Russian Journal of Applied Chemistry, Vol. 77, No. 1, 2004, pp. 1–4. Translated from Zhurnal Prikladnoi Khimii, Vol. 77, No. 1, 2004, pp. 3–6.

INORGANIC SYNTHESIS AND INDUSTRIAL INORGANIC CHEMISTRY

Kinetics of the Reaction of Cubic Boron Nitride with a Melt of Sodium Hydroxide

A. V. Lapshin, A. M. Germanskii, and S. P. Bogdanov

St. Petersburg State Technological Institute, St. Petersburg, Russia

Received October 9, 2003

Abstract—Kinetics of the reaction of cubic boron nitride with a melt of sodium hydroxide in the temperature range 380–480°C was studied. Kinetic parameters of the reaction were determined.

Intermediate products of the synthesis of cubic boron nitride (CBN), so-called cakes, are polydisperse mixtures of two polymorphic modifications of hexagonal graphite-like boron nitride (HBN) and CBN [1]. Crystals of cubic boron nitride are extracted from intermediate products in two stages. In the first stage, a cake is treated with an acid to remove compounds of the metal initiating the synthesis, after which the residue of nonrecrystallized HBN is removed by treatment with a melt of alkali [2]. The CBN extraction in the second stage is based on the difference in rates of reactions of CBN and HBN with a melt of alkali. The degree of CBN decomposition in this reaction, yielding ammonia and the corresponding metal borate, increases as the sample grain size decreases. For example, at 400°C and process duration of 30 min, a CBN micropowder with the particle size from 5 to 3 μm (5/3) decomposes to 55%, and that with the particle size of 250/200, only to 6%. At 700°C, a 5/3 micropowder and also samples with the main fraction particle size from 50 to 40 μm decompose completely, whereas CBN with the particle size of 100/80 and 250/200 decompose to 90 and 88%, respectively. Thus, the treatment with a melt of alkali, which is used to remove HBN during enrichment of the primary product of the synthesis with CBN, even at low temperatures results in considerable losses of this expensive material, especially of its small-size fractions [3].

Furthermore, the following data on the reaction of CBN with alkali melts are available in the literature. According to [4], edges of CBN crystals with nitrogen atoms on the surface have a higher activity in reactions with a KOH melt than edges with boron atoms. However, quantitative characteristics of CBN chemical stability were not given in that work. Mishina and Filonenko [5] have correlated the observed cracking of CBN bicrystals on etching by a KOH melt with the presence of a mass defect on grain boundaries; however, it seems more probable that this phenomenon results from the chemical decomposition of impurities segregating on interfaces. Thus, according to [6], the degradation of CBN crystals on their etching by an alkali results from the chemical decomposition of HBN inclusions contained in the crystals and of impurities captured during their growth. At the same time, it is known [2] that the content of impurities (in particular, of carbon and oxygen) on the surface of LO-grade CBN crystals is higher than in LKV-grade crystals having a more perfect structure and also higher strength and crack resistance. Therefore, we can conclude that the chemical stability of CBN toward an alkali melt depends on both the shape of crystals and the state of their surface.

Such conclusion seems to be important, because wearing of tools equipped with CBN crystals depends on their chemical interaction with a material under treatment and with the environment [7]. Klimenko *et al.* [7] have found that chemical compounds consisting of elements of contacting materials and environment arise in the region of the contact between CBN and the material under treatment. It is probable that the parameter of CBN chemical inertness to oxidants can serve as one of criteria in selection of a type of CBN to be used as a tool material.

We failed to find in the literature a quantitative description of the kinetics of CBN reactions with melts of alkalis. At the same time, the knowledge of the kinetic relationships of the process is required to improve the process for the enrichment of primary products of the CBN synthesis.

The aim of this work was to determine the rate constants of the CBN reaction with an NaOH melt.

1070-4272/04/7701-0001 © 2004 MAIK "Nauka/Interperiodica"

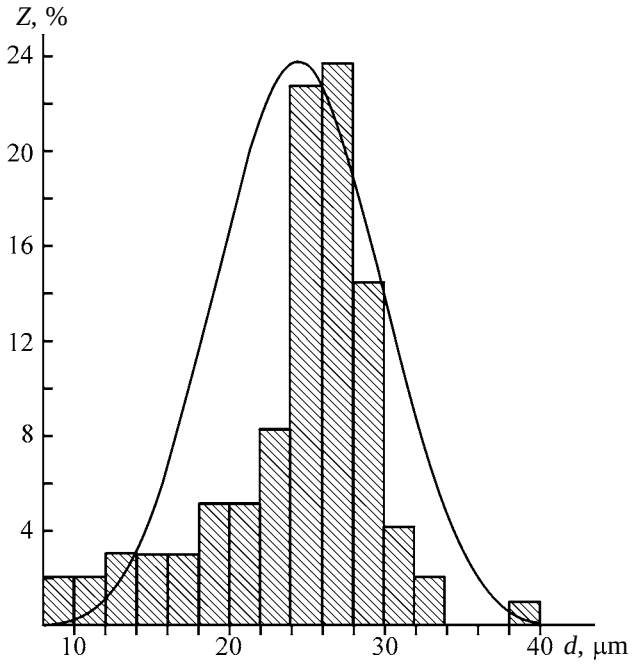

Fig. 1. Particle-size distribution of B-3 28/20 CBN powder. Mean size 24.48 μm; number of particles 97; specific surface area 200.03 $m^2 kg^{-1}$. (*Z*) Proportion of particles and (*d*) equivalent diameter.

EXPERIMENTAL

We used the following CBN samples: LKV-40 grinding powder and LM micropowder [OST (Branch Standard) 2MT 79-2–88]; B-5 grinding powder (amber) and B-3 micropowder synthesized using lithium and magnesium initiators, respectively (Borei corporation, St. Petersburg); Borazon V-500 and Borazon-I grinding powders (General Electric, the United States); and EBN 20-30 micropowder (EID Ltd, the United Kingdom). The samples were treated with NaOH [GOST (State Standard) 4328–77].

A preliminary study of products of the reaction between CBN and an NaOH melt (1 : 1 by weight) by the X-ray phase analysis has shown that they contain residual CBN and the borate Na_3BO_3, which agrees well with the data of [3, 4]. This allows us to state that this reaction is described by the equation

$$BN + 3NaOH \rightarrow Na_3BO_3 + NH_3\uparrow.$$

We studied the chemical reaction of CBN with an NaOH melt on an installation allowing continuous recording of variation in time of the total weight of an NaOH melt and a CBN sample under isothermal conditions. Before the measurements, the melt of alkali was heated to the required temperature in an SShOL-1.1.6/12-M3-U42 shaft furnace, then a CBN sample was placed in the crucible with the melt, and the weight variation during the reaction was recorded with an ADV-200M analytical balance arranged over the furnace. The temperature was determined with an accuracy of ±1°C with a TL-3 thermometer (GOST 21 593) arranged over the melt surface. The reaction time was measured with a stopwatch; the treatment duration was 1 h. The weight of the non-decomposed CBN residue was determined in each experiment.

To determine the rate constants of the reactions of various CBN types with NaOH, we used the generally accepted initial-rate method, according to which the slopes of the initial portions of the concentration vs. time plots correspond to the initial rates at certain initial concentrations and reaction surface areas [8].

The rate constant *K* ($kg\ s^{-1}\ m^{-2}$) of the boron nitride reaction with an NaOH melt was determined using the main equation for topochemical processes given in [9–11] in various forms:

$$d\alpha/d\tau = KS_{sp}c_{NaOH}^{n}, \quad (1)$$

where $\alpha = (m_0 - m_\tau)/m_0$ is the degree of conversion; m_τ, CBN weight (g) to an instant τ; m_0, initial CBN weight (g); S_{sp}, specific surface area of CBN powder ($m^2\ g^{-1}$); c_{NaOH}, NaOH concentration ($g\ g^{-1}$); and *n*, reaction order.

Provided that the NaOH concentration is constant, Eq. (1) in an integral form for spherical particles is converted to the form

$$1 - (1 - \alpha)^{1/3} = \frac{K\tau c_{NaOH}^{n}}{R_0\rho}, \quad (2)$$

where R_0 is the initial particle radius (m), and ρ is the particle density ($g\ cm^{-3}$).

In all the experiments, we took NaOH in a 50-fold excess as compared to the stoichiometric amount of CBN (the weight of NaOH exceeded the weight of a CBN sample by a factor of 50 and more). Therefore, when calculating the degree of conversion by Eq. (2) in the whole range of its variation (from 0 to 1), we accepted $C_{NaOH} \approx 1$ in the case of the reaction with pure NaOH and as a constant value for the reaction with NaOH containing Na_3BO_3.

The initial specific surface area was determined by the Video-Test method [12] from the size distribution of powder particles (Fig. 1).

The reaction conditions and rate constants with the corresponding errors are given in the table. The ex-

perience of using this technique for studying the kinetics of reactions of other BN modifications with an alkali melt has shown that the error in the rate constants is caused mainly by the temperature variation during the experiment [13]. Therefore, we estimated the error taking into account the known temperature dependence of the rate constant

$$K = K_0 \exp(-E_a/RT).$$

For the reaction of B-5 CBN with a melt as an example, we show the characteristic kinetic curves in Fig. 2 together with the kinetic curves calculated by Eq. (2) with the constants obtained. It is seen that the experimental and calculated data on the degree of CBN sample transformation in the reaction with a melt coincide within the limits of the experimental error; therefore, this process is limited by the reaction on the interface.

To determine the reaction order in Eq. (1), we found experimentally the rate of the reaction of LM 28/20 CBN with an NaOH melt containing 10 mol % Na_3BO_3 (C_{NaOH} = 0.738 g g^{-1}) at 440°C. Using these data (the rate was 1.5×10^{-4} s^{-1}) and also the known rate constant of the CBN reaction with a pure NaOH melt at the same temperature, we have calculated the reaction order to be 3.5.

The apparent activation energy of the reaction was determined by the Arrhenius equation. The Arrhenius plot for the grinding powder is linear. The coefficients of the Arrhenius equation for B-5 were found to be as follows: K_0 = 8.2 ± 0.6 kg s^{-1} m^{-2}, E_a = 92.3 ± 12.9 kJ mol^{-1}. The obtained value of the apparent activation energy additionally proves the fact that the reaction is kinetically controlled.

The dependence of $\ln K$ on $1/T$ for a B-3 micropowder is shown in Fig. 3. The fracture of the curve can be accounted for as follows. The relatively high specific surface area of the powder contacting with the melt determines the high reaction rate. As the process is exothermic, the steady-state heat removal from the reaction zone is not ensured. The heat evolution leads to a considerable heating in the zone of the melt–particle contact, and the actual reaction temperature appears to be higher than the temperature detected by a thermometer arranged above the melt surface. Therefore, the determination of the activation energy for micropowders is possible only in the region of temperatures lower than 420°C and requires additional experiments to be carried out.

The data obtained on the degree of CBN decomposition in its reaction with an NaOH melt are in good agreement with the data of [3], where the degree of decomposition of CBN with the particle size of 100/80 upon treatment with NaOH at 400°C for 1 h was 11.2%, and at 460°C and the treatment time of 30 min it was 25%. According to our data, the degree of the decomposition of B-5 grinding powder at 420°C and the treatment time of 50 min was 13.7%, and at 460°C and the treatment time of 30 min it was 20.6%. The degree of the decomposition of an LKV-40 100/80 powder upon treatment with a melt at 420°C for 1 h was 11.1%.

Experimental and calculated rate constants of the reaction of CBN with an NaOH melt

Sample	m_0, g	$S_0 \times 10^3$, m^2	T, °C	$K \times 10^7$, kg s^{-1} m^{-2}
B-5 100/80	0.959	50.3 ± 3.4	420 ± 1	9.1 ± 0.1
	0.500	26.3 ± 1.8	446 ± 1	16.5 ± 1.7
	0.500	26.3 ± 1.8	456 ± 1	19.7 ± 2.1
	0.500	26.3 ± 1.8	460 ± 1	22.2 ± 2.4
B-3 28/20	0.93	186 ± 12.5	393 ± 1	1.8 ± 0.2
	0.93	186 ± 12.5	420 ± 1	3.0 ± 0.3
	0.50	100 ± 6.7	460 ± 1	20.2 ± 2.2
	0.58	116 ± 7.8	480 ± 1	54.7 ± 6
LM 28/20	2.00	410 ± 27.5	380 ± 1	10.1 ± 1.1
28/20	2.00	410 ± 27.5	420 ± 1	16.2 ± 1.7
	2.00	410 ± 27.5	440 ± 1	22.1 ± 2.4
	2.00	410 ± 27.5	460 ± 1	32.7 ± 3.5
EBN 20-30	0.672	141 ± 9.5	415 ± 1	7.7 ± 0.8
LKB-40 100/80	0.99	52 ± 3.5	420 ± 1	5.8 ± 0.6
Borazon B-500 124/105	0.236	9.9 ± 0.7	455 ± 1	15.6 ± 1.7
Borazon-I 145/124	0.35	12.6 ± 0.8	458 ± 1	12.8 ± 1.4

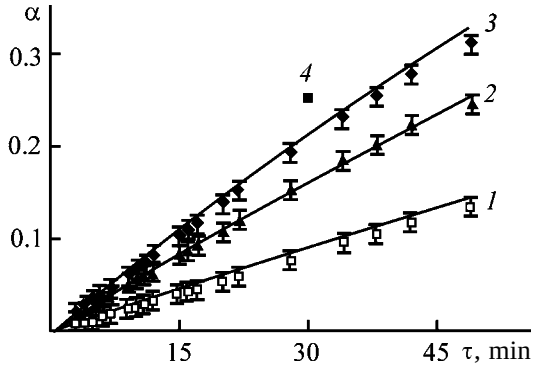

Fig. 2. Degree α of CBN B-5 100/80 conversion upon fusion with NaOH as a function of time τ at various temperatures. Temperature (°C): (*1*) 420, (*2*) 446, and (*3*) 460; (*4*) data of [3] for 460°C. Points are experimental; straight lines correspond to calculation by Eq. (2).

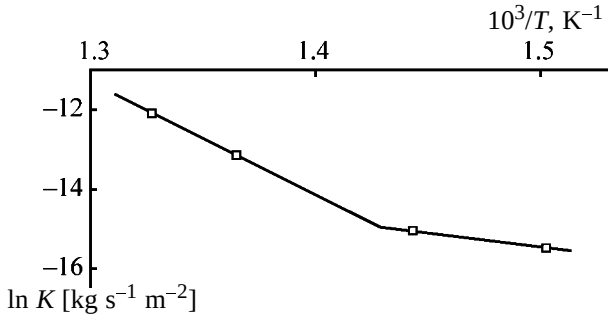

Fig. 3. Rate constant K of the reaction of B-3 28/20 CBN with an NaOH melt as a function of temperature T.

It should be noted that the rate constants of the reactions of various types of CBN with an NaOH melt allow us to judge their chemical inertness at the same temperature. The powders can be ranked in the following order with respect to the chemical stability at low temperatures (less than 420°C): B-3 > LKV-40 > B-5 > LM. The difference in the inertness of various CBN types toward an alkali melt seems to be associated with variations in the defectiveness of their structure, in the development of a microrelief, and in the chemical composition of their surface. It was impossible to determine within the framework of this study what factor was of crucial importance in each particular case. It is probable that such a parameter of chemical stability as the rate constant of the reaction with a corrosive medium can serve as one of criteria for the selection of a CBN type to be used as a tool material. The values of the constants obtained can be used to simulate mathematically the enrichment of intermediate products in the synthesis of abrasive CBN grains using, e.g., the algorithm from [14].

CONCLUSIONS

(1) Rate constants of reactions of various types of cubic boron nitride with an NaOH melt at various temperatures were estimated. The apparent activation energy of the process was determined.

(2) The $\ln K$–$1/T$ dependence for micropowders deviates from linearity. This phenomenon was attributed to the pronounced exothermic effect caused by a high specific surface area of the powders.

(3) Various types of cubic boron nitride differ from each other in the stability to an NaOH melt.

REFERENCES

1. Prikhna, A.I., *Sverkhtverd. Mater*., 1994, nos. 5–6, pp. 14–17.
2. Neshpor, V.S., Denisov, E.P., Ponomarenko, V.A., and Davidenko, V.M., *Sverkhtverd. Mater*., 1995, no. 6, pp. 3–6.
3. Kharitonova, M.V. and Rivlin, I.Ya., *Abraz.: Nauch.-Tekh. Ref. Sb. NIImash*, 1968, no. 5, pp. 8–11.
4. Nikitina, T.P. and Mishina, L.I., *Abraz.: Nauch.-Tekh. Ref. Sb. NIImash*, 1970, no. 3, pp. 5–7.
5. Mishina, L.I. and Filonenko, N.E., *Abraz.: Nauch.-Tekh. Ref. Sb. NIImash*, 1978, no. 1, pp. 8–10.
6. Filonenko, N.E. and Mishina, L.I., *Abraz.: Nauch.-Tekh. Ref. Sb. NIImash*, 1978, no. 12, pp. 8–11.
7. Klimenko, S.A., Mukovoz, Yu.A., Vashchenko, A.N., and Ivas'kevich, Ya.V., *Sverkhtverd. Mater*., 1993, no. 3, pp. 40–43.
8. Avery, H.E., *Basic Reaction Kinetics and Mechanisms*, London: Macmillan, 1974.
9. Tret'yakov, Yu.D., *Tverdofaznye reaktsii* (Solid-Phase Reactions), Moscow: Khimiya, 1978.
10. Ospanov, Kh.K., *Kinetika gomogennykh i geterogennykh khimicheskikh protsessov: Uchebnoe posobie* (Kinetics of Homogeneous and Heterogeneous Chemical Processes: A Textbook), Almaty: Kazakh. Univ., 1997, 2nd ed.
11. Romankov, P.G., Rashkovskaya, N.B., and Frolov, V.F., *Massoobmennye protsessy khimicheskoi tekhnologii* (Mass-Exchange Processes of Chemical Technology), Leningrad: Khimiya, 1975.
12. Panteleev, V.G., Strui, A.V., and Ledyukov, M.A., *Steklo Keram*., 1990, no. 9, pp. 14–15.
13. Lapshin, A.V., Germanskii, A.M., and Bogdanov, S.P., *Komp'yuternoe modelirovanie i optimizatsiya tekhnologicheskikh protsessov elektrotermicheskikh proizvodstv: Svornik trudov Nauchno-tekhnicheskogo soveshchaniya "Duga-200"* (Computer Simulation and Optimization of Electrothermal Production Processes: Proc. Scientific and Technical Conf. "Duga-200"), Udalov, Yu.P., Ed., St. Petersburg: Sankt-Peterb. Gos. Tekhnol. Inst., 2002, pp. 170–175.
14. Lapshin, A.V., Germanskii, A.M., Bogdanov, S.P., and Goryanskii, V.G., *Komp'yuternoe modelirovanie i optimizatsiya tekhnologicheskikh protsessov elektrotermicheskikh proizvodstv: Svornik trudov Nauchno-tekhnicheskogo soveshchaniya "Duga-200"* (Computer Simulation and Optimization of Electrothermal Production Processes: Proc. Scientific and Technical Conf. "Duga-200"), Udalov, Yu.P., Ed., St. Petersburg: Sankt-Peterb. Gos. Tekhnol. Inst., 2002, pp. 176–184.

Russian Journal of Applied Chemistry, Vol. 77, No. 1, 2004, pp. 5–10. Translated from Zhurnal Prikladnoi Khimii, Vol. 77, No. 1, 2004, pp. 7–12.

INORGANIC SYNTHESIS AND INDUSTRIAL INORGANIC CHEMISTRY

Fusibility of Formulations Based on Phases of the System Constituted by Spinel, Mullite, and Aluminum Titanate

S. A. Suvorov, V. N. Fishchev, D. B. Shadricheva, T. V. Firsanova, and N. V. Alekseeva

St. Petersburg State Technological Institute, St. Petersburg, Russia

Received January 15, 2003

Abstract—A set of physicochemical analytical methods was applied to study fusion and crystallization of magnesia–alumina spinel, aluminum titanate, mullite, and their binary and ternary formulations. The feasibility of elucidating phase transformations that occur when phases containing ions with variable oxidation level are fused in an inert gas medium was analyzed.

Of particular interest in developing heat-resistant refractory formulations are materials based on phases of the system $MgO–Al_2O_3–TiO_2–SiO_2$, in which a triangle formed by three refractory phases stands out. These phases are magnesia–alumina spinel, aluminum titanate, and mullite, each of which possesses unique properties. In particular, magnesia–alumina spinel combines high melting point (2135°C) with enhanced resistance to the action of slag melts and high-temperature strength [1, 2]. Owing to the shape of its crystals and low thermal expansion coefficient, mullite improves the heat resistance and makes higher the softening onset temperature of refractories under mechanical load [1, 3]. Aluminum titanate is one of a few materials with negative thermal expansion coefficient, which makes it promising as a base for structural ceramics [3, 4]. However, data on fusibility and phase relationships in the above-mentioned three-component system are virtually lacking.

The aim of this study was to establish the minimum temperature at which a melt appears in the triangle $MgAl_2O_4–Al_6Si_2O_{13}–Al_2TiO_5$ and to determine how the melting occurs.

The melting points of solid phases and crystallization temperatures of melts were determined by high-temperature differential thermal analysis (DTA) [5]. The high-temperature DTA can be performed either in a vacuum or in an inert gas. In this study, the analysis was carried out in helium. To reveal the extent of the reducing influence exerted by the inert gas medium on the behavior of the basic phases in melting–crystallization, a thermodynamic analysis of the stability of the spinel, mullite, and aluminum titanate under partial oxygen pressure of 0.1 Pa at 730–2130°C was made using the thermodynamic characteristics of solid and liquid phases represented in the IVTANTERMO database and reported in [6]. It was found that the magnesia–alumina spinel is stable over the entire temperature range studied, mullite is unstable in the inert medium at temperatures above 1730°C and decomposes into the constituent oxides, and aluminum titanate is unstable below 1300°C and above 1700°C and decomposes into TiO_2 and Al_2O_3. The results obtained are in agreement with the data of [7, 8].

In view of the aforesaid, it was necessary, to attain the formulated goal, to verify the adequacy of high-temperature DTA in an inert gas as applied to oxide compounds containing ions with variable oxidation level. For this purpose, the process of melting of the individual phases (spinel, mullite, and aluminum titanate) and binary systems delimiting the triangle under consideration was studied.

The tetrahedrization of the system $MgO–Al_2O_3–TiO_2–SiO_2$ was given by Berezhnoi in [9]. Data on the structure of the phase diagrams of the systems constituted by spinel and aluminum titanate, spinel and mullite, and mullite and aluminum titanate were reported in [10–13].

The section from spinel to aluminum titanate in the system $MgO–Al_2O_3–TiO_2$ is quasi-binary with a eutectic containing 45 wt % $MgAl_2O_4$ and eutectic temperature of no less than 1730°C [10, 11].

The system constituted by the spinel and mullite has a eutectic that contains 24.7 wt % spinel and melts at 1810°C [12].

The section from aluminum titanate to mullite in the ternary system $Al_2O_3–SiO_2–TiO_2$ is not quasi-

1070-4272/04/7701-0005 © 2004 MAIK "Nauka/Interperiodica"

Table 1. Synthesis conditions and properties of the compounds obtained*

Material	T_{max}, °C	Time of keeping, h	γ_{true}, g cm^{-3}	$\alpha \times 10^6$, K^{-1}	H_μ, MPa
$MgAl_2O_4$	1600	2	3.59	8.46	15 200
Al_2TiO_5	1500	4	3.89	–0.4	6100
$Al_6Si_2O_{13}$	1650	4	3.27	5.15	8800

* γ_{true} is the true density; α, coefficient of linear thermal expansion; H_μ, microhardness.

binary because of the presence of corundum, but has eutectic nature [13]. The minimum temperature of the melt appearance corresponds to the melting temperature of the reaction point (1710°C) [13]. The eutectic contains 48 wt % mullite.

The position of the eutectic in the ternary system constituted by the spinel, aluminum titanate, and mullite was estimated theoretically to be at (mol %) 37 spinel, 55 aluminum titanate, and 8 mullite, using the method developed on the basis of geometric thermodynamics, taking into account changes in the Gibbs energy of a mixture of components [14, 15].

The high-temperature DTA was performed on a VTA-981 derivatograph calibrated against the melting points of well-known substances in helium of A brand [TU (Technical Specification) 6-21-12–94], with temperature raised at a rate of 80 deg min^{-1}. The samples studied were melted in molybdenum crucibles. The temperature corresponding to the onset of a thermal effect was determined at the bending point of a curve. In those cases when the bending of the differential curve was smooth, the beginning or end of an effect was determined as the point of intersection of the baseline with the tangent to the corresponding branch of the peak.

X-ray diffraction patterns were obtained at room temperature on a DRON-3 installation with CuK_α radiation at scanning rate of 2 deg min^{-1}. The X-ray phase analysis consisted in phase identification by comparing the interplanar spacings d/n, measured in the X-ray diffraction patterns, and the corresponding relative intensities I/I_0 of diffraction peaks with the reference values from the ASTM database, using the Ident 4 software package.

The microstructure and microhardness of samples were studied on polished sections. Images of the microstructure of the samples, obtained in reflected light, were analyzed on an EPIQANT automated image analyzer connected to a video camera, which made it possible to view images on the monitor screen. The microhardness of the formulations was measured with a PMT-5M microhardness meter equipped with an FOM-2 photoelectric ocular micrometer. The thermal expansion coefficient was determined on a DKV-5A quartz dilatometer, using sintered samples in the form of 45 × 5 × 5-mm prisms. The pycnometric density was measured in accordance with GOST (State Standard) 2211–65.

As starting materials for solid-state syntheses of the spinel, mullite, and aluminum titanate we used powdered technical-grade alumina (TU 6-09-3916–75), basic magnesium carbonate $m MgCO_3 \cdot Mg(OH)_2 \cdot nH_2O$ (TU 6-09-01-353–78) (characterized by calcination loss of 57.28%), TiO_2 (TU 6-09-05-03-37–75), and quartz glass (GOST 9428–73), taken in amounts corresponding to the stoichiometry of the desired products. Aluminum titanate was synthesized using corundum obtained by firing of technical-grade alumina at 1750°C.

Mixtures of starting compounds were subjected to joint grinding in a vibration mill with corundum balls at balls : material ratio of 4 : 1 to particle size of 4–6 μm. The powders obtained were used to prepare briquettes, which, after drying at room temperature for 48 h, were calcined in air in an electric furnace with molybdenum disilicide heaters at heating rate to the final temperature of 10 deg min^{-1}. Data on the heating modes used are listed in Table 1.

The calcined briquettes were crushed, ground, and recalcined under the same conditions. The completeness of synthesis was judged from XPA data.

Samples for measuring the thermal expansion coefficient and microhardness and preparing polished sections were obtained by compacting powders with particle size of 4–6 μm, which were moistened with a 5% aqueous solution of polyvinyl alcohol to 4% moisture content under a pressure of 50 MPa, with subsequent drying at room temperature for 24 h and calcination at 1600°C for 1 h.

The characteristics of the compounds synthesized, which are listed in Table 1, are in good agreement with published data on the properties of the phases under study [1, 16, 17].

Mixtures of the compounds synthesized, taken in prescribed ratios (Tables 2, 3), were used for DTA. The phase transformations that occurred in melting were judged from the results of XPA (Figs. 1, 2).

Derivatograms of the compounds synthesized are shown in Fig. 3. The fact that the onset temperatures of the effects that can be interpreted as melting and

Table 2. DTA data for binary formulations

Composition, mol %			Phase transformation temperature, °C
$MgAl_2O_4$	Al_2TiO_5	$Al_6Si_2O_{13}$	
25.0	–	75.0	1805, 1865
50.0	–	50.0	1815, 1835
75.0	–	25.0	1825, 1915
–	25.0	75.0	1695, 1860, 1880
–	50.0	50.0	1740, 1840
–	70.0	30.0	1720, 1800, 1850
–	75.0	25.0	1730, 1755, 1830
–	80.0	20.0	1700, 1750, 1810
25.0	75.0	–	1760, 1860
30.0	70.0	–	1760, 1790
50.0	50.0	–	1730, 1750
75.0	25.0	–	1750, 1900

Table 3. DTA data for ternary formulations

Composition, mol %			Phase transformation temperature, °C
$MgAl_2O_4$	Al_2TiO_5	$Al_6Si_2O_{13}$	
47.0	37.0	16.0	1640, 1720, 1800, 1870
33.3	33.3	33.3	1630, 1710, 1775, 1850
47.0	39.0	14.0	1640, 1690, 1800
7.5	70.0	22.5	1660, 1760, 1800, 1870
15.0	70.0	15.0	1630, 1700, 1870
22.5	70.0	7.5	1660, 1775, 1860
30.0	30.0	40.0	1640, 1695, 1760
37.0	55.0	8.0	1600, 1750
12.0	53.0	35.0	1710, 1785

crystallization do not coincide in a single heating–cooling cycle, which is characteristic of some of the formulations under consideration, can be attributed either to overheating of the mixture in melting or to overcooling of a melt in crystallization. It is known [7] that oxide melts tend to be overcooled, and, therefore, preference was, as a rule, given to onset temperatures of the melting effects. To obtain more reliable results, two heating–cooling cycles were performed for each formulation. Visual inspection of the samples after DTA revealed that crystalline samples containing aluminum titanate turned black. The color of the other crystallized melts was light gray.

In melting of the magnesia–alumina spinel, complete melting could not be achieved. The onset temperature of melting, recorded in the thermogram, was 2090°C, with no other effects revealed.

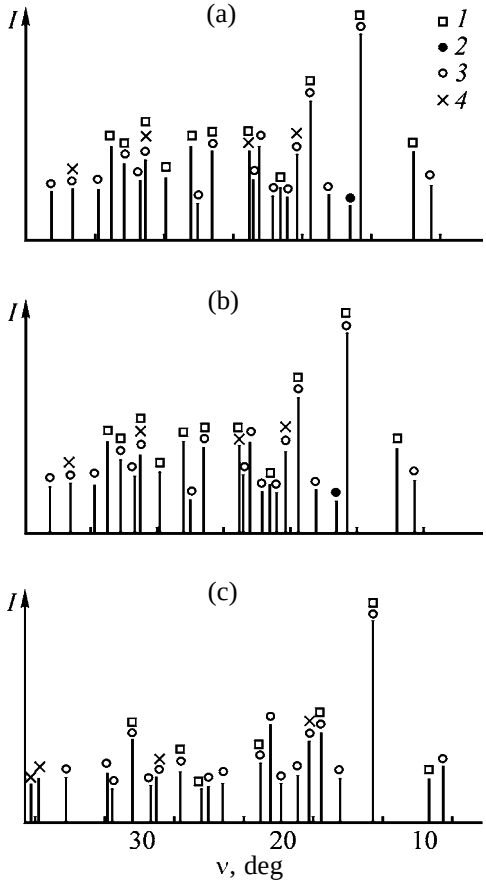

Fig. 1. X-ray diffraction patterns of binary formulations. Composition (mol %): (a) 75 Al_2TiO_5 and 25 $Al_6Si_2O_{13}$; (b) 50 Al_2TiO_5 and 50 $Al_6Si_2O_{13}$; (c) 25 Al_2TiO_5 and 75 $Al_6Si_2O_{13}$. (*I*) Intensity and (ν) angle of slide; the same for Fig. 2. (*1*) Al_2TiO_5, (*2*) TiO_2, (*3*) $Al_6Si_2O_{13}$, and (*4*) SiO_2.

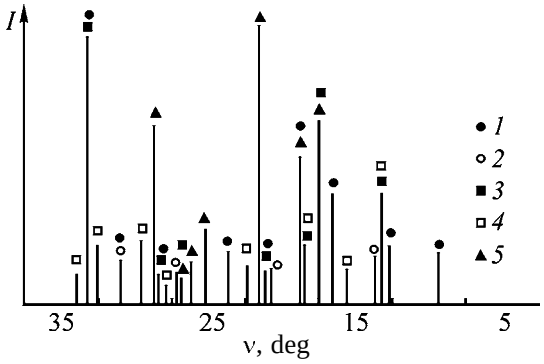

Fig. 2. X-ray diffraction pattern of a ternary formulation. Composition (mol %): 7.5 $MgAl_2O_4$, 70 Al_2TiO_5, and 22.5 $Al_6Si_2O_{13}$. (*1*) Al_2TiO_5, (*2*) TiO_2, (*3*) $Al_6Si_2O_{13}$, (*4*) $MgAl_2O_4$, and (*5*) SiO_2.

In melting of mullite, the endothermic peak has a rather complex structure (Fig. 3a). The onset of melting is recorded at 1845°C; a clearly pronounced superposition of two endothermic effects that begin at 1885

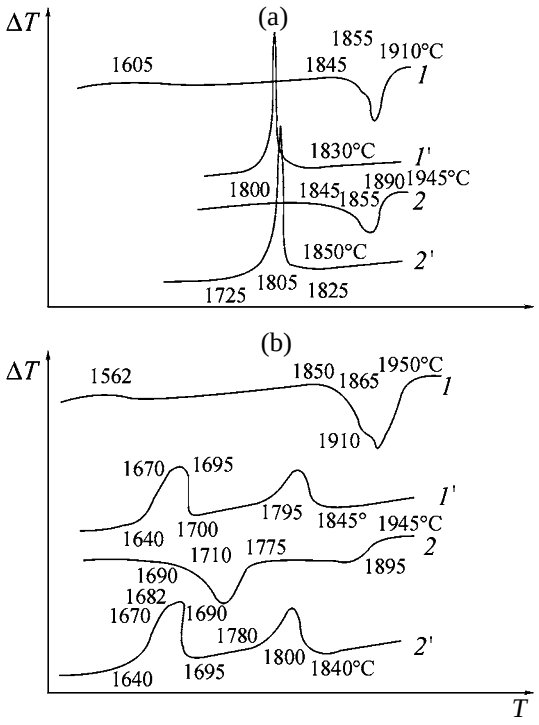

Fig. 3. Thermograms of the synthesized samples of (a) mullite and (b) aluminum titanate. (*T*) Temperature and (Δ*T*) difference between the temperatures of the sample and reference. (*1*, *2*) First and second heating and (*1*', *2*') first and second cooling, respectively.

and 1910°C is observed. In a second heating, the general pattern was preserved, but the peaks were broadened somewhat and the onset temperature of the high-temperature effect slightly decreased (to 1890°C). In cooling, most part of heat is released in both cycles in a narrow temperature range (about 20°C). This is presumably due to the occurrence of crystallization by the reaction mechanism, according to which the primarily formed aluminum oxide reacts with the melt to give mullite [13]. XPA data for a melted sample confirm the assumption made.

In the first heating of aluminum titanate, an endothermic effect that is a superposition of three effects with onset temperatures of 1850, 1870, and 1910°C was recorded (Fig. 3b). However, already the subsequent cooling reveals a group of exothermic effects at lower temperatures. This indicates that the phase composition of aluminum titanate changes significantly in melting–crystallization in an inert gas medium, which is confirmed by the results of XPA indicating that oxides of the general formula TiO_{2-x}, corundum, and anosovite solid solution based on aluminum titanate are present in the crystallized sample. The experimentally obtained phase transformation temperatures of 1690 and 1850°C are in agreement with published data [18].

The results of DTA for two- and three-component formulations are listed in Tables 2 and 3; XPA data, in Figs. 1 and 2; and results of microstructural studies, in Fig. 4.

It follows from the results obtained that the temperature at which a melt appears in the mullite–spinel system is 1815 ± 10°C, with the minimum difference between the solidus and liquidus temperatures observed for a mixture composed of 50 mol % spinel and 50 mol % mullite. Only two phases can be seen in polished section images [19]. The presence of a pronounced dendrite structure in a sample containing equal amounts of spinel and mullite also gives reason to state that this composition is close to the eutectic composition. An X-ray phase analysis of melted formulations and microhardness measurements (15 200 and 8800 MPa) did not reveal any phases except mullite and spinel.

The solidus temperature in the system constituted by aluminum titanate and spinel is 1745 ± 15°C. An X-ray phase analysis of melted samples did not reveal any foreign phases. Presumably, aluminum titanate does not decompose in the first heating in the presence of spinel (under the experimental conditions) because of its stabilization by the spinel [20]. A microstructural analysis of the formulations revealed eutectic colonies in a sample with 25 mol % spinel, on which a fine spherical porosity, characteristic of eutectics, and colonies with dendritic structure can be seen [18].

The DTA curves of the formulations constituted by aluminum titanate and mullite contain three groups of peaks each, for all the compositions studied. The low-temperature effects correspond to the minimum temperature of appearance of a melt, equal to 1715 ± 20°C for the given system, which is close to the temperature reported in [13]. The intermediate heat effects are, in all probability, associated with reactions between solid phases and the melt. The X-ray diffraction patterns of the formulations under study (Figs. 3a and 3b) show, in addition to the initial phases, the presence of corundum in all the samples (reflections with *d*/*n* 0.208 and 0.255 nm). Measurements of the microhardness of the formulations also revealed the presence of corundum (21 000 MPa), mullite (8800 MPa), and aluminum titanate (6100 MPa). Thus, it was confirmed that the system in question is not quasi-binary. Analysis of the microstructure of the formulations under consideration shows that eutectic colonies are

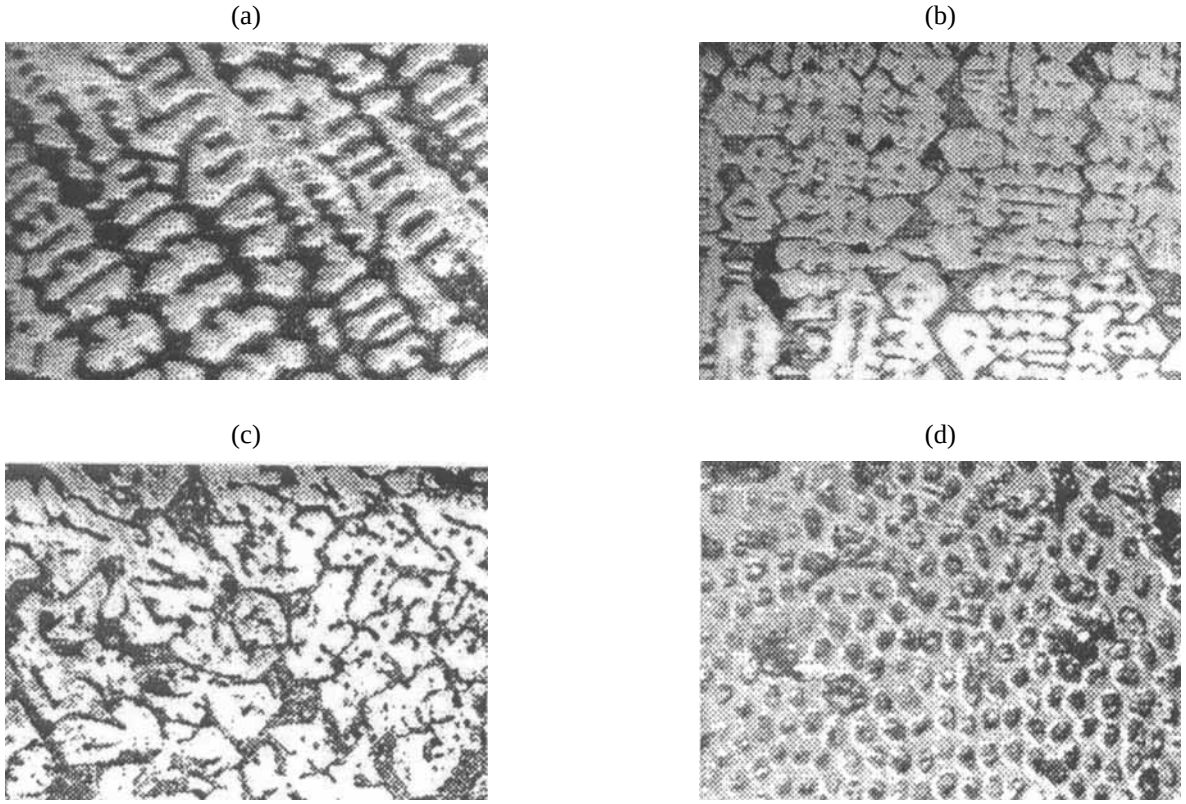

Fig. 4. Photographs of the microstructure of melted samples. Composition (mol %): (a) 70 Al_2TiO_5, 22.5 $Al_6Si_2O_{13}$, and 7.5 $MgAl_2O_4$; (b) 70 Al_2TiO_5, 15 $Al_6Si_2O_{13}$, and 15 $MgAl_2O_4$; (c) 70 Al_2TiO_5, 7.5 $Al_6Si_2O_{13}$, and 22.5 $MgAl_2O_4$; (d) 57 Al_2TiO_5, 34 $Al_6Si_2O_{13}$, and 9 $MgAl_2O_4$. Magnification: (a) 300, (b, c) 100, and (d) 400.

present in the sample containing 25 mol % mullite [19]. This formulation is close in composition to that corresponding to the point of intersection of the conode passing through the apex corresponding to corundum and the reaction point with the tie line connecting aluminum titanate and mullite in the system Al_2O_3–SiO_2–TiO_2.

The satisfactory agreement between published data on the fusibility of the individual phases and the binary systems constituted by spinel and mullite, aluminum titanate and spinel, and aluminum titanate and mullite in helium gave reason to expect that the given technique would be applicable to ternary formulations.

As points to be studied in the ternary system under consideration were chosen those corresponding to the calculated eutectic composition and to the compositions of the equimass, equivolume, and equimolar formulations, with the first two of these latter being so close that they can be regarded as virtually the same composition (Table 3). In addition, compositions with 70 mol % aluminum titanate and varied content of spinel and mullite were studied, and also some others. The results of DTA of the ternary formulations are listed in Table 3.

It follows from the data obtained that the minimum temperature of appearance of a liquid phase in the system under study, 1645 ± 15°C, is virtually composition-independent. An X-ray phase analysis of multiple-phase formulations (Fig. 2) demonstrated the presence of mullite, aluminum titanate, and spinel in all the compositions, and indications of the presence of corundum in samples with high content of aluminum titanate and mullite.

It can be seen from the microstructures of melted samples, shown in Fig. 4, that these samples have structure characteristic of eutectic colonies. Combined with the results of DTA and XPA, this gives reason to believe that the composition completely fusible at the above-mentioned minimum temperature lies near the point corresponding to the composition (mol %) 55 Al_2TiO_5, 8 $Al_6Si_2O_{13}$, and 37 $MgAlO_4$.

At the same time, the fact that the DTA curves obtained for compositions in the region adjacent to the Al_2TiO_5–$Al_6Si_2O_{13}$ side contain more than two thermal effects associated with melting–crystallization processes, taken together with the results of XPA, indicates that the plane constituted by aluminum titanate, mullite, and spinel in the system MgO–Al_2O_3–

SiO_2–TiO_2 cannot be regarded as strictly quasi-ternary.

CONCLUSIONS

(1) The applicability of high-temperature differential thermal analysis in an inert medium to systems containing metal oxides with variable oxidation levels was demonstrated in an experimental study of fusibility of refractory phases in the system $MgAl_2O_4$–$Al_6Si_2O_{13}$–Al_2TiO_5.

(2) A set of physicochemical analytical methods was used to establish that the minimum temperature at which a melt appears in the system under study is 1645 ± 15°C.

(3) The plane constituted by aluminum titanate, mullite, and spinel in the system MgO–Al_2O_3–SiO_2–TiO_2 is not quasi-ternary.

REFERENCES

1. Lang, S.M., Properties of High-Temperature Ceramics and Cermets: Elasticity and Density at Room Temperature, *Monograph 6 of the National Bureau of Standards*, 1960, p. 46.
2. Perepelitsin, V.S., Kormina, I.V., Sivash, V.G., *et al*., *Nov. Ogneupory*, 2002, no. 1, pp. 89–95.
3. FRG Patent 4 029 166.
4. Tarasovskii, V.P. and Lukin, E.S., *Ogneupory*, 1995, no. 11, pp. 8–10.
5. Al'myashev, V.I. and Gusarov, V.V., *Termicheskie metody analiza: Uchebnoe posobie* (Thermal Methods of Analysis: Textbook), St. Petersburg: Sankt-Peterb. Gos. Elektrotekh. Univ. (LETI), 1999.
6. *Termodinamicheskie konstanty veshchestv: Spravochnik* (Thermodynamic Constants of Substances: Handbook), Glushko, V.P., Ed., Moscow: VINITI Akad. Nauk SSSR, 1974.
7. Eitel, W., *The Physical Chemistry of Silicates*, Chicago: Univ. of Chicago Press, 1954.
8. Battacharyya, B.N. and Sudhiz Sen, *Centr. Glass Ceram. Res. Inst. Bull*., 1965, no. 2, pp. 92–103.
9. Berezhnoi, A.S. and Gul'ko, N.V., *Mnogokomponentnye sistemy oksidov: Trudy Ukrainskogo instituta ogneuporov* (Multicomponent Oxide Systems: Coll. of Scientific Works of the Ukrainian Inst. of Refractories), Kharkov: Metallurgizdat, 1961.
10. Berezhnoi, A.S. and Gul'ko, N.V., *Ukr. Khim. Zh*., 1955, vol. 21, no. 2, pp. 158–164.
11. Gul'ko, N.V., *Trudy 6-go soveshchaniya po eksperimental'noi tekhnike mineralogii i petrografii* (Proc. 6th Meet. on Experimental Techniques in Mineralogy and Petrography), Moscow: Nauka, 1962, pp. 287–294.
12. Logvinkov, S.M., Semchenko, G.D., and Kobyzeva, D.A., *Ogneupory Tekh. Keram*., 1996, no. 11, pp. 4–8.
13. *Diagrammy sostoyaniya sistem tugoplavkikh oksidov: Spravochnik* (Phase Diagrams of Refractory Oxide Systems: Handbook), Galakhov, F.Ya., Ed., Leningrad: Nauka, 1985, issue 5, part 1.
14. Suvorov, S.A., Vladimirskaya, L.V., Gorshkova, O.K., *et al*., Abstracts of Papers, *Nauchno-tekhnicheskaya konferentsiya LTI im. Lensoveta* (Scientific and Practical Conf. of Lensovet Technological Institute, Leningrad), Leningrad, 1970, p. 21.
15. Suvorov, S.A. and Novikov, V.K., *Izv. Akad. Nauk SSSR, Neorg. Mater*., 1971, vol. 9, no. 2, pp. 279–281.
16. *Fiziko-khimicheskie svoistva okislov: Spravochnik* (Physicochemical Properties of Oxides: Handbook), Samsonov, G.V., Ed., Moscow: Metallurgiya, 1978.
17. Hummel, F.A., *J. Am. Ceram. Soc*., 1950, vol. 33, no. 3, pp. 1074–1082.
18. Berezhnoi, A.S., *Mnogokomponentnye sistemy okislov* (Multicomponent Oxide Systems), Kiev: Naukova Dumka, 1970.
19. Shadricheva, D.B., Substantiation of the Technology of Heat-Resistant Materials Based on Corundum–Spinel Refractories with Phases Having Low Thermal Expansion Coefficient, *Cand. Sci. Dissertation*, St. Petersburg, 2000.
20. Li Zhijan, Guo Yuxiang, and Wang Linlin, *Naihuo Cailio* (Refractories), 2001, vol. 35, no. 2, pp. 87–88.

Russian Journal of Applied Chemistry, Vol. 77, No. 1, 2004, pp. 11–14. Translated from Zhurnal Prikladnoi Khimii, Vol. 77, No. 1, 2004, pp. 13–16.

INORGANIC SYNTHESIS AND INDUSTRIAL INORGANIC CHEMISTRY

Production of Magnetic Supports Coated with Silica Layer from Dispersed Cobalt and Zinc–Nickel Ferrites

S. S. Airapetyan and A. G. Khachatryan

Yerevan State University, Yerevan, Armenia

Received March 12, 2003

Abstract—The possibility of obtaining dispersed powders of cobalt and zinc–nickel ferrites with particle size of 1–4 μm by thermal treatment of the corresponding oxalates was analyzed. Changes in porous characteristics of the ferrites obtained in their thermal treatment were studied.

Sorbents and supports with magnetic properties have their specific application fields, with the isolation and purification of substances of this kind, including those biologically active, carried out using a magnetic field. The use of sorbents and supports depends on whether soft- or hard-magnetic is a given material.

The sorption properties of sorbents and supports are determined by functional groups deposited onto the surface of one or another layer (of either organic or inorganic origin). Sorbents and supports with magnetic properties are commonly obtained using finished magnetic materials with certain unchanging magnetic characteristics.

In some cases, it is appropriate to use semifinished magnetic materials and, in particular, powders of various ferrites whose thermal treatment is not completed (as shown below, such materials show a certain extent of porosity), which is due to specific features of methods used to deposit a protective coating or a layer with necessary functional groups onto the surface of ferrites. This poses the question of control over the properties of the starting magnetic materials. In the authors' opinion, synthesis of magnetic materials to be used as a magnetic component of magnetic sorbents and supports may become a key issue.

Up to now, magnetite of both natural [1] and synthetic origin [2] has been most frequently used as the magnetic constituent of the systems mentioned above.

Commonly, magnetic sorbents and supports are synthesized by embedding magnetic materials in various macromolecular compounds: agarose and polyamide gel [1, 3], ion-exchange resins [4], etc. In some cases, coatings of organic origin restrict the possible application field of such systems. Therefore, magnetic supports with inorganic coatings become the most promising [5].

The possible promising magnetic materials for obtaining sorbents and supports with magnetic properties are dispersed ferrite powders. The magnetic properties of ferrites are widely diverse and can be controlled in the course of synthesis. Moreover, ferrites may be soft- or hard-magnetic.

In some cases, it is important to know what structural transformations occur in ferrite particles in their thermal treatment. Ferrites of various metals, which are of interest mainly as magnetic materials, are commonly obtained by sintering of metal oxides at high temperature (about 1000°C and more) [6, 7].

EXPERIMENTAL

Dispersed powders of cobalt(II) ferrite and mixed zinc–nickel(II) ferrite were obtained by thermal treatment of powders of the corresponding oxalates under the process conditions listed in the table. Similar results are obtained in precipitation of mixed oxalates of iron(II) and cobalt(II). The oxalates were synthesized by adding concentrated solutions of Me^{2+} (M = Fe, Co, Ni, Zn) to a dilute (0.2–0.4 N) solution of oxalic acid under continuous agitation. After the solution became turbid, the agitation was stopped, the suspension was kept for additional 40–50 min, and then the oxalate powder was separated from the mother liquor by filtering and dried with acetone on the filter.

A silica layer was deposited onto the surface of the ferrite powders obtained by a procedure described in [5]. Powdered cobalt(II) ferrite was suspended under continuous agitation in distilled water heated to the

1070-4272/04/7701-0011 © 2004 MAIK "Nauka/Interperiodica"

Basic process parameters in obtaining iron(II) and zinc–nickel(II) oxalates. Volume of oxalic acid solution 800 ml

Run no.	Oxalic acid concentration, M	M^{2+} volume, ml	M^{2+} concentration, M	Particle size, μm
1	0.1	62.5	Fe 0.80, Ni 0.20, Zn 0.20	1–2
2	0.2	500	Fe 0.40, Ni 0.10, Zn 0.10	4.0
3	0.2	250	Fe 0.40, Ni 0.10, Zn 0.10	2–3
4	0.2	206	Fe 0.5, Ni 0.125, Zn 0.125	2.0
5	0.2	155	Fe 0.667, Ni 0.167, Zn 0.167	1–3
6	0.2	125	Fe 0.80, Ni 0.20, Zn 0.20	2.0
7	0.4	300	Fe 0.667, Ni 0.167, Zn 0.167	2–3
8	0.4	250	Fe 0.80, Ni 0.20, Zn 0.20	2.0

boiling point. To the resulting suspension was added dilute water glass (2.0 wt % in terms of SiO_2, silicate ratio $M \geq 3$), with the volume of the initial suspension maintained constant. After the whole calculated amount of the water glass solution was introduced, the heating was terminated, and the suspension obtained was cooled to room temperature and washed with distilled water on the filter. The resulting powder was dried at 150°C and subjected to thermal treatment at 800–1000°C.

The sorption volume of pores in ferrite samples obtained under various thermal treatment conditions was found from benzene sorption [8].

The porous characteristics of the materials obtained were determined by the BET procedure on a Micromeritics Accusorb 2300A instrument.

It is known [9] that, in obtaining highly dispersed materials, it is necessary to mix reagents in the following order: more concentrated solutions are to be added to a dilute solution. The tendency toward a decrease in the particle size of the resulting powdered oxalates is observed with increasing concentration of oxalic acid and decreasing concentration of solutions of bivalent metals (see table).

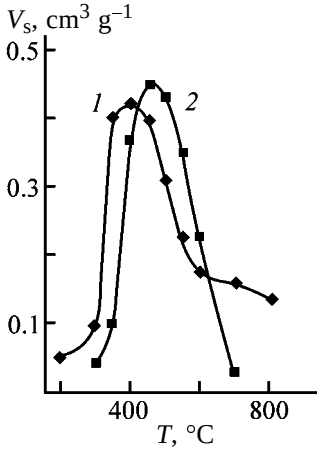

Fig. 1. Sorption volume V_s of pores in (*1*) cobalt and (*2*) zinc–nickel ferrites vs. thermal treatment temperature T.

The oxalates obtained in run no. 4 (see table) and a mixed oxalate of iron and cobalt, synthesized following the same scheme, were used to study the influence exerted by the temperature of thermal treatment on the porosity of ferrites obtained on their base.

Figure 1 shows how the sorption volume of pores in samples of cobalt ferrite (curve *1*) and zinc–nickel ferrite (curve *2*) depends on the temperature of their thermal treatment. It can be seen that the maximum pore volume is observed in samples of these ferrites upon their thermal treatment at 400–500°C. With increasing temperature, the pore volume falls steeply.

A sample of zinc–nickel ferrite has virtually no porosity upon thermal treatment at 600°C, whereas cobalt ferrite behaves somewhat differently. In this sample, residual porosity is still preserved at a temperature of 800–900°C. It is assumed that the presence of zinc oxide ensures fast particle sintering and, as a result, the porosity of zinc–nickel ferrite particles disappears rapidly.

Of particular interest is the fact that thermal treatment of oxalates yields porous ferrite powders (at 400–500°C) that can provide a good adhesion of a film being deposited to the surface. Ferrites with a silica coating were calcined at 800–1000°C for 4–5 h. The presence of silica in the ferrite powder prevents total shrinking of the skeleton, with the result that the samples obtained show a certain amount of porosity.

Deposition of thin inorganic coatings on the surface of magnetic powders makes it possible to obtain magnetic sorbents and supports with a minimum amount of ballast and completely shielded surface.

Ferrites subjected to thermal treatment at 400°C

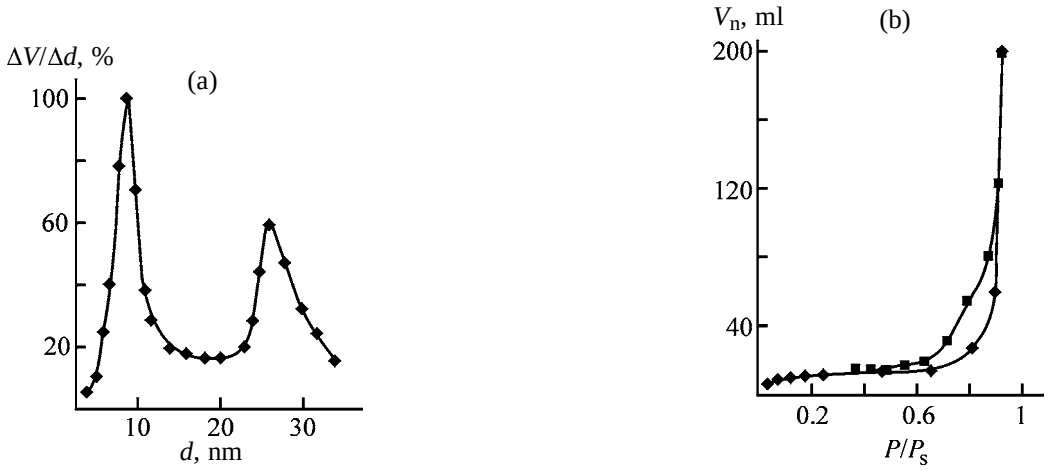

Fig. 2. (a) Pore distribution $\Delta V/\Delta d$ with respect to size d and (b) isotherm of capillary condensation of nitrogen, V_n, on porous cobalt ferrite.

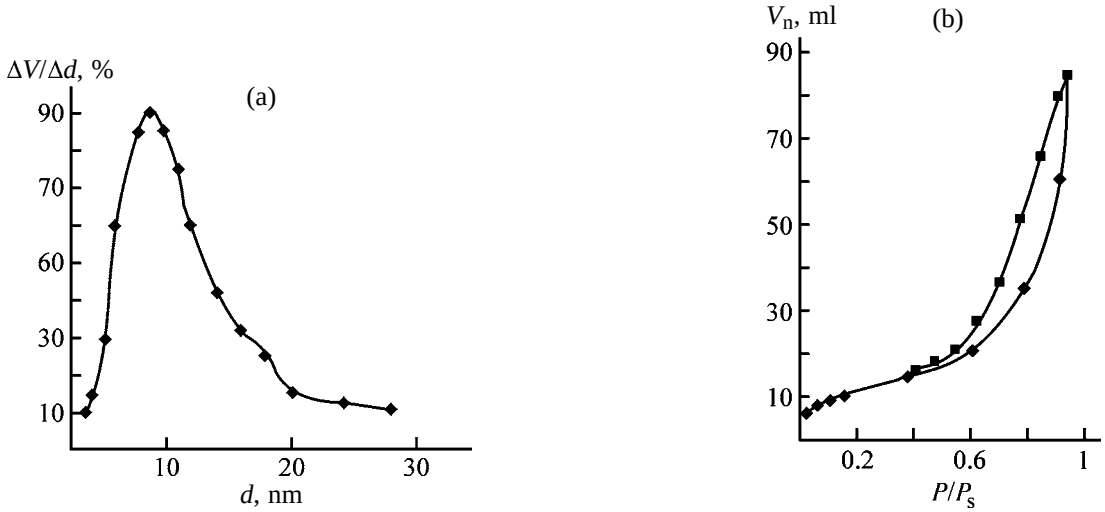

Fig. 3. (a) Pore distribution $\Delta V/\Delta d$ with respect to size d and (b) isotherm of capillary condensation of nitrogen, V_n, on porous cobalt ferrite coated with 15 wt % silica.

were used to produce magnetic supports coated with layers composed of silica.

In contrast to the case of silica deposition onto the surface of nonporous ferrite particles, that onto the surface of porous ferrite particles proceeds at a higher rate. It was demonstrated experimentally that about 20 wt % silica can be deposited onto the surface of the above ferrites thermally treated at 400–500°C. The porosity of the ferrite particles makes it possible to vary the amount of silica deposited onto their surface.

Figures 2a and 2b show isotherms of capillary condensation of nitrogen on porous cobalt(II) ferrite and the pore size distribution for this ferrite sample.

Figure 3 shows isotherms of capillary condensation of nitrogen on cobalt ferrite coated with silicon dioxide (15 wt %) and the pore size distribution for this material.

The pore size distributions were calculated from the desorption branch of the hysteresis loop in the isotherm of capillary condensation.

Interestingly, the initial cobalt ferrite sample shows biporosity, with average pore sizes of 9 and 26 nm. The average pore diameter in cobalt ferrite coated with 15 wt % silica is 9 nm.

It follows from Fig. 3 that the biporosity virtually disappears upon deposition of silica onto the cobalt ferrite surface. It seems strange that the number of coarse pores decreases to a greater extent than that of fine pores. Presumably, the fine pores become in-

accessible to the silica being deposited, since, in a solution with silicate ratio M = 3.25, sodium silicate is hydrolyzed to give colloid varieties of silica, which have limited access into fine pores. Therefore, the major part of silica being deposited remains in coarsely porous regions of the porous ferrite.

CONCLUSIONS

(1) Thermal treatment of mixed oxalate yields porous ferrite particles. The largest pore volume (0.40–0.45 $cm^3 g^{-1}$) is observed in the case of thermal treatment of oxalates in the temperature range 400–500°C.

(2) It is shown that a silica coating can be deposited onto the surface of porous ferrites. In this case, the biporosity of the initial porous ferrite disappears, with the coarse parts of pores diminishing to a greater extent.

REFERENCES

1. Turkin, S.I., Markvicheva, E.A., Lukin, Yu.V., *et al*., *Tr. Mosk. Khim.-Tekhnol. Inst. im. D.I. Mendeleeva, Biotekhnol. Prom. Ekol*., 1986, no. 135, pp. 41–50.
2. Bibik, E.E., *Reologiya dispersnykh sistem* (Rheology of Disperse Systems), Leningrad: Leningr. Gos. Univ., 1981.
3. Osterman, L.A., *Khromatografiya belkov i nukleinovykh kislot* (Chromatography of Proteins and Nucleic Acids), Moscow: Nauka, 1985.
4. *Sintez i primenenie ferromagnitnykh sorbentov: Trudy Gos. nauchno-issledovatel'skogo i proektnogo inst. po obogashcheniyu rud tsvetnykh metallov "Kazmekhanobr"* (Trans. Kazmekhanobr State Research and Designing Inst. for Dressing of Nonferrous Metal Ores), Alma-Ata, 1971, coll. no. 5.
5. Airapetyan, S.S., Balayan, G.G., and Khachatryan, A.G., *Zh. Prikl. Khim*., 2001, vol. 74, no. 3, pp. 507–510.
6. Letyuk, K.M. and Zhuravlev, G.M., *Khimiya i tekhnologiya ferritov* (Chemistry and Technology of Ferrites), Leningrad: Khimiya, 1983.
7. Rabkin, L.A., Soskin, S.A., and Epshtein, B.I., *Ferrity: stroenie, svoistva, tekhnologiya proizvodstva* (Ferrites: Structure, Properties, and Manufacture Technology), Leningrad: Energiya, 1988.
8. Galimov, Zh.B., Dubinina, G.G., and Masagurov, R.N., *Metody analiza katalizatorov neftepererabotki* (Methods for Analysis of Catalysts for Oil Refining), Moscow: Khimiya, 1973.
9. Fridrikhsberg, D.A., *Kurs kolloidnoi khimii* (A Course of Colloid Chemistry), Leningrad: Khimiya, 1984.

Russian Journal of Applied Chemistry, Vol. 77, No. 1, 2004, pp. 15–19. Translated from Zhurnal Prikladnoi Khimii, Vol. 77, No. 1, 2004, pp. 17–21.

INORGANIC SYNTHESIS AND INDUSTRIAL INORGANIC CHEMISTRY

Structure Formation and Conduction of Nanosized Nickel Oxide in Porous Glass

V. N. Pak, O. Yu. Solomatina, T. M. Burkat, and I. Yu. Tikhomirova

Herzen Russian State Pedagogical University, St. Petersburg, Russia

Received April 16, 2003

Abstract—Nickel(II) oxide was deposited on the surface of a porous glass in the amount of 0.5–7.0 mmol g^{-1} by impregnation of the glass with an aqueous solutions of $Ni(NO_3)_2$, followed by decomposition of the salt at 673 K. The size features of the formation of the oxide structure were characterized by the data of optical and X-ray photoelectron spectroscopy and by measurements of density and electrical conductivity.

Transition metal oxides are used for preparing a wide range of electrical materials, from high-ohmic dielectrics to high-temperature superconductors. The intensive development of the chemistry and physics of nanosized functional components and devices for electronics poses a problem of directional synthesis and study of special properties of oxide systems devoid of a formed band structure [1–5]. Of special interest is the specificity of electron exchange and transfer in the case of a small number of atoms (10^{15}–10^{16} at cm^{-2}) making up oxides of *d* elements in the initial stage of filling a surface of typical dielectric supports [1–3, 6, 7]. Apart from its own importance, the study of the electrical conduction should reveal forms of existence and size features of the supported oxides.

To continue our previous studies [6–11], in this work we have studied in the same context the state and electrical conduction of nanosized nickel(II) oxide in porous glass (PG). The technique of the nickel oxide deposition by impregnation of PG with $Ni(NO_3)_2$ aqueous solutions, followed by removal of water and decomposition of the salt at 673 K, appeared the most accessible and reliable. The many-time repetition of these operations using solutions of various concentrations allowed us to smoothly control the oxide content in the glass. The changes in the oxide state in a series of NiO/PG systems were monitored by optical and X-ray photoelectron spectroscopy and by measurements of the density and electrical conductivity.

EXPERIMENTAL

To find specific features of early stages of filling of the PG silica surface with nickel oxide, we carried out experiments using glasses obtained by known techniques [12–14] as laminas of the size $10 \times 10 \times 1$ mm with the following structural parameters: pore radius r_p = 10 nm, porosity ε = 0.30 $cm^3\ g^{-1}$, and specific surface area S_{sp} = 46 $m^2\ g^{-1}$. For the aim of this work it was essential that the developed surface and porosity of the glass provided a possibility for reliable control of the weight of an oxide synthesized in it. The impregnation of PG with $Ni(NO_3)_2$ solutions was intended to ensure the maximal and reproducible filling of the pore space with the electrolyte. The actual molar amount of the salt introduced in a PG (and consequently of nickel oxide *Q*) per gram of the glass linearly correlates with the concentration of the impregnating solution *c* and volume of pores in the glass ε:

$$Q = c\varepsilon\gamma, \quad (1)$$

where $\gamma < 1$ is a coefficient reflecting the deviation from an ideal filling.

We determined the actual γ value as the ratio of the nickel oxide content introduced in the PG, which was measured by the gravimetric method, to its limiting value calculated by Eq. (1) under the condition $\gamma = 1$. Numerous experiments have shown poor efficiency of the impregnation of glass laminas by immersing in solutions, as in this case γ values did not exceed 0.6–0.7. The impregnation of the glass at the expense of capillary rise of a liquid in through pores appeared to be much more complete and reproducible. In this case, the solution was taken up through one of parallel plate surfaces of a lamina, providing free displacement of air through another surface. This mode provided an average value γ = 0.9 describing in essence the frac-

1070-4272/04/7701-0015 © 2004 MAIK "Nauka/Interperiodica"

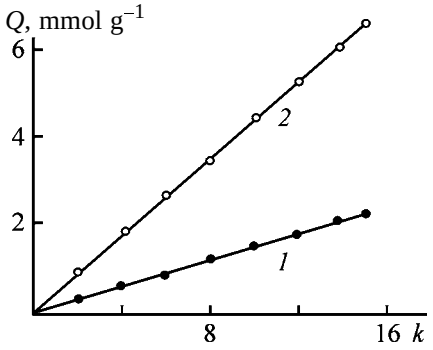

Fig. 1. Dependence of the nickel oxide content in PG Q on the number of deposition operations k using (*1*) 0.5 and (*2*) 1.5 M $Ni(NO_3)_2$ solutions.

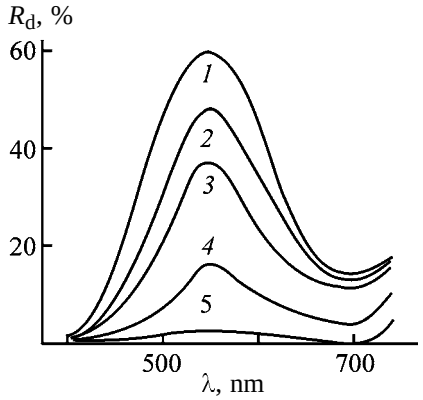

Fig. 2. (*1*) Electronic diffuse reflection spectrum of PG impregnated with 1.5 M $Ni(NO_3)_2$ solution and (*2*–*5*) its variation on subsequent calcination in air at 673 K. (R_d) Diffuse reflection coefficient and (λ) wavelength. Heat treatment duration (h): (*2*) 0.5, (*3*) 1.0, (*4*) 2.0, and (*5*) 3.0.

tion of the total pore volume in which an $Ni(NO_3)_2$ solution was distributed during the capillary impregnation.

Gradual building up of nickel oxide mass in PG can be achieved by repeated impregnation–thermolysis operations using $Ni(NO_3)_2$ solutions of various concentrations (Fig. 1). A series of NiO/PG systems with nickel oxide content Q from 0.5 to 7.0 mmol per gram of the porous glass (hereinafter, mmol g^{-1}) was obtained by this technique.

Samples of NiO/PG were insufficiently transparent to be studied in transmitted light. The optical electronic spectra in the visible range (400–800 nm) were obtained using powders of specially prepared NiO/PG samples; the spectra were recorded in the diffuse reflection mode on an SF-10 double-beam spectrometer with a spherical photometer using the initial PG as a reference. The X-ray photoelectron spectra were taken on an ES-2401 instrument using MgK_α excitation radiation with the energy of 1253.6 eV in a band of removal of inner Ni $2p$ electrons.

Electrical measurements were carried out on direct current using the circuit and instruments described earlier [6–11]. Plates of NiO/PG were placed between pinching (with a constant pressure of 200 g cm^{-2}) electrodes having the form of massive copper disks with polished silver-coated surfaces. In this way we measured the currents passing across the laminas, i.e. along the walls of PG channels with NiO distributed on their surface. The specific electrical conductivity was calculated for the NiO/PG systems taking into account actual sizes of the laminas without recalculation to the nickel oxide content and corrections for the porosity.

The data on the weight loss during the thermal decomposition of $Ni(NO_3)_2$ in PG at 673 K reliably pointed to the formation of NiO on the surface. Characteristic changes in the diffuse reflection spectra accompanying the thermolysis are shown in Fig. 2. The spectrum of the deposited salt is well resolved; the absorption maximum at γ = 710 nm corresponds to one of three bands characteristic of Ni^{2+} cations in the octahedral oxygen surrounding. The maximum corresponds to the spin-allowed electronic transition $^3A_{2g} \rightarrow {}^3T_{1g}(F)$ [15]. The band shape suggests that the second maximum corresponding to the transition $^3A_{2g} \rightarrow {}^3T_{1g}(P)$ is close to 400 nm, which also agrees with the published data (λ = 395 nm [15]). We failed to observe the third d–d transition $^3A_{2g} \rightarrow {}^3T_{2g}(F)$ with $\lambda > 1000$ nm because of the limited working range of the spectrometer. The octahedral nickel(II) coordination with oxygen atoms is retained in all stages of the salt thermolysis (Fig. 2). However, in the process, the absorption in the central part of the visible range rapidly progresses. Thus, even upon depositing the first "portions" of NiO, a broad structureless band covering the whole visible range is formed. Nevertheless, we can judge the presence of nickel(II) in the composition of $[NiO_6]$ polyhedra by a weak maximum at 700 nm. The nature of the observed spectrum broadening is not quite clear and may be due to both strengthening of vibronic coupling in the solid phase and partial $3d_\pi$–$2p_\pi$ conjugation of electrons along Ni–O–Ni bonds in small nickel oxide clusters.

The measured pore volume and density of deposited nickel oxide in the series of NiO/PG systems (Fig. 3) suggest that the free volume would monotonically decrease as the NiO content in the glass increases. This trend is, indeed, observed experimentally; however, it is clearly seen that the rate ε of the

decrease is not constant, and bends in the ε–*Q* dependence are clearly seen. The data of reliable measurements of the NiO weight and volume allow us to make a physically justified estimation of its density

$$\rho = Q/(\varepsilon_0 - \varepsilon), \quad (2)$$

where ε_0 and ε are the volumes of pores of pure and oxide-containing glasses, respectively.

Thus, in the case of a particular sample we obtain the value of density averaged over all types of variously sized oxide formations actually existing in the sample. Building up NiO to the content Q = 2 mmol g^{-1} takes place with preservation of a low density (approximately 4 g cm^{-3}); in the range 2–4 mmol g^{-1}, the density increases to 6.5 g cm^{-3}, after which it continues to increase less noticeably, gradually approaching the reference value of ρ = 7.45 g cm^{-3} for bulk NiO. The results obtained suggest that the state of deposited NiO considerably changes when its content increases.

Measurements of the electrical conductivity σ (Fig. 3) furnish important information on the character of filling of the PG surface with nickel oxide. The shape of the log σ–*Q* dependence is in good agreement with trends in variation of the free volume and density, clearly confirming the presence of stages of oxide growth. In the initial stage, separate nickel-containing polyhedra and(or) their small ensembles (clusters) are fixed on the silica surface. The lowest measurable conductivity appears only when the content of nickel oxide Q = 1.5 mmol g^{-1} is reached, causing origination of primary "channels" of through conductivity. The subsequent small increase in the oxide content to Q =2.0 mmol g^{-1} is accompanied by a jump of σ, which in general agrees with the concept of electrical conduction of small-size systems [1–3, 6–10, 16] and characterizes a high probability of the layer-by-layer filling of the silica surface with nickel-containing polyhedra. It should be noted that, in this case, the content of poorly conducting oxide is low, so the detection of a clear step on the log σ–*Q* plot is rather indicative. The preferential two-dimensional structure of the forming oxide layer is confirmed by an estimate of its effective thickness, which, to a first approximation, can be represented as

$$h = Q/\rho S_{sp}. \quad (3)$$

Thus obtained value h = 8 Å (at Q = 2.0 mmol g^{-1}) closely corresponds to the size of the nickel-containing polyhedron [NiO_6]. The prolongation of

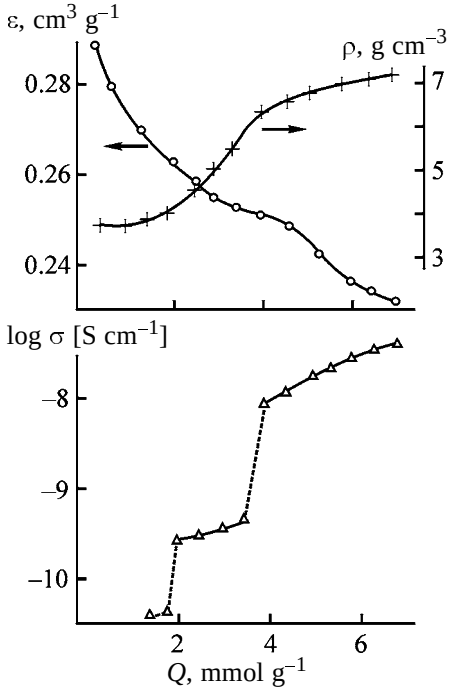

Fig. 3. Variations of the pore volume ε, specific electrical conductivity σ of modified PG, and density ρ of synthesized nickel oxide with increasing nickel oxide content Q in the glass.

supermonolayer growth ensures slow rate of the conductivity growth in the middle segment, Q = 2–3.5 mmol g^{-1}, corresponding to a considerable increase in the density of the synthesized nickel oxide; this is followed by the second jump of σ in the narrow range of oxide content 3.5–4.0 mmol g^{-1}. Further on (Q > 4 mmol g^{-1}), ρ and σ grow monotonically.

The following explanation of the observed experimental relationships seems to be the most probable. The conventional monolayer of nickel-containing polyhedra formed in the first stage is fixed directly on the walls of through channels of a glass and actually is surface nickel silicate. This is responsible for a low "packing density" of the polyhedra and their separation in space, determining the extremely low electrical conductivity. Formation of the second layer of [NiO_6] polyhedra is accompanied by a considerable density increase, which corresponds to the possibility of gradual formation of a structure with the parameters (bond length and bond angles) approaching those for NiO. The completion of this process in the range Q = 3.5–4.0 mmol g^{-1} is accompanied by strengthening of collective electronic interactions in the dense oxide layer and, correspondingly, by a sharp growth of the conductivity. The results obtained allow us to rule out formation of the island (three-dimensional) oxide structure, as at the achieved PG surface filling the islands would inevitably remain separate, remote from

Position of maxima in the X-ray photoelectron spectra of NiO/PG systems in the band of ionization of nickel inner 2*p* levels

Q, mmol g^{-1}	E_b, eV	
	$2p_{1/2}$	$2p_{3/2}$
1.54	876.3	859.5
2.10	876.0	859.0
2.96	875.8	858.7
4.10	875.4	858.2
5.20	875.1	858.0
6.00	874.9	857.9

each other, which contradicts the well pronounced steps in the $\log\sigma$–Q plot in the region of the formation of conventional oxide monolayers. Most likely, the formation of multiple "bridging" Ni–O–Ni bonds in the course of joining of polyhedra in a tangential direction appears energetically preferential as compared to the normal (relative to the surface) direction of the growth.

The dimensional features of changes in the steric and electronic structure of nickel oxide in the course of "step-by-step" increase in its content in a PG are reflected in the X-ray photoelectron spectra. The strongest bands of electron removal from filled shells of nickel atoms correspond to its 2*p* electrons [17]. It should be noted that, according to the published data [17], in the case of NiO the binding energy of 2*p* electrons varies within relatively wide limits of

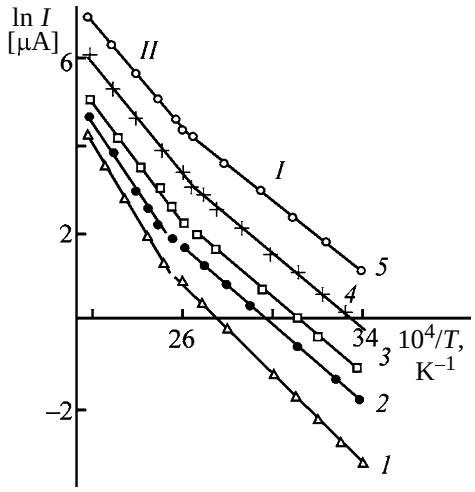

Fig. 4. Temperature dependence of current *I* measured at the voltage of 10 V across laminas of PG containing nickel oxide. NiO content (mmol g^{-1}): (*1*) 4.1, (*2*) 4.5, (*3*) 5.2, (*4*) 5.6, and (*5*) 6.0.

$E_b(2p_{1/2})$ = 871–874 eV. Hence, when studying spectra of NiO/PG systems, the most informative is the binding energy variation with increasing content of the deposited component, rather than the absolute value of the energy. In particular, the increase in E_b is definitely treated as an evidence of the increase in the positive effective charge of metal atoms [17]. The spectra obtained contain two bands of the $2p_{3/2}$ and $2p_{1/2}$ states in the region of removal of nickel inner 2*p* electrons with a distance of about 17 eV between their maxima (see table). The maximal binding energies E_b are observed in the first stage of filling of the glass surface with the oxide ($Q \le 2$ mmol g^{-1}), which is caused by a considerable positive effective charge of nickel atoms in the structure of the surface silicate. An increase in the oxide content over the conventional monolayer is accompanied by a noticeable and uniform shift of the 2*p*-electron maxima to lower energies. In spite of significant shifts of the spectra, they remain two-component, suggesting the electron density redistribution inside the oxide layer as a whole in the direction of lower effective charges of nickel atoms. Thus, the spectral manifestation of the electron-acceptor effect of silica [18, 19] becomes weaker as the weight of the deposited component increases.

Returning to the results of electrical conductivity studies, we note that it has a clear electronic character. In fact, if nickel or oxygen ions took part in the electricity transmission, the samples would be polarized owing to the appearance of an internal field directed against the applied field. In none of the experiments we have observed the emergence of polarization potentials or residual currents after cutting off the external voltage. The linearity of the voltammetric characteristics of all NiO/PG samples in a wide voltage range also suggests the absence of ion transfer. On the whole, relatively low values of σ (Fig. 3) allow us to rule out metal–metal exchange interactions by overlap of the 3*d* orbitals of nickel atoms [6, 7]. The above-mentioned $3d_\pi$–$2p_\pi$ electronic conjugation through Ni–O–Ni "bridges" seems to be the most probable conduction mechanism.

The temperature activation of currents *I* measured across laminas of modified glasses with the density of deposited oxide ρ = 6.4–6.9 g cm^{-3} is shown in Fig. 4. In the range of low temperatures, 293–473 K, the $\ln I$–T plots are of the same shape, which confirms similar structures of the conducting layers and similar features of the electricity transfer. The presence of two activation segments *I* and *II* can result from the fact that, in the vicinity of 380 K, the amplitudes of thermal vibrations are reached, ensuring accelerated

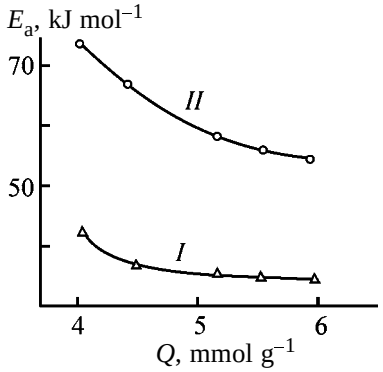

Fig. 5. Influence of NiO content in PG Q on the activation energy E_a calculated for two segments of temperature dependences of conductivity.

growth of the conductivity at the expense of increased electronic conjugation of Ni–O–Ni bonds. The activation energies E_a calculated for the two linear segments of the $\ln I$–T plots are shown in Fig. 5. It is evident that a small decrease in E_a is practically completed in the range of the deposited oxide content Q = 4–6 mmol g^{-1}. This result agrees well with the trends in the density variation (Fig. 3) and confirms the gradual formation and stabilization of structural parameters of a nickel oxide layer on the PG silica surface.

CONCLUSIONS

(1) Variations in the density, electrical conductivity, and optical and X-ray photoelectron spectra of nanosized nickel oxide, accompanying increase in its content on a silica surface, were studied. Based on the results obtained, a probable model of step filling of the porous glass surface was suggested. The process involves formation of a monolayer of nickel silicate in the first stage and uniform building up of predominantly two-dimensional NiO layer in further stages.

(2) Spectroscopic features of nanosized nickel oxide and well-pronounced jumps of the electrical conductivity, corresponding to the phases of its growth on the silica surface, reflect the manifestation of $3d_\pi$–$2p_\pi$ electron conjugation through Ni–O–Ni bonds.

REFERENCES

1. Gusev, A.I. and Rempel', A.A., *Nanokristallicheskie materialy* (Nanocrystalline Materials), Moscow: Fizmatgiz, 2000.
2. Petrov, Yu.I., *Klastery i malye chastitsy* (Clusters and Small Particles), Moscow: Nauka, 1986.
3. Petrov, Yu.I., *Fizika malykh chastits* (Physics of Small Particles), Moscow: Nauka, 1982.
4. Gubin, S.P. and Koksharev, Yu.A., *Izv. Ross. Akad. Nauk, Neorg. Mater.*, 2002, vol. 38, no. 11, pp. 1287–1304.
5. Shevchenko, V.Ya. and Madison, A.E., *Fiz. Khim. Stekla*, 2002, vol. 28, no. 5, pp. 459–464.
6. Tur, T.M. and Pak, V.N., *Zh. Prikl. Khim.*, 2000, vol. 73, no. 1, pp. 48–51.
7. Tur, T.M. and Pak, V.N., *Zh. Prikl. Khim.*, 1999, vol. 72, no. 11, pp. 1801–1804.
8. Pak, V.N., Sukhanov, S.V., and Gavronskaya, Yu.Yu., *Zh. Prikl. Khim.*, 2002, vol. 75, no. 10, pp. 1651–1654.
9. Pak, V.N., Verezhinskaya, R.L., and Burkat, T.M., *Zh. Fiz. Khim.*, 2002, vol. 76, no. 7, pp. 1324–1327.
10. Verezhinskaya, R.L., Burkat, T.M., Pak, V.N., and Rychgorskii, V.V., *Fiz. Khim. Stekla*, 1999, vol. 25, no. 6, pp. 688–692.
11. Verezhinskaya, R.L., Burkat, T.M., and Pak, V.N., *Zh. Obshch. Khim.*, 2000, vol. 70, no. 3, pp. 403–407.
12. Molchanova, O.S., *Natrievoborosilikatnye i poristye stekla* (Sodium Borosilicate and Porous Glasses), Moscow: Oborongiz, 1961.
13. Roskova, T.P. and Tsekhomskaya, T.S., *Fiz. Khim. Stekla*, 1981, vol. 7, no. 5, pp. 513–534.
14. Burkat, T.M. and Dobychin, D.P., *Fiz. Khim. Stekla*, 1992, vol. 19, no. 5, pp. 129–140.
15. Ballhausen, C.J., *Introduction to Ligand Field Theory*, New York: McGraw-Hill, 1962.
16. Chopra, K.L., *Thin Film Phenomena*, New York: McGraw-Hill, 1969.
17. Wagner, C.D., Riggs, W.M., Davis, L.E., *et al.*, *Handbook of X-ray Photoelectron Spectroscopy*, Minnesota: Perkin–Elmer, 1978.
18. Chuiko, A.A., *Teor. Eksp. Khim.*, 1987, vol. 23, no. 5, pp. 597–620.
19. Pak, V.N., Tikhomirova, I.Yu., Burkat, T.M., and Lobov, B.I., *Zh. Fiz. Khim.*, 1999, vol. 73, no. 11, pp. 2024–2028.

Russian Journal of Applied Chemistry, Vol. 77, No. 1, 2004, pp. 20–22. Translated from Zhurnal Prikladnoi Khimii, Vol. 77, No. 1, 2004, pp. 22–24.

INORGANIC SYNTHESIS AND INDUSTRIAL INORGANIC CHEMISTRY

Gas-Sensitive Properties of SnO_2-Based Thin Films Obtained from Film-Forming Solutions

N. V. Postovalova, S. A. Kuznetsova, A. I. Ivanov, and V. V. Kozik

Tomsk State University, Tomsk, Russia

Received July 8, 2003

Abstract—Gas-sensitive properties of SnO_2 thin-film materials doped with antimony(III) with respect to the reducing gases CO, CH_4, and H_2 were studied. The materials were obtained from film-forming solutions of Sn(II) and Sb(III) complexes with acetylacetone.

Environmental protection is one of global problems. First of all it concerns atmosphere pollution, which is determined by emission levels of carbon, sulfur, nitrogen, and heavy metal oxides, radionuclides, and cancerogenic polyaromatic hydrocarbons [1]. Thin-film materials based on SnO_2 with semiconductor properties [2] are widely used as gas-sensitive components for the determination of these combustible and toxic gases in air. It is known that these materials are mainly produced by sputtering; however, these coatings have some drawbacks [3]. Therefore, it is appropriate to perform studies aimed to enhance the SnO_2 sensitivity to gases, which depends on the film structure and composition. Thus, it is necessary to search for new methods of synthesizing film-forming systems, allowing preparation of films with specified structure and composition.

Here we consider the gas-sensitive properties of thin films of tin dioxide doped with antimony. The films were obtained from film-forming solutions of Sn(II) and Sb(III) complexes with acetylacetone as an organic ligand.

EXPERIMENTAL

Film-forming solutions based on complex compounds (FFSCCs) were prepared by dissolving tin(II) chloride (0.297–0.273 M), antimony(III) chloride crystal hydrate (2.9×10^{-3}–2.63×10^{-2} M), acetylacetone (0.6 M), and hydrochloric acid (0.4 M) in alcohol (96 wt %). The antimony content (1, 6, and 9 at. %) in SnO_2 films was chosen on the basis of the published data [4]. Antimony-free FFSCC compositions and the processes occurring in these FFSCCs were considered in detail in [5].

Films of SnO_2–Sb were obtained by centrifugation on an MPW-340 centrifuge (4000–4500 rpm), dried for 1 h in a desiccator at 333 K, and annealed in a muffle furnace at 873 K. Three 1-h annealings were performed to stabilize the electrophysical parameters. Single-crystal silicon was used as support.

The electrical resistance of the films was measured with an E6-13A teraohmmeter in air and in CO and CH_4 atmospheres at 299–673 K. Platinum contacts were used. The ratio of the resistance in air and resistance in a gas was taken as the value of adsorption response R_a/R_g to the action of the CO, CH_4, and H_2 gases. The activation energy of charge carriers E_a was calculated by the procedure described in [6]. The film thickness and refractive index were determined by ellipsometry (LEF-3M). The film composition was determined by X-ray phase analysis on a DRON-3M diffractometer (CuK_α radiation, Ni filter).

The X-ray patterns, interpreted as in [7], show that introduction of antimony(III) into an SnO_2 film results in a shift of interplanar spacings (Table 1), but the rutile-type structure of SnO_2 is preserved. The shift can be caused by formation of a solid solution based on SnO_2.

Table 1. X-ray diffraction parameters of SnO_2–Sb films

c_{Sb} = 1 at. %		c_{Sb} = 9 at. %		SnO_2 [7]	
d, Å	I/I_0	d, Å	I/I_0	d, Å	I/I_0
3.54	100	3.48	100	3.34	100
2.77	88	2.76	90	2.64	63
1.81	56	1.81	80	1.75	18

1070-4272/04/7701-0020 © 2004 MAIK "Nauka/Interperiodica"

The films obtained from these film-forming solutions are conducting. Their thickness is 46–68 nm. Table 2 shows that the electrical resistance and activation energy of charge carriers regularly decrease as the concentration of antimony dopant increases from 1 to 9 at. %. As shown in [4], the rise of the electrical conductivity owing to dopant transition from lattice points to the grain surface is caused by the lifting of the compensation effect of oxygen donor vacancies in SnO_2 by Sb(V) impurity centers.

The conductivity of the films depends not only on the activation energy of charge carriers and their concentration, but also on the structure, which can be judged from the refractive index *n*. Films containing 1 at. % Sb have the lowest *n* value of 1.69. The refractive index of SnO_2 films obtained from antimony-free FFSCC is 1.89 [5], and that of Sb_2O_3 is 2.05 [8]. Such a low *n* value of the SnO_2 film containing 1 at. % Sb antimony suggests its defectiveness. Such films have a fairly high surface resistance of 10^6 Ω. Samples containing 9 at. % Sb have higher $n = 2.13$ and a relatively low surface resistance of about 10^{-3} Ω.

To study the behavior of the films in CO, CH_4, and H_2 atmospheres, we have chosen samples with sharply different physical properties. As seen from Fig. 1, the R_a/R_g ratio increases with temperature. The R_a/R_g curves for SnO_2 film containing 1 at. % Sb have two maxima in CO (curve *1*) and CH_4 (curve *2*) atmospheres: in the low-temperature region at 393 K and in the high-temperature region at 573 K. The low-temperature maximum is caused by surface reactions of oxygen adsorbed on the film with reducing gases, which results in delocalization of electrons [4]. The second peak in the R_a/R_g curves is related to the formation of new chemical bonds corresponding to double-charged tin (SnO) [9]. In contrast to SnO_2, SnO is a narrow-band-gap semiconductor, and, consequently, its presence can lead to a significant change in the electrical conductivity. This film shows no response to hydrogen.

As seen from Fig. 2, R_a/R_g for the SnO_2 film doped with 1 at. % Sb depends on the gas concentration. Its maximal sensitivity corresponds to the CH_4 concentration of 10 vol % ($T = 574$ K). The temperature dependences of R_a/R_g of SnO_2 films doped with 9 and 1 at. % Sb are different (Fig. 1, curves *1* and *2*). No pronounced peaks are observed in the CH_4 atmosphere (Fig. 1, curve *3*). An insignificant sensitivity peak was found for CO concentration of 5 vol % (493 K). It becomes better pronounced after keeping the film for 2 days at the CO concentration of 40 vol % (Fig. 3). The low sensitivity of SnO_2 films doped with 9 at. % Sb is attributable to blocking of the surface states of adsorbed oxygen by a large amount of antimony [5].

Table 2. Properties of SnO_2–Sb* films

c_{Sb}, at. %	E_a, eV	*n*	*R*, Ω
1	0.50	1.69	10^6
6	0.27	2.00	10^6
9	0.19	2.13	10^3

* (*n*) Refractive index and (*R*) surface conductivity.

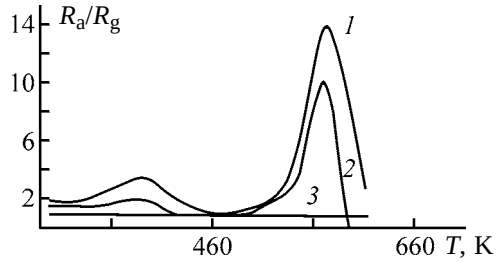

Fig. 1. Temperature dependence of the adsorption response R_a/R_g of SnO_2–Sb films to (*1*) 5 vol % CO and (*2*, *3*) 5 vol % CH_4. Sb concentration (at. %): (*1*, *2*) 1 and (*3*) 9.

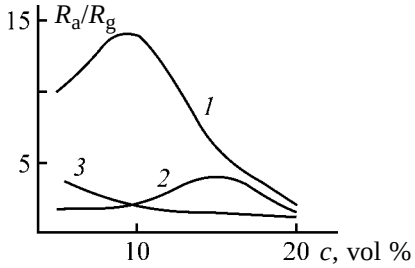

Fig. 2. Adsorption response R_a/R_g of SnO_2 films doped with 1 at. % Sb as a function of concentration *c* of (*1*, *2*) CH_4 and (*3*) CO. Temperature (K): (*1*) 574 and (*2*, *3*) 393.

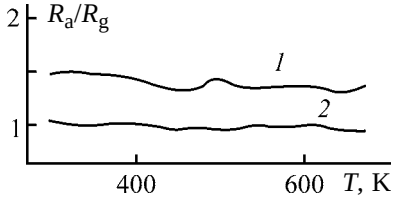

Fig. 3. Temperature dependence of the adsorption response R_a/R_g of SnO_2 films doped with 9 at. % Sb to CO. CO concentration (vol. %): (*1*) 40 and (*2*) 5.

CONCLUSIONS

(1) High-resistance thin SnO_2 films doped with Sb (1, 6, and 9 at. %) were prepared by centrifugation on

silicon supports from film-forming solutions based on tin(II) and antimony(III) complexes with acetylacetone.

(2) The sample containing 1 at. % Sb shows the greatest adsorption response to the reducing gases CO and CH_4. The low-resistance sample containing 9 at. % Sb does not show such a behavior. The films are stable and are able to operate at relatively low temperatures. Their gas-sensitive properties compare well with those of thin-film materials prepared by more laborious and expensive techniques. It is proposed to use the films obtained as components sensitive to CO and CH_4 in the presence of H_2.

REFERENCES

1. Myasoedov, B.F. and Davydov, A.V., *Zh. Anal. Khim.*, 1990, vol. 45, no. 7, pp. 1259–1266.
2. Suikovskaya, N.V., *Khimicheskie metody polucheniya tonkikh prozrachnykh plenok* (Chemical Procedures for Obtaining Thin Transparent Films), Moscow: Nauka, 1971.
3. Orlik, D.R., Ivanovskaya, M.I., and Kol', K.D., *Zh. Anal. Khim.*, 1995, vol. 50, no. 11, pp. 1173–1177.
4. Buturlin, A.I., Gabuzyan, T.A., Golovanov, N.A., *et al.*, *Zarubezhn. Tekh.*, 1983, no. 10. pp. 3–40.
5. Kuznetsova, S.A., Skorik, N.A., and Kozik, V.V., *Zh. Prikl. Khim.*, 1997, vol. 70, no. 12, pp. 2071–2073.
6. *Praktikum po poluprovodnikam i poluprovodnikovym priboram* (Manual on Semiconductors and Semiconductor Apparatus), Shalimova, K.V., Ed., Moscow: Vysshaya Shkola, 1968.
7. *American Society for Testing Materials Inorganic Plain Cards*, Philadelphia, 1946–1969.
8. *Fiziko-khimicheskie svoistva okislov: Spravochnik* (Physicochemical Properties of Oxides: Handbook), Samsonov, G.V., Ed., Moscow: Metallurgiya, 1978.
9. Safonova, O.V., Rumyantseva, M.N., Kozlov, R.I., *et al.*, *Zh. Prikl. Khim.*, 2000, vol. 73, no. 8, pp. 1250–1255.

Russian Journal of Applied Chemistry, Vol. 77, No. 1, 2004, pp. 23–25. Translated from Zhurnal Prikladnoi Khimii, Vol. 77, No. 1, 2004, pp. 25–27.

PHYSICOCHEMICAL STUDIES OF SYSTEMS AND PROCESSES

Iteration Methods for Calculating Physicochemical Properties of Molecular Inorganic Compounds

I. B. Sladkov and M. V. Uchaneva

St. Petersburg State Polytechnic University, St. Petersburg, Russia

Received May 26, 2003

Abstract—Iteration schemes for highly reliable prediction of physicochemical properties of molecular inorganic compounds were proposed.

The most reliable prediction of physicochemical properties of molecular liquids is achieved using methods based on the thermodynamic similarity theory. These methods use relationships between the physicochemical properties expressed in the dimensionless form. Passing to dimensionless values requires data on the critical parameters of substances. Therefore, the above methods employ critical parameters as input data. Because the experimental data on the critical constants are rather limited, the calculation methods of their determination have became practically significant. First, this concerns the molecular inorganic compounds that have found wide practical application [1] but are, however, little studied.

Reliable data on the critical parameters can be obtained by the iteration methods. These methods involve successive approximations to obtain the closest agreement between the required parameter and other previously known physicochemical properties of a substance. The fact that not only the critical parameters but also other physicochemical properties of a substance can be determined in the course of iteration is a significant advantage of the iteration methods.

In this study we developed an iteration scheme for highly reliable prediction of the critical parameters of molecular inorganic compounds. It is based on relationships employing the determining criterion, which reliably describes the thermodynamic similarity of any molecular inorganic compounds. The latter is referred to as the factor of the complexity of intermolecular interaction (or ψ-factor) and is considered in detail in [1].

Let us list the equations used in the iteration scheme proposed (iteration 1). For the critical temperature and critical pressure, we used the equation obtained by integrating the Clausius–Clapeyron equation between the boiling and critical temperatures [2]. In this case, the pressure varies from a value at the boiling point P_b to a value at the critical point P_{cr}. In the literature [3], this equation is known as the van der Waals equation

$$\ln(P_{cr}/P_b) = f(T_{cr}/T_b - 1). \quad (1)$$

The parameter

$$f = \Delta H_b/(RT_{cr}) \quad (2)$$

is referred to as the generalized constant, because its variations from substance to substance lie within very narrow limits. ΔH_b is the enthalpy of vaporization at the boiling point.

To leave only one unknown parameter (critical temperature) in Eq. (1), the known relationship for the critical pressure is used:

$$P_{cr} = RT_{cr}/(8b), \quad (3)$$

where b is the van der Waals constant.

Then, Eq. (1) becomes

$$\ln[RT_{cr}/(8bP_b)] = f(T_{cr}/T_b - 1). \quad (4)$$

The critical temperature appearing in the expression for f can be calculated by the equation [1]

$$T_{cr} = T_b + 0.89(T_b)^{0.92+0.2\psi}, \quad (5)$$

where ψ is the factor of the complexity of intermolecular interaction.

The ψ factor is the determining criterion of thermodynamic similarity, which extends the applicability of

1070-4272/04/7701-0023 © 2004 MAIK "Nauka/Interperiodica"

Error in predicting critical parameters by iteration methods

Calculation method	Error, %*		
	T_{cr}	P_{cr}	V_{cr}
Iteration 1 (set of data for 60 substances)**	0.9	2.2	1.1
Iteration 2 (set of data for 50 substances)***	1.6	2.4	2.0

* Averaged (in the absolute value) for the whole set of substances.
** For any molecular inorganic compounds.
*** For nonpolar and weakly polar substances.

the correlations obtained using the similarity theory [1]. After that, f can be calculated by the equation

$$f = \Delta H_b/\{R[T_b + 0.89(T_b)^{0.92+0.2\psi}]\}$$

and considered constant in Eq. (4).

Taking into account the dimensionalities of b ($cm^3\ mol^{-1}$) and P_b (MPa), we obtain the following expression for the critical temperature:

$$T_{cr} = T_b[(1/f)\ln(10.255T_{cr}/b) + 1]. \quad (6)$$

We start the iteration from calculation of the complexity factor

$$\psi = 0.1\ln T_b - 0.122\ln V_b + 0.006$$

and the van der Waals constant [1]

$$b = mV_b + n,$$

where $m = 1.27$ and $n = -6$ if $\psi \le 0.1$; $m = 1$ and $n = 11$ if $\psi \ge 0.1$; V_b is the molar volume at the boiling point ($cm^3\ mol^{-1}$).

The van der Waals constant b ($cm^3\ mol^{-1}$) can be calculated from the given values of m and n.

The critical temperature, to a first approximation, is calculated by Eq. (5) and, as a second approximation, by Eq. (6).

If the difference between the obtained T_{cr} values is less than the preset accuracy (e.g., 0.001), then we go to calculating the other critical parameters. Otherwise, we return to Eq. (6) using the specified T_{cr} value.

After the critical temperature is determined, the critical pressure should be calculated from Eq. (1):

$$P_{cr} = P_b \exp[f(T_{cr}/T_b - 1)]. \quad (7)$$

The critical volume can be calculated by the Benson equation [4]:

$$V_{cr} = V_b(2.4 + 0.1833\ln P_{cr}]. \quad (8)$$

The iteration is suitable for calculating critical parameters of any molecular inorganic compounds, from nonpolar to strongly polar substances.

The accuracy of the method proposed in this work (iteration 1) was verified on a set of data for 60 substances, including hydrides (B_2H_6, CH_4, GeH_4, SnH_4, NH_3, and N_2H_4), fluorides (CF_4, PF_3, MoF_6, WF_6, UF_6, and PtF_6), chlorides (CCl_4, $SiCl_4$, $GeCl_4$, $SnCl_4$, $TiCl_4$, BCl_3, PCl_3, PCl_5, $BiCl_3$, $SbCl_3$, S_2Cl_2, $MoCl_5$, and HCl), bromides (BBr_3, $SnBr_4$, $GeBr_4$, PBr_3, $AsBr_3$, and $SbBr_3$), iodides (BI_3, SiI_4, and SnI_4), mixed halides ($SiCl_3F$, $SiCl_2F_2$, $SiClF_3$, CBr_2F_2, $CBrF_3$, PCl_2F, $PClF_2$, $SiBr_2Cl_2$, $SiBrCl_3$, and $NClF_2$), hydrohalides ($CHClF_2$, $SiHCl_3$, $SiHBr_3$, and NHF_2), oxohalides (PCl_3O, PBr_3O, SCl_2O, SOF_2, $SeCl_2O$, WCl_4O, VCl_3O, and ClO_3F), and oxides (CO, SO_2, OsO_4, and H_2O). Among these compounds are 10 strongly polar substances (SO_2, NH_3, H_2O, and others).

All the input data were taken from [1]. The calculated and experimental values of the critical parameters (critical temperature T_{cr}, critical pressure P_{cr}, and critical volume V_{cr}) are given in Table 1 to demonstrate the accuracy of the iteration method proposed. The data presented show that the iteration method proposed is highly reliable for predicting the critical parameters.

It should be noted that the method proposed has two essential advantages. First, it employs only accessible input data (boiling point of a substance, its molar volume, and the enthalpy of vaporization at the boiling point). Second, it is suitable for any molecular inorganic compounds, from nonpolar and weakly polar substances to strongly polar substances and associated liquids.

The iteration method based on the minimal number of the experimental input data is important for little studied substances. We developed the iteration scheme (iteration 2) using the boiling point as the only experimental input parameter. The molar volume and the enthalpy of vaporization at the boiling point, apart from the critical parameters, can be determined by this method.

This iteration employs the following relationships between the physicochemical properties of molecular inorganic compounds [1]: (1) $\Delta S_b = 88$ (Trouton rule), (2) $\theta = T_b/T_{cr} = 0.772 - 12.27/\Delta S_b$, (3) $T_{cr} = T_b/\theta$,

(4) $V_b = 116\prod^{1/2}/T_b^{0.3} + 0.5$, (4) $b = 1.27V_b - 6$, (5) $P_{cr} = 1.039T_{cr}/b$, (6) V_b (second approximation) = $85T_{cr}P_{cr} + 2$, (7) $\Delta H_b = T_b[73 + 2.09\ln(T_bM/V_b)]$, and (8) ΔS_b (second approximation) = $\Delta H_b/T_b$.

If the difference between the calculations of ΔS_b by steps 1 and 8 is smaller than a preset accuracy (e.g., 0.001), then the calculation is finished. Otherwise, the calculation by step 1 is performed again, with the new value assigned to ΔS_b.

The iteration converges sharply (the number of steps does not commonly exceed three). The iteration can be applied to nonpolar and weakly polar substances. To judge whether the compound under study belongs to such substances, it is sufficient to compare its boiling point and parachor $\prod$. For nonpolar and weakly polar substances, the following inequality [1] is fulfilled:

$$T_b < 100\prod.$$

The iteration was verified with 50 molecular inorganic substances. It employs the minimal number of easily accessible input data (boiling point) and ensures quite reliable prediction of the critical parameters (see table). Moreover, the iteration can predict the increased number of properties. Apart from the critical parameters, it can also determine (with the mean average error given in parentheses) the molar volume of a liquid at the boiling point (1.7%) and the enthalpy of vaporization at the boiling point (2.2%).

REFERENCES

1. Morachevskii, A.G. and Sladkov, I.B., *Fiziko-khimicheskie svoistva molekulyarnykh neorganicheskikh soedinenii* (Physicochemical Properties of Molecular Inorganic Compounds), St. Petersburg: Khimiya, 1996.
2. Sladkov, I.B., *Zh. Prikl. Khim*., 1993, vol. 66, no. 6, pp. 1206–1209.
3. Heukelom, W., *Recl. Trav. Chim. Pays-Bas*, 1949, vol. 68, nos. 9–10, p. 661.
4. Stolyarov, E.A., and Orlova, N.G., *Raschet fiziko-khimicheskikh svoistv zhidkostei* (Calculation of the Physicochemical Properties of Liquids), Leningrad: Khimiya, 1976.

Russian Journal of Applied Chemistry, Vol. 77, No. 1, 2004, pp. 26–29. Translated from Zhurnal Prikladnoi Khimii, Vol. 77, No. 1, 2004, pp. 28–31.

PHYSICOCHEMICAL STUDIES OF SYSTEMS AND PROCESSES

Kinetic Characteristics of Xylitol Crystallization from Aqueous-Ethanolic Solutions

V. V. Vyglazov

St. Petersburg State Forestry Engineering Academy, St. Petersburg, Russia

Received July 10, 2003

Abstract—The kinetics of xylitol crystallization from aqueous-ethanolic solutions as a function of the initial solution supersaturation, solvent composition, and temperature was studied. The effect of solvent composition on the rate of the xylitol bulk crystallization was considered.

Among sugar substitutes, an important role belongs to pentahydric aliphatic polyol, xylitol, prepared by reductive transformation of *D*-xylose [1]. Inclusion of xylitol in the list of food additives (E 967) [2] and confirmation of its anticarious properties extended applications of this polyol. The main branches of xylitol use are food production, perfumery, pharmaceutics, and chemistry.

The technology of food xylitol production consists of the following main stages: hydrolysis of hemicellulose polysaccharides of pentosan-containing plant raw materials (birch wood, cotton husk, corn cob shanks); pentosan hydrolyzate preparation for hydrogenation; hydrogenation of xylose solution; purification and concentration of xylitol solution; and xylitol crystallization. Crystallization is an important stage of xylitol production, since in many respects it determines the yield and quality of the target product. The possibilities of increasing the xylitol yield and quality by optimization of the known technology of xylitol crystallization from concentrated aqueous solutions are practically exhausted.

The method of xylitol separation including preliminary crystallization from supersaturated aqueous solution and subsequent crystallization in the ethanol–water mixture is more efficient [3]. The optimum mode of xylitol crystallization can be determined from the data on the process statics and kinetics. Previously, on the basis of the solubility data, we developed a model of the statics of xylitol crystallization from aqueous-ethanolic solutions [4]. In this work, we studied the kinetics of polyol crystallization.

EXPERIMENTAL

The xylitol crystallization from aqueous-ethanolic solutions was studied as a function of the degree of solution supersaturation (characterized by supersaturation coefficient *S*), solvent composition, and temperature at a constant stirring rate of 100 rpm. Xylitol crystallization was studied under the isothermal conditions at 5, 25, and 40°C. The compositions of water–ethanol mixtures were taken with regard to probable values of the liquid-to-solid ratio *M* [i.e., the ratio of 95.3% ethanol weight to the weight of dry substances of the crystallizate (massecuite)]. It was 60–90 vol % (or 53.9–87.5 wt %) with respect to ethanol, which corresponds to the $0.10 < M < 0.50$ range used in industrial xylitol crystallization. The initial supersaturation was reached by heating. The degree of supersaturation was selected with regard to polyol solubility [4] by the formula $S = c_{in}/c_s$, where *S* is supersaturation coefficient and c_{in} and c_s are the xylitol initial concentration and solubility (g per 100 g of the solvent), respectively.

Food xylitol used [TU (Technical Specifications) 64-10-04–89] was preliminarily recrystallized and dried to the moisture content of 0.03%. The xylitol purity determined by GLC [5] was 99.9%, mp of crystals 93.5–94.0°C. The solvent was prepared by mixing of ethanol (rectificate) with distilled water at 20°C. The refractive indices of water–ethanol mixtures prepared agree with data of [6]. Xylitol crystallization was performed in a three-necked flask equipped with a stirrer and thermometer. The temperature was controlled with 0.1°C accuracy.

Crystallization was monitored through a change in the refractive index of a liquid phase sample. Preliminarily, the n_D^T–c_{et} calibration plots were built for each ethanol concentration and temperature. A linear dependence n_D^T–c_{et} was observed for the concentration range corresponding to supersaturated metastable state of the solution. This is characteristic also for other

1070-4272/04/7701-0026 © 2004 MAIK "Nauka/Interperiodica"

substances [7]. The error in determination of xylitol concentration in aqueous-ethanolic solution by the refractive index was 0.05 g per 100 g of the solvent, which corresponds to the interval from ±0.25 (in 60% ethanol) to ±2 rel% (in 90% ethanol) at 5°C.

The crystalline products obtained were examined microscopically to estimate the granulometric composition. Linear dimensions of a large number of particles (>60) were measured under a microscope equipped with a special scale. Each crystal was measured along two mutually perpendicular directions, and the average value L was taken as its linear size. Microscopic analysis allowed determination of the size distribution of particles in the fraction (%) [8].

The data on xylitol crystallization under various conditions in the form of typical kinetic curves are shown in Fig. 1. The xylitol solubility c_s at fixed temperature and solution composition is shown by a dashed line. The analysis of the kinetic curves showed that the increase in the ethanol concentration c_{et} in the intercrystallite liquor of the xylitol suspension accelerates xylitol separation into the solid phase. For example, at 25°C, xylitol crystallization proceeds by a factor of 11 faster in 90% than in 60% ethanol (Table 1). The time of decrease in the degree of solution supersaturation from 1.86 to 1.10 was taken as the time of xylitol crystallization.

The initial period of xylitol crystallization is satisfactorily described by the equation [9]

$$J = K_N c_{in}^n, \quad (1)$$

where J is the nucleation rate; K_N, nucleation rate constant; c_{in}, initial xylitol concentration (g per 100 g of solvent); and n, nucleation order.

When the crystallization has an induction period, Eq. (1) transforms into Eq. (2):

$$\log t_{ind} = K_{ind} - n\log(c_{in}/c_s), \quad (2)$$

where t_{ind} is the induction period (min); K_{ind}, induction period constant; and c_s, xylitol solubility (g per 100 g of solvent).

The slope of the linear dependence of $\log t_{ind}$ on $\log(c_{in}/c_s)$ is equal to the nucleation reaction order n; the latter changes for xylitol from n = 7 at c_{et} = 60 vol % and 5°C to n = 30 at c_{et} = 90 vol % and 40°C.

The rate of xylitol nucleation increases with increasing temperature and c_{et}, especially at M > 0.3, which is connected with changes in the mixed solvent structure. Extrapolation of the linear dependences described by Eq. (2) to the range of greater supersaturation, where t_{ind} = 1, allows evaluation of maximum supersaturations S_{lim} characterizing the upper boundary of metastability and determination of the region of stability of xylitol solutions as a whole. In

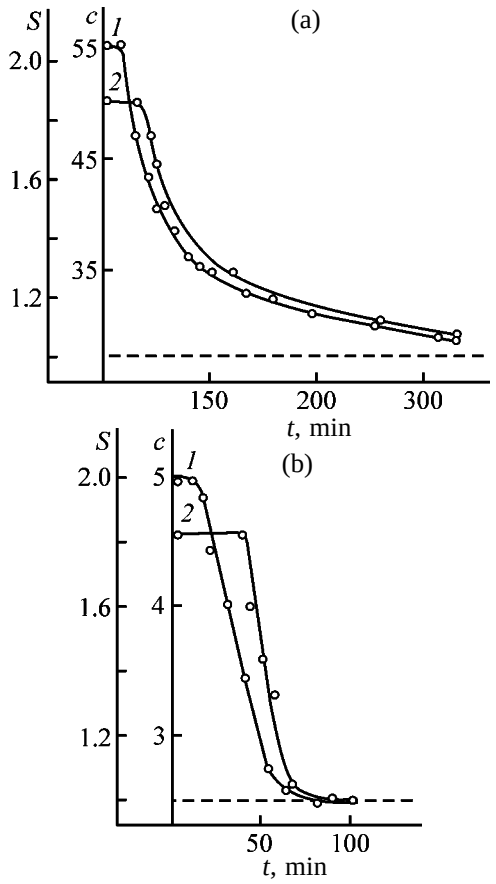

Fig. 1. Kinetics of xylitol crystallization in aqueous–ethanolic solutions at 5°C. (*S*) Degree of supersaturation and (*c*) xylitol concentration (g per 100 g of the solvent). Initial *c*: (a) (*1*) 55.0 and (*2*) 50.2; (b) (*1*) 5.0 and (*2*) 4.6. c_{et} (vol %): (a) 60 and (b) 90.

Table 1. Duration of xylitol crystallization t from aqueous-ethanolic solutions*

c_{et}, vol %	t, min, at indicated temperature, °C		
	5	25	40
60	285	345	930
70	110	122	380
80	70	80	117
90	25	32	85

* c_{et} is the ethanol concentration in water–ethanol mixture; the same for Table 2.

Table 2. Fractional composition of xylitol crystals at various crystallization temperatures

c_{et}, vol %	Content, %, of crystals of indicated size, mm					
	>0.15	<0.15	>0.15	<0.15	>0.15	<0.15
	5°C		25°C		40°C	
60	82	18	58	42	54	46
70	66	34	50	50	41	49
80	40	60	42	58	18	82
90	0	100	0	100	5	95

60% ethanol, S_{lim} changes from 2.99 at 5°C to 2.12 at 40°C, and in 90% ethanol, from 2.40 at 5°C to 1.86 at 40°C. The decrease in the width of the metastable zone with increasing c_{et} satisfactorily agrees with the theory connecting a decrease in S_{lim} with decreasing solvent permittivity (ε_{H_2O} = 82.1 and $\varepsilon_{C_2H_5OH}$ = 25.0 at 20°C [11]).

The second stage of bulk xylitol crystallization from aqueous-ethanolic solutions involves direct formation of crystalline precipitates. At fairly high solution supersaturation, when the rate of back dissolution from the surface of growing crystals can be neglected and the surface area after attaining the maximal rate of the process changes insignificantly, the expression derived from the chemical kinetics equation for heterogeneous reactions [9]

$$\Delta t = A - B\log(c/c_s), \quad (3)$$

is valid. Here $\Delta t = t - t_{ind}$, $A = (1/K_1)\log(c_{in}/c_s)$, $B = 1/K_1$, t is the total time of observation (min), and K_1, the rate constant of xylitol crystal growth (min^{-1}).

The applicability of Eq. (3) to xylitol crystallization from aqueous-ethanolic solutions is confirmed by the linear dependence of $\log(c/c_s)$ on the crystallization time Δt (Fig. 2).

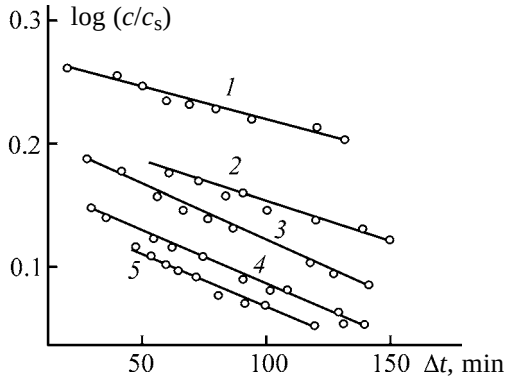

Fig. 2. Logarithm of the degree of supersaturation of xylitol aqueous-ethanolic solutions c/c_s as a function of crystallization time Δt at various temperatures. c_{et} (vol %): (*1*, *2*) 60, (*3*) 70, and (*4*, *5*) 80. Temperature (°C): (*1*, *5*) 25 and (*2*–*4*) 5.

The first order of the crystallization reaction under isothermal conditions shows that the xylitol crystallization rate is limited by the rate of diffusion of polyol molecules to the surface of growing crystals.

It was found that, as the ethanol concentration in the mixed solvent is increased, e.g., from 80 to 90 vol %, the xylitol crystallization rate increases by a factor of approximately 3 (K_1 increases from 1.7×10^{-3} to 4.9×10^{-3} min^{-1}). For c_{et} = 80–90 vol %, the linear dependence of $\log(c/c_s)$ on Δt keeps at S 1.1–1.3, and for c_{et} = 60–70 vol %, at S = 1.2–1.5.

These S values characterize the width of the first zone of metastability in the xylitol–ethanol–water phase diagram. In this region of supersaturation, already existing crystals grow without formation of new crystallization centers, which is very important for the technology of xylitol crystallization.

A microscopic estimation of the fractional composition of xylitol crystals prepared in kinetic experiments showed that the crystal size substantially depends of c_{et} and T (Table 2). At c_{et} < 80 vol %, larger crystals are formed.

Under industrial conditions, massecuite crystals should be capable of further growth in the ethanolic solution characterized by supersaturations corresponding to the first metastable zone.

To prevent the secondary nucleation, ethanol should be introduced into the crystallizing system gradually. To obtain larger crystals, the c_{et} value in the intercrystalline liquor should not exceed 80 vol % (Table 2).

CONCLUSIONS

(1) A study of xylitol crystallization as a function of the degree of the initial solution supersaturation,

solvent composition, and temperature revealed the main kinetic characteristics of this process: maximal supersaturation of solutions in the form of the first and second metastability boundaries, induction period, nucleation reaction order, and the rate constant of xylitol crystal growth.

(2) The data obtained were used to choose the optimum mode of xylitol crystallization on the laboratory and semicommercial scale and were taken into consideration when designing the crystallization apparatus.

REFERENCES

1. Khol'kin, Yu.I., *Tekhnologiya gidroliznykh proizvodstv* (Technology of Hydrolytic Production), Moscow: Lesn. Prom–st., 1989.
2. Sarafanova, L.A., *Pishchevye dobavki: Entsiklopediya* (Food Additives: Encyclopedia), St. Petersburg: GIORD, 2003.
3. USSR Inventor's Certificate no. 810 661.
4. Vyglazov, V.V. and Khol'kin, Yu.I., *Zh. Prikl. Khim.*, 1984, vol. 57, no. 7, pp. 1651–1654.
5. Vyglazov, V.V., Yaropolova, O.M., and Khol'kin, Yu.I., *Gidrolizn. Proizv.*, 1979, no. 7, pp. 14–16.
6. Ioffe, B.V., *Refraktometricheskie metody khimii* (Refractometric Methods in Chemistry), Leningrad: Khimiya, 1974.
7. Nikitina, S.D. and Khamskii, E.V., *Zh. Prikl. Khim.*, 1973, vol. 46, no. 11, pp. 2563–2564.
8. Matusevich, L.I., *Kristallizatsiya is rastvorov v khimicheskoi promyshlennosti* (Crystallization from Solutions in Chemical Industry), Moscow: Khimiya, 1968.
9. Khamskii, E.V., Podozerskaya, E.A., Freidin, B.M., *et al.*, *Kristallizatsiya i fiziko-khimicheskie svoistva kristallicheskikh veshchestv* (Crystallization and Physicochemical Properties of Crystalline Substances), Leningrad: Nauka, 1969.
10. Khamskii, E.V., *Kristallizatsiya v khimicheskoi promyshlennosti* (Crystallization in Chemical Industry), Moscow: Khimiya, 1979.
11. *Kratkii spravochnik fiziko-khimicheskikh velichin* (Concise Handbook of Physicochemical Quantities), Mishchenko, K.P. and Ravdel', A.A., Eds., Leningrad: Khimiya, 1972.

Russian Journal of Applied Chemistry, Vol. 77, No. 1, 2004, pp. 30–33. Translated from Zhurnal Prikladnoi Khimii, Vol. 77, No. 1, 2004, pp. 32–35.

SORPTION AND ION-EXCHANGE PROCESSES

Ion-Exchange Properties and IR Spectra of Natural Clinoptilolite Modified with Titanium Hydroxophosphates

V. S. Aleksandrova, O. P. Zykova, and E. Ya. Markiv

Institute of Sorption and Endoecological Problems, National Academy of Sciences of Ukraine, Kiev, Ukraine

Received July 22, 2002; in final form, March 2003

Abstract—A method for modification of a natural zeolite, a clinoptilolite-containing tuff, with compounds based on titanium phosphate is suggested. The results obtained in a comparative study of sorption of heavy metal ions on the initial and modified clinoptilolite are presented. The modifying effect of an additive is discussed on the basis of IR and X-ray fluorescence spectroscopic data.

The selectivity of a natural zeolite, clinoptilolite, toward ions of heavy and transition metals makes promising its use for recovery of these elements from aqueous solutions, industrial wastewater, and potable water. However, the clinoptilolite-containing material is rarely used in practice in its natural form, being, as a rule, subjected to additional chemical pretreatment to improve its sorption, mainly ion-exchange properties [1].

The most widely used method for directed modification of a zeolite sorbent is cation-exchange modification, which consists in that the polycationic natural material is transformed into a monocationic (H^+, Na^+, Ca^{2+}, NH_4^+, etc.) form [2].

In contrast to the commonly accepted approach [2], in this work we examined the possibility of improving the performance of natural clinoptilolite by chemical grafting of a modifying agent with good sorption and selective properties. We believe that the most promising in this regard are compounds based on titanium hydroxophosphates [3].

EXPERIMENTAL

As starting sorbent we took samples of a clinoptilolite-containing tuff from the Sokirnitskoe deposit (Transcarpathia). The modification was performed by impregnating the polycationic matrix with a 1 M aqueous solution of $TiCl_4$ in 1 M HCl (pH 0) with subsequent drying and further treatment with a 1 M H_3PO_4 solution. The resulting sorbent was washed with distilled water to remove excess acid and salts and dried at 100–110°C.

An analysis of the elemental composition of the surface layer of the modified clinoptilolite samples by X-ray fluorescence spectroscopy (VG ESCA-3 spectrometer with reference for determining the core electrons, C1*s* line 284.4 eV) demonstrated that the Ti : P ratio is within the range (1 : 3)–(1 : 1). The observed scatter is probably due to inhomogeneity of the starting natural material.

Sorption experiments were carried out under dynamic conditions on a filtering column 0.8 cm in diameter with the sorbent bed height of 10 cm (0.5–1.0-mm fraction) and sorbent charge volume [1 c.v. (column volume)] of 5 cm^3. The filtration rate was chosen to be 2.0 m h^{-1} (100 cm^3 h^{-1}, i.e., 20 c.v. h^{-1}). Model solutions containing 1–2 mg dm^{-3} of copper(II), lead(II), and cadmium(II) ions were prepared from potable tap water with total hardness of 3.7–4.2 mg-equiv dm^{-3}, which contained (mg dm^{-3}) 60–65 Ca^{2+} ions, 10–15 Mg^{2+} ions, and 0.3 iron ions; pH 6.8–7.1. Preliminary studies revealed that no precipitation of heavy metal ions occurs in the working range of concentrations ($\leq 10^{-5}$ M) and pH values (6.8–7.1). The results obtained are in agreement with the data of [3–5].

A comparative analysis of the output curves of sorption of copper(II), cadmium(II), and lead(II) ions, which were obtained on natural and modified clinoptilolite under the same conditions, demonstrated that the degree of recovery of these elements with a modified sorbent is 2–2.5 times that with the natural material. Data on the influence exerted by modification on the sorption of Cd^{2+}, Cu^{2+}, and Pb^{2+} ions in the dynamic mode are presented in Fig. 1. It can be seen that, even on the background of a manyfold excess

1070-4272/04/7701-0030 © 2004 MAIK "Nauka/Interperiodica"

(by a factor of 50–100 for Ca^{2+} only) of alkaline-earth elements present in tap water, the degree of recovery of the ions under study is sufficiently high. In this case, as also in the case of titanium hydroxophosphates, the ions can be arranged in the order of increasing degree of recovery as follows: Cu ≤ Cd < Pb.

To reveal how the modifying agent is bound to the natural zeolite, at what centers the modification occurs, and what is reason for higher sorption of heavy metal ions on the sorbent obtained, we examined the IR spectra of the starting clinoptilolite and its modified form before and after sorption of ions. Samples were in the form of KBr pellets or a mull in mineral oil. The weighed portions taken for preparing KBr pellets were chosen so that the bands under study were peaked at 80–20% transmission. The spectra were recorded on a Carl Zeiss Specord M80 instrument in the spectral range 4000–400 cm^{-1}. Since the spectral manifestation of the processes that occur on the surface is diffuse, the method of baseline and internal reference [6] was used to ensure the adequacy of the analysis performed. As the internal reference we chose the band associated with bending vibrations of water (ν ~1635 cm^{-1}) [7]. Its shape, position, and intensity are virtually the same for all of the samples studied (Fig. 2).

It is known [7] that the strongest absorption in the IR spectrum of clinoptilolite is observed in the range 900–1300 cm^{-1}. This absorption is due to intra- and extratetrahedral asymmetric stretching vibrations of O–Si(Al)–O bonds. The absorption bands in the range 400–8500 cm^{-1} range are attributed to symmetric stretching and bending vibrations of structural groups of the aluminum–silicon–oxygen framework. An isolated absorption band peaked at ν ~1635 cm^{-1} is due to bending vibrations of sorbed water, and a broad medium-intensity band of complex shape at ν ~3400 cm^{-1} is associated with stretching vibrations of hydroxy groups [7].

The results obtained in mathematical processing of the spectral data in the region of absorption associated with stretching vibrations of the O–H bonds (2900–4000 cm^{-1}) and the main absorption band of the zeolite framework (850–1550 cm^{-1}) are shown in Figs. 3 and 4, respectively. As seen from Fig. 3, modification of clinoptilolite with titanium hydroxophosphate leads to a decrease in the intensity of the high-frequency (3600–3800 cm^{-1}) wing of the absorption band associated with stretching vibrations of hydroxy groups possessing basic properties [8–10].

The modification of clinoptilolite also manifests itself in an increase in the intensity and halfwidth of the main absorption band of O–Si(Al)–O bonds, peaked at ν ~1075 cm^{-1} (Fig. 4). Figure 4 also shows the difference of the optical densities of the modified and unmodified forms of clinoptilolite, which is a

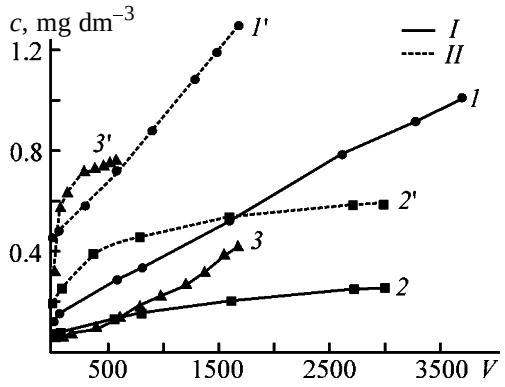

Fig. 1. Output curves of sorption of (*1*, *1'*) Cu^{2+}, (*2*, *2'*) Pb^{2+}, and (*3*, *3'*) Cd^{2+} on (*I*) natural and (*II*) modified clinoptilolite. (*c*) Concentration of Cu^{2+}, Pb^{2+}, and Cd^{2+} in solution; (*V*) number of column volumes.

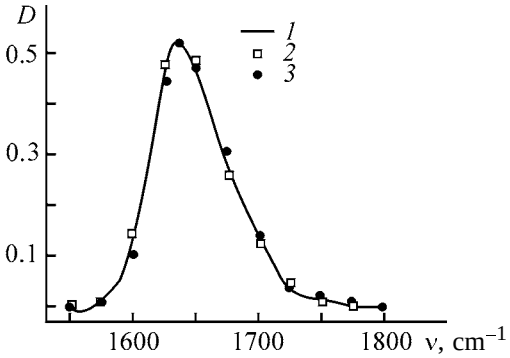

Fig. 2. Absorption associated with bending vibrations of water in (*1*) natural clinoptilolite and in its modified form (*2*) before and (*3*) after sorption of Pb^{2+}. (*D*) Optical density and (ν) wave number; the same for Figs. 3 and 4.

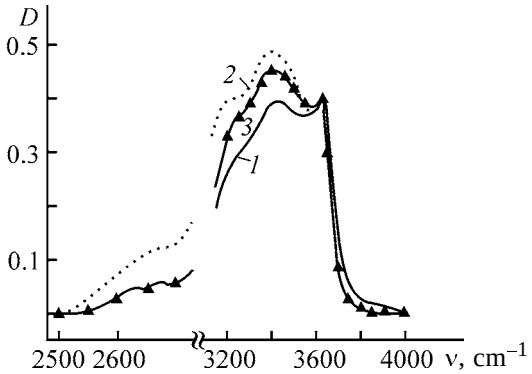

Fig. 3. Range of absorption associated with stretching vibrations of OH groups in (*1*) natural clinoptilolite and that modified with titanium hydroxophosphate, (*2*) before and (*3*) after sorption of Pb^{2+}.

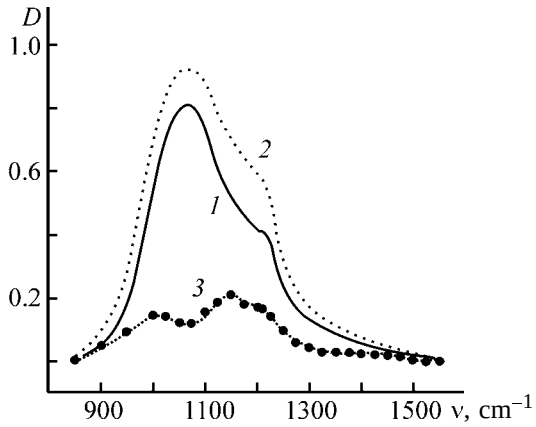

Fig. 4. Absorption bands of aluminum–silicon–oxygen framework of (*1*) natural and (*2*) modified clinoptilolite and (*3*) difference of these two.

curve with two clearly pronounced peaks. The low-frequency peak at ν ~1020 cm^{-1} is related to absorption of the modifying agent, since the main absorption band in the IR spectrum of amorphous titanium hydroxophosphate is recorded in this spectral range. The high-frequency peak (with ν ~1150 cm^{-1}) arises in the spectral range of absorption by strong aluminum–silicon–oxygen bonds of the zeolite framework. The appearance of additional O–Si(Al)–O bonds upon modification indicates that the bonding between clinoptilolite and the modifying agent is covalent.

The decrease in the amount of hydroxy groups of basic nature (Fig. 3, 3600–3800 cm^{-1}), with simultaneous appearance of additional O–Si(Al)–O bonds (Fig. 4, ν ~1150 cm^{-1}), points to the active role of these groups in the formation of covalent bonds between the modifying agent and the starting zeolite.

Figure 3 also shows that the intensity of the low-frequency wing of the absorption band associated with OH groups with pronounced protonogenic properties increases substantially in the course of modification. After the modified clinoptilolite is used as sorbent for ion recovery, the intensity of the low-frequency wing of the absorption band associated with the OH groups responsible for the acid properties of the surface decreases. This decrease is shown for the example of sorption of lead(II) ions in Fig. 3, curve *3*. The decrease (compared with the modified sample before sorption) in the intensity of the low-frequency component responsible for the acid properties of the surface points to the cationic mechanism of sorption. Here, only the following detail of interest should be noted: the stronger the hydrogen in the protonogenic OH group is covalently bound to oxygen (3500–3150 cm^{-1} range), the lower its reactivity toward cations [curve *3* occupies an intermediate position between the absorption curves of the starting clinoptilolite (*1*) and its modified form (*2*)]. With increasing ionic component in the bonding between hydrogen and oxygen (2700–2500 cm^{-1} range), all the protonogenic groups acquired in modification are "consumed" for sorption of lead(II) ions (curve *3* coincides with curve *1* of the starting clinoptilolite). It should also be noted that OH groups are not involved at all in cation sorption: the high-frequency wing (3800–3600 cm^{-1} range) of the absorption band of OH groups of modified clinoptilolite before sorption of lead(II) ions (curve *2*) completely coincides with that upon sorption of these ions (curve *3*).

The following should be taken into account when analyzing the reaction of the modifying agent with the surface of clinoptilolite: (a) IR data (role of basic hydroxy groups in grafting of the modifying agent); (b) the fact that titanium tetrachloride even at pH 0 is hydrolyzed in aqueous sulfuric acid solutions to give hydroxochlorides and hydroxo complexes [11], which form poorly soluble titanium hydroxophosphates in their subsequent reaction with phosphoric acid [3]; (c) elemental ratio Ti : P in the surface layer. Then this reaction can be represented as the following scheme:

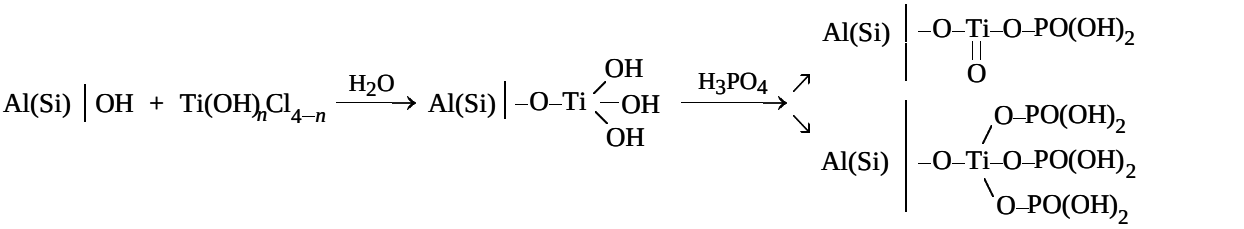

where n = 0, 1, 2, and 3.

Additional sorption of cations on modified clinoptilolite is due to protons of grafted dibasic groups of phosphoric acid, with different dissociation constants [5]. The ionization of phosphoric acid groups mainly by the first step at working pH values of 6.8–7.1 predetermines the involvement of three equivalent protonogenic groups in the ion exchange.

CONCLUSIONS

(1) A new, highly efficient sorbent for heavy metal ions, with sorption characteristics exceeding those of the initial sorbent, was obtained by modifying a natural zeolite, clinoptilolite, with titanium hydroxophosphate.

(2) The results of IR studies, X-ray fluorescence spectroscopy, and sorption measurements led to a conclusion that the modification of clinoptilolite consists in grafting to its surface of titanium hydroxophosphate compounds with increased concentration of OH groups, which can exchange their protons for cations of heavy metals. It is the additional contribution of this cation exchange to the ion exchange commonly observed in natural zeolites that gives rise to improved sorption properties of modified clinoptilolite samples.

REFERENCES

1. Semmens, M.J. and Sayfarth, M., in *Natural Zeolites: Occurence, Properties, Use*, Pergamon, 1976, pp. 517–526.
2. Nikashina, V.A., Tyurina, V.A., and Senyavin, M.M., in *Povyshenie kachestva pit'evoi vody* (Improving the Quality of Potable Water), Moscow: Znanie, 1977, pp. 91–96.
3. Bortun, A.I., Khainakov, S.A., Strelko, V.V., and Farbun, J.A., *Ion Exchange Developments and Applications*, Greig, J.A., Ed., Cambridge: SCI, 1996, pp. 305–312.
4. Schwarzenbach, G. und Flaschka, H., *Die Komplexometrische Titration*, Stuttgart: Ferdinand Enke, 1965.
5. Ashirov, A., *Ionoobmennaya ochistka stochnykh vod, rastvorov i gazov* (Ion-Exchange Purification of Wastewater, Solutions, and Gases), Leningrad: Khimiya, 1983.
6. Babushkin, A.A., Bazhulin, P.A., Korolev, F.A., *et al*., *Metody spektral'nogo analiza* (Methods of Spectral Analysis), Moscow: Mosk. Gos. Univ., 1962.
7. Tsitsishvili, G.V., Andronikashvili, T.G., Kirov, G.N., and Filizova, L.D., *Prirodnye tseolity* (Natural Zeolites), Moscow: Khimiya, 1985.
8. Goncharov, G.N., Zorina, M.L., and Sukharzhevskii, S.M., *Spektroskopicheskie metody v geokhimii* (Spectroscopic Methods in Geochemistry), Leningrad: Leningr. Gos. Univ., 1982.
9. Balicheva, T.G. and Lobanova, O.A., *Elektronnye i kolebatel'nye spektry neorganicheskikh i koordinatsionnykh soedinenii* (Electronic and Vibrational Spectra of Inorganic and Coordination Compounds), Leningrad: Leningr. Gos. Univ., 1983.
10. Kotorlenko, L.A. and Aleksandrova, V.S., *Usp. Khim*., 1984, vol. 53, no. 12, pp. 1959–1984.
11. Sharygin, L.M., Vovk, S.M., and Gonchar, V.F., *Zh. Neorg. Khim*., 1988, vol. 33, no. 7, pp. 1706–1712.

Russian Journal of Applied Chemistry, Vol. 77, No. 1, 2004, pp. 34–40. Translated from Zhurnal Prikladnoi Khimii, Vol. 77, No. 1, 2004, pp. 36–42.

CATALYSIS

Development of a Supported Catalyst for Decomposition of Spent Sulfuric Acid

N. A. Dobrovinskaya, E. I. Dobkina, and S. M. Kuznetsova

St. Petersburg State Technological Institute, St. Petersburg, Russia

Received May 8, 2003

Abstract—A technology for manufacture of a high-strength catalyst for decomposition of spent sulfuric acid is presented.

One of the most difficultly utilizable industrial wastes is spent sulfuric acid (SSA), which is mainly composed of H_2SO_4 and organic or inorganic impurities and water. More than one third of spent sulfuric acid is produced by oil refining and petrochemical industries.

The domestic and foreign experience demonstrates that the most efficient method for SSA utilization is thermal decomposition of sulfuric acid wastes to SO_2 in a fluidized bed of a thermally stable wear-resistant catalyst [1, 2]. This method is versatile, since it can be used to decompose SSA of various qualitative and quantitative compositions. The catalyst operation under the process conditions is affected not only by the fluidized bed mode, but also by temperature and high corrosive activity of the medium. Therefore, stringent requirements are imposed upon catalysts for SSA decomposition. This, in the first place, refers to such a constituent of the catalysts as supports.

It has been shown [2, 3] that the most effective catalysts for thermolysis of sulfuric acid are Fe_2O_3, V_2O_5, CuO, and Cr_2O_3. The activity of a catalyst is determined not only by its chemical composition, but also by the surface area accessible to reagents, i.e., by its pore structure.

It is virtually impossible to directly use metal oxides in high-temperature processes such as thermolysis of sulfuric acid. This is due to the fact that their initially not-too-large specific surface area decreases rapidly because of the agglomeration of fine particles to give coarser aggregates. As a result, the activity of such catalysts decreases in the course of time. The performance of a catalyst and its thermal stability can be raised by distributing a metal oxide over the surface of an appropriate porous support.

In [3], SiO_2 (silica gel, diatomite, Aerosil) and γ-Al_2O_3 were tested as supports for iron oxide catalysts. These supports are not inert toward decomposition of sulfuric acid. It has been demonstrated that silica gel is the most active in the process in question, apparently because of its more developed surface. For example, the activity of the Fe_2O_3 catalyst on SiO_2 is approximately 3 times that of Fe_2O_3 on γ-Al_2O_3. However, after 45 h of operation, the specific surface area of the catalyst on silica gel decreased by a factor of approximately 12, and that of the catalyst supported by aluminum oxide, by a factor of only 4. The predominant pore radius changed from 6–10 to 80–400 nm in the first catalyst, and from 8–10 to only 10–30 nm in the second. Apparently, the higher melting point of γ-Al_2O_3 results in that its microstructure changes in catalyst operation at a considerably slower rate, compared with that of silica gel, i.e., the thermal stability of γ-Al_2O_3 is higher.

It should be remembered here that phase equilibrium conditions may change in objects including small-size particles. One of manifestations of this effect is the depression of the melting point of dispersed particles, which can be described by the equation [5]

$$T = T_m(1 - 2\omega\Delta\alpha/R\theta_m), \quad (1)$$

where T_m is the melting point of a bulk sample; ω, volume per particle; $\Delta\alpha$, change in the surface energy across the interface; R, particle radius; and θ_m, heat of melting.

It follows from Eq. (1) that the smaller the particle radius, the stronger the depression of its melting point. In a real catalyst, which contains particles of various size, finer particles will undergo melting earlier, the melt will fill spaces between coarser particles, and solid–liquid agglomeration will begin [5–7].

According to Hüttig [5], the onset temperature of agglomeration is about 0.45 of the melting point:

$$T_{\text{onset aggl.}} \cong 0.45T_m. \quad (2)$$

1070-4272/04/7701-0034 © 2004 MAIK "Nauka/Interperiodica"

Table 1. Parameters of aluminum oxide

Fraction, mm	ρ_{bulk}, kg m^{-3}	S_{sp}, m^2 g^{-1}	Π_{wear}, %	V_w, cm^3 g^{-1}	Na_2O	Fe_2O_3
					wt %	
1.5–2.0	640	128	0.1	0.48	0.05	0.05
0.8–1.0	710	250	0.2	0.90	0.02	0.05

To synthesize thermally stable catalysts, it is advisable to use substances whose agglomeration onset temperature exceeds the process temperature. When considering silica gel (T_m = 1725°C) and aluminum oxide (T_m = 2050°C) in this regard, preference should be given to the latter.

Thermocatalytic decomposition of SSA, and especially that in a fluidized bed, imposes specific requirements upon a catalyst to be used, with account of the very severe operation conditions (corrosive medium, high temperature, collisions and friction of grains). Therefore, it is the support and only the support that can ensure high stability of a catalyst under these conditions. Such a support should possess, in addition to the necessary macrostructure, high mechanical strength that is preserved during a long service life.

Silica gel, whose porous structure is transformed significantly, fails to meet this requirement even in the initial period of its operation. As for other alternative supports of silicate nature, such as diatomite, Aerosil [6], aluminosilicate, and zeolite [6], all of these show the same shortcomings as silica gel. Under the reaction conditions, they undergo intensive agglomeration, lose their strength, and their active component is carried away, with the resulting loss of activity. All this gives no way of considering silicate materials to be promising supports of catalysts for thermal decomposition of SSA.

As regards the strength and thermal stability of aluminum oxide, it may be stated that they depend on a variety of factors, which can be combined in a single notion of preparation conditions. These include both the synthesis of Al_2O_3 itself and its further modification to obtain the required properties.

EXPERIMENTAL

Fabrication of a support for a catalyst for SSA decomposition was based on the best, for the case in question, properties of aluminum oxide and silica gel. As starting material was taken spherical granulated γ-Al_2O_3 whose main parameters are listed in Table 1 (bulk density ρ_{bulk}; specific surface area S_{sp}; wear resistance Π_{wear}; pore volume for water V_w; content of Na_2O and Fe_2O_3 impurities).

Since aluminum oxide rapidly loses its strength in SSA decomposition under the action of water and SO_3 vapors, it was of interest to protect its surface from the influence of these factors. In this case, SiO_2 may prove to be a good modifying agent because of its chemical stability under the conditions of SSA decomposition. There have been several reports [8, 9] on the strengthening, hydrophobizing, and protective action of film coatings based on polyorganosiloxanes. Among monomeric oxygen-containing organosilicon compounds, the most widely used in practice are pure esters of orthosilicic acid, especially tetramethoxysilane and tetraethoxysiliane (TEOS). Organosilicon–aluminum compounds containing an Si–O–Al group are of particular interest, since they are models of highly stable compounds, aluminosilicates, which widely occur in the Earth's crust.

The binding of hydrophobic films to materials is a result of their interaction with the reactive groups of the surface. For example, treatment of inorganic materials that contain a surface Al–OH group with silicon-functional organic compounds yields a firmly adhering film that covers the surface being treated as a monomolecular layer. The film is so thin that it does not close even the finest pores of the material [8].

Silicon dioxide was deposited by treating the starting spherical γ-Al_2O_3 with ethyl ester of orthosilicic acid, TEOS. A weighed portion of aluminum oxide was placed in a glass reactor with a reflux condenser and a thermometer. A calculated amount of TEOS and a diluent were charged into the same reactor to liquid to solid ratio l : s = 1.15–1.20, so that aluminum oxide was completely covered with the solution. Since TEOS undergoes deep hydrolysis in water, to the point of formation of a sol of silicic acid, ethanol, which can be mixed with TEOS in any ratio, was used as diluent. The presence of a solvent favored more uniform deposition of SiO_2 onto the support surface. The filled reactor was heated on a sand bath to 80–

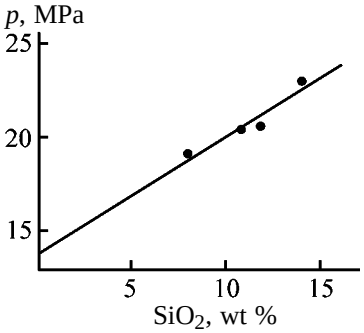

Fig. 1. Crushing strength *P* of a support calcined in an air flow vs. the amount of deposited modifying agent SiO_2.

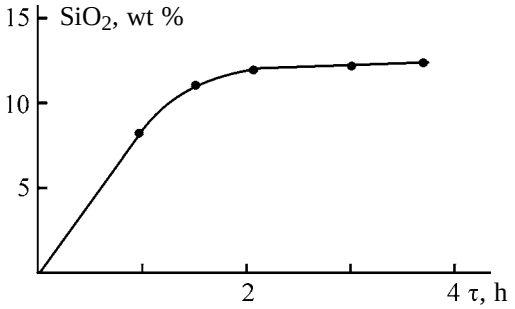

Fig. 2. Amount of deposited SiO_2 vs. the treatment duration τ.

85°C and kept at this temperature for 1–3 h. After the siliconizing was over, the support was discharged and dried at room temperature in the course of 8–10 h. The dried support contained in its pores a small amount of diethyl ether, which was completely burned out in the subsequent calcination of the sample in an air flow at 500–550°C.

The necessary amount of TEOS was approximately determined with account of the amount of SiO_2 (%) to be deposited:

$$V_{TEOS} = m_{SiO_2}/m_{AlO_3}$$

$$= m_{SiO_2} M_{TEOS} G_{Al_2O_3}/(100 - m_{SiO_2}) M_{SiO_2} \rho_{TEOS}, \quad (3)$$

where V_{TEOS} is the calculated volume of TEOS (ml); m_{SiO_2} and $m_{Al_2O_3}$, amounts of substances (%); M_{TEOS} and M_{SiO_2}, molecular masses of TEOS and silicon dioxide; $G_{Al_2O_3}$, weighed portion of aluminum oxide (g); and ρ_{TEOS}, TEOS density (g cm^{-3}).

To determine the amount of the actually deposited SiO_2, siliconized samples were subjected to chemical analysis. To find the optimal amount of the modifying agent, a set of γ-Al_2O_3 samples with varied content of SiO_2 was prepared. Tests demonstrated that modification markedly improves the strength characteristics of the support, with its crushing strength increasing virtually in direct proportion to the amount of the modifying agent deposited (Fig. 1). It was found that, in the case of calcination of samples treated with TEOS in a muffle furnace, their strength is 2–3 MPa lower than that in calcination at the same temperature in an air flow.

This can be explained by taking into account the fact that the ether is oxidized with an increase in volume. In calcination in an air flow, most part of the ether, which is highly volatile, is carried away from its pores at the very beginning of heating, when the oxidation rate of the ether is low and its combustion actually occurs outside a support grain. In the case of the "stagnant" zone of a muffle furnace, some part of diethyl ether has enough time to be oxidized directly within the support pores. The products formed in the process exert a disjoining effect on its structure, so that some contacts of the structure disintegrate and the strength of the support decreases. Thus, to obtain catalysts with the highest strength, it is advisable to use supports calcined in an air flow. The results of experiments demonstrated that it is impossible to deposit more than 16–18 wt % SiO_2 by the procedure suggested. Attempts to raise the content of SiO_2 by longer treatment of aluminum oxide with TEOS failed to produce any significant results. As seen from Fig. 2, the greatest amount of SiO_2 is deposited in the first 1.5–2 h of treatment. Extending the duration of siliconizing to 3–3.5 h made it only possible to deposit additional ~0.5 wt % SiO_2.

Originally, this fact was attributed to the possible consumption of the whole amount of TEOS. Therefore, one of samples was subjected to three successive treatments (for 1.5 h each), every time in a fresh TEOS solution in ethanol.

This method made it possible to raise the content of SiO_2 in the sample to a somewhat greater extent than in the case of a longer single treatment. However, in this case also, the gain was too small in relation to expenditure. For example, the first siliconizing run produced 11 wt % SiO_2 on the Al_2O_3 surface, whereas the contributions of the second and third runs were only 3.3 and 1.9 wt % SiO_2, respectively.

The limitations on the amount of deposited SiO_2 can only be attributed to the presence on the surface of Al_2O_3 of a limited number of functional groups that can react with TEOS by the molecular layer deposition mechanism [10]. A certain increase in the content of SiO_2 upon several successive siliconizing runs can be accounted for by the fact that, after all the available surface OH groups are spent, there remains

a fraction of unshielded Al_2O_3 surface containing aluminum ions with unsaturated coordination. These ions are Lewis acid centers [1]. Thus, the limit on the amount of SiO_2 directly bound to the Al_2O_3 surface depends on specific features of the surface of aluminum oxide, which, in turn, is a function of process parameters of Al_2O_3 synthesis.

A study of the silicon distribution in a siliconized sample by X-ray fluorescence microanalysis demonstrated that this distribution is uniform across the entire grain. Figure 3 shows typical concentration profiles of aluminum and silicon along the grain diameter, obtained with an electron-beam microprobe.

However, this method tells nothing about how silicon is distributed with respect to the Al_2O_3 phase. Comparison of the concentration ratios c_{Si}/c_{Al} of silicon and aluminum, calculated using results of chemical analysis and data on elemental composition, furnished by X-ray photoelectron spectroscopy (XPS), confirms the surface distribution of silicon on Al_2O_3 (Table 2).

The XPS technique yields information about the qualitative and quantitative elemental composition of the surface layer (with thickness of several nanometers, usually 2–5 nm) of the sample, whereas the conventional chemical analysis determines the content of an element related to the whole bulk of the sample under study. The clearly overestimated XPS data, compared with the results of chemical analysis (Table 2), suggest that silicon is concentrated just in the surface layer of the sample. This fact, in combination with the data of X-ray fluorescence spectroscopy (Fig. 3), demonstrates that silicon is rather uniformly distributed over the entire external and internal surface of Al_2O_3.

The whole body of the data obtained suggests that the increase in the sample strength is due to strengthening of a number of individual contacts via deposition of SiO_2 at connection points of grains with Al_2O_3.

To make a final choice of a support, catalysts were synthesized both on the initial and on the siliconized γ-Al_2O_3. Iron and copper oxides were used as active components of the catalyst for SSA decomposition.

The catalysts for carrying out this process in a fluidized bed were prepared by impregnating a support with solutions of salts of the active components at 90°C in the course of 3 h with intermittent agitation. The liquid to solid phase ratio was taken to be 1.5. The samples obtained after the impregnation and separation of the solid phase from the liquid were dried at 110°C and then calcined at 700–800°C for 3 h. The calcination temperature was chosen with account of the working temperature of the catalyst.

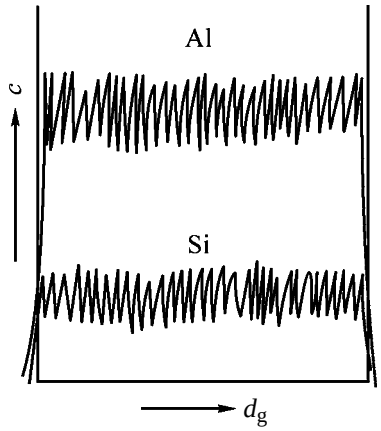

Fig. 3. Aluminum and silicon concentration profiles c along the diameter d_g of a siliconized support grain.

It is known that finely grained catalysts should be used to obtain an effective fluidized bed. The experience of numerous researchers shows that, with a catalyst supported by 0.8–1.0-mm Al_2O_3 fraction, thermal decomposition of SSA is kinetically controlled. Since virtually the entire surface of the catalyst works in this case, its composition should be uniform across the whole grain to improve its performance to the maximum possible extent. Such a uniformity is also important in connection with the abradability of the catalyst in the fluidized bed. Therefore, it is important to reveal how the distribution of active components is affected by siliconizing.

To determine the influence exerted by the support and method of its impregnation on the distribution of the active components in a catalyst grain, two sets of samples were fabricated: set 1 on the starting γ-Al_2O_3 and set 2 on siliconized γ-Al_2O_3. In both sets, aqueous solutions of iron and copper nitrates, $Fe(NO_3)_3 \cdot 9H_2O$ and $Cu(NO_3)_2 \cdot 3H_2O$, with concentrations of 150 and 100 g l^{-1}, respectively, were used as impregnating media. The methods of impregnation

Table 2. Content of silicon in siliconized aluminum oxide

Sample no.	c_{Si}/c_{Al} ratio	
	surface	bulk
1	0.25	0.10
2	0.42	0.17

Table 3. Methods of impregnation and content of active components, CuO and Fe_2O_3, in catalyst samples

Set 1, support γ-Al_2O_3			Order of impregnation	Set 2, support γ-Al_2O_3 + 15 wt % SiO_2		
sample no.	CuO	Fe_2O_3		sample no.	CuO	Fe_2O_3
	wt %				wt %	
1-1	5.42	–	$Cu(NO_3)_2$	2-1	5.40	–
1-2	–	5.85	$Fe(NO_3)_3$	2-2	–	5.00
1-3	2.82	5.30	Simultaneously from a solution of $Fe(NO_3)_3$ and $Cu(NO_3)_2$	2-3	3.46	4.15
1-4	4.17	5.63	Successively (1) $Fe(NO_3)_3$, (2) $Cu(NO_3)_2$	2-4	4.20	4.86
1-5	5.36	4.23	Successively (1) $Cu(NO_3)_2$, (2) $Fe(NO_3)_3$	2-5	5.32	3.71

and the results of a chemical analysis of the samples obtained are listed in Table 3.

Measurements of the strength of the samples obtained demonstrated that it corresponds to the strength of the supports used, being equal to 13.0–14.2 MPa for samples of set 1 and 20.5–22.0 MPa for samples of set 2.

The results of chemical analyses are very close for the samples of both sets and give no way of making choice in favor of one of the two supports. However, a study of these samples revealed the following remarkable pattern. The distribution of copper in catalysts 1-1 and 2-1 is virtually uniform across a grain of each of the supports, whereas the concentration profiles of iron along the grain diameter are strongly different in samples 1-2 and 2-2 (Fig. 4). In "pure" γ-Al_2O_3, this distribution is of typical "crust" nature, whereas in the siliconized sample it is nearly uniform. The same characteristic features are observed for the distribution of active components in binary catalysts (Fig. 5).

The nonuniform distribution of iron is, in contrast to that of copper in pure γ-Al_2O_3, a consequence of the ability of iron(III) hydroxide, which appears in the impregnating solution through hydrolysis of $Fe(NO_3)_3$, to form a colloid system. In this case, the size of aggregates of $Fe(OH)_3$ sol particles is in the range 1–100 nm [12]. If account is taken of the fact that the predominant pore radius of the Al_2O_3 used is

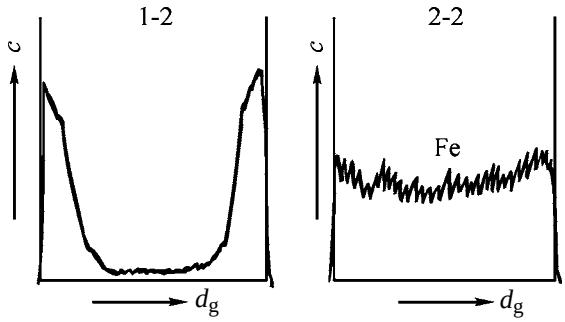

Fig. 4. Iron concentration profiles c along catalyst grain diameter d_g (Table 3).

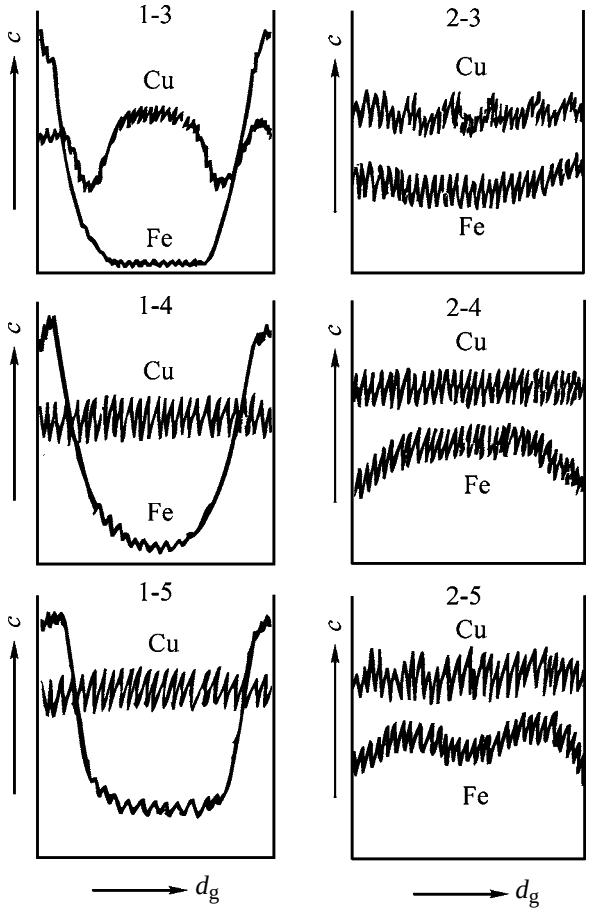

Fig. 5. Iron and copper concentration profiles c along catalyst grain diameter d_g (Table 3).

6–10 nm, it becomes understandable why iron hydroxide cannot penetrate inside a grain. The finest colloid particles penetrate into the accessible pores and block the way for other, coarser particles. The situation is aggravated by a sol–gel transition that occurs as a result of heating in the course of impregnation. In this case, the main part of $Fe(OH)_3$ deposited is concentrated in the surface layer of grains in the form of a ring (Fig. 4, sample 1-2). If the impregnating $Fe(NO_3)_3$ solution is sufficiently concentrated, a thick layer of $Fe(OH)_3$ is accumulated on the outer surface of a support grain. In thermal treatment of the sample, this layer is converted to an Fe_2O_3 layer which is poorly bound to the substrate and is easily lost even in charging into apparatus, not to mention the operation in a fluidized bed.

In the case of binary samples fabricated by impregnation with a solution that contains two salts simultaneously, formation of coarse colloid particles of $Fe(OH)_3$ hinders uniform distribution of copper (Fig. 5, sample 1-3). In this case, the total content of CuO in sample 1-3 is lower than that in samples 1-1, 1-4, and 1-5 (Table 3), in which the copper compound is deposited from solutions that contain no other cations. If a support is first impregnated with an $Fe(NO_3)_3$ solution and calcined, after which copper(II) nitrate is deposited, then, in the absence of $Fe(OH)_3$, copper is distributed uniformly (Fig. 5, sample 1-4), as in the case of a "pure" support. If impregnations are performed in reverse order, the iron concentration profile changes somewhat (Fig. 5, sample 1-5), but its distribution is still far from being uniform.

To obtain a uniform distribution of iron, it is, apparently, necessary to preclude formation of a colloid solution, i.e., to suppress hydrolysis occurring by the reaction

$$Fe(NO_3)_3 + H_2O = Fe(OH)_3 + HNO_3.$$

This equilibrium can be shifted to the left by introducing a strong acid into the reaction zone. However, this may exert disintegrating influence on aluminum and thereby impair its strength. The problem was resolved by siliconization of the support.

An IR study of pyridine adsorption onto the surface of pure and siliconized γ-Al_2O_3 made it possible to establish the nature of acid centers present on the surface. Only Lewis acid centers are present on the surface of Al_2O_3. Siliconizing leads to appearance of additional Brønsted centers, whose amount is the greater, the larger amount of SiO_2 is bound to the surface of Al_2O_3.

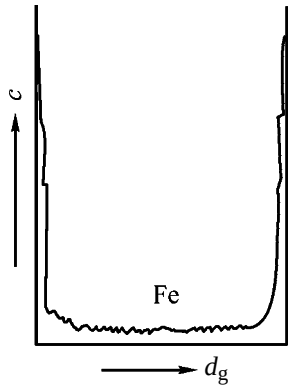

Fig. 6. Iron concentration profile c along the diameter d_g of α-Al_2O_3 grain.

Comparison of the iron concentration profiles in catalysts based on pure and siliconized γ-Al_2O_3 (Figs. 4 and 5) suggests that it is the presence of Brønsted acid centers on the support surface in samples of set 2 that is responsible for the uniform distribution of iron across a grain.

This conclusion is confirmed by the iron distribution on porous corundum α-Al_2O_3 (Fig. 6). The corundum was obtained by calcination of the starting γ-Al_2O_3 at 1300°C for 3 h. Similarly to pure γ-Al_2O_3, α-Al_2O_3 has no Brønsted acidity. Of interest is the fact that, despite the very large pore size in this sample (100–1000 nm), only trace amounts of iron can be introduced inside its grains in the form of a thin concentrated ring on the grain surface. Such a distribution of iron is favored by the visually observed process of coagulation of the $Fe(NO_3)_3$ sol, which occurs in α-Al_2O_3 impregnation with exceedingly high intensity and leads to clogging of even so coarse pores.

In impregnation of siliconized γ-Al_2O_3, nothing, apparently, prevents the occurrence of $Fe(OH)_3$ hydrolysis in the bulk of the impregnating solution. However, the forming $Fe(OH)_3$ aggregates approach the surface exhibiting a Brønsted acidity and experience there its peptizing effect. In this case, coarse colloid particles of $Fe(OH)_3$ disintegrate into finer particles, which freely penetrate into the support pores.

Thus, the advantage of siliconized γ-Al_2O_3 over a pure support is not limited to an increase in mechanical strength. One more important advantage is that active components can be uniformly deposited throughout the catalyst grains.

To find the optimal impregnation method, kinetic characteristics of the catalysts of set 2 were studied on

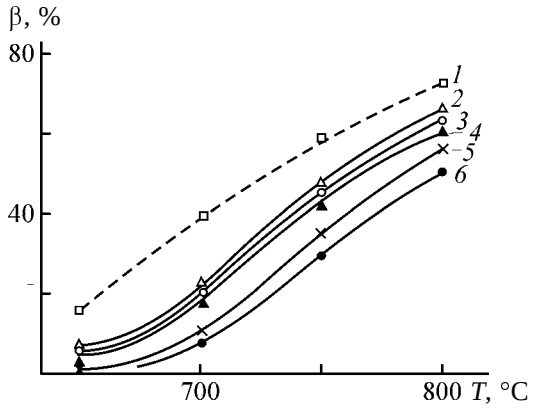

Fig. 7. Degree β of sulfur trioxide SO_3 decomposition on various catalysts vs. temperature *T*. Catalyst: (*1*) platinum, (*2*) 2-3, (*3*) 2-4, (*4*) 2-1, (*5*) 2-5, and (*6*) 2-2 (Table 3).

a laboratory installation in a process that models the thermocatalytic decomposition of SSA. The results obtained are presented in Fig. 7. For comparison, the activity of a platinum catalyst is shown in the same figure.

As for single-component samples, contrary to the existing opinion, the catalyst based on copper oxide much exceeded in activity the iron oxide catalyst (Fig. 7, samples 2-1 and 2-2).

Among the binary catalysts, the highest activity was observed for sample 2-3 fabricated by simultaneous impregnation with a solution of salts of both metals. Catalysts 2-4 and 2-5, which contain an even greater amount of active components than sample 2-3 (Table 3) and are characterized by a similar distribution of these components across a grain (Fig. 5), but were fabricated by successive impregnation have lower activity than catalyst 2-3 (Fig. 7, samples 2-3, 2-4, and 2-5).

An XPS study of the samples demonstrated that the active components are formed in the form of copper ferrite, with a minor amount of free oxides CuO and Fe_2O_3.

The enhanced activity of ferrites, compared with that of individual oxides, is known [6]. Taking into account this fact, it can be assumed that the highest activity of sample 2-3 is due to the existence of the optimal conditions for formation of the copper ferrite phase in simultaneous impregnation of the support with a solution of two salts.

CONCLUSIONS

(1) A catalyst for utilization of spent sulfuric acid with low content of organic impurities was developed. It was established that it is advisable to use copper and iron oxides supported by siliconized γ-Al_2O_3 as active components.

(2) Electron microprobe analysis was applied to study the distribution of the active components in a catalyst grain.

(3) The optimal method for depositing active components consists in simultaneous impregnation of a support with a solution of iron and copper salts. In this case, copper ferrite, which exhibits enhanced catalytic activity, is formed in the final stage of catalyst fabrication, its calcination.

REFERENCES

1. Naishuller, T.M. and Tikhonova, R.A., *Khim. Prom–st. Rubezh.*, 1976, no. 10, pp. 39–51.
2. Vasil'ev, B.T., Spiridonova, N.V., Novikov, A.A., *et al.*, in *Sernokislotnyi kataliz: Materialy Mezhdunarodnoi shkoly* (Sulfuric Acid Catalysis: Proc. Int. Workshop), Novosibirsk: Inst. Kataliza Sib. Otd. Akad. Nauk SSSR, 1982, part 2, pp. 188–194.
3. Maslenshchikov, B.M., Vasil'ev, B.T., and Spiridonova, N.V., *Vopr. At. Nauki Tekh., Ser.: Atomnovodorodn. Energ. Tekhnol.*, 1981, no. 2(9), pp. 23–25.
4. Vasil'ev, B.T., Maslennikov, B.M., Kagramanov, G.G., *et al.*, *Vopr. At. Nauki Tekh., Ser.: Atomnovodorodn. Energ. Tekhnol.*, 1979, no. 1(5), pp. 148–151.
5. Geguzin, Ya.E., *Fizika spekaniya* (Physics of Sintering), Moscow: Nauka, 1984.
6. Mukhlenov, I.P., Dobkina, E.I., Deryuzhkina, V.I., and Soroko, V.E., *Tekhnologiya katalizatorov* (Technology of Catalysts), Leningrad: Khimiya, 1989.
7. Dobkina, E.I., Kuznetsova, S.M., Nefedova, L.A., and Lavrishcheva, S.A., *Zh. Prikl. Khim.*, 2002, vol. 75, no. 11, p. 1855.
8. Pashchenko, A.A. and Tishchenko, V.T., *Gidrofobnoe i zashchitnoe pokrytie na osnove poliorganosiloksanov dlya alyuminiya i ego splavov* (Hydrophobic and Protective Coating Based on Polyorganosiloxanes for Aluminum and Its Alloys), Kiev: Tekhnika, 1966.
9. Pashchenko, A.A. and Voronkov, M.G., *Kremniiorganicheskie zashchitnye pokrytiya* (Organosilicon Protective Coatings), Kiev: Tekhnika, 1969.
10. Malygin, A.A. and Kol'tsov, S.I., *Napravlennyi sintez tverdykh veshchestv: Mezhvuzovskii sbornik nauchnykh trudov* (Directed Synthesis of Solids: Intercollegiate Coll. of Scientific Works), Leningrad: Leningr. Gos. Univ., 1983, no. 1, pp. 17–50.
11. Postnova, A.M., Zhdanova, T.N., and Kol'tsov, S.I., *Izv. Vyssh. Uchebn. Zaved., Khim. Khim. Tekhnol.*, 1985, vol. 28, no. 3, pp. 69–70.
12. Pasynskii, A.G., *Kolloidnaya khimiya* (Colloid Chemistry), Moscow: Vysshaya Shkola, 1968.

Russian Journal of Applied Chemistry, Vol. 77, No. 1, 2004, pp. 41–45. Translated from Zhurnal Prikladnoi Khimii, Vol. 77, No. 1, 2004, pp. 43–47.

CATALYSIS

Cleaning of the Surface of Silver Crystals Used as Catalysts of Gas-Phase Oxidation of Ethylene Glycol to Glyoxal

A. S. Knyazev, O. V. Vodyankina, L. N. Kurina, S. V. Koshcheev, and A. I. Boronin

Institute of Petroleum Chemistry, Siberian Division, Russian Academy of Science, Tomsk, Russia
Tomsk State University, Tomsk, Russia
Institute of Catalysis, Siberian Division, Russian Academy of Science, Novosibirsk, Russia

Received June 16, 2003

Abstract—The procedure for cleaning polycrystalline fibers of electrolytic silver used as a catalyst for gas-phase oxidation of ethylene glycol to glyoxal was developed with the aid of X-ray photoelectron spectroscopy.

Unsupported compact metals are used as catalysts of some important industrial reactions. The typical feature of the catalytic reactions performed under rigid conditions is segregation of impurities on the catalyst surface. These impurities can partially or completely poison the catalyst. As a result, the behavior of the catalytic system at varied external parameters (temperature and pressure of reactants) becomes irreproducible. As a rule, the catalyst is contaminated by the impurities contained in the initial material used for the catalyst production or by impurities introduced in the course of the catalyst production. The problem of the surface cleanness arises for both pilot and industrial catalysts. Measurements of physicochemical properties of contaminated compounds can be incorrect. Purification of these samples under rigorous conditions (calcination, etching, etc.) can also make their properties worse.

Silver is one of widely used metallic catalysts for preparing ethylene oxide [1], formaldehyde, acetaldehyde, and glyoxal [2] by heterogeneous oxidation. Practically important vapor-phase oxidation of ethylene glycol into glyoxal is catalyzed by both compact and supported silver [3].

The best catalyst for glyoxal synthesis is polycrystalline silver fiber prepared by electrolysis of a silver chloride melt [4]. This catalyst has a unique nano- and microstructure stable to reactive chemical media at 800–900 K. The results of the study of these silver catalysts prepared by the electrolytic procedure make a great contribution to the theory of heterogeneous catalysis with metals. Fibrous silver catalysts should be free of process and other impurities. However, investigation of their surfcae by surface-sensitive methods shows the presence of various impurities.

In this work, the states of surface atoms and the chemical composition of the surface of silver fiber samples taken in different steps of their preparation, purification, and application as catalysts were studied by X-ray photoelectron spectroscopy (XPS). Based on the experimental data, a nondestructive procedure for cleaning the surface of silver crystals with preservation of their morphological and structural features was proposed. As determined by XPS, the surface of the silver catalyst treated under actual catalytic conditions is almost free of impurities.

EXPERIMENTAL

Filamentary silver crystals were prepared by electrolysis of an $AgNO_3$ melt in an open electrolysis bath with a rotating cathode (T = 543–560 K, 32–34 wt % $AgNO_3$ in a KNO_3–$NaNO_3$ melt) [4]. A scanning electron microscopic (SEM) study shows that these samples consist of silver needles with a smooth surface (Fig. 1), which are formed by topochemical processes occurring in the course of electrolysis of the melt of metal nitrates. Silver crystals formed under these conditions have a developed dendrite structure with a great number of surface defects [4].

The chemical composition of the surface of silver catalyst was studied by XPS using a VG ESCALAB spectrometer. The spectra were recorded by the procedure described in detail in [5–7].

Electrons were emitted from the samples under the action of soft AlK_α X-ray radiation. The free path of the electrons λ was in the range 20–30 Å depending on their energy, which allowed the study of the sample surface to a depth of 3λ, i.e., 60–90 Å.

The samples were fixed in air in a holder with a

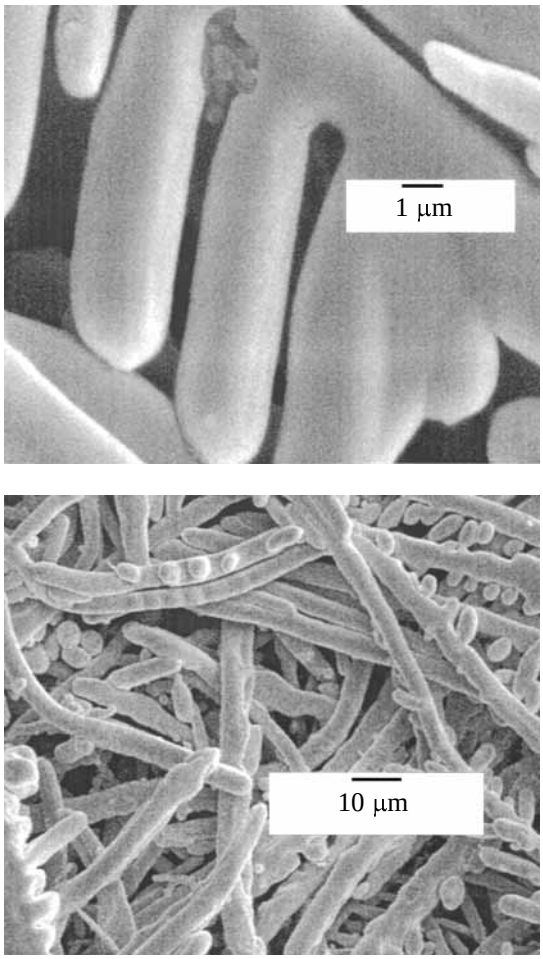

Fig. 1. Surface morphology of silver crystals prepared by electrolysis of $AgNO_3$ melt (SEM pattern).

conducting two-side scotch tape stable in a vacuum. Prior to recording XPS spectra, the samples were evacuated in a pretreatment chamber to a residual pressure of $P = 10^{-2}$ mPa. Then they were moved into the analyzer chamber and evacuated to the residual pressure of about 10^{-4} mPa. The main background gases were CO, CO_2, and H_2O.

The spectral data were treated with the aid of the conventional graphical packages and CALC special original software. To estimate the chemical composition quantitatively, the precision spectra of the most intense bands of the elements were recorded. The concentration ratio of the elements in the samples was determined from the integral intensities of the bands of definite atomic levels, taking into account the tabulated empirical factors of atomic sensitivities [8].

Silver samples (2 cm catalyst bed) were treated in a flow catalytic reactor with a mixture of EG (ethylene glycol), O_2, N_2, and H_2O in different molar ratios. The reactor made from stainless steel tube 15 cm long and 2 cm in diameter was connected with a contact condenser arranged below the catalyst bed. The reaction products were analyzed chromatographically [9].

The total XPS spectra of one of the silver fiber samples is shown in Figs. 2*I*a, and the detailed spectra, in Figs. 2*I*b and 2*I*c. The spectrum of the initial sample prepared by the electrolytic procedure contains the bands of bismuth, zinc, chlorine, and copper impurities along with the major bands of silver, carbon, and oxygen.

Carbon and oxygen are present in all the silver samples and are not considered as impurities for catalytic oxidation of organic molecules. Chlorine can be removed by preliminary heating of the catalyst in an oxygen atmosphere, or it disappears in the course of the catalytic process. Other impurities, Bi, Cu, and Zn, cannot be removed by the redox treatment. In the course of the catalytic processes, their concentration on the silver surface increases owing to diffusion of these elements from the bulk of the catalyst (Fig. 2*I*, curve *2*). In addition, sodium appears on the catalyst surface.

The concentration ratios of these elements were determined by XPS assuming that they are uniformly distributed in the catalyst (Table 1). As seen from Table 1, these ratios are relatively high. It should be noted that the metal impurities are accumulated on the silver surface owing to their segregation and under the action of the oxidative media promoting capture of metal atoms and their oxidation. As a result, the impurity/silver concentration ratio on the surface increases by a factor of 5–6. Thus, as seen from Table 1, large area of the surface of the initial samples is coated by impurity metals. In the course of the catalytic reaction, almost the whole surface can be coated with these impurities, and the catalyst can be partially and completely deactivated.

Thus, effective cleaning of the crystal surface with preservation of the unique morphological and defective structure of silver fiber is an urgent problem. In this case, etching of the surface with nitric acid does not furnish the desired result, since the impurities are present not only on the surface but also in the bulk of the sample.

To remove impurities from the sample, we treated its surface with hydrofluoric acid. This acid does not react with silver and selectively dissolves the impurities. The treatment was performed as follows.

(1) Filamentary silver crystals are sintered with an organic filler at 923 K for 3 h in an air flow to form

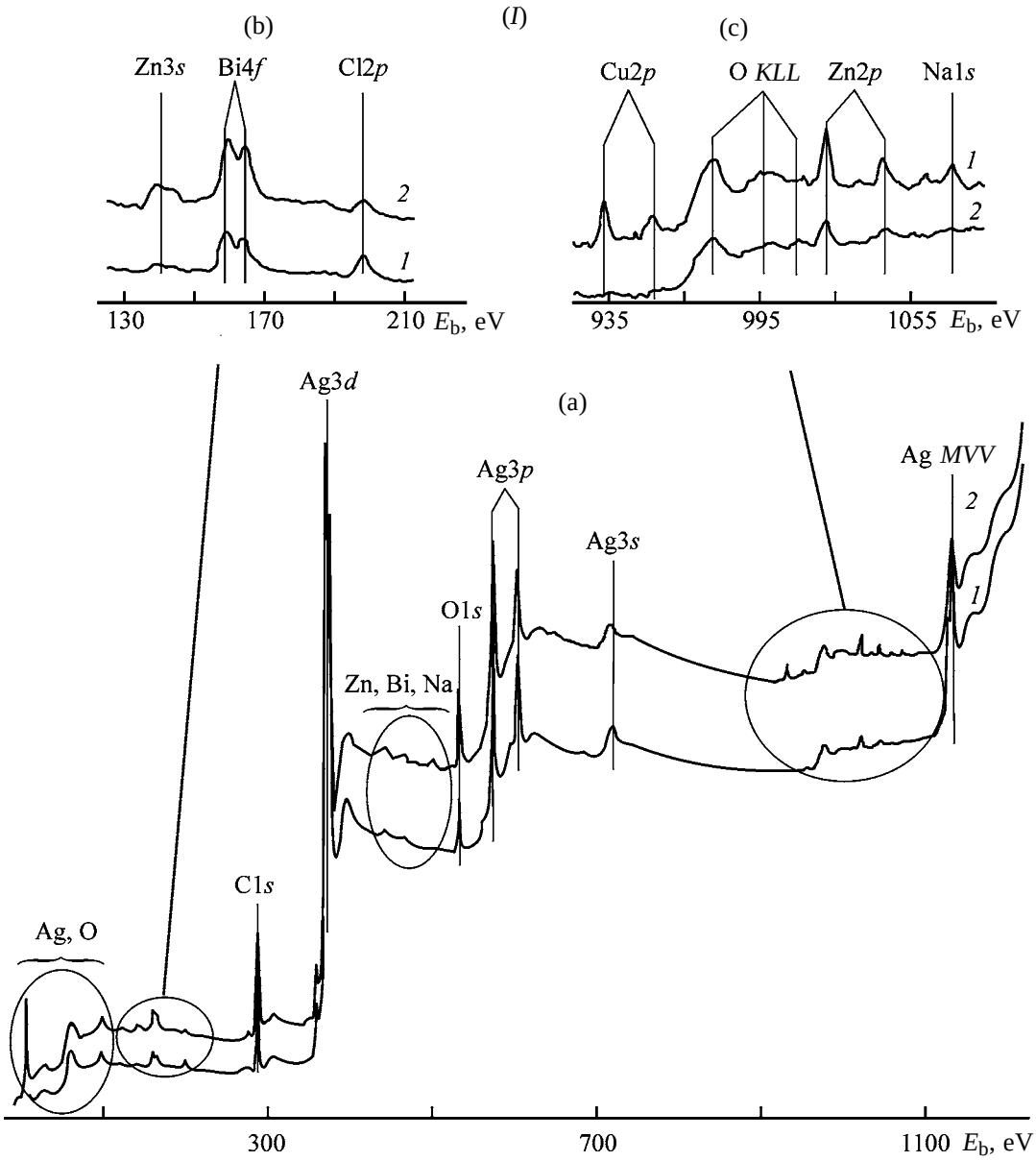

Fig. 2. (a) Total XPS recorded and (b, c) fragments of these spectra containing characteristic bands of the surface impurities. (E_b) Binding energy. (*I*) (*1*) initial silver crystals and (*2*) silver treated with an $O_2 : N_2 : EG : H_2O = 1.0 : 10.0 : 1.0 : 3.4$ reaction mixture; (*II*) (*1*) initial silver crystals, (*2*) silver surface treated with hydrofluoric acid (40 wt %, 1 h, $T = 353$ K), and (*3*) silver treated with HF and then $O_2 : N_2 : EG : H_2O = 1.0 : 10.0 : 1.0 : 3.4$ reaction mixture.

granules of equal size. As noted above, on heating, the impurities are segregated on the catalyst surface, which favors their more complete removal from the sample.

(2) Granulated silver catalyst is treated with 40% aqueous HF at 353 K for 1 h with continuous stirring.

(3) The cleaned catalyst is washed with double-distilled water and calcined at 873 K for 3 h.

We used various acids (HCl, CH_3COOH, and HF) to remove the metal impurities. All the examined acids remove Zn and Cu. However, appreciable amount of Bi is present on the surface after treatment with HCl and CH_3COOH (Table 1). In addition, the content of sodium atoms (common impurity in HCl) and chlorine increases after the treatment with hydrochloric acid probably owing to formation of difficulty soluble AgCl.

Treatment with hydrofluoric acid meets to the greatest extent the requirements to silver cleaning. The

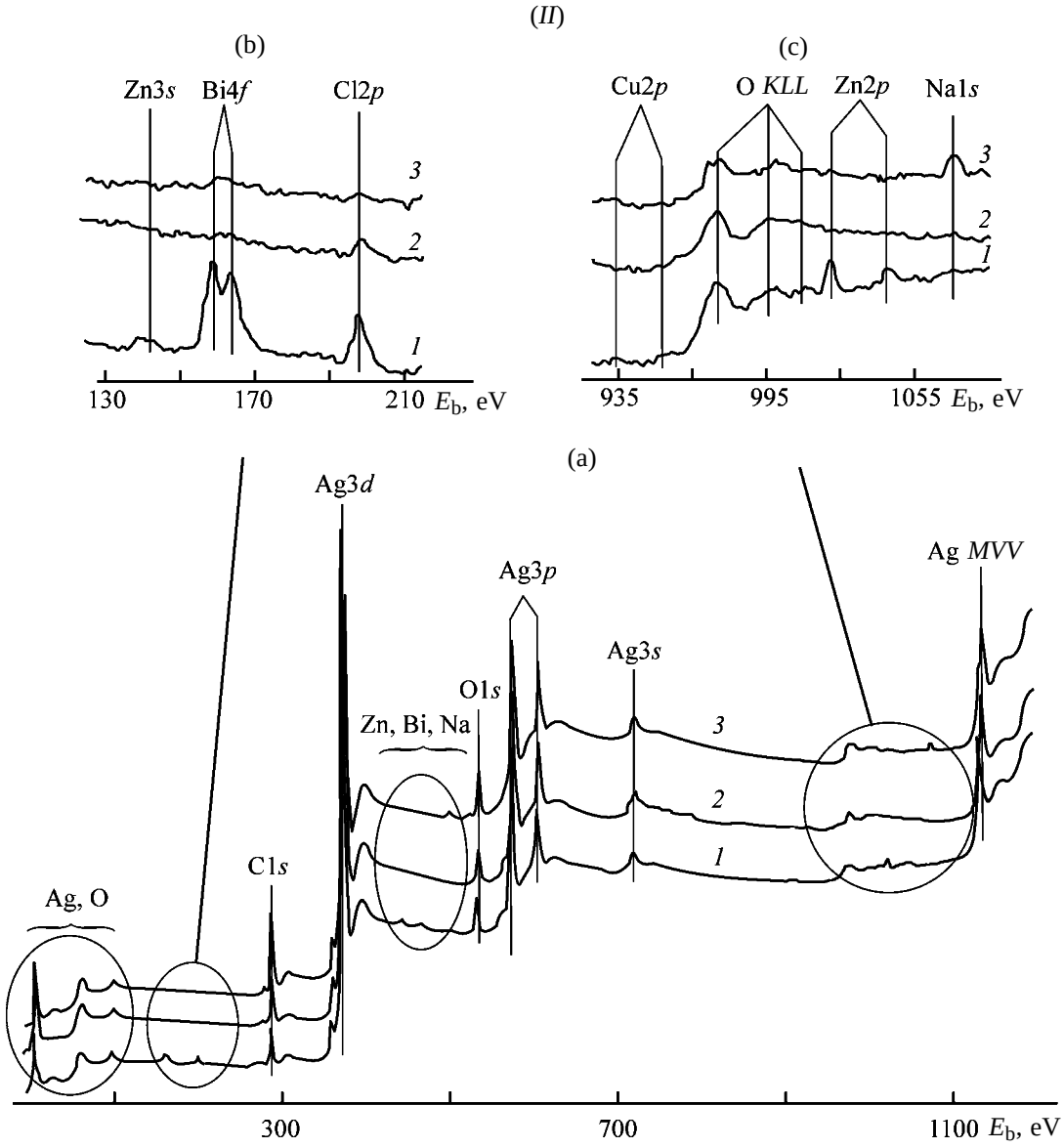

Fig. 2. (Contd.)

Table 1. Relative atomic concentrations of elements on the surface of fibrous silver

Silver sample	Relative atomic concentration*						
	Bi	Cl	C	O	Cu	Zn	Na
Initial	0.10	0.25	1.26	0.59	0.00	0.11	0.00
Treated with the reaction mixture without cleaning the surface	0.15	0.16	2.37	0.85	005	0.23	0.20
With cleaned surface	0.00	0.08	1.15	0.56	0.00	0.00	0.07
Treated with the reaction mixture after cleaning the surface	0.00	0.00	2.6	0.64	0.00	0.00	0.10

* Per silver atom.

Table 2. Main parameters of partial oxidation of ethylene glycol to glyoxal in the presence of cleaned fibrous silver

T, K	EG : O_2 : N_2 : H_2O molar ratio	EG conversion, %	Selectivity of glyoxal formation, %
227	1.0 : 1.0 : 10.0:3.4	81.4	49.9
277	1.0 : 1.0 : 0.0 : 3.4	89.3	62.8
227	1.0 : 1.12 : 30.0 : 5.2	87.7	38.65
277	1.0 : 1.12 : 30.0 : 5.2	89.0	58.7

XPS spectrum recorded in a wider energy range after the treatment with hydrofluoric acid (Fig. 2*II*, curve *1*) contains neither fluorine bands nor bands of new impurity elements. The bands of zinc and bismuth virtually completely disappeared after the treatment. As seen from the XPS spectra (Fig. 2*II*), the impurities of the above elements were not accumulated on the surface of the treated sample after its use as a catalyst of vapor-phase oxidation of ethylene glycol (723–923 K, 4–5 h).

The activity and selectivity of cleaned fibrous silver catalysts (Table 2) are high and are comparable with those reported in [10].

CONCLUSION

Precision analysis of the chemical composition of the surface of compact silver catalysts was performed by surface-sensitive X-ray photoelectron spectroscopy. A number of impurity elements were detected. To remove these impurities, the procedure involving treatment with hydrofluoric acid and preserving the unique defective and morphological structure of filament silver crystals was developed. The cleaned catalysts are thermally stable and exhibit high activity and selectivity in glyoxal synthesis.

ACKNOWLEDGMENTS

This work was financially supported by the Federal Research Program “Basic Research of Higher School in the Field of Natural Philosophy and Humanities. Russian Universities” (project no. 015.05.01.008).

The authors are grateful to A.N. Salanov for assistance in obtaining SEM patterns.

REFERENCES

1. Van Santen, R.A. and Kuipers, H.P.C.E., *Adv. Catal*., 1987, vol. 35, pp. 265–319.
2. Brailovskii, S.M., Temkin, O.N., and Trofimova, I.V., *Probl. Kinet. Katal*., 1985, vol. 19, pp. 146–175.
3. Vodyankina, O.V., Kurina, L.N., Boronin, A.I., and Salanov, A.N., *Stud. Surf. Sci. Catal*., 2000, Vol. 130B, pp. 1775–1781.
4. Samoilenko, V.N., Petrov, L.A., Boronin, A.I., *et al*., *Zh. Fiz. Khim*., 2001, vol. 75, no. 10, pp. 1759–1766.
5. *Practical Surface Analysis by Auger and X-ray Photoelectron Spectroscopy*, Biggs, D. and Seach, M.P., Chichester: Wiley, 1983.
6. Boronin, A.I., Bukhtiyarov, V.I., Vishnevskii, A.L., *et al*., *Surf. Sci*., 1988, vol. 201, pp. 195–203.
7. Bukhtiyarov, V.I., Boronin, A.I., and Savchenko, V.I., *J. Catal*., 1994, vol. 150, pp. 262–267.
8. Moulder, J.F., Stickle, W.F., Sobol, P.E., and Bomben, K.D., *Handbook of X-ray Photoelectron Spectroscopy*, Eden Prairie, MN: Perkin–Elmer, 1992.
9. Vodyankina, O.V. and Galanov, S.I., *Zavod. Lab*., 1995, no. 8, pp. 12–13.
10. Deng, J., Wany, J., and Xu, X., *Catal. Lett*, 1996, vol. 3, pp. 207–214.

Russian Journal of Applied Chemistry, Vol. 77, No. 1, 2004, pp. 46–50. Translated from Zhurnal Prikladnoi Khimii, Vol. 77, No. 1, 2004, pp. 48–53.

CATALYSIS

Catalytic Properties of Mechanically Activated Humic Substances in Electroreduction of Oxygen

N. V. Yudina, A. V. Savel'eva, A. A. Ivanov, E. I. Korotkova, and O. I. Lomovskii

Institute of Petroleum Chemistry, Siberian Division, Russian Academy of Sciences, Tomsk, Russia
Institute of Solid State Chemistry and Mechanochemistry, Siberian Division, Russian Academy of Sciences, Novosibirsk, Russia

Received July 21, 2003

Abstract—Effect of mechanical treatment of peat on the yield of the major fractions (polysaccharides, polyphenols, water-soluble compounds, and humic acids) and catalytic activity of humic substances in oxidation processes is studied. Conditions of formation of substances with the maximal antioxidant and initiating activities are determined. The antioxidant and initiating activities of the polysaccharide and humic fractions is studied, in relation to the structure and iron content.

Humic substances obtained from peat, coals, and sapropel are bioactive. Their physiological action is associated with the effect on the photosynthesis and oxygen, protein, and carbohydrate exchange kinetics [1, 2]. Attempts were made to link the bioactivity of humic substances to their reactivity toward free radicals and also to their structural features, e.g., the hydrophilic to hydrophobic group ratio in humic acid macromolecules [3]. However, results obtained by various authors are not always consistent, most likely, because of an inhomogeneity of the chemical composition of preparations studied, which depends on the starting raw material and preparation, isolation, purification, and bioactivity characterization procedures.

It is clear that study and application of bioactive humic compounds cannon be realized without solving such problems as recovery of humic substances from raw materials, their separation into fractions, and physicochemical characterization. One of the most efficient methods for preparation of humic substances at the maximal yield of water-soluble fractions is mechanical activation of peat in the presence of chemicals. The composition of the resulting products with respect to the major classes of bioactive agents depends on the mechanochemical conditions [4]. The catalytic properties of the products may be characterized using oxygen electroreduction. The inhibiting activity of a compound in this reaction can be considered as a measure of such a performance characteristic as the antioxidant activity, which is important in view of application of the compound as a protector against oxidative degradation of polymers, asphaltization of fuel, rancidity of fats, and, maybe, aging of living organisms and tumorogenesis. The activity of growth stimulants depends on their ability to initiate oxidation. Expansion of the spectrum of compounds used as inhibitors of promoters of oxidation is a topical scientific and practical problem.

In this work we studied the catalytic effect of humic substances obtained using mechanochemical activation on oxygen electroreduction.

EXPERIMENTAL

Humic substances were extracted from two kinds of peat collected from the Tomsk oblast: valley wood peat of the Tagansk deposit (degree of degradation 5%; ash content 3.7%) and high-moor dust peat of the Temnoe deposit (ash content 25.5%). Effect of the mechanochemical treatment procedure on the composition and properties of the resulting humic substances was studied using a VTsM-10 flow planetary mill activator with 10-mm steel balls developed by the Institute of Solid State Chemistry and Mechanochemistry, Siberian Division, Russian Academy of Sciences, Novosibirsk. The ball acceleration was 180 $m\ s^{-2}$ and treatment time, 2 min. The samples studied in this work were as follows. Sample nos. 1, 6: initial peat; nos. 2, 7: peat mechanically activated (dispersed) in the absence of chemicals; nos. 3, 8: peat mechanically activated in the presence of the cellulolytic enzyme celloviridine (CV) (0.5%); nos. 4, 9: peat mechanically activated in the presence of 3% NaOH; and nos. 5, 10: peat mechanically activated in the presence of 3% NaOH + 0.5% CV.

1070-4272/04/7701-0046 © 2004 MAIK "Nauka/Interperiodica"

Table 1. Evolution of peat composition upon mechanochemical activation

Sample no.	Additive, wt %	HA content, wt %		Content in peat, wt %			
		Fe	Ti	polysaccharides	polyphenols	WS	HA
1 (initial)	–	0.18	0.059	0.2	1.1	1.3	3.1
2	–	0.93	0.043	2.4	3.4	5.8	8.7
3	0.5CV	0.29	0.040	3.0	6.1	9.1	10.5
4	3NaOH	0.13	0.055	4.4	2.8	7.1	6.3
5	0.5CV + 3NaOH	0.19	0.040	0.7	4.3	5.0	7.4
6 (initial)	–	0.84	0.018	0.1	0.4	0.5	6.4
7	–	2.27	0.041	0.4	1.8	2.2	12.0
8	0.5CV	1.37	0.062	1.0	1.5	2.5	12.0
9	3NaOH	2.42	0.062	0.7	8.1	8.8	3.7
10	0.5CV + 3NaOH	1.63	0.060	0.6	8.3	15.4	2.3

From the initial and activated peat samples we extracted water-soluble compounds (WS), polysaccharides, polyphenols, and humic acids (HA). Chemical transformations in the separated HA fractions were monitored by ^{13}C NMR. Metals were determined by X-ray fluorescence spectroscopy.

The catalytic activity of the fractions with respect to oxygen electroreduction was determined voltammetrically [5]. Current-voltage curves were obtained over the voltage range 0–2.0 V on a polarograph in alkaline solutions at pH 10–12 (direct-current or differential pulse voltammetry mode; scan rate 20 mV s^{-1}). To determine the initial peak current of oxygen, corresponding to its solubility in a given solvent, we measured the voltammogram of the supporting electrolyte in the absence of a humic substance. Then the electrolyte was purged with an inert gas under pressure to remove oxygen from the solution, and the voltammogram of the supporting electrolyte was registered in the absence of oxygen in the solution. A solution containing a humic substance was added to a fresh portion of the electrolyte, and the proportional change in the oxygen electroreduction current was measured. The differential pulse voltammetry allows determination of the concentration at a level of 10^{-6}–10^{-7} mg l^{-1} to within 10%.

Mechanical activation in a planetary mill alters the content, physicochemical properties, and reactivity of the major components of peat. The degree of the observed transformations and their trends depend on the botanical type of peat and activation conditions. The yields of humic components at various mechanical activation conditions are given in Table 1. Analysis of the group composition of the initial and activated peat samples revealed that, irrespective of the type of peat and activation conditions, the content of water-soluble compounds increases by a factor of 6–15. Similar trends were observed also in the yield of humic acids from various types of peat: mechanical activation in the absence of the reagent increases and the reaction with NaOH decreases the HA content.

The carbohydrate and polyphenol fractions and humic acids representing polyconjugated systems with a wide spectrum of functional groups [4] are expected to be highly reactive. Being introduced in the model system, they act as initiators or inhibitors, changing the oxygen electroreduction rate. The direction of oxygen electroreduction depends on pH, metal salts, structural features of the components, and intermolecular interactions between them.

We plotted the difference of the oxygen reduction current density $I/(I_{lim} - I_{res})$ as a function of the concentration of a humic component in the solution. The resulting curves (Fig. 1) mostly consist of two sections corresponding to groups of different activity. The activity factors of these groups K_1 and K_2 can be evaluated from the slopes of the corresponding sections:

$$K = \frac{\Delta I/(I_{lim} - I_{res})}{\Delta c},$$

where ΔI is the difference of the running oxygen reduction current density with addition of an organic additive; I_{lim}, limiting oxygen reduction current in the absence of additives; I_{res}, residual current in the deoxygenated solution at a constant potential; and Δc, difference of the organic additive concentration.

The results show that the polyphenol, polysaccharide, WS, and HA fractions differently affect the cath-

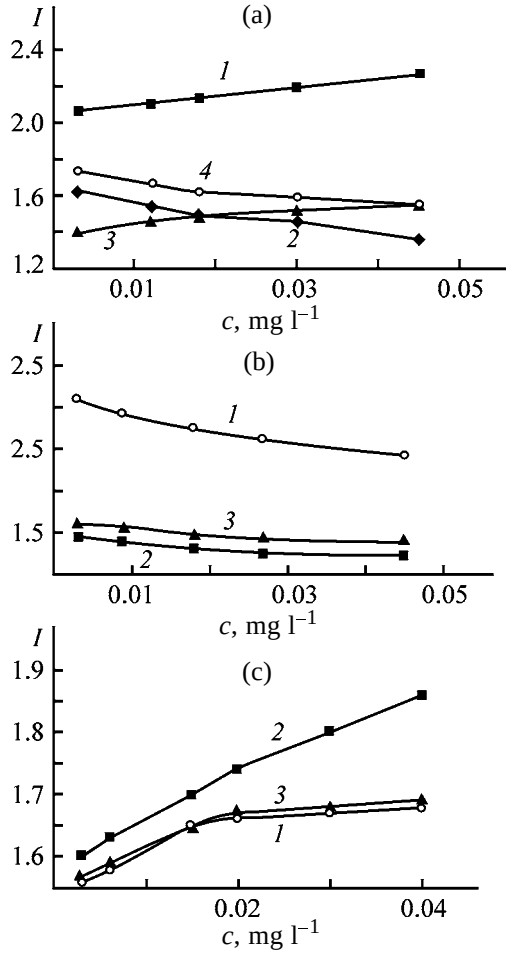

Fig. 1. Current density I of oxygen reduction as a function of the concentration c of (a) polysaccharides, (b) polyphenols, and (c) humic acids. Samples: (*1*) initial, (*2*) dispersed (mechanically activated in the absence of reagents), (*3*) activated in the presence of celloviridine, and (*4*) initial sample of polysaccharides treated with EDTA.

odic current. The polysaccharide fractions separated from the initial peat and that treated with NaOH (Fig. 1a, curves *1*, *3*) and all the HA fractions (Fig. 1c) increase the reduction current, while the polyphenol (Fig. 1b) and WS fractions decrease it. The initiating and inhibiting effects are most clearly pronounced at the humic fraction concentration of 0.01–0.02 mg l^{-1}. The cathodic current decreases with increasing c. Evidently, at low c, the degree of association of humic substances is low, and free active group can contribute to redox reactions.

The catalytic activity factors of humic components separated from the initial and mechanically activated peat samples are given in Table 2. For polysaccharides, activation increases the K values. Among the fractions separated from the initial samples, the maximal initiating activity is observed in polysaccharides from valley peat. The activity of polysaccharides depends on the mechanical treatment procedure. Dispersion and mechanical activation in the presence of celloviridine produce structural transformations in polysaccharides, increasing the antioxidant properties. In this case, the antioxidant activity of polysaccharides from disperse high-moor peat considerably exceeds that of polyphenols. Base hydrolysis enhances the initiating properties of the polysaccharide fractions from both valley and high-moor peats. The change in their catalytic activity seems to be associated with redistribution of WS components: base hydrolysis results in a strong increase in the polyphenol fraction, whereas the polysaccharide fraction decreases.

It is well known that most of native antioxidants are of the phenolic nature (substituted phenols, polyphenols, flavonoids, etc.). Among the mechanically treated samples, the total of the WS and polyphenol fractions separated from both kinds of peat inhibits oxygen electroreduction (antioxidant activity is higher in polyphenols from high-moor peat). Mechanical activation decreases the antioxidant activity of polyphenols, irrespective of the mechanical treatment conditions, except for mechanical activation with the enzyme in the presence of NaOH (sample nos. 5 and 10). The combined WS fractions (total of polysaccharides and polyphenols) demonstrate a synergistic effect, i.e., under various treatment conditions, their antioxidant activity is higher as compared to polyphenols. The WS fraction from high-moor peat shows higher antioxidant activity that that from valley peat. Base hydrolysis considerably increases the activity of the latter.

The HA fraction demonstrates the initiating properties in all cases, regardless of the mechanical activation conditions. The maximal catalytic activity of humic components was observed at their concentration of 0.001–0.003 wt %. With increasing concentration above the indicated value, the cathodic current changes only slightly (Fig. 1c). In all cases, except base hydrolysis, we observed an increase in the activity factors of humic acids. The maximal activity was shown by humic acids from disperse peats.

Catalytic properties of humic components are probably due to the presence of some metals, particularly iron, in them. The X-ray fluorescence analysis revealed (Table 1) that iron dominates in the HA fraction as compared to Mn, Ti, Ca, and Si compounds. Mechanochemical treatment results in redistribution of iron among the fractions (Table 1). However, as we demonstrated previously [6], a decrease in the iron content by a factor of 2–10 through acid treatment has

Table 2. Activity factors of polysaccharides, polyphenols, and humic acids in oxygen electroreduction

Sample no. (Table 1)	Polysaccharides		Polyphenols		WS		HA	
	K_1	K_2	K_1	K_2	K_1	K_2	K_1	K_2
High-moor peat								
1	–6.0	–	+23.0	+1.0	+6.0	+1.2	–5.1	–2.6
2	+33.0	+19.0	+9.7	+2.1	+12.0	+7.4	–40.0	–6.6
3	+14.0	+2.8	+8.5	+2.6	+10.0	+2.8	–9.7	–5.0
4	–7.2	–2.1	+11.0	–	+12.0	+2.9	–5.0	–1.2
5	–4.0	–1.5	+22.0	+6.7	+8.0	+1.4	–6.5	–2.8
EDTA*	+7.4	+2.8	–5.0	–1.7				
Valley peat								
6	–15.0	–5.0	+5.6	+2.7	+5.6	+1.1	–2.5	–1.5
7	+3.0	+1.4	+5.5	–	+22.0	+0.2	–15.0	–0.2
8	+15.0	–	+4.9	+3.5	+26.0	+1.6	–7.7	–1.7
9	–67.0	–12.0	+4.6	–	+20.0	–	–7.7	–3.2
10	–12.0	–1.7	+26.0	12.0	+6.6	+3.3	–8.1	–3.5
EDTA	+70.0	+6.0					–2.6	–1.3

* Ethylenediaminetetraacetic acid.

Table 3. ^{13}C NMR analysis of humic acids

Sample no. (Table 1)	Relative intensity of signals of carbon atoms in indicated structural fragments, %							
	C=O, 220–160 ppm	$C_{ar}O$, 160–140 ppm	$C_{ar}C,H$, 140–113 ppm	$C_{alk}O$, 106–93 ppm	$C_{\alpha,\beta}–O^4$, $C_{alk}O$, 93–66 ppm	$C_{alk}O$, CH_3O, 66–54 ppm	C_{alk}, 54–0 ppm	Fa
1	12.0	2.3	18.5	6.5	14.1	11.3	35.1	21
2	12.9	4.7	16.1	6.1	20.8	14.6	27.5	21
3	11.0	2.1	16.9	11.0	17.4	12.0	29.6	19
4	8.9	2.2	19.0	6.4	18.8	12.2	32.5	21
6	11.0	4.5	30.8	3.5	5.5	7.7	37.4	35
7	13.2	5.6	30.1	3.9	4.0	12.1	29.1	35
8	13.7	4.8	31.6	5.3	4.5	12.8	27.3	36
9	10.5	5.8	29.5	4.0	4.5	8.5	35.2	35

no effect on the catalytic activity of humic acids. Furthermore, Table 2 shows that the highest catalytic activity is shown by humic acids from high-moor peat having lower iron content.

To elucidate the contribution of iron to the catalytic activity, humic components were treated with EDTA. It was suggested that EDTA as a strong complexing agent for Fe(III) should suppress its catalytic activity. After treatment with EDTA, polysaccharides demonstrated a clearly pronounced inhibiting action. Therefore, removal of Fe(III) decomposes the associates in the polysaccharide fraction, making free functional groups with the inhibiting activity. As for HA fractions, their initiating activity remained practically unchanged after treatment with EDTA (Table 2).

Catalytic properties of humic acids depend on the features of their structure which includes carboxy groups, phenolic hydroxy groups, and quinoid fragments. In alkaline solutions, it is typical of humic acids to form a great amount of semiquinone radicals highly active in oxidation reactions [7]. The ^{13}C NMR analysis (Table 3) shows that mechanochemical activation of peats alters the structural characteristics of humic acids. For peat of both kinds, we observed a decrease in the fraction of alkyl carbons and increase in the amount of oxygen-containing fragments $C_{alk}O$ of various natures, which is most clearly pronounced in high-moor peat after mechanical dispersion and treatment with the enzyme. In the samples after base hydrolysis, the dealkylation is less pronounced. The

composition of oxygen-containing groups in humic acids depends on the treatment conditions. The amount of carbohydrate fragments increased in all the mechanically activated samples, which can be attributed to break of the glycoside bonds. The amount of the methoxy groups remained virtually unchanged, as well as the aromatic core structure (Fa) in both types of peat. Dispersion and mechanical treatment with celloviridine increase the amount of the carboxy groups in humic acids, except for the case of base hydrolysis (sample nos. 4, 9). In the latter case, we observed a considerable decrease in the fraction of carboxy groups at the expense of formation of the carboxylate ions.

Finally, removal of iron strongly affects the catalytic activity of the polysaccharide fractions, but only slightly, that of the HA fraction.

CONCLUSIONS

(1) The fraction composition of peat can be altered by mechanochemical treatment. The content of polysaccharides can be varied from 0.2 to 4.4%; that of polyphenols, from 1.1 to 6.1%; that of water-soluble compounds, from 1.3 to 9.1%; and that of humic acids, from 3.1 to 10.5%.

(2) Base hydrolysis enhances the antioxidant action of the polyphenol and water-soluble fractions.

(3) The polysaccharide fraction separated from valley peat, after removal of iron by treatment with EDTA, demonstrates the highest inhibiting activity. Base hydrolysis eliminates the antioxidant action of this fraction because of redistribution of functional groups among the water-soluble fractions.

(4) The inhibiting activity of humic acids is independent of treatment conditions and removal of iron, being controlled by the structural features of their macromolecules.

REFERENCES

1. *Guminovye udobreniya: Teoriya i praktika ikh primeneniya* (Humic Fertilizers: Theory and Applications), Khristeva, L.A., Ed., Dnepropetrovsk, 1977, vol. 6.
2. Komissarov, I.D., Klimova, A.A., and Loginov, A.F., in *Guminovye preparaty* (Humic Substances), Malov, A.V., Ed., Tyumen, 1971, pp. 200–212.
3. Kalabin, G.A., Kanitskaya, L.V., and Kushnarev, D.F., *Kolichestvennaya spektroskopiya YaMR prirodnogo organicheskogo syr'ya i produktov ego pererabotki* (Quantitative NMR Analysis of Natural Organic Raw Materials and Their Processing Products), Moscow: Khimiya, 2000.
4. Yudina, N.V., Zvereva, A.V., and Lomovskii, O.I., *Khim. Tverd. Topl.*, 2002, no. 5, pp. 3–10.
5. Korotkova, E.I., *Zh. Fiz. Khim.*, 2000, vol. 74, no. 9, pp. 1704–1707.
6. Yudina, N.V., Zvereva, A.V., Korotkova, E.I., and Avramchik, O.A., *Izv. Vyssh. Uchebn. Zaved., Khim. Khim. Tekhnol.*, 2002, vol. 45, no. 3, pp. 106–108.
7. Dudarchuk, V.M., Prokhorov, S.G., Smychnik, T.P., *et al.*, *Kolloidn. Zh.*, 1977, vol. 59, no. 3, pp. 313–316.

Russian Journal of Applied Chemistry, Vol. 77, No. 1, 2004, pp. 51–56. Translated from Zhurnal Prikladnoi Khimii, Vol. 77, No. 1, 2004, pp. 54–59.

CATALYSIS

Catalytic Oxidation of Cyclohexane with Ozone–Oxygen Mixtures

A. M. Syroezhko, O. Yu. Begak, and V. P. Proskuryakov

St. Petersburg State Technological Institute, St. Petersburg, Russia
Mendeleev Russian Research Institute of Metrology, Federal State Unitary Enterprise, St. Petersburg, Russia

Received March 20, 2003

Abstract—Selective oxidation of cyclohexane with ozone in the presence of chromium(0) hexacarbonyl and sodium naphthenates–Cr(III) mixtures was studied.

Since cyclohexane is an intermediate of caprolactam oxidation, an increase in the selectivity of cyclohexane oxidation to cyclohexanone [1] is an urgent problem.

Previously we showed [2] that noncatalytic oxidation of cyclohexane to cyclohexanone with ozone is more selective that industrial oxidation of cyclohexane with atmospheric oxygen to form a mixture of cyclohexanol and cyclohexanone.

The selectivity of oxidation of alkanes and cycloalkanes to the corresponding carbonyl compounds appreciably increases in the presence of catalysts of heterolytic decomposition of hydroperoxides, such as chromium(III) and chromium(VI) compounds [3–5]. The catalytic effect in the course of high-temperature liquid-phase oxidation of alkanes and cycloalkanes in manifested mainly in the step of hydroperoxide decomposition. When the process is performed at low temperature in the presence of a strong oxidizing agent (O_3 and O_2), variable-valence metal compounds can appreciably affect the mechanism of chain initiation, propagation, and termination and the contribution of radical and nonradical pathways. To control the selectivity of these processes, the features of the mechanism of these steps should be determined.

The procedures for oxidizing cyclohexane and for analyzing the reaction products were described previously [2, 3].

Cyclohexane ozonolysis was performed at 20–60°C in the presence of 2×10^{-2}–2×10^{-3} M stearates, naphthenates, and acetylacetonates of Co(II), Co(III), Cr(III), Mn(II), and $Cr(CO)_6$ as catalysts. The typical kinetic curves of accumulation of the oxidation products are shown in Fig. 1. The classes of compounds formed in this reaction are identical to those formed in oxidation of cyclohexane with ozone–oxygen mixtures. The kinetics of the overall cyclohexane consumption is of the first order irrespective of the catalyst (Figs. 2, 3). This is confirmed by the constancy of the accumulation rates of cyclohexanol, cyclohexanone, cyclohexyl hydroperoxide, and the acids in cyclohexane ozonolysis in the presence of cobalt(II) stearate (Fig. 1). Hence, the selectivity of formation of the target product (cyclohexanone) is almost constant

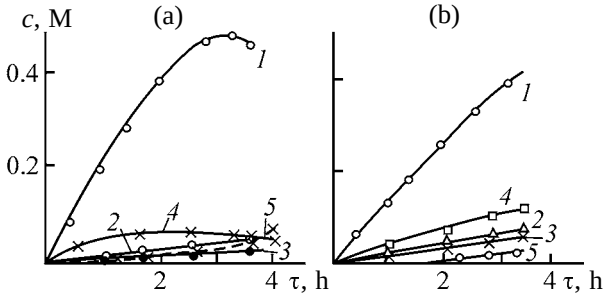

Fig. 1. Kinetic curves of accumulation of (*1*) cyclohexanone, (*2*) cyclohexanol, (*3*) cyclohexyl hydroperoxide, (*4*) acids, and (*5*) esters in catalytic oxidation of cyclohexane with ozone in the presence of (a) $Cr(CO)_6$ and (b) $Co(St)_2$. 40°C, $[O_3]$ = 4 vol %, [cat] = 2×10^{-4} M; the same for Fig. 2. (*c*) Concentration of reaction product and (τ) time.

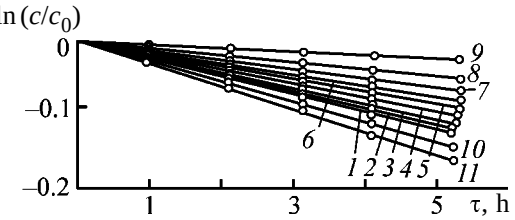

Fig. 2. Kinetic curves of cyclohexane consumption. (c_0, c) Initial and current cyclohexane concentrations and (τ) time; the same for Fig. 3. (*1*) $Cr(CO)_6$; (*2*) $Co(acac)_2$; (*3*) no catalyst; (*4*) $Cr(St)_3$; (*5*) $[Cr(CO)_6] = 2 \times 10^{-5}$ M; (*6*) $Mn(acac)_3$; (*7*) $Co(St)_2$; (*8*) $Cr(CO)_6$, $[O_3]$ = 3 vol %; (*9*) $Cr(CO)_6$, $[O_3]$ = 2 vol %; (*10*) cyclohexane; and (*11*) cyclohexanol ($[Cr(CO)_6] = 2 \times 10^{-4}$ M).

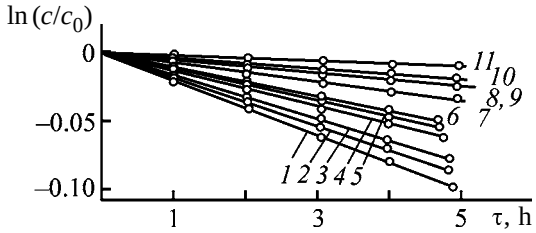

Fig. 3. Kinetic curves of cyclohexane consumption {[O_3] = 2–4 vol %; [$Cr(CO)_6$] = 2×10^{-5}–2×10^{-3} M}. [O_3], vol %: (*1–9*) 4 and (*10, 11*) 20. *T*, °C: (*1–3, 7–10*) 60 and (*4–6, 11*) 2. [$Cr(CO)_6$], M: (*1, 6, 7*) 2×10^{-3}, (*2, 5, 8, 11*) 2×10^{-4}, (*4, 9*) 2×10^{-5}, and (*3, 10*) 0.

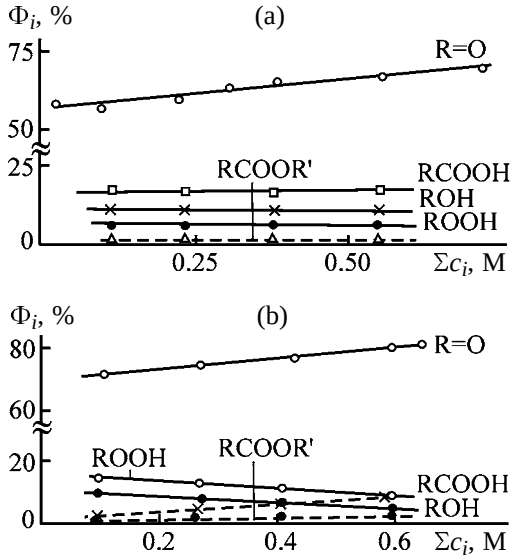

Fig. 4. Total selectivity Φ_i of formation of cyclohexane oxidation products as a function of cyclohexane conversion. 40°C; [O_3] = 4 vol %; (a) [$Cr(St)_3$] = 2×10^{-4} and (b) [$Cr(CO)_6$] = 2×10^{-4} M. (Σc_i) Total concentration of the oxidation products.

in the examined conversion range (~10%). In the presence of $Cr(CO)_6$, the accumulation rates of the hydroperoxide, alcohol, and ketone are also constant in the first oxidation steps (Figs. 1–3). The kinetic curve of accumulation of the acids is nonlinear. However, since the content of these acids in less than 0.05 M, the contribution of this pathway is insignificant and has small effect on the kinetic curve of cyclohexane consumption.

Chromium hexacarbonyl catalyzes the oxidation, whereas $CoSt_2$, $Mn(acac)_3$, and $CrSt_3$ appreciably inhibit the cyclohexane ozonolysis. Clearly, this is not due to homolytic or heterolytic catalytic decomposition of cyclohexyl hydroperoxide. First, at 20–40°C cyclohexyl hydroperoxide is relatively stable to thermocatalytic decomposition [4, 5]. Second, the steady-state concentration of cyclohexyl hydroperoxide in the course of cyclohexane ozonolysis is low owing to its fast consumption in the reaction with ozone (catalysis of this reaction is possible). The inhibiting effect is most likely due to reaction of the peroxy radicals with the catalyst. The rate constant of the reaction between the peroxy radicals and 3*d*-metal compounds is high [6]. The catalysis with $Cr(CO)_6$ and $Co(acac)_3$ can be related to their reaction with ozone, cyclohexane, and its oxidation products.

The selectivity of cyclohexanone formation is maximal in the presence of $Cr(CO)_6$. We studied the rate and selectivity of cyclohexane ozonolysis as influenced by the temperature, ozone concentration, and catalyst. The apparent activation energies of the overall cyclohexane consumption and cyclohexanone formation, determined by varying the reaction temperature in the range 20–60°C, are 34.5 ± 3 and 27.5 ± 2.5 kJ mol^{-1}, respectively, and are close to those of the noncatalytic process. The noticeable difference in the activation energies under conditions of consecutive and parallel reactions suggests a strong temperature effect on the reaction selectivity, which is confirmed experimentally (Figs. 4a, 4b).

The experimental kinetic curves measured at different concentrations of ozone and the catalyst and at different temperatures are shown in Figs. 2 and 3, respectively. The ozone concentration and the temperature have the strongest effect on the reaction rate. As the ozone concentration increases by a factor of 2 (from 2 to 4 vol %), the cyclohexane consumption accelerates by a factor of 2.4 {20°C, [O_3] = 2–4 vol %, [$Cr(CO)_6$] = 2×10^{-4} M}. Hence, bimolecular nonchain reaction of cyclohexane with ozone [1] is accompanied by chain oxidation of cyclohexane or decomposition of ozone with acceleration of initiation and progress of cyclohexane ozonolysis. The dependence of the rate of cyclohexane (RH) oxidation with ozone in CCl_4 at 22°C on [RH], [O_3], and [O_2] is described by the equation [7]

$$v = 3.2 \times 10^{-3}[RH][O_3] + 0.3[RH]^{1/2}[O_3]^{3/2} + 0.75[RH][O_3]^2/[O_2]_{gas}.$$

The third component of this equation is responsible for chain decomposition of O_3 [7] under the action of cyclohexyl radicals. The chain propagates by the equation $R^{\cdot} + O_3 \rightarrow RO^{\cdot} + O_2$, $RO^{\cdot} + RH \rightarrow ROH + R^{\cdot}$ and is terminated by the reaction $R^{\cdot} + O_2 \rightarrow RO_2^{\cdot}$ provided that the reaction between two cyclohexylperoxy radicals is faster than the reaction of RO_2 with ozone. In this case (no solvent, bubbling reactor, [RH] ≫ [O_3] ~ [O_2]), cyclohexyl radicals are almost

quantitatively oxidized to cyclohexylperoxy radicals. However, in the first steps of cyclohexane ozonolysis [7], the major oxidation product, cyclohexanol, is rapidly converted into cyclohexanone by the nonchain mechanism. The reaction of cyclohexylperoxy radicals with ozone and quadratic chain termination with the peroxy radicals should be taken into account in the kinetic equation of cyclohexane consumption by the chain mechanism. The experimental kinetic curves of cyclohexane consumption in $\ln(c/c_0)$–τ coordinates (c_0 and c are the initial and current cyclohexane concentrations, respectively; τ is the reaction time), measured in the first reaction step at low cyclohexane conversion (up to 8%) and small contribution of the chain pathway, are almost linear (Figs. 2, 3). The effect of $Cr(CO)_6$ concentration is significantly weaker. As $[Cr(CO)_6]$ increases from 2×10^{-5} to 2×10^{-3} M (20–60°C), the rate of cyclohexane consumption increases by more than 30% as compared to the noncatalytic reaction. As shown above, the mechanism of ozonolysis of saturated hydrocarbons is radical chain.

Catalytic oxidation of cyclohexane with ozone occurs also by the radical chain pathway. To gain insight into the mechanism of this process, we studied accumulation of the main reaction products. To determine the influence of various catalysts [mainly $Cr(CO)_6$] on the yield of each product, we measured the dependence of the selectivity of its formation on the hydrocarbon conversion. The reaction selectivity was taken as the ratio of the concentration of a definite reaction product to the total concentration of the reaction products.

The dependences of the total selectivity of formation of each product on the hydrocarbon conversion in catalytic ozonolysis of cyclohexane at $[O_3]$ = 4 vol %, 40°C, and the catalyst concentration of 2×10^{-4} M are shown in Figs. 4a and 4b. As the conversion increases, the selectivity of formation of the hydroperoxide and cyclohexanol linearly decreases, as a rule, and that of cyclohexanone formation increases owing to conversion of cyclohexanol and cyclohexyl hydroperoxide into the ketone. When the conversion is lower than 10%, the selectivity of cyclohexanone formation ranges from 69 to 73% without catalyst and reaches 81% in the presence of $Cr(CO)_6$. In addition, in the presence of $Cr(CO)_6$, the yield of cyclohexyl hydroperoxide and cyclohexanol decreases more sharply with increasing cyclohexane conversion. Hence, $Cr(CO)_6$ catalyzes the conversion of these compounds into cyclohexanone. An ozone–chromium(III) stearate system also exhibits high catalytic activity with respect to cyclohexanone (Fig. 4a). In this case, the ketone yield is as high as 70% at 6.5% conversion. When chromium(III) acetate poorly soluble in the reaction mixture is used, the selectivity of the ketone formation does not exceed 31%, but the selectivity of the hydroperoxide formation reaches 48%.

The catalytic effect of ozone–$CoSt_2$, ozone–$Co(acac)_3$, and ozone–$Mn(acac)_3$ systems on the selectivity is considerably lower than that of the ozone–chromium(III) and ozone–chromium(0) systems. In the presence of $Mn(acac)_3$, cyclohexane is rapidly converted into the acids and ε-caprolactone and the total yield of peroxides grows with increasing cyclohexane conversion. This dependence passes through a maximum.

Although the selectivity of cyclohexanone formation is maximal in the presence of the ozone–$Cr(CO)_6$ catalytic system, the selectivity and rate of the reaction considerably change in the examined temperature range (20–60°C). Cyclohexane ozonolysis with ozone–air mixtures containing 2% ozone is slow. In 4 h, the hydrocarbon conversion is as low as 2.2%, and the selectivity of cyclohexanone formation reaches 42–51%. Under these conditions, the catalyst affects the ratio of the main classes of the ozonolysis products. The selectivity of the cyclohexanone formation in the presence of 2×10^{-5} M $Cr(CO)_6$ is relatively high (up to 65%). The total yield of the hydroperoxides slightly grows with increasing catalyst concentration.

This is the case at elevated temperatures (60°C). Under these conditions, the selectivity of cyclohexanone formation is no higher than 60%. At 60°C, the conversion of cyclohexanol and cyclohexyl hydroperoxide into cyclohexanone and parallel conversion of cyclohexanone into the acids and lactone are accelerated. The almost optimal conditions of catalytic ozonolysis of cyclohexane are as follows: $[O_3]$ = 4 vol %, 40°C, $[Cr(CO)_6] = 2 \times 10^{-4}$ M, cyclohexane conversion 7–10%. The ketone yield reaches 81%. Ozone–sodium naphthenate, chromium(III) naphthenate, and ozone–chromium(III) naphthenate catalytic systems [8, 9] provide 85–90% selectivity of the ketone formation at the cyclohexane conversion of 5.3–6.5%.

Thus, as the cyclohexane conversion increases, the selectivity of formation of the main reaction products (R'C=O, ROOH, and ROH) is constant, decreases, or increases depending on the reaction conditions (temperature, concentrations of ozone and the catalyst). At low temperature (20°C), the selectivity of formation of these products decreases with increasing ozone

concentration owing to acceleration of the consumption of the alcohol and hydroperoxide. The selectivity of the ketone formation grows with increasing cyclohexane concentration. At 60°C, cyclohexanone oxidation is accelerated and the selectivity of its formation remains constant in the whole examined conversion range. The selectivity of formation of acids and esters increases. In the course of cyclohexane ozonolysis at 40°C in the presence of the ozone–$Cr(CO)_6$ catalytic system, the total selectivity of cyclohexanone formation regularly increases, the selectivity for the hydroperoxide and alcohol decreases, and the selectivity for the acids is constant. In the presence of ozone–NaNph–$Cr(Nph)_3$ (Nph is the naphthenate anion) catalytic system, the total selectivity of formation of cyclohexanol and cyclohexanone mixture is high [10]. To gain deeper insight into the mechanism of cyclohexane oxidation, let us consider the transformation of the catalyst, hydroperoxide, alcohol, and ketone under these conditions.

The rate constant of reaction of ozone with Co(II), Fe(II), Mn(II), and Cr(III) acetates is higher by 2–3 orders of magnitude than that of reaction of ozone with cyclohexyl hydroperoxide [1, 3, 11]. Ozone reacts with the catalysts by the reaction [12]

$$O_3 + M(II) \rightarrow M(III) + O_2 + O^- \text{ (or } O_3^-).$$

Negatively charged oxygen atom rapidly reacts with a proton of the acid present in the reaction mixture to form ·OH radical. In addition, the reaction of a saturated hydrocarbon with ozone [1] yields R· and ·OH radicals. Hydroxy radicals oxidize the reduced form of a variable-valence metal:

$$\cdot OH + M(II) \rightarrow M(III) + {}^-OH.$$

The oxidation potential of Me(III)/Me(II) is sufficient for Me(III) to oxidize hydroperoxides, alcohols, and ketones. If the activation energy of the reaction of the initial or intermediate compound with the oxidized form of the catalyst is high, more active ·OH radical can initiate the oxidation. In addition, in the course of cyclohexane oxidation with an ozone–air mixture, variable-valence metal carboxylates in the oxidized or reduced forms coordinate the oxygen-containing reaction products (ROOOH, ROH, R'C=O). The overall rate of catalytic ozonolysis of cyclohexane should depend on the stability of these complexes, and the selectivity of ketone formation, on the ratio of the rates of formation and consumption of these complexes. The main sources of cyclohexanone in noncatalytic ozonolysis of cyclohexane are unstable hydrotrioxide, cyclohexanol, cyclohexyl hydroperoxide, and $RO_2^{\cdot}$ radical [1].

Let us consider the influence of $Cr(CO)_6$ catalyst on the conversion of the above intermediates of cyclohexane ozonolysis. In the presence of chromium compounds, cyclohexyl hydroperoxide is selectively converted into cyclohexanone mainly by the nonradical mechanism [4]. Indictor *et al*. showed [5] that Cr(III) is oxidized with the hydroperoxide to Cr(VI). Antonovskii suggests [13] that the O–O bond of the peroxy ester is homolytically ruptured to form the ketone

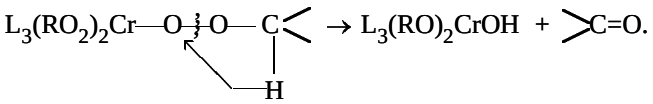

As found in [4], decomposition of *tert*-butyl hydroperoxide in the presence of Cr(III) acetylacetonate is described by the scheme

$$Cr(III) + yt\text{-BuOOH} \rightleftarrows \text{Complex},$$

$$\text{Complex} \rightarrow Cr(III + l) + y(t\text{-BuO}^{\cdot} + {}^-OH),$$

$$Cr(III + l) + Cr(III) \rightarrow Cr(VI) + Cr(l),$$

where y is the stoichiometric coefficient, and l is an integer equal to the change in the chromium oxidation state.

Bibichev [14] also suggests that the selective conversion of a secondary hydroperoxide into the ketone in the presence of chromium(III) stearate also passes through formation of the complex $Cr(St)_3 \cdot n$ROOH, where $n > 1$. When a hydroperoxide molecule is coordinated to the Cr(III) atom, the electron density from the α-oxygen atom of the hydroperoxide is transferred to the *d* orbital of Cr(III). As a result, the O–O bond of the hydroperoxide is weakened and then homolytically ruptured to form alkoxy and hydroxy radicals. The liberated OH radical, without escaping into the bulk of solution, can attack the C–H bond of the coordinated hydroperoxide to form the ketone and water by the molecular (cryptoradical) mechanism.

The apparent rate constant of cyclohexyl hydroperoxide decomposition in the presence of 2×10^{-4} M $Cr(CO)_6$ is $7.6 \times 10^7 \exp(-67\,000 \pm 2000)/RT$ min^{-1}. If the steady-state concentration of ROOH is 0.1 M, the rate constant of cyclohexanone formation from hydroperoxide at 40°C is 0.0046 mol l^{-1} h^{-1}. Hence, the contribution of the catalytic decomposition of cyclohexyl hydroperoxide to cyclohexanone formation is no higher than 2 and 8.2% at 40 and 60°C, respectively, i.e., is low.

The steady-state concentration of hydrotrioxide at 20°C is 2.2×10^{-3} M. The strength of the O–O bond in this compound is close to that in cyclohexyl hydroperoxide. Hence, the contribution of the catalytic decomposition of the hydrotrioxide to the overall process can be neglected. Both inner- and outer-sphere coordination of cyclohexyl hydroperoxide is typical of 3*d* transition metals [15]; however, coordination-saturated $Cr(CO)_6$ can form only outer-sphere complexes with ROOH [$Cr(CO)_6 \cdot ROOH$]. Chromium hexacarbonyl is stable up to 120–140°C. Since carbonyl groups in $Cr(CO)_6$ are substituted by the dissociative mechanism with a high activation energy (ΔE_a = 163 kJ mol^{-1}), occurrence of these reactions under our conditions is unlikely.

Carbonyl ligands are strongly bonded to the chromium atom in $Cr(CO)_6$. The donor–acceptor σ bond in carbonyls is formed by interaction of the *d* orbital of the metal, e.g., $d_{x^2-y^2}$, with *n* electrons of CO on the *sp*-hybrid σ_n orbital. The carbonyl group donates the α-electron pair localized on the carbon atom. The dative π bond in carbonyls is formed by donation of the electron density form *d* orbitals of the metal, e.g., d_{xy}, to unoccupied antibonding π orbitals of CO.

However, zero-valent chromium in $Cr(CO)_6$ is rapidly oxidized with ozone to Cr(III) and Cr(VI). A sharp band at 336 nm typical for Cr(III) appears in the electronic absorption spectra of $Cr(CO)_6$ solutions in $CHCl_3$ and cyclohexane (1.2×10^{-3} M) after bubbling of an ozone–oxygen mixture for 0.5–1 min ($[O_3]$ = 4 vol %, 25°C). As determined by ESR, the steady-state concentration of Cr^{5+} [18] is very low. Hexavalent chromium was qualitatively determined by the reaction with diphenylcarbazide [19].

The overall process of $Cr(CO)_6$ oxidation with ozone can be described by the following reactions:

$$Cr(CO)_6 + mO_3 \xrightarrow[-CO,\ -CO_2,\ -O_2]{} Cr(III)L_3 + 3O^{\cdot-},$$

$$O^{\cdot-} + H^+ \overset{K_e}{\rightleftarrows} {}^{\cdot}OH, \quad K_e = 10^{12} \text{ [3]},$$

$${}^{\cdot}OH + Cr(III) \rightarrow Cr(IV) + {}^{-}OH,$$

$${}^{-}OH + H^+ \rightleftarrows H_2O,$$

$$Cr(III) + RO_2^{\cdot} \rightarrow Cr(IV) + RO_2^-,$$

$$Cr(IV) + O_3 \rightarrow Cr(V) + O^- + O_2,$$

$$Cr(III) + O_3 \rightarrow Cr(IV) + O^- + O_2,$$

$$Cr(V) + O_3 \xrightarrow[-O_2]{} Cr(VI) + O^-,$$

$$RO_2^- + H^+ \rightarrow ROOH.$$

It is known [20] that Cr(VI) selectively oxidizes alcohols to carbonyl compounds:

$$Cr(VI) + ROH \rightarrow R{=}O + Cr(IV).$$

Probably, Cr(IV) is reduced to Cr(III) with cyclohexanol hydroxy hydroperoxide or the hydroxyperoxy radical 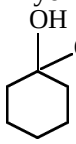 exhibiting redox properties [6]. In addition, reactions between chromium atoms in different oxidation states are also possible. The steady-state concentration of cyclohexanol in the products of catalytic ozonolysis of cyclohexane is low (Fig. 4). The cyclohexanol yield in the course of the ozonolysis decreases owing to its conversion into cyclohexanone [21, 22].

Probably, the fact that the total yield of cyclohexanol and cyclohexanone and the concentration ratio of these products vary a wide range (Fig. 4) is due not only to the catalysis of the alcohol oxidation to the ketone with Cr(VI). Special experiments show slow consumption of cyclohexanol and cyclohexanone in the course of cyclohexane ozonolysis catalyzed with $Cr(CO)_6$ in a bubbling reactor. Slow consumption of cyclohexanol is caused by its self-accociation. We suggest that the increased cyclohexanol yield in the presence of chromium-containing catalysts is due to a change in the reactivity of the peroxide and alkoxy radicals in the chromium(III) coordination sphere. The transformations of these radicals in the course of cyclohexane ozonolysis are discussed in [1].

CONCLUSION

Ozone–chromium(0) hexacarbonyl, ozone–chromium(III) naphthenate–sodium naphthenate, and chromium(0) hexacarbonyl–cyclohexyl hydroperoxide systems are catalytically active in cyclohexane oxidation. In the presence of these catalysts, the selectivity of formation of cyclohexanol–cyclohexanone mixture and of the target product, cyclohexanone, is high.

REFERENCES

1. Tedder, J.M., Nechvatal, A., and Jubb, A.H., *Basic Organic Chemistry*, London: Wiley, 1975.

2. Syroezhko, A.M., Proskuryakov, V.A., and Begak, O.Yu., *Zh. Prikl. Khim.*, 2002, vol. 75, no. 9, pp. 1480–1484.
3. Syroezhko, A.M., Liquid-Phase Oxidation of Alkanes, Cycloalkanes, and Their Oxygen-Containing Derivatives with Oxygen and Ozone in the Presence of *s*- and 3*d*-Element Compounds, *Doctoral Dissertation*, Leningrad, 1984.
4. Pustarnakova, G.F., Solyanikov, V.M., and Denisov, E.T., *Izv. Akad. Nauk SSSR, Ser. Khim.*, 1975, no. 3, pp. 547–552.
5. Indictor, N., Yochsberger, T., and Kurnit, D., *J. Org. Chem.*, 1969, vol. 34, no. 10, pp. 2855–2861.
6. Denisov, E.T. and Kovalev, G.I., *Okislenie i stabilizatsiya reaktivnykh topliv* (Oxidation and Stabilization of Propellants), Moscow: Khimiya, 1983.
7. Denisov, E.T., *Inogi Nauki Tekh., Ser.: Kinet. Katal.*, 1981, vol. 9.
8. Bibichev, V.M., Syroezhko, A.M., and Svirkin, Yu.Ya., in *Issledovanie v oblasti khimii i tekhnologii produktov pererabotki goryuchikh iskopaemykh* (A Study in the Field of Chemsitry and Technology of Reprocessing Products of Fossil Fuels), Leningrad: Leningr. Tekhnol. Inst. im. Lensoveta, 1980, pp. 99–102.
9. USSR Inventor's Certificate no. 692 826.
10. Korotkova, N.P., Syroezhko, A.M., and Proskuryakov, V.A., *Zh. Prikl. Khim.*, 1981, vol. 54, no. 4, pp. 885–889.
11. Rakovski, S.K., Chernyaeva, D.F., and Shopov, D.N., *Izv. Akad. Nauk SSSR, Ser. Khim.*, 1979, no. 9, pp. 1991–1995.
12. Gorbenko-Germanov, D.S., *Neorganicheskie perekisnye soedineniya* (Inorganic Peroxides), Moscow: Nauka, 1975.
13. Antonovskii, V.L., *Organicheskie perekisnye initsiatory* (Organic Peroxide Initiators), Moscow: Khimiya, 1972.
14. Bibichev, V.M., A Study of Liquid-Phase Oxidation of *n*-Paraffins to Acids in the Presence of Multicomponent Catalysts, *Cand. Sci. Dissertation*, Leningrad, 1979.
15. Yablonskii, O.P., Complexation and Its Role in Oxidation and Separation of Hydrocarbons, *Doctoral Dissertation*, Ivanovo, 1979.
16. Makashev, Yu.A. and Zamyatkina, V.M., *Soedineniya v kvadratnykh skobkah* (Compounds in Brackets), Moscow: Khimiya, 1976.
17. Skorik, N.A. and Kumok, V.N., *Khimiya koordinatsionnykh soedinenii* (Coordination Chemistry), Moscow: Vysshaya Shkola, 1975.
18. Popova, N.M and Sokol'skii, D.V., *Glubokoe kataliticheskoe okislenie uglevodorodov (Problemy kinetiki i kataliza)* (Exhaustive Catalytic Oxidation of Hydrocarbons (Problems of Kinetics and Catalysis)), Moscow: Nauka, 1981, vol. 18, pp. 133–142.
19. Marczenko, Z., *Kolorymetryczne oznaczanie pierwiastkow*, Warsaw: Wydawnictwa Naukowa-Techniczne, 1968.
20. Candlin, J.P, Taylor, K.A., and Thompson, D.T., *Reactions of Transition Metal Complexes*, Amsterdam: Elsevier, 1968.
21. Yakovlev, A.S., Syroezhko, A.M., Vikhorev, A.A., and Proskuryakov, V.A., *Izv. Vyssh. Uchebn. Zaved., Khim. Khim. Tekhnol.*, 1983, vol. 1, no. 3, pp. 122–124.
22. Semenchenko, A.E., Solyanikov, V.M., and Denisov, E.T., *Kinet. Katal.*, 1972, vol. 13, no. 5, pp. 1153–1159.

Russian Journal of Applied Chemistry, Vol. 77, No. 1, 2004, pp. 57–61. Translated from Zhurnal Prikladnoi Khimii, Vol. 77, No. 1, 2004, pp. 60–64.

APPLIED ELECTROCHEMISTRY AND CORROSION PROTECTION OF METALS

Cathodic Deposition of Copper from Dilute Solutions

V. S. Kolosnitsyn and O. A. Yapryntseva

Institute of Organic Chemistry, Ufa Scientific Center, Russian Academy of Sciences, Ufa, Bashkortostan, Russia

Received May 22, 2003

Abstract—The cathodic deposition of copper onto stationary and smooth rotating disc electrodes from dilute aqueous solutions [copper(II) concentration up to 100 mg l^{-1}] was studied.

In extraction and dressing of polymetallic sulfide ores, a large amount of stripping rock dumps, lean ores, and dressing tails containing heavy metal sulfides are formed. In the course of prolonged exposure to atmospheric oxygen, sparingly soluble heavy metal sulfides are gradually oxidized with formation of well soluble compounds, sulfites and sulfates, which enter subdump, pit, and mine waters as a result of natural leaching. The volumes of their formation at each plant are between $(50–100) \times 10^3$ and $(5–6) \times 10^6$ m^3 yearly and depend on seasonal and weather conditions. The content of heavy metals in subdump waters is also dependent on seasonal and weather conditions and varies from a few milligrams to 1 g and more per liter, which exceeds by several orders of magnitude the maximum permissible concentration (MPC). The approximate composition of the subdump, mine, and pit waters is given in Table 1. Presently, most of mining plants have no water treatment facilities, and the above waters enter natural reservoirs without any purification.

The sewage from mining plants can be purified by chemical, physicochemical, and biological methods [1–5]. However, all the above methods have drawbacks impeding their application.

A promising method is direct electrolysis (cathodic deposition), which allows recovery of metals from aqueous solutions in the form of target products. It is also important that the electrolysis involves no chemicals. This makes it possible to develop low-waste and wasteless processes [6]. However, the electrodeposition of metals from the sewage from mining plants involves a number of problems caused by complex composition of the wastewaters and low concentration of target components. Among the main problems is intensification of the electrolysis, since electrodeposition of metals from dilute solution is limited by the transport processes.

One of the simplest methods to intensify the electrodeposition of metals is the use of a fast flow of electrolyte in the interelectrode space [7–10]. Porous and cellular cathodes made of carbon fibers also make the process more intense owing to increased deposition area [11–15]. One more way to intensify the electrolysis is the use of fluidized cathodes [15]. However, ensuring fluidization conditions requires special expensive equipment and involves additional power consumption.

We believe that the most efficient method for intensifying cathodic deposition of metals from dilute solutions is the use of a smooth rotating cathode, which makes it possible to lift diffusion restrictions and recover metals at a rate sufficient for commercial application.

Table 1. Content of ions in subdump and mine waters from UOMPP*

Component	Content, mg l^{-1}	
	subdump water	mine water
Cu	83	10
Zn	582	105
Co	1	1
Ni	1	0
Mn	76	18
Pb	0	1
Cd	2	1
Ca	391	310
Mg	1136	217
Sulfates	4730	2131
Chlorides	64	93
Nitrates	5	11
pH	3	5

Note: * Uchaly Ore Mining and Processing Plant.

1070-4272/04/7701-0057 © 2004 MAIK "Nauka/Interperiodica"

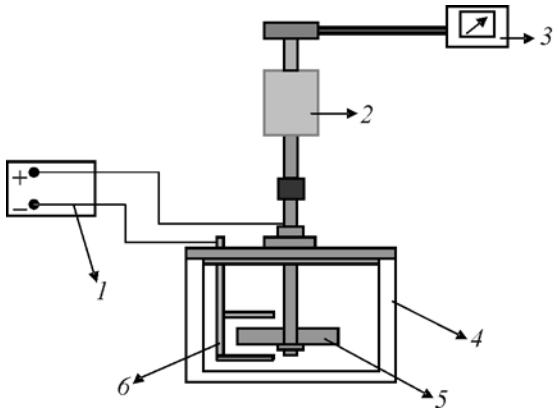

Fig. 1. A setup for studying cathodic deposition of metals on a rotating disc electrode: (*1*) stabilized current source, (*2*) electric motor, (*3*) tachometer, (*4*) electrolyzer, (*5*) smooth rotating cathode, and (*6*) insoluble anodes.

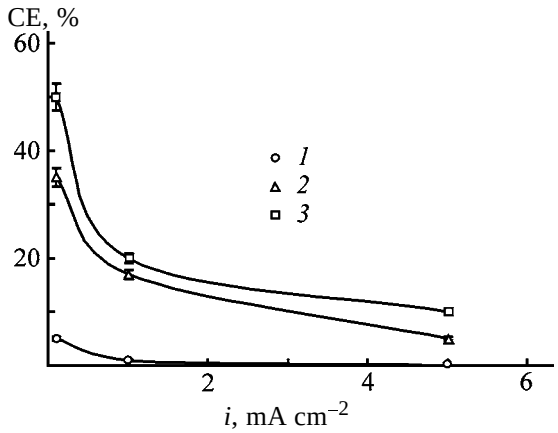

Fig. 2. Current efficiency CE by copper in deposition on a stationary electrode vs. current density *i* at various initial concentrations of Cu^{2+} in solution. Supporting electrolyte 0.5 M Na_2SO_4, pH 3. Copper(II) concentration, g l^{-1}: (*1*) 0.001, (*2*) 0.1, and (*3*) 1.

In this work, the influence of various factors on the cathodic deposition of copper onto a smooth rotating electrode was studied to estimate the potentialities of this method.

EXPERIMENTAL

The features of the cathodic deposition of copper on a stationary electrode were studied by taking chronopotentiometric curves in a YaSE-2 temperature-controlled three-electrode cell with separated electrode compartments. A platinum plate was the working electrode, a silver chloride electrode was reference, and a platinum wire, auxiliary electrode. The study was performed in the galvanostatic mode with the use of an automated potentiostatic-galvanostatic device.[1] The current efficiency (CE) of the cathodic deposition of copper was determined from the ratio of the lengths of the plateaus corresponding to deposition and dissolution potentials of copper in the cathodic and anodic chronopotentiograms.

The features of copper deposition on a smooth rotating electrode were studied in a specially designed cell (Fig. 1). The electrolyzer was polarized in the galvanostatic mode with a stabilized B5-49 voltage and current source. The voltage and current values were controlled with a B7-27 A/1 digital voltmeter. The time of the cathodic deposition of the metal was measured with a stopwatch. The rate of rotation of the disc cathode was measured and adjusted with a tachometer. The cathode was a stainless steel disc, and the anodes were made of the lead–antimony alloy. The cathode area was 160 cm^2. Prior to the test, the cathodes were trimmed with an emery paper (no. 0) and washed in the electrolyte to be studied. The amount of copper deposited on the cathode, CE, and the degree of recovery (DR) were calculated from difference in the copper content in the electrolyte before and after the electrolysis.

The electrolysis time was always chosen so that the amount of the electricity passed corresponded to 100% of the initial copper content.

The model solutions of subdump and mine waters were prepared from chemically pure grade reagents and distilled water. The copper concentration in solutions was determined by direct complexometric titration.

Because copper is an electropositive metal, the rate of the copper deposition will be determined by the ratio of the rates of only two processes: copper deposition and hydrogen evolution. The dissolution of copper from the electrode surface under the action of corrosion is virtually absent.

The preliminary tests showed that, in electrodeposition of copper on a stationary electrode from dilute solutions (Fig. 2), the current efficiency strongly depends on the density of the polarizing current. The acceptable level of CE for solutions containing 0.1 and 1.0 mg l^{-1} copper(II) is attained at a current density of about 0.1 mA cm^{-2}. For the solution containing 0.01 mg l^{-1} copper(II), the acceptable current efficiency in electrodeposition of copper was attained at the current densities as low as 0.01–0.05 mA cm^{-2}.

[1] The device was developed at the laboratory of electrochemistry, Institute of Organic Chemistry, Ufa Scientific Center, Russian Academy of Sciences.

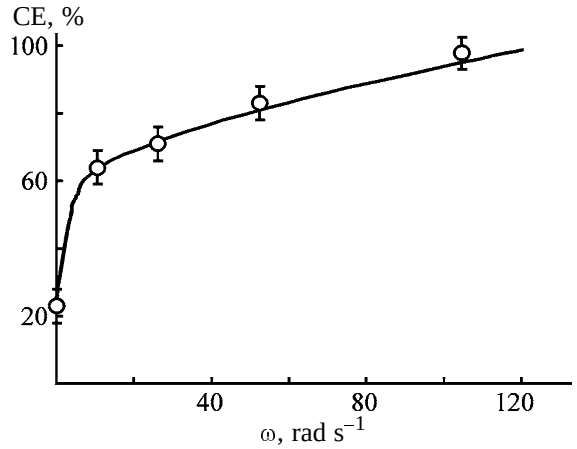

Fig. 3. Current efficiency CE vs. cathode rotation rate ω. Supporting electrolyte 0.5 M Na_2SO_4, i = 0.5 mA cm^{-2}, $c_{Cu^{2+}}$ = 100 mg l^{-1}, pH 3.

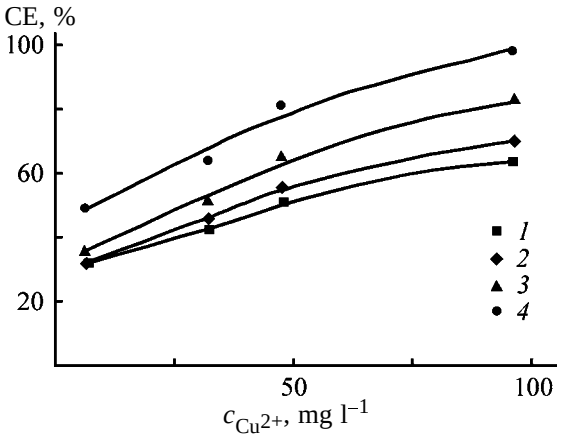

Fig. 4. Current efficiency CE vs. the concentration of copper ions $c_{Cu^{2+}}$ in electrolyte at various rates of rotation of the electrode. Supporting electrolyte 0.5 M Na_2SO_4, i = 0.5 mA cm^{-2}, pH 3. Electrode rotation rate, rad s^{-1}: (*1*) 10.5, (*2*) 26, (*3*) 52.3, and (*4*) 105.

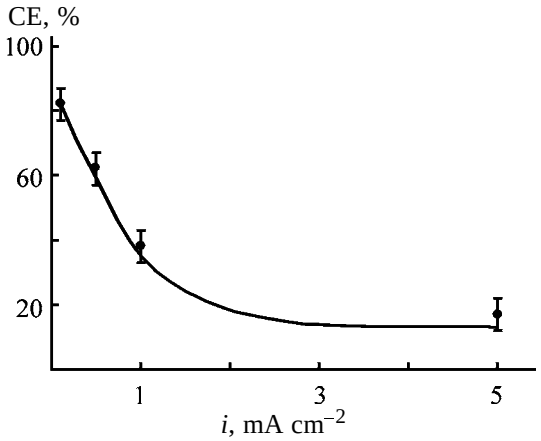

Fig. 5. Current efficiency CE by copper in deposition onto a rotating cathode vs. current density i. Supporting electrolyte 0.5 M Na_2SO_4, ω = 52.3 rad s^{-1}, $c_{Cu^{2+}}$ = 100 mg l^{-1}, pH 5.

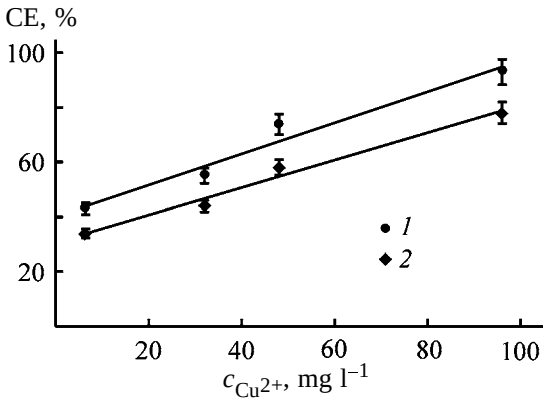

Fig. 6. Current efficiency CE of copper cathodic deposition vs. copper(II) concentration in solution $c_{Cu^{2+}}$ at various pH. Supporting electrolyte 0.5 M Na_2SO_4, i = 0.5 mA cm^{-2}, ω = 52.3 rad s^{-1}. Electrolyte pH: (*1*) 3 and (*2*) 5.

It should be noted that, owing to alkalization of the near-electrode layer upon hydrogen evolution at the cathode, copper(II) hydroxide flakes always appeared on the cathode upon copper deposition. Therefore, the copper deposition from dilute solutions onto a stationary electrode can occur in a quantitative yield only at a very low rate (i < 0.1 mA cm^{-2}), unacceptable for commercial applications.

The current efficiency of the copper deposition on the rotating electrode is considerably higher than on the stationary electrode (Fig. 3). With increasing rotation rate, CE increases to virtually 100%, which for solutions containing 100 mg l^{-1} Cu^{2+} is achieved at a rotation rate of 105 rad s^{-1}. As shown above, copper can be deposited in the form of hydroxides without stirring and at a low rotation rate owing to alkalization of the near-electrode layer of the electrolyte. As a result, the Cu^{2+} concentration on the electrode surface decreases, and the ratio of rates of the copper deposition and hydrogen evolution changes. Increasing the rotation rate decreases the concentration of the cathodically formed alkali. Therefore, $Cu(OH)_2$ is formed to a lesser extent or is not formed at all, which results in increased CE.

With decreasing copper(II) concentration in the solution, the current efficiency decreases also (Fig. 4). For example, at $C_{Cu^{2+}}$ decreased by an order of magnitude, CE decreases by 50%.

The current efficiency of the copper deposition on the rotating electrode, as on the stationary electrode, strongly depends on the polarizing current density (Fig. 5). For example, at the Cu^{2+} concentration in

Table 2. Composition of subdump, mine, and pit waters before and after electrolysis

Object	pH	Content of metal cations, mg l^{-1}			
		Cu	Zn	Fe	Mn
Mine water (UOMPP):					
before electrolysis	6.0	2.45	3.83	0.25	2.06
after electrolysis		0.74 (70)*	2.33 (39)	0.04 (84)	0.04 (98)
Subdump water:					
before electrolysis	2.5	83	582	–	76
after electrolysis		0.1 (99.98)	582 (0)	–	42 (45)

Note: * The degree of recovery (%) is given in parentheses.

solution of 100 mg l^{-1}, pH 5, and rotation rate of 52.3 rad s^{-1}, as the current density is increased from 0.1 to 2 mA cm^{-2}, CE sharply decreases from 82 to 22%; as the current density is increased further, CE decreases insignificantly.

The solution pH plays an important role in electrodeposition of metals. On the one hand, it is responsible for the form in which the metal exists in a solution, and, on the other hand, CE by hydrogen is higher at lower pH. Upon cathodic deposition of copper from neutral solutions of copper(II) sulfate, a sharp increase in pH in the near-cathode layer is observed even at low current densities, which leads to the precipitation of copper hydroxides [16]. As expected, as pH is decreased from 5.0 to 3.0, CE by copper increases by 10–20% on the average in the case of a rotating electrode also (Fig. 6).

In all cases, precipitation of copper hydroxide flakes was not observed on the rotating cathode, though the cathodic deposits obtained at various current densities, pH values, and rotation rates markedly differed in quality.

It can be readily seen from the comparison of the data obtained on stationary and rotating electrodes that the use of a rotating cathode allows the rate of copper electrodeposition to be increased by a factor of 5–10, with CE increasing by 70% in the process.

The data obtained were confirmed in tests on the copper deposition from subdump and mine waters of the Uchaly Ore Mining and Processing Plant (UOMPP). The experimental results show that the degree of copper deposition from subdump and mine waters is 98 and 70%, respectively.

CONCLUSIONS

(1) It was shown by an example of the cathodic deposition of copper that the current efficiency achieved with a rotating electrode is higher than that with a stationary electrode.

(2) The use of a rotating cathode allows the rate of copper electrodeposition from dilute solutions to be increased 5–10-fold, with the high current efficiency retained.

REFERENCES

1. Meinck, F., Stoff, H., and Kohlschütter, H., *Industrie-Abwässer*, Stuttgart: Fisher, 1960, 3rd ed.
2. Smirnov, D.N., and Genkin, V.E., *Ochistka stochnykh vod v protsessakh obrabotki metallov* (Sewage Treatment in Metal Machining), Moscow: Metallurgiya, 1989.
3. Kostyuk, V.I., and Karnaukh, G.S., *Ochistka stochnykh vod mashinostroitel'nykh predpriyatii* (Treatment of Sewage from Machine-Building Plants), Kiev: Tekhnika, 1990.
4. Sidel'nikova, L.I., *Ekol. Prom. Proizv.*, 1994, no. 2, pp. 32–35.
5. Koganovskii, A.M., Kul'skii, A.A., Sotnikova, E.V., and Shmaruk, V.L., *Ochistka promyshlennykh stochnykh vod* (Treatment of Industrial Sewage), Kiev: Tekhnika, 1974.
6. Zapol'skii, A.K., and Obraztsov, V.V., *Kompleksnaya pererabotka stochnykh vod gal'vanicheskogo proizvodstva* (Complex Treatment of Sewage from Electroplating Shops), Kiev: Tekhnika, 1989.
7. Davydov, A.D., Levit, M.L., and Tsvetkov, I.V., *Elektrokhimiya*, 1982, vol. 18, no. 9, pp. 1170–1174.
8. Davydov, A.D. and Krylov, V.S., *Elektrokhimiya*, 1983, vol. 19, no. 3, pp. 397–401.
9. Varentsov, V.K., Zherebilov, A.F., and Bek, R.Yu., *Elektrokhimiya*, 1982, vol. 18, no. 3, pp. 366–370.
10. Bek, R.Yu. and Zherebilov, A.F., *Zh. Prikl. Khim.*, 1995, vol. 8, no. 9, pp. 1470–1473.

11. Koshcheev, O.P., Kichigin, V.I., Antsiferov, V.N., *et al*., *Zh. Prikl. Khim.*, 1995, vol. 68, no. 11, pp. 1809–1813.
12. Koshcheev, O.P., Kichigin, V.I., Antsiferov, V.N., and Gabdrakhmanova, R.M., *Zh. Prikl. Khim.*, 1995, vol. 68, no. 11, pp. 1804–1807.
13. Koshcheev, O.P., Kichigin, V.I., Antsiferov, V.N., *et al*., *Zh. Prikl. Khim.*, 1996, vol. 69, no. 9, pp. 1484–1490.
14. *Intensifikatsiya elektrokhimicheskikh protsessov. Sbornik nauchnykh trudov* (Intensification of Chemical Processes. Coll. of Scientific Works), Tomilov, A.P., Ed., Moscow: Nauka, 1988, pp. 94–98.
15. Kublanovskii, V.S., Gorodyskii, A.V., Belinskii, V.N., and Glushchuk, T.S., *Kontsentratsionnye izmeneniya v prielektrodnykh sloyakh v protsesse elektroliza* (Concentration Variations in Near-Electrode Layers in the Course of Electrolysis), Kiev: Naukova Dumka, 1972.

Russian Journal of Applied Chemistry, Vol. 77, No. 1, 2004, pp. 62–66. Translated from Zhurnal Prikladnoi Khimii, Vol. 77, No. 1, 2004, pp. 65–69.

APPLIED ELECTROCHEMISTRY AND CORROSION PROTECTION OF METALS

Electrochemical Recovery of Silver from Secondary Raw Materials

O. G. Gromov, A. P. Kuz'min, G. B. Kunshina, E. P. Lokshin, and V. T. Kalinnikov

Tananaev Institute of Chemistry and Technology of Rare Elements and Mineral Raw Materials, Kola Scientific Center, Russian Academy of Sciences, Apatity, Murmansk oblast, Russia

Received April 3, 2003

Abstract—Electrolysis of silver in 95–84 wt % sulfuric acid with addition of 40 g l^{-1} of silver sulfate was studied at electrolyte temperature of 40°C. The optimal conditions of silver electrolysis in 84–85 wt % sulfuric acid were determined. Semicommercial tests of the electrochemical recovery of silver from silver coatings on copper, brass, aluminum, and steel articles were performed.

The market demand poses an acute problem of recovery of noble metals from scrap and electronic waste by new economically efficient and environmentally clean technologies. It is known [1] that the electrochemical recovery of noble metals from solutions of complex composition is one of the most economically efficient techniques. However, the existing schemes for processing of secondary raw materials are not always effective because of the low noble metal recovery, high power consumption, and, occasionally, poor environmental characteristics. For example, electrolytic recovery of silver from a silver coating on copper base [2] involves two stages of electrolytic processing. In the first stage, the solder is dissolved in a sulfamic electrolyte, with lead, tin, and zinc deposited at the cathode in the form of powders. In the second stage, the copper-containing base is dissolved in a sulfuric acid electrolyte, with copper powder obtained at the cathode and copper concentrated in the anode slime. The disadvantages of this technique are high power consumption and impossibility of obtaining high-purity silver.

In electrolytic recovery of silver from a silver coating on iron base [3], silver is anodically dissolved in an electrolyte containing 86 vol % concentrated sulfuric acid, 12 vol % ethanol, and 2 vol % mononitrobenzene at 40°C, voltage of 8 V, and current density of 12 A dm^{-2}. The disadvantages of this technology are the presence of strongly toxic aromatic compounds (mononitrobenzene, in particular) and the necessity for subsequent recovery of silver from the electrolyte solution.

The aim of this study was to examine selective recovery of silver from electrotechnical scrap by electrolysis in concentrated sulfuric acid to give high-purity silver metal as the final product.

EXPERIMENTAL

As starting materials we used 95 wt % H_2SO_4 and Ag_2SO_4, both of pure grade, and 6 cm^2 plates of metallic silver, St.3 steel, 1Cr18Ni9Ti stainless steel, and glassy carbon. The electrochemical cell had the form of a glass vessel 50 mm in diameter and 80 mm high, charged with 50 cm^3 of sulfuric acid and Ag_2SO_4 additive. The cathode and anode were placed at a distance of 40 mm and connected to an unconventional dc power supply providing current of 0–30 A, with voltage continuously variable in the range 0–5 V. To maintain the electrolyte temperature at 40–50°C, the cell was placed in an electric furnace. The phase composition of the products obtained was determined by X-ray phase analysis on a DRON-2 diffractometer with CuK_α radiation and graphite monochromator.

Initially, a plate of metallic silver was used as the anode, and a glassy carbon plate, as the cathode. The voltage across the power supply terminals was 1.5 V under no-load conditions; the electrolyte temperature, 40°C; and the concentration of Ag_2SO_4 in sulfuric acid, 40 g l^{-1}. On applying voltage to the cell, the current changed stepwise to 0.6–0.7 A and then decreased to a constant value of 0.4–0.35 A. A silver deposit of black color was formed at the cathode, with small gas bubbles seen on the surface of this deposit. After 3–5 min, the cathode silver turned lighter, and a lilac cloud appeared in the electrolyte near the upper part of the cathode and then, gradually, occupied the whole volume of the electrolyte.

1070-4272/04/7701-0062 © 2004 MAIK "Nauka/Interperiodica"

It was established that the amount of silver obtained at the cathode is 17–18% relative to that dissolved at the anode, with the quantity of electricity passed through the electrolyte being equivalent to the mass of silver dissolved at the anode, i.e., there are no side processes at the anode. The electrolysis product contained, in addition to metallic silver, a black substance. This substance was isolated by dissolving metallic silver in 20% nitric acid. An X-ray phase analysis demonstrated (Fig. 1) that this substance is a mixture of $Ag_8S_3SO_4$ and Ag_2S. The compound $Ag_8S_3SO_4$ can be represented as $3Ag_2S \cdot Ag_2SO_4$. The formation of these compounds in electrolysis can be explained as follows. It is known [4] that silver used as the cathode material reduces hot concentrated sulfuric acid to SO_2, which is readily reduced electrochemically to the sulfide ion S^{2-}. S^{2-} ions react with silver cations to give Ag_2S. In this case, freshly deposited cathodic silver exhibits high chemical activity and partly reacts with concentrated sulfuric acid at relatively low temperature. This reaction yields silver sulfide at the cathode as follows:

$$2Ag + 2H_2SO_4 = Ag_2SO_4 + SO_2 + 2H_2O, \quad (1)$$

$$SO_2 + 2e = S^{2-} + O_2\uparrow, \quad (2)$$

$$2Ag - 2e + S^{2-} = Ag_2S. \quad (3)$$

When combined, these reactions constitute the overall reaction

$$4Ag + 2H_2SO_4 = Ag_2S + Ag_2SO_4 + 2H_2O + O_2\uparrow. \quad (4)$$

The forming silver sulfide is partly dissolved in the electrolyte via reaction with silver sulfate, which is readily soluble in concentrated sulfuric acid, to give double compounds $nAg_2S \cdot Ag_2SO_4$, where n = 1–3. At n = 3, the compound precipitates and is mixed with peeled-off cathodic silver.

By gradual dilution of sulfuric acid, it was found that, at its concentration $c \le 85$ wt %, electrolysis of silver proceeds without any change in the color of the electrolyte, with white deposit of silver formed at the cathode. The mass of the cathodic silver corresponds to the mass of silver dissolved at the anode. The cathodic silver contains no Ag_2S impurity, i.e., reaction (4) does not occur. All the subsequent studies were performed with 84–85% H_2SO_4.

It is inappropriate to use glassy carbon, which is an excellent catalyst for reduction of H_2SO_4, as cathode material in electrolysis of silver. To select a cathode material, plates of Cr18Ni9Ti stainless steel, St.3 steel, and silver were tested. The best result was obtained with metallic silver: a dense layer of finely crystalline silver was formed on the cathode. With St.3 steel used as the cathode material, silver cementation occurred on the steel surface, with simultaneous formation of iron sulfate, which is insoluble in H_2SO_4 of the given concentration and results in that the cathode silver has the form of a very loose, readily peeling layer. In the case of stainless steel, silver cementation also occurred, but a rather dense layer of cathodic silver was formed in the course of electrolysis. The stainless steel cathode is nearly as good as that made of metallic silver. The disadvantages of this cathode are the partial consumption of Ag_2SO_4 dissolved in sulfuric acid and the possible contamination of the electrolyte with iron and alloying components.

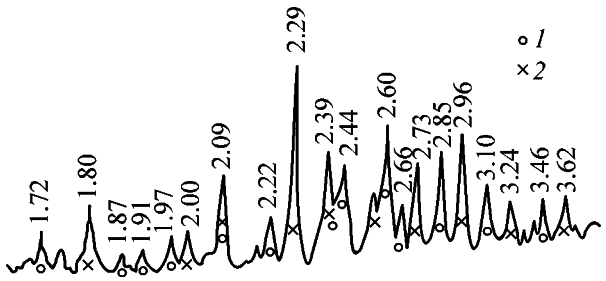

Fig. 1. X-ray diffraction pattern of the black product obtained in electrolysis of silver in concentrated H_2SO_4: (*1*) Ag_2S and (*2*) $Ag_8S_3SO_4$.

With a stainless steel cathode and silver anode, the optimal conditions of silver electrolysis in 84% H_2SO_4 were determined. The intensity of electrolysis was evaluated by the current flowing through the electrolyte. Figure 2a shows the current as a function of the Ag_2SO_4 content in the electrolyte at a working voltage of 1.5 V and electrolyte temperature of 40°C. It was found that a loose, X-ray amorphous deposit of silver is formed at an Ag_2SO_4 concentration of 15 g l^{-1}, and a dense finely crystalline deposit of silver, at 30 g l^{-1}. At Ag_2SO_4 concentration of 40 g l^{-1}, the current is lower and, on cooling the electrolyte to room temperature, Ag_2SO_4 partly precipitates. The recommended Ag_2SO_4 concentration in the electrolyte is 30 ± 5 g l^{-1}.

The dependence of the electrolysis intensity on the electrolyte temperature was studied at a working voltage of 1.5 V and Ag_2SO_4 concentration in the electrolyte of 30 g l^{-1}. It was found that electrolysis virtually does not occur at all at room temperature, since the current strength is 0.05–0.06 A. The plot of the current strength vs. the electrolyte temperature has an inflection point at 40°C (Fig. 2b). Taking into account

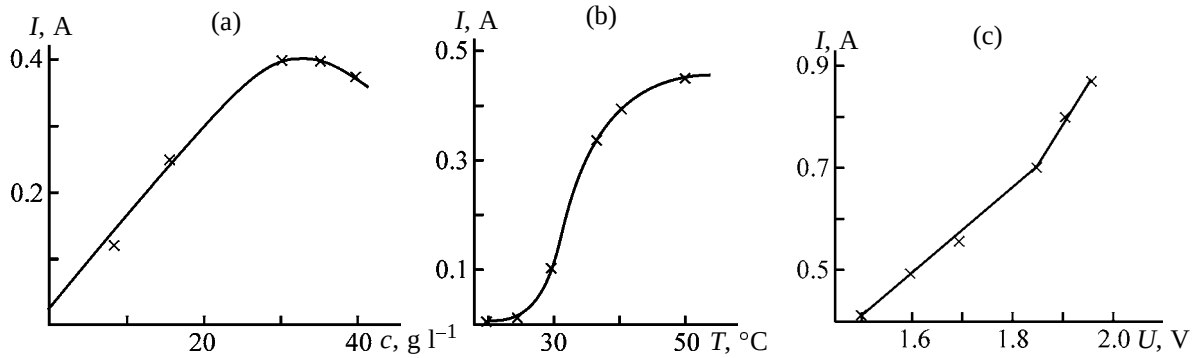

Fig. 2. Current strength I vs. (a) Ag_2SO_4 concentration c in the electrolyte, (b) electrolyte temperature T, and (c) initial voltage U.

the fact that the probability of reaction between the cathodic silver and H_2SO_4 increases with temperature, the optimal electrolyte temperature was taken to be 40 ± 5°C.

The dependence of the electrolysis intensity on the working voltage was studied at the optimal electrolyte temperature and Ag_2SO_4 content (Fig. 2c). As the voltage increases from 1.5 to 1.85 V, the dc current grows proportionally, and at 1.9 V the current starts to rise more steeply and gas evolution begins at the cathode and anode. This can be attributed to electrochemical decomposition of water at voltages of 1.9 V and higher. Consequently, the working voltage should not exceed 1.85 V.

The silver-containing electronic scrap is composed of various articles with silver coatings on copper, brass, bronze, aluminum alloys, and stainless steel. A study of the behavior of these materials as an anode yielded the following results. On submerging a copper plate in the electrolyte, silver cementation occurs. On switching on the voltage, the current increases stepwise to 0.2 A and then, after 10–15 s, falls to zero. This can be accounted for by the anodic dissolution of cemented silver, which terminates when the plate is completely coated with a thin layer of copper sulfate, which is insoluble in the electrolyte. With brass and bronze, the process occurs in a similar way. In the case of stainless steel, its surface is also coated with a protective layer, whose composition was not determined. With plates of aluminum alloys, there is no silver cementation and the current is zero on applying voltage to the cell, since the surface of these alloys is coated with a protective film of aluminum oxide from the very beginning.

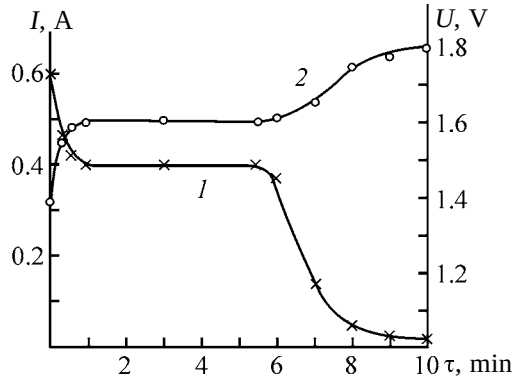

Fig. 3. (*1*) Current I and (*2*) working voltage U vs. electrolysis duration τ.

Since some of silver-plated articles are partly coated with POS 61 solder, its behavior in electrolysis was also studied. For this purpose, a copper plate was completely coated with the solder. On submerging this plate in the electrolyte, there is no silver cementation, and, on switching on the voltage, the current is zero. A similar result was obtained with Sn and Pb plates. This means that the surface of the solder, Sn, and Pb is coated with protective films of the corresponding oxides.

Thus, the presence of Cu, Sn, Pb, Fe, and Al has no effect on the electrolysis of silver, since these metals are passivated.

In studying the electrochemical recovery of silver from silver coatings, the articles to be processed, suspended on a copper wire, were used as the anode. The voltage across the power supply terminals was 1.8 V under no-load conditions. Figure 3 shows typical dependences of the current and working voltage on electrolysis duration. It is noteworthy here that the current rises steeply and the voltage falls on closing the electric circuit. Then, during 1 min, the current decreases and the voltage increases somewhat and remains constant until the article surface starts to be freed of the silver coating. After that, the voltage starts to increase, and the current, to decrease steeply. The electrolysis was terminated when the current reached a value of 0.01 A. The articles were with-

Process conditions and results obtained in electrolysis of silver coatings*

Substrate material	Ag content in articles, wt %	Charge mass, kg	Current, A		τ, h	Mass of cathodic Ag, g	Ag recovery, %
			initial	final			
Copper	0.65	2.985	12.2	0.1	0.81	9.25	99.2
Brass	1.18	2.740	11.8	0.1	1.4	32.00	99.0
Aluminum alloy	1.4	1.434	8.1	0.1	1.25	19.9	99.1
Stainless steel	0.73	1.370	8.5	0.1	0.6	9.89	98.9

* Article surface after electrolysis shows no traces of silver coating and no signs of corrosion.

drawn from the electrolyte, washed with water, and dried in air. An inspection with an MBS-1 microscope (25 × magnification) revealed that the silver coating was completely removed and there were no indications of corrosion on the article surface. The cathodic silver was easily detached from the cathode. The studies performed demonstrated that, with the parameters chosen, electrolysis provides selective dissolution of the silver coating, with simultaneous deposition of metallic silver from the electrolyte at the cathode.

Semicommercial tests of the electrochemical recovery of silver from silver coatings were carried out on an electrolyzer shown schematically in Fig. 4. The electrolyzer casing, which is a metallic (Cr18Ni9Ti stainless steel) tank 180 mm in diameter and 260 mm high, served as the cathode. Silver-plated articles, taken in amount of 1–3 kg, were placed in the anode basket suspended within the casing on a copper rod. As the anode basket served a fluoroplastic vessel 115 mm in diameter and 155 mm high. The cylindrical surface and the bottom of the vessel were perforated (aperture diameter 10 mm) so that the openings occupied 75–80% of the surface. The silver obtained was scraped off the cathode and separated from the electrolyte by decanting and then by centrifuging on a TsLS-3 centrifuge. The results listed in the table demonstrate that the duration of electrolysis is 0.6–1.4 h, depending on the type and amount of the charge with articles; silver coatings are anodically dissolved completely and selectively, which is indicated by their total absence on the article surface after electrolysis; the whole amount of silver dissolved is deposited at the cathode, which is confirmed by the 99% recovery of silver into the final product. It was found that the silver powder obtained is composed of metallic silver with purity of 99.9 wt % and impurity content (wt %): Cu 0.03, Sn 0.01, Pb 0.01, Fe 0.006, and Al 0.02.

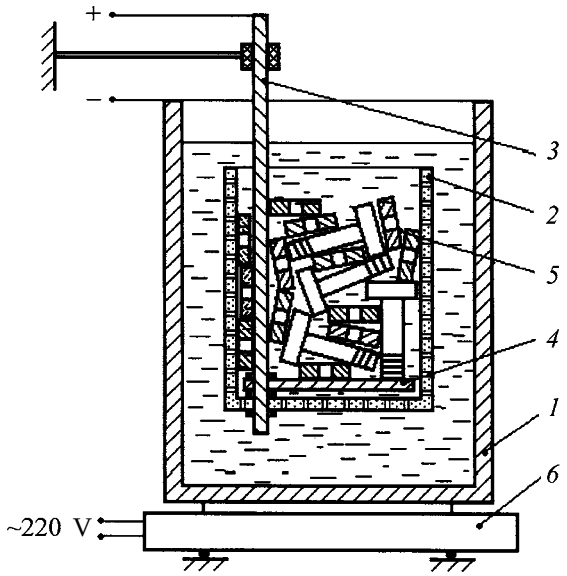

Fig. 4. Scheme of the electrolyzer: (*1*) casing-cathode, (*2*) fluoroplastic anode basket, (*3*) copper rod, (*4*) copper current-leading disc, (*5*) silver-containing scrap, and (*6*) electric hot plate.

CONCLUSIONS

(1) A study of silver electrolysis in sulfuric acid with concentration of 95 wt % and addition of 40 g l^{-1} Ag_2SO_4 at electrolyte temperature of 40°C demonstrated that the electrolysis proceeds with metallic silver and Ag_2S deposited at the cathode.

(2) It was shown that Ag_2S is not formed at the cathode at sulfuric acid concentrations $c \le 85$ wt %.

(3) The optimal silver electrolysis conditions in sulfuric acid with concentration of 84–85 wt % were determined: Ag_2SO_4 content in the electrolyte 30 ± 5 g l^{-1}, initial voltage 1.85 V, and electrolyte temperature 40°C.

(4) It was established that Cu, Sn, Pb, Fe, and Al are passivated under these conditions at the anode

because of the formation on their surface of protective films composed of the corresponding sulfates or oxides.

(5) Semicommercial tests of the method suggested for electrochemical recovery of silver from silver coatings on copper, brass, aluminum, and steel articles were carried out. Metallic silver with 99.9 wt % purity was obtained with the average degree of recovery of 99.0%.

REFERENCES

1. Baimakov, Yu.V. and Zhurin, A.I., *Elektroliz v gidrometallurgii* (Electrolysis in Hydrometallurgy), Moscow: Metallurgizdat, 1962.
2. Gaidarenko, O.V., Drobot, D.V., and Chernyshev, V.I., *Izv. Vyssh. Uchebn. Zaved., Tsvetn. Metall.*, 1997, no. 4, pp. 18–22.
3. US Patent 3788958.
4. German Patent 19718923.

Russian Journal of Applied Chemistry, Vol. 77, No. 1, 2004, pp. 67–70. Translated from Zhurnal Prikladnoi Khimii, Vol. 77, No. 1, 2004, pp. 70–74.

APPLIED ELECTROCHEMISTRY AND CORROSION PROTECTION OF METALS

Gas Evolution and Absorption in a Sealed Nickel–Zinc Battery with Nickel Oxide Electrode Fabricated from Spherical Nickel Hydroxide

Z. P. Arkhangel'skaya, M. M. Loginova, T. B. Kas'yan, and D. A. Vinogradova

Rigel' Battery Company, Open Joint-Stock Company, St. Petersburg, Russia

Received July 22, 2003

Abstract—The range of variation of the barometric parameters of a sealed nickel–zinc battery with nickel oxide electrode made of spherical nickel hydroxide was studied under the conditions of cycling and exposure in charged and discharged states.

Interdependent functioning of nickel oxide (NOE) and zinc electrodes in a nickel–zinc (NZ) system is complicated by the oxygen and hydrogen evolution occurring on the electrodes, when their potentials are in the region of thermodynamic instability of water. Unbalance of main and side processes on the counter-electrodes leads to unbalance between the degrees of their charging. The balance can be maintained for a long time only in a sealed battery owing to efficient methods of recombination of released gases.

Formation of a sealed nickel–zinc (SNZ) battery is based on positive results achieved in study and exploitation of sealed nickel–cadmium (SNC) and sealed lead–acid (SLA) batteries. The most efficient method of the recombination of accumulating gases in NZ battery, which has found practical application, involves the ionization of oxygen on the zinc electrode and the oxidation of hydrogen on the NOE [1].

Presently, SNZ batteries based on this principle use a porous zinc electrode with gauze or a foamed-metal support and a metal-ceramic nickel oxide electrode (MC NOE), which ensure insignificant gas evolution and necessary gas recombination.

The oxygen ionization in chemical alkaline power sources is well studied for the case of a sealed nickel–cadmium battery. It was established in [2, 3] that the rate of the electrochemical recovery of oxygen on the cadmium electrode reaches 5–8 mA cm^{-2}. At limited rate of its delivery into the pores of cadmium electrode, this process is diffusion-controlled. The most important result of these works is a conclusion that the ionization current can be increased considerably by creating conditions for displacement of a part of electrolyte from the electrode pores under the pressure of gas penetrating through separator pores.

The rate of the oxygen ionization on zinc (0.1–0.2 mA cm^{-2}) [4] is less than that on cadmium. A study of the current variations on a half-immersed electrode showed that the dependences typical of diffusion mode are not implemented on the zinc electrode. Apparently, the process occurs by the mixed mechanism.

The conditions of gas delivery to the counterelectrode are more complex in SNZ battery than in SNC battery, which apply microporous separators to impede growth of zinc dendrites. At the same time, though the rate of oxygen ionization on the zinc electrode is low, the balance between the evolved and absorbed oxygen at a low internal gas pressure can be ensured during each cycle (charging, pause, discharge, and pause) by optimizing the battery design and applying efficient charging methods [5]. In this case, in batteries with MC NOE, 60–70% of oxygen is absorbed during charging, and the rest, during the subsequent periods of a cycle.

The interaction of hydrogen with NOE was mainly studied in a nickel–hydrogen battery and at a pressure higher than that in SNZ battery. The voltammetric method was used to show that hydrogen is oxidized at a marked rate only on the charged NOE, whereas on the discharged NOE the oxidation rate is virtually zero [6].

A study of the dynamics of hydrogen accumulation in the SNZ battery showed that the pressure can be stabilized depending on the ratio of the rates of its evolution on the zinc electrode and absorption upon

1070-4272/04/7701-0067 © 2004 MAIK "Nauka/Interperiodica"

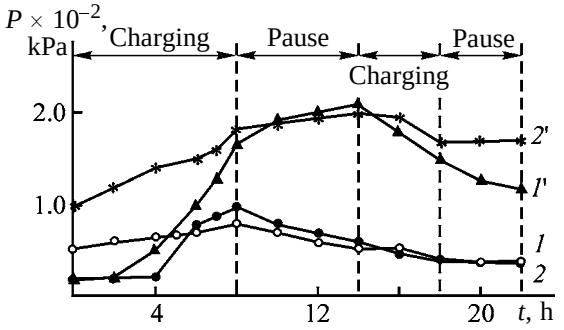

Fig. 1. Variation of the gas pressure P in sealed NTs-25 batteries of types (*1*, *2*) I and (*1'*, *2'*) II during cycling. (t) Time; the same for Figs. 2–4. (*1*, *2*; *1'*, *2'*) successive cycles for types I and II, respectively.

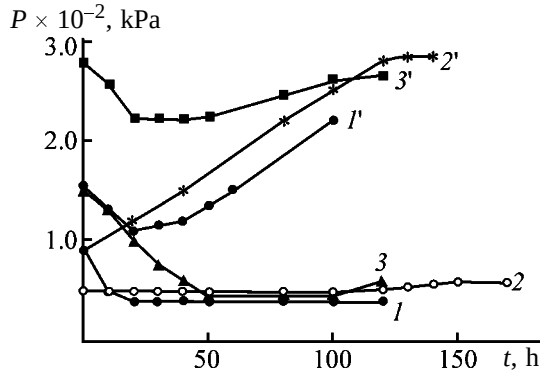

Fig. 2. Variation of the gas pressure P in sealed NTs-25 batteries of types (*1–3*) I and (*1'–3'*) II, when (*1*, *1'*) charged, (*2*, *2'*) discharged, and (*3*, *3'*) charged again.

interaction with NOE [7]. With hydrogen pressure in the gas volume of the battery increased from 1×10^2 to 2.5×10^2 kPa, the rate of its oxidation on the MC NOE increased by a factor of more than 3, in fundamental agreement with the conclusions of [2, 3].

In view of recent development of new materials such as spherical nickel hydroxide and foamed metal supports, it seemed appropriate to use the compacted electrodes fabricated from these materials in NZ batteries [8].

EXPERIMENTAL

To determine the internal pressure appearing in using such electrodes, we studied in this work the gas absorption and evolution in a sealed NTs-25 nickel–zinc battery, in which NOE on foamed nickel (FN) support was used instead of MC NOE. The battery design, including electrode thickness, zinc electrodes, number of electrodes, set of separators, and electrolyte volume, was the same as in a battery with MC NOE. The electrolyte used had the volume V = 90 cm^3 and contained (M) KOH 7 and LiOH 1. At the same time, because the active paste of the FN-supported NOE was denser, the ratio of theoretical capacities of the negative and positive electrodes in a battery with FN-supported NOE was 2.2 : 1 instead of a 3 : 1 ratio in a battery with MC NOE (theoretical capacity of negative and positive electrodes is 112 and 50 A h, respectively).

We studied two types of NTs-25 batteries containing different corrosion inhibitors: 1% HgO and 0.25% PbO (type I) and 2% CdO and 1% PbO (type II).

The batteries were formed during two cycles in the modes recommended in [9]. The discharge capacity imparted in the first and the second cycles was 18 and 35–36 A·h, respectively, and the coefficient of utilization of the active paste was 54–58%. Later on, manometers or valves with an opening pressure of 2×10^2 kPa were mounted on the cycled batteries. The charging capacity was 26–24.5 A h, which corresponds to the rated capacity of sealed NTs-25 battery with MC NOE. The discharge was done with a current of 0.2C = 5 A and sometimes with a current of 1C = 25 A (C is rated capacity).

The obtained data on the barometric parameters of the sealed NTs-25 batteries were recalculated to the volumes of evolved and absorbed gases, based on the internal gas volume of the battery (80 cm^3). The proportions of oxygen and hydrogen were determined from pressure drops in various periods of the cycle using previously obtained data on hydrogen evolution on the zinc electrode in batteries with MC NOE having the same negative electrodes and containing the same corrosion inhibitors [4, 7].

The peculiar features of the processes in the batteries studied can be judged from variations of the gas pressure in them in cycling (Fig. 1) and during the pauses (Fig. 2).

The barometric data presented in Fig. 1 belong to the steady-state conditions, which are well reproduced from cycle to cycle. The value and character of pressure variations in batteries of types I and II differ essentially. This is associated with the different hydrogen evolution, because, except for the inhibitor composition in the zinc electrode, the oxygen evolution on the NOE and the conditions of oxygen absorption on the zinc electrode were the same in both cases.

In type I batteries containing the HgO and PbO additives, the pressure increases only slightly with charging and does not exceed a value of 1×10^2 kPa even when the subsequent charging is done in the intense mode with a current of 1.0C (Fig. 3). In this case, the gas evolution in the different cycles is 45–

Evolution and absorption of oxygen and hydrogen in sealed NTs-25 batteries during different periods of the cycle

Cycle period	Oxygen volume, cm^3			Hydrogen volume, cm^3					
	types I and II			type I			type II		
	evolved	absorbed	accumulated	evolved	absorbed	accumulated	evolved	absorbed	accumulated
Charging	80–120	40–70	40–60	15–25	–	–	80–100	–	–
Pause		30–35	–		10–15	–	60–80	–	–
Discharge		15–20	–		5–10	–	–	40–70	–
Pause		5–10	0		0–5	0	–	0–5	80–100

70 cm^3, including 15–25 cm^3 of hydrogen (see table). The oxygen evolution in charging (80–100 cm^3) minus the oxygen absorption during this period (50–60%) is less by 20–25% than gas evolution in a battery with MC NOE charged under the similar conditions [5]. In the subsequent periods of each cycle, including pause, discharge, and pause, the oxygen is ionized virtually completely, which is confirmed by the gas analysis.

Hydrogen released in charging is absorbed during the time of residence of the battery without current (pause) and during the discharge, but absorption is incomplete. Its residual pressure (of about 0.4×10^2 kPa) corresponds to a value established when batteries of this type reside without current in both charged and discharged states (Fig. 2).

The hydrogen accumulation in charging is larger by a factor of 4–5 in the type II batteries containing CdO and PbO than in the type I batteries (see table, Fig. 1). Figure 1 shows that the hydrogen evolution also increases during the pause between charging and discharge, since the gas evolution in the course of this period exceeds the volume of ionizing oxygen. This result is also consistent with the data of Fig. 2.

A main decrease in the hydrogen pressure, considerably dependent on its value in the battery, occurs in the course of discharge. The gas pressure increases from cycle to cycle to a constant value, with the maximum pressure established within $(2.7–2.8) \times 10^2$ kPa (Fig. 4). This corresponds to a value established in this type of batteries without current in both charged and discharged states (Fig. 2).

Thus, the value of the maximum pressure in a cycled SNZ battery is determined by hydrogen accumulation, which depends on the efficiency of inhibitors in the zinc electrode and on the structure of active paste of NOE, which determines the surface area accessible to hydrogen oxidation.

The effect of the NOE structure on hydrogen recombination can be estimated by comparing the character of pressure variations in cycling for sealed NTs-25 battery of type I and for batteries with MC NOE and a zinc electrode containing the same inhibitors (1% HgO and 0.25% PbO) (Fig. 5). Whereas in the type I battery studied here the pressure initially increases, then decreases to a value of 1×10^2 kPa after cycling for a short time, and then varies within $(1–0.4) \times 10^2$, in a battery with MC NOE both the maximal and the final (minimal) pressures increase gradually to a constant value of $(2.3–2.7) \times 10^2$ kPa to the 50–60th cycle.

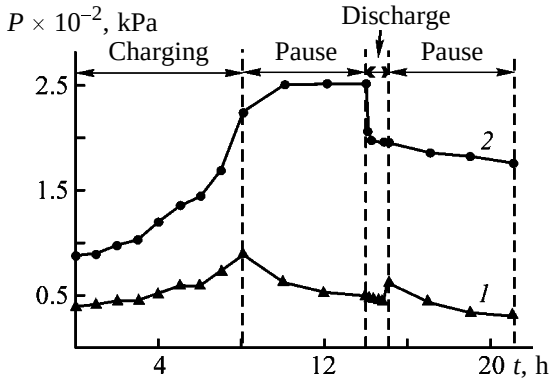

Fig. 3. Variation of the gas pressure P in sealed NTs-25 batteries of types (*1*) I and (*2*) II during cycling at the discharge current of 1.0*C*.

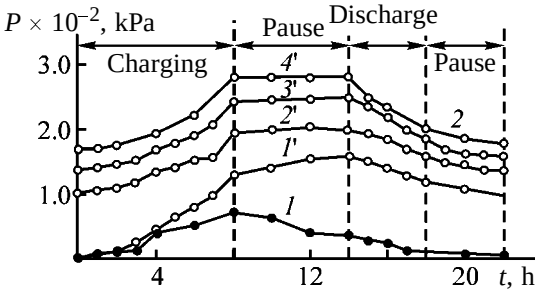

Fig. 4. Variation of the gas pressure P in sealed NTs-25 batteries of type II in succesive cycles (*1'*–*4'*), as compared to the type I battery (*1*).

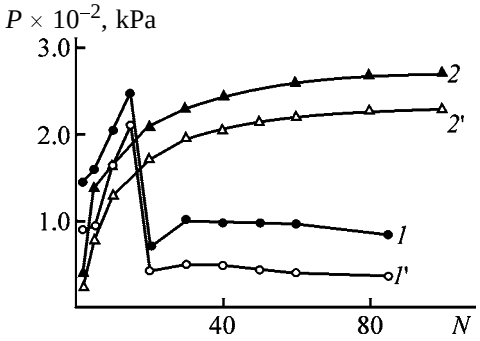

Fig. 5. Variation of the (*1*, *2*) maximal and (*1'*, *2'*) minimal gas pressures in the sealed NTs-25 type I batteries (*1*, *1'*) with NOE on FN support and (*2*, *2'*) with MC NOE electrode during cycling. (*P*) Pressure and (*N*) number of cycles.

The pressure increase in the start of cycling of a battery with MC NOE is associated with insufficient value of the internal surface area of those gas sections of a dosed NOE which are accessible to hydrogen oxidation. As the gas pressure increases, the displacement of electrolyte from the MC NOE, which has the gradual porometric characteristic, is observed starting from coarser pores. As a result, the NOE reveals the properties of a self-dosing electrode. In this period, the rate of the hydrogen oxidation increases and at a certain pressure reaches the evolution rate.

In the NOE with an FN support, unlike MC NOE, small closed pores formed in compacting 1–10-μm spherical particles prevail. The displacement of the electrolyte from these pores is made difficult, especially in the initial cycles, while the electrode surface after compaction is smooth. Therefore, the battery pressure increases stepwise during several cycles, reaches a value of 2×10^2 kPa, at which a valve opens, and after 20 cycles, as active paste becomes loosened, decreases to a constant value, depending on the rate of hydrogen evolution, which is determined by the performance of the corrosion inhibitor in the zinc electrode.

With hydrogen evolution as large as 2–3 cm^3 per 1 A h during one cycle, most of hydrogen can recombine. Apparently, the residual amount giving a pressure of $(0.4-0.6) \times 10^2$ kPa corresponds to the equilibrium concentration established in a contact with nickel(III) hydroxide without current.

If corrosion inhibitors are less efficient (as in type II batteries), only a part of hydrogen, released during the cycle in an amount of 5–8 cm^3 per A h, recombines, and hydrogen accumulates in the battery. In this case, the pressure increase associated with the specificity of NOE structure is sharper than in the battery with MC NOE (Figs. 4, 5). The pressure stabilizes in the range $(2.2–2.7) \times 10^2$ kPa, which corresponds to the steady-state value for the open-circuit state of the discharged or charged battery (Fig. 2).

CONCLUSIONS

(1) A sealed nickel–zinc battery with a nickel oxide electrode fabricated from spherical nickel hydroxide on a foamed nickel support has the barometric parameters dependent on the performance of corrosion inhibitors in the zinc electrode.

(2) The oxygen evolution in charging is 4–5 cm^3 per 1 A h of rated capacity, of which about 60% is absorbed during charging and the rest, during the cycle (discharge and pause). The maximum value of the oxygen pressure does not exceed 1×10^2 kPa. At hydrogen evolution as large as 2–3 cm^3 per 1 A h during one cycle, most of it is absorbed at the total gas pressure varied within $(1.2–0.4) \times 10^2$ kPa. At larger hydrogen evolutions, the pressure increases to a constant value of $(2.3–2.8) \times 10^2$ kPa, at which a battery with nickel oxide electrode passes from the dosed state to the self-dosing state.

REFERENCES

1. Zdyrenkova, T.V., Arkhangel'skaya, Z.P., and Reshetova, G.N., *Issledovaniya v oblasti elektricheskikh akkumulyatorov* (Studies of Electrical Batteries), Leningrad: Energoatomizdat, 1988.
2. Khomskaya, E.A., Kolosov, A.S., Terent'ev, N.K., and Burdanova N.F., *Elektrokhimiya*, 1976, vol. 12, no. 8, pp. 1241–1244.
3. Mokhnatkin, V.M., Khomskaya, E.A., Chirkov, Yu.G., and Pesenson, M.Z., *Elektrokhimiya*, 1979, vol. 15, no. 12, pp. 1807–1812.
4. Zdyrenkova, T.V., Arkhangel'skaya, Z.P., and Mordakov, S.V., *Issledovaniya v oblasti tekhnologii proizvodstva KhIT* (Studies of Processes for Production of Chemical Power Sources), Leningrad: Energoatomizdat, 1986, pp. 72–82.
5. Alekseeva, M.E., Arkhangel'skaya, Z.P., Ivanova, R.P., *et al.*, *Zh. Prikl. Khim.*, 1995, vol. 68, no. 9, pp. 1492–1497.
6. Tsenter, B.I., and Lyzlov, N.Yu., *Metallovodorodnye elektrokhimicheskie sistemy* (Metal–Hydrogen Electrochemical Systems), Leningrad: Khimiya, 1989.
7. Alekseeva, M.E., Arkhangel'skaya, Z.P., Ivanova, R.P., *et al.*, *Zh. Prikl. Khim.*, 1995, vol. 68, no. 9, pp. 1487–1491.
8. Arkhangel'skaya, Z.P., Kas'yan, T.B., Loginova, M.M., and Raikhel'son, L.B., *Zh. Prikl. Khim.*, 2003, vol. 76, no. 6, pp. 953–958.
9. Arkhangel'skaya, Z.P., Kas'yan, T.B., Loginova, M.M., and Raikhel'son, L.B., *Zh. Prikl. Khim.*, 2003, vol. 76, no. 12, pp. 1981–1986.

Russian Journal of Applied Chemistry, Vol. 77, No. 1, 2004, pp. 71–73. Translated from Zhurnal Prikladnoi Khimii, Vol. 77, No. 1, 2004, pp. 75–77.

APPLIED ELECTROCHEMISTRY AND CORROSION PROTECTION OF METALS

Electrolytic Deposition of Molybdenum Oxide from Aqueous Solutions at Room Temperature

V. M. Nagirnyi, R. D. Apostolova, A. S. Baskevich, and E. M. Shembel'

Ukrainian State University of Chemical Engineering, Dnepropetrovsk, Ukraine

Received April 24, 2003

Abstract—The conditions of electrolytic deposition of molybdenum oxide from aqueous solutions at room temperature were studied and the optimal parameters of electrolysis, which provide deposits with necessary physical and structural characteristics, were chosen.

Previously, we demonstrated the possibility of synthesizing molybdenum oxide quantitatively with rather high current efficiency by cathodic deposition from aqueous solutions of ammonium molybdate $(NH_4)_6Mo_7O_{24}\cdot 4H_2O$ at 80–85°C [1]. The deposits obtained, which were tested in a secondary lithium cell in the form of ballast-free and composite ("pasted") cathodes, were distinguished by satisfactory discharge characteristics and cyclability, which indicates that the materials obtained by the method under consideration are promising [2]. However, the issues concerning the electrolytic deposition of molybdenum oxide from an aqueous solution of its salt at low temperature, i.e., under common electrolysis conditions, remained unconsidered. The low-temperature conditions are rather attractive, as considerably simplifying the electrolysis.

Here we report the results of studies in this area. We found no data of this kind in the literature. The electrochemical characteristics of the materials in question, which are an independent issue, were beyond the scope of this study.

The investigation was performed using the procedure described in [1]. As object of the study we used 0.005, 0.01, 0.02, 0.04, and 0.08 M $(NH_4)_6Mo_7O_{24}\cdot 4H_2O$ solutions with pH 6.0 and 9.0. All the experiments were conducted at 22 ± 2°C. The efficiency of the cathodic process was evaluated by the conditional current efficiency (CE_{cond}) calculated with account of the results of X-ray diffraction analysis. According to these data, the phase composition of the deposits is mostly described by the formula of nonstoichiometric molybdenum oxide $Mo_4O_{11}\cdot nH_2O$, which contains 2.75 atoms of oxygen per atom of molybdenum, i.e., is an intermediate oxide compound between the pentavalent, Mo_2O_5, and hexavalent, MoO_3, molybdenum oxides. To a first approximation, it can be regarded as doubled molybdenum pentoxide $2Mo_2O_5$ in which the atoms of molybdenum and oxygen are structurally bound in the above ratio. The reaction of Mo_2O_5 formation at the cathode can be represented as

$$2MoO_4^{2-} + 6H^+ + 2e \rightarrow Mo_2O_5 + 3H_2O.$$

Hence,

$$E = [Mo_2O_5]/2\times 26.8 = 272/2\times 26.8 = 5.07\ \text{g (A h)}^{-1}.$$

Since dehydration at 250°C for 7–10 h affects the weight of the deposits only slightly, compared with the initial weight after electrolysis (0.15–0.2 mg per 2.0–2.5 mg of deposit), the water component was disregarded, which is quite acceptable for CE_{cond} calculation.

The CE_{cond}–I_c dependences are shown in Fig. 1 for different ammonium molybdate concentrations and solution pH values. The dependences exhibit extrema at the points corresponding to current densities of 2.5 and 2.0 mA cm^{-2}, respectively, for the solutions with pH 6.5 and 9.0. The conditional current efficiency grows with the concentration of ammonium molybdate in solution increasing from 0.005 to 0.02 M and markedly decreases in solutions with higher concentrations (Fig. 1, curves *1*–*5* and *1*', *3*', and *5*' for pH 6.5 and 9.0, respectively). All the curves are characterized by descending portions gradually falling to a certain minimum value, which depends only slightly on the current density, with the corresponding portions of the curves nearly merging together for solutions with concentrations higher than 0.01 M (pH 6.5). The same behavior is observed for the dependences of the limiting values of CE_{cond} on the solution concentration at different pH values, shown in Fig. 2.

1070-4272/04/7701-0071 © 2004 MAIK "Nauka/Interperiodica"

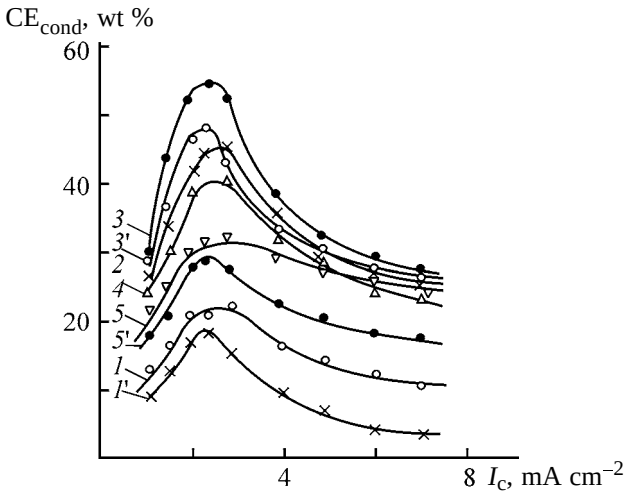

Fig. 1. Conditional current efficiency CE_{cond} by moybdenum oxide vs. the current density I_c in electrolysis of $(NH_4)_6Mo_7O_{24}\cdot 4H_2O$ solutions at 20°C. Solution concentration, M: (*1*, *1*') 0.005, (*2*) 0.01, (*3*, *3*') 0.02, (*4*) 0.04, and (*5*, *5*') 0.08. pH: (*1*–*5*) 6.5 and (*1*', *3*', *5*') 9.0.

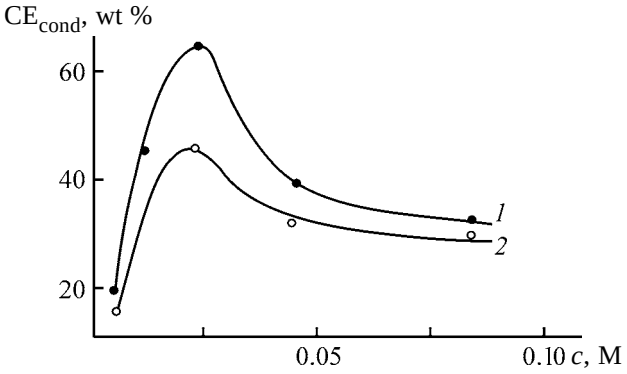

Fig. 2. Maximal value of the conditional current efficiency CE_{cond} vs. the solution concentration c at 20°C. pH: (*1*) 6.5 and (*2*) 9.0. I_c, mA cm^{-2}: (*1*) 2.5 and (*2*) 2.0.

Thus, the shape and relative positions of the curves are largely determined by the concentration and pH value of the solutions used. The rise in CE_{cond} with increasing solution concentration at its relatively low values (0.005–0.02 M) is due to enhanced diffusion of molybdate ions toward the cathode and higher hydrogen overvoltage. This overvoltage is lower in solutions with higher pH (9.0), in agreement with the data of [3]. This results in the corresponding increase in the rate of hydrogen evolution and lowering of the CE_{cond} by the cathode deposit, which to a certain extent accounts for the fact that the CE_{cond} decreases at high ammonium molybdate concentrations in solution ($\geq$0.04 M) (Figs. 1, 2). Apparently, the parallel rise in the concentration of ammonium ions in solution is responsible for their accumulation in the near-cathode layer and to its corresponding alkalization, which, in the end, results in leading acceleration of the hydrogen evolution. As for the equalization of the values of CE_{cond} at high current densities and their coincidence for the solutions with high ammonium molybdate concentration (pH 6.5), this is presumably due to the attainment of close, and independent of electrolysis parameters, ratios of the rates of hydrogen evolution and cathodic deposit formation.

The data presented are in satisfactory agreement with the current–voltage characteristics of the process under study (Fig. 3). The overall I_c–E dependences have the form of steeply ascending branches of a concave parabola, whose position with respect to the cathode potentials depends on the concentration and pH value of the solution and the type of substrate. At the same pH values, the cathodic polarization markedly increases as the salt concentration in solution becomes lower (Fig. 3, curves *1* and *2*). Correspondingly, at the same concentration and pH of the solution, the potential on the cathode surface preliminarily coated with a solid oxide layer is considerably higher than that of the initial steel surface (Fig. 3, curves *1*, *1*' and *3*, *3*'). Raising the solution pH (all other conditions being the same) leads to a decrease in the cathodic polarization of the initial surface of the stainless steel support and, contrariwise, to an increase in the polarization of the surface preliminarily coated with an oxide layer (Fig. 3, curves *1*, *3* and *1*', *3*').

Comparison of the overall and partial curves of cathodic deposit formation and hydrogen evolution (Fig. 3, curves *1*" and *1*'") shows that hydrogen evolution is the potential-determining process in the overall cathodic process. This is also indicated by the run of the partial curve of oxide deposition. This curve reaches the limiting plateau, which is independent of the cathode potential, at relatively low current densities. This results in that, with increasing polarizing current, the relative rates of oxide deposition and hydrogen evolution change continuously in favor of the latter, which also follows from the CE_{cond}–I_c dependences considered above. Hence, the lower the overvoltage and the higher the rate of hydrogen evolution, the lesser the extent of polarization of the cathodic process. For example, the hydrogen overvoltage on the initial surface of the cathode is relatively low and the corresponding overall curves are arranged in the order of decreasing cathode potentials for processes with higher hydrogen evolution rates. This is clearly seen when curves for solutions with higher and lower pH values and salt concentrations are compared (Fig. 3, curves *3* and *1*, and *1* and *2*). These curves are characterized by higher current efficiency by hydrogen in the former case. On a surface preliminarily coated

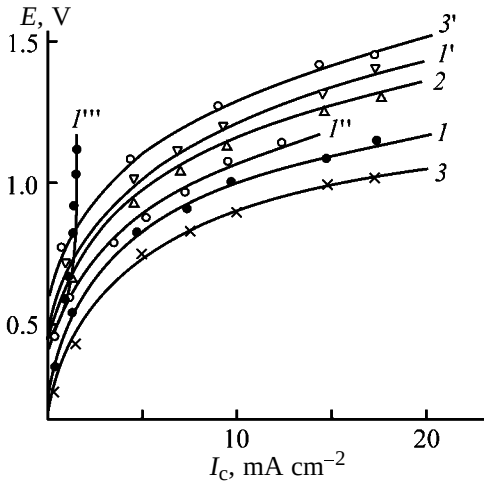

Fig. 3. Cathode potential E vs. the current density I_c in electrolysis of $(NH_4)_6Mo_7O_{24}\cdot 4H_2O$ solutions at 20°C. Cathode: 12Cr18Ni9Ti steel. Solution concentration, M: (*1*, *1*', *1*'', *1*''') 0.04 [(*1*') on a film of molybdenum oxide; (*1*'', *1*''') partial curves of hydrogen evolution and molybdenum oxide deposition, respectively], (*2*) 0.02, and (*3*, *3*') 0.04 [(*3*') on a film of molybdenum oxide]. pH: (*1*, *1*', *1*'', *1*''', *2*) 6.5 and (*3*, *3*') 9.0.

with a solid molybdenum oxide layer, the hydrogen overvoltage increases substantially, which leads to an adequate enhancement of the cathodic polarization (Fig. 3, curves *1*, *1*' and *3*, *3*').

Nearly irrespective of the electrolysis conditions, the resulting molybdenum oxide deposits are obtained on the smooth surface of a stainless steel support as compact semilustrous black coatings with bluish tint, without any deviations in the external appearance. Oxide coatings up to 25 μm thick, dried at room temperature, exhibit satisfactory adhesion to the support surface and good mechanical stability (they sustain sample bending by 180° without cracking at the bending line). On being heated in air to 180–250°C, coatings thicker than 5–7 μm tend to undergo brittle failure and are easily removed when touched with hand. At the same time, thermal treatment at this temperature removes the crystallization water and makes more ordered the structure of the material, which may exert positive influence on its electrochemical characteristics. According to X-ray diffraction analysis, the phase composition of the deposits mainly corresponds to the formula Mo_4O_{11} with inclusions of the Mo_9O_{23} phase. On heating in air to above 60°C, the phase composition of the deposits changes fundamentally, with transition to single-phase MoO_3.

CONCLUSION

High-quality molybdenum oxide deposits are formed as compact uniform coatings up to 25 μm thick and more, exhibiting satisfactory mechanical stability and adhesion to the base, with sufficiently high current efficiency on a substrate made of 12Cr18Ni9Ti stainless steel from ammonium molybdate solutions with concentration of 0.005 to 0.08 M at 20±2°C, pH 6.5–9.0, and cathode current density of 1.5–7.5 mA cm^{-2}. Dispersed deposits may also be formed.

REFERENCES

1. Nagirnyi, V.M., Apostolova, R.D., Baskevich, A.S., *et al*., *Zh. Prikl. Khim*., 2000, vol. 73, no. 3, pp. 412–415.
2. Tysyachny, V., Shembel, E., Apostolova, R., *et al*., Abstracts of Papers, *53rd Annual Meet. of Int. Soc. of Electrochemists*, Dusseldorf, September 15–20, 2002, p. 326.
3. Frumkin, A.N., Bagotskii, V.S., Iofa, Z.A., and Kabanov, B.N., *Kinetika elektrodnykh protsessov* (Kinetics of Electrode Processes), Moscow: Mosk. Gos. Univ., 1952.

Russian Journal of Applied Chemistry, Vol. 77, No. 1, 2004, pp. 74–78. Translated from Zhurnal Prikladnoi Khimii, Vol. 77, No. 1, 2004, pp. 78–82.

ENVIRONMENTAL PROBLEMS OF CHEMISTRY AND TECHNOLOGY

Selective Recovery of Nonferrous Metal Cations from Wastewater with Weakly Basic Anion Exchangers

P. N. Chelnakova and V. A. Kolodyazhnyi

Obninsk State Technical University of Atomic Power Engineering, Obninsk, Kaluga oblast, Russia

Received February 13, 2003

Abstract—Selective recovery of transition metals (Ni^{2+}, Cu^{2+}, and Cr^{2+}) with weakly basic anion exchangers from aqueous solutions simulating naturally mineralized water was studied. The exchange capacity of anion exchangers for these cations was determined. The technique for efficient resin regeneration was developed.

Due to corrosion of construction materials of atomic reactors, the wastewater formed in operation of nuclear power plants can contain traces of radionuclides, in particular, radioactive isotopes of transition metals (Ni^{2+}, Co^{2+}, Cr^{3+}, etc.) [1, 2]. These low-level wastes (10^{-4}–10^{-5} Ci l^{-1}) must be concentrated to obtain small volumes of solid or liquid waste. The ionic contaminants can be efficiently removed and concentrated with ion-exchange resins, in particular, cation exchangers [3–5]. Ion exchangers were widely used also for neutralization of wastewater and wash waters from electroplating production, in which the metal content varies from tens to thousands of milligrams per liter [6–9]. However, in the presence of cations of natural mineralization (in particular, Na^+, K^+, Ca^{2+}, and Mg^{2+}), the exchange capacity of resins for target metals sharply decreases, and conditioning of regeneration solutions is hindered. Therefore, we must choose such ion exchanger which would allow selective recovery of the transition metals. The comparative analysis of the complexing power of resins was published in [10]. It was noted that anion exchangers containing electron-donor groups sorb cations of transition metals due to formation of coordination bonds.

In this work we examined the possibility of removal of transition metals from aqueous solution containing cations of natural mineralization with complexing anion exchangers. The main attention was given to the choice of such a resin that would have sufficiently high sorption capacity and could be regenerated with obtaining highly concentrated solution of the target metals (radionuclides), from which the target metals could be quantitatively recovered in the form of metals or their appropriate compounds.

EXPERIMENTAL

In our experiments, we used the model solutions prepared by dissolution of copper(II), nickel(II) and chromium(III) salts in distilled and tap water. The water hardness was varied from 4 to 6 mg-equiv l^{-1}. The metal concentration was varied from 50 to 2000 mg l^{-1}.

The metal ion content in solutions was determined spectrophotometrically on an SF-46 spectrophotometer. Before determination, the transition metal ions were converted into colored complexes with the following reagents: lead diethyldithiocarbamate for Cu^{2+}, diphenylcarbazide for Cr^{3+} (after preliminary conversion of Cr^{3+} into chromate anion), and dimethylglyoxime (in the presence of bromine as oxidant) for Ni^{2+} [11]. The water hardness was determined by complexometric titration [12]. The acidity of solutions was measured on an EV-74 ionometer.

The spent anion exchangers were regenerated by metal elution with 30–40% aqueous H_2SO_4. After removal of the metals, the anion exchangers were treated with alkali and then washed with water.

Under static conditions, the sorption experiments were carried as follows. A weighed sample of an anion exchanger was placed into a flask (250 ml), and an aqueous solution of a transition metal salt was added. This mixture was kept for 2–4 days at intermittent stirring. After the equilibrium was attained, the residual metal concentration was determined.

The sorption of transition metals under dynamic conditions was studied by passing of their model solutions through a column packed with the anion exchanger until the transition metal concentration be-

1070-4272/04/7701-0074 © 2004 MAIK "Nauka/Interperiodica"

Table 1. Sorption of Cu^{2+} and Ni^{2+} from model solutions.* c_0 = 100 mg l^{-1}, pH 5.5

Sorbent	Distilled water			Tap water		
	c_e, mg l^{-1}	g, mg-equiv g^{-1}	η, %	c_r, mg l^{-1}	g, mg-equiv g^{-1}	η, %
			Cu^{2+} cation			
AV-17	32.7	0.15	59	31.25	0.15	61.1
AN-31	16.98	0.20	79	12.66	0.21	84.2
AM-7	3.39	0.242	95	3.08	0.243	96.2
AN-221	2.48	0.245	97	2.74	0.245	96.5
			Ni^{2+} cation			
AV-17	94.34	0.0213	6.26	85.57	0.0185	6.01
AN-31	52.68	0.162	47.6	43.98	0.159	51.7
AM-7	35.98	0.219	64.2	25.78	0.221	71.7
AN-221	18.53	0.278	81.6	10.97	0.271	87.9

* c_0 is the Cu^{2+} and Ni^{2+} concentration in solution, c_e is the residual (equilibrium) Cu^{2+} and Ni^{2+} concentration, g is the sorption capacity, and η is the degree of metal recovery.

came equal at the inlet and outlet of the column. In these experiments, the height of the anion exchanger bed was 12.2 cm, and the volume of the swollen resin was 46.4 ml. The metal content in the eluate at the outlet of the column was determined at regular intervals.

In order to choose an anion exchanger ensuring both the selective sorption of the transition metals under consideration in the presence of salts of natural mineralization and the maximal sorption capacity for them, the sorption of the metals at their concentration of 100 mg l^{-1} was studied under static conditions. The results of these experiments are listed in Table 1.

The sorption capacity of the resin for metals g (mg-equiv g^{-1} of dry resin) was calculated by the equation

$$g = V(c_0 - c_e)/(Em), \quad (1)$$

where V is the sorbate volume (l), E is the metal mg-equivalent (31.75 and 29.5 mg for Cu^{2+} and Ni^{2+}, respectively), and m is the dry resin weight (g).

The degree of metal recovery η (%) was calculated by the equation

$$\eta = (c_0 - c_e)/c_0. \quad (2)$$

Among anion exchangers tested by us, the maximal sorption capacity for transition metals under consideration is exhibited by weakly basic AM-7 and AN-221 polyfunctional resins. These resins were used in all the experiments. We found that, under identical experimental conditions, Cr^{3+} cations are identically sorbed on both weakly and moderately basic anion exchangers. For example, in sorption of Cr^{3+} from its solutions in both distilled and tap water with the initial concentration $c_0(Cr^{3+})$ 250 mg l^{-1} on AM-7, AN-221, AN-31 resins, their sorption capacity was 0.9 mg-equiv g^{-1}. The strongly basic AV-17 anion exchanger does not noticeably sorb Cr^{3+}.

Table 1 shows that the salts of natural mineralization do not noticeably affect the sorption recovery of Ni^{2+} and Cu^{2+}. The degree of sorption of Cu^{2+} and Ni^{2+} on weakly basic resins reaches 97 and 88%, respectively. These data show that the resins tested ensure selective recovery of the transition metals concerned.

We believe that transition metal cations are sorbed on weakly basic anion exchangers by coordination of the electron-donor groups of the resin (–NH_2, =NH, and ≡N) with metal cations by the donor–acceptor mechanism [10]. Thus, in sorption of transition metals, the anion exchanger acts as macromolecular complexone:

$$\equiv N\colon + \square M^{n+} \longrightarrow \equiv N\colon M^{n+}.$$

In order to determine the maximal sorption capacity of the anion exchangers for metal cations, the sorption of the metals was studied as a function of their concentration. Aqueous solutions of the transition metals were prepared in both distilled and tap water. All the sorption experiments were carried out under static conditions. An accurately weighed sample of the anion exchanger was placed in an aqueous solution of the transition metal salt and kept for approximately

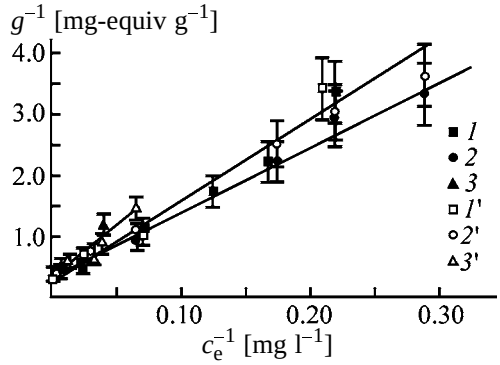

Fig. 1. Sorption of transition metal cations on weakly basic anion exchangers under static conditions as a function of the reciprocal equilibrium metal concentration in the solution. (*g*) Sorption capacity and (c_e) equilibrium metal concentration in the solution. Solvent: (*1*–*3*) tap water and (*1*'–*3*') distilled water. Metal ion: (*1*, *1*') Cu(II), (*2*, *2*') Ni(II), and (*3*, *3*') Cr(III). Solid lines are approximation of the experimental results for tap water.

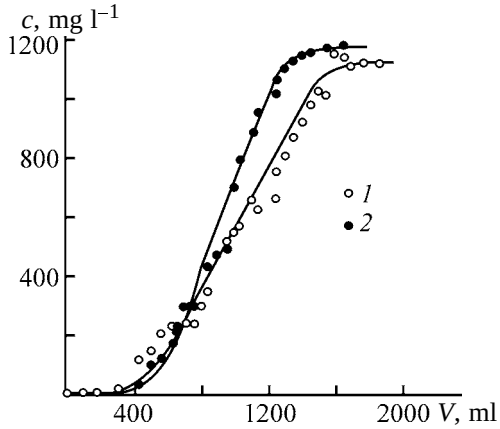

Fig. 2. Sorption of Cu(II) ions from (*1*) distilled and (*2*) tap water on AN-221 anion exchanger under dynamic conditions. (*c*) Cu(II) concentration in the eluate and (*V*) sorbate volume.

48 h. Thereafter, the equilibrium metal concentration in the sorbate was determined. From these data, the static sorption capacity of the resin for transition metals was calculated by Eq. (1). The experimental results on sorption of Ni^{2+}, Cu^{2+}, and Cr^{2+} depending on the equilibrium metal concentration were analyzed in terms of the Langmuir theory [13]

$$g = \alpha c_e/(1 + \beta c_e), \quad (3)$$

where g is the sorption capacity of the resin (mg-equiv g^{-1} dry resin), c_e is the equilibrium metal cation concentration in the solution (mg l^{-1}), and α and β are the empirical constants.

Equation (3) shows that sorption in the coordinates $1/g$ vs. $1/c_e$ is a straight line:

$$1/g = \alpha/\beta + 1/\alpha c_e. \quad (4)$$

Figure 1 shows that the experimental data on sorption of transition metals on anion exchangers are fairly well fitted to the Langmuir equation. These data show also that, in the limits of the determination error, the cations of natural mineralization do not interfere with sorption of the transition metals, i.e., the transition metals can be selectively removed from the initial solution. In sorption of the transition metals from tap water, the maximal sorption capacity of anion exchangers for these metals calculated by Eq. (4) at $c_e \to \infty$ was as follows (mg-equiv g^{-1} resin): Ni^{2+} (AN221) 2.05 ± 0.20, Cu^{2+} (AM-7) 3.5 ± 0.30, and Cr^{3+} (AM-7) 2.86 ± 0.25.

These calculated maximal sorption capacities reasonably agree with their experimental values: Ni^{2+} (AN-221) 1.9, Cu^{2+} (AM-7) 3.42, and Cr^{3+} (AM-7) 3.12 mg-equiv g^{-1} resin. Comparison of the experimental and calculated sorption capacities shows that the maximal sorption capacity of the resins for transition metal cations can be calculated from the data of sorption experiments by the Langmuir equation.

In sorption under static conditions, the equilibrium metal content in the sorbate was attained within three days. Under these conditions, the selective recovery of the transition metals was reached. In sorption under industrial conditions, the equilibrium sorption of metals must be attained within a period required for passing purified water through ion-exchange column. This time is considerably shorter then the time of attainment of the equilibrium sorption. Therefore, we studied the selectivity of sorption of the transition metals [by example of copper(II)] under dynamic conditions. In these experiments, Cu^{2+} solutions in tap and distilled water were passed through a column packed with AN-221 anion exchanger in the OH form. The elution velocity was 1.08 m h^{-1}. Figure 2 shows the output curves (Cu^{2+} content in eluate vs. eluate volume). The characteristics of Cu^{2+} sorption under dynamic conditions are listed in Table 2.

Table 2 shows that the sorption capacity of AN-221 anion exchanger for Cu^{2+} under dynamic conditions is considerably less than that under static conditions. We believe that this decrease in the sorption capacity is caused by the fact that the time of the sorbate–resin contact is insufficient for attainment of the sorption equilibrium. Therefore, we can suggest that, on optimization of the sorption column length, the sorption capacity can significantly increase. Our experimental

Table 2. Characteristics of Cu^{2+} sorption from its solutions in distilled and tap water on AN-221 anion exchanger*

Water	c_0, mg l^{-1}	V_b, ml	Σm, mg	m	g	m	g
				mg cm^{-3} swollen resin		mg-equiv cm^{-3} swollen resin	
Distilled	1150.5	330	1025.9	8.2	22.1	0.26	0.70
Tap	1139.3	340	1089	8.3	23.5	0.26	0.74

* (c_0) Cu^{2+} concentration in the initial solution, (V_b) eluate volume by the moment of Cu^{2+} breakthrough, (Σm) Cu^{2+} weight in the resin saturated with Cu^{2+}, (m) sorption capacity of the resin for copper(II) by the moment of Cu^{2+} breakthrough, and (g) sorption capacity of resin at complete resin saturation with Cu^{2+}, respectively.

data show that the efficiency of copper(II) recovery from both tap and distilled water is virtually identical (within the limits of determination error). This fact shows that salts of natural mineralization do not interfere with copper(II) sorption under dynamic conditions.

In order to regenerate the anion exchanger, aqueous H_2SO_4 was passed through a column at a flow velocity of 1.05 m h^{-1} and the metal concentration in the eluate was determined at a certain intervals. We found that the optimal regeneration is reached in washing the column with aqueous H_2SO_4 of the concentration $c \geq 30$ wt %. The degree of regeneration was determined as the ratio of the weight of copper(II) contained in the regeneration solution Σm_r to the total weight of copper(II) sorbed on the anion exchanger Σm (Table 2). After completion of regeneration, the anion exchanger was washed successively with water and alkali to convert the resin to the OH form. Figure 3 shows the degree of resin regeneration η, the copper(II) content in the regeneration solution Σm_r, and the copper(II) concentration in the regeneration solution c as functions of aqueous sulfuric acid volume passed through the column.

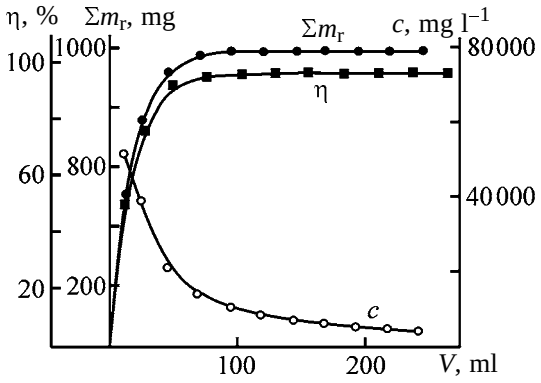

Fig. 3. Regeneration parameters of AN-221 anion exchanger as functions of the sulfuric acid volume V passed through column. (η) Degree of regeneration, (Σm_r) copper(II) content in regeneration solution and (c) copper(II) concentration in the regeneration solution.

Figure 3 shows that the degree of regeneration η > 90% is reached on passing approximately one volume of 30% H_2SO_4 through one volume of resin. Under these conditions, the regeneration solution contains more than 40 g l^{-1} of copper(II). Owing to such a high copper concentration, the utilization of the regeneration solutions becomes expedient from practical and economical viewpoints. Copper can be recovered from this regeneration solution by electrolysis. In our experiments, the regeneration solution (250 ml) was electrolyzed at the current strength of 5 A and voltage of 3 V. On electrolysis for 2 h, 7.4 g of copper was recovered (current efficiency 62%) and the copper concentration in the regeneration solution decreased from 30 to 0.1 g l^{-1}. After such a treatment, the regeneration solution was repeatedly used for regeneration of the anion exchanger saturated with copper(II).

Thus, our sorption experiments under dynamic conditions showed suitability of anion exchange for wastewater treatment to remove copper(II). This technique allows the selective recovery of copper(II) and obtaining of highly concentrated copper-containing solutions suitable for utilization.

CONCLUSIONS

(1) The sorption of copper(II), nickel(II), and chromium(III) from model solutions on anion exchangers was studied under static conditions. In sorption recovery of the nonferrous metals, the AN-221 and AM-7 weakly basic anion exchangers in the OH form exhibit the highest selectivity, and the salts of natural mineralization do not interfere with sorption.

(2) The sorption of copper(II) on AN-221 weakly basic anion exchanger under dynamic conditions and regeneration of this resin with aqueous H_2SO_4 were studied. The salts of natural mineralization do not in-

terfere with sorption. On treatment of copper-containing solutions with the anion exchanger, the residual copper content does not exceed the maximum permissible concentration.

(3) The weakly basic anion exchangers can be used for selective recovery of nonferrous metals from industrial wastewater.

REFERENCES

1. *Corrosion and Wear. Handbook for Water Cooled Reactors*, Paul, D.J., Ed., New York: McGraw–Hill, 1957.
2. Ampilogova, N.I., Simanovskii, Yu.M., and Trapeznikov, A.A., *Dezaktivatsiya v yadernoi energetike* (Decontamination in the Nuclear Power Engineering), Sedov, V.M., Ed., Moscow: Energoizdat, 1982.
3. Khonikevich, A.A., *Dezaktivatsiya sbrosnykh vod* (Decontamination of Wastewater), Moscow: Atomizdat, 1966.
4. Richardson, J.A., *Nucl. Eng. Int.*, 1974, vol. 19, no. 212, pp. 31–37.
5. Gerasimov, V.V., Kasperovich, A.I., and Martynova, O.I., *Vodnyi rezhim atomnykh elektrostantsii* (Water Operation of Atomic Power Plants), Moscow: Atomizdat, 1976.
6. Izmailova, D.R., Voitovich, V.B., and Kurolap, N.S., *Vodosnabzh. Sanit. Tekh.*, 1980, no. 4, p. 709.
7. JPN Patent no. 55-39 993.
8. JPN Patent no. 55-32 796.
9. Kolodyazhnyi, V.A. and Chelnakova, P.N., Abstracts of Papers, *Vserossiskaya nauchno-prakticheskaya konferentsiya "Laboratornoe delo: Organizatsiya i metody issledovanii"* (Russian Scientific and Practical Conf. "Laboratory Practice: Organization and Investigation Techniques"), Penza, 2001, p. 49.
10. Saldadze, K.M. and Kopylova-Valova, V.D., *Kompleksoobrazuyushchie ionity (kompleksity)* (Complexing Ion Exchangers (Complexites)), Moscow: Khimiya, 1980.
11. *Unifitsirovannye metody analiza vod* (Standardized Methods for Water Analysis), Lur'e, Yu.Yu., Ed., Moscow: Khimiya, 1971.
12. Lur'e, Yu.Yu. and Rybnikova, A.I., *Khimicheskii analiz proizvodstvennykh stochnykh vod* (Chemical Analysis of Industrial Wastewater), Moscow: Khimiya, 1978, 4th ed.
13. Daniels, F. and Alberty, R.A., *Physical Chemistry*, New York: Wiley, 1975, 4th ed.

Russian Journal of Applied Chemistry, Vol. 77, No. 1, 2004, pp. 79–82. Translated from Zhurnal Prikladnoi Khimii, Vol. 77, No. 1, 2004, pp. 83–86.

ENVIRONMENTAL PROBLEMS OF CHEMISTRY AND TECHNOLOGY

Deep Purification of Aqueous Solutions To Remove Iron(III) with Carbonate-Containing Industrial Waste

T. G. Lupeiko, M. O. Gorbunova, and E. M. Bayan

Rostov State University, Rostov-on-Don, Russia

Received June 13, 2002; in final form, June 2003

Abstract—The possibility of using a carbonate-containing industrial waste in purification of aqueous solutions to remove iron(III) ions to below the maximum permissible concentration was analyzed. The sorbent capacities were calculated for iron(III) solutions with various initial concentrations. The influence exerted by the time, temperature, anionic composition of iron(III) salt solutions, and other factors on sorption was assessed.

The problem of purification of industrial wastewater that contains metal ions has always been, and still is rather topical in view of their adverse effect on the environment and human health. Of particular interest in this regard is the possibility of using solid industrial wastes as sorbents for heavy metals. To advantages of this method can be referred the ready availability and low cost of the sorbent (waste) and the environmental expediency of its use.

Previously, the composition and physicochemical properties of wastes formed in water treatment at heat and power plants have been studied for the example of the Rostov Heat and Power Plant no. 2 (TETs-2); it was shown that the slime mainly contains calcium and magnesium carbonates, is homogeneous and finely dispersed, has relatively constant composition, and is chemically and radiologically safe [1]. It has also been shown that the waste under study exhibits sorption capacity and can be successfully used to purify aqueous solutions to remove toxic ions of copper [2] and chromium [3].

This study is concerned with the possibility of purification of aqueous solutions to remove iron(III) ions, which can be found most frequently in industrial wastewater. The sorbent suggested is based on calcium and magnesium carbonates. When it is placed in the water medium, an excess amount of OH groups is formed because of the partial hydrolysis of the anion, which is confirmed by the fact that the pH of solutions of the waste is 8.7 [3]. Industrial wastewater from electroplating shops, including iron-containing solutions, is acidic and contains anions of strong acids (Cl^-, SO_4^{2-}, NO_3^-), i.e., Fe^{3+} is present in wastewater in the form of aqua hydroxo complexes formed in hydrolysis of the cation. Therefore, addition of the industrial waste to acid solutions of iron must enhance the hydrolysis, with iron hydroxide, which is the least soluble under the given conditions, formed and carbon dioxide evolved, by the scheme

$$Fe^{3+} \xrightarrow[-H^+]{HOH} Fe(OH)^{2+} \xrightarrow[-H^+]{HOH} Fe(OH)_2^+ \xrightarrow[-H^+]{HOH} Fe(OH)_3\downarrow,$$

$$CO_3^{2-} \xrightarrow[-OH^-]{HOH} HCO_3^- \xrightarrow[-OH^-]{HOH} H_2CO_3 \longrightarrow H_2O + CO_2\uparrow.$$

Thus, it would be expected that the carbonate-containing waste will allow deep purification of aqueous solutions to remove iron ions. In this case, the low solubility product of $Fe(OH)_3$ (6.3×10^{-38} [4]) will result in that the residual concentration of iron will not exceed the maximum permissible concentration (MPC) equal to 0.5 mg l^{-1} [5].

EXPERIMENTAL

In this work we studied the sorption capacity of a carbonate-containing waste in sorption of iron(III) from solutions with various initial concentrations and analyzed the influence exerted by the sorption time, temperature, and other factors on the degree of iron(III) recovery and sorbent expenditure.

The concentration of iron(III) was determined complexometrically by the commonly accepted procedure [6] to within 0.2%. For low concentrations, a spectrophotometric technique with *o*-phenanthroline was used [5]. The optical density was measured on a KFK-2MP photometer to within 4%. The acidity of the solutions

1070-4272/04/7701-0079 © 2004 MAIK "Nauka/Interperiodica"

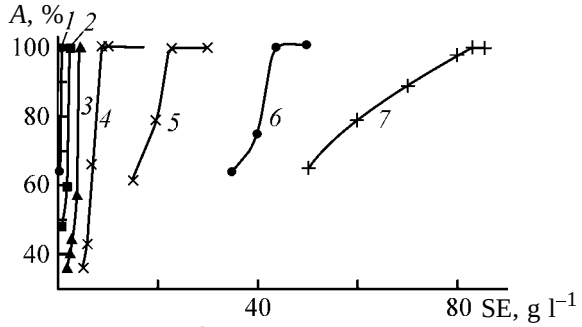

Fig. 1. Degree of Fe^{3+} recovery, *A*, vs. sorbent expenditure SE. Fe^{3+} concentration in solution, mg l^{-1}: (*1*) 200, (*2*) 500, (*3*) 1000, (*4*) 2000, (*5*) 5000, (*6*) 10000, and (*7*) 20000.

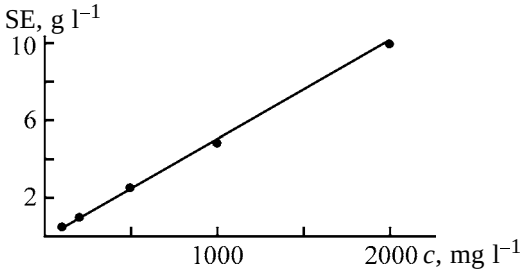

Fig. 2. Optimal sorbent expenditure SE vs. Fe^{3+} concentration *c* in the initial solution.

used was monitored potentiometrically with an I-120M pH meter to within ±0.05 pH units. Model solutions were prepared from a concentrated $FeCl_3$ solution with account of the Fe^{3+} content in wastewater from various industries. The solutions were strongly acidic, which is also characteristic of real wastewater [7]. The sorbent fraction used had particle size of 0.25–0.50 mm, which mainly constitutes the powdered industrial waste [3].

The range within which the content of iron(III) in industrial wastewater varies is rather wide: from several milligrams per liter at nonferrous metallurgical plants to tens of grams per liter at shops for etching of ferrous metals. Therefore, the optimal sorbent expenditure was determined for solutions with different concentrations. For this purpose, a weighed portion of the sorbent was placed in 100 ml of a solution to be purified, kept at 25°C. The amount of sorbent taken for Fe^{3+} precipitation was varied from 0.1 to 8 g (i.e., from 1 to 80 g l^{-1}). The sorption was carried out under static conditions with agitation in the course of 15 min, a time sufficient for the sorption process to be complete. The concentration of Fe(III) in a solution was determined before and after its contact with the sorbent, and the degree of metal recovery was calculated from the difference of the initial and residual concentrations. As the optimal sorbent expenditure was taken the minimum amount of the sorbent that was necessary under the given conditions for iron(III) to be removed to below MPC_{Fe}.

Effect of concentration $c_{Fe^{3+}}$ and pH of the initial $FeCl_3$ solution on expenditure and capacity of the sorbent

$c_{Fe^{3+}}$, mg l^{-1}	pH	Expenditure, g l^{-1}	Capacity, mg g^{-1}
100	2.41	0.5	200
200	2.37	1.0	200
500	2.32	2.5	200
1000	2.11	4.8	208
2000	1.83	10	200
5000	1.63	23	217
10000	1.40	44	227
20000	1.05	83	241

Apparently, the sorbent expenditure becomes higher as the initial content of iron(III) in solution increases (Figs. 1, 2). For example, purifying to below MPC_{Fe} requires 0.5 g l^{-1} of the sorbent for a solution with the initial iron concentration of 100 mg l^{-1} and 80 g l^{-1} for that with the concentration of 20 g l^{-1}. The optimal values of the sorbent expenditure and capacity are listed in the table.

For solutions with not-too-high iron(III) concentration, the sorbent capacity is 200 mg of Fe^{3+} per gram of the sorbent. With increasing iron content, the sorbent capacity grows somewhat, which is presumably due to the formation of a larger amount of difficultly soluble metal hydroxide and to the noticeable contribution to sorption from iron(III) ions additionally coprecipitated on the hydroxide. The dependence of the optimal sorbent expenditure on the Fe^{3+} concentration in the starting solution was processed using the least-squares technique with the use of the experimental data obtained (Fig. 2). In the concentration range 100–2000 mg l^{-1}, the plot can be interpreted as a straight line with 99.9% probability, which makes it possible to calculate the optimal sorbent expenditure for solutions with intermediate concentrations.

As would be expected, the pH values of the initially strongly acidic solutions being purified increased upon their contact with the sorbent (Fig. 3). This process was accompanied by evolution of carbon dioxide. In this case, the higher the iron(III) concentration in solution and the lower the pH of the starting solution, the stronger the gas evolution. It is also noteworthy that pH exceeds 4.5 in filtrates with Fe^{3+} content below the MPC_{Fe} level. This is due to the fact that, in weakly acidic, neutral, and alkaline media ($4.1 < pH < 14$), iron mainly exists in the form of a

difficultly soluble hydroxide, $Fe(OH)_3$ [4]. Hence follows that, indeed, purification of aqueous solutions to remove Fe^{3+} ions is based on their neutralization with a carbonate-containing waste, which leads to mutual enhancement of hydrolysis of the carbonate component of the sorbent and the iron salt to the point of precipitation of iron(III) hydroxide and evolution of carbon dioxide.

To evaluate the influence exerted by the time of contact between a solution being purified and the sorbent on the sorption process, weighed portions of the sorbent (0.25 and 1.0 g) were placed in 100 ml of a solution with the initial Fe^{3+} concentration of 500 and 2000 mg l^{-1}, respectively. The time of sorption was varied from 1 to 10 min. At the iron concentration of 500 mg l^{-1}, 2 min is sufficient for recovery of the metal to the MPC level. With increasing concentration of Fe^{3+} in solution, the sorption duration grows to become 3 min at 2000 mg l^{-1} (Fig. 4). As seen from the data presented, the purification of aqueous solutions to remove Fe^{3+} ions is complete much earlier, compared with ions of other metals. For example, the optimal time of sorption is 60 min for a 10 g l^{-1} copper(II) solution [2]. In all probability, this is due to the fact that, in the case of Cu^{2+}, there exist a number of phases with close solubility products, which can be formed in sorption and in the accompanying processes of neutralization, hydrolysis, etc. In the first stage, when the pH values are relatively low, only the least soluble, under the given conditions, phases are formed. Then, in the course of prolonged neutralization, these phases are converted into other, still less soluble phases, and this solid $\rightarrow$ solid transition cannot be fast. Thus, the fast sorption of iron(III) is apparently related to a simple mechanism of the process, which, in turn, is due to the presence of the $Fe(OH)_3$ phase, predominant in the solubility product in a wide pH range.

In order to study the influence exerted by the sorbent particle size on the extent of purification, three sorbent fractions were used: 0.1–0.25, 0.25–0.5, and 0.5–1.0 mm. The sorption was carried out from a solution with iron(III) concentration of 2 g l^{-1} under static conditions with agitation, in the course of 15 min. It was found that Fe^{3+} ions are removed to the greatest extent at particle size of 0.1–0.25 mm (Fig. 5). In all probability, this is due to higher solubility of finer particles in an aqueous solution and larger working surface area of the sorbent. Taking into account the fact that the sorbent is mainly composed of the 0.25–0.5-mm fraction, preliminary grinding of the sorbent is advisable. However, it was difficult to determine in this study which of the following two ways is more economically efficient: to grind the sorbent, with its expenditure thereby diminished, or to use its greater amounts without preliminary grinding.

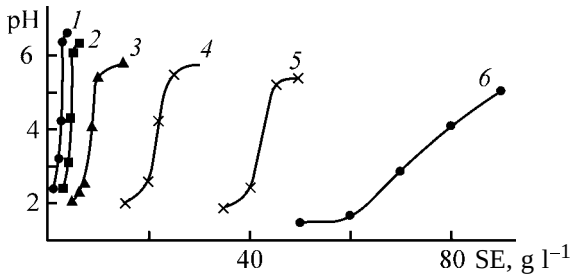

Fig. 3. Solution pH vs. sorbent expenditure SE. Fe^{3+} concentration in solution (mg l^{-1}): (*1*) 500, (*2*) 1000, (*3*) 2000, (*4*) 5000, (*5*) 10 000, and (*6*) 20 000.

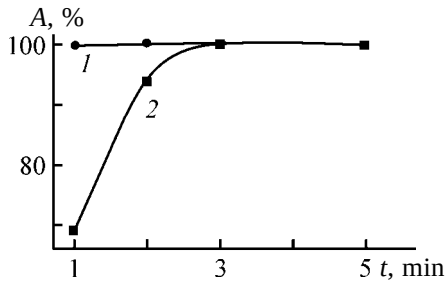

Fig. 4. Degree of Fe^{3-} recovery, *A*, vs. time *t*. Fe^{3+} concentration in solution (mg l^{-1}): (*1*) 500 and (*2*) 2000.

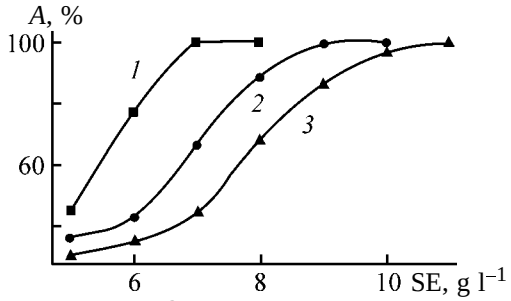

Fig. 5. Degree of Fe^{3+} recovery, *A*, vs. sorbent expenditure SE. Sorbent particle diameter (mm): (*1*) 0.1–0.25, (*2*) 0.25–0.5, and (*3*) 0.5–1.0.

The influence of the solution temperature on sorption was studied with a 2000 mg l^{-1} iron solution at a sorbent expenditure of 8 g l^{-1} (amount of sorbent somewhat smaller than the optimal value) and time of static sorption equal to 15 min. As seen from Fig. 6, sorption is markedly more effective at higher temperatures. This can be attributed to enhancement of hydrolysis and to an increase in the solubility of carbonates contained in the sorbent, which is also confirmed by more vigorous evolution of carbon dioxide. Thus, purification of the starting solution with 2 g l^{-1}

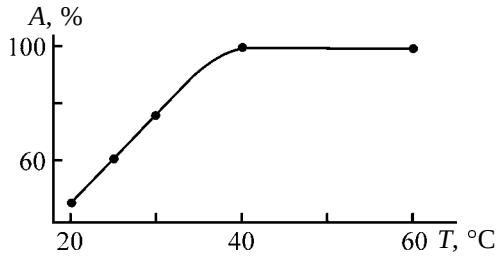

Fig. 6. Degree of Fe^{3-} recovery, *A*, vs. solution temperature *T*.

of iron(III) requires 10 g l^{-1} of the sorbent at 25°C (Fig. 2), whereas, upon heating to 40°C, 8 g l^{-1} of the sorbent is sufficient, i.e., the sorbent expenditure is lower in Fe^{3+} sorption from heated solutions.

In view of the fact that industrial wastewater has varied anionic composition, we analyzed the influence exerted on sorption by the anion component. It was found that processes of purification of chloride, nitrate, and sulfate solutions to remove Fe^{3+} occur in much the same way, with the sorbent capacities coinciding.

The results presented here indicate that the carbonate-containing industrial waste under study can well be used for purification of acid aqueous solutions (e.g., wastewater) to remove iron(III) ions. Moreover, the pH values of purified solutions conform to sanitary regulations concerning purified wastewater.

CONCLUSIONS

(1) The possibility of using a carbonate-containing sorbent for deep purification of aqueous solutions to remove Fe^{3+} ions was demonstrated.

(2) It was confirmed that the main mechanism of sorbent operation is neutralization of strongly acidic solutions with precipitation of Fe^{3+} in the form of a difficultly soluble hydroxide.

(3) The optimal time of contact of the sorbent with a solution being purified and sorbent expenditure for iron(III) salt solutions with various initial concentrations were determined, and the optimal sorbent capacity was calculated to be about 0.2 g of Fe^{3+} per gram of the sorbent.

(4) The sorbent expenditure is lower at finer dispersity of sorbent particles and in the case of sorption from heated solutions.

REFERENCES

1. Lupeiko, T.G., Bayan, E.M., Gorbunova, M.O., and Tsapkova, N.N., *Izv. Vyssh. Uchebn. Zaved., Sev.-Kavk. Region, Estestv. Nauki*, Supplement, 2003, no. 3, pp. 75–79.
2. Lupeiko, T.G., Ivleva, T.I., and Solov'ev, L.A., *Zh. Prikl. Khim.*, 2001, vol. 74, no. 4, pp. 567–570.
3. Lupeiko, T.G., Gorbunova, M.O., and Bayan, E.M., *Zh. Prikl. Khim.*, 2001, vol. 74, no. 10, pp. 1648–1650.
4. Lur'e, Yu.Yu., *Spravochnik po analiticheskoi khimii* (Handbook of Analytical Chemistry), Moscow: Khimiya, 1989.
5. *Rukovodstvo po khimicheskomu analizu poverkhnostnykh vod sushi* (Manual of Chemical Analysis of Surface Land Water), Semenov, A.D., Ed., Leningrad: Gidrometeoizdat, 1977.
6. *GOST* (State Standard) *26449.5–85: Stationary Distillation Installations for Desalination: Methods for Chemical Analysis of Washing Solutions in Equipment Cleansing*.
7. Zhukov, A.I., Mongait, I.L., and Rodziller, I.D., *Kanalizatsiya promyshlennykh predpriyatii* (Sewerage at Industrial Plants), Moscow: Gosstroiizdat, 1962.

Russian Journal of Applied Chemistry, Vol. 77, No. 1, 2004, pp. 83–87. Translated from Zhurnal Prikladnoi Khimii, Vol. 77, No. 1, 2004, pp. 87–91.

ENVIRONMENTAL PROBLEMS OF CHEMISTRY AND TECHNOLOGY

Use of Carbonate-Containing Industrial Waste for Treatment of Aqueous Solutions To Remove Nickel(II) Ions

T. G. Lupeiko, E. M. Bayan, and M. O. Gorbunova

Rostov State University, Rostov-on-Don, Russia

Received July 15, 2003

Abstract—The possibility of using a carbonate-containing industrial waste formed in water-treatment units of thermal power plants for treatment of aqueous solutions to remove nickel(II) ions was analyzed. The influence exerted by the time, temperature, and other factors on the degree of recovery of nickel(II) ions and sorbent expenditure was established. The possibility of separating nickel(II) and iron(III) ions simultaneously present in solution, using the waste under study, was demonstrated.

One of burdensome, large-tonnage wastes produced by thermal power plants is the carbonate-containing precipitate formed at shops for chemical water treatment. The suspended precipitate (slime) is periodically removed to slime collectors, which occupy large area and affect adversely the natural landscape and water-bearing horizons. The water-treatment waste can be used as raw material in manufacture of unfired bricks and as additive in production of ceramic articles and fertilizers. The waste is used most massively in landscape leveling and reclamation of strip pits. Despite the active search for various methods for utilizing slime and diminishing its amount, the problem is far from being resolved.

Previously, the composition and physicochemical properties of wastes formed in water treatment have been studied for the example of the Rostov heat and electric power plant TETs-2, and it was shown that the slime mainly contains calcium and magnesium carbonates, is homogeneous and finely dispersed, has relatively constant composition, and is chemically and radiologically safe [1]. It has also been shown that the waste under study has sorption capacity and can be successfully used to purify aqueous acid solutions to remove iron, copper, and chromium ions [2, 3].

This study is concerned with the possibility of treatment of aqueous solutions to remove nickel(II) ions, which can be found most frequently in wastewater of electroplating shops and are very toxic. Particularly dangerous are spent concentrated nickel-plating solutions (electrolytes) whose discharge to sewage disposal plants can disrupt their operation. Moreover, a great amount of the valuable metal is lost. In this study, we examined the possibility of recovering nickel(II) ions with a carbonate-containing industrial waste.

EXPERIMENTAL

Model solutions were prepared from $NiCl_2 \cdot 6H_2O$ of chemically pure grade; their concentration corresponded to the content of Ni^{2+} ions in wastewater from various plant shops [4]. The sorption was performed under static conditions as follows. A weighed portion of the sorbent (slime) with particle size in the range 0.25–0.50 mm was added to 100 ml of a solution to be purified, with a concentration c_{in} (mg l^{-1}) (calculated in terms of nickel). The resulting mixture was agitated for a time τ (min), and then the solutions were filtered. The pH value and the Ni^{2+} concentration in solution were determined before and after a solution was brought in contact with the sorbent, and the degree of recovery of the metal was determined from the difference of its initial and residual concentrations. The Ni^{2+} concentration was found by a spectrophotometric method with dimethylglyoxime, using the commonly accepted procedure [5]. The optical density was measured on a KFK-2MP photometer to within 5%. The acidity of the solutions used was monitored potentiometrically with an I-120M pH meter to within ± 0.05 pH units.

The content of nickel in industrial wastewater varies widely, and, therefore, the optimal sorbent expenditure was found for solutions with various concentrations c_{in} of 115, 50, 25, 10, and 1 mg l^{-1}. The sorption was carried out at 20°C for 60 min (Table 1, Fig. 1a).

1070-4272/04/7701-0083 © 2004 MAIK "Nauka/Interperiodica"

Table 1. Degree of nickel recovery (DR) at varied sorbent expenditure (SE)

SE, g l^{-1}	$pH_{filtrate}$	c_{res}^{Ni}, mg l^{-1}	DR, %
	c_{in} = 115 mg l^{-1} pH_{in} 5.11		
20	7.80	33.4	71.7
25	7.82	19.8	82.4
30	7.98	8.7	92.4
35	8.01	7.8	93.2
45	8.09	5.5	95.2
50	8.14	5.2	95.5
	c_{in} = 50 mg l^{-1} pH_{in} 5.24		
15	7.88	9.79	80.4
20	8.09	3.90	92.2
25	8.18	1.18	97.6
30	8.19	1.02	97.8
35	8.21	0.87	98.3
	c_{in} = 25 mg l^{-1} pH_{in} 5.36		
5	7.93	6.5	74.0
6	8.01	3.20	87.2
8	8.14	1.71	93.2
10	8.24	0.75	97.0
15	8.26	0.36	98.6
20	8.41	0.17	99.3
	c_{in} = 10 mg l^{-1} pH_{in} 5.47		
2	8.15	2.52	74.8
3	8.37	0.91	90.9
4	8.41	0.48	95.2
5	8.49	0.27	97.3
6	8.52	0.11	98.9
8	8.54	0.08	99.2
	c_{in} = 1 mg l^{-1} pH_{in} 5.61		
1	8.31	0.155	84.5
1.5	8.36	0.119	88.1
2	8.38	0.094	90.6
3	8.44	0.052	94.8
4	8.46	0.011	98.9
5	8.49	0.008	99.2
6	8.52	0.005	99.5

As seen from Table 1, 95% degree of recovery is achieved for a solution with the initial Ni^{2+} concentration of 115 mg l^{-1} at the sorbent expenditure of 50 g l^{-1}. For solutions with lower initial concentration of nickel(II), sufficiently high degree of purification is obtained at lower amounts of the sorbent. For example, 10 g l^{-1} of the sorbent is sufficient for 97% recovery of the metal from a solution with c_{Ni} = 25 mg l^{-1}, and 4 g l^{-1}, for 95% recovery of nickel(II) from a solution with c_{Ni} = 10 mg l^{-1}.

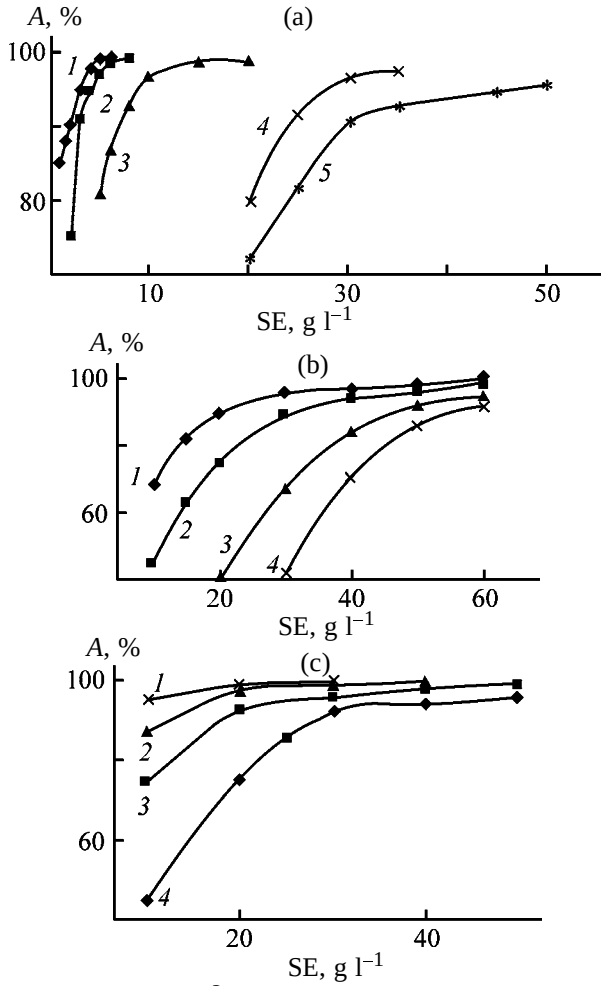

Fig. 1. Degree of Ni^{2+} recovery, *A*, vs. sorbent expenditure SE. (a) Nickel concentration in solution (mg l^{-1}): (*1*) 1, (*2*) 10, (*3*) 25, (*4*) 50, and (*5*) 115. (b) Particle diameter (mm): (*1*) 0.1–0.25, (*2*) 0.25–0.5, (*3*) 0.5–1.0, and (*4*) 1.0–2.0. (c) Temperature (°C): (*1*) 20, (*2*) 40, (*3*) 60, and (*4*) 80.

Analysis of data on the pH values of the starting and purified solutions shows that the sorption is accompanied by neutralization and alkalization of the initially acid solutions. It was noticed that the pH value of the purified solutions conforms to sanitary regulations concerning purified wastewater. The maximum degree of nickel recovery is achieved at pH > 8. Apparently, this is due to hydrolysis of the carbonates contained in the slime, which is confirmed by evolution of carbon dioxide. The higher the concentration of nickel ions and the lower the initial pH of a solution being purified, the more vigorous are the dissolution of the carbonate-containing waste and the gas evolution. The sorption capacity is, apparently, also related to exchange of magnesium(II) ions for nickel(II) in an aqueous solution to give a less soluble nickel carbonate in accordance with their solubility

products: $SP_{MgCO_3} = 2.1 \times 10^{-5}$, whereas $SP_{NiCO_3} = 1.3 \times 10^{-7}$. Formation of nickel carbonate via decomposition of calcium carbonate is unlikely, since $SP_{CaCO_3} = 3.8 \times 10^{-9}$.

In view of the aforesaid, nickel sorption (removal from the solution bulk) can be represented as a set of several reactions.

(1) Partial dissolution of the sorbent with subsequent formation of hydroxide anions

$$CO_3^{2-} + H_2O \rightleftarrows HCO_3^- + OH^-,$$

$$HCO_3^- + H_2O \rightleftarrows OH^- + H_2CO_3,$$

$$H_2CO_3 \rightarrow H_2O + CO_2\uparrow.$$

(2) Formation on the sorbent surface and near it of poorly soluble nickel hydroxide

$$Ni^{2+} + H_2O \rightleftarrows NiOH^+ + H^+,$$

$$NiOH^+ + H_2O \rightleftarrows Ni(OH)_2\downarrow + H^+.$$

The mutual enhancement of hydrolysis of the nickel(II) salt and the carbonate component of the sorbent results in that carbon dioxide is evolved and a precipitate of poorly soluble nickel hydroxide is formed.

(3) Formation on the sorbent surface and near it of poorly soluble nickel carbonate

$$MgCO(s) + Ni^{2+} \rightarrow NiCO_3(s) + Mg^{2+}.$$

In addition, nickel(II) ions can be adsorbed on the surface of an undissolved sorbent and on freshly formed particles. Thus, the interaction with the carbon-containing waste consists in "mild" neutralization of acid solutions and ends in self-adjusting establishment of a weakly acid medium, which rules out excessive alkalization of solutions. In this regard, the waste acts as a material self-adjusting the pH value. In this case, the process itself is constituted by precipitation of nickel(II) hydroxide, exchange interactions that lead to carbonate and mixed hydroxo carbonate phases, and, presumably, adsorption of nickel(II) by the amorphous particles formed and particles of an undissolved sorbent. Since the equilibration process is long, the initially formed solid phases are nonequilibrium and are further transformed into equilibrium phases (similarly to the previously studied sorption of Cu^{2+} [2]).

The above interactions provide nickel recovery from aqueous solutions. However, in view of the low efficiency of this process, it is to be optimized by adjusting its conditions. For this purpose, the influence exerted on the process by various factors was studied.

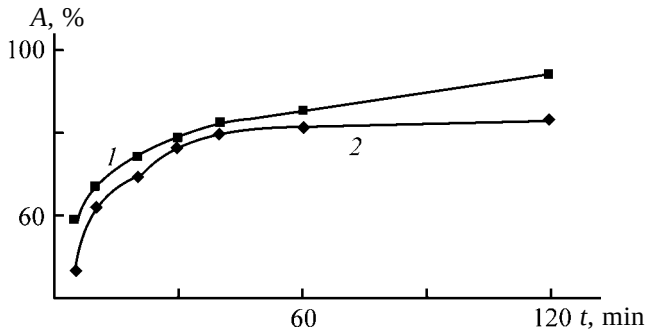

Fig. 2. Degree of Ni^{2+} recovery, A, vs. time t. Sorption conditions: (*1*) $c_{Ni} = 200$ mg l^{-1}, SE = 50 g l^{-1}; (*2*) $c_{Ni} = 25$ mg l^{-1}, SE = 5 g l^{-1}.

Since an air-dry slime sample is a powder with various particle diameters [1], the study was commenced with assessment of the influence exerted on the efficiency of nickel recovery by dispersity of sorbent particles. For this purpose, the main fractions of a carbonate-containing waste with grain sizes of 0.1–0.25, 0.25–0.5, 0.5–1.0, and 1.0–2.0 mm were used. The sorption was performed from solutions with nickel(II) concentration of 100 mg l^{-1}, at sorption time of 30 min. As expected, the degree of sorption is higher, and the sorbent expenditure is lower, with finely dispersed fractions, e.g., 0.1–0.25 mm (Fig. 1b). In all probability, this is due to easier dissolution of finer particles in the aqueous solution and larger working surface area of the sorbent. However, at high sorbent expenditure, which is necessary for achieving >90% nickel(II) recovery, the particle size affects the process only slightly, because the solution is supersaturated with the slime. Moreover, use of a finely dispersed fraction makes difficult the separation of the sorbent contaminated with nickel from the purified solution. Therefore, the sorbent fraction with grain size of 0.25–0.5 mm, whose content in the sorbent exceeds 45% [3], was used in further experiments.

An important specific feature of the process is that the sorption equilibrium is attained slowly (Fig. 2), even though the major part of the metal is recovered already during the first several minutes. For example, for a solution with $c_{in} = 200$ mg l^{-1} (curve *1*), the main part of nickel(II) (58%) is sorbed at the sorbent expenditure of 50 g l^{-1} during the first 5 min. For a solution with the initial concentration of 25 mg l^{-1} (curve *2*), more than 60% of the metal is recovered at the sorbent expenditure of 5 g l^{-1} in 10 min. In this

Table 2. Stage-by-stage purification of solutions. Duration of each purification stage 5 min

c_{in}, mg l^{-1}	First stage of purification		Second stage of purification		DR, %
	SE, g l^{-1}	c_{res}, mg l^{-1}	SE, g l^{-1}	c_{res}, mg l^{-1}	
200	50	72	30	1.44	99
100	20	32	15	0.38	99
25	5	11	5	0.41	98

case, sorption proceeds actively during the first hour, and then the process passes into a less intensive stage, with virtually complete recovery (99%) achieved in 3 days. If a markedly greater amount of sorbent, e.g., 10 mg l^{-1}, is taken for a solution with c_{in} = 25 mg l^{-1}, more than 90% of nickel(II) is recovered in the first 5 min.

In view of this fact, the optimal sorption conditions for achieving a high degree of purification are to be chosen depending on the task to be accomplished. For example, at low sorbent expenditure, the time of contact with a solution being purified should be relatively long, and fast and efficient purification is achieved at a large excess of the sorbent. Taking into account the low cost of the sorbent, the second way seems to be more efficient. Also possible is stage-by-stage purification of solutions. This is particularly important for strongly concentrated solutions, for which "rough" purification will be the first stage, and, if necessary, additional purification, the second stage. Table 2 illustrates a possible course of stage-by-stage purification. As for the choice of conditions and modes of treatment of particular real kinds of wastewater from electroplating shops, it is determined, in the first place, by their qualitative and quantitative composition and the task to be accomplished at a plant (rough purification of spent concentrated electrolytes or fine purification of wastewater).

One more result of interest was that the expenditure of the carbonate-containing sorbent is markedly lower in sorption from hot solutions. In this case, the precipitation of nickel(II) ions is markedly accelerated and a high degree of purification is achieved. For example, upon heating to 40°C, nickel ions are virtually completely removed from a solution (c_{in} = 100 mg l^{-1}) in the presence of 40 g l^{-1} of slime in 15 min, and if the sorption is carried out at 80°C, 95% recovery of nickel requires a 5 times smaller amount of the sorbent (SE = 50 g l^{-1} at 20°C and 10 g l^{-1} at 80°C (Fig. 1c). In all probability, the higher efficiency of purification in sorption from hot solutions is due to increased solubility of the slime and to enhanced hydrolysis of its constituents, such as calcium and magnesium carbonates. This conclusion is confirmed by more vigorous evolution of carbon dioxide from hot solutions.

The qualitative and quantitative compositions of industrial wastewater strongly vary, and, therefore, the influence exerted by various ions on the sorption of nickel(II) was analyzed. A study of sorption from sulfate, chloride, and nitrate solutions revealed that changes in the anionic composition of solutions have virtually no effect on the sorption of nickel(II). At the same time, the presence of metal cations strongly affects the amount of sorbent necessary for solution purification, since the sorbent is also consumed for recovery of other metals. The influence of cations was studied for the example of iron, which is a cation that most frequently occurs in wastewater. Taking into account the fact that sorption of nickel(II) proceeds successfully only at a sufficiently high expenditure of the sorbent (Table 1) and iron(III) is sorbed virtually instantaneously at low sorbent consumption [sorbing capacity 200 mg iron(III) per 1 g sorbent], it is possible to separate solutions that contain these ions. This is particularly important in nickel plating of iron articles, when the nickel-plating electrolyte is contaminated with iron(III) ions. Table 3 lists the results of sorption from solutions containing nickel(II) and iron(III) ions in ratios of 1 : 2, 1 : 4, and 1 : 6, i.e., solutions with c_{in}^{Ni} = 100 mg l^{-1} and c_{in}^{Fe} = 200, 400, and 600 mg l^{-1}, respectively. The sorption was carried out from acid solutions (pH 2–3) for 5 min. As seen from Table 3, 90% of nickel remains in a solution that initially contained a mixture of aqua ions of the metals in a ratio Ni : Fe = 1 : 6 upon complete precipitation of iron(III). For less concentrated solutions, precipitation of iron(III) with virtually zero loss of nickel(II) is possible.

Finally, it should be noted that, under certain conditions, the carbonate-containing waste formed in water treatment at thermal power plants can be used for recovery of nickel(II) ions from dilute and concen-

Table 3. Separation of solutions containing Ni(II) and Fe(III) ions

SE, g l^{-1}	Degree of metal recovery, %					
	Ni : Fe = 1 : 2		Ni : Fe = 1 : 4		Ni : Fe = 1 : 6	
	Fe(III)	Ni(II)	Fe(III)	Ni(II)	Fe(III)	Ni(II)
1.0	76	0	–	–	–	–
1.5	100	0	48	0	–	–
2.0	100	1.2	63	0.1	49	2.3
2.5	–	–	99	1.5	57	5.2
3.0	–	–	100	1.6	77	5.8
4.0	–	–	–	–	100	9.9

trated solutions, and also for partial or virtually complete separation of mixed solutions that contain both Ni(II) and Fe(III) ions.

CONCLUSIONS

(1) The possibility of using the slime formed in water-treatment units of thermal power plants for purification of aqueous solutions to remove nickel(II) ions was demonstrated.

(2) The optimal process duration and sorbent expenditure were found for solutions with various concentrations. Several purification schemes were suggested.

(3) It was established that the sorbent expenditure decreases as the temperature of a solution being purified is raised, sorption duration is made longer, and more finely dispersed sorbent fraction is used.

(4) The possibility of partly or virtually completely separating mixed solutions that contain various amounts of Ni(II) and Fe(III) with the use of the waste was demonstrated.

REFERENCES

1. Lupeiko, T.G., Bayan, E.M., Gorbunova, M.O., and Tsapkova, N.N., *Izv. Vyssh. Uchebn. Zaved., Sev.-Kavk. Region, Estestv. Nauki*, Supplement, 2003, no. 3, pp. 75–79.
2. Lupeiko, T.G., Ivleva, T.I., and Solov'ev, L.A., *Zh. Prikl. Khim.*, 2001, vol. 74, no. 4, pp. 567–570.
3. Lupeiko, T.G., Gorbunova, M.O., and Bayan, E.M., *Zh. Prikl. Khim.*, 2001, vol. 74, no. 10, pp. 1648–1650.
4. Zhukov, A.I., Mongait, I.L., and Rodziller, I.D., *Kanalizatsiya promyshlennykh predpriyatii* (Sewerage at Industrial Plants), Moscow: Gosstroiizdat, 1962.
5. *Rukovodstvo po khimicheskomu analizu poverkhnostnykh vod sushi* (Manual of Chemical Analysis of Surface Land Water), Semenov, A.D., Ed., Leningrad: Gidrometeoizdat, 1977.

Russian Journal of Applied Chemistry, Vol. 77, No. 1, 2004, pp. 88–91. Translated from Zhurnal Prikladnoi Khimii, Vol. 77, No. 1, 2004, pp. 92–95.

ORGANIC SYNTHESIS AND INDUSTRIAL ORGANIC CHEMISTRY

Interrelation between Self-Diffusion, Viscosity, and Optical Properties of Organic Liquids

I. V. Skomorokhov and V. I. Skomorokhov

Tupolev Kazan State Technical University, Kazan, Tatarstan, Russia

Received May 16, 2003

Abstract—The possibility of general correlation analysis of the self-diffusion coefficients and dynamic viscosity coefficients of low-molecular-weight liquid organic nonelectrolytes was studied. An attempt was made to obtain common dependences suitable for calculating the self-diffusion and viscosity coefficients.

Optical methods of investigations, in particular, refractometry, are widely used in physicochemical analysis. Refractometric constants are closely related to many physical properties of substances. Combined measurements of optical and other properties of liquids reveal their interrelation.

There are virtually no published data on a correlation between the kinetic coefficients characterizing the mass and momentum transfer processes, on the one hand, and refractometric constants, on the other. Only Suryanarayana [1] estimated the dynamic viscosity coefficient of liquids η, mPa s^{-1}, from the refractive index n:

$$\eta = C\left[\frac{(n_D^{20})^2 - 1}{(n_D^{20})^2 + 2}\right], \quad (1)$$

where C is the proportionality coefficient with the dimensionality identical to that of η, and n_D^{20}, refractive index for the D line of sodium (λ = 589.3 nm) at 20°C.

There are no published data on interrelation between the self-diffusion coefficients (SDCs), characterizing the thermal (random) motion of molecules in liquids, and the refractometric constants.

Figure 1 presents the D vs. n_D^{20} plots constructed for the experimental self-diffusion coefficients D available from the literature. It is seen that the data for isomeric homologs and liquids from different homologous series cannot be fitted by a single correlation curve.

General correlation analysis is possible only for liquids from the same group (homologous series). For example, for liquid *n*-alkanes from pentane to decane, we obtained the following linear equation:

$$D = an_D^{20} + b, \quad (2)$$

where a = –77.36 (–79.62) and b = 110.23 (113.55) for T = 293.15 (298.15 K). The SDCs calculated by this equation and those measured experimentally differ by less than 5%.

With lengthening molecular chain of *n*-alkanes, Eq. (2) gets nonlinear (Fig. 1, curve *1*). Regular trends in variation of the SDCs with the refractive index along a homologous series are also exhibited by primary alcohols C_1–C_8 (Fig. 1, curve *2*) and cyclanes, namely, *cyclo*-C_5, *cyclo*-C_6, and methyl-*cyclo*-C_6 (Fig. 1, curve *3*). No common equation directly interrelating D and n_D^{20} parameters of liquids from different classes was revealed.

The light wave affects the mobility of the charges (electrons and nuclei in atoms) constituting the molecule. As a result, molecules of liquid nonpolar dielec-

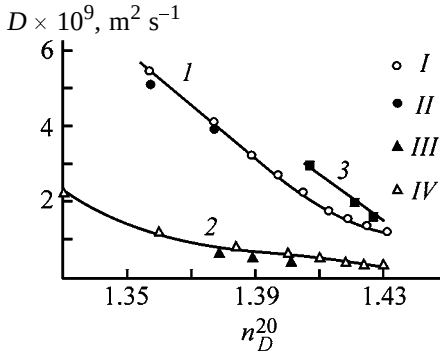

Fig. 1. Correlation of D with n_D^{20} for selected organic liquids at 293.15 K: (*1*) (*I*) *n*-C_5–*n*-C_{17} and (*II*) *iso*-C_5, *iso*-C_6; (*2*) (*III*) primary alcohols C_1–C_8, (*IV*) *iso* alcohols C_3–C_5, and (*3*) cyclanes.

1070-4272/04/7701-0088 © 2004 MAIK "Nauka/Interperiodica"

trics get polarized, acquiring a dipole moment $\vec{\mu} = \alpha\vec{E}$. Here, μ is the dipole moment of the molecule, D; $\vec{E}$, electric field strength, V m^{-1}; and α, polarizability, characterizing the electric-field-induced deformability of the molecule, D m^4 V^{-1}.

The equation for molar polarization corrected for the dipole interaction of molecules in the limit of a very weak field has the form [2, 3]

$$\frac{\varepsilon - 1}{\varepsilon + 2} = \frac{4}{3}\pi n\alpha[1 + S(n, T)], \quad (3)$$

where n is the number of molecules per unit volume (numerical density) in the same limit, m^{-3}, and $S(n, T)$, a function of the numerical density and temperature.

We will introduce the designation $n_0 = (4/3)\pi n\alpha$ into Eq. (3) and thus obtain

$$\frac{\varepsilon - 1}{(\varepsilon + 2)n_0} - 1 = S(n, T). \quad (4)$$

Transfer of particles in liquids is, essentially, a sequence of their random displacements. Diffusion motion of a particle in a medium is usually characterized by an rms displacement $\langle r^2\rangle$ from the initial position within the time $\Delta\tau$. In the three-dimensional space, the rms displacement is defined as follows [4, 5]:

$$\langle r^2\rangle = 6D\Delta\tau. \quad (5)$$

Under isobaric conditions, the rms displacement of a molecule within a certain time interval $\Delta\tau$, like the $S(n, T)$ functional, is a function of the numerical density and temperature. Therefore, SDC can be expressed as

$$D = \frac{\langle r^2\rangle}{6\Delta\tau} = f(n, T). \quad (6)$$

Comparison of Eqs. (4) and (6) suggests that the self-diffusion coefficient can be expressed as a function of the left-hand side of Eq. (4), which is the molar polarization P_m

$$D = \varphi\left[\frac{(\varepsilon - 1)}{(\varepsilon + 2)}\frac{M}{\rho}\right]\varphi(P_m). \quad (7)$$

where φ is the function designation; M, molecular weight, kg mol^{-1}; ρ, density of liquid, kg m^{-3}; and ε, dielectric permittivity (dimensionless).

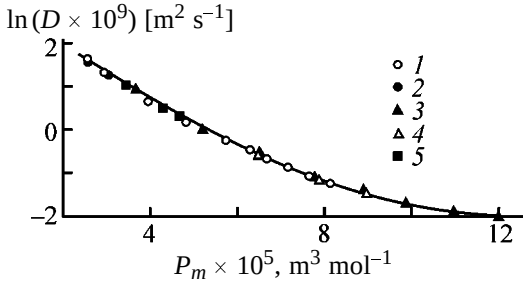

Fig. 2. Common dependence of D on P_m for organic liquids: (*1*) *n*-C_5–*n*-C_{17}; (*2*) *iso*-C_5, *iso*-C_6; (*3*) primary alcohols C_1–C_8; (*4*) *iso* alcohols C_3–C_5; and (*5*) cyclanes.

To test the hypothesized existence of a correlation between the self-diffusion coefficient and molar polarization, we took advantage of the SDCs, densities, refractive indices [6–9], and dielectric permittivities [10] of liquids from various homologous series.

We constructed the $\ln D$ vs. P_m plots for the experimental SDCs of liquid *n*-alkanes (C_5–C_{17}), isopentane, isohexane (with the dipole moment $\mu = 0$ and association number $\psi = 1$), as well as for diethyl ether and diisopropyl ether ($\mu > 0$, $\psi = 1$), benzene, toluene, *m*-xylene, cyclopentane, cyclohexane, methylcyclohexane ($\mu \sim 0$, $\psi > 1$), and homologous series of primary alcohols (C_1–C_8), 2-propanol, and 3-butanol ($\mu > 0$, $\psi > 1$). These points are well fitted by a common curve (Fig. 2).

Comparison with Fig. 1 clearly shows that general correlation analysis of the experimental SDC values in the $\ln D$ vs. P_m coordinates is advantageous.

The molar polarization of liquids whose dielectric permittivity $\varepsilon \neq (n_D^{20})^2$ was calculated by the formula

$$P_m = \frac{(\varepsilon - 1)}{(\varepsilon + 2)}\frac{M}{\rho}, \quad (8)$$

and that of liquids with $\varepsilon = (n_D^{20})^2$, by the formula

$$P_m = \psi R_d, \quad (9)$$

where ψ is the correction for association of the molecules, which is equal to the association number determined using the viscosities [11], and R_d, molar refraction determined by the equation

$$R_d = \frac{(n_D^{20})^2 - 1}{(n_D^{20})^2 + 2}\frac{M}{\rho}. \quad (10)$$

By regression analysis, we obtained the analytical expression describing most adequately the experimental self-diffusion coefficients D, m^2 s^{-1}, for the

liquids studied at 293.15 K:

$$D = 10^{-9}\exp(a_1P_m^2 + b_1P_m + c_1), \quad (11)$$

where $a_1 = 2.791 \times 10^{-4}$ mol^2 cm^{-6}, $b_1 = -8.157538 \times 10^{-2}$ mol cm^{-3}, $c_1 = 3.5155$ for nonpolar and weakly polar liquids (alkanes, cyclanes, aromatic hydrocarbons); and $a_1 = 2.4006 \times 10^{-4}$ mol^2 cm^{-6}, $b_1 = -7.31926 \times 10^{-2}$ mol cm^{-3}, $c_1 = 3.16715$ for polar liquids (primary alcohols); P_m has the dimensionality of cm^3 mol^{-1}.

The discrepancies (per cent) between the SDCs calculated by Eq. (11) and determined experimentally were estimated at 6.6 (maximal) and 2.36 (average) for alkanes, cyclanes, and aromatic hydrocarbons, respectively; and 3.7 (maximal) and 1.63 (average) for primary alcohols.

Unfortunately, the limited number of the experimentally determined SDCs for organic liquids prevents more comprehensive analysis; there are no SDCs for polar molecules of fatty acids and esters having high intrinsic dipole moments ($\mu > 2$ D).

Thus, with lacking experimental SDCs for organic liquids, Eq. (10) can be recommended for calculating these parameters.

We also studied how the dynamic viscosity coefficients (DVCs) vary with the molar refraction and molar polarization of *n*-alkanes and primary alcohols. The experimental viscosities were represented in the $\eta M^{2/3}$ vs. R_d, $\ln\eta$ vs. P_m, and $\ln\eta$ vs. R_d coordinates. The most precise correlation was obtained in the case of the $\ln\eta$ vs. P_m coordinates.

By parabolic regression we obtained equations for calculating the viscosities η, mPa s, of liquid *n*-alkanes,

$$\eta = \exp(a_2P_m^2 + b_2P_m + c_2), \quad (12)$$

with the parameters $a_2 = -2.7358 \times 10^{-4}$ mol^2 cm^{-6}, $b_2 = 8.06 \times 10^{-2}$ mol cm^{-3}, $c_2 = -3.3875$, and viscosities of primary alcohols,

$$\eta = \exp(a_3R_d + c_3), \quad (13)$$

with the parameters $a_3 = 5.62 \times 10^{-2}$ mol cm^{-3} and $c_3 = -2.227$; P_m and R_d have the dimensionality of cm^3 mol^{-1}.

The relative mean deviations of the DVCs calculated by Eqs. (12) and (13) from those determined experimentally were estimated at 0.875 and 1.73% for nonassociated alkanes and associated alcohols, respectively. The average deviation was calculated as the ratio of the sum of the absolute values of the relative deviations for all the N processed experimental points to their number

$$\delta_{mean} = \frac{\sum_{n=1}^{N}|\delta_i|}{N}, \quad (14)$$

where δ_{mean} is the average relative deviation of the calculated DVCs from the experimental data; δ_i, relative deviation for individual experimental points; and N, number of points.

The maximal deviations of the calculated DVCs from the experimental data were estimated at 1.6 and 4.75% for *n*-heptane and primary alcohols, respectively. The maximal deviation $\max\{\delta_i\}$, %, corresponds to the largest deviation among those calculated by the formula

$$\max\{\delta_i\} = \left[\frac{(\eta_{i,calc} - \eta_{i,exp})}{\eta_{i,exp}}\right] \times 100, \quad (15)$$

where $\eta_{i,calc}$ is the viscosity calculated by Eqs. (12) or (13), and $\eta_{i,exp}$, the experimental viscosity.

In view of the fact that the SDCs and DVCs can be precisely described by similar dependences, we can estimate the rotational component of the activation energy of viscous flow $E_{rot} = E_\eta - E_{trans}$ for *n*-alkanes by the equation

$$A_\eta A_D T\exp(E_{rot}/kT) = \exp[(a_1 + a_2)P_m^2 + (b_1 + b_2)P_m + (c_1 + c_2)], \quad (16)$$

where k is the Boltzmann constant; E_{rot}, rotational component of the activation energy of viscous flow; A_η and A_D, pre-exponential factors in the equations for SDC and DVC [12], respectively; constants a_1, a_2, b_1, b_2, c_1, and c_2 are identical to those in Eqs. (11) and (12).

CONCLUSIONS

(1) A correlation was established between the self-diffusion coefficients D and molar polarization P_m of liquid low-molecular-weight organic nonelectrolytes, $\ln D = f(P_m)$, as well as between their dynamic viscosity coefficients η and molar polarization, $\ln\eta = f(P_m)$. These correlations yield common dependences suitable for calculating the self-diffusion [Eg. (11)] and dynamic viscosity [Eqs. (12) and (13)] coefficients.

(2) For a series of homologous substances, common dependences can be obtained for the refractive index.

REFERENCES

1. Suryanarayana, C.V., *Monatsh. Chem*., 1960, vol. 91, no. 1, pp. 139–147.
2. Isihara, A., *J. Chem. Phys*., 1963, vol. 38, no. 10, pp. 2437–2444.
3. Isihara, A., *Physica*, 1964, vol. 30, no. 1, pp. 265–270.
4. Einstein, A., *Ann. Phys*., 1906, vol. 19, no. 1, p. 371.
5. Smoluchowski, M., *Z. Phys. Chem*., 1917, vol. 92, p. 129.
6. *Khimicheskii entsiklopedicheskii slovar'* (Chemical Encyclopedic Dictionary), Knunyants, I.L, Ed., Moscow: Sov. Entsiklopediya, 1983.
7. *Svoistva organicheskikh soedinenii: Spravochnik* (Properties of Organic Compounds: Handbook), Potekhin, A.A., Ed., Leningrad: Khimiya, 1984.
8. Rabinovich, V.A. and Khavin, Z.Ya., *Kratkii khimicheskii spravochnik* (Concise Chemical Handbook), Leningrad: Khimiya, 1977.
9. Krestov, G.A., Afanas'ev, V.N., and Efremova, L.S., *Fiziko-khimicheskie svoistva binarnykh rastvoritelei: Spravochnoe izdanie* (Physicochemical Properties of Binary Solvents: Handbook), Leningrad: Khimiya, 1988.
10. Akhadov, Ya.Yu., *Dielektricheskie svoistva chistykh zhidkostei: Spravochnik* (Dielectric Properties of Pure Liquids: Handbook), Moscow: Izd. Standartov, 1972.
11. Skomorokhov, V.I. and Dregalin, A.F., *Zh. Fiz. Khim*., 1992, vol. 66, no. 11, pp. 2947–2953.
12. Frenkel', Ya.I., *Sobranie izbrannykh trudov* (Coll. of Selected Works), vol. 2: *Nauchnye stat'i* (Research Articles), Moscow: Akad. Nauk SSSR, 1958.

Russian Journal of Applied Chemistry, Vol. 77, No. 1, 2004, pp. 92–97. Translated from Zhurnal Prikladnoi Khimii, Vol. 77, No. 1, 2004, pp. 96–101.

ORGANIC SYNTHESIS AND INDUSTRIAL ORGANIC CHEMISTRY

Synthesis of Tetrafluoromethane by Graphite Fluorination with Elemental Fluorine

D. S. Pashkevich, D. A. Mukhortov, V. B. Petrov, Yu. I. Alekseev, V. S. Asovich, and V. G. Barabanov

Prikladnaya Khimiya Russian Scientific Center, Federal State Unitary Enterprise, St. Petersburg, Russia

Received November 29, 2002; in final form, May 2003

Abstract—Formation of high-temperature inverse wave of the filtration combustion of graphite fixed bed in fluorine was studied. Scientific principles of the industrial process of the tetrafluoromethane synthesis from graphite and fluorine were developed.

Tetrafluoromethane (TFM), CF_4, is widely used in the industry for plasma-chemical production of integrated circuits, as refrigerant, flame inhibitor, etc. [1]. The annual world consumption of TFM is about 1000 t today, which determines urgency of the development of its commercial synthesis.

Various methods of TFM preparation are known: fluorination of methane, its chloro and fluoro derivatives, silicon carbide, and polyfluoroethylene with elemental fluorine and fluorination of tetrachloromethane with various inorganic fluorides [1]. However, the synthesis from the elements is the most promising; fluorine is a commercial product, and electrode graphite, which is characterized by high purity and appropriate physicomechanical properties, can be used as a carbon material.

It was found [2–11] that, depending of fluorination conditions and kind of carbon raw material, the products of fluorine reaction with carbon are liquid, solid, and gaseous substances:

$$C(s) + F_2(g) \rightarrow (CF)_n(s) + CF_4(g) + C_2F_6(g) + C_3F_8(g) + C_4F_{10}(g) + C_5F_{12}(g) + \ldots \quad (1)$$

It was shown in [8, 9] that, at 1000–1500°C, TFM is the single product of the fluorine reaction with graphite. At lower temperatures, hexafluoroethane, octafluoropropane, and higher-molecular-weight perfluorinated carbons are also formed. At the temperatures lower than 500°C, fluorographite $(CF)_n$ is the main product. At temperatures lower than 100°C, fluorine does not react with graphite, as indicated in numerous papers.

The TFM formation in the fluorine reaction with carbon is accompanied by a heat release (932 kJ mol^{-1}) sufficient for graphite heating up to the required temperatures. Powdered graphite has effective heat conductivity of about 10^{-2} W m^{-1} K^{-1}. The filtration combustion mode is realized when fluorine is passed through a heated graphite bed. The combustion wave has inverse structure, since graphite burns out completely, and all the reaction heat is distributed in the graphite bed below the reaction zone along the gas flow direction. In the inverse wave of the filtration combustion, the zone of fluorine uptake is narrower than the zone of highly heated graphite. Therefore, unreacted graphite is subject to prolonged heating before it appears in the reaction zone, and, as a result, volatile impurities (e.g., sulfur) are eliminated. This fact favors preparation of high-purity TFM. It should be noted that, in the inverse wave of the filtration combustion, fluorine breakthrough through the reaction zone is excluded, and thus complete fluorine conversion is provided [12].

As mentioned above, at temperatures lower than 500°C, solid fluorocarbon $(CF)_n$ is the single reaction product [10, 11]. On heating above 500°C, it decomposes to form C_2F_6, C_3F_8, C_4F_{10}, etc. [10, 11]. Therefore, to obtain pure TFM, the thermal interaction of the graphite packing in the fluorine-containing area with heat-bearing surfaces should be excluded. This can be realized by feeding fluorine directly into the graphite bed depth.

However, at the reactor startup, fluorine is (in the simplest case) fed into the graphite bed at room temperature, and, in the course of formation of the high-temperature synthesis wave, fluorographite initially

1070-4272/04/7701-0092 © 2004 MAIK "Nauka/Interperiodica"

accumulates, which then decomposes to form C_2F_6, C_3F_8, C_4F_{10}, etc. In addition, since fluorographite is a thermolabile condensed compound, its accumulation is undesirable from the viewpoint of safety of the reactor functioning. Thus, the stage of formation in the graphite packing with the initial temperature of 10–20°C of a high-temperature wave (1000–1500 K) in which the synthesis proceeds is the most important for production of maximally pure CF_4 in an industrial reactor and the process safety.

We found no studies of carbon ignition in fluorine. Such important characteristics of the industrial process as the time of ignition delay and time of attainment of the reactor operating mode ensuring production of pure TFM (at the content of fluorocarbon impurities no more than 0.1%) are virtually unknown.

In this work, we determined the conditions of formation of a high-temperature wave of filtration combustion of graphite or its mixtures with activated birch charcoal in fluorine and a method for safe and reliable reactor startup.

EXPERIMENTAL

To study the combustion process, we developed a laboratory device (see figure).

A graphite powder was charged into a cylinder (*1*) with an inner diameter of 68 mm and height of 164 mm. Fluorine was fed into the reactor through a thick-walled copper nozzle (*2*). In the reactor volume 700 mm in diameter, Chromel–Alumel thermocouples T1–T3 without protective cases were placed. The distance (along the vertical) between the nozzle outlet and thermocouple junction was 14 mm, and the distance between the thermocouple junctions, 30 mm.

In the experiments, the constant fluorine consumption was preset, and samples of the reaction gas for chromatographic analysis on a katharometer were taken from a sampler (*3*) with a syringe. In addition, the fluorine breakthrough through the sampler (*3*) was monitored. A KI aqueous solution was used as an indicator.

Formation of the high-temperature zone of the synthesis was judged from the thermograms obtained. The time interval from the beginning of fluorine introduction to attainment of the temperature of 400°C near the junction of thermocouple T1 was considered as the ignition delay time t_{id}.

Fluorine and an F_2 + HF mixture[1] were used as

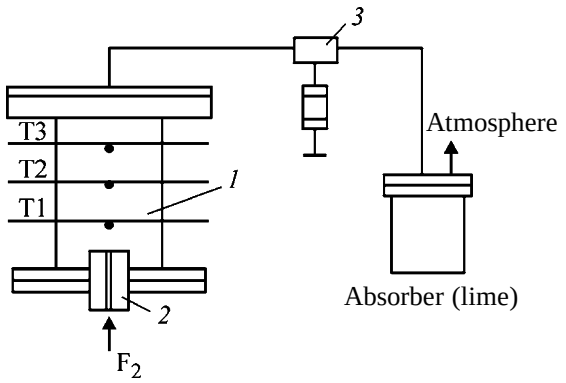

Scheme of the laboratory device for studying carbon combustion in fluorine.

fluorinating agents, and ground VAZ grade graphite (TU 48-20-54–84) produced by the MEZ (Moscow Electrode Plant) Joint-Stock Company and a mixture of 90% graphite and 10% activated birch charcoal (ABC), as carbon raw materials.

The first series of experiments was performed with VAZ graphite and fluorine. The initial graphite and graphite already used in high-temperature synthesis of CF_4 were used. The results of measurements of the ignition delay time as influenced by fluorine consumption are listed in Table 1. The nozzle outlet diameter *d* and the linear velocity of the fluorine flow at the nozzle outlet also presented. It should be noted that the high-temperature reaction zone could not be formed with spent graphite.

The results of chromatographic analysis of the reaction gas samples, qualitative monitoring of the fluorine breakthrough, and measurement of temperature as a function of time from the beginning of fluorine feeding are given in Table 2.

It follows from Tables 1 and 2 that heat accumulation and ignition proceed in the area between thermo-

Table 1. Time of ignition delay t_{id} at different flow rates W_{F_2} and linear velocities U_{F_2} of fluorine at the nozzle outlet, d = 0.85 mm

Raw material	W_{F_2}, $cm^3\ s^{-1}$	U_{F_2}, m s^{-1}	t_{id}, s
Graphite	40	71	540
	27	48	No ignition
Graphite*	45	79	〃
	26	46	〃
Graphite+ ABC	40	71	250
Graphite + ABC*	15	26	No ignition

* After use in high-temperature synthesis of CF_4.

[1] This mixture simulates an anodic gas produced by the Angarsk Electrolysis Chemical Combine.

Table 2. Composition of the reaction gas and temperatures of thermocouples T1–T3 at various times of the synthesis t_s and fluorine flow rates W_{F_2}

Raw material	W_{F_2}, $cm^3\ s^{-1}$	t_s, s	T, °C			Content, vol %					Breakthrough of F_2
			T1	T2	T3	CF_4	C_2F_6	C_2F_4	CO_2	C_3F_8	
Graphite	40	83	36	42	44	11.5	0.70	–	87.8	–	+
	40	165	36	42	71	80.1	3.12	–	15.5	1.20	+
	40	140	31	45	96	95.6	3.11	–	–	1.27	+
	40	330	29	15	168	98.2	1.22	–	–	0.48	+
	40	435	27	678	281	99.2	0.54	–	–	0.26	+
	40	540	>1100	637	358	96.6	2.68	–	–	0.81	+
	40	623	>1100	627	369	99.3	0.45	–	–	0.14	+
	40	735	>1100	1072	358	99.4	0.41	–	–	0.11	+
	40	825	>1100	>1200	350	99.6	0.25	–	–	0.18	+
	7	68	40	35	37	–	–	–	–	–	+
	7	112	45	35	40	–	23.8	75.7	–	–	+
	7	435	40	26	29	–	–	–	–	–	+
Graphite*	45	53	45	23	25	67.6	–	10.9	19.2	–	+
	45	135	55	25	28	88.1	–	11.9	–	–	+
	45	270	55	25	26	–	–	100	–	–	+
	45	360	55	24	25	–	–	100	–	–	+
	45	570	54	21	23	–	–	100	–	–	+
	26	98	20	25	22	–	–	–	100	–	+
	26	210	22	26	34	–	–	–	100	–	+
	26	298	22	26	34	–	–	–	100	–	+
	26	383	29	25	34	–	–	–	–	–	+
	26	495	29	25	32	–	–	–	–	–	+
	26	600	29	24	24	–	–	–	–	–	+
Graphite + ABC	40	120	57	–	–	100	–	–	–	–	+
	40	278	452	–	–	95.8	3.28	–	–	0.73	+
	40	330	713	–	–	90.5	7.83	–	–	1.65	–
	40	405	748	–	–	91.6	5.69	–	0.5	1.87	–
	40	623	–	–	–	99.2	0.55	–	–	0.22	–
	40	675	–	–	–	99.4	0.58	–	–	–	–
Graphite + ABC*	40	180	39	–	–	–	–	–	100	–	+
	40	255	35	–	–	–	–	–	100	–	+
	40	375	35	–	–	49.8	34.9	–	15.3	–	+

* After the use in high-temperature synthesis of CF_4.

couples T2 and T3, and, as a result, a counterwave of the filtration carbon combustion in fluorine is formed. It propagates upwards the flow, is stabilized in the region of fluorine outlet from the nozzle, and transforms into the inverse wave. The counterwave of carbon combustion in fluorine propagates in the filtration mode; there is no fluorine breakthrough beyond the reaction front. The wave linear velocity between thermocouples T2 and T1 is 900 mm h^{-1} with respect to the level of 600°C.

The time of ignition delay of the initial graphite is several hundreds of seconds. In this time, carbon polyfluoride is accumulated, which then decomposes with formation of gaseous fluoroalkanes containing CF_4. Under the laboratory conditions, after the first 900 s of the synthesis, the product containing 99.5 vol % CF_4 was prepared. The main impurities were C_2F_6 and C_3F_8.

To control the possibility of shutdown and startup of the industrial reactor of the TFM synthesis after cooling the reaction zone, we made experiments with graphite treated with fluorine in the high-temperature zone and found that, under laboratory conditions at the initial temperature of 15°C, such graphite was not ignited.

Hence, to obtain pure TFM and provide stable reactor startup, special measures are required to intensify the ignition.

One of the methods of the ignition intensification is adding certain amount of activated charcoal to the graphite packing. The charcoal has substantially larger specific surface area as compared to graphite and provides higher reaction rate. We performed a series of experiments with graphite + ABC mixture using the above method. The results are given in Tables 1 and 2.

The time of ignition delay for freshly prepared graphite + ABC mixture was 250 s at fluorine flow rate of 40 $cm^3 s^{-1}$; there was fluorine breakthrough through the graphite bed. After 700 s of the synthesis, pure CF_4 was not obtained; the hexafluoroethane impurity was 0.6 vol %. In the case of spent mixture and at fluorine flow rate of 15 $cm^3 s^{-1}$, no ignition was observed.

The above facts show that the time of the ignition delay with ABC as initiator decreases, but the problem of the startup period (accumulation of thermolabile carbon polyfluoride under the synthesis conditions) remains. In addition, the spent graphite + ABC mixture, similarly to pure graphite, has startup characteristics differing from those of the freshly prepared mixture.

Using ABC as initiator in an industrial reactor may have the following substantial disadvantage. In the case of faster ABC burn-out as compared to graphite, the ABC in the region of fluorine feeding into the carbon bed can get exhausted after prolonged reactor functioning, which worsens the reactor startup parameters (time of ignition delay, time of attaining the steady-state mode).

In this work, we suggest the following method of the reactor startup. At startup, a gas forming with fluorine a self-igniting pair is introduced into the graphite bed coaxially to the fluorine flow. After formation of high-temperature (> 1000 K) zone, owing to heat liberated in oxidation of this gas with fluorine, feeding of the gas is turned off, and the TFM synthesis is performed.

Taking into account high reactivity of fluorine, readily available methane, propane, ethylene, etc. can be used as a gaseous fuel.

Among the above gases, ethylene is the most reactive with respect to fluorine, since in the fluorine–ethylene system a branched chain reaction mechanism is realized [13]. Therefore, in laboratory trials of this method, we used a mixture consisting of 85 vol % H_2 and 15 vol % ethylene and VAZ graphite (initial and spent). The nozzle for feeding fluorine and gas fuel consists of two coaxial tubes. Fluorine was fed through the axial channel, and a mixture consisting of hydrogen and ethylene, through the ring channel.

Table 3. Time t_{350} at various flow rates of fluorine W_{F_2} and ethylene + hydrogen mixture W_{mix}, d = 0.85 mm

Mixture	W_{mix}, $cm^3 s^{-1}$	W_{F_2}, $cm^3 s^{-1}$	U_{F_2}, $m s^{-1}$	t_{350}, s
$H_2 + C_2H_4$	13	26	46	188
	13	13	23	270
$C_3H_8 + C_4H_{10}$	3.7	26	46	128
	1.8	14	25	173

The gaseous fuel was fed for 10 s, and then fluorine feeding at a preset flow rate was started. When the temperature near the thermocouple T2 junction reached 350°C, feeding the gaseous fuel was stopped, while feeding fluorine with the preset flow rate was continued.

The time intervals between the beginning of fluorine feeding and attainment of 350°C near the thermocouple T2 junction, t_{350}, for various flow rates of fluorine and gas mixture are listed in Table 3. The compositions of the reaction products after stopping feeding of the ethylene + hydrogen mixture and measurement of the temperature of the graphite bed are listed in Table 4.

At the instant of fluorine feeding into the graphite bed, thermocouple T1 recorded a jump of temperature from the initial value to more than 1300°C, after which it burnt down. Thermocouples T2 and T3 recorded smooth temperature rise, and after approximately 5 min, thermocouple T2 recorded the temperature of 150–300°C.

Table 4 shows that, after stopping the supply of the gaseous fuel, a stable high-temperature inverse wave of the CF_4 synthesis is formed in the graphite bed. The time interval from stopping the gaseous fuel feeding to obtaining pure CF_4 (more than 99.9 vol %) does not exceed 500 s.

No fluorine breakthrough through the graphite bed was observed. All experiments of this series were performed with graphite that worked in the high-temperature zone of the synthesis.

Thus, the use of gaseous fuel allows stable startup of the wave reactor of TFM synthesis without ac-

Table 4. Composition of the synthesis products and temperatures of thermocouples T1–T3 at various synthesis times t_s after stopping supply of ethylene + hydrogen or propane–butane mixture*

t_s, s	*T*, °C			Content, vol %				
	T1	T2	T3	CF_4	C_2F_6	C_3F_8	CO_2	HF
				$H_2 + C_2H_4$ mixture				
45	>1300	548	29	97.2	–	2.8	–	–
90	>1300	644	30	98.8	–	1.2	–	–
157	>1300	822	39	99.7	–	0.3	–	–
202	>1300	974	51	99.9	–	0.1	–	–
270	>1300	>1100	67	99.96	–	0.04	–	–
300	>1300	>1100	71	99.94	–	0.06	–	–
15	>1300	207	26	94.48	–	5.52	–	–
90	>1300	373	26	97.16	–	2.84	–	–
150	>1300	693	28	99.91	0.06	0.3	–	–
225	>1300	1189	30	99.96	0.03	0.02	–	–
315	>1300	>1100	32	99.95	0.03	0.02	–	–
465	>1300	>1100	48	100.0	–	–	–	–
600	>1300	>1100	68	99.99	0.01	–	–	–
743	>1300	>1100	94	99.96	0.03	0.01	–	–
840	>1300	–	30	99.97	–	0.03	–	–
150	>1300	–	–	99.50	–	4.50	–	–
330	>1300	–	–	99.50	–	0.50	–	–
420	>1300	–	–	100.0	–	–	–	–
225	>1300	–	–	94.20	–	5.60	–	–
360	>1300	–	–	99.50	–	0.50	–	–
472	>1300	–	–	99.90	–	0.10	–	–
630	>1300	–	–	100.0	–	–	–	–
105	>1300	–	–	88.50	–	11.50	–	–
225	>1300	–	–	96.70	–	3.30	–	–
315	>1300	–	–	99.50	–	0.50	–	–
405	>1300	–	–	99.90	–	0.10	–	–
555	>1300	–	–	100.0	–	–	–	–
				$C_3H_8 + C_4H_{10}$ mixture				
30	>1300	589	28	–	0.50	–	–	–
83	>1300	960	29	96.13	0.08	–	0.32	2.75
150	>1300	>1100	29	99.38	0.03	–	0.04	0.50
210	>1300	>1100	28	99.75	–	–	–	0.23
300	>1300	>1100	44	99.92	–	–	–	0.08
360	>1300	>1100	62	99.95	–	–	–	0.05
30	>1300	489	30	93.14	0.77	–	0.18	5.42
105	>1300	>1100	31	87.85	1.31	–	0.24	9.62
240	>1300	>1100	38	98.78	0.13	–	0.07	0.94
315	>1300	>1100	52	99.29	0.09	–	0.06	0.56
480	>1300	>1100	80	99.64	0.03	–	0.03	0.30
750	>1300	>1100	207	99.91	–	–	0.02	0.07
855	>1300	>1100	267	99.94	–	–	0.01	0.05
1065	>1300	>1100	402	99.99	–	–	–	0.01

* No F_2 breakthrough.

cumulation of carbon polyfluoride in the reactor in the starting period.

Fluorine produced at electrolysis plants contains impurities of HF, N_2, and O_2. To reveal the effect of HF on the TFM synthesis, we made experiments with an F_2 + 9 vol % HF mixture simulating electrolysis gas produced by the Angarsk electrolysis chemical combine and found that HF does not affect the starting characteristics and the composition of the synthesis products.

Propane–butane mixture is the most widespread commercial gaseous fuel. Therefore, we performed some experiments on its use to obtain high-temperature zone of TFM synthesis. The scheme of the laboratory device and experimental procedure were the same as above. The results are presented in Tables 3 and 4.

Thermocouple T1 at the instant of fluorine feeding recorded a temperature jump from the initial value to that higher than 1300°C. The pattern of formation of the high-temperature zone was similar to that observed with ethylene–hydrogen mixture.

The above data show that, under the industrial conditions, startup of the reactor of the TFM synthesis from electrode graphite and F_2 in the mode of the inverse wave of the filtration combustion is the most reliable when a gaseous fuel is used. In this case, the process can be organized so as to minimize accumulation of carbon polyfluoride in the reactor volume in the time of formation of the high-temperature zone and ensure the time of attainment of working conditions not exceeding 10 min. The propane–butane mixture can be recommended as the most readily available.

CONCLUSIONS

(1) A laboratory device was developed, and conditions of formation of high-temperature wave of filtration combustion in fluorine of graphite and its mixtures with activated birch charcoal were studied.

(2) At temperatures higher than 1000°C, tetrafluoromethane is the single product of fluorine reaction with graphite.

(3) At the initial temperature of the bed of graphite (or its mixture with activated birch charcoal) of 20°C, the ignition process is instable, and formation of the high-temperature zone of the synthesis depends of the fluorine flow velocity and carbon raw material history.

(4) The method of formation of the high-temperature synthesis zone with a gaseous fuel, which forms with fluorine a self-igniting pair in the graphite bed, was suggested and experimentally examined. This method allows formation of a stable wave of graphite filtration combustion in fluorine. Propane–butane mixture can be recommended for industrial use.

REFERENCES

1. Maksimov, B.N., Barabanov, V.G., Serushkin, I.L., *et al.*, *Promyshlennye ftororganicheskie produkty: Spravochnik* (Industrial Organofluorine Products: Handbook), St. Petersburg: Khimiya, 1996.
2. Ruff, O. and Keim, R., *Z. Anorg. Chem.*, 1930, vol. 192, pp. 249–256.
3. Ruff, O. and Brettschneider, O., *Z. Anorg. Chem.*, 1934, vol. 717, pp. 1–19.
4. Ruff, O., *Trans. Farad. Soc.*, 1930, vol. 34, pp. 1022–1025.
5. Kuriakose, A.K. and Margrave, J.L., *J. Phys. Chem.*, 1965, vol. 69, pp. 2772–2775.
6. Ruddorff, O. and Ruddorff, G., *Z. Anorg. Allg. Chem.*, 1947, vol. 253, pp. 281–285.
7. Simons, H.J. and Dlock, L.P., *J. Am. Chem. Soc.*, 1939, vol. 61, pp. 2962–2966.
8. Timofeev, N.V., *Sbornik rabot po sintezy i svoistvam ftoruglerodnykh soedinenii* (Coll. of Papers on Synthesis and Properties of Fluorocarbon Compounds), Leningrad: GIPKh, 1967, issue 2, pp. 3–11.
9. Timofeev, N.V. and Stepanov, V.P., *Materialy 1 Mezhvedomstvennoi konferentsii po khimii i tekhnologii soedinenii ftora* (Proc. 1st Interdepartmental Conf. on Chemistry and Technology of Fluorine Compounds), Leningrad: GIPKh, 1973, pp. 23–27.
10. Kita, Y. and Watanabe, N., *J. Am. Chem. Soc.*, 1979, vol. 101, no. 14, pp. 3832–3841.
11. Watanabe, N., Koyama, S., and Imoto, H., *Bull. Chem. Soc. Jpn.*, 1980, vol. 53, pp. 3093–3099.
12. Aldushin, A.P. and Merzhanov, A.G., in *Rasprostranenie teplovykh voln v geterogennykh sredakh* (Propagation of Heat Waves in Heterogeneous Media), Novosibirsk: Nauka, 1988, pp. 8–52.
13. Semenov, N.N., *Khimicheskaya fizika (fizicheskie osnovy khimicheskikh prevrashchenii)* (Chemical Physics (Physical Principles of Chemical Transformations)), Moscow: Nauka, 1978.

Russian Journal of Applied Chemistry, Vol. 77, No. 1, 2004, pp. 98–101. Translated from Zhurnal Prikladnoi Khimii, Vol. 77, No. 1, 2004, pp. 102–105.

ORGANIC SYNTHESIS AND INDUSTRIAL ORGANIC CHEMISTRY

Synthesis and Use of Partially Fluorinated Dialkyl Ethers Derived from Hexafluoropropylene

A. A. Il'in, Yu. L. Bakhmutov, L. M. Ivanova, G. G. Furin, T. G. Tolstikova, and V. S. Sukhinin

Galogen Open Joint-Stock Company, Perm, Russia
Vorozhtsov Novosibirsk Institute of Organic Chemistry, Siberian Division, Russian Academy of Sciences, Novosibirsk, Russia
Perm State Technical University, Perm, Russia

Received June 19, 2003

Abstract—A procedure was developed for preparing partially fluorinated dialkyl ethers by the reaction of hexafluoropropylene with aliphatic and polyfluorinated alcohols in the presence of KOH. On treatment with concentrated sulfuric acid, these ethers form alkyl esters of acids, and on treatment with KOH, alkenyl ethers.

The problems in development of new ozone-friendly solvents are largely determined by the need in replacement of Freon 113, widely used as solvent. The main drawback of this Freon is that hydrocarbon oils are limitedly or poorly soluble in it, and organofluorine and organosilicon liquids are insoluble. Major efforts in this direction have not led to success. Orlov *et al.* [1] suggested as one of alternatives hexafluorocyclobutane, which is an efficient solvent for various azeotropic compositions. This compound can be prepared on the commercial scale from dichlorohexafluorocyclobutane, which, in turn, is obtained by dimerization of trifluorochloroethylene. At the same time, partially fluorinated dialkyl ethers are also of interest. The 3M company developed Freon HFE 7110, $CH_3OCF_2CF_2CF_2CF_3$, but it also has certain drawbacks, whereas tetrafluoroethyl difluoromethyl ether $CHF_2CF_2OCHF_2$ can replace Freon 11 as a foaming agent in production of foamed plastics and can be used in microelectronics in dry etching instead of perfluorocarbons [2]. Ethers like $C_4F_9OCH_3$ (bp 61°C), $(CF_3)_2CFCF_2OC_2H_5$, and others, used for extraction of lavender essential oils, showed good performance with respect to the quality of the extracted product and the purity of the oils obtained therefrom [3]. These ethers were used as solvents in chemical reactions, in particular, in synthesis of amides derived from fluoropolyalkyl ethers for magnetic reproducing media [4] and in oxidation of tetrafluoroethylene [5].

Partially fluorinated ethers were prepared by reactions of hexafluoropropylene with alcohols in the presence of alkali [6, 7] or with metal alcoholates in toluene [8], dioxane [9], or methanol [10]. Polyoxaalkylene glycols add to hexafluoropropylene in the presence of water traces across the olefin double bond; the resulting adducts are used as compression, motor, and vacuum oils [11]. Fully fluorinated dialkyl ethers prepared by reactions of octafluoroisobutylene with alcohols, followed by further electrochemical fluorination in anhydrous HF, e.g., $(CF_3)_2CFCF_2OC_nF_{2n+1}$, are used as solvents for cleaning electronic circuits, as refrigerants, as foaming agents, and as polymerization media [12–14].

The goal of this study was to develop a commercially acceptable procedure for synthesis of partially fluorinated dialkyl ethers from available and relatively cheap hexafluoropropylene and to examine the possibilities of using these ethers as ozone-friendly solvents and as intermediates in organofluorine synthesis.

When gaseous hexafluoropropylene is passed at 20–40°C through alcohols containing catalytic amounts of sodium alcoholates or alkalis (the reaction can also be performed in a pressure vessel), the alcohol adds across the double bond. The reaction pathway only slightly depends on the conditions. The byproducts are alkenyl ethers formed by substitution of the terminal fluorine atom at the double bond by alkoxy groups and alkyl 2,3,3,3-tetrafluoropropionates; their amount does not exceed 5% (cf. data from [15]):

$$CF_3CF{=}CF_2 \xrightarrow[ROH]{5\%\ KOH} CF_3CHFCF_2OR$$

$$+\ CF_3CF{=}CFOR + CF_3CHF{-}\underset{OR}{\overset{O}{\langle\!\!\langle}},$$

where R = Me (**I**, **V**, **VII**), Et (**II**, **VI**, **VIII**), Pr-*i* (**III**), $CHF_2CF_2CH_2$ (**IV**).

1070-4272/04/7701-0098 © 2004 MAIK "Nauka/Interperiodica"

Table 1. ^{1}H, ^{13}C, and ^{19}F NMR spectra of new partially fluorinated dialkyl ethers

Compound	^{1}H NMR spectrum, δ_H, ppm (J, Hz)	^{13}C NMR spectrum, δ_C, ppm (J_{C-F}, Hz)	^{19}F NMR spectrum, δ_F, ppm (J, Hz)
I	4.72 td (H^2, 36.4, 9.2), 3.63 (H^4)	120.4 (C^1, $^1J_{CF}$ 255.9, $^2J_{CF}$ 25.5), 118.8 (C^3, $^1J_{CF}$ 249.9, $^2J_{CF}$ 45.1), 87.6 (C^2, $^1J_{CF}$ 200.6, $^2J_{CF}$ 35.9), 50.0 (C^4, $^3J_{CF}$ 7.1)	88.4 (F^1), *AB* system (F^3) 80.4 and 77.7 (J_{FF} 151.6), –48.2 (F^2)
II	4.71 td (H^2, 43.2, 5.5), 4.03 (H^4, 7.1), 1.29 (H^5, 7.1)	120.3 (C^1, $^1J_{CF}$ 280.0, $^2J_{CF}$ 25.4), 118.7 (C^3, $^1J_{CF}$ 265.9, $^2J_{CF}$ 25.4), 85.1 (C^2, $^1J_{CF}$ 200.0, $^2J_{CF}$ 35.7), 60.7 (C^4, $^2J_{CF}$ 6.2), 14.2 (C^5)	87.5 (F^1), *AB* system 83.5 and 80.5 (J_{FF} 153.4), –48.3 (F^2)
III	4.66 (H^2, 50), 4.65 (H^4, 6.5), 1.29 ($H^{5,6}$, 6.5)	120.1 (C^1, $^1J_{CF}$ 309.8, $^2J_{CF}$ 26.0), 118.7 (C^3, $^1J_{CF}$ 277.3, $^2J_{CF}$ 21.9), 85.2 (C^2, $^1J_{CF}$ 200.3, $^2J_{CF}$ 37.6), 77.7 (C^4), 22.8 ($C^{5,6}$)	88.2 (F^4), *AB* system 85.9 and 82.1 (J_{FF} 152.5), –48.1 (F^2, J_{FH} 40, J_{FF} 12.5)
IV	4.29 t (H^4, 50), 4.65 (H^2, 6.5), 1.29 ($H^{5,6}$, 6.5)	119.9 (C^1, $^1J_{CF}$ 281.4, $^2J_{CF}$ 27.6), 114.1 (C^6, $^1J_{CF}$ 220.6, $^2J_{CF}$ 28.0), 109.1 ($C^{3,5}$, $^1J_{CF}$ 250.1, $^2J_{CF}$ 35.8), 85.0 (C^2, $^1J_{CF}$ 201.9, $^2J_{CF}$ 34.9), 60.5 (C^4, $^2J_{CF}$ 30.8),	88.4 (F^1), *AB* system 38.8 (F^5) and 25.2 (F^6) (J_{FF} 149.7), *AB* system (F^3) 82 and 79.8 (J_{FF} 148.9), –48.4 (F^2)
VII	5.27 (H^2, 44.0, 6), 3.88 (H^4), 1.33 (H^5)	120.5 (C^1, $^1J_{CF}$ 281.9, $^2J_{CF}$ 25.8), 84.1 (C^2, $^1J_{CF}$ 199.5, $^2J_{CF}$ 35.8), 53.3 (C^4)	87.6 (F^1, 8, 12), –41.2 (F^2, 32, 10)
VIII	5.10 (H^2, $^1J_{HF}$ 45, $^2J_{HF}$ 7) 4.36 (H^4, $^2J_{HH}$ 7.1), 1.34 (H^5, $^2J_{HH}$ 7.1)	120.5 (C^1, $^1J_{CF}$ 281.9, $^2J_{CF}$ 27.8), 84.1 (C^2, $^1J_{CF}$ 199.2, $^2J_{CF}$ 35.6), 63.0 (C^4), 13.2 (C^5)	86.5 (F^1, 8, 12), –42.2 (F^2, 45, 10)

The reaction involves the attack of the alkoxy anion at the carbon atom of the hexafluoropropylene double bond, with generation of the intermediate carbanion. This species abstracts the proton from the solvent to form the main reaction product **I**–**IV**. Stabilization of the carbanion by elimination of the fluoride ion from the α-position (from the CF_2 fragment) yields the product of formal substitution of fluorine at the double bond (compounds **V**, **VI**). The hydrogen fluoride released in the process reacts with the alkali, and water participates in formation of the addition product and can induce hydrolysis of both by-products **V**, **VI** and target products **I**–**IV**. This is suggested by isolation of HF from the mixture of reaction products and formation of alkyl 2,3,3,3-tetrafluoropropionates **VII** and **VIII**:

$$CF_3CF{=}CF_2 \xrightarrow{RO^-} [\,CF_3\bar{C}F\,CF_2OR\,]$$

$$\xrightarrow{H^+} CF_3CHF\,CF_2OR \xrightarrow{H_2O}$$

$$\xrightarrow[-F^-]{} CF_3CF{=}CFOR \xrightarrow{H_2O} CF_3CHF{-}\overset{\displaystyle O}{\overset{\|}{C}}{-}OR\,.$$

Indeed, heating of **I** and **II** with concentrated sulfuric acid at 40°C for 1 h, followed by treatment of the reaction mixture with water, causes formation of compounds **VII** [6] and **VIII** in quantitative yield, and heating with solid KOH in dioxane affords **V** and **VI**:

$$CF_3CHF\,CF_2OR \xrightarrow[(2)\ H_2O]{(1)\ H_2SO_4} CF_3CHF{-}\overset{\displaystyle O}{\overset{\|}{C}}{-}OR$$

$$CF_3CHF\,CF_2OR \xrightarrow[\text{Dioxane}]{KOH} CF_3CF{=}CFOR\,,$$

where R = Me or Et.

The structures of the new compounds were confirmed by ^{1}H, ^{13}C, and ^{19}F NMR (Table 1), IR, and mass spectrometry.

For partially fluorinated dialkyl ethers, telomeric alcohols, and partially fluorinated carboxylic acid ester, we evaluated the toxicological parameters. The results are listed in Table 2. It is seen that the compounds belong to hazard class III (moderately toxic) or IV (weakly toxic substances).

Table 2. Some toxicological parameters of organofluorine compounds

Compound	LD_{50}	LD_{100}	Hazard class
	mg kg^{-1}		
$CF_3CHFCF_2OCH_2CF_2CHF_2$	5000		IV
$HCF_2CF_2CH_2OCH_2CH_3$	3420	6000	III
$HCF_2CF_2CH_2OH$	2320	3000	III
$HCF_2CF_2CF_2CF_2CH_2OH$	1180	2000	III
$CF_3CHFC(O)OCH_2H_5$	5000		IV

EXPERIMENTAL

The ^1H, ^{13}C, and ^{19}F NMR spectra were recorded on a Bruker WP 400 SY spectrometer (400, 100, and 188 MHz, respectively) relative to internal HMDS and C_6F_6 (J_{CH} was not measured). The IR spectra were taken on a Specord M-80 spectrometer (CCl_4), and the mass spectra (ionizing electron energy 70 eV), on a Hewlett–Packard G 1800 A GCD gas chromatograph with a mass-selective detector [30 m × 0.25 mm capillary column coated with a 0.25-μm layer of 5% diphenylsiloxane–95% dimethylsiloxane copolymer (HP-5); carrier gas helium, 1 ml min^{-1}; vaporizer temperature 280°C; column temperature schedule: 50°C, 2 min; heating to 280°C at a rate of 10 deg min^{-1}; 280°C, 5 min]. The progress of all the reactions was monitored by ^{19}F NMR spectroscopy. The reaction mixtures were analyzed on an LKhM 72 chromatograph (15% SE-30, SKTF-803, QF-1 on Chromosorb W, 4000 × 4-mm column).

The characteristics of the new compounds and analytical data are listed in Table 3.

Synthesis of partially fluorinated dialkyl ethers. (1) A 100-ml flask equipped with a magnetic stirrer, a thermometer, a tube for input of gaseous reactants, and a reflux condenser was charged with 40 ml of absolute methanol, and 1 g of sodium metal was added in portions at room temperature. After complete dissolution of sodium, gaseous hexafluoropropylene was passed at a rate chosen so as to minimize the breakthrough of the gas. The process was performed for 1.5 h, after which the reaction mixture was poured into 300 ml of water and shaken; the lower organic layer was separated and dried over CaCl2. The mixture was analyzed by ^{19}F NMR spectroscopy and gas chromatography–mass spectrometry. The mixture was distilled with collection of the 54–55°C fraction (33 g).

(2) A similar flask was charged with 50 ml of an alcohol (methanol, ethanol, isopropanol, 2,2,3,3-tetrafluoropropanol) and 5 g of KOH. A flow of gaseous hexafluoropropylene was passed at atmospheric pressure; in the process, the mixture warmed up from 20 to 40°C. After the heat release ceased, passing of hexafluoropropylene was stopped, the mixture was poured into 400 ml of cold water and shaken, and the lower organic layer was separated, washed with 100 ml of water, and dried over $CaCl_2$. The products were distilled and analyzed.

(3) A 100-ml rotating autoclave was charged with 10 ml of methanol and 11.2 g of solid KOH; then the autoclave was sealed, and 30 g of hexafluoropropylene was condensed into it through a valve. The autoclave was heated at 50°C for 1 h (the pressure rose to 4 atm), cooled, and opened; the contents were poured into water. Compound **I** was obtained; yield 34.2 g (94%), bp 54–55°C.

Table 3. Characteristics of partially fluorinated dialkyl ethers and analytical data

Compound	Yield, %	T_b, °C	n_D^{20}	d_4^{20}	Found, %			m/z $[M-H]^+$	Formula	Calculated, %			M
					C	H	F			C	H	F	
I	98	54–55	1.3470	1.4200				181	$C_4H_4F_6O$				182
II	99	64–65	1.3460	1.3040	31.79 31.64	3.19 3.05	57.73 57.91	196*	$C_5H_6F_6O$	30.61	3.06	58.16	196
III	88	85–86	1.3230	1.280				210*	$C_6H_8F_6O$				210
IV	87	102–103	1.2930	1.578	26.11 25.88	1.73 1.69	67.11 67.28	282*	$C_6H_4F_{10}O$	25.53	1.42	67.38	282
VII	60	95–96	1.3200	1.358	29.78 30.08	2.46 2.31	46.86 46.61	159	$C_4H_4F_4O_2$	30.00	2.50	47.50	160
VIII	94	103–104	1.3340	1.3040	34.36 34.43	3.44 3.55	44.30 44.67	174*	$C_5H_6F_4O_2$	34.48	3.45	43.68	174

* $[M^+]$.

Hydrolysis of partially fluorinated dialkyl ethers. (1) A 20-ml flask equipped with a magnetic stirrer and a reflux condenser was charged with 15 g of **I** (with **II**, the procedure was similar), and 15 g of concentrated sulfuric acid was added. The mixture slightly warmed up. Then the mixture was heated with stirring for 1 h at 40°C and poured onto 50 g of ice; the organic layer was separated, washed with water, and dried over $CaCl_2$.

By this procedure, we prepared 10 g of compound **VIII** to be used in the subsequent studies as intermediate.

(2) A similar flask was charged with 27 g of SbF_5, and 15 g of **II** was added in portions with stirring, so as to avoid warming up above room temperature. The mixture was stirred at room temperature for 1 h and poured into 50 g of ice; the organic layer was separated, washed with cold water, and dried over $CaCl_2$. The product was distilled, with collection of the fraction boiling at 95–96°C; yield 8 g.

Reaction of KOH with partially fluorinated dialkyl ethers. A 100-ml flask equipped with a magnetic stirrer, a thermometer, and a reflux condenser was charged with 40 g of **I** (with **II**, the procedure was similar) and 50 ml of dry dioxane, after which finely divided KOH was added in portions with stirring at room temperature. The mixture warmed up. Then the mixture was heated with stirring for 2 h at 40°C, and the reaction products were distilled off. Compound **V**: yield 82%, bp 51–52°C, n_D^{20} 1.3208, d_4^{20} 1.3601 (published data [8]: bp 51.5°C/743 mm Hg, n_D^{20} 1.2970, d_4^{20} 1.3595); **VI**: yield 78%, bp 71–72°C, n_D^{20} 1.3210, d_4^{20} 1.2930 (published data [8]: bp 71–72°C/743 mm Hg, n_D^{20} 1.3103, d_4^{20} 1.2884).

CONCLUSIONS

(1) The possibility of preparing partially fluorinated dialkyl ethers by reaction of hexafluoropropylene with alcohols (methanol, ethanol, isopropanol, 2,3,3,3-tetrafluoropropanol) in the presence of KOH was examined. These ethers are formed by addition of an alcohol across the double bond in hexafluoropropylene.

(2) Partially fluorinated dialkyl ethers are converted to alkyl 2,3,3,3-tetrafluoropropionates by treatment with concentrated H_2SO_4 and to alkyl pentafluoropropenyl ethers by treatment with KOH.

ACKNOWLEDGMENTS

The study was financially supported by grant no. 47 (2002) for innovation projects of the Siberian Division, Russian Academy of Sciences.

REFERENCES

1. Orlov, A.P., Shchavelev, V.B., and Korol'kov, D.N., Abstracts of Papers, *3-ya Mezhdunarodnaya konferentsiya "Khimiya, tekhnologiya i primenenie ftorsoedinenii"* (3rd Int. Conf. "Chemistry, Technology, and Use of Fluoro Compounds"), St. Petersburg (Russia), June 6–9, 2001, report R 1-34, p. 170.
2. Orlov, A.P., Shchavelev, V.B., Barabanov, V.G., and Korol'kov, D.N., Abstracts of Papers, *3-ya Mezhdunarodnaya konferentsiya "Khimiya, tekhnologiya i primenenie ftorsoedinenii"* (3rd Int. Conf. "Chemistry, Technology, and Use of Fluoro Compounds"), St. Petersburg (Russia), June 6–9, 2001, report R 1-36, p. 172.
3. FR Patent Appl. 2 771 408.
4. US Patent 6 187 954.
5. RF Patent Appl. 97 102 618/04.
6. Knunyants, I.L., Shchekotikhin, A.I., and Fokin, A.V., *Izv. Akad. Nauk SSSR, Otd. Khim. Nauk*, 1953, no. 2, pp. 282–289.
7. US Patent 2 862 024.
8. Bargamova, M.D., Cheburkov, Yu.A., Dyatkin, B.L., *et al.*, *Izv. Akad. Nauk SSSR, Ser. Khim.*, 1967, no. 3, pp. 611–614.
9. Dyatkin, B.L., Konstantinov, Yu.S., Lantseva, L.T., *et al.*, *Zh. Org. Khim.*, 1967, vol. 3, no. 6, pp. 1006–1011.
10. England, D.C., Solomon, L., and Krespan, C.G., *J. Fluorine Chem.*, 1973, vol. 3, no. 1, pp. 63–89.
11. Popova, L.M., Vinogradova, V.N., Prytkova, O.A., *et al.*, Abstracts of Papers, *2-ya Mezhdunarodnaya konferentsiya "Khimiya, tekhnologiya i primenenie ftorsoedinenii"* (2nd Int. Conf. "Chemistry, Technology, and Use of Fluoro Compounds"), St. Petersburg (Russia), September 23–26, 1997, report Z 3-9, p. 123.
12. US Patent 5 474 657.
13. US Patent 5 516 946.
14. Novikova, M., Zakharov, V., Denisov, A., and Jukova, V., *J. Fluorine Chem.*, 1992, vol. 58, nos. 2–3, p. 169.
15. Gubanov, V.A., Tumanova, A.V., and Dolgopol'skii, I.M., *Zh. Obshch. Khim.*, 1965, vol. 35, no. 2, pp. 398–399.

Russian Journal of Applied Chemistry, Vol. 77, No. 1, 2004, pp. 102–105. Translated from Zhurnal Prikladnoi Khimii, Vol. 77, No. 1, 2004, pp. 106–108.

ORGANIC SYNTHESIS AND INDUSTRIAL ORGANIC CHEMISTRY

Ozonolysis of Methylcyclohexanols and Methylcyclohexanones

A. M. Syroezhko and O. Yu. Begak

St. Petersburg State Technological Institute, St. Petersburg, Russia
Mendeleev Research Institute of Metrology, Federal State Unitary Enterprise, St. Petersburg, Russia

Received March 20, 2003

Abstract—Ozonolysis of isomeric methylcyclohexanols and methylcyclohexanones was studied.

Oxidation of methylcyclohexane with ozone–oxygen mixtures involves formation of isomeric methylcyclohexanols (MCHLs) and methylcyclohexanones (MCHNs), which subsequently transform into acids and esters. Previously we studied ozonolysis of cyclohexanol [1], cyclohexanone [2], and 1-methylcyclohexanol [3].

Here we consider ozonolysis of secondary alcohols (MCHLs) and the corresponding isomeric MCHNs. The oxidation and analytical procedures are described in [4].

In ozonolysis of methylcyclohexane (MCH), the accumulating secondary and tertiary alcohols are actively consumed. For example, the rate of ozonolysis of 2-methylcyclohexanol grows from 8.3×10^{-3} to 22.2×10^{-3} mol l^{-1} min^{-1} as the temperature is increased from 40 to 100°C ([O_3] = 4 vol %).

Ozonolysis of secondary MCHLs yields the corresponding isomeric MCHNs (see table), hydroxy hydroperoxides, hydrogen peroxide, esters, and acids [5, 6]. The composition of the acids was studied in detail in [7–9]. The selectivity of ozonolysis of isomeric MCHLs is higher compared to their oxidation with oxygen [6, 10–18]; the yields of the target products are given in the table.

Recombination of hydroperoxy radicals and their reaction with ozone can yield hydroxyalkoxy radicals, which isomerize to form mono- and dicarboxylic acids [19–22]. The acids are also formed by reaction of hydroxy hydroperoxides derived from MCHLs with ozone [6, 15, 16]. The $RO^{\cdot}$ radical is also a source of acids at elevated temperatures. It is formed from the adduct $2ROH \cdot H_2O_2$ [18] with the activation energy of 19 kJ mol^{-1}. In the developed ozonolysis of isomeric MCHLs, the accumulating MCHNs are actively oxidized into acids [20–22] and lactones.

The abnormally high reactivity of ozone toward nonassociated primary and secondary alcohols [8, 9], along with the reactivity of ozone with alcoholic C–H bonds, discussed in this paper, may also be due to concerted detachment of hydrogen from the alcoholic hydroxy group with ozone [23]:

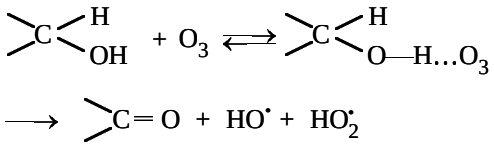

Yield of ozonolysis products of secondary MCHLs* ([O_3] = 4 vol %)

T, °C	MCHL conversion, %	Acid content, mol % relative to sum of acids	Yield of MCHN based on converted MCHL, %
		4-MCHL	
40	10	80	79
	25	76	75
80	10	79	83
	25	74	73
100	10	83	75
	25	71	72
	50		66
		2-MCHL	
40	10	93	
	25	90	
80	10	89	80
	25		75
100	15	88	74
	30	87	63
		2-MCHL	
80	10	75	68
	25	72	42

* Major products: 4-MCHL, β-methyladipic acid and 4-methylcyclohexanone; 2-MCHL, ε-ketoenanthic acid and 2-methylcyclohexanone; and 3-MCHL, sum of α- and β-methyladipic acids and 3-methylcyclohexanone.

1070-4272/04/7701-0102 © 2004 MAIK "Nauka/Interperiodica"

This reaction is exothermic (ΔH –46 kJ mol^{-1} [23]) at the C–H bond energy of 360 kJ mol^{-1}. Simple hydrogen detachment from the C–H group is endothermic (ΔH 40 kJ mol^{-1}). Most probably, ozone reacts with alcohols not only by the radical mechanism discussed above, but also by the mechanism of 1,3-dipolar insertion. The primary molecular product, MCHL hydrotrioxide, can be formed by the mechanism of the hydride ion transfer, with formation of an intermediate ion pair:

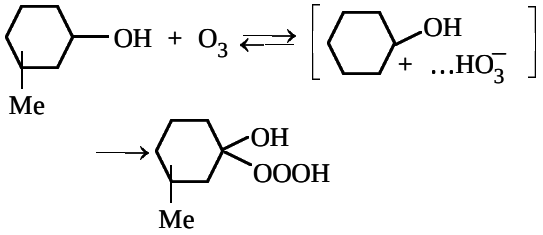

In ozonolysis of methanol, the activation energy of formation of the related ion pair is about 5 kJ mol^{-1} [24]. The ionization potential and hence the probability of formation of ion pairs are determined by the structure and concentration of the starting alcohols and by the polarity of the medium. In formation of the intermediate cyclohexanol hydrotrioxide or isomeric secondary MCHLs, the transition state will be stabilized owing to formation of a relatively stable six-membered ring:

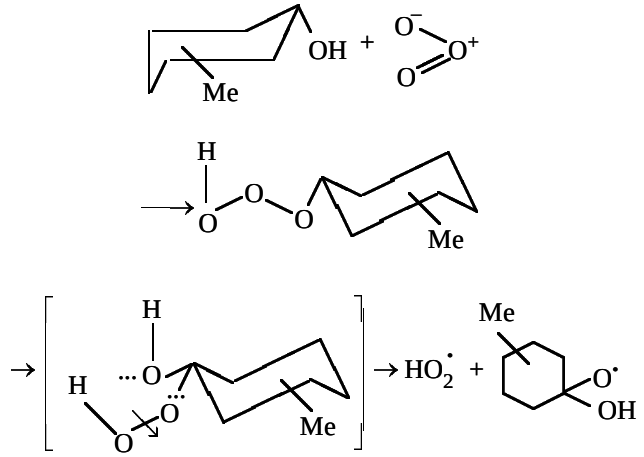

The mechanisms of ozonolysis of cyclohexanone and isomeric MCHLs are similar [2]. The major reaction products are lactones and acids. α-Keto hydrotrioxide, polyozonides, and isomeric methyl-1-hydroxycyclohexan-2-ones and methyl-1,2-cyclohexanediones are accumulated in smaller amounts.

The mechanism of their formation is schematically shown below:

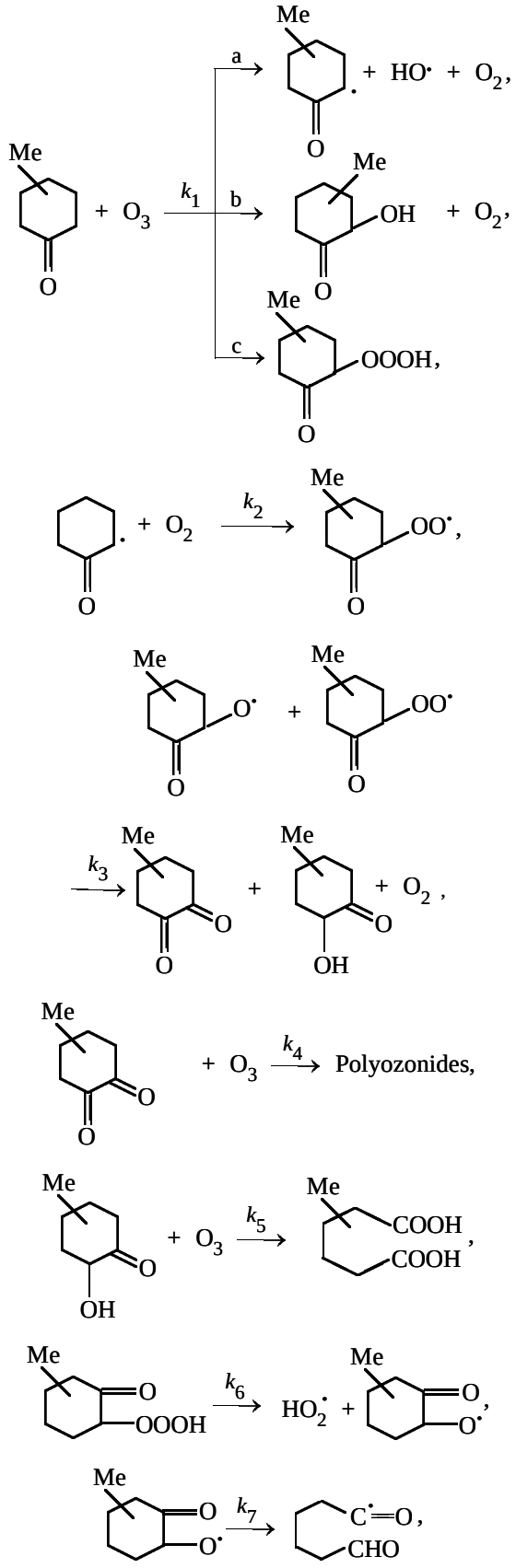

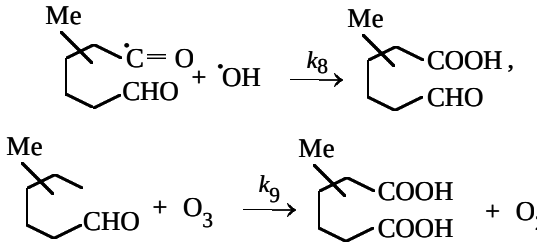

At lower temperatures (15–20°C), the yield of lactones reaches 52% [25]. As the temperature is elevated (40–80°C), the reaction selectivity with respect to acids grows by 12–16% compared to oxidation with oxygen. Ozonolysis of 4-methylcyclohexanone yields mainly β-methyladipic and β-methylglutaric acids [20–26]. In acidic products of 3-methylcyclohexanone ozonolysis, the major components are α- and β-methyladipic and α-methylglutaric acids [6]. In ozonolysis of 2-methylcyclohexanone, the major acidic products are α-methyladipic, ε-ketoenanthic, and caproic acids. Formation of acids [15, 21] at elevated temperatures presumably occurs via isomeric α-keto oxy radicals tending to isomerize with ring opening:

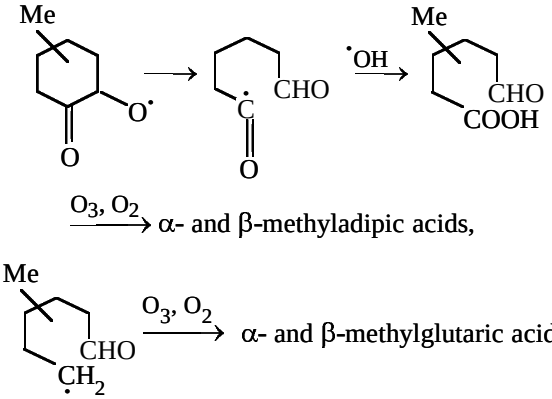

Ozonolysis of MCHNs is more selective than their oxidation with oxygen [14].

CONCLUSIONS

(1) Ozonolysis of isomeric secondary methylcyclohexanols to the corresponding isomeric methylcyclohexanones is more selective than oxidation with atmospheric oxygen.

(2) Ozonolysis of isomeric methylcyclohexanones mainly yields lactones and acids: monocarboxylic, dicarboxylic, and keto carboxylic.

REFERENCES

1. Syroezhko, A.M., Proskuryakov, V.A., and Begak, O.Yu., *Zh. Prikl. Khim.*, 2002, vol. 75, no. 9, pp. 1480–1485.
2. Syroezhko, A.M., Begak, O.Yu., and Proskuryakov, V.A., *Zh. Prikl. Khim.*, 2003, vol. 76, no. 5, pp. 814–820.
3. Syroezhko, A.M. and Begak, O.Yu., *Zh. Prikl. Khim.*, 2003, vol. 76, no. 6, pp. 990–995.
4. Korotkova, N.P., Syroezhko, A.M., and Proskuryakov, V.A., *Zh. Prikl. Khim.*, 1981, vol. 54, no. 3, pp. 660–665.
5. Vikhorev, A.A., Syroezhko, A.M., and Proskuryakov, V.A., *Zh. Prikl. Khim.*, 1976, vol. 49, no. 7, pp. 1592–1597.
6. Vikhorev, A.A., Syroezhko, A.M., and Proskuryakov, V.A., *Zh. Prikl. Khim.*, 1976, vol. 49, no. 3, pp. 588–592.
7. Vikhorev, A.A., Syroezhko, A.M., and Proskuryakov, V.A., *Izv. Vyssh. Uchebn. Zaved., Khim. Khim. Tekhnol.*, 1976, vol. 19, no. 10, pp. 1499–1503.
8. Syroezhko, A.M., Korotkova, N.P., Vikhorev, A.A., and Proskuryakov, V.A., *Zh. Prikl. Khim.*, 1978, vol. 51, no. 11, pp. 2562–2567.
9. Syroezhko, A.M., Korotkova, N.P., Vikhorev, A.A., and Proskuryakov, V.A., *Zh. Prikl. Khim.*, 1978, vol. 51, no. 12, pp. 2743–2754.
10. Sukharev, B.N., Liquid-Phase Oxidation of Isomeric Methylcyclohexanols with Atmospheric Oxygen, *Cand. Sci. Dissertation*, Leningrad, 1978.
11. USSR Inventor's Certificate no. 555084.
12. Vikhorev, A.A., Syroezhko, A.M., and Proskuryakov, V.A., *Zh. Prikl. Khim.*, 1976, vol. 49, no. 5, pp. 1178–1181.
13. Vikhorev, A.A. and Syroezhko, A.M., in *Issledovaniya v oblasti khimii i tekhnologii produktov pererabotki goryuchikh iskopaemykh* (Studies in the Field of Chemistry and Technology of Products of Fossil Fuel Processing), Leningrad: Leningr. Tekhnol. Inst. im. Lensoveta, 1975, issue 2, pp. 43–45.
14. Serov, V.V., Syroezhko, A.M., Proskuryakov, V.A., and Martynov, Yu.N., *Osn. Org. Sint. Neftekhim.* (Yaroslavl), 1976, no. 5, pp. 9–18.
15. Vikhorev, A.A., Syroezhko, A.M., and Proskuryakov, V.A., *Izv. Vyssh. Uchebn. Zaved., Khim. Khim. Tekhnol.*, 1976, vol. 19, no. 10, pp. 1499–1503.
16. Vikhorev, A.A., Syroezhko, A.M., and Proskuryakov, V.A., *Izv. Vyssh. Uchebn. Zaved., Khim. Khim. Tekhnol.*, 1977, vol. 20, no. 5, pp. 672–676.
17. Vikhorev, A.A., Syroezhko, A.M., and Proskuryakov, V.A., *Zh. Prikl. Khim.*, 1977, vol. 50, no. 6, pp. 1310–1314.
18. Vikhorev, A.A., Syroezhko, A.M., and Yakovlev, A.S., in *Issledovaniya v oblasti khimii i tekhnologii produktov pererabotki goryuchikh iskopaemykh* (Studies in the Field of Chemistry and Technology of Products of

Fossil Fuel Processing), Leningrad: Leningr. Tekhnol. Inst. im. Lensoveta, 1975, issue 2, pp. 39–43.

19. Vikhorev, A.A., Syroezhko, A.M., and Kutuev, R.Kh., in *Issledovaniya v oblasti khimii i tekhnologii produktov pererabotki goryuchikh iskopaemykh* (Studies in the Field of Chemistry and Technology of Products of Fossil Fuel Processing), Leningrad: Leningr. Tekhnol. Inst. im. Lensoveta, 1975, issue 2, pp. 38–39.
20. Vikhorev, A.A., Syroezhko, A.M., and Proskuryakov, V.A., *Zh. Prikl. Khim.*, 1975, vol. 48, no. 9, pp. 2059–2062.
21. Nonhebel, D.C. and Walton, J.C., *Free-Radical Chemistry. Structure and Mechanism*, Cambridge: Univ. Press, 1974.
22. Vikhorev, A.A. and Syroezhko, A.M., in *Issledovaniya v oblasti khimii i tekhnologii produktov pererabotki goryuchikh iskopaemykh* (Studies in the Field of Chemistry and Technology of Products of Fossil Fuel Processing), Leningrad: Leningr. Tekhnol. Inst. im. Lensoveta, 1975, issue 2, pp. 33–37.
23. Denisov, E.T., Mechanism of Homolytic Cleavage of Molecules in the Liquid Phase, *Itogi Nauki Tekh., Ser.: Kinet. Katal.*, 1981, vol. 9.
24. Nangia, P.S. and Benson, S.W., *J. Am. Chem. Soc.*, 1970, vol. 102, no. 9, pp. 3105–3115.
25. Korotkova, N.P., Syroezhko, A.M., and Proskuryakov, V.A., *Zh. Prikl. Khim.*, 1981, vol. 54, no. 4, pp. 861–867.
26. Komissarov, V.D., Gerchikov, A.Ya., Galimova, L.G., and Denisov, E.T., *Dokl. Akad. Nauk SSSR*, 1973, vol. 213, no. 4, pp. 881–883.

Russian Journal of Applied Chemistry, Vol. 77, No. 1, 2004, pp. 106–109. Translated from Zhurnal Prikladnoi Khimii, Vol. 77, No. 1, 2004, pp. 109–112.

MACROMOLECULAR CHEMISTRY AND POLYMERIC MATERIALS

Polyacrylonitrile–Fullerene C_{60} System as Laser Radiation Limiter

A. V. Novoselova, E. Yu. Melenevskaya, V. N. Zgonnik, I. M. Belousova, V. P. Belousov, E. A. Gavronskaya, T. D. Murav'eva, and A. G. Skobelev

Institute of Macromolecular Compounds, Russian Academy of Sciences, St. Petersburg, Russia
Institute of Laser Physics, St. Petersburg, Russia

Received July 17, 2003

Abstract—Fullerene-containing media, including polyacrylonitrile and acrylonitrile copolymers, were tested as candidates for application in protective devices for optical limitation of the laser radiation energy generated by a YAG-Nd laser.

Development of laser technologies makes urgent protection of eyes and optical devices against laser radiation. In review [1] we discussed in detail the mechanism of limitation by fullerenes and their derivatives. Janot *et al*. [2] found (like previously for porphyrins [3]) that the energy absorption depends on the strength of interaction between the fullerene molecules.

Guldi and Prato [4] reported that, upon absorption of an energy quantum, the monomeric form of fullerene occurs in the excited state within several hundreds of microseconds, and in the aggregated form the lifetime of the excited state sharply decreases to <1 μs. As revealed by light and neutron scattering studies [5, 6], in the majority of organic solvents C_{60} exists as aggregates occurring in equilibrium with the monomeric form. The energy-absorbing power of fullerene is increased by conversion to the monomeric form. To this end, Guldi and Prato [4] suggested incorporation of fullerene into regular structures such as zeolites, porous silicate matrices, or micelles or its functionalization by linking with various species (low- or high-molecular-weight) forming covalent bonds. Such modification affects the electronic structure of fullerene and decreases its energy-absorbing power. An increase in the number of the monomeric C_{60} molecules in solution upon derivatization compensates the energy intensity loss. Fullerene associates can disaggregate without disturbing the electronic structure via formation of nonvalence bonds in complex, e.g., fullerene–polymer, compounds [7, 8].

Chemically and thermally stable polymers like commercial polyacrylonitrile (PAN) and acrylonitrile copolymers [9], as well as polyamido acids (films, fibers), can be made suitable for creation of protective devices by incorporating fullerenes into their composition. In this work, we studied the energy-absorbing properties of fullerene-containing polymers and copolymers of acrylonitrile (AN), including composites, differing in the composition and synthesis procedure.

EXPERIMENTAL

Polyacrylonitrile (a-PAN) and copolymers of AN with methacrylate (AN–MA) and butyl acrylate (AN–BA) with the acrylate content of up to 10% were synthesized by anionic polymerization, via the action of alkoxides. Low-temperature homogeneous polymerization in dimethylformamide (DMF) yields polymers of AN with a narrow molecular-weight distribution pattern [10], having the stereoblock microstructure [11]. They are characterized, in particular, by enhanced thermal stability compared to the PAN synthesized by radical polymerization (r-PAN). Anionic polymerization allows preparation of AN–acrylate copolymers with the desired composition, as well as partially cyclized polyacrylonitrile (c-PAN), in which up to 40% of the nitrile [–C≡N] groups are converted into imine [>C=N–] groups, forming ladder structures [12].

Covalently bound fullerene C_{60} was incorporated into a-PAN, in particular, via deactivation of "living" polyacrylonitrile chains by introducing a fullerene solution in toluene to terminate polymerization [13].

The polymers under study, except for c-PAN, are able of film and fiber formation. Consequently, the energy-absorbing properties of these polymers were

1070-4272/04/7701-0106 © 2004 MAIK "Nauka/Interperiodica"

studied mostly with their films. The latter were obtained by casting on cover glasses a combined solution of the polymer and fullerene prepared by mixing the solutions of the components that were prepared beforehand; the films were dried at 20°C.

Figure 1 shows schematically the YAG-Nd laser-based experimental setup for studying optical limitation of the laser radiation energy by fullerene-containing media. The working parameters of the setup are as follows: radiation wavelength λ = 532 nm, pulse length 10 ns, pulse energy 0.35 J, and density of incident radiation energy 0–4 J cm^{-3}.

The samples under study were (a) solutions of a straight polymer or of a polymer doped with C_{60} in DMF (we used cells with a 3-mm liquid layer) and (b) polymer films differing in the composition and C_{60} content.

Figures 2a and 2b show how the energy density of the radiation that passed through the sample E_{out} varies with the energy density of the incident radiation E_{in}. The onset of nonlinear transmission for DMF solutions of a-PAN–C_{60} and c-PAN–C_{60} is approximately at E_{in} = 0.5 J cm^{-2}.

The compositions of the samples studied by us and their laser radiation limitation properties are summarized in the table.

For comparison, we present the energy-absorbing properties of solutions of a-PAN (run no. 1) and c-PAN (run no. 3), as well as of the AN–BA film (run no. 8) without fullerene. Clearly, a-PAN solution and AN–BA film absorb nearly a half of the incident laser beam energy. In the case of the solution of c-PAN containing conjugated >C=N–C=N– double bonds (run no. 3), absorption is somewhat greater [11].

These functional groups not only impart a yellow-brown color to the polymer but also are responsible for participation of c-PAN in various complex formation reactions. In solutions of c-PAN, the existence of such structures favors mutual arrangement of the macrochains, yielding crystalline structures in the polymer in the course of removal of the solvent. The same moieties in c-PAN are, evidently, responsible for interaction of the polymer with C_{60} and for its disaggregation. This is confirmed by the fact that, upon introduction of C_{60} into c-PAN (run no. 4), the incident laser energy decreases 20-fold.

Significant nonlinear energy absorption was observed in the case of the a-PAN–C_{60} solution (run no. 2). In this experiment, we studied a-PAN containing covalently bound fullerene. The polymer was prepared by introducing a toluene solution of fullerene during "living" polymerization of AN to terminate the propagating chains, which resulted in its covalent bonding. The part of the C_{60} introduced that has not reacted with the anionic reactive center can interact with a-PAN by the complex formation mechanism.

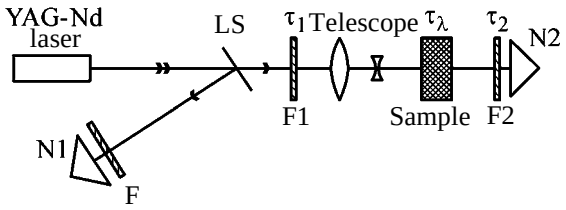

Fig. 1. Schematic of the setup for studying the dynamic range of optical limitation of laser radiation: (LS) light splitter, (F, F_1, F_2) filters, and (N_1, N_2) energy meters.

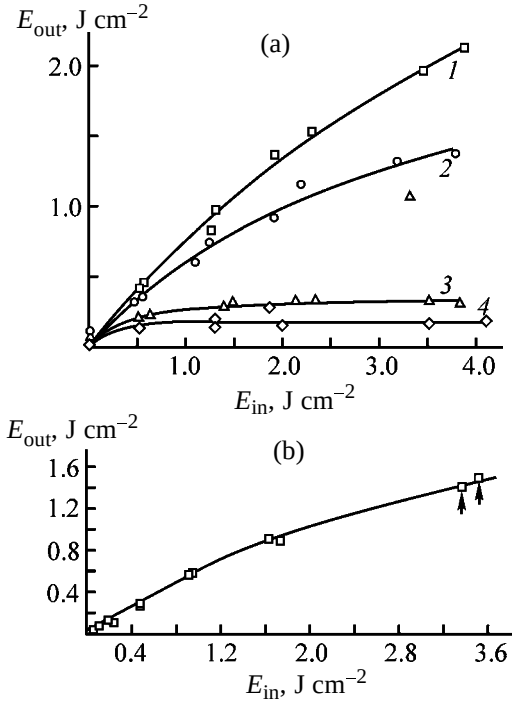

Fig. 2. Radiation energy density at the outlet E_{out} vs. the radiation energy density at the inlet E_{in}. Run no.: (a) 1, (*2*) 3, (*3*) 2, and (*4*) 4; (b) 7. (a) (*1*) a-PAN, (*2*) c-PAN, (*3*) a-PAN–C_{60}, and (*4*) c-PAN–C_{60}; (b) r-PAN–C_{60}. *T*, %: (a) (*1*) 80, (*2*) 69, (*3*) 53, and (*4*) 48; (b) 80.

Studies of the film coatings obtained from the combined solutions of a-PAN–C_{60} and r-PAN–C_{60} (run nos. 5–7) revealed weak optical limitation for these films (Fig. 2a). Evidently, under the actual conditions of combining the polymer (high-viscosity solutions) and fullerene, the components did not interact efficiently. This means that the energy of interaction between the polymer chains was higher than in the

Energy-absorbing properties of the fullerene C_{60}–polymer systems*

Run no.	Composition of the sample**	C_{60}, %	Transmission, %		Limitation coefficient		E_{in}, J cm^{-2}
			T_{in}	T_{non}	K_{abs}	K_{rel}	
	DMF solutions, %:						
1	a-PAN, 2.5	–	80	53	1.8	1.5	
2	a-PAN–C_{60}, 2.5	0.7	53	8	11.4	6.6	
3	c-PAN, 1.2.	–	69	35	2.8	2	
4	c-PAN–C_{60}, 1.2	1.1	48	4.5	22	11	
	Films:						
5	a-PAN–C_{60}	1.0	50	26	3.8	2.6	2
6	a-PAN–C_{60}	0.5	70	50	2	1.4	>2
7	r-PAN–C_{60}	0.5	80	60	1.7	1.3	>2
8	AN–BA	–	87	26	3.8	3.3	>3
9	AN–BA–C_{60}	0.5	60	6	17.0	10.0	2.1
10	AN–BA–C_{60}	1.4	50	21	4.8	2.4	1.0
11	AN–BA–C_{60}	0.9	50	18	2.7	5.5	1.8
12	AN–BA–C_{60}–P	0.9	33	5	20.0	7.2	0.5
13	AN–BA–C_{60}–P	0.9	36	5	20.0	6.6	0.5
14	AN–MA–C_{60}	1.0	30	11	9.0	2.7	0.7
15	AN–BA–(AN–AC)–C_{60}	1.0	77	40	2.5	1.9	>2
17	AN–BA–(AN–AC)–C_{60}	1.6	40	11	9.0	3.6	1.5
18	PAA PM–C_{60}	0.6	60	30	3.3	2.0	>3
19	PAA PM–C_{60}	0.3	67	26	38	2.6	>3

* Transmission $T = E_{out}/E_{in}$; T_{in} is transmission of the sample at small E_{in}; T_{non}, transmission under nonlinear absorption; K_{abs} and K_{rel}, absolute and relative limitation coefficients, respectively; $E_{in.f.}$, energy density at which the sample fails.

** *S* is solvent (*N*-methyl-2-pyrrolidone); AA, acrylic acid; and PAA PM, polymer derived from diaminodiphenyl ether and pyromellitic acid.

case of the polymer–fullerene system. It is known [8] that the PAN macromolecules in solutions exhibit a tendency to cross-linking and gelation.

By changing from PAN to copolymers of AN with acrylates less prone to intermolecular interaction of chains in solutions, it is possible to obtain their films with C_{60} able of more efficient limitation of laser radiation (run nos. 9–14). This suggests that, in these systems, fullerene is significantly disaggregated. However, composite films based on AN–acrylate copolymers are less thermally stable than PAN-based films. The limiting failure energy for these films tended to increase with decreasing C_{60} content in them. This was accompanied by enhancement of the optical-limitation power of the films. Thus, introduction of fullerene in amounts exceeding that sufficient for efficient interaction with the polymer increases the number of C_{60} aggregates and decreases both the transparency and thermal stability of the films. These properties of the films are also deteriorated by incomplete removal of the solvent (run nos. 12, 13) which imparts plasticity to the films.

We intended to enhance the thermal stability of the films prepared from AN–acrylate copolymers by introducing a commercial polymer, polyamido acid, in the solution preparation stage. For comparison, we prepared films from the combined solutions of the polymer of diaminodiphenyl ether and pyromellitic acid (PAA PM) with fullerene C_{60} in DMF. These films (run nos. 18, 19) exhibited a good strength but poor optical properties. Poor nonlinear-optical properties of these films are, evidently, due to chemical reactions of fullerene with the functional groups of amido acids.

To strengthen the AN–BA-based films, we additionally introduced the AN–AA copolymer prepared by partial hydrolysis of a-PAN (degree of hydrolysis 5–10%). The thermal stability of such composite films (run nos. 15–17) actually tended to increase, with certain energy capacity being preserved.

CONCLUSIONS

(1) Fullerene-containing composites based on polyacrylonitrile and acrylonitrile copolymers with alkyl

arcylates offer promise for preparing materials suitable for creation of laser-radiation-protecting devices.

(2) Acrylonitrile–alkyl acrylate copolymers afford more uniform, than homopolymers, distribution of C_{60} fullerene in the composites owing to weakening of interchain interaction.

(3) A relatively low content of C_{60} (0.5%) in composites with copolymers affords optimal limitation properties, with the transparency and thermal stability of the films being preserved.

ACKNOWLEDGMENTS

This work was financially supported by the "Topical Lines in Condensed Matter Physics" State Scientific and Technical Program, "Fullerenes and Atomic Clusters" direction, and by the Russian Foundation for Basic Research (project no. 03-03-32633).

REFERENCES

1. Belousov, V.P., Belousova, I.M., Gavronskaya, E.A., *et al*., *Opt. Zh.*, 1999, vol. 66, no. 8, p. 50.
2. Janot, J.M., Edaou, H., Seta, P., *et al*., *Chem. Phys., Lett.*, 1999, vol. 302, pp. 103–107.
3. Redmond, R., Land, E.J., and Truscott, T.G., *Methods in Porphyrin Sensitization*, Kessel, D., Ed., New York: Plenum, 1985, pp. 293–307.
4. Guldi, D. and Prato, M., *Acc. Chem. Res.*, 2000, vol. 33, pp. 695–703.
5. Torok, G.Y., Lebedev, V.T., and Cser, L., *Fiz. Tverd. Tela*, 2002, vol. 44, no. 3, pp. 546–547.
6. Rudalevige, T., Francis, A.H., and Zand, R., *J. Phys. Chem., A*, 1998, vol. 102, pp. 9797–9802.
7. Konarev, D.V. and Lyubovskaya, R.N., *Usp. Khim.*, 1999, vol. 68, no. 1, pp. 23–44.
8. Jamakoshi, J.N., Jagami, T., Fukuhara, K., *et al*., *J. Chem. Soc., Chem. Commun.*, 1994, pp. 517–518.
9. *Entsiklopediya polimerov* (Encyclopedia of Polymers), Kargin, V.A., Ed., Moscow: Sov. Entsiklopediya, 1977, vol. 3, p. 670.
10. Novoselova, A.V., Nefedov, P.P., Frenkel', S.Ya., *et al*., *Vysokomol. Soedin., Ser. B*, 1974, vol. 16, no. 10, pp. 751–756.
11. Khachaturov, A.S., Abramenko, E.L., and Novoselova, A.V., *Vysokomol. Soedin., Ser. B*, 1988, vol. 30, no. 12, pp. 891–896.
12. Novoselova, A.V., Zgonnik, V.N., Spirina, T.N., *et al*., *Vysokomol. Soedin., Ser. A*, 1993, vol. 35, no. 5, pp. 510–514.
13. Novoselova, A.V., Vinogradova, L.V., and Zgonnik, V.N., *Vysokomol. Soedin., Ser. A*, 2001, vol. 43, no. 7, pp. 1109–1114.

Russian Journal of Applied Chemistry, Vol. 77, No. 1, 2004, pp. 110–115. Translated from Zhurnal Prikladnoi Khimii, Vol. 77, No. 1, 2004, pp. 113–118.

MACROMOLECULAR CHEMISTRY AND POLYMERIC MATERIALS

Chromatographic Characteristics of Adamantyl Silicone Stationary Phase

V. G. Berezkin, S. V. Kurbatova, E. E. Finkel'shtein, O. I. Maryashina, A. A. Korolev, and E. A. Kolosova

Samara State University, Samara, Russia
Institute of Petroleum Chemical Synthesis, Russian Academy of Sciences, Moscow, Russia

Received June 16, 2003

Abstract—Chromatographic characteristics of adamantyl silicone stationary phase were studied.

Adamantane derivatives attract steady interest caused by specific structure of their hydrocarbon framework and also by their biological activity [1, 2]. The structure and hydrophobicity (lipophilicity) of adamantane provide favorable conditions for its transport through biological membranes. Linking of adamantyl radical to organic compounds modifies their biological activity, in many cases enhancing it. It was found [3, 4] that adamantyl radical affects hypoglycemic, antitumor, immunodepressive, antibacterial, and other types of biological activity. Much promise is shown by polymeric materials based on adamantane, characterized by high thermal stability, resistance to corrosive media, and high hardness [5]. Adamantane derivatives are of some interest as a model in solving many problems in theoretical chemistry, such as the influence of the electronic structure and topology of molecules on physicochemical characteristics and influence of induction and steric factors on the reactivity and stability of compounds. However, many problems related to the reactivity, biological activity, structure, and its correlation with physicochemical characteristics of framework compounds, especially with their chromatographic behavior, are not completely understood. Chromatographic characteristics of some adamantane derivatives as sorbates in gas–liquid and liquid chromatography were studied [6–8], but data on the use of sorbents and stationary phases based on adamantane are virtually lacking. There are only evidences that introduction of adamantane fragment into stationary phases should enhance their selectivity, at least with respect to polynuclear aromatic hydrocarbons [9]. In this connection, we studied in this work the chromatographic characteristics of adamantyl silicone stationary phase under conditions realized in capillary gas chromatography.

EXPERIMENTAL

The experiments were performed on a Halls-311 gas chromatograph equipped with a flame-ionization detector in the isothermal mode at temperatures from 100°C to 200°C with the interval of 20°C. The vaporizer temperature was varied from 150°C to 250°C. The analysis was carried out on a steel capillary column (22 m × 0.22 mm) with cross-linked alkyladamantane (film thickness d_f = 0.2 μm). Nitrogen was used as a carrier gas with the flow division at the column inlet of 1 : 60. To characterize the column, we studied the chromatographic retention of various organic substances. Solid substances were introduced into the chromatograph in the form of solutions in ethanol or toluene. The retention indices (RIs) were evaluated by the Kovats formula [10]. The experimental indices averaged over 7–10 values are listed in Table 1. The reproducibility of RI was 1–2 index units (i.u.). The contribution of alkyl to retention $\delta I(R)$ for substances under consideration was evaluated by the scheme $\delta I(R) = I(R_{n+1}) - I(R_n)$, where $I(R_{n+1})$ and $I(R_n)$ are RIs of the neighboring homologs [11]. The differential molar free energy of sorption ΔG was evaluated according to [12]. The Rohrschneider polarity factors were determined from the experimental data by the well-known procedure [10]: x = 0.132, y = 0.993, z = 0.543, and s = 0.210. The selectivity factor of the stationary phase and separation factor for estimation of the *meta–para* selectivity were evaluated by the relationships given in [11].

According to the resulting values of Rohrschneider factor, the phase in hand is nonpolar and its chromatographic characteristics should be close to those of Apiezon-L (Ap-L) or silicones OV-1 and SE-30. To

1070-4272/04/7701-0110 © 2004 MAIK "Nauka/Interperiodica"

Table 1. Retention characteristics of sorbates of various structures on adamantyl silicone

Substance	100°C		120°C		140°C		160°C		200°C	
	RI	ΔG, kJ mol^{-1}	RI	ΔG, kJ mol^{-1}	RI	ΔG, kJ mol^{-1}	RI	ΔG, kJ mol^{-1}	RI	ΔG, kJ mol^{-1}
Cyclohexane	681.1	3.06	685.1	5.23	665.9	7.29	663.6	9.08	660.8	11.6
Benzene	676.2	3.17	676.8	4.82	666.5	7.32	700.5	7.81	837.3	8.88
Toluene	777.0	1.00	778.4	2.81	780.1	5.06	796.1	6.12	892.3	8.03
Ethylbenzene	870.1	–0.99	873.0	0.94	877.1	3.14	887.2	4.52	965.3	6.89
o-Xylene	911.7	–1.88	915.9	0.09	924.3	1.99	931.1	3.75	990.38	6.50
p-Xylene	886.8	–1.35	889.6	0.61	890.9	2.64	903.5	4.23	945.9	7.19
m-Xylene	886.4	–1.34	888.9	0.62	895.2	2.55	902.2	4.25	969.2	6.83
Naphthalene	–	–	–	–	1080	–0.89	1015	2.27	1063	5.38
Anthracene	–	–	–	–	–	–	1104	0.70	1166	3.78
Adamantane	–	–	1105	–3.35	1119	–1.77	1138	0.11	1212	3.03
1-Adamantanol	–	–	–	–	1260	–4.21	1272	–2.22	1326	1.49
Phenol	–	–	967.8	–1.07	969.6	1.12	979.3	2.90	1055	5.49
2-Methylphenol	–	–	1043	–2.07	1043	–0.15	1064	1.41	1112	4.62
3-Methylphenol	–	–	1064	–2.50	1060	–0.49	1080	1.12	1128	4.36
4-Methylphenol	–	–	1062	–2.47	1059	–0.48	1076	1.20	1124	4.36

characterize the properties of adamantyl silicone we studied the chromatographic retention of some representatives of various classes of organic compounds. As follows from Table 1, RIs virtually regularly vary with variation of the molecular weight of sorbates. At the same time, since chromatographic method is based on high sensitivity to differences in the thermodynamic characteristics of sorption of substances, caused by molecular structure of stationary phase and sorbate, the RI values adequately reflect their structural features.

As follows from Fig. 1, the correlation between RI and molecular weight of normal alcohols can be approximated by a linear dependence with the correlation factor of 0.998.

The features of chromatographic retention of organic compounds of various types are the most clearly pronounced in consideration of homomorphism factors and differences in RIs of substances with polar and nonpolar stationary phases. In this case, functional groups, rings, and hydrocarbon radicals can act as homomorphs.

As known, within homologous series of organic compounds, the RIs increase; according to the well-known Kovats rule, the increments of CH_2 δI should be approximately 100 i.u. for a nonpolar stationary phase. For nonbranched alkanes, the experimentally determined contribution of methylene unit to RI on adamantyl silicone is 100 i.u. The contribution to the free energy of sorption was approximately –2 kJ mol^{-1}, decreasing to –1.55 kJ mol^{-2} as the temperature was increased to 200°C. As a whole, for adamantyl silicone ΔG grows with increasing molecular weight of sorbates.

As follows Table 2, $\delta I(CH_3)$ of linear alcohols is in the range 90–100 i.u., somewhat decreasing with increasing temperature. As for normal alkanes, the contribution to the sorption energy $\delta(\Delta G)$ is approximately –2 kJ mol^{-1} and varies from –1.27 to –1.46 kJ mol^{-1} at 200°C. The dependence of ΔG of 1-propanol on operating temperature is shown in Fig. 2. The dependences for other members of this homologous series are similar.

For benzene homologs, the contribution of methylene unit is approximately 90 i.u., as for Apiezon-L.

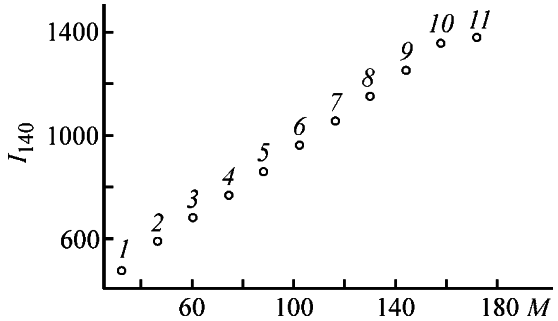

Fig. 1. RI of normal alcohols I_{140} as a function of molecular weight M. T = 140°C, stationary phase adamantyl silicone, r = 0.998, (*1*)–(*11*) C_1–C_{11}, respectively.

Table 2. Contribution of hydrocarbon radicals into RI (δI) and ΔG of sorption [$\delta(\Delta G)$] for adamantyl silicone stationary phase

Substance	Ap-L, δI	Ad-R									
		100°C		120°C		140°C		160°C		200°C	
		δI	$-\delta(\Delta G)$	δI	$-\delta(\Delta G)$	δI	$-\delta(\Delta G)$	δI	$-\delta(\Delta G)$	δI	$-\delta(\Delta G)$
Toluene	108	100.8	2.17	101	2.01	114	2.26	96	1.69	55.0	0.85
Ethylbenzene	93	93.1	1.99	94	1.87	97	2.02	91	1.60	73.0	1.14
o-Xylene	137	134.7	2.88	137	2.72	144	3.07	135	2.37	98.1	1.53
p-Xylene	110	109.8	2.35	111	2.20	111	2.42	107	1.89	53.6	0.84
m-Xylene	111	109.4	2.34	110	2.19	115	2.51	106	1.87	76.9	1.20
Ethanol	83	58.1	1.25	74	1.48	119	2.15	110	1.90		0.61
1-Propanol	105	77.0	1.65	82	1.63	88	1.63	90	1.64		0.44
1-Butanol	120	94.9	2.04	101	2.01	91	1.72	99	1.75	60.6	–1.35
1-Pentanol	107	99.6	2.14	102	2.01	94	1.80	97	1.70	80.5	1.27
1-Hexanol	105	166.9	1.56	101	2.01	95	1.88	103	1.81	93.6	1.46
1-Heptanol	101	163.2	2.29	100	2.00	97	1.84	99	1.75	90.5	1.40
2-Methyl-1-propanol	171	104.4	2.24	110	2.18	134	2.43	105	1.82	79.9	1.24
2-Methyl-1-butanol	78	101.4	2.18	108	2.14	116	2.17	101	1.77	63.1	0.98
Butanone	98	92.1	1.96	116	2.31	84	0.17	73	1.32	58.6	0.90
2-Pentanone	149			119	2.14	182	–6.20	69	1.22	37.3	0.58

The increment of CH_3 groups depends on their number and relative positions in the benzene ring. With increasing number of methyl groups, alkylbenzene molecule remains planar and, hence, can be oriented in the sorbent surface in the manner optimal for sorption [13]. Lengthening of alkyl chain results in nonplanar orientation of the alkylbenzene molecule; therefore, as a rule, the retention of monoalkylbenzenes is worse than the retention of polyalkylbenzenes with the same number of carbon atoms in the substituent.

In particular, for toluene, *m*-, and *p*-xylenes, $\delta I(CH_3)$ at 160°C is in the range 100–160 i.u., while for *o*-xylene this value is significantly greater (from 130 to 140 i.u.). The contribution to the sorption energy is from –2.72 to –2.37 for *o*-xylene and from –2.19 to –1.87 kJ mol^{-1} for *m*- and *p*-xylenes depending on temperature. The similar trends take place with other compounds with vicinal arrangement of methyl groups on both polar and nonpolar stationary phases. The vicinal arrangement of methyl groups causes an increase in the internal energy of the molecule; therefore, the contribution of neighboring methyl groups to the energy of dispersion interaction with the stationary phase is greater than that in the case of more remote arrangement of these groups [14]. Heating increases the *meta*–*para* selectivity of adamantyl silicone, with the contributions of methyl groups to RI somewhat decreasing and becoming different for *ortho*-, *meta*-, and *para*-positions, 98, 54, and 77 i.u., respectively, and the contributions to ΔG of sorption of sorption becoming essentially different: –153, –0.84, and –1.20 kJ mol^{-1} (it should be noted that for normal alkanes this value is practically constant and varies in the homologous series by no more than 0.1–0.2 kJ mol^{-1}). Weaker retention of the *para* isomer in comparison with *meta*-substituted derivatives may be due to the fact that, in symmetrical arrangement of substituents, the benzene ring somewhat rises over the sorbent surface [13]. Heating enhances this process, which is apparently favored by the presence of bulky adamantyl fragment in the stationary phase. It should be noted that nonmonotonic variation of RI with

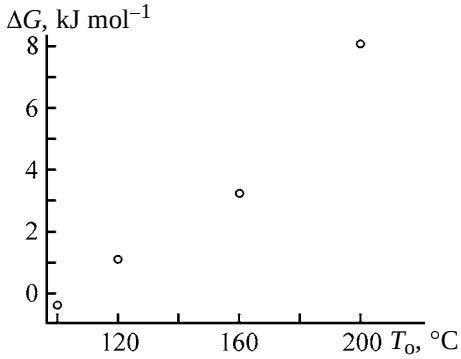

Fig. 2. ΔG of 1-hexanol as a function of operating temperature T_o. Stationary phase is adamantyl silicone, r = 0.982.

Table 3. Differences between RIs on polar and nonpolar stationary phases ΔI, temperature increments dI/dT, and contributions of functional groups to RI (δI) and ΔG of sorption [$\delta(\Delta G)$] of some organic compounds

Substance	$\delta I_{\text{Ap-L}}$	δI_{OV101}	$\delta I_{\text{Ad-R}}$	$\delta(\Delta G)_{\text{Ad-R}}$	$dI/dT_{\text{Ad-R}}$	$\Delta I_{\text{CW-Ap-L}}$	$\Delta I_{\text{CW-OV101}}$	$\Delta I_{\text{CW-Ad}}$
Ethanol	204	264	394	–	2.49	545	485	472
1-Propanol	209	278	381	–	2.76	526	457	475
1-Butanol	229	296	372	–	2.66	488	421	455
1-Pentanol	236	303	366	–	2.52	491	424	463
1-Hexanol	241	308	362	–6.94	0.73	491	424	467
1-Heptanol	242	311	359	–6.89	–0.925	494	425	470
1-Octanol	243	312	358	–6.90	–	498	429	460
Cyclohexanol	204	–	239	–4.64	–	486	–	472
Phenol	401	337	303	–6.20	–	–	–	–
2-Methylphenol	347	222	263	–5.21	–	–	–	–
3-Methylphenol	–	229	280	–5.55	–	–	–	–
Benzaldehyde	279	–	325	–4.36	–	–	–	–
1-Adamantanol	117	–	141	–2.44	–	–	–	558
Nitrobenzene	402	–	420	–8.55				
o-Nitrotoluene	361	–	401	–7.92				
p-Nitrotoluene	418	–	429	–8.47				

temperature (nonconstancy of temperature increment dI/dt) is fairly frequently observed in chromatographic analysis of representatives of various homologous series and is apparently caused by the difference in the energy equivalents of one unit of the index ΔG_{iu}, determined according to [15], and nonlinear variation of this value with increasing RI [16].

It is well known that cyclization significantly increases RI on both polar and nonpolar stationary phases. As follows from Table 1, in passing from hexane to cyclohexane, RI on adamantyl silicone increases by 60–80 i.u. (on Apiezon-L, by 96 i.u.), which is equivalent to addition of one methylene unit in the homologous series. Passing from decane to adamantane results in increase in RI by 120–140 i.u., which is somewhat greater than the increment of the methylene unit. In this case, the sorption energy varies from –1.56 to –3.35 kJ mol^{-1}. Substitution of the benzene ring for a saturated six-membered ring does not result in significant variations in the retention with the adamantane phase, similar to Apiezon. In passing from benzene to naphthalene and then to anthracene, RIs on Apiezon-L significantly increase and are 686, 1309, and 1869 i.u., respectively. On the adamantane stationary phase, these variations are not so great: for these compounds, RIs are 677, 1080, and 1104. It is believed that in this case the steric effect of the adamantane fragment of the stationary phase becomes significant. This is suggested by the fact that, for adamantane, RI on adamantyl silicone is somewhat lower than that on Apiezon (1119 and 1216 i.u., respectively).

The contributions of functional groups to retention with adamantyl silicone are different depending on the nature of the group (Table 3). Contrary to retention on Apiezon-L, the contribution of the OH group of adamantyl silicone stationary phase δI is greater for linear (260–280 i.u., and 204–240 i.u. on Apiezon-L) and cyclic alcohols (228 and 204 i.u., respectively). On methyl silicone SE-30, the contribution of OH groups is 240–260 i.u. It is believed that linear alcohols are retained on adamantyl silicone predominantly owing to formation of a hydrogen bond between the OH group of alkanols and silanol groups of the stationary phase. Apparently, the presence of adamantane fragment is favorable for redistribution of the electron density in molecules of the stationary phase. It was shown previously that 1-adamantyl radical exhibits strong induction increasing the effective negative charge on the oxygen atom bonded to adamantyl [17]. It is likely that this effect results in strengthening of the hydrogen bond of alcoholic hydroxyl with the stationary phase.

For phenol on adamantyl silicone, $\delta I(\text{OH})_{\text{i.u.}}$ decreases in comparison with Apiezon-L (290 and 335 i.u., 337 i.u. on methyl silicone phase), which is apparently caused by the predominant contribution of phenyl radical, interacting nonspecifically with the adamantyl fragment of the stationary phase, to adsorption. For phenol homologs, the contribution of OH group is governed by its position relative to alkyl.

In particular, for 2-methylphenol δI(OH) on adamantyl silicone is 265, and for 3- and 4-methylphenol, 286. For Apiezon, these values are 347 and 379 i.u., and for methyl silicone, 250 and 280. In other words, the contribution of functional group located in *ortho*-position to methyl is less than that for *meta*- and *para*-positions remote from the alkyl. Similarly, the contribution of the CH_3 group in 2-methylphenol is less (73 i.u.) than that in 3- and 4-methylphenols (96 i.u.), which is caused by intramolecular interaction of methyl with hydroxyl in *ortho*-position. Similar trends are observed for other vicinal substituents and functional groups [18]. For example, the contribution of nitro group to retention of *ortho*-nitrotoluene is less (401 i.u.) compared to *para*-nitrotoluene (429 i.u.). For nitrobenzene, this value is 420 i.u. The contribution of OH group of alkylphenols to the adsorption energy does not noticeably vary with heating from 100 to 160°C and decreases by nearly 1.5 kJ mol^{-1} at 200°C, being practically equal to the contribution of OH group of phenol.

The value of δI(OH) of 1-adamantanol is much less and equal to 140 i.u. The contribution of OH group to the adsorption energy is less than the contribution of phenolic and cyclohexanol OH groups by a factor of almost 2 and less than the contribution of OH groups in linear alkanols by a factor of 3. This is largely due to the steric effect of adamantane fragments, present in molecules of both the stationary phase and sorbate and hindering participation of hydroxy group in retention.

The results of this study show that adamantyl silicone exhibits a fairly high selectivity in separation of structural isomers. The selectivity factor of adamantyl silicone varies from 0.53 to 0.73 depending on temperature. In estimation of the *meta–para* selectivity of this stationary phase, the separation factor is 1.18 (for comparison, the selectivity of some liquid crystals with respect to *meta–para* isomers is 1.03–1.09 [19]). The selectivity in separation of isomers of 1-methyl-1,2-dicyclopropylcyclopropane, whose *cis* and *trans* isomers are not always separable on standard stationary phases, is equal to 1.1. High selectivity of adamantyl silicone manifests itself in separation of homologs of normal alkanes and alkylbenzenes (α 2, 1.9), which was used in analysis of naphtha hydrocarbons. These studies also suggest enantioselectivity of this phase, since adamantyl cross-linked with silicone apparently can form chiral cavities. However, this suggestion calls for further investigations.

Thus, our results show that retention of sorbates of various structures with adamantyl silicone is governed by dispersion interactions, which depend essentially on deformability of molecules and, hence, their volume. According to additivity of the free energy of interaction, an increase in the molecular size by one methylene unit results in virtually equal increase in dispersion forces, which is reflected in the equality of contributions of alkyls to the retention and sorption energy. At the same time, it is evident that the presence of the adamantane fragment in molecules of the stationary phase results in redistribution of the electron density in its silanol groups and strengthening of interaction of electron-acceptor functional groups of sorbates with the stationary phase. This is confirmed by an increase in the contribution of these groups to retention with adamantyl silicone in comparison with methyl silicone and Apiezon-L. Apparently, the stationary phase studied can be suitable for solving chromatographic problems and for studying the structure of sorbates and intermolecular interactions of these sorbates.

CONCLUSIONS

(1) The retention indices of primary alcohols, aromatic hydrocarbons, alkylphenols, and some adamantane derivatives and the thermodynamic characteristics of their sorption with adamantyl silicone were compared to the respective characteristics of known silicone stationary phases.

(2) The selectivity of adamantyl silicone phase in separation of low-boiling naphtha hydrocarbon fraction and isomers of 1-methyl-1,2-dicyclopropylcyclopropane was shown. The possible enantioselectivity of the phase was suggested.

REFERENCES

1. Kovalev, I.E., *Khim.-Farm. Zh.*, 1994, vol. 28, no. 5, pp. 19–27.
2. Shvekhgeimer, M.-G.A., *Usp. Khim.*, 1996, vol. 65, no. 7, pp. 603–647.
3. Plakhotnik, V.M., Kovtun, V.Yu., and Leont'eva, N.A., *Khim.-Farm. Zh.*, 1982, vol. 16, no. 7, pp. 42–46.
4. Spasov, A.A., Khamidova, T.V., Bugaeva, L.I., and Morozov, I.S., *Khim.-Farm. Zh.*, 2000, vol. 34, no. 1, pp. 3–9.
5. Bagrii, E.I., *Adamantany: Poluchenie, svoistva, primenenie* (Adamantanes: Synthesis, Characteristics, Application), Moscow: Nauka, 1989.
6. Hala, S., Eyem, J., Burchard, J., and Landa, S., *J. Chromatogr. Sci.*, 1970, vol. 8, no. 1, pp. 203–209.
7. Suslov, I.A., Rudenko, B.A., and Arzamastsev, A.P., *Zh. Anal. Khim.*, 1988, vol. 43, no. 2, pp. 328–332.

8. Kurbatova, S.V., Moiseev, I.K., and Zemtsova, M.N., *Zh. Anal. Khim.*, 1998, vol. 53, no. 3, pp. 307–311.
9. Yang, S.S. and Gilpin, R.K., *J. Chromatogr.*, 1988, no. 3, pp. 414–416.
10. Gol'bert, K.A. and Vigdergauz, M.S., *Vvedenie v gazovuyu khromatografiyu* (Introduction to Gas Chromatography), Moscow: Khimiya, 1990.
11. Vigdergauz, M.S., Semenchenko, L.V., Ezrets, V.A., and Bogoslovskii, Yu.N., *Kachestvennyi gazokhromatographicheskii analiz* (Qualitative Gas-Chromatographic Analysis), Moscow: Nauka, 1978.
12. Ettre, L.S., *Chromatographia*, 1993, vol. 33, no. 3, pp. 73–77.
13. Kiselev, A.V., *Mezhmolekulyarnye vzaimodeistviya v adsorbtsii i khromatografii* (Intermolecular Interactions in Adsorption and Chromatography), Moscow: Vysshaya Shkola, 1986.
14. Golovnya, R.V. and Samusenko, A.L., *Izv. Akad. Nauk SSSR, Ser. Khim.*, 1983, no. 9, pp. 1993–2000.
15. Golovnya, R.V. and Grigor'eva, D.N., *Zh. Anal. Khim.*, 1985, vol. 40, no. 3, pp. 515–523.
16. Grigor'eva, D.N., Vasil'ev, A.V., and Golovnya, R.V., *Zh. Anal. Khim.*, 1993, vol. 48, no. 7, pp. 1167–1173.
17. Kurbatova, S.V., Yashkin, S.N., Moiseev, I.K., and Zemtsova, M.N., *Zh. Fiz. Khim.*, 1999, vol. 73, pp. 1659–1662.
18. Grigor'eva, D.N., Vasil'ev, A.V., and Golovnya, R.V., *Zh. Anal. Khim.*, 1991, vol. 46, no. 2, pp. 283–291.
19. Vigdergauz, M.S., Vigalok, R.V., and Dmitrieva, G.V., *Usp. Khim.*, 1981, vol. 50, no. 5, pp. 943–969.

Russian Journal of Applied Chemistry, Vol. 77, No. 1, 2004, pp. 116–118. Translated from Zhurnal Prikladnoi Khimii, Vol. 77, No. 1, 2004, pp. 119–121.

MACROMOLECULAR CHEMISTRY AND POLYMERIC MATERIALS

Effect of Vinylchlorosilane on Polymerization Modification of the Surface of Nonporous Microspheric Silica Gel

S. S. Airapetyan and A. G. Khachatryan

Khimtekh Research Institute, Yerevan, Armenia
Yerevan State University, Yerevan, Armenia

Received December 3, 2002; in final form, June 2003

Abstract—Formation of a polymeric coating in the course of preparation of polymer-containing silica gel as influenced by preliminary activation of the surface of nonporous silica gel with vinylchlorosilane was studied.

Nonporous silica gel supports with various grafted functional groups find expanding application in chromatography and immobilization of biopolymers [1, 2]. Before coating of the solid support or sorbent with a polymeric layer, its surface is activated by various procedures. Active centers formed by grafting of organic compounds on the support surface containing –OH groups allow their subsequent polymerization modification with various functional groups. Such active centers, which affect the kinetics of the initiator degradation and monomer polymerization [3, 4], can be prepared by grafting of compounds with unsaturated bonds, e.g., vinylchlorosilanes (VCSs) and vinyltrichlorosilanes, to the hydroxyl-containing support surface [5–8]. Polymerization in these systems is initiated by the agent occurring in the monomer bulk or sorbed on the surface of modified solid support [3–8].

Formation of a continuous polymeric coating protecting the support surface is urgent for preparing packing materials for high-performance liquid chromatography (HPLC). Uncontrolled cross-linking during deposition of the polymeric coating can deteriorate the chromatographic properties of the packing materials.

In this work we studied nonporous silica gel microspheres to eliminate the effect of structural features of the matrix (in particular, support porosity) on the polymeric coating deposition.

EXPERIMENTAL

As starting compounds for preparing packing materials with a polymeric coating we used nonporous microspheric silica gel with a particle size of 2 μm and residual pore volume of no more than 0.03 $cm^3\ g^{-1}$; it was prepared by the procedure given in [1]. The surface of this material was modified with VCS and octadecylchlorosilane (ODCS) with additional silanization with trimethylchlorosilane (TMCS) according to published procedure [9].

Copolymer of octadecyl methacrylate (ODMA) and methyl methacrylate (MMA) was used as polymeric material. The ODMA–MMA copolymer was prepared and deposited on the silica gel surface according to [10] using dicumyl peroxide initiating agent.

The HPLC analysis was performed on a Gilson device equipped with a double-beam UV detector (λ = 254 nm) using acetonitrile–water mobile phase (3 : 7 volume ratio). The tests were performed with 4.6×50- and 4.6×33-mm columns.

We used chemically pure grade reagents and chromatographic grade acetonitrile, water, and uracil–pyridine–phenol–toluene test mixture.

The sorption capacity factor of the material with respect to toluene can be determined as

$$k = (\tau_t - \tau_u)/\tau_u,$$

where τ_t and τ_u are the retention times of toluene and uracil, respectively (min).

The chromatographic parameters of the columns packed with nonporous supports (2 μm particle size) and different content of the polymeric coating are listed in the table. The particle surface was not preliminarily modified with VCS. The chromatographic properties of the columns packed with nonporous silica gel microspheres modified with ODCS (C_{18}) are given for comparison.

Let us consider the chromatographic properties of

1070-4272/04/7701-0116 © 2004 MAIK "Nauka/Interperiodica"

Chromatographic properties of HPLC columns packed with polymer-containing nonporous silica gel supports, column diameter 4.6 mm

Column height, mm	Modifying agent	Flow rate, ml min^{-1}	Pressure, Pa	Retention time, min				k with respect to toluene	Polymer content, wt %
				uracil	pyridine	phenol	toluene		
33	ODCS (C_{18}) + TMCS	0.33	183	0.934	–	1.047	1.680	0.798	–
50	–	1.0	177	0.473	0.520	0.570	1.045	1.209	3.10
50	–	1.0	167	0.508	0.543	0.557	0.958	0.885	2.06
33	–	0.5	113	0.607	0.713	0.890	1.068	0.759	1.57
50	–	0.5	172	0.954	1.055	1.147	1.605	0.682	1.11
50	VCS	1.0	183	0.474	0.505	0.565	1.060	1.24	1.25
33	″	1.0	131	0.358	0.395	0.405	0.872	1.30	1.38
50	″	0.5	191	0.500	0.565	0.606	1.437	1.87	1.91
50	″	1.0	193	0.467	0.526	0.546	1.573	2.37	2.53
50	″	1.0	207	0.492	0.507	0.575	2.278	3.63	2.64
50	″	1.0	197	0.465	0.547	0.555	1.730	2.72	2.72
50	″	1.0	121	0.970	1.135	1.335	3.633	2.75	2.78
33	″	1.0	180	0.363	0.412	0.460	1.260	2.47	2.98
50	″	1.0	217	0.439	0.498	0.526	2.133	3.86	3.12
50	″	1.0	198	0.496	0.570	0.835	1.977	2.99	3.40
50	″	1.0	177	0.455	0.540	0.595	2.323	4.10	5.98
33	″	1.0	200	0.356	0.533	1.824	1.824	4.21	6.24

the columns packed with microspheric silica gel containing C_{18} phase as a reference. The data given in the table show that, in the course of polymerization modification without VCS pretreatment, the continuous polymeric coating is formed only when the polymer content does not exceed 2 wt %. It should be noted that this content of the polymer on the nonporous surface significantly exceeds the amount required to form a monomolecular layer. Slight rise of k to 1.21 corresponds to the increase in the content of the polymeric coating to 3.1 wt % relative to the support weight. The main chromatographic properties of the columns packed with nonporous supports (2 μm particle size) preliminarily modified with VCS and differing in the content of the polymer coating are also listed in the table.

The mandatory requirement to the resulting polymer-containing composites is complete shielding of all the silanol groups on the support surface, eliminating two major disadvantages of silica matrices: high solubility in alkaline medium and so-called "silanol" interaction on the surface.

At complete shielding of the silanol groups, the retention time of pyridine is shorter than that of phenol (see table). Although the polymeric coating completely shields all the surface silanol groups, in some cases secondary cross-linking is observed, which is illustrated by increasing sorption capacity factor k with respect to toluene. This increase in k with increasing content of the polymeric coating confirms the fact that the polymeric coating with certain porosity is formed on the vinylated surface.

The sorption capacity factor increases with increasing content of the polymer (see figure). As seen from the comparison of dependences *1* and *2*, a continuous polymeric coating is formed in the course of deposition of the polymer layer on the silica gel surface pre-

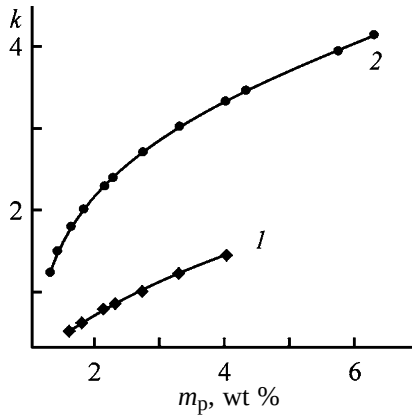

Sorption capacity factor with respect to toluene k as a function of the content of the polymer deposited m_p. Polymer (*1*) without VCS modification and (*2*) preliminarily modified with VCS.

liminarily modified with VCS. In this case, an increase in k with increasing polymer amount is less pronounced than without VCS pretreatment. The chromatographic parameters of the columns, obtained in this case, are similar to those for the columns packed with microspheric nonporous supports modified with ODCS (k values are nearly equal).

Since it is believed that k increases owing to the appearance of additional surface, then it can be concluded that secondary pores are formed in the course of silica gel coating with the polymer. It should be noted that the polymerization initiator (dicumyl peroxide) passes from the pentane solution to the support surface simultaneously with ODMA–MMA oligomer.

Secondary pores on the surface of a support preliminarily modified with VCS are formed as follows. In the course of polymerization on the surface containing vinyl groups, the sections with double bonds react first, because oligomers and silanol groups are less reactive. These vinyl-containing sections on the support surface become the centers of cross-linking of the oligomer fragments, forming a network which gives rise to secondary porosity. Simultaneously, free radicals are generated by thermal degradation of the initiator:

$$\mathrm{ROOR} \rightarrow 2\mathrm{RO}^{\bullet} \text{ and } \mathrm{ROOR} \rightarrow \mathrm{ROO}^{\bullet} + \mathrm{R}^{\bullet}.$$

These free radicals primarily attack the sections with double bonds and generate a large amount of free radicals on the support surface, causing random cross-linking of oligomeric fragments and formation of the porous polymer. Due to the high rate of the radical formation and random linking of oligomers with surface groups, a porous polymeric layer is formed instead of a continuous coating. Moreover, linking of separate oligomeric fragments with each other is hindered, because the main fraction of the initiator is consumed in the opening of the double bonds. It should be noted that, since cross-linking proceeds only with vinyl-containing sections of the support surface, the vinyl-free surface sections remain uncoated.

When the support surface was not preliminarily modified with VCS, the oligomeric fragments of copolymers react with radicals first. Oligomeric fragments are cross-linked, and the degree of additional polymerization is greater than in the above case. In the latter case, the polymer most likely covers silica gel particles and does not interact with their surface. The efficiency of additional polymerization is lower, which causes formation of a more uniform and relatively nonporous polymeric coating. With increasing polymer content, k also grows, but this trend is less pronounced than in the previous case.

CONCLUSIONS

(1) Preliminarily activation of the silica gel surface with vinylchlorosilane provides formation of secondary pores.

(2) The polymeric coatings with decreased porosity can be obtained without preliminary modification when the secondary porosity is insignificant.

REFERENCES

1. Hanson, M., Unger, K.K., and Schomburg, G., *J. Chromatogr.*, 1990, vol. 517, pp. 269–284.
2. Hanson, M. and Unger, K.K., *Evaluation of Advanced Silica Packings. Part 1. Synthesis and Characterization of Nonporous Silica Packings for HPLC*, LG–GG Int., Oct. 1996, pp. 650–656.
3. Rychly, J., Matiscka-Pychler, L., and Lazar, M., *Coll. Czech. Chem. Commun.*, 1975, vol. 40, no. 3, pp. 865–874.
4. Brik, M.T., *Polimerizatsiya na tverdoi poverkhnosti neorganicheskikh veshchestv* (Polymerization on the Solid Surface of Inorganic Compounds), Kiev: Naukova Dumka, 1981.
5. Ivanchev, S.S., Dmitrienko, A.V., Demidova, V.A., and Dabagova, A.G., *Vysokomol. Soedin., Ser. A*, 1985, vol. 27, no. 5, pp. 1086–1093.
6. Ivanchev, S.S., Dmitrienko, A.V., Polozov, B.V., *et al.*, *Plast. Massy*, 1982, no. 10, pp. 20–21.
7. Zubakova, L.B., Borisova, V.N., Koroleva, S.K., *et al.*, *Zh. Prikl. Khim.*, 1987, vol. 60, no. 7, pp. 1491–1494.
8. Zubakova, L.B., Borisova, V.N., Koroleva, S.K., *et al.*, *Zh. Prikl. Khim.*, 1986, vol. 59, no. 5, pp. 1182–1184.
9. *Modifitsirovannye kremnezemy v sorbtsii, katalize i khromatografii* (Modified Silicas in Sorption, Catalysis, and Chromatography), Lisichkin, G.V., Ed., Moscow: Khimiya, 1986.
10. Hanson, M., Unger, K.K., Manti, C.T., and Hodges, R.S., *J. Chromatogr.*, 1992, vol. 599, pp. 65–75.

Russian Journal of Applied Chemistry, Vol. 77, No. 1, 2004, pp. 119–123. Translated from Zhurnal Prikladnoi Khimii, Vol. 77, No. 1, 2004, pp. 122–127.

MACROMOLECULAR CHEMISTRY AND POLYMERIC MATERIALS

Activating Mixing in Preparation and Modification of Polymeric Composites

V. P. Britov, V. V. Bogdanov, O. O. Nikolaev, and A. E. Tubolkin

St. Petersburg State Technological Institute, St. Petersburg, Russia

Received February 4, 2003

Abstract—The concept of activating mixing as a procedure for preparing and modification of polymeric composites was developed. A new classification and generalized parameters of mixing, characterizing conditions of the energy supply to polymeric composition through the device working elements, were proposed. The dependence for determining the treatment modes providing controllable development of chemical transformations in a polymer system, which is invariant with respect to treatment modes and working installation, was obtained.

Formation and modification of polymeric composites by mixing is one of the ways for preparing new materials. Theoretically valid approach to this process was formulated in the middle of the past century [1]. It was suggested that laminar mixing increases the interface area of the components under the shear strain.

Since that time, despite considerable amount of works on various aspects of mixing (technology, installations, procedures to evaluate the system state, quantitative evaluation of the process performance), the phenomenological concept of the process remained unchanged. One of the reasons of this lag in the theoretical interpretation of the processes occurring during mixing was due to the concept of the process objective taken *a priori.*

Until recently, mixing was considered as a process whose "objective is transformation of the initial system, characterized by the ordered distribution of the components, into a system with disordered random distribution" [1].

This concept is obviously restricted [2], as seen from the following example. An active filler is added to a system in which the polymeric matrix is a mixture of elastomers. The required set of the material properties is provided only at the optimal distribution of the filler between the phases. In this case, "optimal distribution" is not identical with the uniform distribution of the filler in the entire system, because the filler content ensuring the highest strengthening is specific for each polymer.

The restriction of the classical concept of the mixing objective is confirmed by the analysis of the other polymeric systems. For example, in polymer engineering (as in other chemical processes) mixing should also be performed in single-component systems. In this case, mixing provides formation of the temperature-uniform material. In particular, a set of devices for rubber treatment is known, which provide heating and temperature uniformity in the material (cold-feeding screw machines).

The known classification of mixing processes should be also refined. These processes are often classified by the phase composition of the working medium and the process kind. As regards the phase composition, mixing can be performed in liquid, viscous-flow, and powder states [3]. In preparation of polymeric composite materials (PCMs), processes of the second group (viscous-flow mixing) are used most widely. However, only a few processes fit in the above classification. In the strict sense, these are only processes based on mixing of two thermoplastic components in a melt. A thermoplastic material is mixed with a rubber when one of the components (rubber) occurs not only in the viscous-flow but also in the hyperelastic state.

The real PCM preparation is based on mixing of powdered and high- and low-viscosity components added in the specific order and in definite time. Preparation of rubber stocks is the most typical example. Hence, we should consider not the process occurring in the viscous-flow state, but mixing of the components in different physical and phase states.

At present, the process results are not taken into account in classification, though the definitions such as "homogenization" and "dispersion" are used. It is

1070-4272/04/7701-0119 © 2004 MAIK "Nauka/Interperiodica"

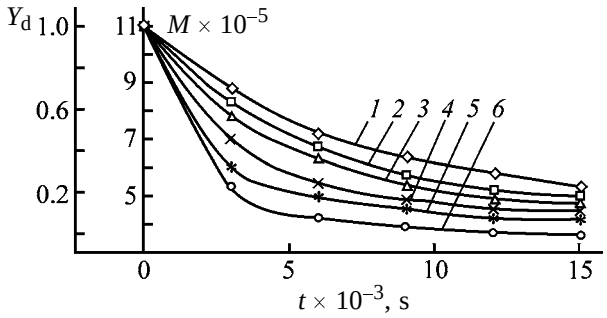

Fig. 1. Kinetic curves of NR degradation. (Y_d) Degree of degradation, (M) molecular weight of the polymer, and (t) time. H_0 (mm): (*1, 4*) 2; (*2, 5*) 1.5, and (*3, 6*) 1. φ_w: (*1, 3*) 0 and (*2, 4–6*) 0.3.

assumed that, in the first case, only the uniform distribution of particles is attained, whereas in the second case this is accompanied by a decrease in the component particle size. The above subdivision was made about 40 years ago [4], it seems valid, but separation of these processes in practice is very difficult. For example, the majority of compositions with addition of various components are prepared using impeller and rotary mixers in which the dispersion of the components is accompanied by homogenization of the entire system.

The most serious disadvantage of the existing approach to the mixing process is that it is considered as a combination of physical processes, whereas occurrence of chemical reactions due to the mechanical impact on the polymers in the course of their treatment is well known [5]. At present, a great body of data on mechanochemical transformations in polymers is available, but it is still not systemized. Moreover, due to the absence of the general criterion of the external effect on a polymer, it is difficult to compare the data given by different authors. In most cases, this effect is evaluated by changes in a separate process parameter, e.g., transition number through the rolls gap, grinding time in mills, etc. This approach does not take into account the process modes and design parameters of the installation in their combination, though they affect the material simultaneously [6].

Mechanochemical transformations in polymers are often described by an equation characterizing changes in the molecular weight with time proposed by Baramboim [5]:

$$M_t = (M_0 - M_\infty)\exp(-kt) + M_\infty, \quad (1)$$

where M_t is the current molecular weight at time t, M_0 is the initial molecular weight of the polymer, M_∞ is the limiting molecular weight of the smallest chain section, and k is a constant.

Casale and Porter [6] believed that constant k depends on the chemical nature of the polymer and packing density of its chains and determines the rate of mechanical degradation. Hence, k is a function of the polymer properties and is independent of the treatment conditions. However, k depends not only on the polymer nature, but also on the conditions of the energy supply to the material. The nature of the medium and temperature mode of dispersion are important but insufficient parameters to characterize the process conditions. Certain changes in the shear rate will cause changes in the shear stress and degradation rate in the system. This fact is confirmed by the data of the same authors on the relationship between the kinetics of ultrasonic degradation and experimental conditions.

This assumption was also confirmed by our experiments illustrating the development of mechanical degradation processes in natural rubber (NR). The kinetic dependences of NR degradation under various treatment conditions (H_0 is the minimal gap between the rolls) on the rolls with a wedge intensifying attachment [3] and without it are shown in Fig. 1. The depth of the wedge dipping is $\varphi_w = 0.3$ and $\varphi_w = 0$, respectively. As seen, the parameter k changes with changes in the treatment conditions. Thus, comparison of the data on mechanical degradation of similar polymers under different experimental conditions is meaningless, because different results will be obtained at different treatment modes. At the same time, comparison of the parameters of mechanical degradation obtained at rigidly fixed treatment modes is also impossible because of differences in the mixer design, providing different parameters of the mechanical field affecting the given material.

Thus, novel criteria allowing comparison of various polymers using parameters of mechanical degradation are required; moreover, these criteria should be invariant with respect to the treatment modes and design features of the installations.

We believe that classification of mixing processes by their effect on the mixed materials is the most promising. In this case, the objective of mixing (as a main procedure for PCM preparation) is to provide the optimal conditions in which the most valuable properties of the material (depending on its composition) will be manifested. For this purpose, new processes and equipment should be developed. Mixing should be organized so that the energy supplied to the components will initiate their chemical interactions

hindered under the other conditions or accelerate these reactions. Obviously, we consider only the components between which these reactions can proceed.

Practical problems which could be solved in this case are (1) development of new high-performance processes for preparing common compositions from viscous chemically reactive components and (2) preparation of new materials in the course of initiation of mechanochemical transformations and(or) controllable chemical modification of the polymers.

We suggest the term "activating" to define mixing under the conditions of initiated and controllable mechanochemical transformations.

The activating mixing differs from the other mixing modes (including those accompanied by mechanochemical transformations) in that in this case, along with increasing interface area between the components, the corresponding chemical reactions in the system are directly initiated or their rate considerably increases.

Activating mixing also differs from the other types of mechanical treatment causing mechanochemical effects (e.g., ultrasonic) by the specific effect of the mechanical field (shear strain), which increases the interface area between the components.

Thus, homogenization and dispersion mixing and the other mechanical procedures initiating chemical transformations can be considered as particular cases of activating mixing. This assumption can be illustrated using the classical Arrhenius equation in which the reaction rate constant K is determined by two variables (activation energy E_a and space steric factor pz):

$$K = pz e^{-E_a/RT}, \quad (2)$$

where z is the factor proportional to the collision number between the interacting particles.

At activating mixing, the reacting compounds obtain certain energy and the activation barrier of chemical reactions decreases. Moreover, during treatment some portion of mechanical energy is transformed in the heat, which also increases the reaction rate.

Finally, under the effect of stresses and shear rates, causing dispersion and homogenization, the interface area between the components increases and, thus, the probability of favorable mutual orientation of components (parameter pz) promoting the chemical reaction also increases. The latter condition of the activating mixing is advantageous as compared with the other modes of mechanochemical initiation and makes it efficient for practical implementation.

Our concept of the activating mixing allows the following classification of processes by the result of their effect on the mixed component.

Simple homogenizing mixing is a process that decreases the concentration heterogeneity in the system without chemical transformations. Mixing of granulated polymers with powdered or granulated additives without changes in the particle size and preparation of temperature-uniform media are the examples of this process.

Simple dispersion mixing is a process that causes breakdown of the disperse phase agglomerates in the system without chemical transformations These processes include formation of oil–water emulsions, breakdown of agglomerates of inert fillers in rubbers, etc.

Homogenizing mixing is a process that decreases the concentration heterogeneity in the system and is accompanied by chemical transformations that are not initiated in the course of the given process. Mixing of liquid media able of chemical reaction is an example of the process.

Dispersion mixing is a process that causes breakdown of the disperse phase agglomerates in the system and is accompanied by chemical transformations that are not initiated in the course of the given process.

Activating mixing is a process of initiation of chemical transformations in the system accompanied by its homogenization and dispersion of the separate phases.

It is advisable to describe each of the above processes by its own parameters (generalized parameters) of the external effect on the material.

The homogenizing mixing can be described using the common concept of the shear strain γ and its variance, which are directly related to the interface area between the components [3].

As for dispersion mixing, along with shear strain, we should evaluate the shear stresses τ appearing in the system and causing dispersion of one polymer in a another, breakdown of filler agglomerates, etc.

To develop the generalized parameters of activating mixing, we used the available experimental data on mechanochemical transformations in polymers processed on different installations. The correlation between the intensity of mechanical energy supply and the rate of mechanical degradation during treatment of rigid carbon-chain polymers (e.g., polystyrene, polyvinyl acetate, and polymethyl methacrylate) in a vibrating mill was found in [5]. With some assumptions, the strike energy of the grinding bodies of cer-

tain generalized weight is taken to be proportional to $(\alpha f)^2$, where α and f are the amplitude and frequency, respectively.

It was found that the rate constant of degradation is proportional to $\log(\alpha f)^2$. This suggests that

$$k_d = \log[(\alpha f)^2/(\alpha_0 f_0)^2], \quad (3)$$

where $\alpha_0 f_0$ is the certain deformation limit at which the rate constant of degradation decreases to zero.

For this process, it is convenient to use the energy E (J m^{-3}) per unit volume of the medium (energy density) as a criterion of the external effect:

$$E = 2\pi^2\rho(\alpha f)^2. \quad (4)$$

The process described above is physically similar to the process of shearing flow as predominant in both mixing and the other process of the polymer treatment.

It is known that the greater the internal friction (determined by the internal friction coefficient, or viscosity μ, Pa s), the greater the shear stress τ (Pa) required to preserve the steady-state motion in a laminar flow with a constant rate gradient γ' (s^{-1}); the relationship of these parameters is shown by the Newton equation $\tau = \mu\gamma'$. The energy intensity of the solution motion in a laminar flow per unit volume Y (W m^{-3}) is determined by the following equation:

$$Y = \mu\gamma'^2. \quad (5)$$

The amount of energy supplied to the material in certain time t (commonly, the period of the material treatment), or the density of the strain energy, can be given as

$$E = \mu\gamma'^2 t. \quad (6)$$

Equation (6) can be presented by various expressions:

$$E = \mu\gamma'^2 t = \mu\gamma'\gamma' t = \mu\gamma'\gamma = \tau\gamma, \quad (7)$$

where $\gamma = \gamma' t$ is the shear strain.

The density of the strain energy can be expressed in various dimensions: $U = E V_m$ [J mol^{-1}, cal mol^{-1}]; $U = EM_{av}/\rho$ [J mol^{-1}] = $0.24EM_{av}/\rho$ [cal mol^{-1}], where V_m and M_{av} are the average molar volume and average molecular weight, respectively. In this case, the value of the external mechanical effect can be compared with the energy of chemical bond.

It can be readily shown that the parameters in Eqs. (3) and (7) are physically identical. In the case of unidimensional motion, the rate gradient U/H can be used instead of the strain rate $d\gamma/dt$, i.e., the strain and shear rate correspond to the amplitude and frequency of the external mechanical field, respectively.

Thus, we proposed two generalized parameters to characterize the activating mixing, namely, the density of the strain energy and its intensity.

The possibility of using the intensity of the shear energy to analyze the mechanical degradation was first proposed in [6], but this parameter was not applied to mixing procedures, polymer treatment, and setup utilized. Hence, it was advisable to verify our generalized parameters with experimental data.

The tests were carried out using laboratory devices (Weissenberg rheogoniometer, Brabender plastograph) and industrial equipment (roller-bending machine, rotary mixers, vibrating mills, rotary-pulsating units). The resulting materials were analyzed by IR and UV spectroscopy, sol–gel analysis, and the other methods allowing evaluation of the molecular weight and molecular-weight distribution. In the course of the tests, we studied the relationships between the generalized parameters of the external effect on the system and parameters of mechanochemical transformations determined independently. The degree of mechanical degradation was studied using a dimensionless parameter (degradation index):

$$I_d = \frac{M_0 - M_t}{M_0 - M_\infty}. \quad (8)$$

In Fig. 2, our experimental data (see Fig. 1) are shown in the "degradation index–strain energy density" coordinates. The kinetic dependences of the index of mechanical degradation of natural rubber fall on a common straight line described by the following equation:

$$I_d^* = 1 - I_d = \frac{M_0 - M_t}{M_0 - M_\infty} = e^{-k^*\tau\gamma}, \quad (9)$$

where k^* is the degradation rate constant.

The curves of mechanical degradation of some other rubbers, obtained by similar procedure, are also shown in Fig. 2. Mutual position of the kinetic curves in the I_d^*–$\tau\gamma$ coordinates allows comparison of the rates of mechanical degradation of various polymers irrespective of the conditions of their treatment. In this case, k^* describes only the material properties. Thus, by determining the dependences of the parameters of

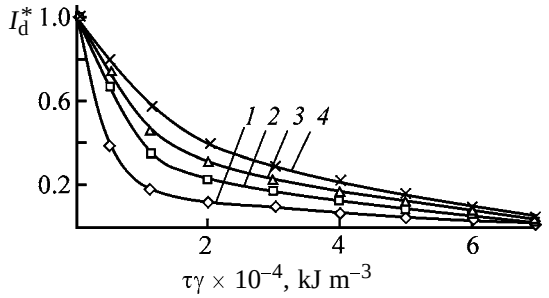

Fig. 2. Kinetic curves of degradation of some rubbers. (I_d^*) Index of mechanical degradation and ($\tau\gamma$) strain energy density. (*1*) NR, (*2*) SKN-40, (*3*) Nairit P, and (*4*) Nairit PNK.

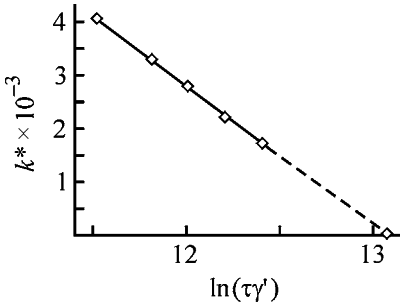

Fig. 3. Rate constant of degradation as a function of the intensity of mechanical effect $\tau\gamma'$.

mechanical degradation on $\tau\gamma$, we can obtain a correlation for a given material that is invariant with respect to the treatment modes and design features of the installation. At the same time, even significant density of the strain energy is not sufficient to cause mechanical degradation. The other necessary requirement is the energy supply. Actually, $\tau\gamma$ can be realized in an infinite period, with no mechanical degradation. This is due to the dispersion of the supplied mechanical energy through the polymer chains; this phenomenon was analyzed by Enikolopov [7]. The author studied ultrafast reactions in solids and formulated the following conclusion: At relatively low loading rates, the contribution of the elastic strain is negligible (1%) as compared to the total strain. As a result, at small shear rates in the working zone of the installation, the elastic energy accumulated in a solid is small. With increasing loading rate, the contribution of the elastic strain grows.

The above results can also be applied to our systems, because the polymer, irrespective of its molecular weight, can be considered as solid at certain intensity of the mechanical field. This fact explains the requirement of high shear rates at mechanochemical modification of polymers, reclaim of rubber crumbs from tire crushing, etc.

In practice, the required intensity of the strain effect can be determined as follows. First, the dependence of the degradation rate constant k^* on the logarithm of the shear stress intensity $\tau\gamma'$ is plotted, and then, extrapolating the resulting curve to the zero rate, the $\tau\gamma'$ value required to initiate the degradation is determined (Fig. 3).

Our theoretical results on the activating mixing were used in the development of processes for physicochemical modification of conducting siloxane compounds [8] and medical-purpose preparations [9]. However, it should be noted that the above processes are accompanied by predominantly physical transformations.

CONCLUSIONS

(1) Traditional concepts on the objective, nature, and classification of the mixing process were significantly refined. Classification of the mixing procedure based on the results of its effect on the mixed materials is the most valid. In accordance with this classification, the following mixing modes were distinguished: simple homogenizing, simple dispersion, homogenizing, dispersion, and activating mixing.

(2) The generalized parameters of the activating mixing characterizing the conditions of the energy supply to the material are the strain energy density and its intensity.

REFERENCES

1. *Processing of Thermoplastic Materials*, Bernhardt, E.C., Ed., New York: Reinhold, 1959.
2. Bogdanov, V.V. and Krasovskii, V.N., *Zh. Prikl. Khim.*, 1984, vol. 57, no. 9, pp. 2020–2025.
3. Bogdanov, V.V., Torner, R.P., Krasovskii, V.N., and Reger, E.O., *Smeshenie polimerov* (Mixing of Polymers), Leningrad: Khimiya, 1979.
4. McKelvey, J.M., *Polymer Processing*, New York: Wiley, 1962.
5. Baramboim, N.K., *Mekhanokhimiya vysokomolekulyarnykh soedinenii* (Mechanochemistry of Macromolecular Compounds), Moscow: Khimiya, 1978, 3rd ed.
6. Casale, A. and Porter, R.S., *Polymer Stress Reactions*, New York: Academic, 1978–1979.
7. Enikolopov, N.S., *Zh. Fiz. Khim.*, 1989, vol. 63, no. 9, pp. 2289–2290.
8. Lazarev, D.N., Britov, V.P., and Bogdanov, V.V., *Zh. Prikl. Khim.*, 2001, vol. 74, no. 11, pp. 1875–1880.
9. Nikolaev, O.O., Britov, V.P., and Bogdanov, V.V., *Zh. Prikl. Khim.*, 2001, vol. 74, no. 6, pp. 982–988.

Russian Journal of Applied Chemistry, Vol. 77, No. 1, 2004, pp. 124–127. Translated from Zhurnal Prikladnoi Khimii, Vol. 77, No. 1, 2004, pp. 128–131.

MACROMOLECULAR CHEMISTRY AND POLYMERIC MATERIALS

Control of Penetration of Macroglobules from Polymer Solution into the Bulk of a Porous Solid

N. V. Volkova, D. N. Emel'yanov, T. S. Kiseleva, and Yu. M. Ananicheva

Lobachevsky Nizhni Novgorod State University, Nizhni Novgorod, Russia

Received November 11, 2002; in final form, April 2003

Abstract—Penetration of poly(butyl methacrylate) macroglobules into solid porous samples of chalk, clay, cement, and cement–river sand mixtures was studied as influenced by the macroglobule size.

Important aspects in impregnation and reinforcement of porous solids (particularly, loose materials typical of historical and cultural monuments) are the depth of penetration and uniformity of distribution of the fixing agent (e.g., polymer) in the bulk of these solids. Naturally, the above-mentioned characteristics will be governed by the properties of the impregnating solution and, above all, by the polymer macroglobule size.

The aim of this work was to study penetration of poly(butyl methacrylate) (PBMA) macroglobules from solutions in solvents of different solvency into the bulk of solid porous samples such as models of historical and cultural monuments. Poly(butyl methacrylate) is widely used for conservation and restoration of art monuments made of various materials [1].

EXPERIMENTAL

We studied suspension PBMA [TU (Technical Specifications) 6-01-240–76] with the molecular weight $M = 3.5 \times 10^5$. As solvents for PBMA served toluene, *o*-xylene, acetone, butanol, and isopropanol. The quality of the solvents with respect to the polymer used was estimated by comparison of their solubility parameters δ [2] summarized in the table below. The table shows that, in changing from toluene to alcohols, the difference in δ increases. This means that, along this series, the quality of the solvent with respect to PBMA tends to deteriorate. The quality of the solvent was also worsened by introducing a precipitating agent for PBMA [3.5 to 10.5% (hereinafter, wt %) distilled water] into isopropanol. In this case, worsened solubility of PBMA in the mixed solvent was evidenced by increased turbidity of the solution, which was estimated nephelometrically.

The rms distance between the ends of the PBMA macromolecule in θ-solvent, isopropyl alcohol, was calculated by the Flory–Fox formula [3]

$$(\bar{h}_\theta^2)^{3/2} = \frac{[\eta]_\theta \bar{M}}{\Phi}, \quad (1)$$

where Φ is the Flory constant; $\bar{M}$, viscosity-average molecular weight of PBMA; and $[\eta]_\theta$, intrinsic viscosity of the PBMA solution in θ-solvent (isopropanol), l g^{-1}, measured at the θ-temperature of 21.5°C [2].

The swelling coefficient α^3 of the macroglobule and the rms distance $(\bar{h}^2)^{1/2}$, nm, between the ends of the macromolecule in different solvent were calculated by the formula

$$\alpha^3 = \frac{[\eta]}{[\eta]_\theta} = \frac{(\bar{h}^2)^{3/2}}{(\bar{h}_\theta^2)^{3/2}}. \quad (2)$$

Influence of the solubility parameter δ on the intrinsic viscosity $[\eta]$ of the PBMA solutions, swelling coefficient α^3 of the macroglobule, and rms distance between the ends of the PBMA macromolecule $(\bar{h}^2)^{1/2}$ [δ_{PBMA} = 8.70 (cal cm^{-3})$^{1/2}$]

Solvent	δ, (cal cm^{-3})$^{1/2}$	α^3	$(\bar{h}^2)^{1/2}$, nm	$[\eta]$, l g^{-1}
Toluene	8.97	5.30	46.0	0.080
o-Xylene	9.03	5.53	46.7	0.083
Acetone	9.74	2.53	36.0	0.038
Butanol	10.77	1.67	31.3	0.025
Isopropanol*	–	1.0	26.4	0.015

* For propanol, δ = 12.06 (cal cm^{-3})$^{1/2}$.

1070-4272/04/7701-0124 © 2004 MAIK "Nauka/Interperiodica"

The polymer content in the solutions was varied from 1 to 16%.

As solids we used $10 \times 10 \times 100$-mm cement–sand samples (CSSs), as well as $10 \times 10 \times 80$-mm pressed chalk (TU 458-15-14–89) and clay samples. The cement–sand samples were prepared by mixing grade 400 Portland cement [GOST (State Standard) 10178–85, particle size from 50 (65%) to 150 (7%) μm] with river sand [average particle size from 100 (5%)–300 (25%) to 400 (20%)–500 (15%) μm] in 18 ml of distilled water. The sand content in the samples was varied from 0 to 90%. The samples were molded at room temperature for 14 days. Clay samples were prepared by room-temperature molding, through mixing fine clay particles [from 1 (28%) to 60 (61%) μm in size] in 18 ml of water, followed by drying to constant weight at 200°C. Next, the pore size of the solid samples was estimated. To this end, we measured the rate of penetration of isopropanol into the sample pores. Then, the average pore radius r_{av}, nm, was calculated by the Washburn equation [4].

The pore radius of the solid samples r_{av}, nm, was estimated at 0.63, 0.48, 0.14, and 1.80 for chalk, clay, CSS-0, and CSS-90, respectively (the figure at the CSS designation corresponds to the river sand percentage).

The porous samples were impregnated until complete saturation with the polymer solutions in closed vessels, by immersing samples, suspended by wires from their face side, by 1 cm of their height in the impregnating liquid. Next, the samples were dried at room temperature under slow solvent evaporation. The uniformity of distribution of the polymer in the bulk of the porous samples was monitored by the procedure from [5]. It is underlain by the fact that the water absorption in the open pore space of the solid sample varies with the extent of pore filling with the penetrated polymer.

The solvent quality will, above all, affect the size of the polymer macroglobule. Grosberg and Khokhlov [6] found that, with deteriorating solvent quality, the macromolecular globule gets contracted. The volume occupied by the macromolecule decreases by a factor of several tens. The table below shows that, in changing from "good" (*o*-xylene or toluene) to "bad" (butanol or isopropanol) solvents, the rms distance between the ends of the PBMA macromolecule decreases by a factor of 1.5–2.

It could be expected with a good reason that, the smaller the globule, the easier and faster its penetration into pores (capillaries) of a solid. However, our

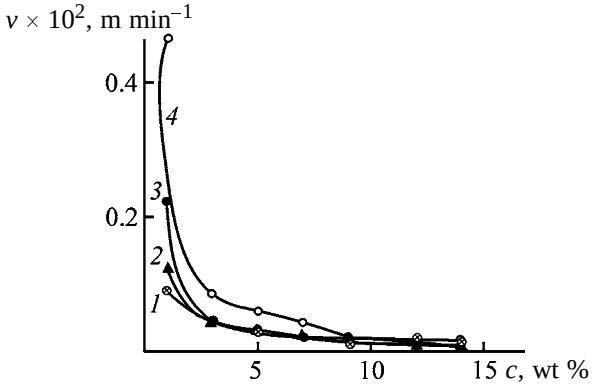

Fig. 1. Influence of the PBMA concentration c in the impregnating solutions in different solvents on the rate of their capillary rising v in CSSs containing 90% river sand. (*1*) Isopropanol, (*2*) butanol, (*3*) *o*-xylene, and (*4*) toluene.

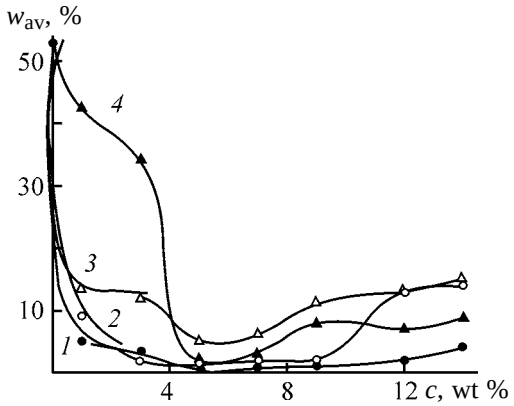

Fig. 2. Average water capacity w_{av} of CSSs containing 90% river sand as a function of the concentration of the impregnating solution c. (*1*) *o*-Xylene, (*2*) acetone, (*3*) butanol, and (*4*) isopropanol.

study showed that the rate of the capillary rising of the solution is larger (Fig. 1) and the degree of penetration of the polymer into CSSs with larger pores is greater (Fig. 2) when the PBMA macroglobules occur in the swollen state. The degree of penetration of the polymer into pores of solid samples was estimated from the amount of water w, %, able of penetration into the sample pores that remained open after impregnation with the polymer. The larger the amount of water absorbed by the sample, the lesser the amount of the polymer it contains. Evidently, in the case of loose globules, the globules extend and get oriented along the flow under the influence of the capillary pressure of absorption. This favors faster and deeper penetration of the globule into the sample pores.

When penetrating into surface pores of the sample, compressed PBMA macroglobules in isopropanol, evidently, plug them, thus preventing further penetration of PBMA into porous solids. This assumption is

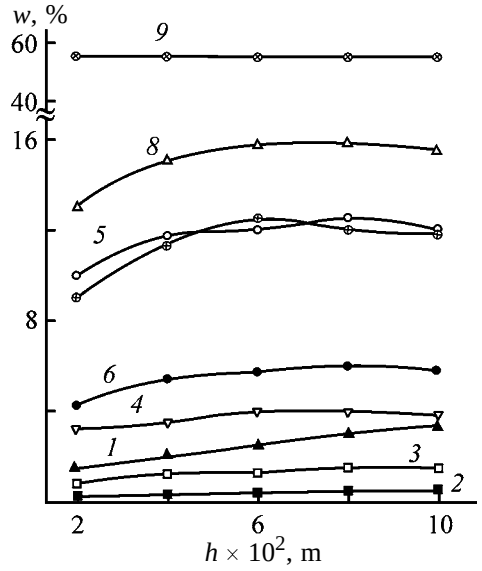

Fig. 3. Variation of the moisture capacity *w* of CSSs containing 90% river sand along the sample height *h*. (*1*–*4*) *o*-Xylene, (*5*–*8*) butanol, and (*9*) unimpregnated sample. Impregnating solution concentration, %: (*1*, *5*) 3, (*2*, *6*) 5, (*3*, *7*) 9, and (*4*, *8*) 14.

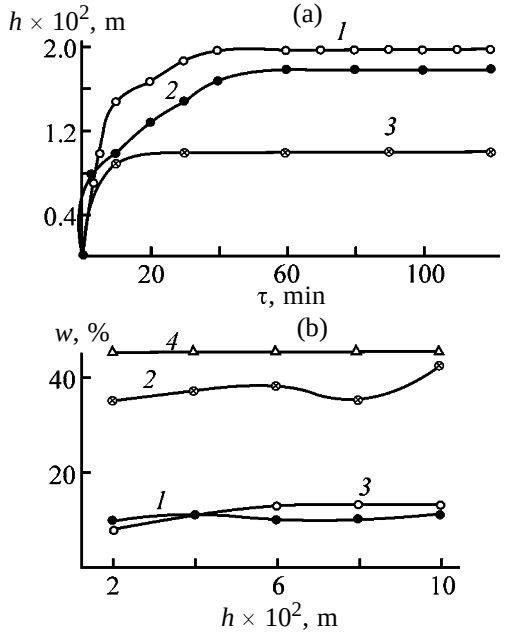

Fig. 4. (a) Kinetic curves of the capillary rising *h* of 3% PBMA solutions into cement samples and (b) variation of the moisture capacity *w* of the samples impregnated with 3% PBMA solutions along their height *h*. (τ) Time of rising of PBMA solutions into the samples, min. (*1*) *o*-Xylene, (*2*) isopropanol, (*3*) butanol, and (*4*) samples untreated with PBMA solution.

confirmed by Fig. 3 which suggests that the moisture capacity of the CSSs impregnated with PBMA solutions in *o*-xylene (a "good" solvent) is virtually invariant along the sample height. This means that the polymer is uniformly distributed over the sample. At the same time, the samples impregnated with PBMA solutions in butanol (a "bad" solvent) are characterized by a much lower moisture capacity of that segment of the sample through which impregnation was performed, compared to that at the opposite end. This suggests that the polymer is nonuniformly distributed over the CSS height and is, most probably, concentrated primarily in the surface pores. Evidently, the internal pores occurring in the middle part of the sample remained unimpregnated with the polymer. This is also confirmed by the fact that the moisture capacity of the samples impregnated with PBMA solutions in butanol significantly exceeds that of the samples impregnated with PBMA solutions in *o*-xylene.

In the case of impregnation of solid samples having small pores, the difference in the rates of rising of solutions in solvents with low and high solvency is virtually leveled off (Fig. 4a). The polymer is uniformly distributed along the height of the samples from both "bad" and "good" solvents (Fig. 4b). However, the degree of its penetration into the sample from the *o*-xylene solution significantly decreases, approaching that of the polymer penetrating from solutions in "bad" solvents. Thus, in both cases the polymer occurs in the surface pores of solids. Penetration of the polymer into sample pores is evidenced by a significant decrease in the moisture capacity relative to the untreated sample.

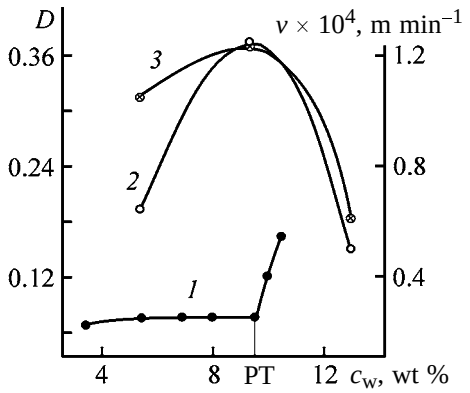

Fig. 5. (*1*) Optical density *D* of 2% PBMA solution and (*2*, *3*) rate of capillary rising of solutions *v* into (*2*) clay and (*3*) chalk samples as functions of the water content c_w in mixtures with isopropanol. (PT) Precipitation threshold for the polymer.

When a precipitating agent is added to a "bad" solvent for PBMA (e.g., water to isopropanol), the macroglubules get contracted, and the solution becomes turbid. We found that, in this state, the rate of impregnation of solid clay and chalk samples with small pores sharply increases (Fig. 5). Decrease in the rate of impregnation of the clay and sand samples after passing the precipitation threshold can be explained by formation of large agglomerates from adhering globules.

Thus, the penetrability of the pores of a solid with large pores by the polymer can be increased by converting the macroglobules into the swollen state. In the case of samples with small pores, the globules should be compressed to the maximal extent.

CONCLUSIONS

(1) In changing from good (*o*-xylene, toluene) to bad (butanol, isopropanol) solvents, the rms distance between the ends of the poly(butyl methacrylate) molecule decreases by a factor of 1.5–2.

(2) The rate of the capillary rising of the poly(butyl methacrylate) solution is higher, and the penetration depth and uniformity of distribution of the polymer within the bulk of a solid with large pores is greater in the case of a swollen globule, i.e., that penetrating from a good solvent.

(3) For samples with small pores, the impregnation rate and uniformity of distribution of poly(butyl methacrylate) along the sample height is independent of the quality of the solvent: The polymer occurs in the surface pores of the samples. Impregnation of the samples with small pores sharply accelerates upon contraction of poly(butyl methacrylate) globules.

REFERENCES

1. Fedoseeva, T.S., *Materialy dlya restavratsii zhivopisi i predmetov prikladnogo iskusstva* (Materials for Restoration of Painting and Applied Arts Items), Moscow: Redaktsionno-Izd. Otd., Nauchno-Issled. Inst. Restavratsii, 1999.
2. Lipatov, Yu.S., Nesterov, A.E., Gritsenko, G.M., and Veselovskii, R.A., *Spravochnik po khimii polimerov* (Handbook on Polymer Chemistry), Kiev: Naukova Dumka, 1971.
3. Semchikov, Yu.D., Zhil'tsov, S.F., and Kashaeva, V.N., *Vvedenie v khimiyu polimerov* (Introduction to Polymer Chemistry), Moscow: Vysshaya Shkola, 1988.
4. Voyutskii, S.S., *Fiziko-khimicheskie osnovy proniknoveniya i impregnirovaniya voloknistykh sistem vodnymi dispersiyami polimerov* (Physicochemical Principles of Penetration and Impregnation of Fibrous Systems by Aqueous Polymer Dispersions), Leningrad: Khimiya, 1969.
5. Ivanova, A.V., *Khudozh. Nasled.*, 1977, issue 2(32), pp. 33–41.
6. Grosberg, A.Yu. and Khokhlov, A.R., *Statisticheskaya fizika makromolekul* (Statistical Physics of Macromolecules), Moscow: Nauka, 1989.

Russian Journal of Applied Chemistry, Vol. 77, No. 1, 2004, pp. 128–130. Translated from Zhurnal Prikladnoi Khimii, Vol. 77, No. 1, 2004, pp. 132–134.

MACROMOLECULAR CHEMISTRY AND POLYMERIC MATERIALS

IR and NMR Study of the Structure of Dextran Polyaldehyde

A. L. Neishlos, E. V. Novikova, B. V. Passet, and A. V. Moskvin

St. Petersburg State Chemical and Pharmaceutical Academy, St. Petersburg, Russia

Received January 24, 2003

Abstract—The structure of samples of dextran polyaldehyde synthesized at various pH was studied by IR and ^{13}C NMR spectroscopy and PM3 semiempirical quantum-chemical method.

As shown previously [1], the structure of dextran polyaldehyde (DPA) depends on the synthesis conditions, in particular, pH value in oxidation of dextran with sodium metaperiodate. Since DPA is used for production of polymeric drugs, its conformity to the standards is one of the important conditions of synthesis. Therefore, the aim of this work was to study the structure of the DPA samples described in [1] by modern physicochemical methods.

It was suggested [2–4] that the DPA samples recovered from a solution with the certain pH can occur in various forms:

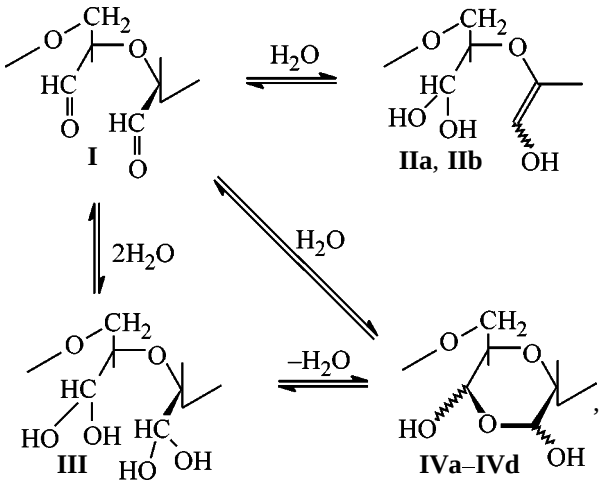

where **I** is aldehyde form, **IIa** and **IIb** are aldoenol forms, **III** is hydrated form, and **IVa**–**IVd** are hemiacetal forms.

Solid samples of DPA were prepared by oxidation of dextran with sodium metaperiodate at pH from 2.78 to 5.34 and isolated from the solution by the procedure described in [1].

Quantum-chemical evaluation of molecules of **I**–**IV** were carried out by semiempirical PM3 method using the GAMESS software [5]. The ^{13}C NMR spectra of solid samples were recorded on a Chemagnetic spectrometer operating at 74.7 MHz with magic angle spinning at 3.6 kHz. The spectra were interpreted using the ACD software. The IR reflection spectra were recorded on a Perkin–Elmer Fourier spectrophotometer.

To determine the energetically more favorable DPA forms, we calculated quantum-chemically the enthalpies of formation of structures **I**–**IV**, $\Delta_f H_0^0$, in a vacuum at 0 K and determined the heat effects of mutual transformations of these forms, $\Delta_r H_0^0$ (Table 1). For **II** and **IV**, the enthalpies of formation of their stereoisomers **IIa, IIb**, and **IVa**–**IVd** were evaluated:

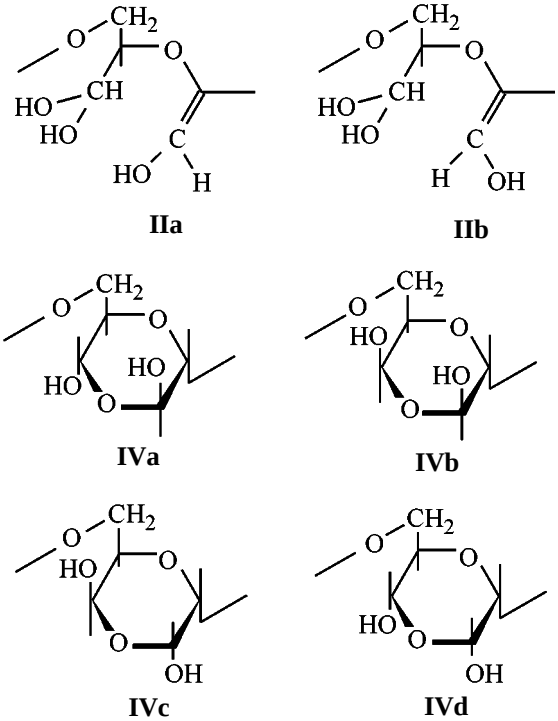

According to quantum-chemical calculations, in the

Table 1. Enthalpies of formation of various DPA forms $\Delta_f H_0^0$ in a vacuum at 0 K and heat effects of their mutual transformations $\Delta_r H_0^0$ (results of PM3 calculations)

DPA form	$\Delta_f H_0^0$, kJ mol^{-1}	Transformation	$\Delta_r H_0^0$, kJ mol^{-1}
I	–830.645	**I → II**	–9.167
IIa	–1053.632	**I → III**	–103.982
IIb	–1063.860	**I → IV**	–71.261
III	–1382.723	**III → IV**	–32.721
IVa	–1125.954		
IVb	–1118.075		
IVc	–1113.874		
IVd	–1116.407		

gas phase hydrated DPA forms **II**–**IV** are more favorable than nonhydrated form **I**. The most probable is hydrated form **III**, and the least probable, aldoenol form **IIb**. Among the considered hemiacetal structures, the most favorable is **IVa**.

The ^{13}C NMR data for DPA samples and the initial dextran are presented in Table 2. The lines in the spectra of dextran were assigned according to published data [6, 7].

The numbering of the carbon atoms of monosaccharide units in the initial dextran and various forms of its oxidation products **I**–**IV** is presented below.

In the ^{13}C NMR spectra of DPA samples, the signals of $C^{1'}$–$C^{5'}$ atoms are shifted upfield relative to the corresponding signals in the spectrum of dextran.

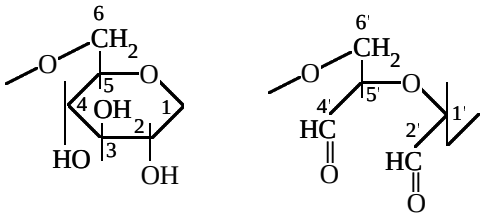

This is usually observed in spectra of carbohydrates substituted in position 2, 3, or 4 [7].

According to the ^{13}C NMR spectra, oxidation of dextran proceeds across the C^2–C^3 and C^3–C^4 bonds, and there are no signals in the range 70.2–71.7 ppm corresponding to the signal of $C^{3'}$.

The aldehyde form **I** in the samples studied is apparently absent, since in the ^{13}C NMR spectra there are no signals in the region of 200 ppm characteristic of the –CHO group.

In the spectra of the DPA sample prepared at pH 2.78 and 4.88, there are signals in the region of 122.1 and 122.7 ppm, respectively, corresponding to the signal of $C^{2'}$ of aldoenol **II**; however, the signal of $C^{1'}$ in the region of 150 ppm is absent.

In the ^{13}C NMR spectra of all the DPA samples synthesized in the pH range 2.78–5.34, there are signals in the range 87.9 and 92.4–93.3 ppm, corresponding to the signals of $C^{2'}$ and $C^{4'}$ of hydrated **III** or hemiacetal **IV** forms.

Thus, the ^{13}C NMR spectra show that the DPA samples prepared at pH from 2.78 to 5.34 are mix-

Table 2. Assignment of signals in the ^{13}C NMR spectra of dextran and DPA samples

Atomic position	^{13}C chemical shift							
	calculated* for indicated form				experiment at indicated pH			
	I	**II**	**III**	**IV**	2.78	3.00	4.88	5.34
C^1	95 ± 4	95 ± 4	95 ± 4	95 ± 4	96.0	96.0	96.0	96.0
$C^{1'}$	103.72 ± 3.1	150.45 ± 13	96.05 ± 8.2	95.4 ± 7.6	101.1	101.4	101.4	100.8
C^2	72.4 ± 0.9	72.4 ± 0.9	72.4 ± 0.9	72.4 ± 0.9	71.4	70.2	71.7	71.7
$C^{2'}$	196.88 ± 8	119.73 ± 8.5	89.6 ± 2.1	90.83 ± 3	87.9	87.9	87.9	87.6
					122.1	144.4	122.7	
C^4	71.23 ± 2.8	68.45 ± 3.1	70.81 ± 4.5	70.81 ± 4.5	71.4	70.2	71.7	71.7
$C^{4'}$	199.83 ± 2	94.72 ± 7.8	94.87 ± 7.5	98.76 ± 4.9	92.7	92.4	92.7	93.3
C^5	73.13 ± 1	71.76 ± 3.1	71.7 ± 2.1	71.71 ± 2.1	71.4	70.2	71.7	71.7
$C^{5'}$	81.95 ± 0.8	74.19 ± 11.3	77.65 ± 10	77.01 ± 10	80.4	80.7	80.4	80.7
C^6	66.21 ± 2.7	62.78 ± 5.2	67.28 ± 1.9	67.28 ± 1.9	66.9	66.6	66.6	66.6
$C^{6'}$	58.81 ± 4.6	60.99 ± 2.1	60.72 ± 2.4	60.72 ± 2.4	58.8	66.6	58.8	58.8

* Calculated with the ACD software.

tures of hemiacetal, hydrated, and (at pH 2.78 and 4.88) aldoenol forms.

The IR reflection spectra were interpreted according to published data [8]. In the IR spectra of all the DPA samples, the stretching modes ν(C–C) and ν(C–O) of nonoxidized dextran ring were observed in the range 950–1080 cm^{-1}.

The IR reflection spectra of the samples synthesized at pH 2.57, 2.78, 4.86, and 5.34 show that aldehyde form **I**, manifested as a sharp band at 1700 cm^{-1}, was present in small amounts only in the samples prepared at pH 5.34. In the spectra of the other DPA samples, the absorption bands in this range are much less strong. In addition, water, which is always present in polysaccharides, absorbs in this range, hampering determination of aldehyde groups by IR spectroscopy.

In all the samples, the absorption bands at 1610 and 1500 cm^{-1} were found, suggesting the presence of aldoenol form **II**, whose content is maximal in the sample synthesized at pH 4.88. Certain decrease in the intensity of these bands in the sample with pH 5.34 is apparently due to a decrease in the total amount of oxidized units [1].

The maximum content of hydrated form **III** is observed in the sample prepared at pH 2.57. In its IR spectrum, there are strong absorption bands in the range 1250–1310 cm^{-1}. In the samples synthesized at higher pH its content decreases, and in the sample prepared at pH 5.34 hydrated form **III** is absent.

Thus, the IR spectra of DPA samples prepared by oxidation of dextran at various pH show that solid DPA is a mixture of hydrated form **III** with a small content of aldoenol form **II** and, at pH 5.34, of aldehyde form **I**.

CONCLUSIONS

(1) Dextran polyaldehyde prepared by solid-phase oxidation of dextran at pH < 5.34 contains no aldehyde form **I** and exists predominantly in the form of a mixture of hydrated **III** and hemiacetal **IV** forms.

(2) The content of hydrated form **III** in the samples of dextran polyaldehyde decreases with increasing pH from 2.57 to 4.88.

(3) Aldoenol form **II** is present in all the samples prepared at pH 2.57–5.34, and its content increases with pH.

REFERENCES

1. Novikova, E.V., Tishchenko, E.V., Iozep, A.A., and Passet, B.V., *Zh. Prikl. Khim.*, 2002, vol. 75, no. 6, pp. 1003–1006.
2. Drobchenko, S.N., Isaeva-Ivanova, L.S., Grachev, S.A., and Bondarev, G.N., *Vysokomol. Soedin., Ser. B*, 1990, vol. 32, no. 4, pp. 254–258.
3. Drobchenko, S.N., Isaeva-Ivanova, L.S., Kulintseva, I.V., *et al.*, *Vysokomol. Soedin., Ser. B*, 1991, vol. 33, no. 3, pp. 220–224.
4. Bondarev, G.N., Drobchenko, S.N., and Isaeva-Ivanova, L.S., *Vysokomol. Soedin., Ser. A*, 1994, vol. 36, no. 7, pp. 1109–1112.
5. Schmidt, M.W., Baldridge, K.K., Boatz, J.A., *et al.*, *J. Comput. Chem.*, 1993, vol. 14, pp. 1347–1363.
6. Usmanov, T.I., Karimova, U.G., and Sarymsanov, A., *Vysokomol. Soedin., Ser. B*, 1990, vol. 32, no. 6, pp. 1176–1183.
7. Seymour, F.R., Knapp, R.D., and Bishop, S.H., *Research*, 1976, vol. 51, no. 2, pp. 179–194.
8. Zhbankov, R.G., *Infrakrasnye spektry i struktura uglevodov* (IR Spectra and Structure of Carbohydrates), Minsk: Nauka i Tekhnika, 1972.

Russian Journal of Applied Chemistry, Vol. 77, No. 1, 2004, pp. 131–135. Translated from Zhurnal Prikladnoi Khimii, Vol. 77, No. 1, 2004, pp. 135–139.

MACROMOLECULAR CHEMISTRY AND POLYMERIC MATERIALS

Antioxidative Stabilization of Polyethylene Glycol in Aqueous Solutions with Herb Phenols

V. M. Mikhal'chuk, T. V. Kryuk, L. V. Petrenko, O. A. Nelepova, and A. N. Nikolaevskii

Donetsk National University, Donetsk, Ukraine

Received September 28, 2001

Abstract—The effect of compounds extracted from herbs on oxidation of polyethylene glycol in aqueous solutiuons was studied.

Polyethylene glycols (PEGs) of various molecular weights, which show no biological activity and are not involved in metabolism, are used in drug and cosmetic formulations [1].

Polymers based on ethylene oxide are characterized by high concentration of $-CH_2-$ groups in which the C–H bond is relatively labile owing to the presence of adjacent ether oxygen atoms. These substances are readily oxidized with atmospheric oxygen [2], which negatively affects the physiological and toxicological properties of drugs based on them. Therefore, PEG-based systems should be stabilized against oxidation. Data on antioxidative stabilization of PEG aqueous solutions are lacking, which makes urgent the studies of PEG oxidation in aqueous solution and the search for optimal inhibitors (InH) of the polymer oxidation.

Preliminary studies of the kinetics of oxygen uptake with 30% solutions of PEG in water and chlorobenzene showed that, in contrast to saturated hydrocarbons and carbon-chain polymers, PEG is oxidized at a high rate ($>5 \times 10^{-6}$ mol l^{-1} s^{-1}) even at 70–90°C. In the initial steps, the oxidation develops with autoacceleration, and the oxygen uptake grows in proportion to time squared; the kinetic curves are linearized in the parabolic coordinates (Fig. 1), which corresponds to the known equation of polymer autooxidation [3]:

$$\Delta O_2 = \frac{\alpha \sigma k_2^2 k_3 [RH]^3}{8k_6} t^2 = \Phi t^2,$$

where ΔO_2 is the amount of oxygen taken up by the polymer; Φ, autoacceleration factor; k_2, k_3, and k_6, rate constants of chain propagation, branching, and termination, respectively; σ, probability of escape of free radicals in breakdown of hydroperoxy groups; and α, yield of hydroperoxide based on the oxygen taken up.

In the course of oxidation, the rate of oxygen uptake monotonically grows, reaches a maximum, and then decreases (Fig. 1). A maximum or plateau in the time dependence of the oxidation rate is due to attainment, at certain instant, of a steady-state concentration of hydroperoxide, primary oxidation product, whose thermal decomposition results in branching of the oxidation kinetic chains [3]. As the temperature is elevated and the PEG content in solution is increased from 30 to 50%, the maximal oxidation rate V_{max} and the autoacceleration factor (Table 1), as expected, grow. An increase in the oxygen partial pressure from 0.02 to 0.1 MPa has virtually no effect on the kinetics

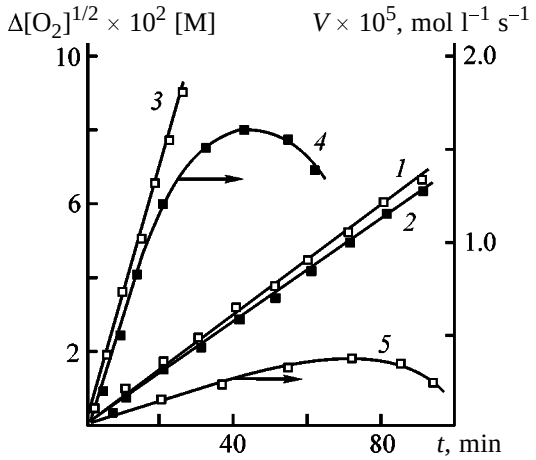

Fig. 1. Kinetic curves of PEG oxidation in water at (*1–4*) 90 and (*5*) 80°C and oxygen pressure of (*1, 3–5*) 0.1 and (*2*) 0.02 MPa. ($\Delta[O_2]$) amount of oxygen taken up by the polymer, (*V*) oxidation rate, and (*t*) time. PEG concentration, %: (*1, 2, 4, 5*) 30 and (*3*) 50.

1070-4272/04/7701-0131 © 2004 MAIK "Nauka/Interperiodica"

Table 1. Autoacceleration factors Φ and maximal oxidation rates V_{max} in oxidation of PEG solutions at 80°C

Conditions, inhibitor	$\Phi \times 10^5$, mol l^{-1} s^{-2}	$V_{max} \times 10^6$, mol l^{-1} s^{-1}
No phenols added		
30% PEG solution in water at *T*, °C:		
70	1.8	–
80	3.1	3.7
90	7.5	16
30% PEG solution in chlorobenzene	8.3	25
50% PEG solution in water	7.0	5.7
Solutions with 5×10^{-3} M phenols added		
Ethyl 3,4,5-trihydroxybenzoate	2.1	3.7
1,3,5-Trihydroxybenzene (phloroglucinol)	1.9	3.7
4-Hydroxy-3,5-dimethoxybenzoic acid (syringic acid)	1.0	1.3
2,3-Dihydroxyphenylpropenoic acid (caffeic acid)	0.67	0.90

of oxygen uptake (Fig. 1). Our results show that oxidation of the polymer in aqueous solution can be considered as a kinetically controlled degenerate branched process.

Oxidation of PEG in aqueous solution is characterized by lower Φ and V_{max} compared to oxidation in chlorobenzene at the same temperature and polymer concentration (Fig. 1). This is due to solvation of PEG [4]. A water molecule forms a hydrogen-bonded radical complex with a peroxy radical,

$$RO_2^{\cdot} + H_2O \rightarrow ROO^{\cdot}\cdots HOH,$$

which is less reactive in chain propagation and termination than nonsolvated $RO_2^{\cdot}$.

Despite relatively low reactivity in water of radicals leading the oxidation chains, PEG is oxidized much faster than hydrocarbons. For example, medical Vaseline oil is oxidized at a noticeable rate only above 200°C [5]. As inhibitors of PEG oxidation, we tested phenols from herb extracts. Such compounds efficiently inhibit oxidation of liquid hydrocarbons, in particular, ethylbenzene [6], and are readily soluble in aqueous systems, in contrast to traditional inhibitors of oxidation of nonpolar hydrocarbons (sterically hindered phenols, aromatic amines, etc.).

The inhibiting power of phenolic antioxidants is usually evaluated by the rate constants of the reaction

$$RO_2^{\cdot} + PhOH \xrightarrow{k_7} ROOH + PhO^{\cdot},$$

which are determined under conditions of initiated oxidation at constant rate of generation of $RO_2^{\cdot}$ radicals. For the system under consideration, it seems impossible to determine the rate constant k_7 of phenol-inhibited oxidation of PEG experimentally, since autooxidation of PEG occurs even at relatively low temperatures (<70°C), and even at high concentrations of an initiator, azobis(isobutyronitrile) ($>1 \times 10^{-2}$ M), the oxygen uptake occurs under conditions of mixed initiation. This is indicated by the absence of linear concentration dependences of the induction periods τ of PEG oxidation in the presence of antioxidants. For example, the induction period in the kinetic curves of the oxygen uptake becomes longer on adding increasing amounts of syringic acid (Fig. 2a), but the $\tau = f([InH])$ dependence shows a pronounced curvature (Fig. 2b) characteristic of phenol-inhibited oxidation

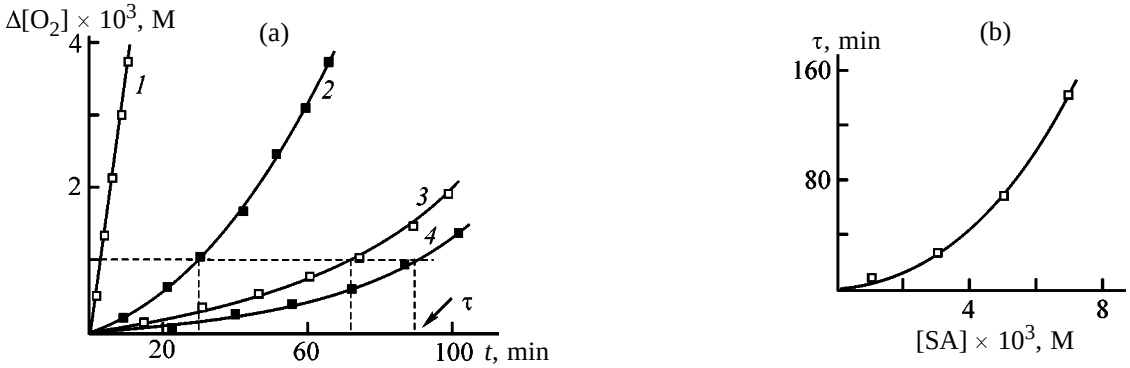

Fig. 2. (a) Kinetic curves of oxygen uptake with 30% PEG solution in water at (*1–3*) 75 and (*4*) 90°C in the presence of (*1–3*) azobis(isobutyronitrile), (*2, 3*) syringic acid, and (*4*) a mixture of syringic acid with phloroglucinol; (b) induction period of initiated oxidation of PEG as a function of syringic acid concentration [SA]. ($\Delta[O_2]$) Amount of oxygen taken up by the polymer, (τ) induction period of oxidation, and (*t*) time. (a) Inhibitor concentration, M: (*2*) 3×10^{-3} and (*3*) 5×10^{-3}; (*4*) 70 : 30 ratio of syringic acid to phloroglucinol at their total concentration of 1×10^{-2} M.

of polymers in the autoaccelerating mode [3]. Therefore, the antioxidative performance of the phenols in hand can be assessed only by the autoacceleration factor and maximal autooxidation rate.

Experiments on the effect of herb phenols on the autooxidation kinetics revealed pronounced antioxidative power of these compounds with respect to PEG. Addition of ethyl gallate, phloroglucinol, syringic acid, and caffeic acid decreases the autoacceleration factor. Furthermore, additions of carboxyl-containing phenols considerably decrease the maximal oxidation rate (Table 1). The phenols in hand can be ranked in the following order with respect to the antioxidative power: ethyl gallate < phloroglucinol < syringic acid < caffeic acid.

As shown in [6], the same compounds are also effective antioxidants for ethylbenzene, which suggests that the stabilizing effect of phenols in polar and nonpolar media is similar. At the same time, data of [6] show that the antioxidative performance of the phenols in hand in aqueous solution is lower than in a nonpolar hydrocarbon medium. For example, in oxidation of PEG and ethylbenzene in the presence of syringic acid under similar experimental conditions (initiator concentration 1×10^{-2} M, 75°C), the 60 min induction period of oxygen uptake is attained at the inhibitor concentration of 5×10^{-3} and 1.5×10^{-5} M, respectively. The lower antioxidative performance of the inhibitors in water may be due to solvation of both phenols and peroxy radical of the polymer [4].

The higher stabilizing performance of carboxyl-containing phenols (syringic and caffeic acids) is, apparently, due to the fact that the antioxidants inhibit the PEG oxidation not only by reacting with peroxy radicals, but also by participating in some other reactions inhibiting the oxidation. The presence of an acid group in InH molecules suggests that such reaction may be decomposition of the primary products of the polymer oxidation. It is known [4] that decomposition of many organic hydroperoxides under the influence of Brønsted acids yields molecular products (alcohols, ketones, aldehydes, acids) incapable of leading the radical-chain oxidation process, which results in the reaction deceleration.

To confirm the assumption that the antioxidative effect of phenols containing acid groups is due to decomposition of hydroperoxides effected by these compounds, we examined the effect of inhibitors on decomposition of the hydroperoxide derived from PEG. We found that ethyl gallate and phloroglucinol containing no COOH groups do not activate the hydroperoxide decomposition. In the presence of syringic and caffeic acids, the hydroperoxide decomposes at a rate exceeding 10^{-6} mol l^{-1} s^{-1} even at 37°C. In the process, the kinetic curves of consumption of hydroperoxy groups are linearized in the coordinates of a second-order reaction with the correlation factor of 0.997 (Fig. 3). At the same time, the rate constant of the bimolecular reaction, calculated at different initial concentrations of the hydroperoxide and syringic acid (from 1×10^{-3} to 1×10^{-2} M) in the temperature range 37–57°C, takes different values depending on reactant concentrations (Table 2). This fact suggests that decomposition of PEG hydroperoxide, apparently, occurs via preliminary complexation and is described by the general relationships of acid decomposition of hydroperoxides following the Michaelis–Menten scheme [7]:

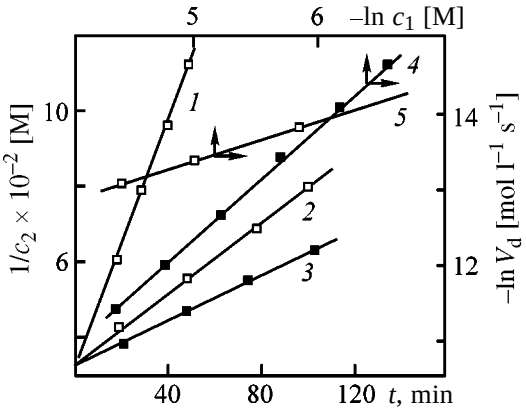

Fig. 3. (*1–3*) Variation with time of the concentration of PEG hydroperoxide in the course of its decomposition in the presence of 5×10^{-3} M syringic acid; initial rate of the hydroperoxide decomposition as a function of the (*4*) hydroperoxide and (*5*) syringic acid concentrations. Temperature, °C: (*1*) 57, (*2*, *4*, *5*) 47, and (*3*) 37. (V_d) Rate of hydroperoxide decomposition, (c_1) hydroperoxide or syringic acid concentration, (c_2) hydroperoxide concentration, and (t) time.

$$\mathrm{ROOH} + \mathrm{H^+} \underset{}{\overset{K_e}{\rightleftharpoons}} \mathrm{ROOH \cdots H^+} \xrightarrow{k_d} \mathrm{H^+} + \text{products}.$$

In this case, the hydroperoxide decomposition rate at $[\mathrm{ROOH}] \ll [\mathrm{H^+}]$ is described by the equation

$$V = \frac{k_d K_e [\mathrm{ROOH}][\mathrm{H^+}]}{1 + K_e[\mathrm{H^+}]},$$

where K_e is the complexation constant, and k_d is the rate constant of hydroperoxide decomposition.

This equation shows that the hydroperoxide decomposition is a first-order reaction with respect to the hydroperoxide, and the reaction order with respect to the catalyst can vary from 0 to 1 depending on K_e.

Table 2. Rate constants k_d of decomposition of PEG hydroperoxides (HP) in aqueous solution in the presence of syringic acid (SA)

c, M	$k_d \times 10^4$, l mol^{-1} s^{-1}, at indicated T, °C		
	37	47	57
[HP] = 5×10^3 M			
[SA] $\times 10^3$, M:			
1	1.4	2.2	1.3
3	–	–	1.5
5	1.6	2.8	1.6
7	2.1	3.7	3.1
10	3.3	8.7	5.8
[SA] = 5×10^3 M			
[HP] $\times 10^3$, M:			
1	0.28	0.28	0.75
3	0.48	1.1	–
5	1.4	3.2	3.0
7	3.4	3.7	5.0
10	4.9	6.2	7.3

Since the integral method is insufficiently sensitive for reliable determination of the reaction order, we calculated the reaction orders with respect to each component using the LeGore differential method [8]. We found that the dependence of the initial reaction rate on the initial concentration of additives is linearized in the $\ln V = f(\ln c)$ coordinates with the slopes of 0.8–1.2 for the hydroperoxide and 0.6 for syringic acid (Fig. 3), i.e., the order with respect to the hydroperoxide is close to unity, and that with respect to the catalyst is less than unity. Hence, indeed, PEG hydroperoxides decompose in aqueous solutions in the presence of carboxy phenols via formation of a complex.

From the temperature dependence of the rate constant of the reaction of syringic acid with PEG hydroperoxide, we determined the reaction activation energy E_a. The values of the rate constants and E_a (98 kJ mol^{-1}) allow comparison of the activating effect of syringic acid with that of such effective catalysts of organic peroxide decomposition as, e.g., quaternary onium salts, for which k_d varies in the range 10^{-4}–10^{-5} l mol^{-1} s^{-1}, and the activation energy of decomposition of cumyl hydroperoxide is 74–95 kJ mol^{-1} (depending on cation) at a catalyst concentration of 0.1 M [9]. Thus, the carboxy phenols studied in this work efficiently decompose hydroperoxides in aqueous solution.

Since decomposition of hydroperoxides in aqueous solutions in the presence of Brønsted acids mainly occurs without generation of active radicals [4], the phenols studied in this work probably decelerate various steps of PEG oxidation (chain propagation and branching). Addition to the polymer of compounds scavenging $RO_2^{\bullet}$ radicals and decomposing hydroperoxides ensures simultaneously small length and small number of kinetic chains. As a result, both functional groups protect each other from fast consumption and, acting in combination, provide prolonged protection of the polymer [3], i.e., an "internal synergism" of the functional groups of the stabilizer is observed. At the same time, enhancement of the antioxidative power of such inhibitors is due to the fact that the functional group that suppresses degenerate chain branching decreases the autoinitiation rate. As a result, syringic and caffeic acids exceed in the antioxidative power phloroglucinol and ethyl gallate.

When typical radical acceptors are introduced together with an inhibitor capable simultaneously of interacting with $RO_2^{\bullet}$ and decomposing hydroperoxides, the mutual effect of the stabilizers can be both synergistic and antagonistic. For example, in the presence of mixtures of ethyl gallate or phloroglucinol with syringic acid, the induction period in the kinetic curves of the oxygen uptake increases (Fig. 2a). The greatest stabilizing effect is attained on adding a mixture of phloroglucinol with syringic acid. In this case, an increase in τ is accompanied by a decrease in the oxidation rate in deep steps. These effects are the most pronounced at the component ratio from 30 : 70 to 70 : 30.

EXPERIMENTAL

Our experiments were performed with pure grade PEG, H–$(OCH_2CH_2)_n$–OH, molecular weight 3000, purchased from Merck (Germany), mp 55–58°C, hydroxyl number 34–43, and with products of its autooxidation at 120°C containing hydroperoxy groups in concentrations of 0.1–1.1 $\times 10^{-2}$ M. Decomposition of the hydroperoxides was performed under argon at 37–57°C. The inhibitors listed in Table 1 were used without additional purification (Merck, chemically pure grade). The content of ROOH groups was determined by iodometric titration. The rate of the oxygen uptake at its partial pressure of 0.10 and 0.02 MPa was determined on an automatic laboratory unit with the sensitivity of 1.0×10^{-6} mol l^{-1} s^{-1}.

CONCLUSIONS

(1) The kinetics of oxygen uptake with polyethylene glycol of molecular weight 3000 in aqueous solu-

tion at temperatures above 70°C are typical of radical-chain processes with degenerate chain branching.

(2) Carboxy phenols catalyze decomposition of hydroperoxides in aqueous solution. The reaction involves complexation of the reactants; the reaction order is 1 with respect to the hydroperoxide and 0.6 with respect to the catalyst.

(3) Herb phenols decomposing hydroperoxides are antioxidants of combined effect: They terminate kinetic chains of oxidation and simultaneously suppress degenerate branching. As a result, these compounds efficiently inhibit oxidation of polyethylene glycol in aqueous solutions: The autoacceleration factor in oxidation decreases by a factor of 3–5, and the maximal rate of the oxygen uptake by the polymer, by a factor of 3–4.

REFERENCES

1. Blatun, L.A., Svetukhin, A.M., Pal'tsin, A.A., *et al.*, *Antibiot. Khimioter.*, 1999, vol. 44, no. 7, pp. 25–31.
2. Grassie, N. and Scott, G., *Polymer Degradation and Stabilisation*, Cambridge: Cambridge Univ. Press, 1985.
3. Emanuel', N.M. and Buchachenko, A.L., *Khimicheskaya fizika stareniya i stabilizatsii polimerov* (Chemical Physics of Aging and Stabilization of Polymers), Moscow: Nauka, 1982.
4. Emanuel', N.M., Zaikov, G.E., and Maizus, Z.K., *Rol' sredy v radikal'no-tsepnykh reaktsiyakh okisleniya organicheskikh soedinenii* (Role of the Medium in Radical-Chain Oxidation of Organic Compounds), Moscow: Nauka, 1973.
5. Farzaliev, V.M., Allakhverdiev, M.A., Akperov, N.A., and Kuliev, A.F., *Neftekhimiya*, 1990, vol. 30, no. 5, pp. 706–711.
6. Bazykina, N.I., Bovkunenko, O.P., and Nikolaevskii, A.N., Abstracts of Papers, *Simpozium "Suchasni problemi katalizu"* (Symp. "Modern Problems of Catalysis"), Donetsk, 2000, p. 41.
7. Antonovskii, V.L., *Zh. Prikl. Khim.*, 1968, vol. 41, no. 1, pp. 233–235.
8. Spiridonov, V.P. and Lopatkin, A.A., *Matematicheskaya obrabotka fiziko-khimicheskikh dannykh* (Mathematical Treatment of Physicochemical Data), Moscow: Mosk. Gos. Univ., 1970.
9. Turovskii, N.A., Antonovskii, V.L., Nikolaevskii, A.N., and Shufletyuk, V.N., *Khim. Fiz.*, 2001, vol. 20, no. 2, pp. 41–45.

Russian Journal of Applied Chemistry, Vol. 77, No. 1, 2004, pp. 136–140. Translated from Zhurnal Prikladnoi Khimii, Vol. 77, No. 1, 2004, pp. 140–144.

MACROMOLECULAR CHEMISTRY AND POLYMERIC MATERIALS

Effect of Nitrosodurene on Radical Copolymerization of Styrene with Acrylic Monomers

E. V. Kolyakina, V. V. Polyanskova, M. A. Lopatin, T. I. Liogon'kaya, A. A. Shchepalov, L. L. Semenycheva, and D. F. Grishin

Research Institute of Chemistry, Nizhni Novgorod State University, Nizhni Novgorod, Russia
Razuvaev Institute of Organometallic Chemistry, Russian Academy of Sciences, Nizhni Novgorod, Russia

Received July 10, 2003

Abstract—The effect of nitrosodurene as a source of stable nitroxyl radicals on radical copolymerization of styrene with methyl methacrylate and butyl acrylate was studied.

An urgent problem of the polymer chemistry is development of efficient methods for controlling the growth of the polymeric chain with the aim to prepare macromolecular compounds of required structure and molecular weight, and hence with the required set of properties [1–5]. This goal can be accomplished, in particular, by the use of stable radicals or other active additives as chain-terminating agents. In polymerization of styrene, the most widely used chain-terminating agents are stable nitroxyl radicals, e.g., 2,2,6,6-tetramethylpiperidinyl-1-oxyl (TEMPO) and its derivatives [1, 3, 4, 6]. These agents are effective only at elevated temperatures (100–150°C). Therefore, to perform controlled polymerization under the conditions similar to those of the industrial process, it seems very promising to use, along with traditional radical initiators, active additives generating stable nitroxyl radicals directly in the polymerization system (*in situ*). Suitable additives for this purpose are nitroso compounds and nitrones, which can react with polymeric radicals to give sterically hindered nitroxyl spin adducts acting as chain-terminating agents [7–10]. The controllable mode is ensured in this case under milder temperature conditions, similar to those of commercial synthesis of vinyl polymers (50–80°C).

From the practical viewpoint, it is particularly interesting to develop efficient methods for controllable synthesis of copolymers under the conditions of radical initiation, since copolymerization plays a crucial role in production of polymeric materials with preset properties.

In this work we studied how nitrosodurene (ND) as a source of stable nitroxyl radicals affects the radical copolymerization of styrene (ST) with methyl methacrylate (MMA) and butyl acrylate (BA). On the one hand, these monomers have similar relative activities (r_1 = 0.52 and r_2 = 0.46 for the ST–MMA pair; r_1 = 0.76 and r_2 = 0.19 for the ST–BA pair [11]) and have an azeotropic point. On the other hand, the reactivities of ST, BA, MMA, and the corresponding propagating radicals are essentially different. In this connection, it is of both theoretical and applied interest to study regular trends in copolymerization of these monomers.

EXPERIMENTAL

The monomers were purified as described in [12] by repeated washing with 5–10% alkali solution, washing with distilled water to neutral reaction, drying over $CaCl_2$, and distillation at reduced pressure. Nitrosodurene was prepared by the procedures described in [13–15]. The physicochemical constants of the compounds agree with published data. The polymerization kinetics was monitored gravimetrically, dilatometrically [12], and thermographically [16]. The samples were prepared as follows: A monomer was placed in glass ampules, degassed by three freeze–pump–thaw cycles, and polymerized at a residual pressure of 1.3 Pa. Copolymerization of ST with MMA and of ST with BA was studied at the monomer molar ratios of 53 : 47 and 77 : 23, corresponding to the azeotropic compositions. The intrinsic viscosity of ST–MMA and ST–BA copolymers was determined in chloroform by dilution at 25°C [17]. The molecular-weight distribution (MWD) of ST–MMA and ST–BA was analyzed by gel permeation chromatography (GPC) on an installation equipped with a set of five Styrogel columns with the pore diameter of

1070-4272/04/7701-0136 © 2004 MAIK "Nauka/Interperiodica"

1×10^5, 3×10^4, 1×10^4, 1×10^3, and 250 Å (Waters, the United States). An R-403 differential refractometer (Waters) was used as detector; the eluent was tetrahydrofuran. Close-cut polystyrene fractions were used as references for calibration [18]. The molecular weights of ST–MMA and ST–BA copolymers was calculated using polystyrene references. The composition of the copolymers was determined by IR (Specord 75 IR) and UV (Perkin–Elmer Lambda 25) spectroscopy.

The effect of ND on copolymerization of ST with acrylic monomers was studied with azeotropic compositions, i.e., with monomer mixtures at which the ratio of the monomeric units in the copolymer is equal to the initial monomer ratio [11]. The use of such mixtures allowed us to eliminate the possible effect exerted by variation of the composition of the monomer mixtures on the copolymerization kinetics and molecular-weight characteristics of the products.

We found that addition of 0.2 mol % ND results in total degeneration of the gel effect in ST–MMA and ST–BA copolymerizations. With ND, in contrast to copolymerization in the presence of TEMPO as chain-terminating agent [6], the total reaction time increases only slightly. This is illustrated by differential curves shown in Fig. 1 for copolymerization of ST with MMA, initiated with azobis(isobutyronitrile) (AIBN), as example.

The initial portions of the kinetic curves of homo- and copolymerization, plotted on the basis of dilatometric data, show that introduction of ND in various concentrations causes appearance of an induction period (Table 1), which is due to reaction of ND with the initiator radicals and macroradicals to form a stable spin adduct terminating propagation of the polymeric chain:

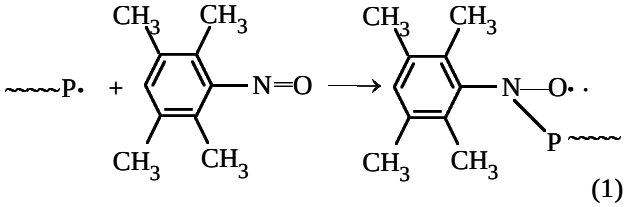

(1)

In homopolymerization of ST and its copolymerization with MMA, additions of ND do not affect significantly the initial reaction rate, and it remains comparable with the copolymerization rate on AIBN (Table 1). It should be noted that, according to the data obtained, the initial rate of ST–MMA copolymerization is controlled by the step of addition of ST to the macroradical. In ST–BA copolymerization, addition of 0.2 mol % ND gives rise to a considerably longer induction period (~230 min) than in the ST–MMA system (~40 min). The initial rate of the ST–BA copolymerization decreases under the influence of ND (relative to copolymerization in the presence of AIBN) more significantly than that of the ST–MMA copolymerization (Table 1).

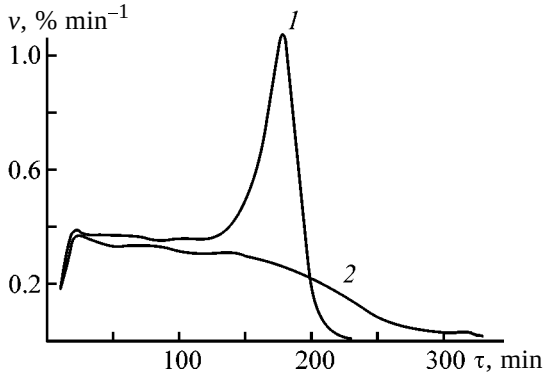

Fig. 1. Differential kinetic curves of ST–MMA copolymerization in the presence of ND at 70°C. Initiator AIBN, 0.8 mol %. (*v*) Polymerization rate and (τ) polymerization time. ND concentration, mol %: (*1*) 0 and (*2*) 0.2; the same for Fig. 2.

Study of the molecular-weight characteristics of the ST–MMA and ST–BA copolymers prepared shows that, in the presence of ND, the intrinsic viscosity of the samples linearly grows with conversion (Figs. 2a, 2b). At the same time, the copolymers prepared in the presence of AIBN without addition of ND are characterized by spontaneous uncontrollable growth of the intrinsic viscosity and molecular weight *M* with the conversion. The number-average molecular weights of the copolymers, calculated from the GPC data, also linearly grow with conversion in the entire conversion range in the case when the copolymers were prepared

Table 1. Kinetic characteristics of styrene homopolymerization and copolymerization with MMA and BA in the presence of ND. Initiator AIBN, 0.8 mol %, 60°C

Monomer	[AIBN] : [ND]	Induction period, min	$v \times 10^4$, mol l^{-1} s^{-1}
ST	1 : 0	–	1.6
	1 : 0.05	~55	1.6
	1 : 0.1	~120	1.5
	1 : 0.25	~280	1.5
ST–MMA	1 : 0	–	1.7
	1 : 0.25	~40	1.6
ST–BA	1 : 0	–	2.0
	1 : 0.25	~230	1.2

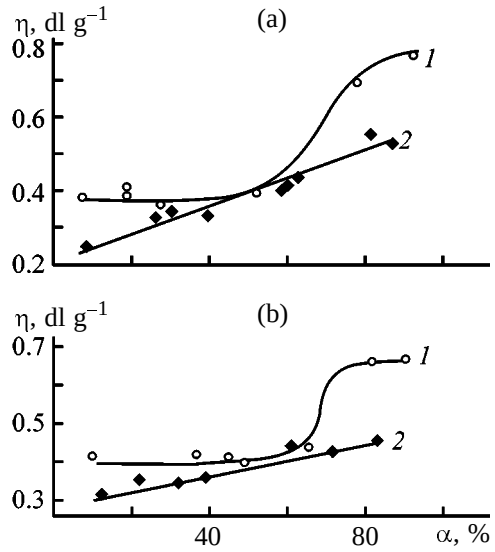

Fig. 2. Intrinsic viscosity η of (a) St–MMA and (b) ST–BA copolymers as a function of conversion α. Initiator AIBN, 0.8 mol %; samples prepared at 70°C.

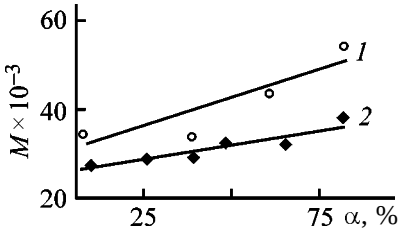

Fig. 3. Number-average molecular weight *M* of (*1*) ST–MMA and (*2*) ST–BA copolymers as a function of conversion α. Initiator AIBN, 0.8 mol %; ND concentration 0.2 mol %; samples prepared at 70°C; the same for Fig. 4.

Table 2. Molecular-weight characteristics of ST–MMA and ST–BA copolymers. Initiator AIBN, 0.8 mol %; samples prepared at 70°C

[AIBN] : [ND]	*P*, %	$M_n \times 10^{-3}$	$M_w \times 10^{-3}$	M_w/M_n
	ST–MMA copolymer*			
1 : 0	78.1	75.0	149.5	2.0
1 : 0.25	10.1	27.3	38.6	1.4
	26.2	28.7	43.1	1.5
	39.4	29.3	45.7	1.6
	48.5	31.5	50.2	1.6
	65.3	32.4	54.6	1.7
	ST–BA copolymer*			
1 : 0	81.4	67.5	176.0	2.6
1 : 0.25	7.9	34.7	52.5	1.5
	8.9	33.8	54.9	1.6
	61.0	43.5	70.0	1.6
	82.7	51.4	94.2	1.8

* The molecular weights of the copolymers were calculated with the polystyrene reference.

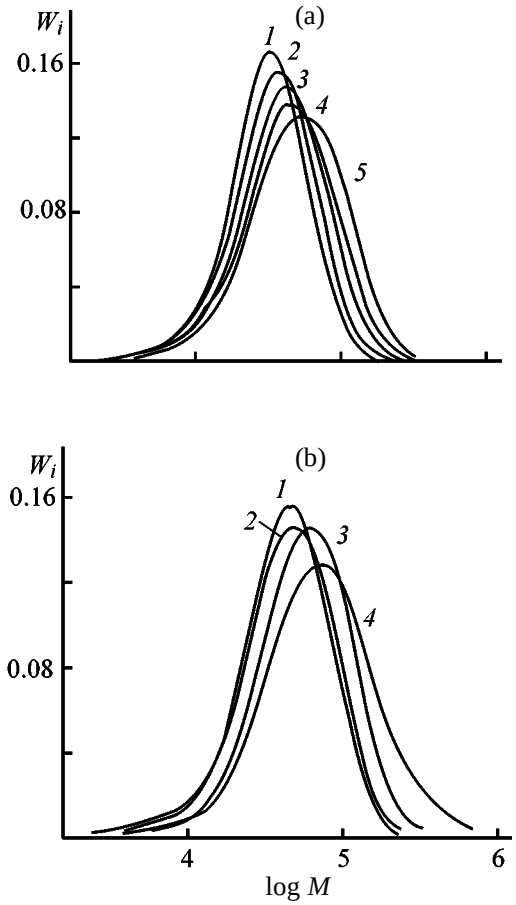

Fig. 4. MWD curves for samples of (a) ST–MMA and (b) ST–BA copolymers. (W_i) weight proportion of the fraction and (log *M*) logarithm of the molecular weight. Conversion, %: (a) (*1*) 10.1, (*2*) 26.2, (*3*) 48.5, (*4*) 65.3, and (*5*) 81.8; (b) (*1*) 7.9, (*2*) 38.9, (*3*) 61.0, and (*4*) 82.7.

in the presence of ND as chain-terminating agent (Fig. 3).

Figures 4a and 4b show how the MWD of copolymers prepared in the presence of the system ND–AIBN at a fixed concentration of the nitroso compound varies with conversion. It is seen that, with increasing conversion, the mode steadily shifts toward higher molecular weights and MWD becomes broader. However, the polydispersity coefficients remain considerably lower than those of the copolymers prepared in the presence of AIBN without ND (Table 2). The observed increase in the polydispersity of the polymer prepared in the presence of ND may be due to occurrence of bimolecular chain termination, along with the mechanism involving ND. As the ND concentration in the system is relatively low, the probability of dimerization of the propagating radicals seems to be fairly high, resulting in formation of the "dead" polymer and increased polydispersity.

Table 3. Results of spectrophotometric determination of the compositions of ST–MMA and ST–BA copolymers. Conditions of copolymer synthesis: azeotropic compositions; initiator AIBN, 0.8 mol %; 70°C

[AIBN] : [ND]	α, %	ST content, mol %	
		IR spectroscopy	UV spectroscopy
ST–MMA copolymer			
1 : 0	9.2	54 ± 2	57 ± 4
	57.3	52 ± 2	46 ± 4
	93.0	53 ± 2	46 ± 4
1 : 0.25	13.0	54 ± 2	56 ± 4
	23.8	52 ± 2	54 ± 4
	47.6	52 ± 2	51 ± 4
	83.8	49 ± 2	44 ± 4
ST–BA copolymer			
1 : 0	11.0	74 ± 3	85 ± 5
	27.2	74 ± 3	83 ± 5
	53.0	72 ± 3	80 ± 5
	66.2	69 ± 3	77 ± 5
1 : 0.25	13	72 ± 3	79 ± 5
	39	73 ± 3	73 ± 5
	61	72 ± 3	71 ± 5
	83	73 ± 3	69 ± 5

The composition of the synthesized copolymers at various conversions was studied by IR and UV spectroscopy. At the molar ratio of the monomers ST : MMA = 53 : 47 and ST : BA = 77 : 23, under the conditions of our experiments, the composition of the copolymer is similar to that of the starting mixture (Table 3). Thus, ND as a source of stable nitroxyl radicals acting as chain-terminating agents does not affect the composition of copolymers of ST with acrylic monomers. On addition of ND, the conditions remain azeotropic up to high conversions.

Our experimental results—degeneration of the gel effect, linear growth of the intrinsic viscosity and number-average molecular weight with conversion, relatively narrow molecular-weight distribution of the copolymer—suggest realization of the reversible inhibition mechanism in copolymerization of ST with MMA and BA in the presence of ND as a source of stable nitroxyl radicals ($T^{\cdot}$):

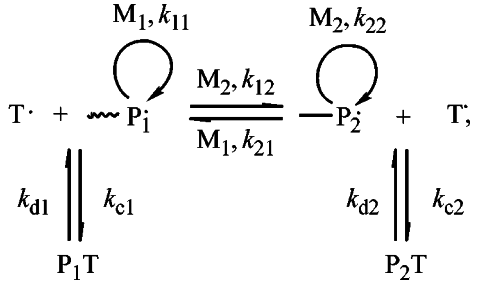

where M_1 and M_2 are the molecules of the monomers, MMA (or BA) and ST, respectively; $T^{\cdot}$ is the nitroxyl radical generated by Eq. (1); $P^{\cdot}$ is the propagating radical; k_{d1} and k_{d2} are the rate constants of dissociation of adducts P_1T and P_2T, respectively; k_{c1} and k_{c2} are the rate constants of recombination of nitroxyl radical $T^{\cdot}$ and macroradicals $P_1^{\cdot}$ and $P_2^{\cdot}$, respectively; k_{11}, k_{22}, k_{12}, and k_{21} are the rate constants of chain propagation (addition of the corresponding monomer to the corresponding macroradical).

CONCLUSIONS

(1) Nitrosodurene as a source of stable nitroxyl radicals acting as chain-terminating agents does not affect the composition of copolymers of styrene with acrylic monomers.

(2) Nitrosodurene can efficiently control the kinetic parameters of copolymerization of styrene with butyl acrylate and methyl methacrylate at relatively low temperatures (70°C), similar to those used in commercial synthesis of polymers.

(3) Addition of nitrosodurene to the polymerization system results in degeneration of the gel effect, uniform growth of the molecular weight of the copolymers, and shift of the molecular-weight distribution curves toward higher molecular weights with increasing conversion.

ACKNOWLEDGMENTS

The study was financially supported by the Competitive Center for Basic Natural Science at the RF Ministry of Education and by the Russian Foundation for Basic Research (project no. 02-03-32427).

REFERENCES

1. Otsu, T. and Matsumoto, A., *Adv. Polym. Sci.*, 1998, vol. 136, pp. 75–137.
2. Smirnov, B.R., *Vysokomol. Soedin., Ser. A*, 1990, vol. 32, no. 3, pp. 583–589.
3. Matyjaszewski, K., *Controlled/Living Radical Polymerization*, Oxford: Oxford Univ. Press, 2000.
4. Korolev, G.V. and Marchenko, A.P., *Usp. Khim.*, 2000, vol. 69, no. 5, pp. 447–475.
5. Grishin, D.F. and Semenycheva, L.L., *Usp. Khim.*, 2001, vol. 70, no. 5, pp. 486–509.
6. Zaremskii, M.Yu. and Golubev, V.B., *Vysokomol. Soedin.*, 2001, vol. 43, no. 9, pp. 1689–1728.

7. Grishin, D.F., Semenycheva, L.L., and Kolyakina, E.V., *Dokl. Ross. Akad. Nauk*, 1998, vol. 362, no. 5, pp. 634–638.
8. Grishin, D.F., Semionicheva, L.L., and Koliakina, E.V., *Mendeleev Commun.*, 1999, no. 6, pp. 250–252.
9. Grishin, D.F., Semenycheva, L.L., and Kolyakina, E.V., *Vysokomol. Soedin., Ser. A*, 1999, vol. 41, no. 4, pp. 609–614.
10. Kolyakina, E.V., Grishin, D.F., and Semenycheva, L.L., *Vysokomol. Soedin., Ser. A*, 2001, vol. 43, no. 12, pp. 2092–2096.
11. Odian, G., *Principles of Polymerization*, New York: McGraw-Hill, 1970.
12. *Praktikum po khimii i fizike polimerov* (Practrical Course of Polymer Chemistry and Physics), Kurenkov, V.F., Ed., Moscow: Khimiya, 1990.
13. Makarova, L.G. and Nesmeyanov, A.N., *Metody elementoorganicheskoi khimii: Rtut'* (Methods of Organometallic Chemistry: Mercury), Moscow: Nauka, 1965.
14. Smith, L.J. and Taylor, F.L., *J. Am. Chem. Soc.*, 1935, vol. 57, no. 8, pp. 2461–2463.
15. *Organic Synthesis*, Blatt, A.H., Ed., New York: Wiley, 1946, 2nd ed., coll. vol. 2.
16. Arulin, V.I. and Efimov, L.I., *Tr. Khim. Khim. Tekhnol.* (Gor'kii), 1970, no. 2, pp. 74–77.
17. Rafikov, S.R., Pavlov, S.A., and Tverdokhlebova, I.I., *Metody opredeleniya molekulyarnykh vesov i polidispersnosti vysokomolekulyarnykh soedinenii* (Methods for Determination of the Molecular Weights and Polydispersities of Macromolecular Compounds), Moscow: Khimiya, 1963.
18. Belen'kii, B.G. and Vilenchik, L.Z., *Khromatografiya polimerov* (Chromatography of Polymers), Moscow: Khimiya, 1978.

Russian Journal of Applied Chemistry, Vol. 77, No. 1, 2004, pp. 141–143. Translated from Zhurnal Prikladnoi Khimii, Vol. 77, No. 1, 2004, pp. 145–147.

MACROMOLECULAR CHEMISTRY AND POLYMERIC MATERIALS

Radical Grafting of Octafluoropentyl Acrylate to a Polycaproamide Thread

N. A. Storozhakova, V. A. Korotkikh, A. I. Rakhimov, and T. I. Danilenko

Volgograd State Technical University, Volgograd, Russia
Institute of Chemical Problems of Ecology, Russian Academy of Natural Sciences, Volgograd, Russia

Received August 13, 2003

Abstract—Grafting of octafluoropentyl acrylate to polycaproamide PCA-6 in the presence of *tert*-butyl hydroperoxide containing 0.87–1.33% fluorine was studied. The specific feature of radical grafting of the polyfluorinated acrylate is participation of terminal groups of PCA-6 macromolecules.

Fluoro acrylates are grafted under conditions of plasma treatment to the surface of polycaproamide (PCA-6), enhancing its fire resistance [1]. Furthermore, the material modified with polyfluorinated compounds acquires hydrophobic and dust-repelling properties [2]. However, radical grafting of monomers to a polycaproamide thread decreases its strength [3, 4].

As polyfluorinated monomer we chose octafluoropentyl acrylate $H(CF_2CF_2)_2CH_2OC(O)CH=CH_2$ (**I**), which is prepared from octafluoropentyl alcohol [5], a by-product in production of tetrafluoropropyl alcohol used in CD production. We intended to develop a procedure alternative to that described in [1]. We believed that radical grafting of **I** to the PCA-6 surface in the presence of commercially available initiator $(CH_3)_3COOH$ (**II**) should occur under mild conditions and with a fairly high selectivity owing to the polar structure of **I**, electrophilic character of the reaction of radicals with polyfluorinated fragments, and nucleophilic properties of polycaproamide radicals and radicals generated from hydroperoxide **II**.

Our goal was grafting of polyfluorinated acrylate **I** to the surface of PCA-6 thread under conditions of minimal homopolymerization of the monomer and preparation of the high-strength modified thread.

EXPERIMENTAL

Acrylate **I** was prepared by the method described in [5]; bp 85°C at 40 mm Hg, n_D^{20} 1.3462, d_4^{20} 1.4460. Samples of polycaproamide (14.54 tex) thread, 1.2–1.5 m long, were placed in a 1% solution of hydroperoxide **II** in acrylate **I** (1 : 75 excess of the monomer) and heated at 80°C for 1–4 h, with the analysis for the fluorine content in the thread and determination of physicomechanical properties of the thread performed every hour.

The fluorine content in modified PCA-6 was determined potentiometrically with an F-selective electrode. For this purpose, the sample was catalytically burnt in an oxygen atmosphere, the combustion products were dissolved in distilled water, and the potential was measured. Then the pF value ($pF = -\log[F^-][M]$) corresponding to this potential was found from the calibration plot. The physicomechanical parameters of the initial and grafted thread samples were determined with an RM-3 machine.

Thermal decomposition of hydroperoxides results in generation of alkoxy and hydroxy radicals, which abstract a hydrogen atom from a substrate or add to the C=C double bond of an unsaturated compound [6]. Experiments with model compounds [7, 8] showed that the hydrogen atom in the $-NH(CH_2)_5C(O)-$ fragment is abstracted from the α-position relative to the NH group. The arising macroradical **III** subsequently reacts with polyfluorooctyl acrylate **I** (which is facilitated by the electrophilic character of the terminal CH_2 group) to form transition state **IV**. It is stabilized by the polyfluorinated ester group and by the terminal NH group, which is associated with the ester group. As a result, copolymer **VI** is formed as final product:

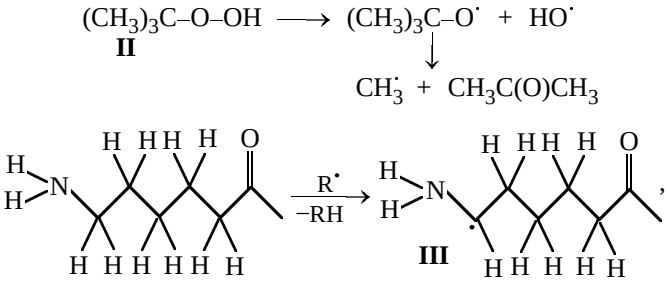

1070-4272/04/7701-0141 © 2004 MAIK "Nauka/Interperiodica"

Variation of physicomechanical properties (data averaged over five runs) of PCA-6 thread upon treatment with polyfluorinated acrylate **I**

Grafting time, h	Breaking load, N	Relative elongation at break	Elongation set
		%	
0	9.1	14.4	4.6
1	9.4	16.5	6.6
2	9.3	15.6	6.2
3	9.3	14.0	5.5
4	9.7	21.8	8.7

R = $(CH_3)_3C–O^{\cdot}$, $^{\cdot}CH_3$, $^{\cdot}OH$.

III + CH_2=CH–C(O)$OCH_2(CF_2CF_2)_2H$

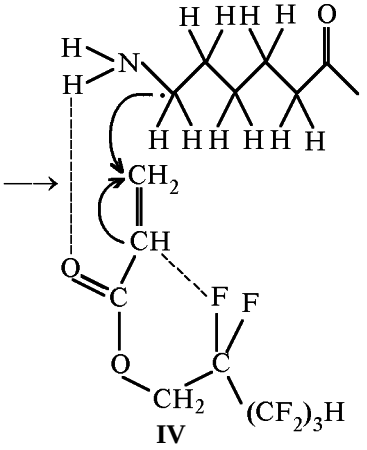

IV

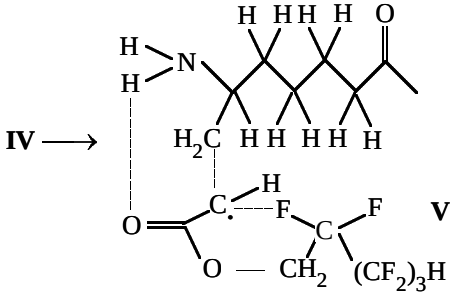

In radical **V**, the unpaired electron density is delocalized with the participation of the ester group and fluorine atoms. Radical **V** participates in radical chain transfer in reactions with the hydroperoxide and with water molecules associated with PCA-6. The reaction of radical **V** with a new molecule of the polyfluorinated monomer can be prevented by shielding of the radical center with the difluoromethylene group, whereas hydroxyl-containing reagents (hydroperoxide, water), associating with the fluorine atoms of the CF_2 group and radical center, are effective chain-transfer agents:

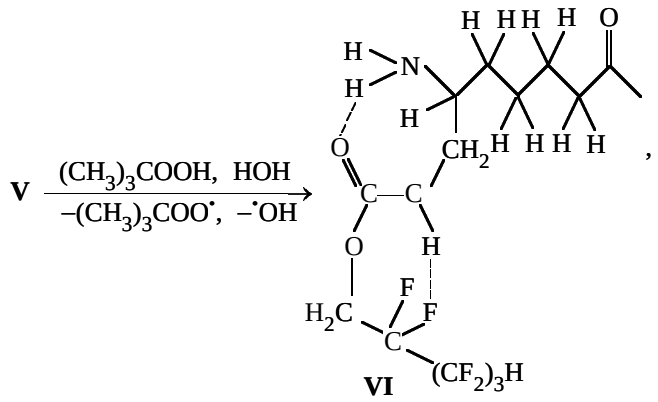

VI

A specific feature of the observed grafting of polyfluorinated acrylate **I**, in contrast to grafting of nonfluorinated acrylates, is that the thread strength grows rather than decreases (see table).

This trend may be due to the above-considered grafting mechanism involving terminal groups of PCA-6 macromolecules. The cyclic (due to associative interactions) structure of the forming terminal groups suggests the possibility of stronger molecular orientation in the amorphous phase of the polymer, which usually enhances the strength. The participation of the terminal groups in the radical grafting is suggested by the fact that grafting for 4 h does not result in a significant increase in the fluorine content in PCA-6 as compared to grafting for 2 h:

Grafting time, h	Fluorine content, %
2	0.87
3	1.19
4	1.33

Another specific feature of grafting of acrylate **I** to PCA-6 is that the homopolymer is not formed in significant amounts under the grafting conditions (the starting monomer was isolated by vacuum distillation). This is due to active reactions of macroradicals **III** with radicals generated from the polyfluorinated monomer, resulting in cross chain termination. This is consistent with the data of [8] according to which the ratio of the rate constants of polymeric chain propagation and chain termination decreased by a factor of 2 when polymerization of methyl methacrylate was performed in the presence of a model compound containing an –$NH(CH_2)_5C(O)$– fragment.

CONCLUSION

A specific feature of radical grafting of octafluoropentyl acrylate to a polycaproamide thread in the pres-

ence of *tert*-butyl hydroperoxide is active participation of terminal groups of polycaproamide in the process, which results in enhancement of the thread strength, probably due to higher degree of molecular orientation in the amorphous phase of the polymer as a result of formation of cyclic associates.

REFERENCES

1. Errifai, I., Jama, C., Delobel, R., *et al.*, in *Fire Retardancy and Protection of Materials: Proc. 9th Eur. Meet.*, Lille (France), 2003.
2. *Novoe v tekhnologii soedinenii ftora* (Fluorine Compounds. Modern Technology and Application), Ishikawa, N.M., Ed., Moscow: Mir, 1984.
3. Khardin, A.P., Zheltobryukhov, V.F., Mkrtychev, K.N., *et al.*, *Khim. Volokna*, 1983, no. 3, pp. 40–42.
4. RF Patent 2011718.
5. Rakhimov, A.I. and Vostrikova, O.V., *Zh. Prikl. Khim.*, 2002, vol. 75, no. 7, pp. 1185–1188.
6. Rakhimov, A.I., *Khimiya i tekhnologiya organicheskikh perekisnykh soedinenii* (Chemistry and Technology of Organic Peroxides), Moscow: Khimiya, 1979.
7. Rakhimov, A.I., Ozerov, A.A., Zheltobryukhov, V.F., and Mkrtychev, K.N., *Khim. Volokna*, 1986, no. 4, pp. 20–22.
8. Lavnikova, I.V., Zheltobryukhov, V.F., Rakhimov, A.I., and Storozhakova, N.A., *Zh. Prikl. Khim.*, 2002, vol. 75, no. 2, pp. 311–313.

Russian Journal of Applied Chemistry, Vol. 77, No. 1, 2004, pp. 144–147. Translated from Zhurnal Prikladnoi Khimii, Vol. 77, No. 1, 2004, pp. 148–151.

MACROMOLECULAR CHEMISTRY AND POLYMERIC MATERIALS

Intensification of Preparation of Modified Polycaproamide Fiber

E. A. Perevalova, V. F. Zheltobryukhov, and S. M. Moskvichev

Volzhskii Polytechnic Institute, Branch of the Volgograd State Technical University, Volzhskii, Volgograd oblast, Russia

Received February 10, 2003

Abstract—A procedure was developed for graft polymerization of dimethylaminoethyl methacrylate onto polycaproamide using a redox system whose components are added to the reaction mixture sequentially. A scheme of radical graft polymerization of dimethylaminoethyl methacrylate onto polycaproamide was suggested. The properties of the copolymers were studied. The materials based on modified polycaproamide show promise as chemisorbents.

Purposeful modification of existing macromolecular compounds is the most promising line in development of a wide set of polymeric materials for various purposes. One of the main procedures for chemical modification of macromolecular compounds, including manmade fibers, is synthesis of graft copolymers of appropriate composition. Graft polymerization allows wide variation of the chemical composition, structure, and properties of polymers. Therefore, development of highly efficient and environmentally sound processes for production of graft copolymers derived from polycaproamide (PCA), one of the most abundant manmade polymers, remains an urgent problem.

In graft polymerization onto PCA, the regular structure of the polymer backbone remains intact [1], and the grafted polymer is distributed on the surface of the modified fiber, which enhances the adhesiveness between the fibers and improves the efficiency of the subsequent processing.

The commercially implemented procedure for production of graft copolymers of PCA with poly(dimethylaminoethyl methacrylate) (PDMAEMA) in the form of KM-A1 chemisorption fiber using polycaproamide fiber peroxidized with atmospheric oxygen and a solution of copper sulfate [2, 3] does not ensure production of fibers with the sufficiently high sorption capacity (1.0–1.5 mg-equiv g^{-1}); the degree of grafting does not exceed 25–30%.

Another procedure for preparing a PCA graft copolymer [4, 5] involves preliminary activation of the polycaproamide fiber with a 0.5–2% solution of hydrogen peroxide in the presence of a copper salt (10.2–10.4 wt % Cu^{2+} relative to the reaction mixture) at 50–80°C for 30–60 min. As a copper-containing compound we used copper sulfate. The activated polycaproamide fiber is treated with a 20% DMAEMA solution at 20–30°C for 60–120 min. After grafting completion, the fiber is washed to remove the monomer and homopolymer by treatment with ethanol in a Soxhlet apparatus for 12 h, with subsequent drying.

The drawbacks of this procedure are relatively low content of the grafted polymer (no more than 40–45%) and formation of an undesirable by-product, PDMAEMA (homopolymer), complicating the subsequent processing of the fiber and decreasing the efficiency of graft polymerization.

Our goal was to intensify the existing commercial batch process. To increase the amount of the grafted polymer and enhance the sorption capacity, we developed a procedure for preparing graft copolymers with the Cu^{2+}–H_2O_2 redox system (with copper ions introduced in the form of aqueous copper sulfate solution). The fiber was activated in steps. First, the fiber peroxidized with atmospheric oxygen was treated with a copper sulfate solution, then hydrogen peroxide was added, and the fiber activation was continued.

EXPERIMENTAL

The raw material was ready staple polycaproamide fiber. It is prepared from polycaproamide fiber production waste: substandard textile and cord threads, which are stored and, when accumulated in sufficient amounts (approximately every 2–3 months), are processed on a staple unit.

To prepare the peroxidized PCA, the starting fiber was treated for 5 h with hot (70°C) air in a dryer.

1070-4272/04/7701-0144 © 2004 MAIK "Nauka/Interperiodica"

The same amount of hydroperoxy groups (10^{-3} wt % relative to the fiber) is formed in storage of PCA fiber in air for 60–120 days [6]. The latter procedure for preparing peroxidized fiber is more appropriate for industrial conditions, as it involves no expenditures, and production of modified fibers is performed today in the batch mode.

The fiber peroxidized with atmospheric oxygen was placed in a flask, and 0.04–0.05% (relative to the fiber weight) aqueous solution of copper sulfate was added at room temperature. Fifteen minutes later, an aqueous H_2O_2 solution was added in amount corresponding to the H_2O_2 content of 0.20–0.25% relative to the fiber weight. The H_2O_2 solution was added in portions over a period of 15 min at 1-min intervals; the subsequent fiber activation was performed for 25–30 min. The activated PCA was thoroughly washed with water to remove excess H_2O_2 and copper sulfate and then squeezed. After that, it was treated with 20% aqueous DMAEMA in a temperature-controlled flask equipped with a reflux condenser for 20–30 min at 45–55°C. After grafting completion, the polymer was treated with ethanol in a Soxhlet apparatus to remove the monomer and homopolymer, dried, and weighed.

The fact that the PDMAEMA content in the modified fiber is higher than that attained previously [3, 5], in combination with published data on decomposition of H_2O_2 and hydroperoxy groups of PCA with variable-valence metal ions, suggests that our activation procedure makes reactive not only the sections of PCA macromolecules containing hydroperoxy groups, but also the sections that remained unaffected by atmospheric oxygen. Such a result cannot be attained by introducing Cu^{2+} and H_2O_2 simultaneously. In this case, the reaction primarily occurs between the components of the redox system, so that the sections of PCA molecules that contain no peroxy groups are not activated.

If the copper ions are added first, this induces decomposition of the hydroperoxy groups of the fiber with generation of active macroradicals, and the subsequent addition of H_2O_2 activates the sections of macromolecules that contain no hydroperoxy groups. Thus, the amount of active centers in PCA capable of graft polymerization grows, resulting in increased amount of the grafted polymer.

In the case of sequential addition of the components of the redox system, the reaction will probably follow the scheme

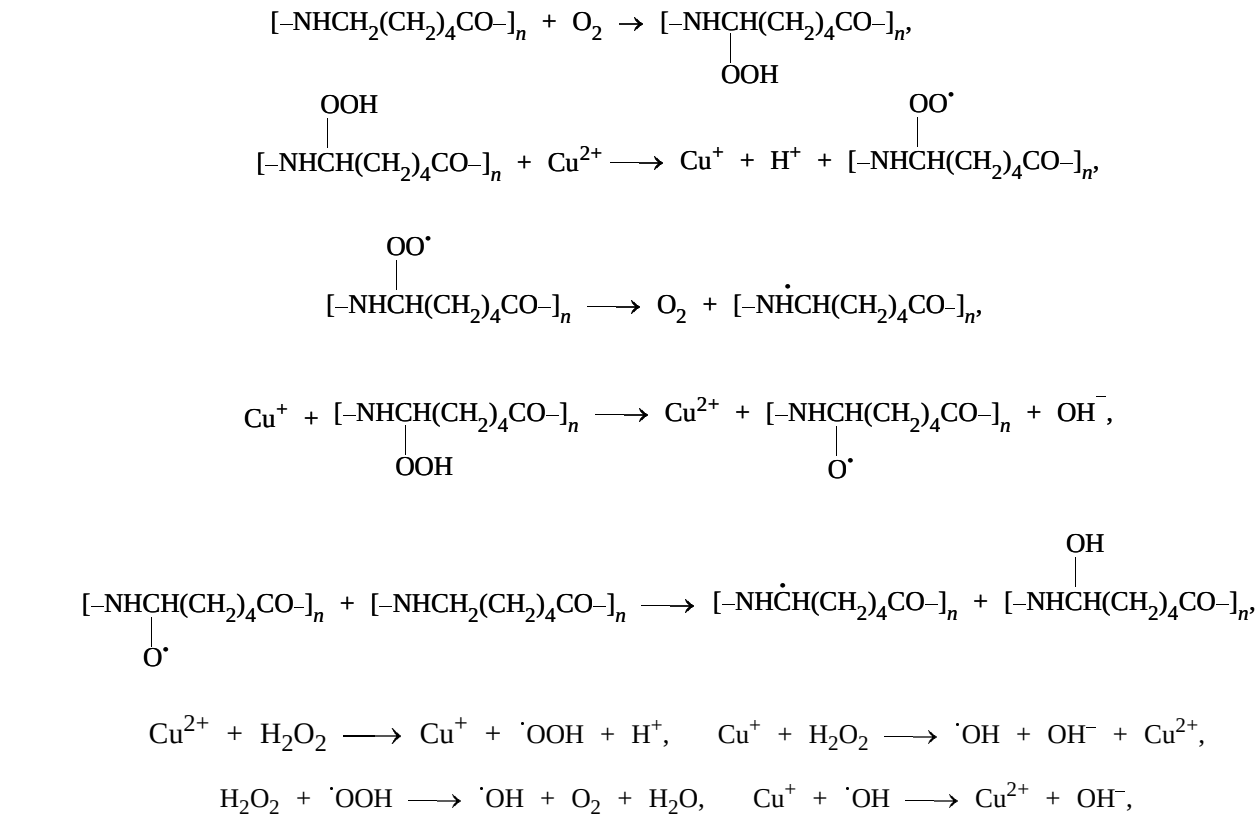

RUSSIAN JOURNAL OF APPLIED CHEMISTRY Vol. 77 No. 1 2004

Table 1. Static exchange capacity (SEC) of the PCA–PDMAEMA graft copolymer

Grafted PDMAEMA content, %	SEC, mg-equiv g^{-1} dry fiber	Tertiary nitrogen content, wt %
20	1.0	1.07
36	1.65	2.00
46	2.1	3.28
58	2.51	3.41
70	3.06	4.32

Table 2. Sorption power of fibers under dynamic conditions*

Gas–air mixture			Mean time, h			
			to breakthrough		to saturation	
gas	*H*, %	c_g, $cm^3\ m^{-3}$	KM-A1	fiber**	KM-A1	fiber**
HCl	82	100	12.37	14.23	13.07	15.03
HCl	82	250	3.45	5.97	3.58	6.12
HF	82	2.5	25.27	29.06	26.13	30.05
SO_2	90	150	2.03	3.34	2.15	3.48

* (*H*) Humidity and (c_g) gas concentration.
** 65–70% PDMAEMA.

$$[\text{–NHCH}_2(\text{CH}_2)_4\text{CO–}]_n + {}^{\bullet}\text{OH} \longrightarrow [\text{–NHC}^{\bullet}\text{H}(\text{CH}_2)_4\text{CO–}] + \text{H}_2\text{O},$$

$$[\text{–NHC}^{\bullet}\text{H}(\text{CH}_2)_4\text{CO–}] + \text{H}_2\text{C}{=}\underset{\displaystyle \text{CH}_3}{\underset{|}{\text{C}}}\text{–COO}(\text{CH}_2)_2\text{N}(\text{CH}_3)_2 \longrightarrow [\text{–NHCH}(\text{CH}_2)_4\text{CO–}]_n,$$

$$[\text{H}_2\text{C–}\underset{\displaystyle \text{COO}(\text{CH}_2)_2\text{N}(\text{CH}_3)_2}{\underset{|}{\text{C}}}(\text{CH}_3)\text{–}]_m\ .$$

Separate introduction of the components of the redox system increases the amount of the grafted polymer, so that it becomes feasible to reach the desirable level of 65–70%.

The content of PDMAEMA obtained by graft polymerization was monitored gravimetrically and by the content of tertiary nitrogen, which was determined from variation of the amount of HCl consumed for binding of tertiary nitrogen in the test samples. The results are listed in Table 1.

To evaluate the performance of PCA–PDMAEMA copolymers as chemisorption materials, we prepared filtering units from the modified polycaproamide fiber containing 65–68% PDMAEMA by processing the fiber into a needle-punctured material 1.2 cm thick, with the fiber packing density of 0.15 $g\ cm^{-3}$.

The chemisorption properties were evaluated by the capability of the ion exchanger to sorb acidic gases (HCl, SO_2, HF) on passing the gas–air mixture containing these gases in varied concentrations through the fibrous filter at a rate of 1.4×10^{-4} $m^3\ s^{-1}$ (0.5 $m^3\ h^{-1}$). The characteristics of the sorption power of the material under dynamic conditions are given in Table 2 in comparison with the data for filtering units from KM-A1 fiber (PDMAEMA content 20–25%).

Table 2 shows that, as the content of the grafted polymer is increased to 65–68%, the sorption power grows, on the average, by 30%. The static exchange capacity of the fiber prepared by our procedure (65–70% PDMAEMA) is as high as 2.8–3.2 mg-equiv g^{-1}.

An important characteristic determining the performance of a chemisorbent is variation of the static

Table 3. Variation of properties of the modified polycaproamide fiber (65–68% PDMAEMA) in the course of service

Parameter	Fiber		
	initial	after 20 sorption–regeneration cycles	after 30 sorption–regeneration cycles
SEC, mg-equiv g^{-1}	3.0	3.0	3.0
Tensile strength, cN tex^{-1}	25.2	25.1	25.2
Wear resistance, cycles	29.2	29.2	29.0
Elongation at break, %	78	78	79

exchange capacity and mechanical properties in the sorption–desorption cycles. The chemisorbent was regenerated with 2% aqueous NaOH solution.

Table 3 shows that both the static exchange capacity and the mechanical properties of the fiber remain unchanged after 20–30 sorption–regeneration cycles, i.e., the fiber shows high stability toward regenerating agents.

CONCLUSIONS

(1) A promising procedure for preparing polycaproamide–poly(dimethylaminoethyl methacrylate) graft copolymer was suggested. The procedure involves sequential addition of the components of the redox system; it ensures increased (65–70%) content of poly(dimethylaminoethyl methacrylate) in the modified fiber and more efficient production of the chemisorption fiber.

(2) The chemisorbent obtained from the modified fiber shows high sorption power, high resistance to repeated regeneration, and long service life.

REFERENCES

1. Sugak, V.N., *Khim. Volokna*, 1998, no. 3, pp. 10–13.
2. Zheltobryukhov, V.F. and Tatarnikov, M.K., *Izv. Vyssh. Uchebn. Zaved., Tekhnol. Legk. Prom–sti.*, 1985, no. 1, pp. 36–38.
3. Tatarnikov, M.K., Zheltobryukhov, V.F., and Morin, B.P., *Khim. Volokna*, 1986, no. 6, pp. 35–36.
4. Khardin, A.P., Zheltobryukhov, V.F., and Tatarnikov, M.K., *Khim. Volokna*, 1984, no. 3, pp. 33–34.
5. Smirnova, N.V. and Gabrielyan, G.A., *Khim. Volokna*, 1995, no. 1, pp. 27–30.
6. Zaikov, V.G., Druzhinina, T.V., and Gal'braikh, L.S., *Khim. Volokna*, 1992, no. 3, pp. 11–12.

Russian Journal of Applied Chemistry, Vol. 77, No. 1, 2004, pp. 148–153. Translated from Zhurnal Prikladnoi Khimii, Vol. 77, No. 1, 2004, pp. 152–157.

MACROMOLECULAR CHEMISTRY AND POLYMERIC MATERIALS

Structurization and Optical Activity in Cellulose Triacetate Modified with Trifluoroacetic Acid Vapor

A. B. Shipovskaya, G. F. Mikul'skii, and G. N. Timofeeva

Chemistry Faculty, Chernyshevsky State University, Saratov, Russia
Research Institute of Chemistry, Chernyshevsky State University, Saratov, Russia
Saratov Military Institute of Radiation, Chemical, and Biological Protection, Saratov, Russia

Received May 16, 2003

Abstract—Structurization in cellulose triacetate modified with trifluoroacetic acid vapor and its effect on the optical activity are studied.

Liquid–crystal (LC) cellulose triacetate (CTA) solutions in trifluoroacetic acid (TFAA) are used for preparing highly oriented films and fibers with improved mechanical characteristics [1, 2]. The anisotropic state is realized only at high (>25%) polymer concentration [3, 4]. Preparation and processing of such concentrated solutions are difficult because of high viscosity of mesomorphic phases [5]. Therefore, development of new processes allowing formation of a highly ordered polymeric matrix through realization of LC state in the system CTA–TFAA is a topical problem.

Previously we demonstrated that an oriented structure in cellulose acetates could be obtained by exposing the polymer to vapor of a solvent in which the polymer forms a lyotropic mesophase [6, 7]. In this case, orientational transformations manifest themselves in, e.g., spontaneous elongation of acetate fibers [6], which can be attributed to transition of the polymer–solvent system into the LC state [8], and also in sustained induced optical anisotropy and decreased grain-boundary angle in acetate films [7], etc. The effect of mesogenic vapor on the structure of condensed (films, fibers) and powdered polymers appeared to be identical: the samples are characterized by abnormal sorption and swelling curves, not obeying the Fick's law [9], and the intensity of their X-ray diffraction peaks increases [10].

It should be pointed out that exposure to vapor of a solvent capable of forming mesophases with cellulose derivatives affects the optical activity of the cellulose esters, suggesting structural changes not only at the supramolecular, but also at the conformation level [7, 9, 11]. In this case, the effect of a solvent vapor on the structure of a cellulose ester is considerably more pronounced as compared to that initiated by the same solvent added in the equivalent amount as liquid [9, 11].

By now, a great body of knowledge is gained on cellulose and its esters as polymers with increased chain rigidity, and there is a steady intense interest in these materials. However, the fact that cellulose acetates, like many natural organic polymers, demonstrate the optical activity varying over a wide range [7, 9, 11] was not given due attention in polymer design. Our recent results showed that it is the optical asymmetry that could be the key point in designing polymers with desirable 3D structure [12], having not only preset, but even some unique characteristics [13].

In [14] we reported the effect of small TFAA additions on the properties of concentrated cellulose acetate solutions. In this work we studied the effect of TFAA vapor on the structure and optical activity of powdered CTA.

EXPERIMENTAL

In the experiments we used the initial and modified samples of powdered CTA, and also solutions and films on its basis.

We employed commercial wood CTA used for producing triacetate fiber (Khimvolokno Joint–Stock Company, Engels, Russia). The characteristics of the polymer are as follows: granule size 4–6 mm, bulk density 1.28 g cm^{-3}, bound acetic acid content 61.2%, and viscosity-average molecular weight 7.5×10^4. For dissolution of the samples we used the conventional process solvent, a 90 : 10 mixture of methylene chloride with ethanol (both of analytically pure grade).

1070-4272/04/7701-0148 © 2004 MAIK "Nauka/Interperiodica"

The bulk polymer was modified by isobaric-isothermal exposure to a solvent vapor at 5–35°C in a hermetically sealed vessel partly filled with a solvent. As a sorbate we used the dipolar amphiprotic solvent, trifluoroacetic acid (analytically pure grade) [15]. Cellulose triacetate was placed on a 2-mm sieve arranged 5 cm above the solvent table. The vapor uptake was determined gravimetrically on a WT torsion balance to within 0.0002 g. The TFAA uptake varied from 0.5 to 100 wt %. The samples of the polymer were taken as it was saturated with the solvent vapor.

The optical rotation of 0.5 g l^{-1} solutions of the initial and modified CTA samples was measured to within 0.04° on an SM-2 circular polarimeter at λ_{Na} = 589 nm and 25°C [16]. The light source was a DNAS18-04-2 lamp.

The polymer films were prepared from 7 wt % solutions by coating onto a preliminarily degreased smooth glass surface in a dust-controlled box. Formation was carried out at room temperature and the same solvent removal rate for all the samples. The film thickness was measured with a TIB-2 thickness gauge to be 100–150 μm. The strength [tensile strength σ_t (MPa)] and elastic properties [elongation at break ε_b (%)] of the CTA films were determined to within 3% on a 2148R-5 tensile-testing machine according to GOST (State Standard) 17316–71.

Differential thermal analysis was performed over the temperature range 200–400°C on a DSC-D differential scanning microcalorimeter at a heating rate of 8 deg min^{-1} with calcined alumina as a reference. The peak positions were registered to within 2° with a KSP-4 logger at a paper speed of 720 mm min^{-1}. X-ray diffraction patterns were obtained on a DRON-3 diffractometer (FeK_α radiation) over the range 2θ = 5°–30°.

Previously we demonstrated [9] that sorption on cellulose acetates of vapor of specific solvents capable of forming lyotropic mesophases with the polymers does not obey the Fick's law. Also the system CTA–TFAA vapor is characterized by abnormal swelling curves (Fig. 1a). At low temperatures, the kinetic curves of sorption pass through extrema (curve *1*), and at room temperature, they are S-shaped (curve *2*). High sorption capacity of CTA for TFAA vapor does not allow equilibrium saturation to be attained even at lowered temperature; swelling is unrestricted and is followed by polymer dissolution. Over the entire experimental temperature range we observed a sorption/desorption hysteresis. Desorption proceeds at a higher rate, and the desorption curve (curve *3*) is no longer abnormal, lying under the swelling curve.

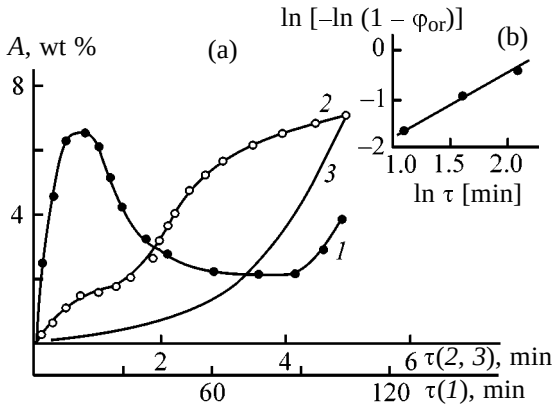

Fig. 1. Kinetic curves of TFAA vapor sorption/desorption on CTA: (a): (*1*) sorption at 8°C, (*2*) sorption at 20°C, and (*3*) desorption at 20°C; (b) descending branch of curve *1* plotted in the coordinates of the Avrami equation. (*A*) Uptake of TFAA vapor, (τ) time, and (1 – φ_{or}) fraction of disordered polymer.

It is known that abnormal kinetics of sorption may be caused by various factors, including structural transformations occurring in the polymer matrix in the course of diffusion of a low-molecular-weight component [17, 18]. To elucidate structural transformations in CTA, initiated by uptake of TFAA vapor, the descending branch of the kinetic curve of swelling (Fig. 1a, curve *1*) was plotted in the coordinates of the Avrami equation (Fig. 1b) [17]. The parameter *n* characterizing the structurization mechanism in the polymer–solvent system was estimated from this equation to be 1.4, suggesting that some orientational transformations occur in the polymer matrix in the presence of TFAA. Similar results were obtained by Azizov and Sadykova [19] for the system cellulose acetate–nitromethane, which, like TFAA, is a mesogenic solvent for cellulose acetates. They suggested orientation of the macromolecules in the course of nitromethane vapor uptake, resulting in modification of the initial polymer structure. Furthermore, they presented abnormal swelling curves similar to those obtained in this work. These curves were interpreted using the concept of structural transitions in the system cellulose acetate–nitromethane proposed by us in [6].

Comparison of two systems (cellulose acetate–nitromethane and CTA–TFAA) appears to be logical, as both systems form lyotropic mesophases [3] under similar conditions [1, 20]. In both systems, formation of anisotropic structures follows the initial gelation [4, 21]. In both systems, an alteration of the optical activity of a cellulose ester was observed [7, 9] as well as initiation of orientational processes accom-

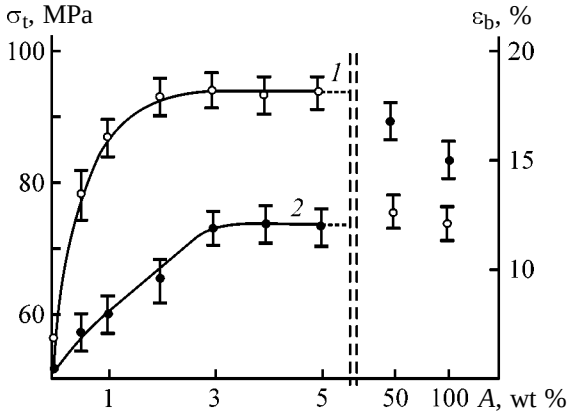

Fig. 2. (*1*) Tensile strength σ_t and (*2*) elongation at break ε_b of CTA films as functions of the TFAA uptake *A*.

panied by considerable improvement of the mechanical characteristics [2, 22]. Finally, both nitromethane and TFAA have an active polar group, high dipole moments, and similar Hildebrand solubility parameters [15, 23]. All the aforesaid allow expansion of the concept proposed in [9] to the system CTA–TFAA vapor. Thus, TFAA vapor uptake modifies the CTA structure. The extrema or inflection points in the kinetic curves (Fig. 1a) reflect alterations in the swelling mechanism. Let us analyze curve *1*. Note first that, in the incompletely acetylated CTA used ($\gamma < 3$), both inter- and intramolecular hydrogen bonds occur, despite the predominance of the acetate groups in the glucopyranose units over the hydroxy groups [24]. The initial stage of polymer swelling (uptake of the first portions of TFAA in amount of no more than 6–8 wt %) involves a break of the intermolecular H bonds. In this case, nonassociated macromolecules, by virtue of their intrinsic rigidity and thanks to the newly realized flexibility, tend to take thermodynamically favorable straightened conformations. Such a self-orientation results in compaction of the polymer chains and, correspondingly, in partial desorption of the solvent, as demonstrated by the decline in curve *1*. Further uptake proceeds in the already modified polymer and is followed by CTA dissolution. The plateau in the curve could be referred to the equilibrium of these two processes. Uptake of the first small amounts of TFAA vapor results in degradation of the system of intermolecular contacts restraining the macrochain flexibility. At the same time, the system of intramolecular hydrogen bonds responsible for high rigidity of the macromolecules is retained. All these factors allow the macromolecules to be oriented [6, 9] up to formation of mesophases [3, 8].

Swelling of a polymer in a solvent vapor is mostly a complex process involving not only a break of intermolecular bonds, but also simultaneous interaction of the solvent with functional groups (specific solvation). Since the sorption capacity of cellulose acetates for TFAA is considerably higher than that for nitromethane, the first of the indicated processes in the system CTA–TFAA vapor can be realized separately only at low temperatures or in a short time corresponding to the uptake of a small amount of the solvent. Therefore, the S-shaped curve obtained at 20°C (Fig. 1a, curve *2*) is a resultant of the structurization and solvation processes. Nevertheless, the inflection points in the swelling curve, the sorption/desorption hysteresis (curve *3*), and the induced optical anisotropy observed previously [7] in acetate films—all these findings suggest dominating structurization in the system with formation of a more ordered polymer matrix.

In further experiments, modified CTA samples were obtained by exposure to TFAA vapor at room temperature. It should be pointed out that CTA samples after uptake of less that 10–15 wt % of TFAA did not differ in their appearance from the initial polymer, in contrast to the case of uptake of 50 wt % of TFAA and more. In the latter cases, the samples represented highly concentrated, transparent, gel-like solutions, which readily formed thin layers on shearing or putting pressure with an object-plate. Such systems are optically anisotropic in a polarized light, demonstrating an iridescent fluorescence.

From modified CTA, we formed films. As a reference we used a film formed from unmodified CTA. Experiments showed that structural transformations induced by TFAA uptake had a strong effect on the mechanical characteristics of the polymer films (Fig. 2). The tensile strength σ_t and elongation at break ε_b of modified CTA films were considerably higher than those of the reference. As the amount of absorbed TFAA increased to about 3 wt %, the mechanical characteristics increased, approaching maximal values. Further increase in the extent of modification ($A > 3$ wt %) no longer affected σ_t and ε_b. For the films formed from CTA after uptake of 50 and 100 wt % of TFAA, we observed certain decrease in σ_t as compared to the films with *A* from about 3 to 5 wt %, but ε_b was found to be higher in the TFAA-rich films. Compared to the reference, the tensile strength and elongation at break of such TFAA-rich films are higher by 30–40 and 200–220%, respectively. In the films with TFFA uptake of 3–5 wt %, the maximal σ_t and ε_b values are higher by 65 and 120%, respectively. These are somewhat unexpected results, since increasing strength of films mostly results in decreasing elasticity, and vice versa. How-

ever, we also observed similar increase in the strength and elastic characteristics in acetate fibers prepared from the polymer modified with TFAA vapor under the same conditions [25]. In this case, the TFAA uptake of 2–3 wt % was sufficient to reach the maximal tensile strength and elongation at break.

The results show that mechanical characteristics of the films correlate with structural transformations in the polymer. These characteristics increase with uptake of small (up to 3–4 wt %) amounts of the solvent vapor, which corresponds to orientational transformations of the macromolecules (Fig. 1, section of curve *2* extending to the inflection point). Note that similar trends were observed in the system cellulose diacetate–nitromethane [25]. It may be suggested that simultaneous increases in σ_t and ε_b in the modified CTA films are caused by the formation of highly ordered domains in the polymer matrix, which, on the one hand, favors increase in the strength and, on the other hand, does not prevent from increase in the elasticity of a film, as such domains do not form a continuous oriented matrix.

The orientational effect of TFAA on the CTA structure was also supported by direct structural methods. Figure 3a shows the X-ray diffraction patterns of the triacetate films. For the modified CTA films, the intensity and area of the peak at $2\theta = 20°–21°$ increase, and those of the peak at 10°–11° decrease. In this case, the total area of the peaks decreases against the reference, giving an additional evidence in favor of the fact that structural transformations occurring in the polymer matrix under the effect of TFAA vapor do not prevent from orientation of the macromolecules, but hinder crystallization of the polymer. Note also that the modified samples are characterized by a higher (by 15°C) decomposition temperature (Fig. 3b).

It is well known that natural polysaccharides, among them cellulose, are optically active. Previously we demonstrated [9, 11] that exposure of cellulose acetates to vapor of a solvent, capable of forming lyotropic mesophases with these polymers, produces strong effects on both their structure and optical activity. The specific optical rotation [α] appeared to be changed in the course of modification of CTA with TFAA vapor.

The unmodified CTA dissolved in a mixture of methylene chloride and ethanol has a negative [α] (–50°, Fig. 4). The absolute [α] values of modified samples are considerably higher. With increasing TFAA uptake, [α] decreases below –200°, which is higher in the absolute value by a factor of 4 than that of the unmodified sample.

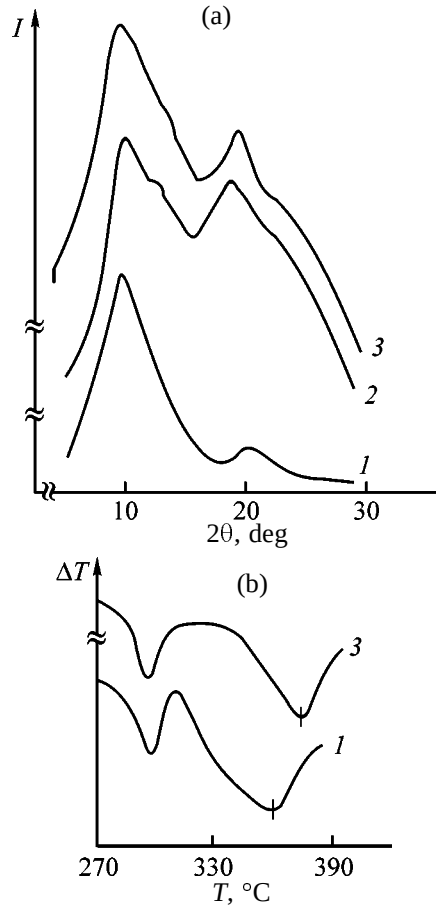

Fig. 3. (a) X-ray diffraction patterns and (b) DTA curves of TCA films: (*1*) reference and (*2*, *3*) TFAA-modified CTA films containing 1 and 3 wt % TFAA, respectively. (*I*) Intensity, (2θ) Bragg angle, (*T*) temperature, and (Δ*T*) difference in the temperature of the test and reference samples.

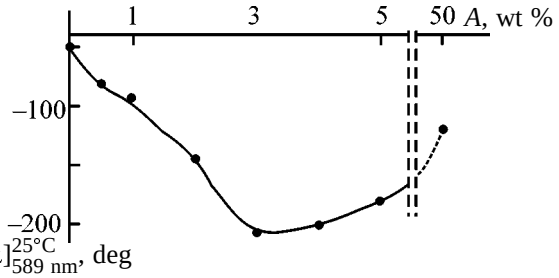

Fig. 4. Specific optical rotation $[\alpha]^{25°C}_{585\,nm}$ of CTA solutions in a mixture of methylene chloride and ethanol as a function of TFAA uptake *A*.

Note that the observed dependence of the specific optical rotation of CTA in the process solvent on the TFAA uptake (Fig. 4) is similar to the concentration dependence of [α] of CTA in TFAA, which was obtained by Meeten and Navard in studying the formation of mesophases in this system [4]. It was demonstrated in the cited work that, with increasing CTA

concentration in TFAA, the negative [α] decreases until the anisotropic transition. In other systems cellulose acetate–mesogenic solvent, the mesophases formed also demonstrated higher absolute values of [α] [3].

Finally, our results show that a strong increase in [α] is typical of the CTA samples modified with small (<3 wt %) amounts of the sorbate vapor (Fig. 4). It is the uptake of such a small amount of TFAA that produces the essential structural transformations (Fig. 1) and improvement of the mechanical characteristics of the films (Fig. 2). It is known that the optical rotation in cellulose esters is controlled by their molecular structure [16], particularly, by the presence of chiral centers in the glucopyranose units and their spatial arrangement, which, in turn, promotes strong inter- and intramolecular hydrogen bonding, and, finally, by the conformation of macromolecules. Uptake of small amount of TFAA initiates a break of intermolecular, but not intramolecular H bonds, providing, as suggested in [3], optimal conditions for highly oriented LC structures to be realized on the basis of cellulose and its derivatives. Furthermore, such an uptake promotes spatial rearrangements in the macromolecules or other structural subunits, strongly changing the optical activity of the polymer. Maybe this is one of the necessary conditions for transition of an optically active polymeric system into LC state. Further uptake of TFAA vapor proceeds with the already modified polymer, which is accompanied by solvation of unbound functional groups. In this case, the induced [α] no longer changes significantly. Similar interrelation between the optical activity and structural ordering was observed also for other natural polymers, e.g., collagen and gelatin [26, 27].

CONCLUSIONS

(1) Modification of cellulose triacetate with trifluoroacetic acid vapor as a mesogenic agent for cellulose derivatives opens the door for directed design of polymers with not only highly ordered, but also even differently organized 3D structure. It is of particular importance that the maximal effects on the structure and optical activity are attained at low TFAA uptake.

(2) The fact that the performance characteristics of the modified cellulose triacetate films are determined by the specific features of the "induced" 3D structure of the ester allows preparation of materials with a controlled structure and desired properties.

ACKNOWLEDGMENTS

The work was financially supported by the Russian Foundation for Basic Research (project no. 00-03-33058a).

REFERENCES

1. Yunusov, B.Yu., Khanich, O.A., Shablygin, M.V., *et al*., *Vysokomol. Soedin., Ser. B*, 1983, vol. 25, no. 4, pp. 292–294.
2. US Patent 4501886.
3. Kulichikhin, V.G. and Golova, L.K., *Khim. Drev*., 1985, no. 3, pp. 9–27.
4. Meeten, G.H. and Navard, P., *Polymer*, 1983, vol. 24, no. 7, pp. 815–819.
5. Belov, S.Yu., Myasoedova, V.V., and Krestov, G.A., *Zh. Prikl. Khim*., 1989, vol. 62, no. 1, pp. 135–139.
6. Timofeeva, G.N. and Tolkunova, E.B., *Vysokomol. Soedin., Ser. A*, 1986, vol. 28, no. 4, pp. 869–872.
7. Timofeeva, G.N., Fedusenko, I.V., Lashek, N.A., and Shipovskaya, A.B., *Vysokomol. Soedin., Ser. B*, 1995, vol. 37, no. 6, pp. 1093–1095.
8. Flory, P.J., *Proc. R. Soc. London, Ser. A*, 1956, vol. 234, no. 1, pp. 60–72.
9. Shipovskaya, A.B. and Timofeeva, G.N., *Vysokomol. Soedin., Ser. A*, 2001, vol. 43, no. 7, pp. 1237–1244.
10. Shipovskaya, A.B. and Timofeeva, G.N., in *Struktura i dinamika molekulyarnykh system: Sbornik statei* (Structure and Dynamics of Molecular Systems: A Collection of Papers), Moscow: Inst. Fiz. Khim. Ross. Akad. Nauk, 2000, issue 7, pp. 319–322.
11. Shipovskaya, A.B. and Timofeeva, G.N., *Vysokomol. Soedin., Ser. B*, 2003, vol. 45, no. 1, pp. 101–105.
12. Shipovskaya, A.B. and Timofeeva, G.N., Abstracts of Papers, *Vtoroi Rossiiskii Simpozium "Khimiya i fizika polimerov v nachale XXI veka"* (2nd Russian Symp. "Chemistry and Physics of Polymers at the Beginning of the 21st Century"), Chernogolovka (Moscow oblast, Russia), 2000, p. C4-87.
13. RF Patent 2174130.
14. Fedusenko, I.V., Shipovskaya, A.B. and Timofeeva, G.N., *Izv. Vyssh. Uchebn. Zaved., Khim. Khim. Tekhnol*., 1997, vol. 40, no. 4, pp. 81–84.
15. Reichardt, Ch., *Solvents and Solvent Effects in Organic Chemistry*, Weinheim: VCH, 1988.
16. Kettering, Ch.F., *New Methods of Polymer Characterization*, New York: Wiley, 1964.
17. Malkin, A.Ya. and Chalykh, E.A., *Diffuziya i vyazkost' polimerov* (Diffusion and Viscosity of Polymers), Moscow: Khimiya, 1979.

18. Popova, E.D. and Chalykh, A.E., *Vysokomol. Soedin., Ser. A*, 1991, vol. 33, no. 12, pp. 2574–2584.
19. Azizov, Sh.A. and Sadykova, L.A., *Vysokomol. Soedin., Ser. B*, 1991, vol. 33, no. 6, pp. 429–432.
20. *Fizicheskaya modifikatsiya polimerov* (Physical Modification of Polymers), Gembitskii, L.S., Ed., Saratov: Saratov. Gos. Univ., 1983, pp. 28–35.
21. Timofeeva, G.N. and Aver'yanova, V.M., *Kolloidn. Zh.*, 1980, vol. 42, no. 2, pp. 393–397.
22. USSR Inventor's Certificate no. 1171580.
23. Kesting, R.E., *Synthetic Polymeric Membranes*, New York: Wiley, 1985.
24. Panina, N.I., Paneikina, T.P., Aver'yanova, V.M., and Zelenev, Yu.V., *Vysokomol. Soedin., Ser. B*, 1978, vol. 20, no. 1, pp. 14–16.
25. Shipovskaya, A.B., Physicochemical Modification of Cellulose Acetates with Solvent Vapor Capable of Forming a Lyotropic Mesophase with the Polymer, *Cand. Sci. Dissertation*, Saratov, 1996.
26. Izmailova, V.N. and Rebinder, P.A., *Strukturoobrazovanie v belkovykh sistemakh* (Structure Formation in Protein Systems), Moscow: Nauka, 1974.
27. Godard, P., Biebuyck, J.-J., Barriat, P., and Naveau, H., *Makromol. Chem.*, 1980, vol. 181, no. 9, pp. 2009–2018.

Russian Journal of Applied Chemistry, Vol. 77, No. 4, 2004, pp. 154–158. Translated from Zhurnal Prikladnoi Khimii, Vol. 77, No. 4, 2004, pp. 158–162.

CHEMISTRY OF FOSSIL FUEL

Flash Pyrolysis and Kinetic Parameters of Decomposition of Oil Shales

Kh. M. Kerimov

Azerbaijan State Petroleum Academy, Baku, Azerbaijan

Received December 6, 2002; in final form, October 2003

Abstract—Flash pyrolysis of oil shales and distribution of the organic matter in the volatile products and solid residue at various pyrolysis temperatures were studied. The concentrations of aliphatic hydrocarbons and naphthenes + arenes in the volatile products were determined.

Inevitable exhaustion of traditional power resources calls for a search for new sources of hydrocarbon raw materials. Among materials showing promise in this respect are oil shales [1].

The assortment of substances produced by shale processing includes tens of items, without taking into account wastes that can be processed. From the viewpoint of energy production, the most important component of shale oils is the organic matter; its base is kerogen. Kerogen is mainly recovered from the inorganic matrix by pyrolysis. Alternative procedures (extraction, biochemical methods) are less suitable for commercial application [2].

Pyrolytic decomposition of oil shale kerogen involves a set of parallel and consecutive reactions following the scheme

$$\text{Kerogen} \xrightarrow[E_1, A_1]{k_1} \text{gas, bitumen} \xrightarrow[E_2, A_2]{k_2} \text{gas, tar, coke,} \quad (1)$$

where k_1 and k_2 are the rate constants, min^{-1}; E_1 and E_2 are the activation energies, kJ mol^{-1}; and A_1 and A_2 are the preexponential terms (min^{-1}) of the corresponding reactions.

Ballice *et al.* studied decomposition of kerogen thermogravimetrically [3] and concluded that the process occurs in two steps: decomposition of kerogen proper at 300–375°C and secondary decomposition and condensation processes at 375–500°C.

The kinetics of thermal decomposition of kerogen is described by a first-order equation

$$\mathrm{d}x/\mathrm{d}\tau = kf(x), \quad (2)$$

$$x = \frac{m_0 - m_\tau}{m_0 - m_f}, \quad (3)$$

where m_0, m_τ, and m_f are the initial, intermediate, and final sample weights, respectively (mg); k is the rate constant, min^{-1}; and x is the degree of decomposition.

Since

$$\mathrm{d}\ln k/\mathrm{d}T = E/RT^2,$$

and, for first-order reactions, $f(x) = 1 - x$, Eq. (2) can be written as follows:

$$\frac{\mathrm{d}x}{\mathrm{d}T}\frac{\mathrm{d}T}{\mathrm{d}\tau} = A\exp(-E/RT)(1 - x), \quad (4)$$

or

$$\frac{\mathrm{d}x}{\mathrm{d}T} = (A/b)\exp(-E/RT)(1 - x), \quad (5)$$

where $b = \mathrm{d}T/\mathrm{d}x$.

Integration of Eq. (5) gives

$$\ln\{[(E + 2RT)/T^2]\ln[1/(1 - x)]\} = \ln(AR/b) - E/RT. \quad (6)$$

This equation is the Chen–Nuttall equation [4]. The kinetic parameters of oil shale decomposition can be determined by the Coats–Redfern graphical method [5]. The activation energy can be determined from the slope of the straight line plotted in the coordinates $-\ln[-\ln(1 - x)/T^2]$ vs. $1/T$ [3].

In this work, to evaluate the kinetic parameters of decomposition of oil shales from the Dzhangichai deposit, we used a combination of the above methods. From the values of x [Eq. (3)] for definite temperatures, we calculated E by the Coats–Redfern method. These values of E were substituted in Eq. (6), and the preexponential term was determined.

1070-4272/04/7701-0154 © 2004 MAIK "Nauka/Interperiodica"

EXPERIMENTAL

The Fischer analysis was performed on a standard installation by the ISO-647 procedure [6]. The elemental analysis of the initial shales and of the tar and residue formed from them was performed according to [7] on an LECO CHNS-932 apparatus. The results are listed in Table 1.

Samples of oil shales were finely divided in a laboratory mill prior to flash pyrolysis. The fraction with the particle size less than 0.1 mm was taken for the experiments; it was dried in a nitrogen atmosphere at 105°C to constant weight.

The scheme of the experimental installation for flash pyrolysis is shown in Fig. 1. A reactor, 120 cm high and 5 cm i.d., is made from stainless steel of grade 316. The dosing unit is arranged in the upper part of the reactor. The temperature of the pyrolysis zone in the lower part of the reactor is controlled with a digital temperature-control unit. The solid residue is collected on the metallic filter arranged in the lower part of the pyrolysis zone. The middle part of the reactor was kept at 300°C for the sample preheating. To prevent condensation of high-molecular-weight hydrocarbons in a flow of decomposition products, the sampling unit arranged after the pyrolysis zone was kept at 200°C. Nickel–chromium thermocouples were used for controlling and measuring the temperatures in the heated zones of the reactor.

In flash pyrolysis, shale samples were placed in the sample inlet unit. Pyrolysis was performed in a nitrogen flow (80 ml min^{-1}) at 450, 500, 550, 600, and 650°C. After attainment of the required temperatures in all the heated zones, the shale sample was input into the pyrolysis zone by turning the arm of the sample inlet unit. The reference, 0.507 vol % neopentane in N_2, was introduced at a flow rate of 20 ml min^{-1} into the flow of products going out from the pyrolysis zone. Samples of products leaving the reactor were taken into evacuated glass ampules. The sampling procedure and chromatographic analysis of the multicomponent vapor–gas mixture are described in [8].

The pyrolysis products were analyzed on a Hewlett–Packard HP 6890 capillary gas chromatograph equipped with a flame-ionization detector. A 100 m × 0.25 mm capillary column was coated with methyl silicone OV-1. The carrier gas was hydrogen, flow rate 25 ml min^{-1}. The detector temperature was 350°C, and the injector temperature, 290°C. The column temperature schedule was as follows: –80°C, 5 min; heating at a rate of 30 deg min^{-1} to –30°C; –30°C, 1.5 min; heating at a rate of 25 deg min^{-1} to 0°C; 0°C, 2 min; heating at a rate of 10 deg min^{-1} to 25°C; 25°C, 1 min; heating at a rate of 10 deg min^{-1} to 280°C; 280°C, 3 min.

Table 1. Elemental analysis and Fischer analysis of oil shales

Component	Content, wt %
Initial shales	
Moisture	2.8
Total carbon	21.93
Organic carbon	20.70
H	2.56
N	0.92
Total sulfur	3.24
Organic sulfur	1.2
Fischer analysis	
Tar	14.75
Water from decomposition	2.62
Solid residue	71.54
Gas + loss, including:	11.09
CO	3.43
CO_2	14.51
CH_4	45.46
C_2–C_4	3.6
Elemental analysis of tar	
C	77.46
H	11.31
N	1.24
S	1.53
Elemental analysis of residue	
C	17.76
H	1.07
N	0.86
S	4.48

The mixture components were identified with a computer by comparing the retention times with the data stored in the memory.

For each temperature, we determined the weight of the solid residue, treated it with 5 M HCl, washed with water on a filter to neutral reaction for chloride ions, and dried to constant weight at 105°C. The solid residue free of mineral carbon was analyzed for C and H on an LECO CHNS-932 apparatus [7]. The yield of volatiles was determined as the weight loss of the sample dry matter. The degree of decomposition of the organic matter X (wt %) was determined by the formula

$$X = \frac{(G_1 - G_2) \times 100}{G_1 (B/100)}, \quad (7)$$

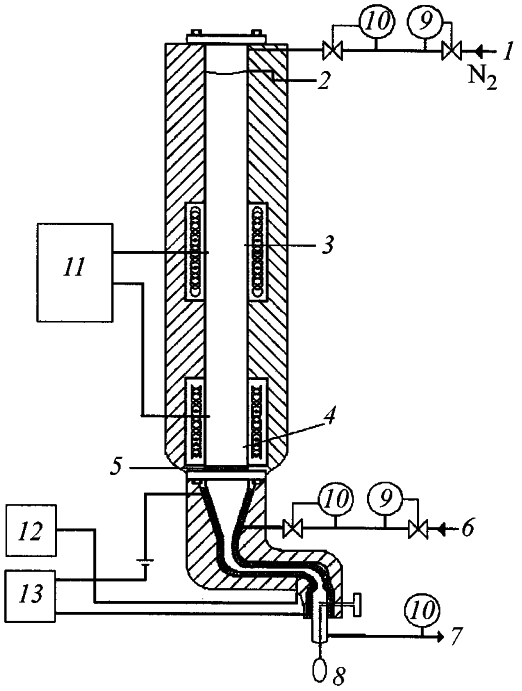

Fig. 1. Scheme of experimental installation: (*1*) carrier gas, (*2*) sample inlet unit, (*3*) preheating zone, (*4*) pyrolysis zone, (*5*) metallic filter, (*6*) reference (0.507 wt % neopentane in N_2), (*7*) outlet of vapor–gas mixture, (*8*) evacuated glass ampule, (*9*) pressure gage, (*10*) unit for dosing the substance to be pyrolyzed, (*11*) temperature measurement and control unit, (*12*) temperature measurement unit, and (*13*) volume measurement unit.

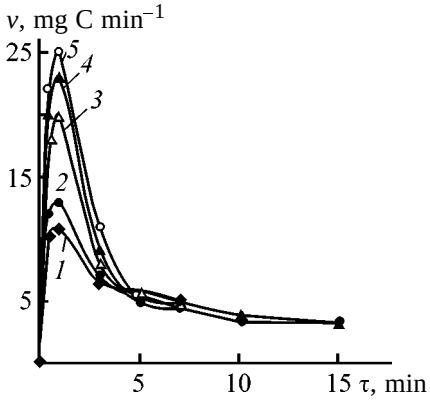

Fig. 2. Rate of conversion of kerogen organic carbon *v* as a function of time τ. Pyrolysis temperature, °C: (*1*) 450, (*2*) 500, (*3*) 550, (*4*) 600, and (*5*) 650.

where G_1 is the weight of a dry shale sample, g; G_2, weight of the solid residue obtained, g; and *B*, organic substance content in the shale, wt %.

Thermogravimetric study was performed with a Netzsch apparatus in a nitrogen flow (15 ml min^{-1}) in the temperature range 30–1000°C at a heating rate of 5 deg min^{-1}.

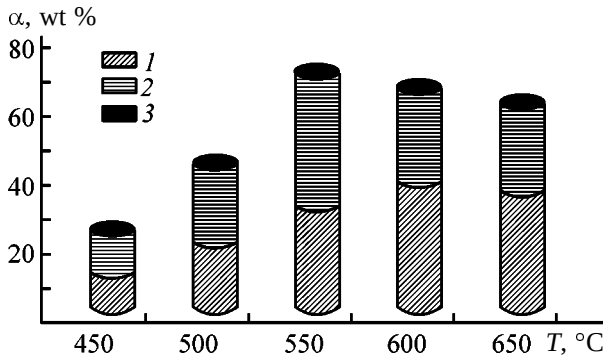

Fig. 3. Yield of hydrocarbons α as a function of pyrolysis temperature *T*: (*1*) alkanes, (*2*) alkenes, and (*3*) naphthenes + arenes.

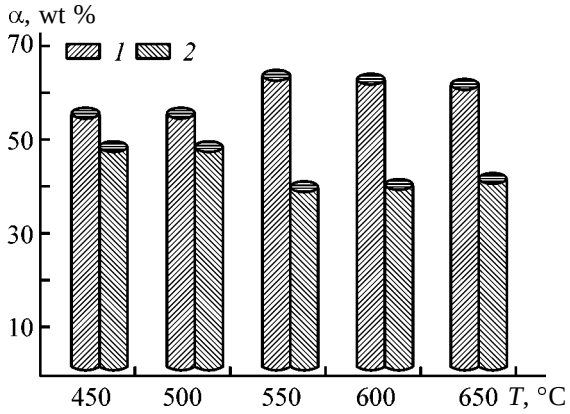

Fig. 4. Distribution of organic carbon: (α) yield and (*T*) temperature. (*1*) Volatiles and (*2*) solid residue.

At all the temperatures studied, the products are formed at a maximal rate (Fig. 2) within the first minutes, after which the rate decreases, which may be due to a decrease in the concentration of the initial organic matter of shale and occurrence of slow reactions of secondary decomposition. Integration of the kinetic curves allowed determination of the amounts of products that could be analyzed by our procedure. Figure 3 shows that the major products are alkanes and olefins. As the pyrolysis temperature is increased, the yield of alkanes grows, the yield of alkenes passes through a maximum at 550°C, and the amount of naphthenes + arenes varies insignificantly.

The yield of volatiles determined as the dry matter weight loss for each temperature was used to evaluate the degree of decomposition of the shale organic matter by formula (7). Figure 4 shows that, with increasing pyrolysis temperature, the total yield of volatiles increases, reaches a maximum at 550°C, and then

Table 2. Characteristics of the solid residue and composition of volatiles

Pyrolysis temperature, °C	Solid pyrolysis residue			Aliphatic hydrocarbons in volatiles, wt %
	C, wt %	H, wt %	C/H atomic ratio	
450	9.62	0.66	1.21	31.5
500	9.24	0.63	1.22	32.4
550	7.89	0.49	1.43	35.2
600	8.01	0.45	1.54	42.1
650	8.27	0.40	1.72	45.3

slightly decreases. At higher temperatures, the volatiles get enriched in aliphatic hydrocarbons. Whereas at 450°C aliphatic hydrocarbons make up 31.5 wt % of volatiles, at 650°C their content reaches 45.3 wt % (Table 2). Apparently, elevated temperatures promote condensation, as evidenced by the C/H ratio in the solid residue. Table 2 shows that, as the pyrolysis temperature is increased from 450 to 650°C, the C/H ratio increases by a factor of almost 1.5.

The TGA data (Fig. 5) show that the weight loss occurs in four steps. Moisture is removed at 120–200°C. The peak at 440°C is assigned to pyrolysis of kerogen. The weight loss at 520°C is due to secondary decomposition and condensation of the heavy fraction of kerogen decomposition products. The weight loss at temperatures above 650°C is due to decomposition of the mineral matrix (primarily carbonates).

To determine the kinetic parameters, we assumed that the decomposition occurs as a first-order reaction with respect to the kerogen concentration. Separate application of the Chen–Nuttall method requires setting of an assumed value of the activation energy to calculate the left part of Eq. (6), after which repeated regression analysis is performed until the desired accuracy of the activation energy and preexponential term is attained. The Coats–Redfern method is simple and allows relatively accurate determination of E. The use of E determined by this procedure in the Chen–Nuttall equation eliminates the need in the repeated calculations.

Using the conversions calculated by Eq. (3), we constructed the plot of $-\ln[-\ln(1 - x)/T^2]$ vs. $1/T$ (Fig. 6). Two linear portions with different slopes suggest the occurrence of two different reactions in the temperature range 300–520°C. Primary reactions of kerogen decomposition occur at 280–380°C, and secondary decomposition processes, at 380–520°C, which is in good agreement with data of [2–5].

The activation energies of the primary (E_1) and secondary (E_2) reactions are 13.95 and 29.86 kJ mol^{-1}, respectively. The calculated activation energies were used to determine the preexponential terms for the primary (A_1) and secondary (A_2) reactions by formula (6): 0.21 and 4.58 min^{-1}, respectively.

The low activation energy E_1 of the kerogen decomposition suggests that the primary decomposition reactions yielding bitumen (pyrolysis tar) and gases involve cleavage of relatively weak chemical bonds in the shale organic matter. The decomposition and condensation of primary pyrolysis products occur with a higher activation energy E_2 at temperatures above 380°C, yielding the final decomposition products.

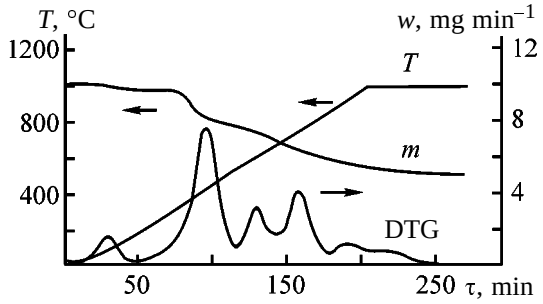

Fig. 5. Thermogravimetric analysis of shale: (T) temperature, (m) weight of residue, (w) decomposition rate, and (τ) time.

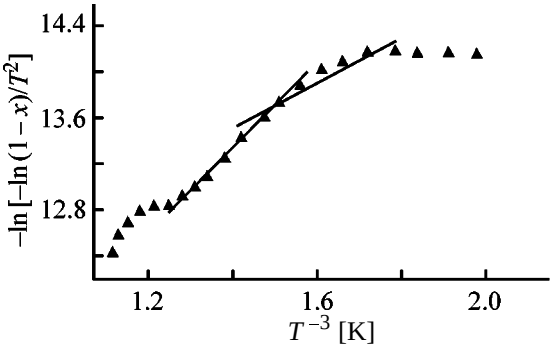

Fig. 6. Analysis of the thermogravimetric data by the combined Coats–Redfern/Chen–Nuttall method. (T) Temperature.

CONCLUSIONS

(1) A study of flash pyrolysis of oil shales from the Dzhangichai deposit showed that, as the temperature is increased, the yield of volatile products passes through a maximum at 550°C, with the relative content of aliphatic hydrocarbons in the volatiles growing and the yield of naphthenes and arenes varying insignificantly.

(2) The occurrence of two consecutive decomposition reactions was revealed, and their kinetic parameters were determined.

ACKNOWLEDGMENTS

The study was performed at the Engineering Faculty, EGE University, Izmir, Turkey, under financial support of NATO-PC TUBITAK.

REFERENCES

1. Blokhin, A.I., Zaretskii, M.I., Stel'makh, G.P., and Eivazov, T.S., *Novye tekhnologii pererabotki vysokosernistykh slantsev* (New Processes for Treatment of High-Sulfur Shales), Moscow: Svetlyi Stan, 2001.
2. Ballice, L., Yuksel, M., Saglam, M., and Schulz, H., *Fuel*, 1996, vol. 75, pp. 453–458.
3. Ballice, L., Yuksel, M., Saglam, M., *et al.*, *Fuel*, 1995, vol. 74, pp. 1618–1623.
4. Thakar, D.S. and Nuttal, N.E., *Ind. Eng. Chem. Res.*, 1987, vol. 26, pp. 1351–1356.
5. Skala, D., Kopsch, H., Sokic, M., *et al.*, *Fuel*, 1990, vol. 69, pp. 490–496.
6. *Int. Standard ISO-647: Determination of the Yields of Tar, Water, Gas, and Coke Residue by Low Temperature Distillation*, 1997.
7. *ASTM D-3178–94: Test Method for Carbon and Hydrogen in the Analysis Sample of Coal and Coke*, 1994.
8. Schulz, H., Boringer, W., Kohl, C.P., *et al.*, Entwicklung und Anwendung der Kapillar-GC-Gesamtprobentechnik für Gas/Dampf-Vielstoffgemische, *Deutsche Gesellschaft für Mineralölwissenschaft und Kohlechemie, DGMK-Forschungbericht*, Hamburg, 1984, vol. 320, pp. 4–20.

Russian Journal of Applied Chemistry, Vol. 77, No. 4, 2004, pp. 159–161. Translated from Zhurnal Prikladnoi Khimii, Vol. 77, No. 4, 2004, pp. 163–165.

CHEMISTRY OF FOSSIL FUEL

Chemical Structure of Asphaltene Compounds from G17 Coal Semicoking Tar

V. V. Platonov, A. N. Kudrya, and S. V. Proskuryakov

Leo Tolstoy Tula State Pedagogical University, Tula, Russia
St. Petersburg State Technological Institute, St. Petersburg, Russia

Received July 3, 2002; in final form, June 2003

Abstract—The chemical structure of asphaltene compounds from the semicoking tar of coal belonging to the G17 processing group was studied in detail.

Detailed data on the chemical composition of semicoking tars formed under conditions excluding to a maximal extent high-temperature pyrolysis furnish information about the native structure of fragments of coal organic matter (COM), their genetic relationship with the initial biomaterial, and pathways of its biogeochemical transformation in the course of coal formation. Knowledge of the specific features of the chemical structure of various COM components is important for wide involvement of coals in production of synthetic fuel, raw materials for organic and petrochemical synthesis, and metallurgical coke.

Asphaltenes (APs) are the least studied components of tars formed by thermal degradation of coals, which is due to relatively high molecular weight and polyfunctional composition of these compounds [1–7].

In this work we studied the chemical structure of APs from the semicoking tar of G17 coal from the Kuznetsk coal fields.

EXPERIMENTAL

Characteristics of the coal: moisture content W^d = 2.9, ash residue A^c = 8.7, yield of volatiles V^{daf} = 36.6% of air-dry coal; elemental composition, %: C 80.8, H 5.7, N 1.0, O 11.7, S_{tot} 0.8. Yield of semicoking tar (% COM) 15.1; its chemical group composition, % of anhydrous tar: organic bases 1.15; carboxylic acids 0.85; phenols 18.96; hydrocarbons 32.9; neutral oxygen-, nitrogen-, and sulfur-containing compounds 25.11; asphaltenes 8.6; resinous substances and losses 12.43 [8].

AP characteristics: molecular weight M = 277.5; elemental composition, %: C 77.8, H 8.2, N 2.6, O 11.4; functional composition, g-equiv mol^{-1}: phenolic groups 0.42, quinoid groups 0.40, keto groups 0.27, alcoholic groups 0.38, alkoxy groups 0.22, and heterocyclic oxygen 0.76.

The IR spectra of APs contain bands (ν, cm^{-1}) of the following fragments: aromatic rings (3030–3080, 1600, 1500, 1440–1465), with the increased intensity of the bands at 1600 and 1500 suggesting the presence of fused aromatic systems; CH_2 groups (stretching modes: 2840, 2940, 2925, 2850; bending modes: 720–740, 970, 1470), with the high intensity of these bands suggesting high content of hydrogenated rings; phenolic hydroxyls (3580–3670, 1140–1230, 1310–1410); methoxy (2850) and quinoid (1645, 1665, 1675, 1745) groups; cyclic and naphthenic alcohols (1030–1120, 1260–1350, 3630–3700); oxygen- and nitrogen-containing heterocycles (1565, 1500, 1015–1030, 845–870, 740–800).

Emission spectrum and X-ray fluorescence analyses revealed the following elements in the AP mineral matter: Fe, Mg, Al, Si, Ti, Ni, Sn, Sb, V, Mn, Cr, Zn, Zr, Pt, Rh, Ge, Ga, Hg, Pb, Na, K, Ca, Co, and Nd.

The whole set of IR, UV–Vis, emission, and X-ray fluorescence spectroscopic data and results of elemental, quantitative functional, and structural-group analyses and cryoscopic measurements allows a conclusion that the APs from G17 coal semicoking tar are a complex mixture of compounds of high molecular weight, containing various oxygen-containing functional and alkyl groups and organometallic structures.

To examine the structure of AP components in more detail, we separated APs into two fractions: those soluble (1) and insoluble (2) in boiling acetone. Fraction 1 after separation from fraction 2 was cooled to room temperature and thus was separated into frac-

1070-4272/04/7701-0159 © 2004 MAIK "Nauka/Interperiodica"

tions 1.1 and 1.2 soluble and insoluble in cold acetone, respectively.

By adsorption liquid chromatography on silica gel ASKM, fraction 1.1 was separated into fractions 1.1.1, 1.1.2, and 1.1.3, eluted with benzene, acetone, and acetic acid, respectively. Fractions 1.1.1, 1.1.2, and 2 were further separated by preparative thin-layer chromatography (TLC) on standard Silufol plates (20 × 20 cm) activated at 105–110°C, with the following optimal eluent systems (the volume ratio is given in parentheses): fraction 1.1.1, hexane–diethyl ether–acetone (5 : 5 : 1); fraction 1.1.2, chloroform–hexane–acetone (50 : 10 : 2); and fraction 2, trichloroethylene–diethyl ether–benzene–acetone–acetic acid (3 : 3 : 3 : 2 : 1).

The AP fractions isolated by fractional dissolution in acetone, adsorption liquid chromatography, and preparative TLC were studied by a set of physicochemical methods; from the results obtained, the molecular and hypothetical structural formulas of APs were calculated.

Fraction 1.1 is major (78.0 wt % of the initial APs); the amounts of its subfractions 1.1.1, 1.1.2, and 1.1.3 are, respectively, 44.2, 31.8, and 2.0 wt %. The yield of APs insoluble in boiling acetone (fraction 2) is 19.5 wt %.

The molecular weight of AP fractions varies from 205 (1.1.1) to 398 (2). AP compounds insoluble in boiling acetone (fraction 2) are characterized by lower aromaticity, which is confirmed by the relative intensity of the IR absorption bands (cm^{-1}) of aromatic (3030–3080, 1500, 1600, 1440–1464) and naphthenic (2840, 2925, 720–740, 970, 1470) rings. Fraction 1.1.2 is rich in phenolic components; the content of alcoholic hydroxyls is maximal in fractions 2 and 1.2. Asphaltenes insoluble in boiling acetone (fraction 2) are characterized by the highest content of methoxy groups and heterocyclic oxygen.

From fraction 1.1.1, we isolated 21 compounds with the molecular weight varying from 157 to 283; C content, from 77.7 to 86.1%, H content, from 7.1 to 12.2%, O content, from 1.9 to 14.1%; H/C ratio, from 1.05 to 1.70; and degree of aromaticity, from 0.20 to 0.60. The following functional groups are prevailing (g-equiv mol^{-1}): quinoid (0.20–1.24), keto (0.30–0.72) groups, and oxygen heterocycles (0.25–1.27); the content of naphthenic alcohols is significant.

Structures with the linear fusion type (hydrogenated benzo- and dibenzofuran, benzofluorene, and benzofluorenone derivatives) prevail in fraction 1.1.1; also, structures linked via –CO– groups were identified.

From fraction 1.1.2, we isolated 23 components; their molecular weight varies from 196 to 405; C content, from 68.6 to 86.2; H content, from 6.7 to 12.8; O content, from 1.0 to 23.3%; H/C ratio, from 1.09 to 1.78; and degree of aromaticity, from 0.15 to 0.58. The H/C ratio and the IR data indicate that the components of this eluate are naphthenoaromatic compounds, and some of them are even fully hydrogenated. The main functional groups revealed (g-equiv mol^{-1}) are as follows: phenolic (0.32–1.86), quinoid (0.10–0.80), and alcoholic (0.31–1.06).

Fraction 1.1.2 consists of highly condensed compounds containing mainly three or four rings, although even components with six fused rings are detected. The fusion is almost exclusively angular. We identified methyl homologs of perhydrophenanthrene and octahydrophenanthrol, and also compounds with oxygen and nitrogen atoms incorporated in five-membered heterocycles of the furan and pyrrole type (in the condensed state), substituted with phenolic and alcoholic groups. A distinctive feature of eluate 1.1.2 is relatively low content of keto groups.

Asphaltenes insoluble in hot acetone (fraction 2) were separated into 15 components. Their molecular weight varies from 257 to 589; C content, from 62.5 to 77.7; H content, from 7.6 to 10.8; N + O content, from 12.0 to 28.0%; H/C ratio, from 1.25 to 1.92; and degree of aromaticity, from 0.07 to 0.48.

According to the results of emission spectrum and X-ray fluorescence analyses, the metals present in the initial APs are mainly concentrated in this fraction. Apparently, the metals are partially incorporated in organic complexes containing phenolic and quinoid groups and nitrogen heterocycles.

The AP components from fraction 2 mainly consist of fragments of two or three fused rings (aromatic, hydrogenated, O- and N-heterocyclic), linked with each other via –O–, $–CH_2–$, –CO–, and –NH– groups. The high molecular weight and long linear chain of the compounds are responsible for their low solubility in the majority of organic solvents.

To confirm the structural features of APs, we subjected each fraction to pyrolysis at 800°C and 3 s residence time of vapor in the heated zone; the AP vapor was diluted with Ar (1 : 25). The liquid products were analyzed by capillary gas–liquid chromatography.

In the liquid pyrolysis products of fraction 1.1.1, we detected diphenyl, naphthalene, its methyl and

dimethyl homologs, diphenylene oxide, and derivatives of fluorene, benzene, quinoline, and isoquinoline; pyrolysis of fraction 1.1.2 yielded naphthalene, phenanthrene and its alkyl homologs, diphenyl, dibenzanthracenes, benzo- and dibenzofurans, phenol, cresols, dimethylphenols, and naphthols; pyrolysis of fraction 2 yielded diphenyl, diphenylene oxide, and carbazole.

These facts convincingly prove that the suggested structural formulas are largely adequate to the major components of the initial APs.

CONCLUSIONS

(1) A scheme was suggested for separation of asphaltenes from G17 coal semicoking tar, involving extraction and adsorption liquid and preparative thin-layer chromatography. It allows isolation of a large number of close-cut fractions.

(2) Asphaltenes contain compounds with cyclic fragments linked via bridging groups or fused in the linear or angular mode, including alicyclic, aromatic, and heterocyclic fragments substituted with various oxygen-containing functional groups and alkyl chains.

REFERENCES

1. Posadov, I.A., Sirotkin, N.V., Pokonova, Yu.V., and Proskuryakov, V.A., *Zh. Prikl. Khim.*, 1977, vol. 50, no. 9, pp. 1978–1980.
2. Platonov, V.V., Mazurov, V.V., and Klyavina, O.A., *Goryuch. Slantsy*, 1987, vol. 4, no. 3, pp. 304–314.
3. Platonov, V.V., Mazurov, V.V., and Klyavina, O.A., *Goryuch. Slantsy*, 1989, vol. 6, no. 4, pp. 411–415.
4. Platonov, V.V., Proskuryakov, V.A., and Ryl'tsova, S.V., *Zh. Prikl. Khim.*, 1998, vol. 71, no. 10, pp. 1729–1736.
5. Speight, J.G. and Pokonova, Yu.V., *Neftekhimiya*, 1982, vol. 22, no. 1, pp. 3–20.
6. Posadov, I.A., Pokonova, Yu.V., Popov, D.G., and Proskuryakov, V.A., *Zh. Prikl. Khim.*, 1978, vol. 51, no. 7, pp. 1977–1980.
7. Platonov, V.V., Proskuryakov, V.A., and Rozental', D.A., *Zh. Prikl. Khim.*, 2001, vol. 74, no. 5, pp. 858–862.
8. Kamneva, A.I. and Korolev, Yu.G., *Laboratornyi praktikum po khimii topliva* (Laboratory Manual on Fuel Chemistry), Moscow: Mosk. Khim.-Tekhnol. Inst. im. D.I. Mendeleeva, 1976.

Russian Journal of Applied Chemistry, Vol. 77, No. 1, 2004, pp. 162–164. Translated from Zhurnal Prikladnoi Khimii, Vol. 77, No. 1, 2004, pp. 166–167.

BRIEF COMMUNICATIONS

Phase Separation of Ternary Liquid Systems Tetradecane–Cyclohexanone–Lanthanide(III) Nitrate Solvates with Tri-*n*-butyl Phosphate

A. K. Pyartman, A. V. Kudrova, and V. A. Keskinov

St. Petersburg State Technological Institute, St. Petersburg, Russia

Received May 6, 2003

Abstract—The phase separation diagrams of ternary liquid systems tetradecane–cyclohexanone–lanthanide(III) nitrate solvates with tri-*n*-butyl phosphate {$[Ln(NO_3)_3(TBP)_3$, Ln is Nd or Sm} at T = 298.15 K were studied.

Extraction of rare-earth metals(III) (REM) with tri-*n*-butyl phosphate (TBP) in hydrocarbon diluents is widely used in industrial recovery and separation of REM [1]. When saturating extractant with REM, the organic phase can be separated into two phases, one of which is enriched in $Ln(NO_3)_3(TBP)_3$. This phenomenon was thoroughly studied for actinides [2]. The phase diagrams of the ternary systems tetradecane–cyclohexanone–lanthanide(III) nitrate solvates with tri-*n*-butyl phosphate {$Ln(NO_3)_3(TBP)_3$, Ln is Nd or Sm} were not studied by now. Such data are required for choosing the diluent and the extractant composition ensuring homogeneity of the organic phase in REM extraction with TBP.

The density of organic phases was determined pycnometrically at 298.15 K. The organic components used in our experiments were as follows: TBP distilled under vacuum (ρ = 0.9727 g cm^{-3}), cyclohexanone (ρ = 0.9502 g cm^{-3}), and tetradecane (ρ = 0.7592 g cm^{-3}). The solvates $Ln(NO_3)_3(TBP)_3$ were prepared by triple contact of TBP with Ln(III) nitrate aqueous saturated solution [3]. The solvate concentration in the organic solutions was 1.08–1.12 M (ρ = 1.2745 ± 0.0012 g cm^{-3}). The binodal curves were obtained by improved Alekseev's visual technique [3]. The $Ln(NO_3)_3(TBP)_3$ concentration in the organic solutions was determined by complexometric titration [4]. The compositions of coexisting phases were determined from the weight fraction of $Ln(NO_3)_3(TBP)_3$ in the ternary phase by the technique reported in [5]. We found that, on mixing all the components of the ternary system, the total volume differs from the sum of volumes of the separate components by no more than ±0.2 vol %. Our experimental results were presented as the phase diagrams (Fig. 1) built in the form of the first Roozeboom's triangle. The determination error of the weight fraction of the components did not exceed ±(0.001–0.002).

The phase diagrams and the data listed in the table show that the components of the binary systems $Ln(NO_3)_3(TBP)_3$–$C_{14}H_{30}$ and $(CH_2)_5CO$–$C_{14}H_{30}$ have limited mutual solubility. The $Ln(NO_3)_3(TBP)_3$–$C_{14}H_{30}$ mixtures are separated into two liquid phases. Phases I and II are enriched in $C_{14}H_{30}$ and $Ln(NO_3)_3 \cdot (TBP)_3$, respectively. The $Ln(NO_3)_3(TBP)_3$ solubility in $C_{14}H_{30}$ (weight fraction 0.081) is virtually independent of particular lanthanide. The $(CH_2)_5CO$–$C_{14}H_{30}$ mixtures are also separated into two liquid phases. In this case, phase I is virtually pure tetradecane containing less than 0.001 (wt fraction) of cyclohexanone, and binary phase II contains $C_{14}H_{30}$ (wt fraction 0.339) and $(CH_2)_5CO$ (wt fraction 0.661).

The phase diagrams of the system $Ln(NO_3)_3 \cdot (TBP)_3$–$(CH_2)_5CO$–$C_{14}H_{30}$ contain the region *B* of homogeneous solutions and the two-phase region *A*. These regions are separated by the binodal curve. The ternary mixtures related to region *A* are separated into two liquid phases like the binary system $Ln(NO_3)_3 \cdot (TBP)_3$–$C_{14}H_{30}$. Phase I is the solution of lanthanide nitrate solvate in $C_{14}H_{30}$, and phase II is the equilibrium ternary solution. The point on the binodal curve corresponding to a solution with approximately equal content of each component is the critical point of the ternary system. This point is practically independent of particular lanthanide (see table).

Our results show that, in extraction of lanthanide nitrates of the cerium group with TBP solution in

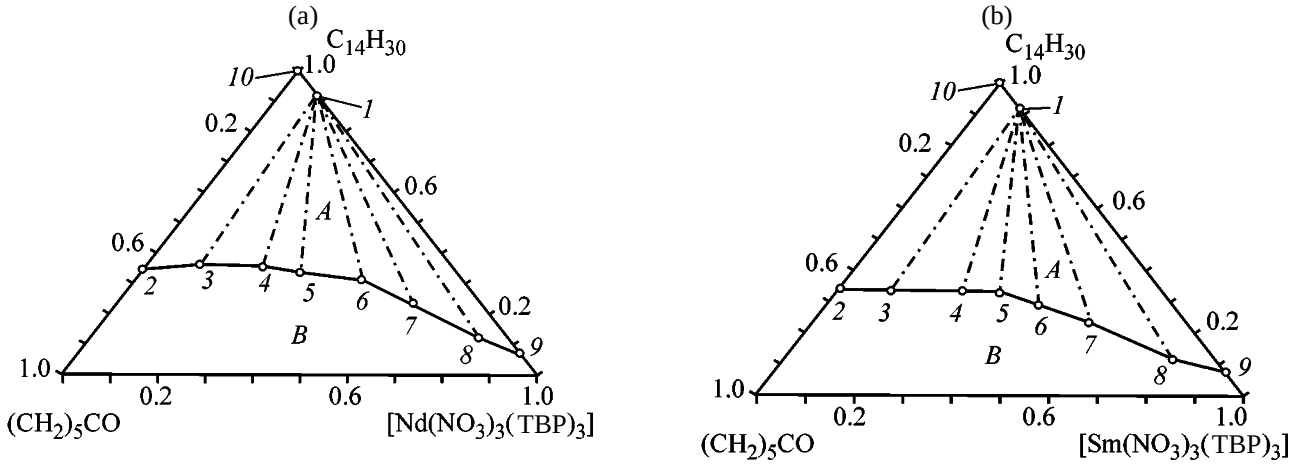

Fig. 1. Phase diagrams of the ternary systems $Ln(NO_3)_3(TBP)_3$–$(CH_2)_5CO$–$C_{14}H_{30}$, Ln is (a) Nd and (b) Sm, at T = 298.15 K. (*A*) Region of coexistence of two liquid phases, (*B*) region of homogeneous solutions, (*2*–*9*) points on the binodal curve, and (*5*) the point on the binodal curve corresponding to the critical composition of the ternary system (ternary system containing equal amounts of each component).

Composition of coexisting phases in the system $Ln(NO_3)_3 \cdot (TBP)_3$–$(CH_2)_5CO$–$C_{14}H_{30}$ at T = 298.15 K

ρ, g cm^{-3}	[$Ln(NO_3)_3(TBP)_3$]	$C_{14}H_{30}$	$(CH_2)_5CO$	Point*
	wt fraction			
	Ln–Nd			
1.2135	0.925	0.075	0	9
1.1552	0.815	0.121	0.064	8
0.9942	0.479	0.309	0.212	6
0.9251	0.244	0.355	0.401	4
0.8961	0.117	0.359	0.524	3
0.8754	0	0.340	0.660	2
0.7849	0.081	0.919	0	1
0.7591	0	1	0	10
0.9512	0.335	0.335	0.330	5
1.0542	0.620	0.236	0.144	7
	Ln–Sm			
1.2136	0.925	0.075	0	9
1.1499	0.795	0.116	0.089	8
0.9881	0.435	0.289	0.276	6
0.9324	0.255	0.334	0.411	4
0.8999	0.109	0.332	0.559	3
0.8754	0	0.339	0.661	2
0.7849	0.081	0.919	0	1
0.7592	0	1	0	10
0.9525	0.335	0.330	0.335	5
1.0396	0.564	0.233	0.203	7

* Points on the binodal curve belonging to nodes [see phase diagrams in Fig. 1].

cyclohexanone–tetradecane mixture, the saturation of the extractant with lanthanide nitrate results in phase separation of the organic extract. To prevent this negative phenomenon deteriorating extraction, the tetradecane weight fraction in the mixed diluent should not exceed 0.30 – 0.35.

CONCLUSIONS

(1) $Ln(NO_3)_3(TBP)_3$–$C_{14}H_{30}$ mixtures are two-phase systems. Phase I is enriched in $C_{14}H_{30}$ and phase II, in $Ln(NO_3)_3(TBP)_3$. The $Ln(NO_3)_3(TBP)_3$ solubility in $C_{14}H_{30}$ is practically independent of particular lanthanide(III). Binary $(CH_2)_5CO$–$C_{14}H_{30}$ mixtures also separate into two liquid phases. Phase I is virtually pure tetradecane containing less than 0.001 (wt fraction) of cyclohexanone, and phase II consists of $C_{14}H_{30}$ (wt fraction 0.339) and $(CH_2)_5CO$ (wt fraction 0.661).

(2) The ternary mixtures belonging to region *A* separate into two liquid phases. Phase I is the solution of lanthanide nitrate solvate in $C_{14}H_{30}$, and phase II is the ternary solution containing all the components of the system, $Ln(NO_3)_3(TBP)_3$–$(CH_2)_5CO$–$C_{14}H_{30}$.

(3) To prevent phase separation of the organic extract in extraction of lanthanide nitrates with TBP solution in the cyclohexanone–tetradecane mixture, the tetradecane weight fraction in the mixed diluent should not exceed 0.30 – 0.35.

REFERENCES

1. Pyartman, A.K., Kopyrin, A.A., Puzikov, E.A., and Bogatov, K.B., *Radiokhimiya*, 1995, vol. 37, no. 1, pp. 52–55.
2. Nikolotova, Z.I., *Ekstraktsiya neitral'nymi fosfororganicheskimi soedineniyami: Aktinidy: Spravochnik* (Extraction with Neutral Organophosphorus Compounds: Actinides: Handbook), Moscow: Energoatomizdat, 1987.
3. *Ekstraktsiya neorganicheskikh veshchestv (Diagrammy rassloeniya, raspredeleniya, vysalivaniya i razdeleniya)* (Extraction of Inorganic Compounds (Diagrams of Phase Separation, Distribution, Salting-Out, and Separation)), Nikolaev, A.V., Ed., Novosibirsk: Nauka, 1970.
4. Přibil, R., *Analytical Applications of EDTA and Related Compounds*, Oxford: Pergamon, 1972.
5. Treybal, R.E., *Liquid Extraction*, New Uork: McGraw-Hill, 1963.

Russian Journal of Applied Chemistry, Vol. 77, No. 1, 2004, pp. 165–167. Translated from Zhurnal Prikladnoi Khimii, Vol. 77, No. 1, 2004, pp. 168–170.

HISTORY OF CHEMISTRY AND CHEMICAL TECHNOLOGY

Academician Georgii Grigor'evich Urazov (to 120th Anniversary of His Birthday)

G.G. Urazov, one of the closest associates and disciples of Academician N.S. Kurnakov, made a major contribution to the development of physicochemical analysis of metallic systems, organization of the domestic aluminum industry, study of natural salts and salt equilibria, nonferrous metallurgy, and training of specialists in chemical technology and nonferrous metallurgy.

Georgii Grigor'evich Urazov was born on January 6 (18), 1884, in Shatoi village of the former Terskaya oblast (North Caucasus) into the family of a physician. He received his secondary education at Yerevan classical education gymnasium, from which he graduated with gold medal in 1903. In the same year, having passed a competition of school-leaving certificates, he was admitted to the metallurgical department of St. Petersburg Polytechnic Institute. Among those who taught chemical sciences at that time were such well-known scientists as N.S. Kurnakov (1860–1941), N.A. Menshutkin (1842–1907), and V.A. Kistyakovskii (1865–1952); courses of lectures on metallurgy were delivered by A.A. Baidakov (1870–1946), M.A. Pavlov (1863–1958), and V.E. Grum-Grzhimailo (1864–1928). The laboratory of general chemistry, headed by Kurnakov, possessed all the necessary equipment for study of physicochemical properties of metallic and other systems. The laboratory comprised three departments: thermal analysis and metallography, electrical measurements and calorimetry, physical measurements and microphotography [1]. When still being a student, Urazov commenced experimental studies of metal alloys under supervision of S.F. Zhemchuzhnyi (1873–1929). In 1906–1908, the results obtained in studying alloys of manganese with copper and nickel, and of magnesium with copper and gold, were published in *Zhurnal Russkogo fiziki-khimicheskogo obshchestva (chast' khimicheskaya)* [Journal of Russian Physicochemical Society (Chemistry)] and *Izvestiya Sankt-Peterburgskogo politekhnicheskogo instituta* (Bulletin of St. Petersburg Polytechnic Institute). Studies of the last two systems were presented is Urazov's graduation thesis, which he defended in 1909 to become engineer metallurgist. Already the very first Urazov's studies, which were

thoroughly carried out and produced reliable results and rigorous conclusions, attracted the attention of specialists. The young scientist was left to work at the chair of general chemistry of the Polytechnic Institute and became Kurnakov's lecture assistant in 1912. In June 1921, the Council of Petrograd Polytechnic Institute elected Urazov a professor of the chair of nonferrous metallurgy. In 1914, the Department of chemistry of the Russian Physicochemical Society awarded the Mendeleev Prize to Urazov for his investigations of metal alloys.

Simultaneously with teaching, Urazov conducted research at quite a number of institutions: in 1918–1920, he was a research worker at the Committee for Analysis of Productive Forces in Russia of the Academy of Sciences; in 1919–1924, head of laboratory at the Department of Industrial Surveys of the Northern Region; in 1924–1940, head of physicochemical laboratory, and later a consultant, at the Geological Committee; in 1931–1940, a consultant and head of

1070-4272/04/7701-0165 © 2004 MAIK "Nauka/Interperiodica"

a research group for chlorination of ores of nonferrous and rare metals at the State Institute of Applied Chemistry. In 1918, Kurnakov initiated foundation in Petrograd of the Institute for Physicochemical Analysis, which united organizationally his disciples and coworkers who had worked at the Polytechnic and Mining institutes and at the chemical laboratory of the Academy of Sciences [2]. Urazov occupied at the new institute the position of research worker. Later, after the Institute of General and Inorganic Chemistry, USSR Academy of Sciences, was organized and Urazov moved to Moscow, he became head of the Department of Chemical Equilibria in 1934 and head of the Department of Physicochemical Analysis at this institute. In June 1934, a scientific degree of doctor of engineering was conferred on Urazov by decision of the Higher Qualification Committee without defense of a dissertation, and in June 1935, the Presidium of the USSR Academy of Sciences conferred on him the degree of doctor of chemistry. Urazov was elected a corresponding member of the USSR Academy of Sciences by its general meeting in January 1939, and academician, in 1946.

From 1938 till 1957, Urazov headed the Chair of Technology of Fine Inorganic Products at the Lomonosov Institute of Fine Chemical Technology in Moscow and organized there the training of specialists in processing of mineral salts. During the period of time from 1943 till 1955, Urazov also headed the Chair of Metallurgy of Heavy Nonferrous Metals at the Kalinin Institute of Nonferrous Metals and Gold in Moscow.

Urazov's scientific activities during more than 50 years were diverse and fruitful. The main areas of his research were analyzed in [3–5]. The scientist's autobiography, published in a historical sketch by Yu.I. Solov'ev [6], read: "All my research activities aimed at diverse objects of study are unified and governed by a common scientific method developed by my teacher Kurnakov, physicochemical analysis."

Immediately after having graduated from the Polytechnic Institute, Urazov continued investigations of metallic systems by studying the magnesium–cadmium system. In view of the division of intermetallic compounds into daltonides and berthollides, suggested by Kurnakov, Urazov studied silicides, antimonides, and sulfides of a number of metals and alloys of iron with silicon. Kurnakov also enlisted the services of his disciple to solution of a number of problems of primary economic importance. As far back as 1914, Kurnakov and Urazov published a study "Toxic Properties of Commercial Brands of Ferrosilicon," in which they established, using methods of physicochemical analysis, the causes of accidents in storage and transportation of ferrosilicon of certain composition. On Kurnakov's initiative, Urazov took part in a survey of salt lakes of the Apsheron Peninsula (Azerbaijan) to determine the possibility of obtaining iodine from brines of these lakes. The results obtained were reported in the article "Baku Iodine Lakes" (1919). A number of lakes were recommended for industrial use. Later, Urazov developed, together with V.P. Il'inskii (1885–1964), an electrochemical technique for recovery of iodine from natural water (1919).

Urazov took an active part in chemical studies of brines from boreholes of the Upper-Kama region, carried out in 1916–1919 under Kurnakov's supervision. After the discovery of a deposit of potassium and magnesium salts by P.I. Preobrazhenskii (1874–1944) in 1925 [7], Urazov continued research in this area. Based on a study of crystallization processes in the quaternary system KCl–NaCl–$MgCl_2$–H_2O, the scientist made suggestions about the conditions of formation of salt seams in deposits of this kind (1930). Urazov was directly involved in studies of salt resources in other regions of the country. He permanently paid much attention to integrated use of the Inderskoe deposit of borate and other salts (western Kazakhstan) and the unique salt basin Kara-Bogaz-Gol (Turkmenistan).

In 1920–1921, at the laboratory of general chemistry of Petrograd Polytechnic Institute, Urazov studied in detail bauxites from the Tikhvin deposit and suggested a method of proximate analysis on the basis of heating curves. The results obtained in these studies were summarized by Kurnakov and Urazov in a paper "Chemical and Thermal Analysis of Tikhvin Bauxite Rock" (1924). Later, Urazov and coworkers developed procedures for recovery of alumina from high-silica bauxites. Systematic studies carried out by the scientist in this area favored the development of an industrial technology for processing of low-grade bauxites.

A large series of investigations by Urazov and coworkers were concerned with quite a number of aluminum-based alloys. Of scientific and practical importance were studies of the physicochemical properties of the ternary systems aluminum–silicon–copper, aluminum–magnesium–copper, and aluminum–silicon–magnesium. Of particular importance for the development of the theory and practice of pyrometallurgical processes were investigations concerned with reactions of metals with sulfur, systems comprising a metal and its halide, equilibria in chloride–sulfate

systems, chlorination of ores of nonferrous and rare metals and mattes, and studies of oxide systems, carried out by Urazov and coworkers.

Urazov's investigations of binary systems formed by silver and copper with sulfur, and also of antimony, initiated studies of physicochemical properties of semiconductor compounds in our country. In communications published in 1919–1921, specific features of the electrical conductivity in the compounds Ag_2S and Cu_2S were noted. The scientist analyzed in detail the publications devoted to unipolar conduction in compounds since M. Faraday (1791–1867) till 1918 and outlined ways to study the nature of conduction in semiconductor compounds.

Urazov's monograph *Metallurgiya nikelya* (Metallurgy of Nickel) ran into two editions (1931 and 1935); he wrote quite a number of articles for *Tekhnicheskaya entsiklopediya* (Technical Encyclopedia) and *Bol'shaya Sovetskaya entsiklopediya* (Great Soviet Encyclopedia), spacious reviews, recollections about his teachers, Zhemchuzhnyi and Kurnakov. The range of Urazov's scientific interests was exceedingly wide, it covered numerous problems of inorganic chemistry, halurgy, and metal science. The scientific and pedagogical activities of Academician Urazov were distinguished by a number of highest State awards.

An outstanding chemist and metallurgist, scientist and pedagogue, Grigorii Grigor'evich Urazov died on April 27, 1957, at the age of 73.

REFERENCES

1. Pogodin, S.A., *Vopr. Istor. Estestvozn. Tekh.*, 1981, no. 1, pp. 121–129.
2. Pogodin, S.A., *Issledovaniya po teoreticheskoi i prikladnoi neorganicheskoi khimii* (Investigations in Theoretical and Applied Inorganic Chemistry), Moscow: Nauka, 1971, pp. 29–42.
3. Pogodin, S.A. and Lepeshkov, I.N., *Izv. Sekt. Fiz.-Khim. Anal.*, 1954, vol. 25, pp. 7–16.
4. *Georgii Grigor'evich Urazov: Materialy k biobibliografii uchenykh* (Georgii Grigor'evich Urazov: Materials on Biobibliography of Scientists), Moscow: Akad. Nauk SSSR, 1957.
5. *Vestn. Akad. Nauk SSSR*, 1954, no. 3, pp. 59–61.
6. Solov'ev, Yu.I., *Inst. obshchei i neorganicheskoi khimii im. N.S. Kurnakova Akad. Nauk SSSR: Istoricheskii ocherk* (Kurnakov Inst. of General and Inorganic Chemistry, USSR Acad. Sci.: Historical Sketch), Moscow: Nauka, 1993.
7. Morachevskii, A.G., *Ocherki ob uchenykh-khimikakh Sankt-Peterburgskogo politekhnicheskogo inst.* (Essays about Chemists of the St. Petersburg Polytechnic Inst.), St. Petersburg: Sankt-Peterb. Gos. Politekh. Univ., 2002.

A. G. Morachevskii

Russian Journal of Applied Chemistry, Vol. 77, No. 1, 2004, pp. 168–169. Translated from Zhurnal Prikladnoi Khimii, Vol. 77, No. 1, 2004, pp. 171–172.

ANNIVERSARIES

Petr Grigor'evich Romankov (to Centennial Anniversary of His Birthday)

A hundred years has elapsed since the birthday of Petr Grigor'evich Romankov, a corresponding member of the USSR Academy of Sciences, professor, a remarkable person, excellent pedagogue and prominent scientist, whose talent and most valuable experience had served for more than half a century the cause of training of high-skilled specialists for domestic science and industry. In the most important field of the science of processes and apparatus of chemical technology, he created the Leningrad scientific school of chemical technologists, which successfully combined in-depth theoretical investigations with their practical implementation and became widely known both in our country and abroad.

P.G. Romankov was born on January 17, 1904, in the town of Eisk, into the family of an office worker. In 1923, he finished rabfak (educational establishment set up to prepare workers and peasants for higher education) at Petrograd State University and entered the chemical faculty of the Technological Institute. In 1929, Petr Grigor'evich graduated from the Leningrad Technological Institute with diploma of engineer chemist-technologist, rejected a tempting offer of post-graduate studentship by Academician A.E. Porai-Koshits, moved to Moscow, and, during the following six years, worked at Dorogomilovskii plant first as a shift chemist and then as a head of a designing shop, which later became a part of Aniloob"edinenie. Simultaneously, Romankov commenced his pedagogical activities at the Chemical Faculty of the Moscow Higher Technical School (1929–1933), chair of processes and apparatus of the Mendeleev Institute of Chemical Technology in Moscow (1929–1934), and at the chair of aniline-dye industry of the Moscow Institute of Chemical Machine-Building (1932–1934).

Beginning in 1934 and till the end of Romankov's life (1990), his active creative, scientific, and educational activities had been associated with the Lensovet Technological Institute (now St. Petersburg State Technological Institute—Technical University).

In 1934, Petr Grigor'evich became a postgraduate student at the chair of processes and apparatus of chemical technology; in 1938, he defended his candidate dissertation devoted to development of methods

for calculation of process modes of drying of milled peat and continued scientific and pedagogical work at the chair.

During the years of the Leningrad siege (1941–1944), Romankov remained in the besieged city; a method for vacuum drying of blood plasma was developed and manufacture of a number of preparations necessary for those at the front line and in the city was set up under his supervision. In 1943, teaching at the chair was resumed and reconstruction of the first country's laboratory of chemical apparatus, organized in 1936, was commenced.

In 1943, Romankov replaced professor K.F. Pavlov, whose investigations in the field of linearity of chemical-technological functions became classical, as head of the Chair of Processes and Apparatus of Chemical Technology, one of the leading chairs for higher education in chemical technology at the Technological Institute. He headed this chair for nearly 50 years.

In 1947, Romankov defended his doctoral dissertation, in which he formulated the concept of unified kinetic patterns of chemical technology as the basis of the modern science of processes and apparatus and

1070-4272/04/7701-0168 © 2004 MAIK "Nauka/Interperiodica"

thereby continued and developed fruitful ideas of such his predecessors as D.I. Mendeleev, A.K. Krupskii, D.P. Konovalov, L.F. Fokin, and K.F. Pavlov.

Since 1950, Romankov had been deputy rector for scientific work of the Technological Institute for 30 years (1950–1980). He desired to combine the achievements of science and technology on the basis of modern foundations of chemical technology, following D.I. Mendeleev's statement: "Education, science, and industry make our state economically strong."

In 1964, Romankov was elected a corresponding member of the USSR Academy of Sciences, and an honorary title of Honored Scientist and Technologist of the Russian Soviet Federative Socialist Republic was conferred on him.

Romankov understood as the main purport of his life to work so as to be of maximum possible benefit to the Motherland and to enhance the prestige of the science of processes and apparatus. Under his supervision, more than 25 doctors and 200 candidates of science, whose investigations made an essential contribution to the development of engineering chemistry and theoretical foundations of chemical technology, were trained. Original methods for carrying out and calculating a number of hydromechanical, thermal, and mass-exchange processes of drying, gas purification, adsorption, extraction, distillation, and agitation were developed. To problems associated with design of high-intensity continuous apparatus for drying of finely dispersed and paste-like materials, adsorption in fluidized bed, separation of heterogeneous systems, etc. were devoted more than 300 scientific publications and inventions and a number of monographs by Romankov and coworkers: *Gidromekhanicheskie protsessy khimicheskoi tekhnologii* (Hydromechanical Processes of Chemical Technology) (1982), *Massoobmennye protsessy khimicheskoi tekhnologii* (Mass-Exchange Processes of Chemical Technology) (1990), and *Metody rascheta protsessov i apparatov khimicheskoi tekhnologii* (Methods for Calculation of Processes and Apparatus of Chemical Technology) (1994).

Much attention was given by Romankov to the development of the students' laboratory and to writing of educational literature. In the 1950s, the students' laboratory at the Chair of Processes and Apparatus of the Technological Institute became a model laboratory in the country. In 1947, the first edition of the textbook *Primery i zadachi po kursu protsessov i apparatov khimicheskoi tekhnologii* (Examples and Problems for the Course of Processes and Apparatus of Chemical Technology) by Pavlov, Romankov, and L.A. Noskov was published. In the following 40 years, this textbook was translated into 12 foreign languages and ran into 10 editions of more than 300 thousand copies. *Rukovodstvo po laboratornomu praktikumu* (Manual of Laboratory Work) written by the staff members of the chair was republished six times.

Romankov's services in the development of international relationships of the domestic higher school were distinguished by honorary titles and State awards of not only our country, but also other European countries (Bulgaria, Hungary, Poland, Czechoslovakia, Yugoslavia).

Romankov liked literary work despite its labor-intensiveness and psychological tension. He worked actively at a journal *Teoreticheskie osnovy khimicheskoi tekhnologii* (Theoretical Foundations of Chemical Technology), published by the Academy of Sciences of the USSR, as deputy editor-in-chief and was a member of the editorial board of *Zhurnal prikladnoi khimii* (Russian Journal of Applied Chemistry). Beginning in 1976, Petr Grigor'evich headed for more than 12 years the editorial board of *Zhurnal prikladnoi khimii*, published by the Academy of Sciences of the USSR, regularly conducted meetings of the Editorial Board in a business-like, friendly climate of confidence and mutual respect, which resulted in that any, even conflicting situations were easily resolved.

As many talented persons, Romankov was an idea man for his colleagues, whose opinion was highly estimated and respected by him, and an exceedingly obliging and good-wishing person. He belonged to the cohort of those Russian scientists whose scientific longevity became legendary and the scope of whose interests seemed to be unbounded.

N. N. Smirnov and E. S. Postnikova

Russian Journal of Applied Chemistry, Vol. 77, No. 2, 2004, pp. 171–172. Translated from Zhurnal Prikladnoi Khimii, Vol. 77, No. 2, 2004, pp. 177–178.

ANNIVERSARIES

Vladimir Stepanovich Shpak (To His 95th Birthday)

On February 20, 2004, Vladimir Stepanovich Shpak, full member of the Russian Academy of Sciences, councilor of the Director general of Prikladnaya Khimiya Russian Scientific Center, and Editor-in-chief of *Zhurnal Prikladnoi Khimii* (Russian Journal of Applied Chemistry), Russian Academy of Sciences, is 95.

V.S. Shpak is a prominent scientist specializing in technical chemistry. He has initiated, organized, and supervised large-scale investigations into new classes of chemical compounds and fields of their application, and the work on development of new types of technological processes for synthesizing most important special purpose substances.

Under Shpak's supervision, and with his direct participation, fundamental studies have been performed and numerous processes of basic organic synthesis have been developed and put in practice at plants of chemical and petrochemical industries. In particular, manufacture of high-molecular-weight amines from nitroparaffins has been organized, a new method for synthesis of esters has been developed, and investigations of hydrazine derivatives and other classes of chemical compounds, such as oxidizing agents, surfactants, and catalysts for various processes, have been performed. Shpak was among originators of a new, most important branch of chemical industry, specifically, the manufacture of organofluorine compounds. His investigations of transformations in various chemical compounds under the impact of high energy yielded initial data for the development of novel kinds of defense equipment.

Vladimir Stepanovich Shpak commenced his working activities in 1931, after having graduated from the Leningrad Technological Institute as a specialist in explosives. Till 1977, he was engaged in pedagogical activities at this institute, occupying successively the positions of an assistant, docent, and professor. Among Shpak's teachers was professor S.P. Vukolov (1863–1940), one of the most prominent Russian specialists in explosives and powders, D.I. Mendeleev's pupil and coworker, originator and the first head of the chair of explosives at the Leningrad Technological

Institute. During several years, Shpak was his deputy. In 1941–1944, Shpak was evacuated, together with the Institute, to Kazan, where he was engaged in teaching and production activities. Shpak was deputy director of the State Institute of Applied Chemistry (GIPKh) for science and technology in 1948–1953 and director of this Institute in 1953–1977. Under his supervision GIPKh became the largest country's chemical institute with unique technological base and a number of branches. Shpak, together with the staff members of the Institute headed by him, could create a new, modern type of a research organization that comprises a research institute, a designing office, and a plant.

1070-4272/04/7702-0171 © 2004 MAIK "Nauka/Interperiodica"

From 1977 till 1992, Shpak was Chief chemist for heavy organic synthesis at the Ministry of Chemical Industry and, simultaneously, headed the Leningrad research center for interbranch activities. He paid much attention to preparation of suggestions, as well as to planning and coordination of joint research works by organizations of the Ministry of Chemical Industry, Ministry of Fertilizers, institutes of the Russian Academy of Sciences, and higher-school institutions of Leningrad. From 1992 till the present time, Shpak has been councilor of the Director general of Prikladnaya Khimiya Russian Scientific Center.

Shpak has always given much of his time to public and scientific-organizational activities. From 1977 till 1992, he was vice-president of the Mendeleev All-Union Chemical Society. At present Shpak is chairman of the Northwestern division of the Scientific Council for combustion, Russian Academy of Sciences. With the strong sense of responsibility, so characteristic of him, Shpak pays much attention to coordination of R&D works in the field of combustion, which are carried out at research organizations, higher-school institutions, and industrial plants of Northwestern Russia. The following areas of research are distinguished as priority issues: "Chemistry for Engine-making and Transportation in Russia," "Chemistry for the Fuel-and-Energy Complex," "Problem of Hydrogen as a Fuel of the Future," etc. Shpak continues to be most actively engaged in the activities of the Prikladnaya Khimiya Russian Scientific Center, being a member of its scientific and thesis councils.

For many years Shpak was a member of the Editorial board of *Zhurnal Prikladnoi Khimii*, Russian Academy of Sciences; from 1998 to the present day, he has been the Editor-in-chief of the Journal.

Shpak's scientific activities are reflected in more than 500 papers and scientific project reports, their scientific novelty has been confirmed by 57 Inventor's certificates and patents. Shpak's pupils include more than 30 doctors and candidates of science. In 1955, a scientific degree of a doctor of science was conferred on Shpak, and in 1956, he became a professor. He was elected a corresponding member of the Academy of Sciences of the USSR in 1968, and a full member of the Academy, in 1981. Shpak became Honored worker of science and technology of the Russian Soviet Federative Socialist Republic (RSFSR) in 1968, and Honorary chemist of the RSFSR in 1974.

For outstanding achievements in the development of rocket engineering, making possible the human flight to the outer space, Vladimir Stepanovich Shpak was given a title of the Hero of Socialist Labor in 1961. His many years' scientific, organizational, and pedagogic activities have been honored with quite a number of highest State awards.

The staff members of the of Prikladnaya Khimiya Russian Scientific Center, St. Petersburg State Technological Institute, and St. Petersburg department of Nauka Publishing House, as well as the Editorial Board and staff members of the Editorial office of Zhurnal Prikladnoi Khimii, congratulate Vladimir Stepanovich on his glorious jubilee and wish him sound health, many happy returns of the day, and success in implementation of his always numerous new scientific ideas.

Prikladnaya Khimiya Russian Scientific Center
St. Petersburg State Technological Institute
St. Petersburg Nauka Publishing House
Editorial Board and staff members of the Editorial office of *Zhurnal Prikladnoi Khimii*

Russian Journal of Applied Chemistry, Vol. 77, No. 2, 2004, pp. 173–177. Translated from Zhurnal Prikladnoi Khimii, Vol. 77, No. 2, 2004, pp. 179–183.

INORGANIC SYNTHESIS AND INDUSTRIAL INORGANIC CHEMISTRY

Granulation of Calcium Sulfate Hemihydrate and Its Topochemical Transition to Dihydrate in Grains in the Presence of Copper, Cobalt, and Molybdenum Salts

L. P. Firsova

Lomonosov State University, Moscow, Russia

Received July 21, 2003

Abstract—The influence exerted by admixtures of ammonium molybdate and copper or cobalt sulfate in humidifying solutions on the granulation of calcium sulfate hemihydrate and its topochemical transformation to calcium sulfate dihydrate in granules was studied experimentally.

Phosphogypsum is a waste formed in industrial processing of phosphate raw materials and production of phosphoric acid. Annually its dumps grow in the world by millions of tons, polluting the environment. Therefore, it is still important to develop new methods for utilization of phosphogypsum, including that formed in manufacture of phosphoric acid by the sulfuric acid hemihydrate method. In particular, it has been suggested to use granulated phosphogypsum as a land-improving agent and carrier of nutritious substances, trace elements, and biologically active materials useful for plant cultivation [1–4].

This study is concerned with the physicochemical effects associated with introduction of biologically active microelements [copper(II), cobalt(II), and molybdenum(VI)] into calcium sulfate hemihydrate, which is a waste formed in manufacture of phosphoric acid. The deficit of these microelements in soil adversely affects agricultural plants. To effects of this kind belongs the influence exerted by admixtures on the formation of granules from a wet powder of the hemihydrate and on the topochemical transition of the hemihydrate to $CaSO_4 \cdot 2H_2O$, both directly in hemihydrate granulation and in the subsequent ripening and hardening of the grains.

By now, a certain amount of data on the mechanisms and kinetics of calcium sulfate hemihydrate–dihydarate transitions has been accumulated [5–7]. These transitions underlie such practically significant processes as, e.g., production and application of cementing materials based on gypsum. However, insufficient attention has been given in the literature [8, 9] to the dependence of the phase transition and granulation parameters on the presence of admixtures. At the same time, topical problems associated with utilization of large-tonnage industrial phosphogypsum wastes require a more detailed study of the effect of admixtures on the phase transitions and granulation and on the properties of the resulting grains, including their strength. It also seems expedient to supplement the list of admixtures to be studied, e.g., by including biologically active microelements (copper-, cobalt-, and molybdenum-containing compounds).

EXPERIMENTAL

The pretreatment of commercial calcium sulfate hemihydrate (manufactured by Voskresensk plant of mineral fertilizers) in order to produce grains containing the necessary admixtures, consisted in that hygroscopic water and, simultaneously, the residual amount of phosphoric acid were removed from the initial phosphogypsum powder by its successive treatment with several portions of a hot solution of calcium sulfate and with acetone. After that, acetone was removed when drying a washed powder in air. This precluded the transition of calcium sulfate hemihydrate to the dihydrate before granulation.

The $CaSO_4 \cdot 0.5H_2O$ powder obtained by this technique consisted of hexagonal prisms 1 to 30 μm long, aggregated into druses 10 to 300 μm in size. The $CaSO_4 \cdot 0.5H_2O$ powder contained (wt %): H_2O 6.5–7.0, CaO 39–40, SO_3 56–57, P_2O_5 0.9–1.1, F 0.3–0.4, SiO_2 0.7–0.8, and R_2O_3 0.5–0.6. The porosity of the powder was $65.1 \pm 2.1\%$, and that of druses,

1070-4272/04/7702-0173 © 2004 MAIK "Nauka/Interperiodica"

43.5 ± 1.3%; the bulk weight of the powder was 0.95–1.0 g cm^{-3}. The content of copper(II) and molybdenum(VI) in the initial hemihydrate was below the limit of their detection by photometry (based on the intensity of yellow coloration of phosphomolybdenum-vanadium heteropolyacid and the blue-violet coloration of copper ammonium complex, respectively).

Immediately before granulation, the washed air-dry powder of calcium sulfate hemihydrate was wetted with specially prepared aqueous solutions containing admixtures of nitric and sulfuric acids (0.5–7.0%) or copper(II) and cobalt(II) sulfates and also that of ammonium molybdate (up to 1–5%). The amount of solution used for humidifying the hemihydrate was varied within the range 20–40%.

The powder and the solution were mixed in the course of 30–60 s and then the wet stock was directly transferred to a plate-type granulator. The stainless steel granulator plate 250 mm in diameter had side walls of height 75 mm. To control the growth and abrasion of grains, the tilt angle of the plate was varied from 20 to 40°; the rotation rate, from 50 to 80 rpm; and the granulation time, from 2 to 30 min.

After the process was complete, the resulting deformable grains were carefully transferred for strengthening (ripening in the course of formation of dihydrate crystals) to a wet atmosphere of a desiccator filled with water-wetted calcium sulfate dihydrate. Within 60–120 min after the beginning of the exposure in the desiccator, grains with a strength higher than 2 kg cm^{-2} were transferred to vessels with aqueous solutions identical to the humidifying solutions. The time of full ripening of the grains was 8 to 30 h.

During the granulation and ripening, portions of grains were taken for analysis. The amount of hygroscopic and crystallization water in the grains was determined. The grain strength determined both by dynamic compacting loads in the rotating plate in the course of stock granulation and by the topochemical transition in the substance of the granules. For a portion of grains with strength more than 2–3 kg cm^{-2}, the size distribution of grains and the average grain diameter were determined.

The content of hygroscopic water in grains and powders was determined from the difference of weights of the initial samples and those washed with acetone and then dried to constant weight. The content of crystallization water in air-dry powders and grains was determined by thermogravimetry. The relative amounts of hygroscopic and crystallization water in the samples made it possible to examine the kinetics of the topochemical transformation and to estimate the degree of conversion of calcium sulfate hemihydrate to the dihydrate.

The grain strength was determined in relation to the presence of admixtures in calcium sulfate from the force required for their crushing under a uniaxial compression. Prior to the tensometric measurements, the surface of wet grains was dried with a filter paper. For grains of specified size and composition, 15–20 parallel measurements were carried out.

A screen analysis was carried out for powders (initial and produced by abrasion of grains in granulation), as well as for dried granules with a strength greater than 2 kg cm^{-2}, in order to determine the average size and particle size distribution in relation to the presence of admixtures in calcium sulfate, humidity, and nodulization conditions. Standard sets of metallic soil sieves (0.25 to 7 mm mesh) and nylon sieves (14 to 300 μm) were used in the screen analysis. The powders and grains were also analyzed with an MBI-14 microscope.

The experiments on granulation of wet hemihydrate powder have shown that the optimal stock humidity W, at which granulation is possible, lies within the range 27–35%. Changing the composition by introduction of various admixtures into the humidifying liquid virtually did not change the optimal humidity limits. At a humidity less than 27–28% (W_{min}), no grains greater than 1 mm in diameter were formed. At the humidity exceeding 35%, large lumps of irregular shape were formed instead of spherical grains. This is in agreement with published data on the influence exerted by the weight ratio of liquid and solid phases on the formation and growth of grains. For example, it was shown in [10] that there exists a rather narrow range of optimal l/s values for granulation, at which formation of spherical grains is possible. However, the influence exerted by the composition of the liquid phase on the range of l/s values at which spherical grains can be formed, and on the value of W_{min}, was not analyzed. The experimental results obtained in the present study show that the presence of admixtures in amounts of several percent in the aqueous solutions used to humidify phosphogypsum affects the value of W_{min} only slightly. For example, the lower humidity limit for the granulation was 28.0 ± 0.7% at 1–5% $(NH_4)_2MoO_4$ in a humidifier, W_{min} = 27.0 ± 0.8% at 1–5% $CuSO_4$, and W_{min} = 27.0 ± 0.5% in the presence of 2.5% H_2SO_4.

The value of W or the l/s ratio determines the mechanism by which grains are formed and the time de-

pendence of the grain size [10]. When the stock contains the minimum amount of a humidifier, which is present only on the surface of solid particles at places of their contact, a rather slow growth of the diameter of granules is observed. This results from the agglomeration of powder particles to give protograins and from the deposition of the powder onto the protograins under the action of surface tension forces at the phase boundary. If the amount of moisture is sufficient for filling of pores in the solid phase, the agglomeration of the initial small-sized powder particles to give protograins and the deposition of powder particles onto the surface of protograins mainly occur via formation of a binding liquid network and under the action of capillary forces. When the amount of the liquids is so large that it completely covers solid particles, adhesive fusion of small-sized grains into larger ones becomes the main mechanism of fast grain growth.

The influence exerted by the content of the liquid phase in a stock on the variation of the grain size with time and on the particle size distribution in granulation within the optimal humidity range is described by the equation [10]:

$$d_t = d_0 \exp(\nu t). \quad (1)$$

Here d_t is the mean size of grains at stock humidity $W > W_{min}$ for granulation time t; d_0, the mean size of the initial druses in the phosphogypsum powder; and ν, the frequency of adhesive sticking of protograins or particles of a powder being granulated, which is dependent on the stock humidity.

Taking into account the experimental dependence of the sticking frequency on the stock humidity and the existence of the lower humidity limit at which grain formation becomes possible and assuming that $\nu = m(W - W_{min})^n$, Eq. (1) can be written as

$$d_t = d_0 \exp[m(W - W_{min})^n t]. \quad (2)$$

Here m and n are empirical constants, which are independent of the stock humidity and account for the properties of solid and liquid phases, e.g., surface tension parameters.

Equations (1) and (2) suggest that $\ln(d_t/d_0)$ depends linearly on t. This assumption is confirmed by the experimental data (Fig. 1). Indeed, the expected linear behavior of the dependence of $\ln(d_t/d_0)$ on t is observed at a short granulation time (1–8 min). Introduction of nitric acid into a humidifying solution, instead of $CuSO_4$, at the same stock humidity leads

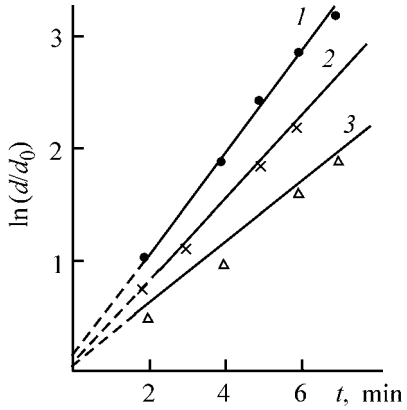

Fig. 1. Dependence of $\ln(d_t/d_0)$ on time t at various compositions of the humidifying solution. Humidifying solution (%): (*1*) 0.5 H_2SO_4, (*2*) 1.0 HNO_3, and (*3*) 2.0 $CuSO_4$. Stock humidity (%): (*1*) 33; (*2*) and (*3*) 30.

to a change in the slopes (or tan α) of straight lines in the coordinates $\ln(d_t/d_0)$–t and in the values of ν. A change in the slope is also characteristic of the case when the humidity of the stock is raised by adding H_2SO_4 solution.

The slope ratio of the straight lines can be represented as

$$\tan\alpha_1/\tan\alpha_2 = \nu_1/\nu_2 = \ln(d_t/d_0)_1/\ln(d_t/d_0)_2 = (m_1/m_2)\,[(W_1 - W_{min})^n/(W_2 - W_{min})^n]. \quad (3)$$

It is essential that, according to (3), the quantities ν and tan α should depend on the properties of solid and liquid phases and on the stock humidity. It is also not improbable that they may depend on the content of impurities in the humidifier, which modify the properties of a material being granulated, as is confirmed by the experimental data presented in Fig. 1 and in the table.

On the assumption that the properties of the solid and liquid phases are predominantly reflected by the coefficients m and n, respectively, several particular cases follow from Eq. (1). For example, if the nodulization of one and the same solid phase, phosphogypsum, is performed with two humidifiers of different

Values of $\ln(d_t/d_0)$ and ν at different humidities W of a stock wetted with 2.5% $CoSO_4$ solution

W, %	$W - W_{min}$	$\ln(d_t/d_0)$	t, min	ν
34	7	3.35	5	0.67
30	3	1.90	5	0.38
28	1	1.50	9	0.17

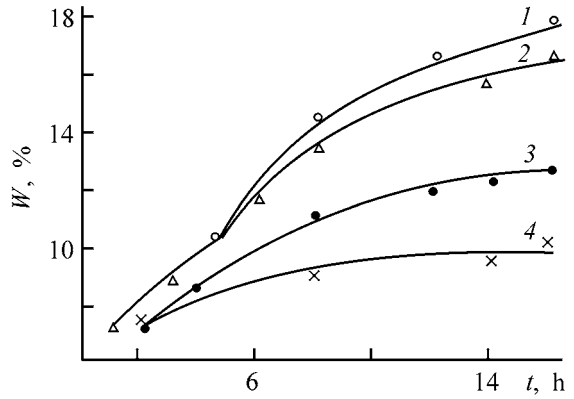

Fig. 2. Variation of the content of crystallization water and of the degree of phase transition in grains in the course of ripening within time *t*. (*W*) Humidity. Humidifying solution (%): (*1*) 5 H_2SO_4 (ripening in solution), (*2*) 2.5 $CoSO_4$ (ripening in solution), (*3*) 5 H_2SO_4 (ripening in a desiccator), and (*4*) 2.5 $CuSO_4$ (ripening in a desiccator).

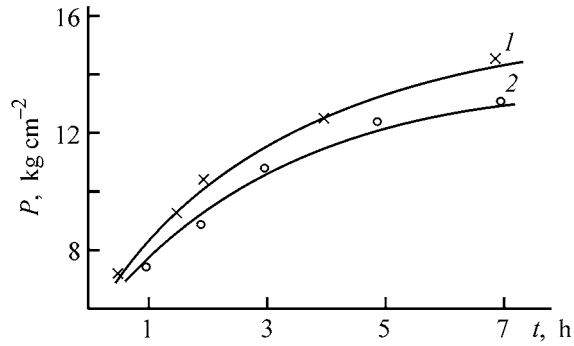

Fig. 3. Change in the mechanical strength of granules *P* in the course of ripening within time *t*. (*1*) H_2O and (*2*) 2.5% $(NH_4)_2MoO_4$.

compositions, i.e. at $m_1 = m_2$ and $W_2 = W_1 = W$ and $W_{min1} = W_{min2} = W_{min}$, then

$$\log(\tan\alpha_1/\tan\alpha_2) = (n_1 - n_2)\log(W - W_{min}). \quad (4)$$

Here $\tan\alpha_1$ and $\tan\alpha_2$ are the slopes of the straight lines in the coordinates $\ln(d_t/d_0)$–t.

In the case when the compositions of humidifiers and the l/s ratios are the same ($W_2 = W_1$), but the solid phases are different, with $m_1 \neq m_2$, but $n_1 = n_2$, it follows that

$$\tan\alpha_1/\tan\alpha_2 = m_1/m_2. \quad (5)$$

If the compositions of the humidifiers are identical, but the l/s ratios are different, i.e., $n_1 = n_2$ (nature of admixtures in liquid phases and their concentration are the same), and also $m_1 = m_2$ and $W_{min1} = W_{min2}$, but W_1 and W_2 are different ($W_2 \neq W_1$), then

$$\log(\tan\alpha_1/\tan\alpha_2) = n\log[(W_1 - W_{min})/(W_2 - W_{min})]. \quad (6)$$

Expressions (3)–(6) can be used to estimate n or m and to verify various hypotheses concerning the mechanisms of grain formation and the particle size distribution. The experimental data in the table correspond to Eq. (6) as regards the granulation conditions and the stock composition. Consequently,

$$n = \log(\tan\alpha_1/\tan\alpha_2)/\log[(W_1 - W_{min})/(W_2 - W_{min})]. \quad (7)$$

A calculation based on the data in the table and expression (7), in which each pair from the experimental series with different degrees of humidification, yielded the coefficients n for the 2.5% solution of cobalt sulfate. For example, $n = 0.68$ at $W_1 = 34$ and $W_2 = 30\%$; $n = 0.71$ at $W_1 = 34$ and $W_2 = 28\%$; $n = 0.73$ at $W_1 = 30$ and $W_2 = 28\%$. The average value of n is 0.71. These data point to a weak dependence of n on the stock humidity. However, this conclusion was not confirmed by estimation of coefficients n for the case of an $(NH_4)_2MoO_4$ solution introduced into the stock. It is necessary to note that the estimates aimed, among other things, to determine the reliability of the technique suggested for analysis of granulation processes and to verify the assumptions made are tentative and require a refinement with other examples.

The effect of $CuSO_4$ and $CoSO_4$ admixtures contained in the humidifying solution also manifests itself in the kinetics of the solid-phase transition of calcium sulfate hemihydrate to the dihydrate, which is accompanied by an increase in the fraction of crystallization water and a decrease in the rate at which this parameter changes within grains. (Fig. 2).

As follows from the experimental data obtained, the nature of an admixture virtually does not affect the rate of grain strengthening in the initial stage, in the course of granulation, when a strength of less than 1.5–2.0 kg cm^{-2} is reached mainly under the action of compacting loads in the rotating plate of the granulator plate. However, admixtures of $(NH_4)_2MoO_4$ notably decelerate the subsequent stage of grain strengthening, which results from a topochemical transition of calcium sulfate hemihydrate to dihydrate in grains in a moist air (Fig. 3). A similar effect has been observed previously in the case of admixtures of salts of manganese and zinc and also boron in the form of a boric acid [11]. By contrast, the introduction of nitric and sulfuric acids into solutions used to humidify phosphogypsum accelerated the grain strengthening.

It was shown in [5–9] that the dihydrate crystals originate on the surface of single crystals of calcium sulfate hemihydrate, which have the form of elongated hexagonal or pseudo-hexagonal prisms (up to 30 μm long) with H_2O molecules contained in channels parallel to the hexagonal axis *c*. Dihydrate crystals can further grow, with the initial monoclinic crystal system retained and a phase transition zone formed on the periphery of the initial hemihydrate single crystal. This zone migrates from the surface to the center. In the process, the dihydrate crystals in grains penetrate through one another to form a rather strong structure. If impurity ions are sorbed on the surface of the crystals, defects originate in the block dihydrate layer that grows on the hemihydrate. Subsequently, these defects are not overgrown as the phase transition boundaries go deeper. Therefore, the dihydrate crystals may be more defective and shorter in the presence of impurity cations, compared with the case of their absence. Accordingly, the grain strength decreases. Impurities can also change the stability limits of the phases of calcium sulfate hemihydrate and dihydrate. For example, according to [8, 9], calcium sulfate dihydrate appears in the presence of an admixture of a rare earth under conditions of hemihydrate stability. The change in stability limits of calcium sulfate hemihydrate and dihydrate can also affect the rate and degree of the phase transition.

CONCLUSION

It was found that admixtures of molybdenum(VI), copper(II), and cobalt(II) compounds exert influence on the mean size of granules obtained by granulation of humidified calcium sulfate hemihydrate, on the kinetics of the topochemical transition of the hemihydrate to the dihydrate in grains, and, accordingly, on the kinetics of grain strengthening in the the phase transition or on the maximum achievable strength of the grains upon ripening.

REFERENCES

1. RF Patent 2079475.
2. USSR Inventor's Certificate, no. 1724655.
3. USSR Inventor's Certificate, no. 1724654.
4. RF Patent 2077524.
5. Melikhov, I.V., Rudin, V.N., and Vorob'eva, L.J., *Mendeleev Commun.*, 1991, vol. 1, pp. 33–34.
6. Melikhov, I.V., Rudin, V.N., and Vorob'eva, L.J., *Neorg. Mater.*, 1988, vol. 24, no. 3, pp. 448–452.
7. Melikhov, I.V., Rudin, V.N., and Vorob'eva, L.J., *Teor. Osn. Khim. Tekhnol.*, 1985, vol. 19, no. 6, pp. 742–745.
8. Berdonosova, D.G., Burlakova, E.V., Yasenkova, M.A., *et al.*, *Zh. Prikl. Khim.*, 1989, vol. 62, no. 2, pp. 245–250.
9. Melikhov, I.V., Berdonosova, D.G., Fadeev, V.V., and Burlakova, E.V., *Zh. Prikl. Khim.*, 1991, vol. 64, no. 2, pp. 334–340.
10. Klassen, P.V., Grishaev, I.G., and Shomin, I.P., *Granulirovanie* (Granulation), Moscow: Khimiya, 1991.
11. Firsova, L.P., *Zh. Prikl. Khim.*, 2003, vol. 76, no. 3, pp. 353–355.

Russian Journal of Applied Chemistry, Vol. 77, No. 2, 2004, pp. 178–181. Translated from Zhurnal Prikladnoi Khimii, Vol. 77, No. 2, 2004, pp. 184–187.

INORGANIC SYNTHESIS AND INDUSTRIAL INORGANIC CHEMISTRY

Heat Conductivity of Zirconium and Alkali Metal (Na, Cs) Phosphates of the $NaZr_2(PO_4)_3$ Family

V. I. Pet'kov, V. N. Loshkarev, and E. A. Asabina

Lobachevskii State University, Nizhnii Novgorod, Russia

Received August 6, 2003

Abstract—The heat conductivity of porous $Zr_3(PO_4)_4$, $NaZr_2(PO_4)_3$, $CsZr_2(PO_4)_3$, and $Na_5Zr(PO_4)_3$ samples was studied in the range 298–673 K. The heat conductivity coefficients of the zero-porosity phosphates under study were calculated and prospects for their application were considered.

A great number of structural analogues of $NaZr_2(PO_4)_3$ (NZP) are known among inorganic orthophosphates [1–3]. The extensive crystallization field of compounds and solid solutions of the NZP structural type is determined by the broad isomorphism in positions of cations located in voids of the 3*D* skeleton of the structure and also by the possibility of isomorphous substitutions in the octahedra and tetrahedra forming the skeleton [4, 5].

It is known [6, 7] that NZP phosphates have high melting points, chemical stability, radiation hardness, and resistance to thermal shocks of any practically achievable intensity.

Thermal properties (heat expansion, specific heat, and heat conductivity) largely determine the high value of ceramic materials. A great number of publications [8–11] have been devoted to experimental determination of the heat expansion of NZP materials, which characterizes the relative change in the volume or linear dimensions of a body upon a certain change in its temperature. Analysis of the thermal coefficients of linear expansion of these materials suggests that the behavior of an NZP structure under thermal impact is determined by the nature, relative size, and number of cations occupying various crystallographic positions, by the number of vacant positions, and also by the unit cell symmetry. A set of empirical relationships governing the heat expansion of NZP phosphates was suggested in [4] on the basis of a crystal-chemical approach. These relationships make it possible to predict existence of new materials with controllable, including ultralow, heat expansion at an almost zero expansion anisotropy.

A precise determination of the specific heat (amount of thermal energy necessary for a certain change in the temperature of a substance) and heat conductivity (amount of heat passing through a material at a specified temperature gradient) is a rather labor-consuming operation. For this reason, the data on the specific heat and heat conductivity of representatives of the NZP family are limited to publications [7, 12–20], and the compounds studied are few in number. Data on the heat conductivity of ceramic materials are available for the following ceramic materials: $(Ca_{1-x}Mg_x)Zr_4(PO_4)_6$ [18, 19], $Ca_{0.9}Li_{0.2}Zr_4(PO_4)_6$ [19], $Ca_{0.9}Zr_{4.05}(PO_4)_6$ [19], and $(Sr_{1-x}K_{2x})Zr_4(PO_4)_6$ [20].

There is an imbalance between the fast accumulation of the information on the structure and heat expansion of NZP materials and the much slower study of their heat conductivity and specific heat. It is evident that the rate at which the temperature of an article varies during its heat treatment in the course of its fabrication or use depends on the heat conductivity and specific heat of the material used. It is the heat conductivity coefficient, alongside with the thermal coefficients of linear and volume expansion, that determines the heat resistance of a material. Therefore studying the heat conductivity of NZP materials in a wide temperature range is an topical scientific and practical task.

The aim of this study was to examine experimentally the temperature dependence of the heat conductivity of porous samples of crystalline NZP phosphates $Zr_3(PO_4)_4$, $NaZr_2(PO_4)_3$, $CsZr_2(PO_4)_3$, and $Na_5Zr(PO_4)_3$ in the temperature range 298–673 K, to

1070-4272/04/7702-0178 © 2004 MAIK "Nauka/Interperiodica"

Characteristics of NZP phosphates

Formula	Space group	Z	Unit cell parameters			ρ_X	ρ_a	P, %
			a, Å	c, Å	V, Å^3	g cm^{-3}		
$Zr_{2.25}(PO_4)_3$	$R\bar{3}c$	6	8.825(4)	23.09(2)	1557	3.13	2.03	35
$NaZr_2(PO_4)_3$	$R\bar{3}c$	6	8.801(1)	22.77(1)	1527	3.20	2.23	30
$CsZr_2(PO_4)_3$	$R\bar{3}c$	6	8.576(1)	24.91(1)	1587	3.77	2.33	38
$Na_5Zr(PO_4)_3$	$R32$	6	9.162(9)	22.15(2)	1610	3.04	2.25	26

estimate the heat conductivity coefficients of such zero-porosity materials, to compare the data obtained with published experimental data on high-density NZP ceramics, and also to consider prospects for their application on the basis of their thermal properties. The objects of study were chosen taking into account the availability of experimental data on the temperature dependence of their specific heat in the above-mentioned temperature range.

EXPERIMENTAL

The compounds $Zr_3(PO_4)_4$ [$Zr_{0.25}Zr_2(PO_4)_3$], $NaZr_2(PO_4)_3$, $CsZr_2(PO_4)_3$, and $Na_5Zr(PO_4)_3$ were synthesized by the sol–gel method [7, 15]. For this purpose, stoichiometric amounts of aqueous solutions of zirconium oxychloride salts and a chloride of an alkali metal were poured together with permanent stirring at a temperature of about 295 K, and then a stoichiometric amount of a solution of orthophosphoric acid was added slowly with stirring. The resulting gel was dried at 353 K, heat treated at 873 and 1073 K with a free access of air for no less than 24 h at each stage. The stepwise heating alternated with dispersion. The maximum calcination temperature of the phosphate $CsZr_2(PO_4)_3$ was 1273 K.

The composition and structure of the resulting phosphates were confirmed by X-ray phase and X-ray fluorescence microprobe analyses and by IR spectroscopy. The X-ray phase analysis (DRON-3M, Cu_{K_α} radiation, 2θ = 10–50°) and the X-ray fluorescence microprobe analysis (Camebax analyzer with a Link AN-10000 energy-dispersion detector) of the samples demonstrated that they are homogenous, have nearly theoretical compositions, and their structure is NZP-like. The sets of interplanar spacings and unit cell parameters of the phosphates (see table) agree with the data in the PDF2 file. The positions and shapes of bands in the IR spectra of the samples are similar to those in [21] and are typical of orthophosphates.

To make samples suitable for heat conductivity measurements, the powders synthesized were compacted into cylinders. The porosity P (%) was estimated using the formula $P = (1 - \rho_a/\rho_X) \times 100$, where ρ_a and ρ_X are the apparent and X-ray densities of a sample, respectively. These densities and the porosity of the samples under study are listed in the table.

The heat conductivity of the phosphates was measured according to the technique [22] on cylindrical samples of diameter 15.0–16.1 mm and height 2.25–2.34 mm, using an IT-λ-400 device. The inaccuracy of the heat conductivity measurements was 8%.

The heat conductivity of the crystalline phosphates $Zr_{2.25}(PO_4)_3$, $NaZr_2(PO_4)_3$, $CsZr_2(PO_4)_3$, and $Na_5Zr(PO_4)_3$ was determined in air in the temperature range 298–673 K at 16 experimental points for each sample, with a temperature step of 25 K. The temperature dependences of the heat conductivity coefficient λ of the samples are shown in the figure. It is seen that, within the entire temperature range under study, the dependences show no features and the heat conductivity coefficient smoothly increases with temperature. The heat conductivities of $Zr_{2.25}(PO_4)_3$,

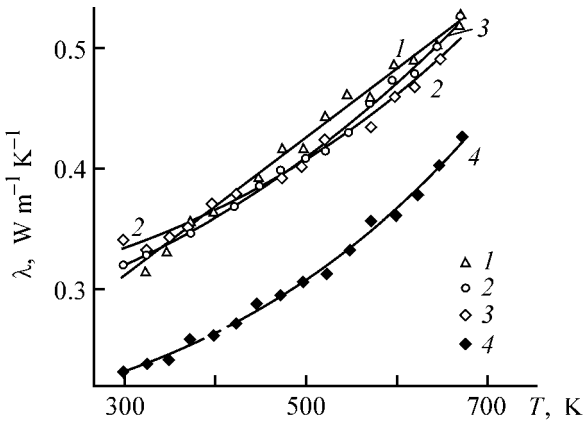

Heat conductivity coefficient λ of porous samples of NZP phosphates vs. temperature T. (*1*) $Zr_{2.25}(PO_4)_3$, (*2*) $NaZr_2(PO_4)_3$, (*3*) $CsZr_2(PO_4)_3$, and (*4*) $Na_5Zr(PO_4)_3$.

$NaZr_2(PO_4)_3$, and $CsZr_2(PO_4)_3$ are close to each other. Pentasodium-zirconium triphosphate has a somewhat lower heat conductivity, mainly owing to a different distribution of sodium ions in the crystal lattice as compared with other phosphates under study.

The temperature dependences of the heat conductivity coefficient λ–T of the samples studied can be described by the following semiempirical formulas:

$$\lambda_{Zr_{2.25}(PO_4)_3} = 0.14 + 0.00057T,$$

$$\lambda_{NaZr_2(PO_4)_3} = 0.23 + 2.58 \times 10^{-4}T + 3.88 \times 10^{-10}T^3,$$

$$\lambda_{CsZr_2(PO_4)_3} = 0.28 + 1.49 \times 10^{-4}T + 4.30 \times 10^{-10}T^3,$$

$$\lambda_{Na_5Zr(PO_4)_3} = 0.18 + 1.13 \times 10^{-4}T + 5.29 \times 10^{-10}T^3.$$

For each sample, the maximal deviation of experimental points from a smoothed λ–T curved did not exceed the inaccuracy of heat conductivity measurements.

The dashed line in the range 389–424 K in the curve describing the temperature dependence of the heat conductivity of $Na_5Zr(PO_4)_3$ corresponds to the region of a phase transition (T_{pt} = 406.9 K), which is associated with a change in the position ordering of sodium cations in voids of the structure skeleton under the action of temperature [23] and manifests itself in the temperature dependence of the specific heat [15, 17]. The transition was not seen in the curve for the heat conductivity of the sample under study, which seems to be due to a small change in energy in the phase transition ($\Delta_{pt}H^0$ = 4.32 kJ mol^{-1} [15, 17]) and to a 8% inaccuracy of the heat conductivity measurements.

The porosity of a system is an important factor, in addition to temperature, that determines its thermal characteristics. An increase in the porosity improves the heat-insulating properties of systems, and a decrease in this parameter enhances the corrosion resistance of the system. To make tentative conclusions concerning the value of high-density NZP ceramics for heat engineering, the heat conductivity of the samples under study at zero porosity was determined using the formula [24]

$$\lambda = \lambda_0 \frac{1 + 2V_a \dfrac{1 - \lambda_0/\lambda_a}{2\lambda_0/\lambda_a + 1}}{1 - V_a \dfrac{1 - \lambda_0/\lambda_a}{\lambda_0/\lambda_a + 1}}.$$

Here λ, λ_0, and λ_a are the heat conductivity coefficients of a porous body, solid phase, and gas (air) in pores, respectively; V_a is the volume fraction of pores in the porous body.

The calculated heat conductivity coefficients (W m^{-1} K^{-1}) at zero porosity in the range 298–673 K are as follows: 0.6–1.1 for $Zr_{2.25}(PO_4)_3$, 0.6–0.9 for $NaZr_2(PO_4)_3$, 0.7–1.1 for $CsZr_2(PO_4)_3$, and 0.4–0.7 for $Na_5Zr(PO_4)_3$.

In [18–20], densely sintered NZP ceramics (P < 5%) were used to measure the heat conductivity. For example, the heat conductivity of ceramics based on $Ca_{0.5}Zr_2(PO_4)_3$ was studied in [19]. It was found that, in the temperature range 298–873 K, the heat conductivity coefficient of $Ca_{0.9}Li_{0.2}Zr_4(PO_4)_6$, $Ca_{0.9}Mg_{0.1}Zr_4(PO_4)_6$, and $Ca_{0.9}Zr_{4.05}(PO_4)_6$ ceramic samples is 1.1–1.4 W m^{-1} K^{-1}. The heat conductivities of $Ca_{0.4}Mg_{0.1}Zr_2(PO_4)_3$ and $Ca_{0.25}Mg_{0.25}Zr_2(PO_4)_3$ ceramics, reported in [18] (λ = 0.6–0.7 W m^{-1} K^{-1} at 873 K), are much lower than those obtained in [19]. The heat conductivity coefficient of the dense ceramic $Sr_{0.5(1+x)}K_xZr_2(PO_4)_3$ at 298 K is 1.0 W m^{-1} K^{-1} [20]. The published values of the heat conductivity coefficients of NZP materials under study show a significant scatter, which is due to their chemical and phase composition, specific features of their crystal structure (valence state of ions, their distribution in a crystal lattice, kind and quantities of defects, and chemical bond nature) and microstructural organization (size, dispersity, and shape of grains; type of porosity), and methodological features of measurements. It is of interest that, despite this circumstance, NZP ceramics have a lower heat conductivity than the industrial stabilized zirconium dioxide (1.95–2.44 W m^{-1} K^{-1} in the range 373–1673 K [25]), which is the main ceramics-forming component of widely used refractories for heat-resistant elements of high-temperature furnaces.

The high melting points, low heat conductivity, ultralow heat expansion at almost zero expansion anisotropy, chemical stability, and radiation hardness allow NZP ceramics to be regardered as promising highly resistant refractories and heat insulators with a low heat conductivity, which outperform the known materials in their ability to withstand thermal shocks.

CONCLUSIONS

(1) The temperature dependences of the heat conductivity of porous phosphates $Zr_3(PO_4)_4$, $NaZr_2(PO_4)_3$, $CsZr_2(PO_4)_3$, and $Na_5Zr(PO_4)_3$, which crystallize in the structural type of sodium-dizirconium triphosphate (NZP), were studied in air in the temperature range 298–673. The temperature dependences of the heat

conductivity can be described with semiempirical linear and cubic equations.

(2) The calculated heat conductivity at zero porosity are equal to 0.6–1.1 W m^{-1} K^{-1} and are close to the heat conductivity of the known high-density NZP ceramics.

(3) Judging from their thermal properties, NZP ceramics are promising highly resistant refractory and heat-insulating materials, which are capable of working under conditions of abrupt temperature changes and high temperature gradients.

ACKNOWLEDGMENTS

This study was financially supported by the Russian Foundation for Basic Research (project nos. 02-03-32181 and 03-03-32538).

REFERENCES

1. Alamo, J., *Solid State Ionics*, 1993, vols. 63–65, pp. 547–561.
2. Hong, H.Y.-P., *Mater. Res. Bull.*, 1976, vol. 11, no. 2, pp. 173–182.
3. Scheetz, B.E., Agrawal, D.K., Breval, E., and Roy, R., *Waste Management*, 1994, vol. 14, no. 6, pp. 489–505.
4. Pet'kov, V.I. and Orlova, A.I., *Neorg. Mater.*, 2003, vol. 39, no. 10.
5. Pet'kov, V.I., Orlova, A.I., Sukhanov, M.V., *et al.*, *J. Mater. Sci. Lett.*, 2002, vol. 21, no. 6, pp. 513–516.
6. Roy, R., Agrawal, D.K., Alamo, J., and Roy, R.A., *Mater. Res. Bull.*, 1984, vol. 19, no. 4, pp. 471–477.
7. Pet'kov, V.I., Kir'yanov, K.V., Orlova, A.I., and Kitaev, D.B., *J. Therm. Anal. Cal.*, 2001, vol. 65, no. 2, pp. 381–389.
8. Breval, E. and Agrawal, D.K., *British Ceramic Transactions*, 1995, vol. 94, no. 1, pp. 27–32.
9. Govindan Kutty, K.V., Asuvathraman, R., and Sridharan, R., *J. Mater. Sci.*, 1998, vol. 33, no. 15, pp. 4007–4013.
10. Woodcock, D.A. and Lightfoot, P., *J. Mater. Chem.*, 1999, vol. 9, no. 11, pp. 2907–2911.
11. Pet'kov, V.I., Orlova, A.I., Kazantsev, G.N., *et al.*, *J. Therm. Anal. Cal.*, 2001, vol. 66, no. 2, pp. 623–632.
12. Warhus, U., Maier, J., and Rabenau, A., *J. Solid State Chem.*, 1988, vol. 72, no. 1, pp. 113–125.
13. Abello, L., Chlor, K., Barj, M., *et al.*, *J. Mater. Sci.*, 1989, vol. 24, no. 9, pp. 3380–3386.
14. Pet'kov, V.I., Kir'yanov, K.V., Orlova, A.I., and Kitaev, D.B., *Neorg. Mater.*, 2000, vol. 36, no. 4, pp. 478–483.
15. Pet'kov, V.I., Kir'yanov, K.V., and Asabina, E.A., *Zh. Fiz. Khim.*, 2003, vol. 77, no. 5, pp. 797–802.
16. Krishnaiah, M.V., Jose Joseph, Seenivasan, G., and Govindan Kutty, K.V., *J. Alloys Comp.*, 2003, vol. 351, no. 1–2, pp. 212–216.
17. Pet'kov, V.I., Asabina, E.A., Markin, A.V., and Kir'yanov, K.V., *Thermochim. Acta.*, 2003, vol. 403, no. 2, pp. 185–196.
18. US Patent 5102836.
19. Liu, D.-M., *J. Mater. Sci. Lett.*, 1994, vol. 13, no. 2, pp. 129–130.
20. Chem, C.-J., Lin, L.-J., and Liu D.-M., *J. Mater. Sci.*, 1994, vol. 29, no. 15, pp. 3733–3737.
21. Kurazhkovskaya, V.S., Orlova, A.I., Pet'kov, V.I., *et al.*, *Zh. Strukt. Khim.*, 2000, vol. 41, no. 1, pp. 74–79.
22. Platunov, E.S., *Teplofizicheskie izmereniya v monotonnom rezhime* (Thermal Measurements in a Monotonic Mode), Leningrad: Energiya, 1973.
23. Boilot, J.P., Collin, G., and Comes, R., *Solid State Commun.*, 1983, vol. 45, no. 3, pp. 231–235.
24. Kingery, W.D., *Introduction to Ceramics*, New York: Wiley, 1960.
25. Shevchenko, V.Ya. and Barinov, S.M., *Tekhnicheskaya keramika* (Technical Ceramics), Moscow: Nauka, 1993.

Russian Journal of Applied Chemistry, Vol. 77, No. 2, 2004, pp. 182–186. Translated from Zhurnal Prikladnoi Khimii, Vol. 77, No. 2, 2004, pp. 188–192.

INORGANIC SYNTHESIS AND INDUSTRIAL INORGANIC CHEMISTRY

A Study of Physicochemical Processes in Film-forming Ethanol Solutions of Zirconium and Cobalt Salts and Properties of Thin Films Obtained on Their Base

V. V. Kozik, E. B. Chernov, L. P. Borilo, O. V. Turetskova, and A. M. Shul'pekov

Tomsk State University, Tomsk, Russia

Received March 26, 2003

Abstract—The main physicochemical processes that occur in film-forming solutions based on zirconium oxochloride $ZrOCl_2 \cdot 8H_2O$, cobalt salts $CoCl_2 \cdot 6H_2O$ and $Co(NO_3)_2 \cdot 6H_2O$, and ethanol were studied. The intermolecular interaction in film-forming solutions was analyzed qualitatively and quantitatively.

Thin films find wide use as light-redistributing, protective, and decorative coatings [1]. Extensive studies intended to obtain new compositions of films, analyze their structure and properties, and extend application fields are being carried out in this country and abroad [2, 3]. Particular attention is paid to composite thin-film materials based on binary and ternary systems constituted by oxides of Group-IV elements [4, 5]. The properties of coatings of this kind are determined by the properties of the constituent oxides and their relative amounts. Films based on zirconium dioxide are promising because of their practically valuable properties: transparency and high refractive index, adhesion, thermal resistance, and chemical stability. However, the use of thin films based on zirconium dioxide is limited by the occurrence of polymorphic transformations, which affects the service characteristics and quality of films. Introduction of cobalt oxide into thin-film materials based on zirconium dioxide makes it possible to stabilize its structure and properties and vary widely the optical characteristics of the films.

This study is concerned with physicochemical processes that occur in film-forming solutions (FFS), qualitative and quantitative analysis of intermolecular interactions in solution, formation of thin films of the system ZrO_2–CoO, and examination of their properties.

EXPERIMENTAL

Thin films of double oxides of zirconium and cobalt were obtained by deposition from FFS based on 99% ethanol, zirconium oxochloride $ZrOCl_2 \cdot 8H_2O$, and cobalt salts $CoCl_2 \cdot 6H_2O$ or $Co(NO_3)_2 \cdot 6H_2O$. Ethanol was preliminarily dehydrated with calcium oxide, using the known procedure [6]. This is necessary for removing excess water, since the salts used contain crystallization water and its amount is sufficient to ensure a minor degree of hydrolysis in FFS. The excess amount of water, introduced with nondehydrated ethanol, enhances the hydrolysis, with the result that the working life of FFS becomes substantially shorter and a polymer is formed rapidly. The total concentration of the salts in the solutions was 0.4 M, the content of zirconium oxochloride was varied within the range 20–100 mol %.

The processes that occur in FFS were studied using viscometry (Ostwald viscometer), and the optical density of the solutions was measured with a KFK-2 photocolorimeter. The concentration dependence of reduced viscosity η_{sp}/c of an FFS based on zirconium oxochloride and cobalt nitrate was measured by diluting the initial FFS with ethanol, in the zirconium oxochloride concentration range 0.5–3.3 g dl^{-1}. The resulting concentration dependences of η_{sp}/c were processed using the method described in [7, 8].

Films were obtained on glass [GOST (State Standard) III-2001] and quartz substrates by centrifugation (rate of substrate rotation 1000–4000 rpm) and pulling from solution (pulling velocity 5 mm min^{-1}) at a temperature of 290–300 K. A thermal treatment of the films was done in two stages at 330 and 770–870 K. The optical characteristics of the films were studied on an LEF-3M laser ellipsometer and Specord-M40

1070-4272/04/7702-0182 © 2004 MAIK "Nauka/Interperiodica"

spectrophotometer; the adhesion was determined with a PMT-3 device.

The film-forming solutions based on $ZrOCl_2 \cdot 8H_2O$ are colorless; addition of cobalt chloride leads to appearance of a blue coloration, and that of cobalt nitrate makes the solution blue and violet. The composition of cobalt complexes in the FFS based on zirconium(IV) oxochloride and cobalt(II) nitrate was determined using data on the varied coloration of complex compounds of cobalt [9] and the Ostromyslenskii–Zhoba method [10]. Figure 1 shows how the optical density D of FFS at a wavelength of 670 nm varies with the content of cobalt nitrate. Probably, the existence of a varied coloration of FFS is associated with changes in the coordination of H_2O molecules and Cl^- ions around a Co^{2+} ion, with the blue color pointing to the presence of chloride complex anions $[CoCl_4]^{2-}$, and violet color, to that of a mixed complex $[Co(H_2O)_4Cl_2]$ [9]. It may be assumed that chloride complex species of composition $[CoCl_4]^{2-}$ predominate at a cobalt nitrate content in FFS lower than 33 mol %, and mixed-ligand complexes of composition $[Co(H_2O)_4Cl_2]$, at a higher content of cobalt nitrate (Fig. 1). The presence of cobalt(II)chloride complex species in FFS based on zirconium oxochloride and cobalt nitrate is accounted for by the high content of chloride ions formed in dissociation of zirconium oxochloride and also by the affinity of Co(II) for chloride ions.

The stability of the FFS viscosity with time is technologically important for obtaining films with reproducible properties. Therefore, the viscosity can serve as a criterion of suitability of a solution for film formation. The viscosity of FFS commonly varies with time in three stages, which correspond to ripening, region of stable properties, and aging through gelation and polymerization [11]. For the FFS based on zirconium oxochloride the three stages are preserved; the variation of the specific viscosity of this solution is shown in Fig. 2, curve *1*. The solution ripening takes 4 days, during which alcoholysis and hydrolysis occur, and oxozirconium(IV) ions, which exhibit high affinity for oxygen, are bound together by the alcohol molecules by ol (–OH) and oxol (–O–) bonds. The film-forming capacity of alcoholic solutions based on zirconium oxochloride is due to the presence of hydroxo complex of zirconium of the composition $[Zr(OH)_2(C_2H_5OH)_x(H_2O)_{4-x}]Cl_2$ [11]. Since Zr(IV) shows strong tendency toward formation of polynuclear compounds, particle condensation occurs in FFS to give more complex macromolecules, and, consequently, the viscosity changes.

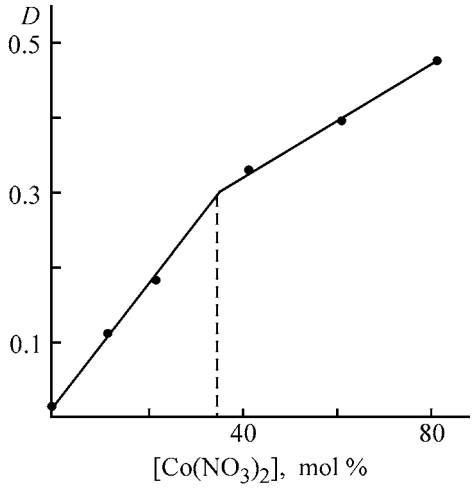

Fig. 1. Optical density D of an FFS based on zirconium oxochloride vs. the content of cobalt nitrate, $[Co(NO_3)_2]$.

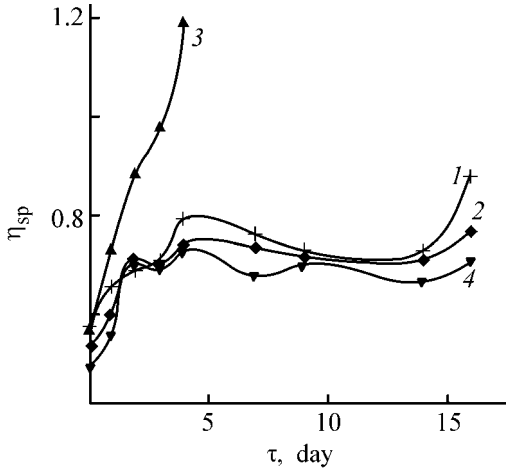

Fig. 2. Specific viscosity η_{sp} of an FFS based on zirconium oxochloride and cobalt chloride vs. the storage time τ. $CoCl_2$ content (mol %): (*1*) 0, (*2*) 50, (*3*) 80, and (*4*) 100.

Introduction of cobalt(II) chloride into an FFS based on zirconium oxochloride in amount of up to 70 mol % has no pronounced effect on the variation of viscosity with time (Fig. 2, curve *2*). At $CoCl_2$ content in FFS of 80 or 90%, the specific viscosity is anomalously high, and these solutions turn into gels already after 1.5 months (Fig. 2, curve *3*). In an FFS with 80 mol % $CoCl_2$, there are four cobalt atoms per zirconium atom, and, therefore, a complex tetrameric particle, in which each zirconium atom is bound to four cobalt atoms, can serve as a polymerization center [12]. The alcoholysis processes that occur in parallel lead to formation of larger macromolecules.

The affinity of cobalt for oxygen is low, and the probability of formation of ol and oxol bonds is considerably lower as compared with zirconium. There-

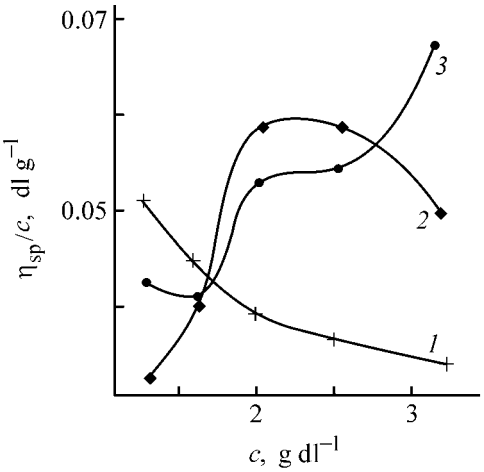

Fig. 3. Reduced viscosity of FFS, η_{sp}/c, vs. its concentration c. $Co(NO_3)_2$ concentration (g dl^{-1}): (*1*) 0, (*2*) 10, and (*3*) 20.

fore, the specific viscosity is lower, too (Fig. 2, curve *4*). The aging of a solution of this kind begins after 14 months.

It should be noted that processes in FFS with zirconium(IV) oxochloride and cobalt(II) nitrate are similar to those in film-forming solutions with zirconium(IV) oxochloride and cobalt(IV) chloride salts.

Taking into account the fact that the FFS based on zirconium oxochloride are polymer solutions, the approach described in [7] can be used to obtain quantitative characteristics of the interaction of macromolecules in solution. To describe the concentration dependence of the reduced viscosity η_{sp}/c, the authors of [7] employed a linear extrapolation equation (Huggins equation)

$$\eta_{sp}/c = [\eta]a + k'[\eta]^2c \quad (1)$$

and nonlinear extrapolation equations

$$\eta_{sp}/c = a + b\exp(-dc), \quad (2)$$

$$\eta_{sp}/c = a + b_1\exp(-d_1c) + b_2\exp(-d_2c), \quad (3)$$

where a, b_i, and d_i are empirical solvation coefficients, which depend on the dipole momentum and donor and acceptor numbers of a solvent and have a dimensionality of molar volume.

Various functions applicable to description of empirical concentration dependences of viscosity make it possible to determine the numerical values of the characteristic viscosity $[\eta]$.

The variation of the reduced viscosity of an FFS based on zirconium(IV) oxochloride (Fig. 3, curve *1*) can be described using Eqs. (1)–(3). The Huggins constants k' and the characteristic viscosities, calculated for this solution by three equations, are listed in Table 1. The Huggins constant has an unrealistic value ($k' = -2.41$), which is probably due to the presence of hydrogen bonds in solution. As indicated by variances and correlation coefficients, Eq. (3) describes the given experimental dependence the most precisely, and, consequently, the significant value of the characteristic viscosity is 0.102 dl g^{-1}. The variation of the reduced viscosity of an FFS based on zirconium oxochloride with addition of cobalt nitrate (Fig. 3, curves *2* and *3*) is also described more precisely by Eq. (3). The Gibbs energies of solvation (kJ mol^{-1}), calculated using the values of $[\eta_{sp}]$ for the FFS under study, are listed in Table 2. The interaction of the forming hydroxo complex of zirconi-

Table 1. Viscometric parameters of FFS based on zirconium(IV) oxochloride

Equation	η, dl g^{-1}	k'	Equation	η, dl g^{-1}	Equation	η, dl g^{-1}
(1)	0.059	–2.41	(2)	0.137	(3)	0.102

Table 2. Effect of the composition of an FFS based on zirconium(IV) oxochloride and cobalt(II) nitrate on the viscometric parameters

$Co(NO_3)_2$, mol %	a	b_1	b_2	ΔG_a	ΔG_{b_1}	ΔG_{b_2}	d_1	d_2	$[\eta]$, dl g^{-1}
				kJ mol^{-1}					
0	0.145	–0.150	0.107	3.5	–3.64	2.60	0.063	0.686	0.102
10	0.310	–0.301	0.018	28.4	–27.60	1.65	0.050	0.046	0.027
20	0.114	–0.222	0.129	13.4	–26.18	15.21	0.160	0.050	0.021

um(IV) with the solvent occurs by both the donor–acceptor and ionic mechanisms. In an FFS that contains only zirconium(IV) oxochloride, there are insignificant electrostatic (ΔG_a = 3.5 kJ mol^{-1}) and specific donor–acceptor interactions (ΔG_{b_1} = 3.61, ΔG_{b_2} = 2.60 kJ mol^{-1}). This circumstance is accounted for by the fact that zirconium(IV) tends to form complex 3*D* polymeric structures to a greater extent and has high characteristic viscosity. Introduction of cobalt(II) nitrate strongly affects the Gibbs energies (Table 2): ΔG_a, ΔG_{b_1}, and ΔG_{b_2} increase and the characteristic viscosity decreases, which is due to the lower ability of cobalt(II) to form polymeric structures and to the enhancement of intermolecular interaction forces in solution. Thus, the film-forming capacity is characterized by formation of a microheterogeneous system in the FFS, and this may affect the thickness of the films obtained and their adhesion to a substrate.

Applying an FFS to a substrate and carrying out a thermal treatment yields thin films of zirconium(IV) and cobalt(II) oxides [12]. It has been established in previous studies (X-ray phase analysis) that films with cobalt(II) oxide content below 10 mol % are solid solutions based on the cubic modification of zirconium dioxide, and those with >10 mol % cobalt(II) oxide, a mixture of zirconium(IV) and cobalt(II) oxides [5]. The physicochemical properties of the films obtained are listed in Table 3. The tendency for zirconium to produce 3*D* polymeric structures leads to formation of thicker films. Raising the content of Co(II) oxide yields thinner films and makes lower their adhesion to a substrate, in agreement with the change in the structure of the hydroxo complex and the decrease in viscosity. The less pronounced affinity of cobalt for oxygen and the high extent of intermolecular interactions in solution lead to a poor adhesion of cobalt oxide films to glass substrates.

Table 3. Physical properties of films obtained from FFS based on zirconium(IV) oxochloride and cobalt(II) nitrate (substrate, glass)

CoO, mol %	Refractive index *n*	Film thickness *d*, nm	Adhesion, kg mm^2
0	2.1600	105.0	69.3
10	2.0875	102.5	56.5
20	2.0211	100.2	56.5
60	1.9907	80.9	31.0
80	1.8916	63.1	28.2

The absorption edge of zirconium oxide films lies at 220 nm, which allows their use as cutoff filters that eliminate the hard UV radiation. By changing the relative amounts of zirconium and cobalt oxides, the transmission coefficient of the films in the UV and in the visible can be varied widely (Fig. 4). Introduction of cobalt(II) oxide makes stronger the absorption not only in the UV range, but also in the visible, with the films remaining uniform and homogeneous. In this case, the color of a glass substrate with a deposited film of zirconium(IV) and cobalt(II) oxides changes from transparent to dark brown, which makes it possible to control the intensity of sunlight, obtain coatings with sun-protective effect, and adjust the spectral composition of light sources in the UV range and in the visible [13. 14].

Figure 5 shows how the refractive index of the films depends on their thickness. Films of thickness 50–100 nm have a higher refractive index. Probably, this

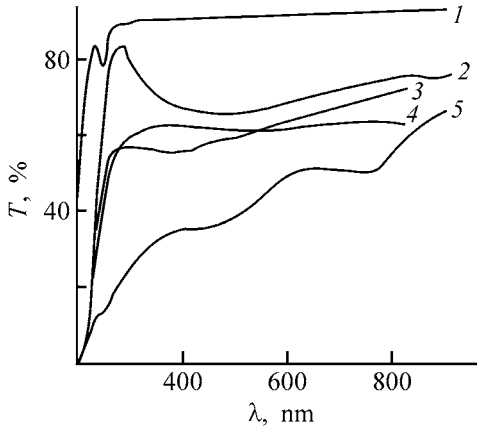

Fig. 4. Transmission spectra of films on quartz substrates. (λ) Wavelength. (*1*) Quartz substrate; films obtained from FFS with varied content of cobalt(II) nitrate (mol %): (*2*) 0, (*3*) 20, (*4*) 30, and (*5*) 50.

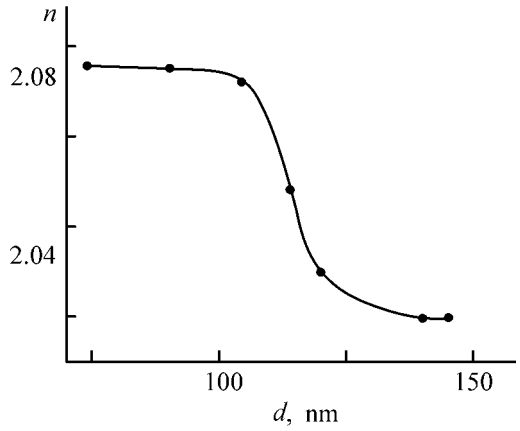

Fig. 5. Refractive index *n* of films obtained from FFS with cobalt chloride content of 10 mol % vs. the film thickness.

Table 4. Influence exerted by the content of cobalt(II) chloride and nitrate on the refractive index of films obtained from FFS based on zirconium(IV) oxochloride (substrate, glass)

CoO, mol %	Refractive index *n* obtained with a salt indicated		CoO, mol %	Refractive index *n* obtained with a salt indicated	
	$CoCl_2 \cdot 6H_2O$	$Co(NO_3)_2 \cdot 6H_2O$		$CoCl_2 \cdot 6H_2O$	$Co(NO_3)_2 \cdot 6H_2O$
20	2.075	2.021	40	2.025	1.881
30	2.089	1.950	50	1.959	1.930

occurs because of the formation of a metastable cubic modification of zirconium dioxide, which may be due to a manifestation of a confinement effect, which leads to stabilization of high-temperature phases in nanosystems [15].

The choice of the starting cobalt(II) salt (chloride, nitrate) has no effect on the chemical stability and color of a film. However, use of cobalt(II) chloride makes the refractive index of the films approximately 4.5% higher (Table 4), which indicates that the films obtained have higher density. This may be due to different compositions of cobalt complexes in the FFS (chloride, mixed-ligand), whose decomposition under thermal treatment affects the structure of a forming oxide film.

CONCLUSIONS

(1) Thin films of the system ZrO_2–CoO were obtained by deposition from film-forming solutions and their physicochemical properties (refractive index, thickness, transmission spectra, adhesion to substrate) were determined.

(2) It was shown that the composition of the starting cobalt salt (chloride, nitrate) and the film thickness affect the refractive index. Films of the system ZrO_2–CoO are promising as coatings protecting biological objects from the UV radiation and as decorative and sunlight-protecting coatings.

REFERENCES

1. Saifulin, R.S., *Neorganicheskie kompozitsionnye materialy* (Inorganic Composite Materials), Moscow: Khimiya, 1983.
2. Min'ko, N.I., Mikhal'chuk, I.N., and Lipko, M.Yu., *Steklo Keram.*, 2000, no. 4, pp. 3–7.
3. Borilo, L.P., *Tonkoplenochnye neorganicheskie nanosistemy* (Thin-Film Inorganic Nanosystems), Tomsk: Tomsk. Univ., 2003.
4. Mal'chik, A.G., Borilo, L.P., and Kozik, V.V., *Zh. Prikl. Khim.*, 1996, vol. 69, no. 2, pp. 224–227.
5. Borilo, L.P., Shul'pekov, A.M., and Turetskova, O.V., *Steklo Kerami.*, 2002, no. 4, pp. 30–31.
6. Voskresenskii, P.I., *Tekhnika laboratornykh rabot* (Manual of Laboratory Works), Moscow: Khimiya, 1973.
7. Safronov, S.M., Berezina, E.M., Terent'eva, G.A., *et al.*, *Vysokomol. Soedin.*, 2001, vol. 43B, no. 4, pp. 751–754.
8. Bogoslovskii, A.Yu., Pribytkov, E.G., Terent'eva, G.A., *et al.*, *Zh. Prikl. Khim.*, 1998, vol. 71, no. 2, pp. 294–300.
9. Nekrasov, B.V., *Osnovy obshchei khimii* (Fiundations of General Chemistry), Moscow: Khimiya, 1973, vol. 2.
10. Kumok, V.N. and Skorik, N.A., *Laboratornye raboty po khimii kompleksnykh soedinenii* (Laboratory Works on Chemistry of Complex Compounds), Tomsk: Tomsk. Univ., 1983.
11. Kozik, V.V., Borilo, L.P., and Shul'pekov, A.M., *Zh. Prikl. Khim.*, 2000, vol. 73, no. 11, pp. 1872–1876.
12. *Khimiya i tekhnologiya redkikh i rasseyannykh elementov* (Chemistry and Technology of Rare and Trace Elements), Bol'shakov, K.A., Ed., Moscow: Vysshaya Shkola, 1976, part 2.
13. Suikovskaya, N.V., *Khimicheskie metody polucheniya tonkikh prozrachnykh pokrytii* (Chemical Methods for Obtaining Thin Transparent Coatings), Leningrad: Khimiya, 1971.
14. *Physics of Thin Films. Advances in Research and Development*, vol. 5, Hass, G. and Thun, R.E., Eds., New York: Academic, 1967.
15. Uvarov, N.F. and Boldyrev, V.V., *Usp. Khim.*, 2001, vol. 70, no. 4, pp. 307–329.

Russian Journal of Applied Chemistry, Vol. 77, No. 2, 2004, pp. 187–191. Translated from Zhurnal Prikladnoi Khimii, Vol. 77, No. 2, 2004, pp. 193–196.

INORGANIC SYNTHESIS AND INDUSTRIAL INORGANIC CHEMISTRY

Continuous Process for Obtaining Carbon Nanofibers

E. G. Rakov, S. N. Blinov, I. G. Ivanov, E. V. Rakova, and N. G. Digurov

Mendeleev Russian University of Chemical Engineering, Moscow, Russia

Shubnikov Institute of Crystallography, Russian Academy of Sciences, Moscow, Russia

Received July 1, 2003

Abstract—A continuous laboratory installation with a horizontal reactor for obtaining carbon nanofibers by catalytic pyrolysis of methane was developed and tested. The conversion of methane at 600°C was studied and the nanofiber output capacity of the continuous installation under the optimal conditions on a Ni–La_2O_3 catalyst was determined.

Carbon nanofibers and nanotubes exhibit a number of properties which have attracted close attention of scientists and technologists in recent years. These materials have a developed surface and possess good mechanical and emission characteristics, are electrically conducting, and can be used as catalyst supports, sorbents, and components of supercapacitors and composites [1, 2]. However, the application of these materials is hindered by their high cost, which is due to the expensiveness of some preparation techniques (e.g., spark procedure [3]) and poor development of simpler methods. Moreover, the overwhelming majority of articles, reports, and patents devoted to synthesis of carbon nanofibers and nanotubes describe batch methods of synthesis, despite that use of continuous techniques makes it possible to diminish dramatically the production cost [4].

The most promising in this regard are pyrolytic methods, which can use low-cost hydrocarbons as starting compounds and do not require high temperature [1, 2, 5]. Fluidized-bed reactors can be used for performing the process. The fluidized-bed reactors for catalytic pyrolysis have been created in China [6–9]; laboratory installations have been tested in the Netherlands [10] and in France [11, 12]. The daily output capacity of the Chinese reactors has been brought to 50 kg of a carbon material containing 70–80% nanotubes.

However, the continuous process in a fluidized bed involves hydrodynamic limitations, since the initial particles of the catalyst are "overgrown" with the product, markedly increase in volume, and their density changes. In the process, the bed volume increases manyfold. The authors of designs mentioned above partly eliminated these limitations by the "nanoagglomeration" method [6–9]. It remains unclear whether or not this could ensure a truly continuous operation. The author of [10] mentioned the difficulties encountered in developing a stable pseudo-fluidized bed in the stage of catalyst reduction by hydrogen and carried out the reduction in a fixed filter bed. Chinese researchers also separated the process into two stages: catalyst reduction and pyrolysis proper, which made the procedure batch-like.

A simpler way to perform continuous pyrolytic synthesis with considerably less pronounced hydrodynamic limitations (or without any limitations at all) consists in use of horizontal tubular reactors with a continuous motion of a bed of a solid material. Preliminary calculations demonstrated that reactors of this kind may have a relatively high output capacity at comparatively small dimensions [13, 14].

The aim of the present study was to test a continuous installation with a horizontal tubular reactor for obtaining carbon nanofibers.

EXPERIMENTAL

Carbon fibers were synthesized by deposition of carbon from the gas phase on a Ni–La_2O_3 catalyst with Ni content of 23 wt %. The catalyst was prepared from $Ni(NO_3)_2 \cdot 6H_2O$ (analytically pure), $La(NO_3)_3 \cdot 6H_2O$, and citric acid (both chemically pure). As starting carbon-containing raw material was

1070-4272/04/7702-0187 © 2004 MAIK "Nauka/Interperiodica"

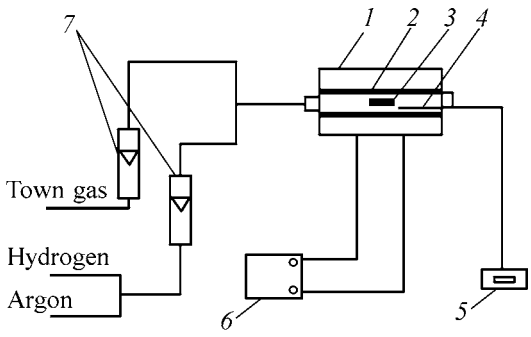

Fig. 1. Schematic of a batch installation for carbon deposition from the gas phase. (*1*) Electric furnace, (*2*) reactor, (*3*) boat with catalyst, (*4*) thermocouple, (*5*) millivoltmeter, (*6*) transformer, and (*7*) rotameters.

used town gas containing 98–99% methane and admixtures of water vapor and mercaptans. Distilled water was used to prepare solutions and wash the product to remove the acid.

The composition of the catalyst and methods of its synthesis were closely similar to those described in [15], with the only exception that the Ni : La atomic ratio was taken to be 5 : 6, against 1 : 2 in [15]. The catalyst was prepared by two procedures. In the first variant, 1.94 g of $Ni(NO_3)_2 \cdot 6H_2O$, 3.45 g of $La(NO_3)_3 \times 6H_2O$, and 2.00 g of citric acid were mixed, and the mixture was dissolved in 20 ml of water. Water was evaporated from the solution, and the residue was dried at 80°C. The resulting powder was calcined in air at 700°C for 5 h to give catalyst no. 1. The second variant of catalyst preparation consisted in burning of the initial mixture. A mixture of nitrates and citric acid was dissolved in water, with 1 ml of water taken per 1.2 g of the mixture, to give a transparent solution. The solution was placed in a furnace heated to 600°C. The product was extracted 15 min after the combustion was complete (catalyst no. 2). To test the continuous reactor, 100 g of the catalyst was synthesized by the second procedure, with the above-mentioned reagent proportions and modes preserved.

An installation comprising a feeding and gas-flow controlling unit, a temperature controlling unit, and a stainless steel reactor was used in the study (Fig. 1). The experiment was performed by passing successively from a small batch reactor (inner diameter 28 mm, length 200 mm) to a larger batch reactor (54 and 400 mm, respectively), and then to a continuous reactor (54 and 1000 mm). A Kipp generator or a cylinder with a nitrogen–hydrogen mixture served as sources of hydrogen. The gas flow rate was monitored with flow meters or rotameters. The temperature in the reactors was monitored with a Chromel–Alumel thermocouple connected to an MPShchPr-54 millivoltmeter with scale-division value of 20°C.

A quartz or ceramic boat with a weighed portion of a catalyst prepared by the first method was placed in batch reactors. The catalyst was reduced in a flow of hydrogen or a nitrogen–hydrogen mixture, with a reactor heated from 20°C to a required temperature and kept for varied time. Then methane was fed into the reactor and, after a prescribed time elapsed, the reactor was cooled in a flow of methane.

The resulting product was weighed and washed with 10% nitric acid at 60°C for 4 h, to remove the catalyst. The purified product was washed with distilled water to remove nitric acid. The amount of the product formed was determined by weighing the samples before and after an experiment.

An X-ray phase analysis was carried out on a DRON-3M diffractometer (Cu_{K_α} radiation, nickel filter, accelerating voltage 20 kV). The morphology and structure of the product were studied with a JEM-100C transmission electron microscope and Tesla BS-340 scanning electron microscope. A derivatographic analysis was performed on an MOM derivatograph (Hungary) at a rate of temperature rise in the range from 1 to 10 deg min^{-1}. The specific surface area of the samples was determined by the method of thermal desorption of nitrogen.

Catalyst samples prepared using different methods were subjected to an X-ray phase analysis. An analysis of the diffraction patterns obtained demonstrated that sample no. 1 is composed of a phase to which a formula $LaNiO_3$ corresponds, with rhombohedral crystal lattice [16]. Catalyst no. 2 contains, in addition to the $LaNiO_3$ phase, trace amounts of other phases. The specific surface area of catalyst nos. 1 and 2 was 36 and 25 $m^2 g^{-1}$, respectively.

Experiments in the small batch reactor at a temperature of 600°C and conditional linear flow velocity of methane of 70 cm min^{-1} (calculated without taking into account the thermal expansion of the gases) with sample no. 1 of mass 0.4 g demonstrated that making longer the process duration leads to a rise in the specific output of the solid product, with this rise terminating in 20–30 min. The catalyst was preliminarily reduced in a flow of the nitrogen–hydrogen mixture, with the reactor heated to 600°C and kept at this temperature for 15 min. The resulting solid product was in the form of bent nanofibers 15–60 nm in di-

ameter (prevalent diameter 25–35 nm), with ~96% purity. Catalyst particles were present at the ends of nearly all the fibers. The final specific output of the fibers was 4.6 g g_{cat}^{-1}.

To determine the dependence of the specific output of fibers on the catalyst bed thickness, different weighed portions of catalyst no. 1 were distributed uniformly over the same area and placed in the reactor (five different samples at a time), with the sample weight increasing or decreasing along the direction of gas flow in the reactor. The experiment was performed at a temperature of 600°C and a conditional linear flow velocity of methane equal to 70 cm min^{-1} in the course of 30 min, with the catalyst preliminarily reduced in a flow of the nitrogen–hydrogen mixture. It was found that this dependence shows an extremum (Fig. 2), with the run of the curve independent of the order in which the samples studied are arranged along the gas flow direction and the maximum reached at a bed thickness of about 1 mm). The rise in the specific output with increasing bed thickness is presumably due to the influence of intermediates formed in methane pyrolysis, and the decrease after reaching the maximum value, to hindered delivery of methane to lower layers of the catalyst bed.

Raising the conditional linear flow velocity of methane within the range 10–30 cm min^{-1} at a catalyst bed thickness of about 1 mm, temperature of 600°C, and preliminary reduction of the catalyst in a flow of H_2 at 600°C for 20 min led to an increase in the specific output, which was as high as 8.8 g g_{cat}^{-1} at a flow velocity of 30 cm min^{-1}. At the same time, raising the flow rate entails a decrease in methane conversion (Fig. 3). The optimal conditional linear flow velocity of methane is 20 cm min^{-1}, at which the specific output is 7.0–8.4 g g_{cat}^{-1}. In this case, the methane conversion is close to 65%.

It is noteworthy that experiments without preliminary reduction of the catalyst yielded the same results. The method used to synthesize the catalyst also affects the specific output and the characteristics of the carbon product only slightly.

The results obtained for the batch reactors were used in testing a continuous reactor (Fig. 4), in which a counterflow motion of gaseous and solid products was organized. The latter were moved by means of vibration.

An output capacity of 5 g h^{-1} or 3.2 g g_{cat}^{-1} h^{-1} was achieved at a temperature of 600°C, conditional linear flow velocity of methane equal to 20 cm min^{-1},

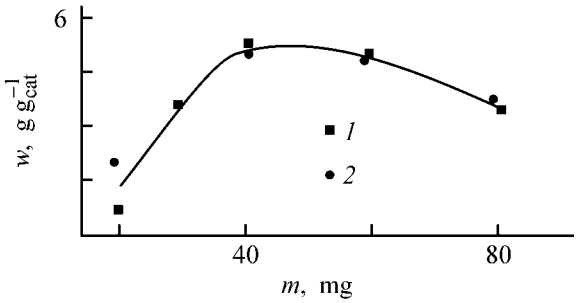

Fig. 2. Specific output *w* of the solid product vs. catalyst mass *m*. Fixed distribution area 220 mm^2, *T* = 600°C, linear flow velocity of methane 70 cm min^{-1}, τ = 30 min. Sample arrangement along the direction of methane flow in the reactor: (*1*) in order of increasing catalyst bed thickness and (*2*) in decreasing order.

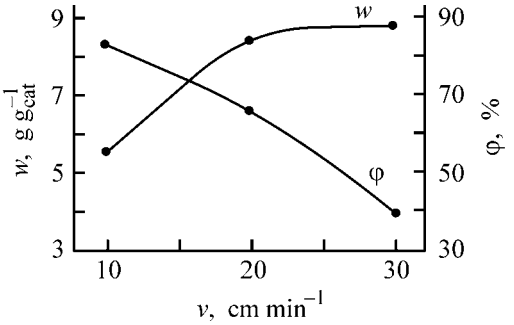

Fig. 3. Effect of the conditional flow velocity *v* of methane on pyrolysis characteristics: specific output *w* and methane conversion φ. τ = 30 min, *T* = 600°C.

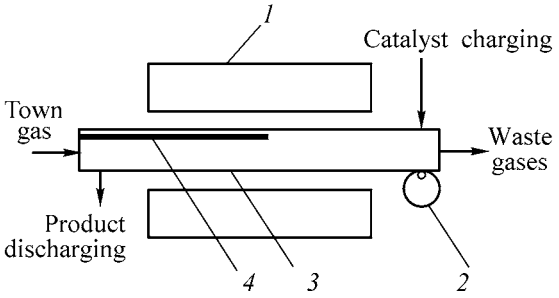

Fig. 4. Schematic of a continuous installation for carbon deposition from the gas phase. (*1*) Electric furnace, (*2*) vibration generator, (*3*) reactor, and (*4*) thermocouple.

catalyst bed thickness of about 1 mm, and a duration of residence of the solid material in the working zone of the reactor equal to 30 min. This value was 10 times that for the batch installations.

The particles of the product obtained in the continuous reactor are rounded and have sizes ranging from 1 to 10 mm. An analysis of their micrographs demonstrated that the particles are constituted by in-

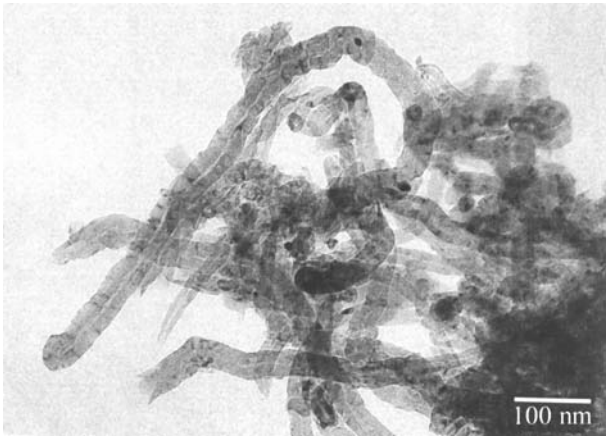

Fig. 5. Micrograph of nanofibers obtained on the continuous installation by pyrolysis of methane on the catalyst Ni–La_2O_3.

terwoven fibers with conical walls (Fig. 5). The fibers show wide scatter in diameter, from 15 to 60 nm, and, occasionally, even 100 nm and more. Catalyst particles not dissolved in washing are contained within some of the fibers.

The specific surface area of the fibers obtained was 105 $m^2 g^{-1}$. The X-ray diffraction patterns of the fibers show a signal corresponding to an angle of 26.25°, which is characteristic of the interplanar spacing d_{002} of multilayer carbon nanotubes and nanofibers, and exceeds somewhat that of graphite.

As follows from the derivatograms obtained, active oxidation of the samples in air begins at a temperature of about 450°C. The content of amorphous carbon and sorbed gases, which are removed at temperatures that are considerably lower than the combustion onset temperature of the product, does not exceed 2% of the original mass of a sample. The incombustible residue, whose content is about 0.5–1.0%, is composed of the catalyst undissolved in washing (nickel particles).

CONCLUSIONS

(1) Pyrolysis of methane was studied in laboratory horizontal tubular batch reactors at a temperature of 600°C and a conditional linear flow velocity of methane equal to 70 cm min^{-1} on a fixed bed of a Ni–La_2O_3-based catalyst preliminarily reduced in a flow of a nitrogen–hydrogen mixture. It was found that the specific output of a solid product reaches its maximum value of 4.6 g g_{cat}^{-1} in 30 min.

(2) It was established, using scanning and transmission electron microscopy, that carbon is deposited onto the catalyst in the form of nanofibers 15 to 60 nm in diameter, with conical walls. Catalyst particles are situated at fiber ends.

(3) It was found that the dependence of the specific output on the catalyst bed thickness shows an extremum, with the highest output capacity at a bed thickness of 1 mm.

(4) It was established that raising the conditional linear flow velocity of methane at a temperature of 600°C and catalyst bed thickness of about 1 mm leads to an increase in the specific output of fibers, which reaches its maximum value at a velocity of 30 cm min^{-1}. In this case, the conversion of methane is 40%. The optimal combination of the output capacity of the catalyst and of the conversion of methane is achieved at methane flow velocity of 20 cm min^{-1}.

(5) The process of pyrolysis in a continuous reactor was tested. The maximum output capacity was 5 g h^{-1} or 3.2 g g_{cat}^{-1} h^{-1}.

ACKNOWLEDGMENTS

The study was in part supported financially by the Russian Foundation for Basic Research (grant no. 01-03-33225) and Ministry of Education of the Russian Federation (“Chemical Technology” Program, project no. 06.06.017).

REFERENCES

1. Fenelonov, V.B., *Poristyi uglerod* (Porous Carbon), Novosibirsk: Inst. Kataliza, 1995.
2. Rakov, E.G., *Usp. Khim.*, 2001, vol. 70, no. 10, pp. 934–972.
3. Rakov, E.G., *Usp. Khim.*, 2000, vol. 69, no. 1, pp. 41–59.
4. De Jong, K.P. and Geus, J.W., *Catal. Rev. Sci. Eng.*, 2000, vol. 42, no. 4, pp. 481–510.
5. Chesnokov, V.V. and Buyanov, R.A., *Usp. Khim.*, 2000, vol. 69, no. 7, pp. 675–692.
6. Luo, G., Li, Z., Wei, F., *et al.*, *Physica B*, 2002, vol. 323, pp. 314–317.
7. Wang, Y., Wei, F., and Luo, G., *Physica B*, 2002, vol. 323, pp. 327–329.
8. Li, Z., Luo, G., Wei, F., and Wang, Y., *Chinese J. Process Eng.*, 2002, vol. 2, no. 3, pp. 224–229.
9. Wang, Y., Wei, F., Luo, G., *et al.*, *Chem. Phys. Lett.*, 2002, vol. 364, nos. 5–6, pp. 568–572.
10. Nijkamp, M., Hydrogen Storage Using Physisorption: Modified Carbon Nanofibers and Related Materials, *Dissertation*, Utrecht, 2002.

11. Venegoni, D., Serp, Ph., Feurer, R., *et al.*, *Carbon*, 2002, vol. 40, no. 10, pp. 1799–1807.
12. Morançais, A., Corrias, M., Serp, Ph., *et al.*, *203rd Meeting Electrochem. Soc.*, Paris, France, Apr. 27–May 2, 2003, *Preprint.*
13. Abashev, R. *et al.*, Nanotechnologies in the Area of Physics, Chemistry and Biotechnology, *5th ISTC SAC Seminar: Proc.*, St. Petersburg, Russia, May 27–29, 2002, St. Petersburg: Ioffe Inst., 2002, pp. 171–174.
14. Rakov, E.G. *et al.*, Abstracts of Papers, *1-aya Mezhdunarodnaya konferentsiya "Uglerod: fundamental'nye problemy nauki, materialovedenie, tekhnologiya" 17–19 oktyabrya 2002 g., Moskva* (1st Int. Conf. "Carbon: Fundamental Problems of Science, Materials Science, and Technology," Moscow, October 17–19, 2002), Moscow, 2002, p. 170.
15. Liang, Q., Gao, L.Z., Li, Q., *et al.*, *Carbon*, 2001, vol. 39, no. 6, pp. 897–903.
16. Golub, A.M., Sidorik, L.S., Nedil'ko, S.A., and Fedoruk, T.I., *Izv. Akad. Nauk SSSR, Neorg. Mater.*, vol. 14, no. 10, pp. 1866–1869.

Russian Journal of Applied Chemistry, Vol. 77, No. 2, 2004, pp. 192–195. Translated from Zhurnal Prikladnoi Khimii, Vol. 77, No. 2, 2004, pp. 197–200.

INORGANIC SYNTHESIS AND INDUSTRIAL INORGANIC CHEMISTRY

Influence Exerted by Pyrite Impurity in the Initial Graphite on Properties of Residual Graphite Hydrosulfates

A. P. Yaroshenko, M. V. Savos'kin, A. N. Magazinskii, and L. Ya. Galushko

Litvinenko Insitute of Physicoorganic Chemistry and Coal Chemistry, Ukrainian National Academy of Sciences, Donetsk, Ukraine

Received September 8, 2003

Abstract—The influence exerted by the particle size and the distribution of sol impurities in the initial graphite, and also by pyrite additives, on the properties of residual graphite hydrosulfates synthesized by oxidation in the CrO_3–H_2SO_4 system was studied.

Graphite hydrosulfate compounds, which expand under heating, are widely used in diverse areas [1–3]. Commonly, compounds of this kind are obtained by liquid-phase chemical oxidation of natural flaked graphite with a strong inorganic oxidant [e.g., HNO_3, CrO_3, $K_2Cr_2O_7$, $(NH_4)_2S_2O_8$, H_2O_2, and O_3] in a concentrated sulfuric acid to give a graphite hydrosulfate $C_{24n}^{+} \cdot HSO_4^{-} \cdot mH_2SO_4$, where n is the stage of the graphite intercalation compound (number of graphene layers between two adjacent intercalate layers). Further, the resulting graphite hydrosulfate is commonly treated with water and dried [4]. The final product is residual graphite hydrosulfate (RGH), a compound in which the sulfuric acid molecules solvating a hydrosulfate anion in the interlayer space of the graphite matrix are replaced with water molecules.

Data on the influence exerted by sol impurities in the initial natural flaked graphite on the expansion coefficient K_{sw} of RGH obtained from it are scarce. In all probability, this is due to the fact that the RGH produced is mostly intended for fabrication of flexible sheet graphite, with thermally or chemically decalcified natural flaked graphite commonly used as raw material. Another possible reason is that a large excess of oxidant and sulfuric acid with respect to graphite has been used previously to perform oxidation of the initial graphite in RGH production. In these conditions, the presence of sol impurities has virtually no effect on the K_{sw} of the final product.

Recently, a number of economical high-tech methods for manufacture of RGH have been developed, in which the consumption of reagents in production of graphite hydrosulfate (GH) is extremely low, i.e., less than 100 parts (by weight) of oxidant and concentrated sulfuric acid per 100 parts by weight of initial graphite. Such low-consumption methods have been developed, in particular, for the intercalating systems HNO_3–H_2SO_4 [5] and CrO_3–H_2SO_4 [4, 6, 7]. For the latter system, it was of interest to study the influence exerted by the particle size and ash content of the initial natural graphites on the course of oxidation and on the characteristics of the resulting product.

As raw material for synthesis of RGH were used samples of GT-1 [GOST (State Standard) 4596–75], GL-1 (GOST 5279–74), and GE-1 (GOST 7478–75) natural flaked graphites from the Zaval'evskoe deposit, differing in the sieve analyses and contents of sol impurities. The granulometric composition and ash content of the natural graphite samples conformed to GOST 17818.2–90 and GOST 17818.4–90, respectively. A FRITSCH GMBH Analysette 3 vibration sizing screen was used. A chemical analysis of sol residues obtained by heating of the initial graphite samples in air at 900°C to constant mass was done according to GOST 2642.0-14–86. Graphite hydrosulfates were synthesized using a 50% aqueous solution of chromium(IV) oxide (ρ = 1.501 g cm^{-3}) and chemically pure sulfuric acid with 95.8 wt % pure substance (ρ = 1.835 g cm^{-3}).

The initial graphite and its fractions were oxidized under the standard conditions in a cylindrical glass reactor equipped with a T-shaped stainless steel stirrer. The process was performed at room temperature without forced heating or cooling. The reactor was charged with 25 g of graphite powder, the stirrer was switched on, and 2.5 cm^3 of chromium(VI) oxide aqueous solu-

1070-4272/04/7702-0192 © 2004 MAIK "Nauka/Interperiodica"

Table 1. Granulometric composition P and ash content A^d of GT-1, GE-1, and GL-1 graphite samples

Particle size, mm	GT-1		GE-1		GL-1	
	P	A^d	P	A^d	P	A^d
	wt %					
–1.000 + 0.630	0.10	5.10	0.00	–	0.00	–
–0.630 + 0.315	22.10	5.21	1.90	6.12	0.80	6.26
–0.315 + 0.200	74.30	5.31	9.80	5.09	7.50	7.04
–0.200 + 0.160	3.30	5.30	15.30	5.29	20.10	7.75
–0.160 + 0.100	0.10	6.15	27.50	6.14	32.70	8.29
–0.100 + 0.063	0.05	8.40	23.90	8.39	24.70	11.35
–0.063	0.05	20.22	21.60	20.23	14.20	23.20
Initial graphite		5.68		9.68		10.43

tion was added. After the graphite was stirred with an aqueous solution of oxidant for 10 min, 12 cm^3 of sulfuric acid was added, and the mixture was continuously stirred for 10 min more. Then, 1.5 dm^3 of water was added to the oxidized graphite, and the resulting mixture was allowed to stay for 24 h, for hydrolysis to occur. The solid phase was filtered in a vacuum of a water-jet pump and washed with water to pH 5–6. The washed product was dried at 100–110°C to moisture content not exceeding 1.0 wt %.

The influence exerted by pyrite additives in the initial graphite on the properties of the RGH obtained were studied with natural pyrite from the Uchaly deposit (Ural, Russia). The pyrite fraction with 97 wt % pure substance and 0.074 + 0.043-mm particles was used. A weighed portion of pyrite was added to the initial graphite, the mixture obtained was stirred for 10 min, and RGH was synthesized under the standard conditions.

For the RGH samples synthesized, the yield and the expansion coefficient at 500°C, K_{sw}^{500} ($cm^3\ g^{-1}$), were determined. The intercalate content of the product, m_i (wt %), was calculated from the product yield on the assumption that phase oxidation of graphite does not occur under the synthesis conditions [8], i.e., the whole amount of carbon passes from the graphite matrix into the final product.

The expansion coefficient was calculated by the following procedure. A weighed portion (m = 0.2–0,3 g) of the product was introduced into a stainless steel container, which was preliminarily installed in a muffle furnace preheated to 500°C, and was kept there for 5 min till complete expansion. The container with the thus expanded graphite was withdrawn from the furnace, its contents were carefully transferred to a volumetric glass cylinder, and the volume V (cm^3) occupied by the expanded graphite was measured. The expansion coefficient was calculated from the expression $K_{sw}^{500} = V/m$ as the arithmetic mean of three parallel measurements.

The granulometric composition, content of sol impurities, and their fractional distribution for natural flaked graphite of the brands studied are listed in Table 1, and the chemical composition of the ash residues in GT-1, GE-1 and GL-1 graphites, in Table 2.

The dependence of the expansion coefficient of RGH on the average size of the initial graphite particles used for RGH synthesis is shown in Fig. 1. If the particles of the initial graphite have the same size, the expansion coefficients of the RGH samples synthesized from different brands of natural graphites virtually coincide. To a first approximation, two linear portions, 0–0.2 and 0.2–0.5, can be distinguished in

Table 2. Chemical composition of sol residues in natural flaked graphite from the Zaval'evskoe deposit

Ash component	Content in graphite, wt %		
	GT-1	GE-1	GL-1
SiO_2	56.60	56.00	53.80
Al_2O_3	24.00	22.80	20.80
Fe_2O_3	11.30	12.80	16.50
MgO	3.40	3.30	3.40
CaO	2.50	2.80	2.20
TiO_2	0.65	0.72	0.86
P_2O_5	0.40	0.50	0.90
Na_2O, K_2O	0.60	0.50	1.00
Residue	0.55	0.58	0.54

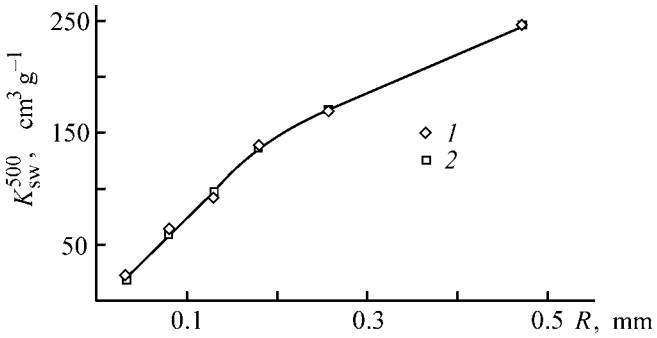

Fig. 1. Expansion coefficient K_{sw}^{500} of residual graphite hydrosulfates vs. the average particle size R of the initial graphite used for its synthesis. Initial graphite: (*1*) GL-1 and (*2*) GE-1.

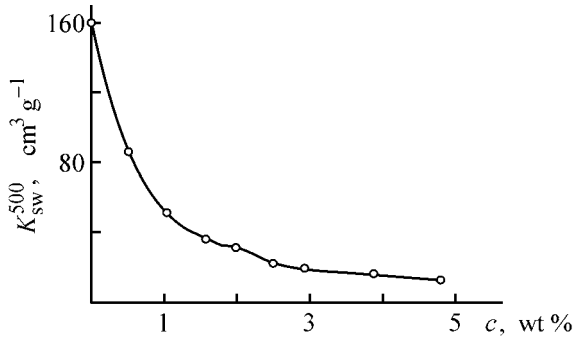

Fig. 2. Expansion coefficient K_{sw}^{500} of residual graphite hydrosulfates vs. the pyrite content c in its mixture with GT-1 initial graphite.

the dependence in question, with the slope of the first portion exceeding that of the second.

It may be assumed *a priori*, that, in the course of graphite intercalation, particles of different sizes interact with the intercalating solution independently. In this case, the expansion coefficient should be an additive quantity, i.e., the relation $K_{sw} = \Sigma(K_{swi}\alpha_i)$ should be valid for the overall expansion coefficient of RGH. In this relation, K_{swi} is the expansion coefficient of the RGH sample obtained from *i*th graphite fraction, and α_i is its share in the graphite. Unexpectedly, the additivity law is not obeyed for the GL-1 and GE-1 initial graphites. The experimental expansion coefficients were found to be substantially lower than the calculated additive values (Table 3). Successive removal of fractions from the initial graphite showed that, when the finest fraction (particle size less than 0.063 mm) is removed, the additivity law is fulfilled completely, i.e., the calculated values well coincide with the experimental data (Table 3). This indicates that all the graphite fractions, except that with particle size less than 0.063 mm, exhibit independent behavior in the course of intercalation. However, the presence of this fine fraction makes smaller the expansion coefficient of RGH obtained from coarser fractions. Such a behavior of the fine fraction may be due to the fact that its ash content exceeds by a factor of 2–4 that in other fractions (Table 1).

Table 3. Experimental and calculated expansion coefficients of RGH samples synthesized from Gl-1, GE-1, and GL-1 initial graphites and from those with the <0.063-mm fraction removed

Graphite	K_{sw}^{500}, cm^3 g^{-1}	
	Experimental	Calculated
Initial:		
GL-1	62	92
GE-1	45	88
Without <0.063-mm fraction		
GL-1	103	104
GE-1	105	107

Analysis of the mineral composition of sol residues of the graphite samples studied (Table 2) suggests that such a behavior of the fine fraction is associated with the increased content of pyrite in it. This assumption is confirmed by the high content of iron oxide (11–16 wt % Fe_2O_3) in the sol residue. Pyrite is a strong reducing agent: oxidation of 1 mol of pyrite requires up to 6 mol of chromium(VI) oxide. This means that, under the synthesis conditions used in this study, virtually the whole amount of the oxidant may be spent for oxidation of pyrite present in the finest graphite fraction. As a result, a considerable amount of oxidant introduced into the reaction zone is spent for side processes, rather than for the main reaction of graphite intercalation. Removal of the finest fraction from the initial graphite decreases the ash content in it by 30–50 wt %. This leads to a virtually twofold increase in the expansion coefficient (Table 3) [9] and to fulfillment of the additive law mentioned above.

To confirm the above argumentation concerning the negative influence exerted by pyrite present in the initial graphite on the formation of graphite hydrosulfate, a number of artificial mixtures of GT-1 graphite with a fine-grained natural pyrite were oxidized. GT-1 graphite was chosen because it is virtually free of the fine fraction (Table 1).

As can be seen from the data obtained (Fig. 2), the intercalate content in the final product and the expansion coefficient steeply decrease as the content of pyrite in the mixture with initial graphite grows. On adding even about 0.5 wt % pyrite to graphite,

the expansion coefficient of RGH decreases by approximately a factor of 2.

CONCLUSIONS

(1) In synthesis of residual graphite hydrosulfate in the CrO_3–H_2SO_4 system, the expansion coefficient grows with increasing particle size of the initial graphite.

(2) The sol impurities are distributed in natural flotation graphites nonuniformly. Approximately half of sol impurities is concentrated in particles less than 0.063 mm in size.

(3) Owing to the increased content of sol impurities, the fine graphite fraction (≤0.063 mm) suppresses the intercalation of coarser particles.

(4) Removal of particles less than 0.063 mm in size from the initial graphite leads to an increase in the expansion coefficient of the final product.

(5) The main mineral component of graphite, which is responsible for the consumption of an oxidant in the side reactions and for suppression of the graphite intercalation, is pyrite. The presence of even a minor amount of pyrite in the reaction mass results in a sharp decrease in the expansion coefficient of the residual graphite hydrosulfate.

ACKNOWLEDGMENTS

The authors are grateful to V.A. Sapunov for the provision of a sample of natural pyrite.

REFERENCES

1. Inagaki, M., *J. Mater. Res.*, 1989, vol. 4, no. 6, pp. 1560–1568.
2. Setton, R., *Synth. Met.*, 1989, vol. 23, nos. 1–4, pp. 267–273, 511–524.
3. Chung, D.D.L., *J. Mater. Sci.*, 1987, vol. 22, no. 12, pp. 4190–4198.
4. Yaroshenko, A.P., Popov, A.F., and Shapranov, V.V., *Zh. Prikl. Khim.*, 1994, vol. 67, no. 2, pp. 204–211.
5. US Patent 4895713.
6. Yaroshenko, A.P., and Savos'kin, M.V., *Zh. Prikl. Khim.*, 1995, vol. 68, no. 8, pp. 1302–1306.
7. RF Patent 2058261.
8. Horn, D., and Boehm, H.-P., *Z. anorg. allgem. Chem.*, 1979, vol. 456, no. 9, pp. 117–129.
9. Ukrainian Patent 35711.

Russian Journal of Applied Chemistry, Vol. 77, No. 2, 2004, pp. 196–200. Translated from Zhurnal Prikladnoi Khimii, Vol. 77, No. 2, 2004, pp. 201–205.

INORGANIC SYNTHESIS AND INDUSTRIAL INORGANIC CHEMISTRY

Effect of Phase Composition on Sulfuric Acid Leaching of Tantalum-containing Alloys

S. A. Krasikov, V. M. Chumarev, M. N. Sviridova, L. Yu. Udoeva, M. V. Timofeev, A. V. Safonov, V. D. Fedorov, and O. A. Arzhatkina

Institute of Metallurgy, Ural Division, Russian Academy of Sciences, Yekaterinburg, Russia
"All-Union Research Institute of Chemical Technology" State Unitary Enterprise, Moscow, Russia

Received July 3, 2002; in final form, September 2003

Abstract—Phase composition of iron-based tantalum–niobium alloys (Ta 2–5, Nb 3–6, Si up to 12, C 1.4–2.4%) was studied. The kinetics of leaching of ferroalloys with H_2SO_4 aqueous solutions and with mixtures of sulfuric and hydrofluoric acids was considered. The conditions of hydrochemical treatment of the alloys, which make it possible to concentrate niobium and tantalum in the solid residue through dissolution of up to 94% of Fe, 90% of Mn, and 70% of Si, were found.

In pyrometallurgical dressing of low-grade tantalum–niobium raw materials of complex composition, rare metals are isolated into an iron-based alloy [1, 2]. Such alloys can be converted to chemical tantalum-niobium concentrates by their direct leaching with mineral acid solutions [1]. However, the processes of acid dissolution of such alloys have been insufficiently studied.

Among the known studies are those devoted to a formal-kinetic description of leaching of a carbidized tantalum–niobium ferroalloy with a mixture of hydrochloric and nitric acids [3] and to analysis of the phase composition of the products formed in decomposition of niobium-containing ferrophosphorus with oleum [4]. According to published data, the intensity and the order of dissolution of alloy components strongly depend on the composition of the metal phase, temperature, and reagent expenditure.

The aim of this study was to analyze the phase composition of silicon-containing iron-based tantalum–niobium alloys and to determine the optimal conditions of their leaching with solutions of H_2SO_4 and mixtures of H_2SO_4 and HF.

EXPERIMENTAL

The chemical composition of the alloys under study is illustrated in Table 1. The alloys were powdered by spraying a liquid metal with compressed air [5]. This technique is effective in alloy preparation for hydrochemical treatment, because it is insensitive to mechanical properties of a metal (hardness and ductility) and yields powders with grain size of 80 to 150 μm.

Table 1. Chemical composition of alloys

Alloy no.	Content, wt %							
	Ta	Nb	W	Ti	Fe	Mn	Si	C
1	4.8	3.2	0.7	1.5	71.3	3.8	12.0	1.4
2	5.5	4.9	0.5	1.5	70.8	5.2	6.4	2.4
3	4.0	3.3	0.4	0.7	79.7	3.9	0.7	2.0
4	2.9	5.6	0.3	0.6	59.2	20.3	4.1	2.0

1070-4272/04/7702-0196 © 2004 MAIK "Nauka/Interperiodica"

Table 2. Results of X-ray fluorescence microprobe analysis of alloys

Alloy no.	Phase	Content, wt %						
		Ta	Nb	W	Ti	Fe	Mn	Si
1	Base	0.1	1.1	0.5	0.5	75.3	4.5	12.7
	Carbide	40.1	40.1	1.4	14.2	1.6	0.05	<0.1
2	Base	–	0.9	0.4	0.1	75.9	6.0	6.7
	Carbide	25.2	54.1	0.8	9.4	0.7	0.05	0.1
3	Base	<0.1	<0.1	–	<0.1	84.6	1.3	0.8
	Carbide	49.6	37.2	–	2.1	<0.1	<0.1	0.01
4	Base	<0.1	<0.1	–	<0.1	58.4	23.6	5.6
	Carbide	35.4	45.4	–	4.6	<0.1	<0.1	<0.1

An examination of alloy particles on a Cameca X-ray fluorescence microanalyzer demonstrated that the constituent elements are selectively distributed between two phases (Table 2). The first phase ("base") contains mainly iron, manganese, and silicon. In the second phase (carbide), which forms irregularly shaped inclusions 3–25 μm in size, the total tantalum, niobium, and tungsten constitute more than 99%.

The results of an X-ray diffraction analysis were in agreement with the data of the X-ray fluorescence microanalysis. According to the X-ray diffraction patterns obtained on a DRON-2.0 diffractometer, iron and manganese are contained in the samples as metals and silicides, and niobium and tantalum, as carbides. The revealed phase distribution of elements and the known resistance of tantalum and niobium carbides to mineral acids [6] confirmed that tantalum and niobium can be concentrated by a hydrochemical technique in a solid residue, a carbide cake.

Alloys were leached in a fluoroplastic temperature-controlled reactor with a mechanical stirrer and a reflux condenser. The stirring rate was 95 rpm. The pulp formed in leaching was filtered, and the solid residue was washed with water and dried. The resulting cakes were analyzed for the content of iron, silicon, tantalum, niobium, and other elements contained in the alloys under study.

It was found in leaching of alloy no. 1 with sulfuric acid solutions that, at a solid-to-liquid ratio s : l = 1 : 5, varying the H_2SO_4 concentration in the range from 50 to 300 g l^{-1}, leaching duration from 2 to 6 h, and temperature from 60 to 100°C affects the dissolution process only slightly. The degree of leaching, α (%), expressed as a relative change in the weight of a solid, $\alpha = 100(G_0 - G)/G_0$, does not exceed 10%, with mainly iron dissolved. The pulps formed are poorly filterable owing to the gelation of the silicic acid. Addition of oxidizing agents, H_2O_2 or HNO_3, to the solution scarcely affects the value of α. Moreover, addition of nitric acid results in an appreciable decrease in the concentration of iron in the solution.

Additional grinding of alloy nos. 1 and 2 in a vibratory mill to a grain size of 20–40 μm made it possible to increase the degree of their leaching (concentration of H_2SO_4 300 g l^{-1}, s : l = 1 : 10, T = 100°C, τ = 6 h) to 20 and 50%, respectively (Fig. 1, curves *1* and *2*). Under these conditions, but without additional grinding, the degree of leaching of alloy nos. 3 and 4 was 70–80%. It should be noted that the reaction of the alloy with the H_2SO_4 solution is the most intensive during the first 60 min. By the end of this period, the degree of leaching at 100°C was 9% for alloy no. 1, 43% for alloy no. 2, and 60–70% for alloy nos. 3 and 4.

The temperature dependences of the leaching rate $\Delta\alpha/\Delta\tau$ during the first 60 min of the process at

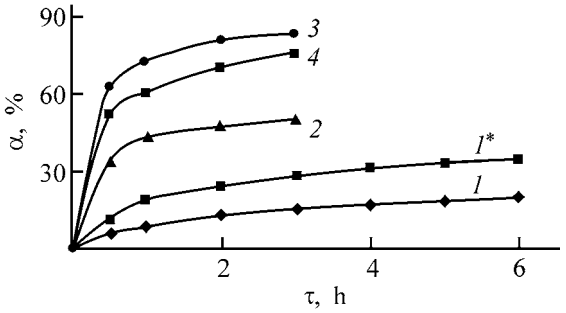

Fig. 1. Kinetics of leaching of tantalum–niobium ferroalloys in sulfuric acid solutions at 100°C. (α) Degree of leaching and (τ) time. Grain size (μm): (*1*, *2*) 20–40, (*1**) less than 20, and (*3*, *4*) 80–100. *Digits at the curves* correspond to alloy numbers in Table 1; the same for Fig. 2.

Table 3. Leaching of alloy no. 4 with H_2SO_4 solutions (T = 100°C, s : l = 1 : 10, τ = 1 h)

Experiment no.	Grain size, μm	H_2SO_4, g l^{-1}	α, %	Content in solid residue, wt %		Degree of recovery into solution, %	
				Fe	Mn	Fe	Mn
1	<30	50	15	43.2	16.3	39.4	32.0
2	<30	150	60	27.9	5.3	81.6	89.6
3	<30	300	74	13.3	–	94.3	–
4	80–150	150	41	28.5	–	72.3	–
5	80–150	300	60	13.9	5.7	90.8	88.8

80–100°C were described using the Arrhenius equation (Fig. 2).

The apparent activation energies E^* of leaching were found to be 32.1 and 29.9 kJ mol^{-1} for alloy nos. 1 and 2, respectively; and less than 15 kJ mol^{-1} for alloy nos. 3 and 4. These values indicate that the process occurs in the intermediate region, which is typical of complex heterogeneous systems. The diffusion hindrance is predominant in the case of alloy nos. 3 and 4, and chemical resistance, which grows with increasing silicide content [7], dominates for alloy nos. 1 and 2.

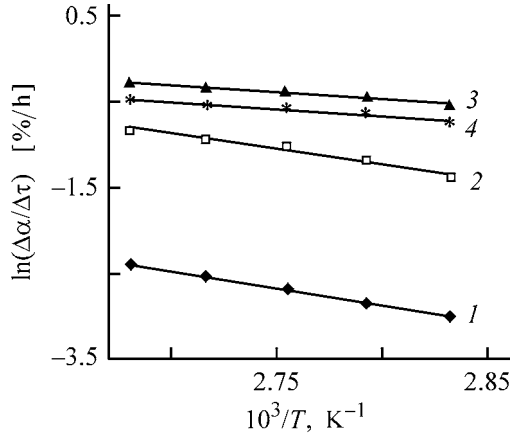

Fig. 2. Effect of temperature T on the rate of alloy leaching, $\Delta\alpha/\Delta\tau$.

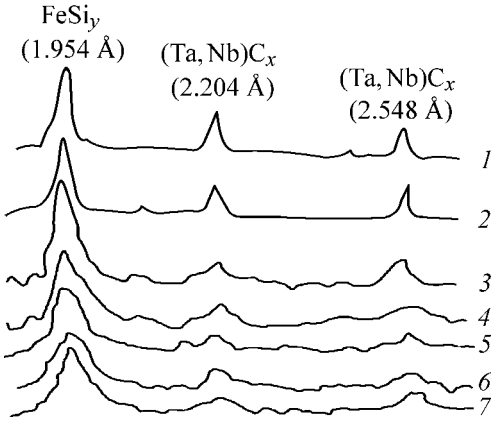

Fig. 3. X-ray diffraction patterns of alloy no. 1 ground to varied extent. Grain size (μm): (*1*) 150 (liquid-phase dispersion), (*2*) 20–40 (vibratory mill) and (*3–7*) <20 (planetary mill). Duration of treatment in a planetary mill (min): (*3*) 1, (*4*) 3, (*5*) 5, (*6*) 6, and (*7*) 9.

To raise the process rate, alloy no. 4 was ground in a vibratory mill to a particle size ≤30 μm, which resulted in an increase in the degree of leaching by 14–19%. The recovery of iron and manganese into solution was 90–94%, whereas rare metals and silicon were concentrated in the solid residue (Table 3).

The influence exerted by the duration of mechanical activation on the process of leaching with sulfuric acid solutions was studied using samples of the most acid-resistant alloy no. 1. A significant disruption of intercrystallite bonds in an alloy treated in a planetary mill, compared with the initial state, were revealed by X-ray phase analysis (Fig. 3). The number of active centers on the particle surface increases as the duration of activation in a planetary mill is made longer, which is manifested in the X-ray patterns as "smoothening-out" of the peaks related to iron silicides. The most pronounced changes were observed when the particle size was reduced to 20 μm and less. As can be seen from Fig. 1 (curve *1**) acid treatment of samples ground in a planetary mill for 8–12 min results that the degree of leaching increases to 35%.

Thus, the study of sulfuric-acid leaching demonstrated that the presence of silicon in an amount exceeding 10% prevents satisfactory dissolution of the components of the alloy even when it is finely ground. This hinders practical use of sulfuric leaching of alloys with high content of silicon.

In this context, it was of interest to study the leaching of alloy nos. 1 and 2 with a mixture of H_2SO_4 and HF. It was found that raising the concentration of hydrofluoric acid in the mixture H_2SO_4 + HF does not

Table 4. Leaching of alloy no. 1 with a mixture of sulfuric and hydrofluoric acids (T = 100°C, s : l = 1 : 10, τ = 1 h)

Experiment no.	H_2SO_4, g l^{-1}	HF, g l^{-1}	α, %	Content in solid residue, wt %			Degree of recovery into solution, %		
				Fe	Mn	Si	Fe	Mn	Si
1	50	2	5.8	71.9	–	12.6	5.3	–	1.3
2	50	4	6.7	71.4	–	12.5	6.9	–	3.1
3	50	12	10.0	70.1	3.8	12.6	11.7	8.8	5.7
4	50	20	18.9	63.8	–	11.9	27.6	–	19.6
5	50	40	28.5	50.3	3.6	9.5	49.7	32.2	43.5
6	300	2	11.0	69.1	3.7	14.3	14.0	12.7	0.1
7	300	4	12.4	70.0	3.6	13.5	14.3	16.4	1.5
8	300	12	17.0	66.1	3.5	12.2	23.3	22.3	15.6
9	300	20	34.0	57.6	–	11.6	46.9	–	36.1
10	300	40	54.0	41.1	3.5	8.1	73.6	57.8	69.2

Table 5. Leaching conditions of tantalum–niobium ferroalloys (T = 80–100°C)

Silicon content in alloy, wt %	Treatment procedure
10–15	Grinding in a planetary mill to <20 μm grain size; concentration, g l^{-1}: 150–300 H_2SO_4, 20–40 HF
5–10	Vibratory grinding to a <70 μm grain size; concentration, g l^{-1}: 150–300 H_2SO_4, 5–10 HF
<5	Dispersion of liquid alloys or crushing to <200 μm; concentration of H_2SO_4 150–300 g l^{-1}

intensify appreciably the leaching of ground alloys with particle size of 20–40 μm (Fig. 4). The effect is enhanced as the concentration of H_2SO_4 is raised from 50 to 300 g l^{-1} (Table. 4).

Silicon passes into the liquid phase in considerable amounts at HF concentrations of 20 g l^{-1} or more. The maximum recovery of silicon into solution in leaching of alloy no. 1 is about 70%.

As expected, the recovery of rare elements into solution in all the experiments was not greater than 0.4%, and their content in solid residues increased as the duration of alloy treatment was prolonged and the concentration of acid solutions was made higher. For example, a 6-h leaching of alloy no. 2 with a mixture of H_2SO_4 and HF resulted in that the content of Ta and Nb in the cakes formed was 27.4 and 23.8%, respectively.

The conditions under which a carbide cake 3–5-fold enriched with tantalum and niobium is obtained are listed in Table 5.

The experimental data on leaching of alloy nos. 1, 2 in mixtures of sulfuric and hydrofluoric acids indicate that the components interact in a certain order: fluoride ions react with iron and manganese silicides to form readily soluble compounds [8] only after removal of metal iron and manganese from the alloys. Hence, the treatment of the alloys should be started with a H_2SO_4 solution only, and continued with a

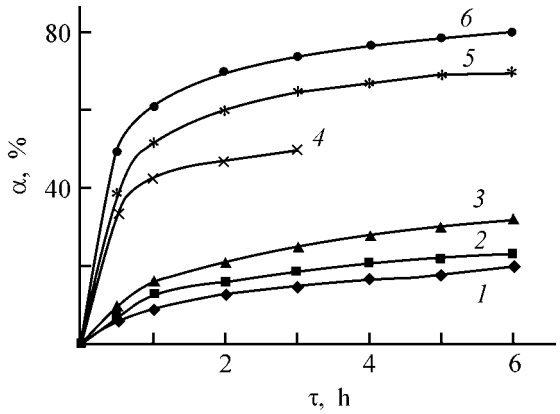

Fig. 4. Degree α of leaching of alloy nos. 1 and 2 with a mixture of H_2SO_4 and HF at various HF concentrations vs. time τ. H_2SO_4 concentration 300 g l^{-1}. HF concentration (g l^{-1}): (*1*, *4*) 0, (*2*, *5*) 5, and (*3*, *6*) 10. Alloy: (*1*–*3*) no. 1, and (*4*–*6*) no. 2.

mixture of H_2SO_4 and HF, which should appreciably decrease the consumption of hydrofluoric acid for leaching of high-silica alloys.

The expenditure for leaching can be diminished by a partial replacement of hydrofluoric acid with fluorine-containing compounds that form complex ions $[MF_x]^{n-}$ (M = Si, Fe, etc., $x > 1$). The experiments performed in this study demonstrated that, when H_2SiF_6 (10% relative to the alloy mass) is employed as a fluorine-containing reagent, the degree of leaching is virtually the same as in the case when an equivalent (in terms of fluorine ions) amount of hydrofluoric acid is used.

CONCLUSIONS

(1) The main phases of tantalum–niobium ferroalloys are carbides of rare metals, metallic iron and manganese, and their silicides. Tantalum, niobium, and tungsten constitute more than 99% in the carbide phases, whereas the total content of other elements is not greater than 1%.

(2) Leaching of tantalum-niobium-silicon-containing ferroalloys with sulfuric acid solutions occurs in the outer-diffusion region. As the silicon content in an alloy increases, its chemical resistance grows, which is due to the higher strength of chemical bonding in silicides.

(3) Extra grinding and addition of hydrofluoric acid and(or) fluorine-containing reagents to a sulfuric acid solution intensify the leaching of alloys that contain more than 5% Si.

(4) Leaching with a mixture of sulfuric and hydrofluoric acids makes it possible to transfer into solution up to 94% of iron, 90% of manganese, and 70% of silicon and to obtain a product 3–5-fold enriched with Ta and Nb, depending on the initial content of silicon in the alloys.

REFERENCES

1. Rockenbauer, W. and Starck, H.C., *Metal "W.–Berlin,"* 1984, vol. 38, no. 2, pp. 156–159.
2. Chumarev, V.M., Okunev, A.I., Krasikov, S.A., *et al.*, *Tsvetn. Met.*, 1995, no. 2, pp. 22–24.
3. Baram, I.I. and Yarkov, A.A., *Izv. Vyssh. Uchebn. Zaved., Tsvetn. Metal.*, 1971, no. 2, pp. 79–81.
4. Gromov, P.B., Lebedeva, L.P., and Lagunova, V.F., *Zh. Prikl. Khim.*, 1994, vol. 67, no. 5, pp. 730–736.
5. Akimenko, V.B., Bulanov, V.Ya., Zalazinskii, G.G., and Gulyaev, I.A., *Metallurgiya zheleznykh i legirovannykh poroshkov* (Metallurgy of Iron and Alloyed Powders), Moscow: Metallurgiya, 1992.
6. Kolchin, O.P., *Niobii i tantal: Oblasti osvoennogo i vozmozhnogo primeneniya* (Niobium and Tantalum: Areas of Commercial and Prospective Applications), Moscow: VINITI, 1959.
7. Vol'dman, G.M. and Zelikman, A.N., *Teoriya gidrometallurgicheskikh protsessov* (Theory of Hydrometallurgical Processes), Moscow: Metallurgiya, 1993.
8. Zelikman A.N., *Metallurgiya tugoplavkikh redkikh metallov* (Metallurgy of Refractory Rare Metals), Moscow: Metallurgiya, 1986.

Russian Journal of Applied Chemistry, Vol. 77, No. 2, 2004, pp. 201–204. Translated from Zhurnal Prikladnoi Khimii, Vol. 77, No. 2, 2004, pp. 206–209.

INORGANIC SYNTHESIS AND INDUSTRIAL INORGANIC CHEMISTRY

Composition and Properties of Magnesium-containing Metallurgic Slimes

I. N. Lipunov, A. S. Teploukhov, M. S. Kovel', I. A. Yupatov, V. V. Tetyukhin, and V. I. Alikin

Ural State Forestry Engineering University, Yekaterinburg, Russia

Academy of Standardization, Metrology, and Certification, Ural Branch, Yekaterinburg, Russia

Verkhne-Salda Metallurgical Industrial Association Open Joint-Stock Company, Verkhnyaya Salda, Yekaterinburg oblast, Russia

Received September 11, 2003

Abstract—Elemental, chemical, phase, and radionuclide composition of magnesium-containing slimes formed in the electrolytic production of metallic magnesium was studied. The binding properties of the slime were analyzed and the possibility of its use as a chloromagnesian binder was demonstrated.

One of ecological problems of large Russian industrial centers is the increasing amount of nonutilizable solid waste. Its storage and disposal have negative ecological, economical, and social impacts on both the environment and the human health.

Among industrial wastes of plants of nonferrous metallurgy, magnesium-containing slimes formed in the production of metallic magnesium are of special interest from the viewpoint of their being involved into further technological processing to give technical-grade products [1, 2]. The electrolytic production of magnesium involves a two-stage dehydration of carnallite:

$$KCl \cdot MgCl_2 \cdot 6H_2O = KCl \cdot MgCl_2 \cdot 2H_2O + 4H_2O$$

(first stage, 90°C),

$$KCl \cdot MgCl_2 \cdot 2H_2O = KCl \cdot MgCl_2 + 2H_2O$$

(second stage, 240°C).

When carnallite is fused and the melt is heated in chlorinators to 750–800°C, the remaining water is removed. In this case, $MgCl_2$ is partly hydrolyzed to give MgO, which is separated from the melt by settling. The slime formed in the process is poured into an ingot mold and, after cooling, stored in the form of a monolithic stock in slime pits.

One of possible ways to utilize slime consists in its reprocessing into a chloromagnesian binder. Inorganic binders with magnesian type of hardening are known [3, 4] to have good physicotechnical characteristics. They have found wide application in the metallurgical, chemical, and refractory branches of industry. Recently, magnesian binders have also been used to prepare wood-mineral composite construction materials [5, 6]. However, the increased sensitivity of the technology of magnesian binders to the activity of magnesium oxide and also the insufficient knowledge of the mechanisms by which basic processes of magnesian stone formation occur require special investigations of magnesium-containing waste as a raw material of technological origin.

This communication reports the results obtained in chemical, X-ray, and gamma-spectrometric studies, which make it possible to assess the prospects for processing of slimes into powders of magnesian binders that can be used in production of composite building materials, along with caustic magnesites.

EXPERIMENTAL

The study was performed with slime samples from a magnesium production shop (AVISMA Closed Joint-Stock Company, Berezniki). The content of Mg, Ca, K, Na, Cl, Fe, Si, Al, and Ba in the slime was determined quantitatively by atomic-absorption photometry, spectrophotometry, and plasma photometry. The content of magnesium-containing compounds (MgO, $MgCl_2$) and alkali metal chlorides (NaCl and KCl)

1070-4272/04/7702-0201 © 2004 MAIK "Nauka/Interperiodica"

Table 1. Mass fraction of chemical compounds in slime samples under study

Sample no.	Chemical analysis				X-ray phase analysis		
	content, wt %						
	MgO	$MgCl_2$	KCl	NaCl	MgO	$KMgCl_3 \cdot 6H_2O$	NaCl
1	1.72	47.36	18.13	2.73	0.0	78.2	5.9
2	35.05	27.28	10.00	1.72	31.4	64.7	3.8
3	56.65	18.10	6.28	1.08	72.6	26.1	1.3
4	42.60	22.46	16.58	2.05	63.3	34.6	2.2

was found quantitatively by chemical and X-ray analyses. The phase composition of the slime was determined by X-ray phase analysis. The samples were tested for radioactivity by gamma spectrometry on an SEG-1P γ-spectrometer. The specific effective activity A_{eff} of natural radionuclides was calculated by the formula

$$A_{eff} = A_{Ra} + 1.31A_{Th} + 0.085A_K,$$

where A_{Ra}, A_{Th}, A_K are the specific effective activities of radium, thorium, and potassium, respectively.

The binding properties of the slime were studied by the procedure recommended by GOST (State Standard) 310.3–76, and the compression strength of the magnesian cement obtained from the slime, in accordance with GOST 310.4–81. A slime with a particle size of 100–150 μm was used in the experiments. To prepare a magnesian paste, the slime was mixed with water, since carnallite was contained in the slime. The thickness of the magnesian paste was determined with a Vicat device.

Preliminary elemental analysis demonstrated that the slime is mainly composed of Mg, O, Cl, K, and Na.

The main chemical compounds contained in the slime are MgO, $MgCl_2$, KCl, and NaCl; their total content is 98.4 wt %. The accompanying admixtures of Si, Fe, and Al oxides, and Ca and Ba chlorides, constitute 4×10^{-1}, 2.7×10^{-1}, 9×10^{-2}, 2×10^{-3}, and 4.3×10^{-4} wt %, respectively. Up to 80 wt % falls on main magnesium-containing components (MgO, $MgCl_2$), which are involved in the reactions of magnesian stone formation and hardening.

With account of the existing industrial technology for casting of the slime melt, it would be expected that the distribution of chemical compounds along the height of an ingot being formed in the mold is nonuniform. To verify this assumption, slime was sampled along a vertical cross-section of its ingot, approximately from each third of its height. Representative samples were taken from each part of the slime ingot in equal amounts (by mass) and carefully averaged. The content of magnesium oxide and magnesium, potassium, and sodium chlorides was determined quantitatively by chemical and X-ray phase analyses (Table 1).

The results of chemical analysis (Table 1) point to a nonuniform distribution of the active components MgO and $MgCl_2$ (main components involved in the formation of Sorel cement) along the height of the slime ingot formed. As the temperature of the melt decreases, the water-soluble components ($MgCl_2$, KCl, and NaCl) are "salted out" in the upper part of the slime ingot (sample no. 1). In the bottom part of the ingot (sample no. 3), the mass fraction of MgO is the largest. In the middle part (sample no. 2), the chemical composition is represented by magnesium oxide and magnesium chloride, their content being 35.05 and 27.28 wt %, respectively. The mass ratio MgO : $MgCl_2$ in this sample is 1 : 0.7, which is close to the optimal ratio of these components in mixing of caustic magnesite with an aqueous solution of $MgCl_2$ to obtain magnesian cement [7].

The use of the slime as a chloromagnesian binder requires its crushing and subsequent grinding to an apprpriate degree of dispersion. In the process, the chemical composition will also be averaged over the whole volume. A chemical analysis demonstrated that the averaged slime sample (sample no. 4) contains MgO and $MgCl_2$ in a mass ratio that allows its use as a magnesian binder and a mixing agent simultaneously.

An X-ray phase analysis of the slime samples not only confirmed the nonuniform distribution of chemical components along the height of a slime ingot (Table 1), but also made it possible to determine

Table 2. Specific activity of natural radionuclides in the slime

Sample	Specific activity, Bq kg^{-1}			A_{eff}, Bq kg^{-1}	Sample	Specific activity, Bq kg^{-1}			A_{eff}, Bq kg^{-1}
	A_{Ra}	A_{Th}	A_K			A_{Ra}	A_{Th}	A_K	
1	<10	<15	4800 ± 500	430	2	<10	<15	3000 ± 500	290

their phase state in the slime (Fig. 1). The samples under study contain chemical components as three individual phases: magnesium oxide MgO, carnallite $KMgCl_3 \cdot 6H_2O$, and sodium chloride NaCl. Sample no. 1 contains carnallite hexahydrate $KMgCl_3 \cdot 6H_2O$ (*d* 0.478, 0.386, 0.360, 0.332, 0.303, 0.297, 0.293, 0.239, 0.234, and 0.201 nm), anhydrous $KMgCl_3$ (*d* 0.349, 0.285, 0.248, and 0.174 nm), and NaCl (*d* 0.282, 0.199, and 0.163 nm) (Fig. 1, curve *1*). Sample nos. 2–4 also contain the MgO phase, as evidenced by the diffraction lines with *d* 0.242, 0.211, and 0.148 nm (Fig. 1, curves *2–4*).

The contents of individual phases in the slime samples under study are different, in good agreement with the data of chemical analysis.

The slime was found to be nontoxic, and ecologically and radiation safe as regards its chemical and radionuclide composition.

According to the specific effective activity of natural radionuclides (A_{eff} = 430 Bq kg^{-1}) contained in the slime, it belongs to class-II materials (Table 2, sample 1) and can be used for manufacture of construction materials suitable for industrial use and for construction of roads in residential areas and zones of future building.

A mixture of the slime with dispersed organic fillers of vegetable origin and, in particular, with shredded wood wastes (sawdust and shavings) in a mass ratio of 1 : (1–0.8) (Table 2, sample 2) belongs to class-I materials as regards the value A_{eff} = 290 Bq kg^{-1}. According to GOST 30 108–94, such a mixture can be used as a wood-mineral composite in manufacture of materials suitable for construction of residential and public buildings.

A study of hardening of magnesian cement showed that the setting time of the cements depends on the amount of water added: as the solid : liquid ratio decreases, the setting time becomes shorter. At the commonly accepted optimal ratio s : l = 1 : (0.42–0.43) (42–43 ml of water are added per 100 g of the slime) the initial and the final time of setting of magnesian cement was 20 and 40 min, respectively.

The dependence of the compressive strength of the samples under study on the amount of mixing water is shown in Fig. 2.

The highest compressive strength after 3 and 7 days of hardening was exhibited by samples formed from a magnesian paste with s : l = 1 : 0.37. In this case, the compression strength was 72.3 and 89.1 MPa,

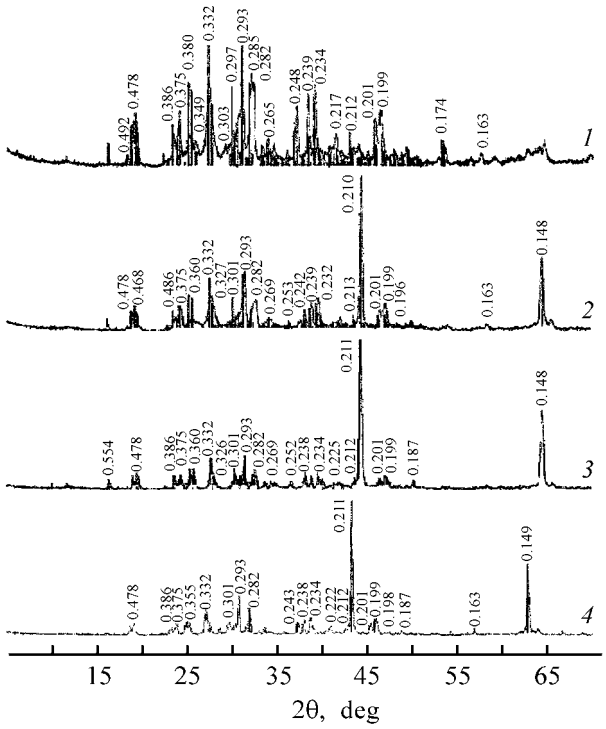

Fig. 1. X-ray diffraction patterns of slime samples taken at different heights of the vertical cut of an ingot. (2θ) Bragg angle. (*1*) Upper part, (*2*) middle part, (*3*) bottom part, and (*4*) thoroughly averaged sample.

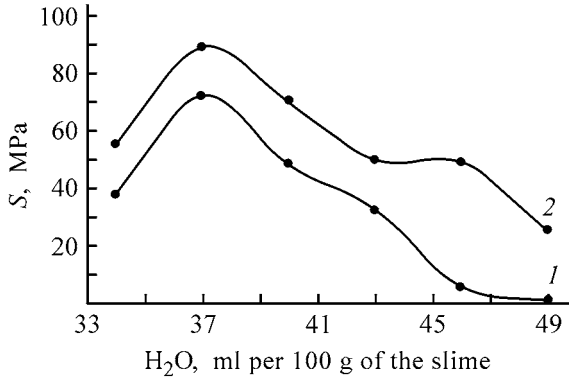

Fig. 2. Compressive strength *S* of the magnesian stone formed in the slime–H_2O system vs. the amount of water added. Time of hardening (days): (*1*) 3 and (*2*) 7.

respectively; however, the setting time of these mixtures was short (<5 min). At s : l = 1 : 0.43, the compressive strength of the samples after 3 and 7 days of hardening was 32.4 and 50 MPa, which is somewhat lower than the compressive strength of the samples formed from caustic magnesite.

The strength characteristics of the magnesian stone obtained from the slime can be improved by adding caustic magnesite to the chloromagnesian mixture. Adding even minor amounts (8–10%) of a PMK-75 caustic magnesite to the slime accelerated the formation of the oxochloride phase and increased the mechanic strength of the magnesian stone. For example, adding 8 and 10% caustic magnesite with s : l = 1 : 0.43 raised the strength of the magnesian stone formed after 28 days of hardening to 59.4 and 70.9 MPa, respectively, in good agreement with the strength characteristics of samples of caustic magnesite mixed with a $MgCl_2$ solution [8].

The microstructure of the solidified magnesian stone formed from the slime is that of a dense conglomerate with reduced porosity.

CONCLUSIONS

(1) Magnesium-containing metallurgical wastes formed in manufacture of metallic magnesium are a valuable raw material of technological origin for production of a magnesian binder.

(2) In mixing of the slime with water, hardening occurs rather actively by the reaction of magnesium oxide and chloride contained in the slime. However, the resulting magnesian stone has a reduced compressive strength, which can be substantially raised by addition of caustic magnesite. Adding caustic magnesite in an amount of 10% makes it possible to obtain samples of a construction material with a compressive strength of up to 70.9 MPa at a high hardening rate.

ACKNOWLEDGMENTS

This study was financially supported by the Scientific-and-Technological Program "Researches at the Higher School in the Priority Areas of Science and Technology" of the Ministry of Education of the Russian Federation and by an individual grant of the Ministry of Education of the Russian Federation for support of research carried out by postgraduate students at higher school institutions (AOZ-3.21-451).

REFERENCES

1. Strelets, Kh.L., Taits, A.Yu., and Gulyanitskii, V.S., *Metallurgiya magniya* (Metallurgy of Magnesium), Moscow: Metallugizdat, 1960.
2. Vetyukov, M.M., Tsyplakov, A.M., and Shkol'nikov, S.P., *Elektrometallurgiya alyuminiya i magniya* (Electrometallurgy of Aluminum and Magnesium), Moscow: Metallurgiya, 1987.
3. Brut, Yu.M., Bogomolov, B.N., and Dvorkin, L.I., *Vyazhushchie materialy Sibiri i Dal'nego Vostoka* (Binders of Siberia and Far East), Novosibirsk, 1970.
4. Volzhenskii, A.V., Burov, V.S., and Kolokol'nikov, V.S., *Mineral'nye vyazhushchie veshchestva* (Mineral Binders), Moscow: Stroiizdat, 1973.
5. Fefelov, N.K. and Svit, G.F., *Ekologicheskie tekhnologii: Pererabotka promyshlennykh otkhodov v stroitel'nye materialy* (Ecological Technologies: Processing of Industrial Waste into Construction Materials), Sverdlovsk, 1984.
6. Lipunov, I.N., Vlasov, P.S., Vasilenko, L.V., *et al.*, *Ekologicheskie problemy i khimicheskie tekhnologii* (Ecological Problems and Chemical Technologies), Yekaterinburg: Ural'sk. Gos. Lesotekhn. Akad., 2000, pp. 142–151.
7. Nanazashvili, I.Kh., *Stroitel'nye materialy iz drevesnotsementnoi kompozitsii* (Structural Materials Manufactured from Wood-Cement Formulations), Leningrad: Stroiizdat, 1990.
8. Zyryanova, V.I., Savinkina, M.A., Logvinenko, A.T., *et al.*, *Sibirskii Khim. Zh.*, 1992, no. 3, pp. 116–119.

Russian Journal of Applied Chemistry, Vol. 77, No. 2, 2004, pp. 205–208. Translated from Zhurnal Prikladnoi Khimii, Vol. 77, No. 2, 2004, pp. 210–213.

SORPTION AND ION-EXCHANGE PROCESSES

Composite Sorbing Materials Based on Porous Carbon Powders

N. V. Sych, N. T. Kartel', V. V. Strelko, V. A. Denisovich, and Yu. P. Zaitsev

Institute of Sorption and Endoecology Problems, National Academy of Sciences of Ukraine, Kiev, Ukraine

Received May 5, 2003

Abstract—The possibility of synthesizing composite sorbing materials on the basis of porous carbon powders was studied. The sorption and porosimetric characteristics of the composites were examined.

The rapid development of sorption technologies imposes increasingly stringent requirements upon the properties of sorbents: adsorption selectivity, physicochemical and physicomechanical characteristics. The acute need for widely diverse and highly efficient adsorbents becomes particularly pressing in connection with the problems of purification, concentration, separation, and accumulation of technological gases in modern high-output processes. The possibilities of varying widely the required sorbent properties are opened up by the creation of the so-called composite sorbing materials (CSM) on the basis of highly porous carbon powders with addition of a binder [1–3].

By distributing and binding monodisperse powders in a certain way, in conformity with the closest-packing law, one can obtain sorbing carbon materials with high specific pore volume of ~0.5 $cm^3\ cm^{-3}$ and narrow distribution of this volume over equivalent radii [3–6].

Creating mixed sorbents on the basis of finely ground porous powders, formed as by-products at plants that manufacture activated carbon, and ultradispersed additives makes it possible to obtain novel CSM, which contain particles with narrow size distribution, a kind of "binder," in spaces between packed particles of activated carbon (see scheme).

Depending on the CSM preparation conditions, the pores of the carbon powder are 30–70%-filled with this ultradispersed component, which determines the volume and radius of mesopores [7].

In order to develop this concept further, the possibility of obtaining carbon sorbents with high porosimetric characteristics and strength from half-products to be utilized and wastes formed in manufacture of activated carbon was studied. An attempt was made to develop technological foundations for synthesis of microporous CSM from porous carbon (activated and oxidized anthracite, activated salted carbon) and ultradispersed powders (technical-grade carbon–carbon black, activated carbon fiber). The choice of just these combinations is based on the authors' opinion that coal must improve the strength characteristics of the resulting formed material, and the ultradispersed powder additives introduced must contribute significantly to the development of porosity.

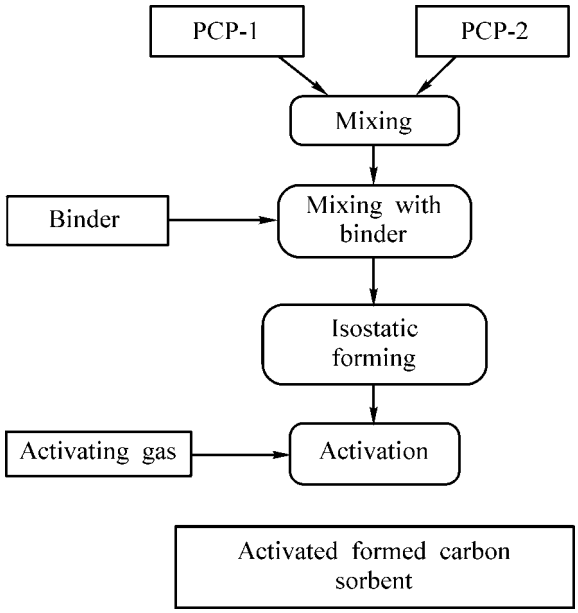

Table 1 lists characteristics of the starting components used to obtain formulations. The stock for synthesizing composite sorbing materials was prepared by mixing the main components with a binder in certain mass ratios and then subjected to forming.

1070-4272/04/7702-0205 © 2004 MAIK "Nauka/Interperiodica"

Table 1. Characteristics of starting components used to prepare the stock

Starting component	Dispersity, μm	Pore volume for benzene, W_s, $cm^3\ g^{-1}$
Anthracite:		
activated	63–100	0.41
oxidized	63–100	0.39
Technical-grade carbon (carbon black)	≤50	0.44
Dispersed activated fiber	≤50	0.45
Activated salted carbon	63–100	0.56
Binder	≤50	0.016

It is known [8] that the conventional forming techniques fail to satisfy the requirements to the structural homogeneity of these materials. The development of new binders (polymeric resins) and forming techniques open up wider opportunities for synthesis of high-porosity materials.

High-porosity materials with uniformly distributed pore structure were synthesized by the isostatic forming method [9, 10]. This was done using a phenol-formaldehyde resin binder whose amount in the molding powder ensured a sufficient mechanical strength of the resulting half-finished articles.

The material formed was activated with water vapor and/or carbon dioxide. When activating the CSM, the method with temperature gradually raised at a rate of 10 deg min^{-1} was used in order to preserve their strength characteristics. The temperature was raised within the range 150–850°C.

In activating the formed material, the combustion loss during certain intervals of time was recorded, and the sorption pore volume for benzene and methanol was measured [11]. In some cases, the sorption activity toward iodine and Methylene Blue was studied; isotherms of nitrogen adsorption were measured, with the corresponding specific surface area evaluated on a Quantochrome Autosorb Automated Gas Adsorption System instrument (USA); adsorption of methane under elevated pressure and its subsequent desorption on relieving the pressure to its atmospheric value were carried out on a volumetric installation.

The variation of the texture characteristics and sorption properties of the composites in the course of their activation is illustrated by Table 2.

Table 2. Variation of texture characteristics and sorption properties of composites in the course of activation

Composite	Activating gas	τ, h	Combustion loss, %	Sorption pore volume W_s, $cm^3\ g^{-1}$		Sorption activity		Specific surface area S_{sp} for N_2, $m^2\ g^{-1}$
				for C_6H_6	for CH_3OH	for MB mg g^{-1}	for I_2, %	
KSM-1	H_2O	0.5	37	0.49	0.48			
	H_2O	1.0	53	0.56	0.61	68	66	854
KSM-2	H_2O	0.5	27.5	0.38	0.37			
	H_2O	1.0	42	0.47	0.45	60	62	756
KSM-3	H_2O	0.5	14.7	0.57	0.53			
	H_2O	0.85	25.2	0.59	0.59			
	H_2O	1.0	35.4	0.60	0.61	118	68	942
	CO_2	0.5	50.1	0.68	0.7	78	76	874
KSM-4	H_2O	0.66	54.5	0.67	0.60	124	78	936
KSM-5	CO_2	0.5	37	0.54	0.51			
	CO_2	0.75	45.7	0.51	0.48	56	66	831
KSM-6	H_2O	0.66	67.2	0.39	0.41	196	62	803
	CO_2	0.5	38.2	0.47	0.47	133	52	650
KSM-7	CO_2	0.5	50.8	0.60	0.56	47	69	800
	H_2O	0.66	18.2	0.42	0.40			
	H_2O	1.0	31	0.455	0.48			
	H_2O	1.4	44.5	0.56	0.50	120	70	944
KSM-8	H_2O	0.66	54.3	0.54	0.50	114	74	952
	CO_2	0.5	37.3	0.49	0.58			
	C_2O	0.75	39.2	0.44	0.46	46	64	798
KSM-9	H_2O	0.66	56.2	0.60	0.57	74	78	923

The chosen forming method yields CSM with good sorption characteristics (W_s = 0.5–0.7 $cm^3\ g^{-1}$, S_{sp} = 790–950 $m^2\ g^{-1}$) and sufficiently high mechanical strength.

It should be noted that, when composites are activated with water vapor, higher sorption of nitrogen is achieved, compared with the case of activation with CO_2, and the accordingly larger specific surface area is developed. The best sorption characteristics are observed for composites that contain activated anthracite and carbon black, as well as activated anthracite and carbon fiber. Introduction of a dispersed powder of activated salted carbon into a composite does not make such a significant contribution as the components mentioned above do.

Figure 1 shows isotherms of low-temperature adsorption of nitrogen, typical of the composites obtained, and Fig. 2 presents the differential distribution of pore volumes over equivalent pore radii. Analysis of the isotherms shows that the CSM obtained exhibit developed microporosity and small-size mesoporosity, and the adsorption and capillary condensation in these pores determines the run of the curves. Analysis of the differential sorption isotherms shows that the range of effective radii is 8–60 Å.

Table 3 lists comparative porosimetric characteristics of the best of the formed CSM samples obtained and commercial granulated carbon of SKT brands, prepared from a mixture of peat and coal dust by chemical activation with K_2S. It can be seen that the CSM obtained are distinguished by higher micropore volumes.

The ability of the samples with high sorption characteristics to absorb gaseous methane was studied. Typical amounts of adsorbed gas as a function of the number of adsorption–desorption cycles are shown in Fig. 3. It can be seen that the adsorption of methane on a composite that contains carbon fiber differs significantly from that for samples that contain carbon black as an additive. Adsorption of natural gas on porous carbon materials is accompanied by condensation of higher hydrocarbons (homologues of methane, propane, and butane) in the micropores of a sample, which leads to lower sorption capacity of the sorbents for methane in subsequent cycles of gas adsorption. The same behavior is observed in Fig. 3. For a composite that contains carbon fiber as an ultradispersed additive, the activity falls dramatically (by a factor of 2) in going from the first cycle to the second and sorption of methane is virtually constant in the subsequent cycles. For all other samples, a gradual filling of micropores with the condensate is observed, and only after the fourth cycle the adsorption of methane becomes virtually constant. Such a dependence indicates, in the authors' opinion, that the porous structure of the additive introduced affects the sorption properties of the composite as a whole.

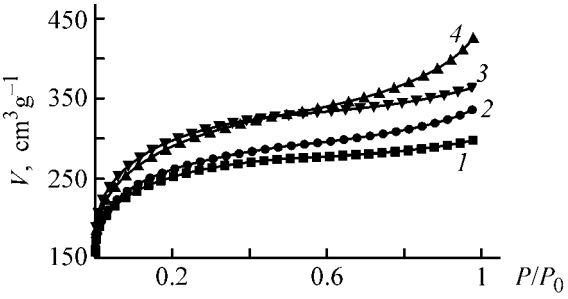

Fig. 1. Integral curves of nitrogen sorption. (V) Volume of nitrogen sorbed, and (P/P_0) relative pressure. Sample: (*1*) KSM-8 (activating gas CO_2), (*2*) KSM-5, (*3*) KSM-8 (activating gas H_2O), and (*4*) KSM-4; the same for Fig. 2.

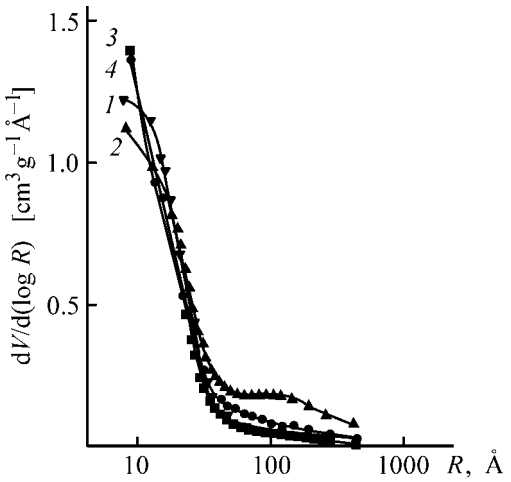

Fig. 2. Differential curves of nitrogen sorption. (V) Sorbent pore volume and (R) pore radii in the sorbent.

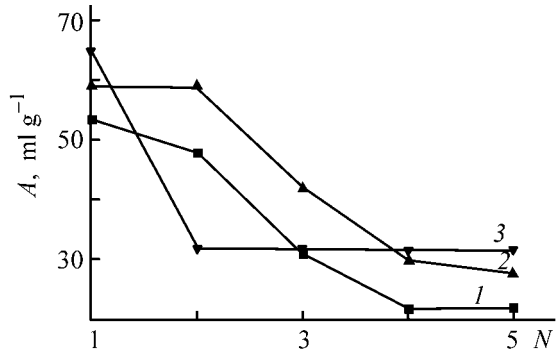

Fig. 3. Amount of adsorbed methane, A, vs. the number N of adsorption–desorption cycles. Sample: (*1*) KSM-5, (*2*) KSM-9, and (*3*) KSM-8 (activating gas CO_2).

Table 3. Comparative porosimetric characteristics of the CSM obtained and industrially manufactured SKT carbon

Carbon brand	Specific pore volume, $cm^3\ g^{-1}$				S_{sp} for N_2, $m^2\ g^{-1}$
	V_Σ	V_{micro}	V_{meso}	V_{macro}	
KSM-4	0.73	0.60	0.07	0.06	936
KSM-8	0.61	0.50	0.04	0.07	952
KSM-9	0.68	0.57	0.03	0.08	923
SKT	0.85–0.98	0.51	0.20	0.27	–
SKT-2	0.75	0.45	0.09	0.21	–
SKT-3	0.80	0.46	0.09	0.25	–
SKT-6	1.11	0.60	0.28	0.23	–

CONCLUSIONS

(1) The method of isostatic forming was applied to demonstrate the possibility of obtaining highly porous (with predominance of a microporous structure) composite sorbing materials, which have good sorption characteristics (W_s = 0.5–0.7 $cm^3\ g^{-1}$, S_{sp} = 790–950 $m^2\ g^{-1}$) and retain sufficiently high mechanical strength, from porous dispersed carbon materials. The sorption and porosimetric characteristics of the materials obtained are comparable with, and in some case even surpass those of commercial industrial carbon of the SKT brand.

(2) The resulting formed adsorbents can be effectively used to accumulate methane in cylinders, which makes it possible to raise the adsorption capacity of a unit volume and to diminish the pressure without lowering the cylinder capacity.

REFERENCES

1. Fenelonov, V.B., *Poristyi uglerod* (Porous Carbon), Novosibirsk: Inst. Katal. Sib. Otd. Ross. Akad. Nauk, 1995.
2. Kuznetsov, B.N., *Soros. Obrazovat. Zh.*, 1999, no. 12, pp. 29–34.
3. Mukhin, V.M., Tarasov, A.V., and Klushin, V.N., *Aktivnye ugli Rossii* (Activated Carbons of Russia), Moscow: Metallurgiya, 2000.
4. Gorlov, E.G., Zummerov, S.R., and Paushkin, Ya.M., *Khim. Tverd. Topl.*, 1977, no. 1, pp. 3–16.
5. Fedorov, N.F., Ivakhnyuk, G.K., and Babkin, O.E., *Zh. Prikl. Khim.*, 1990, vol. 63, no. 4, pp. 787–791.
6. Babkin, O.E. and Ivakhnyuk, G.K., *Sorbenty i sorbtsionnye protsessy* (Sorbents and Sorption Processes), Leningrad: Len. Tekhnol. Inst. im. Lensoveta, 1990, pp. 3–13.
7. Fedorov, N.F., Ivakhnyuk, G.K., and Babkin, O.E., Abstracts of Papers, *V Vsesoyuznoe soveshchanie "Uglerodnye adsorbenty i ikh promyshlennoe primenenie v promyshlennosti"* (V All-Union Symp. "Carbon Adsorbents and Their Industrial Use"), Perm, 1991, pp. 26–28.
8. Butyrin, G.M., *Vysokoporistye uglerodnye materialy* (Highly Porous Carbon Materials), Moscow: Khimiya, 1976.
9. Chalykh, E.F., *Tekhnologiya uglegrafitovykh materialov* (Technology of Carbon-Graphite Materials), Moscow: Metallurgizdat, 1963.
10. Mustafina, F.N. and Solyakov, V.K., *Konstruktsionnye uglegrafitovye materialy* (Carbon-Graphite Construction Materials), Moscow: Metallurgiya, 1964, no. 1, pp. 48–57.
11. Kel'tsev, N.K., *Osnovy adsorbtsionnoi tekhniki* (Fundamentals of Adsorption Technology), Moscow: Khimiya, 1984.

Russian Journal of Applied Chemistry, Vol. 77, No. 2, 2004, pp. 209–214. Translated from Zhurnal Prikladnoi Khimii, Vol. 77, No. 2, 2004, pp. 214–218.

SORPTION AND ION-EXCHANGE PROCESSES

Influence of Humus Acids on Physicochemical Features of KU-2 × 8 Cation Exchangers

G. V. Slavinskaya

Voronezh State University, Voronezh, Russia

Received March 12, 2003

Abstract—In prolonged industrial desalination of natural water with KU-2 × 8 cation exchanger, humic and fulvic acids are accumulated on the resin, which deteriorates its sorption characteristics and desalination efficiency.

In the late 1950s, the Dutch production engineers reported for the first time that the dynamic sorption capacity of strongly ionized anion exchangers used for industrial water desalination is deteriorated because of the sorption of natural organic substances [1]. As for cation exchangers, it was believed for a long time that organic matter does not affect their sorption capacity. However, several experimental facts show that this is not the case. For example, in water treatment with a cation exchanger, approximately 10% of organic impurities oxidizable with potassium permanganate is accumulated on the resin [2]. Accumulation of colored substances (most likely humus substances) on a cation exchanger was observed in [3]. In regeneration of spent cation exchangers with aqueous acid, the filtrates have high oxidizability, which is caused by removal of organic substances accumulated on the resin [4].

In this study, we examined how humic (HA) and fulvic (FA) acids accumulated on KU-2 × 8 cation exchanger in the course of prolonged desalination of natural water affect the physicochemical characteristics of resin and its desalination efficiency.

EXPERIMENTAL

The dimeneralization of natural water was carried out in two stages by passing it through different ion-exchange filters of an industrial desalination installation: cation exchanger I → anion exchanger I → cation exchanger II → anion exchanger II or cation exchanger I → anion exchanger I → MF (mixed cation exchange–anion exchange filter). The samples of cation exchanger were taken from filters I and II and also from MF filter used for exhaustive desalination of

Table 1. Content of organic substances in natural water*

Characteristic	Water		
	Artesian	Bystritsa river	Neva river
Oxidizability, mg O l^{-1}	1.2–2.0	1.4–2.6	6.5–10.6
Color index, degree by the Cr–Co scale	5	5–10	20–40
Humic acids, mg l^{-1}	0.02–0.05	0.06–0.13	0.35–0.54
Fulvic acids, mg l^{-1}	1.1–2.4	1.0–2.9	9.8–13.2
Amino acids, μg N l^{-1}	20–27	–	6–11
Sugars, mg l^{-1}	0.66–0.84	–	0.27–0.78
Esters, μg-equiv l^{-1}	85–95	–	75–100
Carboxylic acids, μg-equiv l^{-1}	8–10	–	20–25
Total salt content, μg-equiv l^{-1}	4.8	2.5	1.1

* A note to Table 1 was be omitted because it refers to the references cited in this paper (see references [5–7]).

1070-4272/04/7702-0209 © 2004 MAIK "Nauka/Interperiodica"

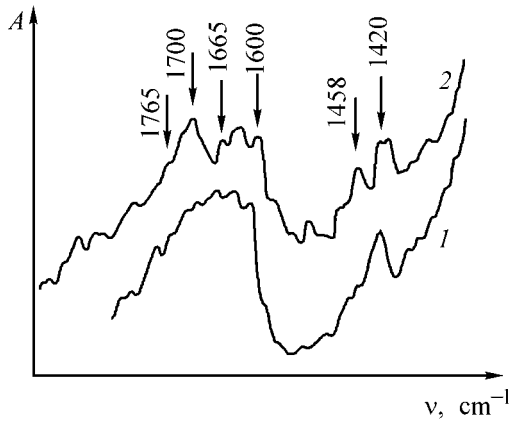

Fig. 1. IR spectra of (*1*) fresh commercial KU-2 × 8 cation exchanger and (*2*) cation exchanger after its prolonged use for industrial desalination of natural water. (*A*) absorption and (ν) wave number.

water. The content of main organic impurities in natural water desalinated using the above ion-exchange technique is given in Table 1. All the analyses were carried out by the methods reported in [5–7].

Table 1 shows that the main organic matter present in the natural water is composed of HA and FA, and their content varies in parallel with the color index. We found that, irrespective of the concentration of organic matter in natural water, the color of the cation-exchange filters changes from yellow to brown in the course of prolonged desalination. We believe that this color change is caused by accumulation of humus substances on the resin. The accumulation of humus substances on KU-2 × 8 was confirmed by the following experimental data.

(1) After desalination of natural water with KU-2 × 8 during five years (Fig. 1), a noticeable band of the C=O stretching vibrations at 1700 cm^{-1} appears in its IR spectra, along with the absorption bands at 1458, 1420, 1510, and 1605 cm^{-1} typical of sulfonic cation exchangers [8]. The enhancement of intensity of the absorption bands at 1665 and 1635 cm^{-1} can be attributed to amino groups [9, 10]. We believe that these carboxy and amino groups enter the composition of the peripheral amino acid groups of HA and FA macromolecules accumulated on the spent resin [11, 12].

(2) Accumulation of humus substances on the cation-exchange resin was confirmed by their recovery with chemical reagents. In these experiments, a KU-2 × 8 sample preliminarily used for desalination of an artesian water for eight years was treated for 15 and 30 days with solutions of the following composition (wt %): NaCl (10), NaOH (2) + NaCl (10), $Na_4P_2O_7$ (5), HCl (7), NaOH (2) + NH_4OH (2), water–acetone (1 : 1), water–dimethyl sulfoxide (1 : 4), and water–ethanol (1 : 5). It was found that treatment of the resin with alkali ensures the maximum recovery of humic substances. In order to separate humic acids from fulvic acids, the alkaline eluates were acidified with 1 M HCl to pH ~2.

In studies of molecular structure of HA and FA, these substances are subjected to acid hydrolysis to recover separate chemical constituents of these macromolecules. From the molecular species determined in the hydrolyzate, the initial humus substance structure can be reconstructed [13]. In our experiments, the colored organic substances recovered from the cation exchanger were hydrolyzed with 6 M HCl on heating in a sealed tube at 120 °C for 24 h.

The hydrolyzate was analyzed by descending paper partition chromatography using butanol-acetic acid-water mixture (4 : 1 : 5) as eluent and ninhydrin (0.05% aqueous solution) as developer. The particular amino acids were identified by comparison of the chromatograms of the hydrolyzate with those of model reference system containing twenty amino acids. The chromatograms of the hydrolyzates contain six bands with R_f from 0.05 to 0.88, related to the amino acid groups of natural HA and FA [12] (Table 2).

(3) After partial removal of HA and FA from spent KU-2 × 8, the resin becomes lighter. After removal of humus substances from the resin with a salt-alkali solution, the intensity of the absorption bands of humic acids at 1690, 1560, 1533, 1470, 1400, and 1300 cm^{-1} decreases (relative to the intensity of the most stable absorption band at 826 cm^{-1}) (Table 3). These spectroscopic data show that, in extraction with alkali, the structural fragments of HA and FA containing the aliphatic and aromatic amino acid groups,

Table 2. Amino acids recovered from humus substances accumulated on KU-2 × 8 cation exchanger

Humus substances	Amino acids recovered from hydrolyzate of humus acids
Humic acids	Cysteine, lysine, glycine, leucine, arginine, histidine, asparagine, aspartic acid, alanine, valine
Fulvic acids	Cysteine, lysine, glycine, leucine, arginine, histidine, asparagine, aspartic acid, glutamine

Table 3. Relative intensity of the absorption bands in the IR spectra of KU-2 × 8 cation exchanger before and after removal of organic impurities

Wave number, cm^{-1}, and assignment of absorption bands [9, 10]	Relative intensity of absorption bands		
	before treatment	after treatment, days	
		15	30
1760, C=O in COOH dimers	4.0	3.0	0
1690, C=O in aromatic acids and	15.0	14.0	10.0
1673, C=O in COOH	16.0	10.0	5.0
1560, C=O in COO^-	5.0	4.0	1.0
1533, C=O in COO^-	3.5	1.0	1.0
1470, C–H in CH_2	15.0	8.0	5.0
1400, C=O in COO^-	18.5	7.0	5.0
1346, C–H	4.5	1.0	1.0
1300, NH_3 in salts of amino acids	1.5	1.0	1.0

Table 4. Content of organic substances in river water before and after desalination with KU-2 × 8 cation exchanger !

Water volume, m^3	FA content, ±20 μg l^{-1}		Increase of c_{FA}, μg l^{-1}	HA content, ±20 μg l^{-1}		Increase of c_{HA}, μg l^{-1}
	before cation exchanger	after cation exchanger		before cation exchanger	after cation exchanger	
80	860	200	660	70	270	200
400	300	1300	1000	140	300	160
1000	850	1750	900	60	190	130
1600	880	1040	160	80	160	80
1800	910	1030	120	50	75	25

benzene rings with different substituents, aldehide groups, etc, are removed from the resin. On removing HA and FA, the content of the methyl and methylene groups in the side aliphatic chains (1346 cm^{-1}) decreases.

(4) To elucidate how treatment of natural water with KU-2 × 8 cation exchanger affects the chemical composition of organic impurities, we recorded the IR spectra of dry residues of the initial river water (sample 1) and of the water treated with the cation exchanger (sample 2). The IR spectrum of the initial natural water contains absorption bands of the amino (3400–3300, 1650–1630 cm^{-1}) and carboxy (2800, 1720, 1700, 1460 cm^{-1}) groups [9, 10]. After contact with the cation exchanger, all these absoprtion bands virtually completely disappear, and new absorption bands at 3030, 1600, 1550, 1450 and 690 cm^{-1} appear, which can be assigned to the stretching vibrations of the C–H, C=C, =C, and =C–H bonds in the aromatic ring. This spectrum also contains absorption bands of stretching vibrations of sulfonic groups (1200–1100 cm^{-1}). These data show that, in water treatment with cation exchanger, the resin not only accumulates the ionic groups of organic impurities, but simultaneously enriches water with products formed in destruction of the resin itself.

We found that, in treatment of water of the Bystritsa river with KU-2 × 8 resin, desalinated water is additionally contaminated with organic matter. In these experiments, natural water was passed through KU-2 × 8 cation exchanger preliminarily regenerated with aqueous acid. In the course of this experiment, 1-l water samples were taken at regular intervals at the inlet and outlet of the filter throughout the operation period. The filtered water was neutralized with 0.1 M KOH and dried, and the content of HA and FA in the dry residue was determined. The results of these analyses are listed in Table 4.

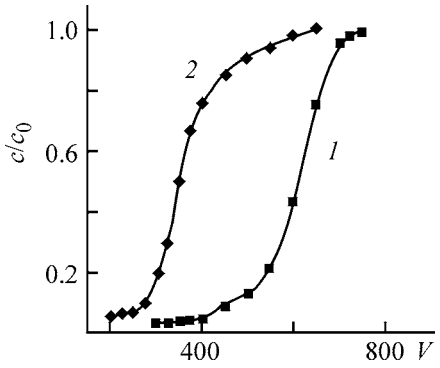

Fig. 2. Output curves of sorption of calcium cations on (*1*) fresh commercial KU-2×8 cation exchanger and (*2*) KU-2×8 after prolonged water desalination. (c and c_0) Concentration of calcium cations in water after and before treatment with cation exchanger in the H form; (V) number of the column volumes of water passed.

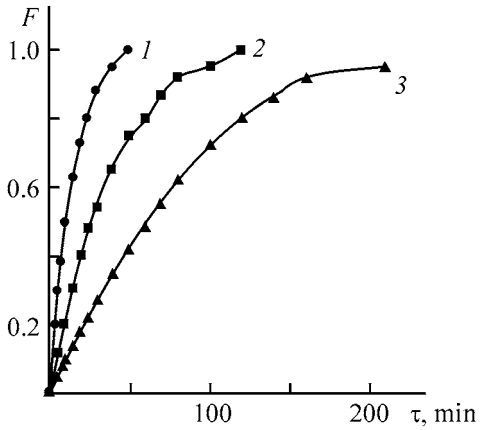

Fig. 3. Kinetic curves of sorption of sodium cations on (*1*) fresh commercial KU-2×8 cation exchanger, (*2*) KU-2×8 from spent industrial filter after treatment with salt-alkali solution and (*3*) KU-2×8 from spent industrial filter. (F) Degree of saturation of the resin and (τ) time.

Table 4 shows that the content of HA and FA in the desalinated water exceeds that in the initial river water. We believe that this excess of humus acids was accumulated on the resin in the stage of its regeneration with aqueous acid and was then gradually released in the course of desalination of the river water. Thus, the natural organic impurities are accumulated in ion-exchange water desalination, not only on anion, but also on cation-exchange resins.

Our experimental results show that HA and FA accumulated on the sulfonic cation-exchange resin in the course of water desalination deteriorate its physicochemical properties and performance.

We found that, after service in desalination for 2–5 years, the operative exchange capacity (OEC) of the cation exchanger to breakthrough of cations $c/c_0 = 0.03$ (c and c_0 are the contents of cations in the desalinated and initial water, respectively) decreased by 10–30%. The same decrease was observed for the total exchange capacity. In sorption of calcium on fresh commercial KU-2×8 cation exchanger, the shape of the output curve of sorption (Fig. 2, curve *1*) shows that the mass transfer is controlled by external diffusion [14] (extended initial part and shortened late stage of sorption). In sorption of calcium on the spent cation exchanger, the shape of the output curve of sorption (Fig. 2, curve *1*) shows that the mass transfer is largely controlled by the internal diffusion (reduced initial part of the sorption curve and its extension in the final stage of sorption when the eluate contains a rather large amount of calcium).

We believe that the appearance of a certain contribution of the internal diffusion control to the total mass transfer of calcium, along with the common external diffusion mechanism typical of ion-exchange sorption under dynamic conditions, is caused by accumulation of HA and FA on the cation exchanger. These humus acids produce the diffusion resistance to transfer of mineral cations to cation-exchange sites, which deteriorates the kinetic characteristics of the resin. As a result, the OEC of the spent resin decreases under dynamic conditions. The humus substances accumulated on the resin fill its porous space and decrease the moisture content (from 1.020 to 0.885 g H_2O/g).

To elucidate how prolonged desalination affects the kinetic characteristics of KU-2×8 cation exchanger, we studied the sorption of Na^+ from aqueous 0.003 M NaCl on a fresh commercial resin and on a resin used for desalination of Neva water in the first stage of the desalination installation for five years. Figure 3 shows that prolonged industrial use of the resin noticeably deteriorates its kinetic characteristics: the half-sorption time increases from 10 to 60 min. In a separate experiment, an aliquot of the cation exchanger used for five years for desalination of Neva water was treated with a salt-alkali aqueous solution for 35 days to remove humus substances. The content of HA and FA in this resin was found to be 68.4 mg and 12.0 mg FA per gram of air-dry resin, respectively. Our experiments showed that, after removal of humus substances, the half-sorption time of Na^+ decreased to 26 min (Fig. 3, curve *2*) , i.e. the sorption rate somewhat increased.

In separate model experiments, we found that contamination of commercial cation exchanger with FA

of Neva water increases the time to half-cation exchange from 10 to 16 min. This negative effect of humus substances on the kinetic characteristics of the ion exchanger is consistent with the pattern of deterioration of the kinetic characteristics observed in functioning of the industrial desalination filter.

We found also that humus substances accumulated on the resin hinder the removal of HCl from regenerated KU-2 × 8. Figure 4 shows that, in the case of fresh commercial KU-2 × 8 treated with HCl, HCl is removed with five column volumes of distilled water. At the same time, HCl was not removed even with 200 column volumes of water from spent KU-2 × 8 cation exchanger. If humus acids were preliminarily partially removed from the spent industrial filter with a salt-alkali solution, HCl was removed with 140 column volumes of water (i.e., the wash water volume decreased by 30%) (Fig. 4, curve *2*).

The presence of the amino groups in HA and FA imparts to them anion-exchange features. The anion-exchange capacity of resins from different ion-exchange filters varies from 0.15 to 0.70 mg-equiv cm^{-3} swollen resin. In regeneration of cation-exchange filters with HCl, the amino acids are protonated to form salts $Cl^-[N^+H_3–CHR–COOH]$. In washing with water, these salts are hydrolyzed by the reaction

$$Cl^-[N^+H_3–R–COOH] + H_2O \rightleftarrows OH^-[N^+H_3–R–COOH] + HCl,$$

to give the zwitterion, which is the most stable amino acid species in neutral solutions [15]. Because of this reaction, the wash water is acidified and, therefore, the larger water volume is required for complete removal of the mineral acid. Since the cation-exchange filters are washed to remove the mineral acid under industrial conditions with natural mineralized water, this procedure decreases the exchange capacity of the resin. This decrease is the larger, the higher the mineralization of natural water.

CONCLUSIONS

(1) In desalination of natural water with a sulfonic cation exchanger in the H form, the resin is contaminated with humic and fulvic acids, irrespective of their content in natural water and position of the cation-exchange filter in the process chain.

(2) The humus acids accumulated on the spent cation exchanger fill its pores and decrease the moisture content. These factors increase the diffusion resistance to transfer of mineral cations from the bulk to the cation-exchange sites and, as a result, decrease the sorption capacity of the resin and deteriorate its kinetic characteristics.

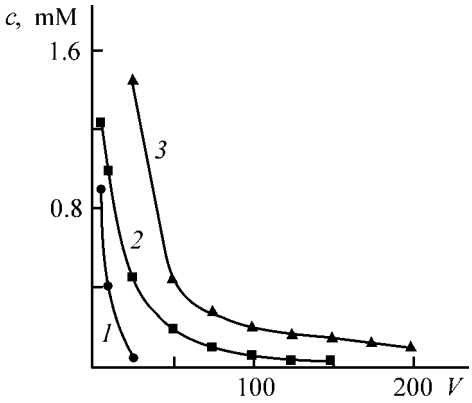

Fig. 4. Washing of KU-2 × 8 with water to remove HCl after regeneration: (*1*) fresh commercial KU-2 × 8 cation exchanger, (*2*) KU-2 × 8 from spent industrial filter treated with a salt-alkali solution, and (*3*) KU-2 × 8 from spent industrial filter without treatment. (*c*) HCl concentration and (*V*) number of column volumes of distilled water passed through the column.

(3) In regeneration of spent cation-exchange filters with hydrochloric acid, hydrogen chloride form salts with the amino groups of HA and FA. In washing the resin with water to remove HCl, these salts are hydrolyzed and, therefore, a larger water volume is required to remove the acid.

(4) To prevent poisoning of ion-exchange filters in desalination of mineralized natural water, humus acids should be preliminarily removed.

REFERENCES

1. Ianssen, C., *Mitt. Verein. Grosskesselbesitzer*, 1959, no. 60, pp. 172–178.
2. Granovskaya, G.L., Mazo, A.A., and Spirina, A.F., *Tr. Lab. Ionoobmenn. Prots. Sorb.*, Voronezh Univ., 1966, no. 1, pp. 147–154.
3. Kruithof, J.C., *Aqua*, 1985, no. 2, pp. 89–99.
4. Wiktorowski, S., Legedz, E., and Ksawczyk, G., *Gosp. Wod.*, 1980, vol. 40, no. 8–9 , pp. 267–270.
5. Ivleva, I.N., Semenov, A.D., and Datsko, V.G., *Gidrokhim. Mater.*, 1965, vol. 38, pp. 144–147.
6. Goncharova, I.A., Khomenko, A.N., and Semenov, A.D., *Gidrokhim. Mater.*, 1966, vol. 39, pp. 114–115.
7. Varshal, G.M., Velyukhanova, T.K., and Sirotkina, I.S., *Gidrokhim. Mater.*, 1973, vol. 59, pp. 143–151.
8. Polyanskiy, N.G., Gorbunov, G.V., and Polyan-

skaya, N.L., *Metody issledovaniya ionitov* (Methods for Study of Ion Exchangers), Moscow: Khimiya, 1976.

9. Bellamy, L.J., *The Infra-Red Spectra of Complex Molecules*, London: Methuen, 1954.
10. Kazitsyna, L.A. and Kupletskaya, N.B., *Primenenie UV, IR, NMR-spektroskopii v organicheskoi khimii* (Application of UV, IR, and NMR Spectroscopy to Organic Chemistry), Moscow: Vysshaya Shkola, 1985.
11. Malyarenko, V.V., *Khim. Tekhn. Vody*, 1994, vol. 16, no. 5, pp. 592–606.
12. Orlov, D.S., *Khimiya pochv* (Soil Chemistry), Moscow: Mosk. Gos. Univ., 1985.
13. Vinogradova, R.P., Tsudzevich, B.A, and Khrapunov, B.N., *Fiziko-khimicheskie metody v biokhimii* (Physicochemical Methods in Biochemistry), Kiev: Vishcha Shkola, 1983.
14. *Ionoobmennye metody ochistki veshchestv* (Ion-Exchange Methods for Purification of Substances), Chikin, O.N. and Myagkoi, O.N., Eds., Voronezh: Voronezh. Gos. Univ., 1984.
15. Chchibabin, A.E., *Osnovnye nachala organicheskoi khimii* (The Main Principles of Organic Chemistry), Moscow: Goskhimizdat, 1965.

Russian Journal of Applied Chemistry, Vol. 77, No. 2, 2004, pp. 215–217. Translated from Zhurnal Prikladnoi Khimii, Vol. 77, No. 2, 2004, pp. 219–221.

SORPTION AND ION-EXCHANGE PROCESSES

Determination of Metal Traces in Polypropylene by Gas Chromatography

Yu. G. Slizhov and M. A. Gavrilenko

Tomsk State University, Tomsk, Russia

Received May 10, 2001; in final form, December 2003

Abstract—A procedure was developed for determination of metal traces in polypropylene on chromatographic sorbents and phases of various polarities. The thermal stability of volatile aluminum, chromium, and gallium acetylacetonates under the conditions of gas chromatography was studied. The influence exerted on the determination process by the column material, temperature, and polarity of phases was examined.

Polyolefins, and polypropylene in particular, are produced on catalysts containing complexes of Al, Ti, Cr, and other metals [1–3]. Evaluation of the quality of the finished product involves determination of the residual catalyst, which is commonly done photometrically. The capability of many metals to form thermally stable volatile β-diketonates [4] offers an opportunity to use gas chromatography for determining metals in polyolefins [5, 6]. Therefore, study of chromatographic properties of metal β-diketonates and assessment of the possibility of using them to determine impurities in polyolefins is topical problem.

In this study, we examined the possibility of determining metals at their content of 10^{-3}–10^{-4} wt % by gas chromatography with a simplified sample preparation procedure.

EXPERIMENTAL

The metal acetylacetonates $Al(acac)_3$, $Ga(acac)_3$, and $Cr(acac)_3$ were prepared as described in [7]. The sample purity was checked by IR spectroscopy (400–4000 cm^{-1}, Specord M80 spectrophotometer). The thermal analysis was performed with a Q-1500 derivatograph in the temperature range 20–500°C at a heating rate of 10 deg min^{-1}, using Al_2O_3 as reference. The sample weight was 50 mg. Chromatographic experiments were performed with a Chrom 5 chromatograph equipped with a flame ionization detector. Glass and Teflon columns were packed with Tsvetosil M-SKT and Tsvetosil SKTFT diatomite supports modified with chemically grafted silicone rubbers, or with Chromosorb G AW DMDS impregnated with SE-30, OV-1, or SKTFV-803 (phenylvinylsilicone phase) liquid phases.

The metal impurities in polypropylene were determined as follows. A weighed portion of the polyolefin powder (4 g) was placed in a 100 cm^3 three-necked round-bottomed flask, 12 cm^3 of acetylacetone was added, and the mixture was heated at 60°C for 60 min. After cooling, the solution was filtered through a finely porous glass frit and vacuum-evaporated to dryness. The dry residue was dissolved in 6 cm^3 of CCl_4. The sample volume was 0.4 μl. The chromatographing conditions were as follows: column, vaporizer, and detector temperatures 140, 190, and 180°C, respectively; carrier gas flow rate 35 $cm^3\,min^{-1}$. The total analysis time was 1.5 h.

The possibility of direct reaction of β-diketones, including acetylacetone, with metals embedded in a polymeric matrix was demonstrated in [8, 9]. The metal transforms into the corresponding acetylacetonate on treatment of the polymer powder with the hot β-diketone. The IR spectra of the compounds thus prepared agreed with published data [10]. The strong bands at 1545 and 1590 cm^{-1}, characteristic of metal acetylacetonates, are indicative of the presence of a conjugated system of C=O and C=C bonds. The CH_3 bending vibration band is observed at 1390 cm^{-1}. The IR data allow the compounds obtained to be identified as acetylacetonates of the corresponding metals.

According to thermal gravimetric analysis, aluminum, gallium, and chromium acetylacetonates are stable up to temperatures exceeding 170°C (Table 1).

1070-4272/04/7702-0215 © 2004 MAIK "Nauka/Interperiodica"

Table 1. Thermal stability of metal acetylacetonates

Chelate	Temperature, °C		Degree of evaporation at 500°C, %
	onset of weight loss	weight loss maximum	
$Al(acac)_3$	185	290	94
$Ga(acac)_3$	175	275	75
$Cr(acac)_3$	200	335	93

Table 2. Kovats retention indices *I* at 150°C on various stationary phases

Chelate	SE-30	OV-1	SKT	SKTFT	SFTFV-803
$Al(acac)_3$	1647	1678	1480	1730	1658
$Cr(acac)_3$	1844	2429	2134	1871	1995
$Ga(acac)_3$	1695	1579	1642	1770	1720

The thermal stability of acetylacetonates correlates with their electronic structure. Chromium acetylacetonate stabilized owing to the involvement of vacant *d* orbitals in coordination sublimes at a higher temperature than aluminum and gallium acetylacetonates; gallium acetylacetonate, characterized by the filled 3*d*-electron shell of Ga, shows the lowest sublimation temperature and the strongest tendency to decompose. Aluminum acetylacetonate, in which vacant 3*d* orbitals may take part in donor–acceptor interaction [10], occupies an intermediate position. The gas-chromatographic determination of Al, Ga, and Cr in the form of acetylacetonates is possible at temperatures of up to 170°C.

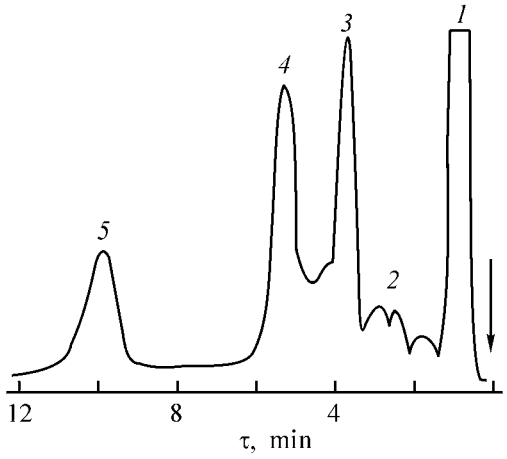

Chromatogram of a mixture of acetylacetonates on a 60 × 0.4-cm Teflon column. Stationary phase 5% SE-30 on Chromosorb G AW DMDS. Temperatures, °C: column 150, vaporizer 250, and detector 200; carrier gas He, flow rate 60 $cm^3\,min^{-1}$. (τ) Retention time. (*1*) CCl_4, (*2*) products of $Al(acac)_3$ decomposition, (*3*) $Al(acac)_3$, (*4*) $Ga(acac)_3$, and (*5*) $Cr(acac)_3$.

The Teflon columns are advantageous over the glass columns because of the more inert column material. On Teflon columns, $Al(acac)_3$ and $Cr(acac)_3$ gave reproducible peaks even in the first injections, whereas on glass columns the first peaks appear after repeated injections. Steel columns are wholly unsuitable for this purpose because of the catalytic degradation of the complexes on the column walls, to give large amounts of degradation products.

We found that the chromatographic separation of the β-diketonates under consideration is largely influenced by the solvent. With chloroform, resolution of the chelate and solvent peaks is unsatisfactory, and with acetone, the chromatographic peaks are resolved incompletely, probably because of the coordination interaction with possible outer-sphere ligand exchange. The best results were obtained with CCl_4.

For $Al(acac)_3$, $Ga(acac)_3$, and $Cr(acac)_3$, we calculated the Kovats retention indices. The results are listed in Table 2.

The retention index depends on the sorbate structure and strength of metal coordination in the chelate ring. The retention indices of $Al(acac)_3$ and $Ga(acac)_3$ are similar, which is consistent with the fact that the ionic radii of Al^{3+} and Ga^{3+} are approximately equal. The specific features of the electronic structure of chromium (presence of 3*d* electrons) are apparently responsible for the appreciably longer retention time of the acetylacetonate and increased logarithmic retention index. The minimal values of the Kovats index are observed on the SE-30 nonpolar phase. With this phase, the metal acetylacetonates can be determined most quickly, without loss in the accuracy of analysis. Acetylacetonates can also be separated on SKTFT and SKTFV-803 phases. In the case of SKT and OV-1, the high polarity of the phases results in a significant increase in the retention time of $Cr(acac)_3$ and in broadening of its chromatographic peak. The chromatogram of $Ga(acac)_3$, $Al(acac)_3$, and $Ga(acac)_3$, obtained on a Teflon column with the SE-30 phase, is shown in the figure.

The chromatogram reveals broadening of the peaks due to decomposition of gallium and aluminum acetylacetonates. As the vaporizer temperature is decreased, the peaks of decomposition products decrease in intensity and finally disappear. With chromium acetylacetonate, which is more stable thermally, we detected no decomposition products. Thus, the tem-

Table 3. Comparison of the suggested gas-chromatographic procedure for Al determination in polyolefins with the results obtained by independent methods (n = 4–5, P = 0.95)

Method	Sr	Detection limit, wt %	Analysis time, h
Spectrophotometry	0.06	>0.005	>4
Atomic emission spectroscopy	0.11	10^{-6}	>4
Gas chromatography	0.05	to 0.001	~1.5

perature conditions of the analysis should be chosen so as to minimize the degree of the chelate decomposition, but, at the same time, ensure short time of analysis (10 min retention time of the last component).

Using the introduced–found method, we compared our procedure with the most frequently used procedure for photometric determination of residual Al in polyolefins with Xylenol orange [11] and with atomic emission analysis. The results of chromatographic determination of the Al content (Table 3) coincide, within a random error, with the results of independent determinations, with the analysis time being appreciably curtailed.

CONCLUSIONS

(1) The study of the gas-chromatographic behavior of volatile aluminum, chromium, and gallium acetylacetonates in packed columns showed that these complexes can be determined quantitatively without appreciable degradation when the temperatures are relatively low and the columns are sufficiently short. The retention parameters of the compounds on various phases were measured experimentally.

(2) A procedure, based on the data obtained, was developed for determination of metal traces in polypropylene. The metrological characteristics of this procedure were compared with those of commonly used procedures.

REFERENCES

1. Boreskov, G.K., *Geterogennyi kataliz* (Heterogeneous Catalysis), Moscow Nauka, 1988.
2. *Kataliticheskie svoistva veshchestv: Spravochnik* (Catalytic Properties of Substances: Handbook), Kiev: Naukova Dumka, 1968.
3. Sokolovskii, V.D., Yur'eva, T.M., Matros, Yu.M., *et al., Usp. Khim.*, 1989, vol. 58, no. 1, pp. 38–55.
4. Moshier, R.W. and Sievers, R.E., *Gas Chromatography of Metal Chelates*, Oxford: Pergamon, 1965.
5. Sokolov, D.N., Nesterenko, G.N., and Golubeva, L.K., *Zavod. Lab.*, 1973, vol. 39, no. 8, pp. 939–944.
6. Slizhov, Yu.G. and Gavrilenko, M.A., *Primenenie vnutrikompleksnykh soedinenii v gazovoi khromatografii* (Use of Chelates in Gas Chromatography), Tomsk: Tomsk. Gos. Univ., 2000.
7. Slizhov, Yu.G., Berezkin, V.G., and Arkhipova, I.M., *Zh. Anal. Khim.*, 1991, vol. 46, no. 4, pp. 736–740.
8. Genty, C., Harin, C., and Malherbe, P., *Anal. Chem.*, 1971, vol. 43, no. 2, p. 235.
9. Sokolov, D.N. and Nesterenko, G.N., *Zavod. Lab.*, 1976, vol. 42, no. 10, pp. 1172–1174.
10. Kazitsyna, L.A. and Kupletskaya, N.B., *Primenenie UF-, IK i YaMR-spektroskopii v organicheskoi khimii* (Application of UV, IR, and NMR Spectroscopy to Organic Chemistry), Moscow: Vysshaya Shkola, 1971.
11. Cotton, F.A. and Wilkinson, G., *Advanced Inorganic Chemistry*, New York: Interscience, 1966.

Russian Journal of Applied Chemistry, Vol. 77, No. 2, 2004, pp. 218–221. Translated from Zhurnal Prikladnoi Khimii, Vol. 77, No. 2, 2004, pp. 222–225.

CATALYSIS

Catalytic Activity of Manganese-containing Layers Formed by Anodic-Spark Deposition

M. S. Vasil'eva, V. S. Rudnev, N. B. Kondrikov, L. M. Tyrina, A. A. Reshetar', and P. S. Gordienko

Far-Eastern State University, Vladivostok, Russia

Institute of Chemistry, Far-Eastern Division, Russian Academy of Sciences, Vladivostok, Russia

Received April 10, 2003

Abstract—The catalytic activity of manganese oxide–containing anodic layers formed on titanium at room temperature in CO oxidation to CO_2 was studied.

Systems that contain MnO_2, Mn_2O_3, and Mn_3O_4 catalyze numerous gas- and liquid-phase reactions [1–4]. In particular, they are used as catalysts for CO oxidation to CO_2 [3, 5]. Manganese oxides are commonly obtained by various chemical methods; for example, Mn_2O_3 and Mn_3O_4 are prepared by heating salts, oxides, or hydroxides of manganese to 700 and 1000°C, respectively [2].

Previously, surface structures with thickness of up to 60 μm, which contained, together with TiO_2, oxides Mn_2O_3 and Mn_3O_4, have been obtained on titanium by anodic-spark deposition at room temperature from an electrolyte containing sodium tetraborate and salts of manganese [6]. In the process, both the phase composition and the content of manganese in the coatings (0–40 at.%) could be purposefully altered by varying the concentration of manganese salts and the forming modes.

This communication reports the results obtained in evaluating the catalytic activity in CO oxidation of manganese-containing structures formed on titanium.

EXPERIMENTAL

Electrolytes were prepared using distilled water and commercial reagents $Na_2B_4O_7 \cdot 10H_2O$ and $Mn(CH_3COO)_2 \cdot 4H_2O$ of chemically pure grade. Anodic films were formed by means of electric breakdowns on VT1-0 titanium samples in the galvanostatic mode (i = 0.2 A cm^{-2}) in the course of 4 or 10 min. As current source served a thyristor converter with unipolar current pulses. The process was performed in the temperature range 13–40°C. The specific features of electrolyte preparation, the design of the electrochemical cell and units for solution cooling and agitation, and the method for electrode pretreatment were described in [6].

The phase composition of the coatings was determined on a DRON-2.0 diffractometer (Cu_{K_α} radiation), and the elemental composition, on a JXA-5A X-ray fluorescence microanalyzer, with measurement error of about 10%.

The molar ratio of the gaseous components changes when the reaction $2CO + O_2 \rightarrow 2CO_2$ occurs. Therefore, a setup that comprised a 400-cm^3 quartz reactor and a pressure gage connected to it was used for evaluating the catalytic activity of the structures synthesized, in the reaction of CO oxidation to CO_2. The pressure gage provided measurements in the range –0.1–0 MPa with an accuracy of 5×10^{-3} MPa. Samples with a total area of 40 cm^2 were placed in the reactor. Preliminarily, a 2 : 1 gas mixture of oxygen and carbon(II) oxide with a total volume of 300 cm^3 was prepared volumetrically in a separate vessel. A rarefaction was created in the reactor with a fore pump. Then, the gas mixture prepared was admitted into the reactor at room temperature and heated at a rate of 20 deg min^{-1}. Simultaneously, the variation of pressure within the reactor was recorded.

The composition of the gas mixture at the reactor outlet was determined with an LKhM-8MD chromatograph.

Figure 1a shows how the pressure in the reactor varies with temperature in the presence (curves *1*, *2*) and in the absence (curve *3*) of titanium with manganese oxides in its surface layer. It can be seen that, in the presence of manganese-containing layers,

1070-4272/04/7702-0218 © 2004 MAIK "Nauka/Interperiodica"

the pressure in the reactor decreases in the range 250–350°C despite the rise in temperature. This indicates that the molar ratio of the gaseous components in the reactor changes because of the occurrence of the reaction $2CO + O_2 \rightarrow 2CO_2$. This conclusion is confirmed by the results presented below and by an analysis of these.

Figure 2 shows chromatograms of a gas mixture kept at 340°C in the absence (a) and in the presence (b) in the reactor of titanium with manganese oxides in its surface layer, c_{Mn} = 35.7 at.%. The decrease in the area of the peaks related to CO directly indicates that the reaction of CO oxidation to CO_2 occurs in the temperature range under study on manganese-containing layers formed by the anodic-spark deposition method.

Similar $P = f(T)$ dependences were obtained with a platinum grid with an area of 8 cm^2 charged into the reactor with the gas mixture (Fig. 1b). In this case, the conversion temperature was in the range 180–250°C.

When titanium or titanium that contains only TiO_2 in its surface layer is placed in the reactor, the temperature dependence of the pressure in the reactor is similar to that obtained in the absence of manganese-containing layers (Fig. 1a, curve *3*). This result, on the one hand, means that titanium and anodic-spark layers that contain only TiO_2 do not catalyze the reaction of CO oxidation in the absence of manganese oxides, and on the other, indicates that the influence exerted by the oxidation of the titanium base on the variation of the pressure in the reactor is insignificant at the given temperatures.

The results obtained in measuring the catalytic activity in five successive cycles of measurements on one and the same sample demonstrate that the dependences $P = f(T)$ are identical to those shown in Fig. 1a (curves *1*, *2*) as regards both the temperature range and the magnitude of changes in pressure. In this case, the phase (Fig. 3) and elemental (Table 1) composition of the coatings changed only slightly. The crystallinity of the coatings increased somewhat, and no new crystalline phases appeared. The minor decrease in the content of manganese, the increase in the content of titanium, and the corresponding change in the calculated amount of oxygen in the surface layer being analyzed (analysis to a depth of 3–5 μm) may be due both to the possible measurement errors and to processes of thermal diffusion of elements across the layer thickness and influence of crystallization processes, which lead to cracking. Undoubtedly, the problems of stability and working life of the systems in question under the conditions mentioned invite further investigation.

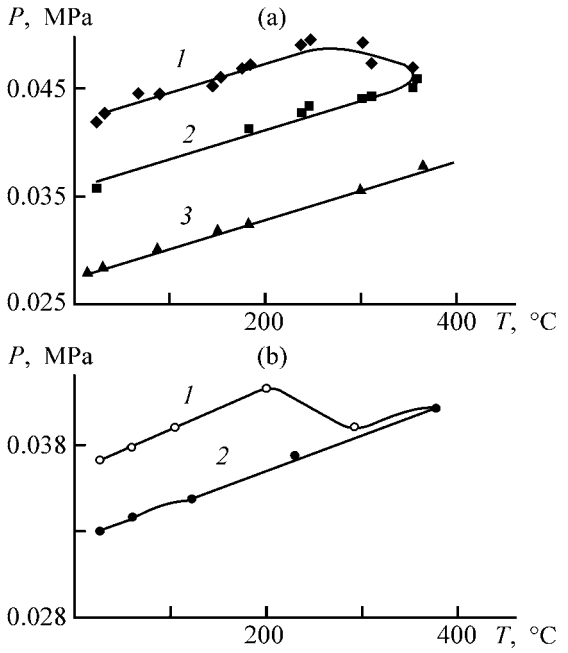

Fig. 1. Pressure *P* of the gas mixture vs. *T*, (*1*, *2*) in the presence and (*3*) in the absence of (a) titanium with manganese oxides in its surface layer and (b) platinum grid. (*1*) Heating, (*2*) cooling, and (*3*) heating–cooling.

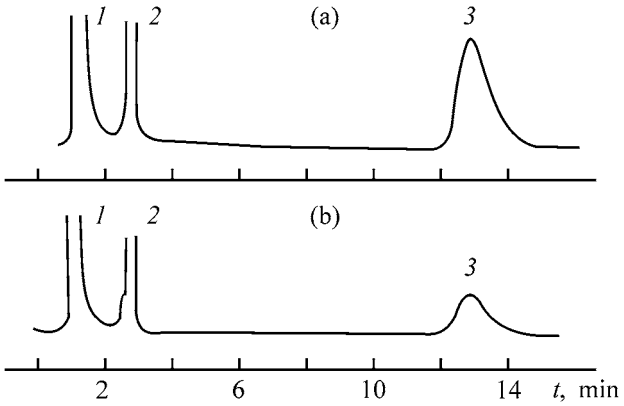

Fig. 2. Chromatograms of a gas mixture kept in the reactor at 340°C for 30 min (a) in the absence and (b) in the presence of titanium with manganese oxides in its surface layer. c_{Mn} = 35.7 at.%. (*t*) Time. (*1*) O_2, (*2*) N_2, and (*3*) CO.

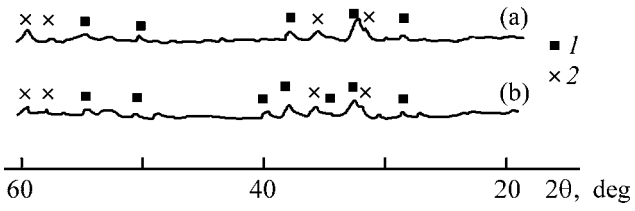

Fig. 3. X-ray diffraction patterns of anodic-spark layers formed on titanium: (a) initial layers and (b) those after catalysis. (2θ) Bragg angle. (*1*) Mn_2O_3 and (*2*) Mn_3O_4.

Table 1. Elemental composition of coatings

Composition	Content, at.%			
	Mn	Ti	Na	O*
Initial	39.7	1.9	0.3	58.2
After five measurement cycles	33.0	3.0	0.3	63.3

* Calculated from the difference.

Table 2. Rate constant of CO oxidation on various manganese-containing systems

System	$k \times 10^4$ (s^{-1}) at indicated T, °C	
	260	290
$Mn_2O_3 + Mn_3O_4$, c_{Mn}, at.%:		
22.9	0.15	0.16
31.4	0.19	0.23
35.7	1.75	1.90
39.6	0.24	0.34
β-MnO_2	0.88	0.90

It may be assumed that the change in the pressure in the reactor in the first measurement cycle may be due to oxidation of amorphous oxide MnO contained in the coatings to amorphous MnO_2 in the temperature range 250–350°C. In this case, the content of oxygen in the coatings must substantially increase, and the atomic ratio Mn/O must markedly decrease, after a cycle of heating–cooling in an oxygen-containing gas mixture. At the same time, as follows from the experimental data presented here, no decrease in this ratio was observed. Calculations show that the experimental data on the elemental composition of the coatings correspond to presence of the compounds TiO_2, Mn_2O_3, and Mn_3O_4 both in the initial state and after five cycles of catalytic activity measurements.

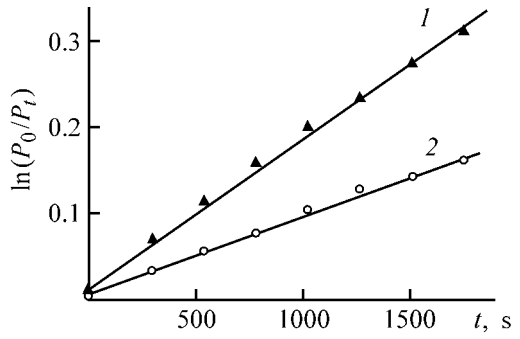

Fig. 4. $\ln(P_0/P_t)$ vs. time t of the process of CO oxidation on anodic layers that contain manganese oxides of various compositions, at 290°C. (P_0, P_t) Partial pressure of CO at the initial instant of time and at the instant of time t, respectively. (*1*) Mn_2O_3, Mn_3O_4 and (*2*) β-MnO_2.

Thus, the experimental data obtained show that, under the experimental conditions, the catalysts formed on titanium by anodic-spark deposition, which contain oxides Mn_2O_3 and Mn_3O_4, catalyze the reaction of CO oxidation to CO_2 in the temperature range 250–350°C.

Figure 4 shows kinetic curves that describe the reaction of CO oxidation at 290°C, plotted in the semilogarithmic coordinates $\ln(P_0/P_t)$–t. The partial pressures of CO, P_0 and P_t, were calculated from the known total pressure and molar ratio of the components. It can be seen that a linear dependence is observed in the presence in the reactor of titanium with a layer of oxides Mn_2O_3 and Mn_3O_4, with a manganese content c_{Mn} = 35.7 at.% (curve *1*), and titanium with a β-MnO_2 layer deposited by the conventional pyrolytic method (curve *2*) [7]. This dependence indicates that, in both cases, the CO oxidation formally proceeds by a first-order reaction and is due to the presence of an excess amount of oxygen in the reaction mixture. The rate constants of the reaction of CO_2 formation at 260 and 290°C, calculated using the equation $\ln(P_0/P_t) = kt$ for titanium with varied content of manganese in the surface layer, are listed in Table 2.

It can be seen that the rate of CO conversion to CO_2 depends on the content of manganese in the anodic layers. Samples that differed in the content of manganese were obtained both by using electrolytes with different concentrations of the components and by varying the forming modes. The optimal content of manganese at the chosen temperatures is 35.7 at.%. This is presumably due to a change in the ratio of the oxides, in their distribution in the surface layer, and in the surface morphology and also to specific features of coating formation by anodic-spark deposition.

CONCLUSIONS

(1) Manganese-containing anodic films on titanium, formed by the anodic-spark method, catalyze the reaction of CO oxidation in the temperature range 250–350°C. The catalytic activity of structures of this kind compares well with that of coatings obtained by the conventional pyrolytic technique.

(2) The rate of CO conversion on the anodic structures formed depends on the content of manganese in these structures.

ACKNOWLEDGMENTS

The study was supported in part by the programs of the Ministry of Education of the Russian Federation "New Materials" (grant no. 02.02.055) and "Universities of Russia" (grant no. UR-05.01.018).

REFERENCES

1. Arena, F., Torre, T., Raimondo, C., and Parmaliana, A., *Phys. Chem. Chem. Phys.*, 2001, vol. 3, pp. 1911–1917.
2. Ocana, M., *Colloid Polym. Sci.*, 2000, vol. 278, pp. 443–449.
3. Zaki, M.I., Hasan, M.A., Paspulety, L., and Kumari, K., *Thermochim. Acta*, 1998, vol. 311, pp. 97–103.
4. Bezouhanova, C. and Al-Zihari, M.A., *Appl. Catal. A*, 1992, vol. 83, pp. 45–49.
5. *Kataliticheskie svoistva veshchestv: Spravochnik* (Catalytic Properties of Substances: Reference Book), vol. 4, Gorokhovskii, Ya.B., Ed., Kiev: Naukova Dumka, 1977, pp. 225–226.
6. Rudnev, V.S., Vasil'eva, M.S., Tyrina, L.M., *et al.*, *Zh. Prikl. Khim.*, 2003, vol. 76, no. 7, pp. 1092–1098.
7. Razina, N.F., *Okisnye elektrody v vodnykh rastvorakh* (Oxide Electrodes in Aqueous Solutions), Alma-ata: Nauka, 1982.

Russian Journal of Applied Chemistry, Vol. 77, No. 2, 2004, pp. 222–225. Translated from Zhurnal Prikladnoi Khimii, Vol. 77, No. 2, 2004, pp. 226–229.

APPLIED ELECTROCHEMISTRY AND CORROSION PROTECTION OF METALS

Cathodic Deposition of Zinc from Dilute Solutions onto a Rotating Disc Electrode

V. S. Kolosnitsyn and O. A. Yapryntseva

Institute of Organic Chemistry, Ufa Scientific Center, Russian Academy of Sciences, Ufa, Bashkortostan, Russia

Received May 22, 2003

Abstract—The cathodic deposition of zinc onto a rotating disc electrode was studied. The influence exerted by various parameters on the process was examined. The observed phenomena were explained in terms of corrosion and the positive difference-effect.

Purification of sewage to remove heavy-metal ions is a problem of current importance for many industries. Various methods can be used for sewage purification, but electrochemical methods, such as electrocoagulation, electroflotation, electrodestruction, and electrodeposition of metals, are of particular interest. The electric treatment makes it possible to purify wastewater of varied composition and dispersity without raising the content of salts in a water being purified and, rather frequently, with precipitates not formed at all or formed in a considerably decreased amount [1]. Among the electrochemical methods mentioned above, the electrolysis is of special interest, since it can be performed without use of chemicals in the course of purification and yields a metal in the form of a target product, which simplifies its further processing.

The electrodeposition of metals from dilute solutions has its own specific features, which consist in that the process rate is limited by delivery of a reagent to the electrode surface. This problem can be solved by using a rotating disc electrode instead of an immobile electrode. As shown previously [2], using a rotating disc cathode allows the rate of copper electrodeposition from dilute solutions to be increased by a factor of 5–10, with a high current efficiency (CE) retained.

In this study, we continue to examine the electrodeposition of metals onto a rotating disc electrode and the cathodic deposition of zinc from solutions with concentrations of up to 1 g l^{-1}.

EXPERIMENTAL

Zinc was electrodeposited in a glass cell with a rotating cathode. The cell volume was 0.5 l. As cathodes were used discs made of stainless steel, sheet copper, and aluminum. The cathode area was 160 cm^2. Semi-discs made of titanium gauze coated with ruthenium(IV) oxide served as anodes. Prior to the experiments, the cathodes were trimmed with an emery paper and washed in the electrolyte solution.

The electrodes were polarized in the galvanostatic mode with a B5-49 source of stabilized current and voltage. The voltage was monitored with a V7-27 A/1 voltmeter.

The rate of rotation of the disc electrode was determined and controlled using a tachometer.

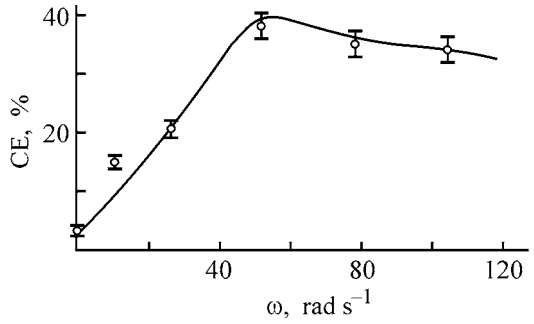

Fig. 1. Effect of the rotation rate ω on the current efficiency CE by zinc in cathodic deposition from dilute solutions. Supporting electrolyte 0.5 M Na_2SO_4, $c_{Zn^{2+}}$ = 100 mg l^{-1}, pH 6, copper cathode.

1070-4272/04/7702-0222 © 2004 MAIK "Nauka/Interperiodica"

The electrolyte solutions were prepared by the gravimetric method by dissolving the appropriate dry salts in distilled water. The current efficiency was determined from the difference of the zinc concentrations before and after the electrolysis. The content of zinc(II) was determined by direct complexometric titration.

The duration of electrolysis was calculated on the basis of the initial concentration of zinc ions in the solution, so that the amount of electricity passed through the cell corresponded to the complete recovery of metal.

The dependence of CE on the rate of cathode rotation is shown in Fig. 1. It can be seen that CE is 5% for the immobile electrode. As the rotation rate is raised to 52.3 rad d^{-1}, CE increases to 35–40%. With the rotation rate raised further, CE somewhat decreases.

The pH value of the electrolyte solutions also affects the current efficiency. The dependence of CE on the solution pH passes through a maximum at pH 7 (Fig. 2).

Irrespective of the initial concentration of zinc ions, the dependences of CE on current density also pass through a maximum (Fig. 3), whose position shifts to higher current densities as the concentration of zinc ions in the electrolyte increases.

With a stainless steel electrode, no zinc is deposited onto the cathode, whereas with copper and aluminum electrodes, the cathodic deposition of zinc is rather effective (Fig. 4).

To account for the dependences obtained, it is necessary to note that the electrodeposition of metals, which stand to the left of hydrogen in the electrochemical series, is almost always complicated by a concurrent reaction of hydrogen evolution. In addition, electronegative metals can displace hydrogen from water, i.e., they may be subject to corrosion with a hydrogen and oxygen depolarization. Therefore, the CE by zinc in cathodic deposition will be determined by the relative rates of three processes: zinc recovery, hydrogen evolution, and corrosion of zinc from the electrode surface. It is also necessary to note that amphoteric metals, such as zinc, exhibit a positive difference-effect in cathodic polarization, which originates from destruction of a protective zinc oxide film upon alkalization of the near-cathode layer of the solution through cathodic evolution of hydrogen.

The flux N of a solution across the boundary diffusion layer, which appears on a rotating cathode and

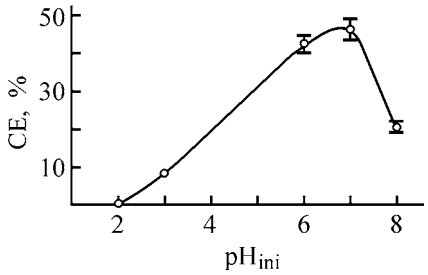

Fig. 2. Effect of the pH of the initial solution on the CE by zinc in cathodic deposition. Supporting electrolyte 0.5 M Na_2SO_4, $c_{Zn^{2+}}$ = 100 mg l^{-1}, i = 1 mA cm^{-2}, ω = 52.3 rad s^{-1}, copper cathode.

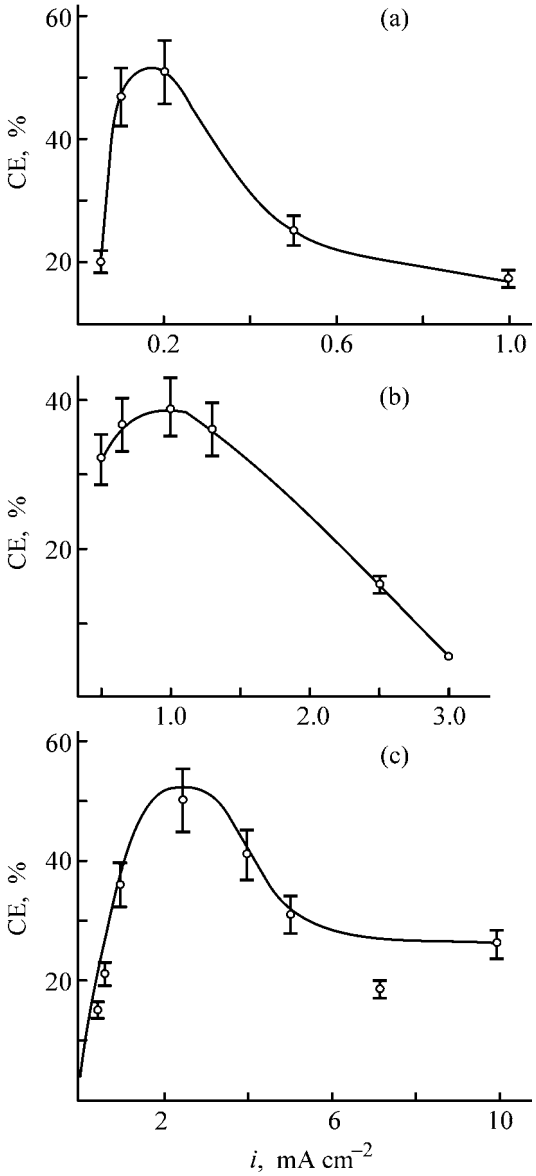

Fig. 3. Current efficiency CE by zinc in cathodic deposition from dilute solutions with various concentrations vs. current density i. Supporting electrolyte 0.5 M Na_2SO_4, pH 6, ω = 52.3 rad s^{-1}, copper cathode. Zinc concentration (mg l^{-1}): (a) 5, (b) 100, and (c) 1000.

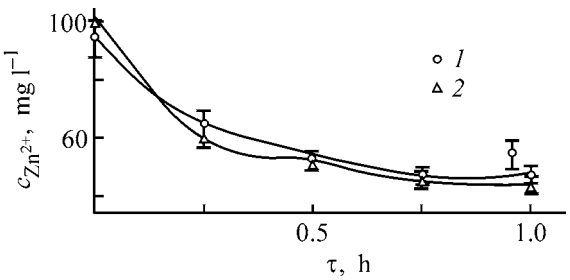

Fig. 4. Variation of zinc concentration $c_{Zn^{2+}}$ in the course of electrolysis with cathodes made of different materials. Supporting electrolyte 0.5 M Na_2SO_4, pH 6, ω = 52.3 rad s^{-1}. Cathode: (*1*) copper and (*2*) aluminum. (τ) Duration of electrolysis.

is at rest with respect to it, is directly proportional to the diffusion coefficient D of the solution and to the gradient of the solution concentration Δc and inversely proportional to the thickness δ of the boundary diffusion layer δ: [3]:

$$N = D\Delta c/\delta. \quad (1)$$

In turn, δ can be calculated as follows [4]:

$$\delta = 1.61 D^{1/3} \nu^{1/6} \omega^{-1/2}, \quad (2)$$

where ν is the kinematic viscosity of the electrolyte solution (cm^2 s^{-1}), and ω is the angular velocity of rotation of the electrode (s^{-1}).

The concentration difference is given by

$$\Delta c = c_0 - c_c, \quad (3)$$

where c_0 is the concentration of ions in the solution bulk, and c_c is the concentration of ions at the electrode surface.

The latter concentration can be calculated as follows:

$$c_c = c_0 - i_c\delta/(DFz_i), \quad (4)$$

where i_c is the current flowing to the cathode, and z_i is the ion charge.

Substituting the expression for the boundary layer thickness into Eq. (4), we obtain

$$c_c = c_0 - 1.62 i_c \nu^{1/6}/(D^{1/3} F z_i \omega^{1/2}). \quad (5)$$

According to (5), the concentration of ions at the cathode surface increases with the rotation rate. This allows electrolysis to be performed at higher current densities.

At the same time, at high flow velocities of the electrolyte, the cathodically formed alkali is removed from, and the oxidant (e.g., oxygen) delivered to the cathode surface. As a result, the surface of freshly deposited zinc has enough time to be covered with a protective oxide film. This explains why CE increases when the rate of cathode rotation is raised to 52.3 rad s^{-1} (Fig. 1). However, as the rotation rate increases further, CE decreases somewhat, which is probably due to the fact that, at higher flow velocities of the electrolyte, the corrosion becomes the so-called impingement corrosion. In this case, the passivating films, which were formed and existed before the onset of corrosion, are torn off the metal surface by a liquid jet, so that the metal without a protective film undergoes intense corrosion [5].

The shape of the obtained CE-vs.-pH curve (Fig. 2) can be accounted for by the influence of acidity on processes of hydrogen evolution and zinc corrosion, which occur simultaneously at the cathode.

It is known that the dependence of the hydrogen overvoltage on the solution pH passes through a maximum at pH 7 [6]. Because zinc is an amphoteric metal, the rate of its corrosion also depends on the solution pH. The corrosion rate is the lowest in neutral solutions and increases dramatically in acid and alkaline solutions [5, 7].

Thus, the appearance of a peak in the CE-vs.-pH curve (Fig. 2) is due to the fact that, in acid and alkaline solutions, the processes of zinc corrosion and hydrogen evolution prevail over the cathodic deposition of zinc.

The effect of current density on the CE by zinc in cathodic deposition was studied in solutions with initial pH 6. The appearance of extrema in the CE–i dependences is probably due to the fact that, at low rates of the cathodic process, the pH of the near-electrode layer increases, but does not exceed 7. Under these conditions, the rates of hydrogen evolution and zinc corrosion are the lowest. Therefore, the CE by zinc in its cathodic recovery increases with current density at low polarizing currents. After the current densities at which pH 7 is established in the near-electrode layer are attained, the rates of cathodic hydrogen evolution and zinc corrosion start to increase. Therefore, CE by zinc starts to decrease after a certain polarizing current density is reached.

Presumably, the shift of the peak positions to higher current densities, observed in the CE–i dependences as the concentration of zinc(II) increases, is due to acceleration of the cathodic recovery of zinc

owing to a decrease in the overvoltage. In this case, the rates of other concurrent processes remain virtually unchanged.

When zinc is deposited onto the surface of metals that have a more positive standard potential than zinc, it forms with them short-circuited galvanic microcells [8], in which the more electropositive metal is a cathode, on which hydrogen evolution occurs, and zinc is a soluble anode. The dissolution of zinc is limited by the cathodic evolution of hydrogen, which, in turn, is dependent on the overvoltage of hydrogen evolution on a given metal.

As is known, the overvoltage of hydrogen evolution on metals that constitute stainless steel (such as iron and nickel) is lower than that on copper and aluminum. Therefore, the rate of electrochemical corrosion of zinc on the surface of a stainless steel electrode is such that we do not observe its deposition. At the same time, the deposition of zinc onto copper and aluminum is rather effective, with the CE by zinc in cathodic deposition being as high as 30–40%.

CONCLUSION

The study performed demonstrated that the deposition of zinc from dilute aqueous solutions onto a rotating disc electrode is complicated by intense corrosion. On an immobile cathode, the current efficiency does not exceed 5%. On a rotating electrode, the current efficiency by zinc grows with the rotation rate, to reach its maximum value (35–40%) at a rate of 52.3 rad s^{-1}. Irrespective of the initial concentration of zinc(II) in a solution, the current efficiency first increases and then decreases as the current density becomes higher. The pH value of the electrolyte solutions, at which the CE by zinc is at a maximum in electrodeposition from dilute solutions with concentration of up to 1 g l^{-1}, is 6–7.

REFERENCES

1. Yakovlev, S.V., Krasnoborod'ko, I.G., and Rogov, V.M., *Tekhnologiya elektrokhimicheskoi ochistki vody* (Electrochemical Purification of Water), Leningrad: Stroiizdat, 1987.
2. Kolosnitsyn, V.S., and Yapryntseva, O.A., *Zh. Prikl. Khim.*, 2004, vol. 77, no. 1, pp. 60–64.
3. Tarasevich, M.P., Khrushcheva, E.I., and Filinovskii, V.Yu., *Vrashchayushchiisya diskovyi elektrod* (Rotating Disc Electrode), Moscow: Nauka, 1987.
4. Kublanovskii, V.S., Gorodyskii, A.V., Belinskii, V.N., and Glushchuk, T.S., *Kontsentratsionnye izmeneniya v prielektrodnykh sloyakh v protsesse elektroliza* (Variation of Concentration in Near-Electrode Layers in the Course of Electrolysis), Kiev: Naukova Dumka, 1972.
5. Akimov, G.V., *Teoriya i metody issledovaniya korrozii metallov* (Theory and Methods of Study of Metal Corrosion), Moscow: Akad. Nauk SSSR, 1945.
6. Antropov, L.I., *Teoreticheskaya elektrokhimiya* (Theoretical Electrochemistry), Moscow: Vysshaya Shkola, 1975.
7. Tomashov, N.D., *Teoriya korrozii i zashchity metallov* (Theory of Corrosion and Protection of Metals), Moscow: Akad. Nauk SSSR, 1960.
8. Pecherskaya, A.G., and Stender, V.V., *Zh. Prikl. Khim.*, 1950, vol. 32, no. 9, pp. 921–935.

Russian Journal of Applied Chemistry, Vol. 77, No. 2, 2004, pp. 226–230. Translated from Zhurnal Prikladnoi Khimii, Vol. 77, No. 2, 2004, pp. 230–234.

APPLIED ELECTROCHEMISTRY AND CORROSION PROTECTION OF METALS

Electrodeposition of CdTe Films from Ammonia-Chloride Buffer Electrolyte

M. B. Dergacheva, V. N. Statsyuk, and L. A. Fogel'

Sokol'skii Institute of Organic Catalysis and Electrochemistry, National Academy of Sciences of the Republic of Kazakhstan, Almaty, Kazakhstan

Received August 4, 2003

Abstract—Voltammetry was applied to a study of joint electroreduction of Cd(II) and Te(IV) on a glassy carbon electrode from an ammonia-chloride buffer electrolyte with pH 8.4. The optimal conditions of electrodeposition of CdTe films were determined and their structure was examined by means of X-ray phase analysis.

The optimal band gap width (E_g = 1.44 eV) and the possibility of obtaining deposits with *p*- and *n*-type conduction allow wide use of electrodeposited CdTe films in photoelectric devices. CdTe films are commonly deposited electrochemically from acid electrolytes at pH 1–3 [1–7]. One of the principal disadvantages of acid electrolytes is that corrosion processes occur and elementary tellurium is codeposited together with the CdTe deposit. This is so because, as it follows from the potential–pH diagram of the CdTe compound in aqueous solutions [8], the stability region of elementary tellurium in acid solutions is wide and becomes narrower as pH increases. To prevent accumulation of elementary tellurium in CdTe films, the concentration of Te(IV) ions in acid solutions is chosen to be much lower than that of Cd(II) ions. The Cd(II)/Te(IV) concentration ratio should be about 10^4. In this case, the rate of CdTe formation in the process of deposition is controlled by transport of $HTeO_2^+$ ions to the electrode surface. The deposition is performed at 363 K. Under these conditions, uniform CdTe films with good adhesion cannot be always obtained. The difficulties encountered can be eliminated by using a complex electrolyte with high pH values.

The processes of CdTe formation affect the reaction kinetics in two ways. First, the equilibrium potential of the system $HTeO_2^+$/Te depends on the pH value, whereas that of the system (Cd^{2+} + Te)/CdTe is independent of this parameter. Second, the rate of electron transfer at the potential of $HTeO_2^+$ reduction decreases as pH increases. If the stage that governs the stoichiometry is potential-independent (e.g., if this is the subsequent chemical reaction), then the deposit quality will improve with decreasing rate of the electrochemical reaction.

The electrochemical deposition of CdTe films on a glassy carbon was carried out using an ammonia-chloride buffer electrolyte with pH 8.4, buffer capacity π = 0.4, and ionic strength μ = 2. This electrolyte enhances the proton-donor capacity of aqueous solutions and hinders hydrolysis of Cd(II) ions because of the formation of $Cd(NH_3)_n^{2+}$ ammonia complexes. The electrochemical processes that occur at the electrode in electrodeposition of CdTe were studied by means of voltammetry and X-ray phase analysis (XPA).

EXPERIMENTAL

The voltammetric studies were performed using a PI-50.1.1 potentiostat, with *I*–*E* curves recorded with a PDA-1 XY recorder. The potential sweep rate was 20 mV s^{-1}. A three-electrode electrochemical cell was in the form of a hermetically sealed thermostated Pyrex glass vessel with separated anode and cathode spaces. As working electrode served a glassy carbon disc electrode with an apparent surface area of 0.07 cm^2. As auxiliary electrode was used a platinum wire with an apparent surface area of 1.5 cm^2. All the potentials are given in this paper relative to a saturated silver chloride reference electrode.

The working solution was agitated with a magnetic stirrer. Measurements on the disc electrode were performed at a temperature of 30°C, CdTe films on

1070-4272/04/7702-0226 © 2004 MAIK "Nauka/Interperiodica"

glassy carbon electrodes with an apparent surface area of 1 cm^2 were obtained at 80°C. Prior to experiments, the glassy carbon was cleaned with a finely dispersed Al_2O_3 powder and then washed with ethanol and distilled water. X-ray analysis of the films was made on a DRON-3 instrument with Co radiation. Reagents of special-purity and chemically pure grades were used in the study. The solutions used were prepared with twice-distilled water.

Figure 1 compares potentiodynamic voltammetric curves of cathodic reduction of Te(IV) and Cd(II) ions and their reverse runs (curves *1*) in an ammonia-chloride buffer solution at pH 8.4 with voltammetric curves of their codeposition (curves *2*). The cathodic voltammetric curve obtained in a solution containing 3.8×10^{-4} M of Te(IV) (Fig. 1a, curve *1*) shows a region of limiting current, which is due to Te(IV) reduction to Te(0), with peak current at a potential $E_m = -0.6$ V [Eq. (1)], and a peak of cathodic current at a potential $E_p = -0.9$ V, which is associated with further reduction of elementary tellurium to a telluride [Eq. (2)]. When the direction of potential sweep is changed in the anodic region, elementary tellurium is oxidized to Te(IV) ($E_p = 0.09$ V) in accordance with Eq. (3):

$$TeO_3^{2-} + 6H^+ + 4e \rightarrow Te^0 + 3H_2O, \quad (1)$$

$$Te^0 + 2e + H^+ \rightarrow Te^{2-}, \quad (2)$$

$$Te^0 - 4e + 3H_2O \rightarrow TeO_3^{2-} + 6H^+. \quad (3)$$

As the concentration of Te(IV) ions in the solution bulk increases, the limiting current associated with electroreduction of Te(IV) to Te(0) and the current in the anodic peak at $E_p = 0.09$ V become higher.

Figure 1b shows the voltammetric curves of discharge–ionization of Cd(II) ions on a glassy carbon electrode in an ammonia-chloride buffer solution with pH 8.4. The voltammetric curve shows a wave associated with reduction of Cd(II) ($E_p = -0.9$ V) and a current peak related to oxidation of metallic cadmium ($E_p = -0.87$ V) in reverse sweep of the potential. The process of Cd(II) discharge–ionization in an ammonia-chloride buffer solution is reversible. This is indicated by the potential difference of the current peaks of reduction and oxidation, $\Delta E = 0.03$ V. With increasing Cd(II) concentration, the heights of the current peaks related to reduction of Cd^{2+} ions and oxidation of metallic cadmium grow linearly.

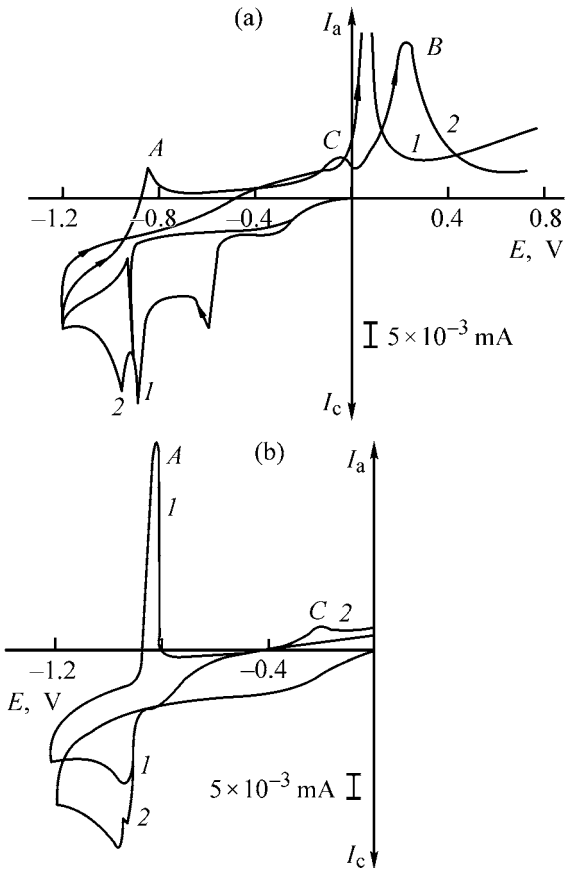

Fig. 1. Voltammetric curves of joint discharge–ionization of Te(IV) and Cd(II) ions on a glassy carbon electrode in an ammonia-chloride buffer electrolyte of varied composition at pH 8.4. (*I*) Current and (*E*) potential; the same for Figs. 2–4. (a) $c_{Te(IV)} = 3.8 \times 10^{-4}$ M. $c_{Cd(II)}$ (M): (*1*) 0 and (*2*) 4.58×10^{-4}. (b) $c_{Cd(II)} = 3.8 \times 10^{-4}$ M. $c_{Te(IV)}$ (M): (*1*) 0 and (*2*) 6.3×10^{-4}.

On addition of 4.58×10^{-4} M of Cd(II) to a solution that contains 3.8×10^{-4} M of Te(IV) (Fig. 1a, curve *2*), the wave of Cd(II) reduction is strongly shifted to negative potentials, to $E = -0.9$ V, and a new peak of cathodic current appears at $E = -0.94$ V. In this case, the wave of Te(IV) reduction coincides with that of Cd(II) reduction. The strong shift of the wave of tellurium reduction to negative potentials may be due to adsorption on the electrode surface of outersphere complexes $Cd(NH_3)_4^{2+} \cdot TeO_3^{2-}$, which hinder tellurium reduction.

At the reverse run of the voltammetric curve of codeposition of Te(IV) and Cd(II), there appear a current peak (peak *A*) related to oxidation of metallic cadmium that is unbound into the compound CdTe [Eq. (4)], a minor peak (peak *C*) associated with oxidation of the compound CdTe to elementary tellurium by Eq. (5), and a peak (peak *B*) related to oxidation of

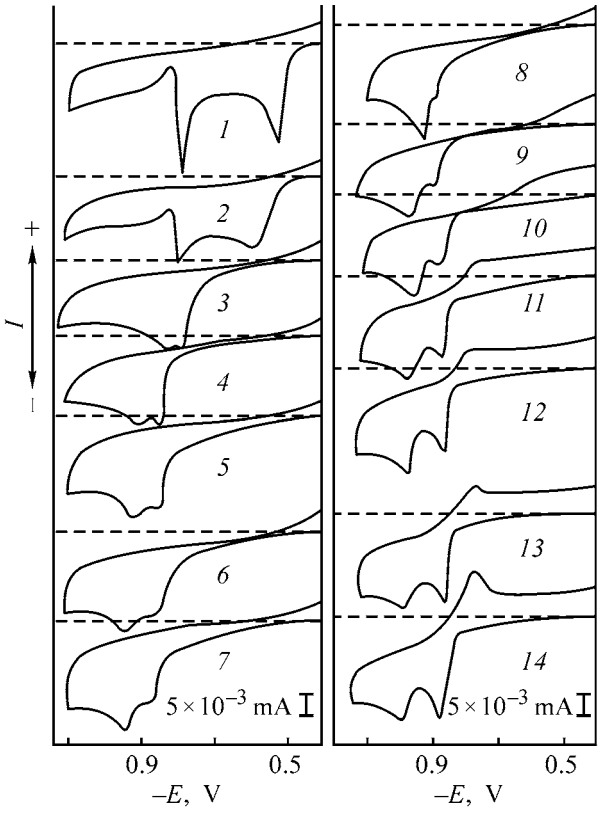

Fig. 2. Effect of Cd(II) concentration on the voltammetric curves of joint discharge–ionization of Te(IV) and Cd(II) ions on a glassy carbon electrode in an ammonia-chloride buffer electrolyte. pH 8.4, $c_{Te(IV)} = 3.8 \times 10^{-4}$ M; the same for Fig. 3. $c_{Cd(II)}$ (M): (*1*) 0, (*2*) 1.9×10^{-5}, (*3*) 3.8×10^{-5}, (*4*) 5.7×10^{-5}, (*5*) 7.6×10^{-5}, (*6*) 9.5×10^{-5}, (*7*) 1.1×10^{-4}, (*8*) 1.3×10^{-4}, (*9*) 1.7×10^{-4}, (*10*) 2.2×10^{-4}, (*11*) 2.9×10^{-4}, (*12*) 3.3×10^{-4}, (*13*) 3.7×10^{-4}, and (*14*) 4.6×10^{-4}.

tellurium contained in the compound CdTe to TeO_3^{2-} at $E = 0.22$ V [Eq. (6)]:

$$Cd^0 - 2e \rightarrow Cd^{2+}, \quad (4)$$

$$CdTe + 4NH_3^{2-} - 2e \rightarrow Cd(NH_3)_4^{2+} + Te^0, \quad (5)$$

$$CdTe + 4NH_3 + 3H_2O - 6e \rightarrow TeO_3^{2+} + Cd(NH_3)_4^{2+} + 6H^+. \quad (6)$$

The potential of the current peak *B* depends on the Cd(II) concentration in the electrolyte solution and varies within the range 0.1–0.22 V. As the concentration of Cd(II) increases, the potential of the current peak related to oxidation of the compound CdTe is shifted to more positive potentials.

On addition of a solution of 6.3×10^{-4} M of Te(IV) to a solution that contains 3.8×10^{-4} M of Cd(II), the current of the joint wave of reduction of Cd(II) and Te(IV) ions grows (Fig. 1b, curve *2*), with the current of this wave lower than the total current of Te(IV) and Cd(II) reduction at their corresponding concentrations in the electrolyte. In the cathodic voltammetric curve, as also in the voltammetric curve shown in Fig. 1a (curve *2*), there appears a current peak at $E = -0.94$ V, which is associated with the reduction of the CdTe compound formed by the equation

$$CdTe + 2H^+ + 2e \rightarrow Cd + H_2Te. \quad (7)$$

In the reverse run of the voltammetric curve (Fig. 1b, curve *2*), no current peak related to oxidation of elementary cadmium is observed, since the concentration of Te(IV) exceeds that of Cd(II) as compared with the 1 : 1 stoichiometric composition.

In order to consider in more detail the influence of Cd(II) ions on the electrochemical reduction of Te(IV) in an ammonia-chloride buffer solution, voltammetric curves were measured at a constant Te(IV) concentration of 3.8×10^{-4} M and various concentrations Cd(II) ions. On adding to the electrolyte solution even a minor amount of Cd(II) (1.9×10^{-5} M), the wave of Te(IV) reduction is shifted to more negative potentials, the current of Te(IV) reduction decreases, and the current peak related to further reduction of Te(0) to Te(–2) by reaction (2) becomes lower (Fig. 2, curve *2*). Raising the concentration of Cd(II) to 3.8×10^{-5} M leads to further shift of the wave of Te(IV) reduction to the region of negative potentials (Fig. 2, curve *3*).

At a Cd(II) concentration of 5.7×10^{-5} M, the wave of Te(IV) reduction reaches a potential of –0.9 V and coincides with the wave of Cd(II) reduction (Fig. 2, curve *4*). Under these conditions, Te(IV) is reduced directly to Te(–2), with addition of six electrons, and enters into chemical reaction with Cd^{2+} situated in the near-electrode layer to give the compound CdTe.

$$TeO_3^{2-} + Cd(NH_3)_4^{2+} + 6H^+ + 6e \rightarrow CdTe + 4NH_3 + 3H_2O. \quad (8)$$

At potentials more negative than that of the joint wave of Te(IV) and Cd(II) reduction, there appears a minor peak related to formation of the CdTe compound by Eq. (7). As the concentration of cadmium in the electrolyte solution becomes higher, the potential of this peak is shifted to more negative potentials and the current grows.

As the Cd(II) concentration increases, the potential at which the wave of joint reduction of Te(IV) and Cd(II) remains constant, but the shape of this wave changes: the current peak of reduction disappears and

a limiting current appears at a Cd(II) concentration of 9.5×10^{-5} M (Fig. 2, curve *6*). The current of this wave decreases gradually as the concentration of Cd(II) ions is raised to 1.3×10^{-4} (Fig. 2, curve *8*). With the Cd(II) concentration increasing further, to 1.7×10^{-4}, a minor peak reappears in the wave at a potential of –0.9 V (Fig. 2, curve *9*), and the current of the joint wave increases with Cd(II) concentration. At $c_{Cd(II)} = 2.9 \times 10^{-4}$ M, a minor peak associated with oxidation of metallic cadmium to Cd(+2) by reaction (4) appears in the reverse run of the voltammetric curve (Fig. 2, curve *11*), which indicates that free, elementary cadmium, unbound to tellurium, appears on the electrode surface. In this case, the peak of CdTe reduction reaches its maximum magnitude.

Consequently, as the concentration of cadmium grows, the total current of the reduction wave decreases, passes through a minimum, and again starts to increase, with the total current not additive to the currents of Te(IV) and Cd(II) reduction. The phenomenon observed is due to the reaction of the product formed in Te(IV) reduction with cadmium ions present in solution, to give a poorly soluble compound CdTe, which diminishes the flow of cadmium ions toward the electrode. A similar phenomenon has been observed in reduction of As(3+) and ions of bi- and trivalent metals (Cd^{2+}, Zn^{2+}, In^{3+}) on a mercury electrode in neutral solutions [9].

Raising the Cd(II) concentration to 2.98×10^{-4} M (Fig. 2, curve *11*) and more leads to an increase in the current of the joint reduction wave of Cd(II) and Te(IV) ions at $E = -0.9$ V, and the current of reduction of the CdTe formed decreases. Consequently, it may be assumed that the concentration ratio Cd(II) : Te(IV) = 1 : 1–0.8 : 1 in the electrolyte solution is the optimal for formation of the CdTe compound. The results obtained are confirmed by the dependence of the magnitudes of the anodic peaks related to CdTe electrooxidation on the concentration ratio of Cd(II) and Te(IV) ions in solution (Fig. 3). The current peak observed in the anodic portion of the voltammetric curves at potentials of 0.1–0.22 V, which correspond to oxidation of tellurium contained in the compound CdTe, reaches its maximum magnitude at a concentration ratio Cd(II) : Te(IV) = 0.8 : 1. With increasing content of Cd(II) ions in the electrolyte, the maximum current decreases.

The dependence of the current of the anodic peak of CdTe oxidation, observed at potentials of 0.15–0.3 V, on the potential of electrodeposition of this compound on a glassy carbon electrode in an ammonia-chloride buffer electrolyte with pH 8.4 was

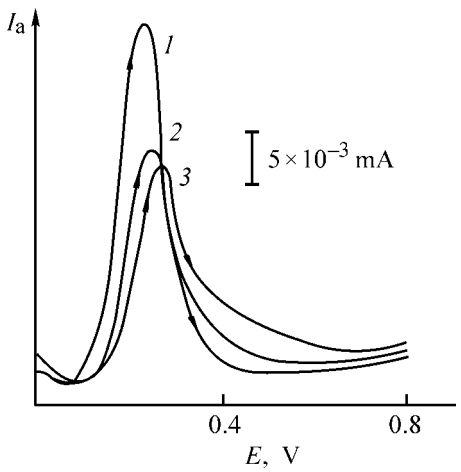

Fig. 3. Anodic voltammetric curves of CdTe ionization in an ammonia-chloride buffer electrolyte of varied composition. $c_{Cd(II)} \times 10^4$ (M): (*1*) 2.8, (*2*) 3.7, (*3*) 4.5.

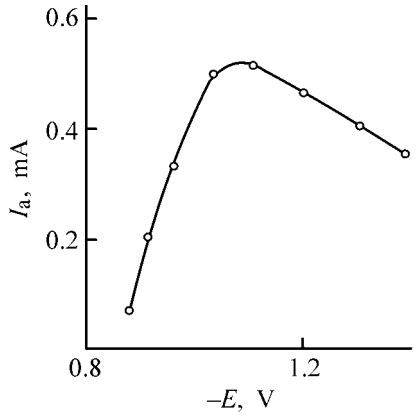

Fig. 4. Effect of the potential of CdTe deposition in an ammonia-chloride buffer electrolyte on the current of the anodic peak observed at potentials of 0.15–0.3 V at pH 8.4.

determined (Fig. 4). The electrodeposition was carried out at different cathode potentials (plotted in the figure along the abscissa axis), in the course of 30 s, with stirring. It was found that the maximum oxidation current of the compound formed is observed when CdTe is deposited onto the electrode surface at a potential of –1.1 V.

The data obtained are confirmed by the results of XPA. The X-ray phase analysis was carried out for CdTe films electrodeposited in the potentiostatic mode onto glassy carbon substrates with an apparent surface area of 1 cm^2. The electrodeposition of CdTe was performed from an ammonia-chloride buffer electrolyte with pH 8.4 at 80°C in the course of 20 min, with agitation of the electrolyte. The resulting films were annealed at 400°C for 10 min.

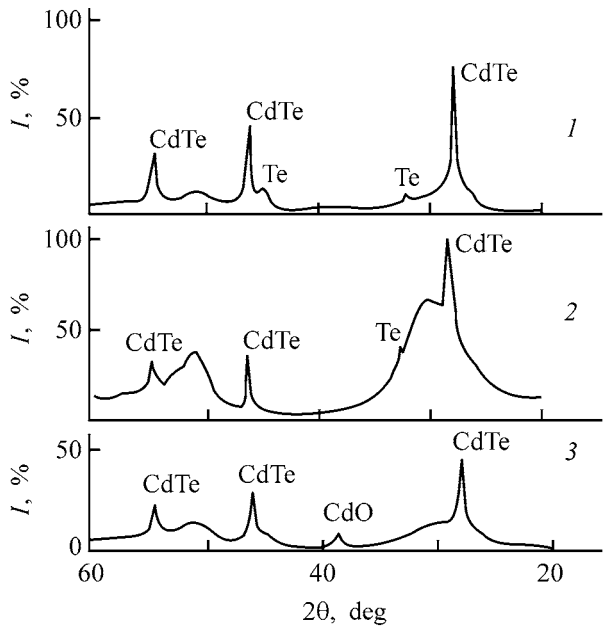

Fig. 5. X-ray diffraction patterns of CdTe films on a glassy carbon electrode. (*I*) Intensity and (2θ) Bragg angle. Concentration (M): (*1*) 1.2×10^{-3} Cd(II) and 1.2×10^{-3} Te(IV); (*2*) 1.17×10^{-3} Cd(II) and 1.47×10^{-3} Te(IV); and (*3*) 3.7×10^{-4} Cd(II) and 3.7×10^{-4} Te(IV). Deposition time (min): (*1, 2*) 20 and (*3*) 60.

Figure 5 (curves *1*, *2*) shows X-ray diffraction patterns of CdTe films electrodeposited at a potential of –1.1 V from an ammonia-chloride buffer electrolyte at a concentration ratio of Cd(II) and Te(II) in the electrolyte equal to 1 : 1 (diffraction pattern *1*) or 0.8 : 1 (diffraction pattern *2*). The clearly pronounced reflections of the compound CdTe can be seen in the figure. The three main reflections, which correspond to the interplanar spacings of 3.74, 2.29, and 1.95 Å, are in agreement with the ASTM file data for CdTe. Using an ammonia-chloride buffer electrolyte with pH 8.4 makes it possible to diminish the content of elementary tellurium in the CdTe deposit to CdTe : Te = 1 : 0.079–1 : 0.08, as indicated by the relative intensities of the main peaks of CdTe and Te in the X-ray diffraction patterns. In the widely used sulfate electrolytes, the CdTe : Te ratio is 1 : 0.30–1 : 0.31 [10]. Lowering the content of tellurium in the deposit of the compound obtained improves its semiconducting properties. It was shown, based on the relative intensities of the main reflections in the X-ray diffraction patterns, that CdTe films obtained from the ammonia-chloride buffer electrolyte have a regular cubic structure.

The effect of making longer (60 min) the time of CdTe electrodeposition was studied (Fig. 5, diffraction pattern *3*). The content of cadmium and tellurium in the ammonia-chloride solution was $c_{Cd(II)} = c_{Te(IV)} = 3.7 \times 10^{-4}$ M. It was found that sufficiently thick semiconducting CdTe films, which contain no elementary tellurium, are obtained at longer electrodeposition times. The reflections from the substrate are weakly pronounced, but there appear minor reflections corresponding to the CdO compound.

Thus, the use of an ammonia-chloride buffer electrolyte with pH 8.4 made it possible to obtain pure films of the semiconducting CdTe, which contain no elementary tellurium, and thereby to improve the semiconducting properties of the films obtained.

CONCLUSIONS

(1) In codeposition of cadmium(II) and tellurium(IV) from an ammonia-chloride buffer electrolyte with pH 8.4 onto a glassy carbon electrode, the potential of Te(IV) reduction is substantially shifted to more negative potentials, so that the reduction potentials of Cd(II) and Te(IV) coincide.

(2) The optimal conditions of CdTe electrodeposition from an ammonia-chloride electrolyte with pH 8.4 are as follows: deposition potential –1.1 V, temperature 80°C, concentration ratio Cd(II) : Te(IV) = 1 : 1–0.8 : 1.

(3) Using the ammonia-chloride electrolyte with pH 8.4 makes it possible to eliminate virtually totally the codeposition of elementary tellurium together with the CdTe deposit.

REFERENCES

1. Panicker, M.P.R., Knaster, M., and Kroger, F.A., *J. Electrochem. Soc.*, 1978, vol. 125, no. 4, pp. 566–572.
2. Sella, K., Boncorps, P., and Vedel, J., *J. Electrochem. Soc.*, 1986, vol. 133, no. 12, pp. 2043–2047.
3. Engelken, R.D. and Van Doren, T.P., *J. Electrochem. Soc.*, 1985, vol. 132, no. 12, pp. 2910–2919.
4. Verbrugge, M.W. and Tobias, C.W., *J. Electrochem. Soc.*, 1987, vol. 134, no. 12, pp. 3104–3109.
5. Lyons, L.E., Morris, G.C., Horton, D.H., and Keyes, J.G., *J. Electroanal. Chem. Interfacial Electrochem.*, 1984, vol. 168, no. 1, 2, pp. 2043–2047.
6. Takahashi, M., Uosaki, K., and Kita, H., *J. Appl. Phys.*, 1984, vol. 55, no. 10, pp. 3879–3881.
7. Meulenkamp, E.A. and Peter, L.M., *J. Chem. Soc. Faraday Trans.*, 1996, vol. 92(20), pp. 4077–4082.
8. Kuniaki Murase, Hiroto Watanabe, Tetsuji Hirato, and Yasuhiro Awakura, *J. Electrochem. Soc.*, 1999, vol. 146, no. 5, pp. 1798–1803.
9. Vasil'eva, E.G., Zhdanov, S.I., and Kryukova, P.A., *Elektrokhimiya*, 1969, vol. 5, no. 11, p. 1279.
10. Dergacheva, M.B., Statsyuk, V.N., Fogel', L.A., and Pen'kova, N.V., *Zh. Prikl. Khim.*, 2003, vol. 76, no. 6, pp. 947–952.

Russian Journal of Applied Chemistry, Vol. 77, No. 2, 2004, pp. 231–235. Translated from Zhurnal Prikladnoi Khimii, Vol. 77, No. 2, 2004, pp. 235–238.

APPLIED ELECTROCHEMISTRY AND CORROSION PROTECTION OF METALS

Oxide Compounds of Chromium as Cathode Material for Pulsed Power Cells

N. D. Ivanova, E. I. Boldyrev, and S. V. Ivanov

Vernadskii Institute of General and Inorganic Chemistry, National Academy of Sciences of the Ukraine, Kiev, Ukraine
National Aviation University, Kiev, Ukraine

Received October 21, 2003

Abstract—The optimal composition of a cathode material based on films of an oxide chromium compound for a pulsed lithium chemical power cell that provides current densities of 80–140 mA cm^{-2} was determined.

Development of lithium chemical power cells that operate in pulsed mode is one of the most important tasks in view of the expanding range of their application in electronics. The operation of electronic devices (especially in its initial stage) frequently requires a very short high-current pulse. With account of this circumstance, the main requirement to chemical power cells is that they should provide high current densities (>50 mA cm^{-2}) in discharge through low external loads of the order of tens of ohms.

Commonly, lithium-based chemical power cells of pulsed type are fabricated using a thin-film technology for obtaining a cathode material on the basis of oxide systems of molybdenum, aluminum, and vanadium. The specific power of a power cell of this kind may be as high as 100 W g^{-1} [1]. The use of oxides is preferable, compared with compounds of other classes, since oxides are more stable in aprotic electrolytes, less toxic, and undergo only slight structural changes during operation of a chemical power cell.

At present, chemical power cells with a lithium anode and a manganese dioxide cathode are being commercially produced on a large scale. To their advantages belong the possibility of obtaining a rather high specific power (up to 200 W h kg^{-1}), stability of the discharge characteristic, and capacity for operation at low temperatures (below –20°C). A disadvantage of such a cell is the low discharge current (<1 mA cm^{-2}) [2].

The operation of lithium-based chemical power cells is based on solid-phase reduction of oxide materials, whose rate-determining stage is lithium diffusion in the solid phase. The diffusion coefficients are low (10^{-9}–10^{-13} cm^2 s^{-1} [3], and, as a result, the maximum current densities are low, too (commonly, ≤2 mA cm^{-2}).

To make higher the discharge current of lithium cells, a number of technological procedures have been advanced. It particular, it was suggested to assemble cells based on manganese dioxide into batteries, e.g., thin batteries with a voltage of 6 V. The discharge current of batteries of this kind may vary within the range 0.03–150 mA in their operation in the continuous mode (with the battery capacity being, in this case, 13 A h) and be as high as 1 A in the pulsed mode (with the battery capacity not exceeding 0.85 A h) [4].

In the recent 10–15 years, a close attention has been given to oxide compounds of nonstoichiometric composition as possible electrode materials. It has been established that the rate of electrochemical reactions and, consequently, the achievable current density are the higher, the stronger the deviation of the composition of a compound from the stoichiometry, which determines the type of conduction, the defectiveness of the structure, and the catalytic activity of a compound [5–7].

Using the nonstoichiometric oxides makes it possible to raise the specific capacity of the electrode, and varying the deviation of composition from the stoichiometry allows control over the rate of introduction of the lithium cation into the cathode material [8]. An important additional advantage of such oxides is their mixed conductivity with a considerable share of the electronic component [9]. In some cases, this obviates the necessity for introduction of electrically conducting additives (carbon black, graphite) into the cathode material, which not only simplifies the fabri-

1070-4272/04/7702-0231 © 2004 MAIK "Nauka/Interperiodica"

cation technology of chemical power cells and, accordingly, lowers its cost, but also makes it possible to raise the utilization factor of the cathode material.

Of particular interest among representatives of this class of compounds are nonstoichiometric oxide compounds of chromium [10–13]. For example, lithium cells with a cathode material based on $CrO_{2.66}$, which have a specific power of 300–1000 W h l^{-1} and a specific capacity of 370–410 A h kg^{-1}, have been suggested [13]. However, the technology for synthesis of this compound is rather complicated [14]: it is commonly obtained by removing a required amount of oxygen from a stoichiometric chromium(VI) oxide.

It is known that chemical methods for obtaining compounds of nonstoichiometric composition fail to ensure its due reproducibility, require long time, and are labor-consuming. Electrochemical synthesis yields virtually compositionally reproducible compounds and can be readily controlled with electrolysis parameters.

The aim of this study was to select a cathode material for pulsed lithium-based chemical power cells and to optimize its composition.

EXPERIMENTAL

The method of electrochemical synthesis from fluorine-containing electrolytes has been used to obtain a number of oxide compounds of copper, molybdenum, nickel, and chromium of nonstoichiometric composition [9]. Preliminary studies of these compounds as cathode materials for chemical power cells with a lithium anode demonstrated that oxide compounds of chromium and molybdenum are of particular interest. The peak currents in a pulse at discharge time of 10 s and load of 1 kΩ are given below for lithium power cells with cathodes made of the compounds under study:

Oxide	Cu(I)	Cr	Mo	Ni	Mn
Peak current in a pulse, mA	15	70	35	30	22

The highest discharge currents in the pulsed mode were obtained for a cathode material based on chromium compounds, and this material was chosen for the further study. An additional advantage is that oxide compounds of chromium can be deposited in the form of thin films that firmly adhere to the base, which obviates the necessity for introduction of a binder and electrically conducting additives into the cathode material. As a result, the fabrication technology of the lithium-based chemical power cell is strongly simplified because of the elimination of a number of technological procedures.

The oxide compounds of chromium were obtained from an electrolyte containing 250 g l^{-1} of chromium(VI) oxide and 0.1 to 0.8 g l^{-1} of hydrofluoric acid [9]. The thickness of a film of an oxide chromium compound, deposited onto the base, was 12–15 μm. The composition of the oxide compounds obtained was determined using the atomic-absorption and neutron activation methods of analysis. The latter technique was used to determine the total oxygen, including that contained in H_2O and in OH^- groups, in oxide compounds of chromium [15]. Taking into account the fact that the compounds under study are not stoichiometric and, consequently, their density differs from the tabulated values, the apparent and true densities of the oxide compounds synthesized were determined. The specific surface area of this compounds was found using the BET method.

The conductivity (ionic and electronic) is a structure-sensitive parameter that governs the electrical characteristics of a material. The total conductivity and its constituents were found using the procedure described in [16]. Also, the effect of the duration and the mode of thermal treatment on these quantities and on the peak current in a pulse of a lithium power cell was studied.

The electrical characteristics of prototype lithium power cells were determined with an S8-13 oscilloscope in the form of a 100-ms pulse on a load of 10 Ω. The prototype samples of lithium-based chemical power cells of standard size 23 × 25 were assembled in a box in the atmosphere of argon; as electrolyte served a 1 M solution of lithium fluoroborate in γ-butyrolactone.

The data on the composition of oxide compounds of chromium and the peak current in a pulse are listed in Table 1 in relation to the concentration of the ligand in the electrolyte. For example, raising the concentration of the F^- ion in the electrolyte leads to an increase in both the total and metallic chromium in the samples. In the same order decreases the amount of oxygen and OH groups, which stabilize the redox systems $M^{n+}/M^{(n-1)}$ in oxide compounds of this type [4].

The peak current in a pulse of a lithium power cell and the composition of an oxide compound used to fabricate the cathode are determined by the concentration of the ligand in the electrolyte: the maximum current is observed for sample no. 1 and decreases on passing to sample nos. 2–4, i.e., with increasing concentration of the ligand in the electrolyte. In the same way decreases the share of ionic conductivity in the

Table 1. Composition, share of ionic conductivity of oxide compounds of chromium obtained in HF solutions of various concentrations, and peak current in a pulse of a lithium power cell on their base

Sample no.	c_{HF}, g l^{-1}	Composition of oxide compounds of chromium, %				O_2, %	Peak current in a pulse, mA	Share of ionic conductivity σ, %
		ΣCr	Cr(0)	Cr(II)	Cr(III)			
1	0.2	70.0	30.0	18.0	22.0	29.0	190	11.3
2	0.4	73.0	41.0	13.0	19.0	22.0	170	10.8
3	0.6	82.0	55.0	11.0	16.0	18.0	160	10.5
4	0.8	89.0	68.0	10.0	11.0	11.0	100	9.5

Table 2. Density of oxide compounds of chromium at various HF concentrations in the electrolyte

c_{HF}, g l^{-1}	Density, g cm^{-3}		c_{HF}, g l^{-1}	Density, g cm^{-3}	
	true	apparent		true	apparent
0.2	2.1	1.41	0.6	2.27	1.65
0.4	2.25	1.58	0.8	2.29	1.78

compounds studied. The data in Table 1 were used to determine the optimal electrolyte composition for obtaining a cathode material for a pulsed lithium-based chemical power cell. In the same order grow the true and apparent densities of oxide compounds of chromium (Table 2), which is due to an increase in the content of metallic chromium in the samples studied. The specific surface area of the compounds obtained varies from 0.5 $m^2 g^{-1}$ for pelletized samples to 1.9 $m^2 g^{-1}$ for powdered samples.

To create lithium power cells that allow high discharge rate, it seems necessary to study the conductivity of the cathode materials used, since it is this parameter that largely determines the rate of the electrochemical process that occurs in operation of a chemical power cell. It is known that the conductivity of a substance is strongly temperature-dependent. To optimize the thermal treatment mode, temperature dependences of conductivity were studied. The peak currents in a pulse (current–time dependences) were examined for a lithium power cell with a cathode material based on an oxide chromium compound of the optimal composition no. 1 (Table 1).

The figure shows how the share of ionic conductivity of the oxide compounds of chromium, synthesized in this study, depends on the temperature of thermal treatment and on the electrolyte composition. It follows from an analysis of these data that, as the concentration of the F^- ion in the electrolyte increases in electrosynthesis of oxide compounds of chromium, the share of the ionic constituent of the conductivity decreases. A similar influence is exerted by the temperature of their subsequent thermal treatment. Moreover, after thermal treatment at 300°C the share of the ionic constituent of conductivity is virtually zero.

The results obtained suggest that the ionic conduction is due to the presence of hydroxy groups, which, in turn, predetermines the difference between the ionic components of samples with different compositions. This conclusion is confirmed by results of a thermogravimetric analysis and IR spectroscopy, according

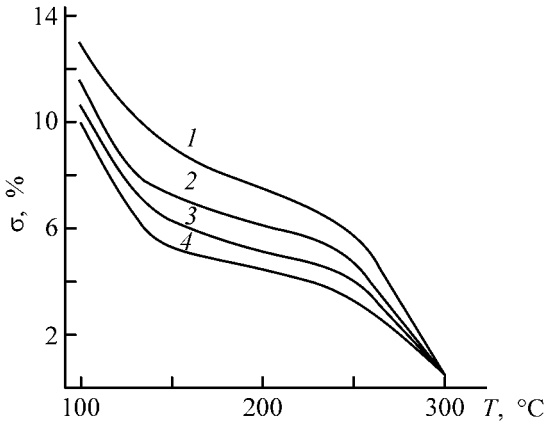

Share of ionic constituent of the conductivity σ of oxide compounds of chromium vs. temperature T of their thermal treatment at different concentrations of the ligand in the electrolyte in synthesis of these compounds. Concentration (g l^{-1}): (*1*) 0.1, (*2*) 0.2, (*3*) 0.4, and (*4*) 0.8.

Table 3. Peak current in a pulse of a lithium power cell (23 × 25 standard size) in relation to the thermal treatment mode of an oxide chromium compound and to the discharge duration (external load R = 10 Ω)

T, °C	Peak current in a pulse (mA) at indicated discharge duration		T, °C	Peak current in a pulse (mA) at indicated discharge duration	
	100 ms	100 μs		100 ms	100 μs
100	20–40	200	200	100–120	260
140	50–60	220	250	170–180	290
			300	120–140	130

Table 4. Peak current in a pulse at varied number of successive switch-ons of a lithium power cell (23 × 25 standard size)

τ, ms	Peak current in a pulse, mA, at indicated resistance, Ω and number of successive switch-ons											
	7			8			10			12		
	1	10	20	1	10	20	1	10	20	1	10	20
10	280	275	260	260	250	240	220	200	190	180	160	130
15	280	275	260	260	250	240	220	200	190	180	160	130
20	280	275	260	260	250	240	220	200	190	180	160	125
100	230	220	200	230	200	190	180	175	165	150	140	110

to which the crystallization water and OH^- groups are completely removed at 300–320°C. It should be noted that a correlation is observed between the modes of thermal treatment and the peak currents in the I–T dependences for the prototype samples of lithium power cells. The variation of the peak current in a pulse with the temperature of thermal treatment of oxide compounds of chromium are is illustrated in Table 3 for different pulse durations. According to these data, the optimal temperature of thermal treatment of oxide compounds of chromium is 250–260°C. The share of the ionic conductivity for the given cathode material should not exceed 4–5%.

A lithium-based chemical power cell of this kind allows multiple switch-ons (Table 4). Up to 20 successive switch-ons of a power cell were carried out, with the current pulse recorded. The peak current in a pulse decreases only slightly during the first ten successive switch-ons, but starts to fall more steeply after 20th switch-on of the chemical power cell. However, the discharge current density of the lithium-based power cell under study remains, even under these conditions, 20–30 times the discharge current density of the known lithium power cells.

Thus, there appears an opportunity to test preliminarily both the potential electrode materials and the systems as a whole for possible use in power cells providing high (up to 140 mA cm^{-2} for a short interval of time) discharge current densities at low external loads.

CONCLUSION

The data obtained indicate that oxide compounds of chromium can be used as cathode materials in lithium-based chemical power cells that provide high current densities (80–110 mA cm^{-2}) in discharge through low external loads during a short period of time.

REFERENCES

1. Yoshizava, S., Takehara, Z., and Nishimura, T., *32nd Meet. Int. Soc. Electrochem.: Ext. Abstr.*, Dubrovnic, 1981, no. 2, pp. 1, pp. 864–867.
2. Yoshio, M., Nakamura, H., and Xia, Y., *Electrochim. Acta*, 1999, vol. 45, nos. 1–2, pp. 273–283.
3. Brenet, J.P., *J. Power Sources*, 1979, vol. 4, no. 2, pp. 183–190.

4. Cohen, F.S., *Progr. Batteries Sol. Cells*, 1984, no. 5, pp. 95–98.
5. Zlomanov, V.P., *Soros. Obrazov. Zh.*, 2001, no. 5, pp. 29–35.
6. Kovtunenko, P.V., *Fizicheskaya khimiya tverdogo tela: Kristally s defektami* (Physical Chemistry of Solids: Crystals with Defects), Moscow: Vysshaya Shkola, 1993.
7. Ivanova, N.D., Boldyrev, E.I., Ivanov, S.V., *et al.*, *Zh. Prikl. Khim.*, 2002, vol. 75, no. 6, pp. 953–955.
8. Ivanova, N. D., Mishchenko, A.B., Boldyrev, E.I., *et al.*, *Elektrokhimiya*, 1995, vol. 31, no. 1, pp. 85–87.
9. Ivanova, N.D. and Ivanov, S.V., *Functional Materials*, 2000, vol. 7, no. 1, pp. 5–25.
10. Ivanova, N.D. and Ivanov, S.V., *Ukr. Khim. Zh.*, 1986, vol. 52, no. 11, pp. 1160–1163.
11. Takeda, Y., Kanno, R., and Tsuji, Y., *J. Electrochem. Soc.*, 1984, vol. 131, no. 9, pp. 2006–2010.
12. Jakubec, I., Vondrak, J., and Bludska, J., *J. Power Sources*, 1992, vol. 39, no. 2, pp. 133–145.
13. Lauck, H. and Nijhawen, S.C., *Progr. Batteries Sol. Cells*, 1984, vol. 5, pp. 61–63.
14. Alpen, U., Nijhawen, S.C., and Lauck, H., *15th Int. Telecommun. Energy Conf. INTELEC 83, Tokyo, 18–21 Oct., 1983*, Tokyo, 1983, pp. 349–352.
15. Beckurts, K.H. and Wirtz, K., *Neutron Physics*, Berlin: Springer, 1964.
16. Ivanova, N.D., Filatov, K.V., Boldyrev, E.I., *et al.*, *Dokl. Akad. Nauk Ukrainy*, 1992, no. 11, pp. 136–139.

Russian Journal of Applied Chemistry, Vol. 77, No. 2, 2004, pp. 236–240. Translated from Zhurnal Prikladnoi Khimii, Vol. 77, No. 2, 2004, pp. 239–243.

APPLIED ELECTROCHEMISTRY AND CORROSION PROTECTION OF METALS

Electroless Nickel and Copper Plating of Carbon Fibers with the Use of Sulfur-containing Reducing Agents

I. N. Terskaya, V. V. Budanov, S. V. Makarov, and L. V. Ermolina

Ivanovo State University of Chemical Engineering, Ivanovo, Russia

Received April 3, 2003

Abstract—The fundamental aspects of electroless nickel and copper plating of carbon fibers with the use of sodium hydroxymethane-sulfinate and thiourea dioxide as reducing agents were studied.

The development of modern technology requires that new materials with special properties, including electrically conducting metallized fibers, should be created [1]. The efficiency of metallization depends on the state of the fiber surface. Surface pretreatment includes stages of cleaning, degreasing, etching, sensitization, and activation. Tin compounds are commonly used as sensitizing agents; the activation is done by treatment of a sensitized surface with solutions of compounds of platinum-group metals, most frequently with palladium salts [1, 2]. Of economic interest are activation methods that use no palladium. A disadvantage of the known techniques of this kind is that the composition of the activating solution is rather complex and the process is labor-consuming because of the great number of successive technological procedures involved [3, 4].

Of interest for further improvement of the existing methods and development of new techniques for electroless metallization is expansion of the number of the reducing agents used. The conventionally employed sodium borohydride and hypophosphite give no way of obtaining impurity-free metal coatings, and their solutions are insufficiently stable, especially in acid media [5]. In [6], it was suggested to use thiourea dioxide (TDO) and sodium hydroxymethane-sulfinate (SHMS) for electroless nickel plating of polyacrylonitrile (PAN) fibers. In this case, coatings with high adhesion can be obtained without activation with palladium salts.

The aim of the present study was to examine the possibility of using TDO and SHMS (technical name rongalite) for metallization of carbon fibers and to analyze the physicomechanical aspects of formation of metal coatings.

EXPERIMENTAL

Samples of black-reinforced epoxy plastic were prepared from UUT-2 fabric with carbon fiber content of 60% by the standard procedure [7, 8]. Thiourea dioxide $(NH_2)_2CSO_2$ was synthesized from thiourea of chemically pure grade by oxidation with hydrogen peroxide by the known technique [9], or a technical-grade product was used after double recrystallization. Sodium hydroxymethane-sulfinate $HOCH_2SO_2Na \cdot 2H_2O$ was obtained by double recrystallization of a technical-grade product from water. The content of the main substance in the reducing agents prepared, monitored iodometrically [10], was no less than 99.8%. Etching, activation, and metallization solutions were prepared from Ni, Cu, and Cd salts, potassium dichromate of chemically pure grade, and H_2SO_4 acid of analytically pure grade. Carbon fiber samples were preliminarily treated with concentrated sulfuric acid (d = 1.83 g ml^{-1}) with various additives for 3–10 min, with subsequent washing with water as described in [11]. The reaction of Ni^{2+}, Cu^{2+}, and $Cr_2O_7^{2-}$ with SHMS or TDO was performed in air. The content of Ni^{2+} ions in solution was monitored by trilonometry, and that of Cu^{2+} ions, by spectrophotometry (SF-46 spectrophotometer, λ_{max} = 740 nm), using the known procedures [12]. The amount of metal deposited was determined gravimetrically, with correction made for the content of sulfides and sulfites [12].[1] Additionally,

[1] Admixtures of sulfides and sulfites may appear through decomposition of sulfur-containing reducing agents.

1070-4272/04/7702-0236 © 2004 MAIK "Nauka/Interperiodica"

the metal deposit was analyzed for the content of Ni and Cu by atomic-adsorption spectrometry (Saturn spectrometer); the size of metal powder particles was determined with a Tesla BS-300 electron microscope. The adhesion strength of metal coatings with a black-reinforced plastic substrate was evaluated by the "thermal shock" and ultrasonic methods. The metal coatings were subjected to the action of high-frequency sound vibrations in a liquid medium, using a UD-20 ultrasonic integrator.[2]

In the experiments, the instant of time at which disintegration of a metal film started and the time of its complete disintegration (disintegration spot diameter 5 mm) were recorded.

A study of reduction of Ni^{2+}, Cu^{2+}, and $Cr_2O_7^{2-}$ with SHMS and TDO demonstrated that, in the absence of a substrate, the decrease in the concentration of the ions of the oxidizing agents at fixed concentration of a reducing agent, taken in excess, is described by the kinetic equation of a pseudo-monomolecular reaction. The effective rate constants of the reaction are listed in Table 1. The data in the table were used to calculate the activation energies and logarithms of the pre-exponentials in the Arrhenius equation; the dependences obtained are shown in Fig. 1. The strong influence of temperature on the reaction rate and the accordingly high activation energies of the process (84–187 kJ mol^{-1}) can be accounted for as follows.

It has been established previously [10, 13–15] that the reactions of reduction of organic and inorganic oxidizing agents with hydroxy and amine derivatives of sulfinic acids proceed by two parallel pathways: via direct interaction of reactant molecules (associative pathway) and via cleavage of the reducing agents at the C–S bond (dissociative pathway):

$$HOCH_2SO_2^- + H_2O = HSO_2^- + CH_2(OH)_2, \quad (1)$$

$$NH_2(NH)CSO_2H + OH^- = HSO_2^- + (NH_2)_2CO. \quad (2)$$

In the latter case, the role of reducing agents is played by sulfoxylate ions HSO_2^{2-} or secondary products of reactions (1) and (2), dithionite ions $S_2O_2^{2-}$. The occurrence of these pathways and their contribution to the overall rate of reduction processes were determined experimentally from the decrease in the reaction rate in the presence of an admixture of formaldehyde, which binds sulfoxylate to $HOCH_2SO_2^-$

[2] A sample was placed in a vessel with distilled water and the focusing attachment of the vibrator was mounted at a distance of 10 mm from the sample surface.

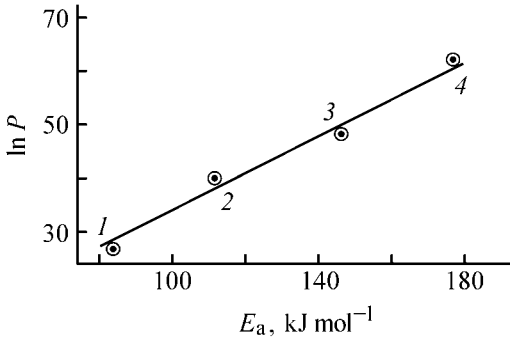

Fig. 1. Dependence of $\ln P$ on the activation energy E_a of the reaction of reduction of nickel and copper salts with (*1, 2*) SHMS and (*3, 4*) TDO in the presence of powdered (*1, 4*) copper and (*2, 3*) nickel. (*P*) Pre-exponential in the Arrhenius equation.

by a reverse reaction (1). It was established in [14] that an activation energy of more than 100 kJ mol^{-1} corresponds to the dissociative pathway, whereas in the case of an associative pathway, this quantity is about 20 kJ mol^{-1}, on average. The results obtained in a study of the influence exerted by formaldehyde additives [15] and a comparison of the activation energies indicate that the concepts developed are also applicable to reactions in which salts of transition

Table 1. Rate constants of redox reactions in the absence of substrate, found under various conditions from the loss of the oxidizing agent in a solution

Solution composition		pH value	T, K	$K_{eff} \times 10^2$, min^{-1}
Ox	Red			
Cu^{2+}	TDO	4.0	313	0.8
		4.0	323	8.5
		4.0	333	72.5
	SHMS	4.0	313	1.7
		4.0	323	3.2
		4.0	333	13
Ni^{2+}	TDO	4.0	313	0.4
		4.0	323	2.0
		4.0	333	9.8
Ni^{2+}*	SHMS	4.0	323	0.025
Ni^{2+}		4.0	333	0.11
$Cr_2O_7^{2-}$	TDO	4.0	323	81
		6.0	323	149.5
		12.0	323	245
	SHMS	4.0	323	145
		6.0	323	90
		12.0	323	60

* Data of [6].

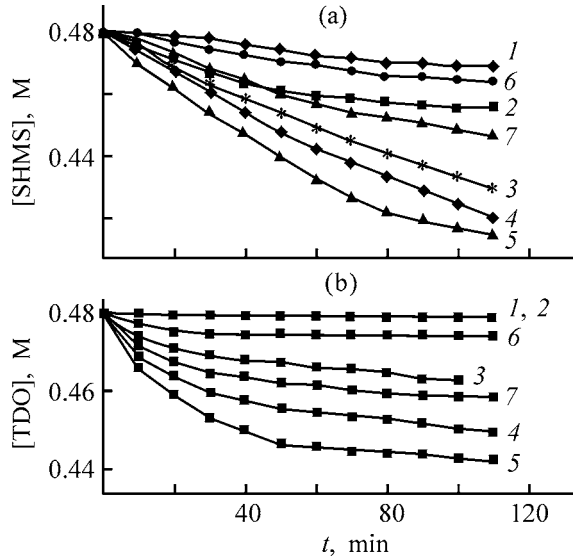

Fig. 2. Variation of the concentration of (a) SHMS and (b) TDO in the course of decomposition (*1*) in the absence of carbon fibers and in the presence of (*2*–*5*) carbon fibers and (*6*) Ni and (*7*) Cu powders. [TDO] = [SHMS] = 0.48 M, T = 298 K, pH 4.0. Carbon fiber: (*2*) untreated and (*3*–*5*) activated in conc. H_2SO_4 (*3*) without additives and with addition of 0.01 M of (*4*) Cd^{2+} and (*5*) $Cr_2O_7^{2-}$.

metals, nickel and copper, are reduced, with the dominant role played in this case by the dissociative pathway. It follows from Fig. 1 that, with allowance made for the rather high errors in measuring these quantities ($\Delta E_a = \pm 20$ kJ mol^{-1}, $\ln P = \pm 10$), the activation parameters $\ln P$ and E_a are correlated in terms of the compensation effect. This indicates that the rate-determining stages (1) or (2) proceed via intermediate states with configurations of the same type [16].

Table 2. Influence exerted by the mode of carbon fiber activation on the amount m of metal being deposited (metallization conditions: $[Ni^{2+}] = [Cu^{2+}] = 0.2$ M, T = 343 K, t = 10 min, [SHMS] = [TDO] = 0.4 M)

Metal	Solution composition, M	T, K	t, min	m, mg g^{-1} of fiber
Cu	H_2SO_4 conc.	293	6	1.2
	H_2SO_4 conc. + $CdSO_4$, 0.01	293	6	2.8
	H_2SO_4 conc. + $CdSO_4$, 0.3	353	6	3.8
	The same	353	10	2.4
Ni	H_2SO_4 conc.	293	6	2.3
	H_2SO_4 conc. + $K_2Cr_2O_7$, 0.3	293	6	4.4
	The same	353	6	5.8
	"	353	10	2.2

An important specific feature of the process of reduction with thiourea dioxide in a weakly acidic medium at temperatures lower than 333 K, in contrast to the process with SHMS, is that products of decomposition of the reducing agent, sulfite and sulfide ions, are virtually totally absent in the reaction system. This circumstance leads to a significant advantage of TDO over SHMS, since it furnishes an opportunity to obtain high-purity metal powders and coatings [17]. It can be seen from Table 1 that the rate constants of $Cr_2O_7^{2-}$ reduction are, on average, an order of magnitude higher than those of Ni^{2+} and Cu^{2+} reduction. Hence follows that, in the case of joint presence of Ni^{2+}, Cu^{2+}, and $Cr_2O_7^{2-}$ ions, the last type of ions will be more rapidly reduced to Cr^{3+} and Cr_2O_3. Being adsorbed on the surface of carbon fibers, these species may act as active centers in chemical deposition of metals [18].

In order to elucidate the mechanism by which carbon fibers affect the rate of redox reactions, decomposition of the reducing agents was studied in the presence of carbon fibers and Cu and Ni powder additives or without these (Figs. 2a, 2b). It can be seen that, in the presence of carbon fibers, the decomposition rate of SHMS (Fig. 2a) and TDO (Fig. 2b) increases. This is particularly pronounced in the case of a carbon fiber etched in conc. H_2SO_4 with addition of Cd^{2+} and $Cr_2O_7^{2-}$ (Figs. 2a, 2b; curves *4*, *5*). In the presence of Ni and Cu powders (Figs. 2a, 2b; curves *6*, *7*), the decomposition rate also increases, even though to a lesser extent than in the presence of an activated carbon fiber. It is known that Cu and Ni metals catalyze the decomposition of SHMS [6].

The data in Fig. 2 are in good agreement with the results obtained in determining the rates of redox reactions in the presence of carbon fibers. It has been found [11, 15] that, in reduction of Cu^{2+}, the highest rate is observed in the presence of a carbon fiber etched in conc. H_2SO_4 with addition of Cd^{2+} ($K_{eff} = 3.6 \times 10^{-3}$ min^{-1}), whereas in reduction of Ni^{2+}, the most efficient treatment is that with conc. H_2SO_4 with addition of $Cr_2O_7^{2-}$ ($K_{eff} = 9.3 \times 10^{-3}$ min^{-1}). At the same time, the effective rate constants of reduction of Cu^{2+} and Ni^{2+} ions in the absence of carbon fibers are 1.4×10^{-3} and 3.4×10^{-3} min^{-1}, respectively.[3] It is known that etching of carbon fibers leads to a certain surface roughness, with simultaneous appearance of –C=O and –C–O– groups involved in redox processes of formation of primary metal crystallization centers [7]. The data in Table 2 indicate that a sufficiently high content of copper and nickel in car-

[3] All values of K_{eff} are related to a temperature of 298 K.

bon fiber samples (up to 3.8–5.8 mg g^{-1}) is achieved in etching the substrate in conc. H_2SO_4 with addition of Cd^{2+} (in Cu deposition) or $Cr_2O_7^{2-}$ (in Ni deposition) for 6 min. It can be seen from Table 3 that the optimal concentration of the additives in the etching bath should be 0.3 g l^{-1} at the etching time of 6 min.

Thus, comparison of the data on the decomposition rates of the reducing agents and the rates of redox reactions in the presence and in the absence of a carbon fiber substrate gives reason to believe that the influence of the substrate on the rate of metal deposition is determined by the following two factors. On the one hand, there is a growing contribution from the dissociative pathway and increasing quasi-stationary concentration of intermediates, sulfoxylate ions. On the other hand, the Cd(0) and Cr(III) species formed on the substrate surface upon its activation exert an accelerating action.

Figure 3 compares the adhesion strengths of nickel coatings formed upon different kinds of pretreatment of carbon fiber substrates. The data obtained indicate that the adhesion strength of the nickel coating formed using the suggested procedure is high. A sample treated with conc. H_2SO_4 with addition of $Cr_2O_7^{2-}$ significantly surpasses the samples treated with salts of tin and palladium in the time of beginning and completion of coating disintegration. Thus, the method of simultaneous etching and activation of carbon fibers, suggested here, leads to enhanced localization of the redox process on the surface and to improved adhesion strength of the coating.

Analysis of the experimental data obtained makes it possible to recommend a rather simple method for electroless nickel plating of carbon fibers, protected by a patent [19]. The procedure is as follows. The surface of an article made of carbon fibers is etched for 6 min at a temperature of 353 K with a 0.3 M solution of potassium dichromate in concentrated sulfuric acid (d = 1.83 g cm^{-1}). After that the article is placed, without washing or removal of the etching mixture remaining on its surface, in a metallization bath with an aqueous solution of nickel chloride and SHMS or TDO. The duration of this stage is 3–5 min, after which the article is washed and dried. The method can produce nickel coatings with a layer thickness of 4.5–5.2 μm at an average metallization rate of 24 μm h^{-1}. The technique suggested makes the process less labor-consuming. This is achieved by combining the stages of activation and chemical metallization into a single stage, eliminating the stages of washing and preparation of a special activating formulation, and excluding the use of highly expensive components (Sn and Pd). Moreover, if sodium borohydrate is used, the coating contains, in addition to the main substance, a boron impurity. However, a keen interest in obtaining pure metal coatings has aroused recently [2, 3, 5]. In this context, more promising reducing agents are SHMS and TDO, which provide a 99.0–99.9% content of the main metal in a coating.

Table 3. Influence exerted by the concentration of Cd(II) and Cr(IV) additives in the etching solution on the mass of the metal being deposited (metallization conditions: $[Cu^{2+}] = [Ni^{2+}] = 1.0$ M, t = 6 min, [SHMS] = [TDO] = 0.2 M)

Metal*	Additive, g l^{-1}	m, mg g^{-1} of fiber
	Cd^{2+}	
Cu	0.005	0.47
	0.3	2.76
	0.6	0.81
	$Cr_2O_7^{2-}$	
Ni	0.005	0.57
	0.3	4.46
	0.6	0.97

* Deposition of Cu or Ni onto carbon fibers activated with a solution containing Cd(II) or Cr(IV), respectively.

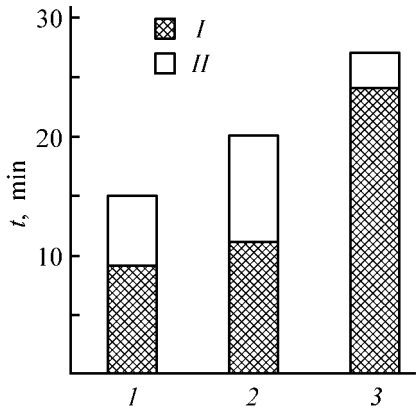

Fig. 3. Influence exerted by method used for pretreatment of carbon fibers on the adhesion properties of a nickel coating. (*I*) Time elapsed before the beginning of film disintegration and (II) that before completion of film disintegration. Carbon fiber treatment: (*1*) with a $PdCl_2$ solution (0.5 g l^{-1}), (*2*) *1* + sensitization with a colloid solution of $SnCl_2 \cdot 2H_2O$ (0.25%), and (*3*) conc. H_2SO_4 containing 0.01 M of $Cr_2O_7^{2-}$ + sensitization with a 0.01 M solution of $CuCl_2$ with addition of 0.1 M of TUDO or HMSS.

CONCLUSION

A study of the influence exerted by a carbon fiber substrate and methods of its activation on the rate of chemical deposition of nickel and copper demonstrated that use of sulfur-and-oxygen-containing reducing agents, rongalite and thiourea dioxide, yields coatings with high adhesion to the substrate and makes the metallization process simpler and less expensive.

REFERENCES

1. Shalkauskas, M.V and Kashkyalis, A., *Khimicheskaya metallizatsiya plastmass* (Chemical Metallization of Plastics), Leningrad: Khimiya, 1972.
2. Golovchanskaya, R.G. and Kruglikova, S.S., *Itogi nauki i tekhniki: Elektrokhimiya* (Advances in Science and Technology: Electrochemistry), Moscow: VINITI, 1987, vol. 25, pp. 79–143.
3. Lyatok, L.V., Gomadov, V.N., and Orekhova, T.V., *Resursosberegayushchaya tekhnologiya v elektrokhimicheskikh proizvodstvakh: Materialy Respublikanskoi konferentsii* (Proc. Republ. Conf. on Resource-saving Technology in Electrochemical Industry), Kharkov, 1987, p. 5.
4. Lomovskii, O.M. and Boldyrev, V.V., *Zh. Prikl. Khim.*, 1989, vol. 62, no. 11, pp. 2444–2455.
5. *Khimicheskoe osazhdenie metallov iz vodnykh rastvorov* (Chemical Deposition of Metals from Aqueous Solutions), Sviridov, V.V., Ed., Minsk: Universitetskoe, 1987.
6. Budanov, V.V., Akbarov, D.N., Makarov, S.V., and Egorova, E.V., *Metallizatsiya nemetallicheskikh materialov i problemy promyshlennoi gal'vanoplastiki* (Metallization of Nonmetallic Materials and Problems of Industrial Galavanoplasty), Moscow: Mosk. Dom Nauchn.-Tekhn. Propagandy im. F.E. Dzerzhinskogo, 1990, pp. 62–67.
7. Novikova, O.A. and Sergeev, V.P., *Modifikatsiya poverkhnosti armiruyushchikh volokon v kompozitsionnykh materialakh* (Modification of the Surface of Reinforcing Fibers in Composites), Kiev: Naukova Dumka, 1989.
8. Andreevskaya, G.D., Gorbatkina, Yu.A., Ivanova-Mumzhieva, V.G., and Epifanova, S.S., *Mekh. Polimerov*, 1974, no. 1, pp. 37–42.
9. Budanov, V.V., *Khimiya i tekhnologiya vosstanovitelei na osnove sul'foksilovoi kisloty: Rongalit i ego analogi* (Chemistry and Technology of Reducing Agents Based on Sullfoxylic Acid: Rongalite and Its Analogues), Moscow: Khimiya, 1984.
10. Budanov, V.V. and Makarov, S.V., *Khimiya serosoderzhashchikh vosstanovitelei (rongalit, ditionit, dioksid tiomocheviny)* [Chemistry of Sulfur-containing Reducing Agents (Rongalite, Dithionite, Thiourea Dioxide)], Moscow: Khimiya, 1994.
11. Ermolina, S.V., Terskaya, I.N., Budanov, V.V., and Makarov, S.V., *Izv. Vyssh. Uchebn. Zaved., Khim. Khim. Tekhnol.*, 2000, vol. 43, no. 1, pp. 35–38.
12. Alekseev, V.N., *Kolichestvennyi analiz* (Quantitative Analysis), Moscow: Khimiya, 1972.
13. Polenov, Yu.V., Budanov, V.V., and Egorova, E.V., *Zh. Prikl. Khim.*, 2001, vol. 74, no. 10, pp. 1664–1671.
14. Budanov, V.V., *Koord. Khim.*, 2002, vol. 28, no. 4, pp. 314–320.
15. Ermolina, S.V., Terskaya, I.N., Makarov, S.V., and Budanov, V.V., *Izv. Vyssh. Uchebn. Zaved., Khim. Khim. Tekhnol.*, 1993, vol. 36, no. 6, pp. 52–55.
16. Basolo, F. and Pearson, R.G., *Mechanisms of Inorganic Reactions. A Study of Metal Complexes in Solution*, New York: Wiley, 1967.
17. Terskaya, I.N. and Budanov, V.V., *Zh. Neorg. Khim.*, 1995, vol. 40, no. 9, pp. 1466–1469.
18. Ermolina, S.V., Terskaya, I.N., Makarov, S.V., and Budanov, V.V., *Izv. Vyssh. Uchebn. Zaved., Khim. Khim. Tekhnol.*, 1996, vol. 39, nos. 1–2, pp. 47–49.
19. RF Patent 2063461.

Russian Journal of Applied Chemistry, Vol. 77, No. 2, 2004, pp. 241–248. Translated from Zhurnal Prikladnoi Khimii, Vol. 77, No. 2, 2004, pp. 244–252.

APPLIED ELECTROCHEMISTRY AND CORROSION PROTECTION OF METALS

Amperometric Cholinesterase Biosensors with Carbon Paste Electrodes Modified with Cobalt Phthalocyanine

L. G. Shaidarova, S. A. Ziganshina, E. P. Medyantseva, and G. K. Budnikov

Kazan State University, Kazan, Tatarstan, Russia

Received April 14, 2003

Abstract—Biosensors based on a carbon paste electrode with immobilized cholinesterase and cobalt(II) phthalocyanine as a mediator are studied. Electrochemical characteristics of the biosensors are investigated in relation to the carbon paste composition, the enzyme and mediator immobilization procedures, nature of the protective film and procedure of its application, and also storage conditions of the electrodes. A method is suggested for fabricating a cholinesterase biosensor with cobalt(II) phthalocyanine mediator, providing the maximum electrocatalytic response in electrooxidation of butyrylthiocholine iodide (substrate for cholinesterase).

The development of various biosensors has attracted much attention [1–4]. Biosensors differ from each other in the composition and design of their biosensing elements, and also in the design of the detection system [5]. Among diverse existing biosensors, those with electrochemical detection systems have found wide application [6–8]. The use of biocatalytic and electrochemical reactions in combination allows development of highly sensitive and fast methods for determining various bioactive compounds [2–8]. One of the lines in this area is the development of electrochemical biosensors with immobilized mediators [9, 10]. Mediators serve to provide facilitated electron transfer between active centers of the enzyme and a transducer. The use of mediators in biosensors allows an increase in the electrochemical response and selectivity by virtue of a decrease in the electrode potential.

Biosensors with electron-transfer mediators can be improved in different ways: development of novel mediating systems and elaboration of advanced methods for immobilizing a mediator and an enzyme and new techniques for fabricating a sensing element of the electrode. The development of biosensors with carbon paste electrodes is regarded as a promising way for improving analytical characteristics of amperometric enzyme sensors [11]. The sensitivity of amperometric determinations with carbon paste electrodes (CPE) is limited by the background interference and also by noises generated in electrochemical transducers. The signal-to-noise ratio can be improved by lowering the residual current in such ways as development of new sensing materials, modification of the electrode surface, and immobilization of a redox mediator.

Metals, metal oxides, complexes of metals, and polymers can be used as mediators [5]. Ferrocene-like compounds are frequently used for this purpose [10]. For example, ferrocenes have been successfully used in glucose oxidase biosensors [12]. The same mediator has been employed for amperometric determinations with the cholinesterase enzyme system [13]. Quinone has been used as a mediator in glucose oxidase biosensors for determination of, e.g., glucose [10]. Amperometric biosensors based on inorganic polycrystalline materials show interesting properties too [14, 15]. The use of electrodes modified with Prussian Blue in biosensors [14] allowed an increase in the current density of hydrogen peroxide reduction and a decrease in the potential of the working electrode, thus reducing the sensitivity of the biosensor to oxygen, ascorbic acid, and other reducing agents. However, iron(II) ferrocyanide films obtained by electrochemical deposition are insufficiently stable, especially, in alkaline solutions. The stability of a glucose oxidase biosensor can be improved by making use of, e.g., synthetic copper(II) ferrocyanide incorporated into the carbon paste in addition to glucose oxidase [15]. Such an electrode may operate at the physiological pH ~7.4. In contrast to the above-indicated mediators, metallophthalocyanines (MPc) are charac-

1070-4272/04/7702-0241 © 2004 MAIK "Nauka/Interperiodica"

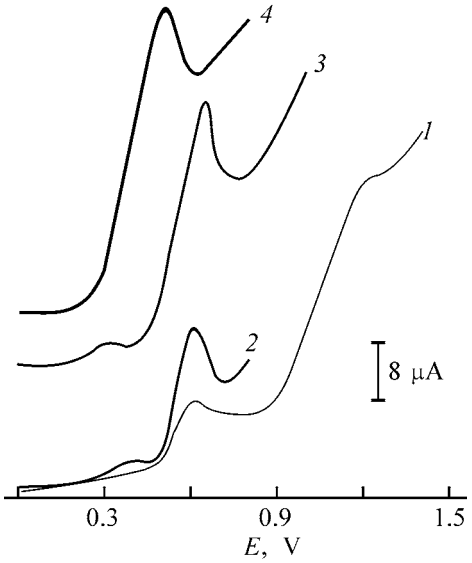

Fig. 1. Voltammograms of BTCH oxidation on (*1*) CPE and (*2*–*4*) CPE-based CHE biosensors: (*2*) immobilized CHE, (*3*) immobilized CHE + CoPc, and (*4*) the initial carbon material pretreated with butyl acetate. (*E*) Potential. Solution: 2×10^{-3} M BTCH in borate buffer (pH 9.0); the same for Figs. 2–4.

terized by both high catalytic activity in various electrochemical reactions and sufficient chemical stability [16, 17]. Therefore, metallophthalocyanines have been used as mediators for biosensors too [18, 19]. The catalytic activity of metallophthalocyanines depends on the ligand structure and the nature of a metal. Among 3*d* metal complexes, Co(II) and Fe(II) phthalocyanines demonstrate the highest catalytic effect in oxidation of organic hydrosulfides [20]. In studying the electrocatalytic properties of metallophthalocyanines-modified electrodes in the system constituted by cholinesterase (CHE) and thiocholine ester, we also demonstrated that the highest catalytic effects are observed on CoPc- and FePc-modified electrodes [21].

In this study, we examined how the composition of the sensing element of the electrode and the procedure of its formation affect the performance of CPE-based biosensor with immobilized CHE and CoPc as a mediator.

In developing an amperometric CHE biosensor with CoPc, we compared various methods for immobilization of the enzyme and mediator, such as incorporation of all or some of components into carbon paste or their application as films on the CPE surface.

It is known [22] that butyrylthiocholine (BTCH) iodide is a specific substrate for CHE. Enzymatic hydrolysis of BTCH produces butyric acid and thiocholine (TCH) iodide:

$$C_3H_7C(O)SCH_2CH_2N^+(CH_3)_3I^- + H_2O \xrightarrow{CHE} C_3H_7COOH + HSCH_2CH_2N^+(CH_3)_3I^-.$$

The CHE activity was determined by amperometric measurement of TCH iodide as a product of enzymatic hydrolysis of BTCH. Anodic voltammograms were recorded in 2×10^{-3} M BTH in borate buffer solution (pH 9.0) over the potential range 0.0–1.0 V. We observed two steps in the anodic oxidation curve of BTCH, measured with CPE after spontaneous hydrolysis (Fig. 1, curve *1*). The first peak (E_p = 0.60 V), corresponding to oxidation of TCH, was used as the analytical response. Previously, we demonstrated [21] that, in this potential range, TCH is oxidized and iodide acts as a mediator:

$$I^- - e \rightleftarrows I, \quad I + RSH \rightarrow I^- + \tfrac{1}{2}RSSR + H^+,$$

where $R = -CH_2CH_2N^+(CH_3)_3$.

In the presence of both native CHE [21] and that immobilized on carbon paste (Fig. 1, curve *2*), the intensity of the peak at E_p ~0.60 V increased because of the enzymatic hydrolysis of BTCH. Figure 1 (curve *3*) shows the curve of anodic oxidation of BTCH, obtained with a biosensor fabricated using simultaneous immobilization of CHE and CoPc, as a mediator, on CPE. In this case, the anodic peak is observed within the same potential range as that without mediator, but it has higher intensity. In the presence of CoPc, heterogeneous electrocatalytic oxidation of TCH occurs in addition to the above-described electrochemical reaction. In this case, the electrochemically generated Co(III)Pc acts as a catalyst [21]:

$$M(II)Pc \rightleftarrows M(III)Pc + e, \quad M(III)Pc + RSH \rightarrow M(II)Pc + \tfrac{1}{2}RSSR + H^+.$$

The structure of the CHE biosensor and the procedure of its fabrication also affect the peak potential and TCH oxidation current.

The CPE performance, including the residual current, depends on a conducting carbon-based material and a binder used. We used various types of carbon materials such as spectroscopy-grade graphite powder, activated carbon, and flake graphite. The current–voltage characteristics of the electrodes were compared using the TCH oxidation data (Table 1). Globular graphite powders (spectroscopy-grade graphite and activated carbon) demonstrated better electrochemical performance: lower peak potentials and higher anodic peak currents. Carbon-paste electrodes fabricated from

Table 1. Structure and electrochemical characteristics of carbon paste electrodes in BTCH oxidation

Carbon	Binder	Solvent	Electrode resistance, kΩ	*E*, V	*I*, μA
Spectroscopy-grade graphite	Nujol	Butyl acetate	0.04	0.50	10.8
Activated carbon	"	"	0.01	0.52	7.5
Flake graphite	"	"	0.4	0.58	6.0
Spectroscopy-grade graphite	Paraffin	"	0.1	0.58	4.6
	Polyethylene	"	4.0	0.82	1.9
	Nujol	Methylene chloride	20.0	0.80	6.4
	"	Acetone	6.6	0.65	7.2
	"	Acetonitrile	3.0	0.60	8.8
	"	Toluene	1.9	0.58	10.0
	"	Ethanol	1.4	0.55	9.6

Table 2. Voltage–current characteristics of BTCH oxidation on electrodes with differently immobilized CHE*

Experiment no.	Immobilization procedure	Order of reagent deposition on the electrode surface		*E*, V	*I*, μA
		first layer	second layer		
1	Adsorption of CHE**	–	–	0.48	16.2
2	Incorporation of CHE into CPE	–	–	0.74	20.8
3	Covalent binding of CHE to GA:				
	(a) in carbon paste CHE + GA	–	–	0.50	20.4
	(b) on CPE surface	CHE + GA	–	0.48	26.8
		CHE	GA	0.62	20.2
		GA	CHE	0.45	21.6
		GA	CHE**	0.68	32.8
	(c) in GA vapor	CHE	GA vapor***	0.65	30.8
4	Incorporation into polymer films	NC	CHE + GA	0.58	22.8
		NC + CHE + GA	–	0.50	20.2
		CHE + GA	NC	0.53	10.2
		The same	Gelatin	0.52	28.0
		CHE + GA + gelatin	–	0.60	25.2
		CHE + GA	Agar-agar	0.50	27.7
		The same	Chitosan	0.58	26.2

* (GA) Glutaraldehyde and (NC) nitrocellulose. ** CHE was adsorbed from a 22.5 mg ml^{-1} solution for 15 min. *** At 4°C for 12 h.

flake graphite show a lower conductivity and, as a result, higher peak potentials, lower peak currents, and worse reproducibility of the electrochemical response. The nature of a binder influences the ohmic resistance of the electrode and, therefore, the detection sensitivity. The finer a powder, the larger amount of a binder is needed. But an increase in the amount of a binder results in that the ohmic resistance of the electrode becomes higher. The TCH oxidation current decreases in the order Nujol > paraffin > polyethylene. The ohmic resistance of the electrode and the residual current are at a minimum for the electrode fabricated from spectroscopy-grade graphite with Nujol as a binder (Table 1).

The CPE characteristics are strongly affected by pretreatment of the initial carbon material with an organic solvent. Such a pretreatment, followed by removal of a solvent, occasionally leads to a considerable decrease in the electrode polarization. We compared properties of CPEs treated with various solvents, such as butyl acetate, ethanol, toluene, acetonitrile, acetone, and methylene chloride (Table 1). As can be seen, the best characteristics (lower resistance and higher peak current) were provided by pretreatment with butyl acetate. Furthermore, pretreatment of activated carbon with butyl acetate shifts the peak potential by 150 mV (Fig. 1, curve *4*).

The crucial point in development of biosensors is to properly arrange an enzyme molecule on the electrode surface. We tested various methods of CHE immobilization such as adsorption on the electrode surface, incorporation into carbon paste, chemical (covalent) binding, and incorporation into a polymeric film (Table 2).

Immobilization of CHE by adsorption on the electrode surface (Table 2, experiment no. 1) or by in-

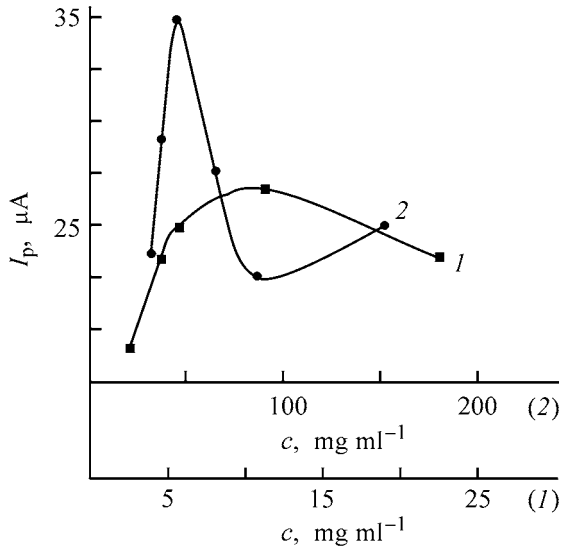

Fig. 2. Peak current I_p of BTCH oxidation on CHE biosensor vs. (*1*) CHE and (*2*) glycerol concentration c in the film.

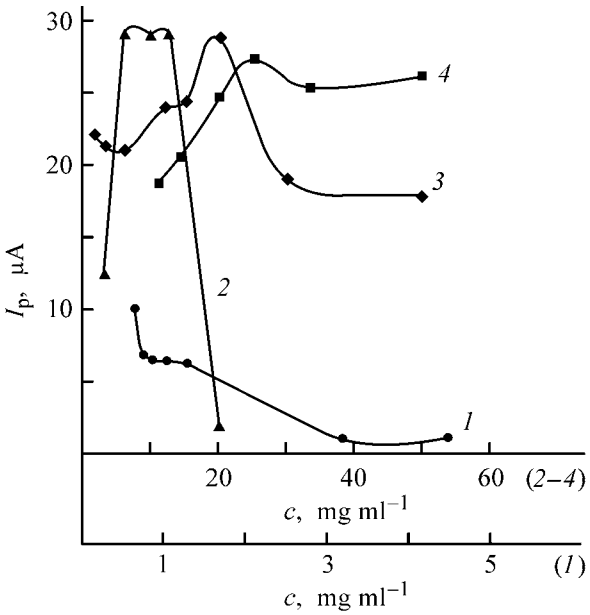

Fig. 3. Peak current I_p of BTCH oxidation on CHE biosensor vs. (*1*) NC, (*2*) gelatin, (*3*) agar-agar, and (*4*) chitosan concentration c in the film.

corporation into the carbon paste (Table 2, experiment no. 2) resulted in a low and poorly reproducible (S_r > 10%) TCH oxidation current, because of the rapid washout of the enzyme from the electrode surface.

To more tightly fix CHE in the electrode matrix, we employed covalent binding with a bifunctional agent, glutaraldehyde (GA) (Table 2, experiment no. 3). The carbon powder was impregnated with butyl acetate and then with a mixture of CHE and GA, followed by removal of the solvent. The optimal CHE to GA ratio has been established previously [23]. The resulting biosensor demonstrated better metrological characteristics (S_r < 5%) and a satisfactorily low E_p = 0.50 V (Table 2, experiment no. 3a). In fabricating a biosensing element in the form of a layer on CPE (Table 2, experiment no. 3b), a drop of an aqueous solution containing CHE and GA was deposited onto the electrode surface. We also varied the order of CHE and GA deposition: the CHE layer was deposited first, and the GA layer, second, and vice versa. One more variant of immobilization was deposition of the GA layer, followed by adsorption of CHE from its aqueous solution. In this case, the optimal CHE concentration on the electrode surface was created by adsorption from a 5 mg ml^{-1} solution (Fig. 2, curve *1*). The best electrochemical (E_p and I_p) and metrological (S_r < 5%) characteristics were obtained with a sensor fabricated by deposition of a mixture of CHE and GA on the electrode surface.

Another procedure used for CHE immobilization was exposure of the electrode, modified with adsorbed CHE, to a GA vapor [24]. Varying the temperature, we established that the highest response is observed with CHE covalently bound to GA at 4–7°C (Table 2, experiment no. 3c). However, we observed an increase in E_p in this case.

To stabilize the electrochemical response and catalytic activity of immobilized CHE, the electrode surface was coated with a film of various polymeric materials, such as nitrocellulose, gelatin, agar-agar, and chitosan (Table 2, experiment no. 4). The films were obtained by deposition of 0.1 ml of a solution with various polymer concentrations on the electrode surface with subsequent removal of the solvent. A mixture of butyl acetate and toluene was used as a solvent for NC, and water, for the other polymers. The optimal NC concentration in the solution used for the film preparation was established from the dependence of the TCH oxidation current on the polymer concentration to be 1 mg ml^{-1} (Fig. 3). The optimal concentrations of gelatin, agar-agar, and chitosan were found to be 6–15, 20, and 25 mg ml^{-1}, respectively (Fig. 3).

In a series of experiments (Table 2, experiment no. 4) we varied the sequence of reagent deposition on the electrode surface. Adsorption of CHE over the NC layer did not increase the TCH oxidation peak; in addition, in this case, CHE is rapidly washed out from the electrode surface. The immobilization of CHE bound to GA in an NC film improved the reproducibility of the peak current, but strongly decreased the enzyme activity, which was reflected in a decreased

Table 3. Current–voltage characteristics of BTCH oxidation on biosensors with CPE variously modified with CoPc mediator

Experiment no.	Mode of incorporation into a film				
	first layer	second layer	third layer	*E*, V	*I*, μA
1	CoPc	CHE + GA	–	0.50	40.8
	CoPc	The same	Gelatin	0.50	41.2
	CoPc + CHE + GA	–	–	0.54	32.4
2	NC + CoPc	CHE + GA	–	0.63	34.0
	NC	CoPc	CHE + GA	0.54	21.4
3	CoPc + PVP (electrochem.)	CHE	Gelatin	0.52	29.8
	CoPc + PVP	CHE	〃	0.53	35.0
	Mode of incorporation into a paste				
	paste composition	first layer	second layer	*E*, V	*I*, μA
4	CoPc	CHE + GA	–	0.60	43.2
	CoPc	The same	Gelatin	0.62	44.0
5	CoPc + CHE + GA	–	–	0.50	30.8
	The same	Gelatin	–	0.52	31.8
6	NC + CoPc + CHE + GA	–	–	0.52	29.5
	The same	Gelatin	–	0.54	31.2

analytical response. The deposition of an NC film over the layer of CHE, covalently bound to GA, totally inactivated CHE, i.e., the peak current was equal in this case to that in the absence of CHE, which is probably due to the inhibiting effect of the organic solvent used for NC dissolution.

In a similar experiment, but with gelatin instead of NC, we also observed a decrease in the enzyme activity, but it was considerably less pronounced. A higher response was obtained on an electrode successively coated with a layer of CHE + GA and a layer of gelatin. With the use of agar-agar and chitosan, better results were also obtained when polymeric films were applied over the enzyme-containing layer (Table 2, experiment no. 4).

Thus, application of a polymeric film improved the reproducibility of the electrochemical response of the biosensors, but decreased the catalytic activity of the enzyme. The use of films of natural polymers favored tight binding of CHE to the electrode matrix, and, unlike NC, had no inhibiting effect on the catalytic activity of immobilized CHE.

It should be pointed out that the storage conditions also influence the electrochemical characteristics of the biosensors. The activity of biosensors decays with time. However, if stored under conditions of increased humidity, the biosensors demonstrated even better metrological characteristics, and their lifetime increased to a week.

Introduction of some "water-like" compounds into the enzyme-containing layer of a biosensor increases the activity of immobilized CHE, including that upon in storage. For example, introduction of glycerol considerably increases the CHE activity. In [25, 26], it was demonstrated for the example of proteins other than CHE that raising the sorbitol content in a chymotrypsin preparation leads to a higher enzyme activity, and the absence of glycerol in the immobilized enzyme results in a total loss of activity [26]. Most likely, such compounds as sorbitol [25] and glycerol [26] provide a favorable environment for an enzyme in dehydration compensating hydrogen bonds. Evidently, that is why the introduction of glycerol into the film considerably increases the CHE activity. In special experiments, we established the optimal glycerol to CHE ratio in the sensing element (Fig. 2).

In development of biosensors with mediators, it is important to provide conditions for facilitated electron transfer between an enzyme and a transducer. This can be done through optimal orientation of enzymes and mediators on the electrode surface. Therefore, we studied various immobilization modes of the enzyme (CHE) and mediator (CoPc) on CPE.

In fabricating biosensors, we used various electrode modification procedures, such as successive deposition of layers of the mediator, enzyme, and other components or formation of a biosensing membrane containing all these components (Table 3, experiment no. 1).

Table 4. Parameters of flow-injection analysis for heavy metals with CHE biosensor with CoPc mediator (regression equation: $\log I = a + b \log c$; I, μA; c, M)

Cation	Concentration, M	a	b	R	c_{min}, μg l^{-1}	MPC, μg l^{-1} [29]
Zn^{2+}	1×10^{-6}–1×10^{-3}	0.94 ± 0.02	–0.180 ± 0.005	0.9991	8×10^{-7} (52)	1000
Cd^{2+}	1×10^{-8}–1×10^{-5}	1.05 ± 0.02	–0.048 ± 0.002	0.9995	5×10^{-9} (0.56)	100
Cu^{2+}	5×10^{-10}–1×10^{-6}	2.20 ± 0.04	–0.150 ± 0.006	0.9997	1×10^{-10} (0.01)	500

In this case, higher currents were observed for electrodes manufactured by successive application of the layers of CoPc, CHE covalently bound to GA, and gelatin, or of CoPc, CHE, and gelatin. The decrease in the TCH oxidation current observed with CPE modified with CoPc and CHE + GA can be attributed to decreasing number of enzyme active sites or lesser accessibility of the substrate for the enzyme. To fix the mediator on the electrode surface, we used a nonconducting film of NC and polyvinylpyridine (PVP), which were obtained electrochemically or by deposition of a drop of an organic solution on the CPE surface followed by solvent removal. However, incorporation of CoPc into the film did not increase the TCH oxidation current (Table 3, experiment nos. 2, 3).

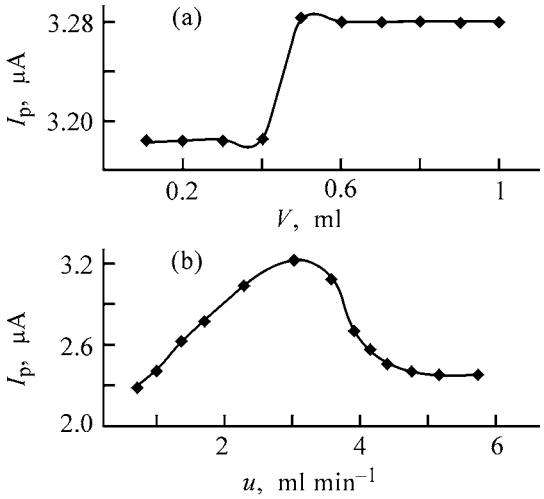

Fig. 4. FIA response to BTCH oxidation on CHE biosensor vs. (a) injected sample volume V and (b) flow rate u. (I_p) Current.

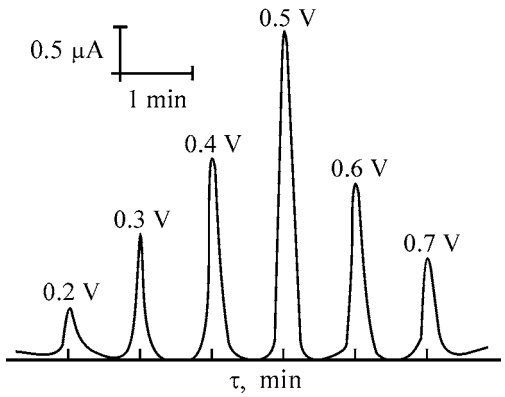

Fig. 5. FIA response to BTCH oxidation on CHE biosensor with CoPc mediator vs. the applied potential E. Initial BTCH concentration 2×10^{-3} M; injected sample volume V = 0.5 ml; and flow rate u = 3.0 ml min^{-1}. (τ) Time.

In developing carbon paste electrodes, special efforts are made to provide high stability and reproducibility of the analytical response and easy renewability of the electrode surface. For this purpose, we incorporated in this study CoPc, taken in various combinations with other components, into the carbon paste (Table 3, experiment nos. 4–6). Deposition of the CHE + GA layer over the CoPc-modified CPE provided high and reproducible response (Table 3, experiment no. 4). A lower response was obtained with the biosensor fabricated by successive incorporation of CoPc and CHE + GA into the carbon paste (Table 3, experiment no. 5). However, this procedure allowed a decrease in E_p to 0.50 V. Furthermore, is becomes possible in this case to mechanically renew the electrode surface. Incorporation of NC into the paste improved the reproducibility of the response, but impaired the sensitivity of the biosensor (Table 3, experiment no. 6).

Finally, the best characteristics were obtained with biosensors fabricated using immobilization of CHE bound to GA on the surface of a CoPc-modified CPE or over a CoPc layer deposited on the CPE surface. Evidently, the optimal coupling of the enzymatic and electrocatalytic reactions is achieved in these cases. Application of a protective gelatin film in all cases improved the stability of the electrochemical response.

The biosensor in its optimal version was tested under conditions of flow-injection analysis (FIA). The maximum FIA response was obtained at a flow rate u = 3.0 ml min^{-1} and injected sample volume V = 0.5 ml (Fig. 4). Since the FIA response was recorded in the controlled potential mode, we studied the effect of the applied potential on the BTCH oxidation current. Figure 5 shows that the maximum response is observed at E = 0.50 V.

The FIA response is a linear function of the BTCH concentration over the concentration range 1×10^{-5}–2×10^{-3} M, and it can be fitted with the equation $I = a + bc$ (I, μA; c, M) with $a = (7.78 \pm 0.09) \times 10^{-3}$ and $b = (1.65 \pm 0.08) \times 10^{3}$ (r 0.9992). The detection limit was found to be 4×10^{-6} M. Within the working concentration range, the standard deviation was within 5% at $n = 10$.

It is known that many metal ions inhibit the activity of both native and immobilized CHE [27]. In this study we used a CHE biosensor with a CoPc mediator, to assess the inhibiting effect of such heavy metal cations as Cu(II), Cd(II), and Zn(II) on immobilized CHE. The reversible inhibiting effect of the metal cations was evaluated by the decrease in the FIA response initiated by injection of a metal-containing sample in the presence of BTCH, compared to the blank experiment without a metal. The results of determinations of metal cations are listed in Table 4. Like other CHE biosensors [28], the biosensor with CoPc mediator is the most susceptible to the effect of copper(II). The concentration ranges in which the FIA response is a linear function of the concentration of the metals studied coincide with those obtained previously in determining the inhibiting ranges for of the CHE activity by these ions [28]. Incorporation of the mediator into the biosensing element has more a pronounced effect on the inhibitors detection sensitivity. The detection limits of the metal ions on the CHE biosensor with CoPc mediator are lower by several orders of magnitude as compared to the corresponding maximum permissible concentrations.

EXPERIMENTAL

DC votammograms were recorded on a PU-1 polarograph with a three-electrode cell. The working electrodes were CPE, chemically modified electrode (CME), and biosensor with a mediator. The reference electrode was Ag/AgCl, and the anode, Pt wire. The CPE fabrication procedure was described elsewhere [20]. The surface was renewed by mechanical polishing of the electrode surface with filter paper and tracing paper. In constructing CME, we used CoPc (2 wt %) in addition to the common CPE components (carbon powder and Nujol). The modifier was either incorporated into the carbon paste or deposited onto CPE. In manufacturing the biosensor, the enzyme (CHE) was also incorporated either into CPE or into the films applied onto the CPE surface.

The flow-injection analysis system included a DLV-1 peristaltic pump, an injector, a mixer, a flow-through electrochemical cell (V = 0.2 ml), and a polarograph as a recording device.

In manufacturing a biosensing element of the sensor, we used a cholinesterase preparation (EC 3.1.1.8) with an activity of 110 units per mg protein (Biomed Research and Production Association, Perm, Russia). As a specific substrate for CHE, we used recrystallized BTCH. Other chemicals used were CoPc (Fluka, Switzerland), GA (Reanal, Hungary), glycerol (chemically pure grade), NC $[C_6H_7O_2(OH)_{3-x}(ONO_2)_x]_n$ of the colloxylin type with a nitrogen content from 10.7 to 12.2%, gelatin, agar-agar, and chitosan (chemically pure grade). As analytes, we used Cd(II), Cu(II), and Zn(II) as chlorides.

Solutions were prepared gravimetrically using double-distilled water or organic solvents (butyl acetate, ethanol, toluene, acetonitrile, acetone, and methylene chloride). Nitrocellulose was dissolved in a mixture of butyl acetate and toluene. Gelatin and agar-agar were dissolved on heating on a water bath until complete dissolution. Chitosan was dissolved in 1% acetic acid, then 1% KOH was added, and the resulting gel was filtered off, washed with water, dried a little, and repeatedly dissolved in 1% acetic acid. An electrode with a poly(2-vinylpyridine) membrane modified with CoPc was fabricated by the procedure described in [30].

Amperometric determinations were carried out in a borate buffer solution (pH 9.0). The solution pH was measured with a pH-150 pH-meter.

CONCLUSIONS

(1) The composition of cholinesterase biosensor with CoPc mediator has been optimized. The biosensor was constructed by immobilization of cholinesterase chemically bound to glutaraldehyde on the carbon-paste electrode surface modified with CoPc, followed by application of a gelatin layer. Another fabrication procedure involved successive deposition of the layers of CoPc mediator, a mixture of cholinesterase with glutaraldehyde, and gelatin.

(2) The cholinesterase biosensor with Co(II) phthalocyanine mediator was used for flow-injection determination of butyrylthiocholine iodide (substrate for cholinesterase) and Zn(II), Cd(II), and Cu(II) (cholinesterase inhibitors).

(3) The flow-injection analysis response was recorded at the applied potential E = 0.50 V, flow rate u = 3.0 ml min^{-1}, and injected sample volume V = 0.5 ml. The response is a linear function of the buty-

rylthiocholine iodide concentration over the concentration range 1×10^{-5}–2×10^{-3} M. In metal determinations, linear logarithmic dependences of the response on the metal concentrations were observed over the concentration ranges 1×10^{-6}–1×10^{-3}, 1×10^{-8}–1×10^{-5}, and 5×10^{-10}–1×10^{-6} M for Zn(II), Cd(II), and Cu(II), respectively ($S_r < 0.07$).

(4) High analytical and metrological performance of the cholinesterase biosensor with CoPc mediator makes it suitable for determination of cholinesterase substrates and inhibitors.

ACKNOWLEDGMENTS

The study was financially supported by the Russian Foundation for Basic Research (project no. 00-03-32389).

REFERENCES

1. *Biosensors: Fundamentals and Applications*, Turner, A.P.F., Karube, I., and Wilson, G.S., Eds., Oxford: Oxford Univ., 1987.
2. Karube, I. and Namura, Y., *Trends Anal. Chem.*, 1995, vol. 14, no. 7, pp. 295–301.
3. Paddle, B.M., *Biosensors Bioelectron.*, 1996, vol. 11, pp. 1079–1113.
4. Albareda-Sirvent, M., Merkoci, A., and Alegret, S., *Sensors Actuators, Ser. B*, 2000, vol. 69, nos. 1–2, pp. 153–163.
5. Budnikov, G.K., Maistrenko, V.N., and Murinov, V.I., *Voltamperometriya s modifitsirovannymi i ul'tramikroelektrodami* (Voltammetry with Modified and Ultramicroelectrodes), Moscow: Nauka, 1994.
6. Tarasevich, M.R., Bogdanovskaya, V.A., and Zhutaeva, G.V., *Elektrokhimiya*, 1993, vol. 29, no. 12, pp. 1505–1560.
7. Ivnitskii, D.M., Kurochkin, I.N., and Varfolomeev, S.D., *Zh. Anal. Khim.*, 1991, vol. 46, no. 8, pp. 1462–1479.
8. Budnikov, G.K., Medyantseva, E.P., and Babkina, S.S., *Usp. Khim.*, 1991, vol. 60, no. 4, pp. 881–910.
9. Kano, K. and Ikeda, T., *Anal. Sci.*, 2000, vol. 16, no. 10, pp. 1013–1021.
10. Bobrin, S.V., Atanasov, P., Iliev, I., *et al.*, *Elektrokhimiya*, 1993, vol. 29, no. 8, pp. 1013–1016.
11. Bogdanovskaya, V.A., Evstefeeva, Yu.E., Tarasevich, M.P., *et al.*, *Elektrokhimiya*, 1997, vol. 33, no. 2, pp. 150–154.
12. Cass, A.E.G., Davis, G., Francis, G.D., *et al.*, *Anal. Chem.*, 1984, vol. 56, no. 4, pp. 667–671.
13. Evtyugin, G.A., Budnikov, G.K., Galyametdinov, Yu.G., and Suntsov, E.V., *Zh. Anal. Khim.*, 1996, vol. 51, no. 4, pp. 424–426.
14. Karyakin, A.A. and Karyakina, E.E., *Zh. Vseross. Khim. O–va im. D.I. Mendeleeva*, 1998, vol. 42, nos. 1–2, pp. 86–95.
15. Wang, J., Zhang, X., and Prakash, M., *Anal, Chim. Acta*, 1999, vol. 396, no. 1, pp. 11–16.
16. Berezin, B.D., *Koordinatsionnye soedineniya porfirinov i ftalotsianina* (Porphyrin and Phthalocyanine Complexes), Moscow: Nauka, 1978.
17. Tarasevich, M.R. and Radyushkina, K.A., *Kataliz i elektrokataliz metalloporfirinami* (Catalysis and Electrocatalysis with Metalloporphyrins), Moscow: Nauka, 1982.
18. Skladal, P., *Anal. Chim. Acta*, 1992, vol. 269, no. 2, pp. 281–287.
19. Nunes, G.S., Barcelo, D., Grabaric, B.S., *et al.*, *Anal. Chim. Acta*, 1999, vol. 399, no. 1, pp. 37–49.
20. Shaidarova, L.G., Budnikov, G.K., and Zaripova, S.A., *Zh. Anal. Khim.*, 2001, vol. 56, no. 8, pp. 839–845.
21. Shaidarova, L.G., Fomin, A.Yu., Ziganshina, S.A., *et al.*, *Zh. Anal. Khim.*, 2002, vol. 57, no. 2, pp. 178–184.
22. Yakovlev, V.A., *Kinetika fermentativnogo kataliza* (Kinetics of Enzymatic Catalysis), Moscow: Nauka, 1965.
23. USSR Inventor's Certificate, no. 1296913, *Byull. Izobret.* 1986, no. 10.
24. Kumaran, S., Meiser, H., Danna, A.M., and Tran-Minh, C., *Anal. Chem.*, 1991, vol. 63, no. 18, pp. 1914–1918.
25. Triantafyllou, A.O., Wehtje, E., Adlerceutz, P., and Mattiasson, B., *Biotechnol. Bioeng.*, 1997, vol. 54, no. 1, pp. 67–76.
26. Lorenzo, E., Pariente, F., Hernandez, L., *et al.*, *Biosensors Bioelectronics*, 1998, vol. 13, nos. 3–4, pp. 319–332.
27. Medyantseva, E.P., Vertlib, M.G., and Budnikov, G.K., *Usp. Khim.*, 1998, vol. 67, no. 3, pp. 252–260.
28. Medyantseva, E.P., Budnikov, G.K., and Li Fa-Shen, in *Khimicheskii analiz pishchevykh produktov i zagryaznenii okruzhayushchei sredy* (Chemical Analysis of Foods and Environmental Pollutions), Moscow: TsRDZ, 1992, pp. 42–45.
29. Bespamyatkov, G.P. and Krotov, Yu.A., *Predel'no dopustimye kontsentratsii (PDK) khimicheskikh veshchestv v okruzhayushchei srede: Spravochnik* [Maximal Permissible Concentrations (MPC) of Chemicals in the Environment: A Reference Book], Leningrad: Khimiya, 1985.
30. Shaidarova, L.G., Gedmina, A.V., and Budnikov, G.K., *Zh. Anal. Khim.*, 2003, vol. 58, no. 2, pp. 193–198.

Russian Journal of Applied Chemistry, Vol. 77, No. 2, 2004, pp. 249–253. Translated from Zhurnal Prikladnoi Khimii, Vol. 77, No. 2, 2004, pp. 253–258.

ENVIRONMENTAL PROBLEMS OF CHEMISTRY AND TECHNOLOGY

Comparison of Fibrous Carboxylic Ion Exchangers in Water Treatment to Remove Heavy Metal Ions

A. A. Shunkevich, R. V. Martsinkevich, G. V. Medyak, V. P. Sokol, L. P. Filanchuk, and V. S. Soldatov

Institute of Physical Organic Chemistry, National Academy of Sciences of Belarus, Minsk, Belarus

Received March 4, 2003

Abstract—Treatment of drinking water to remove heavy metal ions Pb^{2+}, Cu^{2+}, Cd^{2+}, Co^{2+}, Ni^{2+}, and Zn^{2+} with commercial fibrous carboxylic ion exchangers FIBAN Kh-1, K-3, K-4, and K-5 was studied. Features of metal ion sorption from two-component solutions were determined. A comparative evaluation of the sorption selectivity of FIBAN fibrous ion exchangers with respect to heavy metal ions was made.

Fibrous carboxylic ion exchangers are of interest in treatment of natural water and wastewater to remove heavy metal ions [1–4]. However, methods usually used in studying metal sorption with both fibrous and granulated ion exchangers do not allow assessment of their practical efficiency in water purification. These methods give too optimistic estimations and reveal no significant differences between various carboxylic ion exchangers. The capacity with respect to an ion being recovered, which is the criterion of the sorptive power, is determined by a static method at a preset volume ratio of the sorbent to the solution containing a metal in a too high concentration [5, 6]. The model solution containing 1–5 g l^{-1} heavy metal ions is prepared with distilled water with addition of 0.5 M supporting ions, usually Na^+. Carboxylic ion exchangers are very weakly selective with respect to these ions as compared to double-charged ions. Thus, the data obtained are related to the systems far from the real water for which the sorbents are intended. In such experiments, the amount of sorbed ions is actually determined by the total ion-exchange capacity and pH of the initial and equilibrium solutions.

In natural water, the concentration of heavy metal ions is usually substantially lower than that used in the model solution, and the content of these ions should be monitored at the maximum permissible concentration (MPC) limit. As a rule, water to be purified contains a background of metal ions (Na^+, Ca^{2+}, Mg^{2+}, Fe^{2+}/Fe^{3+}) with the concentrations exceeding the concentration of toxic ions by 2–5 orders of magnitude. The problem of water treatment to remove iron is solved separately, and then water containing Na^+, Ca^{2+}, and Mg^{2+} is usually subjected to purification. Water with moderate hardness contains 1.5–3 mM (Ca^{2+} + Mg^{2+}) ions, which are also selectively sorbed by carboxylic ion exchangers and compete with heavy metal ions for ion-exchange centers. In the static method of sorption, pH and concentrations of supporting and target ions change simultaneously in the equilibrium solutions, and hence each point of the sorption curve is related to different conditions. Therefore, the static method of determination of the ion exchanger sorption power in a multicomponent solution inadequately characterizes the sorbent behavior in purification of real drinking water.

In this study, real possibilities of commercial FIBAN carboxylic ion exchangers in treatment of drinking water to remove heavy metal ions Pb^{2+}, Cu^{2+}, Cd^{2+}, Co^{2+}, Ni^{2+}, and Zn^{2+} were assessed under the dynamic conditions.

EXPERIMENTAL

FIBAN Kh-1, K-4, and K-3 ion exchangers produced by the Institute of Physical Organic Chemistry and FIBAN K-5 ion exchanger produced by Ekofil-Deko Research and Production Association in the form of a staple with single fibers about 30 μm in diameter and 66 mm long were used in the experiments. FIBAN Kh-1, K-3, and K-5 ion exchangers are products of chemical modification of Nitron polyacrylonitrile (PAN) fiber. They contain several kinds of carboxy groups and a certain amount of various basic groups.

1070-4272/04/7702-0249 © 2004 MAIK "Nauka/Interperiodica"

Table 1. Properties of FIBAN fibrous ion exchangers

Ion exchanger	Functional groups of an ion exchanger	SEC,* mmol g^{-1}		Swelling in H^+ form, g H_2O per g of ion exchanger
		–COOH	$-NR_2$	
Kh-1	–COOH, $-N(CH_2COOH)_2$	3.76	0.6	0.60
K-4	–COOH	4.25	–	0.85
K-3	–COOH, =NH, ≡N	5.3	1.8	0.46
K-5	–COOH, $-NH_2$, =NH, ≡N	5.6	1.3	0.44

* SEC is the static exchange capacity of an ion exchanger.

FIBAN K-4 is the product of radiation grafting of acrylic acid to polypropylene (PP) fiber and contains carboxy groups only. The main characteristics of the ion exchangers studied are listed in Table 1.

The acid–base properties of the ion exchangers were studied by a potentiometric titration procedure described in [7, 8], and titration curves were interpreted in terms of acidity parameters by computer analysis [9]. Staple fibers were additionally cut to 1–3 mm length. Titration was performed by the method of a single sample with 1.0 M KOH + 1.0 M KCl titrant. Initially, the ion exchanger sample based on Nitron fiber was introduced into a cell containing HCl solution to completely convert the carboxy groups into the H^+ form, and amino groups, into the Cl^- form, with the same supporting electrolyte. The cell was isolated from ambient air to prevent penetration of CO_2 into the solution during titration. A FIBAN K-4 fiber sample was used in the H^+ form. The titrant was added to the solution in weighed portions at 20-min intervals (time sufficient for the equilibrium to be attained in the system). After reaching pH 12, the back-titration of certain ion exchangers with 1 M HCl in 1 M KCl supporting electrolyte was performed. pH was measured with an OP 211/1 digital laboratory pH-meter equipped with an OP-0808P combination pH electrode.

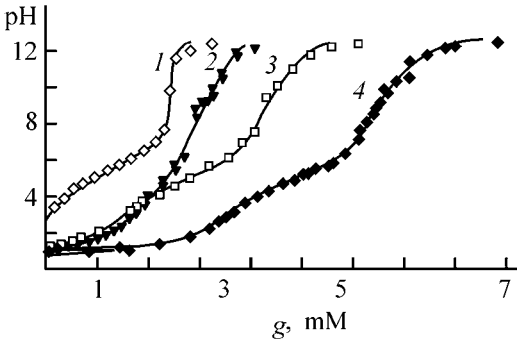

Fig. 1. Experimental points and calculated curves of potentiometric titration of FIBAN fibrous sorbents. Supporting electrolyte 1.0 M KCl. (*g*) Titrant amount. Sorbent: (*1*) K-4, (*2*) Kh-1, (*3*) K-5, and (*4*) K-3. Sample weight, g: (*1*) 0.6169, (*2*) 0.6067, (*3*) 0.5285, and (*4*) 0.535. Initial HCl excess, mM: (*2*) 2.74, (*3*) 2.54, and (*4*) 6.6. Initial solution volume V_0, ml: (*1*) 19.4, (*2*) 20.5, (*3*) 22.0, and (*4*) 20.

To study the sorption of heavy metal ions, two kinds of salt solutions were prepared. The first was a binary solution containing 2 mM of any heavy metal ion (Cu^{2+}, Pb^{2+}, or Ni^{2+}) and 2 mM of Ca^{2+} background. Sorption was performed at optimal pH 4–7 adjusted by adding small amounts of NaOH or HNO_3 solutions. The second is a multicomponent solution containing Pb^{2+}, Cu^{2+}, Cd^{2+}, Co^{2+}, Ni^{2+}, and Zn^{2+} ions (each in a concentration of 2×10^{-2} mM) and 2 mM of Ca^{2+}. Sorption of each heavy metal ion was determined at pH 6.

The metal ion sorption was studied under dynamic conditions. In the first series of experiments, a 0.2-g ion exchanger sample in the H^+ form was placed in a glass column, and a binary solution containing 2 mM of one of heavy metal ions (Cu^{2+}, Pb^{2+}, or Ni^{2+}) and 2 mM of Ca^{2+} was passed through it at optimum pH at a flow velocity of about 1.5 cm min^{-1}. The salt solution was passed in an amount of 4 l through each sample to attain equilibrium, when the ion concentrations and pH in the initial solution and in the solution outflowing from the column become equal. Heavy metal and calcium ions sorbed were eluted with 1 M HNO_3.

In the second series, a dilute solution containing heavy metal ions and 2 mM calcium background was pumped through a column 12.5 mm in diameter and 30 mm high, packed with an ion exchanger (packing density 0.13–0.23 g cm^{-3}). The solution flow velocity was 9.5 cm min^{-1}. The ion exchanger was preliminarily treated with acetate buffer solution with pH 6 to convert it into a mixed $H^+ + Na^+$ form. After sorption, the excess solution was removed by blowing air through the sorbent bed, and then metal ions were desorbed with 1 M HCl or 1 M HNO_3 with the linear flow velocity of 0.8 cm s^{-1}. The metal ion contents were determined on a Vista PRO atomic-emission spectrometer with inductively coupled plasma (Varian) under the following conditions: RF plasma 1.1 kW, plasma-forming argon flow 15, axial argon flow 1.5, and argon flow to the sprayer 1.2 l min^{-1}.

The curves of potentiometric titration of FIBAN Kh-1 chelate ion exchanger and weakly acidic FIBAN K-4, K-3, and K-5 ion exchangers are shown in Fig. 1.

Table 2. Acidity parameters of FIBAN ion exchangers

Ion exchanger	E_1	pK_1	Δpk_1	E_2	pK_2	Δpk_2	E_3	pK_3	Δpk_3	E_4	pK_4	Δpk_4
Kh-1	1.5	3.2	0.8	1.1	5.0	0.4	1.5	9.0	0.6	0.7	11.5	0.3
K-4	–	–	–	4.85	5.3	2.0	–	–	–	–	–	–
K-3	0.7	4.0	0.35	5.2	5.0	2.0	0.5	8.7	0.25	1.7	10.5	0.85
K-5	0.6	3.0	0	5.6	5.0	2.0	0.7	9.0	0.3	1.1	10.5	0.4

To calculate the potentiometric titration curves (CPT), computer simulation described in [9] was used. The software developed allows determination from the experimental titration curve of exchange capacities with respect to each type of E_i groups and of the ion exchanger acidity parameters pK_i and Δpk_i, where K_i is the H^+–Me^+ exchange constant and k_i, equilibrium constant:

$$\Delta\text{p}k_i = \text{p}k_{i(x=1)} - \text{p}k_{i(x=0)}.$$

The titration curve was reconstructed by the inverse calculation; its coincidence with the experimental curve indicates reliability of the parameters found. In all calculations of the kind, the parameters E_i, pK_i, and Δpk_i cannot be determined unambiguously. Therefore, to interpret the results, independent data on properties, chemical composition, and synthesis method of ion exchangers should be invoked. However, in simple cases, the acidity parameters are determined with a high degree of reliability. This is confirmed by practical coincidence in all the details between the experimental and calculated titration curves shown in Fig. 1.

Among the ion exchangers considered, FIBAN K-4 ion exchanger has the simplest structure. It is a monofunctional ion exchanger containing carboxy groups only (this follows from the synthesis method) and is well described by a single set of acidity parameters (Table 2). In contrast to it, all the other ion exchangers studied, which were synthesized on the basis of PAN fibers, are inevitably polyfunctional and contain not only carboxy groups but also anion-exchange (various nitrogen-containing) groups protonated in the acid medium. Carboxy groups are formed by hydrolysis of the nitrile groups, and amino groups, during treatment of PAN fibers with hydrazine or polyamines [10], which are used to cross-link the polymer chains to prevent the polymer dissolution after hydrolysis. Thus, ion exchangers based on PAN fibers are polyampholytes. At definite pH, they form intramolecular salts or strong associates of $RCOO^- + R_3HN^+ = RCOOH \cdot R_3N$ type, which substantially complicates the shape of the titration curve.

To obtain the total curves of polyampholyte titration, it is necessary to start from one pure ionic form of the ion exchanger: completely protonated or completely deprotonated. This means that, in the first case, the ion exchanger should contact with a solution containing excess acid, and in the second, with a solution with excess alkali. The excess amount of these reagents can be arbitrary and can be determined by a computer analysis of the titration curve described above [9]. We titrated ion exchangers based on PAN fibers in the presence of excess hydrochloric acid. Under these conditions, the ion exchanger contains undissociated carboxy groups –COOH and protonated basic groups $\equiv N \cdot HCl$, or, at higher HCl concentrations, associates of the $\equiv N \cdot (HCl)_n$ type [11]. Titration of this system includes the following reactions:

$$HCl + KOH \rightarrow KCl + H_2O, \quad (1)$$

$$R{\equiv}N \cdot HCl + KOH \rightleftarrows R{\equiv}N + KCl + H_2O, \quad (2)$$

$$R{\equiv}N + R\text{–}COOH \rightleftarrows R{\equiv}N \cdot HOOC\text{–}R, \quad (3)$$

$$R\text{–}COOH + KOH \rightleftarrows RCOOK + H_2O, \quad (4)$$

$$R{\equiv}N \cdot HOOC\text{–}R + KOH \rightleftarrows R{\equiv}N + R\text{–}COOK + H_2O. \quad (5)$$

Reaction (1) corresponds to titration of excess HCl. Reaction (2) is the reaction of an alkali with HCl bound with weakly protonated basic groups, which then form an intramolecular bond with carboxy groups [reaction (3)]. In the case of excess carboxy groups with respect to basic groups, their neutralization is the next stage [reaction (4)]. Finally, carboxy groups incorporated in intramolecular complexes and showing the weakest acidity are neutralized [reaction (5)].

In real systems, as in our case, the pattern is further complicated by the presence in the ion exchanger phase of different kinds of carboxy and weakly basic groups. The results of the computer analysis of ion exchangers studied are listed in Table 2. It follows from Tables 1 and 2 that the ion exchangers strongly differ in the acidity parameters, although having com-

Table 3. Total dynamic capacity of FIBAN ion exchangers with respect to metal ions in sorption from binary M^{2+}–Ca^{2+} solutions as a function of pH (metal ion concentration in the solution 2 mM)

Ion exchanger	Total dynamic capacity (mmol g^{-1}) at indicated pH							
	4.5*		5.0*		5.0		7.0	
	Cu^{2+}	Pb^{2+}	Cu^{2+}	Pb^{2+}	Ni^{2+}	Ca^{2+}	Ni^{2+}	Ca^{2+}
Kh-1	1.3	1.4	1.8	1.6	1.15	0.3	1.35	0.2
K-4	1.5	1.7	1.75	2.1	1.0	0.45	1.25	0.3
K-3	–	1.35	–	1.45	0.9	0.4	1.2	0.25
K-5	1.45	1.8	1.9	1.7	1.3	0.5	1.6	0.35

* Sorption of Ca^{2+} with the ion exchanger is less than 0.05 mmol g^{-1}.

parable static exchange capacities with respect to carboxy groups. FIBAN K-3 and K-5 ion exchangers are the most similar in the acid-base properties. They contain about 5 mmol g^{-1} carboxy groups with pK 5 and ΔpK 2.0. Among the ion exchangers studied, a special place is occupied by FIBAN Kh-1, which contains more acidic groups with pK 3.2 and ΔpK 0.8, since the existence of functional groups with such acidity parameters cannot be caused by reaction (2) as in the case of FIBAN K-3 and K-5 because of the small capacity of FIBAN Kh-1 with respect to amino groups.

It follows from the above data that all the carboxylic ion exchangers studied strongly differ in the chemical composition, acidity, and set of functional groups. However, in sorption from binary solution with equal concentrations of heavy metal ions and Ca^{2+}, there is no substantial difference in sorption properties of ion exchangers (Table 3). In all the cases, different ion exchangers sorb only heavy metal ions, while Ca^{2+} ions are not appreciably sorbed. This produces an illusion of equal sorption efficiency of any carboxylic ion exchanger in water purification. However, the results substantially changed when the solutions used more closely simulated the real water to be purified.

The outlet curves of sorption are shown in Fig. 2, and the working capacities with respect to heavy metal ions at their concentrations of 2×10^{-2} mM

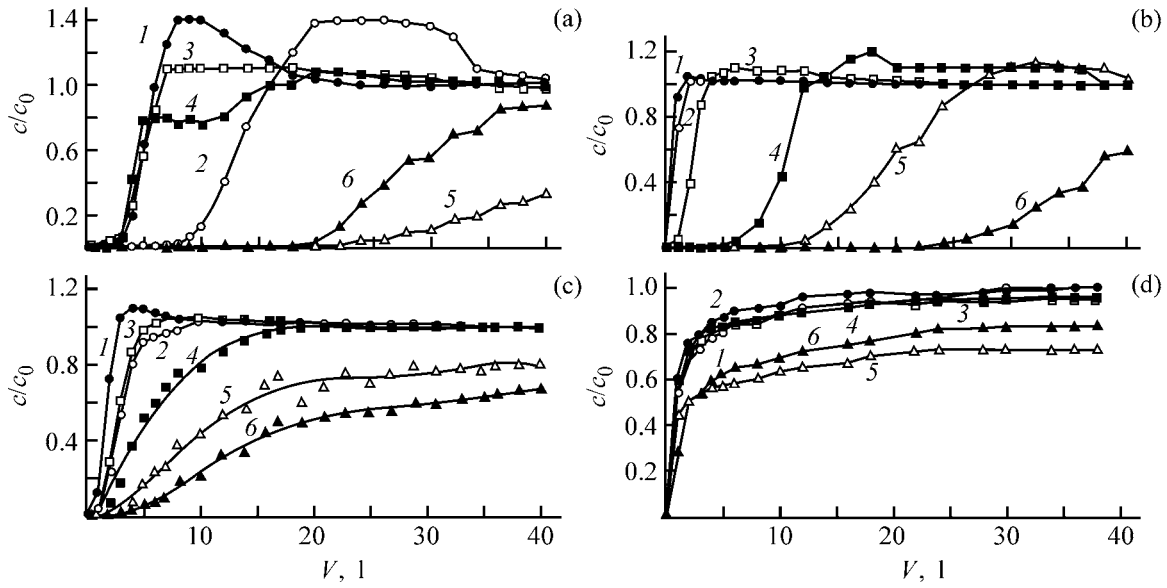

Fig. 2. Outlet curves of sorption of heavy metal ions by fibrous ion exchangers (a) FIBAN Kh-1, (b) FIBAN K-4, and (c) FIBAN K-5 and with (d) ANKB-35 granulated ion exchanger. (c/c_0) Ratio of metal ion concentration in the solution outflowing from the column to the concentration in the initial solution and (V) volume of the solution passed through the column with the ion exchanger. Cation sorbed: (*1*) Co^{2+}, (*2*) Ni^{2+}, (*3*) Zn^{2+}, (*4*) Cd^{2+}, (*5*) Cu^{2+}, and (*6*) Pb^{2+}.

with a higher Ca^{2+} background concentration (2 mM) are listed in Table 4. As can be seen from these data, the ion exchangers show quite specific individual properties. Among fibrous ion exchangers, FIBAN K-3 and K-5 prepared by saponification of cross-linked PAN fibers are the least effective. FIBAN Kh-1 ion exchanger containing chelate groups is the most universal. It showed the best results in water treatment to remove all the heavy metal ions studied. Granulated chelate ion exchanger ANKB35 which is based on styrene and divinylbenzene copolymer and contains functional groups similar to those in FIBAN Kh-1 is ineffective in heavy metal ion sorption from water by the dynamic method. All heavy metal ions studied appear already in the first portions of the eluate in concentrations exceeding 0.05 mg l^{-1}. At the same time, FIBAN K-4 monofunctional fibrous ion exchanger proved to be almost as effective as FIBAN Kh-1 with respect to Cu^{2+} and substantially exceeded the latter in the efficiency of removal of Cd^{2+} and Pb^{2+}. However, FIBAN K-4 is inefficient in water treatment to remove Ni^{2+}, Co^{2+}, and Zn^{2+}. It should be noted that FIBAN Kh-1 has a substantial advantage over the other ion exchangers studied in water treatment to remove Fe^{2+}, which makes it the most suitable ion exchanger for natural water purification to obtain technical and drinking water.

Thus, the study of heavy metal ion sorption from dilute solutions against a background of high Ca^{2+} concentration revealed features of selective sorption of these ions by FIBAN fibrous ion exchangers from multicomponent aqueous solutions. Among the ion exchangers based on PAN fibers, the best results in water treatment to remove heavy metal ions were obtained with FIBAN Kh-1 chelate ion exchanger, which substantially suprasses FIBAN K-3 and K-5 cation exchangers in the dynamic capacity. Good results were also obtained with FIBAN K-4 monofunctional carboxylic cation exchanger based on PP fibers.

CONCLUSIONS

(1) A dynamic study of sorption properties of FIBAN Kh-1, K-3, K-4, and K-5 with respect to heavy metal ions showed that, in sorption from binary M^{2+}–Ca^{2+} solutions containing 2 mM of each cation, all the ion exchangers studied almost equally sorb Pb^{2+}, Cu^{2+}, or Ni^{2+} and do not noticeably sorb Ca^{2+}.

(2) In sorption from a multicomponent system containing heavy metal ions in concentrations close to their maximum permissible concentration (2×10^{-2} mM), with the background of 2.0 mM Ca^{2+}, FIBAN Kh-1 chelate ion exchanger based on polyacrylonitrile fibers is the most universal ion exchanger for water treatment to remove heavy metal ions, while FIBAN K-4 monofunctional carboxylic cation exchanger based on polypropylene fibers is the best for water purification to remove Pb^{2+} and Cd^{2+}.

Table 4. Dynamic capacity (to metal ion breakthrough) of FIBAN fibrous ion exchangers (metal ion concentration in the solution 2×10^{-2} mM)

Ion exchanger	Dynamic capacity (mmol g^{-1}) to breakthrough of 0.05 mg l^{-1}					
	Cu^{2+}	Pb^{2+}	Ni^{2+}	Co^{2+}	Cd^{2+}	Zn^{2+}
Kh-1	0.46	0.35	0.18	0.07	0.05	0.05
K-4	0.45	0.75	0	0	0.15	0
K-3	0.11	0.10	0	0	0.04	0
K-5	0.12	0.12	0.005	0.04	0.05	0

REFERENCES

1. Vernon, F. and Shah, T., *React. Polym.*, 1983, no. 1. p. 301.
2. Burinskii, S.V., *Khim. Volokna*, 1996, no. 6, pp 16–19.
3. Ogorodnikov, V.A., Soldatov, V.S., and Shunkevich, A.A., *Izv. Nats. Akad. Nauk Bel., Ser. Khim. Nauk*, 2000, no. 1, pp. 116–119.
4. Soldatov, V.S., Sergeev, G.I., Martsinkevich, R.V., and Shunkevich, A.A., *Zh. Prikl. Khim.*, 1991, vol. 64, no. 12, pp. 2506–2510.
5. Nemilova, T.V., Emets, L.V., Nemilov, V.N., and Nachinkin, O.I., *Khim. Volokna*, 1996, no. 6, pp. 22–27.
6. Myasoedova, G.V., Nikashina, V.A., Molochnikova, N.P., and Lileeva, L.V., *Zh. Anal. Khim.*, 2000, vol. 55, no. 6, pp. 611–615.
7. Soldatov, V.S., Sosinovich, Z.I., and Korshunova, T.A., *Dokl. Nats. Akad. Nauk Bel.*, 2001, vol. 45, no. 2, pp. 71–75.
8. Soldatov, V.S., in *Ion Exchange at the Millenium*, Greig, J.A., Ed., Imperial College, 2000, pp. 193–200.
9. Soldatov, V.S., *React. Function. Polym.*, 1998, vol. 38, nos. 2/3, pp. 73–112.
10. Vol'f, L.A. and Meos, A.I., *Volokna spetsial'nogo naznacheniya* (Special Fibers), Moscow: Khimiya, 1971.
11. Polkhovskii, E.M., Sosinovich, Z.I., and Soldatov, V.S., *Dokl. Nats. Akad. Nauk Bel.*, 2002, vol. 46, no. 6, pp. 57–59.

Russian Journal of Applied Chemistry, Vol. 77, No. 2, 2004, pp. 254–259. Translated from Zhurnal Prikladnoi Khimii, Vol. 77, No. 2, 2004, pp. 259–264.

ENVIRONMENTAL PROBLEMS OF CHEMISTRY AND TECHNOLOGY

Recovery of Lipids from Aqueous Dispersions with Chitosan Solutions

I. N. Konovalova, V. Yu. Novikov, N. V. Stepanova, and K. V. Reut

Murmansk State Technical University, Murmansk Russia

Knipovich Arctic Research Institute of Fishery and Oceanography, Murmansk, Russia

Received July 10, 2003

Abstract—Binding of lipids from aqueous protein-lipid suspensions with a natural polysaccharide, chitosan, was studied in order to develop a procedure for removal of impurities from water. The physicochemical nature of this process was analyzed. The mechanism involving formation of structurally ordered chitosan precipitates, and adsorption and solubilization of lipids with chitosan macromolecules was discussed. The best conditions for defatting of aqueous protein-lipid dispersions with the aid of chitosan were determined.

Removal of proteins and lipids from industrial wastewater is being studied extensively. The conventional physicochemical procedures used to remove proteins and lipids from aqueous dispersions with high content of these impurities (e.g., wasterwater of fish industry and hydrobiont reprocessing) are sorption on various sorbents and flotation with preliminary coagulation of proteins and lipids with inorganic electrolytes and macromolecular flocculants. Inorganic coagulants, such as aluminum and iron salts, calcium compounds, and dry lime, are ineffective for purification of aqueous dispersions with low lipid content (e.g. protein hydrolyzates). Moreover, some of these compounds are toxic. Proteins and lipids recovered with the aid of synthetic flocculants (e.g., polyacrylamides and polymeric quarternary ammonium salts) cannot be used as forage additives without additional purification [1, 2].

Hence, a search for new nontoxic biodegradable reagents suitable for exhaustive removal of peptides and lipids from aqueous dispersions is a topical problem. Natural macromolecular polysacharides including a cationic polysacharide, chitosan, can be used for this purpose. Chitosan is produced by deacetylation of the natural biopolymer, chitin [3]; it consists of residues of 2-deoxy-2-amino-*D*-glycose bound via β-1,4-bonds. Chitosan contains reactive free amino groups. This polysacharide coagulates peptide-lipid colloids [4–6] and can be used for efficient recovery of lipids from aqueous dispersions [7], e.g., from peptide hydrolyzates. Peptide hydrolyzate is a dispersion containing low-molecular-weight peptides, suspended substances, free amino acids, and lipids. Peptide hydrolyzates are mainly used for preparing microbiological culture media [8, 9]. Lipids and, in particular, fatty acids are toxic for most of bacterial cultures [10].

The interaction mechanism in the systems containing peptides and lipids and macromolecular compounds has been recently studied [11–13]. It is known [11] that macromolecular compounds can solubilize small amounts of oleophilic compounds to form colloids. Probably, the solubilization of lipids can affect the quality of purification of peptide hydrolyzates with chitosan.

The aim of this study was to examine sorption of lipids from aqueous peptide-lipid dispersions on chitosan and to determine the physicochemical mechanism of this process.

EXPERIMENTAL

Protein hydrolyzates of wastes from processing of northern shrimp fishery (SFW), king crab (KCW), Icelandic comb (ICW), and sea cucumber (cucumaria) (CW) were prepared and characterized by the conventional procedures [14, 15]. The wastes were treated with a Model 1094 (Tecator) homogenizer. The proteins were hydrolyzed for 6 h in the presence of proteinases at 50°C and a protein : water weight ratio of 1 : 1. Proteinases were synthesized from hepatopancrease of king crab [16, 17].

Protein hydrolyzates were treated with chitosan solutions in the ratio of 0.125–1.000 g of the polymer

1070-4272/04/7702-0254 © 2004 MAIK "Nauka/Interperiodica"

Table 1. Influence of chitosan concentration c on the quality of protein hydrolyzate prepared from ICW

c, g l^{-1}	Effect observed	
	before centrifuging	after centrifuging
0.125	No changes in the solution	Turbid solution, lipid film on its surface
0.250	Slight turbidity of the solution	The same
0.375	Flocculation in the whole solution volume, formation of fat drops on the surface	Transparent solution, thinner lipid film
0.500	Flocculation in the whole solution volume, fat in completely bound with chitosan	Transparent solution, traces of lipid film
0.750	Large readily precipitated flakes	Transparent solution, no lipid film
1.000	The same	The same

per 1 l of the hydrolyzate solution. The degree of deacetylation of the chitosan samples with average molecular weight of 285, 265, and 255 kDa was 75.1, 91.2, and 99.8%, respectively. Chitosan was dissolved in 1% acetic acid or 0.1 N hydrochloric acid. A chitosan solution was added to protein hydrolyzate acidified to pH 6.5 and the mixture was stirred. Chitosan was precipitated by addition of a 1% NaOH solution to pH 7–9.5. The resulting dispersion was left to coagulate for a time of 10 min to 3 h. The precipitate was separated by centrifuging. To determine the protein concentration in the hydrolyzate, the optical density of the solution at 280 nm was measured on a UV 3101 PC Shimadzu spectrophotometer by the conventional procedure [18].

Lipids were extracted from hydrolyzates with hexane. The optical density of the extract in the UV–Vis range was measured relative to pure hexane.

The degree of defatting of the hydrolyzate was estimated from the relative optical density D_{rel} (%) at 195 nm.

$$D_{rel} = D/D_0 \times 100,$$

where D is the optical density of the extract of the hydrolyzate treated with a chitosan solution; D_0 is the optical density of the extract of hydrolyzate without chitosan addition.

To study the solubilizing power of chitosan, we used oleophilic lipid, cod-liver oil, prepared from cod liver [GOST (State Standard) 3714–72].

The solubilzation of cod-liver oil with chitosan solutions was determined by the degree of solution turbidity [19], which, in turn, was measured on a KFK-3 photocolorimeter in 5-cm cells at the wavelength of 540 nm. This method is based on the following phenomenon. When a saturated solution of an oleophilic compound in an aqueous solution of a macromolecular compound (MMC) is formed, excess MMC is emulsified and the turbidity of the system increases. The saturation point of the system with the oleophilic component, taken as the measure of the solubilizing power of the solution at a definite polysaccharide concentration, was determined from the inflection point in the dependence of the optical density on the concentration of the oleophilic component.

The Gibbs energy $\Delta G^0_{T,P}$, enthalpy $\Delta H_{T,P}$, and entropy $\Delta S_{T,P}$ of binding of the solubilizate were calculated by the equations given in [11].

In preliminary experiments, we studied the influence of chitosan additives on the concentration of low-molecular-weight proteins contained in the hydrolyzate and not precipitated with 10% trichloroacetic acid. We found that chitosan did not precipitate these compounds under the experimental conditions and hence did not decrease the yield of the target hydrolyzate.

Chitosan is completely coprecipitated with lipids and insoluble proteins (Table 1) after its addition in amount of 0.75 g l^{-1} of the incubation solution (1.5 g kg^{-1} of the initial hydrolyzate).

The efficiency of defatting of protein hydrolyzates was studied at different pH values. The relative optical density D/D_0 of the hydrolyzate containing 1 g of chitosan per 1 kg of the solution was constant (65%) at pH from 5.5 to 9.5. Hence defatting of the hydrolyzate is independent of pH in this range. However, at higher pH, the transparency of the solution increased and the lipid film formed on the solution surface after centrifuging decreased and then disappeared at all.

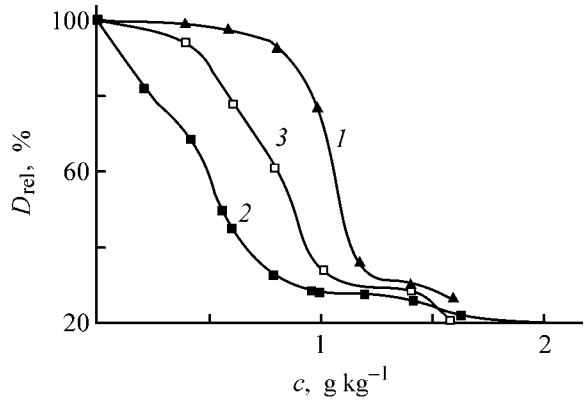

Fig. 1. Efficiency of defatting of ICW hydrolyzates with chitosan deacetylated to (*1*) 75.1, (*2*) 90.1, and (*3*) 99.8% vs. chitosan concentration *c*. Precipitated at pH 8.3. (D_{rel}) Relative optical density; the same for Fig. 2.

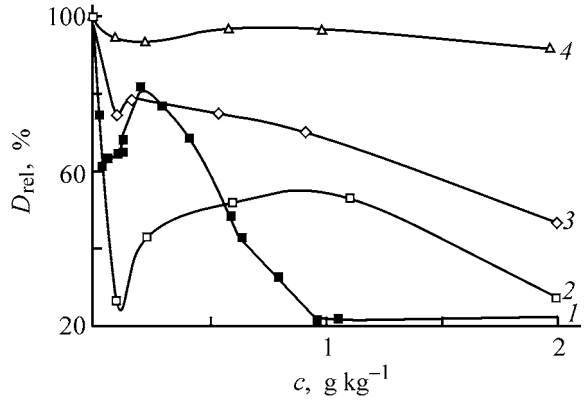

Fig. 2. Efficiency of defatting of (*1*) ICW, (*2*) NSW, (*3*) KCW, and (*4*) CW hydrolyzates vs. the concentration *c* of chitosan with 90.1% degree of deacetylation. pH of precipitation 8.3.

The influence of the degree of chitosan deacetylation on the efficiency of defatting of the hydrolyzates is shown in Fig. 1. Chitosan deacetylated to 90% provides the maximum defatting. At lower or higher degree of deacetylation, the degree of defatting decreases.

Probably, the sorption capacity of chitosan for lipids is determined by its degree of deacetylation and the presence of inter- and intramolecular chemical bonds.

As the degree of deacetylation increases, the number of active sorption centers grows. However, in the samples with a high degree of deacetylation, intra and intermolecular interaction of chitosan molecules is observed. As a result, the number of sorption centers decreases owing to both globulation of the macromolecules and formation of strong intermolecular bonds to give ordered structures. The sorption properties of chitin and chitosan depends on their crystallinity. It is known [20, 21] that the sorption capacity of chitosan increases with a decrease in the degree of its crystallinity, i.e., with an increase in the content of the amorphous phase of the polymer. At a high degree of deacetylation (from 91 to 96%), the mechanical and spectral properties of chitosan appreciably change owing to an increase in its crystallinity [22].

In the initial stages, lipids are probably bound with dissolved chitosan molecules. In the course of precipitation, the chitosan structure is ordered owing to the formation of intermolecular bonds. As the degree of chitosan deacetylation increases, the intramolecular bonds between amino and hydroxy groups are strengthened, and foreign molecules (in our case lipids) are "forced out" from the internal structure and are sorbed on the free surface of the precipitate. As a result, the concentration of centers capable of sorbing lipids decreases.

The chitosan concentration optimal for defatting of ICW hydrolyzates is 1 g kg^{-1} of the solution. Defatting of hydrolyzates of king crab and cucumaria production wastes by chitosan treatment is less efficient.

The dependence of the relative optical density of the NSW hydrolyzates on the chitosan concentration passes through a sharp minimum at low chitosan concentration and has a maximum at the higher concentration (Fig. 2).

The abnormal decrease in the optical density at low chitosan concentration (about 0.1 g kg^{-1} solution) is of interest. In this case, the hydrolyzate remains turbid, as also does the reference sample without chitosan additive. The dependences observed with the other hydrolyzates examined are similar to some extent (Fig. 2).

At a low chitosan concentration, the dissolved macromolecules partially bind lipids. However, this concentration is insufficient for complete precipitation. Probably, only free lipids are extracted in hexane. The growth of D_{rel} with increasing chitosan concentration is caused by two factors. On the one hand, at a high concentration of chitosan, it is precipitated from the solution and hence the concentration of dissolved chitosan capable of binding the lipids decreases. On the other hand, lipids and proteins probably compete for the sorption centers of chitosan macromolecules.

The increase in the relative optical density is most likely due to the formation of a dense precipitate with an ordered structure at high chitosan concentration, which results in lipid desorption. This is confirmed

by a gradual increase in D/D_0 during aging of the precipitate, probably accompanied by its ordering.

As the chitosan concentration growths further, D/D_0 increases owing to a rise in the adsorption surface area of the chitosan precipitate.

Thus, the mechanism of interaction of lipids with chitosan is complex. Probably, sorption of lipids on chitosan macromolecules is caused by electrostatic interaction of positively charged functional groups of chitosan and deprotonated carboxy groups of lipids, which is indicated by a rise in the lipid sorption with increasing degree of chitosan deacetylation (Fig. 1). In addition, the shape of $D_{rel} = f(c)$ curve depends not only on the sorption but also on solubilization of lipids with chitosan macromolecules. Probably, extraction of solubilized lipids in hexane is more difficult.

One of the processes responsible for binding of lipids with chitosan is the solubilization of lipids. To study the solubilizing effect of chitosan, we used a model system containing cod-liver oil as the lipid component. The chitosan concentration varied from 0 to 0.5 g l^{-1}. At this concentration, chitosan macromolecules do not precipitate in the pH range examined (1.2–9.5). Chitosan solutions were prepared in 1% acetic acid.

The solubilization of cod-liver oil grows with increasing chitosan concentration. Clearly, the total capacity of the hydrophobic regions grows with increasing chitosan concentration.

The solubilization of oleophilic compounds with the polymer is due to the formation of hydrophobic "intramolecular micelles" of the macromolecules bound by the hydrophobic bonds [11]. Probably, binding of lipids with chitosan is caused by this phenomenon.

Solubilization can be regarded as distribution of a third component among two immiscible phases. This approach makes it possible to calculate of the thermodynamic parameters of solubilization, estimate the free energy of solubilizate binding, and determine the solubilization mechanism. We calculated the thermodynamic parameters of solubilization of the examined systems by the procedure used in [11] for calculations system constituted by a protein and low-molecular-weight hydrocarbons. The results are presented in Figs. 3 and 4.

A calculation of ΔS and ΔG in solubilization of cod-liver oil with chitosan solution demonstrated that $\Delta G < 0$ and $\Delta S > 0$ in the whole range of pH. The Gibbs energy is at a minimum in acidic and neutral solutions. In alkaline solutions (pH > 10), ΔG increases owing to a decrease in the solubilizing power of chitosan and deterioration of the solubilization conditions.

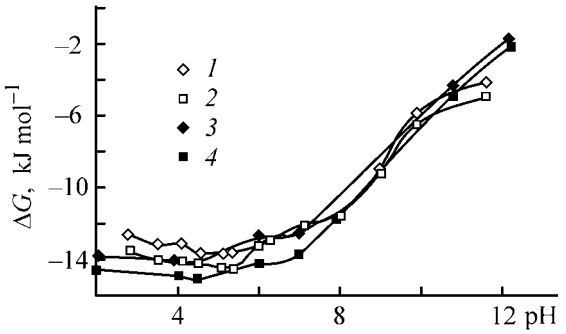

Fig. 3. Gibbs energy ΔG of solubilization of cod-liver oil with chitosan solutions at (*1*, *3*) 20 and (*2*, *4*) 40°C vs. pH. Chitosan concentration (mg l^{-1}): (*1*, *2*) 25 and (*3*, *4*) 250.

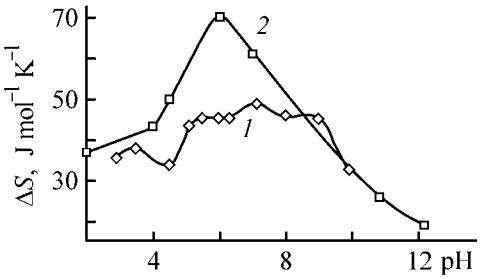

Fig. 4. Entropy ΔS of solubilization of cod-liver oil in chitosan solution with chitosan concentration of (*1*) 25 and (*2*) 250 mg l^{-1} vs. the solution pH.

The sign of the thermodynamic parameters ($\Delta G < 0$; $\Delta S > 0$) is in agreement with the statistic thermodynamic model of hydrophobic bonding. These parameters are close to those of transfer of nonpolar substances from polar to nonpolar medium [23]. Thus, these calculations and analysis of the published data show that the solubilization of cod-liver oil in chitosan solutions, as well as that of other oleophilic compounds, is a spontaneous thermodynamically favorable process. In this case, cod-liver oil penetrates into internal hydrophobic regions formed by chitosan macromolecules.

The dependence of the degree of defatting of protein hydrolyzates on the chitosan concentration and on the precipitation time can also be understood in terms of the solubilization mechanism. We found that lipids are desorbed from the precipitate formed in more than 1 h. Freshly prepared amorphous chitosan gradually crystallizes with time. As a result, the number of amorphous hydrophobic regions in the chitosan precipitate decreases and lipids are desorbed into the solution.

Table 2. Chemical composition of the hydrolyzates before and after treatment with chitosan solutions

Component content, wt %	NSW hydrolyzates		ICW hydrolyzate		Component content, wt %	NSW hydrolyzates		ICW hydrolyzate	
	no chitosan	after precipitation	no chitosan	after precipitation		no chitosan	after precipitation	no chitosan	after precipitation
Moisture	3.00	3.67	1.7	0.43	Ash	4.60	4.28	12.80	12.60
Lipids	1.84	0.33	2.30	0.56	Proteins	90.56	91.72	83.20	86.40

Thus, small amounts of chitosan can be effectively used for clarification and defatting of protein hydrolyzates of NSW and ICW.

As can be seen from Fig. 2, the weight fraction of lipids in WSF and ICW hydrolyzates treated with chitosan under the optimal conditions decreases by a factor of 4–5.

The chemical composition of the hydrolyzates before and after treatment with chitosan is listed in Table 2.

CONCLUSIONS

(1) The degree of clarification and defatting of protein hydrolyzates depends on the degree of deacetylation of chitosan. The relative optical density D_{rel} of the extract of the hydrolyzates treated with chitosan deacetylated to 90% is at a minimum. At higher degree of deacetylation, D_{rel} increases again.

(2) The degree of defatting is determined as influenced by pH of the solution, chitosan concentration, and time of treatment of the hydrolyzate with a chitosan solution. The best conditions of the chitosan treatment are as follows: chitosan concentration from 1.0 to 1.5 g kg^{-1} of hydrolyzate, precipitation at pH 8.0–8.5, and time of incubation after addition of chitosan shorter than 1 h.

(3) The suggested mechanism of defatting of protein hydrolyzates involves crystallization of chitosan precipitate, adsorption, and solubilization of lipids with chitosan macromolecules.

REFERENCES

1. Babenkov, E.D., *Ochistka stochnykh vod koagulyantami* (Treatment of Wastewater with Coagulating Agents), Moscow: Nauka, 1977.
2. Baran, A. A., *Polimersoderzhashchie dispersnye sistemy* (Polymer-containing Dispersions), Kiev: Naukova Dumka, 1986.
3. Bogdanov, V.D., *Materialy 3-i Vsesoyuznoi Konferentsii* (Proc. Of Third All-Union Conf.) Moscow: VNIRO, 1992, pp. 76–79.
4. FRG Patent 2036672.
5. RF Patent 2137390.
6. Prabhu, P.V., Radhakrishnan, A.G. , and Iyer, T.S.G., *Fish. Technol.*, 1986, vol. 13, no. 1, pp. 69–72.
7. Hwang, D.-C. and Damodaran, S., *J. Agr. Food Chem.*, 1995, vol. 43, no. 1, pp. 33–37.
8. Kovchik, N.A. and Litvinenko, I.I., *Razrabotka i standartizatsiya bakteriologicheskikh pitatel'nykh sred* (Development and Standardization of Bacteriological Culture Medium), Moscow: Nauchno-Issledovatel'skii Inst. Vaktsin i Syvorotok im. I.I. Mechnikova, 1980, pp. 120–123.
9. *Bakteriologicheskie sredy dlya sanitranoi i klinicheskoi mikrobiologii, biotekhnologii i kontrolya lekarstvennykh sredstv: Katalog* (Bacteriological Media for Sanitary and Clinical Microbiology, Biotechnology, and Drug Control: Catalog), Obolensk, 1999.
10. Semenov, S.M., *Peptony, ispol'zuemye v mikrobiologii: Proizvodstvo i primenenie produktov mikrobiologicheskikh proizvodstv: Obzor informatsii* (Peptones for Microbiology: Production and Application of Microbiological Products: Information Review), Moscow: VNIISENTI, 1988, issue 4.
11. Izmailova, V.N. and Rebinder, P.A., *Strukturoobrazovanie v belkovykh sistemakh* (Structurization in Peptide Systems), Moscow: Nauka, 1974.
12. Tarasevich, B.N., Izmailova, V.N., and Ivashchuk, Yu.A., *Vestn. Mosk. Gos. Univ., Ser. 2: Khim.*, 1996, vol. 37, no. 3, pp. 287–290.
13. Shchipunov, Yu.A., *Usp. Khim.*, 1997, vol. 66, no. 4, pp. 328–352.
14. Artyukhin, V.I., Shepelin, A.P., and Kiseleva, N.V., *Belkovye gidrolizaty v proizvodstve pitatel'nykh sred: Proizvodstvo i primenenie produktov mikrobiologicheskikh proizvodstv: Obzor informatsii* (Peptide Hydrolyzates in Production of Culture Media: Production and Application of Microbiological Products: Information Review), Moscow: VNIISENTI, Min. Med. Prom. SSSR, 1990, issues 9–10.
15. *GOST* (State Standard) *7636–85: Fish, Marine Mammals, Marine Invertebrates, and Products of Their Processing*, 1985, Moscow: Izd. Standartov.

16. Mukhin, V.A. and Novikov, V.Yu., Abstracts of Papers, *10-ya Nauchno-tekhnicheskaya konferentsiya professorsko-prepodavatel'skogo sostava MGTU* (10th Scientific and Technical Conf. of Teaching Staff of Murmansk State Technical University), Murmansk: Murmansk. Gos. Tekh. Univ., 1999, pp. 354–355.
17. Mukhin, V.A. and Novikov, V.Yu., Abstracts of Papers, *Mezhdunarodnaya konferentsiya vyezdnaya sessiya Otdeleniya obshchei biologii RAN* (Int. Conf. and Out-of Town Session of the Department of General Biology of Russian Acad. of Sci.), Petrozavodsk, September 6–10, 1999, pp. 243–244.
18. Alekseenko, L.P., *Sovremennye metody v biokhimii* (Modern Biochemical Methods), Moscow: Meditsina, 1968, vol. 2.
19. Neiman, R.E., *Praktikum po kolloidnoi khimii (kolloidnaya khimia lateksov and poverkhnostno-aktivnykh veshchestv* [Practical Course of Colloid Chemistry (Colloid Chemistry of Latexes and Surfactants)], Neiman, R.E., Ed., Moscow: Vysshaya Shkola, 1971.
20. Mar'in, A.P., Feofilova, E.P., Genin, Ya.V., *et al.*, *Vysokomol. Soedin., Ser. B*, 1982, vol. 24, no. 9, pp. 658–662.
21. Feofilova, E.P., *Prikl. Biokhim. Mikrobiol.*, 1984, vol. 20, no. 2, pp. 147–160.
22. Mima, S., Miya, M., Iwamoto, R., and Yoshikawa, S., *J. Appl. Polym. Sci.*, 1983, vol. 28, no. 6, pp. 1909–1917.
23. Nemethy, J. and Scheraga, H., *J. Phys. Chem.*, 1992, vol. 66, no. 5, p. 1773.

Russian Journal of Applied Chemistry, Vol. 77, No. 2, 2004, pp. 260–262. Translated from Zhurnal Prikladnoi Khimii, Vol. 77, No. 2, 2004, pp. 265–267.

ORGANIC SYNTHESIS AND INDUSTRIAL ORGANIC CHEMISTRY

Acylation of Amines with Carboxyethyl Dextran Azides

A. V. Krasnikova, Yu. L. Vasil'eva, and A. A. Iozep

St. Petersburg State Academy of Pharmaceutical Chemistry, St. Petersburg, Russia

Received July 9, 2003

Abstract—The stability and reactivity of carboxyethyl dextran azides toward amines, and also the influence exerted by the pH of the reaction medium and pK_a of the amine on the number of amide groups in acylation products were studied.

The assortment of physiologically active polymers (PAPs) used in medicine steadily grows. Among the routes to PAPs, the "carboxyethyl" route is the least studied. At the same time, the use of longer spacers between the polymer and a biologically active substance (BAS) can make the active fragment more accessible and enhance the effect of the biopolymer. Therefore, development of procedures for preparing carboxyethyl polysaccharide derivatives and study of their reactivity is a topical problem from both theoretical and applied viewpoints.

The carboxyethyl route suggested in [1–3] for modification of polysaccharides with amines with the aim to develop new physiologically active polymers has a number of significant darwbacks: The H form and esters of carboxyethyl dextran (CED) react with amines at high temperature, which is unacceptable for binding to polysaccharides of such BASs as antibiotics and enzymes. At the same time, more reactive CED azides are poorly studied.

Therefore, our goal was to study the stability and reactivity of CED azides in reactions with amines.

EXPERIMENTAL

The chemical scheme for acylation of amines with CED azides is as follows:

$$[C_6H_7O_2(OH)_{3-m}(OCH_2CH_2COONa)_{m-k}(OCH_2CH_2CONHNH_2)_k]_m$$
A

$$\xrightarrow{NaNO_2,\ HCl}$$

$$[C_6H_7O_2(OH)_{3-m}(OCH_2CH_2COOH)_{m-k}(OCH_2CH_2CON_3)_k]_m$$
B

$$\xrightarrow{RNH_2}$$

$$[C_6H_7O_2(OH)_{3-m}(OCH_2CH_2C\overset{-}{O}O\overset{+}{N}H_3R)_{m-k}(OCH_2CH_2CONHNR)_k]_m$$
C

$$\xrightarrow{NaOH}$$

$$[C_6H_7O_2(OH)_{3-m}(OCH_2CH_2COONa)_{m-k}(OCH_2CH_2CONHR)_k]_m,$$
D

R = $PhCH_2$, Ph, *p*-$MeOC_6H_5$, *p*-MeC_6H_5, *p*-$NO_2C_6H_5$, *p*-BrC_6H_5.

CED hydrazides **A** containing 0.3–0.35 hydrazide group and 1.0–0.9 carboxyethyl group per monosaccharide unit of the polymer were prepared from CED amides and hydrazine hydrate at 10–15°C [3]. These products were dissolved in a 0.5 N solution of sodium nitrite; the mixture was acidified with HCl to pH 2 and stirred for 1.5 h at 0–5°C. To the resuilting solution of CED azide **B**, an appropriate amine was added, pH 2–10 was adjusted with an acid or alkali, and the reaction was performed for 1–18 h at 15–20°C; the molar ratio of the amine to the monosaccharide units was 5 : 1. The reaction product **C** was

1070-4272/04/7702-0260 © 2004 MAIK "Nauka/Interperiodica"

precipitated with ethanol and reprecipitated from 0.1 N NaOH solution to decompose the ammonium salt whose absence in the product **D** was checked by TLC. Amides **D** were vacuum-dried (20–25 mm Hg) at 61°C. The substituted amides **D** are colorless or yellow amorphous powders readily soluble in water but insoluble in ethanol, acetone, diethyl ether, and most of other organic solvents.

The IR spectra of CED azides **B** contain a $\nu(N_3)$ stretching band at 2150 cm^{-1}, disappearing on treatment of azides with amines. The IR spectra of amides **D** treated with an acid contain the absorption bands at 1540–1550, 1650–1670, and 1490–1610 cm^{-1}, characteristic of δ(N–H) (amide **II**), ν(C=O) (amide **I**), and ν(C⋯C) of the benzene ring, respectively, and absent in the spectra of the starting polysaccharides; the carboxy group band at 1720–1730 cm^{-1} is preserved. In the IR spectra of sodium salts **D**, the bands of amide groups are obscured by the strong absorption band of the carboxylate ion (1570 cm^{-1}).

The UV spectra of the synthesized amides **D** in 0.1 N NaOH contain absorption peaks characteristic of aromatic compounds. The position of the peaks in the UV spectra of CED *N*-benzylamide, benzylamine, and *N*-benzylacetamide is the same. The UV spectra of CED *N*-arylamides also coincide with those of the respective anilides, but the λ_{max} values for the free amines are different. CED azides **B** show no absorption in this range. Hence, UV spectroscopy is a convenient method for analysis and evaluation of the purity of the compounds. The calibration plots were constructed using benzylamine and the corresponding anilides.

Amides **D** were characterized by the degree of aminocarbonylethylation N_{ace} (number of amide groups per monosaccharide unit of the polysaccharide), which was calculated from the UV and elemental analysis data. The reactions of CED azides **B** with different amines were characterized by the degree of amidation, N_{am} (%), which was calculated by the formula $N_{am} = (N_{ace}/N_{hce}) \times 100$, where N_{hce} is the number of hydrazide groups per monomeric unit of hydrazide **A**.

To find the best conditions for the reactions of azides **B** with amines, we studied the stability of aqueous solutions of azide **B** in time, as influenced by the temperature and pH. The concentration of azides **B** in solutions was determined spectrophotometrically after addition of hydroxylamine and $FeCl_3$ [4] (Fig. 1).

Azides **B** are stable in strongly acidic aqueous solutions. At pH 2, the content of azide groups decreases with time only slightly (by 5–10%). The difference between the losses of azide groups observed at 0 and 20°C is insignificant, which allows the acylation to be performed at a higher temperature (and hence at a higher rate). However, as the solution pH is increased, the content of azide groups capable of acylating amines drastically decreases. At 0°C, it decreases within several minutes to 85% at pH 6 and to 40% at pH 10. Therefore, the order of adding the reactants in acylation of amines with CED azides is essential. When aniline is added first and then KOH is added to adjust the required pH, the degree of amidation is approximately 30% higher than when KOH is added first.

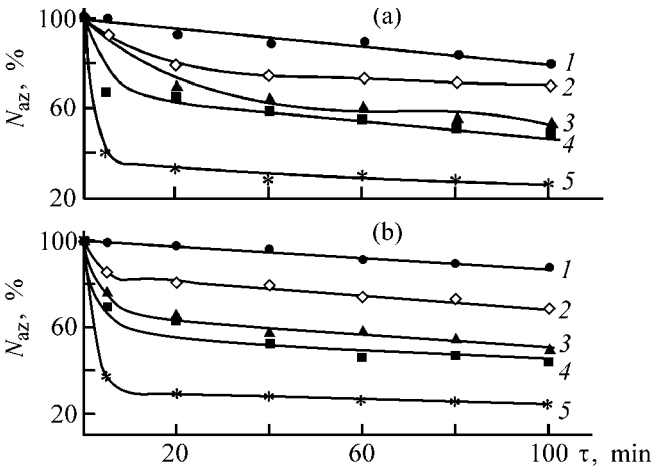

Fig. 1. Content of azide groups N_{az} (relative to the initial content of azide groups in CED azide) vs. time τ of keeping CED azide in solution at (a) 0 and (b) 20°C. pH: (*1*) 2, (*2*) 4, (*3*) 6, (*4*) 8, and (*5*) 10.

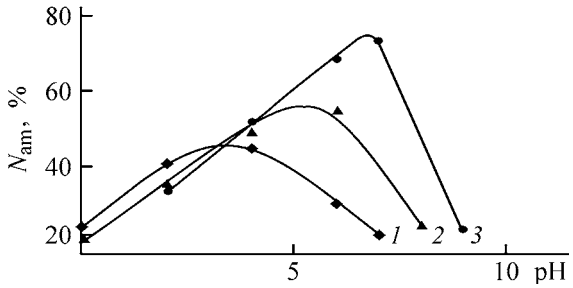

Fig. 2. Degree of amidation N_{am} of azides **B** with (*1*) *p*-bromoaniline, (*2*) aniline, and (*3*) *p*-phenetidine vs. pH. 17–20°C; 18 h; 5 mol of amine per mole of monosaccharide units; the same for Fig. 3.

When studying the acylating power of azides **B** toward amines, we expected that, similarly to carboxymethyl dextran azides [5], the solution acidity would exert a major influence on the degree of conversion of the azide groups into amide groups. The optimal pH is specific to each particular amine, in accordance with pK_a of the amine. Indeed, acid–base transforma-

Optimal pH values of solution (pH_{opt}) and degrees of conversion of azide groups into amide groups in reactions of azides **B** with amines (17–20°C; 18 h; 5 mol of amine per mole of monosaccharide units)

Amine	pK_a	σ_p	pH_{opt}	N_{am}	Amine	pK_a	σ_p	pH_{opt}	N_{am}
$PhCH_2NH_2$	9.37	–	10	70	$PhNH_2$	4.6	0	5.5	50.1
p-$EtOC_6H_4NH_2$	5.25	–0.24	7	72.0	*p*-$BrC_6H_4NH_2$	3.9	0.232	4	37.5
p-$MetC_6H_4NH_2$	5.12	–0.17	6	61.9	*p*-$NO_2C_6H_4NH_2$	1.02	0.778	0	10.0

tions of amines in the reaction medium exert a major effect on the reaction results (Fig. 2). When the pH deviates from the optimal value, N_{am} may decrease by a factor of 10. The lower the nucleophilicity of the amine, the lower the pH at which the degree of amidation of azides **B** is maximal. By contrast, strong bases better react with azides **B** in neutral and alkaline media. For example, the optimal pH is 10 for benzylamine and 5–6 for aniline. The optimal pH values at which the degrees of amidation of CED azides with aromatic amines are maximal linearly correlate with pK_a of the amines: pH = 1.5636 pK_a – 1.7201; n = 5, R^2 = 0.9833) (Fig. 3). With this correlation, it is possible to estimate the optimal acylation conditions from the known pK_a value of an amine without preliminary experiments.

As in the case of carboxymethyl dextran [5], the degree of conversion of azide groups into amide groups in reactions of azides **B** with aromatic amines also depends on the substituent in the benzene ring. Electron-donor substituents increase, and electron-acceptor substituents decrease N_{am} as compared to the reaction of azide **B** with aniline (see table). For example, the degree of amidation of azides **B** with aromatic amines increases from 10% with *p*-nitroaniline to 72% with *p*-phenetidine, which may be due to increasing nucleophilicity of the amines. The correlation of N_{am} with the Hammett constants of substituents σ_p is linear: $N_{am} = -58.05\sigma_p + 53.266$ (n = 5, R^2 = 0.9812).

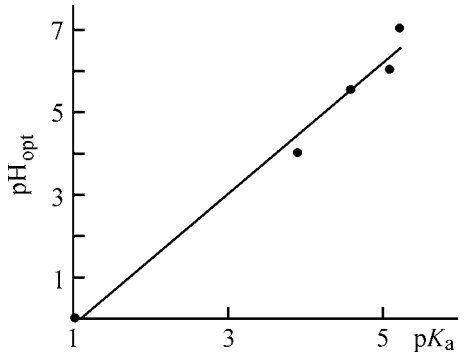

Fig. 3. Correlation between pK_a of aromatic amines and optimal pH (pH_{opt}) of their reaction with azides **B**.

CONCLUSIONS

(1) Aqueous solutions of carboxyethyl dextran azides can be used for acylation of aromatic and aliphatic amines in acidic and alkaline solutions at 0–20°C.

(2) The pH at which the degree of conversion of carboxyethyl dextran azide into amide passes through a maximum is specific to each particular amine and, in the case of aromatic amines, correlates with pK_a of the amine.

(3) The degree of amidation of azides with carboxyethyl dextran grows with increasing pK_a of the aromatic amine and linearly correlates with the Hammett σ_p constants of substituents.

REFERENCES

1. Iozep, A.A., Bessonova, N.K., and Passet, B.V., *Zh. Prikl. Khim.*, 1998, vol. 71, no. 2, pp. 320–323.
2. Iozep, A.A., Bessonova, N.K., and Passet, B.V., *Zh. Prikl. Khim.*, 1998, vol. 71, no. 6, pp. 995–998.
3. Iozep, A.A., Bessonova, N.K., and Passet, B.V., *Zh. Prikl. Khim.*, 1998, vol. 71, no. 6, pp. 998–1003.
4. Iozep, A.A., Ponomarenko, M.N., Kupriyanova, L.V., *et al.*, *Zh. Prikl. Khim.*, 1996, vol. 69, no. 9, pp. 1537–1542.
5. Iozep, A.A., Ponomarenko, M.N., and Passet, B.V., *Zh. Prikl. Khim.*, 1998, vol. 71, no. 1, pp. 140–145.

Russian Journal of Applied Chemistry, Vol. 77, No. 2, 2004, pp. 263–266. Translated from Zhurnal Prikladnoi Khimii, Vol. 77, No. 2, 2004, pp. 268–270.

ORGANIC SYNTHESIS AND INDUSTRIAL ORGANIC CHEMISTRY

Reactions of Carboxymethyl Polysaccharides and Their Ethyl Esters with Amines

O. V. Sibikina, A. A. Iozep, and B. V. Passet

St. Petersburg State Academy of Pharmaceutical Chemistry, St. Petersburg, Russia

Received September 23, 2003

Abstract—The reaction of carboxymethyl polysaccharides and their ethyl esters with amines was studied with the aim to determine how the structure of the polymeric acylating agent affects the composition of the reaction products.

Previously, we heve studied the reactions of carboxymethyl dextran and its ethyl esters with aliphatic and aromatic amines [1, 2] and, based on these results, developed procedures for designing physiologically active polymers (PAPs) with the aim to prepare new biologically active substances and improve the existing drugs [3]. In view of the fact that PAPs are prepared with polysaccharides of different structures, we studied the reactions of amines with carboxymethyl polysaccharides (CMPs) and their ethyl esters, aiming to determine how the structure of the polymeric acylating agent affects the composition of the reaction products.

Our experiments were performed with aubasidan [branched β-1,3-β-1,6-α-1,4-*D*-glucan produced by *Aureobasidium pullulans*, molecular weight $(5–9) \times 10^6$]; corapulan (linear β-1,3-*D*-glucan prepared from aubasidan by Smith degradation); amylose (isolated from potato starch by the procedure described in [4], mean molecular weight 4×10^5); rhodexman (linear β-1,3-β-1,4-*D*-mannan produced by *Rhodotorula rubra*, molecular weight 6.5×10^4); cellulose [molecular weight $(1.5–2) \times 10^4$]; and also dextran commercially produced in Russia (used in production of Poliglyukin plasma-substituting antishock agent), with the average molecular weight of $(6 \pm 1) \times 10^4$.

Chemical modification of polysaccharides was performed by the scheme

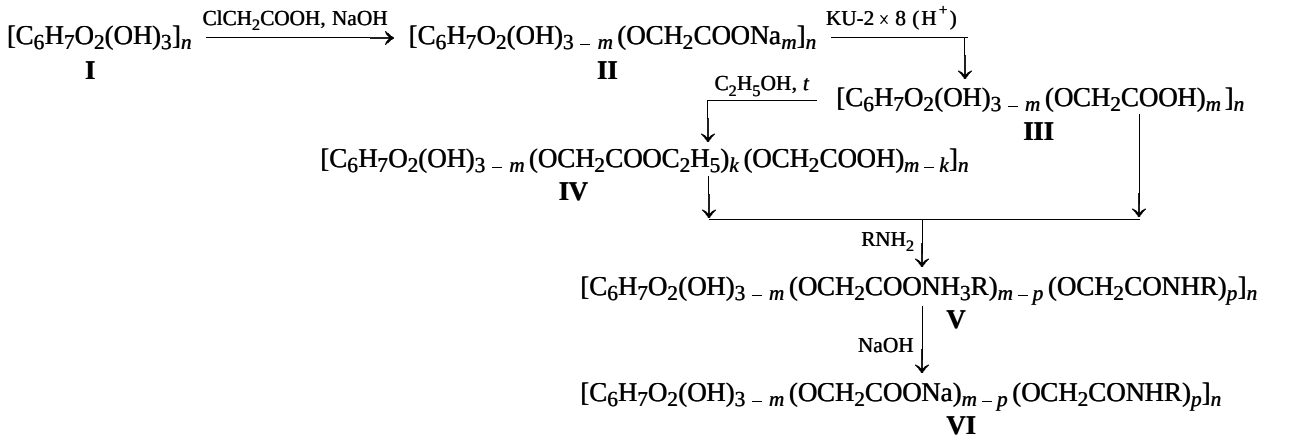

Carboxymethyl polysaccharides and their ethyl esters (CMPEEs) were prepared as described in [4, 5]. Polysaccharide **I** was alkylated with monochloroacetic acid in isopropanol in the presence of alkali [4]. Poly acid **III** was prepared by treatment of aqueous solutions of CMP salt **II** with KU-2 × 8 cation exchanger.

1070-4272/04/7702-0263 © 2004 MAIK "Nauka/Interperiodica"

Table 1. Ionization constants of carboxymethyl polysaccharides

Polysaccharide	C_{cm}	$K_a \times 10^5$	pK_a
Carboxymethyl dextran	0.94	9.772	4.01
Carboxymethyl rhodexman	1.07	7.079	4.15
Carboxymethyl amylose	1.61	4.57	4.32
Carboxymethyl cellulose	0.91	3.715	4.43
Carboxymethyl corapulan	1.73	2.512	4.60
Carboxymethyl aubasidan	1.11	1.259	4.90

Table 2. Degree of esterification C_e of carboxymethyl polysaccharide samples as influenced by pK_a of the poly acid

Polysaccharide	C_{cm}	pK_a	C_e, %
Carboxymethyl dextran	1.09	4.01	49
Carboxymethyl aubasidan	1.11	4.90	48
Carboxymethyl rhodexman	1.07	4.15	37
Carboxymethyl cellulose	0.91	4.43	37
Carboxymethyl amylose	1.61	4.32	34
Carboxymethyl corapulan	1.04	4.60	28

To prepare CMP ethyl ester **IV**, the poly acid was refluxed in excess ethanol under conditions of autocatalysis [5]. The resulting CMP and CMPEE samples were characterized by the degree of carboxymethylation, C_{cm}, and degree of alkoxycarbonylmethylation, C_{acm} (numbers of carboxymethyl and ester groups, respectively, per polysaccharide monomeric unit).

CMP sodium salts are white amorphous powders soluble in water (solubility: carboxymethyl aubasidan Na salt 10%; carboxymethyl rhodexman Na salt 15%; carboxymethyl dextran Na salt 20%) but insoluble in alcohol, acetone, ether, and most of other organic solvents.

For the CMP samples synthesized, we determined the acid ionization constants. Solutions of the poly acids were prepared by passing CMP sodium salts through a cation-exchange column, which was followed by potentiometric titration of the acid. The content of carboxy groups was determined by volumetric titration. The acid ionization constant was calculated as described in [6]. The relative error of the mean result did not exceed 4% (Table 1).

The apparent ionization constants of the carboxymethyl derivatives of dextran and cellulose coincided with the published values [7, 8].

One of the factors responsible for a decrease in the ionization constants in going from carboxymethyl dextran to carboxymethyl aubasidan (Table 1) may be different positions of substituents in the monomeric units of the polysaccharides. The effects of the monosaccharide unit on the carboxy group in positions C^2–O, C^3–O, C^4–O, and C^6–O are different. The ionization constant of the C^2–O-carboxymethyl group is higher, compared to the other positions. The electron-withdrawing effect of the carbonyl group of the monosaccharide unit is in this case the strongest. Hence, the higher the content of carboxymethyl group in the C^2–O position of the monosaccharide unit, the higher the ionization constant of the poly acid.

It should be noted that the capability of linear CMPs to form esters in reactions with ethanol correlates with pK_a of the poly acids (Table 2), except in the case of carboxymethyl amylose. Carboxymethyl dextran reacts with alcohol the most readily, and carboxymethyl corapulan, the least so. However, taking into account that, at $C_{cm} > 1$, C_e decreases, on the average, by 20–25% with increasing degree of substitution of CMP [5], carboxymethyl amylose, as expected, reacts with the alcohol more readily than carboxymethyl cellulose.

Acylation of amines with CMPs and their esters was performed in dioxane at 50–100°C for 4–16 h at a fivefold excess of the amine. The compounds were precipitated and reprecipitated with ethanol, acetone, or their mixtures with ether from aqueous solution of an alkali to remove low-molecular-weight impurities. The absence of low-molecular-weight impurities in the reaction products was checked by TLC. The CMP amides were examined by IR and UV spectroscopy, conductometric titration, and elemental analysis. The IR spectra of the reaction products in the H form contain absorption bands at 1535–1590 and 1640–1685 cm^{-1}, which are absent in the spectra of the starting substances and are characteristic of δ(N–H) (amide **II**) and ν(C=O) (amide **I**).

The content of amide groups in polysaccharide samples was determined by elemental analysis and UV spectroscopy. The acylation was characterized by the degree of amidation, C_{am} (percentage of acyl groups of the polysaccharide converted into amide groups).

Table 3. Results of reactions of carboxymethyl polysaccharides with aniline and benzylamine in dioxane (100°C, 6 h, molar ratio of amine to carboxy groups 5 : 1)

Polysaccharide	C_{cm}	C_e, %	C_{am} (%) in reaction with	
			benzylamine	aniline
Carboxymethyl dextran	0.9	49	26	43
Carboxymethyl aubasidan	1.11	48	18	39
Carboxymethyl rhodexman	0.91	37	14	27
Carboxymethyl cellulose	1.06	37	10	26
Carboxymethyl amylose	1.61	34	–	26
Carboxymethyl corapulan	1.04	28	10	11

Table 4. Degree of amidation of carboxymethyl polysaccharide ethyl esters in reactions with benzylamine (50°C, 4 h) and aniline (70°C, 16 h) in dioxane (fivefold excess of amine)

Ethyl ester of	C_{cm}	C_{acm}	C_{am} (%) in reaction with	
			benzylamine	aniline
Carboxymethyl dextran	0.36	0.56	38	82
Carboxymethyl aubasidan	0.58	0.53	45	72
Carboxymethyl cellulose	0.57	0.34	35	56
Carboxymethyl amylose	1.06	0.55	31	55
Carboxymethyl rhodexman	0.67	0.39	31	49
Carboxymethyl corapulan	0.75	0.29	31	45

The results of acylation of benzylamine and aniline with CMPs and their ethyl esters are given in Tables 3 and 4.

These results show that the reactivity of CMPs toward amines varies approximately similarly to the reactivity of the poly acids toward ethanol (Table 3). The dextran and aubasidan derivatives are modified with amines the most readily. The reactivities of the rhodexman, amylose, and cellulose derivatives toward amines are similar and somewhat lower than that of the dextran and aubasidan derivatives. Carboxymethyl corapulan reacts with amines the most difficultly. The same trend, with a minor exception (Table 4), is observed in acylation of benzylamine and aniline with ethyl esters of carboxymethyl polysaccharides under the conditions when only esters react with the amines. The influence of the polymer structure on the reactivity of CMPs and their ethyl esters is probably also associated with different arrangements of substituents in the monosaccharide unit and with structural features and properties of these polysaccharides.

Experiments on acylation of benzylamine and aniline with different CMPs showed that, in all the cases, aniline reacts under equal conditions with CMPs almost a factor of 2 faster than benzylamine. This is probably due to the higher stability of benzylammonium salts of polymeric carboxylic acids under acylation conditions and hence to lower concentrations of the acid (H form) and free amine in the reaction mixture (the carboxylate ion does not acylate amines). With CMP ethyl esters, benzylamine, being a stronger nucleophile, reacts considerably faster than aniline.

CONCLUSIONS

(1) Carboxymethyl derivatives of polysaccharides of different structures and their esters are simple and convenient acylating agents in reactions with amines.

(2) The apparent ionization constant of carboxymethyl polysaccharides depends on the position of the carboxymethyl groups in the monosaccharide unit of the polymer.

(3) The acylating activity of carboxymethylated linear polysaccharides and their ethyl esters grows with decreasing pK_a of the poly acid.

REFERENCES

1. Il'ina, T.Yu., Sibikina, O.V., and Iozep, A.A., *Zh. Org. Khim.*, 1994, vol. 30, no. 9, pp. 1326–1330.
2. Iozep, A.A., Sibikina, O.V., Kuznetsova, T.E., and

Passet, B.V., *Zh. Prikl. Khim.*, 1995, vol. 68, no. 2, pp. 307–311.

3. Ponomarenko, M.N., Iozep, A.A., and Passet, B.V., *Zh. Prikl. Khim.*, 1999, vol. 72, no. 5, pp. 823–827.
4. *Methods in Carbohydrate Chemistry*, Whistler, R.L. and Wolfrom, M.L., Eds., New York: Academic, 1962–1965, vols. I, II, IV, V.
5. Iozep, A.A., Il'ina, T.Yu., and Passet, B.V., *Zh. Prikl. Khim.*, 1993, vol. 66, no. 5, pp. 1106–1110.
6. Evstratova, K.I., Kupina, N.A., and Malakhova, E.E., *Fizicheskaya i kolloidnaya khimiya: Uchebnik dlya farmatsevticheskikh vuzov i fakul'tetov* (Physical and Colloid Chemistry: Textbook for Higher Pharmaceutical Institutions and Faculties), Moscow: Vysshaya Shkola, 1990.
7. Petropavlovskii, G.A., Larina, E.I., and Borisova, T.I., *Cellul. Chem. Technol.*, 1984, vol. 18, no. 3, pp. 283–292.
8. Tolmachev, V.N. and Polovinkina, L.I., *Vysokomol. Soedin., Ser. A*, 1985, vol. 27, no. 2, p. 251.

Russian Journal of Applied Chemistry, Vol. 77, No. 2, 2004, pp. 267–270. Translated from Zhurnal Prikladnoi Khimii, Vol. 77, No. 2, 2004, pp. 271–274.

MACROMOLECULAR CHEMISTRY AND POLYMERIC MATERIALS

Theoretical Description of Physical Aging of Amorphous Polymers

G. V. Kozlov, I. V. Dolbin, and G. E. Zaikov

Kabardino-Balkarian State University, Nalchik, Kabardino-Balkaria, Russia

Emanuel Institute of Biochemical Physics, Russian Academy of Sciences, Moscow, Russia

Received August 20, 2002; in final form, December 2003

Abstract—Physical aging of amorphous polymers was studied, and a theoretical description of the process in terms of fractal analysis was attempted.

Physical aging of polymers involves modification of their structure and properties with time and reflects the thermodynamically nonequilibrium nature of these materials. Physical aging typically results in increased brittleness of polymeric materials, which makes it important to forecast how the structural characteristics vary with time, so as to estimate the safe service life of polymeric articles. For network polymers, Kozlov *et al.* [1, 2] quantitatively estimated the structural changes in terms of the fractal analysis [3] and of the cluster model of the structure of polymers in the amorphous state [4, 5]. In the present, these models were applied to description of physical aging of polycarbonate (PC) based on bisphenol A. Also, we examined in more detail the behavior of PC during physical aging by using the concept of the quasiequilibrium state of the polymer structure [6] and to the model of a thermal cluster [7], which is a variant of the percolation theory.

EXPERIMENTAL

We studied granulated commercial PC of the Lexan brand (USA). The reduced viscosity η_{red} of a 0.5% chloroform solution of PC, measured on an Ubbelohde viscometer at 298 K, was 0.12 $m^3\ kg^{-1}$. We prepared $4 \times 6 \times 50$-mm samples by pressing at ~7 MPa and 490 K. The physical aging of the PC samples was carried out at T_{ag} = 403 K, which is below the glass-transition point of 423 K for PC [8]. The aging continued for 1000 h, during which time mechanical tests were run at 200-h intervals. Also, the reduced viscosity η_{red} was measured at 200-h intervals for the same samples and proved to be constant, which suggests the lack of thermal-oxidative degradation. Impact tests were carried out at 293 K by the Charpy technique on a UT-1/4 pendulum impact machine equipped with a piezoelectric load sensor. This installation records the load–time, P–τ, diagrams suitable for calculating the elasticity modulus E [9] and the yield stress σ_y [10]. These parameters, in turn, allow calculation of the Poisson coefficient ν by the relationship [11]

$$\frac{\sigma_y}{E} = \frac{1 - 2\nu}{6(1 + \nu)}. \quad (1)$$

In terms of the model [4, 5], the PC structure can be characterized by the relative proportion of the domains exhibiting local ordering (clusters), φ_{cl}, which is an order parameter in the strict physical sense [12]. For the starting PC, φ_{cl} is calculated by the relationship [12]

$$\varphi_{cl} = 0.03(T_g - T)^{0.55}, \quad (2)$$

where T is the test temperature (K); and T_g, the glass-transition point (K).

In terms of fractal analysis [13], the polymer structure is characterized by the fractal (Hausdorfian) dimensionality d_f and by the dimensionality of the excess energy localization domains, D_f, which characterizes the degree of the energetic excitation of loosely packed areas of the polymer structure and the size distribution of microcavities of the fluctuation free volume [6]. The dimensionalities d_f and D_f can be calculated by the equations [13]

$$d_f = 2(1 + \nu), \quad (3)$$

$$D_f = \frac{2(1 - \nu)}{1 - 2\nu}. \quad (4)$$

1070-4272/04/7702-0267 © 2004 MAIK "Nauka/Interperiodica"

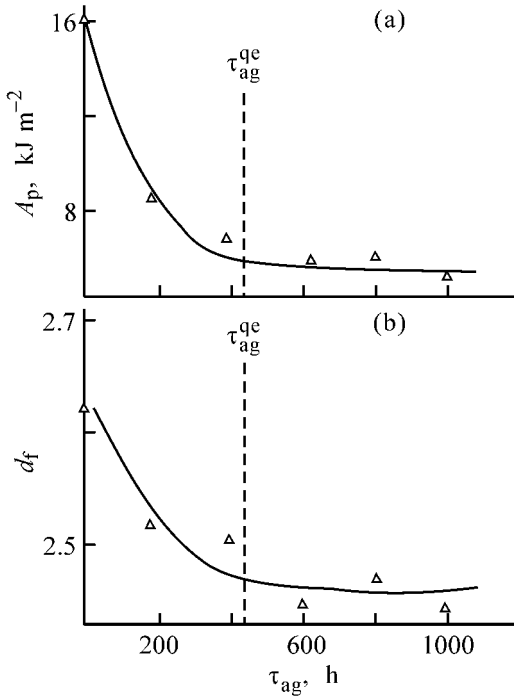

Fig. 1. (a) Resilience A_p and (b) fractal dimensionality of the structure d_f vs. the aging time τ_{ag} for PC. The vertical dashed line indicates the τ_{ag}^{qe} parameter calculated by Eq. (11).

Common knowledge [14] suggests that physical aging involves a decrease in the plasticity of PC, which is manifested in a decrease in the resilience A_p with the aging time τ_{ag} (Fig. 1). Figure 1a shows that A_p tends to decrease during the first 500 h of aging, whereupon the A_p-vs.-τ_{ag} plot flattens out with minor absolute values of A_p of ~4.5 kJ m^{-2}. Such a run of this plot may be due to the fact that the structure attains a certain limiting state which is defined as a quasiequilibrium state [6]. In terms of the model [4, 5], the tendency toward thermodynamic equilibrium, exhibited by the nonequilibrium structure of the polymer during physical aging, is expressed by an increase in the degree of local (short-range) order, φ_{cl} [1, 2]. In a certain stage of aging, however, the entropy-related chain tension counterbalances this tendency, and φ_{cl} ceases to increase [6], thus yielding the quasiequilibrium state. The dimensionality of the domains characterized by excess energy localization for this state, D_f^{qe}, is defined by the equation [6]

$$D_f^{qe} = \frac{4\pi T}{\ln(1/f_{ff})T_g}, \quad (5)$$

where f_{ff} is the relative fluctuation free volume, and T, test temperature.

Novikov and Kozlov [15] have found earlier that the polymer structure can be modeled as a thermal cluster whose formation is governed by both geometric and thermal interactions. The order parameter φ_{cl} for such a cluster is defined by the equation [7]

$$\varphi_{cl} = \left(\frac{T_g - T}{T_g}\right)^{\beta_t}, \quad (6)$$

where β_t is the critical index of the thermal cluster; T, test temperature (K); and T_g, the glass transition point (K).

Novikov and Kozlov [15] have shown earlier that β_t is generally a function of the degree of molecular mobility of the polymer and that $\beta_t \geq \beta$, where β is the corresponding critical index of the percolation cluster whose formation is controlled by geometric interactions only [16]. The $\beta_t = \beta$ equality is attained only when molecular mobility is totally suppressed, i.e., in the quasiequilibrium state.

Figure 1b shows the d_f–τ_{ag} plot calculated by Eqs. (1) and (3), which illustrates the evolution of the PC structure during physical aging. It is seen that, at $\tau_{ag} > 500$ h, the plot flattens out, with A_p attaining a value of ~2.46. The parameter f_{ff} for this case [$\nu = 0.23$ from Eq. (3)] can be calculated by the equation [11]:

$$f_{ff} \approx 0.017\frac{(1+\nu)}{(1-2\nu)}. \quad (7)$$

Next, we can calculate D_f^{qe} by Eq. (5) and then estimate the corresponding d_f^{qe} using the relationship [13]

$$D_f^{qe} = 1 + \frac{1}{3 - d_f^{qe}}. \quad (8)$$

Using Eqs. (5) and (8), we obtain $D_f^{qe} = 2.68$ and $d_f^{qe} = 2.41$. The latter value agrees well with the above-cited d_f value for the asymptotic branch of the d_f–τ_{ag} plot (Fig. 1b). Thus, the fact that the plot for resilience A_p (kJ m^{-2}) flattens out (Fig. 1a) is due to the attainment of a quasiequilibrium state by the PC structure in the course of physical aging.

Next, we estimate φ_{cl} in the quasiequilibrium state, using Eq. (6) and determining $\beta_t = \beta$ as [17]:

$$\beta_t = \beta = 1/d_f, \quad (9)$$

where β is the critical index of the percolation cluster.

Calculation by Eq. (6) yields $\varphi_{cl}^{qe} = 0.619$. Next, a_f^{qe} can be estimated from the expression [6]

$$d_f = 3 - 6\left(\frac{\varphi_{cl}}{SC_\infty}\right)^{1/2}, \quad (10)$$

where S is the cross-section area of the macromolecule (for PC, S = 30.7 Å^2 [18]), and C_∞, a characteristic ratio that reflects the statistical flexibility of the chain [19] (for PC, C_∞ = 2.4 [21]).

Calculation by Eq. (10) yields d_f^{qe} = 2.45, which agrees well with the above-cited values. Thus, the thermal cluster model adequately describes the polymer structure and, in particular, the conditions of realization of the quasiequilibrium state.

Using Eqs. (4), (5), and (8), we estimated D_f^{qe} to be 2.85, 2.68, and 2.82, respectively, which also shows that the techniques mentioned give well consistent results.

Let us estimate the time of physical aging, τ_{ag}^{qe}, required for attainment of the quasiequilibrium state. To this end, we use the equation derived by Aharoni [20]:

$$\varphi_{cl}^{qe} = k\varphi_{cl}\tau_{ag}^{(d_f - 2)(d_f - d_f^{qe})}, \quad (11)$$

where k is a constant equal to 0.14 [2], and φ_{cl}, the relative fraction of the clusters for the initial polymer; τ_{ag} is given in seconds.

The parameters in Eq. (11) can be estimated as follows. The parameter φ_{cl}^{qe} is calculated at T_{ag} by Eq. (6), and φ_{cl}, also at T_{ag} according to Eq. (2). Next, d_f and d_f^{qe} at T_{ag} can be calculated by Eq. (10) for the corresponding φ_{cl} and φ_{cl}^{qe}. The τ_{ag}^{qe} value of ca. 438 h, calculated in the given conditions by Eq. (11), is indicated in Figs. 1a and 1b with a vertical dashed line. It is seen that τ_{ag}^{qe} agrees well with τ_{ag} that corresponds to flattening out of the A_p–τ_{ag} and d_f–τ_{ag} plots. Thus, we can estimate the transient (nonstationary) period τ_{ag}^{tr} (h) during which the structure and properties of the polymer are modified by physical aging ($\tau_{ag}^{tr} \le \tau_{ag}^{qe}$).

It is known [14] that A_p grows with increasing molecular mobility associated with the mobility of the chains in loosely packed domains of the polymer structure [21]. The model discussed in [4, 5] treats such a domain as a loosely packed matrix in which the clusters are embedded. The relative proportion of such a domain φ_{lm} can be determined by the equation [11]

$$\varphi_{lm} = 1 - \varphi_{cl}. \quad (12)$$

Figure 2 presents the A_p–φ_{lm} plot, which has the expected shape. According to Aharoni [14], A_p tends to linearly grow with increasing φ_{lm}, and A_p = 0 corresponds to $\varphi_{lm} \approx 0.352$, rather than to the expected φ_{lm} = 0. According to Eq. (12), $\varphi_{lm} \approx 0.352$ corresponds to $\varphi_{cl} \approx 0.648$, which is fairly close to $\varphi_{cl} \sim 0.619$ at 293 K. This is consistent with the postulated total extension of the chains in the quasiequilibrium state, which restrict the growth of φ_{cl}, and with the resulting total suppression of the molecular mobility, which yields A_p = 0, i.e., totally brittle polymer.

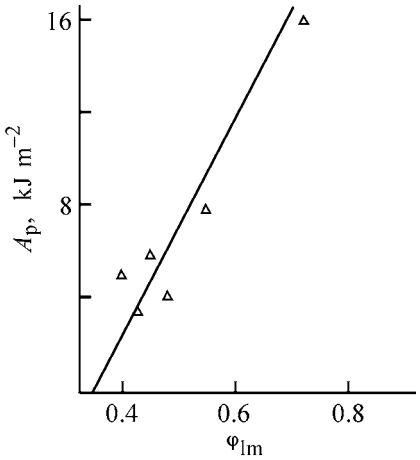

Fig. 2. Resilience A_p vs. the relative proportion of the loosely packed matrix φ_{lm} for PC.

CONCLUSION

Physical aging of amorphous polymers was theoretically described in terms of the fractal analysis and the thermal cluster model, taking polycarbonate as a typical example. It was shown that, during physical aging, the polymer structure attains a quasiequilibrium state. The evolution of the structure and properties of polymers during this process can be quantitatively described.

REFERENCES

1. Kozlov, G.V., Beloshenko, V.A., Gazaev, M.A., and Lipatov, Yu.S., *Vysokomol. Soedin., Ser. B.*, 1996, vol. 38, no. 8, pp. 1423–1426.
2. Kozlov, G.V., Beloshenko, V.A., and Lipatpv, Yu.S., *Ukr. Khim. Zh.*, 1998, vol. 64, no. 3, pp. 56–59.
3. Blumen, A., Klafter, J., and Zumofen, G., Fractals in Physics, *Proc. Sixth Trieste Int. Symp. on Fractals in Physics*, CTP, Trieste, Italy, July 9–12, 1985, Pietronero, L. and Tosatti, E., Eds., Amsterdam: North-Holland, 1986. Translated under the title Blumen, A., Klafter, J., and Zumofen, G., *Fraktaly v fizike*, Pietronero, L. and Tosatti, E., Eds., Moscow: Mir, 1988, pp. 561–574, 553–560.

4. Sanditov, D.S., Kozlov, G.V., Belousov, V.N., and Lipatov, Yu.S., *Ukr. Polym. J.*, 1992, vol. 1, nos. 3–4, pp. 241–258.
5. Kozlov, G.V., Beloshenko, V.A., Varyukhin, V.N., and Lipatov, Yu.S., *Polymer*, 1999, vol. 40, no. 7, pp. 1045–1051.
6. Kozlov, G.V. and Novikov, V.U., *Sinergetika i fraktal'nyi analiz setchatykh polimerov* (Synergetics and Fractal Analysis of Network Polymers), Moscow: Klassika, 1998.
7. Family, F., *J. Stat. Phys.*, 1984, vol. 36, nos. 5/6, pp. 881–896.
8. Kalinchev, E.L. and Sakovtseva, M.B., *Svoistva i pererabotka termoplastov* (Properties and Processing of Thermoplastics), Leningrad: Khimiya, 1983.
9. Kozlov, G.V., Shetov, R.A., and Mikitaev, A.K., *Vysokomol. Soedin., Ser. A*, 1987, vol. 29, no. 5, pp. 1109–1110.
10. Kozlov, G.V., Shetov, R.A., and Mikitaev, A.K., *Vysokomol. Soedin., Ser. A*, 1987, vol. 29, no. 9, pp. 2012–2013.
11. Kozlov, G.V. and Sanditov, D.S., *Angarmonicheskie effekty i fiziko-mekhanicheskie svoistva polimerov* (Anharmonic Effects and Physicomechanical Properties of Polymers), Novosibirsk: Nauka, 1994.
12. Kozlov, G.V., Gazaev, M.A., Novikov, V.U., and Mikitaev, A.K., *Pis'ma Zh. Teor. Fiz.*, 1996, vol. 22, no. 16, pp. 31–38.
13. Balankin, A.S., *Sinergetika deformiruemogo tela* (Synergetics of Deformed Body), part 1, Moscow: Ministerstvo Oborony SSSR, 1991.
14. Kausch, H.H., *Polymer Fracture*, Berlin: Springer, 1978.
15. Novikov, V.U. and Kozlov, G.V., *Usp. Khim.*, 2000, vol. 69, no. 6, pp. 572–599.
16. Sokolov, I.M., *Usp. Fiz. Nauk*, 1986, vol. 150, no. 2, pp. 221–256.
17. Bobryshev, A.N., Kozomazov, V.N., Babin, L.O., and Solomatov, V.I., *Sinergetika kompositnykh materialov* (Synergetics of Composite Materials), Lipetsk: ORIUS, 1994.
18. Aharoni, S.M., *Macromolecules*, 1985, vol. 18, no. 12, pp. 2624–2630.
19. Budtov, V.P., *Fizicheskaya khimiya rastvorov polimerov* (Physical Chemistry of Polymer Solutions), St. Petersburg: Khimiya, 1992.
20. Aharoni, S.M., *Macromolecules*, 1983, vol. 16, no. 9, pp. 1722–1728.
21. Bartenev, G.M. and Zelenev, Yu.V., *Fizika i mekhanika polimerov* (Polymer Physics and Mechanics), Moscow: Vysshaya Shkola, 1983.

Russian Journal of Applied Chemistry, Vol. 77, No. 2, 2004, pp. 271–275. Translated from Zhurnal Prikladnoi Khimii, Vol. 77, No. 2, 2004, pp. 275–279.

MACROMOLECULAR CHEMISTRY AND POLYMERIC MATERIALS

Radiation Aging of Cross-Linked Poly(Methyl Methacrylates)

V. N. Salimgareeva, S. P. Pivovarov, S. V. Kolesov, L. Kh. Bikchurina, A. I. Vorob'eva, and G. V. Leplyanin

Institute of Organic Chemistry, Ufa Scientific Center, Russian Academy of Sciences, Ufa, Bashkortostan, Russia

Received July 29, 2003

Abstract—Radiation aging of poly(methyl methacrylate) and copolymers of methyl methacrylate with *trans*-1,2-di(methacryloxy)cyclohexane, 3,4-di(methacryloxy)sulfolane, and 9,10-di(methacryloxymethyl)anthracene was studied.

The radiation resistance of polymers is influenced by the chemical structure of a polymer, its supramolecular structure, and chain mobility. Any of these factors can be decisive, depending on conditions. Studies of the radiation resistance of ionomers (copolymers of ethylene with acrylic acids, in which the carboxy groups are partially converted to Mn, Pb, and Cd salts) showed that, upon irradiation, these copolymers exhibit higher strength than polyethylene (PE) irradiated with the same doses (PE macromolecules cross-link under the action of high-energy radiation [1]).

The crystallinity decreases in going from PE to the ionomer [2], which should result in lower radiation resistance [3]. The higher, compared to PE, resistance of the ionomers to radiation (at doses of up to 70 Mrad [4]) cannot be accounted for by the presence of metal-containing fragments only (as these fragments protect the polymers only at irradiation doses not exceeding 0.1 Mrad [4]) but can be explained in terms of structural protection. In ionomers, the macromolecules (and also separate fragments of a macromolecule) form with each other not only common van der Waals and hydrogen bonds, but also ionic bonds [2] decreasing the molecular mobility. As a result, the probability of radiation-induced intermolecular cross-linking, impairing the PE properties, decreases.

It seems interesting to evaluate the effect of intermolecular cross-links on the radiation aging of a polymer degrading under high-energy radiation, poly(methyl methacrylate) (PMMA). To this end, we examined in this study the radiation resistance of copolymers of methyl methacrylate (MMA) with *trans*-1,2-di(methacryloxy)cyclohexane (DMCH), 3,4-di(methacryloxy)sulfolane (DMS), and 9,10-di(methacryloxymethyl)antracene (DMMA). The main macromolecular chains in these copolymers are cross-linked with cyclohexane, sulfolane, and dimethylanthracene bridges. The cross-links have the following structure:

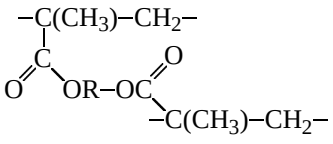

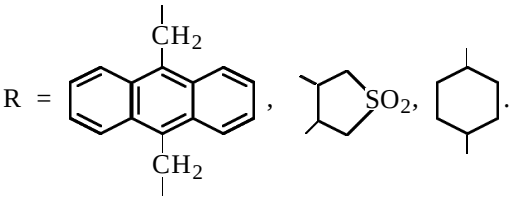

EXPERIMENTAL

The radiation resistance of MMA copolymers was evaluated by comparing the accumulation curves and radiation-chemical yields of radicals and the thermomechanical properties of irradiated samples with the respective characteristics of the homopolymer.

Polymer samples were prepared by bulk polymerization, performed to full conversion, at 40°C in the presence of dicyclohexyl peroxydicarbonate initiator with various amounts of DMCH or DMMA, or at

1070-4272/04/7702-0271 © 2004 MAIK "Nauka/Interperiodica"

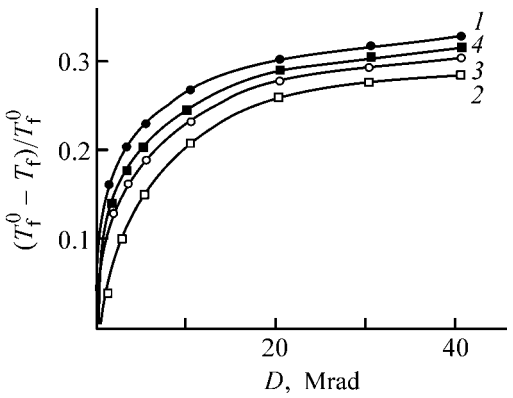

Fig. 1. Relative change in the flow point, $(T_f^0 - T_f)/T_f^0$, of (*1*) PMMA and copolymers of MMA with (*2*) DMMA, (*3*) DMS, and (*4*) DMCH vs. the absorbed dose *D*. Content of the second comonomer in the polymer 0.7 mol %; the same for Fig. 5. (T_f^0, T_f) Flow points (°C) of the unirradiated and irradiated samples, respectively.

50°C in the presence of azobis(isobutyronitrile) and DMS. DMCH, DMMA, and DMS were prepared according to [5–7] and were added to the polymerization mixture in amounts of 0–5.1, 0–1.3, and 0–4.5 mol %, respectively. The copolymers are insoluble in organic solvents. The molecular weight of PMMA is 9.11×10^5.

From the polymer blocks, we cut disks 3 mm in diameter and 4 mm high and irradiated them with ^{60}Co γ-rays at 25°C on an Issledovatel' installation (dose rate 0.15 Mrad h^{-1}, absorbed dose 0–60 Mrad).

The ESR spectra of the irradiated samples were recorded on an RE-1301 spectrometer at 77 K; the relative error in determination of the macroradical concentration was 5–10%.

The radiation-chemical yields of radicals (per 100 eV of absorbed energy) were determined from the slopes of the linear portions of the radical-accumulation curves.

Thermomechanical tests were performed on an installation providing progammed heating of the sample, by the method of constant loading. The load was 0.13 MPa, and the heating rate, 0.04 deg s^{-1}. The glass transition (T_g) and flow (T_f) points were determined by the method of interception of tangents to the initial portions of the thermomechanical curves.

Poly(methyl methacrylate) degrades under the action of ionizing radiation, with scission of the backbone at the quaternary carbon atom. These scissions are random, and the molecular weight of the polymer considerably decreases even in the initial step of irradiation. A similar pattern is observed with MMA copolymers: Their T_f (which directly correlates with the molecular weight, the parameter that is the most sensitive to irradiation) drastically decreases (Fig. 1). However, with MMA–DMCH and MMA–DMS copolymers this trend is appreciably less pronounced than with PMMA (cf. curves *1*, *3*, *4* in Fig. 1). Neither dissipation of the absorbed energy nor deactivation of the intermediate reactive states can be responsible for the observed protection effect. In the sulfolane groups of DMS–MMA copolymers, all the six valence electrons of the S atom involved in the formation of the S=O and C–S bonds. In contrast to bivalent sulfur compounds, sulfolane has no electrons capable of excitation to the *d* level. The cyclohexane fragment in the MMA–DMCH copolymer contains no conjugated double bonds and, similarly to the sulfolane group, cannot be involved in redistribution of the absorbed energy. In radiolysis, these groups do not generate species able to deactivate macroradicals. The stabilization of the polymer is apparently due to structural features of the macromolecules. The cross-links decrease the mobility of the macromolecules, and radicals arising in a macromolecule cannot cause degradation of another macromolecule, as it takes place, e.g., in PMMA [8].

The radicals decay by interaction with the radiation field (leading to the polymer degradation) and recombination (inhibiting degradation) [9]. Cross-links favor stabilization of radicals by complicating their decay both via thermal recombination and via direct interaction with the radiation (e.g., by dissociation to form stable molecules and hydrogen atoms recombining with the nearest radicals [9]). The rate constant of radical decay in irradiated MMA–DMS copolymer by direct interaction with the radiation is 0.23 $Mrad^{-1}$, whereas in PMMA it is 0.37 $Mrad^{-1}$ [10]. The activation energy of bimolecular radical decay in 110 kJ mol^{-1} in PMMA [10] and 146 kJ mol^{-1} in the copolymer. The inhibition of radical recombination in the copolymer is apparently due to a decrease in their "rotational" mobility in a cage and to the decreased probability of their escape from the cage.

The cross-linking of PMMA macromolecules of the sulfolane group causes a stronger radiation-protective effect than cross-linking with the cyclohexane fragment (curve *3* in Fig. 1 lies below curve *4*). This is apparently due to the lower concentration of free radicals accumulating in the MMA–DMS copolymer, compared to the copolymer with DMCH, in the exam-

ined ranges of the irradiation doses (Fig. 2) and comonomer concentrations in the copolymers (Fig. 3). As seen from the table, the radiation-chemical yield of free radicals G in the MMA–DMS copolymer is lower than in the MMA–DMCH copolymer.

The cross-links decrease the mobility of separate fragments of polymeric chains and give rise to mechanical stresses. Therefore, in the cross-linked polymers, compared to PMMA, the probability of macromolecule scission, the concentration of radicals, and their radiation-chemical yield increase. Furthermore, the comonomers can increase the concentration of defects of macromolecular packing owing to the steric effect, which may also be responsible for the experimentally observed growth of the radical concentration in proportion to the amount of the comonomer (Fig. 3).

Despite the higher, compared to PMMA, radiation-chemical yields and concentrations of radicals in the cross-linked samples, these samples appear to be more resistant to high-energy radiation. This means that, for the copolymers in hand, the macromolecular mobility is the major factor affecting the radiation aging, although the effect of the first two factors is also noticeable.

In real network polymer samples, not all the molecules are cross-linked, i.e., the sol fraction is present. The macromolecules that are not incorporated in the network exhibit not only hyperelastic but also viscous-flow properties. The contribution of the viscous-flow deformation depends on the content of such macromolecules. In copolymers of MMA with DMCH, DMS, and DMMA, the content of non-cross-linked PMMA macromolecules should be significant, since the concentrations of the comonomers are low (≤5.1 mol %). Furthermore, apparently, not all the comonomer molecules are involved in cross-linking of the macromolecules in the course of the synthesis. Some of them can be present as fragments of the linear copolymer chain and can participate in cross-linking by radiation-induced copolymerization of the pendant methacryloxysulfolane (or -cyclohexane, -methylanthracene) group with PMMA. This process may be responsible for the fact that T_g of the MMA–DMS copolymer, in contrast to T_g of PMMA, tends to increase upon γ-irradiation with small doses (Fig. 4).

Cross-linking with anthracene groups (in MMA–DMMA copolymer) enhances the radiation resistance of the polymer to a still greater extent. DMMA, compared to DMCH and DMS, inhibits to a greater extent the decrease in the flexibility of the whole macromolecule (factor responsible for the polymer flowability,

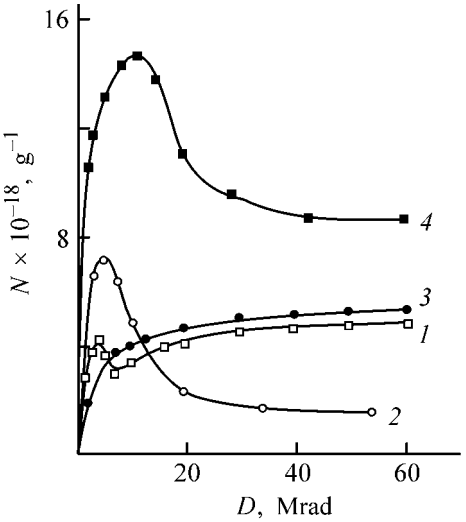

Fig. 2. Curves of radical accumulation in (*1*) PMMA and copolymers of MMA with (*2*) DMMA, (*3*) DMCH, and (*4*) DMS. Comonomer concentration 0.7 mol %. (*N*) Concentration of radicals and (*D*) irradiation dose.

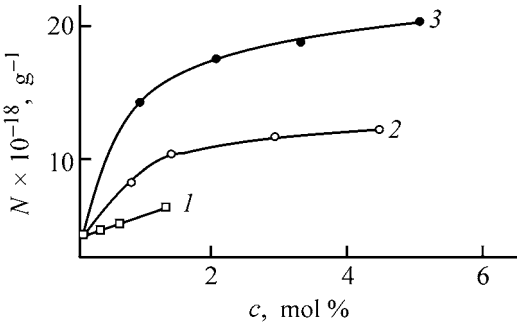

Fig. 3. Concentration of macroradicals *N* in the maximum of the accumulation curve vs. the content *c* of (*1*) DMMA, (*2*) DMS, and (*3*) DMCH in the copolymer.

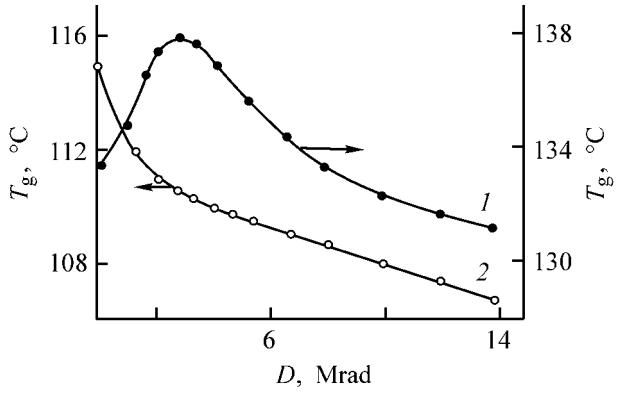

Fig. 4. Glass transition point T_g of (*1*) PMMA and (*2*) MMA–DMS copolymer (0.7 mol % DMS) vs. the irradiation dose *D*.

Radiation yield of radicals *G* (per 100 eV) in irradiated homo- and copolymers of MMA (25°C)

Comonomer	Concentration, %	*G*
–	–	2.6
DMCH	0.7	3.2
	3.0	4.2
	5.1	5.3
DMS	0.7	3.0
	1.4	3.5
	3.0	3.9
	4.5	4.1
DMMA	0.25	0.4
	0.7	1.4
	1.3	2.3

Fig. 1) and in the mobility of separate chain segments (factor responsible for the glass transition, Fig. 5), occurring upon γ-irradiation.

The curves of radical accumulation in MMA–DMMA copolymers upon irradiation at 25°C level off at $D > 30$ Mrad, whereas for PMMA and the other copolymers they pass through a maximum (Fig. 2). The descent of the curve after the accumulation of a certain concentration of radicals in PMMA and copolymers of MMA with DMS and DMCH is apparently due to the fact that the radiation-induced degradation of the polymers appreciably alters the macrochain mobility, making possible subsequent thermal transformations of the radicals since irradiation is performed at a relatively high temperature. When PMMA is irradiated at low temperatures, such transformations are impossible, and the plot of the radical concentration vs. irradiation dose levels off [9]. In MMA–DMMA copolymers, the transformations of radicals are hindered by the high rigidity of the anthracene core and of macromolecules containing it.

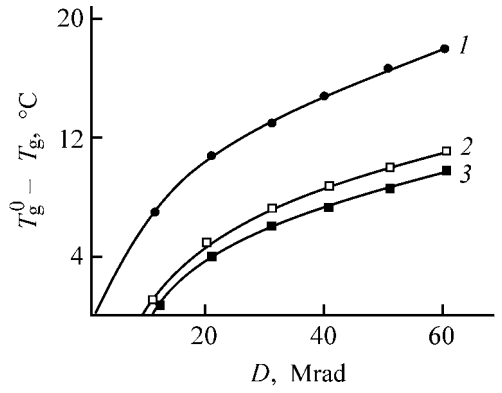

Fig. 5. Change in the glass transition point, $T_g^0 - T_g$, of (*1*) PMMA and copolymers of MMA with (*2*) DMS and (*3*) DMMA vs. the irradiation dose *D*.

The maximal concentration of free radicals, attained in irradiation of this copolymer, is lower than that attained in MMA–DMCH and MMA–DMS copolymers (Fig. 1). This relationship is preserved when the content of DMMA units in the copolymer is increased to 1.3 mol % (Fig. 3; the upper concentration limit corresponds to the limit of DMMA solubility in MMA).

The anthracene groups present in the MMA–DMMA copolymer are capable to absorb the incident energy by the system of conjugated double bonds and to dissipate it in the form of heat and light so rapidly that the polymer has no time to degrade. Apparently, owing to this protective effect ("radiation sponge"), the radiation-chemical yield of radicals in this copolymer appears to be lower, compared to MMA–DMS and MMA–DMCH copolymers and to PMMA (see table). The anthracene fragments, on the one hand, protect the polymer from radiation and, on the other hand, when present in certain concentration, alter its supramolecular structure, stabilizing the macroradicals: As the DMMA content in the copolymer is increased, the radiation-chemical yield of the radicals and their concentration grow.

Mechanical blending ot antracene with PMMA, compared to preparation of MMA–DMMA copolymers, provides the same radioprotective effect at 5–10 times higher content of anthracene. This fact is indicative of a complex protection mechanism in the copolymer, involving both the redistribution of the absorbed energy by aromatic cores and the structural protection due to cross-linking of the macromolecules.

Thus, in copolymers of MMA with monomers that act as cross-linking agents, radiation-induced degradation is inhibited.

CONCLUSIONS

(1) Cross-linking of poly(methyl methacrylate) macromolecules with cyclohexane and sulfolane bridging groups in copolymers of methyl methacrylate with *trans*-1,2-dimethacryloxycyclohexane and 3,4-dimethacryloxysulfolane enhances the radiation resistance of the polymer owing to a decreased mobility of macromolecules, despite the higher radiation-chemical yields and concentrations of the radicals, compared to the homopolymer.

(2) Introduction of anthracene fragments into poly(methyl methacrylate) enhances the radiation-protec-

tive effect of cross-linking owing to the capability of aromatic cores to participate in redistribution of the incident energy.

REFERENCES

1. Andrusenko, A.A., Nurmukhametov, F.N., Sevast'yanova, O.S., and Sankina, Z.A., Abstracts of Papers, *Simpozium po radiatsionnoi khimii* (Symp. on Radiation Chemistry), Tbilisi, November 13–15, 1978, pp. 16–17.
2. Aleksandrovich, K.V., Berezin, I.A., Gorbachev, V.M., *et al.*, *Tekh. Radiats. Eksp.*, 1978, no. 6, pp. 87–89.
3. Rafikov, S.R. and Andrusenko, A.A., in *Sintez i svoistva polimerov* (Synthesis and Properties of Polymers), Ufa: Bashkir. Filial Akad. Nauk SSSR, 1974, pp. 4–48.
4. *Radiatsionnaya khimiya polimerov* (Radiation Chemistry of Polymers), Kargin, V.A., Ed., Moscow: Nauka, 1973.
5. Leplyanin, G.V., Bikchurina, L.Kh., and Rafikov, S.R., *Vysokomol. Soedin., Ser. B*, 1977, vol. 19, no. 1, pp. 11–14.
6. Rafikov, S.R., Korobeinikova, V.N., Lotnik, S.V., *et al.*, *Vysokomol. Soedin., Ser. A*, 1978, vol. 20, no. 4, pp. 766–771.
7. USSR Inventor's Certificate, no. 481615.
8. Rafikov, S.R., Ibragimov, Sh.Sh., Leplyanin, G.V., *et al.*, *Khim. Vys. Energ.*, 1981, vol. 15, no. 4, pp. 333–337.
9. Pshezhetskii, S.Ya., Kotov, A.G., Milinchuk, V.G., *et al.*, *EPR svobodnykh radikalov v radiatsionnoi khimii* (ESR of Free Radicals in Radiation Chemistry), Moscow: Khimiya, 1972.
10. Pivovarov, S.P., Poljakov, A.I., Rjabikin, Yu.A., *et al.*, *Radiat. Eff.*, 1982, vol. 59, pp. 179–182.

Russian Journal of Applied Chemistry, Vol. 77, No. 2, 2004, pp. 276–280. Translated from Zhurnal Prikladnoi Khimii, Vol. 77, No. 2, 2004, pp. 280–284.

MACROMOLECULAR CHEMISTRY AND POLYMERIC MATERIALS

Influence of Chemical Modification of the Surface on the Electret Properties of Polytetrafluoroethylene

A. A. Rychkov, A. A. Malygin, S. A. Trifonov, and D. A. Rychkov

St. Petersburg State Technological Institute, St. Petersburg, Russia
Herzen Russian State Pedagogical University, St. Petersburg, Russia

Received April 7, 2003

Abstract—Thermal stability of the electret state of polytetrafluoroethylene films with element oxide structures on the surface was studied. The frequency factor and the activation energies of the newly formed groups of deep centers that capture the electret charge were determined.

As is known [1], when irradiated with charged particle fluxes, polymer insulators accumulate a positive or a negative charge on their surface, yielding an electret state. Such materials are called electrets, and the charge on their surface can be preserved for a fairly long time, depending on the external conditions and properties of the polymer. This effect finds application in electroacoustic transformers and sensors, as well as in nonlinear-optics components [2]. Of great practical importance for such systems is the stability of the electret state. For nonpolar polymers, such a stability is afforded by creation on their surface of deep charge capture centers, using specially developed procedures [3]. For example, fluoropolymers are characterized by extremely low mobility of charge carriers [1–3]. Their equilibrium concentration is so small, compared to that of the injected charges, that the deciding role in relaxation of the electret state is played by the surface traps [3]. Therefore, it is not surprising that, the stability of the nonequilibrium charge injected into nonpolar polymers during charging in the corona discharge, is strongly dependent on the chemical structure of the surface [3–5]. Rychkov and Boitsov [3] showed that, with increasing degree of hydration of the surface of nonpolar fluoropolymer films, the curves of thermoinduced relaxation of the surface potential tend to regularly shift to higher temperatures. X-ray photoelectron spectroscopic (XPS) studies revealed major defluorination of the surface being modified [3]. Thus, chemical modification of the surface can efficiently control the electret characteristics of polymers.

Modification of the energy spectrum of the surface traps is the most pronounced in hydration of the polytetrafluoroethylene (PTFE) surface. Rychkov *et al.* [3, 6] revealed a correlation between the thermal stability of the surface potential and the concentration of the OH groups on the film surface. At the same time, it is known that the concentration of the active sites chemisorbing the OH groups on the film surface can be significantly increased by molecular layer deposition (MLD). This method is based on chemical reactions between the functional groups of the solid-phase matrix and volatile low-molecular-weight reagents [7, 8].

EXPERIMENTAL

In this study, we examined the nature of the centers that capture the electret charge in PTFE films with element oxide nanostructures on their surface and also determined the microscopic parameters of the forming surface traps of the positive homocharge.

We studied 10-μm-thick F4-EA grade PTFE films coated with aluminum on one side. The desired composition of the surface was achieved by using chemical nanotechnology based on the MLD principles.

The element oxide groups were synthesized in a flow reactor, by treating 50×20-mm film samples of the polymer material with a PCl_3 vapor. The choice of PCl_3 as the modifying agent was dictated by the high hydrolytic activity of polar phosphorus-containing groups. After synthesis, the physisorbed PCl_3 and HCl were removed by a dried air flow until they ceased to evolve at the reactor outlet. To replace the chloride ions with OH groups in the products of the reaction of

1070-4272/04/7702-0276 © 2004 MAIK "Nauka/Interperiodica"

PTFE with the modifier vapor, the samples were subjected to vapor-phase hydrolysis. The completion of this hydrolysis was ascertained by ceased evolution of HCl at the reactor outlet. The modification temperature was 180°C, the times of treatment of the samples with PCl_3 and H_2O vapor, 1 h and 30 min, respectively, and the flow rate of air dried to a dew point (from –50 to –55°C), 100 $cm^3\ min^{-1}$.

The electret state in the initial and modified films was created by charging in a positive corona discharge on a setup shown schematically in Fig. 1. The initial surface potential V_0 = +500 V was set by the voltage on grid *2*. The charging time was 1 s, and the charging temperature, 290 K.

The electret properties of the samples were studied by the method of thermoinduced relaxation of the surface potential (TIRSP) [3] in the linear heating mode at β_1 = 0.10 and β_2 = 0.17 deg s^{-1}. This method allows recording of the temperature dependences of the surface potential of electrets. Simmons *et al.* [9] suggest that, for nonpolar fluoropolymers, the TIRSP curves can be described by the expression [3]

$$\frac{V(T)}{V_0} = 1 - \frac{1}{\beta}\int_{T_0}^{T} D f_0^*(E_s)\, N^*(E_s)\, dT', \qquad (1)$$

$$E_s = T\left(\log\frac{\omega_s}{\beta} + a\right)b - c. \qquad (2)$$

Here, E_s is the activation energy of surface traps; $f_0^*(E_s)N(E_s)$, distribution function of the filled surface traps with respect to activation energies; $D = 1.2\beta E_s T^{-1}$, a weakly temperature-dependent coefficient [9]; and ω_s, frequency factor of surface traps.

The constants *a*, *b*, and *c* are determined by the system of units chosen. For E_s measured in eV, and *T*, ω_s, and β, in International System units, these constants take the following values: a = 1.66, $b = 1.92 \times 10^{-4}$, and c = 0.015 [9].

Equations (1) and (2) show that, in terms of the model accepted, TIRSP of the electret state is fully determined by the parameters of the energy spectrum of the surface traps. The d*V*/d*T* dependence on the temperature *T* reflects the distribution of the traps with respect to energies. Thus, to derive the distribution function of the filled surface traps with respect to activation energies from the experimental data, it is sufficient to transform the d*V*/d*T* scale to the $f_0^*(E_s)N(E_s)$ scale, and the temperature scale, to the energy scale. These transformations present no difficulties, since the required frequency factor ω_s can be determined experimentally from the shift of the maximum of

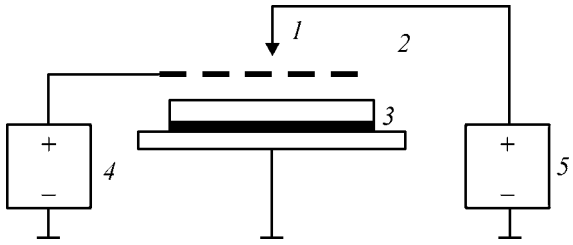

Fig. 1. Schematic of the setup for polarization in a corona discharge: (*1*) corona discharging electrode, (*2*) grid, (*3*) sample being charged, (*4*) stabilized power supply, and (*5*) high-voltage source.

the derivative of the TIRSP signal with respect to temperature depending on the heating rate, using the formula [9]

$$\log\omega_s = \frac{T_2^*\log\beta_2 - T_1^*\log\beta_1}{T_2^* - T_1^*} - a, \qquad (3)$$

where T_1^* and T_2^* are the temperatures corresponding to the peaks of the d*V*/d*T*–*T* curves recorded at the heating rates β_1 and β_2, respectively.

Chemical modification, evidently, involves grafting of phosphorus-containing groups to the polymer matrix surface. According to the XPS data [3], the chemical structure of PTFE includes $–CF_2–CF{=}CF–CF_2–$ groups incorporating double bonds, which can be active in reactions with PCl_3:

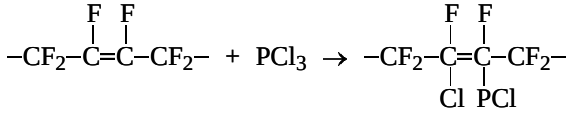

A chemical analysis showed that the phosphorus concentration in the modified samples is insignificant (ca. 0.01 wt %).

In our earlier communication [10], we reported similar chemical transformations, namely, addition of phosphorus-containing groups to the surface of nonpolar low-density polyethylene via scission of the C=C bond, as revealed by various methods (chemical analysis, IR spectroscopy). The subsequent vapor-phase hydrolysis of the modified films results in replacement of the chloride ions and an increase in the concentration of OH groups.

Also, the surface of real polymers contains chemisorbed molecules strongly fixed to certain moieties of the polymer chains. These moieties include OH, CO, C–C, C=C, CH_2, CH_3, and other groups, among which oxygen-containing groups result from polymeric material the contact of an air [11]. These defects are, evidently, reactive and can exhibit activity during

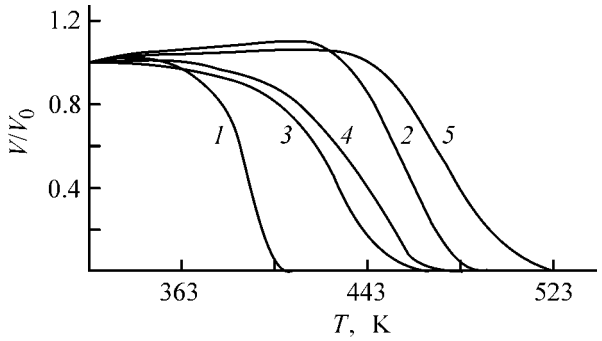

Fig. 2. Thermoinduced relaxation of the surface potential V/V_0 as influenced by the surface modification modes for the electret structures of PTFE-A1. (T) Temperature. (*1*) Initial sample; (*2*) treatment in water; (*3*) gas-phase modification with PCl_3 vapor; (*4*) gas-phase modification with PCl_3 vapor, followed by gas-phase hydration; and (*5*) sample no. 3 subjected to additional treatment with water; the same for Fig. 3.

surface modification of the PTFE film with PCl_3 vapor. Thus, the chemical structure of the modified polymer can be represented schematically as follows:

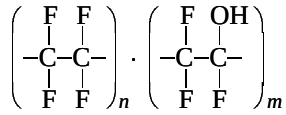
(a)

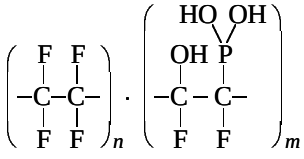
(b)

Figure 2 shows the TIRSP of the samples depending on the surface treatment modes. Curve *1* corresponds to relaxation of the potential of the initial PTFE film. As already mentioned, the sample treated by the known hydration procedure (the time of contact between the film surface and water 10 s [3]) exhibits a much greater thermal stability of the surface potential (Fig. 2, curve *2*).

Chemical modification of the polymer with PCl_3 vapor is also responsible for the increased thermal stability of the potential of electret structures (Fig. 2, curve *3*) relative to untreated samples (curve *1*). However, the highest thermal stability is achieved in the case of a complex treatment, when the polymer films with element oxide surface nanostructures are additionally hydrated by 10-s contact with water (Fig. 2, curve *5*). Notably, the kinetics of the relaxation processes is less affected by the gas-phase treatment of phosphorus-containing PTFE-A1 with water vapor (Fig. 2, curve *4*).

Our results suggest that chemical modification of the surface of the PTFE films yields additional centers that of the electret charge. The deciding role in homocharge accumulation belongs to surface traps, by which are usually meant specific surface defects such as, e.g., chain breaks, adsorbed molecules, oxidation products, etc. Sessler [1] distinguished three types of such traps, namely, primary, secondary, and tertiary. Thermal activation of charge carriers from these traps occurs in different temperature ranges. The least thermally stable are primary traps which are represented by atoms incorporated in macromolecules. The release of charge from them is limited by small-scale motions of the macromolecular chain. The tertiary traps are activated at higher temperatures, when the crystal structure of the polymer is rearranged. Our experimental data suggest (Fig. 2) that treatment with water yields charge capture sites at the interface between a crystallite and a amorphous phase, which is specifically responsible for the high thermal stability of the potential of the electret structures (Fig. 2, curve *2*).

Thus, it can be assumed that the chemical modification of the PFTE film surface with PCl_3 vapor yields new charge capture centers in the near-surface layers of the polymer film, which can be treated as primary traps.

The theoretical concepts being developed in this study regard the thermal stability of the electret state in the PTFE films as being strongly dependent on the degree of surface hydration. The steady-state contact angles θ were estimated at 92° for the initial sample, at 88° and 79° for samples treated with PCl_3 vapor and water, respectively, and at 57° for the sample subjected to complex treatment (gas-phase modification with PCl_3 vapor, followed by treatment with water). The contact angles were determined by a standard technique [3] involving the contact of a microdrop (1–2 mg) of distilled water with the sample surface. The above-mentioned data are average values obtained for no less than seven points on the sample surface.

It is seen that, whatever the treatment procedure, the contact angle tends to decrease after treatment, most profoundly in the case of the complex treatment, which suggests a high surface energy of the modified film [11].

Thus, introduction of chemisorbed reactive phosphorus-containing groups into the polymer chain of PTFE increases the concentration of the OH groups on the surface being modified. The structures being

formed act as deep centers that capture the electret charge. Therefore, it is of interest to determine the microscopic parameters characterizing these capture sites.

To this end, we carried out the following experiments. We varied the heating rates for samples during TIRSP and, using formulas (1)–(3), determined the frequency factor and reconstructed the energy spectrum of the surface traps. Notably, in a number of cases, the TIRSP curves exhibit initial rise in the surface potential during heating. Rychkov and Boitsov found earlier [3] that the rise in the potential is due exclusively to a decrease in the electric capacitance of the fluoropolymers with rising temperature rather than to relaxation of the electret charges. Therefore, to determine the distribution functions, we normalized the experimental curves, taking into account the temperature dependence of the electric capacitance of the film.

Figure 3 demonstrates how the distribution of the electret charge capture centers with respect to energy varies with the modification mode. It is seen that modification of the PTFE film surface yields new groups of capture centers lying deep in energy. For example, for unmodified sample (Fig. 3, curve *1*) the frequency factor ω_s was estimated at 7×10^{13} s^{-1}, and the energy at the distribution maximum E_s^*, at 1.23 eV, and for the sample treated with water, at 1×10^{13} s^{-1} and 1.39 eV, respectively (Fig. 3, curve *2*). Upon chemical modification of the film surface with PCl_3 vapor, ω_s decreases to 8×10^{12} s^{-1}, E_s^* being 1.26 eV (Fig. 3, curve *3*). Additional gas-phase modification with H_2O vapor of the surface modified with PCl_2 groups favors formation of traps characterized by $\omega_s = 9 \times 10^{12}$ s^{-1} and $E_s^* = 1.34$ eV (Fig. 3, curve *4*). However, the spectrum of the surface capture centers is the most profoundly affected by the complex treatment of PFTE films (Fig. 3, curve *5*). In this case, $\omega_s = 6 \times 10^{12}$ s^{-1}, $E_s^* = 1.4$ eV, and also a new group of traps with $E_s^* = 1.48$ eV is formed.

The rise in the efficiency of capture of positive electret homocharge on the polymer surface is usually attributed to the structures having a higher affinity for holes. In the given case, the $P(OH)_2$ groups occurring in the polymer chain of PTFE can well act as such capture centers. At the same time, the resulting functional groups can indirectly affect the thermal stability of the electret charge. Specifically, the nonstoichiometric defects such as new surface functional groups introduced into the macromolecules can significantly decrease the molecular mobility via an increase in the chain packing density and growth of the

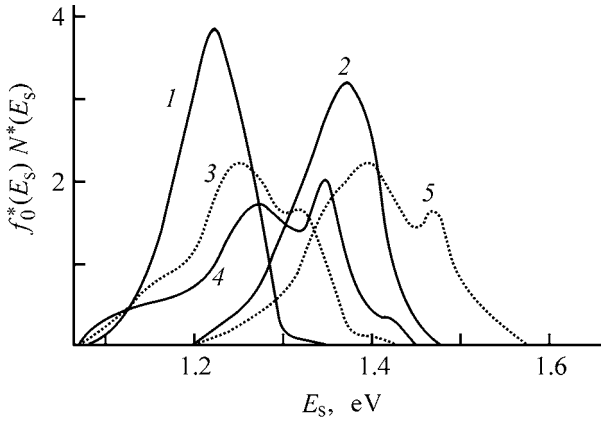

Fig. 3. distribution function $f_0^*(E_s)N^*(E_s)$ of the surface traps with respect to the activation energies E_s for PTFE films depending on the surface modification procedure.

effective length of the kinetic segments. The resulting capture centers can be treated as secondary traps responsible for a growth of the glass-transition temperature of the amorphous phase on the polymer surface [2]. From the viewpoint of charge accumulation and retention, this should be manifested in a decreased frequency factor of the capture centers owing to increased moment of inertia of the kinetic units [12]. This was actually revealed by our TIRSP experiments.

CONCLUSIONS

(1) Chemical modification of the polytetrafluoroethylene film surface is an efficient means for controlling its electret characteristics.

(2) Introduction of phosphorus-containing nanostructures into the surface layer of the polymer films presumably increases the concentration of the OH groups. These groups form new deep centers that capture positive electret charge; they are characterized by a quasicontinuous distribution with respect to the activation energies.

ACKNOWLEDGMENTS

The study was financially supported in part by the Russian Foundation for Basic Research (project no. 01-03-32 345).

REFERENCES

1. *Electrets*, Sessler, G.M., Ed., Berlin: Springer, 1980. Translated under the title Sessler, G., *Elektrety*, Moscow: Mir, 1983, pp. 25–104.
2. *Electrets*, Gerhard, R., Ed., California: Mulhaupt-Laplacian, 1999.

3. Rychkov, A.A. and Boitsov, V.G., *Elektretnyi effekt v strukturakh polimer–metall* (Electret Effect in Polymer–Metal Structures), St. Petersburg, Ross. Gos. Pedagog. Univ., 2000.
4. Rychkov, A.A., Boitsov, V.G., and Shvets, B.B., *Proc. 9th Int. Symp. on Electrets (ISE-9)*, Shanghai, 1996, pp. 89–92.
5. Boitsov, V.G., Rychkov, A.A., and Rozhkov, I.N., *Funct. Mater.*, 1995, vol. 2, no. 2, pp. 296–298.
6. Rychkov, A.A. and Dergachev, V.F., Abstracts of Papers, *II Vserossiiskaya konferentsiya "Khimiya poverkhnosti i nanotekhnologiya"* (II Russian Conf. "Surface Chemistry and Nanotechnology"), Sept. 23–28, 2002, Khilovo (Pskov oblast), St. Petersburg: Redakts.-Izd. Otd., Sankt-Peterb. Gos. Tekhnol. Inst., 2002, pp. 49–51.
7. Malkov, A.A., Malygin, A.A., and Trifonov, S.A., *Metod molekulyarnogo naslaivaniya – osnova noveishei pretsizionnoi tekhnologii* (Molecular Layer Deposition Method as a Basis for Advanced Precision Technology), 1992, St. Petersburg, Available from VINITI, Ross. Akad. Nauk, July 8, 1992, no. 2205-V92.
8. Malygin, A.A., *Zh. Prikl. Khim.*, 1996, vol. 69, no. 10, pp. 1585–1593.
9. Simmons, J.G., Taylor, G.W., and Tam, M.C., *Phys. Rev. B*, 1973, vol. 7, no. 8, pp. 3714–3719.
10. Trifonov, S.A., Lapikov, V.A., and Malygin, A.A., *Vliyanie khimicheskogo modifitsirovaniya khloridom fosfora(III) poverkhnosti polietilena na ego termookislitel'nuyu stoikost'* (Influence of Chemical Modification with Phosphorus(III) Chloride of the Surface of Polyethylene on Its Thermooxidation Stability), 2002, St. Petersburg, Available from VINITI, Ross. Akad. Nauk, February 26, 2002, no. 374-V2002.
11. Povstugar, V.I., Kodolov, V.I., and Mikhailov, S.S., *Stroenie i svoistva poverkhnosti polimernykh materialov* (Structure and Properties of Polymeric Material Surface), Moscow: Khimiya, 1988.
12. Bartenev, G.M. and Frenkel', S.Ya., *Fizika polimerov* (Polymer Physics), Leningrad: Khimiya, 1990.

Russian Journal of Applied Chemistry, Vol. 77, No. 2, 2004, pp. 281–284. Translated from Zhurnal Prikladnoi Khimii, Vol. 77, No. 2, 2004, pp. 285–288.

MACROMOLECULAR CHEMISTRY AND POLYMERIC MATERIALS

Morphological Features of the First Growth Steps of Polymeric Coatings from the Active Gas Phase on the Activated Surface

A. A. Rogachev

Belarussian State University of Transport, Gomel, Belarus

Received May 14, 2003

Abstract—Morphological features of the first growth stages of polytetrafluoroethylene films from the active gas phase on the silicon surface treated by various methods were studied. The influence of the surface energy of the support on the distribution of polymer microparticles in these stages and on the distribution kinetics was determined.

Thin films with unique properties can be grown from an active gas phase formed by electron-beam dispersion of initial polymer [1–3]. This method is used to solve complex technical problems, including dressing and coloration of fiber-fabric materials, growth of 0.1–5.0 μm polymeric films with a low constant of friction and high resistance to wear, and preparation of thin-film recording systems [1–4].

Growth of a polymeric coating on the support surface involves sorption of low-molecular-weight particles of the dispersion, their migration along the surface, and subsequent polymerization. The structure and physicochemical properties of these films are mainly determined by the features of the initial stages of formation of the polymer-support interface, density and orientation of polymeric particles, kinetics of their growth, intermolecular interactions, etc. Nucleation of the polymeric phase, unlike that of the solid phase, is a nonequilibrium process [5]. The parameters of the surface particle size distribution and the changes in the particle density in the course of deposition indicate that the density of polymerization nuclei depends on the presence of surface defects. Chemisorption of molecular fragments on the support surface is also possible and the interface shows strong structural nonuniformity.

In this context procedures that affect the state of the surface can be effectively used to control the structure and properties of the coatings.

The aim of this study was to examine the structural and morphological features of nucleation and the first growth stages of polytetrafluoroethylene (PTFE) coatings on the surface of single-crystalline silicon activated by various methods.

The morphology and adsorption properties of PTFE coating in the first deposition stages were studied as influenced by the pretreatment conditions of the support. The coatings were grown from the active gas phase obtained by electron-beam dispersion of the initial polymer in a vacuum [6]. The thickness of PTFE coating was controlled with the aid of a special device with a controllable shutter. The growth rate was measured with a quartz thickness gage (QTG) by the conventional procedure. Single-crystalline silicon wafers treated with an organic solvent and a beam of N^+ and Ar^+ ions (ion energy 3 keV and flux density 1.2 A m^{-2}) for 5 min was used as the supports.

To eliminate the influence of the nonuniformity of the flux density in the cross section of the ion beam on the treatment efficiency, the radial distribution of ions in the flux was preliminarily estimated with the aid of a Faraday cylinder. The experimental data were processed with account to this correction.

The adsorption activity of the support was determined from the surface energy and its Livshits–van der Waals, acid, and base constituents which, in turn, were calculated from the angle of contavt between the sample surface and twice-distilled water, glycerol, and dimethyl sulfoxide [7].

The morphology of the surface of the treated films was studied by atomic force microscopy (AFM) on

1070-4272/04/7702-0281 © 2004 MAIK "Nauka/Interperiodica"

Surface energy of silicon E, MJ m^{-2}

Surface energy components	Treatment agent		
	solvent	N^+	Ar^+
Livshits–van der Waals	19.9	27.6	27.5
Acid	40.5	66.2	53.8
Base	3.1	1.4	1.6
Total	63.5	95.2	82.9

a NANOTOP-203 setup. The scanning was performed in the tapping mode. To determine the features of formation of three-dimensional supramolecular structures, thick films were etched with nitrogen ions. A fractal analysis on the surface structures was performed by Feder's procedure [8].

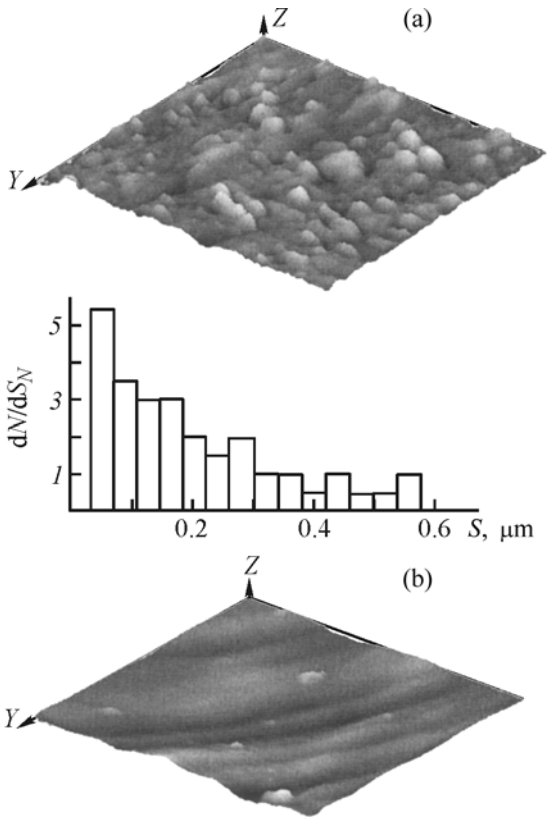

Fig. 1. AFM image of the surface of a PTFE coating on (a) active and (b) inactive regions of the silicon surface treated with the solvent and the distribution of microparticles with respect to the base surface area S, corresponding to section (a). Apparent thickness of the coating 3.8 nm. The image was scanned in a 12.6×12.6 μm area; the same for Figs. 2–4.

The total surface energy of single-crystalline silicon wafers and its components dramatically change after the treatment with nitrogen and argon ions (see table).

The maximum increase in the surface energy (by a factor of 1.5) and especially in its acid component was observed after the treatment of the silicon surface with nitrogen ions.

The morphology and properties of PTFE coatings depend on the conditions of the support activation. Adsorption and nucleation of polymeric microparticles on the silicon surface treated with the solvent are nonuniform. There are surface regions on which relatively large particles are formed even in the first deposition stages (Fig. 1a).

For example, at an apparent film thickness of 3.8 nm, particles growing on these regions are dome-shaped with a base area of 0.6 μm^2 and a height of up to 20 nm. The calculated fractal dimension of these structures ($D = 2.73 \pm 0.19$) is close to that of nonfractal surfaces ($D = 3$). There are also surface regions in which virtually no microparticles are observed in this deposition stage (Fig. 1a). These results agree with our previous data [5] and indicate that adsorbed molecular fragments can easily move along the surface and the growth of polymerization nuclei is mainly lateral. We also conclude that the aerosol mechanism fails to describe the formation of volatile dispersion products under these conditions [9].

In the course of further deposition of the polymeric coating, the particles grow and, what is the most important, they are nucleate on less active surface regions (Fig. 2).

At the apparent film thickness greater than 10 nm, the monotonic particle distribution with respect to the base area transforms into a curve with a sharp peak, suggesting a change in the deposition mechanism. The first non-steady-state stage of continuous nucleation of the particles gives way to the stage in which the bases of deposited stable particles predominantly grow. This is confirmed by the calculated fractal dimension. The fractal dimension calculated at the apparent thickness of PTFE layer d = 7.6, 11.5, and 15.3 nm is $D = 2.84 \pm 0.12$, 2.66 ± 0.14, and 2.38 ± 0.29, respectively.

The mechanism of deposition of volatile dispersion products on the silicon surface treated with nitrogen and argon atoms is different (Fig. 3, *I*, *II*).

Formation of morphologically discrete structures typical of a solvent-treated silicon surface was not

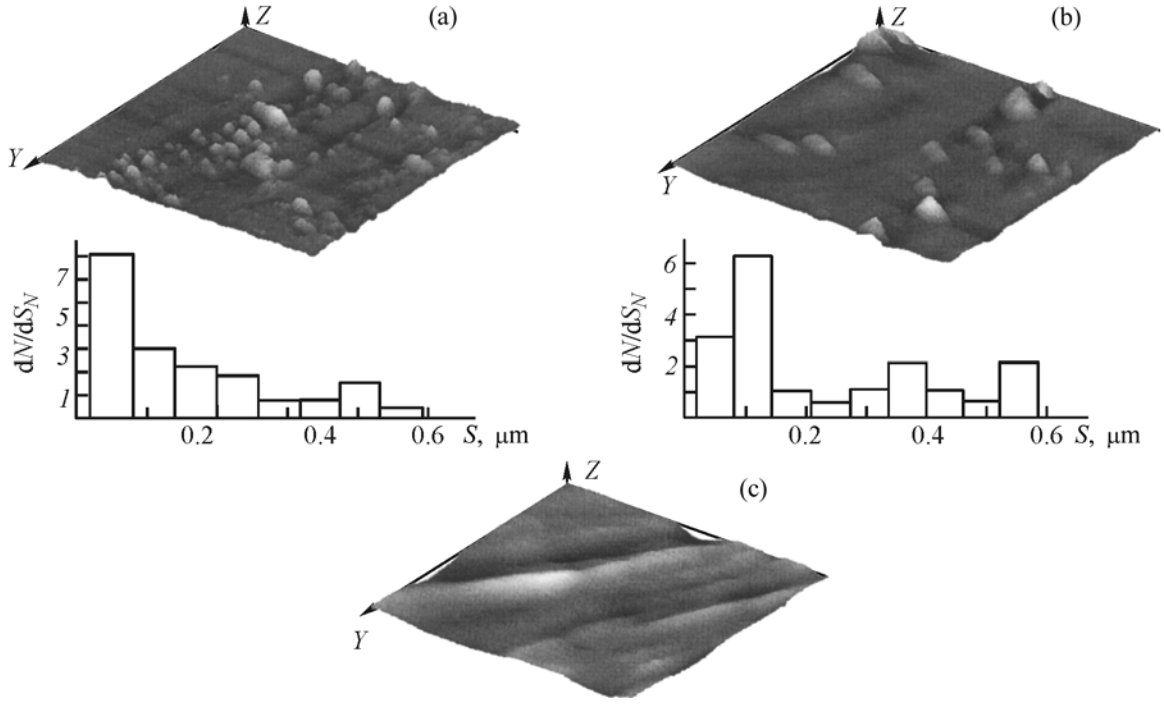

Fig. 2. AFM image of the surface of a PTFE coating with an apparent thickness of (a) 7.6 , (b) 11.5, and (c) 15.3 nm on the silicon surface treated with the solvent and the corresponding distributions of microparticles with respect to the base surface area *S*.

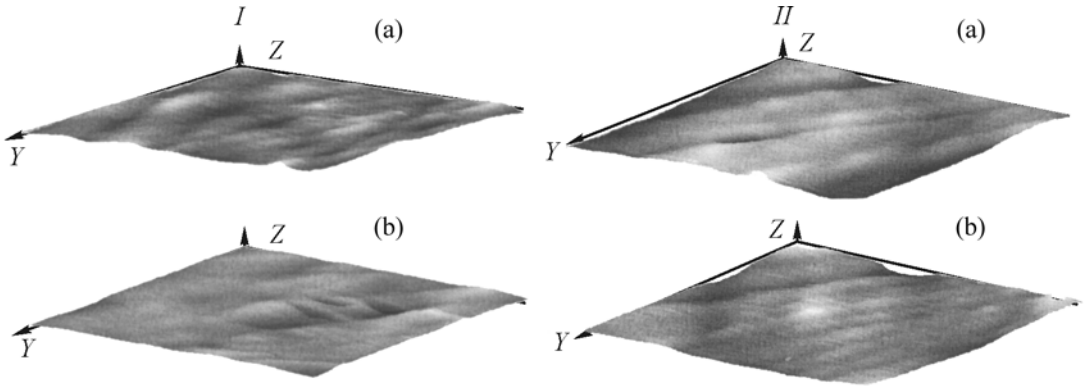

Fig. 3. AFM image of the surface of a PTFE coating with an apparent thickness of (a) 3.8 and (b) 19.1 nm on the silicon surface treated with (*I*) argon and (*II*) nitrogen ions.

detected in the first deposition stages on the ion-treated surface.

In this case, the energy of the silicon surface treated by different procedures (see table) correlates with the microrelief parameters of the deposits. The higher the surface energy, the denser the coatings, i.e., the adsorption growth mechanism prevails.

Thick PTFE coatings contain alternating relief structures formed by intermolecular interaction to give primary supramolecular structures. This is confirmed by the morphology of these coatings etched in a glow discharge plasma (Fig. 4).

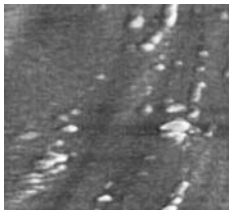

Fig. 4. AFM image (phase contrast mode) of the surface of a silicon-supported PTFE coating etched in a glow discharge plasma.

We found that supramolecular structures more than 20 nm in size and stable to ion etching are formed in the bulk of the polymeric coating. These structures can be regarded as macromolecular plates.

Thus, we have studied the morphological features of the growth of PTFE coatings on the silicon surface activated by different methods and the adsorption properties of these coating. On the solvent-treated silicon surface, the polymeric coating is deposited selectively. This is due to nonuniform adsorption properties of the silicon surface. The deposition on the silicon surface treated with nitrogen and argon ions is characterized by low activation energy and yields continuous polymeric layers even at a low apparent thickness.

ACKNOWLEDGMENTS

This study was financially supported by the Belarussian Republic Foundation for Basic Research (project no. T03M-158).

REFERENCES

1. Tkachuk, B.V. and Kolotyrkin, V.M., *Poluchenie tonkikh polimernykh plenok is gazovoi fazy* (Deposition of Thin Polymeric Films from the Gas Phase), Moscow: Khimiya, 1977.
2. Bruk, M.A. and Pavlov, S.A., *Polimerizatsiya na poverkhnosti tverdykh tel* (Polymerization on Solid Surfaces), Moscow: Khimiya, 1990.
3. Krasovskii, A.M. and Tolstopyatov, E.M., *Poluchenie tonkikh plenok raspyleniem polimerov v vakuume* (Preparation of Thin Films by Dispersion of Polymers in a Vacuum), Minsk: Nauka i Tekhnika, 1989.
4. Zadorozhnyi, V.G., Deposition of Thin Films and Coatings of Fluorinated Polymers in a Vacuum and Study of Their Properties, *Cand. Sci. Dissertation*, Leningrad, 1978.
5. Rogachev, A.V., Egorov, A.I., and Kazachenko, V.P., *Trudy 3-go mezhdunarodnogo simpoziuma "Vakuumnye tekhnologii i oborudovanie"* (Proc. Third Int. Symp. "Vacuum Technologies and Vacuum Equipment") Kharkov: MNTsKhFTI, 1999, pp. 29–32.
6. Rogachev, A.V., Kazachenko, V.P., and Egorov, A.I., *Plasma Phys. and Plasma Technol.*, 1997, vol. 3, pp. 511–514.
7. Lee, Lieng-Huang, *J. Adhesion Sci. Technol.*, 1993, vol. 7, no. 6, pp. 583–634.
8. Feder, J., *Fractals*, New York: Plenum, 1988.
9. Yablokov, M.Yu. and Trofimchuk, E.V., Abstracts of Papers, *2nd Conf. "Natural and Anthropogenic Aerosols,"* St. Petersburg, September 27–October 1, 1999, pp. 35–36.

Russian Journal of Applied Chemistry, Vol. 77, No. 2, 2004, pp. 285–289. Translated from Zhurnal Prikladnoi Khimii, Vol. 77, No. 2, 2004, pp. 289–293.

MACROMOLECULAR CHEMISTRY AND POLYMERIC MATERIALS

Thermal and Thermal-Oxidation Stability of Permethylpolysilane-Siloxanes and Permethylpolyoxysilane

A. I. Chernyavskii, D. Yu. Larkin, M. I. Buzin, E. G. Kononova, and N. A. Chernyavskaya

Nesmeyanov Institute of Heteroorganic Compounds, Russian Academy of Sciences, Moscow, Russia

Received March 4, 2003

Abstract—Thermal and thermal-oxidation stability of organosilicon copolymers with linear or/and cyclic oligosilane fragments in the backbone was studied by thermal gravimetric analysis in an inert gas and in air. The dependence of the thermal characteristics of polysilane-siloxanes on the number of $SiMe_2$ units in the oligosilane fragment of copolymers was established.

The development of modern branches of industry (mechanical engineering, machine building, aircraft industry, etc.) requires production of new construction materials with high strength and high thermal characteristics. Of particular interest are silicon carbide and silicon carbide oxide construction ceramics having unique properties, untypical of the traditional structural materials [1, 2].

In this connection, development of new precursors of ceramic materials is an important scientific and practical problem. At present, polycarbosilanes are of the most practical importance as precursors of silicon carbide ceramics [1]. For production of silicon carbide oxide ceramics, polysilane-siloxanes of various structures may be of certain interest. New permethylpolysilane-siloxanes with linear and cyclolinear structure of the backbone and permethylpolyoxysilane have been synthesized previously [3–8] (see table). In this study, we examined the thermal and thermal oxidation stability of the synthesized copolymers with the aim to assess the prospects for their use as precursors of Si–O–C ceramic materials.

EXPERIMENTAL

Linear polysilane-siloxanes **Ia**–**Ie** were synthesized by heterofunctional polycondensation of α,ω-dichlo-

Yields, viscosities, molecular weights*, and spectral (UV) characteristics of copolymers

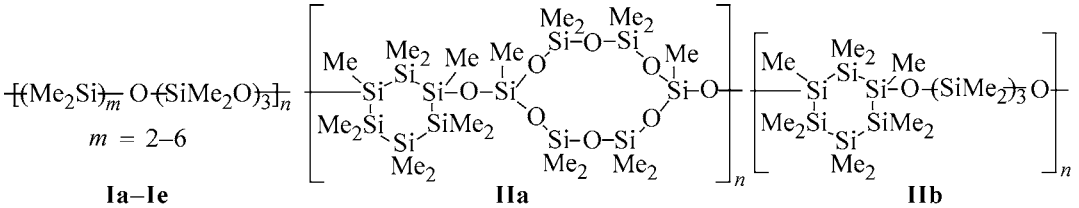

Ia–Ie **IIa** **IIb**

Copolymer	Yield, %	[η], dl g^{-1}	$M_w \times 10^{-3}$	$M_n \times 10^{-3}$	M_w/M_n	λ_{max}, nm	Coke residue (air/argon), %
Ia	35.2	0.05	7.6	4.9	1.55	201	62/28
Ib	34.4	0.10	11.6	7.7	1.51	223	41/–
Ic	57.3	0.11	14.1	8.4	1.68	238	58/24
Id	52.4	0.07	8.6	5.0	1.72	258	38/8
Ie	57.9	0.25	31.1	15.3	2.03	265	49/12
IIa	70.2	0.08	3.4	1.4	2.42	280	67/32
IIb	67.1	0.10	4.7	3.2	1.47	280	66/27

* Data of gel-permeation chromatography.

1070-4272/04/7702-0285 © 2004 MAIK "Nauka/Interperiodica"

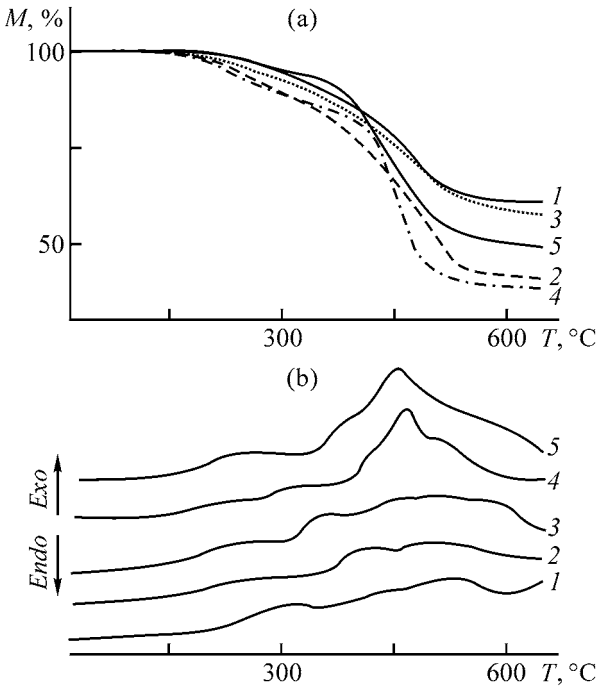

Fig. 1. (a) TGA and (b) DTA curves of (*1*–*5*) copolymers **Ia**–**Ie**, respectively, in air. (*M*) Weight of residue, (*T*) temperature, the same for Figs. 2 and 4.

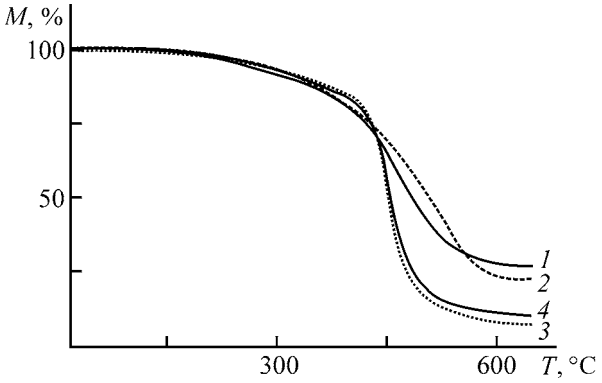

Fig. 2. (*1*–*4*) TGA curves of copolymers **Ia** and **Ic**–**Ie**, respectively, in argon.

ropermethyloligosilanes $Cl(Me_2Si)_mCl$ (m = 2–6) with 1,5-dihydroxyhexamethyltrisiloxane [5, 6, 8]. Cyclolinear polysilane-siloxane **IIa** and permethylpolyoxysilane **IIb** were synthesized by heterofunctional polycondensation of 1,3-dihydroxydecamethylcyclohexasilane with 1,7-dichlorododecamethylcyclohexasiloxane and 1,3-dichlorohexamethyltrisilane, respectively [3, 4, 6, 7]. Some characteristics of the resulting copolymers are listed in the table.

The thermal and thermal-oxidation stability of copolymers **Ia**–**Ie**, **IIa**, and **IIb** was studied by thermal gravimetric analysis (TGA) and differential thermal analysis (DTA) on a Q-1500D MOM derivatograph (Hungary). The 60–80-mg samples were heated in argon or air in the range 20–700°C at a heating rate of 10 deg min^{-1}.

The IR spectra were recorded on a Specord M-82 spectrophotometer in the range 400–3700 cm^{-1}, using thin films on a KBr support or compacted KBr pellets. The UV spectra were recorded on a Specord M-40 spectrophotometer from thin films on a quartz support.

Thermal oxidative degradation of copolymers **Ia**–**Ie** in air (Fig. 1) proceeds in two stages: the first at 200–300°C, and the second at 300–560°C. Comparison of the TGA curves (Fig. 1a) shows that, in the range 200–300°C, the weight loss of copolymers with an even number of $SiMe_2$ units in the oligosilane fragment (copolymers **Ia**, **Ic**, and **Ie** with m 2, 4, and 6; curves *1*, *3*, and *5*) is approximety 9 wt %, which is less than that for copolymers with an odd number of $SiMe_2$ units, copolymers **Ib** and **Id** with m 3 and 5 (curves *2* and *4*). These trends are retained in the second stage of degradation of copolymers in the range 300–560°C, i.e., the copolymers with an even number of $SiMe_2$ units give a larger amount of the coke residue, 50–60% against 40% (see table). At a higher temperature, the amount of coke residue for all the copolymers studied remains virtually the same. It should be noted that, in the series of the copolymers with both even and odd number of $SiMe_2$ units, the thermal stability of the copolymers decreases with increasing m. With respect to the thermal oxidation stability dependent on the number of $SiMe_2$ units in the oligosilane fragment, copolymers **Ia**–**Ie** can be ranked in the following order: $m = 2 > m = 4 > m = 6 > m = 3 > m = 5$.

The DTA curves of copolymers **Ia**–**Ie** are shown in Fig. 1b. The weight loss in copolymers is accompanied by exothermic effects, which suggests that of atmospheric oxygen is involved in chemical transformations that proceed in the copolymers at elevated temperatures. The shapes of exothermic peaks are similar for copolymers with m = 1, 2, and 3 (Fig. 1b, curves *1*–*3*). In the case of copolymers with m = 5 and 6 (Fig. 1b, curves *4* and *5*), the pattern is different: A strong exothermic peak is observed at about of 460°C, which may be due to a decreased thermal oxidation stability of copolymers with the length of dimethylsilane fragment increased to five or six units.

The TGA curves of copolymers **Ia** and **Ic**–**Ie** under argon are shown in Fig. 2. The main weight loss is observed in the range 350–550°C; at higher temperatures, the weight of the samples remains virtually

unchanged. The trends in thermolysis of the copolymers are the same as in the case of thermal oxidative degradation: the thermal stability of copolymers decreases with increasing number of $SiMe_2$ units in the copolymer chain and the thermal stability falls in passing from copolymers with even *m* to copolymers with odd *m*. Similar trends have been observed previously in thermolysis of permethylpolyoxysilanes $–[(SiMe_2)_mO]_n–$ [9].

The chemical transformations that occurr in the oligosilane fragment of linear copolymers **Ia**–**Ie** in thermolysis were studied by IR spectroscopy for the example of copolymer **Ic** (Fig. 3). The main weight loss of copolymer **Ic** in the range 350–550°C (Fig. 2) is accompanied by degradation, cross-linking, and transition to an insoluble form. This is apparently caused by the abstraction of methyl groups from the silicon atoms in the copolymer chain and rearrangement of the skeleton of the copolymer chain, which is suggested by the appearance of Si–H stretching bands in the spectrum of copolymer **Ic** in the region of 2110 cm^{-1} after heating at 450°C for 0.5 h (Fig. 3, spectrum *2*) and $Si–CH_2–Si$ bending bands in the region of 1360 cm^{-1}, and also by broadening of the absorption band in the range 1100–1000 cm^{-1}. The broadening is apparently caused by superposition of Si–O–Si stretching bands (1085 and 1034 cm^{-1}) and $Si–CH_2–Si$ bending bands (1050 cm^{-1}). The appearance of abnormal Si–H bonds and $–Si–CH_2–Si–$ units in the copolymer chain is apparently caused by Yajima rearrangement in the oligosilane fragment of the copolymer at 450°C [10–12]:

$$-\left(Me_2Si\right)_n- \xrightarrow{450°C,\ Ar} -\left(\begin{array}{c}H\\|\\Si\\|\\Me\end{array}-CH_2\right)_n-.$$

After heating at 1000°C for 0.5 h, copolymer **Ic** loses the majority of methyl groups and transforms into a silicon carbide oxide material: In the IR spectrum (Fig. 3, spectrum *3*), there are absorption bands of the residual CH_3 groups in the region of 2960 and 2900 cm^{-1}, a broad band corresponding to the $Si–CH_2–Si$ vibrations, and overlapping Si–O–Si vibrations, and also an absorption band of the Si–C bonds. At the same time, the Si–H absorption band is absent. As judged from the IR spectra, thermolysis of the other linear copolymers proceeds similarly.

Similar processes, the Yajima rearrangement and formation of silicon carbide oxide material, have been observed in thermolysis of linear permethylpolyoxysilanes, in which the oligosilane fragments of the macromolecule are linked by oxygen bridges [9].

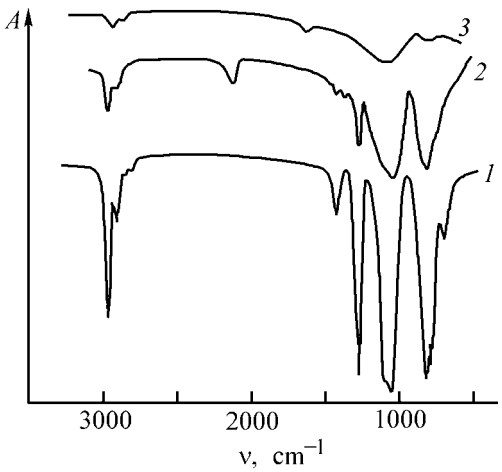

Fig. 3. IR spectra of copolymer **Ic** (*1*) before and after heating at (*2*) 450, and (*3*) 1000°C. (*A*) Transmission and (ν) wavenumber.

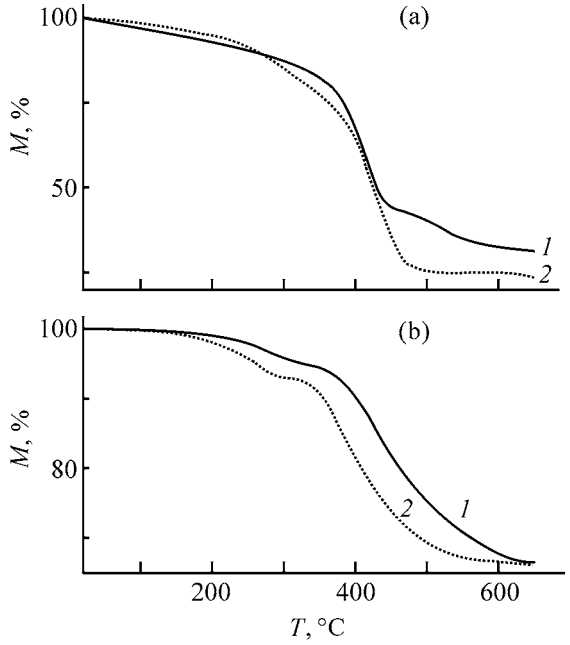

Fig. 4. DTA curves (a) in air and (b) in argon of copolymers (*1*) **IIa** and (*2*) **IIb**.

The spectra, similar to spectra *2* and *3* in Fig. 3, were recorded after heating of these polymers for 2 h at 500°C and 1000°C, respectively. The ^{29}Si MAS NMR spectra of the coke residue of copolymers contained the signals of the SiC, $SiCO_3$, SiC_2O_2, and SiC_3O fragments.

Similarly to linear copolymers **Ia**–**Ie**, thermal oxidative degradation of cyclolinear copolymers **IIa** and **IIb** proceeds in two stages: the first at 200–300°C and the second at 300–530°C, at which the main weight loss of the copolymers is observed (Fig. 4a). Further

heating of the copolymers does not result in a decrease in the amount of the coke residue. Cyclolinear copolymers **IIa** and **IIb**, whose backbone consists of a cyclohexasilane fragment linked by oxygen bridges to cyclohexasiloxane or to linear trisilane fragments, respectively, exceed linear copolymers **Ia**–**Ie** in the thermal oxidation stability, which is apparently due to the presence of the cyclohexasilane unit in the macromolecules of copolymers **IIa** and **IIb**.

The TGA curves of copolymers **IIa** and **IIb** in argon are shown in Fig. 4b. The main weight loss of the copolymers is observed in the range 300–500°C, and at higher temperatures the weight of the samples remains the same. The coke residue of copolymers **IIa** and **IIb** was approximately 30% and exceeded the similar characteristic of linear copolymers **Ia**–**Ie**.

Owing to the presence of oligosilane fragments in the polymer chain, copolymers **Ia**–**Ie**, **IIa**, and **IIb** retain the UV absorption characteristic of oligo- and polysilanes [13, 14]. The wavelength λ_{max} of the absorption peak in the spectra of linear copolymers **Ia**–**Ie** grows with increasing number of $SiMe_2$ groups in the oligosilane fragment of the copolymer (see table).

The UV absorption of copolymers **IIa** and **IIb** is caused by the presence of the cyclohexasilane fragment in the copolymer chain. In the UV spectrum of copolymer **IIb**, there is an absorption peak at 280 nm, characteristic of the cyclohexasilane unit of the copolymer, and the absorption peak corresponding to the linear trisilane fragment is absent. A similar pattern (the presence of the absorption peak of the cyclic fragment and the absence of the absorption peaks of linear fragments) has been observed previously in the UV spectra of cyclolinear compounds on the purely silane structure, α,ω-bis(cyclopentasilanyl)oligodimethylsilanes [15].

It has been shown previously [16] that oligodimethylsilanoxanes, oligomers in which $(Me_2Si)_n$ fragments alternate with $(Me_2SiO)_m$ groups, are effective vulcanizing agents in photolytic curing of silicone rubbers. The synthesized copolymers **Ia**–**Ie**, **IIa**, and **IIb** are transparent viscous liquids readily soluble in polydimethylsiloxanes. The trial experiments showed that, similar to oligosilanoxanes, copolymers **Ia**–**Ie**, **IIa**, and **IIb** can cause vulcanization of polymethylvinylsiloxanes: under UV radiation of a mixture of liquid siloxane rubber with polysilanesiloxane and polyoxysilane copolymers (3–5 wt %), silicone rubber was cured within a few minutes.

CONCLUSIONS

(1) The thermal and thermal oxidation stability of linear permethylpolysilane-siloxanes is governed by the number of dimethylsiloxane units in the oligosilane fragment of the copolymers. In passing from copolymers with an even number of $SiMe_2$ units to copolymers with an odd number of $SiMe_2$ units in the oligosilane fragment of copolymers, and also with increasing number of $SiMe_2$ units, the thermal and thermal oxidation stability of the copolymers decreases.

(2) A study of the thermal and thermal oxidation stability of permethylated linear and cyclolinear polysilane-siloxanes and polyoxysilanes showed that copolymers **IIa** and **IIb** with cyclolinear structure of the backbone have the best thermal characteristics: the amount of coke residue was approximately 65% in air and 30% in argon. These copolymers are of interest as precursors of Si–O–C ceramic materials.

(3) The linear and cyclolinear copolymers studied show promise as polymeric photoinitiators of cross-linking of organosilicon rubbers and as cross-linking agents for compounds based on these.

ACKNOWLEDGMENTS

This study was financially supported by the Science and Technology Committee of the Department of Science and Industrial Policy of the Moscow Government (grant nos. GA-38/02 and GA-62/03) and Russian Foundation for Basic Research (project nos. 00-03-33189 and 02-03-06443).

REFERENCES

1. Tsirlin, A.M. and Popova, N.A., *Keramikoobrazuyushchie kremniiorganicheskie polimery – polikarbosilany: Obzornaya informatsiya, Elementoorganicheskie soedineniya i ikh primenenie* (Ceramic-Forming Organosilicon Compounds, Polycarbosilanes: A Review, Heteroorganic Compounds and Their Application), Moscow: NIITEKHIM, 1990.
2. Langley, N.R., LeGrow, G.E., and Lipowitz, J., *Fiber Reinforced Ceramic Composite*, Mazdiyasni, K.S., Ed., Park Ridge, NJ: Noyes, 1990, pp. 63–98.
3. Chernyavskii, A.I., Larkin, D.Yu., and Chernyavskaya, N.A., *Izv. Ross. Akad. Nauk. Ser. Khim.*, 2002, no. 1, pp. 165–169.
4. Chernyavskii, A.I., Larkin, D.Yu., Kolesova, I.A., and Chernyavskaya, N.A., *Sbornik nauchnykh trudov 4-go Mezhdunarodnogo simpoziuma po khimii i primeneniyu fosfor-, sero-, i kremniiorganicheskikh soedinenii "Peterbugskie vstrechi" (ISPM-4)* (Proc. 4th Int.

Symp. on Chemistry and Application of Organophosphorus, Organosulfuric, and Organosilicon Compounds "Petersburg Meetings" (ISPM-IV)), St. Petersburg, May 26–31, 2002, p. 204.

5. Chernyavskii, A.I., Buzin, M.I., Kononova, E.G., and Chernyavskaya, N.A., *Sbornik nauchnykh trudov 4-go Mezhdunarodnogo simpoziuma po khimii i primeneniyu fosfor-, sero-, i kremniiorganicheskikh soedinenii "Peterbugskie vstrechi" (ISPM-4)* (Proc. 4th Int. Symp. on Chemistry and Application of Organophosphorus, Organosulfuric, and Organosilicon Compounds "Petersburg Meetings" (ISPM-IV)), St. Petersburg, May 26–31, 2002, p. 205.
6. Chernyavskii, A.I., Larkin, D.Yu., and Chernyavskaya, N.A., Abstracts of Papers, *Vserossiiskaya konferentsiya s mezhdunarodnym uchastiem "Sovremennye problemy khimii vysokomolekulyarnykh soedinenii: vysokoeffektivnye i ekologicheski bezopasnye protsessy sinteza prirodnykh i sinteticheskikh polimerov i materialov na ikh osnove"* (Russian Conf. "Modern Problems of Chemistry of Macromolecular Compounds: Highly Efficient and Environmentally Safe Procedures of Synthesis of Natural and Synthetic Polymers and Materials Based on These"), Ulan-Ude, August 20–27, 2002, p. 179.
7. Larkin, D.Yu., Chernyavskaya, N.A., and Chernyavskii, A.I., Abstract of Papers, *Vos'maya Mezhdunarodnaya konferentsiya po khimii i fizikokhimii oligomerov "Oligomery-2002"* (8th Int. Conf. on Chemistry and Physical Chemistry of Oligomers "Oligomers-2002"), Chernogolovka, September 9–14, 2002, p. 75.
8. Chernyavskii, A.I., Kononova, E.G., Buzin, M.I., and Chernyavskaya, N.A., *Izv. Ross. Akad. Nauk., Ser. Khim.*, 2003, no. 4, pp. 903–907.
9. Kurjata, J., Scibiorek, M., Fortuniak, W., and Chojnowski, J., *Organometallics*, 1999, vol. 18, no. 7, pp. 1259–1266.
10. Yajima, S., Hayashi, J., and Omori, M., *Chem. Lett.*, 1975, no. 9, pp. 931–934.
11. Yajima, S., Okamura, K., and Hayashi, J., *Chem. Lett.*, 1975, no. 12, pp. 1209–1212.
12. Yajima, S., Liaw, C.-F., Omori, M., and Hayashi, J., *Chem. Lett.*, 1976, no. 5, pp. 435–436.
13. West, R., J. *Organomet. Chem.*, 1986, vol. 300, nos. 1–2, pp. 327–346.
14. Miller, R.D. and Michi, J., *Chem. Rev.*, 1989, vol. 89, no. 6, pp. 1359–1410.
15. Hengge, E. And Jenkner, P.K., *Z. Anorg. Allg. Chem.*, 1988, vol. 560, pp. 27–34.
16. Semenov, V.V., Ladilina, E.Yu., Cherepennikova, N.F., and Chesnokova, T.A., *Zh. Prikl. Khim.*, 2002, vol. 75, no. 1, pp. 128–134.

Russian Journal of Applied Chemistry, Vol. 77, No. 2, 2004, pp. 290–294. Translated from Zhurnal Prikladnoi Khimii, Vol. 77, No. 2, 2004, pp. 294–298.

MACROMOLECULAR CHEMISTRY AND POLYMERIC MATERIALS

Acetic Acid in Sol–Gel Process of Hydrolytic Polycondensation of Tetramethoxysilane

N. N. Khimich, B. I. Venzel', L. A. Koptelova, and I. A. Drozdova

Grebenshchikov Institute of Silicate Chemistry, Russian Academy of Sciences, St. Petersburg, Russia

Received March 7, 2003

Abstract—The possibility of using acetic acid in the organic sol–gel synthesis of a monolithic SiO_2 gel both in the presence of water and in an anhydrous medium was studied.

The science of organic-inorganic nanohybrids is a new area of research that has appeared at the interface between organic chemistry, macromolecular chemistry, and colloid chemistry. The rapid development of this field, especially in the last ten years, has resulted in the synthesis of novel materials, whose distinctive feature is the nanosize of their structural elements.

One of the simplest and, consequently, promising, from the preparative standpoint, methods for obtaining hybrids of this kind is the sol–gel synthesis [1]. Unfortunately, the standard sol–gel technique for obtaining inorganic materials, which involves hydrolysis of silicon alkoxides and polycondensation of the forming compounds, requires that polar solvents, strong inorganic acids (in performing the sol–gel process in an acid medium), and water should be used as the necessary components of the sol–gel system [2]. This considerably restricts the possibility of varying the organic component of the hybrid. The reason is that the overwhelming majority of organic compounds (with both low and high molecular weight) are sparingly soluble in water-containing systems. Therefore, the variety of organic components introduced into the inorganic SiO_2 matrix in the sol–gel synthesis of nanocomposites is commonly limited to a number of strongly polar organic substances, such as polyalcohols [3], polyamines [4], and other organic compounds of varied molecular weight, soluble in water–alcohol systems.

At the same time, the possibility of obtaining polyorganosiloxanes by various methods of heterofunctional condensation of silicon alkoxydes in the absence of water has been studied previously [5–7]. The studies performed demonstrated that heating of a number of monocarboxylic acids (formic, acetic, chloroacetic, propanoic, and butyric) with diethyldiethoxysilane yields polydiethylsiloxanes in up to 98% yield [6]. With account of this fact, the possibility of synthesizing a monolithic inorganic SiO_2 matrix, with tetramethoxysilane (TMOS) solutions in the above organic acids without addition of water used as the sol–gel system, has been studied [8].

There also exist, however, a great number of practically promising compounds, which are soluble solely in strongly polar solvents (alcohol, water, organic amides, etc.). To these belong, e.g., complexes of transition metal ions (Cu^+, Cd^{2+}, Pt^{2+}, Ru^{2+}, Er^{3+}, etc.) with various ligands (2,2'-dipyridine, 1,10-phenanthroline, diacetyl, etc.), which are of great practical importance. Being stable in a neutral medium, some of them (e.g., Cu^+ complexes) are decomposed in the presence of strong mineral acids. But even when these organometallic complexes are stable at any acidity of the medium (e.g., Ru^{2+} complexes), the so-called drying control chemical additives (DCCA) should be introduced into a sol–gel system to obtain a monolithic organic-inorganic hybrid [9, 10].

Despite the fact that the total amount of these reagents can be considerably reduced, their use leads to formation of low-volatile organic impurities in gel pores [11], which impairs the mechanical and, especially, optical properties of the monoliths obtained. That is why a novel catalyst, trifluoroacetic acid, has been suggested for organic sol–gel process [8]. Its use instead of a strong inorganic acid enabled optimization of the processes of TMOS hydrolysis and polycondensation of the forming compounds without DCCA reagents [8]. This optimization is done by means of gradual removal of trifluoroacetic acid from

1070-4272/04/7702-0290 © 2004 MAIK "Nauka/Interperiodica"

Table 1. Physicochemical characteristics of the gels obtained

Sample no.	t, h, at 60°C	SiO_2	C	d, g cm^{-1}	W_{op}	W_t	T, kg mm^{-2}
		wt %			%		
1	60*	77.5	4.46	1.25	28.0	38.2	34.0
2	45*	77	1.53	1.07	45.8	53.48	15.1
3	44*	77.5	1.10	0.97	50.7	57.83	11.6
4	1.15	83.5	1.10	1.39	30.9	39.6	82.4
5	1.25	82	1.0	1.45	30.6	36.7	83.5
6	1.25	81.5	1.65	1.39	31.6	39.5	83.5
7	1.35	81	3.38	1.37	32.0	40.5	80.3
8	1.45	80	4.15	1.29	36.6	43.8	51.3
9	1.50	79.5	1.46	1.16	40.5	49.7	33.2
10	1.60	78.5	1.85	1.01	46.7	55.08	22.6
11	1.95	89	0.35	1.48	15.3	35.6	103

* t as obtained at 70°C.

the sol–gel system in the form of its volatile methyl ester. With acetic acid used as solvent, methylacetate is also present, in addition to methyl trifluoroacetate, in the dispersion medium, i.e., acetic acid itself reacts with methanol under the conditions of a sol–gel process. This reaction suppresses alcoholysis of the Si–O–Si bond, promotes condensation, ensures fast removal of residual amounts of the low-volatile acetic acid, and leads to the minimum content of carbon in the gel matrix. To make the sol–gel system even simpler, a decision was made to abandon use of trifluoroacetic acid as a catalyst and to study the possibility of synthesizing a monolithic SiO_2 gel in a two-component system constituted by TMOS and acetic acid (AcOH) or in a three-component system, TMOS–AcOH–H_2O.

EXPERIMENTAL

To study the gelation of TMOS in the presence of acetic acid, we prepared sample nos. 1–10, which contained (per 1 mol TMOS) 4 mol water (nos. 4–10) and different amounts of AcOH (mol):

Sample no.	1	2	3	4	5	6	7	8	9	10
AcOH	4	6	8	0.2	0.5	0.7	1	2	3	4

The resulting solutions were placed in hermetically sealed polypropylene test tubes and heated at 70°C for 4 days. Then the hermetic stoppers of the test tubes were replaced with stoppers with apertures (d ~1.5 mm), and humid gels were dried in the following temperature mode: heating from 70 to 100°C for 6 h, keeping at 100°C for 20 h, heating from 100 to 120°C for 4 h, and keeping at 120°C for 30 h. Samples of gel no. 11 were obtained by gelation of solution no. 7 in the presence of 0.1 mol CF_3COOH catalyst and were additionally dried at 150°C for 20 h.

For the resulting samples were determined the open and total porosity, W_{op} and W_{tot}, and the apparent and true, d_a and d_t, density (by the Archimedes method with toluene as saturating fluid and water as second working fluid). The gelation point t (h) was found as the time after which the gel lost its fluidity. The hardness T of the samples was measured on a PMT-3 microhardness meter. A thermal analysis was done on a Q-1500D derivatograph (Hungary) at temperatures of up to 1000°C at a heating rate of 20 deg min^{-1}. The content of SiO_2 (wt %) in the gels obtained was determined thermogravimetrically, and the carbon content was found from the change in the electrical conductivity of a $Ba(OH)_2$–CO_2 solution that served as absorber of CO_2 formed in burning of the samples in oxygen. The porous structure of the gels obtained was studied by analyzing the adsorption–desorption of ethanol on a McBain spring vacuum balance. The pore volumes V (cm^3 g^{-1}), specific surface area S (m^2 g^{-1}), and predominant pore radii r (Å) were calculated by the standard procedures [12] from the adsorption data. An electron-microscopic study of the gels was performed on an EM-125 microscope at an accelerating voltage of 75 kV, with cellulose replicas prepared on freshly cleaved surfaces of the gels studied.

All the gels synthesized were monolithic transparent cylinders; sample nos. 4–11, colorless, and sample nos. 1–3, yellow-pale. Table 1 lists the physicochemical characteristics of gel nos. 1–11.

The data presented show that raising the amount of AcOH in the sol–gel system makes lower the hardness

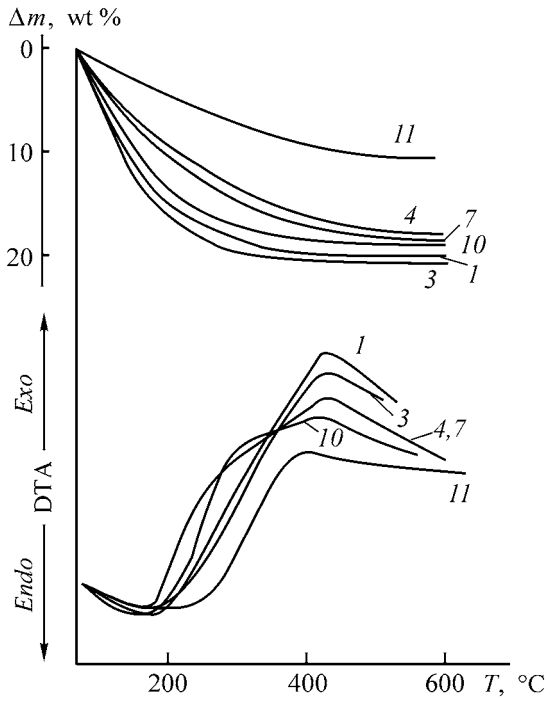

Fig. 1. TG and DTA curves of the gels.(Δm) Mass loss and (T) temperature. The *curve numbers* denote the gel numbers.

and density of the gels synthesized. It should be noted that this is true both for sol–gel processes that occur in the presence of water (gel nos. 4–11) and for those proceeding in an anhydrous medium (gel nos. 1–3), although the mechanisms of both the processes are fundamentally different.

The standard sol–gel system consists of four components: e.g., TMOS, water, alcohol (solvent), and acid (catalyst). As is known, the rate of tetramethoxysilane hydrolysis in an acidic medium is proportional to the concentration of protons. This predetermines the use of strong inorganic acids as catalysts [2]. Raising the amount of AcOH, which is a weak acid ($K = 1.75 \times 10^{-5}$), in the sol–gel system from 0.2 mol (sample no. 4) to 4 mol (sample no. 10) should not substantially affect the rate of TMOS hydrolysis. In this case, as indicated by kinetic studies, AcOH is an inefficient catalyst for TMOS hydrolysis, i.e., the content of the unhydrolyzed product and low-molecular-weight siloxanes is very high even in the vicinity of the gelation point. It appears that trifluoroacetic acid ($K = 0.23$) is a considerably more efficient catalyst for the sol–gel process [8]. Despite this circumstance, gel nos. 4–7 are only slightly inferior to sample no. 11 in hardness and density. The reason for such a high efficiency of acetic acid is that the following reaction occurs

$$CH_3COOH + CH_3OH \rightarrow CH_3COOCH_3 + H_2O.$$

Acetic acid reacts with the residual methanol (as confirmed by a study of the dispersion medium of the sol–gel process), with the volatile methyl acetate $CH_3COOOCH_3$ removed from the system in drying of the xerogel. The occurrence of this reaction suppresses alcoholysis of silanols formed in hydrolysis of TMOS and promotes their condensation.

In this study, AcOH served not only as a catalyst, but as a solvent, too. Water and TMOS, which are mutually insoluble, are soluble in AcOH. Moreover, raising the AcOH concentration, which leads to a slight acceleration of the hydrolysis, makes higher the concentration of methanol, the product of TMOS hydrolysis. Methanol is also a solvent for the sol–gel process. Therefore, the initial hydrolysis of TMOS and the homogenization of the system occur virtually instantaneously at an AcOH amount in the sol–gel system equal to 1 mol and more, whereas at an AcOH amount decreased to 0.2 mol, the heterogeneous system is to be vigorously stirred for a long time.

At the same time, AcOH is a low-volatile compound. Therefore, raising its concentration in the system to above 0.5–1.0 M leads to a drastic deterioration of the physicochemical properties (gel nos. 8–10 in Table 1). In this case, the content of SiO_2 in the gel matrix falls, despite a decrease in the total content of carbon and in the number of unhydrolyzed methoxy groups in it. This is confirmed by thermogravimetric data (Fig. 1) and by analysis of the silica gel for the content of carbon.

Taking into account the results obtained, we suggested a novel method for sol–gel synthesis, which does not require introduction of water into the initial sol–gel system. This method enables synthesis of a monolithic SiO_2 gel in the two-component system TMOS–AcOH in the absence of water. In this case, acetic acid serves not only as the catalyst and the solvent, but also as a reagent of the sol–gel process. Attempts to use other organic acids, such as monochloroacetic, propionic, butyric, and oxalic acid, failed. Use of formic acid was also unsuccessful: owing to the low thermal stability of this compound, the SiO_2 matrix obtained contained a too large amount of thermally decomposed organic impurities and did not possess the necessary strength, although the possibility of using this acid in the sol–gel process has been reported [13]. It should be emphasized that the sol–gel synthesis in the two-component system TMOS–AcOH differs fundamentally from that described in the literature [14, 15], in which water is

generated *in situ* and methanol is introduced into the sol–gel system, along with AcOH. In this case, gradual formation of water through the reaction of methanol with the acid ensures hydrolysis and polycondensation by the standard mechanism.

The mechanism of processes that occur when two-component system TMOS–AcOH is used in sol–gel synthesis is more complex. In any case, the first stage of the process is condensation of tetraalkoxysilane with acetic acid [6, 7]:

$$Si(OMe)_4 + AcOH \rightarrow (MeO)_3SiOAc + MeOH.$$

The forming methanol can either enter into a further reaction with acetoxysilane or esterify acetic acid, with water released in the process also leading to formation of silanols through hydrolysis. In this study, the occurrence of these chemical reactions was confirmed by addition to the initial sol–gel system of methanol in one case and acetic anhydride in another, as it was done in [14, 16]. The addition of methanol makes considerably shorter the gelation time, whereas acetic anhydride (which reacts with methanol in quantitative yield) inhibits the sol–gel process.

A study of the porosity of some of the gels synthesized (Table 2) demonstrated that the nanostructure of the samples obtained is about the same, although raising the AcOH concentration always leads to an increase in the average pore radius.

The drastic drop in the hardness and density of the samples, which occurs in this case, can be understood by comparing their electron micrographs, shown in Fig. 2. The dense and uniform structure of gel no. 11 (and the closely similar structure of gel no. 7), with the average size of visible pores of about 80–120 Å (Fig. 2a), becomes much looser, channel-like (with the size of visible pores of about 180–220 Å) on passing to gel no. 10 (Fig. 2b). A similar conclusion can be made when comparing gel nos. 1 (Fig. 2b) and 3 (Fig. 2c), which were obtained in an anhydrous medium.

CONCLUSIONS

(1) A novel method for sol–gel synthesis without addition of water or polar solvents (alcohol) to the system is suggested. The method employs acetic acid as solvent, catalyst, and reagent simultaneously, which makes a sol–gel system considerably simpler and allows synthesis of organic-inorganic hybrids from components insoluble in polar systems.

Table 2. Porosity characteristics of the gel samples

Sample no.	V, $cm^3\ g^{-1}$	S, $m^2\ g^{-1}$	r,* Å
1	0.316	530	12.0
3	0.595	660	18
7	0.29	490	12.0
10	0.51	620	16–17
11	0.061	–	–

* Isotherm for sample no. 11 has no adsorption hysteresis, and, therefore, the pore size cannot be determined ($r \geq 10$).

(2) It is demonstrated that the traditional sol–gel synthesis in the system TMOS–solvent–catalyst–water can be performed with acetic acid used as a solvent and a catalyst. In this case, the low efficiency of AcOH as a catalyst is compensated for by its reaction with methanol formed in the sol–gel system, which suppresses the alcoholysis of the Si–O–Si bond and promotes condensation processes.

(3) Monolithic gels formed in hydrolytic polycondensation do not crack in drying and have a high hardness and density, which are comparable with the analogous characteristics of gels synthesized in the presence of trifluoroacetic acid.

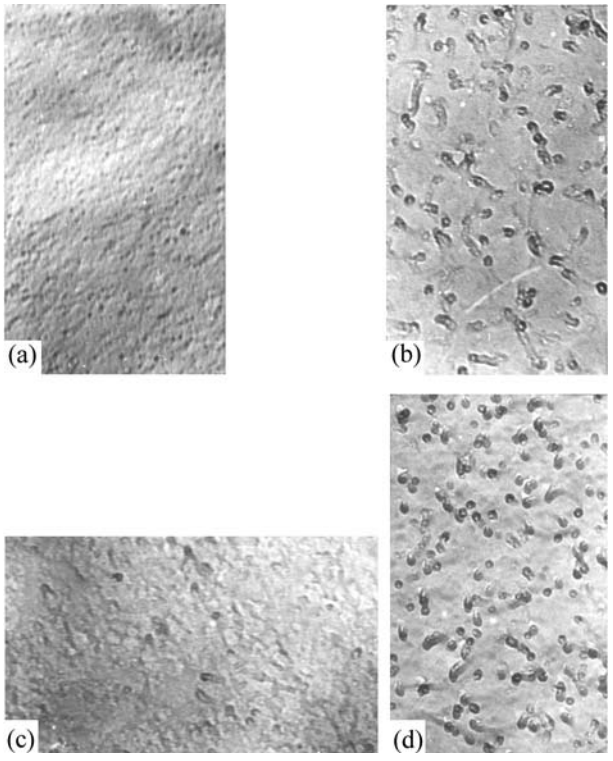

Fig. 2. Electron micrographs of gel nos. (a) 11, (b) 10, (c) 1, and (d) 3. Magnification: (a, b, d) 60 000 and (c) 80 000.

REFERENCES

1. Pomogailo, A.D., *Usp. Khim.*, 2000, vol. 69, pp. 60–88.
2. Brinker, C.I. and Scherer, G.W., *Sol–Gel Science*, New York: Acad., 1990.
3. Tamaki, R. and Chujo, Y., *Appl. Organomet. Chem.*, 1998, vol. 12, pp. 755–762.
4. Gong, A., Chen, Y., Zhang, XI, Liu, H., Chen, C., and Fu, XI, *J. Appl. Polym. Sci.*, 2000, vol. 78, pp. 2186–2190.
5. Andrianov, K.A., Sokolov, N.N., and Khrustaleva, E.N., *Zh. Obshch. Khim.*, 1955, vol. 25, pp. 1102–1107.
6. Leznov, N.S., Sabun, L.A., and Andrianov, K.A., *Zh. Obshch. Khim.*, 1959, vol. 29, pp. 1508–1515.
7. Leznov, N.S., Sabun, L.A., and Andrianov, K.A., *Zh. Obshch. Khim.*, 1959, vol. 29, pp. 1518–1522.
8. Khimich, N.N., Venzel', B.I., Drozdova, I.A., and Koptelova, L.A., *Zh. Prikl. Khim.*, 2002, vol. 75, no. 7, pp. 1125–1130.
9. Orcel, G. and Hench, L., *J. Non-Cryst. Solids*, 1986, vol. 97, pp. 177–194.
10. Adachi, T. and Sakka, S., *J. Non-Cryst. Solids*, 1988, vol. 99, pp. 118–128.
11. Khimich, N.N. and Stolyar, S.V., *Zh. Prikl. Khim.*, 1998, vol. 71, no. 10, pp. 1590–1594.
12. *Eksperimental'nye metody v adsorbtsii i molekulyarnoi khromatografii* (Experimental Methods in Adsorption and Molecular Chromatography), Kiselev, A.V., and Drevint, V.P., Eds., Moscow: Mos. Gos. Univ., 1973.
13. Sharp, G., *J. Sol–Gel Sci. Technol.*, 1994, vol. 2, pp. 35–41.
14. Jada, S., *J. Am. Ceram. Soc.*, 1987, vol. 70, pp. 298–300.
15. Munoz-Aguado, M.J., Gregorkiewitz, M., and Larbot, A., *Mat. Res. Bull.*, 1992, vol. 27, pp. 87–97.
16. Post, W.H., and Hofrichter, H.C., *J. Org. Chem.*, 1940, vol. 5, pp. 443–448.

Russian Journal of Applied Chemistry, Vol. 77, No. 2, 2004, pp. 295–298. Translated from Zhurnal Prikladnoi Khimii, Vol. 77, No. 2, 2004, pp. 299–301.

MACROMOLECULAR CHEMISTRY AND POLYMERIC MATERIALS

Polymerization of 1-Hexene on Catalytic System $TiCl_4$–$Al(C_6H_{13})_3 \cdot Mg(C_6H_{13})_2$

I. V. Vasilenko, S. V. Kostyuk, L. V. Gaponik, and F. N. Kaputskii

Research Institite of Physicochemical Problems, Belarussian State University, Minsk, Belarus

Received October 1, 2003

Abstract—Polymerization of 1-hexene on the catalytic system $TiCl_4$–$Al(C_6H_{13})_3 \cdot Mg(C_6H_{13})_2$ was studied.

Copolymerization of ethylene and propylene with a small amount of higher α-olefins yields polymeric materials with a wide range of consumer characteristics (density, melting point, crystallinity) [1–4]. Data on homopolymerization of higher α-olefins allow better understanding of their behavior in copolymerization. At the same time, homopolymers based on higher α-olefins with high molecular weight (MW) show promise as depressing agents, w3hich improve the rheological characteristic of crude oil. Among the catalysts tested, the most efficient catalysts for production of these materials are supported titanium–magnesium catalytic systems [5, 6]. By contrast, metallocene catalysts, which have rather high activity, favor formation of polymers with low MW [2, 7–10].

It has been shown previously [11] that the use of higher magnesium aluminum alkyls (MAA) as organometallic components of Ziegler catalysts significantly increases the yield, MW, and isotacticity of polystyrene in comparison with the classic systems. The catalytic systems based on MAA are also effective in synthesis of ultra-high-molecular-weight polyethylene and its copolymers with higher α-olefins [12]. In this context it was interest to study the polymerization of 1-hexene on the system $TiCl_4$–$Al(C_6H_{13})_3 \cdot Mg(C_6H_{13})_2$.

Data on the polymerization of 1-hexene on the catalytic system $TiCl_4$–$Al(C_6H_{13})_3 \cdot Mg(C_6H_{13})_2$ at various temperatures are presented in Figs. 1 and 2. Figure 1 shows that the process decelerates on heating, whereas in polymerization of styrene the reaction rate on this system decreases with as the temperature is lowered [11, 13]. The maximum rate of hexene-1 polymerization is reached at 25°C. At this same temperature, the catalytic system exhibits the highest activity,

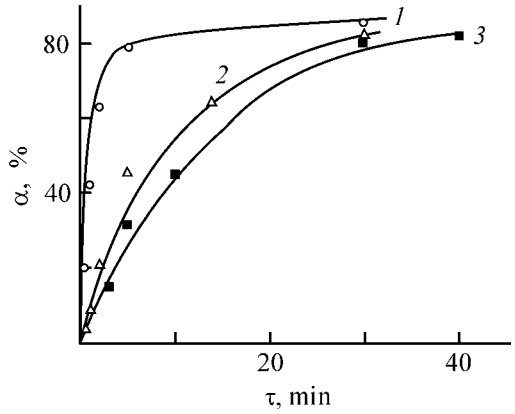

Fig. 1. Kinetic curves of polymerization of 1-hexene on the system $TiCl_4$–$AlMg(C_6H_{13})_5$ at (*1*) 25, (*2*) 15, and (*3*) 45°C. Polymerization conditions: $[TiCl_4]$ = 0.028 M, [1-hexene] = 2.24 M, $[TiCl_4] : [AlMgR_5]$ = 1 : 1, solvent hexane; the same for Figs. 2 and 3. (α) Degree of conversion and (τ) time.

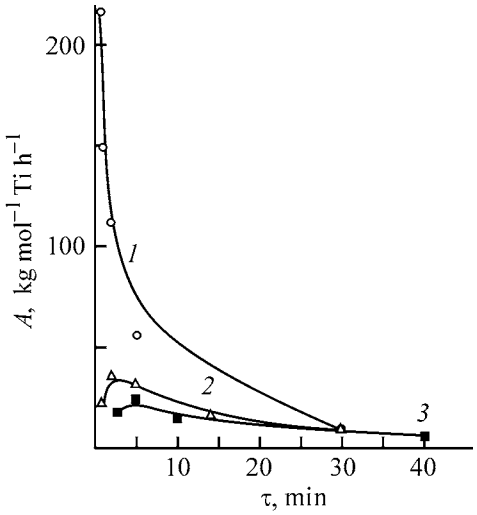

Fig. 2. Activity of the catalyst $TiCl_4$–$AlMg(C_6H_{13})_5$, *A*, vs. the polymerization time τ at (*1*) 25, (*2*) 15, and (*3*) 45°C.

1070-4272/04/7702-0295 © 2004 MAIK "Nauka/Interperiodica"

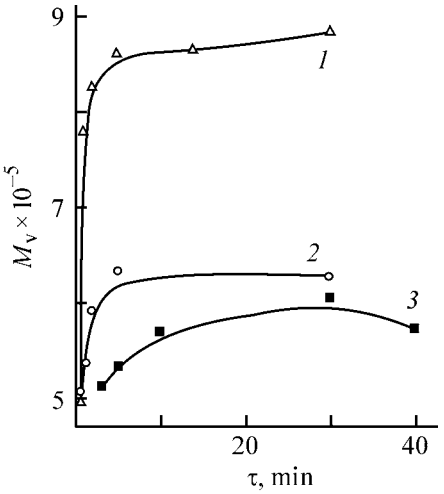

Fig. 3. Molecular weight of poly-1-hexene, M_w, vs. the polymerization time τ at (*1*) 15, (*2*) 25, and (*3*) 45°C.

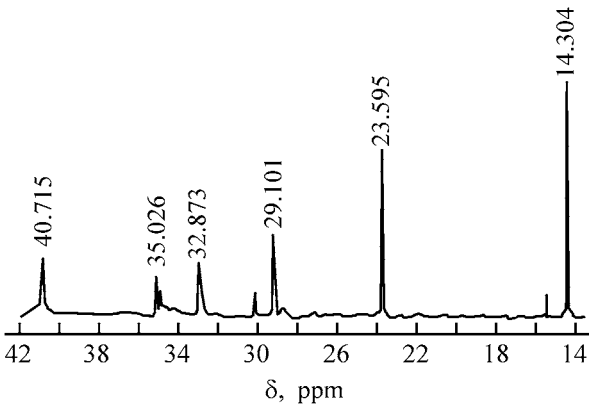

Fig. 4. ^{13}C NMR spectrum of poly-1-hexene prepared on the $TiCl_4$–al$Mg(C_6H_{13})_5$ system at 25°C. (δ) Chemical shift; the same for Fig. 5.

which abruptly decreases with time (Fig. 2). This abrupt decrease in the catalyst activity may be due to hindered diffusion of the monomer to the active centers, since within 10–15 s after the beginning of polymerization the reaction mixture becomes viscous. At other temperatures, the activity reaches a maximum within 2.5–5 min and then slightly decreases and tends to a constant value. The low activity of the catalyst is apparently caused at high temperatures by a high rate of deactivation of the active centers of polymerization, and at low temperatures, by slow activation of the catalyst. A similar temperature dependence of the catalyst activity was observed in polymerization of 1-hexene on post-metallocene catalyst (maximum activity of the catalyst was reached at 28°C) [14]. In polymerization of higher α-olefins on supported titanium-magnesium catalyst in the range 25–60°C, the polymerization rate and the catalyst activity increase steadily with temperature [5, 6].

It should be noted that, in polymerization of 1-hexene, the catalytic system $TiCl_4$–$Al(C_6H_{13})_3 \cdot Mg(C_6H_{13})_2$ is more active (30–100 kg mol^{-1} Ti h^{-1}) than the supported titanium-magnesium catalysts (15–35 kg mol^{-1} Ti h^{-1}) [5]. We showed that the maximum activity of the catalyst is reached at the $AlR_3 : MgR_2$ ratio in MAA equal to 1 : 1, and a decrease or increase in the content of magnesium dialkyl results in a decreased activity of the catalytic system [15]. This is apparently due, on the one hand, to higher alkylating power of MAA, compared to the equivalent amount of AlR_3, which result from involvement of two radicals from MgR_2 in this process, whereas in the case of AlR_3 only one alkyl radical participates in the process [16]. On the other hand, at a high content of magnesium dialkyl in the organometallic component, the low activity can be caused by overreduction of $TiCl_4$ with excess MgR_2 [17]. It should be noted that the molecular-weight distribution (MWD) of the polymer synthesized is rather wide (M_w/M_n = 28–29) and suggests the presence of several types of active centers, which can alter their activity in the course of polymerization [18]. This fact also confirms participation of both AlR_3 and MgR_2 in alkylation of $TiCl_4$.

Figure 3 shows that the molecular weight of poly-1-hexene is significantly higher at lower synthesis temperature. The MW of the polymer increases with polymerization time [19]. This is apparently caused by stabilization of the Ti–C bond owing to formation of triple Ti–Al–Mg complexes, which hinders the deactivation of active centers and hampers the chain termination and transfer. It was found that the weight-average molecular weight of the synthesized polymer M_w, similarly to M_w of poly-1-hexene prepared on supported titanium-magnesium catalyst, is 2×10^5–6×10^5, which is significantly higher than the molecular weight of the polymer synthesized on metallocene catalysts [7–10].

It has been shown previously that polymerization of styrene on the catalytic system $TiCl_4$–$Al(C_6H_{13})_3 \cdot Mg(C_6H_{13})_2$ yields the polymer with a high degree of isotacticity [11]. Here, we studied the structure of the forming polymers by ^{13}C NMR (Fig. 4). The ^{13}C NMR spectrum of poly-1-hexene prepared at 25°C consists of six resonance lines. The chemical shifts of six carbon atoms well correlate with published data [8, 14]. As a rule, the degree of isotacticity of higher α-olefins is evaluated as the ratio of the intensity of

the C-3 line at approximately 35.0 ppm (Fig. 5) to the total intensity of the signals at 34.0–35.0 ppm [8, 14]. The degree of isotacticity of the polymer, evaluated by this method, was 35%.

It should be noted in conclusion that the resulting polymers can be efficiently used as depressants for crude oils with a high solidification point.

EXPERIMENTAL

Polymerization of 1-hexene was carried out in hexane at 15–65°C. The catalyst was prepared by reduction of $TiCl_4$ with an $AlMg(C_6H_{13})_5$ solution for 10 min at 20°C. The components were added in the following order: $TiCl_4$, metallorganic component and solution of monomer in hexane. The reaction was terminated by adding a mixture of ethanol and HCl. The polymer was separated from the reaction mixture, washed with ethanol, and dried in a vacuum at 60–75°C to constant weight. The compounds $Al(C_6H_{13})_3$ and $Al(C_6H_{13})_3 \cdot Mg(C_6H_{13})_2$ were prepared by the procedure described in [20]. All manipulations in synthesis of the catalysts and polymerization were performed under argon. 1-Hexen and hexane were dried and twice distilled from CaH_2. The viscosity-average molecular weight M_v of poly-1-hexene was evaluated by the equation $[\eta] = 2.05 \times 10^{-4} M_v^{0.72}$ (cyclohexane, 25°C) [21]. The weight-average molecular weight and MWD of polymers were determined by gel-permeation chromatography on a Waters device equipped with three Styro-gel columns with the pore size of 1×10^3, 5×10^4, and 5×10^5 Å. THF was used as a solvent. The elution rate was 1.2 ml min^{-1}. The structure of the resulting polymers was studied by ^{13}C NMR on a Bruker AC-400 spectrometer operating at 100.6 MHz. The spectra were recorded in CD_2Cl_2 at 25°C.

CONCLUSIONS

(1) The catalytic system $TiCl_4 - Al(C_6H_{13})_3 \cdot Mg(C_6H_{13})_2$ is more active in polymerization of 1-hexene than supported titanium-magnesium catalysts and favors synthesis of the polymer with a high molecular weight ($M_w = 2 \times 10^5 - 6 \times 10^5$). The activity of the catalytic system and the molecular weight of the resulting polymers strongly depend on the polymerization temperature.

(2) The microstructure of the synthesized polymers was studied by ^{13}C NMR. It was found that this system yields polymers with degree of isotacticity of approximately 35%.

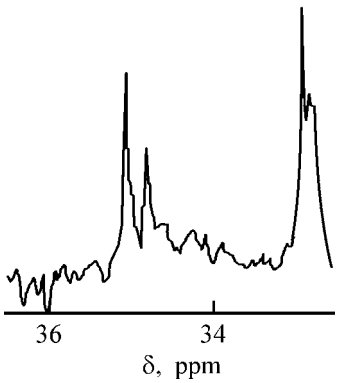

Fig. 5. C-3 region of the ^{13}C NMR spectrum of poly-1-hexene prepared on the $TiCl_4$–$AlMg \cdot (C_6H_{13})_5$ catalyst at 25°C.

ACKNOWLEDGMENTS

The authors are grateful to P.N. Gaponic for the help in discussion of the results.

REFERENCES

1. Bialek, M. and Czaja, R., *Polymer*, 2000, vol. 41, pp. 7899–7904.
2. Ivanchev, S.S., Badaev, V.K., Ivancheva, N.I., *et al.*, *Vysokomol. Soedin., Ser. A*, 2000, vol. 42, no. 2, pp. 200–206.
3. Ivanchev, S.S., Badaev, V.K., Ivancheva, N.I., *et al.*, *Vysokomol. Soedin., Ser. A*, 2000, vol. 42, no. 12, pp. 2097–2103.
4. Nomura, R., Oya, R., and Imanishi, Y., *Polymer*, 2000, vol. 41, pp. 2755–2764.
5. Saxena, P.K., *Eur. Polym. J.*, 1999, vol. 35, pp. 1313–1317.
6. Kothandaraman, H. and Saroja Devi, M., *J. Polym. Sci., Part A: Polym. Chem.*, 1994, vol. 32, pp. 1283–1294.
7. Asanuma, T., Nishimori, Y., Ito, M., *et al.*, *Polym. Bull.*, 1991, vol. 25, pp. 567–570.
8. Frauenrath, H., Keul, H., and Hocker, H., *Macromol. Rapid Commun.*, 1998, vol. 19, pp. 391–395.
9. Janiak, C., Lange, K.C.H., and Markquardt, P., *J. Mol. Catal., Ser. A*, 2002, vol. 180, pp. 43–58.
10. Quijada, R., Guevara, J.L., Yazdani-Pedram, M., *et al.*, *Polym. Bull.*, 2002, vol. 49, pp. 273–280.
11. Gaponik, L.V., Antipova, A.M., Morozova, T.K., and Mardykin, V.P., *J. Appl. Polym. Sci.*, 1989, vol. 38, pp. 1975–1985.
12. GDR Patent no. 243171.
13. Antipova, A.M., Morozova, T.K., Gaponik, L.V., and Mardykin, V.P., *Vysokomol. Soedin., Ser. B*, 1986, vol. 28, no. 3, pp. 182–185.
14. Manivannan, R. and Sundarajan, G., *Macromolecules*, 2002, vol. 35, no. 21, pp. 7883–7890.

15. Kaputskii, F.N., Vasilenko, I.V., Kostyuk, S.V., and Gaponik, L.V., *Vestn. Bel. Gos. Univ., Ser. 2*, 2002, no. 2, pp. 15–17.
16. Chirkov, N.M., Matkovskii, L.E., and D'yachkovskii, F.S., *Polimerizatsiya no kompleksnykh metalloorganicheskikh katalizatorakh* (Polymerization on Complex Organometallic Catalysts), Moscow: Khimiya, 1976.
17. Mori, H., Hasebe, K., and Terano, M., *Polymer*, 1999, vol. 40, pp. 1389–1394.
18. Sigaeva, N.N., Shirokova, E.A., Mullagaliev, I.R., *et al.*, *Vysokomol. Soedin., Ser. A*, 2000, vol. 42, no. 8, pp. 1269–1274.
19. Kostjuk, S.V., Vasilenko, I.V., Gaponik, L.V., and Kaputsky, F.N., *Modern Trends in Organometallic and Catalytic Chemistry*, Moscow, May 18–23, 2003, p. 80.
20. Mardykin, V.P., Gaponik, L.V., and Morozova, T.K., *Vestsi Akad. Navuk Bel. SSR, Ser. Khim. Navuk*, 1987, no. 2, pp. 67–71.
21. Lin, F.S., Stivala, S.S., and Beisenberger, J.A., *J. Appl. Polym. Sci.*, 1973, vol. 17, pp. 1073–1090.

Russian Journal of Applied Chemistry, Vol. 77, No. 2, 2004, pp. 299–302. Translated from Zhurnal Prikladnoi Khimii, Vol. 77, No. 2, 2004, pp. 302–305.

MACROMOLECULAR CHEMISTRY AND POLYMERIC MATERIALS

Formation of Reaction Mixture in the Course of Preparation of *cis*-1,4-Polyisoprene in the Turbulent Mode

V. P. Zakharov, I. V. Sadykov, K. S. Minsker, A. A. Berlin, and Yu. B. Monakov

Bashkir State University, Ufa, Bashkortostan, Russia

Institute of Organic Chemistry, Ufa Scientific Center, Russian Academy of Sciences, Ufa, Bashkortostan, Russia

Semenov Institute of Chemical Physics, Russian Academy of Sciences, Moscow, Russia

Received July 1, 2003

Abstract—The effect of a piperylene modification of Ziegler–Natta catalytic systems was studied by sedimentation analysis in the gravity field. The rate of isoprene polymerization was analyzed as influenced by additional crushing of catalyst particles and formation of uniform reaction mixture in mixing of the initial components in a tubular turbulent prereactor of the diffuser-confuser design.

The production cost of synthetic products is determined by the cost of raw materials and power consumption in separate stages of industrial production. In synthesis of polymers, in particular, the cost of treatment of the final product to remove the catalyst residues reaches 30–40% of the overall production cost. Thus, to improve the profitability of the polymer production by catalytic polymerization, the consumption of expensive catalysts should be decreased, which would simultaneously decrease the production coast due to simpler polymer treatment to remove the catalyst residues. It has been found [1] that, in stereospecific polymerization of isoprene using Ziegler–Natta catalytic systems, the reaction rate grows and, as a result, the catalyst consumption decreases with increasing stirring rate of the reaction mixture. However, intensive turbulent mixing of a high-viscosity reaction mixture directly in the reaction zone is difficult to ensure by mechanical stirring. In this case, the use of small tubular diffuser-confuser reactors with a high output capacity [2], which provide intensive turbulent mixing of the reaction mixture in catalytic (co)polymerization of olefins and dienes, seems promising [3, 4].

In this study we examined the disperse composition and activity of the catalyst as influenced by the turbulent mixing in the stage of formation of the reaction mixture and microheterogeneous $TiCl_4$–$Al(i\text{-}C_4H_9)_3$ Ziegler–Natta catalytic systems in stereospecific polymerization of isoprene.

A schematic of the experimental setup for isoprene polymerization is shown in Fig. 1. The starting reagents were purified by standard procedures commonly used in stereospecific polymerization of dienes in the presence of Ziegler–Natta catalysts. Under similar polymerization conditions [Ti : Al : piperylene molar ratio 1 : 1.25 : 2], piperylene modifying agent (M) was added to a solution of the catalytic system in the course of its keeping prior to the process [keeping time τ_{ck} 30 min at 273 K , polymerization temperature

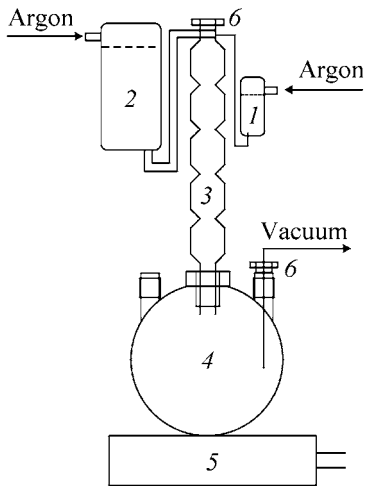

Fig. 1. Schematic of the experimental installation: (*1, 2*) vessels for reagents, (*3*) prereactor, (*4*) 500 cm^3 reactor, (*5*) magnetic stirrer, and (*6*) three-way valve.

1070-4272/04/7702-0299 © 2004 MAIK "Nauka/Interperiodica"

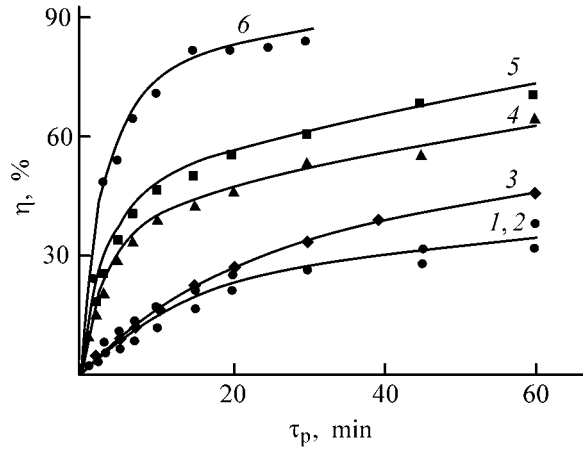

Fig. 2. Isoprene polymerization in the presence of catalytic systems: (*1–3*) $TiCl_4$–Al(*i*-$C_4H_9)_3$ and (*4–6*) $TiCl_4$–Al(*i*-$C_4H_9)_3$–piperylene. c_{Ti} = 6 mM, c_M = 1.5 M, Ti : Al : piperylene = 1 : 1.25 : 2, τ_{ck} = 30 min at 273 K, toluene solvent, 298 K. (η) Product yield and (τ_p) polymerization time. (*1, 4*) Blank tests; polymerization modes: (*2, 5*) 1, (*3*) 2, and (*6*) 3.

298 K, toluene solvent, c_{Ti} = 6 mM, c_M = 1.5 M]. Several process modes were tested.

Mode 1. Pretreated two- or three-component catalytic system [$TiCl_4$–Al(*i*-$C_4H_9)_3$ or $TiCl_4$–Al(*i*-$C_4H_9)_3$–piperylene] and solvent from vessels *1* and *2*, respectively, were mixed in the tubular turbulent unit *3* at a linear flow velocity in the wide section (diffuser) of no less than 0.5 m s^{-1} and a residence time of the reactants in the mixing zone of 2–3 s (hydrodynamic treatment the catalytic system in the turbulent mode). Then, the catalyst solution from unit *3* was fed into the 500-cm^3 vessel *4*, isoprene was added, and polymerization was carried out with slow agitation.

Mode 2. Solutions of $TiCl_4$ and Al(*i*-$C_4H_9)_3$ from vessels *1* and *2*, respectively, were fed through unit *3* into reactor *4*, in which the catalytic system was kept at 273 K for 30 min with subsequent monomer addition (formation of the catalytic system in the turbulent mode).

Mode 3. Solutions of the pretreated three-component catalytic system and monomer from vessels *1* and *2*, respectively, were mixed in unit *3* and then fed into unit *4* (formation of the reaction mixture in the turbulent mode). Polymerization of isoprene was carried out under slow agitation with a magnetic stirrer *5* (100 rpm) under the standard conditions; in this case, the tubular turbulent unit *3* worked as a prereactor (Fig. 1).

For each of the above experimental modes we performed blank tests, simulating the traditional process (the starting reagents without mixing in prereactor *3* are fed directly into reactor *4*). The conversion curves of isoprene polymerization were recorded by a gravimetric procedure. The quality of microheterogeneous catalytic systems after hydrodynamic treatment in the turbulent mode (mode 1) and blank test was determined by sedimentation using a torsion balance [5]. The sediment accumulation curves were graphically differentiated, and these results were used to evaluate the equivalent weight-average radius r_e (radius of the spherical particle settling at the same rate).

Hydrodynamic treatment of the separately prepared Ti–Al catalytic system in the turbulent mode (mode 1) does not noticeably affect the rate of isoprene polymerization as compared to the standard process modes (blank test; Fig. 2, curves *1*, *2*). In this case, the catalyst can be activated owing to formation of the catalytic system in mixing of the initial components directly in the tubular turbulent prereactor with subsequent keeping at 273 K (mode 2, Fig. 2, curve *3*). A somewhat different pattern is observed in modification of the Ti–Al catalytic system with diene (piperylene) additives. In the presence of the modified Ti–Al catalyst, the rate of isoprene polymerization significantly increases even in the blank tests (Fig. 2, curves *1*, *4*). This phenomenon is widely used in industry for activation of the Ziegler–Natta catalytic systems for diene polymerization.

Hydrodynamic treatment of the three-component catalytic system in its mixing with the solvent in the turbulent mode (mode 1) at maximum activity in the blank tests (Fig. 2, curves *1*, *4*) increases the yield of the final product by nearly 10% at a polymerization time of 1 h (Fig. 2, curve *5*). A more pronounced acceleration of isoprene polymerization is provided by a hydrodynamic treatment of the reaction mixture in the course of its formation, i.e., in mixing of the solution of the monomer and catalytic complex in the turbulent mode (mode 3). In this case, the yield of isoprene reaches ~80% at a polymerization time as short as 20 min (Fig. 2, curve *6*). The acceleration of isoprene polymerization, observed in the above tests, is obviously due to the fragmentation of the particles of microheterogeneous catalysts based on $TiCl_4$. To verify this assumption, we performed a dispersion analysis of particles of the catalytic systems prepared.

When the Ti–Al catalytic system is formed without diene modification, relatively coarse catalyst particles are formed (~3–4 μm average radius). As compared with the standard process, hydrodynamic treatment of the two-component Ti–Al catalytic system in the turbulent mode (mode 1) does not noticeable af-

fect the size of the catalyst particles and, hence, its specific surface area (Fig. 3, curves *1*, *2*). As a result, the rates of isoprene polymerization are similar (Fig. 2, curves *1*, *2*).

When the Ti–Al catalytic system is formed in the presence of piperylene (three-component system), the size of the catalyst particles decreases to $r_e \sim 1.5$ μm (Fig. 3, curve *3*). Since the active centers of stereospecific polymerization are located at the defects of the catalyst crystal structure (in our case, β-$TiCl_3$ [6]), the increase in the specific surface area of the catalyst should increase the polymerization rate, which is observed experimentally (Fig. 2, curve *4*). A hydrodynamic treatment of the modified Ti–Al catalytic system in the turbulent mode (mode 1) also decreases the catalyst particle size to $r_e \approx 1$ μm (Fig. 3, curve *4*), providing an increase in the polymerization rate as compared with the traditional process (Fig. 2, curves *4*, *5*). Apparently, when the catalyst is formed in the presence of dienes, macrochains of piperylene fragments start to form on the active particles, which decreases the strength of the solid phase structure and, thus, simplifies its fragmentation in the turbulent flow. The hydrodynamic treatment in the tubular turbulent prereactor (mode 1) is similar to fragmentation of heterogeneous Ziegler–Natta catalysts in the course of polymerization [6]. The increased polymerization rate in the case when the catalytic system is formed in the turbulent mode (mode 2; Fig. 2, curve *3*) and $TiCl_4$ and Al(*i*-$C_4H_9)_3$ solutions are mixed directly in the tubular turbulent prereactor; is also accounted for by a simultaneous increase in the specific surface area of the catalyst. In this case, at high rate of micromixing attained in the turbulent prereactor, the rate ratio of the crystal nucleus formation and crystal growth increases, so that the number of the crystal nuclei grows and r_e decreases.

Our experimental data show that the increase in the specific surface area of the catalyst in stereospecific polymerization of dienes is a necessary but insufficient factor to accelerate the polymerization. Significant activity of the catalyst system is achieved by premixing of the catalyst and monomer solutions in the turbulent mode (mode 3; Fig. 2, curve *6*). In this case, the catalyst particles are disintegrated (Fig. 3, curve *4*) and uniformly distributed in the reaction mixture. Moreover, the effect can be enhanced by elimination of the diffusion limits to linking of the first monomer molecule with the active center (initiation proceeding at a high rate [3]).

Thus, the process rate strongly depends on the mode of isoprene polymerization in the presence of the Ziegler–Natta catalytic systems. High reaction rate

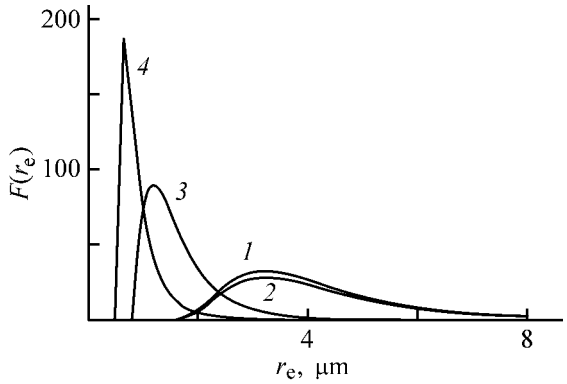

Fig. 3. Differential size distribution of particles in the catalytic systems (*1*, *2*) $TiCl_4$–Al(*i*-$C_4H_9)_3$ and (*3*, *4*) $TiCl_4$–Al(*i*-$C_4H_9)_3$–piperylene. (r_e) Particle size. c_{Ti} = 12 mM, Ti : Al : piperylene = 1 : 1.25 : 2, τ_{ck} = 30 min at 273 K, 298 K. (*1*, *3*) Blank tests and (*2*, *4*) polymerization mode 3.

is attained using a simple tubular turbulent prereactor, which provides a residence time of the reaction mixture of 2–3 s in the mixing zone. Modification of the Ti–Al catalytic systems with dienes increases the specific surface area in the case of catalyst and, in turn, the polymerization rate. This effect can be enhanced by additional fragmentation of the catalyst particles under hydrodynamic treatment in the turbulent mode. The polymerization rate in the case of premixing of the monomer and catalyst solutions in the turbulent mode is the highest, which is due to the increase in the specific surface area of the catalyst and its more uniform distribution in the reaction mixture. The modes of isoprene polymerization in the presence of microheterogeneous Ti–Al catalytic system given above allow the catalyst consumption and, thus, the production cost of the final product to be decreased.

CONCLUSIONS

(1) Turbulent premixing of the components of the reaction mixture and Ziegler–Natta catalytic system in isoprene polymerization using a tubular turbulent diffuser-confuser prereactor allows the process rate to be varied widely and the catalyst consumption to be decreased.

(2) The dispersion composition and the activity of microheterogeneous Ziegler–Natta catalysts can be improved by their modification with dienes, and the strongest effect is observed in the case of hydrodynamic pretreatment of the reaction mixture in the turbulent mode.

ACKNOWLEDGMENTS

This study was financially supported by the Russian Foundation for Basic Research (project no. 02-

01-97913) and "Leading Scientific Schools" program (project no. NSh-728.2003.03).

REFERENCES

1. Buder, S.A., Perlin, B.A., Solodskii, V.V., and Egova, L.S., *Prom–st. Sint. Kauch.*, 1983, no. 7, pp. 9–11.
2. Minsker, K.S., Zakharov, V.P., and Berlin, Al.Al., *Teor. Osn. Khim. Technol.*, 2001, vol. 35, no. 2, pp. 172–177.
3. Minsker, K.S., Zakharov, V.P., Berlin, Al.Al., and Monakov, Yu.B., *Dokl. Ross. Akad. Nauk*, 2001, vol. 381, no. 3, pp. 373–376.
4. Takhavutdinov, R.G., Mukhametzyanova, A.G., D'yakonov, G.S., *et al.*, *Vysokomol. Soedin., Ser. A*, 2002, vol. 44, no. 7, pp. 1094–1100.
5. *Laboratornye raboty i zadachi po kolloidnoi khimii* (Laboratory Works and Problems on Colloidal Chemistry), Frolov, Yu.G. and Grodskii, A.S., Eds., Moscow: Khimiya, 1986.
6. Grechanovskii, V.A., Andrianova, L.G., Agibalova, L.B., *et al.*, *Vysokomol. Soedin., Ser. A*, 1980, vol. 22, no. 9, pp. 2112–2120.

Russian Journal of Applied Chemistry, Vol. 77, No. 2, 2004, pp. 303–306. Translated from Zhurnal Prikladnoi Khimii, Vol. 77, No. 2, 2004, pp. 306–309.

MACROMOLECULAR CHEMISTRY AND POLYMERIC MATERIALS

Spontaneous Polymerization of *N*-(3-Dimethylaminopropyl)methacrylamide Salts in Concentrated Aqueous Solutions

O. A. Kazantsev, K. V. Shirshin, A. P. Sivokhin, N. A. Kuznetsova, and A. P. Malyshev

Dzerzhinsk Branch, Nizhni Novgorod State Technical University, Dzerzhinsk, Nizhni Novgorod oblast, Russia

Received March 12, 2003

Abstract—Spontaneous polymerization of *N*-(3-dimethylaminopropyl)methacrylamide in concentrated aqueous solutions in the presence of inorganic and organic acids was studied. A common mechanism of initiation of spontaneous polymerization of amine-containing (meth)acrylamides and (meth)acrylic acid esters in water was suggested.

Much attention has been given recently to spontaneous polymerization of (meth)acrylic monomers in concentrated aqueous solutions. The process was studied for acrylamide [1], 2-acrylamido-2-methylpropanesulfonic acid [2], and *N*,*N*-dialkylaminoethyl methacrylate salts [3–5]. The reaction was shown to occur by the radical mechanism, with the monomer molecules being the sources of radical [1]; the initiation mechanism was suggested in [5].

In this study, we examined spontaneous polymerization of *N*-(3-dimethylaminopropyl)methacrylamide (**I**) salts in concentrated aqueous solutions.

Our preliminary experiments showed that spontaneous polymerization of amide **I** in water at 50–70°C occurs at a noticeable rate in weakly alkaline, neutral, and acidic solutions (pH ≤ 8) at the monomer concentration exceeding 20 wt %. The process is suppressed by adding inhibitors of radical polymerization (hydroquinone, phenothiazine).

Figure 1 shows the kinetic curves of consumption of C=C bonds in the course of spontaneous polymerization of **I** at various degrees of its neutralization with sulfuric acid. It is seen that, without acid additions or with insufficient amounts of the acid (curves *1*, *2*), no reaction occurs. The polymerization becomes noticeable only after 80% of the amino groups of the monomer are neutralized (pH 8). However, even under these conditions, the reaction is slower than that in an acidic solution (curves *5*–*7*). The influence of the ratio of the acid and amino components of the system on the initial rate is illustrated by Fig. 2. The curve

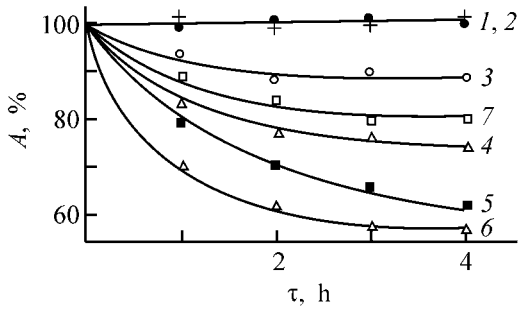

Fig. 1. Variation of the content of C=C bonds *A* (relative to the initial content) with time τ in the system amide **I**–H_2SO_4, as influenced by the amount of sulfuric acid. $[\mathbf{I}]_0$ = 50 wt %, 70°C; the same for Fig. 2. $[\mathbf{I}]_0 : [H^+]_0$ ratio: (*1*) 1 : 0, (*2*) 1 : 0.5, (*3*) 1 : 0.8, (*4*) 1 : 1, (*5*) 1 : 1.1, (*6*) 1 : 1.5, and (*7*) 1 : 2.

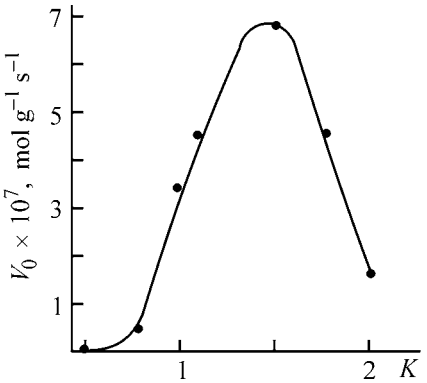

Fig. 2. Initial rate of amide **I** polymerization V_0 in the presence of sulfuric acid vs. the ratio of the acid and amine, $K = [H^+] : [\mathbf{I}]$.

1070-4272/04/7702-0303 © 2004 MAIK "Nauka/Interperiodica"

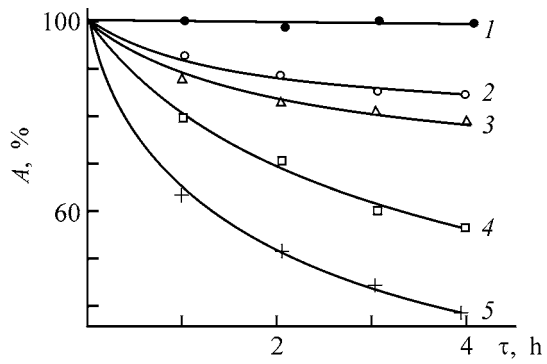

Fig. 3. Variation of the content of C=C bonds *A* (relative to the initial content) in amide **II** with time τ, as influenced by temperature. $[\mathbf{II}]_0$ = 66 wt %. *T*, °C: (*1*) 25, (*2*) 50, (*3*) 60, (*4*) 70, and (*5*) 90.

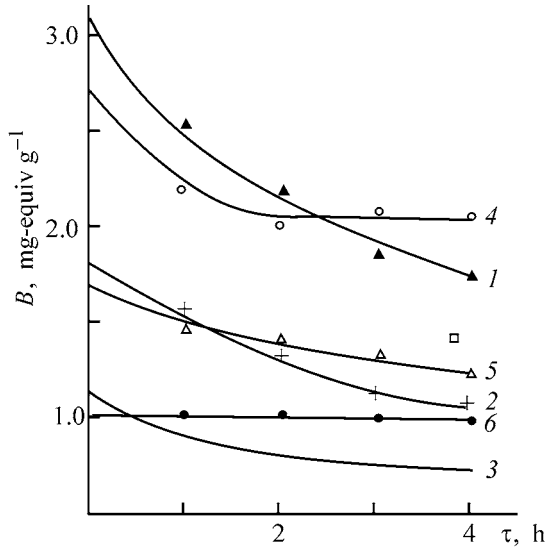

Fig. 4. Variation with time τ of the content of C=C bonds *B* in amides (*1–3*) **II** and (*4–6*) **III** in the course of spontaneous polymerization in the presence of H_2SO_4, as influenced by the amide concentration. $[H^+]$ = 0.4 mg-equiv g^{-1}, 70°C; (τ) time. $[Amide]_0$, wt %: (*1*) 70, (*2*) 41, (*3*) 25, (*4*) 80, (*5*) 50, and (*6*) 30.

passes through a maximum at approximately 50% excess of the acid groups relative to amino groups. It should be noted that a similar maximum in the pH dependence of the initial reaction rate was observed in spontaneous polymerization of 2-acrylamido-2-methylpropanesulfonic acid [2].

Figures 3 and 4 illustrate the influence of temperature and initial monomer concentration on the course of polymerization in solutions of *N*,*N*-dimethylammoniopropylmethacrylamide sulfate **II** and *N*,*N*,*N*-trimethylammoniopropylmethacrylamide methyl sulfate **III**. As the temperature and monomer concentration are increased, the reaction dramatically accelerates. From the temperature dependences, we determined the overall activation energy of spontaneous polymerization of **II**: 51 kJ mol^{-1}. This value is close to that obtained in [4] for spontaneous polymerization in water of a related ester, *N*,*N*,*N*-trimethylammonioethyl methacrylate methyl sulfate (63.5 kJ mol^{-1}). Figure 4 shows that tertiary salt **II** polymerizes more actively than quaternary salt **III**. In particular, a decrease in the concentration of **II** from 70 to 25 wt % causes only deceleration of the process, whereas in the case of **III**, spontaneous polymerization does not occur at all at a monomer concentration of 30 wt % (Fig. 4).

The influence exerted by the solution acidity and by the initial concentration and structure of the monomer on the spontaneous polymerization should be analyzed, in our opinion, taking into account the association of the compounds in water. The association has been detected previously in aqueous solutions of acrylamide [6] and *N*,*N*-dimethylaminoethyl methacrylate [7] on the basis of viscosity and surface tension data. Furthermore, we showed in [5] that the spontaneous polymerization of amino methacrylate salts is largely governed by association of the monomers. To evaluate the tendency of amino amide **I** and its salts to associate in water, we measured the concentration dependences of the viscosity (Fig. 5).

We found that, at a monomer concentration of 10–15 wt %, the linearity of the dependences is disturbed, and the viscosity sharply grows, suggesting an association of the monomeric molecules. It should be noted that both the amino amide salts and free monomer **I** tend to associate. Since spontaneous polymerization occurs only in concentrated solutions, it can be concluded that the necessary condition for the polymerization is the formation of monomeric associates of a definite structure. In dilute solutions, conditions for the association are unfavorable. Therefore, apparently, the polymerization does not occur if the monomer concentration is below a certain limit. However, the association of the amides does not necessarily lead to their polymerization. For example, amide **I** and *N*,*N*,*N*-dimethylbenzylammoniopropylmethacrylamide **IV** do not undergo spontaneous polymerization under the conditions indicated in the caption to Fig. 4, despite their strong tendency to associate in water. Such a difference in the behavior of the monomers may be due, e.g., to "favorable" or "unfavorable" molecular packing in the associate (following the terminology of [8]). Hence, the association of monomers is a necessary but insufficient condition for spontaneous polymerization.

The acid anion exerts a significant effect on the polymerization of **I** (Fig. 6). The reaction occurs in the presence of not only strong mineral acids, but also weaker organic acids. Furthermore, acetic and formic acids appeared to be more active than strong hydrochloric acid, and with hydrofluoric acid the reaction did not occur at all. Hence, the acid strength is not the major factor affecting the polymerization.

The experimental results, combined with published data, show that, in the absence of anions, there is no self-initiation of radical polymerization of acrylic monomers in aqueous solutions. For example, upon dissolution of free amide **I** in water, no spontaneous polymerization occurs, despite the association in concentrated solutions. Additions of inorganic salts do not induce polymerization of the amides either. For example, no changes in the concentration of **I** were observed in 4.1 M solution of **I** containing 0.5 M Na_2SO_4 upon keeping for 5 h at 70°C.

To sum up, we can state that the influence of the initial monomer concentration, solution acidity, and nature of the acid added, observed in our systems, is largely similar to the trends observed previously in spontaneous polymerization of amino methacrylate salts [5], for which a hypothesis was put forward that the polymerization is initiated in monomeric associates by a redox reaction of the anions present in the system with the C=C bonds. A similar mechanism of radical generation was suggested in [9] for polymerization of acrylamide in surfactant micelles in the presence of Na_2SO_3. Thus, presumably, the spontaneous polymerization of (meth)acrylic monomers occurs by a similar mechanism in all the cases.

EXPERIMENTAL

Amino amide **I** was twice distilled in a vacuum before use. Quaternary ammonium salts were prepared from amide **I** and the corresponding alkylating agents in toluene or acetone. Tertiary salts were prepared by mixing of equivalent amounts of the amine-containing monomer and protonic acid with cooling.

Spontaneous polymerization of the monomeric salts was studied at 50–90°C and initial reactant concentrations of 25–80 wt %.

The course of the polymerization was monitored by measuring the concentration of C=C bonds and by isolating the reaction products. The products were isolated by precipitation into acetone, followed by separation of the unchanged starting compounds by repeated washing. After washing, the polymers were dried in a vacuum (20°C, 2 mm Hg) to constant weight.

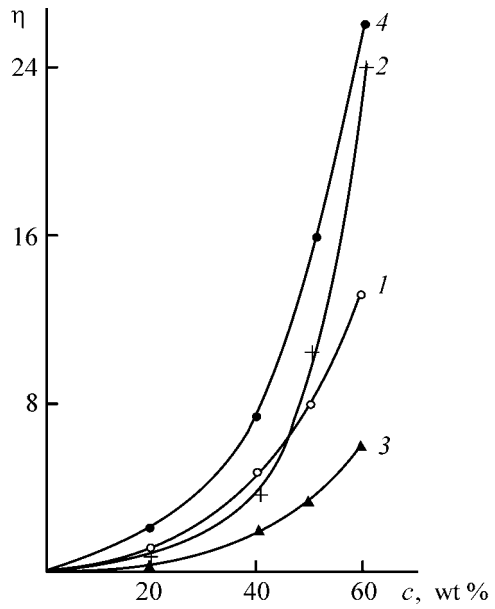

Fig. 5. Specific viscosity η of aqueous solutions of amides (*1*) **I**, (*2*) **II**, (*3*) **III**, and (*4*) **IV** at 25°C vs. the amide concentration.

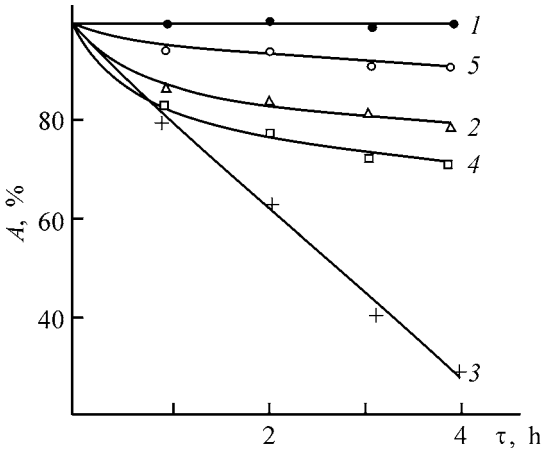

Fig. 6. Spontaneous polymerization of amide **I** in the presence of different acids. $[\mathbf{I}]_0 : [HAn]_0 = 1 : 1$, 70°C. (*A*) Amount of monomeric salt of **I** (relative to the initial amount) and (τ) time. Acid: (*1*) HF, (*2*) HCl, (*3*) HCOOH, (*4*) CH_3COOH, and (*5*) CH_3CH_2COOH.

The concentration of C=C bonds was determined by bromide–bromate titration. The intrinsic viscosity of the monomers was measured in an Ubbelohde viscometer with the capillary diameters of 0.56, 0.73, and 0.99 mm at 25°C. The ^{13}C NMR spectra were recorded on a Varian Gemini-300 Fourier spectrometer (75 MHz, solvent D_2O, reference DMSO).

Poly-*N*,*N*-dimethylammoniopropylmethacrylamide sulfate. To 7.12 g (0.0419 mol) of amide **I** in

1.4 ml of water, we added with stirring and cooling 4.62 g of 50% sulfuric acid. The solution was heated at 70°C for 4 h, and the resulting polymer was precipitated into acetone, washed twice with acetone, and vacuum-dried (20°C, 2 mm Hg). Yield 3.21 g (35%). The product contained no C=C bonds. The ^{13}C NMR spectrum contained the following signals, δ_C, ppm: 179.6–179.2 (–CONH–), 55.7 (–CH_2N–), 54.0–53.8 (–CH_2– in the chain), 45.6–45.3 (–C– in the chain), 43.1 (CH_3–N), 37.5 (–CH_2–NH–), 24.6 (–C–CH_2–C–), 18.5–17.2 (CH_3–C–).

CONCLUSIONS

(1) Spontaneous polymerization of tertiary and quaternary salts of *N*-(3-dimethylaminopropyl)methacrylamide occurs in concentrated aqueous solutions at pH $\leq$ 8.

(2) The initial reaction rate is the highest at a 50% excess of the acid relative to the amide and depends on the anions present in the system.

(3) The presence of anions and association of *N*-(3-dimethylaminopropyl)methacrylamide salts are necessary conditions for spontaneous polymerization.

REFERENCES

1. Kurlyankina, V.I., Ushakova, I.L., Molotkov, V.A., *et al.*, *Zh. Obshch. Khim.*, 1999, vol. 69, no. 1, pp. 97–100.
2. Kazantsev, O.A., Igolkin, A.V., Shirshin, K.V., *et al.*, *Zh. Prikl. Khim.*, 2002, vol. 75, no. 3, pp. 476–480.
3. Efimova, D.Yu., Shibalovich, V.G., and Nikolaev, A.F., *Zh. Prikl. Khim.*, 2000, vol. 73, no. 5, pp. 815–819.
4. Kurlyankina, V.I., Molotkov, V.A., Dobrodumov, A.V., *et al.*, *Dokl. Ross. Akad. Nauk*, 1995, vol. 341, no. 3, pp. 358–363.
5. Kazantsev, O.A., Kuznetsova, N.A., Shirshin, K.V., *et al.*, *Vysokomol. Soedin., Ser. A*, 2003, vol. 45, no. 4, pp. 572–580.
6. Arutyunyan, R.S., Grigoryan, Dzh.D., Simonyan, G.S., *et al.*, *Zh. Fiz. Khim.*, 2002, vol. 76, no. 5, pp. 846–849.
7. Shibalovich, V.G., Efimova, D.Yu., and Nikolaev, A.F., *Plast. Massy*, 2000, no. 3, pp. 25–27.
8. Korolev, G.V., *Usp. Khim.*, 2003, vol. 72, no. 3, pp. 222–244.
9. Zeng, X., Wang, Q., Cheng, S., and Zhang, Y., *J. Dispersion Sci. Technol.*, 1999, vol. 20, no. 4, pp. 1263–1271.

Russian Journal of Applied Chemistry, Vol. 77, No. 2, 2004, pp. 307–312. Translated from Zhurnal Prikladnoi Khimii, Vol. 77, No. 2, 2004, pp. 310–315.

MACROMOLECULAR CHEMISTRY AND POLYMERIC MATERIALS

Copolymerization of Sodium 2-Acrylamido-2-methylpropanesulfonate with *N*-Vinylpyrrolidone in Water and Dimethyl Sulfoxide

V. F. Kurenkov and T. A. Zhelonkina

Kazan State Technological University, Kazan, Tatarstan, Russia

Received July 21, 2003

Abstract—The kinetics of radical copolymerization of sodium 2-acrylamido-2-methylpropanesulfonate with *N*-vinylpyrrolidone in water and dimethyl sulfoxide at pH 9 and 50°C in the presence of potassium peroxodisulfate initiator were studied dilatometrically.

The interest in synthesis of copolymers of 2-acrylamido-2-methylpropanesulfonic acid (H-AMS) salts with *N*-vinylpyrrolidone (VP) is due to unusual and insufficiently studied features of radical copolymerization of ionic monomers [1, 2] and VP [3–5] in various media, and also to prospects for diverse applications of these copolymers in industry and medicine as flocculants [6], adhesives, antistatic agents [7], thickeners, and complexing agents [4, 8]. Previously we have studied some features of copolymerization of H-AMS sodium salt (Na-AMS) with VP in aqueous solutions [9–11] and evaluated the effect of the solution ionic strength and kind of single- [12, 13] and double-charged [13, 14] cations on the copolymerization. In this study, we revealed new features of radical copolymerization of Na-AMS with VP in water and dimethyl sulfoxide (DMSO).

EXPERIMENTAL

Na-AMS was prepared by neutralization of H-AMS [Lubrizol 2404 (Lubrizol, the United Kingdom), mp 185°C, main substance content 99%) solutions with NaOH to pH 9. VP (Merck, Germany) was used after double distillation in a vacuum from 0.1% KOH, n_D^{20} 1.5117, main substance content (GLC) >99%. Potassium peroxodisulfate (PP) was recrystallized twice from aqueous solutions; the main substance content, as determined by the redox method, was 97.8%. The other chemicals were of chemically pure or analytically pure grades.

The kinetics of copolymerization of Na-AMS (M_1) with VP (M_2) was studied in 10 and 15% solutions in water and DMSO at pH 9 and 50°C. The reaction was initiated by thermal decomposition of PP ([PP] 7.4×10^{-4} M). The pH was maintained with the aim to prevent hydrolysis of VP [15] and to ensure the effectiveness of PP as initiator [16] and a constant initiation rate under the conditions when the solution ionic strength varies in the course of copolymerization owing to variation of the Na-AMS concentration [17]. The copolymerization was performed under homogeneous conditions, and no spontaneous polymerization was observed. However, in concentrated solutions of the monomers in DMSO, partial microheterogeneity of the process was not excluded.

The kinetic information on the process was obtained dilatometrically. The initial copolymerization rates V_0 were determined at low conversions ($x < 3\%$) from the slope of the linear portions of the kinetic curves. The experimental procedures are similar to those described in [10].

After the synthesis, Na-AMS–VP copolymers were precipitated from reaction solutions with acetone, washed with acetone, and dried in a vacuum at 50°C to constant weight. The yields of the copolymers were determined gravimetrically. The molecular weights of the copolymers were judged from the intrinsic viscosities [η], which were determined in 0.5 M NaCl at 30°C with a VPZh-3 viscometer (capillary diameter 0.43 mm).

The content of ionic units in the VP–Na-AMS copolymer

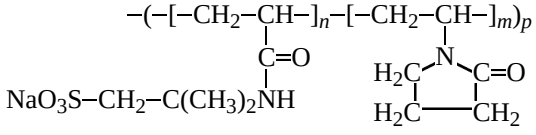

1070-4272/04/7702-0307 © 2004 MAIK "Nauka/Interperiodica"

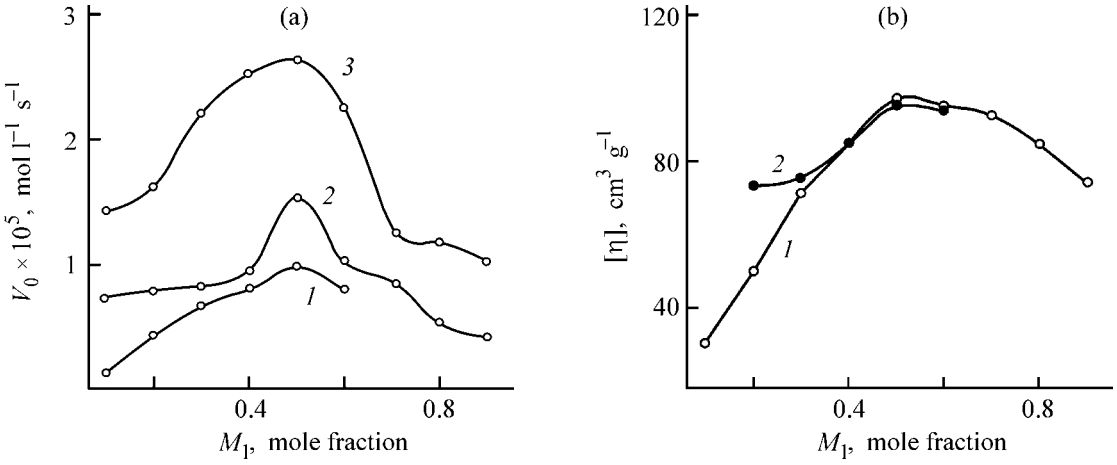

Fig. 1. (a) Initial rate V_0 of copolymerization of Na-AMS with VP and (b) intrinsic viscosity [η] of copolymers vs. Na-AMS mole fraction M_1 in the starting monomeric mixture. Solvent: (*1*) water and (*2*, *3*) DMSO. [M_1 + M_2], %: (*1*, *2*) 10 and (*3*) 15.

was determined by elemental analysis for sulfur, performed as described in [18].

The electrical conductivity of solutions of mixtures of the monomers and copolymer was measured at 25°C with an Anion-410A ionomer–conductometer equipped with a DKV-1 sensor.

The pH was determined at 25°C with a pH-121 pH-millivoltmeter using an ESL-63-07 glass indicator electrode and an EVL 1M3 silver chloride reference electrode.

To examine how the copolymerization of Na-AMS with VP is influenced by the composition of the starting monomeric mixture, we performed the reaction in concentrated solutions of the monomers ([M_1 + M_2] 10 and 15%) in water and in DMSO under equal other conditions. Figure 1 shows the dependences of V_0 and [η] of the resulting copolymers on the Na-AMS mole fraction in the starting monomeric mixture M_1. As seen, V_0 and [η] vary with M_1 similarly. Both the dependences, $V_0 = f(M_1)$ (Fig. 1a) and [η] = $f(M_1)$ (Fig. 1b) in water (curves *1*) and DMSO (curves *2*), pass through maxima at the equimolar ratio of the monomers in the starting mixture ([M_1] : [M_2] = 1 : 1). This is in good agreement with published data [9, 10] and confirms the donor–acceptor character of the reaction of Na-AMS with VP [19]; Na-AMS shows a medium electron-acceptor power, and VP, a medium electron-donor power. Figure 1a shows that the rate of copolymerization in DMSO grows with increasing total concentration of the comonomers (curves *2*, *3*), which is well consistent with the general relationships of radical copolymerization.

Table 1. Yield of Na-AMS–VP copolymer in copolymerization in water and DMSO as influenced by the Na-AMS mole fraction in the starting monomeric mixture M_1 ([M_1 + M_2] = 10%)

M_1	Yield, %	
	in H_2O	in DMSO
0.1	–	21
0.2	23	30
0.3	26	31
0.4	31	38
0.5	47	50
0.6	46	51
0.7	47	47
0.8	52	56
0.9	58	67

Comparison of data in Fig. 1a at [M_1] = const shows that, in a wide range of compositions of the starting monomeric mixture, V_0 increases in going from water to DMSO. At the same time, the intrinsic viscosities of the copolymers obtained in water and DMSO differ insignificantly (Fig. 1b) because of the negligible contribution of the chain transfer to DMSO molecules. Such a loss of the capability of compounds to participate in chain transfer has been noted previously for alternating copolymerization in other systems [20].

The yields of Na-AMS–VP copolymers in copolymerization are listed in Table 1. It is seen that, both in water and DMSO, the copolymer yield grows with increasing content of Na–AMS in the starting mixture;

it also grows somewhat in going from water to DMSO (at the same $[M_1]$).

To obtain an equation of the overall rate of copolymerization of Na-AMS with VP in DMSO, we performed experiments at various concentrations of Na-AMS, VP, and PP under equal other conditions. The influence exerted on the copolymerization by the Na-AMS concentration was examined in the range 0.110–0.661 M. The V_0 values found in this experimental series are plotted in Fig. 2, and the intrinsic viscosities and yields of the copolymers are listed in Table 2. As the Na-AMS concentration is increased, V_0 (the reaction order with respect to Na-AMS is 1.0, Fig. 2, straight line *1*), [η], and the yield of the copolymer grow (Table 2).

The influence of VP on the copolymerization was examined in two concentration ranges, 0.145–3.112 and 0.437–4.298 M, under equal other conditions. We found that V_0 grows with increasing VP concentration (Fig. 2, straight lines *2*, *3*); in both experimental series, the reaction order with respect to VP was 0.5. It should be noted that an unusual (lower than unity) reaction order with respect to the monomer has also been observed previously in radical polymerization of VP at $1 < [VP] < 6$ M [3, 21] and in graft polymerization of VP on chitosan [22].

As the initiator (PP) concentration was increased in the range $(1.57–7.4) \times 10^{-4}$ M, V_0 grew (Fig. 2, straight line *4*); the reaction order with respect to the initiator was 1. The intrinsic viscosity decreased with increasing PP concentration (Table 2), in agreement with the general relationships of radical polymerization.

From the above data, we obtained an empirical equation for the overall rate of copolymerization of Na-AMS with VP in DMSO:

$$V = k_c[M_1]^{1.0}[M_2]^{0.5}[PP]^{1.0}, \quad (1)$$

where k_c is the copolymerization rate.

Below is given for comparison the corresponding equation for the copolymerization in water, obtained in [10]:

$$V = k_c[M_1]^{0.9}[M_2]^{0.7}[PP]^{0.5}. \quad (2)$$

Comparison of Eqs. (1) and (2) shows that the kinetic orders of the reaction with respect to the comonomers change insignificantly in going from water to DMSO, whereas the order with respect to the initiator changes appreciably. Similar changes in the reaction orders with respect to $[M_1]$ and [PP] in going from water to DMSO have been observed previously in copolymerization of acrylamide with Na-AMS [23] and with another strong unsaturated electrolyte, sodium *p*-styrenesulfonate [2]. The reaction order of 0.5 with respect to the initiator in Eq. (2) suggests a bimolecular termination of the kinetic chains, and the first order with respect to the initiator in Eq. (1) suggests a monomolecular chain termination due to partial microheterogeneity of the process in concentrated solutions of the monomers in DMSO.

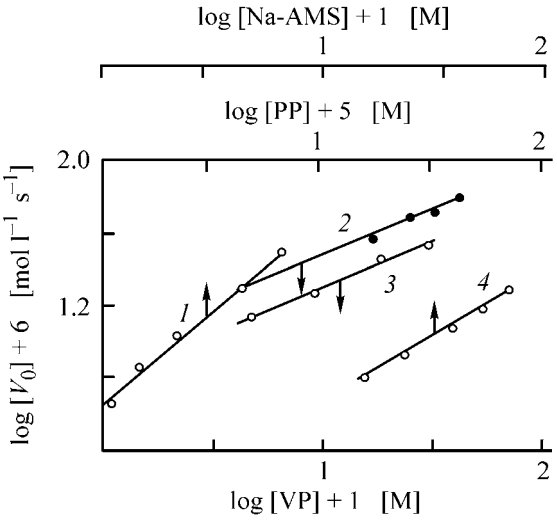

Fig. 2. log–log plot of the rate V_0 of copolymerization of Na-AMS with VP in DMSO vs. concentration of (*1*) Na-AMS, (*2*, *3*) VP, and (*4*) PP. Concentrations, M: VP (*1*, *4*) 0.44; PP (*1*–*3*) 7.4×10^{-4}; Na-AMS (*2*, *4*) 0.44 and (*3*) 0.53.

To explain the kinetic effects revealed in copolymerization of Na-AMS with VP in water and DMSO,

Table 2. Intrinsic viscosity [η] and yield of Na-AMS–VP copolymer at various concentrations of Na-AMS and PP ([VP] = 0.437 M; $[M_1 + M_2]$ = 10%)

[Na-AMS]	[PP] × 10^4	[η], $cm^3\ g^{-1}$	Yield, %
M			
0.11	7.4	66	39
0.15	7.4	70	40
0.22	7.4	86	–
0.44	7.4	119	64
0.66	7.4	124	90
0.44	2.4	134	72
0.44	4.1	126	–
0.44	7.4	119	–

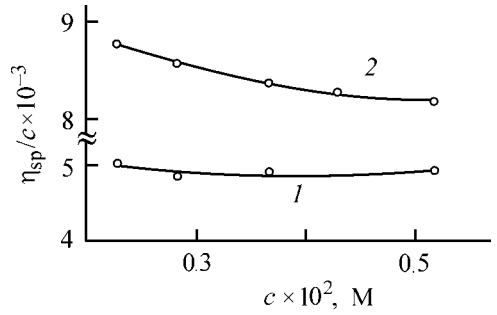

Fig. 3. Reduced viscosity η_{sp}/c of Na-AMS–VP copolymer vs. the copolymer concentration c in (*1*) water and (*2*) DMSO at 30°C. $[\eta] = 260$ cm^3 g^{-1}; content of Na-AMS units 34 mol %.

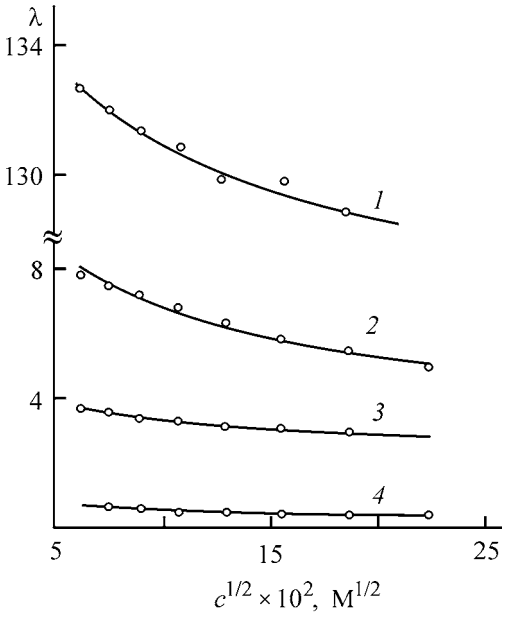

Fig. 4. Equivalent electrical conductivity λ of (*1, 2*) mixture of the monomers ($[M_1] : [M_2] = 20 : 80$) and (*3, 4*) Na-AMS–VP copolymer ($[m_1] : [m_2] = 20 : 80$, $[\eta] = 260$ cm^3 g^{-1}) (*1, 3*) in water and (*2, 4*) in DMSO vs. the square root of the concentration of the monomer mixture or copolymer $c^{1/2}$ at 20°C.

let us consider the ionization equilibrium of ionic groups of Na-AMS and their units in macromolecules:

$$\underset{\textbf{I}}{A^-X^+} \rightleftarrows \underset{\textbf{II}}{A^- \,||\, X^+} \rightleftarrows \underset{\textbf{III}}{A^- + X^+}, \qquad (3)$$

where A^- is the monomer anion or macroanion and X^+ is the cation; **I**, **II**, and **III** are, respectively, the contact ion pairs, solvent-separated ion pairs, and free ions.

As the solvent polarity decreased in going from water to DMSO, the effective degree of ionization of the sulfonate groups of the monomer and macroradicals decreased, with equilibrium (3) shifted to the left. As a result, the ratio of different ionic species in the reaction mixture and the intensity of their electrostatic interactions changed, affecting the relative activities of the monomer (copolymerization constants r_1 and r_2). Along with the multicomponent composition of the system, the nonisoionic synthesis conditions (due to variations in the content of the ionic monomer in the starting mixture and with conversion) could also cause changes in r_1 and r_2. Thus, copolymerization involving an ionic monomer cannot be described by fixed values of r_1 and r_2 [2].

The change in the effective degree of ionization of sulfonate groups in Na-AMS and macromolecules of Na-AMS–VP copolymer on replacement of water with DMSO is confirmed by viscometric (Fig. 3) and conductometric (Fig. 4) data. The concentration dependences of η_{sp}/c (Fig. 3) and electrical conductivity λ (Fig. 4) are typical of polyelectrolytes and indicative of an appreciable electrostatic interaction of the sulfonate groups in Na-AMS and its copolymer with VP in water and DMSO. In going from water to DMSO, η_{sp}/c (at c = const) and the effective size of macromolecular globules of Na-AMS–VP copolymer decrease (Fig. 3). The electrical conductivities λ of the Na-AMS–VP copolymer (Fig. 4, curves *1*, *2*) and a mixture of the monomers of a similar composition (Fig. 4, curves *3*, *4*) decrease also. Figure 4 shows that, in the same solvent and at c = const, λ decreases in going from the monomeric mixture to the copolymer. This is due to the lower effective degree of ionization of the sulfonate groups in the copolymer, compared to Na-AMS monomer, owing to the specific binding of Na^+ ions with the copolymer macromolecules [24].

In view of these facts, it can be noted that the electrostatic repulsion between the similarly charged Na-AMS monomer and macroradical with the terminal Na-AMS unit in the chain propagation events should decrease in going from water to DMSO. Therefore, an increase in the rate constant of chain propagation k_{11} was the decisive factor responsible for the growth of V_0 of Na-AMS–VP copolymerization in going from water to DMSO. Another possible factor could be the complexation between VP as electron donor and DMSO as electron acceptor. The presumed structure of the complex is as follows:

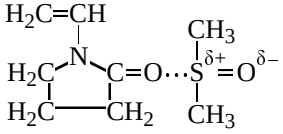

(4)

We also studied how the composition of the Na-AMS–VP copolymer correlates with the composition of the starting monomeric mixture, for the process performed in water and DMSO (Fig. 5, curves *1* and *2*, respectively). From the experimental data, we calculated the effective relative activities of the monomers $r_1 = k_{11}/k_{12}$ (for Na-AMS) and $r_2 = k_{22}/k_{21}$ (for VP) using the Mayo–Lewis equation. The $m_1 = f(M_1)$ plot for copolymerization in water corresponds to $r_1 = 0.35 \pm 0.01$ and $r_2 = 0.15 \pm 0.08$, $r_1r_2 = 0.05$, and that for copolymerization in DMSO, to $r_1 = 0.11 \pm 0.07$ and $r_2 = 0.44 \pm 0.36$, $r_1r_2 = 0.05$. These values of the relative activities of the monomers r_1 and r_2 show that, both in water and in DMSO, both kinds of macroradicals react considerably faster with the monomer of the other kind than with the "own" monomer, owing to complexation between the monomers. This results in the formation of alternating copolymers of regular composition, which is confirmed by the r_1r_2 values. In both solvents, the system has an azeotropic point (Fig. 5). Figure 5 shows that, at $[M_1]$ = const, the content of the ionic units in the copolymer decreases in going from water to DMSO (going from curve *1* to curve *2*) in a wide range of compositions of the starting monomeric mixtures. Apparently, DMSO molecules compete with Na-AMS in complexation with VP [scheme (4)], enhancing the activity of VP in copolymerization and increasing the content of VP units in the copolymer.

The intrinsic viscosities and compositions of the Na-AMS–VP copolymers in the course of copolymerization in DMSO at Na-AMS mole fractions in the starting monomeric mixture of 0.5 and 0.7 are shown in Fig. 6. It is seen that [η] increases with conversion (curves *1*', *2*'). Similar dependences have also been observed in other systems with alternating copolymerization [20]. The composition of the copolymer at M_1 0.5 varies with conversion only slightly (curve *1*), whereas at M_1 0.7 the variation is significant (curve *2*). One of the possible factors responsible for the variation of the copolymer composition with conversion is that the synthesis conditions are not isoionic, which affects the activity of the ionic comonomer in copolymerization [2].

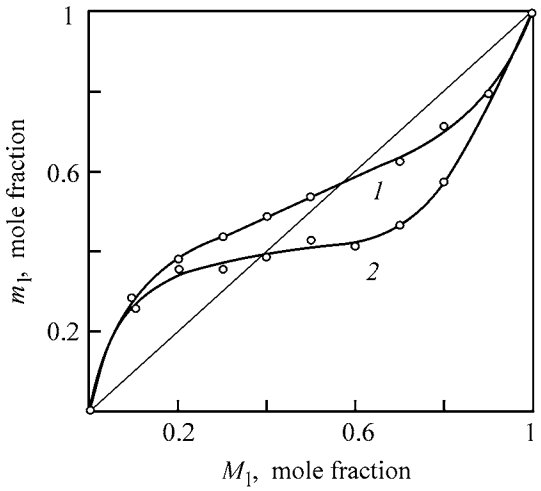

Fig. 5. Mole fraction m_1 of Na-AMS units in the copolymer with VP at <3% conversion vs. the mole fraction M_1 of Na-AMS in the starting monomeric mixture. Solvent: (*1*) water and (*2*) DMSO. $[M_1 + M_2]$ = 10%; the same for Fig. 6.

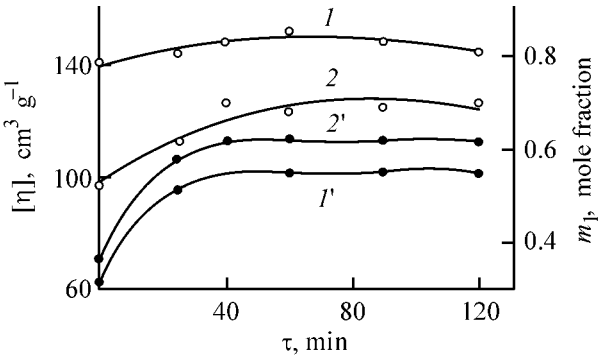

Fig. 6. (*1*', *2*') Intrinsic viscosity [η] and (*1*, *2*) mole fraction m_1 of Na-AMS units in the copolymer with VP vs. time τ of copolymerization in DMSO. Na-AMS mole fraction M_1 in the starting monomeric mixture: (*1*, *1*') 0.5 and (*2*, *2*') 0.7.

CONCLUSIONS

(1) In radical copolymerization of sodium 2-acrylamido-2-methylpropanesulfonate with *N*-vinylpyrrolidone in water and dimethyl sulfoxide, V_0 grows as the concentrations of M_1, M_2, their sum, and initiator increase and passes through a maximum (at equimolar ratio of the comonomers) with variation of $[M_1] : [M_2]$; V_0 also increases in going from water to dimethyl sulfoxide.

(2) The intrinsic viscosities of the copolymers pass through a maximum with variation of $[M_1] : [M_2]$ and grow as the $[M_1]$ and conversion increase and in the initiator concentration decreases.

(3) The content of ionic units in the copolymer decreases on replacement of water with dimethyl sulfoxide and as the conversion becomes lower.

ACKNOWLEDGMENTS

The study was financially supported by the Research and Development Foundation of the Republic of Tatarstan (project no. 07-7.1-104/2003).

REFERENCES

1. Kabanov, V.A. and Topchiev, D.A., *Polimerizatsiya ionizuyushchikhsya monomerov* (Polymerization of Ionizable Monomers), Moscow: Nauka, 1975.
2. Kurenkov, V.F. and Myagchenkov, V.A., *Zh. Prikl. Khim.*, 1999, vol. 72, no. 6, pp. 881–890.
3. Topchiev, D.A., Martynenko, A.I., Kabanova, E.Yu., and Timofeeva, L.M., *Vysokomol. Soedin., Ser. A*, 1997, vol. 39, no. 7, pp. 1129–1139.
4. Gromov, V.F., Bune, E.V., and Teleshov, E.N., *Usp. Khim.*, 1994, vol. 63, no. 6, pp. 530–541.
5. Sivtsov, E.V., Lavrov, N.A., and Nikolaev, A.F., *Plast. Massy*, 2001, no. 10, pp. 32–42.
6. Kurenkov, V.F., Sharapova, Z.F., and Khairullin, M.R., *Zh. Prikl. Khim.*, 1999, vol. 72, no. 8, pp. 1374–1378.
7. Shevtsova, S.A., Borkhanova, T.A., Zhelonkina, T.A., and Kurenkov, V.F., Abstracts of Papers, *Materialy konferentsii "III Kirpichnikovskie chteniya"* (Proc. Conf. "III Kirpichnikov Readings"), Kazan: Kazan. Gos. Tekh. Univ., 2003, pp. 303–311.
8. Lisovtsev, V.V., Rostokin, G.A., and Kulikova, A.E., *Khimicheskaya promyshlennost'. Akrilaty i polivinilkhlorid* (Chemical Industry. Acrylates and Polyvinyl Chloride), Moscow: NIITEKhIM, 1984, pp. 1–20.
9. Schulz, D.N., Kitano, K., Danik, J.A., and Kaladas, J.J., *Polym. Mater. Sci. Eng.*, 1987, vol. 57, pp. 149–153.
10. Kurenkov, V.F., Sirotkin, R.O., Beryachkova, E.A., and Khairullin, M.R., *Zh. Prikl. Khim.*, 1999, vol. 72, no. 8, pp. 1533–1537.
11. Kurenkov, V.F., Khabibullina, G.A., and Zaitseva, N.N., *Zh. Prikl. Khim.*, 2002, vol. 75, no. 11, pp. 1892–1895.
12. Kurenkov, V.F., Zaitseva, O.A., and Karyagina, S.V., *Vestn. Kazan. Tekhnol. Univ.*, 2000, nos. 1–2, pp. 121–126.
13. Kurenkov, V.F., Zaitseva, O.A., Khartan, Kh.G., and Lobanov, F.I., *Vestn. Kazan. Tekhnol. Univ.*, 2001, Supplement, pp. 1684–1687.
14. Kurenkov, V.F., Zaitseva, O.A., and Isaeva, N.V., *Zh. Prikl. Khim.*, 2001, vol. 74, no. 10, pp. 1374–1378.
15. Sidel'kovskaya, F.P., *Khimiya N-vinilpirrolidona i ego polimerov* (Chemistry of *N*-Vinylpyrrolidone and Its Polymers), Moscow: Nauka, 1970.
16. Kholodnova, L.V., Pavlyuchenko, V.N., Alekseeva, Z.M., and Andreeva, A.I., in *Kataliticheskie i initsiiruyushchie sistemy dlya sinteza i modifikatsii polimerov* (Catalytic and Initiating Systems for Synthesis and Modification of Polymers), Leningrad: Plastpolimer, 1984, pp. 90–104.
17. Kolthoff, I.M. and Miller, I.K., *J. Am. Chem. Soc.*, 1951, vol. 73, pp. 3055–3059.
18. Charlot, G., *Les methods de la chimie analytique. Analyse quantitative minerale*, Paris: Masson, 1961, 4th ed.
19. Olson, K.G. and Butler, G.B., *Macromolecules*, 1984, vol. 18, pp. 2486–2498.
20. Kabanov, V.A., Zubov, V.P., and Semchikov, Yu.D., *Kompleksno-radikal'naya polimerizatsiya* (Coordination Radical Polymerization), Moscow: Khimiya, 1987.
21. Karaputadze, T.M., Shumskii, V.I., and Kirsh, Yu.E., *Vysokomol. Soedin., Ser. A*, 1978, vol. 20, no. 8, pp. 1854–1859.
22. Nud'ga, L.A., Petrova, V.A., Klishevich, N.V., *et al.*, *Zh. Prikl. Khim.*, 2002, vol. 75, no. 10, pp. 1712–1716.
23. Kurenkov, V.F., Antonovich, O.A., Demina, T.A., and Selezneva, O.Yu., *Vysokomol. Soedin., Ser. A*, 2003, vol. 45, no. 8, pp. 1246–1252.
24. Marina, N.G. and Monakov, Yu.B., in *Khimiya vysokomolekulyarnykh soedinenii* (Chemistry of Macromolecular Compounds), Ufa: Inst. Khimii Bashkir. Filiala Akad. Nauk SSSR, 1976, pp. 116–146.

Russian Journal of Applied Chemistry, Vol. 77, No. 2, 2004, pp. 313–318. Translated from Zhurnal Prikladnoi Khimii, Vol. 77, No. 2, 2004, pp. 316–320.

MACROMOLECULAR CHEMISTRY AND POLYMERIC MATERIALS

Properties of Some Chitosan-containing Blends and Films Therefrom

N. G. Bel'nikevich, N. V. Bobrova, S. V. Bronnikov, L. M. Kalyuzhnaya, and T. V. Budtova

Institute of Macromolecular Compounds, Russian Academy of Sciences, St. Petersburg, Russia

Received May 7, 2003

Abstract—Mixed solutions of chitosan and polymers with different chain rigidities (polyvinyl alcohol and methyl cellulose) in 2% acetic acid, at various component ratios, were studied viscometrically. The compatibility of the components in solutions and in the solid phase was assessed, and the mechanical characteristics of films prepared from these blends were determined.

Chitosan is a nontoxic biocompatible and biodegradable polymer used in various fields of medicine and cosmetics as a drug carrier and as a material for separation membranes and sutures [1–5]. However, fibers and films prepared from pure chitosan are relatively brittle, and making them more elastic is an topical problem. One of the ways to improve the performance of polymers is their modification with other polymers. Blending allows preparation of systems with properties significantly differing from those of the starting components, without sophisticated chemical modification procedures or synthesis of new macromolecular compounds. Forming of articles from polymer blends in a common solvent is a relatively simple and accessible procedure.

Published data show that addition of some polymers to chitosan improves the mechanical characteristics of films therefrom. As modifying additives have been used oligomers [6], polyvinyl alcohol (PVA) [7–10], polyoxyethylene (POE) [10], polyethylene glycol [11], polygalacturonic acid [12], polyvinylpyrrolidone [13], and disperse cellulose [14]. Additions of chitosan considerably decrease the solubility and water absorption of PVA–chitosan films [7]. Mukhina *et al.* [8] revealed a certain enhancement of the mechanical characteristics of films prepared from chitosan–PVA blends: The strength and elongation at break increased by 10–30% at 20% content of PVA. However, strengthening of chitosan films with PVA was not observed in other studies [7, 9]. It has been shown previously that the strength of films prepared from chitosan–POE blends at a stoichiometric ratio of the components is two times higher, and the elongation at break, six times higher as compared to the films prepared from blends of other compositions or from pure components [15]. It was also shown [15] that this pair of polymers is only partially compatible, and it was suggested that the improvement of the deformation-strength characteristics of the polymers is due to a favorable steric arrangement and to ordering of polymeric chains in the films, rather than to formation of interpolymeric complexes, suggested in [10].

It seemed appropriate to continue systematic studies of blends of chitosan with macromolecular modifiers, with the aim to obtain promising chitosan-containing materials and reveal correlations between the properties of modifying polymeric additives and the deformation-strength characteristics of films prepared from these blends.

In this study, we used as polymeric additives two water-soluble polymers: a flexible-chain film- and fiber-forming polymer, PVA, and a semirigid-chain polymer, methyl cellulose (MC).

EXPERIMENTAL

We used the following polymers: chitosan (Aldrich, the United States), $M_w = 2.5 \times 10^5$, degree of deacylation 0.75–0.85; PVA (Plastpolimer, St. Petersburg, Russia), $[\eta] = 0.86$, $M_\eta = 1.2 \times 10^5$ (evaluated by the formula $[\eta] = 7.5 \times 10^{-4} M^{0.6}$ in water at 25°C [16]), 3% acetate groups; and MC (Aldrich), $M_n = 8.6 \times 10^4$, degree of substitution 1.6–1.8.

1070-4272/04/7702-0313 © 2004 MAIK "Nauka/Interperiodica"

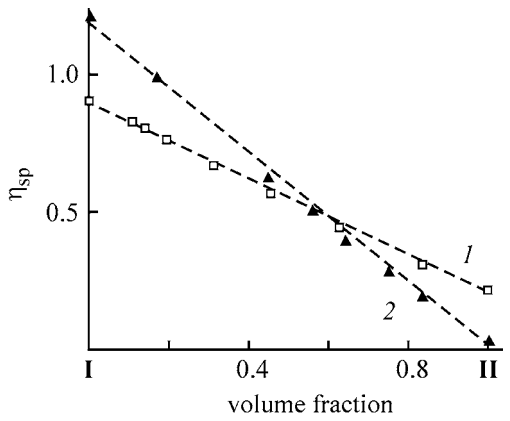

Fig. 1. Specific viscosity η_{sp} of mixed solutions of chitosan (component **I**) with (*1*) MC and (*2*) PVA (component **II**) in 2% acetic acid vs. the mixture composition. Total concentration of solutions, %: chitosan–MC 0.028 and chitosan–PVA 0.035. *Dashed lines* are calculated additive values.

In all the experiments, we used 2% acetic acid as common solvent (hereinafter, solvent).

Films were prepared from 1.5% solutions of the components. It should be particularly noted that, since PVA is soluble in 2% acetic acid only on heating, we initially dissolved it in distilled water with heating, to avoid changes in the solvent composition. The concentration of the aqueous solution was about 3%. Then the cooled solution was diluted with a more concentrated solution of acetic acid, so as to obtain a solution containing 2% acetic acid and 1.5% polymer. Then the solutions of the components were mixed in volume ratios of 0.9 : 0.1, 0.8 : 0.2, 0.6 : 0.4, 0.4 : 0.6, 0.2 : 0.8, and 0.1 : 0.9. The mixed solutions were stirred and kept until air bubbles fully disappeared. Films were prepared by casting onto silicone-coated glass support, followed by drying in air to constant weight. All the films were homogeneous and transparent; their thickness was 30–50 μm.

The occurrence of intermolecular interactions in dilute mixed solutions of the polymers was judged viscometrically. Measurements were performed in a capillary Ubbelohde viscometer at a solvent outflow time of about 125 s at 25 ± 0.1°C. The measurement error did not exceed 3%.

The intermolecular interactions in films were studied by sorption of solvent vapor with films of various compositions (chitosan–PVA and chitosan–MC), using an experimental installation with a quartz spring balance at a saturated vapor pressure of the solvent at room temperature. Our approach was based on studying the equilibrium sorption of vapor by a polymer blend, which furnishes information on the polymer–polymer interactions. The experimental error did not exceed 5%.

Mechanical tests of the films were performed with a UMIV-3 tensile-testing machine in the extension mode at a rate of 5 mm min^{-1} (sample length 25 mm, width 2 mm, interclamp distance 15 mm). The tensile strength, relative elongation at break, and Young's modulus of the films were determined from the experimental stress–strain curves with a ≤10% error.

Specific intermolecular interactions of polymeric components in solutions (e.g., formation of interpolymeric complexes) are usually studied viscometrically, as this method is relatively simple and furnishes rich information. If the measured specific (or relative) viscosity of a polymer blend in a common solvent, η_{exp}, differs from the calculated additive value η_{ad}, this is regarded as an evidence of complexation. The procedure is well known [17–19]. The additive values are calculated from the experimental concentration dependences of the specific viscosities η_{sp}, measured for each component in the course of dilution with a pure solvent (2% acetic acid in our case) [19]:

$$\eta_{sp,\,ad} = \eta_{sp,\,\mathbf{A}}(c_{\mathbf{A}}) + \eta_{sp,\,\mathbf{B}}(c_{\mathbf{B}}), \qquad (1)$$

where $\eta_{sp,\,\mathbf{A}}(c_{\mathbf{A}})$ and $\eta_{sp,\,\mathbf{B}}(c_{\mathbf{B}})$ are the specific viscosities of polymers **A** and **B** at their concentrations $c_{\mathbf{A}}$ and $c_{\mathbf{B}}$, respectively; $c_{\mathbf{A}} + c_{\mathbf{B}} = c$, where c is the total concentration of the polymers in the blend.

Deviation of the experimental dependence of η_{sp} from the calculated additive dependence suggests the formation of complexes. A coincidence of the experimental and additive dependences means that interactions between the components are not pronounced: either the complexes are not formed, or the hydrodynamic volume of the complex macromolecule is equal to the sum of the hydrodynamic volumes of the components (which is most often due to the low molecular weight of one of the components). The same criterion is used as the criterion of compatibility of the polymers in solutions.

The experimental specific viscosities of 0.028% chitosan–MC and 0.035% chitosan–PVA solutions are plotted in Fig. 1 vs. the component ratio. It is seen that the calculated additive values coincide with the experimental values for all the polymer blends studied. These results suggest that strong specific intermolecular interactions in the chitosan–MC system are absent, and complexation is insignificant. In chitosan–PVA blends, the specific viscosities of PVA solutions at this concentration are extremely low (in contrast to

MC having η_{sp} comparable with that of chitosan). Therefore, it is difficult to make any definite conclusions about the occurrence or absence of complexation between chitosan and PVA.

Similar results for chitosan–PVA blends have been obtained previously [9]. However, Mukhina *et al.* [8] and Mucha [10] did detect formation of interpolymeric complexes of chitosan with PVA. This discrepancies may be due to the fact that, firstly, the sources of chitosans were evolutionarily different (from crab shells, Russia [8]; from Antarctic crill, Poland [10]; from crab shells, Japan [9]; chitosan purchased from Aldrich, this study), and, secondly, different solvents were used (0.33 M CH_3COOH + 0.3 M NaCl [8]; 1% CH_3COOH for chitosan and water for PVA and POE [10]; and 2% CH_3COOH for all the polymers in this study). Since chitosan–PVA and chitosan–MC blends remain transparent at concentrations of up to 1.5% and any component ratios, and the experimental η_{sp} of the blends do not differ from the calculated additive values, we can conclude that there is no phase segregation of the components in the concentration range studied.

The compatibility of the polymeric components in the blends was judged from the polymer–polymer interaction parameter χ_{23} [20], calculated from the results of experiments on sorption of saturated vapor by films cast from mixed 1.5% chitosan–MC and chitosan–PVA solutions in 2% acetic acid. The curves of solvent vapor sorption by films formed from polymer blends with various component ratios were obtained, and the equilibrium values of the specific sorption A ($g\,g^{-1}$) were determined. The polymer–polymer interaction parameters for films of each composition were calculated as follows [20]:

$$\chi_{23} = \frac{[\ln\Phi_1 + (1 - \Phi_1) + (1 - \Phi_1)(\chi_{12}\Phi_2 + \chi_{13}\Phi_3)]}{\Phi_2\Phi_3}, \quad (2)$$

where subscript 1 refers to the solvent (2% acetic acid), 2, to chitosan, and 3, to the modifying polymer (PVA or MC); χ_{23} is the polymer–polymer (chitosan–MC or chitosan–PVA) interaction parameter characterizing interactions of segments of different polymers; Φ_1 is the volume fraction of the solvent absorbed by the film in the course of the experiment; Φ_2 and Φ_3 are the volume fractions of the respective polymers in the swollen film; and χ_{12} and χ_{13} are the Flory–Huggins polymer–solvent (e.g., chitosan–2% aqueous acetic acid) interaction parameters.

The parameters χ_{12} and χ_{13} were calculated from the results of separate sorption experiments with films cast from solutions of the respective polymers, taken separately, in 2% acetic acid:

$$\chi_{12} = -(\ln\Phi_1^* + \Phi_2^*)/(\Phi_2^*)^2,$$
$$\chi_{13} = -(\ln\Phi_1^* + \Phi_3^*)/(\Phi_3^*)^2, \quad (3)$$

where Φ_1^*, Φ_2^*, and Φ_3^* are, respectively, the volume fractions of the solvent, chitosan, and modifying polymer (PVA or MC) in the swollen film cast from the solution of the separately taken polymer.

The polymer volume fractions Φ_2^* and Φ_3^* (in the films cast from solutions of the separate components) and Φ_{pol} ($\Phi_{pol} = \Phi_2 + \Phi_3$ in the films cast from the polymer blend; Φ_2 and Φ_3 were calculated from the initial component ratio in the blend) were calculated from the specific sorption A for each film:

$$\Phi_2^* = (1 + A\rho_2/\rho_1)^{-1},$$
$$\Phi_3^* = (1 + A\rho_3/\rho_1)^{-1}, \quad (4)$$
$$\Phi_{pol} = (1 + A\rho_{pol}/\rho_1)^{-1},$$

where ρ_2, ρ_3, and ρ_{pol} are the polymer densities determined gravimetrically; ρ_1 is the solvent density determined with a densimeter; and A is the specific sorption for each film.

The dependence of the specific sorption A on the film composition is shown in Fig. 2a. It is seen that, in chitosan–MC films with the fraction of MC exceeding 0.8 (Fig. 2a, curve *1*), the specific sorption of acetic acid vapor is appreciably decreased. All the other values differ insignificantly. The χ_{23} values calculated by formula (2) (Fig. 2b, curve *1*) are close to zero at an MC fraction in the films of up to 0.4 and positive at larger MC additions. These data show that, in blends with the MC fraction of 0.1–0.4, all the polymer–polymer and polymer–solvent interactions are identical to those occurring in solutions of each component, taken separately, in 2% aqueous acetic acid. An increase in the MC fraction above 0.4 makes this polymer incompatible with chitosan. Taking into account the viscometric data, these polymers can be concluded to be partially compatible in the blend.

For chitosan : PVA = 0.9 : 0.1 blends, addition of PVA drastically (by a factor of 2.5) decreases the specific sorption (Fig. 2a, curve *2*). As the PVA content in the system is increased further, the specific sorption smoothly decreases. The calculated χ_{23} values for these films are negative at any compositions (Fig. 2b, curve *2*), unambiguously suggesting full compatibility of this pair of the polymers.

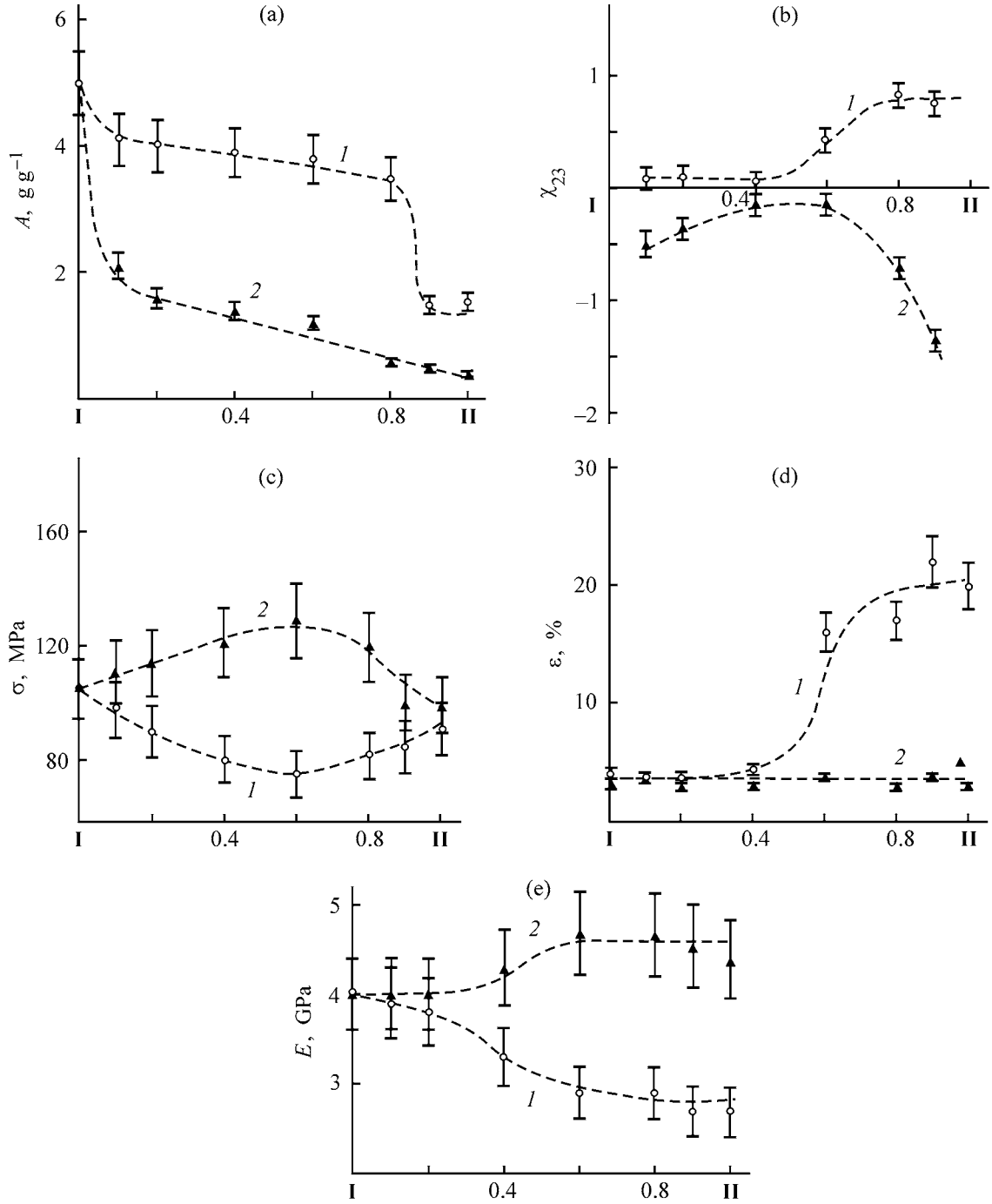

Fig. 2. (a) Specific sorption of the solvent (2% aqueous acetic acid), *A*; (b) polymer–polymer interaction parameter χ_{23}; (c) strength σ; (d) elongation at break, ε; and (e) Young's modulus *E* of (*1*) chitosan (**I**)–MC (**II**) and (*2*) chitosan (**I**)–PVA (**II**) films vs. their composition.

The results of mechanical tests of the films cast from blends of different compositions are shown in Figs. 2c–2e. The composition dependences of the elongation at break, strength, and Young's modulus deviate from the additivity. As the MC fraction in a chitosan–MC blend is increased to 0.5, the strength σ (Fig. 2c, curve *1*) and Young's modulus *E* (Fig. 2e, curve *1*) decrease to a similar extent (by approximately a factor of 1.4), compared to pure chitosan, whereas the elongation at break remains unchanged (Fig. 2d, curve *1*). At larger amounts of the MC added, the Young's modulus varies insignificantly (Fig. 2e,

curve *1*), but the strength (Fig. 2c, curve *1*) and especially elongation at break (Fig. 2d, curve *1*) grow: by approximately factors of 1.2 and 4.8, respectively. Thus, the MC fraction in chitosan–MC blends of 0.6 and higher is preferable.

In the chitosan–PVA system, no significant changes in the mechanical properties were revealed at any component ratios. As the PVA fraction in the blend was increased to 0.6, the strength (Fig. 2c, curve *2*) and Young's modulus (Fig. 2e, curve *2*) increased by a factor of approximately 1.2 compared to pure chitosan. Further increase in the PVA fraction in the blend caused a decrease in the strength and no changes in Young's modulus as compared to the above-indicated maximal values. The elongation at break varies insignificantly with the composition of chitosan–PVA films (Fig. 2d, curve *2*).

Comparison of the data obtained for the chitosan–MC and chitosan–PVA systems with those obtained previously for the chitosan–POE system [14] shows that the elastic properties of chitosan-containing films are improved at relatively high weight fraction of the second component: 0.6 MC in chitosan–MC films and 0.17 POE in chitosan–POE films. Actually we deal with polymer blends and films therefrom, rather than with modification of chitosan. Despite good fiber- and film-forming properties of PVA, the chitosan–PVA system is of no interest from the viewpoint of improving the elasticity of the films.

It should be noted that the weight fraction of the second component (MC or POE) that provides the best elastic properties of chitosan-containing films approximately corresponds to the stoichiometric ratio of the components in the blend. Furthermore, the components in the above systems are only partially compatible, and improvement of the elastic properties of the films is observed just in the composition range at which the components become incompatible (stoichiometric ratio; Fig. 2b, curve *1*). Thus, the improvement of the mechanical properties of films cast from solution and, in particular, the appreciable increase in their elongation at break, are due to combination of a favorable steric arrangement of macromolecules of different kinds and their partial compatibility, rather than to thermodynamic rigidity of the polymeric additive or specific interactions with chitosan (complexation with chitosan was not detected). Specifically the partial compatibility of the components, which does not result in their phase segregation, favors the ordering of the different macromolecules. Apparently, further search for chitosan-containing films and fibers with improved mechanical properties should be performed taking into account the polymer–polymer interaction parameter.

CONCLUSIONS

(1) In the systems chitosan–methyl cellulose and chitosan–polyvinyl alcohol, strong specific intermolecular interactions that would lead to formation of interpolymeric complexes do not occur.

(2) Experiments on sorption of solvent vapor show that chitosan and methyl cellulose are partially compatible, whereas chitosan and polyvinyl alcohol are compatible in the entire composition range.

(3) The strength of films cast from chitosan–methyl cellulose blends at any component ratio does not exceed that of the films cast from separate components.

(4) At a stoichiometric ratio of the components in the chitosan–polyvinyl alcohol system, the strength grows, but Young's modulus and elongation at break are close to those for films obtained from pure polyvinyl alcohol.

REFERENCES

1. Fang, Y.E., Cheng, Q., and Lu, X.B., *J. Appl. Polym. Sci.*, 1998, vol. 68, pp. 1751–1756.
2. Singh, D.K. and Ray, A.R., *J. Membr. Sci.*, 1999, vol. 155, no. 1, pp. 107–110.
3. Wang, X.P., Shen, Z.Q., and Zhang, F.Y., *J. Appl. Polym. Sci.*, 1998, vol. 69, pp. 2035–2041.
4. Nam, S.Y. and Lee, Y.M., *J. Membr. Sci.*, 1999, vol. 153, pp. 155–159.
5. Dutta, P.K., Ravikumar, M.N.V., and Dutta, J., *J. Macromol. Sci., Polym. Rev.*, 2002, vol. 42, no. 3, pp. 307–354.
6. Fuentes, S., Retuert, P.J., Ubilla, A., *et al., Biomacromolecules*, 2000, no. 1, pp. 239–243.
7. Nikolaev, A.F., Prokopov, A.A., Shul'gina, E.S., *et al., Plast. Massy*, 1987, no. 6, pp. 1406–1409.
8. Mukhina, V.R., Pastukhov, N.V., Semchikov, Yu.D., *et al., Vysokomol. Soedin., Ser. A*, 2001, vol. 43, no. 10, pp. 1797–1804.
9. Cho, Y.-W., Nam, C.-W., Jang, J., and Ko, S.-W., *J. Macromol. Sci. Phys., Ser. B*, 2001, vol. 40, no. 1, pp. 93–104.
10. Mucha, M., *React. Funct. Polym.*, 1998, vol. 38, pp. 19–25.
11. Jiamg, W.H. and Han, S.J., *J. Polym. Sci., Part B: Polym. Phys.*, 1998, vol. 36, pp. 1275–1281.

12. Arguelles-Monal, W., Cabrea, G., Peniche, C., and Rinaudo, M., *Polymer*, 2000, vol. 41, pp. 2373–2378.
13. Sakurai, K., Maegawa, T., and Takahashi, T., *Polymer*, 2000, vol. 41, pp. 7051–7056.
14. Rogovina, L.Z., Vikhoreva, G.A., Akopova, T.A., and Erina, N.A., *Vysokomol. Soedin., Ser. B*, 1999, vol. 41, no. 11, pp. 1839–1842.
15. Budtova, T., Belnikevich, N., Kalyuzhnaya, L., *et al.*, *J. Appl. Polym. Sci.*, 2002, vol. 84, pp. 1114–1122.
16. *Polymer Handbook*, Brandrup, J. and Immergut, E.H., Eds., New York, 1966.
17. Nikolaeva, O., Budtova, T., Alexeev, V., and Frenkel, S., *J. Polym. Sci., Part B: Polym. Phys.*, 2000, vol. 38, pp. 1323–1330.
18. Antipina, A.D., Baranovskii, V.Yu., Papisov, I.M., and Kabanov, V.A., *Vysokomol. Soedin., Ser. A*, 1972, vol. 14, pp. 941–949.
19. Bel'nikevich, N.G., Budtova, T.V., Nikolaeva, O.V., and Vesnebolotskaya, S.A., *Vysokomol. Soedin., Ser. B*, 2002, vol. 44, no. 2, pp. 341–346.
20. *Polymer Blends*, Paul, D.R. and Newman, S., Eds., New York: Academic, 1978, vol. 1.

Russian Journal of Applied Chemistry, Vol. 77, No. 2, 2004, pp. 319–322. Translated from Zhurnal Prikladnoi Khimii, Vol. 77, No. 2, 2004, pp. 321–323.

MACROMOLECULAR CHEMISTRY AND POLYMERIC MATERIALS

Influence of the Chemical Structure of Oligodienourethanoepoxide on Its Rheological Properties

S. A. Imankulova, V. A. Val'tsifer, L. L. Khimenko, and I. A. Fedotov

Institute of Technical Chemistry, Ural Division, Russian Academy of Sciences, Perm, Russia
Research Institute of Polymeric Materials, Perm, Russia

Received October 17, 2003

Abstract—Rheological properties of urethane-containing oligomers as influenced by intermolecular interactions in them were studied.

The great diversity of structures of urethane-containing oligomers and the complex nature of their synthesis reactions present a severe problem in studying the composition, final structure, and properties of these polymers [1].

The properties of urethane-containing oligomers are primarily governed by specific intermolecular interactions in them. Published data [1–4] suggest that intermolecular interactions and, in particular, hydrogen bonding, largely affect the physicochemical properties of oligomers containing reactive groups. A parameter highly sensitive to structural changes is viscosity of oligomers [5].

Romanovskii *et al.* [6, 7] have shown that the viscosity of oligomers whose molecules contain groups capable of hydrogen bonding significantly exceeds that of the oligomers of comparable molecular weights, but lacking such groups. It is believed that the major factor affecting the rheological properties of urethane-containing polymers, e.g., oligodienourethanoepoxide, are intermolecular interactions involving functional groups.

In this study, we examined the rheological properties of urethane-containing oligomers as influenced by intermolecular interactions. This seems to be a topical task in view of the development of studies of the structure and properties of polymers characterized by strong intermolecular interactions, as well as in view of the growing applications of such oligomers.

EXPERIMENTAL

Our experimental studies were performed with oligodienourethanoepoxide samples differing in the content of epoxy groups (see table).

The rheological properties were studied on a Rheotest 2.1 rotary viscometer at 25–60°C at shear rates of 0.024 to 70 s^{-1}.

Band intensities of the epoxy groups and bound and free carboxy groups, ratio of the band intensities of bound and free epoxy groups, and ratio of room-temperature viscosities at shear rates of 0.024 and 2.33 s^{-1}

Sample no.	Content of epoxy groups	I_{1223} (epoxy group)	I_{1735} (–C=O free)	I_{1710} (–C=O bound)	$\frac{I_{1735}}{I_{1710}}$	$\frac{\eta_{0.024}}{\eta_{2.33}}$
1	1.84	0.570	0.466	0.374	1.25	1.93
2	1.80	0.570	0.473	0.374	1.26	1.25
3	1.84	0.431	0.435	0.342	1.27	1.23
4	1.84	0.693	0.555	0.454	1.22	2.62
5	1.97	0.621	0.510	0.417	1.22	0.24
6	1.79	0.653	0.530	0.444	1.19	14.1
7	2.00	0.646	0.539	0.454	1.19	4.55
8	1.90	0.635	0.533	0.453	1.19	4.33

1070-4272/04/7702-0319 © 2004 MAIK "Nauka/Interperiodica"

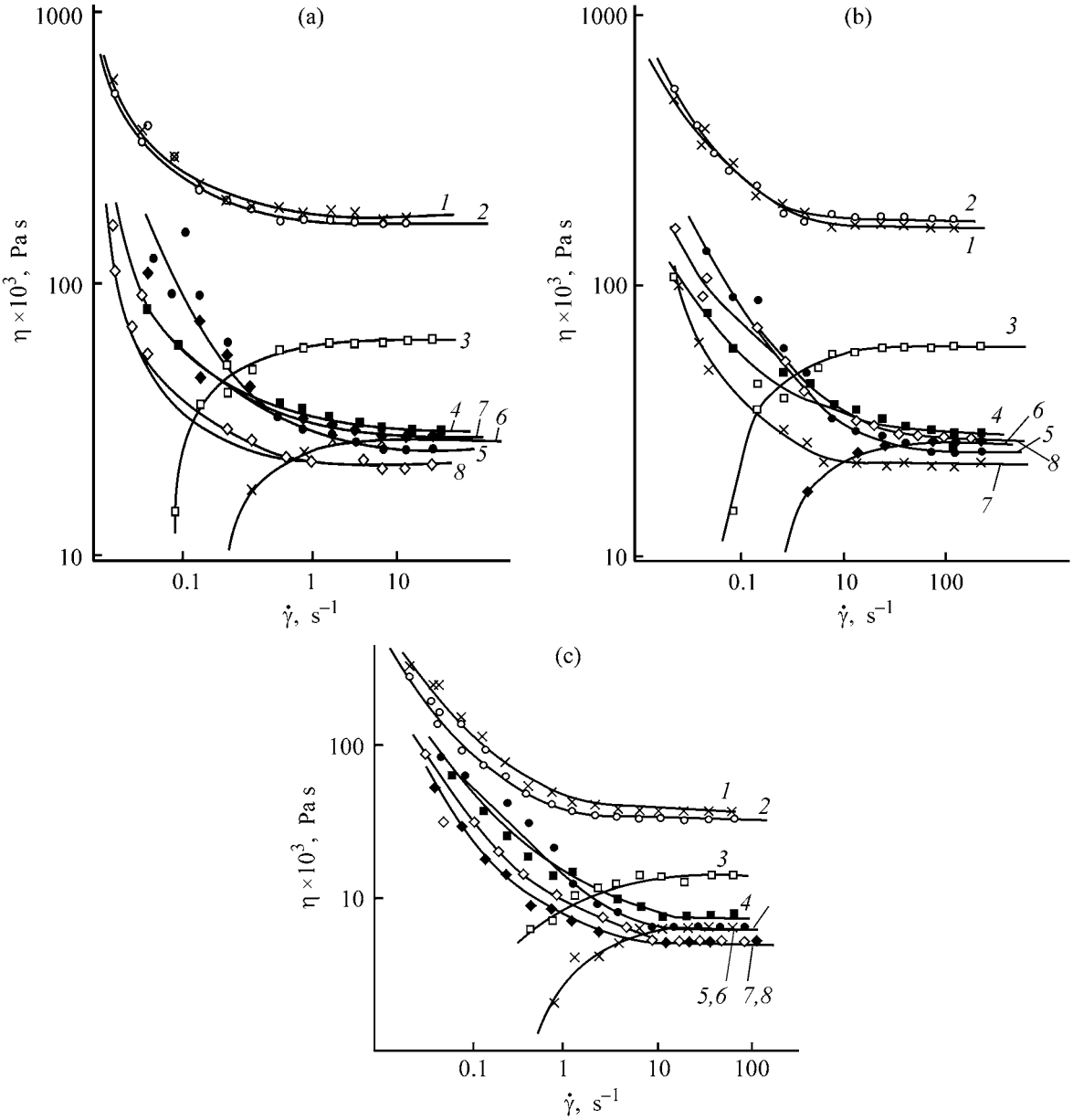

Fig. 1. Viscosity η of the oligodienourethanoepoxide samples vs. the shear rate $\dot{\gamma}$ at (a) 25, (b) 40, and (c) 60°C. *Figures at curves* correspond to sample nos. in the table; the same for Fig. 2.

The chemical structure of the samples was studied by infrared multiple attenuated total internal reflection (IR MATIR) spectroscopy on a Bruker IFS 66/S Fourier spectrometer using a KRS-5 crystal (α = 45°).

Figures 1a–1c show the results of the rheological studies. It is seen that the oligomer of interest is a non-Newtonian liquid. The maximum viscosity at high shear rates at all the temperatures was exhibited by sample nos. 1–3. Also, sample nos. 3 and 5 showed an abnormal rheological behavior: their viscosity tended to grow with increasing shear rate. This may be due to the branched structure of the molecules of these samples.

We determined the optical density ratio of the analytical to the reference band. As the reference served the band of the component whose concentration is known and invariable under the actual conditions [8, 9], in our case, the band at 2915 cm^{-1}, belonging to $-CH_2-$ groups.

For oligodienourethanoepoxide samples under study, the Amide I band lies 1760–1680 cm^{-1}. As

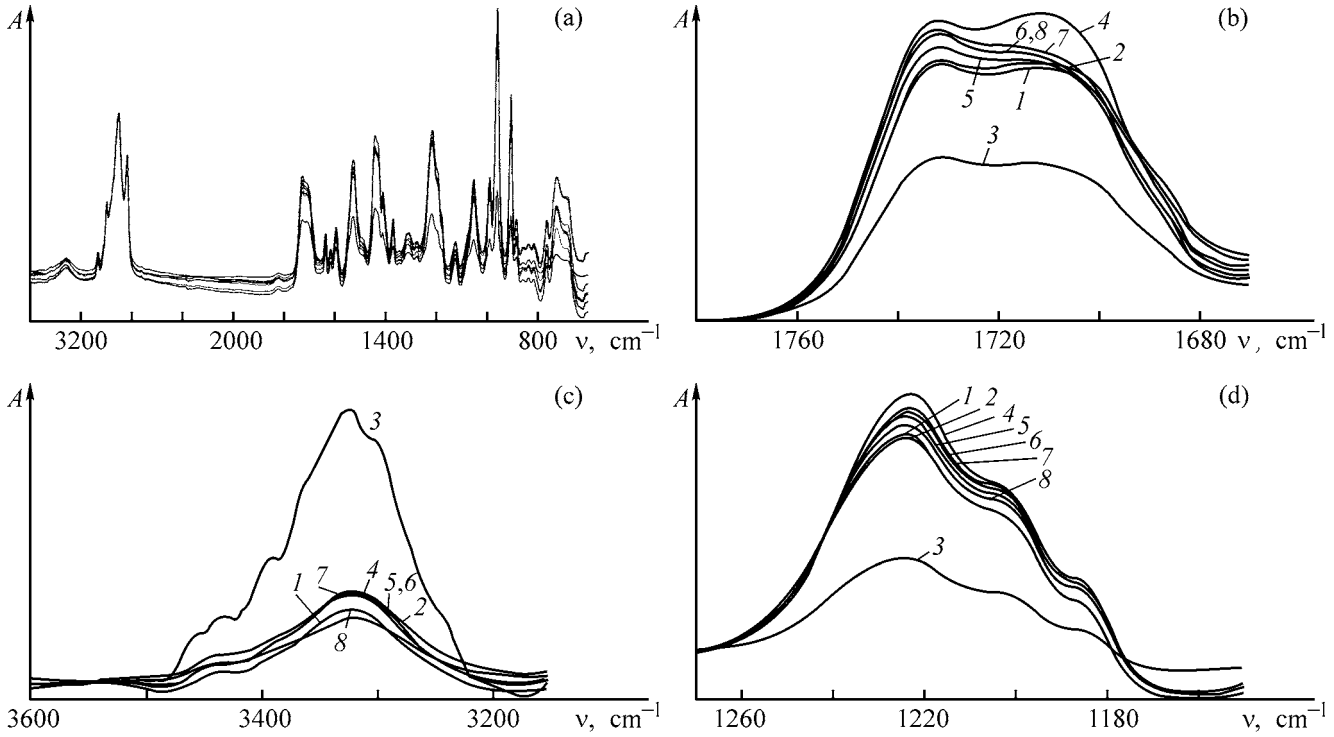

Fig. 2. (a) Total IR spectrum and (b, c, d) fragments corresponding to (b) Amide-I vibrations, (c) stretching vibrations of NH groups, and (d) vibrations of epoxy groups in different oligodienourethanoepoxide samples.(*A*) Absorption and (ν) wave number.

seen from the spectrum (Figs. 2a, 2b), this region contains a band at 1710 cm^{-1} (C=O). This band belongs to associates of urethane groups and can surpass in intensity the band at 1735 cm^{-1}, characteristic of the free C=O group. For the batch under study, the band at 1710 cm^{-1} is rather intense for all the samples, which suggests the presence of associates of urethane groups [10, 11].

The existence of three-dimensional associates in the oligomers under study is also evidenced by the IR data for the region corresponding to urethane groups, namely, bands at 3200–3500 cm^{-1} characteristic of stretching vibrations of the NH groups (Fig. 2c). It is seen from Fig. 2c that, in the spectra of sample nos. 1–5, the band corresponding to "free" NH groups (3440 cm^{-1}) is virtually lacking.

The tabulated data suggest that the relatively weak dependence of the viscosity of oligodienourethanoepoxides on the shear rate for sample nos. 1–3 is due to a lower concentration of hydrogen bonds (I_{1735}/I_{1710}) in these samples. At the same time, the high viscosities of these samples are, apparently, due to increased molecular weight of the product, as evidenced by the lower content of epoxy groups in these samples (see table; Figs. 2a, 2d).

CONCLUSIONS

(1) The rheological properties of oligodienourethanes that differ in the content of epoxy groups are strongly influenced by the chemical structure and intermolecular interactions. A decrease in the number of epoxy groups increases the molecular weight and, thus, the viscosity of the oligomer.

(2) A high content of hydrogen bonds is responsible for the increased viscosity and stronger influence of the shear rate on the non-Newtonian rheological behavior of the rubber.

REFERENCES

1. *Entsiklopediya polimerov* (Encyclopedia of Polymers), Moscow: Sov. Entsiklopediya, 1977.
2. Lipatov, Yu.S., Panov, Yu.N., Sushko, L.S., and Frenkel', S.Ya., *Dokl. Akad. Nauk SSSR*, 1967, vol. 176, pp. 1341–1343.
3. Zharkov, V.V., Kopusov, L.I., and Kozlova, T.V., *Plast. Massy*, 1981, no. 9, pp. 41–45.
4. Berlin, A.A. and Matveeva, N.G., *Uspekhi kimii i fiziki polimerov* (Advances in Polymer Chemistry and Physics), Moscow: Khimiya, 1970.

5. Berlin, A.A., Kondrat'ev, A.G., Tvorogov, N.N., *et al.*, *Vysokomol. Soedin., Ser. B*, 1973, vol. 15, pp. 740–744.
6. Romanovskii, G.K., Rappoport, L.Ya., Pavlov, N.G., *et al.*, *Vysokomol. Soedin., Ser. A*, 1972, vol. 14, no. 10, pp. 2241–2245.
7. Romanovskii, G.K., Tsitokhtsev, V.A., Rappoport, L.Ya., and Petrov, G.N., *Vysokomol. Soedin., Ser. A*, 1975, vol. 17, no. 11, pp. 2512–2516.
8. Imankulova, S.A., Kondyurin, A.V., Val'tsifer, V.A., and Klyachkin, Yu.S., *Vysokomol. Soedin., Ser. B*, 1994, vol. 36, no. 7, pp. 1197–1200.
9. Imankulova, S.A., Val'tsifer, V.A., and Klyachkin, Yu.S., *Plast. Massy*, 1999, no. 5, pp. 26–27.
10. Zharkov, V.V., Strikovskii, A.G., and Verteletskaya, T.E., *Vysokomol. Soedin., Ser. A*, 1992, vol. 34, no. 5, pp. 142–147.
11. Tereshatov, V.V., Tereshatova, E.N., Makarova, M.A., and Tereshatov, S.V., *Vysokomol. Soedin., Ser. A*, 2002, vol. 44, no. 5, pp. 433–451.

Russian Journal of Applied Chemistry, Vol. 77, No. 2, 2004, pp. 323–326. Translated from Zhurnal Prikladnoi Khimii, Vol. 77, No. 2, 2004, pp. 324–327.

MACROMOLECULAR CHEMISTRY AND POLYMERIC MATERIALS

Solvent Effect in Swelling of Butyl Rubber and Polybutadiene

R. G. Makitra, E. A. Zaglad'ko, A. A. Turovskii, and G. E. Zaikov

Division of Physical Chemistry of Fossil Fuels, Pisarzhevskii Institute of Physical Chemistry, National Academy of Sciences of Ukraine, Lviv, Ukraine

Emanuel' Institute of Biochemical Physics, Russian Academy of Sciences, Moscow, Russia

Received June 3, 2003

Abstract—Relationship between the swellabilities of butyl rubber and polybutadiene in organic solvents and the physicochemical characteristics of solvents, including their capability for nonspecific and specific solvation, was studied.

The problem of quantitative evaluation of the solvent effect on the swellability of polymers in organic solvents is not yet satisfactorily solved. This is, evidently, due to the fact that the swelling process is attempted to be described using one-parameter equation. For example, the most commonly used relationships between the swellability and Hildebrand's solubility parameter δ, based on the regular solution theory and Flory–Huggins theory [1], yield fuzzy bell-shaped curves with strong deviations [2]. More or less acceptable correlation factors have been obtained only for homologous series of solvents [3]. This is true also for correlations with the molar volume of solvents [4]. It is well known, however, that the integral solvent effect is a resultant of a number of particular solvation effects. Therefore, in the chemistry of solutions, the solvent effect is treated in terms of the principle of linear free energies, using multiparametric equations that take into account the total change in the thermodynamic potential: $\Delta G = \Sigma \Delta g_i$ [5–8].

Such an approach appeared to be suitable for analysis of data on swellability of polyethylene [9] and natural carbonaceous polymers (coals) [10]. However, these polymers have relatively simple structures, and it was appropriate to check the applicability of multiparametric correlations to generalization of the swellability data for polymers of more complex structure.

Therefore, we applied in this study this approach to generalization of data on the swellability of vulcanized butyl rubber and polybutadiene in various organic solvents. Unlike other synthetic rubbers, these polymers contain no cycles or polar groups, so that their structures are, in principle, similar to the structure of polyethylene, which permits comparison of the swellability data. Rostler and White [11] studied the swellability of polyethylene in ten solvents. However, as they themselves noted, only qualitative conclusion like "the similar swells in the similar" could be drawn from their results (data were presented only graphically could not be used for quantitative processing). Reviewing this study, we only note that the maximum swelling to above 300 vol % was observed in cyclohexane. The increase in the volume in alkanes, dichloroethane, and CS_2 was determined to be above 200, and that in benzene, about 150 vol %. At the same time, in polar solvents, such as aniline, acetone, and hexanol, the swelling is less than 10 vol %, i.e., virtually no swelling is observed. Diethyl ether stands intermediately.

Bristow and Watson [2] the studied swelling of butyl rubber in more detail. They used Butyl-400 commercial polymer containing 5% ZnO, 2% S, 1% tetramethylthiuram disulfide, and 1% stearic acid, vulcanized at 150°C, and then extracted with acetone. The density of the sample was 0.91 g ml^{-1}. The 0.25-g samples were swollen for three days at 25°C, dried, and weighed. The results were represented as the polymer volume fraction V_2 in the swollen sample (Table 1). However, analysis of these data in terms of Flory's theory appeared to be unsuccessful: even in a series of *n*-alkanes C_5–C_{16}, the dependence of V_2 on the Hildebrand's solubility parameter δ was represented by a fuzzy broken-line function with a minimum for *n*-heptane.

Bristow and Watson [2] wrote that the cohesion energy density may be only an available indication of a certain mutuality in the system polymer–sol-

1070-4272/04/7702-0323 © 2004 MAIK "Nauka/Interperiodica"

Table 1. Polymer volume fraction V_2 in swollen butyl rubber [2] and solvent uptake S_M (mol), determined experimentally and estimated by Eq. (2)

Solvent	V_2	S_M	log S_{exp}	log S_{calc}	ΔS_{calc}
n-Pentane	0.3616	0.0169	–1.7737	–1.6079	0.1658
n-Hexane	0.2670	0.0231	–1.6398	–1.6361	0.0037
n-Heptane	0.2320	0.0248	–1.6078	–1.6791	–0.0712
n-Decane	0.2930	0.0136	–1.8665	–1.7927	0.0738
n-Hexadecane	0.2886	0.0093	–2.0356	–2.0792	0.0435
Isooctane	0.3175	0.0143	–1.8444	–1.6589	0.1855
Cyclohexane	0.1818	0.0458	–1.3396	–1.4752	–0.1356
Methylcyclohexane	0.1959	0.0365	–1.4517	–1.5251	–0.7334
Benzene	0.3891	0.0194	–1.7144	1.7458	–0.0314
Toluene	0.2786	0.0269	–1.5746	–1.7611	–0.1865
Dichloromethane	0.2778	0.0446	–1.3503	–1.2990	–0.1865
Chloroform	0.2361	0.0446	–1.3549	–1.4651	–0.1102
Tetrachloromethane	0.1942	0.0472	–1.3256	–1.4646	0.1390
Bromoethane	0.2907	0.0359	–1.4325	–1.2302	0.2024
1,2-Dibromoethane	0.7119	0.0052	–2.2875	–2.7206	–0.1225
Bromoform	0.6820	0.0059	–2.2320	–2.4916	0.2310
Pyridine	0.8439	0.0025	–2.5981	–1.6386	0.6802
1,4-Dioxane	0.8719	0.0006	–2.7226	–1.4765	0.7556

vent, but only a rather approximate indication, as, generally, other significant factors exert influence too.

It is noteworthy here that the use of the polymer volume fraction in a swollen polymer as a correlating factor is incorrect: if swelling is considered a thermodynamically reversible process, it is necessary to use the mole fraction of a solvent as a parameter. Therefore, we recalculated V_2 to the solvent uptake in moles S_M (Table 1). Because of the high average molecular weight of the polymer, we did not recalculate the polymer volume to the moles.

We generalized data from [6] using Eq. (1).

$$\log S_M = a_0 + a_1\frac{n^2-1}{n^2+2} + a_2\frac{\varepsilon-1}{2\varepsilon+1} + a_3B + a_4E_T + a_5\delta^2 + a_6V_M, \quad (1)$$

where n is the refractive index; ε, the dielectric constant; B, Palm's basicity [5]; E_T, Reichardt's electrophilicity index [2]; δ, Hildebrand's solubility parameter; and V_M, molar volume of a solvent.

The first four terms of the equation reflect the effects of specific and nonspecific solvation. They are commonly used in the chemistry of solutions to reproduce the solvent effect on the chemical reaction rate, some spectroscopic characteristics, etc. The cohesion energy density characterizes self-association of a solvent and, correspondingly, the energy consumption for detachment of its molecule from the structure. High molar volume of a solvent, as a rule, hinders penetration of solvent molecules to the polymer structure, thereby decreasing the swellability. However, Aminabhavi *et al*. [4] have demonstrated that these are correlated, but not proportional parameters. Accordingly, for all the 18 solvents studied, calculation by Eq. (1) gives the multiple correlation factor $R = 0.876$, which is unacceptably low [1]. After excluding from consideration data for only two solvents, bromoform and dibromoethane, as the most outlying, R increased to 0.977. In this case, we obtain Eq. (2) reproducing the solvent effect on the swellability of butyl rubber with an acceptable accuracy.

$$\log S = -0.911 + (6.45 \pm 1.50)f(n^2) + (4.32 \pm 0.74)f(\varepsilon) - (3.47 \pm 0.25) \times 10^{-3}B - (0.07 \pm 0.03)E_T - (1.69 \pm 0.93) \times 10^{-3}\delta^2 - (3.62 \pm 0.54) \times 10^{-3}V_M; \quad (2)$$

$$R = 0.977, \; s \pm 0.09.$$

This equation, as well as all the equations presented below, is adequate, as demonstrated by comparison of the estimated Fisher test parameter F with the tabulated values for the corresponding number of degrees of freedom at a 95% confidence level [12]. Analysis of the signs at separate terms of the equation shows that the capacity of the solvents for specific interaction prevents their penetration into the nonpolar struc-

Table 2. Solvent volume fraction V_2 in swollen polybutadiene [14] and solvent uptake S_M (mol), determined experimentally and estimated by Eq. (5)

Solvent	V_2	$S_{M(exp)}$	log $S_{M(exp)}$	log $S_{M(calc)}$	Δlog S
Hexane	1.40	0.0110	–1.9731	–1.9325	0.0406
Heptane	1.48	0.0100	–1.9983	–1.9483	0.0499
Octane	2.14	0.0130	–1.8831	–1.9729	–0.0898
Cyclohexane	3.05	0.0280	–1.5494	–1.5486	0.0886
Tetrachloromethane	4.35	0.0450	–1.3460	–1.3861	–0.0401
p-Xylene	3.84	0.0310	–1.5123	–1.4829	0.0294
Ethylbenzene	3.63	0.0300	–1.5280	1.4998	0.0281
Toluene	3.91	0.0370	–1.4366	–1.4175	0.0191
Benzene	3.51	0.0390	–1.4060	–1.4365	–0.0305
Choroform	4.50	0.0560	–1.2525	–1.2534	–0.0875
Nitrobenzene	0.98	0.0098	–2.0186	–0.4917	–0.0153
1,4-Dioxane	1.32	0.0150	–1.8099	–1.8167	–0.0068

ture of the polymer; as expected, an increase δ^2 and V_M has an antiswelling effect. At the same time, nonspecific solvent–rubber interactions favor swelling. However, low pair correlation factors (r_1 = 0.176, r_2 = 0.549, r_3 = 0.804, r_4 = 0.664, r_5 = 0.302, and r_6 = 0.08) do not permit evaluation of the separate contributions of the equation parameters, and high standard deviations of some regression coefficients suggest their nonsignificance.

The significance of contributions of particular factors to log S_M was examined by alternate exclusion of separate terms of the equation, with R determined in each case [12]. The calculation revealed nonsignificance of the cohesion energy: its exclusion has no considerable effect on R.

$$\log S_M = -0.07 + (4.84 \pm 1.34) f(n^2) + (4.59 \pm 0.80) f(\varepsilon) - (3.55 \pm 0.27) \times 10^{-3} B - (0.10 \pm 0.02) E_T - (3.48 \pm 0.59) \times 10^{-3} V_M; \quad (3)$$

$$R = 0.972, \; s \pm 0.10.$$

But exclusion of any other term, especially V_M or B, decreases R to below the acceptable value R 0.95.

As can be seen from Table 1, for all the solvents studied, except $CHBr_3$ and $C_2H_4Br_2$, the ΔS values ($\Delta\log S = \log S_{calc} - \log S_{exp}$) are within the determination error ($s \pm 0.10$) or only slightly exceed it.

Therefore, generalization of data on the swellability of butyl rubber in various solvents allows prediction of swelling of butyl rubber in other solvents. Also, multiparametric analysis of the solvent effect provides a better insight into the swelling mechanisms.

To validate our approach, we similarly generalized data on swelling of polybutadiene, reported by Scott and Magat [13]. They determined the solvent uptake in 5 days at 25°C. The density of the initial cross-linked sample was 0.976, and the average molecular weight of the polymer units between cross-links, 5600, i.e., the cross-links are arranged at average intervals of 400 carbon atoms.

The solvent uptake in volumes per unit volume of the polymer (V_2) and in moles (S_M), and also log S_M values are listed in Table 2.

The initial value R 0.909, obtained for the entire set of 13 solvents, is unsatisfactory. According to the IUPAC recommendations for generalization of correlation analysis data [8], we excluded from consideration the data for nitrobenzene as the most outlying, and obtained Eq. (4) characterized by an excellent R 0.996, s ±0.02, and the following pair correlation factors: r_1 = 0.707, r_2 = 0.702, r_3 = 0.064, r_4 = 0.570, r_5 = 0.598, and r_6 = 0.703.

$$\log S_M = -1.17 + (3.24 \pm 0.63) f(n^2) + (5.08 \pm 0.89) f(\varepsilon) - (1.85 \pm 0.43) \times 10^{-3} B - (0.10 \pm 0.02) E_T + (4.03 \pm 0.84) \times 10^{-3} \delta^2 - (1.56 \pm 0.77) \times 10^{-3} V_M. \quad (4)$$

As in the case of polyethylene [9], the higher the solvent molar volume V_M and its capacity for specific interaction, the lower the swellability of polybutadiene. At the same time, the strong tendency of a solvent toward nonspecific solvation promotes swelling.

The terms of the cohesion energy density $f(\delta^2)$ and basicity (B) in Eq. (4) are nonsignificant, and the solvent effect on swelling of polybutadiene can be sat-

isfactorily reproduced using a four-parameter equation (5).

$$\log S_M = -0.51 + (5.77 \pm 0.61) f(n^2) + (6.39 \pm 0.71) f(\varepsilon) - (0.11 \pm 0.01) E_T - (4.63 \pm 0.76) \times 10^{-3} V_M; \quad (5)$$

$$R = 0.988, \; s \pm 0.04.$$

Further decrease in the number of parameters is unacceptable, as resulting in an abrupt decrease in *R*.

The sign and significance of separate terms of Eqs. (2) and (4), and (3) and (5) only slightly differ from each other, suggesting that, despite the difference in the polymer structure (methyl branching in butyl rubber and double bonding in polybutadiene), the swelling mechanisms are quite similar, being controlled essentially by their backbone structure.

CONCLUSIONS

(1) The swellability of a polymer in organic solvents depends on the integral solvent effect, which can be estimated on the basis of the principe of linear free energies, using multiparametric equations.

(2) Swelling of butyl rubber and poly(isobutylene) is controlled essentially by the molar volume of a solvent. Both nonspecific and specific solvation effects also contribute significantly, but not the cohesion energy density of a solvent.

REFERENCES

1. Flory, P.J., *Chem. Phys.*, 1956, vol. 18, no. 1, pp. 108–120.
2. Bristow, S.M. and Watson, W.F., *Trans. Faraday Soc.*, 1958, vol. 54, no. 11, pp. 173–174.
3. Erede, L., *Macromolecules*, 1986, vol. 19, no. 6, pp. 1522–1526.
4. Aminabhavi, R.H., Harogoppad, S.B., Khinnavar, R.C., and Balundgi, R.H., *JMS Rev. Macromol. Chem. Phys., Ser. C*, 1991, vol. 31, no. 4, pp. 433–498.
5. Koppel, L.A. and Palm, V.A., *Advances in Linear Free Energies Relationships*, New York: Plenum, 1973, pp. 203–300.
6. Richards, R.B., *Trans. Faraday Soc.*, 1946, vol. 42, no. 1, pp. 20–28.
7. Kamlet, M.J., Abboud, J.L.M., and Taft, R.W., *Progr. Phys. Org. Chem.*, 1981, vol. 13, pp. 485–630.
8. Mayer, U., *Monatsh. Chem.*, 1978, no. 2, pp. 421–433.
9. Makitra, R., Pyrih, Y., Zagladko, E., *et al.*, *J. Appl. Polym. Sci.*, 2001, vol. 81, no. 7, pp. 3133–3190.
10. Makitra, R.G. and Pristanskii, R.E., *Khim. Tverd. Topl.*, 2001, no. 5, pp. 3–16.
11. Rostler, F.S. and White, R.M., *Rubber Age*, 1997, vol. 61, no. 3, pp. 421–433.
12. Recommendations for Reporting the Results of Correlation Analysis in Chemistry Using Regression Analysis, *Quant. Struct. Act. Relat.*, 1946, vol. 4, p. 29.
13. Scott, R.L. and Magat, M., *J. Polym. Sci.*, 1949, vol. 4, pp. 555–571.

Russian Journal of Applied Chemistry, Vol. 77, No. 2, 2004, pp. 327–332. Translated from Zhurnal Prikladnoi Khimii, Vol. 77, No. 2, 2004, pp. 328–334.

CHEMISTRY OF FOSSIL FUEL

Formation of Consolidated Bed by Carbon Sorbent and Oil in Removal of Spilled Oil

N. A. Samoilov, R. N. Khlestkin, M. I. Osipov, and O. P. Chichirko

Ufa State Oil Technical University, Ufa, Bashkortostan, Russia

Balykles Joint-Stock Timber Company, Pyt'-Yakh, Khanty-Mansi Autonomous District, Russia

Received October 8, 2003

Abstract—Formation of a consolidated bed by carbon sorbent and oil in sorption removal of spilled oil was observed and substituted experimentally; the dynamics of this process was analyzed. A process for eliminating oil spills on the water surface using a carbon sorbent was developed.

Large-scale spills of oil and petroleum products upon mechanical or corrosion failure of pipelines and upon incidents on water, railway, and motor transport are important sources of environmental pollution, often causing real ecological catastrophes. The environmental damage on spilling of 1 ton of oil in water and soil can be estimated at 3 104 500 and 3 528 000 rubles, respectively (costs as of 1997) [1]. Removal of oil and petroleum products spilled over the soil and, especially, water surfaces is rather complex and laborious technical problem. Oil is removed from the water surface using barrier and pump systems, oil-spill boats, and various sorbents [2–6], including both special sorbents or industrial and agricultural wastes [7–10] (Table 1).

Finely dispersed sorbents, e.g., chopped straw and cane, peat, moss, buckwheat husk, rubber crumb, and special sorbents (Lessorb, Peat Sorb) allow relatively simple collection of spilled oil. This procedure includes two main stages: distribution of the sorbent over the oil–spill surface and collection of the sorbent with adsorbed oil from the surface using gauze frames, shovels, scoops, and other instruments, with the collected matter in special tanks. However, analysis of the physical interaction of various sorbents with oil layer revealed rather important dynamic changes in the sorbent–oil system upon their contact.

A fine sorbent added to an oil layer forms a specific three-dimensional structure between the upper surface of the oil layer and water surface (Fig. 1). Within several minutes, oil fills these free voids, and the resulting sorbent–oil system can be recovered using, e.g., gauze apparatus. However, the resulting sorbent–oil system is unstable, and in the course of removal not only water, but also certain fraction of sorbed oil escape through the gauze. In this case, the sorbent–oil system acts as a non-Newtonian liquid and spreads from the zone of treatment of the oil spill to the zone of removal of the spent sorbent (Fig. 2). As a result, the total area of the oil spill remains unchanged, with only result that the sorbent bed layer containing oil on the water surface becomes thinner. In this case, manual labor expenditures are very high, because multiple treatment to remove diffluent spent

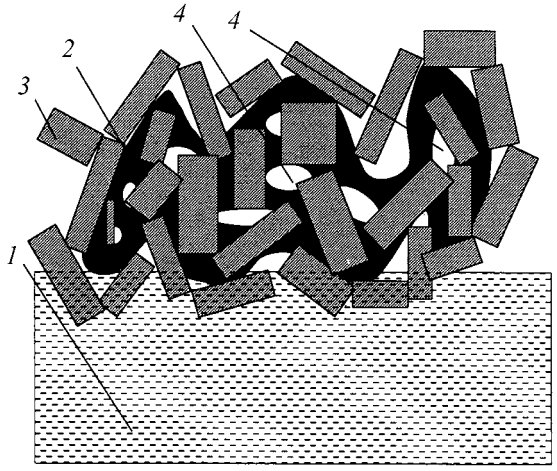

Fig. 1. Formation of an unstable layer of the sorbent–oil system on the water surface: (*1*) water, (*2*) oil, (*3*) sorbent, and (*4*) voids in the unstable layer.

1070-4272/04/7702-0327 © 2004 MAIK "Nauka/Interperiodica"

Table 1. Sorption capacity of some sorbents with respect to oil and water

Sorbent	Sorption capacity for oil	Sorption capacity for water	Oil extraction ratio, %
	g g^{-1}		
Industrial organic sorbents			
Polystyrene foam plastic (granules)	9.26	4.45	0
Polypropylene (granules)	1.60	0.80	0
Tire crumb	3.58	7.20	55
Rubber crumb	5.11	0.30	0
Urea-formaldehyde resin:			
fragments	23.30	0.10	0
powder	39.60	–	60
Phenol-formaldehyde resin (powder)	4.42	14.54	0
Sheet foam-rubber, mm	14.50	1.30	75
3	35.2	25.92	85
18	36.89	30.71	–
Foam-rubber granulated (5–8 mm)	46.31	42–52	94
Sin-tepon	46.31	42–52	–
Ground lignite	≈1	–	–
Ground bitumen	4–4.5	0.2–1	–
SINTAPEKS (wastes of spinning industry)	24.45	0.20	83
Nonwoven fabric (Lav-san):			
sample A	14.05	13.91	82
sample B	7.27	7.08	66
sample C	4.71	4.33	60
Agril A:			
smooth surface	13.90	1.46	0
rough surface	13.60	1.80	0
Agril B:			
smooth surface	8.20	1.48	0
Sheet wadding	24–27	0.5	87
Cotton coiled linen	3.2	–	–
Industrial inorganic sorbents			
Foamed Nickel (5 mm thick)	2.91	3.03	0
Fiber glass	5.42	1.72	60
Agricultural wastes			
Chopped wheat straw	4.10	4.30	35
Chopped cane	8.20–2.66	4.68	18–30
Saw dust	1.72	4.31	10–20
Buckwheat husk	3.05–3.50	2.20	44
Wastes of cotton wool production	8.30	0.26	60
Dried moss:			
unbroken	3.5	3.1	–
chopped	5.8	3.5	–
peat	17.71	24.28	74
Special oil sorbents			
Lessorb (treated peat dust)	9.10	2.50	66
Peat Sorb (Clon Ink. Co., Germany)	6.19	0.71	0

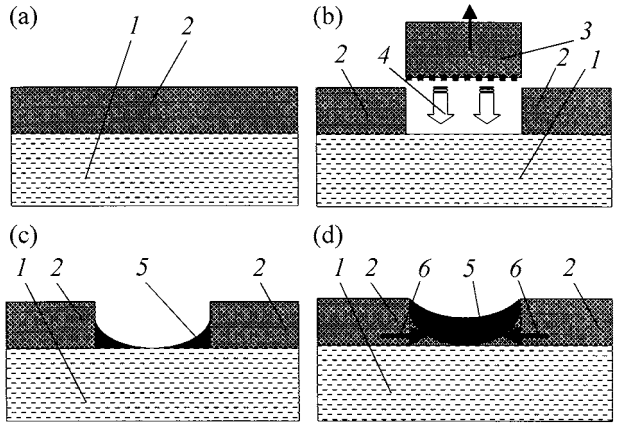

Fig. 2. Removal of the unstable sorbent–oil layer from the water surface. (a) Initial layer, (b) removal of a certain fraction of the layer, (c) oil spilling from the layer over cleaned water surface, and (d) spreading of the unstable layer over the water surface. (*1*) Water, (*2*) unstable layer, (*3*) removal of a certain fraction of the layer with a scoop, (*4*) spill of oil and water from the scoop onto the cleaned water surface, (*5*) oil spill from the layer, and (*6*) spreading of the layer.

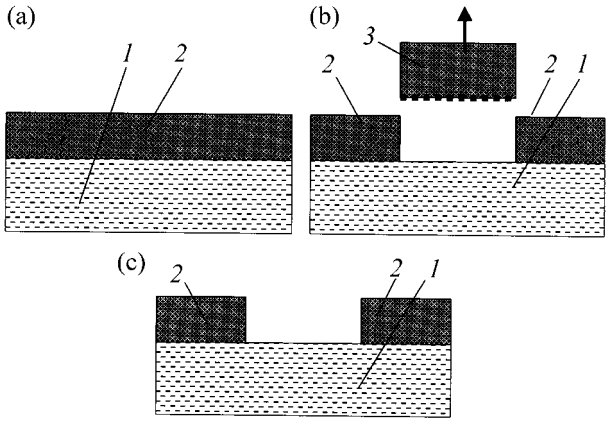

Fig. 3. Removal of the consolidated bed formed by carbon sorbent and oil from water surface: (a) initial layer, (b) removal of a certain fraction of the bed, and (c) steady state of the system. (*1*) Water, (*2*) consolidated bed, and (*3*) removal of a certain fraction of the bed with a scoop.

from the same section of the oil spill is required. For the same reason, the efficiency of mechanical devices in removal of spent sorbent, e.g., bucket elevator with gauze ladles, is also low.

Quite a different pattern is observed in sorption of spilled oil using carbon sorbents. The carbon sorbent (CS), being a product of carbonization of the wastes of merchantable wood treatment, is produced on an industrial scale [11]. Finely dispersed macroporous carbon sorbent (technical carbon) produced in this process is characterized by 0.170 g cm^{-3} bulk density and free volume of 4.18 cm^3 per gram of sorbent. This sorbent, consisting predominantly of needle-like particles (3.5–6 mm long and 0.47–0.71 mm thick), exhibits high hydrophobic and lipophilic properties, and it can sorb up to 4 g oil per gram of sorbent (Table 2). Hence, it is rather competitive compared with the other sorbents studied (Table 1).

The data on the oil removal performed on the model systems with oil spill 0.5 m in diameter and in the course of pilot tests of the carbon sorbent at an accidental oil spill near Pyt'-Yakh town (Khanty-Mansi Autonomous District) showed that the system consisted by a carbon sorbent and oil is characterized by some specific features untypical of other sorbents. Removal of the CS–oil system in 1–5 min after treatment of the oil spill proceeds similarly to that with the other fine sorbents (Fig. 2), whereas keeping this system on the water surface for several hours causes formation of a rather strong sorbent–oil system, which prevents spill of oil from the recovered spent sorbent over the cleaned water surface; this is also the case when the spent sorbent is removed from the water surface using gauze frames (Fig. 3). We also observed no spreading of the layer remaining on the water surface toward the cleaned zone. Such a strong CS–oil layer was named consolidated bed. The strength of this bed is so high that it holds branches and boards on the surface, though its density is smaller that that of the load (wood).

Two concepts concerning the mechanism of formation of this consolidated bed were suggested. (1) Evaporation of the light oil fractions in the course of keeping of the CS–oil system provides strengthening of the system owing to increasing viscosity of the oil remaining in the consolidated bed. (2) Formation of the "carpet" CS–oil system is related to slow diffusion of oil in microchannels at the particle interface due to capillary forces, which "glues" sor-

Table 2. Sorption capacity of carbon sorbent in removal of petroleum products from the water surface, 5 min contact time

Petroleum product	Sorption capacity, g per gram of sorbent
Oil from Tyumen field	4.27–4.34
Oil from Shaim field	4.13–4.35
Oil from Arlan field	4.4–4.5
Diesel oil	4.04–4.13

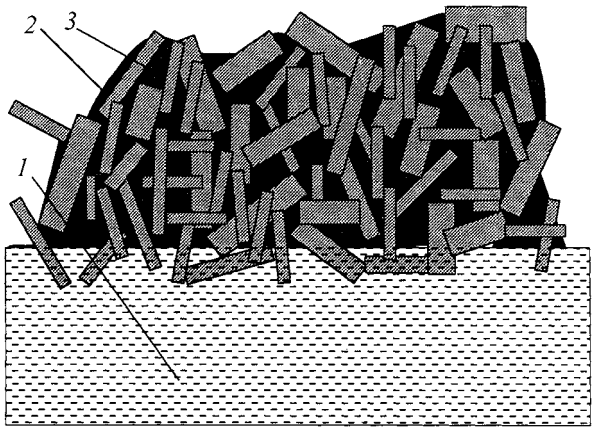

Fig. 4. Formation of a consolidated CS–oil bed on the water surface: (*1*) water, (*2*) oil, and (*3*) sorbent.

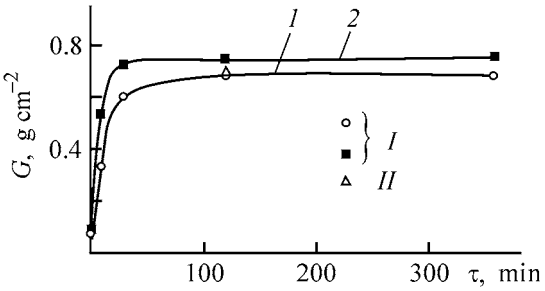

Fig. 5. Force of adhesion in the CS–oil system, *G*, vs. the consolidation time τ for (*1*) fresh and (*2*) aged oil at layer thickness of (*I*) 10 and (*II*) 20 mm.

bent particles and improves the retention of oil in the free voids of the sorbent (Fig. 4).

The mechanism of the sorbent–oil consolidation on the water surface was studied on a laboratory setup equipped with a different-arm balance allowing registration of the forces appearing in removal of a fragment of the sorbent–oil system from the water surface with a gauze. In the course of the experiments, we determined the force of adhesion between the gauze and water, the force required to remove certain fragment of the sorbent–oil system from the whole layer of the spent sorbent, the weight of this removed fraction, the force acting at the perimeter and over the area of the boundary between the whole sorbent–oil system and its removed fragment. In our experiments, we used both fresh oil of the Arlan field (801 kg m^{-3} density, 30 mm^2 s^{-1} viscosity) and oil artificially aged by evaporation in air for 2 weeks in a hood, whose viscosity was greater than that of the fresh oil by a factor of 15 (920 kg m^{-3} density, 450 mm^2 s^{-1} viscosity).

It was found that, with increasing contact time in the CS–oil system, the degree of consolidation of the system increases to a certain level for both fresh and aged oil (Fig. 5). The reliability of experimental data in a series of replicate tests was confirmed by statistical analysis in accordance with Student's test [12].

In both cases, the stable consolidated CS–oil system is formed in 2 h. Our experimental data showed that the formation of this consolidated CS–oil bed is not due to partial evaporation of the oil and the related increase in its density and viscosity on keeping for 2–6 h, because the consolidation of the aged oil proceeds similarly to that of the fresh oil. If evaporation of the light oil fractions were responsible for the bed consolidation, then, for the aged oil, the dependence of the force acting at the perimeter and over the area of the boundary between the whole sorbentoil system and its removed fragment would be nearly constant in time. However, as can be seen from the experimental data, these dependences are similar for both aged and fresh oil.

The second concept of fuller impregnation of the sorbent bed with oil in the course of the system keeping as the reason for bed consolidation was not confirmed either, because our additional studies of the kinetics of oiling of a 60–70-mm sorbent bed on bringing its bottom in contact with an oil layer showed that, already after 10 min of contact, the height of the oil lift was 10–20 mm. The kinetics of sorption of the oil of Arlan field aged for 1 month (67 mm sorbent bed, 531.5 mm s^{-1} viscosity) on the carbon sorbent is illustrated below:

Height of the oil lift in the sorbent, mm	Contact time of oil and sorbent, min
2	2
5	5
10	10
20	15
30	17
40	19
50	21
60	23

In the studies of the consolidation of the CS–oil system, the layer thickness was 10 mm. A twofold increase in the layer thickness after the same contact time of the sorbent and oil did not change the specific disruptive force at the boundary between the whole sorbent–oil system and its fragment being removed.

Our experimental data suggest that an additional intermolecular interaction appears between the sorbent surface and oil in narrow slits between the fine sorbent particles. This concept is confirmed by computer simulation of nanostructures formed by spread-

Table 3. Evaluation of the oil spill capacity

Area of the oil spill, m^2	Volume of the oil spill (m^3) at indicated oil layer thickness, mm							
	50	20	10	5	3	1	0.5	0.1
1	0.05	0.02	0.01	0.005	0.003	0.001	0.0005	0.0001
3	0.15	0.06	0.03	0.015	0.009	0.003	0.0015	0.0003
5	0.25	0.1	0.05	0.025	0.015	0.005	0.0025	0.0005
10	0.5	0.2	0.1	0.05	0.03	0.01	0.005	0.001
30	1.5	0.6	0.3	0.15	0.09	0.03	0.015	0.003
50	2.5	1	0.5	0.25	0.15	0.5	0.025	0.005
100	5	2	1	0.5	0.3	0.1	0.05	0.01
300	15	6	3	1.5	0.9	0.3	0.15	0.03
500	25	10	5	2.5	1.5	0.5	0.25	0.05
1000	50	20	10	5	3	1	0.5	0.1
3000	150	60	30	15	9	3	1.5	0.3
5000	250	100	50	25	15	5	2.5	0.5
10000	500	200	100	50	30	10	5	1

Table 4. Consumption of carbon sorbent for removal of oil (0.85 g cm^{-3} oil density)

Area of the oil spill, m^2	Sorbent charge (kg) at indicated oil layer thickness, mm							
	50	20	10	5	3	1	0.5	0.1
1	10.7	5.66	3.2	2.12	1.8	0.85	0.7	0.4
3	32.1	17	9.6	6.7	5.4	2.55	2.1	1.2
5	53.5	28.3	16	10.6	9	4.25	3.5	2.1
10	107	56.6	32	21.2	17.6	8.5	7.1	4.2
30	321	170	96	67	54	25.5	21	12
50	535	283	160	106	90	42.5	35	21
100	1070	566	320	212	176	85	71	42
300	3210	1700	960	670	540	255	210	120
500	5350	2830	1600	1060	900	425	350	210
1000	10700	5660	3200	2120	1760	850	710	420
3000	32100	17000	9600	6700	5400	2550	2100	1200
5000	53500	28300	16000	10600	9000	4250	3500	2100
10000	107000	56600	32000	21200	17600	8500	7100	4200
Rated sorbent capacity, g oil per g sorbent	4	3	2.5	2	1.5	1	0.6	0.2

ing of small drops over microheterogeneous supports [13]. These data show that four compact "legs" are formed in the microdrop, which support its upper section and provide strong and stable contact between the nanoobject and heterogeneous solid surface. At low- and high-energy sections of the surface the molecular clusters are formed, which round low-energy sections or link high-energy sections. This concept is confirmed by the fact that the cogesion energy (energy necessary for rupture of the oil layer) determined from the surface tension of the fresh and aged oil, respectively, constitutes 0.08–0.10 g cm^{-2}, which is smaller by a factor of 5–7 than the specific disruptive energy at the boundary between the whole sorbent–oil system and its fragment being removed (0.68–0.75 g cm^{-2}).

This phenomenon of consolidation of the CS–oil system allows the process of oil removal to be simplified by elimination of a multiple treatment of the oil spill with sorbent the consumption of the sorbent and labor and the cost of the process thereby lowered.

We suggest the following scheme for removing oil spill with the use of a dispersed carbon sorbent.

(a) Evaluation of the oil spill capacity by its area and oil layer thickness according to Table 3.

(b) Evaluation of the amount of carbon sorbent required, using Table 4.

(c) Uniform distribution of the dispersed carbon sorbent over the oil spill area with a pneumatic batcher to provide complete oiling of the sorbent.

(d) Keeping of the sorbent bed with sorbed oil for at least 2 h to form a consolidated sorbent–oil system.

(e) Removal of the consolidated sorbent–oil bed by scoops or mechanical elevators or drags and storage of the spent sorbent in special tanks.

(f) If necessary, secondary treatment of the water surface with a small amount of dispersed carbon sorbent to remove separate spots and films of oil.

(g) Transportation of the spent sorbent to special installation for oil recovery.

(h) Further regeneration of the spent sorbent, e.g., burning out of residual oil.

CONCLUSIONS

(1) At a contact time of no less than 2 h, a consolidated CS–oil bed is formed upon treatment with carbon sorbent of an oil spill on the water surface; this bed is easily removed from water without its secondary pollution.

(2) The specific disruptive energy at the boundary between the whole sorbent–oil system and its fragment being removed is greater by a factor of 5–7 than the cohesion energy (energy of the oil layer rupture).

(3) A scheme of the process for removal of spilled oil from the water surface using a carbon sorbent to form a consolidated sorbent–oil bed is suggested.

REFERENCES

1. Isaeva, L.K. *Transp. Khran. Nefteprod.*, 1998, nos. 2–3, pp. 11–15.
2. Mochalova, O.S., Nesterova, M.P., and Antonova, N.M., *Neft. Khoz–vo.*, 1992, no. 3, pp. 33–35.
3. Borodavkin, P.P., *Okhrana okruzhayushchei sredy pri stroitel'stve i ekspluatatsii magistral'nykh nefteprovodov* (Environmental Protection at Building and Operation of Oil–Trunk Pipelines), Moscow: Nedra, 1981.
4. Mironov, O.G., *Obzornaya informatsiya VNIIOENG, Ser.: Korroziya i zashchita v neftegazovoi promyshlennosti* (VNIIOENG Information review. Ser.: Corrosion and Protection in Oil–and–Gas Industry), Moscow: VNIIOENG, 1980, pp. 31–32.
5. Kormak, D., *Bor'ba s zagryazneniem morya neft'yu i neftekhimicheskimi veshchestvami* (Control of Sea Pollution with Oil and Petroleum Products), Moscow: Transport, 1989.
6. Samoilov, N.A., Khlestkin, R.N., Shemetov, A.V., and Shamazov, A.A., *Sorbtsionnyi metod likvidatsii avariinykh razlivov nefti i nefteproduktov* (Sorption Method for Elimination of Spills of Oil and Petroleum Products), Moscow: Khimiya, 2001.
7. Khlestkin, R.N., Samoilov, N.A., and Shemetov, A.V., *Neft. Khoz-vo.*, 1999, no. 2, pp. 46–49.
8. Khlestkin, R.N. and Samoilov, N.A., *Neft. Khoz–vo.*, 2000, no. 5, pp. 51–52.
9. Khlestkin, R.N. and Samoilov, N.A., *Ecol. Congr. Int. J. USA*, 1999, vol. 3, no. 1, pp. 33–37.
10. Khlestkin, R.N. and Samoilov, N.A., *J. Fushin Petrol. Inst. (China)*, 2000, vol. 20, no. 3, pp. 156–162.
11. RF Patent 2181073.
12. Batuner, L.M. and Pozin, M.E., *Matematicheskie metody v khimicheskoi tekhnike* (Mathematical Methods in Chemical Engineering), Moscow: Goskhimizdat, 1963.
13. Samsonov, V.M., Dronnikov, V.V., Murav'ev, S.O., *et al.*, *Zh. Fiz. Khim.*, 2002, vol. 76, no. 11, pp. 2052–2056.

Russian Journal of Applied Chemistry, Vol. 77, No. 2, 2004, pp. 333–335. Translated from Zhurnal Prikladnoi Khimii, Vol. 77, No. 2, 2004, pp. 335–337.

BRIEF COMMUNICATIONS

Partial Pressure of Saturated Sodium Nitrite Vapor over the System $NaNO_2$–$NaNO_3$

V. I. Glazov, G. P. Dukhanin, M. Kh. Dkhaibe, and V. A. Losev

Volgograd State Technical University, Volgograd, Russia

Received November 13, 2003

Abstract—The partial pressure of sodium nitrite was measured in the system $NaNO_2$–$NaNO_3$ at temperatures of 798, 823, and 848 K and the logarithm of the $NaNO_2$ pressure was obtained as a function of inverse temperature. The coefficients A and B of the Clausius–Clapeyron equation and the partial molar heats of evaporation were calculated. The activities and activity coefficients of sodium nitrite were determined for various compositions of the system $NaNO_2$–$NaNO_3$.

In continuation of studies of the physicochemical and thermodynamic properties of molten nitrite–nitrate systems [1–4], the partial pressure of saturated sodium nitrite vapor was measured over the system $NaNO_2$–$NaNO_3$.

The procedure of salt preparation, the experimental setup, and the method used for analyzing the condensate of the vapor phase have been described previously [1, 4]. The saturated vapor pressure of sodium nitrite over liquid $NaNO_2$–$NaNO_3$ mixtures was measured at 798, 823, and 848 K. The temperature dependence of the sodium nitrite vapor pressure is described by the Clausius–Clapeyron equation $\log P = B - A/T$.

The results obtained in measuring the vapor pressure of sodium nitrite over melts of various compositions, as well as the calculated coefficients of the Clausius–Clapeyron equation and partial molar heats of $NaNO_2$ evaporation, are listed in Table 1. The logarithm of the vapor pressure of sodium nitrite at its varied content in the melt is shown as a function of inverse temperature in Fig. 1.

The coefficient of linear correlation of $\log P$ as a function of $1/T$ is in the range from 0.78 (at low sodium nitrite concentrations) to unity.

As shown previously [4], the concentration behavior of the curves for partial pressures of sodium

Table 1. Saturated vapor pressure P_{NaNO_2}, coefficients A and B of the Clausius–Clapeyron equation, and partial molar heats of sodium nitrite evaporation, $\Delta H_{evap}^{NaNO_2}$, in the system $NaNO_2$–$NaNO_3$

c_{NaNO_2} in melt, mol %	P_{NaNO_2} (Pa) at indicated temperature, K			Coefficients of equation		$\Delta H_{evap}^{NaNO_2} \times 10^{-3}$, J mol^{-1}
	798	823	848	$A \times 10^{-3}$, K	B	
10	1.20	2.78	5.36	8.781	11.083	168.13
20	2.76	5.75	11.30	8.308	10.850	159.07
40	6.65	13.67	25.95	7.986	10.831	152.91
50	9.05	18.06	33.73	7.716	10.627	147.74
60	11.71	22.95	42.39	7.541	10.520	144.39
80	17.83	34.17	61.40	7.256	10.345	138.93
90	22.35	41.50	74.39	7.054	10.193	135.06
100	26.61	48.82	86.50	6.934	10.114	132.77

1070-4272/04/7702-0333 © 2004 MAIK "Nauka/Interperiodica"

Table 2. Activities a and activity coefficients γ of sodium nitrite in the system $NaNO_2$–$NaNO_3$ at various temperatures

T, K	Values of a and γ at indicated $NaNO_2$ content in the melt, mol %						
	10	20	40	50	60	80	90
798	0.045* / 0.45	0.11 / 0.54	0.25 / 0.63	0.34 / 0.68	0.44 / 0.73	0.67 / 0.84	0.84 / 0.93
823	0.057 / 0.57	0.12 / 0.61	0.28 / 0.69	0.37 / 0.73	0.47 / 0.78	0.70 / 0.87	0.85 / 0.94
848	0.062 / 0.62	0.13 / 0.66	0.30 / 0.75	0.39 / 0.78	0.49 / 0.81	0.71 / 0.89	0.86 / 0.96

* a, numerator; γ, denominator.

nitrite and nitrate shows negative deviations from the Raoult law. Under isothermal conditions, the vapor pressure of sodium nitrite grows steadily with decreasing content of the second component.

As the content of sodium nitrite in the system decreases, the heat of its evaporation becomes higher, which points to increasingly enhanced interaction of particles in the melt.

The experimental values of the saturated vapor pressure over a pure component, P_i^0, and partial pressures of this component, P_i, in the system were used to calculate the activities a_i and activity coefficients γ_i of sodium nitrite in the system $NaNO_2$–$NaNO_3$. The results obtained are listed in Table 2.

The activities and activity coefficients of sodium nitrite in the system under study have been reported previously [4].

Figure 2 shows the temperature dependences of the activity and activity coefficient of sodium nitrite and nitrate vs. the content of $NaNO_3$ in the system at 798 and 848 K.

It can be seen from Fig. 2 that the activities of sodium nitrite and nitrate show negative deviations from the concentrations expressed in mole fractions, and, therefore, the calculated activity coefficients are less than unity. The isotherms of sodium nitrite activity show large negative deviations. The negative deviations point to a certain extent of complexing in

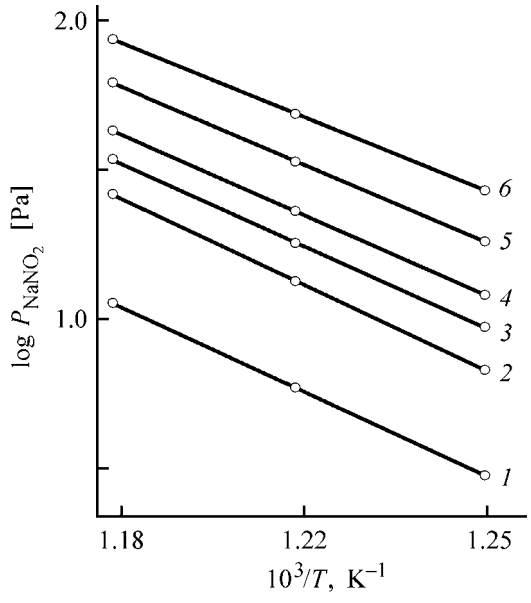

Fig. 1. Vapor pressure of sodium nitrite, P_{NaNO_2}, in the system $NaNO_2$–$NaNO_3$ vs. temperature T. $NaNO_2$ content in the melt (mol %): (*1*) 20, (*2*) 40, (*3*) 50, (*4*) 60, (*5*) 80, and (*6*) 100.

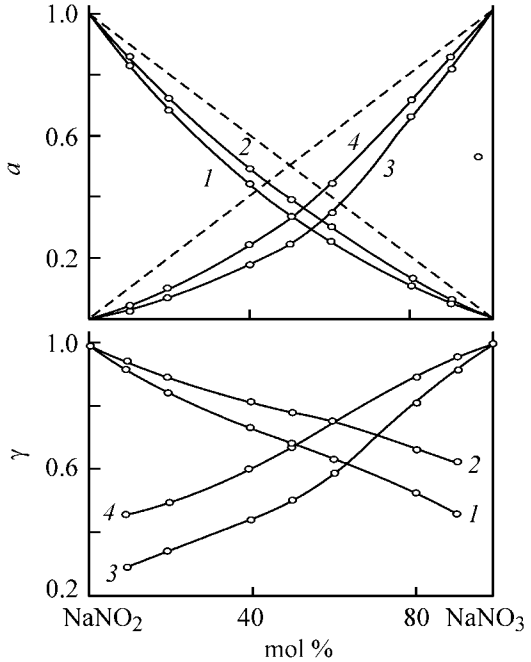

Fig. 2. Activity a and activity coefficient γ of sodium nitrite and nitrate in the system $NaNO_2$–$NaNO_3$ at temperatures of (*1*, *3*) 798 and (*2*, *4*) 848 K.

the system [4, 5]. With increasing temperature, the negative deviations become less pronounced.

CONCLUSIONS

(1) The partial pressure of sodium nitrite in the system $NaNO_2$–$NaNO_3$ was determined at 798, 823, and 848 K. The temperature dependence of the vapor pressure was found to be described by the Clausius–Clapeyron equation.

(2) The experimental values of the saturated vapor pressures over pure components and the partial pressures of these components over the system were used to calculate the activities and activity coefficients of sodium nitrite. It was established that the activities of both the components show negative deviations from the ideal behavior, and the activity coefficients are less than unity. This points to a certain extent of complexing in the system.

REFERENCES

1. Glazov, V.I., Golod, V.F., and Golovanov, P.S., *Zh. Prikl. Khim.*, 1984, vol. 57, no. 6, pp. 2351–2352.
2. Glazov, V.I., Golovanov, P.S., and Dukhanin, G.P., *Zh. Prikl. Khim.*, 1990, vol. 63, no. 1, pp. 193–195.
3. Glazov, V.I., Dukhanin, G.P., and Losev, V.A., *Zh. Prikl. Khim.*, 2002, vol. 75, no. 6, pp. 908–910.
4. Glazov, V.I., Dukhanin, G.P., and Dkhaibe, M.Kh., *Zh. Prikl. Khim.*, 2003, vol. 76, no. 9, pp. 1445–1447.
5. Bergman, A.G., Berul', S.N., and Nikonova, I.N., *Izv. Sekt. Fiz.-Khim. Analiza*, 1953, vol. 23, p. 183.

Russian Journal of Applied Chemistry, Vol. 77, No. 2, 2004, pp. 336–338. Translated from Zhurnal Prikladnoi Khimii, Vol. 77, No. 2, 2004, pp. 338–339.

BRIEF COMMUNICATIONS

Catalytic Transformations of Bornyl Chloride under the Action of $AlCl_3$

E. V. Vishnyakova, V. A. Utsal', and D. A. Ponomarev

St. Petersburg State Forestry Academy, St. Petersburg, Russia

Received June 2, 2003

Abstract—The composition of products formed in catalytic transformations of bornyl chloride under the action of $AlCl_3$ was studied.

Turpentine, which is a mixture of monoterpenes $C_{10}H_{16}$, is one of the main products of the wood-chemical industry and serves as starting raw material for synthesis of various substances, e.g., those used in the perfumery-cosmetic industry [1]. In some cases, obtaining the target product involves a preliminary isomerization of the starting monoterpenes, which yields substances with various types of carbon skeletons. In the course of isomerization under the action of acid catalysts, the double bonds of monoterpenes are frequently involved in polymerization processes, which leads to a decrease in the output of the target product [2, 3]. Therefore, it seemed appropriate to study acid-catalytic transformations of mono halogen derivatives of monoterpenes. In this case, the polymerization processes mentioned above do not occur, which makes it possible to synthesize valuable products in good yield from the available vegetable raw materials.

EXPERIMENTAL

Bornyl chloride (BCh), *endo*-2-chloro-1,7,7-trimethyl[2.2.1]bicycloheptane, which can be easily synthesized from α- and β-pinenes [4, 5], was chosen as object of study. As catalysts were taken $AlCl_3$ (Aldrich) and $ZnCl_2$ (prepared by calcination of $ZnCl_2$ in the presence of several drops of concentrated HCl), which are a strong and a relatively weak Lewis acids, respectively. It was assumed that treatment of BCh with these acids leads to formation of a mixture of halogenocycloalkanes $C_{10}H_{17}Cl$ (isomeric to BCh), whose structure and relative amounts depend on the process conditions. Despite the fact that the isomerization transformations of hydrochlorides of bicyclic monoterpenes have been already studied for 80 years [6], the mechanisms of the rearrangements observed remain open to question [7].

The starting BCh was obtained by addition of HCl to α-pinene [4] and, after recrystallization from petroleum ether (40–70°C) and further purification by column adsorption chromatography (silica gel, petroleum ether as eluent), had melting point of 135–136°C [96% main substance according to gas–liquid chromatography (GLC)]. As solvent in the reaction of catalytic treatment served hexane or trichloroethylene. The conditions of the catalytic treatment are listed in the table.

After decomposition and drying, the composition of the reaction mixture was analyzed on a Hewlett–Packard 5995 mass-spectrometer in the programmed-temperature mode. The chromatogram was recorded as the total ion current in the range of masses 50–300.

An analysis of the composition of the reaction products by chromato-mass-spectrometry demonstrated that the catalytic transformations of BCh yield multicomponent mixtures, in which it is difficult to distinguish any main component. The peaks in the chromatograms can be distinctly divided, depending on their retention time, into several groups, among which groups with retention times of 5.5–1.5, 13–18, 20–23, and 33–45 min were distinguished.

An analysis of the mass spectra of the compounds that correspond to each of the groups distinguished showed that the first group comprises hydrocarbons of composition $C_{10}H_{16}$ and $C_{10}H_{18}$, for which the corresponding peaks of molecular ions were recorded. By comparison with a spectrum contained in the database of the spectrometer, one of the compounds was identified as *trans*-decaline, which was additionally confirmed by GLC. A comparison of the mass-spectra obtained with those of trimethyl bicyclo[2.2.1]heptanes, reported in [8], revealed the presence of *endo*-1,2,4-trimethyl, *exo*-1,2,4-trimethyl, and 1,4,7-trimethyl de-

1070-4272/04/7702-0336 © 2004 MAIK "Nauka/Interperiodica"

Influence of reaction conditions on the composition of products formed in catalytic transformations of bornyl chloride under the action of $AlCl_3$ and $ZnCl_2$

Run no.	BCh : catalyst : solvent mole fraction	τ, h	*T*, °C	Products
1	1 : 1 : 20	24	20	$C_{10}H_{18}$, $C_{20}H_{32}$, $C_{20}H_{34}$
2	1 : 1 : 20	48	20	$C_{10}H_{18}$, $C_{20}H_{32}$, $C_{20}H_{34}$
3*	1 : 1 : 20	24	20	–
4	1 : 1 : 20	4	20	$C_{10}H_{16}$, $C_{10}H_{18}$, $C_{10}H_{17}Cl$, $C_{10}H_{16}Cl_2$, $C_{20}H_{32}$, $C_{20}H_{34}$, $C_{20}H_{33}Cl$
5	1 : 3 : 4	4	20	$C_{10}H_{16}$, $C_{10}H_{18}$, $C_{10}H_{17}Cl$, $C_{10}H_{16}Cl_2$, $C_{20}H_{32}$, $C_{20}H_{34}$, $C_{20}H_{33}Cl$
6	1 : 3 : 20	4	20	$C_{10}H_{16}$, $C_{10}H_{18}$, $C_{10}H_{17}Cl$, $C_{10}H_{16}Cl_2$, $C_{20}H_{32}$, $C_{20}H_{34}$, $C_{20}H_{33}Cl$
7	1 : 3 : 200	4	20	$C_{10}H_{16}$, $C_{10}H_{18}$, $C_{10}H_{17}Cl$, $C_{10}H_{16}Cl_2$, $C_{20}H_{32}$, $C_{20}H_{34}$, $C_{20}H_{33}Cl$
8	1 : 3 : 20	4	0	$C_{10}H_{16}$, $C_{10}H_{18}$, $C_{10}H_{17}Cl$, $C_{10}H_{16}Cl_2$, $C_{20}H_{32}$, $C_{20}H_{34}$, $C_{20}H_{33}Cl$
9	1 : 3 : 4	4	0	$C_{10}H_{16}$, $C_{10}H_{18}$, $C_{10}H_{17}Cl$, $C_{10}H_{16}Cl_2$, $C_{20}H_{32}$, $C_{20}H_{34}$, $C_{20}H_{33}Cl$

* $ZnCl_2$ was used as catalyst.

rivatives of bicyclo[2.2.1]heptane in the products of catalytic transformations of BCh. 1,7,7-Trimethyl bicyclo[2.2.1]heptane (bornane), whose formation by transfer of the hydride ion to the bornyl cation would be expected, was not found among the reaction products.

In the next (as ranked with respect to retention time, 13–18 min) group of chromatographic peaks, bicycloalkyl chlorides were found. It was impossible to attribute the components of this group to halogenoalkanes by means of mass-spectrometry, because of the absence of peaks related to molecular ions. For this group of compounds, the greatest mass number m/z = 137 corresponds to a fragment ion $[M–Cl]^+$. These compounds were identified as halogenoalkanes by GLC, according to the presence of the peak corresponding to the starting BCh in this group of peaks.

An analysis of the mass-spectra of the compounds responsible for the group of chromatographic peaks with retention time of 33–45 min made it possible to identify these compounds as hydrocarbons of composition $C_{20}H_{32}$ and $C_{20}H_{34}$. The presence of doublet peaks of molecular ions, which are characteristic of chloroderivatives, also revealed compounds of composition $C_{20}H_{33}Cl$ in this group.

Thus, a study of the qualitative composition of a mixture of reaction products made it possible to suggest the following scheme of catalytic transformations of BCh under the action of $AlCl_3$:

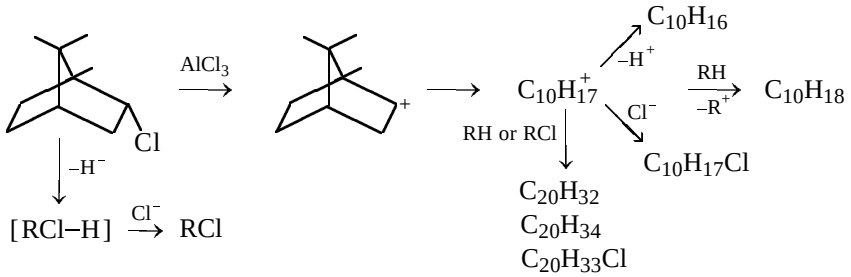

CONCLUSIONS

(1) Treatment of bornyl chloride with $AlCl_3$ at 0–20°C yields a complex mixture of bicycloalkanes and bicycloalkyl chlorides. Changing the temperature and concentration of the reaction mixture has no effect on the qualitative composition of the products.

(2) By making smaller, within certain limits, the amount of the catalyst, the reaction time, and the concentration of the reaction mixture, the reaction can be directed toward formation of bicycloalkyl chlorides, whose content in the reaction mixture is at a maximum (60%) under the conditions of run no. 7 (see table).

REFERENCES

1. Osadchii, S.A. and Tolstikov, G.A., *Khim. Interes. Ustoich. Razv.*, 1997, vol. 5, no.1, pp. 79–93.
2. Vyrodov, V.A., Kislitsyn, A.N., Glukhareva, M.I., *et al.*, *Tekhnologiya lesokhimicheskikh proizvodstv* (Technology of Wood-Chemical Industry), Moscow: Lesn. Prom–st., 1987.
3. Markevich, R.M., Lamotkin, A.I., and Reznikov, V.M., *Khim. Dreves.*, 1987, no. 1, pp. 3–20.
4. Peshekerova, M.S., *Prakticheskie raboty po khimii drevesiny s uklonom v khimiyu terpenov* (Practical Works in Chemistry of Wood with Emphasis on Chemistry of Terpenes), Leningrad: Goskhimizdat, 1932.
5. Erickson, G. and Fry, J.L., *J. Org. Chem.*, 1987, vol. 52, no. 3, pp. 462–464.
6. Meerwein, H. and van Emster, K., *Chem. Ber.*, 1922, vol. 55, no. 3, pp. 2500–2528
7. Smith, W.B., *J. Org. Chem.*, 1999, vol. 64, no. 1, pp. 60–64.
8. Rusinova, G.V., Matveeva, I.A., Sokolova, I.M., *et al.*, *Izv. Akad. Nauk SSSR, Ser. Khim.*, 1981, no. 2, pp. 313–319.

Russian Journal of Applied Chemistry, Vol. 77, No. 2, 2004, pp. 339–341. Translated from Zhurnal Prikladnoi Khimii, Vol. 77, No. 2, 2004, pp. 340–342.

BRIEF COMMUNICATIONS

Controlled Release of Farmazin from Thermosensitive Gels Based on Poly(*N*-vinylcaprolactam)

R. M. Iskakov, S. V. Sedinkin, G. K. Mamytbekov, E. O. Batyrbekov, E. A. Bekturov, and B. A. Zhubanov

Bekturov Institute of Chemical Sciences, Almaty, Kazakhstan

Received July 1, 2003

Abstract—With the aim to prolong the effect of a wide-spectrum antimicrobial agent, Farmazin (tylosine tartrate), this drug was immobilized on a gel of *N*-vinylcaprolactam–sodium itaconate copolymer, which undergoes a phase transition on heating. The phase transition, accompanied by a change in volume, in aqueous solutions of the pure copolymer gel and that with the immobilized drug was studied.

Hydrophilic network polymers (hydrogels), thanks to the set of their unique physicochemical properties, are widely used in various fields of medicine, agriculture, biotechnology, and electronics [1–5]. For example, some representatives of this class, owing to favorable balance of the hydrophilic and hydrophobic units, undergo thermally induced collapse upon slight variation of the temperature of the ambient [6, 7]. Such polymers find growing applications in pharmaceutics for thermally controlled drug release [8–10].

The goal of this study was to prepare hydrogels based on vinylcaprolactam–sodium itaconate copolymer and containing an immobilized antimicrobial agent, Farmazin, with the aim to provide the release of the drug controlled by the ambient temperature.

EXPERIMENTAL

Hydrogels based on vinylcaprolactam and sodium itaconate (1, 2, and 3 wt %), in the form of disc samples (10 mm in diameter), were placed in a 5 wt % Farmazin solution for 24 h at 10°C for the equilibrium adsorption of the drug. Then the discs were washed with 50 ml of distilled water and placed on a small sieve in stirred saline (250 ml) to monitor the drug release. The Farmazin release was performed under equilibrium conditions at various temperatures. The drug concentration was determined at regular intervals by taking 2-ml samples of the solutions and UV detection (Jasco UV VIS 7850 spectrophotometer, Japan) at 260 nm.

The phase transition temperature of polymer solutions was determined in a stirred temperature-controlled cell heated with a TC Jasco attachment at 0.5°C temperature steps, with spectrophotometric detection at 500 nm.

The vinylcaprolactam–sodium itaconate (1 wt %) hydrogel, when heated, passes into the water-insoluble form at 36°C, collapsing to the nontransparent state (Fig. 1). The photographs of the copolymer gel colored with Malachite Green are shown in Fig. 2 for two different states of the gel: swollen at 22°C and collapsed at 37°C. The complexes of this copolymer with Farmazin also show a phase transition, but the degree of collapsing increases, and the lower critical solution temperature (LCST) decreases to 33°C. Farmazin contains urea groups capable of forming hydro-

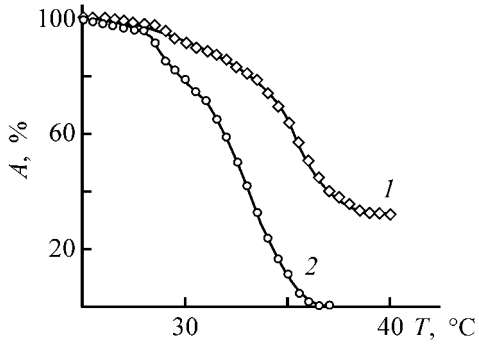

Fig. 1. Determination of LCST of (*1*) vinylcaprolactam–sodium itaconate (1 wt %) copolymer and (*2*) its complex with Farmazin (2.0 wt %). (*A*) Transmission and (*T*) temperature.

1070-4272/04/7702-0339 © 2004 MAIK "Nauka/Interperiodica"

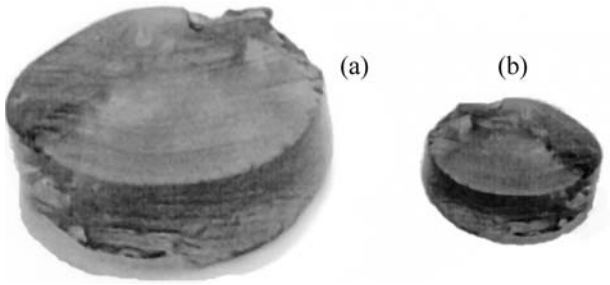

Fig. 2. Photographs of a sample of *N*-vinylcaprolactam–sodium itaconate hydrogel at (a) 22 and (b) 37°C.

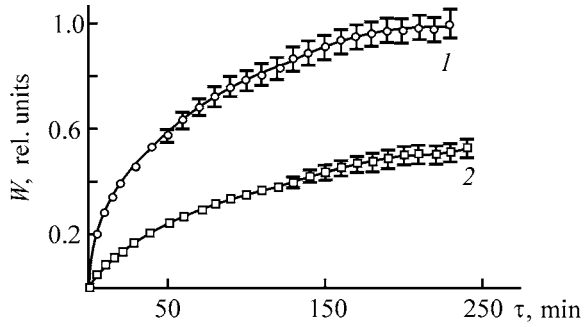

Fig. 3. Release of Farmazin from copolymer gels at (*1*) 22 and (*2*) 37°C into saline (the initial gel temperature corresponded to the temperature of the saline). (*W*) Degree of drug release and (τ) time.

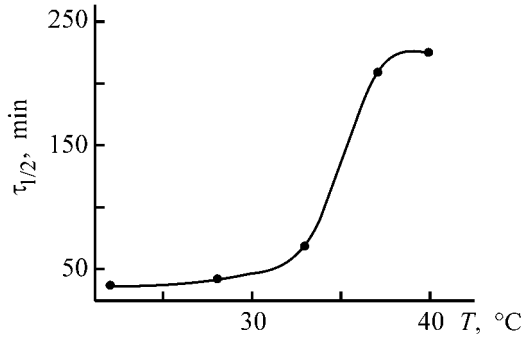

Fig. 4. Half-time $\tau_{1/2}$ of Farmazin release into saline from a vinylcaprolactam copolymer gel vs. temperature *T*.

gen bonds between the copolymer and the drug or between the oxygen of the lactam ring of amide group and the Farmazin. Such interactions are manifested in the IR spectra as a shift of the amide band of Farmazin isolated from aqueous solutions from 1640 to 1670 cm^{-1}. The increased degree of collapsing may be due to an increase in the polymer hydrophobicity upon complexation with Farmazin, causing LCST to decrease.

After immobilization of Farmazin antibiotic on the hydrogels based on a copolymer of vinylcaprolactam and sodium itaconate by equilibrium adsorption, we studied its desorption. At 22°C, the hydrogel is swollen and releases Farmazin (Fig. 3) by the mechanism of equilibrium diffusion into the surrounding solution. As the temperature is elevated to 37°C, the hydrogel collapses to a hard nontransparent state, and the diffusion rate decreases by a factor of 4.5. The weight of the compact gel is 5.5 times lower than that of the swollen gel. Whereas at low temperature Farmazin is fully released within 200–210 min, the gel compacted at elevated temperature releases in this time less than 50% of the drug. Apparently, the major factor responsible for the decreased diffusion in the gel is its phase transition from the swollen state at low temperatures to the compact state at high temperatures. The morphology of the collapsed gel prevents free diffusion of the hydrophilic drug to the environment. At the same time, a well hydrated gel with a low degree of crosslinking, in our case a polyvinylcaprolactam hydrogel, is essentially an aqueous solution of the polymer with a limited degree of freedom of macromolecular segments [11]. The drug diffusion in such a system is essentially the diffusion of Farmazin in water.

We examined the influence of temperature on the rate of Farmazin release the from the hydrogel. We found that, above 35°C, the drug diffusion rate sharply decreases (Fig. 4). The half-time of Farmazin release increases from 60 min at 34.5°C to 220 min at 37°C. It is seen that the ambient temperature is the major factor affecting the diffusion rate, and the effect is exerted in a very narrow temperature range. The suggested design of the gel–polymer–drug system potentially allows its use for controlled release of drugs, stimulated by the ambient temperature or by a discrete temperature factor. Such systems show promise for pharmaceutics, medicine, and biotechnology.

CONCLUSIONS

(1) Immobilization of Farmazin antibiotic on a gel of a copolymer of *N*-vinylcaprolactam and sodium itaconate afforded a new thermosensitive polymeric material allowing control of the rate of drug diffusion from a polymeric matrix by varying the temperature. The half-time of drug release is 32 min at 22°C and 210 min at 37°C.

(2) The shift of the phase transition temperature of the gel with adsorbed tylosine tartrate by 2.5°C to lower temperatures, compared to the gel without the drug, is due to hydrogen bonding of the lactam oxygen atom of the polymer to amino groups of tylosine tartrate.

REFERENCES

1. Osada, Y., Gong, J., Uchida, M., and Isogai, N., *Jpn. J. Appl. Phys.*, 1995, vol. 34, pp. 511–516.
2. Bektenova, G.A., Sulekeshova, G.K., Sigitov, V.B., *et al.*, *Izv. Minist. Nauki–Akad. Nauk Resp. Kaz., Ser. Khim.*, 1997, no. 3, pp. 65–68.
3. Budtova, T.V. and Suleimenov, I.E., *Appl. Polym. Sci.*, 1995, vol. 57, pp. 1653–1658.
4. Katono, H., Sanui, K., Ogata, N., *et al.*, *Polym. J.*, 1991, vol. 10, pp. 1179–1184.
5. Aoyagi, T., Ebara, M., Sakai, K., *et al.*, *J. Biomater. Sci. Polym. Ed.*, 2000, vol. 11, no. 1, pp. 101–110.
6. Galaev, I.Yu., *Usp. Khim.*, 1995, vol. 64, no. 5, pp. 505–524.
7. Yuk, S.H. and Bae, Y.H., *Crit. Rev. Therap. Drug Carrier Syst.*, 1999, vol. 16, no. 4, pp. 385–412.
8. Zhubanov, B.A., Batyrbekov, E.O., and Iskakov, R.M., *Polimernye materialy s lechebnym deistviem* (Polymeric Materials with a Therapeutic Effect), Almaty: Kompleks, 2000.
9. Okano, T.R. and Yoshida, T., *Adv. Polym. Biomat. Sci. Yearbook*, Akaike, T., Okano, T., Akashi, M., *et al.*, Eds., 1997, pp. 603–614.
10. Filippova, O.E., *Vysokomol. Soedin.*, 2000, vol. 42, no. 12, pp. 2328–2352.
11. Bekturov, E.A. and Suleimenov, I.E., *Polimernye gidrogeli* (Polymeric Hydrogels), Almaty: Gylym, 1998.

Russian Journal of Applied Chemistry, Vol. 77, No. 2, 2004, pp. 342–345. Translated from Zhurnal Prikladnoi Khimii, Vol. 77, No. 2, 2004, pp. 343–346.

Academician Lev Vladimirovich Pisarzhevskii (To 130th Anniversary of His Birthday)

L.V. Pisarzhevskii, a scientist, pedagogue, research organizer, and public figure, is one of the most prominent Russian physical chemists of the first half of the XX century. His studies covered a wide variety of problems: chemistry and structure of metal peroxides, nonaqueous solutions, electronic theory of redox processes, and theory of catalysis.

Lev Vladimirovich Pisarzhevskii was born on February 14, 1874, in Kishinev, Bessarabia Province, into the family of a notary. In 1882, after his father's death, the family moved to Odessa, where Pisarzhevskii finished a classical gymnasium and entered the natural-medical faculty of Novorossia University (Odessa). Soon afterwards, however, he went to the chemical department of the physicomathematical faculty and all his subsequent scientific and pedagogical activities were associated with chemistry. Among his teachers at the University were such well-known scientists of that time: A.A. Verigo (1837–1905), P.G. Melikishvili (1850–1927), S.M. Tanatar (1849–1917), and P.I. Petrenko-Kritchenko (1866–1944). Already beginning with his second term at the University, Pisarzhevskii commenced research work under the supervision of professor Melikishvili, analyzed the composition of a meteorite, and later studied peroxy compounds. In 1896, Pisarzhevskii graduated from Novorossia University with first-degree diploma and, on recommendation of professors Verigo and Melikishvili, was left at the university to be trained for professorship.

In 1898, the young scientist passed master's examinations and gained a right to deliver lectures as privatdocent. The courses of lectures, planned to be delivered by him, covered the topical problems of physical chemistry, which originated at that time. In 1899, Melikishvili and Pisarzhevskii were awarded the Lomonosov Prize for the monograph *Issledovaniya nad perekisyami* (Studies of Peroxides). In January 1901, Pisarzhevskii was sent to a business trip to Leipzig, to the laboratory headed by W. Ostwald (1853–1932, 1909 Nobel Prize in chemistry), which was the renowned center of novel ideas and research in physical chemistry at that time. Quite a number of young Russian scientists worked in Leipzig in different years [1, 2]. In the early XX century, the main areas of research conducted by Ostwald and his closest associates were kinetics and catalysis.

At Ostwald's laboratory Pisarzhevskii finished work on his master's dissertation "Peroxides and Peracids," which he successfully defended at Novorossia University on November 20, 1902 [3].

Various peroxide compounds, objects of study of inorganic chemistry, were examined using physicochemical methods, electrical conductivity measurements, as well as thermochemical and kinetic techniques. As a theoretical substantiation served Arrhenius's theory of solutions and the laws of thermochemistry. Melikishvili and Pisarzhevskii studied a wide variety of peroxide compounds, including quite a number of substances synthesized by them for the first time. The structural similarity of hydrogen peroxide, metal peroxides, and peracids was demonstrated. Metal peroxides were regarded as salts of hydrogen peroxide, in which it plays the part of a mono- or dibasic acid. Peracids were regarded as mixed anhydroacids of common acids and hydrogen peroxide. D.I. Mendeleev was much interested in the studies of peroxide compounds. In 1897–1899, Melikishvili and Pisarzhevskii published in co-authorship 16 studies con-

1070-4272/04/7702-0342 © 2004 MAIK "Nauka/Interperiodica"

cerned with peroxide compounds; 11 more investigations in this area were published by Pisarzhevskii alone in 1900–1903. The scientist reverted to the subject of peroxide compounds more than once in the subsequent years. A detailed analysis of investigations carried out at Novorossia University by the founders of chemistry of peroxide compounds was made in Turchenko's monograph [4] and in [5, 6].

On January 1, 1903, were commenced diverse Pisarzhevskii's pedagogical activities at Novorossia University. He delivered courses of lectures in inorganic and analytical chemistry to students of various specialties and supervised practical studies in physical chemistry, organized by himself. It so turned out that Pisarzhevskii's work at Novorossia University was not long. In 1903, G. Tammann (1861–1938) moved to Germany, to Göttingen University, and freed the chair of chemistry at Yur'ev (Tartu) University. In the second half of the year of 1904, Pisarzhevskii was invited to this chair as extraordinary professor. Already in the 1904/1905 academic year, he delivered all the lectures in chemical disciplines at the physicomathematical faculty. However, the unfavorable conditions for research work, the lack of necessary equipment, the political circumstances of that time, and the Baltic climate, taken together, resulted in that Pisarzhevskii returned to the Ukraine at the beginning of 1908 to fill a vacant position of a professor of inorganic and analytical chemistry at Kiev Polytechnic Institute.

Nevertheless, Pisarzhevskii in fact started at Tartu the second series of his experimental studies of chemical interaction of solutes with a solvent [5, 7]. In 1904–1908, he published five papers in this field. The area of research, chosen by the scientist, was characteristic and rather important for the understanding of the nature of solutions at the turn of the XX century. Undoubtedly, this choice was affected by the two years' stay of Pisarzhevskii at Ostwald's laboratory. The theoretical concepts of solutions, developed by J. Vant-Hoff (1852–1911, 1901 Nobel Prize in chemistry) and S. Arrhenius (1859–1927, 1903 Nobel Prize in chemistry) provoked objections of a number of leading Russian scientists. Being a supporter of Arrhenius's theory, Pisarzhevskii was aware of the necessity for supplementing this theory with account of Mendeleev's views on the chemical nature of solutions. In his publications, Pisarzhevskii aimed at avoiding the extreme opinions of advocates of the physical and chemical theories of solutions. A detailed analysis of the nature of the difference in opinions was made in Solov'ev's monograph [8] and in some other publications [3–5, 9].

To elucidate the role of chemical factors in solution formation, Pisarzhevskii did not restrict his consideration to a study of solutions in various solvents, as it was done by other scientists concerned with this problem. Contrariwise, he undertook wide-scale investigations of the influence exerted by the solvent on the chemical equilibrium. He studied nine ionic reactions in 47 simple and mixed solvents and calculated more than 100 equilibrium constants [5, 9]. The equilibria were studied both analytically and by measuring the electromotive forces of appropriate circuits. When necessary, the electrical conductivity and viscosity were also measured. It was established that the solvent strongly affects the state of equilibrium. Pisarzhevskii himself formulated the basic conclusion made on the basis of this series of investigations as follows: "... it is necessary to recognize the chemical interaction between the solvent and solutes and to regard the dissolution process as purely chemical phenomenon" [10, 11]. This chemical phenomenon consists in solvation.

Having started lecturing at Kiev Polytechnic Institute in April 1908, Pisarzhevskii paid considerable attention to improvement of the teaching process. He introduced a theoretical course "Introduction into Analytical Chemistry," delivered lectures in terms of the ionic theory, and redesigned the system of practical works in analytical chemistry. In 1908–1911, Pisarzhevskii finished work on his doctoral dissertation "Free Energy of a Chemical Reaction and the Solvent" [10], which he defended successfully at St. Petersburg University in 1913.

Already when being a professor in Tartu, Pisarzhevskii belonged to a revolutionary all-Russian Akademicheskii Soyuz (Academic Society). In 1911, in connection with political unrest in quite a number of higher-school institutions, Pisarzhevskii resigned, together with a group of professors of the Polytechnic Institute, and moved to Moscow, to become there one of founders and editors of a popular-science journal *Priroda* (Nature). At that same time, Pisarzhevskii delivered lectures at Bestuzhev school and Institute of Psychoneurology in St. Petersburg.

In 1913, Pisarzhevskii was elected a professor of general and physical chemistry at the Mining Institute in Yekaterinoslav (now Dneropetrovsk), and all the subsequent pedagogical and scientific activities of the scientist were associated with this institute. Already during the first years of his work there, the third and, probably, the main area of Pisarzhevskii's research was formed: the electron in chemistry and the nature of redox processes. He published a series of articles

"The Electron in Chemistry of Solutions and in Electrochemistry" (1921–1924) and a monograph under the same title (together with M.A. Rozenberg, 1923). As far back as 1914, Pisarzhevskii demonstrated that all chemical processes can be regarded as a result of electron transfer from some atoms or molecules to others, with the interaction of the free electric charges that are generated in the process [9]. The oxidation and reduction processes were interpreted as transfer of electrons from an oxidant to a reducing agent. All these approaches were introduced by Pisarzhevskii and his closest associates into the teaching process and described in understandable form in the textbooks *Vvedenie v khimiyu na osnove stroeniya atoma i elektronnogo stroeniya molekul, chast' 1* (Introduction into Chemistry on the Basis of Atomic Structure and Electronic Structure of Molecules, Part 1) (Dnepropetrovsk, 1928) and *Neorganicheskaya khimiya* (Inorganic Chemistry) (together with Rozenberg; Dnepropetrovsk, 1930; Kharkov, 1933 and 1934).

The concept of redox processes was extended to reactions in solutions, heterogeneous catalysis, and electrochemistry. For his investigations in the field of electronic chemistry, Pisarzhevskii was awarded a Lenin Prize in 1930.

In addition to the Mining Institute, Pisarzhevskii taught at other higher-school institutions of Yekaterinoslav: Institute of People's Education and Medical Institute. In 1923–1926, he held the position of rector of the Mining Institute. In 1922, on Pisarzhevskii's initiative, a research chair of electronic chemistry was created at the Mining Institute. Already in 1927, this chair was reorganized into Ukrainian Research Institute of Physical Chemistry, and in 1934, into the Institute of Physical Chemistry, Academy of Sciences of the Ukrainian SSR (Soviet Socialist Republic). In 1936, the institute was named for L.V. Pisarzhevskii.

In 1925, Pisarzhevskii was awarded a title of Honored professor of the Ukrainian SSR. In the same year, he was elected a full member of the Academy of Sciences of the Ukrainian SSR. He was elected a corresponding member of the Academy of Sciences of the USSR in 1928, and a full member of the Academy in 1930. The contribution made by the scientist to the development of higher technical education in the Ukraine is remarkable. On Pisarzhevskii's initiative, a faculty of chemical engineering was opened at the Mining Institute and the metallurgical faculty was developed further. In 1930, during the period of reorganization of the higher-school institutions in the country, the Institute of Chemical Engineering and Metallurgical Institute were created on the basis of these faculties.

In 1929, Pisarzhevskii was invited to Georgia to create at Tbilisi a chemical research center. This aspect of the scientist's activities has been considered in detail by A.Sh. Avaliani and co-authors [12]. In 1928, the State Polytechnic Institute of Georgia was organized in Tbilisi. This institute, in particular, included a mining-chemical faculty with two departments, mining and chemical. The chemical department was intended to train chemists-technologists and metallurgists. Pisarzhevskii and his closest associate Rozenberg were entrusted with organization of teaching of all the chemical disciplines at the due level. Simultaneously, Pisarzhevskii was engaged in organization of the Research Institute of Chemistry, officially opened on October 1, 1929. Pisarzhevskii was appointed the director of the Institute, and Rozenberg, the head of the department of electronic chemistry. As suggested by the director, the Institute was named after Melikishvili. The stay of Pisarzhevskii in Tbilisi was not long; it coincided with the reorganization of the higher school and scientific institutions in the country, but exerted strong influence on the subsequent development of chemical research in Georgia [12]. In the summer of 1931, Pisarzhevskii returned to Dnepropetrovsk, with, however, his intimate contacts with Georgian colleagues maintained. In 1934, Pisarzhevskii again headed the Institute, which was then already a part of the Georgian branch of the Academy of Sciences of the USSR, for a short time.

Among Pisarzhevskii's pupils and closest associates in the Ukraine were the following, later well-known scientists: A.I. Brodskii (1895–1969, academician of the Academy of Sciences of the Ukrainian SSR since 1939, corresponding member of the Academy of Sciences of the USSR since 1943), a prominent specialist in chemistry of isotopes and author of the textbook *Fizicheskaya khimiya* (Physical Chemistry), which ran into numerous editions; V.A. Roiter (1903–1974, academician of the Academy of Sciences of the Ukrainian SSR since 1961), author of the monograph *Vvedenie v teoriyu kinetiki i kataliza* (Introduction into Theory of Kinetics and Catalysis) (1971); and S.Z. Roginskii (1900–1970, corresponding member of the Academy of Sciences of the USSR since 1939), the founder of a prominent scientific school specialized in the theory of catalysis.

Pisarzhevskii was actively involved in public and political activities in the country and was a member of executive Soviet bodies: he became an alternate member of the Central Executive Committee of the

USSR in 1928, was elected a member of the Central Executive Committee of Georgia in 1930 and 1935, and became a member of Central Executive Committee of the Ukraine in 1935.

Academician Lev Vladimirovich Pisarzhevskii died of a severe illness on March 23, 1938, in Dnepropetrovsk. A vast literature is devoted to his life and scientific activities. Of particular value are papers written by the closest associates of the scientist: Rozenberg, Brodskii, B.Ya. Dain, Roiter, and S.Z. Roginskii [3, 5, 13–15]. Considerable attention was given to Pisarzhevskii's works in the well-known monographs devoted to the development of chemical science in Russia [8, 9, 16, 17] and in the Ukraine [4, 18, 19]. A popular-science sketch of Pisarzhevskii's life and scientific activities has been written by Yu.S. Lyalikov [20]; other popular-science publications are also available [6, 21, 22].

REFERENCES

1. Rodnyi, N.I. and Solov'ev, Yu.I., *Vil'gel'm Ostval'd* (Wilhelm Ostwald), Moscow: Akad. Nauk SSSR, 1959.
2. Morachevskii, A.G., *Zh. Prikl. Khim.*, 2003, vol. 76, no. 10, pp. 1751–1755.
3. Rozenberg, M.A., Brodskii, A.I., Dain, B.Ya., *et al.*, *Usp. Khim.*, 1948, vol. 17, no. 4, pp. 502–515.
4. Turchenko, Ya.I., *Osnovnye puti razvitiya obshchei, neorganicheskoi i fizicheskoi khimii na Ukraine* (Main Trends in the Development of General, Inorganic, and Physical Chemistry in the Ukraine), Kiev: Kiev. Gos. Univ., 1957.
5. Brodskii, A.I., *Zh. Obshch. Khim.*, 1939, vol. 9, no. 1, pp. 86–96.
6. Sheptunova, Z.I., *Khim. Shkole*, 1999, no. 7, pp. 82–84.
7. Ryago, N.Ya., *Trudy Inst. Istor. Estestvozn. Tekhn.*, 1956, vol. 12, pp. 105–134.
8. Solov'ev, Yu.I., *Istoriya ucheniya o rastvorakh* (History of the Theory of Solutions), Moscow: Akad. Nauk SSSR, 1959.
9. Solov'ev, Yu.I., *Istoriya khimii v Rossii* (History of Chemistry in Russia), Moscow: Nauka, 1985.
10. Pisarzhevskii, L.V., *Svobodnaya energiya khimicheskoi reaktsii i rastvoritel'* (Free Energy of a Chemical Reaction and a Solvent), Moscow, 1912.
11. Pisarzhevskii, L.V., *Izbrannye trudy* (Selected Works), Kiev: Akad. Nauk UkrSSR, 1936.
12. Avaliani, A.Sh., Chagunava, R.V., and Tikhonova, N.F., *Stanovlenie khimicheskoi nauki v Sovetskoi Gruzii 1921–1931* (The Development of Chemical Science in Soviet Georgia in 1921–1931), Tbilisi: Metsniereba, 1980.
13. Roiter, V.A. and Moskovich, S.M., *Izv Akad. Nauk SSSR, Ser. Khim.*, 1938, no. 4, pp. 763–774.
14. Brodskii, A.I., *Vyssh. Shkola*, 1938, vol. 5, pp. 91–95.
15. Roginskii, A.I., *Vestn. Akad. Nauk SSSR*, 1938, no. 5, pp. 90–97.
16. Kipnis, A.Ya., *Razvitie khimicheskoi termodinamiki v Rossii* (The Development of Chemcal Thermodynamics in Russia), Moscow: Nauka, 1964.
17. Solov'ev, Yu.I., *Ocherki po istorii fizicheskoi khimii* (Studies in the History of Physical Chemistry), Moscow: Nauka, 1964.
18. Atroshchenko, V.I., Berezhnoi, A.S., Boyarskaya, L.A., *et al.*, *Razvitie neorganicheskoi khimii na Ukraine* (The Development of Inorganic Chemistry in the Ukraine), Gorodyskii, A.V., Ed., Kiev: Naukova Dumka, 1987.
19. Barchuk, L.P., Beloded, A.A., Boyarskaya, L.A., *et al.*, *Razvitie fizicheskoi khimii na Ukraine* (The Development of Physical Chemistry in the Ukraine), Pokhodenko, V.D., Ed., Kiev: Naukova Dumka, 1989.
20. Lyalikov, Yu.S., *Chelovek, kotoryi "videl" elektrony* (A Man Who "Saw" Electrons), Kishinev: Kartya Moldovenyaska Publishing House, 1978.
21. Balezin, S.A. and Beskov, S.D., *Vydayushchiesya russkie uchenye-khimiki* (Outstanding Russian Scientist Chemists), Moscow: Prosveshchenie, 1972.
22. Shingarev, G., *Khim. Zhizn'*, 1973, no. 3, pp. 17–19.

A. G. Morachevskii

Russian Journal of Applied Chemistry, Vol. 77, No. 2, 2004, p. 346. Translated from Zhurnal Prikladnoi Khimii, Vol. 77, No. 2, 2004, p. 347.

BOOK REVIEWS

Chokhonelidze, A.N., Galustov, V.S., Khlopanov, L.P., and Prikhod'ko, V.P., *Spravochnik po raspylivayushchim, orositel'nym i kapleulavlivayushchim ustroistvam* (A Reference Book of Spraying and Drop-Catching Devices), Moscow: Energoatomizdat, 2002, 608 pp.

Apparatus for spraying and dispensation of liquids are widely used in chemical industry for making larger the contact area in performing a wide variety of heat- and mass-exchange processes. However, the presently available reference literature devoted to the operation of these apparatus has become markedly outdated. The introduction of new types of apparatus and methods for intensification of dispersion processes is hindered, in particular, by the lack of a full-value information that could be used by designers and developers. In the reference book by A.N. Chokhonelidze and co-authors, the domestic and foreign designs in the field of spraying and drop-catching are systematized and generalized for the first time, with the whole material presented in a form convenient for practical use. The book comprises seven parts, which include 25 chapters.

The first part (pp. 7–108, chapters 1–4) presents general evidence that concerns the spraying of liquids, drop carry-over and catching of liquid aerosols, and methods for monitoring of the occurring processes. A refined classification of methods for liquid spraying is presented, the basic parameters of devices employed for liquid spraying are considered, and the influence exerted by various external factors on the characteristics of the gas-liquid flare are analyzed. Of particular interest is chapter 3, which describes stands for determining experimentally the characteristics of spraying devices.

The second part (pp. 109–221, chapters 5–11) contains data on the design and operation of atomizers for hydraulic spraying. Centrifugal, single-flare, jet, and impact-jet atomizers, as well as some other designs of hydraulic atomizers, are described. Considerable attention is given by the authors to apparatus classification and to terminology.

The third part of the reference book (pp. 222–290; chapters 12, 13) is devoted to gas-spraying atomizers (pneumatic and acoustic). A vast body of evidence concerning the principles of their operation, design and application features, and calculation procedures is presented. The fourth part (pp. 291–336; chapters 14, 15) considers the design, application fields, and methods for calculation of mechanical atomizers. The fifth part (pp. 337–383; chapters 16, 17) describes unconventional spraying devices which either have limited application (ultrasonic atomizers or those with electrostatic spraying) or are being developed at present. Also considered are devices for pulsating spraying, atomizers with preliminary gas-saturation, and devices for combined spraying.

The sixth part (pp. 384–476, chapters 18–20) contains extensive evidence concerning the spraying devices and spraying systems used in technological practice. Sprinklers and liquid dispensers, choice of spraying devices, design of spraying systems, and their operation are described. The seventh part (pp. 477–595, chapters 21–25) discusses various drop-catching devices: centrifugal separators, nozzle separators, and also gravitational and combined separators. Fabrication, setting-up, and operation of drop-catchers are described; the efficiency and reliability of their operation is assessed and the fabrication and assembling costs are estimated.

The bibliographic list contains 89 references to publications of exclusively domestic authors. As mentioned in the foreword to the reference book, only those references were included in the bibliographic list, which contain wide generalizations or a previously undiscussed material. In the reviewers' opinion, the number of references should have been considerably greater for such a fundamental publication as the reference book under consideration.

The book is of interest for a wide audience of specialists from a great variety of industries, those who are engaged in design or operation of spraying or dropcatching devices. It may also be of use for lecturers and post- and undergraduate students of higher school institutions specialized in chemical engineering, metallurgy, and power engineering. The reference book is well published and contains a large number of illustrations.

I.N. Beloglazov and A.G. Morachevskii

1070-4272/04/7702-0346 © 2004 MAIK "Nauka/Interperiodica"

Russian Journal of Applied Chemistry, Vol. 77, No. 3, 2004, pp. 347–352. Translated from Zhurnal Prikladnoi Khimii, Vol. 77, No. 3, 2004, pp. 353–358.

INORGANIC SYNTHESIS AND INDUSTRIAL INORGANIC CHEMISTRY

Reactions of Oxides of Some 3*d* Elements with Ammonium Hydrogen Difluoride

V. T. Kalinnikov, D. P. Nesterov, D. V. Makarov, E. A. Steshin, and E. L. Tikhomirova

Institute of Chemistry and Technology of Rare Elements and Mineral Raw Materials, Kola Scientific Center, Russian Academy of Sciences, Apatity, Murmansk oblast, Russia

Received June 11, 2003

Abstract—Reactions of iron, manganese(II), manganese(IV), copper, and zinc oxides with ammonium hydrogen difluoride were studied by thermogravimetry, X-ray phase analysis, IR spectrometry, and chemical analysis.

Fluorides of 3*d* elements find use as active components of solid lasers and phosphors, as components of chemical current sources and fluoride glasses, and as catalysts in organic synthesis [1]. On the other hand, recently there has been a considerable progress in processing of oxide–silicate raw materials containing 3*d*-metal oxides using ammonium hydrogen difluoride NH_4HF_2 [2]. Therefore, study of reactions of 3*d*-element oxides with NH_4HF_2 is of scientific and practical importance. It is known that NH_4HF_2 is close to anhydrous hydrogen fluoride in reactivity, but has a number of advantages: it can be easily dehydrated and regenerated from gaseous components, and fluoridation reactions can be carried out without sophisticated equipment [3]. In this work we have studied the fluoridation of manganese(II) and (IV), iron(III), copper, and zinc oxides with ammonium hydrogen difluoride by thermogravimetry, chemical and X-ray phase analyses, and crystal optics. The chemically pure grade oxides and double-recrystallized NH_4HF_2 (analytically pure grade) were used as the starting substances.

The thermogravimetric study was carried out on a Q-1500D (Hungary) derivatograph in platinum crucibles using 200–400-mg samples and calcined Al_2O_3 as reference. The experiments were carried out in dynamic and quasi-isothermal modes at the heating rate of 2.5–10 deg min^{-1}.

The X-ray phase analysis of reaction products was performed on a DRON-2 diffractometer with the CuK_α radiation. The IR absorption spectra were recorded on a UR-20 spectrophotometer.

The content of iron was determined by the flame-emission spectrometry, and that of fluoride, by pyrohydrolysis followed by potentiometric determination (using a F^--selective electrode). The ammonia content was determined by Kjeldahl's method.

The following methods of synthesizing FeF_3 have been described in the literature: reaction of $FeCl_3$ with anhydrous HF [4] yielding an amorphous product, which is heated to 1000°C to form a crystalline product; calcination of Fe_2O_3 or hydrated FeF_3 in an HF flow at 1000°C [5]; and thermal decomposition of $(NH_4)_3FeF_6$ at 400–500°C [6], including the reaction in an F_2 atmosphere [7].

These procedures require sophisticated equipment, and the fluoridation proceeds at high temperatures in several stages. It was pointed out in [7] that the absence of iron(II) impurities in the final product is an advantage of obtaining FeF_3 by decomposing $(NH_4)_3FeF_6$ in an F_2 atmosphere.

When $(NH_4)_3FeF_6$ is synthesized by the reaction of natural pyrrhotines $Fe_{1-x}S$ with NH_4HF_2 [7], iron(II)-containing compounds are inevitably formed, which makes necessary the subsequent treatment with F_2. The preparation of $(NH_4)_3FeF_6$ by the reaction of FeF_3 with NH_4F in an inert atmosphere [6] or by the reaction of $FeBr_3$ with NH_4F in methanol [8] was also described.

The derivatogram of a mixture of Fe_2O_3 with NH_4HF_2 in the molar ratio of 1 : 10 is shown in Fig. 1. The DTA curve reveals a number of endothermic effects. The first of them at approximately 115°C corresponds to the melting of NH_4HF_2 [9]. The endothermic effect at 166°C results from the formation of $(NH_4)_3FeF_6$ by reaction (1).

$$Fe_2O_3 + 6NH_4HF_2 = 2(NH_4)_3FeF_6 + 3H_2O. \quad (1)$$

1070-4272/04/7703-0347 © 2004 MAIK "Nauka/Interperiodica"

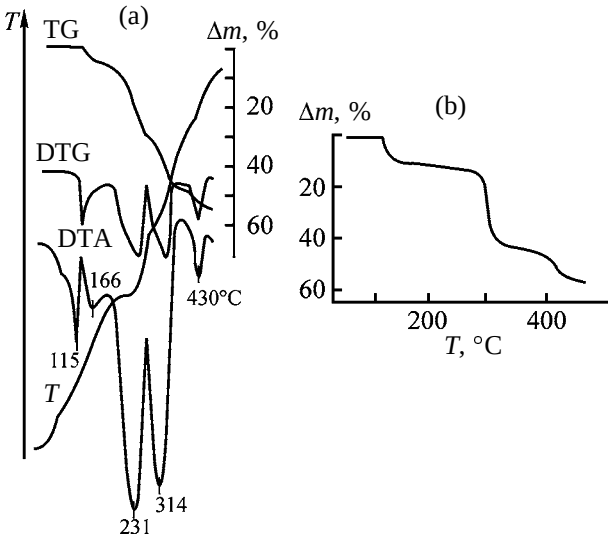

Fig. 1. (a) Derivatogram of a mixture $Fe_2O_3 : NH_4HF_2$ = 1 : 10 and (b) thermogravigram of a mixture $Fe_2O_3 : NH_4HF_2$ = 1 : 6 recorded in the quasi-isothermal mode. (*T*) temperature and (Δ*m*) weight loss; the same for Figs. 3, 5, and 6.

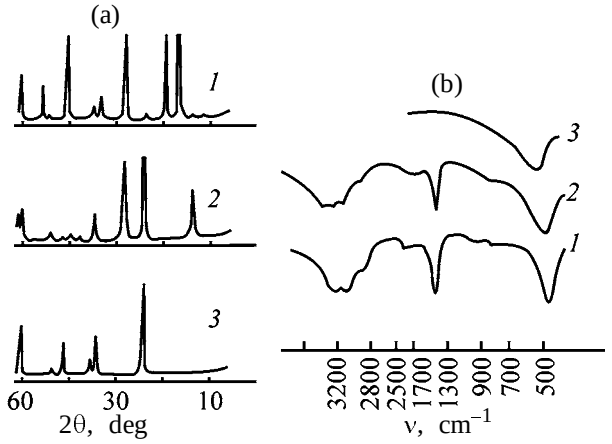

Fig. 2. (a) X-ray patterns of cakes of $Fe_2O_3 : NH_4HF_2$ = 1 : 6 mixtures and (b) IR absorption spectra of the same samples. (2θ) Bragg's angle and (ν) wave number. *T*, °C: (*1*) 180, (*2*) 320, and (*3*) 430.

On further heating, $(NH_4)_3FeF_6$ decomposes by the scheme

$$(NH_4)_3FeF_6 = NH_4FeF_4 + 2HF + 2NH_3. \quad (2)$$

The decomposition is completed at 314°C, as proved by a series of the corresponding endothermic effects. Boiling of excess NH_4HF_2 at approximately 231°C [3, 9] is accompanied by the corresponding endothermic effect. The final stage (3) of the synthesis is completed at approximately 430°C by the formation of anhydrous iron(III) fluoride.

$$NH_4FeF_4 = FeF_3 + HF + NH_3. \quad (3)$$

The thermogravigram obtained in the quasi-isothermal mode contains three plateaus corresponding to the formation of $(NH_4)_3FeF_6$, NH_4FeF_4, and FeF_3, respectively (Fig. 1b). The calculated weight loss in each stage of the synthesis (10.8, 40.3, and 55.0 wt %, respectively) agrees well with the loss observed experimentally (Fig. 1b). The derivatographic results were confirmed by X-ray phase analysis. The X-ray patterns of $Fe_2O_3 : NH_4HF_2$ mixtures with the molar ratio of 1 : 6 at 180, 320, and 430°C are shown in Fig. 2a. It is seen from Fig. 2a, curve *1* that $(NH_4)_3FeF_6$ is the reaction product at 180°C, and at 320°C it decomposes to give NH_4FeF_4 (Fig. 2a, curve *2*). Curve *3* in Fig. 2a is the X-ray pattern of anhydrous FeF_3. Its heating in air results in the following pyrohydrolysis reactions:

$$2FeF_3 + H_2O = Fe_2F_4O + 2HF, \quad (4)$$

$$2FeF_3 + 3H_2O = Fe_2O_3 + 6HF. \quad (5)$$

The formation of Fe_2O_3 was confirmed by X-ray phase analysis. The X-ray patterns of the synthesized compounds coincide with the data given in [6].

The IR absorption spectra of ammonium fluoroferrates(III) and FeF_3 are given in Fig. 2b. The absorption bands in the regions of 2800–3400 and 1430 cm^{-1} in the spectra of ammonium fluoroferrates(III) are assignable to the stretching and bending vibrations of N–H bonds. The absorption band at 450–550 cm^{-1}, which is observed in all the IR spectra under consideration, is characteristic of the Fe–F stretching vibration. A weak absorption band in the region of bending vibrations of water molecules is present in the spectrum of ammonium tetrafluoroferrate(III) at 1630 cm^{-1}. This is apparently hygroscopic water appearing owing to fine dispersity of the substance.

Thus, we found the conditions for obtaining anhydrous FeF_3 by the reaction of Fe_2O_3 with NH_4HF_2. It should be taken into account that a 1.5–2-fold excess of NH_4HF_2 relative to the stoichiometry is required to obtain FeF_3 as a final product free from iron(III) oxide formed by pyrohydrolysis. Depending on the requirements to FeF_3 purity, it is appropriate to synthesize it either in inert or in fluorinating atmosphere, the repeated treatment with a fluorinating agent being possible.

The main method of obtaining MnF_2 is the reaction of $MnCO_3$ with HF [4].

The derivatogram of an $MnO : NH_4HF_2$ mixture with the molar ratio of 1 : 2 is shown in Fig. 3a. A number of peaks corresponding to endothermic effects

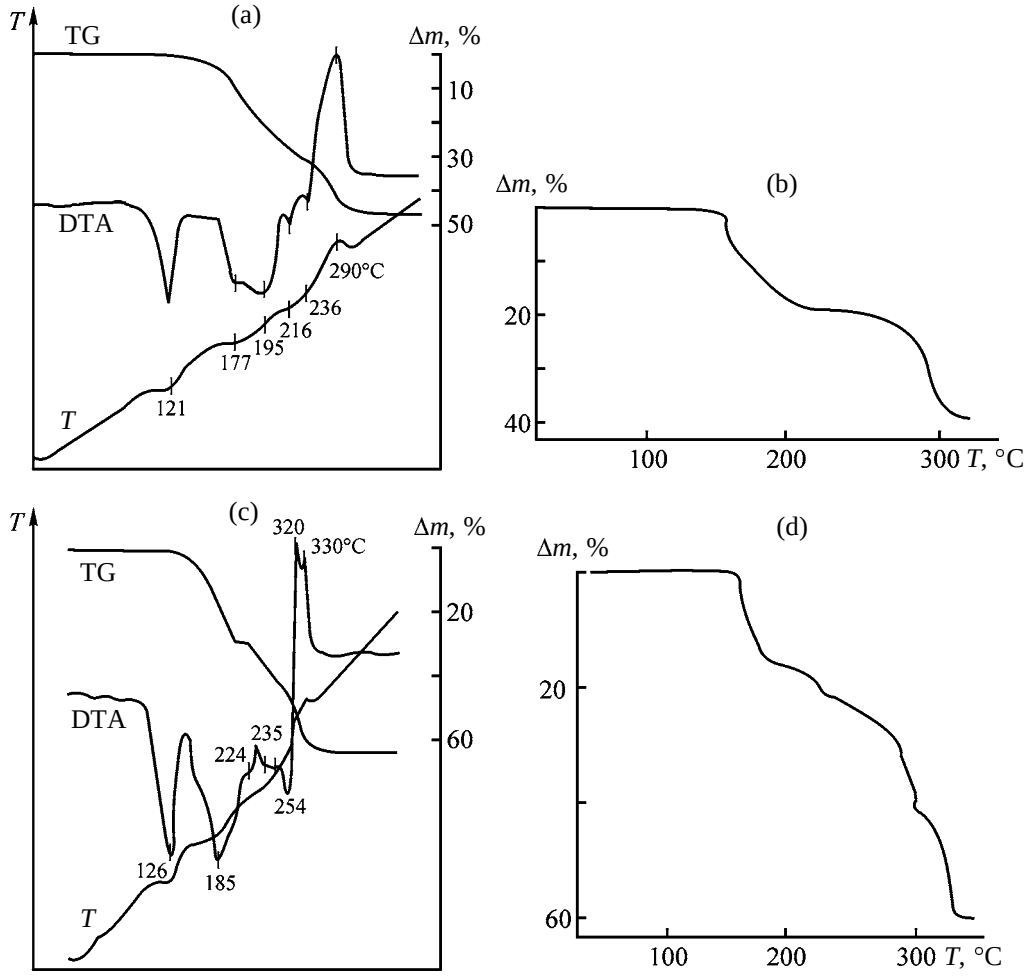

Fig. 3. (a) Derivatogram of an $MnO : NH_4HF_2 = 1 : 2$ mixture; (b) thermogravigram of an $MnO : NH_4HF_2 = 1 : 1.5$ mixture recorded in the quasi-isothermal mode; (c) derivatogram of an $MnO : NH_4HF_2 = 1 : 4$ mixture; and (d) thermogravigram of an $MnO_2 : NH_4HF_2 = 1 : 2.5$ mixture recorded in the quasi-isothermal mode.

are observed in the DTA curve. The endothermic effect at 195°C corresponds to the formation of the complex NH_4MnF_3 by the reaction

$$MnO + 2\ NH_4HF_2 = NH_4MnF_3 + H_2O. \quad (6)$$

As the temperature is increased to 350°C, NH_4MnF_3 decomposes to give MnF_2:

$$NH_4MnF_3 = MnF_2 + HF + NH_3. \quad (7)$$

The scheme of the MnO fluoridation is confirmed by the thermogravigram taken in the quasi-isothermal mode at the molar ratio of components $MnO : NH_4HF_2 = 1 : 1.5$. The experimental weight losses of 17.6 and 42%, respectively, agree well the calculated losses of 17.4 and 41% (Fig. 3b). Compounds identified as NH_4MnF_3 and MnF_2 by X-ray phase and chemical analyses [10] were synthesized at 200 and 325°C, respectively (Figs. 4a and 4b).

The reaction of MnO_2 with NH_4HF_2 was studied by Rakov and co-workers [11]. They found that the reaction proceeded stepwise to give $(NH_4)_2MnF_5$, NH_4MnF_4, and MnF_2 at 175, 230, and 300°C, respectively. Another reaction scheme was given in [12], where the reaction of iron-manganese concretions with NH_4HF_2 was studied. The product of the exothermic reaction of MnO_2 and NH_4HF_2 is a compound isostructural to $(NH_4)_3MnF_6$ but having a 10% deficiency of fluorine as compared to this stoichiometry owing to the isomorphous replacement of fluorine by hydroxide ions. The final stage of the process at 320°C is the formation of MnF_2.

The thermogram of a mixture of MnO_2 with NH_4HF_2 in the molar ratio of 1 : 4 is shown in Fig. 3c. The reaction proceeds in several stages (endothermic effects at 185 and 224°C). The process can be described by the equation

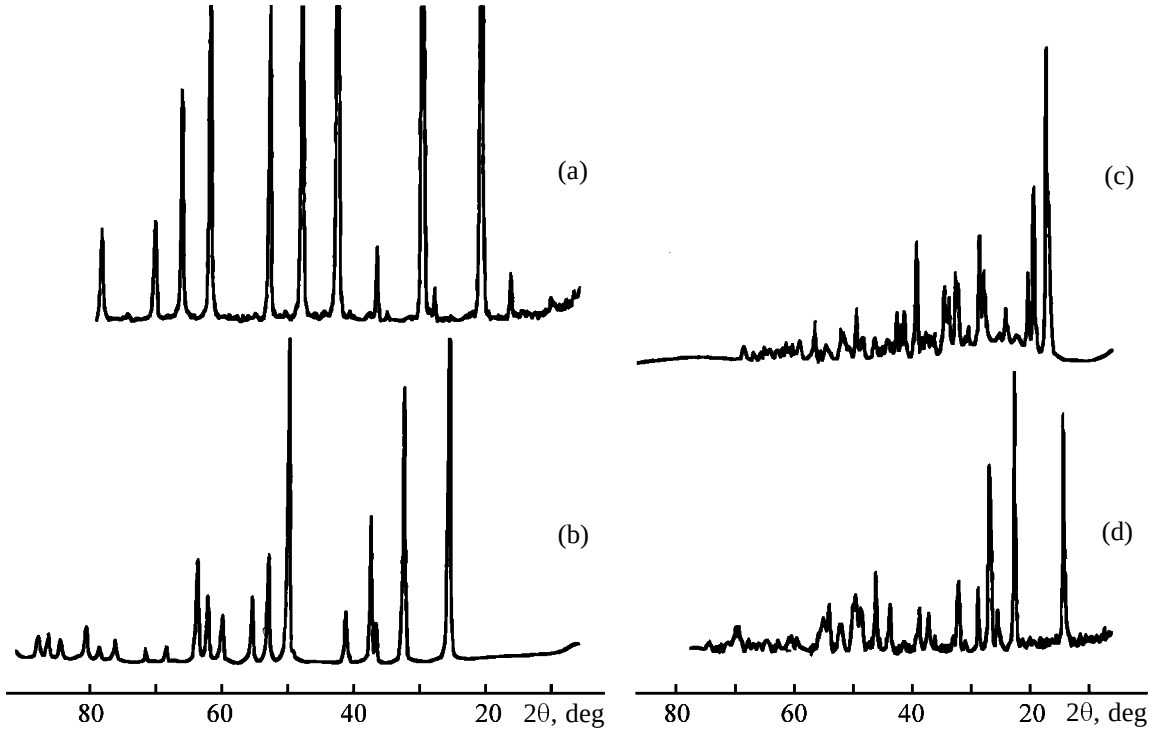

Fig. 4. X-ray patterns of $MnO : NH_4HF_2$ and $MnO_2 : NH_4HF_2$ mixtures at various temperatures: (a) NH_4MnF_3 (200°C), (b) MnF_2 (325°C), (c) $(NH_4)_2MnF_5$ (200°C), and (d) NH_4MnF_4 (300°C).

$$6MnO_2 + 24NH_4HF_2 = 6(NH_4)_2MnF_5 + 18HF + 10NH_3 + N_2 + 12H_2O. \quad (8)$$

A series of endothermic effects observed on further heating (Fig. 3c) correspond to the reactions

$$(NH_4)_2MnF_5 = NH_4MnF_4 + HF + NH_3, \quad (9)$$

$$NH_4MnF_4 = MnF_2 + HF + 1/2F_2 + NH_3. \quad (10)$$

The thermogravigram obtained in the quasi-isothermal mode is shown in Fig. 3d. It contains three plateaus corresponding to the formation of $(NH_4)_2 \cdot MnF_5$, NH_4MnF_4, and MnF_2, respectively. The thermogravimetric data obtained are confirmed by the results of the X-ray phase analysis [13] (Figs. 4c and 4d). The compounds $(NH_4)_2MnF_5$, NH_4MnF_4, and MnF_2 were isolated at 200, 300, and 320°C.

Thus, the established reaction scheme of the fluoridation of manganese(IV) oxide coincides with the results of [11].

The nature of exothermic effects (Figs. 3a, 3c) remains to be elucidated. They may be due to the crystallization of the forming amorphous manganese fluoride.

Preparation of anhydrous copper(II) fluorides is complicated by the reaction with materials of crucibles and by the pyrohydrolysis [14]. The following methods for preparing CuF_2 have been described in the literature: fluoridation of dehydrated $CuCl_2$ crystal hydrates using F_2 or ClF_3 at 400°C [4], dissolution of CuO or $(CuOH)_2CO_3$ in excess 40% hydrofluoric acid with the subsequent dehydration of crystal hydrates of copper(II) compounds ($CuF_2 \cdot 2H_2O$ or $CuF_2 \cdot 5H_2O \cdot 5HF$ according to the data of various authors) in a dry HF flow [4, 14], and the reaction of CuS with SF_4 in an autoclave at 190°C followed by treatment of the resulting products with anhydrous carbon disulfide to remove sulfur [15]. The dehydration of $CuF_2 \cdot 2H_2O$ crystal hydrate both in air and in an inert atmosphere with heating results in the formation of mixtures of CuOHF, CuO, and CuF_2 [16, 17].

Typical thermogravimetric curves of a mixture of CuO with NH_4HF_2 in the molar ratio of 1 : 2 are shown in Fig. 5a. The DTA curve contains a number of endothermic effects. The first effect at 125°C corresponds to the melting of NH_4HF_2 [3, 9]. The endothermic effect at 200°C corresponds to the formation of the complex $(NH_4)_2CuF_4$ by reaction (11):

$$CuO + 2NH_4HF_2 = (NH_4)_2CuF_4 + H_2O. \quad (11)$$

Further heating causes thermal decomposition of $(NH_4)_2CuF_4$ according to scheme (12), completed at 230°C.

$$(NH_4)_2CuF_4 = NH_4CuF_3 + HF + NH_3. \quad (12)$$

The final stage (13) of the synthesis is completed at approximately 290°C by the formation of anhydrous CuF_2.

$$NH_4CuF_3 = CuF_2 + HF + NH_3. \quad (13)$$

At 200, 230, and 290°C, we have synthesized the compounds identified by X-ray phase and chemical analyses as $(NH_4)_2CuF_4$, NH_4CuF_3, and CuF_2 [17]. Three steps corresponding to the formation of $(NH_4)_2 \cdot CuF_4$, NH_4CuF_3, and CuF_2 (Fig. 5b) are detected in the TG curve obtained in the quasi-isothermal mode. The weight loss for process (11) in the established temperature range takes place even under conditions of the quasi-isothermal measurement. An increase in temperature results in the pyrohydrolysis of CuF_2 and in the contamination of the product with copper oxide. In the copper(II) difluoride obtained, the atomic ratio $F : Cu \le 2$. According to the data from [14], the formula of copper(II) fluoride is CuF_{2-x} ($0 \le x \le 0.33$); the stoichiometric samples were synthesized by treatment of CuF_{2-x} with xenon difluoride.

The thermal decomposition of NH_4CuF_3 to anhydrous CuF_2 occurs at a lower temperature than the corresponding processes for NH_4CoF_3 and NH_4NiF_3 (340 and 370°C) [18].

The complete fluoridation is reached with a certain excess of NH_4HF_2 as compared to the stoichiometry of Eq. (11). This is associated with possible partial decomposition of NH_4HF_2 [9]. To obtain the pure product from copper oxide, it is better to perform the synthesis in an inert atmosphere.

Anhydrous ZnF_2 is obtained by the reaction of $ZnCO_3$ with excess hot hydrofluoric acid, followed by heating of the precipitate at 800°C without air access [4]. According to the review [3], zinc(II) forms the complex compounds $(NH_4)_2ZnF_4 \cdot H_2O$ and NH_4ZnF_3. The temperature of NH_4ZnF_3 decomposition is 250°C.

It is seen from Fig. 6a that the reaction in the mixture of ZnO with NH_4HF_2 (molar ratio 1 : 2) starts even before NH_4HF_2 melting and is accompanied by a weight loss. It results in the formation of $(NH_4)_2ZnF_4$:

$$ZnO + 2NH_4HF_2 = (NH_4)_2ZnF_4 + H_2O. \quad (14)$$

Further increase in the temperature above 178°C leads

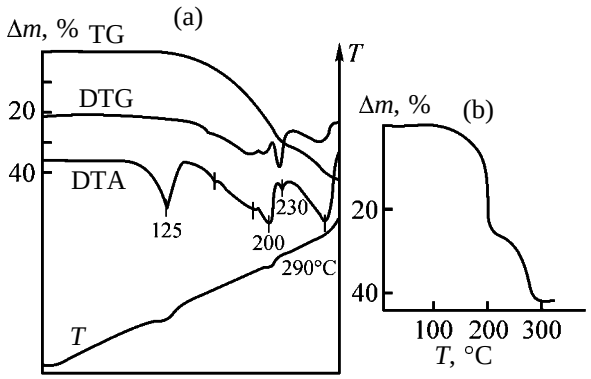

Fig. 5. (a) Derivatogram of a mixture $CuO : NH_4HF_2 = 1 : 2$ and (b) thermogravigram of a mixture $CuO : NH_4HF_2 = 1 : 2$ recorded in the quasi-isothermal mode.

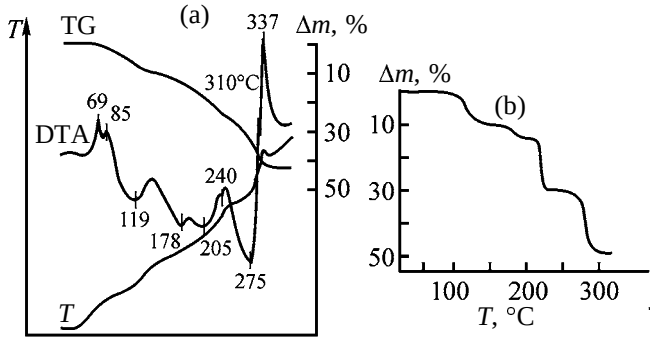

Fig. 6. (a) Derivatogram of a mixture $ZnO : NH_4HF_2 = 1 : 2$ and (b) thermogravigram of a mixture $ZnO : NH_4HF_2 = 1 : 2$ recorded in the quasi-isothermal mode.

to the thermal decomposition of $(NH_4)_2ZnF_4$:

$$(NH_4)_2ZnF_4 = NH_4ZnF_3 + HF + NH_3. \quad (15)$$

It is completed at 240°C, which is confirmed by a series of the corresponding endothermic effects. The final stage (16) of the synthesis proceeds up to approximately 337°C.

$$NH_4ZnF_3 = ZnF_2 + HF + NH_3. \quad (16)$$

Three steps corresponding to the formation of $(NH_4)_2ZnF_4$, NH_4ZnF_3, and ZnF_2 (Fig. 6b) are observed in the TG curve obtained in the quasi-isothermal mode. These compounds were synthesized and isolated at the corresponding temperatures and identified by X-ray phase and chemical analyses.

CONCLUSION

The reaction of ZnO with NH_4HF_2 proceeds similarly to the reactions of NH_4HF_2 with nickel, cobalt, and copper oxides considered in the literature [18].

REFERENCES

1. Churbanov, M.F., Abstracts of Papers, *Simpozium po khimii neorganicheskikh ftoridov* (Symp. on the Chemistry of Inorganic Fluorides), Moscow: Dialog-MGU, 1998, p. 192.
2. Mel'nichenko, E.I., Ammonium Oxyfluorides and Fluorometallates in the Chemistry and Technology of Rare Metals, *Doctoral (Chem.) Dissertation*, Vladivostok, 1999.
3. Rakov, E.G., Ammonium Fluorides, *Itogi Nauki Tekh., Ser.: Neorg. Khim.*, 1983, vol. 15.
4. *Handbuch der präparativen anorganischen Chemie*, Brauer, G., Huber, F., *et al*., Eds., Stuttgart: Ferdinand Enke, 1978, vol. 1.
5. Ryss, I.G., *Khimiya ftora i ego neorganicheskikh soedinenii* (Chemistry of Fluorine and Its Inorganic Compounds), Moscow: Goskhimizdat, 1956.
6. Shinn, D.B., Crocet, D.S., and Haendler, H.M., *Inorg. Chem.*, 1966, vol. 5, no. 11, pp. 1927–1933.
7. RF Patent 2034786.
8. Volodkovich, L.M., Petrov, G.S., Dalidovich, S.V., *et al*., Abstracts of Papers, *VI Vsesouyznyi simpozium po khimii neorganicheskikh ftoridov* (VI All-Union Symp. on the Chemistry of Inorganic Fluorides), Novosibirsk: Sib. Otd. Ross. Akad. Nauk, 1981, p. 147.
9. Rakov, E.G. and Mel'nichenko, E.I., *Usp. Khim.*, 1984, vol. 53, no. 9, pp. 1463–1492.
10. *Ref. National Bureau of Standards*, Monograph 25, Section 5, 1967.
11. Rakov, E.G., Khaustov, S.V., and Ostropikov, V.V., *Zh. Neorg. Khim.*, 1997, vol. 42, no. 2, pp. 196–198.
12. Kurilenko, L.N., Reaction of Silicon-Containing Minerals with Ammonium Hydrogen Difluoride, *Cand. Sci. (Chem.) Dissertation*, Vladivostok, 2003.
13. Bukovec, P. and Šiftar, J., *Thermochim. Acta*, 1977, vol. 21, no. 1, p. 117.
14. Fadeeva, E.E., Ardashnikova, E.I., Borzenkova, M.P., and Popovkin, B.A., *Zh. Neorg. Khim.*, 1991, vol. 36, no. 4, pp. 839–842.
15. Kostyuk, A.P. and Yagupol'skii, L.M., *Ukr. Khim. Zh.*, 1982, vol. 48, no. 4, pp. 437–438.
16. Nirsha, B.M., Allakhverdov, R.G., Velikodnyi, Yu.A., and Olikova, V.A., *Zh. Neorg. Khim.*, 1983, vol. 28, no. 11, pp. 2756–2759.
17. Wheeler, C. and Haendler, H.M., *J. Am. Chem. Soc.*, 1954, vol. 76, no. 1, pp. 263–264.
18. Ikrami, D.D., Levina, N.N., and Okhunov, R., *Izv. Akad. Nauk SSSR, Neorg. Mater.*, 1983, vol. 19, no. 9, pp. 1549–1553.

Russian Journal of Applied Chemistry, Vol. 77, No. 3, 2004, pp. 353–359. Translated from Zhurnal Prikladnoi Khimii, Vol. 77, No. 3, 2004, pp. 359–365.

INORGANIC SYNTHESIS AND INDUSTRIAL INORGANIC CHEMISTRY

Formation of the Structure of C–SiC–Si–Al Composites

E. A. Belenkov and E. M. Baitinger

Chelyabinsk State University, Chelyabinsk, Russia
Chelyabinsk State Pedagogical University, Chelyabinsk, Russia

Received January 29, 2002; in final form, December 2002

Abstract—Transmission electron microscopy and X-ray structural analysis were applied to study the fundamental aspects of formation of the crystal structure of C–SiC–Si–Al composites. The reasons why spatially heterogeneous regions are formed were revealed.

C–SiC composites are commonly obtained by reaction of porous carbon supports with molten silicon [1–3]. To modify the properties of such materials, metal impurities are added to the silicon melt. However, these additives frequently lead to appearance of spatial heterogeneities, which adversely affects the strength properties of composites [4]. This study is concerned with the structure of C–SiC–Si composites with admixture of aluminum.

EXPERIMENTAL

As objects of study were chosen the composites PG–AS, GP–0.5AS, and MG–AS [5], synthesized by reaction of PG-50, PROG-2400, and ARV porous carbon materials with an Si + Al melt. The content of aluminum in the melt was ~10 wt % in synthesizing the PG–AS and MG–AS composites and ~5 wt % in the case of GP–0.5AS. Selected properties and the composition of the composites and the carbon supports, taken from [3, 5], are listed in Table 1.

Samples for comparative X-ray studies were prepared in the form of $100 \times 14 \times 14$-mm slabs. Samples for analysis of how the phase composition varies across the cross section of the MG–AS composite were obtained using a diamond saw in accordance with the scheme shown in Fig. 1.

The X-ray diffraction analysis was carried out with a DRON-3 diffractometer (CuK_α radiation with λ = 0.15418 nm). The phase analysis and indexing of X-ray diffraction patterns were performed using the ASTM file. The profiles of the diffraction peaks were measured at a scanning rate of 0.25 deg min^{-1}. The interplanar spacings d were calculated from the centers of gravity of the diffraction peaks [6]. The average size L of the coherent domains was determined from the integral width β of diffraction peaks [6], with silicon and silicon carbide used as references. The electron-microscopic studies were carried out with a PEM-100 electron microscope.

Typical electron diffraction patterns of C–SiC–Si–Al composites are shown in Fig. 2. An analysis of the

Table 1. Properties and compositions of the samples studied

Material	Support	Pore radius,* μm	Porosity,* cm^3 g^{-1}	Composition,** wt %				ρ**	ρ***
				C	Si	SiC	Al	g cm^{-3}	
PG-50	–	3.98–8.95	0.46–0.517	100	–	–	–	1.00	–
ARV	–	3.76–4.50	0.173–0.182	100	–	–	–	1.55	–
PROG-2400	–	4.42–7.33	0.10–0.147	100	–	–	–	1.65	–
PG–AS	PG-50	–	–	22–23	15	55	7–8	2.63	2.59
MG–AS	ARV	–	–	22–23	15	55	7–8	2.30	2.16
GP–0.5AS	PROG-2400	–	–	–	–	–	–	–	2.47

* Data of [5].
** Data of [3].
*** Determined in this work.

1070-4272/04/7703-0353 © 2004 MAIK "Nauka/Interperiodica"

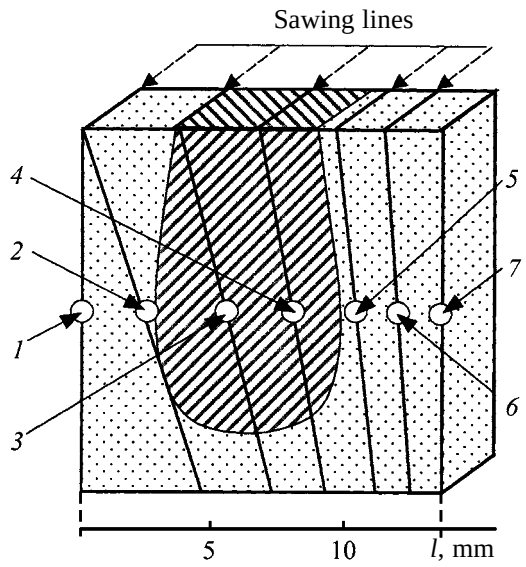

Fig. 1. Schematic of a study of how the phase composition and crystal structure varies across a sample of the MG–AS composite. (*1–7*) Region for which X-ray diffraction patterns were measured. (*l*) Distance; the same for Fig. 4.

electron diffraction patterns demonstrated that they can be related to microdiffraction from turbostratic carbon, silicon carbide, silicon, and aluminum. The probability of observing electron diffraction patterns of various phases widely varies across a sample. Regions that differ in contrast from the bulk of the material can be seen even visually on the edge cross sections of the GP–0.5AS and MG–AS composites. In Fig. 3, they are marked schematically with dark hatching and denoted by symbol C. Only electron diffraction patterns characteristic of carbon are recorded within these regions.

A comparative analysis performed for the MG–AS composite demonstrated that the crystal structure of carbon in the bulk of the composite is markedly different from the structure of carbon in C inclusions. Indeed, four basic types of electron diffraction patterns of turbostratic carbon are observed in the composites under study: (1) annular [characteristic of microscopic volumes occupied by crystals ~1 nm in size (Fig. 2a)], (2) annular with small number of discrete reflections [characteristic of a mixture of crystals ~1 and ~10 nm in size (Fig. 2b)], (3) discrete–ring-like [characteristic of microscopic volumes occupied by crystals ~10 nm in size (Fig. 2c)], and (4) discrete-periodic (characteristic of electron scattering by separate coarse crystals with size of ~100 nm and more (Fig. 2d)].

The probability of observing electron diffraction patterns of various types can be evaluated using the

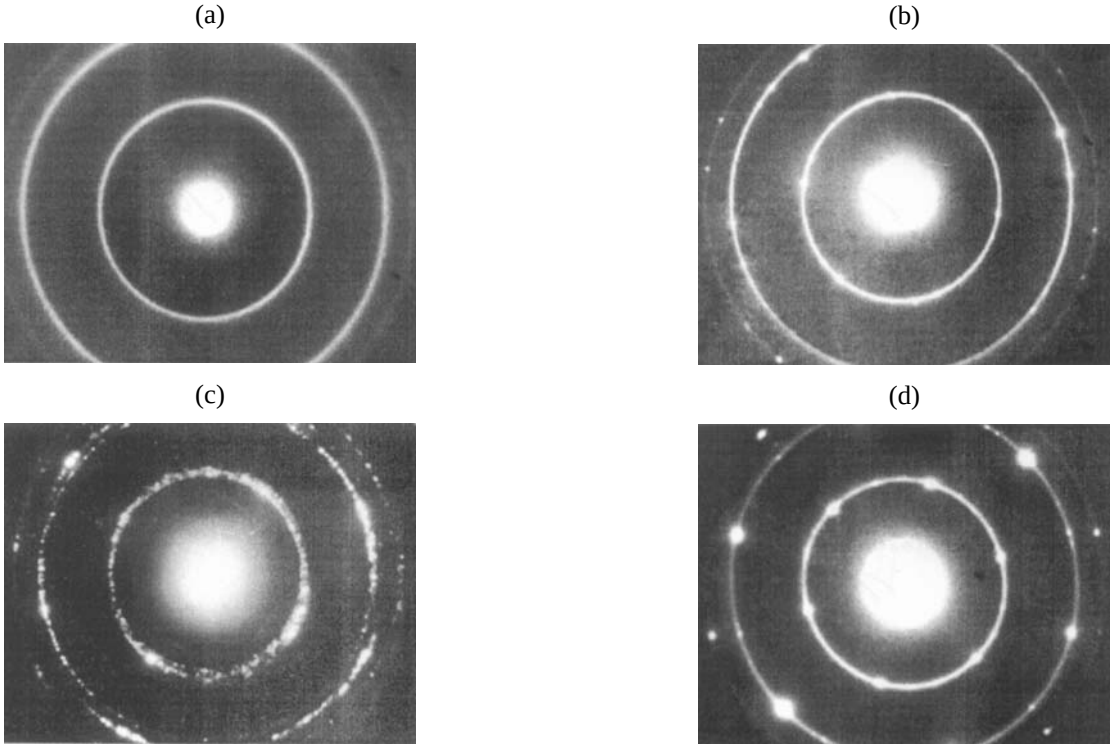

Fig. 2. Typical electron diffraction patterns of turbostratic carbon contained in C–SiC–Si–Al composites. Electron diffraction pattern: (a) ring-like, (b) ring-like with small number of discrete reflections, (c) discrete, and (d) discrete-periodic.

Table 2. Occurrence frequency of various types of electron diffraction patterns of turbostratic carbon in different regions of the MG–AS composite (Fig. 2)

Type of electron diffraction pattern	Bulk		Carbon inclusion C	
	number of electron diffraction patterns	%	number of electron diffraction patterns	%
1	8	8	44	41
2	18	17	27	25
3	9	8	16	15
4	72	67	20	19
Σ	107	100	107	100

data in Table 2. The annular electron diffraction patterns of the first type occur five times more frequently in the C regions of the composite. Contrariwise, electron diffraction patterns of the fourth type, which are characteristic of coarse crystals, are found 3.5 times more frequently in the bulk of the composite. The aforesaid suggests that the carbon region C is a volume into which the Si–Al melt did not penetrate and its structure and composition remained similar to those of the starting carbon material. The increase in the share of the coarsely crystalline component in the carbon remaining in the bulk of the composite (Table 2) is presumably due to the following: the finely crystalline component of the graphite phase is the first to be involved in carbide formation.

Part of discrete electron diffraction patterns obtained from the bulk of the composite is attributed to silicon carbide and silicon with a coherent domain size of more than 50 μm. The appearance of the electron diffraction patterns of silicon is virtually the same over the entire cross section of the samples. The interplanar spacings calculated from these diffraction patterns are in good agreement with the ASTM file. Direct measurements of the coherent domains with the use of dark-field images obtained using the reflection 111 demonstrated that they are 70 nm and more in size. The interplanar spacings of silicon exceed by approximately 0.001 nm those from the ASTM file, which indicates the existence of solid solutions of aluminum in silicon. Deviations from the interplanar spacing listed in the ASTM file are observed in the vicinity of the C regions. This may be due to an increase in the concentration of the aluminum impurity. The size of the coherent domain in silicon, measured using the dark-field images obtained with the reflection 110, varies within the range 50–400 nm.

Characteristically, the electron diffraction patterns of aluminum are constituted by nearly solid rings and can only be recorded at the interface between the bulk of the composite and the C regions. The sizes of aluminum crystals, measured from the light-field image, are 8–12 nm.

The X-ray diffraction patterns obtained from the bulk of the PG–AS, GP–0.5AS, and MG–AS composites (Fig. 3, light hatching) show reflections characteristic of β-SiC, turbostratic carbon, and silicon. The intensities of reflections from different phases in the composites (peak heights) are listed in Table 3. It can be seen that the lowest intensity of the diffraction reflections of β-SiC, which is contained in the composites, is observed for PG–AS. For the other two of the materials studied (GP–0.5AS and MG–AS), the intensities of the diffraction peaks of β-SiC are by a factor of approximately 1.3 higher. This indicates that the amount of silicon carbide grows as the density of the starting carbon supports and the concentration of aluminum in the melt become higher (Tables 1, 3).

Table 3 shows that the intensity of carbon lines increases, on the average, by a factor of 1.4 and 2 for GP–0.5AS and MG–AS, respectively, as compared to the PG–AS composite. Such a change in the intensities indicates that the amount of residual carbon, which has not reacted with the silicon melt, becomes greater. The possible reason is the same: the increased density of the carbon materials and higher concentration of aluminum (Tables 1, 3).

The relative intensities of the silicon reflections

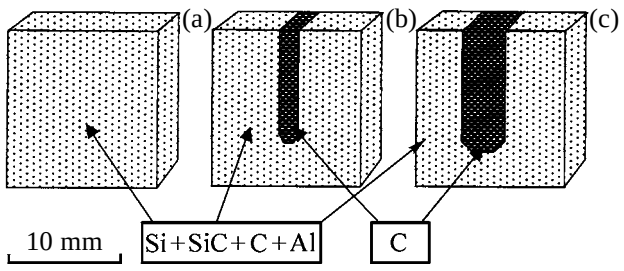

Fig. 3. Schematic of edge surfaces of C–SiC–Si–Al composites: (a) PG–AS, (b) GP–0.5AS, and (c) MG–AS.

Table 3. Structural characteristics of the main phases of C–SiC–Si–Al composites, determined from the profiles of reflections with 100% intensity, and the intensities of reflections from the main phases in the X-ray diffraction patterns of the composites, measured under the identical conditions

Composite			PG–AS		GP–0.5AS		MG–AS	
SiC								
d_{111}, nm			0.2518		0.2518		0.2518 (0.2521*)	
L_{111}, nm			230		260		220 (140*)	
I_{111}, rel. units			1677		2079		2053 (194*)	
ASTM SiC								
d, Å	*I*, %	*hkl*	*I*, rel. units	*I*, %	*I*, rel. units	*I*, %	*I*, rel. units	*I*, %
2.51	100	111	158	100	200	100	201	100
2.18	20	200	20	12.7	30	15	28	14
1.54	63	220	45	28.5	75	37.5	66	32.8
1.31	50	311	38	24	48	24	52	25.8
1.26	5	222	8	5	11	5.5	10	5
Σ			269	100	368	135	357	132
C:								
d_{002}, nm			0.3371		0.3387		0.3373 (0.3388**)	
L_{002}, nm			38.1		33.5		37.7 (333.5**)	
I_{002}, rel. units			377		713		876 (9117**)	
ASTM C								
3.348	100	002	65	100	99	100	141	100
2.127	3	100	3	4.6	3	3	6	4.3
2.027	15	101	5	4.6	4	4	6	3.5
1.647	6	004	3	4.6	2	2	5	3.5
1.228	4	110	5	7.7	3	3	8	5.6
Σ			81	100	111	137	166	205
Si:								
d_{111}, nm			0.3147		0.3146		0.3145 (0.3153*)	
L_{111}, nm			230		>500		>500 (420*)	
I_{111}, rel. units			1156		836		416 (227*)	
ASTM Si								
3.1355	100	111	250	100	22	100	30	100
1.9201	55	220	47	18.8	4	18.2	21	70
1.6375	30	311	38	15.2	6	27.3	9	30
1.3577	6	400	18	7.2	–	–	–	–
1.2459	11	331	5	2	–	–	3	10
Σ			358	1118	32	100	63	193

* Boundary of the carbon region C.
** Carbon region C.

Table 4. Variation of the relative intensity of the strongest reflections from the main phases across a sample of the MG–AS composite

Measurement point	*l*, nm	C(002)			Si(111)		SiC(111)	
		I, rel. units	*L*, nm	*d*, nm	*I*, rel. units	*d*, nm	*I*, rel. units	*d*, nm
1	0.00	23	37.7	0.3376	3.5	0.3145	30	0.2518
2	3.60	139	35.4	0.3384	2.5	0.3153	12	0.2521
3	6.65	229	33.5	0.3388	0	–	0	–
4	9.10	221	33.9	0.3388	0	–	1	–
5	11.05	48	34.6	0.3386	4	0.3153	25	0.2520
6	12.45	32	36.4	0.3382	9	0.3149	30	0.2519
7	14.25	31	37.6	0.3376	5.5	0.3145	28	0.2518

are in disagreement with those in the ASTM files (Table 3). In addition, a minor rotation (by ~5°) of the section of a composite leads to a strong (severalfold) change in the intensities of the diffraction peaks of Si. This indicates that the silicon crystals formed in the composites are textured, which hinders a correct comparative analysis. However, judging from the total intensity Σ of all the reflections, it can be stated that the highest concentration of Si is observed in the PG–AS composite (Σ_{PG-AS} exceeds by a factor of approximately 11 the total intensity of the Si lines in the GP–0.5AS composite).

The structural characteristics of the main phases (β-SiC, C, and Si) were determined by analyzing the profiles of the strongest reflections from these phases (Table 3). It was established that the interplanar spacings d_{002} of the carbon phase are in the range 0.3371–0.3377 nm, and the average sizes of the coherent domain, 30.2–37.7 nm. The differences are presumably due to the different structures of the starting carbon materials. Strong differences are observed between the characteristics of crystalline carbon in the bulk of the MG–AS composite and in the carbon region C (Table 4). Table 4 shows that the interplanar spacings and the integral intensity in the C region are larger, and the average size of the coherent domains smaller, than those in the bulk of the composite. In all probability, the finely crystalline component of the carbon material has the highest reactivity and is the first to enter into the reaction with silicon to form a carbide. Noteworthy is one more specific feature of crystal formation: the coherent domains of silicon carbide at the boundary of the C region are smaller than in the bulk of the composite (Table 3). This is due to the fact that β-SiC is formed in the boundary region under the conditions of silicon deficiency.

The interplanar spacings d_{111} of silicon in the composites are 0.3145–0.3153 nm, which exceeds the tabulated value (0.3135 nm) and points to the formation of solid solutions of aluminum in silicon. The average size of the coherent domains exceeds 200 nm.

To elucidate the mechanism of formation of those regions of the composites into which the silicon melt does not penetrate, the variation of the phase composition across a sample of a composite was studied in accordance with the scheme in Fig. 1. The results obtained are listed in Table 4 and shown in Fig. 4. It was established that the content of silicon carbide and silicon in the carbon region C of the composite is

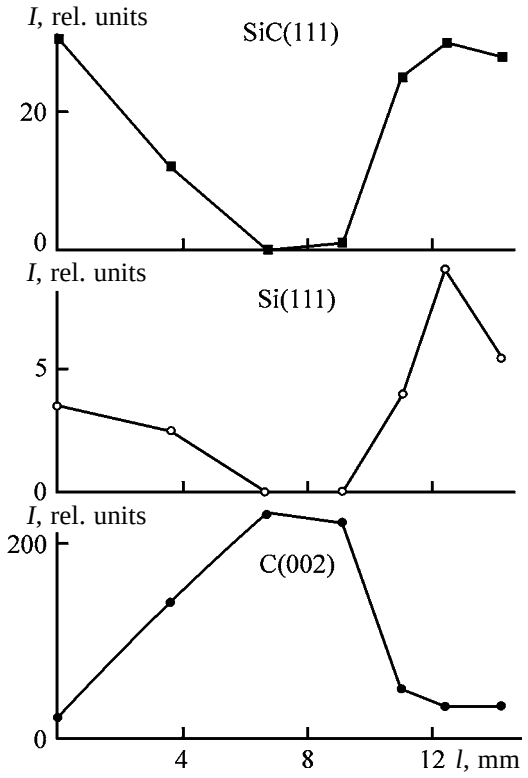

Fig. 4. Variation of the intensity *I* of the reflections 111 for silicon carbide, 111 for silicon, and 002 for carbon across a sample of the MG–AS composite.

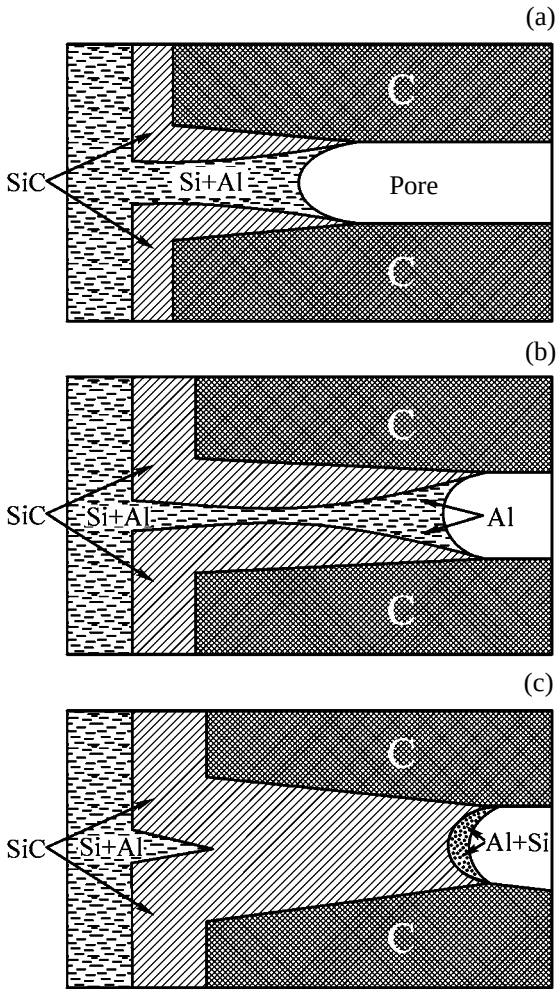

Fig. 5. Mechanism of formation of carbon regions in C–SiC–Si–Al composites: (a) Motion of the Si–Al melt along a pore at the beginning of the process, (b) overgrowth of the pore, and (c) formation of an SiC layer beyond the overgrowth point through spreading of the remaining part of the melt that penetrated into the pore.

virtually zero and their content in the bulk of the composite decreases toward the boundary of the purely carbon region. Contrariwise, the intensity of the line 002 of carbon increases and reaches its maximum value in the C region.

The results obtained suggest the following formation mechanism of the structure of the four-component composite C–SiC–Si–Al. The composites are formed by reaction with the Si–Al melt, which spreads along the capillaries (pores) of the starting carbon supports. Since silicon is constantly spent in the process for SiC formation, the concentration of the impurity (aluminum) at the melt motion front must increase, as it occurs when C–SiC–Si–Cu is formed [4]. This is confirmed by the experimentally observed dependence of the interplanar spacings d_{111} of metallic silicon present in the composite on the cut depth (Table 4). The average interplanar spacing d_{111} varies from 0.3145 to 0.3153 nm and exceeds that for pure silicon (0.3135 nm). The hypothesis is also confirmed by the formation of aluminum crystals at the boundary of the carbon region C. The concentration of aluminum in silicon on the surface of the MG–AS composite, evaluated using Vegard's law [6], is two times smaller than that at the boundary of the volume of the composite in which the reaction with the Si–Al melt did not occur. The increase in the concentration of aluminum at the front of the melt moving along the capillaries must lead to a proportional acceleration of the crystallization of SiC. The catalytic effect of aluminum on the growth rate of SiC is confirmed by the results of comparative studies of carbide formation in Si, Si–Al, and Si– Cu melts brought in contact with a carbon surface in the initial stage (2 to 120 s) of the process, reported in [7].

The motion of the front of the Si–Al melt is illustrated by the scheme in Fig. 5. The amount of SiC formed at the beginning of the interaction between the silicon melt and carbon gradually increases, so that at a small diameter of the pores they must be overgrown with a layer of rapidly formed SiC. As a result, further supply of the melt along the capillaries is terminated (Fig. 5b). Regions into which no melt has penetrated are formed in the composite. A part of the unreacted melt, which is beyond the clogging point, gradually flows toward the defective region (Fig. 5c), with the result that the boundary of this region becomes less abrupt and the amount of SiC formed gradually varies in going from the surface of the composite to the C region. This mechanism of formation of structural heterogeneities differs from that for the case of four-component composites and copper, in which the melt motion terminates as a result of an increase in the contact angle [4]. Strongly different effects of Cu and Al on the phase boundaries of other semiconductors have also been reported [8].

The acceleration of carbide formation at the interface between the Si–Al melt and carbon, compared to that for a system with no aluminum additives, is presumably due to a higher rate of carbon dissolution in the melt at the beginning of the interaction between the melt and the carbon surface. After an SiC layer is formed on the carbon surface, the rate of carbide formation is limited by diffusion of carbon across the carbide layer and the impurities present in the melt cannot affect the process to any noticeable extent. However, at the beginning of the interaction, when the SiC layer is not formed yet, the surface tension at the

melt–carbon phase boundary decreases to zero, and even becomes negative [9]. This may lead to diffusion of carbon particles into the melt, to form a colloid solution [9]. The thickness of the primary SiC layer formed on the carbon surface must be proportional to the amount of carbon dissolved in the melt at the beginning of the interaction. Therefore, the catalytic effect of aluminum on the formation of a carbide is, in the authors' opinion, due to the fact that its presence in the silicon melt leads to dissolution of a greater amount of carbon at the beginning of the interaction between the melt and the carbon surface.

CONCLUSION

Spatially heterogeneous regions are formed in C–SiC–Si–Al composites as a result of a catalytic action of aluminum on the process of carbide formation. The formation of regions into which no melt penetrates can be precluded by lowering the concentration of aluminum in the silicon melt and making larger the capillaries (pores) in the starting carbon support.

REFERENCES

1. Tarabanov, A.S. and Kostikov, V.I., *Silitsirovannyi grafit* (Siliconized Graphite), Moscow: Metallurgiya, 1977.
2. Gnesin, G.G., *Karbidokremnievye materialy* (Silicon Carbide Materials), Moscow: Metallurgiya, 1977.
3. Virgil'ev, Yu.S., *Izv. Ross. Akad. Nauk, Neorg. Mater.*, 1997, vol. 33, no. 6, pp. 683–690.
4. Belenkov, E.A., Tyumentsev, V.A., Koshelev, Yu.I., and Sheinkman, A.I., *Izv. Ross. Akad. Nauk, Neorg. Mater.*, 1992, vol. 28, no. 10/11, pp. 2096–2099.
5. Nagornyi, V.G., Kotosonov, A.S., Ostrovskii, V.S., *et al.*, *Svoistva konstruktsionnykh materialov* (Properties of Structural Materials), Moscow: Metallurgiya, 1975.
6. Umanskii, Ya.S., Skakov, Yu.A., Ivanov, A.N., and Rastorguev, L.N., *Kristallografiya, rentgenografiya i elektronnaya mikroskopiya* (Crystallography, X-ray Diffraction Analysis, and Electron Microscopy), Moscow: Metallurgiya, 1982.
7. Belenkov, E.A., Tyumentsev, V.A., and Fotiev, A.A., *Izv. Ross. Akad. Nauk, Neorg. Mater.*, 1997, vol. 33, no. 3, pp. 324–328.
8. Bechstedt, F. and Enderlein, R., *Semiconductor Surface and Interface: Their Atomic and Electronic Structure*, Berlin: Akademie, 1988.
9. Elyutin, V.P., Kostikov, V.I., Maurakh, M.A., *et al.*, *Konstruktsionnye materialy na osnove ugleroda* (Carbon-Based Structural Materials), Moscow: Metallurgiya, 1974, vol. 9, pp. 190–200.

Russian Journal of Applied Chemistry, Vol. 77, No. 3, 2004, pp. 360–363. Translated from Zhurnal Prikladnoi Khimii, Vol. 77, No. 3, 2004, pp. 366–369.

INORGANIC SYNTHESIS AND INDUSTRIAL INORGANIC CHEMISTRY

Structure of Silica Formed by Carbonation of Alkaline Silicate Solution

K. B. Oganesyan, S. S. Karakhanyan, and E. B. Oganesyan

Institute of General and Inorganic Chemistry, National Academy of Sciences of Armenian Republic, Yerevan, Armenia

Received August 6, 2003; in final form, December 2003

Abstract—The structure of silica formed by carbonation of alkaline silicate solution was studied by adsorption, electron microscopy, and sedimentation analysis.

This study continues our previous work [1] and concerns the structure of silica formed by carbonation of alkaline silicate solution [2]. This kind of silica is considerably less studied than silicas prepared by the reaction of sodium or potassium silicate with acid mineral reagents [3–6].

Silica of pilot-plant production containing ~75 wt % SiO_2 and ~25 wt % Na_2CO_3 was washed with water to remove Na_2CO_3. According to spectral analysis, the washed sample contained about 3.4×10^{-2} wt % sodium ions. The product was studied by adsorption methods (with krypton, methanol, and water as adsorbates) [7], electron microscopy [8], and sedimentation analysis. The fractionation was done under the standard conditions: powder in the form of a turbid aqueous suspension (solid-to-liquid ratio 100 : 10) was poured into a glass cylinder (12 cm in diameter and 20 cm high), and the precipitate was separated from the suspension at regular intervals with a bottom rubber tube. The precipitate (fraction) was dried, weighed, and examined under an optical microscope (magnification 500). The fragments of the micrographs and results of their statistical treatment in the form of particle-size distribution curves are presented in Figs. 1 and 2 and in the table.

The initial (reference) silica had polydispersed granulation and consisted of oval or spherical particles from 2 to 100 μm in size (Fig. 1a). Most (about 85%) of the polydispersed system consisted of 30–50-μm particles (Fig. 1b); about 10%, of 10–20-μm particles (Fig. 1c); and 1%, of 5-μm and finer particles (Fig. 1d).

The comparison of the specific surface areas of the initial silica and its fractions, as calculated from the krypton adsorption isotherms S_{Kr}, $m^2\ g^{-1}$ (true surface

Fractional composition and adsorption-structural characteristics of the initial silica and constituent fractions

Sample no.	Fraction	Fraction percentage, %	Effective particle diameter, d_{eff}, μm	Specific surface area S, $m^2\ g^{-1}$ by adsorption*		
				Kr	CH_3OH	H_2O
1	Initial sample	–	–	420	500	760
2	2-min	45	50	380	465	730
3	4-min	25	40	370	480	675
4	8-min	14	30	400	460	750
5	40-min	8	20	500	555	745
6	80-min	1.5	15	510	570	700
7	2-h	0.6	5	540	545	760
8	24-h	0.5	2	560	570	775

* S_{CH_3OH} and S_{H_2O} are the formal surface areas calculated from the corresponding adsorption isotherms of methanol and water vapor. The plateau ω occupied by the adsorbate molecules in a dense monolayer on the surface of silica at saturation is taken as 21.5 $Å^2$ for krypton and 25 $Å^2$ for methanol and water [7].

1070-4272/04/7703-0360 © 2004 MAIK "Nauka/Interperiodica"

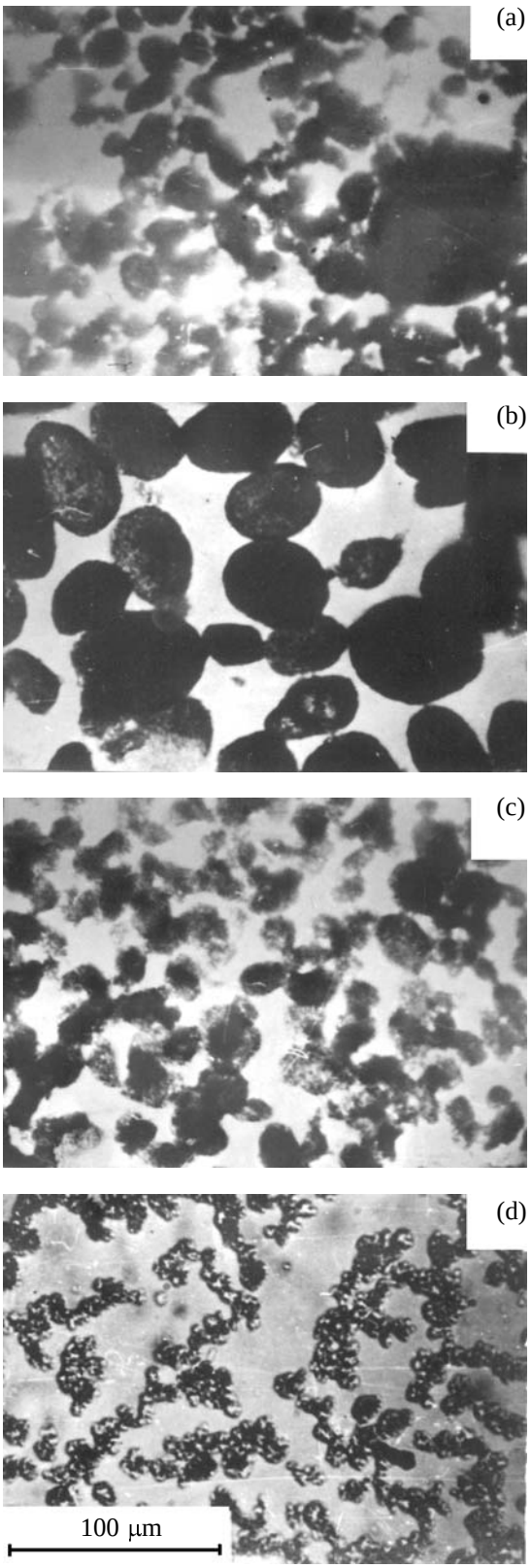

Fig. 1. Micrographs of the samples: (a) initial silica; fractions: (b) 2-min, (c) 40-min, and (d) 120-min. Magnification 500.

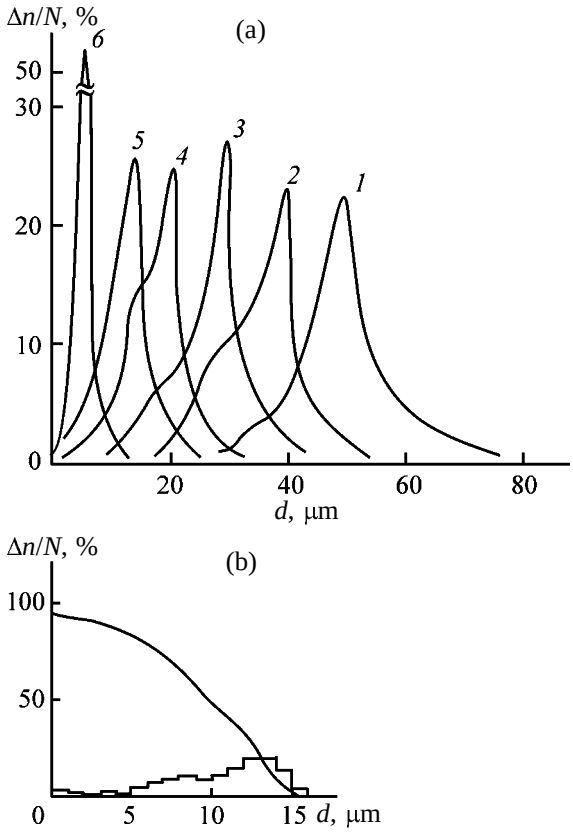

Fig. 2. (a) Particle size distribution curves ($\Delta n/N$ vs. d) and (b) differential and integral curves of the particle size distribution taken on a Kaulter T2A 16-channel analyzer for a sample of the 80-min fraction. (a) Fraction: (*1*) 2-min, (*2*) 4-min, (*3*) 8-min, (*4*) 40-min, (*5*) 80-min, and (*6*) 120-min.

area corresponding to the nonspecific dispersion interaction in the adsorbent–adsorbate system [9]) shows that, though sample nos. 1–8 have different S_{Kr} values, they can be subdivided into two groups (see table). The first group includes coarsely dispersed fractions having somewhat lower S_{Kr} values compared to the initial sample, and the second group, finely dispersed fractions having a more developed surface compared to the initial sample. The similar dependence of the specific surface area on the fraction fineness is also clearly revealed when comparing with S_{Kr} the formal S_{H_2O} and S_{CH_3OH} values as calculated from the corresponding adsorption isotherms of water and methanol vapors. The increased adsorption activity with respect to methanol and water is observed for all the samples, especially for coarse fractions (S_{H_2O}/S_{Kr} = 1.9 and S_{CH_3OH}/S_{Kr} = 1.3).

According to the electron-microscopic study, the initial silica has a corpuscular skeleton formed by corpuscules of size from 70 to 150 Å and aggregated

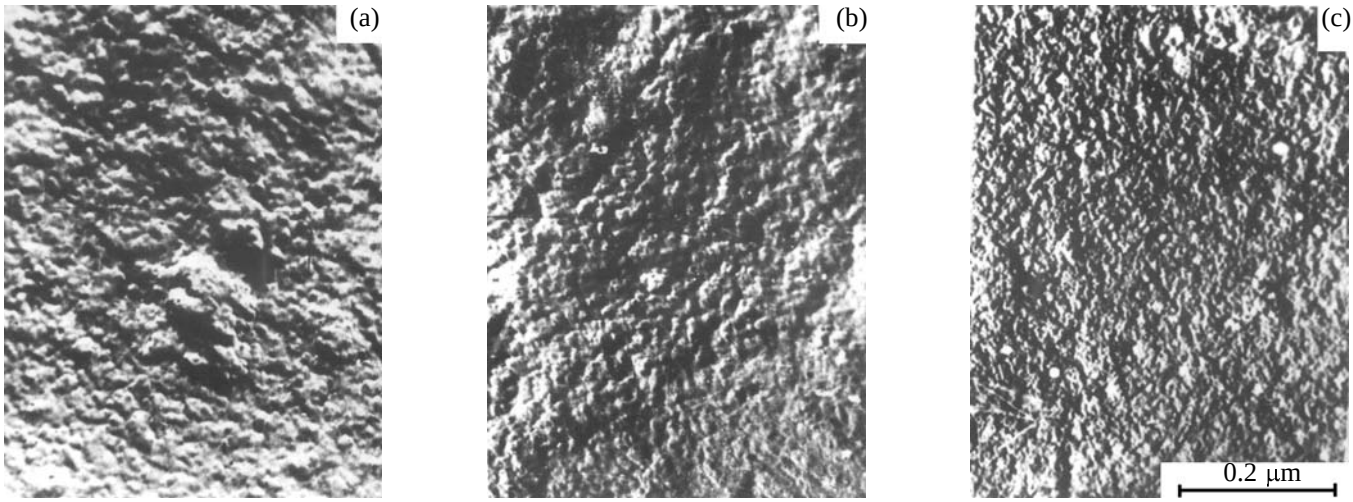

Fig. 3. Electron micrographs taken with self-shaded Pt–carbon replicas prepared on surfaces of the samples. (a) Initial silica; fraction: (b) 8-min and (c) 80-min.

globules of smaller (up to 50 μm) size (Fig. 3a). The coarsely dispersed fractions have the similar skeleton. The micrograph of a sample of the 8-min fraction is given as example (Fig. 3b, sample no. 4). The samples of finely dispersed fractions have the pronounced close-packed skeleton (Fig. 3a) formed by fine globules 30–50 μm in diameter. The average pore volume is from 0.45 to 0.58 and ~0.35 $cm^3\ g^{-1}$ for the samples of the first and second groups, respectively. To these values correspond the average pore diameters of 60 and 30 Å, respectively.[1]

As known, the structure of the silica corpuscular skeleton, globule size and packing, and, consequently, surface area, pore volume, and pore diameter depend on the synthesis conditions (solution pH, reagent concentrations, and temperature [3, 4]). Therefore, it may be suggested that the silica fractions of the first group (the major part of the initial sample) were formed under somewhat different synthesis conditions than samples of finely dispersed fractions. In the traditional method of the synthesis of amorphous SiO_2 [3, 4], the acid is fed into alkaline silicate solution at once (i.e., formation and growth of silica sol occur simultaneously throughout the volume). At the same time, in an alternative method described in [2, 5, 6], silicic acids form and polymerize into more complex cross-linked structures gradually, as CO_2 is fed into the solution. The process is complete at a 104–108% carbonation. Therefore, the conditions of the nucleation and growth of silica sol at each subsequent moment are different.

In the first stages of carbonation, when the concentration of Na_2SiO_3 solution is high and concentration of the acidic reagent is low ($CO_2 + H_2O \rightleftarrows H^+ + HCO_3^-$), the amount of the forming silicic acids cannot ensure bulk polycondensation and solation. As CO_2 is fed, the content of silicic acids increases. However, up to 80–85% carbonation, the degree of polymerization is so low that the solution remains transparent even after prolonged storage (so-called sol phase [3]). After a slight amount of CO_2 is then fed, the solution becomes turbid within a short time, i.e., gelation and subsequent precipitation take place.

The formation, growth, and aggregation of the macromolecules of silicic acids accompany each other during the whole process of the carbonation of alkaline silicate solution. This suggests that most (up to 85%) of the precipitated SiO_2 (namely, coarsely dispersed fractions) is formed in the first stage of the carbonation. Finely dispersed fractions (~10% of the total SiO_2 amount) having finely globular close-packed skeleton are formed in the final stages, when the residual amount of Na_2SiO_3 in the reaction medium is low [4].

The persorption phenomenon, revealed as preferential adsorption of CH_3OH and H_2O in comparison with large spherical Kr atoms, shows that, apart from coarse pores, i.e., voids between the SiO_2 globules in contact, there are very fine pores (ultrapores) accessible mainly to water molecules. The ultrapores or voids of molecular size can be formed in the volume of macromolecules under the certain conditions of the

[1] The average pore volume was determined by the "desiccator" method, i.e., by keeping the sample in benzene vapor till saturation, i.e., at $p/p_S = 1.0$; the average pore diameter was calculated from the $d_{av} = 4V_{av}/S_{cr}$ ratio [9] for corpuscular structures.

silica synthesis or hydrothermal treatment (when, e.g., the polymeric chain terminates upon attachment of the ≥Si–ONa group and continues to grow in another direction) [10, 11]. Such incorporation of the ≥Si–ONa groups into the silica polymeric network is facilitated by the long carbonation time and by gradual accumulation of silicic acids in the bulk. The washout and removal of sodium ions results in the formation of ultravoids in the volume of globules. The extent of termination of the polymeric chain determines the linear size of the ultrapore.

The fact that S_{CH_3OH} slightly exceeds S_{Kr} (corresponding to the true value of the surface area) indicates that a part of ultrapores is also accessible to CH_3OH molecules. When a CH_3OH molecule is favorably oriented with respect to the ultrapore aperture, it can partly enter the ultrapore with its hydroxy group (S_{H_2O}/S_{Kr} is ~1.9 and ~1.1 for coarsely dispersed and finely dispersed fractions, respectively).

According to the experimental data (see table), small H_2O molecules in perceptible amounts penetrate into the silica ultrapores. The amount of such defects in the macromolecule structure is the largest in the samples of coarsely dispersed fractions. The additional surface area accessible for H_2O molecules inside the silica ultrapores is 300–340 $m^2 g^{-1}$ (for fine fractions, 200 $m^2 g^{-1}$). With all the samples without exception, the adsorption equilibrium was attained within 40–45 min for krypton, 1–2 h for methanol, and 10–20 h for water. The long time of attainment of the adsorption equilibrium in adsorption of H_2O vapor shows that the ultrapore length is large.

Silica with the similar structural characteristics can be used as drying agent for various gaseous systems and in manufacture of special-purpose glasses (their production process allows preparation of silica containing ~10^{-3} wt % color impurities [2, 6]).

CONCLUSIONS

(1) Study of the structure and granulometric composition of silica formed by carbonation of alkaline silicate solution showed that the product is a finely dispersed powder system. Most (~85%) of the powder is in the form of 30–50-μm particles having the similar corpuscular skeleton formed by globules 70–150 Å in diameter (S = 360–400 $m^2 g^{-1}$). The remainder is finely dispersed fractions 20 μm in size and less, with close-packed skeleton.

(2) The silica corpuscular skeleton with a pore volume from 0.30 to 0.58 $cm^3 g^{-1}$ and pore diameter in the range 30–60 Å, depending on the fraction dispersion, has the ultrapore structure, i.e., it consists of molecular-size pores accessible to water molecules.

(3) The long time of the formation and polymerization of silicic acids, associated with the prolonged carbonation of alkaline silicate solution, is mainly responsible for the inhomogeneity of the silica structure and granulometric composition.

REFERENCES

1. Oganesyan, K.B., Karakhanyan, S.S., and Oganesyan, E.B., *Zh. Prikl. Khim.*, 1999, vol. 72, no. 3, pp. 374–378.
2. Manvelyan, M.G., *Trudy Vsesoyuznogo soveshchaniya po glinozemu* (Proc. All-Union Meet. on Alumina), Yerevan, 1964, pp. 421–429.
3. Iler, R.K., *The Chemistry of Silica*, New York: Wiley–Interscience, 1979.
4. Neimark, I.E., and Sheinfain, R.K., *Silikagel', ego svoistva i primenenie* (Silica Gel. The Properties and Application), Kiev: Naukova Dumka, 1971.
5. Manvelyan, M.G., and Badalyan, S.B., *Arm. Khim. Zh.*, 1969, vol. 22, no. 10, pp. 943–945.
6. Manvelyan, M.G., Abadzhyan, K.S., and Mikaelyan, V.O., *Arm. Khim. Zh.*, 1971, vol. 24, no. 12, pp. 1069–1073.
7. *Eksperimental'nye metody v adsorbtsii i molekulyarnoi khromatografii* (Experimental Methods in Adsorption and Molecular Chromatography), Kiselev, A.V., Ed., Moscow: Mosk. Gos. Univ., 1973.
8. Manvelyan, M.G., Oganesyan, E.B., and Oganesyan, K.B., *Arm. Khim. Zh.*, 1973, vol. 26, no. 2, pp. 378–381.
9. *Kurs fizicheskoi khimii* (Course of Physical Chemistry), Gerasimov, S.Ya., Ed., Moscow: Goskhimizdat, 1963.
10. Vysotskii, Z.Z., Zhuravlev, L.T., Kiselev, A.V., *et al.*, *Kolloidn. Zh.*, 1971, vol. 33, no. 1, pp. 51–56.

Russian Journal of Applied Chemistry, Vol. 77, No. 3, 2004, pp. 364–368. Translated from Zhurnal Prikladnoi Khimii, Vol. 77, No. 3, 2004, pp. 370–374.

INORGANIC SYNTHESIS AND INDUSTRIAL INORGANIC CHEMISTRY

Combustion in a System of Conjugated Layers and High-Temperature Synthesis of Materials

G. I. Ksandopulo and A. N. Baidel'dinova

Plamya Research and Production Association, Almaty, Kazakhstan
Institute of Combustion Problems, Almaty, Kazakhstan

Received August 29, 2002; in final form, July 2003

Abstract—The possibility of constructing layered systems for high-temperature synthesis of materials is demonstrated. The cases of vertical and horizontal arrangement of layers, which ensure different types of a technological combustion of the initial reactant mixtures with or without subsequent interaction of the reaction products formed, are considered. The conditions are found for the synthesis of alkaline-earth metal titanates and aluminum borides in the layered systems.

The temperature of the combustion wave front in metal–oxide systems may be as high as $(3–4) \times 10^3$ K under quasi-adiabatic conditions. In order to perform a high-temperature synthesis, conditions of this kind can be created if the mixture of reacting components is formed as a layer receiving thermal energy from the side of parallel energy-carrying layers [1].

A stack of layers selected with account of the task to be accomplished is arranged horizontally or vertically (perpendicularly to the horizontal or vertical axis, respectively). In some cases, it can be subjected to the action of a centrifugal force, or an electric or a magnetic field.

This article is concerned with the fundamental aspects of combustion of complex stacks in relation to the mutual arrangement of the constituent layers, their orientation, etc. It is not aimed to establish a strict relationship between the kinetic parameters that govern the chemical process and the parameters determining the removal of heat from the reaction zone. The goal is to consider the phenomenology of combustion in the layers and the propagation of the combustion front in the adjacent layers.

Combustion of a horizontal stack of layers. In the horizontal variant, when the layers are arranged perpendicularly to the horizontal axis (Fig. 1a), the products formed in combustion of oxide system and, in particular, reduced metals, do not penetrate into the adjacent layers. In this case, only conductive heat transfer occurs, since the horizontal stack is composed of chemically independent layers. To ensure a quasi-adiabatic course of the process in the layered system, ignition is performed simultaneously in the adjacent layers. Then the synthesis layers can be repeatedly alternated with the layers that serve as sources of heat, with the maximum heating achieved.

The macrokinetics of combustion in a layer is determined not only by the reactant concentrations, temperature, and pressure, but also by external forces, e.g., those due to centrifugal acceleration in the case of axial rotation.

The characteristic time τ of combustion of a stack is constituted by the times τ_k of burning-through of all

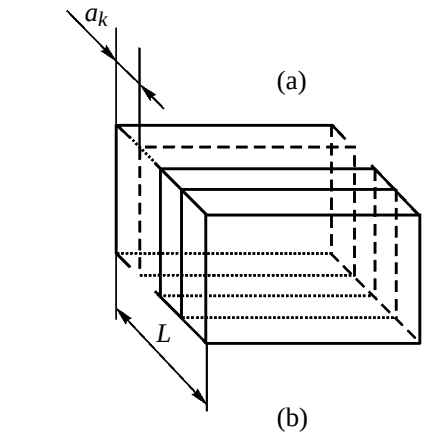

Fig. 1. Schematic of a horizontal stack of layers. Stack: (a) that in the general case and (b) that with a repetitive system of three layers, in which layer no. 2 is the synthesis layer.

1070-4272/04/7703-0364 © 2004 MAIK "Nauka/Interperiodica"

the k layers of the stack:

$$\tau = \sum_{k=1}^{i} \tau_k = \sum_{k=1}^{i} (n\bar{M}/W_k), \quad (1)$$

where n is the number of moles; $\bar{M}$, average molecular weight of the starting substances; and W_k, mass rate of the overall reaction in the kth layer.

The normal combustion velocity U_k in a layer is equal to the thickness of each layer (a_k) divided by the time τ_k of its combustion, and, consequently, the average linear velocity of combustion of the whole stack ($\bar{U}$) in the case of successive ignition of the layers is given by

$$\bar{U} = \tau^{-1} \sum_{k=1}^{i} a_k. \quad (2)$$

Let us assume that the optimal result of synthesis is determined by the average mass velocity of combustion of a stack with substance density ρ_k in the kth layer:

$$\bar{U}_m = S\tau^{-1} \sum_{k=1}^{i} a_k \rho_k. \quad (3)$$

The quantity $\bar{U}_m$ differs from the additive $\bar{U}_{am}$, which is equal to the average velocity of separate combustion of each layer of the stack at average temperature T_{av},

$$\bar{U}_{am} = S \sum_{k=1}^{i} (a_k \rho_k / \tau_k).$$

Let us name the ratio

$$\varphi = \bar{U}_m / \bar{U}_{am} \quad (4)$$

the coefficient of conjugation of layers in a stack. This coefficient characterizes the rise in the rate of the overall reaction in a stack, caused by changes in the heat transfer conditions, number and distribution of ignition points, and mutual arrangement of layers in the stack:

$$\varphi = f(\lambda, \rho, S, P_n), \quad (5)$$

where λ is the heat conductivity; S, cross-sectional area of the stack; P_n, nth permutation, whose total number P_n in a stack composed of k layers is given, with account of the fact that the 1st, 2nd, 3rd, ..., and kth layers are repeated α, β, γ, ... times, by

$$P_n = k!/\alpha!\ \beta!\ \gamma!,... \quad (6)$$

It is noteworthy that the quantity φ we introduced also characterizes the synthesis layers. In this case, the quantity $\bar{U}_{am}$ is equivalent to the rate of accumulation of the product at T_{av}, and $\bar{U}_m$, to the rate of its accumulation in a layer within a stack.

Thus, for any composition of the stack, the value of φ depends on the arguments in expression (5), whose variation mainly affects $\bar{U}_m$. If the parameters λ, ρ, and S are constant within the limits of variations, then the only reason why the coefficient φ changes is transition from one arrangement of the layers to another. The best synthesis effect, to which corresponds the maximum value of φ, is achieved at a certain average value of the mass velocity.

Let us consider a three-layer system repeated in the stack k times (see Fig. 1b). Layer 2, in which the strongest heating conditions are to be created, is in contact with layer 1 on the left and layer 3 on the right. In the case of a simple, nonchain reaction in layer 2, the degree of conversion of the reaction mixture at any point of this layer along the stack axis is determined by the temperature distribution on the left and on the right, attained by the instant of time τ_k. The value of φ in layer 2 is determined in this case by the velocity U_m of the heat wave that arrives from the adjacent layers.

The resulting value of φ for the three layers combined is given by

$$\varphi = \overrightarrow{\varphi_1} - \varphi_2 + \overleftarrow{\varphi_3}.$$

The strongest effect ($\varphi' = 0$, $\varphi'_2 = 0$) corresponds to a numerical equality of the velocities of the oppositely propagating combustion waves in layers 1 and 3:

$$|U_{m_1}| = |U_{m_3}|.$$

The temperature distribution within layer 2 is set by the propagation of the heat waves from the left and from the right. If it is assumed that the total content of enthalpy in layers 1 and 3 much exceeds the heat consumed by the reaction in layer 2, then the reaction rate profile in the synthesis layer is determined by the existing temperature distribution. If, further, the characteristic time of the reaction in the synthesis layer is of the same order of magnitude as the time of propagation of the heat wave (the reaction begins at

its front), then the temperature profile is approximately described by the known Michelson distribution:

$$T_{(x)} \approx T_0 + (T_c - T_0)\exp UXC_t\rho/\lambda. \quad (7)$$

At the point x where the temperature increases by a factor of approximately e ($T_x/T_0 \approx 2.718$ at $T_0 \approx 300$ K), but the reaction rate can still be neglected,

$$(T_x - T_0)/(T_c - T_0) \approx e, \quad (8)$$

$$x \approx \lambda/(UC_p\rho).$$

For the TiO_2–Al reaction mixture diluted with graphite, $C_p = 170$ J g^{-1} deg^{-1}, $\lambda = 0.05$ J cm^{-1} deg^{-1} s^{-1}, $\rho = 2.3$ g cm^{-3}, $U = 0.02$ cm s^{-1}, and the increase in temperature to $T_x/T_0 \approx 2.718$ will occur at a distance $x = 1.5 \times 10^{-3}$ cm from the plane that divides the reaction and heating layers.

In various mixtures of metal oxides with the specific heat $C_p \approx 80$–130 J g^{-1} deg^{-1}, all other conditions being the same, the value $x \approx (1–2) \times 10^{-2}$ is reached within 1 s, and at $U = 1$ cm s^{-1}, at 10^{-3} s. Extrapolation suggests that a layer of thickness 10 cm is heated in 1 s. Since the synthesis layer can be heated both from the left and from the right, the yield of the reaction product is the highest at the boundary of the heat source and the lowest in the middle of the synthesis layer.

The ratio (4) of the mass velocities characterizes rather effectively the relationship between the thermal properties of layers for a three-layer stack, in which the yield of the product is determined by temperature.

Let us assume that at a furnace temperature T_1 the reaction rate in the synthesis layer is infinitely small and the velocity of the combustion wave in the auxiliary layer is U_1. The combination of two auxiliary layers and the synthesis layer that lies in between is a system in which several pathways of the process are possible, depending on the heat-exchange conditions. If the synthesis layer considerably exceeds in mass the auxiliary layers and the contact area is small, then the middle layer acts as a heat insulator, the relative yield of the reaction product in this layer is nearly zero, and φ tends to unity. As the mass of the synthesis layer decreases and the contact area increases, the conditions can be created under which the reactions in the layers of the system go to completion and the velocity of the combustion wave in isolated auxiliary layers is zero. This is the ideal, hardly achievable in practice, case, when φ tends to infinity.

Real layered systems include auxiliary layers in which, when these layers are in the isolated state, the combustion process occurs in the steady-state mode without any change in their shape or disruption of the integrity of their surface, the loss of heat across the lateral surface is at a minimum, and the amount of thermal energy released is sufficient for initiating or maintaining reactions in the synthesis layer.

Synthesis of titanates of alkaline-earth elements in a horizontal stack. The reaction of titanium and barium oxides occurs in the temperature range 1350–1450°C. The composition and parameters of the auxiliary layer were chosen taking into account the endothermic effect of the reaction between the components in the main layer and its geometric dimensions [2].

The starting mixtures were thoroughly mixed. A hydraulic press equipped with a pressure gage for recording the compaction force was used to fabricate samples in the form of cylinders of various diameters or prisms, depending on the aim of a particular experiment. The samples were used to form layered systems, which were then placed in a furnace heated to the temperature of self-ignition of the mixtures used. After the combustion in the auxiliary layers was complete, a sample was either extracted for cooling in air or left in the furnace until equalization of temperatures.

In the case of synthesis of materials of prescribed composition for electronics, the requirements imposed on the product purity are high, and not only chemical interaction between the layers, but even mechanical penetration of the combustion products formed in the auxiliary layer into the synthesis layer are unacceptable. Therefore, the layers were arranged vertically, along the common horizontal axis. The cylindrical shape of the multilayer compound structure was chosen in order to diminish the area of contact with the substrate and, accordingly, to make lower the unproductive heat expenditure. These conditions ensure a sufficiently high ratio of the total weight of the reactants to the total area of the sample surface, across which heat is consumed, and the maximum possible area of contact between the layers. As a result, a steady-state combustion wave was obtained in the auxiliary layer and the most complete energy transfer from one layer to another was achieved. The furnace temperature was maintained at 850°C.

In the course of the experiments, auxiliary layer compositions Al–Cr_2O_3 with varied content of the reducing agent were studied. At a constant layer diameter of 20 mm and an auxiliary to synthesis layer mass ratio of 2, it was found that the temperature to which

the reagent mixture in the synthesis layer is heated varies with the composition and mass of the auxiliary layer. The results obtained are listed in Tables 1 and 2.

The limiting mass ratio in a synthesis layer of composition TiO_2–$BaCO_3$ and an auxiliary layer of composition Al–Cr_2O_3 was 1 : 2 at an aluminum content in the initial composition of the auxiliary layer of 15% and 1 : 1 at 23%. An X-ray phase analysis demonstrated that the finished product in the synthesis layer is the tetragonal modification of barium titanate.

In a similar way, with a minimum energy expenditure, we synthesized magnesium and calcium titanates. In this case, experimental selection of the composition and weight of the layers ensured that, in accordance with a calculation, the temperature in the synthesis layer was as high as 1650–1700°C at the furnace temperature of 850–900°C.

Synthesis of pure strontium titanate is hindered by the inertia of the process. To bring its rate in correspondence with the reaction rates in the auxiliary layers, the stock of the main layer was mechanically activated (the efficiency of this process was demonstrated in preliminary experiments for the example of an Al–Cr_2O_3 mixture [3]).

Thus, the approach developed for synthesis of materials in a layered system was used to obtain a number of compounds whose conventional synthesis involves complicated preparation of starting reactants and prolonged thermal treatment at high temperature. Combining the layer technique with such methods as, e.g., compaction or mechanochemical activation of the starting mixtures makes it possible to improve the control over the process.

Synthesis of aluminum borides in a stack of layers with protective interlayers. In contrast to the case of synthesis of alkaline-earth metal titanates, when it is only important to observe the lower temperature limit, synthesis of aluminum borides of certain compositions, AlB_2, AlB_{10}, and AlB_{12}, is complicated by its rather narrow temperature range (°C):

AlB_2	1000–1100
α-AlB_{12}	1100–1550
β-AlB_{12}	1550–1660
AlB_{10}	1660–1850

Moreover, aluminum borides are, as a rule, formed in the presence of carbon, which takes the uncompensated free bonds of complex boride molecules, and contamination of the finished product with other impurities, which diffuse from the auxiliary layers, significantly changes the electrotechnical properties of the borides.

Table 1. Heating temperature T_{comb} of the synthesis layer in relation to the stock composition of the auxiliary layer

C_{Al}, wt %	Forming density ρ, g cm^{-3}	T_{comb}, °C
12.0	2.726	1250
15.0	2.828	1382
18.0	2.830	1510
20.0	2.726	1648
23.0	2.725	1650
26.5	2.718	1618
32.0	2.692	1600

Table 2. Heating temperature T_{comb} of the substance in the synthesis layer in relation to the weight m of the auxiliary layer at aluminum content in this layer of 18%

m, g	Cylinder height h, mm	T_{comb}, °C
1.84	2.55	1406
3.80	4.46	1470
5.74	6.84	1538
7.64	8.98	1550
9.81	11.0	1580

The low-temperature boride AlB_2 was synthesized in a furnace heated to 870°C in an Al–B_2O_3 layer with additional heating from the side of an auxiliary layer composed of a stoichiometric mixture (Al + V_2O_5): Al_2O_3 (20–25%)–(Al + V_2O_5) (80–75%) or V_2O_5 (20–25%)–(Al + V_2O_5) (80–75%). AlB_{12} was synthesized using a three-layer system with two auxiliary layers situated on both sides of the main layer in which the Al–B_2O_3 mixture is also used as the synthesis layer, and the Al–TiO_2 system with nearly stoichiometric composition, as the auxiliary layer. The furnace temperature was 950°C, and the temperature in the combustion wave, 1500–1600°C.

Further rise in temperature enhances the diffusion interaction between the layers. Titanium penetrates from the auxiliary layer into the main layer and reacts with boron to give titanium boride. To preclude this process in synthesizing AlB_{10}, insulating interlayers of activated carbon were used. The use of inert high-melting interlayers enables a choice of the spatial arrangement of the layered compound structure, a horizontal or a vertical stack. The temperature in the reaction zone was raised by increasing the number of alternating layers in the order 1–2–3–2–1–2–3– etc.

(see Fig. 1b). To improve the mechanical strength of the system, a horizontal arrangement of the layers along a common vertical axis was used. Placing this multilayer system in a cylindrical graphite reactor ensures that the combustion process is highly adiabatic.

CONCLUSIONS

(1) The combustion of layered compound structures with characteristic conjugation of chemical processes in the layers was analyzed.

(2) It was shown that the main and fundamental distinctive feature of the layered combustion is the possibility of performing reactions in deep layers in a quasi-adiabatic mode. The temperatures that can be reached are as high as $(3–4) \times 10^3$ K.

(3) It was demonstrated that, in a horizontal stack with layers arranged perpendicularly to a horizontal axis, the combustion products of oxide system do not penetrate into adjacent layers, the layers are chemically independent, with only conductive heat exchange existing between them. As a characteristic of the compound structure was introduced the coefficient of layer conjugation, which is determined by the relative positions of the layers, changes in the combustion conditions in the case of combustion in a stack, and the number and distribution of ignition points; it characterizes the rise in the rate of the overall reaction. At a furnace temperature of 850°C, alkaline-earth metal titanates and aluminum borides were synthesized.

(4) With the layers lying one above another perpendicularly to a vertical axis, heavy reaction products in a melt pass from upper layers to lower ones and enter into a reaction with new reagents. This scheme is efficient in the case of a stage-by-stage formation of a multicomponent product and can also be used when insulating interlayers are introduced between the layers.

REFERENCES

1. Strunin, V.A., D'yakov, A.P., Nikolaeva, L.I., and Manelis, G.B., *Izv. Ross. Akad. Nauk, Neorg. Mater*., 1999, vol. 35, no. 3, pp. 57–61.
2. Baideldinova, A.N., Kanakidi, M.P., Korobova, N.E, and Ksandopulo, G.I., Abstracts of Papers, *Int. Symp. "Chemistry of Flame Front,"* Almaty: Inst. of Combustion Problems, 1997, pp. 65–66.
3. Kanakidi, M.P., Korobova, N.E., Ksandopulo, G.I., and Baidel'dinova, A.N., in *Problemy goreniya gazov i kondensirovannykh sistem* (Problems Associated with Combustion of Gases and Condensed Systems), Almaty: Inst. Problem Goreniya, 1998, issue 6, pp. 61–67.

Russian Journal of Applied Chemistry, Vol. 77, No. 3, 2004, pp. 369–375. Translated from Zhurnal Prikladnoi Khimii, Vol. 77, No. 3, 2004, pp. 375–381.

INORGANIC SYNTHESIS AND INDUSTRIAL INORGANIC CHEMISTRY

Thermal Expansion of Mixed Zirconium Phosphates

G. N. Kazantsev, A. I. Orlova, M. V. Zharinova, S. G. Samoilov, V. I. Pet'kov, and V. S. Kurazhkovskaya

Institute of Energy Physics, State Scientific Center of the Russian Federation, Obninsk, Kaluga oblast, Russia
Lobachevsky State University, Nizhni Novgorod, Russia
Moscow State University, Moscow, Russia

Received June 2, 2003

Abstract—A series of framework phosphates with varied ratio of cations $Na_{5-2x}B^{II}_xZr(PO_4)_3$, B^{II} = Mg, Ca, Sr, Ba ($0 \le x \le 2$) and $Na_{5-3x}Fe_xZr(PO_4)_3$ ($0 \le x \le 1.33$) were synthesized and studied under heating. The coefficients of thermal expansion along crystal axes α_a and α_c were calculated, and their dependences on the cationic composition (nature and concentration) and on the occupancy of out-of-framework structural positions were established.

Structural analogs of $NaZr_2(PO_4)_3$ (NZP, or Nasicon) are most studied among framework compounds characterized by the structural motif $[T_2(PO_4)_3]^f$, where T are elements in the oxidation states 1+, 2+, 3+, 4+, and 5+ (A, B, R, M, and C), and f is the framework charge taking values from 0 to 4. These compounds have a number of useful properties, which are often combined successfully in materials based on them. One of such properties is that, when heated in a wide temperature range, these compounds expand only slightly, sometimes do not expand, or even contract.

Phosphates of the NZP structural type (trigonal system, rhombohedral cell) are described by the crystal-chemical formula $(M1)(M2)_3L_2(PO_4)_3$, where L are cationic positions of an anionic framework, and M1 and M2 are positions in framework voids. As cations with varied size, oxidation state, and electronegativity can enter into various nonequivalent crystallographic positions of the structure, formation of wide isomorphous series becomes possible. Iso- or heteropolyvalent replacement of cations, on condition that their ratio is controlled, allows the physical and physicochemical characteristics of the compounds to be regularly varied.

The majority of works on the thermal expansion of phosphates concern double phosphates containing quadrivalent elements M^{IV} (Ti, Zr, Hf, Ge, Sn) in the framework and uni, bi-, or trivalent elements in voids. These phosphates are grouped in series according to the principle of isovalent replacement of A^I, B^{II}, and R^{III} cations. Among them, the following isoformula phosphates were studied: $A^IM^{IV}_2(PO_4)_3$, M^{IV} = Ti, A^I = Na, K [1–5]; M^{IV} = Zr, A^I = Li, Na, K, Rb, Cs [1, 3–8]; M^{IV} = Hf, A^I = Na, K, Rb, Cs [5, 9]; M^{IV} = Ge, A^I = Li, K [10, 11]; M^{IV} = Sn, A^I = Na [1, 5]; $B^{II}_{0.5}Zr_2(PO_4)_3$, A^{II} = Mg, Ca, Sr, Ba, Cd [3, 8, 12–20]; $R^{III}_{1/3}Zr_2(PO_4)_3$, R^{III} = La, Pr, Nd, Sm, Eu, Gd, Tb, Er, Tm, Yb [21].

As the metal–oxygen bonds in L positions do not noticeably elongate with increasing temperature and phosphorus–oxygen bonds become slightly shorter, the framework of such compounds does not noticeably expand on heating, and the thermal behavior of the structure as a whole depends on the nature and number of cations filling the framework cavities. It follows from the equation $\alpha = 32.9(0.75 - zp) \times 10^{-6}$ [22] [α is mean thermal expansion coefficient of the metal–oxygen bond (K^{-1}); z; cation charge; and p, coordination number] that the thermal expansion decreases as the cation charge increases. Increase in the size of cations located in positions of M, as shown for the above-given series with the same frameworks $[Zr_2(PO_4)_3]^-$, causes a decrease in the parameter α_c and an increase in the parameter α_a of a rhombohedral cell (hexagonal setting) with increasing temperature. In this case, the lattice parameters themselves change differently with increasing ionic radii of out-of-framework ions: c increases and a decreases. An increase in the number of M positions not occupied by cations often reduces the thermal expansion, as it was found when studying the phosphates $Sr_{0.5}Ti_2(PO_4)_3$ [23], $Cs_{1.3}R_{0.3}Zr_{1.7}(PO_4)_3$ [24], and the phosphates of the series with varied concentrations of cations and vacan-

1070-4272/04/7703-0369 © 2004 MAIK "Nauka/Interperiodica"

cies $Na_{1-x}Nb_xZr_{2-x}(PO_4)_3$, $Na_{1+x}Y_xZr_{2-x}(PO_4)_3$, and $A_{5-4x}Zr_xZr(PO_4)_3$. The role of vacancies has been considered in [23] when discussing the mechanism of thermal expansion of the phosphate $Sr_{0.5}\cdot Ti_2(PO_4)_3$.

The system of zirconium phosphates of the series $A^I_{5-x}A^I_xZr(PO_4)_3$, $A^I_{5-x}B^{II}_xZr(PO_4)_3$, $A^I_{5-3x}R^{III}_x\cdot Zr(PO_4)_3$, $A^I_{5-4x}M^{IV}_xZr(PO_4)_3$, and $A^I_{5-5x}C^V_x\cdot Zr(PO_4)_3$ is of interest for the estimation of contributions of the concentrations n and ν of cations and vacancies, respectively, to the thermal expansion. Variations in the concentration x of cations B^{II}, R^{III}, M^{IV}, and C^V in these series upon their heterovalent substitution for cations A^I are accompanied by a change in the concentration ν of vacancies ($\square$) by the scheme

$$A^+ \rightleftarrows 1/2B^{2+} + 1/2\square,\quad A^+ \rightleftarrows 1/3R^{3+} + 2/3\square,$$
$$A^+ \rightleftarrows 1/4M^{4+} + 3/4\square,\quad A^+ \rightleftarrows 1/5C^{5+} + 4/5\square.$$

Earlier thermal expansion was studied for such series of phosphates with zirconium as M^{IV}, namely, $Na_{5-4x}Zr_xZr(PO_4)_3$ [$Na_{5-4x}Zr_{1+x}(PO_4)_3$] and $K_{5-4x}\cdot Zr_xZr(PO_4)_3$ [$K_{5-4x}Zr_{1+x}(PO_4)_3$] at x varied from 0 up to 1, i.e., from $Na_5(K_5)Zr(PO_4)_3$ to $Na(K)\cdot Zr(PO_4)_3$, and also for the phosphate $NbZrNb(PO_4)_3$ with C^V. The dependences of the thermal expansion parameters on the number of occupied crystallographic out-of-framework positions and, therefore, on the concentration of M^{IV} were revealed [27]. In this work we studied the series with bi- and trivalent elements. We examined the thermal expansion of the phosphates $Na_{5-2x}B_xZr(PO_4)_3$ for B = Mg, Ca, Sr, Ba and $Na_{5-3x}Fe_xZr(PO_4)_3$ with x 0–2 and 0–1.33, respectively, in the range from room temperature to 750°C. For this purpose we prepared the following phosphates of these series:

$Na_5Zr(PO_4)_3$	$x = 0$	$Na_5Zr(PO_4)_3$	$x = 0$
$Na_4Mg_{0.5}Zr(PO_4)_3$	$x = 0.5$	$Na_4Fe_{0.33}Zr(PO_4)_3$	$x = 0.33$
$Na_3MgZr(PO_4)_3$	$x = 1.0$	$Na_3Fe_{0.66}Zr(PO_4)_3$	$x = 0.66$
$Na_2Mg_{1.5}Zr(PO_4)_3$	$x = 1.5$	$Na_2FeZr(PO_4)_3$	$x = 1.0$
$NaMg_2Zr(PO_4)_3$	$x = 2.0$	$NaFe_{1.33}Zr(PO_4)_3$	$x = 1.33$

and similar compounds with Ca, Sr, and Ba.

Apparently, the numbers of occupied (n) and vacant (ν) positions in framework voids of the phosphates change from $n = 4$ and $\nu = 0$ (in this case the positions in the framework voids are fully occupied by cations) to $n = 2$ and $\nu = 2$ for the phosphates with bivalent elements and to $n = 1.33$ and $\nu = 2.67$ for the phosphates with Fe (in this case, the possible number of vacant positions in the framework voids is maximal).

EXPERIMENTAL

The phosphates were precipitated from 1 M solutions of appropriate salts by adding 1 M phosphoric acid. The solution over the precipitate was evaporated, and the precipitate was heated in several stages: at 600, 800, and 1000°C for 24 h in each stage, with intermediate grindings.

The resulting compounds and intermediate products were studied by IR spectroscopy and X-ray phase analysis (XRPA).

The IR spectra were recorded on a Specord 75-IR spectrophotometer in the range of wave numbers 1800–400 cm^{-1} at room temperature. Samples were deposited on a KBr support as finely dispersed suspension in isopropanol. A clean cell was used as a reference (100% transmission).

The X-ray patterns of powder samples were recorded on a DRON-3M diffractometer in filtered CoK_α or CuK_α radiation (λ_1 1.78892 and 1.54078 Å, respectively). The unit cell parameters were determined using Al_2O_3 as reference (a = 4.758, c = 12.991 Å, crystal planes [113] and [116]) in the range of angles 2θ = 10°–80°. The parameters were calculated by the least-squares method, the measurement error being no more than 0.015°. It gave an error in the hexagonal lattice parameters of 0.005 Å for the a-axis and 0.01 Å for the c-axis.

Thermal expansion of the phosphates was studied by high-temperature X-ray diffraction. The coefficients of linear thermal expansion were determined from the shifts of the reflections from crystalline planes [hkl] at varied temperature. The temperature was measured with a Pt–Pt/Rh thermocouple. The temperature readings were checked by simultaneous recording of the reference (Al_2O_3) pattern. The axial coefficients α_a and α_c were calculated using a technique based on the least-squares method.

The samples obtained were colorless finely crystalline powders. Their IR spectra are similar to each other (Figs. 1a and 1b). The character of the spectra points to the presence of orthophosphate groups: the bands in the ranges 1140–900 and 630–540 cm^{-1} correspond to antisymmetric stretching and bending vibrations of PO_4 tetrahedra. The IR data indicate that the compounds under study belong to the class of orthophosphates.

The positions of diffraction peaks and their relative intensities in the X-ray patterns are similar to each

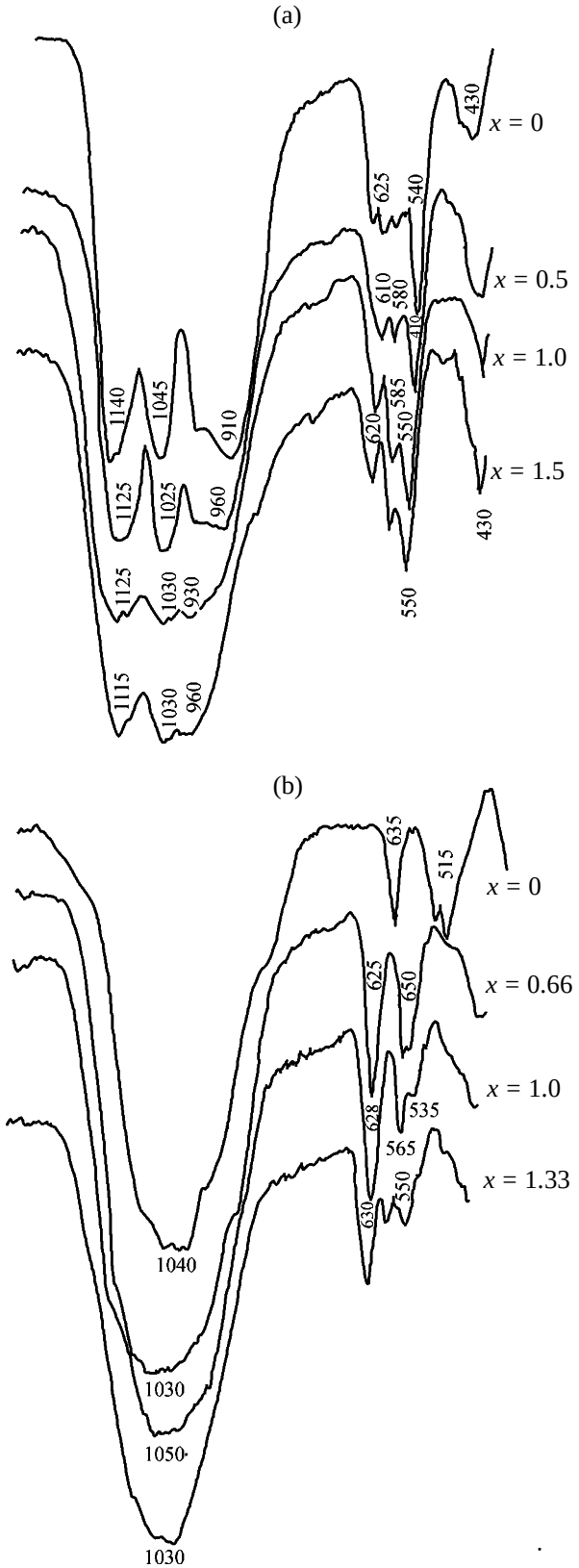

Fig. 1. IR spectra of (a) $Na_{5-2x}Sr_xZr(PO_4)_3$ and (b) $Na_{5-3x}Fe_xZr(PO_4)_3$ (ν, cm^{-1}).

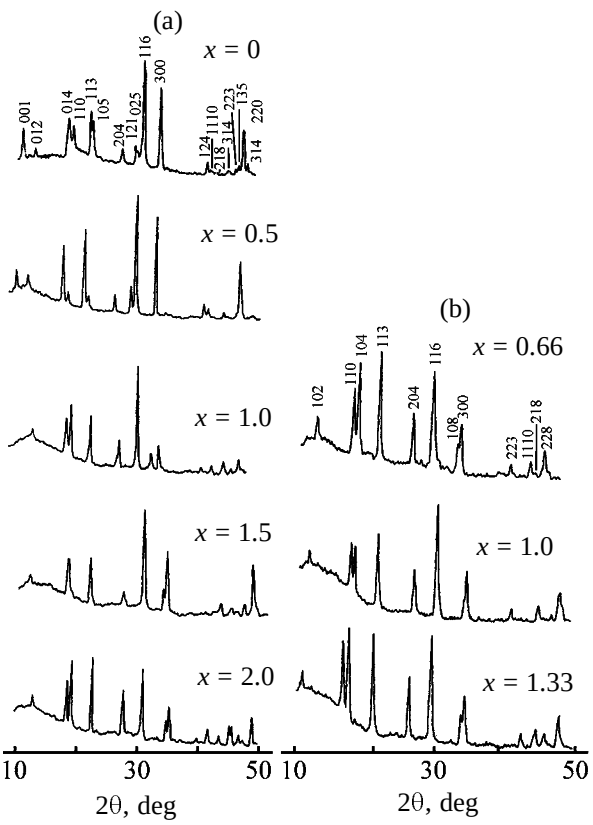

Fig. 2. X-ray patterns of (a) $Na_{5-2x}Sr_xZr(PO_4)_3$ and (b) $Na_{5-3x}Fe_xZr(PO_4)_3$. (2θ) Bragg's angle.

other (Fig. 2). They were indexed using two crystalline modifications of $Na_5Zr(PO_4)_3$ as structural analogs. It was found that the phosphates under study crystallized in two structural forms of trigonal system (space groups $R32$ and $R\bar{3}c$).

Phosphates $Na_{5-2x}B^{II}_xZr(PO_4)_3$ (B^{II} = Ca, Sr, Ba). The phosphate $Na_5Zr(PO_4)_3$, which is an extreme member of the series $Na_{5-2x}B^{II}_xZr(PO_4)_3$ (B^{II} = Ca, Sr, Ba), is characterized, as mentioned above, by two structural modifications with space groups $R\bar{3}c$ and $R32$, with ordered (space group $R32$) and disordered (space group $R\bar{3}c$) arrangement of the NaO_6 and ZrO_6 polyhedra along the c-axis.

According to the XRPA data, the $R32$ modification is formed in the phosphates with a small content of calcium and strontium [up to $x = 0.5$, which corresponds to $Na_{4.5}B_{0.5}Zr(PO_4)_3$]. This conclusion agrees with the IR data. The IR spectra of the phases with space group $R\bar{3}c$ (according to the XRPA data), containing Ca and Sr in concentrations $x > 0.5$ and Ba in concentration $x = 1.0$, exhibit bands typical of the $R32$ modification: 4–5 of five bands allowed by selection rules appear in the region of stretching and bend-

Unit cell parameters and thermal expansion coefficients for $Na_{5-2x}B_xZr(PO_4)_3$ (B = Mg, Ca, Sr, Ba) and $Na_{5-3x}\cdot Fe_xZr(PO_4)_3$

Phosphate	x	n	Unit cell parameters			Thermal expansion coefficients $\alpha \times 10^6$, K^{-1}		
			a, Å	c, Å	V, Å^3	α_a	α_c	$\alpha_{av} = 2/3\alpha_a + 1/3\alpha_c$
				$Na_{5-2x}B_xZr(PO_4)_3$				
B = Mg	0	4.0	9.160	21.80	1584	–5.82	20.73	3.03
	1.0	3.0	8.867	22.52	1533	–1.30	25.18	7.53
	1.5	2.5	8.863	22.50	1531	–1.09	23.20	7.01
	2.0	2.0	8.800	22.78	1526	–0.74	16.70	5.07
B = Ca	0	4.0	9.158	21.78	1582	12.08	60.18	38.55
	0.5	3.5	9.130	22.51	1625	9.95	24.80	14.90
	1.0	3.0	9.073	22.38	1595	9.87	27.30	15.68
	1.5	2.5	8.795	22.74	1523	9.35	29.50	16.07
	2.0	2.0	8.804	22.74	1526	–5.53	28.80	5.91
B = Sr	0	4.0	9.158	21.78	1582	12.08	60.18	38.55
	0.5	3.5	9.146	22.39	1622	13.18	44.30	23.55
	1.0	3.0	9.028	22.48	1587	3.65	21.83	9.71
	1.5	2.5	9.029	22.50	1589	2.91	18.90	8.24
	2.0	2.0	8.804	22.80	1530	–2.20	18.68	4.76
B = Ba	1.0	3.0	9.128	22.82	1575	–	–	–
				$Na_{5-3x}Fe_xZr(PO_4)_3$				
R = Fe	0	4.0	9.160	21.80	1584	–5.82	20.73	3.03
	0.66	2.66	8.779	22.75	1518	–4.13	23.00	4.91
	1.0	2.0	8.775	22.37	1485	–0.57	21.90	6.92
	1.33	1.33	8.767	22.71	1512	–0.58	13.40	4.08

ing vibrations. Hence, as x increases, the ordered arrangement of Na and Zr atoms in the columns of the structure (space group $R32$) is gradually converted to their disordered state (space group $R\bar{3}c$). These structural changes are not obvious from the XRPA data, but the more sensitive IR data reveal them.

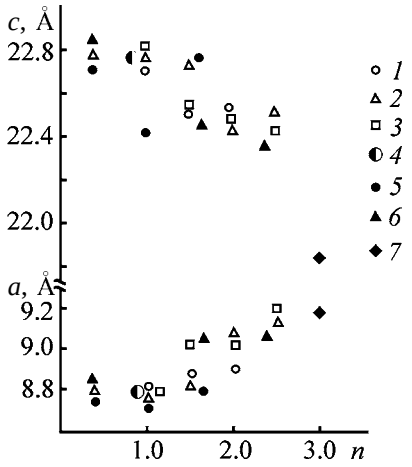

Fig. 3. Unit cell parameters a and c as functions of the occupancy n of M positions in phosphates $Na_{5-qx}T_x\cdot Zr(PO_4)_3$, where T = B = (*1*) Mg, (*2*) Ca, and (*3*) Sr; T = R = (*4*) Al, (*5*) Fe, and (*6*) Dy; (*7*) $Na_5Zr(PO_4)_3$.

Phosphates $Na_{5-2x}Mg_xZr(PO_4)_3$ and $Na_{5-3x}\cdot Fe_xZr(PO_4)_3$. Phosphates of the series $Na_{5-2x}Mg_x\cdot Zr(PO_4)_3$ and $Na_{5-3x}Fe_xZr(PO_4)_3$ with x values covering the whole range were assigned, according to XRPA, to space group $R\bar{3}c$. The observed IR spectra are similar to those of the phases of space group $R\bar{3}c$, which confirms the conclusions on the structure symmetry, made from the XRPA data.

The XRPA and IR data show that, among the phosphates synthesized, there are compounds with the higher concentrations of alkaline-earth cations than those in any known phosphates of the NZP-like structure. These are the phosphates $NaMg_2Zr(PO_4)_3$, $NaCa_2Zr(PO_4)_3$, $NaSr_2Zr(PO_4)_3$, and $Na_3BaZr(PO_4)_3$. Earlier attempts to incorporate alkaline-earth cations into zirconium compounds in greater amounts than in $B_{0.5}Zr_2(PO_4)_3$ failed [29]. The NZP structure of the new compounds seems to be stabilized by sodium cations. A similar effect was also observed for the Li-containing zirconium phosphates $NaLi_4Zr(PO_4)_3$ and $KLi_4Zr(PO_4)_3$ [30].

We calculated the unit cell parameters from the indexing data (see table). It is evident (Fig. 3) that the parameter a increases and the parameter c decreases

as the concentrations of alkaline-earth elements and iron decrease (n increases and ν decreases). The minimal value of the unit cell parameter c and the maximal value of a correspond to the phosphate $Na_5Zr(PO_4)_3$ (all structural positions are occupied and vacancies are absent).

The phosphates were studied in the range from room temperature to 750°C. Changes in their structure on heating were judged from the coefficients of linear thermal expansion $\alpha_a = \Delta a/a\Delta T$ and $\alpha_c = \Sigma c/c\Delta T$. It follows from the coefficients α_a and α_c calculated from the X-ray diffraction data (see table) that the thermal expansion anisotropy characteristic for NZP phosphates is also observed in the compounds obtained. As is the case with the majority of known NZP phosphates, $\alpha_a < 0$ and $\alpha_c > 0$. The expansion along the c-axis is greater than the contraction along the a-axis ($|\alpha_a| < |\alpha_c|$).

At the same time, both coefficients α_a and α_c were positive for certain phosphates in the series under study; these are the phosphates $Na_5Zr(PO_4)_3$ (space group $R32$) and $Na_{5-2x}B_xZr(PO_4)_3$ (B = Ca, Sr) at $0 < x < 1.5$. Especially strong elongation of the structure along the c-axis was observed in the case of the phosphate $Na_5Zr(PO_4)_3$ ($x = 0$, $n = 4$, $\nu = 0$): $\alpha_c = 60.18 \times 10^{-6}$ K^{-1}. In the case of the phosphates of the $R32$ modification with Ca and Sr, α_a and α_c tended to decrease (Fig. 4) as the concentration x of these elements increased and, hence, the number of occupied M positions decreased (and, correspondingly, the number of vacant positions increased); also, growing disordering of the Na and Zr octahedra took place.

The dependences $\alpha_a = f(n)$ and $\alpha_c = f(n)$ for $Na_{5-2x}Mg_xZr(PO_4)_3$ and $Na_{5-3x}Fe_xZr(PO_4)_3$ crystallizing in space group $R\bar{3}c$ are plotted in Fig. 5. The published data for $Na_{5-4x}Zr_xZr(PO_4)_3$ [27] and $NbZr(PO_4)_3$ [28] are also given. These compounds belong to the above-given system of zirconium phosphates: zirconium with M^{IV} and zirconium with C^V cations.

We found that our experimental data for the series with bi- and trivalent B^{II} and R^{III} cations are consistent with published data for the series with quadri- and quinquivalent elements M^{IV} and C^V [26–28]. For all the phosphates of the $R\bar{3}c$ structural modification, the contraction along the a-axis and the expansion along the c-axis took place on heating (Fig. 5). The dependences $\alpha_a = f(n)$ for the phosphates $A^I_{5-2x}Mg_xZr(PO_4)_3$, $A^I_{5-3x}Fe_xZr(PO_4)_3$, $A^I_{5-4x}Zr_xZr(PO_4)_3$, and $A^I_{5-5x}Nb_xZr(PO_4)_3$ with B^{II} (Mg), R^{III} (Fe), M^{IV} (Zr), and C^V (Nb) are very close to each other.

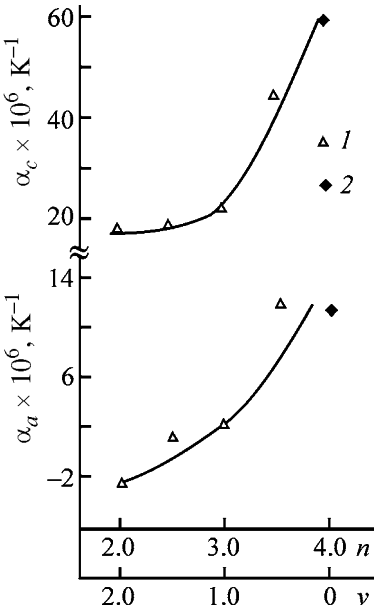

Fig. 4. Plot of axial thermal expansion coefficients α_a and α_c vs. occupancy n of M positions and number ν of vacancies for (*1*) $Na_{5-2x}Sr_xZr(PO_4)_3$ and (*2*) $Na_5Zr(PO_4)_3$.

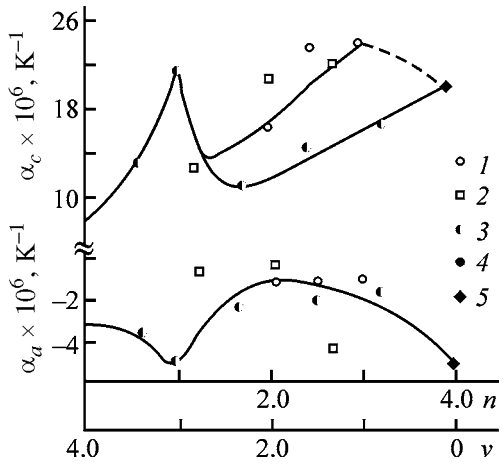

Fig. 5. Plot of axial thermal expansion coefficients α_a and α_c vs. occupancy n of M positions and number ν of vacancies for mixed zirconium phosphates, according to data of various authors: (*1*) $Na_{5-2x}Mg_xZr(PO_4)_3$, (*2*) $Na_{5-3x}Fe_xZr(PO_4)_3$, (*3*) $Na_{5-4x}Zr_xZr(PO_4)_3$ [28], (*4*) $NbZr(PO_4)_3$ [27], and (*5*) $Na_5Zr(PO_4)_3$ [28].

At the same time, the plot of $\alpha_c = f(n)$ for the phosphates $Na_{5-4x}Zr_xZr(PO_4)_3$ [26] lies somewhat lower than that for the phosphates with Mg and Fe. This agrees with the generally accepted mechanism of thermal expansion of phosphates with a $[T_2(PO_4)_3]^f$ framework based on the crystal-chemical model: with increasing cation charge in TO_6 octahedra forming chains along the c-axis, the thermal expansion along this axis decreases (it is assumed that multicharged

cations in the above-mentioned series occupy L positions together with zirconium at $2 \le n < 4$).

The nonmonotonic course of the dependences of α_a and α_c on n (ν) for both newly studied and previously described series is attributable to different effects exerted by multicharged cations (B^{II}, R^{III}, M^{IV}, and C^{V}) and vacancies in occupation of various crystallographic positions of the NZP structure.

(1) An increase in the concentration of multicharged cations in the L-positions upon replacement of sodium by magnesium, iron, and zirconium causes a decrease in α_c and, correspondingly, an increase in α_a.

(2) An increase in the number of vacant M2 positions upon replacement of sodium by magnesium, iron, and zirconium ($4 \le n \le 1$) causes a decrease in α_a (vacancies behave as small-size cations), as noted above when considering the parameters a and c (Fig. 3). They expand to a lesser extent on heating than cation–oxygen bonds in the same positions, which facilitates elongation of bonds along the c-axis (α_c increases).

At $n \le 1$ ($\nu \ge 3$), when all M2 positions are free ($\nu \ge 3$) and the number of free M1 positions decreases, the increase in the number of vacancies causes a decrease in α_c [26]. This causes the O–P–O angles in the PO_4 tetrahedra to decrease and facilitates elongation of bonds along the a-axis (α_a increases) (Fig. 5). This can be followed in the sections of the curves at $n \le 1$ (with the number of vacant positions, correspondingly, varying in the range $3 \le \nu \le 4$). This result agrees well with published data [23] on the behavior of vacancies on heating of $Sr_{0.5}Ti_2(PO_4)_3$. A similar behavior of vacancies in M2 positions should result in the structure contraction along the a-axis, which also agrees with the above-given facts.

The vacancies in the phosphates of $R32$ modification (Fig. 4) affect the structure more strongly along the a-axis (an increase in their number results in a decrease in α_a), whereas an increase in the concentration of multicharged ions in M positions affects the structure more strongly along the c-axis (α_c also decreases).

On the whole, it follows from the experiment that many factors affect the behavior of the structure on heating: the nature of cations T, their concentration, the number of vacant positions, and also the unit cell symmetry. It should be noted that their roles are ambiguous. Their better understanding can be reached only using structure analysis methods allowing estimation of the distribution of cations over three types of nonequivalent positions of the structure.

It should also be noted that our experimental data on the thermal expansion of phosphates allow control of the thermal expansion characteristics of zirconium phosphate materials by choosing appropriate cations and their ratios and concentrations. It is important for practice that $Na_{5-qx}T_xZr(PO_4)_3$ phosphates can be either low-expanding ($\alpha_{av} \le 2 \times 10^{-6}$ K^{-1}), medium-expanding ($2 \times 10^{-6} < \alpha_{av} \le 8 \times 10^{-6}$ K^{-1}), or highly expanding ($\alpha_{av} > 8 \times 10^{-6}$ K^{-1}), so that structurally related substances with a wide range of thermal expansion characteristics become available.

CONCLUSIONS

(1) The thermal expansion of new zirconium phosphates with uni-, bi-, and trivalent elements was studied. These phosphates belong to the family of structural analogs of $Na_5Zr(PO_4)_3$, namely, $Na_{5-2x} \cdot B^{II}_xZr(PO_4)_3$ (B^{II} = Mg, Ca, Sr, Ba) and $Na_{5-3x}Fe_x \cdot Zr(PO_4)_3$.

(2) The dependences of the linear and cubic expansion coefficients on the composition of phosphates with varied combinations and quantitative ratios of Na and Mg, Ca, Sr, Ba, Fe cations were determined. By choosing appropriate cationic composition, the thermal expansion characteristics of zirconium phosphates in the series under study can be adjusted in the following ranges: α_a, from -6 to 13×10^{-6} K^{-1}, α_c, from 17 to 60×10^{-6} K^{-1}; and α_{av}, from 3 to 38×10^{-6} K^{-1}.

ACKNOWLEDGMENTS

This work was financially supported by the Russian Foundation for Basic Research (project nos. 01-03-33013 and 02-03-32181).

REFERENCES

1. Rodrigo, J.L. and Alamo, J., *Mater. Res. Bull*. 1991, vol. 26, pp. 475–480.
2. Rodrigo, J.L., Carrasco, P., and Alamo, J., *Mater. Res. Bull*., 1989, vol. 24, pp. 611–618.
3. Roy, R., Agrawal, D.K., Alamo, J., and Roy, R.A., *Mater. Res. Bull*., 1984, vol. 19, pp. 471–477.
4. Yamai, I. and Ota, T., *J. Am. Ceram. Soc*., 1992, vol. 75, no. 8, pp. 2276–2282.
5. Alamo, J. and Rodrigo, J.L., *Solid State Ionics*, 1989, vols. 32/33, pp. 70–76.
6. Dhas, A.N. and Patil, K.C., *J. Mater. Chem*., 1995, vol. 5, no. 9, pp. 1463–1468.

7. Lenain, G.E., McKinstry, H.A., Limaye, S.Y., and Woordward, A., *Mater. Res. Bull.*, 1984, vol. 19, pp. 1451–1456.
8. Breval, E. and Agrawal, D.K., *Brit. Ceram. Trans.*, 1995, vol. 94, no. 1, pp. 27–32.
9. Samoilov, S.G., Kryukova, A.I., Kazantsev, G.N., and Artem'eva, G.Yu., *Izv. Ross. Akad. Nauk, Neorg. Mater.*, 1992, vol. 28, nos. 10/11, pp. 2197–2202.
10. Alami, M., Brochu, R., Soubeyroux, J.L., *et al.*, *J. Solid State Chem.*, 1991, vol. 90, pp. 185–193.
11. Brochu, R., Louer, M., Alami, M., *et al.*, *Mater. Res. Bull.*, 1997, vol. 32, pp. 116–122.
12. Limaye, S.Y., Agrawal, D.K., and McKinstry, H.A., *J. Am. Ceram. Soc.*, 1987, vol. 70, no. 10, pp. 232–236.
13. Agrawal, D.K. and Stubican, V.S., *Mater. Res. Bull.*, 1985, vol. 20, pp. 99–106.
14. Lee, W.E., Cooley, K.M., Berndt, C.C., *et al.*, *J. Am. Ceram. Soc.*, 1996, vol. 79, no. 10, pp. 2759–2762.
15. Agrawal, D.K., Harshe, G., Breval, E., and Roy, R., *J. Mater. Res.*, 1996, vol. 11, no. 12, pp. 3158–3163.
16. Limaye, S.Y., Agrawal, D.K., Roy, R., and Menrotra, Y., *J. Mater. Sci.*, 1998, vol. 26, pp. 93–98.
17. Brewal, E., McKinstry, H.A., and Agrawal, D.K., *J. Am. Ceram. Soc.*, 1998, vol. 81, no. 4, pp. 926–932.
18. Ota, T., Jin, P., and Yamai, I., *J. Mater. Sci.*, 1989, vol. 24, pp. 4239–4245.
19. Brochu, R., El-Yacoubi, M., Louer, M., *et al.*, *Mater. Res. Bull.*, 1996, vol. 32, no. 1, pp. 15–22.
20. Rega, D.A., Agrawal, D.K., Huang, C-Y., and McKinstry, H.A., *J. Mater. Sci.*, 1992, vol. 27, pp. 2406–2412.
21. Talbi, M.M., Brochu, R., Parent, C., *et al.*, *J. Solid State Chem.*, 1994, vol. 110, pp. 350–355.
22. Govindan Kutty, K.V., Asuvathraman, R., and Sridharan, R., *J. Mater. Sci.*, 1998, vol. 33, pp. 4007–4013.
23. Woodcock, D.A., Lightfoot, Ph., and Ritter, C., *Chem. Commun.*, 1998, pp. 106–107.
24. Orlova, A.I., Kazantsev, G.N., and Samoilov, S.G., *High Temp.—High Press.*, 1999, vol. 31, pp. 105–111.
25. Yamai, I., Ota, T., and Jib, P., *J. Ceram. Soc. Jpn.*, 1988, vol. 96, no. 10, pp. 1019–1020.
26. Oota, I. and Yamai, I., *J. Am. Ceram. Soc.*, 1986, vol. 69, no. 1, pp. 1–6.
27. Orlova, A.I., Kemenov, D.V., Samoilov, S.G., *et al.*, *Izv. Ross. Akad. Nauk, Neorg. Mater.*, 2000, vol. 36, no. 8, pp. 995–1000.
28. Ni, Y-X., Haghes, J., and Mariano, A., *Am. Mineral.*, 1995, vol. 80, pp. 21–26.
29. Pet'kov, V.I., Orlova, A.I., and Kapranov, D.A., *Zh. Neorg. Khim.*, 1998, vol. 43, no. 9, pp. 1534–1540.
30. Orlova, A.I., Trubach, I.G., Pet'kov, V.I., *et al.*, *Radiokhimiya*, 1999, vol. 41, no. 4, pp. 304–310.

Russian Journal of Applied Chemistry, Vol. 77, No. 3, 2004, pp. 376–379. Translated from Zhurnal Prikladnoi Khimii, Vol. 77, No. 3, 2004, pp. 382–385.

SORPTION AND ION-EXCHANGE PROCESSES

Adsorption of Thiophene Vapor on Sodium and Polyhydroxoaluminum Montmorillonites

S. Z. Muminov, D. B. Gulyamova, and A. A. Agzamkhodzhaev

Institute of General and Inorganic Chemistry, Academy of Sciences of the Republic of Uzbekistan, Tashkent, Uzbekistan

Received June 3, 2003

Abstract—Changes in the surface properties and pore structure of montmorillonite in substitution of inorganic exchange cations by polyhydroxoaluminum cations were studied by measuring the adsorption of thiophene vapor.

One of the main goals of oil refining and gas processing is to develop efficient processes for removal of sulfur from oil and natural gas, with the sorption method having particular importance [1–4]. Of the three adsorbents (silica gel, alumogel, salica clay) tested in purification of natural gas to remove mercaptans, silica gel has the highest adsorption capacity [2]. According to [3, 4], thiophene is adsorbed by silica gel, alumogel, and zeolite, with its molecules having planar orientation in the monolayer of the adsorbate. Thiophene molecules form in the interlayer space of montmorillonite coordination bonds with exchange cations via sulfur atoms [5]. Elucidating the mechanism of sorption interaction in systems constituted by an organosilicon compound and an adsorbent remains a topical task. Substitution of exchange cations of montmorillonite by polyhydroxoaluminum cations promotes formation of a microporous structure [6]. Data on adsorption and heat of adsorption of a number of polar molecules on the initial and polyhydroxoaluminum montmorillonites (PHAMt) were reported in [7–9].

In this work we studied adsorption of thiophene vapor on dehydrated sodium and polyhydroxoaluminum forms of montmorillonite.

As the initial sorbent we took white bentonite from the Azkamar deposit, which is mainly composed of a sodium montmorillonite mineral (NaMt) and has a cation-exchange capacity E = 0.82 mg-equiv g^{-1} and the following chemical composition (wt %): SiO_2 52.51, Al_2O_3 17.92, Fe_2O_3 3.56, CaO 1.20, MgO 3.62, SO_3 0.28, K_2O 0.27, Na_2O 5.16, and calcination loss 17.16.

The polyhydroxoaluminum montmorillonite was prepared by treating a suspension of Na-montmorillonite with a polyhydroxoaluminum complex [10]. The substitution of the Na^+ ions of the mineral with bulky complex hepta-charged polyhydroxoaluminum cations (PHAC) $[Al_{13}O_4(OH)_{24}(H_2O)_{12}]^{7+}$ leads to an increase in the interlayer spacing along the c axis by Δd_{001} = 0.85 nm.

As adsorbate we used thiophene of pure grade, carefully purified and dried with NaA zeolite. Prior to performing adsorption experiments, thiophene was degassed, so that its saturated vapor pressure corresponded to the tabulated value [11].

The adsorption was measured by the gravimetric and isosteric [7] methods. Before measuring the adsorption, NaMt and PHAMt were vacuum-treated at 423 and 773 K for 6–8 h (at a residual pressure in the system of about 1.33×10^{-4} Pa). At these temperatures, the structure of NaMt undergoes characteristic changes: at 423 K it undergoes partial dehydration (this sample is designated as NaMt-1), with exchangeable Na^+ ions introduced into ditrigonal cavities of the aluminosilicate layer; at 773 K, NaMt is totally dehydrated, the structure collapses, and partial dehydroxylation occurs (NaMt-2). Thermal treatment of PHAMt at these temperatures, i.e., below and above the temperature of PHAC transformation into aluminum oxide clusters [12], is accompanied by dehydration and dehydroxylation (samples designated as PHAMt-1 and PHAMt-2). In accordance with the structural changes in the sorbents, it would be expected that the adsorption interaction should change, too, compared to that in NaMt and PHAMt.

The isotherms of thiophene vapor adsorption on Na-montmorillonite (Fig. 1) are S-shaped, with

1070-4272/04/7703-0376 © 2004 MAIK "Nauka/Interperiodica"

hysteresis loops in a wide range of relative pressures P/P_s. Raising the temperature of vacuum treatment of NaMt within the range 423–773 K leads to lower accessibility of the exchange ions to thiophene molecules, and, therefore, the adsorption decreases and the hysteresis loop in the isotherm becomes somewhat narrower. The most probable reason for the change in the width of the hysteresis loop in the isotherms is formation of various ion–molecule complexes with or without residual water molecules, which coordinate the exchange ions. The structural-sorptive properties of NaMt samples, found from the isotherms of thiophene sorption, are listed in Table 1.

In calculating the specific surface areas of NaMt-1 and NaMt-2 by the BET equation, the surface area occupied by a thiophene molecule was taken to be 0.39 nm^2 [1].

It follows from Table 1 that raising the NaMt treatment temperature within the range 423–773 K leads to a decrease in the capacity of the monolayer and, consequently, in the specific surface area by a factor of more than 3; the sorption volume in the state saturated to the maximum possible extent decreased in this case by a factor of approximately 2.2. Undoubtedly, all this is due to differences in the surface properties and in the pore structure of NaMt forming as a result of dehydration and dehydroxylation. The role played by the internal and external surfaces of montmorillonite can be revealed by comparing the adsorption of benzene, whose molecules are mainly adsorbed on the external surface of the mineral (without being incorporated into the interlayer space) with that of thiophene. It was found that the adsorption capacity of NaMt-1 for thiophene exceeds that for benzene by a factor of 3.7. Consequently, thiophene molecules are adsorbed on NaMt-1 not only on the external surface, but also within the internal pore volume. The specific surface areas of NaMt-2 for both the adsorbates are close, which suggests that the adsorption of thiophene and benzene is limited in this case to the external surface of NaMt-2.

Polyhydroxoaluminum montmorillonite is a thermally stable clayey adsorbent [6]. Thermal treatment in a vacuum at 423 K leads to full opening of the sorption volume as a result of dehydration. The transfer of modifying cations into aluminum oxide clusters does not lead to any noticeable change in the interlayer spacing in the mineral [7]. The isotherm of thiophene adsorption on PHAMt-1 (at $P/P_s < 0.01$) has a steeper initial portion (Fig. 1) than that for PHAMt-2. The difference in thiophene adsorption between PHAMt-1 and PHAMt-2 is due to specific

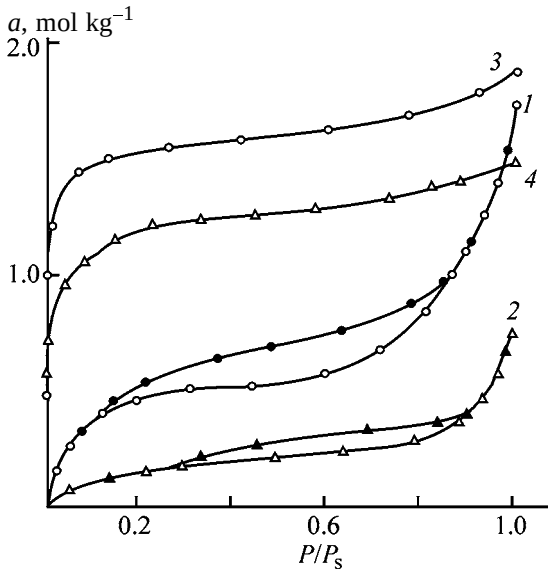

Fig. 1. Isotherms of thiophene vapor adsorption on (*1, 2*) NaMt and (*3, 4*) PHAMt dehydrated at (*1, 3*) 423 and (*2, 4*) 773 K. (*a*) Adsorption and (P/P_s) relative pressure.

adsorption interaction of thiophene molecules with PHAC and aluminum oxide clusters. The fact that both isotherms are virtually Γ-shaped and the adsorption increases only slightly within the range $P/P_s \approx 0.05–0.9$ indicates that the structure of PHAMt is not deformed in the course of thiophene adsorption.

The sorption volumes of PHAMt for thiophene ($m^3\ kg^{-1}$) at P/P_s = 0.2 (W), 0.4 (W_0), and 1.0 (V_s) and the mesopore volumes $W_{me} = V_s - W_0$ calculated from the adsorption isotherms are listed in Table 2.

Table 1. Sorption characteristics of Na-montmorillonite for thiophene*

Adsorbent	a_m, mol kg^{-1}	$S \times 10^{-3}$, $m^2\ kg^{-1}$	a_s, mol kg^{-1}	$V_s \times 10^{-3}$, $m^3\ kg^{-1}$
NaMt-1	0.53	105	1.76	0.133
NaMt-2	0.14	29	0.78	0.061

* a_m is the monolayer capacity; S, specific surface area; a_s, limiting adsorption; and V_s, limiting sorption volume.

Table 2. Sorption volumes ($m^3\ kg^{-1}$) of polyhydroxoaluminum montmorillonite for thiophene

Adsorbent	$W \times 10^3$	$W_0 \times 10^3$	$V_s \times 10^3$	$W_{me} \times 10^3$
PHAMt-1	0.118	0.123	0.147	0.024
PHAMt-2	0.093	0.098	0.116	0.018

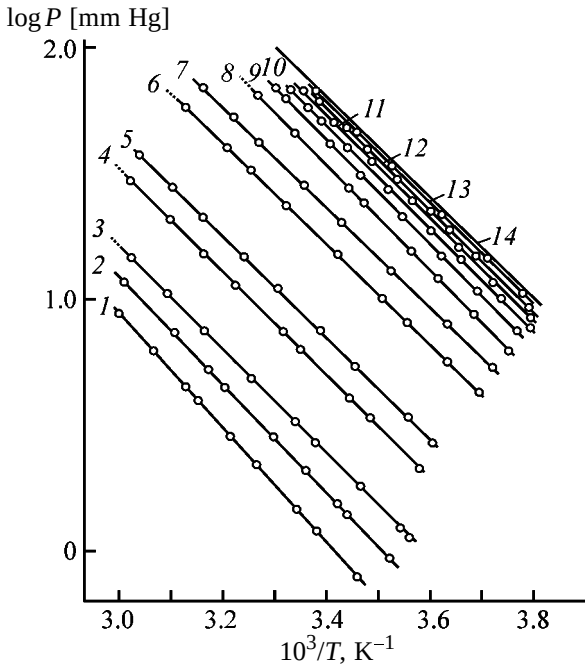

Fig. 2. (*1–13*) Isosteres of thiophene adsorption on NaMt-1 at different amounts of adsorbed thiophene. (*P*) Pressure and (*T*) temperature. Amount of thiophene (mol kg^{-1}): (*1*) 0.009, (*2*) 0.13, (*3*) 0.23, (*4*) 0.35, (*5*) 0.43, (*6*) 0.52, (*7*) 0.80, (*8*) 1.03, (*9*) 1.08, (*10*) 1.20, (*11*) 1.29, (*12*) 1.45, and (*13*) 1.55; (*14*) $\log P_s$ vs. T^{-1} curve for unadsorbed thiophene.

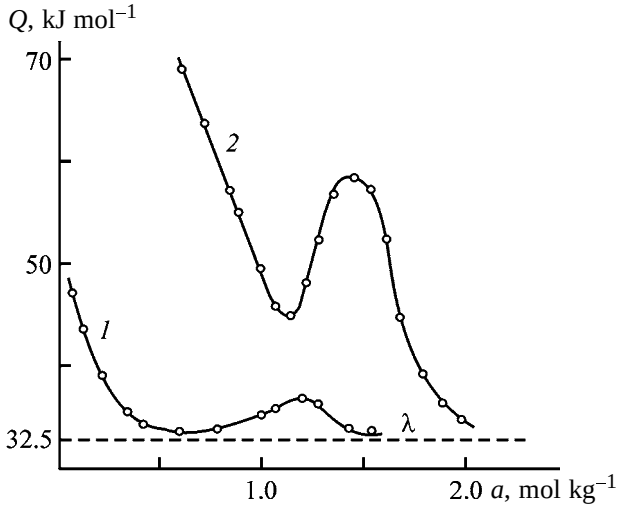

Fig. 3. Differential isosteric heat of thiophene adsorption on (*1*) NaMt-1 and (*2*) PHAMt-1 vs. the amount of substance adsorbed. (*Q*) Heat of sorption, (*a*) adsorption, and (λ) heat of condensation.

It can be seen that the volume of micropores, W_0, and that in saturation of PHAMt-1, V_s, markedly exceed the sorption volumes of PHAMt-2. The adsorption of thiophene vapor at P/P_s mainly proceeds with filling of the mesopore volume. Thermal treatment of PHAMt at 773 K, i.e., at a temperature exceeding the onset temperature of aluminum oxide cluster formation, leads to a decrease by 20–25% in the pore volume, compared to the volume of PHAMt dehydrated at 423 K. Comparison of the sorption volumes of PHAMT for thiophene and benzene shows that they are rather close. This indicates that molecules of these organic substances are adsorbed on PHAMt via volume filling of micropores.

The changes in the nature of the surface and in the pore structure of montmorillonite upon substitution of Na^+ ions by $[Al_{13}O_4(OH)_{24}(H_2O)_{12}]^{7+}$ can be judged by comparing the heats of thiophene adsorption on NaMt-1 and PHAMt-1. The heats of adsorption were found from the temperature dependence of thiophene adsorption, i.e., from a set of isosteres of thiophene adsorption, measured in the temperature range 260–320 K at fillings from a fraction of V_s to complete saturation. As an example, Fig. 2 shows a family of isosteres of thiophene adsorption, measured on NaMt-1 and plotted in the $\log P$–T^{-1} coordinates. In these coordinates, the isosteres are approximated with straight lines, which indicates that the heat of adsorption is temperature-independent in the temperature range studied. The upper line in Fig. 2 represents the dependence of the logarithm of the saturated vapor pressure on T^{-1} for the bulk phase of thiophene. It can be seen that the slopes of the isosteres vary with the amount of adsorbed thiophene.

The change in the slope of the isosteric straight lines for the systems thiophene–NaMt-1 and thiophene–PHAMt-1 was used to calculate, using the Clausius–Clapeyron equation, the differential isosteric heats of adsorption, *Q* (Fig. 3). For the systems studied, the dependences of *Q* on the amount of substance adsorbed abruptly descend at small fillings, reach a minimum, then pass through maxima at medium adsorption levels, after which the value of *Q* decreases, gradually approaching the heat of condensation of the bulk phase of thiophene (λ = 32.5 kJ mol^{-1}). In this range of fillings, the adsorption in the system thiophene–NaMt-1 mainly occurs at the surface of NaMt-1, but penetration of its molecules into the interlayer space of the mineral cannot be ruled out, either. When thiophene molecules are adsorbed with the plane of their ring parallel to aluminosilicate stacks, Δd_{001} of the mineral remains virtually unchanged [5]. Further, *Q* increases somewhat, to reach its maximum value $Q^{max} \approx 36.5$ kJ mol^{-1} at $a \approx 1.25$ mol kg^{-1}. Beyond the maximum, the value of *Q* gradually decreases, again approaching λ. The increase in *Q* and its extremal behavior can be accounted for by intermolecular interaction in the polylayers.

The minimum in the dependence $Q = f(a)$ is observed for the system thiophene–PHAMt-1 at an adsorption approximately equal to 1.10 mol kg^{-1} (i.e., at micropore volume filling $a/a_0 = 0.68$, where a_0 is the adsorption at $P/P_s = 0.4$), with the minimum value $Q^{min} \approx 45.0$ kJ mol^{-1}. The initial decrease in the heat of thiophene adsorption on PHAMt could have been even more abrupt, if it were not partly compensated for by a rise in the heat because of the increasing intensity of interaction between molecules adsorbed in micropores. At higher adsorption levels, the heat of adsorption increased from 45.0 to its maximum value $Q^{max} \approx 58.5$ kJ mol^{-1} (at $\theta = 0.86$). In this adsorption range, the increase in the heat of thiophene adsorption was about 13.5 kJ mol^{-1}. At $\theta > 0.86$, the heat of thiophene adsorption on PHAMt-1 decreases abruptly to 47.5 kJ mol^{-1} (at $\theta = 1.0$). In the range of mesopore filling at $1.0 < \theta < 1.18$, the value of Q continues to decrease and approaches λ at adsorbent saturation.

The higher heat of adsorption for the system thiophene–PHAMt-1, compared to that for thiophene–NaMt-1, is presumably due to the enhancement of the adsorbate–adsorbent interaction because of structural changes that occur in montmorillonite under modification. As active centers in PHAMt-1 act free hydroxy groups and external oxygen atoms in polyhydroxoaluminum cations, oxygen surface of the silica layer, Al^{3+} ions that isomorphically substitute silicon in the silica layer, and Na^+ ions that are not substituted by polyhydroxoaluminum cations; as active centers in NaMt-1 serve Na^+ ions, surface hydroxy groups, oxygen surface of the silica layer, etc.

CONCLUSIONS

(1) The influence exerted by substitution of Na^+ ions with polyhydroxoaluminum cations on the adsorption properties of dehydrated montmorillonite clay was studied. A set of isosteres of thiophene vapor adsorption were obtained. The changes in the parameters of the adsorption equilibrium in a wide range of fillings were used to calculate the differential isosteric heats of adsorption.

(2) It was established that the increase in the heat of thiophene adsorption on replacing Na^+ ions with polyhydroxoaluminum cations results from the formation of a developed system of slitlike micropores in the interlayer space of montmorillonite; adsorption of thiophene on polyhydroxoaluminum montmorillonite mainly occurs in micropores to give ion–molecule complexes.

REFERENCES

1. Kel'tsev, N.V., *Osnovy sorbtsionnoi tekhniki* (Fundamentals of Sorption Technology), Moscow: Khimiya, 1984.
2. *Adsorbtsiya glinistymi mineralami iz uglevodorodnoi sredy azot-, kislorod i serosoderzhashchikh soedinenii nefti: Tematicheskii sbornik* (Adsorption of Nitrogen-, Oxygen-, and Sulfur-Containing Compounds of Oil on Clayey Minerals from a Hydrocarbon Medium; Topical Coll.), Vladivostok, 1976.
3. Usmanova, D.A., *Cand. Sci. Dissertation*, Tashkent, 1974.
4. Norton, C., *Chem. Ind.*, 1962, no. 6, pp. 258–262.
5. Varfolomeeva, E.K. and Zgadzai, L.K., *Kolloidn. Zh.*, 1981, vol. 43, no. 4, pp. 633–638.
6. Muminov, S.Z., Gulyamova, D.B., and Aripov, E.A., *Zh. Prikl. Khim.*, 1992, vol. 65, no. 6, pp. 1292–1294.
7. Muminov, S.Z. and Gulyamova, D.B., *Zh. Fiz. Khim.*, 1997, vol. 71, no. 10, pp. 1834–1837.
8. Muminov, S.Z. and Gulyamova, D.B., *Uzb. Khim. Zh.*, 1998, no. 3, pp. 23–28.
9. Muminov, S.Z. and Gulyamova, D.B., *Zh. Fiz. Khim.*, 2000, vol. 74, no. 6, pp. 1085–1088.
10. Matsumoto, M., Shinoda, S., Takahashi, H., and Saito, I., *Bull. Chem. Soc. Jpn.*, 1984, vol. 57, no. 7, pp. 1795.
11. Stull, D.R., Vapor Pressure of Pure Substances, *Ind. Eng. Chem.*, 1947, vol. 39, N 4, pp. 517–550.
12. Muminov, S.Z., Gulyamova, D.B., and Aripov, E.A., *Zh. Fiz. Khim.*, 1993, vol. 67, no. 12, pp. 2436–2438.

Russian Journal of Applied Chemistry, Vol. 77, No. 3, 2004, pp. 380–384. Translated from Zhurnal Prikladnoi Khimii, Vol. 77, No. 3, 2004, pp. 386–390.

APPLIED ELECTROCHEMISTRY AND CORROSION PROTECTION OF METALS

Electrically Conducting Formulations Based on Ultradispersed Powders of Copper, Obtained by Reduction of Its Salts with the Hypophosphite Ion

I. I. Obraztsova, G. Yu. Simenyuk, and N. K. Eremenko

Kemerovo Branch, Institute of Solid-State Chemistry and Mechanochemistry, Siberian Division, Russian Academy of Sciences, Kemerovo, Russia

Received July 29, 2003

Abstract—Powders of copper were obtained by reducing its various salts with hypophosphorous acid and sodium hypophosphite. The influence exerted by various factors on the stability and electrical conductivity of composites on their base was studied.

Thanks to unique physicochemical, electrical, magnetic, and optical properties, polymeric formulations with an ultradispersed metallic filler find wide application in modern science and technology in developing current-conducting pastes, photo- and X-ray-sensitive resists, shielding coatings, and electrodes. Silver is most commonly used in electrically conducting formulations because of its high electrical conductivity and resistance to oxidation [1, 2]. Recently, steadily increasing attention has been given to development of copper-based formulations [3], whose production cost is lower. In this context, the problems associated with stabilization of ultradispersed powders (UDP) of copper and improvement of the service life and electrical conductivity of composites on their base are of current interest.

Previously, methods were developed for obtaining copper UDP with average particle size of 20–40 nm by reducing various copper salts with glycerol and making formulations on their base with epoxy and novolak resins [4–8]. The most efficient is the reduction of basic carbonate, acetate, and tartrate of copper with glycerol, and formulations on their base with novolak resin exhibit higher electrical conductivity [resistivity $\rho = (0.6–1.9) \times 10^{-6}$ Ω m] and stability (more than 6 years).

In addition, it was found that, with appropriate stabilizing agents, it is also possible to prepare formulations based on copper sulfate with the electrical conductivity and stability comparable with those of pastes based on copper UDP obtained by reduction of readily decomposing copper salts. Introduction of organic acid reductants (ascorbic, citric, formic, and acetylsalicylic acids) leads to an increase in the reaction rate by a factor of 5–10, decrease in the process temperature by 20–40°C, and improvement of the stability and electrical conductivity of the pastes.

It was found that epoxy formulations with addition of stabilizers (1-naphthol and *p*-aminophenol) in amount of 1% (relative to the mass of the copper UDP) retain high electrical conductivity without changes for more than 10 years, and formulations with 1-naphthol have the lowest resistivity of $(0.8–1.2) \times 10^{-6}$ Ω m, which is close to that characteristic of metals. It was also found that 1-naphthol is the best oxidation inhibitor for the novolak resin, and addition of glycerol as a plasticizer in a 1 : 3 ratio yields formulations whose electrical conductivity (resistivity 1.2×10^{-6} Ω m) is comparable with that of the best samples with epoxy resin. Pastes based on the novolak resin are only slightly inferior to the above formulations in stability, but they are less expensive and more readily available, and, therefore, primary attention will be given here to novolak formulations.

The study is concerned with reduction of various copper salts with hypophosphorous acid and sodium hypophosphite at a molar ratio $\nu(Cu) : \nu(H_2PO_2^-) = 1 : (1.5–4.0)$. The promise of this method is in that the reduction with hypophosphite ions is carried out under milder conditions (reaction temperature not higher than 95°C, reaction time 2–35 min) than those in reduction with glycerol (130–200°C, 15–240 min). The copper UDP obtained was used to prepare formulations with phenol–formaldehyde novolak resin. The influence exerted by various factors on the stability and electrical conductivity of the formulations ob-

1070-4272/04/7703-0380 © 2004 MAIK "Nauka/Interperiodica"

tained was studied. These materials were compared with samples obtained previously by reduction with glycerol and with industrially used pastes based on noble metals.

EXPERIMENTAL

The copper salts were reduced with sodium hypophosphite as follows: into a vessel with a solution of a copper(II) salt heated to 80–90°C, we gradually poured with continuous agitation a solution of sodium hypophosphite heated to 50–60°C. Then the reaction mixture was heated to 80–95°C [depending on a copper(II) salt used] and kept at this temperature until an ultradispersed copper powder precipitated. After that, the UDP was washed with water to neutral reaction of the washing water, treated with solutions of hydroquinone and stearic acid in ethanol, and stored under a layer of the solution of stearic acid in ethanol. According to small-angle X-ray scattering data (Fig. 1), the copper UDP obtained has particle size in the range 8–100 nm, with 45% of the particles (by mass) being less than 30 nm in size. The formulations prepared from SF-010 phenol–formaldehyde resin and copper UDP (with 80 wt % metallic phase) were kept at 140–145°C for 4 h. The dc resistance of the pastes was measured (12 V, 2.5 mA) at room temperature (20–25°C).

To improve their resistance to oxidation, all the copper UDP samples were treated with solutions of hydroquinone and stearic acid in ethanol, as suggested in [4]. The ultradispersed powders of copper obtained by reduction of copper(II) salts (and $CuSO_4 \cdot 5H_2O$, in particular) with sodium hypophosphite are highly active and are readily oxidized in air because of their increased dispersity. As a result, the formulations on their base have relatively high resistivity (10^{-2} Ω m) and are very unstable in storage (Fig. 2, curve *1*). However, it was found that treatment of copper UDP with formic acid leads to a dramatic increase in the electrical conductivity and stability of the formulations (Fig. 2, curve *2*). This is due to the fact that treatment with formic acid removes the oxide film from the surface of UDP particles and stabilizes metallic copper against further oxidation.

Inorganic (nitrate, sulfate, chloride) and organic (acetate, formate, citrate) salts of copper(II) were reduced with sodium hypophosphite. The results are listed in Table 1. It can be seen that the highest reduction rate is observed for copper nitrate, sulfate, and formate (Table 1, sample nos. 1, 2, 5, 6, 8). Copper acetate and nitrate (sample nos. 3, 4, 9) are reduced

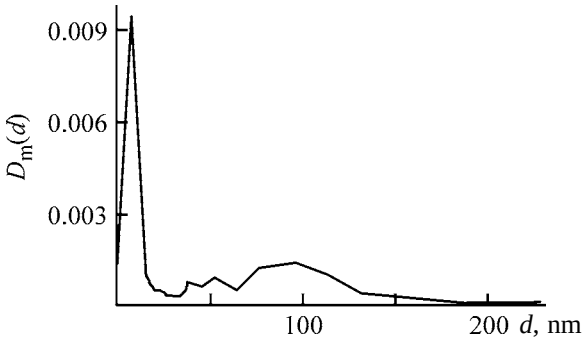

Fig. 1. Mass function $D_m(d)$ of the size (d) distribution of ultradispersed copper particles, calculated from small-angle X-ray scattering curves in the approximation of uniform spherical particles.

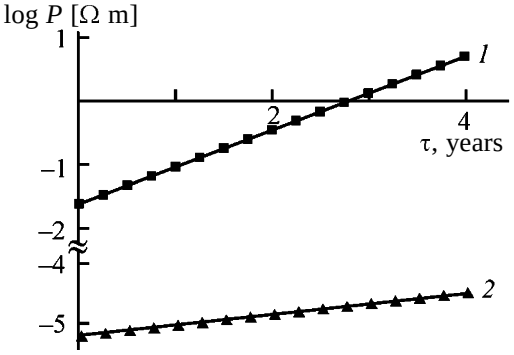

Fig. 2. Electrical resistivity ρ of the formulation (copper UDP + novolak resin SF-010) (*1*) in the initial state and (*2*) after additional treatment with formic acid, vs. the testing time τ.

at a lower rate because of their lower solubility in water. With $CuCl_2$ used, copper UDP was formed, in contrast to the case of reduction with glycerol [8], but formulations on its base could not be obtained because of the decreased stability and increased reactivity of the powder. Before being introduced into formulations, all the copper UDP samples obtained were treated with formic acid.

The copper UDP samples obtained were used to prepare formulations with a novolak resin at a copper UDP to novolak resin ratio of 100 : 25. The highest electrical conductivity and stability were observed for a formulation based on copper formate, since in this case the reaction products (formate ion etc.) stabilize copper (sample no. 8). Only slightly inferior in electrical conductivity to this sample are formulations based on copper sulfate (sample nos. 5, 6) and copper citrate (sample no. 9), but they are unstable in storage. The formulations based on copper nitrate and acetate have even lower electrical conductivity and stability.

Apparently, the presence of an excess amount of sodium hypophosphite leads to higher electrical con-

Table 1. Reduction of copper(II) salts with sodium hypophosphite in an aqueous medium.* SF-010 novolak resin : copper UDP = 25 : 100

Sample no.	Copper salt	Cu(II) : NaH_2PO_2, mol : mol	τ_r, min	T_r, °C	$\rho \times 10^6$, Ω m, at indicated testing time, years				
					1 day	1	2	3	4
1	$Cu(NO_3)_2 \cdot 3H_2O$	1 : 1.5	7	85	11.2	15.6	22.5	31.8	40.2
2	〃	1 : 2	5	85	8.5	11.8	16.9	22.4	28.2
3	$Cu(OAc)_2 \cdot H_2O$	1 : 1.5	35	90	18.2	22.6	32.4	44.2	55.8
4	〃	1 : 2	30	90	10.8	14.3	19.8	27.2	34.6
5	$CuSO_4 \cdot 5H_2O$	1 : 1.5	10	85	8.2	10.6	16.8	24.4	32.6
6	〃	1 : 2	7	85	6.8	8.2	12.0	16.4	21.2
7	$CuCl_2 \cdot 6H_2O$	1 : 3	10	90	–	–	–	–	–
8	$Cu(COOH)_2$	1 : 2	10	85	4.2	4.4	4.6	4.7	–
9	$Cu_2(Citr) \cdot 2.5H_2O$	1 : 3	15	95	7.4	8.6	11.8	14.5	–

* τ_r and T_r are the time and temperature of the reduction of copper(II) salt with sodium hypophosphite.

ductivity and stability of copper formulations. This is presumably due to an additional stabilizing effect of unreacted hypophosphite ions, which decompose in the course of the reaction under the action of water, to give hydrogen [9].

We also studied the influence exerted by stabilizers introduced directly into the novolak resin on the electrical conductivity and stability of copper powders. It was noted in [8] that the best stabilizer (for both epoxy and novolak resins) is 1-naphthol, and additional introduction of glycerol as a plasticizer leads to a considerable increase in the stability and electrical conductivity. In this work, we analyzed the effect of the ratio between UDP, novolak resin, 1-naphthol, and glycerol on the stability and electrical conductivity of pastes with novolak resin (Fig. 3). Ultradispersed copper powders were obtained by reducing copper sulfate with sodium hypophosphite at a ratio $\nu(Cu) : \nu(H_2PO_2^-) = 1 : 1.5$ (Table 1, sample no. 5). It was found that, after introduction of 1-naphthol and glycerol, phenol–formaldehyde novolak formulations based on copper UDP obtained by the hypophosphite method become comparable in stability and electrical conductivity with copper ultradispersed powders prepared by reduction with glycerol.

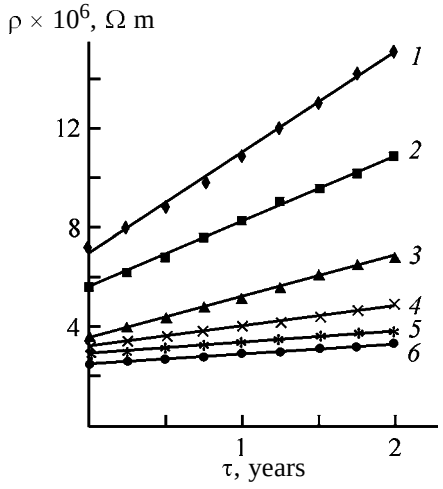

Fig. 3. Effect of stabilizers on the electrical resistivity ρ of formulations with an SF-010 phenol–formaldehyde novolak resin. (τ) Testing time. Weight ratio of copper UDP, SF-010, 1-naphthol, and glycerol (plasticizer): (*1*) 100 : 25 : 0.5 : 1.5, (*2*) 100 : 25 : 0.5 : 3, (*3*) 100 : 25 : 1.0 : 1.5, (*4*) 100 : 25 : 1.0 : 3, (*5*) 100 : 25 : 2.0 : 1.5, and (*6*) 100 : 25 : 2.0 : 3.

It can be seen that the optimal content of 1-naphthol in the formulations is 2 wt % relative to the amount of copper UDP (sample nos. 5, 6). A smaller amount of 1-naphthol is insufficient for obtaining stable formulations with nearly metallic electrical conductivity (sample nos. 1–4). As for the use of a larger amount, it is unfeasible because the electrical conductivity and stability increase in this case only slightly. Apparently, the stability and electrical conductivity also become higher as the amount of glycerol is raised (sample nos. 2, 4, 6). However, a large excess of glycerol may impair the properties of the pastes, because they show poorer hardening and become less stable in storage. Introduction of glycerol in an amount of 1.5–3% (relative to the mass of copper UDP) diminishes the brittleness of the novolak resins. The highest stability and electrical conductivity are exhibited by sample no. 6, stabilized with 2 wt % naphthol and 3 wt % glycerol. The higher optimal content of 1-naphthol in the formulations, compared to that in formulations prepared on the basis of ultradispersed copper powders obtained by reduction with glycerol,

Table 2. Reduction of copper(II) salts with sodium hypophosphite in a water–hexanol medium. SF-010 novolak resin : copper UDP = 25 : 100

Sample no.	Copper salt	Water : hexanol, v/v	Cu(II) : NaH_2PO_2, mol : mol	τ_r, min	T_r, °C	$\rho \times 10^6$, Ω m, at indicated testing time, years				
						1 day	1	2	3	4
1	$Cu(NO_3)_2 \cdot 3H_2O$	10 : 1	1 : 2	2	85	6.4	7.4	8.6	9.8	10.7
2	〃	5 : 1	1 : 2	4	85	4.2	4.8	5.6	6.2	6.8
3	$Cu(OAc)_2 \cdot H_2O$	10 : 1	1 : 2	35	90	7.8	8.9	10.2	11.8	13.2
4	〃	5 : 1	1 : 2	30	90	5.6	6.2	7.1	7.9	9.2
5	$CuSO_4 \cdot 5H_2O$	10 : 1	1 : 2	5	85	3.8	4.2	5.1	5.8	6.4
6	〃	5 : 1	1 : 2	4	85	2.6	2.8	3.1	3.4	3.8
7*	〃	5 : 1	1 : 2	4	85	2.8	3.0	3.2	3.5	–
8	$CuCl_2 \cdot 6H_2O$	10 : 1	1 : 4	4	90	–	–	–	–	–
9	$Cu(COOH)_2$	10 : 1	1 : 2	7	85	2.1	2.2	2.4	2.5	–
10	〃	5 : 1	1 : 2	5	85	1.7	1.8	2.0	2.1	–

* Formulation prepared on the basis of copper(II) (sample no. 6) a year after UDP synthesis.

is due to the higher dispersity and reactivity of the UDP synthesized by reduction with sodium hypophosphite.

Copper(II) compounds were reduced with sodium hypophosphite both in an aqueous medium and in a mixture of solvents, polar (distilled water) and less polar (hexyl alcohol), at a water : hexanol volume ratio of 5 : 1 and 10 : 1. The reduction was carried out as follows: into a vessel containing a copper(II) salt solution was poured a sodium hypophosphite solution, the mixture was agitated, a necessary amount of hexyl alcohol was added, and the resulting mixture was heated to the reaction temperature of 80–90°C and kept at this temperature for 2–35 min, depending on the copper(II) salt used. Then, the hexanol layer was decanted, and the UDP formed was washed with water and treated with solutions of hydroquinone and stearic acid in ethanol. It was found that the stability of the UDP is enhanced as the amount of hexyl alcohol is increased.

The copper UDP samples synthesized were used to prepare formulations with novolak resin. The results obtained are listed in Table 2. It can be seen that all the samples prepared in the system water–hexanol have higher electrical conductivity and stability, compared to the samples synthesized in an aqueous medium (Table 1). The highest stability and electrical conductivity were observed for the UDP samples based on copper(II) formate and sulfate (even when the UDP was stored for a year). This is due to the action of hexanol, which, being adsorbed on the surface of copper UDP, prevents its oxidation and aggregation. However, the copper UDP samples obtained from copper chloride (Table 2, sample no. 10) are rather unstable, are rapidly oxidized, and formulations based on these UDP samples are not electrically conducting. This is probably due to the presence of chloride ions adsorbed on the UDP surface.

Copper(II) acetate, sulfate, formate, basic carbonate, and oxide were reduced with hypophosphorous acid in a water–hexanol medium at a water : hexanol volume ratio of 5 : 1. It was found that basic copper carbonate and copper oxide can only be reduced in the presence of excess hypophosphorous acid [$\nu(H_3PO_2)$: $\nu(Cu) = 4$], and, being poorly soluble in water, these compounds do not react with sodium hypophosphite. The results obtained are listed in Table 3. Apparently, the reduction of copper(II) compounds with H_3PO_2 occurs more actively than that with sodium hypophosphite.

Comparison of Tables 2 and 3 shows that the highest electrical conductivity is exhibited by formulations based on copper UDP samples obtained by reduction with hypophosphorous acid. This is due to the fact that, according to the results of X-ray phase analysis, virtually no oxides could be found in the samples reduced with hypophosphorous acid even in an aqueous medium, in contrast to the samples synthesized by reduction with sodium hypophosphite. Thus, the highest electrical conductivity and stability of formulations based on copper UDP are attained in the case of reduction of copper(II) formate or sulfate with hypophosphorous acid, and also upon introduction of 2 wt % 1-naphthol and 3 wt % glycerol into the formulations.

These formulations are only slightly inferior in electrical conductivity and stability to those ob-

Table 3. Reduction of copper(II) salts with hypophosphorous acid in a water–hexanol medium. Volume ratio water : hexanol = 5 : 1, SF-010 novolak resin : copper UDP = 25 : 100

Sample no.	Copper salt	Cu(II) : H_3PO_2, mol : mol	τ_r, min	T_r, °C	$\rho \times 10^6$, Ω m, at indicated testing time, years				
					1 day	1	2	3	4
1	$Cu(OAc)_2 \cdot H_2O$	1 : 2	20	90	4.2	4.6	5.4	6.2	6.6
2	$CuSO_4 \cdot 5H_2O$	1 : 2	3	85	2.0	2.2	2.5	2.8	3.2
3	$Cu(COOH)_2$	1 : 2	4	85	1.5	1.6	1.7	1.8	–
4	$CuCO_3 \cdot Cu(OH)_2$	1 : 4	15	90	2.4	2.7	3.1	3.6	4.1
5	CuO	1 : 4	25	90	2.5	2.7	3.0	3.4	3.9

tained by reduction with glycerol and stabilized with 1-naphthol and glycerol, but their synthesis is characterized by lower consumption of energy and materials (milder conditions, low expenditure of the reducing agent, lower expenditure of a solvent for UDP washing).

Thus, it is preferable to perform the reduction of copper(II) compounds with sodium hypophosphite and hypophosphorous acid in the system water–hexanol, rather than in the aqueous medium. Adsorption of hexyl alcohol on the surface of copper particles substantially improves their stability and raises the electrical conductivity, so that formulations based on the UDPs of this kind become comparable with those prepared on the basis of UDPs synthesized by reduction with glycerol [4–8] and can compete with similar materials based on silver [1–2].

CONCLUSIONS

(1) Ultradispersed copper powders and formulations based on them were synthesized by reducing various copper salts with sodium hypophosphite and hypophosphorous acid.

(2) The ultradispersed copper powders obtained by reduction with sodium hypophosphite and hypophosphorous acid become more stable and electrically conductive upon treatment with formic acid.

(3) The ultradispersed copper powders synthesized in a water–hexanol medium show higher stability and electrical conductivity.

(4) The increased stability and low production cost of these materials make them promising for use in modern nanoelectronics instead of composites based on noble metals.

REFERENCES

1. US Patent 5 891 367.
2. US Patent 5 929 141.
3. JPN Patent Appl. 3 239 767.
4. RF Patent 2 031 759.
5. RF Patent 2 115 516.
6. Obraztsova, I.I., Efimov, O.A., Eremenko, N.K., and Simenyuk, G.Yu., *Izv. Ross. Akad. Nauk, Neorg. Mater*., 1995, vol. 31, no. 4, pp. 798–799.
7. Obraztsova, I.I., Simenyuk, G.Yu. and Eremenko, N.K., *Inorg. Mater*., 1999, vol. 35, no.. 8, pp. 792–794.
8. Obraztsova, I.I., Simenyuk, G.Yu., and Eremenko, N.K., *Zh. Prikl. Khim*., 2002, vol. 75, no. 11, pp. 1772–1775.
9. Chernogorenko, V.B. and Tasybaeva, Sh.B., *Zh. Prikl. Khim*., 1995, vol. 68, no. 4, pp. 529–533.

Russian Journal of Applied Chemistry, Vol. 77, No. 3, 2004, pp. 385–391. Translated from Zhurnal Prikladnoi Khimii, Vol. 77, No. 3, 2004, pp. 391–398.

APPLIED ELECTROCHEMISTRY AND CORROSION PROTECTION OF METALS

Solvent and Solute Effects on Electrokinetic Potentials at Interfaces between Air and Aqueous or Formamide Solutions of Alkali Metal Chlorides and Sodium Alkyl Sulfates

K. P. Tikhomolova and T. V. Luzyanina

St. Petersburg State University, St. Petersburg, Russia

Received October 10, 2003

Abstract—Electrokinetic flow in a hydrophilic capillary of a model direct emulsion consisting of a polar liquid (water or formamide) containing an alkali metal chloride or sodium alkyl sulfate and air is studied. The interfacial electrokinetic potentials are determined.

This work is aimed at understanding the constant electric field driven flow of a direct emulsion in a thin capillary wetted with a polar fluid. This problem is of interest not only for chemists, but also for medical men, ecologists, geologists, technologists, etc. For actual systems, parameters of the emulsion flow in a capillary can be predicted only on the basis of experimental data and mostly even qualitatively, because for actual systems exact analytical solution is quite difficult. As a result, in the majority of theoretical works, any mathematical approach developed to reproduce the motion of two fluids in a capillary (regardless of the driving force of this motion) is based on the simplest model (see figure) [1–8]. The same model is also used in experimental works [1, 4, 9–13].

The model system represents a cylindrical or slot-like capillary containing a single fine particle of a nonpolar fluid (liquid or gas). The whole residual volume of the capillary is filled with a dispersion medium (polar liquid). The capillary surface is wetted with the polar liquid. The particle of the nonpolar fluid is a cylinder with the long axis along the capillary axis, faced with half-spheres. The length of the cylindrical part of the particle is larger than the capillary radius. In their experimental works, researchers mostly used cylindrical glass capillaries, an aqueous solution as the polar fluid, and air or a hydrocarbon as the nonpolar fluid.

By virtue of wetting of the capillary with a polar liquid and the occurrence of electrical double layers at the interfaces between the polar fluid and the inner surface of the capillary and also between the polar and nonpolar fluids, a thin film of the polar fluid is formed between the capillary wall and the cylindrical surface of the nonpolar particle (hereinafter, the film of the corresponding dispersion medium). The thickness of this film r_f, assumed constant throughout the surface of the cylindrical part of the particle, ranges from several to thousands nanometers. The thickness depends, particularly, on the nature and concentrations of the components of the polar phase and also on the applied external fields [8, 12–16].

Applying external constant electric field initiates electrokinetic motion of the particle, the velocity of which can be strongly influenced by the film thickness.

The actual structure of the film can be far from the ideal, especially in the initial period after formation of the system, when the film can be strongly nonuniform in its thickness. However, with time, the film shape approaches that predicted by the theory, as demonstrated by the experimental (indirect) data [12–15].

Previously [7] we theoretically considered the problem of steady-state electrokinetic flow in such a model system. As a result, we derived a relationship between the electrokinetic flow velocity u_c with the film thickness r_f and electrokinetic potentials at the interface between two fluids ζ^{p-np} and between the polar phase and the capillary wall ζ^{p-s}.

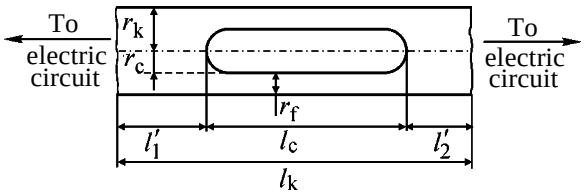

Schematic of the model emulsion in a capillary (for explanation, see text).

1070-4272/04/7703-0385 © 2004 MAIK "Nauka/Interperiodica"

$$\zeta^{p-np} = \zeta^{p-s} + \frac{\mu^p u_c l'}{\varepsilon^0 \varepsilon^p \Delta H} \frac{(1 - r_{rel}^4 + l_{rel})(1 - r_{rel}^2 + l_{rel})}{(1 - r_{rel}^2)^2 + l_{rel}}, \quad (1)$$

where μ^p is the viscosity of the polar phase; l^1, length of the capillary filled with the polar phase only; ε^0 and ε^p, dielectric constant and dielectric permittivity of the polar phase; ΔH, strength of the external constant electric field at the ends of the capillary; $r_{rel} = (r_k - r_f)/r_k = r_c/r_b$; r_k, capillary cross section; $l_{rel} = l_c/l^1$; and l_c, the length of the particle.

Equation (1) allows estimation of ζ^{p-np}. In addition to this parameter, this equation includes *a priori* unknown r_f. The latter was estimated by Eq. (2) representing the Ohm law for the model system in hand [17]:

$$\frac{\Delta H}{I} = \frac{2}{\chi\pi} \frac{1}{[r_k^2 - (r_k - r_f)^2]^{1/2}} \arctan \frac{(r_k - r_f)}{[r_k^2 - (r_k - r_f)^2]^{1/2}} + \frac{l_c - 2(r_k - r_f)}{\chi\pi[r_k^2 - (r_k - r_f)^2]} + \frac{l_k - l_c}{\chi\pi r_k^2}, \quad (2)$$

where I is the current; χ, specific conductivity of the polar phase; and l_k, length of the capillary.

The main goal of this work is to study the effect of the polar phase components on the interfacial electrokinetic potential ζ^{p-np}. Changing nature of the polar phase components, in principle, can influence the thickness of the polar fluid film, which, in turn, significantly affects the electroosmotic flow velocity and, correspondingly, the reliability of the estimated ζ^{p-np}. In view of the basic principles of the colloid chemistry, it could be suggested that the film thickness is influenced by the structural and mechanical properties of the p–np interface, which, in their turn, depend on the solvent and the presence of organic surfactants in the system. Therefore, among the goals of this work was also to check Eq. (1) for consistency with wide variation in the polar phase composition. Selection of a series of inorganic salts and organic diphilic compounds as electrolytes allowed us to affect various structural and mechanical properties of the p–np interface.

In experiments we used quartz glass capillaries, air as the nonpolar fluid, and water and formamide as the polar solvents. Formamide is one of the most polar liquids ($\varepsilon = 111$; $\mu = 11.24 \times 10^{-30}$ C m). For water, the corresponding values are 81 and 6.5×10^{-30} C m [18]. As inorganic electrolytes, we used Li, Na, K, and Cs chlorides, and as organic electrolytes, sodium alkyl sulfates with 10, 12, 13, and 15 carbon atoms in the hydrocarbon radical (hereinafter, SAS_{10}, SAS_{12}, SAS_{13}, and SAS_{15}) (Table 1). The chlorides (analytically pure grade) were additionally purified by recrystallization. The alkyl sulfates were synthesized and recrystallized from benzene at the Academy of Technology and Design (St. Petersburg). The concentration of the inorganic salts was 0.1 M in aqueous solutions and 0.15 M in formamide. Such a decision on the salt concentration in the aqueous systems was caused by the accuracy of measurement of the characteristic parameters included in Eqs. (1) and (2) [15–17]. The inorganic salt concentrations in formamide were selected so that the specific conductivities of the corresponding aqueous and formamide solutions be equal.

Table 1. Zeta-potential ζ^{p-s} in working systems

System no.	Solvent	Electrolyte	SAS*	ζ^{p-s}, mV
1	Water	LiCl	–	–21
2	″	NaCl	–	–23
3	″	KCl	–	–28
4	″	CsCl	–	–28
5	Formamide	LiCl	–	–32
6	″	NaCl	–	–34
7	″	KCl	–	–41
8	Water	NaCl	SAS_{10}	–23
9	″	″	SAS_{12}	–24
10	″	″	SAS_{13}	–22
11	″	″	SAS_{15}	–29
12	Water	NaCl	SAS_{10}	–25
13	″	″	SAS_{12}	–24
14	″	″	SAS_{13}	–27
15	″	″	SAS_{15}	–29
16	Formamide	NaCl	SAS_{10}	–32
17	″	″	SAS_{12}	–38
18	″	″	SAS_{13}	–35
19	″	″	SAS_{15}	–40
20	Formamide	NaCl	SAS_{10}	–34
21	″	″	SAS_{12}	–37
22	″	″	SAS_{13}	–36

* For system nos. 8–11 and 16–19, the SAS concentrations correspond to those for the first series, and for system nos. 12–15 and 20–22, those for the second series.

The SAS concentrations were taken equal in both aqueous and formamide solutions. Two different concentrations were taken for each SAS in both solvents. In the first series, the SAS concentrations were selected to meet the condition of equal amounts of SAS adsorbed on the solution–air interface Γ (mol m^{-2}),

and in the second series, the concentrations were considerably (by a factor of 3–5) higher. Regardless of the solvent, the SAS concentrations in the first and second series were as follows (mM): SAS_{10} 0.3 and 1.7, SAS_{12} 0.24 and 1.2, SAS_{13} 0.23 and 0.7, and SAS_{15} 0.22 and 0.7. Naturally, the surface tensions σ were different in the aqueous and formamide solutions of each series (64–65 and 53–54 mN m^{-2}, respectively, for the first series). The Γ values were also different, depending on the solvent, being 2.8×10^{-6} and 2×10^{-6} mol m^{-2} in the aqueous and formamide solutions, respectively. All the SAS-containing aqueous solutions were prepared with 0.1 M NaCl as a supporting electrolyte, and all the formamide solutions, with 0.15 M NaCl. Note that the SAS concentrations were lower by 2–3 orders of magnitude than the chloride concentrations. It is clear that the contribution of SAS to the conductivity of the working solutions was negligible as compared to the contribution of NaCl.

The procedures of formulation of the working systems and electrokinetic measurements were described elsewhere [13, 14]. The surface tension σ was determined by the Rebinder's method, and the adsorption Γ was estimated from σ by the Gibbs equation [19].

First of all, note that, in all experiments, we observed some variance of the measured particle velocity and current *I*, i.e., u_c and r_f. Specifically, here we are dealing with the least experimentally obtainable values. Following our previous works [13, 14], these velocities and film thicknesses are referred to as instantaneous and designated hereinafter as u_c^x and r_f^x. The observed behavior of the working systems could be referred to as labile. Previously [13] we reported on the lability of the electrokinetic flow of a nonpolar fluid in a glass capillary filled with an aqueous solution. At the same time, we have demonstrated [13, 14] that, with the use of the average u_c and r_f values, the estimated electrokinetic potentials at the interface between two fluids are reliable from the standpoint of their consistence with ζ^{p-np} as a theoretical physical parameter. However, it should be pointed out that we observed such a lability, even considerably less pronounced, for the average ζ^{p-np} values also. The estimated mean ζ^{p-np} values could range within more or less wide intervals: the more labile is the system, the greater the variance of the estimated potential for a given pair of fluids (Table 2). Even in the experiments with similar geometric parameters of the working systems, the mean u_c and r_f values could appear different, as well as the ζ^{p-np} values (Table 2). Nevertheless, the spread in the potentials estimated from the mean u_c and r_f is a result of experimental errors, and it can be reduced using standard methods, i.e., through performing a series of replicate runs.

The mean velocities are estimated from the path length and the time required for the particle to pass "a sufficiently long path" along the capillary; and the mean film thickness, by averaging over all the instantaneous values measured throughout "a sufficiently long capillary" [14]. In experiments we mostly used capillaries 23–25 cm in length. The instantaneous velocities and the corresponding instantaneous film thicknesses allowed only qualitative characterization of the effect of solution components on the electrokinetic behavior of the working systems. In quantitative estimates of ζ^{p-np}, we used the mean u_c and r_f values.

The equation for ζ^{p-np} includes the potential at the polar phase–glass interface ζ^{p-s}. It was determined as an electroosmotic potential. For this purpose, a capillary was filled with a given solution (without dispersed particle), and the electroosmotic flow velocity was measured [20]. The experiments were carried out with working capillaries of various lengths and cross sections. The ζ^{p-s} was estimated according to the procedure described in [19]. The resulting ζ^{p-s} values were shown to be well reproducible, being independent of the capillary size. The maximal deviations from the mean ζ^{p-s} values in the systems with various salts were as follows: LiCl ±5%, NaCl ±7%, and KCl and CsCl ±10%. The mean ζ^{p-s} values are given in Table 1.

The ζ^{p-s} values obtained in aqueous solutions of alkali metal chlorides, generally, reasonable agree with the published data [21].[1] This parameter slightly depends on the kind of the alkali metal, increasing in the absolute value with the molar weight of the cation. The ζ^{p-s} series obtained in this work differs from that known from the literature, where it was noted that $|\zeta^{p-s}|$ increases with increasing hydration of a cation. This distinction is probably due to different material of the capillaries (we use quartz glass, but not quartz).

The ζ^{p-s} values obtained in the formamide solutions of alkali metal salts have the same sign (minus) as in the aqueous solutions, being considerably higher in their absolute value.[2] The kind of the cation only slightly influences ζ^{p-s}, which changes in the same order as in the aqueous solutions.

[1] Published data mostly refer to KCl or NaCl.

[2] We found no published data on the formamide solutions. Since the formation mechanism of the electrical double layer at the glass–formamide interface is unknown, we offer no explanation for the disagreement.

Table 2. Electrokinetic potentials at the air–alklai metal chloride solution interface

System no.	Electrolyte	r_k, μm	l_c, μm	l_k, cm	ζ^{p-np}, mV, at indicated applied voltage, V	
					45	90
			Water			
1	LiCl	91	1000	26	–25	–24
2		145	964	26	–29	–29
3		109	1100	21	–32	–32
4		109	2000	27	–29	–30
				Mean	–29	–29
5	NaCl	93	1520	25	–29	–28
6		93	1250	25	–33	–35
7		157	1100	25	–25	–25
8		126	1000	23	–35	–37
				Mean	–30	–31
9	KCl	109	1820	25	–35	–37
10		95	2000	21	–39	–40
11		109	1350	22	–45	–44
12		90	1950	22	–48	–48
				Mean	–42	–42
13	CsCl	109	2000	28	–43	–43
14		120	1600	24	–25	–27
15		127	2000	28	–51	–52
16		100	1360	26	–33	–32
				Mean	–38	–39
			Formamide			
17	LiCl	109	1500	26	–38	–41
18		98	1600	25	–33	–32
19		95	1500	25	–25	–29
20		94	500	26	–54	–52
				Mean	–38	–38
21	NaCl	109	1500	26	–29	–28
22		91	1000	24	–36	–36
23		145	1500	26	–46	–44
24		109	1300	26	–25	–28
				Mean	–34	–34
25	KCl	118	500	29	–45	–44
26		127	1420	27	–39	–37
27		109	1500	27	–43	–48
28		109	960	20	–50	–48
				Mean	–44	–44

Introduction of SAS into both aqueous and formamide solutions has practically no effect on ζ^{p-s}. The only exception is the system with SAS_{15}. The results suggest that SAS_{10}–SAS_{13} are not noticeably adsorbed on glass, which is consistent with data from [14, 22] for SAS_{12}. SAS_{15} is adsorbed very slightly.

Analysis of the electrokinetic behavior of the systems consisting of two fluids with the polar phase containing only inorganic chlorides shows that, in the cases of both aqueous and formamide solutions, this behavior was labile. Although the lability was observed in all the systems studied, the trends of variation in u_c^x and I^x (correspondingly, r_f^x) were different, depending on the cation. In aqueous LiCl, the electrokinetic flow oscillated [13] with 10–20% deviation from the mean value. Similar behavior was observed for r_f^x. In the cases of CsCl, NaCl, and KCl, the trends in variation of u_c^x and r_f^x were very diverse. The difference between the maximal and minimal velocities in the CsCl solutions reached 50%, while that in the NaCl and KCl solutions was considerable smaller.

The trends of variation in u_c^x and I^x (correspondingly, r_f^x) as well as their limiting values also depend on the solvent. The orders of variation of these values in the series of cations was the same for both aqueous and formamide solutions. However, the formamide systems were much more labile. In the formamide solutions of CsCl, the characteristic parameters so much widely ranged that we could not realize a statistic representation of the experimental data for estimating ζ^{p-np}. The estimated ζ^{p-np} values are given in Table 2.

The mean r_f values in the working systems approached several thousands of nanometers, which is close to the values reported in [13, 14] for similar systems.

Table 2 shows that, in all the systems with given electrolyte and solvent, the ζ^{p-np} values were mostly somewhat different, even in the cases of practically identical or close geometric parameters of the capillary and the particle. This suggests that the estimated potentials are independent of these parameters, and their variations are determined by labile behavior of the working systems. The independence of the estimated ζ^{p-np} from the geometric parameters is a clear indication of the fact that each of the mean ζ^{p-np} values in Table 2 corresponds (within the experimental error) to ζ^{p-np} as the theoretical physical parameter characterizing the interface between two fluids in each of the systems studied. The reliability of the ζ^{p-np} values obtained in this work is additionally evidenced by the fact that these values are well consistent with the available data on the 0.1 M NaCl–air interface, obtained by various methods. The ζ^{p-np} variation range observed in the working systems depended on the cation, being the wider, the heavier the cation. In each of the solvents, $|\zeta^{p-np}|$ slightly decreased with decreasing molar weight of the cation. Explanation of this finding requires further investigations.

In the systems with the same cation, but different solvents, $|\zeta^{p-np}|$ is slightly higher in the case of formamide solutions, which can be associated with two factors.

(1) Assuming that the intensive properties of the solvents used are constant behind the solution–air interface, the higher ζ^{p-np} values observed in formamide can be attributed to the fact that, in this case, the chloride concentration in the interfacial electrical double layer is higher as a result of the higher dielectric constant of formamide.

(2) Assuming that, in the interfacial layer, water and formamide are structured (structures can be different), deceleration of the electrokinetic flow, caused by structurization, is more strongly pronounced in water, presumably, as a result of stronger interactions of components.

The question about occurrence and properties of structured interfacial layers in aqueous solutions is actively discussed in the literature for a long time. In the case of formamide, such a question has not been raised yet.

Tables 3 and 4 show ζ^{p-np} in SAS-containing systems at various geometric parameters of the capillary and particle.

Tables 3 and 4 show that introduction of SAS into the systems decreases the mean r_f by an order of magnitude. In this case, the variance of the ζ^{p-np} values is considerably lower than in systems without SAS. Therefore, the electrokinetic behavior of SAS-containing systems is more stable as compared to that in the systems containing inorganic electrolytes only.

The estimated ζ^{p-np} values are independent of the geometric parameters of the capillary and particle, also evidencing that the estimated values are consistent with the theoretical physical parameter.

Introduction of SAS did not change the sign of ζ^{p-np} (it remained negative), but its absolute value increased significantly, as compared to the systems containing inorganic chlorides only. All these findings reveal a considerable adsorption of the organic anion

Table 3. Electrokinetic potentials at the air–aqueous solution interface in the presence of SAS

System no.	SAS*	r_k, μm	l_c, μm	l_k, cm	ζ^{p-np}, mV
1	SAS_{10}	109	1620	26	–100
2		135	1000	29	–98
3		129	1400	28	–108
4		98	1550	25	–99
5		145	1260	21	–104
				Mean	–102
6	SAS_{12}	119	1250	26	–113
7		95	1650	25	–105
8		75	960	24	–102
9		109	1540	26	–92
10		129	1570	25	–98
				Mean	–102
11	SAS_{12}	109	2000	24	–105
12		100	1450	21	–103
13		109	1380	23	–106
14		109	1550	23	–108
15		128	1100	24	–123
				Mean	–109
16	SAS_{15}	85	1850	21	–110
17		100	1570	25	–107
18		127	2500	23	–109
19		120	1200	27	–108
20		109	1100	22	–114
				Mean	–112
21	SAS_{10}	100	1500	27	–110
22		109	1650	25	–98
23		120	1300	24	–95
24		109	1450	26	–115
25		98	1500	21	–105
				Mean	–105
26	SAS_{12}	127	1350	25	–120
27		109	1460	24	–118
28		95	1200	25	–126
29		85	1140	25	–113
30		100	1250	23	–108
				Mean	–117
31	SAS_{13}	109	1240	21	–109
32		120	950	29	–115
33		127	1350	25	–110
34		109	1440	26	–128
35		0	1580	25	–120
				Mean	–118

* For system nos. 1–20, the SAS concentrations correspond to those for the first series, and for system nos. 21–35, to those for the second series.

Table 4. Electrokinetic potentials at the air–formamide solution interface in the presence of SAS

System no.	SAS*	r_k, μm	l_c, μm	l_k, cm	ζ^{p-np}, mV
1	SAS_{10}	109	1250	24	–60
2		98	1400	26	–59
3		109	1260	25	–64
				Mean	–61
4	SAS_{12}	127	1740	25	–64
5		108	1960	25	–67
6		94	1570	25	–59
				Mean	–63
7	SAS_{13}	100	1100	23	–69
8		127	1220	26	–67
9		93	780	25	–69
				Mean	–68
10	SAS_{15}	85	1850	24	–70
11		100	1540	25	–59
12		95	1360	25	–64
				Mean	–64
13	SAS_{10}	109	1550	25	–70
14		84	1930	24	–75
15		79	1570	25	–69
				Mean	–71
16	SAS_{12}	91	1200	25	–71
17		145	1530	25	–74
18		127	2000	23	–73
				Mean	–73
19	SAS_{13}	109	1550	25	–70
20		109	1620	25	–78
21		74	2040	24	–72
				Mean	–73

* For system nos. 1–12, the SAS concentrations correspond to those for the first series, and for system nos. 13–21, to those for the second series.

on the interface between air and any polar fluid used. At the same time, the increase in ζ^{p-np} in the absolute value ($\Delta|\zeta^{p-np}| = |\zeta^{p-np}|_{SAS} - |\zeta^{p-np}|$) was considerably higher in the aqueous systems (70 mV against 30 mV in the formamide systems). This difference, without question, can be attributed to the properties of the boundary layers and also to the fact that the adsorption of SAS from aqueous solutions is higher than that from formamide solutions. The higher adsorption of SAS on the aqueous solution–air inter-

face is caused by the hydrophobic effect and arrangement of the SAS molecules in the surface layer, controlled by the hydrophilic–lipophilic balance [23, 24]. Both effects, as known, are typical of water only. As a result of interaction between the polar group of SAS and replacement of the hydrocarbon radical from water (hydrophobic effect), a part of the hydrophobic radical of SAS becomes bound to water molecules [24], promoting strong ordering of the water structure. The thickness of this layer corresponds to the length of the hydrocarbon radical occurring in the solution [23].

CONCLUSIONS

(1) Electrokinetic flow in a hydrophilic capillary of model direct emulsions air–polar fluid (water or formamide) containing alkali metal chlorides was labile in all cases, which was more pronounced in formamide solutions and with cations of higher molar weight. Introduction of sodium alkyl sulfates into solutions stabilizes the electrokinetic flow.

(2) Electrokinetic potentials on the interface between air and aqueous (or formamide) solution of Li, Na, K, or Cs chloride are determined. The zeta-potential increases on passing from aqueous to formamide systems.

(3) Introduction of sodium alkyl sulfates (C_{10}–C_{15}) to both aqueous and formamide solutions does not noticeably influence the zeta-potential at the glass–liquid interface, but strongly increases that at the air–liquid interface, suggesting that sodium alkyl sulfates are not adsorbed on glass but are strongly adsorbed on the air–liquid interface. In this case, the absolute values of the zeta-potential were demonstrated to be considerably higher in the aqueous solutions as compared to the formamide solutions.

SASKNOWLEDGMENTS

The work was financially supported by the Russian Federation President's grant "Leading Scientific Schools of the Russian Federation" (no. NSh-789.2003.3).

REFERENCES

1. Bretherton, F.P., *J. Fluid Mechan*., 1961, vol. 51, pp. 166–188.
2. Kalinin, V.V. and Starov, V.M., *Kolloidn. Zh*., 1989, vol. 51, no. 6, pp. 1094–1098.
3. Park, C.W. and Homsy, G.G., *J. Fluid Mechan*., 1984, vol. 139, pp. 291–308.
4. Schwartz, L.W., Princen, H.V., and Kiss, A.D., *J. Fluid Mechan*., 1986, vol. 172, pp. 259–275.
5. Stebe, K.J. and Barthes-Biesel, D., *J. Fluid Mechan*., 1995, vol. 286, pp. 25–42.
6. Tikhomolova, K.P. and Kokorina, O.V., *Kolloidn. Zh*., 1993, vol. 55, no. 2, pp. 147–152.
7. Tikhomolova, K.P. and Kokorina, O.V., *Kolloidn. Zh*., 1993, vol. 55, no. 3, pp. 167–171.
8. Tikhomolov, D.V. and Slyadneva, O.N., *Int. J. Multiphase Flow*, 2000, vol. 26, pp. 1891–1903.
9. Faierbrother, F. and Stabbs, A., *J. Chem. Soc*., 1935, pp. 527–529.
10. Gintley, G.M. and Radke, C.J., *ACS Symp. Ser*., 1989, vol. 396, pp. 480–495.
11. Hirasaki, J. and Lawson, J.B., *Soc. Petr. Eng. J*., 1986, vol. 25, pp. 176–193.
12. Tikhomolova, K.P. and Slyadneva, O.N., *Kolloidn. Zh*., 1997, vol. 59, no. 6, pp. 819–826.
13. Tikhomolova, K.P. and Slyadneva, O.N., *Kolloidn. Zh*., 1998, vol. 60, no. 1, pp. 89–96.
14. Tikhomolova, K.P., Kokorina, O.V., and Voznaya, E.E., *Kolloidn. Zh*., 1993, vol. 55, no. 3, pp. 174–182.
15. Tikhomolov, D.V., Krasikov, N.N., and Marmorshtein, L.M., *Kolloidn. Zh*., 1986, vol. 48, no. 5, pp. 1034–1037.
16. Tikhomolova, K.P., Arndt, N.S., Tikhomolov, D.V., and Voznaya, E.E., *Kolloidn. Zh*., 1990, vol. 52, no. 5, pp. 805–808.
17. Tikhomolov, D.V., *Zh. Prikl. Khim*., 1993, vol. 66, no. 3, pp. 519–524.
18. *Spravochnik khimika* (Chemist's Handbook), Nikol'skii, B.P., Ed., Leningrad: Goskhimizdat, 1962, vol. 1.
19. Grigorov, O.N., Karpova, I.F., Koz'mina, Z.P., *et al*., *Pukovodstvo k prakticheskim rabotam po kolloidnoi khimii* (Practical Manual on Colloid Chemistry), Leningrad: Khimiya, 1964.
20. Tikhomolova, K.P., *Electroosmosis*, New Jersey: Horwood, 1993.
21. Bogdanova, N.F., Sidorova, M.P., Ermakova, L.E., and Savina, I.A., *Kolloidn. Zh*., 1997, vol. 59, no. 4, pp. 452–459.
22. Schulze, H. and Cichos, Chr., *Z. Phys. Chem*., 1972, vol. 251, nos. 3–4, pp. 252–261.
23. Izmailova, V.N. and Rebinder, P.A., *Strukturoobrazovanie v belkovykh sistemakh* (Structure Formation in Protein Systems), Moscow: Nauka, 1974.
24. Rusanov, A.I., *Mitselloobrazovanie v rastvorakh poverkhnosno-aktivnykh veshchestv* (Micelle Formation in Surfactant Solutions), Leningrad: Khimiya, 1992.

Russian Journal of Applied Chemistry, Vol. 77, No. 3, 2004, pp. 392–396. Translated from Zhurnal Prikladnoi Khimii, Vol. 77, No. 3, 2004, pp. 399–403.

ENVIRONMENTAL PROBLEMS OF CHEMISTRY AND TECHNOLOGY

Kinetics of Decomposition of Water-Dissolved Phenol under the Action of Ozone and Electric Field

A. G. Bubnov, V. I. Grinevich, A. A. Gushchin, and V. V. Kostrov

Ivanovo State University of Chemical Engineering, Ivanovo, Russia

Received July 29, 2003

Abstract—Kinetics of phenol decomposition in aqueous solution under the combined action of weak electric field and ozone is studied. The possible reaction mechanism is suggested and analyzed.

According to the data obtained by foreign researchers [1], the human health may be 80% determined by the quality of potable water. Therefore, much attention is being given in the United States, Canada, and West Europe both to manufacture of bottle water of improved quality (from Artesian wells) and to problems associated with water treatment. One of the most important tasks of water treatment is to diminish the content of phenol, which is virtually always present in natural surface water basins and in water streams used as sources of potable water (1–5 $\mu g\ l^{-1}$ in natural water reservoirs in Russia [2]), to the level specified by regulations. This is primarily due to the fact that chlorination of phenol-containing water leads to formation of extremely toxic organochlorine compounds [3]. Therefore, introduction of new efficient energy-saving methods for purification of wastewater of various kinds (industrial, municipal, and surface) to remove phenols can improve the quality of water in natural water streams, which receive the above wastewater, and, consequently, can improve the quality of potable water [4]. However, both new, efficient, and old, known since the late 1940s, methods for water purification frequently fail to find wide use only because of the insufficient knowledge of the fundamental aspects of the physicochemical processes and reactions inherent in these techniques. Therefore, the aim of this study was to examine the kinetics of phenol decomposition in aqueous solutions under the action of electric field and ozone.

EXPERIMENTAL

As object of study was chosen an aqueous solution of phenol with an initial concentration of 0.5 $mg\ l^{-1}$. The initial solution was delivered to a feeding tank *1* (Fig. 1) and further, through cock *2*, to the electrochemical cell *3* of "comb" type with rectangular electrodes. The cell casing, anodes, and cathodes were made of 2-M fluoroplastic, titanium, and aluminum, respectively. The flow rate of the phenol solution was varied from 0.07 to 0.8 $ml\ s^{-1}$, which corresponded to a time of contact between the solution and the electrodes in the range from 130 to 1500 s. Ozone was generated using a laboratory ozonizer with coaxial arrangement of electrodes (maximum output of ozone of 0.146 and 0.454 $\mu mol\ s^{-1}$ with the use of air and oxygen, respectively).

The setup was connected to a dc power source *4*. The current strength *I* in the cell was varied from 0.1 to 10 mA (current density of 0.01 to 1.1 $A\ m^{-2}$), and the voltage, from 15 to 65 V.

A solution after treatment was delivered to the receiving vessel *5*. The concentration of phenol in the aqueous solution and in the gas phase at the reactor outlet was monitored photometrically (KFK-2MP colorimeter) by the reaction with 4-aminoantipyrine [5] (λ = 455 nm). The content of ozone in the gas and liquid phases was measured by absorption spectroscopy on the basis of light absorption at λ = 253.7 nm, which corresponds to the maximum cross section of

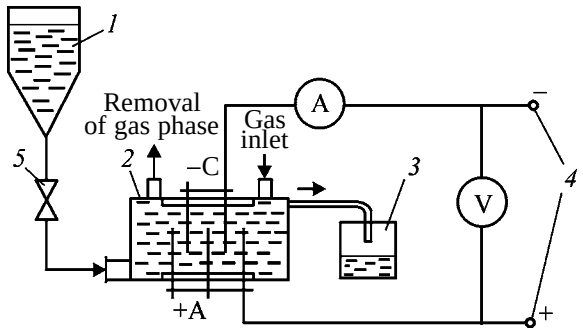

Fig. 1. Schematic of the experimental setup.

1070-4272/04/7703-0392 © 2004 MAIK "Nauka/Interperiodica"

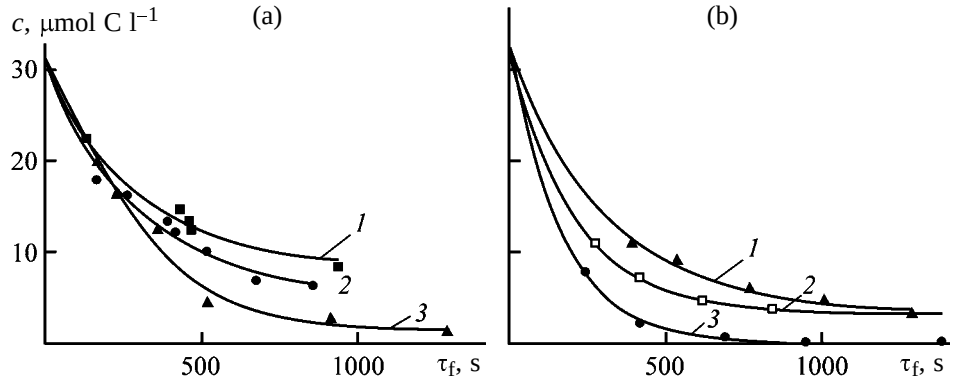

Fig. 2. Kinetics of phenol decomposition. (*c*) Concentration of phenol in terms of carbon and (τ_f) process time. Carrier gas: (a) air and (b) O_2; the same for Figs. 3 and 4. Type of treatment: (*1*) O_3, (*2*) O_3 + electric field, and (*3*) O_3 + electric field in a weakly mineralized medium; the same for Figs. 3 and 4.

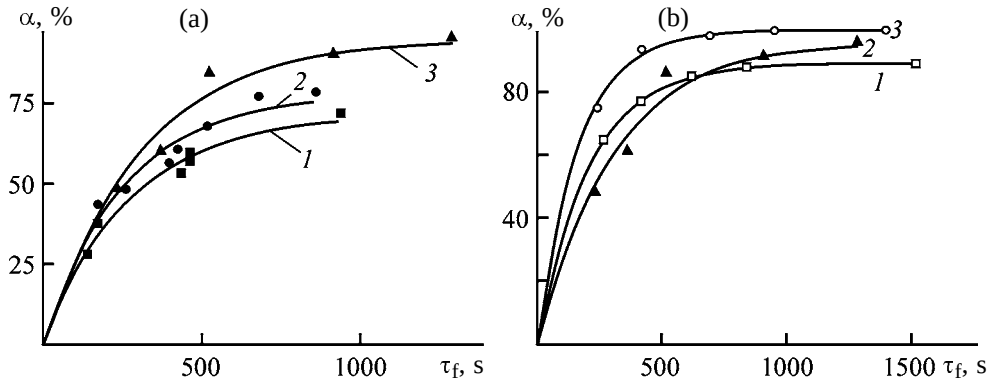

Fig. 3. Efficiency α of phenol decomposition. (τ_f) Time.

photoabsorption by O_3 ($\sigma = 7.8 \times 10^{-18}$ cm^2 [6]). The concentration of ozone, N_{O_3} (cm^{-3}), was calculated using the formula

$$N_{O_3} = \frac{\ln(I_0/I)}{\sigma l},$$

where I_0 is the initial intensity of the resonance emission line of Hg without ozone (rel. units); I, the same, but in the presence of ozone (rel. units); σ, cross section of photoabsorption (cm^2); and l, length of a cell with quartz windows (5.9 and 0.999 cm for the cases of measurement of the O_3 concentration in the gas phase and in the aqueous solution, respectively).

The concentration of carbon dioxide (in terms of the bicarbonate ion) was determined potentiometrically [5]. The pH value of the solution before and after electrochemical treatment was measured with an EV-746 pH meter.

The efficiency α (%) of phenol decomposition was determined using the formula

$$\alpha = \frac{c_{in} - c_f}{c_{in}},$$

where c_{in} and c_f are the concentrations of phenol in terms of carbon before and after treatment (μmol C l^{-1}).

Figures 2 and 3 show the kinetics and efficiency of phenol decomposition in water both in the case of ozonation and under a combined action of ozone and an electric field. It follows from the data presented that the decomposition of phenol is in all cases described by a pseudo-first-order reaction. The efficiency of phenol decomposition under the action of O_3 obtained from air is the lowest, about 60%, and that in the case of a combined action of ozone and an electric field is as high as 75%. If the process is carried out in a weakly mineralized medium (addition of 10 mg l^{-1} of KCl), the decomposition efficiency increases to 85%. The rate of phenol oxidation in the case of a combined purification method (weakly mineralized aqueous medium) exceeds that with only ozonation by a factor of more than 1.8 (Table 1). The efficiency of phenol decomposition in a weakly mineralized medium, with O_2 used to generate O_3, was as high as 99%, and the rate of phenol decomposition increased by a factor of 2.8, compared to that under the action of O_3 obtained from air.

Table 1. Effective rate constants k_{eff} of decomposition of phenol and formation of the final oxidation product in aqueous solution

Type of solution treatment	k_{eff}, s^{-1}			
	air		O_2	
	from decrease in phenol concentration	from increase in HCO_3^- concentration	from decrease in phenol concentration	from increase in HCO_3^- concentration
O_3	$(13 \pm 1.5) \times 10^{-4}$	$(10 \pm 1.1) \times 10^{-4}$	$(17 \pm 1.8) \times 10^{-4}$	$(13 \pm 2.4) \times 10^{-4}$
O_3 + electric field	$(18 \pm 1.5) \times 10^{-4}$	$(11 \pm 1.8) \times 10^{-4}$	$(25 \pm 3.6) \times 10^{-4}$	$(15 \pm 2.4) \times 10^{-4}$
O_3 + electric field in weakly mineralized medium (10 mg l^{-1} KCl)	$(24 \pm 2.7) \times 10^{-4}$	$(18 \pm 4.2) \times 10^{-4}$	$(38 \pm 6.0) \times 10^{-4}$	$(20 \pm 6.4) \times 10^{-4}$

It is known [7] that the yield of ozone increases as the power, which is directly proportional to the voltage applied across the ozonizer electrodes, is raised. Consequently, the efficiency of phenol decomposition in aqueous solutions must increase, too, and this was observed in the experiment.

However, if the conversion is found from the decrease in the concentration of phenol, the completeness of its decomposition cannot be determined adequately. The final products of total breakdown of organic compounds are H_2O and dissolved CO_2. Measurements of the concentration of CO_2 in solution (pH varied in all the experiments within the range 5.2–6.8, and, consequently, the carbonate system is ~90% represented in this case by HCO_3^-) demonstrated that this concentration remains virtually unchanged as the concentration of ozone in solution grows. It is noteworthy that the maximum yield of the final product in ozonation is very low and does not exceed 4% of the initial concentration of phenol, i.e., total decomposition of phenol under the action of O_3 is virtually not observed. This suggests that the rate-determining stage of phenol decomposition in water under the action of ozone is the decomposition of intermediates formed in its oxidation to the final products, i.e., CO_2 (k_3):

$$C_6H_5OH \xrightarrow{k_1} RC(O)H \xrightarrow{k_2} RC(O)OH \xrightarrow{k_3} CO_2 + H_2O.$$

Similar measurements in the case of a combined action on phenol solutions indicate that, at the same doze of ozone, additional application of an electric field leads to an increase in the degree of phenol decomposition to CO_2 by a factor of approximately 3 (at the maximum current density of 1.1 A m^{-2}), i.e., to 15%; however, in this case, too, the yield of HCO_3^- is low.

Combined action of ozone and an electric field on a phenol solution in a weakly mineralized medium (10 mg l^{-1} of KCl) is equivalent to an increase in the current density at the same voltage applied across the ozonizer electrodes. This results in that the efficiency of phenol decomposition to the final products grows to 45% (Fig. 4). The yield of the final oxidation prod-

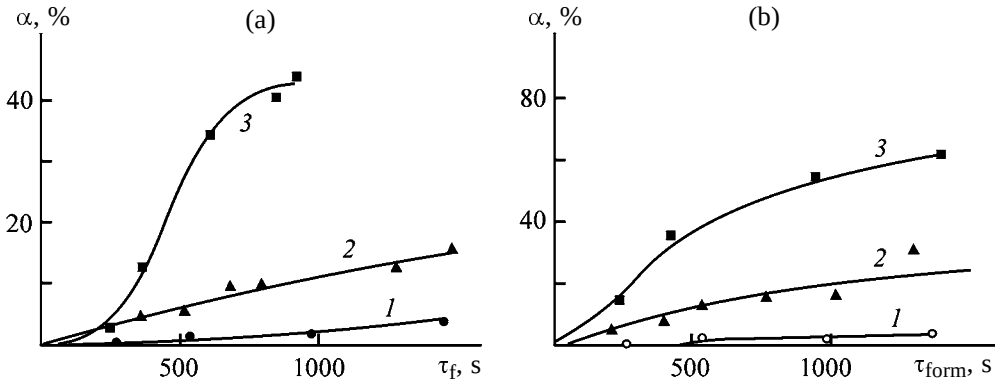

Fig. 4. Efficiency α of phenol decomposition to HCO_3^-. (τ_f, τ_{form}) Time.

uct increases in this case as compared to the treatment of phenol with only ozone by a factor of more than 7.

With oxygen used to generate ozone, the yield of the final product of phenol decomposition (HCO_3^-) was as high as 60% (Fig. 4). Consequently, use of O_2 to obtain O_3 is in this case justified, since the yield of HCO_3^- increases by a factor of 15, compared to treatment of a phenol solution with a mixture of ozone and air.

Consequently, application of electric fields leads to an increase in the concentration of active species initiating decomposition of phenol molecules. The arising additional active species (solvated electrons, hydroxy and hydroperoxy radicals, and chlorine oxides formed by the reaction $Cl + O_3 \rightarrow ClO + O_2$) mostly react with intermediates formed in decomposition of phenol and cause their oxidative breakdown to CO_2 (HCO_3^-).

Table 2 lists the results obtained in measuring the concentration of ozone in the gas (at the reactor inlet) and liquid (at the reactor outlet) phases, with ozone generated from air and O_2 and all other experimental conditions being the same.

The concentration of ozone in the liquid phase in the reactor is proportional to that in the gas phase at the reactor inlet. Only unreacted ozone remains in the liquid phase at the reactor outlet. Complete oxidation of 5.5 μmol of phenol requires 25.7 μmol of O_3, which constitutes 58% of the amount of ozone fed into the reactor in the case of ozone generation from air. The conversion of phenol with ozone obtained from air, measured for different types of treatment, varied between 62 and 88%. With account of the fact that a part of ozone, undissolved in water, is carried away from the reactor by discharged gases, complete decomposition of phenol must not occur in this case, which is confirmed by the experimental data presented above (the yield of the final oxidation products varied from 4 to 40%). With oxygen used to generate ozone, complete oxidation of phenol dissolved in water requires only 18% of O_3 fed into the reactor (Table 2). Consequently, the available O_3 is quite sufficient for complete oxidation of phenol. The experiments performed demonstrated that the yield of the final oxidation products was in this case substantially higher (60%). With aqueous solutions of phenol treated with only ozone, the yield of the final decomposition products was the same (about 4%), with both air and oxygen used to generate O_3. The decomposition rate of phenol is approximately 30–60% higher with O_2 used as the plasma-forming medium in the ozonizer

Table 2. Concentration of ozone in the gas and liquid phases for different methods of treatment of phenol solutions (c_{ph}^{in} = 5.5 μM)

Type of solution treatment	Air		O_2	
	gas	liquid	gas	liquid
O_3	44	3.4	153	5.9
O_3 + electric field	44	0.2	153	1.1
O_3 + electric field in weakly mineralized medium	44	0.6	153	1.0

(Table 1), irrespective of a method used for treatment of the aqueous solution. The experimental data obtained suggest the following: (1) the mechanism of phenol decomposition, including the rate-determining stages of the process, does not vary significantly between different types of solution treatment or different plasma-forming media in the ozonizer; (2) changing the plasma-forming medium in the ozonizer alters only the concentration of active species that initiate decomposition of phenol in an aqueous solution; and (3) use of combined methods for treatment of aqueous solutions results in that the composition of the active species, which cause decomposition of phenol molecules, changes not only quantitatively, but also qualitatively [e.g., chlorine oxides with high oxidizing capacity (ClO and ClO_2) are formed in addition to the OH and HO_2 radicals].

An estimation of the energy expenditure (main component for determining the environmental and economic efficiency of any purification method) for water purification to remove phenol by combining ozonation and application of an electric field in a weakly mineralized medium demonstrated that it does not exceed 3.4 kW h m^{-3}, which is only 1.2 kW h m^{-3} greater compared to treatment by only ozonation (2.2 kW h m^{-3}). Consequently, to reduce the concentration of intermediates formed in oxidative decomposition of phenol in purification of real wastewater or in water conditioning is combined treatment with ozone and an electric field (since wastewater is commonly mineralized to a sufficient extent).

CONCLUSIONS

(1) The degree of phenol decomposition in an aqueous solution in joint ozonation and electrochemical treatment in a mineralized medium is 2.3 times that in ozonolysis.

(2) The yield of CO_2 does not exceed 4% in ozonation of model solutions of phenol and increases to 60% (by a factor of 15) in the case of combined electrochemical treatment and ozonolysis, with the energy expenditure increasing by a factor of only 1.5.

ACKNOWLEDGMENTS

The study was supported by the Russian Foundation for Basic Research (grant no. 12.G-RF.03).

REFERENCES

1. Bocharov, V.L. and Smirnova, A.Ya., Abstracts of Papers, *III nauchno-tekhnicheskii seminar "Problemy pit'evogo vodosnabzheniya i puti ikh resheniya"* (III Scientific and Technical Workshop "Problems of Potable Water Supply and Ways of Their Solution"), Moscow, 1997, pp. 54–55.
2. *Gosudarstvennyi doklad "O sostoyanii okruzhayushchei prirodnoi sredy Rossiiskoi Federatsii v 1997 godu"* (State Report "On the State of the Environment in the Russian Federation in 1997"), Moscow: Gos. Tsentr Ekol. Programm, 1998.
3. Kuzubova, L.I. and Kobrina, V.N., *Khimicheskie metody podgotovki vody (khlorirovanie, ozonirovanie, ftorirovanie): Analiticheski obzor* (Chemical Methods of Water Treatment (Chlorination, Ozonation, Fluorination): Analytical Review), Novosibirsk: Sib. Otd. Ross. Akad. Nauk, 1996.
4. *Chemistry of Wastewater Technology*, Rubin, A.J., Ed., Ann Arbor: Ann Arbor Science, 1978.
5. Novikov, Yu.V., Lastochkina, K.O., and Boldina, Z.N., *Metody issledovaniya kachestva vody vodoemov* (Methods for Analysis of the Quality of Water in Water Basins), Shitskova, A.P., Ed., Moscow: Meditsina, 1990.
6. Sabadil, H., Bachmann, P., and Kastelewicz, H., *Beitr. Plasmaphys.*, 1980, vol. 20, no. 4, p. 283.
7. Lunin, V.V., Popovich, M.P., and Tkachenko, S.N., *Fizicheskaya khimiya ozona* (Physical Chemistry of Ozone), Moscow: Mosk. Gos. Univ., 1998.

Russian Journal of Applied Chemistry, Vol. 77, No. 3, 2004, pp. 397–401. Translated from Zhurnal Prikladnoi Khimii, Vol. 77, No. 3, 2004, pp. 404–408.

ENVIRONMENTAL PROBLEMS OF CHEMISTRY AND TECHNOLOGY

Fundamental Aspects of Recovery of Components from Acid Wastewater in Its Treatment by Galvanocoagulation

L. P. Sokolova, V. V. Skornyakov, and G. S. Beklemisheva

Tsvetmetobrabotka Institute, Open Joint-Stock Company, Moscow, Russia

Received November 3, 2003

Abstract—The mechanism and fundamental aspects of recovery of ions of nonferrous metals, chromium(III), and sulfate ions in galvanocoagulation treatment of acid wastewater from plants for processing of nonferrous metals were studied.

At present, the galvanocoagulation method is widely used for treatment of wastewater of various compositions.

This work continues studies concerned with the mechanism of recovery of components in galvanocoagulation treatment (GCT) of acid wastewater (washing water from etching shops) formed at plants for processing of nonferrous metals, with the use of an iron–coke voltaic couple [1, 2].

Acid wastewaters from plants for processing of nonferrous metals have the following average chemical composition (mg l^{-1}): copper(II) ions 100, nickel(II) 5.0, zinc(II) 50, chromium(III) 50, iron(III) 15, sulfate ions 990–2200; pH 1.8–3.5.

Thus, the main contaminating components of acid wastewater are ions of nonferrous metals, chromium(III), and sulfate ions.

It has been shown experimentally [1, 2] that the main mechanism by which ions of nonferrous metals and chromium(III) are recovered from a solution of an acid wastewater in GCT is formation of their ferrites by the reaction with iron oxide and hydroxide compounds. Sulfate ions are recovered from acid wastewater in GCT mainly through their reaction with iron(III) hydroxide compounds, with the positive charge of a micelle of the aquahydroxo complex of iron(III) neutralized by the negative charge of the sulfate ion to form a complex compound of the type $Fe_2(SO_4)_{3-0.5m}(OH)_m(H_2O)_n$.

A minor part of sulfate ions is recovered in the form of poorly soluble iron sulfide (pyrrhotine) [1] through reduction of sulfur(VI) to sulfide.

Ferrites are complex oxides of the general formula $MO \cdot Fe_2O_3$. They can also be regarded as derivatives of hypothetical ferrous acid $H_2Fe_2O_4$, in which hydrogen ions are substituted by metal ions. Ferrites, as a rule, exhibit ferromagnetic properties; their crystals have a cubic structure of the spinel type [3, 4].

The main method for obtaining ferrites is sintering of iron(III) oxide with the oxide of the corresponding metal [3]. Considerably less frequent is the "wet method" in which an alkali solution is added to a solution that contains salts of iron and some nonferrous metal, with joint precipitation of the metal hydroxides in the presence of oxygen and their subsequent dehydration. The wet synthesis of ferrites is a complex process which includes reactions of solid-phase coordination and crystallographic structuring. Lyubman *et al*. [5] describe the formation of ferrites by the "wet method" by the following scheme:

$$M(OH)_2 + Fe(OH)_2 \xrightarrow{O_2} \left[\begin{array}{ccccc} & OH & & OH & \\ Fe & & M & & Fe \\ & OH & & OH & \end{array}\right]_n \longrightarrow MFe_2O_4 \cdot 2H_2O. \quad (1)$$

Apparently, such a scheme is operative in the case of ferrite purification. The key stage of the process is its initial stage, when ions of the metals being recovered are fixed with iron(III) hydroxide by the coordination mechanism. The solid complex compounds formed in the process have a tunnel structure, which favors an additional incorporation of the contaminating components to form clathrates.

A similar "wet technique" of ferrite formation, based on adsorption of ions of bivalent metals (Fe, Zn, Co, Ni, Cu, Cd) on particles of γ-oxyhydroxide of iron(III), γ-FeOOH, was described in [6].

The GCT of acid wastewater using an iron–coke voltaic couple involves anodic dissolution of iron

1070-4272/04/7703-0397 © 2004 MAIK "Nauka/Interperiodica"

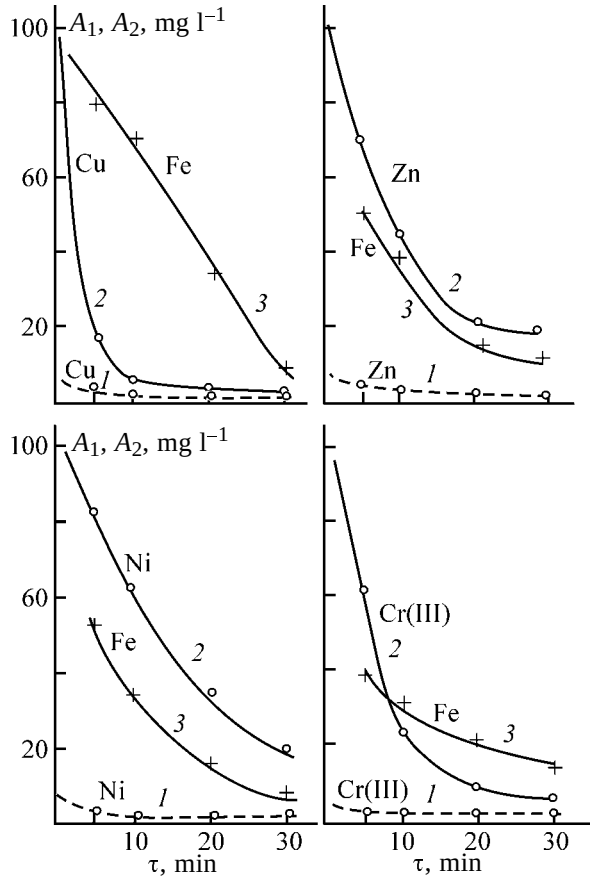

Fig. 1. Effect of the time τ of galvanocoagulation on the concentrations A_1 of copper(II), zinc(II), nickel(II) and chromium(III) and A_2 of iron in the solution after galvanocoagulation. Initial concentration (mg l^{-1}): (*1*) 5 and (*2*) 100.

to form iron(II) ions, which are then oxidized by atmospheric oxygen to iron(III). Simultaneously occurs chemical dissolution of iron in the acid contained in wastewater. In the process, the acid contained in wastewater is neutralized and the pH value increases to 4.0–6.5. As a result, a complex precipitate is formed, which contains a mixture of oxides and hydroxides of bi- and trivalent iron in various modifications, both magnetic and nonmagnetic [1]. At pH 5.0–6.5, hydroxides of nonferrous metals and chromium(III) start to precipitate.

Further, presumably, iron(II) hydroxide reacts with hydroxides of nonferrous metals and chromium(III) in the presence of atmospheric oxygen [5], and Cu(II), Zn(II), Ni(II), Cr(III) ions are adsorbed on γ-FeOOH particles. All these processes lead to formation of ferrites of the corresponding metals, which are thereby recovered from a wastewater solution.

It was shown in [5, 7] that the mixture of hydroxides of bi- and trivalent iron, which is formed both upon addition of an alkali solution to a solution of iron salts and in operation of an iron–coke voltaic couple, is highly active. Under various conditions (pH value, temperature) it gives a number of oxide and hydroxide compounds, both magnetic and nonmagnetic. In [1, 4, 5], it was established that only magnetic oxide and hydroxide compounds of iron are involved in the formation of ferrites. These compounds have a cubic crystal structure of the spinel type [3, 4], which is also typical of ferrites of nonferrous metals and chromium(III).

The aim of this work was to determine the optimal conditions of recovery by the galvanocoagulation method of ions of nonferrous metals and chromium(III), and also sulfate ions, from a solution of an acid wastewater of the composition specified above, to make it conform to the MPC (maximum permissible concentration) requirements imposed on purified water to be discharged into Moscow municipal sewage [8].

EXPERIMENTAL

The components of acid wastewater were recovered by the galvanocoagulation method under dynamic conditions, with the wastewater solution passed through a laboratory electrocoagulator (length 35 cm, diameter 10 cm, working zone volume 0.5 l) charged with a mixture that is an iron–coke (5 : 1) voltaic couple.

The concentration of ions of nonferrous metals and chromium(III) in the solutions before and after galvanocoagulation was determined by atomic absorption spectroscopy on a Perkin–Elmer spectrophotometer [9], and that of sulfate ions, by the volumetric method.

The kinetics of recovery of ions of nonferrous metals and chromium(III) was studied with individual sulfate solutions of these components, which contained 100 and 5 mg l^{-1} of the corresponding metals and had pH 2.5–2.7, which corresponds to the pH of acid wastewater.

The solutions under study were passed through the galvanocoagulator at different flow rates, with the time of contact between the solution being purified and the voltaic couple varied from 5 to 30 min. The results obtained (Fig. 1) indicate that, for copper(II), nickel(II), zinc(II), and chromium(III) ions to be effectively recovered in the course of galvanocoagulation, a 20–30-min time of contact between the solution being purified and the voltaic couple is sufficient at the ion concentration in the starting solution equal to both 5 and 100 mg l^{-1}. Figure 1 also shows that the concentration of iron decreases dramatically as the time

of contact is made longer, from 50–80 mg l^{-1} at a time of contact of 5 min to 5–10 mg l^{-1} at 20–30 min. This means that, as complete recovery of the corresponding elements is achieved, iron precipitates to form magnetic oxide and hydroxide compounds, including ferrites. The results of an X-ray phase analysis of this precipitate, performed on a DRON-2 diffractometer, demonstrate that it contains (%): lepidocrocite γ-FeOOH, 30–60; magnetite Fe_3O_4, 10–25; ferrites, 3–10; and goethite α-FeOOH, trace amounts.

A study of the kinetics of recovery of sulfate ions was studied with sulfuric acid solutions that contained 500 mg l^{-1} of sulfate ions, which corresponds to pH 3.0–3.5. The solution was passed through the galvanocoagulator, with the time of contact between the solution and the voltaic couple varied from 5 to 30 min. The results shown in Fig. 2 indicate that the recovery of sulfate ions in the time range specified is insignificant. At a time of contact between the solution under study and the voltaic couple equal to 30 min, the concentration of sulfate ions in a solution subjected to galvanocoagulation decreases from 500 to 300 mg l^{-1}. In this case, the concentration decreases from 300 to 60 mg l^{-1}.

Thus, the we found that the rate at which ferrites and also the sulfate–hydrate complex of iron (form in which sulfate ions are recovered in the galvanocoagulation process) is very low. For complete recovery of components from acid wastewater, the time of its contact with the voltaic couple should be 20–30 min. This time was used in our further experiments aimed to find how the recovery depends on the pH of the starting solution and on the concentrations of components in it.

Also, we studied how the galvanocoagulation recovery of copper(II), nickel(II), zinc(II), and chromium(III) ions from individual sulfate solutions containing 100 mg l^{-1} of each component depends on pH, which was varied from 1.5 to 5.5. The results obtained are shown in Fig. 3. It can be seen that copper is rather efficiently recovered in a wide range of pH values, 1.5–5.5. The most efficient recovery of chromium(III) is observed at pH 2.0–2.5, and that of zinc(II), at pH 2.7. Nickel(II) is an exception: it is recovered to the maximum extent at pH 3.0–4.0.

As seen from Fig. 3, the pattern is the same as before (Figs. 1, 2): At the instant when the maximum recovery of all the components is achieved, the concentration of iron in solution abruptly decreases, because iron passes into a precipitate in the form of oxide and hydroxide compounds. The pH of the solutions increases from 1.5–5.5 to 3.0–8.5 after galvanocoagulation.

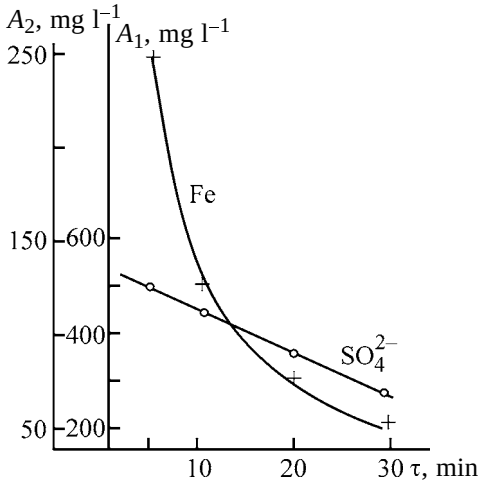

Fig. 2. Effect of the galvanocoagulation time τ on the concentrations A_1 of sulfate ions and A_2 of iron in the solution.

The dependence of the galvanocoagulation recovery of ions of nonferrous metals and chromium(III) on their concentration in the starting solution was studied by varying the concentration of each component in individual sulfate solutions from 50 to 200 mg l^{-1}. In doing so, the pH of the sulfate solutions of copper, zinc, and chromium(III) was maintained at 2.5–2.7, and that of nickel solutions, at 3.5–3.7, which corresponds to the pH value at which the recovery of these components from sulfate solutions is at a maximum.

Figure 4 shows that copper(II) and chromium(III) ions are efficiently recovered in the concentration range studied, 50–200 mg l^{-1}. Nickel(II) ions are well recovered in a rather narrow concentration range 50–100 mg l^{-1}, and recovery of zinc(II) ions is efficient only at low concentrations of ≤50 mg l^{-1}. These data allow the components of acid wastewater to be ranked in the following order of their decreasing recoverability in GCT with an iron–coke voltaic couple: Cu = Cr(III) > Ni > Zn, which corresponds to the series of ferrite-forming ability of nonferrous metal ions, reported in [5].

A study of how the recovery of sulfate ions in GCT depends on the concentration and pH of sulfate solutions showed (see table) that, at equal concentrations in the starting solution, the recovery of sulfate ions is the most efficient at pH of the starting solution equal to 2.0–4.0.

Zolotova and Ass [7] established that, in hydrolysis of a mixture of salts of bi- and trivalent iron, the following species are at equilibrium in the solution: Fe^{2+}, $Fe(OH)^+$, $Fe(OH)_2^0$, $Fe(OH)_3^-$, Fe^{3+}, $Fe(OH)^{2+}$,

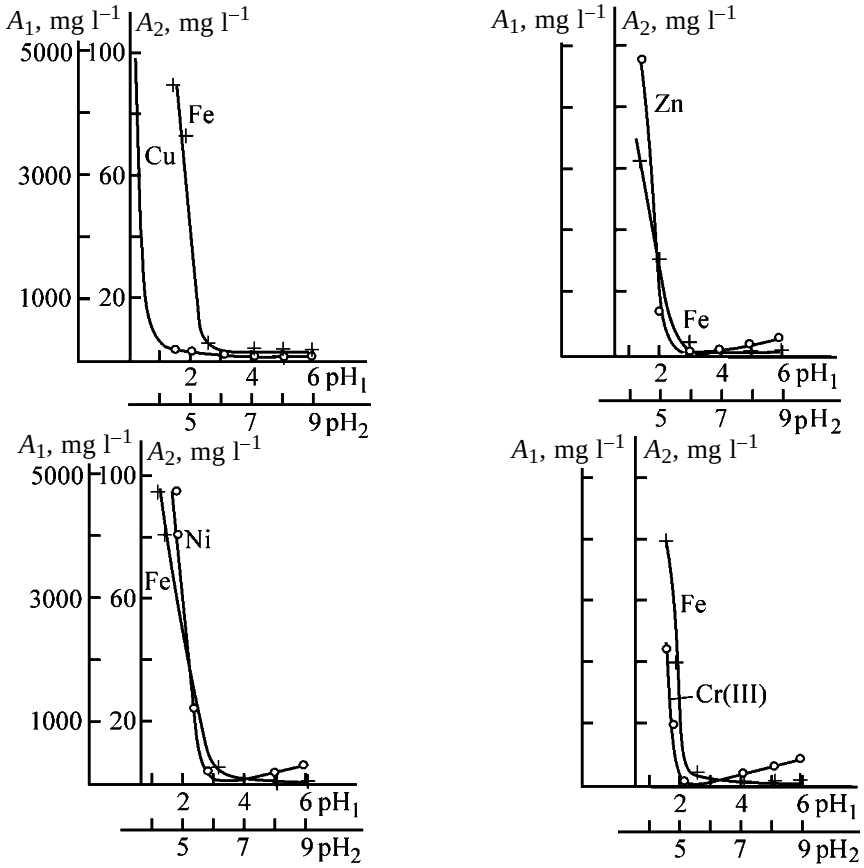

Fig. 3. Effect of the pH_1 of the starting solution on the content A_1 of copper(II), zinc(II), nickel(II), and chromium(III) ions and A_2 of iron in the solution after galvanocoagulation, with pH_2.

$Fe(OH)_2^+$, $Fe(OH)_3^0$, $Fe(OH)_4^-$, and $Fe(OH)_4^{2-}$.

It has been shown previously [1] that the main part of sulfate ions is recovered in GCT through their reaction with iron(III) hydroxo compounds, in which the positive charge of the aquahydroxo complex of iron(III) is neutralized by the negative charge of the sulfate ion. Therefore, it may be assumed that sulfate ions react with $Fe(OH)^{2+}$ and $Fe(OH)_2^+$ ions. It was shown in [10] that the maximum amounts of these ions are present in products of hydrolysis of iron salts at various concentrations of iron in aqueous solutions at pH 2.0–4.0. Thus, the pattern of recovery of sulfate ions in galvanocoagulation, revealed in this study, is in good agreement with these data.

The fundamental aspects of recovery of acid wastewater components, studied under laboratory conditions, made it possible to develop a process for purification of this wastewater and test it on the semicommercial scale. As a result, facilities for GCT of acid wastewater from the Moscow plant for processing of nonferrous metals were designed and constructed.

Galvanocoagulation recovery of sulfate ions at varied pH and concentration of the starting solution

Concentration of sulfate ions, mg l^{-1}		pH		Recovered amount of sulfate ions	
in the starting solution	after galvanocoagulation	of the starting solution	after galvanocoagulation	mg	%
520	208	3.5	6.0	312	60
532	364	6.0	8.5	168	30
1020	504	2.85	5.5	516	50
1030	950	5.8	8.0	80	12

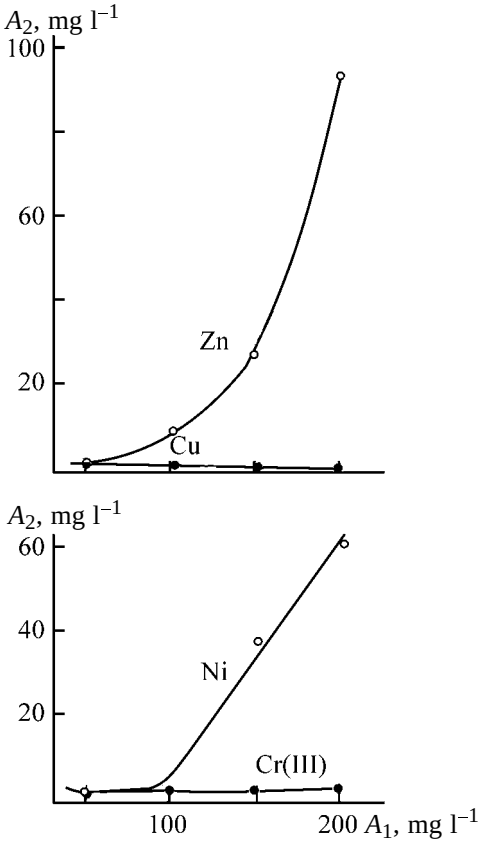

Fig. 4. Effect of the initial concentration A_1 of copper(II), zinc(II), nickel(II), and chromium(III) ions on the concentration A_2 of these components in a solution subjected to galvanocoagulation.

However, the dependences presented in this communication cannot be used for developing a process for GCT of acid wastewater of other compositions without a preliminary experimental study.

CONCLUSIONS

(1) The minimum time required for galvanocoagulation treatment of sulfate solutions to remove ions of copper(II), nickel(II), zinc(II), and chromium(III) and sulfate ions is 20–30 min.

(2) Copper(II) ions are efficiently recovered by galvanocoagulation treatment in a wide range of pH values and concentrations of the starting solution; chromium(III) ions, at pH of the starting solution equal to 2.0–2.5 in a wide range of initial concentrations; zinc(II) and nickel(II) ions, in a narrow range of pH values of the starting solution (2.7 for zinc and 3.0–4.0 for nickel) at their concentrations in the starting solution equal to 50–100 mg l^{-1}.

(3) The components of the acid wastewater from plants for processing of nonferrous metals can be ranked in the following order of decreasing recoverability in galvanocoagulation treatment: Cu = Cr(III) > Ni > Zn.

(4) In galvanocoagulation treatment, sulfate ions are efficiently recovered at pH 2.0–4.0.

(5) The revealed pattern is used in galvanocoagulation treatment of acid wastewater from the Moscow plant for processing of nonferrous metals.

ACKNOWLEDGMENTS

The authors thank A.K. Samsonov for help in semicommercial trials.

REFERENCES

1. Sokolova, L.P., Smurova, E.S., Kokorina, E.B., *et al.*, *Zh. Prikl. Khim.*, 1991, vol. 64, no. 3, pp. 551–555.
2. Sokolova, L.P., Kokorina, E.B., and Smurova, E.S., *Tsvetn. Metall.*, 1992, no. 9, pp. 56–60.
3. Letyuk, L.M. and Zhuravlev, G.I., *Khimiya i tekhnologiya ferritov* (Chemistry and Technology of Ferrites), Leningrad: Khimiya, 1983.
4. Pilat, B.V., Zaitseva, V.I., and Romanenko, L.T., *Metody izvlecheniya blagorodnykh metallov iz rastvorov stochnykh vod* (Methods for Recovery of Noble Metals from Wastewater Solutions), Moscow: TsNIITsMEI, 1983.
5. Lyubman, N.Ya., Imangazieva, G.K., and Kim, Z.I., in *Organizatsiya besstochnoi tekhnologii i sovershenstvovanie metodov ochistki stochnykh vod na predpriyatiyakh tsvetnoi metallurgii* (Organization of Wastewater-Free Technology and Improvement of Methods for Purification of Wastewater at Plants of Nonferrous Metallurgy), 1981, no. 24, pp. 25–32.
6. Mel'nichuk, V.P. and Popov, V.V., *Poluchenie kobal'tsoderzhashchikh oksidov zheleza* (Synthesis of Cobalt-Containing Iron Oxides), Moscow: NIITEKhIM, 1990.
7. Zolotova, E.F. and Ass, T.Yu., *Ochistka vody ot zheleza, margantsa, ftora i serovodoroda* (Purification of Water To Remove Iron, Manganese, Fluorine, and Hydrogen Sulfide), Moscow: Stroiizdat, 1975.
8. *Pravila priema proizvodstvennykh stochnykh vod v Moskovskuyu gorodskuyu kanalizatsiyu* (Regulations Concerning Admission of Industrial Wastewater to the Moscow Municipal Sewage), Moscow: Mosvodokanal, 1984.
9. Price, W.J., *Analytical Atomic Absorption Spectrometry*, London: Heyden, 1974.
10. Zapol'skii, A.K. and Baran, A.A., *Koagulyanty i flokulyanty v protsesse ochistki vody* (Coagulants and Flocculants in Water Treatment), Leningrad: Khimiya, 1987.

Russian Journal of Applied Chemistry, Vol. 77, No. 3, 2004, pp. 402–406. Translated from Zhurnal Prikladnoi Khimii, Vol. 77, No. 3, 2004, pp. 409–413.

ENVIRONMENTAL PROBLEMS OF CHEMISTRY AND TECHNOLOGY

Solubility and Stability of Peroxo Solvates $KF \cdot nH_2O_2$ in Organic and Aqueous-Organic Media

K. V. Titova, V. P. Nikol'skaya, V. V. Buyanov, I. P. Suprun, and O. B. Pudova

State Research Institute for Biological Instrument Making, Federal State Unitary Enterprise, Moscow, Russia

Institute for Problems of Chemical Physics, Russian Academy of Sciences, Chernogolovka, Moscow oblast, Russia

Received April 22, 2003

Abstract—The solubility and stability of the peroxo solvates $KF \cdot nH_2O_2$ ($n \geq 1$) and disinfectants based on them was studied in organic and aqueous-organic solvents. Polyhydric alcohols (glycerol and ethylene glycol) and Tosol (commercial antifreeze) were used as solvents.

Potassium fluoride peroxo solvates (PFP) $KF \cdot nH_2O_2$ (n = 1–3) are well soluble in water. The solubility of the monoperoxo solvate $KF \cdot H_2O_2$ is 51.5 wt % at 0°C and 60.7 wt % at 20°C. The solutions are stable [1]. The PFP disinfectants developed on the basis of peroxo solvates (aqueous solutions) show a wide spectrum of antimicrobial activity. The preparations are effective against bacteriological and virus infections (including hepatitis and AIDS) [2]. At the same time, for treating many objects, it is appropriate to use disinfectants in the form of solutions in viscous organic or aqueous-organic solvents. A viscous organic medium ensures a better contact with the object to be treated. Slow evaporation of a viscous solvent results in the formation of a stock of hydrogen peroxide, which diffuses from the solvent to the treated surface gradually, thus prolonging the exposure. Aqueous-organic compositions with low freezing point allow the use of disinfectant solutions at negative temperatures.

In this work, we studied the solubility and stability in organic solvents and aqueous-organic media of the peroxo solvates $KF \cdot nH_2O_2$ ($n \geq 1$) and PFP disinfectant prepared on their basis with a potassium hydrofluoride stabilizing additive, which were obtained on a pilot-plant installation made of 12Cr18Ni10Ti steel. As solvents were studied glycerol, ethylene glycol, and Tosol (commercial antifreeze), which is a promising solvent of PFP preparations to perform the disinfection of various objects, including military objects, at low temperatures.

EXPERIMENTAL

Glycerol in the form of an 85% medical preparation (which has an optimal viscosity), chemically pure ethylene glycol, and the A40M grade Tosol (Rospolimer, Podolsk, Moscow oblast, Russia) were used without additional dehydration and purification. The liquid base of Tosol is aqueous ethylene glycol; it also contains a set of environmentally clean additives, which are not specified by the producer.

Since preparation of saturated solutions with a magnetic stirrer resulted in the decomposition of a part of hydrogen peroxide, solutions were prepared by the following procedure. To solid peroxo solvates or PFP preparations, the solvent prepared in advance was added in an amount ensuring preservation of one third of the solid bottom phase. The mixture prepared was manually stirred for 1–2 h and kept for a day. In so doing, the solid phase slowly precipitated onto the bottom. Then, the solution was stirred again to constant content of hydrogen peroxide, filtered through a polymer film with small apertures, and placed into polymer vessels for storage. The solutions were analyzed for the content of H_2O_2 by permanganometric titration. The content of potassium fluoride was determined gravimetrically. In ethylene glycol containing systems, the volatile components were removed by keeping the weighed portions of the solution at 130–150°C and by calcining the residual KF at 200°C to constant weight (temperature of complete dehydration of $KF \cdot 2H_2O$ is 40°C). Because of the high boiling temperature of glycerol, removal of volatile components in glycerol-containing systems at

1070-4272/04/7703-0402 © 2004 MAIK "Nauka/Interperiodica"

Table 1. Solubility and stability of $KF \cdot nH_2O_2$ and PFP disinfectants in water–glycerol solvents at 20 ± 2°C

Glycerol, wt %	Solubility at τ = 0, wt % H_2O_2	Storage time, day	$k \times 10^4$, h^{-1}	Average rate of H_2O_2 loss, % day^{-1}
$KF \cdot H_2O_2$, $[H_2O_2]_s^*$ = 36.9 wt %				
85.0	9.06	33	1.1 ± 0.1	0.30 ± 0.006
76.5	10.88	25	1.6 ± 0.5	0.49 ± 0.20
68.0	13.56	14	2.2 ± 0.8	0.65 ± 0.35
59.5	14.53	28	4.3 ± 1.4	1.56 ± 1.10
$KF \cdot 1.23H_2O_2$, $[H_2O_2]_s$ = 41.9 wt %				
85.0	11.32	39	1.9 ± 0.4	0.42 ± 0.07
76.5	15.39	39	3.0 ± 1.1	0.69 ± 0.24
68.0	18.60	24	3.8 ± 1.7	0.82 ± 0.32
59.5	21.61	25	4.0 ± 1.9	1.05 ± 0.31
PFK-1 ($KF \cdot 0.87H_2O_2$), $[H_2O_2]_s$ = 33.8 wt %				
85.0	7.51	51	0.6 ± 0.4	0.10 ± 0.09
76.5	9.14	50	0.4 ± 0.2	0.11 ± 0.03
85.0	11.39	43	0.6 ± 0.2	0.19 ± 0.08
59.5	12.66	42	0.5 ± 0.1	0.23 ± 0.15
PFK-2 ($KF \cdot 1.41H_2O_2$), $[H_2O_2]_s$ = 45.1 wt %				
85.0	12.58	34	2.1 ± 0.3	0.50 ± 0.10
76.5	13.24	27	0.7 ± 0.4	0.18 ± 0.08
68.0	16.64	27	0.7 ± 0.5	1.6 ± 1.3
59.5	18.66	27	–	1.5 ± 0.9

* $[H_2O_2]_s$ is H_2O_2 content in solid product.

200°C is accompanied by the appearance of carbon black traces on the surface of residual potassium fluoride. Therefore, the analysis for the content of potassium was done by atomic absorption spectrophotometry [AAS-1(3) abhvs spectrophotometer, Carl Zeiss, Jena]. The decomposition rate constant was calculated by the equation $\ln(c_0/c) = k(\tau - \tau_0)$, where c_0 is the concentration of the initial solution and c, the solution concentration in time τ. The hydrogen peroxide concentration in the stored solutions was measured at 5–7-day intervals. The values averaged over 5–8 measurements are given in Tables 1–4.

It was established that the solubility of $KF \cdot H_2O_2$ in a mixed glycerol–water solvent at a ratio (wt %) $C_3H_8O_3 : H_2O$ 85.0 : 15.0 is 9.06 wt % in terms of H_2O_2. As the content of water in the solvent increases, the $KF \cdot H_2O_2$ solubility grows, reaching the value of 14.5 wt % for the glycerol–water ratio of 59.5 : 40.5 (Table 1).

The solubility of $KF \cdot 1.23H_2O_2$ and samples of PFK-1 and PFK-2 preparations increases similarly.

The analysis of $KF \cdot H_2O_2$ solutions in water–glycerol systems for the content of KF showed that, at all water–glycerol ratios, hydrogen peroxide passes into the solution in excess compared to the value calculated from the KF content. For example, in $KF \cdot H_2O_2$ solution in 85% glycerol, the KF content is 11.22%, which corresponds to 6.58% H_2O_2. The

Table 2. Composition of water–glycerol and water–ethylene glycol solutions

Alcohol, wt %	Solution composition, wt %			
	$KF \cdot nH_2O_2$	H_2O_{2ex}	$C_nH_{2n+2}O_n$	H_2O
$KF \cdot H_2O_2$, glycerol				
85.0	17.80	2.48	67.76	11.96
76.5	19.41	3.71	58.81	18.07
68.0	23.24	5.04	48.82	22.97
59.5	23.82	5.73	41.92	28.53
$KF \cdot 1.31H_2O_2$, ethylene glycol				
100	20.26	0.68	79.08	0
90	22.60	1.63	68.19	7.6
80	29.60	3.80	53.36	13.34
70	33.10	4.54	43.64	18.70

Table 3. Solubility and stability of $KF \cdot nH_2O_2$ and PFP disinfectants in ethylene glycol and in water–ethylene glycol mixtures

Ethylene glycol, wt %	Solubility at $\tau = 0$, wt % H_2O_2	Storage time, days	$k \times 10^4$, h^{-1}	Average rate of H_2O_2 loss, % day^{-1}
		$KF \cdot 0.97H_2O_2$, $[H_2O_2]_s$ = 36.3 wt %		
100	5.83	51	2.5 ± 0.2	0.57 ± 0.14
90	6.90	52	1.8 ± 0.2	0.40 ± 0.05
80	8.48	51	2.2 ± 0.2	0.50 ± 0.20
70	9.52	34	1.6 ± 0.6	0.54 ± 0.15
		$KF \cdot 1.23H_2O_2$, $[H_2O_2]_s$ = 41.9 wt %		
100	8.85	27	2.0 ± 0.7	0.45 ± 0.18
90	9.45	27	1.6 ± 0.5	0.38 ± 0.12
80	11.73	26	2.0 ± 0.3	0.36 ± 0.10
70	14.30	26	7.6 ± 2.2	1.66 ± 0.54
		PFK-1 ($KF \cdot 0.89H_2O_2$), $[H_2O_2]_s$ = 34.1 wt %		
100	4.91	28	2.9 ± 0.8	0.63 ± 0.16
90	6.04	28	2.4 ± 1.2	0.59 ± 0.29
80	8.20	28	2.4 ± 0.3	0.55 ± 0.08
70	10.0	40	1.7 ± 0.2	0.34 ± 0.04
		PFK-2 ($KF \cdot 1.31H_2O_2$), $[H_2O_2]_s$ = 43.5 wt %		
100	9.46	35	1.8 ± 0.3	0.41 ± 0.08
90	11.47	35	1.1 ± 0.2	0.18 ± 0.08
80	16.60	34	1.2 ± 0.4	0.34 ± 0.07
70	18.92	34	2.1 ± 0.3	0.49 ± 0.06

found content of H_2O_2 (9.06%) exceeds the calculated value by 2.48%.

The data obtained confirm both the sufficiently high solubility of the $KF \cdot H_2O_2$ peroxosolvate in a water–glycerol mixture (9–22 wt % in terms of H_2O_2) and the ability of the water–glycerol solvent to extract into a solution excess hydrogen peroxide owing to the dissociation:

$$KF \cdot H_2O_2(s) \rightleftarrows KF(s) + H_2O_2(sol). \quad (1)$$

As the water content in the solvent grows, the solubility of $KF \cdot H_2O_2$ itself and the amount of excess hydrogen peroxide passing into the solution increase (Table 2).

We believe that the ability of the solvent to extract hydrogen peroxide from the solid peroxo solvate depends on the following factors: difference in the solubilities in the chosen solvent of H_2O_2 and the solvated salt itself, solvent polarity, and the binding energy of hydrogen peroxide in the peroxo solvates. For example, complete extraction of H_2O_2 with water from $BaF_2 \cdot 2H_2O_2$ is mainly determined by the difference in the hydrogen peroxide and BaF_2 solubilities in water [3]. The binding energy of H_2O_2 in $BaF_2 \cdot 2H_2O_2$ does not play a significant role, though, according to our estimates, it is fairly high. On heating the barium fluoride peroxo solvate at 100°C in a vacuum, no more than 30% of hydrogen peroxide is evolved into the gas phase [3]. The amount of H_2O_2 evolved from $KF \cdot H_2O_2$ at this temperature is similar (50%). The enthalpy of the $KF \cdot H_2O_2(s)$ dissociation into KF(s) and $H_2O_2(g)$ is 85.5 kJ mol^{-1} [4]. Apparently, the enthalpy of dissociation of $BaF_2 \cdot 2H_2O_2$ is close to this value.

The solutions of $KF \cdot nH_2O_2$ and PFP preparations in glycerol–water mixed solvents are stable. The $KF \cdot H_2O_2$ and $KF \cdot 1.23H_2O_2$ samples obtained under laboratory conditions in the (85.0 : 15.0)–(68.0 : 32.0) range of the solvent compositions and stored for 14–24 days decompose at the average rates of 0.3–0.8 % day^{-1} relative to the initial content of H_2O_2. At the glycerol–water ratio of 59.5 : 40.5, the rate of the H_2O_2 decomposition somewhat increases (to 1.0–1.6 % day^{-1}). The PFK-1 sample obtained in the presence of the KHF_2 stabilizing additive appeared to be

Table 4. Solubility and stability of $KF \cdot nH_2O_2$ and PFP disinfectants in Tosol and in water–Tosol mixtures

Tosol, wt %	Solubility at $\tau = 0$, wt % H_2O_2	Storage time, day	$k \times 10^4$, h^{-1}	Average rate of H_2O_2 loss, % day^{-1}
$KF \cdot 0.97H_2O_2$, $[H_2O_2]_s$ = 36.5 wt %				
100	14.09	65	9.5 ± 1.5	1.5 ± 0.1
90	15.65	38	9.9 ± 1.4	1.8 ± 0.2
80	16.54	63	8.6 ± 2.6	1.3 ± 0.2
70	17.07	63	4.0 ± 1.3	0.8 ± 0.2
PFK-1 ($KF \cdot 0.82H_2O_2$), $[H_2O_2]_s$ = 32.5 wt %				
100	13.53	35	1.9 ± 0.4	0.43 ± 0.02
90	13.67	42	4.5 ± 0.7	0.95 ± 0.15
80	15.43	48	1.1 ± 0.3	0.25 ± 0.07
70	16.14	41	1.5 ± 0.4	0.35 ± 0.07

Tosol, wt %	Solubility at $\tau = 0$, wt % H_2O_2	Exposure time, day	H_2O_2 concentration in solution, wt %	Mixture appearance
$KF \cdot 1.23H_2O_2$, $[H_2O_2]_s$ = 41.9 wt %				
100	30.46	5	31.1	Solution + precipitate
		29	41.0	
90	29.43	5	30.3	Solution + precipitate
		19	33.5	
80	26.44	5	26.7	Solution + precipitate
		27	31.2	
70	27.56	3	27.9	Solution + precipitate
		27	32.9	
PFK-2 ($KF \cdot 1.36H_2O_2$), $[H_2O_2]_s$ = 44.5 wt %				
100	24.70	5	24.9	Solution + precipitate
		29	25.0	
90	27.32	5	28.1	Solution + precipitate
		36	28.8	
80	28.19	5	28.5	Solution + precipitate
		36	30.8	
70	29.17	5	28.6	Solution + precipitate
		21	31.4	

the most stable. The PFK-1 preparation loses H_2O_2 at an average rate not exceeding 0.23 % day^{-1}. The PFK-2 preparation is less stable.

According to published data [5], glycerol, hydrogen peroxide, and water under certain concentrations form explosive mixtures. The method of internal ignition in a tin tube showed that only compositions containing more than 40% H_2O_2, from 0 to 45% water, and from 0 to 15% glycerol are explosive. The solutions obtained by us contain hydrogen peroxide and water in small concentrations [9.1–21.6 and 12–28%, respectively)] and glycerol in high concentration (42–68%), i.e., the solutions are far from being explosive. Such solutions are not dangerous for practical use.

Potassium fluoride peroxosolvates are also soluble in another polyhydric alcohol, ethylene glycol. The solubility of the monoperoxo solvate $KF \cdot H_2O_2$ in anhydrous ethylene glycol is 5.83 wt % in terms of hydrogen peroxide. The solutions are stable: in 50 days of storage, the average rate of the H_2O_2 decomposition does not exceed 0.6 % day^{-1}. At the ethylene glycol : water ratio of 70 : 30, the decomposition rate somewhat increases (to 1.66 % day^{-1}, Table 3).

The solubility and stability of the PFK-1 and

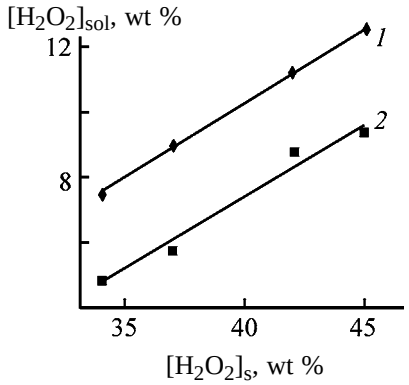

Dependence of the hydrogen peroxide concentration in solution $[H_2O_2]_{sol}$ on its content in the solid product $[H_2O_2]_s$. Solvent composition: (*1*) 85 wt % glycerol–15 wt % water and (*2*) anhydrous ethylene glycol.

PFK-2 preparations in ethylene glycol mixtures are of the same order as those of the peroxo solvate samples obtained under laboratory conditions.

For all the solvates studied, the hydrogen peroxide concentration in ethylene glycol solutions and in glycerol solutions are the higher, the higher its concentration in the solid preparation (see figure). A study of the ethylene glycol systems using PFK-2 preparation showed that excess hydrogen peroxide passes into both water–glycerol solutions and water–ethylene glycol solutions (Table 2). The amount of excess H_2O_2 in ethylene glycol is lower than that in glycerol, though glycerol was studied with individual $KF \cdot H_2O_2$, in which the binding energy of H_2O_2(g) is 85.5 kJ mol^{-1}, whereas ethylene glycol was studied with the PFK-2 preparation, a mixture of monoperoxo solvate $KF \cdot H_2O_2$ and diperoxo solvate $KF \cdot 2H_2O_2$. The second H_2O_2 molecule in the diperoxo solvate has a lower binding energy (70.88 kJ mol^{-1}) [4], which must assist the dissociation. Evidently, the weaker capability of ethylene glycol to dissolve $KF \cdot nH_2O_2$ and extract excess hydrogen peroxide into a solution owing to dissociation mainly results from the fact that ethylene glycol is less polar than glycerol: the dielectric constant ε is 42.5 for glycerol and 37.7 for ethylene glycol [6].

Potassium fluoride peroxo solvates and PFP preparations are soluble in water–Tosol mixtures. In the case when the content of hydrogen peroxide in the peroxo solvates is higher than unity, the admixtures contained in Tosol produce a slight catalytic effect on the decomposition of peroxo solvates and a more considerable effect on their dissociation (Table 4).

The average rate of the $KF \cdot H_2O_2$ decomposition is 0.8–1.8 % day^{-1}. The PFK-1 preparation is more stable. In the same composition range, the average rate of the PFK-1 decomposition is 0.2–0.9 % day^{-1}. The peroxo solvate containing more than one hydrogen peroxide molecule and the PFK-2 preparation, while dissolved, undergo fast dissociation, with passing of excess hydrogen peroxide into the solution. In storage of such solutions, potassium fluoride gradually precipitates owing to further dissociation, without decrease in the hydrogen peroxide concentration. The PFK-1 solutions formed in the Tosol systems and the PFK-2 heterogeneous mixtures can be used in disinfectology.

CONCLUSIONS

(1) Potassium fluoride peroxosolvates and disinfectants based on them are soluble in polyhydric alcohols, such as glycerol and ethylene glycol, and in Tosol (commercial antifreeze).

(2) The solutions are reasonable stable. The average rate of the H_2O_2 decomposition does not exceed 1.7 % day^{-1} in solvents containing from 100 to 60 wt % alcohol.

(3) The dissolution of peroxosolvates is accompanied by the additional dissociation $KF \cdot nH_2O_2$(s) = KF(s) + H_2O_2(sol), with the excess hydrogen peroxide passing into the solution. In Tosol and its mixtures with water, the dissociation is accompanied by KF precipitation.

(4) The fact that potassium fluoride peroxosolvates and preparations based on them are soluble and stable in organic and aqueous-organic mixtures extends the range of their application in disinfectology.

REFERENCES

1. Titova, K.V., Nikol'skaya, V.P., Buyanov, V.V., *et al*., *Zh. Prikl. Khim*., 2001, vol. 74, no. 6, pp. 886–890.
2. *Dezinfitsiruyushchie sredstva* (Disinfectants), Ivanova, S.I. and Shandala, M.G., Eds., Moscow: InterSEN, 2001, vol. 1, no. 3.
3. Titova, K.V., Kolmakova, E.I., and Rosolovskii, V.Ya., *Zh. Neorg. Khim*., 1990, vol. 35, no. 10, pp. 2483–2487.
4. Titova, K.V., Nikol'skaya, V.P., and Buyanov, V.V., *Koordinatsionnye soedineniya peroksida vodoroda* (Hydrogen Peroxide Coordination Compounds), Chernogolovka: Inst. Problem Khim. Fiz., Ross. Akad. Nauk, 2000.
5. *Gmelins Handbuch der anorganischen Chemie, Sauerstoff*, 1966, vol. 3, issue 7.
6. Gordon, A.J., and Ford, R.A., *The Chemist's Companion. A Handbook of Practical Data, Techniques, and References*, New York: Wiley–Interscience, 1972.

Russian Journal of Applied Chemistry, Vol. 77, No. 3, 2004, pp. 407–413. Translated from Zhurnal Prikladnoi Khimii, Vol. 77, No. 3, 2004, pp. 414–420.

ENVIRONMENTAL PROBLEMS OF CHEMISTRY AND TECHNOLOGY

Performance Criteria for Compositions Based on Cationic Polyelectrolytes as Reagents for Treating Wastewaters from Pulp-and-Paper Works

N. B. Mel'nikova, V. G. Sokolov, and L. I. Molvina

Nizhni Novgorod State Technical University, Nizhni Novgorod, Russia

Received February 11, 2003

Abstract—Colloid-chemical properties of cationic polyelectrolytes and their mixtures with iron(III) chloride are studied, including the viscosity, adsorption on the cellulose surface, capillary imbibition and rise, and apparent charge density on the polymer. Selection criteria are proposed for polyelectrolytes as reagents for thickening and compaction of sludge from pulp-and-paper works.

Cationic polyelectrolytes are widely used in pulp-and-paper industry for treating wastewaters by flocculation and also in paper-making [1, 2]. Wastewaters from pulp-and-paper works contain negatively charged cellulose dispersions. Flocculation of such dispersions with polyelectrolytes proceeds through aggregation of particles by virtue of neutralization of the charge and bridge formation, and also as a result of mosaic binding [2, 3]. Low-molecular-weight fractions of cellulose are involved in the formation of a structured gel network capable of retaining particles of the disperse phase [2, 3]. In selecting polyelectrolytes as flocculants, such factors should be taken into account as the cationic demand of cellulose suspensions, apparent cationic charge, adsorption a polyelectrolyte on a given dispersion, viscosity, and other characteristics of both polyelectrolytes and the disperse system as a whole.

In this work we developed criteria for evaluating the performance of polyelectrolyte-based compositions as flocculants for treating wastewaters derived from paper making and also express tests for these compositions.

In formulating the compositions we used copolymers of acrylamide with nitrogen-containing bases such as Polymin KP, Kat-floc-487F, Praestol (MW > 500 000); a series of polymers of various natures with MW 10 000–30 000 (modified polyimines Polymin SK and Katiofast SF); and also poly(dimethyldiallylammonium chloride).

It was demonstrated previously that blends of cationic polyelectrolytes and inorganic coagulants show promise as flocculants [4]. Therefore, in this work we studied compositions based on a cationic polyelectrolyte and iron(III) chloride, which showed high performance in flotation treatment of wastewaters derived from paper-making.

EXPERIMENTAL

In the work we used $FeCl_3$ [pure grade, GOST (State Standard) 4147–74]; concentrated hydrochloric acid (chemically pure grade, GOST 3118–77); cationic polymers Praestol-644BC, 650BC, 611BC, 851, and 853 (Moscow–Stockhausen–Perm Closed Corporation, Russian–German Enterprise); Polymin SK, Katiofast SF, Polymin KP (BASF, Germany), Katfloc-487F (KEM-TRON Inc., Germany); decyldimethylbenzylammonium chloride $[(C_{10}H_{21})(CH_3)_3N(C_7H_7)Cl]$; poly(diallyldimethylammonium chloride) (poly-DADMAC); Toluidine Blue O; anionic polymer, potassium polyvinyl sulfate (PVSK) (MW 162.2, n = 1500, Lot/Contr. no. 04290, Serva Feinbiochemica GmbH & Co K G); and paper filter [TU (Technical Specifications) 6-09-1678–95].

The specific viscosity η_{sp} of polymer solutions was measured on an Ubbelohde viscometer with a 0.56-mm capillary. The correction factor due to the flow kinetic energy was estimated to be no more than 1.5%, and was neglected in estimating the viscosity number η_{sp}/c ($l^3\ g^{-1}$) (c is the polymer concentration in the solution, $g\ l^{-1}$).

The specific viscosity is defined as

$$\eta_{sp} = \eta_{rel} - 1,$$

1070-4272/04/7703-0407 © 2004 MAIK "Nauka/Interperiodica"

where $\eta_{rel} = \tau/\tau_0$, and τ and τ_0 are the outflow times of the colloid solution and water, respectively.

The cationic demand (CD) of cellulose dispersions was determined by colloid titration as follows. 25 ml of the filtrate of cellulose suspension (pulp + wastewater derived from paper-making) was charged into a 250-ml flask, and 10 ml of a cationic polymer solution (0.5 g l^{-1}) and 5 ml of Toluidine Blue (40 mg l^{-1}) were added. The volume was adjusted to 100 ml with distilled water, and the mixture was titrated with 65 mg l^{-1} PVSK until the color changed to violet.

In the blank experiment, we similarly titrated distilled water. The cationic demand (mg l^{-1}) was estimated by Eq. (1).

$$CD = \frac{(V^0_{PVSK} - V_{PVSK})x_p}{V_f}, \quad (1)$$

where V^0_{PVSK} is the volume of the PVSK solution (l) consumed for blank titration; V_{PVSK}, that consumed for titration of the working sample (l); x_p, concentration of the polymer solution (mg l^{-1}); and V_f, volume of the filtrate sample (l).

Also CP of the cellulose dispersion was determined by radio-frequency titration with a TV-6L1 radio-frequency conductometer. A pulp suspension (100 ml; 0.666 mg l^{-1}) containing a cationic polymer was placed into a cell of the radio-frequency conductometer. As a titrant we used 65 mg l^{-1} PVSK solution. The end point was determined graphically [5, 6].

The specific charge of the macromolecules was determined by colloid titration of 0.01% polyelectrolyte solution with 0.000388 N PVSK (MW 243 000) in the presence of Toluidine Blue [5]. The PVSK concentration was initially determined more precisely by colloid titration with a standard solution of decyldimethylbenzylammonium chloride. Assuming

$$N_{PVSK}V_{PVSK} = N_p V_p, \quad (2)$$

where N_p is the polymer concentration in the polyelectrolyte (g-equiv l^{-1}); N_{PVSK}, PVSK concentration (g-equiv l^{-1}); and V_p, volume of the polymer (l), the apparent density of the cationic charge on the macromolecules ρ (mg-equiv g^{-1}) was estimated by Eq. (3).

$$\rho = \frac{N_p \times 10^3}{m}, \quad (3)$$

where m is the polymer weight (g).

To determine the adsorption of the polymers, a piece of paper filter of a fixed area was immersed into 10 ml of 0.01% polymer solution. The paper was taken out after 30 s, and the volume of the residual solution was measured. The adsorption A_{eff} (g-equiv cm^{-2}) was estimated by Eq. (4).

$$A_{eff} = \frac{N_{cat}(V_{in} - V_{fin})}{S}, \quad (4)$$

where N_{cat} is the concentration of the cationic charges in 0.01% polymer solution (g-equiv ml^{-1}); V_{in} and V_{fin} are the volumes of the polymer solution before immersing and after removal of the paper filter, respectively (ml); and S is the area of the paper piece (cm^2).

In control experiments, we titrated the polymer before and after adsorption with 65 mg l^{-1} PVSK. The A_{eff} (g-equiv cm^{-2}) was estimated by Eq. (5):

$$A_{eff} = \frac{N_{PVSK}(V^0_{in} - V^0_{fin})}{S}, \quad (5)$$

where N_{PVSK} is the PVSK concentration (g-equiv ml^{-1}) and V^0_{in} and V^0_{fin} are the volumes of the PVSK solution (ml) consumed for titration of the initial 0.01% polymer solution and that after adsorption on paper, respectively.

The UV absorption spectra of aqueous solutions were recorded on an SF-46 spectrophotometer over the range 190–700 nm against water as a reference using 1-cm cells. The influence of oxygen on the optical density of the polymer solutions over the range 190–230 nm was studied by comparison of the UV spectra with those obtained on a Specord M-40 instrument after thorough purging of the sample with argon.

The efficiency of sludge thickening was characterized by the velocity of the motion of the interface between the clarified and unclarified volumes in a 2-l volumetric cylinder.

The capillary imbibition was determined as follows. A sample of filter paper (S = 20.4 cm^2) was fastened with a lifting holder arranged on a stand. A 0.01% polymer solution (10 ml) was charged into a 50-ml beaker. The paper sample was immersed in the solution to a depth of 0.5 cm, and the capillary rise was monitored as a function of time. The total experiment time was no more than 5 min.

The solution pH was measured with a pH 320 SET pH-meter (Wissenschaftlich–Technische–Werkstatten GmbH).

The method for determination of the absorption of a cationic polyelectrolyte by a negatively charged surface of cellulose fibers was proposed in [5]. Its essence is that, in solutions, negatively charged polymers react with cationic polymers practically stoichiometrically, forming a precipitate. For example, it was demonstrated that colloid titration of a cationic polymer, methyl glycol chitosan, with PVSK results in formation of an insoluble nonionic precipitate near the isoelectric point [5, 7]. The end point is determined using Toluidine Blue O as an indicator, which is adsorbed on the surface of an anionic polymer, changing its color from blue to purple or rosy at the end point.

If a fixed volume of a standard solution of the test cationic polymer is added to a cellulose suspension in distilled water and contacted for a sufficiently long time, the above-described method can be used for determination of the excess of a cationic polymer remaining in the solution after the cellulose precipitate was filtered out. Using PVSK as a titrant and knowing the stoichiometry of interaction of a cationic polymer with PVSK, we can estimate the adsorption of the polymer on cellulose and determine the adsorption characteristics of the cellulose dispersion such as the cationic demand, adsorption power, and apparent cationic charge density.

The adsorption properties of cationic polymers were evaluated using two parameters: the adsorption on filter paper and cationic demand of the cellulose dispersion, the latter corresponding to the amount of a cationic polymer bound to the carboxy groups of cellulose in unit volume of the dispersion. In determining both parameters, colloid titration was used to measure the excess amount of the cationic polymer remaining in the solution after a sufficiently long contact time.

The PVSK to test polymer stoichiometric ratio was determined by UV spectroscopy. It was demonstrated that the light absorption D_{rel} of an aqueous solution of a mixture of the modified cationic polyimine, Polymin SK, and PVSK in the UV range (190–220 nm) is an additive function of the concentrations of the individual components (Fig. 1). Titration of an aqueous solution of Polymin SK with PVSK in the presence of Toluidine Blue, which changes its color from blue to violet at the end point, revealed 1 : 1 stoichiometry. The UV spectra showed that the absorption follows the Beer–Lambert–Bouguer law over the concentration range from 0 to 1×10^{-3} g-equiv l^{-1} for both the initial polyelectrolytes and their mixtures with PVSK (Fig. 2).

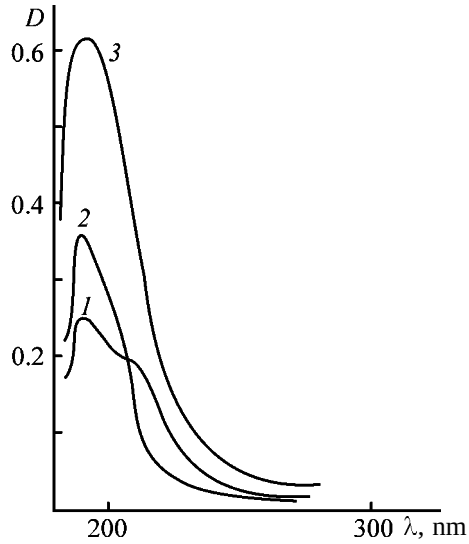

Fig. 1. UV spectra of polymer solutions: (*1*) 4.615×10^{-4} g-equiv l^{-1} PVSK, (*2*) 5×10^{-4} g-equiv l^{-1} Polymin SK, and (*3*) 5×10^{-4} g-equiv l^{-1} Polymin SK + 4.615×10^{-4} g-equiv l^{-1} PVSK. (*D*) Optical density and (λ) wavelength; reference: water; the same for Fig. 3.

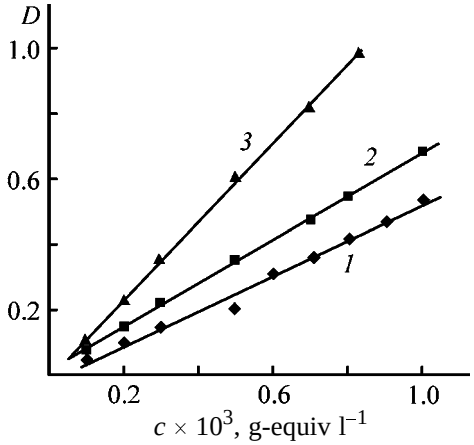

Fig. 2. UV absorption *D* (λ = 190–210 nm) as a function of the polymer concentration in solutions *c*: (*1*) PVSK, (*2*) Polymin SK, and (*3*) Polymin SK + PVSK, at the end point.

Therefore, colloid titration with PVSK allows determination of the amount of a cationic polymer in the system over the indicated concentration ranges. Table 1 shows the characteristics of polyelectrolyte solutions, determined by colloid titration.

Note that cationic polymers with high molecular weight (nos. 1–5) have a low concentration of charged nitrogen-containing groups (ρ = 1–3 mg-equiv g^{-1}), and their 0.05% solutions demonstrate weakly acidic pH. Cationic polymers with relatively low molecular

Table 1. Characteristics of cationic polyelectrolytes

Flocculant	pH of 0.5% solution	ρ, mg-equiv g^{-1}	$A_{eff} \times 10^9$, g-equiv cm^{-2} (0.01% solution)
Polymin KP	4.64	1.0	1.7
Kat-floc-487F	4.60	1.5	2.0
Praestol 611BC	4.91	1.4	3.5
Praestol 851BC	4.15	1.5	3.6
Praestol 853C	4.15	2.9	3.6
Katiofast SF	6.85	14.0	26.0
Polymin SK	7.17	5.5	15.0
Poly-DADMAC	7.00	5.9	12.0

Table 2. Cationic demand (CD) of the filtrate of cellulose suspension, determined by colloid (CT) and high-frequency (HFT) titration*

Experiment no.	Polymer	*m*,** g	CD of filtrate, mg l^{-1}		$(\Delta CD/CD_{in}) \times 100$, %
			CT	HFT	
1	Polymin KP	–/2.5	559.4/452.0	562.0/450.0	19
2	Katiofast SF	–/4.5	520.0/500.0	516.0/498.5	4
3	Kat-floc-487F	–/2.5	546.1/500.0	540.0/446.0	18
4	Katiofast SF + Polymin KP	–/2.0 + 1.25	546.1/412.9	540.0/400.3	24
5	PDMDAAC + Polymin KP	–/2.0 + 1.20	559.4/432.8	563.3/538.0	23

* Data on the initial cellulose suspension in water are given in the numerator, and those on cellulose suspension containing a polymer, in the denominator.

** (*m*) Amount of a polymer required to thicken 1 l of a suspension.

weight from 10000 to 30000 g mol^{-1} (nos. 6–8) are characterized by high ρ and neutral pH.

In addition, the cationic demand was determined by high-frequency titration of the paper suspension [6, 8].

Table 1 shows that the adsorption of polymers with low apparent charge density (nos. 1–5) is considerably lower than in those with high ρ (nos. 6–8). Therefore, in the latter case, larger amount of the cationic polymer is required to neutralize the net negative charge of the cellulose surface. This conclusion is also supported by data on the cationic demand (Table 2).

The results show (Table 2) that the decrease in the cationic demand for Polymin KP (ρ = 1.0 mg-equiv g^{-1}) from 559.4 to 452 mg l^{-1} ($\Delta CD/CD_{in}$ = 19%) is more significant as compared to Katiofast SF having ρ = 14 mg-equiv g^{-1} (from 520 to 500 mg l^{-1}; $\Delta CD/CD_{in}$ = 4%). Correspondingly, the consumption of a cationic polymer is much higher for polymers with high charge density. At the same time, the highest effect toward decrease in CD was obtained with a mixture of cationic polymers with high and low ρ (Table 2, no. 4).

Table 2 reveals satisfactory agreement of data obtained by colloid and high-frequency titration methods. The cationic demand depends on both the structure of the polyelectrolyte and composition of the polyelectrolyte system.

The mechanism of interaction of a cationic polyelectrolyte with a negatively charged cellulose surface is shown in the picture below.

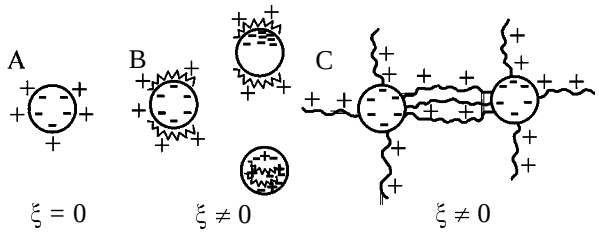

It is a common view that fixation of a cationic polymer on cellulose particles is a resultant of two simultaneous processes, namely, ionic interaction of accessible surface carboxy groups (A, B) and adsorption through van der Waals or hydrogen bonding (C). Ionic mechanism dominates in the case of highly charged cationic polymers, e.g., Katiofast SF, representing, in essence, organic coagulants. Adsorption of such kind of polyelectrolytes was attributed in [9] to neutralization of the surface charge (B). Combined effect of high-molecular-weight polymers Polymin KP

Table 3. Treatment efficiency of cellulose suspensions by a three-mark scale (initial COD 3300 mg l^{-1}; polymer concentration 0.5%)

Composition	Thickening test*	Clarification test**	COD, mg l^{-1} (by O_2)
	mark		
Polymin KP	3	2	1600
Polymin KP + $FeCl_3$, 10 g l^{-1}	3	3	500
Kat-floc-487F	3	2	1500
Kat-floc-487F + $FeCl_3$, 10 g l^{-1}	3	3	450
Katiofast SF	0	0	2800
Katiofast SF + $FeCl_3$, 10 g l^{-1}	1	1	2500
Polymin SK	0	0	2500
Polymin SK + $FeCl_3$, 10 g l^{-1}	2	2	1000

* Mark 0: no thickening; mark 3: efficient thickening (stable floccules).
** Mark 0: turbid medium; mark 3: total clarification.

and Katiofast SF with a low specific charge is, most likely, associated with bridging according to scheme C. In the case of efficient flocculation, smaller amount of the polyelectrolyte is consumed for neutralization of negatively charged cellulose particles, and, larger amount of the polyelectrolyte remains in the filtrate. Correspondingly, the amount of PVSK consumed for colloid titration of the filtrate will be higher than in the case of weak flocculation, and CD, according to Eq. (1), will decrease more strongly.

Evidently, in using polymers like Katiofast SF, poly-DADMAC, and high-molecular-weight polymers in combination, neutralization of negatively charged cellulose particles occurs most efficiently. Polyelectrolytes form complexes with the carboxy groups of cellulose and functional groups of hemicelluloses and lignin [2], resulting in formation of associates of various kinds. These associates, in turn, can form labile 3D networks, promoting flocculation. In order to further improve the efficiency of wastewater treatment, we proposed to use a composition based on a low-charged polyelectrolyte and the highly effective coagulant, $FeCl_3$, capable of forming polyelectrolyte complexes, as flocculants for cellulose suspensions. Our results showed that better flocculation and higher degree of decontamination are realized with a mixture of Kat-floc-487F and Polymin KP in combination with $FeCl_3$ (Table 3).

The UV spectra show that addition of $FeCl_3$ to Polymin KP and Kat-floc-487F polymer solution increases the absorption at 190–220 nm by a factor of about 1.5, the component concentrations in the solution being the same (Figs. 3a, 3b).

At the same time, in the case of highly charged

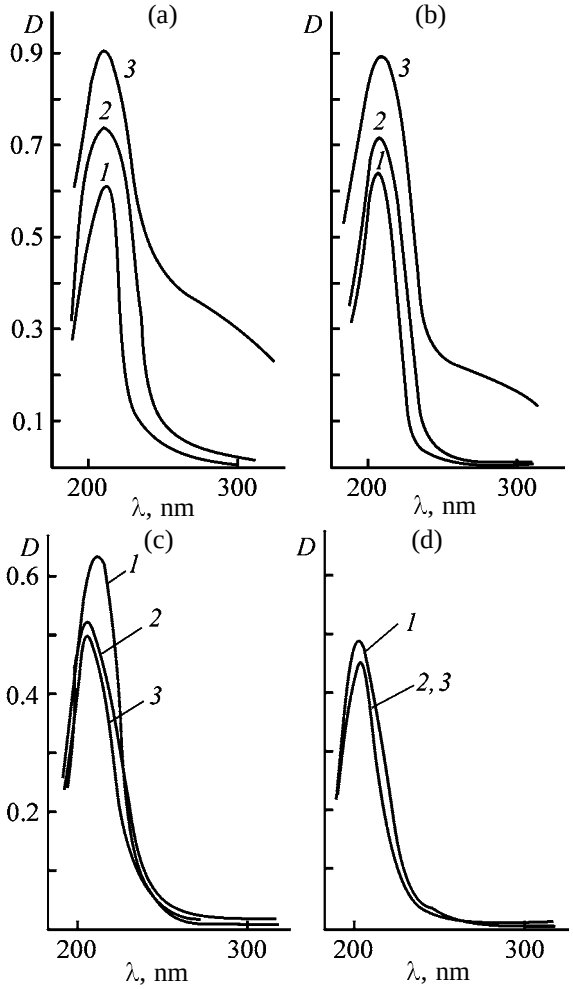

Fig. 3. UV spectra of polymer solutions: (a) Kat-floc-487F, (b) Polymin KP, (c) Katiofast, and (d) Polymin SK. Initial polymer concentration (g l^{-1}): (a, b) 0.5 and (c, d) 0.2. (*1*) Initial polymer, (*2*) initial polymer + 0.5 g l^{-1} HCl, and (*3*) initial polymer + 2.5 g l^{-1} $FeCl_3$.

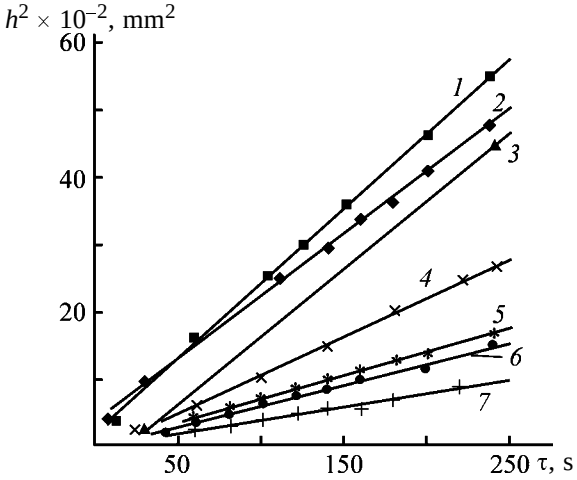

Fig. 4. Capillary rise h^2 of 0.01% polyelectrolyte solutions as a function of the time τ and polyelectrolyte composition: (*1*) Polymin SK, (*2*) Katiofast SF, (*3*) Praestol 611BC, (*4*) Praestol 650BC, (*5*) Polymin KP, (*6*) Kat-floc-487F, and (*7*) Kat-floc-487F + $FeCl_3$. *K* (mm^2 s^{-1}): (*1*) 23.0, (*2*) 20.0, (*3*) 19.0, (*4*) 11.0, (*5*) 7.0, (*6*) 6.0, and (*7*) 4.2.

low-molecular-weight polyelectrolytes like Katiofast SF and Polymin SK, addition of $FeCl_3$ does not changes significantly the UV spectra (Figs. 3c, 3d).

Since hydrolysis of $FeCl_3$ produces hydrochloric acid, we studied the effect of addition of 0.5 g l^{-1} HCl on the properties of polyelectrolyte solutions. As seen from Fig. 3, HCl has no significant effect on the optical density over the range 190–220 nm.

The influence of atmospheric oxygen on the UV absorption of cationic electrolyte solutions was insignificant, since we used water as a reference.

The observed considerable changes in the optical density, initiated by addition of $FeCl_3$ to solutions of cationic polymers with low ρ (1–3 mg-equiv g^{-1}), are probably due to formation of polyelectrolyte complexes with $FeCl_3$.

Another practically significant characteristics of the polyelectrolyte-based compositions is their viscosity. In this work, the viscosity of 0.2% polymer solutions (120–130 m^3 kg^{-1}) remained unchanged at 10°C for a year. Also, we observed no noticeable changes in the flocculating properties of the compositions.

The efficiency of flocculation of cellulose particles depends on their wettability with a polymer solution. Therefore, we studied this effect by the kinetic method, i.e., by measuring the capillary rise along the paper [2]. The features of capillary imbibition of a liquid into a porous body can be described as follows.

On immersing a porous body into a liquid, a capillary pressure arises in the pores, given by the Laplace equation (6).

$$P_{cap} = (2\sigma\cos\theta)/r, \quad (6)$$

where *r* is the pore radius; σ, surface tension of the liquid; and θ, contact angle.

If a body has a hydrophilic surface, a fluid in pores forms concave meniscus, and the capillary pressure initiates capillary rise of the liquid in a capillary (imbibition).

The equilibrium height of the liquid rise in the case of ideal wetting (θ = 0) can be estimated by Eq. (7)

$$\eta_{max}c = 2\sigma/(r\rho g), \quad (7)$$

where *g* is the gravity acceleration.

The kinetics of capillary rise is described by the Poiseuille and Washburn equations:

$$dh/d\tau = (2\sigma\cos\theta/r - \rho gh)r^2/(8\eta h). \quad (8)$$

where η is the polyelectrolyte viscosity.

Since the hydrostatic pressure driven by the gravity is mostly considerably lower than the capillary pressure, the product ρ*gh* can be neglected, and Eq. (8) can be reduced to obtain Eq. (9).

$$dh/d\tau = 2\sigma r\cos\theta/(8\eta h). \quad (9)$$

Integrating (9) gives

$$h^2 = K\tau. \quad (10)$$

The empirical constant *K* reflects the capillary rise velocity, being controlled by the ratio between the surface tension and polyelectrolyte viscosity.

We studied capillary rise of 0.1% polyelectrolyte solutions using filter paper as a porous body. The measured height of the liquid rise as a function of the time is shown in Fig. 4.

The results were fit to the form of Eq. (11).

$$h^2 = a + K\tau, \quad (11)$$

where *a* is the constant reflecting the nonlinearity of imbibition in the initial period of time.

These results in combination with data given in Table 3 show that polyelectrolytes demonstrating the best flocculating action in thickening and clarification of cellulose suspensions have $K = 5 \pm 2$ mm^2 s^{-1}. The flocculating action decreases as *K* increases.

The capillary imbibition method can also be used for estimating the adsorption of a polyelectrolyte on the cellulose surface. In this case, the same batch of filter paper should be used as a support.

CONCLUSIONS

(1) The wastewater treatment efficiency increases if a composition based on a low-charged polyelectrolyte and an inorganic coagulant, $FeCl_3$, capable of forming polyelectrolyte complexes is used as a flocculant.

(2) The effective adsorption of a polymer as well as the cationic demand difference of cellulose, obtained by colloid titration, can be used as criteria in evaluating the flocculation efficiency of wastewater treatment and pulp thickening.

(3) An express method is proposed for testing the flocculating action, based on the capillary rise measurements. The empirical constant K in Eq. (11) should be 5 ± 2 $mm^2\ s^{-1}$ for polyelectrolytes having a considerable flocculating action in cellulose suspensions.

REFERENCES

1. Kopylov, V.A., *Ochistka stochnykh vod i uplotnenie osadka tsellyulozno-bumazhnogo proizvodstva* (Wastewaster Treatment and Pulp Thickening in Paper Making), Moscow: Lesn. Prom–st., 1983.
2. Akim, E.L., *Sinteticheskie polymery v bumazhnoi promyshlennosti* (Synthetic Polymers in Pulp-and-Paper Industry), Moscow: Lesn. Prom–st., 1986.
3. Lapin, V.V. and Shtreis, E.F., *Sb. Tr. Tsentr. Nauchno-Issled. Inst. Bum. Prom–sti*, 1977, no. 14, pp. 86–91.
4. RF Patent 2114068.
5. Rouger, J. and Matue, P., *Proc. Symp. Polymer-83*, Varna (Bulgaria), 1983, pp. 1–14.
6. Lapin, V.V., Sokolova, B.I., Shpender, N.P., *et al.*, *Zh. Prikl. Khim.*, 1977, vol. 50, no. 9, pp. 2079–2084.
7. Baran, A.A. and Gregory, J., *Kolloidn. Zh.*, 1996, vol. 58, no. 1, pp. 13–18.
8. Lapin, V.V., Sokolova, B.I., and Talmud, S.A., *Zh. Prikl. Khim.*, 1979, vol. 52, no. 7, pp. 1672–1674.
9. Edeline, F., *L'epuration physico-chemique des eaux. Theorie technologie*, Paris: CEBEDOC, 1998.

Russian Journal of Applied Chemistry, Vol. 77, No. 3, 2004, pp. 414–422. Translated from Zhurnal Prikladnoi Khimii, Vol. 77, No. 3, 2004, pp. 421–429.

ORGANIC SYNTHESIS AND INDUSTRIAL ORGANIC CHEMISTRY

Aggregation of Rhodamine B in Water

N. O. Mchedlov-Petrosyan and Yu. V. Kholin

Karazin Kharkov National University, Kharkov, Ukraine

Received March 4, 2003

Abstract—Protolytic and associative equilibria in aqueous solutions of rhodamine B were studied. The curves of potentiometric titration with NaOH solution of the dye hydrochloride within the 5×10^{-4}–3×10^{-2} M range and at an ionic strength of 0.1 M (NaCl or KCl) were treated by chemometric methods of successive modification of the equilibrium system models with regard to spectrophotometric data. The most probable value of the equilibrium constants of the reaction $i\mathrm{H}^+ + j\mathrm{R} \rightleftarrows \mathrm{H}_i\mathrm{R}_j^{i+}$ were determined.

Thanks to the unique spectral-luminescence properties, rhodamine dyes are widely used as markers and probes in studies of various objects including biological systems [1], in sensors [2], including those based on Langmuir–Blodgett films [3], in supramolecular chemistry [4], and in studies of nanoobjects prepared by the sol–gel method [5]. The most part of rhodamines in aqueous solutions show deviations from Bouguer–Beer's law even at concentrations of 10^{-4} M. Spectrophotometry and the other methods show dye association [6–8]. Nevertheless, in many cases, e.g., in laser beam technology, concentrated solutions of rhodamines are required. As a rule, dyes are characterized by step (but not cooperative) association [6, 7], i.e., by successive formation of dimers, trimers, etc. Therefore, the state of dyes in solutions in the concentration range between the infinitely dilute and concentrated solutions is of interest.

In this work, the state of rhodamine B in water within the 2×10^{-6}–3×10^{-3} M concentration range was studied spectrophotometrically and potentiometrically. In water, HRCl salt dissociates with formation of the HR^+ cation.

In contrast to many other rhodamines, such as rhodamines 6Zh and 3B, rhodamine B participates in acid–base reaction not only at pH < 1.7 but also in less acidic medium because of the presence of a carboxy group. Its dissociation produces zwitterion $R^{\pm}$, which is the main form of the neutral species R in aqueous solution:

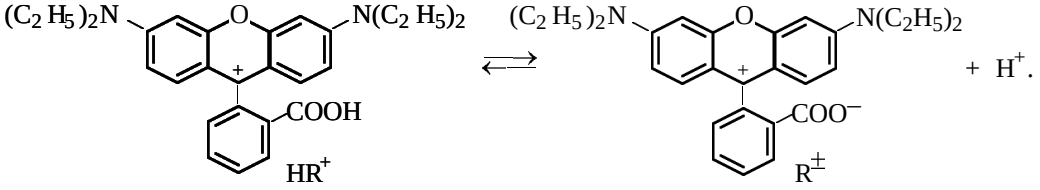

The fraction of molecules R converting in water into a colorless, low-polarity lactone R^0 amounts to 0.5–1% [10]. In general, rhodamine B transformations in the solution, depending on the acidity and dye concentration c_d, can be expressed by the equation

$$i\mathrm{H}^+ + j\mathrm{R} \rightleftarrows \mathrm{H}_i\mathrm{R}_j^{i+};\ \beta_{ji}, \qquad (1)$$

where β_{ji} is the equilibrium constant.

Although in aqueous solution the absorption bands of HR^+ and $R^{\pm}$ are ill-resolved (λ_{max} = 556–557 and 553–554 nm, respectively, at virtually the same extinction coefficient), it is possible to determine $\log\beta_{11}(\mathrm{R} + \mathrm{H}^+ = \mathrm{RH}^+)$ spectrophotometrically at $c_d \le 10^{-5}$ M ($\log\beta_{11}$ = 3.22 [9]; thermodynamic value at the ionic strength $I \to 0$). The $\log\beta_{11}$ values obtained potentiometrically are necessarily determined at substantially greater c_d. Because of association (dimerization), the standard method gives substantial difference in $\log\beta_{11}$ values measured at different rhodamine concentrations (from 3.2 to 4.1) [11–13] and drift of the calculated $\log\beta_{11}$ along the titration curve [14].

Dimerization of rhodamines was studied spectrophotometrically in [9, 11, 15–17]. Structural features of rhodamine B allow complete conversion of the HR^+ cation into the readily soluble in water zwitterion $R^{\pm}$, which prevents precipitation of HR^+X^- on adding salts and allows complete transformation of the dye

1070-4272/04/7703-0414 © 2004 MAIK "Nauka/Interperiodica"

into the dimer even at $c_d \sim 10^{-4}$ M [15]. The dimerization constants β_{20} at high I produced by inert salts[1] are listed in Table 1:

$$2R \rightleftarrows R_2;\ \beta_{20}. \quad (2)$$

A typical spectrum of the dimer R_2 is shown in Fig. 1a. In accordance with [9, 11, 18], the HR^+ cation can also dimerize in water. Variation of the dye concentration at pH 1.8–2.0 reveals a typical dimer band in the spectrum; however, in this case, λ_{max} is 526–527 nm, against 524 nm for R_2 [9, 15] (Fig. 1b). In dilute solutions, in which HR^+ species prevails (the fraction of H_2R^{2+} species is less than 3%), the band maximum lies at 556–557 nm as compared to 553–554 nm for R. The equilibrium constant of the $2HR^+ \rightleftarrows H_2R_2^{2+}$ equilibrium is calculated by standard procedure [15], $(1.6 \pm 1.1) \times 10^3$ [19], which agrees with the known value of 1.4×10^3 [18]. The band maximum at 526 nm was observed at pH 1.3 and I = 1.0 (KCl) [11].

We suggested previously [14, 19] that HR_2^+ species are formed along with cation dimers. Such complexes between the base and its protonated form, similarly to those between the acid and its anion, are usually formed in bipolar aprotic solvents, e.g., acetonitrile [20]. However, formation of $C_6H_5COOH\cdots {}^-OOCC_6H_5$ and $FH\cdots F^-$ species in water is also known [21]. We suggested that systematic deviations in calculations of $\log\beta_{11}$ made by simplified methods from the results of the pH-metric titration in water can be used as a source of information on association processes (dimerization in the simplest case). In this work, we studied rhodamine B association using data of HRCl titration with alkali and simulated the equilibria by the methods of quantitative physicochemical analysis (QPCA) [22].

EXPERIMENTAL

Chromatographically pure grade rhodamine B (as HRCl) [9, 10, 23, 24] was used. Chemically pure grade salts were additionally purified by recrystallization. An NaOH reference solution prepared from carbonate-free alkali solution and standardized by titration with double-recrystallized adipic acid was protected from atmospheric CO_2. β-Cyclodextrin (β-CD) produced by the Chinoin Company (Hungary) was used; in calculation of its concentration, it was assumed that this preparation contained 9 water molecules per macrocycle molecule. The absorption spectra of solutions were measured previously [9, 23]; additional measurements were performed on an SF-46 spectrometer. The pH values were measured with a glass electrode in an electric circuit with transfer vs. AgCl or calomel electrode; the bridge (contacting through a ground-glass joint) was filled with a KCl saturated solution (in special experiments, 1 M KCl solution was used). The electric circuit was standard-

[1] Here and hereinafter, dimensions of the constants are not indicated; the M concentration scale was used.

Table 1. Dimerization constant of rhodamine B zwitterions [15] at 20°C

I, M	λ_{max} (R),* nm	Isobestic point	$\log\beta_{20}$ (±0.05)
NaOH**	553–554	532	3.31 (25°C)
1.0 (KCl)	555	533	3.36
3.9 (LiCl)	557	535	4.00
4.6 ($NaClO_4$)	556	533	4.40
9.7 (LiCl)	559	539	5.17

* Molar absorption coefficient of monomer in absorption maximum, $\varepsilon(R) = (106–108) \times 10^3$ l cm^{-1} mol^{-1}.

** NaOH added to obtain pH 10–12 in all the systems.

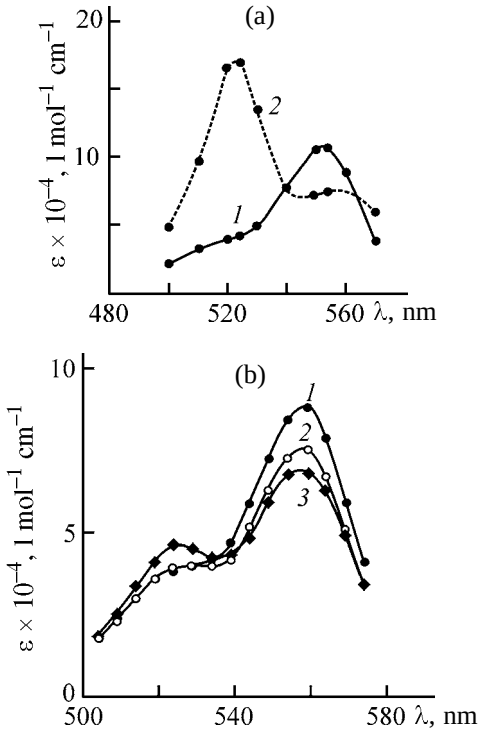

Fig. 1. (a) Absorption spectra of rhodamine B (*1*) monomer R and (*2*) dimer R_2 in 4.6 M $NaClO_4$ solution at pH 10–11, and (b) rhodamine B spectra at pH 2 (HCl) at various dye concentrations, M: (*1*) 1×10^{-4}, (*2*) 3×10^{-4}, and (*3*) 7×10^{-4}. (ε) Molar extinction coefficient and (λ) wavelength.

ized using reference buffer solutions with pH 1.68, 4.01, and 6.86. The hydrogen function of ESL-63-07 and ESL-43-07 glass electrode corresponded to the calculated function. In some cases, titration was performed in the presence of salts (NaCl, KCl), total I values were 0.05, 0.08, or 0.1 M; higher Cl^- concentrations can precipitate the dye as HRCl. The results were well reproduced; equilibria were reached virtually instantly. Prolonged contact of the solutions with glass surfaces causes adsorption of up to 5% of dye within 3 h under unfavorable conditions. A total of 55 titrations were performed at various dye (from 5×10^{-4} to 3×10^{-2} M) and alkali (from 1×10^{-3} to 3×10^{-2} M) concentrations, excluding preliminary experiments.

The number of species, stiochiometry, and stability constants of complexes are calculated from the dependence of any property (light absorption, concentration or activity of a system component) of the equilibrium system on its composition (composition–property dependences) [22]:

$$A_{lk} = \zeta(\lambda_l, n_{*k}), \quad (3)$$

where A is a property of the equilibrium system; k, the number of the mixture measured, $1 \le k \le N$; N, the number of mixtures measured; λ, analytical position (e.g., wavelength of the light absorbed in the method of multiwave spectrophotometry); l, the number of the analytical position, $1 \le l \le A$; A, the total number of analytical positions (channels of the simultaneous measurement of the properties of the equilibrium system); n_{*k}, vector of the initial (known from the conditions of mixing) reagent amounts in kth mixture studied; and ζ, any function whose form is determined by the features of the system studied and experimental method taken.

In studying equilibria in the solutions by pH-metry or spectrophotometry, the model structure is set by three groups of equations: connection of a measured property A with equilibrium composition, material balance, and law of mass action. Mixed equilibrium constants are calculated when estimations of hydrogen ion activities $h = 10^{-\mathrm{pH}}$ are used as approximated property A, and concentration constants, when the equilibrium concentration $[H^+] = 10^{-\mathrm{pH}} f_H^{-1}$ (where f_H is the hydrogen ion activity coefficient) is approximated by the model.

In this work, to find the number of species and stoichiometric composition of reaction products in rhodamine B solutions, we used the method of "successive correction of trial models" [25] for the case when experimentally measured quantities are the equilibrium concentrations of one of reagents [M]. In modeling, we formulated a trial hypothesis on reactions proceeding in the system, calculated for it the unknown equilibrium constants and reactant concentrations in all the experimental points, found weighted discrepancies $\xi_k = w_k^{1/2}$ {where k is the number of the experimental point, $\Delta_k = [M]_k^{cal} - [M]_k^{exp}$; $w_k + \sigma^{-2}(\Delta_k)$, statistic weight of kth measurement; and $\sigma^2(\Delta_k)$, variance of Δ_k}, and checked the model adequacy. When the statistic criteria showed lack of fit of the trial model to the experiment, parts of the experimental plan with higher absolute values of discrepancies $|\xi_k|$ were considered.

To compensate large discrepancies ξ_k, the model was supplemented with a new chemical species L_{new}, whose inclusion *a fortiori* improves the experiment description. Rules of the selection of L_{new} stoichiometric composition are described in [25, 26] in detail. Then, the calculation procedure was repeated.

It should be noted that the composition–property dependences are preset in the tabulated form, the arguments and responses contain errors, with information on only "typical" errors of the experimental values being accessible, and in this case the calculation of the parameters becomes a mathematically incorrect task. As a result, inclusion of excess chemical species in the models, wrong choice of the criterion of the mismatching between the model and experiment, erroneous estimation of the confidence intervals of parameters, uncritical estimation of the model adequacy, and other defects substantially decreasing reliability of the proposed models of the equilibrium systems are possible.

The work with fairly concentrated rhodamine B solutions caused the choice of pH-metric titration as the method of investigation, although the above disadvantages are characteristic of it in full measure. To make maximally reliable the information obtained from titration curves, in the stages of calculation of unknown stability constant, check of the model adequacy, and estimation of parameter significance, we used the methods of the data analysis theory. The traditional least-squares techniques was supplemented by Huber's robust M-assessments of the model validity (cross validation), singular analysis, and combining of local and global criteria of the model adequacy. Detailed description of the calculation methods used and CLINP 2.1 computer software is presented in [26–28].

To assess the adequacy of the models, we used the global criterion χ^2 (after preliminarily introducing the

necessary corrections when M-assessments were used) [29]. The model was considered to be adequate if

$$\chi^2_{\text{exp}} = s_0^2 f < \chi^2_f(\alpha), \quad (4)$$

where $f = N - z$ is the number of degrees of freedom; z, the number of unknown parameters of the model;

$$s_0^2 = f_k^{-1} \sum_{k=1}^{N} \xi_k^2, \quad (5)$$

residual variance; $\chi^2_f(\alpha)$, 100α% point of the distribution of χ^2 for f degrees of freedom at the preset significance level $\alpha = 0.05$ [30].

Additionally, we used cross validation [31]. For this purpose, we eliminated the gth dimension from N experimental points, calculated from the remaining data the fitting parameters, and found A_k^{cal} and weighted discrepancy of cross validation $d_g = w_k(A_k^{\text{cal}} - A_k^{\text{exp}})$. Calculations were performed for all N possible subdivisions of the set of experimental points, and cross-validation variance was found:

$$\bar{s}_0^2 = (N - z)^{-1} \sum_{g=1}^{N} d_g^2. \quad (6)$$

Cross validation reveals the presence in the model of "risk parameters" found using measurements only in one or in a few experimental points ("out-of-balance").

After our publication [15], along with monomers and dimers, the existence of rhodamine B trimers in concentrated ethanolic solutions was reported [32]. We additionally treated previously published spectrophotometric measurements [15] by the method of equilibrium model. It was found that, at c_d within the 4×10^{-4}–9×10^{-4} M range, pH 10–11, and the absence of the supporting electrolyte $\log\beta_{20} = 3.275(0.08)$[2] and $\varepsilon(R_2) \times 10^{-3} = 93(4)$ and 225(6) l cm^{-1} mol^{-1} for 524 and 554 nm, respectively. For the monomer, the $\varepsilon(R) \times 10^{-3}$ values are equal to 108 and 40 l cm^{-1} mol^{-1}, respectively. Thus, the result obtained previously was confirmed (Table 1). The model including only monomers and dimers well describes the experiment. At c_d within the 6×10^{-5}–6×10^{-4} M range, pH 10–11, and $I = 1.0$ M (KCl), similar procedure gave $\log\beta_{20} = 3.25(0.08)$, also without including more complex species.

In simulating the equilibria in more concentrated solutions (Fig. 2), the thermodynamic values of $\log\beta_{11} = 3.22$ and $\log\beta_{20} = 3.25$ (at $I = 0.1$ M, 3.30 and 3.30, respectively) found earlier from spectrophotometric data [9, 15] were considered to be known precisely. Variation of $\log\beta_{11}$ and $\log\beta_{20}$ within ± 0.3 had virtually no effect on the results of simulating the equilibria in the concentrated solutions because of low yield of HR^+ and R_2 species.

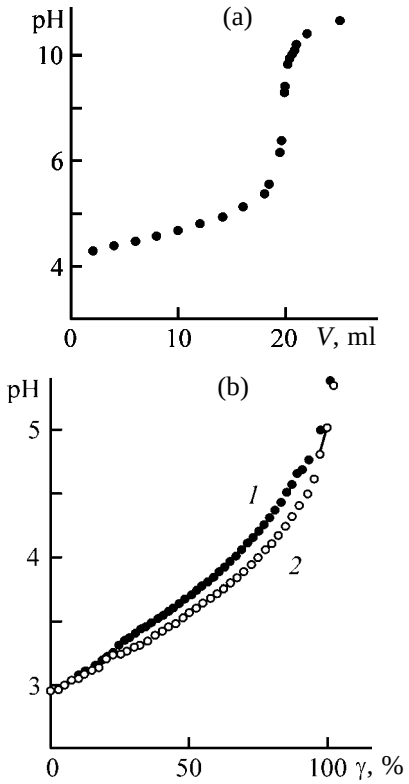

Fig. 2. Curves of titration of 20 ml of (a) 1.958×10^{-2} M rhodamine B (HRCl) solution with NaOH solution of the same concentration and of (b) 3.9×10^{-3} M rhodamine B solution with NaOH solution of the same concentration (*1*) in the presence of β-cyclodextrin and (*2*) without it. (V) Volume of NaOH solution added and (γ) degree of titration.

The estimated equilibrium hydrogen ion concentration $[H^+]$ was taken as a property approximated by the models. The experimental pH and f_H taken from the monograph [33] (for 0.1 M solutions of the supporting electrolytes NaCl and KCl, f_H is equal to 0.85 and 0.83, respectively) were used in calculation of $[H^+] = 10^{-\text{pH}} f_H^{-1}$. Prescribing the statistic weights w_k, we assumed the relative standard deviations $\sigma_r([H^+]) = 0.069$. This corresponds to the standard deviations in measuring pH $\sigma(\text{pH}) = 0.03$. In calculations, unless otherwise stated, unknown parameters were calculated by the nonlinear least-squares method.

[2] Here and hereinafter, the rms deviations of parameters are given in parentheses.

Table 2. Calculation of logarithms of the concentration equilibrium constants in solutions of rhodamine B. Supporting electrolyte concentration 0.1 M

c^0(R), M	Supporting electrolyte	$\log\beta_{21}$	$\log\beta_{22}$	$\log\beta_{30}$	$\log\beta_{31}$	χ^2_{exp}	f	$\chi^2_f(\alpha = 0.05)$
5×10^{-4}	NaCl	7.40(0.01)	–	–	–	9.4	5*	9.5*
1.6×10^{-3}	KCl	7.27(0.01)	–	–	–	13.5	16	26.3
4.0×10^{-3}	–	7.25(0.01)	10.32(0.01)	–	–	9.2	35	49.8
5.0×10^{-3}	KCl	7.22(0.02)**	10.35(0.05)**	–	–	1.8	15	25.0
2.0×10^{-2}	NaCl	7.27***	10.4(0.4)	6.5(0.5)	11.0(0.6)	13.5	7	14.1
3.0×10^{-2}	NaCl	7.27***	10.1(0.15)	6.40(0.18)	9.9(0.5)	11.5	8	5.5

* Values obtained using Huber parameters of M-assessment.
** Logarithms of mixed equilibrium constants.
*** Values were not refined.

For the equilibrium in the solution with the initial HRCl concentration of 5×10^{-4} M (supporting electrolyte 0.1 M NaCl), a set of the permissible chemical species in the initial model was restricted to H^+, HR^+, R, and R_2, and a single parameter $-\log\beta_{11}$ ($H^+ + R = HR^+$) was calculated. Testing of the trial model gave $\log\beta_{11} = 3.50$, $\chi^2_{exp} = 42.3 > \chi^2_{f=10}(\alpha = 0.05) = 18.3$, i.e., the model is inadequate to the experiment. The local adequacy criteria, weighted discrepancies ξ_k, are large and systematic (Fig. 3, curve *2*). In Fig. 3, the vertical straight line divides the titration curve in two parts: In part *A*, the prevailing species are H^+ and R, while in part *B*, where ζ_k values are maximal, H^+ and R_2. To compensate the largest discrepancies, we supplemented the model by the HR_2^+ species, which is a product of the reaction between H^+ and R_2. After parametric identification of the supplemented model, we obtained the following results. $\log\beta_{11}$ cannot be determined from the data obtained (the yield of HR^+ in any point of the titration curve does not exceed 0.01% of the total rhodamine B concentration); $\log\beta_{21} = 7.37$; $\chi^2_{exp} = 16.7 < \chi^2_{f=9}$ ($\alpha = 0.05$) = 16.9, i.e., the model is adequate to the experiment with respect to χ^2 test. The local adequacy criteria ξ_k also substantially decreased (Fig. 3, curve *3*); only in the last point, the discrepancy ξ_k was still abnormally high. This result can be interpreted in two ways: either measurement in the last point of the titration curve is erroneous, or, with increase in pH, along with HR_2^+, other rhodamine B associates are formed.

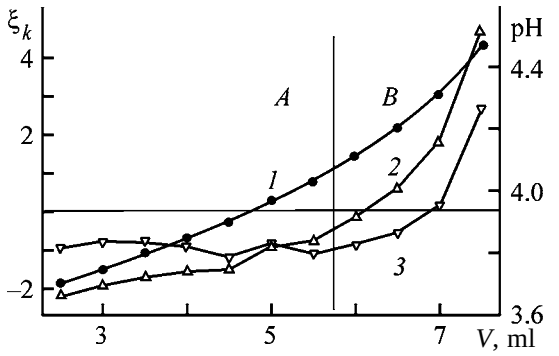

Fig. 3. Weighted discrepancies ξ_k for the initial model of equilibria. (*V*) Volume of NaOH solution added. (*1*) experimental titration curve; (*2*), (*3*) ξ_k.

In the end of the titration curve, the chemical species R and HR_2^+ prevail; the large positive discrepancy in the last experimental point is compensated by inclusion in the model of the product of reaction between them, HR_3^+. Testing of the model with a set of H^+, HR^+, R, R_2, HR_2^+, and HR_3^+ showed that the quality of the experiment approximation increased: $\chi^2_{exp} = 14.5 < \chi^2_{f=9}$ ($\alpha = 0.05$) = 16.9, and the HR_3^+ species is a significant component of the model; its yield exceeds 10% of total c_d. However, cross validation showed that $\log\beta_{31}$ ($H^+ + 3R \rightleftarrows HR_3^+$) is a risk parameter, since elimination of only one (last) point from the set of data treated drastically changes its value. Thus, it is impossible to make any reliable conclusion on formation of the HR_3^+ species under these conditions. The use of M-assessment gave the robust estimation of $\log\beta_{21} = 7.40$ (Table 2).

Spectrophotometric measurements performed at pH 1.8–2.0 for solutions within the $c_d = 1.0\times10^{-4}$–$1.0\times$

Table 3. Molar extinction coefficients ε of rhodamine B species

Species	ε, l cm^{-1} mol^{-1}, at indicated λ, nm	
	554	524
R	1.08×10^5	4.03×10^4
R_2	1.0×10^5	2.24×10^5
HR^+	1.1×10^5*	4.0×10^4**

* At 559 nm. ** At 529 nm.

10^{-3} M range at λ 559 and 529 nm (0.013 cm cell length) allowed verification of the above model. The previously found [9, 15] values of ε for various rhodamine B species are listed in Table 3.

Considering that $\log\beta_{20}$, $\log\beta_{21}$, and molar extinction coefficients of the above chemical species are known precisely, we calculated $\log\beta_{11}$($H^+ + R = HR^+$) and the extinction coefficient of HR_2^+ from the spectrophotometric data. The value found, $\log\beta_{11} = 3.5(0.05)$, coincides within the determination error with the value published in [9]; the model is adequate to the experiment: estimation of the relative standard deviation of the light absorption gave $s_r(A) = 0.05\chi^2_{exp} = 18.25 < \chi^2_{f=10}(\alpha = 0.05) = 18.31$. The equilibrium model proposed is also applicable to describing the potentiometric titration curve of rhodamine B solution with $c_d = 1.6 \times 10^{-3}$ M (supporting electrolyte 0.1 M KCl) (Table 2).

For the initial HRCl concentrations of 0.004 M (without supporting electrolyte) and 0.005 M (supporting electrolyte 0.1 M KCl), the simplest model with R, R_2, and HR_2^+ species fails to describe the experimental results. For instance, for the system with $c_d = 0.005$ M, $\chi^2_{exp} = 43.3 > \chi^2_{f=10}(\alpha = 0.05) = 18.3$, with substantial positive discrepancies ξ_k being concentrated in the region of the experiment plan with the prevailing species H^+ and HR_2^+. After supplementing the model with the reaction

$$H^+ + HR_2^+ \rightleftarrows H_2R_2^{2+},$$

we obtained an adequate model (Table 2). Similar results were obtained for the titration curve at the initial HRCl concentration of 4.0×10^{-3} M (Table 2).

Let us consider equilibria with the initial HRCl concentrations of 2×10^{-2} and 3×10^{-2} M (supporting electrolyte 0.1 M NaCl). Using the method of "successive correction of trial models," we reached in several steps the model adequate to the experiment (Table 4). Nevertheless, for this model, the weighted discrepancies ξ_k in the region with the prevailing species R and HR_3^+ are also systematic. At [R] < [HR_3^+], $\xi_k < 0$, and vice versa, at [R] > [HR_3^+], $\xi_k > 0$. This means that associates consisting of more than three rhodamine B molecules probably occur in the solutions. We tested the corresponding hypotheses (Table 4) and found that inclusion of these species, indeed, improves the agreement between the model and experiment; however, differences in the values of the criterial function χ^2_{exp} for different models are not so large to prefer one model to the others. Under these

Table 4. Procedure for construction of the model of equilibria in solutions with $c_d = 2 \times 10^{-2}$ M

Step of modeling*	Species	$\log\beta$	χ^2_{exp}	f	χ^2_f ($\alpha = 0.05$)
1	R	–			
	HR	3.22**	46.5	9	16.9
	R_2	3.25**			
	HR_2^+	7.27**			
	$H_2R_2^{2+}$	9.70(0.15)			
2	R	–			
	R_2	3.25**			
	HR_2^+	7.27**	23.4	8	15.5
	$H_2R_2^{2+}$	9.62(0.12)			
	R_3	4.9(0.4)			
3 (accepted model	R	–			
	HR	3.22**			
	R_2	3.25**	13.5	7	14.1
	HR_2^+	7.27**			
	$H_2R_2^{2+}$	10.4(0.4)			
	R_3	6.8(0.5)			
	HR_3^+	11.1(0.6)			
4	R	–			
	HR	3.22**			
	R_2	3.25**	10.8	7	14.1
	HR_2^+	7.27**			
	$H_2R_2^{2+}$	10.12(0.15)			
	R_4	9.31(0.20)			
	HR_4^+	13.73(0.25)			
5	R	–			
	HR	3.22**			
	R_2	3.25**	7.9	7	14.1
	HR_2^+	7.27**			
	$H_2R_2^{2+}$	10.01(0.10)			
	R_5	12.15(0.14)			
	HR_5^+	16.72(0.20)			
6	R	–			
	HR	3.22**			
	R_2	3.25**	5.7	7	14.1
	HR_2^+	7.27**			
	$H_2R_2^{2+}$	9.96(0.08)			
	R_6	15.05(0.14)			
	HR_6^+	19.17(0.15)			

* It was suggested to supplement the model with the reactions between the prevailing components, which improves the quality of the experiment description in the region of the experiment plan with maximal discrepancies ξ_k: $3R = R_3$ (step 1), $H^+ + R_3 = HR_3^+$ (step 2).

** Parameter was not refined.

Table 5. Parameters of equilibria in 3.9×10^{-3} M rhodamine B solutions with additions of 0.01 M β-CD at 25°C

Reaction	log β	χ^2_{exp}	f	χ^2_f ($\alpha = 0.05$)
$H^+ + R \rightleftarrows HR^+$	3.45(0.005)			
$2R \rightleftarrows R_2$	Parameter is insignificant: R_2 is absent	18.3	45	59.3
$H^+ + 2R \rightleftarrows HR_2^+$	6.03(0.02)			

conditions, we prefer the simplest hypothesis on the composition of the reaction products, though understanding that this hypothesis is approximate and partially conventional. Figure 4 shows the degrees of formation α_c(%) of rhodamine B chemical species H_iR_j (charges are omitted), calculated in the points of the titration curve.

$$\alpha_c = \frac{j[H_iR_j]}{\sum_j j[H_iR_j]} \times 100.$$

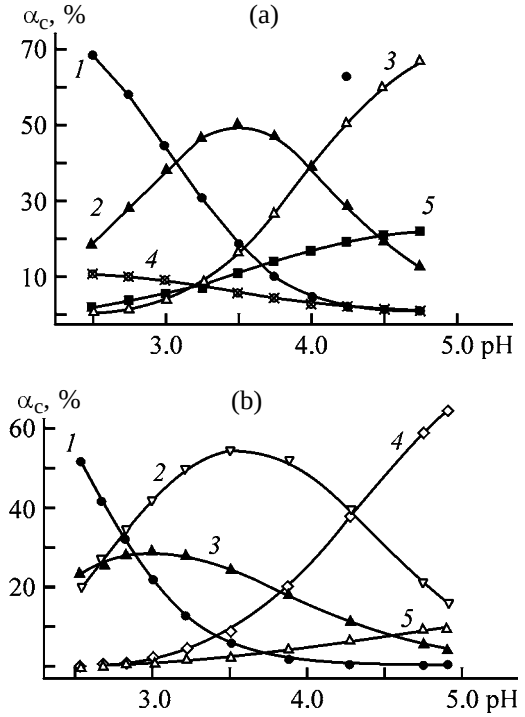

Fig. 4. pH dependence of the degree of formation α_c of various rhodamine B species. c_d (M): (a) 4×10^{-3} and (b) 2×10^{-2}. (a) (*1*) $H_2R_2^{2+}$, (*2*) HR_2^+, (*3*) R_2, (*4*) HR^+, and (*5*) R. (b) (*1*) $H_2R_2^{2+}$, (*2*) HR_3^+, (*3*) HR_2^+, (*4*) R_3, and (*5*) R_2; the degree of formation of HR^+ does not exceed 3.9%, and that of R, 6.7% (not shown in Fig. 4b).

It is interesting to determine how the presence of β-CD in the highest possible concentration of 0.01 M will affect the equilibria in HRCl solutions. It is known that β-CD forms complexes with rhodamine B monomers, decomposing the dimers [16].

Using the same scheme, we studied equilibria in the solutions with $c_d = 3.9 \times 10^{-3}$ M by titration with an NaOH solution of the same concentration (Fig. 2b). The simulation results (Table 5) convincingly show that, indeed, the association processes are sharply suppressed: R_2 fully disappears, and the HR_2^+ stability constant decreases by a factor of more than 10.

On the whole, the simulation results prove the fact that association of rhodamine B molecules in aqueous solutions is not limited to formation of the dimers R_2, HR_2^+, and $H_2R_2^{2+}$. With increasing c_d, the composition of the prevailing species changes: from monomers and dimers in dilute solutions to at least trimers in concentrated solutions. Additions of β-CD do not completely decompose the HR_2^+ species, but substantially suppress rhodamine B association.

The steric structure of rhodamine B dimers was considered in [17, 32, 34]; in all the cases, the mutual orientation of the chromophoric systems is close to parallel. Such an orientation does not exclude the interaction of carboxyphenyl fragments with each other. Probably, this causes association of R with HR^+ with the highest constant of 1.2×10^4 exceeding the constant of R dimerization (2×10^3). It is likely that, along with hydrophobic and π–π electronic interaction of the chromophoric systems, the $-C_6H_5-COOH\cdots OOC-C_6H_5-$ coupling, similar to that occurring between benzoic acid molecule and benzoate ion, makes a significant contribution.

However, stronger, as compared to R dimerization, association of HR^+ with HR^+ (equilibrium constant 5×10^3) is still difficult to explain (and this is in conflict with certain spectrophotometric data [11, 18, 34]). In this case, participation of Cl^- in formation of more complex associates can be assumed. However, experiments performed with a membrane ion-selective electrode in the absence of supporting electrolyte do not allow reliable conclusion because of insufficient reproducibility of pCl measurements under these conditions. As to the steric structure of R_3 or HR_3^+, we cannot make any definite assumptions. As a whole, within the concentration range studied, rhodamine B solutions can be considered as systems intermediate between solutions of monomers and of aggregates with less ordered structures and size approaching that of colloid particles.

CONCLUSIONS

(1) In 5×10^{-4} M solutions of rhodamine B (R), the pH-metric study revealed, along with neutral molecules R and cations HR^+, also the dimeric species R_2 and HR_2^+.

(2) Within the intermediate concentration range (~0.004–0.005 M), the dimeric species R_2, HR_2^+, and $H_2R_2^{2+}$ prevail in the solution, while the content of the monomeric species does not exceed 25%.

(3) In concentrated solutions of rhodamine B, associates consisting of at least three dye molecules exist, with the content of monomeric species being less than 10%.

(4) Using chemometric methods, the most probable values of the equilibrium constants of reaction (1) were determined: $\log\beta_{21}$ = 7.25–7.4, $\log\beta_{22}$ = 10.1–10.4, $\log\beta_{30} \approx 6.4-6.8$, and $\log\beta_{31} \geq 10$.

(5) β-Cyclodextrin introduced into the dye solution decomposes the dimers R_2 and decreases the stability constant of HR_2^+ by more than an order of magnitude.

(6) On the whole, solutions of rhodamine B in the concentration interval studied can be considered as transition systems between solutions of monomers and aggregates with less ordered structure and the size approaching that of colloid particles.

REFERENCES

1. Krasovitskii, B.M. and Bolotina, B.M., *Organicheskie lyuminofory* (Organic Luminophores), Moscow: Khimiya, 1984.
2. Preininger, C., Mohr, G.J., Klimant, I., and Wolfbeins, O.S., *Anal. Chim. Acta*, 1996, vol. 334, pp. 113–123.
3. Shtykov, S.N., Klimov, B.N., Naumenko, G.Yu., *et al.*, *Zh. Fiz. Khim.*, 1999, vol. 73, no. 9, pp. 1689–1691.
4. Zhang, Y.-Z., Cao, W.-X., and Xu, J., *Chin. J. Chem.*, 2002, vol. 20, no. 4, pp. 322–326.
5. Geddes, C.D., *J. Fluorescence*, 2002, vol. 12, no. 3/4, pp. 343–367.
6. Burgett, B.C., in *Aggregation Processes in Solution*, 1983, pp. 241–270.
7. Kessler, Yu.M. and Zaitsev, A.L., *Sol'vofobnye effekty* (Solvophobic Effects), Leningrad: Khimiya, 1989.
8. Murakami, K., *Dyes Pigm.*, 2002, vol. 53, no. 1, pp. 31–43.
9. Adamovich, L.P., Mel'nik, V.V., and Mchedlov-Petrosyan, N.O., *Zh. Fiz. Khim.*, 1979, vol. 53, no. 2, pp. 356–359.
10. Mchedlov-Petrossyan, N.O., Kukhtik, V.I., and Bezugliy, V.D., *J. Phys. Org. Chem.*, 2003, vol. 16, pp. 380–397.
11. Ramette, R.W. and Sandell, E.B., *J. Am. Chem. Soc.*, 1956, vol. 78, no. 19, pp. 4872–4878.
12. Kalousek, I., Jandarova, D., and Vodrazka, Z., *Int. J. Biol. Macromol.*, 1980, vol. 2, no. 4–6, pp. 284–288.
13. Woislawski, S., *J. Am. Chem. Soc.*, 1953, vol. 75, no. 21, pp. 5201–5203.
14. Mchedlov-Petrossyan, N.O. and Mel'nik, V.V., *Sopostavlenie razlichnykh metodov issledovaniya kislotno-osnovnykh svoistv rodamina B* (Comparison of Methods for Studying Rhodamine B Acid–Base Properties), Available from ONIITEKhim, Cherkassy, February 20, 1979, no. 2395-79.
15. Mchedlov-Petrosyan, N.O., *Zh. Fiz. Khim.*, 1982, vol. 56, no. 1, pp. 94–98.
16. Degani, Y., Willner, I., and Haas, Y., *Chem. Phys. Lett.*, 1984, vol. 104, no. 5, pp. 496–499.
17. Gal, M.E., Kelly, G.R., and Kurucsev, T., *J. Chem. Soc., Faraday Trans.*, 1972, vol. 69, pp. 395–402.
18. Lopez Arbeloa, I. and Ojeda, P.R., *Chem. Phys. Lett.*, 1981, vol. 79, no. 2, pp. 347–350.
19. Mchedlov-Petrosyan, N.O., A Study of Ionic Equilibria of Xanthene Series Analytical Reagents, *Cand. Sci. (Chem.) Dissertation*, Kharkov, 1979.
20. Kolthoff, I.M., *J. Am. Chem. Soc.*, 1965, vol. 87, no. 20, pp. 4428–4436.
21. Martell, A. and Smith, R., *Critical Stability Constants*, New York: Plenum, 1982, vol. 5.
22. Anosov, V.Ya, Ozerova, N.I., and Fialkov, Yu.Ya., *Osnovy fiziko-khimicheskogo analiza* (Foundations of Physicochemical Analysis), Moscow: Nauka, 1976.
23. Mchedlov-Petrosyan, N.O., Chemical Equilibria of Multifunctional Compounds of Xanthene and Triphenylmethane Series in Nonaqueous Media, *Doctoral (Chem.) Dissertation*, Ivanovo, 1992.
24. Mchedlov-Petrosyan, N.O., Vodolazkaya, N.A., and Doroshenko, A.O., *J. Fluorescence*, 2003, vol. 13, no. 3, pp. 235–248.
25. Bugaevsky, A.A. and Kholin, Yu..V., *Anal. Chim. Acta*, 1991, vol. 249, pp. 353–365.
26. Kholin, Yu.V., *Kolichestvennyi fiziko-khimicheskii analiz kompleksoobrazovaniya v rastvorakh i na poverkhnosti khimicheski modifitsirovannykh kremnezemov: soderzhatel'nye modeli, matematicheskie metody i ikh prilozheniya* (Quantitative Physicochemical Analysis of Complex Formation in Solutions and on the Surface of Modified Silicas: Substantial Models, Mathematical Methods, and Their Applications), Kharkov: Folio, 2000.
27. Mernyi, S.A., Konyaev, D.S., and Kholin, Yu.V., *Vestn. Khar'k. Univ., Khim.*, 1998, pp. 112–120.

28. Kholin, Yu.V., Konyaev, D.S., and Mernyi, S.A., *Vestn. Khar'k. Univ., Khimiya*, 1999, pp. 17–35.
29. Vuchkov, I., Boyadzhieva, L., and Solakov, E., *Prilozhen lineen regresonen analiz* (Applied Linear Regression Analysis), Sofia: Tekhnika, 1984.
30. Bol'shov, Kh.N. and Smirnov, N.V., *Tablitsy matematicheskoi statistiki* (Tables of Mathematical Statistics), Moscow, Nauka, 1983.
31. Osten, D.W., *J. Chemometrics*, 1988, vol. 2, pp. 39–48.
32. Lopez Arbeloa, F., Ruiz Ojeda, P., and Lopez Arbeloa, I., *Chem. Phys. Lett.*, 1988, vol. 148, nos. 2–3, pp. 253–258.
33. Komar', N.P., *Khimicheskaya metrologiya* (Chemical Metrology), vol. 1: *Gomogennye ionnye ravnovesiya* (Homogeneous Ionic Equilibria), Kharkov: Vishcha Shkola, 1983.
34. Lopez Arbeloa, F., Rodriguez Liebana, Y., Cordero Fernandez, E., and Lopez Arbeloa, I., *Spectrochim. Acta, Part A*, 1989, vol. 45, no. 12, pp. 1201–1206.

Russian Journal of Applied Chemistry, Vol. 77, No. 3, 2004, pp. 423–426. Translated from Zhurnal Prikladnoi Khimii, Vol. 77, No. 3, 2004, pp. 430–433.

ORGANIC SYNTHESIS AND INDUSTRIAL ORGANIC CHEMISTRY

Reactivity of Arylhydrazones toward Molecular Oxygen

E. I. Khizhan, T. A. Filippenko, and A. N. Nikolaevskii

Donetsk National University, Donetsk, Ukraine

Received September 30, 2003

Abstract—The kinetics and mechanism of reaction of arylhydrazones with molecular oxygen were studied by gas volumetry. The reaction rate was studied in relation to the structure of arylhydrazone and kind of the solvent. The inhibiting power of the compounds toward initiated oxidation of ethylbenzene was evaluated, and the most effective compounds were found, judging from the ratio of the rate constants of the reactions with molecular oxygen and with peroxy radicals arising in the course of ethylbenzene oxidation.

We found previously [1, 2] that arylhydrazones derived from aromatic and heterocyclic aldehydes exhibit pronounced antioxidant properties. The inhibiting effect of these compounds in radical chain oxidation of organic substances is due to termination of oxidation chains by reaction with the peroxy radicals $RO_2^{\bullet}$ arising in the course of the substrate oxidation. However, despite the high activity of virtually all the tested arylhydrazones toward peroxy radicals, the stoichiometric inhibition coefficient *f* (number of radicals decaying on one antioxidant molecule) and induction period τ (time during which the agent inhibits oxidation), characterizing their overall antioxidant effect, are relatively low and depend on the structure of the compounds. This may be due to participation of antioxidant molecules in side reactions (nonproductive consumption). Since the reaction system in the course of oxidation contains not only $RO_2^{\bullet}$ radicals but also other oxidants such as molecular oxygen, partial consumption of hydrazones in reaction with this oxidant should be expected.

Studying oxidation of arylhydrazones with molecular oxygen is necessary for gaining better insight into the mechanism of the effect of such active radical scavengers as arylhydrazones. Furthermore, studying the reactivity of arylhydrazones toward oxygen is closely related to the problem of stabilization of organic compounds, since this reaction largely determines the performance and service life of these oxidation inhibitors. Available data [3] on the mechanisms and kinetics of oxidation of arylhydrazones with molecular oxygen are scarce and do not allow definite conclusions concerning the influence of the structure of arylhydrazones and oxidation conditions on their reactivity and the role of this reaction in inhibited oxidation processes. This problem is considered in our paper.

EXPERIMENTAL

The reactivity of arylhydrazones of the general formula $R^2R^3C{=}NNHR^1$ (R^1 = Ph; R^2 = Ar; R^3 = H, Me) toward molecular oxygen was studied in the temperature range 303–358 K in various solvents (chlorobenzene, ethylbenzene, ethanol) by gas volumetry [4]. The antioxidant activity of arylhydrazones in initiated [azobis(isobutyronitrile) initiator] oxidation of ethylbenzene was studied by a chemiluminescence method [4]. The products of arylhydrazone oxidation with molecular oxygen were identified by UV spectroscopy (Specord UV VIS spectrophotometer, chloroform solutions) and TLC (Silufol plates, eluent chloroform–benzene–hexane–methanol, 30 : 6 : 1 : 1).

The kinetic curves of oxygen uptake in oxidation of various arylhydrazones (Fig. 1a) show that these compounds actively react with oxygen. In the initial portions of the curves, oxidation occurs at a constant rate depending on the structure of the compound and its initial concentration. As judged from the dependences of the reaction rates on the oxygen and arylhydrazone concentrations, with all the arylhydrazones studied the reaction is first-order with respect to both reactants. The reaction rate constants are listed in Table 1. The inertness of the disubstituted hydrazone toward molecular oxygen suggests that the oxidation primarily involves the NH group of the hydrazone moiety. The autooxidation of hydrazones occurs by the radical mechanism [3]; the primary reaction is formation of the *N*-hydrazonyl radical:

$$R^2R^3C{=}N{-}NHR^1 + O_2 \xrightarrow{k_{O_2}} R^2R^3C{=}N{-}\dot{N}R^1 + HO_2^{\bullet}.$$

This radical occurs in an equilibrium with the

1070-4272/04/7703-0423 © 2004 MAIK "Nauka/Interperiodica"

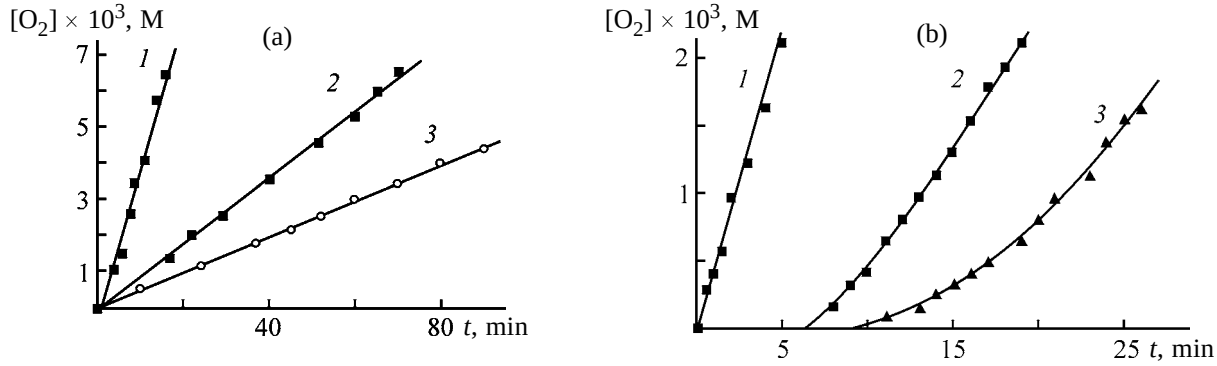

Fig. 1. Kinetic curves of oxygen uptake in oxidation of phenylhydrazones. (*t*) Time; the same for Fig. 2. Temperature, K: (a) 343 and (b) 323. Solvent: (a) chlorobenzene and (b) benzene. Phenylhydrazone derived (a) from (*1*) benzaldehyde, (*2*) cinnamaldehyde, and (*3*) 4-chlorobenzaldehyde; (b) from (*1*, *3*) benzaldehyde and (*2*) 3,5-di-*tert*-butyl-4-hydroxybenzaldehyde. Hydrazone concentration, M: (a) (*1*, *2*) 2×10^{-2} and (*3*) 5×10^{-2}; (b) (*1*) 2×10^{-2}, (*2*) 5×10^{-2}, and (*3*) $2 \times 10^{-2} + 2 \times 10^{-3}$ Ionol.

Table 1. Kinetic parameters of the reactions of arylhydrazones derived from aromatic aldehydes and acetophenone with molecular oxygen (k_{O_2}) and with peroxy radicals generated from ethylbenzene (f, $k_{RO_2^{\bullet}}$), T = 343 K

Hydrazone	k_{RO_2}	$k_{RO_2^{\bullet}}$	f	D_{N-H}, kJ mol^{-1}
	l mol^{-1} s^{-1}			
Ph–NH–N=CH–Ph Benzaldehyde phenylhydrazone	$(2.93 \pm 0.09) \times 10^{-2}$	$(1.20 \pm 0.07) \times 10^{6}$	1.0	267
Ph–NH–N=CH–C_6H_4Cl-4 4-Chlorobenzaldehyde phenylhydrazone	$(8.6 \pm 0.4) \times 10^{-3}$	$(1.18 \pm 0.09) \times 10^{6}$	1.1	267
Ph–NH–N=CH–C_6H_4OMe-4 4-Methoxybenzaldehyde phenylhydrazone	$(3.7 \pm 0.2) \times 10^{-2}$	$(1.24 \pm 0.09) \times 10^{6}$	1.3	266
Ph–NH–N=CH–$C_6H_4(NMe_2)$-4 4-*N*,*N*-Dimethylaminobenzaldehyde phenylhydrazone	$(4.17 \pm 0.17) \times 10^{-2}$	$(1.3 \pm 0.1) \times 10^{6}$	1.3	266
Ph–NH–N=CH–C_6H_4OH-2 2-Hydroxybenzaldehyde phenylhydrazone	$(6.4 \pm 0.2) \times 10^{-4}$	$(1.3 \pm 0.1) \times 10^{6}$	1.4	266
Ph–NH–N=CH–$C_6H_3(OH)_2$-2,4 2,4-Dihydroxybenzaldehyde phenylhydrazone	$(1.75 \pm 0.05) \times 10^{-3}$	$(2.7 \pm 0.2) \times 10^{6}$	2.1	256
Ph–NH–N=CH–C_6H_3OH-2-Br-5 5-Bromo-2-hydroxybenzaldehyde phenylhydrazone	$(4.1 \pm 0.2) \times 10^{-4}$	$(7.7 \pm 0.4) \times 10^{5}$	1.4	–
Ph–NH–N=CH–C_6H_2OH-4-(Bu-*t*)$_2$-3,5 3,5-Di-*tert*-butyl-4-hydroxybenzaldehyde phenylhydrazone	$(4.2 \pm 0.2) \times 10^{-3}$	$(2.6 \pm 0.3) \times 10^{6}$	1.9	–
Ph–NH–N=C(CH_3)–C_6H_5 Acetophenone phenylhydrazone	$(7.50 \pm 0{,}27) \times 10^{-2}$	–	–	–
Ph–NH–N=CH–CH=CH-Ph Cinnamaldehyde phenylhydrazone	$(1.6 \pm 0.3) \times 10^{-2}$	$(1.1 \pm 0.1) \times 10^{6}$	1.2	268
Ph–N(–CH_2Ph)–N=CH–Ph	Does not react with O_2 and ethylbenzene peroxy radicals			

C-radical:

$$R^2R^3C{=}N{-}\dot{N}R \rightleftarrows R^2R^3\dot{C}{-}N{=}NR.$$

Then the radicals add oxygen to form azo hydroperoxides or recombine to form dimeric products. UV spectroscopic and chromatographic study shows that the final product of benzaldehyde phenylhydrazone oxidation is N^1,N^3-diphenyl-N^4-benzylidenebenzhydrazidine (λ 288, 345 nm; R_f 0.87) formed by recombination of the *C*- and *N*-radicals.

Table 1 shows that electron-acceptor substituents in the aldehyde moiety decelerate, and electron-donor substituents accelerate oxidation of arylhydrazones with O_2.

In contrast to other electron-donor substituents, the hydroxy group introduced into the aldehyde moiety considerably enhances the resistance of the arylhydrazone to oxidation with molecular oxygen. The kinetic curves of the oxygen uptake with hydroxybenzaldehyde arylhydrazones show well-defined induction periods (Fig. 1b), which is apparently due to participation of phenolic hydroxyl in inhibition of the radical oxidation of the NH group with oxygen. This assumption is confirmed by the fact that the kinetic curve of the oxygen uptake in oxidation of benzaldehyde phenylhydrazone in the presence of Ionol (well-known phenolic antioxidant) has a similar shape.

The higher, compared to other hydrazones, rate constant of the reaction of acetophenone phenylhydrazone with oxygen is apparently due to existence of this hydrazone in the enehydrazine form, which is more readily oxidizable than the hydrazone form [3].

A study of the solvent effect on the oxidation rate shows (Fig. 2) that the reaction of phenylhydrazones with O_2 in ethanol is considerably slower than in aromatic solvents, which is due to hydrogen bonding of ethanol with the reaction center of arylhydrazone. Oxidation of arylhydrazone with oxygen in ethylbenzene does not lead to additional chain initiation and hence to acceleration of the hydrocarbon oxidation. This fact indicates that the radicals generated in oxidation of arylhydrazones show no initiating effect, since they recombine with each other to form a dimer; this dimer was detected experimentally.

In the course of ethylbenzene oxidation inhibited with arylhydrazones, the inhibitor will be consumed both in the reaction with peroxy radicals generated from the hydrocarbon [5]

$$R^2R^3C{=}N{-}NHR^1 + RO_2^{\bullet} \xrightarrow{k_{RO_2^{\bullet}}} R^2R^3C{=}N{-}\dot{N}R^1 + ROOH,$$

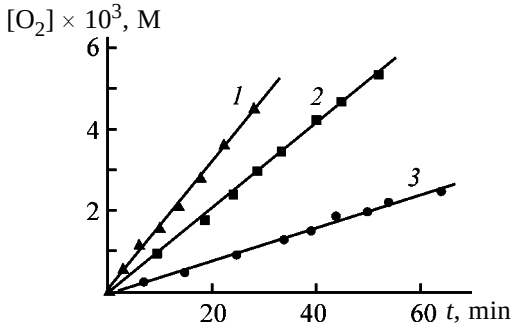

Fig. 2. Kinetic curves of oxygen uptake in oxidation of 4-chlorobenzaldehyde phenylhydrazone (5×10^{-2} M) in (*1*) chlorobenzene, (*2*) ethylbenzene, and (*3*) ethanol. T = 343 K; $[O_2] = 10^{-2}$ M.

and in the reaction with oxygen. Comparison of the rate constants of the reactions of arylhydrazones with oxygen and peroxy radicals (Table 1) shows that the contribution of the reaction with oxygen to the total consumption of arylhydrazones is in some cases low. This primarily concerns phenylhydrazones containing hydroxy groups in the aldehyde moiety, namely, the derivatives of 5-bromo-2-hydroxybenzaldehyde and salicylaldehyde. Specifically these compounds, being fairly active toward peroxy radicals generated from ethylbenzene, are of practical interest as antioxidants.

The majority of the arylhydrazones studied are relatively reactive toward molecular oxygen. As oxidation of arylhydrazones involves homolytic cleavage of the N–H bond, the rate constants k_{O_2} and $k_{RO_2^{\bullet}}$ linearly correlate with the dissociation energy of the N–H bond, D_{N-H}. This quantity was calculated by the PM3 semiempirical method using MOPAC-97 software. The low dissociation energies of the N–H bonds (Table 1), on the one hand, are responsible for the high reactivity of arylhydrazones toward radicals, but, on the other hand, result in nonproductive consumption of the antioxidants in side reactions.

Therefore, to develop new antioxidants of the hydrazone series, it would be appropriate to decrease somewhat the activity of the NH group in oxidation by increasing the strength of the N–H bond. This can be done by introducing heterocyclic substituents into the hydrazine moiety. As seen from Table 2, good results are obtained with hydroxybenzaldehyde quinoxalinohydrazone **III**. This compound is characterized by high rate constant of peroxy radical termination $k_{RO_2^{\bullet}}$ and high stoichiometric coefficient of inhibition; at the same time, it shows low reactivity toward molecular oxygen. Furthermore, antioxidants of such a structure exhibit biological activity. Our results will be useful in further search for effective antioxidants of the hydrazone series.

Table 2. Parameters of the antioxidant effect of hydrazones in initiated oxidation of ethylbenzene (V_i = 5.4 × 10^{-7} mol l^{-1} s^{-1}, T = 343 K)

Hydrazone	f	$k_{RO_2^\bullet}$, l mol^{-1} s^{-1}
I	0.2	$(3.5 \pm 0.1) \times 10^4$
II	0.8	$(3.60 \pm 0.16) \times 10^4$
III	1.7	$(9.4 \pm 0.4) \times 10^4$

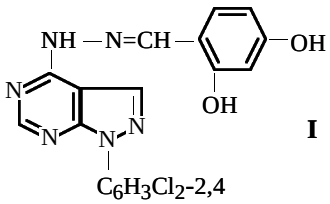

I

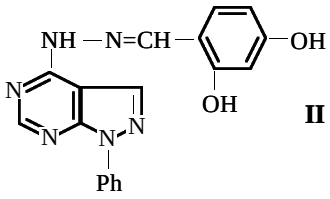

II

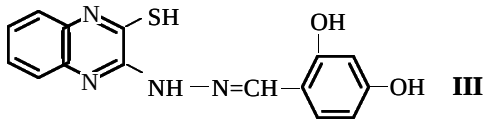

III

CONCLUSIONS

(1) A kinetic study of the reaction of arylhydrazones with molecular oxygen showed that the reactive fragment is the NH group of the hydrazone moiety.

(2) Electron-donor substituents in the aldehyde moiety enhance the activity of arylhdyrazones, and electron-acceptor substituents decrease it.

(3) The strength of the N–H bond in hydrazone molecules correlates with their reactivity in oxidation with both peroxy radicals and oxygen. High reactivity toward O_2 decreases the performance of antioxidants.

(4) Arylhdyrazones derived from hydroxybenzaldehydes are more resistant to oxidation with oxygen and are therefore effective antioxidants.

REFERENCES

1. Pleskushkina, E.I., Nikolaevskii, A.N., and Filippenko, T.A., *Zh. Prikl. Khim.*, 2001, vol. 74, no. 5, pp. 770–774.
2. Nikolaevskii, A.N., Pleskushkina, E.I., and Filippenko, T.A., *Neftekhimiya*, 2000, vol. 40, no. 2, pp. 145–148.
3. Kitaev, Yu.P. and Buzykin, B.I., *Gidrazony*, Moscow: Nauka, 1974.
4. Emanuel', N.M., Denisov, E.T., and Maizus, Z.K., *Tsepnye reaktsii okisleniya uglevodorodov v zhidkoi faze* (Chain Reactions of Liquid-Phase Oxidation of Hydrocarbons), Moscow: Nauka, 1965.
5. Pleskushkina, E.I., Filippenko, T.A., and Artemova, V.V., *Visn. Donets'k. Univ., Ser. A: Prirodn. Nauki*, 2001, no. 1, pp. 185–191.

Russian Journal of Applied Chemistry, Vol. 77, No. 3, 2004, pp. 427–429 Translated from Zhurnal Prikladnoi Khimii, Vol. 77, No. 3, 2004, pp. 434–436.

ORGANIC SYNTHESIS AND INDUSTRIAL ORGANIC CHEMISTRY

Kinetics of Hydroxyethylation of Dimethylamine

S. M. Danov, V. A. Kolesnikov, R. V. Efremov, and D. Yu. Mezhenin

Dzerzhinsk Branch, Nizhni Novgorod State Technical University, Dzerzhinsk, Nizhni Novgorod oblast, Russia

Received October 6, 2003

Abstract—The kinetics of hydroxyethylation of dimethylamine with oxirane was studied in the temperature interval 20–50°C at the oxirane : dimethylamine molar ratio of 1 : 3. The influence exerted on the reaction rate by the reaction product, dimethylethanolamine, was examined.

Dimethylethanolamine (DMEA), hydroxyethylation product of dimethylamine (DMA), is widely used in basic organic synthesis, as solvent in paint-and-varnish production, and as a component of cleansing, degreasing, preserving, hydraulic, and cutting fluids.

DMEA is synthesized in industry by liquid-phase hydroxyethylation of DMA. At one of the enterprises, the synthesis is performed in a coaxial-pipe reactor at 80–175°C, pressure of 5–6 MPa, and DMA : oxirane (OX) molar ratio of 3 : 1.

However, the quality of the DMEA produced is poor, because the conditions in the reactor are far from being optimal. Because of inefficient heat exchange, the temperature in the reactor rises to 175°C, whereas the available papers recommend much lower synthesis temperatures.

In this work we studied the kinetics of DMA hydroxyethylation with the aim to obtain data required for optimizing the reactor design and operation conditions. It is known that, in the absence of proton donors, amines do not react with oxirane or react very slowly [1]. Lebedev and Smirnova [2–5] studied the reaction of oxirane with various amines manometrically. They found that proton donors (water, alcohol, phenols, acids) accelerate the reaction and that the reaction follows the first-order kinetic equation. The amino alcohol formed in the reaction also acts as a proton donor, causing an autocatalytic effect. The reaction follows the Brønsted relationship, and for each type of proton donors the logarithms of the rate constants correlate with the pK_a values.

In experiments without catalysts, in agreement with data of [1], no reaction initially occurred; the induction period became shorter with increasing temperature, but fully disappeared only at 230°C. After the end of the induction period, the reaction rate sharply grew, and the nitrogen atom underwent fast and selective hydroxyethylation. After completion of the substitution, at temperatures above 110°C, the reaction decelerated again, and above 150°C it almost fully stopped. However, at 70–100°C the reaction continued after substitution completion, yielding polyoxyethylated products. This phenomenon was explained by Sorokin and Shode [6–8]. They reported on formation of minor amounts of quaternary ammonium bases which catalyze successive hydroxyethylation as efficiently as do, e.g., alkali metal alcoholates. However, quaternary ammonium bases are unstable and decompose above 100°C with the regeneration of the tertiary amine.

It is also known that, in DMA hydroxyethylation, formation of the desired DMEA is accompanied by side reactions such as formation of dimethylaminoethoxyethanol (DMAEE), isomerization of oxirane into acetaldehyde, and dimerization and polymerization of oxirane [9]. The resulting products can undergo further transformations.

Preliminary experiments showed that the side reactions were insignificant at 20–60°C and DMA : oxirane molar ratio of 3 : 1. This ratio is used in the commercial synthesis, and therefore we chose it in our kinetic experiments.

The reaction rate was evaluated from accumulation of DMAE in the reaction mixture, monitored chromatographically. Figure 1 shows the kinetic curves of DMEA formation at various temperatures.

It is seen that the kinetic curves are S-shaped, which is typical of autocatalytic reactions. The DMEA formed in the process can donate protons activating the oxirane molecule. To confirm the occurrence of autocatalysis, we performed some experiments at 30°C with addition of DMEA to the starting mixture. The results are shown in Fig. 2.

1070-4272/04/7703-0427 © 2004 MAIK "Nauka/Interperiodica"

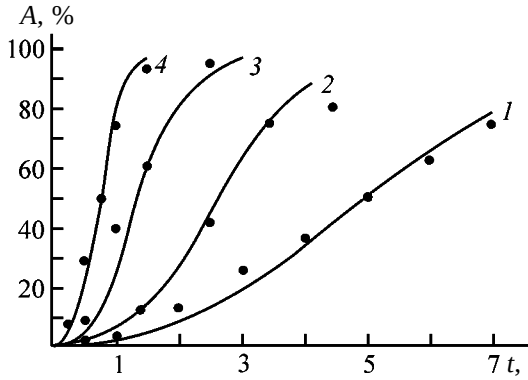

Fig. 1. Kinetic curves of DMEA formation at various tempereatures. (*A*) DMEA yield and (*t*) time; the same for Fig. 2. *T*, °C: (*1*) 20, (*2*) 30, (*3*) 40, and (*4*) 50. $n^0_{OX} \times 10^4$, mol: (*1*) 309.4, (*2*) 203.4, (*3*) 270.9, and (*4*) 317.0. $n^0_{DMA} \times 10^4$, mol: (*1*) 850.1, (*2*) 613.4, (*3*) 743.4, and (*4*) 903.7. Points are experimental data, and lines are calculated; the same for Fig. 2.

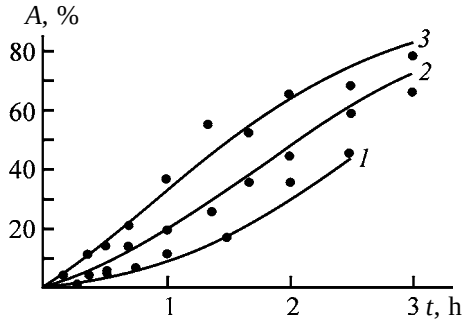

Fig. 2. Kinetic curves of DMEA formation at 30°C with addition of the target product to the starting mixture. $n^0_{OX} \times 10^4$, mol: (*1*) 203.4, (*2*) 420.1, and (*3*) 334.1. $n^0_{DMA} \times 10^4$, mol: (*1*) 613.4, (*2*) 1187.0, and (*3*) 965.8. $n^0_{DMEA} \times 10^4$, mol: (*1*) 0, (*2*) 30.1, and (*3*) 82.6.

Figure 2 shows that, as the concentration of DMEA in the starting mixture is increased, the curves lose their S-shape, and the reaction rate grows, confirming the occurrence of autocatalysis.

When developing a kinetic model, we assumed the reaction orders with respect to OX and DMA to be unity, in accordance with [2–5]. The reaction order with respect to DMEA was calculated from the experimental data. Thus, the rates of the noncatalytic (r_1) and catalytic (r_2) reactions were described by the equations

$$r_1 = k_1 c_1 c_2, \qquad r_2 = k_2 c_3^n c_1 c_2,$$

where k_1 is the rate constant of the noncatalytic reaction; k_2, that of the catalytic reaction; c_i, concentration (M) of component *i* (1, OX; 2, DMA; 3, DMEA); and *n*, reaction order with respect to DMEA.

The number of moles decreases in the course of the reaction; this decrease reaches 12% at complete conversion of OX. Therefore, the material balance equations for the components

$$dVc_i/dt = \nu_i V(r_1 + r_2),$$

were solved simultaneously with the equation for the volume change in the course of the reaction,

$$dVc_i/dt = \sum_{i=1}^{3} \nu_i V(r_1 + r_2)/\rho_i,$$

where *V* is the reaction mixture volume; *t*, time (min); ν_i, stoichiometric coefficient at component *i* ($\nu_1 = -1$, $\nu_2 = -1$, $\nu_3 = 1$); and ρ_i, molar density of component *i*.

The system of equations was integrated numerically by the fourth-order Runge–Kutta method. The order of the catalytic reaction with respect to DMEA was estimated from the kinetic curves (Fig. 2) obtained at different initial concentrations of DMEA in the reaction mixture. The reaction order with respect to DMEA *n* and the rate constants of the noncatalytic (k_1) and catalytic (k_2) reactions at $T = 30$°C were calculated so as to minimize the sum *F* of squared deviations between the calculated (b_i^c) and experimental (b_i^e) yields of DMEA in each point *i* for all the kinetic curves, taking into account the weight factors w_i ($T = 30$°C):

$$\min_{n,k_1,k_2} F = \sum_{i=1}^{N} w_i (b_i^c + b_i^e)^2,$$

where *N* is the number of experimental points.

To find the minimum of the function *F*, we used the modified gradient method.

We obtained the following values: $k_1 = 9.41 \times 10^{-5}$, $k_2 = 3.95 \times 10^{-4}$, and $n = 0.92$. As seen from Fig. 2, the calculated and experimental yields are well consistent. Since the reaction order with respect to DMEA is close to unity, in the subsequent calculationed we assumed $n = 1$.

The rate constants calculated similarly from the experimental data for various temperatures (Fig. 1) with $n = 1$ are listed in the table.

The parameters of the temperature dependence of the rate constants [$k = A\exp(-E/RT)$] of the noncatalytic (A_1, E_1) and catalytic (A_2, E_2) reactions were calculated so as to minimize the sum *F* of squared deviations between the experimental and calculated DMEA yields for all the experimental points shown

Rate constants k_i at various temperatures

T, °C	k_1, l mol^{-1} min^{-1}	k_2, l^2 mol^{-2} min^{-1}
20	2.85×10^{-5}	2.87×10^{-4}
30	9.41×10^{-5}	3.95×10^{-4}
40	6.13×10^{-5}	1.80×10^{-3}
50	2.96×10^{-4}	1.53×10^{-3}

in Figs. 1 and 2 and obtained at T = 20, 30, 40, and 50°C and different initial compositions of the reaction mixture:

$$\min_{A_1, E_1, A_2, E_2} F = \sum_{i=1}^{N} w_i (b_i^c + b_i^e)^2.$$

The calculated parameters of the Arrhenius equation are given below:

Rate constant	A	E, kJ mol^{-1}
k_1	9.25×10^5	58 800
k_2	1.75×10^5	49 800

The points in Fig. 1 show the experimental yields of DMEA, and lines correspond to the values calculated with these parameters.

Thus, our kinetic model adequately describes the experimental data and can be used to optimize the reaction unit for DMEA production.

EXPERIMENTAL

Oxirane [GOST (State Standard) 7568–88] and dimethylamine (GOST 9967–74) were used without additional purification. Dimethylethanolamine [TU (Technical Specifications) 6-02-1086–91] was purified by distillation on a 20 TP laboratory column. The moisture content in the purified product did not exceed 0.05%.

The starting mixture was prepared in a hermetically sealed glass ampule at –20°C. The mixture was charged into 0.5–0.7-ml ampules 5 mm in diameter, precooled to –20°C. The ampules were sealed and kept for a prescribed period in a water thermostat. Then the ampules were quickly cooled with water and then with an ice–salt mixture to –20°C. A 0.1–0.2-g sample was withdrawn from each ampule and transferred into a hermetically sealed vessel with a solvent (hexane, 10 ml). The solution was analyzed chromatographically (2000 × 3-mm column; stationary phase 3% OV-225 on Inerton; flame ionization detector; carrier gas N_2, flow rate 2 l h^{-1}; vaporizer and detector temperatures 170°C; programmed heating: 80°C, 3 min; heating to 140°C, 20 deg min^{-1}; and 140°C, 3 min).

CONCLUSIONS

(1) Hydroxyethylation of dimethylamine is an autocatalytic reaction. At the dimethylamine : oxirane molar ratio of 3 : 1, in the temperature interval 20–50°C, the reaction selectivity is close to 100%.

(2) A kinetic model of dimethylamine hydroxyethylation, adequately describing the experimental data, was suggested. The parameters of the temperature dependence of the rate constants of the catalytic and noncatalytic reactions were calculated.

REFERENCES

1. Schönfeldt, N., *Grenzflachenaktive Äthyleneoxid-Addukte*, Stuttgart: Wissenschaftliche, 1976.
2. Lebedev, N.N. and Smirnova, M.M., *Izv. Vyssh. Uchebn. Zaved., Khim. Khim. Tekhnol.*, 1960, vol. 3, no. 1, p. 104.
3. Lebedev, N.N. and Smirnova, M.M., *Kinet. Katal.*, 1961, vol. 2, no. 3, p. 519.
4. Lebedev, N.N. and Smirnova, M.M., *Kinet. Katal.*, 1965, vol. 6, no. 3, p. 457.
5. Lebedev, N.N. and Smirnova, M.M., *Zh. Obshch. Khim.*, 1969, vol. 39, no. 12, p. 2732.
6. Sorokin, M.F. and Shode, L.G., *Zh. Org. Khim.*, 1966, vol. 2, no. 8, p. 1463.
7. Sorokin, M.F. and Shode, L.G., *Zh. Org. Khim.*, 1966, vol. 2, no. 8, p. 1469.
8. Sorokin, M.F. *et al.*, *Kinet. Katal.*, 1968, vol. 9, no. 3, p. 548.
9. Zimakov, P.V., *Okis' etilena* (Ethylene Oxide), Moscow: Goskhimizdat, 1946.

Russian Journal of Applied Chemistry, Vol. 77, No. 3, 2004, pp. 430–434. Translated from Zhurnal Prikladnoi Khimii, Vol. 77, No. 3, 2004, pp. 437–441.

ORGANIC SYNTHESIS AND INDUSTRIAL ORGANIC CHEMISTRY

NMR Determination of the Total Composition of Commercial Absorbents Based on Monoethanolamine

V. P. Talzi

Omsk Branch, Boreskov Institute of Catalysis, Siberian Division, Russian Academy of Sciences, Omsk, Russia

Received October 10, 2003

Abstract—The composition of aqueous solution of monoethanolamine used in various units of gas treatment of the Omsk Oil-Refining Plant, Joint-Stock Company, was studied by the ^{13}C NMR spectroscopy. The components of the gases to be purified and the reactions producing the impurities were established.

Recently we studied by NMR the composition of absorbents used for treatment of processing gases to remove acidic impurities CO_2, H_2S, CS_2, and COS at the Omsk Oil-Refining Plant (ORP) [1]. This paper completes the development of a procedure for analysis of the total composition of absorbents produced on the basis of aqueous solutions of monoethanolamine (MEA), substantially refining the published data [1] on identification of components and schemes of side reactions.

As known, the absorption capacity and corrosive and surface activities of MEA solutions, which govern the efficiency of absorber operation, depend on the content of MEA decomposition products. Despite the lack of a procedure for direct analysis of the total composition of the absorbents in hand, decades of operation of amine gas treatment units resulted in correct identification of the absorbent components and development of a correct concept of their formation pathways. A practically complete review on the problem in hand was published 40 years ago in [2]. According to published data [1, 2], under the conditions of industrial gas treatment, carbamates and thiocarbamates **I**–**III**, respectively, are formed in the reaction of MEA with CO_2, COS, and CS_2:

$[HOCH_2CH_2NHCO_2^-][H_3N^+CH_2CH_2OH]$ (**I**),

$[HOCH_2CH_2NHCOS^-][H_3N^+CH_2CH_2OH]$ (**II**),

$[HOCH_2CH_2NHCSS^-][H_3N^+CH_2CH_2OH]$ (**III**).

Sulfide, a product of the reaction of hydrogen sulfide with MEA, gives a total NMR signal averaged with the amine signal; therefore, its content in the solution cannot be determined from the NMR data. Among compounds **I**–**III**, only carbamate **I** is contained in industrial absorbents. As a rule, it is a main component of saturated and regenerated MEA solutions at various treatment units.

Thio analogs of carbamate **I** are much more stable with respect to decomposition under conditions of absorbent regeneration into COS or CS_2 and MEA; therefore, Kohl and Riesenfeld believe [2] that any reaction of MEA with carbonyl sulfide and carbon disulfide results in irreversible loss of the absorbent. However, as mentioned in [1], after absorption of COS and CS_2, MEA can be regenerated by hydrolysis of thiocarbamates **II** and **III** to form carbamate **I**. The latter decomposes in regeneration to form MEA and carbon dioxide practically without by-products:

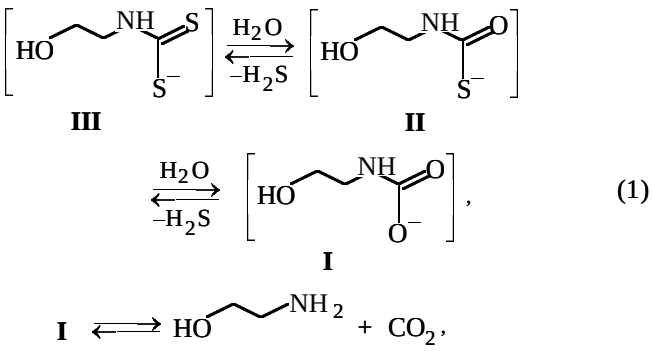

(1)

In our earlier work [1] we have not clearly formulated the established fact that compounds **IV**–**VII** are formed by the reaction of MEA with COS or CS_2 and subsequent transformations of the resulting carbamate **II**. In particular, it was suggested that carbamate **I** can also give impurities not removed in regen-

1070-4272/04/7703-0430 © 2004 MAIK "Nauka/Interperiodica"

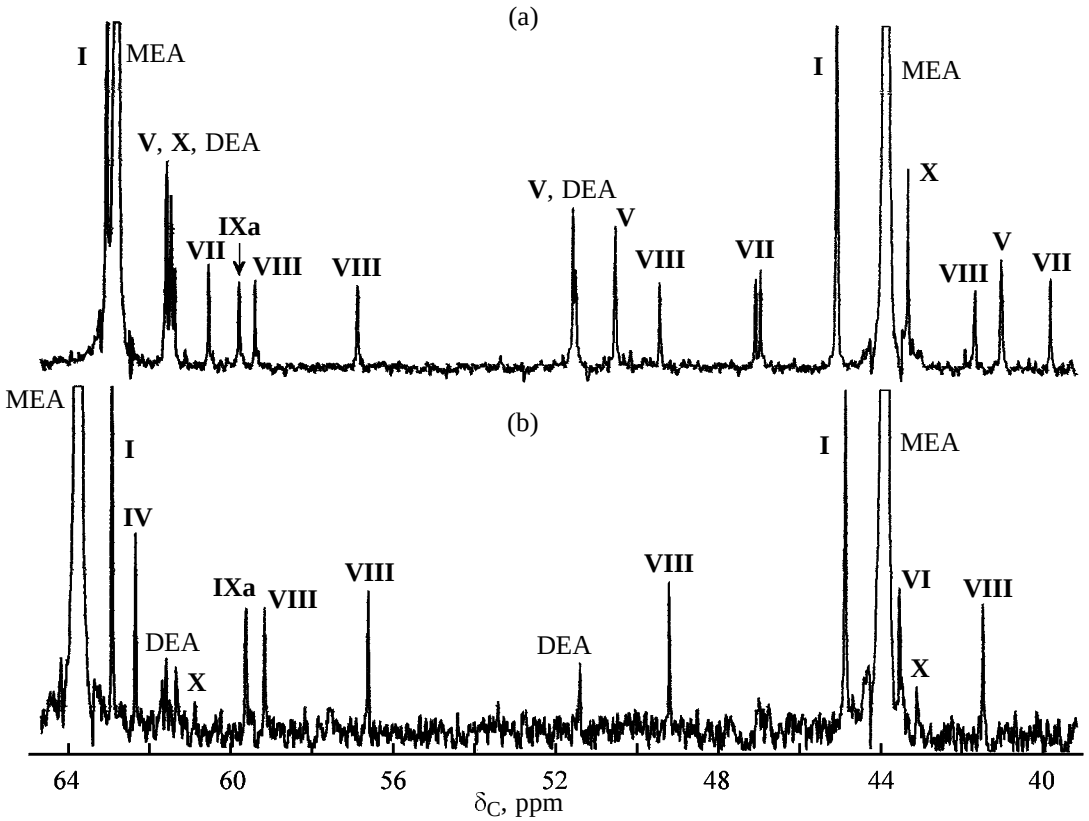

Fig. 1. Fragments of ^{13}C NMR spectra of the samples of (a) regenerated absorbent (AGFU) and (b) aqueous solution of MEA after regeneration (SPU). (δ_C) Chemical shift; the same for Fig. 2.

eration, e.g., **IV**, in a noticeable yield:

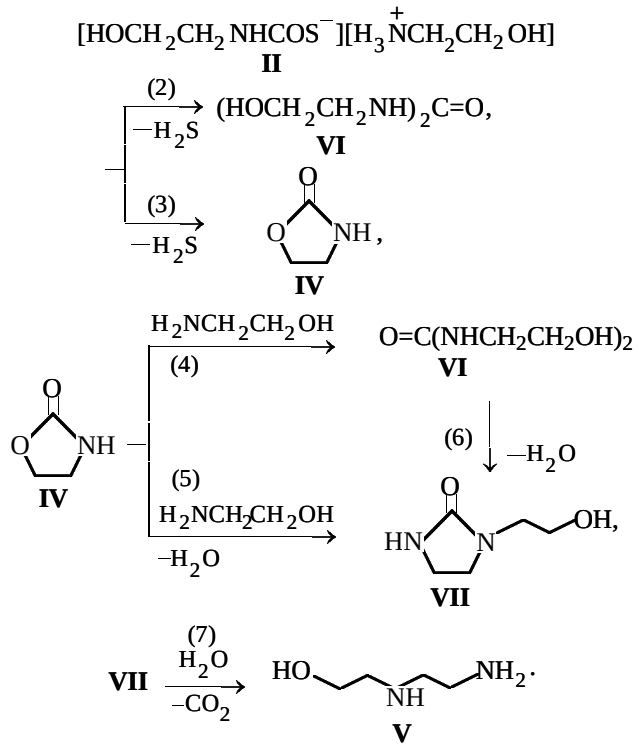

The above pathways of formation of impurities **IV**–**VII** [2, 3] were confirmed in [1] with significant refinement considering that, in the industrial saturated and regenerated absorbents, compound **IV** is absent completely and the main impurity originating from thiocarbamate **II** is urea analog **VI**. According to the NMR spectra, the concentrations of impurities **V**–**VII** are approximately 0.1–0.5%. Significant amounts of **V** and **VII** were detected only in a certain period of operation of absorption gas-fractionation unit (AGFU) at the Omsk ORP [1], and also small concentrations of **V** and **VII** were found in the similar absorbers used for gas treatment in catalytic cracking. We think that the most probable pathway of formation of **VII** is pathway (6), since at high intensities of the NMR signals of **V** and **VII** in the corresponding spectra the signals of **IV** are absent (Fig. 1a). Factors favoring conversion of **VI** to **VII** and then to diamine **V** are not exactly established. Under laboratory conditions, the attempts to attain reproducible formation of **V** and **VII** by heating of mixtures formed in saturation of MEA solutions with carbonyl sulfide failed [1]. It is likely that the catalyst of this reaction is iron chloride.

Thus, the content of **VI** or, more precisely, the total

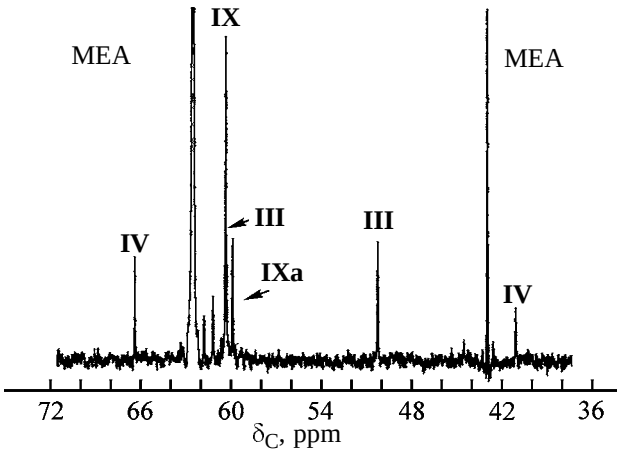

Fig. 2. Fragment of the ^{13}C NMR spectrum of carbon disulfide solution in aqueous MEA (15%) after keeping at 90°C for 0.5 h. Signals of **IV** appear as a result of hydrolysis of **III** with formation of **II**; ^{13}C signals of OCH_2 fragments of **III** and **IX** overlapp.

content of **V**–**VII** in MEA solutions varies in parallel with the concentration of carbonyl sulfide and carbon disulfide in the gases to be purified. In absorption of carbon disulfide, these compounds are formed by hydrolysis of dithiocarbamate **III** to thiocarbamate **II**.

The ^{13}C NMR spectra of two samples of the absorbent taken from the AGFU and the sulfur production unit (SPU) of the Omsk ORP are shown in Fig. 1. The concentrations of absorbent components can be estimated from the integral intensities of the corresponding signals by the standard procedure. In so doing, the contents of MEA and carbamate **I** can be determined fairly accurately from the ^{1}H NMR spectra discussed previously [1].

The series of compounds whose signals were correctly identified previously [1] in the spectra shown in Fig. 1 (see table) is restricted to **I**, **V**–**VII**, and diethanolamine (DEA). It turned out that one of the most typical groups of the signals at approximately 39, 49, 56, 58, and 59 ppm, observed in the spectra of the samples withdrawn from all the gas-treatment units at the Omsk ORP with exception of the hydrorefining unit, belongs to two compounds, as suggested previously [1]. The signals at 39, 49, 56, 58, and 172 ppm correspond to one compound, and the signal at 59 ppm, to another compound. This fact was established by analyzing the spectra of various absorbents and model solutions obtained by heating a mixture of aqueous MEA and carbon disulfide at 80–100°C.

According to reference data and reactions (2)–(6) [4], the signals at 39, 49, 56, 58, and 172 ppm belong to **VIII**, which is thio analog of **VII** and was identified in bottoms of a unit for amine treatment of coke-chemical gases [3]. The identification of the second compound formed owing to the presence of carbon disulfide in the gases to be purified is not so evident as in the case of **VIII**. The signal at 59 ppm was initially assigned to the CH_2OH group of a thiourea analog **IX**. We assumed that the signals of carbon atoms of the fragments C=S and NCH_2 structure (**IX**) are not observed because of broadening caused by hindered rotation around the thioamide bond N–CS. The similar phenomenon was observed in studying the ^{13}C NMR spectra of thiocarbamates derived from secondary amines [5]. Actually, in the spectrum of the model system formed by heating of a mixture of aqueous MEA and carbon disulfide to 100–120°C (Fig. 2), only the signal at 60 ppm corresponds to **IX**. At the same time, there is less strong signal at 59 ppm, which apparently belongs to analog **IXa** formed from **IX** by elimination of ethylene oxide molecule [reaction (9)]. Thus, the signal at 59 ppm observed in the spectra of absorbents presented in Figs. 1a and 1b can be assigned to **IXa**. This assumption is indirectly confirmed by signals at 162.2, 61.75, and 42.51 ppm, constantly appearing in the ^{13}C NMR spectra of MEA solutions saturated with carbonyl sulfide under laboratory conditions upon their heating at 120°C for approximately 0.5 h. These signals are observed along with much stronger signals of **VI** (see table) and apparently belong to an urea analog $NH_2(C{=}O)NHCH_2CH_2OH$ (**IVa**) formed from **VI** by elimination of ethylene oxide molecule.

Only some spectra of similar laboratory samples obtained by heating of a mixture of carbon disulfide and MEA contain the above signals at 39, 49, 56, and 58 ppm of **VIII**, and these signals are very weak:

$$[HOCH_2CH_2NHCSS^-][H_3\overset{+}{N}CH_2CH_2OH]$$

III

$$\xrightarrow[-H_2S]{(8)} (HOCH_2CH_2NH)_2C{=}S,$$

IX

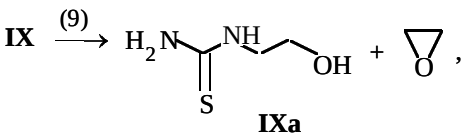

IXa

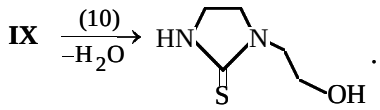

VIII

Thus, the content of **VIII** and **IXa** in the ab-

sorbents varies in parallel with the concentration of carbon disulfide in the gases to be treated.

Diethanolamine was correctly identified in the composition of the commercial absorbents previously [1], but a too complicated pathway of its formation was suggested. Actually, under conditions of gas treatment, MEA apparently decomposes to form ammonia and ethylene oxide. The latter gives DEA and also ethylene glycol [reactions (11)–(13)]. A weak signal at 64 ppm observed in the spectra of some samples corresponds to ethylene glycol but not to dioxolane considered in [1], which was proved by addition of the corresponding reagent to the absorbent:

$$HOCH_2CH_2NH_2 \xrightarrow{(11)} NH_3 + \text{ethylene oxide},$$

$$HOCH_2CH_2NH_2 + \text{ethylene oxide} \xrightarrow{(12)} \underset{\text{DEA}}{HN(CH_2CH_2OH)_2},$$

$$\text{ethylene oxide} + H_2O \xrightarrow{(13)} HOCH_2CH_2OH.$$

Under the conditions of gas treatment, decomposition of MEA to ammonia and ethylene oxide is catalyzed by acidic impurities to be absorbed. This conclusion was made based on the spectra of MEA solutions saturated with hydrogen sulfide and then regenerated under laboratory conditions. In some absorbers of the hydrofining unit, which purify hydrogen sulfide gases containing no carbonyl sulfide and carbon disulfide, the impurities in MEA solutions include only DEA and carbamate **I** (less than 0.1%). On other columns of this unit, an oxidation product of MEA, substituted oxamide **X**, is also detected.

Oxidation of MEA is one of the main causes of absorbent loss and deterioration of its performance. Oxidation of MEA yields oxalic acid and its amides [2]. The signal of oxalic acid at 174 ppm in the spectra of absorbent samples was correctly assigned previously, while the signals of **X** (see table, Fig. 1) were incorrectly assigned to another compound [1]. Under laboratory conditions the signals of **X** at 42.5 and 60.4 ppm and also signals with chemical shifts close to that of the corresponding monooxamide were observed in heating of a mixture of MEA and oxalic acid to approximately 150°C. With increasing excess of MEA with respect to oxalic acid, the intensity of signals of diamide increases relative to the monoamide and the intensity of carbonyl signals of amides at approximately 166–167 ppm decreases, so that at the concentration of **X** in the commercial absorbents of approximately 0.1% this signal of carbonyl, as a rule, is not observed:

Assignment of signals in the ^{13}C NMR spectra of model compounds and samples of industrial absorbents, aqueous solutions of monoethanolamine

Compound	Assignment of ^{13}C NMR signals, δ_C, ppm		
	NCH_2	CH_2OH	COX, X = O, S
MEA	43.89	63.57	
I	44.93	63.00	166.1
II	44.70	60.41	185.3
III	51.34	60.21	213.2
IV	40.52	66.71	163.3
V	50.75, 51.23, 39.05	60.30	
VI	43.59	62.41	161.8
VIa	42.51	61.75	162.2
VII	38.34, 46.82, 47.03	60.02	165.9
VIII	39.52, 49.20, 56.48	58.93	172.1
IX	None*	60.24	None
IXa	″	59.13	″
DEA	51.24	60.32	
X	42.5	60.37	None

* Signals not detected for various reasons considered in the text.

$$H_2NCH_2CH_2OH \xrightarrow[\text{Oxidation, } +O_2]{(14)} HOOCCOOH$$

$$2H_2NCH_2CH_2OH \xrightarrow[-2H_2O]{(15)}$$

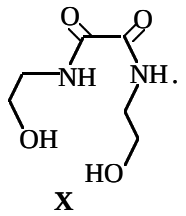

X

The content of amide **X** in the absorbent varies in parallel with the degree of its oxidative decomposition under the conditions of gas treatment.

The strongest signals in the ^{13}C NMR spectrum of the absorbent withdrawn from AGFU after regeneration (excluding MEA) (Fig. 1a) are the signals assigned to amide **X**; in this case, the signal of carbamate **I** is weak. According to process information for the absorbent in hand, the absorption of carbon dioxide was low. It is reasonable to explain this fact by the general acid catalyst of carbamate **I** decomposition to form MEA and CO_2 under the action of acids present in the absorbent. These acids can be oxalic

acid, since the content of oxamide **X** in these samples is noticeably higher than that in the samples withdrawn from the SPU (compare Figs. 1a and 1b), or hydrogen chloride present in these samples.

Actually, the spectrum of absorbents withdrawn from AGFU contains the signals of two carbon atoms of methyl groups (24 and 25 ppm) and associated signal of a quaternary carbon atom at approximately 182 ppm. The signals of methyl groups belong to different compounds, according to their relative intensities in the spectra. The intensity of these signals is comparable with the intensity of other signals in Fig. 1a. In the ^{1}H NMR spectra, the corresponding methyl protons give two singlets in the region of 1.8 ppm.

It is likely that the signals in hand belong to trimethylsulfonium chloride **XI** and the corresponding ylide **XII** formed in alkaline medium of the absorbent, which arise from chloromethane and dimethyl sulfide present in gases to be purified:

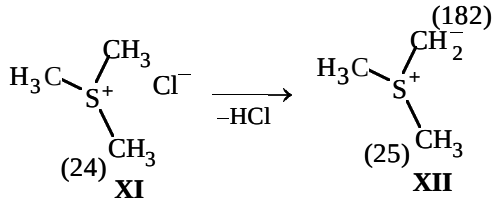

EXPERIMENTAL

The ^{13}C NMR spectra of absorbents and model mixtures were recorded by the standard procedures on a Bruker ACP 200-P spectrometer.

Under laboratory conditions, the gas treatment process was simulated on a setup consisting of a flask for generation of gases and absorption bottles. CO_2 and COS were generated by the action of sulfuric acid on sodium hydrocarbonate and potassium (or ammonium) thiocyanate, respectively. H_2S, CS_2, and ethylene glycol, used for synthesis and identification, were commercial chemicals of chemically pure grade.

Regeneration of absorbents was simulated ether by heating on a water bath or by boiling.

CONCLUSION

An NMR-based procedure was developed for determination of the total composition of industrial absorbents based on aqueous solutions of monoethanolamine. The impurities formed from carbonyl sulfide, carbon disulfide, oxygen, dimethyl sulfide, and chloromethane present in the gases to be purified, not removed in regeneration, were identified. These results allow better understanding of the dependence of the operation characteristics of the absorbent on its composition.

REFERENCES

1. Talzi, V.P. and Ignashin, S.V., *Zh. Prikl. Khim.*, 2002, vol. 75, no. 1, pp. 80–85.
2. Kohl, A.L. and Riesenfeld, F.C., *Gas Purification*, New York: McGraw-Hill, 1960.
3. Dmitrikov, V.P. and Nabichev, V.M., *Khim. Koks*, 1999, no. 10, pp. 21–25.
4. Levy, G.C. and Nelson, G.L., *Carbon-13 Nuclear Magnetic Resonance for Organic Chemists*, New York: Wiley, 1972.
5. Savin, V.P., Talzi, V.P., and Bek, N.O., *Zh. Org. Khim.*, 1984, vo. 20, no. 9, pp. 1842–1851.

Russian Journal of Applied Chemistry, Vol. 77, No. 3, 2004, pp. 435–437. Translated from Zhurnal Prikladnoi Khimii, Vol. 77, No. 3, 2004, pp. 442–444.

ORGANIC SYNTHESIS AND INDUSTRIAL ORGANIC CHEMISTRY

Process Parameters of Oxidative Chlorination of Benzene with the Participation of Nitrogen(IV) Oxide

A. I. Morozovskii, A. B. Solomonov, and V. I. Skudaev

Perm State Technical University, Perm, Russia

Received May 16, 2003

Abstract—The efficiency of replacing oxygen with nitrogen(IV) oxide in oxidative chlorination of benzene was studied. The optimal process parameters: temperature, time of contact, and relative content of reagent, were determined.

Synthesis of organochlorine compounds involves heavy loss of hydrogen chloride. Utilization of hydrogen chloride is possible in some cases, e.g., in synthesis of trichloroethylene and tetrachloroethylene by oxidative chlorination of hydrocarbons [1]. In these processes, a hydrocarbon is chlorinated with a mixture of hydrogen chloride with oxygen on a catalyst. Wide introduction of these processes is hindered by their low output capacity. Oxidative chlorination can be intensified by using oxidizing agents with activity exceeding that of oxygen. In this work we studied oxidative chlorination of benzene with a mixture of hydrogen chloride and nitrogen(IV) oxide on a solid catalyst based on copper(II) chloride.

EXPERIMENTAL

Nitrogen(IV) oxide obtained in the first oxidation reactor by mixing nitrogen(II) oxide with oxygen at room temperature was fed into the second oxidation reactor together with hydrogen chloride. The gaseous products (nitrosyl chloride, chlorine, and excess oxygen) and also benzene were delivered to a heated quartz reactor 1.4 cm in diameter and 50 cm high, packed with a fixed bed of a catalyst. The products obtained were analyzed chromatographically for the content of chlorobenzene. The efficiency of an oxidizing agent and a catalyst was evaluated by the conversion *A* of hydrogen chloride and specific yield *B* of chlorobenzene per 1 kg of the supported catalyst in 1 s.

Table 1 shows how the catalyst composition affects the specific yield of chlorobenzene at 250°C and benzene : hydrogen chloride : nitrogen(II) oxide : oxygen molar ratio of 5 : 2 : 1 : 1. The content of a supported catalyst is given in weight percents. The time of contact was 3 s at 250°C and reagent feeding rate of 390 μmol s^{-1}. It was found that the optimal catalyst is that containing copper(II) chloride (10%) and potassium chloride with $Cu^{2+} : K^+$ molar ratio of 1 : 1 on a KSS-3 support with the specific surface area of about 500 $m^2 g^{-1}$. Potassium chloride does not enhance the activity of the catalyst, but markedly prolongs its service life. It was established experimentally that the activity of the catalyst does not decrease during 42 h.

Data on the efficiency of replacing oxygen with nitrogen(IV) oxide at a time of contact of 1.6 s are listed in Table 2. The use of nitrogen(IV) oxide leads to a 17-fold increase in the conversion of hydrogen chloride at 250°C and to the corresponding rise in the yield of chlorobenzene. If account is taken of the fact that, in contrast to nitrogen(IV) oxide, oxygen can be used at higher temperatures without being decomposed, the intensification of oxidative chlorination can be estimated as tenfold.

Table 1. Influence exerted by the $CuCl_2$ content in supported catalyst on the specific yield of chlorobenzene *B*

Support	$CuCl_2$ content, wt %	*B*, mg $kg^{-1} s^{-1}$
INA-53 aluminosilicate	–	6.1
Coke	–	21.1
TZK diatomite	–	64.6
KSS-3 silica gel	–	67.8
INA-53	10	26.4
TZK	10	103
KSS-3	6	107
	10	112
	20	112

1070-4272/04/7703-0435 © 2004 MAIK "Nauka/Interperiodica"

Table 2. Influence exerted by the temperature and the type of an oxidizing agent on the conversion of hydrogen chloride *A*

T, °C	Oxidizing gent	*A*, %
200	Oxygen	1.8
250	"	2.5
300	"	3.9
250	Nitrogen(IV) oxide	42.9

Oxidative chlorination of benzene can be described by the following basic set of reactions:

$$C_6H_6 + 2CuCl_2 = C_6H_5Cl + 2CuCl + HCl, \quad (1)$$

$$2NO_2 + 4HCl = 2NOCl + Cl_2 + 2H_2O, \quad (2)$$

$$NOCl + CuCl = CuCl_2 + NO, \quad (3)$$

$$2CuCl + Cl_2 = 2CuCl_2, \quad (4)$$

$$C_6H_6 + 2NOCl = C_6H_5Cl + 2NO + HCl, \quad (5)$$

$$C_6H_6 + Cl_2 = C_6H_5Cl + HCl, \quad (6)$$

$$2CuCl + NO_2 = CuOCuCl_2 + NO, \quad (7)$$

$$CuOCuCl_2 + 2HCl = 2CuCl_2 + H_2O, \quad (8)$$

$$2NO + O_2 = 2NO_2. \quad (9)$$

Chlorobenzene can be formed both at the catalyst surface, by reaction (1), and in the gas phase, by reactions (5) and (6). Regeneration of copper(II) chloride may occur in a reaction of copper(I) chloride with nitrosyl chloride (3) and chlorine (4) or with nitrogen(IV) oxide (7) and then with hydrogen chloride (8). Reactions (2) and (9) may proceed not only in the oxidation reactors, but also in chlorination reactors.

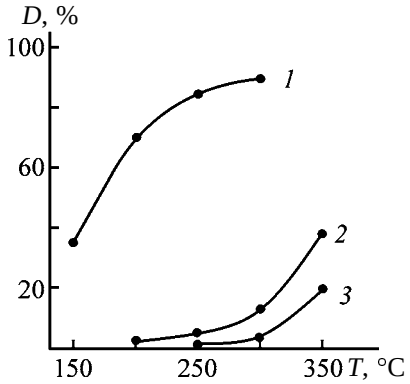

Fig. 1. Conversion *D* of chlorine and nitrosyl chloride vs. temperature *T*. Chlorination: (*1*) catalytic with nitrosyl chloride, (*2*) gas-phase with chlorine, and (*3*) gas-phase with nitrosyl chloride.

To evaluate the contribution of the gas-phase reactions, processes of separate chlorination of benzene with chlorine and nitrosyl chloride were studied in a reactor without catalyst at flow rates of benzene, chlorine, and nitrosyl chloride of 207, 21, and 42 μmol s^{-1}, respectively. Nitrosyl chloride was obtained using the known method [2] by the reaction of chlorine and nitrogen(II) oxide at 60°C, followed by condensation of the product at –20°C. The conversion *D* of the reactants at different temperatures, calculated from the amount of the chlorobenzene formed, is plotted in Fig. 1. The contribution of the gas-phase chlorination becomes noticeable only at temperatures higher than 250°C, whereas in catalytic chlorination the conversion at this temperature exceeds 80%. Consequently, chlorobenzene is mainly formed by reaction (1). It is more probable that the catalyst regeneration occurs by reactions (3) and (4), rather than by reactions (7) and (8), since the rate of oxidation of copper(I) chloride with nitrogen(IV) oxide exceeds that with oxygen by a factor of only 2 [3].

A number of process parameters were studied. It was found that, in catalytic oxidative chlorination, raising the linear flow velocity of gases from 0.1 to 0.4 m s^{-1} and the grain size of the support from 0.3 to 5 mm did not lead to any change in the yield of chlorobenzene and, consequently, outer or inner diffusion is not the rate-determining stage of the process.

The influence exerted by the time of contact between the gases and the catalyst on the conversion of hydrogen chloride was studied at varied height of the catalyst bed and flow rate of reactants. The results obtained are shown in Fig. 2a. It can be considered that 2.5–3 s is a sufficient time of contact at 250°C.

An excess of nitrogen(II) oxide or oxygen over the stoichiometric amount in reaction (9) strongly affects the process. To study this influence, nitrogen(II) oxide and oxygen, taken in the stoichiometric ratio of 2 : 1, were fed into the oxidation reactor, and additional amounts of these reagents were delivered directly to the chlorination reactor, bypassing the oxidation reactor. The reagent excess factor *q*, equal to the ratio of the total volume of a reagent to the volume of this reagent fed into the oxidation reactor, was varied from 1 to 2.5. In this case, the other conditions were as follows: flow rate of reactants 330 μmol s^{-1}, benzene : hydrogen chloride : nitrogen(IV) oxide molar ratio 5 : 2 : 1, temperature 250°C, time of contact 1.6 s; the results obtained are shown in Fig. 2b.

With an excess amount of nitrogen(II) oxide, the conversion of hydrogen chloride decreases, which is accounted for by partial binding of chlorine into nitro-

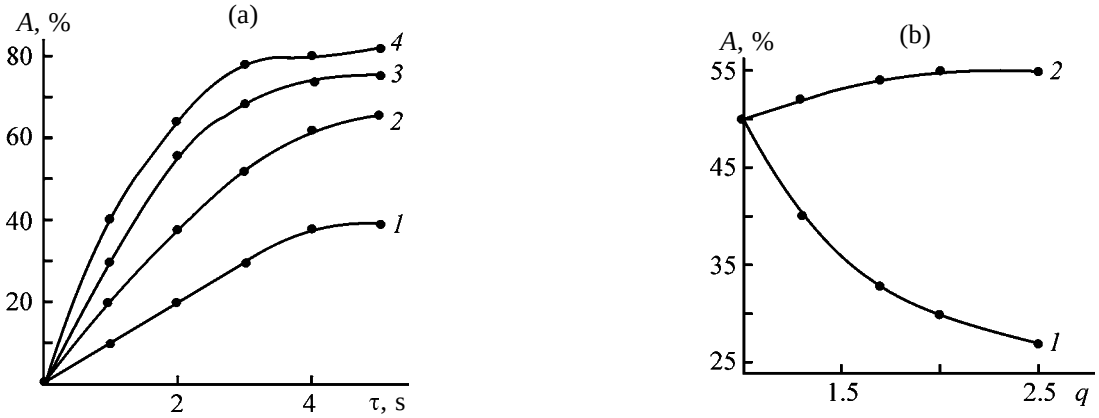

Fig. 2. Conversion *A* of hydrogen chloride vs. (a) the time τ of contact between the reactants and the catalyst and (b) reagent excess factor *q*. (a) *T* (°C): (*1*) 150, (*2*) 180, (*3*) 210, and (*4*) 250. (b) (*1*) Nitrogen(II) oxide and (*2*) oxygen.

syl chloride, which is a less active chlorinating agent. An increase in the content of nitrosyl chloride at the reactor outlet was revealed by IR spectroscopy. By contrast, an excess amount of oxygen leads to an increase in the conversion of hydrogen chloride because of the oxidation of nitrogen(II) oxide and secondary hydrogen chloride formed by reaction (1) directly in the chlorination reactor. It is advisable to use a twofold excess of oxygen over its stoichiometric amount.

The selectivity *S* of the process with respect to monochlorobenzene as a function of the conversion *R* of benzene is plotted in Fig. 3. The main product formed in oxidative chlorination, even at high conversion of benzene, is chlorobenzene.

Nitrogen(II) and nitrogen(IV) oxides are not among the products formed. The absence of nitrobenzene in the products was established by gas chromatography. In the process flowsheet, nitrogen(II) oxide, secondary hydrogen chloride, and unchanged benzene should be recycled after separation of the target products.

The output capacity of the reactor for oxidative chlorination of benzene with the use of nitrogen(IV) oxide is about 350 kg h^{-1} per 1 m^3 of the reactor volume. This value is no less than the output capacity of the reactor for direct chlorination of benzene [4]. At the same time, use of waste hydrogen chloride, instead of the more expensive chlorine, makes lower the manufacture cost of the product.

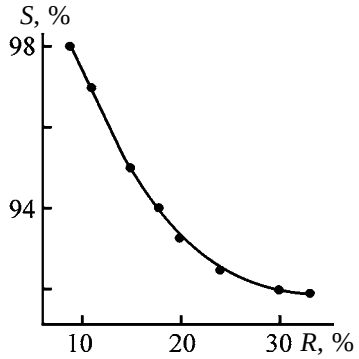

Fig. 3. Selectivity *S* with respect to monochlorobenzene vs. the conversion *R* of benzene.

CONCLUSIONS

(1) Use of nitrogen(IV) oxide, an active oxidizing agent, instead of oxygen makes it possible to intensify the oxidative chlorination of benzene by a factor of more than 10.

(2) The optimal catalyst for intensive oxidative chlorination of benzene is copper(II) chloride supported by KSS-3 silica gel and stabilized with potassium chloride at $Cu^{2+} : K^{+}$ molar ratio of 1 : 1.

(3) The optimal conditions for the synthesis of monochlorobenzene are as follows: temperature 250°C, time of contact 2.5–3 s, nitrogen(II) oxide : oxygen molar ratio 1 : 1, and conversion of benzene <30%.

REFERENCES

1. Treger, Yu.A., Kartashov, L.M., and Krishtal', N.F., *Osnovnye khlororganicheskie rastvoriteli* (Main Organochlorine Solvents), Moscow: Khimiya, 1984.
2. Beckam, L.J., Fessler, W.A., and Kise, M.A., *Chem. Rev.*, 1951, vol. 48, no. 3, pp. 320–396.
3. Skudaev, V.I., Gertsen, P.P., Solomonov, A.B., *et al.*, *Zh. Prikl. Khim.*, 1990, vol. 63, no. 1, pp. 19–23.
4. Oshin, L.A., Treger, Yu.A., Motsarev, G.V., *et al.*, *Promyshlennye khlororganicheskie produkty: Spravochnik* (Industrial Organochlorine Products: Reference Book), Moscow: Khimiya, 1978.

Russian Journal of Applied Chemistry, Vol. 77, No. 3, 2004, pp. 438–440. Translated from Zhurnal Prikladnoi Khimii, Vol. 77, No. 3, 2004, pp. 445–447.

MACROMOLECULAR CHEMISTRY AND POLYMERIC MATERIALS

Physicochemical properties of Water-Soluble Fullerene C_{60}–Carbohydrate Composites

L. S. Litvinova, A. V. Gribanov, M. V. Mokeev, and V. N. Zgonnik

Institute of Macromolecular Compounds, Russian Academy of Sciences, St. Petersburg

Received October 22, 2003

Abstract—Water-soluble composites of fullerene C_{60} with carbohydrates (saccharose, fructose, and dextrans) prepared by the mechanochemical procedure were analyzed by electronic absorption and ^{13}C NMR spectroscopy, thin-layer chromatography, and differential scanning calorimetry.

Fullerenes and their derivatives readily form complexes with electron donors [1–7]. In particular, some complexes of fullerene C_{60} are water-soluble and can be used in medicine and biochemistry. A series of water-soluble fullerene-containing compounds has been prepared. In this work we studied water-soluble composites prepared by solid-phase reaction of C_{60} with low and high-molecular-weight carbohydrates. The fullerene concentration in the samples ranged from 0.1 to 30 wt %. Prominence was given to the mechanism of C_{60}–carbohydrate interactions and its strength as influenced by the molecular weight of the carbohydrate.

The C_{60}–carbohydrate composites were prepared by a mechanochemical procedure [6]. Appropriate carbohydrate was suspended in a definite volume of 0.1 mg ml^{-1} C_{60} solution in CCl_4. The solvent was evaporated in air, and the residue was ground in an agate mortar and dried in a vacuum oven at 40°C for 48 h. A water aliquot (3–5 ml) was added to the resulting fine powder. The mixture was stirred for 1 min and centrifuged. The solution was decanted from the precipitate.

To determine the concentration and extinction coefficients of the water-soluble fullerene by spectrophotometry, the fullerene was isolated from an aqueous solution of the composite by semipreparative thin-layer chromatography (TLC). For this purpose, an aliquot of the aqueous solution was applied in the form of a band on a chromatographic paper (6 × 10 cm). The sample was dried and eluted with toluene to the height of 6 cm. The fullerene was eluted with the solvent front. The fullerene-containing section of the paper was cut out, and the fullerene was extracted with carbon tetrachloride. The solution was weighed and its volume was calculated. Then the spectrum of the solution was recorded. Given the extinction coefficient of C_{60} solution in CCl_4 at 330 nm, the concentration and the extinction coefficient of the aqueous solution of the fullerene–carbohydrate composite were determined. The relative standard deviation s_r of the calculated concentration was no more than 15% at $n = 3$. The extinction coefficients of the water-soluble fullerene complexes depends on its concentration in water (see table). Hence, the composition of the water-soluble forms depend on the fullerene content in the composite.

The water-soluble fraction of the composite was studied by electronic absorption spectroscopy on a Specord M40 spectrophotometer (Carl Zeiss, Jena, Germany). As compared to the UV spectrum of the initial C_{60}, the following transformations were observed: broadening of the bands, bathochromic shift of their maximum, change in the intensity ratio, and change in the absorption in the long-wave region (λ 440 and 470 nm). These transformations suggest aggregation of the fullerene in the aqueous phase [8, 9], i.e., occurrence of the fullerene–fullerene interaction. The optical density of the solution depends on the fullerene content in the initial composite (see table). When the content of saccharose and monosaccharides in the composite increases to more that 90% (molar ratio 1 : 20) and that of dextran increases to more than 98% (molar ratio 1 : 1) at a constant C_{60} content, the optical density increases: first sharply and then smoothly. The optical densities and the concentration of the water-soluble fractions for the dextran composites are lower than those for the saccharose composite.

It should be noted that aqueous solutions of the

1070-4272/04/7703-0438 © 2004 MAIK "Nauka/Interperiodica"

Parameters of aqueous solutions of C_{60} composites with saccharose and dextran (40 kDa)*

C_{60} content, wt %	C_{60}–saccharose					C_{60}–dextran, 40 kDa			
	n	λ, nm	*D*	$c \times 10^4$, M	$\varepsilon \times 10^{-4}$ (λ = 440 nm), l mol^{-1} cm^{-1}	*n*	λ, nm	*D*	$c \times 10^4$, M
30	5	336.9	0.009	0.03	2.76	0.04	–	–	–
10	19	342.5	0.031	–	–	0.15	340.6	0.036	0.19
4	50	339.7	0.431	1.32	0.74	0.43	344.9	0.041	0.29
3	67	341.2	0.448	0.94	0.88	0.6	–	–	–
2	103	341.2	0.481	0.43	2.14	0.9	342.5	0.063	–
1	208	341.0	–	–	–	1.8	343.9	0.07	0.21
0.75	280	342.3	0.43	0.44	2.17	2.4	–	–	–
0.5	419	339.2	0.712	0.31	1.88	3.6	343.8	0.163	0.26
0.25	840	341.7	0.619	0.79	1.36	7.2	345.0	0.248	0.33
0.125	1628	341.0	0.814	0.66	2.06	14.4	344.4	0.286	0.35
0.1	2080	341.8	0.78	0.86	1.50	18	–	–	–

* *n* is the carbohydrate/C_{60} molar ratio in the initial solid composite; *D* is the optical density.

fullerene–carbohydrate composites are stable to toluene and chloroform used as solvents for C_{60}. This can be due to shielding or protection of fullerene in the composite by the carbohydrate.

The fullerene–carbohydrate interaction in the solid state was studied by ^{13}C NMR spectroscopy. High-resolution ^{13}C NMR spectra of solid samples were recorded at room temperature on a Bruker CXP-100 spectrometer using the magic angle spinning (MAS) and cross polarization (CP MAS) techniques. The MAS spectrum of the 20% C_{60}-dextran composite contains the signal typical for C_{60} (δ = 143.6 ppm). The half-width of this signal is larger (1.2 ppm) compared to pure fullerene (0.16 ppm). The CP MAS spectra also contain the C_{60} signal, suggesting the presence of proton-containing groups near the fullerene surface. The C_{60} signal in the MAS NMR spectrum of 20% C_{60}–saccharose composite is also broadened (half-width 1.2 ppm) and is shifted upfield in the spectra recorded by both procedures (δ_{MAS} = 141.3 ppm).

The upfield region of the CP MAS spectrum contain a new signal with a lower intensity ($\delta_{CP\ MAS}$ = 139.2 ppm). The splitting of the C_{60} signal and its upfield shift can be due to interaction of the fullerene with hydroxy groups of the carbohydrate. This assumption agrees with results of [2, 10, 11]. Thus, the fullerene–carbohydrate interaction occurs in the examined composites. Probably the hydroxy groups of the carbohydrate form donor–acceptor bonds with the fullerene.

The comparative study of the fullerene–carbohydrate interaction was performed by TLC. Since there are no solvents in which both C_{60} and the carbohydrates are soluble, we failed to determine the stability constants of the complexes by the conventional methods [12, 13]. The complexation was examined by TLC [14]. TLC plates (Sorbfil, Sorbpolimer JSC, Krasnodar) were impregnated with 0.5–5% solutions of the carbohydrates in hand and dried. The fullerene was chromatographed on the resulting plates using hexane as eluent. The change in the retention factor of C_{60} on the initial and impregnated plates was calculated by the equation

$$\Delta hR_f = hR_{f(SiO_2)} - hR_{f(carbohydrate)}.$$

As seen from the figure, ΔhR_f increases with increasing concentration of the impregnating solution. At the concentration at which the curves flatten out

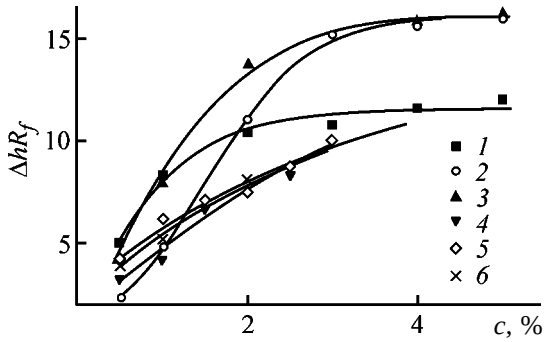

Change in the retention factors of C_{60} ΔhR_f in elution with hexane of TLC plates impregnated with 0.5–10% solutions of (*1*) glucose, (*2*) fructose, (*3*) saccharose, and (*4*–*6*) dextrans with molecular weight $M \times 10^{-3}$: (*4*) 20, (*5*) 40, and (*6*) 110, as a function of the solution concentration *c*.

(~3%), the interaction strength decreases in the following order: saccharose > fructose > glucose > dextrans. The higher the molecular weights of dextrans, the weaker complexes with C_{60} are formed.

The 20% C_{60}–saccharose composite was studied by DSC (Mettler–Toledo DSC 20, heating rate 10 deg min^{-1}). It was found that the transition temperature of the A form increases, and that of the B form decreases in the presence of C_{60}.

Based on the features of preparation of water-soluble fullerene, the dependence of the extinction coefficients of the aqueous solutions on the fullerene concentration, and the features of electronic absorption spectra of aqueous solutions of the composites, we suggest that the water-soluble form consists of fullerene aggregates surrounded by carbohydrate molecules. The fullerene–carbohydrate interaction in the solid phase was detected by DSC and ^{13}C NMR spectroscopy. Thus, two main interaction types in the solid composites and in the water-soluble fractions were revealed: formation of donor–acceptor bonds between the fullerene and carbohydrate and fullerene–fullerene interaction in C_{60} aggregates. As determined by TLC, the fullerene–carbohydrate interaction with monosaccharides and saccharose are stronger than that with dextrans. The procedure developed in this work for determining the fullerene content in the aqueous phase shows that monosaccharides and saccharose are more efficient than dextrans for preparing water-soluble fullerene forms.

CONCLUSIONS

(1) Water-soluble fullerene C_{60}–carbohydrate composites were prepared by the mechanochemical procedure and were studied by electronic absorption spectroscopy, NMR, TLC, and DSC.

(2) The water-soluble fraction consists of C_{60} aggregates coated by carbohydrate molecules, which are bound to the fullerene core by van der Waals bonds.

(3) A procedure for determining the fullerene content in water was developed. The concentration of C_{60}–saccharose composite in the aqueous phase is higher than that of C_{60}–dextran composite.

(4) The energy of fullerene–carbohydrate interaction decreases in the following order: saccharose > fructose > glucose > dextrans.

REFERENCES

1. Anderson, T., Nilsson, K., Sundahl, M., *et al*., *J. Chem. Soc., Chem. Commun*., 1992, pp. 604–606.
2. Yoshida, Z.-i., Takekuma, H., Takekuma, S.-i., and Matsubara, Y., *Angew. Chem., Int. Ed. Engl*., 1994, vol. 33, nos. 15/16, pp. 1597–1599.
3. Yamakoshi, Y.N., Yagami, T., Fukuhara, K., *et al*., *J. Chem. Soc., Chem. Commun*., 1994, pp. 517–518.
4. Atwood, J.L., Koutsantonis, G.A., and Raston, C.L., *Nature*, 1994, vol. 368, no. 6468, pp. 229–231.
5. Komatsu, K., Fujiwara, K., Murata, Y., and Braun, T., *J. Chem. Soc., Perkin Trans. 1*, 1999, no. 20, pp. 2963–2966.
6. Litvinova, L.S. and Zgonnik, V.N., Abstracts of Papers, *IWFAC'99*, St. Petersburg, October 4–8, 1999, p. 294.
7. Melenevskaya, E.Yu., Reznikov, V.A., Litvinova, L.S., *et al*., *Vysokomol. Soedin., Ser. A*, 1999, vol. 41, no. 5, pp. 864–869.
8. Bensasson, R.V., Bienvenue, E., Dellinger, M., *et al*., *J. Phys. Chem*., 1994, vol. 98, no. 13, pp. 3492–3500.
9. Mrzel, A., Mertelj, A., Omerzu, A., *et al*., *J. Phys. Chem*., 1999, vol. 103B, no. 51, pp. 11 256–11 260.
10. Sun, D., Tham, F.S., Reed, C.A., *et al*., *J. Am. Chem. Soc*., 2000, vol. 122, no. 43, pp. 10 704–10 705.
11. Ikeda, A., Yoshimura, M., Udzu, H., *et al*., *J. Am. Chem. Soc*., 1999, vol. 121, no. 117, pp. 4296–4297.
12. Job, P., *Ann. Chem. Phys*., 1928, vol. 9, no. 1, pp. 113–203.
13. Benesi, A. and Hildebrand, J.H., *J. Am. Chem. Soc*., 1949, vol. 71, no. 8, pp. 2703–2707.
14. Litvinova, L.S. and Zgonnik, V.N., *J. AOAC Int*., 1999, vol. 82, no. 2, pp. 227–230.

Russian Journal of Applied Chemistry, Vol. 77, No. 3, 2004, pp. 441–444. Translated from Zhurnal Prikladnoi Khimii, Vol. 77, No. 3, 2004, pp. 448–451.

MACROMOLECULAR CHEMISTRY AND POLYMERIC MATERIALS

Quantitative Aspects of the Competition of Substitution and Addition Pathways in Polyisobutylene Chlorination

A. A. Goryacheva, V. A. Alferov, and V. A. Aver'yanov

Tula State University, Tula, Russia

Received February 19, 2003

Abstract—The competition of the substitution and addition chlorination pathways was studied. A quantitative model was developed to describe the rate ratio of the substitution and addition pathways in chlorination of polyisobutylene.

In the world polymer industry, the modern trends in development of new valuable polymeric materials are toward chemical modification of known polymeric products, rather than toward construction of facilities for large-scale production of new synthetic polymers by polymerization and polycondensation [1]. Modification of known polymers allows substantial saving of material and power resources and does not require large capital investments, as it is based on successfully mastered, economically efficient, and environmentally sound processes. One of the main routes of chemical modification of polymers, which is being actively developed today, is chlorination. Production of new materials by this method offers an opportunity to replace expensive materials by more durable and cheaper formulations showing higher performance. In this context, it becomes urgent to study quantitative characteristics of polymer chlorination. In this work we studied quantitatively the competition of substitution and addition pathways in chlorination of P-1 polyisobutylene.

The properties of the chlorination products can be optimized by properly choosing the balance between the contents of chlorine and residual double bonds in the polymer. The presence of chlorine enhances the fire resistance, chemical stability, and elasticity of materials, but, as the extent of chlorination grows, the content of residual double bonds responsible for the strength of the finished items decreases. At deficiency of residual double bonds, a chlorinated polymer becomes less capable of covulcanization with nonchlorinated analogs. In this connection, it seems necessary to study the competition of substitution and addition chlorination pathways as a factor controlling the ratio of the amounts of incorporated chlorine and residual double bonds.

EXPERIMENTAL

Chlorination of polyisobutylene was performed in chloroform without initiation. The polyisobutylene concentration in chloroform was 5 wt % in all cases. The reaction was performed in a glass vessel equipped with a temperature-control jacket, a bubbler for feeding chlorine, a reflux condenser, and a thermometer. Gaseous chlorine from a cylinder was passed through a Tishchenko bottle with concentrated H_2SO_4 and mixed in an equimolar ratio with argon; the resulting gas mixture was fed to the reactor. The constant flow rate of chlorine was maintained with a manostat and monitored with a rheometer. The required temperature was provided by circulation of water from a thermostat through the reactor jacket. Hydrogen chloride and unchanged chlorine present in off-gases were absorbed in a bottle filled with aqueous KI and arranged at the reactor outlet. After chlorination completion, the setup was purged with argon for 40 min to quantitatively remove Cl_2 and HCl from the reactor. The solvent was removed from the reaction mixture on a rotary evaporator, and the bottoms were kept in a vacuum to constant weight and then weighed. The iodine released from the KI solution under the action of Cl_2 was titrated with a 0.1 N $Na_2S_2O_3$ solution, after which the absorbed HCl was titrated with a 0.2 N NaOH solution in the presence of phenolphthalein. From this value, we estimated the content of C–Cl bonds formed in the polymer by the substitution pathway. The contents of total chlorine and chlorinated double bonds in the samples were determined by the difference between the actual sample weight and the value calculated from the content of C–Cl bonds formed by substitution.

Preliminary experiments showed that, in the initial

1070-4272/04/7703-0441 © 2004 MAIK "Nauka/Interperiodica"

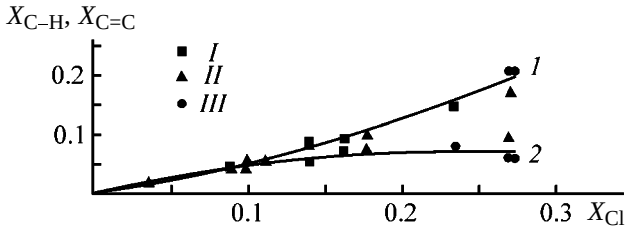

Fig. 1. Influence of the rate of feeding chlorine on the yields of polyisobutylene chlorination by (*1*) substitution and (*2*) addition pathways. ($X_{C=C}$, X_{C-H}) Amounts of chlorinated C=C and C–H bonds (mole per mole of monomeric units), respectively; (X_{Cl_2}) amount of chlorine taken up (mole per mole of monomeric units); the same for Fig. 2. Rate of feeding Cl_2, mol min^{-1}: (*I*) 0.9×10^{-3}, (*II*) 1.26×10^{-3}, and (*III*) 9.3×10^{-3}.

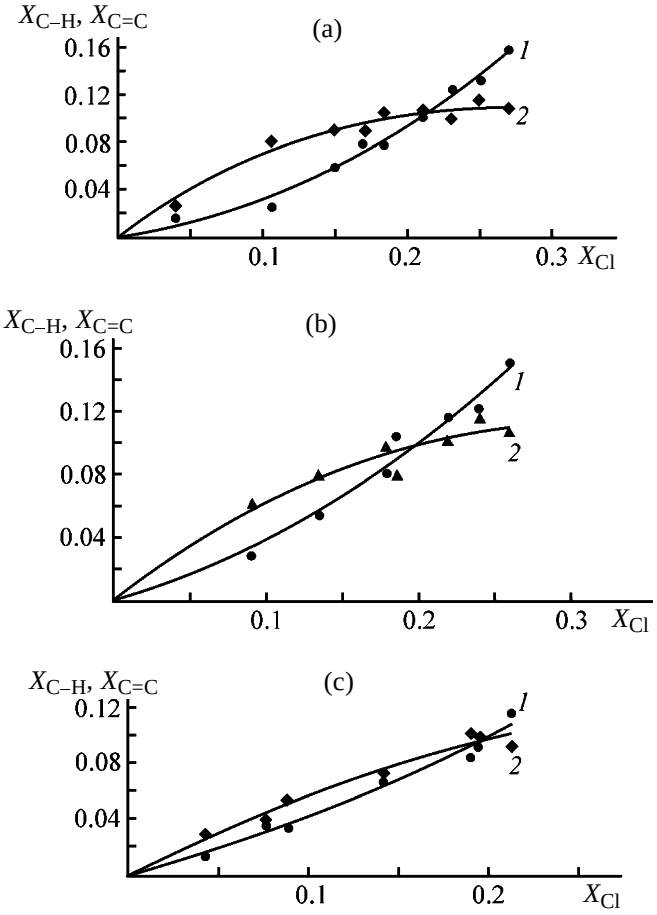

Fig. 2. Degrees of chlorination of (*1*) C–H (substitution pathway) and (*2*) C=C bonds (addition pathway) as functions of the degree of chlorination at (a) 10, (b) 35, and (c) 58°C.

chlorination period, the concentration of molecular chlorine in the reaction mixture is appreciably lower than the solubility of chlorine in chloroform. This fact suggests that the reaction is diffusion-controlled. Under these conditions, the chlorine concentration should depend on the intensity of its bubbling through the reaction mixture. In this connection, we first studied how the rate of feeding chlorine affects the ratio of substitution and addition products. Typical results are shown in Fig. 1 as the amounts (mole) of the C=C and C–H bonds per mole of monomeric units of polyisobutylene ($X_{C=C}$, X_{C-H}) vs. amount (mole) of chlorine taken up per mole of monomeric units (X_{Cl_2}).

It is seen that the data corresponding to different rates of feeding molecular chlorine fall on common curves, i.e., the ratio of the products formed by the competing chlorination pathways is insensitive to the rate of feeding chlorine. This fact indicates that the orders of both reactions with respect to chlorine are equal. Correspondingly, the ratio of the contributions of the substitution and addition pathways does not depend on whether the process is performed under conditions of diffusion or kinetic control; therefore, our results are valid for any mode of liquid-phase chlorination.

Then we studied how the contributions of the substitution (X_{C-H}) and addition ($X_{C=C}$) pathways of polyisobutylene chlorination depend on temperature and degree of chlorination (X_{Cl_2}). Typical results are shown in Figs. 2a–2c as plots of X_{C-H} and $X_{C=C}$ vs. X_{Cl_2} at various temperatures.

These data show that, with increasing conversion, the content of chlorinated double bonds monotonically grows, flattening out at certain X_{Cl_2}. At the same time, the content of chlorinated C–H bonds grows with autoacceleration, suggesting the free-radical mechanism of the process: For the reaction to develop, a certain autocatalytic period is required for accumulation of active radical centers. At the same time, this result is consistent with the growth of the inducing power of double bonds with accumulation of chlorine atoms in their surrounding; this trend is typical of free-radical chlorination of organic compounds [2].

The plots of X_{C-H} and $X_{C=C}$ vs. X_{Cl_2} were approximated by polynomials of the second degree,

$$X_{C-H} = a + bX_{Cl_2} + c(X_{Cl_2})^2, \quad (1)$$

$$X_{C-C} = m + nX_{Cl_2} + p(X_{Cl_2})^2, \quad (2)$$

using the least-squares method. The results are listed in the table.

Differentiation of Eqs. (1) and (2) leads to the

expressions

$$\frac{d[X_{C-H}]}{d[X_{Cl_2}]} = b + 2cX_{Cl_2}, \quad (3)$$

$$\frac{d[X_{C=C}]}{d[X_{Cl_2}]} = n + 2pX_{Cl_2}. \quad (4)$$

By dividing Eq. (3) by Eq. (4), we obtain

$$\frac{d[X_{C-H}]}{d[X_{C=C}]} = \frac{b + 2cX_{Cl_2}}{n + 2pX_{Cl_2}}. \quad (5)$$

Apparently, the left side of Eq. (5) corresponds to the rate ratio of the substitution and addition chlorination pathways. Then Eq. (5) takes the form

$$\frac{r_s}{r_{ad}} = \frac{b + 2cX_{Cl_2}}{n + 2pX_{Cl_2}}. \quad (6)$$

Expression (6) allows calculation of the rate ratio of the substitution and addition chlorination pathways in the examined range of X_{Cl_2} using data from the table. The calculated ratios r_s/r_{ad} are plotted in Fig. 3 vs. the content of residual double bonds $Y_{C=C}$ (mole per mole of monomeric units of polyisobutylene).

It is seen that the relative contribution of the substitution pathway monotonically grows as the content of double bonds in the polymer increases. This means that the substitution pathway has a higher order with respect to the double bond concentration than the addition pathway, which indirectly confirms the free-radical mechanism of induced substitution chlorination. The plots in Fig. 3 can be approximated by

$$r_s/r_{ad} = \alpha + \beta Y^n_{C=C}. \quad (7)$$

The values of α determined by extrapolation of the r_s/r_{ad} vs. $Y_{C=C}$ plots to zero concentration of the double bonds are given below:

T, °C	α	β	*n*
10	0.168	11.74	1.20
35	0.379	11.74	1.20
58	0.512	11.74	1.20

To determine the parameters β and *n*, Eq. (7) was transformed to

$$\log(r_s/r_{ad} - \alpha) = \log\beta + n\log Y_{C=C}. \quad (8)$$

The plots of $\log(r_s/r_{ad} - \alpha)$ vs. $\log Y_{C=C}$ are shown in Fig. 4.

Parameters of Eqs. (1) and (2)

T, °C	Eq. (1)			Eq. (2)		
	a	*b*	*c*	*m*	*n*	*p*
10	–	0.141	1.660	–	0.859	–1.660
35	–	0.274	1.145	–	0.726	–1.145
58	–	0.338	0.844	–	0.662	–0.844

It is seen that the results obtained for polyisobutylene at different temperatures fall on a common straight line characterized by the same values of β and *n*. These values, determined from the slope and the portion intercepted on the ordinate, are given above. The Arrhenius treatment of the α values gives the expression

$$\alpha = 10^{2.63}\exp(-18.25 \text{ kJ mol}^{-1}/RT).$$

This difference between the activation energies of the competing substitution and addition chlorination pathways is consistent with the difference between the activation energies of these pathways under conditions of molecular reaction mechanism [3]. This fact is natural, as the parameter α reflects the competition of the substitution and addition chlorination pathways

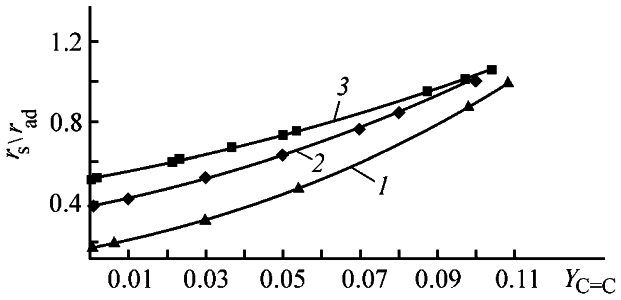

Fig. 3. Rate ratio of the substitution and addition chlorination pathways r_s/r_{ad} as a function of the content of residual double bonds $Y_{C=C}$. Temperature, °C: (*1*) 10, (*2*) 35, and (*3*) 58.

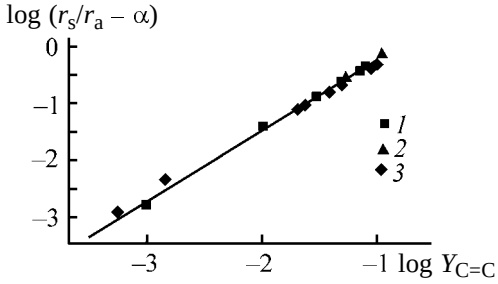

Fig. 4. Determination of the parameters β and *n*. Temperature, °C: (*1*) 35, (*2*) 10, and (*3*) 58.

under conditions when double bonds inducing the radical chlorination mechanism are virtually absent.

Thus, we have obtained an expression for the rate ratio of substitution and addition pathways in chlorination of P-1 polyisobutylene.

REFERENCES

1. Ronkin, G.M., Mazanko, A.F., and Romashin, O.P., in *Nauchnye trudy NII "Sintez"* (Transactions of the Sintez Research Institute), Moscow, 1996, pp. 445–503.
2. Serguchev, Yu.A., Barabash, V.V., and Stetsyuk, T.A., Abstracts of Papers, *IV Vsesoyuznaya nauchnaya konferentsiya "Sovremennoe sostoyanie i perspektivy razvitiya teoreticheskikh osnov proizvodstva khlororganicheskikh produktov"* (IV All-Union Scientific Conf. "Modern State and Prospects for Development of Theoretical Principles of Production of Organochlorine Products"), Baku, 1985, pp. 31–32.
3. Mkhitaryan, S.A., Smirnov, V.V., Shilina, M.I., *et al.*, *Kinet. Katal.*, 1988, vol. 29, no. 1, pp. 70–76.

Russian Journal of Applied Chemistry, Vol. 77, No. 3, 2004, pp. 445–448. Translated from Zhurnal Prikladnoi Khimii, Vol. 77, No. 3, 2004, pp. 452–455.

MACROMOLECULAR CHEMISTRY AND POLYMERIC MATERIALS

Specific Features of Thermal Degradation of Polypropylene in the Presence of Magnesium Hydroxide

E. V. Koverzanova, S. V. Usachev, N. G. Shilkina, S. M. Lomakin, K. Z. Gumargalieva, and G. E. Zaikov

Semenov Institute of Chemical Physics, Russian Academy of Sciences, Moscow, Russia
Emanuel' Institute of Biochemical Physics, Russian Academy of Sciences, Moscow, Russia

Received October 10, 2003

Abstract—Specific features of thermal oxidative degradation of polypropylene and its composite with $Mg(OH)_2$ were studied by pyrolytic gas chromatography–mass spectrometry and thermal gravimetric analysis.

An urgent problem of the modern polymer industry is to reduce the combustibility of polymers and polymeric materials. Of particular interest are fireproofing agents that combine high performance with environmental safety. One of a few fire retardants meeting these criteria is magnesium hydroxide, $Mg(OH)_2$. It is commonly believed that its fireproofing effect is due to dilution of gaseous pyrolysis products with water vapor formed by endothermic (ΔH 1450 J kg^{-1}) decomposition of $Mg(OH)_2$ above 340°C [1]:

$$Mg(OH)_2 = MgO + H_2O\uparrow.$$

The heat consumed in this reaction considerably decreases the temperature on the surface of the degrading polymer. On the other hand, large amount of the released water vapor dilutes the mixture of volatile degradation products, altering the thermal balance in the combustion zone.

Since the decomposition point of $Mg(OH)_2$ is higher than the temperatures of industrial processing of such polymers as ethylene–vinyl acetate copolymer, polypropylene, and polyamides and corresponds to the temperatures at which these polymers start to degrade, there are no problems with preparing composites of reduced combustibility from these components.

Polymeric composites of polypropylene, Nylon 6, and ethylene–vinyl acetate copolymer, containing 50 wt parts of $Mg(OH)_2$ and more, showed considerably decreased combustibility, as determined from the oxygen index and concalorimeter method [2].

In this work, the fire-retarding effect of $Mg(OH)_2$ on polypropylene was evaluated by mass-spectrometric analysis of polypropylene pyrolysis products.

The mechanism of thermal degradation of polypropylene (PP) at temperatures close to the processing temperatures had been comprehensively studied [3–7]. It is known that, in the absence of oxygen, PP decomposes without residue to give large amounts of aliphatic compounds: alkanes, alkenes, and dienes. The primary thermal degradation of the polymeric chain involves scission of the weakest bonds. Oxygen chemisorbed on the polymer surface initiates radical formation at approximately 250°C and causes ignition at 470–540°C:

$$RH + O_2 \rightarrow R^{\bullet} + HO_2^{\bullet}.$$

Furthermore, peroxy radicals are formed at approximately 350°C:

$$-R^{\bullet} + O_2 \rightarrow -ROO^{\bullet}.$$

Above this temperature, dehydrogenation of polymeric radicals results in formation of a polyene and $HO_2^{\bullet}$:

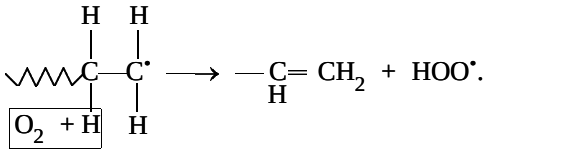

This reaction pathway prevails in the range 350–500°C.

According to the classical scheme of radical initiation [7], the peroxy radicals initiate the following reactions of chain propagation:

$$HOO^{\bullet} + RH = H_2O_2 + R^{\bullet},$$

$$HOO^{\bullet} + CH_4 = H_2O_2 + CH_3^{\bullet},$$

1070-4272/04/7703-0445 © 2004 MAIK "Nauka/Interperiodica"

$$HOO^{\bullet} + H_2 = H_2O_2 + H^{\bullet},$$

$$H_2O_2 = 2HO^{\bullet},$$

$$HO^{\bullet} + RH = R^{\bullet} + H_2O,$$

$$HO^{\bullet} + H_2 = H^{\bullet} + H_2O,$$

and chain branching:

$$H^{\bullet} + O_2 \rightarrow HO^{\bullet} + O^{\bullet},$$

$$O^{\bullet} + H_2 \rightarrow HO^{\bullet} + H^{\bullet},$$

$$ROOH \rightarrow RO^{\bullet} + HO^{\bullet}.$$

It is generally accepted that fire retardants can actively participate in pyrolytic reactions and inhibit radical generation in the combustion zone or directly before it. Jha *et al.* [8] subdivided fire retardants with respect to the mechanism of their effect into two groups: (1) additives acting in the gas phase (terminating generation of free radicals in the preliminary flash and combustion front zones); (2) additives acting in the solid phase (decelerating common pyrolysis by increasing the amount of coke, thus insulating the polymer melt from the intense high-temperature flame flow or ignition source, or altering the pyrolysis course so as to prevent dropping of the polymer melt).

It is commonly believed that magnesium hydroxide belongs to the first group.

In this work we studied how magnesium hydroxide affects solid-phase coke formation enhancing the fire resistance of polypropylene.

EXPERIMENTAL

Polypropylene was of BE677MO brand (Borealis), and its composite with magnesium hydroxide (FD905-U brand, Borealis) contained 40% $Mg(OH)_2$.

Pyrolysis of pure polypropylene and its composite with $Mg(OH)_2$ was performed at 300, 500, and 700°C in a tubular flow-through pyrolytic cell in air (flow rate ~40 ml min^{-1}). The outflowing gases were passed through a bubbler filled with 4 ml of hexane and cooled on an ice bath, to trap the pyrolysis products.

The thermal gravimetric analysis of PP and its composite with $Mg(OH)_2$ was performed on a 950Q derivatograph in air at a heating rate of 10 deg min^{-1}.

The screening analysis of the pyrolysis products was performed on a Tsvet 500 M gas chromatograph (electron capture detector, ECD; 4000 × 3-mm packed glass column; stationary phase OV-17 phenylmethylsilicone; column and injector temperatures 230°C; detector temperature 290°C; carrier gas nitrogen, flow rate 16 ml min^{-1}; sample volume 2 μl).

Analysis of the most representative samples by gas chromatography–mass spectrometry was performed on a laboratory complex consisting of a Varian 3300 gas chromatograph, a Finnigan MAT ITD 800 mass spectrometric detector of the ion trap type, and a computer system for data processing. Separation was performed on a quartz capillary column (30 m long, 0.32 mm i.d.) coated with a 0.25-μm film of DB-5 phenylmethylsilicone. The column was heated at a 10 deg min^{-1} rate from 50 to 270°C; the injector temperature was 200°C. The carrier gas was helium (inlet pressure 0.1 MPa). Samples (1 μl) were injected without flow division; the time before the start of purging of the sample inlet unit was 30 s. The mass spectra were taken with the electron impact (70 eV) ionization mode at a scanned rate of 1 mass spectrum per minute; the scanning range was 40–650 amu.

At 300 and 500°C, the major reaction products are alkenes, alkanes, dienes, and also alcohols and ketones. The composition and percent content of components in pyrolysis products of PP and its composite with $Mg(OH)_2$ are given in the table. The strongest peaks in the chromatograms correspond to 2,4-dimethyl-1-heptene, 4-methyl-2-heptanone, 2,6-dimethyl-4-heptanone, isomers of dimethyloctanol, and some other hydrocarbon derivatives. At low pyrolysis temperatures, $Mg(OH)_2$ exerts no noticeable effect on the composition of pyrolysis products, whereas at higher temperatures this effect becomes significant. Benzene derivatives appear at 500°C. At this temperature, we identified allylbenzene. Its content in the pyrolysis products of the composite (1.5%) was lower compared to pure PP (2.8%). At 700°C, the number and content of aromatic compounds grow. We identified toluene, ethylbenzene, xylenes, and isomeric ethyltoluenes and methylstyrenes. As seen from the table, their content in pyrolysis of the composite is considerably higher compared to pure PP. As for compounds with fused benzene rings, the pyrolysis products of pure PP contain no methylnaphthalene and dihydronaphthalene isomers detected in pyrolysis of the composite. The content of naphthalene in the pyrolysis products of the composite was two times higher compared to pure PP. In pyrolysis products of the composite, we also identified biphenyl. Thus, in the presence of $Mg(OH)_2$ formation of aromatic compounds (mononuclear compounds, naphthalenes, biphenyls) is more intense.

The TG analysis of the composite revealed forma-

Composition and content of components in pyrolysis products of PP and its composite with $Mg(OH)_2$

Pyrolysis products	Time, min/s	Content, wt %, at indicated pyrolysis temperature, °C					
		300		500		700	
		PP	composite	PP	composite	PP	composite
Toluene	3/16	–	–	–	–	16.2	19.3
2,4-Dimethyl-1-heptene	4/01	7.0	4.6	33.2	18.2	7.9	–
Ethylbenzene	4/23	–	–	–	–	6.9	9.9
Trimethylcyclohexene	4/26	–	1.0	0.6	1.4	–	–
Xylenes	4/42	–	–	–	–	5.3	7.6
4-Methyl-2-heptanone	5/17	7.5	6.8	1.2	0.9	–	–
	5/42	–	–	–	–	1.4	2.0
Ethyltoluene isomers	6/01	–	–	–	–	1.2	1.3
Dimethyloctene	6/05	5.6	3.8	–	–	–	–
Allylbenzene	6/12	–	–	2.8	1.5	3.8	–
2,6-Dimethyl-4-heptanone	6/15	10.2	8.5	4.4	3.6	–	–
α-Methylstyrene	6/15	–	–	–	–	4.1	5.0
β-Methylstyrene	7/01	–	–	0.2	–	1.9	4.7
	7/26	4.7	2.0	–	0.3	1.0	–
	7/30	5.1	3.5	9.8	7.4	2.8	–
Dimethyloctanol isomers	7/34	4.5	3.4	5.9	3.9	1.5	–
2-Methyl-4-phenyl-1-butene	8/42	–	–	–	–	1.6	4.6
Dihydronaphthalenes	8/48	–	–	–	–	–	2.8
	8/58	–	–	–	–	–	1.1
Naphthalene	9/17	–	–	–	–	6.8	14.6
Methylnaphthalenes	10/59	–	–	–	–	–	5.5
	11/15	–	–	–	–	–	3.3
2,4,6,8-Tetramethylundecene	11/00	5.1	4.3	6.7	11.5	18.0	–
Biphenyl	12/12	–	–	–	–	–	3.2
Hydrocarbons:							
$\leq C_{10}$	–	17.4	15.1	17.5	16.3	6.1	2.3
C_{10}–C_{16}	–	30.5	26.2	13.9	25.7	24.6	5.3
$\geq C_{16}$	–	2.5	20.5	5.0	6.5	2.6	3.1
Unidentified aromatic compounds	–	–	–	1.0	2.8	2.4	1.9
	–	100.0	100.0	100.0	100.0	100.0	100.0

tion of a coke residue under conditions of thermal oxidative degradation, whereas with pure PP virtually no residue was obtained (see figure). The amount of the coke residue was about 15%. To account for formation of the coke residue and aromatic compounds, we suggested a scheme of solid-phase catalysis. Magnesium hydroxide starts to decompose at 340°C. The nonvolatile magnesium oxide formed on the polymer surface protects deeper layers of the material. Thus, at elevated temperatures magnesium oxide starts to behave as active fire retardant. Due to the weak basic properties and large active surface area, magnesium oxide is used as additive to oxide catalysts for dehydrogenation of aliphatic compounds [9]. In pyrolysis of polypropylene, apparently, MgO behaves similarly.

The possible mechanism of formation of aromatic compounds and coke with nonfused and fused benzene rings is shown in the scheme:

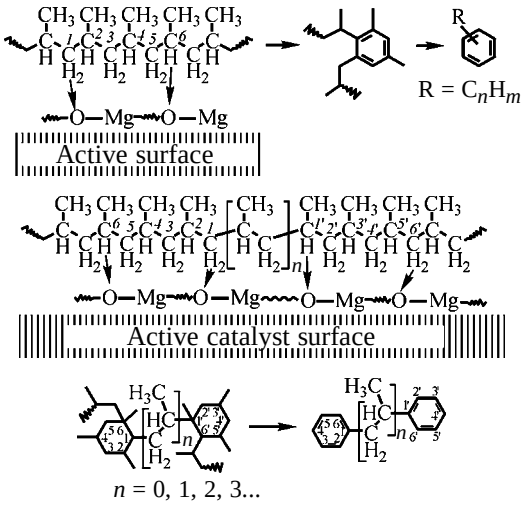

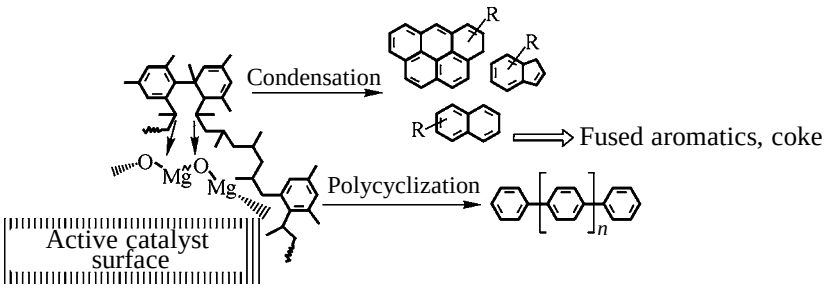

The products of PP thermal degradation undergo dehydrogenation on the active MgO surface, yielding aromatic compounds. A similar mechanism involving catalysis with MgO explains formation of structures with benzene rings linked by an alkyl bridge. Then two pathways are possible. The first pathway is formation of diphenylalkanes. The second pathway involves catalytic solid-phase condensation followed by polycyclization, yielding coke on the MgO surface via intermediates with fused benzene rings, such as naphthalene and its derivatives. The detection of naphthalene, methylnaphthalenes, azulene, and biphenyl, and also of benzene derivatives shows that this process is primary.

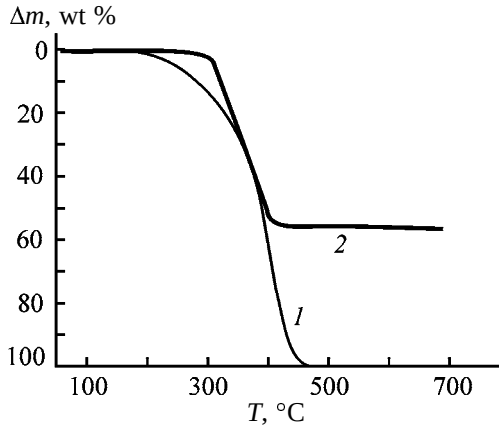

TG curves of (*1*) PP and (*2*) PP–40 wt % $Mg(OH)_2$ composite, recorded in air. Heating rate 10 deg min^{-1}. (Δm) Weight loss and (T) temperature.

CONCLUSION

Compounding polypropylene with $Mg(OH)_2$ enhances its resistance to combustion in both the gas and solid phases; one of the factors responsible for this effect is MgO-catalyzed coke formation on the polymer surface.

REFERENCES

1. Shigeo, M., Takeshi, I., and Hitoshi, A., *J. Appl. Polym. Sci*., 1980, vol. 25, nos. 1–3, pp. 415–425.
2. Lomakin, S.M. and Zaikov, G.E., in *Ecological Aspects of Polymer Flame Retardancy*, Utrecht (the Netherlands): VSP, 2001.
3. Bockhorn, H., Hornung, A., Hornung, U., and Schawaller, D., *J. Anal. Appl. Pyrol.*, 1999, vol. 48, pp. 93–109.
4. Hornung, U., Hornung, A., and Bockhorn, H., *Chem. Ind.*, 1998, vol. 70, pp. 145–148.
5. Hornung, U., Hornung, A., and Bockhorn, H., *Chem. Eng. Technol.*, 1998, vol. 21, pp. 332–337.
6. Bockhorn, H., Hornung, A., and Hornung, U., *J. Anal. Appl. Pyrol.*, 1998, vol. 46, pp. 1–13.
7. Tkáč, A. and Špilda, I., *J. Polym. Sci., Polym. Chem. Ed.*, 1981, vol. 19, pp. 1495–1508.
8. Jha, N.K., Misra, A.C., and Bajaj, P., *J. Macromol. Sci., Rev. Macromol. Chem. Phys.*, 1984, vol. C24, no. 1, pp. 69–116.
9. Isagulyants, G.V., Rozengart, M.I., and Dubinskii, Yu.G., *Kataliticheskaya aromatizatsiya alifaticheskikh uglevodorodov* (Catalytic Aromatization of Aliphatic Hydrocarbons), Moscow: Nauka, 1983.

Russian Journal of Applied Chemistry, Vol. 77, No. 3, 2004, pp. 449–453. Translated from Zhurnal Prikladnoi Khimii, Vol. 77, No. 3, 2004, pp. 456–460.

MACROMOLECULAR CHEMISTRY AND POLYMERIC MATERIALS

Antiturbulent Powers of Higher Polyolefins and Olefin Terpolymers

V. N. Manzhai, L. G. Echevskaya, A. V. Ilyushnikov, A. N. Ochered'ko, V. A. Zakharov, T. B. Mikenas, and S. A. Sergeev

Institute of Oil Chemistry, Russian Academy of Sciences, Tomsk, Russia
Institute of Catalysis, Siberian Division, Russian Academy of Sciences, Novosibirsk, Russia

Received April 10, 2003

Abstract—Terpolymers of ethylene with propylene and higher α-olefins with various compositions and molecular weights were synthesized, as well as copolymers with higher poly-α-olefins with various molecular weights. The possibility of laboratory assessment of the antiturbulent power of polymers and turborheometric determination of the volumes and molecular weights of poly-α-olefin macromolecules was examined.

Introduction of polymer additives to a turbulent flow of a liquid increases its viscosity but decreases the hydrodynamic resistance coefficient and, thus, increases the average flow rate or decreases the friction loss of the pressure (Toms effect [1]).

The mechanism of this somewhat unusual phenomenon remains the subject of heated discussions, but the ability of polymers to decrease the turbulent flow resistance has found wide application, in particular, in oil and oil product transportation via pipelines [2, 3].

By now, hydrodynamic properties of a large number of polymer samples of different chemical nature have been studied. It was found that many of them exhibit the Toms effect [4] under laboratory conditions, but only a few proved to be suitable for and demanded by commercial oil and oil product pipelines. The divergence between the results of laboratory and field experiments can be explained in part as follows. The Toms effect, %, is quantitatively described by the formula

$$DR = (\lambda_s - \lambda_p)/\lambda_s \times 100, \quad (1)$$

commonly used in hydrodynamics. Here, *DR* is the magnitude of the Toms effect, and λ_s and λ_p, hydrodynamic resistance coefficients for pure solvent and polymer solution, respectively.

The coefficients λ_s and λ_p can be determined only after conducting appropriate experiments and processing the experimental data by the Darcy–Weissbach equation.

The main drawback of formula (1) is that it does not implicitly reflect the dependence of the Toms effect on numerous hydrodynamic flow parameters and physicochemical characteristics of polymer solutions (shear stress and Reynolds number, concentration and molecular weight of the polymer additive, and temperature, density, viscosity, and thermodynamic quality of the solvent) affecting the structure of the turbulent flow and, thus, is unsuitable for predicting the effect before experiments.

Comparative assessment of the antiturbulent powers of polymer additives is typically based on analysis of the plots of the Toms effect, *DR*, vs. the polymer concentration in solution, constructed after laboratory bench experiments. Hydrodynamic studies of a wide spectrum of polymers (polystyrene, polyisobutylene, polybutadiene, polymethacrylates, polysiloxanes, etc.) showed that, with increasing amount of the additive, *DR* initially tends to linearly increase within the range corresponding to very dilute solutions and attains a maximal value DR_{max} at a certain optimal concentration c_{opt}, whereupon it slowly decreases with increasing concentration. Samples having the greatest DR_{max} at the smallest c_{opt} are regarded as the most effective.

Figure 1 presents a typical concentration dependence of *DR*, obtained after a laboratory test with oil solutions of two natural rubber (polyisoprene) samples with different molecular weights (MWs). It is seen that, at identical concentrations of solutions, *DR* is the greater, the higher the MW of the sample (Fig. 1, curves *2, 3*) and the greater the shear stress τ_ω on the tube wall (Fig. 1, curves *1, 3*), c_{opt} being the smaller,

1070-4272/04/7703-0449 © 2004 MAIK "Nauka/Interperiodica"

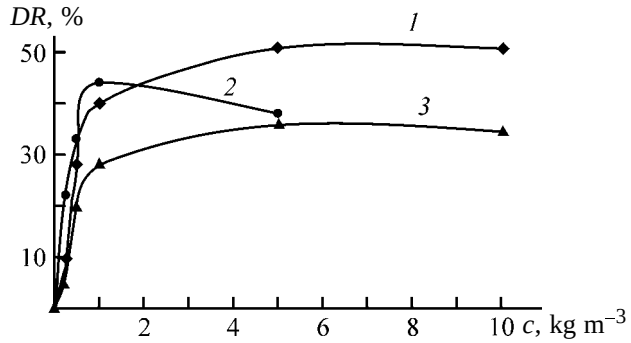

Fig. 1. Hydrodynamic resistance reduction effect *DR* as a function of the concentration *c* of natural rubber in oil. Molecular weight: (*1*, *3*) 2.4×10^5 and (*2*) 5.5×10^5. Intrinsic viscosity [η], $m^3\,kg^{-1}$: (*1*, *3*) 0.20 and (*2*) 0.35. Shear stress τ, Pa: (*1*) 240 and (*2*, *3*) 120.

the higher the MW. From the technological and economical viewpoints, the polymer additive concentration within $0–c_{opt}$ seems optimal for commercial pipeline applications. Thus, practically applicable are polymers with very low optimal concentrations (c_{opt} < 0.05 kg m^{-3}).

Figure 1 presents the results of hydrodynamic tests for three natural rubber samples, which not only show poor performance, not satisfying the concentration criterion (a high-molecular-weight polyisoprene sample has c_{opt} of 1 kg m^{-3} and a sample with a lower molecular weight, 5 kg m^{-3}), but also show no promise for commercial pipelines characterized by typical shear stresses no greater than 10 Pa. These natural rubber samples were studied under the laboratory conditions at arbitrarily chosen and much higher shear stresses (120 and 240 Pa), which are not limited by expression (1).

A change in the quantitative description of the Toms effect from *DR* to a relative parameter $(Q_p - Q_s)/Q_s$ (where Q_p and Q_s are the flow rates of the polymer solution and solvent, respectively) obviates the drawbacks of formula (1). The $\Delta Q/Q_s$ ratio, %, characterizes the increase in the throughput of a tube in which the liquid flow rate increases from Q_s of a pure solvent to Q_p upon introduction of a polymer additive. The dependence of the flow rate increment on various hydrodynamic and physicochemical factors of flowing polymer solutions [5] is described by the equation

$$\Delta Q = S\Psi\tau_\omega\left(\frac{V_g}{\rho kT}\right)^{1/2}\left[1-\left(\frac{kT}{\tau_\omega V_g}\right)^{1/2}\right], \qquad (2)$$

where $\Delta Q = Q_p - Q_s$ is the flow rate increment of a polymer solution relative to the solvent; $S = \pi R_\omega^2$, cross-section area of the cylindrical channel; $\Psi = [\eta]c_p/(1 + [\eta]c_p)$, volume fraction of the macromolecular globules in solution, which depends on the intrinsic viscosity [η] and concentration of the polymer solution c_p; $\tau_\omega = \Delta P R_\omega/2L$, shear stress on the wall of a tube with radius R_ω and length L at a given pressure gradient ΔP; V_g, volume of a macromolecular globule with immobilized solvent; ρ, density of the solvent; *k*, Boltzmann constant; and *T*, temperature.

It is seen that Eq. (2) is consistent with the currently available empirical data and allows predicting not only the magnitude of the effect (i.e., increase in the average flow rate), but also the conditions of its manifestation. It was found experimentally that the Toms effect is observed in the turbulent region of flow (Re > 2300, where Re is the Reynolds number) at shear stresses exceeding a certain "threshold" parameter τ_{thr} which for each particular sample is the smaller, the higher the MW. Clearly, Eq. (2) suggests that the effect ($\Delta Q > 0$) can be manifested only at $[1 - (kT/\tau_\omega V_g)^{1/2}] > 0$, or at $\tau_\omega V_g > kT$. Using the latter inequality, we can estimate the minimal (threshold) shear stress above which the turbulent flow rate of the polymer solution will exceed the flow rate of the solvent:

$$\tau_{thr} = kT/V_g. \qquad (3)$$

Using the well-known Flory–Fox formula $V_g \approx M[\eta]/N_a$ connecting the volume of the macromolecule with its molar mass *M*, intrinsic viscosity [η], and Avogadro number N_a, we can modify expression (3) into

$$\tau_{thr} = RT/M[\eta]. \qquad (4)$$

Thus, the threshold shear stress for a particular polymer sample is the smaller, the larger its molar mass and intrinsic viscosity or their proportional globule volume. For the two natural rubber samples (Fig. 1) with molar masses M_1 = 240 kg mol^{-3} (MW = 2.4×10^5) and M_2 = 550 kg mol^{-3} (*MW* = 5.5×10^5) and intrinsic viscosities $[\eta]_1 = 0.2$ and $[\eta]_2 = 0.35$ $m^3\,kg^{-1}$ at *T* = 293 K, the threshold shear stresses were estimated at $\tau_{thr1} \approx 50$ and $\tau_{thr2} \approx 13$ Pa. These exceed the actual shear stresses in main pipelines ($0 < \tau_\omega < 10$ Pa), which suggests that introduction of these polymer additives into pipelines will not increase the flow rate.

In the case of developed turbulent flows, i.e., at fairly large Reynolds numbers and shear stress on the wall τ_ω, when the algebraic sum $[1 - (kT/\tau_\omega V_g)^{1/2}]$ in

Eq. (2) tends to unity, this equation acquires a simpler form

$$\Delta Q = S\Psi\tau_\omega\left(\frac{V_g}{\rho kT}\right)^{1/2}. \quad (5)$$

Therefore, the flow rate increment for a polymer solution is the larger, the larger the size and concentration of the macromolecules with the solvent immobilized, as well as the shear stress. Based on the data of a turborheometric test with polymer solutions, the volume of the macromolecular globules can be calculated by Eq. (5). Next, it is possible to estimate the molar mass of the polymer sample by the modified Flory–Fox formula

$$M = V_g N_a/[\eta]. \quad (6)$$

EXPERIMENTAL

The above analysis of the flow rate increment as dependent on various factors allows formulation of economically and technologically sound requirements for candidate agents decreasing the hydrodynamic resistance in main oil pipelines. These requirements include a fairly low prime cost (which is primarily determined by the price of the monomer); no adverse effect on oil processing; a fairly high molecular weight; and a good compatibility (solubility) with oil and its individual fractions, that is, the polymer additive must have fairly high intrinsic viscosities in hydrocarbon liquids of different polarities.

Among a great number of well-characterized polymers of different chemical nature, these requirements are most adequately satisfied by higher poly-α-olefins and their X-ray amorphous copolymers prepared using Ziegler catalysts. It is well known [6] that the rate of polymerization proceeding by the ion-coordination mechanism and the molecular weight of the resulting product are governed by numerous factors such as the chemical nature of the monomer and of the catalytic system, concentration of the monomer in the initial reaction mixture and its conversion (the degree of the monomer conversion into polymer within a certain period), temperature, and some other parameters.

High-molecular-weight X-ray amorphous terpolymers (ethylene/propylene/α–olefin) were prepared using a highly active vanadium-magnesium catalyst. It was synthesized by the procedure from [7], by applying vanadium compounds (VCl_4, $VOCl_3$) onto finely dispersed magnesium chloride (the vanadium content in the catalyst was 2–3 wt %). High-molecular-weight homopolymers of higher poly-α-olefins were synthesized using two modifications of titanium–magnesium catalysts. They were prepared by applying $TiCl_4$ onto finely dispersed magnesium chloride containing modifying additives (2–4 wt % titanium in the samples).

The olefins were polymerized in a 1-l steel autoclave under vigorous stirring at 293–323 K. As cocatalyst served triethylaluminum or triisobutylaluminum. The concentration of the catalyst was 0.4 g l^{-1}, and that of the cocatalyst, 5 mM.

The composition of terpolymers (C_2, C_3, C_α) was determined by ^{13}C NMR spectroscopy on a Bruker DRX-250 instrument at 393 K and 62.91 MHz. The samples were prepared in the form of solutions in 1,2-dichlorobenzene with a polymer concentration of 0.07–0.12 g ml^{-1}.

The hydrodynamic properties of terpolymers and poly-α-olefins were studied in the laminar and turbulent flow modes. The intrinsic viscosities of poly-α-olefins in benzine and of terpolymers in three solvents (heptane, benzine, and toluene) were determined by capillary viscometry. The use of different solvents allows estimation of the degree of crystallinity of the resulting products. Terpolymers with a high ethylene content and, consequently, prone to formation of crystallinity zones, are well soluble in toluene and less soluble in heptane. Benzine, which is a mixture of alkanes and aromatic compounds, is intermediate in solvency.

We determined the flow rates Q_s and Q_p at the shear stress on the tube wall τ_ω = 4 Pa in a turbulent rheometer [8] measuring flow rates of solvents and polymer solutions of different concentrations in a cylindrical channel in the turbulent flow mode (Re > 2300). Then, we calculated the $\Delta Q/Q_s$ parameters. The choice of benzine as the solvent was dictated by two reasons. First, as one of oil fractions, benzine is close in solvency to the mixed oil transported by main pipelines. Second, being a low-viscosity solvent, benzine is suitable for measurements in a turbulent-flow region at shear stresses close to those actually occurring in commercial main pipelines. The parameters V_g, M, and τ_{thr} were calculated by formulas (5), (6), and (3).

Polyolefins and their copolymers prepared at lower temperatures usually have higher molecular weights [6]. This is true for the samples of ethylene-, propylene-, and 1-dodecene-based terpolymers synthesized at 293–323 K (Table 1).

Table 1 shows that the intrinsic viscosity of solu-

Table 1. Composition and hydrodynamic properties of solutions of terpolymers synthesized at different temperatures T_s

T, K	Composition of copolymer, wt %			Intrinsic viscosity [η], $m^3\ kg^{-1}$			$V_g \times 10^{21}$, m^3	τ_{thr}, Pa	c_{opt}, $kg\ m^{-3}$	$(\Delta Q/Q_s)_{max}$, %
	C_2	C_3	C_{12}	heptane	benzine	toluene				
323	33	36	31	0.14	0.16	0.17	0.19	21.3	–	0
313	39	37	24	0.31	0.33	0.38	1.15	3.5	0.55	44
303	50	30	20	0.29	0.34	0.41	1.61	2.5	0.25	47
293	56	29	15	0.26	0.28	0.42	1.45	2.8	0.35	46

tions in toluene tends to increase with decreasing temperature of the sample synthesis, which, most probably, suggests a growth of the molecular weight. The intrinsic viscosity of the same samples in heptane exhibits an opposite trend. Visual examination of the solutions in toluene and heptane revealed the absolute transparency of the former (which allows their classification with true solutions) and pronounced opalescence of the latter (suggesting the presence of heterogeneous inclusions of microgels). A decrease in the solubility in heptane for the terpolymers prepared at relatively low temperatures is due to a decrease in the content of propylene and 1-dodecene units in them and to a growth in the proportion of ethylene units (Table 1) enhancing the microblock structure.

Benzine is intermediate in solvency between toluene and heptane; consequently, the hydrodynamic properties of solutions of terpolymers in benzine are determined by the ratio of the molecular weight of the samples to the content of α-olefin units in them (Table 1). It is seen that the maximal antiturbulent power is exhibited by the polymer prepared at T = 303 K. Further decrease of the synthesis temperature, though affording higher molecular weights of terpolymers, decreases the proportion of 1-dodecene. This worsens the solubility and thus decreases both the volumes of macromolecular globules with the solvent immobilized and the resistance reduction effect $(\Delta Q/Q_s)_{max}$.

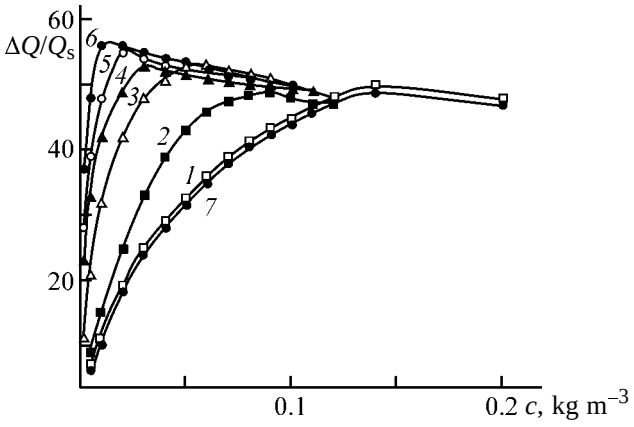

Fig. 2. Flow rate increment $\Delta Q/Q_s$ as a function of the polymer concentration c. Polyolefin: (*1*–*6*) poly-1-hexene (for characteristics of the samples, see Table 2), (*7*) $C_2/C_3/C_6$ ternary copolymer ([η] = 0.41 $m^3\ kg^{-1}$, V_g = 3.79×10^{-21} m^3).

A change to a monomer with a lower molecular weight (from 1-dodecene to 1-hexene) in copolymerization at 293 K allowed preparation of a terpolymer with enhanced content of α-olefin in the polymer chain (25 wt %). This improved the solubility of the terpolymer in benzine ($[\eta]_{benz}$ = 0.41 $m^3\ kg^{-3}$), increased the volume of the macromolecular globule ($V_g = 3.79 \times 10^{-21}$ m^3), and decreased the "threshold" shear stress (τ_{thr} = 1.1 Pa).

The resulting ternary copolymer has the highest hydrodynamic power $(\Delta Q/Q_s)_{max}$ = 48% at τ_ω = 4 Pa) among all the terpolymers synthesized. At the same time, the maximal (by a factor of nearly 1.5) increase in the flow rate is achieved at a too high concentration of 0.14 $kg\ m^{-3}$ (Fig. 2, curve *7*). This sends us in a further search for optimal catalytic systems and copolymer combinations, as well as for conditions of synthesis of well soluble terpolymers with the aim to prepare samples with a maximal $\Delta Q/Q_s$ at concentrations under 0.05 $kg\ m^{-3}$.

Experiments on polymerization of individual 1-hexene, 1-octene, and 1-dodecene in heptane showed that the maximal activity and, thus, the rate of conversion into polymer are exhibited by 1-hexene, which made specifically this monomer preferable for homopolymerization.

Test syntheses at various temperatures also showed that the MW of the resulting product increases with decreasing temperature and that polymers with molecular weights over 10^6 are formed below 300 K. Therefore, we carried out polymerization of 1-hexene at 293 K, which yielded a suitable product ($M[\eta] > RT/\tau_\omega$) at an acceptable rate.

Table 2 presents the results of a hydrodynamic test

Table 2. Synthesis conditions and hydrodynamic properties of poly-α-hexene samples

Sample no.	c, M	τ_s, min	$[\eta]_{benz}$, $m^3\ kg^{-1}$	$V_g \times 10^{21}$, m^3	M, kg mol^{-1}	τ_{thr}, Pa	c_{opt}, kg m^{-3}	$(\Delta Q/Q_s)_{max}$, %
1	1	300	0.42	3.8	5450	1.06	0.14	49
2	1.8	300	0.69	6.5	5670	0.62	0.09	50
3	2.5	300	0.87	9.3	6440	0.36	0.05	51
4	2.5	180	1.25	14.6	7030	0.28	0.03	53
5	2.5	120	1.41	21.6	9220	0.19	0.02	54
6	2.5	60	1.62	28.4	10560	0.15	0.01	55

of poly-1-hexene samples prepared in a number of synthesis runs at varied initial concentration of the monomer in the reaction medium c_m and synthesis time τ_s.

Table 2 and Fig. 2 show that the concentration of the polymer additive c_{opt} corresponding to the maximal flow rate increment $(\Delta Q/Q_s)_{max}$ is the smaller, the larger the size of its macromolecular globules with the solvent immobilized. In accordance with the kinetic relationships in the polymerization process, the molecular weight of the forming macromolecules (globule volume) is the larger, the higher the monomer concentration in the reaction medium. Therefore, the antiturbulent power of the resulting samples increases with increasing initial concentration of the monomer charged into the reactor and decreasing synthesis time (conversion). Figure 2 (curve *7*) shows that the most effective terpolymer is surpassed in hydrodynamic properties by all the homopolymers synthesized. Table 2 and Fig. 2 also suggest that the samples of poly-1-hexene (sample nos. 3–6) are suitable for commercial application in main oil pipelines.

CONCLUSIONS

(1) A procedure, based on two criteria, was proposed for assessing under the laboratory conditions the suitability of candidate agents to reduce the hydrodynamic resistance. The necessary condition is a turbulent flow mode (Re > 2300) in the experimental setup, and the sufficient condition, measurement of the antiturbulent properties of polymer additives at shear stresses in the turborheometer equivalent to those actually occurring in main pipelines.

(2) Terpolymers (ethylene/propylene/α-olefin) synthesized on vanadium–magnesium catalysts are able of reducing the hydrodynamic resistance by 40–50% when introduced into turbulent flow in amounts of 0.15–0.55 kg m^{-3}.

(3) Samples of homopolymer (polyhexene) synthesized on titanium–magnesium catalysts below 300 K and having a molecular weight of $(1–10) \times 10^6$ are able of reducing the hydrodynamic resistance by 50–55% at concentrations of $(10–50) \times 10^{-3}$ kg m^{-3}.

REFERENCES

1. Toms, B.A., in *First Int. Congr. on Rheology*, Amsterdam: North Holland, 1949, vol. 2, pp. 135–141.
2. Small, S.R., *Neft', Gaz Neftekhim. Rubezh.*, 1983, no. 6, pp. 58–60.
3. Nesyn, G.V., Manzhai, V.N., Popov, E.A., *et al.*, *Truboprov. Transp.*, 1993, no. 4, pp. 28–30.
4. Belousov, Yu.P., *Protivoturbulentnye prisadki dlya uglevodorodnykh zhidkostei* (Antiturbulent Additives to Hydrocarbon Liquids), Moscow: Nauka, 1986.
5. Manzhai, V.N., in *Teoreticheskie i prikladnye osnovy fiziko-khimicheskogo regulirovaniya svoistv neftyanykh dispersnykh sistem* (Theoretical and Applied Principles of Physicochemical Control of the Properties of Oil Disperse Systems), Tomsk: Tomsk. Gos. Univ., 2001, part 3, pp. 71–81.
6. Chirkov, N.M., Matkovskii, P.E., and D'yachkovskii, F.S., *Polimerizatsiya na kompleksnykh metalloorganicheskikh katalizatorakh* (Polymerization on Complex Organometallic Catalysts), Moscow: Khimiya, 1976.
7. RF Patent 2047355.
8. Malkin, A.Ya., Nesyn, G.V., Manzhai, V.N., and Ilyushnikov, A.V., *Vysokomol. Soedin., Ser. B*, 2000, vol. 42, no. 3, pp. 377–383.

Russian Journal of Applied Chemistry, Vol. 77, No. 3, 2004, pp. 454–457. Translated from Zhurnal Prikladnoi Khimii, Vol. 77, No. 3, 2004, pp. 461–464.

MACROMOLECULAR CHEMISTRY AND POLYMERIC MATERIALS

Energy Characteristics of the Surface of Modified Phosphorus-Containing Epoxy Polymers

L. M. Amirova and A. F. Magsumova

Tupolev Kazan State Technical University, Kazan, Tatarstan, Russia

Received April 22, 2003

Abstract—The Fowkes and van Oss–Good approaches were used for assessing the energy characteristics of the surface of the epoxy–amine systems modified with triglycidyl phosphate. Variation of these characteristics with the modifier content and polymer curing conditions was studied.

Modification of the initial oligomer systems allows control of the surface properties of cured polymers. It is known [1, 2] that the components of compounds differ in the adsorbability, which can be responsible for differences in their distribution in the bulk and at interfaces [1, 2]. This allows formation of surfaces with desired energy characteristics.

The surface energy γ_S of solids at the solid–liquid or solid–gas interfaces is often assessed using the Fowkes–Owens [3, 4] and van Oss–Good [5, 6] approaches. They are based on measuring the contact angles of wetting of the surface with test liquids. The surface energy and its components were estimated for a number of epoxy polymers [1, 2, 7, 8]. Rudoi and co-workers [1] and Chalykh and co-workers [2] showed that the surface activity of modified epoxy systems is governed by a number of factors such as ratio of the rates of the chemical reaction and diffusion, molecular weight, and the curing mode chosen. However, the above-cited works, even though concerned with the same epoxy systems, report different surface energies. Van Oss and co-workers [5, 6] assessed the acid–base properties of the surface of epoxy polymers and revealed their basic nature.

We found earlier [9–13] that modification of epoxy–4,4'-isopropylidenediphenol oligomers with glycidyl esters of phosphorus-containing acids (GEPs) yields materials with enhanced thermophysical, physicomechanical, and optical properties. At the same time, when the developed phosphorus-containing epoxy compounds are intended as adhesives, preparation of coatings requires knowledge of the surface and interphase properties of both uncured oligomer systems and polymers thereof.

The aim of this work is to quantitatively estimate the energy characteristics of the surface of polymers based on ED-20 epoxy-4,4'-isopropylidenediphenol oligomer modified with triglycidyl phosphate.

EXPERIMENTAL

We used ED-20 epoxy–4,4'-isopropylidenediphenol oligomer **I**, triglycidyl phosphate $P(O)(OCH_2\text{–}\underset{\backslash\ /}{CH}\text{–}CH_2)_3$ **II**, and 4,4'-diaminodiphenylmethane (DADPM).

Oligomer **I** was vacuum-treated at 80–90°C, whereupon the contents of epoxy and hydroxy groups were estimated by chemical methods [14] (at 21.5 and 1.3%, respectively). Triglycidyl phosphate **II** was synthesized as described by Rizpolozhenskii *et al.* [15], purified by vacuum distillation, and kept in sealed glass ampules. The compound was identified by elemental analysis and IR and ^1H, ^{13}C, and ^{31}P NMR spectroscopy.

The compatibility of **I** and **II** was checked by microinterferometry on an MI-2 instrument. Based on the data obtained, we constructed phase diagrams.

Mixtures of **I** and **II** of different compositions were cured with a stoichiometric amount of DADPM in a stepwise mode (heating to 60°C and curing for 6 h at 20°C) and postcured in a stepwise mode as well (heating for 1 h at 100–170°C with a 10°C step).

The surface energy of the resulting polymers and its components were estimated from the angle of wetting with test liquids. The contact wetting angles were determined using a horizontal microscope equipped with a goniometric accessory, under saturated liquid

1070-4272/04/7703-0454 © 2004 MAIK "Nauka/Interperiodica"

Energy characteristics of the test liquids

Test liquid	Energy characteristic, mJ m^{-2}, taken from indicated works							
	[3, 4]			[5, 6]				
	γ	γ^d	γ^p	γ	γ^{LW}	γ^{SR}	γ^+	γ^-
Water	72.2	22.0	50.2	72.8	21.8	51.0	25.5	25.5
Glycerol	64.0	34.0	30.0	64.0	34.0	30.0	3.92	57.4
Formamide	58.3	32.3	26.0	58.0	39.0	19.0	2.28	39.6
Diiodomethane	50.8	48.5	2.3	50.8	50.8	0	0	0
Ethylene glycol	48.3	29.3	19.0	48.0	29.0	19.0	1.92	47.0

vapor in a chamber kept at a constant temperature of 20°C. The test liquids were chosen by the criteria suggested by Kwok *et al*. [16]. The surface energy components and the equilibrium contact wetting angle θ for the contacting solid and liquid phases are linked by the Owens–Wendt relationship [3, 4]

$$(\cos\theta + 1)\gamma_L = 2(\gamma_S^d\gamma_L^d)^{1/2} + 2(\gamma_S^p\gamma_L^p)^{1/2}, \quad (1)$$

where, γ_L is the surface tension at the liquid–gas interface; γ_S^d and γ_L^d are the dispersion, and γ_S^p and γ_L^p, polar components of the surface energy of a solid and a liquid, respectively.

The total surface energy γ_S can be represented as

$$\gamma_S = \gamma_S^d + \gamma_S^p. \quad (2)$$

The polar component γ^{SR} of the surface energy of cured polymers and its acidic γ_S^+ and basic γ_S^- constituents were estimated taking into account the Lifshits–van der Waals nonpolar component γ^{LW} which is virtually identical to the dispersion component γ^d in terms of the approach suggested in [5, 6]. This approach implies that the polar component of the surface energy γ^{SR} is due to electron donor–acceptor (acid–base) interactions and is determined by the relationship

$$\gamma^{SR} = 2(\gamma^-\gamma^+)^{1/2}, \quad (3)$$

where γ^- and γ^+ are the donor (basic) and acceptor (acidic) components of the surface energy, respectively.

The major equation linking the acid–base and nonpolar interactions with the contact wetting angle θ is

$$(\cos\theta + 1)\gamma_L = 2[(\gamma_S^{LW}\gamma_L^{LW})^{1/2} + (\gamma_S^+\gamma_L^-)^{1/2} + (\gamma_S^-\gamma_L^+)^{1/2}], \quad (4)$$

where the subscripts "S" and "L" refer to the solid and liquid phases, respectively.

The surface energies of the **I**–**II**–DADPM solid polymers yielded by curing of the oligomer systems were estimated from the contact angles of wetting with a number of test liquids (see table). Figure 1 (curves *1*–*3*) shows how the energies of the surface formed at the epoxy polymer–air interface, estimated by Eqs. (1) and (2), vary with the content of triglycidyl phosphate **II** for epoxy polymers postcured in a stepwise mode to 150°C.

It is seen that γ_S is virtually independent of triglycidyl phosphate concentration up to 70 wt %. At the same time, at the modifier content within 0–10 wt %, the dispersion component γ_S^d tends to significantly decrease, and the polar component γ_S^p, to increase. Figure 1 shows that the increased surface energy of the polymers containing over 70 wt % triglycidyl phosphate **II** is due to increased contribution from the polar component, the dispersion component being virtually unchanged.

Dogan *et al*. [7] and Chung *et al*. [8] showed that the surface of epoxy–amine polymers is virtually monopolar and basic. Our data (Fig. 2) suggest that the surface basicity is enhanced by introduction of triglycidyl phosphate **II** into the polymer. This is evidently due to increases in the number of oxygen atoms in the polymer network and of secondary hydroxy groups and to appearance of phosphoryl groups.

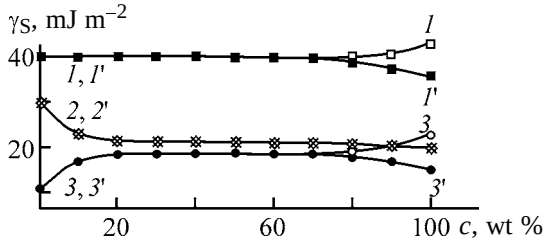

Fig. 1. (*1*, *1*') Surface energy γ_S and its (*2*, *2*') dispersion, γ_S^d, and (*3*, *3*') polar, γ_S^p, components as functions of the triglycidyl phosphate concentration *c* in the epoxy–amine polymer heat-treated at (*1*–*3*) 150 and (*1*'–*3*') 170°C.

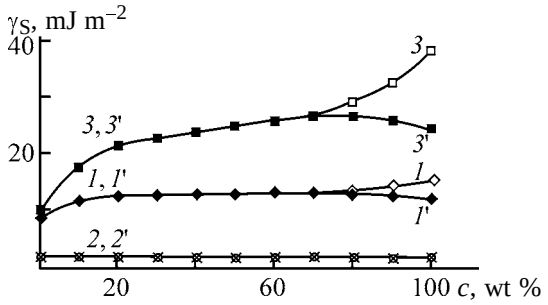

Fig. 2. Variation of (*1*, *1*') polar component γ_S^{SR} and (*2*, *2*') acidic, γ_S^+, and (*3*, *3*') basic, γ_S^-, constituents of the surface energy γ_S with the triglycidyl phosphate concentration *c* in the epoxy–amine polymer heat-treated at (*1*–*3*) 150 and (*1*'–*3*') 170°C.

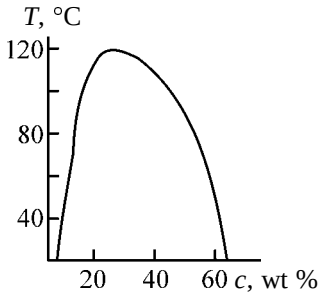

Fig. 3. Phase diagram of the **I**–**II** system. (*T*) Temperature and (*c*) triglycidyl phosphate concentration.

To explain the nonuniform variation of the energy characteristics of the epoxy polymer surface with increasing content of triglycidyl phosphate **II**, we will turn to the phase diagram of the **I**–**II** system (Fig. 3). It is seen that, with <8 and >65 wt % **II**, the system is compatible, and within 8–65 wt %, incompatible with the upper critical solution point (UCSP) of 120°C. Similar phase diagrams were obtained previously by Amirova *et al*. [13] for a number of GEPs and E-40 epoxy polymer. It was shown that, in the region of incompatibility of the epoxy oligomer–GEP system, stratifying emulsions are formed, whose curing yields polymers exhibiting a composition gradient over the sample cross section. The upper layer of such polymer is formed from the epoxy–4,4'-isopropylidenediphenol oligomer containing ca. 10 wt % GEP. The lower layer is formed by GEP saturated with the dissolved epoxy–4,4'-isopropylidenediphenol polymer. Elemental analysis suggested similar segregation and formation of a gradient polymer in the **I**–**II** system studied by us.

Thus, invariant energy characteristics of the surface of epoxy–amine polymers of the **I**–**II** system with the triglycidyl phosphate content within 10–70 wt % (Figs. 1, 2) are due to invariant composition of their surface containing 8–10 wt % triglycidyl phosphate **II**. In the regions of compatibility, enhancement of the polarity (and basicity) of the surface of these polymers with increase in the concentration of **II** is due to increase in the concentration of **II** in the upper layer.

Recently, Amirova [17] showed that heat treatment at 170°C of the triglycidyl phosphate based epoxy polymer cured with DADPM results in water elimination and decrease in the content of the secondary hydroxy groups. This is accompanied by increases in the glass transition point and elastic modulus. A similar effect is also observed for polymers prepared by curing mixtures of **I** and **II** with DADPM, whose glass transition points are above 170°C. This holds for polymers containing over 10 wt % triglycidyl phosphate **II** [10]. In this connection, it was of interest to elucidate how such heat treatment affects the energy characteristics of the surface of the polymers under study.

Figure 1 (curves *1*'–*3*') shows the plots of the surface energy for the polymer–air interface formed by epoxy polymers with different contents of triglycidyl phosphate **II**, cured stepwise to 150°C and heat-treated at 170°C. It is seen that heat treatment does not noticeably affect the run of curves *1* and *3* for triglycidyl phosphate concentrations within 0–70 wt % and the run of curve *2* throughout the modifier concentration range. At 70–100 wt % content of triglycidyl phosphate, the polar component γ_S^p and, thereby, the surface energy of the polymer as a whole, significantly decrease (Fig. 1).

The runs of the curves for the polar component and its basic constituent as calculated by Eqs. (3) and (4) were also different in the region of 70–100 wt % triglycidyl phosphate (see curves *1*' and *3*' in Fig. 2), while the acidic constituent remained unchanged (Fig. 2, curve *2*'). Weakening basicity of the surface of polymers with these compositions during heat treatment can be probably explained by the above-mentioned decrease in the amount of polar hydroxy groups on the polymer surface during annealing at 170°C. The fact that the heat treatment does not affect the nature of the surface of the polymers containing up to 10 wt % triglycidyl phosphate **II** is evidently due to the lacking water elimination and unchanged content of the surface polar groups. As mentioned above, for polymers containing 10–70 wt % triglycidyl phosphate **II**, the surface layer was formed by epoxy–4,4'-isopropylidenediphenol oligomer with a constant content of triglycidyl phosphate which is unaffected by heat treatment at 170°C. In our opinion, this adequately explains the fact that the energy character-

istics of the surface of polymers containing 0–70 wt % triglycidyl phosphate **II** are unaffected by annealing at 170°C.

CONCLUSIONS

(1) Triglycidyl phosphate introduced into epoxy–4,4'-isopropylidenediphenol oligomer modifies the energy characteristics of the resulting polymer in the region of compatibility of epoxy compounds.

(2) Heat treatment of the resulting polymer decreases the polar component of the surface energy and its basic constituent at triglycidyl phosphate concentrations above 70 wt %.

ACKNOWLEDGMENTS

This study was supported in part by the Russian Universities program of the RF Ministry of Education (project no. UR.05.01.034).

REFERENCES

1. Rudoi, V.M., Okulova, I.A., and Ogarev, V.A., *Kolloidn. Zh.*, 1989, vol. 51, no. 2, pp. 310–317.
2. Chalykh, A.E., Stepanenko, V.Yu., and Avgonov, A., *Lakokras. Mater.*, 2000, no. 6, pp. 3–7.
3. Fowkes, F.M., *Ind. Eng. Chem.*, 1964, vol. 56, no. 12, pp. 40–52.
4. Owens, D.K. and Wendt, R.C., *J. Appl. Polym. Sci.*, 1969, vol. 13, no. 8, pp. 1741–1747.
5. Oss, C.J. van, Chaudhury, M.K., and Good, R.J., *Chem. Rev.*, 1988, vol. 88, no. 6, pp. 927–941.
6. Oss, C.J. van, Good, R.J., and Chaudhury, M.K., *Langmuir*, 1988, vol. 4, no. 4, pp. 884–891.
7. Dogan, M., Eroglu, M.S., and Erbil, H.Y., *J. Appl. Polym. Sci.*, 1999, vol. 74, no. 12, pp. 2848–2855.
8. Chung, T.S., Chen, W.Y., Lin, Y.H., and Pramoda, K.P., *J. Polym. Sci, Part B: Polym. Phys.*, 2000, vol. 38, no. 11, pp. 1449–1460.
9. Amirova, L.M., *Low Flammability Polymeric Materials*, Zaikov, G.E. and Khalturinskii, N.A., Eds., New York: Nova Science, 1999, ch. 7, pp. 257–277.
10. Amirova, L.M., Shageeva, I.K., and Stroganov, V.F., *Zh. Prikl. Khim.*, 2001, vol. 74, no. 8, pp. 1328–1331.
11. Amirova, L.M. and Sakhabieva, E.V., *Zh. Prikl. Khim.*, 2001, vol. 74, no. 10, pp. 1692–1695.
12. Amirova, L.M., Saifutdinov, R.Kh., Magsumova, A.F., and Amirov, R.R., *Zh. Prikl. Khim.*, 2001, vol. 74, no. 11, pp. 1881–1884.
13. Amirova, L.M., Andrianova, K.A., Bukharaev, A.A., and Fomin, V.P., *Zh. Prikl. Khim.*, 2002, vol. 75, no. 9, pp. 1505–1508.
14. Lee, H. and Nevill, K., *Handbook of Epoxy Resins*, New York: McGraw-Hill, 1967.
15. Rizpolozhenskii, N.I., Boiko, L.V., and Zvereva, M.A., *Dokl. Akad. Nauk SSSR*, 1964, vol. 155, no. 6, pp. 1137–1139.
16. Kwok, D.Y., Ng, H., and Neumann, A.W., *J. Colloid Interf. Sci.*, 2000, vol. 225, no. 2, pp. 323–328.
17. Amirova, L.M., *Vysokomol. Soedin., Ser. A*, 2003, vol. 45, no. 6, pp. 896–902.

Russian Journal of Applied Chemistry, Vol. 77, No. 3, 2004, pp. 458–462. Translated from Zhurnal Prikladnoi Khimii, Vol. 77, No. 3, 2004, pp. 465–469.

MACROMOLECULAR CHEMISTRY AND POLYMERIC MATERIALS

Polyfunctional Anion Exchangers Based on Copolymers of Allyl Glycidyl Ether and Polyamines

E. E. Ergozhin, T. K. Chalov, R. A. Iskakova, and T. V. Kovrigina

Bekturov Institute of Chemical Sciences, Ministry of Education and Science of Kazakhstan Republic, Almaty, Kazakhstan

Received April 16, 2003

Abstract—Polyfunctional anion exchangers were prepared by copolymerization of allyl glycidyl ether with polyamines in the presence of a promoter. The synthesis conditions were optimized. The composition and physicochemical features of the resins prepared were studied.

It is known that, in storage, pretreatment, and practical application of sorbents, their characteristics are deteriorated. Therefore, development of polymeric sorbents with stable physicochemical and sorption characteristics is an urgent problem. In this respect, allylic resins show much promise. These polymers are formed by slow radical polymerization of allyl monomers. Their molecular weight is usually low because of degradation chain transfer to the monomer [1]. This process is widely used for preparating polymers with stable physicochemical features [2, 3].

In this work we prepared polyfunctional anion exchangers by copolymerization of allyl glycidyl ether (AGE) and polyamines [polyethylenimine (PEI), poly-2-methyl-5-vinylpyridine (PMVP) in the presence of initiator (H_2O_2)]. The composition, structure, and acid–base properties of the anion exchangers were studied by IR and ^{13}C NMR spectroscopy and potentiometric titration.

EXPERIMENTAL

The AGE–PEA (or PMVP) copolymers were prepared in dimethylformamide (DMFA) at 70–80°C. Before polymerization, a portion of 30% aqueous hydrogen peroxide was added as initiator into the reaction mixture. The initially formed gel-like polymer was cured at 80–120°C. The solid polymer was crushed, and the fraction with the granule size of 0.25 mm was separated by sifting [4, 5].

The pretreatment of the polymer and determination of its physicochemical characteristics were carried out by common technique [6].

The IR spectra of polimerization products formed in the initial, intermediate, and final polymerization stages were recorded on a Specord M80/M85 spectrophotometer [KBr pellets (200 mg KBr + 1 mg polymerization product), thin film of the product placed between plates]. The ^{13}C NMR spectra of polymerization products were recorded in dimethyl sulfoxide solution on a Mercury-300 NMR spectrometer (75 MHz) at room temperature.

The potentiometric titration of the anion exchanger was carried out by contact of its air-dry weighed samples (0.20–0.25 g) with different amounts of 0.1 N aqueous HNO_3 at the ionic strength (KNO_3) of 1 M. After the equilibrium was attained (within 7–10 days), the pH was measured on an EV-74 universal ionometer.

In order to optimize the conditions for preparing the polyelectrolytes, their static exchange capacity (SEC) and swelling (V_{sp}) were studied in relation to the main preparation parameters: AGE : polyamine ratio, polyamine type, temperature, and prepolymerization time.

We found (Table 1) that, with increasing the polyamine : AGE weight ratio in the reaction mixture above unity, both the SEC of anion exchanger (prepared in the presence of H_2O_2) for HCl and its swelling decrease. The increase in the H_2O_2 concentration in the reaction mixture from 0.1 to 0.3% also negatively affects the polyelectrolyte characteristics.

Table 1 shows that the polymer prepared without adding H_2O_2 has a lower anion-exchange capacity and higher swelling as compared to the anion exchanger prepared in the presence of hydrogen peroxide. Thus, introduction of hydrogen peroxide into the reaction mixture improves the resin characteristics.

1070-4272/04/7703-0458 © 2004 MAIK "Nauka/Interperiodica"

Table 1. Influence of AGE : polyamine ratio in the reaction mixture on the SEC and swelling of anion exchangers, T = 80°C, τ = 4 h

AGE : polyamine weight ratio	C_N in anion exchanger	$c_{H_2O_2}$ in reaction mixture	SEC, mg-equiv g^{-1}, for Cl^- in 0.1 M solution		V_{sp}, ml g^{-1}
	%		HCl	NaCl	
		AGE–PEI			
1.0 : 1.0	13.6	0.1	9.5	0.1	5.5
1.0 : 1.5	14.0	0.1	9.5	0.2	5.1
1.0 : 2.0	14.6	0.1	8.8	0.2	5.0
1.0 : 2.5	15.7	0.1	7.5	0.2	2.7
2.5 : 1.0	12.8	0.1	8.6	0.3	5.4
3.0 : 1.0	12.3	0.1	7.9	0.2	7.4
1.0 : 2.5	15.4	0.2	6.6	0.3	1.5
1.0 : 2.5	15.9	0.3	5.4	0.3	1.1
1.0 : 1.5	13.2	–	6.6	0.2	12.9
1.0 : 2.5	14.6	–	5.1	0.2	10.0
		AGE–PMVP			
1.0 : 1.0	5.4	0.1	4.6	1.2	3.4
1.0 : 2.0	6.5	0.1	5.3	0.9	5.6
1.0 : 3.0	6.1	0.1	6.2	0.7	5.9
2.0 : 1.0	6.6	0.1	3.4	0.8	6.4
1.0 : 1.0	7.0	–	4.2	1.0	8.7
1.0 : 2.0	7.7	–	3.7	0.7	9.0

Table 2. Influence of temperature and reaction time on SEC of AGE–PEI and AGE–PMVP anion exchangers

Parameter	T, °C			τ, h				
	70	80	90	1	2	3	4	5
				AGE–PEI				
SEC_{HCl}, mg-equiv g^{-1}	7.3	7.5	5.2	2.3	4.1	5.9	7.5	7.2
V_{sp}, ml g^{-1}	6.3	2.7	2.6	7.9	6.3	3.7	2.7	2.2
				AGE–PMVP				
SEC_{HCl}, mg-equiv g^{-1}	5.2	4.6	3.4	1.3	2.7	3.5	4.6	4.4
V_{sp}, ml g^{-1}	5.8	3.4	2.5	8.3	7.7	5.8	5.4	5.2

We found that EGA–PEI anion exchanger exhibits higher sorption exchange capacity for chloride anions than AGE–PMVP resin. The EGA–PEI resins also have increased nitrogen content c_N, apparently due to the fact that PEI contains larger amount of primary and secondary amino groups than PMVP. What is more, the branched PEI structure is favorable for the formation of chemically and thermally stable polymers.

It is known [7] that polymerization time and temperature strongly affect the physicochemical characteristics of polymeric sorbents. Table 2 shows that AGE–PEI copolymer prepared at 80°C has the highest anion-exchange capacity. In copolymerization under these conditions, the opening of the epoxy rings is the most complete. In polymerization at temperatures higher than 80°C, the static exchange capacity of the polymer decreases. We found that the optimal polymerization time is 4 h. In further keeping of the reaction mixture under these conditions, the sorption characteristics of the resin did not change. The yield of the polymeric sorbent exceeds 80%.

Table 3. Chemical shifts in the ^{13}C NMR spectra of PEI

Structural fragment	Chemical shift, ppm	
	this work	data of [10]
$-NH_2CH_2CH_2N(CH_2-)(CH_2-)$	40.0; 57.4	39.5; 57.0
$-NHCH_2CH_2N(CH_2-)(CH_2-)$	47.2; 54.2	47.3; 54.4
$-NH_2CH_2CH_2NH-$	41.2; 52.2	41.7; 52.0
$-NHCH_2CH_2NH-$	48.9	48.9

Table 4. Assignment of signals in the ^{13}C NMR spectra of AGE–PEI and AGE–PMVP anion exchangers (before postcuring)

Chemical shift, ppm	Assignment
53.2 broad signal	$-H_2C$ (53.2) $NCH_2CH_2N(CH_2)(CH_2)$ $-H_2C$
	$-H_2C$ (54.2) $NCH_2CH_2N(CH_2)(CH_2)$ H
48.0 broad signal	H_2C (46.7) $NCH_2—CH_2N(CH_2-)(CH_2-)$ H
68.4 broad signal	OH $-OCH_2-CH-CH_2-N(CH_2-)(H)$ 68.7
	OH $-OCH_2-CH-CH_2-N(CH_2-)(CH_2-)$ 68.7
20.1; 27.2; 32.4; 33.7; 36.3; 37.6; 42.8; 44.0	$-CH_2$ $-CH_2$ $N-CH_2-CH_2-$
72.4 broad signal	OH $-OCH_2-CHCH_2-N(CH_2-)(H)$
	OH $-OCH_2-CHCH_2-N(CH_2-)(CH_2-)$

The IR spectrum of AGE–PEI anion exchanger contains no absorption bands at 760 and 848 cm^{-1} belonging to the epoxy ring. This spectrum contains the absorption bands of the N–H bending vibrations (3200–3500 and 1600–1700 cm^{-1}) and the bands of C–N stretching vibrations of polymeric anion exchangers (1020–1220 cm^{-1}). The asymmetric and symmetric stretching vibrations of the CH_2 groups are manifested as the absorption bands at 2940 and 2840 cm^{-1}, respectively. The absorption at 1460–1470 cm^{-1} is due to the bending vibrations of the C–H bonds. The IR spectra show that polymerization sharply decreases the intensity of the absorption bands of the out-of-plane vibrations of the vinyl groups at 910 cm^{-1}.

The precondensation of AGE and PEI was studied by ^{13}C NMR technique (Table 3, 4). The signals in the ^{13}C NMR spectra of AGE–PEI copolymers (prior to postcuring) in DMSO were assigned to particular structural fragments by their comparison with the ^{13}C NMR spectra of AGE

$$\overset{116.2}{CH_2}=\overset{134.9}{CH}-\overset{71.1}{CH_2}-O-\overset{70.7}{CH_2}-\overset{50.2}{CH}(O)-\overset{43.3}{CH_2}$$

and PEI [8, 9] (Table 3).

The ^{13}C NMR spectra show that AGE–PEI anion exchanger (prior to postcuring) contains significant amount of linear-branched fragments containing secondary and tertiary amino groups.

One of important physicochemical characteristics of polymeric sorbents is their chemical and thermal stability. These characteristics were evaluated by changes in the sorption capacity of the resins after their treatment with 5 M aqueous H_2SO_4, 5 M aqueous NaOH, and 10% H_2O_2 (Table 5). Taking into account that replacement of OH anions in the polymeric anion exchanger by other anions increases its stability, we tested for chemical and thermal stability the anion exchangers in the OH form. The chemical and thermal stability of resins prepared by polymerization for 4 h in the presence of H_2O_2 exceeds that of the polymers prepared without H_2O_2. We believe that enhanced thermal stability of anion exchangers prepared in this work as compared to that of commercial anion exchangers (EDE-10P, AV-17 and AN-31) is caused by more regular structure of AGE–PEI resins and uniformity of functional groups in them. We found that AGE–PEI anion exchanger is less stable against aqueous acids, alkalis, and oxidants than AGE–PMVP resin, apparently owing to the presence of the aromatic ring in the PMVP molecule.

Table 5. Chemical and thermal stability of AGE–PEI anion exchangers

AGE : PEI weight ratio	$c_{H_2O_2}$ in reaction mixture, %	SEC_{HCl} before treatment, mg-equiv g^{-1}	SEC_{HCl} after treatment, mg-equiv g^{-1}/decrease in SEC_{HCl} after treatment, %						
			chemical treatment			thermal treatment			
			5 N H_2SO_4	5 N NaOH	10% H_2O_2	3 h	5 h	7 h	12 h
AGE–PEI									
1.0 : 1.5	0.1	9.5	6.6/30	7.6/20	7.2/24	8.5/10	8.0/16	7.1/25	7.1/25
1.0 : 2.5	0.1	7.5	6.8/9	7.07	6.6/12	7.3/3	7.2/4	7.1/5	7.1/5
3.0 : 1.0	0.1	7.9	5.5/30	5.8/27	2.5/68	7.6/4	7.3/8	7.1/10	6.7/15
1.0 : 1.5	–	6.6	3.5/47	4.0/40	Dissolves	5.9/11	5.5/17	4.8/27	4.7/28
1.0 : 2.5	–	5.1	2.5/50	2.6/48	″	4.5/12	4.2/18	3.7/28	3.6/30
AGE–PMVP									
1.0 : 1.0	0.1	4.6	4.2/8	4.3/6	4.3/7	4.5/2	4.5/3	4.4/4	4.4/4
1.0 : 2.0	0.1	5.3	4.9/7	5.1/4	5.0/5	5.2/2	5.2/2	5.1/3	5/1/4
2.0 : 1.0	0.1	3.4	3.1/10	3.1/10	2.9/15	3.2/6	3.1/8	3.1/10	3.1/10
1.0 : 2.0	–	3.7	3.1/15	3.2/13	3.0/18	3.3/10	3.2/13	3.1/16	3.1/16

The basicity of particular amino groups in anion exchangers was determined by potentiometric titration. The pK_a values of ionic groups of the anion exchangers and the empirical coefficients *m* were determined graphically (Figs. 1, 2). It is known [11] that low and medium-basic anion exchangers exhibit the highest complexing power. Therefore, the content of particular amino groups of different basicity was determined by titration of separate weighed samples of anion exchanger in aqueous supporting electrolyte.

Since anion exchangers under consideration contain secondary and tertiary amino groups, they are polyfunctional resins. However, due to small difference in pK_a of particular amino groups, there is only one inflection point in the potentiometic titration curve, which reflects the total content of functional groups in the resin.

The pK_a values of the functional groups of the resins were calculated from the potentiometric titration curve by the Henderson–Hasselbach method [12]. The factor *m* (empirical coefficient reflecting interunit interactions in polymeric chain) was calculated graphically. The *m* and pK_a values obtained in this work are given below:

Anion exchanger	*m*	pK_a
AGE–PEI	1.9	5.3
AGE–PMVP	2.2	4.9

The pK_a values calculated by us are fairly well consistent with the published data [13]. Considerably

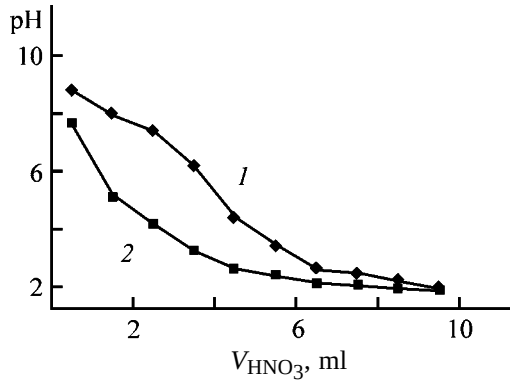

Fig. 1. Curves of potentiometric titration of (*1*) AGE–PEI and (*2*) AGE–PMVP anion exchangers. (V_{HNO_3}) 0.1 M HNO_3 volume.

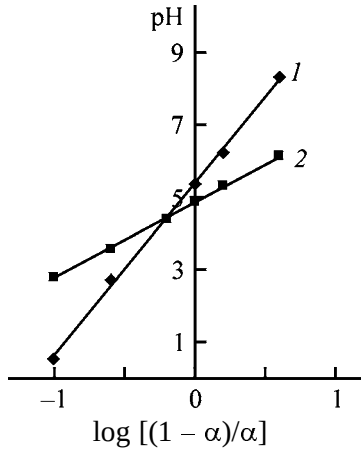

Fig. 2. Plot of pH vs. log[(1 – α)α] for (*1*) AGE–PEI and (*2*) AGE–PMVP anion exchangers.

Table 6. Sorption capacity of AGE–PEI and AGE–PMVP anion exchangers

AGE : PEI weight ratio in reaction mixture	$c_{H_2O_2}$ in reaction mixture, %	Sorption capacity, mg-equiv g^{-1}		
		Cu^{2+}	Ni^{2+}	Co^{2+}
AGE–PEI				
1.0 : 2.5	0.1	6.1	4.8	4.3
3.0 : 1.0	0.1	3.6	0.7	0.5
1.0 : 2.5	–	2.3	0.8	0.5
AGE–PMVP				
1.0 : 1.0	0.1	4.3	2.5	2.2
2.0 : 1.0	0.1	3.1	1.6	1.2
1.0 : 2.0	–	2.2	0.8	0.6

decreased basicity of AGE–PEI and AGE–PMVP anion exchangers in comparison with the basicity of the corresponding initial polyamines is apparently due to increased degree of substitution at the nitrogen atom, i.e., increased content of the secondary and tertiary amino and substituted pyridinium groups in the polymers.

As seen from Table 6, AGE–PEI and AGE–PMVP anion exchangers have fairly high sorption capacity for transition metals (Table 6). These data show that anion exchangers prepared by us are promising sorbents for recovery of transition metals from wastewater from hydrometallurgical plants.

CONCLUSIONS

(1) The sorption characteristics and stability of polyfunctional anion exchangers prepared by copolymerization of allyl glycidyl ether and polyamines are dependent on their ratio in the initial reagent mixture, polymerization time, and temperature. The anion exchangers prepared in the presence of hydrogen peroxide as promoter have improved characteristics.

(2) The use of allyl glycidyl ether allows preparation of three-dimensionally cross-linked highly permeable polymeric sorbents suitable for use in hydrometallurgical production.

REFERENCES

1. Sutyagin, V.M. and Lyapkov, A.A., *Izv. Vyssh. Uchebn. Zaved., Khim. Khim. Tekhnol.*, 2002, vol. 45, no. 3, pp. 113–123.
2. Ergozhin, E.E., Chalov, A.K., Iskakova, R.A., *et al.*, *Zh. Prikl. Khim.*, 2002, vol. 75, no. 11, pp. 1826–1829.
3. Ergozhin, E.E., Chalov, A.K., Iskakova, R.A., *et al.*, *Zh. Prikl. Khim.*, 2001, vol. 74, no. 4, pp. 629–633.
4. Ergozhin E.E., Chalov, A.K., and Kovrigina, T.V., in *Trudy Mezhdunarodnoi nauchnoprakticheskoi konferentsii "Problemy khimicheskoi tekhnologii neorganicheskikh, organicheskikh, silikatnykh i stroitel'nykh materialov i podgotovka inzhenernykh kadrov"* (Proc. Int. Scientific and Practical Conf. "Problems of Chemical Technology of Inorganic, Organic, Silicate, and Structural Materials, and Engineering Staff Training"), Shymkent, 2002, vol. 3, pp. 141–145.
5. Ergozhin, E.E., Chalov, A.K., Iskakova, R.A., *et al.*, in *Proc. Int. Monitoring Conf. "Development of Rehabilitation Methodology of Environment of the Semipalatinsk Region Polluted by Nuclear Tests,"* Semipalatinsk, 2002, pp. 94–96.
6. *GOSTs* (State Standards) *10898–84, 10898.2–74, and 10898.5–84.*
7. Helfferich, F., *Ionenaustauscher*, Weinheim: Chemie, 1959, vol. 1.
8. Ergozhin, E.E., Chalov, A.K., Iskakova, R.A., *et al.*, *Zh. Prikl. Khim.*, 2002, vol. 75, no. 1, pp. 103–106.
9. Klepikova, S.G., Iskakova, R.A., Chalov, A.K., *et al.*, *Izv. Min. Obraz. Nauki Resp. Kaz., Nats. Akad. Nauk Resp. Kaz., Ser. Khim.*, 2001, no. 4, pp. 88–90.
10. Ionin, B.I., Ershov, B.A., and Kol'tsov, A.I., *YaMR-spektroskopiya v organicheskoi khimii* (NMR Spectroscopy in Organic Chemistry), Leningrad: Khimiya, 1983.
11. Saldadze, K.M. and Kopylova-Valova, V.D., *Kompleksoobrazuyushchie ionity (kompleksity)* (Complexing Ion Exchangers (Complexites)), Moscow: Khimiya, 1980.
12. Grissbach, R., *Austauschadsorption in Theorie und Praxis*, Berlin: Akademie, 1957.
13. Ergozhin, E.E. and Menligaziev, E.Zh., *Polyfunktsional'nye ionoobmenniki* (Polyfunctional Ion Exchangers), Alma-Ata: Akad. Nauk Kaz. SSR, 1986.

Russian Journal of Applied Chemistry, Vol. 77, No. 3, 2004, pp. 463–466. Translated from Zhurnal Prikladnoi Khimii, Vol. 77, No. 3, 2004, pp. 470–473.

MACROMOLECULAR CHEMISTRY AND POLYMERIC MATERIALS

Flocculation Activity (with Respect to Ocher) of Anionic Copolymers of Acrylamide in the Mode of Restricted Sedimentation as Influenced by Their Chemical Heterogeneity

V. A. Myagchenkov and V. E. Proskurina

Kazan State Technological University, Kazan, Tatarstan, Russia

Received October 22, 2003

Abstract—The kinetics of sedimentation of an aqueous ocher suspension in the presence of ionic (anionic) acrylamide copolymers in the mode of restricted sedimentation was studied; the effect of composition and of the composition polydispersity of the copolymer on the flocculation activity with respect to ocher was evaluated.

Search for practicable and effective ways for direct control of the aggregation and sedimentation stability of disperse systems is of particular interest in many branches of national economy [1]. In this connection, synthetic or natural macromolecular compounds being added in small amounts and acting as flocculants or stabilizers of a disperse system [2, 3] show much promise. The direction (decrease or increase in the sedimentation stability of the system) and magnitude of the resultant effect in addition of polymeric compounds depend on numerous parameters of the dispersion medium, dispersed phase, (co)polymer-flocculant, and process characteristics [4]. Ionic and nonionic copolymers of acrylamide find wide use as flocculants thanks to their high performance and availability.

Proceeding with systematic studies aimed to improve the flocculation parameters of this promising class of water-soluble copolymers, we examined in this paper the sedimentation stability of concentrated ocher solutions as influenced by the concentration, composition, and chemical heterogeneity of random copolymers of acrylamide and sodium acrylate. Available data on the effect of copolymer composition polydispersity on the flocculation characteristics of model and real disperse systems are scarce [4].

EXPERIMENTAL

In our work we used an ocher suspension ["golden" brand, TU (Technical Specifications) 301-10-019–90] with the average particle radius $R = 9.25 \times 10^{-6}$ m. The sedimentation kinetics of the 10% ocher suspension in the mode of restricted sedimentation in the presence of polymeric additives was studied in 100-ml cylinders by the shift of the boundary between the clarified and unclarified fractions of the suspension. The samples of acrylamide anionic copolymers were prepared by base hydrolysis (NaOH) of the initial polyacrylamide (hydrolysis degree α = 1.5% and molecular weight $\overline{M}_\eta = 7.4 \times 10^6$) under mild conditions. Hydrolysis was performed at 35°C for 180 min using 0.5% polymer solution; a total of seven different copolymer samples were obtained.

The simplified scheme of base hydrolysis of polyacrylamide can be presented as follows:

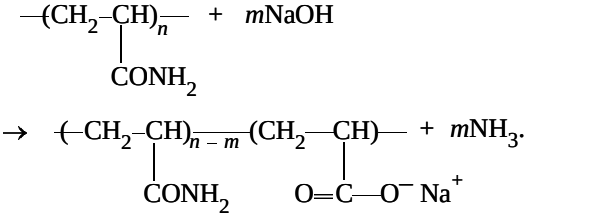

The degree of hydrolysis α was calculated from Eq. (1):

$$\alpha = \frac{7.1(V - V_0)N}{0.01cq - 0.023(V - V_0)N}, \qquad (1)$$

where V and V_0 are the volumes of NaOH solution in the working and blank tests (cm^3), N is the molarity of the alkali solution (M), c is the concentration of the copolymer (wt %), and q is the volume of the copolymer solution sample (cm^3).

The potentiometric measurements were carried out

1070-4272/04/7703-0463 © 2004 MAIK "Nauka/Interperiodica"

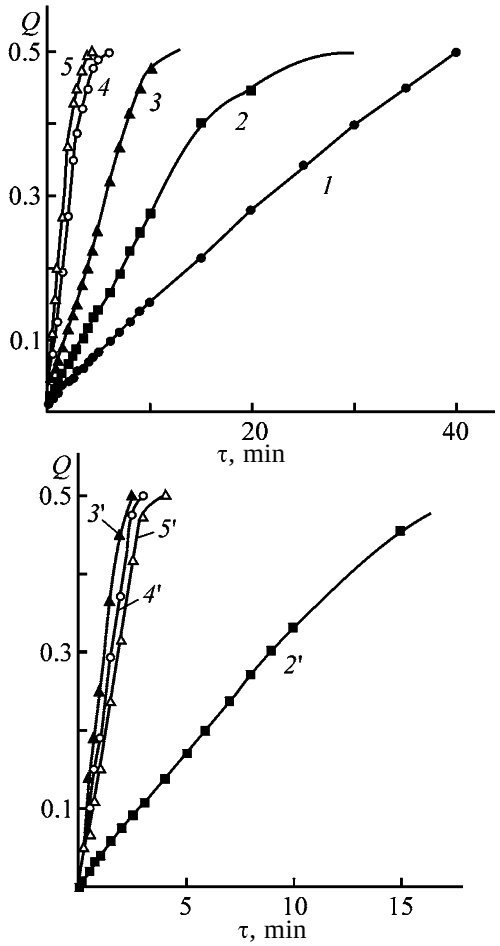

Fig. 1. Kinetic curves of sedimentation of the ocher suspension (*1*) in the absence and (*2*–*5*, *2*'–*5*') in the presence of acrylamide copolymers with the (*2*–*5*) minimal (α = 1.5%) and (*2*'–*5*') maximal (α = 63.7%) degree of hydrolysis α. (*Q*) Clarification ratio and (τ) time. $c \times 10^4$ (wt %): (*1*) 0, (*2*, *2*') 0.999, (*3*, *3*') 5.96, (*4*, *4*') 11.9, and (*5*, *5*') 19.6.

on an I120-M digital pH-meter. The viscosity of the aqueous solutions of acrylamide anionic copolymers was measured on an Ubbelohde viscometer (0.56 mm capillary diameter). The correction for the kinetic flow energy was lower than 2% and was neglected in the calculations of the reduced viscosity η_{sp}/c.

In general case, in preparation of copolymers by polymerization or polycondensation, the products at final stages of conversion are nonuniform in molecular weight and composition of macromolecules [5–7]. Data for a wide range of carbon- and heterochain copolymers show that the main properties (including flocculation parameters) of copolymers and composites based them depend on both the molecular weight *M* and degree of hydrolysis α [4, 5]. The dependence of the flocculation properties on the copolymer composition α becomes more pronounced with increasing difference in the properties of the repeating units in the copolymer macromolecules, in particular, on passing from nonionic to ionic acrylamide copolymers [4]. As seen, all the seven samples studied strongly differ in α (from 1.5 to 63.7%) and in the properties of the repeating units in the copolymer macromolecules: from nonionic (acrylamide) to ionic (acrylate). These two factors obviously caused more pronounced dependence of the flocculation activity on the composition and on the composition polydispersity of acrylamide copolymers and formulations based on them. The dependence of the flocculation effect *D* on *M* and α was observed in a series of model and real dispersed systems based on anionic copolymers of acrylamide and sodium acrylate. This suggests that the correct dependences $D = f(M)$ can be obtained in the experiments at constant α, and vice versa, $D = f(\alpha)$, at constant *M*. Fulfillment of the latter condition for acrylamide anionic copolymers ("warranted" by the mild hydrolysis conditions) was confirmed by the data on the viscosity of the samples in question using constants *K* and *a* in the Staudinger–Mark–Houwink equation tabulated for various α [8]:

$$[\eta] = KM^a. \quad (2)$$

To evaluate the effect of the copolymer composition on the flocculation parameters, we first studied the kinetics of the ocher sedimentation as influenced by concentration and composition of polymeric flocculants. For example, the kinetic data registered for acrylamide copolymer samples with minimal and maximal α are shown in Fig. 1. From these kinetic curves, we calculated the flocculation effect *D*:

$$D = \bar{v}/\bar{v}_0 - 1, \quad (3)$$

where $\bar{v}$ and $\bar{v}_0$ are the average rates of the ocher sedimentation to the clarification ratio $Q = 0.5$ in the presence of polymer flocculant (concentration *c*) and without it, respectively.

When comparing the flocculation properties of copolymers with various *c* and α, it is advisable to use not the parameter *D*, but the flocculation activity λ [4]:

$$\lambda = (\bar{v}/\bar{v}_0 - 1)c^{-1}. \quad (4)$$

The selected data on the concentration dependences of the flocculation activity of three samples of hydrolyzed polyacrylamide with different α are shown in Fig. 2. The maximum in the $\lambda = f(c)$ curve is indicative, on the one hand, of certain deficiency of the polymeric component in the course of formation of

three-dimensional aggregates at small concentrations $c < c_{max}$, and, on the other hand, of certain trend to stabilization on addition of new portions of the copolymer at its relatively high concentrations ($c > c_{max}$). In terms of the modern concepts of the flocculation by the bridging mechanism [3], appearance of a maximum in the dependences of the flocculation activity on the concentration α of ionic groups in the copolymer macromolecule (Fig. 2, curves *1–3*) is quite natural, especially taking into account significant differences in the macroscopic processes of adsorption of the ionic and nonionic fragments of acrylamide copolymer macromolecules [9].

The generalized dependences of the flocculation activity of acrylamide copolymers as influenced by their composition for three test series (with fixed c) are shown in Fig. 3. As seen, the experimental dependences $\lambda = f(\alpha)$ have well-defined maxima. Analysis of experimental data show that changes in the molecular parameters of the flocculant samples of various composition produce no problems. The maxima in the $D = f(\alpha)$ and $\lambda = f(\alpha)$ dependences at flocculation with ionic copolymers of acrylamide in a series of real and model disperse systems were revealed previously in [4]. The nonmonotonic dependences of λ on the composition of macromolecules of anionic acrylamide copolymers are not unambiguously due to the specific features of macroscopic processes of adsorption and formation of structural elements (aggregates) from dispersed particles and copolymer macromolecules [3, 10–12]. Obviously, the conformation of macromolecules noticeably affects the $\lambda = f(\alpha)$ dependences, especially taking into account that the concentration of the ionic units in the copolymer macromolecules was varied in a wide range. This is also confirmed by the pronounced maxima in the dependences of the viscosity numbers η_{sp}/c [and thus of the root-mean-square size of the macromolecule globules $(\bar{R}^2)^{0,5}$] on the degree of hydrolysis α (Fig. 4). We should note that the quantities η_{sp}/c and $(\bar{R}^2)^{0,5}$ vary in similar direction [13].

The maxima in the dependences $\lambda = f(\alpha)$ (Fig. 3) and $\eta_{sp}/c = f(\alpha)$ (Fig. 4) and complex mechanism of macroscopic processes of adsorption and flocculation suggest the possibility that the flocculation properties of the systems in question can also depend on the composition polydispersion of anionic acrylamide copolymers. The copolymer samples with various composition polydispersion were prepared using several standard samples with fixed α (the average composition $\bar{\alpha}$ being constant 14]).

For example, for the simplest binary composition

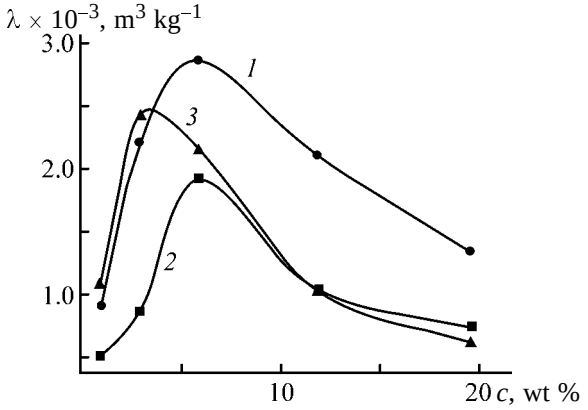

Fig. 2. Flocculation activity λ as a function of the copolymer concentration c. α (%): (*1*) 36.2, (*2*) 47.93, and (*3*) 63.7.

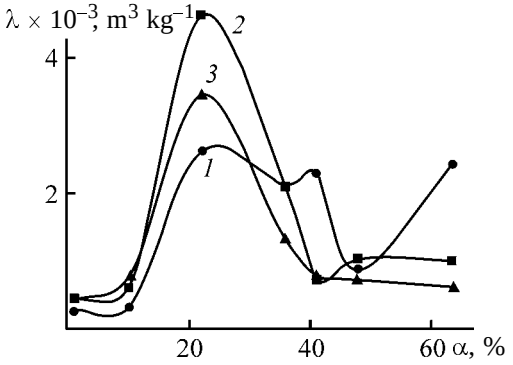

Fig. 3. Flocculation activity λ as a function of the composition of acrylamide copolymers with sodium acrylate α. $c \times 10^4$ (wt %): (*1*) 2.99, (*2*) 11.9, and (*3*) 19.6.

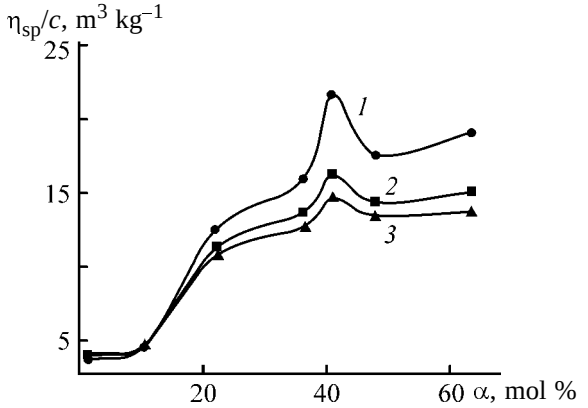

Fig. 4. Viscosity number η_{sp}/c of copolymers as influenced by the copolymer composition α. c (kg m^{-3}): (*1*) 0.4, (*2*) 0.2, and (*3*) 0.1.

with $\bar{\alpha} = \alpha_a$, the weight fraction of the reference sample w_1 with a small degree of hydrolysis $\alpha_1 < \alpha_a$ was calculated from the following expression:

$$\alpha_a = w_1\alpha_1 + (1 - w_1)\alpha_2, \quad (5)$$

where α_2 is the degree of hydrolysis of the reference

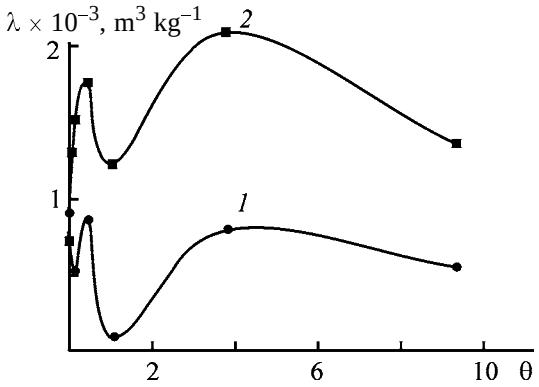

Fig. 5. Flocculation activity λ as a function of parameter θ in the presence of mixed acrylamide copolymers with $\bar{\alpha}$ = 41.02 mol %. $c \times 10^4$ (wt %): (*1*) 0.999 and (*2*) 11.9.

sample with a high degree of hydrolysis (obviously, $\alpha_2 > \alpha_a$).

The criterion θ was used to characterize the chemical heterogeneity of the mixed systems:

$$\theta = \sum_{i=1}^{k} w_i \alpha_i \sum_{i=1}^{k} w_i/\alpha_i - 1, \qquad (6)$$

where α_i and w_i are the degree of hydrolysis and weight fraction of the *i*th reference sample in the mixture and *k* is the number of the reference components in the mixture.

As seen from expression (6), θ parameter is essentially similar to the composition dispersion of copolymers [15, 16] often used for quantitative evaluation of the chemical heterogeneity of copolymers.

For mixed copolymers with $\bar{\alpha}$ = 41.02% ($\overline{M}$ being constant), Fig. 5 shows the dependence of the flocculation activity with respect to ocher as influenced by the chemical heterogeneity of the hydrolyzed polyacrylamide copolymers. Based on general considerations, we believe that the effect of chemical heterogeneity of the ionic copolymers of acrylamide on the flocculation parameters of the system will be more pronounced with complication of the disperse system [e.g., on passing from the model (ocher) to the real systems] and dispersion medium.

CONCLUSIONS

(1) Seven samples of ionic (anionic) acrylamide copolymer with identical molecular weights *M* and *M* polydispersity, but different compositions were prepared by hydrolysis of polyacrylamide under mild conditions using sodium hydroxide.

(2) The effect of composition and of the composition polydispersity of anionic acrylamide copolymers of constant molecular weight on the flocculation activity with respect to ocher was analyzed. The extrema in these dependences are largely due to the conformation state of copolymer macromolecules in the dispersion medium.

REFERENCES

1. Bokris, O.M., *Khimiya okruzhayushchei sredy* (Environmental Chemistry), Moscow: Khimiya, 1982.
2. Rebinder, P.A., *Poverkhnostnye yavleniya v dispersnykh sistemakh: Kolloidnaya khimiya* (Surface Phenomena in Disperse Systems: Colloidal Chemistry), Moscow: Nauka, 1978.
3. Baran, A.A., *Polimersoderzhashchie dispersnye sistemy* (Polymer-Containing Disperse Systems), Kiev: Naukova Dumka, 1986.
4. Myagchenkov, V.A., Baran, A.A., Bekturov, V.A., and Bulidorova, G.V., *Poliakrilamidnye flokulyanty* (Polyacrylamide Flocculants), Kazan: Kazan Tekhnol. Univ., 1998.
5. Shur, A.M., *Vysokomolekulyarnye soedineniya* (Macromolecular Compounds), Moscow: Vysshaya Shkola, 1981.
6. Plate, N.A., Litmanovich, A.D., and Noa, O.V., *Makromolekulyarnye reaktsii* (Macromolecular Reactions), Moscow: Khimiya, 1977.
7. Myagchenkov, V.A. and Frenkel', S.Ya., *Kompozitsionnaya neodnorodnost' polimerov* (Composition Heterogeneity of Polymers), Leningrad: Khimiya, 1988.
8. Klein, J. and Conrad, K.D., *Makromol. Chem.*, vol. 179, pp. 1635–1638.
9. Lipatov, Yu.S. and Sergeeva, L.M., *Adsorbtsiya polimerov* (Adsorption of Polymers), Kiev: Naukova Dumka, 1984.
10. Proskurina, V.E., Akhmetova, L.A., and Myagchenkov, V.A., *Zh. Prikl. Khim.*, 2003, vol. 76, no. 4, pp. 632–638.
11. Lipatov, Yu.S., *Kolloidnaya khimiya polimerov* (Colloidal Chemistry of Polymers), Kiev: Naukova Dumka, 1984.
12. Navrotskii, A.V., Dryabina, S.S., Malysheva, Zh.N., and Novakov, I.A., *Kolloidn. Zh.*, 2003, vol. 65, no. 3, pp. 368–373.
13. Gennes, P.-G. de, *Scaling Concepts in Polymer Physics*, Ithaca: Cornell Univ. Press, 1979.
14. Myagchenkov, V.A., Proskurina, V.E., Gromova, E.Yu., and Bulidorova, G.V., *Colloid Polym. Sci.*, 2001, vol. 279, no. 5, pp. 468–478.
15. Izyumnikov, A.L. and Vyrskii, Yu.P., *Vysokomol. Soedin., Ser. A*, 1967, vol. 9, no. 9, pp. 1996–2000.
16. Myagchenkov, V.A., Kurenkov, V.F., and Frenkel', S.Ya., *Dokl. Akad. Nauk SSSR*, 1968, vol. 181, no. 1, pp. 141–150.

Russian Journal of Applied Chemistry, Vol. 77, No. 3, 2004, pp. 467–470. Translated from Zhurnal Prikladnoi Khimii, Vol. 77, No. 3, 2004, pp. 474–477.

MACROMOLECULAR CHEMISTRY AND POLYMERIC MATERIALS

Influence of Acidity and Uranyl Nitrate Concentration on the Efficiency of Recovery of Uranium(VI) from Aqueous Solutions with Hydrolytic Wood Lignin

N. G. Rachkova, I. I. Shuktomova, and A. I. Taskaev

Institute of Biology, Komi Scientific Center, Ural Division, Russian Academy of Sciences, Syktyvkar, Komi Republic, Russia

Received August 18, 2003

Abstract—The efficiency of recovery of uranium(VI) from aqueous solutions with hydrolytic lignin and strength of binding of uranium to lignin were studied in relation to the uranium concentration and acidity. The mechanisms of sorption of uranium were analyzed by the methods of sequential leaching of uranium from lignin and IR spectroscopy.

In recent years it was repeatedly reported that hydrolytic lignin efficiently sorbs lead, zinc, and copper [1–4]. The possibility of using hydrolytic lignin for decontamination of aqueous solutions from natural heavy radionuclides was analyzed in [5–7]. These works show that hydrolytic lignin is a promising material for this purpose. For example, it was found [6] that hydrolytic lignin prepared from coniferous wood practically completely recovers uranium(VI) from 1×10^{-2} g l^{-1} aqueous $UO_2(NO_3)_2$. The high affinity of lignin for uranium(VI) is manifested in formation of very stable chelates between uranium(VI) and products of lignin humification [8]. Taking into account the availability of hydrolytic lignin and the fact that lignin is a precursor of humus substances in soils, recovery of uranium with lignin from aqueous media of different composition, among them from soil solutions, deserves attention. The urgency of this problem increases due to growing contamination of environment with natural radionuclides.

In this work we studied recovery of uranium(VI) with hydrolytic wood lignin from aqueous solutions as influenced by acidity and uranium concentration.

EXPERIMENTAL

In our experiments we used fractions of hydrolytic lignin with granule size of 0.25–0.5 mm. The content of Komarov's lignin in these samples was 82.5%, and their ash residue was 6%. The sorption of uranium(VI) was studied under static conditions at room temperature. The acidity of the initial uranium aqueous solutions was adjusted by adding concentrated (13 M) aqueous $NH_3 \cdot H_2O$. The pH was measured on an Inolab pH Level I pH meter (Wissenschaftlich–Technische Werkstatten GmbH, Germany). Before contact with uranium(VI)-containing aqueous solution, the samples of hydrolytic lignin were kept in distilled water for a day. This procedure facilitates access of lignin sorbent sites for uranium. To ensure high specific surface area of the sorbent, we used the fractions of lignin of small size. After contact of lignin with uranium-containing aqueous solution, lignin was separated from solution by filtration, and uranium concentration in the liquid phase was determined. The sorption capacity of lignin, the uranium distribution coefficient, and the degree of uranium recovery were determined by the difference between the uranium concentrations in the liquid phase before and after contact with lignin. Saturation of lignin with uranium was reached by its repeated contact with uranium-containing solution. In order to determine the strength of uranium association with lignin, its sample saturated with uranium was separated from aqueous solution and sequentially treated with different leaching solutions: distilled water (water-soluble uranium species), 1 M aqueous CH_3COONH_4 (exchangeable uranium species), and HCl (acid-soluble species). This leaching technique, widely used in soil science, allows isolation of relatively uniform fractions of uranium species associated with lignin by particular mechanisms and bound to lignin with a certain strength.

The IR spectra of hydrolytic lignin saturated with

1070-4272/04/7703-0467 © 2004 MAIK "Nauka/Interperiodica"

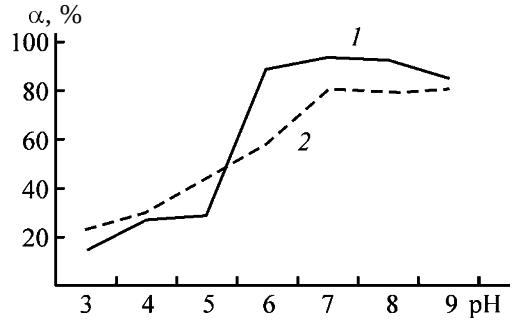

Degree of recovery of uranium(VI) with hydrolytic lignin α from aqueous solution as function of pH. U(VI) concentration (mg ml^{-1}): (*1*) 0.1 and (*2*) 0.01.

uranium (VI) were recorded in the range 400–4000 cm^{-1} on a Specord M-80 IR spectrometer (KBr pellets). The quantitative calculation of the relative optical density was carried out by the baseline method. The band at 1518 cm^{-1} was used as the internal reference. The uranium content was determined by luminescent technique [9]. The HCO_3^- content was determined by the back-titration [10].

The efficiency of metal sorption on proton-exchange sorbents is a function of acidity of the aqueous phase. In sorption of heavy natural radionuclides on hydrolytic lignin, the sorption is complicated by hydrolysis of these radionuclides. It is known that uranium(VI) is present in the form of UO_2^{2+} cations only in acid solutions free of complexing agents. At low acidity, uranium(VI) forms several coexisting mononuclear and polymeric (among them colloid) hydrolyzed species [5, 11–15]. In neutral and alkaline carbonate-containing media, stable uranyl carbonate anionic complexes are formed. When the carbonate concentration exceeds $n \times 10^{-3}$ M, the hydrolysis of uranium(VI) is completely suppressed by formation of uranyl carbonate complexes [16]. Another reason hindering the sorption of uranium on lignin is the competitive uranium complexation with fulvic and humic acids always present in lignin in sufficiently large amount [17]. It is known that approximately one fifth of organic carbon of hydrolytic lignin belongs to humus substances present in lignin. Therefore, recovery of uranium from aqueous solution with hydrolytic lignin to some extents models the recovery of uranuim from soil solutions containing humus acids.

Our experiments showed (see figure) that from 59 to 93% of uranium is recovered with hydrolytic lignin from neutral and alkaline solutions containing 0.1 and 0.01 mg ml^{-1} U. In acid solutions (pH < 5), the degree of recovery of uranium does not exceed 29%. We believe that the decrease in uranium recovery is caused by suppression of ionization of the acid ion-exchange groups in lignin. Therefore, in sorption of uranium from acidic media, the fraction of its exchangeable species considerably decreases (see table).

Another reason for decreased uranium recovery from acidic solutions is specific behavior of fulvic acids in the systems under consideration. On the contact of lignin with acidic uranium-containing aqueous solution, the fulvic acids associated with lignin pass into the aqueous phase. Since fulvic acids do not form complexes with uranium in acid solutions [18–22], their liberation from lignin does not affect the recovery of uranium with lignin. However, fulvic acids liberated from lignin can be repeatedly sorbed on the lignin surface. As a result, the sorption centers of lignin get shielded with fulvic acid molecules, and uranium sorption on lignin becomes suppressed.

To elucidate how uranium(VI) carbonate complexes formed in the presence of atmospheric CO_2 influence the recovery of uranium(VI) with lignin, the uranium(VI)-containing aqueous solutions were kept in air for 24 h before introduction of lignin. We found that, under these conditions, the CO_2 concentration in aqueous solutions was 1.6, 1.7, and 2.6 mM at pH 7, 8 and 9, respectively. The equilibrium concentrations of CO_3^{2-} and HCO_3^- calculated by common methods do not exceed $n \times 10^{-3}$ M. These results showed that, under our experimental conditions, the contribution of uranium(VI) carbonate complexes is very small, and hydrolyzed uranium species prevail [16]. Therefore, in further analysis of uranium(VI) recovery with lignin, the contribution of uranium carbonate complexes was not taken into account.

With increasing pH, the content of soluble hydrolyzed uranium species [$UO_2(OH)^+$, $(UO_2)_3(OH)_5^+$, $(UO_2)_3(OH)_4^{2+}$, $(UO_2)_4(OH)_7^+$] and $UO_2(OH)_2$ sol increases. All these species exhibit enhanced sorbability on lignin. With increasing pH, ionization of both the carboxy and phenolic hydroxy groups of lignin and humus acids associated with it increases and, as a result, sorption of uranium on lignin by ion-exchange mechanism is enhanced. Due to ion-exchange sorption, the aqueous phase is acidified, and the content of the exchangeable uranium species associated with lignin increases to 19%.

We found that, at pH within 5–8, the fraction of uranium species strongly bound to lignin increases. This effect can be caused by formation of stable uranium(VI) complexes with humus acids entering into the composition of lignin. Among these species,

Influence of acidity and uranyl nitrate concentration on efficiency of uranium(VI) recovery from aqueous solutions with hydrolytic lignin (lignin to aqueous phase ratio 1 : 20)

pH of initial solutions	U(VI) concentration, $c \times 10^5$, g ml^{-1}		Uranium sorbed, $c \times 10^4$, g g^{-1}	Distribution coefficient, ml g^{-1}	Uranium(VI) desorbed, % of its amount sorbed			Strongly bound U(VI), % of total U(VI) sorbed
	before sorption	after sorption			distilled water	1 M solution		
						CH_3COONH_4	HCl	
3	1.00	0.89 ± 0.01	0.45 ± 0.01	5.1 ± 0.01	38.40 ± 0.40	18.20 ± 0.47	44.53 ± 0.44	(n/f)*
4	1.00	0.80 ± 0.02	0.60 ± 0.03	7.49 ± 0.45	19.78 ± 1.58	16.51 ± 1.41	44.24 ± 0.63	19.48 ± 3.61
5	1.00	0.65 ± 0.05	0.86 ± 0.09	13.29 ± 2.15	15.09 ± 2.03	10.94 ± 0.16	42.63 ± 4.72	31.35 ± 5.8
6	1.00	0.47 ± 0.04	1.18 ± 0.07	25.38 ± 3.65	7.27 ± 1.50	7.18 ± 0.77	46.98 ± 1.27	38.56 ± 3.55
7	1.00	0.22 ± 0.01	1.62 ± 0.02	73.62 ± 4.14	1.98 ± 0.02	7.81 ± 0.76	47.65 ± 2.55	42.71 ± 1.92
8	1.00	0.23 ± 0.002	1.59 ± 0.003	67.89 ± 0.64	5.94 ± 0.82	7.67 ± 0.11	53.24 ± 3.26	33.15 ± 3.96
9	1.00	0.23 ± 0.003	1.60 ± 0.004	70.44 ± 0.95	4.91 ± 0.40	7.40 ± 1.13	48.72 ± 6.69	38.97 ± 7.42
3	10.00	9.80 ± 0.01	2.85 ± 0.01	2.91 ± 0.01	64.33 ± 0.63	3.78 ± 0.02	31.92 ± 0.63	(n/f)
4	10.00	8.50 ± 0.70	5.22 ± 1.14	6.31 ± 1.83	46.93 ±13.47	3.30 ± 0.05	34.86 ± 1.51	15.00 ± 1.20
5	10.00	8.20 ± 0.50	5.74 ± 0.09	7.05 ± 0.16	29.81 ± 1.74	6.00 ± 0.05	53.44 ± 3.35	10.75 ± 5.14
6	10.00	1.30 ± 0.20	17.73 ± 0.35	140.12 ± 24.25	1.26 ± 0.02	13.88 ± 1.66	51.34 ± 2.91	33.52 ± 4.58
7	10.00	0.90 ± 0.20	18.52 ± 0.27	234.40 ± 51.90	1.10 ± 0.12	16.39 ± 0.43	51.2 ± 2.92	31.12 ± 3.23
8	10.00	1.00 ± 0.10	18.34 ± 0.09	193.64 ± 11.14	0.84 ± 0.10	18.65 ± 0.61	58.78 ± 1.19	21.73 ± 1.90
9	10.00	1.80 ± 0.20	16.94 ± 0.26	97.65 ± 9.86	2.30 ± 0.07	14.75 ± 1.49	62.46 ± 3.17	20.50 ± 1.60

* (n/f) Not found.

poorly soluble stable compounds can be formed [8, 19–22, 24]. Beyond the above-noted pH range, the total recovery of uranium and its fraction strongly bound to lignin slightly decrease.

Our experiments showed that recovery of uranium with lignin is dependent on uranium concentration in the aqueous phase. At low uranium concentrations, the pH range of optimal recovery of uranium is shifted to alkaline region, the sorption curve flattens, and the uranium fraction strongly bound to lignin substantially increases. These results are consistent with the well-known effect of dilution of aqueous solution on the behavior of hydrolyzable metals. According to this effect, we can expect that, in dilution of uranium solution, the hydrolysis of uranium is facilitated, its hydrolyzed species are stabilized in solution, and deposition of $UO_2(OH)_2$ sol on the lignin surface is hindered. It is known that hydrolyzable metals form the most stable complexes with natural organic compounds in the range of formation of hydrolyzed metal species [5, 25].

To elucidate the mechanism of uranium recovery with hydrolytic lignin, we studied its IR spectra before and after saturation with uranium. On saturation of lignin with uranium from aqueous uranyl nitrate (0.1 mg l^{-1}) at pH 6, the intensity of the absorption band of the stretching vibrations of the carboxy groups at 1716 cm^{-1} decreases. The absorption band at 1600 cm^{-1} becomes 21% more intense and is shifted, presumably due to structural changes in the phenolic fragments of lignin macromolecule. The broadening of the band of the OH stretching vibrations with 8% change in its asymmetry index suggests that more kinds of hydrogen bonds are formed. The formation of the carboxylate groups is manifested as a new absorption band at 1390 cm^{-1}. Thus, our spectroscopic data show that one of the main mechanisms of recovery of uranium with lignin is substitution of protons of carboxy and phenolic groups by uranim-containing cations. Therefore, in recovering uranium with lignin, the aqueous phase is acidified.

CONCLUSIONS

(1) Hydrolytic lignin efficiently recovers uranium(VI) from weakly acidic and alkaline solutions.

(2) The IR spectra of hydrolytic lignin saturated with uranium and the data on uranium speciation obtained by sequential leaching show that lignin recovers uranium from aqueous solutions not only by the mechanism of ion exchange of uranium(VI)-containing cationic species for acid protons of carboxy and phenolic groups of lignin and humus acids as-

sociated with them, but also by donor–acceptor interaction of lignin oxygen atoms with uranyl ions.

(3) Hydrolytic lignin recovers uranium(VI) most efficiently from weakly acidic and neutral solutions. Under these conditions, uranium is recovered by various mechanisms: ion exchange of uranim(VI)-containing cationic species for protons of carboxy and phenolic groups, sorption of $UO_2(OH)_2$ sol on the lignin surface, and formation of insoluble uranium(VI) compounds with humus acids entering into the lignin composition.

(4) In dilution of uranium solution, the pH of optimal recovery of uranium is shifted to alkaline range and the fraction of uranium(VI) species strongly bound to lignin substantially increases.

REFERENCES

1. Belyaev, Yu.A. and Belyaeva, L.E., *Khim. Inter. Ustoich. Razv*., 2000, no. 8, pp. 763–772.
2. Quick, S.Y., Wase, A.J., and Foster, C.F., *Water S. Afr*., 1998, vol. 24, no. 3, pp. 251–256.
3. Ravich, B.M., Okladnikov, V.P., Lygach, V.N., *et al*., *Kompleksnoe ispol'zovanie syr'ya i otkhodov* (Integrated Use of Raw Materials and Wastes), Moscow: Khimiya, 1998.
4. Fedorova, A.A., Sineva, A.V., and Mashkova, L.P., Abstracts of Papers, *III S"ezd obshchestva pochvovedov* (III Congr. of Society of Soil Scientists), Suzdal, Moscow, 2000, book 1, p. 312.
5. Kuznetsov, Yu.V., Shchebetkovskii, V.N., and Trusov, A.G., *Osnovy ochistki vody ot radioaktivnykh zagryaznenii* (Fundamentals of Water Decontamination from Radioactive Pollutants), Moscow: Atomizdat, 1974.
6. Andreev, P.F., Andreeva, I.V. and Rogozina, E.M., *Geokhimiya*, 1962, no. 4, pp. 313–317.
7. Nikiforov, A.F., Smirnova, M.V., Eremina, L.N., *et al*., in *Radiatsionnaya bezopasnost' Urala i Sibiri: Materialy Vserossiiskoi nauchno-prakticheskoi konferentsii* (Radiation Safety of Ural and Siberia: Proc. Scientific and Practical Conf.), Yekaterinburg, September 18–20, 1997, pp. 43–44.
8. Manskaya, S.M. and Kodina, L.A., *Geokhimiya lignina* (Geochemistry of Lignin), Moscow: Nauka, 1975.
9. Dobrovol'skaya, T.S., in *Analiticheskaya khimiya urana* (Analytical Chemistry of Uranium), 1962, pp. 143–165.
10. *Metodika vypolneniya izmerenii kontsentratsii gidrokarbonatov v poverkhnostnykh vodakh titrimetricheskim metodom. Metodicheskie ukazaniya RD 52.24.493–95* (Technique of Titrimetric Determination of Hidrocarbonate Concentration in Surface Waters: Guideline RD 52.24.493–95), Rostov-on-Don: Rosgidromet, 1995.
11. Starik, I.E., *Osnovy radiokhimii* (Fundamentals of Radiochemistry), Leningrad: Nauka, 1969.
12. *Transuranic Elements in the Environment*, Hanson, W.C., Ed.; Oak Ridge, TN: Technical Information Center, 1980.
13. Bond, K.A., Cross, J.E., and Ewart, F.T., *Radiochim. Acta*, 1991, vol. 52/53, pp. 433–437.
14. Dent, A.J., Ramsay, J.D.F., and Swanton, S.W., *J. Colloid Interf. Sci*., 1992, vol. 150, no.1, pp. 45–60.
15. Barnett, M.O., Jardine, P.M., Brouks, S.C., and Selim, H.M., *Soil Sci. Soc. Am. J*., 2000, vol. 64, pp. 908–917.
16. Arkhipov, N.P., Medvedev, V.P., Grishina, L.A., and Fedorova, T.A., *Radiokhimiya*, 1985, vol. 27, no. 6, pp. 812–817.
17. Ponomareva, V.V. and Plotnikova, T.A., *Gumus i pochvoobrazovanie (Metody i rezul'taty izucheniya)* (Humus and Soil Formation (Methods and Results of Study)), Leningrad: Nauka, 1980.
18. Buffle, J., *Complexation Reaction in Aquatic Systems: An Analytical Approach*, New York, 1988.
19. Voskresenskaya, N.T., *Izv. Akad. Nauk Kirg. SSR, Ser. Estestv. Tekh. Nauk*, 1960, vol. 2, no. 5, pp. 57–65.
20. Lopatkina, A.P., *Geokhimiya*, 1967, no. 6, pp. 708–719.
21. Szalay, A., *Geochim. Cosmochim. Acta*, 1964, vol. 28, no. 11, pp. 1605–1614.
22. Szalay, A., *Ark. Mineral. Geol*., 1969, vol. 5, no. 3, pp. 23–36.
23. Zakis, G.F., Mozheiko, L.N., and Telysheva, G.M., *Metody opredeleniya funktsional'nykh grupp lignina* (Methods for Determination of Functional Groups of Lignin), Riga: Zinatne, 1975.
24. *The Chemistry of the Actinide Elements*, Katz, J.J., Seaborg, G.T., and Morss, L., Eds., New York: Chapman and Hall, 1986, 2nd ed.
25. Serov, V.A., Afanas'ev, N.I., Brovko, O.S., and Zasukhina, L.V., *Khim. Inter. Ustoich. Razv*., 1997, nos. 5–6, pp. 613–618.

Russian Journal of Applied Chemistry, Vol. 77, No. 3, 2004, pp. 471–475. Translated from Zhurnal Prikladnoi Khimii, Vol. 77, No. 3, 2004, pp. 478–482.

MACROMOLECULAR CHEMISTRY AND POLYMERIC MATERIALS

Complexation of Chromium, Aluminum, and Iron Ions with Monocarboxy Cellulose

N. K. Yurkshtovich, N. V. Golub, F. N. Kaputskii, T. L. Yurkshtovich, and R. I. Kosterova

Research Institute of Physicochemical Problems, Belarussian State University, Minsk, Belarus

Received November 28, 2003

Abstract—Complexation of iron(III), aluminum(III), and chromium(III) cations with monocarboxy cellulose was studied by potentiometric titration and IR spectroscopy. The composition and stability constants of the complexes were determined.

Monocarboxy cellulose is used as a suture material in surgery and as a sorbent of heavy metals. Therefore, the study of reactions of metal ions with functional groups of monocarboxy cellulose and determination of factors affecting the metal sorption on monocarboxy cellulose are of both scientific and practical interest.

Cellulose containing hydroxy and carboxy groups is prepared by oxidation with nitrogen(IV) oxide. Oxidized cellulose selectively sorbs some multicharged metal cations which behave as cross-linkers [1, 2].

In this work we studied complexation of Al^{3+}, Cr^{3+}, and Fe^{3+} with monocarboxy cellulose (MCC). No data are available on the stability of complexes of these metals with functional groups of MCC.

EXPERIMENTAL

The mechanism of sorption of the multicharged cations on MCC was studied by potentiometric titration in the presence and in the absence of the metal and by IR spectroscopy.

We used oxidized viscose cord threads (184 tex) and cotton threads (100 tex) containing from 0.4 to 1.4 mmol g^{-1} of carboxy groups in the H form. The threads were prepared by treatment with 5 or 10% solutions of nitrogen(IV) oxide in tetrachloromethane for 7 h [3]. Some physicochemical properties of the samples are summarized in Table 1.

The procedure for calculating the stability constants and the experimental procedure are described in [4, 5].

The MCC samples were titrated under static conditions. The ionic strength was kept constant (0.5) by adding Na_2SO_4 and NaCl to the solutions of metal sulfates and metal chlorides, respectively. The total solution volume was 40 ml; the sample weight was 0.3 g. After the equilibrium was attained (24 h), pH of the solution and the metal concentration in the sorbent were determined.

To analyze the cellulose samples for Al^{3+}, Cr^{3+}, and Fe^{3+}, they were dissolved in H_2SO_4 solution containing H_2O_2. The content of these metals in the resulting solution was determined, respectively, by complexometric titration with Dithizone indicator, chromatometric titration, and colorimetry in the presence of sulfosalicylic acid [6].

The procedure for preparing KBr pellets of cellulose samples was described in [7]. The IR spectra were recorded on a Specord 75-IR spectrophotometer.

The OH bands in the range 3000–3700 cm^{-1} were characterized by the following parameters: ν_{OH}, frequency of the absorption maximum; a/b, symmetry index equal to the ratio of the right (a) and the left (b) parts of the band at the half-maximum [8, 9].

Table 1. Ion-exchange properties of MCC samples at $I = 0.5$

$c_{Na_2SO_4}$ = 0.17 M			c_{NaCl} = 0.5 M		Degree of swelling in water, ml g^{-1}
EC_{COOH}, mmol g^{-1}	pK_a	n	pK_a	n	
0.8	3.5	0.85	3.0	1.10	0.73
1.4	3.5	0.85	3.0	1.05	0.95

1070-4272/04/7703-0471 © 2004 MAIK "Nauka/Interperiodica"

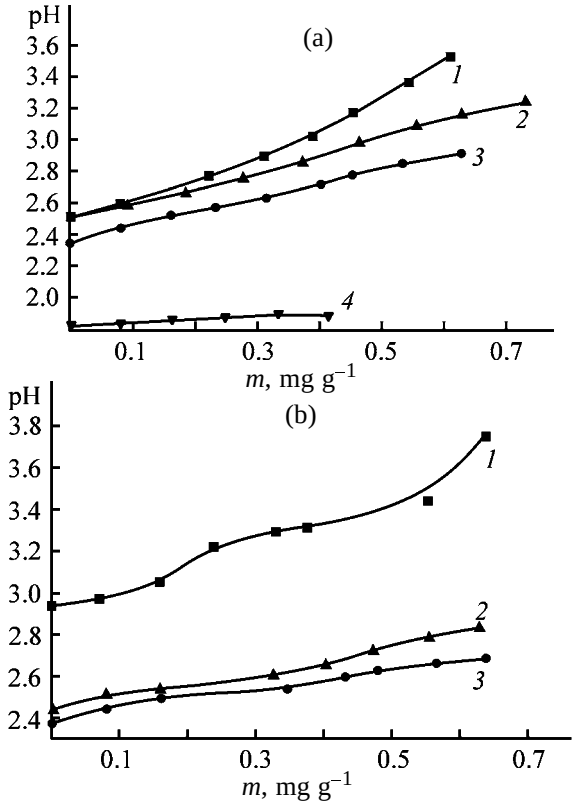

Fig. 1. Potentiometric titration curves of MCC (EC_{COOH} = 0.8 mmol g^{-1}) (*1*) in the absence of triple-charged cations and in the presence of (*2*) Al^{3+}, (*3*) Cr^{3+}, and (*4*) Fe^{3+} cations. Ionic strength I = 0.5 was produced by (a) hydrochloric acid and (b) sulfuric acid solutions of the metals(III) and sodium. (*m*) NaOH amount.

Sorption of Al^{3+}, Cr^{3+}, and Fe^{3+} cations on the cellulose cation exchanger is caused by both electrostatic attraction and formation of strong donor–acceptor bonds.

Formation of MCC–M^{3+} intrapolymeric complex can be described by the following equilibrium:

$$n\overline{\text{celCOOH}} + M^{3+} \rightleftarrows \overline{[(\text{celCOO})_nM]^{(3-n)}} + n^+H^+,$$

where M^{3+} is the metal cation; n is the mean content of carboxy groups coordinated to one metal cation.

The concentration equilibrium constant K of complexation is related to the stability constant of the complex in the sorbent phase K_{st}:

$$K = \frac{\bar{c}_M(H^+)^n}{c_M\overline{(COO^-)^n}} = K_{st}(H^+)^n.$$

To calculate these constants, n should be determined by the equation

$$n = \frac{EC - [COOH] - [COO^-]}{\bar{c}_M},$$

where EC is the exchange capacity of the cation exchanger (mmol g^{-1}); [COOH] and [COO$^-$] are the concentration of protonated and deprotonated (coordination-active) carboxy groups (mmol g^{-1}), respectively; $\bar{c}_M$ is the metal concentration in the sorbent phase (mmol g^{-1}).

The pontiometric titration curves of MCC taken in the presence of Al^{3+}, Cr^{3+}, and Fe^{3+} cations are shown in Figs. 1a and 1b. The solubility of iron sulfate was insufficient to construct the curve of MCC titration in the presence of this salt. Furthermore, the potentiometric titration curves were measured only in acidic solution (Fig. 1), since at higher pH metal hydroxides precipitated. Based on the results obtained, the relative stability of MCC–M^{3+} complexes can be ranked in the following order: $Fe^{3+} > Cr^{3+} > Al^{3+}$. It should be noted that more stable chromium and aluminum complexes with MCC are formed when these metals are sorbed from sulfuric acid solutions.

This may be due to the fact that the composition of Al^{3+} and Cr^{3+} complexes substantially depends on the nature of anions of their salts, all other conditions being the same [10–13]. It is known [13] that these metal cations form aqua complexes in aqueous solutions, which hydrolyze with increasing pH.

$$[M(H_2O)_6]^{3+} \rightleftarrows [M(H_2O)_5OH^-]^{2+} + H^+.$$

The hydroxo complexes can condense to form polynuclear species.

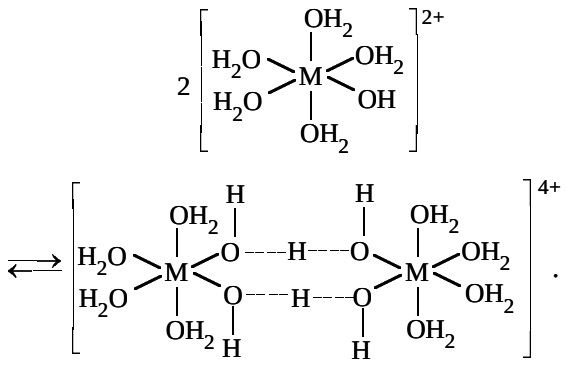

Unlike $CrCl_3$ solution, positively charged hydroxosulfate complexes are formed along with hydroxocomplexes in equilibrium $Cr_2(SO_4)_3$ solution [12].

Table 2. Results of titration of MCC (EC_{COOH} = 0.8 mmol g^{-1}) in the presence of Al^{3+}, Cr^{3+}, and Fe^{3+} cations

Salt concentration, M	pH	c_M, mmol g^{-1}	K_d	n	[COO^-], mmol g^{-1}	log K_1*	log K_2*
0.09 $FeCl_3$	1.92	0.51	10.9	2.3	1.0×10^{-2}	–	5.0
	1.93	0.54	11.0	2.3	6.0×10^{-3}	–	5.0
	1.95	0.55	11.8	2.4	2.5×10^{-3}	–	6.3
	1.98	0.56	11.2	2.5	1.0×10^{-3}	–	7.0
0.05 $Cr_2(SO_4)_3$	2.37	0.15	3.2	2.3	6.6×10^{-3}	–	4.9
	2.45	0.16	3.3	2.3	7.9×10^{-3}	–	4.7
	2.50	0.17	3.4	2.5	7.4×10^{-3}	–	4.8
	2.66	0.21	3.7	–	1.0×10^{-4}	–	8.5
0.022 $Cr_2(SO_4)_3$	2.53	0.13	6.8	1.8	1.9×10^{-2}	–	4.3
	2.61	0.16	7.7	2.5	1.4×10^{-2}	–	4.6
	2.83	0.22	8.1	–	3.6×10^{-3}	–	5.8
0.107 $CrCl_3$	2.39	0.07	1.5	2.1	0.197	–	1.6
	2.44	0.11	2.4	1.8	0.196	–	1.8
	2.50	0.14	3.1	1.8	0.202	–	1.9
	2.56	0.18	3.9	1.7	0.196	–	2.0
	2.83	0.22	4.1	–	8.6×10^{-2}	–	2.8
	2.89	0.22	4.0	–	2.1×10^{-2}	–	4.0
0.05 $Al_2(SO_4)_3$	2.44	0.29	6.2	1.0	1.2×10^{-2}	2.8	–
	2.51	0.31	6.7	1.1	1.1×10^{-2}	2.8	–
	2.53	0.33	6.9	1.3	0.9×10^{-2}	2.9	–
	2.79	0.39	6.8	–	1.4×10^{-3}	3.7	–
	2.84	0.41	6.7	–	5.4×10^{-5}	5.1	–

* K_1 and K_2 are the stability constants of complexes with the composition M : COO^- = 1 : 1 and 1 : 2, respectively.

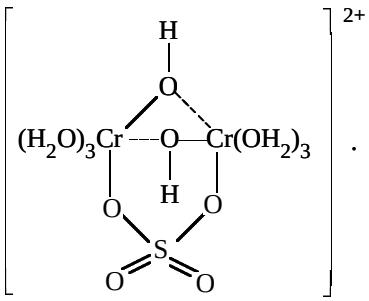

Hence, higher selectivity in sorption of Al^{3+} and Cr^{3+} cations on MCC from sulfuric acid solutions, as compared to the sorption from hydrochloric acid solutions, may be due to different absorption energy of the aqua, hydroxo, and polynuclear complexes whose relative content depends on the anion.

The composition and stability constants of the complexes were calculated from the results of potentiometric titration (Table 2). Complexes with the composition M(III) : COO^- = 1 : 2 are mainly formed in the Fe(III)–MCC and Cr(III)–MCC systems at pH of equilibrium solutions $pH_{eq} \le 1.98$ and $pH_{eq} \le 2.50$, respectively. Aluminum cation ($pH_{eq} \le 2.51$; $pH_{in} \le 3.60$) mainly coordinates a single carboxy group. Determination of the composition of the intrapolymeric complexes at higher pH failed owing to substantial influence of the hydrolysis and polycondensation on the equilibrium. The stability constants in a wider pH range can be calculated assuming that their composition in the sorbent phase remains the same [13, 14].

As seen from Table 2, the stability of M(III)–MCC complexes depends on the pH of the solution. This is due to the fact that the fraction of stable six-membered rings

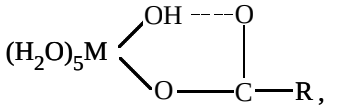

(where R is cellulose residue) formed by the hydroxo complexes in the sorbent phase increases with pH.

The calculated stability constants of the polymeric complexes at pH_{eq} from 1.98 to 2.51 are as follows:

pK_2	System	EC, mol g^{-1}	pH
7.0	$FeCl_3$–MCC	1.4	1.98
4.8	$Cr_2(SO_4)_3$–MCC	0.7	2.50
1.9	$CrCl_3$–MCC	0.7	2.50
2.8(pK_1)	$Al_2(SO_4)_3$–MCC	0.7	2.51

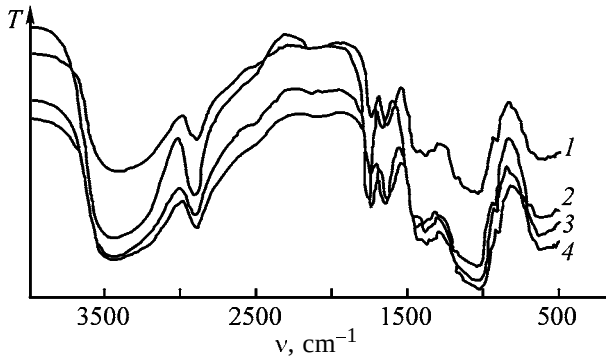

Fig. 2. IR spectra of (*1*) MCC (EC_{COOH} = 0.7 mmol g^{-1}), and its complexes (*2*) Fe^{3+}–MCC (c_{Fe} = 0.34 mmol g^{-1}), (*3*) Al^{3+}–MCC (c_{Al} = 0.50 mmol g^{-1}), and Cr^{3+}–MCC (c_{Cr} = 0.41 mmol g^{-1}). (ν) Wave number and (*T*) transmission; the same for Fig. 3.

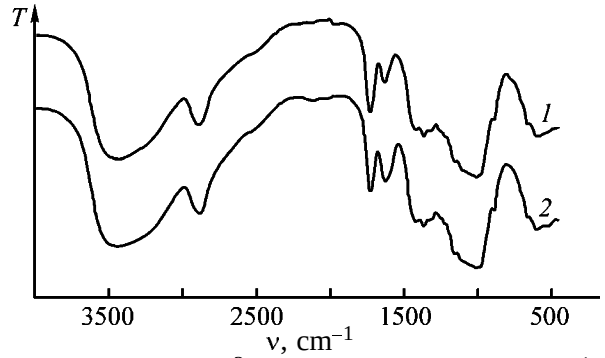

Fig. 3. IR spectra of Cr^{3+}–MCC (EC_{COOH} = 0.7 mmol g^{-1}) with c_{Cr} (mmol g^{-1}) (*1*) 0.19 and (*2*) 0.41.

Table 3. Parameters of the OH band in the spectra of MCC containing metal cations

Cation	Metal content, mmol g^{-1}	ν_{OH}, cm^{-1}	*a*/*b*
MCC (EC = 0.4 mmol g^{-1}) viscose fiber			
H^+	–	3390	0.77
Cr^{3+}	0.18	3395	0.79
Al^{3+}	0.21	3395	0.78
Fe^{3+}	0.16	3395	0.79
MCC (EC = 0.8 mmol g^{-1}) viscose fiber			
H^+	–	3430	0.48
Cr^{3+}	0.40	3450	0.43
Fe^{3+}	0.34	3430	0.46
Al^{3+}	0.50	3440	0.45
MCC (EC = 1.4 mmol g^{-1}) viscose fiber			
H^+	–	3350	0.88
Cr^{3+}	0.11	3395	0.80
Fe^{3+}	0.42	3425	0.61

To confirm the proposed composition of Fe(III)–MCC intramolecular complex, let us consider complexation of Fe^{3+} cations with dicarboxylic acids. The pK_2 of $FeOx^+$ complexes formed in the Fe(III)–oxalic acid (H_2Ox) system is 7.54 (the hydrolytic equilibrium was not considered). At the same time, the stability constants of Cr^{3+} complexes with anions of malonic, succinic, and phthalic acids [Cr(III) : L = 1 : 2] are 12.85, 10.99, and 10.00 [15] (pH of the solution was not reported).

The IR spectra of Cr(III)–MCC and Al(III)–MCC complexes isolated form sulfuric acid solutions and those of Fe(III)–MCC complexes isolated from hydrochloric acid solutions are shown in Figs. 2 and 3, respectively. The intensity of the band at 1720 cm^{-1} decreases and that of the band at 1610 cm^{-1} increases after treatment of MCC with the metal salt. The appearance of absorption in the ranges 1610–1550 and 1450–1350 cm^{-1} with simultaneous weakening of the C=O band at 1750–1720 cm^{-1} was believed [1, 7] to be due to the ion-exchange reaction. However, as the metal content in the MCC increases, the intensity of the absorption with the main maximum at 1610 cm^{-1} grows, but the intensity of the $\nu_{C=O}$ band at 1720 cm^{-1} does not decrease. This trend is the most pronounced in the IR spectra of Cr–MCC complexes (Fig. 3).

As the Cr^{3+} content in the samples increases by a factor of 2, the intensity of the band at 1610 cm^{-1} increases, whereas the intensity of the band at 1720 cm^{-1} decreases negligibly. These results confirm our assumption that the OH group of the coordinated metal hydroxo complexes forms hydrogen bonds with carboxy group of MCC to give a stable six-membered ring.

The parameters of the OH band of MCC salts are presented in Table 3. Intramolecular bonds of MCC are partially ruptured after introduction of the metal cation into the sorbent phase. The higher the content of carboxy groups in MCC, the stronger is this effect. However, the symmetry indices and the frequencies at the maxima of bands of the OH groups forming hydrogen bonds depend mainly on the content of carboxy groups in the oxidized cellulose rather than on the nature of the sorbed metal cation.

The 40 cm^{-1} shift of the OH band to high frequencies and the decrease in the symmetry index with an increase in the content of carboxy groups of MCC indicate that the sample structure becomes not only looser but also less uniform [8, 9].

The higher the content of carboxy groups in MCC, the stronger the high-frequency shift of the OH bands

in the spectra of MCC salts. The 10–70 cm^{-1} high-frequency shift of the OH bands in the spectra of MCC salts containing more that 0.8 mmol g^{-1} carboxy groups suggests partial rupture of the H bonds in the cellulose matrix after introduction of the metal cations. At the same time, the parameters of the OH band in the spectra of MCC samples with a low content of carboxy groups (EC = 0.4 mmol g^{-1}) change insignificantly after the metal sorption, suggesting preservation of the polymer structure.

CONCLUSIONS

(1) As determined by IR spectroscopy, Al^{3+}, Cr^{3+}, and Fe^{3+} cations are sorbed on monocarboxy cellulose by ion exchange and formation of hydrogen bonds between the OH group of the hydroxo complex and carboxylate anion of the sorbent. Intramolecular bonds in monocarboxy cellulose are partially ruptured after metal sorption.

(2) The stability constants of the complexes of Al^{3+}, Cr^{3+}, and Fe^{3+} cations with monocarboxy cellulose increase with increasing pH of the solution. The stability of these complexes at pH 1.98–2.51 decreases in the following order: $Fe^{3+} > Cr^{3+} > Al^{3+}$.

REFERENCES

1. Ermolenko, I.N., *Spektroskopiya v khimii okislennykh tselyulloz* (Spectroscopy in the Chemistry of Oxidized Celluloses), Minsk: Akad. Nauk Bel. SSSR, 1959.
2. Kaputskii, V.E., Study of Physicochemical Properties of Monocarboxy Cellulose, *Cand. Sci. Dissertation*, Minsk, 1971.
3. Yurkshtovich, N.K., Chekhovskii, A.K., Kaputskii, F.N., and Golub, N.V., *Vestn. Bel. Gos. Univ., Ser. Khim.*, 2000, no. 3, pp. 29–30.
4. Tabakova, S.V., Kiseleva, E.D., and Chmutov, K.V., *Zh. Fiz. Khim.*, 1978, vol. 5, no. 9, pp. 2361–2365.
5. Saldadze, K.M. and Kopylova-Valova, V.D., *Kompleksoobrazuyushchie ionity* (Complexing Ion Exchangers), Moscow: Khimiya, 1980.
6. Charlot, G., *Les methods de la chimie analytique. Analyse quantitative minerale*, Paris: Masson, 1961, 4th ed.
7. Zhbankov, R.G., *Infrakrasnye spektry tsellyulozy i ee proizvodnykh* (Infrared Spectra of Cellulose and Its Derivatives), Minsk: Nauka i Tekhnika, 1964.
8. Dzhumbaeva, M.S., *Fosforsoderzhashchie proizvodnye tsellyulozy* (Phosphorous-Containing Cellulose Derivatives), Bishkek: Ilim, 1992.
9. Petropavlovskii, G.A., *Gidrofil'nye chastichno zameshchennye efiry tsellyulozy i ikh modifikatsiya putem khimicheskogo sshivaniya* (Hydrophilic and Partially Substituted Cellulose Esters and Ethers and Their Modification by Chemical Cross-Linking), Leningrad: Nauka, 1988.
10. Radion, E.V., Zalevskaya, T.L., and Baev, A.K., *Vestsi Akad. Navuk Bel., Ser. Khim. Navuk*, 1994, no. 1, pp. 7–14.
11. Radion, E.V., Zalevskaya, T.L., and Baev, A.K., *Vestsi Akad. Navuk Bel., Ser. Khim. Navuk*, 1994, no. 4, pp. 5–8.
12. Matusevich, A.N., *Vestsi Akad. Navuk Bel. SSR, Ser. Khim. Navuk*, 1985, no. 6, pp. 6–8.
13. Mikhailov, A.N., *Khimiya dubyashchikh veshchestv i protsessov dubleniya* (Chemistry of Tanning Agents and Tanning Process), Moscow: Legrprom, 1953, p. 794.
14. Perevozchikova, N.B. and Korneev, V.I., *Koord. Khim.*, 1999, vol. 25, no. 11, pp. 2371–2374.
15. Lavrukhina, A.K. and Yukina, L.V., *Analiticheskaya khimiya elementov: Khrom* (Analytical Chemistry of Elements: Chromium), Moscow: Nauka, 1979.

Russian Journal of Applied Chemistry, Vol. 77, No. 3, 2004, pp. 476–479. Translated from Zhurnal Prikladnoi Khimii, Vol. 77, No. 3, 2004, pp. 483–486.

MACROMOLECULAR CHEMISTRY AND POLYMERIC MATERIALS

Viscosity of Cellulose Ether Solutions as Influenced by Mechanical Impact Intensity

O. V. Alekseeva, O. V. Rozhkova, A. N. Prusov, V. A. Padokhin, and Ya. A. Anikin

Institute of Chemistry of Solutions, Ivanovo, Russia

Received July 8, 2003

Abstract—Structuring and viscosity of solutions of cellulose derivatives as influenced by mechanical treatment under high shear stresses were studied.

In exploitation and processing, polymer systems are exposed to various mechanical impacts modifying the structure of their solutions and affecting the compatibility of their components, which, in turn, affects the properties of films and coatings thereof. Prediction of such changes requires knowledge on the influence of mechanical impacts on structuring in polymer solutions.

In this work, we consider how the mechanical activation parameters affect the structure and viscosity of aqueous solutions of cellulose ethers, namely, hydroxypropyl cellulose (HOPC), methyl cellulose (MC), hydroxyethyl cellulose (HOEC), and methyl hydroxypropyl cellulose (MHPC).

EXPERIMENTAL

We studied samples of HOPC, MC, HOEC, and MHPC with the degrees of polymerization of 810, 800, 920, and 840, respectively, synthesized by Politsell Closed Joint-Stock Company (Vladimir). Double-distilled water served as solvent. The solutions were prepared by dissolving weighed portions of polymers in water under continuous stirring with a magnetic stirrer at 298 K. To attain an equilibrium, the solutions were kept for 3 days. The resulting systems were treated on a rotary-pulse installation for 1 min at the activator rotor rate w within 500–3000 rpm. This corresponded to shear strain rate varying from 0.5×10^3 to 3×10^3 s^{-1}. The viscosity of the initial and mechanically treated solutions was measured on a Rheotest 2.1 rheoviscometer (coaxial-cylinder working unit) at shear rates within 0.0167–145.8 s^{-1} at 293–318 K. Before measurements, the treated solutions were kept at rest for 4 h. The heterogeneity parameters of aqueous solutions of cellulose ethers (turbidity t_λ, disperse phase particle size r, and content of disperse particles in 1 m^3 N) were determined by the turbidity spectrum method on a Specord M-40 spectrophotometer in the wavelength range from 240 to 450 nm.

The radius of the disperse phase particles and the content of disperse particles in 1 m^3 were determined by the formulas [1]

$$r = \alpha\lambda_0/2\pi n_0, \quad (1)$$

$$N = \tau_\lambda/K_1\pi r^2, \quad (2)$$

respectively. Here, r is the disperse phase particle radius; α, relative particle size; λ_0, average wavelength in the measurement range; n_0, refractive index of the disperse phase under study; N, content of disperse particles in 1 m^3; t_λ, turbidity at the wavelength λ; and K, dissipation constant.

Figure 1 presents the log–log plots of the viscosity η vs. shear stress τ for aqueous solutions of cellulose

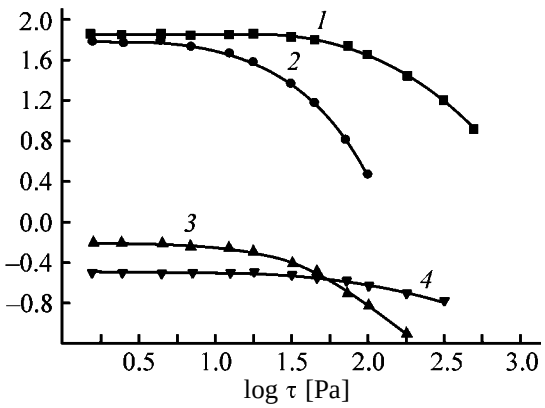

Fig. 1. Viscosity η as a function of the shear stress τ for aqueous solutions (5 wt %) of cellulose ethers at 298 K. (*1*) HOEC, (*2*) MC, (*3*) HOPC, and (*4*) MHPC.

1070-4272/04/7703-0476 © 2004 MAIK "Nauka/Interperiodica"

ethers at 293 K. The systems under study are non-Newtonian liquids. The viscosities of equiconcentrated aqueous solution of cellulose ethers (Fig. 1) increase in the series MHPC < HOPC < MC < HOEC. The lowest viscosity is characteristic of aqueous solutions of MHPC which exhibit a close-to-Newtonian flow under shear stress throughout the temperature range studied. Increase in viscosity along the above-mentioned series of systems is accompanied by deterioration of the polymer affinity for the solvent. This is confirmed by increase in the structuring coefficient (from 1.07 for MHPC solutions to 1.49 for MC solutions) as calculated by the formula [2]

$$\gamma = K\tau^n, \quad (3)$$

where n is the structuring coefficient; γ, shear rate; τ, shear stress; and $K = 1$ for Newtonian liquids.

It was shown in [3–5] that the main contribution to the mechanical impacts exerted on liquid-phase systems when treated in rotary-pulse activators comes from shear stress, cavitation, and its accompanying physical and physicochemical phenomena. Figure 2 presents the plots of extremal viscosity vs. mechanical impact for the cellulose ether solutions at 298 K. It is seen that mechanical treatment strongly affects the shear viscosity of all the systems studied. Solutions of MC, MHPC, and HOPC are characterized by a maximum, η_{max}, in the plot of the viscosity vs. mechanical impact, the largest viscosity increment being observed at w = 1000 rpm. Increase in the viscosity is evidently due to unfolding of the macromolecular chains in a flow, which yields additional intermolecular hydrogen bonds in the system. This, in turn, yields a new, larger, supramolecular structure. For the HOEC–water system, the viscosity tends to sharply decrease with increasing w. The decline in viscosity is due to disturbed intermolecular interaction of the macromolecules in solution, which is responsible for conformational changes. Khailenko *et al*. [6] reported similar results for structuring in cellulose ether solutions as influenced by mechanical treatment.

The more developed structure of polymers is confirmed by the structuring coefficients calculated from the rheological data and by the microheterogeneity parameters of the solutions. The plots of the structuring coefficients n vs. the rotor rotation rate w for HOPC, MC, and MHPC (but not HOEC) exhibited a maximum near 1000 rpm (Fig. 3). This suggests that the mechanically treated cellulose ethers (1000 rpm) are liquids that surpass the initial polymers in the degree of structuring.

Table 1 lists the sizes of the supramolecular forma-

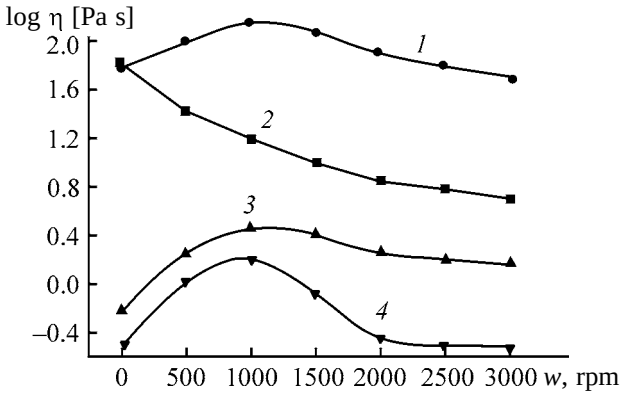

Fig. 2. Extremal viscosity η of 5 wt % cellulose ether solutions at 298 K as a function of the activator rotor rotation rate w. (*1*) MC, (*2*) HOEC, (*3*) HOPC, and (*4*) MHPC.

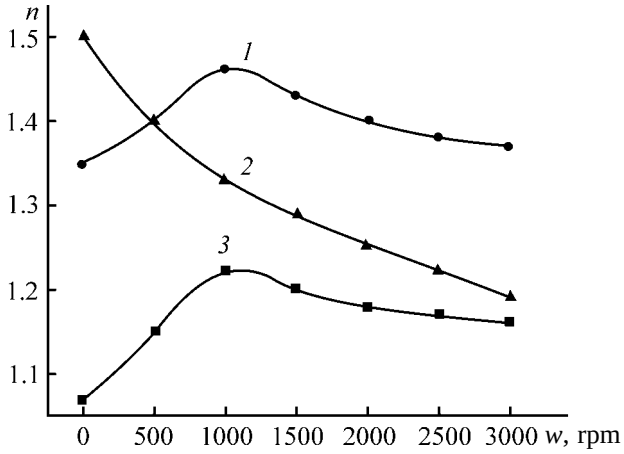

Fig. 3. Structuring coefficient n of cellulose ether solutions as a function of the rotor rotation rate w. (*1*) HOPC, (*2*) HOEC, and (*3*) MHPC.

Table 1. Size of the supramolecular formations in aqueous solutions (5 wt %) of cellulose ethers

Cellulose ether	w, rpm	$\tau_\lambda \times 10^{-2}$, m^{-1}	$r \times 10^8$, m	$N \times 10^{-17}$
MHPC	0	1.6	4.6	68
	1000	1.8	5.1	40
	2000	1.5	4.8	68
	3000	1.1	4.5	69
HOPC	0	1.5	5.9	38
	1000	1.8	6.9	23
	2000	1.4	6.5	34
	3000	1.4	5.1	48
MC	0	1.8	12.0	0.7
	1000	1.9	12.7	0.6
	2000	1.8	12.1	0.7
	3000	1.7	11.4	0.8

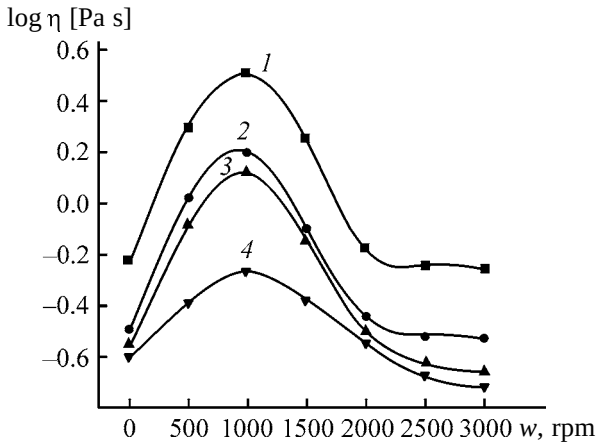

Fig. 4. Viscosity η of the aqueous solution (5 wt %) of MHPC at (*1*) 293, (*2*) 298, (*3*) 303, and (*4*) 308 K as a function of the rotor rotation rate *w*, rpm.

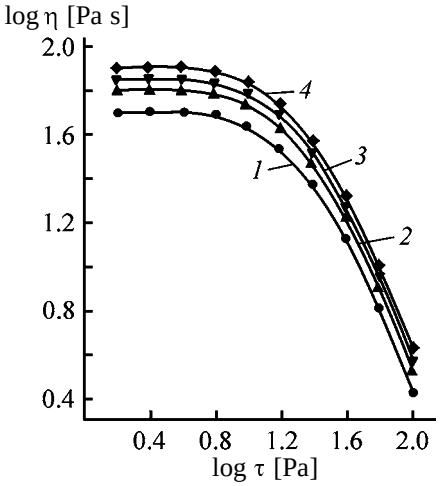

Fig. 5. Viscosity η as a function of the shear stress τ of aqueous solutions (5 wt %) of MC at (*1*) 293, (*2*) 298, (*3*) 303, and (*4*) 308 K.

tions in aqueous solutions of cellulose ethers. For systems based on MC, MHPC, and HOPC, the largest supramolecular formations are observed at w = 1000 rpm, which agrees well with the $\eta = f(w)$ plots. In the HOEC–water system, the size of these formations tends to decrease with increasing mechanical impact.

Table 2. Viscous flow activation energy for cellulose ether solutions (5 wt %) at different rotor rotation rates

w, rpm	E_a, kJ mol^{-1}			
	MHPC	MC	HOEC	HOPC
0	30.6	25.0	63.3	22.4
1000	73.3	71.1	43.7	35.6
2000	26.4	34.0	17.2	30.6
3000	13.3	31.5	5.6	27.9

Further information about the structure of polymer solutions can be derived from the temperature dependences of the viscosity. Figure 4 shows as an example the plot of the viscosity vs. rotor rotation rate for 5 wt % MHPC solution at different temperatures. With increasing temperature, the viscosity of both the initial and mechanically activated solutions of MHPC, HOPC, and HOEC tends to decrease, suggesting a change in their degree of structuring, and the maximum in the η_{max} vs. w plot gets more flattened (Fig. 4).

Solutions of MC exhibit an opposite trend (Fig. 5), i.e., the viscosity of the system tends to increase with rising temperature. As known, heating of aqueous MC solutions results in degradation of, above all, the weakest H-bonds linking the oxygen atoms in the methoxy groups with water molecules. This enhances hydrophobic interactions (association) and changes the size and shape of the associates in solution. Further increase of temperature can result in gelation [7]. However, our experiment showed that methyl cellulose solutions within the temperature range studied, both with and without strong mechanical impact, did not form gels, as confirmed by polarization-microscopic examination.

We found that the dependence of E_a on w is nonlinear (Table 2). With rotor rotation rate w increasing to 1000 rpm, the solutions of MHPC, MC, and HOPC exhibited an increase in E_a, but E_a tended to decrease with further enhancement of the mechanical impact. The viscous flow activation energy is associated with scission of the secondary bonds or temporary contact points of the fluctuation network. Therefore, increase in the absolute value of E_a suggests formation of new, stronger, bonds. The hydrodynamic field near 1000 rpm, evidently, modifies the structural organization (shape and size of associates) of the solutions. In the case of HOEC solutions, enhancement of the mechanical impact tends to decrease E_a.

CONCLUSION

At certain shear stresses, systems based on MC, MHPC, and HOPC exhibit a maximal increase in viscosity due to increase in the size of supramolecular formations, which tends to increase the viscous flow activation energy. This pattern is not characteristic of hydroxyethyl cellulose solutions.

REFERENCES

1. Petropavlovskii, G.A., Vasil'eva, G.G., Brestkin, Yu.V., *et al.*, *Zh. Prikl. Khim.*, 1983, vol. 56, no. 2, pp. 366–370.
2. Matveeva, N.A., Ostrovskaya, L.D., Klenkova, N.I., *et al.*, *Cellulose Chem. Technol.*, 1984, vol. 18, pp. 155–168.
3. Baramboim, N.K., *Mekhanokhimiya vysokomolekulyarnykh soedinenii* (Mechanochemistry of Macromolecular Compounds), Moscow: Khimiya, 1971.
4. Agranat, B.A., Dubrovin, M.N., Khavskii, N.N., *et al.*, *Osnovy fiziki i tekhniki ul'trazvuka* (Fundamentals of Ultrasound Physics and Techniques), Moscow: Vysshaya Shkola, 1987.
5. Fridman, V.M., *Ul'trazvukovaya khimicheskaya apparatura* (Ultrasonic Chemical Instrumentation), Moscow: Mashinostroenie, 1967.
6. Khailenko, L.V., Kercha, Yu.Yu., Lipatov, S.Yu., *et al.*, *Kompoz. Polim. Mater.*, 1987, no. 32, pp. 24–27.
7. Bochek, A.M., Zabivalova, N.M., Lavrent'ev, V.K., *et al.*, *Zh. Prikl. Khim.*, 2001, vol. 74, no. 8, pp. 1322–1327.

Russian Journal of Applied Chemistry, Vol. 77, No. 3, 2004, pp. 480–483. Translated from Zhurnal Prikladnoi Khimii, Vol. 77, No. 3, 2004, pp. 487–489.

MACROMOLECULAR CHEMISTRY AND POLYMERIC MATERIALS

Effect of Thermal Treatment on the Fine Structure of Cellulose Materials

T. V. Smotrina, A. T. Kynin, and S. F. Grebennikov

Mari State Technical University, Ioshkar-Ola, Mari-El Republic, Russia
St. Petersburg State University of Technology and Design, St. Petersburg, Russia

Received March 21, 2003

Abstract—The effect of thermal treatment in the range 110–250°C on the structural and sorption characteristics of cellulose was studied by ^{1}H NMR and sorption methods.

Production of composite materials based on renewable raw materials is an urgent problem. One of the most abundant natural materials suitable for production of various items in the form of composites and in the pure state are cellulose materials, among them wastes formed in production of these materials. These materials are widely used in many branches of industry. One of the problems in production of efficient cellulose-containing composites is estimation of relaxation characteristics of macromolecules and the number of active centers in cellulose material, since precisely these characteristics govern the adhesion and ultimately consumers' characteristics of finished products.

In production of textiles and their service, the materials based on cellulose are subjected to thermal action (drying, ironing, and fixation of dyes), which can result in degradation of the polymer and, hence, deterioration of its performance. Under the action of elevated temperatures, the least ordered areas of the cellulose matrix are altered first. These variations in the amorphous component of cellulose can be significant even under the action of temperatures that do not exceed the point at which cellulose starts to actively degrade.

Despite the publications [1–3] devoted to thermal degradation of cellulose, variation of its fine structure and hydrophilic and relaxation characteristics as a result of thermal action was not studied in detail.

Here, the effect of thermal treatment on the state of amorphous areas of cellulose and its water absorption capacity was analyzed on the basis of NMR relaxation data and sorption data.

EXPERIMENTAL

For the samples of cotton cellulose heat-treated at 105, 150, and 175°C (below the point of intense thermal degradation of cellulose), the dependences of the proton spin–spin relaxation time of the sorbate T_{2d} on the equilibrium moisture content coincide within the limits of the experimental error, i.e., under these conditions the thermal treatment does not noticeably affect the structure of amorphous areas of cellulose and, hence, the mobility of sorbed water. The general shape of the dependences of T_{2d} on the moisture content shows two linear portions (Fig. 1, curves *1–3*), corresponding to fractions of firmly bound (the initial portion) and relatively weakly bound water, which is characteristic of native cellulose fibers. Further increase in the treatment temperature (200–250°C)

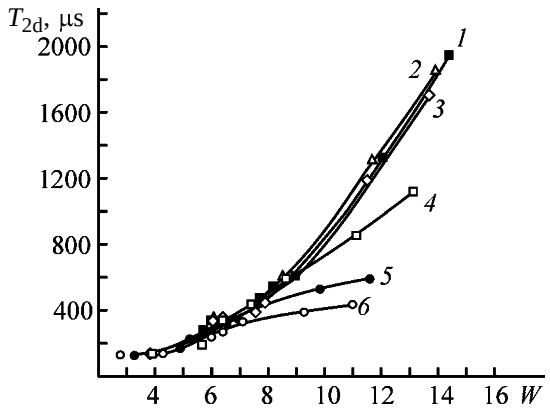

Fig. 1. Spin–spin relaxation time of water T_{2d} as a function of equilibrium moisture content W (g H_2O per 100 g cellulose) for cotton cellulose. (*1*) Initial cellulose; treatment temperature, °C: (*2*) 150, (*3*) 175, (*4*) 200, (*5*) 225, and (*6*) 250.

1070-4272/04/7703-0480 © 2004 MAIK "Nauka/Interperiodica"

results in changes in the curve shape (Fig. 1, curves *4* and *5*). Relatively stable values of spin–spin relaxation time of sorbate protons at moisture content above 5–6 wt % (up to the maximum moisture capacity from the vapor phase) suggest transformation of the cellulose structure as a result of thermal treatment. In our opinion, thermal treatment under the above conditions is favorable for formation of stable microareas with bounded geometry, hindering development of rotation mobility of water molecules with increasing moisture content of cellulose.

Above 200°C, the mobility of macromolecules increases due to devitrification of a significant fraction of the amorphous phase of the polymer, which provides favorable conditions for the mutual approach of the macromolecules and intermolecular dehydration with formation of cross-links. The presence of strong interchain bonds provides the stability of the resulting quasi-network microstructure and, hence, low mobility of sorption water even at high relative vapor pressure. The similar results were obtained for wood cellulose with the only difference that the mobility of water sorbed on wood cellulose is somewhat lower compared to cotton cellulose and stabilization of the microstructure is observed at lower temperatures, which is caused by lower thermal stability of wood cellulose in comparison with cotton cellulose.

The experimental dependences of spin–lattice relaxation time of cellulose protons T_{1c} on the equilibrium moisture content is typical for cellulose materials (Fig. 2). The position of the minimum of T_{1c} depends on the accessibility of the sorption surface for sorbate molecules and its nature. An increase in the treatment temperature results in a shift of the T_{1c} minimum toward lower W, which is caused by partial changes in the nature of relaxation centers, in particular, by formation of carboxy groups as a result of thermal oxidation [4]. The shift of the left branches of the dependences toward lower moisture content suggests an increase in the number of functional groups available in the initial stages of sorption, more pronounced at temperatures above 200°C. At treatment temperatures below 175°C, this is apparently caused by compaction of amorphous areas of cellulose due to removal of the fraction of residual water most firmly bound to the polymer and not removed in drying [5].

Additional data on variation of supramolecular and chemical structure of the cellulose samples were obtained in processing of sorption isotherms of water with the use of thermal equation of sorption (1) [5, 6]

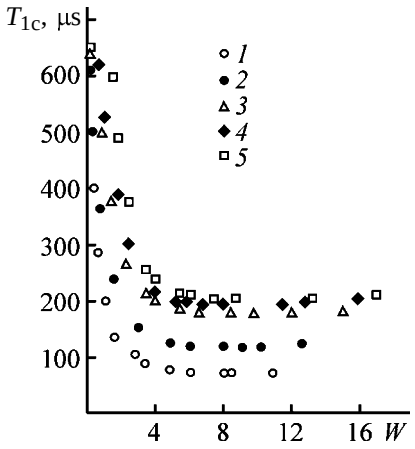

Fig. 2. Spin–lattice relaxation time of thermally treated cotton cellulose T_{1c} as a function of equilibrium moisture content W (g H_2O per 100 g cellulose). Treatment temperature, °C: (*1*) 150, (*2*) 175, (*3*) 200, (*4*) 225, and (*5*) 250.

and equation for quasi-chemical model of sorption equilibrium (2) [7]:

$$a = a_0^a(1 - X_c)\exp[-(-\Delta\mu_1/E)^n + \alpha(T - T_0)], \quad (1)$$

$$a = a_m\alpha' h/\{(1 - \beta h)[1 + (\alpha' - \beta)h]\}, \quad (2)$$

where a_0^a is the limiting sorption in amorphous areas of the fiber at the standard temperature T_0 = 293 K and the pressure of saturated vapor p_0, X_c is the degree of crystallinity, E (the characteristic energy of sorption) and n = 0.7 are the equation parameters, $\Delta\mu_1 = RT\ln h$, α is the thermal factor of sorption, β and α' are the parameters of the quasichemical model of the sorption equilibrium, a_m is the concentration of active centers in the free volume of the polymer, $h = p/p_0$, and β is a constant mostly related to the rigidity of the polymer structure: the lower the mobility of the macromolecule, the lower the constant.

In Eq. (1), a_0^a, E, and α allow estimation of the integral heat of sorption

$$q_i = \frac{E a_0^a}{M_{H_2O} n}(1 - \alpha T)\Gamma(n^{-1}), \quad (3)$$

where Γ is gamma-function (for cellulose Γ = 0.8861) and M_{H_2O} is the molecular weight of water.

We found that a_0^a and E remain unchanged up to the treatment temperature of approximately 175°C and then regularly decrease. This causes the constancy of the heat of sorption, i.e., the energy of the interaction of water with the polymer is constant up to the above temperature (Fig. 3a) and then decreases. The latter

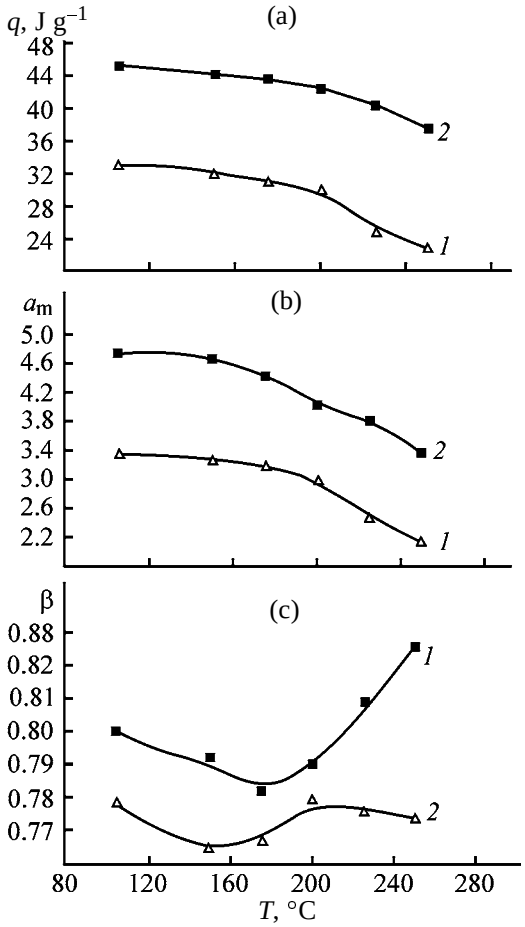

Fig. 3. Variation of (a) heat of sorption q and (b, c) constants a_m and β of Eq. (2) in thermal treatment of (*1*) cotton and (*2*) wood cellulose. (a_m) Concentration of active centers (g H_2O per 100 g cellulose) and (T) temperature.

can be caused by changes in the chemical structure of cellulose, e.g., by formation of carboxy groups.

The a_m value regularly decreases in thermal treatment of cellulose materials (Fig. 3b), which correlates with the NMR data and suggests that these changes in the cellulose structure are observed even at low temperatures, while the main changes begin at a temperature above 180–200°C. It is seen from Fig. 3c that, with increasing temperature to 150–170°C, β somewhat decreases, which can be caused by the transition of cellulose into a more equilibrium state. At higher temperatures, dehydration and thermal oxidation processes begin, which are accompanied by formation of carboxy groups and rupture of intermolecular hydrogen bonds; therefore, β somewhat increases.

Higher heats of sorption of wood cellulose and lower values of β in comparison with cotton cellulose suggest higher strength of bonds of water molecules with active groups of the polymer [7], which is confirmed by the NMR data.

EXPERIMENTAL

We used samples of cotton cellulose [GOST (State Standard) 595–79] and whitened sulfate cellulose (GOST 9571–89). The samples were subjected to isothermal drying at 105°C to constant weight (GOST 6839–54), after which the samples were heat-treateded in air at 150, 175, 200, 225, and 250°C for 1 h. Under these conditions, the temperature affects only amorphous areas of cellulose and does not noticeably affect the crystalline areas. For moistening, the thermally treated cellulose samples were placed over saturated solutions of crystal hydrates producing constant water vapor pressure. The amount of sorbed water was determined gravimetrically. The ^1H NMR relaxation parameters were measured on an NMR spectrometer operating at 42 MHz with an amplitude detector; the 90° pulse length was 3 μs. The free induction delay for the system cellulose–water is two-component. There are short (fast relaxation) and long (slow relaxation) components corresponding to relaxation of cellulose protons and water protons, respectively. The values of transverse relaxation time for each components differ by two orders of magnitude; therefore, approximation by two exponents is justified. The proton spin–spin relaxation time of sorbed water was determined by the Carr–Purcell method (the determination error did not exceed 5%). The spin–lattice relaxation time of cellulose protons was determined by measuring the curve of reduction of longitudinal magnetization [4] (the determination error did not exceed 3%).

CONCLUSION

Data furnished by ^1H NMR and sorption methods allow elucidation of changes in the chemical and supramolecular structure of cellulose materials under thermal treatment in the range 110–250°C and the influence of these changes on the state of sorbed water.

REFERENCES

1. *Metody issledovaniya tsellyulozy* (Methods of Cellulose Study), Karlivan, V.P., Ed., Riga: Zinatne, 1981.
2. Soares, S., Ricardo, N., Jones, S., and Heatley, F., *Eur. Polym. J.*, 2001, vol. 37, pp. 737–739.

3. Scheirs, J., Camino, G., and Tumiatti, W., *Eur. Polym. J.*, 2001, vol. 37, pp. 933–937.
4. Grunin, L.Yu. and Smotrina, T.V., Abstracts of Papers, *5th Vsesoyuznaya konferentsiya* (Fifth All-Union Conf.), Ioshkar-Ola: Mari Gos. Tekh. Univ., 1998, part 3, p. 97.
5. Grebennikov, S.F., Perepelkin, K.E., and Kynin, A.T., *Obzornaya Informatsiya. Ser.: Promyshlennost' khimicheskikh volokon* (Review Information, Ser.: Chemical Fibers Industry), 1989.
6. Grebennikov, S.F. and Kynin, A.T., *Zh. Prikl. Khim.*, 1982, vol. 55, no. 10, pp. 2299–2303.
7. Klyuev, L.E. and Grebennikov, S.F., *Zh. Fiz. Khim.*, 1999, vol. 73, no. 9, pp. 1700–1702.
8. Chizhik, V.I., *Yadernaya magnitnaya relaksatsiya* (Nuclear Magnetic Relaxation), Leningrad: Lening. Gos. Univ., 1991.

Russian Journal of Applied Chemistry, Vol. 77, No. 3, 2004, pp. 484–487. Translated from Zhurnal Prikladnoi Khimii, Vol. 77, No. 3, 2004, pp. 490–493.

MACROMOLECULAR CHEMISTRY AND POLYMERIC MATERIALS

Acid Hydrolysis of Chitin and Chitosan

V. Yu. Novikov

Knipovich Arctic Research Institute of Fishery and Oceanography, Murmansk, Russia

Received December 17, 2002; in final form, January 2004

Abstract—Acid hydrolysis of chitin and chitosan recovered from shells of sea Crustacea was studied by exclusion high-performance liquid chromatography.

Antiarthrosis preparations based on chitin oligomers and glucosamine salts attract growing attention [1, 2]. The yield and quality of glucosamine hydrochloride produced from chitin[1] depend in a complex manner on the chitin properties [3]. To understand this dependence, the mechanism of acid hydrolysis of chitin was studied in more detail.

Acid hydrolysis of chitin (CTN) and chitosan (CSN) was examined in [4–8]. The aim of this work was to determine the limiting degree of chitosan deacetylation suitable for preparing glucosamine. For this purpose, the influence of the degree of chitosan deacetylation on its acid hydrolysis was studied by exclusion high-performance liquid chromatography (HPLC).

EXPERIMENTAL

We used CTN prepared by deproteinization and demineralization of shell of North shrimp (*Pandalus borealis*) by the procedure in [9]. The chitosan content in the sample was 97 wt %; the ash content was lower than 0.1 %; the particle size was no larger than 2 mm.

The chitosan samples were prepared by deacetylation of CTN and CSN. Chitosan with the 68.0% degree of deacetylation (DD) (CSN-1) was obtained by treatment of CTN with 50% aqueous NaOH at 95 ± 5°C for 30 min. The samples with DD of 88.0 (CSN-2) and 92.0% (CTN-3) were prepared under similar conditions from CSN-1 and CSN-2, respectively.

Chitin and chitosan were hydrolyzed with 36.5% HCl at 50 and 70°C. The resulting hydrolyzates were diluted with distilled water, neutralized to pH 3, and filtered through a glass filter with pore diameter of no more than 10 μm (POR 10).

The degree of CSN deacetylation was determined by potentiometric titration of a 2% CSN solution with 0.1 M HCl by the procedure in [10]. The absolute error of the determination was 0.5%.

The hydrolysis products of CTN and CSN were separated by HPLC on an $LC10A_{vp}$ chromatograph (Shimadzu, Japan) with TSK-gel Alpha-2500 (30 × 0.78 cm) column and TSK-guardcolumn Alpha (6 × 0.4 cm) precolumn (TOSOH, Japan). The hydrolyzate samples were applied in the form of 0.1% solutions in the eluent (0.3 M NaCl acidified with HCl to pH 3). The hydrolysis products were detected by the absorption at 210 nm.

The UV detection of the hydrolysis products allowed us to monitor changes in the concentration of acetylated compounds and acetic acid. The considerably weaker absorption of deacetylated CSN oligomers and *D*-glucosamine (GA) was obscured by the strong band of the acetylated products. Monomeric *N*-acetylated glucosamine (AcGA) was identified by comparing its retention time (9.78 min) with that of pure GA (9.86 min). For this purpose, a 5% GA solution in the eluent was used.

Based on the published chromatographic data on CTN oligomers [5–7], we assigned the other chromatographic peaks to the acetylated oligomers (Fig. 1). If peak *2* is due to AcGA, then peaks *3* and *4* are assigned to *N*,*N*'-diacetylchitobiose and *N*,*N*',*N*''-triacetylchitotriose, respectively. The semilog plot of the molecular weight (MW) of these compounds on the elution time τ is linear. The nonlinear deviation for GA can be due to either characteristics of the linearity the column or structural difference of the deacetylated monomer from AcGA. Hence, GA cannot be used to construct the calibration curve.

[1] Ekobiotek-Murmansk Research and Technical Center, Limited Liability Company.

1070-4272/04/7703-0484 © 2004 MAIK "Nauka/Interperiodica"

It is known [4, 8] that the rate of formation of AcGA and GA in the course of acid hydrolysis of CTN and CSN decreases with an increase in their DD.

The influence of DD on the rate of acid hydrolysis of CTN and CSN is seen from the chromatograms of their hydrolyzates. At 50°C, CTN is hydrolyzed incompletely to form a mixture of macromolecular and low-molecular-weight products (Fig. 2). As the hydrolysis time increases, the peaks of the macromolecular products shift toward lower molecular weights and decrease in the integral intensity; the intensity of the peaks of the oligomers and monomers increases. It should be noted, however, that the integral intensity of peaks cannot be a measure of chitin depolymerization, since depolymerization is accompanied by formation of deacetylation products whose molar extinction coefficient is lower than that of the acetylated products.

The content of the macromolecular compounds in the products of hydrolysis of CTN and CSN-1 (DD = 68%) at 70°C sharply decreases (Fig. 3). The products of hydrolysis performed for more than 10 min contain mainly oligomers, monomers, and acetic acid; the polymer concentration is very low.

In the products of hydrolysis of CSN-2 and -3 (DD 88 and 92%), the peak of macromolecular fractions is preserved even after hydrolysis for 300 min. It should be noted that a chitosan precipitate in the form of a fine dispersion and with the outward appearance of the initial sample was observed after 5-h hydrolysis of CSN-2 and CSN-3, respectively.

The degree of hydrolysis was estimated from the AcGA yield. The AcGA amount was recalculated to the number of acetyl groups in CTN with DD = 0%, taking the initial DD into account. The AcGA yield increases in the first hydrolysis steps owing to cleavage of glycoside bonds of the macromolecules and then decreases owing to deacetylation (Fig. 4). The AcGA yield in hydrolysis of CTN and CSN, performed for the same time, sharply decreases with an increase in DD of the polysaccharide (Fig. 5).

This result agrees with the fact that the glycoside bond in acetylated monomeric chains is more readily hydrolyzed than the bond in deacetylated chains [8]. Based on relative deceleration of depolymerization with respect to the deactylation rate at high acid concentrations, Varum *et al*. [8] suggested different hydrolysis mechanisms of *N*-acetyl and glycoside bonds. Probably the *N*-acetyl bond is hydrolyzed by the S_4N2 mechanism in which the rate-determining step is addition of water molecule to the carbocation. As the acid concentration increases, the concentration of water

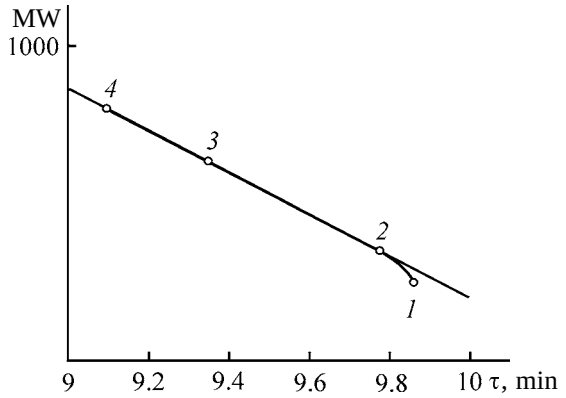

Fig. 1. Calibration curve for chromatographic determination of mono- and polysaccharides. (MW) Molecular weight and (τ) retention time. (*1*) GA, (*2*) AcGA, (*3*) chitobiose, and (*4*) chitotriose.

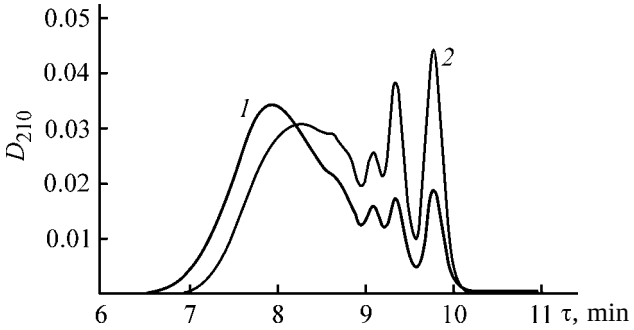

Fig. 2. Chromatograms of CTN hydrolyzates obtained at 50°C, normalized to the equivalent amount of acetyl groups corresponding to DD = 0%; the same for Fig. 3. (D_{210}) Optical density at 210 nm, and (τ) retention time. Hydrolysis time, min: (*1*) 20 and (*2*) 40.

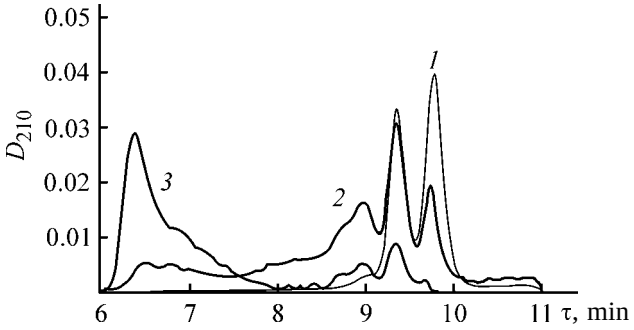

Fig. 3. Chromatograms of hydrolyzates of (*1*) CTN, (*2*) CSN-2, and (*3*) CSN-3 at 70°C (120 min). (D_{210}) Optical density at 210 nm and (τ) retention time.

molecules decreases and the reaction decelerates. The glycoside bond is hydrolyzed by the S_N1 mechanism in which the rate-determining step is the proton attack to form carbocation. In this case, the reaction rate is independent of the water concentration.

However, the influence of the acetyl substituent at the nitrogen atom of a CTN molecule on the depoly-

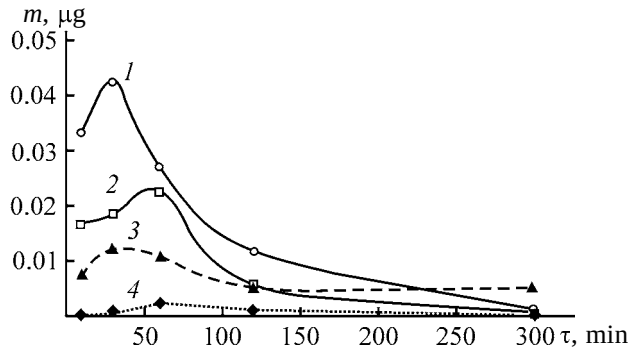

Fig. 4. Kinetics of AcGA formation in hydrolysis of (*1*) CTN, (*2*) CSN-1, (*3*) CSN-2, and (*4*) CSN-3. Temperature 70°C; the same for Figs 5 and 6. (*m*) AcGa weight and (τ) hydrolysis time.

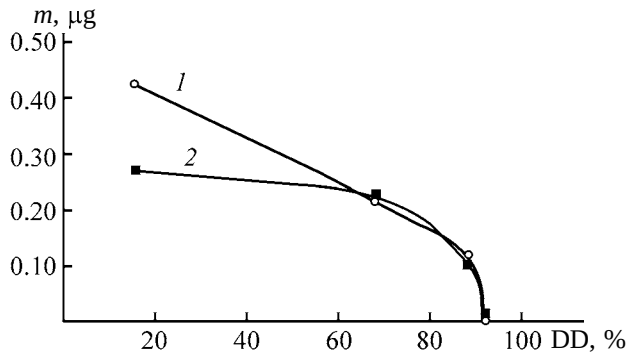

Fig. 5. Yield of AcGA as a functions of DD of CTN and CSN hydrolyzed for (*1*) 30 and (*2*) 60 min. (*m*) AcGa weight and (DD) degree of deacetylation.

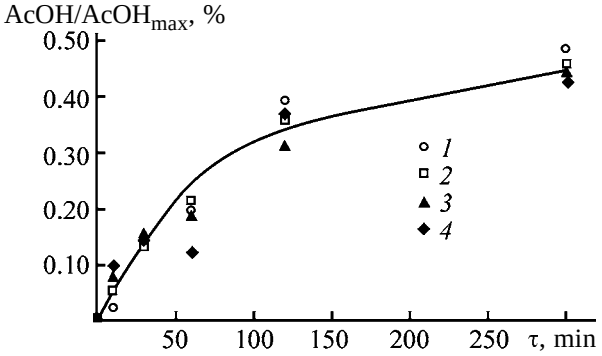

Fig. 6. Rate of AcOH formation in hydrolysis of (*1*) CTN, (*2*) CSN-1, (*3*) CSN-2, and (*4*) CSN-3. ([AcOH]/[AcOH]$_{max}$) Relative AcOH concentration and (τ) hydrolysis time.

merization rate cannot be explained within the framework of the proposed hydrolysis mechanism of the glycoside bond. Computer simulation of the electron density distribution in the molecule showed no appreciable increase in the excess negative charge on the atoms of the glycoside bond after acetylation of the amino group. This charge promotes the proton attack. To understand the hydrolysis mechanism of glycoside bonds in a chitin molecule, more comprehensive studies are required.

It is of practical importance that partially deacetylated CTN or CSN are completely hydrolyzed to AcGA and GA in a time longer than that required for hydrolysis of CTN with minimal DD.

The GA concentration in the CTN hydrolyzate is low, and this product cannot be detected by UV absorption since its molar extinction coefficient is small. Therefore, deacetylation of the acetylated products was monitored by the rate of acetic acid formation (Fig. 6).

The AcOH amount was estimated in relative units from chromatographic peak area (retention time 14.14 min). The amount of AcOH that could be released upon complete acid hydrolysis of CTN with DD = 0% was taken as the maximal. A sample containing the calculated amount of AcOH was introduced in the column, and the peak area was measured.

As seen from Fig. 6, the deacetylation rate is almost independent of the initial DD. This is also the case for the deacetylation of CTN and CSN in alkaline solution [11].

Thus, Figs. 4 and 6 show that depolymerization of CTN and CSN depends on the initial degree of their deacetylation. The higher DD, the lower is AcGA yield. The deacetylation course depends only on the experimental hydrolysis conditions and is independent of DD of CTN and CSN. Hence, the steps of deproteinization and demineralization of chitin production should be performed with care to avoid uncontrolled deacetylation affecting the GA yield.

The limiting degree of deacetylation providing optimal hydrolysis of CTN can be estimated from the dependence of the AcGA yield on DD, assuming that this dependence is linear in the DD range from 15 to 68%. We suggest that a decrease in the monomer yield in the course of hydrolysis should not exceed 10% of its yield in hydrolysis of commonly used CTN with DD ~15%. Our calculations show that the DD of CTN should not exceed 26%. The yield estimated by extrapolation to zero DD is higher by 14% than that of AcGA formed in hydrolysis of commonly used CTN. Hence, the production process of glucosamine can be further improved.

CONCLUSIONS

(1) The study of acid hydrolysis of chitin and chitosan by HPLC shows that accumulation of oligomers and monomers of chitin and chitosan decelerates with

increase in the degree of deacetylation and the deacetylation rate is independent of the initial degree of deacetylation of chitin and chitosan.

(2) The minimal degree of deacetylation of chitin suitable for glucosamine production is 26%.

ACKNOWLEDGMENTS

We are grateful to Yu.B. Ripak (Ekobiotek-Murmansk Scientific and Technical Center) for putting HPLC columns (TOSHO, Japan) at our disposal.

REFERENCES

1. Reginster, J.Y., Deroisy, R., Rovati, L.C., *et al*., *Lancet*, 2001, vol. 357, no. 9252, pp. 251–256.
2. Matheson, A.J. and Perry, C.M., *Drugs Aging*, 2003, vol. 20, no. 14, pp. 1041–1060.
3. Ripak, Yu.B. and Novikov, V.Yu., *Mezdunar. Akad*., 2002, no. 18, pp. 76–78.
4. Horowitz, S.T., Roseman, S., and Blumental, H.J., *J. Am. Chem. Soc*., 1957, vol. 79, no. 18, pp. 5046–5049.
5. Capon, B. and Foster, R.L., *J. Chem. Soc., Sect. C*, 1970, no. 12, pp. 1654–1655.
6. *Chitin Handbook*, Muzzarelli, R.A.A. and Peter, M.G., Eds., Grottamare (Italy): Atec, 1997, pp. 195–198.
7. Chang, K.L.B., Lee, J., and Fu, W.-R., *J. Food Drug Anal*., 2000, vol. 8, no. 2, pp. 75–83.
8. Varum, K.M., Ottoy, M.H., and Smidsrod, O., *Carbohydr. Polym*., 2001, vol. 46, no. 1, pp. 89–98.
9. *Chitin Handbook*, Muzzarelli, R.A.A. and Peter, M.G., Eds., Grottamare (Italy): Atec, 1997, pp. 475–489.
10. Nud'ga, L.A., Plisko, E.A., and Danilov, S.H., *Zh. Obshch. Khim*., 1973, vol. 43, no. 12, pp. 2752–2756.
11. Novikov, V.Yu., Orlova, T.A., and Voronina, I.E., *Izv. Vyssh. Uchebn. Zaved., Ser. Pishch. Tekhnol*., 1990, no. 5, pp. 64–67.

Russian Journal of Applied Chemistry, Vol. 77, No. 3, 2004, pp. 488–492. Translated from Zhurnal Prikladnoi Khimii, Vol. 77, No. 3, 2004, pp. 494–498.

MACROMOLECULAR CHEMISTRY AND POLYMERIC MATERIALS

Preparation and Properties of Blends of Ion-Containing Polyurethane with Polyvinylpyrrolidone

L. V. Stepanenko, A. A. Brovko, T. I. Novikova, L. M. Sergeeva, and A. A. Chernobai

Institute of Chemistry of Macromolecular Compounds, National Academy of Sciences of Ukraine, Kiev, Ukraine

Received June 6, 2003; in final form, January 2004

Abstract—Binary blends of linear polymers, segmented polyurethane [derived from oligooxytetramethylene glycol (MW 1000), toluene diisocyanate (65 : 35 isomer mixture), and magnesium *p*-hydroxybenzoate] and poly-*N*-vinylpyrrolidone (MW 10 000), were prepared and studied.

Polymer blends and interpenetrating polymer networks (IPNs) whose components are capable of forming a three-dimensional system of stable physical bonds offer wide opportunities for preparing composite materials with diverse properties, which can be readily processed in any step [1–3]. Segmented polyurethanes (SPUs) show much promise as such components. In these polymers, microphase segregation results in formation of hydrogen-bonded aggregates of rigid blocks, domains, acting as centers of cross-linking [4, 5]. This accounts for the rubber-like properties of SPUs. When ion-containing SPUs are used for preparing blends or IPNs, not only hydrogen bonds but also ionic bonds can participate in formation of the material structure, significantly affecting the microphase structure and properties of the composite [1–3, 6, 7]. Therefore, the researchers' interest in polyurethane ionomers is steadily high. However, data on blends based on SPUs with ionic groups in the backbone are extremely scarce. We have recently initiated studies in this field [7, 8].

Proceeding with this research, we have studied blends of an ion-containing polyurethane with polyvinylpyrrolidone.

EXPERIMENTAL

The polyurethane component was a linear polyurethane ionomer (PUI) derived from oligooxytetramethylene glycol (OTMG, MW 1000), toluene diisocyanate (TDI), and magnesium *p*-hydroxybenzoate (Mg-PHOB). The PUI was prepared in two steps following the general procedure described in [8]. In the first step, a prepolymer with terminal NCO groups was prepared by the reaction of OTMG with TDI (65 : 35 isomer mixture) in the molar ratio OH : NCO = 1 : 2. In the second step, the prepolymer was extended with Mg-PHOB, and ionic magnesium dicarboxylate fragments were thus introduced. The polyurethane ionomer had MW ~40 000; the anionic group content was about 2%. The second component of the blends was a linear polymer with a pendant five-membered heteroring, commercially available polyvinylpyrrolidone (PVP, **A**) with mean MW 10 000:

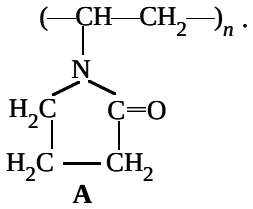

A

Blends were formed by chemical mixing of the two polymers [1]. The starting prepolymer and the chain-extending agent were added to a solution of PVP in dimethylformamide, and PUI was formed in a PVP solution upon vigorous stirring at room temperature for 2 h. The reaction mixture was cast on Teflon supports, and the reaction was completed by drying for 5–7 days at 353 K. The weight fraction of PVP in the blend samples was varied from 0 to 90%.

To study intermolecular interactions in polymer blends, we recorded the IR spectra of blend samples in KBr on a Specord M-80 spectrophotometer in the range 600–4000 cm^{-1}. To study the viscoelastic properties of the blend samples and qualitatively estimate the extent of their microheterogeneity, we used a relaxometer with automatic recording of the phase shift angle [9]. Measurements were performed at a

1070-4272/04/7703-0488 © 2004 MAIK "Nauka/Interperiodica"

100 Hz frequency of induced sinusoidal vibrations in the temperature range 173–513 K. The dynamic modulus of elasticity E' (MPa) and modulus of loss E'' (MPa) were calculated from the experimental values of the complex modulus of elasticity and mechanical loss tangent $\tan\delta$. The glass transition points T_g were determined graphically from the temperature dependences of tthe viscoelastic characteristics. The sample length, width, and thickness were about 0.06, 0.03, and 0.005 m, respectively. We also evaluated the physicomechanical properties of films prepared from the blends.

The polyurethane ionomer is a segmented polyether urethane; its flexible segments (or blocks) are formed by oligooxytetramethylene glycol **B**:

$$\sim[\text{—O(CH}_2)_4\text{—}]_n\sim .$$

B

The rigid blocks of PUI are formed by reaction of the terminal isocyanate groups of the prepolymer with the chain-extending agent; their structure can be schematically shown as structure **C**:

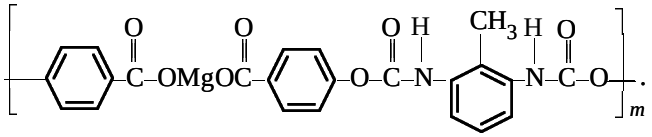

C

Various kinds of intermolecular bonds (H bonds, ion–ion, ion–molecule bonds) are possible in this PUI. These bonds can be revealed by IR spectroscopy [7].

Figures 1 and 2 show the IR spectra of the starting polymers and some blends therefrom. We analyzed in more detail the range 1800–1500 cm^{-1} corresponding to stretching vibrations of various kinds of carbonyl groups (urethane, ester, ionic, heterocyclic).

The spectrum of PUI (Fig. 1, spectrum *1*) in the range 1600–1730 cm^{-1} contains weak ill-resolved bands at 1730, 1710, and 1675 cm^{-1}; also, there is a band at 1610 cm^{-1} with a shoulder at 1630 cm^{-1}. It is known [7] that the carbonyl group in urethane fragments of SPUs gives bands at 1730 (free C=O groups) and 1710 cm^{-1} (C=O groups involved in H bonding with NH groups). It is also known that the carbonyl group in polymers can interact with metal ions, especially with those having high ionic potential such as, e.g., Mg^{2+} [7]. Such interaction gives rise to a new, lower-frequency C=O stretching band in the IR spectra. Therefore, we believe that the band at 1675 cm^{-1} characterizes the ion–molecule bonds $C{=}O\cdots Mg^{2+}$ in PUI. The band at 1630 cm^{-1}, observed as a shoulder, is due to vibrations of the carboxylate anions $RCOO^-$ coordinated with the metal ion [7]. The nonassociated carboxylate anions absorb at 1580–1610 cm^{-1} [7]. The benzene rings also absorb in this range; therefore, the band at 1610 cm^{-1} is the strongest in this part of the spectrum.

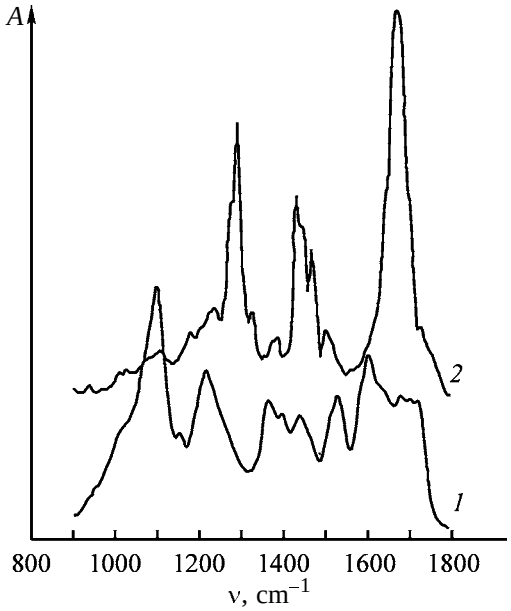

Fig. 1. UR spectra of (*1*) PUI and (*2*) PVP. (*A*) Absorption and (ν) wave number; the same for Fig. 2.

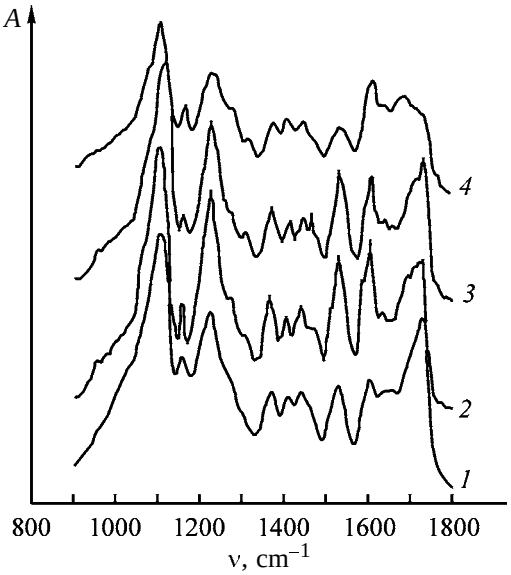

Fig. 2. IR spectra of PUI–PVP blends with the PVP content (wt %) of (*1*) 10, (*2*) 20, (*3*) 30, and (*4*) 70.

The most characteristic bands in the spectrum of PVP (Fig. 1, spectrum *2*) are those of the lactam carbonyl groups at 1680–1690 cm^{-1} and of the pyrrolidone ring [10] at 1290 cm^{-1}.

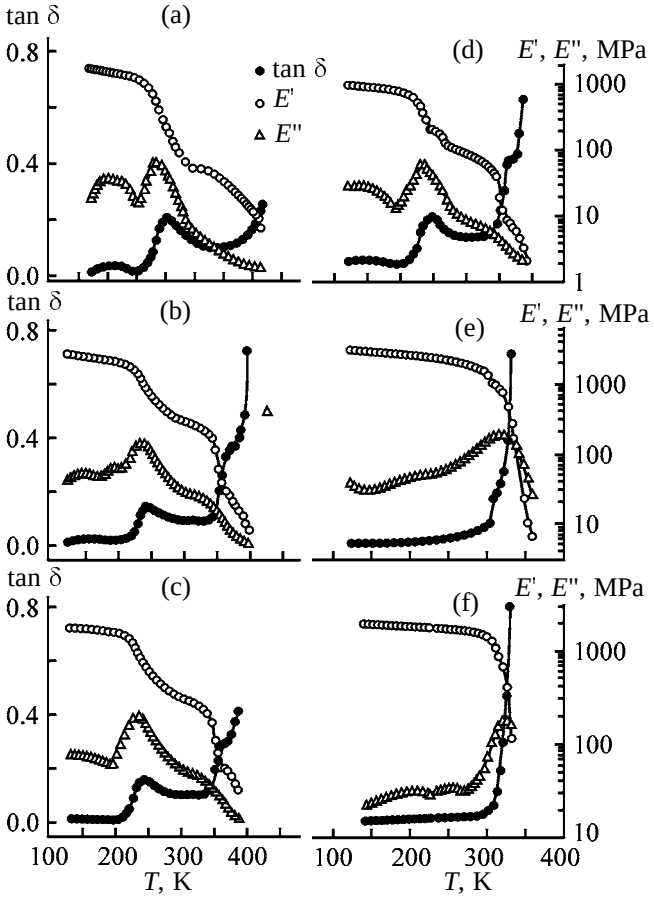

Fig. 3. Temperature dependences of the mechanical loss tangent tan δ, dynamic modulus of elasticity E', and modulus of loss E'' for PUI–PVP blends. PVP content, wt %: (a) 0, (b) 10, (c) 20, (d) 30, (e) 90, and (f) 100.

Comparison of the IR spectra of the polymer blends and their components reveals appreciable changes in the carbonyl absorption pattern depending on the component ratio (Fig. 2). In the spectrum of the blend containing 10 wt % PVP (Fig. 2, spectrum *1*), compared to the spectrum of PUI, the intensity of the band at 1730 cm^{-1} grows, and that of the bands at 1610 and 1630 cm^{-1} sharply decreases. This fact suggests the prevalence of intermolecular interactions between the blend components. For example, the PVP amide group as a strong H-bond acceptor (stronger than the urethane ester group) can participate in hydrogen bonding with the NH groups of urethane fragments. As a result, the content of bound urethane CO groups decreases, and the content of urethane carbonyl groups not involved in hydrogen bonding grows.

A decrease in the intensity of the bands at 1610 and 1630 cm^{-1} may also be due to interpolymer interactions of free $RCOO^-$ groups of PUI with the nitrogen atoms of PVP and of Mg^{2+} ions with the C=O groups of PVP.

As the PVP content in the blend is increased to 20 wt % (Fig. 2, spectrum *2*), the intensity of the band at 1610 cm^{-1} appreciably grows. In the carbonyl absorption range, ill-resolved maxima are observed at 1695, 1710, and 1730 cm^{-1}. These data suggest predominant formation of an ion–molecule bond between the CO groups of PVP and Mg^{2+} ions in PUI. Such interaction is energetically preferable compared to H bonding between two urethane fragments [7].

As the PVP content in the blend is further increased to 30 and 70 wt % (Fig. 2, spectra *3*, *4*), the shape and position of the absorption bands (for all kinds of C=O groups and ionic groups) undergo changes suggesting partial break of the main types of bonds between the components.

The character of intermolecular interactions in polymer blends is closely related to their microstructure. In this connection, we compared the IR data with the viscoelastic properties of the composites, which were studied by dynamic mechanical thermal analysis (DMTA). It is known that the viscoelastic characteristics, especially tan δ, are extremely sensitive to all kinds of relaxation processes, structural nonuniformities, and morphological features of multiphase systems; they can be efficiently used for qualitative characterization of the microphase structure [11]. Figure 3 shows the temperature dependences of tan δ, E', and E'' for PUI, PVP, and a series of blends therefrom.

For PUI (Fig. 3a), the temperature dependence of tan δ shows two relaxation transitions. The first transition in the range 250–275 K corresponds to the flexible (polyester) block. The second transition reflects processes in rigid blocks; it has the shape of an ascending curve in the range 400–420 K.

The temperature dependence of the viscoelastic characteristics of PVP (Fig. 3f) shows a transition in the range 300–330 K.

The temperature dependences of the viscoelastic characteristics of the polymer blends containing 10, 20, and 30 wt % PVP show two temperature transitions: at 230–260 and above 300 K. This unambiguously indicates that two-phase systems are formed. In the blends, the low-temperature (polyether) PUI transition is slightly shifted toward lower temperatures (Figs. 3b–3d, cf. Fig. 3a), and the tan δ peak becomes less pronounced (from the $T > T_g$ side). The temperature dependences of the viscoelastic characteristics of the polymer blends (Figs. 3b–3e) are characterized by

Physicomechanical properties of PUI–PVP blends

Content in blend, wt %		Tensile strength, MPa	Relative elongation at break, %	Modulus of elasticity, MPa	Hardness, arb. units $\times 10^{-1}$
PUI	PVP				
100	–	21.0	300	7.0	1.0
99	1	23.0	290	7.9	1.4
98	2	25.0	280	8.9	1.7
95	5	28.0	240	1.7	2.0
90	10	29.5	100	14.7	2.5
85	15	28.5	180	15.0	2.7
80	20	25.5	150	17.0	2.3
70	30	19.0	100	19.0	1.3
60	40	15.0	100	15.0	0.9
50	50	–	–	–	0.7

a shoulder appearing in the high-temperature branch of the $\tan\delta$ curve ($T > T_g$). This is the temperature range of relaxation processes associated with the mobility in microareas of rigid blocks (rigid domains) and with the breakdown of these domains [12], and also with transition of PVP from the glassy to hyperelastic state. This shoulder is not observed in the temperature dependences of $\tan\delta$ of the starting polymers. These effects may be due to more pronounced microphase segregation in preparation of blends with small (≤20 wt %) PVP content. This, in turn, causes T_g of the polyether blocks to decrease [12].

As shown by the IR spectra, the intermolecular interactions of the two polymers are the strongest specifically in this concentration range. The DMTA data reveal changes in the structure formation: new structural groups arise, favoring more pronounced microphase segregation [12]. It should be noted that the temperatures at which these structural formations are broken down in blends are lower than the temperatures at which rigid PUI blocks are broken down (Figs. 3b–3d, cf. Fig. 3a).

The DMTA results for blends containing 30 wt % PVP and more are also consistent with the IR data. The temperatures and intensities of the peaks of the relaxation processes in the temperature dependences of the dynamic characteristics approach those observed with the starting polymers. The lower stability of the interpolymer structural formations at temperatures above T_g follows from the facts that the temperature of their breakdown decreases to 300–330 K (Figs. 3d, 3e), the shoulder in the temperature dependence of $\tan\delta$ becomes less pronounced, and the modulus of elasticity decreases.

The system of the forming physical bonds and the participation of ionic groups in formation of additional ionic "cross-links" are responsible for formation of a definite microphase structure of the blends, affecting their physicomechanical properties. Elucidation of the interrelation of all these factors in multicomponent polymer sysrtems is very important, as being related to development of new valuable materials [1–3, 8, 11]. The physicomechanical properties of films prepared from some PUI–PVP blends are listed in the table.

It is seen that the physicomechanical parameters of blends depend on the ratio of the polymeric components. At a PVPO content of 1–20 wt %, the strength of the composites exceeds that of the components taken separately. The maximal tensile strength is attained in the 5–15 wt % range of PVP content. As noted above, at these compositions the redistribution of intermolecular bonds is the most pronounced, and the active groups of both polymers are involved in the interaction to the greatest extent. As a result, according to DMTA data, the extent of microphase segregation increases. As the PVP content in blends is increased to 40 wt %, the strength decreases significantly, and the modulus of elasticity decreases slightly. These results are also consistent with the IR and DMTA data.

CONCLUSIONS

(1) According to the IR spectrum, the synthesized segmented polyurethane ionomer is characterized by a system of intermolecular interactions such as urethane–urethane hydrogen bonds, ion–ion bonds, and ion–molecule bonds. These interactions are responsible for formation of a two-phase microstructure.

(2) In blends of the polyurethane ionomer with small amounts (up to 20 wt %) of polyvinylpyrroli-

done, the intermolecular interactions between the polymers are the strongest. As follows from the results of dynamic mechanical thermal analysis, these interactions cause formation of structural groups that are less stable than domains of rigid polyurethane blocks. The network of intermolecular interactions and the microphase structure of the systems in this composition range ensure the maximal tensile strength of the composites.

(3) As the polyvinylpyrrolidone concentration in the blends is increased above 40 wt %, the main intermolecular bonds between the polymers are gradually broken down, the microphase structure of the blends becomes similar to that of the individual polymeric components, and the strength of the material decreases.

REFERENCES

1. Sperling, L.H., *Interpenetrating Polymer Networks and Related Materials*, New York: Plenum, 1982.
2. Lipatov, Yu.S. and Sergeeva, L.M., *Usp. Khim.*, 1986, vol. 40, no. 12, pp. 2086–2106.
3. Sergeeva, L.M., Karabanova, L.V., and Grigor'eva, O.P., *Ukr. Khim. Zh.*, 1997, vol. 63, no. 11, pp. 65–69.
4. *Uretanovye elastomery* (Urethane Elastomers), Apukhtina, N.P. and Mozzhukhina, L.V., Eds., Leningrad: Khimiya, 1971.
5. Bonart, R., *Angew. Makromol. Chem.*, 1977, vols. 58–59, no. 849, pp. 259–297.
6. Tsonos, C., Apekis, L., Viras, K., *et al.*, *J. Macromol. Sci. Phys. B*, 2000, vol. 2, pp. 155–174.
7. Stepanenko, L.V., Novikova, T.I., Sergeeva, L.M., *et al.*, *Zh. Prikl. Khim.*, 2002, vol. 75, no. 8, pp. 1341–1345.
8. Stepanenko, L.V., Kolodnitskaya, Z.A., Brovko, A.A., *et al.*, *Kompoz. Polim. Mater.*, 1990, no. 45, pp. 31–36.
9. *Fizicheskie metody issledovaniya polimerov* (Physical Methods for Studying Polymers), Privalko, V.P., Ed., Kiev: Naukova Dumka, 1981, pp. 85–93.
10. Dechant, J., Danz, R., Kimmer, W., *et al.*, *Ultrarotspektroskopische Untersuchungen an Polymeren*, Berlin: Akademie, 1972.
11. Nielsen, L.E., *Mechanical Properties of Polymers and Composites*, New York: Marcel Dekker, 1974.
12. Kercha, Yu.Yu., *Fizicheskaya khimiya poliuretanov* (Physical Chemistry of Polyurethanes), Kiev: Naukova Dumka, 1979.

Russian Journal of Applied Chemistry, Vol. 77, No. 3, 2004, pp. 493–496. Translated from Zhurnal Prikladnoi Khimii, Vol. 77, No. 3, 2004, pp. 499–502.

MACROMOLECULAR CHEMISTRY AND POLYMERIC MATERIALS

Activating Mixing in Modification of Rubbers in Solution

B. L. Smirnov, A. E. Tubolkin, V. P. Britov, O. O. Nikolaev, and V. V. Bogdanov

St. Petersburg State Technological Institute, St. Petersburg, Russia

Received February 4, 2003

Abstract—The applicability of the previously developed principles of activating mixing to modification of rubbers in solutions was tested, and a process was developed for mechanochemical modification of *cis*-1,4-polyisoprene in rotary pulsation apparatus.

Activating mixing can significantly intensify processes involved in production of synthetic rubber. Among such processes are distribution of catalyst suspensions in the monomer and solvent prior to polymerization, deactivation, stabilization, activation, and washing. Activating mixing may be of particular importance in chemical modification of rubbers in the step of polymer preparation (these processes will be considered below for modification of *cis*-1,4-polyisoprene as example).

Progress of studies on rubber modification allowed development of commercial brands of modified *cis*-1,4-polyisoprene (SKI-3-01 and DKI-3-OK rubbers). Their production involves reactions with aromatic *C*-nitroso compounds. Nitroso derivatives are widely used as modifying agents, stabilizers, and promoters of the interaction of rubber with carbon black in the course of preparation of rubber stocks and vulcanizates. Among numerous *C*-nitroso amines and nitroso compounds tested as modifying agents, much promise is shown by *p*-nitrosodiphenylamine (PNDPA) owing to a wide spectrum of its modifying effect and insignificant contribution of side reactions to the molecular structure of the final product.

The diphenylamine fragment, which can bind to the polymeric chain via nitrogen atom, shows antioxidant properties; therefore, PNDPA can act not only as modifier, but also as stabilizer [1].

It is very interesting to prepare *cis*-oligoisoprene with nitroso amine groups (SKI-3-NA) formed by reactions of high-molecular-weight *cis*-1,4-polyisoprene (SKI-3) with nitroso compounds. The reaction of *cis*-1,4-polyisoprene with PNDPA in solution involves successive and parallel addition of the nitroso compound dimer, cleavage of the resulting tetrahydrooxadiazole ring, and branching of the polymeric chain with the participation of double bonds and groups [2, 3].

The use of SKI-3-NA in preparation of tire stocks not only improves such propertiers of tires as heat and ozone resistance but also considerably enhances the fatigue resistance, stability in prolonged vulcanization, and tear resistance—the parameters responsible for the quality and service characteristics of large tires. Nevertheless, no high-capacity process for production of SKI-3-NA have been developed up to now.

We noted recently [4] that rotary pulsation apparatus (RPA) show much promise in modification of polymers using activating mixing. This fully concerns the modification of SKI-3. The use of activating mixing opens wide prospects for the process intensification and improvement of the product quality.

The goals of this study are to analyze the possibilities of modifying rubbers under conditions of activating mixing and to reveal qualitative and quantitative correlations between the criteria of mechanochemical transformations and criteria describing the external mechanical field acting on a material.

EXPERIMENTAL

We used the substances required for development of a process for modification of isoprene rubber: solutions of *cis*-1,4-polyisoprene in hexane of various concentrations, solutions of *p*-nitrosodiphenylamine sodium salt of various concentrations, phosphoric acid (grades A, B), and other solvents (isopentane, toluene).

Modification of isoprene rubber was performed on an installation schematically shown in Fig. 1.

The starting components for modification of isoprene rubber were prepared as follows. First, we pre-

1070-4272/04/7703-0493 © 2004 MAIK "Nauka/Interperiodica"

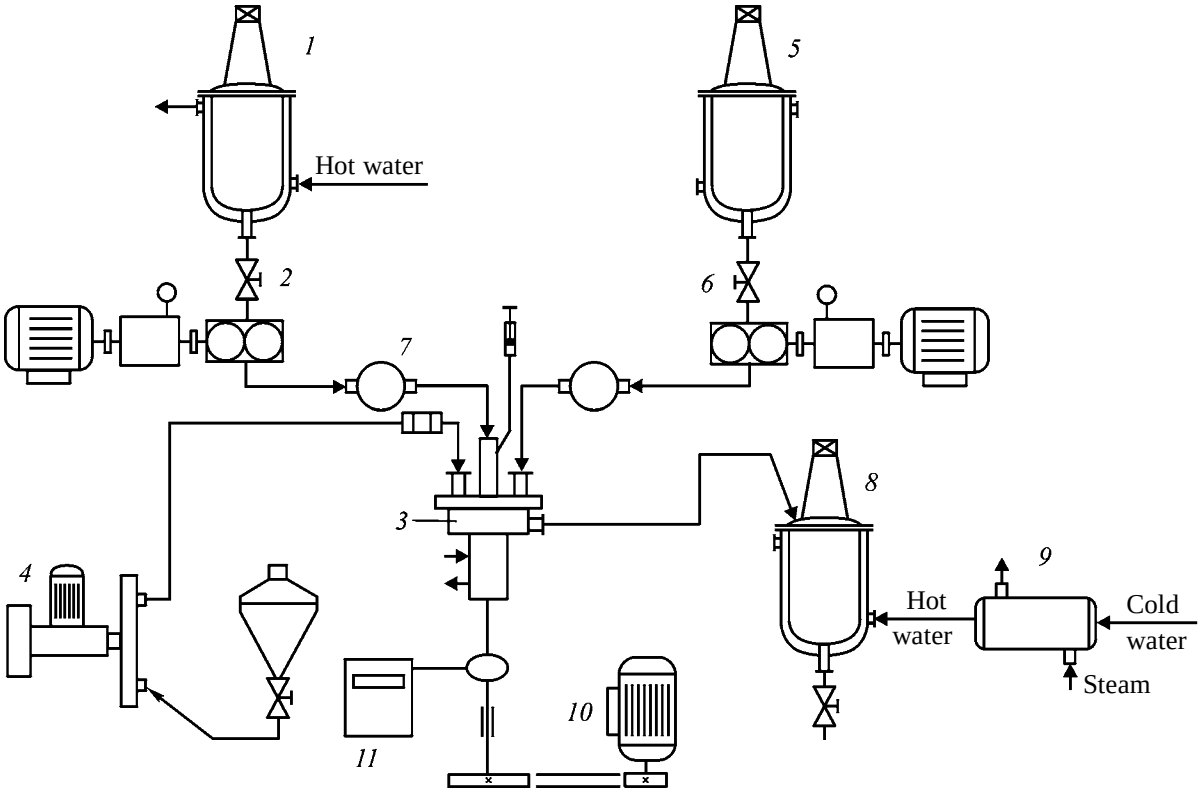

Fig. 1. Installation for modification of isoprene rubber.

pared in stirred vessels a 10% solution of SKI-3 rubber in hexane and a 20% solution of the PNDPA salt. Phosphoric acid was added in amount of 1 mol per mole of PNDPA sodium salt to convert the salt to free *p*-nitrosodiphenylamine. Toluene was added in an amount of 150 ml per liter of solution. The sodium salt was added in an amount of 15 wt % relative to the rubber.

A solution of the rubber in hexane was fed from reactor *1* with a gear pump *2* to RPA *3*. An aqueous solution of PNDPA sodium salt was also fed to the RPA with a piston pump *4*. Feeding of phosphoric acid from reactor *5* with a gear pump *6* to RPA was also provided. The process was monitored visually through a window *7*. After passing RPA, the modified rubber solution was collected in reactor *8* in which it was heated to 80°C for 5 h under stirring with an anchor stirrer (n = 500 rpm). The temperature in the reactor was maintained by passing hot water heated in a heat exchanger *9* through the reactor jacket. The rate of RPA rotor rotation was varied from 1000 to 4400 rpm with a hydraulic drive *10* connected to a hydrosystem. The rotation rate was measured with a digital tachometer *11*. The temperature of the medium was measured with a Chromel–Copel thermocouple connected to a PM-66 potentiometer. Samples for quantitative determination of the extent of physicochemical transformations were taken after 1, 3, and 5 h. Analyses were performed spectrophotometrically [5]. The physicomechanical and service properties of the materials were determined according to the corresponding GOSTs (State Standards): 270–75, 10722–76, 19338–90, 19816.4–74, and 27109–86.

First, we analyzed the effect of various solvents on the structure and properties of oligoisoprenes. The oligoisoprenes prepared in different solvents appreciably differed in the molecular characteristics. For example, samples prepared in toluene had lower values of the intrinsic viscosity, weight-average molecular weight, and polydispersity.

The range of molecular weights of oligoisoprene fractions prepared in a 100 : 200 isopentane : toluene is considerably wider, especially for high-molecular-weight fractions. The differential molecular-weight distribution (MWD) curves calculated from the gel chromatograms show significant differences in the position of the maximum and number of fractions for the oligomers prepared in different solvents. The differences in the MWD parameters of oligoisoprenes can significantly affect the course of modification. Significant microheterogeneity observed with the

isopentane–toluene mixture used as solvent can lead, upon mechanical treatment, to formation of both the initial SKI-3 rubber fractions (high-molecular-weight MWD branch) and oligomeric molecules formed by degradation (low-molecular-weight MWD branch).

At large extents of degradation, the MWD should tend to that characteristic of random bond cleavage ($M_w/M_n \to 2$). The fact that the MWD of oligoisoprenes is considerably wider suggests abnormal process conditions due to heterogeneity of the system; this ultimately depends on the solvent used.

The second step of our study concerned features of chemical modification. The chemical degradation of SKI-3 with PNDPA occurs under microheterogeneous conditions. Therefore, different fractions of the rubber participate in the reaction to different extents, depending on the solubility of PNDPA in these fractions. In particular, Fig. 2 shows that the PNDPA concentration in oligoisoprene fractions can vary from 9 to 50–60 wt % in the range of molecular weights from 500 to $(40–50) \times 10^3$. The functionality of the fractions increases from 1.5–1.7 to 15–20 in the same range of molecular weights. Hence, the low-molecular-weight fraction is polyfunctional to a significant extent.

In the third step of our study, we analyzed the possibility of activation of polymer solutions. It is known that mixing, along with equalization of the concentrations of the component being distributed and with its dispersion, can induce mechanochemical transformations in the system. Such transformations are often undesirable. In our case, however, they allow the SKI-3 modification process to be considerably intensified.

We studied solutions of isoprene rubber in various solvents to reveal their tendency to degrade. By subjecting the material to various actions in an RPA, we determined the percentage of free and bound PNDPA. The material was analyzed after keeping the solution in the reactor for 1, 3, and 5 h.

Figure 3 shows the results obtained as a correlation between the extent of mechanochemical modification and parameters describing the external effect on the system. It is seen that treatment in an RPA, even at relatively low strain energy densities $\tau\gamma$, considerably increases the amount of bound PNDPA, thus decreasing the residence time of the solution in the reactor.

This effect is determined by the mechanism of the treatment process in an RPA. Modifying agents are mixed with the polymer matrix to form a system with a large interface area, due to dispersion and homogenization. The mixed system moves from the apparatus

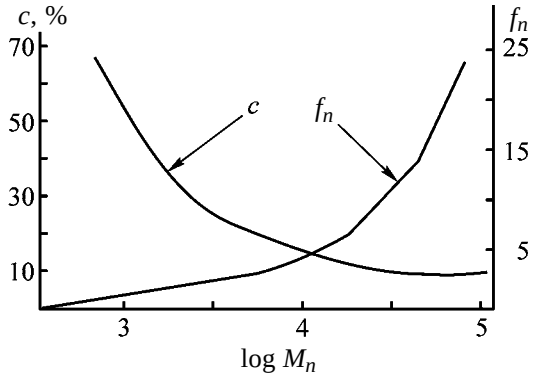

Fig. 2. PNDPA content c and functionality f_n vs. the molecular weight M_n of the oligomer fractions (oligomer prepared in toluene).

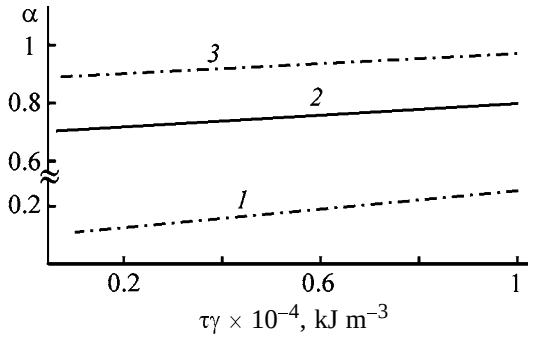

Fig. 3. Influence of the strain energy density $\tau\gamma$ on the reaction of 10% SKI-3 solution in hexane with PNDPA. (α) Fraction of bound PNDPA. Reaction time, h: (*1*) 1, (*2*) 3, and (*3*) 5.

center to the region of increasing shear rates and stresses. In the process, the polymer gets activated, which may cause both generation of active radicals and redistribution over the polymer chains of the vibration energy of the initial highly active state that arose upon local supply of excess mechanical energy. Thus, favorable conditions are created for the reaction of the polymer with modifying agents.

The results of our study were used in development of a flowsheet for producing SKI-3-OK rubber–oligomer formulation for big tires, using RPA as the main equipment. The efficiency of using RPA for modifying *cis*-1,4-polyisoprene is confirmed by the results of industrial tests at the Sintezkauchuk Production Association (Togliatti, Samara oblast, Russia).

The activating mixing in RPA ensured satisfactory agreement between the amount of PNDPA sodium salt added and the sum of free and bound PNDPA in the reaction mixture after mixing the components. Without RPA treatment, the PNDPA content in the reaction mixture was lower by a factor of 1.5–2, indicating that mixing was unsatisfactory; furthermore,

the PNDPA salt precipitated, and its significant fraction was lost in side reactions. With activating mixing, the reaction temperature could be decreased from 65 to 50°C, the polymer concentration could be increased from 11 to 13%, and two vessels could be eliminated from the polymerization battery.

CONCLUSIONS

(1) Activating mixing in rotary pulsation apparatus, used in modification of *cis*-1,4-polyisoprene, allows significant intensification of the process: increase in the polymer concentration from 11 to 13%, elimination of a part of equipment from the flowsheet, decrease in the process temperature, and shortening of the treatment cycle.

(2) Intensification of the modification by activating mixing is due to the following factors: (a) formation of a large interface area between the modifying agents and polymer matrix as a result of homogenization and dispersion; (b) activation of the polymer, which can cause generation of active radicals or redistribution over the polymer chains of the vibration energy of the initial highly active state that arose on local supply of excess mechanical energy.

REFERENCES

1. Kogan, L.N., Krol', V.A., Monastyrskaya, N.B., and Fikhtengol'ts, V.S., *Kauchuk Rezina*, 1979, no. 10, pp. 20–23.
2. Kogan, L.N. and Krol', V.A., *Zh. Vses. Khim. O–va. im. D.I. Mendeleeva*, 1981, no. 3, pp. 272–280.
3. Estrin, A.S., Kogan, L.N., and Krol', V.A., *Sinteticheskii kauchuk* (Synthetic Rubber), Garmonov, I.V., Ed., Leningrad: Khimiya, 1983, pp. 180–183.
4. Britov, V.P., Bogdanov, V.V., Nikolaev, O.O., and Tubolkin, A.E., *Zh. Prikl. Khim.*, 2004, vol. 77, no. 1, pp. 122–127.
5. Fikhtengol'ts, V.S., Kogan, L.M., Krol', V.A., and Monastyrskaya, N.B., *Prom–st. Sint. Kauchuka*, 1979, no. 4, pp. 6–9.

Russian Journal of Applied Chemistry, Vol. 77, No. 3, 2004, pp. 497–500. Translated from Zhurnal Prikladnoi Khimii, Vol. 77, No. 3, 2004, pp. 503–506.

MACROMOLECULAR CHEMISTRY AND POLYMERIC MATERIALS

Optimization of Coagulation and Flocculation in Fat-Containing Highly Dispersed Systems

A. F. Dobrynina, G. G. Faizullina, and V. P. Barabanov

Kazan State Technological University, Kazan, Tatarstan, Russia

Received April 22, 2003

Abstract—The coagulation activity of aluminum sulfate and products of its hydrolysis was analyzed. Formation of particles in fat-containing disperse systems in the presence of both the coagulant and its mixtures with flocculants based on polyacrylamide was studied.

Treatment to remove impurities from wastewater of food and light industry is an important environmental problem. The most difficult is removal of emulsified fats, which is often performed using traditional coagulants [sulfates and chlorides of aluminum, iron(III), etc.] and mixtures of coagulants with various flocculants, in particular, water-soluble polyacrylamide copolymers [1]. However, due to unpredictable results obtained with aluminum oxysulfate (AOS) coagulant, it is necessary to find empirically the optimal conditions of coagulation and flocculation [2, 3].

EXPERIMENTAL

In this work, we used the wastewater from a fur-processing plant; its average composition is given Table 1.

As seen from the IR spectra [4] (Specord 71-IR spectrophotometer), before treatment the disperse phase contains both aliphatic (methyl and methylene) structural groups and heteroatomic groups (sulfoxides, acids, and esters). The broad band of OH vibrations confirms the presence of fatty (e.g., oleic, palmitic, and, partially, stearic) acids. The group of bands in the 1240–1170 cm^{-1} range indicates the presence of various oxygen-containing compounds. Among the organic components, polyfunctional heteroatomic compounds are predominant.

In our work we used AOS [GOST (State Standard) 3758–65] containing 15.3 ± 0.4 wt % aluminum oxide as coagulant, and anionic (PAA1 and PAA2) and cationic (PAA3) polyacrylamide copolymers as flocculants. The average molecular weight M_η of PAA1 and PAA2 was 12.6×10^6 (Technical Certificate) and 4.46×10^6, respectively; and the molecular weight of the acrylamide copolymer with dimethylaminoethyl methacrylate hydrochloride (PAA3) was 3.5×10^6. The content of the ionic units in PAA1, PAA2, and PAA3 was 19.8, 20, and 42%, respectively [5, 6].

The systems in question were studied by sedimentation [7], optical microscopy [7], and colorimetry [8]. The kinetics of sedimentation in the presence of coagulant and flocculants was studied on a VT-500 torsion balance using 1000-ml beakers. The particle-size distribution in the untreated disperse system was studied by optical microscopy (Biolam microscope). The experimental data obtained by this method in 20 series of measurements were treated according to the procedure given in [9]. The particle size in the untreated disperse system was 2.76×10^{-6} m. The colorimetric measurements were carried out on a KFK-2 photocolorimeter (λ = 440 nm, l = 10 mm) using the middle supernatant fraction.

The flocculation power of polyacrylamide copolymers can be quantitatively evaluated using the dimensionless parameter D:

$$D = V/V_0 - 1, \quad (1)$$

Table 1. Chemical composition of wastewater

Parameter	Average content, mg l^{-1}
Formaldehyde	0.2–1.1
Chlorides	1800–2500
Sulfates	100–500
Detergents	80–170
COD	900–2000
Fats	400–600
Soaps	60–100
Suspended compounds	2000–2500
Chromium(III)	5–10
Chromium(VI)	2

1070-4272/04/7703-0497 © 2004 MAIK "Nauka/Interperiodica"

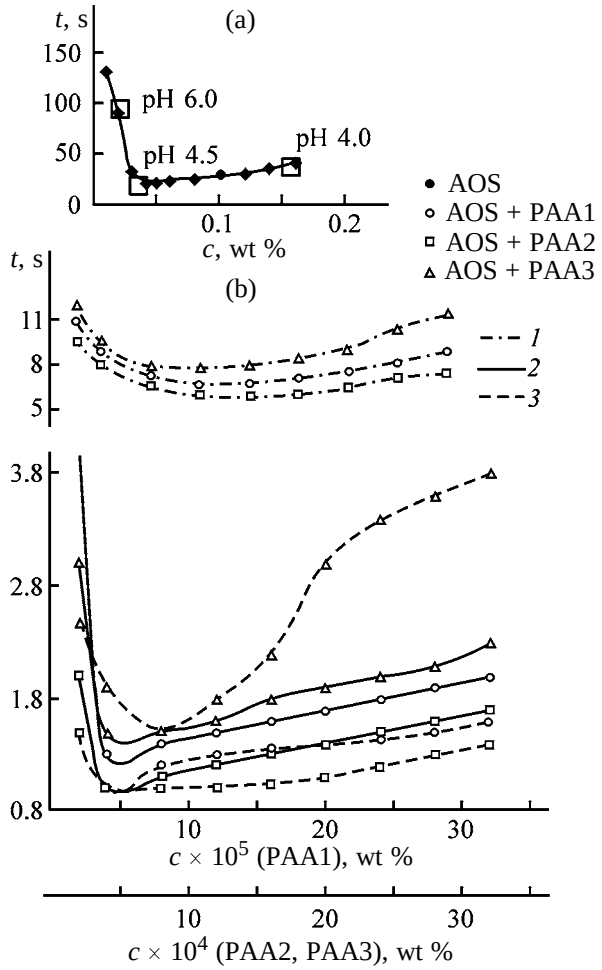

Fig. 1. Time of formation of primary flakes t as influenced by the concentration c of (a) AOS and (b) PAA additives (c_{AOS} = 0.04 wt %). The flocculant was added after AOS coagulant in (*1*) 10 s, (*2*) 20 s, and (*3*) 10 min.

where V and V_0 are the sedimentation rates of the dispersed phase in the presence of the flocculant and without it [10]. We also calculated the flocculating activity λ of each additive:

$$\lambda = D/c = (V/V_0 - 1)c^{-1}, \quad (2)$$

where c is the flocculant concentration.

Available data on the coagulation and flocculation in model and real multicomponent disperse systems [11] show that the study of the mechanisms of interaction involving the dispersed phase (e.g., between the coagulant aggregates and dispersed particles or between the flocculant and coagulant macromolecules, etc.) is of particular importance. The mechanisms of the interparticle interactions between the dispersed phase and dispersion medium can be judged from such macroscopic parameters as the rate of formation of primary flakes, sedimentation rate, etc.

In this work we attempted to evaluate the correlations between the kinetic parameters of flocculation and sedimentation in the presence of AOS and polyacrylamide flocculants.

The dependences of the time of formation of the primary flakes in the disperse system on the concentration of various flocculants and coagulant are shown in Fig. 1. The curve in Fig. 1a exhibits pronounces steep section, which, in our opinion, is probably due to the latent coagulation and formation of the adsorption-active centers and primary aggregates of aluminum hydroxide. The flat section of the curve is related to structuring of the resulting particles and formation of the products of AOS hydrolysis with various size and density parameters, lime factors, and other characteristics [12]. The coagulant concentration corresponding to the inflection in the curve determines the boundary of the optimal concentration range of the coagulant for the given disperse system; the solution pH in this point is 4.5.

As seen from the IR data, the content of paraffin (especially branched) structures strongly decreases after treatment of the disperse system with AOS coagulant. Simultaneously, the contribution of the carboxy groups belonging to acids and esters also decreases, which suggests predominant coagulation of branched aliphatic oxygen-containing compounds.

Thus, we determined the optimal concentration of the coagulant it the stage of formation of the primary flakes (c = 0.04%). Now, by adding flocculant in various time intervals (10 s, 20 s, and 10 min) after the coagulant, we can determine the optimal concentration range of flocculants (Fig. 1b). The flocculant shows high activity, probably related to the intensity and diversity of intermolecular interactions of the flocculants with primary and relatively open mosaic structure of the coagulant. Formation of the secondary particle structures in the presence of the coagulant after prolonged exposure (10 min) does not noticeably affect the interparticle interactions between the coagulant and flocculants as compared to the experiment in which the flocculant was added in 20 s after coagulant addition.

The second series of flocculation experiments was carried out at various pH using different concentrations of the coagulant. As seen from Fig. 2 (pH 6.0, 5.4, 4.0), the flocculation rate is relatively high. Moreover, we can determine the optimal concentrations of flocculants already in the initial stage of flocculation, which is probably due to the properties of aluminum hydroxo complexes.

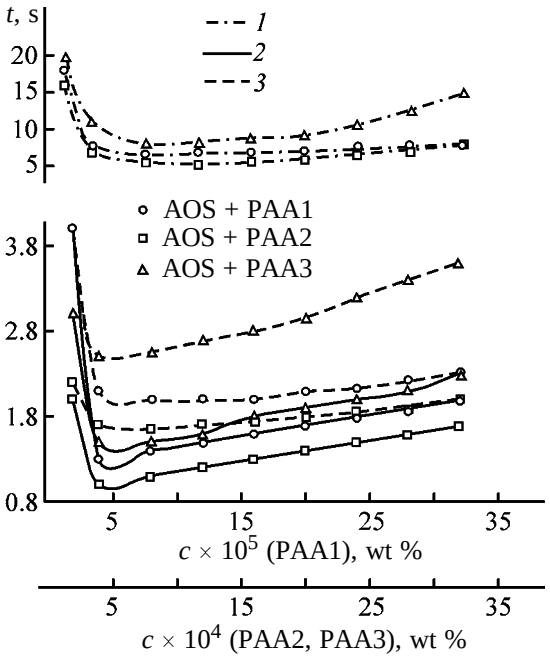

Fig. 2. Time of formation of primary flakes *t* as influenced by the concentration of additives *c*. pH: (*1*) 6.0, (*2*) 4.5, and (*3*) 4.

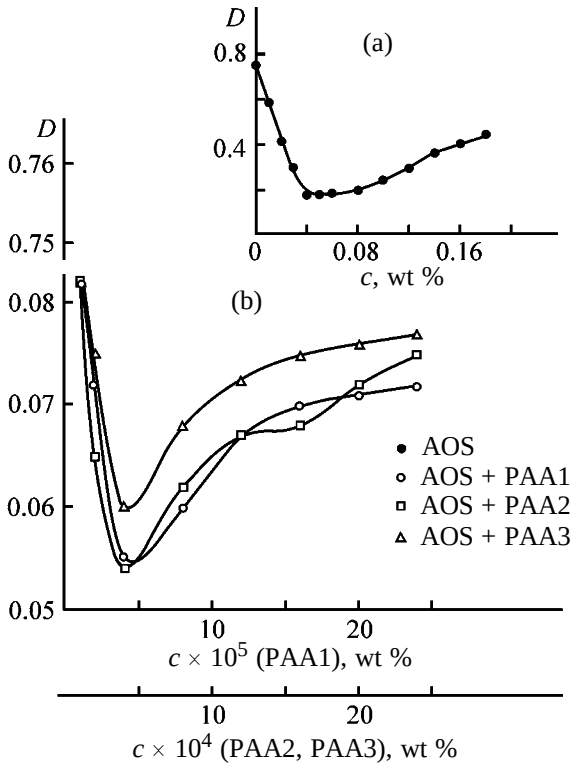

Fig. 3. Optical density *D* of a fat-containing disperse system as influenced by the concentration of additives *c*. Optimal concentration, wt %: AOS 0.04, PAA1 4×10^{-5}, PAA2 4×10^{-4}, and PAA3 4×10^{-4} (recorded 30 min after flocculant addition).

The dependences of the optical density of a fat-containing dispersion on the concentrations of the coagulant and its mixtures with flocculants allow determination of the optimal concentration range for AOS (Fig. 3a). The maximal coagulation power of the reagent is observed in the concentration range 0.04–0.08 wt %; thus, addition of the coagulant to the smallest optimal concentration would considerably decrease its consumption in industry.

Addition of flocculants to the disperse system containing coagulant in the optimal concentration strongly improves the purification quality. The optimal concentrations of the flocculants correspond to the minimum in the curves plotted in the optical density–flocculant concentration coordinates (Fig. 3b).

Further stage in purification of a disperse system is related to formation of the chain structures and coarser aggregates. The curves of the particle sedimentation in the presence of the coagulant and flocculants added in the optimal amounts are shown in Fig. 4.

As seen from Fig. 4, addition of both cationic or anionic flocculants increases the rate of the particle sedimentation. The flocculation power increases with increasing polymer concentration to some optimal value and then decreases (Fig. 5).

Our results (Fig. 5) showed that, at optimal coagulant concentration, the flocculation power of

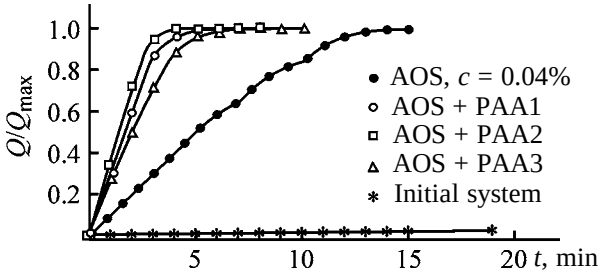

Fig. 4. Kinetic curves of sedimentation of fat dispersions at optimal doses of coagulant and flocculants; (*Q*) sediment amount and (*t*) time. Optimal concentration, wt %: AOS 0.04, PAA1 4×10^{-5}, PAA2 4×10^{-4}, and PAA3 4×10^{-4}; the same for Fig. 5.

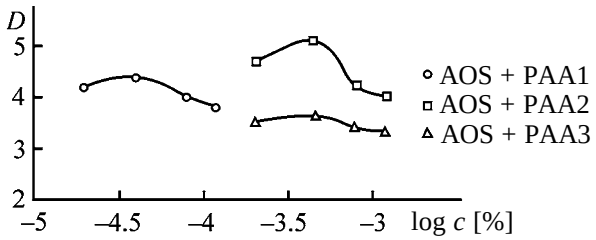

Fig. 5. Flocculation parameter *D* as a function of the flocculant concentration *c*.

anionic acrylamide copolymers is higher than that of the cationic compound. This difference is probably due to the nature of interactions between the negatively charged copolymer macromolecules and positively charged products of coagulant hydrolysis. Formation of hydrogen bonds between the functional groups of the copolymer with the AOS hydroxy groups can also be considered. The repulsion between the dispersed particles and similarly charged flocculant particles levels off the interaction with the primary coagulant structure. Comparison of the flocculation data for similarly charged copolymers PAA1 and PAA2 reveals that the molecular weight of the copolymer strongly affects formation of intermolecular bridges between the flocculant particles and coagulant structures.

The effect of the cationic flocculant added to the disperse system containing coagulant (c_C = const) is slightly lower that that of the anionic copolymers. This is probably due to some "blocking" effect of the positively charged AOS particles and repulsion of similarly charged flocculant and coagulant structures. In this case, the role of hydrogen bonds between the coagulant structures and cationic copolymer macromolecules in the course of flocculation is predominant.

Analysis of the composition of organic compounds remaining in the system after its treatment with AOS and flocculants indicates strong decrease in the optical density of solutions in the 1240–1170 cm^{-1} range.

CONCLUSIONS

(1) Data on sedimentation, primary flocculation, and optical density of fat-containing disperse system demonstrate the possibility of using aluminum oxysulfate as coagulant. The optimal concentration range of the coagulant was determined.

(2) The optimal properties of the coagulant are due to the primary coagulant structure formed by the products of aluminum sulfate hydrolysis.

(3) The data on sedimentation, primary flocculation, and optical density demonstrate rapid particle formation in the presence of flocculants in the stage of flake formation.

(4) The strongest flocculation effect is observed for anionic flocculants. At similar content of the ionic units in macromolecules, the flocculation power of polyacrylamide copolymers increases with increasing molecular weight of the polymer.

REFERENCES

1. Veitser, Yu.I. and Mints, D.M., *Vysokomolekulyarnye flokulanty v protsessakh ochistki prirodnykh i stochnykh vod* (Macromolecular Flocculants in Purification of Natural and Waste Waters), Moscow: Stroiizdat, 1984.
2. Zapol'skii, A.K. and Baran, A.A., *Koagulyanty i flokulyanty v protsessakh ochistki vody* (Coagulants and Flocculants in Water Treatment), Leningrad: Khimiya, 1987.
3. Babenkov, E.D., *Ochistka vody koagulyantami* (Water Treatment with Coagulants), Moscow: Nauka, 1977.
4. Bellamy, L.J., *The Infra-Red Spectra of Complex Molecules*, New: York: Wiley, 1957.
5. Kurenkov, V.F., Snigirev, S.V., Dervoedova, E.A., and Churikov, F.I., *Zh. Prikl. Khim.*, 1999, vol. 72, no. 11, pp. 1892–1896.
6. Churikov, F.I., Snigirev, S.V., and Kurenkov, V.F., *Zavod. Lab.*, 1998, vol. 64, no. 6, pp. 9–10.
7. Frolov, Yu.G., *Kurs kolloidnoi khimii* (Course of Colloidal Chemistry), Moscow: Khimiya, 1982.
8. Bazaz'yan, I.V., Kushekova, O.I., and Il'icheva, I.A., *Zavod. Lab.*, 1972, vol. 38, no. 4, p. 415.
9. Croxton, C.A., *Liquid State Physics: A Statistical Mechanical Introduction*, London: Univ., 1974, p. 421.
10. Myagchenkov, V.A. and Bulidorova, G.V., *Khim. Tekhnol. Vody*, 1993, vol. 15, no. 2, p. 100.
11. Myagchenkov, V.A., Baran, A.A., Bulidorova, G.V., and Berkutov, E.A., *Poliakrilamidnye flokulyanty* (Polyacrylamide Flocculants), Kazan: Kazan Gos. Tekhnol. Univ., 1988.
12. Gerasimenko, N.G., Solomentseva, I.M., and Teselkin, V.V., *Khim. Tekhnol. Vody*, 1994, vol. 16, no. 1, pp. 12–17.

Russian Journal of Applied Chemistry, Vol. 77, No. 3, 2004, pp. 501–504. Translated from Zhurnal Prikladnoi Khimii, Vol. 77, No. 3, 2004, pp. 507–510.

MACROMOLECULAR CHEMISTRY AND POLYMERIC MATERIALS

Properties of Asphalt–Lime-Containing Mineral Powder System

V. V. Yadykina

Shukhov State Technological University, Belgorod, Russia

Received May 6, 2003

Abstract—Strength and water, frost, and heat resistance of asphalt binding compound were studied in relation to the content of calcium oxide.

Asphalt–mineral composite is the main structural component of asphalt concrete; it acts as binder and strongly affects such properties of concrete as density, strength, deformability, resistance to water, frost, and heat, etc. [1].

The quality of asphalt binder (asphalt–mineral powder binary system) is characterized by structural-mechanical properties and their changes under the action of external factors, especially, temperature and water [2].

The stability of these properties depends on the organic binder and mineral powder and their ratio. Since asphalt binder is an ultimately concentrated disperse system, the interaction of the mineral surface with asphalt provides the decisive effect. Hence, the nature of the boundary and, especially, adhesion interaction between the filler and binder determine the properties of composites and their operation stability [2, 3].

It is known that the adhesion of asphalt to mineral materials is determined by their chemical composition. Numerous studies and factory experience show that the best components are finely ground limestone and dolomite [1, 2] chemically interacting with asphalt. These powders are recommended for production of asphalt concrete by GOST (State Standard) 16557–78.

In some cases, industrial wastes can also be used as fillers in production of asphalt concretes, but, according to GOST 9128–97, the content of active CaO + MgO must not exceed 3 wt %.

This limit has virtually no substantiation. Moreover, to activate acidic mineral fillers (rubble and sand) and improve their adhesion to asphalt, lime is added in asphalt concrete mixture in amounts of 1–2% of the total system weight (i.e., 15–20% of the weight of mineral powder) [1, 4].

The data on utilization of finely dispersed industrial wastes containing 15–25% CaO as mineral filler of asphalt concretes indicate that they improve the concrete properties [5].

The aim of this work was to determine the optimal content of calcium oxide in the mineral powder and to study its effect of structuring and properties of the asphalt–lime-containing mineral powder system.

EXPERIMENTAL

We used limestone from the Elets field and lime purchased from the Stroimaterialy Joint-Stock Company (Belgorod, Russia). These mineral components were thoroughly mixed in certain ratios; the properties of the resulting powders are listed in Table 1.

The size distribution and specific surface area of the mineral powders tested were similar (100% sifting through sieve 0.071, 4500 $cm^2\,g^{-1}$ specific surface area).

The asphalt binder was prepared by mixing of the preheated components at 150–160°C for 5–6 min to obtain a uniform mixture.

The optimal charge of asphalt for each composition was determined by the procedure given in [6]. We used BND-60/90 asphalt with the following properties: penetration 21×10^{-1} and 83×10^{-1} mm at 0 and 25°C, respectively; softening point 41°C; extensibility 3.8 and 70 cm at 0 and 25°C, respectively; brittle point 17°C; and flash point 246°C.

The properties of the asphalt–lime-containing mineral powder binary system were studied using cylindrical samples (25 mm in diameter) according to GOST 12784–78.

The interaction with asphalt and structuring processes as influenced by the properties of mineral

1070-4272/04/7703-0501 © 2004 MAIK "Nauka/Interperiodica"

Table 1. Properties of mineral powders

Parameter	GOST requirements	Mineral powders					
		limestone	studied				
Content of active CaO + MgO, no more than	3	0	20	30	40	50	60
Porosity, vol %	45.00	29.60	33.60	35.00	32.34	29.90	27.01
Capacity for asphalt, g, no more than	100	68	82	89	93	105	123

Table 2. Properties of asphalt binder

Parameter	$CaO : CaCO_3$ ratio in the mineral powder					
	0 : 10	2 : 8	3 : 7	4 : 6	5 : 5	6 : 4
Water saturation, wt %	1.81	1.68	1.52	1.24	1.09	0.75
Average density, kg m^{-3}	2170	2180	2190	2190	2230	2240
Swellability, vol %	2.01	1.88	1.73	1.61	1.55	1.46
Compression strength, MPa, at temperature, °C:						
50	3.1	3.6	4.2	4.25	4.4	4.5
20	5.4	5.8	6.2	6.7	7.15	7.0
at 20°C in water-saturated state	4.59	5.2	6.05	7.0	7.55	7.2

powders were studied by IR spectroscopy and conical plastometry.

The results of physicomechanical tests of the asphalt binder shown in Table 2 and in the figure indicate that calcium oxide contained in the mineral powder noticeable affects the properties of the asphalt–lime-containing mineral powder system. With increasing content of CaO to 60%, the average density of the samples increases from 2170 to 2240 kg m^{-3}. Simultaneously, water saturation and swellability decrease from 1.81 and 2.01 to 0.75 and 1.46%, respectively; the sample strength increases. All these facts suggest more active interaction of asphalt with mineral lime-containing filler as compared to the composite based on limestone. This is probably due to the acid–base reaction of asphaltic and naphthenic acids with calcium oxide in the mineral powder and chemisorption on its surface of aromatic acids and other organic compounds (with unsaturated bonds) contained in asphalt.

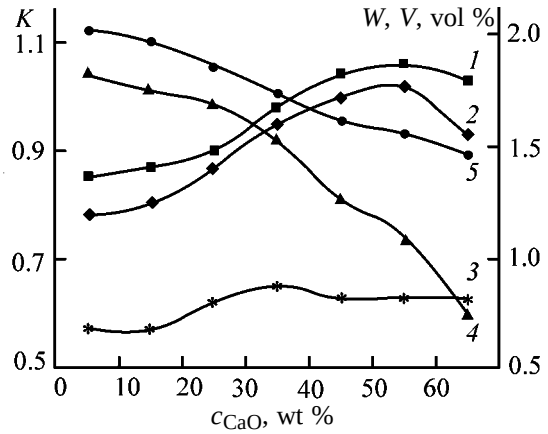

Properties of asphalt binder as influenced by the content of calcium oxide in the mineral powder c_{CaO}. Coefficient *K* of (*1*) water resistance, (*2*) water resistance at prolonged storage, (*3*) heat resistance; (*4*) water saturation *W*, and swellability *V*.

The above assumptions are confirmed by the IR data. The decrease in the intensity of the absorption bands in the 1720–1700 and 1600 cm^{-1} ranges indicates that the content of acids and aromatic compounds participating in the interaction of asphalt with lime-containing mineral powder is smaller than that with the filler based on calcium carbonate.

Formation of calcium hydroxide in the presence of water and mudding of the pores (due to new growths [7]) probably explains the increasing density and decreasing water saturation of the samples.

It was found [1] that free lime, being added in

certain amounts, acts as active filler of asphalt concrete and promotes its structuring.

Our data on structural-mechanical properties of asphalt binder confirmed the above assumption. As seen, in the case of lime-containing mineral powders, the inflection in the dependence of the ultimate shear stress on the degree of filling of the disperse systems is observed at lower degrees of filling as compared to the composites based on limestone. The structuring effect is proportional to the content of calcium oxide in the filler. For example, at 40% content of the limestone-containing mineral powder, the ultimate shear stress was 0.53, and at addition of 20% and 40% lime, the ultimate shear stress increased to 0.69 and 0.79 MPa, respectively. At 60% degree of filling, the ultimate shear stress comprised 1.28, 1.55, and 1.70 MPa, respectively.

With increasing content of calcium oxide in the mineral powder to 50%, the ultimate compression strength at 20°C increases, and at $c_{CaO} > 50\%$ this parameter decreases for samples in both dry and water-saturated states (Table 2).

As seen, maximal increase in the strength of the dry samples is 32.4%, whereas in the case of water-saturated samples it is greater (64.5%); this fact confirms formation of calcium hydrate and filling of the pores.

When the content of lime in the mineral powder is higher than 30%, the compression strength of water-saturated samples at 20°C is greater than that of the dried samples, i.e., the water resistance coefficient is greater than 1 (figure, curve *1*) and reaches a maximum (1.06) at 50 wt % content of CaO in the filler. Though with further increase in the lime content the water resistance coefficient slightly decreases (to 1.03), it does not meet the GOST requirement (no more than 0.8). Similar dependence was registered for the water resistance coefficient at prolonged storage (figure, curve *2*). According to [8], specifically the water resistance of the binary systems exactly determines the intensity of adhesion at the mineral powder–binder boundary.

The ultimate compression strength at 50°C increases in the entire concentration range studied, probably due to the increase in the adhesion, and the maximal increase is 45.2%. This fact is of particular importance, because at 50°C the adhesion of asphalt sharply decreases [9]. The increase in the compression strength at 50°C improves the heat resistance of the samples (figure, curve *3*).

It was found that, after prolonged storage, the strength of the samples based on lime-containing mineral powder with an optimal content of CaO was greater as compared to the limestone-containing samples. For example, the ultimate compression strength of the samples (based on mineral powder containing 40% CaO) stored for 30 days at room temperature and tested at 20 and 50°C increased by 12–14%, whereas the compression strength of the limestone-containing samples remained virtually constant. The tests performed after 6-month storage of the samples showed no changes in the compression strength, i.e., structuring processes were completed.

These results indicate elevated adhesion of the mineral powder and asphalt, which was confirmed in [10], and intensive structuring in the presence of lime. The optimal content of CaO in the mineral powder is 20–50%. At greater content of calcium oxide the parameters of asphalt concrete become worse, probably due to insufficient content of the active components in asphalt, such as naphthenic acids and other oxygen-containing compounds able to bind the reactive mineral component.

CONCLUSIONS

(1) Calcium oxide being added in optimal amounts (20–50 wt %) to the mineral powder increases the strength and water, frost, and heat resistance of the asphalt binder and decreases its water saturation and swellability, which is probably due to the active sorption of asphalt on the mineral powder surface, hydration of lime, and its structuring effect on asphalt.

(2) The experimental data obtained allow prediction of physicomechanical and operation properties of the asphalt concrete pavement at utilization of the lime-containing mineral powder.

REFERENCES

1. *Dorozhnyi asfal'tobeton* (Road Asphalt Concrete), Gezentsvei, L.B., Ed., Moscow: Transport, 1985.
2. Ryb'eva, T.G., *Izv. Vyssh. Uchebn. Zaved., Stroit. Arkhitekt.*, 1960, no. 3, pp. 90–99.
3. Kolbanovskaya, A.S. and Mikhailov, V.V., *Dorozhnye bitumy* (Road Asphalts), Moscow: Transport, 1973.
4. Kuchma, M.I., *Poverkhnostno-aktivnye veshchestva v dorozhnom stroitel'stve* (Surfactants in Road Building), Moscow: Transport, 1980.
5. Gridchin, A.M., Yadykina, V.V., and Vetrov, M.V., *Izv. Vyssh. Uchebn. Zaved., Stroit.*, 2000, no. 10, pp. 50–53.

6. Korolev, I.V., *Dorozhnyi teplyi asfal'tobeton* (Road Warm Asphalt Concrete), Kiev: Vishcha Shkola, 1975.
7. Semirikov, I.S., Vyvarets, L.S., and Vishnevskii, A.A. in *Sbornik dokladov Mezhdunarodnoi nauchno-prakticheskoi konferentsii "Kachestvo, bezopasnost', energo- i resursosberezhenie v promyshlennosti stroitel'nykh materialov i stroitel'stve na poroge XXI veka"* (Coll. of Reports of Int. Scientific-Practical Conf. "Quality, Safety, and Energy- and Resource-Saving in Production of Construction Materials and Building on the Eve of XXI Century"), Belgorod: BelGTASM, 2000, part 2, pp. 353–357.
8. Kovalev, Ya.N., *Aktivatsionno-tekhnologicheskaya mekhanika dorozhnogo asfal'tobetona* (Activation-Technological Mechanics of Road Asphalt Concrete), Minsk: Vysheishaya Shkola, 1990.
9. Ryb'ev, I.A., *Asfal'tovye betony* (Asphalt Concretes), Moscow: Vysshaya Shkola, 1969.
10. Yadykina, V.V., Kuznetsov, D.A., and Vysotskaya, M.A., in *Materialy III Mezhdunarodnoi nauchno-prakticheskoi konferentsii shkoly-seminara molodykh uchenykh, aspirantov i doktorantov "Sovremennye problemy stroitel'nogo materialovedeniya"* (Proc. III Int. Scientific-Practical Conf. Workshop of Young Scientists, Post-Graduate Students, and Persons Working for Doctoral Degree "Modern Problems of Science of Construction Materials"), Belgorod (Russia), October 3–5, 2001, Belgorod: BelGTASM, 2001, part 1, pp. 134–136.

Russian Journal of Applied Chemistry, Vol. 77, No. 3, 2004, pp. 505–506. Translated from Zhurnal Prikladnoi Khimii, Vol. 77, No. 3, 2004, pp. 511–512.

BRIEF COMMUNICATIONS

An Electrochemical Method for Creating a pH Gradient in a Microflow of an Electrolyte

E. A. Ostrovidov and M. N. Ryabova

North-West State Extramural Technical University, St. Petersburg, Russia

Received December1, 2003

Abstract—A method for creating a pH gradient in a microflow of an electrolyte and an installation for the same purpose without any moving parts were developed.

Modern high-performance liquid chromatography (HPLC) is frequently carried out by the method of gradient elution in order to optimize the determinations. In doing so, a modifying substance, which changes the eluting capacity of the mobile phase, is introduced into its flow in the form of a compact zone. By now, introduction techniques based on mechanical agitation of the eluting mixture in mixing chambers of liquid chromatographs have been developed in ample detail [1]. In addition to being technologically complicated, such an approach is hardly possible in microcolumn chromatographic analysis, when the volume of the eluting mixture is several microliters [2]. The method of preformed gradient, which is frequently used in the microcolumn version of HPLC and consists in introducing precisely measured volumes of the eluent of various compositions, is rather laborious [3].

A flow-through porous electrode (FPE) can be used to meter a marker substance into the flow of the mobile phase. In polarization of an FPE made of glassy or activated carbon, there occurs, depending on the polarization sign, a change in the pH of the aqueous mobile phase:

$$\left.\begin{aligned} 2H_2O + 2e &\rightarrow 2OH^- + H_2\uparrow \\ 2H_2O - 4e &\rightarrow 4H^+ + O_2\uparrow. \end{aligned}\right\} \quad (1)$$

The electrochemical method for changing the pH value in a microflow of the electrolyte makes it possible to vary the pH of the mobile phase within six pH units using an FPE with a microvolume of the mobile phase of up to 2–3 μl.

The need in such a method for varying the pH in a microflow of an electrolyte is acute in analysis of amino acids [4]. The schematic of an electrochemical installation that can be used for this purpose is shown in the figure. The mobile phase, which fills vessel *1*, is driven therefrom by compressed helium delivered into the vessel from cylinder *2*. The flow of the mobile phase is directed into the electrochemical cell that contains a graphite FPE through whose pores the mobile phase is filtered. The vessel *1* contains an auxiliary electrode made of platinum-plated titanium and used to polarize the FPE. Depending on the polarization sign, the pH of the mobile phase changes as a result of occurrence of reaction (1) in the pores of the FPE. Further, the modified flow of the mobile phase is delivered to the measuring unit of the installation, which contains a flow-through capillary in-

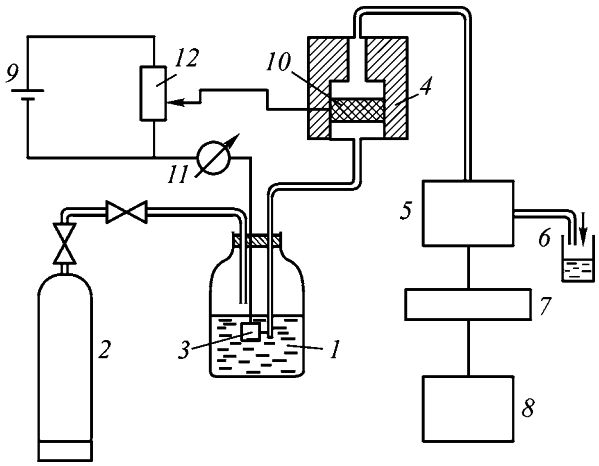

Schematic of an electrochemical acid–alkali generator: (*1*) vessel filled with the mobile phase, (*2*) cylinder with compressed helium, (*3*) titanium electrode, (*4*) casing of the generator cell, (*5*) cell of the control pH-meter with a capillary indicator electrode, (*6*) eluate collector, (*7*) control pH-meter, (*8*) self-recording potentiometer, (*9*) dc power source with variable polarity, (*10*) graphite generator FPE, (*11*) milliammeter, and (*12*) rheostat.

1070-4272/04/7703-0505 © 2004 MAIK "Nauka/Interperiodica"

Experimental and calculated pH values of the mobile phase at different filtration rates

I, mA	$u \times 10^3$, $cm^3\ s^{-1}$	pH of the flow	
		calculation	experiment
0.83	14.2	3.82	3.62
0.91	8.3	3.55	3.58
0.54	8.3	3.77	3.68
0.30	8.3	4.03	4.01
0.11	8.3	4.46	4.50
0.88	5.8	3.40	3.41
0.83	5.8	3.43	3.45
0.61	5.8	3.57	3.52
0.29	5.8	3.89	3.90
0.91	4.2	3.25	3.26
0.90	2.5	3.03	3.05
0.91	1.6	2.83	2.78

dicator electrode made of Corning 015 glass and having a hydrogen function [4].

The volume of the measuring capillary of the transducer was 20 mm^3. The geometric thickness of the generator FPE was found from the condition of decay of the electrochemical process in the porous medium of the electrode. The calculations performed demonstrated that the thickness of the generator FPE should be 0.4–0.5 cm.

With the four-electron mechanism of the electrode reaction, the concentration c of ions being regenerated was calculated using the Faraday law:

$$c = \frac{I}{4Fu},$$

where I is the polarization current; F, the Faraday number; and u, the filtration rate of the mobile phase.

The table lists the calculated and experimental pH values of the mobile phase composed of a 0.1 M KCl solution.

The table shows that the results of calculation coincide with the experimentally measured pH values. In solutions having higher buffer capacity, compared to an aqueous solution of potassium chloride, the current of polarization of the generator FPE should be raised to 200–500 mA, depending on the buffer capacity of the mobile phase used. For example, to change the pH of a citrate buffer solution that contains potassium citrate, hydrochloric acid, thiodiglycol, detergent, and caprylic acid [1] from 4.26 to 8.30 at a filtration rate of the mobile phase equal to 5 $cm^3\ s^{-1}$, it is necessary to maintain the current at about 240 mA.

CONCLUSION

An electrochemical method for creating a pH gradient in a microflow of an electrolyte and an installation for this purpose, which contains no moving parts and makes it possible to vary the pH value within six units, were suggested. The volume of the generation chamber is about 20 mm^3.

REFERENCES

1. *Liquid Column Chromatography: A Survey of Modern Techniques and Applications*, Deyl, Zd., Macek, K., and Janak, J., Eds., Amsterdam: Elsevier, 1975.
2. Kiselev, A.V., Poshkus, D.P., and Yashina, Ya.I., *Molekulyarnye osnovy adsorbtsionnoi khromatografii* (Molecular Foundations of Adsorption Chromatography), Moscow: Khimiya, 1986.
3. Belen'kii, B.G., Gankina, E.S., and Mal'tsev, V.G., *Zh. Vses. Khim. O–va. im. D.I. Mendeleeva*, 1983, vol. 28, no. 1, pp. 43–47.
4. Bates, R.G., *Determination of pH, Theory and Practice*, New York: Wiley, 1964.

Russian Journal of Applied Chemistry, Vol. 77, No. 3, 2004, p. 507. Translated from Zhurnal Prikladnoi Khimii, Vol. 77, No. 3, 2004, p. 513.

BRIEF COMMUNICATIONS

New Cooling Mixtures Containing Sodium Acetate Trihydrate

I. M. Osadchenko and A. P. Tomilov

State Research Institute of Organic Chemistry and Technology, Moscow, Russia

Received December 30, 2003

Abstract—Binary cooling mixtures consisting of $CH_3COONa \cdot 3H_2O$ and NH_4NO_3, $Al(NO_3)_3 \cdot 9H_2O$, or $Ni(NO_3)_2 \cdot 6H_2O$ were developed. They allow the initial temperature to be decreased by 18–19°C. Application of the mixtures does not require additional consumption of water.

Recently there has been an interest in problems of small-scale power engineering for the purpose of power saving. One of the routes to power saving is the development of materials and devices based on the use of physicochemical properties of substances, e.g., of cooling mixtures. Cooling mixtures as autonomous sources of cold are used in laboratory and everyday practice and for cooling and transportation of biological materials (e.g., vaccines, blood, etc.) [1–3].

Numerous compositions of cooling mixtures containing solid salts and water (ice) have been described. A temperature decrease on mixing them is due to the absorption of heat upon salt dissolution [1]. For example, a ternary mixture containing (wt %) NH_4NO_3 40.62, Na_2CO_3 40.62, and $CuSO_4$ 0.76 is produced for everyday use under the Shal'tis brand name [2]. The temperature decrease on dissolving this mixture in water is 10°C (difference in the temperatures before and after mixing). The drawback of this mixture is relatively low performance. A search for new mixtures is an urgent problem.

Mixtures containing $CH_3COONH_4 \cdot 3H_2O$ were tested previously. The test procedure is described in [4].

The tests performed showed that mixtures containing $CH_3COONa \cdot 3H_2O$ and NH_4NO_3, $Al(NO_3)_3 \cdot 9H_2O$, or $Ni(NO_3)_2 \cdot 6H_2O$ are the most effective. It is important that the binary mixtures found are applied without using free water. Evidently, the process occurs with participation of water of crystallization. We found no data on such mixtures in the literature.

Let us give a typical example of application of the cooling mixture. A 100-ml beaker was charged with 5.0 g of $CH_3COONa \cdot 3H_2O$ and then 7.0 g of NH_4NO_3 (as powders), and the temperature was recorded with a thermometer placed inside the beaker. The initial temperature was 21.5°C. The minimal temperature was 2.0°C after stirring for 2.0–2.5 min and 3.0°C after stirring for 4.0–5.0 min. The temperature difference was 19.5°C. The mixture after stirring becomes a suspension. The results of similar tests with mixtures of other compositions are presented in the table. The table shows that, at the component weight ratios from 1 : 0.5 to 1 : 2.9, the temperature decrease is from 17.5 to 29.5°C, i.e., the mixtures show considerably higher performance than Shal'tis. Moreover, the mixture proposed is simpler in use.

Performance of binary cooling mixtures

Second component	CH_3COONa, g	$M(NO_3)_n$, g	CH_3COONa : $M(NO_3)_n$	ΔT, °C
NH_4NO_3	6	6	1 : 1	20.5
	7	4	1 : 0.6	20.0
	8	4	1 : 0.5	17.5
$Ni(NO_3)_2 \cdot 6H_2O$	7	7	1 : 1	25.5
	7	14	1 : 2	26.5
$Al(NO_3)_3 \cdot 9H_2O$	7	20	1 : 2.9	22.5
	7	7	1 : 1	29.0
	7	14	1 : 2	29.5

REFERENCES

1. *Kratkii slovar' khimika* (Concise Chemist's Dictionary), Perel'man, V.I., Compiler, Moscow: Khimiya, 1964.
2. Goryainova, T.S., Isaev, P.V., Manakova, G.V., *et al*., *Tovary bytovoi khimii* (Goods of Household Chemistry), Moscow: Ekonomika, 1975.
3. *Spravochnik po veterinarno-zootekhnicheskomu i laboratornomu oborudovaniyu* (Reference Book on Veterinary-Zootechnic and Laboratory Equipment), Makeev, A.S., Ed., Moscow: Kolos, 1966.
4. Semishin, V.I., *Praktikum po obshchei khimii* (Practical Course of General Chemistry), Moscow: Khimya, 1967.

1070-4272/04/7703-0507 © 2004 MAIK "Nauka/Interperiodica"

Russian Journal of Applied Chemistry, Vol. 77, No. 3, 2004, pp. 508–510. Translated from Zhurnal Prikladnoi Khimii, Vol. 77, No. 3, 2004, pp. 514–516.

BRIEF COMMUNICATIONS

Thermochemical Characteristics of a Series of Terpenoids, Alkaloids, and Flavonoids

B. K. Kasenov, Zh. K. Tukhmetova, Sh. B. Kasenova, A. Zh. Abil'daeva, and S. M. Adekenov

Institute of Phytochemistry, Ministry of Education and Science of the Kazakhstan Republic, Karaganda, Kazakhstan

Received November 13, 2003

Abstract—The heats of combustion and melting of a series of natural terpenoids, alkaloids, and flavonoids were estimated by approximate thermochemical methods. From these quantities, the standard heats of formation of the compounds in the liquid (molten) and solid states were calculated.

Natural terpenoids, alkaloids, and flavonoids exhibit a wide spectrum of biological activity, and valuable drugs have been developed on their basis. However, data on the thermochemical and thermodynamic characteristics of these natural compounds, required to simulate physicochemically their synthesis and to reveal correlations between structural and energy characteristics of these substances, are lacking. Our goal was to estimate the thermochemical characteristics (heats of combustion, melting, and formation) of some terpenoids, alkaloids, and flavonoids using indirect approximate methods.

The standard enthalpies of combustion of the compounds were calculated by the Karash and Frost equations [1] applicable to complex organic substances in the liquid state. The heats of combustion calculated by both methods, and also the mean values, are given in the table.

The Karash method takes into account the presence of lactone rings, various functional groups, and number of shifted electrons. The Frost method takes into account the presence of aromatic rings, cyclenes, and double bonds in rings and side chains of cyclenes.

From the mean values of ΔH^0_{comb}, using the Hess law and proceeding from the reactions

$$C_aH_bO_{c(l)} + (a + b/4 - c/2)O_{2(g)} = aCO_{2(g)} + b/2\,H_2O_{(l)} - \Delta H^0_{comb}, \quad (1)$$

$$C_aH_bN_dO_{c(l)} + (a + b/4 - c/2 + d/4)O_{2(g)} = aCO_{2(g)} + b/2H_2O_{(l)} + d/2N_2 - \Delta H^0_{comb}, \quad (2)$$

we calculated the standard enthalpies of formation of the compounds in the liquid state (see table). The quantities $\Delta_f H^0(298.15)$ for CO_2(g) and H_2O(l) were taken from [2].

Since at the standard temperature (298.15 K) the compounds are in the crystalline state, it is necessary to calculate $\Delta_f H^0(298.15)$ for the solid compounds. To do this, we estimated ΔH^0_m of these compounds by the Gambill equation recommended in [3]:

$$\Delta H^0_m/T_m = 20.72 \times 10^{0.00324M}, \quad (3)$$

where M is the molecular weight of the compound.

The results of calculation of ΔH^0_m are given in the table. The melting points of terpenoids, alkaloids, and flavonoids were taken from [4–10].

From the equations

$$\Delta_f H^0(298.15)\,C_aH_bO_{c(s)} = \Delta_f H^0(298.15)\,C_aH_bO_{c(l)} - \Delta H^0_m, \quad (4)$$

$$\Delta_f H^0(298.15)\,C_aH_bN_dO_{c(s)} = \Delta_f H^0(298.15)\,C_aH_bN_dO_{c(l)} - \Delta H^0_m, \quad (5)$$

we calculated the standard enthalpies of formation of the compounds in the crystalline state (see table).

1070-4272/04/7703-0508 © 2004 MAIK "Nauka/Interperiodica"

Thermochemical characteristics of terpenoids, alkaloids, and flavonoids

Compound	$-\Delta H^0_{comb}$, kJ mol^{-1}			ΔH_m, kJ mol^{-1}	$\Delta_f H^0(298.15)$, kJ mol^{-1}	
	Karash	Frost	mean		liquid	solid
Terpenoids						
Austricin $C_{15}H_{18}O_4$	8256	8556	8406	54.8	74.8	129.6
Artemisin $C_{15}H_{18}O_4$	8256	8556	8406	69.3	74.8	144.1
Anobin $C_{15}H_{20}O_5$	8365	8774	8569	75.0	197.4	272.4
Arborescin $C_{15}H_{20}O_3$	8665	8747	8706	54.3	61.0	115.3
Artausin $C_{15}H_{22}O_3$	8855	8965	8910	63.4	143.0	206.4
Arlatin $C_{15}H_{22}O_4$	8692	8965	8828	71.0	224.4	295.4
Artemin $C_{15}H_{22}O_4$	8474	8937	8706	75.4	347.0	422.4
Artepaulin $C_{15}H_{22}O_3$	8801	8937	8869	57.2	184.0	241.2
Grosshemin $C_{15}H_{18}O_4$	8310	8610	8460	69.3	20.04	90.0
Grossmisin $C_{15}H_{18}O_4$	8256	8556	8406	62.8	74.8	137.6
Gracillin $C_{15}H_{20}O_3$	8610	8747	8679	49.7	88.0	137.7
Tauremisin $C_{15}H_{20}O_4$	8447	8747	8597	66.4	170.0	236.3
Hanphyllin $C_{15}H_{20}O_3$	8719	8828	8774	61.0	6.73	54.3
Alkaloids						
Aconine $C_{25}H_{41}NO_9$	14 022	15 368	14 695	348.0	1013.0	1361.0
Aconitine $C_{34}H_{47}NO_{11}$	18 435	19 191	19 191	1213.0	919.0	2132.0
Harmaline $C_{13}H_{14}N_2O$	6702	7329	7016	53.5	105.2	159.0
Harmalol $C_{12}H_{12}NO$	5981	6675	6328	40.3	113.0	153.3
Glaucine $C_{21}H_{25}NO_4$	11 280	12 043	11 662	110.5	182.0	293.5
3-Deoxyaconitine $C_{34}H_{47}NO_{10}$	18 272	19 946	19 109	1013.2	1001.0	2014.2
9-Deoxylappaconitine $C_{32}H_{44}N_2O_7$	17 901	18 828	18 365	673.0	528.3	1201.3
Deoxypeganidine $C_{14}H_{16}N_2O$	7302	7956	7629	40.0	172.0	212.0
Deoxypeganine $C_{11}H_{12}N_2$	5749	6212	5976	27.0	72.0	99.0
Isolappaconitine $C_{32}H_{44}N_2O_8$	17 698	18 747	18 222	744.0	671.0	1415.0
Caffeine $C_8H_{10}N_4O_2$	3732	4632	4182	44.5	398.3	443.0
Lappaconine $C_{23}H_{37}NO_6$	13 041	14 060	13 550	180.0	798.0	978.0
Lupinine $C_{10}H_{19}NO$	6049	6430	6240	25.0	415.0	440.0
Flavonoids						
Apigenin $C_{15}H_{10}O_5$	6883	7657	7270	95.3	66.8	162.1
Bonanzin $C_{19}H_{18}O_8$	9156	10 272	9714	145.0	342.0	487.0
Isorhamnetin $C_{16}H_{12}O_7$	7400	8311	7855	126.5	161.0	287.5
Casticin $C_{19}H_{18}O_8$	9293	10 229	9761	149.5	295.0	444.5
Kaempferol $C_{15}H_{10}O_6$	6883	7657	7270	96.0	66.8	162.8
Luteolin $C_{15}H_{10}O_6$	6897	7657	7277	105.5	59.7	165.2
Rhamnetin $C_{16}H_{12}O_7$	7400	8311	7855	124.5	161.0	285.5
Rhamnocitrin $C_{16}H_{12}O_6$	7603	8311	7957	96.5	59.5	156.0
Salvigenin $C_{18}H_{16}O_6$	8842	9662	9262	111.0	124.0	235.0
Tricin $C_{17}H_{14}O_7$	7918	8965	8441	135.0	255.0	390.0
Chrysoeriol $C_{16}H_{12}O_6$	7400	8311	7855	117.0	161.0	278.0
Cirsiliol $C_{17}H_{14}O_7$	7918	8965	8441	134.0	255.0	389.0
Cirsilineol $C_{18}H_{16}O_7$	8639	9575	9107	128.4	269.1	397.5

CONCLUSIONS

(1) Previously unknown enthalpies of combustion, melting, and formation of a series of terpenoids, alkaloids, and flavonoids were calculated.

(2) The results are of interest for predicting the thermodynamic properties of related compounds and simulating their synthesis. They can also be included in basic handbooks and data bases.

ACKNOWLEDGMENTS

The study was financially supported by the Grant Agreement of the Science Foundation of the National Academy of Sciences of the Kazakhstan Republic, Research Program PFI 2-2-2.4-2 (31)–II of March 11, 2003.

REFERENCES

1. Kazanskaya, A.S. and Skoblo, V.A., *Raschety khimicheskikh ravnovesii* (Calculations of Chemical Equilibria), Moscow: Vysshaya Shkola, 1974.
2. Viktorov, V.V., *Metody vychisleniya fiziko-khimicheskikh velichin i prikladnye raschety* (Methods for Calculating Physicochemical Quantities and Applied Calculations), Moscow: Khimiya, 1977.
3. Ryabin, V.A., Ostroumov, M.A., and Svit, T.F., *Termodinamicheskie svoistva veshchestv: Spravochnik* (Thermodynamic Properties of Substances: Handbook), Leningrad: Khimiya, 1977.
4. Kagarlitskii, A.D., Adekenov, S.M., and Kupriyanov, A.N., *Seskviterpenovye laktony rastenii Tsentral'nogo Kazakhstana* (Sesquiterpene Lactones from Plants Growing in Central Kazakhstan), Alma-Ata: Nauka, 1987.
5. Irismetov, M.P., Dzhiembaev, B.Zh., Arystanova, T.A., and Baramysova, G.T., *Khimiya i primenenie prirodnoi glitsirrizinovoi kisloty i ee proizvodnykh* (Chemistry and Applications of Natural Glycyrrhizic Acid and Its Derivatives), Almaty, 2002.
6. Arystanova, T.P. and Abdieva, A.K., *Standartizatsiya lekarstvennykh preparatov* (Stadnardization of Drugs), Shymkent, 2001.
7. Shakirov, R., Telezhenetskaya, M.V., Bessonova, I.A., *et al.*, *Khim. Prirodn. Soedin.*, 1996, no. 2, pp. 248–335.
8. Shakirov, R., Telezhenetskaya, M.V., Bessonova, I.A., *et al.*, *Khim. Prirodn. Soedin.*, 1996, no. 3, pp. 421–510.
9. Shakirov, R., Telezhenetskaya, M.V., Bessonova, I.A., *et al.*, *Khim. Prirodn. Soedin.*, 1996, no. 4, pp. 633–800.
10. Pribytkova, L.N. and Adekenov, S.M., *Flavonoidy rastenii roda Artemisia* (Flavonoids of Plants of *Artemisia* Genus), Almaty: Gylym, 1999.

Russian Journal of Applied Chemistry, Vol. 77, No. 3, 2004, pp. 511–512. Translated from Zhurnal Prikladnoi Khimii, Vol. 77, No. 3, 2004, pp. 517–518.

BRIEF COMMUNICATIONS

Hydrogenation of Ethyl *p*-Nitrobenzoate on Carbon-Supported Palladium–Triphenylphosphine Catalyst

I. I. Obraztsova and O. A. Efimov

Kemerovo Branch, Institute of Solid-State Chemistry and Mechanochemistry, Siberian Division, Russian Academy of Sciences, Kemerovo, Russia

Received August 6, 2003

Abstract—Hydrogenation of ethyl *p*-nitrobenzoate on carbon-supported palladium–triphenylphosphine catalyst at 40°C and atmospheric pressure of H_2 was studied.

Hydrogenation of ethyl *p*-nitrobenzoate (ENB) attracts particular attention, since the reaction product is ethyl *p*-aminobenzoate (EAB), which is an anesthetic (medical name Anesthesin) and an intermediate in synthesis of novocaine.

Anesthesin is synthesized in industry by reduction of ENB in aqueous solution with the system iron powder–ammonium chloride [1–3]:

$$p\text{-}NO_2C_6H_4CO_2Et + Fe + NH_4Cl \leftrightarrows p\text{-}NH_2C_6H_4CO_2Et + H_2O. \quad (1)$$

Reaction (1) is performed at 96–98°C; the yield of the target product does not exceed 90%, and it requires additional time-consuming purification. The synthesis is labor-consuming; it is performed under severe conditions, is accompanied by formation of colored by-products, and involves dilution of the reaction mixture with water, washing, and separation of the metallic slime, which gives rise to environmental problems.

The majority of the above problems can be avoided by performing catalytic hydrogenation of ENB with molecular hydrogen:

$$p\text{-}NO_2C_6H_4CO_2Et + H_2 \xleftrightarrow{\text{Cat.}} p\text{-}NH_2C_6H_4CO_2Et + H_2O. \quad (2)$$

Some implementations of this process are reported in [4–8]. In some cases [4–6], classical heterogeneous hydrogenation catalysts based on platinum group metals were used. The reaction was performed at atmospheric or elevated [4] H_2 pressure; the reaction temperature was varied from 20 to 80°C. The yield of Anesthesin did not exceed 90%. The drawbacks of these procedures are high consumption of Pd (5 wt%), its inefficient utilization, the necessity of the catalyst purification after every run, and severe reaction conditions (high pressure, elevated temperature, corrosive medium). In other works [7, 8], EAB was prepared on metal–polymer catalysts such as palladium-containing anion exchangers A-17-8-Pd and AN-1-Pd. The reaction was performed at 30–45°C and H_2 pressure of 1 atm; the yield was 98–100%. The major drawback of the process is relatively low reaction rate on such catalysts (by an order of magnitude lower than on Pd/C catalysts).

Thus, search for new, more effective catalysts of reaction (2) remains an urgent problem. In this connection, we studied hydrogenation of ENB on carbon-supported palladium–triphenylphosphine catalyst.

EXPERIMENTAL

Carbon-supported palladium–triphenylphosphine catalyst was prepared as follows: 2.11 g of palladium acetate and 0.985 g of triphenylphosphine were dissolved in 200 ml of acetone in an inert atmosphere (N_2, Ar), 50 g of a carbon support was added in an inert gas flow, and the mixture was stirred at room temperature until the solution became fully colorless. Then the reactor was purged with H_2 for 5 min, and the catalyst was reduced at 20–40°C for 4–6 h with vigorous stirring. The catalyst was filtered off, dried in a vacuum, and stored in an inert atmosphere. The resulting catalyst contained no more than 2 wt % Pd.

Reduction of ENB was performed in ethanol or 2-propanol at 40°C with H_2 at atmospheric pressure. The reactants were loaded in an inert gas atmosphere.

1070-4272/04/7703-0511 © 2004 MAIK "Nauka/Interperiodica"

Hydrogenation of ENB was also performed at atmospheric pressure in a temperature-controlled reactor at 30–40°C. The components were also loaded in an inert gas atmposphere (N_2 or Ar) to prevent their oxidation with atmospheric oxygen and thus improve the product quality. After loading the catalyst prepared, ENB, and solvent, the whole system was kept at the required temperature for 3–5 min and purged with H_2 for 5 min, after which vigorous stirring was started. After the uptake of the theoretical amount of hydrogen, the reaction stops. The next portion of ENB is fully hydrogenated in the same time. The catalyst can effect hydrogenation of up to 50 portions of ENB without noticeable loss in the activity.

The total amount of converted ENB per gram of Pd is 29250 g on the average. The yield of Anesthesin is quantitative (chromatographic analysis data).

The spent catalyst can be separated, regenerated, and then reused without noticeable loss in the activity.

The high activity and long life of the suggested catalyst are due to its structural features. As shown in [9], deposition of palladium on carbon supports followed by reduction with hydrogen results in formation of cluster complexes in which triphenylphosphine molecules stabilize palladium particles of definite size (optimal ratio $PPh_3/Pd \approx 0.4$), exhibiting the highest catalytic activity. This allows the hydrogenation rate and yield of the target product to be considerably increased; it also ensures long working life of the catalyst without noticeable loss in the activity.

The preservation of the catalyst activity is also favored by mild synthesis conditions (H_2 pressure 1 atm; temperature up to 40°C; anhydrous medium; single-component solvent readily removable by evaporation in isolation of the target product). It is also important that the solvents used are not involved in side reactions and are not so toxic as, e.g., toluene, benzene, or methanol used in alternative procedures [4, 8] (which is very important in preparation of pharmaceuticals); also, they do not require time-consuming washing of the finished product.

It should be noted that, with ultradispersed diamond used as catalyst support, the hydrogenation rate appreciably increases [10].

Thus, we have improved the hydrogenation process: the service life of the catalyst was increased many-fold; the process was made simpler and shorter; the high pharmacopoeia quality of the finished product and its ~100% yield were attained.

CONCLUSIONS

(1) A carbon-supported palladium–triphenylphosphine catalyst was suggested for preparation of Anesthesin of high pharmacopoeia quality in a quantitative yield.

(2) Anesthesin is prepared in one step under mild conditions without by-products. Fifty synthesis runs can be performed with one catalyst portion, after which it can be regenerated and reused.

REFERENCES

1. USSR Inventor's Certificate no. 609278.
2. USSR Inventor's Certificate no. 753069.
3. USSR Inventor's Certificate no. 492514.
4. US Patent 3037046.
5. Simonov, A.P., Chuvilin, A.L., Moroz, E.M., *et al.*, Abstracts of Papers, *II Vsesoyuznaya konferentsiya "Kataliz i kataliticheskie protsessy khimfarmproizvodstva"* (II All-Union Conf. "Catalysis and Catalytic Processes in Production of Pharmaceuticals"), Moscow, October 8–10, 1989, part 2, p. 248.
6. Klyuev, M.V., *Zh. Org. Khim.*, 1984, vol. 20, no. 9, pp. 1908–1912.
7. Abdullaev, M.G., Abstracts of Papers, *12-ya Mezhdunarodnaya konferentsiya molodykh uchenykh po khimii i khimicheskoi tekhnologii, posvyashchennaya 100-letiyu obrazovaniya Rossiiskogo khimiko-tekhnologicheskogo univ.* (12th Int. Conf. of Young Scientists on Chemistry and Chemical Technology, Dedicated to the Centennial of Foundation of the Russian Univ. of Chemical Engineering), Moscow, November–December 1998, p. 90.
8. Morogina, A., Nasibulin, A.A., and Klyuev, M.V., *Neftekhimiya*, 1998, vol. 38, no. 4, pp. 277–281.
9. RF Patent 2203885.
10. Obraztsova, I.I., Efimov, O.A., Simenyuk, G.Yu., and Min'kov, A.I., in *Trudy Mezhdunarodnoi nauchno-prakticheskoi konferentsii "Khimiya – XXI vek: novye tekhnologii, novye produkty"* (Proc. Int. Scientific and Practical Conf. "Chemistry—XXI Century: New Technologies, New Products"), Kemerovo, December 5–8, 2000, pp. 62–66.

Russian Journal of Applied Chemistry, Vol. 77, No. 3, 2004, pp. 513–514. Translated from Zhurnal Prikladnoi Khimii, Vol. 77, No. 3, 2004, pp. 519–520.

BRIEF COMMUNICATIONS

Chloromethylation of Benzyltoluenes with Chlorodimethyl Ether

D. A. Pisanenko and Yu. I. Smirnov-Zamkov

Kiev Polytechnic Institute, National Technical University of Ukraine, Kiev, Ukraine

Received November 6, 2003

Abstract—Chloromethylation of a mixture of benzyltoluenes with chlorodimethyl ether in CCl_4 at 65°C in the presence of Fe, FeO, Fe_3O_4, Fe_2O_3, $ZnCl_2$, $FeCl_3$, and a cation-exchange resin (KU-2 × 8chS) was studied.

Macromolecular chloromethylated derivatives are used for preparing metal corrosion inhibitros, antimicrobial agents, and anion-exchange resins [1–3]; they show increased performance when used in multicomponent mixtures. It is interesting to test as components of such mixtures chloromethylation products of commercial hydrocarbons, e.g., diarylmethanes used as liquid dielectrics and heat carriers [4, 5]. Their chloromethylation with chlorodimethyl ether allows HCl to be eliminated from the process [6].

Here we report on chloromethylation of a 35 : 55 : 10 mixture of mono-, di-, and tribenzyltoluenes (**I**) with chlorodimethyl ether **II** in CCl_4 at 65°C in the presence of various catalysts:

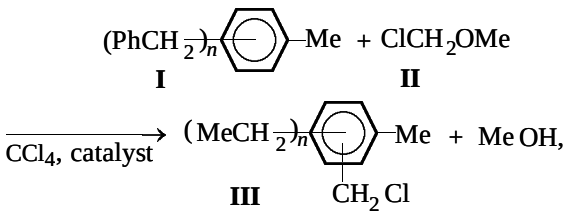

where n = 1–3 (see table).

The chloromethylation efficiency was studied in relation to the molar ratio of benzyltoluenes **I** to chlorodimethyl ether **II**, kind and amount of the catalyst, and reaction time. The number of incorporated CH_2Cl groups was determined from the intensity of the methylene proton signals in the ^1H NMR spectra [7]; both reaction mixtures and final products were sampled. The conditions and results of the experiments are given in the table.

As seen from the table, Fe_2O_3, $FeCl_3$, and $ZnCl_2$ show high catalytic activity in the process; the number of incorporated CH_2Cl groups can be controlled by varying the amount of the catalyst (run nos. 15–21) and the excess of chlorodimethyl ether (run nos. 8–11). At too long reaction time, the content of CH_2Cl

Conditions and results of chloromethylation of benzyltoluenes **I** with chlorodimethyl ether **II**

Run no.	Catalyst, wt % relative to **I**	Excess of **II**, mol	τ, h	Number of incorporated CH_2Cl groups
1	Fe, 3	2.5	4	0.86
2	″	2.5	8	1.02
3	Fe, 1.5	2.5	5	1.85
4	FeO, 1.5	2.5	5	1.80
5	Fe_2O_3, 1.5	2.5	1	1.10
6	″	2.5	2.5	1.70
7	″	2.5	5	1.90
8	Fe_3O_4, 1.5	1.2	5	1.00
9	″	1.5	5	1.20
10	″	2.5	5	1.96
11	″	3.0	5	2.20
12	$FeCl_3$(anhydr.), 1.5	2.5	5	2.10
	$FeCl_3 \cdot 6H_2O$:			
13	1.5	2.5	5	1.63
14	3	2.5	5	1.75
	$ZnCl_2$(anhydr.):			
15	0.1	2.5	6	0.55
16	0.2	2.5	6	0.65
17	1.0	2.5	6	0.85
18	2.0	2.5	5	1.85
19	2.0	2.5	12	1.70
20	5.0	2.5	5	1.90
21	25.0	2.5	5	1.95
	KU-2 × 8chS, 10% moisture content:			
22	10.0	2.5	5	1.10
23	10.0	2.5	12	1.30
24	25.0	2.5	6	1.51
25	KU-2 × 8chS anhydrous, 25.0	2.5	6	1.60
26	″	2.5	12	1.50

1070-4272/04/7703-0513 © 2004 MAIK "Nauka/Interperiodica"

groups starts to decrease (run no. 19), probably owing to condensation of chloromethylated benzyltoluenes. The optimal content of anhydrous $ZnCl_2$ is 2 wt % relative to benzyltoluenes, as with larger amounts of the catalyst (run nos. 20, 21) the content of CH_2Cl groups does not noticeably grow, whereas at smaller amounts (1 wt % and less) it drastically decreases (run nos. 15–17). A cation-exchange resin, KU-2 × 8chS, is also suitable as catalyst, but it should be taken in amount as large as 25 wt % relative to benzyltoluenes (run nos. 24–26).

Iron(III) oxides are promising as catalysts of this reaction, as they show high performance and can be readily separated by filtration. Chloromethylated benzyltoluenes, after purging with nitrogen and distilling off the solvent, can be used in various processes as compounds with a labile chlorine atom [8]; unchanged benzyltoluenes can be reused.

EXPERIMENTAL

Chlorodimethyl ether was prepared by passing HCl through a mixture of paraform and methanol [6]; a 35 : 55 : 10 mixture of mono-, di- and tribenzyltoluenes was prepared by alkylation of toluene with benzyl chloride in the presence of anhydrous $FeCl_3$ [9] or taken as a ready commercial product (used as liquid dielectric) [4]. The GLC analysis was performed on a Biokhrom device (5% SE-30 on Chromosorb W, carrier gas He). The ^{1}H NMR spectra were recorded on a Tesla BS-487 spectrometer (80 MHz); internal reference tetramethylsilane.

Chloromethylation was performed following the procedure from [6]. A reactor was charged with 50 g of a mixture of benzyltoluenes, and 100 ml of CCl_4 and the required amount of the catalyst were added. The mixture was heated with stirring to 65°C, and a solution of the required amount of chlorodimethyl ether in 50 ml of CCl_4 was added over a period of 0.5 h. Then the stirring was continued for the required time. After reaction completion, the catalyst was filtered off, the filtrate was purged with nitrogen, the solvent was distilled off, and a sample was withdrawn for taking a ^{1}H NMR spectrum. Samples of the reaction mixture in the course of the reaction were taken and treated similarly. Characteristic results are given in the table.

REFERENCES

1. Reshetnikov, S.M., *Ingibitory kislotnoi korrozii metallov* (Inhibitors of Acid Corrosion of Metals), Leningrad: Khimiya, 1986.
2. USSR Inventor's Certificate no. 557 793.
3. Talzi, V.P., Ignashin, S.V., Chudinova, I.P., *et al.*, *Zh. Prikl. Khim.*, 1998, vol. 71, no. 11, pp. 1843–1848.
4. Berger, N., Nonpolar Impregnating Formulation Ugilec C-101, *Symp. Boller–Prodelec*, France, November 16, 1983.
5. Matveev, I.G., Gal'perin, N.I., Vil'shau, K.V., *et al.*, *Zh. Prikl. Khim.*, 1958, vol. 31, no. 6, pp. 869–874.
6. Pokonova, Yu.V., *Khimiya i tekhnologiya galogenefirov* (Chemistry and Technology of Halo Ethers), Leningrad: Leningr. Gos. Univ., 1982.
7. Bible, R.H., *Interpretation of NMR Spectra. An Empirical Approach*, New York: Plenum, 1965.
8. Motsarev, G.V. and Rozenberg, V.R., *Zh. Vses. Khim. O–va. im. D.I. Mendeleeva*, 1985, vol. 30, no. 3, pp. 284–294.
9. Germain, J.-E., *Catalytic Conversion of Hydrocarbons*, New York: Academic, 1969.

Russian Journal of Applied Chemistry, Vol. 77, No. 3, 2004, pp. 515–516. Translated from Zhurnal Prikladnoi Khimii, Vol. 77, No. 3, 2004, pp. 521–522.

BRIEF COMMUNICATIONS

Asphaltic Dispersion and Its Evolution in Manufacturing Asphaltic Concrete

E. S. Levchenko, D. A. Rozental', and G. D. Zalishchevskii

St. Petersburg State Technological Institute, St. Petersburg, Russia

Received June 25, 2003

Abstract—Evolution of properties of cold asphalt is investigated. The time required for establishment of adsorption equilibrium in preparation of asphaltic concrete is determined.

The asphaltic dispersion differs from the classical colloidal systems in that its dispersed phase is formed from molecules similar to those of the dispersion medium. The molecules with a polynuclear condensed structure consisting of 3–4 aromatic and 2–3 naphthene rings represent planes with alkyl substituents bound around. Four to six molecules are arranged in parallel to each other to form a quasispherical stack associate.

Thanks to π-electron systems of the aromatic and heteroaromatic rings, the intermolecular bonds in the associate appear to be rather strong, and their dissociation starts only above 300°C. It was demonstrated by X-ray diffraction that, in supramolecular structures of this kind, the stack thickness is well comparable with the diameter of the molecules (~0.8–1.7 nm), that including the solvate shell being about 2.0–2.3 nm [1, 2]. These structures are known as asphaltenes, even though it is not absolutely correct.

In practice, by asphaltenes is meant a mixture of compounds precipitated from a toluene solution of asphalt under the action of *n*-pentane or *n*-hexane. Along with high-molecular-weight aromatic molecules, this mixture can contain low-molecular-weight polar molecules insoluble in the indicated solvents. Therefore, asphaltenes thus isolated can differ significantly from those forming the dispersed phase of asphalt. Furthermore, asphalt contains a great amount of molecules also tending to association, but with a lower energy of intermolecular interaction. In all cases, association proceeds by random diffusion of molecules in the asphalt bulk, until molecules of the appropriate structure come into collision. This requires a time increasing with decreasing temperature, because of increasing viscosity of the system and decreasing energy of the molecules.

Therefore, it takes a long time to form a thermodynamically stable asphalt structure. The lower the temperature of asphalt, the longer this time. This may be clearly demonstrated by measuring the penetration of asphalt without intermediate softening in eight days under oxygen-free conditions in the dark. The results of such experiments are given in the table.

As seen, the penetration of asphalt decreased with time, which is due to solely structural transformations. Such an aging effect was attributed to oxidation in the course of storage. However, in fact, it is a result of high-temperature oxidation of asphalt. Structural transformations accompanying establishment of thermodynamically stable state are very typical of oxidized asphalts. In the course of asphalt oxidation, naphtheno–aromatic oils undergo oxidative dehydrogenation to form asphaltenes. At 220–280°C, this is a kinetically controlled process, while association is controlled by diffusion, proceeding at a considerably lower rate.

Another consequence of aging, but of asphaltic concrete pavements, which has not been taken into consideration until now, is structural transformation of

Variation in the penetration of asphalt in aging at room temperature

Asphalt	Π_{25},* 0.1-mm units, in aging for indicated time, days				
	0	2	4	6	8
BND 40/60	59	57	56	53	50
BND 60/90	88	83	77	74	70
BND 90/130	120	115	110	102	98

* (Π_{25}) Penetration of asphalt at 25°C.

1070-4272/04/7703-0515 © 2004 MAIK "Nauka/Interperiodica"

asphalt caused by adsorption of certain components on the mineral ballast. In fabrication of asphaltic concrete at an asphalt plant, the time of contact of asphalt with mineral ballast is 20 min at 160°C. A short time after asphaltic concrete is laid to the roadbed. Thus, apparently, asphaltic concrete is cooled before reaching the adsorption equilibrium.

It was demonstrated by the hot centrifugation method that the adsorption equilibrium of asphalt on both acidic and basic rocks is established in 3–4 h at 160°C and somewhat more rapidly at higher temperatures. At room temperature, this takes 6–7 months. Adsorption of asphalt on the mineral ballast surface is a selective process, resulting in extraction of the most readily adsorbed components from asphalt, which, in its turn, distorts the thermodynamic equilibrium in the asphaltic dispersion system. As a result, transformation of the asphalt structure changes its characteristics: the penetration considerably decreases and softening point increases.

The effect of heating time τ on the performance characteristics (penetration $\prod_{25}$ and softening point T_s) of centrifuged asphalt is illustrated below.

τ, h	0	1/2	1	2	3	4
$\prod_{25}$, 0.1-mm units	88	71	59	46	39	37
T_s, °C	48	50	54	62	66	67

The observed considerable decrease in the penetration and increase in the softening point suggest an increase in the rigidity of the asphalt structure and decrease in its volume. Detachment of asphalt from a mineral material always proceeds via break of the cohesion bonds, whose strength is lower as compared to the adhesion bonds. Therefore, in asphalt cooled before reaching the adsorption equilibrium, inner stresses are realized in its bulk between the mineral ballast grains, which may result in microcracking, penetration of water, and deterioration of the road pavement. Therefore, the primary cause of deterioration of a road pavement is not an oxidation, but structural transformation of asphalt. Oxidation contributes only at the next stage, i.e., after microcracks are formed in the asphaltic mass.

As a conclusion, our results show that, to improve the durability of asphaltic concrete, it is necessary to hold it at high temperature (160°C) for at least 3–4 h, i.e., until reaching the adsorption equilibrium.

REFERENCES

1. Posadov, I.A., Popov, O.G., Proskuryakov, S.V., *et al*., *Neftekhimiya*, 1985, vol. 25, no. 3, pp. 412–416.
2. Bodan, A.N., *Khim. Tekhnol. Topl. Masel*, 1982, no. 12, pp. 22–24.

Russian Journal of Applied Chemistry, Vol. 77, No. 3, 2004, pp. 517–518. Translated from Zhurnal Prikladnoi Khimii, Vol. 77, No. 3, 2004, pp. 523–524.

BOOK REVIEWS

Beloglazov, I.N., Golubev, V.O., Tikhonov, O.N., Kuukka, J., and Jäskeläinen, Ed., *Fil'trovanie tekhnologicheskikh pul'p* (Filtration of Process Pulps)

Moscow: Ruda i Metally, 2003, 320 pp.

A group of authors, headed by known scientists in the field of simulation of metallurgical processes and apparatus (prof. I.N. Beloglazov) and concentration of mineral resources (prof. O.N. Tikhonov), published, together with the leading specialists of the Finnish Larox Oy company, a manufacturer of filtering equipment, a monograph that summarizes a vast material on dehydration of industrial pulps and slurries. In the four chapters of the book, the authors presented the basic concepts of the theory of dehydration processes and data on technical means used in filtration separation of solid–liquid systems and provided the description with their own recommendations and examples of original engineering decisions from the world practice.

The brief foreword (pp. 3–5) notes the importance of developing, as fast as possible, high-intensity process filters that would meet the requirements of modern industry and enable optimization of the operation modes of the already existing equipment. Tackling with such a task requires a detailed development of appropriate mathematical models and algorithms. The first chapter (pp. 6–109) presents information concerning the theoretical description of filtration processes. A classification of pulps and sediments and of methods for changing their moisture content is given. Reference data on physical properties of various real process pulps, cakes, and gas mixtures and methods for determination of these are presented. The fundamental aspects of hydrodynamic and heat- and mass-exchange processes, which are taken into account by the theory of filtration separation of pulps, are considered. In the main part of the chapter, the fundamental aspects of the processes of filtration, filtration washing, and drying are presented. The authors suggest a unified algorithm for calculating filtration–dehydration processes, based on classical theories of filtration and drying.

The second chapter (pp. 110–143) contains detailed evidence concerning methods for intensifying variously implemented filtration processes. Various methods for improving the filterability of pulps are described, the most effective flocculants lowering the stability of pulps are indicated, and the mechanism by which auxiliary substances affect the course of filtration is analyzed. Also, the main methods for physical or physicomechanical intensification are considered. In particular, studies concerned with the influence exerted by mechanical vibrations with various frequencies, amplitudes, and inducing methods are discussed. A method for improving the filterability of pulps by destruction of the sediment is analyzed.

The third chapter (pp. 144–213) reviews various apparatus implementations of the filtration process. Designs, operation principles, and technical characteristics of a great number of filters are described. These include rotary and plate filters, cartridge and leaf filters, band vacuum filters, plate-and-frame pressure filters, drum and disc filters, automated press filters with horizontal chambers of the FPAKM type, and other special types of filters. The authors note advantages and disadvantages of filters of various designs and give recommendations on choice of the filtration equipment for particular industries. Special attention is given to filtering partitions, their classification is given, and data on their chemical stability and mechanical properties, as well as strength and durability, are given. A summary table of technical characteristics of filtering fabrics of Russian manufacture is presented.

The fourth chapter (pp. 214–305) of the monograph is devoted to recent achievements of world's filter-manufacturing industry. Recently, a tendency toward organization of low-waste plants has been manifested in the development of world's industry, which is due to global economical and environmental problems. This tendency is particularly pronounced for plants of mining, concentrating, and metallurgical industries. In this context, the requirements to particular processes, including separation of process pulps by

1070-4272/04/7703-0517 © 2004 MAIK "Nauka/Interperiodica"

filtration, become increasingly stringent. The authors formulate the requirements to modern filters. The contribution of Russia's specialists to the creation of new filtering technologies and development of the FPAKM family of filters is noted. Modern varieties of filters of this kind are represented by those manufactured by a Finnish company Larox Oy. The manufactured set of press filters is described, with all technical characteristics listed and designs, operation principles of separate units of the filters, and conditions of their industrial use described. Also, the laboratory and pilot equipment for testing of process pulps is described, and results of laboratory tests of pulp samples from a number of domestic and foreign plants are presented. Of particular interest is the material concerning the reconstruction of filtration processes at the largest plants of mining, metallurgical, foodstuff, paint-and-varnish, pharmaceutical, and other industries. Larox LSF filters, which serve for deep purification of various objects: for recovery of solid suspended particles from industrial solutions, electrolytes, and wastewater even at very low content of these particles, are briefly described. The operation of the Larox LSF deep-purification filters is based on the phenomenon of adsorption filtration, which ensures adhesion of micrometer- and submicrometer-size particles to fibers of the filtering fabric, even despite the much smaller size of these particles as compared to the sizes of pores in this fabric. This phenomenon makes it possible to diminish the content of solid particles in media being processed to a level of several ppm (by volume).

The bibliographic list (pp. 306–311) contains 125 references to studies by domestic and foreign researchers. The book is very well printed, it includes illustrative graphical material and useful reference data.

The monograph by Beloglazov and co-authors is of interest for a wide audience of engineers and scientists engaged in process design and modification in a wide variety of industries. The book may be of use for teachers, postgraduate students, masters, and undergraduate students specializing in chemical engineering and metallurgy.

A. G. Morachevskii

Russian Journal of Applied Chemistry, Vol. 77, No. 3, 2004, pp. 519–520. Translated from Zhurnal Prikladnoi Khimii, Vol. 77, No. 3, 2004, pp. 525–526.

BOOK REVIEWS

Krasovitskii, B.M. and Afanasiadi, L.M., *Mono- i bifluofory* (Mono- and Bifluorophores)

Kharkov: Inst. Monokristallov (with Participation of Folio Publishing House), 2000, 448 pp.

The book, published in the framework of the annual series *Sostoyanie i perspektivy razvitiya funktsional'nykh materialov dlya nauki i tekhniki* (State and Prospects for Further Development of Functional Materials for Science and Technology), reviews, systematizes, and generalizes the results of investigations in the field of synthesis, study, and use of organic luminophores, which have been carried out during more than 40 years under supervision of Professor B.M. Krasovitskii at the Institute of Single Crystals, Academy of Sciences of Ukr. SSR (now National Academy of Sciences of Ukraine).

These investigations were commenced at the time when the main task of the Institute of Single Crystals was to provide the nuclear engineering with effective means for monitoring the nuclear radiation. Therefore, the main goal was to obtain luminophores that served as activators of liquid and plastic scintillators. Later, the scope of the investigations was substantially expanded because of the steadily increasing demand for effective luminophores for a wide variety of fields of science and technology. A necessity arose for a search for new classes of luminescent substances, improvement of methods for their synthesis, study of the relationship between their structure and spectral-fluorescent properties, and optimization of conditions of their use. The main feature of the investigations performed was the synthesis of compounds with two fluorophore groups, bifluorophores.

The results obtained in all of these studies are presented in the book, which comprises three parts. The first part ("Monofluorophores") considers successively the synthesis, structure, and use of the following compounds: polycyclic aromatic hydrocarbons and their functional derivatives, vinyl-substituted aromatic hydrocarbons, diaryl-substituted ethylene and polyenes, Schiff bases, dibenzofulvenes and their azomethine derivatives, compounds with five- and six-membered nitrogen-containing heterocyclic rings (derivatives of oxazole, aryl-hetaryl-substituted azoles, imidazoles, and compounds with a pyrazoline ring) and those with carbonyl-containing fluorophore groups (α,β-unsaturated ketones, substituted benzanthrone and anthrapyridone, anthraquinonediazoles, derivatives of oxazolone and imidazolone, benzoxazin-4-ones, substituted 9-akridones), sulfonyl-containing heterocyclic rings, and also derivatives of naphthalimide, *N*-aminoimides, and hydrazides of naphthalic acid, and 1,8-naphthoylene-1',2'- benzimidazole and its derivatives. Thus, the variety of the objects studied is exceedingly wide.

The second part ("Bifluorophores") is devoted to luminophores with conjugated fluorophore groups (both symmetric and asymmetric), polycondensed bifluorophores, luminophores with unconjugated fluorophore groups (with "insulating" groups, with *meta*-position of fluorophore groups in the common aromatic ring, and also with a bridging amide group), as well as to sterically hindered bifluorophores, bifluorophores with ionic structure, and compounds containing more than two fluorophore groups.

The third part ("Luminescent Materials") contains a wide variety of data on day-glo fluorescent and decorative paints and printing inks, use of day-glo fluorescent pigments in translucent screens and in visualization of latent electrostatic images, as well as on day-glo fluorescent pigments and paints based on polyester resins. Luminescent dyes for plastics and synthetic fibers (polystyrene and polymethyl methacrylate, polyethylene, polyvinyl chloride and polyacrylonitrile) and epoxy resins and luminescent organosilicon dyes are considered in detail. Considerable attention is given to organic scintillators, materials for detection and dosimetry of the ionizing radiation. The chapter concerned with fluoroscopic flaw detection considers fluorescent dye penetrant testing, magnetic luminescent materials, and the luminescent technique for determining the chemical stability of rubbers. Further, a review is given of a valuable information about fluorescent markers and probes for biological studies and medical diagnostics. The same chapter considers luminescent markers for indication of proteins and fluorescent probes for fast analysis of cholesterol and triglycerides in the diagnostics of

1070-4272/04/7703-0519 © 2004 MAIK "Nauka/Interperiodica"

atherosclerosis, determination of the binding capacity of albumin, and study of the structure of biomembranes and lipoproteins. Finally, there are special chapters devoted to lasers operating on organic luminophores, to organic luminophores in chemi- and electroluminescent formulations, and to thermoindicating coatings and photographic materials. In a form that is concise, but convenient for readers, the book presents the most important data on synthesis, structure, and spectral-luminescent properties of organic compounds; polarographic studies of the luminophores considered here are also briefly reported. The text is provided with a great number of structural formulas. The book has a particular practical value because of the numerous indications of the application fields of luminophores and vast bibliography: the book contains a total of more than 1200 references, including 45 references to reviews and monographs by Krasovitskii and co-authors.

The scale of investigations whose results are generalized in the book is indicated by the mere fact that only joint investigations, performed in cooperation with other organizations, involved 24 institutes of the Academies of Sciences of the Sovient Union and CIS countries, 28 industrial research institutes and research-and-production associations, 21 higher-school institutions, and 14 industrial plants.

The book will be of use for organic chemists, biohemists, scientists dealing with spectroscopy and laser technology, and specialists working in various fields of applied chemistry, associated with synthesis, study, and use of luminophores.

N. O. Mchedlov-Petrosyan

Russian Journal of Applied Chemistry, Vol. 77, No. 4, 2004, pp. 521–526. Translated from Zhurnal Prikladnoi Khimii, Vol. 77, No. 4, 2004, pp. 529–534.

INORGANIC SYNTHESIS AND INDUSTRIAL INORGANIC CHEMISTRY

Physicochemical Principles of Synthesis of Liquid Fertilizers Based on Potassium Hydrophosphate

A. Sviklas and R. Paletskene

Kaunas Technological University, Kaunas, Lithuania

Received July 15, 2003

Abstract—Technological prerequisites for obtaining special liquid fertilizers with potassium and ammonia hydrophosphates as components were studied. The solubility in the multicomponent $(NH_4)_2HPO_4$–K_2HPO_4–NH_4NO_3–H_2O and $(NH_4)_2HPO_4$–K_2HPO_4–$CO(NH_2)_2$–H_2O systems was studied. The chemical composition of the liquid compound fertilizers obtained was determined.

About 5% of the world output of fertilizers is used to grow vegetable, fruit, and berry cultures [1]. Special types of fertilizers are used with this aim, their main function being to satisfy to the maximum possible extent the needs of plants for mineral nutrition during various periods of their development [2]. Therefore, with regard to a great variety of agricultural crops and their special features, a wide assortment of fertilizers of this kind is necessary. The most efficient for these purposes are liquid compound fertilizers (LCF) that contain ammonium phosphates as the main components [3, 4]. Potassium phosphates are hardly used in the production of LCF owing to their high cost, though they are characterized by a high solubility and high content of potassium and phosphorus [5]. Potassium hydrophosphate contains 40.7% P_2O_5 and 54.0% K_2O and is readily soluble in water. At 20°C, the maximum content of K_2HPO_4 in water is as high as 61.6 wt %. Thus, K_2HPO_4 is a promising source for the production of special liquid fertilizers. When cultivating hot-house cultures, the expenditure for fertilizers is comparatively small, and, therefore, use of potassium phosphates is promising.

The aim of this study was to create technological prerequisites for production of special liquid fertilizers based on potassium hydrophosphates. To this end, it was necessary to solve the following problems: (i) to study the solubility in the multicomponent $(NH_4)_2HPO_4$–K_2HPO_4–NH_4NO_3–H_2O and $(NH_4)_2HPO_4$–K_2HPO_4–$CO(NH_2)_2$–H_2O systems and (ii) to find the chemical composition of liquid compound fertilizers and to determine the physicochemical properties of the products on the basis of solubility data.

To study the solubility, we used K_2HPO_4, $(NH_4)_2HPO_4$, $CO(NH_2)_2$, NH_4NO_3 reagents of analytically pure grade and distilled water. To obtain LCF, we also used technical-grade K_2CO_3, orthophosphoric acid of pure grade (concentration 86%), technical-grade aqua ammonia NH_4OH (concentration 25%), and technical-grade 58% HNO_3.

We determined the composition of substances by chemical and physicochemical methods of analysis. The concentration of ammonia nitrogen was found using the formaldehyde method [6, 7], and that of nitrate nitrogen, by the titration method based on the reduction of nitrates with a titration standard of iron(II) sulfate in an acid medium with the subsequent titration of the excess of iron(II) salt with a potassium permanganate solution in the presence of ammonium molybdate as a catalyst [8], or by the photometric method [9]. The concentration of potassium ions was determined by flame photometry on a Jenway PFP-7 flame photometer, and the concentrations of P_2O_5 and amide nitrogen, by the photometric method [7, 10, 11] on a KFK-2 photocolorimeter.

The solid phases were analyzed using IR spectrometry, thermogravimetry, and X-ray phase analysis.

IR spectra were recorded on a Specord M-80 spectrometer. Samples for recording were compacted into pellets with KBr.

The thermogravimetric experiments were carried out on a Du Pont Instruments 990 Thermal Analyzer, with the temperature raised at a rate of 10 deg min^{-1}.

The X-ray phase analysis was made on a DRON-3 device with a cobalt anode, the interval of diffraction angles was 0°–166.5°, the error did not exceed 0.5%.

1070-4272/04/7704-0521 © 2004 MAIK "Nauka/Interperiodica"

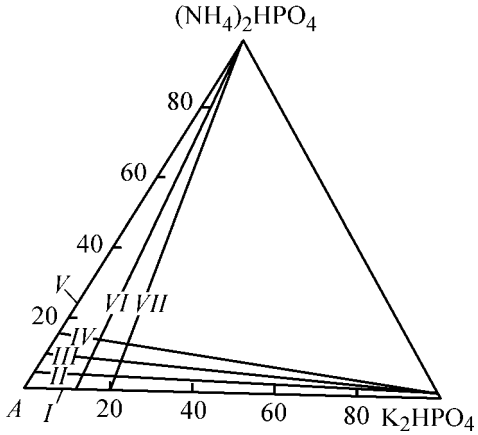

Fig. 1. Sections in the $(NH_4)_2HPO_4$–K_2HPO_4–NH_4NO_3–H_2O system, studied by the polythermic method. Point *A* corresponds to 20% NH_4NO_3 + 80% H_2O; the same for Fig. 3.

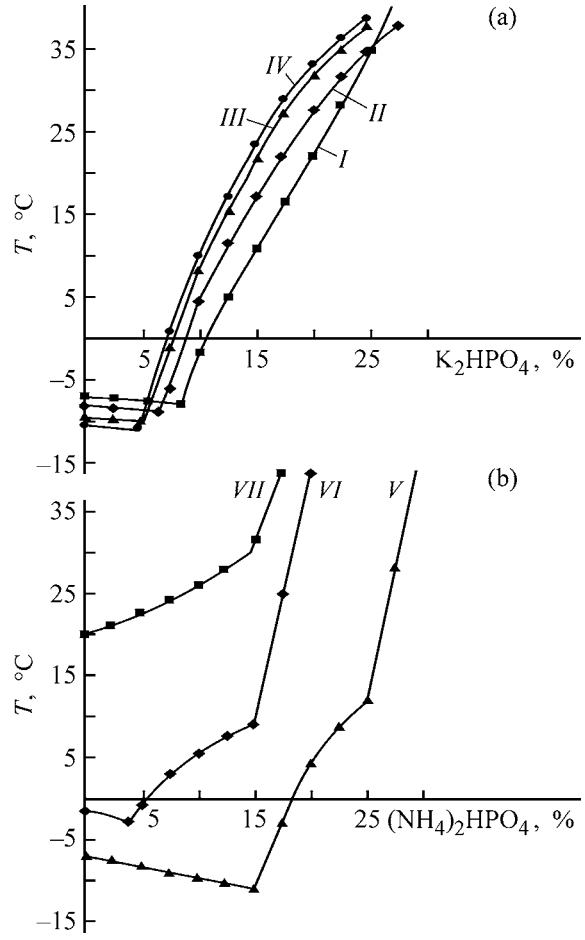

Fig. 2. Polytherms in the $(NH_4)_2HPO_4$–K_2HPO_4–NH_4NO_3–H_2O system. (*T*) Temperature, and K_2HPO_4 and $(NH_4)_2HPO_4$ content of the corresponding compounds; the same for Fig. 4. Section: (a) (*I*) $A \rightarrow K_2HPO_4$, (*II*) [5% $(NH_4)_2HPO_4$ + 95% *A*] $\rightarrow K_2HPO_4$, (*III*) [10% $(NH_4)_2HPO_4HPO_4$ + 90% *A*] $\rightarrow K_2HPO_4$, (*IV*) [15% $(NH_4)_2HPO_4$ + 85% *A*] $\rightarrow K_2HPO_4$; (b) (*V*) $A \rightarrow (NH_4)_2HPO_4$, (*VI*) [10% K_2HPO_4 + 90% *A*] $\rightarrow (NH_4)_2HPO_4$, (*VII*) [20% K_2HPO_4 +80% *A*] $\rightarrow$ $(NH_4)_2HPO_4$.

The properties of solutions and LCF were determined using a pH-673 pH-meter, a VPZh-2 viscometer, a set of AON-1 areometers for measuring the density of solutions of compound fertilizers, an IRF-2 refractometer for finding the refractive indexes, and a Radelkis conductometer for measuring the electrical conductivity.

We determined the solubility of the salts in water by the visual-polythermic method [12, 13]. Depending on a required temperature, a mixture of ice, sodium chloride, and ammonium chloride (nitrate) or a mixture of dry ice and ethanol was used as a cooling agent.

To identify the composition of solid phases, the compounds were isolated in the crystalline state. The crystals obtained at the inflection points and in the characteristic intervals of the resulting polytherms were separated using a centrifuge condenser (at low crystallization temperatures) or a Nutsch filter (at crystallization temperatures higher than 0°C) and subjected to the chemical and instrumental analysis.

To determine the composition of liquid special compound fertilizers, the data on the solubility in the $(NH_4)_2HPO_4$–K_2HPO_4–NH_4NO_3–H_2O and $(NH_4)_2HPO_4$–K_2HPO_4–$CO(NH_2)_2$–H_2O systems were necessary.

We studied each system by the method of inner sections. We constructed solubility polytherms along the sections on the basis of experimental data and then obtained triangular section diagrams for the system in the region under study. All the systems were studied in the range from the temperature of complete freezing to +40°C.

The $(NH_4)_2HPO_4$–K_2HPO_4–NH_4NO_3–H_2O system was studied at concentrations of ammonium hydrophosphate and potassium hydrophosphate in the ranges from 0 to 30 and from 0 to 25 wt %, respectively. The ratio of ammonium nitrate and water was maintained constant at 1 : 4. The study was carried out along seven sections, four of which were directed toward increasing potassium hydrophosphate concentration, and three toward increasing ammonium hydrophosphate concentration. The location of the sections is shown in the triangular diagram in Fig. 1. The curves of solution crystallization are shown in Fig. 2.

Crystallization curves of sections *I–IV* are of the same nature. Each section consists of two crystallization branches. The inflections in the curves occur owing to changes in the phase composition. In sections *V–VI*, two inflection points are formed, and the crystallization from solutions of section *VII* occurs only at positive temperatures.

Table 1. Indices of eutonic points in the $(NH_4)_2HPO_4$–K_2HPO_4–NH_4NO_3–H_2O system

Section	Solution composition, wt %				T_{cr}, °C	Solid phase
	$(NH_4)_2HPO_4$	K_2HPO_4	NH_4NO_3	H_2O		
I	–	9.00	18.20	72.80	–8.5	Ice + NH_4NO_3
II	4.66	6.75	17.72	70.87	–8.8	Ice + NH_4NO_3 + $(NH_4)_2HPO_4$
III	9.45	5.50	17.01	68.04	–10.2	Ice + NH_4NO_3 + $(NH_4)_2HPO_4$
IV	14.36	4.25	16.28	65.11	–10.9	Ice + NH_4NO_3 + $(NH_4)_2HPO_4$
V	15.50	–	16.90	67.60	–11.1	Ice + $(NH_4)_2HPO_4 \cdot 2H_2O$
V	25.00	–	15.00	60.00	12.0	$(NH_4)_2HPO_4 \cdot 2H_2O$ + $(NH_4)_2HPO_4$
VI	4.00	9.60	17.28	69.12	–2.7	NH_4NO_3 + $(NH_4)_2HPO_4$
VI	15.50	8.45	15.21	60.84	9.2	NH_4NO_3 + $(NH_4)_2HPO_4$
VII	14.80	17.04	13.63	54.53	31.0	NH_4NO_3 + $(NH_4)_2HPO_4$

Table 2. Chemical composition of saturated solutions with the crystallization temperature of 0°C in the $(NH_4)_2HPO_4$–K_2HPO_4–NH_4NO_3–H_2O system

Section	Solution composition, wt %				Concentration of nutritious substances, wt %				Ratio $N:P_2O_5:K_2O$
	$(NH_4)_2HPO_4$	K_2HPO_4	NH_4NO_3	H_2O	N	P_2O_5	K_2O	sum	
I	0.00	10.25	17.95	71.80	6.28	4.18	5.53	16.00	1.5 : 1 : 1.3
II	4.56	8.75	17.34	69.35	7.04	6.03	4.72	17.78	1.5 : 1.3 : 1
III	9.23	7.75	16.61	66.42	7.77	8.13	4.18	20.08	1.9 : 1.9 : 1
IV	13.92	7.20	15.78	63.10	8.47	10.43	3.89	22.79	2.2 : 2.7 : 1
V	18.25	0.00	16.35	65.40	9.59	9.82	0.00	19.41	1 : 1 : 0
VI	5.5	9.45	17.01	68.04	7.12	6.82	5.10	19.04	1.4 : 1.3 : 1

The solid compounds formed within the range of the solution concentrations under study were identified using chemical and instrumental analyses and stoichiometric calculations of the composition.

The crystallization temperatures of eutonic points, T_{cr}, and the chemical compositions of precipitated solid phases of the $(NH_4)_2HPO_4$–K_2HPO_4–NH_4NO_3–H_2O system were determined within the indicated range of the component concentrations (Table 1). The eutonic point of section *IV* corresponds to the lowest crystallization temperature (–10.9°C). Its chemical composition corresponds to (wt %): $(NH_4)_2HPO_4$ 14.36, K_2HPO_4 4.25, NH_4NO_3 16.28, and H_2O 65.11. The total concentration of nutritious substances is 20.50%.

Based on the data obtained, we constructed a triangular diagram of the $(NH_4)_2HPO_4$–K_2HPO_4–NH_4NO_3–H_2O system (Fig. 3). The boundary lines of the crystallization fields are plotted in the diagram on the basis of the polythermic and chemical analysis data. A study of the bottom phases precipitated from supersaturated solutions in various regions of the system at the appropriate temperatures, demonstrated that no new compounds are formed in the system. A comparison of derivatograms, X-ray diffraction patterns, and IR absorption spectra confirmed these conclusions.

To determine the chemical composition of liquid compound fertilizers, we calculated the composition of saturated solutions with the crystallization temperature of 0°C. The results are listed in Table 2.

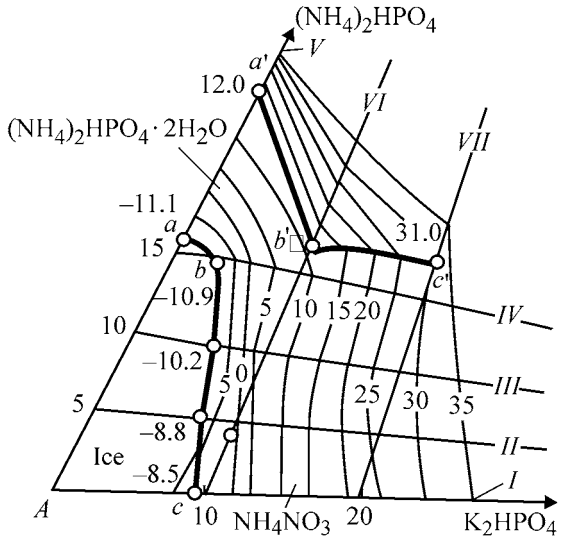

Fig. 3. Solubility polytherm of the $(NH_4)_2HPO_4$–K_2HPO_4–NH_4NO_3–H_2O system.

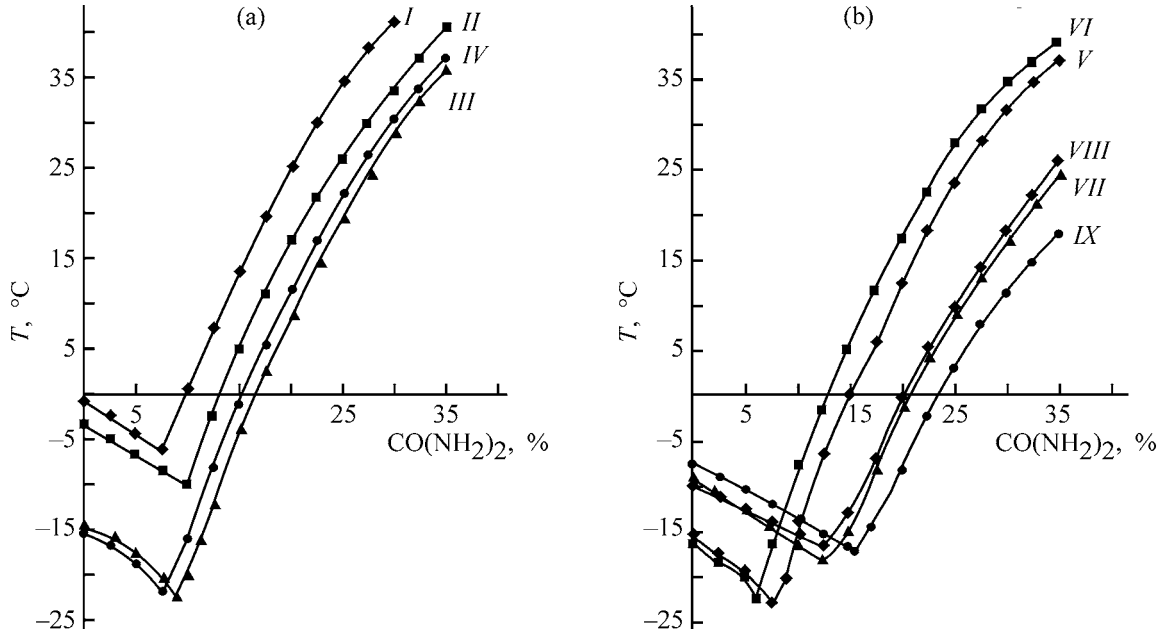

Fig. 4. Polytherms of the $(NH_4)_2HPO_4$–K_2HPO_4–$CO(NH_2)_2$–H_2O system. Section: (a) (*I*) [5% $(NH_4)_2HPO_4$ + 55% K_2HPO_4 + 40% H_2O] → $CO(NH_2)_2$, (*II*) [55% $(NH_4)_2HPO_4$ + 45% H_2O] → $CO(NH_2)_2$, (*III*) [5% $(NH_4)_2HPO_4$ + 45% K_2HPO_4 50% H_2O] → $CO(NH_2)_2$, (*IV*) [10% $(NH_4)_2HPO_4$ + 40% K_2HPO_4 + 50% H_2O] → $CO(NH_2)_2$, (b) (*V*) [15% $(NH_4)_2HPO_4$ + 35% K_2HPO_4 + 50% H_2O] → $CO(NH_2)_2$, (*VI*) [25% $(NH_4)_2HPO_4$ + 25% K_2HPO_4 + 50% H_2O] → $CO(NH_2)_2$, (*VII*) [5% $(NH_4)_2HPO_4$ + 35% K_2HPO_4 + 60% H_2O] → $CO(NH_2)_2$, (*VIII*) [10% $(NH_4)_2HPO_4$ + 30% K_2HPO_4 + 60% H_2O] → $CO(NH_2)_2$, (*XI*) [5% $(NH_4)_2HPO_4$ + 30% K_2HPO_4 + 65% H_2O] → $CO(NH_2)_2$.

It is seen from Table 2 that the maximum concentration of nutritious substances is 22.79 wt % at the ratio $N : P_2O_5 : K_2O = 2.2 : 2.7 : 1$.

The replacement of ammonium nitrate with carbamide is known to raise, as a rule, the total concentration of nutritious substances in LCFs [3, 14]. With this in mind, we studied the solubility of the $(NH_4)_2HPO_4$–K_2HPO_4–$CO(NH_2)_2$–H_2O system. We analyzed the solutions at ammonium hydrophosphate, potassium hydrophosphate, and carbamide concentrations of 5 to 25, 25 to 55, and 0 to 35 wt %, respectively. The solubility polytherms were plotted using the results of the polythermic studies. The analysis was made for nine sections, with varied chemical composition of the system (wt %):

I: $[5(NH_4)_2HPO_4 + 55K_2HPO_4 + 40H_2O] \rightarrow CO(NH_2)_2$,

II: $[55(NH_4)_2HPO_4 + 45H_2O] \rightarrow CO(NH_2)_2$,

III: $[5(NH_4)_2HPO_4 + 45K_2HPO_4 + 50H_2O] \rightarrow CO(NH_2)_2$,

IV: $[10(NH_4)_2HPO_4 + 40K_2HPO_4 + 50H_2O] \rightarrow CO(NH_2)_2$,

V: $[15(NH_4)_2HPO_4 + 35K_2HPO_4 + 50H_2O] \rightarrow CO(NH_2)_2$,

VI: $[25(NH_4)_2HPO_4 + 25K_2HPO_4 + 50H_2O] \rightarrow CO(NH_2)_2$,

VII: $[5(NH_4)_2HPO_4 + 35K_2HPO_4 + 60H_2O] \rightarrow CO(NH_2)_2$,

VIII: $[10(NH_4)_2HPO_4 + 30K_2HPO_4 + 60H_2O] \rightarrow CO(NH_2)_2$,

IX: $[5(NH_4)_2HPO_4 + 30K_2HPO_4 + 65H_2O] \rightarrow CO(NH_2)_2$.

The general shape of the curves obtained is shown in Fig. 4.

All the crystallization curves are of the same nature. They consist of two crystallization branches. The indices of eutonic points of the crystallization curves are listed in Table 3.

To determine the chemical composition of LCF, we calculated the chemical composition of saturated solutions with the crystallization temperature of 0°C. The data are listed in Table 4.

Use of carbamide instead of NH_4NO_3 sharply increases the concentration of nutritious substances. The maximum sum of nutritious substances in section *I* is 54.94 wt %. High concentrations are attained with popular ratios of nutritious substances. For example, at the ratios $N : P_2O_5 : K_2O$ of 1 : 2 : 2, 1 : 2 : 1, and 1 : 1 : 1 the sum of nutritious substances is 45.61, 43.00, and 35.5%, respectively. This indicates that $(NH_4)_2HPO_4$, K_2HPO_4, and $CO(NH_2)_2$ can be used

Table 3. Indices of eutonic points in the $(NH_4)_2HPO_4$–K_2HPO_4–$CO(NH_2)_2$–H_2O system

Section	Solution composition, wt %				T_{cr}, °C	Solid phase
	$(NH_4)_2HPO_4$	K_2HPO_4	$CO(NH_2)_2$	H_2O		
I	4.61	50.74	7.75	36.9	–6.7	$K_2HPO_4 \cdot 6H_2O$ + $CO(NH_2)_2$
II	–	49.36	10.25	40.39	–10.3	$K_2HPO_4 \cdot 6H_2O$ + $CO(NH_2)_2$
III	4.53	40.72	9.50	45.52	–23.6	$K_2HPO_4 \cdot 6H_2O$ + $CO(NH_2)_2$
IV	9.12	36.50	8.75	45.63	–23.3	$K_2HPO_4 \cdot 6H_2O$ + $CO(NH_2)_2$
V	13.82	32.25	7.85	46.08	–23.1	$(NH_4)_2HPO_4 \cdot 2H_2O$ + $CO(NH_2)_2$
VI	23.44	23.44	6.25	46.87	–22.0	$(NH_4)_2HPO_4$ + $CO(NH_2)_2$
VII	4.32	30.28	13.50	51.90	–19.2	Ice + $CO(NH_2)_2$
VIII	8.62	25.86	13.80	51.72	–17.4	Ice + $CO(NH_2)_2$
IX	4.17	25.05	16.50	54.28	–17.3	Ice + $CO(NH_2)_2$

Table 4. Chemical composition of saturated solutions with the crystallization temperature of 0°C in the $(NH_4)_2HPO_4$–K_2HPO_4–$CO(NH_2)_2$–H_2O system

Section	Solution composition, wt %				Concentration of nutritious substances, wt %				Ratio $N : P_2O_5 : K_2O$
	$(NH_4)_2HPO_4$	K_2HPO_4	$CO(NH_2)_2$	H_2O	N	P_2O_5	K_2O	sum	
I	4.49	49.36	10.25	35.90	5.74	22.56	26.64	54.94	1 : 3.9 : 4.6
II	–	47.58	13.50	39.92	6.30	19.42	24.68	51.40	1 : 3.1 : 4.1
III	4.18	37.57	16.50	41.75	8.59	17.58	20.28	46.45	1 : 2.1 : 2.4
IV	8.45	33.80	15.50	42.25	9.03	18.34	18.24	45.61	1 : 2 : 2
V	12.75	29.82	14.80	42.60	9.62	19.04	16.09	44.75	1 : 2 : 1.7
VI	21.75	21.75	13.00	43.50	10.68	20.58	11.74	43.00	1 : 2 : 1
VII	3.98	27.82	20.50	47.70	10.41	13.50	15.01	38.92	1 : 1.3 : 1.4
VIII	7.98	23.94	20.20	47.88	11.12	14.07	12.92	38.11	1 : 1.3 : 1.2
IX	3.83	23.01	23.30	49.86	11.69	11.45	12.42	35.56	1 : 1 : 1

Table 5. Physicochemical properties of LCFs at 20°C

Type (N–P_2O_5–K_2O)	T_{cr}, °C	pH	Viscosity, mPa s^{-1}	Density, kg m^{-3}	Refractive index	Electrical conductivity, S m^{-1}
12–11–12	–1.2	7.4	3.38	1267	1.405	0.071
11–21–11	–2.5	7.7	8.12	1355	1.421	0.067
7–8–4	–2.5	7.0	1.87	1171	1.378	0.164

Note. Liquid compound fertilizers based on potassium hydrophosphate, ammonium hydrophosphate, and ammonium nitrate or carbamide can be used under both field and greenhouse conditions, irrespective of a plant species and the period of its vegetation.

as components in production of highly concentrated liquid compound fertilizers.

Based on the results of our chemical and physicochemical studies, we developed a procedure and a technology for manufacture of LCF [15]. K_2CO_3, $CO(NH_2)_2$, $NH_3 \cdot H_2O$, H_3PO_4, and HNO_3 as the raw materials for production of special-purpose LCF. Using this procedure, we prepared LCF solutions under laboratory conditions and determined their properties (Table 5). These properties were found to be close to those of standard fertilizers.

CONCLUSIONS

(1) The solubility in the $(NH_4)_2HPO_4$–K_2HPO_4–NH_4NO_3–H_2O and $(NH_4)_2HPO_4$–K_2HPO_4–$CO(NH_2)_2$–H_2O systems was studied within the temperature range from complete solidification to +40°C. The crystal-

lization polytherms and the compositions of liquid and solid phases were determined and also the concentrations of the saturated solutions with the crystallization temperature of 0°C were found.

(2) With carbamide, the concentration of nutritious substances in solution increases to 54.94 wt %, whereas with ammonium nitrate, the concentration of nutritious substances is only 22.79 wt %.

REFERENCES

1. IFA. *The World Agricultural Situation*, Paris, IFA, A/99/125, 1999.
2. Fedyushkin, B.F., *Mineral'nye udobreniya s mikroelementami: tekhnologiya i primenenie* (Mineral Fertilizers with Microelements: Technology and Application), Leningrad: Khimiya, 1989.
3. Kochetkov, V.N., *Proizvodstvo i primenenie zhidkikh kompleksnykh udobrenii* (Production and Application of Liquid Compound Fertilizers), Moscow: Agropromizdat, 1986.
4. *Osnovy tekhnologii kompleksnykh udobrenii* (Fundamentals of the Technology of Compound Fertilizers), Kononov, A.V., Ed., Moscow: Khimiya, 1988.
5. Kochetkov, V.N., *Fosforsoderzhashchie udobreniya: Spravochnik* (Phosphorus-containing Fertilizers: Reference Book), Moscow: Khimiya, 1982.
6. *The Fertilizers (Sampling and Analysis) Regulations, Statutory Instruments, Agriculture*, London: HMSO, 1991, no. 973.
7. *Tekhnicheskie usloviya na mineral'nye udobreniya* (Technical Specifications for Mineral Fertilizers), Shevchenko, K.F., Ed., Moscow: Proizv.-Izd. Kombinat, 1979.
8. *Metody Opredeleniya razlichnykh form azota v mineral'nykh azotnykh udobreniyakh: Instruktsiya* (Methods for Determining Various Forms of Nitrogen in Mineral Nitrogen Fertilizers), Pokhodenko, L.A., Ed., Lvov: LPI, 1986.
9. Williams, W.J., *Handbook of Anion Determination*, London: Butterworths, 1979.
10. *Tekhnicheskii analiz v proizvodstve neorganicheskikh veshchestv* (Technical Analysis in the Production of Inorganic Substances), Trocheshnikov, N.S., Ed., Moscow: Vysshaya Shkola, 1976.
11. *Osnovy analiticheskoi khimii: Prakticheskoe rukovodstvo* (Fundamentals of Analytical Chemistry: Manual), Zolotov, Yu.A., Ed., Moscow: Vysshaya Shkola, 2001.
12. Bergman, A.G. and Luzhnaya, N.P., *Fiziko-khimicheskie osnovy izucheniya i ispol'zovaniya solyanykh mestorozhdenii khlorid-sulfatnogo tipa* (Physicochemical Principles of the Study and Use of Salt Birthplaces of Chloride-Sulfate Type), Moscow: Akad. Nauk SSSR, 1951.
13. Eraizer, L.N. and Kaganskii, I.M., *Zavod. Lab.*, 1967, no.1, p. 119.
14. Paletskene, R., Liquid Fertilizers based on Potassium and Ammonium Phosphates: Physicochemical Properties and Preparation, *Doctoral Dissertation*, Kaunas, 2000.
15. Lithuanian Republic Patent 4697 B (N 99-093).

Russian Journal of Applied Chemistry, Vol. 77, No. 4, 2004, pp. 527–530. Translated from Zhurnal Prikladnoi Khimii, Vol. 77, No. 4, 2004, pp. 535–537.

INORGANIC SYNTHESIS AND INDUSTRIAL INORGANIC CHEMISTRY

Recovery of Palladium(II) from Hydrochloric Solutions with Fullerene Black Impregnated with Trioctylamine

A. N. Turanov and N. K. Evseeva

Institute of Solid-State Physics, Russian Academy of Sciences, Chernogolovka, Moscow oblast, Russia

Received July 8, 2003

Abstract—Distribution of HCl and Pd(II) among aqueous solutions of HCl and the product of electric-arc evaporation of graphite, fullerene black, impregnated with trioctylamine was studied.

Recently, macroporous sorbents impregnated with extracting agents of various classes have found wide application in the analytical and preparative practice of recovery and concentration of metal ions from aqueous solutions [1, 2]. Pd(II) has been recovered from hydrochloric solutions with the use of macroporous polymeric sorbents impregnated with trialkylamines [3], trioctylphosphine oxide [4], sulfoxides [5], dialkylthiophosphoric acids [6], and nitrogen-containing phenolformaldehyde oligomers [7]. Hydrocarbon materials as a matrix for obtaining impregnated sorbents have been studied to a lesser extent. Recovery of Pd(II) from hydrochloric solutions with an intercalated compound of trioctylamine (TOA), based on fluorinated graphite, has been reported [8]. With the development of research aimed to synthesize fullerenes, attention was given to the high specific surface area and sorption capacity of the fullerene black (FB), an amorphous carbon material obtained in exhaustive extraction of fullerenes C_{60} and C_{70} from the product formed in electric-arc evaporation of graphite [9].

In order to assess the possibility of using FB as a matrix for obtaining an impregnated sorbent, some aspects of how Pd(II) is distributed among HCl solutions and FB impregnated with TOA were examined in the present study.

EXPERIMENTAL

The fullerene black was synthesized by exhaustive extraction of fullerenes C_{60} and C_{70} with toluene in a Sohxlet apparatus from a fullerene-containing carbon black. The black was obtained by electric-arc evaporation of graphite on an installation described in [10]. As the active component of the impregnated sorbent was used TOA (Merk) without additional purification. The FB was impregnated with trioctylamine by the procedure similar to that described previously in [7]. The content of TOA in the sorbent was 0.1–11.26 mol kg^{-1} of FB.

The starting aqueous Pd(II) solutions with a concentration of 5×10^{-3} M were prepared by dissolving $PdCl_2$ of pure grade in a 6 M solution of HCl, with subsequent dilution of the resulting solution to obtain required concentrations of Pd(II) and the acid. Sorption experiments were performed under static conditions at a temperature of $18 \pm 2°C$. The aqueous solution with a sorbent was agitated with a magnetic stirrer for 2 h, which is sufficient for constant distribution coefficients D_{Pd} of Pd(II) to be attained. The ratio between the volume of the aqueous phase and the sorbent mass was 300 : 1.

The concentration of Pd(II) in the aqueous solutions before and after sorption was determined photometrically with KNCS [11], and that in the sorbent phase, using the material balance equation. The distribution coefficients of Pd(II) were calculated as a ratio of Pd(II) concentrations in the equilibrium solid and aqueous phases. The concentration of HCl in the equilibrium aqueous phases was determined by potentiometric titration with a NaOH solution.

It is known that, when brought in contact with HCl solutions, TOA forms trioctylammonium chloride (TOAHCl) [12]. Extraction of Pd(II) with TOAHCl solutions in organic solvents has been studied rather well [13–17]. It was established that Pd(II) is extracted into the organic phase from solutions with

1070-4272/04/7704-0527 © 2004 MAIK "Nauka/Interperiodica"

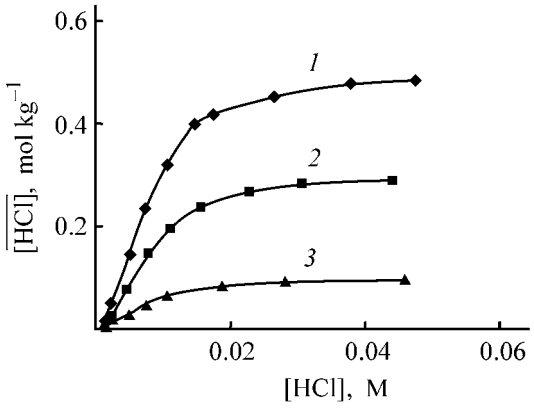

Fig. 1. Distribution of HCl among aqueous solutions of the acid, [HCl], and FB impregnated with TOA, [$\overline{\text{HCl}}$]. Content of TOA (mol kg^{-1}): (*1*) 0.5, (*2*) 0.3, and (*3*) 0.1.

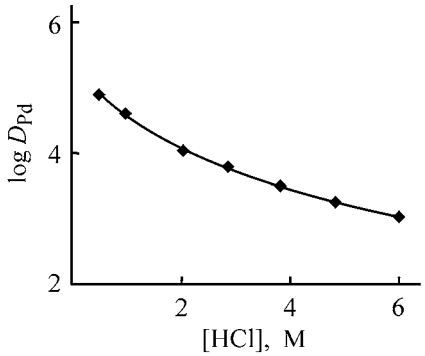

Fig. 2. Distribution coefficient of Pd(II), D_{Pd}, vs. the concentration of HCl in the equilibrium aqueous phase, [HCl], in sorption with a fullerene black containing TOA in amount of 1.26 mol kg^{-1} of FB.

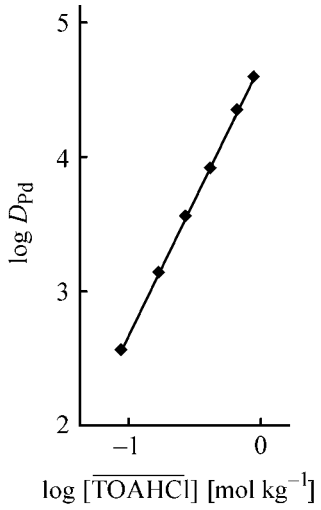

Fig. 3. Distribution coefficient of Pd(II), D_{Pd}, vs. the content of TOAHCl, [$\overline{\text{TOAHCl}}$], in the sorbent phase in sorption from a 1 M solution of HCl.

1–6 M of HCl as a result of occurrence of the anion-exchange reaction

$$PdCl_4^{2-} + 2\overline{TOAHCl} \rightleftarrows [\overline{PdCl_4}](\overline{TOAH})_2 + Cl^-, \quad (1)$$

where the overline designates components in the non-aqueous phase.

In addition, Pd(II) passes into the organic phase in the form of a binuclear complex $[Pd_2Cl_6](TOAH)_2$ under the conditions of deficiency of an extracting agent [15]. It has been shown by means of IR and Raman spectroscopy that complexes of the same kind are also formed upon interaction of hydrochloric solutions of Pd(II) with TOA in the absence of an organic solvent [8].

To study equilibria in the system Pd(II)–HCl–TOA–FB, recovery of HCl from its aqueous solution with an impregnated sorbent was examined preliminarily. Since FB does no extract HCl from a solution in the absence of trioctylamine, the rise in the concentration of HCl in the sorbent phase with increasing concentration of TOA in the solid phase or of HCl in the aqueous phase (Fig. 1) can be attributed to the formation of the complex $\overline{\text{TOAHCl}}$ in the sorbent phase [18]:

$$H^+ + Cl^- + \overline{TOA} \rightleftarrows \overline{TOAHCl}. \quad (2)$$

The equilibrium constant of reaction (2), found from the data in Fig. 1, $K_{HCl} = 1.5 \times 10^4$.

At a constant concentration of TOA in the sorbent phase, the recovery of Pd(II) into the solid phase decreases as the concentration of HCl in the aqueous phase becomes higher (Fig. 2), which is due to a shift of the equilibrium of reaction (1) to the left. The rise in the concentration of TOA in the sorbent phase is accompanied by an increase in the sorption of Pd(II) (Fig. 3), with the slope of the dependence of log D_{Pd} on log [$\overline{\text{TOA}}$] equal to 2, which corresponds to recovery of Pd(II) in the form of the complex $[PdCl_4](TOAH)_2$ by reaction (1). The equilibrium constant of the process of interphase distribution of Pd(II)[Eq. (1)], found from the data in Fig. 3, $K_{Pd} = 5.62 \times 10^4$.

The isotherm of Pd(II) adsorption from a hydrochloric solution with an impregnated sorbent (Fig. 4a) can be described using the Langmuir equation

$$[\overline{Pd}] = \frac{K[\overline{Pd}]_{max}[Pd]}{1 + K[Pd]}, \quad (3)$$

where [Pd], [$\overline{\text{Pd}}$] are the equilibrium concentrations of Pd(II) in the aqueous and solid phases; $[\overline{Pd}]_{max}$,

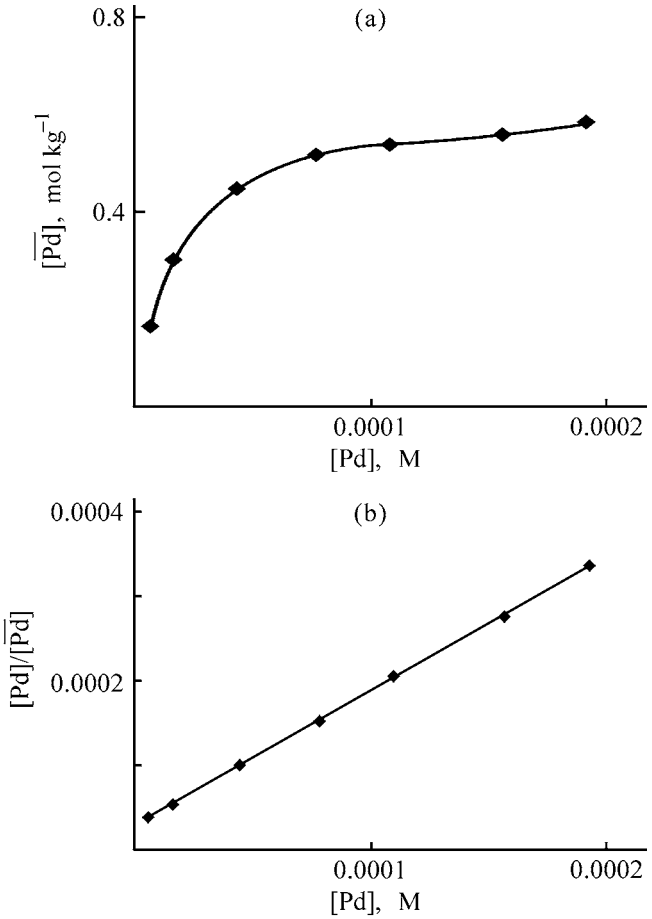

Fig. 4. (a) Distribution of Pd(II) among a 1 M solution of HCl, and an impregnated sorbent containing TOA in an amount of 1.26 mol kg^{-1} of FB, $[\overline{Pd}]$. (b) Linearization of Eq. (3).

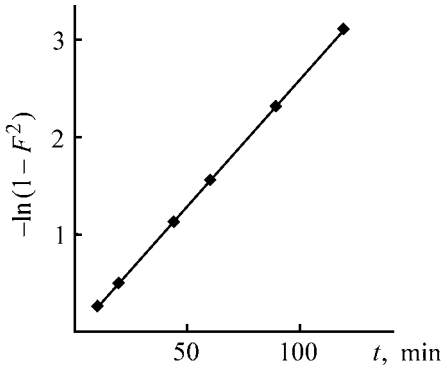

Fig. 5. Sorption of Pd(II) from a 1 M solution of HCl with an impregnated sorbent vs. the agitation time *t*.

maximum concentration of Pd(II) in the sorbent phase under the conditions of monolayer formation; and *K*, the equilibrium constant of the sorbent–sorbate system.

The value of $[\overline{Pd}]_{max}$, found from the data in Fig. 4b upon linearization of Eq. (3), is 0.63 mol kg^{-1} of FB, which corresponds, with account of the initial concentration of TOA (1.26 mol kg^{-1}) to the following stoichiometry of the complex being sorbed: Pd(II) : TOA = 1 : 2. The value $K = 5.88 \times 10^4$ corresponds to the equilibrium constant of the anion-exchange reaction (1), found above. This indicates that at the metal concentrations studied, the process of sorption recovery of Pd(II) from hydrochloric solutions is adequately described, by the equation of reaction (1).

According to the existing concepts [19], a sorbed TOAHCl molecule is oriented so that its hydrophobic moiety is directed toward the carbon matrix, and its polar reaction center, toward the aqueous phase. Thus considerably facilitates the anion exchange at the phase boundary. The rate of Pd(II) sorption is independent of the agitation rate in the range 50–1000 rpm, i.e., it is determined by the diffusion of the tetrachloropalladate anion being recovered within the pores of the sorbent [20]. The experimental dependence of Pd(II) sorption on the time of contact between the phases is described by the equation

$$-\ln(1 - F^2) = \overline{K}t, \qquad (4)$$

where *F* is the degree of completeness of sorption, calculated as a ratio of the sorption capacity at an instant of time t to the equilibrium capacity of the sorbent for Pd(II), and $\overline{K}$ is the apparent rate constant, found from the data in Fig. 5 to be $\overline{K} = 4.3 \times 10^{-4}$ s^{-1}.

The data presented above show that fullerene black impregnated with TOA can be used for recovery of Pd(II) from aqueous solutions.

CONCLUSIONS

(1) Fullerene black impregnated with trioctylamine effectively recovers Pd(II) from hydrochloric solutions.

(2) In the concentration range studied, $[PdCl_4]^{2-}$ is sorbed as a complex $[PdCl_4](TOAH)_2$ through an anion-exchange reaction with trioctylammonium chloride. The equilibrium constant of this reaction is $(5.75 \pm 0.13) \times 10^4$.

REFERENCES

1. Meretukov, M.A., *Ispol'zovanie impregnirovannykh materialov dlya izvlecheniya i razdeleniya tsvetnykh metallov: Obzornay informatsiyua TsNIIEITsM* (Use of Impregnated Materials for Recovery and Separation of Nonferrous Metals: Review by TsNIIEITsM), 1980, issue 2.

2. Cortina, J.L. and Warshawsky, A., *Ion Exch. Solvent Extraction*, 1997, vol. 13, pp. 195–293.
3. Rovira, M., Cortina, J.L., Arnaldos, J., and Sastre, A.M., *Solv. Extr. Ion Exch.*, 1998, vol. 16, pp. 1279–1302.
4. Turanov, A.N., *Zh. Prikl. Khim.*, 1990, vol. 63, no. 11, pp. 2602–2604.
5. Turanov, A.N., *Zh. Prikl. Khim.*, 1992, vol. 65, no. 1, pp. 121–125.
6. Rovira, M., Hurtado, L., Cortina, J.L., *et al*. *Solv. Extr. Ion Exch.*, 1998, vol. 16, pp. 545–564.
7. Turanov, A.N., Karandashev, V.K., and Reznik, A.M., *Zh. Prikl. Khim.*, 2000, vol. 73, no. 5, pp. 744–750.
8. Tatarchuk, V.V., Paasonen, V.M., Korda, T.M., and Shubin, Yu.V., *Zh. Neorg. Khim.*, 2000, vol. 45, no. 4, pp. 732–738.
9. Kulikov, A.V., Kushch, S.D., Fursikov, P.V., and Bogatyrenko, V.R., *Appl. Magn. Reson.*, 2002, vol. 22, pp. 539–550.
10. RF Patent 2121965.
11. Ginzburg, S.I., Ezerskaya, N.A., Prokof'eva, I.V., *et al.*, *Analiticheskaya khimiya platinovykh elementov* (Analytical Chemistry of Platinum-Group Elements), Moscow: Nauka, 1972.
12. Mazurova, A.A. and Gindin, L.M., *Zh. Neorg. Khim.*, 1965, vol. 10, no. 11, pp. 2559–2563.
13. Mazurova, A.A. and Gindin, L.M., *Zh. Neorg. Khim.*, 1965, vol. 10, no. 2, pp. 489–496.
14. Ivanova, S.N., Gindin, L.M., Chernyaeva, A.P., *et al.*, *Izv. Sib. Otd. Akad. Nauk SSSR, Ser. Khim. Nauk*, 1978, no. 14, issue 6, pp. 68–73.
15. Selezneva, I.A., Ivanova, S.N., and Gindin, L.M., *Izv. Sib. Otd. Akad. Nauk SSSR, Ser. Khim. Nauk*, 1982, no. 14, issue 6, pp. 107–110.
16. Belova, V.V., Khol'kin, A.I., Zhidkova, T.I., and Sidorova, T.P., *Zh. Neorg. Khim.*, 1997, vol. 42, no. 11, pp. 1922–1926.
17. Hasegawa, Y., Kobayashi, I., and Yoshimoto, S., *Solv. Extr. Ion Exch.*, 1991, vol. 9, pp. 759–768.
18. Shmidt, V.S., *Ekstraktsiya aminami* (Extraction with Amines), Moscow: Atomizdat, 1980.
19. Gustafson, R.L., Albright, R.L., Heisler, J., *et al.*, *I&C Research Development*, 1968, vol. 7, no. 2, pp. 107–115.
20. Warshawsky, A., *Ion Exch. Solvent Extraction*, 1981, vol. 8, pp. 229–310.

Russian Journal of Applied Chemistry, Vol. 77, No. 4, 2004, pp. 531–537. Translated from Zhurnal Prikladnoi Khimii, Vol. 77, No. 4, 2004, pp. 538–543.

INORGANIC SYNTHESIS AND INDUSTRIAL INORGANIC CHEMISTRY

Synthesis of Micro- and Nanoporous Materials from Silicon Carbide in Ultradisperse Reaction Systems

V. G. Gilev

Scientific Center for Powder Materials Science, Perm', Russia

Received March 20, 2004; in final form, December 2003

Abstract—The synthesis of porous sorption-active materials and membranes from SiC in the reaction system composed of 70% Si and 30% C was studied. The influence exerted by the conditions under which the reaction mixture is dispersed and compacted samples are thermally treated on the porous structure, specific surface area, permeability, and strength of the resulting materials was analyzed.

Silicon carbide is of interest as a basis for sorption-active and membrane materials owing to its chemical activity, abrasion resistance, temperature stability, and ability to sorb organic pollutants from water filtered through filters based on this compound [1–3]. A high temperature stability of micro- and mesoporous materials and nanoporous membranes based on silicon carbide would be expected in view of the high melting point of SiC and the covalent nature of atomic bonds in this compound [4].

Methods for production of membranes and porous materials with pore size of 1–2 μm from silicon carbide have been sufficiently well developed [1–3, 5, 6]. However, it is difficult to obtain a ceramic with a smaller pore size by usual sintering of ceramic powders. For example, when ultradisperse powders (UDP) of the high-melting compounds TiN and AlN are sintered, raising the temperature to $0.45–0.6T_m$ leads to shrinkage, with the pore size simultaneously increasing [5].

To synthesize microporous materials and membranes from silicon carbide, it has been suggested to use the following solid-phase reaction [7]:

$$Si_s + C_s = SiC. \quad (1)$$

The thus obtained silicon carbide materials with pore size of 0.4–0.7 μm demonstrate highly selective properties in purification of water [8]. It has been found [7] that lowering the temperature of synthesis from 1600 to 1300°C results in an increase in the specific surface area of silicon carbide materials to more than 20 $m^2 g^{-1}$, which opens up opportunities for creating sorption-active materials. Furthermore, estimates of the pore size by the formula $r_{ef} = 2\Pi/S_{sp}$ (Π is the porosity, and S_{sp}, the specific surface area) give a value of about 20 nm. At this pore size, free-molecular gas flow or Knudsen diffusion, on which membrane separation of gases is based [9], becomes possible.

The aim of this study was to develop further this method for obtaining sorption-active materials and membranes based on nanoporous silicon carbide with the use of highly dispersed Si–C reaction mixtures with 30% C.

EXPERIMENTAL

Dry mixtures of KR1 silicon and S-1 colloidal graphite with Si : C weight ratio of 70 : 30 were ground with steel balls of diameter 5.2 and 6.8 mm in an AGO-3 high-energy planetary activator for 3–10 min. The weight of the mixture was 100 g, and that of steel balls, 2000 g. In some cases, thermally expanded graphite (TEG) manufactured by Novomet-Perm Closed Joint-Stock Company was additionally introduced into the resulting highly dispersed mixture. Samples of the materials were compacted under a pressure of 50–150 MPa with a technological binder composed of a 5% aqueous solution of polyvinyl alcohol (PVA), in amount of 1–4 ml per 10 g of the mixture. Mixtures with TEG additive were compacted without a binder. A thermal treatment was carried out in argon, nitrogen, and carbon dioxide, and in a vacuum with a residual pressure of 10 Pa in a furnace with a graphite heater.

1070-4272/04/7704-0531 © 2004 MAIK "Nauka/Interperiodica"

Table 1. Sorption characteristics of silicon carbide materials synthesized from Si–C reaction mixtures with 30% C

Duration of grinding, min	S_{sp} of a mixture, $m^2\ g^{-1}$	P, MPa	Sintering			П, %	Gas-permeability coefficient, μm^2	D_{max}, μm	S_{sp}, $m^2\ g^{-1}$
			T, °C	τ, h	medium				
5	88	50	1600	1	Ar	61	0.008	0.5	5.9
5	88	100	1600	1	Ar	58	0.005	0.47	6.5
5	88	150	1600	1	Ar	54	0.002	0.41	11.0
10	32	50	1300	2	Ar	57	0.0025	0.5	24.2
5	88	50	1600	0.5	Ar	57	0.0045	0.36	8.2
10	32	50	1600	0.5	Ar	56	0.02	1.0	2.3
5	88	50	1600	2	Ar	58	0.006	0.56	3.6
6	115	50	1220	0.5	CO_2	56	0.0006	0.38	30.2
4	58	50	1130	0.67	$N_2 + H_2^*$	43	0.00022	<0.3	26.7
4	58	50	1130	0.67	$N_2 + H_2^*$	42	0.00008	<0.3	22.9
6	115	50	1130	0.67	$N_2 + H_2^*$	50	0.00026	<0.3	33.4
6**	115**	25	1130	0.5	Ar	64	0.0005	<0.3	41.0

* Atmosphere of dissociated ammonia.
** Sample with an addition of 17% TEG.

Supports for silicon carbide membranes were prepared from SiC powders with addition of SiO_2 and CaO in amounts of 10 wt % each [10]. The dry mixture was ground with hard-alloy balls for 24 h in a ball mill lined with a hard alloy, compacted using a 5% aqueous solution of PVA as a temporary technological binder under a pressure of 100 MPa, and sintered in argon at 1620°C for 30 min. The preparation of the supports was described in detail in [10]. To obtain double-layer membranes, a layer of highly dispersed reaction mixture containing 17% TEG was fixed by pressing on a support, and a synthesis was carried out in argon at 1100°C for 30 min. Layers of thickness 200 μm, firmly adhering to the supports, were obtained in this way.

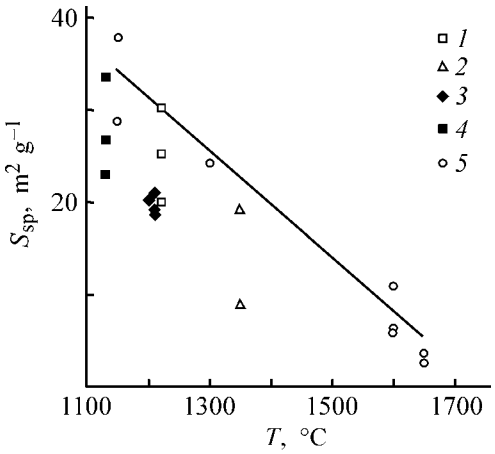

Fig. 1. Specific surface area S_{sp} of a porous silicon carbide material synthesized from a 70% Si–30% C mixture vs. temperature of synthesis, T. (*1*) CO_2, (*2*) vacuum, (*3*) N_2, (*4*) $N_2 + H_2$, and (*5*) Ar.

The gas-permeability was determined in accordance with GOST (State Standard) 25283–82, and the maximum and average sizes of channel pores were found from the gas-driving pressure in accordance with GOST 26849–86 (bubble method).

The phase composition of the samples was analyzed on a DRON-4-13 diffractometer with the λ_{K_a}(Co) radiation and a graphite monochromator. The recording was done point-by-point with a scanning step of 0.02°–0.05° and a 10-s exposure at each point. The specific surface area was determined by the BET method on a GKh-1 gas-meter. Nitrogen adsorption isotherms were obtained on a Carlo Erba Strumentazone Sorbtomatic 1800 device (Italy). The sample strength was determined with a three-point bend on an Instron 1195 test machine on samples in the form of $3 \times 5 \times 40$-mm bars.

The use of a highly dispersed reaction mixture (70% Si–30% C) with S_{sp} of up to 115 $m^2\ g^{-1}$ makes it possible to obtain materials with a specific surface area of pores of up to 48 $m^2\ g^{-1}$ (Fig. 1). The temperature of synthesis strongly affects S_{sp}. Furthermore, S_{sp} increases when the isothermal exposure becomes shorter and when the specific surface area of the initial mixtures increases. The data scatter in Fig. 1 is due to variation of these parameters.

As the compacting pressure is raised from 50 to 150 MPa, S_{sp} increases from 5.9 to 11.0 $m^2\ g^{-1}$ in the case of synthesis in argon at 1600°C for 1 h and from 39.2 to 42.4 $m^2\ g^{-1}$ in synthesis at 1100°C for 0.5 h. The materials synthesized in argon have the highest specific surface area.

The possibility of using these materials as membranes is determined not only by the average pore size r_{ef}, but also by the pore size distribution and especially by the presence of larger pores. When the temperature of synthesis is lowered, the maximum pore size decreases to 0.2–0.3 μm and less (Table 1). Making longer the isothermal exposure at 1600°C results in an increase in the maximum pore size. These changes indicate that the materials obtained with short isothermal exposures are in a nonequilibrium state and, in spite of a rather low temperature {1600°C corresponds to 0.63 T_m (SiC), and sintering of silicon carbide begins at 0.8 T_m (SiC) [4]}, structural transformations take place. Addition of 17% TEG to the 70% Si–30% C mixture with S_{sp} = 115 $m^2 g^{-1}$ leads to an increase in porosity, but the gas permeability and the maximum pore size do not increase significantly in this case (Table 1).

Lowering the temperature and making shorter the duration of isothermal exposure should result in a decelerated and incomplete synthesis and crystallization of a new phase. An X-ray structural analysis demonstrated that, if a 70% Si–30% C mixture is converted to a highly dispersed state with S_{sp} = 115 $m^2 g^{-1}$, the synthesis of SiC is strongly accelerated, and its temperatures decrease substantially. Thus, after a 20-min exposure in argon at 1150°C no graphite lines were found in the X-ray diffraction pattern, with only two weak lines of silicon present. When a mixture with S_{sp} = 61 $m^2 g^{-1}$ is used under the same conditions, a significant amount of unreacted silicon remains (Fig. 2). The X-ray diffraction pattern of a sample of the mixture with S_{sp} = 115 $m^2 g^{-1}$, sintered at 1650°C within 0.5 h, shows that the high-temperature synthesis provides a full expenditure of the reagents, with, however, the ratio of line intensities not coinciding with tabulated data for the equilibrium SiC phases (6H, 15R, 3C).

When a dispersed mixture with S_{sp} = 115 $m^2 g^{-1}$ is subjected to a short (0.17 h) heat treatment at a low temperature (1200°C) in nitrogen, a significant amount of silicon nitride Si_3N_4 is formed alongside with SiC (Fig. 3). It is known [11] that the conventional technologies based on nitriding of silicon involve long exposures at temperatures of at least 1300°C. The content of silicon nitride in the materials synthesized from mixtures with S_{sp} = 61 $m^2 g^{-1}$ is lower, and it does not increase on heating to 1600°C. Apparently, both silicon nitride and silicon carbide are synthesized in early stages of heating. In this case, the amount of silicon nitride is mainly determined by the kinetic opportunities for delivery of nitrogen to within a sample. Therefore, the extent of the nitriding

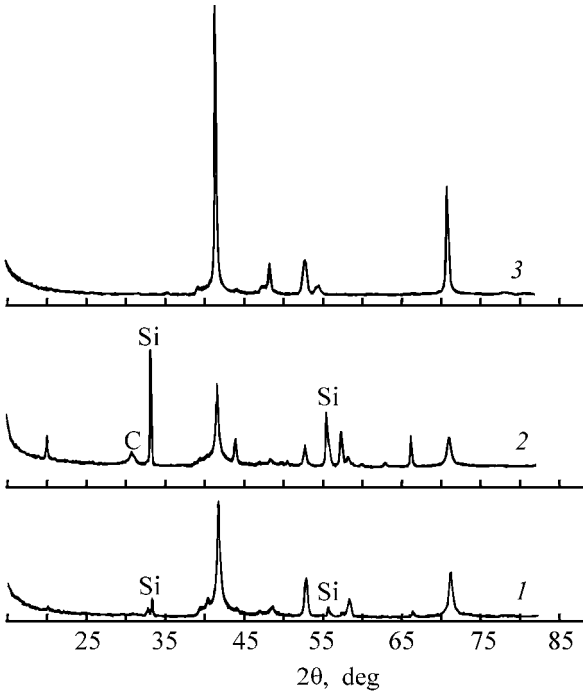

Fig. 2. X-ray diffraction patterns of samples of porous materials based on silicon carbide, synthesized in argon. (2θ) Bragg angle; the same for Fig. 3. Synthesis mode: (*1*) and (*2*) 1150°C, 0.33 h; (*3*) 1650°C, 0.17 h. Specific surface area of the initial reaction mixtures ($m^2 g^{-1}$): (*1*) and (*3*) 115; (*2*) 61.

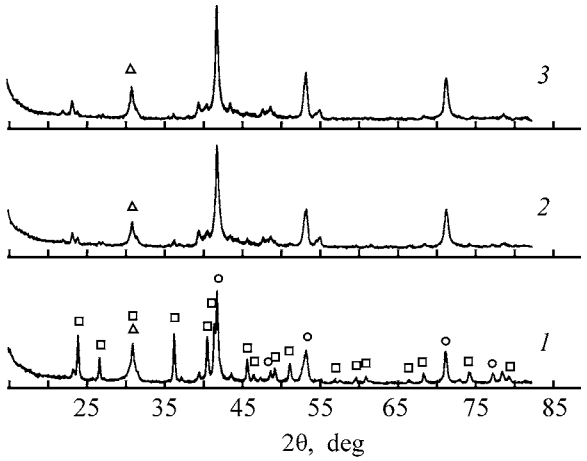

Fig. 3. X-ray diffraction patterns of porous materials synthesized from 70% Si–30% C mixtures in nitrogen. (*I*) SiC, (*II*) α-Si_3N_4, (*III*) graphite. Synthesis regime: (*1*) 1200°C, 0.17 h; (*2*) 1210°C, 0.25 h; (*3*) 1600°C, 0.25 h. Specific surface area of the initial reaction mixtures ($m^2 g^{-1}$): (*1*) 115; (*2*) and (*3*) 61.

reaction in samples of a mixture with S_{sp} = 115 $m^2 g^{-1}$ is greater not only because of the particle size, but also owing to the higher porosity of a sample.

An analysis of the porous structure on the basis of isotherms of nitrogen adsorption demonstrated that

Table 2. Characteristics of porous structure, determined from isotherms of nitrogen adsorption for materials based on silicon carbide as compared with analogous materials*

Technological parameters					Porous structure parameters					
S_{sp} of mixture, $m^2\ g^{-1}$	TEG additive, wt %	T, °C	τ, h	medium	S_{BET}	S_{me}	V_{mi}	V_{me}	W_s	r_p, nm
					$m^2\ g^{-1}$		$cm^3\ g^{-1}$			
87	–	1600	1	Ar	6.1	3.8	0.003	0.008	0.011	3.6
87	–	1600	0.25	Ar	8.6	6.8	0.004	0.012	0.016	3.7
32	–	1300	2	Ar	18.5	16.2	0.007	0.019	0.026	2.8
87	–	1210	0.25	N_2	19.0	13.2	0.008	0.023	0.031	3.3
46	–	1350	0.5	Vacuum	20.7	17.3	0.009	0.029	0.038	3.7
115	–	1150	0.33	Ar	37.2	30.0	0.015	0.045	0.060	3.2
115	–	1220	0.5	CO_2	31.2	23.2	0.013	0.059	0.072	4.6
115	–	1100	0.5	CO_2	48.3	44.7	0.020	0.058	0.078	3.2
115	33	1100	0.5	CO_2	40.9	26.3	0.018	0.059	0.077	3.8
115	17	1350	0.5	Ar	27.4	23.2	0.012	0.098	0.110	8.0
115	33	1350	0.5	Ar	24.9	14.9	0.011	0.086	0.097	7.7
Active coal from FFS [12]							0.1–0.4	0.05–0.2		
Sintered from TiN SDP at 800°C [5]					21.8		0		0.24	
Sintered from AlN SDP at 800°C [5]					20.8		0		0.43	
Sintered from Al_2O_3 SDP [13]							0		0.29	16.8

* Blank places in Table 2 are due to the lack of data.

the total volume of the sorption space of SiC materials is considerably smaller than that of sorbents based on active coals [12] (Table 2). However, a positive point is that they contain an appreciable volume of micropores. Micropores are completely absent in the materials obtained by sintering of UDP of AlN, TiN, and Al_2O_3 [5, 13].

The volume of micropores and the total sorption space grow in proportion to the increase in the specific surface area. Introduction of thermally expanded graphite as an additive to the 70% Si–30% C mixture with S_{sp} = 115 $m^2\ g^{-1}$ in amounts of 17 and 33 wt % changes the shape of adsorption isotherms and raises the total sorption volume W_s mainly because of an increase in the fraction of micropores. Simultaneously, the fraction of micropores decreases somewhat. The effective pore size $r_p = W_s/S_{BET}$ increases when TEG is added. The properties of thermally expanded graphite essentially differ from those of ordinary graphite, and, therefore, the synthesis of silicon carbide in mixtures of silicon and TEG has its own specificity. The authors of [14] believe that the honeycomb structure of particles of thermally expanded graphite, which is retained on its mixing with dispersed silicon, decelerates the exothermic reaction of synthesis. Thus, elevating the temperature and making longer the synthesis leads to a more complete consumption of reagents and, simultaneously, to a decrease in the specific surface area and in the volume of micropores.

There exists an opinion [15] that pores of size 2 nm and less can be obtained only in materials of two types: in those based on carbon and in zeolites. Sorbents based on carbon are produced either by pyrolysis of hydrocarbons [12] or by treatment of carbides with chlorine [6, 16]. Recently, the preparation of silicon carbide with a pore size of less than 1 nm by pyrolysis of organosilicon precursors has been reported [17].

The experimental results obtained in this study and published data suggest that micropores are formed in the carbon phase. In this case, the decrease in S_{sp} and V_{mi} with increasing synthesis temperature and annealing duration are readily attributable to the decrease in the amount of carbon remaining in the course of reaction (1). We can also assume that micropores are formed in silicon carbide, but this microstructural state of SiC is metastable. It is evident that the mechanism of micropore formation is associated with diffusion processes that accompany reaction (1). A more detailed discussion of the micropore formation requires an additional study.

Table 3. Bending strength σ_{fl} of porous silicon carbide materials synthesized from reaction mixtures 70% Si–30% C (compacting pressure P = 50 MPa)

Milling time, min	S_{sp} of mixture, $m^2\ g^{-1}$	Sintering			Π, %	S_{sp}, $m^2\ g^{-1}$	σ_{fl}, MPa
		T, °C	τ, h	medium			
3	61	1150	0.33	Ar	47	28.7	51.4
6	115	1150	0.33	Ar	54	37.9	30.4
6	115	1650	0.17	Ar	59	2.6	12.0
7	46	1650	0.17	Ar	50	3.7	31.9
5	88	1600	0.5	Ar	48	Not determined	12.0
3	61	1350	0.5	Vacuum	52	9.0	36.0
7	46	1350	0.5	″	47	19.3	39.8
3	61	1210	0.25	N_2	43	19.1	63.6
5	88	1210	0.25	N_2	41	20.9	78.7
3	61	1600	0.25	N_2	42	19.9	45.8

Usually, mechanical properties of materials obtained by sintering of powders are improved as the temperature of sintering is raised. However, if materials are synthesized by reactive sintering with the use of reaction (1), the strength increases when the sintering temperature is somewhat lowered (Table 3). The high strength of the materials sintered in the atmosphere of nitrogen results from their greater density and from the presence of silicon nitride in their composition. It is also seen that lowering the temperature of synthesis from 1600 to 1220°C results in a higher strength in this case, too.

Commonly, the limiting stress at which cracks appear in fragile materials is determined by the size of the largest defects. In our case, we cannot attribute the rise in strength on lowering the temperature of synthesis to the corresponding change in the maximum size of channel pores, measured by the bubble method (Table 1), as they are not the largest. The structure contains pores about 1 μm in size (Fig. 4), which are the compaction defects. The microstructure of an Al–SiC composite obtained by impregnation of the pore space of the ceramic under study with a molten aluminum alloy under a pressure is shown in Fig. 4. The increase in the material strength in the case of the low-temperature synthesis seems to be attributable to structural features on a deeper level of the hierarchy. For example, we can assume that the size of SiC crystallites forming the skeleton is comparable with the pore size, i.e., SiC crystals are nanosize.

The materials synthesized can be used in double-layer membranes as a nanoporous selective layer. Double-layer membranes with a coating of nanoporous SiC on silicon carbide supports were fabricated.

To obtain selective layers of double-layer membranes, we used a highly dispersed 70% Si–30% C mixture with a specific surface area of 115 $m^2\ g^{-1}$. We additionally introduced 17% TEG into this mixture. An even layer of the mixture was deposited on a support and fixed on its surface at a pressure of 25 MPa under isostatic conditions. The selective layers were sintered in argon at 1100°C in the course of 30 min. The thickness of the membrane layer, estimated by the weight of the coating deposited, was about 200 μm. The firm adherence of the selective layer to the sup-

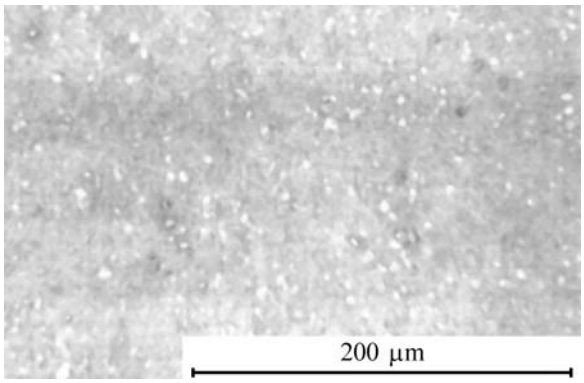

Fig. 4. Structure of an Al–SiC composite obtained by impregnation of the nanoporous ceramic under study with a molten aluminum alloy under pressure. *Light regions* correspond to the largest pores filled with Al alloy; *the gray background* is the nanodispersed Al–SiC mixture.

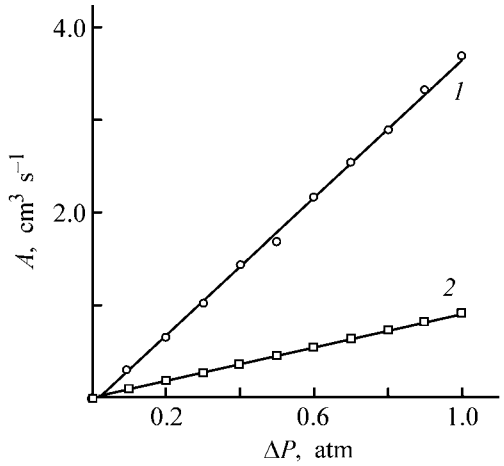

Fig. 5. Flow rate A of (*1*) hydrogen and (*2*) nitrogen vs. the pressure difference ΔP across a double-layer membrane with a silicon carbide support.

port is confirmed by the fact that a silicon carbide double-layer silicon carbide membrane sustained a return gas purging under a pressure of 5 atm.

The gas permeability of double-layer membranes in the case of hydrogen is 3.3 times that for nitrogen (Fig. 5). This ratio is close to a value of 3.7 given by the equation for the Knudsen diffusion coefficient:

$$D_i^K = \frac{l}{3}\sqrt{\frac{8\overline{RT}}{\pi\overline{M_i}}}.$$

Here M_i is mass of molecules; R, the universal gas constant; and T, temperature (K).

The dependence of the gas flow rate on the pressure difference is linear. Usually, deviations from a linear dependence are observed in the case of a viscous flow.

Furthermore, the viscosities of nitrogen and hydrogen differ by no more than a factor of 2 [18]. All the aforesaid suggests that the Knudsen gas flow prevails in the selective layer, which is attained under common pressures only in nanoporous materials.

A double-layer membrane with a silicon carbide support was tested in filtration of artesian water containing 1.2 mg l^{-1} of manganese ions. According to an atomic-absorption analysis carried out on a Proton instrument, the concentration of manganese ions in this water after the filtration decreased to below 0.1 mg l^{-1}.

CONCLUSIONS

(1) It was shown that use of reaction mixtures of silicon with graphite with a specific surface area of 120 $m^2 g^{-1}$ makes it possible to synthesize at rather low temperatures (1100–1200°C) porous silicon carbide materials with a porosity of 45–60%, a high (up to 48 $m^2 g^{-1}$) specific surface area, and a significant fraction of micropores (up to 0.020 $cm^3 g^{-1}$).

(2) Addition of 17 wt % thermally expanded graphite to a reaction mixture results in an increase in the total sorption space W_s to 0.11 $cm^3 g^{-1}$ because of the growing volume of mesopores.

(3) Raising the temperature of synthesis to 1600°C leads to a decrease in the specific surface area of the resulting material, an increase in the pore size, and a decrease in the material strength.

(4) Selective nanoporous layers (200 μm thick) of double-layer membranes firmly adhering to a silicon carbide support were obtained by synthesis of SiC at 1100°C from highly dispersed mixtures of silicon with graphite.

ACKNOWLEDGMENTS

The author is grateful to V.N. Antsiferov for interest in the study and for the discussion of the results obtained.

This study was financially supported by the Russian Foundation for Basic Research (project no. 02-03-32 531).

REFERENCES

1. Artyukhin, O.I., Kravchik, A.E., and Petrova, I.S., *Zh. Prikl. Khim.*, 1999, vol. 72, no. 12, pp. 2029–2031.
2. Tomilina, E.M., Lukin E.S., and Kagramanov, G.G., *Ogneupory Tekhn. Keram.*, 2000, no. 4, pp. 12–14.
3. Matchere, Zh., Merzhanov, A.G., Borovinskaya, I.P., *et al.*, *Ogneupory Tekhn. Keram.*, 1999, nos. 1–2, pp. 43–47.
4. Andrievski, R.A., *J. Mater. Sci.*, 1994, vol. 29, pp. 614–631.
5. Dalidovich, V.V., Fedorov, N.F., and Babkin, O.E., *Zh. Prikl. Khim.*, 1994, vol. 67, no. 6, pp. 942–945.
6. Gordeev, S.K. and Vartanova, A.V., *Zh. Prikl. Khim.*, 1994, vol. 67, no. 7, pp. 1080–1084.
7. Gilev, V.G., *Neorg. Mater.*, 2002, no. 3, pp. 371–377.
8. Gilev, V.G., and Glushankova, I.S., *Konstr. Kompozit. Mater.*, 2001, no. 2, pp. 25–29.

9. Dytnerskii, J.I., Brykov, V.P., and Kagramanov, G.G., *Membrannoe razdelenie gazov* (Membrane Separation of Gases), Moscow: Khimiya, 1991.
10. Gilev, V.G., Busovikova, T.M., and Loginov, M.G., *Izv. Vyssh. Uchebn. Zaved., Tsvetn. Metall.*, 2003, no. 1, pp. 59–64.
11. Andrievskii, R.A. and Spivak, I.I., *Nitrid kremniya i materialy na ego osnove* (Silicon Nitride and Materials on Its Basis), Moscow: Metallurgiya, 1984.
12. Dudarev, V.I., Elshin, V.V., and Oznobikhin, L.M., *Zh. Prikl. Khim.*, 1999, vol. 72, no. 2, pp. 319–321.
13. Dalidovich, V.V. and Fedorov, N.F., *Zh. Prikl. Khim.*, 1997, vol. 70, no. 6, pp. 943–946.
14. Gadzyra, N.F., Gnesin, G.G., and Mihailik, A.A., *Ogneupory Tekhn. Keram.*, 2001, no. 12, pp. 4–9.
15. *Tunable pores: Porous materials, Materials Today*, 2003, vol. 6, no. 10, p. 10.
16. Gordeev, S.K., Kukushkin, S.A., Osipov, A.V., and Pavlov, J.V., *Fiz. Tverd. Tela*, 2000, vol. 42, no. 12, pp. 2245–2248.
17. Ajayan, P.M., Schalder, L.S., and Braun, P.V., *Nanocomposite Science and Technology*, Weinheim: Wiley–VCH GmbH and Co. KGaA, 2003.
18. *Tablitsy fizicheskikh velichin: Spravochnik* (Tables of Physical Quantities: Reference Book), Kikoin, I.K., Ed., Moscow: Atomizdat, 1976.

Russian Journal of Applied Chemistry, Vol. 77, No. 4, 2004, pp. 538–542. Translated from Zhurnal Prikladnoi Khimii, Vol. 77, No. 4, 2004, pp. 544–547.

INORGANIC SYNTHESIS AND INDUSTRIAL INORGANIC CHEMISTRY

Thermal Oxidation and Photochromic Properties of Molybdenum-containing Porous Glasses Obtained by Molecular Layering

V. N. Pak, G. G. Potkina, S. V. Sukhanov, and S. M. Shilov

Gertsen Russian State Pedagogical University, St. Petersburg, Russia

Received December 29, 2003

Abstract—Molybdenum oxide groups were synthesized on a porous glass surface by the molecular layering technique. Kinetic features of Mo(V) $\rightleftarrows$ Mo(VI) transitions in thermal oxidation and photoreduction were studied for a set of samples containing 0.02–0.12 mmol g^{-1} of molybdenum.

Recently, photochromic properties of polyoxomolybdates in solutions, films, and solids have been intensively studied [1–5]. A typical blue color arising under UV irradiation is, as a rule, caused by the transition of a part of Mo(VI) atoms to the Mo(V) state. The appearance, in this case, of an electron on the 4*d* orbitals of the metal makes possible *d*–*d* transitions and gives rise to optical absorption in the visible range. The fact that photochromism is a characteristic feature of molybdenum clusters, which is not observed in the case of the $[MoO_4]^{2-}$ monomer, allows it to be regarded as a "dimensional" property. In this context, it may be assumed that an increase in the number of molybdenum atoms in oxide particles stabilizes the photoreduced form through delocalization of $4d^1$ electrons over its "metal core." However, this assumption has not been confirmed experimentally because of certain difficulties in reliable identification, of molybdenum-oxide clusters in solutions, and especially in their isolation in the solid state [1–5].

In the present study, we examined the influence exerted by collective *d*–*d*-electron interactions on the Mo(V) $\rightleftarrows$ Mo(VI) intervalence transitions via thermal oxidation and photo-reduction of molybdenum-oxide groups grafted to the porous glass surface by the molecular layering technique [6]. Previously, we have shown [7–9] that the reaction of $MoCl_5$ with a completely hydroxylated silica surface presumably occurs by the scheme

$$3(\equiv Si–OH) + MoCl_5 \rightarrow (\equiv Si–O–)_3MoCl_2 + 3HCl. \quad (1)$$

The treatment of the resulting chlorine-containing product with water vapor lead to the formation of Mo(V) hydroxy groups chemically bound to a support:

$$(\equiv Si–O–)_3MoCl_2 + 2H_2O \rightarrow (\equiv Si–O–)_3Mo(OH)_2 + 2HCl. \quad (2)$$

It has been established [7, 8] on the basis of IR spectral data that the thermal oxidation of Mo(V) silica involves the formation of Mo–O–Mo bridging bonds between adjacent molybdenum-oxide groups (in this case, a partial "inner-sphere" condensation of hydroxy groups occurs to give Mo=O molybdenyl bonds). The kinetic features of their oxidation, their possible relationship with the degree of filling of the SiO_2 surface with grafted groups, and the possible photochromic properties of oxidized Mo(VI) silica remain unstudied.

EXPERIMENTAL

Thin polished plates (1 mm thick) of porous glass (PG) were used in the experiments. The porous glass was obtained by leaching of the DV-1M sodium-borosilicate glass thermally pretreated (6 days at 530°C with subsequent annealing at 480°C for 3 h). The specific surface area of PG (80 $m^2 g^{-1}$) was determined from low-temperature adsorption of argon. The average pore radius (4.5 nm) was found from parameters of the hysteresis loop in the region of capillary condensation of water [10].

1070-4272/04/7704-0538 © 2004 MAIK "Nauka/Interperiodica"

The modification reaction (1) was carried out as described earlier [7–9] at room temperature in solutions of $MoCl_5$ in dried CCl_4. After 2 h of contact, the solution was removed, the glass plates were thoroughly washed with the solvent to complete removal of trace amounts of molybdenum(V) in the washout. The content of Mo(V) in the grafted groups was varied by changing the concentration of the working solutions. To carry out a quantitative analysis, the modifying component was dissolved by boiling in 0.1 M sulfuric acid. Molybdenum(V) was determined by photocolorimetry in the presence of ammonium thiocyanate [11]. The surface of the modified PG [reaction (2)] was hydroxylated at 180°C in a flow of nitrogen saturated with a water vapor. The completion of the reaction was judged from the absence of hydrogen chloride at the reactor outlet.

The molybdenum(V)-containing plates were oxidized in air in the temperature range 100–160°C. The oxidation process was monitored by their spectra in the visible range (SF-56 spectrometer). To study the photochromic properties of thermally oxidized glasses, they were irradiated with an unfiltered light of an SVD-120A mercury lamp.

The spectra of glass plates modified with molybdenum(V) oxide groups are shown in Fig. 1. A weak absorption peak at 760 nm is observed for all the samples. The strong band in the short-wavelength region corresponds to charge transfer from pseudo-atomic nonbonding oxygen orbitals to 4*d* molybdenum orbitals $2p^n(O) \rightarrow 4d(Mo)$. The poor resolution of the spectra in the visible range seems to be determined not only by the vibronic, but also by the exchange interaction of Mo(V) $4d^1$ electrons of neighboring groups [9]. For the set of the glasses obtained, the linear dependence of the optical density D at λ = 760 nm on the Mo(V) content in a grafted layer is well observed.

To study the stability of the molybdenum(V) state, we plotted time dependences of D for the oxidation of the modified plates in air. The corresponding experimental data, shown in Fig. 2 for three compositions, are described by the second-order kinetic equation

$$\Delta D/\tau = kD_0(D_0 - \Delta D), \quad (3)$$

where k is the oxidation rate constant and D_0 is the initial optical density.

Linearization of the kinetic curves in the coordinates of Eq. (3) allows us to determine the constants and their temperature dependences, which are shown

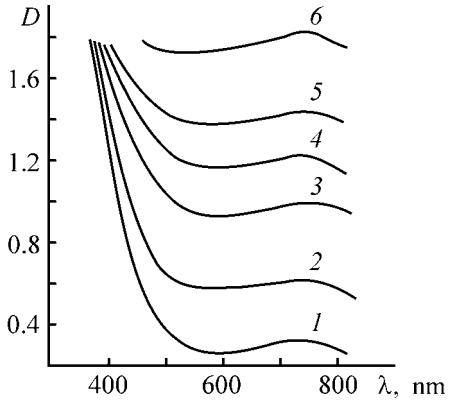

Fig. 1. Spectra of PG plates modified with Mo(V) oxide groups. (D) optical density and (λ) wavelength. Content of molybdenum(V) oxide groups (mmol g^{-1}): (*1*) 0.021, (*2*) 0.043, (*3*) 0.068, (*4*) 0.087, (*5*) 0.098, and (*6*) 0.127.

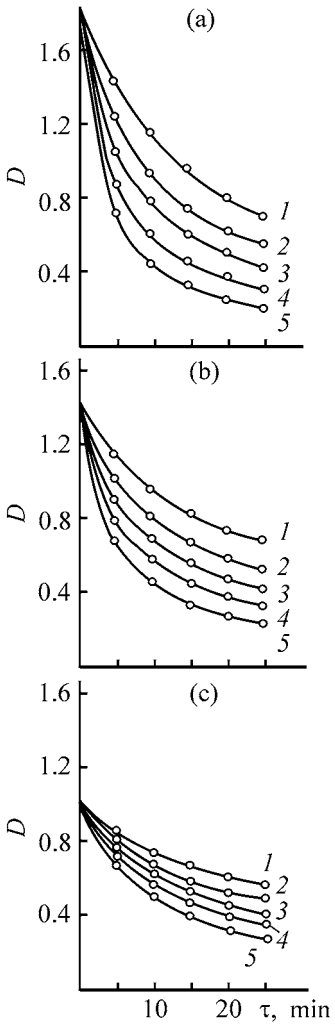

Fig. 2. Kinetic curves for oxidation of Mo(V)-containing PGs at various temperature. (D) optical density and (τ) time; the same for Fig. 5. T (°C): (*1*) 100, (*2*) 110, (*3*) 125, (*4*) 140, and (*5*) 160. Content of Mo(V) in the samples (mmol g^{-1}): (a) 0.127, (b) 0.087, and (c) 0.068.

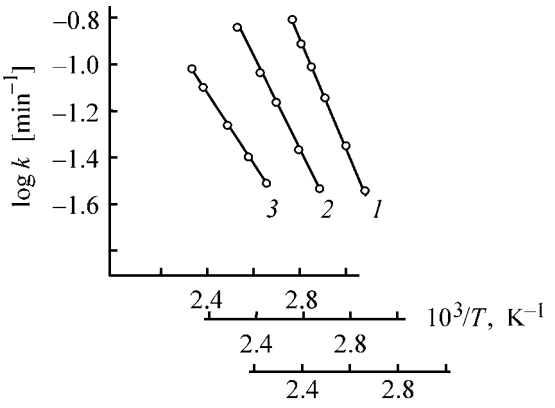

Fig. 3. Logarithm of the rate of oxidation of Mo(V)-containing PGs vs. temperature *T*. Content of Mo(V) in the samples (mmol g^{-1}): (1) 0.127, (2) 0.087, (3) 0.068.

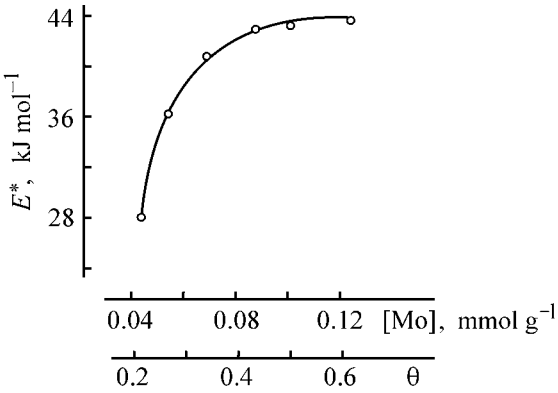

Fig. 4. Activation energy E^* of the oxidation reaction vs. the content of Mo(V) oxide groups, [Mo], and the degree of filling of the porous glass surface with these groups, θ.

for three selected compositions in Fig. 3, and to calculate the activation energies of oxidation, E^*. The fact that these energies are low (Fig. 4) indicates that the reaction occurs in the diffusion region. However, it is not improbable that the values obtained correspond to oxidation, which occurs with an appreciable rate even at moderate temperatures.

The clearly pronounced and characteristic change in the activation energy for the set of samples under study can be interpreted as an evidence of the increasing stability of Mo(V) state at higher concentrations of the component deposited. The most probable reason for the stabilization of molybdenum(V) oxide groups are the lateral Mo(V)···Mo(V) interactions, which predetermine the delocalization of $4d^1$ electrons of molybdenum within the surface layer [9]. In terms of the general theory of conjugated systems, an increase in the conjugation area (chain length) results in a fast manifestation of the basic energetic contribution to the stability. The observed dependence of the activation energy of oxidation on the content of Mo(V) in the grafted layer (Fig. 4) well corresponds to this behavior. The degree of surface filling with grafted groups can be estimated to a first approximation as:

$$\theta = 3[\mathrm{Mo}]/\alpha_{\mathrm{OH}}S_{\mathrm{sp}}. \quad (4)$$

Here [Mo] is the content of molybdenum(V) in the porous glass (μmol g^{-1}); α_{OH} = 7.5 μmol m^{-2}, the average "concentration" of OH groups on a completely hydroxylated surface of silica [12]; S_{sp} = 80 m^2 g^{-1}; and the coefficient 3 corresponds to the dominant grafting mode [reaction (1)].

The role of the "concentration" contribution to the stabilization of molybdenum(V)-containing glasses, discussed here, is also clearly seen when studying the photochromic properties of oxidized samples. It is typical that a prolonged UV irradiation of a glass with a low [Mo(VI)] content of 0.021 mmol g^{-1} does not lead to any observable consequences, whereas an increase in the degree of filling of the PG surface with molybdenum(V) oxide groups leads to the appearance and enhancement of the photochromic properties. In this case, the spectra of plates reduced under UV irradiation are close to those of the initial molybdenum(V)-containing samples.

The kinetics of photoreduction of modified PG plates is illustrated in Fig. 5 by the plots of optical density *D* at λ = 760 nm against the duration of irradiation. It is typical that the *D*–τ curves are almost linear in their main portions and rapidly level off at τ > 40 min. The observed constant oxidation rate may be due to the compensation of the decrease in the content of the oxidized form by the acceleration of the reaction by the progressive Mo(V)···Mo(V) cation–cation interactions. A significant deceleration of the process at τ > 40 min is most likely due to a limited penetration of the UV irradiation into the plate, which corresponds to a strong absorption in the range of charge-transfer transitions (Fig. 1).

The degree of photoreduction can be judged from the parameter

$$\eta = (D^*/D_0) \times 100\%.$$

Here D_0 is the initial optical density of Mo(V)-containing plates and *D* is the optical density after a 1-h irradiation of oxidized samples.

The character of the resulting dependence of η on the content of the photochromic component (Fig. 5) is one more indication of the increasing stability of molybdenum(V) oxide groups at their higher content in the glass.

The photoreduction is completely reversible. The absorption in the visible range is eliminated by annealing the samples in air at 100–150°C. The observed photochromic properties of molybdenum-containing porous glasses are independent of the humidity and possible presence of reducing molecules in air. Moreover, the dehydration of oxidized samples and their subsequent UV irradiation in a quartz cuvette in a flow of helium give rise to a moderate, but clearly observable acceleration of the photoreduction as compared with the photoreduction in air. It is likely that the equilibrium is shifted in the inert gas toward detachment and desorption of the mobile "bridging" oxygen, which determines the state of molybdenum in the grafted groups [9].

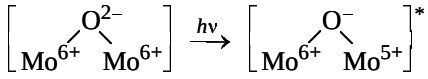

$$\xrightarrow{-\frac{1}{2}O_2} [Mo^{5+}]\cdots[Mo^{5+}].$$

In fact, the Mo(VI) → Mo(V) transition occurs even upon excitation in the charge-transfer band $2p^n(O) \rightarrow 4d(Mo)$. The formation of metal–metal bonds and the delocalization of Mo(V) pseudoatomic $4d^1$ electrons over these bonds stabilize the reduced state.

In conclusion it may be noted that the structural features and the "topographical density" of grafting of molybdenum-oxide groups on the accessible PG surface, which depend on the method of synthesis, determine the clearly pronounced photochromic properties of the samples under study. The photochromism appears to a considerably lesser extent in most of the known molybdenum-oxide media [1–5]. The mobility of oxygen in the Mo–O–Mo bonds in molybdenum-containing porous glasses produced by molecular layering is reflected both in the rate and extent of photoreduction and in the readily occurring thermal regeneration of the oxidized state.

CONCLUSIONS

(1) Molybdenum-oxide groups were synthesized on a porous glass surface in amounts of 0.02–0.12 mmol g^{-1}. The rate constants of oxidation of Mo(V)-containing porous glasses by atmospheric oxygen at 100–160°C were determined. The activation energies of oxidation indicate that the stability of the Mo(V) state grows as the content of grafted groups increases.

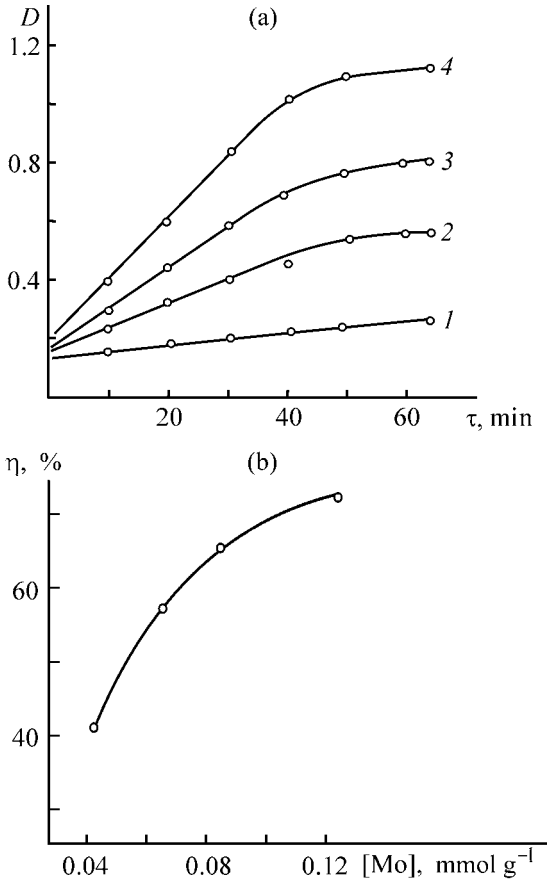

Fig. 5. (a) Kinetics of photoreduction of modified PGs with varied content of Mo(VI) and (b) dependence of the degree of reduction, η, on the content of Mo(VI) in the PG. Content of Mo(V) in the samples (mmol g^{-1}): (*1*) 0.043, (*2*) 0.068, (*3*) 0.087, and (*4*) 0.127.

(2) The photochromic properties of Mo(VI)-containing porous glasses were revealed. The rate and degree of photoreduction are determined by the content of a grafted component. The reversibility of Mo(V) ⇄ Mo(VI) transitions was attributed to the mobility of oxygen in the Mo–O–Mo bonds between the neighboring molybdenum-oxide groups. The attention is called to the possibility of stabilization of the reduced forms through delocalization of molybdenum(V) $4d^1$ electrons within the system of metal–metal bonds.

REFERENCES

1. Gavrilyuk, A.I. and Sekushin, N.A., *Elektrokhromizm i fotokhromizm v oksidakh vol'frama i molibdena* (Electrochromism and Photochromism in Tungsten and Molybdenum Oxides), Leningrad: Nauka, 1990.

2. Andreev, V.N., Nikitin, S.E., Klimov, V.A., *et al.*, *Fiz. Tverd. Tela*, 2001, vol. 43, no. 4, pp. 755–758.
3. He, T., Ma, Y., Cao, Y.A., Jang P., *et al.*, *Langmuire*, 2001, vol. 17, no. 26, pp. 8024 – 8027.
4. Quevedo-Lopez, M.A., Ramirez-Bon, R., Orozko-Teran, R.A., *et al.*, *Thin Solid Films*, 1999, vols. 343–344, no. 1, pp. 202–205.
5. Scarminio, J., Lourenco, A., and Gorenstein, A., *Thin Solid Films*, 1997, vol. 302, nos. 1–2, pp. 66 –70.
6. Aleskovskii, V.B., *Khimiya tverdykh veshchestv* (Chemistry of Solid Substances), Moscow: Vysshaya Shkola, 1978.
7. Pak, V.N., Vorob'eva, G.G., and Ragulin, G.K., *Zh. Fiz. Khim.*, 1986, vol. 60, no. 1, pp. 251–253.
8. Olifirenko, V.V., Davydov, A.A., and Pak, V.N., *Zh. Prikl. Khim.*, 1990, vol. 63, no. 11, pp. 2505–2509.
9. Pak, V.N. and Vorob'eva, G.G., *Zh. Prikl. Khim.*, 1988, vol. 61, no. 10, pp. 2212–2215.
10. *Eksperimental'nye metody v adsorbtzii i katalize* (Experimental Techniques in Adsorption and Catalysis), Nikitin, Yu.S., Ed., Moscow: Mos. Gos. Univ, 1990.
11. *Analiz mineral'nogo syr'ya* (Analysis of Mineral Raw Materials), Knipovich, Yu.N. and Morachevskii, Yu.V., Eds., Leningrad: Khimiya, 1956, pp. 804 – 810.
12. Kiselev, A.V. and Lygin, V.I., *Infrakrasnye spektry poverkhnostnykh soedinenii* (IR Spectra of Surface Compounds), Moscow: Nauka, 1972.

Russian Journal of Applied Chemistry, Vol. 77, No. 4, 2004, pp. 543–548. Translated from Zhurnal Prikladnoi Khimii, Vol. 77, No. 4, 2004, pp. 548–553.

INORGANIC SYNTHESIS AND INDUSTRIAL INORGANIC CHEMISTRY

Kinetics and Thermodynamics of Hardening in Systems $MgO–H_2O$ and $MgO–MgCl_2–H_2O$

I. N. Lipunov, M. S. Kovel', A. S. Teploukhov, V. V. Tetykhin, and V. I. Alikin

Ural State University of Forestry Engineering, Yekaterinburg, Russia

Academy of Standardization, Metrology, and Certification, Ural Branch, Yekaterinburg, Russia

Verkhne-Salda Metallurgical Production Association Open Joint-Stock Company, V. Salda, Yekaterinburg oblast, Russia

Received September 11, 2003; in final form, February 2004

Abstract—The kinetics and thermodynamics of formation of chloromagnesium cements, which involves magnesium oxide, the main component of metallurgical sludge produced in manufacture of magnesium, were studied. The rate constants, activation energy, frequency factor, and thermodynamic constants of the reactions in which crystalline hydrates of composition $3Mg(OH)_2 \cdot MgCl_2 \cdot 8H_2O$ and $5Mg(OH)_2 \cdot MgCl_2 \cdot 2H_2O$ are formed were calculated.

It has been shown previously that metallurgical sludge that contains magnesium oxide MgO and carnallite $KMgCl_3 \cdot 6H_2O$ exhibits binding properties and can be used as a chloromagnesium binder in manufacture of composite wood-mineral construction materials.

In this study, the reactivity of MgO contained in sludge was analyzed by means of thermodynamic calculations and experimentally, as a component of the chloromagnesium cement (Sorel cement).

EXPERIMENTAL

The thermodynamic studies were carried out using the known calculation techniques.

In the experimental part of the study, stoichiometric calculations were performed using the equations of the following chemical reactions

$$MgO + H_2O = Mg(OH)_2, \quad (1)$$

$$3MgO + MgCl_2 + 11H_2O = 3Mg(OH)_2 \cdot MgCl_2 \cdot 8H_2O. \quad (2)$$

The interaction in the system $MgO–H_2O$ was analyzed in order to reveal the part played by reaction (1) in the mechanism of hardening through formation of basic magnesium chlorides, which can occur, in particular, via reaction (2). MgO necessary for reactions (1) and (2) was obtained by washing soluble salts out of the sludge with water at room temperature, with subsequent drying of the resulting solid residue with acetone on a filter. The amount of water in all the experiments corresponded to the mass ratio $MgO : H_2O = 1 : 1.5$. In studying the interaction in the system $MgO–MgCl_2–H_2O$, a stoichiometric amount of $MgCl_2$ of pure grade was dissolved in this amount of water.

Mixtures of MgO with water or a $MgCl_2$ solution were kept in a thermostat at prescribed temperatures and experiment durations. Then the reaction mixture was rapidly freed of the excess amount of water by filtration and washed with acetone on a filter.

The process of MgO hydration was studied by thermogravimetry; the composition of the products formed in the hydration reaction was determined by X-ray phase analysis and IR spectroscopy. Separate samples were subjected to physicomechanical tests.

It is known from the laboratory and industrial practice that the main products of reactions of MgO with $MgCl_2$ are crystalline hydrates of composition $3Mg(OH)_2 \cdot MgCl_2 \cdot 8H_2O$ (I) and $5Mg(OH)_2 \cdot MgCl_2 \cdot 2H_2O$ (II) [2], which are formed in accordance with the equations of the following reactions

$$3MgO + Mg^{2+} + 2Cl^- + 11H_2O = 3Mg(OH)_2 \cdot MgCl_2 \cdot 8H_2O, \quad (3)$$

$$5MgO + Mg^{2+} + 2Cl^- + 7H_2O = 5Mg(OH)_3 \cdot MgCl_2 \cdot 2H_2O. \quad (4)$$

1070-4272/04/7704-0543 © 2004 MAIK "Nauka/Interperiodica"

Table 1. Thermodynamic constants of compounds formed in reaction of MgO with $MgCl_2$ solutions

Compound	$-\Delta H^0_{298.15}$	$-\Delta G^0_{298.15}$	$S^0_{298.15}$	$C^0_{P(298.15)}$
	kJ mol^{-1}		J mol^{-1} K^{-1}	
$3Mg(OH)_2 \cdot MgCl_2 \cdot 8H_2O$	5973.52	5179.28	563.46	589.12
$5Mg(OH)_2 \cdot MgCl_2 \cdot 2H_2O$	6009.90	5396.95	509.11	468.04
$3Mg(OH)_2 \cdot MgCl_2$	3517.71	3200.10	296.09	259.87
$5Mg(OH)_2 \cdot MgCl_2$	5379.20	4882.06	430.99	385.73

Thermodynamic calculations of these and other reactions were carried out using thermodynamic constants obtained by the authors of this study (Table 1) or those taken from [3–6]. The calculated values refer to basic magnesium oxides. The enthalpy and Gibbs energy of formation of basic magnesium chlorides were calculated in terms of the theory of regular solutions, which makes it possible to determine the excess functions of mixing at a minimum amount of experimental data [7, 8].

Actually, the concept of basic salts as isomorphous mixtures of a hydroxide and a neutral salt [$Mg(OH)_2$ and $MgCl_2$ in the case in question] was used in the calculations. Also, account was taken of the fact that the formation of basic chlorides of variable composition is characteristic of hydroxochloride systems [9].

The excess function of mixing of $Mg(OH)_2$ and $MgCl_2$ was found to be 133.98 ± 2.1 kJ mol^{-1} on the basis of the known values of $\Delta H^0_{298.15}$ and $\Delta G^0_{298.15}$ for MgOHCl and $0.5NaCl \cdot MgOHCl$ [5]. The excess functions of addition of crystalline-hydrate water was determined using the known data for $MgCl_2$ crystalline hydrates. The temperature dependences of the Gibbs energy were found using the simplified formula

$$\Delta G_T = \Delta H^0_{298.15} - T\Delta S^0_{298.15}. \quad (5)$$

The equilibrium constants K were determined using the equation

$$\Delta G = -RT \ln K, \quad (6)$$

where ΔG is the energy of the reaction; R, the universal gas constant; and T, temperature (K).

In these calculations, account was taken of the fact that the activities of the solid reactants and liquid water are taken to be unity for the standard conditions and only the activities of the solutes or the partial pressure of gaseous reactants appear in the equation for the equilibrium constants.

To analyze the stability of phases in hydrolysis, solubility, and dehydration, the following reaction equations were considered:

$$3Mg(OH)_2 \cdot MgCl_2 \cdot 8H_2O = \frac{2}{3}[5Mg(OH)_2 \cdot MgCl_2 \cdot 2H_2O] + \frac{2}{3}H^+ + \frac{2}{3}Cl^- + 6H_2O, \quad (7)$$

$$3Mg(OH)_2 \cdot MgCl_2 \cdot 8H_2O = 4Mg(OH)_2 + 2H^+ + 2Cl^- + 6H_2O_l, \quad (8)$$

$$3Mg(OH)_2 \cdot MgCl_2 \cdot 8H_2O = 3Mg(OH)_2 \cdot MgCl_2 + 8H_2O_l, \quad (9)$$

$$3Mg(OH)_2 \cdot MgCl_2 \cdot 8H_2O = 3Mg(OH)_2 \cdot MgCl_2 + 8H_2O_g, \quad (10)$$

$$3Mg(OH)_2 \cdot MgCl_2 \cdot 8H_2O = 4Mg(OH)_2 + 2HCl_g + 6H_2O_g, \quad (11)$$

$$5Mg(OH)_2 \cdot MgCl_2 \cdot 2H_2O = 6Mg^{2+} + 10OH^- + 2Cl^- + 2H_2O_l, \quad (12)$$

$$3Mg(OH)_3 \cdot MgCl_2 \cdot 8H_2O = 4Mg^{2+} + 6OH^- + 2Cl^- + 8H_2O_l. \quad (13)$$

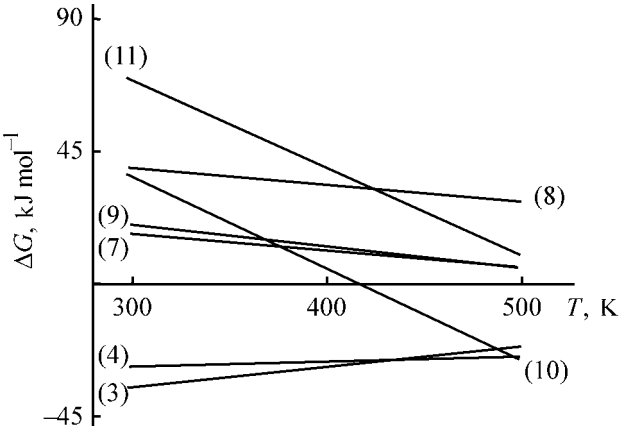

Fig. 1. ΔG for the processes that occur in the system MgO–$MgCl_2$–H_2O by reactions (3), (4), and (7)–(11) vs. temperature T.

Table 2. Results of thermodynamic calculations of chemical reactions

Reaction	$-\Delta H^0_{298.15}$, kJ mol^{-1}	$-\Delta G^0_{298.15}$, J mol^{-1}	$S^0_{298.15}$, J mol^{-1} K^{-1}	log K	Type of equation for K_{eq}
(3)	–224.16	–140.72	–279.89	24.64	$1/[Mg^{2+}][Cl^-]^2$
(4)	–200.51	–168.14	–108.56	29.44	$1/[Mg^{2+}][Cl^-]^2$
(7)	139.17	69.67	233.12	–12.2	$[H^+]^{2/3}[Cl^-]^{2/3}$
(8)	222.11	155.96	219.35	–27.31	$[H^+]^2[Cl^-]^2$
(9)	167.47	80.39	292.07	–	–
(10)	519.83	149.38	1242.47	–26.16	$P^8_{H_2O}$
(11)	636.18	279.72	1195.58	–48.98	$P^2_{HCl}P^6_{H_2O}$
(12)	29.48	352.36	–1082.96	–61.70	$[Mg^{2+}]^6[OH^-]^{10}[Cl^-]^2$
(13)	121.54	251.25	–435.05	–44.00	$[Mg^{2+}]^4[OH^-]^6[Cl^-]^2$

The results obtained in thermodynamic calculations for the standard conditions (298.15 K, 1 atm) are listed in Table 2 and shown in Fig. 1.

The values of ΔG in Fig. 1 refer to one atom of magnesium for all the reactions. For example, $\Delta G^0_{298.15}$ = –140.72/4 = –35.18 kJ mol^{-1} for reaction (3) and –168.14/6 = –28.02 kJ mol^{-1} for reaction (4). In plotting Fig. 1, account was also taken of the fact that the dependences ΔG–T can be represented in the temperature range under study, to a good approximation, as formula (5).

It should be noted that the exothermic effects in the reactions of formation of compounds (I) and (II) [reactions (3), (4)] are strong. For example, calculations by the equation $\Delta T = \Delta H/C_P$ show that the heat of the reaction is sufficient for heating compound (I) by 653 K and compound (II) by 701 K.

Analysis of the data in Tables 1 and 2 leads to a number of technologically important conclusions.

In particular, the data for reactions (12), (13) indicate that compounds (I) and (II) have exceedingly low solubility, which decreases as temperature becomes higher. Compound (I) is thermodynamically stable in the presence of a liquid phase up to 437 K, and, accordingly, its solubility is lower. Possibly, compound (II) is formed as an intermediate metastable phase, which is present in the reaction products at temperatures below 437 K for kinetic reasons only. The thermodynamic stability of compound (I) is also indicated by the data for reaction (7). The presence of a metastable phase in the reaction products, mentioned above, is a widely occurring and well-known fact of formation of a stable phase via metastable intermediates [10].

The thermodynamic calculations also indicate that the compound (I) is stable against loss of crystallization water in the form of a liquid phase in the whole temperature range studied [reaction (9)] and as a gas up to 418 K [reaction (10)]. This compound is also stable against hydrolysis [reactions (7), (11)].

Thus, from the thermodynamic standpoint, the formation of the magnesian stone in a wide temperature range must not be complicated by loss of crystallization water or by hydrolysis.

The influence exerted by the temperature factor on the degree of hydration of magnesium oxide was revealed experimentally. The time dependences of the degree of MgO hydration in the systems MgO–H_2O and MgO–$MgCl_2$–H_2O at different temperatures are shown in Fig. 2. These kinetic curves were used to

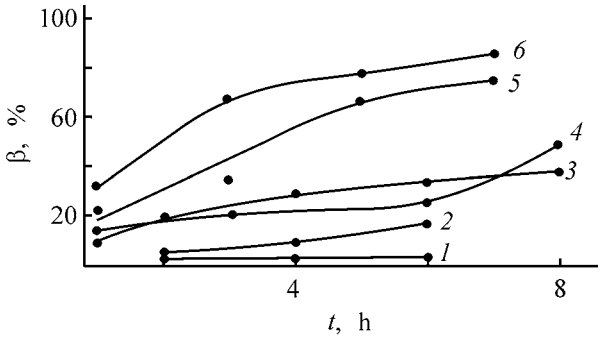

Fig. 2. Degree of MgO hydration, β, in the systems (*1*–*3*) MgO–H_2O and (*4*–*6*) MgO–$MgCl_2$–H_2O vs. time *t*. Temperature (K): (*1*, *4*) 313, (*2*, *5*) 333, and (*3*, *6*) 353.

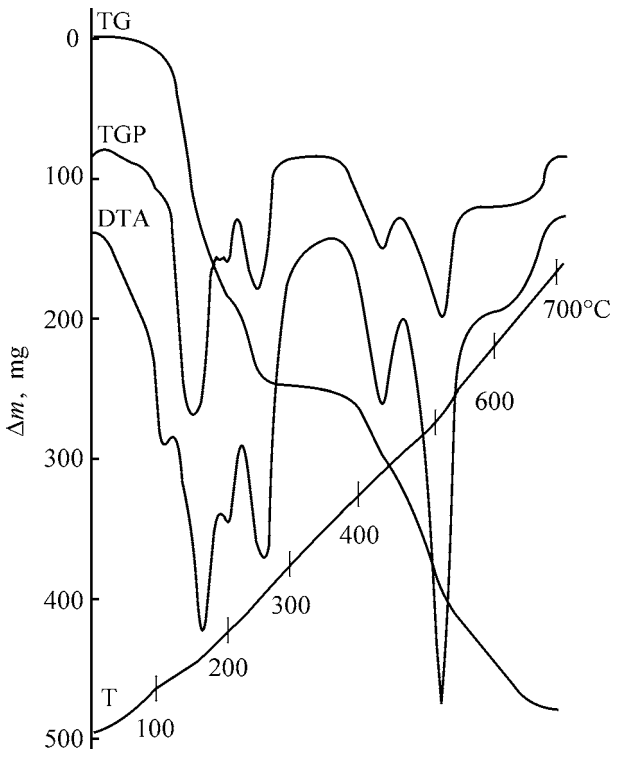

Fig. 3. Derivatogram of the products formed in interaction of MgO in sludge with a $MgCl_2$ solution. (Δm) Loss of mass and (T) temperature.

calculate the rate constants of the reactions of MgO hydration for both of the systems studied. The experimental value of the degree of MgO hydration was calculated on the basis of derivatograms. For this purpose, the total loss of mass by the dried samples was related to the stoichiometric amounts of the products formed in the reactions of thermal decomposition

$$Mg(OH)_2 = MgO + H_2O_g, \quad (14)$$

$$3Mg(OH)_2 \cdot MgCl_2 \cdot 8H_2O = 4MgO + 2HCl_g + 11H_2O_g. \quad (15)$$

The stoichiometric amounts were calculated according to reaction (14) for the system MgO–H_2O and reaction (15) for MgO–$MgCl_2$–H_2O. The assignment of the loss of mass was the simplest for the first of these systems, for which only a single endothermic effect of loss of mass in decomposition of $Mg(OH)_2$ by reaction (14) was present in the derivatograms. For the second system, the derivatograms exhibited several effects. Figure 3 shows a derivatogram of the product formed in interaction of MgO in sludge with a $MgCl_2$ solution at 353 K in the course of 3 h. Published data on the thermal behavior of crystalline hydrates of $MgCl_2$ and also crystalline hydrates of its double salts with sodium and potassium chlorides [11, 12] make it possible to assign the endothermic effects observed in the derivatograms.

At temperatures of 433, 473, and 533 K there occur processes of steplike dehydration, which are mainly associated with removal of physically bound water and are accompanied by partial hydrolysis of $MgCl_2$ with evolution of hydrogen chloride.

$Mg(OH)_2$ formed in interaction of MgO with an aqueous solution of $MgCl_2$ decomposes at a temperature of 693 K. In the process, chemically bound water is removed.

The endothermic effect at 783 K is associated with decomposition of anhydrous basic magnesium chloride MgOHCl to give MgO and HCl.

The assignment of the endothermic effects to the corresponding chemical transformations is also confirmed by thermodynamic calculations, e.g., for the reactions

$$5Mg(OH)_2 \cdot MgCl_2 \cdot 2H_2O = 5Mg(OH)_2 \cdot MgCl_2 + 2H_2O_g, \quad (16)$$

$$5Mg(OH)_2 \cdot MgCl_2 = 6MgO + 2HCl_g + 4H_2O_g. \quad (17)$$

Zero free energy is reached at 490 K for reaction (16) and at 714 K for reaction (17).

Thus, the whole amount of crystallization and hydroxide water, and also chloride ions in the form of HCl, were removed when the samples under study were heated to 1073 K.

The conversion was found as the ratio of the experimental loss of mass to that furnished by calculation. The mathematical processing of the kinetic curves shown in Fig. 2 was performed using the Kolmogorov–Erofeev equation [13]

$$\alpha = 1 - e^{-kt^n}, \quad (18)$$

where α is the conversion; t, the process duration (h); and k, n, temperature-dependent constants.

The reaction rate constants K were found using the Sakovich equation [13]

$$K = nk^{1/n}, \quad (19)$$

where n, k are the constants of the Kolmogorov–Erofeev equation.

The statistical processing of the results obtained was made using the STATGRAPHICS software. In

doing so, the constants k and n were found by approximation of the experimental data with straight lines obtained by rearranging terms and taking double logarithm of Eq. (18):

$$\ln[-\ln(1 - \alpha)] = \ln k + n \ln t. \quad (20)$$

The results of regression and correlation analyses demonstrated that the Kolmogorov–Erofeev equation describes the kinetics of reactions (1) and (2) with high precision: at a 95% confidence level (p-value < 0.05) the correlation coefficients varied within the range 0.91–0.98. The calculated constants are listed in Table 3.

The rate constant of MgO hydration grows as temperature becomes higher, and its values for reaction (2) were found to exceed those for reaction (1). The resulting values of K were used to determine the apparent activation energy ΔE and the frequency factor A by the equation

$$K = Ae^{-\Delta E/RT}. \quad (21)$$

The regression equation $\ln K(1/T)$ was used to determine the values of ΔE and A, which were found to be 14.61 kJ mol^{-1} and 1.196×10^8, respectively, for reaction (2). The activation energy obtained suggests that the heterogeneous processes under study occur in the diffusion region (ΔE < 16.7 kJ mol^{-1}), in which the rate of diffusion is the limiting factor. The same conclusion follows from the relatively low value of the frequency factor. However, the reaction of MgO hydration is not rate-limiting in the process of formation of the magnesian stone. The kinetics of the processes under study is also strongly affected by nucleation of the new phase on the reaction surface.

On the whole, the kinetic studies demonstrated that MgO contained in sludge exhibits a chemical activity that enables its use as a magnesium binder. Mixing MgO with $MgCl_2$ solutions with a density of 1.18–1.20 g l^{-1} leads to formation of the magnesian stone. However, initiation of hardening requires that the magnesian paste should be preheated to 343 K. Control samples formed from such a magnesian paste and hardened for 3, 7, and 28 days were subjected to strength tests. The breaking compression stress was 18.7, 31.2, and 53.1 MPa, respectively.

CONCLUSIONS

(1) The investigation performed demonstrated that magnesium-containing sludge can be used as a mineral binder; a preliminary heating of the reaction mixture to 343–353 K can be recommended for industrial conditions. After that the process may occur in the auto-thermal mode with a transition to the autoclave region, in which the magnesian stone will be formed at a high rate.

Table 3. Constants calculated by the Kolmogorov–Erofeev and Sakovich equations

Constant	Temperature, K		
	313	333	353
Reaction (1)			
k	0.0191	0.0200	0.0227
n	0.416	1.225	1.711
K	3.077×10^{-5}	5.026×10^{-2}	1.871×10^{-1}
Reaction (2)			
k	0.1382	0.2202	0.4009
n	0.618	0.930	0.859
K	2.513×10^{-2}	1.827×10^{-1}	2.964×10^{-1}

(2) At the same time, the high exothermicity of the main reactions requires that special measures should be taken to perform the process under controllable conditions. The thermodynamic and kinetic data obtained make it possible to carry out the necessary technological calculations.

ACKNOWLEDGMENTS

The study was financially supported by the R&D Program "Research by Higher School in Priority Areas of Science and Technology" of the Ministry of Education of the Russian Federation and by an individual grant for support of research by postgraduate students at higher school institutions of the Ministry of Education of the Russian Federation (A03-3.21-451).

REFERENCES

1. Lipunov, I.N., Teploukhov, A.S., Kovel', M.S., *et al.*, *Zh. Prikl. Khim.*, 2004, vol. 77, no. 2, pp. 206–209.
2. Zyryanova, V.I., Savinkina, M.A., Logvinenko, A.T., *et al., Sib. Khim. Zh.*, 1992, no. 3, pp. 116–119.
3. Kelley, K., *Bureau of Mines, Technical Part*, 1945, no. 676, pp. 1–26.
4. Naumov, G.B., Ryzhenko, B.N., and Khodokovskii, I.L., *Spravochnik termodinamicheskikh velichin* (Reference Book of Thermodynamic Quantities), Moscow: Atomizdat, 1971.
5. Orekhova, A.I., Ryabin, V.A., and Lelekova, R.P.,

Khimiya i tekhnologiya mineral'nykh solei (Chemistry and Technology of Mineral Salts), Sverdlovsk: UNIKhIM, 1989, issue 67, pp. 71–78.

6. Orekhova, A.I., Lelekova, R.P., Martsevich, L.P., and Kogan, B.S., *Issledovanie i razrabotka tekhnologii nekotorykh mineral'nykh solei* (Study and Development of Technology of Some Mineral Salts), Sverdlovsk: UNIKhIM, 1988, issue 66, pp. 66–166.
7. Saxena, S.K., *Thermodynamics of Rock-forming Crystalline Solutions*, New York: Springer, 1973.
8. Perchuk, L.L. and Ryabchikov, N.D., *Fazovoe sootvetstvie v mineral'nykh sistemakh* (Phase Correspondence in Mineral Systems), Moscow: Nauka, 1976.
9. Chalyi, V.P., *Gidrookisi metallov* (Hydroxides of Metals), Kiev: Naukova Dumka, 1972.
10. Polak, A.F., *Tverdenie monomineral'nykh vyazhushchikh veshchestv* (Hardening of Monomineral Binders), Moscow: Stroiizdat, 1966.
11. Brut, Yu.M., Bogomolov, B.N., and Dvorkin, L.I., *Vyazhushchie materialy Sibiri i Dal'nego Vostoka* (Binders of Siberia and Far East), Novosibirsk: Nauka Sib. Otd. Ross. Akad. Nauk, 1970.
12. Volzhenskii, V.V., Burov, V.S., and Kolokol'nikov, V.S., *Mineral'nye vyazhushchie veshchestva* (Mineral Binders), Moscow: Stroiizdat, 1973.
13. Boldyrev, V.V., *Metody izucheniya kinetiki termicheskogo razlozheniya tverdykh veshchestv* (Methods for Studying the Kinetics of Thermal Decomposition of Solids), Moscow: Metallurgizdat, 1959.

Russian Journal of Applied Chemistry, Vol. 77, No. 4, 2004, pp. 549–554. Translated from Zhurnal Prikladnoi Khimii, Vol. 77, No. 4, 2004, pp. 554–559.

PHYSICOCHEMICAL STUDIES OF SYSTEMS AND PROCESSES

Dependence of Separation Characteristics of Pervaporation on Parameters of Membranes Composed of Cellulose Myristinate and Polyphenylene Oxide

V. M. Kuznetsov, A. M. Toikka, Yu. P. Kuznetsov, G. A. Polotskaya, and A. K. Khripunov

St. Petersburg State University, St. Petersburg, Russia

Institute of Macromolecular Compounds, Russian Academy of Sciences, St. Petersburg, Russia

Received February 5, 2003

Abstract—Experimental data on evaporation of binary mixtures composed of ethanol and water, ethyl acetate and acetic acid, water and acetic acid, and ethyl acetate and water in a wide range of concentrations, across film membranes composed of cellulose myristinate and polyphenylene oxide are presented.

Membrane separation of substances have attracted increasing attention in recent decades in both technological and scientific regards. In the course of pervaporation, a liquid mixture is brought in contact with a polymeric or inorganic membrane, commonly nonporous polymeric membrane, with a vapor (permeate) that contains mostly the target component removed from its back side. Therefore, the liquid–vapor phase transition is an integral part of this process. The interface between the liquid and vapor frequently lies within a membrane, and the contribution of this phase transition to selectivity of pervaporation may be significant, compared with the part played by physicochemical interactions between the material of the membrane and molecules transported across the membrane, which are specific to this process.

The aim of this study was to analyze the contribution of the liquid–vapor phase transition to the characteristics of pervaporation and to examine the evaporation across a membrane composed of cellulose myristinate and polyphenylene oxide of binary mixtures of water, ethanol, acetic acid, and ethyl acetate.

Modeling of pervaporation for engineering purposes is commonly based on Fick's law equations, which relate fluxes of substances to gradients of their concentrations. In a more correct form, the gradient or difference of the chemical potentials of substances in the liquid and vapor phases are to be used as driving forces of the process.

The conditions for equilibrium between binary liquid and vapor phases are as follows:

$$\left.\begin{aligned} \mu_1^{(l)} &= \mu_1^{(v)}, \\ \mu_2^{(l)} &= \mu_2^{(v)}, \\ P^{(l)} &= P^{(v)}, \\ T^{(l)} &= T^{(v)}, \end{aligned}\right\} \quad (1)$$

where μ is the chemical potential of substances 1 and 2 in the liquid (l) and vapor (v) phases; P and T are, respectively, the pressure and temperature of the coexisting phases.

When one of these quantities changes, there arise fluxes of substance or heat, which results in that an equilibrium is established. For example, a pressure difference across the membrane gives rise to substance fluxes that compensate for this difference. If the difference is created by a vacuum pump that removes the vapor (permeate), and the feeding liquid is at the atmospheric pressure, then the pressure difference cannot exceed 760 mm Hg. However, there are no data indicating that creating such a pressure difference by raising the pressure in the liquid, with the atmospheric pressure maintained in the permeate, gives rise to any noticeable fluxes. In other words, overcoming the hydraulic resistance of the membrane is not the principal condition for the appearance of significant fluxes.

The role of the vacuum consists to a greater extent in diminishing the partial pressure of substances in the permeate, i.e., in lowering the chemical potentials of the substances in the vapor phase. In Onzager's notation, the flux J_1 of substance 1, assumed to be

1070-4272/04/7704-0549 © 2004 MAIK "Nauka/Interperiodica"

independent of the flux of substance 2, has the form

$$J_1 = K_1(\mu_1^{(l)} - \mu_1^{(v)}), \quad (2)$$

where K_1 is the proportionality factor.

The chemical potential $\mu_1^{(l)}$ of the component 1 in the liquid phase is given by

$$\mu_1^{(l)} = \mu_1^{0(l)}(T, P) + RT \ln \gamma_1 x_1, \quad (3)$$

where $\mu_1^{0(l)}$ is the standard value of the potential in the liquid phase; γ_1, the activity coefficient; x_1, the mole fraction of substance 1 in the liquid phase; and R, the gas constant.

The chemical potential $\mu_1^{(v)}$ of component 1 in the vapor (permeate) is expressed as

$$\mu_1^{(v)} = \mu_1^{0(v)}(T) + RT \ln Py_1, \quad (4)$$

where P is the permeate pressure, and y_1 is the mole fraction of component 1 in the vapor.

In the course of pervaporation, the value of P, which is set by the vacuum pump, is equal to the sum of partial pressures of components 1 and 2.

With account of formulas (3) and (4), the flux J_1 in expression (2) takes the form

$$J_1 = J_1^0 + B(-\ln y_1 - \ln P), \quad (5)$$

where $J_1{}^0 = K_1(\mu_1^{0(l)} - \mu_1^{0(v)})$ is the flux determined by the difference of the standard chemical potentials, and $B = K_1RT$.

In deriving formula (5), it was assumed that the composition of the liquid remains unchanged in the course of its evaporation across the membrane. This assumption is well substantiated, since the fluxes across the membrane are relatively small, and is commonly confirmed in experimental studies.

The separating ability of membranes in pervaporation is commonly characterized by the selectivity factor

$$\alpha_{PV} = (y_1/y_2)/(x_1/x_2), \quad (6)$$

where the concentrations of the substances in the liquid (x) and vapor (y) phases are more frequently expressed in weight percent.

Attempts to prognosticate the selectivity of the process are commonly made in terms of the dissolution–diffusion model. In accordance with this model, the feeding liquid does not wet the membrane and transforms into vapor at the boundary of the membrane on the side of the liquid. In accordance with the concept of a local equilibrium, the composition of the vapor is considered to be in equilibrium with that of the liquid. The vapor selectively diffuses across the membrane and is collected at its back side in the form of the permeate. Thus, the selectivity factor is expressed as the product

$$\alpha_{PV} = (y_2^*)/y_2^*(x_1/x_2)(y_1/y_2)/(y_1^*/y_2^*) = K\alpha_{GS}, \quad (7)$$

where y_1^*, y_2^* represent the composition of the vapor in equilibrium with a liquid of composition x_1, x_2.

The coefficient K, equal to the first multiplier in formula (7), is known in the equilibrium thermodynamics as the coefficient of relative fugacity. The second multiplier, α_{GS}, is the selectivity of gas separation on the membrane of a vapor of composition y_1^*, y_2^* to give a permeate of composition y_1, y_2. Such a representation of the selectivity of pervaporation as a product of the coefficient of relative fugacity by the selectivity of gas separation was made in [1, 2]. In [1], the coefficient α_{GS} was named the pervaporation improvement factor E[1]. The author of the monograph [2] introduced the notion of selectivity β_{evap} of the liquid–vapor phase transition, then equating it, however, to K.

Apparently, with formula (6) used to calculate the selectivity and nonselective membranes ($\alpha_{GS} = 1$), the coefficient α_{PV} may be large and nearly equal to the coefficient of relative fugacity, K. For example, for a mixture of esters with water, K = 100–300. Thus, the high selectivity of some membranes is determined by characteristics of the liquid–vapor phase transition, rather than by the properties of a polymer. Therefore, to ascertain the separation characteristics of the polymer constituting the membrane, it is necessary to divide the selectivity factor found from experimental data by the coefficient of relative fugacity:

$$\alpha_{MS} = \alpha_{PV}/K, \quad (8)$$

where α_{MS} is the selectivity of the process, determined by the interaction of the polymer with flows of liquid and vapor dissolved in it.

In this case, as always, to α_{MS} values greater than unity correspond organophilic properties of the membrane with respect to the readily volatile substance being isolated. If the coefficient α_{MS} is close to, but less than unity, the membrane may be both nonselective (chemically inert or interacting in the same manner with the substances transported across it) and or-

ganophobic with respect to the readily volatile substance being isolated. In the former case, if the flux across the membrane is lowered by making higher the permeate pressure and the compositions of the liquid and vapor approach their equilibrium values, α_{MS} tends to unity. In the latter case, α_{MS} is always smaller than K and may be substantially less than unity.

However, such a comparison, which takes into account the contribution from the selectivity of the liquid–vapor phase transition to the total selectivity of pervaporation is, as a rule, not made. Data on the liquid–vapor equilibrium, presented in some papers, serve for comparison of pervaporation and simple distillation as methods for separation of liquid mixtures.

Meanwhile, the selectivity of the liquid–vapor phase transition can be equated to the coefficient of relative fugacuty if, as it is commonly assumed in the dissolution–diffusion model, such a transition occurs outside the membrane. However, the problem of where the phase transition occurs has not been solved conclusively. The author of the monograph [3] believes that the liquid is transformed into a vapor "along the entire way from the entrance into the membrane to permeate formation" at the exit. In the model of a flow within pores [4], the liquid evaporates at a certain depth within the pores penetrating through the bulk of the membrane. If such a transition occurs within the membrane, the applicability of the concept of a local equilibrium is unobvious.

Indeed, this concept assumes that the fluxes across the phase boundary in the forward (from liquid to vapor) and reverse directions are so large that the resulting flux in the forward direction is small and does not affect the phase compositions on both sides of the surface. These compositions correspond to those in equilibrium. If, however, the phase transition occurs within the membrane, the diffusion resistance of the polymer makes the fluxes smaller, so that the resulting flux may become comparable with them. Then, the composition of the vapor no more corresponds to an equilibrium with the liquid. For a nonequilibrium process, which the pervaporation is, the content of, e.g., the more volatile component in the vapor is lower than the equilibrium value. Therefore, in the case of nonselective membranes, the selectivity is somewhat lower than the coefficient of relative fugacity and approaches it asymptotically as the flux decreases. This point will be confirmed when discussing the experimental results.

The setup for studying the pervaporation process included a 200-ml glass reactor thermostated with an internal heat exchanger. The liquid placed in the reactor was agitated with a magnetic stirrer at a rate of 1000 rpm, which is commonly [1] considered sufficient for preventing concentration polarization near the membrane surface. The bottom of the reactor was in the form of a porous fluoroplastic plate on which a membrane was placed. The under-membrane space was connected by means of a vacuum tube to a glass trap cooled with liquid nitrogen. The trap was connected with a 20-l evacuated vessel, which made it possible to maintain the rarefaction created by the vacuum pump.

The temperature of the liquid mixtures used in all the experiments was maintained equal to $30 \pm 0.1°C$. The residual pressure in the vacuum system was 10 ± 0.5 mm Hg. In the case when the dependence of the flux across the membrane on the vapor (permeate) pressure was studied, this pressure was varied within the range 1–100 mm Hg.

As membranes served 40-μm-thick films of cellulose myristinate and 65-μm-thick films of polyphenylene oxide.

The liquid mixtures were prepared from ethyl acetate, ethanol, and acetic acid of chemically pure grade and distilled water. Evaporation across the membrane of binary mixtures composed of ethanol and water, water and acetic acid, ethyl acetate and acetic acid was studied over the entire range of concentrations. The compositions of the liquid mixtures and the permeate were determined by gas chromatography. The fluxes were calculated gravimetrically with account of the membrane area and experiment duration.

In some reported experimental studies of pervaporation, the selectivity factors α_{PV} do not exceed the coefficients of relative fugacity, K. To membranes of this kind belongs, e.g., a polydimethylsiloxane film in isolation of methanol and ethanol from their 10 and 30 wt % solutions in water. The selectivities of this process, α_{PV}, taken from [5] and the coefficients of relative fugacity, K, [6] are listed below

Alcohol	α_{PV}	K	α_{PV}	K
	10 wt %	10 wt %	30 wt %	30 wt %
MeOH	6.03	8.21	4.72	8.06
EtOH	7.44	7.66	5.79	7.00

A film composed of cellulose myristinate is also distinguished by low values of α_{PV}, compared with K,

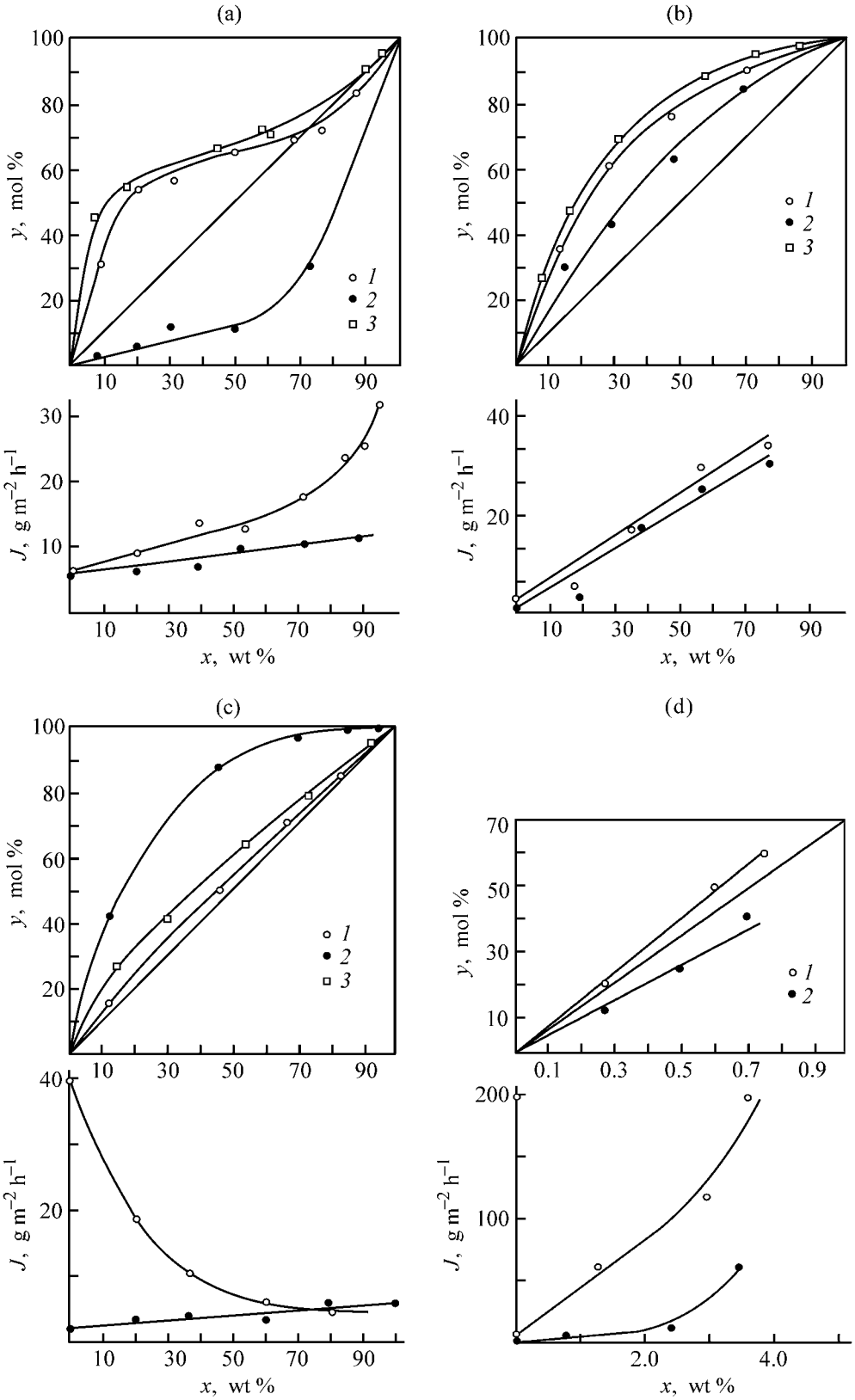

Fig. 1. Composition *y* and flux *J* of the permeate vs. the composition *x* of the liquid in evaporation across a film membrane composed of (*1*) cellulose myristinate and (*2*) polyphenylene oxide; (*3*) vapor composition for a liquid–vapor equilibrium. Liquid mixture: (a) ethanol and water, (b) ethyl acetate and acetic acid, (c) water and acetic acid, and (d) ethyl acetate and water.

for all of the mixtures studied. Figures 1a–1d show how the vapor (permeate) composition depends on the composition of the liquid for the binary mixtures composed of ethanol and water, ethyl acetate and acetic acid, water and acetic acid, and ethyl acetate and water. The same figures show, for comparison, the lines of composition of a vapor that is in equilibrium with the liquid. The plots for pervaporation and an equilibrium with a somewhat lower content of readily volatile substances in the vapor, compared with the equilibrium values, apparently coincide in shape. For example, the azeotropic point characteristic of the equilibrium in the system ethanol–water corresponds to the permazeotropic point with a higher content of water. It is of interest to study how the composition corresponding to the permazeotropic point is related to departure of the process from the equilibrium state.

Figure 2 shows the experimentally determined dependence of the composition of the vapor phase and the flux of ethanol on the permeate pressure. The composition of the liquid phase corresponded to that of the permazeotropic point (28 mol % water, 72 mol % ethanol) at 10 mm Hg and remained constant to within analytical error during the experiments. It can be seen that the flux decreases (which corresponds to an approach to equilibrium) and the composition of the vapor phase (permeate) asymptotically tends to the value in the liquid–vapor system as the flux decreases. Thus, when the flux decreases, the composition of the permazeotropic point shifts toward the equilibrium azeotropic composition. In the process, the selectivity factor α_{MS}, which characterizes the interaction of the polymer constituting this membrane with ethanol and water diffusing across the membrane, becomes equal to unity. When the flux is raised (pressure is lowered from 10 to 1 mm Hg), the content of water at the permazeotropic point increases. With account of the constant composition of the liquid phase, the flux of ethanol can be calculated using formula (5) for $J_1^0 = 0.58$, $B = 0.13$. The results of calculation are shown graphically in Fig. 3.

At the same time, use of expression (5) for calculating the fluxes at constant temperature and pressure and varied compositions of the liquid and vapor phases failed to furnish an agreement with the experimental data at a high content of ethanol in water. Presumably, this is due to strong changes in the properties of the membrane (wettability and plastification) at high concentrations of ethanol. Experimental data on fluxes of substances across cellulose myristinate in the mixtures studied are shown in Figs. 1a–1d. It

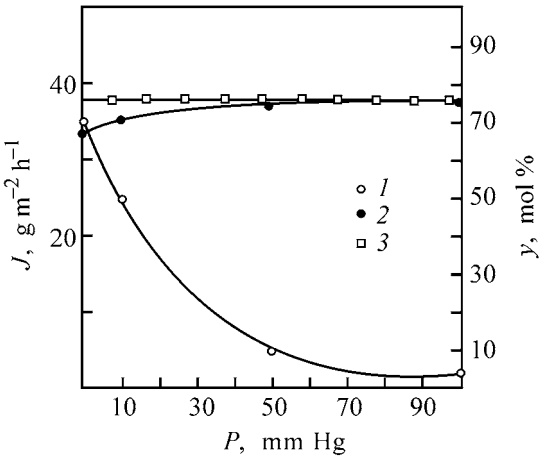

Fig. 2. Effect of the permeate pressure P on (*1*) the permeate composition y and (*2*) the permeate flux J in evaporation of a liquid mixture ethanol–water across a film membrane composed of cellulose myristinate, compared with (*3*) the composition of a vapor in equilibrium with the liquid. Temperature of the liquid 30°C, its composition: 28 mol % water and 72 mol % ethanol; the same for Fig. 3.

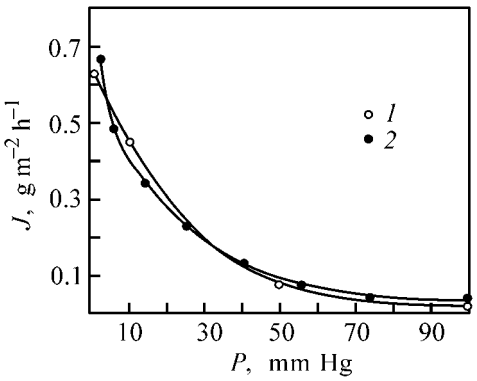

Fig. 3. Ethal flux J vs. the permeate pressure P in evaporation of a liquid mixture ethanol–water across a film membrane composed of cellulose myristinate. (*1*) Experimental data and (*2*) results of calculation by formula (5).

can be seen that the fluxes are only significant for ester-containing liquid mixtures.

In contrast to the film composed of cellulose myristinate, a polyphenylene oxide film exhibits hydrophobic properties, and the permeate formed in evaporation of water-containing binary mixtures of ethanol or acid contains mainly water, as it is shown in Figs. 1a, 1b. For a mixture composed of ethyl acetate and acetic acid, the run of the dependence of the composition of the liquid on that of the vapor is similar to that in the equilibrium case. However, the vapor

contains a smaller amount of the ester, compared with the case of cellulose myristinate (Fig. 1c). Figures 1a–1d show dependences of the mass fluxes of the substances on the composition of the liquid. As in the case of cellulose myristinate, their values are higher for ester-containing mixtures.

CONCLUSIONS

(1) The selective properties of a film membrane composed of cellulose myristinate are determined for the binary mixtures studied by the parameters of the liquid–vapor phase transition. The flux of ethanol across the membrane was calculated at vapor pressures in the range 1–100 mm Hg using the formula of nonequilibrium linear thermodynamics.

(2) A film membrane composed of polyphenylene oxide exhibits similar properties in separation of nonaqueous mixtures, but demonstrates hydrophilicity in the case of organic-aqueous mixtures.

ACKNOWLEDGMENTS

The study was financially supported by the Russian Foundation for Basic Research (grant 03-03-32 379) and Federal Program "Integration" (project B0028).

REFERENCES

1. Ten, P.K. and Field, R.W., *Chem. Eng. Sci.*, 2000, vol. 55, pp. 1425–1445
2. Baker, R.W., *Membrane Technology and Applications*, New York: McGraw–Hill, 2000.
3. Mulder M., *Basic Principles of Membrane Technology*, Dordrecht: Kluwer, 1991.
4. Feng, X. and Huang, R.Y.M., *Ind. Eng. Chem. Res.*, 1997, vol. 36, pp. 1048–1066
5. Uragami, T. and Morikava, T., *J. Appl. Polym. Sci.*, 1992, vol. 44, pp. 2009–2118.
6. Kogan, V.B., Fridman, V.M., and Kafarov, V.V., *Ravnovesie mezhdu zhidkost'yu i parom* (Equilibrium between Liquid and Vapor), Moscow: Nauka, 1966.

Russian Journal of Applied Chemistry, Vol. 77, No. 4, 2004, pp. 555–558. Translated from Zhurnal Prikladnoi Khimii, Vol. 77, No. 4, 2004, pp. 560–563.

PHYSICOCHEMICAL STUDIES OF SYSTEMS AND PROCESSES

Phase Separation in the Systems Constituted by Tetradecane (Hexane, Decane), Tri-*n*-Butyl Phosphate, and Cerium(III) Nitrate Solvate with Tri-*n*-Butyl Phosphate

A. K. Pyartman, A. V. Kudrova, and V. A. Keskinov

St. Petersburg State Technological Institute, St. Petersburg, Russia

Received April 16, 2003

Abstract—Phase diagrams of ternary liquid systems constituted by tetadecane (hexane, decane), tri-*n*-butyl phophate, and cerium(III) nitrate solvate with tri-*n*-butyl phosphate $Ce(NO_3)_3(TBP)_3$ with phase separation into liquid phases I and II were studied at 298.15 K. Phase I is enriched in the hydrocarbon diluent, and phase II, in $Ce(NO_3)_3(TBP)_3$. The distribution of components between phases I and II was considered.

Extraction of rare-earth elements (REE) with neutral organophosphorus compounds, e.g., tri-*n*-butyl phosphate (TBP) in hydrocarbon diluents (HCDs), is widely used in their recovery and separation. The concentration and type of a diluent affect the extraction isotherms and element separation factors [1]. At a low TBP content in HCD, phase separation of the organic phase into two phases is possible. This effect has been studied in detail for actinides [2]. At the same time, phase diagrams of ternary liquid systems constituted by tetadecane (hexane, decane), TBP, and lanthanide(III) nitrate solvate with TBP in the region of phase separation are unknown, although such diagrams can be of practical interest in the choice of HCD and component concentrations for extraction systems.

Vacuum-distilled TBP (density ρ = 0.9727 g cm^{-3} at 298.15 K) and tetradecane (0.7592 g cm^{-3}), decane (0.7263 g cm^{-3}), and hexane (0.6548 g cm^{-3}) of chemically pure grade were used. Cerium(III) nitrate solvate, $Ce(NO_3)_3(TBP)_3$ (S), was prepared by threefold saturation of TBP with fresh portions of a saturated aqueous solution of cerium(III) nitrate [3]. The "concentration" of $Ce(NO_3)_3(TBP)_3$ in pure S was 1.12 M (ρ = 1.2755 g cm^{-3}). The S concentration in the organic phase was determined complexometrically [4]. The phase densities were determined pycnometrically. The binodal curves of the ternary systems were measured by Alekseev's method [3] by titration of binary systems with different compositions with the third component under the temperature control.

Mixtures of tetradecane (hexane, decane) and S taken in various volume ratios (2.5–10 cm^3) (heterogeneous systems) were titrated with TBP, using a microburet, until the system became homogeneous. In parallel experiments, mixtures of TBP and S (homogeneous systems) were titrated with the diluent until the second organic phase formed.

The formation of the second organic phase was additionally monitored by nephelometry with a Kernco 966 R turbidimeter equipped with a color filter (λ = 850 nm). To determine the nodes (compositions of the coexisting phases), the phase volumes were measured (in special experiments, we showed that, within the error of ±0.2%, the system volume is equal to the sum of the component volumes). With regard to binodals and solution densities, the concentrations of TBP and diluent were determined from the S concentration [5]. In this case, a binodal was plotted using volume fractions under the condition that the total volume remains unchanged when the components are mixed. Later on, the phase composition was recalculated to weight fractions to obtain the phase density.

Additionally, the TBP content was determined as the difference between the total TBP concentration and TBP concentration in S, evaluated after cerium stripping into water, the subsequent saturation of the organic phase with cerium(III) nitrate, and determination of the S concentration. The TBP concentration was determined from the phosphorus content measured with an SF-26 spectrophotometer in 1-cm

1070-4272/04/7704-0555 © 2004 MAIK "Nauka/Interperiodica"

Phase separation in the systems $Ce(NO_3)_3(TBP)_3$–TBP–C_nH_{2n+2} at 298.15 K

ρ, g cm^{-3}	$[Ce(NO_3)_3(TBP)_3]$	TBP	C_nH_{2n+2}	Nodes
	weight fraction			
		C_6H_{14}		
0.7169	0.178	0	0.822	*1*
0.7301	0.208	0.006	0.786	*2*
0.7463	0.244	0.012	0.744	*3*
0.7618	0.276	0.019	0.705	*4*
0.7637	0.278	0.022	0.700	*5*
	0.434	0.046	0.520	
	0.475	0.050	0.475	6
0.9205	0.563	0.045	0.392	*5*
0.9498	0.609	0.043	0.348	*4*
0.9919	0.676	0.034	0.290	*3*
1.0247	0.727	0.022	0.251	*2*
1.0897	0.820	0	0.180	*1*
		$C_{10}H_{22}$		
0.7812	0.163	0	0.834	*1*
0.7883	0.177	0.010	0.813	*2*
0.7972	0.195	0.020	0.785	*3*
0.8065	0.214	0.029	0.757	*4*
0.8231	0.245	0.048	0.707	*5*
	0.294	0.077	0.629	
	0.343	0.099	0.557	
	0.443	0.114	0.443	6
	0.545	0.112	0.343	
0.9986	0.569	0.109	0.322	*5*
1.0542	0.669	0.091	0.24	*4*
	0.732	0.080	0.188	
1.1051	0.752	0.075	0.173	*3*
1.1435	0.818	0.050	0.132	*2*
1.2205	0.940	0	0.060	*1*
		$C_{14}H_{30}$		
0.7850	0.081	0	0.919	*1*
0.7912	0.094	0.011	0.895	*2*
0.7993	0.110	0.026	0.864	*3*
0.8089	0.130	0.041	0.829	*4*
0.8184	0.148	0.057	0.795	*5*
	0.182	0.076	0.742	
	0.346	0.160	0.494	
	0.368	0.168	0.464	
	0.403	0.195	0.403	6
	0.475	0.197	0.328	
1.0058	0.499	0.196	0.305	*5*
1.0475	0.586	0.174	0.240	*4*
1.0956	0.679	0.148	0.173	*3*
	0.682	0.142	0.176	
	0.836	0.084	0.080	
1.1829	0.838	0.087	0.075	*2*
1.2281	0.944	0	0.056	*1*

quartz cells after decomposition of samples with sulfuric acid [6].

All the results are presented as phase diagrams, using the second Roozeboom triangle: rectangular coordinates (weight fraction scale) for two components of ternary liquid systems; for the third component, $\omega_3 = 1 - \omega_1 - \omega_2$. Errors in ω determination did not exceed ±(0.001–0.002).

Figure 1 and the table show that the binary systems S-TBP and TBP-HCD are homogeneous at any component ratios. By contrast, the S-HCD system has the solubility limits; between them, the system forms two liquid phases I and II. Phase I is enriched in HCD, and phase II, in S. The solubility (weight fractions) of S in HCD increases in the order: tetradecane (0.081) decane (0.163), and hexane (0.178). The solubilities of tetradecane and decane in S are close (0.056 and 0.060) and lower than the solubility of hexane (0.180).

The phase diagrams of ternary liquid systems S–TBP–HCD consist of fields of homogeneous organic solutions (Fig. 1, field *B*) and fields of separation into two liquid phases (Fig. 1, field *A*) bounded by binodals. In all the cases, the points of critical composition of the ternary system are compositions with approximately equal fractions of S and HCD and different TBP contents depending of HCD chain length. At the point of critical composition, the TBP content (ω_{2cr}) is proportional to the number of the carbon atoms in HCD C_x and, to a first approximation, obeys the equation

$$\omega_{2cr} = -(0.062 \pm 0.013) + 0.0181 \pm 0.0012C_x.$$

This equation allows prediction of the field of phase separation of the ternary system for various HCDs. In practice, HCDs with lower molecular weight are preferable, because in this case, the minimum content of free (not bound in S) TBP is required to prevent phase separation. The analysis of nodes of ternary liquid systems with phase separation (see table and Fig. 1) shows that, along with binary systems of the S–HCD type, two liquid phases I and II are formed. Phase I is enriched in HCD, and phase II, in S. Figure 2 presents a plot of the TBP distribution between phases I and II for hexane, decane, and tetradecane. It was shown that, for the systems with phase separation, the TBP weight fraction in phase II is substantially higher than that in phase I and grows in the order hexane < decane < tetradecane, i.e., with

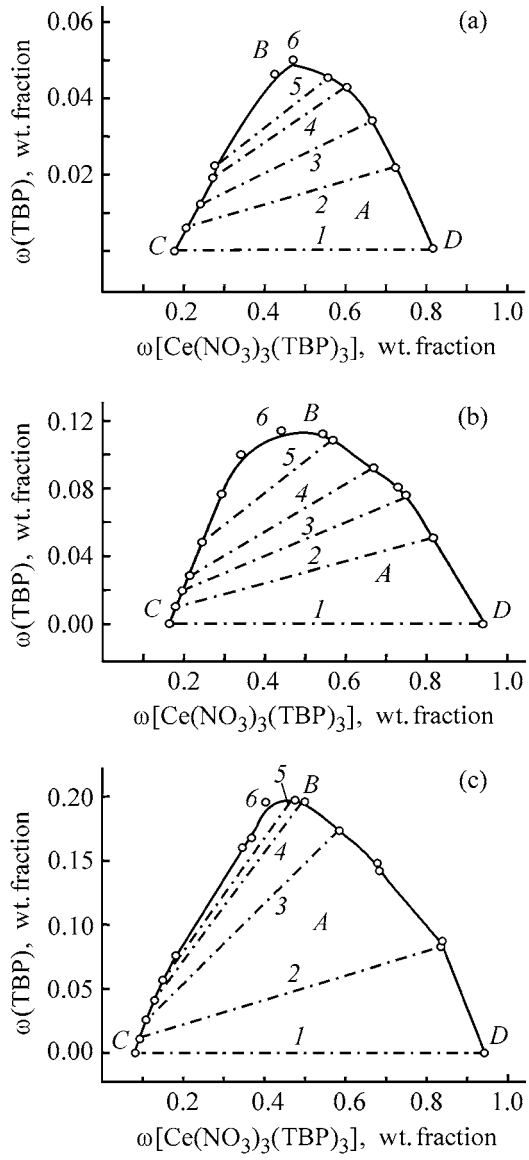

Fig. 1. Phase separation diagram of the ternary systems $Ce(NO_3)_3(TBP)_3$–TBP–C_nH_{2n+2} at 298.15 K. (*A*) Field of phase separation into two liquid phases, (*B*) field of homogeneous organic solutions, (*CD*) binodal, (*1*–*5*) nodes (see table), and (*6*) critical point; (a) hexane, (b) decane, and (c) tetradecane.

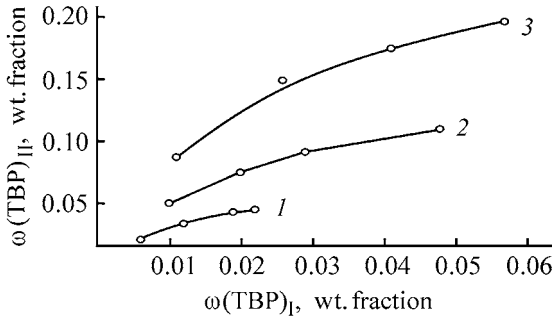

Fig. 2. TBP distribution between phases I and II. $\omega(TBP)_I$ and $\omega(TBP)_{II}$ are the weight fractions of TBP in phases I and II. Phase I is enriched in C_nH_{2n+2}, and phase II, in $Ce(NO_3)_3(TBP)_3$; the same for Figs. 3, 4. (*1*) Hexane, (*2*) decane, and (*3*) tetradecane; the same for Figs. 3, 4.

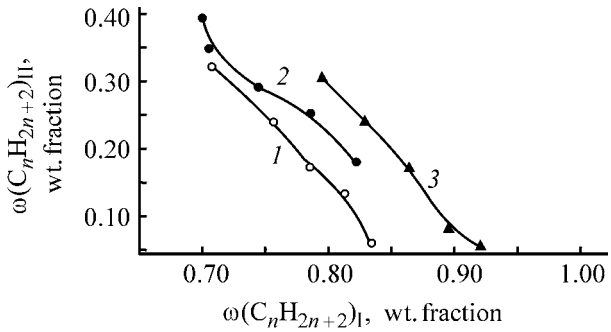

Fig. 3. C_nH_{2n+2} distribution between phases I and II. $\omega(C_nH_{2n+2})_I$ and $\omega(C_nH_{2n+2})_{II}$ are weight fractions of C_nH_{2n+2} in phases I and II.

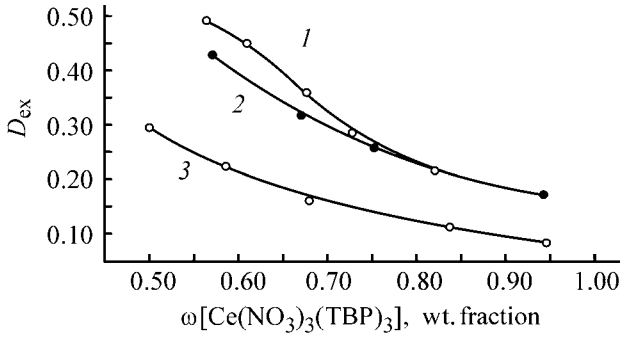

Fig. 4. Dependence of the distribution coefficients, D_{ex}, of $Ce(NO_3)_3(TBP)_3$ between phases I and II on the $Ce(NO_3)_3(TBP)_3$ weight fraction in the phase II.

an increase in the HCD chain length. The curves of HCD distribution between phases I and II are shown in Fig. 3. As can be seen, the HCD weight fraction in phase I is higher than that in phase II and increases in the order: tetradecane < hexane < decane.

The S distribution coefficients between phases I and II for various HCDs are shown in Fig. 4. As can be seen, the S weight fraction in phase II is higher than that in phase I and increases in the order: hexane < decane < tetradecane.

The extraction of cerium(III) nitrate from aqueous-salt solutions with TBP in HCD proceeds by the equation [1]

$$Ce^{3+}_{aq} + 3NO^{-}_{3\,aq} + 3TBP_{org} \rightleftarrows [Ce(NO_3)_3(TBP)_3]_{org},$$

where aq denoted the aqueous phase, and org, the organic phase.

At equilibrium TBP content (weight fraction) higher than 0.2, only one liquid phase exists, which separates into two phases when this fraction decreases.

After saturation of the organic phase with Ce(III) nitrate, two organic liquid phases coexist (phase I is enriched in HCD, and phase II, in S). To use extraction systems based on TBP and HCD in practice, the equilibrium TBP content (weight fraction) should be of 0.17–0.20, i.e., it is necessary to operate with organic phases unsaturated with respect to cerium(III) nitrate, or to use commercial solvents with a low content of long-chain hydrocarbons.

CONCLUSIONS

(1) Phase diagrams of ternary liquid systems constituted by tetradecane (decane, hexane), tri-*n*-butyl phophate, and $Ce(NO_3)_3(TBP)_3$ consist of the field of homogeneous solutions and the field of phase separation (phases I and II). Phase I is enriched in hydrocarbon diluent, and phase II, in cerium nitrate solvate. The phase separation area diminishes in the order tetradecane > decane > hexane with shortening of the hydrocarbon chain length.

(2) At the point of the critical composition of the ternary systems, the TBP content ω_{2cr} is proportional to the number of carbon atoms in the solvent, C_x.

(3) In the phase separation field, the TBP fraction in phase II is substantially higher than that in phase I; the weight fraction of the diluent in phase I is higher and increases in the order: hexane < decane < tetradecane. The solvate weight fraction in phase II tends to increase in the order: tetradecane < decane < hexane.

(4) In practice, to use extraction systems with TBP and hydrocarbon diluent, it is necessary to keep the equilibrium TBP content (weight fraction) no less than 0.17–0.20 or to use commercial solvents with a low content of long-chain hydrocarbons.

REFERENCES

1. Pyartman, A.K., Kopyrin, A.A., Puzikov, E.A., and Bogatov, K.B., *Radiokhimiya*, 1995, vol. 37, no. 1, pp. 52–55.
2. Nikolotova, Z.I., *Ekstraktsiya neitral'nymi fosfororganicheskimi soedineniyami: Aktinoidy: Spravochnik* (Extraction with Neutral Organophophorus Compounds: Actinides, Handbook), Moscow: Energoatomizdat, 1987.
3. *Ekstraktsiya neorganicheskikh veshchestv (Diagrammy rassloeniya, raspredeleniya, vysalivaniya i razdeleniya)* (Extraction of Inorganic Substances (Diagrams of Phase Separation, Distribution, Salting-Out, and Separation)), Nikolaev, A.V., Ed., Novosibirsk: Nauka, 1970.
4. Pribil, R., *Analytical Applications of EDTA and Related Compounds*, Oxford: Pergamon, 1972.
5. Treybal, R.E., *Liquid Extraction*, New York: McGraw–Hill, 1963.
6. Mikhailov, V.A., Kharchenko, S.K., and Nazin, A.G., *Izv. Sib. Otd. Akad. Nauk SSSR*, 1961, no. 7, pp. 50–56.

Russian Journal of Applied Chemistry, Vol. 77, No. 4, 2004, pp. 559–562. Translated from Zhurnal Prikladnoi Khimii, Vol. 77, No. 4, 2004, pp. 564–567.

PHYSICOCHEMICAL STUDIES OF SYSTEMS AND PROCESSES

Phase Separation in Ternary Liquid Systems Containing Rare-Earth Metal(III) Nitrate Solvates with Tri-*n*-butyl Phosphate

A. K. Pyartman, A. V. Kudrova, and V. A. Keskinov

St. Petersburg State Technological Institute, St. Petersburg, Russia

Received April 16, 2003

Abstract—Phase diagrams of ternary liquid systems constituted by tetradecane, tri-*n*-butyl phosphate, and lanthanide(III) nitrate solvates with tri-*n*-butyl phosphate {$[Ln(NO_3)_3(TBP)_3]$, Ln = La, Pr, Nd, Sm} were studied at 298.15 K. The distribution of the components between the phases under stratification conditions was considered.

In this study, we examined phase diagrams of ternary liquid systems constituted by tetradecane, tri-*n*-butyl phosphate, and lanthanide(III) nitrate solvate with TBP in the region of phase separation. Solvates $Ln(NO_3)_3(TBP)_3$ were prepared by a threefold contact of TBP with lanthanide(III) nitrate saturated aqueous solutions [1]. The "concentrations" of $Ln(NO_3)_3(TBP)_3$ in the phase of the pure solvate were 1.08–1.12 mol dm^{-3}, $\rho = 1.2755 \pm 0.0012$ g cm^{-3}. Binodals and nodes were plotted by the method described in [2].

The analysis of the data obtained (see table and Fig. 1) showed that the binary systems $Ln(NO_3)_3(TBP)_3$–

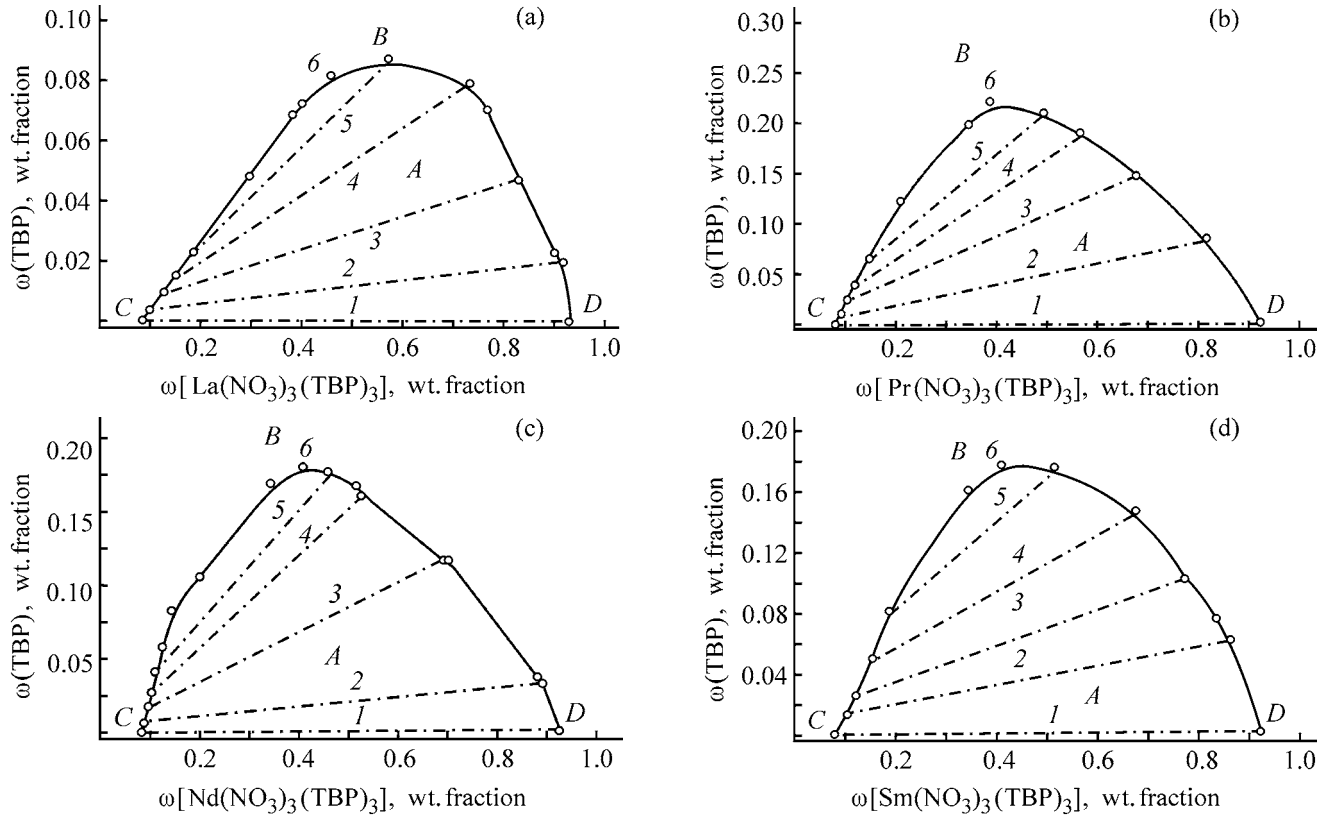

Fig. 1. Phase diagrams of the ternary systems $Ln(NO_3)_3(TBP)_3$–TBP–$C_{14}H_{30}$ at 298.15 K. (*A*) Field of phase separation, (*B*) field of homogeneous organic solutions, (*CD*) binodal, (*1*–*5*) nodes (see table), and (*6*) point of critical composition of the ternary systems; (a) La, (b) Pr, (c) Nd), and (d) Sm.

1070-4272/04/7704-0559 © 2004 MAIK "Nauka/Interperiodica"

Phase separation in the systems $Ln(NO_3)_3(TBP)_3$–TBP–$C_{14}H_{30}$ at 298.15 K

ρ, g sm^{-3}	$[Ln(NO_3)_3(TBP)_3]$	TBP	$C_{14}H_{30}$	Nodes	ρ, g sm^{-3}	$[Ln(NO_3)_3(TBP)_3]$	TBP	$C_{14}H_{30}$	Nodes
	wt. fraction					wt. fraction			
	Ln = La					Ln = Nd			
0.7849	0.081	0	0.919	*1*	0.7850	0.081	0	0.919	*1*
0.7927	0.103	0.004	0.893	*2*	0.7880	0.087	0.006	0.907	*2*
0.8035	0.131	0.010	0.859	*3*	0.7938	0.098	0.018	0.884	*3*
0.8128	0.155	0.015	0.830	*4*	0.7971	0.103	0.027	0.870	*4*
0.8251	0.185	0.023	0.792	*5*	0.8025	0.111	0.041	0.848	*5*
	0.299	0.048	0.653			0.128	0.057	0.815	
	0.383	0.069	0.548			0.144	0.083	0.773	
	0.402	0.072	0.526			0.201	0.106	0.693	
	0.459	0.082	0.459	*6*		0.344	0.168	0.488	
1.0132	0.573	0.087	0.340	*5*		0.410	0.180	0.410	*6*
1.1071	0.733	0.079	0.187	*4*	0.9784	0.458	0.176	0.366	*5*
	0.769	0.070	0.161		1.0062	0.516	0.167	0.317	
1.1613	0.830	0.047	0.123	*3*	1.0099	0.527	0.160	0.313	*4*
	0.900	0.023	0.077		1.0937	0.693	0.116	0.191	*3*
1.2176	0.920	0.019	0.061	*2*	1.1013	0.706	0.115	0.179	
1.2192	0.932	0	0.068	*1*	1.1942	0.880	0.036	0.083	
					1.2027	0.894	0.032	0.074	*2*
	Ln = Pr				1.2135	0.925	0	0.075	*1*
0.7849	0.081	0	0.919	*1*					
0.7909	0.094	0.010	0.896	*2*		Ln = Sm			
0.7987	0.109	0.025	0.866	*3*	0.7849	0.081	0	0.919	*1*
0.8060	0.122	0.04	0.838	*4*	0.7953	0.104	0.015	0.881	*2*
0.8214	0.152	0.065	0.783	*5*	0.8046	0.126	0.025	0.849	*3*
	0.213	0.122	0.665		0.8205	0.157	0.052	0.791	*4*
	0.346	0.198	0.456		0.8370	0.185	0.082	0.733	*5*
	0.390	0.220	0.390	*6*		0.345	0.161	0.494	
1.0076	0.497	0.208	0.295	*5*		0.411	0.178	0.411	*6*
1.0413	0.567	0.189	0.244	*4*	1.0091	0.516	0.177	0.307	*5*
1.0959	0.679	0.148	0.173	*3*	1.0958	0.678	0.149	0.173	*4*
1.1687	0.820	0.085	0.095	*2*	1.1426	0.774	0.102	0.124	*3*
1.2135	0.925	0	0.075	*1*		0.838	0.076	0.086	
					1.1899	0.861	0.062	0.077	*2*
					1.2135	0.925	0	0.075	*1*

TBP and TBP–$C_{14}H_{30}$ the components are homogeneous at any component ratios. The mutual solubility of the components in the $Ln(NO_3)_3(TBP)_3$–$C_{14}H_{30}$ systems is limited, and, as a result, two liquid phases I and II are formed. Phase I is enriched in $C_{14}H_{30}$, and phase II, in $Ln(NO_3)_3(TBP)_3$. The solubility (weight fraction) of $Ln(NO_3)_3(TBP)_3$ in $C_{14}H_{30}$ is virtually independent of a particular lanthanide and amounts to 0.081. The solubility of tetradecane in the solvate is also independent of a particular lanthanide.

The phase diagrams of ternary liquid systems $Ln(NO_3)_3(TBP)_3$–TBP–$C_{14}H_{30}$ consist of fields of homogeneous organic solutions (Fig. 1, field *B*) and fields of phase separation into two liquid phases (Fig. 1, field *A*), bounded by binodals. The points of the critical composition of the ternary systems (ω_{2cr}) are compositions with approximately equal weight fractions of $Ln(NO_3)_3(TBP)_3$ and $C_{14}H_{30}$ and different TBP contents, depending on a lanthanide. At the point ω_{2cr}, the TBP weight fraction tends to increase from La(III) to Pr(III) and then to decrease from Pr(III) to

Nd(III), while the TBP contents in the systems with Nd and Sm are close (see table).

Nodes of ternary liquid systems with phase separation (see table and Fig. 1) show that, as in the case of binary systems $Ln(NO_3)_3(TBP)_3$–$C_{14}H_{30}$, two liquid phases I and II are formed; phase I is enriched in $C_{14}H_{30}$, and phase II, in $Ln(NO_3)_3(TBP)_3$.

The dependences of the solvate distribution coefficients between phases I and II on the solvate weight fractions in phase II are shown in Fig. 2. As can bee seen, the distribution coefficients decrease with increasing solvate weight fraction. At the solvate weight fraction of 0.5, the distribution coefficients depend on a particular lanthanide and decrease in the order La, Sm, Pr, Nd. At the solvate weight fraction in phase II of 0.95, the distribution coefficients are virtually independent of a particular lanthanide.

Figure 3 shows that the TBP weight fraction in phase II is substantially higher than that in phase I. The maximal TBP accumulation in phase II is observed for Pr and Nd solvates, and the minimum accumulation, for La and Sm solvates.

It follows from Fig. 4 that the $C_{14}H_{30}$ weight fraction in phase I is higher than that in phase II.

Lanthanides(III) substantially (La and Nd, more strongly, and Sm and Pr, more weakly) affect the tetradecane distribution between phases I and II. To use extraction systems based on TBP and hydrocarbon diluent in practice, the TBP equilibrium concentration (weight fraction) should be 0.17–0.20, i.e., it is necessary to operate with organic phases unsaturated with respect to lanthanide(III) nitrate, or to use commercial solvents with a low content of long-chain hydrocarbon fractions.

CONCLUSIONS

(1) Phase diagrams of ternary liquid systems constituted by tetradecane, tri-*n*-butyl phophate, and $Ln(NO_3)_3(TBP)_3$ (Ln = La, Pr, Nd, and Sm) consist of the field of homogeneous solutions and the field of phase separation (phases I and II). Phase I is enriched in tetradecane and phase II, in lanthanide(III) nitrate solvate.

(2) At the point of the critical composition of the ternary systems, the weight fractions of $Ln(NO_3)_3(TBP)_3$ and tetradecane are approximately equal at different TBP contents, depending on particular lanthanide. At the point ω_{2cr}, the TBP weight fraction

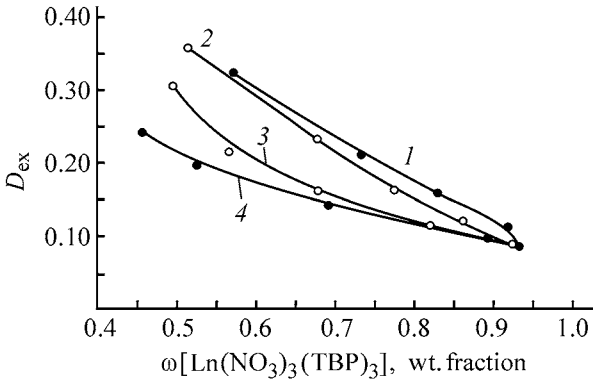

Fig. 2. Distribution coefficients of $Ln(NO_3)_3(TBP)_3$, D_{ex}, between phases I and II vs. ω $Ln(NO_3)_3(TBP)_3$, in phase II. Phase I is enriched in $C_{14}H_{30}$, and phase II, in $Ln(NO_3)_3(TBP)_3$; the same for Figs. 3, 4. (*1*) La, (*2*) Sm, (*3*) Pr, and (*4*) Nd.

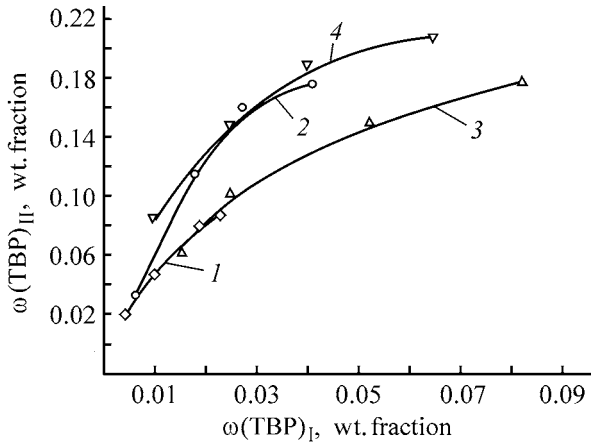

Fig. 3. Distribution of TBP between phases I and II. $\omega(TBP)_I$ and $\omega(TBP)_{II}$ are weight fractions of TBP in phases I and II, respectively. (*1*) La, (*2*) Nd, (*3*) Sm, and (*4*) Pr.

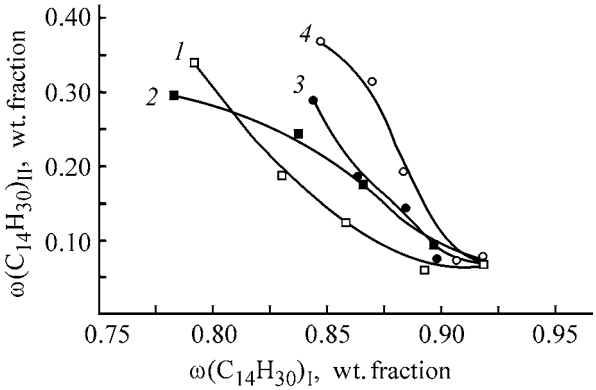

Fig. 4. Distribution of $C_{14}H_{30}$ between phases I and II. $\omega(C_{14}H_{30})_I$ and $\omega(C_{14}H_{30})_{II}$ are weight fractions of tetradecane in phases I and II, respectively. (*1*) La, (*2*) Nd, (*3*) Sm, and (*4*) Pr.

tends to increase from La(III) to Pr(III) and then to decrease from Pr(III) to Nd(III), while the TBP content in the systems with Nd and Sm is about the same.

(3) In the phase separation field, the TBP and $Ln(NO_3)_3(TBP)_3$ weight fractions in phase II are substantially higher than those in phase I; the tetradecane weight fraction in the phase I is higher than that in phase II. The distribution of the components in the ternary systems depends on a particular lanthanide.

(4) In practice, to use extraction systems with TBP and tetradecane, it is necessary to keep the equilibrium TBP content (weight fraction) no less than 0.17–0.20 or to use commercial solvents with a low content of long-chain hydrocarbons.

REFERENCES

1. Pyartman, A.K., Kopyrin, A.A., Puzikov, E.A., and Bogatov, K.B., *Radiokhimiya*, 1995, vol. 37, no. 1, pp. 52–55.
2. Pyartman, A.K., Kudrova, A.V., and Keskinov, V.A., *Zh. Prikl. Khim.*, 2004, vol. 77, no. 4, pp. 560–563.

Russian Journal of Applied Chemistry, Vol. 77, No. 4, 2004, pp. 563–565. Translated from Zhurnal Prikladnoi Khimii, Vol. 77, No. 4, 2004, pp. 568–570.

PHYSICOCHEMICAL STUDIES OF SYSTEMS AND PROCESSES

Effect of Temperature on Phase Separation in Liquid Binary System Constituted by Tetradecane and Samarium(III) Nitrate Solvate with Tri-*n*-Butyl Phosphate and Ternary System Constituted by Tetradecane, Tri-*n*-Butyl Phosphate, and Samarium(III) Nitrate Solvate with Tri-*n*-Butyl Phosphate

A. K. Pyartman, A. V. Kudrova, and V. A. Keskinov

St. Petersburg State Technological Institute, St. Petersburg, Russia

Received May 6, 2003

Abstract—The phase diagrams of a binary liquid system constituted by tetradecane and samarium(III) nitrate solvate with tri-*n*-butyl phosphate and a ternary system constituted by tetradecane, tri-*n*-butyl phosphate, and samarium(III) nitrate solvate with tri-*n*-butyl phosphate were studied at 298.15–355.15 K. The distribution of components between the phases was considered. The points of critical compositions of the ternary system at various temperatures and the upper critical temperature of mixing of the binary and ternary systems were estimated.

The phase diagrams of ternary liquid systems constituted by tetradecane, tri-*n*-butyl phosphate (TBP), and lanthanide(III) nitrate solvate with TBP at 298.15 K were studied in [1]. These diagrams consist of a field of homogeneous solutions and a field of separation into two liquid phases: phase I is enriched in tetradecane, and phase II, in $[Ln(NO_3)_3(TBP)_3]$. Quantitative data on the above binary and ternary phase diagrams in relation to the temperature are lacking, although such an information is of interest for the choice of diluent, component concentrations, and temperature of extractor operation. In this study, we examined the temperature dependences of the above binary and ternary systems with Sm(III).

The phase densities were measured pycnometrically. Vacuum-distilled TBP (density $\rho = 0.9727$ g cm^{-3} at 298.15 K) and tetradecane of chemically pure grade (0.7592 g cm^{-3}) were used. Samarium(III) nitrate solvate $[Sm(NO_3)_3(TBP)_3]$ (S) was prepared by threefold saturation of TBP with fresh portions of a saturated aqueous solution of samarium nitrate [2]. The "concentration" of $[Sm(NO_3)_3(TBP)_3]$ in the phase of pure S was 1.10 M, $\rho = 1.2755 \pm 0.0012$ g cm^{-3}. The binodals of the ternary system were measured with modified Alekseev's method [3] by titration of the binary system with different compositions with the third component under the temperature control. The S concentration in the organic phase was monitored complexometrically [4]. Nodes (compositions of the coexisting organic phases) were determined by the method described in [1, 3]. All the results are presented as phase diagrams in the form of the second Roozeboom's triangle: rectangular coordinates (component weight fractions) for two components of the ternary liquid systems (for the third component, $\omega_3 = 1 - \omega_1 - \omega_2$), depending on temperature. The errors in ω de-

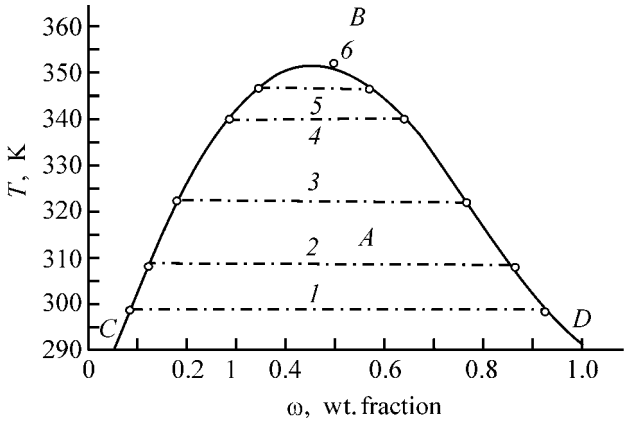

Fig. 1. Effect of temperature on phase separation of the $[Sm(NO_3)_3(TBP)_3]$–tetradecane system. (*T*) Temperature, (ω) weight fraction of $[Sm(NO_3)_3(TBP)_3]$, (*A*) field of separation into two liquid phases, (*B*) field of homogeneous solutions, (*CD*) binodal, (*1–5*) nodes, and (*6*) upper critical temperature of mixing.

1070-4272/04/7704-0563 © 2004 MAIK "Nauka/Interperiodica"

Table 1. Temperature effect on phase separation in the $[Sm(NO_3)_3(TBP)_3]$–tetradecane system

T, K	$[Sm(NO_3)_3(TBP)_3]$	$C_{14}H_{30}$	Nodes (Fig. 1)
	wt. fraction		
298.15	0.081	0.919	*1*
308.15	0.121	0.879	*2*
322.15	0.175	0.825	*3*
340.15	0.289	0.711	*4*
346.15	0.350	0.650	*5*
351.85	0.500	0.500	*6*
346.15	0.568	0.432	*5*
340.15	0.644	0.356	*4*
322.15	0.762	0.238	*3*
308.15	0.87	0.13	*2*
298.15	0.925	0.075	*1*

Table 2. Phase separation in the $[Sm(NO_3)_3(TBP)_3]$–TBP–tetradecane system at 298.15–333.15 K

T, K	$[Sm(NO_3)_3(TBP)_3]$	TBP	$C_{14}H_{30}$	Nodes (Fig. 2)
	wt. fraction			
333.15	0.242	0	0.758	*1*
	0.253	0.003	0.744	*2*
	0.267	0.008	0.725	*3*
	0.305	0.019	0.676	*4*
	0.474	0.052	0.474	*5**
	0.584	0.035	0.381	*4*
	0.638	0.019	0.343	*3*
	0.671	0.008	0.321	*2*
	0.687	0	0.313	*1*
313.15	0.141	0	0.859	*1*
	0.152	0.009	0.839	*2*
	0.183	0.022	0.795	*3*
	0.242	0.048	0.710	*4*
	0.447	0.113	0.440	*5**
	0.566	0.105	0.328	*4*
	0.667	0.069	0.264	*3*
	0.726	0.040	0.234	*2*
	0.824	0	0.176	*1*
298.15	0.081	0	0.919	*1*
	0.104	0.015	0.881	*2*
	0.126	0.025	0.849	*3*
	0.157	0.052	0.791	*4*
	0.185	0.082	0.733	*5*
	0.411	0.178	0.411	*6**
	0.516	0.177	0.307	*5*
	0.678	0.149	0.173	*4*
	0.774	0.102	0.124	*3*
	0.861	0.062	0.077	*2*
	0.925	0	0.075	*1*

* Point of the critical composition of the ternary system.

termination did not exceed ±0.001–0.002, and those of temperature measurement, ±0.2 K.

The binary systems S–TBP and TBP–tetradecane are homogeneous at all the temperatures studied. By contrast, the S–tetradecane system exhibits solubility limits and has a field of separation into two liquid phases I and II. Phase I is enriched in tetradecane, and phase II, in S. With temperature rise, this field narrows (Fig. 1). The upper critical temperature of mixing lies at $T_{cr} = 351.15 \pm 0.2$ K. The compositions of the coexisting phases (nodes) at various temperatures are listed in Table 1. At the T_{cr} point, the component weight fractions are approximately equal (Table 1).

The phase diagram of the ternary liquid system S–TBP–tetradecane at various temperatures is shown in Fig. 2. It consists of the field of homogeneous solutions (Fig. 2, field *B*) and the field of separation into two liquid phases (Fig. 2, field *A*) bounded with binodals. The points of critical composition of the ternary system ω_{2cr} correspond to phases with approximately equal weight fractions of S and tetradecane and varied temperature-dependent TBP content (Table 2). The upper critical temperature of mixing for the binary and ternary systems is the same (Fig. 2). The temperature rise leads to narrowing of the separation field of the ternary system (Fig. 2). The dependence of ω_{2cr} on $1/T$ is shown in Fig. 3. It is virtually linear and can be described by the equation

$$\omega_{2\,cr} = -(0.980 \pm 0.042) + (344 \pm 13)/T. \qquad (1)$$

Dependence (1) allows prediction of the critical compositions of the ternary system at various temperatures.

The nodes of the ternary liquid system S–TBP–tetradecane (Table 2) show that, as in the case of the binary system S–tetradecane, two liquid phases I and II are formed. Phase I is enriched in tetradecane, and phase II, in S. TBP is also concentrated predominantly in phase II, while tetradecane is concentrated in phase I at all the temperatures studied (Table 2).

In practice, to use extraction systems based on TBP and hydrocarbon solvent, it is necessary to keep the TBP equilibrium content (weight fraction) no less than 0.17–0.20 at about 298.15 K, i.e., to operate with the organic phase unsaturated with respect to Ln(III). At 333.15 K, the equilibrium TBP weight fraction can be decreased to 0.05–0.06.

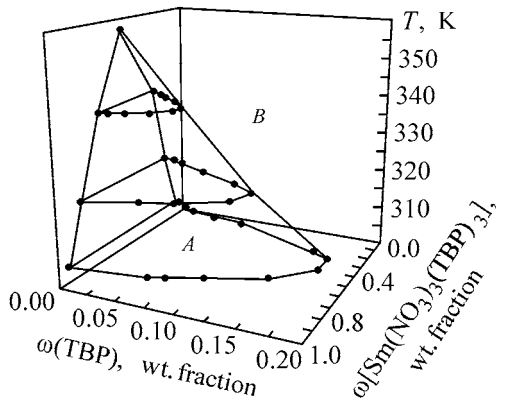

Fig. 2. Phase diagram of the ternary system $[Sm(NO_3)_3(TBP)_3]$–TBP–tetradecane in the 298.15–355.15 K range. $\omega[Sm(NO_3)_3(TBP)_3]$ and ω(TBP) are weight fractions of $[Sm(NO_3)_3(TBP)_3]$ and TBP, respectively; (*A*) field of separation into two liquid phases and (*B*) field of homogeneous solutions.

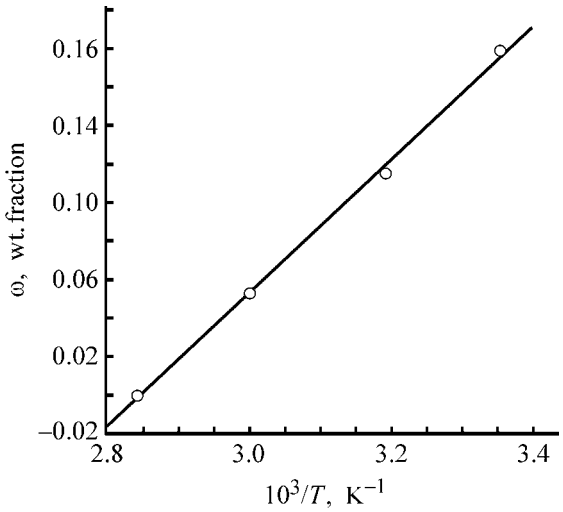

Fig. 3. Dependence of TBP weight fraction ω on the temperature *T* in the points of critical composition of the ternary system $[Sm(NO_3)_3(TBP)_3]$–TBP–tetradecane.

CONCLUSIONS

(1) The binary system S–tetradecane exhibits solubility limits and has a field of separation into two liquid phases I and II. Phase I is enriched in tetradecane, and phase II, in $[Sm(NO_3)_3(TBP)_3]$. With temperature rise, this field narrows (Fig. 1). The upper critical temperature of mixing is $T_{cr} = 351.15 \pm 0.2$ K.

(2) The phase diagram of the ternary liquid system $[Sm(NO_3)_3(TBP)_3]$–TBP–tetradecane at various temperatures consists of the field of homogeneous solutions and the field of separation into two liquid phases. The points of critical composition of ternary system ω_{2cr} correspond to phases with approximately equal weight fractions of $[Sm(NO_3)_3(TBP)_3]$ and tetradecane and varied temperature-dependent TBP content.

(3) Within the field of phase separation, $[Sm(NO_3)_3(TBP)_3]$ and TBP are predominantly concentrated in phase II, while tetradecane, in phase I, at various temperatures.

(4) In practice, to use extraction systems with TBP and hydrocarbon solvent, it is necessary to keep the equilibrium TBP content (weight fraction) no less than 0.17–0.20 at about 298.15 K. At 333.15 K, the equilibrium TBP weight fraction can be decreased to 0.05–0.06.

REFERENCES

1. Pyartman, A.K., Kudrova, A.V., and Keskinov, V.A., *Zh. Prikl. Khim.*, 2004, vol. 77, no. 4, pp. 564–567.
2. *Ekstraktsiya neorganicheskikh veshchestv (Diagrammy rassloeniya, raspredeleniya, vysalivaniya i razdeleniya)* (Extraction of Inorganic Substances (Diagrams of Phase Separation, Distribution, Salting-out, and Separation)), Nikolaev, A.V., Ed., Novosibirsk: Nauka, 1970.
3. Treybal, R.E., *Liquid Extraction*, New York: McGraw–Hill, 1963.
4. Pribil, R., *Analytical Applications of EDTA and Related Compounds*, Oxford: Pergamon, 1972.

Russian Journal of Applied Chemistry, Vol. 77, No. 4, 2004, pp. 566–570. Translated from Zhurnal Prikladnoi Khimii, Vol. 77, No. 4, 2004, pp. 571–575.

PHYSICOCHEMICAL STUDIES OF SYSTEMS AND PROCESSES

Extraction of Aromatic Hydrocarbons from Hydrofined Diesel Fraction with 2-Methoxyethanol in the Presence of Pentane

A. A. Gaile, G. D. Zalishchevskii, L. V. Semenov, A. Ch. Khadartsev, O. M. Varshavskii, and N. P. Fedyanin

St. Petersburg State Technological Institute, St. Petersburg, Russia
Kirishinefteorgsintez Production Association Ltd., Kirishi, Leningrad oblast, Russia

Received April 1, 2003; in final form, December 2003

Abstract—Five-step countercurrent extraction of aromatic hydrocarbons from hydrofined diesel fraction with the 2-methoxyethanol–water–pentane extraction system was studied. The process was performed on a rotary-disk extractor.

In accordance with the demands proclaimed by the World-Wide Fuel Charter for Category 2 diesel fuels (for markets with stringent requirements for emission control or other market demands), the total content of aromatics should be no more than 25 wt % and that of polyaromatics, 5 wt %. The corresponding values for Category 3 diesel fuels (markets with advanced requirements for emissions control or other market demands) are 15 and 2 wt %. The sulfur content should not exceed 300 (Category 2) and 30 ppm (Category 3). Even more restrictions limits were imposed in such countries as the United States and Sweden. For example, the Swedish national standards for the quality of Grade 1 diesel fuel limit the content of total aromatics and polyaromatics to 5 and 0.02 vol %, respectively, and the content of sulfur, to 10 ppm [1].

Such very stringent requirements to the sulfur content are caused not only by undesirability of release of sulfur oxides to the atmosphere, but also by the fact that sulfur has a significant impact on vehicle emissions by poisoning the afterburning catalysts.

Pollution-free diesel fuels can be produced using hydrocracking of vacuum gas oils or hydroreforming of diesel fractions [1, 2]. However, these hydrogenation processes are performed at high pressure and require high specific investment, power consumption, and hydrogen consumption. For example, the consumption of H_2 per 1 vol % of arenes removed is 5–6 $nm^3\ m^{-3}$ raw material, and that per 0.1 wt % of sulfur and nitrogen removed, 2–3 and 4–6 $nm^3\ m^{-3}$ raw material, respectively [3].

The first industrial unit for refining of diesel fuel by solvent extraction was put into service in the United States in 2001 [4]. The extractant composition was not given, but it may be suggested from the reported process flowsheet that it is a high-boiling selective solvent, whose regeneration is performed by aqueous stripping, followed by removal of excess water by distillation. However, in this case, the water consumption for regeneration of the extractant from the extract phase should be high, requiring high power consumption for the subsequent removal of water.

Previously, we have suggested quite efficient extraction systems for refining of the diesel fraction to remove aromatic and organoelement compounds: acetonitrile–water–pentane [5–9] and dimethylformamide (or dimethylacetamide)–water–pentane [10–12]. These systems contain low-boiling polar and nonpolar solvents readily regenerable by distillation. Acetonitrile does not form azeotropic mixtures with components of the diesel fraction, and dimethylformamide and dimethylacetamide form heteroazeotropic mixtures only with saturated hydrocarbons contained in this fraction. Formation of such azeotropic mixtures improves the process selectivity: the major part of saturated hydrocarbons remaining in the extract phase is removed with a selective solvent in the course of its regeneration, and the arene content in the concentrate increases to 98–99.5 wt %.

Acetonitrile, dimethylformamide, and dimethylacetamide are characterized by fairly high selectivity with respect to aromatic hydrocarbons. Their draw-

1070-4272/04/7704-0566 © 2004 MAIK "Nauka/Interperiodica"

back is the hydrolytic instability in the course of regeneration at high temperatures (highly corrosive acetic and formic acids are formed as hydrolysis products). 2-Methoxyethanol is less selective with respect to arenes [13], but demonstrates higher hydrolytic stability and lower corrosive activity. The extraction system 2-methoxyethanol–water–pentane was successfully used for removal of aromatic hydrocarbons from dewaxed fractions 200–320°C [14, 15], for refining of liquid paraffin fractions to remove aromatic hydrocarbons [16], and also for manufacture of hydraulic and transformer oils from light oil fractions of the Troitsk-Anastasievsk oil field [17, 18].

The goal of this study was to check the possibility of manufacturing pollution-free diesel fuel by extraction refining of the hydrofined diesel fraction, using the 2-methoxyethanol–water–pentane extraction system.

As a raw material, we used hydrofined diesel fraction with the characteristics listed in Table 1.

EXPERIMENTAL

Five-step countercurrent extraction was carried out using a system of temperature-controlled separating funnels [20]. The raw material in pentane flowed countercurrent to aqueous 2-methoxyethanol. The experimental conditions are given in Table 2. The decision on five theoretical plates was caused by the fact that the efficiency of industrial extractors used for production of benzene, toluene, and xylenes from reformates corresponds to 6–7 theoretical plates, and that in selective refining of lube cuts, to 3–4 theoretical plates. It would be expected that the efficiency of similar extractors for selective refining of the diesel fraction with a viscosity intermediate between the gas oil and lube fractions corresponds to ca. five theoretical plates. Cycling by the scheme reproducing the operation of a fully charged column was performed until the steady state mode, under which the weights and compositions of the extract and raffinate phases become constant was established. Pentane was recovered from the extract and raffinate phases by distillation on a 15 TP column. 2-Methoxyethanol was entirely removed from the raffinate by multiple aqueous stripping. The most part of 2-methoxyethanol and water that remained after distillation of pentane were removed using the same column. Small residual amounts of 2-methoxyethanol (3–5 wt %) were removed from the extract and raffinate by aqueous stripping. The extract and raffinate were dried over calcined zeolite NaA. The material balance data for

Table 1. Characteristics of hydrofined diesel fraction and raffinate after selective refining

Parameter	Raw material	Raffinate
Yield, wt %	100	81.8
Standard distillation, °C:		
Initial boiling point	213	210
10%	235	249
20%	247	255
30%	256	269
40%	268	277
50%	277	287
60%	290	300
70%	305	313
80%	315	328
90%	360	349
Yield of fraction <360°C, vol %	90.0	94.3
Density ρ_4^{20}, g cm^{-3}	0.840	0.825
Refractive index n_D^{20}	1.4709	1.4598
Kinematic viscosity, mm^2 s^{-1}, at 20°C	6.03	5.72
Cloud point, °C	–5.5	–5.0
Pour point, °C	–12.5	–10.0
Flash point (closed vessel), °C	81	72
Total aromatics content, wt %	25.0	10.4
Polyaromatics content, wt %	5.7	1.9
Sulfur content, wt %	0.045	0.02
Olefin content, wt %	–	1.0
Bromine number, g per 100 g	–	0.706
Acid number, mg KOH per 100 ml fuel	–	0.618
Limiting filterability temperature, °C	–	–1.0
Moisture content by Fischer, ppm	–	46.3
Cetane index**	53	60

* Supplied by the Kirishi Refinery.

** Estimated by the empirical equation given in [19]: $CI = 524 - 20.88\sqrt[3]{0.3t_{10}+0.53t_{50}+0.17t_{96}} - \frac{2605\rho^{20}}{\sqrt[3]{0.3t_{10}+0.53t_{50}+0.17t_{96}}}$, where t_{10}, t_{50}, and t_{96} are the 10, 50, and 96% distillation temperatures, respectively (standard distillation), and ρ^{20} is the density of the fraction at 20°C (g cm^{-3}).

Table 2. Parameters of five-step countercurrent extractive refining and selective extractive distillation on a rotary-disk extractor

Parameter	Five-step extraction	RDE
Temperature, °C	30	15
Moisture content in 2-methoxyethanol, wt %	5.0	5.0
Mass ratio:		
aqueous 2-methoxyethanol : feed	5 : 1	6.9 : 1
pentane : feed	1 : 1	0.96 : 1

Table 3. Material balance in five-step countercurrent extractive refining of the diesel fraction (recalculated to 100 g of raw material)

Component	Feed		Raffinate		Extract	
	g	wt %	g	wt %	g	wt %
Aromatic hydrocarbons	25.0	3.57	9.5	5.56	15.5	2.93
Saturated hydrocarbons	75.0	10.71	74.2	43.39	0.8	0.15
Pentane	100	14.29	68.6	40.12	31.4	5.94
2-Methoxyethanol	475	67.86	18.5	10.82	456.5	86.29
Water	25.0	3.57	0.2	0.11	24.8	4.69
Total:	700	100	171.0	100	529.0	100

the extraction refining of diesel fraction are listed in Table 3.

The process was then performed on a rotary-disk extractor (RDE). It has the form of a column (inner diameter 60 mm; height 1400 mm) with an axle drive shaft supported by a ball thrust bearing. Horizontal disks 40 mm in diameter are fastened on the shaft between the stator rings at a 15-mm spacing. The column consists of 50 sections with a total height of 800 mm. There are settling zones 300 mm high at the top and bottom of RDE. The extractor is equipped with a water jacket. The rotor speed can be finely adjusted within the range 200–1300 rpm. In this study, the extraction was carried out at a rotor speed of 400 rpm. The flows of the feed, extractant, and pentane were set with dosing piston pumps. Watered 2-methoxyethanol having a higher density as compared to the diesel fraction was fed to the top of RDE. The column was charged with the extractant and then the raw material with pentane was started to be fed through a sprayer producing fine droplets. The raffinate and extract phases were run off, respectively, from the top and bottom settling zones to tanks. The raffinate and extract were separated from the equilibrium phases by the procedure described above for the experiment with separating funnels.

The results obtained in the experiments on five-step countercurrent extraction with separating funnels and RDE with the use of the 2-methoxyethanol–water–pentane extraction system are well consistent. The yield of the raffinate in the experiments with separating funnels and RDE was 83.7 and 81.8 wt %, respectively; density of the raffinate at 20°C, 0.822 and 0.823 g cm^{-3}; refractive index at 20°C, 1.4599 and 1.4598; kinematic viscosity at 20°C, 5.98 and 5.72 mm^2 s^{-1}; and total content of aromatics, 11.3 and 10.4 wt %. Since the experiments on RDE were carried out at reduced temperature, a decrease in the solvency of the extractant was compensated for by increasing the extractant-to-feed ratio (Table 2). In the experiments on RDE, we achieved somewhat more exhaustive dearomatization of the diesel fraction at a lower (by 4.4 wt %) arene content in the extract. The similarity of the results obtained in both experiments suggests that the efficiency of RDE is about five theoretical plates.

The conclusions made upon a comparison of the results of this study with those obtained previously with the acetonitrile–water–pentane [6–8] and DMF–water–pentane extraction systems [10, 12] are as follows.

(1) Changing acetonitrile for 2-methoxyethanol in the extraction system allows more exhaustive and selective dearomatization of the diesel fraction. However, this requires an increase in the water content in the extractant from 1 to 5 wt % and in the volume ratio of the extractant to raw material from ca. 2.5 : 1 to (4.35 – 6.0) : 1.

(2) Changing DMF for 2-methoxyethanol provides the same degree of dearomatization, but at a volume ratio of 2-methoxyethanol to raw material, increased by 25–40%.

Despite the somewhat lower efficiency of the 2-methoxyethanol–water–pentane extraction system as compared to the system with DMF, a decision on a polar solvent for the industrial process should be made taking into account such important advantages of 2-methoxyethanol as its lower boiling point and, accordingly, milder temperature conditions required for its regeneration, and also higher thermal and hydrolytic stability of 2-methoxyethanol and, as a result, its lower corrosivity.

Characteristics of the raffinate obtained (Table 1) meet the requirements to summer diesel fuel. The flash point of the diesel fraction after dearomatization decreased, and the cloud and pour points slightly in-

Table 4. Characteristics of the extract from extractive refining of the diesel fraction with 2-methoxyethanol–water–pentane extraction system

Parameter	Five-step extraction	RDE	Parameter	Five-step extraction	RDE
Yield, wt %	16.3	18.2	Degree of recovery, %:		
Density ρ_4^{20}, g cm^{-3}	0.932	0.916	sum of aromatic hydrocarbons	62.0	66.0
Refractive index n_D^{20}	1.5179	1.5173	polycycloarenes	–	72.8
Arene content, wt %	95.0	90.6	sulfur-containing compounds	–	63.6
among them polycycloarenes	–	22.8			

creased. The content of aromatics in the extract was 90.6–95 wt % (Table 4).

The cetane index of the raffinate, which characterizes the ability of diesel fuel to self-ignition and depends on the group hydrocarbon composition, increased by 7 points as compared to the hydrofined diesel fraction. In this parameter (CI = 60) the raffinate meets the demands of the World-Wide Fuel Charter for Category 3 diesel fuels. The sulfur content in the raffinate decreased by a factor of 2.25 as compared to the hydrofined diesel fraction, which meets the requirements for Category 2 diesel fuels.

CONCLUSIONS

(1) Five-step countercurrent extraction of arenes from hydrofined diesel fraction at 5 : 1 weight ratio of aqueous (5% water) 2-methoxyethanol to raw material and 1 : 1 weight ratio of pentane to raw material allowed a decrease in the aromatics content from 25 to 10–11 wt % and in the content of organosulfur compounds from 0.045 to 0.02 wt %. In this case, the arene content in the extract approaches 90–95 wt %.

(2) Extractive refining of the diesel fraction with the 2-methoxyethanol–water–pentane extraction system can be successfully performed on an apparatus with a rotary-disk extractor.

(3) The use of extraction systems with 2-methoxyethanol provides more exhaustive and selective dearomatization of the diesel fraction as compared to that with acetonitrile. In this case, the results are similar to those obtained in refining with DMF–pentane. However, the system with 2-methoxyethanol requires an increased (by 25–40%) weight ratio of polar extractant to raw material. Such advantages of 2-methoxyethanol as higher thermal and hydrolytic stability and lower corrosivity, compared to acetonitrile and DMF, should be taken into account in making a decision on an extraction system for industrial implementation of the process.

REFERENCES

1. Kaminskii, E.F. and Khafkin, V.A., *Glubokaya pererabotka nefti* (Exhaustive Refining of Oil), Moscow: Tekhnika, 2001.
2. Kaminskii, E.F., Osipov, L.N., Khavkin, V.A., *et al.*, *Neftegaz. Tekhnol.*, 2001, no. 1, pp. 36–42.
3. Korelyakov, L.V., *Analiz sushchestvuyushchikh tekhnologicheskikh protsessov polucheniya motornykh i kotel'nykh topliv s tsel'yu vybora i obosnovaniya tekhnologii rekonstruktsii i razvitiya OOO "KINEF" dlya povysheniya glubiny pererabotki nefti, rasshireniya nomenklatury i uluchsheniya kachestva tovarnoi produktsii* (Analysis of the Existing Processes for Production of Petrol and Fuel Oils, Aimed at Selection and Substantiation of Technologies of Reconstruction and Development of the KINEF Limited Liability Company To Increase the Deepness of Oil Refining, To Broaden the Assortment, and To Improve the Quality of Commercial Products), Moscow: OAO "TsNIITEneftekhim", 2001.
4. *Neftegaz. Tekhnol.*, 2002, no. 1, p. 100.
5. RF Patent 2 148 070.
6. Varshavskii, O.M., Gaile, A.A., Semenov, L.V., and Somov, V.E., in *Ekstraktsiya i primenenie arenov srednedistillyatnykh neftyanykh fraktsii: Sbornik trudov OOO PO "KINEF"* (Extraction and Application of Arenes from Middle Oil: Collection of Works of KINEF Production Association, Limited Liability Company), Gaile, A.A. and Somov, V.E., Eds., St. Petersburg: Sintez, 1998, pp. 11–18.
7. Gaile, A.A., Zalishchevskii, G.D., Varshavskii, O.M., *et al.*, in *Ekstraktsionnaya dearomatizatsiya neftyanykh fraktsii: Sbornik trudov OOO PO "KINEF"* (Extractive Dearomatization of Oil Fractions: Collection of Works of KINEF Production Association, Limited Liability Company), Gaile, A.A. and Somov, V.E., Eds., St. Petersburg: Sankt-Peterburg. Gos. Univ., 2002, pp. 102–107.
8. Gaile, A.A., Flisyuk, O.M, Semenov, L.V., *et. al.*, in *Ekstraktsionnaya dearomatizatsiya neftyanykh fraktsii: Sbornik trudov OOO PO "KINEF"* (Extractive Dearomatization of Oil Fractions: Collection of Works of KINEF Production Association, Limited Liability Company), Gaile, A.A. and Somov, V.E., Eds.,

St. Petersburg: Sankt-Peterburg. Gos. Univ., 2002, pp. 114–127.

9. Gaile, A.A., Somov, V.E., Semenov, L.V., *et al.*, *Khim. Tekhnol. Topl. Masel*, 1999, no. 5, pp. 3–7.
10. Gaile, A.A., Zalishchevskii, G.D., Varshavskii, O.M., *et al.*, *Zh. Prikl. Khim.*, 2001, vol. 74, no. 5, pp. 838–842.
11. RF Patent 2 185 416.
12. Gaile, A.A., Zalishchevskii, G.D., Varshavskii, O.M., *et al.*, in *Ekstraktsionnaya dearomatizatsiya neftyanykh fraktsii: Sbornik trudov OOO PO "KINEF"* (Extractive Dearomatization of Oil Fractions: Collection of Works of KINEF Production Association, Limited Liability Company), Gaile, A.A. and Somov, V.E., Eds., St. Petersburg: Sankt-Peterburg. Gos. Univ., 2002, pp. 108–113.
13. Gaile, A.A., Semenov, L.V., Zalishchevskii, G.D., and Varshavskii, O.M., in *Ekstraktsionnaya dearomatizatsiya neftyanykh fraktsii: Sbornik trudov OOO PO "KINEF"* (Extractive Dearomatization of Oil Fractions: Collection of Works of KINEF Production Association, Limited Liability Company), Gaile, A.A. and Somov, V.E., Eds., St. Petersburg: Sankt-Peterburg. Gos. Univ., 2002, pp. 5–34, 164–285.
14. RF Patent 2 139 910.
15. Kaifadzhyan, E.A., Gaile, A.A., Somov, V.E., and Semenov, L.V., *Zh. Prikl. Khim.*, 1998, vol. 71, no. 3, pp. 386–389.
16. Kaifadzhyan, E.A., Gaile, A.A., Somov, V.E., and Semenov, L.V., *Zh. Prikl. Khim.*, 1998, vol. 71, no. 4, pp. 601–603.
17. Gaile, A.A., Dyurik, N.M., Semenov, L.V., *et al.*, *Zh. Prikl. Khim.*, 2003, vol. 76, no. 1, pp. 146–149.
18. Gaile, A.A., Dyurik, N.M., Semenov, L.V., *et al.*, *Zh. Prikl. Khim.*, 2003, vol. 76, no. 1, pp. 150–153.
19. Gureev, A.A., Seregin, E.P., and Azev, V.S., *Kvalifikatsionnye metody ispytanii neftyanykh topliv* (Qualification Tests for Oil Fuels), Moscow: Khimiya, 1984.
20. Alders, L., *Liquid-Liquid Extraction; Theory and Laboratory Practice*, Amsterdam: Elsevier, 1959.

Russian Journal of Applied Chemistry, Vol. 77, No. 4, 2004, pp. 571–575. Translated from Zhurnal Prikladnoi Khimii, Vol. 77, No. 4, 2004, pp. 576–579.

SORPTION AND ION-EXCHANGE PROCESSES

Sorption of Gallium(III) from Alkaline Solutions with a Polymeric Sorbent Impregnated with 1,2-Dioxyanthraquinone

A. N. Turanov and V. K. Karandashev

Institute of Solid-State Physics, Russian Academy of Sciences, Chernogolovka, Moscow oblast, Russia

Institute of Microelectronic Technology and Ultra-High-Purity Materials, Russian Academy of Sciences, Chernogolovka, Moscow oblast, Russia

Received May 26, 2003

Abstract—Distribution of Ga(III) among aqueous solutions of NaOH and a macroporous copolymer of styrene with divinylbenzene, impregnated with 1,2-dioxyanthraquinone in the presence of the trialkylmethylammonium cation, was studied.

The main source of raw materials for manufacture of gallium are alkaline solutions formed in production of alumina [1]. Pointing to the fact that extractive techniques are promising for processing of materials of this kind, the authors of reviews [2, 3] note that the choice of extracting agents for selective recovery of gallium is limited. Extraction of gallium(III) from alkaline solutions with solutions of alkylated 8-oxyquinolines [4–6], pyrocatechols [7, 8], and alkyl phenyl oligomers [9–11] in organic solvents has been reported. The use of hydrophobic reagents of this kind is associated with the decrease in their solubility in aqueous alkaline solutions in the course of extraction [12].

Recently, impregnated materials that combine properties of a sorbent and a selective extracting agent have been finding increasingly wide use in recovery, concentration, and separation of rare, trace, and nonferrous metals [13, 14]. Materials of this kind not only make it possible to eliminate organic solvents, which are frequently toxic, volatile, or fire-hazardous, from the technological scheme, but also ensure a substantial decrease in contamination of aqueous solutions with organic reagents [15]. The use of impregnated materials for recovery of gallium(III) from alkaline solutions has been the subject of a comparatively small number of studies [16]. In these studies, alkylated 8-oxyquinolines, which form with Ga(III) complex compounds in the sorbent phase, served as organic complexing agents. Presumably, the set of such reagents can be supplemented with other phenol derivatives, including those soluble in aqueous alkaline solutions.

For this purpose, the distribution of Ga(III) among aqueous solutions of NaOH and a macroporous polymeric sorbent impregnated with 1,2-dioxyanthraquinone in the presence of the trialkylmethylammonium cation was examined in this study.

EXPERIMENTAL

1,2-Dioxyanthraquinone (alizarin) of analytically pure grade and trialkylmethylammonium nitrate (TAMAN) with the content of the main product of no less than 98% were used in the study. As a matrix for preparing an impregnated sorbent served nonionogenic macroporous copolymer of styrene with divinylbenzene, Wofatite EP-60.[1] The parameters of the material [17] are close to those of similar products of domestic manufacture, polysorbs [18]. The polymeric matrix was impregnated with TAMAN by a procedure similar to that described previously [19] and then the sorbed TAMAN was converted into the OH^- form [20]. The resulting sorbent was mixed with a solution of 1,2-dioxyanthraquinone in a 1 M solution of NaOH, the mixture was agitated for 1 h, and then the sorbent was separated from the aqueous phase by filtration and used to recover Ga(III) from aqueous alkaline solutions.

[1] Manufactured by Bitterfeld Chemical Combine, Germany.

1070-4272/04/7704-0571 © 2004 MAIK "Nauka/Interperiodica"

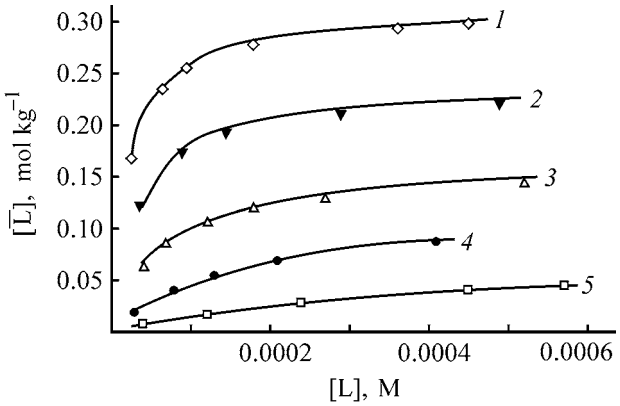

Fig. 1. Distribution of 1,2-dioxyanthraquinone among a 1 M solution of NaOH, [L], and a polymeric sorbent, [$\overline{L}$]. Concentration of ROH in the sorbent phase (mol kg^{-1}): (*1*) 0.75, (*2*) 0.5, (*3*) 0.25, (*4*) 0.1, and (*5*) 0.

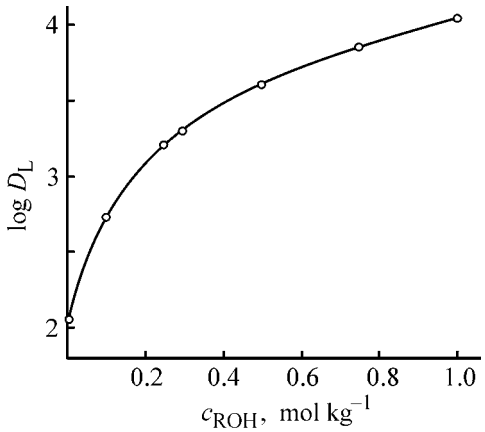

Fig. 2. Distribution coefficient of 1,2-dioxyanthraquinone, D_L, vs. the concentration of ROH, c_{ROH}, in the sorbent phase in sorption of from a 1 M solution of NaOH. Line: calculation by Eq. (5).

The starting aqueous solutions of Ga(III) were prepared by dissolving gallium oxide of pure grade in a 1 M solution of NaOH, with subsequent dilution with water or alkali. The concentration of Ga(III) in the starting solutions was 4×10^{-4} M.

Sorption experiments were performed under static conditions at 18±2°C. The mixture of an aqueous solution and the sorbent was agitated with a magnetic stirrer for 2 h, which is sufficient for constant distribution coefficients of gallium, D_{Ga}, and 1,2-dioxyanthraquinone, D_L, to be attained. The ratio between the volume V (ml) of the aqueous phase and the mass m (g) of the sorbent was 20 : 1.

The content of gallium(III) in the aqueous solutions before and after sorption was determined by mass spectrometry, with ionization of a sample in an inductively coupled plasma (ICP-MS), on a VG Elemental PlasmaQuad mass spectrometer (UK) by a procedure described previously in [21]. The concentration of 1,2-dioxyanthraquinone in the aqueous solutions was determined photometrically at λ = 590 nm on a KFK-2MP photocolorimeter.

The content of gallium(III) and 1,2-dioxyanthraquinone in the sorbent phase was calculated using material balance equations, and the distribution coefficients were found as the ratio of concentrations in the solid and aqueous phases. The concentration of NaOH in equilibrium aqueous solutions was determined by potentiometric titration with a 0.1 M solution of HCl.

Preliminarily, the distribution of 1,2-dioxyanthraquinone (H_2L) among aqueous solutions of NaOH and a polymeric sorbent impregnated with trialkylmethylammonium hydroxide (ROH) was considered. It is known that 1,2-dioxyanthraquinone is soluble in aqueous alkaline solutions because of the dissociation of phenol groups and virtually cannot be extracted with inert organic diluents. By contrast, the nonionogenic macroporous sorbent EP-60 sorbs 1,2-dioxyanthraquinone from solutions of this kind (Fig. 1, curve *5*), presumably as a sodium salt Na_2L. The sorption of 1,2-dioxyanthraquinone is markedly enhanced as the content of ROH in the sorbent phase grows (Fig. 1). This may be due to the formation in the sorbent phase of ionic associates RNaL and R_2L by the following ion-exchange reactions

$$L^{2-} + Na^+ + \overline{ROH} \rightleftarrows \overline{RNaL} + OH^-, \quad (1)$$

$$L^{2-} + 2\overline{ROH} \rightleftarrows \overline{R_2L} + 2OH^- \quad (2)$$

(the overline designates components in the solid phase) with the corresponding equilibrium concentration constants

$$K_1 = \frac{[\overline{RNaL}][OH^-]}{[L^{2-}][Na^+][\overline{ROH}]}, \quad (3)$$

$$K_2 = \frac{[\overline{R_2L}][OH^-]^2}{[L^2][\overline{ROH}]^2}, \quad (4)$$

The variation of the distribution coefficient of 1,2-dioxyanthraquinone with the concentration of ROH in the solid phase and with that of OH^- ions in the aqueous phase can be represented as

$$D_L = \frac{[\overline{RNaL}] + [\overline{R_2L}]}{[L^{2-}]} = \frac{K_1[Na^+][\overline{ROH}]}{[OH]} + \frac{K_2[\overline{ROH}]^2}{[OH]^2}. \quad (5)$$

The equilibrium constants calculated by the least-squares procedure with the use of the data in Fig. 2 are $K_1 = (4.7 \pm 0.2) \times 10^3$ and $K_2 = (6.3 \pm 0.3) \times 10^3$. It follows from these results that the sorbent for recovery of Ga(III), prepared by saturating with 1,2-dioxyanthraquinone a polymeric matrix impregnated with ROH, contains 1,2-dioxyanthraquinone in the form of the associates RNaL and R_2L. The concentration of the latter, relative to the total concentration of 1,2-dioxyanthraquinone in the sorbent phase, is expressed as

$$\alpha = \frac{K_2[\overline{ROH}]}{K_2[\overline{ROH}] + K_1[Na^+][OH]}. \quad (6)$$

Hence follows that raising the concentration of ROH in the solid phase and lowering the concentration of alkali in the aqueous phase favor an increase in the content of such a complex. The sufficiently high hydrophobicity of the associate R_2L ensures that it passes to only a slight extent into the aqueous phase in sorption recovery of Ga(III).

The data on saturation of the sorbent with gallium(III) (Fig. 3) indicate that Ga(III) is recovered into the solid phase in the form of a complex with a ratio Ga : L = 1 : 3, which is characteristic of extraction of this element in the form of intracomplex compounds [1]. It may be assumed that the C=O and OH groups of the molecule of 1,2-dioxyanthraquinone in the positions 9 and 1 of the anthraquinone ring are involved in complexation with Ga(III) [22], and the negative charge of the second phenol group of the reagent is neutralized by the trialkylmethylammonium cation.

Taking into account this fact, the interphase equilibrium of the process of recovery of Ga(III) from alkaline solutions in the form of an ionic associate $GaL_3^{3-} \cdot 3R^+$ can be described by the following equation of the exchange reaction

$$Ga(OH)_4^- + 3\overline{R_2L} \rightleftarrows \overline{Ga(RL)_3} + 3\overline{ROH} + OH^- \quad (7)$$

with an equilibrium constant

$$K_3 = \frac{[\overline{Ga(RL)_3}][\overline{ROH}]^3[OH^-]}{[Ga(OH)_4^-][R_2L]^3}, \quad (8)$$

and the dependence of the distribution coefficient of Ga(III) on the concentrations of components of the aqueous and solid phases can be expressed as

$$D_{Ga} = \frac{K_3[\overline{R_2L}]^3}{[\overline{ROH}]^3[OH]} \quad (9)$$

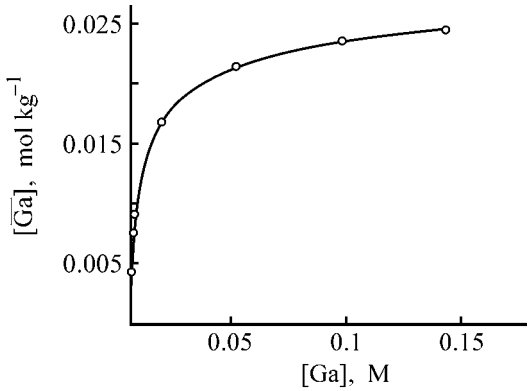

Fig. 3. Distribution of Ga(III) among a 1 M solution of NaOH, [Ga], and the impregnated sorbent, [$\overline{Ga}$]. c_L = c_{ROH} = 0.1 mol kg^{-1}.

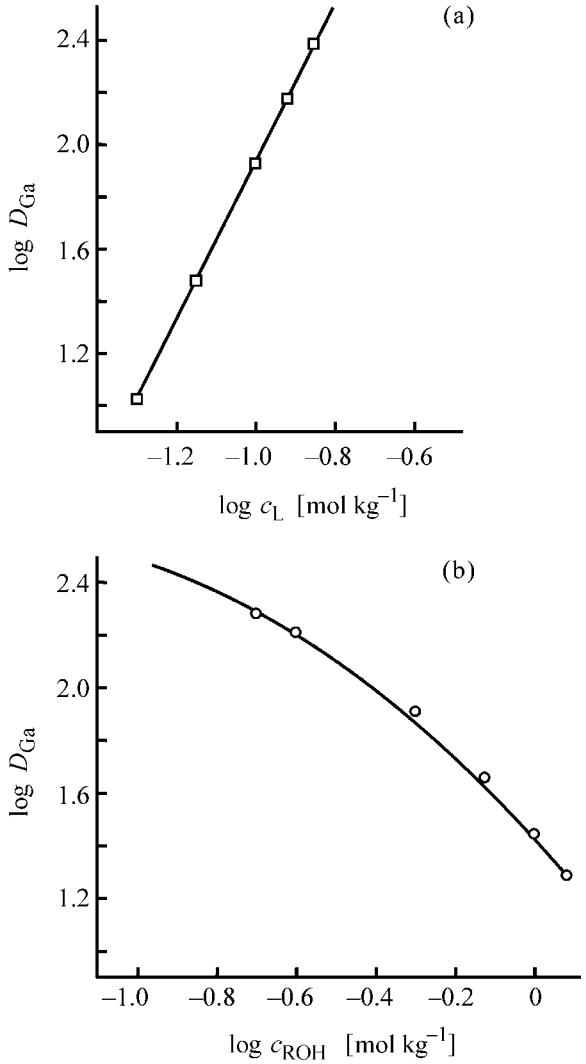

Fig. 4. Distribution coefficient of Ga(III), D_{Ga}, vs. the concentration of (a) 1,2-dioxyanthraquinone, c_L, and (b) ROH, c_{ROH}, in the sorbent phase in sorption from a 1 M solution of NaOH. (a) c_{ROH} = 0.1 mol kg^{-1}, (b) c_L = 0.1 mol kg^{-1}.

or, with account of relation (6),

$$D_{Ga} = \frac{K_3 K_2^3 (c_L - 3[\overline{Ga}])}{[OH](K_2[\overline{ROH}] + K_1[Na^+][OH])^3}, \quad (10)$$

where c_L is the initial concentration of 1,2-dioxyanthraquinone in the sorbent phase, and $[\overline{Ga}]$ is the equilibrium concentration of Ga(III) in the same phase.

The logarithmic dependence of the distribution coefficient of Ga(III) on the concentration of 1,2-dioxyanthraquinone in the solid phase (Fig. 4a) is represented by a straight line with a slope close to 3, which confirms the stoichiometric ratio Ga : L = 1 : 3.

It follows from expression (10) that D_{Ga} decreases as the concentration of ROH in the sorbent phase grows (Fig. 4b). At constant concentrations of NaOH in the aqueous solution and 1,2-dioxyanthraquinone in the solid phase, the dependence of $\log D_{Ga}$ on $\log(K_2[ROH] + K_1[Na^+][OH^-])$ is expressed by a straight line with a slope close to 3, which corresponds to the stoichiometric ratio Ga : R = 1 : 3 in the complex being sorbed. This points to the adequacy of the scheme suggested for describing the recovery of Ga(III) into the sorbent phase. At an invariable initial composition of the solid phase, the recovery of Ga(III) decreases with increasing concentration of NaOH in the aqueous phase, which is due both to the leftward shift of the equilibrium (7) and to a decrease in the fraction of the associate R_2L in the equilibrium solid phase as a result of an increase in the sorption of sodium ions into the sorbent phase.

The data presented here indicate that the macroporous copolymer of styrene with divinylbenzene, impregnated with 1,2-dioxyanthraquinone in the presence of the trialkylmethylammonium cation, effectively sorbs Ga(III) from alkaline solutions and can be used to recover and concentrate Ga(III).

CONCLUSIONS

(1) A sorbent based on a macroporous copolymer of styrene with divinylbenzene, impregnated with 1,2-dioxyanthraquinone (H_2L) in the presence of the trialkylmethylammonium cation (ROH), is suggested for sorption recovery and concentration of Ga(III) from alkaline solutions. The ionic associate R_2L is the active component of the sorbent.

(2) Gallium(III) is recovered from alkaline solutions in the form of the $Ga(LR)_3$ complex.

ACKNOWLEDGMENTS

The authors thank T.A. Orlova and A.E. Lezhnev for assistance in mass-spectrometric measurements.

REFERENCES

1. Reznik, A.M., Ponomareva, E.I., Silaev, Yu.N., *et al.*, *Protsessy ekstraktsii i sorbtsii v khimicheskoi tekhnologii galliya* (Extraction and Sorption in the Chemical Technology of Gallium), Alma-Ata: Nauka, 1985.
2. Bukin, V.I., Zhukovskii, P.V., and Reznik, A.M., *Tsvetn. Met.*, 1984, no. 8, pp. 59–62.
3. Apanasenko, V.V., Bukin, V.I., Zhukovskii, P.V., and Reznik, A.M., *Tsvetn. Met.*, 1987, no. 2, pp. 55–57.
4. Leveque, F. and Helgorsky, J., *Proc. Int. Solvent Extraction Conf.*, Toronto, 1977, vol. 2, pp. 439–442.
5. Sato, T., Nakamura, T., and Oishi, H., *Solv. Extr. Ion Exch.*, 1984, vol. 2, no.. 1, pp. 45–60.
6. Sato, T. and Oishi, H., *Hydrometallurgy*, 1986, vol. 16, pp. 315–324.
7. Tarnopol'skii, Yu.I., Kuznetsova, V.S., and Borbat, V.F., *Izv. Vyssh. Uchebn. Zaved., Khim. Khim. Tekhnol.*, 1974, vol. 17, no. 5, pp. 754–755.
8. Golounin, A.V., Pashkov, G.L., and Aleksandrova, M.V., *Sib. Khim. Zh.*, 1993, no. 1, pp. 43–49.
9. Zhukovskii, P.V., Bukin, V.I., and Reznik, A.M., *Zh. Neorg. Khim.*, 1985, vol. 30, no. 11, pp. 2888–2890.
10. Apanasenko, V.V., Reznik, A.M., Vlasenko, G.V., and Sokolova, V.N., *Zh. Neorg. Khim.*, 1991, vol. 36, no. 11, pp. 2964–2970.
11. Novikov, N.A. and Zhukovskii, P.V., *Tsvetn. Met.*, 1991, no. 8, pp. 64–68.
12. Haragushi, K. and Freiser, H., *Inorg. Chem.*, 1983, vol. 22, pp. 1187–1190.
13. Warshawsky, A., *Ion Exch. Solvent Extraction*, 1981, vol. 8, pp. 229–310.
14. Cortina, J.L. and Warshawsky, A., *Ion Exch. Solvent Extraction*, 1997, vol. 13, pp. 195–293.
15. Meretukov, M.A., *Ispol'zovanie impregnirovannykh materialov dlya izvlecheniya i razdeleniya tsvetnykh metallov: Obzornay informatsiyua TsNIIEITsM* (Use of Impregnated Materials for Recovery and Separation

of Nonferrous Metals: Review by TsNIIEITsM), 1980, issue 2.

16. Cote, G., Laupretre, F., and Chassagnard, C., *Reactive Polymers*, 1987, vol. 5, pp. 141–150.
17. Kremenskaya, I.N., Turanov, A.N., Myul', P., and Gle, K., *Zh. Prikl. Khim.*, 1984, vol. 57, no. 1, pp. 72–76.
18. Polyakova, V.V. and Levchenko, T.M., *Khim. Tekhnol. Vody*, 1981, vol. 3, no. 4, pp. 327–331.
19. Turanov, A.N., Reznik, A.M., Popandopulo, N.V., and Kremenskaya, I.N., *Zh. Neorg. Khim.*, 1984, vol. 29, no. 8, pp. 2075–2079.
20. Sato, T., Sato, K., Oishi, H., and Takenchi, O., *Proc. Int. Solvent Extraction Conf.*, Moscow, 1988, vol. 3, pp. 256–261.
21. Turanov, A.N., Karandashev, V.K., Baulin, V.E., and Tsvetkov, E.N., *Zh. Neorg. Khim.*, 1995, vol. 40, no. 11, pp. 1926–1930.
22. Gorelik, I.S., *Khimiya antrakhinona i ego proizvodnykh* (Chemistry of Anthraquinone and Its Derivatives), Moscow: Nauka, 1987.

Russian Journal of Applied Chemistry, Vol. 77, No. 4, 2004, pp. 576–578. Translated from Zhurnal Prikladnoi Khimii, Vol. 77, No. 4, 2004, pp. 580–582.

SORPTION AND ION-EXCHANGE PROCESSES

Exchange Isotherm of Strontium(II) and Iron(III) Ions on Clay

D. E. Chirkst, T. E. Litvinova, O. V. Cheremisina, and M. V. Ivanov

St. Petersburg State Mining Institute (Technical University), St. Petersburg, Russia

Received April 2, 2003; in final form, September 19, 2003

Abstract—Joint sorption of Sr^{2+} and Fe^{3+} ions on blue Cambrian clay was studied. A relationship between the isotherm of ideal ion exchange and the Langmuir sorption isotherm was revealed. The apparent constant and Gibbs energy of exchange of Sr^{2+} and Fe^{3+} ions on blue Cambrian clay were calculated.

Studying the ion exchange in soil makes it possible to prognosticate the behavior of ^{90}Sr on contaminated territories and to calculate the technological parameters of the process of soil decontamination by ion-exchange washing [1]. Previously, sorption isotherms of strontium(II) and iron(III) ions on clay, which binds most part of ^{90}Sr in soil, have been obtained [2, 3]. The present study is concerned with the exchange isotherm for the case of joint sorption of these cations.

A sample of Cambrian blue clay of composition $K_2Al_4[Al_2Si_6O_{20}](OH,F)_4$ had a specific surface area of 5.86 $m^2\ g^{-1}$ (found from sorption of Methylene Blue) [4]. The exchange capacity of the clay has been determined from the limiting sorption of Sr^{2+} and Fe^{3+} ions separately [2, 3]. The limiting amount of sorption was calculated from experimental data with the use of the Langmuir equation. The capacities of 69 and 78 mequiv kg^{-1} for the limiting sorption of Sr^{2+} and Fe^{3+} ions, respectively, have been obtained [2, 3], with the average value of 73 ± 5 mg-equiv kg^{-1}. A thermal analysis demonstrated that the clay is of the hydromicaceous type. A curve of potentiometric titration of a 0.5-g portion of air-dry clay soaked in 50 ml of water with a 0.01 N solution of NaOH was obtained (Fig. 1). The pH values were measured with a 150M pH-meter with a glass electrode upon addition of the alkali in 0.5-ml portions under agitation with a magnetic stirrer. Three pH jumps can be seen in the titration curve, which indicates that the clay has three functional groups. The equivalence point at pH 4.6 corresponds to an isoelectric state of kaolinite. The jump at pH 7.5–8.0 corresponds to the isoelectric point of hydrargillite and other minerals that are hydrates of aluminum oxide. The equivalence point at pH 9.0–9.2 is presumably due to dissociation of silanol groups.

Prior to determining the amount of sorption of cations, an air-dry sample of clay was ground and soaked in a 1 M solution of HCl for 1 day with agitation at regular intervals. Then the acid solution was replaced with its fresh portion and the soaking was repeated manyfold to negative reaction to iron ions in the aqueous phase. The presence of iron ions was determined by reactions with hexacyanoferrates (II) and (III) and with ammonium thiocyanate NH_4SCN. After that the clay was repeatedly washed with water to pH 3 in an aqueous extract. Then the clay was dried to the air-dry state and ground. The amount of sorption, Γ (mol kg^{-1}), was determined under static conditions at a ratio of the volume of the aqueous phase to the mass of the solid phase, $V/m = 10$ ml g^{-1}, with a 3-g weighed portion of the clay from the difference of concentrations of the initial (c_0) and equilibrium (c_{eq}) solutions by the formula

$$\Gamma = (c_0 - c_{eq})V/m.$$

A solution of a mixture of chlorides, $SrCl_2$ and $FeCl_3$ was acidified to pH 3, mixed with a weighed

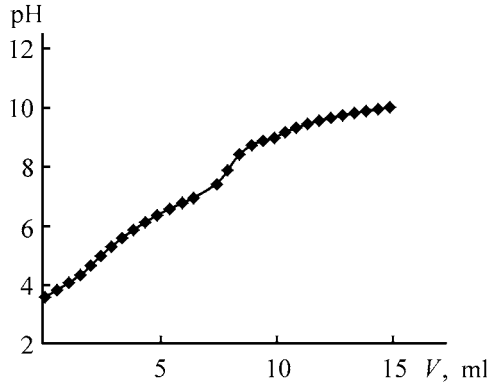

Fig. 1 Potentiometric titration curve of the clay. (V) Volume of the NaOH solution.

1070-4272/04/7704-0576 © 2004 MAIK "Nauka/Interperiodica"

Results of experiments on joint sorption of Sr^{2+} and Fe^{3+} ions on clay

Fe^{3+}				Sr^{2+}			
c_0	c_{eq}	Γ	$\gamma_{Fe^{3+}}$	c_0	c_{eq}	Γ	$\gamma_{Fe^{3+}}$
mM		mmol kg^{-1}		mM		mmol kg^{-1}	
0.217	0.213	0.03	0.622	0.455	0.26	1.95	0.810
0.34	0.28	0.55	0.575	0.60	0.375	2.25	0.782
0.44	0.34	1.04	0.537	0.80	0.52	2.80	0.759
0.60	0.45	1.50	0.493	1.00	0.70	3.0	0.730
1.34	0.94	4.0	0.371	2.00	1.525	4.75	0.644
2.60	2.05	5.5	0.256	4.00	3.35	6.5	0.546
4.43	3.37	10.70	0.191	6.00	5.40	6.0	0.479

portion of clay, and agitated to the equilibrium state. The time in which the equilibrium, which corresponded to a constant concentration of the solution, was attained was 5–6 h, the time of contact between the phases in the experiments performed was no less than 24 h. The initial and equilibrium pH values were 3 and 3.2 ± 0.3, respectively.

After an experiment, a 2- to 10-ml, depending on the content of strontium ions, portion of the solution was filtered through a blue ribbon filter and transferred into a 50-ml vessel. The necessary pH 2.8–3.0 was adjusted using an acetate buffer solution (10 ml). Then 25 ml of a 60% aqueous solution of acetone and 1 ml of a 0.1% solution of Nitroortanile C (nitrochromazo) were added. The content of strontium ions in the solution under study was determined from the intensity of the absorption band at a wavelength of 650 nm. This technique [5] makes it possible to find the content of strontium ions in the range from 2 to 20 μg in a 25-ml portion of a solution. Under these conditions there is no hindering effect by Na^+ and NH_4^+ ions to a 100-fold excess; K^+, to a 30-fold excess; Ca^{2+}, to a 1.5-fold excess; and Mg^{2+}, to a 5-fold excess. The content of iron(III) was determined from the intensity of the absorption band of a complex with thiocyanate at 480 nm. The table lists the following results obtained in the study: the initial and equilibrium concentrations of ions, c_0 and c_{eq}; amounts of sorption, Γ; and activity coefficients γ of cations, calculated using the Davis equation [6].

The exchange of strontium(II) and iron(III) ions was described thermodynamically on the assumption of an ideal solid phase, i.e., with the activity coefficients of ions in the sorbed state disregarded. The equation of the ion-exchange isotherm for the reaction

$$3Sr_s^{2+} + 2Fe_{aq}^{3+} \rightleftarrows 3Sr_{aq}^{2+} + 2Fe_s^{3+}$$

has, in this case, the form

$$K = \frac{\Gamma_{Fe^{3+}}^2 a_{Sr^{2+}}^3}{\Gamma_{Sr^{2+}}^3 a_{Fe^{3+}}^2}, \quad (1)$$

where K is the apparent exchange constant; $\Gamma_{Fe^{3+}}$ and $\Gamma_{Sr^{2+}}$, the amounts of sorption of jointly present ions (mol kg^{-1}); and $a_{Fe^{3+}}$ and $a_{Sr^{2+}}$, the activities of the ions in solution (mol kg^{-1}). It was shown in [7] that the ion-exchange isotherms can be described using equations of the type of the Langmuir isotherm. Now, this method will be applied to the equilibrium under study. The limiting amounts of sorption of the ions $\Gamma_\infty = 3\Gamma_{Fe^{3+}} + 2\Gamma_{Sr^{2+}}$, where Γ_∞ is the limiting amount of sorption of ions in equiv kg^{-1}, and the amounts of sorption of the ions are expressed in mol kg^{-1}. With account of this fact, Eq. (1) can be brought to the form

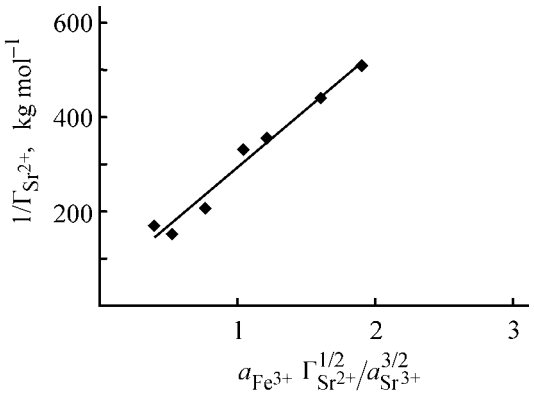

Fig. 2. Linear form of the ion exchange isotherm. (Γ) Amount of sorption and (a) activity of ions (mol kg^{-1}).

$$K = \frac{(\Gamma_\infty - 2\Gamma_{Sr^{2+}})^2 a_{Sr^{2+}}^3}{9\Gamma_{Sr^{2+}}^3 a_{Fe^{3+}}^2}. \quad (2)$$

Equation (2) is transformed into formula (3), which resembles the Langmuir isotherm equation $\Gamma = \Gamma_\infty K_a/(1 + K_a)$:

$$\Gamma_{Sr^{2+}} = \Gamma_\infty \frac{K^{-1/2} a_{Sr^{2+}}^{3/2}}{3a_{Fe^{3+}}\Gamma_{Sr^{2+}}^{1/2} + 2K^{-1/2} a_{Sr^{2+}}^{3/2}}. \quad (3)$$

The linear version of the equation has the form

$$\frac{1}{\Gamma_{Sr^{2+}}} = \frac{2}{\Gamma_\infty} + \frac{3a_{Fe^{3+}}(K\Gamma_{Sr^{2+}})^{1/2}}{\Gamma_\infty a_{Sr^{2+}}^{1/2}} \quad (4)$$

similar to the linear Langmuir equation

$$1/\Gamma = 1/\Gamma_\infty + 1/(\Gamma_\infty Ka).$$

A linear ion-exchange isotherm is shown in Fig. 2. The dependence of the inverse amount of sorption of strontium ions on the argument $\left(a_{Fe^{3+}}\Gamma_{Sr^{2+}}^{1/2}\right)/a_{Sr^{2+}}^{3/2}$ is described by the following linear equation $y = 246.01x + 47.08$, with a correlation factor $R^2 = 0.9744$. This equation was used to calculate $\Gamma_\infty = 42.5$ mg-equiv kg^{-1}, the apparent ion exchange constant $K = 12.14$, and the Gibbs energy of exchange of strontium(II) ions for iron(III) ions on the clay surface, $\Delta G_{298}^0 = -6.19$ kJ mol^{-1}.

The thermodynamic data indicate that the ion-exchange equilibrium is shifted toward displacement of strontium(II) ions from soil by solutions of iron(III) salts.

CONCLUSIONS

(1) The isotherm of ideal ion exchange of strontium(II) and iron(III) ions on blue Cambrian clay is described by a dependence of the type of the Langmuir equation and can be expressed in a linear form with a correlation factor $R^2 = 0.9744$.

(2) The linear Langmuir form of the isotherm was used to determine the apparent ion-exchange constant $K = 12.14$ and the Gibbs energy of exchange, $\Delta G_{298}^0 = -6.19$ kJ mol^{-1}. The exchange equilibrium is shifted toward displacement of strontium from the solid phase by iron(III) ions.

ACKNOWLEDGMENTS

The study was carried out in the framework of the "Research in Higher School in Priority Areas of Science and Technology" Program of the Ministry of Education of the Russian Federation, "Ecology and Efficient Nature Management" subprogram no. 207.

REFERENCES

1. Chirkst, D.E., Litvinova, T.E., Cheremisina, O.V., and Streletskaya, M.I., *Radiokhimiya*, 2001, vol. 43, no. 5, pp. 475–478.
2. Chirkst, D.E., Litvinova, T.E., Cheremisina, O.V., *et al.*, *Zh. Prikl. Khim.*, 2003, vol. 46, no. 5, pp. 755–758.
3. Chirkst, D.E., Litvinova, T.E., Cheremisina, O.V., *et al.*, *Zh. Prikl. Khim.*, 2003, vol. 76, no. 6, pp. 922–925.
4. Chirkst, D.E., Krasotkin, I.S., Litvinova, T.E., *et al.*, *Zh. Prikl. Khim.*, 2003, vol. 46, no. 4, pp. 687–689.
5. *Analiticheskaya khimiya strontsiya* (Analyutical Chemistry of Strontium), Moscow: Akad. Nauk SSSR, 1971.
6. Vasil'ev, V.P., *Termodinamicheskie svoistva rastvorov elektrolitov* (Thermodynamic Properties of Electrolyte Solutions), Moscow: Vysshaya Shkola, 1982.
7. Kokotov, Yu.A. and Pasechnik, V.A., *Ravnovesie i kinetika ionnogo obmena* (Equilibrium and Kinetics of Ion Exchange), Leningrad: Khimiya, 1970.

Russian Journal of Applied Chemistry, Vol. 77, No. 4, 2004, pp. 579–584. Translated from Zhurnal Prikladnoi Khimii, Vol. 77, No. 4, 2004, pp. 583–587.

SORPTION AND ION-EXCHANGE PROCESSES

Dynamic of Exchange Sorption of Transition Metal Ions on Phosphate Cationite KFP-12

L. A. Pimneva

Tyumen State Academy of Architecture and Construction, Tyumen, Russia

Received December 30, 2003

Abstract—The dynamics of ion-exchange sorption of double-charged metal ions on a phosphate cationite KFP-12 was studied. Theoretical calculations of stationary fronts were carried out, the motion velocity of the stationary fronts was calculated, and the rate constant of sorption was evaluated.

The theory of sorption dynamics is a theoretical foundation of modern chromatography. The process of dynamic sorption can be regarded as continuous, and, therefore, all calculations are based on solution of Rachinskii's differential equations [1–5]. Methods for solving differential balance equations make it possible to perform a theoretical analysis of the dynamics of sorption in that stage of transfer, in which the uppermost layer of the sorption column is saturated.

One of the main points in the process of ion-exchange sorption is the equivalence law, according to which ions involved in the exchange are exchanged in equivalent amounts.

The aim of this study is to analyze the dynamics of ion-exchange sorption of double-charged ions on a phosphate cationite KFP-12 from chloride solutions.

EXPERIMENTAL

A phosphate cationite KFP-12 in the hydrogen form with porous structure was used in the study. The structure of the KFP-12 cationite contains phosphonic groups, which dissociate in two stages; the degree of their ionization is characterized by the parameters $pK_1 = 3.5$ and $pK_2 = 8.9$ and total exchange capacity of 7.5 mg-equiv g^{-1}.

The grain size was 0.25–0.50 mm (in the air-dry state). As starting solutions were used 0.2 M $CuCl_2$, $ZnCl_2$, $CdCl_2$, $MnCl_2$, $CoCl_2$, and $NiCl_2$. Two sets of experiments were carried out. In the first of these, output sorption curves were measured at different cationite charges (3.0, 6.0, 9.0, and 12.0 g in terms of absolutely dry resin) in a column with a cross-sectional area of 1.4 cm^2, which corresponds to a bed height of 8.3, 16.5, 24.75, and 33.0 cm, respectively, and constant filtration rate (1.0 ml cm^{-2} min^{-1}). In the second, the filtration rate of the solutions was varied (0.5, 1.0, 2.0, and 3.0 ml cm^{-2} min^{-1}) at an invariable height of the cationite bed (6.0 g) in the column.

The process of ion-exchange sorption of two differently charged ions under dynamic conditions is described by a system of differential material balance equations

$$\frac{\partial c}{\partial t} + \frac{\partial c}{\partial x} + \frac{\partial N}{\partial t} = 0, \quad (1)$$

an equation describing the kinetics of sorption

$$\frac{\partial N}{\partial t} = \beta(c - c_{eq}) \quad (2)$$

and an equation for the ion exchange isotherm

$$\frac{N_1^{1/z_1}}{N_2^{1/z_2}} = K_{1,2}\frac{c_1^{1/z_1}}{c_2^{1/z_2}}. \quad (3)$$

Here c is the concentration of ions being sorbed in a solution (mg-equiv cm^{-1} of column length) at an instant of time t; N, the concentration of ions in the ionite (mg-equiv cm^{-1} of column length) at an instant of time t; x, the distance counted off the inlet of the column packed with the ionite (cm); c_{eq}, the equilibrium concentration of ions being sorbed in the solution (mg-equiv cm^{-1}); β, the mass-exchange coefficient, which characterizes the broadening of the sorption front and depends on inner- and outersphere diffusion and on longitudinal transfer; and $K_{1,2}$, the ion-exchange constant for the ions being exchanged; and z_1, z_2, charges.

1070-4272/04/7704-0579 © 2004 MAIK "Nauka/Interperiodica"

On introducing dimensionless variables $\varphi = n/n_0$, $U\varphi' = n'/n_0$, $V = N/N_0$, $h = n_0/N_0$, the above system of equations takes the form

$$h\frac{\partial\varphi}{\partial t} + Uh\frac{\partial\varphi}{\partial x} + \frac{\partial V}{\partial t} = 0, \quad (4)$$

$$\frac{\partial V}{\partial t} = \beta h(\varphi - \beta'), \quad (5)$$

$$\frac{1 - V}{V^{\lambda}} = B\frac{1 - \varphi}{\varphi^{\lambda}}, \quad (6)$$

where N_0 and n_0 are the initial concentrations of ions in the ionite and solution, respectively; and $\lambda = z_1/z_2$ is the ratio of the charges of the exchanged ions.

This system should be solved with the following boundary conditions

$$\varphi(x, 0) = V(x, 0) = 0;\ \varphi(0, t) = 0;$$

$$V(0, t) = 1;\ \varphi(\infty, \infty) = V(\infty, \infty) = 0.$$

In the standard front, the following condition is satisfied

$$N/N_0 = n/n_0; \quad n = hN \text{ or } V = \varphi.$$

Analysis of the ion-exchange isotherm (6) shows that the shape of the isotherm depends on the constant B, which is the dimensionless exchange constant in a transformed Nikol'skii equation for the case of exchange of two differently charged ions [6]. Thus, the shape of the isotherm and, consequently, the sorbability in the exchange of differently charged ions depend not only on the exchange constant, but also on the ionic ratio (concentration of the solution introduced into the column) and the charge of the exchanged ions.

In the case of dynamics of ion-exchange sorption of differently charged ions, it is possible to select, by varying the ionic ratio, such operating conditions in which the constant $B < 1$, which is the necessary condition for formation of a stationary front of the sorption wave.

Let us introduce the parameter $S = V/\varphi' = \varphi/\varphi'$. Then the equation for the ion-exchange isotherm of differently charged ions takes the form

$$\varphi = \frac{1 - BS^{\lambda}}{S(1 - BS^{\lambda - 1})}, \quad (7)$$

$$(B\sqrt{S})^2 - (1 - \varphi)\sqrt{S} - \varphi B = 0 \quad (8)$$

or

$$\sqrt{S} = \frac{(1 - \varphi) \pm \sqrt{(1 - \varphi)^2 + 4\varphi B^2}}{2B}. \quad (9)$$

For a particular case at $\lambda = 1/2$, the equation of the stationary front has the form

$$x = \frac{h}{1 + h}Ut + \frac{U}{\beta}\frac{1}{1 + h}\left[\frac{B}{1 - B^2}\ln\frac{(\sqrt{S} - 1)^{1 + B}}{(\sqrt{S} + 1)^{(1 - B)}(\sqrt{S} - B)^{B}(1 - B\sqrt{S})^{1/B}} + C\right], \quad (10)$$

where

$$C = \frac{1}{1 + B}\ln(1 - B) + \frac{B}{1 - B}\ln(1 + B) + \frac{B^2 + B - 1}{1 - B^2}, \quad (11)$$

at $B < 1$, $c \approx -1$. From Eq. (10), the following calculational equations are obtained:

(a) equation for the elution curve

$$V = \frac{1 + h}{h}V_0 - \frac{U}{\beta}\frac{Q}{h}\left[\frac{B}{1 - B^2}\ln F(S) + C\right], \quad (12)$$

where V is the filtrate volume; Q, cross-section of the transfer front; V_0, the volume of solution retained within the sorbent column; and $F(S)$, the sublogarithmic function in Eq. (7);

(b) equation for the front width of the sorption wave in the column

$$\delta_V = \frac{U}{\beta}\frac{1}{1 + h}\frac{B}{1 - B^2}\ln\left[\frac{F(S_1)}{F(S_2)}\right], \quad (13)$$

where $F(S_1)$ and $F(S_2)$ are the values of the function $F(S)$ for two concentration points defining the front width;

(c) equation for the front width of the elution curve

$$\delta_V = \frac{U}{\beta}\frac{Q}{h}\frac{B}{1 - B^2}\ln\left[\frac{F(S_1)}{F(S_2)}\right]; \quad (14)$$

(d) equation for the volume passed till breakthrough (by analogy with the time of protective action)

$$V_1 = \frac{1 + h}{h}V_0 - \frac{U}{\beta}\frac{Q}{h}\left[\frac{B}{1 - B^2}\ln F(S) - C\right], \quad (15)$$

where S_1 is the value of the parameter S that corresponds to the breakthrough concentration recorded at the column outlet.

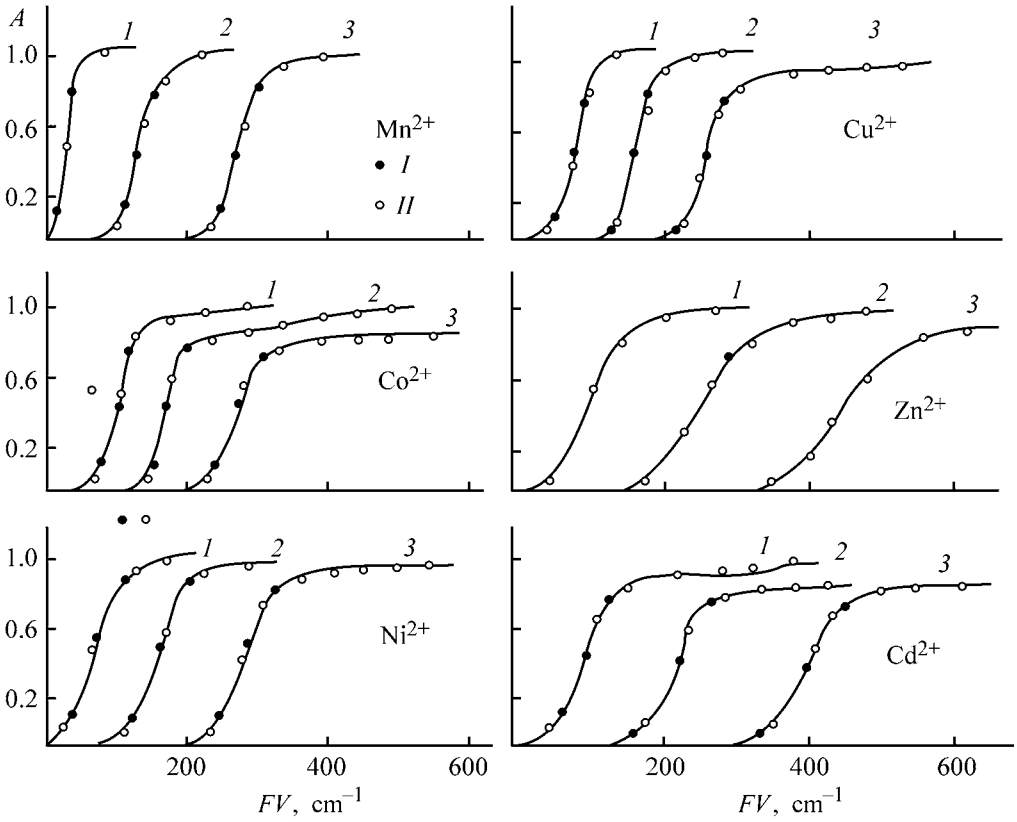

Fig. 1. Elution curves for sorption of double-charged cations from 0.2 M solutions of MCl_2 with a KFP-12 cationite. Filtration rate 1 ml cm^{-2} min^{-1}. Amount of ionite in the column (g): (*1*) 1.0, (*2*) 3.0, and (*3*) 6.0. (*A*) c/c_0 ratio and (*FV*) filtrate volume. Points: (*I*) theoretical and (*II*) experimental.

The experiments were performed at four filtration rates: 0.5, 1.0, 2.0, and 3.0 ml min^{-1}. Figure 1 shows elution curves for sorption of double-charged cations on a phosphate cationite KFP-12 for different column lengths, which were subjected to theoretical analysis. These are ordinary S-shaped frontal curves.

The theoretical analysis of the elution curves consisted in plotting the dependences of the shift of the concentration points at φ equal to 0.15, 0.30, 0.50, 0.70, and 0.85. These dependences confirm the theoretical prediction that stationary fronts are to be formed in the case of a convex isotherm. In all the experiments, the plots that describe the shift of the concentration points of the sorption front are straight lines parallel to one another. The shift plot for φ = 0.50 passes through the origin of the coordinates. Table 1 lists the results of a theoretical analysis of elution curves for sorption of double-charged metal ions. Elution curves for sorption of transition metal ions, constructed using experimental data, are shown in Fig. 1. Theoretical points are plotted on these curves.

To construct the theoretical elution curve for the stationary front, the dynamic constant u/β (where u is the flow velocity) was determined. Such a calculation was carried out using formula (14), and then the corresponding elution curve was calculated by Eq. (15). As can be seen from Fig. 1, the theoretically calculated points satisfactorily fall on the experimental elution curve, which also confirms that the dynamic sorption of double-charged metal ions occurs in this study in the stationary mode.

Calculation of the constant B gives values that are less than unity. According to the theory of sorption dynamics, such a value of the constant confirms the formation of a stationary front.

Let us evaluate the kinetic constant β. The dynamic constant by Todes–Bikson [6] is a sum of three terms:

$$\frac{u}{\beta} = \frac{u}{\beta^*} + \frac{u}{\beta^{**}} + \frac{D^*}{u}, \qquad (16)$$

where β^* is the rate constant of outer-sphere diffusion; β^{**}, that of the inner-sphere diffusion; and D^*

Table 1. Calculated quantities necessary for construction of theoretical elution curves for sorption of double-charged metal cations

Ion	B	V_1, ml min^{-1}	u, cm min^{-1}	δ_V, ml	$\ln F(S_i)$		$\ln \frac{F(S_1)}{F(S_2)}$	u/β	c
					$\varphi_1 = 0.15$	$\varphi_3 = 0.50$			
Cu^{2+}	0.32	0.5	0.42	40	2.54	0.73	7.06	0.53	–80
		1.0	0.83	50				0.66	
		2.0	1.67	60				0.79	
		3.0	2.50	75				0.98	
Zn^{2+}	0.25	0.5	0.42	95	1.72	0.57	5.24	2.25	–0.89
		1.0	0.83	100				2.37	
		2.0	1.67	110				2.60	
		3.0	2.50	125				2.96	
Cd^{2+}	0.24	0.5	0.42	85	1.66	0.55	5.10	2.16	–0.89
		1.0	0.83	90				2.28	
		2.0	1.67	100				2.54	
		3.0	2.50	110				2.79	
Mn^{2+}	0.23	0.5	0.42	75	1.56	0.53	4.88	2.14	–0.91
		1.0	0.83	80				2.29	
		2.0	1.67	90				2.57	
		3.0	2.50	95				2.72	
Co^{2+}	0.29	0.5	0.42	50	2.04	0.64	5.94	0.89	–0.85
		1.0	0.83	60				1.07	
		2.0	1.67	75				1.34	
		3.0	2.50	80				1.43	
Ni^{2+}	0.27	0.5	0.42	45	1.90	0.62	5.64	0.90	–0.86
		1.0	0.83	55				1.10	
		2.0	1.67	60				1.20	
		3.0	2.50	70				1.40	

the effective constant of diffusion and quasi-diffusion longitudinal transfers.

Let us introduce the generalized rate constant of sorption

$$\frac{1}{\beta'} = \frac{1}{\beta^*} + \frac{1}{\beta^{**}}. \quad (17)$$

Then Eq. (16) takes the form

$$\frac{u}{\beta} = \frac{u}{\beta'} + \frac{D}{u}. \quad (18)$$

The rate constants of outer- and inner-sphere diffusion must be virtually independent of the flow velocity. The effective constant of longitudinal transport is proportional to the transport rate $D^* = \alpha u$. Consequently, we have in accordance with Eq. (18)

$$\frac{u}{\beta} = \frac{u}{\beta'} + \alpha. \quad (19)$$

where α = const and β = const.

Substituting Eq. (19) into (14), we obtain

$$\delta_V = \left(\alpha + \frac{u}{\beta}\right)\frac{Q}{h}\frac{B}{1 - B^2}\ln\left[\frac{F(S_1)}{F(S_2)}\right], \quad (20)$$

and then, assuming $u = V/Q$ and

$$G = \frac{\alpha Q}{h}\frac{B}{1 - B^2}\ln\left[\frac{F(S_1)}{F(S_2)}\right],$$
$$H = \frac{1}{\beta h}\frac{B}{1 - B^2}\ln\left[\frac{F(S_1)}{F(S_2)}\right], \quad (21)$$

we come to the equation

$$\delta_V = G + HV. \quad (22)$$

Having determined the experimental values of the coefficients G and H in Fig. 2, we calculated the coefficients α and β', using Eq. (21). Table 2 lists calculated kinetic and quasi-diffusion constants of ion exchange of double-charged metal ions.

The experimental values of the sorption constant β' exceed by an order of magnitude those for porous sorbents, such as silica gel or carbon [5]. This indicates that the mechanism governing the sorption kinetics in ion-exchange resins is different. The higher rate of sorption on the cationite is due to its developed porous structure.

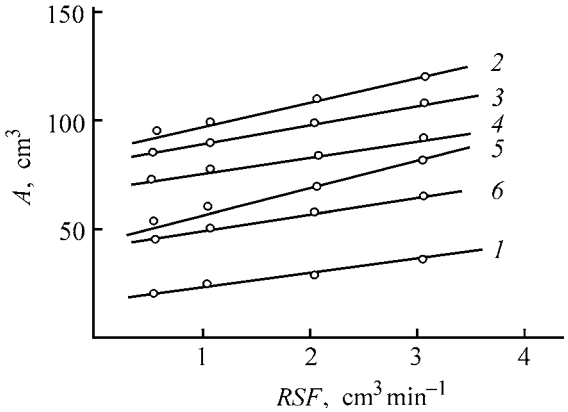

Fig. 2. Front width A of the elution curves for sorption of double-charged ions of (*1*) copper, (*2*) zinc, (*3*) cadmium, (*4*) manganese, (*5*) cobalt, and (*6*) nickel vs. the rate of solution filtration, *RSF*.

CONCLUSIONS

(1) The dynamics of exchange sorption of differently charged ions in the stationary mode was considered. The distribution of ions being sorbed in the stationary mode of dynamic sorption is described by the equation of the stationary front, used to obtain equations for calculating the elution curve and its front width.

(2) A satisfactory agreement between experimental elution curves and the theoretical equation of the elution curve was obtained.

Table 2. Calculated kinetic and quasi-kinetic ion-exchange constants in sorption of double-charged cations by KFP-12 cationite

Ion	u, cm min^{-1}	$1/\beta$, min	G, ml	α, cm	H, min	$1/\beta'$, min	β', s^{-1}	D^*, cm^2 min^{-1}	θ_{calc}, min
Cu^{2+}	0.42	1.25	14.7	0.18	11.7	0.087	0.19	0.151	378
	0.83	0.79							
	1.67	0.47							
	2.50	0.39							
Zn^{2+}	0.42	5.35	93.75	2.22	10.0	0.141	0.12	1.840	389
	0.83	2.85							
	1.67	1.56							
	2.50	1.18							
Cd^{2+}	0.42	5.14	84.40	2.16	8.3	0.127	0.13	1.79	394
	0.83	2.75							
	1.67	1.52							
	2.50	1.12							
Mn^{2+}	0.42	5.11	71.88	2.09	6.7	0.117	0.14	1.74	382
	0.83	2.76							
	1.67	1.54							
	2.50	1.09							
Co^{2+}	0.42	2.13	42.0	0.73	10.0	0.104	0.16	0.61	391
	0.83	1.29							
	1.67	0.82							
	2.50	0.57							
Ni^{2+}	0.42	2.14	41.2	0.81	8.3	0.100	0.17	0.67	396
	0.83	1.32							
	1.67	0.72							
	2.50	0.56							

(3) The rate constant of sorption of double-charged cations by the KFP-12 cationite was evaluated experimentally. The rate constants of sorption have close values for the ions studied.

REFERENCES

1. Rachinskii, V.V., *Zh. Fiz. Khim.*, 1962, vol. 36, no. 9, pp. 2018–2023.
2. Rachinskii, V.V. and Davidova, E.G., *Zh. Fiz. Khim.*, 1966, vol. 40, no. 6, pp. 1190–1195.
3. Rachinskii, V.V. and Rustamov, S.M., *Zh. Fiz. Khim.*, 1966, vol. 40, no. 10, pp. 2436–2439.
4. Rachinskii, V.V. and Garnetskii, V.A., *Zh. Fiz. Khim.*, 1968, vol. 42, no. 10, pp. 2591–2596.
5. Todes, A.M. and Rachinskii, V.V., *Zh. Fiz. Khim.*, 1955, vol. 29, no. 9, pp. 1591–1600.
6. Bikson, Ya.M., *Zh. Fiz. Khim.*, 1953, vol. 27, no. 10, pp. 1530–1537.
7. Todes, A.M. and Bikson, Ya.M., *Dokl. Akad. Nauk SSSR*, 1950, vol. 75, no. 5, pp. 727–735.

Russian Journal of Applied Chemistry, Vol. 77, No. 4, 2004, pp. 585–587. Translated from Zhurnal Prikladnoi Khimii, Vol. 77, No. 4, 2004, pp. 588–590.

PROCESSES AND EQUIPMENT OF CHEMICAL INDUSTRY

A Model of Hydrogen Sulfide Desorption in a Generator of Monodisperse Drops

S. V. Aniskin and I. O. Protod'yakonov

St. Petersburg State Technological University of Plant Polymers, St. Petersburg, Russia

Received December 23, 2003

Abstract—Desorption of hydrogen sulfide in a generator of monodisperse drops from a weakly alkaline solution is considered. A mathematical model of the end effect is suggested. This model takes into account the specific features of formation of a diffusion boundary gas layer at the surface of a drop of increasing volume.

As is known, spraying of fluids is used to tackle with a wide variety of technological problems in chemical, paper-and-pulp, and other industries and, in particular, in purification of gases to remove undesirable impurities.

It should be noted that the mechanisms of substance transfer in spraying mass-exchange apparatus in the region of disintegration of a fluid jet into drops and in that of motion of the already formed drops are different.

When the transfer of the target component in these apparatus is described, an assumption is frequently made, in order to simplify the task of modeling, that the contribution, which comes from the region of disintegration of the fluid jet outflowing from a single-flare atomizer into drops, to the final result of the mass-exchange process can be disregarded because of the comparative smallness of this contribution. However, such an assumption is unjustified, e.g., for desorption in a spraying scrubber in the case when the main resistance to mass transfer is concentrated in the liquid phase.

When this contribution cannot be disregarded, it is said that there exists a pronounced end effect, which is, in the given case, the effect of intensification of mass exchange in the initial region of motion of the liquid phase.

It should be noted that studying the end effect, which is strongly dependent on the specific features of motion of the fluid in drop formation, is a rather complicated task.

Various experimental methods have been used to solve this problem. One of these is based on use of dropping bottles [1]. The main disadvantage of investigations of this kind is that the rate of drop formation with the use of dropping bottles is considerably lower than that from a fluid jet outflowing from an atomizer of a spraying apparatus. Therefore, the results obtained in studying the end effects with the use of dropping bottles are hardly applicable to description of end effects in spraying apparatus.

Studies of end effects with the use of a generator of monodisperse drops (GMD) are devoid of this disadvantage. A generator of this kind makes it possible to obtain a chain of drops of the same size with an outflowing velocity closer to that in the case of spraying of a fluid with atomizers.

The aim of this study is the provide a theoretical description of the end effect examined experimentally with the use of a GMD in desorption of hydrogen sulfide [2].

The way in which a chain of drops is formed when a fluid outflows from a needle-like nozzle of the GMD is shown schematically in the figure. The fluid outflows from a nozzle at a constant velocity v in the form of a jet of radius R_j and length l. Drops of radius R are formed at the end of the jet at intervals of time τ.

The experimental study was carried out at the following characteristic values of the parameters: $v = 1.1\ \mathrm{m\,s^{-1}}$, $R_j = 1.8 \times 10^{-4}$ m, $\tau = 1.045 \times 10^{-3}$ s, and $R = 3.07 \times 10^{-4}$ m. As fluid outflowing from the GMD served a weakly alkaline solution of hydrogen sulfide.

As is known, hydrogen sulfide partly dissociates at low pH to give hydrosulfide ions by the following chemical reaction

$$H_2S + OH^- \rightleftarrows HS^- + H_2O. \qquad (1)$$

1070-4272/04/7704-0585 © 2004 MAIK "Nauka/Interperiodica"

Degree of hydrogen sulfide desorption in drop formation in the GMD*

pH value	$x_0 \times 10^3$, M	A/x_0	η^0_{exp}	η^0_{calc}	η^v_{exp}
		%			
7.5	0.947	0.110	44.0	12.1	42.7
7.55	1.118	0.101	42.1	11.1	39.0
7.70	1.118	0.078	36.7	8.58	30.1
7.75	1.171	0.071	36.4	7.81	27.5

* x_0 is the total concentration of hydrogen sulfide and sodium hydrosulfide in the initial solution; η^0_{exp}, η^0_{calc}, and η^v_{calc}, the degrees of desorption: experimental, theoretically calculated for an immobile drop, and theoretically calculated for a drop that moves at a velocity v; and A, the concentration of hydrogen sulfide in the gas phase at the drop surface.

For this reason, the main forms of existence of sulfur in the alkaline solution mentioned above are the compounds H_2S and NaHS. The end effect in the GMD is manifested in this case as desorption of hydrogen sulfide. The degree of hydrogen sulfide desorption from a drop, before its detachment from the fluid jet, is as high as 40%, as follows from the table.

It was shown in [3] that such a strong desorption of hydrogen sulfide occurs in the conditions under consideration only when a drop is formed at the end of the jet in the GMD. In this case, the desorption of hydrogen sulfide from the surface of this jet can be disregarded.

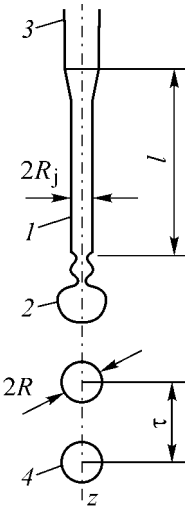

Schematic of drop formation from a solution outflowing from the needle-like nozzle of the GMD. (*1*) Fluid jet, (*2*) forming drop, (*3*) needle-like nozzle of the GMD, and (*4*) formed drop.

With account of such a high degree of desorption and the short time of drop formation (10^{-3} s), it may be assumed that the desorption of hydrogen sulfide occurs during formation of a diffusion boundary layer in the gas phase.

To construct a theoretical model of the process in question, a simpler problem of determining the degree of hydrogen sulfide desorption from an immobile expanding drop will be considered first. The degree of hydrogen sulfide desorption, which is determined relative to the total amount of hydrogen sulfide and sodium hydrosulfide filling the drop volume, can be represented by the formula

$$\eta = \frac{3M}{4\pi R^3 x_0}, \quad (2)$$

where M is the amount of hydrogen sulfide (moles) and x^0 is the total concentration of hydrogen sulfide and sodium hydrosulfide (M).

To find M, it is necessary to formulate and solve a nonstationary boundary-value problem of diffusion from an immobile expanding drop.

The mathematical formulation of this boundary-value problem is as follows:

$$\left[\frac{\partial}{\partial t} - D\left(\frac{\partial}{\partial r} + \frac{2}{r}\frac{\partial}{\partial r}\right) + \frac{R^2}{r^2}\frac{\partial R}{\partial t}\frac{\partial}{\partial r}\right]c = 0, \quad (3)$$

$$0 < r < \infty, \ 0 < t < \infty,$$

$$c\big|_{r=R} = A(t), \quad c\big|_{r=\infty} = 0, \quad c\big|_{t=0} = 0, \quad R\big|_{t=0} = 0, \quad (4)$$

where c is the concentration of hydrogen sulfide (M); D, the diffusion coefficient of hydrogen sulfide in air ($m^2\ s^{-1}$); and r (m) and t (s), the running radius and time, respectively.

This problem has been solved by Koutetsky [4]. The solution is as follows:

$$J = 4\sqrt{\pi D}\left(\frac{3b}{4\pi}\right)^{2/3}\left[1.53t^{1/6} + 1.35\sqrt{\pi D}\left(\frac{4\pi t}{3b}\right)^{1/3}\right]A, \quad (5)$$

where J is the flow of hydrogen sulfide from the entire surface of the expanding drop at an instant of time t (mol s^{-1}), and b is the rate at which the drop volume increases ($m^3\ s^{-1}$).

The quantity b is defined by the formula

$$b = dV/dt, \quad (6)$$

where V is the drop volume (m^3).

To find the sought-for value of M, it suffices to integrate Eq. (5) over a time interval, having preliminarily determined the dependence of A and b on time for given particular conditions. In accordance with the model of fluid flow in drop formation [3], a fresh flow of the fluid with concentration x_0 and constant pH comes to the drop surface. This gives reason to consider that the concentration of hydrogen sulfide at the drop surface is constant during the entire time τ of drop expansion. The quantity b can be expressed by the formula

$$b = \pi R_j^2 v. \quad (7)$$

Then, integration of Eq. (5) with respect to time τ yields the following expression for M:

$$M = 4\sqrt{\pi D}\left(\frac{3b}{4\pi}\right)^{2/3}\left[1.31t^{1/6} + 1.012\sqrt{\pi D}\left(\frac{4\pi\tau}{3b}\right)^{1/3}\right]\tau A. \quad (8)$$

Substitution of (8) into Eq. (2) shows that the final expression for the degree of desorption depends on the ratio of A and x_0. This ratio is given by the formula

$$\frac{x_0}{A} = \frac{1}{\mathrm{He}} + K \times 10^{\mathrm{pH}}, \quad (9)$$

where K is the equilibrium constant defined by

$$K = \frac{[\mathrm{H}^+][\mathrm{HS}^-]}{A}, \quad (10)$$

and $[\mathrm{H}^+]$ and $[\mathrm{HS}^-]$ are the concentrations of hydrogen ions and hydrosulfide ions, respectively.

It follows from [5] that $K = 10^{-6.68}$ at 20°C. The η^0_{calc} calculated with $D = 1.47 \times 10^{-5}$ m^2 s^{-1}, He = 0.38, and $b = 1.159 \times 10^{-7}$ m^3 s^{-1} are listed in the table. The numerical values of these quantities correspond to the experimental conditions of [2]. Comparison of the calculated η^0_{calc} with the experimental η^0_{exp} shows that the actual intensity of desorption substantially exceeds the theoretical value in the conditions under consideration. This can be accounted for by a decrease in the thickness of the diffusion boundary layer because of the drop motion.

The process of formation of a chain of drops in the GMD is characterized by Reynolds numbers that correspond to transition modes of a flow around a drop. This circumstance gives no way of solving analytically the diffusion boundary-value problem formulated.

That is why the present study employs, in order to simplify the solution of the problem in constructing the model of the end effect, the semiempirical Fresling dependence for calculating the mass-transfer coefficient β for the gas phase in that form in which it was presented in [6] when solving the problem for an already formed drop of radius R. This dependence is as follows:

$$\beta/\beta_0 = 1 + 0.275\mathrm{Re}^{1/2}\mathrm{Sc}^{1/3}, \quad (11)$$

where β and β_0 are the mass-transfer coefficients at a drop motion velocity v under conditions of zero relative motion of the gas and fluid phases, respectively; $\mathrm{Re} = 2Rv/\bar{\nu}$, the Reynolds number; $\mathrm{Sc} = \bar{\nu}/D$, the Schmidt number; and $\bar{\nu}$, the kinematic viscosity of air.

The increase in the amount M_v of hydrogen sulfide desorbed from a moving and, simultaneously, expanding drop can be accounted for by the formula

$$M_v = M\beta/\beta_0. \quad (12)$$

The results of calculation of the degree of hydrogen sulfide desorption, η^0_{calc}, for the given case are listed in the table and confirm the good agreement between the theoretical values obtained in this study and experimental data.

CONCLUSIONS

(1) The mathematical model of hydrogen sulfide desorption from a moving drop, constructed in this study, is in agreement with experimental data.

(2) The high degree of hydrogen sulfide desorption from a moving drop is attributed to specific features of a nonstationary diffusion process in motion and simultaneous increase in the volume of a drop in the stage of its formation.

REFERENCES

1. Brounshtein, B.I. and Shchegolev, V.V., *Gidrodinamika, masso- i teploobmen v kolonnykh apparatakh* (Hydrodynamics and Mass and Heat Exchange in Column Apparatus), Leningrad: Khimiya, 1998.
2. Aniskin, S.V., Protod'yakonov, I.O., and Ionov, V.A., *Zh. Prikl. Khim.*, 1998, vol. 71, no. 6, pp. 1158–1160.
3. Aniskin, S.V. and Protod'yakonov, I.O., *Zh. Prikl. Khim.*, 1998, vol. 71, no. 10, pp. 1681–1689.
4. Levich, V.G., *Fiziko-khimicheskaya gidrodinamika* (Physicochemical Hydrodynamics), Moscow: Fizmatgiz, 1959.
5. Yakovlev, V.A., Grigor'eva, N.V., Makarenko, A.A., *et al., Izv. Vyssh. Uchebn. Zaved., Lesn. Zh.*, 1991, no. 2, pp. 92–93.
6. Sherwood, T.K., Pigford, R.L., and Wilke, C.R., *Mass Transfer*, New York: McGraw–Hill, 1975.

Russian Journal of Applied Chemistry, Vol. 77, No. 4, 2004, pp. 588–591. Translated from Zhurnal Prikladnoi Khimii, Vol. 77, No. 4, 2004, pp. 591–594.

PROCESSES AND EQUIPMENT OF CHEMICAL INDUSTRY

A Theoretical Study of Desorption in Disintegration of a Fluid Jet Formed in a Single-Flare Atomizer into Drops

S. V. Aniskin and I. O. Protod'yakonov

St. Petersburg State Technological University of Plant Polymers, St. Petersburg, Russia

Received December 23, 2003

Abstract—A model of desorption in the gas–fluid system for the region of disintegration into drops of a fluid jet outflowing from a single-flare atomizer is suggested.

An issue of current interest in working with black-liquor boilers in manufacture of sulfate pulp is how to make lower the amount of toxic components discharged with fume gases into the atmosphere. This problem is commonly solved by using spraying scrubbers with single-flare atomizers. In scrubber purification of fume gases to remove toxic components, absorption–desorption processes occur on the surface of sprayed fluid. The intensity of these processes predetermines the efficiency of purification of fume gases. As is known, in those cases when the main resistance to mass transfer is concentrated in the liquid phase, the intensity of adsorption and desorption is high in that relatively small region in which the fluid jet disintegrates into drops [1]. This phenomenon has been named the end effect in the scientific literature. By now, no theoretical description of the end effect in spraying of a fluid with single-flare atomizers has been provided.

The aim of the present study was to construct a model of this effect.

Let us consider the process of fluid disintegration in a single-flare atomizer in more detail. In [2], photographic images of various parts of a fluid jet outflowing from a single-flare atomizer were obtained.

The region studied in the jet included both its initial part and that in which the process of jet disintegration into separate parts is complete.

In accordance with the data of [2], despite the diversity and complexity of the process of disintegration of a fluid jet, it reduced to the follows: drops are finally formed by fine jets that appear on the surface of fragments of a disintegrating fluid jet.

In [3], formation of drops of the same size from a separate fine jet outflowing from the nozzle of a generator of monosdisperse drops was analyzed in detail. It was established that the fine fluid jet passes through a drop and comes to its front surface, with vortex flows formed within the drop. As a result, the drop size increases till the instant of drop detachment from the fine jet.

The pronounced end effect in this case is accounted for by mechanical transfer of the fluid to the surface of a growing drop, which leads to a dramatic decrease in the resistance to mass transfer in the fluid phase.

The contribution from the mechanism of diffusion transport in the fluid is negligible under these conditions. Comparison of the results obtained in experimental studies of the process of drop formation from fine jets outflowing from the surface of fragments of a disintegrating fluid jet formed by a single-flare atomizer in a spraying scrubber with the process of drop formation in a generator of monodisperse drops readily reveals a certain analogy between these processes. In this case, it seems natural to assume that the overall end effect that appears in disintegration into drops of a jet formed by a single-flare atomizer in a spraying scrubber is constituted by end effects that arise in the formation of separate drops from these fine jets. This overall end effect can be evaluated by the flux G of a substance, given by the formula

$$G = \Delta M/\Delta t, \quad (1)$$

where ΔM is the total mass of a substance sorbed by drops through the end effect in a certain period of time Δt.

1070-4272/04/7704-0588 © 2004 MAIK "Nauka/Interperiodica"

The quantities ΔM and Δt are found on the basis of the following considerations. Let us analyze a layer Δz in the region of motion of the already formed drops (Fig. 1). Apparently, all the drops in this layer are formed in region *2*. To these drops corresponds a certain value of the quantity G.

The quantity ΔM has the meaning of the characteristic of the overall end effect of drops with the volume ΔV of layer *4* in Fig. 2. The quantity Δt has the meaning of the time in which drops pass across the layer Δz. ΔM can be found from the formula

$$\Delta M = \int_0^\infty M \frac{\partial N}{\partial R} \mathrm{d}R, \quad (2)$$

where M is the value of the end effect for a separate drop of radius R, and N is the number of drops of radius R in the volume ΔV.

The quantity $\partial N/\partial R$ in this formula has the meaning of the numerical drop size distribution function. However, it is more convenient to use in this model the distribution function of drop volumes V over drop sizes

$$\varphi(R) = \frac{1}{\Delta V} \frac{\partial v}{\partial R}. \quad (3)$$

Then, with account of (3), formula (2) takes the form

$$\Delta M = \frac{3\Delta V}{4\pi} \int_0^\infty \frac{M}{R^3} \varphi(R) \mathrm{d}R. \quad (4)$$

Let us express ΔV in terms of the flow rate Q of a fluid emerging from the atomizer:

$$\Delta V = \Delta t Q, \quad (5)$$

where Δt is the time in which drops cross the layer Δz.

From formula (4) can be obtained, with account of (1) and (5), an integral expression for the flux of substance in disintegration into drops of a jet formed by a single-flare atomizer:

$$G = \frac{3}{4\pi} Q \int_0^\infty \frac{M}{R^3} \varphi(R) \mathrm{d}R. \quad (6)$$

An expression for M in (6) was obtained in [4]. This expression takes into account the nonstationary process of formation of a diffusion boundary layer at a drop moving relative to the ambient gas medium. In disintegration of a fluid jet formed by a single-flare atomizer, the density of the forming fluid flow is so high that the gas entrapped by the disintegrating fluid jet moves at virtually the same velocity as the fluid.

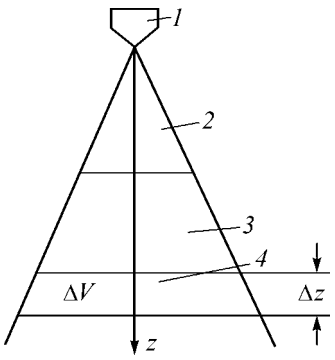

Fig. 1. Schematic of determining the volume ΔV of the fluid in a gas-fluid jet. (*1*) Single-flare atomizer, (*2*) region of disintegration of the fluid jet, (*3*) region of motion of the drops formed, and (*4*) elementary layer of volume ΔV.

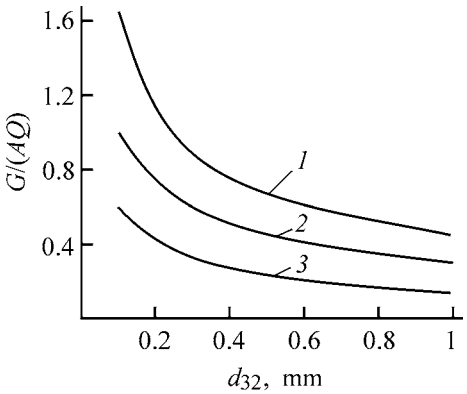

Fig. 2. Relative flux of substance being desorbed in disintegration of a fluid jet into drops vs. the Sauter diameter d_{32}. S = 6.35, D = 1.5–5 $m^2 s^{-1}$. v ($m s^{-1}$): (*1*) 5, (*2*) 10, and (*3*) 30.

Taking into account this circumstance, let us write down the expression for M, obtained in [4], with account of the assumption of the zero relative velocity of motion of the phases:

$$M = \sqrt{4\pi D} \left(\frac{3b}{4\pi}\right)^{2/3} \left[1.31\tau^{1/6} + 1.012\sqrt{\pi D} \left(\frac{4\pi\tau}{3b}\right)^{1/3}\right] \tau A. \quad (7)$$

Here A is the concentration of the substance being desorbed in the gas phase at the drop surface (kmol m^{-3}); D, the diffusion coefficient of the gas A in air ($m^2 s^{-1}$); b, the rate at which the drop volume grows ($m^3 s^{-1}$); and τ, the time in which a drop of radius R is formed (s).

The quantity A is considered to be constant at any instant of time during the formation of a drop of an arbitrary radius R, i.e.,

$$A = \text{const}. \quad (8)$$

The time of drop formation depends on the radius of the drop and on its growth rate:

$$\tau = \frac{4}{3}\pi\frac{R^3}{b}. \quad (9)$$

The rate at which the drop volume grows is a function of the radius R_j of a jet from which the drop is formed:

$$b = \pi R_j^2 v, \quad (10)$$

where v is the motion velocity of the fluid ($m\ s^{-1}$).

Since the motion velocity of the fluid varies only slightly in the region of disintegration of the fluid jet, it is assumed that the motion velocity of fine jets with different radii in the disintegrating fluid jet formed by the single-flare atomizer is the same and equal to the velocity v_n at which the fluid outflows from the nozzle:

$$v = v_n = \text{const}. \quad (11)$$

To integrate the right-hand part of Eq. (6), it is necessary to determine the type of the dependence of M on the final radius R of the drops. For this purpose, let us determine the relationship between the quantities R and R_j in formula (10).

It is known [5] that the wavelength λ of the most probable oscillations of a jet is determined by the radius R_j of this jet by the formula

$$\lambda = SR_j, \quad (12)$$

where S is a coefficient whose value depends on the viscosities of the fluid and gas, and also on the surface tension of the fluid.

For particular conditions of disintegration of a fluid jet, S is a constant:

$$S = \text{const}. \quad (13)$$

With account of the fact that the wavelength λ is that part of a jet of radius R_j, from which a drop is formed, the following equality is valid:

$$\pi R_j^2\lambda = \frac{4}{3}\pi R^3, \quad (14)$$

Comparison of (12) and (14) yields the sought-for relation

$$\frac{R}{R_j} = \sqrt[3]{\frac{4}{3}S}. \quad (15)$$

In accordance with (15), let us write down expressions (9) and (10) in the explicit form:

$$\tau = \left(\frac{4}{3}\right)^{1/3} S^{2/3}\frac{R}{v}, \quad (16)$$

$$\tau = \pi\left(\frac{4}{3}\right)^{2/3} vR^2. \quad (17)$$

The expressions obtained make it possible to find in the explicit form the function M:

$$M = \gamma R^2(\alpha R^{1/2} + \beta)A. \quad (18)$$

The quantities α, β, and γ are calculated using the following formulas:

$$\alpha = 1.33\frac{S^{1/3}}{v^{1/2}}, \quad (19)$$

$$\beta = 1.08\sqrt{\pi D}\,\frac{S^{4/9}}{v^{2/3}}, \quad (20)$$

$$\gamma = 4\sqrt{\pi D}\,\frac{S^{2/9}}{v^{1/3}}. \quad (21)$$

In integrating Eq. (6) with account of (18), we use the Rosin–Rammler distribution [5], which is the most frequently used when describing the dispersion composition of drops of the fluid being atomized. This distribution is described by the formula

$$\varphi(R) = \frac{n}{a}\left(\frac{R}{a}\right)e^{-(R/a)^n}, \quad (22)$$

where a and n are the distribution constants.

Then the sought-for expression for the flux of the substance being desorbed takes the form

$$G = \frac{3\gamma}{4\pi a}\left[\alpha a^{0.5}\Gamma\left(1 + \frac{1}{2n}\right)\right], \quad (23)$$

where Γ is the gamma function.

The constant a of the Rosin–Rammler distribution is uniquely determined in terms of the volume-surface drop diameter (Sauter diameter) by the formula [5]:

$$a = 1.3542d_{32}, \quad (24)$$

where d_{32} is the Sauter diameter.

The constant n of this distribution may be equal or close to 3 [6].

Therefore, the gamma function can be taken to be unity with high precision.

Taking into account the aforesaid and using for-

mulas (19)–(21), we transform expression (23) into the form convenient for analysis:

$$\frac{G}{AQ} = 1.95S^{5/9}\left(\frac{D}{vd_{32}}\right)^{1/2} + 2.39S^{2/3}\left(\frac{D}{vd_{32}}\right)^{1/2}. \quad (25)$$

Relation (25), obtained in the dimensionless form, shows that the relative flux of the substance being desorbed in disintegration of a fluid jet into drops depends mainly on the value of v and on the dispersion composition of the fluid being atomized, which is characterized by the Sauter diameter d_{32}. The calculated values of the function represented by expression (25) are shown in Fig. 2.

It is important to emphasize that G/AQ may exceed unity only in the case of chemisorption, when the substance being desorbed is present in drops in both free and chemically bound states.

It follows from the plots in Fig. 2 that the amount of relative desorption in disintegration of a fluid jet outflowing from a single-flare atomizer may be rather large. This conclusion has been confirmed experimentally, e.g., in [1]. In this study, with the nozzle of the atomizer mounted at a distance of 2 cm from the bottom of a spraying apparatus, the intensity of desorption was so high that the extent to which the equilibrium between the gas and fluid phases was attained exceeded 85%.

CONCLUSIONS

(1) A model of gas desorption in the region of disintegration into drops of a sprayed fluid was constructed with account of its polydisperse composition characterized by the Rosin–Rammler distribution.

(2) The model constructed can be used to evaluate theoretically the efficiency of desorption in spraying apparatus.

REFERENCES

1. Sherwood, T.K., Pigford, R.L., and Wilke, C.R., *Mass Transfer*, New York, McGraw–Hill, 1975.
2. Aniskin, S.V., A Study of Dust Catching in Jet Scrubbers from Gases Discharged in Manufacture of Sulfate Pulp, *Cand. Sci. Dissertation*, Leningrad, 1981.
3. Aniskin, S.V. and Protod'yakonov, I.O., *Zh. Prikl. Khim.*, 1998, vol. 71, no. 10, pp. 1681–1686.
4. Aniskin, S.V. and Protod'yakonov, I.O., *Zh. Prikl. Khim.*, 2004, vol. 77, no. 4, pp. 588–590.
5. Lyshevskii, A.S., *Zakonomernosti drobleniya zhidkostei mekhanicheskimi forsunkami davleniya* (Fundamental Aspects of Fluid Disintegration with Mechanical Pressure Atomizers), Novocherkassk: RIO MPI, 1961.
6. Protod'yakonova, O.I., Aniskin, S.V., and Sleptsov, I.E., *Zh. Prikl. Khim.*, 2002, vol. 75, no. 2, pp. 243–248.

Russian Journal of Applied Chemistry, Vol. 77, No. 4, 2004, pp. 592–594. Translated from Zhurnal Prikladnoi Khimii, Vol. 77, No. 4, 2004, pp. 595–597.

ORGANIC SYNTHESIS AND INDUSTRIAL ORGANIC CHEMISTRY

Oxidation of 2,4-Dinitrotoluene with an Ozone–Oxygen Mixture

P. Yu. Andreev, G. A. Galstyan, A. G. Galstyan, and I. S. Yakunina

Rubezhnoe Branch, Dal East-Ukrainian National University, Rubezhnoe, Lugansk oblast, Ukraine

Received August, 14, 2003

Abstract—Oxidation of 2,4-dinitrotoluene to 2,4-dinitrobenzoic acid with an ozone–oxygen mixture in glacial acetic acid was studied.

2,4-Dinitrobenzoic acid (DNBA) is an intermediate in production of roentgenocontrast agents [1] and is used as a component of light-sensitive materials in electrophotography [2].

2,4-Dinitrobenzoic acid is prepared by oxidation of 2,4-dinitrotoluene (DNT) with sodium dichromate or chromium trioxide in concentrated sulfuric acid at 40–60°C [3, 4]. The disadvantages of this method are the formation of large amounts of toxic and difficultly utilizable wastes and the low yield of the target product (50–70%). In this context, the study of DNT oxidation with ozone is of practical interest.

In this study, we examined the oxidation of DNT with an ozone–oxygen mixture in glacial acetic acid with the aim to develop a low-waste process for DNBA production.

As can be seen from Fig. 1, ozone reacts with the aromatic ring and methyl group of DNT to form peroxides and 2,4-dinitrobenzaldehyde (DNBAld), respectively. These reactions are parallel. As for aromatic products, DNBAld is accumulated in the first oxidation steps and DNBA, in the final steps.

At 30°C, the reaction of ozone with DNT is slow: in 3 h the conversion reaches ~20%, after which the oxidation stops (Fig. 2). The DNBA yield based on the reacted DNT is as low as 34%. The selectivity of oxidation of the methyl group increases on heating. At 100°C, the DNBA yield based on the reacted substrate reaches 48% (Fig. 2). On heating, the oxidation is accelerates and the DNT conversion increases, reaching 100% at 100°C.

It is known [5] that the ratio of alternative reaction pathways in this system is shifted to DNBA formation

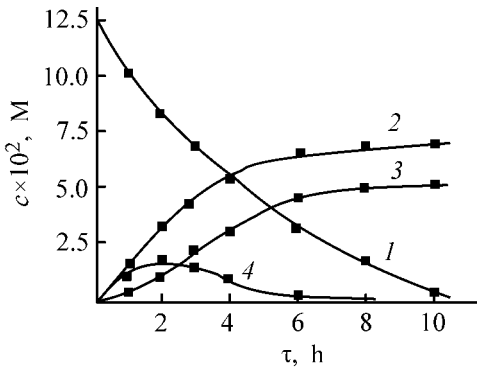

Fig. 1. Content *c* of (*1*) DNT, (*2*) peroxides, (*3*) DNBA, and (*4*) DNBAld in the course of DNT oxidation with an ozone–oxygen mixture vs. time τ. v_{O_2} = 8.3 × 10^{-3} l s^{-1}; $[ArCH_3]_0$ = 0.125, $[O_3]_0$ = 9.5 × 10^{-4} M; 50°C.

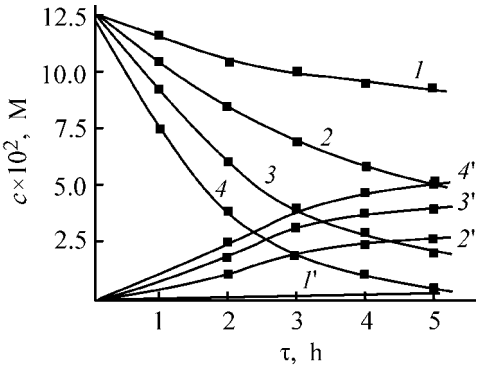

Fig. 2. Kinetic curves of (*1–4*) DNT consumption and (*1'–4'*) DNBA accumulation in DNT oxidation with an ozone–oxygen mixture in acetic acid at (*1*, *1'*) 30, (*2*, *2'*) 50, (*3*, *3'*) 70, and (*4*, *4'*) 100°C. v_{O_2} = 8.3 × 10^{-3} l s^{-1}; $[ArCH_3]_0$ = 0.125, $[O_3]_0$ = 9.5 × 10^{-4} M. (*c*) Concentration and (τ) time; the same for Fig. 3.

1070-4272/04/7704-0592 © 2004 MAIK "Nauka/Interperiodica"

in the presence of catalysts based on salts of metal with variable oxidation state. In this study, we examined the catalytic oxidation of DNT in the presence of cobalt(II) acetate (Fig. 3). Previously, we found that oxidation of DNT with molecular oxygen at 100°C in the presence of cobalt(II) acetate is very slow: only traces of DNBA were detected after 15-h oxidation. Catalytic oxidation with an ozone–oxygen mixture is fast and yields mainly DNBA (Fig. 3). Oxidation at 100°C in the presence of 0.14 M cobalt(II) acetate is complete in 3.5 h; the DNBA yield is 87%.

Selective oxidation of the methyl group with ozone in the presence of cobalt(II) acetate is a two-step process. Under the experimental conditions, ozone oxidizes mainly Co^{2+} (k of $Co^{2+} + O_3$ reaction is 930 [6], and k of the $ArCH_3 + O_3$ reaction is 0.013 $l\,mol^{-1}\,s^{-1}$ at 30°C) to reactive Co^{3+} species which, in turn, rapidly and selectively oxidize the methyl group of DNT:

$$Co^{2+} + O_3 + H^+ \rightarrow Co^{3+} + HO^{\cdot} + O_2, \quad (1)$$

$$ArCH_3 + Co^{3+} \rightarrow Ar\dot{C}H_2 + Co^{2+} + O_2 + H^+. \quad (2)$$

Since $v_1 \gg v_2$ [v_1 and v_2 are the rates of reactions (1) and (2), respectively], cobalt is in the oxidized form throughout the process (Fig. 3). For reaction (1) to occur, ozone should be continuously fed to the system. If the ozone supply is interrupted, the reaction will decelerate and then stop. For the formation of 1 mol of DNBA is spent 95% of the theoretical amount of ozone. This indicates that DNT is mainly oxidized with ozone under the experimental conditions. The role of molecular oxygen is limited to the reaction with benzyl radical

$$Ar\dot{C}H_2 + O_2 \rightarrow ArCH_2O_2^{\cdot}. \quad (3)$$

The amount of oxygen liberated in ozone reduction by reaction (1) is sufficient for reaction (3) to occur. The fact that the rate and selectivity of oxidation of the methyl group are independent of the oxygen concentration in the ozone–oxygen mixture confirms the suggested scheme involving reactions (1)–(3).

Introduction of potassium bromide into the reaction mixture substantially accelerates the DNT oxidation with an ozone–oxygen mixture but has no effect on the selectivity of oxidation of the methyl group (Fig. 3). We suggest that potassium bromide reacts with cobalt(II) acetate to form $Co^{2+}Br^{\cdot}$

$$Co^{3+} + Br^- \rightarrow Co^{3+}Br^- \rightleftarrows Co^{2+}Br^{\cdot}. \quad (4)$$

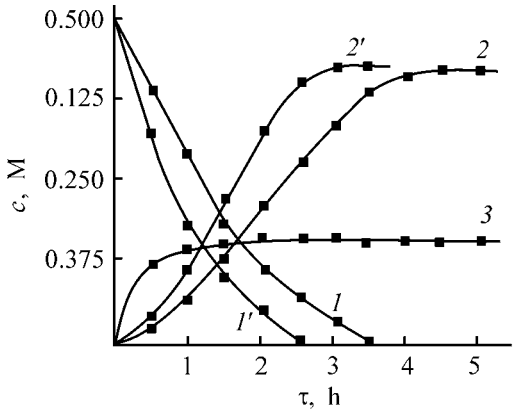

Fig. 3. Kinetic curves of (*1*–*1*′) DNT consumption, (*2*–*2*′) DNBA accumulation, and (*3*) Co^{3+} accumulation in oxidation of DNT with an ozone–oxygen mixture at 100°C. $v_{O_2} = 8.3 \times 10^{-3}$ $l\,s^{-1}$; $[ArCH_3]_0 = 0.5$, $[O_3]_0 = 9.5 \times 10^{-4}$, $[Co(AcO)_2 \cdot 4H_2O]_0 = 0.14$ M. (*1*′, *2*′) [KBr] = 0.1 M.

This complex is more reactive than Co^{3+} and oxidizes DNT by the reaction

$$ArCH_3 + Co^{2+}Br^- \rightarrow Ar\dot{C}H_2 + Co^{3+}Br^- + H^+. \quad (5)$$

EXPERIMENTAL

Dinitrotoluene was oxidized in a glass column with a fine-pore barrier for dispersion of the gas mixture. The reactor was charged with 15 ml of glacial acetic acid and a weighed portion of DNT of chemically pure grade. Then it was heated to the required temperature, and an ozone–oxygen mixture was fed at a rate of 8.3×10^{-3} $l\,s^{-1}$. The concentrations of unchanged DNT and of intermediate oxidation products were determined by gas–liquid chromatography on an LKhM-80 chromatograph with a flame-ionization detector, using a 2 m × 3 mm column packed with Chromaton N-AW with PNFS-6 stationary phase. The DNBA concentration was determined by titration with 0.01 N NaOH on an EV-74 ionometer.

CONCLUSIONS

(1) The reaction of 2,4-dinitrotoluene with ozone in acetic acid at 30°C occurs mainly via oxidation of the aromatic ring. The yield of the products of oxidation of the methyl groups does not exceed 34%. At 100°C, the selectivity of oxidation of the methyl group reaches 48%.

(2) The yield of 2,4-dinitrobenzoic acid in catalytic ozonation of 2,4-dinitrotoluene in the pres-

ence of cobalt(II) acetate is 87%. Introduction of potassium bromide into the oxidation system enhances the catalytic activity of cobalt(II) acetate. As a result, the oxidation of the methyl group is accelerated, but the selectivity of this reaction remains the same.

REFERENCES

1. Lebedev, B.A., Dolmatov, V.Yu., Zubarev, P.S., *et al.*, *Khim.-Farm. Zh.*, 1988, no. 5, pp. 589–591.
2. US Patent 4302521.
3. Kunisaburo, T. and Kimie, Ya., *J. Chem. Soc. Japn.*, 1964, vol. 85, no. 1, p. 5.
4. Polish Patent 233328.
5. Galstyan, G.A., Galstyan, T.M., and Sokolova, S.M., *Kinet. Katal.*, 1992, vol. 33, no. 4, pp. 779–787.
6. Galstyan, G.A., Galstyan, T.M., and Pastushenko, E.V., Abstracts of Papers, *Vsesoyuznaya konferentsiya po selektivnomu okisleniyu uglevodorodov i resursosberezheniyu uglevodorodnogo syr'ya* (All-Union Conf. on Selective Oxidation of Hydrocarbons and Saving of Hydrocarbon Raw Material), Kharkov, 1991, pp. 17–18.

Russian Journal of Applied Chemistry, Vol. 77, No. 4, 2004, pp. 595–598. Translated from Zhurnal Prikladnoi Khimii, Vol. 77, No. 4, 2004, pp. 598–601.

ORGANIC SYNTHESIS AND INDUSTRIAL ORGANIC CHEMISTRY

Surface Activity of Fatty Acid Salts in Aqueous Solutions

I. Yu. Averko-Antonovich, L. R. Ziganshina, A. P. Rakhmatullina, and R. A. Akhmed'yanova

Kazan State Technological University, Kazan, Tatarstan, Russia

Received July 22, 2003; in final form, December 2003

Abstract—The surface activity of sodium, potassium and, ammonium salts of fatty acids [stearic, oleic, synthetic fatty acids (C_{13}–C_{15} fractions), higher fatty acids contained in bottoms after separation of volatile fatty acids from cotton oil] in aqueous solutions was studied and analyzed.

Surfactants are widely used in various branches of economy, mostly for improvement of materials and development of their new kinds.

In production of anionic surfactants, narrow fractions of synthetic fatty acids (SFA) (C_{13}–C_{15} and C_{10}–C_{16}) and also individual stearic and oleic acids are used as raw materials. This raw material is expensive and its production is complicated. Therefore, attempts have been made to find alternative sources of fatty acids and their mixtures. For example, anionic surfactant prepared from products recovered from tall oil (one of products of cellulose processing) has been used in emulsion polymerization [1, 2]. It is known also [3, 4] that sodium or potassium salts of higher fatty acids recovered from cotton oil efficiently stabilize bituminous emulsions [3, 4].

In this study, we prepared anionic surfactants from bottoms formed after separation of volatile fatty acids from cotton oil (FACB). These bottoms contain a fairly large amount of fatty acids and are an inexpensive natural raw materials for preparing surfactants. The surface activities of the new and commercial anionic surfactants are compared.

EXPERIMENTAL

The surface activity of fatty acid salts was studied by common technique [GOST (State Standard 20 216–74] [5–9]. The physicochemical features and chemical composition of FACB were determined by the standard method [GOST 5474–5478] [10]. FACB is a dark brown oily liquid with a specific odor, which contains 30 wt % monomeric (stearic, oleic, palmitic, linoleic) and 70 wt % oligomeric fatty acids. The moisture content is 10.2 wt %, ash content 0.6 wt %, the number-average molecular weight 1130, acid number 156.7 mg KOH g^{-1}, saponification number 192.0 mg KOH g^{-1}, and iodine number 76.1 g I_2/100 g.

The fatty acids were converted into their salts by saponification with 30% aqueous sodium, potassium and ammonium hydroxides at 90–100 °C for 2 h. Aqueous solutions of these surfactants have pH 10.0–11.4.

It is known that surfactant molecules have a large excess free energy at the interface between the aqueous solution and air. The specific interfacial excess free energy (σ) (surface tension) of a surfactant is a function of its molecular weight, molecular configuration, and intermolecular interaction features. In order to characterize the surface activity of surfactants based on FACB, we studied their surface tension isotherms (Figs. 1a–1b). The surface tension in these systems was measured by the Du Nouy technique.

The surface tension of aqueous anionic surfactants is dependent on both the molecular structure of the surfactants and the cation type. It is known that branched anionic surfactants exhibit a higher surface tension. As can be seen from the table, the lowest surface tension is exhibited by paraffinates (fraction C_{13}–C_{15}) used as emulsifiers in production of commercial butadiene-vinylidene-chloride latexes. The highest surface tension is exhibited by sodium stearate. We found that the surface activity of salts prepared from FACB containing a mixture of fatty acids is intermediate between the surface activities of particular fatty acid salts, i.e., the multicomponent FACB salt does not show synergism in the surface activity.

1070-4272/04/7704-0595 © 2004 MAIK "Nauka/Interperiodica"

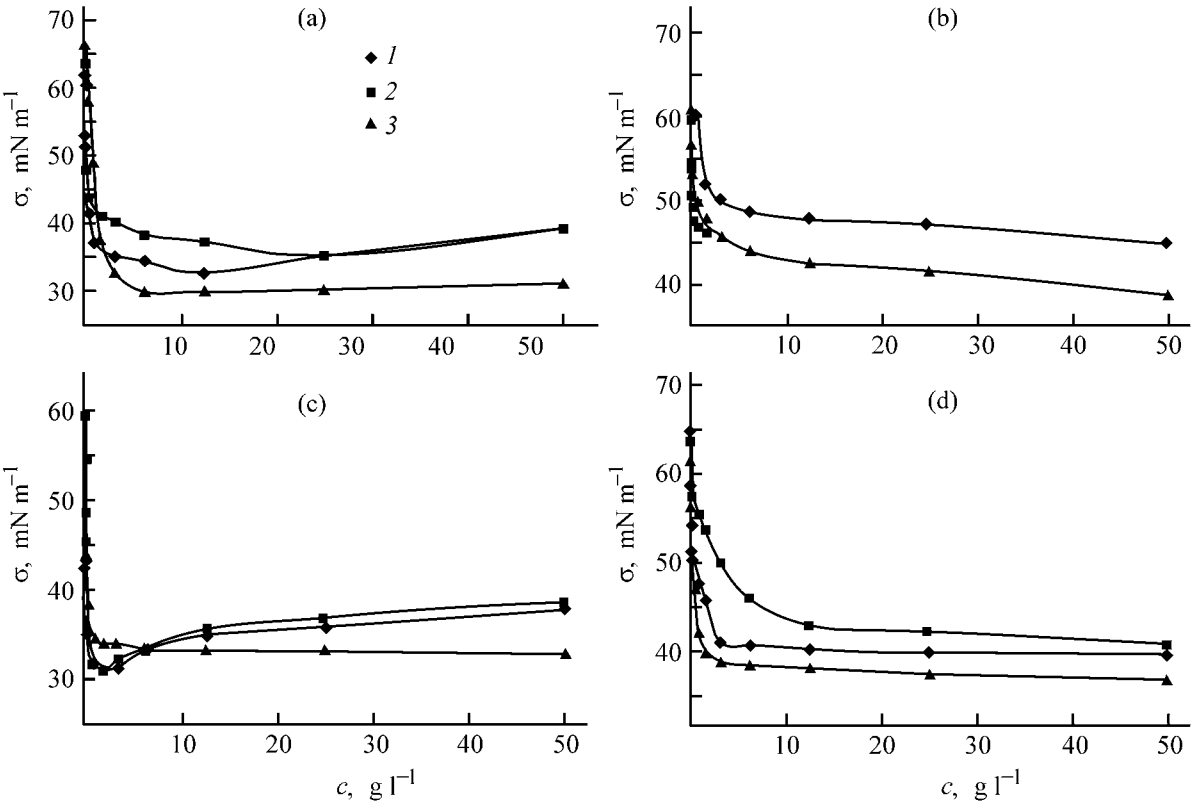

Fig. 1. Surface tension isotherms of aqueous solutions of (a) SFA ($C_{13–15}$ fraction), (b) stearic acid, (c) oleic acid, and (d) FACB salts. (σ) Surface tension and (*c*) surfactant concentration. (*1*) K^+, (*2*) Na^+, and (*3*) NH_4^+.

Along with the surface tension, the surface activity of surfactant can be characterized by the parameter pc_{20} (negative logarithm of the surfactant concentration at which the surface tension decreases by 20 mN m^{-1}). The table shows that this parameter is sensitive to the molecular structure of the hydrocarbon moiety in the surfactant molecule. The sodium SFA salt and sodium oleate have comparable pc_{20} values. In going to sodium stearate and then to FACB salts, this parameter appreciably increases. These data show that, although the multicomponent surfactants based on FACB do not exhibit synergism in surface tension, they are synergistic with respect to the pc_{20} value.

Both dispersing and stabilizing effects of surfactants are due to their interfacial sorption. Therefore,

Characteristics of aqueous surfactants

Surfactant	Cation	σ, mN m^{-1}	pc_{20}, g dm^{-3}	$\Gamma_\infty \times 10^6$, g m^{-2}	*n*	CMC, g dm^{-3}
SFA C_{13}–C_{15}	K^+	32.8	0.25	5.6	0.59	0.6
	Na^+	35.3	0.03	4.8	1.52	0.1
	NH_4^+	29.7	0.78	6.9	1.36	5.0
Stearic acid	K^+	43.2	3.98	3.3	2.18	6.3
	Na^+	47.2	0.32	3.8	1.38	0.8
	NH_4^+	38.7	0.32	2.5	1.76	6.3
Oleic acid	K^+	31.1	–	0.5	4.28	2.6
	Na^+	30.9	0.04	6.0	1.75	0.6
	NH_4^+	32.7	–	7.1	1.76	0.4
FACB	K^+	39.8	0.40	3.0	0.57	0.4, 4.2
	Na^+	41.0	3.16	2.5	1.19	7.9
	NH_4^+	36.9	0.25	2.8	2.54	1.8

the limiting interfacial surfactant sorption (surface concentration of the surfactant, at which its monomolecular surface layer is formed) can be used for characterization of its surface activity. The limiting sorption Γ_∞ of surfactants under consideration was determined from their sorption isotherms (see table). The highest sorption is exhibited by ammonium oleate, and the lowest sorption, by ammonium stearate. The surfactants based on FACB salts have Γ_∞ value close to that of stearates and are virtually insensitive to cation nature. The water solubility of surfactants is dependent on cation nature. The most soluble are potassium salts.The table shows that, irrespective of the cation kind, the stearates and FACB salts are less soluble than the SFA salts and oleates.

The surface activity of surfactants can be characterized also by the slope *n* of the plot of the surface tension against the interfacial sorption. The surfactants belonging to a certain type (water-soluble, nonionic, ionic), have approximately equal colligative parameter *n* irrespective of their molecular structure. Depending on the type of a surfactant, the *n* values vary as follows: water-soluble 1.5, nonionic 1, and ionic 2. The *n* value of ionic surfactants in electrolyte solutions is in the range 1–2. Most part of the surfactants tested by us, apart from their potassium derivatives, belong to the ionic type. Due to weak dissociation of SFA and FACB potassium salts, their *n* parameters are less than unity. At the same time, for completely dissociated potassium stearate and oleate, the *n* value exceeds 2.

The critical micelle concentration (CMC) is one of the most important characteristics of a surfactant. This parameter is sensitive to both the features of surfactant molecular structure and such factors as temperature, electrolyte content, presence of polar organic impurities, etc. The CMC decreases with lengthening of the hydrocarbon radical,[1] and depends on the number, kind, and position of ionic groups and presence of unsaturated functional groups. The surfactants with branched and, especially, cyclic hydrocarbon chains have lower CMC.

Our results (see table) do not show any relationship between the nature of a surfactant and its surface activity. However, these data show some features of FACB salts.

(1) There are two inflection points in the surface tension isotherm corresponding to two different CMC values. We suggest that the appearance of these two CMC values can be caused either by the multicomponent composition of FACB, hindering formation of uniform micelles, or by transformation of the initial spherical micelles into those of another kind. The second CMC can also be due the fact that FACB contains a large amount of oligomeric fatty acids. Their salts are associated at concentrations higher than the first CMC, and this is manifested in the sorption isotherm as the point of critical concentration of association.

(2) The FACB sodium salt has considerably higher CMC than FACB salts with other cations.

(3) The CMC of the FACB ammonium salt is intermediate between those of ammonium stearate (paraffinate) and ammonium oleate.

Thus, our experiments showed that the surface activity of FACB potassium, sodium and ammonium salts is intermediate between the surface activities of unsaturated and saturated acid salts contained in FACB salt. There is a synergistic effect in the slope of the concentration dependence of the surface tension, but the synergism is lacking with respect to other characteristics of surface activity.

CONCLUSION

Anionic surfactants prepared from higher fatty acids contained in bottoms formed after separation of volatile fatty acids from cotton oil are not inferior to commercial industrial surfactants. These surfactants can be applied as emulsifiers in emulsion polymerization, as plasticizers in production of concretes, and as dispersing agents in preparation of suspensions of solids.

REFERENCES

1. Erkova, L.N. and Chechik, O.S., *Lateksy* (Latexes), Leningrad: Khimiya, 1983.
2. Papkov, V.N., Sigov, O.V., Gusev, A.V., *et al.*, Abstracts of Papers, *IX Nauchno-prakticheskaya konferentsiya rezinshchikov "Rezinovaya promyshlennost'. Syr'e, materialy, tekhnologiya"* (IX Scientific and Practical Conf. of Workers in Rubber Industry "Rubber industry. Raw and Auxiliary Materials, Technology"), Moscow, 2002, pp. 107–108.
3. RF Patent no. 2185878.
4. Nagumanova, E.I., Murafa, A.V., Makarov, D.B., *et al., Struktura i dinamika molekulyarnykh sistem "Yal'chik-2002": Sbornik statei* (Structure and Dynamic of Molecular System "Yal'chik-2002"), Collection of Papers, Ufa, 2002, issue 9, vol. 2, pp. 50–52.

[1] Decrease in CMC of SFA (C_{13}–C_{15} fractions) potassium salts by an order of magnitude in comparison with that of potassium stearate (table) is due to the low water solubility of potassium stearate.

5. *Praktikum po kolloidnoi khimii* (Laboratory Manual on Colloid Chemistry), Neiman, R.E., Ed., Moscow: Vysshaya Shkola, 1972.
6. Vyaseleva, G.Ya., Kurmaeva, A.I., and Tret'yakova, A.Ya., *Praktikum po kolloidnoi khimii* (Laboratory Manual on Colloid Chemistry), Kazan: Kazan. Khim.-Tekhnol. Inst., 1979.
7. Rosen, M.J., *Surfactants and Interfacial Phenomena*, New York: Wiley, 1978.
8. Aivazov, V.V., *Praktikum po khimii poverkhnostnykh yavlenii i adsorbtsii* (Laboratory Manual on Chemistry of Surface Phenomena and Adsorption), Moscow: Vysshaya Shkola, 1973.
9. Averko-Antonovich, I.Yu. and Averko-Antonovich, Yu.O., *Metodichiskie ukazaniya po kursu "Tekhnologiya sinteticheskogo kauchuka"* (Methodical Gudeline on the Course "Synthetic Rubber Technology"), Kazan: Kazan. Khim.-Tekhnol. Inst., 1991.
10. Entelis, S.G., Evreinov, V.V., and Kuzaev, A.I., *Reaktsionnosposobnye oligomery* (Reactive Oligomers), Moscow: Khimiya, 1985.

Russian Journal of Applied Chemistry, Vol. 77, No. 4, 2004, pp. 599–602. Translated from Zhurnal Prikladnoi Khimii, Vol. 77, No. 4, 2004, pp. 602–605.

MACROMOLECULAR CHEMISTRY AND POLYMERIC MATERIALS

Synthesis of 2-Methacryloyl-5-hydroxy-3,3,5-trimethylisoxazolidine and Copolymers Thereof

A. Yu. Ershov, N. P. Ivanova, M. V. Mokeev, and E. F. Panarin

Institute of Macromolecular Compounds, Russian Academy of Sciences, St. Petersburg, Russia

Received October 9, 2003

Abstract—Previously unknown 2-methacryloyl-5-hydroxy-3,3,5-trimethylisoxazolidine was prepared by the reaction of 5-hydroxy-3,3,5-trimethylisoxazolidine with methacryloyl chloride. Homopolymers of this compound and its copolymers with *N*-vinylformamide and *N*-vinylpyrrolidone were obtained by radical polymerization.

The targeted transport of a physiologically active substance to a definite organ or tissue of a living body is an important problem of modern pharmacology. Water-soluble copolymers derived from *N*-vinylamides and vinyl saccharides, which exhibit increased affinity for glycoproteins owing to the presence of similar amide and saccharide groups, may be efficient means for such a transport.

Previously, we have prepared polymers derived from *N*-vinylamides (*N*-vinylpyrrolidone; *N*-vinylacetamide and its *N*-alkyl derivatives) and vinylsaccharides (2-*N*-methacryloylglucosamine [1], 3-*O*-methacryloyl-1,2;5,6-di-*O*-isopropylidene-*O*-glucofuranose [2], and 6-*O*-methacryloylglucopyranose [3]).

The main problem arising in preparation of vinylsaccharides, which are the starting comonomers in synthesis of copolymers of vinylsaccharides with *N*-vinylamides, is associated with preliminary protection of hydroxy groups of the glucopyranose ring in regioselective acylation with unsaturated carboxylic acid anhydrides or chlorides [2, 3]. These synthetic limitations can be lifted by using, instead of pyranose and furanose units, oxygen-containing saturated rings (e.g., five-membered isoxazolidine structures) as alternative models of saccharide fragemnts. The presence of the cyclic hemiacetal fragment –O–C–OH suggests an enhanced affinity of these molecules for monosaccharides and thus opens up certain prospects for synthesis of isoxazolidine-containing polymers suitable as structural analogs of polymeric compounds based on vinylsaccharides. It is also known that isoxazolidine derivatives, the so-called "pseudonucleoitides," are used in medicine, e.g., as potential means for treating HIV infections [4–6].

In this context, our goal was to prepare 2-methacryloyl-5-hydroxy-3,3,5-trimethylisoxazolidine **II** by the reaction of readily accessible [7] 5-hydroxy-3,3,5-trimethylisoxazolidine **I** with methacryloyl chloride, and also to study copolymerization of **II** with hydrophilic comonomers, *N*-vinylformamide (VFA) and *N*-vinylpyrrolidone (VP).

It is known that acylation of **I** occurs by several pathways to yield a mixture of cyclic and linear products, 2-acyl-5-hydroxy-3,3,5-trimethylisoxazolidine and 4-(*O*-acylhydroxylamino)-4,4-dimethyl-2-butanone, respectively [8]. However, the reaction of 5-hydroxy-3,3,5-trimethylisoxazolidine **I** with methacryloyl chloride yields the cyclic product only (MAIS, **II**) (see Experimental).

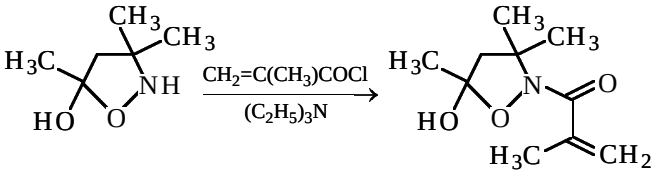

I **II**

The criteria used to prove structure **II** were similar to those applied previously [9–12] to functionally substituted isoxazolidines and were based on NMR spectroscopy. In particular, the ^{1}H NMR spectrum of **II** in $CDCl_3$ contains a set of signals characteristic of a five-membered isoxazolidine ring. Diastereotopic methylene protons give a typical *AB* pattern with a

1070-4272/04/7704-0599 © 2004 MAIK "Nauka/Interperiodica"

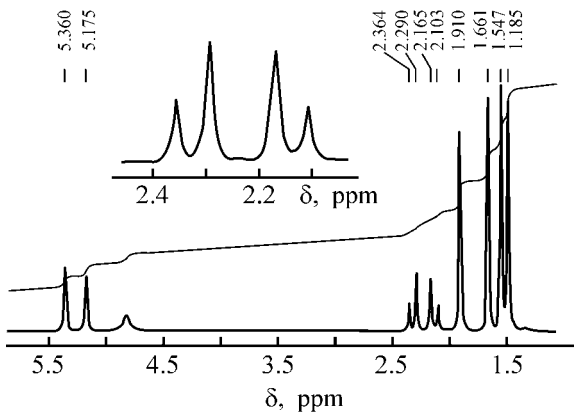

Fig. 1. ^{1}H NMR spectrum of **II** in $CDCl_3$. (δ) Chemical shift; the same for Fig. 2.

coupling constant of 12 Hz. Also, the spectrum contains a set of signals of the methacryloyl moiety, namely, those of the methyl group at 1.91 ppm and two vinyl protons at 5.17 and 5.36 ppm (Fig. 1). The ^{13}C NMR spectrum of **II** in $CDCl_3$ contains a set of signals at 55.7, 63.1, and 102.4 ppm, corresponding to the C^4, C^3, and C^5 atoms of the isoxazolidine ring, respectively (see Experimental). An additional fact confirming the formation of the *N*-acyl group is the violet coloration appearing upon treatment of **II** with an $FeCl_3$ solution, which is typical of cyclic hydroxamic acid derivatives.

Homopolymerization of **II** and its copolymerization with VFA and VP was performed in DMF at 60°C using azobis(isobutyronitrile) as initiator (1 wt % relative to the comonomers). We obtained soluble MAIS–VFA (**IV**) and MAIS–VP (**V**) copolymers, and also MAIS homopolymer, poly-2-methacryloyl-5-hydroxy-3,3,5-trimethylisoxazolidine (PMAIS, **III**):

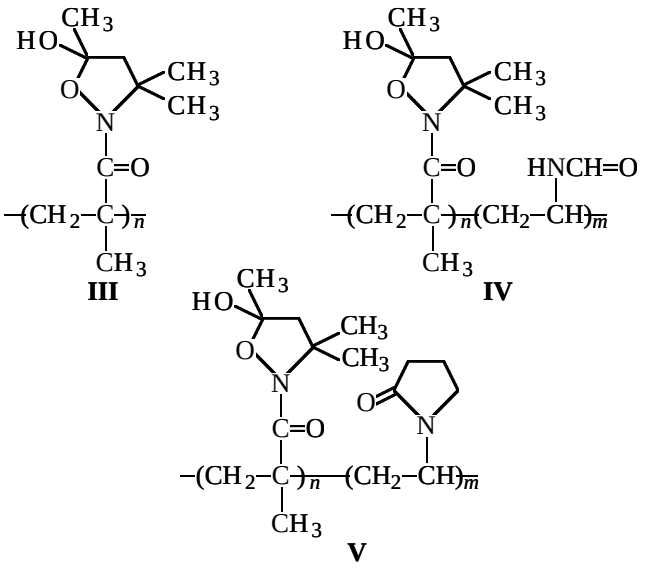

The conditions under which **III**–**V** were prepared and the intrinsic viscosities [η] of these polymers are given in Table 1.

Homopolymer **III** is water-insoluble, which may be due to intrachain hydrophobic interactions of three methyl groups of the isoxazolidine ring. The ^{1}H NMR spectrum of **III** in DMSO-d_6 contains a typical set of signals at about 1.50 ppm, characteristic of the 3- and 5-CH_3 groups of the isoxazolidine ring, and also the signal of the C^4H_2 group at 1.80 ppm (Table 2). As

Table 1. Conditions of synthesis and properties of polymers **III**–**V**

Compound	Composition of comonomer mixture, mol %		Yield, %	Composition of final copolymer, mol %		[η], dl g^{-1}, in 0.1 M AcONa solution
	MAIS	VFA or VP		MAIS	VFA or VP	
III	100	–	50	100	–	0.09*
IV	15	85	75	10	90	0.20
	20	80	70	22	78	0.16
V	30	70	85	30	70	0.33

* Determined in DMF.

Table 2. ^{1}H NMR spectra of **III**–**V** in D_2O

Compound	δ, ppm						
	MAIS				VFA or VP		
	CH_3	3-CH_3	5-CH_3	4-H	H–C=O or 3-H	4-H	5-H
III*	0.88	1.38; 1.49	1.66	1.88	–	–	–
IV	1.15	1.46; 1.53	1.76	2.29	7.98	–	–
V	1.19	1.53 (6H)	1.93	2.36	2.28	2.03	3.26

* Recorded in DMSO-d_6.

compared to the spectrum of **II**, these signals are appreciably shifted upfield, which is due to transformation of the methacryloyl fragment into the saturated isobutyryl unit of the polymer. The ^{1}H NMR spectra of MAIS–VFA (**IV**) and MAIS–VP (**V**) copolymers in D_2O contain a typical set of signals in the range 1.50–1.80 ppm, which are characteristic of the 3- and 5-CH_3 groups in the isoxazolidine ring. The ^{1}H NMR spectrum of **IV** also contains a formyl proton signal at 7.98 ppm (Fig. 2), and the spectrum of **V**, signals of lactam ring protons (4-H, 3-H, 5-H) at 2.03, 2.28, and 3.26 ppm, respectively.

Thus, acylation of 5-hydroxy-3,3,5-trimethylisoxazolidine with unsaturated carboxylic acid anhydrides or chlorides may be a convenient route to new isoxazolidine monomers; their polymers show promise as carriers of biologically active substances.

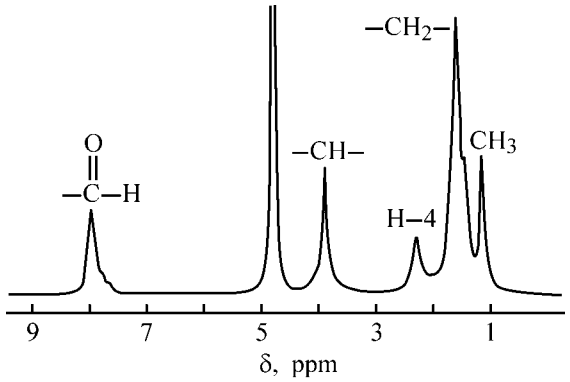

Fig. 2. ^{1}H NMR spectrum of **IV** in D_2O.

EXPERIMENTAL

The ^{1}H and ^{13}C NMR spectra were measured on a Bruker AC 200 spectrometer at 200 and 50 MHz, respectively. The compositions of copolymers **IV** and **V** were determined from the relative intensities of the characteristic ^{1}H NMR signals. The reaction progress was monitored, and the product purity checked, by TLC on Silufol UV 254 plates (eluent benzene : acetone, 2 : 1). The intrinsic viscosity [η] was measured with an Ubbelohde viscometer in 0.1 M sodium acetate solution at 25°C. Compound **I** was prepared as described in [7].

2-Methacryloyl-5-hydroxy-3,3,5-trimethylisoxazolidine II. To a solution of 13.1 g (0.1 mol) of **I** and 15.2 g (0.15 mol) of triethylamine in 250 ml of ether, cooled to 5°C, we added dropwise with stirring 15.7 g (0.15 mol) of methacryloyl chloride. The resulting precipitate was separated, and the ether solution was washed with a saturated $NaHCO_3$ solution. The solvent was removed in a vacuum, and the residue was recrystallized from benzene–hexane, 2 : 1. Yield of **II** 12.9 g (65%), mp 109–111°C.

Found, %: C 60.31, H 8.57, N 6.96.

$C_{10}H_{17}NO_3$.

Calculated, %: C 60.28, H 8.60, N 7.03.

^{1}H NMR spectrum ($CDCl_3$), δ, ppm: 1.49 s, 1.55 s ($2CH_3C^3$), 1.66 s (CH_3C^5), 1.91 s (CH_3C=), 2.13 and 2.32 (4-H, *AB* system, J_{AB} 12 Hz), 4.83 br.s (OH), 5.17 s (CH=), 5.36 s (CH=). ^{13}C NMR spectrum ($CDCl_3$), δ_C, ppm: 19.3 ($\underline{CH_3}C$=), 23.7, 25.4 (3-$\underline{CH_3}$), 27.0 (5-$\underline{CH_3}$), 55.7 (C^4), 63.1 (C^3), 102.4 (C^5), 119.7 (CH_2=), 139.4 (CH=), 172.5 (C=O).

CONCLUSIONS

(1) Reaction of 5-hydroxy-3,3,5-trimethylisoxazolidine with methacryloyl chloride yields a new monomer, 2-methacryloyl-5-hydroxy-3,3,5-trimethylisoxazolidine.

(2) Homopolymers of 2-methacryloyl-5-hydroxy-3,3,5-trimethylisoxazolidine and its copolymers with *N*-vinylformamide and *N*-vinylpyrrolidone, containing 10–30 mol % isoxazolidine units, were prepared. The structures and compositions of the copolymers were confirmed by ^{1}H NMR spectroscopy.

ACKNOWLEDGMENTS

The study was financially supported by the Russian Foundation for Basic Research (project no. 02-03-33110) and by the Ministry of Industry, Science, and Technology of the Russian Federation (project no. NSh-1823.2003.3).

REFERENCES

1. Panarin, E.F., Ershov, A.Yu., Ivanova, N.P., and Efremova, O.N., *Zh. Prikl. Khim.*, 1999, vol. 72, no. 11, pp. 1872–1875.
2. Panarin, E.F., Ershov, A.Yu., and Ivanova, N.P., *Zh. Prikl. Khim.*, 2000, vol. 73, no. 12, pp. 1998–2001.
3. Panarin, E.F., Ivanova, N.P., and Kever, E.E., *Vysokomol. Soedin., Ser. A*, 1998, vol. 40, no. 1, pp. 15–23.
4. Chiacchio, U., Corsaro, A., Pistara, V., *et al.*, *Eur. J. Org. Chem.*, 2002, no. 7, pp. 1206–1212.

5. Merino, P., Franco, S., Merchan, F.L., and Tejero, T., *J. Org. Chem.*, 2000, vol. 65, no. 18, pp. 5575–5589.
6. Chiacchio, U., Corsaro, A., Iannazzo, D., *et al., Eur. J. Org. Chem.*, 2001, no. 10, pp. 1893–1898.
7. Belly, A., Petrus, F., and Verducci, J., *Bull. Soc. Chim. Fr.*, 1973, no. 4, pp. 1395–1398.
8. Bezhan, I.P., Zelenin, K.N., Sviridova, L.A., *et al.*, *Khim. Geterotsikl. Soedin.*, 1989, no. 6, pp. 823–826.
9. Ershov, A.Yu., Gribanov, A.V., Gindin, V.A., and Kol'tsov, A.I., *Zh. Org. Khim.*, 1995, vol. 31, no. 7, pp. 1054–1056.
10. Ershov, A.Yu., Koshmina, N.V., and Dobrodumov, A.V., *Khim. Geterotsikl. Soedin.*, 1999, no. 7, pp. 945–947.
11. Ershov, A.Yu., *Khim. Geterotsikl. Soedin.*, 2002, no. 6, pp. 828–836.
12. Ershov, A.Yu., Koshmina, N.V., Mokeev, M.V., and Gribanov, A.V., *Khim. Geterotsikl. Soedin.*, 2003, no. 9, pp. 1428–1429.

Russian Journal of Applied Chemistry, Vol. 77, No. 4, 2004, pp. 603–607. Translated from Zhurnal Prikladnoi Khimii, Vol. 77, No. 4, 2004, pp. 606–611.

MACROMOLECULAR CHEMISTRY AND POLYMERIC MATERIALS

Copolymerization of *N*-Vinylsuccinimide with Butyl Methacrylate in Pyridine

N. A. Lavrov, A. G. Pisarev, and E. V. Sivtsov

St. Petersburg State Technological Institute, St. Petersburg, Russia

Received January 23, 2004

Abstract—The kinetics of radical copolymerization of *N*-vinylsuccinimide with *n*-butyl methacrylate in pyridine was studied, and the previously unknown copolymerization constants of the monomers were determined. The calculations were performed using appropriate software and a new procedure for approximation of the experimental data, which allow determination of the kinetic parameters at high conversions with the minimum error. The copolymerization kinetics were compared for the reaction systems constituted by *N*-vinylsuccinimide and *n*-butyl methacrylate and by *N*-vinylsuccinimide and *n*-butyl acrylate.

Copolymers of *N*-vinylsuccinimide (VSI) with *n*-butyl acrylate (BA) were suggested as materials for preparing films for medicobiological purposes [1–3]. The acrylic comonomer acting as internal plasticizer makes it possible to prepare elastic films recommended for protection and treatment of skin wounds. However, copolymers containing more than 80–90% BA are sticky liquids incapable of film formation. This drawback can be eliminated by introducing one more comonomer, i.e., by partially replacing BA with *n*-butyl methacrylate (BMA). Papers on preparation of VSI polymers and copolymers, published in the last 50 years [4], contain no data on binary copolymerization of VSI with BMA. In this study, we examined the copolymerization of VSI with BMA in pyridine.

The monomers and initiator, azobis(isobutyronitrile) (AIBN), were purified as described in [5]. Analytically pure pyridine was double-distilled. The copolymerization of the monomers was performed in glass ampules under Ar at 60°C. The total concentration of the monomers in pyridine was 0.7, and that of AIBN, 0.0165 M. The reaction kinetics was studied gravimetrically, as in [5]. After the copolymerization was complete, the ampule contents were poured into distilled water. The precipitated copolymer was filtered off and dried to constant weight at 20°C (660 Pa). The copolymer compositions (Table 1) were determined by IR spectroscopy from the ratio of the optical density at 1700 cm^{-1}, D_{VSI}, to that at 1725 cm^{-1}, D_{BMA}, using a calibration plot constructed according to [6]. The IR spectra of copolymers were recorded on a Perkin–Elmer spectrophotometer. Samples were prepared as films cast on KBr plates or as free films.

Copolymerization of VSI with both BMA and BA [5] in pyridine is relatively fast, which does not always allow isolation of the copolymers at low conversions. With increasing conversion, the viscosity of the reaction mixture grows, thus complicating a quantitative isolation of the product. Copolymerization occurs under homogeneous conditions and yields copolymers soluble in organic solvents, which allows preparation of films by casting.

Comparison of the kinetics of VSI–BMA copolymerization with that of VSI–BA copolymerization and with the results given in [5] shows that the initial rate of VSI–BMA copolymerization is higher as compared to the VSI–BA system (Table 1). This is due to the higher activity of BMA, compared to BA. However, the rate of copolymerization of VIS with BMA decreases with increasing conversion (Table 1). This may be due to changes in the solution viscosity and in conformations of macromolecules in the course of polymerization, and also to steric factors.

The high viscosity of the reaction system may be responsible for the fact that the gravimetric method used to monitor the copolymerization kinetics gives a certain scatter of experimental points. As a result, the error in calculation of the copolymerization constants increases. Therefore, in studying the kinetics of copolymerization of VSI with BMA, we used the approximation procedure [7] allowing correction of

1070-4272/04/7704-0603 © 2004 MAIK "Nauka/Interperiodica"

Table 1. Compositions of copolymers of VSI (M_1) with BMA or BA (M_2), prepared in pyridine at 60°C*

VSI mole fraction in the starting mixture	Comonomer M_2	τ, min	*K*, %	Mole fraction of VSI units in copolymer
0.25	BMA	60	33	0.15
		180	62	0.17
		240	65	0.18
0.50	BMA	60	37	0.30
		180	70	0.37
		240	73	0.38
0.75	BMA	60	42	0.47
		180	80	0.65
		240	82	0.66
0.25	BA	60	29	0.15
		120	52	0.17
		300	84	0.19
0.50	BA	60	35	0.32
		120	61	0.39
		300	89	0.45
0.75	BA	60	38	0.52
		120	70	0.72
		300	98	0.74

* (τ) Copolymerization time and (*K*) conversion.

Table 2. Constants of copolymerization of VSI (M_1) with BMA or BA (M_2) in pyridine (AIBN initiator, 60°C), calculated by the EBR and KT methods

Constant	Comonomer M_2	
	BMA	BA
r_1 (EBR)	0.03 ± 0.04	0.11 ± 0.07
r_1 (KT)	0.03 ± 0.03	0.11 ± 0.07
r_2 (EBR)	1.79 ± 0.04	1.70 ± 0.10
r_2 (KT)	1.79 ± 0.02	1.70 ± 0.09
$1/r_1$	14.2	9.09
$1/r_2$	0.559	0.588
r_2/r_1	25.6	15.5
r_1r_2	0.125	0.187

data on the monomer conversion and copolymer composition by the least-squares method; the error in calculation of the copolymerization constants is thus decreased.

Detailed analysis of the applicability of this procedure to treatment of experimental data obtained at various conversions of the monomers, using computer programs for calculation of the polymerization constants by the Ezrielev–Brokhina–Roskin (EBR) [8] and Kelen–Tüdös (KT) [9] methods, shows that reliable results can be obtained even at conversions exceeding 50%. Using this procedure, we also refined the constants of copolymerization of VSI with BA [5]; the results are listed in Table 2.

In calculation of the VSI–BMA copolymerization constants in pyridine by the EBR and KT methods, the minimum error factor was 0.001. In the system VSI–BA, the copolymerization constants in pyridine could be calculated with an even lower error factor of 0.0001. Calculation of r_1 and r_2 by both methods gives virtually coinciding results (Table 2).

The constants of copolymerization of VSI with BA in pyridine, calculated in [5] ($r_1 = 0.26 \pm 0.05$, $r_2 = 1.86 \pm 0.11$), were determined at a 3–8% conversion of the monomers. However, measurements at low (≤10%) conversions do not always ensure a low error of the copolymerization constants. For example, the error factor was 0.5 in [5].

The use of experimental data for low conversions is quite justified if the methods used for calculating the copolymerization constants are based on solution of differential equations for the copolymer composition. With more up-to-date calculation methods and computer facilities, there is no need to restrict artificially the experimental data. Therefore, we refined in this paper the constants of copolymerization of VSI with BA in pyridine using the approximation treatment of experimental data for <50% conversion (Table 2). The error factor was 0.0001.

The constants of copolymerization of VSI with BMA in pyridine (Table 2) were determined similarly with an error factor of 0.001. Hence, the procedure of approximation of the experimental data on the monomer conversion and copolymer composition allows determination of the copolymerization constants r_1 and r_2 with a minimum error even at conversions exceeding 50% (Table 1). This confirms the conclusion made in [10] that the Kelen–Tüdös method is quite suitable for calculating the copolymerization constants at high conversions. In turn, the copolymerization constants calculated from the approximated experimental data with a very low error factor furnish more reliable information on the reaction kinetics and microstructure of the copolymers.

Using the copolymerization constants for the systems VSI–BMA and VSI–BA (Table 2), we calculated the probability *f* of diad formation and the statistical-mean block lengths *L* in the chains of VSI–BMA and VSI–BA copolymers by the formulas from [11, 12]

Table 3. Probability f of diad formation and statistical-mean block length L in chains of VSI–BMA and VSI–BA copolymers (copolymerization in pyridine, AIBN initiator, 60°C)

VSI–BMA copolymers						VSI–BA copolymers					
VSI mole fraction	f_{11}	f_{22}	$f_{12} = f_{21}$	L_1	L_2	VSI mole fraction	f_{11}	f_{22}	$f_{12} = f_{21}$	L_1	L_2
0.1	0.0002	0.889	0.055	1.003	17.1	0.1	0.0007	0.884	0.058	1.01	16.3
0.2	0.0008	0.781	0.109	1.008	8.16	0.2	0.003	0.770	0.113	1.03	7.80
0.3	0.002	0.675	0.162	1.013	5.18	0.3	0.008	0.660	0.166	1.05	4.97
0.4	0.004	0.571	0.213	1.02	3.69	0.4	0.016	0.552	0.216	1.07	3.55
0.5	0.008	0.469	0.262	1.03	2.79	0.5	0.029	0.446	0.262	1.11	2.70
0.6	0.014	0.369	0.309	1.05	2.19	0.6	0.050	0.344	0.303	1.17	2.13
0.7	0.025	0.270	0.352	1.07	1.77	0.7	0.086	0.244	0.335	1.26	1.73
0.8	0.047	0.174	0.389	1.12	1.45	0.8	0.154	0.148	0.349	1.44	1.43
0.9	0.109	0.081	0.405	1.27	1.20	0.9	0.311	0.059	0.315	1.99	1.19

Table 4. Variation of the VSI (M_1) content in the monomer mixture in the course of copolymerization with BMA or BA (M_2) in pyridine

Comonomer M_2	VSI mole fraction at indicated conversion, %					
	0	10	20	40	50	70
BMA	0.25	0.28	0.30	0.33	0.35	0.40
	0.50	0.54	0.59	0.63	0.66	0.69
	0.75	0.78	0.81	0.83	0.86	0.89
BA	0.25	0.27	0.29	0.32	0.34	0.38
	0.50	0.52	0.55	0.59	0.62	0.65
	0.75	0.77	0.79	0.83	0.85	0.87

Table 5. Probability f of diad formation and statistical-mean block length L in the chains of copolymers of VSI (M_1) with BMA or BA (M_2), calculated taking into account the monomer conversion (copolymerization in pyridine)

Comonomer M_2	Mole fraction of M_1	K, %	f_{11}	f_{22}	$f_{12} = f_{21}$	L_1	L_2
BMA	0.25	0	0.001	0.728	0.136	1.010	6.37
		10	0.002	0.696	0.151	1.012	5.60
		20	0.002	0.675	0.162	1.013	5.18
		40	0.003	0.643	0.177	1.015	4.63
		50	0.003	0.622	0.187	1.016	4.32
		70	0.004	0.571	0.213	1.020	3.69
BA	0.50	0	0.029	0.446	0.262	1.11	2.70
		10	0.032	0.425	0.271	1.12	2.57
		20	0.038	0.395	0.284	1.13	2.39
		40	0.047	0.354	0.299	1.16	2.18
		50	0.056	0.323	0.310	1.18	2.04
		70	0.065	0.293	0.321	1.20	1.92
BA	0.75	0	0.114	0.196	0.345	1.33	1.57
		10	0.128	0.177	0.348	1.37	1.51
		20	0.144	0.158	0.349	1.41	1.45
		40	0.186	0.121	0.347	1.54	1.35
		50	0.213	0.103	0.342	1.62	1.30
		70	0.246	0.085	0.334	1.74	1.25

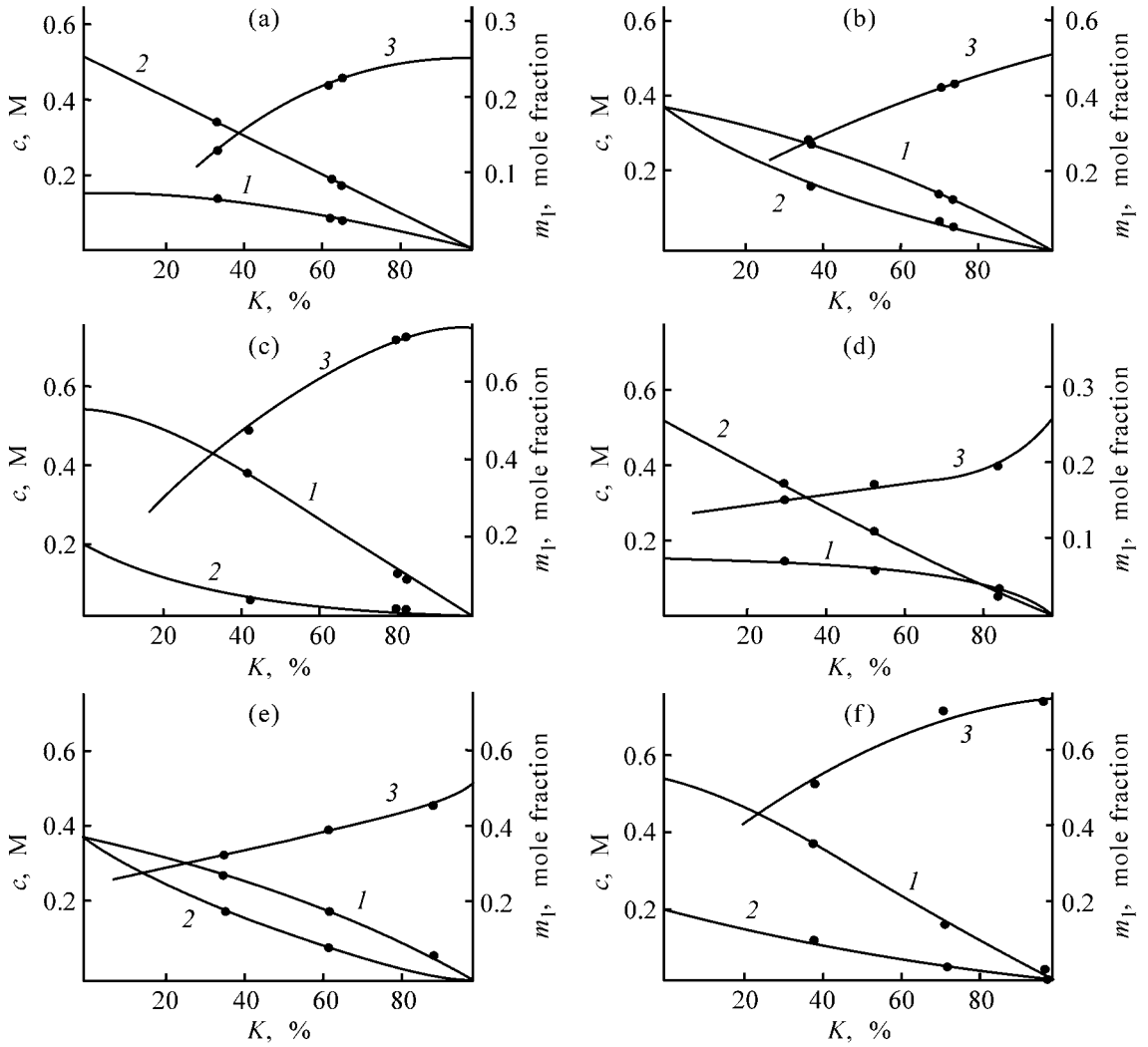

Fig. 1. Concentrations *c* of (*1*) VSI and (*2*) BMA or BA in the reaction mixture and (*3*) the mole fraction of VSI units in the copolymer m_1 vs. the conversion *K*. Solvent pyridine; total monomer concentration 0.7 M; AIBN concentration 0.0165 M; 60°C. VSI mole fraction in the monomer mixture: (a, d) 0.25, (b, e) 0.50, and (c, f) 0.75. Copolymerization: (a–c) VSI + BMA and (d–f) VSI + BA.

using the appropriate software [13]. The results obtained (Table 3) show that the tendency toward formation of alternating copolymers in copolymerization of VSI with BMA in pyridine appears at the VSI mole fraction in the monomer mixture equal to 0.80–0.90, and in the system with BA in the same solvent it appears at the VSI mole fraction of 0.70–0.80.

Taking into account changes that occur in the VSI content in the monomer mixture as the conversion grows from 0 to 70% (Table 4), we determined, according to [14], the probability of diad formation and the statistical-mean block length in the chains of VSI–BMA and VSI–BA copolymers prepared in pyridine at various conversions (Table 5), using the diagrams shown in Fig. 1.

Table 4 shows that the high reactivity of BMA and BA, which determines higher rate of their consumption in the reaction mixture, results in an enrichment of the monomer mixture with the less active monomer, VSI. Therefore, with increasing conversion, the probability of formation of M_1M_2 and M_2M_2 diads ($f_{12} = f_{21}$) grows, and that of formation of diads consisting of BMA or BA units (f_{22}) decreases. Also, with increasing conversion, the statistical-mean block lengths L_1 and L_2 approach each other (Table 5).

Tables 3–5 show that the highest probability of unit alternation, f_{12} = 0.349, in VSI–BA copolymers prepared in pyridine is observed at the VSI mole fraction in the monomer mixture equal to 0.7–0.8. The maximum probability of cross addition of units, f_{12} =

0.349, is attained at the VSI mole fraction of 0.79 and a 20–40% conversion.

The microstructure of VSI–BMA copolymers prepared in pyridine was analyzed similarly. The highest probability of unit alternation, f_{12} = 0.406, is observed at the VSI mole fraction in the monomer mixture equal to 0.7–0.9. The maximum probability of cross addition of units, f_{12} = 0.406, is attained at the VSI mole fraction of 0.87 and a 50–70% conversion.

The BSI–BMA copolymers prepared in pyridine are characterized by better alternation of units than the VSI–BA copolymers prepared in the same solvent. The maximum probability of unit alternation, $f_{12} = f_{21}$, is 0.406 for VSI–BMA copolymers and 0.349 for VSI–BA copolymers. The minimum difference between the mean block lengths L_1 and L_2 (ΔL) for the VSI–BMA copolymers is 0 at VSI mole fraction of 0.88–0.89 and $K \approx 70\%$ (Table 5). For the VSI–BA copolymers, the minimum ΔL is 0.01 at the VSI mole fraction of 0.79–0.80 and $K \approx 20\%$ (Table 5). This fact confirms the conclusion made in [5] that pyridine as a solvent ensures a better compositional uniformity of copolymers, compared to other solvents, e.g., dimethyl sulfoxide.

Our experimental results can be used in planning and simulation of ternary copolymerization of VSI with BA and BMA with the aim to obtain elastic films for medical and biological purposes.

CONCLUSIONS

(1) The kinetics of copolymerization of *N*-vinylsuccinimide with *n*-butyl methacrylate was studied for the first time, and the constants of copolymerization in pyridine were determined: $r_1 = 0.03 \pm 0.04$ and $r_2 = 1.79 \pm 0.04$.

(2) Application of the approximation procedure to data on monomer conversion and copolymer composition made it possible to determine the constants of copolymerization of *N*-vinylsuccinimide with *n*-butyl methacrylate and *n*-butyl acrylate in pyridine with an error factor of 0.0001–0.001.

REFERENCES

1. Lavrov, N.A., Shal'nova, L.I., and Nikolaev, A.F., *Zh. Prikl. Khim.*, 1997, vol. 70, no. 8, pp. 1356–1363.
2. Lavrov, N.A., Shal'nova, L.I., and Nikolaev, A.F., *Plast. Massy*, 2001, no. 10, pp. 5–9.
3. Shal'nova, L.I., Chudnova, V.M., and Trofimova, E.A., *Plast. Massy*, 1989, no. 11, pp. 29–34.
4. Lavrov, N.A., *Zh. Prikl. Khim.*, 2003, vol. 76, no. 9, pp. 1409–1414.
5. Lavrov, N.A., Sivtsov, E.V., and Pisarev, A.G., *Zh. Prikl. Khim.*, 2003, vol. 76, no. 7, pp. 1154–1159.
6. Lavrov, N.A., Sivtsov, E.V., and Nikolaev, A.F., *Zh. Prikl. Khim.*, 1998, vol. 71, no. 12, pp. 2055–2056.
7. Lavrov, N.A., Pisarev, A.G., and Sivtsov, E.V., *Obrabotka dannykh kinetiki radikal'noi (so)polimerizatsii komp'yuternymi metodami* (Computer Processing of Data on Radical (Co)polymerization)), St. Petersburg: Sankt-Peterb. Gos. Tekhnol. Inst. (Tekh. Univ.), 2003.
8. Ezrielev, A.I., Brokhina, E.L., and Roskin, E.S., *Vysokomol. Soedin., Ser. A*, 1969, vol. 11, no. 8, pp. 1670–1680.
9. Kelen, T. and Tüdös, F., *J. Macromol. Sci., Part A*, 1975, vol. 9, no. 1, pp. 1–27.
10. Rao, S.P., Ponzatnam, S., Kapur, S.L., and Lyer, P.K., *J. Polym. Sci., Polym. Lett. Ed.*, 1976, vol. 14, no. 9, pp. 513–516.
11. Gindin, L.M., Abkin, A.D., and Medvedev, S.S., *Dokl. Akad. Nauk SSSR*, 1947, vol. 56, no. 2, pp. 177–180.
12. Gindin, L.M., Abkin, A.D., and Medvedev, S.S., *Zh. Fiz. Khim.*, 1947, vol. 21, no. 11, pp. 1269–1287.
13. Lavrov, N.A., *Raschet cheredovaniya zven'ev v sopolimerakh* (Calculation of Unit Alternation in Copolymers), Leningrad: Leningr. Tekhnol. Inst. im. Lensoveta, 1988.
14. Lavrov, N.A., Sivtsov, E.V., and Pisarev, A.G., *Plast. Massy*, 2001, no. 11, pp. 13–14.

Russian Journal of Applied Chemistry, Vol. 77, No. 4, 2004, pp. 608–612. Translated from Zhurnal Prikladnoi Khimii, Vol. 77, No. 4, 2004, pp. 612–616.

MACROMOLECULAR CHEMISTRY AND POLYMERIC MATERIALS

Influence of the Molecular Structure of Comb-Shaped Photochromic Copolymers on Photoinduced Birefringence

E. B. Barmatov, A. V. Medvedev, and S. A. Ivanov

Lomonosov Moscow State University, Moscow, Russia

Received October 31, 2003; in final form, February 2004

Abstract—A series of mesomorphic and amorphous photochromic copolymers containing azobenzene groups were prepared. The emergence of induced birefringence in films of these copolymers under the action of plane-polarized laser light was studied.

Comb-shaped photochromic mesomorphic polymers (MPs) show promise as media for information recording and storage, as well as for application in various optical elements, including filters, polarizers, switches, etc. [1–3]. Photosensitive MPs are usually obtained from compounds comprising two basic structural elements, photochromic and mesogenic. The primary role in photoorientation of photochromic MPs under linearly polarized laser light belongs, undoubtedly, to photochromic moieties. Mesogenic groups in the mesomorphic copolymers (MCs) not only participate in photoorientation but also perform the following important functions. First, they are responsible for mesomorphic ordering, which in many cases allows significant improvement of the photoinduced order (birefringence enhancement effect [4, 5]). Second, the mesomorphic order substantially enhances the thermal stability of the photoinduced birefringence [6]. This allows preparation of photochromic MCs suitable as advanced information carriers.

Much progress has been achieved in physical chemistry of MPs comprising azobenzene photochromic moieties, but the influence of the chemical structure of photochromic and mesogenic groups on the photooptical properties of copolymers still remains to be elucidated. There are scarce published data on homologous series of comb-shaped MPs with varied length of the aliphatic spacer and invariant structure of the mesogenic units [7, 8]. At the same time, specifically studies of homologous series can provide quantitative information on how the chemical structure of comb-shaped MPs affects the magnitude and kinetic features of photoinduced birefringence.

The aim of this study was to elucidate how the molecular structure of comb-shaped photochromic MPs affects the kinetic features and magnitude of photoinduced birefringence. To this end, we synthesized comb-shaped mesomorphic and amorphous copolymers (ACS) P-1–P-6 with varied photochromic unit polarity and distance separating the azobenzene fragment and the polymer chain:

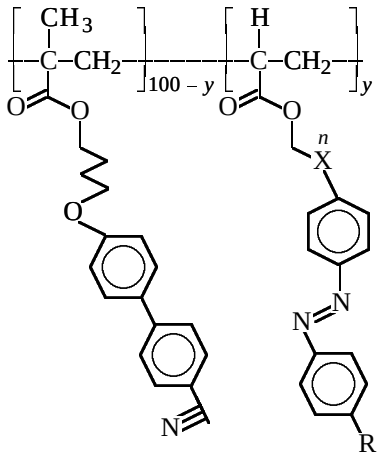

with no X, R = H , n = 0 (P-1); X = O, R = H, n = 4 (P-2); X = O, R = H, n = 10 (P-3); no X, R = CN, n = 0 (P-4); X = O, R = CN, n = 4 (P-5); and X = O, R = CN, n = 10 (P-6); and y = 21 ± 1 mol%.

EXPERIMENTAL

The copolymers were prepared by radical copolymerization from appropriate monomers in absolute tetrahydrofuran with azobis(isobutyronitrile) (AIBN) as initiator. The resulting copolymers were refluxed in ethanol for a long time to exhaustively remove oligomers and low-molecular-weight products. Microcalorimetric studies were carried out on a Mettler differen-

1070-4272/04/7704-0608 © 2004 MAIK "Nauka/Interperiodica"

tial scanning calorimeter (heating rate 10 deg min^{-1}), and microscopic examinations, on a POLAM-P-211 polarization microscope equipped with a Mettler FP-82 heating system. The molecular weight characteristics of the P-1–P-6 copolymers were determined by gel-permeation chromatography on a GPC-2 Waters instrument equipped with an LC-100 column and a Data Modul-370 data processing system. The measurements were made with a UV detector (solvent THF, 1 ml min^{-1}, 25°C; 100, 500, and 10^3 Å columns; calibration against polystyrene).

The kinetic features of the photoinduced birefringence were studied on the photooptical installation described in [9]. The vertically polarized "recording" beam from an argon laser (λ_{rec} = 488 nm, intensity I_0 = 0.035 W cm^{-2}) was directed toward the selected segment of the polymer film. To record the photoinduced alterations in the polymer film, the same segment of the sample was simultaneously illuminated with the probing laser beam from an He–Ne laser (λ_{sens} = 633 nm). The intensity of the probing beam that passed through the sample and analyzer was measured with a photodiode and a special recording system. The photoinduced birefringence Δn_{ind} was estimated from the phase shift $\varphi(\tau)$ between the probing beam components polarized in parallel and perpendicularly to the polarization direction of the recording beam. The absorption of the probing beam passing through the polymer was measured using the monitor channel.

The samples for photooptical measurements were prepared in a glass sandwich cell; the polymer layer thickness was adjusted with Teflon spacers (30 μ). We used amorphous or amorphized samples prepared by rapid cooling of the isotropic melt to the glassy state.

Phase characteristics of P-1–P-6 copolymers. Figure 1 shows the differential-scanning calorimetric (DSC) curves of the copolymers. The P-1 and P-4 copolymers are amorphous, as suggested by the absence of melting peaks of the mesomorphic phase in the DCS curves, as well as by the lack of optical anisotropy of the samples. Copolymer P-5 forms a nematic mesomorphic phase, and P-2, P-3, and P-6 copolymers, a smectic mesophase. The DCS curves of the MCs, recorded in the heating mode, exhibit an endothermic peak with the enthalpy of melting of 1.1–2.1 J g^{-1}. The glass transition points for P-1–P-6 copolymers lie within 61–74°C and are weakly dependent on the nature of the substituent in the azobenzene moiety. Table 1 summarizes the molecular-weight characteristics and phase characteristics of the copolymers.

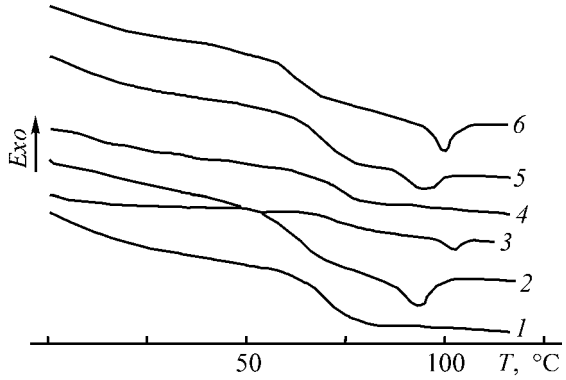

Fig. 1. (*1*–*6*) DCS curves of P-1–P-6 copolymers, recorded in the heating mode. (*T*) temperature.

Photooptical characteristics of the copolymers. To study the photooptical characteristics of the photochromic copolymers P-1–P-6, we recorded the curves of build-up of the photoinduced birefringence in the course of laser irradiation. Specifically, we recorded the time dependence of the phase shift φ/π between the probing beam components polarized parallel and perpendicular to the electric vector of the recording beam. Figure 2 shows a typical dependence of the phase shift on the irradiation time for the P-6 copolymer. For all the copolymers studied, the φ/π phase shift growth curves are typical of photochromic copolymers [1, 9, 10]. Laser irradiation is responsible for the emergence and build-up of the phase shift. Upon termination of irradiation, the birefringence decreases by 15–20% within 1000–3000 s, whereupon it remains unchanged for a long time.

Two segments are distinguishable in the birefringence build-up curves, namely, those corresponding to fast and a slow rise in birefringence (Fig. 2, curves *1*

Table 1. Molecular-weight characteristics, phase transition temperatures, heats of melting, and π–π^*-transition wavelengths for P-1–P-6 copolymers

Sample	$M_w \times 10^3$	M_w/M_n	Phase transition, °C (heat of melting, J g^{-1})	λ_{max}, nm
P-1	11.7	1.7	G 69I	326
P-2	15.5	1.6	G74S103(1.2)I	346
P-3	12.4	1.7	G59S88 (1.2)I	346
P-4	11.9	1.8	G72I	333
P-5	10.8	1.5	G67N97(1.1)I	365
P-6	16.5	1.8	G61S101(1.6)I	365

* M_w is the weight-average molecular weight; M_n, number-average molecular weight; G, glassy state; S, smectic phase; and I, isotropic melt.

Table 2. Characteristics and major kinetic parameters of P-1–P-6 copolymers used in photooptical experiments (laser light intensity 0.04 W cm^{-2}, 25°C)

Sample	Fast build-up segment			Slow build-up segment		
	C, J cm^{-2}	β	$\Delta n \times 10^4$	β	B, s$^{-\beta}$	$\Delta n \times 10^3$
P-1	0.21 ± 0.02	1 ± 0.01	8.8 ± 0.2	0.97 ± 0.05	0.0005 ± 0.0001	9.0 ± 0.3
P-2	0.13 ± 0.01	1 ± 0.01	4.7 ± 0.1	0.50 ± 0.03	0.0037 ± 0.0003	3.8 ± 0.2
P-3	0.22 ± 0.02	1 ± 0.01	11.6 ± 0.2	0.50 ± 0.03	0.01 ± 0.003	12.3 ± 0.4
P-4	0.18 ± 0.02	1 ± 0.01	5.3 ± 0.2	0.73 ± 0.04	0.0025 ± 0.001	4.0 ± 0.2
P-5	0.09 ± 0.01	1 ± 0.01	16.0 ± 0.3	0.66 ± 0.03	0.019 ± 0.001	30.7 ± 0.8
P-6	0.08 ± 0.01	1 ± 0.01	5.9 ± 0.2	0.52 ± 0.03	0.018 ± 0.0005	10.0 ± 0.4

Note. The birefringence Δn is given for the irradiation time of 2400 s.

and *2*). The first segment (Fig. 2, curve *1*) can be closely approximated by the exponential curve [9]

$$\varphi(\tau) = \frac{2\pi}{\lambda_{sens}} \frac{\Delta n_{max}}{\alpha} \left\{ \ln K - \int_1^K \exp\left[-\left(\frac{\hat{\tau}}{z} \right)^{\beta} \right] \frac{dz}{z} \right\}, \quad (1)$$

$$\hat{\tau} = \tau / t_0, \; C = t_g I,$$

where λ_{sens} = 633 nm is the probing beam wavelength; t_g, characteristic time of birefringence growth on the sample surface; α, absorption coefficient of the polymer film for the probing beam ($\ln K = \alpha d$); d, sample thickness; and β, constant in the Kohlrausch–Williams–Watts function

$$\Delta n = \Delta n_{max} \{ 1 - \exp[-(\tau/t)^{\beta}] \}. \quad (2)$$

We described the second segment of the birefringence build-up curve, corresponding to slow, linear, build-up of φ/π (Fig. 2, curve *2*), by the same function (1) for $\hat{\tau} \ll 1$:

$$\varphi/\pi = B\tau^{\beta}, \quad (3)$$

where B is a constant.

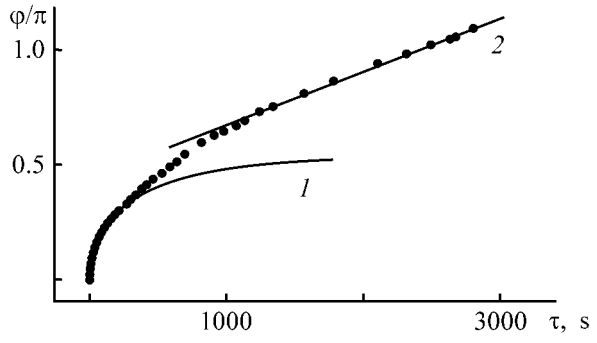

Fig. 2. Variation of the phase shift φ/π for P-6 copolymer in the course of laser irradiation (0.025 J cm^{-2} power). (τ) Time. Approximation of the segments corresponding to (*1*) slow and (*2*) fast birefringence build-up.

Table 2 summarizes the kinetic parameters of P-1–P-6 copolymers, calculated by Eqs.(1)–(3).

Data in Table 2 allow certain conclusions about the kinetic features of the photooptical behavior of the copolymers studied.

It is seen that, for copolymers whose molecules contain the cyano group (R = CN) of the azobenzene moiety (P-4–P-6), the rates in the fast and slow build-up segments of the birefringence curves exceed those of the copolymers with the substituent R = H (P-1–P-3). For example, the constant C [Eq. (1)] for P-3, which is inversely proportional to the birefringence build-up rate, was estimated at 0.22 J cm^{-2}. At the same time, for P-6 containing a polar substituent the constant C is much lower (0.08 J cm^{-2}). Similar trends were observed for the rates B in the slow build-up segments of the kinetic curves of the birefringence. The constants B of copolymers P-4–P-6 exceed those of P-1–P-3, for example, fivefold in the case of P-4 vs. P-1.

Broadening of the spectrum of the relaxation time β in the slow build-up stage suggests gradual complication of the photoorientation process with lengthening of the methylene spacer n. At the same time, β in the fast build-up stage is independent of n, which suggests only one birefringence build-up process in the initial stage of irradiation (up to 100 s). Most probably, this is photoorientation of the dye molecules in defective domains of the sample.

Let us discuss how the polarity of the terminal group R, as well as the length of the aliphatic spacer between the polymer chain and azobenzene moiety, affect the birefringence Δn. Notably, for both fast and slow build-up processes, the photoinduced birefringence of P-4–P-6 copolymers passes through a maximum. The largest birefringence is characteristic of

P-5. This unambiguously suggests a strong influence of the steric factor on the photoorientation process.

To explain the relationships revealed in this study, we will refer to papers by Ho *et al.* [11] and Meng *et al.* [12]. These authors noted that the polarity of the photochromic and mesogenic moieties of macromolecules strongly affect the parameters of the photoorientation process. This influence is the strongest when both the mesogenic and photochromic moieties in the copolymer contain polar cyano groups. Strong Coulomb interaction of the polar fragments increases the efficiency of transfer of the orienting action from the azonbenzene to mesogenic moiety, which suggests cooperativity of the motions of the photoactive groups of the dye and inert mesogenic moieties. At the same time, the birefringence of comb-shaped photochromic copolymers containing both polar and nonpolar side moieties was not enhanced. This allowed Natansohn *et al.* [11, 12] to conclude that, in the copolymer series studied, the deciding influence on the photoinduced birefringence is exerted by specifically dipole interactions between the side groups of the copolymer. The contribution from the cooperativity of the motions of these moieties is less significant.

As mentioned above, our results agree with the conclusions made in [11, 12] and also suggest the importance of dipole interactions between polar photochromic and mesogenic groups. Indeed, the strength of interaction of dipoles is inversely proportional to the cubed distance. Thus, with increasing distance between the photochromic and mesogenic moieties, the strength of their interaction and, hence, the efficiency of transfer of the orienting action from the photochrome to the mesogene will sharply decrease. Therefore, for P-5 copolymer comprising spacers with $n = 4$, the cooperative interaction between the photochromic azobenzene and mesogenic cyanobiphenyl moieties is the strongest, and P-5 is characterized by the largest birefringence. A decrease in the efficiency of interactions because of the less favorable steric arrangement of the interacting polar groups is responsible for much smaller birefringences in the case of P-4 and P-6 copolymers.

For another series of copolymers, P-1–P-3, containing a nonpolar azobenzene moiety we obtained unexpected results. In these copolymers, photoorientation is also strongly affected by the spacer length. However, in contrast to the above-mentioned relationships, the birefringence for P-2 ($n = 4$) copolymer is the smallest for both fast and slow build-up processes. This once again suggests the importance of dipole interactions and the predominance of the dipole factor over the steric factor. Moreover, we found that the maximum birefringence can be achieved for P-5 copolymer in which both factors are favorably combined.

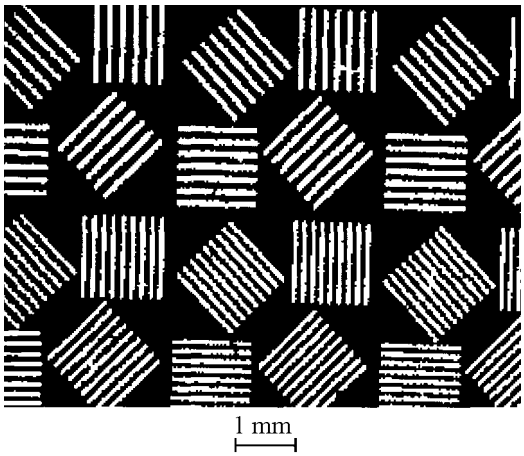

Fig. 3. Image of a standard array recorded on the copolymer P-3 film.

Let us discuss whether the mixtures studied by us are suitable, in principle, as media for optical recording and storage of information. Figure 3 shows as an example the image of a standard test-array obtained upon irradiation of the P-3 copolymer film with unfiltered light from a mercury lamp through a template. The image exhibits reasonable contrast and stability at room temperature.

CONCLUSIONS

(1) A series of comb-shaped photochromic copolymers were synthesized, which contain cyanobiphenyl mesogenic and azobenzene groups differing in the polarity and length of the aliphatic spacer ($n = 0, 4, 10$) between the azobenzene moiety and the polymer backbone.

(2) Kinetic parameters of the birefringence build-up depend on the mutual arrangement of the azobenzene and mesogenic groups, which is manifested in a noticeable influence of the spacer length n on the induced birefringence. For copolymers containing 4-cyanoazobenzene photochromic moieties, the greatest birefringence is achieved for a copolymer in which the mesogenic and photochromic groups are equidistant from the polymer backbone.

REFERENCES

1. *Polymers as Electrooptical and Photooptical Active Media,* Shibaev, V.P., Ed., Berlin: Springer, 1996.

2. Ichimura Kunihiro, *Chem. Rev.*, 2000, vol. 100, no. 5, pp. 1847–1874.
3. Delaire, J.A., and Nakatani Keitaro, *Chem. Rev.*, 2000, vol. 100, no. 5. pp. 1817–1846.
4. Zilker, S.J., Bieringer, T., Haarer, D., *et al.*, *Adv. Mater.*, 1998, vol. 10, no. 11, pp. 855–859.
5. Stracke, A., Wendoff, J.H., Janietz, D., and Mahlstedt, S., *Adv. Mater.*, 1999, vol. 11, p. 667.
6. Barmatov, E.B., Medvedev, A.V., Ivanov, S.A., and Shibaev, V.P., *Polym. Sci., Ser. A*, 2002, vol. 44, no. 1, pp. 50–59.
7. Labarthet, F.L., Freiberg, S., Pellerin, C., *et al.*, *Macromolecules*, 2000, vol. 33, no. 18, pp. 6815–6823.
8. Freiberg, S., Lagugne-Labarthet, F., Rochon, P., and Natansohn, A., *Macromolecules*, 2003, vol. 36, no. 8, pp. 2680–2688.
9. Shibaev, V.P., Kostromin, S.G., and Ivanov, S.A., *Vysokomol. Soedin., Ser. A*, 1997, vol. 39, no. 1, pp. 43–62.
10. Wua, Y., Kanazawaa, A., Shionoa, T., *et al.*, *Polymer*, 1999, vol. 40, no. 17, pp. 4787–4793.
11. Ho, M.-S., Natansohn, A., and Rochon, P., *Macromolecules*, 1996, vol. 29, no. 1, pp. 44–49.
12. Meng, X., Natansohn, A., Barrett, C., and Rochon, P., *Macromolecules*, 1996, vol. 29, no. 3, pp. 946–952.

Russian Journal of Applied Chemistry, Vol. 77, No. 4, 2004, pp. 613–617. Translated from Zhurnal Prikladnoi Khimii, Vol. 77, No. 4, 2004, pp. 617–621.

MACROMOLECULAR CHEMISTRY AND POLYMERIC MATERIALS

Statistical Analysis of the Microstructure and Mechanical Properties of Rolivsans in the Course of Thermal Curing

S. V. Bronnikov, B. A. Zaitsev, and T. E. Sukhanova

Institute of Macromolecular Compounds, Russian Academy of Sciences, St. Petersburg, Russia

Received August 8, 2003; in final form, November 10, 2003

Abstract—The reversible aggregation model was applied to analyze the electron-microscopic data for statistical ensembles of Rolivsan microdomains in the course of thermal curing. The experimentally established correlation between the average size of the microdomains in the ensembles and the dynamic Young modulus of the Rolivsan samples cured at different temperatures was interpreted in terms of the kinetic strength concept.

Rolivsans are polyfunctional monomeric–oligomeric systems whose molecules contain styrene-like and/or methacrylate terminal groups [1, 2]. In the course of curing, they form thermally stable cross-linked polymers of a new type, which find various engineering applications [3, 4].

As known [5–7], the polymer network yielded by three-dimensional copolymerization of the monomeric and oligomeric components of Rolivsan at 100–170°C is converted upon further heating (≥180°C) to a network with a much greater thermal stability. It fundamentally differs from the original (essentially, trivial) network both chemically and topologically; also, their supramolecular structure is different. The main structural unit of the new network of exhaustively cured Rolivsans can be represented as follows:

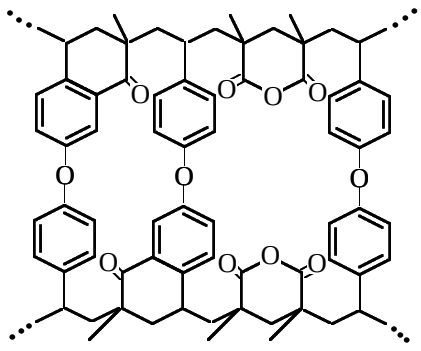

Naturally, rearrangement of such specific densely cross-linked methacrylates under the action of 4,4'-divinyldiphenyl oxide (analogue of *n*-divinylbenzene) into cross-linked polyether-ketones of the Tetralone type affects the properties of new thermosetting binders. In particular, cured Rolivsans surpass the known binders in thermal (softening point 270–330°C and over) and thermooxidative stability.

EXPERIMENTAL

Samples for studies were prepared by open pouring of MV-1 commercial Rolivsan [1–5] into 50 × 50 × 10 mm metallic or Teflon molds, followed by heating at a rate of 5 deg min^{-1} to the end curing temperatures T_0 (150, 160, 180, 200, and 250°C) in the following modes, °C/h: 150/5, 160/5, 170/5, 180/4, 200/4, and 250/9.

Prior to microstructural studies, the Rolivsan samples were cleaved at liquid nitrogen temperature to minimize the plastic deformation at failure. Then, the surfaces of low-temperature chips were etched in a high-frequency oxygen discharge plasma for 15–40 min, depending on T_0. Next, two-stage replicas were prepared by alternately depositing at an angle of 45° to the chip surface (oblique shadow-casting) [8] platinum (Pt) and carbon (C) layers. The Pt/C replicas were detached from the sample surface with an aqueous solution of polyacrylic acid, which was subsequently removed by placing the replicas in distilled water. Next, the Pt/C replicas in the form of thin (30–40 nm) films were deposited onto a copper grid, dried, and examined in a Tesla (Czech Republic) BS-500 transmission electron microscope at the ×20 000 magnification.

The dynamic Young modulus of the cured Rolivsan samples in the form of 34 × 20 × 8-mm parallel-

1070-4272/04/7704-0613 © 2004 MAIK "Nauka/Interperiodica"

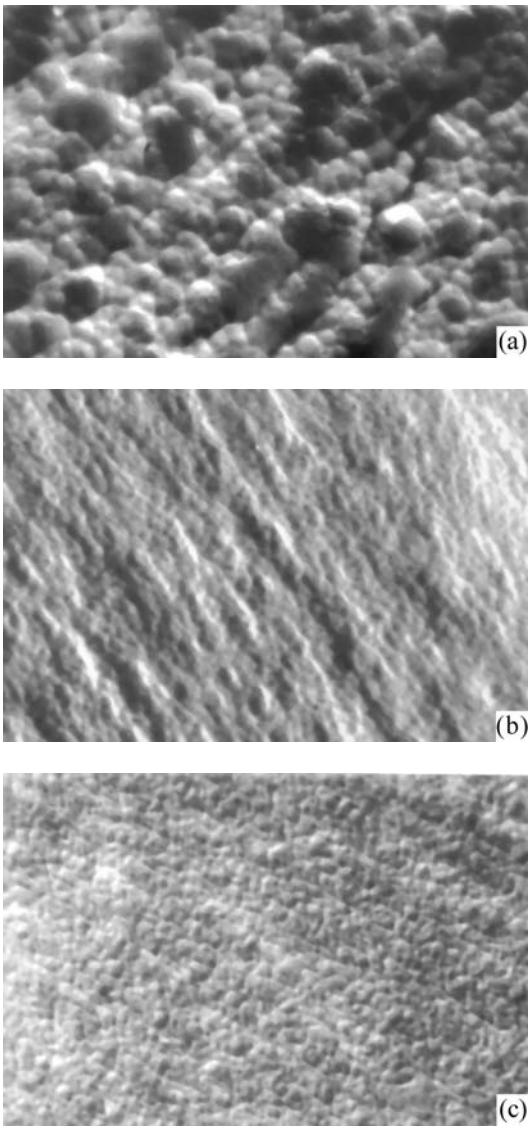

Fig. 1. Electron micrographs of the platinum-carbon replicas from the surface of the Rolivsan samples heated to (a) 150, (b) 190, and (c) 250°C.

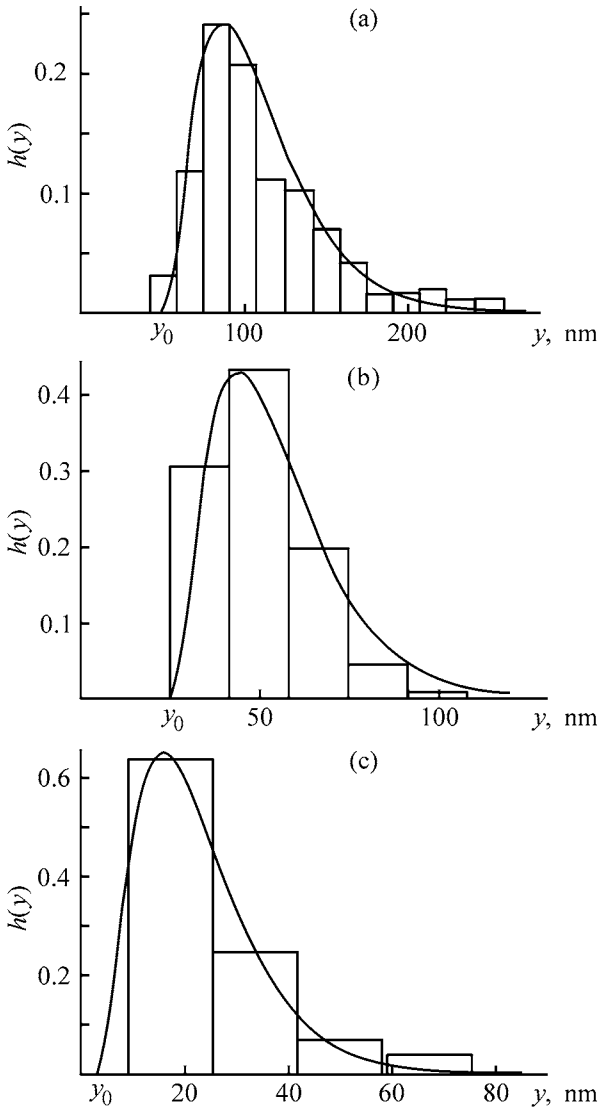

Fig. 2. Statistical distribution $h(y)$ of microdomains over the diameter y, on the surface of Rolivsan samples heated to (a) 150, (b) 190, and (c) 250°C.

epipeds was determined on a facility described in [9] at 20°C at the exciting vibration frequency of 72 Hz.

Figure 1 shows the electron micrographs of the Pt/C replicas from the etched surface of the low-temperature chips of the Rolivsan sample cured at T_0 = 150, 190, and 250°C. It is seen that, like for other cross-linked polymers [5, 6, 10], the surface microstructure of the samples is formed by a set of densely cross-linked microdomains (polymer grains, globules, microdomains) and intergranular layers characterized by a looser polymer network [11–13]. The domains have a close-to-spherical shape, and their linear size (diameter) varies with T_0.

Figure 2 shows the histograms derived from a statistical analysis of the microdomain diameters. From 500 to 4500 microdomains were analyzed in each micrograph. It is seen that, for each T_0, the statistical size distribution patterns for microdomains form common statistical ensembles. For analytical description of these ensembles, we used the reversible aggregation model.

Based on the general principles of chemical kinetics and equilibrium thermodynamics of irreversible processes, we obtained in terms of the reversible aggregation model an expression describing the statistical size distribution $h(y)$ of the structural formations, aggregates [14, 15]:

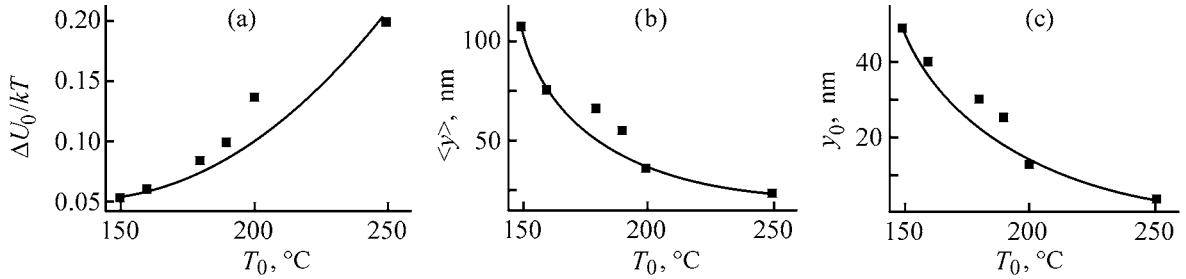

Fig. 3. (a) Reduced aggregation energy $\Delta U_0/kT$ and (b) average $\langle y \rangle$ and (c) nucleation y_0 diameters of microdomains in the Rolivsan samples vs. the heating temperature T_0.

$$h(y - y_0) = A(y - y_0)^m \exp\left[-\frac{(y - y_0)\Delta U}{kT}\right]. \quad (1)$$

Here, A is the normalizing coefficient; $(y - y_0)\Delta U_0$, J, aggregation energy which is a product of the reduced size of an aggregate in the ensemble $(y - y_0)$ by the standard aggregation energy ΔU_0, J m^{-1}; y_0, size of the smallest aggregate; k, Boltzmann constant; T, absolute temperature; and m, dimensionality of the space in which the aggregate grows (for the surface, $m = 2$).

The key role in expression (1) is played by the ΔU_0 parameter determining the equilibrium size distribution of the aggregates.

The lines in Fig. 2 represent the experimental statistical data obtained using Eq. (1). Our results suggest the applicability of the reversible aggregation model to the objects of study. Notably, this model has been successfully applied earlier to derive statistical size distributions for microdomains yielded by solid-phase intramolecular chemical transformations of polyamido acids of various chemical structures to polyimides [16–19]. Our results suggest that this model is suitable for describing the kinetics of various solid-state chemical reactions.

A practically important characteristic of the statistical distribution is the average size of an aggregate in the ensemble, which is defined as the normalized expectancy:

$$\langle y \rangle - y_0 = \frac{\int_0^\infty (y - y_0)\, h(y - y_0)\mathrm{d}y}{\int_0^\infty h(y - y_0)\mathrm{d}y} = \frac{(m + 1)kT}{\Delta U_0} = \frac{3kT}{\Delta U_0}. \quad (2)$$

Figure 3 shows how the reduced standard aggregation energy $\Delta U_0/kT$, as well as the average ($\langle y \rangle$) and nucleation (y_0) diameters of the microdomains, vary with T_0. It is seen that, upon high-temperature heating, the supramolecular structure of cured Rolivsan gets more uniform: $\Delta U_0/kT$ increases approximately fivefold with temperature raized from 150 to 250°C, which means that the statistical distribution of the diameters of the microdomains narrows, and $\langle y \rangle$ and y_0 decrease ten- and fivefold, respectively.

The fact that the size of the polymer grains diminishes in the course of high-temperature curing of Rolivsans is evidently due to chemical and topological rearrangements in the polymer networks constituting these grains. These rearrangements involve scission of polymer chains and cross-links, accompanied by (poly)cyclization, cross-linking, and degradation reactions [5–7]. These processes are responsible for decreased size and denser packing of the polymer grains and forthe resulting optimization of the supramolecular structure.

The optimization of the structure of Rolivsan in the course of thermal curing is confirmed by the results of dynamic mechanical measurements, shown in Fig. 4. It is seen that, with rising T_0, the dynamic Young modulus E' of the Rolivsan samples tends to increase, most steeply at temperatures corresponding to formation of the primary network (T_0 = 150–170°C). To establish the practically important correlation between the microstructure and the macroscopic characteristics, we examined the $\langle y \rangle(T_0)$ and $E'(T_0)$ dependences.

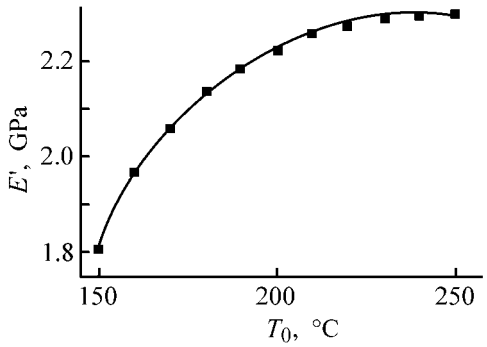

Fig. 4. Dynamic Young modulus E' of the Rolivsan samples vs. the heating temperature T_0.

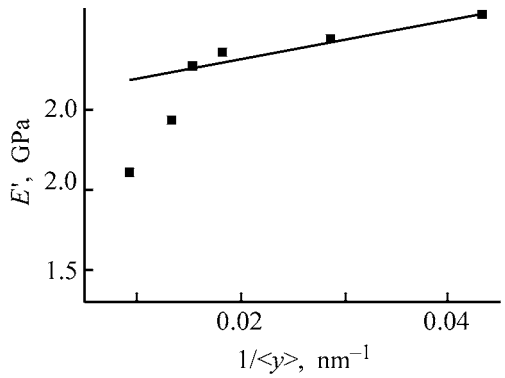

Fig. 5. Dynamic Young modulus E' of Rolivsan samples vs. the inverse average diameter $1/\langle y\rangle$ of microdomains in the course of curing.

In terms of the kinetic failure concept, the strength of a solid, σ, is determined by the characteristics of the interatomic bonds (elasticity E, equilibrium length r_0, and ultimate strain ε^*), free path length of phonons Λ, failure activation energy ΔU_0, and the time before failure τ [20–22]:

$$\sigma = \frac{Er_0\varepsilon^*}{\Lambda}\left(1 - \frac{kT}{U_0}\ln\frac{\tau}{\tau_0}\right), \quad (3)$$

where $\tau_0 \approx 10^{-13}$ s. It can be suggested that, in amorphous substances, including polymers, phonons are scattered at the boundaries of structural (supramolecular) formations, i.e., that the parameter Λ is determined by the average diameter of the microdomains $\langle y\rangle$:

$$\Lambda \cong \langle y\rangle. \quad (4)$$

Vettegren' *et al.* [23, 24] found that the failure and the relaxation of stresses have a common thermal-fluctuation nature, which is manifested in identical kinetic equations describing the temperature and time dependences of the strength and the Young modulus. The common nature of the processes of interest is reflected by the known empirical equation, which relates the dynamic Young modulus E' and the strength [25]:

$$E' = A\sigma + C, \quad (5)$$

where $A \cong 0.1$ and C are empirical parameters. Taking into account Eqs. (3) and (4), we write Eq.(5) as

$$E' = \frac{0.1Er_0\varepsilon^*}{\langle y\rangle}\left(1 - \frac{kT}{U_0}\ln\frac{\tau}{\tau_0}\right) + C = \frac{B}{\langle y\rangle} + C, \quad (6)$$

where

$$B = 0.1Er_0\varepsilon^*\left(1 - \frac{kT}{U_0}\ln\frac{\tau}{\tau_0}\right).$$

Equation (6) was tested in the E'–$1/\langle y\rangle$ coordinates, as illustrated by Fig. 5. It is seen that the experimental data can be fitted with a linear dependence represented by Eq. (6). The fact that the first two points (corresponding to T_0 150 and 160°C) fall out of this dependence is evidently due to the lower ductility (Er_0 parameter) of the polymer chain in the primary network of a weakly cured Rolivsan, compared to that in the final stage of high-temperature curing (densely cross-linked network).

CONCLUSIONS

(1) In the course of thermal curing, microdoamins in Rolivsan form statistical ensembles which can be described in terms of the reversible aggregation model.

(2) With increasing curing temperature, the statistical size distribution parameters of the domains in Rolivsan exhibit the following trends: The aggregation energy tends to grow, and the average and nucleation sizes of the microdomains, to decrease.

(3) A weak inverse proportionality was revealed between the average size of the microdomains and the dynamic Young modulus of thermally cured Rolivsan samples; it was explained in terms of the kinetic strength concept.

REFERENCES

1. Zaitsev, B.A., Khramova, G.I., and Tsygankova, T.S., Abstracts of Papers, *VIII Mezhdunarodnaya konferentsiya "Oligomery-2002"* (VIII Int. Conf. "Oligomers-2002"), Moscow–Chernogolovka, 2002, p. 194.
2. Zaitsev, B.A., Khramova, G.I., and Tsygankova, T.S., *Zh. Prikl. Khim.*, 2003, vol. 76, no. 4, pp. 658–662.
3. Zaitsev, B.A., Khramova, G.I., Dantsig, A.S., *et al.*, *Plast. Massy*, 1981, no. 9, pp. 12–13.
4. Zaitsev, B.A., Khramova, G.I., Tsygankova, T.S., *et al.*, *Mekh. Kompoz. Mater.*, 1982, no. 5, pp. 775–778.
5. Zaitsev, B.A., Relationships in Formation, Structure, and Properties of Polyarylenes, *Doctoral Dissertation*, Leningrad, 1983.
6. Zaitsev, B.A., *Sintez, strutura i svoistva polimerov* (Synthesis, Structure, and Properties of Polymers), Koton, M.M., Ed., Leningrad: Nauka, 1989.
7. Zaitsev, B.A., Abstracts of Papers, *VIII Mezhdunarodnaya konferentsiya "Oligomery-2002"* (VIII Int. Conf. "Oligomers-2002"), Moscow–Chernogolovka, 2002, p. 193.
8. *Techniques for Electron Microscopy*, Kay, D., Ed., Oxford: Blackwell, 1961.
9. Polikarpov, Yu.I., Rudakov, A.P., and Bessonov, M.I.,

Zavod. Lab., 1976, vol. 42, no. 12, pp. 1517–1519.

10. Lukasov, A.A., Zaitsev, B.A., Kenunen, I.V., *et al.*, *Mekh. Kompoz. Mater.*, 1988, no. 5, pp. 771–779.
11. Irzhak, V.I., Rozenberg B.A., and Enikolopyan, N.S., *Setchatye polimery* (Network Polymers), Moscow: Nauka, 1979.
12. Berlin, A.A., Korolev, G.V., Kefeli, T.Ya., *et al.*, in *Akrilovye oligomery i materialy na ikh osnove* (Acrylic Oligomers and Materials Thereof), Moscow: Khimiya, 1983, pp. 57–72.
13. Korolev, G.V., Mogilevich, M.M., and Golikov, I.V., *Setchatye poliakrilaty* (Network Polyacrylates), Moscow: Khimiya, 1995.
14. Kilian, H.G., Metzler, R., and Zink, B., *J. Chem. Phys.*, 1997, vol. 107, pp. 8697–8714.
15. Kilian, H.G., Köpf, M., and Vettegren, V.I., *Prog. Colloid Polym. Sci.*, 2001, vol. 117, pp. 172–181.
16. Bronnikov, S.V., Sukhanova, T.E., and Laius, L.A., *Vysokomol. Soedin., Ser. A*, 2002, vol. 44, no. 6, pp. 940–946.
17. Bronnikov, S.V., Sukhanova, T.E., Meleshko, T.K., *et al.*, *Zh. Prikl. Khim.*, 2003, vol. 76, no. 5, pp. 829–832.
18. Bronnikov, S.V., Sukhanova, T.E., and Goikhman, M.Ya., *Zh. Prikl. Khim.*, 2003, vol. 76, no. 6, pp. 995–999.
19. Bronnikov, S. and Sukhanova, T., *Image Anal. Stereol.*, 2003, vol. 22, no. 2, pp. 105–111.
20. Zhurkov, S.N., *Fiz. Tverd. Tela*, 1983, vol. 25, no. 10, pp. 3119–3123.
21. Petrov, V.A., Bashkarev, A.Ya., and Vettegren', V.V., *Fizicheskie osnovy prognozirovaniya dolgovechnosti konstruktsionnykh materialov* (Physical Basics of Predicting the Service Life of Structural Materials), St. Petersburg: Politekhnika, 1983.
22. Tsoi, B., Kartashov, E.M., and Shevelev, V.B., *Prochnost' i razrushenie polimernykh plenok i volokon* (Strength and Failure of Polymer Films and Fibers), Moscow: Khimiya, 1999.
23. Vettegren', V.I., Bronnikov, S.V., and Frenkel, S.Ya., *Vysokomol. Soedin., Ser. A*, 1984, vol. 26, no. 5, pp. 939–945.
24. Bronnikov, S.V., Vettegren', V.I., Korzhavin, L.N., *et al.*, *Vysokomol. Soedin., Ser. A*, 1986, vol. 28, no. 9, pp. 1963–1970.
25. Perepechko, I.I., *Akusticheskie metody issledovaniya polimerov* (Acoustic Methods of Investigation of Polymers), Moscow: Khimiya, 1973.

Russian Journal of Applied Chemistry, Vol. 77, No. 4, 2004, pp. 618–621. Translated from Zhurnal Prikladnoi Khimii, Vol. 77, No. 4, 2004, pp. 622–625.

MACROMOLECULAR CHEMISTRY AND POLYMERIC MATERIALS

Chemical Modification of Polypropylene with Isocyanate–ε-Caprolactam Mixtures

A. M Gafarov, S. S. Galibeev, A. M. Kochnev, and V. P. Arkhireev

Kazan State Technological University, Kazan, Tatarstan, Russia

Received October 3, 2003; in final form, February 2004

Abstract—Modification of polypropylene with isocyanate–ε-caprolactam mixtures was studied. The effect of these mixtures as influenced by the sequence of introduction of their components was examined.

Physical and chemical modification of polypropylene (PP) is performed to obtain PPs with required performance and process properties, to improve their chemical and supramolecular structure formed under uncontrollable production conditions, and to restore or change the properties of spent articles for their repeated use [1].

In some cases, polypropylenes are modified with mixtures of reactive compounds, as modification with individual additives does not ensure the required result. Previously [2], we have shown that isocyanate (IC)-epoxide (EP) binary mixtures used as modifiers for polyolefins (PO) synergistically affect both the heat resistance and the strength of the samples. This is due to grafting of homo- or copolymers of IC and EP to the terminal unsaturated bonds of PO [3–5].

Thus, a search for other binary systems capable of copolymerization under conditions of PP reprocessing is a topical problem. Among these systems are mixtures of aromatic and aliphatic diisocyanates with ε-caprolactam (ε-CL). Our previous studies have shown that these substances can copolymerize by the anionic mechanism in the presence of sodium organic compounds. The strength and thermal properties of the resulting copolymer can be varied in a wide range [6].

The aim of this study was to examine modification of PP with mixtures of IC [tolulene-2,4-diisocyanate (TDI), diphenylmethane-4,4'-diisocyanate (MDI), and product of reaction of polyoxymethyleneglycol with TDI (SKU-PFL)] with ε-CL, to determine the optimal concentrations, and to develop an efficient procedure for introduction of these modifiers.

EXPERIMENTAL

The IR spectra of PP modified with ε-CL-TDI mixture contain a new band at 3400–300 cm^{-1}, assigned to the N–H bonds of amide and urethane groups formed in opening of the lactam ring; and also the band at 1680–1620 cm^{-1} [–C(O)–N< in the ternary imide group, formed by the rupture of the N=C bond in isocyanate] (Fig. 1). In addition, the band of terminal unsaturated bonds of PP at 888 cm^{-1} is weakened owing to the reaction with isocyanate (Table 1).

The reaction of PP with the binary mixtures probably involves two steps. The first is copolymerization of IC with ε-CL by the anionic mechanism to form

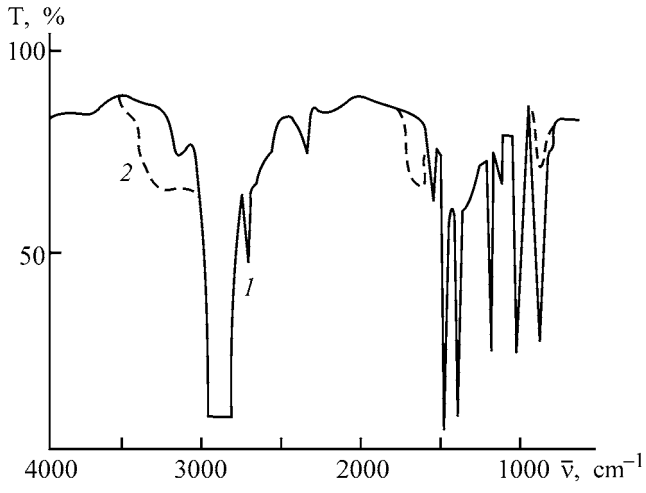

Fig. 1. IR spectra of (*1*) initial PP and (*2*) PP modified with 3 wt % of ε-CL–TDI mixture (1 : 1 weight ratio). (T) Transmission and ($\bar{\nu}$) wave number.

1070-4272/04/7704-0618 © 2004 MAIK "Nauka/Interperiodica"

amides, and the second is grafting of the resulting copolymers via unreacted isocyanate groups to unsaturated bonds of PP.

We studied three sequences of modifier introduction: (1) IC is added to a PP melt, a sample is rolled for 5 min, and ε-CL is added; (2) ε-CL is introduced and then IC is introduced in 5 min; and (3) IC and ε-CL are added simultaneously. Anionic copolymerization of IC and ε-CL was catalyzed by sodium caprolactam.

Since the activities of the modifiers with respect to PO differ, different polymeric structures grafted to PP should be formed at different introduction sequences of the modifier components.

In the first case, IC homopolymerizes to form relatively high-molecular-weight fragments consisting of tertiary polyamides units that can be added via unreacted functional groups to multiple bonds of PP. Introduction of ε-CL enlarges the grafted fragments by reaction with free iocyanate groups to form amide structures.

Since ε-CL ring is not opened in the presence of Na-CA [8], chemical reactions occurring in PP in the case of the second and third introduction sequences are relatively complex. Intense homopolymerization of ε-CL is activated by diisocyanates or *N*-acetylcaprolactam [9]. Hence, ε-CL does not change in the course of the second sequence until diisocyanate is added. In the presence of diisocyanate, ε-CL copolymerizes with lactam to form copolyamides capable of addition via free isocyanate groups to unsaturated bonds of PP.

Thus, the polymer grafted to PP with the first sequence of modifier introduction has mainly the block structure (it consists of tertiary polyimide units bound with the macromolecule via amide groups), whereas the structure of the polymer grafted with the second and the third sequence consists of alternating amide and tertiary imide units.

As can be seen from Table 2, samples with the best performance and process properties were obtained by simultaneous addition of the modifiers.

The ultimate stress σ_u of the samples modified by simultaneous addition of the modifiers is higher than that of the samples prepared by the separate addition of the components. Modification with MDI does not change σ_u and that with ε-CL even decreases σ_u from 34 to 31 Mpa, whereas introduction of a mixture of these compounds increases σ_u to 38 MPa. When MDI is replaced with TDI in the mixture, σ_4 increases to 42.5 MPa (Fig. 2). Introduction of a modifier mixture increases the melt flow index of a polymer (MFI). However, the viscosity of the melt also decreases

Table 1. Change in the content of terminal vinylidene bonds in PP after modification with IC–ε-CL* system

Modifier	log I_{888} : log I_{1380}
–	0.900
3wt % ε-CL	0.900
2 wt % SKU-PFL + 1 wt % ε-CL, 1	0.660
2 wt % 2,4-2,6-TDI + 1 wt % ε-CL	0.685

* I_{888} and I_{1380} are the intensities of the absorption bands at 888 (out-of-plane bending vibrations of the terminal vinylidene group) and 1380 cm^{-1} (symmetrical bending vibrations of the methyl groups), respectively [7].

Table 2. Ultimate stress σ_u of PP modified with MDI and ε-CL introduced in different modes*

Composition content, wt %			σ_u, MPa		
PP	MDI	ε-CL	A	B	C
100	–	–	34.0	33.4	34.0
98	–	2	33.4	33.4	33.4
98	2	–	33.7	33.7	33.7
99	–	1	34.0	34.0	34.0
99	1	–	33.3	33.3	33.3
97	2	1	32.0	36.8	32.5
97	1	2	32.4	36.5	35.8
98	1	1	34.2	34.5	38.5

* (A) IC added first, (B) ε-CL added first, and (C) IC and ε-CL added simultaneously.

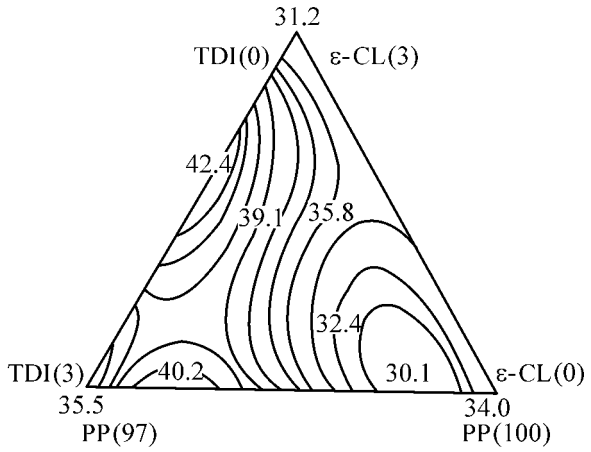

Fig. 2. Composition-ultimate stress diagram for PP + TDI + ε-CL (simultaneous addition of TDI and ε-CL). The weight content of the components is in parentheses TDI, PP, ε-CL.

Table 3. Melt flow index of molten PP modified with CI and ε-CL

Composition, wt %			MFI, $g \times 10^{-1}$ min, with indicated IC		
PP	IC	ε-CL	MDI	TDI	SLU-PFL
100	–	–	2.8	2.8	2.8
98	–	2	3.7	3.7	3.7
98	2	–	3.0	3.7	4.4
99	–	1	3.2	3.2	3.2
99	1	–	2.9	3.0	3.8
97	2	1	4.3	8.1	3.6
97	1	2	3.2	8.0	4.0
98	1	1	3.4	8.5	6.0

Table 4. Induction period τ_{ind} and rate v_{ox} of autooxidation of PP modified with MDI and ε-CL

Composition, wt %			τ_{ind}, min	v_{ox}
PP	MDI	ε-CL		
100	–	–	23	1.7
99	–	1	23	1.5
99	1	–	33	2.0
98	1	1	54	0.8

Table 5. Activation barrier of failure, U_0, and ultimate tensile stress σ_u of PP modified with TDI and ε-CL

Composition, wt %			U_0, kJ mol^{-1}	σ_u, MPa
PP	TDI	ε-CL		
100	–	–	11.2	34.2
100	0	3	11.0	34.8
97	0.2	2.8	11.6	36.3
97	0.3	2.7	12.1	37.3
97	0.6	2.4	12.5	37.2
97	2.7	0.3	12.9	36.6
97	2.8	0.2	12.4	35.9
97	3	0	11.6	36.1

after introduction of IC in amount from 1 to 2 wt % (Table 3).

Modification with the binary mixtures improves also the following thermal properties of PP: induction period τ_{ind} and rate v_{ox} of autooxidation, temperature of 5 and 50% weight loss T_5 and T_{50}, oxidation onset temperature T_{onset}, and equilibrium oxidation temperature T_{ox} (Tables 4, 5). Introduction of a mixture of 1 wt % MDI and 1 wt % ε-CL increases τ_{ind} by 21 min, whereas introduction of 1 wt % MDI increases τ_{ind} by only 10 min. Addition of 1 wt % ε-CL has no effect on this parameter.

The most prominent result of modification with the binary mixtures is a decrease in v_{ox}. The oxidation rate is determined from the slope of the oxidation curve. Oxidation of PP modified with almost all the mixtures examined is slower than that of initial PP and PP modified with IC and ε-CL taken separately (Table 4).

Previously, we have shown that the structure and properties of IC–ε-CL copolymer prepared in the presence of anionic initiators substantially depend on the monomer ratio [7, 10]. In this study, we modified PP with IC–ε-CL binary mixtures with different weight ratios of the components.

As can be seen from Table 5, the flexibility of the macromolecules (estimated from the change in the activation barrier of failure U_0) decreases, and hence the ultimate stress increases.

This is due to the fact that the content of tertiary imide units (which are more rigid than the amide units) in the grafted copolymer increases with increasing IC concentration in the modifying system. In addition, since IC is a bifunctional compound, a more branched copolymer is formed with increasing IC concentration. As a result, the mobility of the grafted macromolecule decreases owing to steric hindrance.

A slight decrease in the ultimate stress after modification with the mixtures with a high IC content (Table 5) is due to a strong acceleration of copolymerization of IC with ε-CL upon PP reprocessing. Clearly, in this case, the number of steps of addition of the isocyanate groups to the double bonds of PO decreases, which deteriorates the modification efficiency.

CONCLUSIONS

Polypropylene was modified with isocyanate–ε-caprolactam mixtures. A synergistic increase in the strength, viscosity, and thermal stability of the modified polymer was observed. We suggest that this is due to the reaction of isocyanate–ε-caprolactam copolymers with unsaturated bonds of polypropylene.

REFERENCES

1. Kochnev, A.M. and Galibeev, S.S., *Izv. Vyssh. Uchebn. Zaved., Khim. Khim. Tekhnol.*, 2003, vol. 46, no. 4, pp. 3–10.

2. Spiridonova, R.R., Galibeev, S.S., Kochnev, A.M., and Arkhireev, V.P., *Zh. Prikl. Khim.*, 2003, vol. 76, no. 2, pp. 298–303.
3. Galibeev, S.S., Influence of Small Additions of Chemically Reactive Compounds on the Efficiency of Modification of Polyolefins, *Cand. Sci. Dissertation*, Kazan, 2000.
4. Shageeva, F.T., Influence of Iscocyanates and Oligourethanes on the Efficiency of Modification of the Structure and Properties of Polyolefins, *Cand. Sci. Dissertation*, Kazan, 1987.
5. Shkalikova, R.R., Trofimov, P.V., Galibeev, S.S., and Kochnev, A.M., Abstracts of Papers, *V Mezhdunarodnaya konferentsiya po intensifikatsii neftekhimicheskikh protsessov "Neftekhimiya-99"* (V Int. Conf. on Intensification of Petrochemical Processes "Petrochemistry-99"), Nizhnekamsk, 1999, pp. 94–95.
6. Bellamy, L.J., *The Infra-red Spectra of Complex Molecules*, London: Methuen, 1954.
7. Galibeev, S.S., Arkhireev, V.P., Varnyagina, O.V., *et al.*, *Izv. Vyssh. Uchebn. Zaved., Khim. Khim. Tekhnol.*, 2003, vol. 46, no. 4, pp. 88–90.
8. *Entsiklopediya polimerov* (Encyclopedia of Polymers), Kabanov, V.A., Ed, Moscow: Sovetskaya Entsiklopediya, 1974, vol. 2.
9. Nikolaev, A.F., *Tekhnologiya plasticheskikh mass* (Technology of Plastics), Leningrad: Khimiya, 1977, p. 279–281.
10. Barnyaguina, O., Fofanova, O., Galibeev, S., and Archireev, V., *Int. Fachtagung "Polymerwerkstoff 2002,"* Halle (Saale), Sept. 25–27, 2002, pp. 45–46.

Russian Journal of Applied Chemistry, Vol. 77, No. 4, 2004, pp. 622–628. Translated from Zhurnal Prikladnoi Khimii, Vol. 77, No. 4, 2004, pp. 626–631.

MACROMOLECULAR CHEMISTRY AND POLYMERIC MATERIALS

Flocculation Properties of Polyelectrolytes Based on 2-(*N*,*N*-Dimethyl-*N*-Benzylammonio)ethyl Methacrylate Chloride

O. O. Kotlyarevskaya, V. A. Navrotskii, M. V. Orlyanskaya, A. V. Navrotskii, and I. A. Novakov

Volgograd State Technical University, Volgograd, Russia

Received October 22, 2003; in final form, January 2004

Abstract—Precipitation of a model kaolin suspension and dehydration of the excess active sludge were studied as influenced by copolymers of 2-(*N*,*N*-dimethyl-*N*-benzylammonio)ethyl methacrylate chloride and its copolymers with acrylamide and 2-(*N*,*N*,*N*-trimethylammonio)ethyl methacrylate methyl sulfate.

Hydrophilic cationic polyelectrolytes based on aminoalkyl (meth)acrylates and their ammonium salts are promising reagents for water treatment [1–3]; among them, poly-2-(*N*,*N*,*N*-trimethylammonio)ethyl methacrylate methyl sulfate, poly-2-(*N*,*N*,*N*-trimethylammonio)ethyl methacrylate chloride and their copolymers with acrylamide are the most widely used compounds. The flocculation power of copolymers simultaneously containing ionic groups and bulky hydrophobic fragments is also of particular importance. It is expected that the flocculation power will increase with enhancement of the polymer-polymer hydrophobic interactions.

In this study, we examined the flocculation power of poly-2-(*N*,*N*-dimethyl-*N*-benzylammonio)ethyl methacrylate chloride (poly-DMAEMA · BC) and copolymers of DMAEMA with nonionic acrylamide (AA) and cationic 2-(*N*,*N*,*N*-trimethylammonio)ethyl methacrylate methyl sulfate (DMAEMA · DMS) using model and real dispersed systems.

EXPERIMENTAL

Poly-DMAEMA · BC and poly-DMAEMA · DMS were synthesized by the ampule procedure (2 M monomer concentration) in aqueous solution at 25 ± 0.5°C. The monomers were prepared by alkylation of dimethylaminoelthyl methacrylate with benzyl chloride and dimethyl sulfate at 0–3°C in acetone with subsequent recrystallization from acetone-acetonitrile mixture; acrylamide was additionally purified by recrystallization from acetone. Copolymerization of DMAEMA · BC with DMAEMA · DMS and AA was performed in aqueous solution at 25 ± 0.5°C at various initial monomer ratios. Polymerization was carried out to 96–98% conversion. *tert*-Butylperoxy-2-propanol initiator was prepared by the procedure described in [4], with subsequent vacuum sublimation. According to the data of potentiometric titration for chloride ions, the copolymer composition corresponded to that of the monomeric mixture. The viscosity of dilute solutions was measured using an Ubbelohde viscometer at 30°C in the presence of sodium chloride (0.1–0.6 M). The intrinsic viscosity was determined by extrapolation of η_{sp}/c to $c \to 0$.

As model dispersion, we used an aqueous kaolin suspension (KSD brand, 7×10^{-6} m particle size) with the concentration of the dispersed phase of 0.8 wt %, which eliminates the effect of hindered sedimentation [5]. The flocculant concentrations were varied in the 0–40 mg g^{-1} range. The flocculation was carried out in 250-ml glass cylinders. The suspensions after polyelectrolyte addition were mixed in sealed vessels with disc stirrers for 2 min (0.3 s^{-1} frequency). After storage for 60 min, the optical density *D* of the supernatant was measured on a KFK-3 device at λ = 490 nm (distilled water reference). The supernatant turbidity τ was calculated from the following expression:

$$\tau = 2.3Dl^{-1}, \quad (1)$$

where *l* is the cell length (cm).

Using the results of measurements, we calculated the optimal polyelectrolyte concentrations c_{opt}, provid-

1070-4272/04/7704-0622 © 2004 MAIK "Nauka/Interperiodica"

Table 1. Properties of homopolymers

Sample	Polymer unit	[η], dl g^{-1} (in 0.1 M NaCl)
PE-2	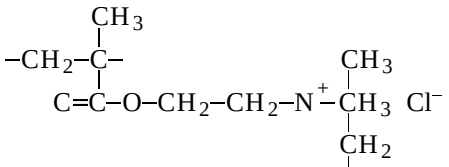	4.2
PE-7		7.0
PE-6.5	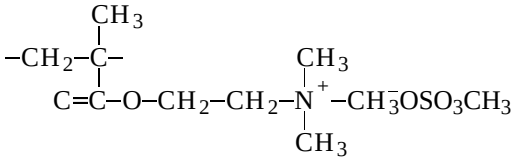	6.5

ing the greatest decrease in the supernatant turbidity, and evaluated the clarification effect D_τ from Eq. (2)

$$D_\tau = \tau_0/\tau - 1, \quad (2)$$

where τ_0 and τ are the supernatant turbidities in the absence of additives and after polyelectrolyte addition, respectively.

The flocculant activity was determined from the following expression:

$$\lambda = D_\tau/c_p^{-1}, \quad (3)$$

where c_p is the polymer concentration.

To study the precipitate dehydration, we used the active sludge from installations for biological treatment of household wastes (Volgogradvodokanal Municipal Unitary Enterprise). The flocculant solution (0.1% concentration) was added to the active sludge (100 ml), and the mixture was stirred by tenfold overflow. After settling for 30 s, the precipitate was filtered off and additionally squeezed for 1 min under a 5-kg load. The water content in the cake was determined by gravimetry [6]. The efficiency of the active sludge dehydration, D_w, was determined as follows:

$$D_w = W_0/W - 1, \quad (4)$$

where W_0 and W are the contents of water in the initial sludge and in the squeezed precipitate upon addition of a certain portion of the polyelectrolyte, respectively.

The approximate intensity of the intermolecular hydrophobic interactions can be evaluated from the behavior of the polyelectrolyte in aqueous salt solutions. The viscometric data (Fig. 1) showed that, with increasing salt concentration in the 0.1–0.6 M range, the thermodynamic quality of the solvent becomes worse, which is confirmed by a nonlinear decrease in the intrinsic viscosity of poly-DMAEMA · BC. According to the modern concepts, this is accompanied by a decrease in the effective charge of macroions and in the number of the polymer–solvent contacts and by an increase in the number of intramolecular contacts, which results in compaction of macromolecular globules. As for poly-DMAEMA · DMS, its intrinsic viscosity also decreases in the above concentration range, but the [η]–C_{NaCl} dependence is characterized by the minimum viscosity of 3.25 dl g^{-1}, corresponding to the conformation of the uncharged globules. In con-

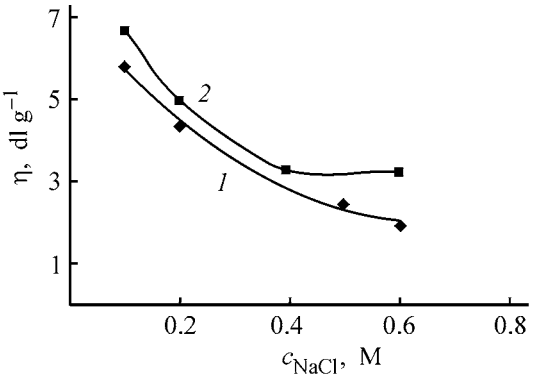

Fig. 1. Intrinsic viscosity of polyelectrolyte η as influenced by the inorganic salt concentration c_{NaCl} in solution. (*1*) PE-7 and (*2*) PE-6.5.

Table 2. Properties of DMAEMA · BC copolymer samples

Sample	*c*, mol %			[η], dl g^{-1}	Sample	*c*, mol %			[η], dl g^{-1}
	DMAEMA · BC	DMAEMA · DMS	AA			DMAEMA · BC	DMAEMA · DMS	AA	
25-AA	75	0	25	4.4	25-DMS	75	25	0	4.6
50-AA	50	0	50	5.3	50-DMS	50	50	0	6.1
75-AA	25	0	75	7.5	75-DMS	25	72	0	6.9

trast to hydrophilic poly-DMAEMA · DMS and poly-1,2-dimethyl-5-vinylpyridinium methyl sulfate (poly-1,2-DM-5-VPMS) [7] soluble even in concentrated aqueous salt solutions (2 M), the solubility of poly-DMAEMA · BC decreases at NaCl concentration of 0.8 M. The phase separation in the system is probably due to intense hydrophobic interactions between the chain units, which become predominant at shielding of the macroion charges. Since no phase separation is observed with poly-DMAEMA · DMS, we assumed that specifically the benzyl substituents in the DMAEMA · BC chain promote the chain association. The hydrophobic interactions can also affect the adsorption of macroions on the particles and formation of interparticle bridges during flocculation.

The flocculation of the kaolin suspension was studied in the presence of DMAEMA · BC homo- and copolymer samples, whose characteristics are listed in Tables 1 and 2.

The experimental dependences of the supernatant turbidity on the flocculant concentration in the system are shown in Figs. 2a–2c. As can be seen, the flocculation of the kaolin suspension with cationic polyelectrolytes based on DMAEMA · BC and DMAEMA · DMS

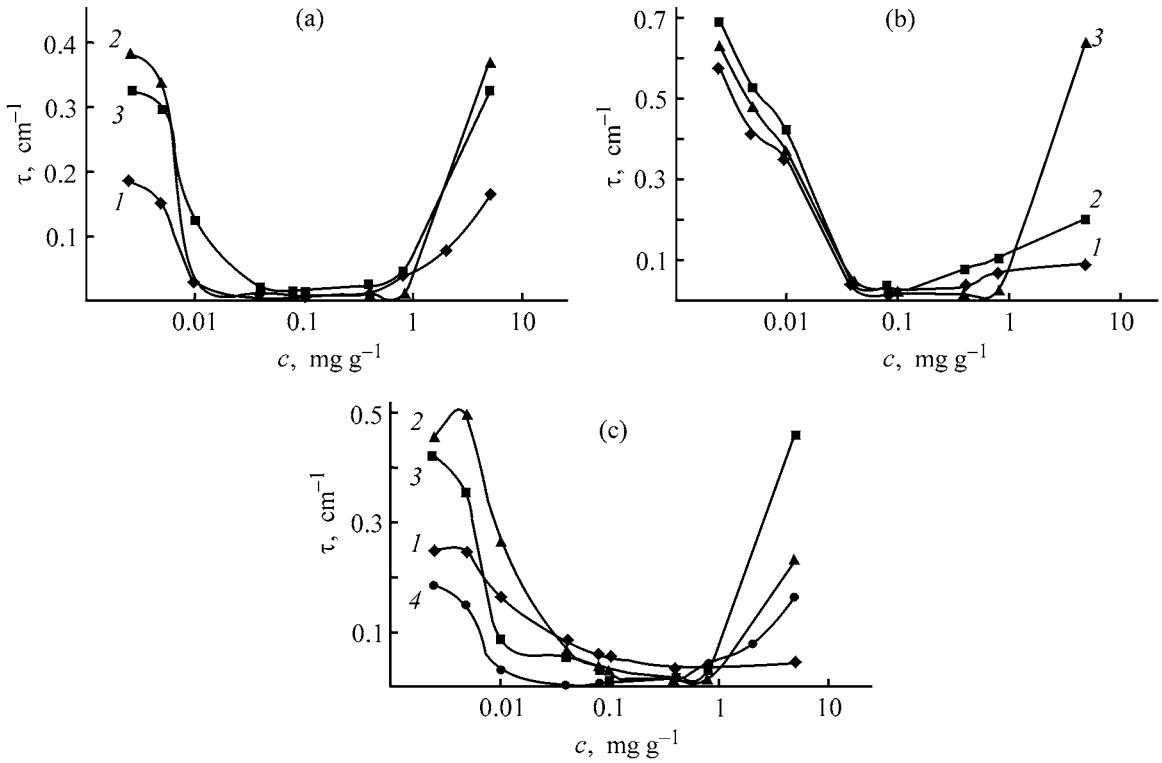

Fig. 2. Supernatant turbidity τ as influenced by the concentration *c* of (*1*) flocculants and copolymers of DMAEMA · BC with (b) AA and (c) DMAEMA · DMS. (a): (*1*) PE-4, (*2*) PE-6, and (*3*) PE-6.5. (b): (*1*) 25-AA, (*2*) 50-AA, and (*3*) 75-AA. (c) (*1*) 25-DMS, (*2*) 50-DMS, (*3*) 75-DMS, and (*4*) PE-4

Table 3. Flocculation of the kaolin suspensions in the presence of homopolymers

Sample	c_{Pe}, mg g^{-1}	τ_{min}, cm^{-1}	D_{max}	λ, g mg^{-1}	Sample	c_{Pe}, mg g^{-1}	τ_{min}, cm^{-1}	D_{max}	λ, g mg^{-1}
PE-4	0.04	0.012	180	566	PE-7	0.04	0.014	152	475
	0.08	0.011	197	308		0.08	0.009	241	351
	0.10	0.009	236	295		0.10	0.01	224	281
PE-6.5	0.04	0.023	95	299					
	0.08	0.015	142	223	poly-1,2-DM-5-VPMS*	0.05	0.017	123	309
	0.10	0.015	142	178					

* $[\eta]$ = 2.3 dl g^{-1}, 0.05 M KBr, 25°C [6].

Table 4. Optimal flocculation parameters of a 0.8% kaolin suspension with DMAEMA · BC copolymers

Sample	η, dl g^{-1}	c_{PE}, mg g^{-1}	τ_{min}, cm^{-1}	D_{max}	λ, g mg^{-1}
25-AA	4.4	0.04	0.035	61	192
		0.08	0.016	134	210
		0.10	0.023	92	115
50-AA	5.3	0.04	0.042	50	159
		0.06	0.032	65	142
		0.10	0.018	120	151
75-AA	7.5	0.08	0.024	88	138
		0.10	0.017	130	163
		0.40	0.014	155	48
25-DMS	4.6	0.08	0.058	37	57
		0.10	0.054	39	48
		0.40	0.033	64	20
50-DMS	6.1	0.08	0.039	55	86
		0.10	0.029	73	91
		0.40	0.014	157	49
75-DMS	6.9	0.08	0.032	66	104
		0.10	0.019	111	139
		0.40	0.016	134	42
poly-1,2-DM-5-VPMS–AA (26 mol % AA)*	1.8	0.08	0.019	111	186
poly-1,2-DM-5-VPMS–AA (53 mol % AA)*	1.6	0.15	0.023	92	76

* Data taken from [6].

proceeds in accordance with classical dependences in the liquid–solid–polyelectrolyte systems. The dependence of the supernatant turbidity on the flocculant concentration is nonmonotonic and consists of three portions. At low flocculant concentrations (>0.08 mg g^{-1}), the supernatant turbidity gradually decreases, which corresponds to destabilization of the dispersed system. In the 0.08–1.00 mg g^{-1} concentration range, the degree of the suspension clarification is the highest. At higher polymer concentrations, the supernatant turbidity sharply increases due to the protective effect of the flocculant. Stabilization is determined by sorption conditions of the excess macromolecules on the solid phase surface; this phenomenon is observed upon recharging of the disperse particle surface as a result of electrostatic repulsion or steric hindrance.

As can be seen from Fig. 1 and Table 3 describing the optimal conditions of kaolin flocculation, the flocculation effects of homopolymers based on DMAEMA · BC (PE-4, PE-7) are similar in the given concentration range, and greater by a factor of 1.1–1.7 than that of PE-6.5. It was found that DMAEMA · BC surpasses poly-1,2-DM-5-VPMS [6] in both the flocculation effect (by a factor of 1.2–1.5) and flocculation activity.

The copolymers of DMAEMA · BC with AA and DMAEMA · DMS also exhibits a fairly high flocculation power (Figs. 2b, 2c). The best results of coagulation of kaolin suspensions with the copolymers are listed in Table 4.

According to the experimental data, the flocculation effect of the kaolin suspension with DMAEMA ·

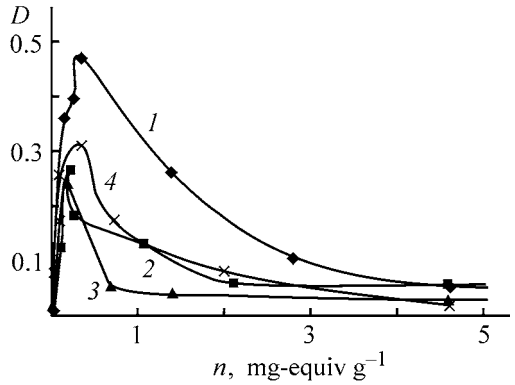

Fig. 3. Flocculation effect *D* of a 0.8% kaolin suspension as influenced by the reduced density of the total charge of macroions *n*. (*1*) PE-4, (*2*) 25-AA, (*3*) 50-AA, and (*4*) 75-AA.

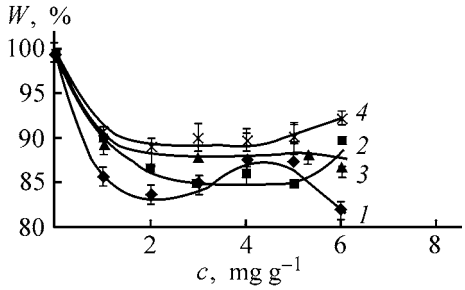

Fig. 4. Residual water content in the cake *W* as influenced by the flocculant charge *c*. (*1*) PE-7, (*2*) PE-6.5, (*3*) 75-DMS, and (*4*) 75-AA.

BC · AA copolymers is 50–155 and does not exceed the optimal values for homopolymers. At the same time, the range of the optimal flocculation conditions becomes narrower and shifts toward higher flocculant concentrations (0.1–1.0 mg g^{-1}). This is probably due to the smaller number of cation-exchange centers in the copolymer (as compared to the homopolymer) involved in sorption of macromolecules on the surface of dispersed particles, whereas the optimal flocculation conditions correspond to the certain and constant ratio of the surface particle charge and total charge of macroions.

Actually, the dependence of the flocculation effect on the total charge of macroions in homo- and copolymers per unit weight of the dispersed phase (Fig. 3) shows that the highest flocculation effect for homopolymers and copolymers of DMAEMA · BC with AA for all the compositions studied corresponds to a rather narrow range of charge densities *n* from 0.176 to 0.350 mg-equiv g^{-1}. A decrease in the flocculation effect of copolymers suggests that the process efficiency is determined by conditions of sorption and fixation of macromolecules on the surface of dispersed particles, which changes as the number of macromolecule chain units containing a bulky hydrophobic fragment and a salt group decreases. The insignificant increase in the flocculation power of 75-AA (Fig. 3) is probably due to the relatively high molecular weight of the sample, which is indirectly confirmed by its intrinsic viscosity.

In the case of DMAEMA · BC–DMAEMA · DMS copolymers (as also for homopolymers), destabilization of the kaolin suspension is observed in the 0.01–1.00 mg g^{-1} concentration range, and the flocculation effect amounts to 55–150, which is comparable with the effect of PE-6.5 and DMAEMA · BC · AA copolymers, but smaller by a factor of 1.8–2.3 than that for poly-DMAEMA · BC.

As can be seen from a comparison of the flocculation parameters of DMAEMA · BC · AA copolymers with a highly active flocculant based on 1,2-DM-5-VPMS (Table 4, [6]), the flocculation effect of acrylamide copolymers based on DMAEMA · BC only slightly exceeds that of the corresponding pyridinium flocculants (by a factor of 1.2–1.3), but, if account is taken of the concentration range studied, their activity is higher than that of the pyridinium analogues by a factor of 1.6–1.9.

The efficient water purification in treatment of household wastes is impossible without use of biological methods employing active sludge. To maintain the operation status of the aeration tanks, the excess sludge biomass should be regularly removed, with subsequent flocculation and filtration. Since the hydrophilic sludge particles strongly retain water in their hydration shells, dehydration of the sludge suspension on the filter is an important problem.

Taking into account the promising data on the flocculation of the model kaolin suspension, the DMAEMA · BC (co)polymers were tested in dehydration of the excess active sludge formed at the sewage treatment plants. The residual water content in the cake was used as a criterion of the flocculant efficiency.

Analysis of the flocculant effect on the water content in the sludge on the filter (Fig. 4) shows that the minimum water content in the cake reaches 83–88%, and it is attained at the polyelectrolyte concentration in the suspension of 2–3 mg g^{-1}. Subsequent increase in the polyelectrolyte charge does not noticeably affect the cake moisture content, and in the presence of PE-7 it even slightly increases. The optimal concentration range of the polymer in flocculation of the active sludge is 2–4 mg g^{-1}, and further increase in the polyelectrolyte concentration is not appropriate. As can be seen from Fig. 4, the minimum water con-

tent of 83.5–85.0% in the cake is attained on adding to the sludge suspension PE-6.5 and PE-7 homopolymers containing hydrophobic benzyl and methyl groups. Addition of hydrophilic AA units to the macromolecular chains, apparently, decreases the number of hydrophobic polymer-sludge contacts, which hinders the sorption of macromolecules on the sludge particles. As a result, the hydrophobicity of the surface layer decreases, which increases the residual water content in the cake to 90% in the sample containing 75 mol % AA.

Since the initial water content in the industrial sludge samples varies in a wide range, the effect of DMAEMA · BC (co)polymers was evaluated with a dimensionless parameter (dehydration power). The data on the sludge dehydration listed in Table 5 show that all the polymers based on DMAEMA · BC are highly active, and the greatest effect on the active sludge dehydration was observed for PE-7 sample (which is greater by a factor of 1.4 than that that for poly1,2-DM-5-VPMS) and for the copolymer of 1,2-DM-5-VPMS and vinylpyrrolidone (1-VP) containing 10% nonionic comonomer. The effect of PE-7 on the active sludge dehydration is also greater by a factor of 1.1 as compared to 1-VP(AA) terpolymer containing 1 mol % AA and 9 mol% vinylpyrrolidone [6].

Our experimental data showed the higher activity of poly-DMAEMA · BC in the dehydration of the active sludge and in flocculation of kaolin suspensions as compared to hydrophilic AA copolymers. This is probably due to different conformation states of homo- and copolymer macromolecules at the phase boundary and conditions of bridging interactions at flocculation. We believe that the hydrophobicity of amphiphilic poly-DMAEMA · BC macromolecules strongly increases due to charge shielding in the course of sorption. In flocculation, new polymer–polymer interactions arise along with the polymer–particle contacts. These interactions can provide additional contacts between the particles with sorbed macromolecules and thus promote flocculation. A similar phenomenon was observed for 1,2-DM-5-VPMS copolymers containing nonionic vinylpyrrolidone units [8]. The efficiency of the active sludge dehydration in the presence of hydrophobic aggregates is greater as compared with that for hydrophilic copolymers.

The sorption of copolymers containing nonionic AA units is probably accompanied by the formation of polymeric bridges in which the content of hydrophobic units is relatively small. As a result, they strongly retain the solvent molecules by Van der Waals interactions. The aggregates that are not stabilized by the polymer-polymer interactions and contain solvent molecule in the interparticle space, are readily broken. As a result, the flocculation with copolymers is less efficient as compared to that with homopolymers.

Table 5. Activity of cationic flocculants in dehydration of excess active sludge

Flocculant	c, mg g^{-1}	W, %	$D_w \times 10^3$
Poly-1,2-DM-5-VPMS*	1.5	87.4	137
1-VP*	2.5	87.5	139
1-VP(AA)*	3.4	84.9	174
PE-7	2.0	83.5	190
PE-3.56	1.0	85.0	169
PE-6.5	3.0	84.9	171
25-DMS	2.0	86.6	148
25-AA	2.0	88.9	117

* Data take from [6].

CONCLUSIONS

(1) The data on the flocculation of model kaolin suspension and dehydration of excess active sludge in the presence of cationic flocculants show that the flocculation performance of poly-2-(*N*,*N*-dimethyl-*N*-benzylammonio)ethyl methacrylate chloride is better than that of copolymers of 2-(*N*,*N*-dimethyl-*N*-benzylammonio)ethyl methacrylate chloride with nonionic acrylamide and cationic 2-(*N*,*N*,*N*-trimethylammonio)ethyl methacrylate methyl sulfate.

(2) The greater flocculation power of homopolymer of 2-(*N*,*N*-dimethyl-*N*-benzylammonio)ethyl methacrylate chloride is probably due to the formation of additional bridges and more complete involvement of the particles in the flocculation, owing to the hydrophobic polymer–polymer contacts.

REFERENCES

1. Zapol'skii, A.G. and Baran, L.A., *Koagulyanty i flokulyanty v protsessakh ochistki vody: Svoistva. Poluchenie. Primenenie* (Coagulants and Flocculants in Water Treatment. Properties. Preparation. Use), Leningrad: Khimiya, 1987.
2. Nebera, V.P., *Flokulyatsiya mineral'nykh suspenzii* (Flocculation of Mineral Suspensions), Moscow: Nedra, 1983.

3. Baran, L.A. and Teslenko, A.Ya., *Flokulyanty v biotekhnologii* (Flocculants in Biotechnology), Leningrad: Khimiya, 1990.
4. Navrotskii, A.V., Novakov, I.A., Lotov, V.V., and Navrotskii, V.A., *Khimiya i tekhnologiya elementoorganicheskikh monomerov i polimernykh materialov: Mezhvuzovskii sbornik nauchnykh trudov* (Chemistry and Technology of Organoelement Monomers and Polymeric Materials: Intercollegiate Collection of Works), Volgograd: Gos. Tekh. Univ., 1995, pp. 13–19.
5. Myagchenkov, V.A. and Bulidorova, G.V., *Khim. Tekhnol. Vody*, 1993, vol. 15, no. 2, pp. 100–105.
6. Novakov, I.A., Navrotskii, A.V., Starovoitova, Ya.M., *et al.*, *Zh. Prikl. Khim.*, 2003, vol. 76, no. 7, pp. 1200–1206.
7. Bekturov, E.A. and Bakaurova, Z. Kh., *Sinteticheskie vodorastvorimye polimery v rastvorakh* (Synthetic Water-Soluble Polymers in Solutions), Alma-Ata: Nauka, 1981.
8. Navrotskii, A.V., Dryabina, S.S., Malysheva, Zh.N. and Novakov, I.A., *Kolloidn. Zh.*, 2003, vol. 65, no. 3, pp. 368–373.

Russian Journal of Applied Chemistry, Vol. 77, No. 4, 2004, pp. 629–632. Translated from Zhurnal Prikladnoi Khimii, Vol. 77, No. 4, 2004, pp. 632–636.

MACROMOLECULAR CHEMISTRY AND POLYMERIC MATERIALS

Influence of Temperature on Formation of Structure and on Mechanical Properties of Plasticized Polyether–Urethane–Urea

V. V. Tereshatov, E. N. Tereshatova, and M. A. Makarova

Institute of Technical Chemistry, Ural Division, Russian Academy of Sciences, Perm, Russia

Received December 9, 2003

Abstract—The influence exerted by temperature and time of curing on the strength and deformation properties of plasticized polyether–urethane–urea was examined. Addition of a plasticizer ensures the optimal rheological properties, and the resulting material cured at a low temperature exhibits high mechanical characteristics.

Polyurethane–ureas (PUUs) derived from polyethers exhibit high strength and deformation properties and resistance to oil, benzine, and many aggressive media. Therefore, articles made of these materials find wide application. The rheological properties and mechanical characteristics of PUUs can be controlled by adding various plasticizers [1–3]. In preparation of PUUs, plasticizers can also act as solvents for powdered diamines whose vapors and dusts are toxic [4].

The elastomers under consideration belong to microheterogeneous polymer systems with incomplete phase segregation of flexible polyether and rigid urethane–urea segments. The structure and properties of PUUs may appreciably depend on the history of their preparation. As a rule, these materials are prepared at temperatures of 80 to 140°C [3–6]. It is believed that the strength of PUUs can appreciably grow when the temperature at which the reaction mixture is cured increases [4]. However, it is impossible to find from the available data any regular trends in the influence of the curing temperature and time on the mechanical properties of plasticized polyurethane–ureas.

In this study, we examined the influence of the curing temperature on the mechanical properties of plasticized PUU and compared the results obtained with those for the nonplasticized samples. Our goal was to find the temperature conditions under which the resulting material exhibits high strength and deformation characteristics. We took into account the fact that, as the curing temperature is increased, the thermal shrinkage of the polymeric material after its cooling to the service temperature grows. This is especially undesirable for big items used for cleaning of oil and gas pipelines.

EXPERIMENTAL

Experiments were performed with PUU derived from SKU-PFL-100 prepolymer ($M \sim 1400$) plasticized with readily available di(2-ethylhexyl) phthalate (DEHP). The prepolymer was prepared by the reaction of oligo(tetramethylene oxide)diol ($M \sim 1000$) with toluene 2,4-diisocyanate taken in a twofold excess. The prepolymer was preliminarily subjected to a vacuum treatment for 20 min in a mixer at 50 ± 1°C. Then a weighed portion of aromatic diamine, 3,3'-dichloro-4,4'-diaminodiphenylmethane (Diamet Kh), dissolved in the plasticizer (or as a melt, in preparing a nonplasticized material) was added. The components were stirred for 3 min at 50 ± 1°C. The resulting mixture was poured into molds, which were subsequently kept at different temperatures. After keeping for the required period, the cured samples were unloaded, and their mechanical properties were determined under equal conditions.

All the experiments were performed at the ratio of the NCO (prepolymer) and NH_2 (diamine) groups less than unity (0.95), taking into account the published data that the dense chemical network negatively affects the mechanical properties of segmented polyurethane materials [4]. This allowed us to decrease the probability of formation of biuret cross-links.

The rheological properties of the reaction mixture were studied with a Rheotest-2 viscometer (cone–plate working unit) at a shear rate of 180 s^{-1}. The mechan-

1070-4272/04/7704-0629 © 2004 MAIK "Nauka/Interperiodica"

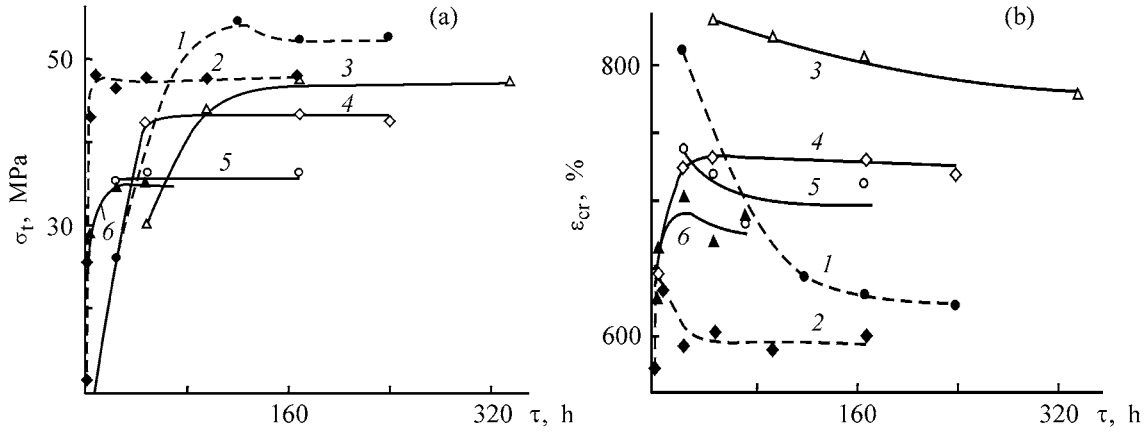

Fig. 1. (a) Strength σ_t and (b) relative critical strain ε_{cr} of (*1*, *2*) nonplasticized and (*3*–*6*) plasticized PUUs vs. the curing time τ. Curing temperature, °C: (*1*, *3*) 35, (*4*) 50, (*2*, *5*) 80, and (*6*) 100.

ical characteristics of PUU {tensile strength σ_t (ultimate stress for the initial cross section of a sample), relative critical strain ε_{cr}, and breaking stress

$$f_b = \sigma_t[(\varepsilon_{cr} + 100)/100],$$

(calculated for the actual cross section of the sample)} were determined at 23 ± 2°C, at the extension rate of 0.28 s^{-1}.

The effective density of the chemical network of PUU, N_c, was calculated with samples subjected to equilibrium swelling in tributyl phosphate, using the procedure described in [7].

The spectroscopic study of association of urea and urethane groups in the PUUs prepared at different temperatures was performed with a Bruker IFS 66/S Fourier spectrometer. The samples were prepared as films without solvents. The amide I band (C=O vibrations, ν 1620–1750 cm^{-1}) was used as analytical band.

The assignment of the components of the amide I band was made in accordance with [8, 9]. For convenience of comparison, the spectral curves were normalized with respect to the band at ν 1575 cm^{-1}. The spectra were compared at complete conversion of the isocyanate groups, as judged from the disappearance of absorption at ν 2275 cm^{-1}.

Figure 1 shows the dependences of the strength and deformation characteristics of PUU samples plasticized with 10% DEHP on the time of their curing at different temperatures (from 35 to 100°C). The corresponding curves for the nonplasticized samples are also shown (curves *1*, *2*). These results indicate that, as the temperature of curing of the plasticized samples is lowered from 80–100 (curves *5*, *6*) to 35–50°C (curves *3*, *4*), the strength and deformation characteristics of PUU are enhanced to a greater extent than in the absence of the plasticizer. Although constant values of σ_t and ε_{cr} are attained in essentially different times, the final mechanical properties of the nonplasticized samples cured at 35 and 80°C differ insignificantly (Fig. 1, curves *1*, *2*).

Comparison of the IR spectra (region of amide I band) of the samples cured at 80°C for different times shows that, as the curing time is increased from 1 to 9 h, the band at ν 1640 cm^{-1} grows in intensity (Fig. 2a). This indicates that the strongest structural formations, self-associates of the urea groups localized in domains of rigid urethane–urea segments [9], grow in amount; accordingly, the elastomer strength increases.

Longer curing at this temperature does not appreciably affect the association of rigid segments and the mechanical properties of the material, as can be clearly seen from comparison of the IR spectra and mechanical characteristics of nonplasticized PUU samples cured for 9 and 168 h at 80°C (Figs. 1, 2a). The results are consistent with the generally accepted views that microphase segregation is the decisive factor affecting the properties of segmented polyurethane materials [10, 11]. In curing of nonplasticized PUUs at 35°C, high mechanical properties are achieved at weakly pronounced microphase segregation. The IR spectra of these samples (Fig. 2b) exhibit in the range 1665–1670 cm^{-1} a well-defined shoulder originating from formation of a large amount of disordered H-bonds between the urea groups of rigid segments mixed with flexible polyether segments, with the intensity of the band at 1640 cm^{-1} being low. The above shoulder is preserved upon prolonged curing.

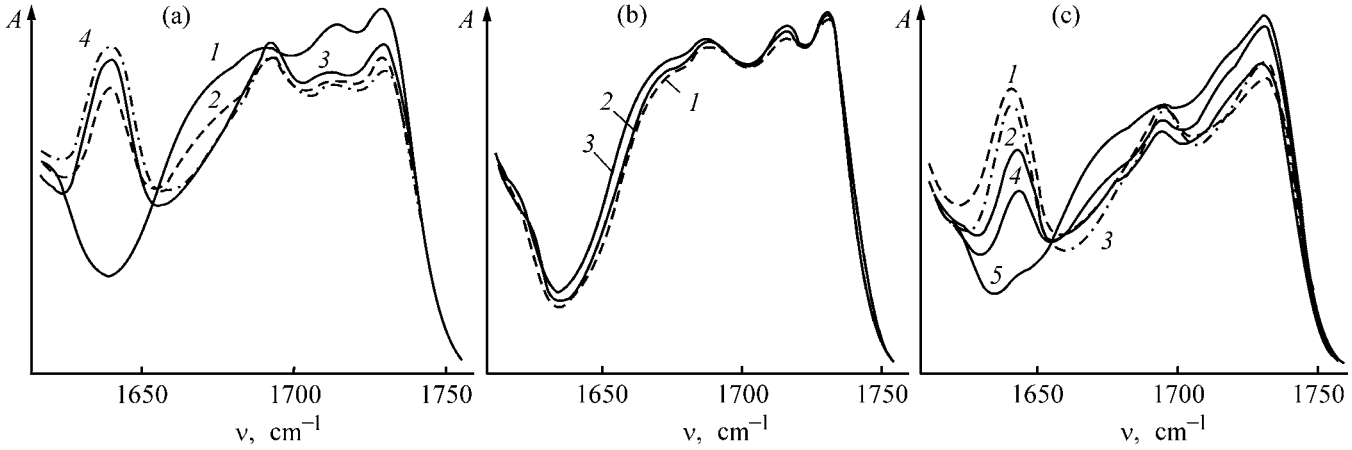

Fig. 2. IR spectra of nonplasticized PUU samples cured at different temperatures. (*A*) Absorption and (ν) wave number. Temperature, °C: (a) 80; (b) 35; (c) (*1*) 80, (*3*) 50, and (*2*, *4*, *5*) 35. Curing time, h: (a) (*1*) 1, (*2*) 2, (*3*) 9, and (*4*) 168; (b) (*1*) 48, (*2*) 120, and (*3*) 240; (c) (*1*, *3*, *4*) 168, (*2*) 336, and (*5*) 48.

The strength of plasticized PUU samples cured for the same time at different temperatures does not grow with the curing temperature but, by contrast, decreases, despite an increase in the amount of associated rigid segments in the material (Fig. 1a, curves *3–5*; Fig. 2c, curves *1*, *3*, *4*).

In curing of plasticized PUU samples at the same temperature, e.g., 35°C, the high strength and deformation properties of the material are achieved when the extent of segregation of rigid blocks is far from the maximum. This is clearly seen from comparison of curves *2* and *4* in Fig. 2a with each other and with curve *1* at $\nu = 1640$ cm^{-1}.

Thus, there is generally no unambiguous correlation between the mechanical propreties of segmented PUU samples prepared under different conditions and the microphase segregation of the flexible and rigid blocks. This may be due to increased defectiveness of the material prepared at elevated curing temperatures when microphase segregation is fast. This effect should be stronger in the presence of a plasticizer enhancing the mobility of flexible and rigid blocks of the polymer.

The enhancement of the interchain interaction in the flexible polymeric matrix due to mixing of flexible polyether segments and rigid urethane–urea blocks acting as proton acceptors positively affects the material strength. Therefore, microphase segregation in a segmented polyurethane material is not undoubtedly the major factor affecting its properties as stated in monographs [10, 11] and many other papers. Our conclusion directly follows from the experimental results shown in Figs. 1 and 2a–2c.

It is known that, under conditions of storage at room temperature, the structure of segmented polyurethanes becomes "frozen," i.e., it can remain in the virtually unchanged state for a long time [12]. The properties of the material should not appreciably

Properties of nonplasticized and plasticized (10% DEHP) PUU samples cured for 7 days, measured immediately after curing and after storage for 120 days at room temperature

Curing temperature, °C	Plasticizer content, %	σ_t, MPa	σ_t^*, MPa	ε_{cr}, %	ε_{cr}^*, %	f_b, MPa	f_b^*, MPa	N_c, kmol m^{-3}	N_c^*, kmol m^{-3}
80	0	48.0	48.9	602	583	337	334	0.04	0.04
	10	34.3	35.1	712	723	279	289	0.02	0.02
50	10	43.2	42.0	730	710	346	340	0.02	0.02
35	0	52.2	51.7	625	609	378	367	0.03	0.03
	10	48	47.9	802	745	433	405	0.02	0.02

* The asterisk refers to samples after storage.

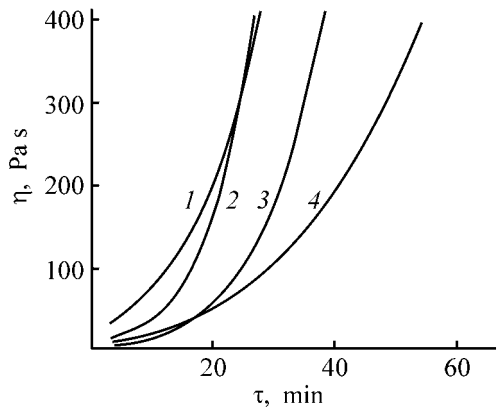

Fig. 3. Dynamic viscosity η of the reaction mixture in curing of (*1*, *2*) nonplasticized and (*3*, *4*) plasticized PUUs vs. time τ. Temperature, °C: (*1*, *4*) 35 and (*2*, *3*) 50.

change in this case. The table shows that, indeed, the mechanical characteristics of PUU samples change insignificantly after storage for 120 days at 20 ± 3°C.

The density of the chemical network, N_c, was low in all the samples (which was preset by the deficiency of the NCO groups in the reaction mixture) and did not noticeably change in storage of the material. The table shows that the trend toward an increase in the strength of the plasticized material with decreasing curing temperature is preserved in prolonged storage of the samples. The strength and deformation characteristics (f_b, ε_{cr}) of plasticized PUU prepared at 35°C exceed those of the nonplasticized material cured at both 35 and 80°C.

The high strength characteristics of the plasticized material obtained under these conditions are combined with the considerably better rheological characteristics of the plasticized reaction mass, compared to the nonplasticized mass (Fig. 3). As a result of plasticization, the shear viscosity of the compound becomes several times lower and the working life of the compound grows, which favors production of block items of higher quality.

CONCLUSIONS

(1) Lower curing temperatures ensure better strength and deformation characteristics of the plasticized material.

(2) Plasticized polyurethane–urea prepared at relatively low temperatures compares well with the nonplasticized material in strength and surpasses it in the deformation and processing characteristics.

(3) There is no unambiguous correlation between the strength of the segmented polymer and microphase segregation in it. The high strength can be achieved at a low extent of microphase segregation of the flexible and rigid blocks.

ACKNOWLEDGMENTS

The study was financially supported by the Russian Foundation for Basic Research (project no. 02-03-96408).

REFERENCES

1. Lyamkin, D.I., Misyuk, K.G., Pasternak, V.Sh., *et al.*, *Vysokomol. Soedin., Ser. B*, 1997, vol. 39, no. 3, pp. 545–550.
2. Baoyan Zhang and Huimen Tan, *Eur. Polym. J.*, 1988, vol. 34, nos. 3–4, pp. 571–580.
3. Tereshatov, V.V., Tereshatova, E.N., Makarova, M.A., and Tereshatov, S.V., *Vysokomol. Soedin., Ser. A*, 2002, vol. 44, no. 3, pp. 443–449.
4. Lyubartovich, S.A., Morozov, Yu.L., and Tret'yakov, O.B., *Reaktsionnoe formovanie poliuretanov* (Reaction Molding of Polyurethanes), Moscow: Khimiya, 1990.
5. Ong, G.J. and Saxon, R., J. *Appl. Polym. Sci.*, 1976, vol. 20, pp. 1695–1710.
6. Rusetskii, V.V. and Kolesnikov, N.M., *Kauchuk Rezina*, 1987, no. 6, pp. 14–16.
7. Tereshatov, V.V., Tereshatova, E.N., Begishev, V.P., and Makarova, M.A., *Vysokomol. Soedin., Ser. B*, 1992, vol. 34, no. 8, pp. 22–25.
8. Zharkov, V.V., Kopusov, L.I., and Kozlova, T.V., *Plast. Massy*, 1981, no. 12, pp. 41–45.
9. Tereshatov, V.V., Tereshatova, E.N., Begishev, V.P., *et al.*, *Vysokomol. Soedin., Ser. A*, 1994, vol. 36, no. 12, pp. 1988–1995.
10. Redman, R.P., *Developments in Polyurethane-1*, London: Applied Science, 1978.
11. Kercha, Yu.Yu., Onishchenko, Z.V., Kutyanina, V.S., and Shelkovnikova, L.A., *Strukturno-khimicheskaya modifikatsiya elastomerov* (Structure-Chemical Modification of Elastomers), Kiev: Naukova Dumka, 1989.
12. Tereshatov, V.V., *Vysokomol. Soedin., Ser. A*, 1995, vol. 37, no. 9, pp. 1529–1534.

Russian Journal of Applied Chemistry, Vol. 77, No. 4, 2004, pp. 633–638. Translated from Zhurnal Prikladnoi Khimii, Vol. 77, No. 4, 2004, pp. 637–642.

MACROMOLECULAR CHEMISTRY AND POLYMERIC MATERIALS

Preparation of Compounds of Epoxy Resins with Low-Molecular-Weight Carboxyl-containing Rubbers by Activating Mixing

V. P. Britov, V. V. Bogdanov, O. O. Nikolaev, A. E. Tubolkin, and T. M. Lebedeva

St. Petersburg State Technological Institute, St. Petersburg, Russia

Received February 4, 2003

Abstract—A process was developed for preparing adhesives from a low-molecular-weight carboxyl-containing rubber and an epoxy resin with different oligomer ratios. The process involves the chemical reaction of the components under conditions of activating mixing.

To develop a process for preparing and modifying compounds under conditions of activating mixing, we chose as objects to be studied epoxy oligomers (EOs) and low-viscosity carboxyl-containing rubbers. This choice was governed by the following facts.

(1) Mixing of epoxy oligomers and low-viscosity carboxyl-containing rubber can initiate their chemical reaction.

(2) These materials have low viscosity, and, in this case, it is especially difficult to provide the strain energy density required to initiate a chemical reaction.

(3) Blends of epoxy polymers with rubbers are of large practical interest as adhesives.

Epoxy oligomers exhibiting high adhesive power are still important for practice, despite the development of new types of adhesives. However, the properties of the existing epoxy adhesives, in particular, their shock resistance and elasticity, do not fully meet the requirements of modern engineering. These characteristics are improved by modifying EOs with liquid rubbers [1–4]. The modification process is based on the high reactivity of carboxy group toward epoxy groups.

Modification of EOs with liquid rubbers is performed by the following procedures: (1) addition of a curing agent to a blend of EO with a rubber, prepared by mechanical mixing; (2) copolymerization of epoxy and rubber oligomers, which occurs simultaneously with curing of the epoxy resin at 120 or 150°C (hot curing); (3) preliminary reaction (esterification) between epoxy groups of the resin and carboxy groups of the rubber, followed by curing of the resulting copolymer at room temperature [5].

In preparation of compounds by the first procedure, there is no chemical reaction of the rubber with the epoxy matrix, which does not allow high mechanical characteristics of the compound to be attained. However, prolonged heating enhances the cracking resistance owing to changes in the phase interaction of the components.

In preparation of compounds by the second procedure, important factors are the selectivity and activity of the functional groups of the rubber, which are necessary for formation of chemical bonds between the components.

Of particular interest is the third procedure for EO modifcation. On mixing of epoxy and rubber oligomers, followed by heating for 2 h at 150°C, a noncatalytic reaction of the carboxy and epoxy groups occurs to yield a hydroxy ester.

The other procedures ensuring the required properties of the materials are more difficult to perform in practice because of the sophisticated equipment required and prolonged process.

Analysis of these methods from the process viewpoint reveals the following contradiction: Mechanical mixing is the simplest and the most convenient procedure, but it does not ensure the required properties of the compound because of the absence of a chemical reaction between the components. Irrespective of a particular procedure of compound preparation, mixing is

1070-4272/04/7704-0633 © 2004 MAIK "Nauka/Interperiodica"

Table 1. Compositions of compounds studied*

Compound no.	Content, weight parts				
	SKN-10KTR	SKD-KTRA	ED-20	XD	UP-583
1		10	100	16	–
2		20	100	–	18
3		20	100	16	–
4		40	100	16	–
5		40	100	–	18
6		60	100	16	–
7		60	100	–	18
8		80	100	16	–
9		80	100	–	18
10		100	100	16	–
11		100	100	–	18
12	10	–	100	15.8	17.8
13	–	10	100	15.0	16.2
14	20	–	100	15.2	17.3
15	–	20	100	14.8	16.0
16	40	–	100	15.0	17.1
17	60	–	100	13.1	15.0
18	–	60	100	11.5	12.3
19	80	–	100	9.2	11.3
20	–	80	100	8.4	10.7
21	100	–	100	6.3	9.9
22	–	10	100	5.0	7.2

* Compound nos. 1–11 are based on oligomer mixtures (content of SKN-10KTR or SKD-KTRA rubber is indicated); compound nos. 12–22 were prepared with preliminary esterification.

an inherent step of the process. In this case, we speak just of activating mixing, since the chemical reaction of the components under consideration requires initiation. We examined the possibility of initiating the chemical reaction of EO with rubber in mechanical-type apparatus.

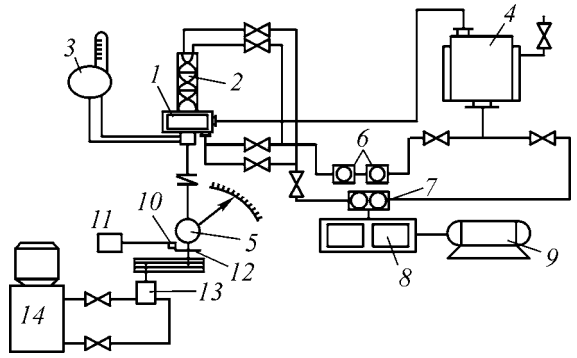

Fig. 1. Scheme of an installation for preparing epoxy–rubber compounds: (*1*) RPA, (*2*) static mixer, (*3*) thermostat, (*4*) tank, (*5*) power meter, (*6*) rotameters, (*7*) gear-type pump, (*8*) universal rate control unit, (*9*) motor, (*10*) sensor, (*11*) frequency meter, (*12*) disc, and (*13*) hydraulic pump.

EXPERIMENTAL

As objects of study served compounds based on EO (oligoether–epoxide) and liquid rubbers with terminal carboxy groups (butadiene–acrylonitrile and butadiene rubbers); also, we studied compounds of EO and liquid butadiene–acrylonitrile rubber with terminal carboxy groups, diluted with furfuryl glycidyl ether (FGE).

The compounds were cured with hardeners traditional for epoxy resins. We studied the materials obtained from blends of EO and liquid rubbers with terminal carboxy groups and those prepared with preliminary esterification of EO with carboxy groups of the rubbers.

Component characteristics: SKN-10KTR oligobutadiene–acrylonitrile rubber with terminal carboxy groups, 10% acrylonitrile units, 2.9% carboxy groups, molecular weight MW 2900 [TU (Technical Specifications) 000-31-24–60]; SKD-KTRA oligobutadiene rubber with terminal carboxy groups, 2.9% carboxy groups, MW 2800 (TU 38-103-327–46); ED-20 oligoether–epoxide, MW 410 [GOST (State Standard) 10597–76); FGE (furfuryl 2,3-epoxypropyl ether), 27% epoxy groups, MW 154.16 (TU 6-09-5208–85); xylylenediamine (XD), MW 150 (pilot product), hardener for ED-20; diethylenetriaminomethylphenol (UP-583), MW 210, hardener for ED-20 (TU 6-05-241-331–82). The compositions of the compounds studied are listed in Table 1.

The compounds were prepared both on traditional equipment (rollers, blade mixer) and on a specially contructed installation with a rotary pulsation apparatus (RPA). Previously, [6] we have formulated common requirements to preparation and modification of compounds under conditions of mechanochemical transformations controlled by mixing: concentration of a definite quantity of energy and its proper utilization in the working volume of the apparatus (creating high shear rates and stresses and controlling them within wide limits; uniformity of the strain action parameters in each elementary volume of the material being processed). We noted that effective small-volume mixers, RPAs, meet these requirements.

The experimental installation is shown schematically in Fig. 1. The installation includes an RPA, a hydraulic drive, a system for flow and pressure head control, and measuring devices. The rotary pulsation apparatus with a vertical shaft was a one-step device with the possibility provided for enhancement of re-

placeable rotors and stators (Fig. 2). This allowed the working clearance to be varied from 0.5 to 6 mm; the number of slits, from 0 to 32; the slit width, from 2 to 12 mm; and the cylinder thickness, from 3 to 12 mm.

The rotor and startor are mounted in a casing. The rotor is fixed on the vertical shaft, and the stator is mounted on a stationary vertical axle with an outlying support with two precision bearings. The outlying support is fixed on the frame of the installation, and on the upper end of the axle there is a horizontal cantilever with the attached system of a rope and a pulley.

Removable weights were fastened at the rope end. The apparatus was driven by an electric motor. We also used another version of the RPA working unit, based on the design from [7] and allowing finer dispersion of the components (Fig. 3).

In the installation scheme, we also used the RPA design from [8], in which the inlet tubes were replaced by a static mixer with screw parts. The installation was equipped with systems for flow and pressure head control for fluids of different viscosities. With low-viscosity fluids, the installation included a tank, a centrifugal pump, two pneumatic rotameters RP-1.6 and RP-10, cut-off and control valves, and a system of pipelines. With more viscous media, the system for flow and pressure head control consisted of the same tank and a gear-type pump with the drive equipped with a universal rate control unit.

The installation worked as follows. The working medium from the tank was withdrawn with a centrifugal (for low-viscosity media) or gear-type (for high-viscosity media) pump. When working with low-viscosity media, the material was fed with the pump through one of rotameters used to set and monitor the required flow rate. After passing through the rotameter, the fluid arrived at the internal volume of RPA and then, after passing through the rotor and stator slits, to the external volume of the apparatus and then moved through the discharge tube to the tank from which, if necessary, it was fed into the RPA again. Thus, the fluid continuously circulated in a closed loop. When working with highly viscous media, the fluid from the apparatus was fed with a gear-type pump preliminarily calibrated with respect to the flow rate. The fluid supply was finely controlled with a universal rate control unit in the pump drive.

Prior to being fed into the RPA, two (or more) polymeric materials were mixed in a static mixer with screw parts. In the experiments, we varied the system of component supply to the static mixer, the number

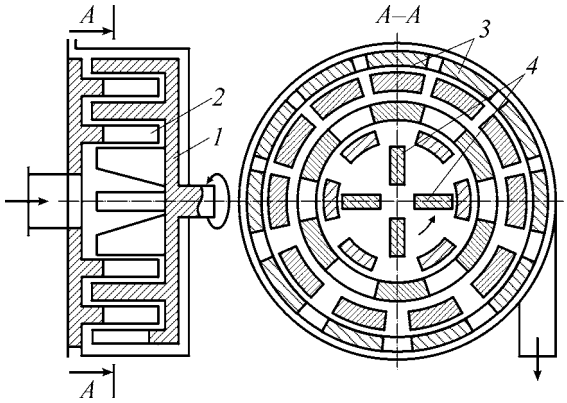

Fig. 2. Scheme of RPA: (*1*) rotor, (*2*) stator, (*3*) teeth, and (*4*) blades.

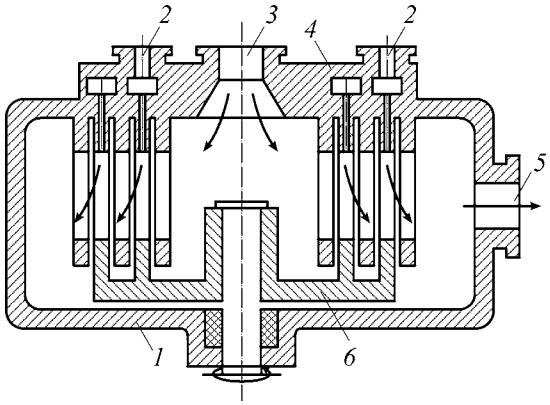

Fig. 3. Rotary pulsation apparatus for fine dispersion of components: (*1*) casing, (*2*, *3*) inlet tubes, (*4*) stator, (*5*) outlet tube, and (*6*) rotor.

of screw parts, the angle of their twisting, etc. This allowed us to analyze how mixing in RPA is affected by the initial interface area.

The power-measuring installation consisted of a stator and a rotor with a rope. The rotor rotation frequency was measured with a frequency meter, which was connected to a magnetic sensor mounted near the disk with slits, with a narrow clearance. The disk was fastened on the rotor shaft. When the disk moved near the sensor, the magnetic flux in it changed in proportion to the number of slits on the disk and frequency of rotor rotation. The induction voltage changed, and this change was transmitted to the frequency meter through the coil in the sensor.

To provide the constancy of the fluid temperature, the tank was equipped with a jacket through which, if necessary, brine (≥15°C) or cold water was passed to maintain the required temperature (20 ± 0.5°C).

The rheological properties of the components and their mixtures were determined with a Rheotest rotary

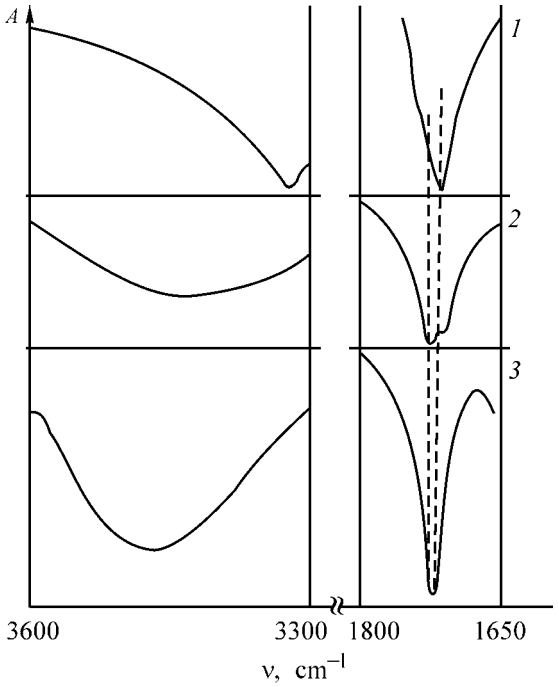

Fig. 4. IR spectra of (*1*) SKN-10KTR rubber, (*2*) blend of SKN-10KTR with EO, and (*3*) product of preliminary esterification. (*A*) Absorption and (ν) wave number.

viscometer. The structure of the uncured compounds was studied with an optical microscope, and that of cured compounds, with an electron microscope (REM-100, V8-500). The chemical and physical transformations of the components were monitored as follows: formation of chemical bonds between the functional groups of rubber and EO, by IR spectroscopy; consumption of EO functional groups, by acid–base back-titration; and the curing kinetics, by the procedure involving evaluation of the temperature effect of curing. The quality of mixing was estimated by optical and dielectric methods.

To elucidate the mechanisms of processes occurring at different compounding procedures, we studied the structure and chemical reactions of the component polymers.

The preliminary esterification product is initially a homogeneous material, but after curing it becomes a two-phase system similar to that obtained from the mechanical mixture.

The following reaction occurs between the carboxy groups of rubbers and epoxy resin [5]:

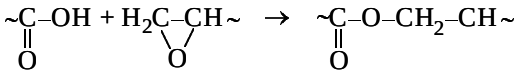

The reaction proceeds until all the carboxy groups are consumed. In the process, intermolecular hydrogen bonds undergo redistribution. Comparison of the IR spectra of SKN-10KTR rubber (Fig. 4, spectrum *1*), its mechanical mixture with EO (spectrum *2*), and product of preliminary esterification shows the following. In the spectrum of SKN-10KTR, the absorption at 1710 cm^{-1} is more pronounced (C=O bonds in hydrogen-bonded carboxy groups). On mixing with EO, the band at 1740 cm^{-1} (free C=O groups) becomes more intense owing to redistribution of hydrogen bonds upon interaction of the hydroxy groups of rubber with proton-acceptor groups of ED-20. The absorption at 1710 cm^{-1} becomes less intense. The IR spectrum of the product of preliminary esterification exhibits a single strong band at 1740 cm^{-1}, suggesting the existence of free carbonyl groups, as all the carboxy groups of the rubber have reacted with the epoxy groups, so that the hydrogen bonds between the rubber molecules have been broken. A strong band at 3300–3600 cm^{-1} in the spectrum of the product of preliminary esterification indicates that all the OH groups are involved in hydrogen bonding.

Thus, in contrast to mechanical mixtures, there is chemical bonding between the phases in the compound prepared by preliminary esterification.

The IR data show that, after the cleavage of the hydrogen bonds with C=O groups, all the OH groups of SKN-10KTR molecules form hydrogen bonds with acceptor groups of ED-20, i.e., a redistribution of intermolecular hydrogen bonds occurs.

The reaction of oligobutadiene–acrylonitrile rubber (SKM-10KTR, $x = 5$, $y = 1$, $z = 10$) with ED-20 resin can be represented as:

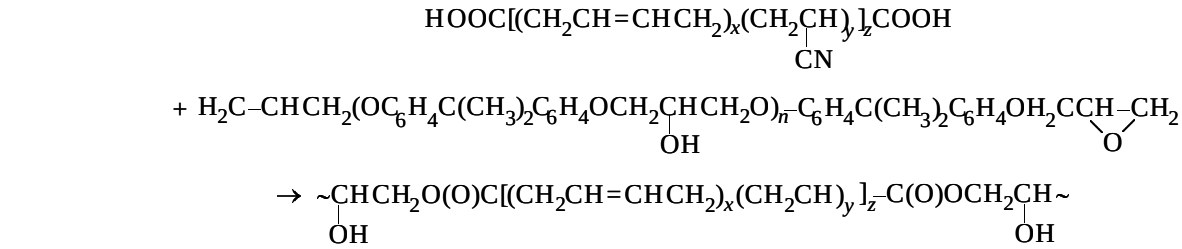

As will be shown below, the occurrence of the chemical interaction determines the difference between the compounds prepared by preliminary esterification and by other procedures in the strength, elastic, and adhesion properties.

Numerous studies have shown that the properties of polymeric systems can be appreciably changed by varying the dispersity of one of the components in the medium of another component in preparation of compounds from polymer blends. One of such properties is the stability of the system (resistance to phase separation). In the first step of this study, we examined the possibility of preparing stable epoxy–rubber systems in an RPA in which it is possible to attain high shear stress by varying the shear rate, and thus to attain fine dispersion of one of the components in the medium of the other component.

Depending on the viscosity and component ratio, it is possible to obtain stable systems in RPA by varying the rotation rate of the working parts or the clearance between the rotor and stator (variation of the shear rate), and also by varying the number of passages through the working zone of the apparatus and the flow rate (variation of the residence time in the treatment zone). In this study, as expected, we obtained the most stable systems at equal amounts of the components. With an RPA of the standard design (without static mixer), a threefold treatment of the SKI-10KTR : ED-20 = 1 : 1 blend yielded a system that did not undergo phase separation in 14 days.

In the second step of our study, we examined the possibility of performing a chemical reaction between the functional groups of the oligomers being mixed. In the first step, we prepared a homogeneous system stable in time and hence provided the most favorable conditions for the reaction between the functional groups; whereas in the second step, we promoted the chemical reaction between the oligomers by making the stirring conditions more "severe." Upon sixfold passage of the components through the working zone of the apparatus (without static mixer), we obtained a system whose analysis suggested the occurrence of the chemical reaction between the components.

As already noted, the spectrum of the blend obtained mechanically without RPA contains two bands at 1710 and 1740 cm^{-1}. In the spectrum of the product of preliminary esterification, the first band is absent. The spectrum of the product obtained in RPA also has an absorption band at 1740 cm^{-1}, but it is less intense than in the previous case. After repeated passages of the blend through the working zone of the mixer, the spectra of the products of preliminary esterification and RPA treatment became virtually identical. The formation of a chemical compound was also confirmed by other methods and by the results of physicomechanical and service tests of the compounds (Table 2).

Table 2. Physicomechanical and service properties of compounds prepared by different procedures

Parameter	Product of RPA treatment	Product of preliminary esterification	Mechanical blend
Tensile strength, MPa	14.0	13.2	4.3
Relative elongation, %	58.0	66.0	10.0
Adhesion strength, MPa	12.2	11.5	4.0

Table 3. Optimal parameterts $\tau\gamma$ for compounds with varied rubber content *c*

c, %	$\tau\gamma$, kJ mol^{-1}	
	ED-20 + SKN-10KTR	ED-20 + SKD-KTRA
10	590–620	600–630
20	650–750	700–800
30	850–950	850–950
40	900–1000	900–1050
50	950–1050	1000–1100

In practice, to obtain a chemical compound, there is no need in repeated passage of the raw materials through the working zone of RPA. On setting the energy of the bond ruptured in chemical modification, it is necessary to estimate the criteria $\tau\gamma$ and $\mu y'$, required for mechanochemical cracking, and to calculate appropriate process modes.

Analysis of the reaction between a carboxyl-containing rubber and an epoxy resin to give a chemical compound, shows that, first, it is necessary to break the C–O bond (according to different sources, its energy varies from 314 to 322.6 kJ mol^{-1}). Thus, $\tau\gamma$ should exceed this value. It is also necessary to take into account the energy consumption for dispersion of one of the components in the other one, their homogenization, etc., which, in turn, depends on the ratio of the component viscosities and concentrations in the two-phase system.

The optimal values of $\tau\gamma$ for compounds with varied rubber content are given in Table 3.

Using the procedure for RPA calculation [6] and knowing the required $\tau\gamma$, we can calculate the appropriate process modes. At the same time, in some cases, a single passage of the material through the RPA working zone is insufficient to perform the process. In this case, the most acceptable way is to improve the apparatus design (e.g., to combine RPA with a static mixer [8]).

CONCLUSIONS

(1) Treatment of blends of low-molecular-weight carboxyl-containing rubbers and epoxy resins in a rotary pulsation apparatus at a definite value of the external energy effect ensures a chemical reaction between the components and preparation of high-quality adhesives.

(2) It is appropriate to use as a criterion of the external energy effect the strain energy density and strain intensity; this allows calculation of process modes for efficient treatment of blends in a rotary pulsation apparatus, depending on the component ratio.

REFERENCES

1. Brower, J., *Adhes. Age*, 1996, vol. 39, no. 9, pp. 16–18.
2. Kang Sung, K. and Purushothman, S., *J. Electron. Mater.*, 1999, vol. 28, no. 11, pp. 1314–1318.
3. Okamatsu, T., *Sci. Ind. (Osaka)*, 1999, vol. 75, no. 5, pp. 240–245.
4. Hasegawa, K., *J. Adhes. Soc. Jpn.*, 1999, vol. 35, no. 11, pp. 531–532.
5. Veselovskii, R.A., *Regulirovanie adgezionnoi prochnosti polimerov* (Control of the Adhesion Strength of Polymers), Kiev: Naukova Dumka, 1988.
6. Bogdanov, V.V., Khristoforov, E.I., and Klotsung, B.A., *Effektivnye maloob"emnye smesiteli* (Efficient Small-Volume Mixers), Leningrad: Khimiya, 1989.
7. USSR Inventor's Certificate, no. 725 691.
8. RF Patent 2 056 154.

Russian Journal of Applied Chemistry, Vol. 77, No. 4, 2004, pp. 639–644. Translated from Zhurnal Prikladnoi Khimii, Vol. 77, No. 4, 2004, pp. 643–648.

MACROMOLECULAR CHEMISTRY AND POLYMERIC MATERIALS

Carbonization of Polyacrylonitrile Composites with Nitrogen-containing Cellulose Derivatives

Yu. N. Sazanov, L. A. Nud'ga, A. V. Novoselova, V. L. Ugolkov, G. N. Fedorova, E. M. Kulikova, and A. V. Gribanov

Institute of Macromolecular Compounds, Russian Academy of Sciences, St. Petersburg, Russia

Institute of Silicate Chemistry, Russian Academy of Sciences, St. Petersburg, Russia

Received February 18, 2004

Abstract—Thermal carbonization of nitrogen-containing cellulose derivatives (chitin, chitosan, cyanoethyl chitosan, cyanoethyl cellulose, copolymers of allyl carboxymethyl cellulose with polyacrylonitrile) as models of probable products of thermal reaction of cellulose with polyacrylonitrile was studied. The quantitative characteristics of carbonization of the model compounds are influenced by the nitrile group.

Polycarylonitrile (PAN) and a number of cellulose derivatives are the most widely used precursors of carbonized products [1]. Numerous materials based on their carbonizates are commercially produced for chemical industry, power engineering, and medicine. It has been shown previously [2–5] that joint carbonization of PAN with other nitrogen-containing polymers, mainly with polyheterocycles, involves thermal reactions between the starting macromolecules. In various steps of these reactions, new compounds are formed, whose carbonization yields products of a polycarbon structure with a number of specific properties. An analysis of these thermal reactions revealed a particular role of nitrogen atoms in formation of the carbonizate structure in the initial step of the reactions of PAN with the polymers examined; nitrogen atoms present in the starting polymers affect the properties of the final carbonization product [6–8]. Since these effects were mainly observed in reactions of PAN with various nitrogen-containing polyheteroarylenes, we examined in this study thermochemical reactions of PAN with nitrogen-containing polysaccharides and their derivatives.

To record changes in the kinetics of thermal reactions of the starting compounds depending on their structure and ratio and on the heat treatment conditions, we used various methods of thermal analysis in the dynamic and isothermal modes in the temperature range 20–1000°C. The reaction products were studied by elemental analysis, pyrolytic gas chromatography (PGC), and spectroscopy.

As nitrogen-containing polysaccharides, we used chitin (CT) and chitosan (CTS), substances with virtually unlimited resources of raw materials, showing much promise as precursors of carbonized products. It should be noted that there are no papers focused on the carbonization of CT and CTS, and also of their blends with other compounds. Certain aspects of thermal degradation of CT, CTS, and their blends with other compounds were considered in [9–16]; according to these papers, their degradation, as that of PAN, involves formation of reactive intermediates which can react by intra- and intermolecular pathways.

The goal of this study was to determine the conditions and mechanism of carbonization of chitin and chitosan and of their blends with PAN. CT and CTS were prepared and pretreated according to [17, 18]; PAN was synthesized using radical (r-PAN) and anionic (c-PAN) catalysts [19].

The kinetics of thermal degradation in a vacuum was studied by thermovolumetric analysis (TVA); the thermal oxidative degradation was monitored by TGA and DTA. The results (Figs. 1, 2) show that the thermal reactions are the most intense in the range 150–350°C.

Thermal degradation in a vacuum (Fig. 1, curve *1*) follows the mechanism of transformation of r-PAN into the cyclic analog of PAN, considered in [19]. At 200°C, vigorous release of volatiles is observed, with a maximum at 215°C and weight loss of 21.5%. These products mainly consist of nitrogen-containing

1070-4272/04/7704-0639 © 2004 MAIK "Nauka/Interperiodica"

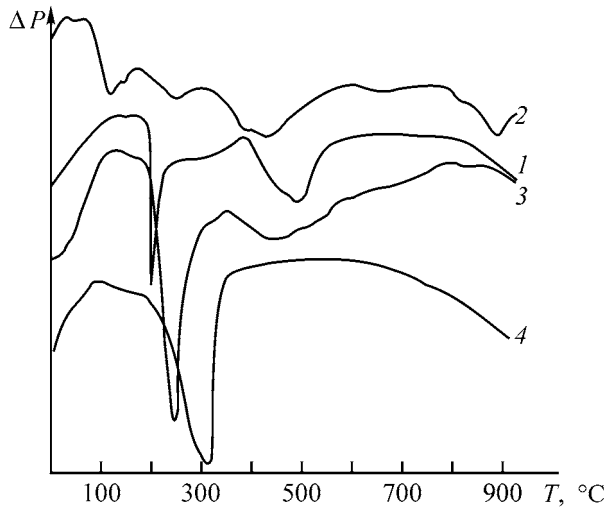

Fig. 1. TVA curves of (*1*) r-PAN, (*2*) c-PAN, (*3*) chitosan, and (*4*) chitin. (Δ*P*) Pressure change and (*T*) temperature.

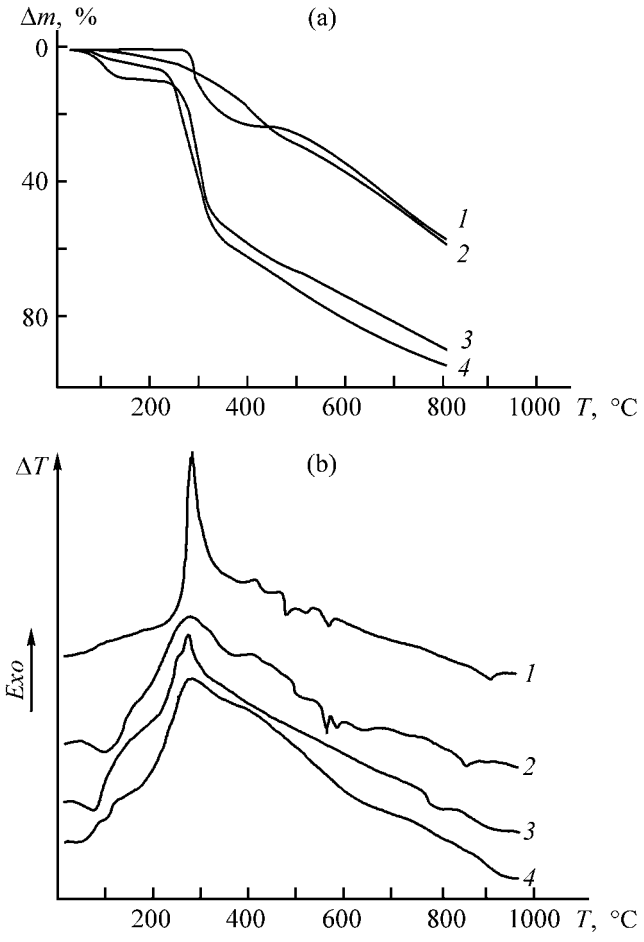

Fig. 2. (a) TG and (b) DTA curves of (*1*) r-PAN, (*2*) c-PAN, (*3*) chitosan, and (*4*) chitin: (Δ*m*) weight loss, (Δ*T*) temperature difference, and (*T*) temperature; the same for Fig. 4.

compounds, such as HCN, NH_3, acrylonitrile, and acetonitrile.

On further heating, at 500–600°C, the rate of the release of volatiles and their amount appreciably decrease, with hydrogen and ammonia becoming prevalent. Under these conditions, degradation prevails over carbonization, and the weight loss of r-PAN reaches 80% at 900°C.

In the case of partially cyclized polyacrylonitrile (c-PAN), the kinetics of gas release under the same heating conditions is appreciably different throughout the temperature range studied (Fig. 1, curve *2*). The gas release occurs with several peaks, but separate steps cannot be distinguished, in contrast to the case of r-PAN.

Unexpectedly, the pattern of thermal degradation of CT and CTS samples, despite the quite different structure of the starting polymers, is qualitatively similar to that of r-PAN as regards the release of low-molecular-weight degradation products. The major amount of volatiles is released in the ranges 150–315°C from CT and 200–260°C from CTS. These effects are related to the breakdown of acetamide- and amine-containing glucopyranose rings, accompanied by the formation of a wide variety of low-molecular-weight oxygen- and nitrogen-containing compounds. The main of these are water, methanol, pyridine, acetamide, levoglucosan, and a number of picoline derivatives. On heating to 320–350°C, CT and CTS lose about 70% of their weight, and at 900°C the amount of the carbonized residue does not exceed 8–10%. According to PGC, whose qualitative aspects will be considered later, the gas release peaks in isothermal heating of CT and CTS samples are shifted to 300–450°C. Thus, the fairly close coincidence of the temperature ranges in which the release of volatile thermal degradation products from PAN, CT, and CTS reaches a maximum suggests that the reactive compounds released from PAN and the polysaccharides may react with each other when these compounds are thermolyzed in a blend.

When these polymers are subjected to thermal oxidative degradation in a self-generated atmosphere, the temperature of intense thermal reactions occurring on heating is still narrower (Figs. 2a, 2b). According to DTA data (Fig. 2b), the peaks of the exothermic reactions of all the four samples are observed at 260 ± 5°C. Hence, this temperature seems to be the best for performing thermal reactions of the intermediate degradation products. Also, curves in Fig. 2 can be considered as reference characteristics of the polymers from which it is possible to evaluate the thermal characteristics of the cocarbonization products. In particular, from the viewpoint of relative heat resistance,

r-PAN is the most stable, showing no weight loss up to almost 300°C; at 800–900°C, its coke residue varies within 40–50%. Contrastingly, c-PAN starts to release low-molecular-weight gaseous products of thermal oxidative degradation even at 150°C; however, its coke residue at 800–900°C is almost equal to that of r-PAN. In addition to these characteristics, recording of thermal effects by DTA reveals differences in intensities of thermal reactions and, in some cases, allows characterization of the reactivity of the intermediates formed in the course of the heat treatment. The DTA curve of r-PAB exhibits a strong exothermic effect at approximately 300°C, accompanied by a 30% weight loss in 5–7 min, whereas the thermal effect observed with c-PAN in the same temperature range is considerably weaker. The endothermic effects observed in the DTA curves for both PAN samples in the range 450–600°C deserve particular consideration with spectroscopic examination of the transformation products. These effects (peaks at 455 and 545°C for r-PAN and at 530 and 550°C for c-PAN) can be assigned to certain partially ordered domains formed at temperatures of PAN precarbonization.

As for the kinetics of thermal degradation of CT and CTS (Fig. 2, curves *3*, *4*), the highest rate of the release of volatiles is observed in the same temperature range as with PAN and is comparable with the rate of thermal oxidative degradation of c-PAN. The values of the total thermal effects of degradation of CT, CTS, and c-PAN are also comparable. It should be noted, however, that the weight loss in degradation of CT and CTS in this temperature range is 45–55%, and on further heating the weight loss in carbonization is almost equal to the rate of carbonization of PAN; at 850–900°C the samples almost fully burn out.

Thus, the results of a thermal analysis of all the samples in hand suggest that, first, all the intermediate degradation products of these polymers can enter thermal reactions with each other and, second, PAN can initiate carbonization of CT and CTS; the specific synergism in cocarbonization with polysaccharides can be manifested through formation of precarbonizates, with a simultaneous increase in the coke residue.

To confirm this conclusion, we prepared a series of polysaccharides whose structure can simulate, to a certain extent, the intermediates formed in reactions of cellulose derivatives, CT, and CTS with PAN and its degradation products. Of particular interest among these compounds are cellulose derivatives containing a nitrile group, in particular, cyanoethyl cellulose (CEC) and cyanoethyl chitosan (CECTS) as products of the initial step of the reaction between the above

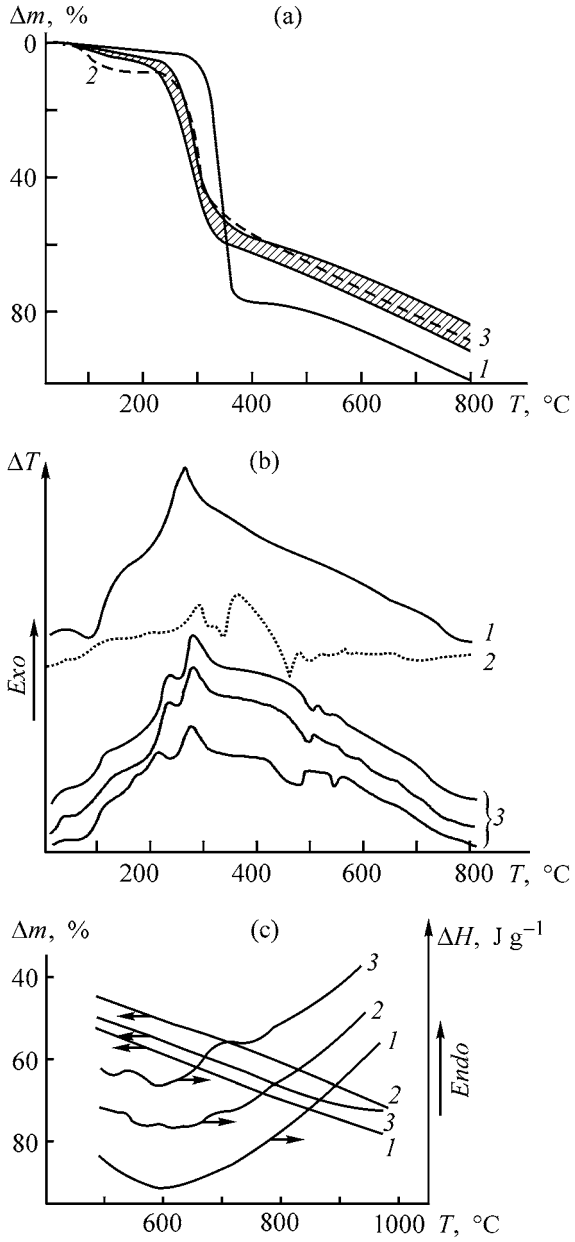

Fig. 3. (a) TG, (b) DTA, and (c) TG + DSC curves of polymers: (Δm) weight loss, (ΔT) temperature difference, (ΔH) heat of reaction, and (T) temperature. (a, b) (*1*) CEC, (*2*) chitosan, and (*3*) CECTS samples with γ = 154–191 (cross-hatched area in Fig. 3a). (c) (*1*) Chitosan; (*2*) CECTS, γ = 166; and (*3*) CECTS, γ = 191.

polymers. For thermochemical studies, we chose several samples of CECTS with the degree of substitution γ, from 51 to 191 and, for comparison, a CEC sample with γ = 280 [18].

Figure 3 shows as examples the TG and DTA curves of CEC and CECTS samples, recorded in a self-generated atmosphere. A comparative kinetic study

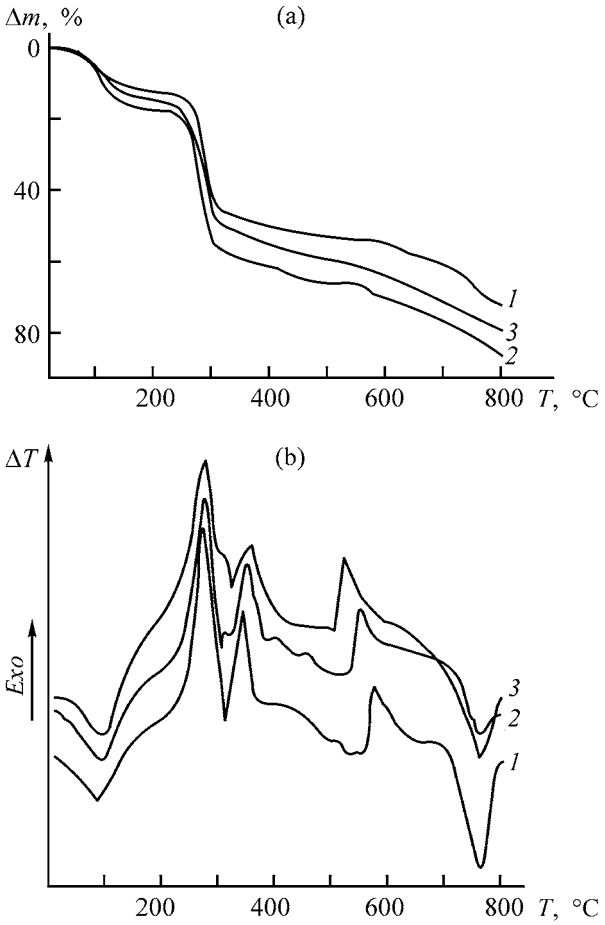

Fig. 4. (a) TG and (b) DTA curves of polymers: (*1*) CMC; (*2*) ACMC, γ = 6; and (*3*) ACMC, γ = 25.

of the thermal oxidative degradation of these compounds demonstrated that the coke residue of CECTS is within 10–18% and grows with increasing degree of substitution. The coke residue is similar to that obtained with unsubstituted CTS; appreciable differences are observed only in the initial step of degradation, corresponding to the release of sorbed water. As for CEC, although it fully burns out at 800°C, it considerably surpasses CECTS in the heat resistance, being comparable with PAN at temperatures below 300°C. This fact shows that the nitrile groups noticeably enhance the heat resistance of cellulose derivatives and affect the carbonization mechanism.

The effect of cyanoethylation of hydroxy groups in the glucopyranose unit of chitosan is still more pronounced when the thermal effects accompanying thermal oxidative degradation of CTS and CEC are considered (Fig. 3b). The degree of substitution in CECTS exerts a certain effect on the shape of the DTA curves (Fig. 3b, curve *3*). These curves noticeably differ from those obtained with CTS and CEC (Fig. 3b, curves *1*, *2*). It should be noted that, with substituted CTS samples, we revealed for the first time noticeable differences in the thermal effects of carbonization above 500°C. A similar pattern is observed in thermal degradation of the same CEC and CECTS samples in a vacuum. Such differences were observed, according to DSC, even in carbonization of small samples in a nitrogen atmosphere (Fig. 3c). It is clearly seen that the CECTS samples with γ = 191 show endothermic effects at 571 and 703°C. The rate of the weight loss in this step of carbonization remains the same for all the samples.

The other compounds simulating the possible products of thermal reactions of PAN with polysaccharides are graft copolymers of PAN with cellulose derivatives. These include copolymers of allyl carboxymethyl cellulose (ACMC) with PAN, prepared using radical catalysts, with the degree of substitution with allyl groups, γ_A = 6, and degrees of grafting, *C*, from 130 to 670. To reveal the role of allyl groups in ACMC and the influence of their content, we studied the samples with γ_A = 20 and 25, and also a CMC sample. According to the TG and DTA curves recorded in the self-generated atmosphere, the course of degradation of these compounds is qualitatively similar to that of cellulose under similar conditions [20], but quantitative differences in the heat resistance are noticeable. The CMC sample is more stable than ACMC with γ_A = 25 but less stable than ACMC with γ_A = 6.

Similar trends were observed in a comparative study of cellulose allyl and sulfoethyl ethers [21]. The allyl groups exert a dual effect. On the one hand, allyl groups form primary cross-links on heating the samples to 120–200°C. On the other hand, these groups are readily oxidized, which results in an accelerated weight loss on heating. Figure 4a shows that, at a higher degree of substitution of ACMC (γ = 25), cross-linking prevails, enhancing the heat resistance of the sample as compared to that with γ = 6. As for CMC (Fig. 4a, curve *1*), this ether degrades to a lesser extent in the initial steps of heat treatment, approaching in the heat resistance unsubstituted cellulose. This is confirmed by comparison of thermal effects observed in thermal oxidative degradation of the samples (Fig. 4b).

As for thermal degradation of ACMC–PAN copolymers (Figs. 5, 6), grafting of PAN to the allyl groups of ACMC appreciably affects the course of the reactions occurring in the samples on heating.

The curves of thermal degradation in a vacuum (Fig. 5) show that the pattern observed with the graft copolymer is a superposition of the patterns characteristic of ACMC and r-PAN. As the degree of PAN grafting to ACMC is increased from 130 to 670, the relative intensities of the corresponding peaks are redistributed. For example, the characteristic peak of thermal transformation of PAN into the cyclic state (peak at 215°C) has almost the same intensity in the case of the PAN–ACMC copolymer with C = 670 and is ill-defined at C = 130. At the same time, the sample with C = 130 (curve *2*) exhibits a well-defined peak of thermal degradation of ACMC (maximum at 182°C). On further heating of the copolymer, certain characteristic features of PAN degradation in the range of low-temperature carbonization are seen (broadened peaks at 450–500°C), but the peaks at 340 and 535°C characteristic of ACMC are fully absent. In the range 750–870°C, the copolymer exhibits gas-release peaks characteristic of high-temperature degradation of the carbonized ACMC residue, but these peaks are somewhat shifted to higher temperatures. A similar pattern is observed with the other copolymer samples with C in the range from 130 to 670.

The TG curves in Fig. 6, recorded under conditions of limited thermal oxidation (self-generated atmosphere), show how the coke residue depends on the degree of PAN grafting to ACMC. As the degree of grafting grows, the coke residue noticeably increases: from 13 for ACMC without grafted PAN to 52 for the copolymer with C = 670. The grafting of PAN to ACMC also enhances the heat resistance of the copolymer in the low-temperature range (75–250°C). It is particularly interesting that, at high degrees of PAN grafting (from 470 to 670) (Fig. 6, curves *5–7*), the coke residue of the copolymers is 10–14% higher, compared to PAN homopolymer. These observations suggest that the carbonization of the graft copolymers above 400°C occurs by the mechanism differing from that observed with PAN and ACMC. This is indicated by the pattern of thermal effects accompanying the carbonization of the homopolymer and copolymers with a high PAN content (Fig. 7). These results suggest the occurrence of a directional carbonization of ACMC, with blocking of the reactive groups of cellulose; this process may occur simultaneously or successively with intramolecular cyclization of PAN side chains in the graft copolymer. Our results show that the bonding of cellulose macromolecules with acrylonitrile (CEC) or polyacrylonitrile (PAN–ACMC) appreciably increases the carbonizate yield under optimal cocarbonization conditions.

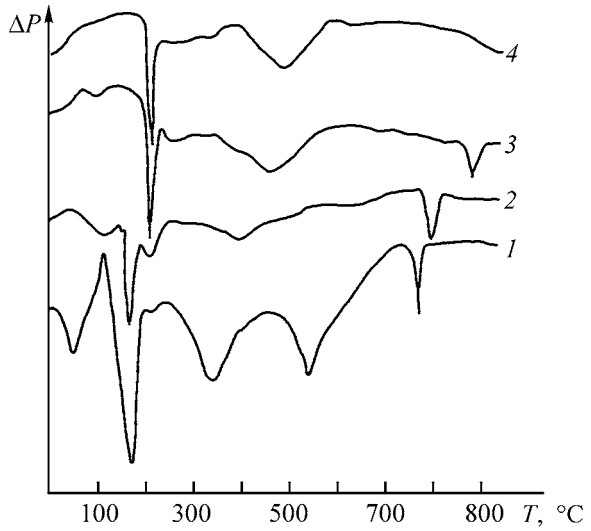

Fig. 5. TVA curves of (*1*) ACMC, γ = 25; (*2*) PAN–ACMC, C = 130; (*3*) PAN–ACMC, C = 670; and (*4*) r-PAN.

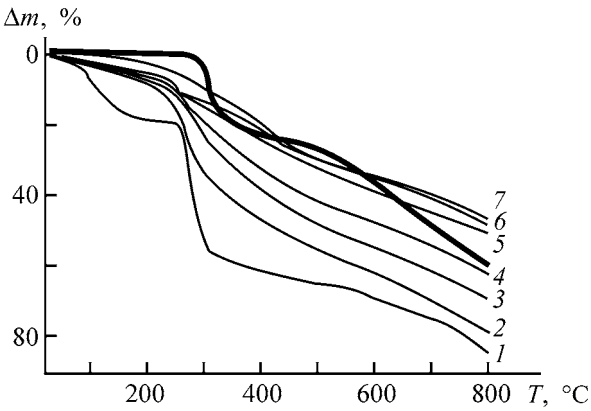

Fig. 6. TG curves of (*1*) ACMC and (*2–6*) ACMC–PAN with C (*2*) 130, (*3*) 220, (*4*) 370, (*5*) 470, and (*6*) 620. (Δm) Weight loss and (T) temperature.

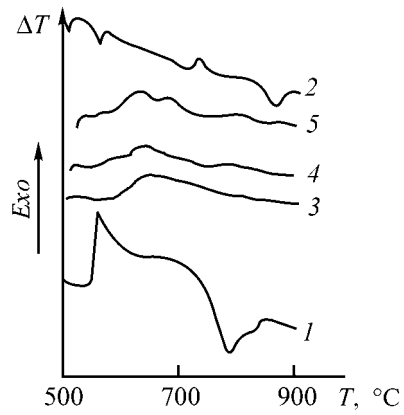

Fig. 7. DTA curves of carbonization of (*1*) ACMC, (*2*) r-PAN, and (*3–5*) r-PAN–ACMC copolymers with C (*3*) 470, (*5*) 620, and (*6*) 670. (ΔT) Temperature difference and (T) temperature.

CONCLUSIONS

(1) In cocarbonization, the carbonized structures of cellulose ethers and polyacrylonitrile affect each other, so that the coke residue becomes higher than that obtained with polyacrylonitrile under the same conditions.

(2) Pathways of thermal reactions of chitin and chitosan with polyacrylonitrile were determined in experiments with the model compounds (cyanoethyl cellulose, cyanoethyl chitosan, and graft copolymers of cellulose ethers and polyacrylonitrile).

REFERENCES

1. Perepelkin, K.E., *Khim. Volokna*, 2002, no. 4, pp. 32–40.
2. Sazanov, Yu.N., Shirokov, N.A., and Goltsin, B.E., *Thermochim. Acta*, 1979, vol. 32, pp. 73–79.
3. Sazanov, Yu.N., Simanovich, I.E., Szekely, T., and Blážo, M., Abstracts of Papers, *Poly Kondensation 1989: XII Int. Microsimp. Poly Kondensation*, Schwerin (GDR), 1989, p. 61.
4. Sazanov, Yu.N., Spirina, T.R., Novoselova, A.V., *et al.*, Abstracts of Papers, *X Vsesoyuznoe soveshchanie po termoanalizu* (X All-Union Meet. on Thermal Analysis), Leningrad, 1989, p. 197.
5. Sazanov, Yu.N., *J. Thermal Anal.*, 1990, vol. 36, no. 2, pp. 361–376.
6. Gribanov, A.V. and Sazanov, Yu.N., *Zh. Prikl. Khim.*, 1997, vol. 70, no. 6, pp. 881–902.
7. Gribanov, A.V. and Sazanov, Yu.N., *Zh. Prikl. Khim.*, 2000, vol. 73, no. 3, pp. 465–469.
8. Gribanov, A.V. and Sazanov, Yu.N., Abstracts of Papers, *Uglerod: fundamental'nye problemy nauki, materialovedenie, tekhnologiya: 2-ya mezhdunarodnaya konferentsiya* (Carbon: Basic Research Problems, Materials Science, Technology: 2nd Int. Conf.), Moscow, 2003, p. 87.
9. Muzzarelli, R.A.A., *Chitin*, London: Pergamon, 1977.
10. Sazanov, Yu.N., Fedorova, G.N., Plisko, E.A., and Nud'ga, L.A., *Zh. Prikl. Khim.*, 1980, vol. 53, no. 9, pp. 2143–2146.
11. Van der Koaden, Boon, J.J., Leeuw, J.W., *et al.*, *Anal. Chem.*, 1984, vol. 56, no. 12, pp. 2160–2166.
12. Alonso, G., J. *Thermal Anal.*, 1983, vol. 27, no. 2, pp. 257–262.
13. Alonso, G. and Vega, D.O., *J. Thermal Anal.*, 1990, vol. 36, no. 4, pp. 1347–1354.
14. Mar'in, A.P. and Shlyapnikov, Yu.A., *Vysokomol. Soedin., Ser. A*, 1980, vol. 22, no. 3, pp. 589–594.
15. Mar'in, A.P., Feofilova, E.P., Genin, Ya.V., *et al.*, *Vysokomol. Soedin., Ser. B*, 1982, vol. 24, no. 9, pp. 658–662.
16. Martin-Gil, E.J., Leal, J.A., Gomez-Meranda, B., *et al.*, *Thermochim. Acta*, 1992, vol. 211, pp. 241–254.
17. Nud'ga, L.A., Plisko, E.A., and Danilov, S.N., *Zh. Obshch. Khim.*, 1971, vol. 41, no. 12, pp. 2555–2559.
18. Nud'ga, L.A., Plisko, E.A., and Danilov, S.N., *Zh. Obshch. Khim.*, 1974, vol. 45, no. 5, pp. 1145–1149.
19. Sazanov, Yu.N., Shirokov, N.A., and Goltsin, B.E., *Thermochim. Acta*, 1978, vol. 24, pp. 81–88.
20. Nud'ga, L.A., Petrova, V.A., Petropavlovskii, G.A., and Sazanov, Yu.N., *Zh. Prikl. Khim.*, 1991, vol. 64, no. 7, pp. 1523–1528.
21. Sazanov, Yu.N., Plisko, E.A., Nud'ga, L.A., *et al.*, *Zh. Prikl. Khim.*, 1981, vol. 54, no. 3, pp. 691–697.

Russian Journal of Applied Chemistry, Vol. 77, No. 4, 2004, pp. 645–648. Translated from Zhurnal Prikladnoi Khimii, Vol. 77, No. 4, 2004, pp. 649–652.

MACROMOLECULAR CHEMISTRY AND POLYMERIC MATERIALS

Oxidative Ammonolysis of Vegetable Raw Materials

M. V. Efanov, D. V. Dudkin, and M. V. Popova

Altai State University, Barnaul, Russia

Received September 10, 2003

Abstract—The influence of the composition of lignocarbohydrate vegetable raw materials, process duration (15–120 min), amount of hydrogen peroxide (0.1–0.9 g per gram of raw materials), and amount of ammonia (0.25–1.5 g per gram of raw materials) on the yield of the target product and on the nitrogen content and the content of functional groups in it in mechanochemical treatment of vegetable wastes with hydrogen peroxide in aqueous ammonia (oxidative ammonolysis) was studied. Sorption and agrochemical testing of the resulting samples as nitrogen-containing ion exchangers and fertilizers was performed.

In treatment of wood and other vegetable raw materials, significant amounts of wastes (bark, sawdust, straw, etc.) are formed. At present, these wastes are not utilized. The promising way of utilization of these wastes is their use as raw materials for production of fertilizers and sorbents [1, 2].

For production of nitrogen-containing fertilizers from wood bark, a procedure involving treatment of raw materials with oxygen in aqueous ammonia (oxidative ammonolysis) has been suggested [1, 3]. The main drawbacks of this procedure are elevated temperature (75–200°C), oxygen pressure of up to 8 MPa, and rather low content of nitrogen in the resulting fertilizer (1–3.5%).

A mechanochemical procedure for production of nitrogen-containing fertilizers and sorbents based on wood by oxidation with ammonia solution of ammonium persulfate at 20°C and atmospheric pressure has been developed previously [4]. However, practical implementation of the procedure is limited by the high cost of ammonium persulfate and its relatively high expenditure. Publications on oxidation of vegetable raw materials with hydrogen peroxide in aqueous ammonia are virtually lacking.

In this study, we examined the influence of the conditions of oxidation with hydrogen peroxide in aqueous ammonia on the yield and characteristics of nitrogen-containing derivatives of lignocarbohydrate materials produced by mechanochemical oxidative ammonolysis.

EXPERIMENTAL

As the raw materials we used air-dry sawdust (0.5-mm fraction) of the following lignocarbohydrate materials (LCHM): birch wood, aspen wood, pine wood, flax shive, and sunflower and buckwheat husk. The raw materials were analyzed by the procedure described in [5]. The data obtained are listed in Table 1. The target product of oxidative ammonolysis is the sol-

Table 1. Characteristics of nitrogen-containing lignocarbohydrate materials (LCHMs) (milling duration 60 min; 0.3 g of H_2O_2 and 0.25 g of NH_3 per gram of raw materials)

Initial LCHM sample	Content in the initial samples, %					Yield, %	Content in modified LCHM, %		
	cellulose	lignin	N	COOH	OCH_3		N	COOH	OCH_3
Wood:									
birch	45.8	19.6	0.5	2.2	5.5	96.5	1.8	3.5	5.1
aspen	49.6	21.2	0.6	2.1	5.7	94.7	2.5	4.2	4.8
pine	53.8	26.1	0.5	2.4	4.8	93.8	3.1	4.9	2.6
Sunflower husk	31.9	29.3	0.7	2.8	3.9	91.5	3.6	6.3	3.1
Flax shive	36.3	31.7	0.7	2.9	3.4	89.4	4.3	7.4	2.7
Buckwheat husk	35.9	34.6	0.9	3.1	3.2	88.3	4.6	7.9	2.4

1070-4272/04/7704-0645 © 2004 MAIK "Nauka/Interperiodica"

Table 2. Influence of duration of mechanochemical synthesis on the characteristics of the products of pine wood oxidation with a mixture of hydrogen peroxide and ammonia (0.3 g of H_2O_2 and 0.25 g of NH_3 per gram of raw materials)

Time, min	Yield, %	Content, %		
		N	COOH	OCH_3
–	–	0.5	2.4	4.8
15	94.6	1.2	2.9	4.1
30	95.2	1.9	3.5	3.5
45	94.3	2.4	4.2	2.9
60	93.8	3.1	4.9	2.6
75	92.5	3.3	5.8	2.3
90	92.1	3.7	6.7	2.2
120	90.6	3.9	7.2	2.1

id residue insoluble in the reaction mixture and containing nitrogen atom and carboxy groups. The process was carried out as follows. A 3.0-g weighed portion of the 0.5-mm fraction of sawdust of vegetable raw materials was placed in a cylindrical reactor of a 300 cm^3 vibrational mill (IV-98B vibrator, frequency 2800 min^{-1}) with 15 steel rods (10 × 100 mm).

Into a temperature-controlled reactor, a 30% solution of hydrogen peroxide (0.1–0.9 g H_2O_2 per gram of the raw materials) and a 25% solution of ammonia (0.25–1.5 g of NH_3 per gram of the raw materials) were introduced, and the mixture was subjected to intensive mechanical grinding at 25°C for 15–120 min. Then, the reaction mixture was discharged from the mill and separated from the milling bodies. The products were washed with distilled water to pH 6–7 and dried in a desiccator to constant weight, and the yield was determined (percent relative to the weight of the raw materials).

The content of bound nitrogen in the product was determined by the Kjeldahl procedure [6]; the content of carboxyl groups, by conductometric back-titration [7]; and the amount of methoxyl groups, by the Zeisel method using gas–liquid chromatography [7]. The agrochemical testing of the resulting products as nitrogen-containing fertilizers for peas was carried out by the method of vegetation experiments, in which the plant height, the weight of the dry substance, and the chlorophyll content in the plant were determined as the growth index [8]. The sorption capacity of nitrogen-containing derivatives of pine wood for cations of some *d* elements was determined under equilibrium conditions, using the p°rocedure described in [2].

As can be seen from Table 1, the ammonolysis products are obtained from various types of wood in a somewhat higher yield than from other lignocarbohydrate materials (nonwood vegetable raw materials), which may be due to oxidative degradation of lignin and polysaccharides contained in these raw materials during mechanochemical oxidation in aqueous ammonia.

It was found that lignocarbohydrate materials containing greater amount of lignin undergo ammonolysis more efficiently. The products of ammonolysis of nonwood vegetable raw materials contain a lower amount of methoxy groups than the products based on various types of wood, excluding pine wood. This may be due to the structural features of lignins of annuals and pine, high content of nonmethoxylated *p*-hydroxyphenylpropane and guaiacyl structures [5], an also their high reactivity in ammonolysis (Table 1). Variation of the functional composition of vegetable raw materials was considered for pine wood as an example. The influence of the duration of mechanochemical treatment on the composition of the products of oxidative ammonolysis of pine wood is illustrated by Table 2.

Table 2 shows that, with increasing duration of mechanical milling of wood in the presence of hydrogen peroxide in the ammonia medium, the content of bound nitrogen and carboxy groups steadily increases, i.e., the oxidative binding of nitrogen takes place. Oxidation of wood in the ammonia medium results in demethylation with the loss of approximately 25–55% of methoxy groups of their initial content. Within 90 min from the beginning of the reaction, up to 3.7% N is incorporated into the wood composition. With increasing process duration, the yield of the resulting products decreases, apparently, due to growing extent of mechanochemical degradation of wood in the ammonia medium (Table 2).

The influence of the amount of oxidizing agent (hydrogen peroxide) on the functional composition of nitrogen-containing derivatives of pine wood was studied. The results obtained (Table 3) show that, with increasing amount of hydrogen peroxide per gram of raw materials, the product yield decreases. This is apparently caused by oxidative mechanochemical degradation of wood. With the content of oxidizing agent increasing from 0.1 to 0.6 g per gram of raw materials, the content of carboxy groups increases from 2.9 to 7.1%, i.e., oxidation of wood is enhanced with parallel binding of nitrogen.

Further increase in the amount of hydrogen peroxide to 0.9 g per gram of raw materials does not result in a significant oxidation of wood. In this case, an in-

crease in content of the hydrogen peroxide results in oxidative demethylation of wood with the loss of 10–65% of methoxy groups relative to their initial amount (Table 3).

The influence of the amount of ammonia on the characteristics of nitrogen-containing derivatives of pine wood is shown in Table 4. With increasing amount of ammonia per gram of raw materials, the yield of nitrogen-containing derivatives of wood somewhat decreases due to degradation.

Raising the ammonia content results in a steady increase in the content of bound nitrogen and carboxy groups in the products of oxidative ammonolysis of pine wood (Table 4). The demethylation of the resulting products is caused by a rise in the degree of ammonolysis with increasing content of ammonia.

To establish the nature of bound nitrogen, the resulting products were hydrolyzed by boiling with 1 M sodium hydroxide [7]. It was found that approximately 15–35% of bound nitrogen (ammonium and amide) is eliminated in hydrolysis, and the remaining amount of nitrogen (65–85%) is firmly bound in organic structures (amine and heterocyclic), in good agreement with published data on oxidative ammonolysis of lignin [7].

The product containing 3.7% bound nitrogen was tested as a nitrogen-containing fertilizer for peas of the "Sakharnyi" variety. It was shown that nitrogen-containing derivatives of pine wood stimulate the pea plant growth by 25–30%, increasing the total biomass by 45–60% and the chlorophyll content in the plants by 58–113%.

Hence, nitrogen-containing derivatives of pine wood stimulate pea growth and can be used as nitrogen-containing organic fertilizers for crops.

Data on sorption capacity of nitrogen-containing derivatives of pine wood with respect to Zn^{2+}, Cd^{2+}, and Cu^{2+} cations are given in Table 5.

As the experimental results show, the sorption capacity of the products of oxidative ammonolysis of wood with respect to the series of the cations studied depends on the content of nitrogen and COOH groups in these products.

The static exchange capacity (SEC) of nitrogen-containing derivatives of wood is fairly high for all the cations studied, which is caused by the high content of carboxy groups (Table 5).

The high sorption capacity of the products of oxidative ammonolysis of wood with a high content of COOH groups, which contain up to 3.7% nitrogen, for multicharged cations is due to their chelating properties.

Thus, the products of oxidative ammonolysis of pine wood can be used as effective sorbents transition metal cations in their recovery from dilute solutions.

Table 3. Influence of the amount of hydrogen peroxide on the characteristics of nitrogen-containing derivatives of pine wood (milling duration 60 min, 0.25 g of NH_3 per gram of raw materials)

Amount of H_2O_2, g g^{-1}	Yield, %	Content, %		
		N	COOH	OCH_3
0.1	97.4	1.8	2.9	4.3
0.2	96.8	2.5	4.1	3.4
0.3	93.8	3.1	4.9	2.6
0.4	92.1	3.4	5.7	2.3
0.5	90.3	3.8	6.5	2.1
0.6	89.5	4.2	7.1	1.9
0.9	87.2	4.7	7.8	1.5

Table 4. Influence of the ammonia amount on the characteristics of nitrogen-containing derivatives of pine wood (milling duration 60 min, 0.3 g of H_2O_2 per gram of raw materials)

Amount of NH_3, g g^{-1}	Yield, %	Content, %		
		N	COOH	OCH_3
0.25	93.8	3.1	4.9	2.6
0.5	92.4	3.7	5.4	2.4
0.75	91.2	4.8	5.9	2.3
1.0	90.5	5.3	6.5	2.1
1.25	89.7	5.8	6.9	2.0
1.5	88.5	6.2	7.4	2.0

Table 5. Sorption power of nitrogen-containing derivatives of pine wood with respect to transition metal ions (concentration of MSO_4 solution 0.05 g-equiv l^{-1})

Sample	Content, %		SEC, mg-equiv g^{-1}		
	N	COOH	Zn^{2+}	Cd^{2+}	Cu^{2+}
Initial	0.5	2.4	0.7	0.8	1.0
1	1.9	3.5	2.5	3.2	3.8
2	3.7	6.7	3.6	4.4	4.7

CONCLUSIONS

(1) In oxidative ammonolysis of various vegetable raw materials with an ammonia solution of hydrogen peroxide, samples of lignocarbohydrate materials containing a larger amount of lignin are oxidized to a greater extent.

(2) Depending on the oxidation conditions, the products of oxidative ammonolysis of pine wood contain up to 6.2% organic bound nitrogen and up to 7.8% carboxy groups. Nitrogen-containing derivatives of wood contain 15–35% weakly bound (ammonium and amide) and 65–85% firmly bound (amine and heterocyclic) nitrogen relative to its total amount.

(3) Oxidative ammonolysis of pine wood with hydrogen peroxide in ammonia medium is accompanied by demethylation with loss of up to 65% of OCH_3 groups of their total amount.

(4) The resulting nitrogen-containing products have a high sorption capacity for Zn^{2+}, Cd^{2+}, and Cu^{2+} cations (SEC 2.5–4.7 mg-equiv g^{-1}) and can also be used as organic fertilizers.

REFERENCES

1. Deineko, I.P., Deineko, I.V., and Kornilova, L.I., *Zh. Prikl. Khim.*, 2002, vol. 75, no. 3, pp. 502–505.
2. Efanov, M.V., Dudkin, D.V., and Galochkin, A.I., *Zh. Prikl. Khim.*, 2002, vol. 75, no. 10, pp. 1745–1746.
3. USSR Inventor's Certificate, no. 545 627.
4. RF Patent no. 2 185 394.
5. Obolenskaya, A.V., Shchegolev, V.P., Akim, G.L., *et al.*, *Prakticheskie raboty po khimii drevesiny i tsellyulozy* (Practical Works on Chemistry of Wood and Cellulose), Moscow: Lesn. Prom–st., 1965.
6. Klimova, V.A., *Osnovnye mikrometody analiza organicheskikh soedinenii* (Main Micromethods of Analysis of Organic Compounds), Moscow: Khimiya, 1975.
7. Zakis, G.F., *Funktsional'nyi analiz ligninov i ikh proizvodnykh* (Functional Analysis of Lignins and Their Derivatives), Riga: Zinatne, 1987.
8. Dospekhov, B.A., *Metodika vegetatsionnogo opyta* (Procedure of Vegetation Experiment), Moscow: Kolos, 1985.

Russian Journal of Applied Chemistry, Vol. 77, No. 4, 2004, pp. 649–652. Translated from Zhurnal Prikladnoi Khimii, Vol. 77, No. 4, 2004, pp. 653–656.

MACROMOLECULAR CHEMISTRY AND POLYMERIC MATERIALS

Preparation of Water-Soluble Sulfur-containing Derivatives of Wood

M. V. Efanov, E. S. Filina, and M. V. Popova

Altai State University, Barnaul, Russia

Received September 30, 2003

Abstract—The influence of conditions of alkaline activation on xanthation of pine wood with mechanochemical preactivation was studied. It was shown that the duration of alkaline preactivation and the amount of sodium hydroxide exert a decisive effect on the degree of conversion of wood. The resulting macromolecular compounds are soluble in aqueous alkaline solutions and form viscous solutions.

Xanthation of cellulose, aimed at production of viscose fibers and films, is based on preparation of cellulose esters by the reaction of alkaline cellulose with carbon disulfide and is widely used in production of chemical fibers [1]. There are published data on the reaction of individual carbohydrate components of wood (cellulose, oligosaccharides, and hemicelluloses) with carbon disulfide in the presence of sodium hydroxide [2]. However, published data on direct xanthation of lignin, wood, and other lignocarbohydrate materials are virtually lacking.

A mechanochemical procedure for xanthation of wood and other lignocarbohydrate materials for production of water-soluble surfactants and fertilizers has been developed previously [3]. Here we describe how the conditions of alkaline pretreatment of pine wood affect the characteristics of water-soluble sulfur-containing polymers produced by its xanthation.

EXPERIMENTAL

A 0.5-mm fraction of air-dry sawdust of pine wood was used as the raw material. Composition of the raw materials (%): lignin determined by the Komarov method, 26.1; cellulose determined by the Kürschner method, 53.8; hemicellulose determined by the Wise method, 17.6. The content of hydroxy groups determined by the Werley acetylation method in the presence of pyridine [4] was 23.5%.

The sulfur content in the resulting products was determined by the Schoeniger method using the procedure described in [5] (error 0.1%). The degree of conversion of hydroxy groups in xanthation, α, was evaluated as the ratio of the content of bound sulfur, determined analytically, to the theoretical content (20.5%) evaluated from the content of hydroxy groups.

The xanthation procedure has been described previously [3]. Xanthation of wood involves mechanochemical activation in the presence of sodium hydroxide with and without addition of water, followed by xanthation proper. The reaction products were washed to remove thio salts with 5% solution of acetic acid in ethanol (50–100 ml) to pH 3–4 an then with ethanol to negative reaction for S^{2-} ion with lead(II) nitrate. The presence of thio salts in the filtrates was tested spectrophotometrically on an SF-46 spectrophotometer at λ = 335 nm (absorption of sodium trithiocarbonate).

The influence of the following factors on the characteristics of products of pine wood xanthation was studied: duration of alkaline pretreatment, amount of reactants, and duration of xanthation. In particular, we determined the solubility of these products in 5% solution of sodium hydroxide and the specific viscosity of the resulting solutions on an Ubbelohde viscometer (d = 0.65 mm) at 20°C according to the procedure described in [6].

The influence of duration of pine wood xanthation on the sulfur content in the resulting products, their solubility in aqueous alkali solution, and specific viscosity of solutions η_{sp} is illustrated in Table 1.

With increasing duration of pine wood xanthation from 10 to 30 min, the sulfur content in the result-

1070-4272/04/7704-0649 © 2004 MAIK "Nauka/Interperiodica"

Table 1. Influence of duration of pine wood xanthation on the characteristics of the resulting products (molar ratio OH : NaOH : CS_2 = 1 : 1 : 1, duration of alkaline activation 10 min)

Xanthation duration, min	Sulfur content, %	Degree of conversion α	Solubility in 5% NaOH, %	η_{sp}
10	1.1	0.05	32	1.02
20	2.1	0.11	34	1.04
30	3.5	0.18	40	1.09
40	3.5	0.18	40	1.09
50	3.0	0.15	39	1.05

Table 2. Influence of duration of alkaline activation on the characteristics of products of pine wood xanthation (molar ratio OH : NaOH : CS_2 = 1 : 1 : 1, xanthation duration 30 min)

Duration of alkaline activation, min	Sulfur content, %	Degree of conversion α	Solubility in 5% NaOH, %
–	2.4	0.12	34
5	2.8	0.14	38
10	3.5	0.18	40
20	3.5	0.18	41
30	3.7	0.18	39
40	3.7	0.18	34

Table 3. Influence of NaOH : OH ratio on the characteristics of xanthation products of pine wood Molar ratio OH : CS_2 = 1 : 1, duration of alkaline activation 10 min, xanthation duration 30 min

Molar ratio OH : NaOH	Sulfur content, %	Degree of conversion α	Solubility in 5% NaOH, %
–	2.3	0.11	30
1 : 0.5	2.7	0.14	33
1 : 1	3.7	0.18	39
1 : 1.5	3.5	0.17	40
1 : 2	3.5	0.17	41
1 : 2.5	2.7	0.14	40
1 : 3	1.9	0.09	39

ing products and the degree of conversion of wood increase. The maximum solubility was observed for the product containing 3.5% S (Table 1).

Further increase in xanthation duration to 40–50 min results in a certain decrease in the content of bound sulfur and in the solubility. This trend is accounted for by side process of formation of thio salts and mechanochemical degradation, disturbing the xanthation equilibrium.

Data on the influence of duration of mechanochemical alkaline pretreatment on the sulfur content, solubility of the resulting products, and degree of conversion of pine wood in xanthation are presented in Table 2.

With the duration of alkaline preactivation increasing from 5 to 30 min, the content of bound sulfur in the xanthation products increases. The degree of conversion of wood varies insignificantly and is 18% after alkaline treatment for 30–40 min. These data show that, with increasing duration of alkaline preactivation, the solubility of the products decreases, which is apparently caused by alkaline degradation occurring upon prolonged mechanochemical action. Therefore, we selected for further studies the optimum duration of alkaline treatment of pine wood equal to 10 min.

Data on the influence of the amount of sodium hydroxide added in the stage of alkaline preactivation on the degree of conversion, solubility, and sulfur content in the xanthation products are presented in Table 3.

It was found that the increase in the molar ratio from 0.5 to 1.5 results in a higher content of bound sulfur in the xanthation products and a higher degree of conversion of wood. Further increase in the amount of sodium hydroxide to 2–3 mol per mole of OH groups of wood is accompanied by a certain decrease in the sulfur content.

An increase in the sodium hydroxide concentration decelerates xanthation of wood, which can be accounted for by binding of free NaOH to form thio salts by the reaction

$$6NaOH + 2CS_2 \rightarrow Na_2S + Na_2CO_3 + Na_2CS_3 + 3H_2O. \quad (1)$$

The optimal molar ratio OH : NaOH is 1 : 1. The influence of the content of water in the reaction mixture, added in the stage of alkaline preactivation, on the xanthation of wood is illustrated by Table 4.

An increase in the amount of water from 1 to 4 mol results in that the content of bound sulfur and the solubility grow, apparently, due to enhancement of hydration. Further increase in the water content in the reaction mixture to above 4 mol is accompanied by a certain decrease in the sulfur content and also in the solubility of the products, apparently due to partial saponification of the resulting wood xanthates and formation of thio salts. The maximum amount of reacted hydroxy groups is 34%.

Table 4. Influence of water content on the characteristics of products of pine wood xanthation (molar ratio OH : $NaOH : CS_2$ = 1 : 1 : 1, duration of alkaline activation 10 min, xanthation duration 30 min)

Molar ratio OH : H_2O	Sulfur content, %	Degree of conversion α	Solubility in 5% NaOH, %
–	3.7	0.18	39
1 : 1	4.1	0.21	41
1 : 2	4.5	0.22	49
1 : 3	5.9	0.30	56
1 : 4	6.9	0.34	60
1 : 5	6.0	0.30	57
1 : 6	6.0	0.30	55

Table 5. Influence of the amount of carbon disulfide on the characteristics of the products of pine wood xanthation (molar ratio OH : NaOH : H_2O = 1 : 1 : 4, duration of alkaline activation 10 min, xanthation duration 30 min)

Molar ratio OH : CS_2	Sulfur content, %	Degree of conversion α	Solubility in 5% NaOH, %
1 : 1	6.9	0.34	60
1 : 1.5	7.0	0.35	65
1 : 2	7.8	0.39	69
1 : 2.5	8.7	0.44	74
1 : 3	8.7	0.44	75
1 : 3.5	8.8	0.44	70
1 : 4	8.8	0.44	68

Data on the influence exerted by the amount of carbon disulfide added on the sulfur content and the solubility of the products of wood xanthation in aqueous alkaline solution are listed in Table 5.

With the amount of carbon disulfide increasing from 1 to 2.5 mol, the content of bound sulfur in the products of wood xanthation grows. Further increase in the amount of this reactant to 3–4 mol per mole does not result in variation of the sulfur content, which is apparently caused by side reactions, namely, by saponification of xanthates and their mechanochemical degradation, and also by formation of thio salts. The degree of conversion of wood in xanthation, evaluated from the sulfur content, suggests that, under the conditions studied, 5–44% of the hydroxy groups of wood had reacted (Tables 1–5).

The influence of various process conditions can be estimated from variation of the specific viscosity of the products of wood xanthation. In prolonged alkaline activation and at high ratios of the reactants, the specific viscosity decreases (figure), which is caused by the prevalence of alkaline and mechanochemical degradation of the main components of wood under these conditions.

As can be seen from the figure, the dependences of the specific viscosity of alkaline solutions of wood xanthate on the main parameters of alkaline activation pass through a maximum. This is apparently caused by the competition of two parallel processes occurring in wood xanthation: formation of xanthates and their degradation with partial dissolution of the main components of wood in the reaction medium with variation of the process conditions.

Thus, the products of wood xanthation have 30–75% solubility in aqueous alkaline solutions and form highly viscous solutions. Alkaline activation of wood significantly affects the characteristics of the xanthation products. The resulting products can be used as polymeric surfactants.

CONCLUSIONS

(1) Macromolecular products containing up to 8.8% bound sulfur and having solubility in aqueous-alkaline solutions of up to 75% were obtained by xan-

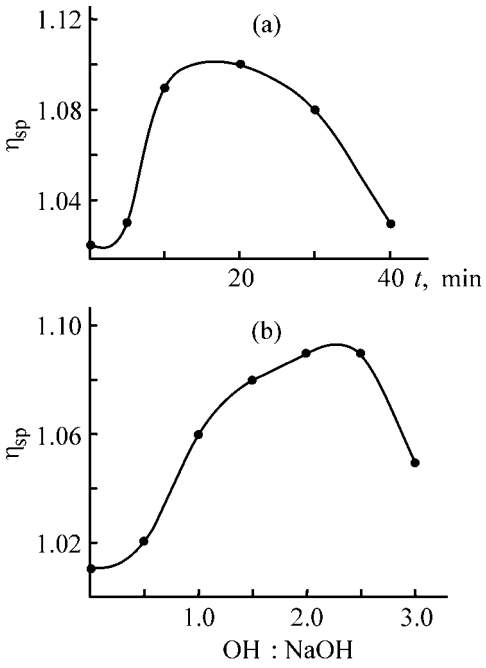

Specific viscosity of the products of pine wood xanthation η_{sp} vs. (a) duration of alkaline pretreatment t and (b) molar ratio OH : NaOH.

thation of pine wood with mechanochemical preactivation.

(2) The stage of alkaline preactivation of raw materials exerts the decisive influence on wood xanthation and characteristics of the resulting products. Within 30 min of xanthation, up to 44% of hydroxy groups of wood react with carbon disulfide.

REFERENCES

1. *Khimicheskie volokna* (Chemical Fibers), Konkin, A.A., Ed., Moscow: Vsesoyuzn. Naucho-Issled. Inst. Volokna, 1968.
2. Rogovin, Z.A., *Khimiya tsellyulozy* (Cellulose Chemistry), Moscow: Khimiya, 1972.
3. Efanov, M.V., *Plast. Massy*, 2002, no. 10, pp. 40–41.
4. Cheronis, N.D. and Ma, T.S., *Organic Functional Group Analysis by Micro- and Semimicro Methods*, New York: Interscience Publ., 1964.
5. Klimova, V.A., *Osnovnye mikrometody analiza organicheskikh soedinenii* (Main Micromethods of Analysis of Organic Compounds), Moscow: Khimiya, 1975.
6. Obolenskaya, A.V., Shchegolev, V.P., Akim, G.L., *et al.*, *Prakticheskie raboty po khimii drevesiny i tsellyulozy* (Practical Works on Chemistry of Wood and Cellulose), Moscow: Lesn. Prom–st., 1965.

Russian Journal of Applied Chemistry, Vol. 77, No. 4, 2004, pp. 653–656. Translated from Zhurnal Prikladnoi Khimii, Vol. 77, No. 4, 2004, pp. 657–660.

CHEMISTRY OF FOSSIL FUEL

Identification of Oxygen-containing Compounds in Benzine and Kerosene Oil Fractions and Determination of Sulfur and Halogen Content in Them

O. Yu. Begak and A. M. Syroezhko

Mendeleev Russian Research Institute of Metrology, Federal State Unitary Enterprise, St. Petersburg, Russia
St. Petersburg State Technological Institute, St. Petersburg Russia

Received April 8, 2003

Abstract—A procedure based on X-ray fluorescence and inductively coupled plasma with mass spectrometric recording was developed for express determination of the content of sulfur and halogen-containing compounds in benzine and kerosene oil fractions. Oxygen-containing compounds in gasolines and reforming products were identified by chromatography-mass spectrometry.

The requirements to the quality of motor fuels (in particular, to gasoline) become increasingly stringent [1]. Heteroatomic compounds (S-, O-, N-, and chlorine-containing products) strongly affect the gasoline quality. The major part of these compounds is removed by hydrofining, but their certain fraction is retained in the final product.

In this study we developed reliable procedures for quantitative determination of heteroorganic compounds in raw materials and benzine components, and also in reforming products from the Ryazan Oil Refining Plant, Joint-Stock Company (RORP).

EXPERIMENTAL

The samples of the initial raw materials, catalyzates, and stable and unstable hydrogenizates were taken from installations for primary (AT-6) and secondary oil refining [hydrofining of benzine, kerosene, diesel oil, and other reforming products, namely, L-35/8-300 (benzene), L-35/5-300 (xylene), L-35/11-300 (12/1, benzine)] and for hydrofining of kerosene (24/600) at the Ryazan Oil Refining Plant. The contents of sulfur and organic chlorine were determined by X-ray fluorescence analysis (RF) [2] using a Spectroscan spectrometer and by the method of inductively coupled plasma with mass spectrometric recording (ICP-MS). The comparative study of products from the entire cycle of production of high-octane gasolines was performed by IR Fourier spectrometry (IR-FS) [3] on an FSM 1201 unit.

The oxygen- and nitrogen-containing compounds in the samples were identified by gas chromatography-mass spectrometry (GC-MS) according to the procedure given in [4], using the MassLab and Amdis software and databases.

The highest content of sulfur was determined in the feed of the 24/600 installation. The 105-140 (feed of L-35/5-300) and 115–180°C fraction contain 0.0353 and 0.0487 wt % sulfur, respectively. The feed of the installation for benzene reforming, (62–85°C, L-35/8-300) and 85–105°C fraction (feed of L-35/6-300) contain 0.0128 and 0.0184 wt % sulfur, respectively.

The content of sulfur in the wide benzine fraction, 85–180°C, supplied to benzine reforming and in benzine from the K-8 fractionating column (AT-6 installation) varies from 0.054 to 0.062 wt %.

Due to hydrofining, the content of sulfur in stable hydrogenates and catalyzates obtained from the above installations decreases to 0.0005 wt%, whereas in imported gasoline, its content is as high as 0.0098 wt %.

The IR spectrum of the straight-run naphtha from the K-8 column (AT-6) exhibits a broad strong absorption band of the methylene groups of alkanes and naphthenes at 2850–2980 cm^{-1}. The presence of methylene groups in alkanes and in paraffins and cyclic compounds (C_5–C_6) is confirmed by a doublet at 1365–1395 and a singlet at 750 cm^{-1}, respectively. The content of arenes in naphtha is low, which is confirmed by a weak band at 1580 cm^{-1}. The carboxy and hydroxy

1070-4272/04/7704-0653 © 2004 MAIK "Nauka/Interperiodica"

Table 1. Content of chlorine, bromine, and iodine in feed, hydrogenizates, and catalyzates from various installations at the RORP Join-Stock Company

Installation, product	Cl	Br	I
	$c \times 10^{-4}$, wt %		
AT-6, desalinated oil	16.0	3.9	6.4
24/600, feed	13.0	1.8	5.5
24/600, hydrofined kerosene	1.8	0.7	2.4
Å™-6, naphtha from K-8	11.0	2.5	5.6
L-35/5-300, feed	10.0	2.1	5.8
L-35/5-300, catalyzate	2.1	0.75	3.2
L-35/5-300, unstable hydrogenizate	1.5	0.6	3.0
L-35/5-300, stable hydrogenizate	1.2	0.5	2.9
L-35/11-300, feed	9.0	1.8	4.6
L-35/11-300, stable catalyzate	3.0	1.0	3.2
L-35/11-300, unstable hydrogenizate	1.7	1.0	0.9
L-35/11-300, stable hydrogenizate	1.3	0.75	0.84
L-35/8-300, feed	8.0	2.5	5.1
L-35/8-300, catalyzate	1.7	1.0	0.9
L-35/8-300, unstable hydrogenizate	1.3	0.65	2.2
L-35/11-300, stable hydrogenizate	1.0	0.6	2.1
12/1, 62–70°C fraction	1.1	0.8	0.9
12/1, 70–115°C fraction	5.0	1.8	1.3
L-35/11-1000, feed	8.0	1.3	1.4
12/1, 115–180°C fraction	7.0	2.0	1.6

groups in naphtha are almost absent; the absorption bands corresponding to these groups are very weak.

As can be seen from the IR spectrum of the catalyzate (L-35/11-300 installation), it is enriched in arenes (1580 cm^{-1}), whereas the content of alkanes is smaller than that in the initial naphtha (180°C dry point).

According to the IR spectra, there are no arenes in light benzine from the E-201 tank (L-35/11-300 installation). The intensity ratio of the absorption bands in the IR spectra of unstable catalyzate sampled from the S-1 separator (L-35/11-300 installation) and hydrogenizate differ from that in the feed. The IR spectrum of the stable catalyzate from this installation exhibits strong absorption bands of arenes at 700–740, 1580, and 3080 cm^{-1}.

The IR data indicate that the 62–70 and 70–115°C fractions contain almost no arenes; these fractions predominantly consist of alkanes, isoalkanes, and naphthenes (strong absorption band at 750 cm^{-1}).

Organic halogens were determined by combustion of the oil product sample, with subsequent absorption of the combustion products with soda and analysis by ICP-MS.

As can be seen from Table 1, the content of organic halides in the feed supplied for secondary oil processing is higher than that in the final products from installations for hydrofining and reforming. The content of chlorine in unstable hydrogenizate is higher than that in the stable product. The chlorine content increases with increasing dry point of the fraction.

It should be noted that, in some cases, the iodine content is much greater than that of bromine. Organic compounds of iodine, bromine, and chlorine strongly accelerate corrosion of installations and pipelines, especially in the presence of water.

The data on the content of organic chlorine in oil and some petroleum products from installations for benzene and benzine reforming at the KINEF Limited Liability Company processing West-Siberian crude oil well agree with the results of an analysis of the feed and products from the RORP installations using the same crude oil.

A typical chromatogram of the 85–180°C fraction, used as the feed at the L-35/11-300 reforming installation, consists of 42 peaks; most of them belong to the compounds listed in Table 2. Nearly 40 and 10 oxygen-containing compounds were iden-

Table 2. Oxygen-containing compounds identified in benzine and its components prepared at the RORP Joint-Stock Company

Compound	Feed, L-35/11-300	K-8 column Naphtha (AT-6)	Hydrogenizate, L-35/11-300
	wt %		
1-Butanol	0.05	0.14	0.07
2-Pentanone	0.02	0.38	
2-Pentanol	0.01	0.18	
2-Methyl-2-pentanol	0.08	0.27	
4-Methyl-2-pentanone	0.12	1.01	
3-Methyl-2-pentanone	0.20	0.44	
4-Methyl-2-pentanol	0.04	0.06	
4,4-Dimethyl-2-pentanone	0.10	0.20	
3-Hexanone,	0.32	0.60	0.07 (0.08)
2-Hexanone	0.59	0.70	0.09 (0.10)
2-Hexanol	0.22	0.13	0.02 (0.05)
Aliphatic alcohol C_6	0.33	0.07	0.01 (0.02)
2-Hexanol	0.32	0.18	0.03 (0.04)
3-Methyl-2-hexanone	0.23	0.27	
Aliphatic alcohol C_7	0.16	0.12	
5-Methyl-3-hexanone	0.16	0.18	0.01
2-Methyl-3-hexanone	0.21	0.22	
2,3-Dimethyl-3-pentanol	0.21	0.16	
3-Ethyl-2-pentanone	0.27	0.24	
4-Methyl-2-hexanone	1.11	1.21	0.01
5-Methyl-2-hexanone	0.15	0.14	
4-Heptanol	0.22	0.23	0.02
Aliphatic ketone C_7	0.23	0.30	0.02
Cyclohexanol	0.05	0.03	
3-Heptanone	0.69	0.61	
2-Heptanone	0.72	0.52	
Aliphatic ketone C_8	0.05	0.06	
Aliphatic ketone C_8	0.07	0.03	
Aliphatic ketone C_8	0.25	0.14	
4-Methyl-2-heptanone	0.48	0.49	
3,4-Dimethyl-2-hexanone	0.21	0.17	
Trimethylcyclohexanone	0.06	0.01	
6-Methyl-3-heptanone	0.09	0.02	
6-Methyl-2-heptanone	0.14	0.04	
Aliphatic ketone C_8	0.06	0.02	
Methyl cyclohexyl ketone	0.06	0.01	
4-Octanone	0.18	0.09	
3-Octanone	0.20	0.03	
Dimethylheptanone	0.43	0.13	
Aliphatic ketone C_8	0.14	0.07	
Cyclopentylpropanone	0.21	0.02	
Cyclohexylpropanone	0.10		
2,2,4-Trimethyl-1,2-dihydroquinoline	0.05		
Total $c \times 10^{-4}$, wt %	9.54	9.92	0.35 (0.37)

tified in the straight-run naphtha sampled from K-8 column (AT-6 installation) and in hydrogenizate of benzine reforming (L-35/11-300), respectively (Table 2).

The data on the content of oxygen-containing compounds in three samples taken from L-35/11-300 and AT-6 installations are also listed in Table 2. According to GC-MS data, the feed supplied to

the L-35/11-300 installation (85–180°C) contains 42 compounds [41 oxygen-containing compounds and insignificant amounts of 2,2,4-trimethyl-1,2-dihydroquinoline (0.05 wt %)]. Aliphatic alcohols and ketones (C_4–C_9) were mainly identified, and the content of ketones is greater than that of alcohols by a factor of 3. The content of alicyclic alcohols is smaller by a factor of 32.4 – 48.0 than that of acyclic compounds. Similar trend is observed for ketones: the acyclic to alicyclic ketone ratio in the samples studied varies from 140 to 205.

As can be seen, aliphatic ketones with methyl substituents at different distance from the carbonyl group are predominant in the samples studied. The fraction of linear ketones C_6–C_8 is smaller. Among alcohols, the major fraction belongs to linear (primary and secondary) aliphatic alcohols.

CONCLUSIONS

(1) The content of sulfur and halogen-containing compounds in benzine and kerosene oil fractions from the RORP Joint-Stock Company was determined using the methods of X-ray fluorescence and inductively coupled plasma with mass spectrometric recording; oxygen-containing compounds were also identified. It was found that the content of ketones is greater than that of alcohols by a factor of 3.

(2) X-ray fluorescence procedure is the best method for express determination of sulfur in benzines and their components and in kerosene. For control of hydrofining and reforming (aromatization) of the benzine and kerosene fractions, the IR Fourier spectrometry is preferable. The method of inductively coupled plasma with mass spectrometric recording is the best for express analysis of halogens in organic compounds contained in oil and petroleum products.

(3) The higher the dry points of the fraction, the greater the content of bromine and iodine in it; in some cases the iodine content is much higher than that of bromine.

REFERENCES

1. Abrosimov, A.A., *Neftepererb. Neftekhim.*, 1999, no. 3, pp. 36 – 41.
2. *GOST* (State Standard) *R 50 442–92, Oil and Petroleum Products: X-ray Fluorescence Analysis of Sulfur*, Moscow: Izd. Standartov, 1993.
3. Bell, R. J., *Introductory Fourier Transform Spectroscopy*, New York: Academic, 1972.
4. Begak, O.Yu. and Syroezhko, A.M., *Zh. Prikl. Khim.*, 2001, vol. 74, no. 11, pp. 1888 –1992.

Russian Journal of Applied Chemistry, Vol. 77, No. 4, 2004, pp. 657–665. Translated from Zhurnal Prikladnoi Khimii, Vol. 77, No. 4, 2004, pp. 661–669.

CHEMISTRY OF FOSSIL FUEL

Relationship between Group Composition of Tars and Asphalts Produced from Various Crude Oils and Their Performance Characteristics

A. M. Syroezhko, O. Yu. Begak, and V. V. Fedorov

Mendeleev Russian Research Institute of Metrology, Federal State Unitary Enterprise, St. Petersburg, Russia
St. Petersburg State Technological Institute, St. Petersburg, Russia

Received October 28, 2003; in final form, January 2004

Abstract—A comparative study is made of the thermodynamic stability of asphalts produced from various crude oils differing in their density, in the content of sulfur, resin, and asphaltene, and in the yield of top paraffins (fraction <350°C). The relationship between the group composition of tars and asphalts produced from these oils and their performance characteristics is analyzed.

It is known that the presence of a fairly large amount of the naphtheno-aromatic rings in the oil fraction of asphalts imparts a colloidal stability and desirable physicochemical characteristics (penetration P_{25} and ductility D_{25}) to bitumens. In the case of an insufficient content of the oil fraction, or when this fraction is of essentially naphtheno-paraffinic nature, the colloidal stability of bitumen decreases, as also do its ductility and mechanical characteristics. Therefore, we examined in this study the effect of the group composition of petroleum tars and asphalts on their performance characteristics.

We examined four petroleum tars (nos. 1–4 in Table 1) and asphalts obtained by their oxidation (nos. 5–9 in Table 1). Tar sample no. 1 was produced at the Kirishi refinery (hereinafter, manufacturer I)

Table 1. Characteristics of tars and asphalts*

Run no.	P_{25}, 0.1 mm units	RV_{80}, s	AN, mg KOH/g	Manufacturer
Tars				
1	305	89	7.8	I
2	390	92	5.0	I
3	320	96	9.6	IV
4	345	93	7.7	III

Run no.	T_s, °C		P_{25}, 0.1 mm units		D_{25}, cm		Asphalt grade	Manufacturer
	initial	after heating	initial	after heating	initial	after heating		
Asphalts								
5	46	47	84	60.3	140	108	BDUS 70/100	I
6	49	49.9	79	39.7	149	96	BND 60/90	I
7	49	49.6	85	72	>100	>100	BDU 70/100	IV
8	49	49.8	67	61	>100	>100	BND 60/90	III
9	48	49.3	86	62	128	102	BND 60/90	II

* (RV_{80}) Relative viscosity at 80°C, (AN) acid number, and (T_s) ring-and-ball softening point.

1070-4272/04/7704-0657 © 2004 MAIK "Nauka/Interperiodica"

Table 2. Content of asphaltenes, malthenes, and polar and nonpolar fractions in tars and asphalts*

Product	Yield, wt %			
	malthenes	asphaltenes	PF	NPF
Tar (no. 1, P_{25} 305 0.1 mm units, RV_{80} 89 s)	89.5	10.5	16.6	83.4
Tar (no. 2, P_{25} 390 0.1 mm units, RV_{80} 92 s)	88.6	11.4	15.0	85.0
BDUS 70/100 (no. 5, P_{25} 84 0.1 mm units, T_s 46°C, D_{25} 140 cm)	80.7	19.3	21.0	79.0
BND 60.90 (no. 6, P_{25} 78 0.1 mm units, T_s 49°C, D_{25} > 150 cm)	79.0	21.0	21.4	78.6
BDU 70/100 (no. 7, Ukhta refinery, T_s 46°C)	78.0	22.0	25.7	74.3
BND 60/90 (no. 8, Norsi refinery, T_s 49°C)	80.5	19.5	19.0	81.0
BND 60/90 (no. 9, Yaroslavl refinery, T_s 48°C)	81.3	18.7	20.2	80.0

* Numbering of samples is the same as in Table 1; the same for text below.

from West-Siberian crude oil; sample no. 2, at the Yaroslavl refinery (II) from West-Siberian crude oil; sample no. 3, at the Norsi Joint-Stock Company (III) from crude oil extracted by the Tatneft' Joint-Stock Company; and sample no. 4, at the Ukhta refinery (IV) from Yarega crude oil.

Tar nos. 1–4 and asphalt nos. 5–9 were deasphalted in a Soxhlet apparatus.

The polar fraction (PF) was extracted from malthenes of the tars and asphalts with DMF. Group separation of polar and nonpolar fractions (NPF) was performed on a silica gel [1, 2].

EXPERIMENTAL

The yields of asphaltenes, malthenes, and polar and nonpolar components, and also the group composition of tars and asphalts under study are listed in Table 2. The yields of malthenes from the tar samples are very close (88.6–89.6%) (Table 2). The yields of polar and nonpolar fractions are about the same (to within 1.5 wt %).

After oxidation of tars into BDUS 70/100 and BDUS 60/90 asphalts, the yield of malthenes from the oxidized samples decreased to 79–80.7%, and that of asphaltenes increased [3].

In the initial tar samples, the asphaltene content is 10.5–11.4 wt %, whereas in the corresponding asphalts (from West-Siberian oil) it ranges from 19.3 to 21 wt %. The yield of the polar fraction from asphalts is higher by 4.3–6.3 wt %, compared to the corresponding tars. Note that tar sample no. 2 [P_{25} 390 (here and hereinafter, 0.1 mm units), RV_{80} 92 s] was oxidized deeper (asphalt sample no. 6, T_s 49°C) than tar no. 1 (P_{25} 305, RV_{80} 89 s). The content of polar components in asphalt no. 6 with a higher softening point increased by 1.8 wt % [3].

Asphalt from Yarega oil differs noticeably in the asphaltene content (22.1 wt %) produced from asphalts from other crude oils. It is also characterized by a high content of the polar component (25.7 wt %). Tar nos. 8 and 9 from the Yaroslavl and Nizhni Novgorod refineries differ from tar nos. 5 and 6 from the Kirishi refinery to a considerably lesser extent.

Tables 3 and 5 shows that the content of oils and resins is essentially different in both the polar and nonpolar fractions of the tars studied and of the corresponding asphalts. In particular, the oils/resins ratio in the nonpolar fraction (NPF) of tar no. 1 (P_{25} 305) is 2.06, whereas that in BDUS 70/100 asphalt (no. 6) is considerably lower (1.73). The resin content in the polar fraction of tar no. 1 and the corresponding asphalt (no. 5) increases, and this ratio is 1.37 and 1.25, respectively.

Tar no. 2 with an increased penetration (P_{25} 390) is distinguished by higher oil content in both polar and nonpolar components.

The oils/resins ratio in the nonpolar fraction of this tar is 2.46, whereas that in tar with P_{25} = 305 is 2.06, and in the polar fraction of the tars under comparison, 1.60 and 1.37, respectively.

It should be pointed out that tar nos. 1 and 2 from West-Siberian oil differ each from other not only in the penetration, but also in the relative viscosity. From tar with P_{25} = 305, BDUS 70/100 quality asphalt was obtained, having the desired T_s, P_{25}, D_{25} and thermal stability (P_{25} and D_{25} after heating). At the same time, from tar no. 2 with higher relative viscosity (92 s), P_{25}, and oils/resins ratio, we were able to obtain only harder BND 60/90 asphalt (no. 6), having not only an increased softening point, but also a lower thermal stability.

Table 3. Group composition of tar no. 1 and the corresponding BDUS 70/100 asphalt no. 5

Fraction	NPF	PF	NPF	PF
	wt % against NPF (or PF)/tar		wt % against NPF (or PF)/asphalt	
	Tar no. 1		Asphalt no. 5	
NPCs	22/16.4	10.6/1.6	14.2/9.0	7.4/1.3
MCACs	18.7/14.0	23.0/3.4	30.0/19.2	30.0/5.1
BCACs (PCACs)	26.6/19.9	23.8/3.5	19.0/12.2	18.7/3.2
TRs	13.2/9.8	18.8/2.8	18.4/11.7	18.0/3.1
ATRs	19.5/14.5	24.0/3.5	18.2/11.6	27.0/4.5
Oils	67.3/50.2	58.3/8.5	63.4/40.3	56.0/9.5
Resins	32.7/24.4	42.7/6.3	36.6/23.3	45.0/7.6
Oil/Resin	2.06	1.37	1.73	1.25
Resin/Σ[MCACs + BCACs (PCACs)]	0.72	0.90	0.74	0.92
TRs/ATRs	0.67	0.80	1.0	0.70
MCACs/BCACs (PCACs)	0.70	0.97	1.6	1.60

* (NPCs) naphtheno-paraffinic compounds, (MCACs, BCACs, PCACs) mono-, bi-, and polycycloaromatic compounds, and (TRs, ATRs) toluene and alcohol-toluene resins.

Table 4. Group composition of tar no. 2 and the corresponding BND 60/90 asphalt no. 6

Fraction	NPF	PF	NPF	PF
	wt % against NPF (or PF)/tar		wt % against NPF (or PF)/asphalt	
	Tar no. 2		Asphalt no. 6	
NPCs	20.1/15.1	10.0/1.34	15.8/9.8	7.2/1.2
MCACs	22.4/16.8	17.0/2.3	22.8/14.2	17.4/2.9
BCACs (PCACs)	28.6/21.5	34.4/4.6	27.8/17.3	32.7/5.5
TRs	11.2/8.4	14.5/1.9	14.0/8.7	15.4/2.6
ATRs	17.7/13.3	24.0/3.2	19.5/12.1	27.3/4.6
Oils	71.0/53.5	61.5/8.2	66.4/41.2	57.3/9.7
Resins	29.0/21.7	38.5/5.1	33.6/20.9	42.7/7.2
Oil/Resin	2.46	1.60	2.0	1.34
Resin/Σ[MCACs + BCACs (PCACs)]	0.57	0.75	0.66	0.85
TRs/ATRs	0.63	0.60	0.70	0.56
MCACs/BCACs (PCACs)	0.78	0.60	0.82	0.53

It is worth noting that BND 60/90 asphalt (no. 6) obtained from tar with P_{25} = 390 0.1 mm units and then oxidized into asphalt with higher T_s is characterized by a higher oils/resins ratio in both the nonpolar and polar fraction as compared to BDUS 70/100 quality asphalt no. 5.

It is known that the thermal stability of asphalts strongly depends on the degree of aromaticity of the starting tars and resulting asphalts. In this case, the thermal stability (defined as the permissible temperature range of variation of the softening point, penetration, ductility, and brittle point) is influenced not only by the deepness of oxidation, but also by the content of oils, resins, asphaltenes, and aromatic compounds.

Not only the total content of these compounds, their ratio, composition (molecular weights and content of polar components depending on the concentration of heteroatoms and paramagnetic centers in the system), and degree of association of the indicated components and their aromaticity are of importance, but also the concentration and nature of trace com-

pounds (metal complexes). It was noted in the literature that, if polycycloarenes dominate among aromatic hydrocarbons of the oil fraction, the packing density of the micellar structures of tars and asphalts is higher, and, correspondingly, such asphalts are characterized by increased thermal stability [3].

According to our results, not so much the content of BCACs and PCACs is important as the degree of aromaticity of these compounds. To obtain thermally stable asphalt, it is also important to meet a desired oils/resins ratio. Because of the increased content of resins in tar no. 2 with $P_{25} = 390$, the resulting asphalt no. 6 also contains undesired excess of resins, compared to asphalt no. 5, so that its degree of structurization (third-type structure of colloidal aggregates by Kolbanovskaya) is lower. With increasing solvency of malthenes and decreasing asphaltenes/resins ratio, the strength of the asphalt structure decreases.

The presence of NPCs in the polar fraction and also of heteroatomic compounds (Tables 3, 4) suggests that the extraction of group components of tar and asphalt proceeds not at the molecular level, but at a level of associates. Evidently, both asphaltenes and malthenes are associated in black oil, the latter forming smaller associates. Dimethylformamide extracts NPCs associated with other more polar molecules. Compounds of hybrid structure (containing both naphthenic and aromatic rings) with long linear alkyl chains can also be extracted, which then behave as NPCs.

Asphalt is a typical dispersion. Its dispersed phase (associates) is distributed throughout the oil fraction, which is the dispersion medium. Because of the strongly different polarities of components, lyophobic dispersions are characterized by weak phase interaction, being thermodynamically unstable. By contrast, lyophilic dispersions are characterized by strong interaction and considerable mutual solubility of components only slightly different in their nature. Such systems are spontaneously formed as abnormally finely dispersed systems (colloid solutions), to which primarily belong emulsions.

The observed deviations in the behavior of tar or asphalt from ideality can be attributed to molecular interactions occurring between numerous compounds contained in structural units. The nature of intermolecular interactions depends on the properties of hydrocarbons (primarily those of hybrid structure) and heteroatomic compounds and on their reactivity.

It is difficult to characterize the chemical organization and to predict properties of such a complex system as tar or asphalt. However, attempts have been made to predict the structure–property trends in a series of polycyclic compounds [4].

The compounds constituting tars and asphalts can be arranged in order of decreasing dipole moment as follows: nitrogen-containing aromatic components of asphaltenes and resins > oxygen-containing components > sulfur-containing components > hybrid-structure condensed PCACs > BCACs > MCACs. The most common and universal forces causing intermolecular interactions are the dispersion forces controlled by the ionization energy and polarizability of molecules.

At an intermolecular distance considerably exceeding the molecular diameter ($r \gg d$), the relative dipole–dipole, induction, and dispersion contributions to the intermolecular interaction energy γ can be determined from comparison of $r^6\gamma_{\text{dip–dip}}$, $r^6\gamma_{\text{ind}}$, and $r^6\gamma_{\text{disp}}$.

For weakly polar molecules, the first two values are lower by several orders of magnitude than $r^6\gamma_{\text{disp}}$. For molecules with higher dipole moment (≥1.5 D), $r^6\gamma_{\text{dip–dip}}$ starts to dominate over the dispersion term.

At an intermolecular distance comparable with the size of molecules, the energy of interaction is no longer an additive value, but, by virtue of electrostatic repulsion, it is lower than it would be if the law $\gamma \approx 1/r^6$ were valid down to these distances.

Brief consideration of certain reactivity issues for representatives of various classes of organic compounds composing tars and asphalts reveals an ambiguity of their predicted contributions to the overall state of aggregation of the system. However, there is no doubt that it is affected by Coulombic interactions between molecules of group components of black oil, association through hydrogen bonding, and π–π interaction between aromatic rings in asphaltenes, resins, PCACs, BCACs, and MCACs.

Furthermore, tars and asphalts contain 3*d* elements capable of forming chelates with heteroatomic (sulfur-, oxygen-, and nitrogen-containing) ligands. Formation of mixed-ligand complexes is also possible, as well as that of donor–acceptor complexes with heteroatoms of resins and asphaltenes, and π complexes with polycycloaromatic compounds.

For a binary mixture consisting of, e.g., resins (r) and asphaltenes (a), we can write

$$\delta_{ra} = \sqrt{\delta_r \delta_a},$$

where δ_r and δ_a are the attractive interactions between unitypical molecules of resins and asphaltenes, respectively; and δ_{ra} is the attractive interaction between resin and asphaltene molecules.

At $\delta_{ra} > \delta_r$ and δ_a, mixing of resins with asphaltenes liberates potential energy, which results in an increase in the temperature and a decrease in the volume and vapor pressure of the mixture. In this case, molecules interact each with other more strongly, and their separation requires higher temperature.

The above considerations are valid for multicomponent systems also. However, in tars and asphalts, asphaltenes occur as associates. Components of oils (arenes) and resins are most likely associated too, but their intermolecular interactions are weaker than those of asphaltenes. Associates of oils and resins are very sensitive to external factors and, in particular, to temperature.

Additionally, to obtain an energetically favorable structure, it is necessary to have the optimal type of interaction between components of the system. Association of complex hybrid structures of BCACs, PCACs, resins, and asphaltenes at ambient temperature results in a slow establishment of the thermodynamic equilibrium in asphalts. To a first approximation (by Hildebrand), the bonding strength between molecules of different types is controlled by the force field of the molecules [$\delta = f(\Delta H_{vap}/V)$, where V is the molar volume]. This parameter is known as the cohesion energy density. The closer the force fields of molecules, the higher the mutual solubility of the compounds. The δ value increases in the order NPCs < MCACs < BCACs < PCACs < TRs < ATRs < asphaltenes, weakly associated polar compounds.

Data on the group composition of BDUS 70/100 thermostable quality asphalt (no. 5) and BND 60/90 substandard asphalt (no. 6) show that they differ in that the resins/total aromatics ratio is higher in the quality asphalt.

Let us compare the group compositions of tars studied and the corresponding asphalts obtained from them. In quality tar no. 1 (P_{25} = 305), the content of NPCs in NPF and PF is 22 and 10.6 wt %, respectively. At the same time, for tar no 2 (P_{25} = 390) the corresponding values are 20.1 and 10 wt %, i.e., both samples are only slightly different in this parameter.

In the corresponding BDUS 70/100 quality asphalts (no. 5) and less thermostable BND 60/90 (no. 6), these values are 14.2 and 7.2 wt %, and 15.8 and 7.2 wt %, respectively. Therefore, although the total content of NPCs in asphalts decreases relative to that in tars, the ratio between the contents of NPCs in NPF and PF remains nearly the same.

There is a tendency toward an increase in the contents of arenes and resins in the polar fraction of both the initial tars and resulting asphalts. The total of MCACs + BCACs in the nonpolar and polar fractions of tar no. 1 and BDUS 70/100 quality asphalt (no. 5) is 45.3–46.9 and 48.7–49.2 wt %, respectively, i.e., the content of aromatic structures increases after oxidation. In less thermostable BND 60/90 (no. 6), the total of MCACs + BCACs is nearly the same as in the initial tar. It ranges from 50.4 to 51.6 wt % in both polar and nonpolar fractions of the tar and asphalt. Note that the MCACs/BCACs ratio in thermostable BDUS 70/100 asphalt (no. 5) is higher than that in less thermostable BND 60/90.

Table 5. Group composition of asphalt no. 9 from West-Siberian oil (Yaroslavl refinery)

Fraction	NPF	PF
	wt %	
NPCs	16.2	8.2
MCACs	20.5	18
BCACs (PCACs)	22.0	24.8
TRs	19.0	19.8
ATRs	22.3	29.2
Oils	58.7	51.0
Resins	41.3	49.0
Oil/Resin	1.40	1.04
Resin/Σ[MCACs + BCACs (PCACs)]	0.97	1.14
TRs/ATRs	0.85	0.68
MCACs/BCACs (PCACs)	0.93	0.73

Finally, the most noticeable differences in the group composition of thermostable (quality) and less thermostable asphalts and the corresponding initial tars are reflected in the resins/total arenes ratio in the oil fraction. This ratio is higher in BDUS 70/100 quality asphalt and the corresponding tar in both polar and nonpolar fractions, compared to less thermostable BND 60/90 asphalt.

The polar fractions of tars and the corresponding asphalts are characterized by higher resins/total arenes ratio, compared to the nonpolar fractions. Furthermore, the TRs/ATRs ratio and, as indicated above, the MCACs/BCACs (PCACs) ratio in the nonpolar and polar fractions are higher in quality asphalt.

Thus, the thermal stability of asphalts depends on the group component ratio in the initial tar and resulting asphalt and also on their structure (structural types 1–3 by Kolbanovskaya). As noted above, the asphalts studied are classified with the third-type structures. Evidently, the presence of a fairly large amount of

Table 6. Group composition of asphalt no. 8 from oil extracted by the Tatneft' Joint-Stock Company

Fraction	NPF	PF
	wt %	
NPCs	14.5	8.1
MCACs	11.8	9.0
BCACs (PCACs)	24.8	25.5
TRs	23.4	28
ATRs	25.5	29.4
Oils	51.0	42.6
Resins	49.0	57.4
Oil/Resin	1.04	0.74
Resin/Σ[MCACs + BCACs (PCACs)]	1.39	1.66
TRs/ATRs	0.92	0.95
MCACs/BCACs (PCACs)	0.48	0.35

Table 7. Group composition of asphalt no. 7 and tar no. 3 from Yarega oil

Fraction	NPF	PF
	wt %	
Asphalt no. 7		
NPCs	11.3	5.2
MCACs	14.8	13.2
BCACs (PCACs)	22.8	25.8
TRs	24.1	26.8
ATRs	27.0	29.0
Oils	49.0	44.2
Resins	51.0	55.8
Oil/Resin	0.96	0.80
Resin/Σ[MCACs + BCACs (PCACs)]	1.36	1.43
TRs/TRs	0.89	0.92
MCACs/BCACs (PCACs)	0.65	0.50
Tar no. 3		
NPCs	18.5*	
MCACs + BCACs + PCACs	35.0*	
TRs	27.0*	
ATRs	10.3*	
Asphaltenes	9.3*	

* Fraction content in tar, wt %.

the oil fraction characterized by a high carbon content in cyclic structures and a high aromaticity imparts the colloidal stability to asphalts. The distribution of atoms plays an important role also [3].

The optimal capacity of asphaltenes and resins for structurization should be combined with the optimal MCACs/BCACs (PCACs) ratio, to obtain the most aggregatively stable and, therefore, less temperature-sensitive structure, in which changes in the penetration and ductility, initiated by the effect of heating (aging) or addition of a mineral ballast, will be at a minimum.

For comparison, Tables 5, 6 show the group composition of asphalts obtained at the Yaroslavl, Norsi, and Ukhta refineries from West-Siberian oil, oil extracted by the Tatneft' Joint-Stock Company, and Yarega oil, respectively (sample nos. 9, 8, and 7). In the group composition, asphalt from the Yaroslavl refinery is close to BDUS 70/100 quality asphalt from the Kirishi refinery, as demonstrated by the oils/resins and resins/Σ[MCACs + BCACs (PCACs)] ratios in the nonpolar and polar fractions, respectively. The most noticeable differences between the asphalt samples are found in the MCACs/BCACs (PCACs) ratio. The increased content of MCACs in BDUS 70/100 asphalt from the Kirishi refinery, i.e., the lower aromaticity, makes this asphalt less thermostable, compared to the asphalt from the Yaroslavl refinery.

In asphalt no. 8 from the Norsi Joint-Stock Company (Table 6), we found increased content of TRs, ATRs, and heavy aromatics (BCACs, PCACs), but lower content of NPCs and MCACs, compared to the quality asphalt from the Kirishi refinery. Therefore, the thermal stability of asphalt from Norsi will be higher.

The most pronounced differences were found between BDUS 70/100 asphalt from Kirishi and BDU 70/100 asphalt from Ukhta (Table 7). The content of MCACs in the nonpolar and polar fractions of asphalt from Yarega oil, manufactured at the Ukhta refinery, is lower by a factor of 2.03 and 2.27, respectively. At the same time, asphalt from Ukhta contains more BCACs (PCACs), TRs, ATRs, and asphaltenes (Table 7). Furthermore, BDU 70/100 from Ukhta contains less naphtheno-paraffinic compounds in NPF and PF. The aromaticity of asphaltenes of asphalts under comparison is 0.395 and 0.5, respectively. Asphalt from Ukhta is characterized by increased concentration of heteroatomic compounds (*O*-, *S*-, *N*-) in both HPF and PF compared to BDUS 70/100 quality asphalt from Kirishi. Asphalts under comparison (nos. 5–7) are obtained from different oils (paraffin-base and asphalt-base oils), which is reflected in the remarkably different group composition of the initial

tars (Table 2). Tar no. 3 from Yarega oil contains more asphaltenes and resins as compared to tars from West-Siberian oils (nos. 1, 2). These tars also differ in the content of the oil fraction. Our results suggest that the performance characteristics of asphalts studied increase in the order West-Siberian paraffin-base oils < oils extracted by the Tatneft' Joint-Stock Company < Yarega oils.

It is obvious that the major factors controlling the aggregative stability of the 3*D* coagulation structure of asphalts are the concentration of asphaltenes in the dispersed phase and its chemical affinity for oils and resins composing the dispersion medium. The formation of a kinetically stable fluctuation state of the asphalt structure is completed in the first several days after it was mechanically or thermally distorted.

It follows from a numerical analysis of small-angle X-ray diffraction patterns that the structure of the asphalt dispersion is characterized by the occurrence of first- and second-order microinhomogeneities. According to [5], the size of these microinhomogeneities does not depend on the group composition of asphalts, which is rather questionable in our opinion. In the cited work, first-order microinhomogeneities are interpreted as primary structural units containing nuclei of the asphaltene phase 2–6 nm in size, and second-order microinhomogeneities, as asphaltene aggregates about 10 nm in size, formed in the course of condensation structurization in the bulk of a complex structural unit.

The aggregative stability of the 3*D* coagulation structure not only depends on the concentration of asphaltenes forming the dispersed phase, but also is caused by the absorption factor, specifically, by the chemical affinity of asphaltenes for oil and resinous components composing the dispersion medium. As a parameter characterizing this affinity, the lyophobicity index *L* is suggested, which is defined as the difference between the aromaticity (fraction of aromatic carbon) of asphaltenes and oils, since it is the presence of condensed aromatic structures in black oil that is the necessary condition for their association into lamellar structures. Posadov *et al.* [6] have demonstrated that *L* is independent of the degree of oxidation of asphalts, but is controlled by the chemical composition of the initial petroleum tars, being 0.18, 0.28, and 0.31 for asphalts obtained by oxidation of tars from West-Siberian, Romashkino, and Arlan oils, respectively. Therefore, the 3*D* coagulation structure of asphalts from Romashkino and Arlan oils should be more stable, and these asphalts, naturally, will be more thermostable, compared to those obtained from West-Siberian oils.

Table 8. Group composition of tars from the AVT-60 plant of the Kirishi refinery

Sample no.	Paraffins (NPCs)	Arenes (BCACs + MCACs)	Resins	Asphaltenes
	wt %			
5	10.3	54.2	24.4	11.1
6	9.8	54.6	22.7	12.9
7	11.4	50.9	26.2	11.5
8	11.9	54.9	20.5	12.7
9	11.9	52.4	24.2	11.5
10	7.6	61.7	20.1	10.6
11	10.5	54.8	23.0	11.7

The correlation between the lyophobicity index and rate constant of condensation structurization *K* can be approximated by the linear relationship

$$K = K_0(L - 0.13),$$

where $K_0 = 8.5 \times 10^{-3}$ yr, suggesting that petroleum disperse systems are thermodynamically stable at $L > 0.13$.

For comparison, we present in Tables 8 and 9 the group composition for an extended sample of tars and asphalts from the Kirishi refinery. The tars were taken from the AVT-6 plant, and the asphalts, from the Bitumnaya-2 plant in May 2000. These data show that the group composition of tars and asphalts only slightly varies samples. In asphalts, the arene content (MCACs + BCACs) decreases and the content of resins and asphaltenes increases as compared to the initial tars.

A higher thermostability, which can be judged from the increase in the softening point (Table 9) and a less pronounced decrease in the penetration and ductility after heating, is observed at the optimal resins/Σ(MCACs + BCACs) ratio from 0.65 to 0.67. Asphalts with $D_{25} < 100$ have a substandard quality after heating for 5 h at 160°C.

In the penetration after heating, all the asphalts from Kirishi (Tables 1 and 9), except sample nos. 5 (Table 1) and 13 (Table 9), meet the requirements only for BND 40/60 hard asphalt, falling outside the range acceptable for the initial BDUS 70/100 and BND 60/90 grades.

Table 9. Characteristics of asphalt nos. 10–16 (Kirishi refinery) obtained by oxidation of tar nos. 5–11 (see Table 8)

Parameter	Sample no.						
	no. 10	no. 11	no. 12	no. 13	no. 14	no. 15	no. 16
T_s, °C	45	45	48	43.5	48.5	48	48.5
Ash content	1.0188	1.023	1.0235	1.0196	1.0218	1.019	1.021
P_{25}, 0.1 mm units	79	76	67	123	84	78	85
D_{25}, cm	150	146	126	118	31	138	128
P_{25} after heating, 0.1 mm units	66	67	71	57	71	60	70
T_s after heating, °C	49	49.5	50	49	52	54	54.3
D_{25} after heating, cm	132	118	54	94	56	81	102
Content, wt %:							
NPCs	10.3	10.0	11.1	10.4	9.4	7.8	9.8
MCACs + BCACs	44.6	43.4	39.1	46.8	46.2	46.44	46.4
resins	29.8	28.3	30.6	28.5	27.1	23.80	23.3
asphaltenes	15.2	18.3	19.2	14.3	16.9	21.95	20.5

Table 9 shows that asphalt nos. 10–16 manufactured from hot charge of West-Siberian crude at the Kirishi refinery (Table 9, tar nos. 5–11) do not demonstrate high thermostability, since their penetration after heating decreases by 29–43%, the softening point increases by 2–6°C, and the ductility decreases considerably. According to requirements for asphalts, the ductility after heating should be no less than 100 cm. Only sample nos. 10, 11 (Table 9), and 5 (Table 5) meet this requirement. Nevertheless, all the asphalts from Table 9 fully meet the requirements of GOST (State Standards) for paving asphalts of BND grade. Asphalts from Yaroslavl, Ukhta, and Nizhni Novgorod refineries correspond to the initial grade after heating. To conclude, we thoroughly studied the group composition of the polar and nonpolar fractions of malthenes of tars from West-Siberian crude and asphalts (thermostable BDUS 70/100 and less thermostable BND 60/90) obtained from them by oxidation at the Kirishi refinery. These tars and asphalts contain virtually equal amounts of dispersed asphaltenes (10.5 and 11.4%, and 19.3 and 21.0%, respectively). The stability of the colloidal structure of asphalts decreases with increasing solvency of malthenes and decreasing asphaltenes/malthenes ratio. Comparison of the compositions of asphalts from West-Siberian oils (Kirishi and Yaroslavl refineries), asphalt from oil extracted by the Tatneft' Joint-Stock Company (Norsi refinery), and asphalt from Yarega oil (Ukhta refinery) shows that asphalt from the Norsi Joint-Stock Company contains heavier aromatic compounds, TRs, and ATRs, compared to asphalts from West-Siberian oil. Asphalt from Yarega oil is characterized by the highest aromaticity of asphaltenes, and the polar and nonpolar fractions of this asphalt contain the largest amount of heteroatomic compounds.

BDUS 70/100 quality asphalt contains more aromatic structures as compared to BND 60/90. In BDUS 70/100 quality asphalt and the corresponding initial tar, the resins/total aromatics ratio is higher in both the polar and nonpolar fractions than that in less thermostable BND 60/90.

The polar components of tars and the corresponding asphalts are characterized by a higher resins/total aromatics ratio as compared to nonpolar components. The quality asphalt is characterized by higher TRs/ATRs and MCACs/BCACs (PCACs) ratios in both polar and nonpolar fractions.

The stability of colloidal structures is the highest if the oil fraction contains a sufficient amount of aromatic carbon in monocycloaromatic compounds and in the toluene fraction of resins, and also if the naphthenic structures have a sufficient carbon content. Factors controlling the aggregative stability of the 3*D* coagulation structure of asphalts are the concentration of the dispersed phase (asphaltenes) and its chemical affinity for oils and resins composing the dispersion medium (lyophobicity index).

Our results revealed no distinct correlation between the group composition of asphalts and their performance characteristics, since the latter depends on a great number of factors.

CONCLUSIONS

(1) The performance characteristics of oxidized petroleum asphalts increase in the order West-Siberian oils < oils extracted by the Tatneft' Joint-Stock Company < Yarega oils.

(2) Heat-resistant quality asphalt (BDUS 70/100 grade) from West-Siberian oil is characterized by a higher content of aromatic structures as compared to the less heat-resistant BND 60/90 asphalt produced from the same raw material. In quality asphalt and the corresponding tar, the resin to total aromatics ratio is higher in both polar and nonpolar components as compared to less heat-resistant BND 60/90 asphalt.

(3) Factors controlling the aggregative stability of the 3D coagulation structure of asphalts are the concentration of the dispersed phase (asphaltenes) and its chemical affinity for oils and resins composing the dispersion medium (lyophobicity index).

REFERENCES

1. Kolbanovskaya, A.S., *Tr. SoyuzdorNII (Moscow)*, 1968, issue 27, pp. 120–125.
2. Pechenyi, B.G., *Bitumy i bitumnye kompozitsii* (Asphalts and Asphaltic Composites), Moscow: Khimiya, 1990.
3. Begak, O.Yu., Syroezhko, A.M., and Fedorov, V.V., *Zh. Prikl. Khim.*, 2002, vol. 75, no. 6, pp. 1032–1037.
4. Rudkevich, M.I., Rudkevich, D.M., and Pyrin, A.I., *Koks Khim.*, 1986, no. 4, pp. 30–32.
5. Posadov, I.A. and Rozental', D.A., *Zh. Prikl. Khim.*, 1985, vol. 58, no. 12, pp. 2713–2719.
6. Posadov, I.A., Rozental', D.A., Abramovich, G.V., and Borisova, L.A., *Kolloidn. Zh.*, 1985, vol. 47, no. 2, pp. 315–322.

Russian Journal of Applied Chemistry, Vol. 77, No. 4, 2004, pp. 666–669. Translated from Zhurnal Prikladnoi Khimii, Vol. 77, No. 4, 2004, pp. 670–673.

BRIEF COMMUNICATIONS

Influence of Enamel Composition and Calcination Conditions on the Corrosion of Steel under a Layer of Enamel Melt

L. G. Protasova and I. G. Kosnyreva

Ural State Technical University, Yekaterinburg, Russia

Received April 16, 2003

Abstract—The influence exerted by introduction of some oxides into the sodium–borosilicate enamel and by calcination conditions on the rate and mechanism of corrosion and on the structure and properties of enamel coatings was studied by thermogravimetric, X-ray phase, and microscopic analyses.

At present, sodium–borosilicate enamels are used as protective coatings on steel pipes for pump-and-compressor stations, oil pipelines, and water lines. Protective enamel coatings are applied onto the inner surface of a pipe by a wet or dry procedure and are calcined at 800–820°C in tunnel-type furnaces for 20–60 min [1]. The calcination is accompanied by iron oxidation, dissolution of iron oxide in the enamel melt, and formation of a transition layer. The corrosion of steel under the layer of an enamel coating was analyzed in [2, 3].

In this study, we examined the corrosion of steel under a layer of a model sodium–borosilicate enamel with a constant component ratio $Na_2O : B_2O_3 : SiO_2 = 1 : 0.5 : 0.48$. The composition of this enamel was made increasingly complex by adding Fe_2O_3, FeO, MnO, CaO, MgO, Li_2O, CaF_2, Al_2O_3, CuO, and ZnO. The compositions of the enamels studied are listed in Table 1. The enamels were synthesized by the method suggested in [4].

EXPERIMENTAL

Samples for study were prepared by the following procedure. An enamel powder (14 mg) with a grain size of 0.8 mm was placed on a 10 × 10 mm 08 KP steel plate. The sample was mounted onto a balance-beam in a derivatograph cell (MOM, Hungary) and heated from 20 to 820°C in the course of 90 min at a rate of 5 deg min^{-1}. Also, a sample was inserted into a furnace preheated to 820°C and kept there for 60 or 90 min. The DTG scale was 200 mg. The temperature

Table 1. Enamel formulations

Enamel	Composition, wt %												
	SiO_2	B_2O_3	Na_2O	Fe_2O_3	FeO	MnO	CaO	MgO	Li_2O	CaF_2	Al_2O_3	CuO	ZnO
1	49.3	26.6	24.1										
2	47.2	25.4	23.1	2.15	2.15								
3	45.1	24.4	22.1	5.6	2.8								
4	42.0	22.7	20.5	5.6	2.8	6.4							
5	39.6	21.3	19.3	5.6	2.8	6.4	5.0						
6	39.6	21.3	19.3	5.6	2.8	6.4	–	5.0					
7	38.3	20.7	18.7	5.6	2.8	6.4	–	5.0	2.5				
8	36.6	19.7	17.9	5.6	2.8	6.4	–	5.0	2.5	3.5			
9	35.9	19.4	17.6	5.6	2.8	6.4	–	5.0	2.5	3.5	1.3		
10	34.6	18.7	16.9	5.6	2.8	6.4	–	5.0	2.5	3.5	1.3	2.7	
11	34.6	18.7	16.9	5.6	2.8	6.4	–	5.0	2.5	3.5	1.3	2.7	2.6

1070-4272/04/7704-0666 © 2004 MAIK "Nauka/Interperiodica"

Table 2. Corrosion of a steel plate under an enamel coating

Composition	τ_1, min	T_1, °C	α_1, mg cm^{-2} min^{-1}	$\Delta m_1/m_0 \times 100$, %	τ_2, min	T_2, °C	α_2, mg cm^{-2} min^{-1}	$\Delta m_2/m_0 \times 100$, %	T_{os}, °C	θ, deg
Plate	29	780	0.167	–	–	–	–	–	–	–
1	52	820	0.333	71.68	82	820	0.222	28.7	800	83
2	27	800	0.187	62.33	75	820	0.080	13.9	800	50
3	22	780	0.570	57.55	36	820	0.167	43.2	850	49
4	16	655	0.250	43.45	40	820	0.083	21.3	780	57
5	16	655	0.286	43.26	37	820	0.061	21.6	760	55
6	16	655	0.231	40.87	42	820	0.102	27.3	790	55
7	30	810	0.226	100	–	–	–	–	740	52
8	27	810	0.176	43.42	61	820	0.120	21.7	700	46
9	26	800	0.103	28.17	50	820	0.216	21.1	730	44
10	24	800	0.122	29.28	61	820	0.026	7.3	800	44
11	24	800	0.360	29.72	35	820	0.167	52.0	800	46

of the enamel spreading and the wetting angle for the melt on the steel surface were determined by the lying-drop method. An X-ray phase analysis (XPA) was made on a DRON-2 instrument (Cu_{K_α}-radiation), and the composition of the corrosion products was identified using the ASTM file. The structure of the enamel coating was studied on an UEMV-100K electron microscope with a resolution of 30 Å (magnification 24000) on carbon replicas of the etched surface of the samples.

The thermogravimetric technique was used to obtain and to process curves describing the change of mass as a function of the temperature and time of the experiment. The characteristic parameters of steel corrosion under a layer of the enamel melt: τ, time; T, temperature; Δm, change in mass; and α, corrosion rate, are listed in Table 2. The corrosion rate was calculated by the formula:

$$\alpha = \Delta m/m_0 \tau S, \quad (1)$$

where m_0 is the initial mass of the sample, and S is the surface area of the metallic plate.

The data in Table 2 show that the corrosion of a steel plate without a coating starts after 29 min of heating at 780°C and proceeds in a single stage: with a gain in mass of 98%. In this case, according to [1], metal oxidation to give scale proceeds by the reactions

$$2Fe + O_2 = 2FeO, \quad (2)$$

$$3Fe + 2O_2 = Fe_2O_3. \quad (3)$$

Except in the case of formulation 7, the corrosion of a steel plate under a layer of enamel melt occurs in two stages. Reactions (2) and (3) proceed in the first stage, before spreading of the enamel; in the second stage, scale starts to dissolve in the enamel melt. Since the diffusion of oxygen to the metal surface is hindered upon spreading of the enamel, the corrosion decelerates. This is indicated by the fact that the corrosion rate in the first stage, α_1, is higher than that in the second stage, α_2. The only exception is formulation 9, for which $\alpha_2 > \alpha_1$ (Table 2).

The composition of the enamel coating affects the corrosion properties of the metallic plate. Under melts of formulations 4–6, metal corrosion starts after 16 min of heating at 665°C (gain in mass, Δm, 41–43%); under melts of formulations 2, 3, and 7–11, it starts after 22–27 min of heating at $T \geq 780$°C (Δm = 36–75%), and under a melt of formulation 1, after 52 min of heating at 820°C (Δm = 71%). As was shown in [3], water dissolved in the enamel melt affects the oxidation of the metal. Apparently, the amount of water in formulation 1 is sufficient for the following reactions to proceed

$$2Fe + 2(OH^-) = 2FeO + H_2, \quad (4)$$

$$2(=B–OH) + Fe = FeO + H_2 + =B–O–B=. \quad (5)$$

As can be seen, these groups of formulations differ mainly in the time and temperature of the onset of corrosion, whereas their remaining parameters (Δm, α) are close. However, the metal corrosion in the second stage depends on the temperature and time of enamel spreading (Table 2). It can be seen that the enamel formulations strongly differ in the onset temperature of spreading, T_{os}. Formulations 2, 3, 10, and 11 are higher-melting (T_{os} = 800–850°C), and the remaining, lower-melting (T_{os} = 700–790°C). On spreading,

Table 3. Results of an X-ray phase analysis of enamel coatings

Enamel	Crystals		
	thermogravimetry	calcination at 820°C	
		60 min	10 min
3	–	α-Fe_2O_3	–
5	$CaMn(SiO_3)_2$, β-$Ca_3Si_3O_9$, Fe_3O_4, α-Fe_2O_3, Fe_2SiO_3	Fe_3O_4	–
8	Fe_3O_4, $MgFe_2O_4$, $(MgFe)SiO_3$	Fe_3O_4	–
9	Fe_3O_4, $MgFe_2O_4$, $(MgFe)SiO_3$	–	–
10	–	$MnLiBO_3$	Fe_3O_4
11	–	Fe_3O_4	Fe_3O_4

all the enamels exhibited good wetting of the metal surface (θ = 44–57°C). Only for formulations 1, 2, 10, and 11, the onset temperature of enamel spreading was the same as the onset temperature of corrosion.

After the experiments, the samples of enamel coatings were markedly different in outward appearance. Solid, uniform, smooth, and shining enamel coatings of green, brown, and black color, respectively, were observed for formulations 1, 3, 10, and 11. For the other formulations, the coatings were uniform, but without shine, more resembling a glass ceramic than a glass. The outward appearance of samples 2 and 5–9 after a thermogravimetric analysis suggests that the corrosion products in these samples are crystallized. Their phase composition, as indicated by XPA, is listed in Table 3.

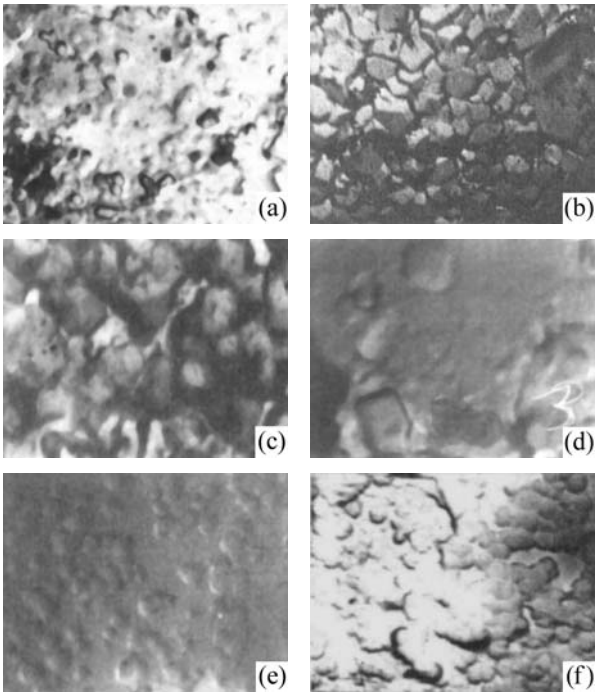

Fig. 1. Electron micrographs of the enamel coatings. Enamel (see Table 1): (a) 1, (b) 2, (c) 3, (d) 7, (e) 9, and (f) 10.

Crystals were revealed only in formulations 5, 8, and 9. Apparently, their concentration in other formulations is low. It is noteworthy that the phase composition is complex: along with the corrosion products, a number of silicates also crystallize.

To reveal the influence exerted by calcination conditions on the composition of corrosion products, samples placed in a muffle furnace preheated to 820°C and kept there for 60 min were subjected to XPA.

The outward appearance of the enamel samples was as follows: coatings of formulations 1, 2, 5–7, and 9 were smooth, shining, light green to black; in coatings of formulations 2 and 4, a great number of pinholes was observed; coatings of formulations 10 and 11 were nonuniform, shining, and black, with small brown inclusions. The results of XPA are presented in Table 3. It can be seen that corrosion products crystallize in coatings of formulations 3, 5, 8, and 11, and, presumably, a binary manganese-lithium borate, in formulation 10. The XPA data in Table 3 refer to enamel coatings on steel plates after calcination at 820°C for 10 min.

The data obtained show that the calcination conditions directly affect the type and amount of corrosion products in enamel coatings. The presence of a great number of crystalline phases in the coatings of formulations 5, 8, and 9, revealed by thermogravimetric analysis in a gradual heating in the course of 90 min, points to a deeper interaction of metal-corrosion products with the enamel melt. Moreover, these phases become crystallization centers, on which silicates crystallize from the melt. Only corrosion products are present in enamel coatings heated for 60 min. Consequently, this time is the optimal for a transition layer to be formed and strong adhesion between a coating and metal ensured. The concentration of the corrosion products in the enamel coating heated for 10 min is too small for a transition layer to be formed in formulations other than 10 and 11.

Electron micrographs of the surface layer of enamel coatings suggest that the microstructure of the coatings is nonuniform (see Fig. 1). However, the degree of nonuniformity is not the same, being at a maximum for formulations 1–3, 9, and 10 and at a minimum for

formulation 7. It may be assumed that the crystals revealed by XPA in formulations 5 and 8–10 are concentrated near the zone of contact between an enamel coating and the metal, rather than on the surface of the coating.

CONCLUSIONS

(1) It was established that the corrosion of the metal under a layer of an enamel melt occurs in two stages, and its parameters are determined by the composition of the enamel, including the concentration of dissolved water, and also by the temperature and time of its spreading.

(2) The extent to which processes of metal corrosion under a layer of Na_2O–B_2O_3–SiO_2 enamels with addition of various oxides are complete depends on calcination conditions. The optimal time of calcination at 820°C is 60 min.

(3) An X-ray phase analysis demonstrated that, in the course of interaction of the enamel melt with the metal, iron oxides dissolve in the enamel coating, which leads, in some cases, to crystallization of α-Fe_2O_3 and F_3O_4 in the coating.

(4) Not only the composition, but also the structure of enamel coatings vary in the course of interaction of an enamel coating with the metal. According to the results of electron microscopic studies, the surface of the coatings is nonuniform at the microscopic level.

REFERENCES

1. Petzold, A., and Poeschmann, H., *Email und Emailliertechnik*, Leipzig: VEB Deutscher Verlag for Grundstoffindustrie, 1986.
2. Buler, P.I. and Lazutkina, O.P., *Zashch. Met.*, 1986, vol. 22, no. 5, pp. 84–86.
3. Buler, P.I., Lazutkina, O.P., and Yushkova, V.A., *Zashch. Met.*, 1987, vol. 22, no. 4, pp. 665–667.
4. Buler, P.I., Protasova, L.G., Kosnyreva, I.G., and Turaikina, E.V., *Steklo Keram.*, 1990, no. 4, pp. 9–10.

Russian Journal of Applied Chemistry, Vol. 77, No. 4, 2004, pp. 670–672. Translated from Zhurnal Prikladnoi Khimii, Vol. 77, No. 4, 2004, pp. 674–676.

BRIEF COMMUNICATIONS

Predicting the Normal Temperature Depression in Boiling of Complex Aqueous Solutions of Nonvolatile Substances

G. M. Mikhailov, V. G. Mikhailov, L. S. Reva, and G. V. Ryabchuk

Volgograd State Technical University, Volgograd, Russia

Received June 26, 2003; in final form, December 2003

Abstract—An equation for predicting the normal temperature depression in boiling of complex aqueous solutions of nonvolatile substances is considered. The constants of the equation are tabulated. The equation is compared with experimental data for a binary solution of caustic soda and sodium chloride.

In the theory and practice of calculations of evaporation installations, the difference in the boiling temperatures of a solution of nonvolatile substances and a pure solvent is commonly referred to as the temperature depression in boiling of solutions. This is because it is a measure of the extent to which the driving force of the heat transfer (i.e., the difference between the temperature of the heating vapor and the boiling point) in boiling of a solution is lower than that in boiling of a pure solvent, all other conditions being the same. The temperature depression in boiling of solutions at an arbitrary pressure is expressed in terms of the normal temperature depression, i.e., the temperature depression at normal pressure [1, 2].

To predict the normal temperature depression for simple aqueous solutions of separate nonvolatile substances, the following equation has been suggested [3]

$$\Delta_n = \frac{327.9}{\dfrac{11.693}{Az + Bz^2 + Cz^3} - 1}, \qquad (1)$$

where $z = x/(1 - x)$ is the relative mass concentration of the solute: x, its mass concentration (kg kg^{-1}); and A, B, and C, tabulated coefficients dependent on the nature of the solute.

However, the importance of Eq. (1) is diminished by the fact that, commonly, complex solutions, i.e., solutions of two or more nonvolatile substances, are used for evaporation in the engineering practice.

We suggest that the normal temperature depression of complex solutions can be predicted using the equation

$$\Delta_n = \frac{327.9}{\dfrac{11.693}{\sum_{i=1}^{n} A_i z_i + \sum_{i=1}^{n} B_i z_i^2 + \sum_{i=1}^{n} C_i z_i} - 1}, \qquad (2)$$

where

$$z_i = \frac{x_i}{1 - \sum_{j=1}^{n} x_j}. \qquad (3)$$

Here i and j are the ordinal numbers of solutes, n, the number of different types of solutes; and z_i, the ratio of the concentration of a given solute to that of water in the complex solution.

In a particular case of simple solutions, i.e., at $n = 1$, Eq. (2) transforms into Eq. (1), whose adequacy as applied to simple solutions was convincingly demonstrated in [3].

It is possible to verify the applicability of Eq. (2) for the example of a solution of two substances, namely, caustic soda and sodium chloride.

According to the data of [3], $A_{NaOH} = 0.7853$, $B_{NaOH} = 1.5828$, and $C_{NaOH} = -1.0365$ at $x > 0.5$, i.e., $z_{NaOH} < 1$; $A_{NaOH} = 1.6272$, $B_{NaOH} = -0.29721$, and $C_{NaOH} = 0.009015$ at $x > 0.5$, i.e., $z_{NaOH} > 1$; $A_{NaCl} = 0.47309$, $B_{NaCl} = 1.02646$, and $C_{NaCl} = -0.7679$ at $z_{NaCl} \le 0.35$.

Table 1 lists the values of the normal temperature depressions in boiling of a binary solution of caustic soda and sodium chloride, calculated using Eq. (2), and compares them with the experimental values from [4].

It can be seen that the maximum deviation of the calculated values from those obtained exper-

1070-4272/04/7704-0670 © 2004 MAIK "Nauka/Interperiodica"

Table 1. Experimental data for a binary solution of caustic soda and sodium chloride [4]

x_{NaOH}	x_{NaCl}	z_{NaOH}	z_{NaCl}	Δ_{exp}	Δ_{calc}	δ
				°C		
0	0.289	0	0.4065	8	8.9	0.9
0.05	0.248	0.0712	0.3533	10	9.37	–0.63
0.10	0.209	0.1447	0.3025	11.5	10.40	–1.1
0.15	0.171	0.2209	0.2519	13.3	11.96	–1.34
0.20	0.138	0.3021	0.2085	15.4	14.32	–1.08
0.25	0.108	0.3894	0.1683	18.4	17.41	–0.99
0.30	0.087	0.4894	0.1420	23.0	21.76	–1.24
0.35	0.074	0.6077	0.1285	28.7	27.51	–1.19
0.40	0.065	0.7477	0.1215	35	34.39	–0.61
0.45	0.059	0.9165	0.1202	41.7	41.78	0.08
0.50	0.056	1.1261	0.1261	50	49.81	–0.19
0.55	0.059	1.4066	0.1509	60.5	60.31	–0.19

Table 2. Coefficients of Eq. (2) for various solutes

Substance	*A*	*B*	*C*	Applicability condition
NH_4NO_3	0.35539	–0.038867	0.0018811	$z_{NH_4NO_3} \le 4$
$(NH_4)_2SO_4$	0.22639	0.023441	0.0084854	$z_{(NH_4)_2SO_4} \le 1$
NH_4Cl	0.54399	0.27418	–0.26985	$z_{NH_4Cl} \le 0.89$
$FeSO_4$	0.080249	0.12026	–0.13557	$z_{FeSO_4} \le 0.54$
KNO_3	0.25488	–0.043002	0.0029882	$z_{KNO_3} \le 4$
K_2CO_3	0.20896	0.40180	–0.12136	$z_{K_2CO_3} \le 4$
KCl	0.36282	0.43950	–0.28904	$z_{KCl} \le 0.54$
$Ca(NO_3)_2$	0.43354	–0.21280	0.12825	$z_{Ca(NO_3)_2} \le 1$
	0.20783	0.17267	–0.032318	$1 \le z_{Ca(NO_3)_2} \le 4$
$CaCl_2$	0.48884	1.0753	–0.56598	$z_{CaCl_2} \le 1.22$
	1.1886	–2.2240	0.02487	$1.22 \le z_{CaCl_2} \le 3.17$
$MgSO_4$	0.094574	0.64733	–0.42599	$z_{MaSO_4} \le 0.75$
$MgCl_2$	0.61987	1.1474	0.69196	$z_{MgCl_2} \le 0.56$
$CuSO_4$	0.041081	0.18426	–0.017624	$z_{CuSO_4} \le 0.82$
$NaNO_3$	0.38315	–0.033788	–0.0010743	$z_{NaNO_3} \le 2.33$
Na_2SO_4	0.26781	–0.29392	0.49946	$z_{Na_2SO_4} \le 0.45$
Na_2CO_3	0.35114	–0.065123	0.099615	$z_{Na_2NO_3} \le 0.54$
NaCl	0.47309	1.02646	–0.76790	$z_{NaCl} \le 0.35$
$ZnSO_4$	0.12376	0.059773	0.033545	$z_{ZnSO_4} \le 0.86$
KOH	0.61604	1.1781	–0.38250	$z_{KOH} \le 1.85$
	1.9668	–0.28020	0.013940	$1.85 \le z_{KOH} \le 4.4$
NaOH	0.78530	1.5828	–1.0365	$z_{NaOH} \le 1$
	1.6272	–0.29791	0.0090152	$1 \le z_{NaOH} \le 2.33$

imentally is –1.34°C, and the average deviation is approximately –0.5°C. Such deviations seem to be acceptable, the more so as they can be attributed to insignificant systematic inaccuracies in determining the concentrations of a complex solution being prepared.

In [3], the constants *A*, *B*, and *C* for solutions of various substances were given together with the conditions for their applicability in the case of Eq. (1). To avoid confusion, the values of these constants in Table 2 are given, with the conditions for their applicability in the case of Eq. (2) specified.

In the case when the constants for a certain substance under consideration are unknown, they can be found from the experimental normal depressions of the corresponding simple solutions of various concentrations, using the formulas presented in [3].

CONCLUSIONS

(1) An equation for analytical prediction of the normal temperature depression in boiling of complex aqueous solutions is suggested.

(2) A table of constants is presented, with the conditions for their applicability in the case of the equation suggested in this study specified.

REFERENCES

1. Shur, V.A., *Khim. Prom–st.*, 1982, no. 11, pp. 677–679.
2. *Osnovnye protsessy i apparaty khimicheskoi tekhnologii: Posobie po proektirovaniyu* (Basic Processes and Apparatus of Chemical Technology: Designing Manual), Dytnerskii, Yu.I., Ed., Moscow: Khimiya, 1983.
3. Mikhailov, G.M., Mikhailov, V.G., Reva, L.S., and Ryabchuk, G.V., *Zh. Prikl. Khim.*, 2002, vol. 75, no. 9, pp. 1438–1442.
4. Yakimenko, L.M., and Pasmanik, M.I., *Spravochnik po proizvodstvu khlora, kausticheskoi sody i osnovnykh khlor-produktov* (Production of Chlorine, Caustic Soda, and Main Chlorine-containing Products: Reference Book), Moscow: Khimiya, 1976, 2nd ed.

Russian Journal of Applied Chemistry, Vol. 77, No. 4, 2004, pp. 673–675. Translated from Zhurnal Prikladnoi Khimii, Vol. 77, No. 4, 2004, pp. 677–679.

BRIEF COMMUNICATIONS

Study of Fusion Diagrams of Two-Component Systems *n*-Tricozane–Pentadecane and *n*-Tricosane–Hexadecane by Low-Temperature Differential Thermal Analysis

I. P. Kalinina, A. Yu. Kopnina, and I. K. Garkushin

Samara State Technical University, Samara, Russia

Received September 16, 2003; in final form, December 2003

Abstract—The two-component systems *n*-tricozane–pentadecane and *n*-tricozane–hexadecane were studied by low-temperature differential thermal analysis. The characteristics of the eutectic compositions were determined.

To predict and study the phase diagrams, the authors analyzed a number of two-component systems formed by *n*-tricosane and *n*-alkanes and determined the specific enthalpies of fusion of the eutectic compositions.

The main method used in the study was low-temperature differential thermal analysis (LDTA) [1–4]. The heating and cooling curves for the compositions studied were measured on an LDTA installation with a TZ 4620 double-line flat self-recorder. As a source of the thermoelectromotive force served a Chromel–Copel thermocouple, with one of its junctions immersed into the mixture under study and the other placed in a test tube filled with a reference indifferent substance (calcined powdered aluminum oxide). The cold junction of the thermocouple was in a Dewar flask filled with a mixture of water and ice, which had a temperature of 0°C. The thermoelectromotive force of the differential thermocouple was amplified with an F 116/1 photoamplifier. The sensitivity of the differential recording was attenuated with an MSR-33 resistance box. The zero line of the differential curve was shifted with an IRN-64 source of variable voltage. The temperature was determined to within ±0.2°C. The compounds studied were cooled and heated in a TK-1 thermal chamber. The study was performed in the temperature range 233–333 K. The rate of cooling and heating of the compounds was 1–2 deg min^{-1}. The starting components were weighed on a VLR-2000 analytical balance with an accuracy of 0.3 mg. The characteristics of the individual substances corresponded to the reference data [5, 6].

n-Tricosane **I** containing 98 wt % pure substance, *n*-pentadecane **II**, and commercial *n*-hexadecane **III** of pure grade were used in the study. The purity of the reagents was confirmed by liquid-phase chromatography (Tsvet-100 chromatograph, 50-m × 0.25-mm and 25-m × 0.25-mm capillary columns). The evaporator temperature was 623 K. As a solvent of solid hydrocarbons served toluene.

To perform a preliminary theoretical analysis of the **I**–**II** and **I**–**III** systems, we calculated the hypothetical eutectic compositions by Schroeder's equation, which is commonly used to describe ideal systems [7]:

$$\ln X_1 = \frac{-\Delta H_{\text{fus},i}(T_{\text{mel},i} - T_\text{e})}{RT_{\text{mel},i}T_\text{e}}, \quad (1)$$

where X_i is the mole fraction of *i*th substance in a mixture; $\Delta H_{\text{fus},i}$ the molar enthalpy of fusion of *i*th component (J mol^{-1}); $T_{\text{mel},i}$, the melting point of *i*th substance (K); T_e, the eutectic temperature (K); and R = 8.314 J mol^{-1} K^{-1}, the universal gas constant.

To confirm the accuracy of determination of the experimentally found specific enthalpies of fusion of the systems, they were calculated by formulas [1, 2]

$$\Delta H_{\text{fus,e}} = x_1 \Delta H_{\text{fus},1} + x_2 \Delta H_{\text{fus},2}, \text{ kJ kg}^{-1}, \quad (2)$$

$$\frac{\Delta H_{\text{fus,e}}}{T_\text{e}} = \frac{x_1 \Delta H_{\text{fus},1}}{T_{\text{mel},1}} + \frac{x_2 \Delta H_{\text{fus},2}}{T_{\text{mel},2}}, \text{ kJ kg}^{-1}, \quad (3)$$

where x_1 and x_2 denote the composition of the eutectic

1070-4272/04/7704-0673 © 2004 MAIK "Nauka/Interperiodica"

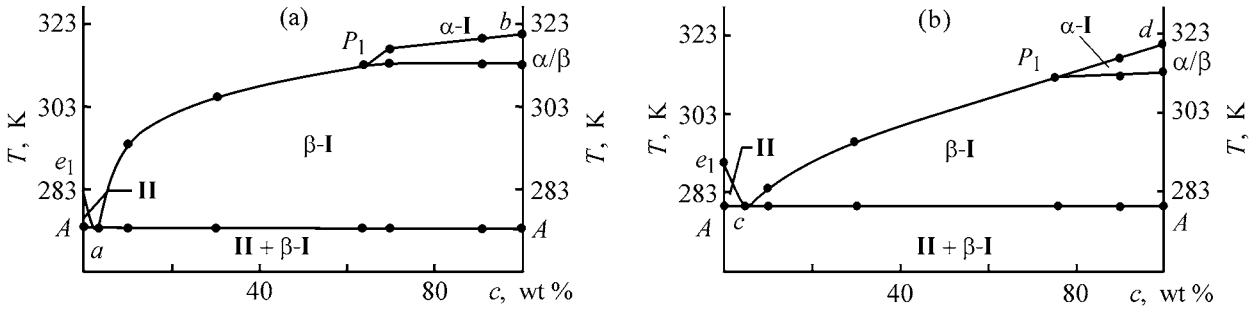

Fig. 1. Phase diagrams of the systems (a) **I**–**II** and (b) **I**–**III**. (*T*) Melting point of components of the system and (*c*) content of *n*-alkane. α-**I**, region of crystallization of α-*n*-tricosane; β-**I**, region of crystallization of β-**I**; **II** + β-**I**, region of crystallization of *n*-alkane and β-*n*-tricosane.

(wt %); $\Delta H_{\text{fus},1}$ and $\Delta H_{\text{fus},2}$ are the specific enthalpies of fusion of compounds **I** and **II** [**III**] (kJ kg^{-1}); and $T_{\text{mel},1}$ and $T_{\text{mel},2}$, the melting points of compounds **I** and **II** [**III**] (K).

Table 1. Calculated and experimental eutectic compositions

System	T_{mel}, K	Eutectic composition, mol %	
		$C_{23}H_{48}$	*n*-alkane
I–**II**	273.5	98.0	2.0
		97.9	2.1
I–**III**	279.6	96.5	3.5
		96.7	3.3

* Numerator: experiment, denominator: calculation by Eq. (1).

Table 2. Calculated and experimental specific enthalpies of fusion of eutectic systems

System	Enthalpy of fusion, kJ kg^{-1}/kJ mol^{-1}		
	calculation		experiment, Eq. (4)
	Eq. (2)	Eq. (3)	
I–**II**	163.18/35.05	82.97/21.57	30/24.76
I–**III**	128.00/19.77	83.52/15.43	72/32.44

Table 3. Phase equilibria in the systems **I**–**II** and **I**–**III**

Point (line)	Equilibrium	Phase equilibrium
Eutectic *AaA*	Nonvariant	l ⇄ **II** + β-**I**
Transition P_1	"	l + α-**I** ⇄ β-**I**
e_1a	Monovariant	l ⇄ **II**
aP_1	"	l ⇄ β-**I**
P_1b	"	l ⇄ α-**I**
Eutectic *AcA*	Nonvariant	l ⇄ **III** + β-**I**
Transition P_1	"	l + α-**I** ⇄ β-**I**
e_1c	Monovariant	l ⇄ **II**
cP_1	"	l ⇄ β-**I**
P_1d	"	l ⇄ α-**I**

The experimental enthalpies of fusion of the systems under study were determined using the equation [1]:

$$\Delta H_{\text{fus, e}} = \frac{\Delta H_{\text{fus},1} T_{\text{e}} S m_1}{T_{\text{mel},1} S_1 m}, \quad (4)$$

where ΔH_{fus} is the enthalpy of fusion of the reference substance (*n*-tetradecane), whose melting point is close to that of the eutectic composition (kJ kg^{-1}); T_{mel}, the melting point of the reference substance (K); S_1 and S, the half areas under the peak in the cooling curve of the pure reference substance and a mixture of eutectic composition, respectively (mm^2); m_1 and m, the weighed portions of the pure reference substance and the eutectic mixture, respectively (kg); T_{e}, the melting point of the eutectic composition in the system (K).

The calculated and experimental data obtained are listed in Tables 1 and 2 and shown in Figs. 1a, 1b.

The liquidus curves are represented by three crystallization branches α-**I**, β-**I**, and **II** [**III**]. The minimum crystallization branch corresponds to the compounds **II** [**III**]. The eutectic compositions found experimentally and those calculated by Eq. (1) are listed in Table 1.

The phase equilibria for points and lines of the given diagrams are indicated in Table 3.

CONCLUSION

The phase diagrams of the two-component systems constituted by *n*-tricosane and pentadecane and by *n*-tricosane and hexadecane were studied. The characteristics of their eutectic compositions were determined: mp 273.5 and 279.6 K, eutectic composition 3.0–97 and 5.0–95.0 wt %, and specific enthalpy of fusion 30 and 72 kJ kg^{-1}, respectively.

REFERENCES

1. Kopnina, A.Yu., Agafonov, I.A., Garkushin, I.K., and Miftakhov, T.T., *Trudy respublikanskoi nauchno-tekhnicheskoi konferentsii molodykh uchenykh "Khimicheskie nauki. Khimicheskie tekhnologii"* (Proc. of Republican Sci. and Eng. Conf. of Young Scientists "Chemical Science. Chemical Engineering"), Samara, 1999, p. 14.
2. Kopnina, A.Yu., Agafonov, I.A., Garkushin, I.K., *Izv. Vyssh. Uchebn. Zaved., Khim. Khim. Tekhnol.*, 2001, vol. 44, no. 5, pp. 84–85.
3. Agafonov, I.A., Garkushin, I.K., and Miftakhov, T.T., *Zh. Fiz. Khim.*, 1999, vol. 73, no. 5, pp. 785–787.
4. Agafonov, I.A., Garkushin, I.K., and Miftakhov, T.T., *Fazovye ravnovesiya v dvukhkomponentnykh sistemakh iz n.-alkanov* (Phase Equilibria in Two-Component Systems of *n*-Alkanes), Samara: Samara Gos. Tech. Univ., 1997.
5. Tatevskii, V.M., *Fiziko-khimicheskie svoistva individual'nykh uglevodorodov* (Physicochemical Properties of Individual Hydrocarbons), Moscow: Gostoptekhizdat, 1959.
6. *Svoistva organicheskikh soedinenii* (Properties of Organic Compounds), Potekhina, A.A., Ed., Leningrad: Khimiya, 1984.
7. Stromberg, A.G. and Semchenko, D.P., *Fizicheskaya khimiya* (Physical Chemistry), Stromberg, A.G., Ed., Moscow: Vysshaya Shkola, 2003.

Russian Journal of Applied Chemistry, Vol. 77, No. 4, 2004, pp. 676–679. Translated from Zhurnal Prikladnoi Khimii, Vol. 77, No. 4, 2004, pp. 680–682.

BRIEF COMMUNICATIONS

Mechanism of Extraction of Vanadium(V) from Sulfuric Acid Solutions with Di-2-ethylhexylphosphoric Acid

L. D. Kurbatova, D. I. Kurbatov, and N. I. Medvedeva

Institute of Solid-State Chemistry, Ural Division, Russian Academy of Sciences, Yekaterinburg, Russia

Received July 22, 2003; in final form, December 2003

Abstract—IR and electronic absorption spectroscopies were applied to a study of the mechanism of extraction of vanadium(V) with di-2-ethylhexylphosphoric acid from sulfuric acid solutions.

Di-2-ethylhexylphosphoric acid (D2EHPA) is an extracting agent widely employed in radiochemistry, analytical chemistry, and chemical engineering. It is used to extract such elements as Nb(V), Ta(V), Ti(III), and V(IV). In [1], it was demonstrated for the first time that D2EHPA can also extract vanadium(V) from weakly acidic solutions by the hydrate-solvate mechanism. Investigations in this area have been continued. The present communication reports the results obtained in studying the mechanism of V(V) extraction with D2EHPA from concentrated sulfuric acid solutions.

EXPERIMENTAL

Extraction of vanadium(V) and spectroscopic measurements were performed at 25 ± 0.5°C. Di-2-ethylhexylphosphoric acid was preliminarily purified to remove mono-2-ethylhexylphosphoric acid. The extraction was carried out with undiluted D2EHPA at $V_o : V_a = 11$ and multiple contact (~4 min) with a sulfuric acid solution of V(V). The working solutions were prepared using sodium metavanadate $NaVO_3$ of chemically pure grade. The concentration of V(V) in aqueous solutions was determined titrimetrically [2]. The content of V(V) in the organic phase was calculated from the difference of concentrations in the aqueous solution before and after extraction.

IR spectra were recorded with a Specord 75-IR spectrometer in the range 400–4000 cm^{-1}. The solutions studied were placed between KRS-6 plates. Electronic absorption spectra of V(V) extracts were recorded with a Specord UV-VIS spectrophotometer in the range 13000–30000 cm^{-1} in cuvettes with the thickness of the absorbing layer $l = 0.1$ cm. Electronic absorption spectra of V(V) solutions in H_2SO_4 were recorded in cuvettes with $l = 1.0$ cm. In this case, the concentration of V(V) was 4×10^{-4} M. ^{51}V NMR spectra were recorded with a Bruker MSL-400 spectrometer at a frequency of 105.24 MHz. The chemical shift δ was determined relative to $VOCl_3$ as external reference.

Of high importance in choosing the conditions of V(V) extraction from sulfuric acid solutions is the stability of the extracting agent. It is known that D2EHPA is stable in acid solutions [1]. It was shown in [2] that, on bringing this extracting agent in contact with sulfuric acid solutions, it is hydrolyzed only slightly. As shown by the investigations performed, D2EHPA is not decomposed, either, in the presence of V(V) up to a concentration of 0.20 M in a 12 M solution of H_2SO_4. The intensity of hydrolysis of D2EHPA increases upon prolonged contact with a 11 M solution of HF, and especially with a mixture of HF and H_2SO_4 [2]. The aforesaid indicates that, in selecting the optimal conditions of V(V) extraction with D2EHPA from solutions with higer H_2SO_4 concentrations. In doing so, however, account should be taken of the fact that the ionic state of V(V) in H_2SO_4 solutions is determined by the concentrations of V(V) and H_2SO_4. At high V(V) concentrations ($c_V \geq 0.12$ M), dimeric complexes of the oxovanadium(V) cation, $[V_2O_3(H_2O)_{8-2x}(SO_4)_x]^{(4-2x)+}$, are formed in concentrated H_2SO_4 solutions [3]. Therefore, it is preferable to extract V(V) from solutions with H_2SO_4 concentrations at which V(V) exists in the form of the above dimeric complexes and no decomposition of D2EHPA occurs.

To establish the concentration range of the monomer–dimer transition, the ionic state of V(V) was studied in H_2SO_4 solutions at the concentrations $c_{H_2SO_4}$ of 1.0–16.8 M.

1070-4272/04/7704-0676 © 2004 MAIK "Nauka/Interperiodica"

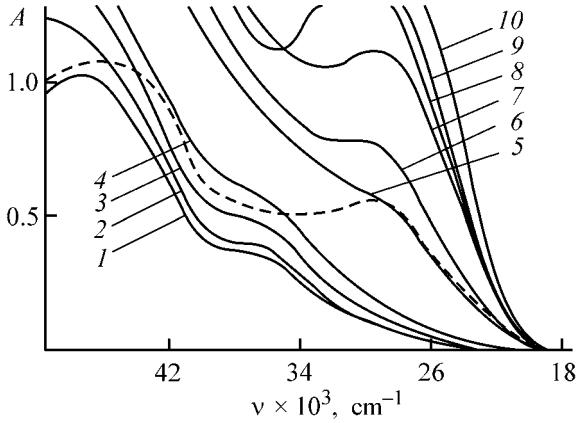

Fig. 1. Electronic absorption spectra of V(V) solutions in H_2SO_4 at l = 1.0 cm. $c_V = 4 \times 10^{-4}$ M; the same for Fig. 2. (*A*) Optical density and (ν) wave number. $c_{H_2SO_4}$ (M): (*1*) 1.0, (*2*) 3.0, (*3*) 5.0, (*4*) 7.0, (*5*) 9.0, (*6*) 10.0, (*7*) 11.0, (*8*) 13.0, (*9*) 15.0, and (*10*) 16.8. *Dashed line*: $c_{H_2SO_4}$ = 12.0 M, $c_V = 1.2 \times 10^{-4}$ M.

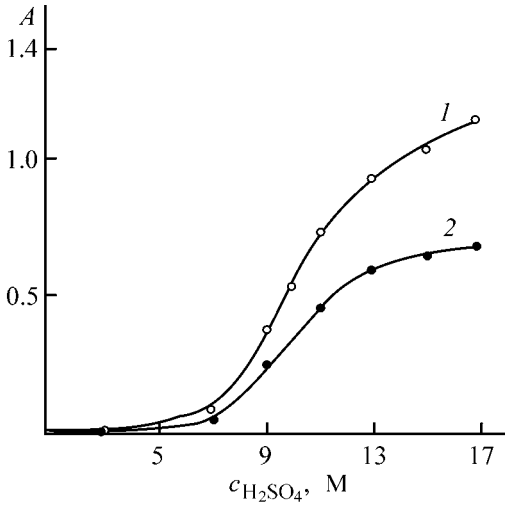

Fig. 2. Optical density A of V(V) solutions vs. the concentration c of H_2SO_4 at l = 1 cm. ν (cm^{-1}): (*1*) 26000 and (*2*) 23000.

Figure 1 shows electronic absorption spectra of V(V) solutions in H_2SO_4. At sulfuric acid concentrations in the range 1.0–7.0 M, absorption bands at 48000, 44000, and 36000 cm^{-1} are observed in the electronic spectra of V(V) solutions, which indicates that V(V) exists under these conditions in the form of complexes in which the dioxovanadium(V) cation is the central group [4]. Raising the concentration of H_2SO_4 further leads to a dramatic increase in the optical density and to a change of the shape of the spectrum. Beginning with a H_2SO_4 concentration of 9.0 M, a new absorption band at 29000 cm^{-1} appears in the electronic spectra of V(V) solutions.

Such a variation of the shape of the spectrum with the H_2SO_4 concentration is probably due to the appearance of another ionic form of V(V). Indeed, beginning with a H_2SO_4 concentration of 7.0 M, the molar absorption coefficients grow abruptly as the concentration of H_2SO_4 or V(V) increases. This is presumably due to the formation of polynuclear forms of V(V).

To confirm these conclusions, ^{51}V NMR spectra of V(V) solutions in H_2SO_4 were recorded. With the concentration of V(V) in the range from 1×10^{-3} to 5×10^{-1} M, a singlet signal with a chemical shift δ = –650 ppm was observed in ^{51}V NMR spectra in H_2SO_4 ($c_{H_2SO_4}$ = 16.0 M), which indicates that dimeric complexes of the oxovanadium(V) cation are formed under these conditions [3] (see table).

At low H_2SO_4 concentrations, ^{51}V NMR spectra of V(V) solutions show a singlet signal with a chemical shift δ = –541 ppm, which indicates that V(V) complexes with the dioxovanadium(V) cation as the central group exist under these conditions [5]. It can be seen from Fig. 2 that the optical density of V(V) solutions increases abruptly at $c_{H_2SO_4} \geq 7.0$ M.

At $c_{H_2SO_4}$ of 11.0 M the optical density starts to level off, which is presumably due to formation of dimeric complexes of dioxovanadium(V) cations in this range of H_2SO_4 concentrations. In the electronic absorption spectrum of the dimeric complex of the dioxovanadium(V) cation in a 12.0 M solution of H_2SO_4 (Fig. 1), two absorption bands at ν 46000 and 29000 cm^{-1} were observed. These bands can be identified as charge-transfer bands. On the basis of the data obtained in analyzing the ionic state of V(V) in H_2SO_4 solutions, and with account of the results of a previous study [6], the optimal conditions of V(V) extraction with D2EHPA are $c_{H_2SO_4} \geq$ 11.00 M.

The extraction of V(V) with D2EHPA from H_2SO_4 solutions was studied using IR and electronic absorption spectroscopies. In the IR spectrum of the extract

Chemical shifts for ^{51}V in sulfuric acid solutions of vanadium(V)

c_V	$c_{H_2SO_4}$	δ, ppm
M		
5×10^{-1}	16.0	–650
5×10^{-2}	16.0	–650
1×10^{-3}	16.0	–648
5×10^{-2}	11.0	–626
1×10^{-3}	1.0	–541

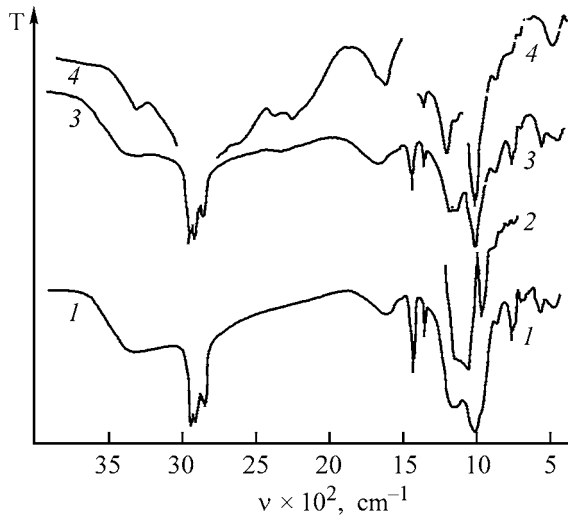

Fig. 3. IR spectra of the system V(V)–H_2SO_4–D2EHPA. (T) Transmission and (ν) wave number. (*1*) V(V) extract with D2EHPA (c_V^{in} = 0.1381 M), (*2*) V(V) extract with D2EHPA after compensation of D2EHPA, (*3*) H_2SO_4 extract with D2EHPA, and (*4*) D2EHPA.

of V(V) with D2EHPA (Fig. 3), the component of the ν_{P-OH} band at 1680 cm^{-1} is shifted to 1630 cm^{-1} as compared with a similar component in the IR spectrum of the H_2SO_4 extract with D2EHPA. The components of the ν_{P-OH} band at 2260 and 2660 cm^{-1} disappear. This indicates that P–OH groups are involved in the coordination of V(V) [7]. Presumably, protons of the extracting agent are replaced with V(V) cations, which exist in concentrated H_2SO_4 solutions. The same behavior is observed in extraction of Sc(III) from concentrated HCl solutions [8]. In this case, the cation-exchange mechanism of extraction predominates up to a HCl concentration of 10 M. In addition, the IR spectra of V(V) extracts with D2EHPA contain absorption bands at 1170 and 1070 cm^{-1}, which are identified as ν_{POO}^{as} and ν_{POO}^{s}, respectively [7]. The shift of the band associated with the POO group, ν_{POO}^{as} in the spectrum of the V(V) extract with D2EHPA, compared with the IR spectrum of the H_2SO_4 extract with D2EHPA, indicates that POO groups are also presumably involved in the coordination of vanadium(V).

An analysis of IR spectra of a V(V) solution in 11 M H_2SO_4 and a V(V) extract with D2EHPA made it possible to identify ions in whose form D2EHPA extracts V(V). As shown above, V(V) exists in 11 M H_2SO_4 solutions in the form of dimeric complexes of the dioxovanadium(V) cation. A band at 988 cm^{-1} and a shoulder at 750 cm^{-1} appear in the IR spectrum of a V(V) solution in 11 M H_2SO_4, measured after the compensation of the acid. The IR spectrum of the V(V) extract with D2EHPA shows a doublet at 970–990 cm^{-1} on the background of the bands associated with D2EHPA and sulfate ions. A strong band at 985 cm^{-1} appears in the IR spectrum of the V(V) extract with D2EHPA after the compensation of D2EHPA. By analogy with the data of [3], this band can be attributed to ν_1-type vibrations of the dimeric oxovanadium(V) cation. The band at 750 cm^{-1} could not be observed because it is, presumably, overlapped with a stronger band of D2EHPA.

The aforesaid shows that D2EHPA extracts V(V) from concentrated H_2SO_4 solutions in the form of a dimeric complex of the oxovanadium(V) cation. The presence of absorption bands at 3450 and 570 cm^{-1} and a shoulder at 600 cm^{-1} in the IR spectrum of the V(V) extract with D2EHPA indicates that the complex being extracted also contains molecules of water and sulfate ions [9]. To confirm the possible formation of mixed-ligand complexes of V(V) in its extraction with D2EHPA, electronic absorption spectra of V(V) solutions in 12 M H_2SO_4 and V(V) extracts with D2EHPA were recorded. The electronic absorption spectrum of a V(V) solution in 12 M H_2SO_4 contains an absorption band at 29 000 cm^{-1}. The electronic absorption spectrum of the V(V) extract with D2EHPA shows a shift of the absorption band to the higher-energy part of the spectrum.

The shift of the absorption peak from 29 000 to 25 000 cm^{-1} on passing from a sulfate dimeric complex if the oxovanadium(V) cation to the V(V) complex with D2EHPA, being extracted, is due to the appearance of upper occupied molecular orbitals, which reflect the π-bond in the PO group. This conclusion follows from an analysis of molecules of the type Alk_3PO (Alk stands for an alkyl radical). It has been established for molecules of this kind that their electronic configuration in the ground state has the form $(1a_1)^2(2a_1)^2(1e)^4(3a_1)^2(2e)^4$, where the high-energy occupied molecular orbital $2e$ is the orbital involved in the π-bonding between oxygen and phosphorus atoms [10].

CONCLUSION

A study of the ionic state of V(V) in H_2SO_4 solutions in the concentration range 1.0–16.8 M resulted in that the optimal conditions of V(V) extraction with di-2-ethylhexylphosphoric acid were determined. It was established that the extraction occurs by the cation-exchange mechanism to give mixed-ligand complexes of the dimeric oxovanadium(V) cation with

anions of sulfuric and di-2-ethylhexylphosphoric acids in the organic phase.

REFERENCES

1. Ignatenko, A.V., Pastukhova, I.V., Petrov, K.M., *et al.*, *Zh. Anal. Khim.*, 1982, vol. 37, no. 4, pp. 744–747.
2. Nikolaev, A.I., Maiorov, V.G., Zozulin, A.P., and Shevyreva, E.V., *Zh. Obshch. Khim.*, 1994, vol. 64, no. 6, pp. 941–946.
3. Madis, C., Begun, G.M., Hahn, R.L., *et al.*, *Inorg. Chem.*, 1984, vol. 23, no. 4, pp. 469–476.
4. Bontchev, P.R. and Nikolov, G.S., *J. Inorg. Nucl.*, 1966, vol. 28, no. 11, pp. 2609–2614.
5. Donnell, S.E.D. and Pope, M.T., *J. Chem. Soc. Dalton*, 1976, no. 21, pp. 2290–2297
6. Kurbatova, L.D., Yatluk, Yu.G., and Kurbatov, D.I., *Analit. Kontrol'*, 2000, vol. 4, pp. 352–353.
7. Stoyanov, E.S., Popov, V.M., and Mikhailov, V.A., *Zh. Prikl. Spektrosk.*, 1984, vol. 40, no. 1, pp. 77–81.
8. Palant, A.A. and Petrova, V.A., *Zh. Neorg. Khim.*, 1997, vol. 42, no. 6, pp. 1044–1046.
9. Nakamoto, K., *Infrared Spectra of Inorganic and Coordination Compounds*, New York: John Wiley & Sons, 1963.
10. Mazalov, L.N. and Yumatov, V.D., *Elektronnoe stroenie ekstragentov* (Electronic Structure of Extracting Agents), Novosibirsk: Nauka, 1984.

Russian Journal of Applied Chemistry, Vol. 77, No. 4, 2004, pp. 680–682. Translated from Zhurnal Prikladnoi Khimii, Vol. 77, No. 4, 2004, pp. 683–684.

BRIEF COMMUNICATIONS

Influence Exerted by H_2SiF_6 on Extraction of Titanium(IV)

V. G. Maiorov, A. I. Nikolaev, V. K. Kopkov, and G. V. Korotkova

Tananaev Institute of Chemistry and Technology of Rare Elements and Mineral Raw Materials, Kola Scientific Center, Russian Academy of Sciences, Apatity, Murmansk oblast, Russia

Received November 4, 2003

Abstract—Extraction of titanium(IV) with octanol and tributyl phosphate from fluoride solutions that contain H_2SiF_6 or H_2SO_4 was studied.

Previously, a significant enhancement of the extraction of Ta(V) and Nb(V) with tributyl phosphate (TBP) from fluoride solutions with high content of impurity ions, Ti(IV), Si(IV), Sn(IV), etc., which form fluoroelement acids, has been observed [1, 2]. These acids can replace mineral acids (sulfuric and others), which are commonly added to improve the efficiency of recovery of Ta(V) and Nb(V) fluorides [3]. The fluoroelement and sulfuric acids can be arranged in order of increasing influence on the extraction of Ta(V) as $H_2TiOF_4 > H_2SiF_6 \geq H_2SO_4$ and in order of increasing effect on the extraction of Nb(V) as $H_2SiF_6 \geq H_2SO_4 \geq H_2TiOF_4$. Of interest is a study of the influence exerted by the acids under consideration, present in the extraction system, on the distribution of fluorides of elements other than Ta(V) and Nb(V).

This study is concerned with the influence exerted by the acid H_2SiF_6 on the recovery of Ti(IV). Naturally, Ti(IV) must also affect the distribution of Si(IV). It has been established that Ti(IV) is extracted from fluoride solutions considerably better than Si(IV) [3], which creates prerequisites for a clearer manifestation of the effect expected. In addition, the content of Ti(IV) in fluoride solutions is more easily determined by chemical analysis than Si(IV). A study of the effect of Si(IV) on the distribution of Ti(IV) is also of practical interest for obtaining pure compounds of Ta(V) and Nb(V) from raw materials with high content of these impurities.

As extracting agents were used octanol-1 (OCL; content of main product ~98%) and TBP of pure grade. The physicochemical properties of OCL were reported in [4], and methods for working with aggressive fluoride solutions and for analytical monitoring, in [1, 2]. The extraction was performed from a solution containing 1 M of Ti(IV) and a varying amount of H_2SiF_6 or (for comparison purposes) H_2SO_4 at two different concentrations of HF_{free}. The designation HF_{free} is adopted for the conditional calculated concentration of HF, which exceeds that necessary for the complexes H_2TiOF_4 and H_2SiF_6 to be formed, since just these complexes are predominant in the system under study [1, 3, 5]. The experimental data obtained are presented in Figs. 1, 2 and in the table ($V_o : V_a$ is the volume ratio of the organic and aqueous phases before extraction).

It has been noted previously [4] that the extracting capacity of OCL for fluoride systems with Ta(V) and Nb(V) is approximately twice lower than that for TBP. Accordingly, the extraction with OCL was performed, in studying the influence exerted by H_2SiF_6 on the distribution of Ti(IV), at $V_o : V_a$ exceeding by a factor of 2 that for TBP. As also in the case of Ta(V) and Nb(V) fluorides, H_2SiF_6 exerts a considerably stronger influence on the extraction of Ti(IV) than

Influence exerted by the concentration of HF on the extraction of Ti(IV) with TBP ($V_o : V_a = 1 : 1$) and OCL ($V_o : V_a = 2 : 1$) from a solution of 1 M of Ti(IV)

HF_{free}, M	Acid, 3.5 M	Recovered Ti(IV), %	
		with TBP	with OCL
0.5	H_2SiF_6	55.5	50.6
3	〃	30.1	50.6
0.5	H_2SO_4	38.4	21.0
3	〃	10.6	13.8

1070-4272/04/7704-0680 © 2004 MAIK "Nauka/Interperiodica"

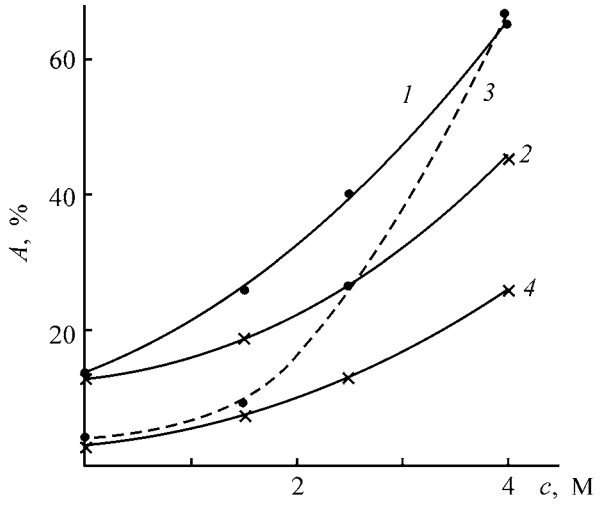

Fig. 1. Effect of (*1*, *3*) H_2SiF_6 or (*2*, *4*) H_2SO_4 on the extraction of Ti(IV) with (*1*, *2*) TBP and (*3*, *4*) OCL from a solution that contains 0.5 M of HF_{free} and 1 M of Ti(IV). (*A*) Recovery of Ti(IV) and (*c*) concentration of H_2SiF_6, H_2SO_4. $V_o : V_a$: (*1*, *2*) 1 : 1 and (*3*, *4*) 2 : 1.

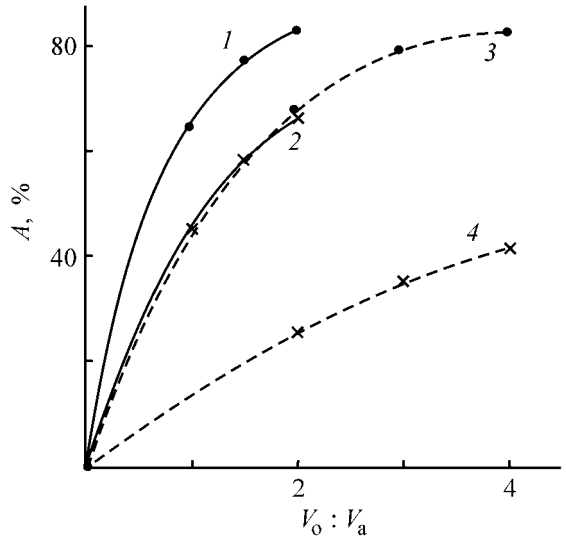

Fig. 2. Effect of the $V_o : V_a$ ratio on the extraction of Ti(IV) with (*1*, *2*) TBP and (*3*, *4*) OCL. Content (M): HF_{free} 0.5, Ti(IV) 1; (*1*, *3*) Si(IV) 4 and (*2*, *4*) H_2SO_4. (*A*) Recovery of Ti(IV).

H_2SO_4 does. The analogy with the data for Ta(V) and Nb(V) is also manifested in that the above effect of enhancement of Ti(IV) extraction from H_2SiF_6 solutions (compared with H_2SO_4 solutions) for OCL at high content of H_2SiF_6 is substantially stronger than that in the case of TBP. For example, replacing H_2SO_4 with H_2SiF_6 in extraction from a 4 M acid solution leads to an increase in the recovery of Ti(IV) with OCL by a factor of 2.6, and that with TBP, by only a factor of 1.4. This indicates that the effect of acids, which supply H^+ ions, on the distribution of H_2TiOF_4 depends not only on the type of an acid, but also on the nature of an organic solvent. This circumstance should be taken into account in studying the influence exerted by fluoroelement acids on the distribution of Ti(IV) and fluorides of other elements present in the extraction system.

Raising the ratio $V_o : V_a$ makes it possible to achieve a Ti(IV) recovery from H_2SiF_6 solutions in a single stage of 80% and more with both OCL and TBP. This value is sufficient for virtually complete extraction of Ti(IV) into the organic phase in the mode of a continuous counterflow extraction. At the same time, complete recovery of Ti(IV) with TBP (and the more so with OCL) from H_2SO_4 solutions under the conditions studied is hardly achievable. It should be noted that the extracting capacity of OCL approaches that of TBP in extraction of Ti(IV) from solutions with high concentration of H_2SiF_6 and large values of $V_o : V_a$, as also in the case of extraction of Ta(V) and Nb(V) [4].

Raising the concentration of HF leads to a decrease in recovery of Ti(IV), presumably, because of the competing extraction of HF (see table). Rather unexpected was the absence of any effect of HF in the concentration range studied on the distribution of Ti(IV) in extraction with OCL from H_2SiF_6 solutions.

The data obtained lead to practically important conclusions. If the objective of a researcher is to ensure complete recovery of Ti(IV) in order to obtain its high-purity compounds [6], then presence of Si(IV) in the extraction system is desirable because this makes it possible to lower the ratio $V_o : V_a$ and, accordingly, to diminish the material flows in the extraction technology. In obtaining high-purity compounds of Ta(V) and Nb(V), the recovery of Ti(IV) should be at a minimum and presence of Si(IV) in solutions is undesirable. To work efficiently with fluoride extraction sys tems, it is necessary to know and take into account the mutual influence of fluoroelement acids of all elements that are present in solutions and can form fluoride complexes that dissociate by the acid type.

CONCLUSIONS

(1) H_2SiF_6 exerts substantially stronger influence on the extraction of Ti(IV) with octanol and tributyl phosphate than H_2SO_4 does.

(2) Conditions are found under which the recovery of Ti(IV) from H_2SiF_6 solutions in a single stage exceeds 80%.

ACKNOWLEDGMENTS

The study was financially supported by the Division of Chemistry and Materials Science (project 10 002-251/OkhNM-06/128-140/200 603-781).

REFERENCES

1. Maiorov, V.G., Nikolaev, A.I., and Kopkov, V.K., *Zh. Prikl. Khim.*, 1999, vol. 72, no. 6, pp. 929–932.
2. Maiorov, V.G., Nikolaev, A.I., and Kopkov, V.K., *Zh. Neorg. Khim.*, 2000, vol. 45, no. 8, pp. 1433–1436.
3. Babkin, A.G., Maiorov, V.G., and Nikolaev, A.I., *Ekstraktsiya niobiya i tantala i drugikh elementov iz ftoridnykh rastvorov* (Extraction of Niobium, Tantalum, and Other Elements from Fluoride Solutions), Leningrad: Nauka, 1988.
4. Maiorov, V.G., Nikolaev, A.I., and Kopkov, V.K., *Zh. Prikl. Khim.*, 2001, vol. 74, no. 3, pp. 357–360.
5. Ryss, I.G., *Khimiya ftora i ego neorganicheskikh soedinenii* (Chemistry of Fluorine and Its Inorganic Compounds), Moscow: Goskhimizdat, 1956.
6. Masloboeva, S.M., Sklokin, L.I., and Budnikova, N.N., *Novye protsessy v metallurgii tsvetnykh, redkikh i blagorodnykh metallov* (New Processes in Metallurgy of Nonferrous, Rare, and Noble Metals), Apatity: Kol'sk. Nauchn. Ts. Ross. Akad. Nauk, 2001, pp. 57–62.

Russian Journal of Applied Chemistry, Vol. 77, No. 4, 2004, pp. 683–684. Translated from Zhurnal Prikladnoi Khimii, Vol. 77, No. 4, 2004, pp. 685–686.

BRIEF COMMUNICATIONS

Synthesis of High-Ratio Mordenite

M. L. Pavlov, R. A. Makhamatkhanov, B. I. Kutepov, F. Kh. Kudasheva, G. I. Apkarimova, and O. S. Buyanova

Institute of Petrochemistry and Catalysis, Academy of Sciences of the Republic of Bashkortostan, Scientific Center of the Russian Academy of Sciences, Ufa, Bashkortostan, Russia

Received April 1, 2003; in final form, February 2004

Abstract—Synthesis of a mordenite-like zeolite from reaction mixtures of composition $2.5R \cdot (2.2–7.3)Na_2O \cdot Al_2O_3 \cdot (12–40)SiO_2 \cdot (300–1200)H_2O$, where R is monoethanolamine, was studied. The crystallization conditions under which mordenite with a SiO_2/Al_2O_3 ratio of 13 to 22 can be synthesized were determined.

Raising the SiO_2/Al_2O_3 ratio in a zeolite improves its thermal stability and resistance to an acid medium [1]. It has been suggested to obtain high-ratio mordenites (with SiO_2/Al_2O_3 molar ratio > 13) by dealumination of low-ratio mordenites (SiO_2/Al_2O_3 = 8–10) [1] or by high-temperature synthesis in the presence of organic additives (templates) [2]. Commonly, quaternary alkyl ammonium bases are used for this purpose. In [3], it was suggested to synthesize mordenite with a ratio of about 20 from reaction mixtures of composition $(10–29)R \cdot (2–20)Na_2O \cdot Al_2O_3 \cdot (30–100)SiO_2 \cdot (600–2500)H_2O$, using a more accessible organic base monoethanolamine (MEA) as a template [3]. As starting reagents served solutions of Na_2SiO_3, $Al_2(SO_4)_3$, and H_2SO_4.

In this study, we made an attempt to synthesize high-ratio mordenite in the presence of MEA from reaction mixtures of another composition, prepared by mixing other types of Si- and Al-containing raw materials, carbon white or wastes produced in manufacture of crystalline silicon (WMSC) [4], with solutions of sodium silicate and aluminate. Not only MEA, but also isobutyl alcohol (IBA), were used as templates.

EXPERIMENTAL

The experiments were performed in an autoclave with a stirrer and a sampling device. The degree of crystallinity and the type of a forming zeolite were determined by X-ray phase analysis. The procedures used to synthesize and study the zeolites were described in more detail in [4].

Reaction mixtures of composition $2.5R \cdot (2.2–7.3)Na_2O \cdot Al_2O_3 \cdot (12–40)SiO_2 \cdot (300–1200)H_2O$ were used for synthesis.

Silica-alumina hydrogels of the above compositions were obtained by mixing a carbon white or WMSC with solutions of sodium silicate and aluminate. To these gels was added MEA or IBA. The crystallization was performed at 130–170°C under continuous agitation.

Preliminary experiments demonstrated that mordenite with a ratio exceeding 13 can be synthesized under the conditions chosen. Further, we studied the kinetics of crystallization of high-ratio mordenites.

The kinetic curves of crystallization of a mordenite-like zeolite at 150°C from the reaction mixtures containing MEA and IBA are plotted in Fig. 1.

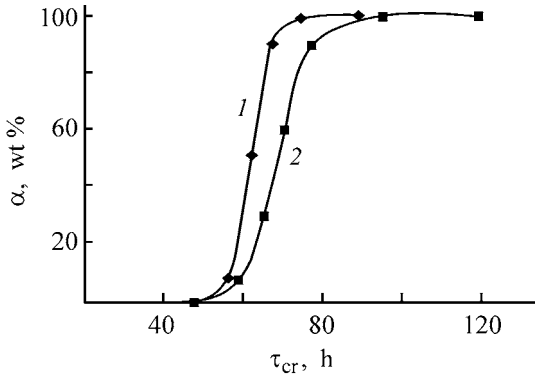

Fig. 1. Crystallinity α of a mordenite-like zeolite vs. the time of crystallization τ_{cr} of a reaction mixture of composition $2.5R \cdot 7.3Na_2O \cdot Al_2O_3 \cdot 40SiO_2 \cdot 1200H_2O$ at 150°C. Organic compound: (*1*) MEA and (*2*) IBA.

1070-4272/04/7704-0683 © 2004 MAIK "Nauka/Interperiodica"

Physicochemical properties of high-ratio mordenites

R	τ_{cr}, %	λ, wt %	Static capacity of a zeolite for an indicated vapor, $cm^3\ g^{-1}$			Composition, wt %		SiO_2/Al_2O_3
			H_2O	C_6H_6	C_7H_{16}	SiO_2	Al_2O_3	
MEA	72	100	0.11	0.07	0.08	88.6	7.1	21.4
IBA	96	100	0.10	0.08	0.08	77.9	7.7	17.2

The duration of the induction period of crystallization is independent of the type of an organic compound, and the period of exponential growth of crystals is longer in the case of IBA. The higher crystallization rate in the case of MEA can be accounted for by its higher basicity as compared with IBA. It should be noted that the crystallinity and adsorption capacity are high for all the zeolites synthesized (see table).

The synthesis of mordenite-like zeolite in the presence of MEA was studied in more detail. The region of crystallization of the zeolite at 150°C from reaction mixtures of composition $2.5\ MEA \cdot (2.2–9.0)Na_2O \cdot Al_2O_3 \cdot (12–50)SiO_2 \cdot (300–1200)H_2O$ is shown in Fig. 2.

The region of crystallization of mordenite-like zeolites, found in this study, corresponds to the following range of compositions of the reaction mixtures: $2.5MEA \cdot (2.2–7.3)Na_2O \cdot Al_2O_3 \cdot (12–40)SiO_2 \cdot (300–1200)H_2O$.

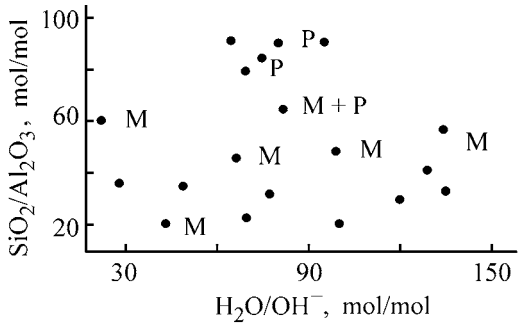

Fig. 2. Regions of crystallization of zeolites from reaction mixtures of composition $2.5MEA \cdot (2.2–9.0)Na_2O \cdot Al_2O_3 \cdot (12–50)SiO_2 \cdot (300–1200)H_2O$. Zeolite: (M) mordenite-like and (P) pentasyl-like.

With the SiO_2/Al_2O_3 ratio raised to 45, two zeolite phases, pentasyl and mordenite, crystallize simultaneously. Crystallization of reaction mixtures with $SiO_2/Al_2O_3 > 50$ yields a pentasyl-like zeolite.

Thus, the results obtained made it possible to develop a procedure for synthesis of mordenite-like zeolites with a ratio of 13–22. This procedure is based on hydrothermal crystallization of silica-alumina hydrogels obtained by mixing a carbon white or WMSC with solutions of sodium silicate and aluminate in the presence of an organic compound, MEA or IBA, at 130–160°C in the course of 72–96 h. The zeolites synthesized have an adsorption capacity of 0.10–0.11 for water vapor and 0.08–0.09 $cm^3 g^{-1}$ for *n*-heptane.

CONCLUSION

A procedure for synthesizing mordenite of high phase purity with a ratio of 13–22 and nearly 100% crystallinity was developed. This procedure is based on crystallization of a silica-alumina hydrogel of composition $2.5MEA \cdot (2.2–7.3)Na_2O \cdot Al_2O_3 \cdot (27–7.30)SiO_2 \cdot (300–1200)H_2O$ at 130–160°C.

REFERENCES

1. Zubkov, A.M., Mishin, I.V., Kapustin, G.I., *et al.*, *Izv. Akad. Nauk SSSR, Ser. Khim.*, 1981, no. 6, pp. 1220–1222.
2. Breck, D., *Zeolite Molecular Sieves*, New York: Wiley, 1974.
3. Limova, T.V. and Meged', N.F., *Katalizatory krekinga i tseolity. Trudy GrozNII* (Catalysts for Cracking and Zeolites. A Collection of Works of GrozNII), Moscow: TsNIITEneftekhim, 1984.
4. Pavlov, L.M., Makhamatkhanov, R.A., and Kutepov, B.I., *Zh. Prikl. Khim.*, 2001, vol. 74, no. 2, pp. 328–329.

Russian Journal of Applied Chemistry, Vol. 77, No. 4, 2004, pp. 685–687. Translated from Zhurnal Prikladnoi Khimii, Vol. 77, No. 4, 2004, pp. 687–689.

BRIEF COMMUNICATIONS

Synthesis and Flocculating Power of Calcium-Containing Polyacrylate

P. A. Podkuiko, L. Ya. Tsarik, and N. V. Zaitsev

Irkutsk State University, Ministry of Education of the Russian Federation, Irkutsk, Russia

Irkutskdortekhkomplekt Private Joint-Stock Company, Irkutsk, Russia

Received February 3, 2003

Abstract—The flocculating power of calcium-containing polyacrylate was studied. The optimal dose of this flocculant and the velocity of clarification of a model process water were determined.

Due to growing hydrosphere pollution, the requirements to wastewater decontamination become increasingly stringent. The commonly used methods for decontamination of wastewater are based on its treatment with coagulating and flocculating agents.

The wastewater treatment with flocculants is more efficient. Their specific consumption in decontamination of process water ranges from 0.5 to 40 g m^{-3}. The consumption of cationic flocculants is in the range from 3 to 8 g kg^{-1} of clay. For anionic flocculants, this parameter varies from 1.0 to 1.5 g kg^{-1}. The clarification efficiency of reused water with flocculants reaches 96–100%.

There are various methods for preparation of polymeric flocculants based on sodium polyacrylate (PA) and polymethacrylate, copolymers of acrylamide with alkali metal acrylates [1, 2] and other cationic and anionic polymers [3–10].

The aim of this study was to elucidate how partial substitution of single-charged Na^+ cations in sodium polyacrylate with double-charged Ca^{2+} cations affects its flocculation characteristics. This problem is important because Ca^{2+} is the main component of wastewater from plants for lime and chalk production. We failed to prepare water-soluble calcium-containing polyacrylate by adding $CaCl_2$ to aqueous sodium polyacrylate. Under these conditions, insoluble calcium polyacrylate is formed. Water-soluble calcium-containing polyacrylate can be prepared by treatment of polyacrylic acid (PAA) ($M = 150 \times 10^3$) with aqueous $CaCl_2$ (0.162–0.625 g Ca^{2+} l^{-1}) at 25–35°C for 16–24 h. At the same time, in treatment of PAA with 400 ml of concentrated $CaCl_2$ (>0.625 g Ca^{2+} l^{-1}) at 50–80°C, insoluble compound is formed.

It is known that several cationic flocculants bind metal cations (Ca^{2+}, Mg^{2+}, Al^{3+}, Sn^{2+}, etc.) from aqueous solution to form poorly soluble complexes. Therefore, the calcium-containing polyacrylates prepared by us were tested in this respect.

Taking into account that introduction of sodium cation into calcium-containing polyacrylates strongly affects their flocculating power, we also tested the polymers with varied Na^+ content. We found that, in complete or half saturation of the carboxy groups of polyacrilic acid with Na^+ cations, stable water-soluble flocculants are formed. However, after replacement of even 0.5% of Na^+ with Ca^{2+} in this flocculant, its viscosity, refractive index, and density significantly increase. The calcium-containing sodium polyacrylate sorbs Ca^{2+}, Mg^{2+}, Al^{3+}, Fe^{2+}, Fe^{3+}, and other cations to form unidentified poorly soluble complexes.

The flocculation performance of water-soluble calcium-containing polyacrylate was tested on a model industrial wastewater contaminated with suspended montmorillonite (Wyoming, USA) (1.0, 5.0, 8.0, 25.0, 60.0, and 100.0 g l^{-1}).

The water clarification velocity W (mm s^{-1}) was determined as the ratio of the height of a clarified water layer S (mm) to the sedimentation time τ (s):

$$W + S/\tau. \quad (1)$$

The approximate flocculant dose D in our experiments was established in accordance with recommendations published in [2]. This dose was then op-

1070-4272/04/7704-0685 © 2004 MAIK "Nauka/Interperiodica"

Table 1. Sedimentation velocity of clay suspension*

c_c, g l^{-1}	Flocculant	S, mm	τ, s	W, mm s^{-1}
1.0	Sanfloc	200	3	67
	Magnafloc	200	2.5	80
	CPA	200	5	40
	$NaPA_{50\%}$	200	4.5	44
	$NaPA_{100\%}$	200	3.5	57
5.0	Sanfloc	250	5.0	50
	Magnafloc	250	3.5	71
	CPA	250	8	31
	$NaPA_{50\%}$	250	7.5	33
	$NaPA_{100\%}$	250	5.5	45
25.0	Sanfloc	200	8	25
	Magnafloc	200	5.5	36
	CPA	200	12	17
	$NaPA_{50\%}$	200	10.5	19
	$NaPA_{100\%}$	200	9	22
60.0	Sanfloc	250	11	23
	Magnafloc	250	8.5	30
	CPA	250	15	17
	$NaPA_{50\%}$	250	14	18
	$NaPA_{100\%}$	250	12.5	20
100.0	Sanfloc	200	12	17
	Magnafloc	200	10.5	19
	CPA	200	18	11
	$NaPA_{50\%}$	200	16.5	12
	$NaPA_{100\%}$	200	15	13

* (CPA) calcium-containing polyacrylate; ($NaPA_{50\%}$, $NaPA_{100\%}$) sodium polyacrylates with 50 and 100% saturation of carboxy groups with sodium cations; (c_c) clay content in aqueous suspension; (S) height of clarified water layer; (τ) sedimentation time of clay suspension from surface layer to a depth S; and (W) water clarification velocity.

timized by its variation in the series of sedimentation tests. The amount of flocculant, required for clarification of 1 m^3 of wastewater, R_f, was determined by the equation [2].

$$R_f = D/(c_f \times 10), \quad (2)$$

where D is the optimal flocculant dose (mg l^{-1}) and c_f is the concentration of the working flocculant solution (g l^{-1}).

The weight Q_f of commercial flocculant, required for preparing V_f (m^3) of aqueous flocculant, was calculated by the equation

$$Q_f = V_f c_f \times 10^2/c_p, \quad (3)$$

where V_f is the volume of the working flocculant solution (m^3), c_f is the concentration of this solution (g l^{-1}), and c_p is the percentage of the main reagent in the commercial flocculant.

Table 2. Optimal flocculant dose D determined by test sedimentation

c_c, g l^{-1}	Flocculant	D, mg l^{-1}	R_f^*, mg
1.0	Sanfloc	2.0–4.0	2.0–4.0
	Magnafloc	0.5–1.0	0.5–1.0
	CPA	0.5–4.0	1.5
	$NaPA_{50\%}$	0.5–3.5	2.8
	$NaPA_{100\%}$	0.5–2.8	1.2
5.0	Sanfloc	1.5	1.5
	Magnafloc	0.5	0.5
	CPA	0.5–2.0	2.0
	$NaPA_{50\%}$	0.5–2.1	1.8
	$NaPA_{100\%}$	0.5–1.5	0.5
25.0	Sanfloc	30	1.2
	Magnafloc	10	1.0
	CPA	10–30	25
	$NaPA_{50\%}$	20	1.5
	$NaPA_{100\%}$	10	1.2
60.0	Sanfloc	30	0.3
	Magnafloc	15	0.5
	CPA	15–25	25
	$NaPA_{50\%}$	5–15	15
	$NaPA_{100\%}$	5–10	6.5
100.0	Sanfloc	30	0.3
	Magnafloc	15	0.5
	CPA	15-20	20
	$NaPA_{50\%}$	15–20	20
	$NaPA_{100\%}$	15–25	15

* (R_f) flocculant consumption (per 1 gram of clay suspension).

EXPERIMENTAL

The sedimentation velocity was measured in 1-l volumetric cylinders with scale divisions on strips of graph paper glued on their walls along a height of 250–300 mm below the water level.

Equal volumes of the model industrial water contaminated with clay suspension were poured into several cylinders, the mixture was stirred and a prescribed dose of the flocculant was added. To randomize the mixture, the cylinders were turned upside down many times. After settling, 100-ml samples of clarified water were taken from a depth of 10 cm, and the amount of suspended matter was determined. After that, the heights of both the clarified water and the sedimented clay layers were measured.

The effect of flocculation on the sedimentation velocity was determined from the time required for sedimentation of the main part of suspended clay, measured with a stopwatch. The clarification velocity was calculated by Eq. (1) (Table 1). The flocculant consumption was calculated by Eq. (2) (Table 2).

The calcium-containing polyacrylate was prepared as follows. Potassium peroxodisulfate [15.5 g (0.057 mol)] was dissolved in distilled water (150 ml) at 30 or 45°C with stirring for 0.4 h. After that, acrylic acid purified by distillation [130.860 g (1.816 mol, 124.5 ml] was added and stirred for 0.5 h. Then 400 ml of aqueous $CaCl_2 \cdot 2H_2O$ (chemically pure grade) (0.375 g ml^{-1}) was added, and this mixture was stirred for 3 h. The resulting solution was diluted with water (1.5 l) and its pH was checked with indicator paper. The pH of this solution was adjusted to 8–9 by adding 1.55 M aqueous NaOH.

The aqueous calcium-containing polyacrylates were kept for 24 h and then dried in a vacuum at 95°C at a residual pressure of 1300 Pa until a solid film of constant weight was formed. The IR spectrum of this film (KBr pellets) contains absorption bands assigned to vibrations of the following groups (cm^{-1}): C–C (800, 850, 900); C–O (1100, 1200, 1250); CH_2, =C(OH)–O (1300, 1410,1470); CH (2920, 2950); and OH (3400, 3500). In the ^1H NMR spectra (working frequency 68.797 MHz) of calcium-containing polyacrylate in D_2O, the following signals were detected (δ, ppm): 1.54 (1H, –C(OH)–CH–), 1.91 (2H, =CH–CH_2–), 4.3 (1H, COOH), and 4.73 (1H, OH).

An elemental analysis of two parallel samples showed the following chemical composition of the calcium-containing polyacrylate films (%): C 21.15, 21.19; H 1.76, 1.80; S 9.40, 9.44; K 11.47, 11.51; Ca 11.76, 11.80; and Na 6.73, 6.77. This elemental composition is close to that of the compound with the stoichiometry $C_6H_6SO_8KCaNa$, %: C 21.17; H 1.78; S 9.42; K 11.49; Ca 11.78; Na 6.75; and O 37.61.

The osmometrically determined molecular weight of the calcium-containing polyacrylate was $(100–125) \times 10^3$.

CONCLUSIONS

(1) Calcium-containing polyacrylate can be used as a flocculant for clarification of process water contaminated with suspended clay.

(2) Partial replacement of Na^+ cations in sodium polyacrylate with Ca^{2+} does not noticeably change its flocculating power.

REFERENCES

1. Timofeeva, S.S., Semenova, V.A., Baiborodina, E.N., *et al.*, Abstracts of Papers, *III Vsesoyuznaya Konferentsiya "Vodorastvorimye polimery i ikh primenenie"* (III All-Union Conf. "Water-Soluble Polymers and Their Application"), Irkutsk, 1987.
2. Lichaev, V.R., Esenovskaya, L.N., and Chikin, Yu.M., *Rukovodstvo po vyboru i proektirovaniyu sistem vodootvedeniya i sposobam vodopodgotovki pri razrabotke rassypnykh mestorozhdenii* (Guide on Choice and Design of Water Supply and Drainage Systems and on Water Treatment in Development of Scattered Deposits), Irkutsk: Irkutsk. Univ., 1990.
3. RF Patent no. 2146230.
4. Moudgil, B.M., Behi, S., and Prakash, T.S., *J. Colloid Interf. Sci.*, 1993, vol. 158, no. 2, pp. 511–512.
5. USSR Inventor's Certificate, no. 123483.
6. US Patent 5919882.
7. US Patent 3488720.
8. USSR Inventor's Certificate, no. 281312.
9. Tsarik, L.Ya., Esenovskaya, L.N., and Fedorin, A.Yu., *Izv. Vyssh. Uchebn. Zaved., Khim. Khim. Tekhnol.*, 1999, vol. 42, no. 5, pp. 69–72.
10. Filatenkov, V.F., *Bum. Prom–st.*, 1978, no. 11, pp. 17–18.

Russian Journal of Applied Chemistry, Vol. 77, No. 4, 2004, pp. 688–690. Translated from Zhurnal Prikladnoi Khimii, Vol. 77, No. 4, 2004, pp. 690–692.

BRIEF COMMUNICATIONS

Rheological and Adhesion Properties of Aqueous Solutions of Corn Dextrin

T. G. Klimets, E. V. Grinyuk, and L. P. Krul'

Research Institute of Physicochemical Problems, Belarussian State University, Minsk, Belarus

Received October 17, 2003; in final form, January 2004

Abstract—Rheological and adhesion properties of aqueous solutions of corn dextrin at widely varied concentrations, obtained at different mixing temperatures, were studied.

Aqueous solutions of natural polysaccharides (ASPs), especially starch and its derivatives, such as, e.g., dextrin, are widely used as adhesives [1]. Dextrin adhesives find extensive application for gluing paper and paper labels [1–3].

Despite the wide use of aqueous solutions of dextrin as adhesives, there are virtually no published data on their rheological and adhesion properties, which specifically determine the main process characteristics of adhesives. Preparation of dextrin glues consists in heating a dextrin–water mixture or in dissolving dextrin in hot water [4]. These operations resemble the pasting stage in preparation of starch paste [5], However, there are no published data on how pasting affects the rheological and adhesion characteristics of dextrin adhesives.

The aim of this study was to examine the rheological and adhesion properties of solutions of corn dextrin (CD) of different concentrations, prepared in hot and, for comparison, in room-temperature water.

EXPERIMENTAL

We studied aqueous solutions of acidic corn dextrin, GOST (State Standard) 6034–74. The solutions were prepared at room temperature or at $65 \pm 5°C$ under continuous stirring for 30 min. The concentration of the solutions was varied from 15 to 70%.

The viscosity of the resulting solutions was measured on a Rheotest 2 rotary viscometer with a coaxial-cylinder working unit at $20 \pm 0.1°C$.

The adhesive properties of ASPs in the glass–adhesive–paper system were studied in an RMU-0.05.-1 tensile-testing machine with the stress measurement range $(0–10) \pm 0.02$ kgf and the rates of motion of the guide rod of the machine from 0 to 100 mm min^{-1} [6, 7].

To keep the glass surface at a constant temperature, we placed it in a metallic flow-through cell whose dimensions were adjusted to those of the glass shell, a fragment of a bottle.

As substrate served samples of KYMULTRA COPY writing paper, A4, 80 g m^{-2}–500, which were cut into 150×10 mm strips. A 100-mm long adhesive layer was manually applied to each strip. The samples were glued to the surface of the bottle fragment kept at $20 \pm 0.5°C$. The free end of the strip was fixed in the stationary clamp of the tensile machine.

Figure 1 presents the log-log flow curves for aqueous solutions of dextrin with different concentrations, prepared by mixing at room temperature. Figure 1a shows that all the aqueous solutions of CD, studied by us, are non-Newtonian liquids. The pseudoplasticity is the most pronounced in the case of 50–70% solutions (Fig. 1a, curves *4*–*6*).

Figure 1b shows the flow curves for the same solutions prepared by mixing at $65 \pm 5°C$. It is seen that pseudoplasticity is characteristic of only 50–70% CD solutions, and 15–30% solutions are virtually Newtonian liquids (Fig. 1b, curves *4*–*6* and *1*–*3*, respectively).

Comparison of the results shows that, at low shear rates ($0.3333–9$ s^{-1}), the CD solutions obtained at $65 \pm 5°C$ are less viscous than those obtained at room temperature, while at high shear rates ($48.6–1312$ s^{-1}) this difference is partly eliminated. Also, heating yields less pseudoplastic solutions.

1070-4272/04/7704-0688 © 2004 MAIK "Nauka/Interperiodica"

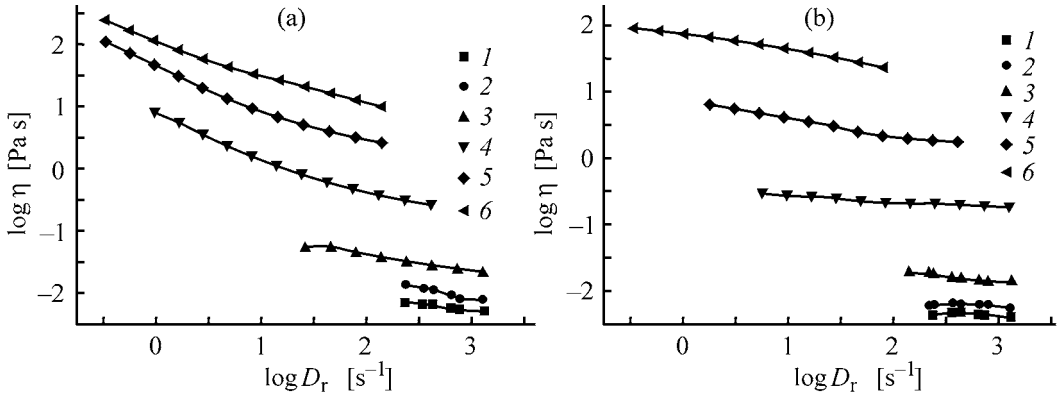

Fig. 1. Log-log plots of the viscosity η, vs. shear rate D_r for aqueous solutions of CD, prepared by mixing at (a) 20 and (b) 65 ± 5°C. Concentration of the solution, %: (*1*) 15, (*2*) 20, (*3*) 30, (*4*) 50, (*5*) 60, and (*6*) 70.

Higher viscosities, as well as lower shear rates and more pronounced pseudoplasticity, of aqueous solutions of CD prepared at room temperature suggest an increased, relative to solutions prepared at 65 ± 5°C, concentration of the points of contact in the fluctuation network [8]. A similar decrease in the concentration of the points of contact in the fluctuation network in aqueous solutions has also been observed for many other water-soluble polymers (polyacrylamide, polyvinyl alcohol, etc.) [9].

As known, the concentration of the points of contact in the fluctuation network in starch (whose hydrolysis yields dextrin) tends to increase with rising temperature. This is usually attributed to degradation of the shells of the natural polymer grains and to the corresponding increase in the effective concentration of macromolecules in solution [6]. Evidently, the starch–dextrin conversion involves grain shell degradation as well. Therefore, with the mixing temperature of dextrin and water rising from room temperature to 65 ± 5°C the viscosity and pseudoplasticity tend to decrease (as in the case of water-soluble polar synthetic polymers), rather than increase (as in the case of starch solutions).

Preliminary studies of the adhesion characteristics of aqueous solutions of CD with concentrations of up to 30 wt % in the glass–adhesive–paper system showed that these solutions are virtually incapable of providing a paper–glass joint. With a 50% aqueous solution of dextrin, the paper can be glued to glass, but this glue joint is so weak that even after 3 min the paper exfoliates from the glass upon attempted application of a load. Figure 2 illustrates the adhesion properties of 60–70% CD solutions. For these solutions, the glue joint strength σ increases with increasing keeping time and approaches in the limit the value corresponding to the breaking strength of a dry paper strip. As can be seen from Fig. 2, the setting time is 2–3 min, which is smaller than that for imported adhesives for gluing labels (4–7 min). The temperature mode of preparation of aqueous solutions of CD only slightly affects their adhesion properties. Evidently, the lack of a direct correlation between the rheological and adhesion properties of aqueous solutions of CD prepared at different temperatures is due to the specific mechanism of glue joint formation. Lower viscosities of the aqueous solution of CD, prepared at 65 ± 5°C, are responsible for the accelerated water removal from the glue joint and, thereby, for an increase in the viscosity of solution to that characteristic of the dextrin solution prepared at room temperature.

Notably, aqueous (especially concentrated) solutions of CD prepared at 65 ± 5°C have better keeping qualities. For example, a 50% solution prepared at room temperature grew moldy even after 3 weeks of keeping in a dry cool place, while the solution prepared at 65 ± 5°C did so only after 2 months of keeping.

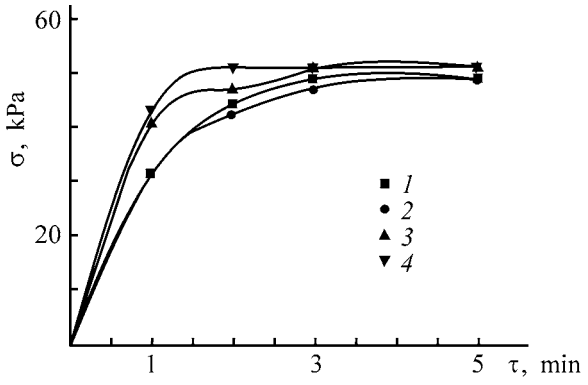

Fig. 2. Variation of the shear strength of glue joint, σ, with the time of keeping τ for aqueous solutions of CD with different concentrations. Concentration of the solution, %: (*1*, *2*) 60 and (*3*, *4*) 70. Mixing temperature, °C: (*1*, *3*) 20 and (*2*, *4*) 65 ± 5°C.

CONCLUSION

Aqueous (60–70%) solutions of corn dextrin are suitable as adhesives for gluing labels. Moreover, they surpass imported analogs in adhesion properties. These properties of aqueous solutions of corn dextrin are virtually unaffected by increase in the temperature of preparation from room temperature to $65 \pm 5°C$, but solutions prepared at $65 \pm 5°C$ are preferable because of better keeping qualities.

REFERENCES

1. Freidin, A.S., *Polimernye vodnye klei* (Polymer Aqueous Adhesives), Moscow: Khimiya, 1985.
2. PCT application, no. 97/00298.
3. US Patent 6280515.
4. Shtyrkova, E.A., Marker, V.E., Goryacheva, A.F., *et al.*, *Proizvodstvo i primenenie pishchevykh dekstrinov* (Production and Application of Food Dextrins), Moscow: TsNII Inform. Tekh.-Ekon. Issled. Pishch. Prom–sti, 1971.
5. *Starch: Chemistry and Technology*, Whistler, R.L. and Pashall, E.F., Eds., New York: Academic, 1965–1967.
6. Brazhnikov, M.M., Grinyuk, E.V., Brazhnikova, L.Yu., and Krul', L.P., *Vestsi Nats. Akad. Navuk Bel., Ser. Khim. Navuk*, 2002, no. 2, pp. 91–93.
7. Brazhnikov, M.M., Grinyuk, E.V., Brazhnikova, L.Yu., and Krul', L.P., *Vestsi Nats. Akad. Navuk Bel., Ser. Khim. Navuk*, 2003, no. 1, pp. 97–100.
8. Brestkin, Yu.V., Frenkel, S.Ya., Zoolshoev, Z.V., *et al.*, *Vysokomol. Soedin., Ser. A*, 1994, vol. 36, no. 8, pp. 1281–1286.
9. Nikolaev, A.F. and Okhrimenko, T.I., *Vodorastvorimye polimery* (Water-Soluble Polymers), Leningrad: Khimiya, 1979.

Russian Journal of Applied Chemistry, Vol. 77, No. 4, 2004, pp. 691–693. Translated from Zhurnal Prikladnoi Khimii, Vol. 77, No. 4, 2004, pp. 693–695.

BRIEF COMMUNICATIONS

Oxidation of Tall Pitch with Atmospheric Oxygen

A. B. Radbil', R. M. Ismagilov, and B. A. Radbil'

Lesma Research-and-Promotion Limited Liability Company, Nizhnii Novgorod, Russia
Ural Wood Chemical Plant Open Joint-Stock Company, Kirovgrad, Sverdlovsk oblast, Russia

Received November 10, 2003

Abstract—Oxidation of tall pitch with atmospheric oxygen was studied as influenced by the oxidation initiator and temperature. Conditions for preparing tall pitch with required physicochemical properties were determined.

Tall pitch (TP), meltable distillation residue of tall oil, is a large-tonnage waste of sulfate cellulose production. This substance contains fatty and resin acids, their esters, and the so-called oxidized compounds and unsaponifiables [1].

Tall pitch is a relatively low-cost renewable phytogenic raw material with valuable properties. However, the major portion of accumulated TP is not used and is burnt in a mixture with mazut. Practical use of TP is prevented by its variable chemical composition and low softening point (T_s = 19–25°C).

Oxidation of TP with atmospheric oxygen at 200–280°C [2–4] improves its physicochemical properties and processing characteristics. The oxidized product with T_s 45–60°C is used in building [4]; that with T_s 60–90°C in metallurgy and in tire and rubber industry [3, 5]; and that with T_s 90–105°C in paint and varnish industry [6].

Clearly, T_s of oxidized TP determines the field of its practical application and depends on the oxidation conditions. In this study, we examine the influence of conditions of TP oxidation on the physicochemical properties of the resulting product.

Tall pitch was oxidized with atmospheric oxygen at 220–280°C in the absence and in the presence of the oxidation initiator. Under these conditions, a brittle dark brown solid product with T_s = 98–102°C was formed in 80–85% yield. Oil, water, and gaseous products with odor of sulfur-containing compounds were liberated, presumably owing to thermolysis of TP components. In addition, the acid number of oxidized TP (38–45 mg KOH g^{-1}) was lower than that of the initial TP (55 mg KOH g^{-1}). Hence, one of the possible pathways of thermolysis can be decarboxylation of resin and fatty acids to form the corresponding hydrocarbons. If this is the case, carbon dioxide should be liberated. Liberation of gaseous products containing CO_2 and sulfur compounds in the course of TP thermolysis has also been observed by Shmidt [2]. Decarboxylation of resin acids in their liquid-phase oxidation was described in [7].

Since the T_s of TP depends on the extent of its oxidation, oxidation of TP was monitored by its T_s. The dependence of T_s of TP oxidized with atmospheric oxygen at different temperatures on the oxidation time is shown in Fig. 1.

As can be seen from Fig. 1, autooxidation of TP by atmospheric oxygen is similar to liquid-phase oxidation of hydrocarbons and their derivatives [8]. As the reaction temperature increases from 220 to 260°C, the induction period shortens and fully disappears at 280°C. The maximum oxidation rate increases. The activation energy of TP oxidation, determined

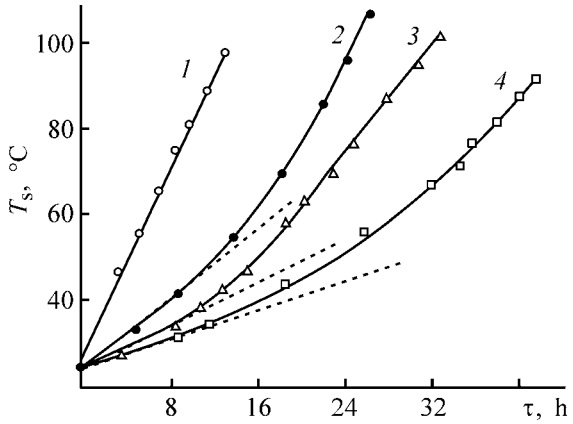

Fig. 1. Softening point T_s of TP oxidized at (*1*) 280, (*2*) 260, (*3*) 240, and (*4*) 220°C vs. the oxidation time τ.

1070-4272/04/7704-0691 © 2004 MAIK "Nauka/Interperiodica"

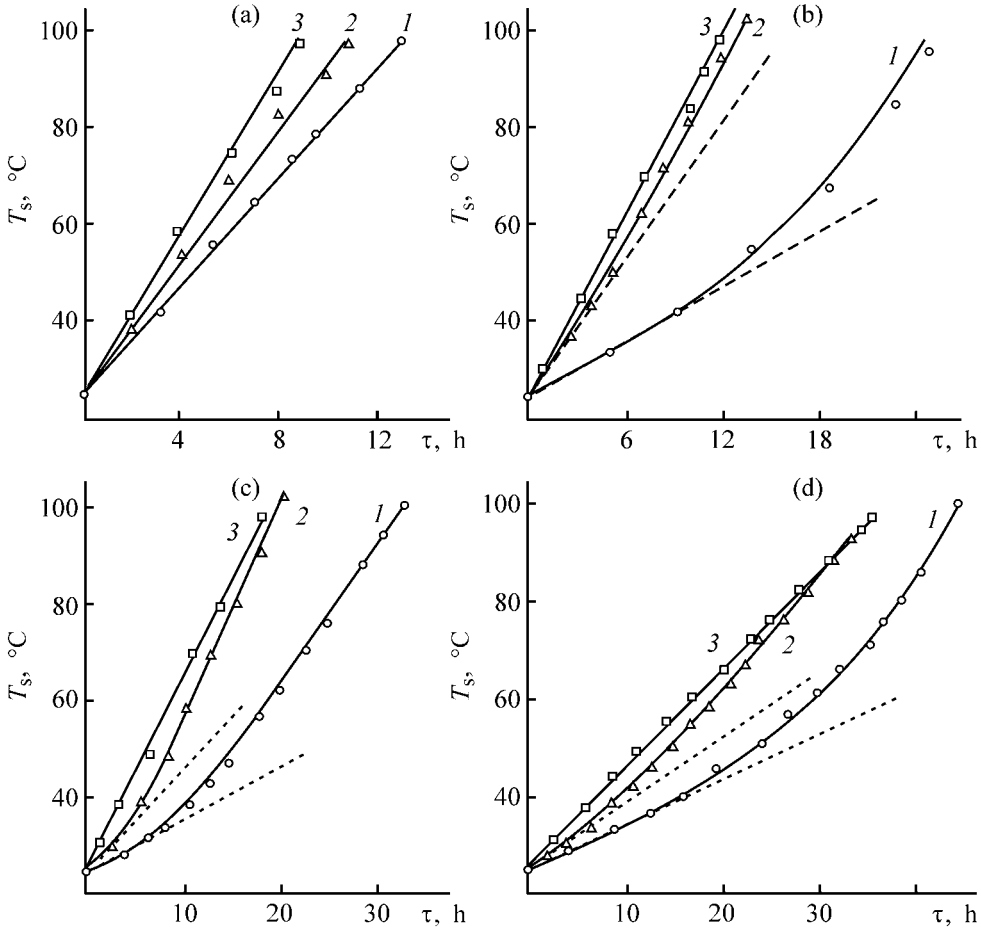

Fig. 2. Softening point T_S of TP oxidized at (a) 280, (b) 260, (c) 240, and (d) 220°C in the presence of (*1*) 0, (*2*) 5, and (*3*) 10 wt % of the initiator vs. the oxidation time τ.

from the slope of the temperature dependence of the initial reaction rate, plotted in the Arrhenius coordinates, is 68.6 ± 0.5 kJ mol^{-1}.

Oxidation of TP is strongly affected by the initiator concentration. As can be seen from Fig. 2, the oxidation substantially accelerates and the induction period of the reaction at 220–260°C shortens with increasing initiator concentration. At the initiator concentration of 10 wt %, the induction period in this temperature range is absent and the dependence of T_s on the oxidation time τ is linear, as that at 280°C (Fig. 2, curve *3*).

The activation energy of TP oxidation in the presence of 5 and 10 wt % initiator, calculated from the slope of the temperature dependence of the initial oxidation rate, plotted in the Arrhenius coordinates, is 62.0 ± 0.5 and 48.6 ± 0.4 kJ mol^{-1}, respectively.

As noted above, the field of practical application of oxidized TP depends on its T_s. The dependence of T_s of oxidized TP on the oxidation conditions (Table 1) can be used for preparing TP with required properties.

Table 1. Oxidation conditions of tall pitch

T_s of oxidized pitch, no less than indicated value, °C	T, °C	Oxidation time at c_{in}^* (wt %) no less than indicated value (h)		
		0 (no initiator)	5	10
45	280	4	3	2.5
	260	10.5	3.5	3
	240	14.5	7.5	5
	220	20	13	10
60	280	6.5	5	4
	260	15	6.5	5
	240	19	11	9
	220	28.5	19.5	17
90	280	11	9	7.5
	260	23	11	10
	240	29	18	16
	220	41.5	31.5	31

* c_{in} is the initiator concentration.

Oxidation of TP was performed at Ural Wood Chemical Plant Open Joint-Stock Company.

EXPERIMENTAL

We used TP [TU (Technical Specification) 13-0281078–84, revision no. 1, Tall Pitch for Road-Building] with T_s 24°C and acid number 55 mg KOH per gram of the product.

Partially oxidized TP containing peroxides was used as the oxidation initiator. It was prepared by oxidation of TP with atmospheric oxygen at 220°C for 10–12 h with subsequent stopping of the air supply and rapid cooling.

Oxidation of TP with atmospheric oxygen was performed in a reactor with a heating jacket. The reactor was equipped with a bubbler for air supply, a descending condenser, and a turbine-type stirrer. The reactor was charged with a weighed portion of TP preheated at ~80°C in the absence or in the presence of the oxidation initiator. The reactor temperature was kept constant (±2°C) by circulating high-temperature heat carrier (organosilicon liquid) between a thermostat and the jacket. When the reactor was heated to the required temperature, the stirrer was switched on and purified air was fed at a rate of 35–36 l h^{-1} per 1 g of the pitch. The air flow rate was measured with a rotameter. The liberated water and oil were removed through a descending condenser into a receiver, and gaseous reaction products were fed into a trap filled with a 15% aqueous solution of NaOH. Samples of the reaction mixture were taken at definite intervals. Their AN and T_s were measured in accordance with GOST (State Standard) 23863–79. The average of three replicate measurements was calculated.

CONCLUSIONS

(1) Oxidation of TP is characterized by an induction period typical of liquid-phase oxidation of hydrocarbons and their derivatives. The induction period shortenes on heating from 220 to 280°C.

(2) Oxidation in the presence of 10 wt % initiator (partially oxidized TP) is substantially faster and is characterized by the absence of the induction period at 220–260°C. The dependence of T_s of oxidized TP on the oxidation time is linear.

(3) The process for production of oxidized tall pitch with different T_s was developed and applied at the Ural Wood Chemical Plant Open Joint-Stock Company.

REFERENCES

1. Golovin, A.I., Trofimov, A.N., Uzlov, G.A., *et al.*, *Lesokhimicheskie produkty sul'fatnotsellyuloznogo proizvodstva* (Wood-Chemical Products of Sulfate Cellulose Industry) , Moscow: Lesnaya Prom–st., 1988.
2. Shmidt, G.G., Lesokhim. Podsochka, *Nauch. Tekh. Ref. Sb.*, 1980, no. 6, p. 13.
3. Kosarev, Yu.N., Golovin, A.I., and Kalugin, E.N., *Gidrolizn. Lesokhim. Prom–st.*, 1984, no. 8, p. 15.
4. Bogomolov, B.D., Butsalenko, V.S., and Mariev, A.A., *Napravleniya ispol'zovaniya tallovogo peka: Obzor informatsii* (Directions of Application of Tall Pitch: Information Review), Moscow: VNIIPIEIlesprom, 1989.
5. Golovin, A.I., Ponomarev, I.A., Khlebov, G.A., *Tallovye produkty i vozmozhnost' ikh primeneniya v retsepture resinovykh smesei: Obzor informatsii* (Tall Products and Possibility of Their Use in Rubber Stock Formulations: Information Review), Moscow: VNIIPIEIlesprom, 1987.
6. Ismagilov, R.M., Radbil' A.B., and Radbil', B.A., in *Novye dostizheniya v khimii i khimicheskoi tekhnologii rastitel'nogo syr'ya: Materialy Vserosiiskogo seminara* (New Advances in Chemistry and Chemical Technology of Vegetable Raw Material: Proc. All-Russia Seminar), Barnaul, March 28–29, 2002, pp. 209–211.
7. Mitskevich, N.I. and Erofeev, B.V., *Sopryazhennoe s okisleniem dekarboksilirovanie karbonovykh kislot* (Decarboxylation of Carboxylic Acids Conjugated with Oxidation), Minsk: Nauka i Tekhnika, 1970.
8. Emmanuel', N.M., *Okislenie uglevodorodov v zhidkoi faze* (Liquid-Phase Oxidation of Hydrocarbons), Moscow: Akad. Nauk SSSR, 1959.

Russian Journal of Applied Chemistry, Vol. 77, No. 4, 2004, pp. 694–696. Translated from Zhurnal Prikladnoi Khimii, Vol. 77, No. 4, 2004, pp. 696–698.

BRIEF COMMUNICATIONS

Effect of Polycaprolactam Fiber on Coagulation of Rubbers and on Properties of Rubbers, Rubber Stocks, and Vulcanizates

S. S. Nikulin and I. N. Akatova

Voronezh State Academy of Forestry Engineering, Voronezh, Russia

Received March 7, 2003

Abstract—The effect of polycaprolactam fiber on the coagulation of butaidene–styrene rubber from the latex was studied.

Large amounts of wastes of fibers and fibrous materials are formed at textile and clothing factories. Utilization of these wastes is a topical problem [1–4].

In industry, fibrous fillers are introduced into polymers on rollers in the course of preparation of rubber stocks [5, 6]. The fillers impart the required rigidity and enhance the strength of rubber items. However, introduction of a fibrous filler on rollers does not ensure its uniform distribution in the bulk of the rubber stock, which negatively affects the physicomechanical parameters of the vulcanizates.

Hence, it is necessary to ensure, with minimum expenditure, a uniform distribution of a fibrous filler in the bulk of a polymeric compound. One of the ways to achieve this goal is introduction of a fibrous filler into a polymer in the latex step in production of emulsion rubbers.

In this study, we analyzed how the polycaprolactam fiber affects the coagulation of a latex of SKS-30 ARK butadiene–styrene rubber (BSR) and the properties of rubbers, rubber stocks, and vulcanizates.

First we considered several modes of pretreatment of a fibrous filler, polycaprolactam, before its mixing with BSR latex. The size and dosage of the filler were kept constant: 2 mm and 0.5 wt % relative to the rubber. The fibrous filler was introduced without pretreatment (dry) and after wetting with various agents: water, tallow soap solution, 24 wt % NaCl solution (coagulant), and 2% H_2SO_4 solution (acidifying agent).

Introduction of the fibrous filler without pretreatment (in the dry form) or after wetting with water does not ensure the desired effect. Better results are obtained after pretreatment of the fiber with a tallow soap solution. However, this involves additional material and economic expenditures. Introduction of the fibrous filler in combination with the coagulating agent does not noticeably affect the coagulation.

Treatment of the fiber with sulfuric acid slightly increases the coagulum yield. This may be due to the fact that the amide groups of polycaprolactam macromolecules react with sulfuric acid molecules. Appearance of quaternary ammonium groups in the macromolecules should stabilize the coagulation process. The possibility of using quaternary ammonium salts for coagulation of rubbers from latexes has been shown previously [7, 8].

Therefore, apparently, the best choice will be introduction of the fibrous filler with an acidifying agent in the final step of coagulation.

Further experiments on the influence exerted on the coagulation by the dosage and length of a polycaprolactam fiber were performed with simultaneous addition of the fiber and the acidifying agent. The fiber length was 2, 5, and 10 mm, and the dosage, 0.1, 0.3, 0.5, 0.7, and 1.0 wt % relative to the rubber. The influence of the fiber length (at a dosage of 0.3 wt % relative to the rubber) and NaCl dosage on the coagulum weight is illustrated by the figure. Similar dependences of the coagulum weight on the NaCl

1070-4272/04/7704-0694 © 2004 MAIK "Nauka/Interperiodica"

Properties of rubbers, rubber stocks, and vulcanizates based on SKS-30 ARK

Parameter	Rubber content, wt % (fiber length, mm)						
	0	0.3 (2)	0.7 (2)	0.3 (5)	0.7 (5)	0.3 (10)	0.7 (10)
Mooney viscosity (1 + 4):							
rubber (100°C)	54.5	59.0	56.0	55.0	57.0	56.5	57.5
rubber stock	57.0	57.0	58.0	59.0	58.0	58.0	58.0
Karrer plasticity, arb. units	0.34	0.33	0.34	0.33	0.36	0.34	0.34
Recovery, mm	1.37	1.30	1.22	1.36	1.19	1.30	1.32
Vulcanization optimum (143°C), min	80	60	60	60	60	60	60
Nominal stress at 300% elongation, MPa	9.4	5.6	7.1	6.1	6.6	5.9	6.0
Nominal tensile strength, MPa	26.3	28.6	22.5	23.1	23.0	23.0	20.5
Relative elongation at break, %	618	680	610	670	640	670	650
Relative residual strain, %	12	16	14	14	14	14	14
Rebound elasticity, %							
20°C	40	38	42	40	42	40	43
100°C	53	50	52	52	50	50	50
Shore hardness A, arb. units	57	57	57	54	55	56	57
Tear resistance, kN m^{-1}	53.0	89.0	90.0	81.0	85.0	66.0	73.0
Resistance to multiple extension, thousands of cycles	69.550	66.700	62.000	93.200	73.100	76.200	77.700
Aging coefficient (100°C, 72 h):							
for strength	0.44	0.65	0.67	0.72	0.69	0.80	0.96
for relative elongation	0.33	0.46	0.40	0.40	0.41	0.45	0.54

dosage were obtained at other dosages of the polycaprolactam fiber.

The experimental data show that addition of the fibrous filler in the course of rubber coagulation from the latex increases the coagulum yield. This is probably due to reduction of losses associated with the removal of a fine rubber crumb with serum and wash waters [9] and to additional introduction of the fibrous filler taken up by the coagulum.

The best results were obtained with the fiber dosage within 0.3–0.7 wt % relative to the rubber and fiber length of about 5 mm. The fiber length affects the coagulum yield insignificantly.

In the second step of our study, we examined the effect of polycaprolactam fibers on the properties of rubber stocks and vulcanizates. The rubber samples filled with polycaprolactam fibers were tested according to GOST (State Standard) 15627–79 for BSR in comparison with a commercial BSR sample.

The table shows that the physicomechanical characteristics of vulcanizates get slightly worse with increasing content and length of polycaprolactam fibers in rubbers. For example, the nominal tensile strength of the rubber containing 0.3 wt % 2-mm-long fibers is 28.6 MPa, and that of the sample containing 0.7 wt % 10-mm-long fibers is 20.0 MPa. By contrast, the rebound elasticity at 20°C slightly increases: from 38 to 43%, respectively. The resistance to thermal aging of vulcanizates and the tear resistance of the filled samples throughout the examined range of fiber dosages are higher than those of the control sample.

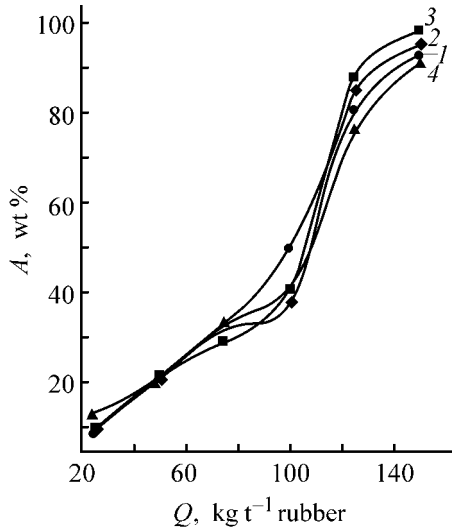

Influence of the polycaprolactam fiber length (dosage 0.5 wt % relative to rubber) and NaCl dosage Q on the coagulum yield A: (*1*) no fiber added; fiber length, mm: (*2*) 2, (*3*) 5, and (*4*) 10.

CONCLUSIONS

(1) Addition of polycaprolactam fiber and an acidifying agent (2% H_2SO_4) in the step of coagulation of butadiene–styrene latex before the final step enhances the tear resistance and resistance to thermal aging of the vulcanizates. The optimal length of the polycaprolactam fibers is 5 mm at the dosage of 0.3–0.7 wt % relative to the rubber.

(2) Introduction of polycaprolactam fibers in the step of latex coagulation ensures its uniform distribution in the bulk of the rubber.

REFERENCES

1. Novikov, Yu.V., *Ekologiya, okruzhayushchaya sreda i chelovek* (Ecology, Environment, and Human), Moscow: Fair, 1999.
2. Chelnokov, A.A. and Yushchenko, L.F., *Osnovy promekologii* (Principles of Industrial Ecology), Moscow: Vysshaya Shkola, 2001.
3. Shein, V.S., Ermakov, V.I., and Norkhin, Yu.G., *Obezvrezhivanie i utilizatsiya vybrosov i otkhodov pri proizvodstve i pererabotke elastomerov* (Making Harmless and Utilizing Effluents and Wastes in Production and Reprocessing of Elastomers), Moscow: Khimiya, 1987.
4. *Otkhody i pobochnye produkty neftekhimicheskikh proizvodstv – syr'e dlya organicheskogo sinteza* (Wastes in By-Products from Petrochemical Industry as Raw Materials for Organic Synthesis), Cherkashin, M.I., Ed., Moscow: Khimiya, 1989.
5. Sadov, F.I., Korchagin, M.V., and Matetskii, V.I., *Khimicheskaya tekhnologiya voloknistykh materialov* (Chemical Technology of Fibrous Materials), Moscow: Legkaya Industriya, 1986.
6. Yagnyatinskaya, E.A., Gol'dberg, B.B., Leonov, V.V., *et al., Tekhnologiya izgotovleniya, svoistva i osobennosti primeneniya rezin s voloknistymi napolnitelyami v RTI* (Rubbers with Fibrous Fillers: Production, Properties, and Features of Application in Rubber Items), Moscow: TsNIITEneftekhim, 1979.
7. Verezhnikov, V.N., Nikulin, S.S., Krutikov, M.Yu., and Poyarkova, T.N., *Kolloidn. Zh.*, 1999, vol. 61, no. 1, pp. 37–40.
8. Nikulin, S.S., Verezhnikov, V.N., Poyarkova, T.N., and Dankovtsev, V.N., *Zh. Prikl. Khim.*, 2000, vol. 23, no. 5, pp. 833–836.
9. Raspopov, I.V., Nikulin, S.S., Garshin, A.P., *et al., Sovershenstvovanie oborudovaniya i tekhnologii vydeleniya butadien(α-metil)stirol'nykh kauchukov iz lateksa* (Improvement of Apparatus and Process for Recovery of Butadiene–(α-Methyl)styrene Rubbers from Latex), Moscow: TsNIITEneftekhim, 1997.

Russian Journal of Applied Chemistry, Vol. 77, No. 4, 2004, pp. 697–699. Translated from Zhurnal Prikladnoi Khimii, Vol. 77, No. 4, 2004, pp. 699–701.

Professor Yurii Konstantinovich Delimarskii (To Centennial Anniversary of His Birthday)

Yu.K. Delimarskii, a known Ukrainian scientist and pedagogue, full member of the Academy of Sciences of the Ukrainian SSR, made a major contribution to the organization and development of research in the field of physical chemistry and electrochemistry of ionic melts in our country; during many years he headed the Scientific Council of the Academy of Sciences of the USSR for physical chemistry of ionic melts and solid electrolytes.

Yurii Konstantinovich Delimarskii was born on April 23, 1904, at Krasnopolka village of Kamenets-Podol'sk Province (now Vinnitsa oblast) into the family of a village teacher. He received his elementary education at Bar nonclassical secondary school (1913–1920) and then at the mechanical school (town of Bar), which he finished in April 1922. Delimarskii started his working activities as metalworker at a machining workshop and then worked as a teacher at a labor school. In 1924–1928, he was a student of Kiev Institute of people's education (physicochemical department). Having graduated from the Institute, Delimarskii became a postgraduate student at Kiev Polytechnic Institute at the chair of the technology of mineral substances, headed by professor D.A. Chernobaev. During the period of time from 1928 till 1934, Delimarskii carried out an extensive series of investigations in the field of synthesis and analysis of physicochemical properties of aluminosilicates of the zeolite type. In 1936, he successfully defended his candidate (Chem. Sci.) dissertation devoted to this research area. From 1932 till 1934, the young scientist worked as a docent at Kiev Polytechnic Institute at the chair of inorganic chemistry, headed by professor V.A. Izbekov (1881–1963, corresponding member of the Academy of Sciences of the Ukrainian SSR since 1939), a prominent scientist in the field of electrochemistry of nonaqueous solutions, including low-melting salt systems.

Beginning in 1934, Delimarskii's scientific activities had been associated with the Academy of Sciences of the Ukrainian SSR and, in particular, with the Institute of General and Inorganic Chemistry, Academy of Sciences of the Ukrainian SSR (IONKh AN USSR, Institute of Chemistry before 1945), where the scientist worked till his dying day, with the exception of the time from September 1941 till March 1944. During this time interval, he headed the laboratory of mineral technology at the Chemical Institute, Uzbek branch of the Academy of Sciences of the USSR, in Tashkent. In 1944, Delimarskii was appointed deputy director of IONKh AN UkrSSR and head of laboratory (department) of electrochemistry of molten salts at the same Institute. In 1949, the scientist completed a large series of investigations, commenced in 1936, of the electrode potentials of metals in molten media and defended his doctoral (Chem. Sci.) dissertation "Electrode Potentials and Electrochemical Series of Metals in Molten Salts." In 1950, he became a professor.

During the period of time from 1938 till 1941, Delimarskii occupied a position of docent at the chair of inorganic chemistry at Kiev State University (KGU). In 1944, he resumed his teaching activities at the University; from 1951 till 1959, he headed the chair of inorganic chemistry at KGU, and in 1960–1964, was a professor of this chair [1].

In January 1957, Delimarskii was elected an academician of the Academy of Sciences of the Ukrainian SSR and chairman of the Bureau of the Department of chemical and geological sciences. He occupied the latter position till March 1960. Since that time, and till March 1973, Delimarskii was director of IONKh AN UkrSSR and, simultaneously, headed (till No-

1070-4272/04/7704-0697 © 2004 MAIK "Nauka/Interperiodica"

vember 1987) the department of electrochemistry of molten salts. Since the end of 1987 he was a councilor of the board of directors of IONKh AN UkrSSR.

The Kiev school of electrochemistry, one of whose brilliant representatives was Delimarskii, owes its origin to a known physical chemist V.A. Plotnikov (1873–1947, academician of the Academy of Sciences of the Ukraine since 1920, corresponding member of the Academy of Sciences of the USSR since 1932). A graduate from Moscow University, he taught from 1899 till 1941 at Kiev Polytechnic Institute, as a professor since 1910. Simultaneously, in 1931–1941, he was director of the Institute of Chemistry, Academy of Sciences of the Ukrainian SSR. The main Plotnikov's investigations were devoted to nonaqueous solutions and, in particular, to their electrochemistry. Among Plotnikov's pupils were such prominent scientists as V.A.Izbekov, Ya.A. Fialkov (1895–1958, corresponding member of the Academy of Sciences of the Ukrainian SSR since 1945), M.I. Usanovich (1894–1981, academician of the Academy of Sciences of Kazakh SSR), and many others [1].

Delimarskii carried out his first studies in the field of electrochemistry of molten salts as early as in 1934–1935 under the supervision of Izbekov. Having graduated from Yur'ev (Tartu) University in 1909, Izbekov commenced his teaching and scientific activities at Kiev Polytechnic Institute and, simultaneously, taught inorganic, physical, and analytical chemistry at other higher school institutions of Kiev. In particular, he taught inorganic chemistry at Kiev University from 1933 till 1950. Already the first joint study by Izbekov and Delimarskii (1936), in which the electrode potentials of metals in molten aluminum bromide were determined, confirmed the phenomenon, previously discovered by Izbekov, that the electrochemical series of metals is specific to each particular solvent. Further investigations by Delimarskii in this area markedly extended the knowledge of the influence exerted by the nature of a solvent on the position of metals in the electrochemical series and revealed the effect of temperature and some other factors. It was established that the difference between electrochemical series in molten electrolytes is primarily due to complexation and to the influence exerted by the nature of anions present in the melts (1955). In the subsequent years, Delimarskii and co-workers paid considerable attention to voltammetric measurements in molten salts (polarography with solid electrodes). Voltammetric measurements were used to study the reduction of cations of the overwhelming majority of metals and to refine their deposition potentials, diffusion coefficients, activation energies of processes, and their reversibility under stationary conditions. Later, pulsed and ac investigation techniques were suggested. A major contribution to the development of stationary and nonstationary methods for studying ionic melts was made by leading staff members of IONKH AN UkrSSR A.V. Gorodyskii (1930–1992; academician of the Academy of Sciences of the Ukrainian SSR since 1978), V.I. Shapoval (1933–1999), corresponding member of the National Academy of Sciences of the Ukraine since 1995), E.V. Panov, N.Kh. Tumanova, and V.F. Grishchenko.

In 1960, a monograph by Delimarskii and Gorodyskii *Elektrodnye protsessy i metody issledovaniya v polyarografii* (Electrode Processes and Investigation Methods in Polarography), largely based on studies of its authors, was published. Delimarskii and B.F. Markov (1912–1992) carried out extensive studies in the field of thermodynamics of molten salts, which were reflected in the monograph *Elektrokhimiya rasplavlennykh solei* (Electrochemistry of Molten Salts, 1960), translated in the United States. Investigations in the field of coordination chemistry in ionic melts were summarized in the monograph *Koordinatsionnaya khimiya solevykh rasplavov* (Coordination Chemistry of Salt Melts) (in co-authorship with S.V. Volkov and V.F. Grishchenko, 1977). The book had no analogues in the domestic and foreign literature.

The research conducted by Delimarskii was of applied nature and promoted the solution of specific technological problems. In particular, considerable attention was given by the scientist to intermetallide electrode processes of refining of heavy nonferrous metals. The main results of these studies were reflected in an original monograph *Elektrolitichеskoe rafinirovanie tyazhelykh metallov v ionnykh rasplavakh* (Electrolytic Refining of Heavy Metals in Ionic Melts) (in co-authorship with O.G. Zarubitskii, 1975). The research in the field of utilization of lead-containing secondary raw materials and separation of lead alloys, conducted under Delimarskii's supervision about 50 years ago, have remained topical and scientifically important up to now. To solution of important technological problems were devoted Delimarskii's monographs *Electrolitichеskoe luzhenie iz solevykh rasplavov* (Electrolytic Tinplating from Salt Melts) (in co-authorship with A.I. Vitkin, A.A. Kolotii, et al., 1967) and *Elektrokhimicheskaya ochistka otlivok v ionnykh rasplavakh* (Electrochemical Cleaning of Castings in Ionic Melts (in co-authorship with I.R. Fishman and Zarubitskii, 1976). Delimarskii supervised numerous investigations of electrolytic recovery of beryllium, titanium, zirconium, silicon, germanium, and carbon from molten salts. The scientist paid prime attention to extending the range of application of ionic liquids in various branches of technology. These issues were

the subject of a special monograph *Ionnye rasplavy v sovremennoi tekhnike* (Ionic Melts in Modern Technology, 1981). The modern state of the theory and practice of electrolysis was considered in a broader sense in Delimarskii's book *Electroliz. Teoriya i praktika* (Electrolysis: Theory and Practice, 1982). There is no escape from mentioning other, widely known monographs by the scientist: *Electrokhimiya ionnykh rasplavov* (Electrochemistry of Ionic Melts, 1976), *Khimiya ionnykh rasplavov* (Chemistry of Ionic Melts, 1980), *Teoreticheskie osnovy electroliza ionnykh rasplavov* (Theoreticval Foundations of Electrolysis of Ionic Melts, 1986), and *Prikladnaya khimiya ionnykh rasplavov* (Applied Chemistry of Ionic Melts, 1988).

The scientific legacy of Delimarskii is immense. The published list of his scientific works, in which the last item is dated by the beginning of 1988 [2], includes 761 titles. Among these, studies in at least three priority areas can be distinguished: electrochemical recovery, separation, and refining of heavy nonferrous metals (18.3% of all the publications); voltammetric (polarographic) studies (15.8%); and studies of the potential series and reference electrodes in molten media (11.2%). A large number of publications were devoted to general problems of electrochemical kinetics in salt melts, methods for study of kinetic characteristics, and techniques for electrodeposition of coatings from melts. A separate series of investigations was devoted to an analysis of the structure of molten salts by measuring their Raman spectra. It was demonstrated for the example of a number of nitrate melts that the ion–ion interactions in these melts are determined both by the crystal structure of the corresponding solid phases and by the nature of the first coordination sphere of the anion.

As already noted, Delimarskii was engaged in pedagogical activities at the chair of inorganic chemistry at KGU during many years. In this connection, he wrote an original textbook *Neorganicheskaya khimiya. Izbrannye glavy* (Inorganic Chemistry: Selected Chapters, 1973), which pays a considerable attention to the Periodic Law. To the centennial anniversary of this law was devoted a monograph by Delimarskii (in coauthorship with G.V. Shilina, in Ukrainian, 1969).

Rather prominent is Delimarskii's contribution to the organization of research in high-temperature inorganic chemistry and physicochemical and electrochemical studies in our country. He initiated the organization in 1969 of the Scientific Council of the Academy of Sciences of the USSR for physical chemistry of ionic melts and solid electrolytes and was its permanent chairman for 20 years.

By the early 1980s, the Council coordinated investigations that involved about 130 research institutions, and higher school institutions as well. All-Union and regional symposia and seminars and scientific workshops were held regularly. At that time, the Soviet Union occupied the leading position in world's science as regards the scale and level of the research in this field.

Delimarskii was also engaged in a variety of other kinds of public activities. He was chairman of the Scientific Council of the Academy of Sciences of Ukrainian SSR for kinetics and thermodynamics of electrode processes from 1967 till 1978, Editor-in-chief of *Ukrainskii Khimicheskii Zhurnal* (Ukrainian Chemical Journal) from 1968 till 1988, and chairman of the Ukrainian republican directorate of the Mendellev All-Union Chemical Society from 1970 till 1983. Delimarskii was a member of a number of international scientific organizations and represented our country at numerous congresses and conferences abroad. During a number of years he headed the Section of high-temperature chemistry of the International Electrochemical Society.

Scientific achievements of Delimarskii were honored with Pisarzhevskii Prize of the Academy of Sciences of Ukraine (1972), Mendeleev gold medal (1980), and a State Prize of the Ukrainian SSR in science and technology (1988). In 1974, Delimarskii was awarded an honorary title of Honored Science Worker of the Ukrainian SSR; he was decorated with a number of State awards.

Yurii Konstantinovich Delimarskii died on June 2, 1990. His pupils and colleagues preserve thankful memory of this remarkable scientist, who had done so much for the development of domestic high-temperature electrochemistry. To the life and activities of Delimarskii were devoted an issue concerned with the biobibliography of scientists of the Ukrainian SSR [2], articles by Gorodyskii [3] and Zarubitskii [4], and other numerous publications listed in [2].

REFERENCES

1. Atroshchenko, V.I., Berezhnoi, A.S., Boyarskaya, L.A., *et al.*, *Razvitie neorganicheskoi khimii na Ukraine* (The Development of Inorganic Chemistry in the Ukraine), Gorodyskii, A.V., Ed., Kiev: Naukova Dumka, 1987.
2. *Yurii Konstantinovich Delimarskii*, Feshchenko, V.G., Ivanova, E.G., and Barchuk, L.P., Compilers, Volkov, S.V., Ed., Kiev: Naukova Dumka, 1991.
3. Gorodyskii, A.V., *Zh. Vses. Khim. O–va im. D.I. Mendeleeva*, 1974, vol. 19, no. 5, pp. 566–567.
4. Zarubitskii, O.G., *Ukr. Khim. Zh.*, 1994, vol. 60, no. 7, pp. 451–455.

A. G. Morachevskii

Russian Journal of Applied Chemistry, Vol. 77, No. 5, 2004, pp. 701–707. Translated from Zhurnal Prikladnoi Khimii, Vol. 77, No. 5, 2004, pp. 705–711.

INORGANIC SYNTHESIS AND INDUSTRIAL INORGANIC CHEMISTRY

Physicochemical Principles and Technology of Processing and Neutralization of Titanium Production Wastes

Yu. P. Kudryavskii

EKO-tekhnologiya Research and Production Ecological Company, Berezniki, Perm oblast, Russia
Berezniki Branch, Perm State Technical University, Berezniki, Perm oblast, Russia

Received July 8, 2003; in final form, December 2003

Abstract—The data on formation of solid, liquid, and dust–gas wastes in various stages of titanium sponge production were generalized and systematized. To prevent environmental contamination by secondary production wastes, the procedures and flowsheets providing solidification of the waste products using gypsum or magnesia binding materials were offered.

The commercial process for production of metallic titanium as titanium sponge consists of three basic stages [1, 2]: (1) reductive ore smelting (ROS) of ilmenite ($FeTiO_3$) and(or) ilmenite–rutile ($FeTiO_3 \cdot TiO_2$) concentrates at 1600–2000°C, which yields titanium slag (80–86% TiO_2) and pig iron alloyed with nonferrous, rare, and scattered metals; (2) chlorination of titanium slags in melts of chlorides of alkali and alkaline-earth metals, mainly in a melt of a spent electrolyte from magnesium production. Thus technical-grade $TiCl_4$ is obtained, which is further purified to remove impurities, in particular, V(V) compounds, to obtain purified $TiCl_4$ and $VOCl_3$ (and/or V_2O_5) as commercial products; and (3) magnesium-thermal reduction of $TiCl_4$ yielding titanium sponge and $MgCl_2$ melt.

Waste products are formed in each of these stages, with the dust from ROS and waste products from the chlorination shop being the most toxic and difficult-to-process. In the course of ROS, almost all micro- and macrocomponents belonging to ilmenite and ilmenite–rutile concentrates are redistributed. Up to 90–96% of Ti, more than 80% of V, Nb, and Ta, and also a significant part of Mn, Cr, Al, Sc, Zr, Hf, Th, and U pass into the slag, whereas Fe mainly passes into pig iron, which is sold as a commercial product. A part of the initial furnace charge and of the products of redox reactions proceeding in the furnace is carried away from the melt surface as a dust–gas mixture to form waste products. The "yield" of the dust is up to 100 kg per ton of commercial titanium sponge [1, 2]. Therefore, production of, e.g., 10000 t/year of spongy titanium involves formation of up to 1000 t/year of the dust in the ROS process.

The composition of the dust in off-gases essentially depends on the operating mode (open, half-closed, and closed), temperature, and time from the beginning of the furnace operation to the end of a cycle. Usually the ROS dust contains (wt %) TiO_2 20–40, Fe_2O_3 30–60, Al_2O_3 1–2, SiO_2 6–7, Cr_2O_3 4–5, V_2O_5 0.2–0.3, MnO_2 1–2, sum of MgO and CaO 2–3, C 2–3, and a small amount of oxides of rare, scattered, and radioactive metals. The size of particles varies within very wide limits from 0.01 to 50 μm. Coarsely dispersed (10–50 μm) dust is entrapped in cyclones and goes then to the process "head" for the preparation of the initial charge for ROS, and finely dispersed dust ("behind-cyclone dust") is caught in bag filters or is ejected into the atmosphere.

It was shown in [3, 4] that the powder is essentially enriched with volatile components Pb, Zn, As, etc., which are evaporated owing to high temperature of the process (up to 2000°C) and are then condensed on dust particles. The degree of their concentration in comparison with the initial raw material ilmenite reaches 25–100%, and their content in the dust is 0.3–0.9%, with the higher degree of concentration of volatile metals being observed in the finely dispersed fraction. At the same time, we note that similar phenomena were also observed [5] when studying various high-temperature processes: gasification of fossilized coal, gaseous fuel and pig iron production, operation of thermal power stations, etc. In view of these facts, we could expect that the secular radioactive balance in the series of uranium and thorium, which are present in the initial ilmenite concentrates, would be disturbed.

1070-4272/04/7705-0701 © 2004 MAIK "Nauka/Interperiodica"

To study the distribution of natural radionuclides among industrial products of ore smelting of ilmenite concentrates, we selected appropriate samples of the initial concentrate, coke, slag, pig iron, dust caught in cyclones, and behind-cyclone dust. The determination of the specific activity of ^{226}Ra, ^{228}Ra, and ^{228}Th has shown that the main γ-emitting radionuclides do not get to a noticeable extent into the smelted pig iron and pass into the slag [3, 4]. The behavior of lead and polonium radionuclides in the ROS process essentially differs from that of their parent radionuclides: both Pb and Po almost completely sublime and are concentrated in the fine fraction. The activity of Pb and Po reached 3000–6000 Bq kg^{-1} in the dust caught in cyclones and 8000–20 000 Bq kg^{-1} in the behind-cyclone dust, which is much higher than the levels prescribed by NRB-99 and OSPORB-99 regulations [6, 7]. The high α-activity of the radionuclides of the behind-cyclone powder essentially complicates its recovery from the dust–gas mixture and subsequent utilization. The concentration of Po and Pb radionuclides in fine dust fractions reaches so high values that, according to the established regulations, the behind-cyclone dust should be classed with radioactive substances, and handling it requires special safety measures.

Thus, it follows from the aforesaid that even in the first stage of the general flowsheet of the spongy titanium production a significant amount of highly toxic radioactive waste products such as ROS dust is formed. Its recovery from a dust–gas mixture and subsequent utilization are of importance for the titanium production as a whole and are pressing problems to be solved urgently. Preliminary study and comparative tests of various ways and devices for the recovery of behind-cyclone dust have shown that, among all the known and commercially available types of dust-removing facilities, the most efficient for the behind-cyclone ROS powder are filters with powdery sintered filter cartridges (PSFCs).[1] The tests have shown that the efficiency of ROS dust removal from gases is more than 99.9%, and the residual concentration of the dust in off-gases does not exceed 0.20–0.34 mg dm^{-3} [8, 9].

In SIOT-type cyclones, only up to 40–50% of ROS dust is trapped. It should be noted that, in this case, the problem of radiation safety of dust recovery under conditions of sealed apparatus does not arise basically. However, this problem inevitably arises further when unloading the dust from the apparatus and when transporting it. According to the existing regulations [6, 7], formation of radioactive aerosols on workplaces during unloading, transportation, dosing, and packaging should be excluded.

The utilization of the trapped dust, especially of the behind-cyclone dust, involves still more problems. Obviously, the direct use of ROS dust, e.g., in formulations of paint-and-varnish materials, as suggested earlier, does not stand up under scrutiny owing to the fact that the powder contains α- and β-emitting radionuclides of Po, Bi, and Pb, volatile daughter products of ^{232}Th and ^{238}U decay. The return of the dust to the process "head," to the stage of charge preparation for ROS, also does not solve all questions concerning the emission of radionuclides into the atmosphere. In this case, radionuclides and stable isotopes of Pb, will inevitably accumulate in the system, and the trapped dust will become richer in Po, Bi, and Pb radionuclides from one cycle to another, being also enriched in stable Pb. We suggest two ways to solve the problem of utilization of the ROS dust [9].

The first way is "burdening up," i.e., addition of a small amount of the dust to the titanium slag to be chlorinated. However, in this case it should be expected that the composition of technical $TiCl_4$ would change, and salt wastes (of spent melt and sublimates from titanium chlorinators) would form. This requires special measures and technical decisions to be undertaken to ensure the necessary purity of $TiCl_4$ and neutralization of waste products.

The second way is mixing of ROS powder with other toxic waste products of titanium production: with the insoluble residue from hydraulic removal of a melt in which Th and Ra are concentrated, or with an oxyhydrate precipitate containing Fe, Cr, Mn, Ti, V, Th, etc., formed upon local neutralization of solutions and(or) pulps from the hydraulic washout of spent melts and sublimates from titanium chlorinators. Then the resulting composition should be solidified using gypsum or predominantly magnesia binding materials [10, 11], in particular, those based on serpentine raw materials, waste products from asbestos production [12]. The chlorination of slags from ROS of ilmenite concentrates enriched in TiO_2 (up to 80–86%) results in the formation of large amounts of waste products in salt chlorinators: spent melt, fusible and "dry" sublimates from titanium chlorinators, acid drains from washing of process equipment, and spent solutions from gas purification. As much as 0.25–0.30 t of the spent melt and up to 0.05–0.10 t of sublimates from titanium chlorinators are formed per ton of $TiCl_4$ (Table 1).

[1] Developed and produced by EKAPOR Ural Research and Production Association (Novouralsk).

Table 1. Composition of raw materials and waste products in $TiCl_4$ production*

Component	Content, wt %								
	Ti	Fe	Cr	Mn	V	Al	Sc	Th	Zr
Ilmenite concentrate	30.0–40.0	23.0–30.0	0.5–1.0	0.7–0.9	0.15–0.25	1.0–2.0	0.005–0.015	0.007–0.035	0.2–0.4
Spent melt	0.2–0.3	8.0–12.0	1.2–3.4	1.2–2.4	0.01–0.1	1.0–4.0	0.01–0.03	0.01–0.05	0.1–1.0
Sublimates	1.0–5.0	8.0–12.0	0.5–1.5	0.1–0.3	0.1–1.0	4.0–10.0	0.005–0.02	0.005–0.01	0.5–5.0

* The content of the water-insoluble phase is 20–30% for melt and 5–10% for sublimates; the content of NaCl/KCl in the spent melt is 38–45%.

Table 2. Composition of wastewater formed in chlorination of titanium slags in salt chlorinators

Component	Concentration, g dm^{-3}			
	hydraulic removal of spent melt	between spent melt discharges (flow-through mode)	hydraulic washout of forehearth sublimates (flow-through mode)	hydraulic washout of dry sublimates in buckets
Fe	13.7	5.5	2.3	17.4
Al	0.9	0.7	1.8	5.1
Ti	0.7	0.3	0.4	9.0
Cr	3.0	1.1	0.2	0.2
Mn	2.9	1.1	0.07	0.1
K	0.11	0.08	0.04	0.20
Na	20.9	9.1	1.9	10.5
Ca	1.9	0.9	0.1	0.08
Mg	1.4	0.6	0.08	0.02
Zn	0.012	0.010	0.005	0.02
Cu	0.05	0.03	0.01	0.01
Th	0.05	0.03	0.01	<0.001
Sc	0.04	0.02	0.001	0.001
Cl^-	64.4	27.9	12.2	93.9
Suspended substances	17.2	7.9	2.2	13.5
Mineralization	115.3	53.1	17.3	117.2
pH	1.1	2.1	2.1	1.3

In the accepted process, these waste products are discharged into water, with the resulting acidic wastes (pulps) forming three independent streams.

The first stream is an acid chloride solution formed directly from hydraulic washout of spent melt: 8–12 m^3 of water per ton of melt. Every day the melt is poured out 5–7 times (per chlorinator), each time in the amount of 2–3 t. Thus, 10–20 t of the melt is poured out from one chlorinator (correspondingly, 20–40 t when two chlorinators work), and 200–450 $m^3\ day^{-1}$ of wastewater is formed. The volume of such dumping reaches 50 $m^3\ h^{-1}$ at the total pouring duration of 9 h.

The second stream from chlorinators is a weakly mineralized solution from hydraulic removal baths. When water is fed to a bath in the flow-through mode, the dumping volume from two chlorinators is up to 150 $m^3\ day^{-1}$ (up to 10 $m^3\ h^{-1}$ at 15 h of the flow).

The third stream is formed by discharges from hydraulic removal baths for sublimates of smelting chambers. Every day 1.5–3.0 t of the sublimate from two chlorinators is discharged, and up to 480 m^3 of water (up to 20 $m^3\ h^{-1}$) is consumed to remove it, with water being fed continuously in the flow-through mode.

The average composition of the above-mentioned solutions, and also the composition of discharges from hydraulic washout buckets with "dry" sublimates are shown in Table 2. Calculations based on the averaged results of the inspection of the wastewater formation

system show that up to 230 000 m^3 of acidic chloride wastewater is formed in the chlorination process stage directly from chlorinators (80 000, 60 000, and 90 000 m^3 per year for the first, second, and third streams, respectively) at the annual output of 10 000 t of spongy titanium.

The discharges from the chlorination stage amount to less than 10% of the total amount of wastewater from the AVISMA Titanium–Magnesium Combine, Joint-Stock Company. At the same time, this wastewater contains the greatest amount of rather toxic metals: nonferrous, rare, scattered, and radioactive (Tables 1, 2).

According to the existing technology, wastewater from the hydraulic washout of spent melt and sublimates of $TiCl_4$ production is discharged into the sewer system, combined with the other wastewaters, and fed to the wastewater treatment facilities (in total, up to 3×10^6 m^3/year and more). The combined discharges are treated with lime milk and Praestol flocculant, settled, and discharged into the so-called "industrial channel" (where practically the whole amount of wastewater from industrial enterprises of the city is discharged) and then into the Kama river.

The scheme accepted for processing wastewater from titanium–magnesium industry has a number of essential drawbacks, the main of which is unsatisfactory removal of Mn(II) and Fe(II) ions and suspended substances. This results in that significant amounts of harmful substances are discharged from the wastewater treatment plant into the industrial channel and then into the Kama river, thus giving rise to secondary environmental pollution. One of the principal causes of the existing situation is that the accepted concept of processing wastewater from the combine is inefficient as a whole. Namely, a relatively small volume of wastewater from chlorinators (up to 10% of the total amount), containing chlorides of polyvalent metal ions, is combined with other wastewaters, mainly those from gas purification units, which are suspensions of solid CaO, $CaCO_3$, SiO_2, etc. in liquid solutions of $CaCl_2$ and $Ca(ClO_3)_2$.

Combining acidic wastewaters from the chlorination stage and alkaline wastewaters from gas purification units results in formation of difficultly settling colloidal and semicolloidal oxyhydrates of metals present in the wastewater from hydraulic washout of spent melt and sublimates of titanium chlorinators. As a result, conditions for the flocculation of all polydisperse suspensions present in the combined pulp get worse, the clarification of solutions becomes unsatisfactory, and hydrophilic precipitates saturated with water (the sum of metal oxyhydrates, hydroxides, oxides, and carbonates) are formed. Their dehydration and utilization is an independent and difficult problem. The results of [13–15] show that these problems can be largely solved by separate processing of wastewaters from chlorinators and those from magnesium production and gas purification as a whole, in particular, by local neutralization of solutions and pulps formed from hydraulic washout of sublimates and especially of spent melt from titanium chlorinators. In this case, the load on wastewater treatment plants is significantly reduced, and the problem of the isolation of suspended substances will consist only in settling of coarsely dispersed phases ($CaCO_3$, "sand" fractions of limy milk, etc.) and the part of solid CaO particles that remained unchanged during removal of Cl_2 and HCl from off-gases owing to relatively large size of the particles, their decreased hydrophilicity, and low chemical activity.

It should be noted that the initial wastewaters from the $TiCl_4$ production are relatively dilute as compared to the maximum possible concentration of the sum of metal chlorides (Table 2). It was found experimentally that 1.8–2.0 m^3 of water per ton of the melt is necessary to obtain solutions saturated with metal chlorides, i.e., when 20–40 $m^3\ day^{-1}$ of the melt is discharged, it is possible to obtain 40–80 $m^3\ day^{-1}$ (instead of 200–450) of the concentrated solutions. To obtain concentrated solutions from the sublimate of melting chambers, 4–5 m^3 of water per ton of the sublimate is necessary. In this case, 15 m^3 of a solution (instead of 480 $m^3\ day^{-}$) is formed daily upon processing 1.5–3.0 t of fusible sublimates. As to water passing through the baths for the hydraulic removal in the flow-through mode, this water should be replaced with recycled solutions to reduce the volume of the forming wastewater. Taken together, these measures will reduce the volume of concentrated chloride solutions discharged from chlorinators from 800–1200 to 50–100 $m^3\ day^{-1}$.

To implement this approach, a flowsheet [13] (see figure) was developed and an installation was constructed, providing for the circulation of solutions obtained from the hydraulic washout of spent melt in a system. The installation consists of a bath for the hydraulic removal: a 40 m^3 water-cooled circulating tank. The experience of the installation operation has shown that, on the one hand, the developed technology significantly reduces the volume of "fresh" water consumed, and, on the other hand, after 4–6-fold circulation it yields solutions concentrated with respect to metal chlorides. These solutions are fairly convenient

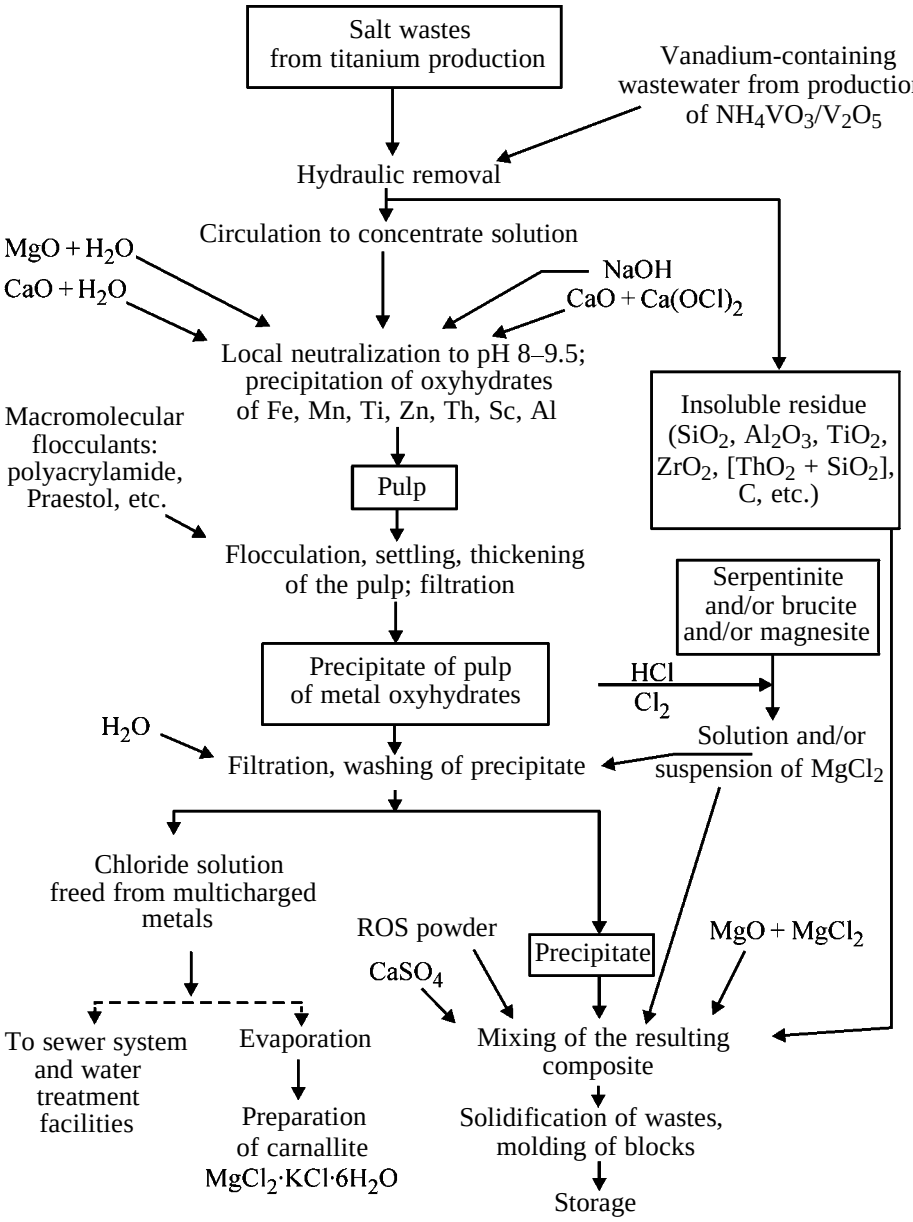

Flowsheet for processing of titanium production wastes.

for subsequent processing, in particular, for the local neutralization [14, 15] and(or) for the complex processing with extraction of valuable components and production of various commercial items [16, 17].

To gain insight into the processes occurring upon neutralizing and rendering harmless acidic wastewaters from chlorination of titanium slags, we studied in detail how the composition of the initial solutions, their concentration, pH, temperature, types of precipitating agents (alkaline reagents) and flocculants, their concentration and amount, and certain specific features of processing and preliminary preparation of a pulp affect the degree of the precipitation of the sum of metal oxyhydrates, the rate of pulp clarification, the aggregative stability, the weight of the forming precipitate, the efficiency of its dehydration, etc. As initial solutions for the experiments and comparative tests we took the initial solutions and pulps from hydraulic washout of the melt and sublimates obtained according to traditional technology, various mixtures of these solutions, and concentrated solutions formed upon their 4–6-fold circulation. These solutions were neutralized with limy milk (100–150 g dm^{-3} of CaO), NaOH solution (40–120 g dm^{-3}), $MgCO_3$, brucite

$Mg(OH)_2$, serpentinite, and(or) their aqueous suspensions. These studies allowed us to develop, test, and run several versions of a process for locally neutralizing and rendering harmless wastes from titanium production, differing in the type of applied alkaline reagents and, correspondingly, in the composition of the resulting precipitates and solutions (filtrates) and in the ways of their further utilization.

The results of the tests and the experience of running the process have convincingly shown that the use of this technology for processing of the whole volume of the forming wastes make it possible to exclude discharge of polyvalent metals to wastewater treatment plants of the combine and creates prerequisites for utilization of wastes as commercial products: concentrates and individual compounds of nonferrous, rare, and scattered metals, in particular, of iron oxide pigments of various color and purpose, selective inorganic sorbents, and commercial scandium compounds [17]. However, in the first stage of the work, it is appropriate to restrict the consideration to local neutralization of acidic wastewater from titanium production by the precipitation of the sum of metal oxyhydrates.

It is doubtful that these precipitates will be claimed by potential consumers because of their relatively poor consumer properties. At the same time, the presence of toxic metals in the precipitates does not allow their open dumping. To utilize secondary waste products of titanium production, including wastes with the increased content of natural radionuclides (Th, Ra, ..., Po, Bi, and Pb), we developed procedures and flowsheets [18] in which the precipitates of metal oxyhydrates are combined with ROS dust and insoluble residue from hydraulic washout of the melt from titanium chlorinators, and the resulting mixture of waste products is treated with gypsum [$CaSO_4$ and(or) $CaSO_4 \cdot 0.5H_2O$] or magnesia ($MgO + MgCl_2$) binders, solidifed, and molded in "blocks" (see scheme). It allows highly toxic wastes to be incorporated into a water-insoluble, nondust-forming matrix, stable to atmospheric precipitates, soil and subsoil waters, fluctuations of the ambient temperature, and wind and water erosion. Storage of such wastes will prevent emission of radioactive dust into the atmosphere and pollution of the environment.

CONCLUSIONS

(1) The processes of formation of solid, liquid, and dust–gas wastes in various stages of titanium sponge production were considered. A significant amount of finely dispersed dust in which toxic metals and radionuclides of the thorium series are concentrated is formed in the course of ore smelting of the ilmenite concentrates.

(2) According to the accepted technology, when titanium slag is chlorinated, the concomitant metals (Fe, Cr, Mn, Zr, Al, Th, Sc, etc.), which are accumulated in the spent melt and sublimates from titanium chlorinators, are discharged into water, and the resulting pulp is discharged to the sewer system and fed to the wastewater treatment facilities. However, owing to the formation of colloidal and semicolloidal metal oxyhydrates upon the neutralization, the pulp does not settle and is not clarified.

(3) To prevent environmental pollution, we suggested and tested a process involving pulp circulation when the spent melt and sublimates from titanium chlorinators are removed. The process yields concentrated solutions and pulps, which are then locally neutralized. The resulting oxyhydrate precipitate is mixed with other toxic wastes from titanium production and with gypsum or magnesia binder for solidification and then molded in blocks in an environmentally safe form.

ACKNOWLEDGMENTS

The study was made within the framework of the 2000–2003 Interbranch Program of Cooperation of the Ministry of Education of the Russian Federation and the Ministry of Atomic Energy of the Russian Federation, Scientific-Innovation Cooperation direction.

REFERENCES

1. Sergeev, V.V., Bezukladnikov, A.B., and Mal'shin, V.M., *Metallurgiya titana* (Metallurgy of Titanium), Moscow: Metallurgiya, 1979.
2. Garmata, V.A., Petrun'ko, A.N., Galitskii, N.V., *et al*., *Titan* (Titanium), Moscow: Metallurgiya, 1983.
3. Grashchenko, S.M., Kudryavskii, Yu.P., and Abramov, D.S., *Radiokhimiya*, 1996, vol. 38, no. 2, pp. 185–189.
4. Grashchenko, S.M., Kudryavskii, Yu.P., and Abramov, D.S., *Radiokhimiya*, 1996, vol. 38, no. 2, pp. 183–184.
5. Grashchenko, S.M., *Ekol. Khim*., 1998, no. 7(4), pp. 268–277.
6. *Normy radiatsionnoi bezopasnosti (NRB-99): Gigienicheskie normativy* (Radiation Safety Regulations (NRB-99): Hygienic Specifications), Moscow: Tsentr Sanitarno-Epidemiologicheskogo Normirovaniya, Gigienicheskoi Sertifikatsii i Ekspertizy Minzdrava Rossii, 1999.

7. *Osnovnye sanitarnye pravila obespecheniya radiatsionnoi bezopasnosti (OSPORB-99)* (Basic Sanitary Rules of Radiation Safety Provision (OSPORB-99)), item 2.6.1: *Ioniziruyushchie izlucheniya: Radiatsionnaya bezopasnost'* (Ionizing Radiations: Radiation Safety), Moscow: Minzdrav Rossii, 1999.
8. Trapeznikov, Yu.F., Vinogradov, M.V., and Kudryavskii, Yu.P., *Intensifikatsiya protsessov tsentrobezhnogo pyleulavlivaniya v titano-magnievom proizvodstve* (Intensification of Centrifugal Dust Catching Processes in Titanium–Magnesium Production), Yekaterinburg: UGLTA, 1999.
9. Kudryavskii, Yu.P., in *Doklady Mezhdunarodnogo ekologicheskogo kongressa "Novoe v ekologii i bezopasnosti zhiznedeyatel'nosti"* (Proc. Int. Ecological Congr. "New in Ecology and Safety of Human Activity"), St. Petersburg: Balt. Gos. Tekh. Univ., 2000, vol. 1, pp. 231–234.
10. Kudryavskii, Yu.P., Trapeznikov, Yu.F., and Rakhimova, O.V., in *Trudy Mezhdunarodnoi nauchnoi konferentsii "Perspektivy razvitiya estestvennykh nauk v vysshei shkole"* (Proc. Int. Scientific Conf. "Prospects for Development of Natural Sciences in the Higher School"), vol. 4: *Ratsional'noe prirodopol'zovanie: Zdorov'e naseleniya* (Rational Nature Management: Health of the Population), Perm: Perm. Univ., 2001, pp. 167–172.
11. Kudryavskii, Yu.P., *Usp. Sovrem. Estestvozn.*, 2002, no. 6, pp. 53–54.
12. Kudryavskii, Yu.P. and Penskii, A.V., in *Problemy i perspektivy razvitiya khimicheskikh tekhnologii na Zapadnom Urale: Sbornik nauchnykh trudov* (Problems and Prospects for Development of Chemical Technologies in Western Urals: Coll. of Scientific Works), Perm: Perm. Gos. Tekh. Univ., 2001, pp. 103–105.
13. Kudryavskii, Yu.P., Freidlina, R.G., and Volkov, V.V., *Tsvetn. Metall.*, 1992, no. 1, pp. 39–41.
14. Kudryavskii, Yu.P., Freidlina, R.G., and Volkov, V.V., *Tsvetn. Metall.*, 1992, no. 6, pp. 39–41.
15. Kudryavskii, Yu.P., *Tsvetn. Metally*, 1998, no. 4, pp. 58–62.
16. Kudryavskii, Yu.P., *Tsvetn. Metally*, 1998, no. 7, pp. 54–58.
17. Kudryavskii, Yu.P., in *Problemy i perspektivy razvitiya khimicheskikh tekhnologii na Zapadnom Urale: Sbornik nauchnykh trudov* (Problem and Prospects for Development of Chemical Technologies in Western Urals: Coll. of Scientific Works), Perm: Perm. Gos. Tekh. Univ., 2001, pp. 110–116.
18. Kudryavskii, Yu.P., *Tsvetn. Metall*, 2003, no. 10, pp. 35–43.

Russian Journal of Applied Chemistry, Vol. 77, No. 5, 2004, pp. 708–710. Translated from Zhurnal Prikladnoi Khimii, Vol. 77, No. 5, 2004, pp. 712–714.

INORGANIC SYNTHESIS AND INDUSTRIAL INORGANIC CHEMISTRY

Possibility of Integrated Processing of the Baddeleyite Concentrate

V. N. Lebedev, E. P. Lokshin, N. A. Mel'nik, T. E. Shchur, and L. A. Popova

Tananaev Institute of Chemistry and Technology of Rare Elements and Mineral Raw Materials, Kola Scientific Center, Russian Academy of Sciences, Apatity, Murmansk oblast, Russia

Received August 21, 2003; in final form, December 2003

Abstract—Main procedures used in integrated processing of baddeleyite, including sintering with calcium carbonate or oxide, decomposition of the cake with hydrochloric acid, and recovery of zirconium in the form of zirconium oxochloride, were studied.

The baddeleyite concentrate (BC) from the Kovdor deposit, which contains no less than 97.5–98.5% ZrO_2 + HfO_2, is used without chemical processing in many fields of technology. Its use for production of zirconium compounds is considered to be inexpedient since the cost of ZrO_2 in the concentrate is nearly twice that in zircon. In view of the decreasing demand for BC because of the saturation of the market with zircon-based synthetic materials [1], a necessity arises for deeper processing of the concentrate. The profitability of such a processing can be substantially improved by recovery of Sc(III), Ta(V), and Nb(V), which are present in the BC in amounts whose cost, at the world prices, is comparable with that of the concentrate. Previously, the distribution of rare and radioactive elements in various flowsheets of BC processing has been studied, and it was shown that simultaneous synthesis of pure zirconium compounds and recovery of rare and radioactive elements into separate concentrates is the most efficient in processing by sintering with CaO or $CaCO_3$ and subsequent transfer of chlorides or nitrates into solution. Here we studied methods for recovery of rare elements into concentrates by sintering of BC with $CaCO_3$ and recovery of zirconium(IV) in the form of an oxychloride.

EXPERIMENTAL

A baddeleyite concentrate conforming to TU (Technical Specification) 48-0572–91 was used in the study. Rare and impurity elements in precipitates were analyzed by X-ray fluorescence and spectral methods, and those in solution, by the emission and atomic-absorption techniques. The specific radioactivity and the content of U and Th were determined by radiometry and γ-ray spectrometry.

The baddeleyite concentrate was ground in a ball mill to grain size of less than 0.054 mm, mixed with $CaCO_3$ and $CaCl_2$ in weight ratio of 10 : 8.2 : 1.2, and sintered at 1150°C for 4 h. The cake was dissolved in hydrochloric acid, and the $ZrOCl_2$ precipitate was separated and washed with counterflow repulpations to required purity. The acid consumed for washing was used to decompose the cake. The degree of concentrate decomposition was 95–97%, which considerably exceeds the value in sintering with CaO [2, 3]. The yield of the mother liquor after isolation of $ZrOCl_2$ was 150–250 ml per 100 g of BC (~150 g of cake) at a composition (g l^{-1}): 40–60 HCl, 120–180 CaO, 2–5 Fe_2O_3, 4–8 ZrO_2, 1.5–3.5 TiO_2, 1.7–3.0 Nb_2O_5, 0.25–0.4 Ta_2O_5, 0.08–0.18 Sc, 0.15–0.6 SiO_2, 0.06–0.12 U, and 0.05–0.1 Th. Iron finds its way into the BC mainly during grinding and is present in solution as Fe(III), with other elements also oxidized to the highest oxidation state.

Rare elements were primarily recovered using extraction techniques. It is known that Sc(III) is best recovered with organophosphorus acids [4, 5]. The possibility of its recovery with a 0.3 M solution of di-2-ethylhexyl hydrogen phosphate (HDEHP) in dodecane was studied. It was found that 99% of Sc(III) is extracted at a phase ratio o : a = 1 : 10, and 92%, at o : a = 1 : 50, in the case of agitation for 5 min and settling for 1 h. The results of a large-scale experiment are listed in Table 1.

The extract was twice washed with a 6 N solution of HCl at o : a = 1 : 1. Zr(IV) and Sc(III) were not noticeably washed out; U(VI), Ti(IV), and Fe(III)

1070-4272/04/7705-0708 © 2004 MAIK "Nauka/Interperiodica"

Table 1. Distribution of elements in extraction with a 0.3 M HDEHP solution

Product	Volume, ml	Concentration, g l^{-1}							
		Sc(III)	ZrO_2	TiO_2	Nb_2O_5	Ta_2O_5	Fe_2O_3	U(VI)	Th(IV)
Initial solution	1000	0.14	4.1	2.3	1.9	0.27	3.3	0.08	0.07
Raffinate	990	0.002	1.8	1.9	1.7	0.3	2.3	0.006	0.02
Washing solution (6 N HCl):									
1st	110	0.01	0.4	1.4	0.1	–	6.8	0.16	0.2
2nd	100	0.001	0.2	0.7	–	–	0.6	0.11	0.25
Extract	95	1.3	16.9	0.4	–	–	0.7	0.2	0.002

Table 2. Composition of precipitates formed in thermal hydrolysis

Run no.	*A*, kBq kg^{-1}	Content of oxides, wt %					
		Nb(V)	Ta(V)	Ti(IV)	Zr(IV)	Fe(III)	Si(IV)
1	52.9	19.7	3.9	26.6	25.6	0.3	6.8
2	570	14.6	2.7	20.8	31.2	1.1	4.7
3	490	15.6	2.9	24.3	32.9	0.01	1.8

were washed out incompletely; all the other elements passed into the aqueous phase. The concentration of Sc(III) in the extract exceeded that in baddeleyite by a factor of nearly 100, and that in solution, by a factor of 10. Use of NaF for back extraction has been recommended [6]. An advantage of such a technique is that the most valuable element is recovered in the first stage; to its disadvantages belong difficult back extraction and distribution of radioactivity among phases.

An experiment on extraction of elements with the most readily available solvents, octanol and tributyl phosphate (TBP), showed that iron(III) can be selectively recovered from solution and the separation factors for other impurities are low.

It would be expected that, at a high concentration of the salting-out agent, $CaCl_2$, the distribution coefficients of Sc(III) should be greater [4, 5]; however, these coefficients were found to be lower and close to those for the other components monitored. Raising the acidity fails to improve the selectivity of the system. Quite the opposite, the distribution coefficient of Sc(III) becomes smaller because of the competing influence of other ions.

We examined the possibility of separating the components using the difference in the pH values of hydroxide precipitation and the tendency for multicharged cations to undergo hydrolysis. In the case of neutralization with ammonia, the pH of the onset of Sc(III) precipitation is 4.8–4.9, whereas Ti(IV), Zr(IV), Nb(V), and Ta(V) precipitate in the pH range from 0.5 to 2.0 [4, 7]. It was established that, upon neutralization to pH 0.5–2.5, virtually unfilterable slurries are formed. At pH 3.5 the precipitate can be filtered off, and not only Ti(IV), Zr(IV), Nb(V), Ta(V), and Fe(III) completely precipitate, but also U(VI), Th(IV), and Sc(III). The coprecipitation of Sc(III) and the radionuclides is due to the sorption properties of the hydrogels of multicharged cations and iron(III).

When thermal hydrolysis is performed in an acid medium, 5–15% of Sc(III) is precipitated, depending on the conditions (acidity, time of thermal treatment, nucleating and other additives). This mainly occurs via capture of the mother liquor. In order of their precipitation, the elements can be ranked as follows: Ta(V) > Nb(V) > Ti(IV) > Zr(IV) > U(VI), Th(IV). By changing the precipitation conditions, it is possible to selectively leave in solution radioactive elements and part of Zr(IV). However, taking into account the separation of Sc(III) and difficulties in filtration, it is advisable to isolate these elements into a collective precipitate. The yield of dry residue is 15–25 g l^{-1} of solution. The compositions of the precipitates obtained by neutralization of the solution with 10 g l^{-1} of HCl, introduction of H_2SO_4 to 1 mol mol^{-1} of ZrO_2, and keeping at 90°C for 2 h are listed in Table 2. In run

no. 3, hydrolysis was performed in solution after separation of Fe(III) by extraction, and in run nos. 1 and 2, before separation of Fe(III). The content of Sc(III) in the washed precipitates was below the detection limit of the X-ray fluorescence analysis (<0.01 wt %). The precipitation was fairly complete: the residual content of Ti(IV) and Nb(V) in solutions formed in run nos. 2 and 3 was less than 0.01 g l^{-1} for each of these components, and that of Zr(IV), less than 0.3 g l^{-1}. Thus, the separation of Sc(III) from multicharged cations was achieved in the experiments, with the only difficulty consisting in the poor filterability of the precipitates formed by hydrolysis.

Further processing of the precipitates can be done using the standard methods in an $HF–H_2SO_4$ medium in order to perform extractive recovery and separation of Ta(V) and Nb(V) [8], with preliminary removal of U(VI) on anion-exchange resins in a sulfuric acid medium [9].

From a solution that contains $CaCl_2$, 85% of Sc(III) is extracted with TBP in a single stage in the absence of competing ions at o : a = 1 : 1. In a counterflow process, 98% recovery was achieved in three stages at o : a = 1 : 2. After backwashing with water and neutralization of the backwash with ammonia, the hydroxides isolated were treated with oxalic acid. The content of Sc_2O_3 in a precipitate calcined at 900°C was 16.5 wt %, with the rest constituted by Ca(II), Fe(III), Mg(II), and Zr(IV). The yield of the precipitate was 0.8–1 g l^{-1} of solution at a direct recovery of Sc(III) from BC in the range 65–78.5%.

CONCLUSION

The study demonstrated the possibility of processing of the baddeleyite concentrate to produce zirconium compounds with recovery of scandium(III), niobium(V), and tantalum(V) into separate concentrates. The process includes sintering with calcium oxide or carbonate in the presence of a modifying agent, breakdown of the cake with hydrochloric acid, recovery and purification of zirconium oxychloride, thermal hydrolysis of the mother liquor, and transfer into a precipitate of basic salts of multicharged cations. Scandium(III) is recovered from solution via extraction with di-2-ethylhexyl hydrogen phosphate or is accumulated in a raffinate in extraction of iron(III) with tributyl phosphate.

REFERENCES

1. *BIKI*, 2000, no. 4 (80486), January 18.
2. Lebedev, V.N., Lokshin, E.P., and Mel'nik, N.A., *Zh. Prikl. Khim.*, 2003, vol. 76, no. 2, pp. 190–195.
3. Kolenkova, M.A., Shumenko, V.N., Dorokhina, M.N., and Safuanova, N.A., *Novoe otechestvennoe syr'e i sposoby ego pererabotki* (New Domestic Raw Materials and Methods for Their Processing), Moscow: TsNII Ekon. Inform. Tsvetn. Metall., 1980, issue 2.
4. Korshunov, B.G., Reznik, A.M., and Semenov, S.A., *Skandii* (Scandium), Moscow: Metallurgiya, 1987.
5. Favorskaya, L.V., *Khimicheskaya tekhnologiya skandiya* (Chemical Technology of Scandium), Alma-Ata: ONTI, 1969.
6. Favorskaya, L.V., Koshul'ko, L.P., and Presnetsova, V.A., *Tekhnologiya mineral'nogo syr'ya* (Technology of Mineral Raw Materials), Alma-Ata: Inst. Miner. Syr'ya, 1975, issue 2, pp. 67–73.
7. Bol'shakov, K.A., *Khimiya i tekhnologiya redkikh i rasseyannykh elementov* (Chemistry and Technology of Rare and Scattered Elements), Moscow: Vysshaya Shkola, 1969, vol. 2.
8. Nikolaev, A.I. and Maiorov, V.G., *Ekstraktsiya niobiya i tantala* (Extraction of Niobium and Tantalum), Apatity: Kol'sk. Nauchn. Tsentr Ross. Akad. Nauk, 1995.
9. Egorov, E.V. and Makarova, S.V., *Ionnyi obmen v radiokhimii* (Ion Exchange in Radiochemistry), Moscow: Atomizdat, 1971.

Russian Journal of Applied Chemistry, Vol. 77, No. 5, 2004, pp. 711–715. Translated from Zhurnal Prikladnoi Khimii, Vol. 77, No. 5, 2004, pp. 715–719.

INORGANIC SYNTHESIS AND INDUSTRIAL INORGANIC CHEMISTRY

Recovery of Thorium(IV) in Utilization of Solutions Formed in Sulfuric Acid Breakdown of Perovskite

V. G. Maiorov, A. I. Nikolaev, V. K. Kopkov, L. A. Safonova, and G. V. Korotkova

Tananaev Institute of Chemistry and Technology of Rare Elements and Mineral Raw Materials, Kola Scientific Center, Russian Academy of Sciences, Apatity, Murmansk oblast, Russia

Received August 21, 2003; in final form, December 2003

Abstract—Extraction of thorium(IV) with di-2-ethylhexyl hydrogen phosphate, octanol, and tributyl phosphate in sulfuric acid processing of perovskite was studied. The main stages of utilization of waste hydrochloric acid solutions were considered.

Russia suffers from permanent shortage of compounds of titanium(IV), niobium(V), and tantalum(V), which is due to the lack of readily available resources of conventional raw materials (ilmenite, columbite–tantalite, pyrochlore, and microlite ores). At the same time, Russia possesses a considerable part of world's mineral resources of titanium-and-rare-metal raw materials; more than half of the domestic resources can be found in the Kola Peninsula. The largest amounts of titanium-and-rare-metal raw materials are contained in loparite ores of the Lovozero deposit and perovskite ores of the Afrikanda and Vuoriyarvi deposits. The loparite concentrate is produced in limited amounts and actually serves as the only important exploited source of raw materials in Russia for manufacture of niobium, tantalum, and rare-earth products. Deposits of perovskite ores deserve closer attention because of the shortage of materials based on titanium and rare metals.

The total amount of ores only at the Afrikanda deposit (the best prepared for industrial use) is 626.2 million tons (52.2 million tons of TiO_2) [1–3]. A characteristic feature of perovskite is its complex multicomponent composition. For example, the perovskite of the Afrikanda deposit contains (wt %) 0.64–2.50 $(Nb,Ta)_2O_5$, 50.8–56.8 TiO_2, 0.12–1.93 SiO_2, 0.15–1.30 Al_2O_3, 0.43–2.00 Fe_2O_3, up to 1.44 FeO, 2.18–10.7 Ln_2O_3 (here and hereinafter, Ln_2O_3 is a sum of oxides of rare-earth elements), 26.3–38.1 CaO, 0.10–2.35 Na_2O, and 0.07–0.14 ThO_2. The complex composition of the raw materials necessitates their integrated processing with recovery of all the valuable components. Various techniques have been developed for processing of perovskite [1]. These techniques make it possible to obtain 0.41–0.47 t of TiO_2 pigment, up to 100 kg of a rare-earth concentrate, 7.7–9.3 kg of Nb_2O_5, and 0.42–0.50 kg of Ta_2O_5 from 1 t of the concentrate. Rather promising is breakdown of perovskite with hydrochloric acid, with Ca(II), La(III), and Th(IV) passing into solution, and Ti(IV), Nb(V), and Ta(V), into the precipitate, which is further processed into commercial products by the known schemes [1–3].

This study is mainly concerned with recovery of Th(IV) in the hydrochloric acid processing of perovskite. The perovskite concentrate contains as undesirable impurities such radionuclides as Th(IV), U(VI), and Ra(II), with Th(IV) predominant among these. A suggestion that Th(IV) compounds can be used in the future in nuclear power engineering has been made in the literature [4]. Naturally, recovery of Th(IV) is also necessary from the standpoint of the environmental safety. Hydrochloric acid solutions obtained by breakdown of perovskite contained, after precipitation of Ti(IV), Nb(V), and Ta(V) by hydrolysis, the following compounds ($g\ l^{-1}$): 100–200 HCl, 100–150 $CaCl_2$, 0.1–0.2 ThO_2, 6–10 Ln_2O_3, 6–10 Fe_2O_3 [Fe(II) + Fe(III) in terms of Fe_2O_3], and 1–10 TiO_2. In addition, Mn(II), V(V) (the perovskite concentrate contains an impurity of titanomagnetite), and Zn(II) [Zn(II) was used in the hydrolysis stage to obtain pigment-grade titanium dioxide] were present in solutions. The system has a complex multicomponent composition, the properties of its constituent elements are strongly different, and it has been poorly studied. All these factors predetermine the complexity and great number of different processes in the scheme to be used for utilization of these solutions, the more so as one of important tasks was to minimize the mass of radioactive products to be disposed of. The solutions

1070-4272/04/7705-0711 © 2004 MAIK "Nauka/Interperiodica"

Table 1. Extraction of thorium with HDEHP at $V_o : V_a = 1 : 1$

Run no.	Composition of the starting solution, g l^{-1}						Extracting agent	Degree of recovery, %			
	HCl	$CaCl_2$	ThO_2	Ln_2O_3	Fe_2O_3	TiO_2		Th(IV)	Ln(III)	Fe(III)	Ti(IV)
1*	pH 0.4	127	0.19	7.5	7.8	0.04	40 vol % HDEHP in OCL	98.9	81.0	–	–
2*	pH 0.4	72	0.10	4.6	5.5	0.4	40 vol % HDEHP in RED-1	95.3	26.9	84.7	99.6
3	73	418	0.60	24.7	28.3	0.08	″	93.0	1.7	60.3	99.0
4	179	129	0.19	8.0	7.5	9.7	″	90.5	1.5	59.9	≥99.9

* Composition of solution after neutralization with NaOH.

Table 2. Extraction of thorium(IV) with OCL

Composition of the initial solution, g l^{-1}						$V_o : V_a$	Degree of recovery, %				
HCl	$CaCl_2$	ThO_2	Ln_2O_3	Fe_2O_3	TiO_2		HCl	Th(IV)	Ln(III)	Fe(III)	Ti(IV)
180	127	0.16	8.0	8.6	5.2	1 : 1	31	<1	<0.1	91.6	12
152	334	0.48	19.8	20.6	0.1	(4–6) : 1	~85	<1	<0.1	–	–
73–109	380–418	0.54–0.60	22–25	26–28	~0.1	(1–1.8) : 1	–	<1	<0.1	79.8–85.5	42–52
106–178	254–317	0.38–0.48	19–24	19–24	1.4–1.7	(2.6–5.3) : 1*	36–65**	≤2	≤1	–	–
98	376	0.54	22.2	17.8	~0.1	0.3 : 1***	–	–	–	83.0	–
98	376	0.54	22.2	17.8	~0.1	0.7 : 1***	–	–	–	98.4	–

* Extraction with OCL containing 153 g l^{-1} of HCl.
** With account of HCl input with OCL.
*** Preliminarily, Fe(II) was oxidized to Fe(III) by addition of H_2O_2.

used in the experiments were either taken immediately after the precipitation of Ti(IV), Nb(V), and Ta(V), or (for the most part) after their evaporation to $CaCl_2$ content of 300 g l^{-1} and more. The evaporation was carried out in order to diminish the process flows, to regenerate HCl [5], which is recycled into the perovskite breakdown stage, and to improve the extraction of Th(IV) and some other components [6].

The distribution of Th(IV) and Ln(III) was monitored by chemical analysis: the sum Th(IV) + Ln(III) was isolated and Th(IV) was determined photometrically; Fe(III) was determined by atomic absorption spectroscopy, and Ca(II), by flame photometry; also, emission spectral, X-ray fluorescence, and X-ray phase analyses were employed. The error in determining the concentrations of the components did not exceed 3–7%, depending on an analytical technique, a chemical element to be determined, and (primarily) the content of this element.

The main method used for recovery of Th(IV) is extraction. As extracting agents we used di-2-ethylhexyl hydrogen phosphate (HDEHP) manufactured by Bayer (content of the main product >98%), octanol (OCL, content of the main product ~98%), and tributyl phosphate (TBP) of pure grade, the diluent was RED-1 (paraffin hydrocarbons C_{12}–C_{16}). The extraction was performed at room temperature (18±2°C); the solutions were kept before extraction (in the case when reagents were introduced into the solutions in order to vary their composition) for no less than 24 h. The extraction time was 10 min. When the precipitation technique was used, neutralization was performed with lime milk containing 20 wt % CaO (CaO containing no less than 97.5 wt % main component was used) or with a solution of 300 g l^{-1} NaOH of pure grade; the pH values were monitored with a standard I-120.2 ion meter with an ESL-45-07 electrode.

Tables 1–3 list the main experimental results obtained in studying the extraction of Th(IV) and concomitant components ($V_o : V_a$ is the ratio of the organic and aqueous phases before extraction). With HDEHP, good results were obtained in recovery of all the components under study; Th(IV), Fe(III), and Ti(IV) could be extracted in a wide range of acidities of the system. Nevertheless, the most complete transfer of the components into the organic phase is ob-

Table 3. Extraction of thorium(IV) with TBP. Solution composition, g l^{-1}: 106 HCl, 317 $CaCl_2$, 0.48 ThO_2, 23.7 Ln_2O_3, 24.0 Fe_2O_3, and 1.7 TiO_2

Run no.	α*	Content in solution fed to extraction, g l^{-1}		$V_o : V_a$	Degree of recovery, %**	
		HCl	$CaCl_2$		HCl***	Th(IV)
1	1.5	226	211	1 : 1	49	59.5
2	2.0	286	158	1 : 1	44	64.9
3	3.0	347	106	1 : 1	43	70.6
4	1	106	317	1.3 : 1****	49	70.4
5	1	106	317	1.9 : 1****	53	73.4
6	1.5	226	211	1.3 : 1****	–	73.2
7	1.5	226	211	1.9 : 1****	47	79.6
8	2.0	286	158	1.3 : 1****	38	76.8
9	2.0	286	158	1.9 : 1****	44	80.8
10	1	106	317	1 : 1	74	85.8
11	1	106	317	3 : 1	84	92.7

* Degree of dilution of the starting solution by adding concentrated HCl (467 g l^{-1} of HCl).
** Extraction with TBP containing 147 g l^{-1} of HCl.
*** Taking into account income of HCl with TBP.
**** Degree of recovery of other elements: Ln(III) ≤10%, Fe(III) >90%, and Ti(IV) about 50%.

served at a low content of HCl, especially for Ln(III). It should also be noted that replacing RED-1 with OCL improves the recovery of Th(IV) and (strongly) Ln(III). However, a disadvantage of HDEHP as an extracting agent is the low selectivity and poor phase separation in the system under study. Moreover, rare-earth elements are easily backwashed from HDEHPA with solutions of acids, whereas backwashing of Th(IV) and Ti(IV) requires use of fluoride or alkaline solutions, which leads to precipitation and gives rise to additional technological problems. Therefore, main attention was focused on neutral organic solvents, OCL and TBP. In the case of extraction with these solvents from the chloride system under study, the distribution of elements is the most strongly affected by changes in the concentrations of HCl and $CaCl_2$ [6].

The use of OCL as an extracting agent for recovery of Th(IV) was found to be inefficient (Table 2): in a wide range of HCl and $CaCl_2$ concentrations and $V_o : V_a$ ratios (including the case when HCl-containing OCL was used), the transfer of Th(IV) into the organic phase did not exceed 2%, presumably as a result of the low basicity of OCL and competition with HCl, which is well extractable with alcohols [7]. However, OCL selectively extracts Fe(III), which was used for its extraction from process solutions in order to simplify their utilization and to diminish the mass of subsequently recovered radioactive precipitates to be disposed of. Preliminary studies demonstrated the possibility of virtually complete extraction of Fe(III) with OCL under conditions of a continuous counterflow process at $V_o : V_a \approx 0.3 : 1$. It should be noted that up to 20 wt % of Fe is present in solutions as Fe(II). Since Fe(II) is not extracted in the system chosen [6], it is necessary to oxidize Fe(II) to Fe(III), e.g., by adding a minor amount of H_2O_2. After washing [mostly performed to remove Ti(IV) and trace amounts of Th(IV)] and back extraction with water ($V_o : V_a$ of 10 : 1 and 3 : 1, respectively), a high-quality concentrate of Fe(III) can be isolated. Further processing of this concentrate by the technique described in [8] yields high-purity compounds of Fe(III), which are used, e.g., in battery industry and for obtaining various types of ferrites [8].

The extraction of Th(IV) with TBP was analyzed in detail. Preliminary studies demonstrated that the transfer of Th(IV) into the organic phase was in the range 40–62% in the case of extraction of Th(IV) from a solution containing 182 g l^{-1} of HCl and 125 g l^{-1} of $CaCl_2$ (the content of other components is give above) immediately after the precipitation of Ti(IV), Nb(V), and Ta(V). This was done in a wide range of concentrations of HCl (182–372 g l^{-1}; concentrated HCl was added to the solution) and $CaCl_2$ (42–125 g l^{-1}; the content of $CaCl_2$ was varied on adding HCl) and varied $V_o : V_a$ ratios [(1–2) : 2; including the case when HCl-containing TBP was used]. The highest degree of Th(IV) extraction was 62% at $V_o : V_a$ = 1 : 1 and a threefold dilution of the solution of con-

centrated HCl to a concentration of 372 g l^{-1} of HCl. These parameters are insufficient for complete recovery of Th(IV) under conditions of an industrial counterflow extraction.

Good results were obtained in extraction of Th(IV) from solutions evaporated to $CaCl_2$ content exceeding 300 g l^{-1} (Table 3). Addition of concentrated HCl to an evaporated solution (run nos. 1–3) made it possible to raise the recovery of Th(IV) in a single stage to 70.6%, despite the decrease in the concentration of $CaCl_2$. Additional "saturation" of the system with HCl because of the use of HCl-containing TBP leads to a further rise in the degree of Th(IV) transfer into the organic phase to 80.8% (run nos. 4–9).

However, the introduction of considerable amounts of HCl into the system has an important disadvantage: HCl itself is rather well extracted with TBP (Table 3) [6], so that the acid binds the extracting agent and successfully competes with Th(IV). This approach, i.e., addition of HCl, can be considered to a certain extent acceptable (or, rather, forced) for systems that contain virtually only HCl, e.g., in processing of solutions in the hydrochloric acid technology of loparite. In the system under study, which contains $CaCl_2$ in high concentrations, it is more appropriate (and more advantageous economically) to extract Th(IV) from solutions with the highest possible (because of the preliminary evaporation) content of $CaCl_2$ (run nos. 10, 11). Even at $V_o : V_a = 1 : 1$, the recovery of Th(IV) is 85.8%, which makes it possible to virtually quantitatively recover Th(IV) from process solutions under the conditions of counterflow extraction. It would be expected that further evaporation of the solutions to a $CaCl_2$ content of, e.g., 450 g l^{-1} will create conditions for even more complete passing of Th(IV) into the extract, with the $V_o : V_a$ ratio simultaneously decreased to less than 1 : 1.

The study also demonstrated that extraction of Th(IV) under the conditions determined, with the subsequent scrubbing and backwashing with water, can be used to obtain a concentrate with the Th(IV) content of up to 10 wt %. Since U(VI) present in a minor amount in perovskite is recovered with TBP from hydrochloric acid solutions better than Th(IV) [6, 9, 10], it passes into the concentrate together with Th(IV). Scrubbing of the Th(IV) extract is necessary for separating such impurities as Ca(II), Ln(III), Ti(IV), Mn(II), etc., because, without scrubbing, the content of oxides of these impurities in the concentrate may be as high as >20, >25, 10–20, and 5–10 wt %, respectively.

Additional purification of Th(IV) to remove impurities can be performed by partial neutralization of its backwash. It is known that the pH of precipitation of element hydroxides strongly depends on the composition of a particular solution and on the type of a precipitating agent. It can be considered that, in the system under study, Ti(IV), Fe(III), Th(IV), U(IV), and U(VI) are completely or fairly completely precipitated at pH 5–6; Ln(III) and Fe(II), at pH ~9; and Mn(II), at pH ~10 [9–13]. Since Fe(III) is readily removed by extraction with OCL before recovery of Th(IV) with TBP, it would be expected that neutralization of the Th(IV) backwash to pH 5–6 will create conditions for the maximum possible purification of Th(IV) to remove Ln(III), Mn(II), and Ca(II), with the content of Th(IV) in the concentrate markedly increasing to values considerably higher than 10 wt %.

The results obtained in this study and published data [1–14] suggest the following scheme for utilization of solutions formed in breakdown of perovskite with hydrochloric acid and precipitation of Ti(IV), Nb(V), and Ta(V), with a Th(IV) concentrate produced: (1) evaporation of a solution (with distillation of HCl) to a $CaCl_2$ content exceeding 300 g l^{-1}; (2) extraction of Fe(III) with OCL, with preliminary oxidation of Fe(II) to Fe(III); (3) extraction of Th(IV) to give its concentrate containing 10 wt % ThO_2 and more [U(VI) is recovered together with Th(IV)]; (4) coprecipitation of Ra(II) on $BaSO_4$; (5) neutralization of the resulting solution to pH 5–6 with the formation of a precipitate that contains mostly Ti(IV); this precipitate is recycled into the stage of perovskite breakdown with hydrochloric acid; (6) neutralization of the solution to pH ~9 to give a commercial product, concentrate of rare-earth elements(III) (with Ln_2O_3 content of up to 90 wt %), which is processed further using the known procedures [1–3, 7].

It should be noted that it is preferable to recover Th(IV) and U(VI) by extraction, rather than by precipitation, since neutralization of solutions may yield soluble carbonate complexes [9, 10, 13] (because of the absorption of atmospheric CO_2), with the resulting distribution of radionuclides over the flowsheet and radioactive contamination of the concentrate of rare-earth elements(III).

According to preliminary data, the recovery of Th(IV) and Ln(III) into the corresponding concentrates exceeds 99%. The $CaCl_2$ solution obtained by neutralization is utilized by its evaporation to dry $CaCl_2$ or processed into gypsum (by addition of H_2SO_4 with evaporation of HCl) [3]. Calcium chloride is widely used as, e.g., a de-icing salt for roads

or a component of drilling muds in petroleum production; gypsum can be potentially used for manufacture of cement clinker and other building materials [1, 3].

The scheme described can be used with minor modifications to recover Th(IV) and Ln(III) in the hydrochloric acid technology of another rare-earth titanoniobate, loparite [15], mainly in utilization of solutions formed in nitric acid breakdown of perovskite and loparite, and also to process other kinds of rare-earth raw materials containing radionuclides.

CONCLUSIONS

(1) The conditions were studied under which thorium(IV) and other valuable components are recovered from hydrochloric acid solutions formed in breakdown of perovskite, after hydrolytic precipitation of titanium(IV), niobium(V), and tantalum(V).

(2) A flowsheet for utilization of hydrochloric acid solutions to give concentrates of thorium(IV), iron(III), and rare-earth elements(III) was suggested.

ACKNOWLEDGMENTS

The study was supported by the Russian Foundation for Basic Research (project no. 03-03-96148).

REFERENCES

1. Nikolaev, A.I., *Pererabotka netraditsionnogo titanovogo syr'ya Kol'skogo poluostrova* (Processing of Unconventuional Titanium Raw Materials from the Kola Peninsula), Apatity: Kol'sk. Nauchn. Tsentr Ross. Akad. Nauk, 1991.
2. Kalinnikov, V.T., Nikolaev, A.I., and Zakharov, V.I., *Gidrometallurgicheskaya kompleksnaya pererabotka netraditsionnogo titano-redkometall'nogo i alyumosilikatnogo syr'ya* (Hydrometallurgical Integrated Processing of Unconventional Titanium–Rare-Earth and Aluminosilicate Raw Materials), Apatity: Kol'sk. Nauchn. Tsentr Ross. Akad. Nauk, 1999.
3. Nikolaev, A.I., Gerasimova, L.G., Lukhton, M.M., *et al.*, *Fundamental'nye problemy kompleksnogo ispol'zovaniya prirodnogo i tekhnogennogo syr'ya Barentseva regiona v tekhnologii stroitel'nykh materialov: Materialy Mezhdunarodnoi nauchnoi konferentsii, Apatity, 1–4 aprelya 2003 g.* (Fundamental Problems of Integrated Use of Natural and Techological Raw Materials of the Barents Sea Region in Technology of Building Materials: Proc. Int. Scientific Conf., Apatity, April 1–4, 2003), Apatity: Kol'sk. Nauchn. Tsentr Ross. Akad. Nauk, 2003, pp. 62–64.
4. Kotova, V.M., *Strategiya ispol'zovaniya i razvitiya mineral'no-syr'evoi bazy redkikh metallov Rossii v XXI veke* (The Strategy of Use and Development of Mineral Resources of Rare Metals in Russia in the XXI Century), Moscow: VIMS, 2000, vol. 1, pp. 91–99.
5. Sklokin, L.I., Muzhdabaeva, M.A., Prokof'eva, T.A., *et al.*, *Novye protsessy v metallurgii tsvetnykh, redkikh i blagorodnykh metallov* (New Processes in Metallurgy of Nonferrous, Rare, and Noble Metals), Apatity: Kol'sk. Nauchn. Tsentr Ross. Akad. Nauk, 2001, pp. 153–157.
6. Zolotov, Yu.A., Iofa, B.Z., and Chuchalin, L.K., *Ekstraktsiya galogenidnykh kompleksov metallov* (Extraction of Metal Halide Complexes), Moscow: Nauka, 1973.
7. Lebedev, V.N., Asseretskova, O.V., and Smirnova, I.P., in *Khimiya i tekhnologiya mineral'nogo syr'ya Kol'skogo poluostrova* (Chemistry and Technology of Mineral Raw Materials of the Kola Peninsula), St. Petersburg: Nauka, 1992, pp. 54–60.
8. Kopkova, E.K. and Sklokin, L.I., *Khim. Tekhnol.*, 2001, no. 11, pp. 20–26.
9. Ryabchikov, D.I. and Gol'braikh, E.K., *Analiticheskaya khimiya toriya* (Analytical Chemistry of Thorium), Moscow: Akad. Nauk SSSR, 1960.
10. Markov, V.K., Vernyi, E.A., Vinogradov, A.V., *et al.*, *Uran: Metody ego opredeleniya* (Uranium: Methods of Determination), Moscow: Atomizdat, 1964.
11. Ryabchikov, D.I. and Ryabukhin, V.A., *Analiticheskaya khimiya redkozemel'nykh elementov i ittriya* (Analytical Chemistry of Rare-Earth Elements and Yttrium), Moscow: Nauka, 1966.
12. Svyatokhina, V.P., Isaeva, O.Yu., Pestrikov, S.V., *et al.*, *Zh. Prikl. Khim.*, 2003, vol. 76, no. 2, pp. 330–332.
13. Zemtsova, L.I., Stepanova, N.A., Zheleznova, E.I., *et al.*, *Opredelenie redkikh i radioaktivnykh elementov v mineral'nom syr'e* (Determination of Rare and Radioactive Elements in Mineral Raw Materials), Moscow: Nedra, 1983.
14. Vdovenko, V.M. and Dubasov, Yu.V., *Analiticheskaya khimiya radiya* (Analytical Chemistry of Radium), Leningrad: Nauka, 1973.
15. Kasikova, N.I., Petrov, V.B., Kasikov, A.G., *et al.*, in *Nauchnye doklady VII Mezhdunarodnoi konferentsii "Ekologiya i razvitie Severo-Zapada Rossii", 2–7 avgusta 2002 g.* (Proc. VII Int. Conf. "Ecology and Development of Northwestern Russia," August 2–7, 2002), St. Petersburg: Mezhdunar. Akad. Nauk Ekologii, Bezopasnosti Cheloveka i Prirody (MANEB), 2002, pp. 275–279.

Russian Journal of Applied Chemistry, Vol. 77, No. 5, 2004, pp. 716–720. Translated from Zhurnal Prikladnoi Khimii, Vol. 77, No. 5, 2004, pp. 720–724.

INORGANIC SYNTHESIS AND INDUSTRIAL INORGANIC CHEMISTRY

New Sensory Materials Based on Chalcogenide Glasses Containing Zinc, Cadmium, and Manganese Sulfides

K. A. Legin, A. M. Bolotov, A. V. Legin, and Yu. G. Vlasov

St. Petersburg State University, St. Petersburg, Russia

Received April 12, 2004

Abstract—New chalcogenide glasses of the system $0.5AgI–(0.5 – x)Sb_2S_{3-x}MS$ containing cadmium, manganese, and zinc sulfides were obtained. The high purity of these materials and their glassy state were proved by X-ray analysis and X-ray fluorescence energy-dispersive spectroscopy. The impedance of the glasses obtained was measured within a wide range of frequencies, and the dependences of the conductivity on the composition of glasses were studied. New potentiometric sensors based the new glasses were developed, and an electrochemical experiment was carried out.

Glassy materials have a number of important advantages when used as chemical sensors [1, 2], in particular, high chemical stability in a number of liquid media and increased sensitivity and selectivity. Furthermore, modification of the glass composition allows their properties to be controlled within wide limits. The development of potentiometric sensors based on glassy systems and sensitive to inorganic ions is an urgent problem. Incorporation of transition metal chalcogenides in various glassy matrixes strongly affects the transport properties, e.g., conductivity parameters [3, 4], surface characteristics, and electrochemical behavior of new glasses [5, 6].

A wide region of glass formation is known to exist in the pseudobinary system $AgI–Sb_2S_3$ [7], and this chalcogenide system is mainly an ionic conductor with respect to silver. Furthermore, such glasses have a sufficiently "flexible" structure allowing their composition to be modified over a wide range, so that glassy materials considerably differing in their properties from the initial glasses can be prepared.

The aim of this work was to study glass formation in the system $0.5AgI–(0.5 – x)Sb_2S_{3-x}MS$ (MS = ZnS, CdS, and MnS), transport characteristics of these glasses, and also their electrochemical sensory properties in aqueous solutions of inorganic salts.

EXPERIMENTAL

The initial substances for the synthesis of glasses of the system $0.5AgI–(0.5 – x)Sb_2S_{3-x}MS$ were cadmium(II) sulfide (99.995%) and manganese(II) sulfide (99.9%) (Aldrich), analytical grade elemental sulfur and metal zinc (Merck), and also silver iodide and antimony sulfide, which were synthesized by standard techniques from chemically pure or ultrapure grade chemicals.

The glasses were synthesized by vacuum melting in quartz ampules evacuated to 0.01–0.1 Pa. The weight of samples for the synthesis was 3 g. The ampules were kept in a furnace at 900°C for a week with daily stirring of the melt, quenched by cooling from 900°C in water with ice, and then annealed for 24 h at 110°C. The amorphous structure of the glasses obtained was checked visually in the case of the compositions containing low amounts of ZnS, CdS, and MnS, and by X-ray phase analysis (XRPA) in the case of the compositions with the mole fraction of these sulfides exceeding 0.05.

To prepare samples for the X-ray phase analysis, they were polished to obtain pellets with the diameter not exceeding 10 mm and thickness, 2 mm. The glasses were washed with double-distilled water and spectroscopic-grade acetone. Samples were prepared just before taking X-ray diffraction patterns in order to prevent surface oxidation.

To control the glassy state, we used a Rigaku GeigerFlex–D/max–RC diffractometric system (Japan). A rotating cobalt anode (radiation wavelength λ = 1.789 Å) with a secondary monochromator on a diffracted beam served as an X-ray source. The current in the tube was 50 mA, and the accelerating voltage, 40 kV. The scanning rate was 1.5 deg min^{-1}, and the scanning step was 0.01°. The crystal phases

1070-4272/04/7705-0716 © 2004 MAIK "Nauka/Interperiodica"

were identified using the Powder Diffraction File, Alphabet Index of Inorganic Phases.

To check the presence of impurities in Sb_2S_3 and in $0.5AgI–0.5Sb_2S_3$ glasses, we analyzed them using X-ray fluorescence energy-dispersive spectroscopy. Weighed samples of Sb_2S_3 and of $0.5AgI–0.5Sb_2S_3$ glasses (2 g) were ground in an agate mortar and pressed in pellets on a boric acid support in a Herzog HTP-40 press. To take the spectra in air, we used a Tracor X-ray Spectrace-5000 X-ray fluorescent energy-dispersive spectrometer equipped with an X-ray tube with an Rh anode. The voltage across the tube was 30 kV, and the current in the tube, 0.10 mA.

Samples for the measurements were polished with an abrasive powder to obtain plane-parallel (with the accuracy of ±0.01 mm) plates 0.08–1.5 mm thick. We deposited contacts of the greatest possible diameter made from Sigma Carbon Paste (up to 40% of black lead in isopropanol + binding agent) on the parallel sides. The deposited contacts were dried for 0.5 h. The error of measuring the surface areas of the contacts did not exceed ±10%. Then the sample was clamped between two gold contacts and placed in a thermostat–cryostat cooled with liquid nitrogen, with a temperature control unit connected. The impedance was measured on alternating current using an Agilent Technologies 4285A LCR electrochemical measuring system controlled with a computer, which allowed us to obtain and accumulate all data in the digital form. The impedance spectra were taken in the temperature range 220–310 K and frequency range from 20 Hz to 1 MHz.

The charge-transfer activation energy E_a (eV), preexponential factor σ_0 (S cm^{-1} K), and also electrical conductivity at 25°C σ_{25} (S cm^{-1}) were calculated by the least-squares method from the dependence

$$\sigma T = \sigma_0 \exp[-E_a/(kT)]. \quad (1)$$

The choice of the calculation formula was determined by the fact that the glasses under study are mainly ionic conductors and the dependence of type (1) adequately describes their characteristics. The error in the determination of E_a was ±0.005 eV on the average, that of the preexponential factor, ±0.1–0.2 $\log\sigma_0$ units, and that of the conductivity at 25°C, ±0.06 $\log\sigma_{25}$ units.

The electrode properties of membranes for sensors with a solid contact were studied by measuring emf of the voltaic cell with transfer

Cu | Ag | AgCl, KCl_{sat} | Solution under study | Glass membrane | Ag | Solid contact | Cu.

For sensors with liquid contact, we used the cell

Cu | Ag | AgCl, KCl_{sat} | KNO_3, 0.1 M | Solution under study | Glass membrane | $AgNO_3$, 0.01 M | Ag | Cu.

An EVL 1M3 saturated silver chloride electrode served as a reference electrode. To measure pH of solutions, we used an ESL-43-07 glass electrode preliminarily calibrated with standard buffer solutions.

All measurements were carried out on a multichannel electronic digital voltmeter with a high input resistance (10^{12} Ω), with computer control and data collection. Standard solutions with the concentration of ions to be determined of 10^{-3} M and more were prepared by successive tenfold dilution of the initial 1 M solutions prepared gravimetrically. The dilution was carried out using a 0.1 M KNO_3 solution. Calibrating solutions were prepared directly before measurements in a Teflon measuring cell by adding fixed small volumes of standard solutions to 100 ml of a 0.1 M solution of a supporting electrolyte, potassium nitrate.

For all the experiments reported here, we have prepared and studied no less than three samples of each composition.

Repeated synthesis of compositions containing zinc, cadmium, and manganese sulfides has shown that the compositions with the mole fractions of ZnS, CdS, and MnS of 0.025, 0.05, and 0.1 had glassy appearance. At the mole fraction of the sulfides of 0.15, the samples are inhomogeneous, and at the mole fraction of zinc, cadmium, or manganese sulfide of 0.2, they apparently contain crystalline inclusions.

The results of the X-ray phase analysis of the glasses and the compositions of the crystallizing phases are given in Table 1. According to the X-ray data, the samples with the CdS mole fraction of 0.025, 0.05, and 0.1 and those with the MnS and ZnS mole fractions of 0.025 and 0.05 are X-ray amorphous.

Comparison of the crystal phases detected in non-X-ray-amrophous samples of all the systems under study shows that the main crystallizing phases are ZnS, CdS, and MnS, and also AgI. The crystallization of AgI at a metal sulfide concentration of 15 mol % and more is attributable to the fact that, when the sulfide of the second metal is introduced in significant amounts, the glass formation limit in the pseudobinary system $AgI–Sb_2S_3$ is approached (the limiting composition in this system is $0.66AgI–0.34Sb_2S_3$).

The analysis of Sb_2S_3 and $0.5AgI–0.5Sb_2S_3$ samples revealed the presence of Fe, Cu, and Ni impuri-

Table 1. Compositions of crystallizing phases as given by X-ray phase analysis

Metal sulfide, mole fraction	Crystallizing phase	
	main	other
ZnS:		
0.05	None	None
0.1	ZnS	ZnI_2, SbSI, AgI
0.15	ZnS	AgI
0.2	ZnS	AgI
MnS:		
0.05	None	None
0.1	None	None
0.15	AgI	SbSI, MnS, $AgSbS_2$
0.2	AgI	SbSI, MnS, $AgSbS_2$
CdS:		
0.05	None	None
0.1	None	None
0.15	AgI	None
0.2	AgI	CdS, $AgSbS_2$, SbSI, AgI(β), Ag_2CdI_4, CdI_2

Table 2. Conductivity at room temperature $\log\sigma_{25}$, conduction activation energy E_a, and preexponential factor $\log\sigma_0$ for the glasses under study

Metal sulfide, mole fraction	$\log\sigma_{25}$	E_a, eV	$\log\sigma_0$
ZnS:			
0.025	–4.29(7)	0.330(5)	3.7(8)
0.05	–4.30(5)	0.337(8)	3.8(1)
0.1	–4.15(8)	0.270(1)	2.8(1)
0.15	–3.97(6)	0.208(7)	1.9(1)
0.2	–4.68(7)	0.257(5)	1.9(1)
CdS:			
0.025	–4.39(3)	0.343(5)	3.8(9)
0.05	–4.75(7)	0.345(9)	3.5(1)
0.1	–4.58(4)	0.357(3)	3.9(6)
0.15	–4.41(5)	0.341(5)	3.8(9)
0.2	–4.63(3)	0.298(5)	2.7(8)
MnS:			
0.025	–4.48(7)	0.334(9)	3.6(1)
0.05	–4.29(7)	0.315(9)	3.4(1)
0.1	–4.01(8)	0.300(2)	3.4(2)
0.15	–3.90(1)	0.200(2)	1.9(2)
0.2	–4.10(1)	0.230(1)	1.9(2)

ties. Their amount is insignificant (no more than several ppm in total). Certain starting reagents, in particular antimony, seem to be the basic source of the impurities. Thus, the physical and chemical properties of the glasses described in this work are determined not by the presence of foreign elements and casual contaminants, but by specific features of structure and properties of the materials.

The results of studying conductivity of the glasses are given in Figs. 1–3 and Table 2. A typical impedance hodograph for the samples under study is shown in Fig. 1. The polarizing branch observed in the hodograph (Warburg's impedance) at low frequencies points to the presence of polarizing phenomena on the glass|graphite boundary and hence proves predominantly ionic character of conductivity in the glasses.

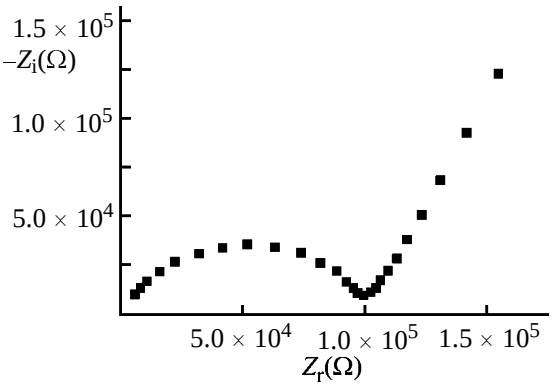

Fig. 1. Impedance hodograph for a sample of the composition $0.5AgI–0.475Sb_2S_3–0.025ZnS$.

The temperature dependences of the electrical conductivity for several glasses with the mole fraction of metal sulfides of 0.05 are given in Fig. 2. These dependences are adequately described by the Arrhenius equation of type (1) in the entire temperature range of the conductivity measurements.

The conductivity parameters of the alloys obtained are summarized in Table 2. The dependences of $\log\sigma_{25}$ on the content of the transition metal sulfide in all the three systems are presented in Fig. 3. The conductivity of glasses containing manganese, cadmium, or zinc sulfide is as high as approximately 10^{-4} S cm^{-1}, exceeding by almost two orders of magnitude that of the initial glass $0.5AgI–0.5Sb_2S_3$ [7]. When the mole fraction of a sulfide is increased to 0.1, the conductivity of the glasses at room temperature tends to increase (Fig. 3). This trend is the most pronounced in the case of the manganese-containing samples.

The preexponential factors and activation energies are virtually independent of the composition for the glassy materials (at the mole fraction of the sulfide in the systems with MnS and CdS of up to 0.1 and in the

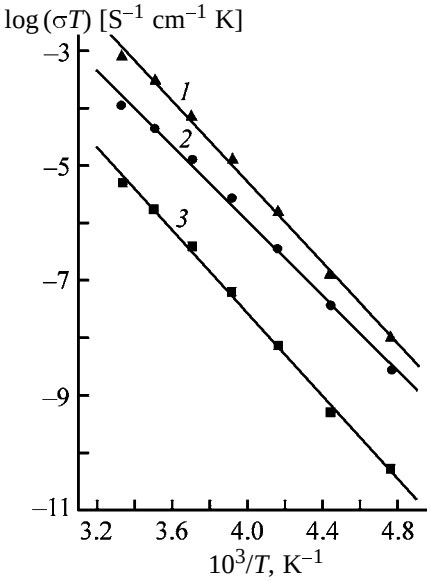

Fig. 2. Temperature dependence of the electrical conductivity σT for certain glasses of the system $0.5AgI–0.45Sb_2S_3–0.05MS$. (*1*) $0.5AgI–0.45Sb_2S_3–0.05ZnS$, (*2*) $0.5AgI–0.45Sb_2S_3–0.05MnS$, and (*3*) $0.5AgI–0.45Sb_2S_3–0.05CdS$.

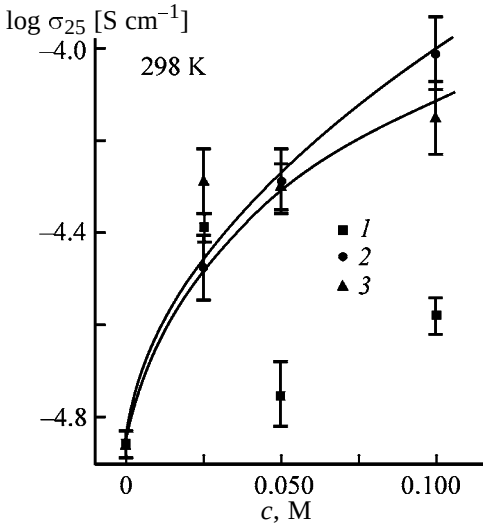

Fig. 3. Conductivity σ_{25} as a function of concentration c of a transition metal sulfide for glasses of various compositions: (*1*) $0.5AgI–(0.5 – x)Sb_2S_3–xCdS$, (*2*) $0.5AgI–(0.5 – x)Sb_2S_3–xMnS$, and (*3*) $0.5AgI–(0.5 – x)Sb_2S_3–xZnS$.

system with ZnS, up to 0.05). At the same time, it should be noted that, as compared to glassy materials, a decrease is observed in the activation energies (by up to 0.1 eV) and preexponential factors (by up to two orders of magnitude) of alloys containing a crystalline phase. This trend is especially pronounced in the case of the alloys containing ZnS and MnS, and is somewhat less pronounced in the cadmium-containing samples. A sharp reduction of E_a and $\log \sigma_0$ in comparison with homogeneous glasses is typical for inhomogeneous glasses and especially for glass–crystals [8], which is attributable to the appearance of additional paths of the facilitated charge transport along grain or phase boundaries.

We have carried out calibrating measurements with solutions of ammonium iodide NH_4I in the concentration range 10^{-6}–10^{-2} using potentiometric sensors manufactured from the glasses obtained. The results of these experiments for sensors of typical composition $0.5AgI–0.4Sb_2S_3–0.1MnS$ are given below:

Membrane	Slope, mV/pI	E^0, mV
I	–51.5 ± 1.4	–16.7 ± 5.6
II	–51.3 ± 1.6	–37.5 ± 2.4
III	–52.8 ± 1.1	–10.7 ± 2.6

The calibration plots are given in Fig. 4.

We have found that the sensors containing manganese sulfide have a good sensitivity to I^- anions with the anionic slope S = 50–57 mV/pI. The electrode functions for halide anions were observed previously only for crystalline sensors or glass–crystal compositions [1, 2]. The iodide function of a homogeneous glassy sensory material was observed here for the first time.

We also found that the sensitivity of chalcogenide glass sensors (the slope of the electrode function),

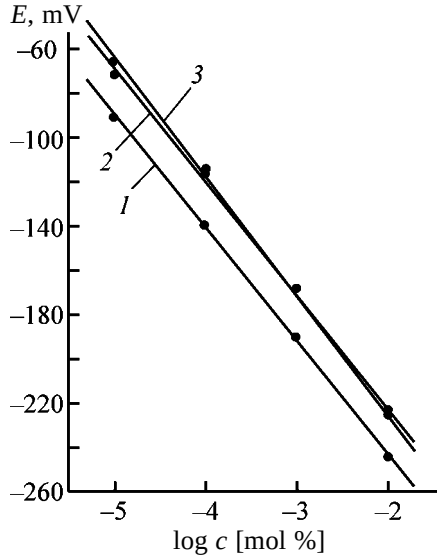

Fig. 4. Typical shape of the calibrating dependence of the sensor potential E on the concentration c of iodide ion in ammonium iodide solutions for potentiometric sensors of the composition $0.5AgI–0.4Sb_2S_3–0.1MnS$. Membrane: (*1*) I (S = –51.5 ± 2.1 mV), (*2*) II (S = –51.3 ± 0.9 mV), and (*3*) III (S = –52.8 ± 0.9 mV).

which was measured twice a day within a week, gradually decreased to S = 40–50 mV/pI. The standard potentials of the electrodes also changed to the side of more negative values as compared to the initial values.

The detection limit for each $0.5AgI–0.4Sb_2S_3–0.1MnS$ sensor was determined by a technique recommended by IUPAC. In this case, measurements were carried out in solutions with the concentrations from 10^{-8} to 10^{-4} M:

Membrane	Detection limit, M
I	8×10^{-7}
II	9×10^{-7}
III	8×10^{-7}

The results obtained show that the sensors containing manganese sulfide and manufactured from the glasses under study have a relatively low detection limit (on the average, 8.5×10^{-7} M).

We found in the course of the work that all the glasses under study containing sulfide of a second metal tend to cracking with time, practically irrespective of the glass composition. The cracking was observed visually after polishing of the glass surface. The glasses were stable during the synthesis and some time after it. Probably, the cracking occurred faster when the glasses were in contact with aqueous solutions. These phenomena could be due to sharp quenching of the glasses or insufficient annealing [9], which is proved by the fact that the mechanical instability of the glasses under study was manifested differently. Rather slow quenching of the glasses during synthsis and the subsequent annealing at temperatures close to T_g enhance their stability, but the causes of the observed cracking are not quite clear. The presence of internal stresses in the glasses obtained, which relax gradually, seems to be the most probable cause. Presumably, especially long and careful annealing is required for these compositions after the synthesis; however, we could not carry out it in this work because of time limitation.

CONCLUSIONS

(1) The study of the glass formation region in the systems $0.5AgI–(0.5 – x)Sb_2S_3–xMS$ (M = Zn, Cd and Mn) has shown that amorphous materials are obtained when the mole fraction of manganese, cadmium, or zinc sulfide is from 0 to 0.1.

(2) The conductivity parameters for all the compositions of the alloys were obtained by the electrochemical impedance spectroscopy, and it was found that introduction of the sulfide of the second transition metal into the glasses increases the conductivity to approximately 10^{-4} S cm^{-1}, which exceeds by two orders of magnitude the conductivity of the initial pseudobinary glass of the composition $0.5AgI–0.5Sb_2S_3$.

(3) The study of sensory characteristics of the synthesized materials in ammonium iodide solutions has shown that the sensors with glassy membranes of the composition $0.5AgI–0.4Sb_2S_3–0.1MnS$ have high sensitivity to iodide ions in aqueous solutions (electrode function slope 50–57 mV/pI) with the detection limit of 8.5×10^{-7} M.

ACKNOWLEDGMENTS

The authors are grateful to John Mortensen (Roskild University, Denmark) for the invaluable organizational help in carrying out the research. This work was financially supported in part by the Council of Ministers of Northern Countries (grant no. 2003-8003-2) and by Russian Foundation for Basic Research (project no. 02-03-32740).

REFERENCES

1. Vlasov, Yu.G., Bychkov, E.A., and Legin, A.V., *Talanta*, 1996, no. 6, pp. 1059–1093.
2. Vlasov, Yu.G. and Bychkov, E.A., *Ion-Selective Electrode Rev*., 1987, vol. 9, pp. 3–92.
3. Sokolov, I.A. and Borisova, Z.U., *Fiz. Khim. Stekla*, 1983, vol. 9, no. 6, pp. 80–83.
4. Vlasov, Yu.G. and Bychkov, E.A., *Solid State Ionics*, 1984, vol. 14, no. 4, pp. 329–335.
5. Borisova, Z.U., *Khal'kogenidnye poluprovodnikovye stekla* (Chalcogenide Semiconductor Glasses), Leningrad: Khimiya, 1983.
6. Myuller, R.L., *Elektroprovodnost' stekloobraznykh veshchestv* (Electrical Conductivity of Glassy Substances), Leningrad: Khimiya, 1968.
7. Daved, M.M., Ionic Processes and Short-Range Order in Sulfide Glasses Doped with Silver Halides, as Given by Radiochemical and Nuclear Spectroscopic Methods, *Cand. Sci. (Chem.) Dissertation*, St. Petersburg, 1992.
8. Kazakova, E.A., Study of Silver-Containing Chalcogenide Glasses, *Cand. Sci. (Chem.) Dissertation*, St. Petersburg, 1980.
9. Ingram, M.D., *J. Non-Cryst. Solids*, 1991, vols. 131–133, pp. 955–960.

Russian Journal of Applied Chemistry, Vol. 77, No. 5, 2004, pp. 721–724. Translated from Zhurnal Prikladnoi Khimii, Vol. 77, No. 5, 2004, pp. 725–728.

INORGANIC SYNTHESIS AND INDUSTRIAL INORGANIC CHEMISTRY

Effects of Potassium Polysilicates on Formation of Hydrogels from Stabilized Silica Sols

S. S. Airapetyan and A. G. Khachatryan

Yerevan State University, Yerevan, Armenia

Received June 27, 2003; in final form, February 2004

Abstract—The effect of introduction of potassium polysilicates with different SiO_2/K_2O ratios (silicate ratios *M*) on the rate of gelation of stabilized silica sols and on the quality parameters of the forming hydrogels was studied.

The problem of gelation of stabilized silica sols is a key issue as regards the formation of porous and other structural characteristics of porous silicas synthesized on their base. Such structural characteristics as the matrix rigidity, pore volume, and pore size distribution are formed in the sol–gel transition.

Occasionally, and in particular when obtaining microspherical silica gels, it is necessary to perform fast gelation. In this case, the high gelation rate is a decisive factor for preservation of the regular shape of the forming microspherical particles of a silica hydrogel. Fast gelation of water-soluble polysilicates (liquid glasses) is not unachievable. It occurs in their neutralization with various acids. However, it is difficult to achieve fast gelation of stabilized silica sols by neutralization, since the gelation processes that occur in this case may take a rather long time (5–6 days).

Fast gelation of stabilized silica sols can be achieved if the pH of the silica sol is preliminarily raised before the gelation. However, only raising the pH of the system fails to ensure fast formation of rigid homogeneous gels. As a rule, silica sols with increased pH yield in gelation inhomogeneous hydrogels or precipitates, i.e., more resemble hydrogels obtained from soluble polysilicates. Raising the pH value of a stabilized silica sol with, e.g., NaOH leads to precipitation of the silica sol before its gelation and fails to ensure the required concentration of the silicate fraction of silica because of the partial dissolution of colloid particles of silica sol. In fast gelation of silica sols to produce homogeneous rigid gels, the presence of such a silicate fraction becomes necessary, as demonstrated below.

Among alkali metal silicates, potassium silicates are the best compatible with stabilized silica sols: in contrast to sodium silicates, they do not cause precipitation of silica sols.

It is known [1, 2] that stable potassium polysilicates have a silicate ratio *M* 3–6 and 11–24. Potassium polysilicates can be obtained by addition of colloid silica to potassium silicate with a smaller silicate ratio (*M* = 3–4) under agitation and heating. As shown by electron microscopy, in synthesis of potassium polysilicates with silicate ratios *M* = 4–20, the particle size of the initial sol falls from 22 to 9–14 nm, which corresponds to a 4–12-fold decrease in the degree of polymerization. In addition, particles 1–7 nm in diameter were found in polysilicate solutions. For solutions with silicate ratios *M* = 4–40, the content of soluble silica is 20–50% of the total silica.

The problem of fast gelation is also associated with reinforcement of the structure of the forming gel, because addition of potassium polysilicate not only raises the pH of the system before its gelation, but also ensures the presence in the system of a reinforcing additive in the form of an active silica formed in gelation of potassium silicate. In the absence of such an additive of silicate origin, the gelation, as a rule, lasts for a considerably longer time (10–15 min), compared to the case when potassium silicate is present in the system (no more than 3 min). This indicates that active silica provides fast "setting" of colloid particles and leads to rapid structurization.

EXPERIMENTAL

As an object of study was used a stabilized silica sol obtained using the procedure described in [4], with

1070-4272/04/7705-0721 © 2004 MAIK "Nauka/Interperiodica"

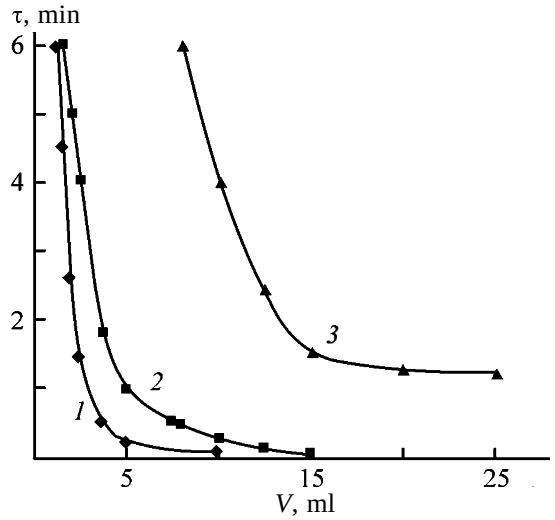

Fig. 1. Duration τ of gelation of stabilized silica sol vs. volume V of potassium polysilicate introduced. M = 15, V_{tot} = 100 ml. Content of SiO_2 in potassium polysilicate (wt %): (*1*) 30, (*2*) 15, and (*3*) 5.

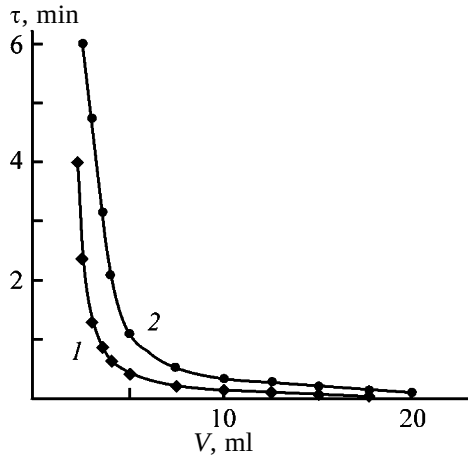

Fig. 2. Duration τ of gelation vs. volume V of potassium polysilicate introduced. M = 6.0, V_{tot} = 100 ml. Concentration of the gelling agent NH_4NO_3 (M): (*1*) 3.0 and (*2*) 1.5.

a particle size of 10 nm (as determined by the Sears method).

Potassium polysilicates with silicate ratios $M > 4$ were obtained from a potassium polysilicate with M = 4 by addition of polysilicic acid (PSA) synthesized according to [5]. The feeding rate of PSA was equal to the rate of moisture removal from the system. Potassium polysilicates with $M < 4$ (M = 3.2) were obtained by adding a certain amount of KOH to potassium polysilicate with M = 4.

Potassium polysilicate with the silicate ratio M = 4 was synthesized in a 1000-ml beaker. A 400-ml portion of distilled water was introduced into the beaker, and 42 g of KOH was dissolved in this water. Then, 100 g of silica gel was introduced in portions into the KOH solution at its boiling point under continuous agitation. The process was continued until silica gel completely dissolved, after which the heating was switched off, the system was allowed to cool under agitation, and the volume of the system was brought to 500 ml by adding distilled water.

As the gelling agent served NH_4NO_3 solution (1.5 or 3 M).

In all the experiments, a silica sol with a volume of 100 ml and concentration of 20 wt % (in terms of SiO_2) was used.

Figure 1 shows how the duration of gelation of a stabilized silica sol depends on the amount of potassium polysilicate with the silicate ratio M = 3.2, introduced into its composition. It can be seen that, as the amount of the potassium polysilicate introduced is increased, the gelation of the silica sol dramatically accelerates. The gelation duration mainly depends on the total amount of potassium polysilicate.

The table lists the basic parameters of the process in which hydrogel samples are prepared and the gelation duration τ. It is seen that, to obtain a rigid gel, the content of active silica (of silicate origin) in the system should exceed 3 wt %. In this case, the gelation duration does not exceed 1.5 min. The final content of silica sol (in terms of SiO_2) upon addition of the gelling agent is 14.5–19.0 wt %, which cannot affect the gelation processes. As a rule, low-strength hydrogels are obtained in systems that contain less than 2.5–3.0 wt % active silica, and the gelation takes a relatively long time.

Figure 2 shows how the duration of silica sol gelation depends on the amount of potassium polysilicate added (with the silicate ratio M = 6.0). It can be seen that, with more concentrated (3 M) NH_4NO_3 solutions used as gelling agents, the gelation is faster than with less concentrated (1.5 M) solutions. The gelation duration mainly depends on the total amount of the electrolyte in the system at the instant of gelation.

The table also shows that, if potassium silicate with M = 6.0 is used, high-strength gels start to form at its content in the silica sol as low as 5.9 wt % in terms of SiO_2.

As the silicate ratio of polysilicates increases (up to M = 15), the amount of colloidal silica, not involved in reinforcement of the hydrogel structure, grows. With increasing silicate ratio of potassium polysilicate, the minimum amount of polysilicate to be introduced to ensure the rigidity of the resulting hydrogel

Basic parameters of gelation of the system composed of silica sol and potassium polysilicate

Volume of potassium silicate, ml	Silica from potassium silicate, g	Total weight of silica, g	Fraction of silica from potassium silicate in total silica, wt %	Volume of NH_4NO_3 solution, ml		Concentration of gelling agent, M	τ, s	pH		Phase*
				1.5 M	3.0 M			pH_{in}	pH_{fin}	
Silicate ratio M = 3.2, 25 wt % in terms of SiO_2										
1.25	0.375	20.375	1.84	–	7.5	0.207	420	8.5	6.5	LSG
2.50	0.750	20.750	3.61	–	10.0	0.267	65	9.5	6.5	HHSG
3.75	1.125	21.125	5.32	–	12.5	0.323	30	10.0	7.0	HHSG
5.0	1.5	21.5	6.98	–	15.0	0.375	5	10.0	7.5	HHSG + A
10.0	3.0	23.0	13.04	–	25.0	0.556	0	11.0	7.5	HSG + A
2.5	0.375	20.375	1.84	–	7.5	0.328	95	10.0	7.0	HHSG + A
5.0	0.75	20.75	3.61	–	10.0	0.261	90	10.0	7.0	HHSG + A
7.5	1.125	21.125	5.32	–	12.5	0.312	30	10.0	7.5	HHSG
10.0	1.50	21.5	6.94	–	15.0	0.360	10	10.0	7.0	HHSG
15.0	2.25	22.25	10.11	–	20.0	0.444	0	10.0	6.5	HHSG
15.0	1.50	21.5	6.98	–	25.0	0.536	30	–	8.0	HHSG + A
15.0	1.50	21.5	6.98	–	30.0	0.621	25	–	8.0	HSG + A
7.5	0.30	20.3	1.48	12.5	–	0.156	480	10.0	7.0	LSG
10.0	0.40	20.4	1.96	15.0	–		240	10.0	7.0	HHSG
15.0	0.60	20.6	2.91	17.5	–		90	10.0	7.0	HHSG + A
25.0	1.0	21.0	4.76	20.0	–		75	10.0	7.5	HSG + A
Silicate ratio M = 6.0, 30 wt % in terms of SiO_2										
2.5	0.625	20.625	3.03	20.0	–	0.245	360	9.0	7.0	LSG
5.0	1.25	21.25	5.88	25.0	–	0.288	65	9.5	7.5	LSG
7.5	1.875	21.875	8.57	27.5	–	0.321	25	10.0	7.5	LSG
10.0	2.50	22.50	11.11	30.0	–	0.305	18	10.0	7.5	A
15.0	3.75	23.75	15.79	32.5	–	0.33	8	11.0	7.5	LSG
20.0	5.0	25.0	20.0	35.0	–	0.338	0	11.0	8.0	LSG
2.5	0.625	20.625	3.03	–	12.5	0.326	80	9.0	7.5	LSG
5.0	1.25	21.25	5.88	–	15.0	0.375	20	9.5	7.5	HHSG
7.5	1.875	21.875	8.57	–	15.0	0.367	15	10.0	7.5	HHSG
10.0	2.50	22.5	11.11	–	15.0	0.36	10	10.0	7.5	HHSG
10.0	3.75	23.75	15.79	–	20.0	0.444	0	11.0	7.5	HHSG
15.0	5.0	25.0	20.0	40.0	–		5	–	–	HHSG
20.0	5.0	25.0	20.0	40.0	–		0	–	–	HSG + A
20.0	5.0	25.0	20.0	–	15.0		0	–	–	HSG + A
20.0	5.0	25.0	20.0	–	30.0		5	–	–	Tendency toward A

* LSG, low-strength gel; HHSG, homogeneous high-strength gel; HSG, high-strength gel; and A, aggregation.

also grows. At M = 3.2, this amount does not exceed 3 wt %, whereas at M = 15 it exceeds 24 wt % in terms of SiO_2. This indicates that, to reinforce the gel structure by addition of active silica into the composition of silica sol before its gelation, it is the most appropriate to use as potassium polysilicates those with silicate ratios M = 4–10. As the silicate ratio increases, the amount of silica of nonsilicate nature grows, i.e., when colloid silica is dissolved to obtain potassium polysilicate with a higher silicate ratio, its particles do not dissolve completely. In all probability, silica of nonsilicate nature is not involved in reinforcement of the hydrogel structure. It may be assumed that soluble silica of silicate nature is the main agent for fast gelation and reinforcement of the hydrogel structure.

In these terms, the mechanism of fast gelation can be understood as follows: At high pH values, soluble silicas are not deposited onto the surface of colloid

particles of the sol; it is soluble silicas that primarily respond to a decrease in pH in gelation. In such a system, a gel network is rapidly formed between colloid particles and the number of contact points between separate particles of the colloid silica grows. This yields a rigid and elastic hydrogel. In the process, silica gels with more open structure are produced.

CONCLUSIONS

(1) Raising the silicate ratio of potassium polysilicates introduced into the composition of stabilized silica sols prior to their gelation leads to an increase in the amount of polysilicates necessary for strengthening of hydrogels in a comparatively short time.

(2) The gelation duration increases as the silicate ratio of the potassium polysilicates used is made higher.

(3) The primary role in the processes of strengthening and fast gelation is played by silica of silicate nature. With increasing silicate ratio, the silicate nature of potassium polysilicates becomes less pronounced and the content of colloid particles grows. These particles are not involved in fast gelation and strengthening of the hydrogel structure.

REFERENCES

1. Iler, R.K., *The Chemistry of Silica*, New York: Wiley–Interscience, 1979.
2. US Patent 4059658.
3. Poddubnyi, N.A., Synthesis of Low-Alkaline Binders Based on Water-Soluble Silicates, *Cand. Sci. Dissertation*, Leningrad, 1985.
4. USSR Inventor's Certificate no. 1174376.248.
5. US Patent 2244325.

Russian Journal of Applied Chemistry, Vol. 77, No. 5, 2004, pp. 725–728. Translated from Zhurnal Prikladnoi Khimii, Vol. 77, No. 5, 2004, pp. 729–732.

PHYSICOCHEMICAL STUDIES OF SYSTEMS AND PROCESSES

Activity of Components in the Surface Layer of Ternary Mutual Melts

B. V. Patrov

St. Petersburg State Polytechnic Institute, St. Petersburg, Russia

Received January 28, 2004

Abstract—The activity of components in the bulk and in the surface layer, considered as individual phase, was calculated from the experimental surface tension values and in terms of the model of regular solutions. The ternary mutual chloride–fluoride, chloride–carbonate, and fluoride–carbonate systems were examined.

Study of the surface tension in ternary mutual systems, which can be used in electroslag remelting as flux and for welding of nonferrous metals, is of practical and theoretical significance. Determination of the activity of melt components is very important for thermodynamic calculations of salt systems [1]. The model of regular solutions is the most commonly used in study of metallurgical systems.

Calculation of the component activity in the bulk of mutual melts from the experimental surface tension values was described previously [2]. For the exchange reaction MA + NB = NA + MB at $\Delta G_T^0 > 0$, the stable diagonal section is the melt MA–NB. The mole fractions x and $(1 - x)$ of MA and NB in the initial mixture become in equilibrium $(x - y)$ and $(1 - x - y)$, i.e, they decrease by the mole fraction y of the reaction products. In terms of the model of regular solutions [3, 4], one can write

$$\ln\gamma_1 = \frac{A}{RT}(1 - x - y)^2, \quad (1)$$

$$\ln\gamma_2 = \frac{A}{RT}(x - y)^2, \quad (2)$$

where γ_1 and γ_2 are the activity coefficients of components along stable diagonals MA and NB and A, the interaction parameter.

The interaction parameter A was determined from experimental data on surface tension described by the Burylev equation [5] for regular solutions:

$$\sigma = \sigma_1 x_1 + \sigma_2 x_2 + C x_1 x_2, \quad (3)$$

where x_1 and x_2 are the mole fractions of MA and NB components, and σ_1 and σ_2 are their surface tensions.

The constant C includes the ion-exchange energy [5] and is related to the interaction parameter A by

$$A = C\omega, \quad (4)$$

where ω is the molar surface area of the component:

$$\omega = V_{\text{mix}}^{2/3} N^{1/3}, \quad (5)$$

N is the Avogadro number, and V_{mix}, the molar volume of the mixture.

To a first approximation, V_{mix} was calculated from the additivity equation $V_{\text{mix}} = xV_{\text{MA}} + (1 - x)V_{\text{NB}}$, and in equilibrium it was calculated as

$$V_{\text{mix}} = xV_{\text{MA}} + (1 - x - y)V_{\text{NB}} + yV_{\text{NA}} + yV_{\text{MB}}.$$

The necessary data on the density of components in the exchange reaction were taken from a reference book [6].

Since the content of the components along unstable diagonal did not exceed 6 mol %, their activities a_{NA} and a_{MB} were accepted equal to mole fraction y. The mole fraction was derived from the equation for the equilibrium constant of the exchange reaction.

$$K_a = y^2(x - y)^{-1}\{\exp[A(1 - x - y)^2(RT)^{-1}]\}^{-1} \times (1 - x - y)^{-1}\{\exp[A(x - y)^2(RT)^{-1}]\}^{-1}. \quad (6)$$

Comparison of the component activities in LiF–NaCl and LiF–KCl systems, as calculated by Fellner method [4] and by the method proposed in [2], showed that the maximal difference between them is 0.008 at the mole fraction $x = 0.5$ and does not exceed 2%, i.e., the activities are the same. Consequently,

1070-4272/04/7705-0725 © 2004 MAIK "Nauka/Interperiodica"

the suggested method of calculating the component activity from data on surface tension furnishes reliable data for the ternary mutual systems.

The activities of components in the surface layer of the solutions were calculated by assuming equilibrium of the component in the surface layer of the solution and in its bulk [7].

$$\mu_i^\omega - \mu_i = \sigma\omega_i, \quad (7)$$

where μ_i^ω are the chemical potentials of the component in the surface layer of the solution and in its bulk, and ω_i is the molar surface area of the ith component.

For a binary solution at the equal molar surface areas,

$$\sigma = \sigma_1 + \frac{RT}{\omega}\ln(a_1^\omega/a_1) = \sigma_2 + \frac{RT}{\omega}\ln(a_2^\omega/a_2). \quad (8)$$

From this relationship, we can derive the component activities in the surface layer of mutual melts:

$$\ln a_1^\omega = \frac{\sigma - \sigma_1}{RT}\omega + \ln a_1, \quad (9)$$

$$\ln a_2^\omega = \frac{\sigma - \sigma_2}{RT}\omega + \ln a_2. \quad (10)$$

The component activities a_1 and a_2 of the systems studied are given in [8, 9]. The surface layer, as the melt bulk, was assumed to be a regular solution. For regular solutions, the activity coefficients of components along the stable diagonal in the surface layer were determined from the equations

$$\ln\gamma_1^\omega = A(a_2^\omega)^2[RT(\gamma_2^\omega)^2]^{-1}, \quad (11)$$

$$\gamma_2^\omega = \exp\{A(a_1^\omega)^2[RT(\gamma_1^\omega)^2]^{-1}\}. \quad (12)$$

where A is the interaction parameter.

After expression for the activity coefficient of the second component in the surface layer is substituted in Eq. (11), we obtain

$$\ln\gamma_1^\omega = \frac{A(a_2^\omega)^2}{RT\{\exp[A(a_1^\omega)^2(RT)^{-1}(\gamma_1^\omega)^{-2}]\}^2}. \quad (13)$$

Consequently, the activity coefficients of components along the stable diagonal in the surface layer can be calculated by Eqs. (13) and (12), and the mole fractions, by the equations

$$x_1^\omega = a_1^\omega/\gamma_1^\omega, \quad x_2^\omega = a_2^\omega/\gamma_2^\omega. \quad (14)$$

The chloride–fluoride systems Ba^{2+}, Na^+ // F^-, Cl^-, and Ba^{2+}, K^+ // F^-, Cl^- were studied first. The stable diagonal sections in these systems are the melts $BaF_2 \cdot BaCl_2$–Na_2Cl_2 and $BaF_2 \cdot BaCl_2$–K_2Cl_2 [10]. Their characteristics (Gibbs energy of exchange reaction, Burylev constant, molar surface area, and interaction parameter) are given below:

System	T, K	ΔG_T^0, J	$-C$, mJ m^{-2}	ω, m^2 mol^{-1}	$-A$, J mol^{-1}
$BaF_2 \cdot BaCl_2$–Na_2Cl_2	1273	47 250	43.4	195 200	8472
$BaF_2 \cdot BaCl_2$–K_2Cl_2	1273	95 240	91.6	219 340	20 092

For these systems, as for simpler chloride–fluoride melts [11], the change in the Gibbs energy is related to the surface activity of chlorides by the interaction parameter. The results of calculation of the component activities in the surface layer of the melts are presented in Table 1.

As seen, the activity of the first component, equimolar compound of barium fluoride and chloride, is considerably lower than its mole fraction in the surface layer. The activity of sodium and potassium chlorides was also less than the mole fraction at their content x_2 in the melt of up to 0.5 and equal to the mole fraction in the surface layer at higher concentrations: $a_2^\omega \sim x_2^\omega$.

The second group of mutual systems comprised chloride– and fluoride–carbonate melts Na_2CO_3–K_2Cl_2 and K_2CO_3–Na_2F_2 [12]. The Gibbs energy, Burylev constant, molar surface area, and the interaction parameter for the given systems are presented below:

System	T, K	ΔG_T^0, J	$-C$, mJ m^{-2}	ω, m^2 mol^{-1}	$-A$, J mol^{-1}
Na_2CO_3–K_2Cl_2	1123	31 300	131.6	153 265	20 170
K_2CO_3–Na_2F_2	1273	55 073	6.72	127 570	857

The second system in this group differs from the above chloride–fluoride melts by the second component, sodium fluoride, which is not surface-active in this system. The interaction parameter A = –857 J mol^{-1} was lower by an order of magnitude,

Table 1. Activity of components in the surface layer in the systems $BaF_2 \cdot BaCl_2(1)$–$Na_2Cl_2(2)$ and $BaF_2 \cdot BaCl_2(1)$–$K_2Cl_2(2)$ at 1273 K

x	a_1^ω	a_2^ω	γ_1^ω	γ_2^ω	x_1^ω	x_2^ω
			$BaF_2 \cdot BaCl_2$–Na_2Cl_2			
0.1	0.0121	0.9300	0.4999	0.9995	0.0242	0.9304
0.2	0.0323	0.8639	0.5490	0.9972	0.0588	0.8663
0.3	0.0619	0.7890	0.6048	0.9916	0.1023	0.7956
0.4	0.1043	0.7079	0.6641	0.9804	0.1571	0.7220
0.5	0.1634	0.6145	0.7298	0.9606	0.2239	0.6397
0.6	0.2453	0.5118	0.7972	0.9270	0.3077	0.5521
0.7	0.3568	0.3961	0.8654	0.8727	0.4123	0.4539
0.8	0.5077	0.2684	0.9288	0.7872	0.5466	0.3410
0.9	0.7129	0.1309	0.9786	0.6538	0.7285	0.2002
			$BaF_2 \cdot BaCl_2$–K_2Cl_2			
0.1	0.0038	0.8858	0.2251	0.9995	0.0169	0.8863
0.2	0.0109	0.7736	0.3201	0.9978	0.0341	0.7753
0.3	0.0235	0.6662	0.4283	0.9943	0.0549	0.6700
0.4	0.0451	0.5616	0.5449	0.9871	0.0828	0.5690
0.5	0.0834	0.4736	0.6441	0.9687	0.1295	0.4889
0.6	0.1400	0.3627	0.7663	0.9386	0.1827	0.3864
0.7	0.2353	0.2678	0.8544	0.8658	0.2754	0.3093
0.8	0.3855	0.1748	0.9222	0.7176	0.4180	0.2436
0.9	0.6253	0.0858	0.9695	0.4538	0.6450	0.1891

Table 2. Activity of components in the surface layer in the systems $Na_2CO_3(1)$–$K_2Cl_2(2)$ and $K_2CO_3(1)$–$Na_2F_2(2)$

x	a_1^ω	a_2^ω	γ_1^ω	γ_2^ω	x_1^ω	x_2^ω
			Na_2CO_3–K_2Cl_2, 1123 K			
0.1	0.0021	0.8643	0.1989	0.9998	0.0106	0.8645
0.2	0.0072	0.7481	0.2979	0.9987	0.0242	0.7490
0.3	0.0168	0.6417	0.4093	0.9964	0.0410	0.6440
0.4	0.0344	0.5387	0.5310	0.9910	0.0648	0.5436
0.5	0.0651	0.4395	0.6527	0.9787	0.0997	0.4491
0.6	0.1171	0.3406	0.7682	0.9510	0.1524	0.3581
0.7	0.2040	0.2441	0.8647	0.8867	0.2359	0.2753
0.8	0.3481	0.1521	0.9346	0.7409	0.3725	0.2053
0.9	0.5905	0.0680	0.9783	0.4550	0.6036	0.1495
			K_2CO_3–Na_2F_2, 1273 K			
0.1	0.0702	0.8139	0.9476	0.9996	0.1103	0.8143
0.2	0.1045	0.6830	0.9627	0.9990	0.2263	0.6837
0.3	0.2179	0.5647	0.9742	0.9960	0.3367	0.5670
0.4	0.3280	0.4573	0.9829	0.9910	0.4416	0.4614
0.5	0.4340	0.3593	0.9890	0.9845	0.5410	0.3649
0.6	0.5350	0.2705	0.9935	0.9768	0.6359	0.2769
0.7	0.6318	0.1897	0.9965	0.9680	0.7264	0.1960
0.8	0.7239	0.1168	0.9984	0.9583	0.8130	0.1219
0.9	0.8117	0.0519	0.9993	0.9480	0.8970	0.0547

compared to the chloride–fluoride and chloride–carbonate melts.

The results of calculation of the component activities in the surface layer of the second-group melts are presented in Table 2. As seen, in the Na_2CO_3–K_2Cl_2 system the activity of the first component, sodium carbonate, in the surface layer is also considerably lower than the mole fraction. As for the first-group melts, the activity of potassium chloride in the surface layer is virtually equal to the mole fraction at the chloride content x_2 more than 0.5.

Of interest are data on the activity, mole fraction, and the activity coefficient of components in the surface layer of the system K_2CO_3–Na_2F_2. The activity of the first component, potassium carbonate, and of the second component, sodium fluoride, is equal to the mole fraction: $a_1^\omega \sim x_1^\omega$, $a_2^\omega \sim x_2^\omega$. The coefficients of component activity are virtually equal to unity. This agrees with the above value of the interaction parameter.

Consequently, for surface-inactive components (sodium carbonate or equimolar compound of barium fluoride and chloride) in more complex chloride–fluoride and chloride–carbonate melts studied, the calculation equation (8) takes the form

$$\sigma = \sigma_1 + \frac{RT}{\omega}\ln(a_1^\omega/a_1). \quad (15)$$

For surface-active components (chlorides), the calculation equation is applicable in the narrower concentration range, $x_2 = 0.5$–1:

$$\sigma = \sigma_2 + \frac{RT}{\omega}\ln(x_2^\omega/a_2). \quad (16)$$

The surface tension of fluoride–carbonate mutual melts K_2CO_3–Na_2F_2 is described by the equations

$$\sigma = \sigma_1 + \frac{RT}{\omega}\ln(x_1^\omega/a_1), \quad \sigma = \sigma_2 + \frac{RT}{\omega}\ln(x_2^\omega/a_2). \quad (17)$$

CONCLUSIONS

The equations for calculating the surface tension of mutual chloride–fluoride, chloride–carbonate, and fluoride–carbonate melts were derived, depending on the content of chlorides, fluorides, and carbonates in the surface layer.

REFERENCES

1. Gorodyskii, A.V., *Termodinamicheskie svoistva rasplavov solevykh sistem: Spravochnoe posobie* (Thermodynamic Properties of Molten Salt Systems. Reference Guide), Kiev: Naukova Dumka, 1985.
2. Patrov, B.V., *Zh. Prikl. Khim.*, 1998, vol. 71, no. 3, pp. 507–508.
3. Hildebrand, J.H., *Solubility of Non-Electrolytes*, New York: Reinhold, 1936.
4. Fellner, P., *Chem. Zvesti*, 1983, vol. 37, pp. 603–607.
5. Burylev, B.P., and Vasil'ev, V.V., in *Fizicheskaya khimiya poverkhnostnykh yavlenii v rasplavakh* (Physical Chemistry of Surface Phenomena in Melts), Kiev: Naukova Dumka, 1971, pp. 144–149.
6. Morachevskii, A.G., *Spravochnik po rasplavlennym solyam* (Reference Book on Molten Salts), Leningrad: Khimiya, 1971.
7. Popel', S.I., *Poverkhnostnye yavleniya v rasplavakh* (Surface Phenomena in Melts), Moscow: Metallurgiya, 1994.
8. Patrov, B.V., *Zh. Prikl. Khim.*, 1998, vol. 71, no. 7, pp. 1206–1207.
9. Patrov, B.V., *Zh. Prikl. Khim.*, 2000, vol. 73, no. 2, pp. 326–328.
10. Posypaiko, V.I., and Alekseeva, E.A., *Diagrammy plavkosti solevykh sistem: Mnogokomponentnye sistemy* (Melting Diagrams for Salt Systems: Multicomponent Systems), Moscow: Khimiya, 1977.
11. Patrov, B.V., *Zh. Prikl. Khim.*, 2003, vol. 76, no. 5, pp. 738–741.
12. Posypaiko, V.I., and Alekseeva, E.A., *Diagrammy plavkosti solevykh sistem: Troinye vzaimnye sistemy* (Melting Diagrams for Salt Systems: Ternary Mutual Systems), Moscow: Khimiya, 1977.

Russian Journal of Applied Chemistry, Vol. 77, No. 5, 2004, pp. 729–731. Translated from Zhurnal Prikladnoi Khimii, Vol. 77, No. 5, 2004, pp. 733–735.

PHYSICOCHEMICAL STUDIES OF SYSTEMS AND PROCESSES

Phase Separation in Ternary Liquid Systems Tetradecane–*n*-Octanol (or *n*-Butanol)–Neodymium(III) Nitrate Solvate with Tri-*n*-Butyl Phosphate

A. K. Pyartman, A. V. Kudrova, and V. A. Keskinov

St. Petersburg State Technological Institute, St. Petersburg, Russia

Received April 17, 2003; in the final form, November 2003

Abstract—The phase diagrams of ternary liquid systems tetradecane–*n*-octanol (or *n*-butanol)–neodymium(III) nitrate solvates with tri-*n*-butyl phosphate [$Nd(NO_3)_3(TBP)_3$] at T = 298.15 K were studied. These diagrams contain the fields of homogeneous solutions and the field of separation into two liquid phases (I, II). The distribution of components between these phases is analyzed.

In this work we studied the phase diagrams of ternary liquid systems tetradecane-*n*-octanol (or butanol)–neodymium(III) nitrate solvates with tri-*n*-butyl phosphate in the field of phase separation.

In our experiments we used *n*-octanol (ρ = 0.8220 g cm^{-3}) and *n*-butanol (ρ = 0.8075 g cm^{-3}, T = 298.15 K). The solvate $Nd(NO_3)_3(TBP)_3$ was prepared by triple contact of TBP with saturated aqueous solutions of Ln(III) nitrates [1]. The solvate concentration in the organic phase was 1.12 M (ρ = 1.2755 ± 0.0012 g cm^{-3}). The binodal curves were obtained by the visual technique reported in [2].

The phase diagrams (Fig. 1) and the data listed in the table show that the components of the binary systems $Nd(NO_3)_3(TBP)_3$–*n*-$C_8H_{17}OH$ (*n*-C_4H_9OH) and *n*-$C_8H_{17}OH$–$C_{14}H_{30}$ have infinite mutual solubility. The $Nd(NO_3)_3(TBP)_3$–$C_{14}H_{30}$ mixtures separate into two liquid phases (I, II). Phases I and II are enriched in $C_{14}H_{30}$ and $Nd(NO_3)_3(TBP)_3$, respectively.

The phase diagrams of the systems $Nd(NO_3)_3 \cdot (TBP)_3$–*n*-$C_8H_{17}OH$ (*n*-C_4H_9OH)–$C_{14}H_{30}$ (Fig. 1) contain field *B* of homogeneous solutions and two-phase field *A*. These fields are separated by the binodal curves. Ternary mixtures related to field *A* separate into two liquid phases (I, II) like the binary system $Nd(NO_3)_3(TBP)_3$–$C_{14}H_{30}$. Phases I and II are enriched in $C_{14}H_{30}$ and $Nd(NO_3)_3(TBP)_3$, respectively. For all the systems, the critical point in the binodal curve (ω_2, crit) corresponds to a solution with approximately equal weight fraction of $Nd(NO_3)_3 \cdot (TBP)_3$ and $C_{14}H_{30}$ and different content of alcohol. As seen from table, in the critical point the $C_8H_{17}OH$ content somewhat exceeds the *n*-butanol content.

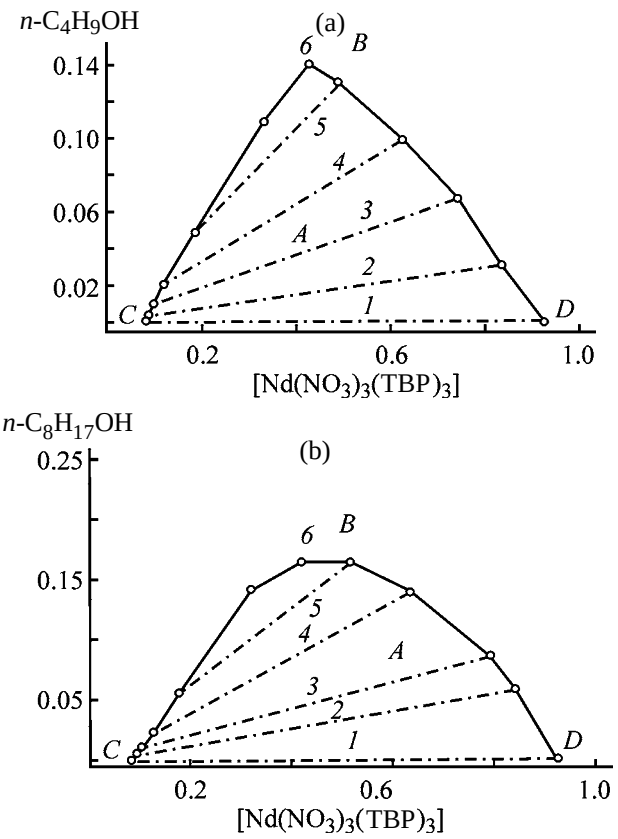

Fig. 1. Phase diagrams (weight fraction scale) of the ternary systems $Nd(NO_3)_3(TBP)_3$–*n*-$C_8H_{17}OH$ (*n*-C_4H_9OH)–$C_{14}H_{30}$ at T = 298.15 K. (*A*) Field of coexistence of two liquid phases, (*B*) field of homogeneous solutions, and (*CD*) binodal curve. (*1*–*5*) Nodes (see table); (*6*) point of the critical composition of the ternary system. Alcohol: (a) *n*-C_4H_9OH and (b) *n*-$C_8H_{17}OH$.

1070-4272/04/7705-0729 © 2004 MAIK "Nauka/Interperiodica"

Table 1. Compositions of coexisting phases in the ternary systems $Nd(NO_3)_3(TBP)_3$–*n*-$C_8H_{17}OH$ (C_4H_9OH)–*n*-$C_{14}H_{30}$ at T = 298.15 K

ρ, g cm^{-3}	$[Nd(NO_3)_3(TBP)_3]$	$C_{14}H_{30}$	Alcohol	Node no.
	weight fraction			
	n-C_4H_9OH			
0.7849	0.081	0.919	0	*1*
0.7870	0.087	0.909	0.004	*2*
0.7913	0.099	0.891	0.010	*3*
0.7993	0.121	0.858	0.021	*4*
0.8246	0.189	0.762	0.049	*5*
	0.335	0.541	0.109	
	0.430	0.430	0.140	*6*
0.9577	0.493	0.377	0.130	*5*
1.0261	0.628	0.274	0.098	*4*
1.0921	0.743	0.190	0.067	*3*
1.1508	0.836	0.133	0.031	*2*
1.2135	0.925	0.075	0	*1*
	n-$C_8H_{17}OH$			
0.7849	0.081	0.919	0	*1*
0.7891	0.092	0.901	0.007	*2*
0.7927	0.103	0.886	0.011	*3*
0.7984	0.118	0.840	0.042	*4*
0.8215	0.177	0.767	0.056	*5*
	0.317	0.540	0.143	
	0.417	0.417	0.166	*6*
0.9652	0.512	0.323	0.165	*5*
1.0508	0.630	0.230	0.140	*4*
1.1258	0.788	0.124	0.088	*3*
1.1846	0.839	0.101	0.060	*2*
1.2135	0.925	0.075	0	*1*

Figure 2 shows the distribution coefficient of $Nd(NO_3)_3(TBP)_3$ between phases I and II as a function of $Nd(NO_3)_3(TBP)_3$ weight fraction in phase II. As seen from these plots, with increasing $Nd(NO_3)_3 \cdot (TBP)_3$ concentration in phase II, the distribution coefficient decreases, i.e., $Nd(NO_3)_3(TBP)_3$ is accumulated in the phase II. This accumulation is virtually independent of the kind of alcohol.

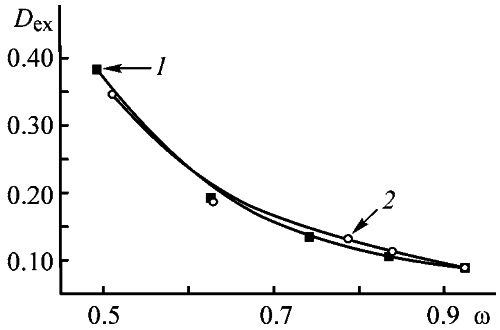

Fig. 2. Distribution coefficient D_{ex} of $Nd(NO_3)_3(TBP)_3$ between phases I and II as a function of the weight fraction ω of $Nd(NO_3)_3(TBP)_3$ in phase II. Alcohol: (*1*) *n*-C_4H_9OH and (*2*) *n*-$C_8H_{17}OH$; the same for Figs. 3 and 4.

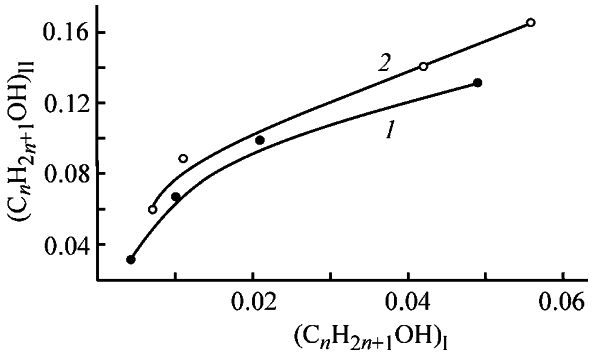

Fig. 3. Distribution of alcohols between phases II and I.

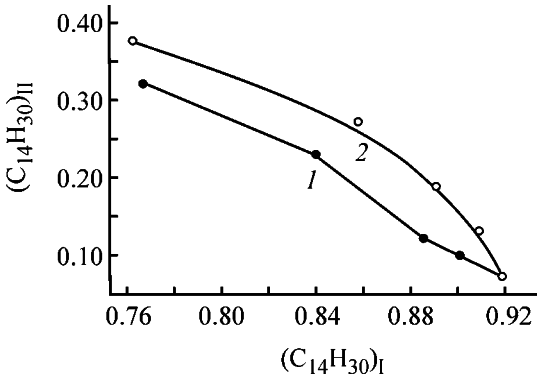

Fig. 4. Distribution of $C_{14}H_{30}$ between phases II and I.

Figure 3 shows the distribution of *n*-octanol (*n*-butanol) (weight fraction) between phases II and I. It is seen that the alcohols are predominantly concentrated in phase II and this tend is more pronounced for *n*-octanol.

Figure 4 shows the distribution of $C_{14}H_{30}$ (weight fraction) between phases II and I. It is seen that $C_{14}H_{30}$ is predominantly concentrated in phase I. The extent of enrichment of phase I with $C_{14}H_{30}$ is dependent on the kind of alcohol and is larger in the *n*-butanol-containing system.

Our results show that, in extraction of neodymium(III) nitrates with TBP in tetradecane–*n*-octanol (or *n*-butanol) mixture, the phase separation of the extracts saturated with neodymium(III) can be prevented if the weight fraction of *n*-octanol or *n*-butanol is no less than 0.15–0.17.

CONCLUSIONS

(1) The phase diagrams of the systems $Nd(NO_3)_3 \cdot (TBP)_3$–*n*-$C_8H_{17}OH$ (*n*-C_4H_9OH)–$C_{14}H_{30}$ contain the

field of homogeneous solutions and the two-phase field. Phases I and II are enriched in $C_{14}H_{30}$ and $Nd(NO_3)_3(TBP)_3$, respectively. The size of the two-phase field is dependent on the kind of alcohol; it somewhat decreases in going from *n*-octanol to *n*-butanol.

(2) In all the systems, the critical point in the binodal curve (ω_2, crit) corresponds to a solution with approximately equal weight fraction of $Nd(NO_3)_3 \cdot (TBP)_3$ and $C_{14}H_{30}$ and different content of alcohol. The *n*-$C_8H_{17}OH$ content in the critical point somewhat exceeds the *n*-butanol content.

(3) In phase separation, both $Nd(NO_3)_3(TBP)_3$ and *n*-octanol (*n*-butanol) are accumulated in phase II. The accumulation of $Nd(NO_3)_3(TBP)_3$ in phase II is virtually independent of the kind of alcohol. $C_{14}H_{30}$ is predominantly concentrated in phase I. This trend is more pronounced in the *n*-butanol-containing system.

(4) In extraction of neodymium(III) nitrates with *n*-TBP in tetradecane–*n*-octanol (*n*-butanol) mixture, the phase separation of the extracts saturated with neodymium(III) can be prevented if the weight fraction of *n*-octanol (*n*-butanol) in the extractant is no less than 0.15–0.17.

REFERENCES

1. Pyartman, A.K., Kopyrin, A.A., Puzikov, E.A., and Bogatov, K.B., *Radiokhimiya*, 1995, vol. 37, no. 1, pp. 52–55.
2. Pyartman, A.K, Kudrova, A.V., and Keskinov,V.A., *Zh. Prikl. Khim.*, 2004, vol. 77, no. 4, pp. 560–563.

Russian Journal of Applied Chemistry, Vol. 77, No. 5, 2004, pp. 732–735. Translated from Zhurnal Prikladnoi Khimii, Vol. 77, No. 5, 2004, pp. 736–739.

PHYSICOCHEMICAL STUDIES OF SYSTEMS AND PROCESSES

Dehydration Kinetics of Sodium Tetraborate Decahydrate

A. I. Sokol'skii, T. V. Basova, S. A. Sokol'skii, and V. Yu. Prokof'ev

Ivanov State University of Chemical Engineering, Ivanovo, Russia

Received April 3, 2003

Abstract—The kinetics of the dehydration of sodium tetraborate decahydrate was studied. The Topley–Smith effect was observed. The dehydration kinetics was described by an equation of contracting sphere. The mass conductivity coefficients were determined, and an empirical equation for calculating them is given.

In thermal decomposition of crystal hydrates, the dependence of the reaction rate on the water vapor pressure in the air supplied for the heat treatment is abnormal [1]. The influence exerted by the product phase on the water removal process is the important feature of the dehydration reaction. The abnormal behavior consists in that the thermal decomposition of crystal hydrates at pressures below equilibrium pressure decelerates with an increase in the deviation of the system from the equilibrium. This phenomenon is known as the Topley–Smith effect. The understanding of specific features of dehydration of crystal hydrates, sodium tetraborate decahydrate (STD) in particular, allows control of the process and preparation of the product of prescribed composition.

Sodium tetraborate decahydrate $Na_2B_4O_7 \cdot 10H_2O$ is obtained by crystallization from aqueous solution. Then, the powder is heat-treated in a heat carrier flow with formation of pentahydrate and anhydrous sodium tetraborate. In this case, it is necessary to obtain the resulting product containing either pentahydrate or anhydrous salt. When two forms of sodium tetraborate are present in the system, the powder tends to rapidly cake, and its consumers' properties get worse.

The kinetics of the topochemical reaction of thermal decomposition is described on the basis of combined solution of the kinetic equation and nonstationary mass-conductivity equation [2]. Thus, the thermal decomposition of dispersed materials in the region of diffusion-kinetic control is described within the nonstationary mass-conductivity boundary-value problem with an internal volume source of mass determined by the kinetics of chemical reaction. The mathematical description of the thermolysis of a spherical particle has the form

$$\frac{\partial c(r,\tau)}{\partial \tau} = k\left[\frac{\partial^2 c(r,\tau)}{\partial \tau^2} + \frac{2}{r}\frac{\partial c(r,\tau)}{\partial \tau}\right] + q, \qquad (1)$$

where c is the concentration of gaseous products (kg m^{-3}); r, particle radius (m); τ, time (s); q, internal volume source of mass (kg m^{-3} s); and k, the mass-conductivity coefficient (m^2 s^{-1}).

EXPERIMENTAL

Technical-grade sodium tetraborate is a white powder having, according to chemical analysis, the formula $Na_2B_4O_7 \cdot 10H_2O$. The dehydration was performed in a flow-through installation. The humidity and temperature of the heat carrier fed into the installation was maintained constant during one test. The flow rate of the heat carrier was chosen so as to eliminate external diffusion hindrance:

$$\mathrm{Bi} = \frac{\beta r}{k} \to \infty,$$

where Bi is the Biot criterion; β, mass-transfer coefficient (m s^{-1}); k, mass-conductivity coefficient (m^2 s^{-1}); and r, particle radius (m).

Fulfillment of this condition ensures constancy of the water vapor pressure over a sample during the whole test.

The change in the sample mass and the material temperature were recorded in the course of the experiment. The content of the main substance was calculated according to the reaction

$$Na_2B_4O_7 \cdot 10H_2O \to Na_2B_4O_7 + 10H_2O. \qquad (2)$$

Zonal method [3, 4] was used to calculate the mass-

conductivity coefficient by the equation

$$k = \frac{m_0[(\alpha_i)^{-1} - (\alpha_f)^{-1}]r}{F\Delta\tau\rho_v}, \quad (3)$$

where m_0 is the mass of the main substance, i.e. $Na_2B_4O_7$, in the weighed portion (kg); F, the surface area of particles of the sample (m^2); ρ_v, water vapor density (kg m^{-3}); α_i and α_f, initial and final contents of the main substance in the sample (%); and $\Delta\tau$, the time interval (s) in which the main substance content changes from α_i to α_f.

The partial water vapor pressure affects, according to the experimental data (Fig. 1), the content of the main product in the heat carrier depending on time. These dependences were obtained at a heat carrier temperature of 150°C and water vapor pressures of 10–20 and 145 mm Hg. Similar curves were also obtained for other temperatures. The rates of the $Na_2B_4O_7 \cdot 10H_2O$ dehydration as functions of water vapor pressure P_w are plotted in Fig. 2. As seen, with increasing water vapor pressure, the rate of reaction (2) first decreases, then increases, and after that passes a maximum at $P_w \cong 15$ mm Hg for all the temperatures. Thus, the Topley–Smith effect is clearly observed in thermolysis of sodium tetraborate decahydrate.

The kinetics of STD decomposition is most adequately described by a contracting volume equation whose integral form [1] is

$$k_0'\tau = 1 - (1 - \alpha)^{1/3}, \quad (4)$$

where k_0' is the rate constant (s^{-1}).

The values of the rate constant for different conditions are given in the table. The data obtained, when treated using the Arrhenius equation (Fig. 3), show that the pre-exponential factor k_0' and activation energy E as functions of water vapor pressure vary similarly with several extrema. The first and the second maxima in the curves correspond to the minimal and maximal dehydration rates, respectively. Thus, a decrease in k_0', rather than increase expected from Fig. 2, is observed for water vapor pressures above 18 mm Hg, with the minimal and maximal values differing by a factor of 3. An increase in the pre-exponential factor is compensated by the growth of the activation energy.

First of all, such phenomena are associated with thermodynamic properties, namely, with the ratio between the water vapor pressure in the heat carrier, its equilibrium pressure in reaction (2), and partial pressure of water vapor over the crystal hydrate.

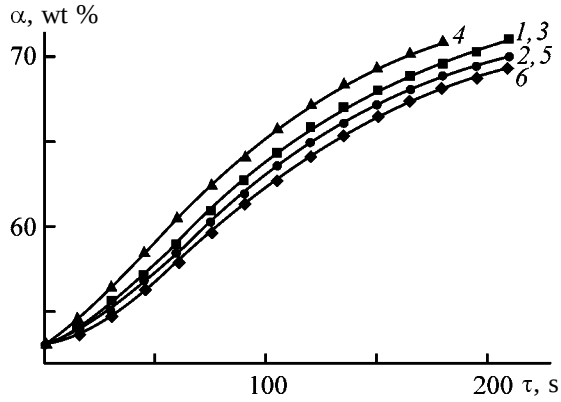

Fig. 1. Content of main substance, $Na_2B_4O_7$, α vs. time τ at 150°C. Partial water vapor pressure in air (mm Hg): (*1*) 10, (*2*) 11.36, (*3*) 13.97, (*4*) 15.26, (*5*) 18.04, and (*6*) 20.145.

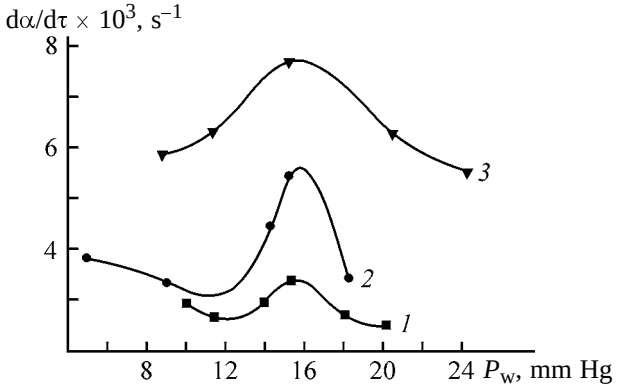

Fig. 2. Dehydration rate of sodium tetraborate decahydrate $d\alpha/d\tau$ vs. water vapor pressure P_w at various temperatures. Temperature (°C): (*1*) 150, (*2*) 200, and (*3*) 250.

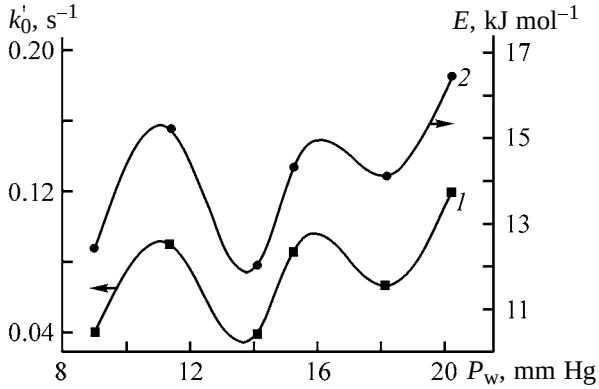

Fig. 3. Pre-exponential factor k_0' and activation energy E vs. water vapor pressure P_w. The parameters are calculated by Eq. (4).

The experimental data (Fig. 4) show that the dependences of the mass-conductivity coefficient k on the conversion α^* pass through a maximum at $\alpha \cong 0.2$, corresponding to the empirical formula $Na_2B_4O_7 \cdot$

Parameters of $Na_2B_4O_7 \cdot 10H_2O$ dehydration

Air temperature, °C	P_p, mm Hg	$k'_0 \times 10^3$, s^{-1}	Material temperature, °C	$k^* \times 10^6$, kg m^{-2} s^{-1}
150	10.00	1.31	99.0	48.4
	11.36	1.21	97.5	47.9
	13.97	1.31	99.0	48.4
	15.26	1.50	92.0	54.9
	18.04	1.21	93.5	47.9
	20.145	1.13	101.0	46.5
200	4.90	1.66	122.0	56.3
	9.00	1.48	113.0	53.5
	14.26	1.88	115.5	62.7
	15.26	2.27	109.5	76.0
	18.27	1.85	115.0	66.2
250	8.73	2.56	120.0	106.0
	11.38	2.76	134.0	98.0
	15.26	3.27	112.0	115.1
	20.42	2.76	134.0	98.0
	24.26	2.45	151.0	86.2

* The values are given at the conversion $\alpha^* = 0.2$.

$8H_2O$. Comparison of the above dependences with the character of variation of the material temperature t_m with conversion (Fig. 4) suggests that the increase in k at $\alpha^* < 0.2$ occurs in parallel with a considerable growth of the material temperature. Consequently, in this period, STD dehydration is accompanied by warming of the material.

With process at $\alpha^* > 0.2$ continued, k decreases gradually and the temperature of the powder grows insignificantly.

As noted above, the dehydration kinetics is described by an equation of contracting volume, i.e., the reaction starts from the outer layers of STD particles and then moves toward the grain centers. Evidently, a layer of the product impedes diffusion of water to the particle surface. As a result, the mass-conductivity coefficient decreases. It should also be noted that the mass-conductivity coefficients as functions of water vapor pressure in the heat carrier correlate with the corresponding rate constants calculated by Eq. (4).

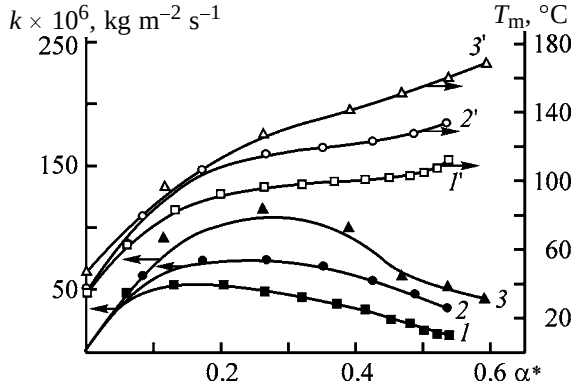

Fig. 4. Mass-conductivity coefficient k and the material temperature T_m vs. conversion α^* at the water vapor pressure of 15.26 mm Hg. Air temperature (°C): (*1*, *1'*) 150, (*2*, *2'*) 200, and (*3*, *3'*) 250.

A slight temperature growth at $\alpha^* > 0.2$, with an appreciable temperature gradient between the material and heat carrier preserved, is assigned to the fact that dehydration is an endothermic process, i.e., the heat supplied with a heat carrier is mainly spent for the chemical reaction.

The mass-conductivity coefficient is a function of many variables, with all these dependences having extrema (see table; Fig. 4). The noticeable effect on the mass-conductivity coefficient is exerted by the degree of dehydration α^*, water vapor pressure P_w, and heat carrier temperature T. Therefore, for analytical description of k, we choose the functional dependence

$$K = f(\alpha^*, P_w, T). \quad (5)$$

The mass-conductivity coefficient can be calculated most accurately by the equation

$$k = a + b\alpha^* + c\alpha^{*2} + d\alpha^{*3} + e\alpha^{*4} + f\alpha^{*5} + gP_w + hP_w^2 + iP_w^3 + jP_w^4 + mP_w^5, \quad (6)$$

where α^* is the degree of conversion by reaction (2); P_w, water vapor pressure (mm Hg); a, b, c, d, e, f, g, h, i, j, and m, the coefficients dependent on the heat-carrier temperature; and T, the heat-carrier temperature (°C):

$$a = \frac{-6297.72}{1 + \exp[(T - 164.17)/14.84]} + 345.91,$$

$$b = 1018.67 - 6.52 \times 10^{-6} T^3,$$

$$c = -7643.67 + 51.38 \exp(T/18.03),$$

$$d = (1.082 \times 10^9 - 68.49T^3)^{1/2},$$

$$e = -49\,398.28 + 69.28 \exp(T/10.18),$$

$$f = 45\,688 - 0.0025T^3,$$

$$g = -113.18 + 1703.02 \exp[-(T - 150)/21.94],$$

$$h = 10.08 + \frac{-332.10}{1 + \exp[(T - 162.79)/12.23]},$$

$$i = 17.10 \exp[-(T - 150)/1.77],$$

$$j = 31\,997.08 \exp[-T/13.79],$$

$$m = -0.0071 - (331.17/T),$$

where T is the heat carrier temperature (°C).

CONCLUSIONS

(1) Dehydration of sodium tetraborate decahydrate is characterized by the Topley–Smith effect, i.e., an irregular dependence of the dehydration rate on the water vapor partial pressure. The optimal content of water vapor in the gas phase is about 15 mm Hg.

(2) The mass-conductivity coefficients were determined. An empirical equation for calculating the coefficients as functions of dehydration conditions was suggested.

(3) The data obtained and the equations suggested for the kinetics of thermal decomposition of sodium tetraborate decahydrate can be used in calculating installations intended for preparation of pentahydrate or anhydrous sodium tetraborate.

REFERENCES

1. Brown, M.E., Dollimore, D., and Galwey, A.K., Reactions in the Solid State, *Comprehensive Chemical Kinetics*, Bamford, C.H., and Tipper, C.F.H., Eds., Amsterdam: Elsevier, 1980, vol. 22.
2. Fedosov, S.V., Zaitsev, V.A., Sokol'skii, A.I., and Tarasova, T.V., in *Voprosy kinetiki i kataliza: Mezhvuzovskii sbornik nauchnykh trudov* (Problems of Kinetics and Catalysis: Intercollegiate Collection of Research Works), Ivanovo, 1987, pp. 8–10.
3. Rudobashta, S.P., *Massoperenos v sistemakh s tverdoi fazoi* (Mass Transfer in Systems with the Solid Phase), Moscow: Khimiya, 1980.
4. Ognev, E.N., Rudobashta, S.P., Planovskii, A.N., and Dmitriev, V.M., *Teor. Osn. Khim. Tekhnol.*, 1975, vol. 9, pp. 491–495.

Russian Journal of Applied Chemistry, Vol. 77, No. 5, 2004, pp. 736–738. Translated from Zhurnal Prikladnoi Khimii, Vol. 77, No. 5, 2004, pp. 740–742.

PHYSICOCHEMICAL STUDIES OF SYSTEMS AND PROCESSES

Thermochemistry of Dissolution of Glucose in Binary Systems *N*-Methylmorpholine *N*-Oxide Monohydrate–Aprotic Solvent

M. P. Kurlykin, N. P. Novoselov, and E. S. Sashina

St. Petersburg State University of Technology and Design, St. Petersburg, Russia

Received March 4, 2003; in final form, January 2004

Abstract—Glucose enthalpies of solution in binary systems *N*-methylmorpholine *N*-oxide monohydrate–aprotic solvent at 75°C are measured.

Since cellulose is the most abundant steadily renewable native polymer, the problem of its dissolution is topical for more than 150 years all over the world. Numerous works in this area are stimulated by the need in processing cellulose fibers through dissolution, to manufacture fibers and films of various purposes. The difficulty of the problem of cellulose dissolution originates from complexity of the structure of its elementary unit bearing hydroxy groups of various natures, and also from the structure of the cellulose macromolecule consisting of crystalline and amorphous regions of different reactivities.

To understand the mechanism of interaction of cellulose macromolecules with solvents, it is advisable to study the reactivity of functional groups of its elementary unit (α-*D*-glucose) under various conditions. In this case, it is rational to perform the study with solvents that dissolve cellulose to form solutions suitable for subsequent processing [1–3]. The capability of individual or mixed solvents to dissolve cellulose can be predicted using the calorimetric method. Not disclosing the nature of interparticle interaction, thermochemical data reveal whether or not components of a mixture are involved in chemical interaction.

The goal of this work is to study dissolution of α-*D*-glucose as a model for the cellulose unit in solvents based on *N*-methylmorpholine *N*-oxide monohydrate (MMO). The decision on the solvent was caused by the fact that MMO is of great practical interest in view of cellulose dissolution [3]. Also we used binary mixtures of MMO with co-solvents. The use of such binary mixtures allows preparation of cellulose solutions suitable for manufacture of speciality fibers and films, making these processes more cost-efficient [4–7].

The enthalpies of solution were determined at 75°C on a Calvet adiabatic calorimeter (calorimetric vessel volume 75 ml) to within 2.5%. As co-solvents for MMO we used dimethyl sulfoxide (DMSO), dimethylformamide (DMF), and dimethylacetamide (DMAA) (all of chemically pure grade). The solvents were dried over a zeolite. The composition of MMO was controlled by the melting point (72–73°C) and also using Fischer titration. In experiments we used glucose (chemically pure grade) with mp 146°C.

The solvency of DMSO, DMF, and DMAA at 75°C with respect to glucose amounts to 15–20%. The solubility of glucose in pure MMO is about 2% at 75°C. Therefore, in this work we studied solutions of glucose in binary mixtures with a concentration no more than 2%.

Our results (Table 1) showed that the enthalpy of glucose solution in DMSO, DMF, and DMAA at 75°C is independent of the glucose concentration.

Table 1. Glucose enthalpies of solution in aprotic solvents at 75°C

Solvent	Glucose concentration, wt %	ΔH_s, J g^{-1}
DMSO	2.2	61.5
	4.3	60.0
	6.1	58.9
	8.7	60.0
	10.2	59.1
DMF	2.1	99.9
	4.2	101.2
	6.1	102.7
	8.4	98.7
	10.1	99.2
DMAA	2.1	115.3
	4.3	117.5
	6.0	114.0
	8.3	113.8
	10.0	114.1

1070-4272/04/7705-0736 © 2004 MAIK "Nauka/Interperiodica"

Table 2. Glucose enthalpies of solution in binary mixtures MMO monohydrate–aprotic solvent at 75°C

Solvent	ΔH_s, J g^{-1}, at indicated solvent concentration, wt %							
	0	20	40	60	70	80	90	100
DMSO	–10	–26	–67	–96	–95	–88	–75	60
DMF	–10	–20	–59	–81	–83	–82	–47	100
DMAA	–10	–39	–82	–109	–110	–107	–73	115

The glucose enthalpies of solution in binary solvents are given in Table 2 as functions of the solvent composition. In straight MMO, glucose dissolves with heat liberation, which can be attributed to hydrogen bonding between the NO group of MMO and OH groups of glucose (specific solvation). The specific solvation contributes significantly to the total enthalpy of solution ΔH_s

$$\Delta H_s = \Delta H_l + \Delta H_{solv}, \quad (1)$$

where ΔH_l is the crystal lattice energy of glucose and ΔH_{solv}, enthalpy of solvation. The observed negative enthalpy of solution is caused by strongly negative value of ΔH_{solv}.

In turn,

$$\Delta H_{solv} = \Delta H_{cav} + \Delta H_{sp} + \Delta H_{nonsp}, \quad (2)$$

where ΔH_{cav} is the enthalpy of cavity formation in a solvent (a positive value) and ΔH_{sp} and ΔH_{nonsp} are the contributions of specific and nonspecific interactions (negative values), with ΔH_{sp} prevailing.

In aprotic dipolar solvents such as DMSO, DMF, and DMAA, solvation occurs through essentially dipole–dipole interactions, whose energy is considerably lower than that of hydrogen bonding (ΔH_{nonsp} is considerably lower than ΔH_{sp}), and solvation appears to be an endothermic process. As a result, dissolution of glucose in aprotic solvents proceeds with heat consumption. The corresponding endothermic effect increases in the order DMSO < DMF < DMAA, being, respectively, 60, 100, and 115 J g^{-1} (Table 2). Therefore, the dominant effects in dissolution of glucose are fusion of the crystal lattice of glucose and cavity formation in a solvent, i.e., break of its structure. It is known [8] that, among the solvents used, DMSO is characterized by the strongest intermolecular interaction. Since ΔH_l is a constant, the contribution of nonspecific interactions between an aprotic solvent and glucose decreases in the order DMSO > DMF > DMAA, which correlates with the order of variation of the dipole moments (4.3, 3.86, and 3.8 for DMSO, DMF, and DMAA, respectively).

In binary solvents, the exothermic effect of glucose dissolution is considerably higher as compared to the individual components (Table 2). This can be attributed to the fact that the aprotic solvents studied have a strong structure-breaking effect on MMO, thus facilitating cavity formation [positive value of ΔH_{cav} in Eq. (2) considerably decreases]. As a result, dissolution of glucose becomes more exothermic. The break of MMO structure by adding an aprotic solvent should increase its solvency with respect to cellulose also.

Comparison of ΔH_s in various binary solvents at the compositions corresponding to the maximal exothermic effect of dissolution shows that the order of decrease in the interaction energy observed for the straight solvents changes: the strongest interaction with glucose is found in the system DMAA–MMO. This is inconsistent also with the results reported in [9] on dissolution of cellulose in the same binary systems. This inconsistency is probably due to specific structural features of cellulose and glucose. The glucose molecules occur in solutions in the cyclic and open forms, the latter containing the aldehyde group [10]. We have demonstrated the presence of the open conformation of glucose in DMSO, DMF, and DMAA. We compared the Ag^0 deposition efficiency upon adding the same amount of $AgNO_3$ to 5% glucose in the indicated aprotic solvents. The lowest deposition was observed in the DMAA solution, and the highest, in DMSO, suggesting that the fraction of glucose with free aldehyde groups increases on passing from DMAA to DMSO. Since the oxygen atom of the C=O group is more polarized and sterically accessible as compared to the oxygen of the ether group C–O–C in the cyclic conformation of glucose, the aldehyde group can produce a repulsive electrostatic effect when a glucose molecule approaches the oxygen atom of the NO group of MMO in a binary solvent. This effect should be reflected in the strength of intermolecular interaction of MMO with glucose and, correspondingly, in ΔH_{sp} and ΔH_{nonsp}, resulting in changing order of the decrease in the exothermic effect of glucose dissolution in the binary solvents.

On the contrary, cellulose does not form open conformations upon dissolution, which explains the results obtained in [9].

CONCLUSIONS

(1) The enthalpies of solution of glucose are determined in DMSO, DMF, DMAA, *N*-methylmorpholine *N*-oxide monohydrate, and their binary mixtures at 75°C.

(2) The observed differences in the thermal effects of solution of cellulose and glucose in binary systems *N*-methylmorpholine *N*-oxide monohydrate–aprotic solvent can be attributed to the occurrence of the open aldehyde conformation of glucose molecules in solutions.

REFEREMCES

1. Golova, L.K., *Khim. Drev*., 1996, no. 1, pp. 12–23.
2. Rozhkova, O.V., Myasoedova, V.V., and Krestov, G.A., *Khim. Drev*., 1985, no. 2, pp. 26–31.
3. Golova, L.K., Kulichikhin, V.G., and Papkov, S.P., *Vysokomol. Soedin., Ser. A*, 1986, vol. 28, no. 8, pp. 1795–1809.
4. Kabrelian, V., Berger, W., Keck, M., and Philipp, B., *Acta Polym*., 1988, vol. 39, no. 12, pp. 710–714.
5. Berger, W., Keck, M., Kabrelian, V., *et al*., *Acta Polym*., 1989, vol. 40, no. 5, pp. 351–358.
6. Berger, W., Kabrelian, V., Keck, M., *et al*., *Acta Polym*., 1990, vol. 41, no. 1, pp. 25–31.
7. Petropavlovskii G.A., Bochek, A.M., and Sheek, V.M., *Khim. Drev*., 1987, no. 2, pp. 2–21.
8. Belousov, V.P. and Morachevskii, A.G., *Teploty smesheniya zhidkostei* (Enthalpies of Mixing of Liquids), Leningrad: Khimiya, 1970.
9. Novoselov, N.P., Sashina, E.S., and Kozlov, I.L., *Zh. Fiz. Khim*., 2001, vol. 75, no. 7, pp. 1254–1257.
10. Stepanenko, B.N., *Khimiya i biokhimiya uglevodov: monosakharidy* (Chemistry and Biochemistry of Carbohydrates: Monosaccharides), Moscow: Khimiya, 1977.

Russian Journal of Applied Chemistry, Vol. 77, No. 5, 2004, pp. 739–744. Translated from Zhurnal Prikladnoi Khimii, Vol. 77, No. 5, 2004, pp. 743–748.

SORPTION AND ION-EXCHANGE PROCESSES

Adsorption of Hydrocarbon Vapors on Activated Carbons Obtained from Vegetable Raw Materials

T. V. Anurova, V. N. Klushin, V. M. Mukhin, V. E. Myshkin, S. A. Anurov, and M. A. Suare

Mendeleev Russian University of Chemical Engineering, Moscow, Russia

Received July 22, 2003; in final form, December 2003

Abstract—The equilibrium adsorption of vapors of benzene, toluene, *o*-xylene, and gasoline in the temperature range 25–100°C and adsorbate content of 0.01–1.80 vol % on activated carbons obtained from plum stones and shells of peanut, walnut, and coconut was studied. The effect of temperature on the adsorption properties of the absorbents were analyzed. The isosteric heats of adsorption were calculated.

The protection of the atmosphere from pollution is an important and complicated environmental problem. Among the most global contaminants discharged into the atmosphere are various hydrocarbons. The most dangerous of these are, because of their prevailing mass, vapors of volatile organic solvents and light petroleum products, such as benzene, toluene, xylenes, gasolines, etc. The negative consequences of discharge of these toxic compounds are well known [1]. However, the economical factor, associated with the loss of valuable chemical compounds so much needed by modern industry, is to be taken into account in addition to the environmental aspect of the problem. According to the available estimates [2], the annual Russia's discharge from only stationary industrial sources is 1.6 million tons of volatile organic compounds and 2.6 million tons of other hydrocarbons even during the period of recession.

The diversity of conditions under which organic solvents and motor fuels are vaporized requires that different methods should be developed for their recovery. Among the rather wide variety of methods of this kind [1], processes of carbon-sorption purification are virtually unrivaled in processing of flows with relatively low content of these components. However, their use is only economical if low-cost and readily available carbon adsorbents can be used.

A technique for obtaining activated carbon from vegetable wastes in the form of plum stones and nutshells has been developed. This method yields microporous adsorbents with an effective half-width of micropores of 0.5–0.7 nm, which is comparable with the size of molecules of the organic compounds mentioned above. This suggests that these adsorbents can serve as rather active absorbents of hydrocarbons from vapor–gas mixtures.

To confirm the efficiency of this approach, it is necessary to study the adsorption properties of these carbons with respect to a number of characteristic hydrocarbons and light petroleum products. This was the aim of our study.

EXPERIMENTAL

As adsorbents served activated carbons obtained by carbonization in a nitrogen atmosphere of plum stones (PS) and shells of peanut (SP), walnut (SW), and coconut (SC) at 800°C for 1 h, followed by steam–gas activation of the carbon matrices under similar temperature and time conditions. The carbonizates of PS and SW were oxidized with water vapor, and those of SP and SC, with a nitrogen–oxygen mixture (2 vol % O_2). As reference were chosen activated carbons of SKT and ART-1 brands, which are recommended as adsorbents for catching vapors of organic solvents [3, 4]. The main technical characteristics of the carbon adsorbents are listed in Table 1.

As adsorbates were used benzene, toluene, *o*-xylene, and gasoline (motor fuel of the AI-95 brand). A number of physical constants of these hydrocarbons are listed in Table 2 [5–7]. It is difficult to specify the physical properties of gasolines because they are mixtures (boiling out at 40–195°C) of cyclic (20–65%), aromatic (2–12%), saturated (25–80%), and unsaturated (1–2%) hydrocarbons whose content in the final product is determined by the composition of the

1070-4272/04/7705-0739 © 2004 MAIK "Nauka/Interperiodica"

Table 1. Characteristics of carbon adsorbents

Adsorbent	Raw material	Activation	Strength	Ash content	Moisture content	Bulk density, g cm^{-3}
			%			
KU-1	SW	H_2O vapor	67	0.5	4.6	0.40
KU-2	PS	H_2O vapor	68	0.5	4.3	0.42
AA-1	SP	N_2 + 2% O_2	65	1.4	4.9	0.39
AK-1	SC	N_2 + 2% O_2	91	1.3	4.5	0.50
SKT	Peat	Chemical	66	14.7	5	0.55
ART-1	Peat, coal	Chemical	70	16	5	0.58

Table 2. Selected properties of the adsorbates studied

Adsorbate	*M*	Critical diameter, nm	Density, g cm^{-3}	Saturated vapor pressure, mm Hg	Heat of vaporization, kJ mol^{-1}	Explosive limit, vol %	
						lower	upper
Benzene	78.10	0.60	0.879	74.8	30.87	1.4	6.7
Toluene	92.14	0.67	0.860	21.6	33.31	1.5	7.7
o-Xylene	106.17	0.69	0.880	4.88	36.96	0.9	7.6
Gasoline	~109	–	0.700–0.780	225–375*	–	1.7	2.9

* At 38°C.

raw materials used and the conditions of their processing [5]. The average molar mass of gasoline M = 109 g mol^{-1} was evaluated using the following empirical equation, which relates this parameter to the average temperature T_{av} of boiling-out of a mixture of hydrocarbons [5]:

$$M = 60 + 0.3T_{av} + 0.001T_{av}^2. \quad (1)$$

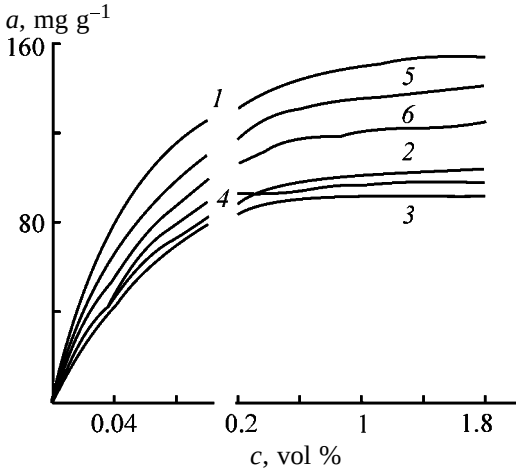

Fig. 1. Isotherms of benzene adsorption on activated carbons: (*a*) adsorbent activity and (*c*) benzene content. Type of carbon: (*1*) KU-1, (*2*) SKT, (*3*) AK-1, (*4*) AA-1, (*5*) ART-1, and (*6*) KU-2.

The adsorption measurements were performed in an evacuated setup with a McBain quartz spring balance in the temperature range 25–100°C. To remove moisture prior to adsorption, the carbons were dried at 120°C to constant weight. The adsorbate concentration was chosen with account of the requirement that, under the real conditions, the content of a hydrocarbon in the gas flow should be at the lower explosive limit in order to ensure explosion and fire safety. If the content of an adsorbate in a flow to be treated exceeds this limit, the technique envisages that it is diluted in an appropriate way with nitrogen or air. As seen from Table 2, these values for the substances used are within the range 0.9–1.7 vol %, and, therefore, the study was performed, irrespective of the nature of the hydrocarbons, at their contents in the range 0.01–1.8 vol %.

One of the most important characteristics used for comparative evaluation of the adsorption properties of solid absorbents and, consequently, for assessment of their suitability for specific processes is the adsorption isotherm. The results obtained in studying the static adsorption of hydrocarbon vapors at 25°C on the activated carbons under study are illustrated by Figs. 1 and 2. These figures show that, virtually in all cases, the isotherms correspond to the first type by Brunauer's classification: the adsorption capacity

grows with increasing content of adsorbates in the gas flow [8]. The highest adsorption capacity for all the systems is exhibited by the KU-1 adsorbent obtained from SW and by industrial carbon SKT. The static adsorption capacity of these adsorbents at a content of benzene, toluene, xylene, and gasoline in the gas mixture equal to 1.0 vol % is 151, 262, 295, 343 and 136, 238, 265, 312 mg g^{-1}, respectively. Less active are the KU-2, ART-1, AA-1, and AK-1 carbons, although their adsorption capacities for these hydrocarbons are rather close to the adsorption capacities of KU-1 and SKT and equal to 75–80% of these.

Also noteworthy is the fact that all the isotherms have a portion of steep initial rise, suggesting that these carbons will efficiently absorb the target components mentioned above from weakly concentrated gas flows.

A mathematical approximation to the adsorption equilibrium in question was made using the classical single-term equation for uniformly porous adsorption, which is derived in the theory of volume filling of micropores (TVFM) by Dubinin and Radushkevich (DR) [9]:

$$a = (W_0/V)\exp[(A/\beta E_0)^2], \quad (2)$$

where a is the amount of an adsorbed substance at a temperature T and relative pressure p/p_s; V, molar volume of the adsorbate; $A = RT\ln(p_s/p)$, differential molar work of adsorption; $\beta = E/E_0$, coefficient of similarity of the substance under study to a reference substance; E_0, characteristic energy of adsorption of the vapor of the reference substance (benzene); E, characteristic energy of adsorption of the vapor of the substance under study; p, partial pressure of the adsorbate; p_s, saturated vapor pressure of the adsorbate; and W_0, volume of micropores.

As shown by the calculations performed, the points characterizing the adsorption of each adsorbate on the activated carbons under study are approximated with a satisfactory accuracy with straight lines in the coordinates of the equation $\log a = f(\log p_s/p)^2$. This confirms unambiguously that the application of TVFM to description of the adsorption equilibrium in the systems under consideration is well justified.

The DR equation makes it possible to determine the volume of micropores in the adsorbents, the characteristic energy of adsorption of a reference substance in the micropores, and their effective half-width, the radius x_0 related to E_0 by

$$x_0 = k/E_0, \quad (3)$$

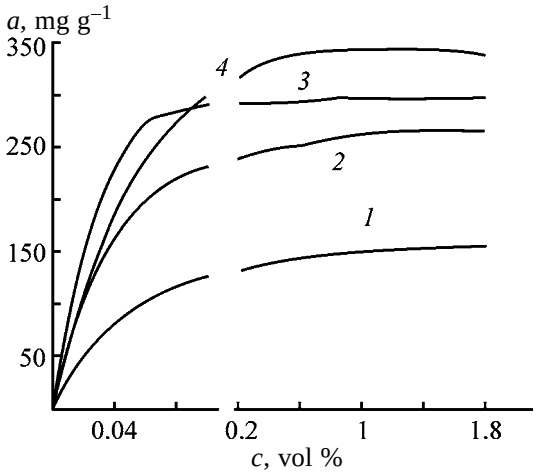

Fig. 2. Isotherms of hydrocarbon vapor adsorption on KU-1 activated carbon: (*a*) Adsorbent activity and (*c*) adsorbate content; the same for Fig. 4. Adsorbate: (*1*) benzene, (*2*) toluene, (*3*) xylene, and (*4*) gasoline; the same for Figs. 3–5.

where k is a coefficient equal to 10–12 kJ mol^{-1} [10, 11].

The volume of mesopores, V_{me}, was found as the difference

$$V_{me} = V_s - W_0, \quad (4)$$

where V_s is the limiting volume of the adsorption space (amount of adsorbed substance at the saturated vapor concentration).

The specific surface area was found from the BET equation [8].

Table 3 lists characteristics of the pore structure of the adsorbents, which were found from isotherms of adsorption–desorption of a benzene vapor using the single-term DR equation. Analysis of these data suggests that all the microporous adsorbents obtained compare well with the industrial activated carbons used as reference. For example, the microporosity of

Table 3. Structural characteristics of the adsorbents

Adsorbent	S_{BET}, m^2 g^{-1}	Pore volume, cm^3 g^{-1}			E_0, kJ mol^{-1}	x_0, nm
		V_s	W_0	V_{me}		
KU-1	932	0.69	0.47	0.22	14.49	0.69
KU-2	915	0.63	0.42	0.21	16.67	0.60
AK-1	583	0.51	0.30	0.21	22.22	0.45
AA-1	560	0.48	0.26	0.22	25.64	0.39
SKT	970	0.67	0.48	0.19	17.54	0.57
ART-1	730	0.65	0.45	0.20	14.93	0.67

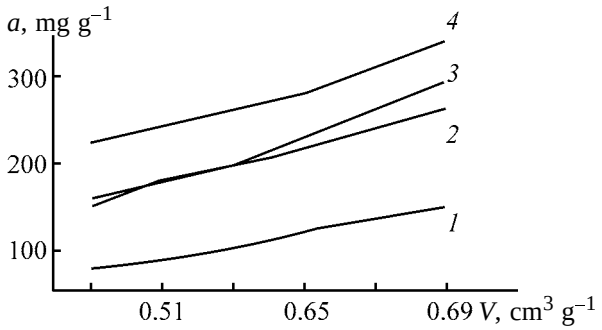

Fig. 3. Activity *a* of the carbons vs. the volume *V* of sorbing pores.

the adsorbents prepared from PS and SW is virtually the same and equal to 0.42–0.48 $cm^3 g^{-1}$. The volume of micropores in the adsorbents prepared by activation with oxygen (AA-1 and AK-1) is somewhat lower, but, nevertheless, quite sufficient: 0.26–0.30 $cm^3 g^{-1}$. The volume of mesopores is virtually the same for all of the adsorbents (0.19–0.22 $cm^3 g^{-1}$).

Comparison of the adsorption capacities of the adsorbents for the hydrocarbons with the parameters of their pore structure shows that this structure governs the adsorption properties. As seen in Fig. 3, the equilibrium activities are directly proportional to the volume of the sorbing pores in the carbons. This fact indicates that the absorption of vapors of aromatic and gasoline hydrocarbons by the carbon adsorbents proceeds in accordance with, exclusively, the laws of physical adsorption, i.e., the binding of adsorbate molecules to the carbon surface is due solely to the van der Waals forces.

The effect of temperature on the equilibrium adsorption capacity of the carbon adsorbents for vapors of the hydrocarbons under study was studied in the temperature range 25–100°C. As an illustration of the results obtained, Fig. 4 shows the isotherms of adsorption of aromatic hydrocarbons and gasoline on an activated carbon prepared from SW. For the other adsorbent–adsorbate systems, the effect of temperature

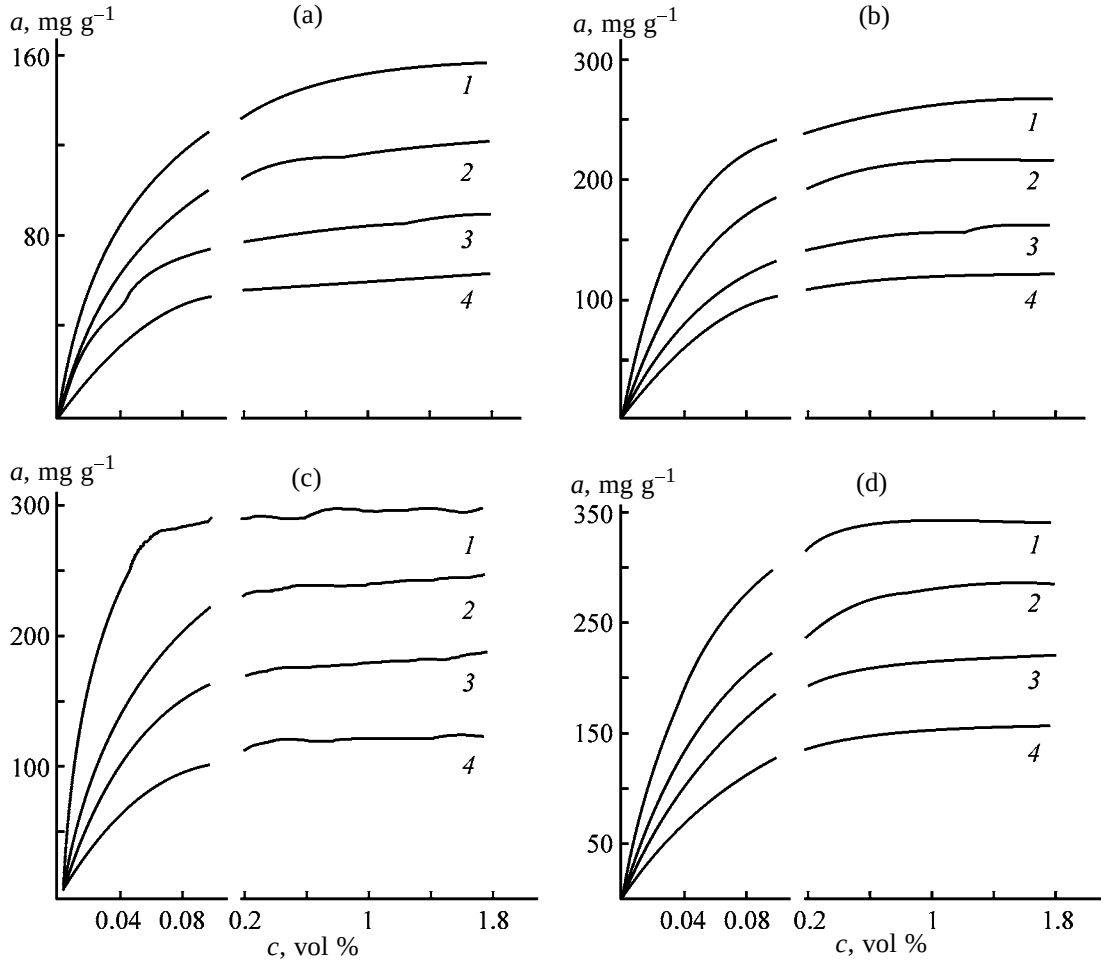

Fig. 4. Effect of temperature on the adsorption of hydrocarbons on KU-1 activated carbon. Temperature (°C): (*1*) 25, (*2*) 50, (*3*) 75, and (*4*) 100. Adsorbate: (a) benzene, (b) toluene, (c) *o*-xylene, and (d) gasoline.

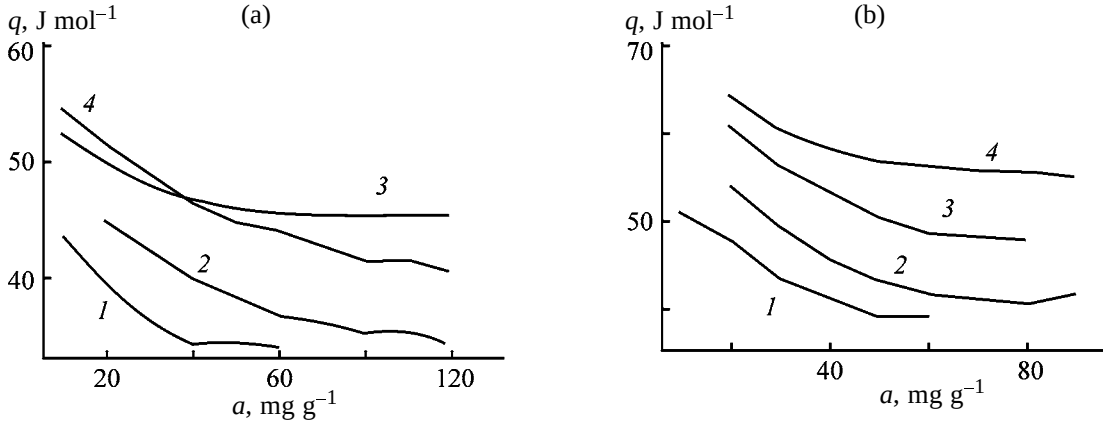

Fig. 5. Heats of adsorption of hydrocarbons on (a) KU-1 and (b) KU-2 activated carbons. (*q*) Differential heat of adsorption and (*a*) activity of an adsorbent.

on the activity of the adsorbents is similar. Apparently, an increase in temperature adversely affects in all cases the total amount of adsorbed hydrocarbons: with the temperature increasing in the range studied, the capacity of the adsorbents falls by 50–80% at a content of adsorbates in the vapor–gas mixtures higher than 1 vol %. However, at a low content of the hydrocarbons (<0.005%) the activity of the carbons is little dependent on the temperature, which indicates that their use for purification of low-concentrated gas flows at elevated temperatures without preliminary cooling is advisable.

The adsorption of vapors and gases is an exothermic process. Together with the equilibrium activity, the heat of adsorption is a parameter that is to be known in a calculation of adsorption processes. One of the simplest methods for calculating the heats of adsorption is based on the Clapeyron–Clausius equation, used in the form [12]

$$q = RT^2(\partial \ln p/\partial T)_{a=\text{const}}. \quad (5)$$

Figure 5 shows how the nature of an adsorbate and the degree of filling of the adsorption capacity affect the heat of adsorption of hydrocarbons on the activated carbons prepared from PS and SW. Analysis of these calculated data shows that, in all cases, the dependences $q = f(a)$ are decsending functions, which indicates that there is no specific interaction in the systems. For degrees of filling that are close to the limiting values, the heats of adsorption are approximately equal to the heats of condensation of the adsorbates, which is also evidence in favor of the physical nature of the adsorption of the hydrocarbons under study on microporous adsorbents. And finally, it should be noted that the isosteric differential heat of adsorption grows as the molecular mass of an adsorbate increases.

The average values of the differential heats of adsorption of benzene, toluene, *o*-xylene, and gasoline vapors on the carbon adsorbents under study are 42, 46, 51, and 57 kJ mol^{-1}, respectively.

CONCLUSION

The activated carbons obtained from waste agricultural vegetable raw materials can be successfully used for purification of vapor–air mixtures to remove vapors of benzene, toluene, *o*-xylene, and gasoline. The absorption of the hydrocarbons obeys the laws of physical adsorption, not complicated by any specific interaction, and the adsorption equilibrium is approximated with a sufficient accuracy with the single-term equation of the Dubinin–Radushkevich theory of volume filling of micropores, which can be used in simulation of purification processes.

REFERENCES

1. Rodionov, A.I., Klushin, V.N., and Sister, V.G., *Tekhnologicheskie protsessy ekologicheskii bezopasnosti* (Processes Ensuring Environmental Safety), Kaluga: Izd. Bochkarevoi, 2000.
2. *Rossiiskii statisticheskii ezhegodnik: Statisticheskii sbornik* (Russia's Statistical Yearbook: Statistical Collection), Moscow: Goskomstat Rossii, 1994.
3. *Aktivnye ugli; Elastichnye sorbenty; Katalizatory; Osushiteli; Khimicheskie poglotiteli: Katalog* (Activated Carbons; Elastic Sorbents; Catalysts; Drying Agents; Chemical Absorbents: Catalog), Cherkassy: NIITEKhIM, 1996.

4. Kolyshkin, D.A. and Mikhailova, K.K., *Aktivnye ugli. Svoistva i metody ispytanii. Spravochnik* (Activated Carbons. Properties and Methods of Testing. Reference Book), Moscow: Khimiya, 1972.
5. *Khimiya nefti i gaza* (Chemistry of Oil and Natural Gas), Proskuryakov, V.A. and Drabkin, A.E., Eds., Leningrad: Khimiya, 1981.
6. Zhorov, Yu.M., *Termodinamika khimicheskikh protsessov: Neftekhimicheskii sintez, pererabotka nefti, uglya i prirodnogo gaza* (Thermodynamics of Chemical Processes: Petrochemical Synthesis and Processing of Oil, Coal, and Natural Gas), Moscow: Khimiya, 1985.
7. *Spravochnik po pozharnoi bezopasnosti i protivopozharnoi zashchite na predpriyatiyakh khimicheskoi, neftepererabatyvayushchei i neftekhimicheskoi promyshlennosti* (Handbook of Fire Safety and Fire Protection at Plants of Chemical, Oil Refining, and Petrochemical Industries), Moscow: Khimiya, 1975.
8. Brunauer, S., *The Adsorption of Gases and Vapors*, Prinston: Prinston Univ. Press, 1943.
9. Dubinin, M.M., *Adsorbtsiya i poristost'* (Adsorption and Porosity), Moscow: Voen. Akad. Khim. Zashch., 1972.
10. Polyakov, N.S., Petukhova, G.A., Stackley, F., *et al*., *Izv. Ross. Akad. Nauk, Ser. Khim*., 1996, no. 5, pp. 1132–1137.
11. Fomkin, A.A., Regent, N.I., and Sinitsyn, V.A., *Izv. Ross. Akad. Nauk, Ser. Khim*., 2000, no. 6, pp. 1018–1022.
12. *Eksperimental'nye metody v adsorbtsii i molekulyarnoi khromatografii* (Experimental Techniques in Adsorption and Molecular Chromatography), Nikitin, Yu.S. and Petrova, R.S., Eds., Moscow: Mosk. Gos. Univ., 1990.

Russian Journal of Applied Chemistry, Vol. 77, No. 5, 2004, pp. 745–749. Translated from Zhurnal Prikladnoi Khimii, Vol. 77, No. 5, 2004, pp. 749–753.

SORPTION AND ION-EXCHANGE PROCESSES

Sorption of Oil by Swollen Graphite: Contributions of Specific Surface Area and Specific Volume

M. V. Savos'kin, A. P. Yaroshenko, V. I. Shologon, and L. Ya. Galushko

Litvinenko Institute of Physical Organic Chemistry and Coal Chemistry, National Academy of Sciences of Ukraine, Donetsk, Ukraine

Received May 13, 2002; in final form, February 2004

Abstract—Sorption of heavy oil by swollen graphites obtained from residual graphite hydrosulfate at 300–900°C was studied. The dependence of the sorption capacity for oil on the specific surface area and specific volume of the swollen graphite sorbent was analyzed.

It has been shown previously that swollen graphite is an extremely effective sorbent for oil and oil products [1–11]. Despite the relatively low specific surface area, its sorption capacity for oil is up to 80 g g^{-1} [12–16]. It was demonstrated in [15] that, to a first approximation, there exists a hyperbolic dependence of the sorption capacity on the bulk density of a sorbent and a directly proportional dependence of the sorption capacity on the total pore volume of the sorbent. No dependence of the sorption capacity on the specific surface area was revealed. On this basis, a conclusion was made that the main contribution to sorption comes from the specific volume of a sorbent, with pores 1–400 μm in size responsible for sorption.

Here we have shown that the sorption determined by the specific surface area of a sorbent makes, together with the sorption governed by the specific volume, an important contribution to sorption of oil by swollen graphite. To distinguish these contributions to the total sorption, a number of sorbents obtained by swelling of the same residual graphite hydrosulfate at 300–900°C [17] were studied. It was found that, for all the samples studied, there exists a strong correlation between the specific surface area S_{sp} and specific volume V_{sp}, which makes impossible any separation of the contributions of these parameters to the total sorption of oil. To diminish the correlation between S_{sp} and V_{sp}, samples of swollen graphite were subjected to a mechanical treatment. This was done on the assumption that such a treatment will not affect S_{sp}, but will strongly diminish V_{sp}, thus making it possible to separate the contributions from the specific surface area and specific volume of the sorbent to the total sorption.

EXPERIMENTAL

The sample of residual graphite hydrosulfate (product formed in hydrolysis of graphite hydrosulfate) used in our study was prepared as follows [17]. Natural flaky graphite of the GT-1 brand (A^d = 5.68 wt %) from the Zaval'evskoe deposit (Ukraine) was used. The initial graphite contained two fractions; 74.3 wt % particles 0.630–0.315 mm in size and 22.1 wt % particles 0.315–0.200 mm in size. As reagents were used a CrO_3 solution in distilled water (50 wt %, d = 1.50 g dm^{-3}) and concentrated H_2SO_4 of chemically pure grade (95.8 wt %). To 25 g of graphite was added with stirring 3.0 cm^3 of the aqueous solution of CrO_3, and the reaction mass was agitated for 10 min. Then, 9.0 cm^3 of H_2SO_4 was introduced into the reactor, and the agitation was continued for 10 min. Further, the contents of the reactor were poured over with 500 cm^3 of water, and the resulting mixture was blended by agitation and allowed to stand for 24 h for hydrolysis to occur. After that, the solid phase was filtered off and washed on the filter with 2 dm^3 of water. The residual graphite hydrosulfate was obtained by drying the moist product at 105°C for 2 h.

Sorbent samples were obtained by heating the residual graphite hydrosulfate in a muffle furnace in the heat-shock mode in the temperature range 300–900°C. The samples were kept in the furnace for 5 min at 300–500°C and for 2 min at 600–900°C. The mechanical treatment of the resulting samples was carried out under the standard conditions by agitation of dry sorbent samples with a T-shaped glass stirrer in a glass vessel at 200 rpm for a time from 0 to 45 min. The values of S_{sp} and V_{sp}, as well as the

1070-4272/04/7705-0745 © 2004 MAIK "Nauka/Interperiodica"

Characteristics of swollen graphite sorbents obtained at different temperatures

T_{sw}, °C	S_{sp}, $m^2\ g^{-1}$	V_{sp}, $cm^3\ g^{-1}$	W_{sp}, $g\ g^{-1}$
20*	0.8	2	1.8
300	2.5	23	7.6
400	5.2	71	18.6
500	22.9	195	22.3
600	34.6	215	26.0
700	43.1	245	67.0
800	46.7	272	75.4
900	47.0	287	71.6

* Initial residual graphite hydrosulfate.

sorption capacity for oil at 20°C, W_{sp}, were determined for all the initial and mechanically treated samples.

The BET specific surface area S_{sp} was determined by low-temperature adsorption of argon in accordance with GOST (State Standard) 13144–79. The specific volume was calculated as a reciprocal of the bulk density of the sorbent, which was determined in accordance with GOST 14922–77. The sorption capacity of a sorbent was determined for heavy oil from Lisichansk oil refinery, with a density of 0.873 $g\ cm^{-3}$ at 20°C. The sorption capacity for oil was determined as follows [18]. To a 0.2–0.6-g weighed portion of the graphite sorbent was added 25 g of oil, the resulting mixture was blended by careful agitation, and, after keeping for 1 h, the unsorbed oil was removed in the course of 24 h using a filter made of a metallic mesh. The swollen graphite sorbent with sorbed oil was weighed and the sorption capacity (g of oil per g of sorbent) was calculated.

The parameters of the untreated sorbents obtained at different swelling temperatures T_{sw} in the range 300–900°C are listed in the table.

Figures 1a–1c show how the specific surface area, specific volume, and sorption capacity for oil depend on the temperature at which swollen graphite sorbents are obtained, before their mechanical treatment.

It is seen that all the three parameters studied for the swollen sorbents depend on the swelling temperature in a similar way; below 300°C, the values of the parameters vary only slightly; beginning with 400°C, a steep rise is observed; and in the range 700–800°C all the three curves tend to level off. An attempt to estimate the contributions from the specific volume and specific surface area to the sorption capacity of swollen graphite sorbents on the basis of the data

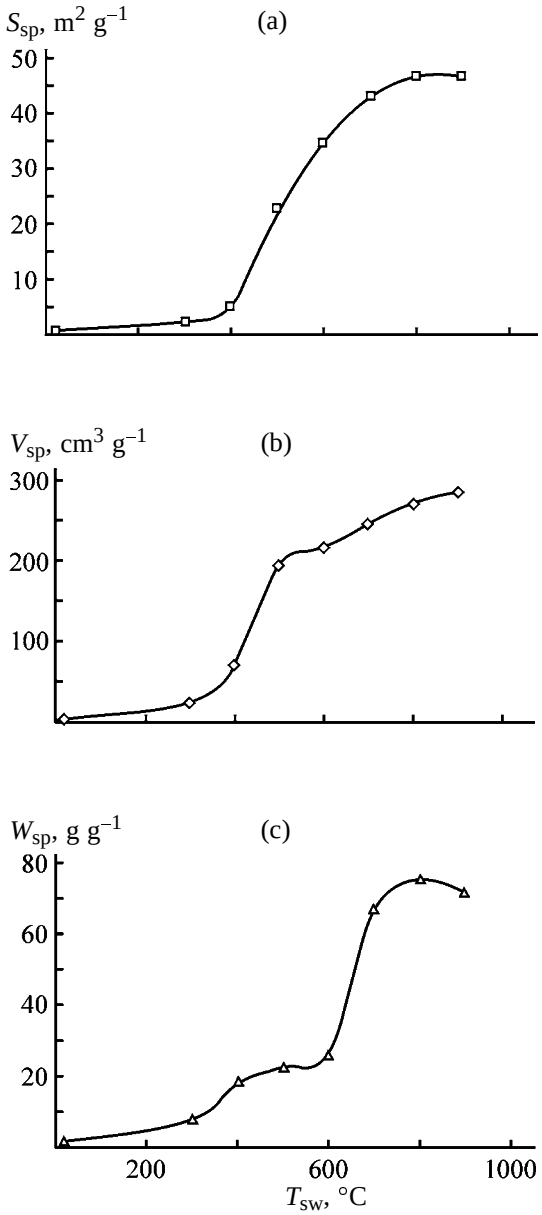

Fig. 1. (a) Specific surface area S_{sp}, (b) specific volume V_{sp}, and (c) sorption capacity of swollen graphite for oil W_{sp} vs. the temperature T_{sw} at which it was obtained.

presented in the table and Figs. 1a–1c by the method of a multiple linear regression failed. This is due to the fact that the presumably independent regression parameters S_{sp} and V_{sp} are actually not independent. As seen from Figs. 1a and 1b, both these parameters depend on the swelling temperature in a similar way, which results in a high coefficient of linear correlation between them: $r = 0.96$.

To diminish the correlation between the parameters S_{sp} and V_{sp}, the sorbent samples obtained at different

temperatures were subjected to a mechanical treatment. It was demonstrated that V_{sp} remains virtually unchanged upon such a treatment of the swollen graphite samples obtained at 300 and 400°C, and steadily decreases by, to a first approximation, a hyperbolic law for samples obtained at 500–900°C. At the maximum time of the mechanical treatment of 45 min, V_{sp} of these samples decreases 2–3-fold. As expected, mechanical treatment does not change the specific surface area of all the samples studied in the whole range of treatment times used. Typical dependences of the specific volume of swollen graphite on the time of its mechanical treatment are shown in Fig. 2.

Figure 3 shows how the sorption capacity for oil depends on the specific volume for samples obtained at 300–900°C and subjected to a mechanical treatment. For the samples prepared at 300 and 400°C, mechanical treatment does not change significantly their sorption capacity for oil, which is indicated by the compact arrangement of the points for these samples. This fact is in agreement with the invariability of the parameters S_{sp} and V_{sp} for these swollen graphite samples in the course of their mechanical treatment. For the samples obtained at higher temperatures (500–900°C), the situation changes dramatically. To a first approximation, the dependences of W_{sp} for oil on V_{sp} can be represented for these samples by straight lines, around which lie, with a significant scatter, experimental points. The slopes of these straight lines are positive, close to zero, and negative for the samples obtained at 700–900, 600, and 500°C. It is noteworthy that the intercepts on the *y*-axis fall within the range 30–40 g g^{-1} for all these straight lines.

For the samples obtained at 700–800°C, the straight lines with a positive slope can be readily accounted for by a decrease in V_{sp} of these samples in the course of a mechanical treatment (Fig. 2), which makes lower their sorption capacity for oil. Unexpectedly, it was found that for the samples obtained at 500 and 600°C the run of these curves is anomalous. For the samples synthesized at 600°C, V_{sp} decreases in the course of a mechanical treatment, but the sorption capacity for oil remains virtually unchanged. For the samples obtained at 500°C, mechanical treatment even raises their sorption capacity for oil.

The anomalous dependences of W_{sp}, observed for the swollen graphite samples obtained at 500 and 600°C, can presumably be accounted for as follows. Heating of the residual graphite hydrosulfate yields

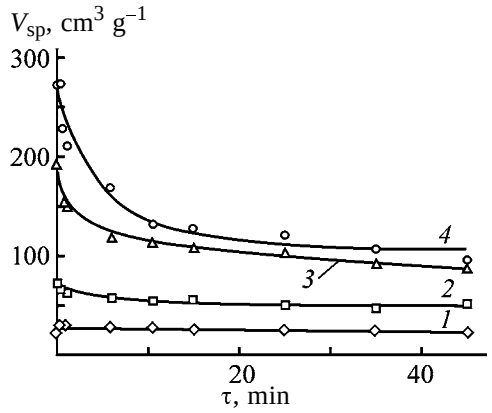

Fig. 2. Specific volume V_{sp} of swollen graphite samples obtained at different temperatures vs. the duration τ of their mechanical treatment. Preparation temperature (°C): (*1*) 300, (*2*) 400, (*3*) 500, and (*4*) 800.

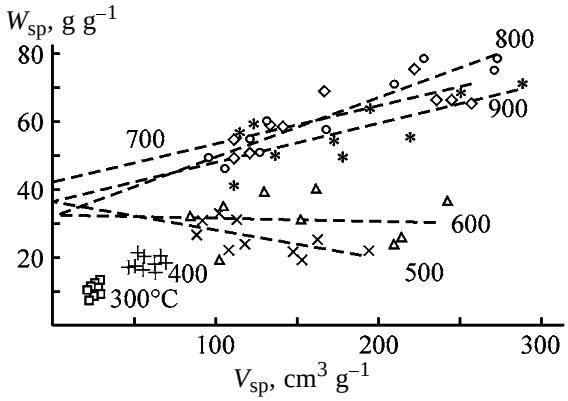

Fig. 3. Sorption capacity for oil, W_{sp}, vs. the specific volume V_{sp} for swollen graphite samples obtained at 300, 400, 500, 600, 700, 800, and 900°C and subjected to a mechanical treatment.

a swollen graphite with a characteristic honeycomb structure [19]. In all probability, this structure is poorly developed at 300–400°C and is mainly composed of closed pores, which are inaccessible to oil. At a swelling temperature of 500–600°C, the honeycomb structure of the swollen graphite is already well developed; however, a considerable fraction of closed pores inaccessible to oil is still present. At swelling temperatures of 700–900°C, virtually all pores in the structure of swollen graphite are open and accessible to oil. It is noteworthy that raising the temperature at which swollen graphite is obtained leads not only to the development of the honeycomb structure, but also to a decrease in its mechanical strength.

Mechanical treatment of swollen graphite obtained at 700–900°C only diminishes the specific volume of the sorbent and, as a consequence, leads to a decrease in its sorption capacity for oil. In the case of swollen

graphites obtained at 500–600°C, mechanical treatment also diminishes the V_{sp} of the sorbent, which leads to a decrease in the W_{sp} of swollen graphite for oil. However, closed pores are, presumably, also opened in this case and, as a result, become accessible to oil. This effect compensates for the decrease in the W_{sp} of the sorbents, which is associated with the lowering of their specific volume. An evidence in favor of this conclusion is the following experimental fact. As regards their behavior in isopropyl alcohol, all the untreated sorbent samples can be divided into two groups: those obtained at 300–500°C float on the alcohol surface, and those prepared at 600–900°C drown. After 45 min of mechanical treatment, the behavior of the samples obtained at 300–400 and 600–900°C remains unchanged. By contrast, the sample prepared at 500°C drowns in the alcohol virtually completely. In the untreated sample obtained at 600°C, all the pores are presumably already opened, but the size of their mouths allows only comparatively small molecules, e.g., those of isopropyl alcohol, to penetrate into the pores. Molecules of substances contained in oil (average molecular mass is about 1000) cannot penetrate through so narrow apertures into the pores. Presumably, the mechanical treatment used makes the pore mouths wider, with the result that pores become accessible to oil.

The honeycomb structure of the swollen graphites obtained at 300–400°C is so strong that the mechanical treatment used neither makes smaller the V_{sp} of the sorbent, nor opens up the closed pores present in its structure. As a result, mechanical treatment leaves virtually unchanged the W_{sp} of these sorbents.

The fact that, upon a mechanical treatment of swollen graphite, its V_{sp} decreases and S_{sp} remains unchanged made it possible to diminish the correlation between these parameters. For the untreated samples of graphites swollen at 300–900°C, the coefficient of linear correlation between the parameters S_{sp} and V_{sp} is $r = 0.96$. At the same time, after a mechanical treatment it decreases to $r = 0.76$. It is noteworthy that, if the samples obtained at 300 and 400°C (whose mechanical treatment does not change the parameters S_{sp} and V_{sp}) are excluded from consideration, the correlation coefficient falls to $r = 0.27$.

Such a weakening of the correlation between these parameters made it possible to estimate, to a first approximation, their separate contributions to the sorption of oil by swollen graphite. An estimate of the regression dependence of the sorption capacity W_{sp} of swollen graphite on the parameters S_{sp} and V_{sp} by means of the method of linear multiparameter regression for the whole body of experimental data yields the equation $W_{sp} = 3.946 + 0.807S_{sp} + 0.0812V_{sp}$ ($r = 0.88$). In this case, the estimate by the *t*-test (at confidence probability of 95%) shows that the coefficients at the parameters S_{sp} and V_{sp} in this equation are significant. Reducing this equation to the standard scale, which makes it possible to compare the absolute values of the regression coefficients, yields the equation $W_{sp} = 0.648S_{sp} + 0.277V_{sp}$. It follows from this equation that both the contributions to the sorption of oil, associated with the specific surface area and the specific volume of swollen graphite, are significant, with 70% of the sorption capacity governed by the specific surface area of swollen graphite, and only 30%, by its specific volume.

CONCLUSIONS

(1) Swollen graphite obtained by heating of the residual graphite hydrosulfate in the thermal-shock mode is a highly effective sorbent of oil. The sorption capacity of swollen graphite grows with increasing swelling temperature to become 70–75 g g^{-1} for the sorbents obtained at 800–900°C.

(2) The strength of the honeycomb structure of the swollen graphite sorbent, which is responsible for sorption of oil, is low. Even a simple mechanical agitation of dry sorbents obtained at 700–900°C leads to a decrease in their specific volume and, as a consequence, makes lower their sorption capacity for oil.

(3) The sorption capacity for oil is determined both by the specific surface area and the specific volume of swollen graphite, with the contribution of the sorption governed by the specific surface area equal to about 70%, and that associated with the specific volume, to about 30%.

REFERENCES

1. US Patent 3357929.
2. US Patent 2536807.
3. UK Patent 2149769.
4. Ukrainian Patent 298.
5. US Patent 5282975.
6. RF Patent 2050972.
7. US Patent 5788865.
8. RF Patent 2117635.
9. Ukrainian Patent 40918.
10. Ukrainian Patent 41858.

11. Cao, N.Z., Shen, W.C., Wen, S.Z., *et al*., Extended Abstracts, *Carbon'96*, July 7–12, 1996, Newcastle upon Tyne (Great Britain): British Carbon Group, 1996, vol. 1, pp. 114–115.
12. Toyoda, M., Aizawa, J., and Inagaki, M., *Desalination*, 1998, vol. 115, no. 2, pp. 199–201.
13. Toyoda, M., Moriya, K., Aizawa, J.-I., *et al*., *Desalination*, 2000, vol. 128, no. 3, pp. 205–211.
14. Toyoda, M. and Inagaki, M., *Carbon*, 2000, vol. 38, no. 2, pp. 199–210.
15. Toyoda, M., Moriya, K., and Inagaki, M., Abstracts and Programme, *EUROCARBON 2000: 1st World Conf. on Carbon*, July 9–13, 2000, Berlin (Germany), 2000, vol. 2, pp. 697–698.
16. Tryba, B., Kalenczuk, R.J., and Morawski, A.W., Program and Abstracts, *11th Int. Symp. on Intercalation Compounds*, May 27–31, 2001, Moscow (Russia), 2001, p. 104.
17. Ukrainian Patent 34777.
18. Savoskin, M.V., Yaroshenko, A.P., Shologon, V.I., *et al*., Abstracts and Programme, *EUROCARBON 2000: 1st World Conf. on Carbon*, July 9–13, 2000, Berlin (Germany), 2000, vol. 2, pp. 673–674.
19. Inagaki, M. and Suwa, T., *Carbon*, 2001, vol. 39, no. 6, pp. 915–920.

Russian Journal of Applied Chemistry, Vol. 77, No. 5, 2004, pp. 750–755. Translated from Zhurnal Prikladnoi Khimii, Vol. 77, No. 5, 2004, pp. 754–759.

SORPTION AND ION-EXCHANGE PROCESSES

Activated Carbons Prepared from Chemically Modified Sapropelites

N. V. Bodoev, V. A. Kucherenko, T. G. Shendrik, and T. A. Bal'burova

Buryat State University, Ulan-Ude, Buryatia, Russia

Received November 25, 2003

Abstract—Changes in sapropelite structure at room temperature in the course of modification with HNO_3, HNO_3–Ac_2O, SO_3–H_2SO_4, and H_2SO_4 were studied. The effect of chemical modification on the development of the specific surface area at thermolysis in the presence of acid (H_3PO_4) or base (KOH) activators was analyzed.

Natural coals are widely used raw materials for preparing carbon sorbents (CS), whose properties are largely determined by the chemical structure and reactivity of the precursor [1]. The fossil coal structure can change under the conditions of chemical modification and, in turn, strongly affect the processes of further physical or chemical activation at the sorbent preparation [2–9].

The most widely used procedures for chemical modification of natural coals involve treatment with various oxidants, e.g., O_2 [2, 4], HNO_3 [3–5], $HClO_4$ [6, 7], acetyl nitrate [8], and others [9]. Conditions of oxidative modification (OM) are chosen on the basis of only two principally different approaches: (1) partial oxidative degradation of the coal organic matter with formation of functional groups (FGs) and (2) reorganization of the steric and molecular structure under the conditions similar to those of graphite intercalation [10].

As a typical heterogeneous process, oxidative degradation starts in the near-surface layer and spreads inside the coal particle; it is accompanied by low-temperature burning-out of organic compounds. Intercalation conditions provide rapid diffusion of the modifying agent into the coal, uniform distribution of the reacting species in the coal matrix (as in formation of solid solutions), and the occurrence of the modification reaction not only in the near-surface layer, but also in the coal bulk, i.e., under the "pseudohomogeneous" conditions.

It should be mentioned that the intercalation method is yet under development. Various procedures and reagents are tested, optimal conditions of intercalation of the natural coals (which are quite different from the conditions for preparing graphite intercalation compounds [11]) are sought for, and data on the reactivity of carbons of various histories are accumulated. The positive effect of intercalation has been shown, but its further development seems promising [5–7, 9].

In this work we studied modification of sapropelite (Sp) under the intercalation conditions and analyzed changes in its structure and their effect on the development of the specific surface area at activation.

The following modifying agents were used.

(1) Fuming HNO_3 (≥99%) is a traditional reagent for preparing graphite nitrate [10], which yields one-electron oxidant (nitronium cation NO_2^+) and intercalating agent (NO_3^- anion) in the course of dissociation: $2HNO_3 = NO_2^+ + HNO_3^- + H_2O$. As reagent, it was tested with anthracite (Donets Coal Fields, Ukraine) [9].

(2) Equimolar HNO_3–acetic anhydride (Ac_2O) mixture, which yields the same oxidant NO_2^+, but different intercalating agent (acetate anion) by the reaction $HNO_3 + Ac_2O \rightarrow NO_2AcO + AcOH \rightarrow NO_2^+ + AcO^- + AcOH$. This reaction was studied using humus coals [12] and tested with sapropelite [8].

(3) Oleum (20% SO_3 in H_2SO_4), containing oxidant (SO_3) and intercalating agent (hydrosulfate anion).

(4) Sulfuric acid (96%) was taken for comparison with oleum.

The first two reagents are nitrating agents [5, 12], and the last two are sulfonating agents [13].

These reagents were selected so as to transform the structural fragments of sapropelite into carbocations

1070-4272/04/7705-0750 © 2004 MAIK "Nauka/Interperiodica"

with subsequent compensation of the positive charge by intercalation of anions (A = NO_3^-, AcO^-, HSO_4^-) in the coal skeleton; as a result, modification reactions can be transferred from the particle surface into the bulk.

EXPERIMENTAL

We studied an Sp sample from the Taimylyr deposit (Lena coal field): particle size $d \le 0.2$ mm, water content $W^a = 1.1\%$, ash content $A^d = 3.5\%$; elemental composition of the organic matter (% daf): C 82.6, H 9.5, S 0.3, N 0.7, O_d 6.9. The contents of alginite and vitrinite was 87 and 13%, respectively.

Preliminarily dried (105°C, 2 h) coal sample was modified at room temperature (20 ± 1°C). The Sp sample (1 g) was contacted with a required amount of reagent R, given in moles of HNO_3 (or H_2SO_4) per kilogram of dry coal. In certain time τ, the reaction mixture was filtered, and the solid product was washed with benzene (30 cm^3) and diethyl ether (30 cm^3) and dried in a vacuum (~2 kPa, 20°C).

The modified coal was isolated by triple washing with water (hydrolysis) and decantation (250 cm^3 H_2O per gram of Sp) with subsequent filtration and drying. We assume that this treatment provides removal of molecules and ions that are not bound with the carbon skeleton by covalent bonds, i.e., the intercalated "guest" species are removed from the coal skeleton. For the coal samples prepared by this procedure, we studied changes in the molecular structure. Coals modified with various reagents are designated as follows: Sp(HNO_3), Sp(NO_2AcO), Sp(SO_3), and Sp(H_2SO_4).

Activated sapropelites (ASps) were prepared by thermal treatment of the modified coals in the presence of various activators (KOH or H_3PO_4) in two steps. The first step involves impregnation of the carbon sample (10 g) with a 50% aqueous solution of KOH or H_3PO_4 in the amount providing the required activator/coal weight ratio R_a (g g^{-1}), where a = KOH or H_3PO_4, storage at 20°C for 20 h, and drying for 3 h at 150 (KOH) or 170°C (H_3PO_4). In the second stage, the impregnated sample (2 g) is heated in a horizontal tubular furnace (heating rate 10 ± 2 deg min^{-1}) in an argon flow (~1 dm^3 h^{-1}) to the activation temperature T_a, kept at this temperature for 2 h, cooled in argon to 50 ± 10°C, washed with water to pH ~ 7, and dried at 105°C for 2 h.

In the course of modification, the relative changes in the coal weight m and volume V were monitored:

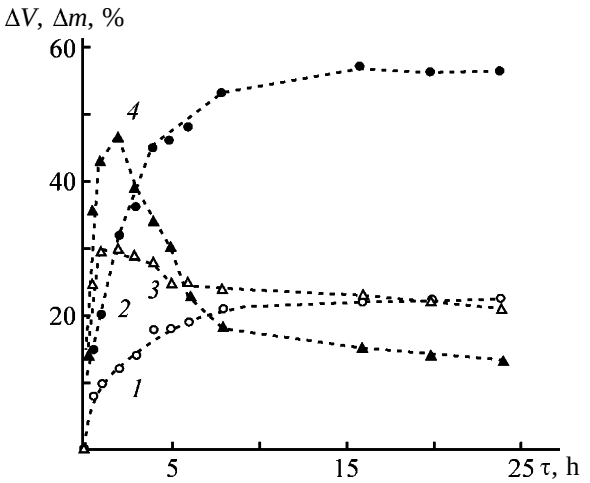

Fig. 1. Changes in the coal (*1*, *3*) weight Δm and (*2*, *4*) volume ΔV in the course of modification with HNO_3–Ac_2O mixture as functions of the reagent/coal ratio R. (τ) Time. R, mol kg^{-1}: (*1*, *2*) 20 and (*3*, *4*) 100.

Δm (%) = $100(m - m_0)/m_0$ and ΔV (%) = $100(V - V_0)/V_0$, where m_0 and V_0 correspond to the initial dry sample.

The IR spectra of coal–KBr (5 : 95 weight ratio) mixture were recorded on a Mattson 3000 FTIR apparatus in the 4000–400 cm^{-1} range (2 cm^{-1} resolution, 500 scans). The absorption bands were assigned by comparative analysis of the IR spectra of individual compounds [14], natural organic compounds [15], and coals [16]. The thermogravimetric analysis was performed on a Setaram TGDTA 92 analyzer (sample weight 50 mg, heating rate 10 deg min^{-1}, argon atmosphere). The IR spectra of the volatile thermolysis products were recorded *in situ* using a Bio-Rad FTS 165 spectrophotometer connected by a tube with the Setaram TGDTA 92 analyzer. The specific surface area S (m^2 g^{-1}) was determined by low-temperature (77 K) sorption of argon and by small-angle X-ray scattering (SAXS) [8].

Irrespective of the reagent type, modification is accompanied by swelling of the coal, changes in its weight, and release of gaseous NO_2 or SO_2. We also recorded exothermic effects, which (in the first 45–60 min) increase the temperature of the reaction mixture to the following values (R = 20 mol kg^{-1}): 63 (HNO_3), 59 (HNO_3–Ac_2O), 73 (oleum), and 67°C (H_2SO_4).

In the examined range of R, the weight and volume of the coal first increase and then reach a plateau (Fig. 1) or pass through a maximum and subsequently decrease to certain constant Δm or ΔV. All the modification reactions are complete in 16–20 h: ΔT values

Table 1. Change in the elemental composition of sapropelite at modification with HNO_3–Ac_2O mixture; R = 20 mol kg^{-1}, isolation by hydrolysis

τ, h	Composition, %				
	C	H	N	S	O_d
0	82.6	9.5	0.7	0.3	6.9
0.5	72.0	8.7	2.3	0.3	16.7
1.0	69.1	8.3	3.2	0.2	19.2
2.0	67.4	7.9	3.8	0.2	20.7
3.0	66.7	8.0	4.7	0.2	20.4
6.0	65.3	8.1	4.6	0.2	21.8
16	64.2	8.1	4.6	0.2	22.9
20	64.4	8.2	4.5	0.2	22.7

tend to zero, gas liberation is terminated, Δm and ΔV values are stabilized, and the elemental composition becomes constant (Table 1). In all the further tests, the modification time was constant (τ = 20 h). The degree of modification (evaluated as Δm and ΔV) depends on the reagent/coal ratio (Fig. 2): with increasing R, the weight and volume of the coal increase, reaching maximal values at R = 20 mol kg^{-1}. In the R = 20–100 mol kg^{-1} range, Δm values either remain constant or decrease after passing a maximum, which is caused by partial oxidative degradation of the organic matter at the reagent excess [8, 12]. The oxidative degradation is the most pronounced in modification with HNO_3 and less pronounced with the HNO_3–Ac_2O mixture; with H_2SO_4 and oleum at 20 ± 1°C, no degradation is observed. Thus, from the viewpoint of maximal weight and volume of the resulting coal, R = 20 mol kg^{-1} is the optimal value. This conclusion can be confirmed by the following facts.

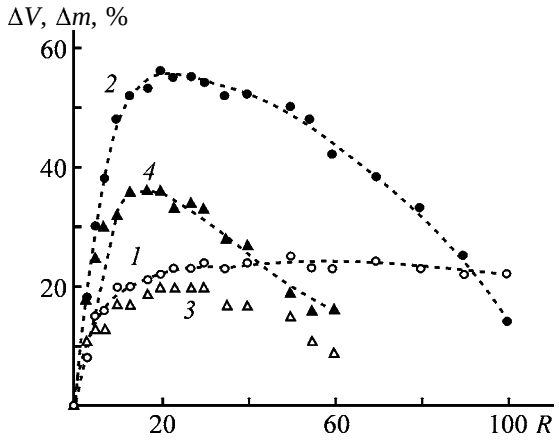

Fig. 2. Changes in the coal (*1*, *3*) weight Δm and (*2*, *4*) volume ΔV as functions of the reagent/coal ratio R. Modifying agent: (*1*, *2*) HNO_3 and (*3*, *4*) HNO_3–Ac_2O.

(1) According to the data of chemical analysis, the main fraction (0.90–0.95) of the covalently bound O, N, and S atoms appear at R = 20 mol kg^{-1}. In the R = 20–100 mol kg^{-1} range, the content of O, N, and S remains nearly constant (±0.1%). The intensity of the IR absorption bands, in particular, those of nitrate (1555 and 1375 cm^{-1}) and sulfate (1060 cm^{-1}) groups remain constant within the measurement error (±10 rel. %).

(2) The DTA data (Table 2) show that the total yield of the solid products and its dependence on the temperature (heating rate 10 deg min^{-1}) of thermolysis of the modified carbons only slightly change with increasing R from 20 to 100 mol kg^{-1}, but strongly differ from those observed in thermolysis of the initial sample.

(3) At small R (≤20 mol kg^{-1}), sapropelite seems visually dry (especially in the case of HNO_3 and HNO_3–Ac_2O reagents). Liquid modifying agent is almost completely absorbed by the coal skeleton, i.e., the modification reactions proceed in the carbon bulk. Moreover, R = 20 mol kg^{-1} was found to be the optimal value in modification of coals of the aromatic nature (humolites) in HNO_3–Ac_2O [17].

In the case of HNO_3-containing reagents, the coal organic matter is nitrated; the IR spectra exhibit the absorption bands of the antisymmetric (1555 cm^{-1}) and symmetric (1375 cm^{-1}) stretching and bending (850 cm^{-1}) vibrations of aliphatic nitro groups (Alk–NO_2). By deconvolution of the IR spectra [8], the fragments with C–N bonds (1580 cm^{-1}) and nitroso and aromatic nitro groups (1530 and 1348 cm^{-1}) were identified, but their amount is small because of small content of aromatic structures in sapropelite [16]. The carboxy groups and ketones with open chain were also detected (increase in the absorption intensity at 1725–1700 cm^{-1}).

Functional groups are formed in reactions with aliphatic sapropelite chains; as a result, the intensity of the absorption bands of the stretching (2926 and 2853 cm^{-1}) and bending (1465 cm^{-1}) vibrations of methylene groups decreases. The IR spectrum of Sp(NO_2AcO) exhibits a strong broad band at 1100 cm^{-1}, typical of dialkyl ethers –CH_2–O–CH_2– [15] and absent in the spectra of Sp and Sp(HNO_3). The bending vibrations of the alcohol hydroxy groups are also observed in this region, but simultaneously with the stretching vibrations of the alcoholic C–O groups (1350–1260 cm^{-1} [14]). In our case, the intensity of the absorption bands of the alcoholic C–O groups is low, and thus the content of alcoholic groups

Table 2. Yield of solid products of thermolysis of the initial and modified sapropelites

Sample	Yield, %, on heating to the indicated temperature, °C							
	200	300	400	500	600	700	800	900
Sp	96	92	84	28	24	19	13	9
$Sp(NO_2AcO)$, R, mol kg^{-1}:								
20	82	64	54	30	28	27	26	25
100	74	55	49	26	24	23	22	20
$Sp(HNO_3)$, R = 20 mol kg^{-1}	83	61	52	29	27	26	25	25

in $Sp(HNO_3)$ and $Sp(NO_2AcO)$ is insignificant. Moreover, these C–O groups can be parts of acetoxy (Alk–OAc) and other ester groups identified by the C=O absorption at 1750–1730 cm^{-1} in the IR spectra of $Sp(NO_2AcO)$. Thus, modification with the HNO_3–Ac_2O mixture probably yields ester groups between the neighboring alkane chains in the carbon skeleton.

If the increase in the nitrogen content after Sp modification (Table 3) is due to the nitration, then the content of the nitro groups comprises 3 and 2.7 mol kg^{-1} for $Sp(HNO_3)$ and $Sp(NO_2AcO)$, respectively. However, the corresponding content of oxygen in the NO_2 groups is 9.6 and 8.6% of the total 23.0 and 22.7%, respectively (Table 3). Thus, nitration of Sp in the course of modification is accompanied by other reactions, primarily, by formation of coal radicals at one-electron oxidation of the sapropelite fragment due to the electron transfer on the nitronium cation. Evolution of gaseous NO_2 directly confirms the occurrence of this reaction.

The oxidative degradation effect of the sulfuric acid reagents is lower. The increase in O_d (Table 3) is close to the oxygen content in the sulfo groups (calculated from S^{daf}), though in $Sp(SO_3)$ the oxygen content is higher. Appearance of new bands in the IR spectra of $Sp(SO_3)$ and $Sp(H_2SO_4)$ confirms formation of the sulfo groups (1225 and 1055 cm^{-1}), sulfones Alk–SO_2–Alk (1310 cm^{-1}), and probably sulfonates Alk–O–SO_2Alk (1360–1170 cm^{-1}). The oxidation and polymerization (dehydropolycondensation), often proceeding at sulfonation of alkanes, are also possible [13].

Our data on the effect of modification on the surface development in the course of sapropelite activation show that the ASp properties depend on the nature of the modifying and activation (KOH or H_3PO_4) agents. The initial sapropelite poorly reacts with aqueous solutions of KOH and H_3PO_4 at impregnation, and its activation yields only low-porous materials (S = 40–60 $m^2\ g^{-1}$). All the modified sapropelites are much more active than the initial substance.

The temperature dependences of the specific surface area S of modified sapropelites at activation with H_3PO_4 are shown in Fig. 3a. With increasing temperature (from 350 to 700°C), the specific surface area increases, whereas at T_a = 700–850°C it tends to decrease. The highest value of $S = 500 \pm 20$ $m^2\ g^{-1}$ is attained at T_a = 700°C; however, the samples with almost the same specific surface area (up to 440 $m^2\ g^{-1}$) can be prepared even at 500°C at activation of $Sp(H_2SO_4)$. A similar pattern is observed with $Sp(NO_2AcO)$; the greatest $S = 390 \pm 20$ $m^2\ g^{-1}$ is reached at T_a = 500°C, and on heating to 850°C it remains constant (within the experimental error). As seen from Fig. 3, H_2SO_4 is the best modification agent to convert sapropelite into porous carbon materials, but the other modifying agents are also effective. The acid activation agent (H_3PO_4) reacts at fairly low temperatures (≤500°C), but it is ineffective for preparing highly porous materials from modified sapropelites.

The activation effect of KOH is more pronounced (Fig. 3b); at T_a = 850°C [R(KOH) = 1.1 g g^{-1}] all

Table 3. Chemical compositions of modified sapropelites; R = 20 mol kg^{-1}, isolation by hydrolysis

Sample	Elemental composition, % daf				
	C	H	N	S	O_d
Sp	82.6	9.5	0.7	0.3	6.9
$Sp(HNO_3)$	64.0	7.9	4.9	0.2	23.0
$Sp(NO_2AcO)$	64.4	8.2	4.5	0.2	22.7
$Sp(SO_3)$	73.1	8.1	0.5	4.4	13.9
$Sp(H_2SO_4)$	75.1	8.2	0.6	3.8	12.3

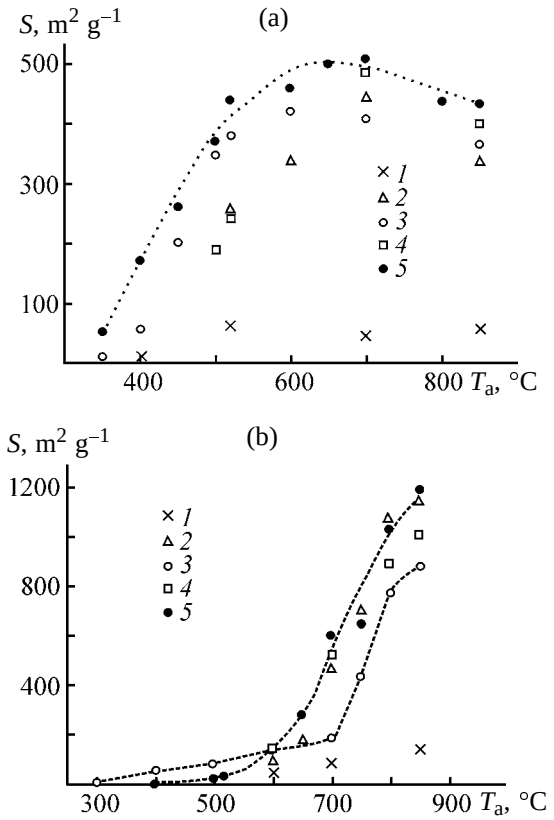

Fig. 3. Specific surface area *S* of sapropelites as influenced by the activation temperature T_a. Activating agents: (a) H_3PO_4 and (b) KOH; $R(H_3PO_4) = R(KOH) = 1.0$ g g^{-1}. Sapropelite: (*1*) Sp, (*2*) Sp(HNO_3), (*3*) Sp(NO_2AcO), (*4*) Sp(SO_3), and (*5*) Sp(H_2SO_4).

the modified sapropelites yield the materials with highly developed surface (S = 900–1200 m^2 g^{-1}). In the 650–850°C range, *S* almost linearly increases with temperature for all the samples, but with Sp(NO_2AcO) this increase is the least, and with Sp(H_2SO_4), the most pronounced, as in activation with H_3PO_4.

High activation temperature (800–850°C) levels off the differences caused by modification with different reagents. Under milder conditions [T_a = 700°C, R(KOH) = 1.0 g g^{-1}], the effect of the modifying agents on the specific surface area changes in the following order [*S* values, m^2 g^{-1}, for ASp (Fig. 3b) are given in parentheses]: HNO_3–Ac_2O (190) < HNO_3 (480) < SO_3–H_2SO_4 (520) < H_2SO_4 (600).

Table 4. Specific surface area as influenced by KOH/coal ratio,* T_a = 800°C, τ = 2 h

Sample	*S*, m^2 g^{-1}, at indicated *R*(KOH), g g^{-1}				
	0.25	0.50	1.0	1.5	2.0
Sp(H_2SO_4)	105	510	1030	1460 (1600)**	1590
Sp(NO_2AcO)	90	360	770	1130 (1200)	1230

* *S* determined by SAXS method [8].
** Measurement error ±8 rel %.

It should be noted that the same order is observed with H_3PO_4, but the *S* values (410, 450, 490, 510 m^2 g^{-1}; Fig. 3a) vary in a narrower range, i.e., the functional groups formed at modification are more sensitive to alkali than to H_3PO_4 (acid activator). With increasing KOH/coal ratio, *S* values increase (Table 4) virtually linearly to R(KOH) = 1.5 g g^{-1}; with further increase in *R*, variations in the specific surface area are negligible. Similar *S*–*R*(KOH) dependences were found previously for humus coals [18]. For two ASp samples (Table 4) we obtained similar *S* values by two independent methods: low-temperature (77 K) sorption of argon and SAXS procedure [8].

As seen, alkali strongly affects the development of the specific surface area in activation of modified sapropelites, which is due to the additional reactions of KOH with functional groups formed by modification. Even in the course of impregnation, various processes occur simultaneously, namely: ion-exchange reactions with acidic functional groups R–OH + KOH → R–O–K$^+$ + H_2O, where R = Alk–, Alk–C(O)–, Alk–SO_2–, formation of *aci*-nitro compounds Alk–CH_2NO_2 + KOH → Alk–CH=$NO_2^-K^+$ + H_2O, saponification of esters, etc.

These reactions promote penetration of KOH into the coal bulk, which is accompanied by swelling of the coal and distribution of KOH (or K^+ and OH^- ions) in the coal skeleton, which is similar to the formation of solid solutions. Upon heating to the activation temperatures, potassium compounds decompose, e.g., R–$NO_2^-K^+$ → R–OK + NO (≤400°C); R–SO_3K → R–OK + SO_2 (300–500°C); R–COOK → ROK + CO (≤500°C). Several new reactive intermediates arise, which form the secondary ASp network due to the polycondensation processes. Free alkali distributed in the coal skeleton also participates in the thermally initiated reactions, e.g., in cleavage of ethers (at 300–400°C [19]) and dehydrogenation CH_2 + KOH → C(H)OK + H_2 (500–700°C) [20].

Reactions involving KOH and various functional groups yield a porous carbon material with highly developed surface (S = 1000–1600 m^2 g^{-1}). The acidic groups do not promote penetration of H_3PO_4 into the coal bulk; as a result, certain fraction of the coal material is converted without H_3PO_4, yielding a more compact three-dimensional secondary lattice

with less developed surface ($S \leq 500$ $m^2 g^{-1}$). It should be noted that the greatest effect was found in modification with H_2SO_4, which exhibits only the sulfonation power at minimal oxidative degradation of the coal. We assumed that, along with formation of the corresponding functional groups, H_2SO_4 promotes low-temperature polycondensation of the alkane chains in sapropelite through the intermediate generation of carbocations [13]. Such reactions prepare the aliphatic carbon skeleton for thermally initiated conversion into the aromatic AC lattice.

CONCLUSIONS

(1) The data on structural changes in the course of sapropelite modification with HNO_3, HNO_3–Ac_2O, SO_3–H_2SO_4, and H_2SO_4 at room temperature showed that the steric structure changes owing to the penetration of reactive species in the coal skeleton and their binding with ionic and covalent bonds. The molecular structure changes as a result of nitration or sulfonation of the alkane chains, transformation of the aliphatic fragments into oxygen functional groups, and cleavage of a part of C–C and C–O bonds of the organic skeleton.

(2) At properly chosen temperature and activator/coal ratio, modified sapropelites transform into porous carbon materials with highly developed surface (1200–1600 $m^2 g^{-1}$).

REFERENCES

1. Schobert, H.H. and Song, C., *Fuel*, 2002, vol. 81, no. 1, pp. 15–32.
2. Pis, J.J., Parra, J.B., Puente, G. de la, *et al*., *Fuel*, 1998, vol. 77, no. 6, pp. 625.
3. Verheyen, V., Rathbone, R., Jagtoyen, M., and Derbyshire, F., *Carbon*, 1995, vol. 33, no. 6, pp. 763–772.
4. Serrano-Talavera, B., Munoz-Guillena, M.J., Linares-Solano, A., and Salinas-Martinez de Lecea, C., *Energy Fuels*, 1997, vol. 11, no. 4, pp. 785–791.
5. Kucherenko, V.A., Khabarova, T.V., Gruber, R., *et al*., Extended Abstracts, *23rd Conf. on Carbon "Carbon'97" (July 18–23, 1997)*, Pennsylvania (USA): Am. Chem. Soc., 1997, vol. 2, pp. 64–65.
6. Albiniak, A., Furdin, G., and Begin, J.F., *Carbon*, 1996, vol. 34, no. 11, pp. 1329–1334.
7. Lyubchik, S.B., Benoit, R., and Beguin, F., *Carbon*, 2002, vol. 40, no. 11, pp. 1287–1294.
8. Bodoev, N.V., Gruber, R., Kucherenko, V.A., *et al*., *Fuel*, 1998, vol. 77, no. 6, pp. 473–478.
9. Kucherenko, V.A., in *Struktura organicheskikh soedinenii i mekhanizmy reaktsii* (Structure of Organic Compounds and Reaction Mechanisms), Donetsk, 1998, pp. 69–72.
10. Chernysh, I.G., Karpov, I.I., Prikhod'ko, G.P., and Shai, V.M., *Fiziko-khimicheskie svoistva grafita i ego soedinenii* (Physicochemical Properties of Graphite and Its Compounds), Kiev: Naukova Dumka, 1990.
11. Khabarova, T.V., Tamarkina, Yu.V., Shendrik, T.G., and Kucherenko, V.A., *Khim. Tverd. Topl*., 2000, no. 1, pp. 45–52.
12. Tamarkina, Y.V., Shendrik, T.G., Krzton, A., and Kucherenko, V.A., *Fuel Proc. Technol*., 2002, vols. 77–78, pp. 9–15.
13. Gilbert, E.E., *Sulfonation and Related Reactions*, New York: Interscience, 1965.
14. Bellamy, L.J., *The Infra-Red Spectra of Complex Molecules*, New York: Wiley, 1957.
15. Orlov, D.S. and Osipova, N.N., *Infrakrasnye spektry pochv i pochvennykh komponentov* (IR Spectra of Soils and Soil Components), Moscow: Mosk. Gos. Univ., 1988.
16. Bodoev, N.V., *Sapropelitovye ugli* (Sapropelite Coals), Novosibirsk: Nauka, 1991.
17. Kucherenko, V.A., Khabarova, T.V., and Chotii, K.Yu., *Zh. Prikl. Khim*., 1996, vol. 69, no. 9, pp. 1462–1467.
18. Tamarkina, Yu.V. and Shendrik, T.G., *Khim. Tverd. Topl*., 2002, no. 6, pp. 3–10.
19. Utz, B.R., Nowak, M.A., and Fauth, D.J., *Proc. Int. Conf. on Coal Science*, Tokyo: IEA, 1989, vol. 1, pp. 197–200.
20. Yoshizawa, N., Maruyama, K., and Yamada, Y., *Fuel*, 2002, vol. 81, no. 15, pp. 1717–1722.

Russian Journal of Applied Chemistry, Vol. 77, No. 5, 2004, pp. 756–758. Translated from Zhurnal Prikladnoi Khimii, Vol. 77, No. 5, 2004, pp. 760–762.

SORPTION AND ION-EXCHANGE PROCESSES

Determining the Mechanism of Formaldehyde Adsorption from an Aqueous Medium on the Basis of the Diffusion Criterion

L. I. Bel'chinskaya and O. A. Tkacheva

Voronezh State Forestry Academy, Voronezh, Russia

Received April 16, 2003; in final form, October 2003

Abstract—Adsorption of formaldehyde from an aqueous medium on acid-treated clayey minerals was studied under conditions of natural convection and under stirring of the solution.

One of important unsolved environmental problems of the woodworking industry is removal of formaldehyde from liquid wastes of furniture factories. The aim of this study was to establish the mechanism of formaldehyde adsorption from an aqueous medium on the basis of the diffusion criterion and to use this parameter to determine ways to intensify the process.

EXPERIMENTAL

Three systems constituted by formaldehyde and clayey microporous minerals (montmorillonite, palygorskite, and clinoptilolite) and having different types of structure [1, 2] were studied.

To determine the specific features of the behavior of the systems under study under conditions of natural convection and under stirring, equilibrium and dynamic processes were studied.

The adsorption of formaldehyde was carried out on 1-g mineral samples (grain size 0.025 cm) from 0.025 l of 0.03 M formaldehyde solution. The time of equilibration was 20 min. The samples were pretreated with a 15% solution of H_2SO_4 to improve their adsorption characteristics [3].

The adsorption value, a (mg g^{-1}), was calculated by the equation [4]

$$a = (c_0 - c)/m, \quad (1)$$

where c_0 and c are the concentrations of the formaldehyde solution before and after adsorption, respectively (mg l^{-1}); m is the adsorbent mass (g l^{-1}).

The values of a were obtained with a high correlation factor ($r = 0.98$).

Typical dependences which supposedly reflect processes of the rate-determining stage of diffusion were analyzed: θ–τ and θ–$\tau^{1/2}$, where $\theta = a/a_{max}$ is the fraction of adsorption in a certain interval of time τ; a and a_{max} are the running and maximum adsorption values, respectively (mg g^{-1}).

The adsorption rate is determined by inner diffusion if the dependence θ–τ is initially linear and then gives way to the linear dependence $\theta = f(\tau^{1/2})$, with the straight lines emerging from the origin of coordinates [5]. The obtained linear dependence $\theta = f(\tau^{1/2})$ assumes that the inner diffusion is the rate-determining factor in adsorption of formaldehyde on palygorskite, montmorillonite, and clinoptilolite.

When the rate of the process is determined by outer diffusion, the dependence $\ln(1 - \theta)$–τ from the equation

$$\ln(1 - \theta) = -\beta\tau, \quad (2)$$

where β is the rate constant (s^{-1}), should be linear [6], which was found to be the case in an analysis of formaldehyde adsorption on the minerals under study. The value of β was determined graphically from the slope of the straight line in the coordinates $\ln(1 - \theta)$–τ.

The bounds of the outer- and inner-diffusion regions were discussed on the basis of an analysis of the Bi criterion with the use of the rate constant β of the adsorption process [4] and the inner-diffusion constant $\bar{D}$. The Bi criterion (ratio of the inner resistance to mass transfer within an adsorbent grain to the outer resistance to mass transfer from the bulk of the liquid to the grain surface) was found from the equation

$$Bi = \beta r^2/\bar{D}, \quad (3)$$

1070-4272/04/7705-0756 © 2004 MAIK "Nauka/Interperiodica"

Table 1. Kinetic, equilibrium, and thermodynamic characteristics of formaldehyde adsorption on modified clayey minerals under conditions of natural convection

Mineral	a, mg g^{-1}	k_d*	$\beta \times 10^3$, s^{-1}	$\bar{D} \times 10^8$, cm^2 s^{-1}	Bi criterion	$-\Delta F^0$, kJ mol^{-1}
Clinoptilolite	3.7**/9.6	0.17/0.62	1.7	2.7	10.1	27.3
Montmorillonite	7.7/15.0	0.44/1.50	2.9	4.6	9.8	31.2
Palygorskite	9.2/17.0	0.58/2.13	3.7	5.8	9.9	32.1

* k_d is the distribution coefficient of formaldehyde between the liquid and solid phases.
** Numerator: data at the minimum fraction of adsorption, θ; denominator: those at the maximum $\theta = 1$.

Table 2. Comparative kinetic characteristics of formaldehyde adsorption on montmorillonite under the conditions of natural convection and under stirring

τ,* s	a, mg g^{-1}					k_d				θ			
	at indicated stirring rate, rpm												
	0	6	20	50	60	0	6	20	50	0	6	20	50
120	7.7	10.0	12.7	16.6	18.5	0.44	0.67	1.03	1.98	0.51	0.53	0.65	0.79
300	11.8	14.3	16.2	19.0	23.0	0.89	1.34	1.84	3.16	0.79	0.75	0.83	0.90
600	14.0	17.0	18.0	20.3	22.0	1.27	2.13	2.57	4.32	0.93	0.89	0.92	0.96
1200	14.7	18.2	19.0	20.8	21.2	1.43	2.68	3.17	4.95	0.98	0.96	0.97	0.98
1800	14.8	18.8	19.4	20.9	21.0	1.45	3.03	3.23	5.10	0.99	0.98	0.98	0.99
2400	14.9	18.9	19.5	21.0	20.7	1.48	3.10	3.55	5.25	0.99	0.99	0.99	0.99
3600	15.0	19.0	19.6	21.1	20.5	1.50	3.17	3.63	5.41	1.00	1.00	1.00	1.00

* τ is the time of adsorption.

where r is the effective radius of sorbent particles (cm) and $\bar{D}$ is the inner-diffusion coefficient $\bar{D}$ (cm^2 s^{-1}) calculated graphically using the Crank equation [4]

$$\ln(1 - \theta) = \ln(6/\pi^2) - (\bar{D}\pi^2\tau/r^2), \quad (4)$$

The values of D, obtained for the systems under study (Table 1), are comparable with published values for natural minerals [6, 7].

On the basis of the values obtained for β and $\bar{D}$, the Bi criterion was calculated (Table 1). This criterion establishes the boundary between the outer and inner types of diffusion: Bi $\leq$ 0.1 corresponds to rate-determining outer diffusion, and at Bi $\geq$ 30, the control is by the inner diffusion. If Bi is within the range from 0.1 to 30, the process may occur by the mixed-diffusion mechanism [4]. For modified minerals, Bi is approximately 10 (Table 1).

The operation of the mixed mechanism of adsorption is confirmed by the fact that the outer-diffusion limitations are partly lifted in the case of formaldehyde adsorption on montmorillonite in the hydrodynamic mode. The solution was agitated at fixed rates V of 6, 20, 50, and 60 rpm.

The free molar energy $-\Delta F^0$ (kJ mol^{-1}) was calculated by the equation

$$-\Delta F^0 = RT\ln K_{se}, \quad (5)$$

where K_{se} is the sorption equilibrium constant found from adsorption isotherms; R, universal gas constant (J mol^{-1} K^{-1}); and T, temperature (K).

The values of $-\Delta F^0$ for palygorskite and montmorillonite (Table 1) differ only slightly, but exceed that for clinoptilolite.

Montmorillonite was chosen as a sorbent of formaldehyde because it shows promise as a material for environmental technologies owing to the presence in Voronezh oblast of rather large and accessible deposits of bentonite enriched in montmorillonite.

The results of a comparative analysis of equilibrium, kinetic, and thermodynamic parameters (Tables 2, 3) under the conditions of natural convection and under stirring indicate that, in the latter case, adsorption of formaldehyde on a modified montmorillonite is intensified. The adsorption capacity grows with increasing rotational speed of the stirring rod

Table 3. Comparative diffusion and thermodynamic characteristics of the process of formaldehyde adsorption on montmorillonite under the conditions of natural convection and under stirring

v, min^{-1}	$\beta \times 10^3$, s^{-1}	$\bar{D} \times 10^8$, $cm^2\ s^{-1}$	$-\Delta F^0$, $kJ\ mol^{-1}$
0	2.9	4.6	31.2
6	2.8	4.4	33.0
20	3.7	5.9	33.3
50	9.3	14.7	34.3

(Table 2). However, the extent of this influence decreases at $\tau > 300$ s, as it becomes probable at n = 60 rpm that the adsorption equilibrium can be disturbed and desorption processes can occur owing to the possible turbulent nature of motion of the solution [8]. Consequently, stirring of the solution enhances sorption (Table 2) and makes higher the rate constant of adsorption and the inner-diffusion coefficient (Table 3).

To partly lift the outer-diffusion limitations, it is suggested to agitate the solution at a rate of 6 to 50 rpm. The stirring raises the adsorption rate and the adsorption value, with only a slight increase in the free molar energy, which makes it possible to identify stirring as a factor that intensifies formaldehyde adsorption from an aqueous medium and to use it to develop promising technologies for wastewater purification to remove formaldehyde.

CONCLUSIONS

(1) Equilibrium, kinetic, and thermodynamic parameters of formaldehyde adsorption on clayey microporous minerals, montmorillonite, clinoptilolite, and palygorskite, were determined.

(2) Under the conditions of natural convection, the adsorption of formaldehyde occurs by the mixed-diffusion mechanism.

REFERENCES

1. Bel'chinskaya, L.I., Leikin, Yu.A., and Tarasevich, Yu.I., *Zh. Prikl. Khim.*, 1994, vol. 65, no. 11, pp. 1855–1858.
2. Tarasevich, Yu.I., *Adsorbtsiya formal'degida na glinistykh mineralakh* (Adsorption of Formaldehyde on Clayey Minerals), Tarasevich, Yu.I. and Ovcharenko, F.F., Eds., Kiev: Naukova Dumka, 1975.
3. Bel'chinskaya, L.I., Tkacheva, O.A., and Sakhokiya, I.A., *Izv. Vyssh. Uchebn. Zaved., Khim. Khim. Tekhnol.*, 1996, vol. 39, no. 6, pp. 65–68.
4. Koganovskii, A.M., Klimenko, N.A., Levchenko, T.M., and Roda, I.G., *Adsorbtsiya organicheskikh veshchestv iz vody* (Adsorption of Organic Substances from Water), Leningrad: Khimiya, 1990.
5. *Zeolite Chemistry and Catalysis*, Rabo, J.A., Ed., Washington: American Chemical Society, 1976.
6. Ashirov, A., *Ionnoobmennaya ochistka stochnykh vod, rastvorov i gazov* (Ion-Exchange Purification of Wastewater, Solutions, and Gases), Leningrad: Khimiya, 1983.
7. Tsitsishvili, G.V., Andronikashvili, T.G., Kirov, G.N., and Felizova, L.D., *Prirodnye tseolity* (Natural Zeolites), Moscow: Khimiya, 1985.
8. Koganovskii, A.M., Levchenko, T.M., Roda, I.G., and Marutovskii, R.M., *Adsorbtsionnaya tekhnologiya ochistki stochnykh vod* (Adsorption Technique of Wastewater Purification), Kiev: Tekhnika, 1981.

Russian Journal of Applied Chemistry, Vol. 77, No. 5, 2004, pp. 759–762. Translated from Zhurnal Prikladnoi Khimii, Vol. 77, No. 5, 2004, pp. 763–766.

SORPTION AND ION-EXCHANGE PROCESSES

Extraction of Molybdenum(VI) from Aqueous–Peroxide Solutions of Sodium Tungstate with Trialkylamine

L. A. Voropanova and N. G. Barvinyuk

North-Caucasian State Technological University, Vladikavkaz, North Ossetia, Russia

Received August 8, 2003; in the final form, January 2004

Abstract—The extraction of molybdenum(VI) from aqueous–peroxide solutions of sodium tungstate with a trialkylamine–isooctyl alcohol mixture in kerosene was studied in relation to the ratio of the organic and aqueous phases, hydrogen peroxide and hydrogen chloride consumption, and the ratio of molybdenum(VI) and tungsten (VI) in the aqueous phase. A method for additional purification of the raffinate to remove molybdenum was developed.

In recovery of tungsten from its ore concentrates, along with the target metal, arsenic(V), phosphorus(V), silicon(IV), and molybdenum(VI) impurities also pass into the solution. This solution can be efficiently purified to remove As(V), P(V), and Si(IV) impurities by well-known methods widely used in industry [1]. In contrast to As(V), P(V), and Si(IV), the purification of W(VI) to remove molybdenum is a more difficult problem, especially at high W : Mo ratios. In order to meet the consumers' requirements, the Mo content in tungsten must not exceed 0.02%. A common technique for tungsten purification to remove molybdenum is based on Mo(VI) precipitation as sulfide MoS_3. However, this procedure does not ensure preparation of tungsten meeting the requirements with respect to molybdenum content. Furthermore, with this technique, 0.2–0.3% of WS_3 is lost due to the coprecipitation of MoS_3 and WS_3. One more drawback of this technique is the hydrogen sulfide liberation. The most efficient tungsten purification to remove molybdenum can be carried out by solvent extraction or ion exchange.

It is known that, in acidification of aqueous solutions containing Mo(VI) and W(VI), mixed polyoxyanions of these metals are formed. When the molybdenum content in these polyanions becomes considerably lower than the tungsten content, the species similar to W(VI)-containing polyanions are formed. The mixed Mo(VI)–W(VI) polyanions can be decomposed with H_2O_2. This agent is relatively cheap and does not contaminate solution with any impurities [2]. Since aqueous–peroxide solutions of W(VI) and Mo(VI) are stable at pH < 2, they can be processed by solvent extraction. For example, in extraction of W(VI) and Mo(VI) from aqueous–peroxide–nitric acid solutions at pH 0.4–0.9 with tributyl phosphate, W(VI) is separated from Mo(VI) with the separation factor $\beta_{Mo/W}$ of about 40 [3]. Currently the most efficient purification of tungstates to remove Mo(VI) is achieved by selective solvent extraction of thio species $[MoS_4]_2^-$ [4–6].

In this work we studied the solvent extraction of Mo(VI) from aqueous–peroxide solutions of Na_2WO_4–Na_2MoO_4 mixture with the Mo(VI) content not exceeding 1% relative to the W(VI) content.

The extraction system used in our experiments contained trialkylamine R_3N [R = $CH_3(CH_2)_6CH_2$, TAA, 7 vol %], isooctyl alkohol $C_8H_{17}OH$ (14 vol %), and kerosene as diluent. This extraction system is used for industrial recovery of W(VI) from aqueous solutions preliminarily decontaminated from impurities, among them from Mo(VI) [7].

The aqueous solutions of W(VI) and Mo(VI) were prepared from chemically pure grade sodium tungstate and molybdate $Na_2MO_4 \cdot 2H_2O$ (M = W, Mo). Immediately after preparation, 33% H_2O_2 was added to the solution and the resulting mixture was acidified with concentrated HCl to the required pH (0–0.7). The HCl amount required for acidification is dependent on the initial tungstate concentration. In the course of extraction, the required pH was maintained at a constant level. The extraction was carried out at continuous stirring of the organic and aqueous phases to attain the equilibrium. The W(VI) and Mo(VI) content in both the initial solution and raffinate was determined colorimetrically. Before analysis, the aqueous solution was boiled to decompose H_2O_2. The metal content in the extract was determined as the difference between its content in the initial solution and raffi-

1070-4272/04/7705-0759 © 2004 MAIK "Nauka/Interperiodica"

Table 1. Parameters of extraction of W(VI) at its different concentrations in the initial aqueous solution. Molar ratio W : Mo = 100 : 1

Parameter	W(VI) concentration, g dm^{-3}					
	120	60	30	15	10	5
Ratio of organic and aqueous phases o : aq	1 : 3	1 : 3.5	1 : 4	1 : 7	1 : 9	1 : 15.5
H_2O_2 content, mol/mol W + Mo	1.76	1.5	0.75	0.75	0.75	0.75
HCl consumption, g dm^{-3}	74.7	48.75	34.5	25.4	34.5	34.5
pH	0	0.3	0.5	0.7	0.5	0.5
Time of extractant saturation with Mo(VI), min	45	30	30	30	15	15
D_W	0.18	0.23	0.49	1.10	1.29	2.24
D_{Mo}	7.19	9.15	14.3	13.33	15.53	20.07
β	38.05	39.44	29.19	12.06	12.02	8.94
ε_W, %	4.35	5.63	11.33	14.49	12.67	13.13
ε_{Mo}, %	63.38	70.19	78.87	67.14	63.51	57.51

nate. The efficiency of extraction of the metals was characterized by their distribution factors D (the ratio of the metal concentration in the organic and aqueous phase), degree of Mo and W separation $\beta = D_{Mo}/D_W$, and degree of recovery ε (wt % relative to the initial content).

The experimental results were statistically treated. The degree of W(VI) and Mo(VI) recovery was calculated from results of three parallel determinations. These results were characterized by the variance of reproducibility, S^2, accuracy of reproducibility S, and confidence interval at 0.95 confidence level X_m.

Parameter	Mo	W
S^2	0.737	0.985
S	0.858	0.992
X_m	±0.572	±0.662

In our experiments, the molybdenum(VI) impurity was extracted from aqueous solutions containing 120, 60, 30, 15, 10 and 5 g dm^{-3} W(IV) at the molar ratio W : Mo = 100 : 1. The extraction conditions and results are listed in Table 1.

With decreasing W(VI) concentration in the initial solution, the consumption of both H_2O_2 and HCl decreases. At the same time, the distribution factors of W(VI) and Mo(VI) increase and, as a result, the degree of the metal recovery grows. However, with increasing degree of tungsten recovery ε_W, the W(VI)/Mo(VI) separation factor β decreases. Thus, in extraction from highly concentrated solutions (C_W 120 and 60 g dm^{-3}), the separation of W(VI) from Mo(VI) is the most efficient, whereas the extraction from less concentrated tungsten(VI) solutions (C_W 30 g dm^{-3}) allows the maximal recovery of molybdenum(VI), with somewhat lower but still high separation factor β of molybdenum from tungsten. With further decreasing the W(VI) concentration, the separation factor sharply decreases.

For all the extraction systems, ε_W and ε_{Mo} increase with increasing extractant volume. With decreasing H_2O_2 concentration below its optimal value, the degree of the metal recovery decreases. In extraction of the metals in the absence of H_2O_2, colloids are formed, deteriorating the phase separation. This phenomenon is the most pronounced in extraction from concentrated metal solutions. Under these conditions, $\varepsilon_W > \varepsilon_{Mo}$ and $\beta < 1$. With increasing H_2O_2 content to 2 mol mol^{-1} W(VI) + Mo(VI), the extraction characteristics do not change noticeably.

With increasing HCl consumption, the H_2O_2 decomposition sharply accelerates, and the W(VI) and Mo(VI) peroxide complexes decompose. Under these conditions, tungstic and molybdic acids coprecipitate. With decreasing acidity of solutions, the Mo recovery ε_{Mo} virtually does not change, whereas the tungsten recovery ε_W strongly increases. We believe that such a behavior of W(VI) and Mo(VI) is due to the fact that, in strongly acidic solutions (pH < 0.5), nondissociated peroxy acids of Mo(VI) and W(VI) prevail, whereas at high pH partly protonated peroxyanions $HMoO_6^-$ and HWO_5^- are predominantly formed [8]. The conditions for extraction of the metals are the most favorable at pH corresponding to conversion of nondissociated species to their anionic forms. This transformation depends on the metal concentration: the lower the metal concentration, the faster is conversion and the higher the required pH. The large HCl consumption in the course of extraction of the metals is caused both by association of Cl^- with the peroxyanions HA^- and by recovery of HCl with TAA.

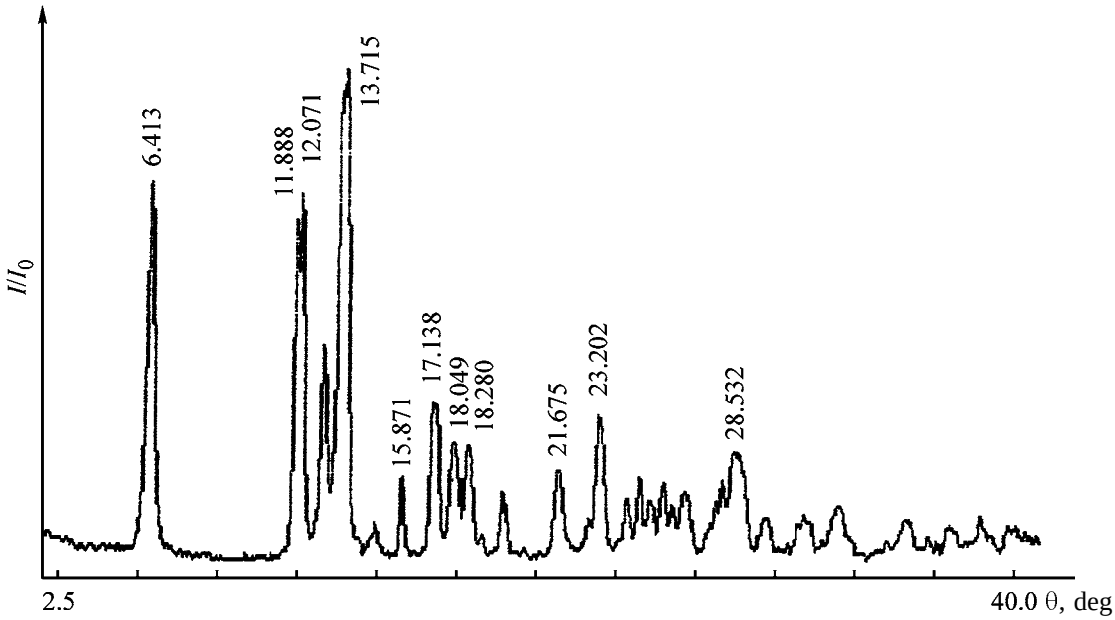

X-ray diffraction pattern of tungstic acid precipitated from a raffinate after extractive recovery of Mo(VI) from the initial solution containing W(VI) (30 g dm^{-3}) and Mo(VI) (0.3 g dm^{-3}). (I/I_0) Relative intensity and (θ) Bragg's angle.

We found that, on saturation of the extractant with Mo(VI), the ratio TAA : (W + Mo) = 1 : 0.35 remains constant irrespective of the metal content in the liquid phase. This fact shows that W and Mo are extracted in the form of an extractable complex of definite composition.

Table 1 shows that the recovery of Mo(VI) as a function of the tungsten concentration in the aqueous phase has a maximum at c_W = 30 g dm^{-3}. (ε_{Mo} = 78.87%). At this maximum, the extraction is characterized by fairly high separation factor $\beta_{Mo/W}$ = 29.19. Furthermore, at c_W = 30 g dm^{-3} the consumption of H_2O_2 and HCl can be decreased to 0.75 mol mol^{-1} (Mo + W) and 34.5 g dm^{-3}, respectively, and the ratio of organic and aqueous phases, to 1 : 4. These data show that the conditions for extraction separation of Mo(VI) from W(VI) are optimal at c_W 30 g dm^{-3} [9].

The extraction of Mo(VI) and W(VI) from aqueous–peroxide solutions with TAA–isooctanol in kerosene is described by following equations of the heterogeneous chemical reactions:

$$HA^- + (R_3NH)^+ \rightleftarrows (R_3NH)HA, \quad (1)$$

$$HA^- + H^+ + 2(R_3NH)HA \rightleftarrows [(R_3NH)HA]_2 \cdot H_2A, \quad (2)$$

where HA^- is HWO_5^- and HWO_6^-.

The extraction of the metals by the mechanism of the addition reaction (Eq. 2) is more characteristic of peroxomolybdic acid which is weaker than peroxotungstic acid. This difference allows the selective recovery of molybdenum impurities from concentrated Na_2WO_4 solutions. With increasing acidity, the dissociation of the peroxy acids is suppressed, which hinders the extraction of the metals by the mechanism of the addition reaction. At a very low Mo(VI) content, its extraction by this mechanism becomes insignificant. Therefore, on the phase contact for 30–45 min, when approximately one third of Mo(VI) remains in the aqueous phase (about 0.26% of c_W), the extraction of Mo(VI) stops, whereas the extraction of tungsten (ε_W) continues.

As noted above, the extraction of W(VI) from highly concentrated solutions is complicated by formation of poorly soluble WO_3 precipitate. This phenomenon can be used for additional purification of tungsten to remove molybdenum [10]. Once the main part of Mo(VI) is removed by extraction, tungstic acid precipitates, and, after a lapse of 2 days, about 92% of W(VI) and slightly more than 40% of Mo(VI) accumulate in the precipitate.

The figure shows the X-ray diffraction pattern (DRON-1 X-ray diffractometer, CuK_α radiation) of tungstic acid precipitated from a raffinate containing 120 g dm^{-3} W(IV) and 1.2 g dm^{-3} Mo(VI).

The relative reflection intensities I/I_0 and the interplanar spacings d calculated from the X-ray diffraction pattern are listed in Table 2 and are compared with those of both synthetic tungstic acid H_2WO_4 and tungsten trioxide WO_3.

This comparison shows (Table 2) that the structural parameters calculated from the most intense reflections

Table 2. X-ray diffraction patterns of tungstic acid precipitated from the raffinate, synthetic tungstic acid and tungstic trioxide

Precipitate		$H_2WO_4 \cdot H_2O$		WO_3	
d, Å	I/I_0	*d*, Å	I/I_0	*d*, Å	I/I_0
6.902	75	6.944	100		
3.742	70	3.774	30		
3.685	74	3.704	30		
3.446	43	3.472	30	3.448	14
3.285	95	3.311	40		
3.251	100	3.257	40		
2.636	32	2.646	15		
2.616	31	2.625	12		
2.526	23	2.525	10		
2.488	8	2.475	10		
2.458	22	2.457	8		
2.451	23			2.445	6
2.415	3	2.410	2	2.415	11
2.392	4			2.392	7
2.298	12	2.304	10		
2.091	17	2.101	8		
		2.066	10		
		1.965	12		
1.957	28	1.957	12		
1.903	4	1.901	12		
1.874	12	1.880	4		
1.839	16	1.845	6		
1.814	11	1.815	6		
1.778	15	1.783	6		
1.725	13	1.730	6	1.730	6
1.712	6			1.724	9
				1.709	8

in the X-ray diffraction patterns of both tungstic acid precipitated from a raffinate and synthetic tungstic acid are identical. At the same time, several weak reflections can be assigned to tungsten trioxide. According to X-ray phase analysis, tungsten precipitated from the raffinate consists to 89.82% of $H_2WO_4 \cdot H_2O$, with the remainder being WO_3.

After precpitation of tungstic acid, the raffinate contains H_2O_2 and HCl (pH ~0) and, therefore, it can be used as a leaching solution for processing of tailing piles and wastes, especially of those containing reduced tungsten and molybdenum species. Ammonium paratungstate (APT) can also be precipitated from this solution.

Spectrum analysis of tungstic acid and APT precipitated from the raffinate showed that these compounds contain no more than 0.016% Mo(VI). However, these compounds are contaminated with relatively large amount of sodium and chlorine impurities, which can be removed by repeated precipitation.

It should be noted that, in the course of extraction treatment of aqueous–peroxide solutions of sodium tungstate, TAA is converted to trialkylamine oxide due to reaction with hydrogen peroxide [11]. This oxidized extractant strongly binds molybdenum and especially tungsten. As a result, these metals gradually accumulate in the organic phase. It was found that Mo(VI) and a considerable part of W(VI) can be backwashed from these organic concentrates with aqueous NaOH, aqueous ammonia, and distilled water. Furthermore, the organic extract saturated with W(VI) and Mo(VI) can be used as a binder in solid-phase reduction of tungsten oxides [12]. To overcome the above-noted problems caused by accumulation of W(VI) and Mo(VI) in the organic phase, quarternary ammonium salts and neutral reagents like TBP can be used as extractants instead of TAA.

CONCLUSIONS

(1) With increasing W(VI) concentration in aqueous hydrogen peroxide solutions contaminated with Mo(VI), the extractive recovery of Mo(VI) impurities with trialkylamine decreases, whereas the separation factor of molybdenum(VI) from tungsten(VI) increases.

(2) After extractive removal of the main part of molybdenum(VI), W(VI) can be precipitated from the raffinate as tungstic acid, which allows the additional purification of tungsten(VI) to decrease the molybdenum(VI) impurity content in the target metal.

REFERENCES

1. Zelikman, A.N., *Metallurgiya tugoplavkikh redkikh metallov* (Metallurgy of Rare Refractive Metals), Moscow: Metallurgiya, 1986.
2. Vol'dman, G.M., Zelikman, A.N., Ziberov, G.N., *et al*., *Dokl. Akad. Nauk SSSR*, 1977, vol. 232, no. 3, pp. 660–662.
3. Vol'dman, G.M., Zelikman, A.N., Ziberov, G.N., and Kagerman'yan, V.S., *Izv. Vyssh. Uchebn. Zaved., Tsvetn. Metall*., 1978, no. 3, pp. 46–49.
4. Blokhin, A.A., Pak, V.I., Pirmatov, E.A., *et al*., *Tsvetn. Met*., 1994, no. 8, pp. 41–42.
5. US Patent 4278642.
6. US Patent 4288413.
7. Giganov, G.P., Tserekova, A.M., Agnokov, T.Sh., *et al*., *Tsvetn. Met*., 1988, no. 5, pp. 67–71.
8. Vol'dman, G.M. and Zelikman, A.N., *Zh. Neorg. Khim*., 1993, vol. 38, no. 7, pp. 1234–1245.
9. Voropanova, L.A. and Barvinyuk, N.G., *Tsvetn. Metall*., 2002, nos. 4–5, pp. 21–25.
10. RF Patent 2186865.
11. Zelikman, A.N., and Kalinina, I.G., *Zh. Neorg. Khim*., 1974, vol. 19, no. 4, pp. 1040–1045.
12. RF Patent 2196862.

Russian Journal of Applied Chemistry, Vol. 77, No. 5, 2004, pp. 763–769. Translated from Zhurnal Prikladnoi Khimii, Vol. 77, No. 5, 2004, pp. 767–773.

APPLIED ELECTROCHEMISTRY AND CORROSION PROTECTION OF METALS

Effect of How Copper Oxide Is Obtained on the Behavior of Copper Oxide Electrodes in Lithium-Ion Power Cells

S. P. Kuksenko

Vernadsky Institute of General and Inorganic Chemistry, National Academy of Sciences of Ukraine, Kiev, Ukraine

Received December 2, 2003

Abstract—The electrochemical parameters of copper oxide electrodes in hermetically sealed lithium power cells were studied in relation to routes of copper oxide preparation, with the aim to diminish the share of side reactions.

Owing to high specific energy parameters, working voltage, and very low level of self-discharge, copper oxide–lithium (COL) power cells have long attracted the attention of development engineers and consumers as an alternative to silver–zinc (SZ) and mercury–zinc (MZ) power cells of cylindrical and button designs of various sizes [1, 2]. Recently, interest has been aroused in improvement of the fabrication technology of COL power cells in view of the increasing requirements to their electrical characteristics [3–5].

As the discharge capacity, the manner in which the voltage varies in the course of discharge, and the output power of COL power cells largely depend on how and under what conditions copper oxide is obtained, it is necessary to continue the search for industrially acceptable methods for preparing copper oxide and also for compositions of cathode pastes on its base that would ensure the required electrical parameters of the cells in various operation modes.

Presently, a wide variety of methods for obtaining copper oxide are known. These methods differ in the compositions of the starting substances and in conditions of their chemical and thermal treatment. However, there is no unambiguous published evidence that would make it possible to estimate the electrochemical parameters of copper oxide prepared by one or another technique as the active component of the positive electrode of COL power cells. Moreover, there are quite opposite assessments of the discharge characteristics of electrodes based on copper oxide obtained using the same starting substance under identical treatment conditions [3–12].

Studying the electrochemical behavior of electrodes based on copper oxide (or on other active materials suitable for fabrication of lithium power cells with a voltage of 1.5 V) involves a number of experimental difficulties because of the necessity for taking into account side reductive processes, which may occur at these electrodes under load (in contrast to oxidative processes at the cathodes of power cells with a voltage of 3 V, which occur at a higher rate under open-circuit conditions [13, 14]). Differing degrees of suppression of side processes can account for the discrepancies in the results of previous experiments.

In the present study, an attempt was made to examine the electrochemical characteristics of electrodes based on copper oxide obtained by different methods, with a minimized contribution from side reactions and electrodes operating in a mode as close as possible to that in lithium power cells working under real conditions.

EXPERIMENTAL

For fabricating copper oxide electrodes we chose copper oxide samples obtained by the following methods.

(1) Thermal decomposition of $Cu(NO_3)_2$. After preliminary drying at 105°C in a vacuum for 8 h in order to remove water of crystallization, copper nitrate was subjected to thermal treatment in air at 400°C for 8 h.

(2) Oxidation of Cu_2O. Copper(I) oxide was heated in an oxygen atmosphere to 400°C and kept at this temperature for 1 h.

(3) Thermal decomposition of $CuCO_3 \cdot Cu(OH)_2$. Copper hydroxycarbonate was dried in a vacuum at

1070-4272/04/7705-0763 © 2004 MAIK "Nauka/Interperiodica"

105°C for 8 h in order to remove water of crystallization and then heated in air to 400°C and kept at this temperature for 4 h.

(3a) The resulting copper oxide was additionally thermally treated in air at 800°C for 1 h.

(3b) Copper oxide was thermally treated at 800°C for 4 h.

(4) Oxidation of spherical copper particles in pure oxygen at 1000°C.

(4a) The resulting copper oxide was additionally thermally treated in air at 800°C for 1 h.

The completeness of conversion of the starting substances into copper oxide was verified by X-ray diffraction analysis, with monitoring the strongest lines.

Commonly, an electrically conducting additive, acetylene black [6–8] or graphite [3, 10, 11], is introduced in the electrode paste with copper oxide characterized by high electrical resistance [11]. In a number of studies [3, 6–8], a binder, Teflon, was also introduced into the paste (in [7], a carbon black hydrophobized with Teflon served as a filler); in [10, 11], no binder was used. It should be kept in mind, when choosing materials for an electrically conducting additive and a binder and deciding upon the amount of these, that these materials may be electrochemically active in the range of copper oxide reduction potentials. Indeed, studies of the cathodic behavior of various carbon materials point to their inherent electrochemical activity [15]. The discharge capacity of such electrodes is the higher, the greater the specific surface area of carbon, and it mainly depends on the structure of the amorphous region, rather than on the crystal structure. Use of a Teflon-containing binder in experiments concerned with the behavior of copper oxide electrodes cannot be considered justified because of the ability of this binder to be electrochemically reduced at potentials of 2.1–1.8 V relative to the lithium reference electrode Li/Li^+ under loads of 1–10 $\mu A\ cm^{-2}$ to give amorphous carbon [16–18]. An electrode made of a mixture of carbon black with 15 wt % Teflon discharged in a 1 M solution of $LiClO_4$ in propylene carbonate (PC) to a potential of 1.0 V with an output capacity of 120 $mA\ h\ g^{-1}$, whereas an electrode without Teflon produced only 8 $mA\ h\ g^{-1}$ under the same conditions [15]. A wave at a potential of 2.1 V was observed in the potentiodynamic curve of an electrode composed of a mixture of graphite with Teflon, measured in a 1 M solution of $LiClO_4$ in a mixture of PC and 1.2-dimethoxyethane (DME) in the first cathodic cycle. In [20], with a graphite electrode without binder in the same electrolyte, the cathodic wave appeared in the first cycle only at 0.8 V relative to Li/Li^+ [21].

In this study, the necessary electrical conductivity was ensured by mixing the copper oxide samples under study with powdered graphite of C1 brand in a weight ratio of 97 : 3 (which constituted approximately 92 : 8 v/v). Copper oxide electrodes without binder were compacted into pellets under a pressure of 2300 $kg\ cm^{-2}$. The absence of a binder did not impair the strength of the pellets and made it possible to raise the capacity of the copper oxide electrodes because of the increased content of the active substance. The pellets were placed in an evacuated cell and kept there at 300°C for 1 h in the atmosphere of dry argon.

The electrochemical behavior of copper oxide electrodes was studied in hermetically sealed cells with a lithium anode. In doing so, it is necessary to take into account the fact that, in the course of discharge, the copper oxide electrode grows in size (swells) because the volume of discharge products somewhat exceeds the initial volume of the electrode (theoretically, by 78%). The thickness of the electrode pellets was chosen so that the cells did not overcome their overall dimensions in discharge. In a hermetically sealed cell, the copper oxide electrode experiences a deficiency of electrolyte, in contrast to the case of tests in an electrochemical cell with an excess of electrolyte [6–8]. The procedure used in this study makes it possible to assess the electrochemical characteristics of copper oxide electrodes under the conditions close to those in practical use of COL power cells.

The anodes were fabricated as disks of rolled lithium. To diminish the contribution of the anode to the voltage drop across the cells in the pulsed mode of its discharge, an alloy of lithium with aluminum was formed on the anode surface, using the procedure described in [22]. The cells were fabricated with an excess of the anode capacity.

Previously, most of studies concerned with the electrochemical behavior of copper oxide electrodes have been performed with electrolytes containing PC (1 M $LiClO_4$/PC [6, 7] and 1 M $LiClO_4$/PC + DME [11]), which are the most readily available. According to [23], PC in 1 M $LiClO_4$/PC is reduced at potentials more negative than 1.3 V; at the same time, there have been numerous reports that a PC + DME mixed electrolyte is stable on a graphite electrode down to 0.8 V relative to Li/Li^+ (see, e.g., [21]). It should be taken into account that oxygen adsorbed by the electrically conducting carbon additive (more by acetylene black, than by graphite) and copper oxide, and also

dissolved in the electrolyte, is reduced at potentials of 2.0–1.8 V relative to Li/Li^+ unless special measures to remove it are taken. At potentials more negative than 1.3 V relative to Li/Li^+, water that was not removed in preparing the electrolyte undergoes reduction [23]. When the discharge behavior of copper oxide electrodes was studied in electrochemical cells with an excess of electrolyte [6–8], this had to lead to increased share of side reactions associated with reduction of oxygen and water dissolved in the electrolyte, in contrast to studies in which electrodes were tested in hermetically sealed lithium cells under the conditions of electrolyte deficiency [10, 11]. Thorough drying of the electrolyte and reliable sealing of a cell are also necessary because dehydrated copper oxide readily adsorbs water. In this study, a 1.4 M solution of $LiClO_4$ in a mixture of PC and DME (42 : 58 w/w) and water content of less than 30 ppm was used as an electrolyte. The electrolyte was subjected to an additional drying by a previously described procedure [24] and bubbled-through with dry argon to remove dissolved oxygen.

The cells were assembled in a glove box filled with dry argon. The results reported here were obtained with cells 9.5 mm in diameter and 2.10 mm high. Discharge curves of the cells were measured after 1 month of aging. The discharge was done through a continuous load of 30 kΩ with a pulsed load of 1 kΩ connected in parallel for 1 s once in 24 h. This procedure rules out any influence of side processes that occur in tests on a continuous high load (when the active cathode substance is reduced at lower potentials). To determine how the components of the total voltage drop across the cell in a pulse, ΔU_Σ, vary during discharge across a continuous load, the voltage drops across the cell were recorded as follows: at the instant of switch-on of the load, as a sum of ohmic components of the polarization resistances of both the electrodes and voltage drop in the interelectrode space, ΔU_r; 1 ms after the switch-on of the load, as a sum of activation polarizations of the electrodes, ΔU_a. The difference between ΔU_Σ and ΔU_r was regarded as a sum of the diffusion polarizations of both the electrodes, ΔU_d, at the end of the 1-s period of time. As the cells were fabricated with an excess of lithium and the type of the anode polarization had to be invariable in the course of the discharge, the relative changes in the electrochemical parameters of the cell were determined during the continuous discharge with the copper oxide electrodes.

The copper oxide electrodes used contain graphite as an electrically conducting additive. For this reason, to evaluate the contribution of side processes that occur at the copper oxide electrodes, cells with a graphite positive electrode containing no copper oxide were fabricated under the same conditions and discharged through a load of 30 kΩ. The capacity of such cells in discharge to a voltage of 1.0 V was less than 1.2 mA h (the corresponding discharge curve is represented by a dotted line in Fig. 1).

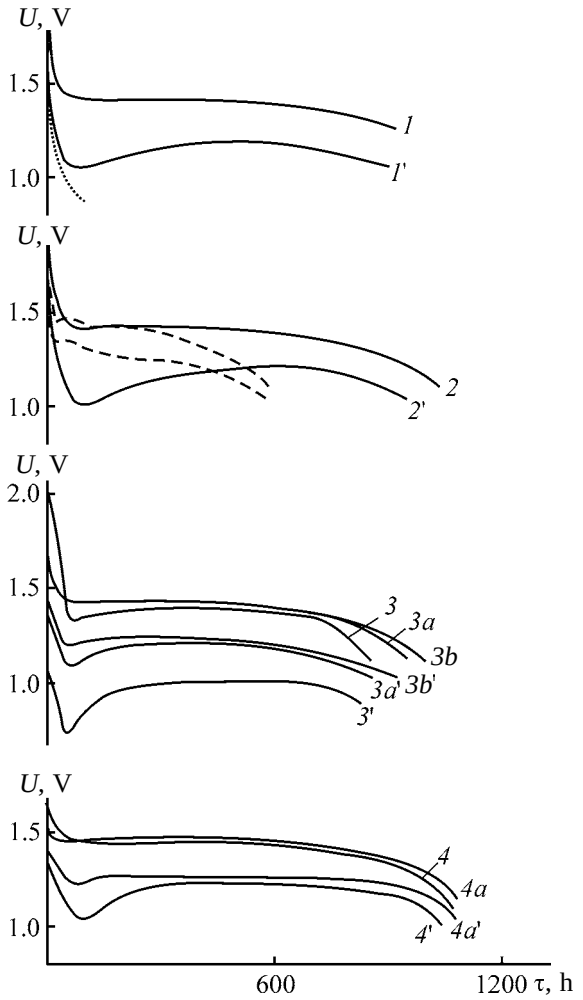

Fig. 1. (*1–4*, *3a*, *3b*, *4a*) Discharge curves of lithium power cells with a copper oxide cathode and (*1'–4'*, *3a'*, *3b'*, *4a'*) dependences of the cell voltage at the end of a load pulse on the duration of a continuous discharge. Cell size type 921, constant load 30 kΩ, pulsed load 1 kΩ s. (*U*) Voltage and (τ) duration of continuous discharge. Digits at curves: methods used to produce copper oxide. Dotted line: discharge curve of a cell with a graphite cathode; dashed lines: discharge curve of a cell with a Cu_2O cathode (upper) and dependence of the cell voltage by the end of a load pulse on the duration of a continuous discharge (lower).

Figure 1 shows the discharge curves and dependences of the cell voltage at the end of a load pulse on the duration of discharge for power cells with cop-

per oxide electrodes for which copper oxide was prepared using procedures 1–4a. The discharge capacity of a cell with copper oxide produced by method 1 was 42 mA h in discharge to a final voltage of 1.2 V, and 46 mA h, to 1.0 V. The utilization factor (UF) for copper oxide was 77 and 83%, respectively. This result is in agreement with the UF of 80% [11] obtained for copper oxide under similar conditions (in hermetically sealed cells of size type 1142 with a copper oxide electrode composed of a mixture of copper oxide obtained by decomposition of copper nitrate and 5 wt % graphite without a binder), but contradicts the data of [6]. According to [6], a copper oxide electrode composed of a mixture of copper oxide (also produced by decomposition of copper nitrate) and 33 wt % acetylene black and 17 wt % fluoroplastic binder is characterized by a UF of 40% for copper oxide in the case of its electrochemical reduction in an excess of electrolyte. Discharge curve 1 is characterized by a relatively prolonged transition portion before that of a stable working voltage, despite the low open-circuit voltage (OCV) of 1.98 V. The dependence of the cell voltage at the end of the pulse on the duration of a continuous discharge (curve *1*) shows a decrease in the pulsed voltage during the first several tens of hours, with the subsequent slow rise till approximately half of the total duration of discharge. The further run of the curve of the pulsed voltage corresponds to that of the discharge curve.

Of the 12 methods for obtaining copper oxide, studied in [6], the best was a short-time (1 to 3 h) oxidation of Cu_2O in an atmosphere of oxygen at 300–500°C. The thus obtained copper oxide had a UF as high as 92%, but the discharge characteristic of the electrode made of this material exhibited a prolonged transition region before a stable discharge plateau (with low average level of potentials of about 1.35 V). In the present study, copper oxide obtained using the same technique as that in [6] (method 2) differed only slightly in its electrochemical characteristics from copper oxide prepared by method 1. Its UF was found to be 79% in the case of cell discharge to 1.2 V (cell capacity was 43.5 mA h) and 89% in discharge to 1.0 V (49 mA h). In discharge curve *2*, as also in curve *1*, the voltage reaches a stable level in a relatively long time; curve *2*' shows, similarly to curve *1*', a decrease in the pulsed voltage in the first half of the discharge. Under the same testing conditions, Cu_2O was reduced in the case of a continuous load at the same potentials as copper(II) oxide synthesized from this material, but the cell with a Cu_2O cathode exhibited no dip in the curve for pulsed voltage (upper and lower dashed lines in Fig. 1, respectively) and was characterized by a lower OCV: 1.90 V, compared to 2.12 for the cell with a cathode made of copper oxide produced by method 2.

As follows from curves *3* and *3*', the cell with copper oxide prepared by method 3 is distinguished by an extremely high initial discharge voltage in discharge on a continuous load (the OCV of the cell was 2.56 V), a dip in curve *2* before the plateau, and the corresponding deep dip in curve *2*' for pulsed discharge. The cell capacity was relatively low: 38 and 41 mA h in discharge to 1.2 and 1.0 V, respectively. An X-ray phase analysis of the copper oxide produced by method 3 did not reveal presence of any other phases.

It is noteworthy that, under the experimental conditions of [6], the electrode based on copper oxide produced by thermal decomposition of copper hydroxycarbonate at 300°C in the course of 76 h also discharged at high initial potentials, but exhibited no stable discharge plateau and had high capacity, more than 90% of the theoretical value (calculated for the reaction of copper oxide reduction).

An even higher discharge capacity (99% of the theoretical value in discharge of the electrode to 1.0 V relative to Li/Li^+ with a current of 0.5 mA) was observed [7] for copper oxide produced by thermal decomposition of $Cu(OH)_2$ at 300°C for 2 h. The discharge curve of the electrode with copper oxide of this kind was also distinguished by a sloping run during the entire course of discharge. Prolonged heating of copper oxide samples decreased the discharge capacity and the reduction potentials of copper oxide electrodes. This was attributed to changes in nonstoichiometry upon removal of residual OH groups from the active form of copper oxide.

Curves *3a* and *3b* indicate that, under the experimental conditions, a prolonged thermal treatment of copper oxide at high temperature (1 and 4 h at 800°C, respectively) improved the electrochemical parameters of copper oxide electrodes. The continuous discharge of cells with thermally treated electrodes proceeded at higher stable voltage (with relatively low initial voltage). The cell capacity increased to, respectively, 43 and 45 mA h (in discharge to 1.2 V), and the OCV decreased to 2.16 and 2.06 V. However, the strongest positive influence was exerted by thermal treatment of copper oxide produced by method 3 on the dependences of the cell voltage by the end of a load pulse on the duration of a continuous discharge (curves *3a*', *3b*'). The average level at which these curves ran increased substantially and the dip in the pulsed voltage

in their initial portions decreased dramatically (more so for curve *3b*'). As the temperature and duration of thermal treatment increased, the peaks in the X-ray diffraction patterns of copper oxide samples became narrower and higher, which indicated that the grain size increased and the crystal lattice perfection was improved.

The positive influence of a prolonged thermal treatment of copper oxide on the specific capacity of copper oxide was observed in [9]: the specific capacity of electrodes based on industrial copper oxide increased from 150–300 to 550 mA h g^{-1} after its thermal treatment in air for 16 h. A correlation was revealed between the ratio of CuO and Cu_2O peak intensities for copper oxide samples and the specific capacity of the electrodes. The specific volume capacity of the electrodes based on industrial copper oxide increased by 50–70% on heating copper oxide samples to 600–800°C followed by fast cooling (quenching) [4]. This was attributed to the appearance of an oxygen nonstoichiometry.

The relatively high electrochemical parameters in a continuous discharge were observed for a cell with copper oxide produced by high-temperature oxidation of spherical copper particles (method 4). The cell had a relatively stable discharge voltage with an average value of 1.40 V (Fig. 1, curve *4*) and high capacity of 48 and 51 mA h in discharge to 1.2 and 1.0 V, respectively. The OCV of the cell was 2.05 V. It is noteworthy that the discharge of a cell with copper oxide produced by controlled oxidation of copper particles (of a certain size and shape) at 400°C [10] proceeded at an average voltage of 1.4 V (at the same current density) and high output capacity, but the discharge curve differed from that obtained in this study in the longer time in which the stable voltage plateau was reached and higher value of OCV of 2.3 V. Under other experimental conditions, a copper oxide electrode made of a copper powder oxidized in air at 400°C for 1 h discharged at an average potential of 1.35 V and a UF of about 78%, and upon oxidation for 10 h, at 1.2 V and UF of 50% [6]. As can be seen from curve *4*' in Fig. 1, short-time oxidation of spherical copper particles by method 4 also leads (as also do methods 1–3) to a dip in the curve for the pulsed voltage in the initial stage of discharge of a COL cell through a continuous load.

Figure 2 shows how the overall voltage drop under pulsed load and its components vary in discharge of the given cell through a continuous load. It can be seen that, in the initial stage, the major contribution to the overall voltage drop comes from the diffusion component, which grows until the cell discharges by approximately 10% relative to the total duration of discharge. Also grows during this period of time the ohmic component, and the activation component does not change its sign. Further, the diffusion and activation components decrease and, after 1/4 discharge of the cell, remain virtually unchanged till 4/5 of the total discharge duration is reached. In the process, the ohmic component makes the most pronounced contribution to the overall voltage drop. In the final stage of discharge, the diffusion component again grows and, at the end of the discharge process, much exceeds the activation and ohmic components.

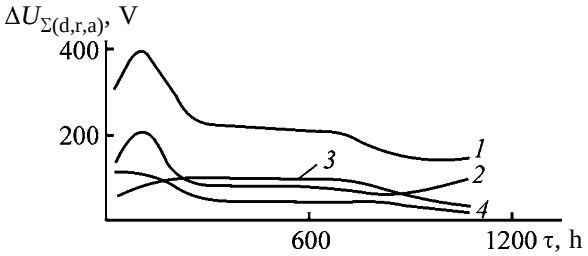

Fig. 2. Variation of the overall voltage drop and its components (diffusion-related, ohmic, activated) $\Delta U_{\Sigma(d,r,a)}$ under pulsed load in discharge through a continuous load of a cell with copper oxide produced by method 4. (τ) Duration of continuous discharge. (*1*) ΔU_{Σ}, (*2*) ΔU_{d}, (*3*) ΔU_{r}, and (*4*) ΔU_{a}.

Curve *4a*' in Fig. 1 shows that additional thermal treatment of copper oxide results in that both the depth and the duration of the dip in the curve for the pulsed voltage decrease substantially. Further discharge of the cell was more stable and proceeded with a higher pulsed voltage. The cell with such a copper oxide was distinguished by a lower OCV of 1.90 V and higher discharge capacity of 50 and 52 mA h in discharge to 1.2 and 1.0 V, respectively. In discharge to 1.2 V, the specific discharge capacity of the copper oxide electrode was 625 mA h g^{-1}, and the UF of copper oxide, 95%. The cell voltage in continuous discharge rapidly reached a stable level (Fig. 1, curve *4a*) at a relatively high average discharge voltage of 1.43 V. In addition, curve *4a* is characterized by a rather strong bend at the end of discharge (the capacity in discharge to a final voltage of 1.35 V was 44 mA h, i.e., 88% of the capacity in discharge to 1.2 V). It was found that a minor dip in the curve for pulsed voltage in the initial stage of a continuous discharge is also associated with the corresponding change in the diffusion component of the overall voltage drop. In the plateau in the dependence of the pulsed voltage on the duration of a continuous discharge, the diffusion and ohmic components were

virtually the same. The X-ray diffraction pattern of a copper oxide sample subjected to an additional thermal treatment showed no peaks of copper(I) oxide, which were observed in the X-ray diffraction pattern of the initial copper oxide sample.

Discharge curves of COL cells are distinguished by a common feature: the longer the delay of the initial voltage in a continuous discharge, the deeper the dip in the curve describing the dependence of the pulsed voltage on the duration of the continuous discharge. This phenomenon is associated with the state of the surface of copper oxide, which depends on the method by which it is produced and on the mode of its further thermal treatment. In a discharge of a copper oxide electrode, lithium cations are introduced into the monoclinic lattice of copper oxide to give $Cu^{II}_{1-x}Cu^{I}_{x}Li_{x}O$ [8]. The reaction occurs at places of contact between copper oxide particles and particles of the distributed current lead (graphite in the given case). This process is preceded by reduction of surface groups, which are inevitably formed when copper oxide is obtained and processed using the methods described here. Possibly, residual OH groups can catalyze reduction of Teflon from a Teflon-containing carbon black and reduction of PC. This probably accounts for the high capacity and discharge potentials of continuously loaded electrodes with copper oxide produced at a relatively low temperature and short time of thermal treatment [6, 7].

In electrochemical reduction of surface groups, a layer of a lithium-conducting solid electrolyte grows on copper oxide particles and the diffusion of lithium cations across this layer is slow. Also slow is the diffusion of lithium cations into the particles via formation of an intermediate compound $Cu^{II}_{1-x}Cu^{I}_{x}Li_{x}O$, whose subsequent reduction gives Cu and Li_2O or Cu_2O and Li_2O [8] and results in disintegration of the primary film of the solid electrolyte under the action of mechanical stresses. In the same range of potentials, Cu_2O enters into an electrochemical reaction (being reduced to Cu and Li_2O). The rise in the diffusion polarization of the electrode in the final stage of the discharge is due to exhaustion of the electrolyte within the micropores of the swollen cathode. According to [7], the removal of chemically bound water and oxygen from copper oxide samples obtained from $Cu(OH)_2$ continues at above 500°C. Controlled oxidation of spherical copper particles at a high temperature in pure oxygen rules out any involvement of water molecules in the synthesis process.

Hydrogen-containing groups on the surface of copper oxide particles presumably appear in the contact of these particles with the ambient atmosphere. Prolonged high-temperature treatment of copper oxide samples in air largely removes the surface groups, improves the crystal perfection, and gives rise to a mosaic structure of grains, which facilitates diffusion of lithium cations into the particles in the course of electrochemical reduction. This leads to a high and stable voltage in discharge through a continuous load and to a pronounced stabilization of the pulsed voltage. Additional ways to completely eliminate the dip in the curve for the pulsed voltage in the initial stage of discharge are to be sought for. Preliminary experiments demonstrated that one of the possible ways is incorporation of lithium into copper oxide in high-temperature treatment with lithium carbonate.

CONCLUSIONS

(1) In studying the electrochemical parameters of copper oxide electrodes, it is necessary to take into account the influence of side reactions that involve the electrically conducting carbon additive, Teflon binder, oxygen, and water.

(2) Under testing conditions that are close to real working conditions of copper oxide–lithium power cells, the highest electrochemical parameters are ensured by copper oxide produced by high-temperature oxidation of spherical copper particles in pure oxygen.

(3) Prolonged high-temperature treatment of copper oxide in air improves the electrical parameters of power cells, but fails to completely eliminate the dip in the curve for the pulsed voltage in the initial stage of discharge through a continuous load.

REFERENCES

1. Skundin, A.M. and Nizhnikovskii, E.A., *Elektron. Komponenty*, 2001, no. 4, pp. 27–31.
2. Kuksenko, S.P., Lugovoi, V.P., and Prokopenko, V.T., *Zh. Prikl. Khim.*, 1997, vol. 70, no. 6, pp. 957–960.
3. Chmilenko, N.A., Prisyazhnyi, V.D., Tkalenko, D.A., *et al.*, in *Fundamental'nye problemy e/kh energetiki: Materialy IV Mezhdunarodnoi konferentsii* (Fundamental Problems of Electrochemical Power Engineering: Proc. IV Int. Conf.), Saratov, 1999, pp. 136–138.
4. Belonenko, S.A., Yalyushev, N.I., and Pugachev, A.Yu., in *Litievye istochniki toka: Materialy VI Mezhdunarodnoi konferentsii* (Lithium Power Cells: Proc. VI Int. Conf.), Novocherkassk, 2000, p. 48.
5. Grugeon, S., Laruelle, S., Herrera-Urbina, R., *et al.*, *J. Electrochem. Soc.*, 2001, vol. 148, no. 4, pp. A285–A292.

6. Podhajecky, P., Klapste, B., Novak, P., *et al*., *J. Power Sources*, 1985, vol. 14, pp. 269–275.
7. Novak, P., Klapste, B., and Podhajecky, P., *J. Power Sources*, 1985, vol. 15, pp. 101–108.
8. Novak, P. and Podhajecky, P., *J. Power Sources*, 1991, vol. 35, pp. 235–247.
9. Breslavets, V.P., Ezikyan, V. I., Pleshakov, M.S., and Khodarev, O.M., Abstracts of Papers, *Yubileinaya nauchno-tekhnicheskaya konferentsiya "Sovremennye e/kh tekhnologii"* (Jubilee Scientific and Technical Conf. "Modern Electrochemical Technologies"), Saratov, 1996, p. 21.
10. Bates, R. and Jumel, Y., *Lithium Batteries*, Gabano, J.-P., Ed., Academic, 1983, pp. 76–85.
11. Iijima, T., Toyoguchi, Y., Nishimura, J., and Ogawa, H., *J. Power Sources*, 1980, vol. 5, pp. 99–109.
12. Fateev, S.A. and Batrakov, Yu.A., in *Fundamental'nye problemy e/kh energetiki: Materialy IV Mezhdunarodnoi konferentsii* (Fundamental Problems of Electrochemical Power Engineering: Proc. IV Int. Conf.), Saratov, 1999, pp. 103–104.
13. Kuksenko, S.P., *Zh. Prikl. Khim*., 1996, vol. 69, no. 10, pp. 1658–1662.
14. Frackowiak, E. and Kuksenko, S., *J. Power Sources*, 1998, vol. 72, pp. 174–177.
15. Watanabe, A., Mori, K., Ishikawa, H., and Nakamura, Y., *J. Electrochem. Soc*., 1987, vol. 134, no. 6, pp. 1318–1321.
16. Barker, D.J., Brewis, D. M., and Dahm, R.H., *Electrochim. Acta*, 1978, vol. 23, no. 10, pp. 1107–1110.
17. Stezeryanskii, E.A., Litovchenko, K.I., and Kublanovskii, V.S., *Ukr. Khim. Zh.*, 1990, vol. 56, no. 1, pp. 29–33.
18. USSR Inventor's Certificate no. 1 342 349.
19. Yang, H., Ai, X., Lei, M., and Li, S., *J. Power Sources*, 1993, vols. 43–44, pp. 399–403.
20. Apostolova, R.D., Shembel', E.M., and Berlizov, Yu.S., *Zh. Prikl. Khim*., 1991, vol. 64, no. 1, pp. 58–64.
21. Fournie, R., Messina, R., and Perichon, J., *J. Appl. Electrochem*., 1979, vol. 9, pp. 329–335.
22. USSR Inventor's Certificate, no. 1 551 183.
23. Aurbach, D., Daroux, M., Faguy, P., and Yeager, E., *J. Electroanal. Chem*., 1991, vol. 297, pp. 225–244.
24. USSR Inventor's Certificate no. 1 667 580.

Russian Journal of Applied Chemistry, Vol. 77, No. 5, 2004, pp. 770–774. Translated from Zhurnal Prikladnoi Khimii, Vol. 77, No. 5, 2004, pp. 774–778.

CATALYSIS

Origin of the Activity of Hydrogenation Catalysts Based on Palladium Complexes and Primary Phosphines

L. B. Belykh, T. V. Goremyka, and F. K. Shmidt

Irkutsk State University, Irkutsk, Russia

Received December 3, 2003

Abstract—The activity of the catalytic system based on palladium bisacetylacetonate and phenylphosphine in hydrogenation catalysis was studied.

The unique capability of transition metals to catalyze hydrogenation of unsaturated organic molecules with gaseous hydrogen is known for a long time and is used in numerous industrial processes [1–3]. Among Group VIII transition metals, much attention is given to palladium-based catalysts. Modification of palladium with nitrogen-containing compounds (quinoline, ethylenediamine, alkaloids) allows preparation of highly selective catalysts for hydrogenation of alkynes, chemoselective hydrogenation of unsaturated aldehydes and ketones, enantioselective hydrogenation of derivatives of α,β-unsaturated acids, etc. [1, 2]. Along with studies of heterogeneous supported palladium catalysts, active efforts have been made in the past three decades to elucidate factors responsible for the activity of palladium complexes with phosphine ligands as hydrogenation catalysts. Whereas the modifying effect of tertiary [4–7] and secondary [8] phosphines on the properties of palladium complexes as hydrogenation catalysts has been studied in detail, primary phosphines have not yet been used in hydrogenation catalysis. Interest in these systems is due to the fact that primary phosphines exhibit simultaneously the properties of Lewis bases and Brønsted acids. Furthermore, primary phosphines, like other three-coordinate phosphorus compounds, are reductants.

The goal of this work was to gain insight into the promoting effect of PH_2Ph in a microheterogeneous hydrogenation catalyst based on $Pd(acac)_2$.

EXPERIMENTAL

The solvents were purified by standard procedures used in organometallic chemistry [9].

Palladium bisacetylacetonate was prepared according to [10].

Phenylphosphine was prepared by reaction of phenylchlorophosphine with lithium aluminum hydride [11] and isolated by vacuum distillation (38°C/5 mm Hg). ^{31}P NMR: δ –122 ppm ($^1J_{PH}$ 200 Hz). The compound was stored in a sealed ampule under argon.

The catalyst based on $Pd(acac)_2$ and PH_2Ph was prepared as follows. To a solution of 0.00304 g (1×10^{-5} mol) of $Pd(acac)_2$ in DMF, prepared in a duck-shaped vessel that had been evacuated and filled with hydrogen, 1 ml of a phenylphosphine solution was added; the P/Pd ratio was 0.1–2.0. The lemon-yellow reaction mixture was stirred in a hydrogen atmosphere at 80°C for 5–15 min. The resulting black-brown "solution" was cooled to 30°C, and a substrate to be hydrogenated was introduced with a syringe. Hydrogenation was performed with vigorous stirring at the initial hydrogen pressure of 1 atm. The reaction progress was monitored volumetrically and by GLC.

Acetylacetone and benzene in the catalyzate were determined by GLC, after evaporation–condensation of the solution in a vacuum unit (20°C/1×10^{-3} mm Hg), on a Chrom-5 chromatograph equipped with a 3.6-m packed column (stationary phase SE-30) and flame ionization detector. The column temperature was 100°C, and the carrier gas was nitrogen. The error in determination of acetylacetone and benzene did not exceed 10%.

The UV spectra were recorded on a Specord UV VIS spectrometer in an all-sealed cell. The concentration of $Pd(acac)_2$ was calculated from the absorption band at 330 nm (ε_{330} = 10 630 l mol^{-1} cm^{-1}), and that of acetylacetone, from the band at 290 nm [for Hacac, ε_{290} = 5000, and for $Pd(acac)_2$, 3090 l mol^{-1} cm^{-1}].

X-ray phase analysis of the catalyst samples was performed on a DRON-3M diffractometer, CuK_α

1070-4272/04/7705-0770 © 2004 MAIK "Nauka/Interperiodica"

radiation. The procedure for determination of Pd(0) was described in [12].

We showed previously that palladium bisacetylacetonate, like palladium(II) acetate [13], is not reduced with hydrogen in aprotic solvents (benzene, toluene) below 80°C in the absence of water. We found that water breaks down the oligomeric species $[Pd(acac)_2]_n$ preserved upon dissolution in benzene and facilitates heterolytic cleavage of the hydrogen molecule. The hydrogenolysis of $Pd(acac)_2$ in DMF occurs under milder conditions. At 30°C, it takes no less than 2 h, whereas at 80°C it is complete in 5–15 min depending on the Pd(II) concentration.

The initial rate of styrene hydrogenation in the presence of the thus generated Pd black is relatively low, and the maximal specific activity W does not exceed 19 mol of styrene per mole of Pd per minute. At low initial concentrations of $Pd(acac)_2$, the catalyst undergoes rapid deactivation in the course of hydrogenation (Table 1). Introduction of water enhances the performance of Pd black.

To obtain a more effective catalytic system, we used PH_2Ph as modifier. Catalytic hydrogenation of styrene in the presence of the system based on $Pd(acac)_2$ + $n PH_2Ph$ (P/Pd = 0.3, 1.0, 2.0) at 30°C in DMF is characterized by a long induction period (40 min) and low reaction rate. The catalyst that is the most active in hydrogenation is formed after preliminary reaction of the system components, $Pd(acac)_2$ + $n PH_2Ph$, with H_2 in DMF at 80°C for 5–15 min. The catalytic system exhibits the highest performance at the $PH_2Ph : Pd(acac)_2$ ratio of 0.3 (Fig. 1).

The specific activity of the system $Pd(acac)_2$ + $0.3PH_2Ph$ does not change upon hydrogenation of no less than 3000 mol of styrene per mole of Pd, after which the activity gradually decreases with formation of a precipitate. The reaction rate as a function of the catalyst concentration nonlinearly grows in the range 0.5–2 mM and starts to decrease at $c_{Pd} > 1.4$ mM (Fig. 2).

In hydrogenation of other unsaturated hydrocarbons and of carbonyl and nitro compounds, the system under consideration also shows high activity and selectivity (Table 2).

In reduction of benzaldehyde on palladium catalysts (Pd/C), the C–O bond in the forming benzyl alcohol usually undergoes further hydrogenolysis, with the rates of both steps being comparable [2]. At the same time, the selectivity of the system $Pd(acac)_2$ + $0.3PH_2Ph$ in benzaldehyde hydrogenation reaches 92%. Nitrobenzene is usually selectively reduced to aniline on palladium catalysts. The advantage of our catalyst is the high reaction rate. The specific activity of our catalyst in reduction of the nitro group exceeds by a factor of 3.5 that of Pd nanoparticles immobilized on the styrene–divinylbenzene copolymer [14] but is lower than that of the Pd catalyst with diphenylphosphine [8].

Table 1. Hydrogenation of styrene in the presence of Pd black formed from $Pd(acac)_2$. Solvent DMF, 30°C, P_{H_2} = 1 atm, substrate concentration $c_{sub} = 8.7 \times 10^{-3}$ M

$Pd(Acac)_2$,* mM	W, mol H_2/(mol Pd min)		Styrene conversion, %	
0.45	2	11**	3	29**
0.90	6	19**	25	61**
2.27	12	16**	62	100**
4.54	9	12**	100	100**

* Reduction of $Pd(acac)_2$ with hydrogen was performed at 80°C.

** Reduction of $Pd(acac)_2$ was performed with addition of 1 wt % H_2O to the solvent.

To gain insight into the promoting effect of PH_2Ph, we studied in more detail the system with P/Pd = 0.3.

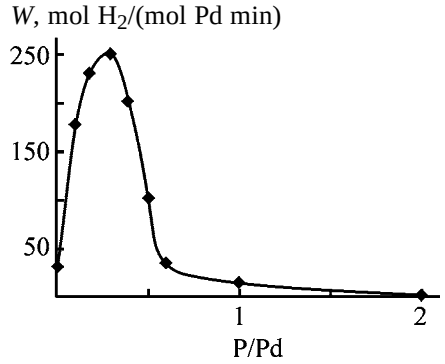

Fig. 1. Hydrogenation of styrene in the presence of the catalytic system $Pd(acac)_2$ + $n PH_2Ph$. (W) Specific activity and (P/Pd) ratio of the starting reactants. Solvent DMF, c_{Pd} = 0.9 mM, 30°C, P_{H_2} = 1 atm.

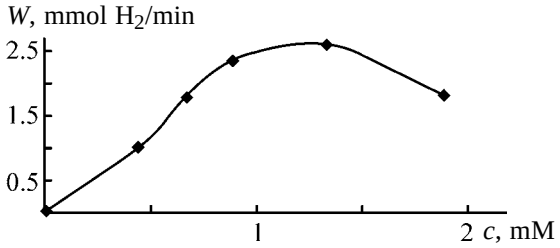

Fig. 2. Rate of styrene hydrogenation W in the presence of the catalytic system $Pd(acac)_2$ + $0.3PH_2Ph$ as a function of the $Pd(acac)_2$ concentration c. Solvent DMF, 30°C, P_{H_2} = 1 atm, $c_{sub} = 8.7 \times 10^{-3}$ M.

Table 2. Catalytic properties of the system $Pd(acac)_2$ + $0.3PH_2Ph$ in hydrogenation. Solvent DMF, c_{Pd} = 0.9 mM, 30°C, P_{H_2} = 1 atm, c_{sub}/c_{Pd} = 870

Substrate	*W*, mol H_2/(mol Pd min)	Conversion, %	Products, %
PhC≡CH	104 (–C≡C–), 112 (–C=C–)	100	Ethylbenzene 85, styrene 15
PhC≡CPh	113 (–C=C–), 21 (–C=C–)	100	Diphenylethane 69, *cis*-stilbene 24, *trans*-stilbene 7
$PhCH=CH_2$	260	100	Ethylbenzene 100
PhC(O)H*	10	70	Benzyl alcohol 92, toluene 8
$PhNO_2$*	48	97	Aniline 100

* c_{Pd} = 5 mM.

Table 3. Conversion of the catalytic system $Pd(acac)_2$ + $n PH_2Ph$ in hydrogen, according to UV and GLC data. Solvent DMF, 80°C, c_{Pd} = 5 mM

$PH_2Ph/Pd(Acac)_2$	Reaction time, min	Concentration, wt %		C_6H_6/PH_2Ph
		$Pd(Acac)_2$	HAcac	
0.3	5	2	99	0.26
0.3	15	0	98	0.50
0.3	40	0	99	0.51
0.5	15	2	87	0.46
0.5	40	0	93	0.45
1.0	15	24	79	0.13
1.0	40	12	83	0.19
1.0	60	–	113	0.20

Phenylphosphine, in contrast to tertiary phosphines, exhibits both base and acid properties. The previous study of the reaction of $Pd(acac)_2$ with PH_2Ph in benzene and DMF in an inert atmosphere [15] showed that the reaction went beyond simple complexation and was accompanied by fast exchange of acetylacetonate ligands for organophoshorus groups, yielding acetylacetone and polynuclear palladium complexes containing μ_3-PPh, μ_2-PHPh, and coordinated PH_2Ph ligands, and also *O*,*O*-chelate acetylacetonate ligands, like

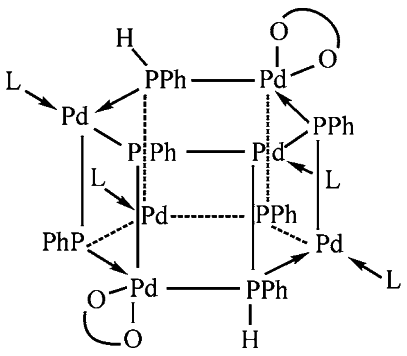

where L = PH_2Ph.

The reaction is complete in 2–3 min. At the P/Pd ratio of 0.3, upon ligand exchange, about 15% of Pd appears in the form of polynuclear complexes, and 85%, in the form of $Pd(acac)_2$. The degree of conversion of $Pd(acac)_2$ to the reaction products grew with an increase in the P/Pd ratio. Quantitative formation of acetylacetone was observed at P/Pd > 2.

Additional treatment of the system $Pd(acac)_2$ + $n PH_2Ph$ with hydrogen results in quantitative formation of acetylacetone (Table 3), i.e., not only $Pd(acac)_2$ but also acetylacetonate ligands incorporated in polynuclear Pd complexes are subject to hydrogenolysis. The catalyzate from the reaction with H_2 contained not only acetylacetone but also benzene originating from decomposition of the organophosphorus ligands. The amount of benzene formed per mole of PH_2Ph grows as the P/Pd ratio is decreased. The content of $Pd(acac)_2$ grows in the same direction. Similar trends were observed with triphenylphosphine [5]. The observed dephenylation is consistent with the previously proposed mechanism according to which degradation of organophosphorus ligands occurs in the coordination sphere of Pd(0) [8]; therefore, the mechanism of benzene formation in the system can be tentatively presented as follows.

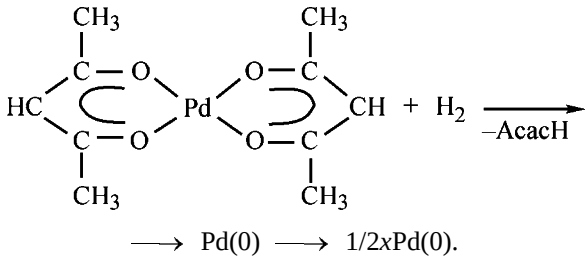

$Pd(acac)_2$ is readily reduced with hydrogen in DMF at 80°C to Pd(0). The Pd(0) atoms arising from hydrogenolysis of $Pd(acac)_2$ can both aggregate to form palladium clusters and react with phenylphosphinylidene ligands in polynuclear palladium complexes. Oxidative addition of Pd(0) to these complexes with hydrogenolysis of the P–C bond yield benzene and, probably, palladium phosphides:

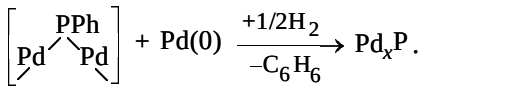

Elemental analysis of the black precipitate (sample 1) isolated from the reaction system $Pd(acac)_2$ + $0.3PH_2Ph$ + H_2 corresponds to the empirical formula $Pd_8P_1C_1H_1$, and the content of Pd(0) determined chemically does not exceed 28%. According to X-ray phase analysis, sample 1 is elemental palladium in the dispersed state; the size of its coherent scattering domain, as estimated from the shape of the Pd line *hkl* 111, is 2 nm. We believe that the results of X-ray phase and elemental analyses do not contradict each other. Sample 1 may contain higher palladium phosphides in the X-ray amorphous state for which the main reflections are observed in the same region as for elemental palladium and overlap with the broadened Pd(111) line. It should be noted that the products formed by the components of the catalytic system in an inert atmosphere, associates of polynuclear palladium complexes, were X-ray amorphous, giving a diffuse maximum (halo) at d/n = 13.556 Å; the size of coherent scattering domains was 2.7 nm. The absence of an amorphous halo at small diffraction angles ($2\theta = 5°–40°$) in the diffraction pattern of sample 1 indicates that the structure of polynuclear palladium complexes is broken down upon treatment of the catalytic system with hydrogen.

It was shown previously that the catalytic activity of the system $Pd(acac)_2$ + $n PPh_3$ in hydrogenation of phenylacetylene was maximal at the P/Pd ratio of 0.3 also [16], and the solid reaction products identified were palladium phosphide Pd_3P and crystalline Pd. However, whereas formation of the system with triphenylphosphine took no less than 24 h, with phenylphosphine the formation time was as short as 5 min.

Our results suggest that, in the course of formation of the catalytic system based on $Pd(acac)_2$ at P/Pd = 0.3, phenylphosphine acts as a structural promoter. Its effect can be described as follows. The reaction of PH_2Ph with $Pd(acac)_2$ yields nanosized associates of polynuclear palladium complexes with organophosphorus ligands. The associates of the polynuclear palladium complexes and palladium phosphides formed in an H_2 atmosphere by decomposition of organophosphorus ligands act as crystallization centers for immobilization and growth of Pd(0) clusters. At higher P/Pd ratios, the content of Pd(I) and Pd(II) complexes with phosphorus-containing ligands increases relative to Pd(0), and the catalytic activity of the system decreases.

CONCLUSIONS

(1) A new high-performance catalyst based on $Pd(acac)_2$ and PH_2Ph was suggested for hydrogenation of unsaturated bonds and of carbonyl and nitro groups.

(2) Transformations of the catalytic system $Pd(acac)_2$ + $n PH_2Ph$ in hydrogen yield nanosized particles (2 nm) containing elemental palladium and, probably, palladium phosphides. Associates of polynuclear palladium complexes and palladium phosphides are crystallization centers for immobilization and growth of Pd(0) clusters. Phenylphosphine acts as a structural promoter.

REFERENCES

1. Colquhoun, H.M., Holton, J., Thomson, D.J., and Twigg, M.V., *New Pathways of Organic Synthesis: Practical Applications of Transition Metals*, New York: Plenum, 1984.
2. Blaser, H.-U., Indolese, A., Schnyder, A., *et al.*, *J. Mol. Catal. A: Chem.*, 2001, vol. 173, pp. 3–18.
3. James, B.R., *Homogeneous Hydrogenation*, New York: Wiley–Interscience, 1973.
4. Collman, J.P., Hegedus, L.S., Norton, J.R., and Finke, R.G., *Principles and Applications of Organotransition Metal Chemistry*, Mill Valley, California: Univ. Science Books, 1987.
5. Shmidt, F.K., Belykh, L.B., and Cherenkova, T.V., *Kinet. Katal.*, 2001, vol. 42, no. 2, pp. 182–194.
6. Cairns, G.R., Gross, R.J., and Stirling, D., *J. Mol. Catal. A: Chem.*, 2001, vol. 172, pp. 207–218.

7. Moiseev, I.I. and Vargaftik, M.N., *Zh. Obshch. Khim.*, 2002, vol. 72, no. 4, pp. 550–560.
8. Shmidt, F.K., Belykh, L.B., and Cherenkova, T.V., *Kinet. Katal.*, 2003, vol. 44, no. 5, pp. 683–691.
9. Gordon, A.J. and Ford, R.A., *The Chemist's Companion. A Handbook of Practical Data, Techniques and References*, New York: Wiley–Interscience, 1972.
10. US Patent 3474464.
11. Kormachev, V.V. and Fedoseev, M.S., *Preparativnaya khimiya fosfora* (Preparative Chemistry of Phosphorus), Perm: Ural. Otd. Ross. Akad. Nauk, 1992.
12. Shmidt, A.F. and Mametova, L.V., *Kinet. Katal.*, 1996, vol. 37, no. 3, pp. 431–433.
13. Mironova, L.V., Levkovskii, Yu.S., Belykh, L.B., *et al.*, *Koord. Khim.*, 1985, vol. 2, no. 12, pp. 1689–1693.
14. Klyuev, M.V. and Nasibulin, A.A., *Kinet. Katal.*, 1996, vol. 37, no. 2, pp. 231–244.
15. Belykh, L.B., Goremyka, T.V., Antipina, D.V., and Schmidt, F.K., Abstracts of Papers, *Symp. "Modern Trends in Organometallic and Catalytic Chemistry,"* Moscow, May 18–23, 2003, p. 145.
16. Bakunina, T.I., Zinchenko, S.V., Khutoryanskii, V.A., *et al.*, in *Metallokompleksnyi kataliz: Sbornik nauchnykh statei* (Coordination Catalysts: Coll. of Scientific Papers), Shmidt, F.K., Ed., Irkutsk: Irkutsk. Gos. Univ., 1989, p. 132.

Russian Journal of Applied Chemistry, Vol. 77, No. 5, 2004, pp. 775–778. Translated from Zhurnal Prikladnoi Khimii, Vol. 77, No. 5, 2004, pp. 779–782.

ENVIRONMENTAL PROBLEMS OF CHEMISTRY AND TECHNOLOGY

Activated Carbons from Waste Wood in Wastewater Treatment To Remove Surfactants

A. O. Eremina, V. V. Golovina, M. Yu. Ugai, and A. V. Rudkovskii

Institute of Chemistry and Chemical Technology, Siberian Division, Russian Academy of Sciences, Krasnoyarsk, Russia

Received December 25, 2003

Abstract—Activated carbons synthesized by steam–gas treatment of charcoal produced from wastes formed in cutting of mixed wood were tested in adsorption of surfactants from aqueous solutions: anionic (Volgonat, Uglepen, neutralized black catalyst) and cationic (Katamin AB). Isotherms of adsorption of these impurities are presented, and a flowsheet of step-by-step wastewater treatment to remove surfactants by adsorption is suggested.

A search for effective methods for wastewater treatment to remove various organic and inorganic impurities is one of the most important problems of environment protection. Among the known contaminants are surfactants, which are widely used in the industry and in households. The problem of wastewater treatment is complicated by the wide variation of the concentration of surfactants: from 20–30 mg l^{-1} in household wastes to 50–1000 mg l^{-1} in industrial wastewater. Particularly severe difficulties are encountered at the very plants that manufacture surfactants because the concentration of surfactants in wastewater is subject to wide fluctuations, which requires that systems for local purification of process wastewater should be created.

Various techniques have found application in the practice of wastewater treatment to remove surfactants: foam separation, pressure flotation, ion exchange, biological treatment, and also membrane, adsorption, destructive (thermal detoxication, ozonation, radiation treatment) and other methods [1, 2]. The efficiency of these techniques depends on a multitude of factors. For example, the key part in adsorption purification is played by the choice of an adsorbent. Surfactants are commonly adsorbed, depending on their nature and concentration in wastewater, with peat, slag, undersized low-temperature coke, limestone, clayey minerals, zeolites, etc. [3]. In the process, the adsorbents are rather rapidly deactivated, which is caused, among other factors, by adsorption of other organic impurities. Activated carbons of various brands, which can be used for adsorption of surfactants, are manufactured in limited amounts by outdated technologies and their cost is high. Rather economical should be use of low-cost adsorbents manufactured from wastes of wood and woodworking industries. This would simultaneously allow utilization of waste wood, which is an important environmental problem.

This study is concerned with purification of aqueous solutions to remove surfactants by adsorption on activated carbons manufactured by steam–gas activation of charcoal that is produced from wastes formed in cutting of mixed wood.

EXPERIMENTAL

As raw materials for manufacture of activated carbons served charcoal produced from waste birch and aspen wood: branches, offcut, and crown posts.[1] The charcoal was produced on a UVP-5B installation. Further, the charcoal was subjected to a steam–gas activation in a fluidized-bed reactor at 850°C for 0.5 h; the content of oxygen and steam in the steam– gas mixture was 5 and 35%, respectively. The commercial fraction of the activated carbon with a particle size of more than 1 mm was isolated from the overall activated product. The yield of the commercial fraction was more than 80%. The main characteristics of the charcoal and of the activated carbon manufactured from it are listed in Table 1. The basic physicochemical and adsorption properties were determined using the known methods [4, 5].

Prior to tests, the activated carbons were dried at

[1] The basin of the Biryusa River in Krasnoyarsk krai.

1070-4272/04/7705-0775 © 2004 MAIK "Nauka/Interperiodica"

Table 1. Basic characteristics of charcoal and activated carbon produced from wastes formed in cutting of mixed wood raw materials

Parameter	Carbon	
	charcoal	activated carbon
Moisture content, %	5.0	7.4
Ash content A^d, %	1.8	2.6
Bulk density, kg m^{-3}	223	186
Total pore volume, cm^3 g^{-1}	0.06	1.80
Adsorption capacity:		
for iodine, %	6.5	63
for Methylene Blue, mg g^{-1}	12.9	77

105–110°C for 2 h and cooled in a desiccator over a drying agent, and their samples (0.1 to 10 g) were weighed with an accuracy of 0.2 mg. Then the activated carbons were saturated with water vapor. For this purpose, the samples were placed in a vessel with the air humidity of 98–99% (over a saturated solution of sodium carbonate) at 40°C and kept under these conditions for 3 h.

The samples of activated carbons were placed in flasks with ground-glass stoppers, each with 150 ml of an aqueous solution of a surfactant, and the flasks were gently shaken for 48 h. The aqueous solution was separated by centrifugation and the residual content of a surfactant was determined by photometry [6].

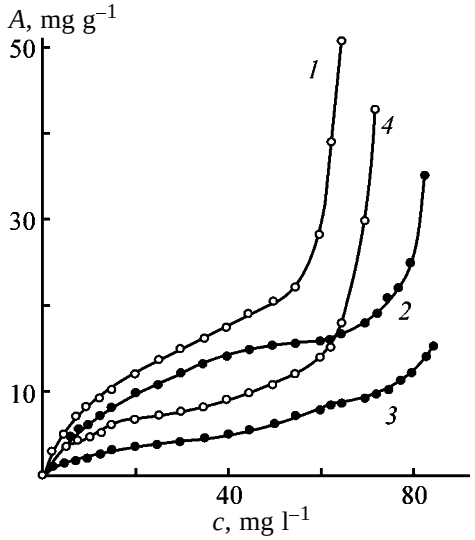

Fig. 1. Isotherms of adsorption *A* of surfactants on activated carbon. (*c*) Equilibrium concentration of surfactants. Surfactant: (*1*) Volgonat, (*2*) Uglepen, (*3*) neutralized black catalyst, and (*4*) Katamin AB; the same for Fig. 2.

Aqueous solutions of anionic (Volgonat, Uglepen, neutralized black catalyst) and cationic (Katamin AB) surfactants with an initial concentration of the main substance of 100 mg l^{-1} were used in the tests.

Figure 1 shows isotherms of adsorption of the surfactants on activated carbons. The isotherms of adsorption have the same shape for all the surfactants and belong to type II by the BET classification [7]. This indicates that the mechanisms of adsorption of the surfactants of varied nature are the same and that the activated carbons contain, together with micropores, also a considerable amount of meso- and macropores. This conclusion is confirmed by the following data: the total volume of pores is 1.80 cm^3 g^{-1} (Table 1), and the volume of micropores, 0.28 cm^3 g^{-1}.

Several regions can be distinguished in the isotherms of adsorption. The first, initial, portion has a convex shape and is due to electrostatic adsorption of separate anions (cations) of a surfactant by positively (negatively) charged centers on the surface of the activated carbons. Raising the concentration of a surfactant leads to enhancement of the mutual attraction of the hydrocarbon radicals in the anions (cations) of the surfactants and to the onset of association in the adsorption layer. In the third region of the isotherms, the rise in adsorption with increasing concentration of a surfactant gradually becomes less pronounced. This is presumably due to increased density of surface filling with adsorbed anions (cations) of the surfactants, to enhanced association of the hydrocarbon radicals and stronger forces of electrostatic repulsion between likely charged anion (cation) groups of the surfactants, and to a change in the sign of the charge at the phase boundary as a result of adsorption (through the van der Waals forces) of the nonpolar part of anions (cations). The fourth region of the isotherms, in which they form nearly a plateau, is due to complete coverage of the surface of the activated carbon with ionic associates or to the fact that the activity of unassociated anions (cations) of the surfactants remains constant despite the increase in the total analytical concentration of these substances. The steep rise exhibited by the isotherms is probably due to formation of a polymolecular adsorption layer, 3D association in the system, and dramatic increase in the enthalpy (build up of the entropy) because of the disintegration of the structure of water around the molecules being associated [3].

The efficiency of purification of contaminated water to remove anionic surfactants decreases in the order Volgonat > Uglepen > neutralized black catalyst. The cationic surfactant, Katamin AB, occupies an

Table 2. Expenditure of the activated carbon in multistage adsorption of surfactants ensuring 99% degree of purification

Surfactant	Expenditure of activated carbon, kg m^{-3}, at indicated number of stages (adsorbers)		
	1	2	3
Volgonat	33.00	11.25 + 3.00 = 14.25	6.76 + 4.25 + 0.67 = 11.68
Uglepen	45.00	15.00 + 4.09 = 19.09	8.25 + 4.48 + 0.91 = 13.64
Neutralized black catalyst	82.50	45.00 + 7.50 = 52.50	22.86 + 12.14 + 1.67 = 36.67
Katamin AB	49.5	20.00 + 4.50 = 24.50	11.76 + 5.31 + 1.00 = 18.07

intermediate position between the last two anionic surfactants: Uglepen and neutralized black catalyst.

The expenditure of activated carbon does not exceed 8–10 kg m^{-3} in purification to remove Volgonat and Uglepen, 15–20 kg m^{-3} in removing Katamin AB, and 25–30 kg m^{-3} for neutralized black catalyst, at a degree of purification of 85–90% (Fig. 2). If 99% purification is required, the expenditure of the activated carbon increases dramatically (Table 2).

The expenditure of the activated carbon can be decreased by performing a step-by-step purification by adsorption in a system of in-series connected adsorbers. In performing the adsorption process in two stages, the concentration of a surfactant in the aqueous solution was to be decreased tenfold, i.e., from 100 to 10 mg l^{-1}, in the first stage and completed, with the concentration of the surfactant diminished from 10 to 1 mg l^{-1} (permissible concentration of a surfactant for industrially used water), in the second. In performing the adsorption in three stages, the surfactant concentration in the aqueous solution was to be decreased from 100 to 20 mg l^{-1} in the first stage, from 20 to 3 mg l^{-1} in the second, and from 3 to 1 mg l^{-1} in the third.

With the two-stage scheme of purification applied, the expenditure of the activated carbon decreases by 36–57% as compared to the single-stage scheme, and with the three-stage scheme, by 16–29% as compared to the two-stage scheme and by 56–70% as compared to the single-stage scheme. As the adsorption capacity of the activated carbon in the first adsorber is exhausted, the adsorber is discharged, filled with a fresh portion of the activated carbon, and connected as the last stage in the system of adsorbers. Naturally, the increasing number of stages (i.e., assembling of additional adsorbers) leads to a directly proportional rise in the cost of the installation. Thus, the introduction of each new stage (if more than two) requires a thorough feasibility study.

It is inexpedient to regenerate spent activated carbon because of its low cost and a dramatic decrease in its mechanical strength upon regeneration. Therefore, it is recommended to burn spent activated carbons in power installations as an improved solid fuel.

Wastewater from a mechanized laundry and a plant for dry-cleaning and dyeing of clothes was purified under laboratory conditions. This was done on an activated carbon from waste wood in a flow-through installation at a specific load of 8–10 h^{-1} (adsorber 40 mm in diameter and 450 mm long). The input wastewater had the following composition (mg l^{-1}): anionic surfactants 52–130, phenols 0–5, chemical oxygen demand 1020–1200 mg O/l. After filtration across a bed of activated carbon, the concentrations of these impurities decreased dramatically to become as follows (mg l^{-1}): anionic surfactants 0.5–2.0, phenols 0–0.01, chemical oxygen demand 510–560 mg O/l. The concentrations of the contaminants in the purified wastewater exceed those permissible for water to be discharged into open water basins, but well conform

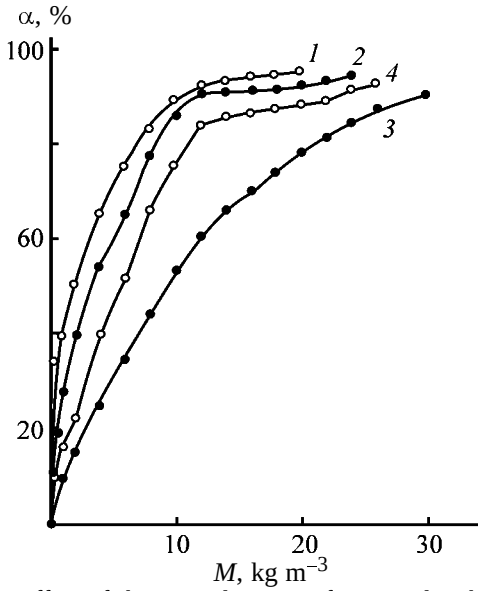

Fig. 2. Effect of the expenditure M of activated carbon on the degree α of purification of aqueous solutions to remove surfactants.

to the regulations concerning discharge of wastewater into municipal sewers for subsequent additional purification.

CONCLUSION

A rather high efficiency of purification of wastewater from some service plants was demonstrated in a study of the fundamental aspects of adsorption of surfactants (anionic: Volgonat, Uglepen, neutralized black catalyst; cationic: Katamin AB) on active carbons from wastes formed in cutting of mixed wood.

REFERENCES

1. Grishchenko, A.S. and Gushchina, L.I., *Metody ochistki stochnykh vod ot PAV: Tematicheskii obzor. Ser.: Okhrana okruzhayushchei sredy* (Methods for Wastewater Treatment To Remove Surfactants: Review. Ser.: Environment Protection), Moscow: TsNIITEneftekhim, 1984.
2. Smirnov, A.D., *Sorbtsionnaya ochistka vody* (Water Purification by Sorption), Leningrad: Khimiya, 1982.
3. Koganovskii, A.M., Klimenko, N.A., Levchenko, T.M., and Roda, I.G., *Adsorbtsiya organicheskikh veshchestv iz vody* (Adsorption of Organic Substances from Water), Leningrad: Khimiya, 1990.
4. Von Kinle, H. und Bader, E., *Aktivkohle und ihre industrielle Anwendung*, Stuttgart: Enke, 1980.
5. Kolyshkin, D.A., *Aktivnye ugli: Spravochnik* (Activated Carbons: Reference Book), Leningrad: Khimiya, 1985.
6. Lur'e, Yu.Yu., *Analiticheskaya khimiya promyshlennykh stochnykh vod* (Analytical Chemistry of Industrial Wastewater), Moscow: Khimiya, 1984.
7. Kel'tsev, N.V., *Osnovy adsorbtsionnoi tekhniki* (Fundamentals of Adsorption Technology), Moscow: Khimiya, 1984.

Russian Journal of Applied Chemistry, Vol. 77, No. 5, 2004, pp. 779–782. Translated from Zhurnal Prikladnoi Khimii, Vol. 77, No. 5, 2004, pp. 783–786.

ORGANIC SYNTHESIS AND INDUSTRIAL ORGANIC CHEMISTRY

Di-*tert*-butylhydroxylamine in Synthesis of Poly(Methyl Methacrylate) and Polystyrene

D. F. Grishin, L. L. Semenycheva, and M. V. Pavlovskaya

Research Institute of Chemistry, Lobachevsky Nizhni Novgorod State University, Nizhni Novgorod, Russia

Received January 9, 2004

Abstract—The effect of di-*tert*-butylhydroxylamine on polymerization of methyl methacrylate and styrene under conditions of radical initiation, similar to the commercial synthesis conditions, was studied.

Radical polymerization remains the main pathway of commercial synthesis of polymeric materials, since the procedure and the required equipment are relatively simple, the synthesis is well reproducible, a wide range of monomers can be involved in the reaction, etc. However, applications of radical polymerization are limited by such a significant drawback as nonuniform reaction progress with the occurrence of the gel effect (spontaneous growth of the molecular weight) impairing the polymer properties. In particular, the products become less heat-resistant, their molecular-weight distribution (MWD) becomes broader, etc. [1, 2]. A possible way to solve this problem is development of efficient methods for controlling the polymer chain propagation under conditions of radical initiation and, primarily, elaboration of theoretical principles and practical applications of so-called controlled radical polymerization [3, 4].

Controlled synthesis of polymers in the living chain mode has recently received much attention of macromolecular chemists. Among processes of this type, polymerization by the reversible inhibition mechanism in the presence of nitroxyl radicals, such as 2,2,6,6-tetramethylpiperidyl-1-oxyl and its analogs, is the most studied [5–7]. When this mechanism is realized in polymerization of vinyl monomers in the presence of nitroxyl radicals, a number of characteristic features are observed: weaker gel effect, linear growth of the molecular weight with conversion, and lower polydispersity coefficients (1.2–1.4).

Previous studies [8, 9] revealed side rections that occur in the course of polymerization in the presence of nitroxyl radicals along with reversible inhibition and temporarily remove nitroxyl from the polymerization sphere. One of the products of such reactions is hydroxylamine, which can generate the nitroxyl radical under the action of peroxy initiators:

$$>\!N\!-\!OH \xrightarrow{(O)} >\!N\!-\!O^{\bullet}. \qquad (1)$$

Also, chain transfer to hydroxylamine with formation of the nitroxyl radical is also possible:

$$>\!N\!-\!OH + R^{\bullet} \longrightarrow >\!N\!-\!O^{\bullet} + RH. \qquad (2)$$

This can be followed by realization of the reversible inhibition mechanism according to the scheme

$$\sim P^{\bullet}_m + A^{\bullet} \underset{k_d}{\overset{k_t}{\rightleftharpoons}} \sim P_m\!-\!A, \qquad (3)$$

where $\sim P^{\bullet}_m$ is the propagating radical; $A^{\bullet}$, nitroxyl spin adduct; k_d, rate constant of adduct reinitiation; k_p, propagation rate constant; and k_t, rate constant of adduct formation.

To develop new effective chain-terminating agents and gain deeper insight into the mechanism of polymerization in the presence of nitroxyl radicals, we studied the synthesis of poly(methyl methacrylate) (PMMA) and polystyrene in the presence of di-*tert*-butylhydroxylamine (DBHA) under conditions of radical initiation.

EXPERIMENTAL

Di-*tert*-butylhydroxylamine was prepared as described in [10, 11]. Dicetyl peroxydicarbonate (DPC), benzoyl peroxide (BP), and azobis(isobutyronitrile) (AIBN) used as initiators, and also the monomers and solvents were purified by standard procedures. The polymerization kinetics was monitored gravimetrically

1070-4272/04/7705-0779 © 2004 MAIK "Nauka/Interperiodica"

Molecular-weight characteristics of poly(methyl methacrylate) and polystyrene prepared in the presence of di-*tert*-butylhydroxylamine

Run no.	Polymer	DBHA, mol %	Initiator, mol %	T, °C	Conversion, %	$M_n \times 10^{-3}$	$M_w \times 10^{-3}$	M_w/M_n
1	PMMA	–	DPC, 0.1	50	72	519	1488	>3.0
2	″	0.015	″	50	10	137	234	1.7
3	″	0.015	″	50	28	168	317	1.9
4	″	0.015	″	50	85	400	1162	2.9
5	PS	–	BP, 1.0	100	91	20	41	2.1
6	″	0.4	″	100	18	6	11	1.9
7	″	0.4	″	100	22	6	11	1.9
8	″	0.4	″	100	45	13	19	1.5
9	″	0.4	″	100	77	16	25	1.5
10	″	–	AIBN, 0.8	70	84	77	246	3.2
11	″	0.5	″	70	13	17	25	1.5
12	″	0.5	″	70	61	25	35	1.5
13	″	0.5	″	70	76	27	53	1.9

[12] and thermographically [13]. The molecular weight M of the polymer was determined viscometrically [14]. Gel permeation chromatography (GPC) was performed on a device equipped with a set of five Styrogel columns with the pore size of 10^5, 3×10^4, 10^4, 10^3, and 250 Å (Waters, the United States). An R-403 differential refractometer (Waters) was used as detector. Tetrahydrofuran (THF) was the eluent. Calibration was performed using close-cut polystyrene references [15]. The ESR spectra were recorded on an AE4700 radiospectrometer. Crystalline MgO doped with Mn^{2+} ions was used as a reference for the magnetic field calibration.

Polymerization of methyl methacrylate (MMA) in the presence of DBHA was performed at 50°C in the presence of DPC, which simultaneously acts as oxidant for DBHA and as initiator of radical polymerization. On introducing 0.005–0.01 mol % DBHA into the system, the gel effect noticeably decreases, which, as noted above, is one of the evidences of polymerization in the living chain mode. The molecular weight of the polymer formed in the presence of DBHA linearly grows with the conversion (Fig. 1, curve *2*), and the unimodal MWD curves shift toward higher molecular weights with increasing conversion. However, the initially low polydispersity coefficient noticeably increases at conversions exceeding 30% (see table).

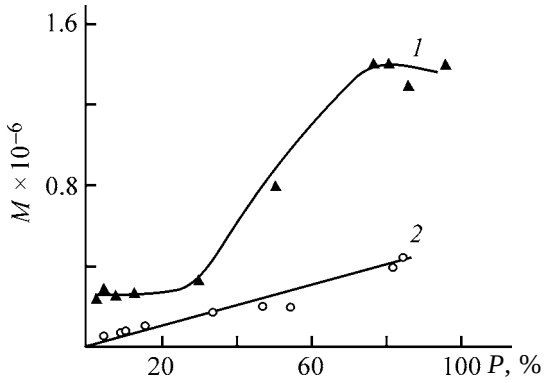

Fig. 1. Variation of the viscosity-averaage molecular weight M of PMMA with conversion P. Initiatior DPC (0.1 mol %), synthesis temperature 50°C. DBHA concentration, mol %: (*1*) 0 and (*2*) 0.015.

Similar results were obtained in polymerization of styrene in the presence of DBHA (0.2–0.4 mol %) and another peroxy initiator, BP (1.0 mol %). Polymerization of styrene at 100°C occurs without gel effect, and the molecular weight of polystyrene (PS) formed in the presence of DBHA also linearly grows with conversion (Fig. 2). The MWD curves are unimodal, and the maximum (mode) somewhat shifts toward higher M with conversion (Fig. 3). It is particularly important that the polydispersity coefficient of the samples prepared in the presence of DBHA is lower compared to the samples prepared without it (see table, run nos. 5–9). Furthermore, the polydispersity of polystyrene decreases with increasing conversion (see table, run nos. 6–9).

Our results give good grounds to suggest that, in polymerization of MMA in the presence of DBHA and DPC, some polymeric chains propagate by the reversible inhibition mechanism [Eq. (3)], but the secondary catalytic inhibition [Eqs. (4), (5)] also

makes a significant contribution:

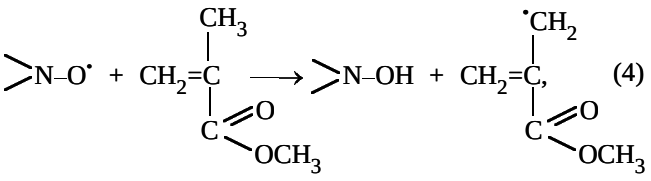

(4)

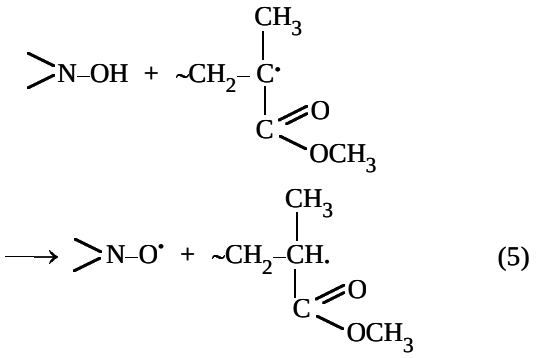

(5)

According to published data [16, 17], reactions (4) and (5) are more typical of methacrylic monomers and virtually do not occur with styrene. Also, in the presence of DBHA formation of the nitroxyl radical (*in situ*) occurs concurrently with chain propagation and termination by the common radical mechanism. The polymer chain propagation by several mechanisms, occurring in the presence of DBHA, results in increased polydispersity of PMMA.

The results of the kinetic studies of styrene polymerization in the presence of DBHA and BP, and also the molecular-weight characteristics of the synthesized polymers suggest predominant realization of the reversible inhibition mechanism in this case [Eq. (3)]. Of particular importance in this case are linear dependence of M on conversion, issuing virtually from the origin, pronounced shift of the MWD curves toward higher M with conversion, and low polydispersity coefficients of the polystyrene samples at high conversions.

To evaluate the contribution of reaction (5) to control of the chain propagation, we studied polymerization of styrene in the presence of a nonperoxy initiator, AIBN, which is incapable of oxidizing hydroxylamine to the nitroxyl spin adduct.

With AIBN used as initiator of styrene polymerization in the presence of DBHA at 70°C, the decreased gel effect, linear growth of the polystyrene molecular weight with conversion (Fig. 4), and shift of MWD curves toward higher M with conversion are observed also. Although the polydispersity coefficient of the samples prepared in the presence of DBHA is somewhat lower compared to the samples prepared without

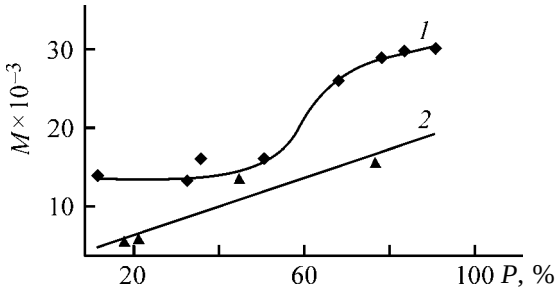

Fig. 2. Variation with conversion P of the (*1*) viscosity-average and (*2*) number-average molecular weight M of polystyrene prepared in the presence of BP (1.0 mol %). Synthesis temperature 100°C. DBHA concentration, mol %: (*1*) 0 and (*2*) 0.4.

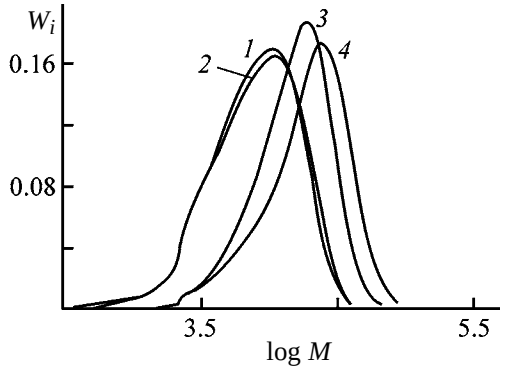

Fig. 3. MWD curves of polystyrene prepared in the presence of BP (1.0 mol %). DBHA concentration 0.4 mol %, synthesis temperature 100°C. (W_i) Fraction of the polymer and (M) molecular weight. Conversion, %: (*1*) 18, (*2*) 22, (*3*) 45, and (*4*) 77.

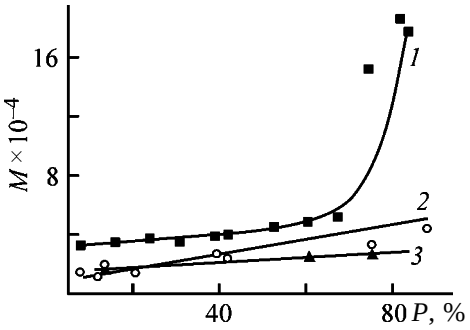

Fig. 4. Variation with conversion P of the (*1*, *2*) viscosity-average and (*3*) number-average molecular weight M of polystyrene. Initiator AIBN (0.8 mol %), synthesis temperature 70°C. DBHA concentration, mol %: (*1*) 0 and (*2*, *3*) 0.5.

it (also with AIBN as initiator; see table, run no. 10), it considerably grows with conversion, exceeding the polydispersity coefficients of the samples prepared in the presence of DBHA with BP as initiator.

Azobis(isobutyronitrile), in contrast to peroxides, does not oxidize DBHA to nitroxyl radical. Nitroxyl

radcal can form in the course of polymerization exclusively by hydrogen abstraction from hydroxylamine with the propagating macroradical [Eq. (5)]. Hence, in this case the concentration of the nitroxy spin adduct as chain-terminating agent [Eq. (3)] is considerably lower than with the peroxy initiator. Furthermore, the half-lives of AIBN and BP differ considerably. For example, AIBN can initiate radical polymerization of styrene throughout the process: The half-life of AIBN at 70°C is longer (300 min) than that of BP at 100°C (25 min). Formation of the "dead" polymer due to decomposition of residual AIBN and the lower concentration of di-*tert*-butylnitroxyl cause the polydispersity coefficient to increase.

In contrast to AIBN, benzoyl peroxide in polymerization in the presence of DBHA not only acts as initiator, but also oxidizes hydroxylamine to nitroxyl spin adduct reinitiating the chain propagation by Eq. (3). Formation of di-*tert*-butylnitroxyl by oxidation of DBHA with benzoyl peroxide was confirmed by ESR. The ESR spectrum contains a triplet with the hyperfine coupling constant a_N = 15.5 Oe, belonging to the di-*tert*-butylnitroxyl radical. Participation of the di-*tert*-butylnitroxyl radical in chain propagation appreciably reduces the contribution of the so-called "dead" process as compared to styrene polymerization in the presence of AIBN.

CONCLUSIONS

(1) Additions of di-*tert*-butylhydroxylamine control the kinetic parameters of polymerization of styrene and methyl methacrylate and the molecular-weight characteristics of the polymers under the conditions similar to those of the commercial synthesis.

(2) The polymerization control with di-*tert*-butylhydroxylamine is the most efficient in polymerization of styrene with peroxy initiators.

ACKNOWLEDGMENTS

The study was financially supported by the Russian Foundation for Basic Research (project no. 02-03-32427) and Competitive Center for Basic Natural Science, Ministry of Education of the Russian Federation (project no. E00-0.5-366).

REFERENCES

1. Ivanchev, S.S., *Radikal'naya polimerizatsiya* (Radical Polymerization), Leningrad: Khimiya, 1985.
2. Kireev, V.V., *Vysokomolekulyarnye soedineniya* (Macromolecular Compounds), Moscow: Vysshaya Shkola, 1992.
3. Matyjaszewski, K., *Controlled/Living Radical Polymerization*, Oxford: Oxford Univ. Press, 2000.
4. Grishin, D.F. and Semenycheva, L.L., *Usp. Khim.*, 2001, vol. 70, no. 5, pp. 486–509.
5. Otsu, T. and Matsumoto, A., *Adv. Polym. Sci.*, 1998, vol. 136, pp. 75–137.
6. Zaremskii, M.Yu. and Golubev, V.B., *Vysokomol. Soedin.*, 2001, vol. 43, no. 9, pp. 1689–1728.
7. Korolev, G.V. and Marchenko, A.P., *Usp. Khim.*, 2000, vol. 69, no. 5, pp. 447–475.
8. Rozantsev, E.G. and Sholle, V.D., *Organicheskaya khimiya svobodnykh radikalov* (Organic Chemistry of Free Radicals), Moscow: Khimiya, 1979, vol. 1.
9. *The Chemistry of the Nitro and Nitroso Groups*, Feuer, H., Ed., New York: Interscience, 1969, part 1.
10. Kornblum, N., Clutter, R.J., and Jones, W.J., *J. Am. Chem. Soc.*, 1956, vol. 78, no. 16, pp. 447–475.
11. Hoffman, A.K. and Henderson, A.T., *J. Am. Chem. Soc.*, 1961, vol. 83, no. 22, pp. 4671–4672.
12. Emel'yanov, D.N., Panova, G.D., and Ryabov, A.V., *Praktikum po metodam issledovaniya vysokomolekulyarnykh soedinenii* (Manual on Methods for Studying Macromolecular Compounds), Gor'kii: Gor'k. Gos. Univ., 1963.
13. Arulin, V.I. and Efimov, L.I., *Tr. Khim. Khim. Tekhnol.* (Gor'kii), 1970, no. 2, pp. 74–77.
14. Rafikov, S.R., Pavlova, S.A., and Tverdokhlebova, I.I., *Metody opredeleniya molekulyarnykh vesov i polidispersnosti vysokomolekulyarnykh soedinenii* (Methods for Determining Molecular Weights and Polydispersities of Macromolecular Compounds), Moscow: Khimiya, 1963.
15. Belen'kii, B.G. and Vilenchik, L.Z., *Khromatografiya polimerov* (Chromatography of Polymers), Moscow: Khimiya, 1978.
16. Smirnov, B.R. and Il'in, A.A., *Vysokomol. Soedin., Ser. A*, 1993, vol. 35, no. 6, pp. 591–597.
17. Il'in, A.A., Smirnov, B.R., Golikov, I.V., and Mogilevich, M.M., *Vysokomol. Soedin., Ser. A*, 1993, vol. 35, no. 6, pp. 597–601.

Russian Journal of Applied Chemistry, Vol. 77, No. 5, 2004, pp. 783–786. Translated from Zhurnal Prikladnoi Khimii, Vol. 77, No. 5, 2004, pp. 787–790.

ORGANIC SYNTHESIS AND INDUSTRIAL ORGANIC CHEMISTRY

Synthesis and Antioxidative Activity of S-Substituted 2-Mercapto-1,4-dihydroxybenzenes

V. M. Farzaliev, M. A. Allakhverdiev, S. A. Shamkhalova, and I. A. Rzaeva

Kuliev Institute of Chemistry of Additives, National Academy of Sciences of Azerbaijan, Baku, Azerbaijan
Baku State University, Baku, Azerbaijan

Received August 4, 2003; in final form, January 2004

Abstract—S-Substituted 2-mercapto-1,4-dihydroxybenzenes were prepared, and their antioxidative activity in autooxidation of cumene and in the reactions with cumylperoxy radicals and cumyl hydroperoxide was studied.

Sulfur-substituted phenols as effective oxidation inhibitors are widely used for stabilization of petroleum products [1]. Their high inhibiting performance is due to the presence in one molecule of two functional groups: phenolic hydroxyl and sulfide sulfur, making these compounds capable to inhibit oxidation by scavenging of peroxy radicals and decomposition of peroxides [2, 3].

Proceeding with studies on synthesis of phenolic sulfides [2–7], we prepared S-substituted 2-mercapto-1,4-dihydroxybenzenes and studied their antioxidative activity in cumene oxidation.

2-Mercapto-1,4-dihydroxybenzene **I** was prepared as follows:

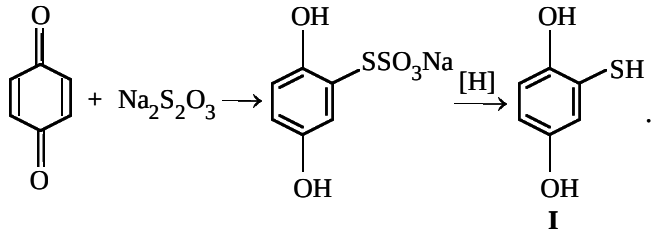

I

S-Methyl (**II**), *S*-ethyl (**III**), *S*-isopropyl (**IV**), *S*-carboxymethyl (**V**), *S*-acetyl (**VI**), *S*-allyl (**VII**), and *S*-benzyl (**VIII**) derivatives of **I** were prepared by the reactions of **I** with the corresponding halides in the presence of NaOH:

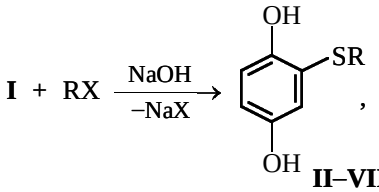

II–VIII

where R = CH_3, X = I (**II**); R = C_2H_5, X = Br (**III**); R = $(CH_3)_2CH$, X = Br (**IV**); R = CH_2COOH, X = Cl (**V**); R = CH_3CO, X = Br (**VI**); R = CH_2=$CHCH_2$, X = Br (**VII**); R = $C_6H_5CH_2$, X = Cl (**VIII**).

S-tert-Butyl (**IX**) and *S*-(2-cyanoethyl) (**X**) derivatives of **I** were prepared, respectively, by addition of **I** to acrylonitrile in the presence of triethylamine and to 2-methylpropene in the presence of catalytic amounts of sulfuric acid:

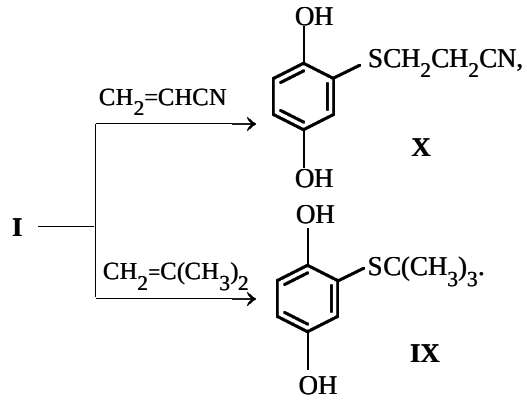

The purity of the compounds was checked by TLC and elemental analysis (Table 1), and their structures were proved by IR and ^{1}H NMR spectroscopy.

The IR spectra of **I**–**X** contain absorption bands at about 1450 (C···C stretching vibrations in the aromatic ring), 3450 (stretching vibrations of the O–H bond involved in hydrogen bonding with the adjacent S atom [8]), and 810–860 cm^{-1} (1,2,4-substituted benzene ring). The ^{1}H NMR spectra of mercaptophenols **I**–**X** contain a proton signal from two hydroxy groups (7.4 ppm). The multiplets of three benzene ring protons are observed at about 5.9 ppm. Compound **I** exhibits a band at 2530 cm^{-1} in the IR spec-

Table 1. Yields, melting points, retention factors (R_f), and elemental analyses of **I**–**X**

Compound	mp, °C	Yield, %	R_f	Found, %			Formula	Calculated, %		
				C	H	S		C	H	S
I	117–117.5	38	0.57	50.83	4.07	22.36	$C_6H_6O_2S$	50.68	4.25	22.55
II	123–124	47	0.82	53.49	5.28	20.32	$C_7H_8O_2S$	53.82	5.16	20.51
III	135–136	35	0.63	56.21	5.75	20.66	$C_8H_{10}O_2S$	56.45	5.92	20.49
IV	142–143	42	0.47	57.83	5.62	17.23	$C_9H_{12}O_2S$	58.67	6.56	17.40
V	147–148	55	0.73	60.73	7.41	16.38	$C_{10}H_{14}O_2S$	60.57	7.12	16.17
VI	140–142	49	0.87	50.72	4.17	15.27	$C_9H_8O_2S$	50.94	3.79	15.11
VII	99–100	60	0.68	52.37	4.61	17.59	$C_8H_8O_3S$	52.16	4.38	17.41
VIII	132–133	26	0.85	59.12	5.74	17.39	$C_9H_{10}O_2S$	59.32	5.53	17.60
IX	97–98	75	0.57	55.52	4.19	16.58	$C_9H_9NO_2S$	55.37	4.65	16.42
X	148–149	36	0.90	67.43	5.39	13.67	$C_{13}H_{12}O_2S$	67.25	5.21	13.80

trum (S–H stretching vibrations), and its NMR spectrum contains an SH proton singlet at 3.3 ppm. The IR and ^{1}H NMR spectra of **II**–**X** exhibit features characteristic of the substituents at the S atom.

To evaluate the inhibiting activity of **I**–**X**, we used as model substrate cumene, as the mechanism of its oxidation is well understood. Experiments on cumene autooxidation in the presence of **I**–**X** revealed their fairly high inhibiting performance. Experiments on oxidation of cumene initiated with azobis(isobutyronitrile) (AIBN; 60°C, [AIBN] = 2×10^{-2} M) showed that these compounds actively terminate oxidation chains, reacting with cumylperoxy radicals. Data for **I** as example are shown in Fig. 1. From the induction period τ_{ind}, we calculated the stoichiometric inhibition coefficient f equal to the number of oxidation chains

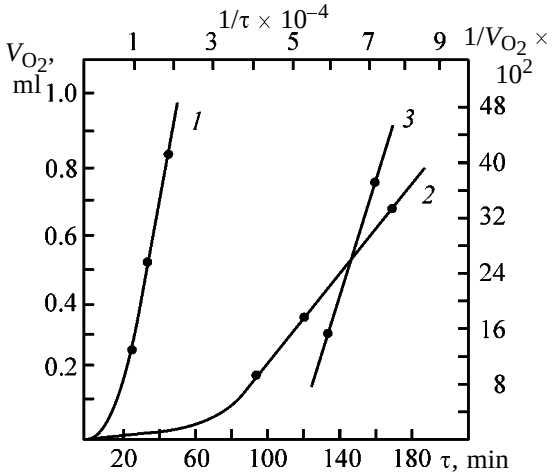

Fig. 1. Kinetic curves of O_2 uptake in initiated oxidation of cumene (*1*) without additives and (*2*) in the presence of **I**. (*3*) Linearization of curve *2* in the coordinates $1/\tau$–$1/V_{O_2}$. (V_{O_2}) Volume of oxygen taken up and (τ) time.

terminated on one molecule of an inhibitor and its transformation products:

$$f = \tau_{ind} v_{ind}/[In]_0,$$

where τ_{ind} is the induction period; v_{ind}, initiation rate; and $[In]_0$, initial concentration of inhibitor In.

From the kinetics of the oxygen uptake, we calculated the rate constants of the reactions of the inhibitors with peroxy radicals k_7 [8, 9]. To do this, we transformed the kinetic curves of the oxygen uptake from the coordinates $[O_2]$–τ to the coordinates $[O_2]^{-1}$–τ^{-1} and from the slope $\tan\alpha$, equal [9, 10] to

$$\tan\alpha = fk_7[In]_0/(k_2[RH]v_{ind}),$$

found the constant k_7:

$$k_7 = \tan\alpha k_2[RH]v_{ind}/f[In]_0,$$

where k_2 is the rate constant of chain initiation [9, 10], equal to 1.51 l mol^{-1} s^{-1}; [RH] = 6.9 M.

Table 2 shows that the constants k_7 for the compounds with electron-donor substituents are higher compared to the compounds with electron-acceptor substituents. As for f, it varies in the range 1.05–2.20.

Reactions of **I**–**X** with cumyl hydroperoxide (CHP) were performed in chlorobenzene under nitrogen at 110°C. All the compounds **I**–**X** decompose CHP. Figure 2 shows (by the example of **I**) that the kinetic curve of CHP decomposition in the presence of mercaptophenols is S-shaped, which is typical of autocatalytic processes. The reaction starts with a certain induction period in which the consumption of CHP is insignificant; this is followed by fast catalytic decom-

position of CHP and then by reaction deceleration due to a decrease in the CHP concentration. Apparently, the inhibitor first reacts with CHP to give a product that catalytically decomposes CHP.

To determine the reaction order, we studied how the initial rate of the catalytic decomposition of CHP depends on the concentrations of the reactants. We found that the initial rate v_0 of catalytic decomposition of CHP under the action of **I**–**X** obeys the kinetic equation

$$v_0 = k[\mathrm{In}][\mathrm{ROOH}]^2.$$

To determine the reaction stoichiometry, we took CHP in excess. The catalytic factor ν characterizes the number of CHP molecules decomposed with one inhibitor molecule; it was calculated by the formula

$$\nu = [\mathrm{ROOH}]_0 - [\mathrm{ROOH}]_\infty/[\mathrm{In}]_0,$$

where $[\mathrm{ROOH}]_0$ and $[\mathrm{ROOH}]_\infty$ are, respectively, the initial and final concentrations of [CHP], and $[\mathrm{In}]_0$ is the initial inhibitor concentration.

Experiments showed that one molecule of **I**–**X** can decompose up to several thousands of CHP molecules (Table 2). The kinetic parameters of the reaction show certain correlation with the properties of substituents at the S atom. In particular, in going to branched alkyl substituents (compounds **II**–**V**) k decreases, probably owing to steric factors; ν is higher for the compounds with electron-donor substituents at the S atom.

EXPERIMENTAL

The IR spectra were recorded on a Specord 75-IR spectrophotometer, and the ^{1}H NMR spectra, on a Varian T-60 spectrometer, with tetramethylsilane as internal reference.

2-Mercapto-1,4-dihydroxybenzene I. A solution of 43.2 g of benzoquinone in 150 ml of glacial acetic acid was heated to 40–50°C, and then a solution of 150 g of $Na_2S_2O_3$ in 200 g of water was gradually added, avoiding warming-up of the reaction mixture by more than 10°C. After short stirring, the transparent and almost colorless solution was saturated with KCl to precipitate sodium *S*-(2,5-dihydroxyphenyl) thiosulfate. A solution of 2.6 g of this salt in 10 ml of water was mixed with 20 ml of concentrated HCl, and 5 g of zinc dust was gradually added; the reaction temperature was maintained at 40–50°C until the gas evolution ceased.

Table 2. Kinetic parameters of the reactions of mercaptophenols **I**–**X** with cumylperoxy radicals k_7 and f (60°C, [AIBN] = 2×10^{-2} M) and of decomposition of cumyl hydroperoxide k and ν (110°C)

Compound	$k_7 \times 10^{-4}$, l mol^{-1} s^{-1}	f	k, l mol^{-1} s^{-1}	ν
I	2.15	1.27	10.45	4500
II	1.53	2.20	3.24	3350
III	1.71	2.11	2.45	2730
IV	2.70	1.92	1.96	1840
V	1.52	1.05	1.62	400
VI	2.17	1.72	2.99	2800
VII	1.05	1.64	3.50	1770
VIII	1.41	1.57	3.10	1050
IX	1.25	1.62	4.63	1500
X	1.15	1.74	4.67	2870

2,5-Dihydroxyphenyl methyl sulfide II. A 2-g portion of NaOH was added at 10–15°C to a solution of 7.1 g (0.05 mol) of **I** in 30 ml of isopropyl alcohol, after which 7.1 g of methyl iodide was added at the same temperature. The reaction was performed under nitrogen. The temperature was raised to 60°C, after which the mixture was stirred for an additional 3 h and washed first with 2 M HCl and then with water to neutral reaction. The organic layer was treated with petroleum ether (30–60°C) and dried over sodium sulfate.

Compounds **III**, **IV**, **VII**, **VIII**, and **X** were prepared similarly.

2,5-Dihydroxyphenyl *tert*-butyl sulfide IX. A 3-ml portion of isobutylene was added to a mixture of 7.1 g of **I** and five drops of concentrated H_2SO_4 saturated with $(NH_4)_2SO_4$, heated to 110–120°C. Then the mixture was neutralized with 13 ml of 2 M NaOH, treated with petroleum ether, and washed three

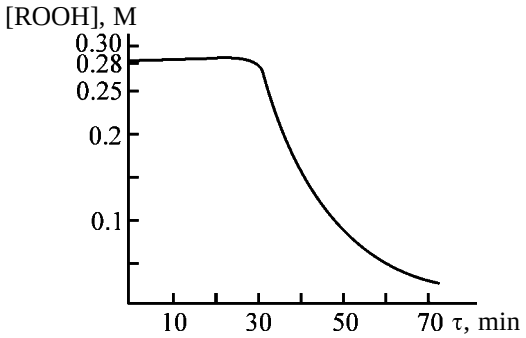

Fig. 2. Kinetic parameters of decomposition of cumyl hydroperoxide (ROOH) under the action of **I**. [In] = 3×10^{-4}, $[\mathrm{ROOH}]_0$ = 0.285 M. (τ) Time.

times with water. After drying over Na_2SO_4, the solvent was distilled off.

2,5-Dihydroxyphenyl 2-carboxymethyl sulfide V. A 7.1-g portion of **I** was added to a solution of 2 g of NaOH in 10 ml of water, and a concentrated solution of 4.7 g of chloroacetic acid, neutralized with sodium hydrogen carbonate, was added with stirring and cooling. After 5 h, the solution was heated, impurities were steam-distilled, and the solution was acidified with dilute H_2SO_4.

2,5-Dihydroxyphenyl 2-cyanoethyl sulfide X. A mixture of 7.1 g of **I**, 20 ml of anhydrous benzene, and a drop of triethylamine was stirred at 60–70°C for 3 h. Then the mixture was washed with water and dried over Na_2SO_4. The solvent was distilled off, and the product was recrystallized from diethyl ether.

CONCLUSIONS

(1) 2-Mercapto-1,4-dihydroxybenzene was prepared and converted into various S-substituted derivatives.

(2) The compounds synthesized exhibit synergism as inhibitors of cumene oxidation and, being polyfunctional antioxidants, terminate cumene oxidation chains by reactions with peroxy radicals and catalytically decompose cumene hydroperoxide.

REFERENCES

1. Kuliev, A.M., *Khimiya i tekhnologiya prisadok k maslam i toplivam* (Chemistry and Technology of Additives to Oils and Fuels), Leningrad: Khimiya, 1985, pp. 31–38.
2. Aliev, A.S., Zolotova, N.V., Denisov, E.T., and Farzaliev, V.M., *Neftekhimiya*, 1974, vol. 14, no. 3, pp. 424–428.
3. Aliev, A.S., Farzaliev, V.M., Abdullaeva, F.A., and Denisov, E.T., *Neftekhimiya*, 1975, vol. 15, no. 6, pp. 890–895.
4. Magerramov, A.M., Sattar-zade, R.I., Farzaliev, V.M., and Allakhverdiev, M.A., *Vestn. Bakin. Univ., Estestv. Nauki*, 2000, no. 3, pp. 26–31.
5. Magerramov, A.M., Sattar-zade, R.I., Farzaliev, V.M., and Allakhverdiev, M.A., *Vestn. Bakin. Univ., Estestv. Nauki*, 2000, no. 4, pp. 5–12.
6. Allakhverdiev, M.A., Farzaliev, V.M., Sattar-zade, R.I., and Rzaeva, I.A., *Zh. Prikl. Khim.*, 2001, vol. 14, no. 12, pp. 2023–2026.
7. Farzaliev, V.M., Allakhverdiev, M.A., Aliev, Sh.R., *et al.*, *Zh. Prikl. Khim.*, 2003, vol. 76, no. 8, pp. 1321–1324.
8. Zuika, I.V. and Bankovskii, Yu.A., *Usp. Khim.*, 1973, vol. 42, no. 1, pp. 39–64.
9. Emanuel', N.M., Denisov, E.T., and Maizus, Z.K., *Tsepnye reaktsii okisleniya uglevodorodov v zhidkoi faze* (Chain Reactions of Liquid-Phase Oxidation of Hydrocarbons), Moscow: Nauka, 1965.
10. Emanuel', N.M. and Denisov, E.T., *Neftekhimiya*, 1976, vol. 16, no. 3, pp. 366–368.

Russian Journal of Applied Chemistry, Vol. 77, No. 5, 2004, pp. 787–789. Translated from Zhurnal Prikladnoi Khimii, Vol. 77, No. 5, 2004, pp. 791–793.

ORGANIC SYNTHESIS AND INDUSTRIAL ORGANIC CHEMISTRY

Some Transformations of 2-Amino-4-phenyl-1,3-thiazole

S. E. Sadigova, A. M. Magerramov, M. A. Allakhverdiev, and T. M. Vekilova

Baku State University, Baku, Azerbaijan

Received December 4, 2003; in final form, March 2004

Abstract—Reactions of 2-amino-4-phenyl-1,3-thiazole with aromatic aldehydes, phenyl isocyanate, and carboxylic acid chlorides were studied.

Various thiazoles exhibit antimicrobial, antihelmintic, antiparasitic, and antipyretic properties [1–3]. Thiazole derivatives are widely used as antioxidants [4], vulcanization accelerators [5], and photochromic compounds [6]. Thiazoles and azomethines derived from them are important analytical reagents [7]. Thiazoles are also used for preparing various heterocycles [8], cyclizing terpenes [9], and concentrating some transition metals. In many cases, the triazoles used contain aryl and basic (amino) groups.

In this context, it seemed appropriate to prepare a thiazole containing simultaneously aryl and amino groups, 2-amino-4-phenyl-1,3-thiazole **I**, and its derivatives.

Compound **I** was prepared according to [10] in two steps: bromination of acetophenone followed by the reaction of the resulting α-bromoacetophenone with thiourea; the yield of the target product was 90%:

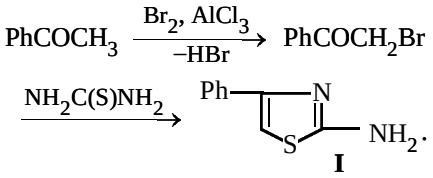

I

Reaction of thiazole **I** with phenyl isocyanate gave urea derivative **II**; hydrogen substitution with bromine in **I** yielded 2-amino-5-bromo-4-phenylthiazole **III**:

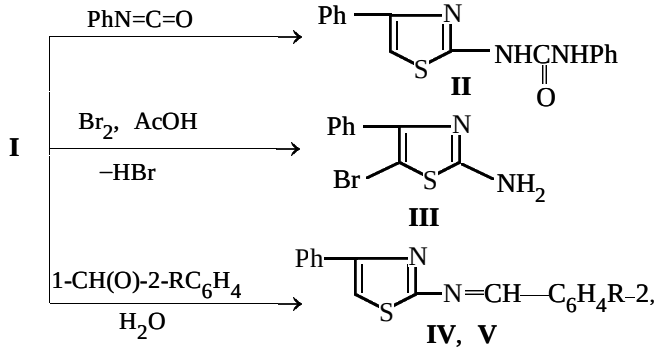

where R = H (**IV**), OH (**V**).

It is known thart condensation of various amines with aldehydes yields Schiff bases. We have studied for the first time the reactions of **I** with benzaldehyde and salicylaldehyde and obtained the corresponding Schiff bases **IV** and **V**.

2-(2-Hydroxybenzylidenimino)-4-phenyl-1,3-thiazole **V** is hydrogenated under mild conditions with sodium borohydride to give 2-(2-hydroxybenzylamino)-4-phenyl-1,3-thiazole **VI**. Treatment of **VI** with HCl gives the corresponding hydrochloride:

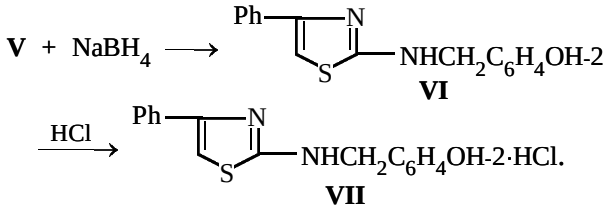

With the aim to synthesize potentially physiologically active derivatives of thiazole **I**, we prepared its hydrochloride **VIII**, which, in contrast to the free base, is readily soluble in water; acylation of **I** gave amide hydrochlorides **IX** and **X**:

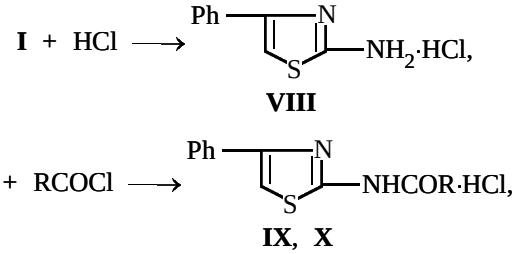

where R = Me (**IX**), Ph (**X**).

The IR spectra of Schiff bases **IV** and **V** are similar to that of thiazole **I**. However, there is a new absorption band at about 3450 cm^{-1} in the spectra of **IV** and **V**, characterizing an intramolecular hydrogen bond between the phenolic hydroxyl and N=CH fragment.

1070-4272/04/7705-0787 © 2004 MAIK "Nauka/Interperiodica"

Yields, melting points, and elemental analyses of 2-amino-4-aryl-1,3-thiazole **I** and its derivatives **II**–**X**

Compound	Yield, %	mp, °C	Found, %				Formula	Calculated, %			
			C	H	N	S		C	H	N	S
I	70	148–150	61.21	4.73	15.51	18.42	$C_9H_8N_2S$	61.34	4.58	15.89	18.19
II	91	209	65.16	4.28	14.08	10.92	$C_{16}H_{13}N_3OS$	65.06	4.44	14.23	10.86
III	65	155–156	42.58	2.44	10.68	12.73	$C_9H_7N_2SBr$	42.37	2.76	10.98	12.57
IV	71	160–161	72.61	4.73	10.75	12.02	$C_{16}H_{12}N_2S$	72.70	4.58	10.60	12.12
V	80	143	68.76	4.13	9.74	11.28	$C_{16}H_{12}N_2OS$	68.55	4.31	9.99	11.44
VI	70	155	67.93	5.14	9.86	11.49	$C_{16}H_{14}N_2OS$	68.06	5.00	9.92	11.36
VII	93	177	60.35	4.57	8.92	10.26	$C_{16}H_{15}N_2OSCl$	60.28	4.74	8.79	10.06
VIII	85	176–177	50.99	4.11	13.45	15.22	$C_9H_9N_2SCl$	50.82	4.27	13.17	15.07
IX	90	168	51.99	4.26	10.78	12.74	$C_{11}H_{11}N_2OSCl$	51.87	4.35	11.00	12.59
X	87	195	60.48	4.03	8.72	10.95	$C_{16}H_{13}N_2OSCl$	60.66	4.14	8.84	10.12

No bands characteristic of NH_2 stretching vibrations were revealed. The bands at about 3300 cm^{-1} in the IR spectrum of **VI** characterize the intramolecular hydrogen bond HN···HO.

The UV spectrum of **V** dramatically differs from that of its hydrogenated analog **VI**. The absorption bands at 208 and 278 nm in **V** belong to conjugated aromatic rings, and the long-wave band at 385 nm is due to the $\pi \rightarrow \pi^*$ transition in the conjugated azomethine fragment C=N. In the spectrum of **VI**, this band is absent. The lack of conjugation between the benzene rings results in this case in the presence of two bands at 260 and 282 nm, assignable to the monosubstituted benzene and phenolic rings, respectively, instead of a single band at 278 nm.

In the ^{1}H NMR spectrum of **V**, the phenolic hydroxyl proton gives a signal at about 3.25 ppm, and the N=CH proton, at 7.85–7.90 ppm. In the hydroxyphenyl moiety, the four nonequivalent protons give a multiplet at 7.2–7.5 ppm.

The yields and melting points of **I**–**X** are listed in the table. The purity of **I**–**X** was confirmed by TLC, and the compositions and structures were proved by elemental analysis and by IR, UV, and ^{1}H NMR spectroscopy.

EXPERIMENTAL

The IR spectra of **I**–**X** were taken on a Specord IR-75 spectrophotometer. Samples were prepared as thin films or mulls in mineral oil. The spectra were recorded in the range 700–3700 cm^{-1} using KBr, NaCl, and LiF prisms. The ^{1}H NMR spectra were taken on a Varian VXR-400S spectrometer (400 MHz, solutions in DMSO-d_6, internal reference TMS). The TLC analysis was performed on Silufol UV-254 plates. A 1 : 1 (by volume) mixture of isopropyl alcohol and heptane was used as eluent. The plates were developed with iodine vapor.

2-(Phenylaminocarbonylamino)-4-phenyl-1,3-thiazole II. A 2.4-g (0.02-mol) portion of phenyl isocyanate was added dropwise with stirring to a solution of 3.4 g (0.02 mol) of **I** in 20 ml of anhydrous toluene. The stirring was continued for 24 h at 60°C. Then the mixture was cooled to room temperature, and the colorless crystalline precipitate was filtered off and recrystallized from acetone.

2-Amino-4-phenyl-5-bromo-1,3-thiazole III. A solution of 3.2 g (0.02 mol) of bromine in 10 ml of acetic acid was added at 20°C to a solution of 3.4 g (0.02 mol) of **I** in 20 ml of glacial acetic acid, and the mixture was stirred at 20°C for 30 min. Then 100 ml of water was added. The yellowish precipitate that formed in 2 h was filtered off and recrystallized from ethanol.

2-Benzylidenamino-2-phenyl-1,3-thiazole IV. A 8.8-g (0.05-mol) portion of **I** was added to 5.3 g (0.05 mol) of benzaldehyde, and the mixture was vigorously stirred for 3 min. Then the mixture was transferred into a beaker, 15 ml of ethanol was added, and the mixture was cooled. The colorless crystalline precipitate that formed in several minutes was filtered off.

2-(2-Hydroxybenzylidenamino)-4-phenyl-1,3-thiazole V. A 8.8-g (0.05-mol) portion of **I** was added to 6.1 g (0.05 mol) of salicylaldehyde, and the mixture was vigorously stirred for 30 min. In so doing, the mixture spontaneously warmed up to 40°C. Then the mixture was transferred into a beaker, 15 ml of ethanol was added, and the mixture was cooled with ice. The crystalline precipitate that formed was filtered off.

2-(2-Hydroxybenzylamino)-4-phenyl-1,3-thiazole VI. A 30-ml portion of ethanol was added to 5.6 g (0.02 mol) of **V**, and the mixture was stirred to obtain a suspension. Then sodium borohydride was added, and the mixture was stirred for an additional 30 min. After that, 100 ml of water was added, and the mixture was acidified to pH 7.5. The colorless crystalline precipitate that formed was filtered off and recrystallized from benzene.

2-Amino-4-phenyl-1,3-thiazole hydrochloride VIII. Dry HCl was passed through a solution of 8.2 g (0.05 mol) of **I** in 30 ml of isopropyl alcohol, cooled to 0°C. The colorless crystalline precipitate that formed was filtered off and washed three times with anhydrous diethyl ether. The resulting hydrochloride was recrystallized from ethanol.

Compound **VII** was prepared similarly.

2-Acetylamino-4-phenyl-1,3-thiazole hydrochloride IX. Freshly distilled acetyl chloride (1.5 g, 0.02 mol) was added dropwise to a solution of 3.4 g (0.02 mol) of **I** in 10 ml of anhydrous toluene, cooled to 0–5°C. The colorless crystalline precipitate that formed was filtered off and recrystallized from acetone.

Compound **X** was prepared similarly.

CONCLUSION

2-Amino-4-phenyl-1,3-thiazole was synthesized in a high yield and converted into various derivatives (azomethines, halides, amides), which may be promising as bioactive substances, antioxidants, and analytical reagents.

REFERENCES

1. Karpov, K.A., Nazarenko, A.V., Pekarevskii, B.V., and Potekhin, B.M., *Zh. Prikl. Khim.*, 2001, vol. 74, no. 6, pp. 971–974.
2. Manian, A.K., Khadse, B.G., Kirticar, P.A., and Sengupta, S.R., *Indian J. Pharm. Sci.*, 1991, vol. 53, no. 3, pp. 102–103.
3. Uchikawa, O., Fukatsu, K., Suno, M., *et al.*, *Chem. Pharm. Bull.*, 1996, vol. 44, no. 11, pp. 2070–2077.
4. Kelarev, V.I., Gracheva, O.G., Silin, M.A., *et al.*, *Neftepererab. Neftekhim.*, 1997, no. 12, pp. 29–32.
5. Kurtzer, F., Sulfur, Selenium and Tellurium, *Specialist Periodical Reports*, London: Chem. Soc., 1973, vol. 2.
6. *Comprehensive Organic Chemistry. The Synthesis and Reactions of Organic Compounds*, Barton, D. and Ollis, W.D., Eds., vol. 4: *Heterocyclic Compounds*, Sammer, P.G., Ed., Oxford: Pergamon, 1974.
7. Sadigova, S.E., Magerramov, A.M., Allakhverdiev, M.A., *et al.*, *Zh. Obshch. Khim.*, 2003, vol. 73, no. 12, pp. 2043–2046.
8. Kuznetsov, V.V. and Prostakov, N.S., *Khim. Geterotsikl. Soedin.*, 1990, no. 1, pp. 5–32.
9. *Khimicheskaya entsiklopediya* (Chemical Encyclopedia), Gorkin, A.P., Ed., Moscow: Bol'shaya Ross. Entsiklopediya, 1995, vol. 4.
10. *Organic Synthesis*, Blatt, A.H., Ed., New York: Wiley, 1946, 2nd ed., coll. vol. 2. Translated under the title *Sintezy organicheskikh preparatov*, Moscow: Inostrannaya Literatura, 1949, coll. 2, pp. 40–41.

Russian Journal of Applied Chemistry, Vol. 77, No. 5, 2004, pp. 790–793. Translated from Zhurnal Prikladnoi Khimii, Vol. 77, No. 5, 2004, pp. 794–797.

ORGANIC SYNTHESIS AND INDUSTRIAL ORGANIC CHEMISTRY

Synthesis and Anticorrosion and Biocidal Activity of Triazoloazepine Derivatives

A. M. Demchenko, K. G. Nazarenko, A. P. Makei, S. V. Prikhod'ko, I. N. Kurmakova, and A. P. Tretyak

Shevchenko State Teacher's Training Institute, Chernigov, Ukraine
Institute of Organic Chemistry, Ukrainian National Academy of Sciences, Kiev, Ukraine

Received February 19, 2003; in final form, March 2004

Abstract—Inhibiting effect on acid corrosion of steel 45 and biocidal activity with respect to sulfate-reducing bacteria are studied for a series of *N*-aryl-*N*-(6,7,8,9-tetrahydro-5*H*-[1,2,4]triazolo[4,3-*a*]azepin-3-ylmethyl)-amines.

Both acid corrosion inhibitors [1] and biocides [2] are known among nitrogen-containing heterocyclic organic compounds. We made an attempt to synthesize compounds demonstrating these properties in combination. Such compounds can find application in developing inhibitor formulations, paint and varnish materials, and protective compositions for metals exploited under the impact of several corrosion factors.

The goal of this work is to study the inhibiting activity of *N*-aryl-*N*-(6,7,8,9-tetrahydro-5*H*-[1,2,4]triazolo[4,3-*a*]azepin-3-ylmethyl)amines in hydrochloric acid solutions and also to characterize the biocidal activity of these compounds with respect to sulfate-reducing bacteria as the major factor of biocorrosion.

EXPERIMENTAL

N-Aryl-*N*-(6,7,8,9-tetrahydro-5*H*-[1,2,4]triazolo-[4,3-*a*]azepin-3-ylmethyl)amines **3a**–**3i** were synthesized by reactions of 7-methoxy-3,4,5,6-tetrahydro-2*H*-azepine with hydrazides of substituted *N*-arylaminoacetic acids [4, 5]. To 0.01 mol of hydrazide **2a**–**2i** in 30 ml of 2-propanol, 0.011 mol of compound **1** was added and the mixture was refluxed for 2 h. The reaction progress was monitored chromatographically. After the reaction completion, the mixture was cooled, and the precipitate was filtered off, washed with 2-propanol, dried, and recrystallized from 2-propanol. The characteristics of the products are summarized in Table 1.

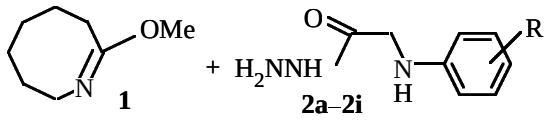

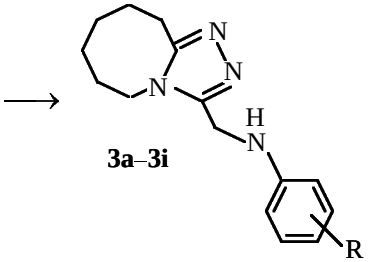

where R = H (**a**), 4-F (**b**), 4-Cl (**c**), 4-I (**d**), 4-CH_3O (**e**), 2,4-$(CH_3)_2$ (**f**), 4-CH_3 (**g**), 2-CH_3 (**h**), and 3-CH_3 (**i**).

The composition and structure of the products were confirmed by ^{1}H NMR. The spectra in DMSO-d_6 were recorded on a Bruker-300 instrument with TMS as internal reference. The reaction was monitored by TLC on Silufol UV-254 in the system chloroform/methanol = 9/1.

The inhibiting activity of the compounds was studied in 1 M HCl at 293 K by the electrochemical method using a P-5845 potentiostat [6]. Polarization curves (80 mV min^{-1}) were recorded at the stationary potential of free corrosion φ_s in a three-electrode glass cell with separated cathode and anode spaces (working steel 45 end face electrode, Ag/AgCl reference electrode, and Pt auxiliary electrode). The potentials were recalculated to the standard hydrogen scale. The concentration of **3a**–**3i** was 2 mM. From the polarization curves, we determined the potential and current of free corrosion φ_f and I_f, and also potentials and currents of cathodic (φ_c, I_c) and anodic (φ_a, I_a) corrosion. Then we estimated the Tafel coefficients a_c, a_a, b_c, and b_a; electrochemical corrosion inhibition coefficients γ_s, γ_c, and γ_a; protective efficiency Z_f, Z_c, and Z_a; and, finally, the shift of the adsorption potential $\Delta\Psi'$ [1].

1070-4272/04/7705-0790 © 2004 MAIK "Nauka/Interperiodica"

Table 1. Characteristics of *N*-aryl-*N*-(6,7,8,9-tetrahydro-5*H*-[1,2,4]triazolo[4,3-*a*]azepin-3-ylmethyl)amines

Compound	Yield, %	mp, °C	Found, %		Formula	Calculated, %	
			N	Hlg		N	Hlg
3a	78	199–200	23.38	–	$C_{14}H_{18}N_4$	23.14	–
3b	76	182–183	21.20	7.02	$C_{14}H_{17}FN_4$	21.05	7.14
3c	81	193–195	20.46	12.95	$C_{14}H_{17}ClN_4$	20.25	12.84
3d	72	214–216	15.04	34.65	$C_{14}H_{17}IN_4$	15.22	34.51
3e	77	175–177	20.76	–	$C_{15}H_{20}N_4O$	20.58	–
3f	76	156–158	20.49	–	$C_{16}H_{22}N_4$	20.74	–
3g	77	184–186	21.98	–	$C_{15}H_{20}N_4$	21.88	–
3h	64	163–164	21.64	–	$C_{15}H_{20}N_4$	21.88	–
3i	70	201–203	22.05	–	$C_{15}H_{20}N_4$	21.88	–

Table 2. Electrochemical parameters of corrosion of steel 45 in 1 M HCl

Compound	Potential, V			Current density, A m^{-2}			Constants in Tafel equation, V				$\Delta\Psi'$, V
	$-\varphi_f$	$-\varphi_a$	$-j_c$	I_f	I_a	I_c	a_c	a_c	b_c	b_a	
–	0.235	0.190	0.365	3.16	50.12	50.12	0.869	–0.002	0.18	0.06	
3a	0.225	0.160	0.410	1.42	14.13	30.20	0.914	+0.008	0.18	0.06	+0.042
3b	0.230	0.160	0.420	1.26	14.13	25.12	0.929	+0.008	0.18	0.06	+0.021
3c	0.195	0.090	0.490	0.33	1.32	10.00	0.994	+0.078	0.18	0.06	+0.169
3d	0.205	0.110	0.465	0.53	2.52	14.45	0.969	+0.058	0.18	0.06	+0.126
3e	0.210	0.145	0.380	1.74	8.92	44.67	0.884	+0.023	0.18	0.06	+0.104
3f	0.225	0.160	0.410	1.42	14.13	30.20	0.914	+0.008	0.18	0.06	+0.042
3g	0.225	0.130	0.500	0.48	5.00	9.13	1.00	+0.038	0.18	0.06	+0.042
3h	0.219	0.120	0.490	0.52	4.17	10.96	0.994	+0.048	0.18	0.06	+0.067
3i	0.225	0.138	0.470	0.70	6.30	13.18	0.974	+0.03	0.18	0.06	+0.042

The kinetics of adsorption was monitored by a decrease in the cathode current (by 0.6 V relative to the stationary current) after adding an inhibitor to the electrolyte solution. To elucidate the most probable mechanism of inhibiting action, we estimated the correlation coefficients r in processing data in the coordinates $\log I$–τ, ΔI–$\log\tau$, $\log\Delta I$–$\log\tau$, $\log\log I/I_\infty$–τ, $\log\gamma$–$\log\tau$, and $\log\log\gamma$–$\log\tau$ [1].

The antibacterial activity was studied by the method of diffusion of the compounds studied to agar using paper disks impregnated with 0.1, 0.2, and 2% alcoholic solutions of **3a**–**3i**. The biocidal effect was characterized by the diameter of the growth suppression area [7]. As a test culture we used a culture of sulfate-reducing bacteria (SRB) separated from ferrosphere of corroding steel and grown in Postgate medium B.

Experimental data were statistically treated at a 0.95 confidence level (three replicates) [8].

The anticorrosive properties of compounds **3a**–**3i** are given in Tables 2–4 and in the figure. Addition of the inhibitor increases the free corrosion potential of steel 45 by 5–40 mV (Table 2), suggesting preferen-

Table 3. Inhibition coefficients and protective efficiency of compounds **3a**–**3i** in corrosion of steel 45 in 1 M HCl

Compound	Inhibition coefficients			Protective efficiency, %		
	γ_f	γ_a	γ_c	Z_f	Z_a	Z_c
3a	2.2	3.6	1.7	55.0	72.0	86.0
3b	2.5	3.6	2.0	60.0	72.0	50.0
3c	9.6	38.0	5.0	89.5	97.0	80.0
3d	6.0	20.0	3.5	83.3	95.0	71.4
3e	1.8	5.6	1.1	44.0	82.0	9.0
3f	2.2	3.6	1.7	55.0	72.0	86.0
3g	6.6	10.0	5.5	84.8	97.0	80.0
3h	6.1	12.0	4.6	83.6	78.2	91.6
3i	4.5	8.0	3.8	77.7	73.7	87.5

Table 4. Correlation analysis of data on the decrease in the cathode current

Coordinates	Correlation coefficient estimated by the Pearson method [8]				
	3a	**3b**	**3c**	**3d**	**3e**
$\log I$–τ	–0.96	–0.96	–0.95	–0.97	–0.94
ΔI–$\log \tau$	0.29	–0.49	–0.81	–0.69	–0.60
$\log \Delta I$–$\log \tau$	0.29	–0.56	–0.87	–0.61	–0.66
$\log\log I/I_\infty$–τ	–0.97	–0.97	–0.97	–0.96	–0.95
$\log \gamma$–$\log \tau$	–0.19	–0.55	–0.76	–0.74	–0.59
$\log\log \gamma$–$\log \tau$	–0.41	–0.60	–0.75	–0.67	–0.65

tial inhibition of anodic dissolution of the metal at φ_f in the presence of the inhibitor. Addition of compounds **3a**–**3i** decreased the free corrosion current by a factor of 1.8–9.6, and the anode and cathode currents, by factors of 3.6–38.0 and 1.1–5.5, respectively. Relatively high protective effect was shown by compound **3c** with a chlorine atom in the *para* position of the benzene ring ($\sigma_p = +0.227$). The inhibition coefficients γ_f, γ_c, and γ_a of **3c** are higher that those of the unsubstituted compound **3a** by factors of 4.3, 2.9, and 10.6, respectively (Table 3). The lowest protective characteristics were shown by **3e** (substituent OCH_3; $\sigma_p = -0.268$).

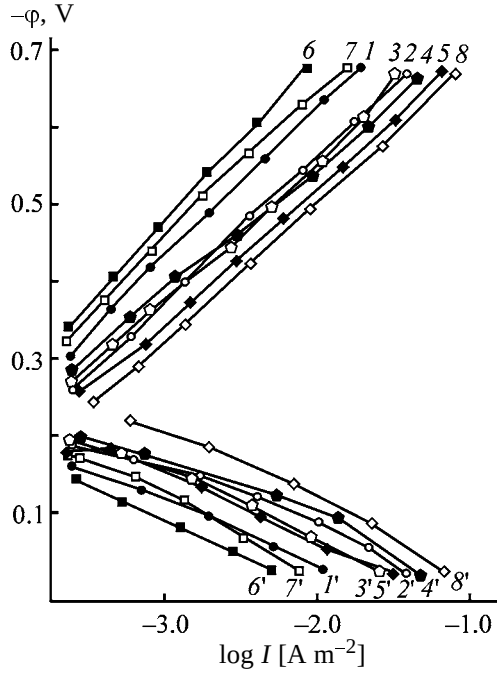

(*1*–*8*) Cathode and (*1*'–*8*') anode polarization curves of steel 45 in 1 M HCl. Inhibitor concentration 2 mM. (φ) Potential and (*I*) current density. Inhibitor: (*1*, *1*') **3d**, (*2*, *2*') **3b**, (*3*, *3*') **3f**, (*4*, *4*') **3a**, (*5*, *5*') **3e**, (*6*, *6*') **3c**, (*7*, *7*') **3g**, and (*8*, *8*') no inhibitor.

Addition of the inhibitors into 1 M HCl changes the electrochemical parameters of electrode processes as follows: the Tafel constant a_c increases by 15–131 mV, and a_a, by 30–100 mV, which is consistent with the inhibition coefficients (Table 3). The overvoltage of electrode reactions increases as a result of increase in the adsorption potential Ψ' by 21–169 mV.

Adsorption of protonated molecules of **3a**–**3i** from the acid solution on the negatively charged metal surface proceeds through electrostatic interaction. In this case, the charge on the adsorption sites of the sorbate, i.e., on the amine nitrogen and nitrogen atom of the triazole ring, is of considerable importance.

The nature of a substituent in the *para* position of the benzene ring affects most significantly the electron density on the amine nitrogen in **3a**–**3i**. A decrease in the electron density on this atom caused by introduction of electron-acceptor substituents into the benzene ring favors adsorption of the inhibitors on the metal surface. As a result, the highest protective efficiency was shown by compound **3c** with a chlorine atom as a substituent.

The adsorption equilibrium of compounds **3a**–**3i** on the negatively polarized metal surface is established in 20–25 s. According to [1], if physical adsorption dominates, purely energetic inhibiting effect may be expected. However, no significant difference was found in the correlation coefficients *r* obtained in treating data on decrease in the cathode current (Table 4) in the coordinates $\log I$–τ and $\log\log I/I_\infty$–τ, suggesting realization of a complex energetic–adsorption-blocking mechanism of inhibition on a uniform metal surface. This suggestion is supported by the lack of a distinct correlation between the anticorrosion characteristics of the compounds studied and the shift of the adsorption potential.

Another practically important characteristic of corrosion inhibitors is their biocidal activity with respect

to sulfate-reducing bacteria as the major factor of biocorrosion. The mechanism of biocidal action involves adsorption of a compound on the negatively charged surface of the bacterial cell and penetration into it to destroy its metabolism. All the compounds studied in this work exhibit a weakly pronounced biocidal effect with respect to iron-reducing bacteria [9].

The biocidal effect with respect to SRB was found only for the compounds with the methyl substituent. In the case of *ortho* substitution in the benzene ring (compound **3h**), the diameter of the growth suppression area is 21.0, 28.0, and 42.7 mm; and in the case of *meta* substitution (**3i**), it is 25.7, 37.3, and 49.3 mm at the inhibitor concentration of 0.1, 0.2, and 2 wt %, respectively. The *para*-substituted compound **3g** practically totally suppresses the growth of SRB. Thus, the position of the methyl substituent in the benzene ring strongly affects the biocidal effect, which increases in the order *ortho* < *meta* < *para*. Introduction of two methyl groups in positions 2 and 4 of the benzene ring (compound **3f**) decreases the biocidal effect on SRB. In this case, the diameter of the growth suppression area was found to be 10.0, 10.0, and 20.0 mm at the inhibitor concentration of 0.1, 0.2, and 2 wt %, respectively.

CONCLUSION

A series of *N*-aryl-*N*-(6,7,8,9-tetrahydro-5*H*-[1,2,4]-triazolo[4,3-*a*]azepin-3-ylmethyl)amines are synthesized. These compounds are acid corrosion inhibitors and demonstrate biocidal activity with respect to sulfate-reducing bacteria, which increases in compounds with a methyl substituent in the benzene ring in the order *ortho* < *meta* < *para*.

REFERENCES

1. Reshetnikov, S.M., *Ingibitory kislotnoi korrozii* (Acid Corrosion Inhibitors), Leningrad: Khimiya, 1986.
2. Pogrebova, I., Kozlova, I., Purish, L., and Yantsevich, K., *Fiziko-Khim. Mekh. Mater*., 2000, vol. 2, special issue, no. 1, pp. 479–481.
3. Romanenko, I.V., *Fiziko-Khim. Mekh. Mater*., 2000, vol. 2, special issue, no. 1, pp. 513–515.
4. Shridhar, O.R., Jogibhurta, M., Ioshi, P.P., and Reddy, P., *Indian J. Chem., Ser. B*, 1981, vol. 20, no. 2, pp. 132–140.
5. Glushkov, R.G. and Granik, V.G., *Usp. Khim*., 1969, no. 11, pp. 1998–2006.
6. Fokin, M.N. and Zhigalova, K.A., *Metody korrozionnykh ispytanii metallov* (Methods for Metal Corrosion Tests), Kolotyrkin, Ya.M., Ed., Moscow: Metallurgiya, 1986.
7. *Rukovodstvo k prakticheskim zanyatiyam po mikrobiologii* (Practical Guide on Microbiology), Egorov, N.S., Ed., Moscow: Mosk. Gos. Univ., 1983.
8. Lakin, G.F., *Biometriya* (Biometry), Moscow: Vysshaya Shkola, 1990.
9. Tretyak, A.P., Smykun, N.V., Prikhod'ko, S.V., *et al*., *Visn. Odes'k. Nats. Univ*., 2001, vol. 6, no. 4, pp. 313–316.

Russian Journal of Applied Chemistry, Vol. 77, No. 5, 2004, pp. 794–796. Translated from Zhurnal Prikladnoi Khimii, Vol. 77, No. 5, 2004, pp. 798–800.

ORGANIC SYNTHESIS AND INDUSTRIAL ORGANIC CHEMISTRY

Synthesis of Cobalt(III) Ammine Complexes as Explosives for Safe Priming Charges

A. V. Smirnov, M. A. Ilyushin, and I. V. Tselinskii

St. Petersburg State Technological Institute, St. Petersburg, Russia

Received October 16, 2003; in final form, March 2004

Abstract—Physicochemical and explosive properties of Co(III) pentammine complexes containing in the inner coordination sphere monodentate polynitrogen heterocyclic ligands, 1-methyl-5-aminotetrazole and 1,5-diaminotetrazole, were studied, and it was shown that these compounds can be used in priming charges.

Domestically produced standard priming explosives (PEs) allow production of reliable priming charges (PCs) meeting the requirements of modern engineering, industry, and building. However, requirements to PCs continuously rise; PCs with elevated safety with respect to mechanical impact and static electricity are required. In addition, environmental safety requires elimination of toxic metal ions from PC formulation. It is impossible to accomplish the above task with standard PCs.

Cobalt(III) tetrazolate pentamminates show promise for development of a new generation of high-performance PEs of increased safety. The use of 5R-tetrazols in PE synthesis is expedient because of their positive enthalpies of formation, while coordination chemistry allows variation of physicochemical and explosive properties within a wide range by varying outer- and inner-sphere ligands.

The synthesis of the compounds of this group and their physicochemical characteristics were reported in [1]. In all the complexes described, a heterocyclic ligand is located in the inner sphere of the complex as an anion, while coordination of the neutral ligand should increase the content of the outer-sphere ion by 1 mol, which will affect the properties of the complex. In this work, we prepared and studied high-energy-capacity cobalt(III) complexes with neutral ligands, (1-methyl-5-aminotetrazole)pentamminecobalt(III) perchlorate (C1M5AT) and (1,5-diaminotetrazole)pentamminecobalt(III) perchlorate (CDAT).

Their synthesis was performed by the scheme

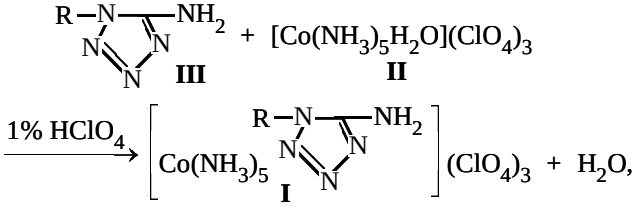

where **I** is C1M5AT (R = CH_3), **I** or CDAT (R = NH_2).

The isolated complexes are yellow-orange crystalline powders soluble in water, DMSO, and DMF and weakly soluble in ethanol, isopropanol, and isobutanol. The physicochemical and explosive properties of C1M5AT and CDAT in comparison to (5-aminotetrazolato-N_2)pentamminecobalt(III) perchlorate (CAT, [2]) are listed in the table.

The densities of the compounds synthesized were calculated using an additive scheme through specific volumes of the molecular fragments with the error of 0.02 g cm^{-3} [2].

The detonation rate of compounds was estimated by fragmentation of the molecule into active (perchlorate ions and ligands) and inert (metal ion) parts followed by calculation using increments of structure fragments, with the average error of ±140 m s^{-1} [2].

A study of the thermal decomposition of the substances obtained under nonisothermal conditions at a heating rate of 5 deg min^{-1} showed that they are fairly heat-resistant, having T_d higher than 210°C (onset of active decomposition). In the initial stage of decomposition of Co(III) ammine complexes, ammonia molecules are eliminated from the inner coordination sphere. This is followed by stepwise decomposition of tetrazole ligands accompanied by their oxidation with outer-sphere perchlorate ion located in the outer sphere [2]. In all cases, the initial endothermic process overlaps with the subsequent exothermic process. C1M5AT has two exothermic peaks at 216 and 238°C in the DTA curve, and CDAT, three peaks at 218, 271, and 300°C.

The IR spectra of complexes contain bands of all their fragments: coordinated ammonia molecules,

1070-4272/04/7705-0794 © 2004 MAIK "Nauka/Interperiodica"

Physicochemical and explosive properties of the compounds synthesized

Characteristic	C1M5AT	CDAT	CAT
Density, ρ (calc.), g cm^{-3}	1.95	2.03	1.95
Oxygen coefficient, α	0.96	1.17	0.86
Detonation rate, D^{ρ} (calc.), km s^{-1}	7.32	7.68	7.14
Temperature of the onset of active decomposition, T_d, °C	218	216	240
Minimal charge (MC) for cyclonite, g (BC no. 8)	0.4	0.2	>0.5
Shock sensitivity, $H_{25\ cm}$, % (weight 2 kg, substance sample 20 mg)	40	12	0

methyl and amino groups, tetrazole ring, and perchlorate ions.

The electronic spectra of C1M5AT and CDAT in aqueous solution are typical for this group of compounds [3] and reflect *d*–*d* transition ($^1T_{1g} \rightarrow {}^1A_{1g}$) at 463 nm, ε = 77 l cm^{-1} mol^{-1} for CDAT and 464 nm, ε = 62 l cm^{-1} mol^{-1} for C1M5AT. The second strong absorption band ($^1T_{2g} \rightarrow {}^1A_{1g}$) in both cases overlaps with the band of the tetrazole ligand. Apparently, the complexes studied, like CAT, contain octahedral chromophore CoN_6.

The ^{1}H NMR spectra of the compounds contain signals at 3.3–3.8 ppm belonging to equatorial (in lower field) and axial (in higher field) ammonia molecules. The difference between the positions of equatorial (3.66 and 3.68 ppm) and axial (3.52 and 3.50 ppm) ammonia molecules for C1M5AT and CDAT, respectively, is the evidence of the *trans* effect of heterocyclic ligands and agrees with their coordination through nitrogen atoms [4]. The heterocycle is the most probably coordinated via N^4 atom [5].

The salts obtained surpass CAT in the shock sensitivity. The shock sensitivity of CDAT is close to that of pentaerythritol tetranitrate (TEN) and somewhat lower than that of C1M5AT [5]. In contrast to CAT, C1M5AT and CDAT are priming explosives. In accordance with the minimal charge with respect to cyclonite within blasting cap no. 8 (BC no. 8) dimension, the priming performance of C1M5AT is approximately close to that of mercury fulminate, and that of CDAT is higher by a factor of approximately 2. CDAT is of most practical interest as PE for safe PCs.

We can suggest that the presence of an additional 1 mol of perchlorate ion as oxidant increases the priming performance and shock sensitivity and decreases the thermal stability of the complexes obtained as compared to CAT.

EXPERIMENTAL

The IR spectra of C1M5AT and CDAT were recorded on a Perkin–Elmer M-457 spectrometer using films or mulls in Nujol or perfluorinated oil on KBr pellets.

The UV spectra were recorded on a Perkin–Elmer LAMBDA 40 spectrometer in quartz cells (l = 1 cm) at analytical concentrations of 10^{-1}–10^{-2} M.

The ^{1}H NMR spectra were recorded on a Bruker AC spectrometer (300 MHz) in DMSO-d_6, internal reference hexamethyldisiloxane (HMDS).

The synthesis progress was monitored by thin-layer chromatography on Silufol UV-254 plates, eluent 3% NaCl.

Thermographic studies were performed on an OD-102 device (20–500°C, heating rate 5 deg min^{-1}). T_d was measured on a thermographic device at a heating rate of 5.3 deg min^{-1}. The shock sensitivity measurements were performed with an impact machine according to GOST (State Standard) 4545–88. The minimal charge of complexes was determined relative to cyclonite within BC no. 8 dimensions (P_{pr} of the compound 300, and P_{pr} of cyclonite, 800 kg cm^{-2}).

Aquapentamminecobalt(III) perchlorate (**II**) was synthesized by the method described in [6]. After drying, the yield of **II** was 77%. IR, ν, cm^{-1}: 3330 s, 3270 s, 1630 m, 1350 m, 830 m (H_2O, NH_3), 1100 s (ClO_4^-). ^{1}H NMR (DMSO-d_6), δ, ppm: 3.75 (3H, NH_3 ax); 4.90 (12H, NH_3 eq).

Found (%): H 3.6; N 15.4; Cl 23.3.
$H_{17}Cl_3CoN_5O_{13}$.
Calculated (%): H 3.7; N 15.2; Cl 23.1.

The properties of this compound agree with data of [6].

(1-Methyl-5-aminotetrazolo)pentamminecobalt(III) perchlorate (C1M5AT). Aquapentammine-

cobalt(III) perchlorate (0.5 g) was dissolved in 5 ml of 1% perchloric acid, and 0.5 g of 1-methyl-5-aminotetrazole synthesized according to [7] was added. The reaction mixture was kept on a boiling water bath for 4 h and cooled to 15°C; the precipitate was filtered off, washed with ethanol (2 × 5 ml), and recrystallized from 1% $HClO_4$. Yield 58%. IR, ν, cm^{-1}: 3328 m, 1354 m (NH_3, Tz), 1100 m (ClO_4^-), 1648 m (C=N), 3112 w, 1660 w (NH_2), 2880 w (CH_3). ^1H NMR (DMSO-d_6), δ, ppm: 3.52 (3H, NH_3 ax); 3.66 (9H, NH_3 eq); 3.90 (3H, CH_3–Tz), 7.58 (2H, NH_2–Tz).

Found (%): C 4.6; H 3.8; N 25.7.
$C_2H_{20}Cl_3CoN_{10}O_{12}$.
Calculated (%): C 4.4; H 3.7; N 25.8.

(1,5-Diaminotetrazolo)pentamminecobalt(III) perchlorate (CDAT) was synthesized similarly to C1M5AT. Yield 62%. IR, ν, cm^{-1}: 3304 m, 1376 m (NH_3, Tz), 1072 m (ClO_4^-), 1628 m (C=N), 3104 w, 1664 w (NH_2). ^1H NMR (DMSO-d_6), δ, ppm: 3.68 (9H, NH_3 eq); 3.52 (3H, NH_3 ax); 6.90 (2H, NH_2–C); 7.45 (2H, NH_2–N).

Found (%): C 2.3; H 3.7; N 28.2.
$C_1H_{19}Cl_3CoN_{11}O_{12}$.
Calculated (%): C 2.2; H 3.5; N 28.4.

CONCLUSION

Two high-energy-capacity coordination compounds, (1-methyl-5-aminotetrazolo)pentamminecobalt(III) perchlorate and (1,5-diaminotetrazolo)pentamminecobalt(III) perchlorate, were synthesized. The second compound in accordance with its properties is a promising priming explosive for safe priming charges.

ACKNOWLEDGMENTS

The work was financially supported by the Ministry of Education of the Russian Federation within the scope of Priority Directions of Development of Science and Engineering intercollegiate program.

REFERENCES

1. Smirnov, A.V., Ilyushin, M.A., Tselinskii, I.V., *et al*., *Zap. Gorn. Inst*., 2001, vol. 148, part 1, pp. 220–224.
2. Ilyushin, M.A., Smirnov, A.V., Kotomin, A.A., and Tselynsky, I.V., *Hanneng cailiao* (Energ. Mater.), 1994, vol. 2, no. 1, pp. 16–20.
3. Fronabarger, J., Schuman, A., Chapman, R.D., *et al*., *Am. Inst. Aeronaut. Astronaut. Pap*., 1995, no. 2858, pp. 1–7.
4. Sheng, D., Ma, F., Sun, F., and Lu. Q., *Hanneng cailiao* (Energ. Mater.), 2000, vol. 8, no. 3, pp. 100–103.
5. Zhilin, A.Yu., Ilyushin, M.A., Tselinskii, I.V., *et al*., *Zh. Prikl. Khim*., 2003, vol. 76, no. 4, pp. 592–596.
6. Novakovskii, M.S., *Laboratornye raboty po khimii kompleksnykh soedinenii* (Laboratory Works on Chemistry of Coordination Compounds), Kharkov: Khar'kov. Univ., 1972.
7. Henry, R.A. and Finnegan, W.C., *J. Am. Chem. Soc*., 1954, vol. 76, no. 3, pp. 923–926.

Russian Journal of Applied Chemistry, Vol. 77, No. 5, 2004, pp. 797–800. Translated from Zhurnal Prikladnoi Khimii, Vol. 77, No. 5, 2004, pp. 801–804.

ORGANIC SYNTHESIS AND INDUSTRIAL ORGANIC CHEMISTRY

Acylation of Amino Acids with Dextran Derivatives

A. V. Krasnikova and A. A. Iozep

St. Petersburg State Academy of Pharmaceutical Chemistry, St. Petersburg, Russia

Received January 15, 2004

Abstract—The conditions of N-acylation of amino acids with carboxymethyl dextran ethyl ester and with carboxymethyl and carboxyethyl dextran azides were studied.

Derivatives of amino acids containing primary amino and carboxy groups receive steady researchers' attention due to a wide spectrum of the biological activity. They are active components of many antibacterial, antitumor, antiphlogistic, antiulcer, and other drugs. Typical examples are ampicillin, oxacillin, cephalexin, cephalotin, etc. [1]. In this context, binding of amino acids with polysaccharides through a peptide bond is also of interest, since it allows, on the one hand, preparation of potentially bioactive substances and, on the other hand, improvement of existing drugs [2].

Polysaccharide–amino acid conjugates are prepared by such methods as azide method, method of activated esters, cyanogen bromide method, and also via dextran dialdehyde [3–5]. The goal of this study was to look for new routes and improve existing routes to polysaccharide–amino acid conjugates (see scheme).

As agents for acylation of amino acids we used carboxymethyl dextran ethyl ester (CMDEE, **I**) and carboxymethyl dextran (CMD) and carboxylethyl dextran (CED) azides. Compound **I** was prepared as suggested in [6] by heating the H form of CMD at 80°C with excess ethanol under the conditions of autocatalysis. CMD hydrazides (**III**) were prepared by acylation of hydrazine with CMDEE in water at 5–15°C for 24 h [7]. CED amides (**II**) and hydrazides (**III**) were prepared by alkylation of dextran with

Chemical modification of dextran

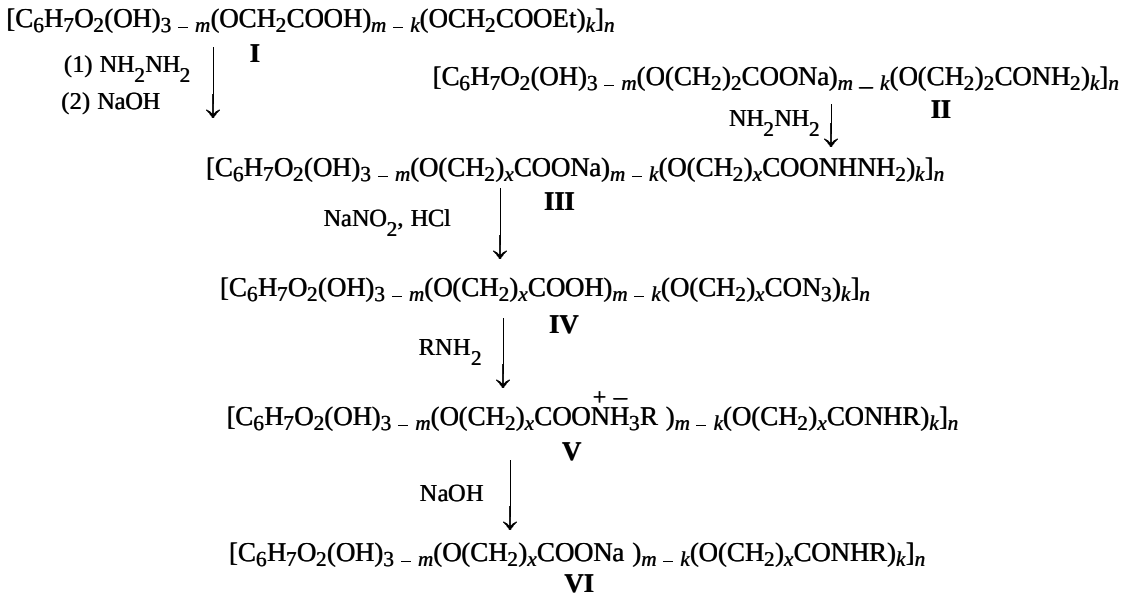

where R = $C_6H_5CH_2$, tryptophan, phenylalanine, tyrosine, diiodotyrosine, histidine, glutamic acid, methionine, lysine; x = 1 or 2.

1070-4272/04/7705-0797 © 2004 MAIK "Nauka/Interperiodica"

Table 1. Results of acylation of amino acids with CMD ethyl ester (C_{cm} = 0.37–0.59, C_{ecm} = 0.33–0.37)* in water and in ethanol (5 and 3 mol of amine per mole of carboxy groups, respectively)

Amino acid	C_{am}, %, under indicated conditions	
	water, pH 8, 16 h, 20°C	ethanol, 5 h, 78°C, TEA
D,L-α-Alanine	21	18 (32, 20 h)
β-Alanine	52	40
γ-Aminobutyric	71	58
ε-Aminocaproic	76	68 (100, 8 h)
D,L-Lysine	94	–
D,L-Tryptophan	7.3	21 (8 h)
D,L-β-Phenyl-α-alanine	29.2	27 (8 h)

* (C_{cm}, C_{ecm}) Number of carboxymethyl and ethoxycarbonylmethyl groups in the polymer per monosaccharide unit.

acrylamide, followed by acylation of hydrazine hydrate with the resulting CED amide as described in [8]. CMD and CED azides (**IV**) were prepared as described previously [8, 9], by dissolving hydrazides **III** in 2.5 M aqueous $NaNO_2$ at 0°C, with subsequent acidification with HCl to pH 2. Dextran azides **IV** were used for acylation of amino acids without isolation from solution.

Acylation of amino acids with CMDEE was performed in aqueous alkaline solution at 0–20°C for 1–24 h or in ethanol in the presence of triethanolamine (TEA) at 78°C for 5–20 h; the amino acid was taken in the amount of 3–5 mol per mole of monosaccharide units. The reactions of amino acids with CMD and CED azides were performed in water; the pH, reactant ratio, and reaction time were varied. To a solution of carboxyalkyl dextran azide, after decomposition of excess HNO_2 with urea, we added a solution of an amino acid sodium salt (1–3 mol per mole of monosaccharide units); then we adjusted pH by adding alkali or acid solution and diluted the mixture with water to the required volume (4–7 ml). The mixture was kept at 0–25°C for 1–24 h. The resulting products were precipitated and reprecipitated with ethanol from aqueous alkali to remove low-molecular-weight impurities. Their absence in the reaction products was checked by TLC.

Substituted carboxyalkyl dextran amides **VI** are white or yellowish white amorphous powders readily soluble in water and insoluble in alcohol, acetone, ether, and the majority of other organic solvents.

The IR spectra of the reaction products in the H^+ form contain bands at 1535–1590 and 1640–1685 cm^{-1} (CMD amides), or at 1540–1550 and 1650–1670 cm^{-1} (CED amides), absent in the spectra of the starting substances and characteristic of δ_{N-H} (amide II) and $\nu_{C=O}$ (amide I) vibrations. In the IR spectra of the sodium salts of the products, the band at 1730 cm^{-1} disappears, and a new band at 1580 (CED amides) or 1600 cm^{-1} (CMD amides) appears. This band, characteristic of the carboxylate ion, obscures the bands of amide groups. The spectra also contain bands characteristic of aromatic rings of the starting amino acids.

UV spectroscopy is a convenient tool in our case, since the spectra of aqueous solutions of N-substituted carboxyalkyl dextran amides and of the starting amino acids are similar, whereas the polysaccharide shows no absorption in this range.

CMD and CED amides were quantitatively characterized by the degree of aminocarbonylalkylation C_{aca} (numbere of amide groups per monosaccharide unit of the polymer), and the acylation reaction, by the degree of amidation C_{am} (percentage of the polysaccharide acyl groups involved in the reaction). The C_{aca} values were calculated from the elemental analysis data and UV spectra.

Since CMDEE readily acylates aliphatic and aromatic amines [10, 11], we studied its reaction with amino acids. As expected, this reagent allows binding of amino acids with dextran, but with α-amino carboxylic acids in water and ethanol CMDEE reacts worse than with other amino acids (Table 1).

This may be due, firstly, to a stronger, compared to other amino acids, effect of the carboxy group in α-amino acids on the nucleophilicity and steric accessibility of the amino group and, secondly, to physicochemical properties of the amino acids, which are poorly soluble or insoluble in water and the majority of organic solvents. Addition of bases to the reaction mixture for solubilization of the substrate in water causes hydrolysis of CMD ester, which occurs faster than acylation. Therefore, in aqueous solutions CMDEE virtually does not acylate tryptophan, which is sparingly soluble even in alkali solutions, and poorly reacts with more soluble β-phenyl-α-alanine. Similar pattern is observed in ethanol in which CMDEE poorly acylates α-amino acids irrespective of their solubility in alcohol.

Lysine and ε-aminocaproic acid are soluble in water and at pH 7–8 react with CMDEE almost as readily as do aliphatic amines. The degree of amidation of CMDEE ester groups in reactions with these

Table 2. Results of acylation of α-amino acids with CMD and CED azides at optimal pH of the medium (4 and 24 h, respectively; 18–20°C; 3 mol of amino acid per mole of monosaccharide units)

Amino acid	Isoelectric point	CMD azide		CED azide	
		pH_{opt}	C_{am}, %	pH_{opt}	C_{am}, %
Glutamic	3.22	11	86	11	88
D,L-β-Phenyl-α-alanine	5.07	8	86	10	80
D,L-Tyrosine	5.66	8	58	10	57
D,L-Diiodotyrisone	–	9	77	12	75
D,L-Tryptophan	5.89	8	34	9	36
D,L-Histidine	7.64	8	54	12	56

amino acids is approximately similar, being somewhat higher with lysine. This fact suggests that the ε-amino group of lysine reacts predominantly, but acylation at the α-amino group cannot be ruled out either.

Experiments on acylation of α-, β-, γ-, and ε-amino acids with CMDEE in water and ethanol showed that, the more remote is the amino group in the substrate molecule from the carboxy group, the higher the degree of conversion of CMD esters into amides. The reaction in water is faster than in ethanol, but the dependences of C_{am} on the position of the amino group are similar in water and ethanol (Fig. 1). Despite lower reaction rate in ethanol, it is, however, preferable to perform the reactions of dextran with amino acids in ethanol. In this case, the reaction is not complicated by hydrolysis of the ester groups and can be performed for longer time, leading to higher C_{am} than in water. For example, with α-amino acids, an increase in the acylation time from 5 to 20 h resulted in a 1.8-fold growth in the conversion of ester groups, and with ε-aminocaproic acid, 100% conversion of CMD ester groups into amide groups was attained in 8 h.

Since modification of polysaccharides with α-amino acids via CMDEE involves serious problems, we examined the suitability for this purpose of CMD and CED azides. The conditions for acylation of amino acids with carboxyalkyl dextran azides were optimized by examining the dependence of C_{am} on the solution acidity, as it was shown previously that the results of similar reactions with amines strongly depend on pH [9, 12]. Indeed, as in the case of amines, in acylation of α-amino acids there is a certain optimal pH at which the degree of conversion of the azide groups in the polysaccharides into the amide groups passes through a maximum. For example, the reactions of CMD and CED azides with phenylalanine are the most efficient at pH 8 and 10, respectively (Fig. 2); under these conditions, the amino acid fully dissolves in water, and the reaction mixture is homogeneous. The optimal pH values for acylation of the other amino acids are listed in Table 2.

We found that the reactions of CMD azide with α-amino acids were the most efficient at approximately the same pH values, pH 8–9, and only with glutamic acid pH 11 was optimal. As in acylation of aromat-

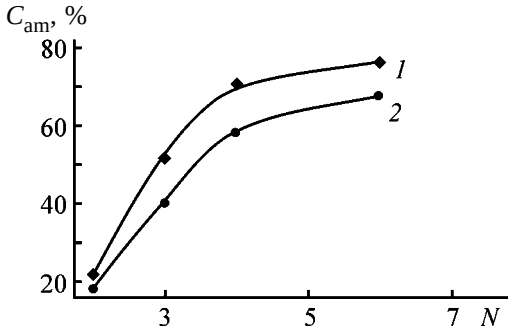

Fig. 1. Degree of amidation C_{am} of CMDEE ester groups in reactions with α- and β-alanine, γ-aminobutyric acid, and ε-aminocaproic acid in (*1*) water and (*2*) ethanol, plotted vs. position of the amino group in the molecule (number of the carbon atom *N*).

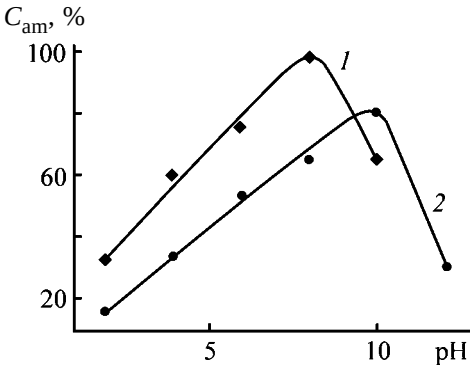

Fig. 2. Degree of amidation C_{am} of azide groups in reactions of β-phenyl-α-alanine with (*1*) CMD and (*2*) CED azides as a function of solution pH (4 and 24 h, respectively; 18–20°C; 3 mol of amino acid per mole of monosaccharide fragment).

ic and aliphatic amines [12], CED azide reacts with amino acids in more alkaline media than does CMD azide, and the optimal pH values in this case are pH 9–12. To compare, replacement of CMD azide by CED azide in reactions with benzylamine and aniline shifts the optimal pH of the reaction mixtures from 8 to 10 and from 2 to 5, respectively. This may be due to lower reactivity of CED azides and higher activity of the nucleophile at higher pH. However, higher stability of CED azides allows the reaction time to be extended to 18–24 h, and the results similar to those of acylation with CMD azides can be obtained. Indeed, in all the cases, under similar other conditions, C_{am} of azide groups in CMD and CED derivatives in reactions with the same α-amino acids is similar (Table 2).

It should also be noted that carboxyalkyl dextran azides acylate α-amino acids better than does CMDEE. Under proper conditions, C_{am} of CMD azide in reactions with the majority of the amino acids studied exceeds 70% and in some cases even 90%. The results of acylation of amino acids with CED azides are somewhat worse but also high. And only with tryptophan, whose acylation occurs in a heterogeneous medium in contrast to the other acids, C_{am} does not exceed 40% in both cases.

We also examined the influence of time on the reaction of carboxyalkyl dextran azides with amino acids. We found that the reaction was complete in 2–4 h with CMD azides and in 16–24 h with CED azides. For example, in acylation of β-phenyl-α-alanine with CMD azide, C_{am} was 57% in 1 h and 98% in 2 h. The molar ratio of amino acids to CMD monosaccharide units should be no less than 2 : 1, at the concentrations of 0.154 and 0.077 M, respectively.

CONCLUSIONS

(1) Carboxymethyl dextran ethyl esters acylate amino acids in water and ethanol and can be used for preparing dextran–amino acid conjugates.

(2) Carboxymethyl and carboxyethyl dextran azides react with α-amino acids more readily than does carboxymethyl dextran ethyl ester. For any particular amino acid, there is a certain optimal pH at which C_{am} is maximal; this pH is in the range 8–11 with carboxymethyl dextran azide and 9–12 with carboxyethyl dextran azide.

REFERENCES

1. Mashkovskii, M.D., *Lekarstvennye sredstva* (Drugs), Moscow: Meditsina, 1993.
2. Plate, N.A. and Vasil'ev, A.E., *Fiziologicheski aktivnye polimery* (Physiologically Active Polymers), Moscow: Khimiya, 1986.
3. Livshits, A.B., Vasil'ev, A.E., Kol'tsova, G.N., *et al.*, *Zh. Obshch. Khim.*, 1977, vol. 47, no. 3, pp. 699–709.
4. Glozman, O.M., Zhmurenko, L.A., Shavyrina, V.V., *et al.*, *Zh. Obshch. Khim.*, 1980, vol. 50, no. 7, pp. 1640–1648.
5. Vasil'ev, A.E., Shishkanova, L.S., Sterligov, D.O., *et al.*, *Zh. Obshch. Khim.*, 1977, vol. 47, no. 7, pp. 1636–1641.
6. Iozep, A.A., Il'ina, T.Yu., and Passet, B.V., *Zh. Prikl. Khim.*, 1993, vol. 66, no. 5, pp. 1106–1110.
7. Iozep, A.A., Kupriyanova, L.N., Ponomarenko, M.N., *et al.*, *Zh. Prikl. Khim.*, 1996, vol. 69, no. 9, pp. 1537–1542.
8. Iozep, A.A., Bessonova, N.K., and Passet, B.V., *Zh Prikl. Khim.*, 1998, vol. 71, no. 6, pp. 998–1003.
9. Iozep, A.A., Ponomarenko, M.N., and Passet, B.V., *Zh. Prikl. Khim.*, 1998, vol. 71, no. 1, pp. 140–145.
10. Iozep, A.A., Il'ina, T.Yu., and Passet, B.V., *Zh. Prikl. Khim.*, 1994, vol. 67, no. 3, pp. 470–474.
11. Iozep, A.A., Sibikina, O.V., Kuznetsova, T.E., and Passet, B.V., *Zh. Prikl. Khim.*, 1995, vol. 68, no. 2, pp. 307–311.
12. Krasnikova, A.V., Vasil'eva, Yu.L., and Iozep, A.A., *Zh. Prikl. Khim.*, 2004, vol. 77, no. 2, pp. 265–267.

Russian Journal of Applied Chemistry, Vol. 77, No. 5, 2004, pp. 801–803. Translated from Zhurnal Prikladnoi Khimii, Vol. 77, No. 5, 2004, pp. 805–808.

ORGANIC SYNTHESIS AND INDUSTRIAL ORGANIC CHEMISTRY

Electronic Spectra and Protonation of 1,4-Di(arylamino)anthraquinones and Their Monodimethylformamidinium Salts in Acid Solutions

V. P. Shapkin, S. I. Popov, and V. V. Marshalova

Rubezhnoe Branch, Dal East-Ukrainian National University, Rubezhnoe, Lugansk oblast, Ukraine

Received August 18, 2003; in final form, January 2004

Abstract—Electronic spectra of arylaminoanthraquinones and their amidinium salts in acids were studied, and experimental data on electrophilic substitution of diarylaminoanthraquinone amidinium salts in acetic and sulfuric acids of various concentrations were considered.

To explain different inhibiting effect of dimethylformamidinium group in acetic and sulfuric acids on the reactivity of 1,4-di(arylamino)anthraquinone aryl core [1–4], we have studied the electronic spectra of these derivatives in the corresponding media.

Monodimethylformamidinium salts of 1,4-di(arylamino)anthraquinone [e.g., monodimethylformamidinium salt of 1,4-di(4-methylanilino)anthraquinone (**1**)] in acetic acid solutions have spectra characteristic for compounds in which one arylamino group is absent or is not involved in conjugation with the anthraquinone core as, e.g., in the case of 1-(4-methylanilino)anthraquinone (**2**) or its acetylamino derivative (**3**) (Fig. 1). This shows that the arylaminodimethylformamidinium group is removed from the conjugation, and its inactivity in electrophilic substitution in acetic acid solutions suggests partial localization of the positive charge on the nitrogen atom bonded to the anthraquinone core:

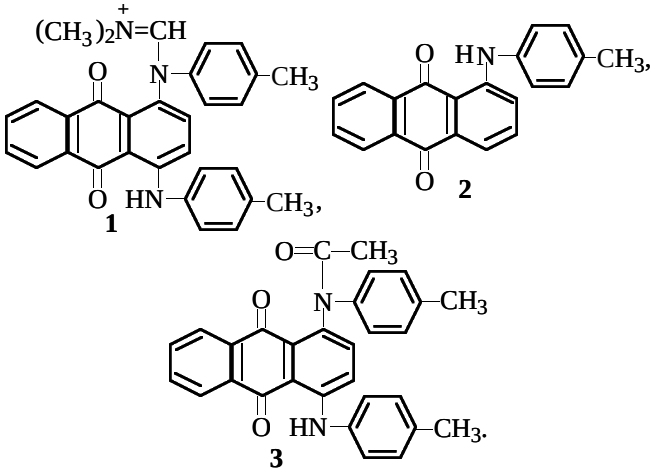

The spectral characteristics of 1,4-di(arylamino)anthraquinones and their monodimethylformamidinium salts in solutions containing sulfuric acid are more complex. Additon of sulfuric acid to a solution of 1,4-di(4-methylanilino)anthraquinone with $c \geq 1 \times 10^{-3}$ M in acetic acid causes appearance of a band at 507 nm and finally leads to a spectrum characteristic of 1-(4-methylanilino)anthraquinone (Fig. 2a, curve *9*). This suggests protonation to the nitrogen atom of one of arylamino groups (**4**). In the region of lower substrate concentrations ($\leq 0.25 \times 10^{-4}$ M), similar increase in the sulfuric acid concentration leads to appearance of a band at 714 nm (Fig. 2b, curve *8*), which can be explained by protonation of the oxygen

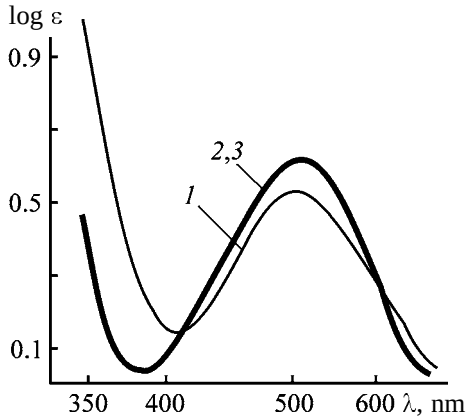

Fig. 1. Electronic spectra of arylaminoantraquinones in acetic acid solutions. (ε) Extinction coefficient and (λ) wavelength; the same for Fig. 2. (*1*) Monodimethylformamidinium salt of 1,4-di(4-methylanilino)antraquinone, (*2*) 1-(4-methylanilino)antraquinone, and (*3*) 1-(*N*-acetyl-4-methylanilino)-4-(4-methylanilino)antraquinone.

1070-4272/04/7705-0801 © 2004 MAIK "Nauka/Interperiodica"

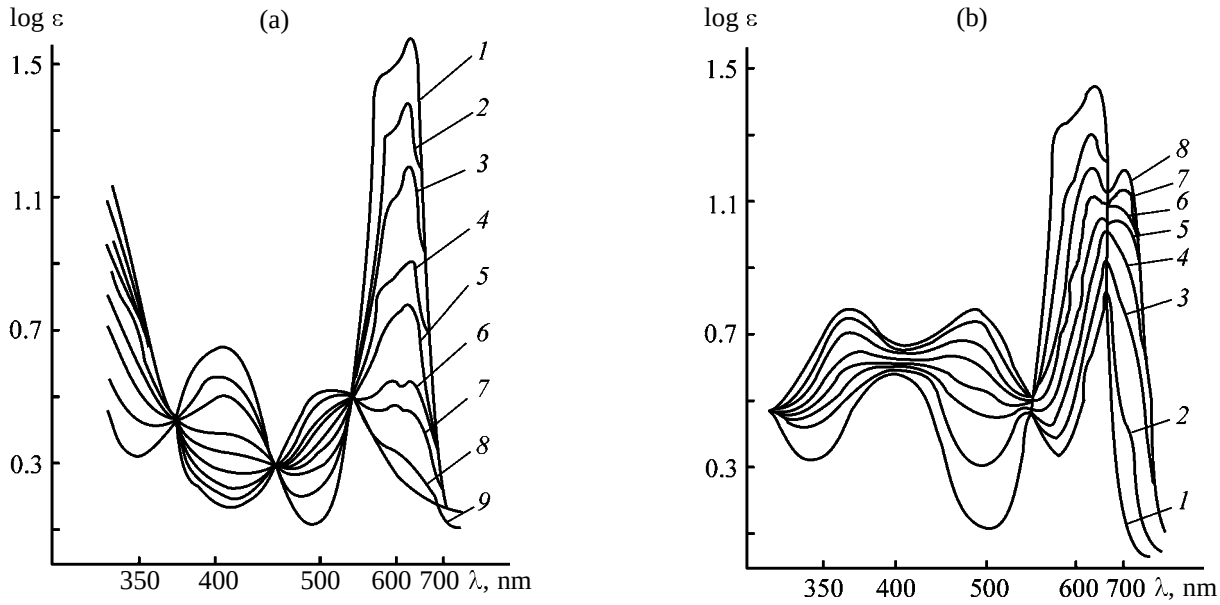

Fig. 2. Electronic spectra of 1,4-di(4-methylanilino)anthraquinone in AcOH–H_2SO_4 mixtures. Substance concentration, (M): (a) 0.96×10^{-3} (l = 0.1 cm) and (b) 0.24×10^{-4} (l = 4 cm). H_2SO_4 concentration (wt %): (a) (*1*) 0, (*2*) 0.33, (*3*) 0.69, (*4*) 1.1, (*5*) 1.5, (*6*) 2.06, (*7*) 2.5, (*8*) 5.0, and (*9*) 7–9; (b) (*1*) 0, (*2*) 0.17, (*3*) 0.36, (*4*) 0.74 (*5*) 1.3, (*6*) 1.26, (*7*) 5.08, and (*8*) 9–16.

atom of the keto group accompanied by redistribution of bonds in the nitrogen(C^4)–oxygen(C^{10}) chain and formation of more deeply colored 1,10-quinonimine structure (**5**):

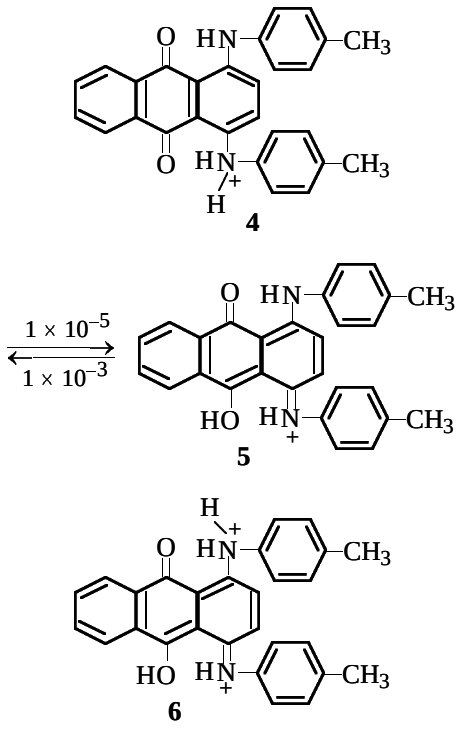

Since data on distribution of the bonds in the protonated species of 1,4-di(arylamino)anthraquinones and their dimethylformamidinium salts are lacking, in the schemes and in the text we show for each case one of possible boundary structures explaining to a certain extent the color transitions observed.

At intermediate concentrations of the substance, 1×10^{-3}–1×10^{-5} M, with correspondingly chosen thicknesses of the absorbing layers, and constant concentration of sulfuric acid, both species are observed. In such solution, the initial 1,4-di(4-methylanilino)-anthraquinone is absent, and the presence of isobestic points indicates equilibrium between two protonated species **4** and **5**. Near the boundary concentrations and outside these boundaries, when only one species exists, the solution obeys Lambert–Beer's law. At higher concentrations of sulfuric acid, species **4** and **5** convert into one diprotonated species **6**.

The calculated values of pK_a for red (**4**) and green (**5**) forms are –1.64 and –1.67, respectively. This demonstrates close properties of protonation centers and possibility of formation of different protonated species when the protonation conditions are changed. At present, this phenomenon has no strict explanation. Presumably, in the more concentrated solutions associates (dimers) exist. Different surrounding of the protonated molecule in this case can cause proton localization on different atoms.

Similar protonation pattern is observed at various concentrations of 1,4-dianilinoanthraquinone (p$K_{a(C=O)}$ = 1.82, p$K_{a(N–H)}$ = 1.81), 1-(2-bromo-4-methylanilino)-4-(4-methylanilino)anthraquinone, and

1-(2-nitro-4-methylanilino)-4-(4-methylanilino)anthraquinone.

In the case of 1,4-di(2-bromo-4-methylanilino)-anthraquinone, addition of sulfuric acid to solution within a wide range of substrate concentrations leads to appearance of the band at 714 nm, suggesting protonation of the carbonyl oxygen atom. In turn, more basic 1-methylamino-4-(4-methylanilino)anthraquinone converts into the red form owing to protonation of the methylamine group at any concentrations.

Different protonated species were also detected for monodimethylformamidinium salt (**1**). At salt concentrations $c \geq 1.6 \times 10^{-3}$ M and addition of sulfuric acid, the red salt solution becomes colorless, and species **7** is formed, while at $c \leq 4.0 \times 10^{-5}$ M, deeply colored blue species **8** appears. Formation of different species is confirmed by the electronic spectra. The calculated values of basicity ($pK_{a(C=O)} = -3.9$, $pK_{a(N-H)} = -3.8$) are also close, but two orders of magnitude lower as compared to pK_a for 1,4-di(4-methylanilino)anthraquinone due to the effect of the positively charged dimethylformamidinium group. Both species **7** and **8** convert into deeply colored form **9** as the sulfuric acid concentration is increased further:

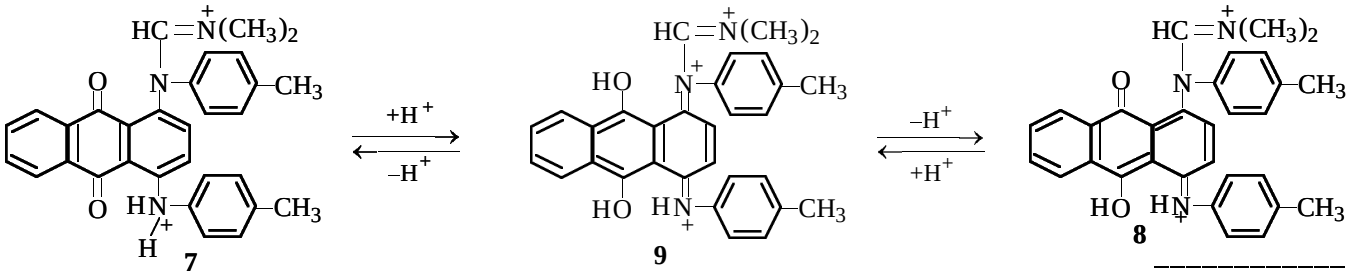

This transition is, most likely, caused by protonation of the oxygen atom at the second (at C^9) keto group. The deep color of diprotonated monodimethylformamidinium salt of 1,4-di(4-methylanilino)anthraquinone (bathochromic shift by 72 nm as compared to species **6**) suggests existence of the 1,4-quinonediimine structure **9**. In this structure, free rotation of the fragment unsubstituted with the dimethylformamidinium group around the N–C bond is, probably, hindered by conjugation through the C=N bond. In this case, only one *o*-position of the 4-methylphenylimino group is free for substitution, while the second position is blocked with the C^3–H fragment of the anthraquinone ring.

The spectral changes observed with monodimethylformamidinium salt of 1,4-di(4-methylanilino)anthraquinone as the sulfuric acid concentration is increased correspond to the color differences of solutions used for bromination. For instance, dibromination of monodimethylformamidinium salt of 1,4-di(4-methylanilino)anthraquinone in 85–87% sulfuric acid yields 1-(4-methylanilino)-4-(2,6-dibromo-4-methylanilino)-anthraquinone, whereas the same reaction in 97% sulfuric acid yields the 2,5-dibromo isomer. In the latter case, only 1-(4-methylanilino)-4-(2-bromo-4-methylanilino)anthraquinone is formed as intermediate.

The spectra were recorded on a Specord spectrophotometer with standard optical cells from 0.1 to 10 cm thick. Analytically and chromatographically pure grade substances were used for preparing solutions.

CONCLUSIONS

(1) In the series of 1,4-di(arylamino)anthraquinones and their monodimethylformamidinium salts, various protonated species are formed in the acid solutions depending on the substance concentration at the same acid concentration.

(2) According to the electronic spectra recorded at different substrate concentrations, in dilute solutions proton is added to the carbonyl oxygen atom, and in more concentrated solutions, to the nitrogen atom of the arylamino group.

REFERENCES

1. Shapkin, V.P. and Popov, S.I., *Zh. Org. Khim.*, 1980, vol. 16, no. 1, pp. 160–167.
2. Shapkin, V.P. and Popov, S.I., *Zh. Org. Khim.*, 1980, vol. 16, no. 1, pp. 230–231.
3. USSR Inventor's Certificate no. 717108.
4. USSR Inventor's Certificate no. 810672.
5. USSR Inventor's Certificate no. 821474.

Russian Journal of Applied Chemistry, Vol. 77, No. 5, 2004, pp. 804–808. Translated from Zhurnal Prikladnoi Khimii, Vol. 77, No. 5, 2004, pp. 809–813.

MACROMOLECULAR CHEMISTRY AND POLYMERIC MATERIALS

Phase Separation in Aqueous Solutions of Binary Copolymers of Acrylamide with Sodium 2-Acrylamido-2-Methylpropanesulfonate and Sodium Acrylate

V. F. Kurenkov, I. N. Nadezhdin, O. A. Antonovich, and F. I. Lobanov

Kazan State Technological University, Kazan, Tatarstan, Russia

Received October 22, 2003

Abstract—Phase separation in aqueous solutions of binary copolymers of acrylamide with sodium 2-acrylamido-2-methylpropanesulfonate and sodium acrylate is studied over the temperature range from 20 to 100°C, as influenced by addition of calcium, magnesium, and sodium chlorides, inorganic salt concentration, and molecular characteristics of the copolymers.

Water-soluble copolymers of acrylamide (AA) with sodium salt of 2-acrylamido-2-methylpropanesulfonic acid (HAMS) demonstrate a wide spectrum of useful properties such as thickening and flocculating activities [1–3], adhesion and antistatic properties [4], and also stabilizing and structuring activities. They are used in oil production, borehole drilling, and water treatment [1, 2, 5]. Water-soluble polymers are often prepared and used in media containing salt additives capable of influencing the conformation and stability of macromolecules in solutions and also the properties of polymers. For example, the viscosity of polyacrylamide (PAA) hydrogels, used in oil production, decreases under the effect of calcium, magnesium, and sodium chlorides from stratal water. Therefore, it is important to study the effect of salt aggression on the stability of polymers, as influenced by various factors.

Previously Ikegami reported on the effect of mixtures of Na and Ca chlorides [6] and Na chloride and Mg, Ca, and Ba nitrates [7, 8] on the phase separation in aqueous solutions of PAA and its hydrolyzed derivatives. Also the effect of calcium chloride on the phase separation in solutions of copolymers of AA with sodium acrylate (NaA) and NaAMS [9], of AA with HAMS and 4-acrylamido-4-methylsulfolane-3-sulfonic acid, and of acrylonitrile with HAMS [10] was studied.

In this work we reported new data on the phase separation in aqueous solutions of copolymers of AA with NaAMS and NaA over the temperature range from 20 to 100°C, as influenced by addition of calcium, magnesium, and sodium chlorides, inorganic salt concentration, and concentration and molecular characteristics of the copolymers. For comparison, the features of phase separation were also studied in solutions of homopolymers: PAA and poly-NaAMS (NaPAMS).

EXPERIMENTAL

In this work we studied copolymers of AA with NaAMS and NaPAMS, obtained by radical polymerization and copolymerization in aqueous solutions [11]. After synthesis, the products were separated by adding acetone, and then they were washed with acetone and vacuum-dried at 50°C to constant weight. The characteristics of the resulting products are given in Table 1.

The structural formulas of the macromolecules of the samples studied are given below.

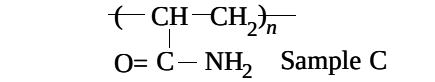

Sample C

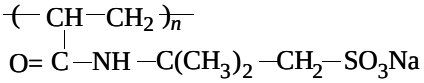

Sample B

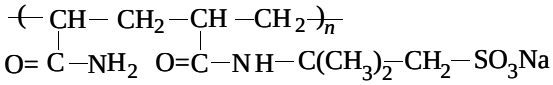

Samples L, M, N, O, P

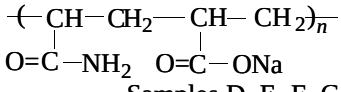

Samples D, E, F, G

1070-4272/04/7705-0804 © 2004 MAIK "Nauka/Interperiodica"

AA/NaAMS copolymers with various molecular weights (MW) and given chemical composition of macromolecules were obtained by degradation of the high-molecular-weight sample R (SNF Flodger, France) (Table 1). Degradation was carried out in 0.2% solutions at 60°C in the presence of a radical-type degrading agent, potassium peroxodisulfate $K_2S_2O_8$, according to the procedure described in [12]. Using the calibration curve $[\eta] = f(t)$ (η is the intrinsic viscosity of the copolymer and t, degradation time) (Fig. 1), we obtained AA/NaA copolymers with various $[\eta]$. The MW of the resulting products was estimated from $[\eta]$ by the Mark–Houwink–Kuhn equation.

In the work we used polyacrylamide and AA/NaA copolymers from Moscow–Stockhausen–Perm Closed Corporation, Russian–German Enterprise. Their characteristics are given in Table 1. The salts NaCl, $MgCl_2$, and $CaCl_2$ were of chemically pure grade.

The content of ionic groups in macromolecules of the AA/NaAMS copolymers was estimated from the sulfur content determined according to the procedure described in [13]. The content of NaA units in the AA/NaA copolymer was determined by potentiometric titration [14]. The intrinsic viscosity of copolymers was measured at 30°C in 0.5 M NaCl using VPZh-3 viscometer (capillary diameter 0.43 mm).

The phase separation was studied in 0.2% solutions of copolymers in distilled water. An inorganic salt was added into the copolymer solution (30 ml), and the mixture was stirred on a magnetic stirrer with slow heating (<1 deg min^{-1}). After the solution became clear, it was cooled, and the cloud point was accepted as the phase separation temperature ($T_{p.s}$), which was determined to within 1°C.

Initially we studied phase separation in AA/NaA copolymers of various chemical compositions (Table 1, samples D, E, F, G), as influenced by the temperature and inorganic salt concentration. The $CaCl_2$ and $MgCl_2$ concentrations varied from 0.25 to 3%, and the NaCl concentration, from 3 to 10%. Figure 2 shows a typical dependence of $T_{p.s}$ in AA/NaA copolymer solutions on the $MgCl_2$ concentration. As seen, in the range of low salt concentrations, $T_{p.s}$ decreases, and in the range of high salt concentrations, increases with increasing $MgCl_2$ concentration. Such a dependence with a lower critical point $T_{p.s}$ was observed for all the salts and AA/NaA copolymer samples, which is well consistent with the published data [5, 8].

For AA/NaA copolymers of various compositions, the effect of the $CaCl_2$, $MgCl_2$, and NaCl concentration on $T_{p.s}$ is shown in Table 2. Phase separation occurs at low $CaCl_2$ and $MgCl_2$ concentrations (0.25–3%), but with NaCl the required concentration is higher (3–10%). The observed effects can be attributed to a decrease in the solubility of the copolymers [15, 16] as a result of specific interaction (chelation) of divalent cations Ca^{2+} and Mg^{2+} with polyanions of the AA/NaA copolymer with formation of strong intra- and intermolecular bonds resulting in decomposition of the hydration shell around the macromolecules. In this case, the electrostatic repulsion between likely charged ions along the chain weakens, decreasing the linear size of coils of the polyions. When the number of salt bonds between the polyanions and cations approached the critical value, the

Characteristics of homo- and copolymers studied

Sample	$[\eta]$, $cm^3\ g^{-1}$	Monomeric unit content, mol %		
		AA	NaA	NaAMS
B	180	–	–	100
C (Praestol 2500)	1550	100	–	–
D (Praestol 2510)	500	93	7	–
E (Praestol 2515)	1500	89	11	–
F (Praestol 2530)	1800	80	20	–
G (Praestol 2540)	1600	72	28	–
L	230	93	–	7
M	190	91	–	9
N	287	83	–	17
O	224	82	–	18
P (AN-125)	570	80	–	20

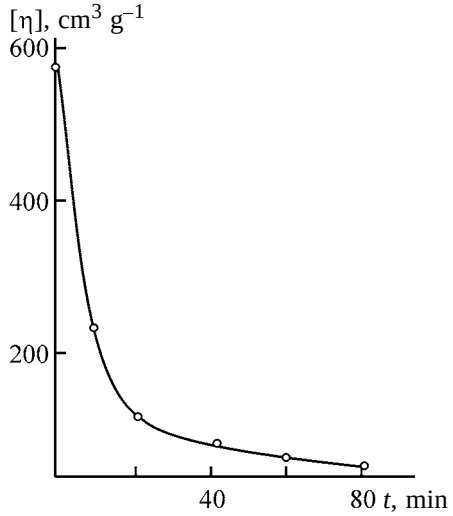

Fig. 1. Intrinsic viscosity $[\eta]$ of AA/NaAMS copolymer (sample P) as a function of the degradation time t. c_p = 0.2%; [initiator]/[copolymer] = 0.04; T = 60°C.

Table 2. Phase behavior of PAA (sample C), NaPAMS (sample B), and AA/AMS (samples L, M, N, O, P) and AA/NaA copolymers (samples D, E, F, G) in salt solutions at 25–100°C

Sample	Ionic unit content, mol %	Phase separation temperature $T_{p.s}$, °C, at indicated salt concentration, %								
		NaCl			$CaCl_2$			$MgCl_2$		
		3	5	10	0.25	1	3	0.25	1	3
D	7.0	–	–	–	76	65	78	–	–	–
E	11.0	75	66	78	56	51	60	80	69	85
F	20.0	59	54	60	50	43	52	66	61	72
G	28.0	48	41	51	–	–	–	52	45	53
C	0	n*	n	n	n	n	n	n	n	n
L	7.0	n	n	n	n	n	n	n	n	n
M	9.0	n	n	n	n	n	n	n	n	n
N	11.4	n	n	n	n	n	n	n	n	n
O	18.2	n	n	n	n	n	n	n	n	n
P	20.1	n	n	n	n	n	n	n	n	n
B	100.0	n	n	n	n	n	n	n	n	n

* (n) No phase separation.

copolymer became insoluble and precipitated. Compared to the divalent metal salts, NaCl demonstrates lower dehydrating capacity, and phase separation of the copolymers occurs at higher salt concentration than in the case of Ca and Mg chlorides (Table 2).

Analysis of data obtained at a fixed concentration of inorganic salts (Table 2) shows that, for all the salt additives studied, $T_{p.s}$ decreases with increasing content of ionic groups in macromolecules of the AA/NaA copolymer, which is consistent with the published data [7, 8]. Increase in the ionic group content in the copolymer increases the concentration of salt bonds between polyanions and cations, decreasing the stability of the macromolecules in solution. This is also favored by the reduced possibility of H-bond blocking of ionic groups of the copolymers in interaction with the amide groups as the content of the NaA units in the AA/NaA copolymers increases.

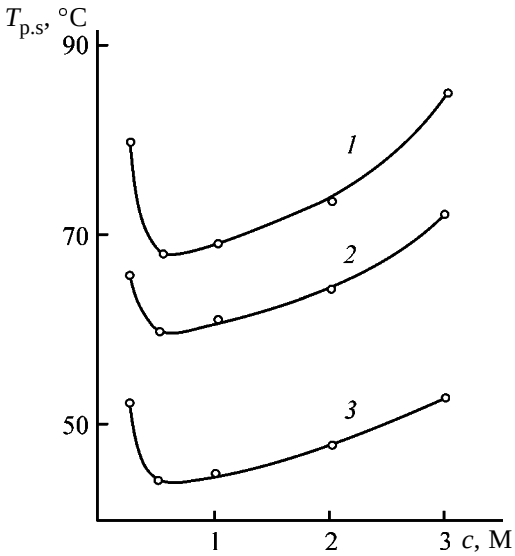

Fig. 2. Phase separation temperature $T_{p.s}$ of AA/NaA copolymers in aqueous solutions as a function of the $MgCl_2$ concentration *c*. c_p = 0.2%; the same for Fig. 3. Samples: (*1*) E, (*2*) F, and (*3*) G.

Let us consider the effect of divalent metal salts, $CaCl_2$ and $MgCl_2$, on the phase separation in solutions of AA/NaA copolymers. The dependence of $T_{p.s}$ on the solution ionic strength μ controlled by salt additions is presented in Fig. 3a (sample E) and Fig. 3b (sample F). Analysis of data obtained at μ = const (Fig. 3) shows that $T_{p.s}$ decreases on passing from Mg^{2+} to Ca^{2+} (curves *1*, *2*). This is probably due to the fact that Ca^{2+} is more strongly bound to polyacrylate anion than Mg^{2+} [17].

The phase behavior in solutions of AA/NaAMS copolymers of different compositions and of the homopolymers, PAA and NaPAMS, was studied in the presence of $CaCl_2$, $MgCl_2$, and NaCl at 25–100°C. Table 2 shows that, over the experimental salt concentration range, the indicated polymers and copolymers remain to be soluble up to 100°C.

The effect of the concentration of AA/NaAMS copolymer on the phase separation was studied at 20 and 100°C over the copolymer concentration range from 0.1 to 0.5% in the presence of 0.25 and 3% $CaCl_2$ (Table 3). At low copolymer concentration (0.1

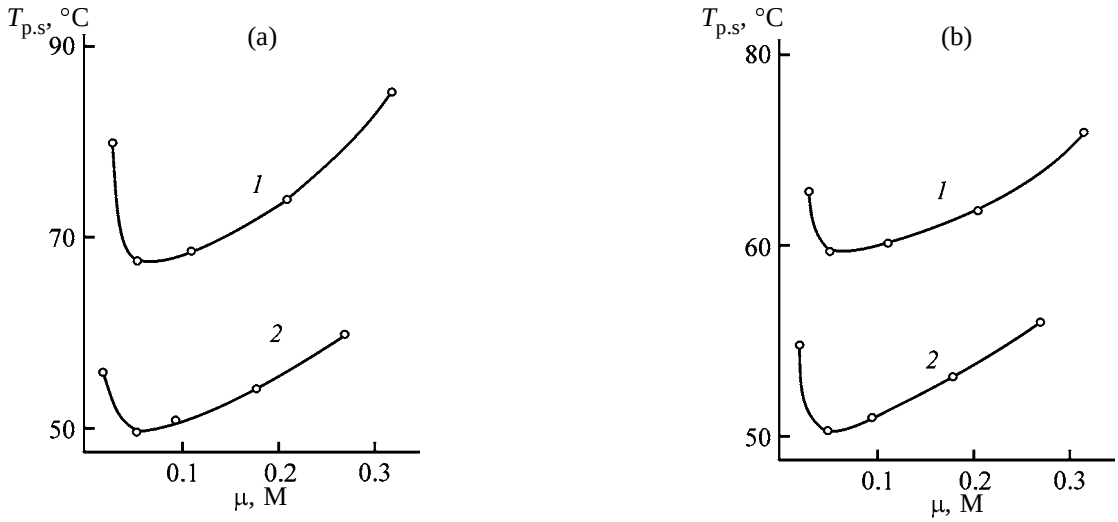

Fig. 3. Phase separation temperature $T_{p.s}$ of AA/NaA copolymers as a function of the solution ionic strength μ: (*1*) $MgCl_2$ and (*2*) $CaCl_2$. Sample: (a) E and (b) F.

and 0.2%), no phase separation was observed. With increasing c_p to 0.3%, we did not observe phase separation only at the lower $CaCl_2$ concentration, and at c_p = 0.5%, phase separation was observed at both $CaCl_2$ concentrations.

We also studied the effect of MW of AA/NaAMS copolymer on the phase separation. Experiments were carried out at c_p = 0.2% and the $CaCl_2$ concentration of 0.25 and 3% over the temperature range 20–100°C. The results obtained for AA/NaAMS copolymers of the same chemical composition showed that, over the [η] range from 50 to 570 $cm^3\ g^{-1}$, no phase separation occurred.

The observed higher phase stability of AA/NaAMS copolymers in the presence of divalent metal salts, compared to AA/NaA copolymers, can be attributed to different geometry of anions in these copolymers. AA/NaAMS copolymer contains longer substituents [–C(O)–NH–C$(CH_3)_2$–CH_2–SO_3Na] as compared to AA/NaA [–C(O)–ONa]. As known, longer substituents provide higher flexibility and lower charge density along the chain. Evidently, this should favor lower degree of bonding of divalent cations with the polysulfonate anions as well as higher phase stability of AA/NaAMS as compared to AA/NaA.

Another reason is different strength of bonding between divalent cations and strong and weak polyelectrolytes. It was demonstrated [17] that specific bonding between the counterions and polyions is untypical of strong polyelectrolytes such as AA/NaAMS copolymer, being significant in the case of weak polyelectrolytes such as AA/NaA copolymer. Therefore, divalent cations, Ca^{2+} and Mg^{2+}, are more readily bound to AA/NaA as compared to AA/NaAMS, providing higher phase stability for the latter.

CONCLUSIONS

(1) Copolymers of acrylamide and sodium 2-acrylamido-2-methylpropanesulfonate demonstrate higher phase stability in the presence of inorganic salts ($CaCl_2$, $MgCl_2$, and NaCl) as compared to copolymers of acrylamide and sodium acrylate.

(2) No phase separation was observed for copolymers of acrylamide and sodium 2-acrylamido-2-methylpropanesulfonate with different ionic group contents and 50 < [η] < 570 $cm^3\ g^{-1}$ over the copolymer concentration range 0.1–0.2%, irrespective of the $CaCl_2$ and $MgCl_2$ concentrations and temperature (20–100°C).

(3) The phase separation temperature of copoly-

Table 3. Effect of the concentration of AA/NaAMS copolymer (sample P) on the phase behavior in $CaCl_2$ solutions

c_p, %	Phase behavior* at indicated c_{CaCl_2}, %			
	0.25	3	0.25	3
	20°C		100°C	
0.1	–	–	–	–
0.2	–	–	–	–
0.3	–	+	–	+
0.5	+	+	+	+

* (–) No phase separation and (+) phase separation takes place.

mers of acrylamide and sodium acrylate decreases with increasing ionic group content in the copolymer and on passing from Mg^{2+} to Ca^{2+}.

REFERENCES

1. Lisovtsev, V.V., Rostokin, G.A., and Kulikova, A.E., in *Khimicheskaya promyshlennost': Akrilaty i polivinilkhlorid* (Chemical Industry: Acrylates and Polyvinyl Chloride), Moscow: NIITEKhim, 1984, pp. 1–21.
2. *2-Acrylamido-2-Methylpropane Sulfonic Acid Monomer*, Wickliffe, Ohio (the United States): Lubrizol, 1994, pp. 1–18.
3. Kurenkov, V.F. and Shipova, L.M., *Zh. Prikl. Khim.*, 1997, vol. 70, no. 1, pp. 153–157.
4. Shevtsova, S.A., Zaitseva, O.A., and Kurenkov, V.F., *Vestn. Kazan. Tekhnol. Univ.*, 2000, vols. 1–2, pp. 126–128.
5. McCormick, C.L., *Macromol. Sci. Chem., Part A*, 1985, vol. 5, pp. 955–982.
6. Ikegami, A., *J. Polym. Sci.*, 1962, vol. 5, p. 544.
7. Kabo, V.Ya., Maslennikov, V.A., and Gorodnov, V.P., *Neftepromysl. Delo*, 1975, no. 12, pp. 191–194.
8. Kabo, V.Ya. and Gorodnov, V.P., *Vysokomol. Soedin.*, 1977, no. 5, pp. 1109–1112.
9. McCormick, C.L. and Elliott, D.L., *Macromolecules*, 1986, vol. 19, pp. 542–547.
10. Maer, Zh.A., Synthesis and Characterization of Copolymers of Sulfonic Amido Acids with Acrylamides and Acrylonitrile as Versatile Stabilizers for Bentonite Dispersions, *Cand. Sci. Dissertation*, Yaroslavl, 1998.
11. Kurenkov, V.F., Khairullin, M.R., and Utikeeva, A.R., *Zh. Prikl. Khim.*, 1999, vol. 72, no. 7, pp. 1177–1181.
12. Kurenkov, V.F., Zaitseva, N.N., Zhelonkina, T.A., and Lobanov, F.I., *Zh. Prikl. Khim.*, 2003, vol. 76, no. 6, pp. 1009–1012.
13. Charlot, G., *Les Methods de la Chimie Analytique. Analyse quantitative Minerale*, Paris: Masson, 1961, 4th ed.
14. Churikov, F.I., Snigirev, S.V., and Kurenkov, V.F., *Zavod. Lab., Diagnost. Mater.*, 1998, no. 6, pp. 9–10.
15. Eisenberg, H. and Ram Mohan, G., *J. Chem. Phys.*, 1959, vol. 63, pp. 671–680.
16. Dubin, P.L., *Structure–Solubility Relationships in Polymers*, Harris, F.W. and Seymour, R.B., Eds., New York: Academic, 1977, pp. 135–140.
17. Marina, N.G. and Monakov, Yu.B., in *Khimiya vysokomolekulyarnykh soedinenii* (Macromolecular Chemistry), Ufa: Inst. Khimii, Bashkir. Fil., Akad. Nauk SSSR, 1976, pp. 116–146.

Russian Journal of Applied Chemistry, Vol. 77, No. 5, 2004, pp. 809–812. Translated from Zhurnal Prikladnoi Khimii, Vol. 77, No. 5, 2004, pp. 814–817.

MACROMOLECULAR CHEMISTRY AND POLYMERIC MATERIALS

Specific Features of Interaction of Polyacrylic and Polymethacrylic Acids with Nanoparticles of Amorphous Selenium

V. V. Kopeikin, S. V. Valueva, A. I. Kipper, A. P. Filippov, G. V. Shishkina, L. N. Borovikova, N. V. Rumyantseva, Ya. I. Nazarkina, and V. K. Lavrent'ev

Institute of Macromolecular Compounds, Russian Academy of Sciences, St. Petersburg, Russia

Received November 25, 2003; in final form, February 2004

Abstract—A study was made of formation of selenium nanoparticles in water from reduction of sodium selenite with ascorbic acid in the presence of polyacrylic and polymethacrylic acids.

It is well known that nanoparticles of zero-valence metals and nonmetals, with their specific structural features and high surface energy, exhibit abnormal physicochemical properties because of the scale effect of matter [1]. Of special interest are nanoparticles of selenium, a chemical element with unique photoelectric, semiconducting, catalytic, and biological properties and X-ray sensitivity.

Ligand-free nanoparticles are metastable and tend to rapidly aggregate in aqueous solutions. Therefore, they are usually stabilized by water-soluble polymers whose interaction with nanoparticles yields nanostructures of various morphologies [2]. However, the nature of this interaction in formation of nanoparticles in aqueous solutions of polymers still remains to be elucidated.

This work was aimed at elucidating the nature of the above-mentioned interactions and their role in polymer stabilization of selenium nanoparticles (nano-Se^0). To this end, we studied for the first time formation of nano-Se^0 particles in the presence of synthetic polymers differing in the hydrophylic–lipophilic balance. Also, we carried out optical studies of the morphological characteristics of the nanostructures being formed.

EXPERIMENTAL

We studied nano-Se^0 nanoparticles prepared by reducing selenious acid (SA) with ascorbic acid, with and without polymer additions.

As polymeric stabilizers of nano-Se^0 served synthetic polymers, polyacrylic acid (PAA) and polymethacrylic acid (PMAA), with molecular weights M_w of 27×10^6 and 25×10^3, respectively. This choice was dictated by close structures and Kuhn segment sizes of these polymers, of which only PMAA has side hydrophobic methyl groups [3].

The ionic selenium species SeO_3^{2-} was reduced at the selenium concentration in solution of 0.01 wt % and the polymer-to-selenium mass ratio of 9 : 1 (i.e., under exhaustive saturation of the adsorption capacity of nanoparticles, as revealed for other selenium–polymer nanostructures [4]).

Using the method of flow birefringence [5], we estimated the molecular dispersity of the solutions of the adsorbates being formed, based on analysis of the gradient dependence of the birefringence Δn. Specifically, we studied the birefringence versus the gradient of the rotor rotation rate g and the polymer concentration c at a fixed selenium concentration of 0.01 wt %. We used titanium dynamooptometer with a 4-cm-high internal rotor and the rotor–stator slit width of 0.03 cm. The solutions for birefringence measurements were kept at a constant temperature of 21°C to prevent variations of their viscosities and optical distortions due to the temperature gradient. The measuring facility was calibrated against 2-phenylethanol having a significant birefringence ($\Delta n/g = 17 \times 10^{-12}$), as well as against the polystyrene–bromoform system. The intrinsic birefringence $[n] = \lim_{g \to 0, c \to 0}(\Delta n/gc\eta_0)$ (η_0 is the viscosity of the solvent) was measured accurately to within 10%. The measurements were carried out at $g < g_k$, where g_k is the rate gradient corresponding to the onset of flow turbulence.

1070-4272/04/7705-0809 © 2004 MAIK "Nauka/Interperiodica"

The experimentally determined intrinsic birefringence $[n]$ in a general case ($dn/dc \neq 0$, where dn/dc is the increment of the refractive index of the solution, estimated for PAA–Se^0–H_2O and PMAA–Se^0–H_2O systems at 0.245 and 0.165, respectively) has three components: $[n] = [n]_e + [n]_{fs} + [n]_f$, where $[n]_e$ is the intrinsic anisotropy; $[n]_{fs}$, microform effect; and $[n]_f$, macroform effect [5]. The full segment anisotropy $[n]_{fs} + [n]_e$ is determined by the equilibrium rigidity A of the polymer chain and by the structure of the polymer unit, and $[n]_f$ is related to the shape asymmetry parameter p of the macromolecule (particle) as

$$[n]_f = [(n_s^2 + 2)/3]^2[M_w(dn/dc)^2 f(p)]/(30\pi RTn_s)$$

$$= \text{const}\, M_w(dn/dc)^2 f(p), \quad (1)$$

where M_w is the molecular weight of the adsorbate macromolecule; n_s, refractive index of the solvent; T, absolute temperature; R, universal gas constant; and $f(p)$, tabulated function of the ratio of the axes of a rigid (impermeable by the solvent) ellipsoid approximating the particle [5].

Relationship (1) is valid both for isolated macromolecule and nanostructure; all what is needed of a particle is to be impermeable by the solvent. Thus, for high-molecular-weight flexible-chain and moderately rigid-chain polymers ($A < 5$ nm), having minor optical anisotropy and low-molecular-weight units, the intrinsic birefringence can be fitted by the approximation $[n] \approx [n]_f$, which allows the parameter p to be estimated directly from the experimentally measured birefringence [5].

Using the elastic (static) light scattering method [6], we estimated M_w and the root-mean-square inertia radii R_g of the polymers and nanostructures, as well as their affinity for solvent, water (from the second virial coefficient A_2). Based on the ratio of the parameters M_w for poly acids and nanostructures they form, we determined the number of the macromolecules adsorbed on the nano-Se^0 surface. The reduced intensity of light scattering by solutions R_0 was measured on a Fica photogoniodiffusometer. The wavelength of the incident, vertically polarized, light was 546.1 nm. The measurements were carried out at light scattering angles θ within 30°–150°.The solutions and solvents were purified by centrifugation at 15×10^3 rpm for 1–1.5 h. The refractive index increment dn/dc was determined from the refractive indices measured on an IRF-23 instrument.

The experimental light scattering data were processed by the Zimm method, by double extrapolation ($c \to 0$, $\theta \to 0$) of the plots of Kc/R_θ vs. $\sin^2(\theta/2) + kc$ (K is the calibration constant, and k, numerical constant).

We determined the average hydrodynamic particle sizes R_H by quasielastic (dynamic) light scattering method [7]. Based on the experimental R_g-to-R_H ratio for the nanostructures, we estimated the parameter ρ^* characterizing the conformation of the nanostructure [8–11].

The optical component of the facility for measuring the dynamic light scattering comprised an ALV-SP (Germany) goniometer (a Spectra-Physics He–Ne laser with a wavelength $\lambda = 632.8$ nm, power ca. 20 mV, as light source). The correlation function of the scattered light intensity was obtained on a 288-channel Photo Cor-FC correlator (Anteks Closed Joint-Stock Company, Russia). Data processing was carried out by standard methods of cumulants and Tikhonov regularization, using appropriate software.

According to the static light scattering data, the parameter M_w remains unchanged ($M_w = 27 \times 10^7$) in going from the PAA–H_2O to PAA–Se^0–H_2O system, i.e., in the presence of PAA, no nanostructure is formed. For the PMAA–Se^0–H_2O system, M_w was estimated at 1.5×10^8, i.e., it increased by a factor of 4300 relative to free PMAA macromolecules. This unambiguously suggests the deciding importance of hydrophobic interactions between macromolecules and nano-Se^0 in formation of nanostructures.

The second virial coefficient A_2 for the PMAA–Se^0–H_2O system is equal to zero, which suggests an ideal thermodynamic quality of the solution. For the PAA–Se^0–H_2O system, A_2 is negative, namely, -0.8×10^{-4} $cm^3\,mol\,g^{-2}$, which suggests a bad thermodynamic quality of the solution. Thus, adsorption of macroions on nano-Se^0 improves the thermodynamic quality of the solution.

The parameter R_H for nano-Se^0 particles obtained without polymeric stabilizer was estimated at 170 nm. The particle size of the PMAA–Se^0 adsorbate, estimated by dynamic and static light scattering methods, is much smaller (root-mean-square inertia radius R_g = 90 nm and mean hydrodynamic radius R_H = 90 nm). The parameter $\rho^* = R_g/R_H$ is equal to unity, which suggests virtually ideal spherical shape of the particles of the adsorbate being formed [8–11].

To determine the radius of the selenium particles occurring in the core of the nanostructure, we lyophilically dried an aqueous solution of PMAA–Se^0,

and the resulting dry pelletized product was examined by small-angle X-ray scattering. We estimated the radius of the spherical Se^0 particles at 15 nm, which is by an order of magnitude smaller than that of selenium particles obtained without polymeric stabilizer. Thus, the nano-Se^0 particles in aqueous solutions have a ca. 75-nm-thick polymer shell.

Optical studies of the PAA and PMAA macromolecules showed that, in the nonionized state, these are Gaussian globules with the asymmetry parameter $p \sim 2$ [12].

Calculation of the parameter p in the $[n] \sim [n]_f$ approximation for the PAA–Se^0–H_2O and PMAA–Se^0–H_2O systems yielded, respectively, $p \sim 1$ (spherical conformation) and $p \sim 2$ (which is inconsistent with the value of the parameter p^*, corresponding to the spherical conformation of the nanostructure) [5]. Also, the fact that the reduced optical anisotropy for the PMAA–Se^0–H_2O system is independent of the concentration (Fig. 1) suggests that the parameter p tends to unity, i.e., that the nanostructure is spherical [5]. The fact that hybrid nanostructures formed by macromolecules and nanoparticles have a spherical shape, even in the case of such a rigid macromolecule as DNA [13], suggests that the $[n] \sim [n]_f$ approximation is invalid for the PMAA–Se^0–H_2O system. Evidently, in this case a significant contribution to the optical anisotropy comes from an effect similar to the microshape effect for an isolated macromolecule (Lyubina [12] showed that the intrinsic optical anisotropy even for PMAA with its high degree of ionization is negligible). This is supported by the fact that the $\Delta n = f(g)$ curves (Fig. 2) for the PMAA–Se^0–H_2O system reach saturation. This suggests an increase in the rigidity of the PMAA macromolecules owing to hydrophobic interactions. Thus, hydrophobic interactions of nonpolar fragments of the macromolecules with one another and with nano-Se^0 constitute the major driving force of adsorption.

In the case of PAA, no nanostructure is formed, and the conformation of the macroions changes, in contrast to nonionic hydrophilic polymers such as polyacrylamide [4]. This is presumably due to dipole–dipole interactions of PAA with selenium nanoparticles.

We showed that selenium nanoparticles are adsorption matrices suitable for accommodating in high local concentrations anionic polyelectrolytes containing hydrophobic methyl groups in the side chains. Our results can be applied to molecular designing of new materials with desired properties.

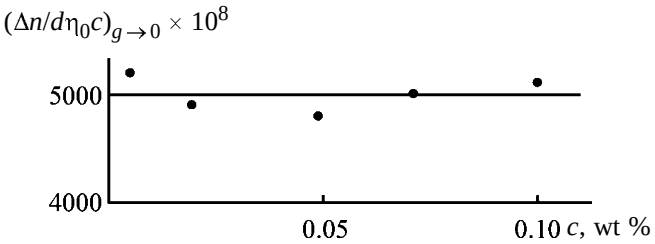

Fig. 1. $(\Delta n/g\eta_0 c)_{g\to 0}$–$c$ dependence for the PMAA–Se^0–H_2O system. (Δn) Dimensionless birefringence of the polymer; (g) flow rate gradient, s^{-1}; (η_0) viscosity of the solvent, cm s g^{-1}; and (c) concentration of the polymer.

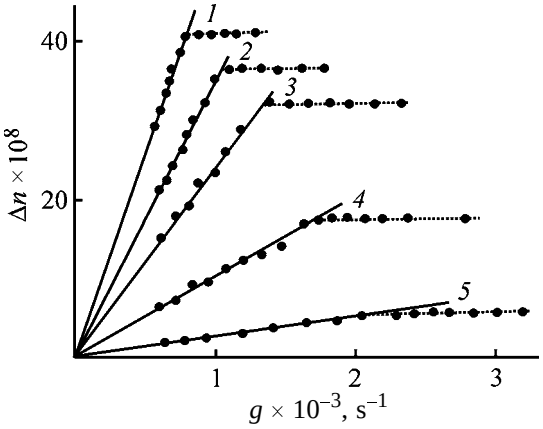

Fig. 2. Variation of the birefringence Δn with the flow rate gradient g for the PMAA–Se^0–H_2O system. c_{PMAA}, wt %: (*1*) 0.1, (*2*) 0.071, (*3*) 0.049, (*4*) 0.0195, and (*5*) 0.0048.

CONCLUSIONS

(1) Reduction of sodium selenite with ascorbic acid in an aqueous solution of polymethacrylic acid yielded spherical nano-Se^0 particles with a size of ca. 15 nm.

(2) Molecular-optical studies showed that the polymethacrylic acid macromolecules adsorbed on nano-Se^0 form an ultra-high-molecular-weight (MW = 150×10^6) spherical nanostructure with a size of ca. 90 nm, comprising over 4000 densely packed macromolecules.

(3) The PMAA–Se^0–H_2O system exhibits an induced conformational transition of polyacrylic acid from a Gaussian globule to a sphere.

(4) The hydrophobic interactions of the macromolecules with nano-Se^0 play the deciding role in their adsorption on nanoparticles.

REFERENCES

1. Pomogailo, A.D., *Nanochastitsy metallov v polimerakh* (Nanoparticles of Metals in Polymers), Moscow: Nauka, 1999.

2. Mayer, A.B.R., *Polym. Adv. Technol.*, 2001, vol. 12, no. 1, pp. 96–106.
3. Nekrasova, T.N., Study of the Structure of Polymethacrylic Acid Molecules in Solution, *Cand. Sci. Dissertation*, Leningrad, 1970.
4. Kopeikin, V.V., Valueva, S.B., Kipper, A.I., *et al.*, *Vysokomol. Soedin., Ser. A*, 2003, vol. 45, no. 4, pp. 615–622.
5. Tsvetkov, V.N., Eskin, V.E., and Frenkel, S.Ya., *Struktura makromolekul v rastvorakh* (Structure of Macromolecules in Solutions), Moscow: Nauka, 1964.
6. Eskin, V.E., *Rasseyanie sveta rastvorami polimerov i svoistva makromolekul* (Light Scattering by Polymer Solutions and Properties of Macromolecules), Leningrad: Nauka, 1986.
7. Brown W., *Dynamic Light Scattering: the Method and Some Applications*, Oxford: Clarendon, 1993.
8. Meewes, M., Ricka, J., De Silva, M., *et al.*, *Macromolecules*, 1991, vol. 24, no. 21, pp. 5811–5816.
9. Hishio, I., Shao Thang Sun, Swislow, G., and Tanaka, T., *Nature*, 1979, vol. 281, no. 5728, pp. 208–209.
10. Konishi, T., Yoshizaki, T., and Yamakawa, H., *Macromolecules*, 1991, vol. 24, no. 20, pp. 5614–5622.
11. *Laser Light Scattering in Biochemistry*, Harding, S.E., Satelle, D.B., and Bloomfild, V.A., Eds., Cambridge: Royal Chem. Soc., Inform. Services, 1992, pp. 3–21.
12. Lyubina, S.Ya., Influence of the Intramolecular Interactions and Secondary Structure on the Dynamooptical Properties of Macromolecules in Solutions, *Cand. Sci. Dissertation*, Leningrad, 1965.
13. Storhoff, J.J., Lazaorides, A.A., Mucic, R.C., *et al.*, *J. Am. Chem. Soc.*, 2000, vol. 122, no. 19, pp. 4640–4650.

Russian Journal of Applied Chemistry, Vol. 77, No. 5, 2004, pp. 813–816. Translated from Zhurnal Prikladnoi Khimii, Vol. 77, No. 5, 2004, pp. 818–821.

MACROMOLECULAR CHEMISTRY AND POLYMERIC MATERIALS

NMR Study of the Structure of Polymers Based on 2,3-Epoxypropyl Methacrylate

E. E. Ergozhin, N. A. Bektenov, and N. N. Chopabaeva

Bekturov Institute of Chemical Sciences, Ministry of Education and Science of Kazakhstan Republic, Almaty, Kazakhstan

Received January 20, 2004

Abstract—The structure of homo- and copolymers of 2,3-epoxypropyl methacrylate and methyl methacrylate was studied by high-resolution NMR. The stereochemical sequences in the polymer chains were established.

High-resolution NMR is an efficient method in study and identification of vinyl monomers and polymers based on these, since it allows determination of molecular distribution in polymer chains and furnishes data on the composition of polymers, microstructure, and stoichiometry of macromolecular chain [1–11].

Here we report on the structure of homo- and copolymers of 2,3-epoxypropyl methacrylate (2,3-EPMA) and methyl methacrylate (MMA) studied by ^{1}H and ^{13}C NMR.

EXPERIMENTAL

Poly-2,3-epoxypropyl methacrylate (poly-2,3-EPMA), polymethyl methacrylate (PMMA), and copolymers based on 2,3-EPMA and MMA (2,3-EPMA–MMA) were synthesized by radical polymerization in 1,4-dioxane in the presence of an initiator, azobis(isobutyronitrile) (AIBM) in a concentration of 5×10^{-3} M at 60°C under argon. The polymers were purified from unchanged monomers by threefold reprecipitation from acetone to ethyl ether and dried in a vacuum oven. The content of epoxy groups in 2,3-EPMA, poly-2,3-EPMA, and 2,3-EPMA–MMA was determined by the chemical method based on their reaction with hydrochloric acid in acetone [12].

The ^{1}H and ^{13}C NMR spectra of 10% solutions of monomers and polymers in dimethyl sulfoxide (DMSO–d_6) with hexamethyldisiloxane (HMDS) as an internal reference were recorded at room temperature on a Varian Mercury-300 spectrometer operating at 300.06 MHz for protons.

The signals in the ^{1}H and ^{13}C NMR spectra of the polymers were assigned using the spectral data for the initial monomer 2,3-EPMA and the structural analogs of 2,3-EPMA–MMA: poly-2,3-EPMA and PMMA (Table 1).

The olefin protons of 2,3-EPMA give multiplets in the range 5.6–6.2 ppm with the geminal constant of 1.5 Hz and constants of remote spin–spin coupling with methyl protons equal to 1.0 and 1.5 Hz in *trans* and *cis* positions with respect to this group, respectively. The signal of the methyl group is observed at 1.89 ppm. The protons of the methylene group adjacent to the ester group are nonequivalent and give two doublets of doublets with the geminal constant of 12.3 Hz and vicinal constants of 2.8 and 6.3 Hz. The signals at 2.65, 2.79, and 3.23 ppm are assigned to the protons of the epoxy ring. The first two of them, a doublet of doublets and a triplet with a broadened central component, belong to protons of the methylene group. They have the same splitting of 5.4 Hz arising from geminal coupling, and the splittings of 2.4 and 4.8 Hz corresponding to *cis* and *trans* coupling with protons of the oxirane ring. A complicated structure of the third signal assigned to the methine proton is caused by its coupling with the protons of the neighboring methylene groups.

In the ^{1}H and ^{13}C NMR spectra of homo- and copolymers of 2,3-EPMA and MMA (Table 1), the signals of methyl groups at the double bond, olefin protons, and corresponding carbon atoms disappear. At the same time, new signals characteristic of α-CH_3 groups at a single bond, methylene groups, and quaternary carbon atoms in the polymer chain appear in the spectrum. The positions of the signals of methoxy groups, epoxy ring, and neighboring methylene group do not change noticeably.

The signals in the ^{1}H and ^{13}C NMR spectra of the

1070-4272/04/7705-0813 © 2004 MAIK "Nauka/Interperiodica"

Table 1. ^{1}H and ^{13}C NMR chemical shifts of PMMA, 2,3-EPMA, and copolymers based on these

Group	δ, ppm							
	2,3-EPMA		poly-2,3-EPMA		PMMA		2,3-EPMA–MMA	
	^{1}H	^{13}C	^{1}H	^{13}C	^{1}H	^{13}C	^{1}H	^{13}C
CH_2	6.05	127.23	1.83	52.40	1.80	53.85	1.81	52.89
	5.71		1.52	54.44	1.44	54.95	1.50	54.54
C_{quat}	–	136.65	–	45.22	–	44.85	–	45.17
				45.56		45.27		45.53
α-CH_3	1.89	18.98	0.79	17.41	0.74	17.20	0.78	17.29
			0.96	19.38	0.93	19.45	0.95	19.46
			1.18		1.13		1.13	
C=O	–	167.34	–	176.94	–	177.29	–	176.94
				177.71		178.12		177.71
				177.95		178.30		177.95
								178.29
								178.49
O–CH_2	4.45	66.16	4.29	66.77	–	–	4.30	66.72
	3.90		3.72				3.72	
CH^{epoxy}	3.23	50.04	3.19	49.60	–	–	3.19	49.56
CH_2^{epoxy}	2.79	44.83	2.79	44.86	–	–	2.80	44.80
	2.65		2.65				2.65	
O–CH_3	–	–	–	–	3.55	52.69	3.55	52.71

polymers have no fine structure and are broadened in comparison with the signals of the initial monomer.

The quantitative content of epoxy groups in the polymer can be estimated from the epoxy number (EN). For the 2,3-EPMA homopolymer synthesized, EN determined by the chemical method [12] coincides with the EN found for the initial 2,3-EPMA and is equal to 30.28%. This suggests complete preservation of oxirane rings in poly-2,3-EPMA. The NMR data suggest that radical homo- and copolymerization of 2,3-EPMA initiated by AIBN involves scission of double bonds without participation of epoxy groups. This is in good agreement with the results of chemical analysis.

The composition of the copolymer 2,3-EPMA : MMA = 66 : 34 mol % found from the relative integral intensities of signals of epoxy and methoxy groups in the ^{1}H NMR spectrum (66 : 34 mol %) practically coincides with the values obtained by elemental and chemical analysis: 68.18 : 31.82 and 65.30 : 34.70 mol %, respectively. In the initial mixture of monomers, [2,3-EPMA] : [MMA] = 60 : 40 mol %.

Found, %: C 59.37, H 7.28, O 33.36; EN 22.04.
Calculated, %: C 59.43, H 7.35, O 33.23: EN 20.61.

It is seen that the copolymer is somewhat enriched with fragments of 2,3-EPMA, which is more active than MMA in accordance with the copolymerization constants ($r_{2,3\text{-EPMA}} = 0.94$, $r_{MMA} = 0.75$) [13].

It is well known [14] that, in polymers synthesized from a vinyl monomer with different α-substituents, the monomer molecules add to the end of the growing chain, as a rule, in the "head-to-tail" manner. In this case, every second carbon atom, being the center of the stereoisomerism, can occur in one of two configurations differing in location of α-substituents with respect to the carbon chain. The knowledge of the fractions of these configurations allows determination of the polymer structure.

It is seen from Table 1 that almost each group in the monomeric unit of the polymer gives several signals whose chemical shifts essentially depend not only on the nature of this group but also on the relative configuration of the neighboring monomeric units. The exceptions are methoxy and epoxy groups and also adjacent methylene group, which are insensitive to the isomerism of the main polymer chain because of relatively remote location.

In the range of proton resonance of α-methyl groups, there are three signals of different intensities. This suggests that the polymers are not highly stereoregular, i.e., there are various configuration sequences

Table 2. Distribution of triad sequences in poly-2,3-EPMA, PMMA, and 2,3-EPMA–MMA

Compound	Triad	^{1}H NMR of α-CH_3 at 0.7–1.2 ppm	^{13}C NMR			P_m	Calculation of triads according to Bernoulli
			C_{quat}, 44–46 ppm	$-CH_3$, 17–20 ppm	C=O, 176–179 ppm		
Poly-2,3-EPMA	*mm*	0.03	0.03	0.03	0.03	0.23	0.05
	mr	0.36	0.37	0.37	0.35		0.36
	rr	0.61	0.60	0.60	0.62		0.59
PMMA	*mm*	0.05	0.05	0.05	0.05	0.24	0.06
	mr	0.37	0.35	0.36	0.39		0.36
	rr	0.58	0.60	0.59	0.56		0.58
2,3-EPMA–MMA	*mm*	0.04	0.04	0.04	–	0.24	0.06
	mr	0.38	0.38	0.37	–		0.36
	rr	0.58	0.58	0.59	–		0.58

in these polymers. The presence of three signals means that the configuration of only short fragments of the chain, containing three monomer units, can be determined from the ^{1}H NMR spectrum. These signals belong to α-methyl groups in the central units of iso- (*mm*), syndio- (*rr*), and heterotactic (*mr*) triads. The signals were assigned considering the influence of magnetic susceptibility anisotropy of carbonyl groups in the terminal units of the triads on the chemical shift. In the syndiotactic triad, whose units occur in opposite configurations, α-methyl group is in the region of shielding effect of two carbonyl groups similarly arranged with respect to this group. As a result of shielding, its signal is shifted upfield relative to the signal of the isotactic triad. The signal of the heterotactic triad is positioned between these signals, with intermediate chemical shift. Thus, three α-methyl signals at 0.74–0.79, 0.93–0.96, and 1.13–1.18 ppm correspond to *rr*, *mr*, and *mm* triads, respectively. It should be noted that a large difference in the chemical shifts of the triads is mainly caused by the characteristics of carbonyl group with α-glycidyl and methoxyl substituents and by orientation. For poly-2,3-EPMA, PMMA, and 2,3-EPMA–MMA, this difference is equal to 0.39 and 0.35 ppm, while for polypropylene [15] having no electronegative and magnetoanisotropic α-substitutents which can noticeably affect the chemical shift, this difference is as small as 0.05 ppm.

The measurements of the integral intensities of the signals of α-methyl groups allow estimation of the relative fractions of stereochemical sequences in the polymers (Table 2). These values suggest predominant formation of syndiotactic polymers and show that the distribution of monomeric units in the macromolecular chain of poly-2,3-EPMA, PMMA, and 2,3-EPMA–MMA, synthesized in the presence of AIBN radical initiator in 1,4-dioxane at 60°C, is described by the Bernoulli statistics and is characterized, within the limits of the experimental error, by the probability of formation of mesodiad $P_m = 0.23 \pm 0.02$.

Along with the signals corresponding to triads, carbonyl carbon gives an additional signal at 177.95 ppm, which belongs to *mrrr* pentads with the probability equal to 0.15.

We failed to distinguish the sequences of comonomer units in 2,3-EPMA–MMA from the evidence of NMR data owing to the fact that the shielding effect of the carbonyl group linked to glycidyl and methyl substituents is practically the same. However, the configuration sequences in the form of *mm*, *mr*, and *rr* triads differ clearly in the signals of α-methyl groups and quaternary carbon atom in the polymer chain. The found distribution of triad sequences in copolymer is the same as in the homopolymers (Table 2).

CONCLUSION

Homo- and copolymers of epoxypropyl methacrylate and methyl methacrylate, produced by radical polymerization in a solution in the presence of azobis(isobutyronitrile) at 60°C, are predominantly syndiotactic and obey the Bernoulli statistics with the probability of isotactic addition $P_m = 0.24 \pm 0.02$.

REFERENCES

1. Grenier-Loustalot, M.F., Andenaert, M., Boutillier, J., *et al.*, *Eur. Polym. J.*, 1989, vol. 25, no. 3, pp. 211–220.
2. Mohan, D., Radhakrishnan, G., Rajadurai, S., and

Thomas, J., *J. Polym. Sci*., 1990, vol. 28, no. 10, pp. 307–314.

3. Dhai Pradeep, K. and Babu, G., *Angew. Makromol. Chem*., 1983, vol. 119, pp. 125–135.
4. Grenier-Loustalot, M.F., *Polym. Commun.*, 1990, vol. 31, no. 8, pp. 329–333.
5. Brar, A.S. and Dutta, K., *Macromolecules*, 1998, vol. 31, no. 15, pp. 4695–4702.
6. Deshpande, S.M. and Athawali, V.D., *J. Chem. Technol*., 1996, vol. 3, no. 2, pp. 121–124.
7. Ozdemir, E., Coskun, M., and Ahmedov, M.A., Abstracts of Papers, *35th IUPAC Congr*., Istanbul, 1995, p. 898.
8. Subraminian, K., Nanjundan, S., and Rami Reddy, A.V., *J. Macromol. Sci., Ser. A*, 2000, vol. 37, no. 10, pp. 1211–1225.
9. Matsuzaki, K., Kawazu, F., and Kanai, T., *Makromol. Chem*., 1982, vol. 183, pp. 185–192.
10. Dhal Pradeep, K., Deshpande, D.D., and Babu, C.N., *IUPAC MACRO'83*, Bucharest, 1983, p. 46.
11. Ergozhin, E.E., Chalov, A.K., Iskakova, R.A., *et al*., *Zh. Prikl. Khim*., 2003, vol. 76, no. 1, pp. 103–106.
12. Toroptseva, A.I., Belogorodskaya, K.V., and Bondarenko, V.M., *Laboratornyi praktikum po khimii i tekhnologii vysokomolekulyarnykh soedinenii* (Practical Guide on Chemistry and Technology of Macromolecular Compounds), Leningrad: Khimiya, 1972.
13. Sorokin, M.F. and Lyalyushko, K.A., *Plast. Massy*, 1963, no. 3, pp. 3–7.
14. Kuchanov, S.I., *Metody kineticheskikh raschetov v khimii polimerov* (Methods of Kinetic Calculations in Polymer Chemistry), Moscow: Khimiya, 1978.
15. Bovey, F.A., *High Resolution NMR of Macromolecules*, New York: Academic, 1972.

Russian Journal of Applied Chemistry, Vol. 77, No. 5, 2004, pp. 817–819. Translated from Zhurnal Prikladnoi Khimii, Vol. 77, No. 5, 2004, pp. 822–824.

MACROMOLECULAR CHEMISTRY AND POLYMERIC MATERIALS

Aqueous Adhesives Based on Dextrin-Containing Polyacrylate Composites

T. G. Klimets, E. V. Grinyuk, E. I. Nareiko, E. D. Skakovskii, L. Yu. Tychinskaya, and L. P. Krul'

Research Institute of Physicochemical Problems, Belarussian State University, Minsk, Belarus

Received January 22, 2004

Abstract—Rheological and adhesion characteristics of water-soluble adhesive composites based on copolymer of acrylamide with sodium acrylate and corn dextrin were studied. The optimum composition of these composites in their use as label adhesives was determined.

High-quality label adhesives should have the following characteristics: high reliability of the adhesive joint in the initial stage of drying, short time of setting, and, desirably, pseudo-plastic character of flow [1].

It is well known that aqueous saline solutions of copolymers of acrylamide with sodium acrylate (CASA) are used as label adhesives [1–3]. However, these adhesives have poorly pronounced pseudo-plasticity and fairly prolonged time of setting; they ensure low reliability of the adhesive joint in the first minutes. These characteristics can be improved by increasing concentration of polymer in the solution. However, increase in the concentration of CASA results in significant increase in the solution viscosity, which hampers its use as adhesive [3].

Another approach to improvement of characteristics of adhesives based on CASA is, apparently, development of composites with other polymers.

Here we studied the possibility of using corn dextrin (CD) for improvement of adhesion and rheological characteristics of glues based on CASA.

EXPERIMENTAL

As the initial materials we used aqueous–saline solution of CASA with the concentration of 27.5% and shear viscosity of 35 Pa s, and also acidic corn dextrin (high grade, pale yellow), GOST (State Standard) 6034–74. Copolymers of acrylamide with sodium acrylate were produced by base hydrolysis of Nitron D polyacrylonitrile fiber according to TU RB (Technical Specification of Belarus Republic) 00 280 198.026–96. The resulting hydrolyzate was neutralized with acetic acid.

The viscosity of the resulting solutions was determined on a Rheotest 2 rotary viscometer with a cylinder–cylinder working unit at $20 \pm 0.1°C$ [4].

To determine adhesion characteristics of the hydrolyzate solutions in the system glass–adhesive–paper, we used an RMU-0.05-1 tearing machine with the limits of load measurements of $(0–10) \pm 0.02$ kgf and velocity of the guide rod of the machine of up to 100 mm min^{-1} [2, 3].

The content of the dry substance was determined gravimetrically by drying in a thermostat at 80°C to constant weight. The polymer concentration was determined by subtraction of the salt concentration from the content of dry substance. The salt content was evaluated by the formula

$$c_{salt} = 82 n_{acid} / m_h,$$

where c_{salt} is the concentration of salt in the neutralized hydrolyzate (%), n_{acid} is the amount of acetic acid consumed for neutralization (mole), and m_h is the weight of the neutralized hydrolyzate (g).

The ^{13}C NMR spectra were recorded on a Tesla BS-587A spectrometer operating at 20 MHz. We used 10% solutions of copolymers in D_2O placed into standard ampules (10 ml). The spectra were recorded without Overhauser effect with pulse delay exceeding $7T_1$, where T_1 is the spin–lattice relaxation time of the most slowly relaxing nuclei. The signals were assigned by the DEPT procedure with the use of model compounds [5]. The chemical shifts were measured using the signal of methyl group of acetone-d_6 added to the reaction mixture as a reference (δ 30.2 ppm).

The composites of aqueous saline solution of CASA with CD were prepared at room temperature and at $65 \pm 5°C$.

1070-4272/04/7705-0817 © 2004 MAIK "Nauka/Interperiodica"

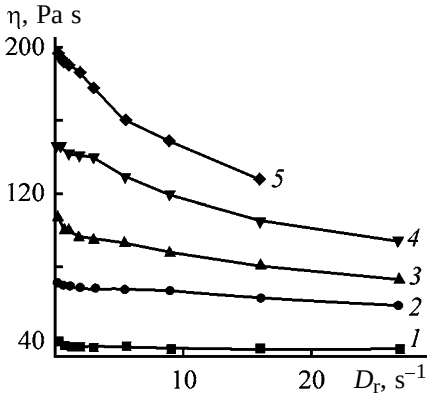

Fig. 1. Flow curves for the hydrolyzate of the polyacrylonitrile fiber and the mixture of the hydrolyzate with CD. Temperature of mixing 20°C; the same for Fig. 2. (η) Viscosity; (D_r) shear rate. Concentration of CD, %: (*1*) 0, (*2*) 10, (*3*) 15, (*4*) 20, and (*5*) 25; the same for Figs. 2 and 4.

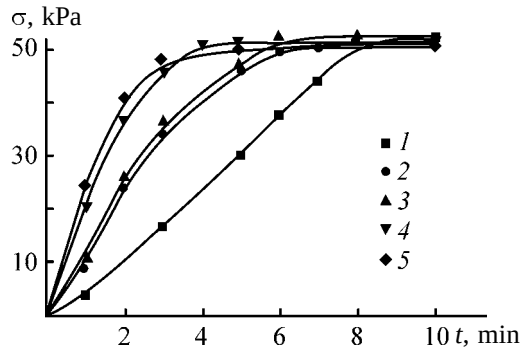

Fig. 2. Shear strength of the glue joint σ as a function of keeping time *t* for hydrolyzate of polyacrylonitrile fiber and mixtures of the hydrolyzate with CD.

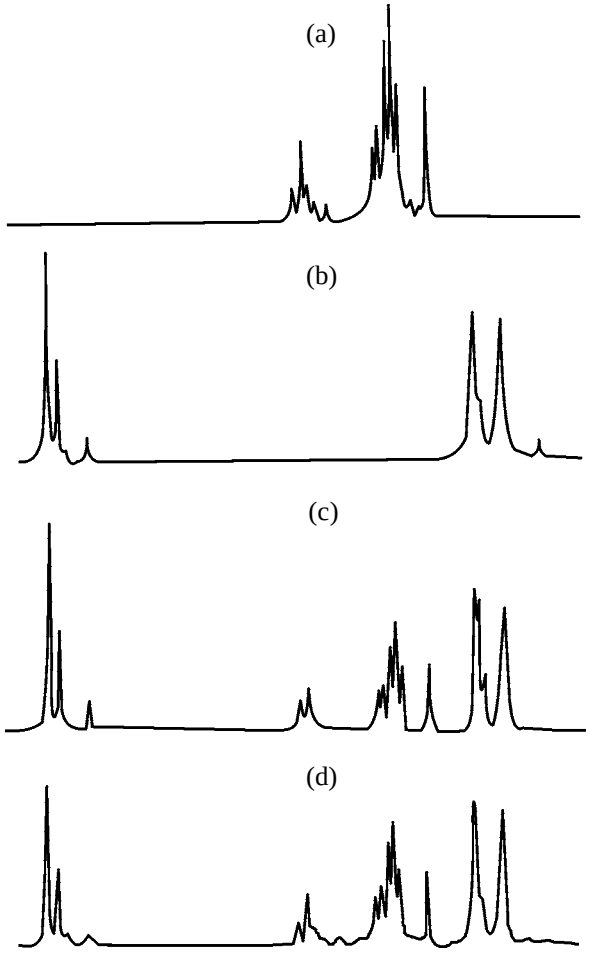

Fig. 3. The ^{13}C NMR spectra of the samples of (a) CD, (b) CASA, and (c, d) composites of CASA with CD prepared at (c) 20°C and (d) 65±5°C.

The flow curves for the mixtures CASA–CD with CD content from 10 to 25%, prepared at room temperature, are shown in Fig. 1. It is seen that, on adding CD to the CASA solution, its viscosity significantly increases (to 146 Pa s at a shear rate of 0.33 s^{-1} and CD content in the composite of 20%). In this case, the viscosity of 20% aqueous solution of CD is as low as 13 mPa s at the same shear rate. Hence, mixing of CD with the hydrolyzate results in superadditive increase in the viscosity.

It can be noted that the resulting solutions of composites have significantly more pronounced pseudoplastic character of flow than the initial solution of CASA.

It should also be noted that mixing of the CASA solution with CD in the concentration exceeding 25% is of no practical interest, since in this case the solutions are highly viscous. In addition, thread formation is observed in using these blends as label adhesives in high-speed label lines.

The results of determination of adhesion characteristics of the mixtures of CASA solution with CD, prepared at room temperature, are shown in Fig. 2. It is seen that addition of CD to aqueous saline solution of CASA results in improvement of the adhesion characteristics. This is primarily manifested in accelerated growth of the glue joint strength. On adding 20% CD, the setting time reaches a minimum equal to 2 min, which corresponds to adhesion characteristics of the best imported glues.

Variation of rheological characteristics of the composites in comparison with CASA solutions can be caused by formation of covalent and noncovalent bonds between CASA molecules and CD. To confirm this assumption, we studied these compositions by ^{13}C NMR.

The ^{13}C NMR spectra of CASA, CD, and composites of CASA with 15% CD, prepared at room temperature and 65±5°C, are shown in Fig. 3. It is seen that the spectrum of CASA–CD composite (Fig. 3c)

Rheological characteristics of CASA–CD composites prepared at various blending temperatures

Content of CD, wt %	T_{bl}, °C	Viscosity,* Pa s
10	20	67.2/60
10	65±5	65.5/61.6
15	20	106.5/80
15	65±5	114.7/91.2
20	20	146/104
20	65±5	143.3/102.3
25	20	197/127
25	65±5	220/147

* Viscosity at the shear rate of 0.33/16.2 s^{-1}.

contains the same signals as in the spectra of the individual components (Figs. 3a, 3b). There are no changes in the positions of signals and their intensities. This suggests no covalent bonding between functional groups of CASA and CD macromolecules. It could be assumed that these bonds would arise in composites produced at elevated temperatures. However, as seen from Fig. 3, the ^{13}C NMR spectra of composites produced at room temperature and at 65± 5°C are the same (Figs. 3c, 3d), i.e., even after heating no covalent bonds between CASA and CD macromolecules are formed.

Hence, the only explanation of variation of the rheological characteristics of the composites in comparison with the initial CASA solution is strengthening of intermolecular interactions in the system with participation of CASA and CD functional groups.

It could be expected that the interchain interactions would change under heating. The shear viscosities of the composites prepared at room temperature and at 65°C are listed in the table. These data show that the blending temperature does not noticeably affect the rheological characteristics of the composites.

The dependences of the strength of glue joints on the duration of keeping for the CASA–CD composites prepared at 65±5°C are shown in Fig. 4. Comparison of Figs. 2 and 4 shows that the curves of strength growth for the composites containing different amounts of CD and prepared at different temperatures practically coincide. Hence, the blending temperature does not affect the adhesion characteristics of the composites.

Comparison of the rheological and adhesion characteristics of the composites prepared at various temperatures shows that an increase in the temperature of composite preparation to 65±5°C does not result in variation of the interchain interaction.

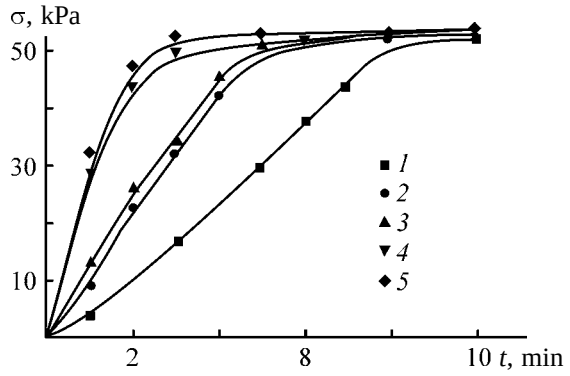

Fig. 4. Shear strength of glue joint σ as a function of keeping time *t* for hydrolyzate of polyacrylonitrile fiber and mixtures of the hydrolyzate with CD. Blending temperature 65±5°C.

CONCLUSION

Mixing of corn dextrin with aqueous saline solution of copolymer of acrylamide with sodium acrylate prepared by base hydrolysis of polyacrylonitrile fibers results in transformation of the hydrolyzate from a Newtonian liquid to a pseudo-plastic liquid, increase in viscosity at any shear rate, and improvement of adhesion characteristics of the composites in the system glass-paper in comparison with the individual components. The composition containing 20% corn dextrin has the optimal adhesion and rheological characteristics for use as a label adhesive. This composition can be produced by mixing at room temperature.

REFERENCES

1. Krul', L.P. and Grinyuk, E.V., *Problemy sovremennogo materialovedeniya: Trudy VII sessii Nauchnogo soveta po novym materialam Mezhdunarodnoi assotsiatsii akademii nauk* (Problems of Modern Materials Technology: Proc. VII Session of the Scientific Committee for New Materials of the Int. Association of Academies of Sciences), Kiev, May 22, 2002, Gomel': IMMS Nats. Akad. Nauk Bel., 2003, pp. 53–57.
2. Brazhnikov, M.M., Grinyuk, E.V., Brazhnikova, L.Yu., and Krul', L.P., *Vestsi Nats. Akad. Navuk Bel., Ser. Khim. Navuk*, 2002, no. 2, pp. 91–93.
3. Krul', L.P., Brazhnikov, M.M., Grinyuk, E.V., and Rybak, A.S., *Izv. Nats. Akad. Navuk Bel., Ser. Khim. Navuk*, 2003, no. 1, pp. 97–100.
4. Brazhnikov, M.M., Brazhnikova, L.Yu., Grinyuk, E.V., *et al.*, *Vestsi Nats. Akad. Navuk Bel., Ser. Khim.*, 2001, no. 3, pp. 117–119.
5. Derome, A.E., *Modern NMR Techniques for Chemistry Research*, Oxford: Pergamon, 1987.

Russian Journal of Applied Chemistry, Vol. 77, No. 5, 2004, pp. 820–825. Translated from Zhurnal Prikladnoi Khimii, Vol. 77, No. 5, 2004, pp. 825–830.

MACROMOLECULAR CHEMISTRY AND POLYMERIC MATERIALS

Dilatometric Characteristics of Polyacrylonitrile in a Mixture with Fullerene C_{60}

A. V. Sidorovich, O. E. Praslova, A. V. Novoselova, and V. N. Zgonnik

Institute of Macromolecular Compounds, Russian Academy of Sciences, St. Petersburg, Russia

Received January 9, 2004

Abstract—Thermal cyclization of polyacrylonitrile, synthesized by anionic and radical polymerization, in films containing 0.5 wt % fullerene C_{60} and without it was studied dilatometrically in the range 20–400°C.

Fullerenes are a family of polyhedral molecules with a closed large-diameter spherical structure built from three-coordinate carbon atoms with an extended π-electron system capable of diverse interactions with molecules of inorganic and organic substances [1–3]. This made fullerenes a subject of active studies aimed to elucidate their promise for modification of the properties of polymers.

Fullerene C_{60} acts as inhibitor in thermal and thermooxidative degradation of polymethyl methacrylate [4–6]. Calorimetric studies revealed enhanced thermal stability of complex and covalent compounds of polymers of *N*-vinylpyrrolidone and ethylene glycol with C_{60} [7, 8]. Much attention has been given to studying the properties of polymers containing fullerene C_{60} in solutions [9, 10].

There are virtually no published data concerning the influence of C_{60} on dilatometric characteristics of polymers under physicochemical transformations, despite scientific and practical importance of this issue.

In this work we studied dilatometrically the thermal cyclization of polyacrylonitrile (PAN) films, with and without fullerene C_{60}, as influenced by the method of synthesis (anionic and radical polymerization) and by the chemical and supramolecular structure of PAN. This is urgent in view of the fact that heat treatment of PAN is essential for preparation of high-modulus heat-resistant fibers, as well as of semiconductor and carbon materials [11].

EXPERIMENTAL

We studied films prepared from PAN with $M_\eta = 8 \times 10^5$ Da, synthesized by anionic (A-PAN) and radical (R-PAN) polymerization. Anionic polymerization was carried out in DMF at –60°C using lithium alkoxide [12], and radical polymerization, by conventional procedure in water at 25°C in the presence of potassium peroxosulfate and $NaHSO_3$. Films of A-PAN exhibited a narrow MWD (M_w/M_η = 1.3), microtacticity with a block structure coefficient $K \sim 1.57$ [13], and virtually perfect chemical structure of the chain due to the lack of side reactions in the case of anionic polymerization [14]. Films of R-PAN exhibited a wide MWD ($M_w/M_\eta \approx 10$) and no microtacticity ($K \sim 1.02$) [13].

To elucidate the influence of C_{60} on the properties of PAN, we took a small amount of C_{60}, since it is known [15] that the properties of polymers are most strongly affected by the monomeric form of C_{60}, which is the most abundant at low concentrations.

The films were cast from solutions of polymers (5 wt %) and their mixtures with fullerene (0.5 wt % with respect to PAN) in DMF containing the desired amount of *N*-methylpyrrolidone (MP) as solvent for C_{60}. The solutions were heated for 1 h at 100°C. After filtration and cooling to room temperature, these solutions, without preliminary keeping, were used for casting R-PAN and A-PAN films onto glasses.

The R-PAN·C_{60} and A-PAN·C_{60} films were cast after keeping the solutions at room temperature for 3 days. Prolonged maturing of the solution favored structuring and improved the mechanical properties. The films cast without preliminary keeping were brittle, virtually unsuitable for cutting out samples for measurements. The films were dried at room temperature for 5 days.

Dilatometric measurements were carried out on an installation capable of recording the changes in the longitudinal linear dimensions of films accurately to

1070-4272/04/7705-0820 © 2004 MAIK "Nauka/Interperiodica"

within 0.01 μm, when the samples are heated at a rate of 10 deg min^{-1} at 20–400°C [16]. The samples were film stripes 30 mm long, 4 mm wide, and 20–35 μm thick, aligned under a small load of 1 kg cm^{-2}.

Calorimetric measurements within 20–400°C were carried out with a DSM-2M microcalorimeter at a scanning rate of 16 deg min^{-1} and the threshold sensitivity of 0.04 mW [17].

The dilatometric curves of the films (Fig. 1) of R-PAN (curve *1*) and A-PAN (curve *2*) exhibit nonmonotonic, complex patterns, which suggests structural transformations during heat treatment. Three sections are distinct in these curves, namely, those corresponding to temperatures below 120, within 120–260, and above 260°C, respectively, for which the size variation patterns strongly differ. Below 260° the dilatometric curves for R-PAN and A-PAN are similar. Below 120°C these samples exhibit contraction (shrinkage), followed by elongation up to 260°C, almost linear for A-PAN and more complex for R-PAN. The R-PAN and A-PAN films differ only in the shrinkage ratio and in the shrinkage onset temperature. In the case of the R-PAN film, contraction began above 60°C; below 60°C, the film elongated. At the same time, the A-PAN film exhibited no initial elongation region, and its contraction began at 50°C. The third sections of the dilatometric curves (heating above 260°) differ significantly: The R-PAN film contracts (this section is restricted by the subsequent failure of the sample), whereas the A-PAN film sharply elongates.

The shapes of the curves in Fig. 1 suggest that there are structural transformations within two temperature regions, namely, in low-temperature (below 120°C) and high-temperature (above 260°C) regions. Low-temperature transformations are virtually complete at 120°C both for R-PAN and A-PAN, as suggested by a shrinkage minimum in the dilatometric curves.

As mentioned above, in the high-temperature region, the R-PAN and A-PAN films substantially differ in the size variation pattern, namely, the A-PAN film elongates (onset of flow) and R-PAN film contracts. In the intermediate region (120–260°C), virtually no physicochemical processes are observed; the polymer structure is fairly stable, since we recorded a linear elongation with rising temperature due to thermal expansion.

Figure 2 shows the dilatometric curves recorded for mixed films, R-PAN·C_{60} (curve *1*) and A-PAN·C_{60} (curve *2*). They differ significantly from the curves

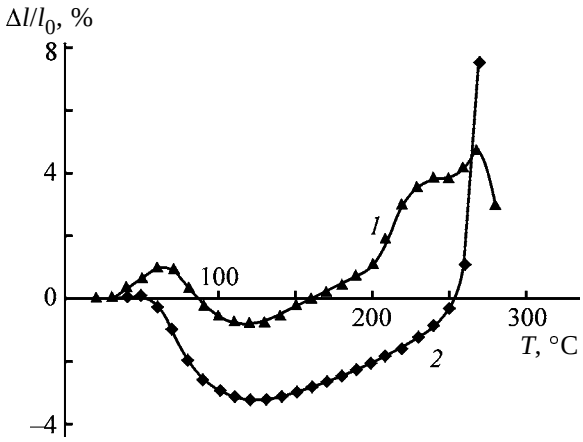

Fig. 1. Dilatometric curves for (*1*) R-PAN and (*2*) A-PAN films. Continuous heating (first run). ($\Delta l/l_0$) Relative change in size, %, and (*T*) temperature, °C; the same for Figs. 2 and 4.

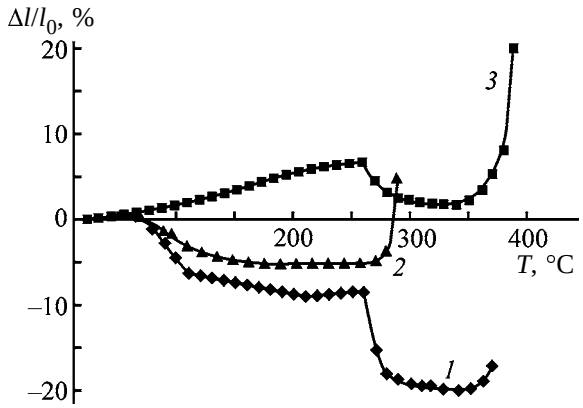

Fig. 2. Dilatometric curves for (*1*) R-PAN·C_{60}, (*2*) A-PAN·C_{60} films (continuous heating, first run), and (*3*) R-PAN·C_{60} [repeated stepwise heating to 160, 260, and 390°C after heating of the initial samples to 160 and 260°C (for explanation, see text)].

recorded for films containing no C_{60} (R-PAN and A-PAN). In the case of the R-PAN·C_{60} film, contraction persists up to 200°C (shrinkage up to 9%), while in the case of the R-PAN film, contraction (no greater than 1%) ceased at 120°C (Fig. 1, curve *1*). Upon heating above 250–260°C, the curves for R-PAN·C_{60} film exhibited a second contraction section, with a total shrinkage of over 20%, and upon rising temperature to 340–250°C, the film, on the contrary, elongated. According to the differential scanning calorimetric (DSC) data, specifically the 260–350°C region corresponds to thermal cyclization (Fig. 3b, curve *1*). Upon introduction of C_{60}, the A-PAN·C_{60} film contracts, similar to R-PAN·C_{60}, though with a smaller total shrinkage of 5%, ceasing at 200°C. This slightly exceeds the shrinkage of the initial A-PAN film, 3% at a maximum, ceasing at 120°C (Fig. 1,

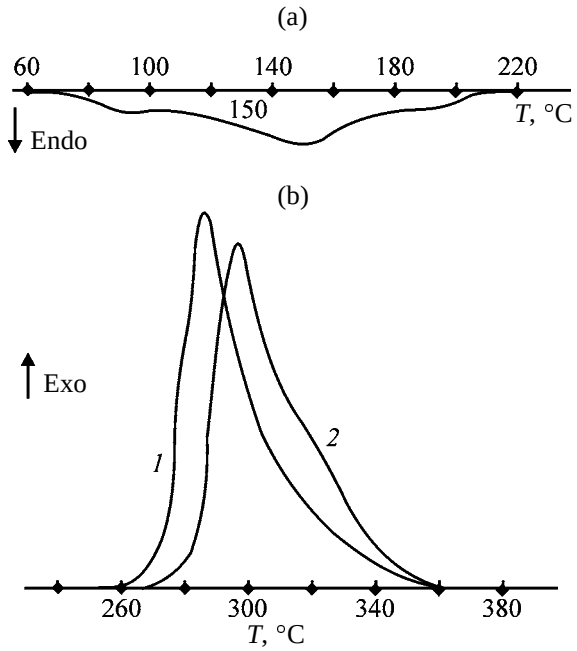

Fig. 3. DSC curves. (*T*) Temperature. Film: (a) R-PAN·C_{60} and (b) (*1*) R-PAN·C_{60} and (*2*) A-PAN·C_{60}.

curve *2*). Further heating from 200 to 270°C corresponds to stabilization, and above 270°C there is an abrupt change to elongation (flow), corresponding to the onset of exothermic effect of thermal cyclization in the DSC curve (Fig. 3b, curve *2*).

The dilatometric curves demonstrate variations of the film size due to thermal expansion and structural transformations yielding new intermolecular bonds, which can be accompanied by a mass loss owing to removal of residual solvents and thermal degradation products.

Therefore, interpretation of the nonmonotonic complex curves describing the primary continuous heating of the initial samples (Figs. 1, 2; curves *1* and *2*) requires understanding of the physicochemical processes occurring during heating.

To this end, we carried out repeated stepwise heating of the films heated to different temperatures in the first run, as illustrated by curve *3* in Fig. 2 for the R-PAN·C_{60} film. Curve *1* was recorded in the first run of continuous heating, and curve *3*, under repeated heating of the two initial samples heated in the first run to 160 and 260°C. Comparison of curves *1* and *3* suggests irreversible changes due to structural transformations, since there is a different monotonic plot of $\Delta l/l_0$ vs. *T*. The above-mentioned data suggest that even primary heating of the initial sample to 160°C is accompanied by structural transformations. When the temperature of primary heating is further risen to 260°C, the monotonic linear dependence observed in the repeated heating run is the same as after heating to 160°C. This suggests that the structural changes that occurred upon heating to 160°C were not followed by further changes on heating to 260°C. However, upon repeated heating above 260°C of the initial sample heated in the first run to 260°C, there appears a section corresponding to sharp contraction followed by elongation. This suggests a second type of structural transformations. Thus, the dilatometric curve *1* provides information about two types of structural transformations, namely, low-temperature transformations up to 260°C and high-temperature transformations above 260°C.

Our calorimetric studies revealed within 80–200°C endothermic low-temperature heat effects with $\Delta H \sim$ 15–20 kJ kg^{-1} and exothermic high-temperature effects with much stronger heat effects $\Delta H \sim$ 650–800 kJ kg^{-1} (Fig. 3). These include an endothermic effect for the R-PAN·C_{60} film (ΔH = 20 kJ kg^{-1}) and exothermic effects for R-PAN·C_{60} (ΔH = 827 kJ kg^{-1}) and A-PAN·C_{60} (ΔH = 623 kJ kg^{-1}).

The calorimetric data concerning the temperature regions of structural transformations correlate with dilatometric data. Opposite signs of the heat effects suggest different types of structural transformations. In the low-temperature region, the endothermic nature of the structural transformations (which is manifested in the dilatometric characteristics as well) is due to a special role played by the cyano groups. On the supramolecular level, they form donor–acceptor bonds with α-hydrogen atom of the polymer and with one another, as well as complexes with the solvent (DMF). This favors numerous interactions of the macromolecules with one another and with the solvent, yielding strong complex bonds, the so-called "physical cross-links" [18]

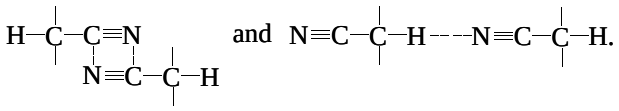

The strength of such interactions reaches 33–35 kJ mol^{-1}, and they can be responsible for insolubility in DMF of the R-PAN and A-PAN films heat-treated to 110°C. The mixed films preserved their solubility in DMF upon heating to higher temperatures: to 150°C in the case of R-PAN·C_{60} and to 160°C in the case of A-PAN·C_{60}. This can be explained by the fact that C_{60} molecules can act in this case as "traps" hindering formation of interchain cross-links [4, 5]. Heating within 80–200°C involves superposition of the heat effects from scission of the

bonds formed by CN groups with one another and with DMF and from the onset of formation of the interchain chromophore moieties. This is evidenced by the fact that the films acquire light brown colors. The heat effects corresponding to the structural changes in the low-temperature regions have opposite signs. While scission of intermolecular bonds with cyano group and removal of the solvent consumes energy, formation of an insoluble colored polycyclic polymer with chromophore groups is accompanied by heat liberation.

Since the energy of nonvalent bonds is 33–35 kJ mol^{-1} and they act as fairly strong cross-links [18], the energy consumption prevails, which is responsible for an endothermic effect. In fact, changes in the supramolecular structure and the initial reaction of cyano groups, yielding moieties comprising chromophore bonds, are the initial steps, preparing the high-temperature cyclization.

Analysis of our results allows the temperature dependence of the dilatometric characteristics to be interpreted as follows. The initial rearrangements of the macrochains, initiating and preparing interactions of the cyano groups, are recorded dilatometrically even upon heating to above 70–80°C. This is evident from the change in the thermal expansion sign, followed by appearance of characteristic sections corresponding to contraction (shrinkage) during the first heating run.

The shrinkage ratios reflect, for the most part, the processes occurring in the first stage of structural transformations which are complete at 200°C in the case of fullerene-containing films and at 120°C in the case of fullerene-free films. Within the same temperature range, the complexes degrade and the solvent is removed. All this exerts the deciding influence on the shrinkage ratio, which reflects the depth of transformation in the first stage. This interpretation is supported by two facts, namely, by irreversible nature of transformation, as directly evidenced by the difference in the dilatometric dependences measured in the repeated heating runs, and by the occurrence of an endothermic effect within 80–200°C, as evidenced by DSC data.

The high-temperature region corresponds to the second stage of transformations, thermal cyclization, which is accompanied by a significant exothermic effect and a sharp change in the film size. This is due to cleavage of the triple bond in the cyano groups of the polymer and formation of ladder structures with conjugated imine sequences [11]:

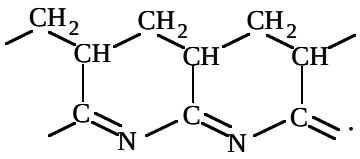

Like C_{60}, such polymer structures are polyunsaturated compounds; they actively react with one another, forming strong intermolecular complex bonds. This is responsible for compaction of the polymer macromolecules, which can result in a sharp contraction, and even in failure, of the PAN films. However, thermal cyclization of PAN, evidently, involves interchain reactions also giving rise to chemical cross-links between rigid ladder structures of cyclic PAN. Possibly, the number of such cross-links and the rate of their formation govern the heat resistance of films in this stage of heat treatment. Our studies showed that the presence of C_{60}, and especially preheating, favor more active formation of chemical "cross-links," which enhances the heat resistance of R-PAN·C_{60} during thermal cyclization (the yield point increases to 390°C). This is the main factor affecting the shape of the dilatometric curve of R-PAN·C_{60} in the high-temperature region.

Our study showed that the dilatometric properties are extremely strongly influenced by the synthesis conditions, since the relationships for the anionic and radical films are completely different. The PAN films prepared by anionic polymerization tend to sharply elongate in the high-temperature region, rather than contract like the films prepared by radical polymerization. Such behavior of A-PAN films can be explained by the structural features of this polymer. Specifically, homogeneity of the molecular weight and chemical structure, as well as the stereoblock character of its macromolecules, can favor their predominant existence in solutions and in films as double helices. In such films, without C_{60}, even at 260°C weaker bonds between the double helices of the macromolecules can be disturbed, making possible the "flow" effect for the PAN film even before thermal cyclization, as we observed in this work.

In the presence of C_{60}, which, most likely, is inserted between the double helices, the bonds linking the helices are strengthened. In the case of the A-PAN·C_{60} film, the onset of flow coincides with the onset of thermal cyclization. In this case, interaction of cyano groups, most preferably, involves one or two A-PAN·C_{60} macromolecules integrated into a double helix. Interaction of the "ladder" moieties of cyclized A-PAN·C_{60} with one another is more efficient than their interaction with C_{60}, and the structures formed

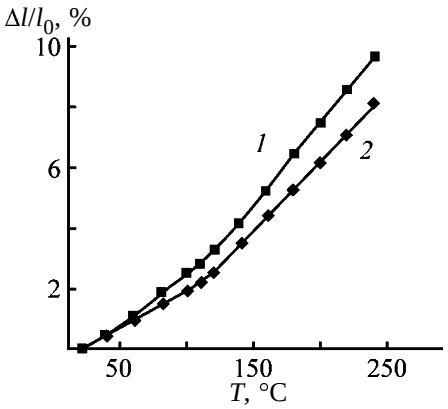

Fig. 4. Dilatometric curves for repeated heating runs with (*1*) A-PAN·C_{60} and (*2*) R-PAN·C_{60} films.

from the double helices flow even in the presence of C_{60}.

Repeated heating of the A-PAN·C_{60} films favors denser contacts between the macromolecules, yielding cross-links between the macromolecules not only inside the double helix. This can be specifically responsible for the fact that the dilatometric curves in this case do not show contraction characteristic of R-PAN·C_{60} (Fig. 2, curve *1*).

Figure 4 presents the data for mixed films, obtained after repeated heating (after primary heating). The dilatometric curves exhibit a prominent inflection at 120°C, which suggests a transition. This can reflect a change in the supramolecular structure due to arising of interchain bonds in the course of formation of chromophore groups. However, elucidation of the real nature of this effect requires special structural studies.

CONCLUSIONS

(1) Thermal cyclization of films of polyacrylonitrile, synthesized by anionic and radical polymerization, with and without fullerene C_{60} (0.5 wt %), were studied by dilatometric method and by differential scanning calorimetry within 20–400°C. Two temperature regions were revealed, which correspond to structural transformations in two stages of transition of PAN from the linear to polycyclic state. Based on analysis of the physicochemical processes in stepwise transformations, the temperature dependence of the dilatometric characteristics was interpreted as due to scission of intermolecular bonds and formation of chromophore groups, followed by transition to the final polycyclic state.

(2) The shape of the dilatometric curves depends on the method of PAN synthesis. The shrinking film samples prepared by radical polymerization contract by up to 20% in the thermal cyclization region, and the film samples prepared by anionic polymerization, on the contrary, elongate, exhibiting flow. This results from the difference in the molecular and supramolecular structures of the polymers.

(3) A procedure was proposed for identifying the temperature regions corresponding to physicochemical transformations, based on comparison of the dilatometric curves recorded after the primary heating and repeated heating runs.

ACKNOWLEDGMENTS

This work was financially supported by the "Topical Lines in Condensed Matter Physics" State Scientific and Technical Program, "Fullerenes and Atomic Clusters" line, and by the Russian Foundation for Basic Research (project no. 03-03-32 633).

REFERENCES

1. Sokolov, V.I., *Dokl. Akad. Nauk SSSR*, 1992, vol. 325, no. 5, pp. 991–993.
2. Sun, Y.P., Bunker, C.E., and Ma, B., *J. Am. Chem. Soc*., 1994, vol. 116, no. 21, pp. 9692–9699.
3. Turanov, I.A. and Kremenskaya, I.N., *Izv. Ross Akad. Nauk, Ser. Khim*., 1995, no. 3, pp. 481–483.
4. Shibaev, L.A., Ginzburg, B.M., Antonova, G.A., *et al*., *Vysokomol. Soedin., Ser. A*, 2002, vol. 44, no. 5, pp. 815–823.
5. Troitskii, B.B., Troitskaya, L.S., Yakhnov, A.S., and Domrachev, G.A., *Dokl. Ross. Akad. Nauk*, 1998, vol. 363, no. 1, pp. 79–81.
6. Troitskii, B.B., Troitskaya, L.S., and Domrachev, G.A., *Dokl. Ross. Akad. Nauk*, 2000, vol. 373, no. 6, pp. 796–798.
7. Sidorovich, A.V., Praslova, O.E., Vinogradova, L.V., *et al*., *Zh. Prikl. Khim*., vol. 75, no. 6, pp. 813–817.
8. Berstein, V.A., Egorov, V.M., and Egorova, L.M., *J. Non-Cryst. Solids*, 1998, vols. 235–237, pp. 476–484.
9. Klenin, S.I., Sushko, M.L., Dumpis, M.A., *et al*., *Zh. Tekh. Fiz*., 2000, vol. 70, no. 3, pp. 27–32.
10. Evlampieva, N.P., Lavrenko, P.N., Zaitseva, I.I., *et al*., *Vysokomol. Soedin., Ser. A*, 2002, vol. 44, no. 9, pp. 1564–1570.
11. *Entisklopediya polimerov*, Kargin, V.A., Ed., Moscow: Sov. Entsiklopediya, 1972.
12. Erussalimsky, B.L. and Novoselova, A.V., *Faser-*

forsch. Textiltechn., 1975, vol. 26, no. 5, pp. 293–297.

13. Khachaturov, A.S., Abramenko, E.A., Novoselova, A.V., *et al*., *Vysokomol. Soedin., Ser. B*, 1988, vol. 36, no. 12, pp. 891–896.
14. Novoselova, A.V., Zgonnik, V.N., Sazanov, Yu.N., *et al*., *Vysokomol. Soedin., Ser. A*, 1992, vol. 34, no. 3, pp. 59–63.
15. Zgonnik, V.N., Vinogradova, L.V., Melenevskaya, E.Yu., *et al*., *Fiz. Tverd. Tela*, 2002, vol. 44, no. 4, pp. 592–593.
16. Sidorovich, A.V. and Kuvshinskii, E.V., *Zavod. Lab*., 1959, vol. 25, no. 9, pp. 778–784.
17. Sidorovich, A.V. and Kotel'nikov, G.V., *Vysokomol. Soedin., Ser. A*, 1983, vol. 25, no. 12, pp. 2623–2625.
18. Beevers, R.B., *Macromol. Rev*., 1968, vol. 3, no. 8, pp. 113–116.

Russian Journal of Applied Chemistry, Vol. 77, No. 5, 2004, pp. 826–829. Translated from Zhurnal Prikladnoi Khimii, Vol. 77, No. 5, 2004, pp. 831–834.

MACROMOLECULAR CHEMISTRY AND POLYMERIC MATERIALS

Molecular Weight and Dynamic Properties of Polystyrene Solutions

B. B. Damdinov, L. U. Bazaron, B. B. Badmaev, D. M. Mognonov, Yu. E. Doroshenko, and T. N. Khamaganova

Department of Problems of Physics, Buryat Scientific Center, Siberian Division, Russian Academy of Sciences, Ulan-Ude, Buryatia, Russia

Baikal Institute for Use of Natural Resources, Buryat Scientific Center, Siberian Division, Russian Academy of Sciences, Ulan-Ude, Buryatia, Russia

Mendeleev Russian University of Chemical Engineering, Moscow, Russia

Received April 4, 2003; in final form, December 2003

Abstract—Eight fractions of polystyrene with linear structure and different molecular weights were prepared by fractional precipitation with methanol from a solution of polystyrene in chloroform. The polystyrene fractions were dissolved in toluene to prepare solutions with different concentrations for dynamic property studies. The dynamic shear modulus and the tangent of the mechanical loss angle for these solutions were measured by the acoustic-resonance method.

The molecular weight of polymers can be determined by numerous methods [1]. They imply studies of both polymers proper and their solutions (flow temperature, relaxation properties, viscosity, etc.). Molecular weight is a major characteristic of macromolecular compounds, since the chemical and physical characteristics of polymers are directly related to the size of their molecules [2].

Dynamic deformations of highly elastic materials typically entail only reversible deformations due to displacements of individual fragments of macromolecules, which make them independent of the molecular weight of the macromolecules as a whole. However, at temperatures below the flow point, irreversible displacements of macromolecules become also prominent. In this case, the dynamic deformation parameters become sensitive to the molecular weight of the polymer and thus can be used for determining the molecular weight.

The aim of this work was to study the dynamic viscoelastic properties of polymer solutions as influenced by the molecular weight and concentration.

For fractional precipitation and estimation of the molecular weight we chose polystyrene (PS) whose samples serve as international standards in checking the accuracy of determining the molecular weights of polymers. Polystyrene is a linear polymer, and its molecular characteristics are most often estimated by studying the properties of its solutions.

EXPERIMENTAL

Fractional precipitation of linear PS yielded eight fractions with a 3.95% weight loss. Based on the intrinsic viscosities of the PS fractions and initial PS, we calculated the molecular weights by the equation $[\eta] = KM^{\alpha}$. For the PS prepared by fractional precipitation we took the empirical coefficients $K = 0.007 \times 10^{-3}$ and $\alpha = 0.93$ [3]; $T = 20°C$; toluene served as solvent because of its relatively low volatility making it especially suitable for determining the dynamic properties of solutions. Table 1 presents the results of fractional precipitation, the intrinsic viscosities of the

Table 1. Results of fractional precipitation. Initial weight 7.5343 g, $[\eta] = 0.80$, $\overline{M}_0 = 3\,240\,000$, 3.95% loss

Fraction no.	m*	$[\eta]$, dl g^{-1}	$\overline{M} \times 10^{-3}$
1	1.5921	1.20	5050
2	1.2447	0.90	3690
3	1.4734	0.82	3350
4	0.2699	0.71	2870
5	1.2570	0.62	2480
6	0.6151	0.48	1860
7	0.5587	0.40	1540
8	0.2258	0.14	480
	$\Sigma_{pi} = 7.2367$	–	3240

*m is the weight of the fraction.

1070-4272/04/7705-0826 © 2004 MAIK "Nauka/Interperiodica"

fractions and the initial polymer, and the molecular weights.

Figures 1a and 1b present the integral and differential curves of the molecular weight distribution (MWD), respectively [4]. The solvents were purified by the known techniques. Polystyrene was subjected to fractional precipitation with methanol from a 2.5% chloroform solution. The resulting PS fractions were dried to constant weight in a vacuum oven at 60°C under residual pressure of 2–5 mm Hg. The intrinsic viscosities of the fractions and the initial PS in a toluene solution were measured on an Ubbelohde capillary viscometer with a suspended level at 20 ± 0.05°C.

In our experiments we used a piezoelectric-crystal resonator filled with the liquid under study, whose working surfaces were preliminarily cleaned in a glow discharge. The dynamic shear modulus G and tangent of the mechanical loss angle $\tan\theta$ were estimated by measuring the acoustic parameters of the resonator; also, the effective viscosity η_{eff} of the PS solutions in toluene was calculated. The acoustic-resonance experiments [5, 6] were carried out at the shear impact frequency of 74 kHz at 19 ± 0.1°C. The resonance method of determining the shear characteristics of liquids consists in the following. The horizontal surface of a piezoelectric crystal (an X-18.5° cut) with a Poisson coefficient of zero, oscillating at the fundamental resonance frequency, contacts the liquid interlayer covered with a solid application. The application with a liquid interlayer occurs at one end of the piezoelectric crystal; the liquid interlayer is subjected to shear strain, and the parameters of the resonance curve of the piezoelectric crystal vary with the liquid interlayer thickness.

Theoretically, when the liquid interlayer thickness is assumed to be much smaller than the shear wavelength and the application is assumed to be virtually at rest, the tangent of the mechanical loss angle and the dynamic shear modulus (estimated by the acoustic-resonance method) can be described by the expressions [5]:

$$G = \frac{4\pi^2 M_p f_0 \Delta f' H}{S}, \qquad (1)$$

$$\tan\theta = \frac{\Delta f''}{\Delta f'},$$

where $\Delta f'$ and $\Delta f''$ are the real and imaginary shifts of the resonance frequency of the piezoelectric crystal, respectively; M_p, piezoelectric crystal mass; S, contact area; H, liquid interlayer thickness; and f_0, resonance frequency of the piezoelectric crystal.

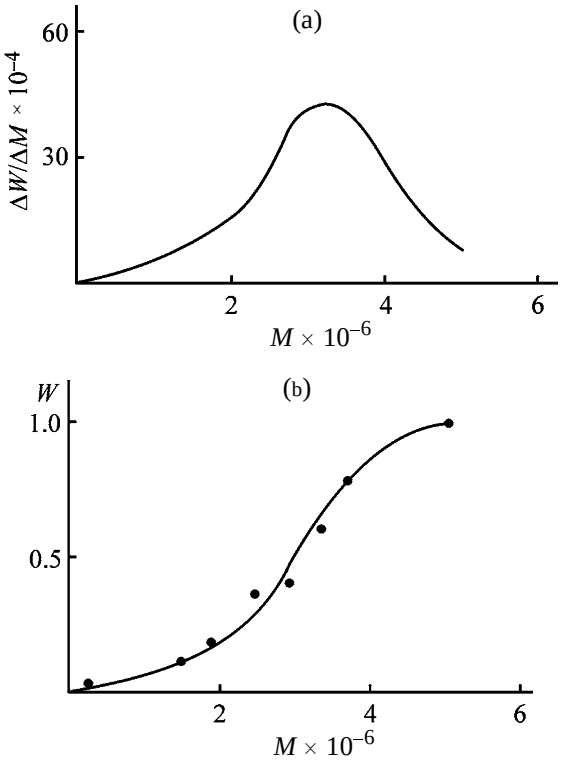

Fig. 1. (a) Differential and (b) integral MWD curves of PS solutions.

The imaginary shift is equal to the change in the resonance curve half-width. Equation (1) shows that, when the liquid under study exhibits shear elasticity, the real frequency shift should be proportional to inverse interlayer thickness.

The resonance experiment was carried out with a piezoelectric crystal with a mass of 6.24 g; the contact surface area was 0.2 cm^2. An important advantage of the resonance method is no limit on the viscosity of the liquids under study (from several hundredth to 10^5 P). A drawback of the method is that it can be realized at a strictly fixed invariable frequency. A positive shift of the resonance frequency of the oscillating system is indicative of a shear elasticity.

Having determined the dynamic shear modulus and tangent of the mechanical loss angle, we can estimate the effective viscosity by the formula

$$\eta_{eff} = \frac{G(1 + \tan^2\theta)}{2\pi f_0 \tan\theta}. \qquad (2)$$

Assuming that the effective viscosity correlates with

Table 2. Viscoelastic properties of 10% solution of PS in toluene

Fraction no.	$\bar{M} \times 10^{-3}$	$G \times 10^5$, Pa	$\tan\theta$	η_{eff}, Pa s	$[\eta]$, dl g^{-1}
1	5050	1.990	0.205	0.221	1.20
2	3690	1.672	0.199	0.190	0.90
3	3350	1.375	0.197	0.185	0.82
4	2870	1.038	0.228	0.085	0.71
5	2480	0.891	0.261	0.064	0.62
6	1860	0.784	0.284	–	0.48
7	1540	0.700	0.354	0.050	0.40
8	480	0.521	0.575	0.026	0.32
9*	330	0.630	0.566	0.032	0.23
10*	68	0.382	0.580	0.019	0.14

* Taken from [7].

the intrinsic viscosity, we can determine the relation between the parameters G and M:

$$\rho M^{\alpha} \sim \frac{G(1 + \tan^2\theta)}{2\pi\eta_w f_0 \tan\theta}, \qquad (3)$$

where ρ is the density of the polymer solution; η_w, viscosity of water; and M, molecular weight of the polymer.

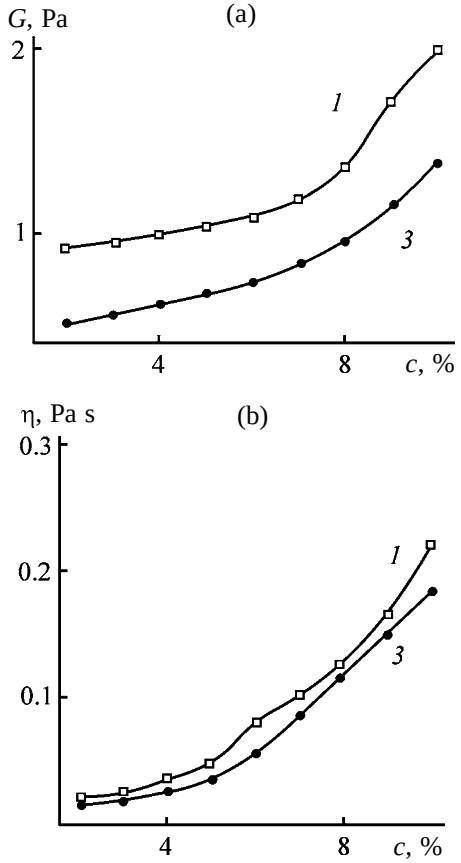

Fig. 2. (a) Shear modulus G and (b) effective viscosity η, as functions of the content c of PS in toluene for fraction nos. 1 and 3, respectively.

Equation (3) suggests that the shear modulus varies with the molecular weight.

Table 2 presents the viscoelastic properties of 10% solutions of PS in toluene for different fractions. It is seen that, with decreasing molecular weight of the polymer, the dynamic shear modulus and effective viscosity tend to decrease. Tangent of the mechanical loss angle tends to increase with decreasing molecular weight. Also, the effective and intrinsic viscosities vary similarly.

Knowing how the viscoelastic properties vary with the molecular weight, we can estimate the molecular weights of various polymers after measurement of the parameters G. The influence of polydispersity on the shear modulus requires special investigation.

Bazaron [5] found earlier that, for high-molecular-weight polymethylsiloxanes, the dynamic shear modulus G linearly varies with the molecular weight. Probably, this will hold for a polymer with a more uniform molecular weight. To elucidate how the dynamic characteristics vary with the concentration of the solution, we studied the properties of various PS fractions. Figures 2a and 2b show the experimental data for fraction nos. 1 and 3 (Table 1). It is seen that, with decreasing PS concentration, the shear modulus and the effective viscosity tend to decrease. The pattern of variation of the dynamic characteristics for PS solutions in toluene is qualitatively similar to that revealed by Moore *et al*. [8] for PS solutions of various concentrations in dibutyl phthalate (at 40 MHz). The dynamic shear moduli of solutions of PS in toluene, estimated by the acoustic-resonance method, are consistent with those measured by the impedance method by Matheson [7]. Moore *et al*. [8] analyzed

the experimental results from the viewpoint of the molecular structure of the polymer solutions. In this article, we restricted ourselves to estimation of the molecular weight of PS by the acoustic method.

CONCLUSIONS

(1) Dynamic viscoelastic properties of solutions of polystyrene in toluene were measured by the acoustic method at 74 kHz. The dynamic shear modulus G and effective viscosity η_{eff} of the solutions decrease with decreasing molecular weight.

(2) The plots of G and η_{eff} vs. molecular weight are nearly linear. The molecular weight of an unknown polymer can be estimated from the dynamic shear modulus of its solution, measured by the acoustic method.

REFERENCES

1. *Entsiklopediya polimerov* (Encyclopedia of Polymers), Moscow: Khimiya, 1985, vol. 2.
2. *Sovremennye fizicheskie metody issledovaniya polimerov* (Modern Physical Methods of Investigation of Polymers), Slonimskii, G.S., Ed., Moscow: Khimiya, 1982.
3. Rafikov, S.R., Pavlova, S.A., and Tverdokhlebova, I.I., *Metody opredeleniya molekulyarnykh vesov i polidispersnosti vysokomolekulyarnykh soedinenii* (Methods of Determination of Molecular Weights and Polydispersities of Polymers), Moscow: Akad. Nauk SSSR, 1963.
4. Shatenshtein, A.I., Vyrskii, Yu.P., Pravikova, N.A., *et al.*, *Prakticheskoe rukovodstvo po opredeleniyu molekulyarnykh vesov i molekulyarno-massovogo raspredeleniya polimerov* (Practical Guide on Determination of Molecular Weights and Molecular-Weight Distribution of Polymers), Moscow: Khimiya, 1964, pp. 22–25.
5. Bazaron, U.B., *Nizkochastotnaya sdvigovaya uprugost' zhidkostei* (Low-Frequency Shear Elasticity of Liquids), Ulan-Ude: Buryat. Nauch. Tsentr Sib. Otd. Ross. Akad. Nauk, 2000.
6. Badmaev, B.B. and Damdinov, B.B., *Akust. Zh.*, 2001, vol. 47, no. 4, pp. 561–563.
7. Matheson, A.J., *Molecular Acoustics*, London, 1970.
8. Moore, R.S., McSkimin, H.J., Ginewsky, C., and Andreatch, P., *J. Chem. Phys.*, 1969, vol. 50, pp. 466–472.

Russian Journal of Applied Chemistry, Vol. 77, No. 5, 2004, pp. 830–834. Translated from Zhurnal Prikladnoi Khimii, Vol. 77, No. 5, 2004, pp. 835–839.

MACROMOLECULAR CHEMISTRY AND POLYMERIC MATERIALS

Flocculation of Butadiene–Styrene Latex with Polymeric Ammonium Salts of *N*,*N*-Dimethylaminoethyl Methacrylate and Mineral Acids

V. N. Verezhnikov, T. V. Min'kova, and T. N. Poyarkova

Voronezh State University, Voronezh, Russia

Received January 14, 2004

Abstract—The flocculation performance of cationic polyelectrolytes (polymeric ammonium salts of *N*,*N*-dimethylaminoethyl methacrylate) and mineral acids (HCl, HNO_3, H_2SO_4, H_3PO_4) in recovery of rubber from SKS-30 ARK butadiene–styrene latex was studied.

Flocculation of latexes using cationic polyelectrolytes is a promising salt-free procedure to recover rubbers after emulsion copolymerization [1]. These flocculants eliminate discharge with wastewater of sodium chloride consumed in significant amounts in coagulation of latexes by the existing procedures (up to 1000 kg per ton of rubber). Therefore, study of latex flocculation with polymers and search for new effective polymeric flocculants are of particular importance; and among them, polymers based on aminoalkyl methacrylates show much promise [2–4] due to their high reactivity in (co)polymerization, simple preparation of monomers and polymers, and their high solubility in water.

As the monomers are bases, it seems the most feasible to prepare flocculants in the form of polymeric ammonium salts of aminoalkyl methacrylates and mineral acids. Synthesis and polymerization of ammonium salts of *N*,*N*-dimethylaminoethyl methacrylate (DM) and mineral acids (HCl, HNO_3, H_2SO_4, H_3PO_4) were studied in [5], and the electrical conductivity of solutions and acid–base properties of poly-DM ammonium salts (PDMASs) were analyzed in [6, 7]. It was found that PDMASs in aqueous solutions are polyelectrolytes with basic properties and, depending on the salt structure, the pH of their half-neutralization, $pH_{0.5}$, is within 6.2–7.2 range [7].

The flocculation power of these polyelectrolytes in recovery of rubber from latexes is of particular importance. In this work we studied the flocculation performance of PDMAS and above mineral acids in their interaction with industrial latex of butadiene–styrene rubber as influenced by the salt structure, concentration of the latex dispersed phase, and solution pH.

We used *N*,*N*-dimethylaminoethyl methacrylate purchased from Metakor company (Yaroslavl, Russia). According to the potentiometric titration data, the content of amino ester in the initial sample was 99.8%. Chemically pure grade mineral acids (HCl, HNO_3, H_2SO_4, H_3PO_4) were used in the experiments.

The poly-DM ammonium salts were prepared by two procedures.

(A) The initial monomeric salts were synthesized in isopropanol according to [5]. The corresponding hydrochlorides were obtained by passing gaseous hydrogen chloride and polymerized in aqueous solution (50% weight fraction) without initiating agent at the following temperatures, °C: 100 $DM \cdot HCl$, 95 $DM_2 \cdot H_2SO_4$, and 80 $DM \cdot H_3PO_4$. Polymerization was performed for 3–4 h until a viscous difficult-to-stir mass was obtained.

(B) The monomeric salts were prepared and polymerized in aqueous solution without isolation of salts from the reaction mixture. Equivalent amounts of DM were added to the aqueous acid solutions at two temperature modes: 0–5 (procedure B_5) and 20–25°C (procedure B_{25}). After neutralization, the concentration of the resulting salt was determined by potentiometric titration, which was performed in aqueous alcohol with a 0.5 M alcoholic solution of potassium hydroxide. For polymerization, the solutions were heated to the same temperatures (as in method A) for 3–4 h.

The intrinsic viscosity (see table) of the resulting polymeric salts $PDMAS \cdot HCl$ (**I**), $PDMAS \cdot HNO_3$ (**II**), $PDMAS \cdot H_2SO_4$ (**III**), and $PDMAS \cdot H_3PO_4$ (**IV**)

1070-4272/04/7705-0830 © 2004 MAIK "Nauka/Interperiodica"

was measured on a VPZh-1 viscometer (capillary diameter 0.86 mm, formamide, 30°C).

For flocculation studies, we chose SKS-30 ARK commercial butadiene–styrene latex prepared using emulsifiers based on salts of disproportionated rosin and fatty and resin acids of tall oil. The latex properties were as follows: dry substance weight fraction 239 g l^{-1}, pH 9.7, surface tension 58.0 mJ m^{-2}, and average particle radius 25.9 nm (light scattering data [8]).

The PDMAS flocculation performance was determined by the fraction of the precipitated rubber φ (wt %) relative to the initial polymer weight in the latex. In these tests, the required amounts of distilled water, acidifying agent (0.1 N H_2SO_4), and flocculant (1.5–3.0 g dl^{-1} aqueous solutions) were added to the latex (5 ml) with stirring up to the total volume of the reaction mixture of 10 ml. The recovered rubber was filtered off, washed, and dried to the constant weight at 80–90°C.

The turbidity of the diluted latex solutions was measured using an NFM visual turbidimeter and solution pH, with an EV-74 pH-meter.

The dependences (flocculation curves) of the degree of rubber recovery φ on the concentration of polyelectrolytes **I**–**IV** are shown in Fig. 1. As seen, in all the cases the polymer yield sharply increases with increasing flocculant concentration c_{PE}, reaching the highest constant value (≥95%). The quantity c_{PE} corresponding to the beginning of the plateau in the flocculation curves [optimal flocculation concentration (OFC)] is almost independent of the anions in polymeric salts **I**–**III**, preparation procedure, and intrinsic viscosity. The OFC values for these salts correspond to the relative flocculant consumption Q of ~10 kg per ton of rubber. In the case of phosphoric acid DM derivative, the consumption is greater and reaches 18–25 kg per ton of rubber.

The flocculation tests reflected in Fig. 1 were performed at constant concentration of the dispersed phase (120 g l^{-1}). However, it was shown [9, 10] that the shape of the flocculation curves can change with changing rubber concentration in the latex c_d. The same phenomenon was observed with PDMAS flocculants. The curves of the latex flocculation in the presence of PDMAS · HNO_3 are shown in Fig. 2. As seen, the shape of the φ–c_{PE} curves significantly changes with decreasing c_d; the dependence with a plateau, obtained for relatively concentrated latex solution (120 g l^{-1}), transforms into the dependences with a maximum, which becomes more pronounced with decreasing polymer concentration in the latex. Similar phenomenon was observed with polystyrene [9], butadiene–styrene, and butadiene–acrylonitrile latexes [10] at their flocculation in the presence of poly-*N*,*N*-dimethyl-*N*,*N*-diallylammonium chloride.

Intrinsic viscosity of PDMAS compositions

PE	Preparation procedure	[η], dl g^{-1}
I	A	2.4
	B_5	1.0
II	B_5	1.5
	B_{25}	4.0
III	A	3.3
	B_5	5.2
	B_{25}	4.7
IV	A	1.8

The maximum appearing in the flocculation curves at small concentration of the dispersed phase is due to

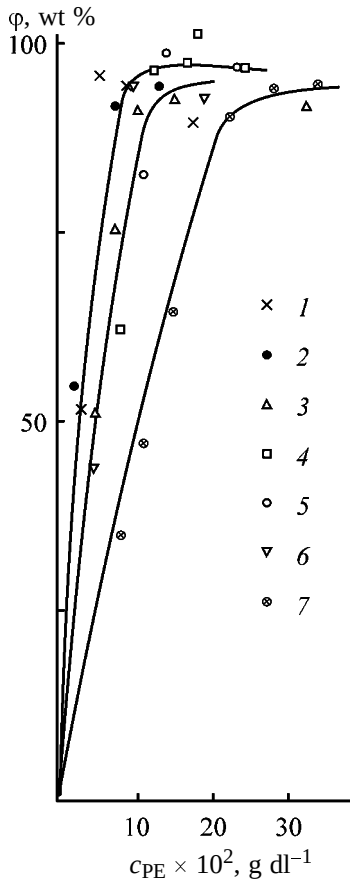

Fig. 1. Degree of rubber recovery φ as a function of PDMAS concentration c_{PE}; dispersed phase concentration in the latex 120 g l^{-1}. Polyelectrolyte: (*1*) **I** (B_5), (*2*) **I** (A), (*3*) **II** (B_5), (*4*) **II** (B_{25}), (*5*) **III** (A), (*6*) **III** (B_5), and (*7*) **IV** (A).

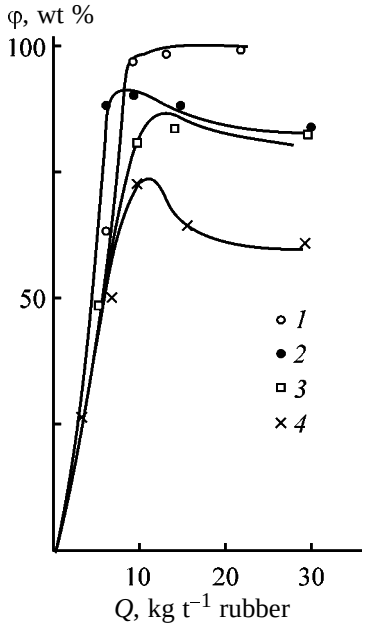

Fig. 2. Degree of rubber recovery φ as a function of $PDMAS \cdot HNO_3$ consumption Q; H_2SO_4 consumption 15 kg per ton of rubber. Dispersed phase concentration in the latex, g l^{-1}: (*1*) 120, (*2*) 50, (*3*) 25, and (*4*) 10.

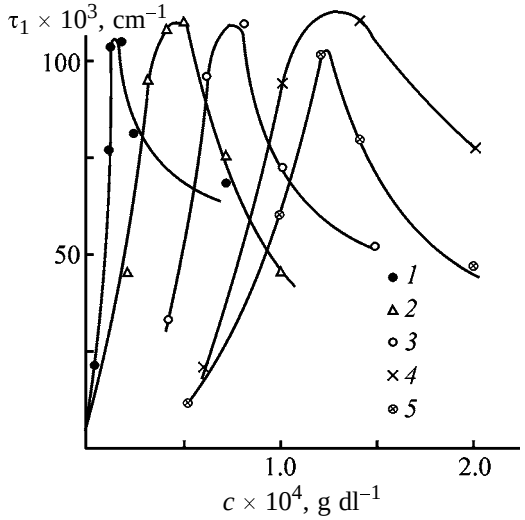

Fig. 3. Initial flocculation rate τ_1 as a function of $PDMAS \cdot H_2SO_4$ concentration c. pH: (*1*) 3.5, (*2*) 5.3, (*3*) 6.8, (*4*) 8.8, and (*5*) 9.2. Latex dilution 1 : 5000.

the features of the flocculation effect of cationic polymeric reagents on negatively charged sols [11, 12]. The interaction involves neutralization of the particle surface charge in the course of interaction of the emulsifier anions (in the case of negatively charged latex particles) with the cationic centers of polyelectrolyte macromolecules to form insoluble ionic complexes. Along with neutralization, the bridging mechanism with simultaneous sorption of macromolecules on several particles also contributes to the flocculation. The flocculation optimum is often attained at complete neutralization of the particle surface charge. Further sorption of the charged polyelectrolyte macromolecules on the particle surface causes recharging and "restabilization" of the system. The recharging effect was confirmed by measurements of the electrophoretic mobility of the latex particles as influenced by c_{PE} [9, 10, 13]. The stabilizing effect of excess flocculant is also due to the formation of a fairly thick layer of the hydrophilic polymer on the particle surface [11, 12].

Disappearance of the restabilization section of the flocculation curves at high concentration of the dispersed latex phase can be due to the relaxation of macromolecules in sorption interaction with the particle surface [14, 15]. The probability of formation of the bridging bonds between the neighboring particles decreases with increasing time of sorption contacts between macromolecules and particle surface. At sufficiently high concentration of the dispersed phase, the "free-path" time of the particles between collisions becomes smaller than the relaxation time of sorbed macrochains and they preserve the capability for bridge formation [14, 16]. In this case, despite recharging, polyelectrolytes exhibit high flocculation activity at their concentrations higher than OFC.

It was shown in [7] that PDMASs exhibit base properties, i.e., the ionization equilibrium is shifted toward charged polymer structures capable to bind emulsifier anions. This equilibrium can be shifted with changing concentration of hydrogen ions, and thus the solution pH can affect the flocculation power of PDMAS. To analyze this effect, we studied the dependence of the initial flocculation rate on the flocculant concentration at various solution pH. The "minute turbidity" τ_1, i.e., the increase in a turbidity of the diluted latex solution (1 : 5000) in 1 min after addition of the flocculant into the latex solution, was used as a measure of the initial flocculation rate [8]. The pH of the flocculating solutions was adjusted by adding 0.1 N solutions of H_2SO_4 and KOH. The dependences of the initial flocculation rates of the latexes on the $PDMAS \cdot H_2SO_4$ concentration at various pH are shown in Fig. 3. In all the cases, the τ_1–c_{PE} curves pass through a maximum at c_m, which shits toward higher concentrations with decreasing solution acidity. Thus, the increase in the solution pH decreases the flocculation performance of the DM polyelectrolytes, which is probably due to the decreasing fraction of charged units (amino ester fragments) in the polymeric chains.

The contribution of the neutralization factor to the latex destabilization decreases with decreasing charge density on the macromolecules.

To verify the above assumptions, we studied the effect of pH on the interaction of PDMAS with anionic latex stabilizer Leukanol (L, a mixture of oligomeric sodium salts of the products of condensation of β-naphthalenesulfonic acid and formaldehyde) by the nephelometric method. Butadiene–styrene latexes often contain Leukanol (about 0.4 wt % relative to the polymer) along with alkaline salts of fatty and resin acids [1]. At coagulation in the presence of mineral acids, the carboxyl-containing emulsifiers lose the stabilizing power because of the hydrolysis, whereas Leukanol remains active even in acidic solutions.

As in the case of the other cationic polyelectrolytes [17], addition of PDMAS into the Leukanol solution makes it turbid owing to the formation of an insoluble nondissociating oligomer–polymer ionic complex. The effect of the solution pH on formation of this complex was studied as follows. The Leukanol solution was added to aqueous solutions of $PDMAS \cdot H_2SO_4$ containing various amounts of H_2SO_4 or KOH, so that the concentrations of Leukanol and polyelectrolyte in the mixture were constant and equal to 8×10^{-4} and 4×10^{-4} M, respectively. The components were quickly mixed, and the minute turbidity of the resulting dispersion was measured. The τ_1–pH dependence is shown in Fig. 4. We also performed potentiometric titration of the polyelectrolyte solution with an alkali solution (Fig. 5). As seen from the τ_1–pH dependence, the amount of the resulting insoluble complex decreases with increasing pH; there are two sections in which the complex formation sharply depends on pH. In the acidic section (pH < 3), the increase in the complex formation with decreasing pH can be due to the suppression of hydrolysis of the polymeric salt of the weak organic base, which increases the number of cationic groups in the polymeric chains and promotes linking with Leukanol. In passing to the alkaline section (pH >~ 6.5), deprotonation of the nitrogen atoms in the amino groups probably begins, and it increases with increasing pH. In the process, the fraction of the neutral units in the polymeric chains increases, decreasing the complexation efficiency up to its complete termination at pH 8.5. As seen from the potentiometric titration curve (Fig. 5), this pH value corresponds to the half-neutralization point of the polymer.

The middle section (plateau) in the τ_1–pH curve, within which the intensity of complexation is constant, corresponds to the pH region from 3 to ~6.5, in which the charge density of macromolecules remains approximately constant.

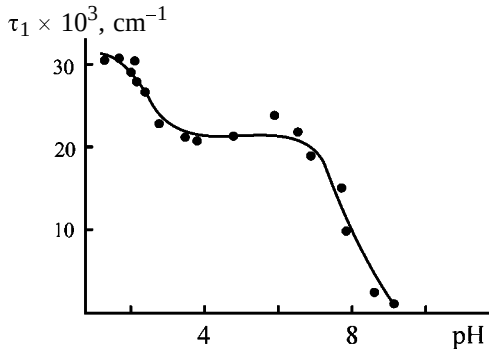

Fig. 4. Minute turbidity τ_1 of the $PDMAS \cdot H_2SO_4$ + L system as a function of pH. Concentrations of Leukanol and polyelectrolyte 8×10^{-4} and 4×10^{-4} M, respectively.

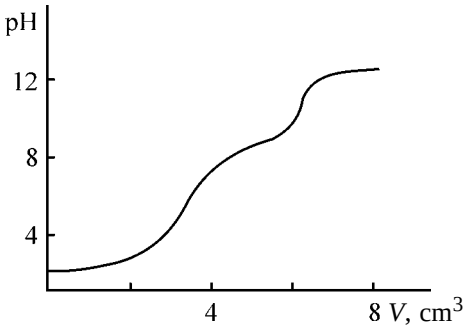

Fig. 5. Potentiometric titration curve of $PDMAS \cdot H_2SO_4$. (V) Volume of 0.5 M KOH solution.

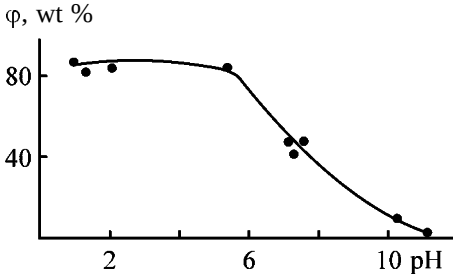

Fig. 6. Rubber fraction φ recovered with $PDMAS \cdot H_2SO_4$ flocculant as a function of pH. Concentration of the dispersed phase 50 g l^{-1}, specific consumption of flocculant 15 kg per ton of rubber.

It was of particular interest to compare the nephelometric data characterizing interaction between the anionic stabilizer and cationic flocculant with the data on the effect of pH on the rubber recovery in the course of the latex flocculation (Fig. 6). The flocculation was carried out at various contents of acid or alkali. After the rubber recovery, the serum pH was determined. As seen from the φ–pH curve, in the acidic section (pH < 6), the degree of rubber recovery is independent of pH, and it decreases in alkaline

solutions virtually to zero at pH ~ 12. Constancy of φ in the initial section (pH < 6) is probably due to the fact that, despite possible changes in the density of the positive charge of macromolecules, Leukanol is completely linked by excess polyelectrolyte under the experimental conditions ([PE] : [L] = 3 : 1). At pH > 6, deprotonation of the polyelectrolyte units increases with simultaneous conversion of the carboxy-containing emulsifiers to the salt form. As a result, the deficiency of the cationic groups required for binding of the stabilizer anions (soap and Leukanol) grows, making the coagulum yield lower.

It should be noted that the flocculation power disappears at higher solution bacisity (pH 12) than that at which the Leukanol binding is terminated (pH ~ 8.5). This fact indicates that the latex flocculation cannot be explained solely by chemical interaction between the flocculant and anionic stabilizer and neutralization of the particle surface charge. In strongly alkaline solutions, the rubber recovery (though not very efficient) is possible by the bridging mechanism of flocculation.

CONCLUSIONS

(1) In rubber recovery from SKS-30 ARK latex with polymeric ammonium salts of *N,N*-dimethylaminoethyl methacrylate and mineral acids, the optimal flocculant concentration is independent of particular mineral acid, procedure of the salt preparation, and intrinsic viscosity of the polyelectrolyte; it corresponds to the specific consumption of the chloride, nitrate, and sulfate of 10 (up to 25 for phosphate) kg per ton of rubber.

(2) The data on the initial flocculation rate and interaction of polymeric ammonium salts of *N,N*-dimethylaminoethyl methacrylate with the latex stabilizer (Leukanol) as influenced by pH of the medium showed that the flocculant performance decreases with decreasing solution acidity. This fact may be due to the decreasing positive charge of macromolecule and contribution of the neutralization factor to the latex destabilization.

REFERENCES

1. Kirpichnikov, P.A., Averko-Antonovich, L.A., and Averko-Antonovich, Yu.O., *Khimiya i tekhnologiya sinteticheskogo kauchuka* (Chemistry and Technology of Synthetic Rubber), Leningrad: Khimiya, 1987.
2. Kabanov, V.A. and Topchiev, D.A., *Polimerizatsiya ioniziruyushchikhsya monomerov* (Polymerization of Ionizable Polymers), Moscow: Nauka, 1975.
3. Askarov, M.A., Mukhitdinova, N.A., and Nazarov, A., *Polimerizatsiya aminoalkilmetakrilatov* (Polymerization of Aminoalkyl Methacrylates), Tashkent: Fan, 1977.
4. *Ionogennye polimery* (Ionic Polymers), Askarov, M.A., Ed., Tashkent: Fan, 1986.
5. Efimova, D.Yu., Shibalovich, V.G., and Nikolaev, A.F., *Zh. Org. Khim.*, 1995, vol. 31, no. 12, pp. 1864–1865.
6. Efimova, D.Yu., Shibalovich, V.G., and Nikolaev, A.F., *Zh. Prikl. Khim.*, 1997, vol. 70, no. 10, pp. 1704–1708.
7. Efimova, D.Yu., Shibalovich, V.G., and Nikolaev, A.F., *Zh. Prikl. Khim.*, 1998, vol. 71, no. 8, pp. 1355–1359.
8. Neiman, R.E., Kiseleva, O.G., Egorov, A.K., *et al*., *Kolloidnaya khimiya sinteticheskikh lateksov* (Colloidal Chemistry of Synthetic Latexes), Voronezh: Voronezh. Gos. Univ., 1984.
9. Verezhnikov, V.N., Poyarkova, T.N., Nikulin, S.S., and Kurbatova, N.A., *Kolloidn. Zh.*, 2000, vol. 62, no. 1, pp. 20–23.
10. Verezhnikov, V.N., Nikulin, S.S., Poyarkova, T.N., and Vostrikova, G.Yu., *Zh. Prikl. Khim.*, 2000, vol. 73, no. 10, pp. 1720–1724.
11. Baran, A.A. and Solomentseva, I.M., *Khim. Tekhnol. Vody*, 1983, vol. 5, no. 2, p. 120–127.
12. Baran, A.A., *Polimersoderzhashchie dispersnye sistemy* (Polymer-Containing Disperse Systems), Kiev: Naukova Dumka, 1986.
13. Solomentseva, I.M., Tusupbaev, N.K., Baran, A.A., and Musabekov, K.B., *Ukr. Khim. Zh.*, 1980, vol. 46, no. 9, pp. 928–932.
14. Gregory, J., *Colloids Surf.*, 1988, vol. 31, nos. 2/3, pp. 231–253.
15. Pelssers, E., Cohen, S., and Fleer, G., *J. Chem. Soc., Faraday Trans.*, 1990, vol. 86, no. 9, pp. 1355–1361.
16. Baran', Sh. and Gregory, J., *Kolloidn. Zh.*, 1996, vol. 58, no. 1, pp. 13–18.
17. Kashlinskaya, P.E., Verezhnikov, V.N., and Poyarkova, T.N., *Zh. Prikl. Khim.*, 1991, vol. 64, no. 1, pp. 218–221.

Russian Journal of Applied Chemistry, Vol. 77, No. 5, 2004, pp. 835–837. Translated from Zhurnal Prikladnoi Khimii, Vol. 77, No. 5, 2004, pp. 840–842.

MACROMOLECULAR CHEMISTRY AND POLYMERIC MATERIALS

Specific Features of Molecular Structure and Viscosity Characteristics of Oligodiene Urethanes

V. I. Valuev, L. N. Mikhailova, M. A. Okhotnikov, and I. V. Dal'gren

Lebedev Research Institute of Synthetic Rubber, Federal State Unitary Enterprise, St. Petersburg, Russia

Received December 29, 2003; in final form, March 2004

Abstract—Polycondensation of bifunctional hydroxyl-containing oligodienes with diisocyanates was studied by gel permeation chromatography, IR spectroscopy, and rheokinetic method. The kinetics of oligodiene urethane formation and the properties of the resulting oligomers, including the molecular-weight distribution and viscosity, were studied in relation to the ratio of the isocyanate and hydroxy groups.

Reactions of diisocyanates with hydroxyl-containing dienes attract particular interest due to their wide use in production of elastomers, urethane foams, adhesives, coatings, and other items. Despite seeming simplicity of such reactions, preparation of oligomers containing terminal isocyanate groups and exhibiting the required set of physicochemical properties is impossible without comprehensive study of the synthesis process, including the kinetic, molecular-weight, and rheological aspects.

In this work, we studied by gel permeation chromatography (GPC), IR spesctorscopy, and rheokinetic method the molecular-weight distribution (MWD) and dynamic viscosity of oligodiene urethanes in relation to the synthesis conditions. Also we examined the kinetic features of polycondensation of diisocyanates with bifunctional oligodienes containing terminal hydroxy groups.

EXPERIMENTAL

As investigation objects we used linear bifunctional oligodienes with terminal hydroxy groups (M_w 3600–3800), prepared by radical polymerization of 1,3-butadiene in the presence of an azo dinitrile initiator, 4,4'-azobis(4-cyanopentanol), and toluene 2,4-diisocyanate (TDI).

The IR spectra were recorded on a Specord IR-75 spectrophotometer. Samples were prepared as films between CaF_2 plates. The kinetics of the reactions of oligodienes with the diisocyanate were studied by monitoring the IR absorption of the NCO groups at ν = 2275 cm^{-1}. One of the oligomer bands [ν(C–H) of the methylene fragment] was used as internal reference.

Chromatography of oligomers was performed on a Waters-244 module-type chromatograph using three Styrogel columns with the pore size of 100, 500, and 1000 Å. The eluent was tetrahydrofuran (elution rate 1 ml min^{-1}). A differential refractometer was used as detector.

The rheological behavior of the reaction mixture in the course of the synthesis and that of the final products were studied with a Hoeppler rheoviscometer.

Synthesis of oligodiene urethanes with terminal isocyanate groups was performed in the bulk in the temperature range 3–70°C to constant content of NCO groups, which differed from the calculated content by no more than 0.05% [1].

The rate of the reaction of functional isocyanate and hydroxy groups depends on their concentrations and reaction temperature, following the common kinetic relationships. At [NCO]/[OH] = 2.05–2.15, the synthesis of oligodiene urethanes is complete in 3–4 h (T = 60°C), whereas at the equimolar ratio of the reacting groups, under similar conditions, the time required to prepare the product containing less than 0.1 wt % NCO groups was as long as 10–12 h.

It should be noted that the rate constants of the reaction of NCO and OH groups are apparent quantities. Actually the kinetics of formation of diene urethane prepolymers from oligodiene diols and TDI can be described by four rate constants because of different reactivities of the NCO groups of TDI at the *o*- and *p*-positions to the methyl substituent [2, 3].

The temperature dependence of the rate constants of the reaction between the isocyanate and hydroxy groups ([NCO]/[OH] = 2.15), plotted in the Arrhenius

1070-4272/04/7705-0835 © 2004 MAIK "Nauka/Interperiodica"

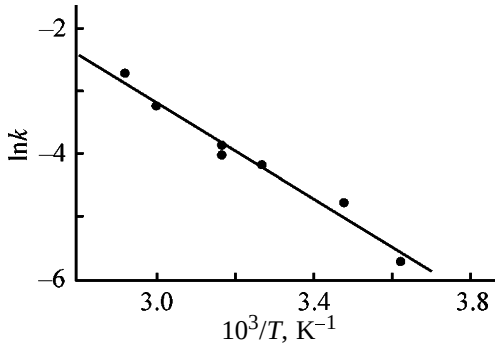

Fig. 1. Temperature dependence of the rate constant k of oligodiene urethane synthesis in Arrhenius coordinates. [NCO]/[OH] = 2.15.

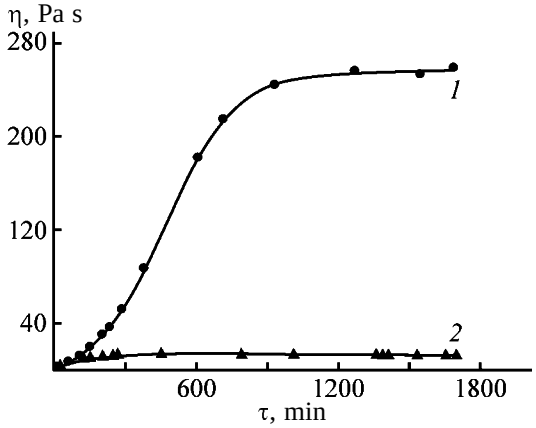

Fig. 2. Dynamic viscosity η of the reaction mixture as a function of time τ at the [NCO]/[OH] ratio of (*1*) 1.5 and (*2*) 2.1.

Molecular-weight and rheological characteristics of the oligodiene urethanes synthesized as influenced by the [NCO]/[OH] ratio (T = 60°C)

[NCO]/[OH]	η^{50}, Pa s	MWD parameters*		
		M_w	M_n	M_w/M_n
3.0	3.3	4100	2530	1.62
2.35	8.2	4510	2680	1.69
2.2	13.2	3800	2540	1.50
2.1	13.0	4740	2740	1.73
2.0	16.8	6100	3400	1.81
1.85	42.7	6170	3410	1.81
1.7	57.0	8290	4330	1.91
1.5	245	12500	5990	2.09
1.33	~1200	21450	7890	2.72
1.2	–	36150	13500	2.68
1.1	–	130700	32760	4.56
0.5	–	6920	3615	1.91

* Calculated for the "polymeric" fraction of the product.

coordinates (Fig. 1), shows that the activation barrier of the reaction is relatively low (activation energy E_a = 3.19 ± 2.6 kJ mol^{-1}), allowing preparation of oligodiene urethanes in a wide temperature range (20–60°C).

Synthesis of the prepolymers is accompanied by an increase in the dynamic viscosity of the reaction mixture due to the growth of M_w of the polymer and to formation of urethane groups capable of strong intermolecular interactions. The rheokinetic data suggest rapid growth of the dynamic viscosity in the initial step of polycondensation (Fig. 2).

Then, as the reactive groups are consumed, the growth of the viscosity decelerates. The plateaus in the η–τ curves correspond to the virtually ready product, indicating that modification of the oligodiene with the diisocyanate has been completed. Comparison of the η–τ dependences for systems with different [NCO]/[OH] ratios shows that the constant viscosity is attained most rapidly at the highest [NCO]/[OH] ratios.

Figure 2 shows that, at [NCO]/[OH] = 1.5, the rheokinetic curve is S-shaped, which may be due to formation of intermediates $(oligomer–TDI)_n$ (n = 1, 2) in the initial step of the process, with an increase in the weight-average molecular weight by a factor of 2–3. Condensation of these intermediates with each other causes active growth of the viscosity without pronounced plateau, in contrast to the pattern observed at [NCO]/[OH] = 2.1.

Quantitative data illustrating the relationship of MWD and viscosity of oligodiene urethanes with the [NCO]/[OH] ratio are given in the table.

The viscosity of the oligomer prepared at [NCO]/[OH] = 3.0 is minimal because of the narrow MWD of the polymeric fraction of the sample and the highest content of the low-molecular-weight component, TDI, in the final product. As the [NCO]/[OH] ratio is decreased, the dynamic viscosity of oligodiene urethanes grows, which is due both to a decrease in the TDI content in the system and to an increase in M_w of the polymeric component.

The average molecular weights and polydispersity coefficient of oligodiene urethanes are minimal in the range of [NCO]/[OH] ratios from 2.0 to 3.0. As the [NCO]/[OH] ratio is decreased to 1.1–1.2, the molecular weights grow substantially, and MWD becomes broader owing to intense chain propagation with no exchange reactions (Fig. 3).

The fact that at [NCO]/[OH] = 1.1–1.2 the experimental polydispersity coefficient appreciably exceeds

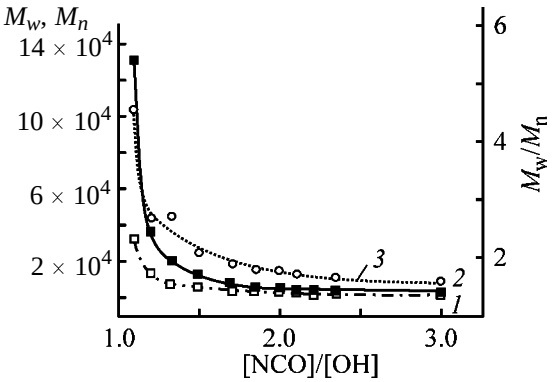

Fig. 3. Influence of the [NCO]/[OH] ratio on the MWD parameters of oligodiene urethanes: (*1*) M_n, (*2*) M_w, and (*3*) M_w/M_n.

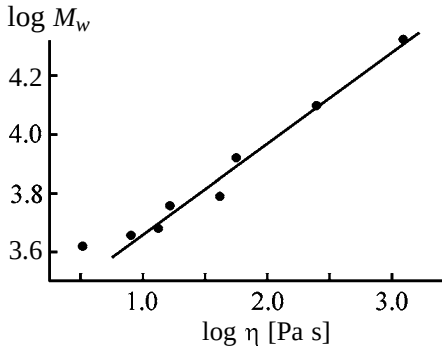

Fig. 4. Logarithmic plot of M_w of oligodiene urethanes vs. their dynamic viscosity η.

the theoretical value for polycondensation processes (M_w/M_n = 2) is also due to development of side reactions yielding branched macromolecules. At substoichiometric [NCO]/[OH] ratios, the average molecular weights and the polydispersity coefficient of the oligodiene urethanes obtained regularly decrease.

The log–log plot of the dynamic viscosity of the oligomers synthesized vs. their weight-average molecular weight is linear (Fig. 4), which is typical of structurallly related liquid polymers in the entire range of molecular weights.

CONCLUSIONS

(1) Hydroxy groups of an oligodiene react with isocyanate groups of toluene 2,4-diisocyanate in the bulk at a fairly high rate with relatively low activation energy, which allows the synthesis of oligodiene urethanes in a wide temperature range.

(2) Oligourethanes prepared at the ratio of the isocyanate and hydroxy groups [NCO]/[OH] = 2.1–2.2 exhibit the best structural and viscosity characteristics required of prepolymers to be used in preparation of urethane elastomers by reaction with cross-linking agents.

REFERENCES

1. Bogatyreva, S.A., Valuev, V.I., Nasonova, T.P., and Safronova, T.V., *Prom–st. Sint. Kauchuka*, 1983, no. 12, pp. 11–12.
2. Sushkina, V.G., Palyutkin, G.M., and Zharkov, V.V., *Kinet. Katal.*, 1985, vol. 26, no. 2, pp. 476–480.
3. Korzyuk, E.L. and Zharkov, V.V., *Kinet. Katal.*, 1981, vol. 22, no. 2, pp. 522–525.

Russian Journal of Applied Chemistry, Vol. 77, No. 5, 2004, pp. 838–841. Translated from Zhurnal Prikladnoi Khimii, Vol. 77, No. 5, 2004, pp. 843–846.

MACROMOLECULAR CHEMISTRY AND POLYMERIC MATERIALS

Structure and Properties of Polyurethane–Ureas Prepared from Blends of Thermodynamically Incompatible Oligomer Diisocyanates

S. V. Tereshatov, V. Yu. Senichev, E. N. Tereshatova, M. A. Makarova, and V. V. Tereshatov

Institute of Technical Chemistry, Ural Division, Russian Academy of Sciences, Perm, Russia

Received October 17, 2003; in final form, January 2004

Abstract—The structure and properties of materials based on oligo(divinyl–isoprene) and oligoether diisocyanates cured with an aromatic diamine were studied.

Preparation of segmented polyurethanes (SPUs) from individual oligomers does not always yield materials with optimal properties. For example, the frost resistance of SPUs with flexible oligodiene segments is high (down to –60°C), but, as compared to SPUs derived from oligoethers, their strength is lower, and the reaction mixture is more viscous and has shorter working life (time in which the system remains in the state of a low-viscosity liquid [1]).

An efficient way to control the properties of such materials is the use in polyurethane formulations of not one but several (usually two) oligomers [2–5]. Oligomers both compatible in any ratios at temperatures of SPU preparation and virtually incompatible [5] can be used. In the latter case, an SPU may have a heterogeneous structure with a disperse phase with flexible blocks incorporated in a polymeric matrix of a different structure, also with flexible blocks. Formation of such a disperse phase in SPUs may both improve and impair the properties of materials, depending on the component ratio.

In this work we studied the structure and properties of SPUs with thermodynamically incompatible polar polyether and nonpolar poly(divinyl–isoprene) flexible blocks.

Our main goal was to examine the possibility of reinforcing the elastomer with nonpolar flexible blocks by introducing polar flexible blocks into the composition of the flexible phase and of controlling the rheological properties of the SPU reaction mixture.

EXPERIMENTAL

We used segmented polyurethane–ureas (SPUUs) with similar rigid blocks and different flexible blocks. SPUUs were prepared from commercial prepolymers: P-10.000 (M ~4500) based on oligo(divinyl–isoprene)-diol (molar ratio of butadiene and isoprene units 70/30, M ~400) and SKU-PFL-100 (M ~1400) based on oligo(tetramethylene oxide)diol (M ~1000). The prepolymers were prepared by reactions of the oligomeric diols with toluene 2,4-diisocyanate taken in a twofold excess. The molecular weight of the oligomers was estimated from the content of isocyanate groups. Blends of the prepolymers were prepared by mixing in a vacuum for 30 min at 60 ± 1°C. Then we added into the mixer the melt of an aromatic diamine, 3,3'-dichloro-4,4'-diaminodiphenylmethane (Diamet Kh) and stirred the components for 3 min under the above-indicated conditions.

The rheological properties of the reaction mixture were determined with a Rheotest-2 device (cone–plate working unit) at a shear rate of 180 s^{-1}.

The samples cured for 4 days at 80 ± 1°C were stored at room temperature for no less than 15 days before tests.

The physicomechanical characteristics of SPUUs [tensile strength σ_t (ultimate stress per initial cross section of the sample) and relative elongation at break ε_b] were determined at 25°C and extension rate of 0.28 s^{-1}.

Because of the lack of an approach to evaluating the parameters of the three-dimensional network of heterogeneous polymer blends, we determined the density of the chemical (N_c) and physical (N_p) networks (the points of the latter are domains of rigid urethane–urea blocks) only for SPUUs with individual flexible blocks. The effective network parameters were estimated following the procedure from [6].

1070-4272/04/7705-0838 © 2004 MAIK "Nauka/Interperiodica"

Composition and properties of SPUUs with different flexible blocks

SPUU	x_2	c_{PFL}, %	ρ, g cm^{-3}	c_r, %	N_p	N_c
					kmol m^{-3}	
SPUU-1	0	0	954	14	0.22	0.02
SPUU-2	0.15	6	960	15	–	–
SPUU-3	0.17	6	961	15	–	–
SPUU-4	0.20	8	964	16	–	–
SPUU-5	0.30	13	973	17	–	–
SPUU-6	0.45	21	993	20	–	–
SPUU-7	0.60	33	1013	22	–	–
SPUU-8	0.75	50	1040	26	–	–
SPUU-9	0.80	57	1048	28	–	–
SPUU-10	0.85	65	1068	30	–	–
SPUU-11	0.90	75	1090	32	–	–
SPUU-12	1.00	100	1129	37	1.51	0.08

The glass transition points T_g^s of flexible SPUU blocks were determined with a DSM-2 differential scanning calorimeter under conditions of slow sample heating (0.02 deg s^{-1}).

The properties of SPUUs were studied in a wide range of the prepolymer ratios. The mole fractions (x_2) and weight percentages (c_{PFL}) of SKU-PFL in prepolymer blends, sample densities ρ, contents of the rigid phase in them (c_r), and effective network parameters N_c and N_p are given in the table.

As expected, because of thermodynamic incompatibility of P-10.000 and SKU-PFL-100, an emulsion of one of the prepolymers in the other is formed already on mixing the components. After adding a curing agent, two phases are formed: phase 1 consisting of P-10.000 and Diamet Kh and phase 2 consisting of SKU-PFL-100 and Diamet Kh. At a stoichiometric ratio of the NH_2 and NCO groups, the calculated weight ratio of the diamine to the prepolymer m is m_1 = 0.059 in phase 1 and m_2 = 0.191 in phase 2.

Our experiments showed that the solubility of the chosen aromatic diamine in the two prepolymers at the mixing temperature (60°C) is essentially different. The experimental values are m_1 = 0.047 and m_2 = 0.350. Comparison of these results with the calculated values shows that the curing agent is in deficiency in phase 1 and in excess in phase 2.

If phase 1 is the dispersion medium in the reaction mixture, then deficiency of the active agent in it should result in preservation of the low viscosity of the polyurethane formulation for a long time, i.e., in longer working life of the formulation, which is the case. For example, the dynamic viscosity η = 20 Pa s of SPUU-1 formulation based on individual P-10.000 at 60°C is attained in 10 min after the compounding. The same viscosity of SPUU-5 and SPUU-6 formulations based on prepolymer blends is attained in 65 and 110 min, respectively (Fig. 1, curves *2*, *4*, *5*). Hence, addition of a small amount of SKU-PFL-100 prepolymer (see table, c_{PFL} = 13–21%) to the reaction mixture containing P-10.000 increases the working life of the formulation by approximately an order of magnitude. If phase 2 is the dispersion medium (c_{PFL} = 65%, x_2 = 0.85), the working life of the reaction mixture, on the contrary, becomes shorter.

Curing of the disperse phase and dispersion medium with an aromatic diamine yields an elastomer with a flexible polymeric matrix incorporating particles of an elastic filler.

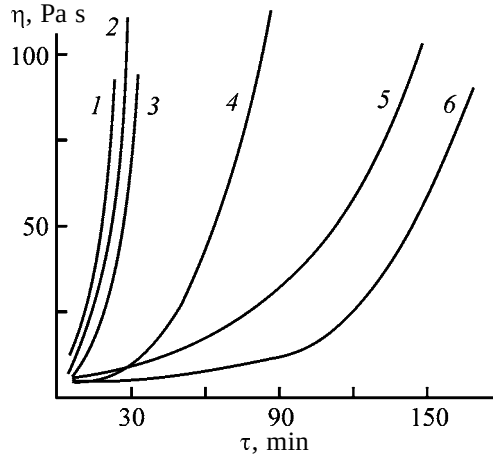

Fig. 1. Variation with time τ of the dynamic viscosity η of polyurethane–urea samples: (*1*) SPUU-10, (*2*) SPUU-1, (*3*) SPUU-12, (*4*) SPUU-4, (*5*) SPUU-5, and (*6*) SPUU-6.

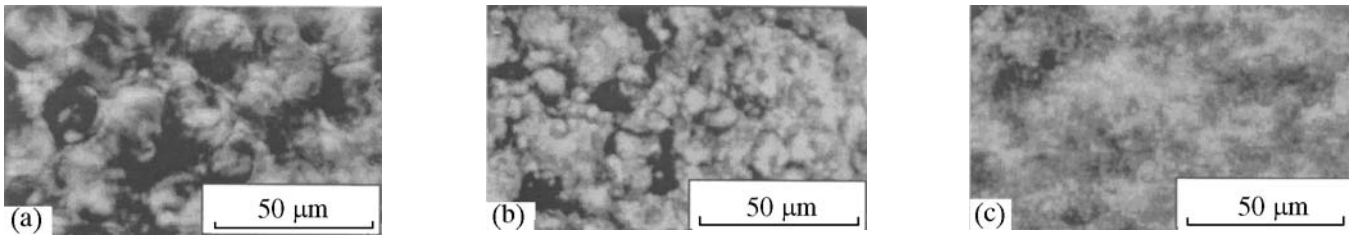

Fig. 2. Photomicrographs of SPUUs based on prepolymer blends with different content of SKU-PFL-100: (a) SPUU-6 (x_2 = 0.3), (b) SPUU-7 (x_2 = 0.6), and (c) SPUU-8 (x_2 = 0.75, c_{PFL} = 50%).

The structure of the cured material depends on the component ratio. At a low content of one of the prepolymers (up to 30%), the filler particles are spherical with a clear phase boundary and size of about 10–25 μm (Fig. 2a). As the filler concentration increases, continuous domains of agglutinated filler particles are formed (Fig. 2b), and at equal content of the prepolymers in the blend (c_{PFL} = 50%, x_2 = 0.75) the phases overlap (Fig. 2c).

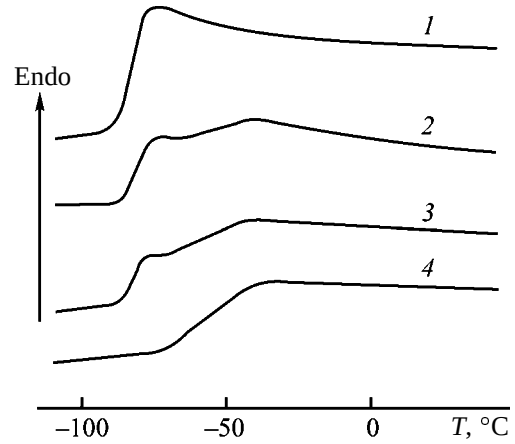

Fig. 3. DSC curves of SPUU samples: (*1*) SPUU-1 (P-10.000), (*2*) SPUU-7 (c_{PFL} = 33%), (*3*) SPUU-10 (c_{PFL} = 65%), and (*4*) SPUU-12 (SKU-PFL-100). (*T*) Temperature.

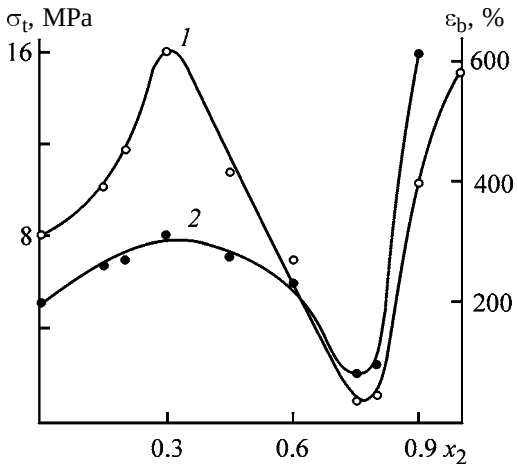

Fig. 4. (*1*) Relative elongation at break ε_b and (*2*) strength σ_t of SPUU as a function of the mole fraction of SKU-PFL-100 x_2 in the prepolymer blend.

The DSC curves (Fig. 3) show that the compounds based on prepolymer blends are characterized by two glass transition points of flexible blocks T_g^s, differing insignificantly from T_g^s of the materials based on the individual prepolymers: –54 (SPUU-12) and –82°C (SPUU-1). This fact indicates that the materials based on the two prepolymers are heterogeneous blends of two polyurethane–ureas in which the flexible blocks do not mix with each other. It should be emphasized that such structures are not necessarily formed in materials with polar and nonpolar flexible blocks. For example, at MW ~200, as shown in [4], polybutadiene and polyether flexible segments are miscible in any ratios.

The mechanical characteristics of polydiene–urethane–ureas based on a single prepolymer, P-10.000, and those of polyether–urethane–ureas based on another single prepolymer, SKU-PFL-100, differ dramatically. The high density of the physical network (N_p = 1.51 kmol m^{-3}) in SPUU-12 with polyether flexible segments and the high concentration of rigid blocks (37%), in combination with dipole–dipole and specific interchain interactions, provide high strength (42 MPa) and high nominal modulus (11.5 MPa at 100% relative strain) of the material. The relative elongation at break, ε_b, reaches 560%. In SPUU-1 with nonpolar flexible segments, low N_p and low concentration of rigid blocks (see table) are responsible for the poor strength (5.4 MPa), low nominal modulus (2.7 MPa), and lower ε_b (320%). The influence of various factors on the mechanical properties of polyurethane materials in considered in detail in [7, 8].

Combination in one material of polyurethane–ureas strongly differing in the mechanical properties results in nonmonotonic dependence of the mechanical characteristics of the heterogeneous polymeric composite on the prepolymer ratio (Fig. 4). On adding SKU-PFL-100 to the reaction mixture containing P-10.000,

the strength and breaking strain grow, reaching a maximum at x_2 = 0.3. The tensile strength σ_t increases from 5.4 to 8.2 MPa, and the relative elongation at break, from 320 to 630%.

The material of the composition corresponding to the inversion point of the filler and polymeric matrix (x_2 = 0.75, c_{PFL} = 50%) has the lowest strength. As the fraction of SKU-PFL-100 is increased further, polyuether–urethane–urea becomes the dispersion medium, and polydiene–urethane–urea, the filler. With decreasing concentration of the low-strength filler in the polyether matrix, the strength of the material regularly grows. Such a pattern is typical of thermodynamically incompatible polymer blends.

Significant enhancement of the mechanical characteristics is observed at such material composition at which, as noted above, the working life of the reaction mixture considerably grows; this is important from the viewpoint of preparation of big polyurethane items of high quality.

CONCLUSIONS

(1) Segmented polyurethane–ureas with polydiene and polyether flexible blocks are heterogeneous blends of two polyurethane–ureas differing in the chemical structure of the flexible chains.

(2) The dependences of the mechanical characteristics of the polyurethane elastomer on the prepolymer ratio pass through extrema, which is due to the heterogeneous structure of the material and to strong difference in the mechanical characteristics of the filler and polymeric matrix.

(3) Introduction of 13–20% oligoether diisocyanate into the polydiene–urethane–urea formulation ensures the 1.5 times higher strength of the material and 2 times larger elongation at break. Furthermore, the working life of the polyurethane compound increases by an order of magnitude owing to depletion in the curing agent of the liquid phase containing oligodiene diisocyanate.

REFERENCES

1. Lyubartovich, S.A., Morozov, Yu.L., and Tret'yakov, O.B., *Reaktsionnoe formovanie poliuretanov* (Reactive Molding of Polyurethanes), Moscow: Khimiya, 1990.
2. Tae Oan Ahn, Soon-Uk Jung, Han Mo Jeong, and Sang Won Lee, *J. Appl. Polym. Sci.*, 1994, vol. 51, pp. 43–51.
3. Shtempel', V.I. and Kercha, Yu.Yu., *Vysokomol. Soedin., Ser. B*, 1996, vol. 38, no. 10, pp. 1776–1779.
4. Tereshatov, V.V., Tereshatova, E.N., Makarova, M.A., and Tereshatov, S.V., *Vysokomol. Soedin., Ser. A*, 2002, vol. 44, no. 3, pp. 443–454.
5. Tereshatova, E.N., Baranets, I.V., and Tereshatov, V.V., *Plast. Massy*, 1998, no. 7, pp. 17–19.
6. Tereshatov, V.V., Tereshatova, E.N., Begishev, V.P., and Makarova, M.A., *Vysokomol. Soedin., Ser. B*, 1992, vol. 34, no. 8, pp. 22–25.
7. Speckhard, T.A. and Cooper, S.L., *Rubber Chem. Technol.*, 1986, vol. 59, no. 3, pp. 405–421.
8. Tereshatov, V.V., Tereshatova, E.N., and Volkova, E.R., *Vysokomol. Soedin., Ser. A*, 1995, vol. 37, no. 11, pp. 1881–1887.

Russian Journal of Applied Chemistry, Vol. 77, No. 5, 2004, pp. 842–845. Translated from Zhurnal Prikladnoi Khimii, Vol. 77, No. 5, 2004, pp. 847–850.

MACROMOLECULAR CHEMISTRY AND POLYMERIC MATERIALS

Preparation of Metal Carboxylates and Their Stabilizing Performance under Intense High-Pressure Shear Treatment

R. M. Akhmetkhanov, S. V. Kolesov, R. G. Kadyrov, A. Yu. Karmilov, and G. E. Zaikov

Bashkir State University, Ufa, Bashkortostan, Russia
Institute of Synthetic Polymeric Materials, Russian Academy of Sciences, Moscow, Russia
Institute of Biophysical Chemistry, Russian Academy of Sciences, Moscow, Russia

Received October 28, 2003

Abstract—Solid-phase synthesis of certain metal carboxylates and their effect on stabilization of polyvinyl chloride under intense high-pressure shear treatment were studied.

Metal carboxylates are widely used as thermal stabilizers and lubricants in development of new materials and goods based on polyvinyl chloride (PVC) [1]. The main method of industrial production of metal carboxylates is the exchange reaction between aqueous solution of metal chloride or nitrate and sodium carboxylate, e.g., stearate, at elevated temperatures. It is characterized by a large amount of wastewater, the need in additional operations to isolate target products, etc. [2]. In known methods of solid-phase synthesis of metal carboxylates [3, 4], sophisticated and power-consuming devices with abrasive, cutting, and impact action are used. The product yields in such procedures are usually low.

A new method of solid-phase synthesis of chemical materials and processing and modification of polymers under intense high-pressure shear treatment (IHPST) at elevated temperatures in special dispersers is being actively developed today [5, 6]. Under IHPST, various chemical reactions can proceed in polymers: change of supramolecular structure, disintegration, and increase in specific surface area of the material treated with formation of a superfine powder.

The goal of this work is to perform solid-phase synthesis of certain metal carboxylates and to study polyvinyl chloride (PVC) stabilization with these carboxylates under IHPST.

EXPERIMENTAL

The solid-phase synthesis of metal carboxylates and processing of polyvinyl chloride compositions under IHPST were performed in a rotary disperser designed at the Institute of Chemical Physics, Russian Academy of Sciences [6]. The yield of metal carboxylates was determined analytically in accordance with TU (Technical Specifications) 6-09-4104–87 from the residual content of carboxylic acids in the reaction mixture and by IR spectrometry on a Bruker IFS-88 spectrometer from the intensity of the absorption bands within the 1400–1650 cm^{-1} range depending on metal. Pure grade stearic, lauric, and palmitic acids and calcium, barium, cadmium(II), lead(II), and zinc(II) oxides or their binary mixtures, and sodium and potassium carbonates were used. The method of determination of the PVC dehydrochlorination rate was similar to that described in [7]. The thermal stability time of polymeric compositions was determined in accordance with GOST (State Standard) 14041–91.

The IHPST method has no disadvantages characteristic for other methods of metal carboxylate synthesis and provides high yield of the reaction products and short reaction time; no catalysts are required. The specific feature of solid-phase reactions with IHPST is that the combined effect of high pressure and shear strain brings solid substances to the plastic flow state. In the process, a great amount of structural defects is formed in the substance, electronic properties of molecules change, and the activation barrier of reactions decreases [8].

The solid-phase synthesis of metal carboxylates proceeds by the reactions

$$MO + 2RCO_2H \rightarrow M(RCO_2)_2 + H_2O,$$

$$M'_2CO_3 + 2RCO_2H \rightarrow 2M'(RCO_2) + H_2O + CO_2,$$

where M = Ca, Ba, Zn, Cd, Pb; M' = K, Na; R = $C_{11}H_{23}$, $C_{15}H_{31}$, $C_{17}H_{35}$.

1070-4272/04/7705-0842 © 2004 MAIK "Nauka/Interperiodica"

The reaction products are formed during passing of the reaction mixture through the rotary disperser for 3–5 min at a single IHPST effect on the reactants. The yield of the target product, which is obtained as a dry superfine powder, was 96–99% of the calculated amount (Table 1). The method allows preparation in the same device of a wide assortment of individual metal carboxylates and their mixtures (including synergistic mixtures).

Estimation of the stabilizing performance of salts of saturated monocarboxylic acids with respect to vinyl chloride polymers (PVC; copolymer of vinyl chloride with 4 wt % propylene, VCPR-4; copolymer of vinyl chloride with 15 wt % vinyl acetate, VCVA-15) showed that, with respect to the "thermal stability time" index, it is not inferior to the performance of stabilizers prepared by the industrial method (Table 2).

The solid-phase method of obtaining metal carboxylates under IHPST has substantial advantages as compared to the industrial synthesis method: it is continuous and single-stage, synthesis can proceed in one apparatus at a high rate without heating, the process is characterized by elevated environmental safety, and the chemical modification of stabilizers and preparation of synergistic mixtures on their base are possible.

The synthesis of metal carboxylates is also possible directly in a polymer matrix, when a mixture of PVC with a metal oxide (or another base) and an equivalent amount of a carboxylic acid is processed in a rotary disperser. The high stabilizing performance of the components under IHPST is apparently due to solid-phase synthesis of metal carboxylates from the initial reactants. It should be noted, however, that, with the carboxylates prepared *in situ*, the thermal stability time is shorter than when PVC is stabilized with the corresponding metal carboxylates prepared in advance (Table 3).

To improve PVC grinding under IHPST, various components, in particular, metal carboxylates can be used as process additives. Joint grinding of PVC mixtures with metal carboxylates under IHPST substantially improves the process efficiency and increases the degree of dispersion of the powder formed.

Joint grinding of PVC with metal carboxylates under IHPST substantially enhances stabilizing performance of additives with respect to thermal stability time index as compared to usual mechanical mixing (Table 3). The stabilizing performance of additives also increases with respect to the "dehydrochlorination rate" index when coordination-unsaturated metal

Table 1. Solid-phase synthesis of metal carboxylates under IHPST

Reactants used		Molar ratio acid : metal oxide (salt)	Product yield, %
acid	metal oxide, salt		
$C_{17}H_{35}CO_2H$	CaO	2 : 1	99
	CaO	2 : 1	98
	CaO	2 : 1	98
	CaO	2 : 1	99
	BaO	2 : 1	96
	ZnO	2 : 1	97
	PbO	2 : 1	96
	CdO	2 : 1	98
$C_{11}H_{23}CO_2H$	CaO	2 : 1	98
	CdO	2 : 1	97
$C_{15}H_{31}CO_2H$	BaO	2 : 1	97
	PbO	2 : 1	96
$C_{17}H_{35}CO_2H$	K_2CO_3	2 : 1	96
	Na_2CO_3	2 : 1	97
	BaO + CaO	4 : 1 : 1	96
	CaO + ZnO	4 : 1 : 1	97

Table 2. Effect of metal carboxylates synthesized under IHPST conditions (2 wt parts per 100 wt parts of polymer) on the thermal stability time of vinyl chloride polymers

Metal carboxylate	Thermal stability time, min		
	PVC	VCPR-4	VCVA-15
–	4	4	3
Stearate of:			
calcium	21(22)*	20(19)	17(18)
barium	57(56)	55(54)	51(52)
zinc	5(5)	4(4)	3(4)
lead	76(75)	72(73)	68(70)
cadmium	31(32)	29(29)	26(27)
Laurate of:			
calcium	25(26)	23(22)	20(19)
cadmium	36(35)	33(34)	29(27)
Palmitate of:			
barium	61(61)	59(58)	55(54)
lead	79(79)	74(72)	70(69)
Stearate of:			
potassium	58(57)	55(56)	52(50)
sodium	62(63)	58(60)	55(56)
Mixture of stearates:			
barium and calcium	46(44)	44(45)	41(42)
calcium and zinc	19(20)	18(18)	15(15)

* The thermal stability time of vinyl chloride polymers (175°C) in the presence of metal carboxylates synthesized by the industrial method is given in parentheses.

Table 3. Change in thermal stability time and rate of PVC dehydrochlorination in the presence of additives after IHPST*

Component	Composition, wt %, for indicated sample												
	1	2	3	4	5	6	7	8	9	10	11	12	13
PVC	100	100	100	100	100	100	100	100	100	100	100	100	100
$(C_{17}H_{19}CO_2)_2Ba$	5	–	–	–	–	–	–	–	–	–	–	–	–
$(C_{17}H_{19}CO_2)_2Ca$	–	3	5	–	–	–	–	–	–	–	–	–	–
$C_{17}H_{19}CO_2Na$	–	–	–	5	–	–	–	–	–	–	–	–	
$(C_{17}H_{19}CO_2)_2Pb$	–	–	–	–	3	5	–	–	–	–	–	–	
$(C_{17}H_{19}CO_2)_2Cd$**	–	–	–	–	–	–	5	–	–	–	–	–	–
$(C_{15}H_{17}CO_2)_2Ba$	–	–	–	–	–	–	–	3	–	–	–	–	–
BaO	–	–	–	–	–	–	–	–	1.08	–	–	–	–
CaO	–	–	–	–	–	–	–	–	–	0.46	–	–	–
NaOH	–	–	–	–	–	–	–	–	–	–	0.64	–	–
PbO	–	–	–	–	–	–	–	–	–	–	–	1.44	–
CdO**	–	–	–	–	–	–	–	–	–	–	–	–	0.94
$C_{17}H_{19}CO_2H$	–	–	–	–	–	–	–	–	4.04	4.70	4.64	3.67	4.20
Thermal stability time at 175°C, min:													
before IHPST	97	24	50	153	64	274	105	74	48	18	115	75	50
after IHPST	109	32	58	171	73	282	118	85	84	43	143	181	88
$V_{HCl} \times 10^6$ at 175°C, mol HCl : mol PVC*:													
before IHPST	1.20	1.20	1.20	1.21	0.32	0.30	0.32	1.19	1.33	1.46	1.70	0.85	1.06
after IHPST	1.21	1.19	1.20	1.22	0.21	0.18	0.24	1.18	1.26	1.28	1.31	0.39	0.52

* Temperature in disperser at IHPST: in compression chamber 115°C and in grinding chamber 60°C; speed of screw rotation 35 min^{-1}.

** Dehydrochlorination rates in the initial period of degradation.

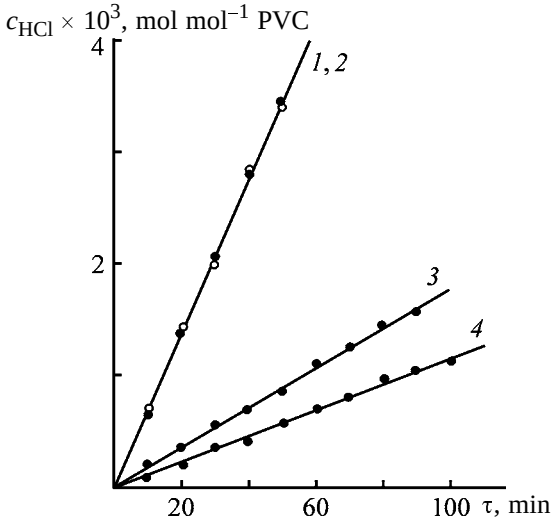

Kinetics of dehydrochlorination (175°C, air) of PVC stabilized (5 wt parts per 100 wt parts of PVC) with (*1*, *2*) barium stearate and (*3*, *4*) lead stearate (*1*, *3*) before and (*2*, *4*) after intense high-pressure shear treatment in a rotary disperser; (c_{HCl}) hydrogen chloride concentration and (τ) time.

[Cd(II) and Pb(II)] stearates are used, which, in addition to HCl scavenging, inhibit PVC dehydrochlorination due to chemical deactivation of the labile groups [7] (Table 3).

The physical and chemical processes occuring under IHPST are characterized by high rate of mass transfer (apparent diffusion coefficient becomes several times higher [8]). In this case, increased stabilizing performance of metal carboxylates can be explained by more uniform distribution of the thermal stabilizer in the polymer and by better accessibility of labile groups in reaction with stabilizing additives.

CONCLUSION

The method of intense high-pressure shear treatment shows promise in solid-phase synthesis of metal carboxylates. It also enhances their stabilizing performance in processing of polymeric compositions based on polyvinyl chloride.

REFERENCES

1. Minsker, K.S. and Fedoseeva, G.T., *Destruktsiya i stabilizatsiya polivinilkhlorida* (Degradation and Stabilization of Polyvinyl Chloride), Moscow: Khimiya, 1979.
2. Gorbunov, B.N., Gurvich, Ya.A., and Maslova, I.P., *Khimiya i tekhnologiya stabilizatorov polimernykh materialov* (Chemistry and Technology of Stabilizers for Polymeric Materials), Moscow: Khimiya, 1981.
3. German Patent 12 117 381.
4. UK Patent 1 573 367.
5. Prut, E.V. and Zelenetskii, A.N., *Usp. Khim.*, 2001, vol. 70, no. 1, pp. 72–87.
6. Akopyan, E.A., Karmilov, A.Yu., Nikol'skii, V.G., *et al.*, *Dokl. Akad. Nauk SSSR*, 1986, vol. 291, no. 1, pp. 133–136.
7. Kolesov, S.V., Berlin, Al.Al., and Minsker, K.S., *Vysokomol. Soedin., Ser. A*, 1977, vol. 19, no. 2, pp. 381–385.
8. Enikolopov, N.S., *Dokl. Akad. Nauk SSSR*, 1985, vol. 283, no. 4, pp. 897–899.

Russian Journal of Applied Chemistry, Vol. 77, No. 5, 2004, pp. 846–847. Translated from Zhurnal Prikladnoi Khimii, Vol. 77, No. 5, 2004, pp. 851–852.

BRIEF COMMUNICATIONS

Adsorption of Ammonia and Sulfur Dioxide by Sorbents Based on Modified Montmorillonite

A. S. Panasyugin, G. V. Bondareva, and A. I. Rat'ko

Research Laboratory on Waste Gas Treatment, Belarussian National Technical University, Minsk, Belarus
Institute of General and Inorganic Chemistry, Belarussian National Academy of Sciences, Minsk, Belarus

Received October 28, 2003

Abstract—The sorption properties of montmorillonite modified with Fe(III) and Al(III) polyhydroxo complexes and with Fe(III)–Zr(IV), Fe(II)–Ni(II), and Fe(III)–Al(III) heteronuclear polyhydroxo complexes with respect to ammonia and sulfur dioxide were examined.

Synthetic sorbents such as activated carbons, zeolites, and ion exchangers used in the majority of adsorption processes can be replaced with inexpensive mineral sorbents based on smectite minerals. Of specific interest are clay minerals with expandable cell, whose layers are intercalated with polyhydroxo complexes (PHCs) of multiply charged metals. After calcination, the above PHCs transform into the oxide clusters, which support certain spacing between clay layers.

In this study, the sorptive properties of montmorillonite (MM) intercalated with PHCs of metals of various origin with respect to acid and base gases were considered by an example of ammonia and sulfur dioxide.

The initial material was montmorillonite clay of Askanskoe deposit (Georgia) containing (wt %) 53.3 SiO_2, 18.1 Al_2O_3, 0.84 Fe_2O_3, 4.9 MgO, 1.65 CaO, 1.1 Na_2O, 0.32 K_2O, and 7.98 H_2O.

The PHCs of metals were prepared and montmorillonite was modified according to the methods proposed in [1–3]. The specific surface area S_{sp} of the modified montmorillonite samples was determined by low-temperature sorption of nitrogen on a Micromeritics 2200 express analyzer. The parameters d_{001} for the first basal reflection from modified clays were determined with a Siemens 5000 diffractometer after drying samples at 120°C. The adsorption-structural characteristics of the obtained samples were calculated using data on the adsorption–desorption isotherms of benzene vapor. The isotherms of ammonia and sulfur dioxide sorption were taken gravimetrically at 20°C.

The table shows that the montmorillonite modification makes the spacing between aluminosilicate layers considerably larger, i.e., the d_{001} parameter for the first basal reflection from the Fe–Ni–MM sample increases to 2.42 nm, compared to the value of 0.95 nm for the initial sample. Noteworthy, S_{sp} of the montmorillonite samples containing heteronuclear PHCs amounts to 250–280 $m^2 g^{-1}$, which is somewhat larger compared to montmorillonite modified with individual iron and aluminum individual complexes (190 and 180 $m^2 g^{-1}$, respectively).

The presence of mesopores of radius larger than 20 nm in the pore structure of the modified samples can be judged from the shape of the isotherms of benzene vapor sorption [4]. Sharp rise of the isotherms in the low-pressure range for the Al–MM and Fe–Al–MM samples is an evidence for the considerable content of micropores.

The NH_3 sorption isotherms in Fig. 1a show that the maximal sorption capacity for NH_3 is exhibited by the Fe–MM sample and the minimal, by the Al–MM

Characteristics of natural and modified montmorillonites

Sample	Amount of modifying metal		d_{001}, nm	S_{sp}, $m^2 g^{-1}$
	Fe	Al, Ni, Zr		
Montmorillonite in Na^+ form	–	–	0.9	60
Al–MM	–	3.18	1.75	180
Fe–Al–MM	0.48	3.4	1.63	250
Fe–Ni–MM	0.82	0.14	2.42	270
Fe–Zr–MM	1.26	0.11	1.65	280
Fe–MM	1.23	–	1.59	190

1070-4272/04/7705-0846 © 2004 MAIK "Nauka/Interperiodica"

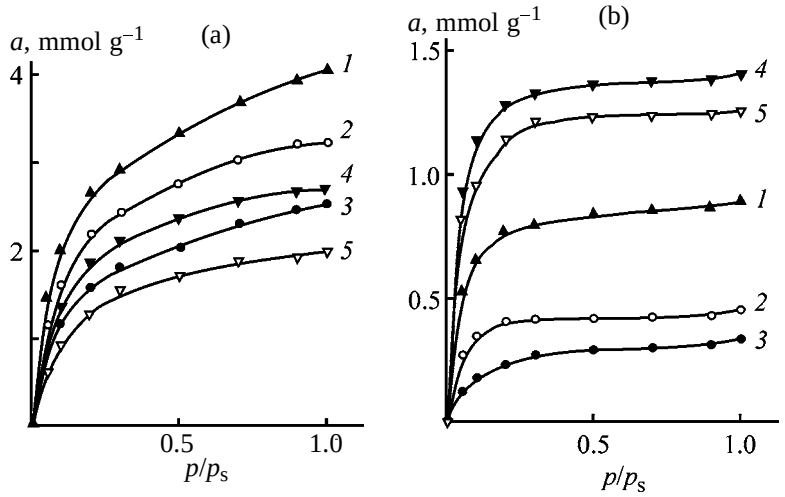

Fig. 1. Isotherms of (a) ammonia and (b) sulfur dioxide sorption a on the montmorillonite samples modified with PHCs of (*1*) Fe(III), (*2*) Fe(III)–Zr(IV), (*3*) Fe(III)–Ni(II), (*4*) Fe(III)–Al(III), and (*5*) Al(III). (p/p_s) Relative pressure.

sample. Adsorption of gaseous NH_3 is commonly used as test method to compare the surface acidity and catalytic activity of catalysts based on natural and synthetic aluminosilicates [5, 6]. Thus, we can suggest that the Fe–MM sample is the most acidic, and the Al–MM sample, the least acidic.

An increase in the acidity of montmorillonite samples modified with metal PHCs, as compared to the initial clay, is usually ascribed to an increase in the interlayer spacing, which, in turn, makes accessible the previously shielded internal acidic centers [7]. Therefore, samples with larger interlayer spacings, i.e., those characterized by higher d_{001} values, should be expected to exhibit higher acidity. However, d_{001} and the adsorption capacity of the samples for NH_3 do not correlate. These facts suggest that the high sorption capacity of the Fe–MM sample is due to the nature of the modifier, rather than to the montmorillonite properties. In such a case, a decrease in the sorption capacity for NH_3 of the Fe–Zr–MM and Fe–Ni–MM samples can be due to a decrease in the amount of intercalating iron agents (see table) and to introduction of Ni(II) and Zr(IV) into the modifier.

The SO_2 adsorption isotherms in Fig. 1b show that all the modified montmorillonite samples as a whole sorb SO_2 worse than NH_3, with the sorbents becoming saturated even at p/p_s ratios close to 0.2–0.3. The best sorption properties with respect to SO_2 are shown by the Al–MM sample. This is quite consistent with the observed trends in the surface acidity of modified montmorillonite samples, i.e., an acid gas is adsorbed to a greater extent by a less acid sample. For SO_2 adsorption, as for NH_3 adsorption, the introduction of additional metal ions into modifying Fe(III) PHC also impairs the sorption properties of modified montmorillonite. This is consistent with the results of [8], according to which catalyst samples containing Ni oxides sorb SO_2 worse than those containing Fe(III) oxides.

To conclude, our study shows that montmorillonite materials modified with iron(III) polyhydroxo complexes are good sorbents for NH_3.

REFERENCES

1. Rat'ko, A.I., Bondareva, G.V., Panasyugin, A.S., and Belyi, O.A., *Kolloidn. Zh.*, 2001, vol. 63, no. 5, pp. 1–5.
2. Panasyugin, A.S., Rat'ko, A.I., Trofimenko, N.E., and Masherova, N.I., *Kolloidn. Zh.*, 1999, vol. 61, no. 5, pp. 1–6.
3. Komarov, V.S., Panasyugin, A.S., Trofimenko, N.E., *et al.*, *Kolloidn. Zh.*, 1995, vol. 57, no. 1, pp. 51–54.
4. Gregg, S.J., and Sing, K.S.W., *Adsorption, Surface Area, and Porosity*, New York: Academic, 1967.
5. Datka, J., and Gil, B., *J. Mol. Struct.*, 2001, vol. 596, pp. 41–45.
6. Brown, D.R., and Rhodes, C.N., *Thermochim. Acta*, 1997, vol. 294, pp. 33–37.
7. Narayanan, S., and Deshpande, K., *Appl. Catal. A: Gen.*, 2000, vol. 193, pp. 17–27.
8. Pàlinkò, I., Làsàr, K., and Kiricsi, I., *J. Mol. Struct.*, 1997, vol. 410, pp. 547–550.

Russian Journal of Applied Chemistry, Vol. 77, No. 5, 2004, pp. 848–850. Translated from Zhurnal Prikladnoi Khimii, Vol. 77, No. 5, 2004, pp. 853–855.

BRIEF COMMUNICATIONS

Surface Tension in Aqueous Dodecylethylaminocarbonyldimethylbenzylammonium Chloride

N. N. Kochurova, O. P. Korotkikh, and M. V. Dmitrovskaya

Chemistry Research Institute, St. Petersburg State University, St. Petersburg, Russia

Received December 17, 2003; in final form, February 2004

Abstract—The surface tension of aqueous solutions of the cationic surfactant dodecylethylaminocarbonyldimethylbenzylammonium chloride is measured for the first time over a wide concentration range from 7.9×10^{-7} to 3.9×10^{-2} M at 20–35°C. The critical micelle concentration of DAEDMBAC as influenced by temperature is determined.

Surfactants are intensively studied because of their wide use in micellar catalysis, organic synthesis, as detergents and components of lubricants, in dyeing, dry cleaning, photographic processes, as models for various biological and physiological objects, etc. [1]. Addition of surfactants to water and other liquids such as oil and petroleum products decreases the expenses for their pipeline transportation and pipeline steel intensity. All these applications are based on the ability of surfactants to decrease the surface tension of solutions.

In this work we reported on the surface tension of a new, practically unstudied surfactant, dodecylethylaminocarbonyldimethylbenzylammonium chloride (DEADMBAC), as influenced by the solution concentration and temperature, and also on the critical micelle concentration (CMC) of the solutions and adsorption of DEADMBAC.

EXPERIMENTAL

The structural formula of the surfactant studied is

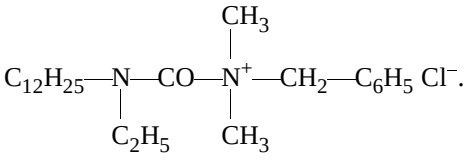

The purity of this compound was confirmed by the shape of the surface tension isotherm (no minimum near CMC). Aqueous DEADMBAC solutions were prepared using double-distilled water.

The surface tension was measured by the ring detachment method with a Markada digital instrument (St. Petersburg) [2]. Initially the instrument was calibrated by measuring the surface tension of hexane, isopropanol, benzene, ethylene glycol, and double-distilled water. The calibration curve (Fig. 1) is linear, allowing determination of the surface tension to within 0.5 mN m^{-1}.

Measurements were conducted at 20, 25, 30, and 35°C and concentrations from 7.9×10^{-7} to 3.9×10^{-2} M. The results are given in Fig. 2. Under the experimental conditions, the surface tension γ decreases by more than 33 mN m^{-1} as the concentration increases, and by 2–3 mN m^{-1} with increasing temperature. Such concentration and temperature dependences are typical of surfactant solutions [1, 3].

From the measured surface tension we estimated the adsorption Γ (mol m^{-2}) by

$$\Gamma = -\frac{1}{2RT}\frac{\partial\gamma}{\partial \ln a}, \qquad (1)$$

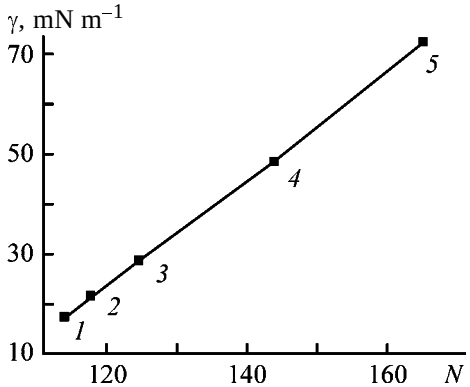

Fig. 1. Calibration curve for determination of the surface tension. (γ) Surface tension and (*N*) scale reading. (*1*) Hexane, (*2*) isopropanol, (*3*) benzene, (*4*) ethylene glycol, and (*5*) water.

1070-4272/04/7705-0848 © 2004 MAIK "Nauka/Interperiodica"

where R is the gas constant; T, absolute temperature; a, activity (M) [$a = cf$, here c is the concentration (M) and f, activity coefficient].

The mean activity coefficient can be estimated by the Debye–Hückel approximation [4] using Eq. (2).

$$\log f_{\pm} = -\frac{AI^{1/2}}{1 + BI^{1/2}}, \quad (2)$$

where the coefficients A and B are the functions of the temperature (they were taken from [4]) and I is the solution ionic strength.

The estimated activity coefficients were demonstrated to be close to unity over the entire concentration and temperature ranges studied in this work, ranging from 0.9990 at 7.9×10^{-7} M to 0.9830 at 4×10^{-3} M.

The experimental dependences $\gamma(\ln a)$ obtained at 20, 25, 30, and 35°C were, respectively, approximated by the following relationships:

$$d\gamma/d\ln a = -17.79 - 1.1\ln a,$$

$$d\gamma/d\ln a = -21.21 - 1.46\ln a,$$

$$d\gamma/d\ln a = -22.82 - 1.56\ln a,$$

$$d\gamma/d\ln a = -21.67 - 0.72\ln a.$$

and then the adsorption was estimated by Eq. (1).

The estimated concentration and temperature dependences of the adsorption are presented in Fig. 3. The adsorption obtained for DEADMBAC (about 10^{-6} mol m^{-2}) is well comparable with that of other surfactants [3].

In parallel to the surface tension measurements we determined CMC. It is 4.5×10^{-4}, 3.4×10^{-4}, 2.6×10^{-4}, and 5.5×10^{-4} M at 20, 25, 30, and 35°C, respectively.

These values are plotted in Fig. 4, demonstrating a clearly pronounced minimum near 30°C. It is known that micelles are formed in aqueous surfactant solutions through hydrophobic interactions with water, resulting in displacement of surfactant molecules from water. Study of the kinetic features of the cation DEADMBAC$^+$ in aqueous solutions of the chloride salt showed that, at 30–35°C, the nature of interaction of the cation with water changed. At temperatures below 30°C, the presence of the surfactant decreases the activation energy of translation motion of the nearest water molecules (negative hydration by Samoilov [5]), decreasing the degree of structurization of water. Above 30°C, the surfactant increases the activation energy and the degree of structurization (positive hydration). Therefore, the temperature of about 30°C corresponds to the minimal CMC. At

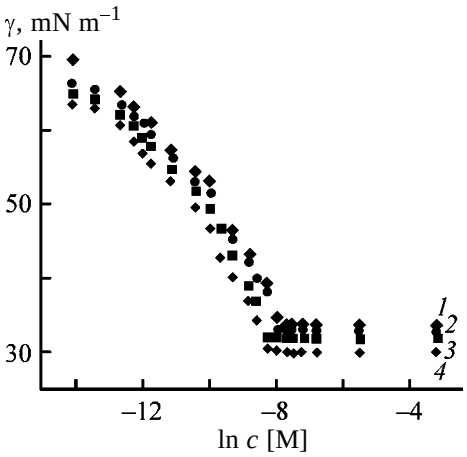

Fig. 2. Isotherms of the surface tension γ in aqueous DEADMBAC solutions. (c) Concentration. Temperature (°C): (*1*) 20, (*2*) 25, (*3*) 30, and (*4*) 35; the same for Fig. 3.

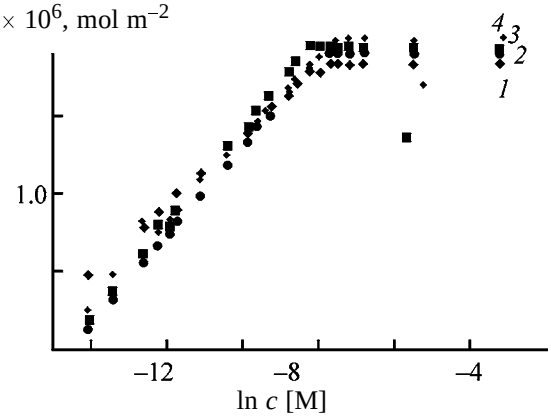

Fig. 3. Adsorption Γ of DEADMBAC as a function of the concentration c.

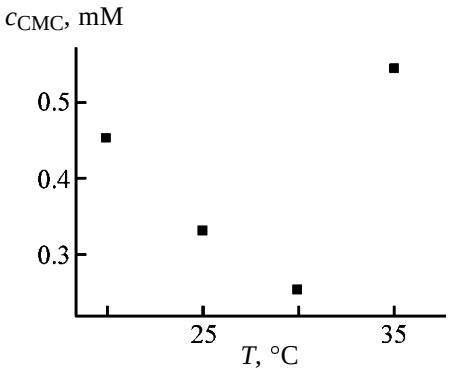

Fig. 4. Critical micelle concentration c_{CMC} as a function of the temperature T.

lower and higher temperatures, higher surfactant concentration is required for micelles to be formed. Similar temperature dependence of CMC was observed for other surfactants (see, e.g., [6]).

CONCLUSIONS

(1) For the first time the surface tension of DEADMBAC is studied at 20, 25, 30, and 35°C over a wide concentration range from 7.9×10^{-7} to 3.9×10^{-2} M.

(2) The critical micelle concentration of DAEDMBAC is determined at various temperatures. The CMC is minimal at about 30°C.

(3) The equilibrium adsorption at 20–35°C is estimated to be approximately 1×10^{-6} mol m^{-2}.

ACKNOWLEDGMENTS

The work was financially supported by the Science and Technology Program "Scientific Research in High School on Foreground Scientific and Technological Tasks" (project no. 205.06.06.035) and RF President Program "Leading Russian Scientific Schools," grant NSh 789.2003.3.

REFERENCES

1. Rusanov, A.I., *Mitselloobrazovanie v rastvorakh poverkhnostno-aktivnykh veshchestv* (Micelle Formation in Surfactant Solutions), St. Petersburg: Khimiya, 1992.
2. Abdulin, N.G., Kochurova, N.N., and Rusanov, A.I., *Kolloidn. Zh.*, 1997, vol. 59, no. 6, pp. 725–728.
3. Abramzon, A.A., *Poverkhnostno-aktivnye veshchestva* (Surfactants), Leningrad: Khimiya, 1962.
4. Burchfield, I.E. and Woolky, E.M., *J. Phys. Chem.*, 1984, vol. 88, no. 10, pp. 2149–2155.
5. Samoilov, O.Ya., *Struktura vodnykh rastvorov elektrolitov i gidratatsiya ionov* (Structure of Aqueous Electrolyte Solutions and Ion Hydration), Moscow: Akad. Nauk SSSR, 1957.
6. Mehrian, T., Keizer, A., Korteweg, A.G. de, and Lyklema, J., *Colloids Surf., Ser. A*, 1993, vol. 71, pp. 255–267.

Russian Journal of Applied Chemistry, Vol. 77, No. 5, 2004, pp. 851–852. Translated from Zhurnal Prikladnoi Khimii, Vol. 77, No. 5, 2004, pp. 856–857.

BRIEF COMMUNICATIONS

Synthesis and Corrosion-Protective Properties of 2,3,5,10*b*-Tetrahydrooxazolo[3,2-*c*][1,3]benzoxazine

B. F. Kukharev, V. K. Stankevich, G. R. Klimenko, V. A. Kukhareva, E. N. Kovalyuk, and V. V. Bayandin

Favorskii Irkutsk Institute of Chemistry, Siberian Division, Russian Academy of Sciences, Irkutsk, Russia

Received October 16, 2003; in final form, February 2004

Abstract—A new method was developed for one-pot synthesis of 2,3,5,10*b*-tetrahydrooxazolo[3,2-*c*][1,3]-benzoxazine in 51% yield by successive reactions of monoethanolamine with salicylaldehyde and paraformaldehyde. The corrosion-protective properties of the title compound and intermediate *N*-(2-hydroxybenzylidene)-2-aminoethanol were studied.

It is known that some oxazolidines exhibit corrosion-protective properties [1–4]. In this work, with the aim to reveal corrosion-protective properties of compounds containing oxazolidine and dihydrooxazine rings, we prepared 2,3,5,10*b*-tetrahydrooxazolo[3,2-*c*]-[1,3]benzoxazine **II** and studied its inhibiting performance in carbon dioxide and hydrogen sulfide acid corrosion of steel.

2,3,5,10*b*-Tetrahydrooxazolo[3,2-*c*][1,3]benzoxazine was prepared previously in 43% yield by condensation of *N*-(2-hydroxybenzylidene)-2-aminoethanol **I** with paraformaldehyde in benzene [5]. 2,3,5,10*b*-Tetrahydrooxazolo[3,2-*c*][1,3]benzoxazine derivatives were prepared in 57–67% yields by condensation of oxazolidines unsubstituted at the N atom with salicylaldehyde [6]. Since the conditions for the synthesis of **II** by both methods and for the synthesis of imino alcohol **I** and oxazolidines are very similar [7], we examined the possibility of one-pot synthesis of oxazolobenzoxazine **II** from monoethanolamine, salicylaldehyde, and paraformaldehyde.

In developing the synthesis, we proceeded from the conditions used for each separate step in [5–7]. As solvent we used benzene. Condensation of monoethanolamine with salicylaldehyde was performed by refluxing an equimolar mixture of the reactants, with the azeotropic distillation of water. After the release of water ceased, a stoichiometric amount of paraformaldehyde was added, and the mixture was further refluxed until the release of the new portion of water ceased:

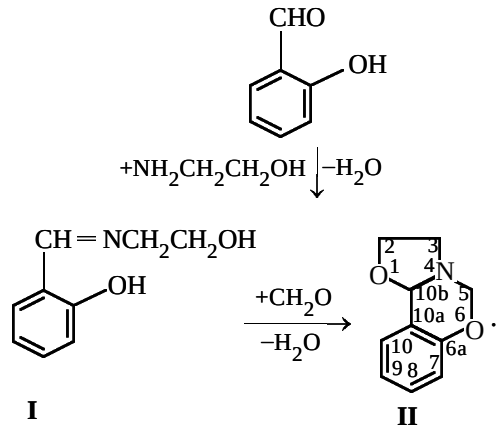

I **II**

The yield of oxazolobenzoxazine **II** under these conditions was 51.2%. When any of the reactants was taken in a small (5–10%) molar excess, the yield of **II** decreased by 5–12%.

Based on the procedure for preparing 2,3,5,10*b*-tetrahydrooxazolo[3,2-*c*][1,3]benzoxazine derivatives [6], we tested another reaction sequence for one-pot synthesis of **II**: initial preparation of oxazolidine from monoethanolamine and paraformaldehyde, followed by condensation of this oxazolidine with salicylaldehyde. However, in this case we obtained only traces of **II**. This may be due to the fact that the simplest oxazolidine formed in the first step readily isomerizes into stable *N*,*N*',*N*"-tris(2-hydroxyethyl)perhydro-1,3,5-triazine [8], which does not react with salicylaldehyde.

Also unsuccessful was our attempt to prepare **II** in one step by mixing all the three components (salicyl-

1070-4272/04/7705-0851 © 2004 MAIK "Nauka/Interperiodica"

aldehyde, monoethanolamine, paraformaldehyde) simultaneously. In this case, monoethanolamine immediately reacts with paraformaldehyde with heat release and formation of *N*,*N*',*N*"-tris(2-hydroxyethyl)perhydro-1,3,5-triazine.

To evaluate the inhibiting power of **II**, we examined its effect on the corrosion of steel under conditions simulating the steel corrosion in oil production [9]. For comparison, we also tested the reaction intermediate, imino alcohol **I**.

The corrosion-protective activity was studied gravimetrically with 2 × 20 × 6-mm samples of St.3 steel according to GOST (State Standard) 9.505–86 in 1% NaCl saturated with CO_2 in the presence of H_2S at 20, 40, and 60°C and contact time of 3 h. When added in a concentration of 10^{-3} M, the compounds showed the following protective effect *Z* (%): 98.1 (20°C), 97.2 (40°C), and 58.5 (60°C) for **II**; 88.2 (20°C), 79.3 (40°C), and 50.1 (60°C) for **I**. Thus, 2,3,5,10*b*-tetrahydrooxazolo[3,2-*c*][1,3]benzoxazine derivatives show promise as corrosion inhibitors.

EXPERIMENTAL

Paraform (99.3% pure), monoethanolamine, and salicylaldehyde were commercial chemicals; the latter two compounds were purified by fractional distillation to no less than 99.8% purity.

2,3,5,10*b*-Tetrahydrooxazolo[3,2-*c*][1,3]benzoxazine II. A mixture of 30.5 g (0.5 mol) of monoethanolamine, 61.1 g (0.5 mol) of salicylaldehyde, and 250 ml of benzene was refluxed with a Dean–Stark trap until the release of water ceased. Then 15.1 g (0.5 mol) of paraform was added, and the mixture was refluxed until the release of water ceased. Then the mixture was cooled and separated by fractional distillation to obtain 90.7 g (51.2%) of **II**; bp 110–112°C at 3 mm Hg; d_4^{20} = 1.2177; n_D^{20} = 1.5624. Published data [5]: bp 111–113°C at 3 mm Hg; d_4^{20} = 1.2180; n_D^{20} = 1.5631. ^{1}H NMR spectrum (400 MHz, $CDCl_3$, HMDS), δ, ppm (*J*, Hz): 3.08 (2H, m, NCH_2), 3.81 (2H, m, OCH_2), 4.67 (1H, d, NCH_2O, ^2J = 9.7), 4.79 (1H, d, NCH_2O, ^2J = 9.7), 5.58 (1H, s, NCHO), 6.84 (1H, d.d, C^7H, $J_{7,8}$ = 8.2, $J_{7,9}$ = 1.2), 6.93 (1H, d.d.d, C^9H, $J_{9,10}$ = 7.6, $J_{8,9}$ = 7.4, $J_{7,9}$ = 1.2), 7.19 (1H, d.d.d, C^8H, $J_{7,8}$ = 8.2, $J_{8,9}$ = 7.4, $J_{8,10}$ = 1.8), 7.24 (1H, d.d, $C^{10}H$, $J_{9,10}$ = 7.6, $J_{8,10}$ = 1.8).

Found, %: C 67.66, H 6.21, N 7.73. $C_{10}H_{10}NO_2$. Calculated, %: C 67.78, H 6.26, N 7.90.

***N*(2-Hydroxybenzylidene)-2-aminoethanol I.** A mixture of 6.1 g (0.1 mol) of monoethanolamine, 12.2 g (0.1 mol) of salicylaldehyde, and 100 ml of benzene was refluxed with a Dean–Stark trap until the release of water ceased. Fractional distillation in a vacuum gave 14.7 g (89%) of **I**, bp 161–163°C at 3 mm Hg; d_4^{30} = 1.1598; n_D^{30} = 1.5957. Published data [7]: bp 137–139°C at 1 mm Hg; d_4^{30} = 1.1547; n_D^{30} = 1.5936.

CONCLUSIONS

(1) Conditions were found for one-pot synthesis of 2,3,5,10*b*-tetrahydrooxazolo[3,2-*c*][1,3]benzoxazine from monoethanolamine, salicylaldehyde, and paraformaldehyde in a higher yield based on the starting reactants than in the two-step synthesis with the intermediate isolation of *N*-(2-hydroxybenzylidene)-2-aminoethanol.

(2) The protective effect of 2,3,5,10*b*-tetrahydrooxazolo[3,2-*c*][1,3]benzoxazine in carbon dioxide and hydrogen sulfide corrosion of steel reaches 98%.

REFERENCES

1. Kukharev, B.F., Stankevich, V.K., Klimenko, G.R., *et al.*, *Zh. Prikl. Khim.*, 1993, vol. 66, no. 7, pp. 1653–1654.
2. Kukharev, B.F., Stankevich, V.K., Klimenko, G.R., and Baranov, A.N., *Zh. Prikl. Khim.*, 1995, vol. 68, no. 1, pp. 142–143.
3. Baranov, A.N., Kovalyuk, E.N., Kukharev, B.F., and Mikhailov, B.N., *Izv. Vyssh. Uchebn. Zaved., Tsvetn. Metall.*, 1998, no. 3, pp. 53–55.
4. Kukharev, B.F., Stankevich, V.K., Klimenko, G.R., *et al.*, *Nauka Proizv.*, 2003, no. 6, pp. 36–37.
5. Kukharev, B.F., *Zh. Org. Khim.*, 1989, vol. 25, no. 11, pp. 2454–2455.
6. Kukharev, B.F., Stankevich, V.K., Klimenko, G.R., and Bayandin, V.V., *Mendeleev Commun.*, 2001, no. 4, pp. 143–144.
7. Bergmann, E.D., Zimkin, E., and Pinchas, S., *Recl. Trav. Chim. Pays-Bas*, 1952, vol. 71, no. 2, pp. 168–191.
8. Riehl, M. and Laurent, P.A., *Bull. Soc. Chim. Fr.*, 1969, no. 4, pp. 1223–1226.
9. Saakiyan, A.S. and Efremov, A.P., *Zashchita neftepromyslovogo oborudovaniya ot korrozii* (Corrosion Protection of Oil-Extraction Equipment), Moscow: Nedra, 1982.

Russian Journal of Applied Chemistry, Vol. 77, No. 5, 2004, pp. 853–854. Translated from Zhurnal Prikladnoi Khimii, Vol. 77, No. 5, 2004, pp. 858–859.

BRIEF COMMUNICATIONS

Synthesis of Condensed Nitrofuroxanes Using Hydroxylamine

O. R. Klyuchnikov, V. I. Starovoitov, F. G. Khairutdinov, and V. V. Golovin

Kazan State Technological University, Kazan, Tatarstan, Russia

Received January 13, 2004

Abstract—The possibility of preparing condensed nitrofuroxanes using hydroxylamine was examined.

Benzofuroxanes exhibit biological activity and are intermediates in synthesis of a number of effective antimicrobial agents; 4,6-dinitrobenzofuroxane in the form of salts is used in priming charges [1]. In this connection, it is interesting to develop relatively safe methods for preparing nitrofuroxanes without using azides.

Previous studies concerning formation of the furoxane ring in synthesis of 4,6-dinitrobenzofuroxane by reaction of picryl chloride, hydroxylamine hydrochloride, and sodium acetate showed that the intermediate in this procedure is picrylhydroxylamine [2]. This finding allowed preparation of 3-nitro[4,5-*c*]pyridofuroxane by the reaction of 4-hydroxylamino-3,5-dinitropyridine with picryl chloride [3]. Similarly, the reaction of 2,4- or 2,6-dinitrophenylhydroxylamine or its potassium salt with picryl chloride also yielded, respectively, 4- or 6-nitrobenzofuroxane and picric acid:

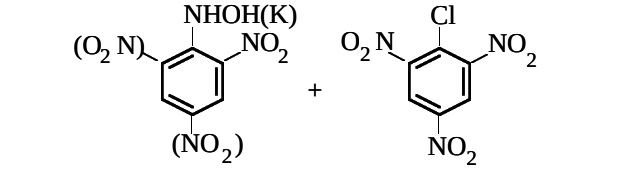

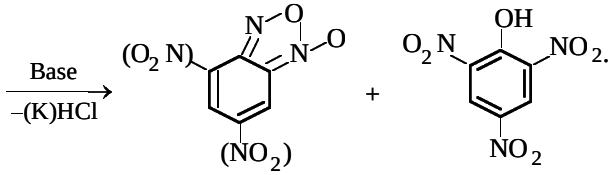

From compounds containing a labile nitro group, 4,6-dinitrobenzofuroxane derivatives are formed also:

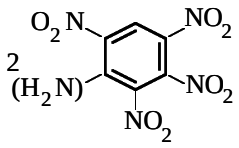

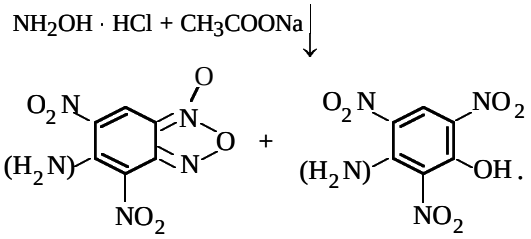

EXPERIMENTAL

4- and 6-Nitrobenzofuroxanes were prepared by adding 2.48 g (0.01 mol) of picryl chloride to a suspension of 2.37 g (0.01 mol) of potassium salt of, respectively, 2,6- and 2,4-dinitrophenylhydroxylamine in 30 ml of MeOH at room temperature with stirring. The mixture was left for 0.5 h and poured into 60 ml of water. The precipitate of 4- or 6-nitrobenzofuroxane was filtered off, washed with water, and dried. Yield of 4-nitrobenzofuroxane 1.67 g (92%), mp 112°C (from EtOH); yield of 6-nitrobenzofuroxane 1.59 g (88%), mp 74–76°C (from EtOH).

4,6-Dinitrobenzofuroxane was prepared by gradual addition of 5.16 g (0.02 mol) of 1,2,3,5-tetranitrobenzene to a suspension of 1.39 g (0.02 mol) of hydroxylamine hydrochloride and 3.28 g (0.04 mol) of sodium acetate in 50 ml of MeOH at 45–50°C with stirring. The mixture was stirred at this temperature for an additional 1 h, after which it was cooled and diluted with water; the precipitate was filtered off, washed with water, and dried. Yield 2.1 g (93%), mp 172°C (from MeOH).

5-Amino-4,6-dinitrobenzofuroxane was prepared similarly by adding 5.46 g (0.02 mol) of 2,3,4,6-tetranitroaniline to a suspension of 1.39 g (0.02 mol) of hydroxylamine hydrochloride and 3.28 g (0.04 mol) of sodium acetate in 50 ml of MeOH at 45–50°C. The reaction mixture was kept at this temperature for an additional 2 h, after which it was cooled, and the pre-

1070-4272/04/7705-0853 © 2004 MAIK "Nauka/Interperiodica"

cipitate was filtered off, washed with water, and dried. Yield 2.0 g (83%), mp 265–266°C (from AcOH).

The physicochemical constants of the compounds prepared coincide with those of the authentic samples prepared by the azide method [4–6].

CONCLUSION

A procedure for preparing condensed nitrofuroxanes in good yields using hydroxylamine was suggested to replace the less safe azide method.

REFERENCES

1. Khmel'nitskii, L.I., Novikov, S.S., and Godovikova, T.I., *Khimiya furoksanov: Reaktsii i primenenie* (Chemistry of Furoxanes: Reactions and Applications), Moscow: Nauka, 1983.
2. Klyuchnikov, O.R., Starovoitov, V.V., Khairutdinov, F.G., and Golovin, V.V., *Khim. Geterotsikl. Soedin.*, 1996, no. 3, p. 428.
3. Klyuchnikov, O.R., Khairutdinov, F.G., Golovin, V.V., and Falyakhov, I.F., *Khim. Geterotsikl. Soedin.*, 2000, no. 8, pp. 1143–1144.
4. Duall, L.K., *Aust. J. Chem.*, 1975, vol. 28, pp. 2147–2159.
5. Hobin, T.P., *Tetrahedron*, 1968, vol. 24, pp. 6145–6148.
6. Khmel'nitskii, L.I., Novikov, S.S., and Godovikova, T.I., *Khimiya furoksanov: Stroenie i sintez* (Chemistry of Furoxanes: Structure and Synthesis), Moscow: Nauka, 1981.

Russian Journal of Applied Chemistry, Vol. 77, No. 5, 2004, pp. 855–857. Translated from Zhurnal Prikladnoi Khimii, Vol. 77, No. 5, 2004, pp. 860–862.

BRIEF COMMUNICATIONS

Orcinol as Inhibitor of Thermal Polymerization in Processing of Pyrolysis Intermediates

A. V. Ivanova, A. F. Gogotov, and V. K. Stankevich

Angarsk Pertochemical Company, Open Joint-Stock Company, Angarsk, Irkutsk oblast, Russia
Favorskii Irkutsk Institute of Chemistry, Siberian Division, Russian Academy of Sciences, Irkutsk, Russia

Received November 20, 2003; in final form, March 2004

Abstract—Fractionation of dihydric phenols from coal-tar chemical productions was studied, and various fractions were tested as inhibitors of thermal polymerization of unsaturated components of pyrocondensates.

Modern pyrolysis production is impossible without using inhibitors [1, 2]. Production of ethylene–propylene and benzene involves the use of such inhibitors as phenols, amines, and various multicomponent formulations in distillation of pyrolysis intermediates. The cheapest and the most readily available inhibitors are phenolic fractions from thermal processing of coal and wood [3, 4]. The most effective phenolic inhibitors are derivatives of dihydric phenols, alkylated hydroquinones and pyrocatechols. Their high inhibiting activity is due to the capability for conformational transition into the corresponding quinones. Among individual phenols, the most widely used polymerization inhibitor is *tert*-butylpyrocatechol (TBPC) [5–7]. The inhibiting activity of FCh-16, an inhibitor widely used in coal-tar chemical industry, and pyrocatechol fraction (PCF) is specifically due to the presence of mono- and dialkyl derivatives of pyrocatechols and hydroquinones [3, 8, 9]. The PCF composition (see table), determined with a Hewlett–Packard gas chromatograph–mass spectrometer using the relevant data bases [8], shows that this fraction contains pyrocatechols, resorcinols, and hydroquinones, with insignificant (~5–6%) content of various monohydric phenols.

We performed fractionation of PCF to closer-cut fractions with the aim to find what groups of dihydric phenols exhibit stronger inhibiting power and to reveal the components (pyrocatechols, resorcinols, or hydroquinones) that inhibit polymerization of pyrocondensates most actively. For this purpose, the fraction of dihydric phenols was subjected to finer fractional distillation. Pyrocatechols and hydroquinones (118–146°C fraction) comprise 84.1 wt % in total, and resorcinols [resorcinol fraction, RF (146–160°C)], 15.9%.

The isolated fractions were tested as inhibitors. The results for RF are shown in Fig. 1. The effect obtained at 0.025–0.030 wt % content of RF was 52–54%, and the maximal effect, 74%, was attained at 0.05 wt % content of RF. The RF (see table) contains in approximately equal amounts unsubstituted resorcinol and methylresorcinol in the form of two isomers with 5- and 2-methyl groups. As for nonphenolic components, RF contains a large set of mono-, di- and trialkylbenzenes. As resorcinol and 3,5-dihydroxytoluene are the major components of RF, they were tested as individual inhibitors. Resorcinol showed poor performance (~20% effect). The performance of 3,5-dihydroxytoluene (orcinol, 5-methylresorcinol) was stud-

Composition of pyrocatechol and resorcinol fractions

Components	Content, wt %
PCF:	
phenol	2.5
cresols	2.7
xylenols + ethylphenols	0.9
pyrocatechol	11.3
3-methylpyrocatechol	7.6
4-methylpyrocatechol	13.8
resorcinol + hydroquinone	8.6
isomeric dimethylhydroquinones	4.3
isomeric methylresorcinols	14.8
dimethyl- and ethylresorcinols	13.7
RF:	
resorcinol	24.4
1,3-dihydroxy-2-methylbenzene	5.2
3,5-dihydroxytoluene (orcinol)	17.3
methylguaiacol	3.4
2-naphthol	0.1

1070-4272/04/7705-0855 © 2004 MAIK "Nauka/Interperiodica"

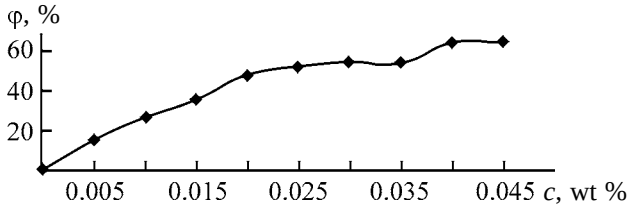

Fig. 1. Efficiency of inhibition of K-27 pyrocondensate φ as a function of the resorcinol fraction content *c*.

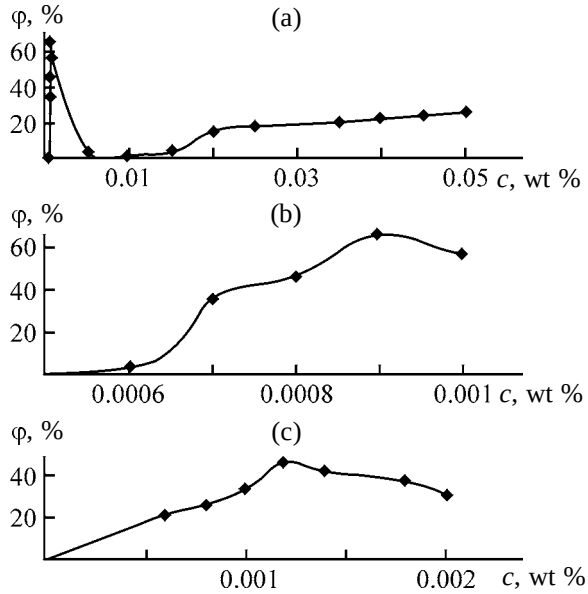

Fig. 2. Inhibiting activity of orcinol φ in polymerization of pyrocondensates as a function of its content *c*: (a) *c* 0–0.05 wt %, K-27 pyrocondensate; (b) *c* 0.0005–0.001 wt %, K-27 pyrocondensate; and (c) *c* 0–0.002 wt %, K-20 pyrocondensate.

ied in the range of its content of 0.0–0.5 wt %; the range 0.0006–0.01 wt % was studied in more detail.

The tests (Figs. 2a, 2b) revealed fairly high performance of orcinol at its extremely low content relative to the weight of the K-27 column pyrocondensate. A specific feature of orcinol is a drastic decrease in the inhibiting activity beyond the range of optimal concentrations; the maximal activity (66% effect) was observed at 0.0009 wt % content or orcinol.

With the K-20 column pyrocondensate, orcinol shows the highest inhibiting activity (45% effect) in the different concentration range (Fig. 2c).

Thus, experiments on inhibition of thermal polymerization revealed extremely high inhibiting activity of some phenolic compounds, comparable only with inhibitors of the last generation, nitroxyl radicals [10]. The high inhibiting activity of resorcinol derivatives in thermal polymerization was also revealed for the first time [11]. As noted above, it was believed until recently that, among dihydric phenols, only pyrocatechols and hydroquinones could show inhibiting activity due to their capability for phenol–quinone redox transformations. Quinones form a well-known class of effective inhibitors of radical processes [12]. The most widely used polymerization inhibitor, TBPC, shows high inhibiting performance at its content of 0.015–0.017 wt %, which is by an order of magnitude higher compared to the optimal content of orcinol. As the TBPC content is decreased to 0.002– 0.004 wt %, its activity drastically decreases, and in concentrations comparable with the optimal concentration of orcinol (0.0008–0.0012 wt %) its activity is as low as 2–3% (against 45–66% for orcinol).

The high inhibiting activity of resorcinol derivatives may be due to possible transformation of these compounds into the diketo tautomer with active methylene group at high temperature. Such transformations are known for 1,3-dihydroxy compounds, and their occurrence depends on the solvent polarity, its acid–base properties, temperature, and mutual location of substituents [13]. The C^2 atom in the 1,3-dioxo form is CH-active, and the activity of such species differs in the nature from the activity associated with the phenol–quinone transformations: responsible for deactivation of radical species are labile hydrogen atoms of the CH_2 groups. It should be noted that orcinol as a methylene-active compound is used in organic analysis for determination of carbonyl groups, e.g., in cellulose (orcinol method) [14].

CONCLUSIONS

(1) Resorcinols exhibit inhibiting activity in thermal polymerization of unsaturated components of pyrocondensates.

(2) Orcinol shows particularly high inhibiting effect (~66%) at its extremely low content, 0.0009–0.0012 wt %, considerably surpassing in the inhibiting performance the widely used inhibitor, *tert*-butylpyrocatechol (added in the same amount).

REFERENCES

1. Mukhina, T.N., Barabanov, N.L., Babash, S.E., *et al.*, *Piroliz uglevodorodnogo syr'ya* (Pyrolysis of Hydrocarbon Raw Materials), Moscow: Khimiya, 1987.
2. Kurbatov, V.A., Liakumovich, A.G., and Kirpichnikov, P.A., *Neftekhimiya*, 1983, vol. 23, no. 1, pp. 118–120.
3. Berents, A.D., Vol'-Epshtein, A.B., Mukhina, T.N.,

and Avrekh, G.L., *Pererabotka zhidkikh produktov piroliza* (Processing of Liquid Pyrolysis Products), Moscow: Khimiya, 1985.

4. Zav'yalov, A.N., Gol'dshmidt, Yu.M., Zav'yalova, Z.A., and Kasilova, L.V., *Drevesnosmolyanoi i drugie ingibitory tsepnykh protsessov* (Wood-Tar and Other Inhibitors of Chain Processes), Moscow: VNIPIEIlesprom, 1978.
5. RF Patent 2154048.
6. RF Patent Appl. 2000119908/04.
7. Gogotov, A.F., Amosov, V.V., Tayurskii, V.A., *et al.*, *Proizv. Elastom.*, 2002, no. 1, pp. 3–9.
8. Gogotov, A.F., Novichikhin, D.N., Bobyleva, E.E., *et al.*, *Neftepererab. Neftekhim.*, 1999, no. 10, pp. 23–27.
9. RF Patent 2127750.
10. RF Patent Appl. 93048468/04.
11. RF Patent 2215728.
12. Kirpichnikov, P.A., Liakumovich, A.G., Pobedimskii, D.G., and Popova, L.M., *Khimiya i tekhnologiya monomerov dlya sinteticheskikh kauchukov* (Chemistry and Technology of Monomers for Synthetic Rubbers), Leningrad: Khimiya, 1981.
13. Levina, R.Ya. and Velichko, F.K., *Usp. Khim.*, 1960, vol. 29, no. 8, pp. 929–971.
14. Obolenskaya, A.V., El'nitskaya, Z.P., Leonovich, A.A., *et al.*, *Laboratornye raboty po khimii drevesiny i tsellyulozy* (Laboratory Works on Wood and Cellulose Chemistry), Moscow: Ekologiya, 1991.

Russian Journal of Applied Chemistry, Vol. 77, No. 5, 2004, pp. 858–860. Translated from Zhurnal Prikladnoi Khimii, Vol. 77, No. 5, 2004, pp. 863–865.

BRIEF COMMUNICATIONS

Use of Nitric Acid for Determination of Lignosulfonates

Yu. G. Khabarov

Arkhangelsk State Technical University, Arkhangelsk, Russia

Received November 25, 2003; in final form, February 2004

Abstract—The possibility of using the reaction of nitric acid with lignosulfonates for their quantitative determination in aqueous solutions was studied.

For photometric determination of lignins, the Pearl-Benson method based on their nitrosation [1] is used most widely. Nitrosation is carried out for 15 min in acidic medium, and the optical density of the solution is measured after alkalization of the reaction medium.

Nitric acid is used in indirect determination of the degree of delignification of lignocellulose materials [2, 3]. The first procedure is based on release of nitrogen oxides in the reaction of a sample being analyzed with HNO_3. Nitrogen oxides are quantitatively collected, and their amount is determined by titration with $KMnO_4$ [2]. In the second procedure, the lignocellulose material after appropriate pretreatment is heated with 14% HNO_3 at 80°C for 15 min. The solid residue is separated by filtration. The yellow filtrate is analyzed photometrically at 425 nm to determine the lignin content in the sample. It is suggested that, under determination conditions, lignin macromolecules are nitrated and degrade, and lignin passes into solution; the products of this process are intensely colored [3].

The use of nitric acid for determination of lignosulfonates (LS) was not reported.

The aim of this work was to assess the possibility of using HNO_3 for photometric determination of LS formed in sulfite cooking of cellulose.

EXPERIMENTAL

We used 14% HNO_3 and a solution with LS concentration of 10 g l^{-1}. The analysis was carried out as follows: Into a 100-ml volumetric flask a certain volume of LS solution and 10 ml of HNO_3 were added. The flask was placed into a boiling water bath for a certain time, after with the solution volume was brought to the mark and the optical density was measured at 315 and 340 nm on a KFK-2MP photocolorimeter.

The UV spectra were recorded in the range 250–400 nm on a Specord M-40 spectrophotometer (Laboratory of Lignin, Institute of Environmental Problems of North, Russian Academy of Sciences, Ural Division).

Upon heating of LS with HNO_3, the color of the reaction mixture significantly changes. To choose the analytical absorption band, we recorded the electronic spectra of a solution of LS prepared by dilution of the

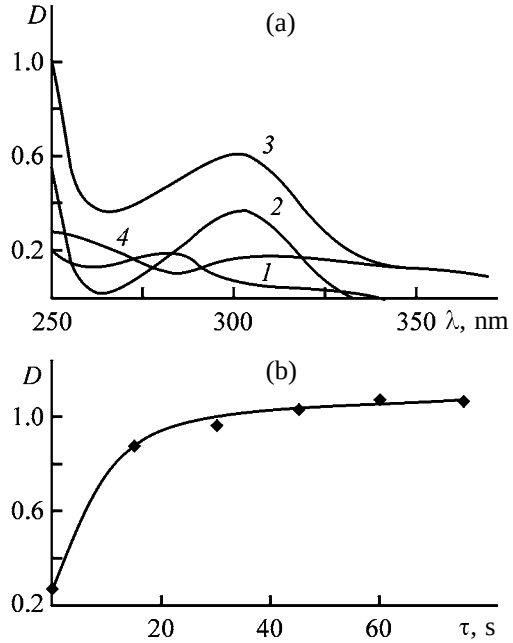

Fig. 1. (a) UV spectra and (b) dependence of optical density D on duration of color reaction τ. (λ) Wavelength. Spectrum: (*1*) solution of the initial LS, (*2*) HNO_3 solution, (*3*) the mixture of the initial LS and HNO_3 after thermal treatment, and (*4*) difference spectrum obtained by subtraction of spectra (*2* + *1*) from spectrum *3*.

1070-4272/04/7705-0858 © 2004 MAIK "Nauka/Interperiodica"

Table 1. Stability of optical density in determination of LS*

τ, min	λ = 315 nm		λ = 340 nm	
	D	variation, %	*D*	variation, %
0	0.929	100.0	0.852	100.0
6	0.925	99.6	0.850	99.8
10	0.924	99.5	0.848	99.5
15	0.922	99.2	0.846	99.3
45	0.919	98.9	0.843	98.9
60	0.917	98.7	0.841	98.7

* (τ) Duration of thermal treatment; (D_{315}, D_{340}) optical densities at 315 and 340 nm, respectively.

initial solution by a factor of 500 (λ_{max} = 280 nm), HNO_3 solution diluted with distilled water by a factor of 50, and a solution prepared by mixing of 1 ml of LS solution and 10 ml of the initial HNO_3 solution and heated on a boiling water bath for 60 s and then diluted with distilled water to 500 ml (Fig. 1a). The spectrum of the reaction products differs essentially from the additive spectrum by increased intensity of absorption at 310 nm (Fig. 1a, spectrum *4*).

In further studies we used the wavelengths of 315 and 340 nm. The band at 340 nm has the advantage that nitric acid does not noteceably absorb at this wavelength. During photometric reaction, the optical density of the solution at 315 nm increases by a factor of 2.44, and at 340 nm, by a factor of 3.5 as compared to the initial LS.

To determine the minimum reaction duration, this parameter was varied from 10 to 75 s in various runs (Fig. 1b). It was found that the maximal optical density is attained within 60 s. The color of the reaction products is stable for a long time (Table 1).

The results listed in Table 2 show that the color reaction is well reproducible. As expected, the coefficient of variation decreases with increasing optical density.

From data listed in Tables 2 and 3, using least-squares technique, we evaluated the coefficients of

Table 2. Reproducibility of the results of photometric determination of optical density*

c_{LS}, mg l^{-1}	λ = 315 nm				λ = 340 nm			
	D_{av}	*n*	$\Delta D \times 10^3$	*V*, %	D_{av}	*n*	$\Delta D \times 10^3$	*V*, %
0.8	0.014	2	1.4	10.1	0.008	2	0.7	9.4
20	0.179	3	2.7	1.4	0.154	3	2.7	1.7
40	0.344	3	6.7	1.9	0.305	3	7.6	2.5
60	0.497	3	6.5	1.3	0.446	3	5.5	1.2
80	0.640	3	11.9	1.8	0.580	3	9.5	1.6
100	0.804	3	7.9	0.9	0.737	3	9.2	1.3

* (c_{LS}) Concentration of lignosulfonates in the solution subjected to photometric determination, (*n*) number of replicate measurements, (Δ*D*) standard deviation, and (*V*) variation.

Table 3. Results of LS* determination

λ = 315 nm						λ = 340 nm					
D_1	D_2	D_{av}	c_{LS}, mg l^{-1}		*S*, %	D_1	D_2	D_{av}	c_{LS}, mg l^{-1}		*S*, %
			given	found					given	found	
0.025	0.026	0.026	2	1.5	24.0	0.017	0.019	0.018	2	1.8	10.2
0.05	0.048	0.049	4.8	4.5	6.7	0.038	0.037	0.038	4.8	4.5	6.9
0.077	0.075	0.076	8	7.9	1.5	0.061	0.059	0.060	8	7.6	5.5
0.432	0.422	0.427	50	52.1	–4.1	0.382	0.373	0.378	50	51.1	–2.2
0.548	0.555	0.552	70	67.7	3.2	0.493	0.497	0.495	70	67.2	3.9
0.718	0.685	0.702	90	86.6	3.7	0.65	0.634	0.642	90	87.4	2.9
0.911	0.929	0.920	120	114	4.9	0.837	0.852	0.845	120	115	4.0

* (*S*) mean relative deviation.

calibration plots for the analytical bands at 315 and 340 nm:

$$D_{315} = 0.007942c_{LS} + 0.013431 \quad (R^2 = 0.9992),$$

$$D_{340} = 0.007289c_{LS} + 0.005916 \quad (R^2 = 0.9996).$$

The large coefficients of pair correlation R^2 suggest that the system in hand obeys the Bouguer–Lambert–Beer law. The possibility of determining the concentration of lignosulfonates was assessed in the experiments; the results are given in Table 3. In a wide range of LS concentrations, a good accuracy of determination was reached. The measurements performed at 340 nm allow determination of LS content with a better accuracy (mean relative deviation 4.5%) than at 315 nm (mean relative deviation 5.7%).

CONCLUSION

Reaction of lignosulfonates with HNO_3 can be used for proximate quantitative analysis of LS. This procedure consists in short thermal treatment of the solution with a nitric acid solution and subsequent photometry at 315–340 nm.

REFERENCES

1. Leithe, W., *Die Analyse der organischen Verunreinigungen in Trink-, Brauch-, und Abwassern*, Stuttgart: Wissenschaftliche, 1972.
2. Fuchs, W., *Die Chemie des Lignins*, Berlin: Springer, 1926.
3. Henriksen, A. and Kesier, R.B., *TAPPI*, 1970, vol. 53, no. 6, pp. 1131–1140.

Russian Journal of Applied Chemistry, Vol. 77, No. 5, 2004, pp. 861–862. Translated from Zhurnal Prikladnoi Khimii, Vol. 77, No. 5, 2004, pp. 866–867.

BRIEF COMMUNICATIONS

Sorption Kinetics of Acid and Reactive Dyes on Wool Fiber in the Presence of Redox Systems

O. V. Petrova, A. A. Burinskaya, and V. V. Kotetskii

St. Petersburg State University of Technology and Design, St. Petersburg, Russia

Received October 28, 2003

Abstract—Low-temperature dyeing with Acid Bordeaux and Reactive Brilliant Red 5CX is studied.

Wool dyeing with acid and reactive dyes is conventionally performed at the boiling temperature of the solution, which may cause unpractical use of expensive raw materials and high energy consumption. Therefore, low-temperature dyeing (at temperature by 15–20°C below the boiling point) is of great practical interest, as allowing minimization of the damage of fiber and decrease in the hydrolysis of reactive dyes, pollution of the environment, and power consumption.

Previously it was demonstrated that addition of redox systems in a dye bath facilitates low-temperature dyeing of wool with acid and reactive dyes [1].

As a substrate we used wool rove with a surface density of 1.32 g cm^{-2}. Dyeing was performed according to the standard procedure [2].

As redox systems we used hydrogen peroxide in a mixture with various reducing agents such as glycerol, glucose, polyoxymethylene, and hexamethylenetetramine.

As demonstrated in [1, 3], the use of redox systems (0.0075–0.015 M) considerably increases the sorption of acid and reactive dyes in the course of low-temperature dyeing. To determine the performance of redox systems in dyeing, we studied the sorption kinetics of acid and reactive dyes on wool fiber. The contact time of the substrate with a dye varied from 15 to 90 min. The sorption was monitored by the residual concentration of dyes in the dye bath. The kinetic curves of Acid Bordeaux and Reactive Brilliant Red 5CX in the presence of various redox systems are given in Figs. 1a and 1b.

In the presence of redox systems, the maximal sorption is observed in the first 60 min. With further increase in the dyeing time, the sorption remains practically unchanged. Thus, the use of any of the redox systems studied facilitates sorption more strongly than does increase in the dyeing temperature from 80°C to the boiling point. To characterize quantitatively the effect of addition of redox systems, we estimated the dyeing rate constants. For this purpose, we plotted the logarithm of the concentration change of a dye against the dyeing time (Figs. 2a, 2b). The observed linearity of the dependence $\log c$–τ suggests the first-order kinetics of dyeing. The rate constants were then estimated by the Stirling's equation [4]. The results are given in the table.

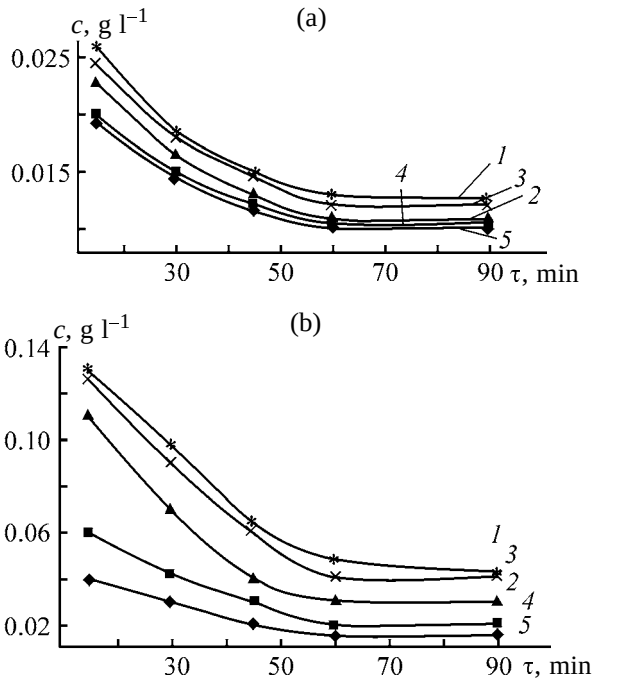

Fig. 1. Kinetic curves of (a) Acid Bordeaux and (b) Reactive Brilliant Red 5CX in the presence of various redox systems: (*1*) no redox system, (*2*) H^2O^{2-}polyoxymethylene, (*3*) H_2O_2–hexamethyleletetramine, (*4*) H_2O_2–glucose, (*5*) H_2O_2–glycerol; the same for Fig. 2. (*c*) Dye concentration and (τ) dyeing time; the same for Fig. 2. Dyeing temperature (°C): (*1*) 100 and (*2*–*5*) 80; the same for Fig. 2.

1070-4272/04/7705-0861 © 2004 MAIK "Nauka/Interperiodica"

Rate constants of dyeing of wool rove with Acid Bordeaux and Reactive Brilliant Red 5CX

Dyeing conditions	Acid Bordeaux		Reactive Brilliant Red 5CX	
	$K \times 10^3$, min^{-1}	E_a, kJ mol^{-1}	$K \times 10^3$, min^{-1}	E_a, kJ mol^{-1}
At bp without redox additive	27.80	133	22.14	119
At 80°C with redox additive:				
H_2O_2–glucose	49.12	116	39.82	106
H_2O_2–glycerol	51.27	113	40.57	86
H_2O_2–hexamethylenetetramine	32.23	123	30.82	113
H_2O_2–polyoxymethylene	46.81	119	32.60	106

$$K = \frac{2.303}{\tau_2 - \tau_1}\log(c_1/c_2),$$

where K is the rate constant (min^{-1}); τ_1 and τ_2 are the times of the start and end of dyeing (min); and c_1 and c_2 are the initial and final dye concentrations in the bath ($g\ l^{-1}$).

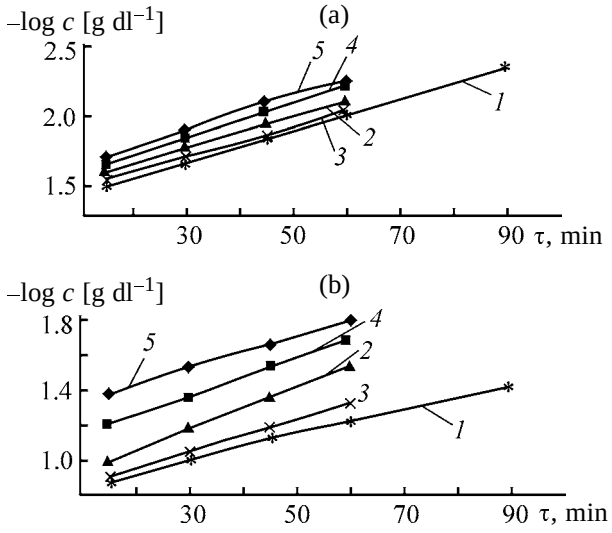

Fig. 2. Concentration change of (a) Acid Bordeaux and (b) Reactive Brilliant Red 5CX in the course of dyeing.

The results show (see table) that introduction of a redox additive increases the sorption rates of the acid and reactive dyes by factors of 1.2–1.9 and 1.5–1.7, respectively, thus creating the necessary prerequisites for reducing the dyeing time. This is also demonstrated by the estimated activation energies.

To conclude, redox additives accelerate sorption of dyes, allowing dyeing with acid and reactive dyes at temperatures below the boiling point of a dyeing liquor and also reduction of the dyeing time.

REFERENCES

1. RF Patent 2 211 265.
2. *Otdelka i krashenie sherstyanykh tkanei: Spravochnik* (Finishing and Dyeing of Wool Fabrics: Reference Book), Molokov, V.L., Ed., Moscow: Legprombytizdat, 1985.
3. Petrova, O.V., Burinskaya, A.A., and Zhukova, A,N., *Tekhlol. Tekstil. Prom-sti.*, 2002, no. 6, pp. 57–60.
4. *Fizicheskaya khimiya* (Physical Chemistry), vol. 2: *Elektrokhimiya: Khimicheskaya kinetika i kataliz* (Electrochemistry: Chemical Kinetics and Catalysis), Krasnov, K.S., Ed., Moscow: Vysshaya Shkola, 1995, pp. 95–113.

Russian Journal of Applied Chemistry, Vol. 77, No. 5, 2004, pp. 863–865. Translated from Zhurnal Prikladnoi Khimii, Vol. 77, No. 5, 2004, pp. 868–870.

HISTORY OF CHEMISTRY AND CHEMICAL TECHNOLOGY

Vladimir Fedorovich Luginin (to 170th Anniversary of His Birthday)

V.F. Luginin, an outstanding Russian thermochemist, a talented experimenter, and a progressive who created the first Russia's Thermal Laboratory at Moscow University at his own expense was the author of quite a number of manuals of calorimetry and head of a prominent scientific school.

Vladimir Fedorovich Luginin was born in Moscow on May 20, 1834, into a rather wealthy nobleman's family. His father, Fedor Nikolaevich Luginin, a former General Staff officer and a participant of the war with Turkey (1825–1829), owned a large forest estate in Vetluga uezd of Kostroma province, which was inherited by his sons. Luginin received an excellent domiciliary education at home. His teacher was H.A. Trautschold (1817–1902), formerly one of Liebig's assistants, later, a known scientist, professor of geology at Petrovskaya (now Timiryazev) academy. As mentioned in [1–3], Trautschold stimulated his pupil's interest in natural sciences and acquainted him with prominent scientific centers, and primarily those in France and Germany, during their trips to West Europe.

In 1849, at the age of 15, Vladimir Luginin entered, on his father's advice, the Mikhail artillery college in St. Petersburg, which was one of the best Russia's military colleges of that time. At that college, as well as at Mikhail artillery academy, taught the most prominent Russian scientists: mathematician M.V. Ostrogradskii (1801–1862), physicist H.F.E. Lenz (1804–1865), and known chemists A.A. Fadeev (1810–1898) and L.N. Shishkov (1830–1909).

In August 1853, Luginin graduated from the cadet department of Mikhail college and was left there to receive higher artillery education as one of the best graduates. However, the war between Russia and Turkey, which began in October 1853, interrupted Luginin's education, and he was assigned to the front-line forces in February 1854. The young officer took part in military action at the Danube River and in the defense of Sevastopol. Only in May 1856, he returned to St. Petersburg and continued his education at the Artillery academy, wherefrom he successfully graduated in April 1858. In 1861, Luginin retired from military service and could commence studies of natural sciences at the best scientific centers of West Europe. For a long time he attended lectures at Heidelberg University (Germany), worked at the chemical laboratory of R.W. Bunsen (1811–1899), studied organic synthesis at the laboratory of J. Wislizenus (1835–1902) in Zurich, attended lectures delivered by Clausius (1828–1888), perfected himself in organic chemistry at the laboratory of C.A. Wurtz (1817–1884) in Paris. In 1866–1867, Luginin published his first studies in organic chemistry. However, his scientific interests switched by that time to physical chemistry, and primarily to thermochemistry. This was favored by scientist's work at the laboratories of H.V. Regnault (1810–1878) and M. Berthelot (1827–1907) in Paris. At Regnault's laboratory, Luginin studied the applicability of the Henry–Dalton law to the solubility of CO_2 in water at various pressures, determined the density of hydrocarbons of the homologous series of benzene in a wide range of temperatures. Further scientist's attention was focused on studies of thermochemical nature. He preserved friendly relationships with M. Berthelot for many years.

1070-4272/04/7705-0863 © 2004 MAIK "Nauka/Interperiodica"

In 1873, Luginin returned to Russia and organized in St. Petersburg a small private laboratory, where he commenced calorimetric measurements. Later, a special laboratory was organized in St. Petersburg, at Luginin's expense and on his initiative, for determining the calorific value of combustible materials.

Beginning in 1882, Luginin worked in Paris. A laboratory aimed to carry out thermochemical studies was organized at the house where his family lived.

At the end of 1888, Luginin again returned to Russia. V.V. Markownikoff (1837–1904), a professor of Moscow University, allowed him to work at his laboratory. In 1889, a group of professors of Moscow University submitted a petition for conferring on Luginin "the degree of a doctor of chemistry without examinations for master's degree and without submitting a dissertation," in acknowledgment of Luginin's achievements in the field of thermochemistry. In January 1890, this move was satisfied. Having received the degree of a doctor of chemistry, Luginin decided to transfer his thermal laboratory from Paris to Moscow, to Moscow University. As mentioned in his memoirs by I.A. Kablukov (1857–1942, honorary member of the Academy of Sciences of the USSR since 1932), a Luginin's disciple and a professor of Moscow State University, Luginin's thermal laboratory "took the first place among thermal laboratories of not only Russia, but West Europe as well" [4]. At that same time, Luginin started to deliver to students of the physicomathematical faculty of Moscow University lectures on thermochemistry, thermometry, and calorimetry. In 1891, Luginin was elected a privatdocent, and in June 1899, he was appointed a supernumerary extraordinary professor of Moscow University by the initiative of a large group of professors.

In 1897, Luginin donated to Moscow University his personal library, which included journals on chemistry and physics, both domestic and foreign, published during several decades, rare publications by foreign scientists, domestic scientific literature, and books on history, philosophy, and agriculture. Luginin had a perfect command of four European languages and was interested in a wide variety of problems. Up to 8000 of books from the "Luginin library" are kept at the library of Moscow University [4].

In 1903, Luginin decided to hand over to Moscow University the whole equipment of the thermal laboratory, purchased by him. The laboratory was named "Professor Luginin thermal laboratory." In recognition of the scientist's services, he was given the rank of an honorary member of Moscow University.

Because of the deterioration of his health, Luginin had to go abroad more and more frequently. He was at his laboratory for the last time in 1906.

Luginin occupied himself with experimental thermochemistry for about forty years and became a prominent specialist in this field; his experimental data were considered highly reliable for that time and cited in world's reference literature. The main Luginin's studies in this field were considered in a monograph by Yu.I. Solov'ev and P.I. Starosel'skii [5] and in quite a number of other review publications [6–8] and in separate communications [9–11].

The first Luginin's communication, carried out in cooperation with M. Berthelot and reporting the results of a thermochemical study of the decomposition of fatty acid halides, was published in France in 1869. Seven more joint studies of these scientists were carried out and published in French journals during the period from 1870 to 1875. The first study carried out independently by Luginin in Russia was aimed to determine the heat effects of formation of potassium and sodium trichloroacetates (1873). Beginning in 1880, the main attention was paid by the scientist to determining the heats of combustion of various organic acids. Using a combustion chamber modified by him, he studied organic compounds of various classes and types. V.F. Luginin described his experimental methods in a paper "On Measurement of the Heats of Combustion of Organic Compounds," published by him first in France (1882) and then in Russia (1884). A series of studies carried out by him together with I.A. Kablukov were concerned with determining the heat of bromine addition to unsaturated compounds.

Luginin wrote a number of textbooks on calorimetry, of which the most important is *Opisanie razlichnykh metodov opredeleniya teplot goreniya organicheskikh soedinenii* (Description of Various Methods for Determining the Heats of Combustion of Organic Compounds, 1894). In this textbook, the newest experimental techniques for determining the heats of combustion were considered. As a supplement to the book, Luginin presented tabulated heats of combustion for about 1000 substances.

In the 1890s, V.F. Luginin carried out extensive studies of the specific heats and the heats of vaporization of various liquid organic substances: alcohols, ketones, esters of dibasic acids, and saturated hydrocarbons. In the process, the scientist used a rather perfect method for determining the heats of vaporization, developed by him. Based on his own experimental data, Luginin came to a conclusion that the known

"Trouton's rule" is not universal and is observed to some extent only for organic compounds of the same class, or, even better so, within the same homologous series of one or another class. Already at the end of his scientific activities, Luginin carried out, together with A.N. Schchukarev (1864–1926), thermochemical studies of copper and magnesium alloys with aluminum (1906).

Together with his scientific activities, Luginin was actively engaged in Russia's public life. Among his close friends were N.G. Chernyshevskii (1828–1889), A.I. Herzen (1812–1870), and N.P. Ogarev (1813–1877). V.F. Luginin and his younger brother Stanislav Fedorovich Luginin (1837–1866), marshal of the nobility of Vetluga uezd, also paid much attention to solution of zemstvo's problems and published a number of papers concerned with this issue.

An honorary doctor of chemistry of Moscow University, Vladimir Fedorovich Luginin died on October 13 (26) in Paris after a severe prolonged illness. To his memory were devoted spacious obituaries written by Kablukov [4] and K.A. Timiryazev [12], and memoirs by professors of Kharkov University Shchukarev and I.P. Osipov [13]. Owing to the scientist's daughter (married name princess M.V. Volkonskaya), V.F. Luginin's works were published in 1917 under the editorship of Kablukov [14]. She also supported financially the publication of the catalog of the library donated by Luginin to Moscow University [15].

Such known thermochemists as Kablukov, Shchukarev, Osipov, P.V. Zubov, V.V. Swietoslawski, M.M. Popov, and others worked at the Luginin Thermal laboratory at Moscow University at different times [8]. To the history of the Luginin laboratory from the time of its foundation till the middle of the 1980s was devoted a publication by G.L. Gal'chenko [10]. The evidence concerning Luginin's life and scientific and public activities is included in all the main Russian encyclopedias and world's biographic reference books [16, 17].

REFERENCES

1. Kablukov, I.A., *Front Nauki Tekh.*, 1935, no. 9, pp. 41–48.
2. Kablukov, I.A., *Usp. Khim.*, 1940, vol. 9, no. 6, p. 733.
3. Kablukov, I.A., *Uch. Zap. Mosk. Gos. Univ., Khim., Yubilein. Ser.*, 1940, issue 53, pp. 47–52.
4. Kablukov, I.A., *Vladimir Fedorovich Luginin*, Moscow, 1912.
5. Solov'ev, Yu.I. and Starosel'skii, P.I., *Vladimir Fedorovich Luginin*, Moscow: Akad. Nauk SSSR, 1963.
6. Kapustinskii, A.F., *Ocherki po istorii neorganicheskoi i fizicheskoi khimii v Rossii* (An Outline of the History of Inorganic and Physical Chemistry in Russia), Moscow: Akad. Nauk SSSR, 1949.
7. Kipnis, A.Ya., *Razvitie khimicheskoi termodinamiki v Rossii* (The Development of Chemical Thermodynamics in Russia), Moscow: Nauka, 1964.
8. Solov'ev, Yu.I., *Istoriya khimii v Rossii* (History of Chemistry in Russia), Moscow: Nauka, 1985.
9. Figurovskii, N.A. and Sokolova, N.D., *X Vsesoyuznaya konferentsiya "Problemy kalorimetrii i khimicheskoi termodinamiki"* (X All-Union Conf. "Problems of Calorimetry and Chemical Thermodynamics"), Chernogolovka, June 12–14, 1984, vol. 1, part 1, pp. 5–10.
10. Gal'chenko, G.L., *X Vsesoyuznaya konferentsiya "Problemy kalorimetrii i khimicheskoi termodinamiki"* (X All-Union Conf. "Problems of Calorimetry and Chemical Thermodynamics"), Chernogolovka, June 12–14, 1984, vol. 1, part 1, pp. 11–18.
11. Sokolova, N.D., *Istoriya khimii: oblast' nauki i uchebnaya distsiplina* (History of Chemistry: Field of Science and Subject), Moscow: Mosk. Gos. Univ., 2001, pp. 245–247.
12. Timiryazev, K.A., *Sochineniya* (Works), Moscow: Sel'khozgiz, 1939, vol. 8, pp. 349–353.
13. *Pamyati Vladimira Fedorovicha Luginina: Sbornik* (In Memory of Vladimir Fedorovich Luginin: Coll. of Works), Kharkov, 1913.
14. *Trudy Vladimira Fedorovicha Luginina, professora Imperatorskogo Moskovskogo universiteta* (Coll. of Works of Vladimir Fedorovich Luginin, Professor of Emperor's Moscow University), Kablukov, I.A., Ed., Moscow, 1917.
15. *Katalog biblioteki imeni Vladimira Fedorovicha Luginina* (Catalog of Vladimir Fedorovich Luginin Library), issue 1: *Matematika i estestvoznanie* (Mathematics and Natural Sciences), Moscow, 1917.
16. Volkov, V.A., Vonskii, E.V., and Kuznetsova, G.I., *Vydayushchiesya khimiki mira. Biograficheskii spravochnik* (World's Outstanding Chemists, Biographic Reference Book), Moscow: Vysshaya Shkola, 1991.
17. Soloviev, Y.I., *Dictionary of Scientific Biography*, Gillespie, C.C., Ed., New York, 1981, vol. 8, p. 545.

A. G. Morachevskii

Russian Journal of Applied Chemistry, Vol. 77, No. 5, 2004, p. 866. Translated from Zhurnal Prikladnoi Khimii, Vol. 77, No. 5, 2004, p. 871.

BOOK REVIEWS

Blinov, L.N., *Khimiya i fizika khal'kogenidnykh, galogenkhal'kogenidnykh i fullerenkhal'kogenidnykh stekloobraznykh materialov* (Chemistry and Physics of Chalcogenide, Halochalcogenide, and Fullerene–Chalcogenide Glassy Materials)

St. Petersburg: Sankt-Peterb. Gos. Univ., 2003, 210 pp.

A small original monograph by L.N. Blinov, a known specialist in solid-state chemistry, is concerned with properties of a number of chalcogenide glassy materials. Also, preparation techniques and application fields of some types of chalcogenide glasses are considered.

The book comprises eight chapters and a supplement. Bibliographic lists are given separately for each chapter, which makes a total of 493 references to studies of domestic and foreign authors for the entire monograph. Chapter 1 (pp. 5–33) presents general concepts of glass formation in chalcogenide systems. Emphasizing the importance of disordered systems for modern science and technology, the author of the monograph regards the chemistry of glass as a new independent branch of chemical science, which is concerned with a purposeful search for glassy materials and with their preparation and study. The relationship between the glass-forming ability of substances and the position of their constituent elements in the periodic table is discussed.

Chapter 2 (pp. 34–56) is devoted to magnetic properties of chalcogenide glasses. A major part of chalcogenide glassy formulations exhibit semiconducting properties. The importance of studying the magnetic properties of systems of this kind was mentioned by professor R.L. Myuller more than 40 years ago. The author of the monograph analyzes the results obtained in studying the magnetochemistry of chalcogenide glasses.

Chapter 3 (pp. 57–103) demonstrates the possibilities of ESR spectroscopy in studying various chalcogenide glassy semiconductors. Studies mostly carried out with the author's participation revealed that the ESR spectroscopy is highly informative as applied to objects discussed in the book. Small Chapter 4 (pp. 104–119) describes the results obtained in analysis of how the magnetic susceptibility of glasses depends on temperature.

Chapter 5 (pp. 120–139) includes evidence concerning the preparation methods and properties of chalcogenide dielectric glassy materials and the possibilities of their application. By varying the relative content of the main components and the concentrations of the additives introduced, one can change the properties of chalcogenide glasses in a required direction and, in particular, improve their dielectric properties. Chapter 6 (pp. 140–155) is devoted to synthesis and properties of fluorine-containing chalcogenide glasses. It is shown that the type of a fluoride introduced affects the nature of conduction in glasses based on chalcogenides. Chapter 7 (pp. 156–175) discusses bromo- and iodochalcogenide glasses. The author of the monograph developed methods, devices, and approaches that provide synthesis of materials of these classes and considers promising fields of their application. The final Chapter 8 (pp. 176–202) summarizes evidence concerning chalcogenide fullerene-containing chalcogenide materials. It is noted that the class of chalcogenide glasses that contain fullerenes may be rather wide. The fact that the structure of fullerenes is preserved in the chalcogenide glass matrices opens up opportunities for obtaining disordered materials with high-temperature superconductivity on their base.

The monograph is largely based on studies of its author, Blinov, and a number of his coworkers. The supplement to the monograph (pp. 203–206) presents in concise form the most important conclusions of these investigations: application fields and main technical characteristics of chalcogenide glasses belonging to the classes studied; main-group elements in the periodic table, which form chalcogenide, halochalcogenide, and fullerene–chalcogenide glassy materials; and a list of binary, ternary, quaternary, and quinary chalcogenide systems analyzed in these studies.

Blinov's book is of indubitable interest for a wide audience of specialists working in the field of inorganic materials science.

A. G. Morachevskii

1070-4272/04/7705-0866 © 2004 MAIK "Nauka/Interperiodica"

Russian Journal of Applied Chemistry, Vol. 77, No. 5, 2004, pp. 867–868. Translated from Zhurnal Prikladnoi Khimii, Vol. 77, No. 5, 2004, p. 872.

BOOK REVIEWS

Flottmann, D., Forst, D., and Roßwag, H., *Chemie für Ingenieure, Grundlagen und Praxisbeispiele*

Berlin: Springer, 2004, Zweite völlig überarbeitete und verbesserte Auflage, 434 pp.

The course of chemistry for engineers, written by three German professors from Fachhochschule Aalen, Fachbereich Chemie, Aalen, Germany, may be, as regards its content and structure, of interest for a wide audience of chemistry teachers at higher school institutions and colleges, specialized schools, and lyceums. The book presents in a concise and well understandable manner the main sections of the conventional general chemistry, with considerable attention given to the most important chemical and related production facilities and environment protection.

The book comprises 12 sections (chapters) and contains a well-compiled illustrative material and numerous examples of calculations.

Chapter 1 (pp. 1–17) includes basic evidence concerning the atomic structure and elementary particles and gives notion of the radioactivity and nuclear fission. Chapter 2 (pp. 18–65) discusses various kinds of chemical bonds and the crystal structure. Chapter 3 (pp. 66–113) is devoted to water and aqueous solutions, describes specific features of water as a liquid, dissolution processes, and methods for expressing the concentration, and gives notion of the water hardness and water treatment. The same chapter includes evidence concerning ionic equilibria, the most important acids and bases, buffer solutions, pH measurements, and redox reactions in aqueous solutions.

Chapter 4 (pp. 114–143) briefly reviews the periodic system. It considers the following elements: alkali and alkaline-earth metals; elements that belong to groups of boron, carbon, and nitrogen; chalcogens and halogens; and transition metals. Special attention is paid in this chapter to complexation processes involving transition metals, gives typical examples, and discusses chelate complexes. Chapter 5 (pp. 144–161) presents basic concepts of thermodynamics and kinetics of chemical reactions. In this chapter, the thermodynamic characteristics of reactants and of the process as a whole: the enthalpy and Gibbs energy of compound formation (the authors uses instead of the Gibbs energy the term "free enthalpy") and the enthalpy, entropy, and Gibbs energy of a reaction are considered in sufficient detail, the directions and boundaries of occurrence of the chemical reaction are determined, and examples of necessary calculations are given. The dependence of the reaction rate on the concentrations of the reactants and the influence exerted by temperature and presence of catalysts on the process rate are discussed.

Chapter 6 (pp. 162–198) presents evidence concerning the main classes of organic compounds: saturated and unsaturated hydrocarbons, benzene and its derivatives, alcohols, ethers, esters, organic acids, organochlorine compounds, and also oil, gasoline, inflammable liquids and ignition temperatures of these substances.

Chapter 7 (pp. 199–249) is devoted to fundamentals of electrochemistry. The concepts of electrolysis as a redox process that occurs under external influence, voltaic cells, Nernst equation, and pH measurements with the use of a glass electrode are given. Considerable attention is paid by the authors to various primary and secondary chemical power cells, including lithium batteries.

Chapter 8 (pp. 250–281) discusses problems of corrosion and corrosion protection: theory of the phenomenon, chemical and electrochemical corrosion, types of corrosion, practical examples, and various methods of corrosion protection. Chapter 9 (pp. 282–320) contains evidence concerning the most important products of chemical industry: ammonia (synthesis and use); manufacture of chlorine, alkali, and hydrogen by electrolysis; glasses; and semiconductors. The same chapter describes the manufacture of metals, with the production of iron, steel, and aluminum considered as examples. Chapter 10 (pp. 321–366) is devoted to problems of industrial processing of organic raw materials: oil, natural gas, biomass, and other substances. The authors also review in sufficient detail the chemistry of polymers.

Chapter 11 (pp. 367–393) gives notion of chemical processes that occur in the environment, the ozone

1070-4272/04/7705-0867 © 2004 MAIK "Nauka/Interperiodica"

layer and the hazard of its destruction, and the greenhouse effect. Chapter 12 briefly reviews the biotechnology, its topical tasks, biological foundations, and related industrial processes.

The book luckily combines the diversity of the material presented and the simplicity of presentation. In each chapter, the main body of the material is preceded by a very brief (15–20 lines) introduction containing some interesting evidence of mainly historical nature, which enlivens the presentation. The assimilation of the material is favored by detailed division of each chapter into sections and subsections. The book is very well published and equipped with subject and author indexes. Translation of the book into Russian would be of interest primarily for its use as an additional textbook by college teachers.

A. G. Morachevskii

Russian Journal of Applied Chemistry, Vol. 77, No. 6, 2004, pp. 869–874. Translated from Zhurnal Prikladnoi Khimii, Vol. 77, No. 6, 2004, pp. 881–886.

INORGANIC SYNTHESIS AND INDUSTRIAL INORGANIC CHEMISTRY

Study and Development of a Technology for Manufacture of Special-Purity Calcium Carbonate

A. A. Fakeev

State Research Institute of Chemical Reagents and Special-Purity Chemicals, Moscow, Russia

Received November, 11, 2003

Abstract—The precipitation of $CaCO_3$ from $Ca(NO_3)_2$ solutions with gaseous CO_2 and NH_3 was investigated. Different variants of purification of $Ca(NO_3)_2$ solutions on hydrated aluminum oxide (collector) were considered.

Special-purity calcium carbonate is used in production of optical glass, fiber-optical materials, luminophores, ferromagnetic ferroelectrics, oxide cathodes, etc. In these cases, stringent requirements are imposed on the content of certain admixtures (10^{-4}–10^{-6} wt %).

Commercial $CaCO_3$ of reagent grade [GOST (State Standard 4530–76)] and special-purity grade 16-2 [TU (Technical Specification) 6-09-895–77] [1] fails to meet the requirements of modern industries.

The known procedures for manufacture of $CaCO_3$ yield technical- and reagent-grade products and can be conditionally divided into the following groups: reactions of $Ca(OH)_2$ with gaseous CO_2 or sodium, potassium, and ammonium carbonates; decomposition of calcium formate, acetate, or oxalate upon heating; precipitation of calcium salts from solutions under the action of gaseous CO_2 and NH_3 (or of their aqueous solutions); and exchange reactions of solutions of calcium salts with sodium, potassium, or ammonium carbonates.

The reaction of $Ca(OH)_2$ (solution or aqueous suspension) with gaseous CO_2 [2, 3] or with Na_2CO_3 solution [4] and the decomposition of calcium formate, acetate, or oxalate in a vacuum or in air at 300–600°C [5] are not promising for obtaining a special-purity product, as the technological processes include no purification stages and sufficiently pure compounds involved in the processes are not manufactured industrially [1].

The last two procedures for obtaining $CaCO_3$ from solutions of calcium salts under the action of gaseous CO_2 and NH_3 or solutions of Na_2CO_3, K_2CO_3, and $(NH_4)_2CO_3$ are widely used in industry to produce technical- or reagent-grade products [6–9]. The technological scheme of the processes can be supplemented with a stage of preliminary purification of the starting reagents.

In liquid conversion of calcium salts under the action of solutions of sodium, potassium, or ammonium carbonates into $CaCO_3$, the process is rather fast; however, the volume of dilute mother liquors that contain the corresponding nitrates or chlorides increases [9–11].

In gaseous conversion of calcium salts (with gaseous CO_2 and NH_3), the consumption of the starting compounds increases and complete precipitation of $CaCO_3$ is not achieved. Therefore, it has been suggested to carry out the process in two stages with gaseous CO_2 and NH_3 and with a solution of $(NH_4)_2CO_3$ successively [12].

Despite the considerable number of publications devoted to the precipitation of $CaCO_3$ with gaseous CO_2 and NH_3 from solutions of calcium salts, the process has been investigated insufficiently. Data on selection of technological parameters (relative amounts and feed rates of reagents, concentration of a calcium salt solution, temperature, and pH), on the mechanism and kinetics of the reactions, and on the behavior of admixtures are lacking.

The aim of this study was to develop a technological process for manufacture of special-purity $CaCO_3$.

EXPERIMENTAL

With account of published data, the reaction of a preliminarily purified $Ca(NO_3)_2$ solution with gaseous CO_2 and NH_3, followed by filtration of the result-

1070-4272/04/7706-0869 © 2004 MAIK "Nauka/Interperiodica"

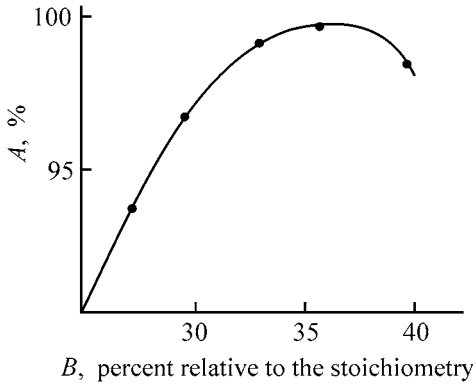

Fig. 1. $CaCO_3$ yield A vs. the excess B of CO_2 and NH_3.

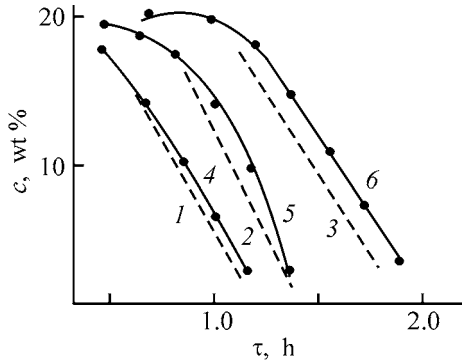

Fig. 2. Kinetics of $CaCO_3$ precipitation from $Ca(NO_3)_2$ solutions. (c) $Ca(NO_3)_2$ concentration and (τ) time. (*1–3*) Calculation, (*4–6*) experiment. CO_2 feed rate ($l\ min^{-1}$): (*1*, *4*) 0.75, (*2*, *5*) 0.55, and (*3*, *6*) 0.35.

ing suspension and washing of the $CaCO_3$ paste with water and its drying, was chosen for experimental verification:

$$Ca(NO_3)_{2(sol)} + 2NH_{3(g)} + CO_{2(g)} + H_2O = \downarrow CaCO_3 + 2NH_4NO_3.$$

The reactions that occur in the precipitation of $CaCO_3$ with gaseous CO_2 and NH_3 point to a complicated character of the process [13, 14]. In addition, the formation of ammonium carbamate NH_4COONH_2 and its hydrolysis proceed in the solution [13, 15–17].

One of the main stages of the technological process, which determines the chemical and granulometric composition of the final product, its quality, and the output capacity of the equipment used, is the stage of $CaCO_3$ precipitation.

In the continuous variant of $CaCO_3$ precipitation, the feed rates of $Ca(NO_3)_2$ solutions and gaseous CO_2 and NH_3 should be selected so that the precipitation is complete at the reactor outlet and the consumption of gaseous precipitants is at a minimum. The output capacity of the stage depends on the concentration of the $Ca(NO_3)_2$ solution. Theoretically, it is preferable to use a concentrated $Ca(NO_3)_2$ solution; however, this would hinder the absorption of gaseous CO_2 and NH_3 by this solution, raise the capture by the $CaCO_3$ solution of the forming NH_4NO_3 at its high concentration in the mother liquor, and, consequently, make more complicated the following stage of washing of the paste. With account of the results of previous studies of purification of $Ca(NO_3)_2$ solutions [18], its concentration was taken to be about 20 wt %.

The effect of the relative amounts and feed rates of the starting reagents and temperature on the yield of the final product was studied experimentally. The installation and the experimental procedure used were described in [19]. The main unit of the installation was a 1.0-l titanium or plexiglass reactor equipped with a stirrer and an external jacket. The feed rates of gaseous CO_2 and NH_3 and the $Ca(NO_3)_2$ solution were measured with rheometers and a rotameter, respectively. The pH values of solutions were determined with a pH-262 instrument, and the $Ca(NO_3)_2$ concentration in the mother liquor, by complexometric titration with trilon B. The feed rates of the gaseous reagents, CO_2 and NH_3, were varied in all the experiments at a constant feed rate of a $Ca(NO_3)_2$ solution.

Introduction of stoichiometric amounts of gaseous reagents (according to the reaction the molar ratio is $NH_3 : CO_2 = 2 : 1$) (Fig. 1) does not lead to complete precipitation of $CaCO_3$, in a satisfactory agreement with published data [12]. A theoretical calculation of the height of a gas-liquid layer in the reactor, which would provide a complete absorption of CO_2 in the reaction, demonstrated that it is necessary to develop rather high bubble-type apparatus (or a cascade) [20], which is not always possible. To achieve a complete precipitation of $CaCO_3$ under real conditions, it is advisable to use a certain excess of CO_2 and NH_3, which is due not only to incomplete dissolution of CO_2 under these conditions, but also to the occurrence of side reactions and the formation of a small constant $(NH_4)_2CO_3$ concentration in solution. Raising the feed rate of CO_2 and NH_3 by more than 35% of the stoichiometry results in an increase in the rates of side reactions and in a certain reduction of the $CaCO_3$ yield (Fig. 1).

Comparison of the calculated and experimental values for three feed rates of CO_2 (Fig. 2) shows that, at a feed rate of 0.35 $l\ min^{-1}$, CO_3^{2-} ions are accumu-

Table 1. Purification of aqueous solutions of $Ca(NO_3)_2$ to remove admixtures of 3*d* elements on a HAO (hydrated aluminum oxides) collector

Purification variant	Coefficient of removal of ions, K_p					
	Fe	Cr	Cu	Mn	Co	Ni
1	800–1000	3000–3100	50–60	20–30	40–50	40–50
2	1000–1200	150–200	120–130	70–80	160–180	80–90
3	800–1000	3000–3100	1000–1100	150–170	150–170	150–170

lated in solution and $CaCO_3$ gradually precipitates (Fig. 2, curve *6*), whereas at a rate of 0.75 l min^{-1} (Fig. 2, curve *2*), a partial breakthrough of the gas is observed. The results obtained show that the best CO_2 feed rate for precipitation of $CaCO_3$ is 0.55 l min^{-1}.

Temperature affects the reactions occurring in solution in the case of $CaCO_3$ precipitation with gaseous CO_2 and NH_3 in different ways: as the temperature increases to 40–45°C, the formation of ammonium carbamate is considerably retarded and the hydrolysis is accelerated [15, 17]; the solubility of CO_2 and NH_3 decreases.

It was established experimentally that the temperature of the reaction medium increases to 40–45°C at a CO_2 feed rate of 0.55 l min^{-1} (Fig. 2) under the conditions of $CaCO_3$ precipitation, which is due to a noticeable exothermic heat effect of the main reaction. This accelerates the hydrolysis of NH_4COONH_2 formed and leads to a more complete precipitation of $CaCO_3$ (Fig. 2).

An analysis of published data on the precipitation of $CaCO_3$ with gaseous CO_2 and NH_3, made with account of the results of this study, demonstrated that the rate-determining reactions are dissolution of CO_2 [13–15, 17, 21], formation of $CaCO_3$ nuclei and their growth [13, 22–24], and hydrolysis of ammonium carbamate [15, 21].

To estimate preliminarily the limiting stages of the technological process, a qualitative theoretical analysis of kinetic equations of the reactions [13–15, 17, 21–24] has been carried out. It has been shown that the rates of all the known reactions considerably exceed the rates of CO_2 dissolution and growth of the $CaCO_3$ crystal [25]. A mathematical model has been developed for describing the $CaCO_3$ precipitation from $Ca(NO_3)_2$ solutions with gaseous CO_2 and NH_3, with the optimization of the total time required for the stages of precipitation, filtration of the resulting suspension, and washing of the $CaCO_3$ paste [20].

To obtain a special-purity product, a preliminary purification of the starting raw materials [$Ca(NO_3)_2$ solution, gaseous CO_2 and NH_3] is necessary.

Earlier studies of the author [18, 26] have shown a high efficiency of inorganic collectors [hydrated aluminum (HAO) or zirconium oxides (HZO) for the purification of $Ca(NO_3)_2$ solutions]. The influence exerted by a number of parameters (weight of the collector, time of contact with the solution, pH of the medium, concentrations of the solution and the admixtures, addition of an oxidizer, and the nature of a collector precipitator) on the efficiency of purification of $Ca(NO_3)_2$ solutions with HAO or HZO has been investigated [18, 26].

On the basis of the investigation performed, three variants of purification of $Ca(NO_3)_2$ solutions on HAO can be considered: (1) precipitation of the collector (HAO) with aqueous ammonia; (2) precipitation of HAO with aqueous ammonia, with preliminary addition of H_2O_2; and (3) precipitation of the collector (HAO) with a NaOH solution (Table 1). The data in Table 1 point to a high efficiency of purification of $Ca(NO_3)_2$ solutions to remove admixtures of 3*d* elements. The precipitation of HAO with aqueous ammonia (variant 1) provides a high efficiency of solution purification to remove admixtures of iron and chromium ions and a considerably lower efficiency for copper, manganese, nickel, and cobalt ions, because of the formation of readily soluble ammino or hydroxoammino complexes with these ions. Addition of H_2O_2 (variant 2) improves the removal of copper, manganese, iron, nickel, and cobalt admixtures, but impairs that of chromium(III) owing to its oxidation to chromium(VI), which coprecipitates with HAO to a much lesser extent in the pH range 7.5–8.0. Precipitation of HAO with an alkali solution (variant 3) results in the highest efficiency of removal of all the admixtures under study. This is due to the formation of hydroxo complexes of 3*d* elements, which rather effectively coprecipitate on the collector, in contrast to

Table 2. Microfiltration of $Ca(NO_3)_2$ solutions across a PVC-0.25 membrane

Solution	Number	Granulometric composition of particles, μm					
		0.5–0.6	0.6–0.7	0.7–0.85	0.85–1.00	1.0–5.0	5.0
Initial	13402	749	2302	1727	1714	6683	227
Purified	60	11	22	10	5	12	0
Initial	12923	1470	4365	2446	1697	2639	306
Purified	64	12	35	9	4	4	0

Table 3. Quality of laboratory $CaCO_3$ samples of special purity and of the best foreign analogues (according to catalogues)

Sample	Content of ions $c \times 10^6$, wt %					
	Fe	Mn	Cu	Cr	Ni	Co
Laboratory:						
HAO	5	1	1	2	1	0.5
purified on HZO and PVC-0.25 membrane	4	0.5	<1	<1	<1	<0.5
E.Merek, Germany:						
Suprapur	5	5	1		1	1
Optipur FO	5	1	5	1	1	1
USA:						
Ultrapure, Ventron	5	10	5		1	5
Ultrex, Baker	3	8	2	3	1	0.6
Great Britain, Optran	<200	<200	30	<200	<500	<20

the readily soluble and rather stable ammino or hydroxoammino complexes.

The efficiency of purification of $Ca(NO_3)_2$ solutions on HZO is somewhat lower [26], which seems to be caused by the difficulty of careful separation of the amorphous superfine precipitate of the collector.

For better separation of the collector, such membranes as SPA, PVC, MFF were used, differing in the supporting material and porosity [27]. A study of the microfiltration of a 20% $Ca(NO_3)_2$ solution purified using HZO [collector weight 2.0% in terms of $Ca(NO_3)_2$, time of contact with the solution 2 h, solution pH 8.0, and temperature 50°C] was carried out in a laboratory cell of diameter 47 mm under a pressure of 0.5 kg cm^{-3}, with the size and number of particles monitored (LAM instrument with a flow-through cell). The data obtained with a preliminary separation of the HZO precipitate on a "blue band" filter and with filtration across a PVC-0.25 membrane are listed in Tables 2 and 3.

Thus, the high efficiency of purification of solutions on a collector (HZO), combined with the membrane technology, was experimentally established. Use of membranes in purification ensures a complete separation of microscopic particles of the collector, which contains certain admixtures at a level of 10^{-1}–10^{-3} wt %. Use of membranes in the final stage of purification of solutions in the technological scheme for obtaining special-purity inorganic substances somewhat complicates the process and decreases its output capacity, but makes it possible to improve dramatically the quality of the products.

The experimental data on the fine separation of the collector, obtained in this study, enable a wider use in technological practice of such effective inorganic collectors as hydrated oxides of manganese(IV), titanium(IV), tin(IV), iron(III), chromium(III), cobalt(III), etc.

Special-purity grade CO_2 and NH_3 required for production of special-purity $CaCO_3$ are not manufactured industrially, but the domestic industry produces in large amounts these products of technical grade, with high content of the main substances (liquefied $CO_2 \geq 98.0$ vol %, and liquefied $NH_3 \geq 99.6$ vol %).

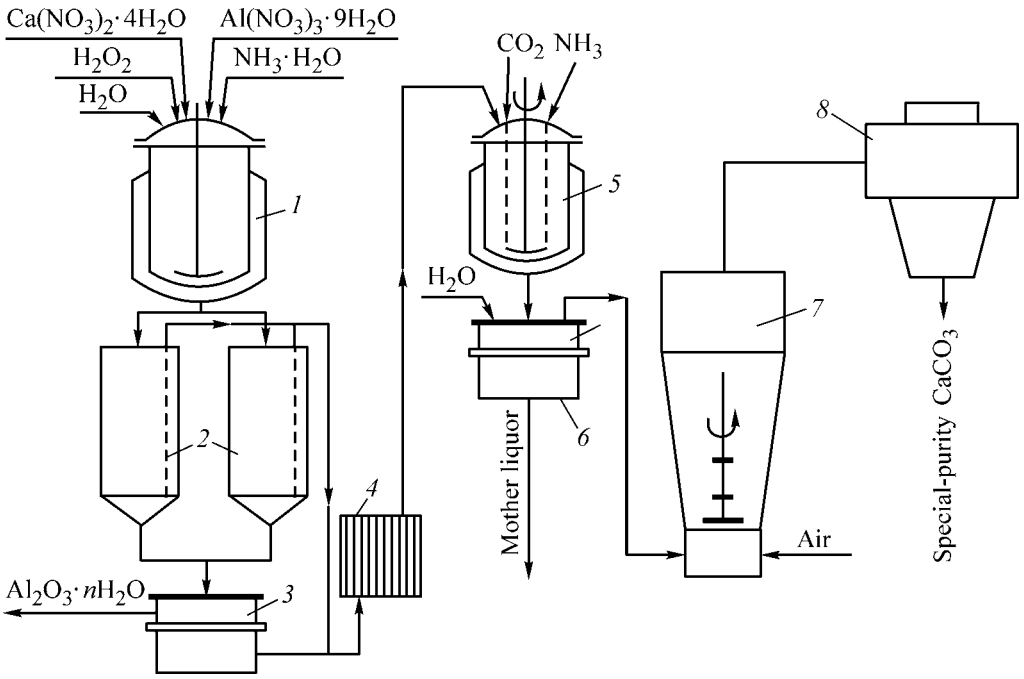

Fig. 3. Technological scheme for manufacture of special-purity $CaCO_3$. (*1*) Reactor for dissolution and purification of the $Ca(NO_3)_2$ solution, (*2*) sedimentation columns, (*3*) filter for collector separation, (*4*) frame fluoroplastic filter, (*5*) reactor for precipitation of $CaCO_3$, (*6*) unit for filtering and washing of the $CaCO_3$ paste, (*7*) fluidized-bed apparatus, and (*8*) cyclone separator.

These products are rather pure as regards the content of admixtures whose content in $CaCO_3$ of special-purity grade is to be limited. For a preliminary purification, gaseous CO_2 and NH_3 are bubbled through a layer of distilled water and an FP filter [28].

The choice of a variant to be used for $Ca(NO_3)_2$ purification is governed by the quality of the starting raw materials and the target product.

Systematic analysis of reagent-grade $Ca(NO_3)_2$ (analytically pure and chemically pure grades, GOST 4142–77) shows a rather low level of 3*d*-element admixtures (10^{-3}–10^{-5} wt %) [26]. If the purification coefficients (Table 1) are taken into account, ingress of impurities into the target product is ruled out, and $Ca(NO_3)_2$ of the above quality and preliminarily purified CO_2 and NH_3 are used, a special-purity $CaCO_3$ containing admixtures at a level of 10^{-5}–10^{-7} wt % can be obtained.

On the basis of the investigation performed, a technological scheme for manufacture of special-purity $CaCO_3$ from preliminarily purified solutions of calcium nitrate (analytically pure and chemically pure grades) and gaseous CO_2 and NH_3 (technical grade) was developed (Fig. 3). The main stages of the technological process are the following: dissolution of $Ca(NO_3)_2$ in distilled water and purification of the solution on a collector (HAO); separation of the collector precipitate; precipitation of $CaCO_3$ with gaseous CO_2 and NH_3; filtering and washing of the precipitate; and drying of the paste. A 20–25% aqueous solution of $Ca(NO_3)_2$ was purified on a collector (HAO), which was precipitated at pH 7.5–8.0 with aqueous ammonia or NaOH. As a collector-forming agent was used analytically pure $Al(NO_3)_3$ (GOST 3757–75) in an amount of 2 g of $Al(NO_3)_3 \cdot 9H_2O$ per 100 g of $Ca(NO_3)_2$. To achieve a deep separation of the resulting HAO gel, which contained 10^{-2}–10^{-3} wt % admixtures of 3*d* elements, and the purified $Ca(NO_3)_2$ solution, the suspension was subjected to aging and settling. The lower condensed layer of the suspension was twice filtered on an ordinary Nutsch filter across two layers of "blue-band" filters, combined with the clarified part of the solution, and filtered on a frame-type microfilter with fluoroplastic filtrating partitions [29]. The rate of filtration of the condensed part of the suspension on a Nutsch filter rapidly decreases, and mechanical removal of the gel-like precipitate of the collector from the filter surface at regular intervals of time is necessary. The precipitation of $CaCO_3$ was carried out in an apparatus, into which purified $Ca(NO_3)_2$ solution and gaseous CO_2 and NH_3 were continuously fed. The suspension of $CaCO_3$ was continuously discharged on-

to a Nutsch filter, where the accumulated and squeezed paste was washed with special-purity water to remove nitrate ions. The washed paste was delivered into a "fluidized-bed" apparatus.

The quality parameters of the resulting special-purity $CaCO_3$ [30] and of the best foreign samples are listed in Table 3.

Comparison of these products shows that the technology developed enables manufacture of special-purity $CaCO_3$, which is comparable in its main characteristics with the best foreign analogues.

CONCLUSIONS

(1) The precipitation of $CaCO_3$ from $Ca(NO_3)_2$ solutions with gaseous CO_2 and NH_3 was studied and the parameters of the process were determined.

(2) A technological scheme was developed for manufacture of special-purity $CaCO_3$ from preliminarily purified $Ca(NO_3)_2$ solutions and gaseous CO_2 and NH_3.

REFERENCES

1. *Khimicheskie reaktivy i vysokochistye khimicheskie veshchestva: Katalog* [Chemical Reagents and High-Purity Chemicals (Catalogue)], Moscow: Khimiya, 1983.
2. Kozlov, A.N., Sysoev, V.A., Valiullin, A.K., and Letyuk, A.I., *Trudy NioKhIM*, 1980, issue 54, pp. 39–44.
3. Söhnel, O. and Markalous, F., *Chem. Prüm.*, 1981, vol. 31, no. 2, pp. 53–56.
4. US Patent 5364610.
5. Glasson, D.R., *J. Appl. Chem.*, 1963, vol. 13, no. 3, pp. 124–127.
6. Gel'perin, N.I. and Glushkov, V.P., *Khim. Prom–st.*, 1976, no. 6, p. 445.
7. Packter, A., *Cryst. Research.*, 1982, vol. 17, no. 6, pp. 693–716.
8. Trendafelova, E., Minasyan, M., and Trendafelov, D., *Farmatsiya*, 1982, vol. 32, no. 2, pp. 1–6.
9. Fridman, S.D., Skum, L.S., Polyakov, N.N., *et al.*, *Trudy GIAP*, 1975, issue 31, p. 8–11.
10. Maruscak, A., Baker, C.G.T., and Bergougnou, M.A., *Canad. J. Chem. Eng.*, 1971, vol. 49, no. 6, pp. 819–824.
11. Richter, A., Petzold, D., Hofmann, H., and Ullrich, B., *Chem. Techn.*, 1995, vol. 47, no. 6, pp. 306–313.
12. Gol'dinov, A.L., Novoselov, F.I., Abramov, O.B., and Afanasenko, B.P., *Khim. Prom–st.*, 1981, no. 2, p. 96–97.
13. Danckwerts, P.V., *Gas-Liquid Reactions*, New York: McGraw–Hill, 1970.
14. Usdowski, E., *Neues Jahrbuch Mineralogie*, 1982, vol. 144, no. 2, pp. 148–171.
15. Faurholt, C., *Z. Anorg. Allgem. Chem.*, 1929, vol. 22, nos. 3–4, pp. 417–425.
16. Szarawar, J., Piotrowski, J., and Zolotajkin, M., *Chem. Stosow.*, 1978, vol. 22, nos. 3–4, pp. 417–425.
17. Sarukhanyan, T.A. and Belopol'skii, A.P., *Zh. Prikl. Khim.*, 1954, vol. 27, no. 7, pp. 712–721.
18. Fakeev, A.A., Kurmanguzhina, L.K., and Sukhanovskaya, A.I., *Zh. Prikl. Khim.*, 2002, vol. 75, no. 5, pp. 724–729.
19. Savel'eva, L.V., Rodimtseva, I.Yu., Novikov, A.N., *et al.*, *Reaktivy i osobo chistye veshchestva: Trudy IREA* (Reagents and Special-Purity Substances: Proc. IREA), Moscow: IREA, 1976, issue 38, p. 52–57.
20. Falin, V.A. and Fakeev, A.A., *Vysokochist. Veshch.*, 1988, no. 6, pp. 52–54.
21. Pinsent, B.R.W. and Roughton, F.J.W., *Trans. Faraday Soc.*, 1951, vol. 47, no. 3, pp. 263–269.
22. Nancollas, G.H. and Reddy, M.M., *J. Colloid. Interface Sci.*, 1971, vol. 37, no. 4, pp. 824–830.
23. Wiechers, H.N.S., Sturrock, P., and Marais, G., *Water Res.*, 1975, vol. 9, no. 9, pp. 835–845.
24. Goodarz-Nia, I. and Motamedi, M., *J. Cryst. Growth.*, 1980, vol. 49, no. 1, pp. 125–131.
25. Fakeev A.A., Knyazev, A.N., Aizin, S.M., *et al.*, *Khim. Prom–st.*, 1987, no. 4, p. 219–221.
26. Fakeev, A.A. and Suhhanovskaya, A.I., *Zh. Prikl. Khim.*, 2001, vol. 74, no. 12, p. 1921–1924.
27. Yasminov, A.A., Gleizer, S.V., Volodin, V.F., *et al.*, *Membrannaya mikrofil'tratsiya v tekhnologii ochistki zhidkikh veshchestv* (Membrane Microfiltration in the Technology of Purification of Liquid Substances), Moscow: NIITEKhIM, 1987.
28. Stepin, B.A., Gorshtein, I.G., Blyum, G.Z., *et al.*, *Metody polucheniya osobo chistykh neorganicheskikh veshchestv* (Methods for Producing Special-Purity Inorganic Substances), Leningrad: Khimiya, 1969.
29. Mel'nikov, V.D., Kudryashov, A.F., Fokin, A.P., *et al.*, *Khimicheskie reaktivy i osobo chistye veshchestva: Trudy IREA* (Chemical Reagents and Special-Purity Substances: Proc. IREA), Moscow: IREA, 1983, issue 45, pp. 175–182.
30. Chupakhin, M.S., Sukhanovskaya, A.I., Krasil'shchik, V.E., *et al.*, *Metody analiza chistykh khimicheskikh reaktivov* (Methods for Analysis of Pure Chemical Reagents), Moscow: Khimiya, 1984.

Russian Journal of Applied Chemistry, Vol. 77, No. 6, 2004, pp. 875–877. Translated from Zhurnal Prikladnoi Khimii, Vol. 77, No. 6, 2004, pp. 887–889.

INORGANIC SYNTHESIS AND INDUSTRIAL INORGANIC CHEMISTRY

Synthesis of High-Purity Calcium Hydride

A. D. Bulanov, O. Yu. Troshin, and V. V. Balabanov

Institute of Chemistry of High-Purity Substances, Russian Academy of Sciences, Nizhni Novgorod, Russia

Received December 4, 2003

Abstract—A procedure for synthesizing high-purity calcium hydride in high yield was suggested. The admixture composition of the resulting CaH_2 was determined by laser mass spectrometry.

CaH_2 is used in laboratory practice as a desiccant that can take away water from crystal hydrates [1]. It is highly efficient in drying of hydrocarbons, ethers, and other solvents. Calcium hydride has found wide application as a reducing agent in preparing powders of certain metals (Ti, Zr, Nb, Ta, Mo, and W) from their oxides and halides [2, 3]. A method is known for converting silicon halide compounds (silicon tetrachloride, trichlorosilane, and silicon tetrafluoride) into silane by their reaction with CaH_2 [4]. In this case, admixtures of F_2, H_2O, O_2, N_2, AsH_3, and PH_3 are removed from SiH_4 via their adsorption on a metal hydride [5]. In [6], calcium hydride was used as a reducing agent to obtain high-purity hydrides of monoisotopic silicon ($^{28}SiH_4$, $^{29}SiH_4$, and $^{30}SiH_4$) from monoisotopic SiF_4 by the reaction

$$SiF_4 + 2CaH_2 \rightarrow SiH_4 + 2CaF_2. \quad (1)$$

The choice of CaH_2 was determined by the fact that, unlike NaF in the reaction with NaH, CaF_2 does not react with monoisotopic SiF_4 to give $CaSiF_6$ in synthesis of silane [7, 8]. Moreover, CaF_2 reacts with a BF_3 admixture in silicon fluoride to give a stable $Ca(BF_4)_2$ complex [4], which favors purification of the resulting SiH_4 to remove boron-containing admixtures. At the same time, CaH_2 is the safest in handling, compared with other hydrides and metal aluminum hydrides.

The compound CaH_2 is a light gray crystalline substance that does not react with oxygen up to 400–500°C [9] and reacts with water to give CaO, $Ca(OH)_2$, and hydrogen [10]. In synthesizing SiH_4 from SiF_4, the reactions of SiF_4 with the products of CaH_2 hydrolysis are thermodynamically allowed [11]. It has been established experimentally that presence of several percent CaO in calcium hydride substantially decreases the yield of SiH_4, and, therefore, there is no point in using commercial-grade CaH_2. Moreover, an admixture of metal calcium in CaH_2 may result in thermal reduction of SiF_4 to give monoisotopic elementary silicon [12]. Therefore, development of a procedure for synthesizing active CaH_2 in high yield is a matter of current interest.

The reaction of Ca with H_2 becomes noticeable at 170–250°C [10], $\Delta H_f^{298}(CaH_2) = -45.1$ kcal mol^{-1} [13]. For practical use, temperatures in the range from 250 to 700°C are recommended [14]. The hydrogenation of solid Ca to give a solid product is a topochemical process. Kinetic studies [15] revealed three stages of the reaction: formation of centers of CaH_2 crystallization on the surface of a sample (induction period), formation of a CaH_2 surface layer precluding a direct contact of H_2 with Ca, and diffusion of H_2 with the subsequent reaction at the Ca–CaH_2 interface (dissolution or formation of a chemical bond). The rate of Ca hydrogenation depends on temperature, H_2 pressure, linear dimensions of a sample, internal structure of the metal, and admixtures present in calcium and hydrogen [15–17].

The admixtures of O_2 and H_2O in hydrogen decrease the hydrogenation rate, because CaO formed on the surface of calcium hinders the diffusion of H_2. It was shown in [18] that 0.5% oxygen decelerates the reaction by a factor of 2.5, and 0.5% H_2O, by a factor of 6.

EXPERIMENTAL

To obtain high-purity CaH_2, we used distilled Ca in the form of 1.5-mm-thick shavings [TU (Technical Specifications) 95.768–80, manufactured by Mashinostroitel'nyi zavod Open Joint-Stock Company (Elekt-

1070-4272/04/7706-0875 © 2004 MAIK "Nauka/Interperiodica"

Results of analysis by laser mass-spectrometry

Element	Content, at.%	
	Ca	CaH_2
B	$<8 \times 10^{-6}$	$<1 \times 10^{-4}$
C	$<3 \times 10^{-2}$	$\leq 8 \times 10^{-2}$
P	$<1 \times 10^{-5}$	1×10^{-4}
F	7×10^{-3}	$\leq 1 \times 10^{-3}$
Mg	1×10^{-3}	1×10^{-3}
Al	5×10^{-5}	4×10^{-5}
Si	2×10^{-3}	2×10^{-4}
Cl	0.12	2×10^{-2}
Fe	1×10^{-3}	5×10^{-4}
Mn	1×10^{-3}	7×10^{-4}
Cu	6×10^{-4}	3×10^{-3}
Zn	2×10^{-4}	$<1 \times 10^{-4}$
Sr	3×10^{-2}	5×10^{-3}
S	1×10^{-3}	3×10^{-4}

rostal')] and H_2 purified by diffusion across a palladium membrane. The content of admixtures in calcium, as determined by laser mass spectrometry, is listed in the table.

The content of O_2 and H_2O admixtures in purified hydrogen does not exceed 10^{-4} mol %.

We synthesized CaH_2 on an installation shown schematically in the figure. The main units of the installation are a cylinder with H_2 *1*, a H_2 purification unit *2*, and a flange reactor *3*. We controlled the pressure of H_2 during the process with vacuum gages *4* and *5*. The temperature of the resistance furnace *6* was set with an R-133 temperature control unit and monitored with a Chromel–Copel thermocouple *7*.

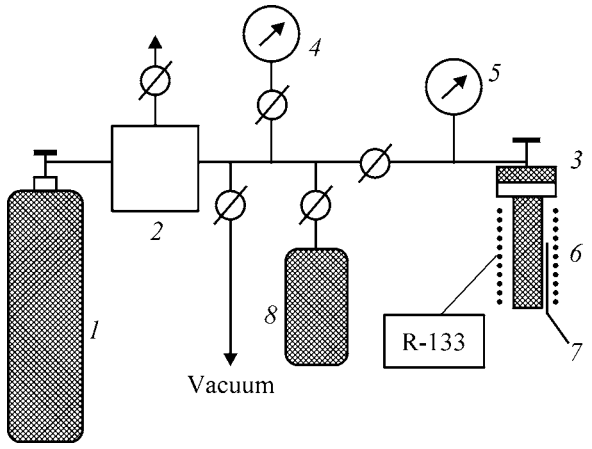

Schematic of the installation for synthesis of CaH_2. (*1*–*7*) For explanations, see text; (*8*) receiver.

We synthesized CaH_2 by the following procedure. A stainless-steel flange reactor was charged with 350–400 g of Ca, connected it to the installation, evacuated to 10^{-1} mm Hg, and heated to 360°C within 0.5 h. According to [16], melted Ca in the form of shavings starts to react with H_2 at 400°C; hence, we hydrogenated Ca in the temperature range 400–450°C. We filled the reactor with purified H_2 to a pressure of 5 atm and kept it for about 5 min. During this time, the pressure of H_2 in the reactor decreased first gradually and then abruptly to 0.05–0.1 atm. The increase in the rate of H_2 absorption is accounted for by the high rate of the hydrogenation reaction on the surface of Ca. In this stage of hydrogenation, we controlled the flow of H_2 into the reactor in such a manner that the pressure of H_2 in the reactor did not exceed 1 atm, since an elevated pressure of H_2 results in a rise in temperature.

A rise in temperature may lead to caking of CaH_2, which impedes its withdrawal from the reactor. After a layer of CaH_2 is formed on the surface of Ca, diffusion of H_2 to the Ca–CaH_2 interface begins, and the rate of H_2 absorption decreases. To complete the hydrogenation, we raised the H_2 pressure in the reactor to 10 atm, and the temperature to 480°C. We judged the completion of the hydrogenation reaction from the cessation of the H_2 absorption.

The yield of CaH_2 was calculated as the ratio of the weight of CaH_2 obtained in the experiment to its theoretical value. The yield of CaH_2 was $99.6 \pm 0.1\%$, i.e., the synthesis procedure results in an almost complete hydrogenation of Ca. The output capacity of the pilot installation for CaH_2 synthesis is 150 g of CaH_2 per hour.

The resulting CaH_2 was analyzed by laser mass spectrometry for the content of admixtures. The results obtained are listed in the table. It can be seen that the main admixtures in CaH_2 are C and Cl, whereas the content of metal admixtures is at the level of 10^{-3} at.%.

After the process was complete, we placed the cooled reactor in a box purged with dried nitrogen and then ground the CaH_2 obtained to powder with particle size of less than 0.6 mm. The powdered CaH_2 was charged into the reactor in a flow of purified H_2 in order to obtain silane.

An effective procedure for removal of carbon from metals [19] is their "washing" with purified H_2. The admixtures of hydrocarbons can be formed in the reaction of H_2 with admixtures of metal carbides present in calcium:

$$M_nC_m(\text{solid}) + 2mH_2 = nM(\text{solid}) + mCH_4(\text{gas}). \quad (2)$$

In [20], CaH_2 was obtained in the reaction of calcium carbide with H_2 at 100–1000oC under an elevated pressure (up to 100 atm):

$$CaC_2 + 5H_2 \rightarrow CaH_2 + 2CH_4. \quad (3)$$

Therefore, side reactions of hydrogenation of carbon and its compounds to give hydrocarbons can occur under the conditions of CaH_2 synthesis.

In this study, we blew CaH_2 with a flow of purified H_2 at 250°C for 8 h in order to diminish the content of carbon admixtures. It was shown that, after contact with CaH_2, the content of hydrocarbon admixtures in H_2 increases by two orders of magnitude, which allowed us to diminish the content of the most difficultly removable admixture of ethylene in silane by an order of magnitude.

CONCLUSIONS

(1) High-purity calcium hydride was obtained by hydrogenation of distilled metallic calcium with purified hydrogen.

(2) The main admixtures in CaH_2 are C and Cl, whereas the content of metal admixtures is at the level of 10^{-3} at.%. The procedure of "washing" of CaH_2 was used to decrease the content of carbon admixture in it.

ACKNOWLEDGMENTS

The study was financially supported by the 6th Competition-examination of scientific projects of young scientists of the Russian Academy of Sciences, in the field of fundamental and applied research (grant no. 165).

REFERENCES

1. Hurd, D.T., *An Introduction to the Chemistry of Hydrides*, New York: Wiley, 1952.
2. Meerson, G.A. and Kolchin, O.P., *Atomnaya Energiya*, 1957, vol. 2, no. 3, pp. 253–259.
3. Bichara, M., *Ann. Chim.*, 1956, vol. 1, p. 399.
4. RF Patent 2077483.
5. Jpn. Patent Aplication 58-120511.
6. Devyatykh, G.G., Dianov, E.M., Bulanov, A.D., *et al.*, *Dokl. Ross. Acad. Nauk*, 2003, vol. 391, no. 5, pp. 638–639.
7. EC Patent 0052808.
8. US Patent 4407783.
9. *Gmelins Handbuch der Anorg Chemie: Calcium*, 1956, vol. 28, pp. 28 and 271.
10. Mikheeva, V.I. and Kuznetsov, V.A., *Zh. Anal. Khim.*, 1965, vol. 20, no. 2, p. 200.
11. Opalovsky, A.A., Labkov, E.U., Torosyan, S.S., and Dzhambek, A.A., *J. Therm. Anal.*, 1979, vol. 15, pp. 67–77.
12. US Patent 4446120.
13. Zhigach, A.F. and Stasinevich, D.S., *Khimiya Gidridov* (Chemistry of Hydrides), Leningrad: Khimiya, 1969.
14. Johnson, W.C., Stubbs, M.F., and Pechukas, A., *J. Am. Chem. Soc.*, 1939, vol. 61, no. 2, p. 318.
15. Krestovnikov, E.P., *Trudy UNIKHIM*, 1958, no. 5, pp. 118–135.
16. Efremkin, V.V. and Fefelova, G.F., *Trudy UNIKHIM*, 1958, no. 5, pp. 136–151.
17. Teplenko, V.G., Kudinova, K.G., and Shikhanova, T.S., *Sbornik trudov TSNIICHermet* (Coll. of Works of TSNIICHermet), 1965, vol. 43, p. 135.
18. US Patent 2702740.
19. Devyatykh, G.G., Yushin, A.S., and Osipova, L.I., *Metally osoboi chistoty* (Special-Purity Metals), Moscow: Nauka, 1976, pp. 105–113.
20. Jpn. Patent Application 61-178401.

Russian Journal of Applied Chemistry, Vol. 77, No. 6, 2004, pp. 878–880. Translated from Zhurnal Prikladnoi Khimii, Vol. 77, No. 6, 2004, pp. 890–893.

INORGANIC SYNTHESIS AND INDUSTRIAL INORGANIC CHEMISTRY

Modern Designs in Modular Technology of Hydrofluoric Acid

G. Z. Blyum, E. A. Ryabenko, A. M. Yaroshenko, V. M. Polosin, S. B. Sobolev, D. A. Bol'shakova, and G. E. Zaikov

State Research Institute of Chemical Reagents and Special-Purity Substances, Moscow, Russia

Emanuel Institute of Biochemical Physics, Russian Academy of Sciences, Moscow, Russia

Received December 9, 2003

Abstract—Prospects for application of a modular technology in manufacture of high-purity hydrofluoric acid to perform automated control of the production process and further improve the quality of the high-purity product are considered.

At present, the existing industrial production of hydrofluoric acids of special purity 27-5 and special-purity 20-6 grades[1] satisfies the demands of widely diverse fields of technology. The technology for manufacture of special-purity hydrofluoric acid, which employs a block-module installation made of fluoroplastic-4 (of the Proton type) makes it possible to obtain a higher-quality product that satisfies the requirements of leading companies, such as Merk, Canto chemical, etc., to the content of the main impurities and particles in conformity with regulations [1].

The modular installation comprises the following units: unit for chemical treatment of the acid with a potassium permanganate solution (to convert microscopic admixtures of volatile compounds of arsenic, phosphorus, sulfur, etc. into nonvolatile compounds); unit for separation of a concentrated acid into the gas (hydrogen fluoride) and liquid (azeotropic solution of HF) phases with a unit for purification of hydrogen fluoride by filtration on a sprinkled self-cleaning filter made of Ftorlon fiber; unit for reactive purification of the azeotropic solution; unit for absorption of purified hydrogen fluoride with a purified azeotropic solution (to give a product with a prescribed concentration of hydrogen fluoride); unit for microfiltration of the acid to remove suspended microparticles; unit for collection and agitation of the finished product; and unit for feeding the high-purity product into the transport unit (with supply of filtered air into the working zone).

[1] Created in accordance with the design by the Institute of Chemical Reagents and Special-Purity Substances at Galogen Production Association.

However, the advances of modern science and technology impose even more stringent requirements on the quality of high-purity hydrofluoric acid. In view of the aforesaid, the existing technology is being further modified in the following scientific and technological areas.

(1) Development and creation of computer systems for optimization of technological units and the whole computerized automated control system.

(2) Development of a new unit for chemical treatment of hydrofluoric acid to oxidize volatile microimpurities to convert them into nonvolatile compounds in order to ensure continuity and closed nature of the entire process.

(3) Development of a new additional unit for finishing purification of the azeotropic solution to remove dissolved impurities (electrolytes).

(4) Creation of a unit for storage and transportation of the finished product.

Let us consider in more detail the chemical and technological aspects of these areas of research. To purify HF_{aq} to remove volatile impurities that possess reducing properties, it was suggested to generate O_3 in solution from dissolved oxygen. The process occurs in accordance with the equation

$$3H_2O \cdot 2HF + 3O_2 \xrightarrow{h\nu,\ T^\circ C} 2H_2O + 2HF + 2O_3\uparrow.$$

UV photons are produced using ultraviolet quartz mercury sources of light with wavelengths of 180–360 nm.

1070-4272/04/7706-0878 © 2004 MAIK "Nauka/Interperiodica"

In contrast to the existing method, a new technique associated with the above photochemical reaction was suggested for oxidation of an arsenic microimpurity.

The process suggested is based on the mainly homogeneous reaction of oxygen dissolved in hydrofluoric acid with molecules of water in azeotropic clusters at a temperature of about –10°C. The ozone formed in the acid solution oxidizes the arsenic(III) microimpurity by the reaction

$$AsF_3 + O_3 + H_2O \rightarrow AsOF_3 \cdot H_2O + O_2,$$

with As(III) converted into a nonvolatile compound. Simultaneously are oxidized other volatile microimpurities, such as compounds of phosphorus, sulfur, etc.

A most important issue of the technique is its optimization. To achieve this goal, the following problems are to be solved: it is necessary to select a construction material that would be chemically stable and transparent to ultraviolet light. As demonstrated by the studies performed, these requirements are satisfied by fluoropolymers F-4, F-4MB, and F-50, whose transparency to UV light exceeds that of quartz (in the wavelength range 150–380 nm). However, irradiation of the hydrofluoric acid solution is complicated by strong scattering and absorption of UV light by this solution. Therefore, the hydrofluoric acid saturated with oxygen at the optimal temperature should be in the form of a thin layer, which can be accomplished by using a special apparatus. One of the possible variants is shown in Figs. 1, 2. In addition, it was necessary to use an appropriate power of the light source and find the optimal temperature of the process that includes chemical reactions of ozone formation and oxidation of arsenic(III) microimpurities.

Figure 3 shows how the optimal yield of O_3 and oxidation of the arsenic(III) microimpurity depend on the process temperature. The optimal time of irradiation of the liquid reaction medium with UV light depends on the apparatus height and the number of cycles of liquid recycling, and also on the velocity of the liquid flow in the reaction zone.

To determine the time dependence of the concentration of O_3 formed, experiments were carried out and the type of the functional dependence $c_{O_3} = f(\tau)$ was found. It was shown that the adequate expression for the differential equation has the following form:

$$\frac{dc_{O_3}}{d\tau} = b - ac,$$

where c_{O_3} is the concentration of ozone; a, the coefficient describing the rate at which the concentration of O_3 increases; and b, the limiting concentration of O_3, which depends on the solubility of oxygen, c_{O_2}.

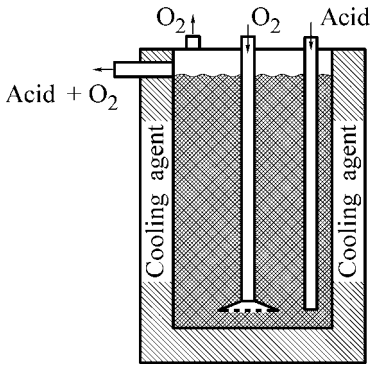

Fig. 1. Apparatus for saturation of hydrofluoric acid with oxygen gas at the optimal temperature.

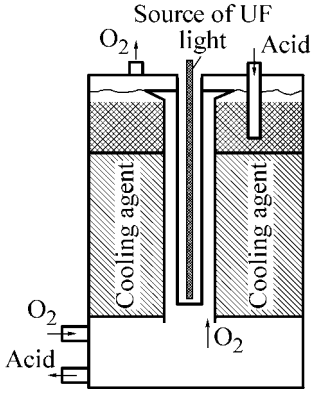

Fig. 2. Apparatus for performing the photochemical reaction of ozone formation with the subsequent oxidation of the arsenic(III) microimpurity.

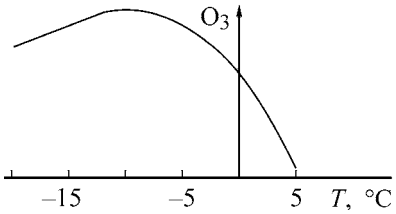

Fig. 3. Concentration of ozone formed in a hydrofluoric acid solution vs. temperature T.

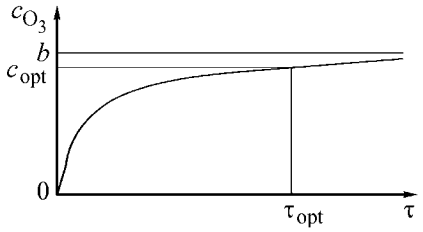

Fig. 4. Graphical optimization of the photochemical process of ozone synthesis.

The integral expression has the form

$$c_{O_3} = b(1 - e^{-a\tau}).$$

Figure 4 illustrates the graphical procedure for kinetic optimization of the photochemical process of ozone synthesis.

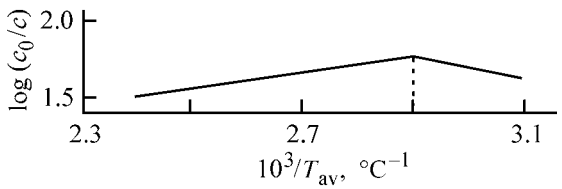

Fig. 5. Optimization of the hydroion convection with respect to temperature.

The necessity for additional purification of the azeotropic solution of hydrofluoric acid to remove admixtures of compounds-electrolytes to a level below 10^{-7}–10^{-8}% is due to the fact that, even in slow boiling or evaporation without boiling, the HF vapor is contaminated with these compounds. This process can be accounted for in its simplest form by ionic carry-over [2, 3]. In solution, ions of microimpurities form hydrates (clusters). These formations are rather stable (binding energy of about 1000 cal mol^{-1}), whereas their binding to other dipoles in the solution is considerably weaker (100 cal mol^{-1}).

In evaporation of the surface layer of the liquid, clusters of impurity ions are the first to evaporate. In this context, another problem arises: how can ionic clusters be supplied to the surface layer of the liquid film flowing down over the inner surface of, e.g., a cylindrical apparatus. For this purpose, two more effects are used in addition to carry-over: ionic repulsion (occurs because of the poor wettability of the fluoropolymeric surface with the liquid) and thermodiffusion transfer. Thus, the total internal work done by the system in the process, ΔE, is constituted by the effects of cluster formation (ΔE_1), ionic repulsion (ΔE_2), and thermodiffusion transfer (ΔE_3): $\Delta E = \Delta E_1 + \Delta E_2 + \Delta E_3$. The driving force of the thermodiffusion transfer is the temperature gradient δ between the inner (adjacent to the apparatus) and outer surface of the downflowing liquid film.

The evaporation of ionic clusters from the surface of the acid solution requires a heat Q, supplied from the outside. The entire process, which is named ionic convection and is associated with a change in the ion concentration in the liquid (azeotropic mixture) being purified can be represented as an exponential

$$c = c_0 \exp(-\Delta E - Q) \quad \text{or} \quad \ln\frac{c_0}{c} = \frac{\Delta E - Q}{RT},$$

where c_0 is the concentration of ions in the initial mixture, and c is the running concentration of ions.

It is known [6] that

$$\Delta E_1 = K_1 \rho \xi,$$

where ρ is the ion charge; ξ, the degree of ion hydration; and K_1, the constant of cluster formation;

$$\Delta E = K_2(1 + \cos\theta_a)/(1 + \cos\theta_w),$$

where θ_a and θ_w are the contact angles between the fluoropolymeric surface and acid or water, and K_2 is the ionic repulsion constant;

$$\Delta E_3 = K_3 \Delta T/\delta,$$

where $\Delta T/\delta$ is the temperature gradient across the thickness of the liquid film, and K_3 is thermodiffusion constant.

Thus,

$$\ln\frac{c_0}{c} = \frac{1}{RT}\left(K_1 \rho \xi K_2 \frac{1 + \cos\theta_a}{1 + \cos\theta_w} K_3 \Delta T/\delta\right).$$

The constants of cluster formation (K_1), hydroionic repulsion (K_2), and diffusion transfer (K_3) are found experimentally.

It was demonstrated that, in the overall process under study, $\ln(c_0/c)$ takes values in the range from 1.5 to 2. This means that the total decrease in the concentration of ion impurities is as high as two orders of magnitude. The total concentration of ion microimpurities in the purified azeotropic mixture is as low as 10^{-8}–10^{-10} wt %.

The optimization of the process performed in the unit in question can be done, as can be seen from the process equation, by choosing the average optimal temperature T and temperature gradient $\Delta T/\delta$ (Fig. 5) and by selecting a construction fluoropolymer with a contact angle θ_a. For hydrofluoric acid, T = 70°C and $\Delta T/\delta \approx$ 30–50°C. The height of a vertical apparatus at a liquid motion velocity of 20–30 cm s^{-1} is about 100 cm. Thus, the residence time of the fluid in the evaporation zone is 3–5 s. At an average thickness of the liquid film of up to 1 mm and diameter of the cylindrical apparatus of 30 mm, the output capacity of a single element of the unit is as high as 2–3 cm^3 s^{-1}, or 30–50 tons year^{-1}. With a multiple-element apparatus used, the output capacity can be raised to the required level.

Using the results of the study performed makes it possible to achieve a sufficiently high (by present standards) quality of high-purity hydrofluoric acid, surpassing the best world's analogues.

REFERENCES

1. Ryabenko, E.A., Blyum, G.Z., Yaroshenko, A.M., *et al.*, *Vysokochist. Veshch.*, 1990, no. 6, pp. 12–28.
2. Ryabenko, E.A., Blyum, G.Z., Yaroshenko, A.M., *et al.*, *Khim. Prom–st'*, 1996, no. 10, pp. 671–675.
3. Blyum, G.Z., Ryabenko, E.A., Yaroshenko, A.M., *et al.*, *Plast. Massy*, 1999, no. 10, pp. 121–124.

Russian Journal of Applied Chemistry, Vol. 77, No. 6, 2004, pp. 881–886. Translated from Zhurnal Prikladnoi Khimii, Vol. 77, No. 6, 2004, pp. 894–899.

INORGANIC SYNTHESIS AND INDUSTRIAL INORGANIC CHEMISTRY

Phase Equilibria in the Systems $Na^+, K^+ \| Cl^- – H_2O$ and $Na^+, K^+ \| Cl^-, H_2PO_4^- – H_2O$ at Temperatures of 0–100°C

K. K. Agilar, B. A. Dmitrevskii, O. V. Arapov, M. V. Charykova, and N. A. Charykov

St. Petersburg State Technological Institute, St. Petersburg, Russia

St. Petersburg State University, St. Petersburg, Russia

Received September 11, 2003

Abstract—Binary and ternary parameters of the Pitzer equation and also the thermodynamic potentials of solid phases and the solubility diagrams of ternary aqueous-salt systems $Na^+, K^+ \| Cl^- – H_2O$ and $Na^+, K^+ \| Cl^-, H_2PO_4^- – H_2O$ in the temperature range 0–100°C, which corresponds to the technological conditions of brine formation, were calculated.

The previously developed thermodynamic model [1–3] makes it possible to quantitatively describe the processes of concentration of natural water and brines, precipitation of salts, interaction of salts with water and brines (congruent and incongruent dissolution), and formation of secondary salts. However, the consideration has been restricted to description of the behavior of macrocomponents of natural water (Na^+, K^+, Mg^{2+}, Ca^{2+}, Cl^-, SO_4^{2-}, etc.) because it is their content that determines the hydrochemical type of a brine, as well as the composition and mass of the crystallizing salt minerals.

The aim of this study was to determine the parameters of the thermodynamic model that makes it possible to take into account the presence of such a component as the $H_2PO_4^-$ ion in natural brines.

The model is thermodynamically based on the conditions for phase and chemical equilibria [4]. Let us consider these conditions for the example of the ternary system M, $N \| X – H_2O$. The liquid phase in such a system is a solution that contains cations M and N and anion X, and the solid phases may be in the form of anhydrous salts MX and NX, their crystal hydrates, and compounds on their base. The general formula of the solid phase whose crystallization is possible in the given system, can be represented as $l_1MX \cdot l_2NX \cdot l_3H_2O$, where l_i is the stoichiometric coefficient of ith component (salt or water) in the solid phase. According to the conditions for a phase or chemical equilibrium for any solution saturated with respect to a given compound in the system M, $N \| X – H_2O$, the linear combination of the logarithms of activities of the components of the system, multiplied by the respective stoichiometric coefficients ($l_1 \ln a_{MX} + l_2 \ln a_{NX} + l_3 \ln a_w$), must be constant at a given temperature and pressure, because it characterizes the logarithm of the solubility product, ln SP, of this compound with account of the activity coefficients of all the components.

The dependences of the excess thermodynamic functions (activity coefficients of electrolytes and osmotic coefficient of water) on the solution composition were approximated using Pitzer equations [5]. These equations, as well as the algorithm for calculating the solubility diagrams and evaluating the saturation of brines, were reported in [1–3].

A description of a binary system by means of the Pitzer method requires no less than four parameters: $\beta^{(0)}$, $\beta^{(1)}$, $\beta^{(2)}$, and $C^{(\varphi)}$, which are independent of the ionic strength and characterize binary ($\beta^{(0)}$, $\beta^{(1)}$, $\beta^{(2)}$) and ternary ($C^{(\varphi)}$) short-range interactions between ions in an electrolyte. They can be determined from experimental values of the activity of water or the activity coefficients of electrolytes in binary systems. The parameters θ and ψ correspond to binary and ternary short-range interactions between ions of different electrolytes and are calculated on the basis of experimental data for ternary systems. On passing to systems with more than three components, no additional

1070-4272/04/7706-0881 © 2004 MAIK "Nauka/Interperiodica"

Table 1. Parameters of the Pitzer equations for binary systems

System	$\beta^{(0)}$	$\beta^{(1)}$	$\beta^{(2)}$	$C^{(\varphi)}$	α_1	α_2	Reference
$NaCl–H_2O$	0.0765	0.2664	0	0.00124	2	–	[5]
$KCl–H_2O$	0.0484	0.2122	0	–0.00084	2	–	[5]
$NaH_2PO_4–H_2O$	0.0158	0.4681	–0.3338	0.00040	2	1	[6]
$KH_2PO_4–H_2O$	–0.1141	0.0690	0	0.02069	2	I	[7]

parameters appear and, in the overwhelming majority of cases, all calculations are performed using data for binary and ternary subsystems. The only exception are the cases when solid phases that were not present in any of the ternary subsystems crystallize in multicomponent systems. This circumstance is an advantage of the Pitzer method over other methods for calculation of the activity coefficients in electrolyte solutions.

Thus, the database for constructing the thermodynamic model of a multicomponent aqueous-salt system with the use of the Pitzer equations includes a set of parameters of the binary and ternary subsystems of the system under study, as well as a set of thermodynamic potentials (ln SP) of solid phases that crystallize in the system.

Table 2. Parameters of the Pitzer equations for ternary systems*

Ion	$\theta^{(0)}$	$\theta^{(1)}$	$\psi^{(0)}$	$\psi^{(1)}$
Cl, H_2PO_4	0	0	–	–
K, Cl, H_2PO_4	–	–	0.038	–0.00040
Na, K	0	0	–	–
Na, K, Cl	–	–	–0.004	–0.00001

* $\mathrm{Par} = \mathrm{Par}^{(0)} + \mathrm{Par}^{(1)}T$; T is temperature, °C.

Table 3. Values of ln SP for solid phases that contain sodium and potassium chlorides and dihydrophosphates*

Solid phase	$\ln \mathrm{SP}_D^{(0)}$	$\ln \mathrm{SP}_0^{(1)}$	T, °C
$NaCl \cdot 2H_2O$	3.04	0.017	–20…0
NaCl	3.58	0.004	0…100
KCl	1.71	0.016	0…+100
$NaH_2PO_4 \cdot 2H_2O$	0.34	0.027	–10…+41
$NaH_2O_4 \cdot H_2O$	0.86	0.024	+41…+58
NaH_2PO_4	0.81	0.032	+58…+100
α-KH_2PO_4	–1.68	0.025	–3…+65
β-KH_2PO_4	–2.71	0.040	+65…+90
H_2O (ice)	0.00	0.011	–20…0

* $\ln \mathrm{SP} = (\ln \mathrm{SP})_0^{(0)} + (\ln \mathrm{SP})_0^{(1)}T$; T is temperature, °C.

As shown previously [1–3], the solubility diagrams of multicomponent systems that model natural brines are described with a satisfactory precision in the temperature range 0–100°C by a set of parameters of binary systems for 25°C. As for the parameters of ternary systems and the values of ln SP for solid phases, it was sufficient, in most cases, to introduce a linear temperature dependence in accordance with the formula $\mathrm{Par}(T) = \mathrm{Par}(T_0) + (\mathrm{dPar}/\mathrm{d}T)(T - T_0)$, where $T_0 = 25$°C.

This study is devoted to calculation of the set of parameters that is necessary for constructing a thermodynamic model of the aqueous-salt system in the temperature range 0–100°C. Tables 1–3 list values of parameters of the binary and ternary subsystems and of ln SP of the solid phases that crystallize in the system, with part of the binary parameters taken from the literature [5–7]. The calculation was performed on the basis of published data on how the activity coefficients of the salt components and the osmotic coefficient of water depend on the composition of binary solutions and data on solubility in three-component aqueous-salt systems Na^+, $K^+ \| Cl^- – H_2O$ and Na^+, $K^+ \| Cl^-$, $H_2PO_4^- – H_2O$. The calculation included processing of a sufficiently large body of experimental data for different temperatures (in the range from 0 to 100°C). The procedure for finding the parameters of the Pitzer equations from data on solubility was described in [8]. The volume of calculation strongly varied between different systems because of the unequal extents to which these systems were studied. The calculation was based on experimental data on solubilities in three-component systems for two or three markedly different temperatures, so that the temperature range under study was covered sufficiently completely. Preference was given to those temperatures, for which an as complete body of experimental data as possible could be found in the literature.

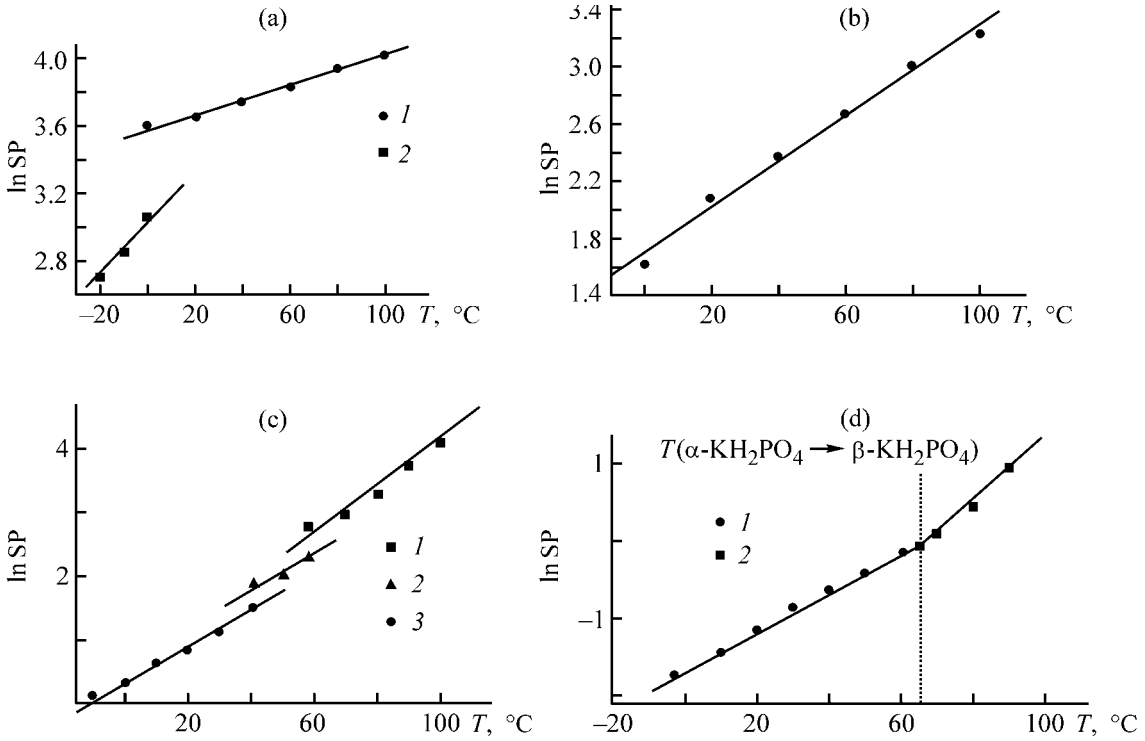

Fig. 1. Thermodynamic potentials of the solid phases, ln SP, vs. temperature *T*. Solid phase: (a) (*1*) NaCl and (*2*) $NaCl \cdot 2H_2O$; (b) KCL; (c) (*1*) NaH_2PO_4, (*2*) $NaH_2PO_4 \cdot H_2O$, and (*3*) $NaH_2PO_4 \cdot 2H_2O$; (d) (*1*) α-KH_2PO_4 and (*2*) β-KH_2PO_4. *Lines*, calculation; *points*, experimental data for binary subsystems.

The binary Pitzer parameters are listed in Table 1. The binary parameters of the system KH_2PO_4–H_2O, which could not be found in the literature, were calculated by the authors of this study on the basis of experimental data on how the osmotic coefficient of water depends on the composition of the binary solution [9]. The root-mean-square deviations σ^{φ} of the calculated φ from the experimental values were 0.005.

Table 2 lists the parameters of the Pitzer equations for three-component systems, and also their temperature dependence. To achieve a better agreement between these parameters in the quaternary mutual system Na^+, $K^+||Cl^-$, $H_2PO_4^-$–H_2O, all parameters of the θ type are set zero.

Table 3 lists values of ln SP for the solid phases that crystallize in the systems under consideration in the temperature range 0–100°C, as well as the quantities that characterize their derivative with respect to temperature. The accuracy of the linear approximation of the function ln SP(*T*) is illustrated in Fig. 1.

The solubility isotherms calculated using the resulting set of Pitzer equation parameters and values of ln SP for three-component systems containing sodium and potassium chlorides and dihydrophosphates are presented in Figs. 2, 3 and Tables 4, 5. The solution compositions are expressed in molalities of salts. Also given are published experimental data on solubility. As can be seen in Figs. 2, 3, an, on the whole, convincing agreement is observed between the results of calculation and experimental values.

In all the figures, nonvariant points are designated in accordance with the terminology introduced in [12, 13]. Letter *E* denotes ternary eutonics, and letter *O*, transfer points corresponding to an equilibrium of a three-component solution with two crystal hydrates of the same salt composition. No ternary peritonics *P* were found in the systems in question in the temperature range under study (0–100°C).

Figures 2a–2e show the solubility diagrams of the system NaCl–KCl–H_2O at 0, 25, 50, 75, and 100°C. In the same figures are plotted the experimental data of [10, 11] for 0, 25, 50, 75, and 100°C. As can be seen from Fig. 2, at all temperatures except 0°C the solubility diagram of the system NaCl–KCl–H_2O is simple eutonic, comprises two branches corresponding to crystallization of NaCl and KCl, and contains one nonvariant eutonic point. At 0°C there appears an additional, very short branch corresponding to crystallization of hydrogalite $NaCl \cdot 2H_2O$, and an additional nonvariant point *O* corresponding to joint crystallization of $NaCl \cdot 2H_2O$ and NaCl.

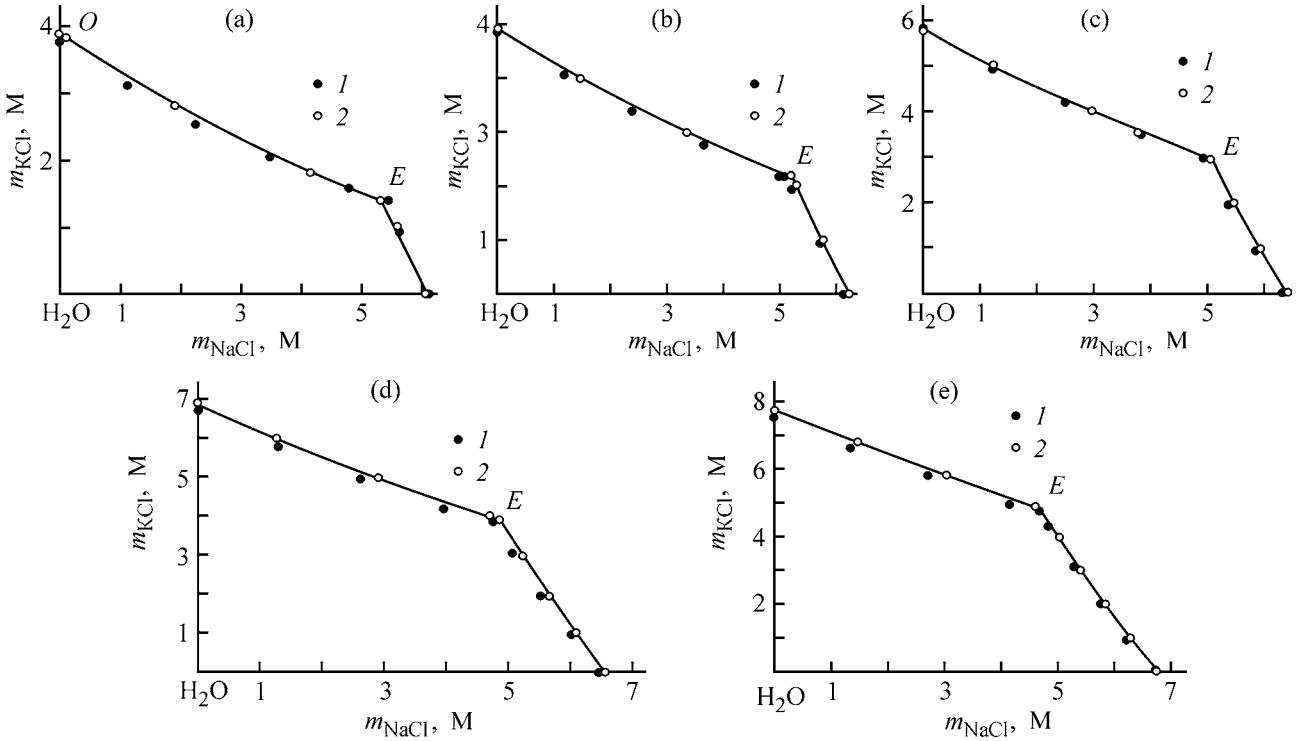

Fig. 2. Solubility diagrams for the system Na^+, $K^+||Cl^-$–H_2O at (a) 0, (b) 25, (c) 50, (d) 75, and (e) 100°C. *Lines*, calculation by the Pitzer method; *points*, experimental data of [10, 11]; the same for Fig. 3. (*m*) Molal concentration of salts; the same for Fig. 3.

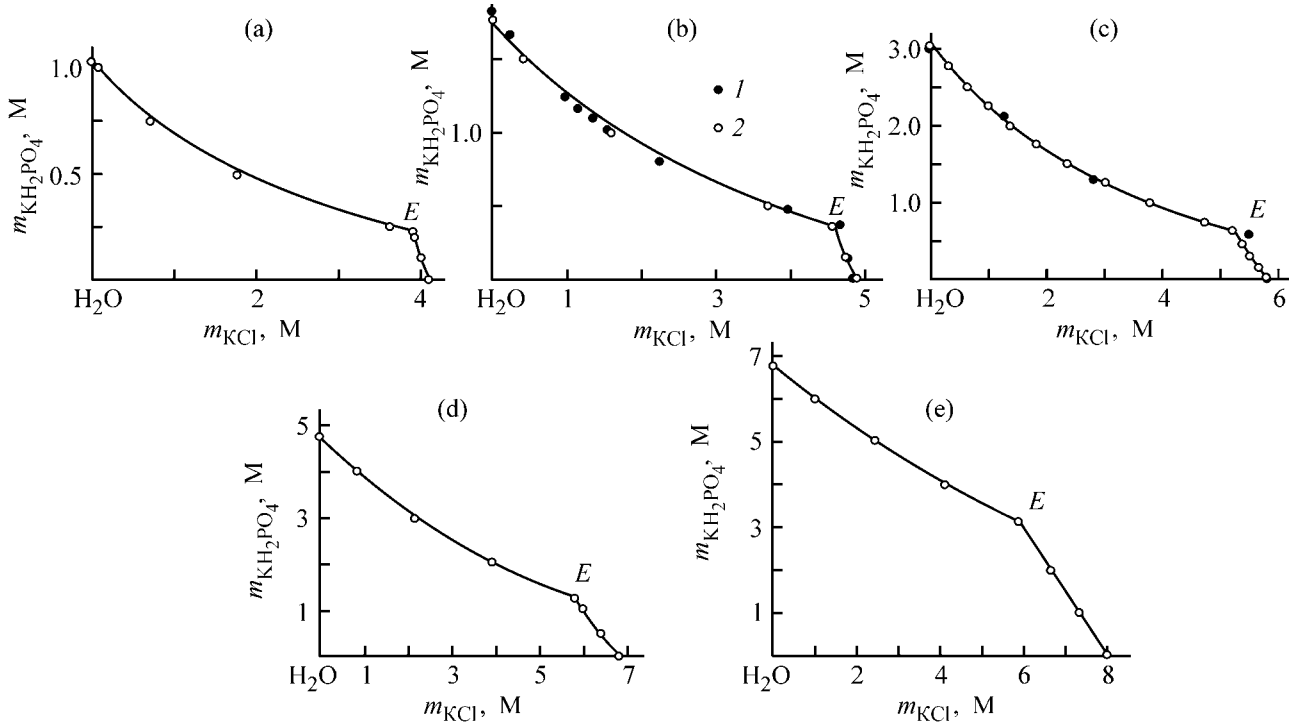

Fig. 3. Solubility diagrams of the system $K^+||Cl^-$, $H_2PO_4^-$–H_2O at (a) 0, (b) 25, (c) 50, (d) 75, and (e) 100°C.

Figures 3a–3e show the solubility diagrams of the system KCl–KH_2PO_4–H_2O at 0, 25, 50, 75, and 100°C. In the same figures are plotted experimental data of [10, 11] for 25 and 50°C. It can be seen in Fig. 3 that, at all the temperatures, the solubility diagram of the system KCl–KH_2PO_4–H_2O is simple

Table 4. Solubility diagram of the system KH_2PO_4–KCl–H_2O

T °C	m_{KCl}, mol kg^{-1}	$m_{KH_2PO_4}$, mol kg^{-1} of H_2O	a_w	Solid phase
0	0	1.03	0.973	α-KH_2PO_4
	0.07	1	0.9718	〃
	0.69	0.75	0.9586	〃
	1.76	0.5	0.9301	〃
	3.61	0.25	0.8728	〃
	3.89	0.23	0.8642	α-KH_2PO_4 + KCl
	3.91	0.2	0.8645	KCl
	3.99	0.1	0.8661	〃
	4.07	0	0.8676	KCl
25	4.56	0.36	0.8348	α-KH_2PO_4 + KCl
	3.69	0.5	0.8619	α-KH_2PO4
	1.59	1	0.9229	〃
	0.42	1.5	0.9506	〃
	0	1.76	0.9583	〃
	4.74	0.15	0.8379	KCl
	4.87	0	0.8401	〃
50	0	3.05	0.9331	α-KH_2PO_4
	0.33	2.75	0.9273	〃
	0	3.05	0.9331	〃
	0.33	2.75	0.9273	〃
	0.64	2.5	0.9215	〃
	0.99	2.25	0.9146	〃
	1.38	2	0.906	〃
	1.84	2.75	0.8952	〃
	2.37	1.5	0.8817	〃
	3	1.25	0.8647	〃
	3.76	1	0.8472	〃
	4.7	0.75	0.8159	〃
	5.24	0.63	0.7996	α-KH_2PO_4 + KCl
	5.39	0.45	0.8021	KCl
	5.52	0.3	0.8042	〃
	5.65	0.15	0.8064	〃
	5.79	0	0.8085	〃
75	0	4.80	0.8865	β-KH_2PO_4
	0.71	4	0.8751	〃
	1.79	3	0.8558	〃
	3.25	2	0.8246	〃
	5.53	1	0.7686	〃
	5.83	0.90	0.7607	β-KH_2PO_4 + KCl
	6.14	0.6	0.7646	KCl
	6.47	0.3	0.7686	〃
	6.81	0	0.7727	〃
100	5.77	1.74	0.7127	β-KH_2PO_4 + KCl
	5.30	2	0.7210	β-KH_2PO4
	3.77	3	0.7459	〃
	2.56	4	0.7637	〃
	1.53	5	0.7777	〃
	0.63	6	0,7897	〃
	0	6.75	0.7980	〃
	6.03	1.5	0.7153	KCl
	6.61	1	0.7208	〃
	7.24	0.5	0.7265	〃
	7.95	0	0.7328	〃

Table 5. Solubility diagram of the system NaCl–KCl–H_2O

T °C	m_{NaCl}, mol kg^{-1}	m_{KCl}, mol kg^{-1} of H_2O	a_w	Solid phase
0	5.31	1.6	0.7347	NaCl + KCl
	5.57	1	0.7434	NaCl
	6.05	0	0.7574	〃
	4.15	2	0.7729	KCl
	1.92	3	0.8317	〃
	0.12	4	0.8657	〃
	0	4.07	0.8660	〃
25	5.23	2.18	0.7180	NaCl + KCl
	5.30	2	0.7207	NaCl
	5.75	1	0.7353	〃
	6.14	0.1	0.7477	$NaCl \cdot 2H_2O$ + NaCl
	6.21	0	0.7491	$NaCl \cdot 2H_2O$
	3.35	3	0.7726	KCl
	1.47	4	0.8150	〃
	0	4.88	0.8400	〃
50	5.08	2.94	0.6984	NaCl + KCl
	5.48	2	0.7126	NaCl
	5.92	1	0.7270	〃
	6.39	0	0.7476	〃
	4.96	3	0.7021	KCl
	2.99	4	0.7533	〃
	1.26	5	0.7882	〃
	0	5.79	0.8085	〃
75	4.87	3.90	0.6754	NaCl + KCl
	5.23	3	0.6895	NaCl
	5.66	2	0.7044	〃
	6.10	1	0.7186	〃
	6.56	0	0.7320	〃
	4.69	4	0.6802	KCl
	2.91	5	0.7223	〃
	1.27	6	0.7533	〃
	0	6.81	0.7727	〃
100	4.60	5.08	0.6484	NaCl + KCl
	5.01	4	0.6660	NaCl
	5.41	3	0.6814	〃
	5.83	2	0.6961	〃
	6.28	1	0.7100	〃
	6.74	0	0.7233	〃
	3.06	6	0.6823	KCl
	1.47	7	0.7112	〃
	0	7.95	0.7327	〃

eutonic, with two branches corresponding to crystallization of KCl and KH_2PO_4 and a single nonvariant eutonic point. However, α-KH_2PO_4 crystallizes at temperatures of 0, 25, and 50°C, and the β-modification at 75 and 100°C.

CONCLUSION

The binary and ternary Pitzer parameters and thermodynamic potentials of solid phases of the binary and ternary subsystems of the quaternary mutual system Na^+, $K^+ \| Cl^-$, $H_2PO_4^-$–H_2O in the temperature range 0–100°C were calculated, which made it possible to construct the solubility diagrams of the subsystems. The results of the thermodynamic calculation are in a good agreement with the available published experimental data.

REFERENCES

1. Kurilenko, V.V., Filippov, V.K., Charykov, N.A., and Shvarts, A.A., *Dokl. Akad. Nauk SSSR*, 1990, vol. 311, no. 1, pp. 193–196.
2. Charykova, M.V., Ruchkov, L.V., Terskaya, L.P., *et al.*, *Zh. Prikl. Khim.*, 1994, vol. 67, no. 9, pp. 1555–1557.
3. Charykov, N.A., Nazarov, S.A., and Puchkov, L.V., *Zh. Prikl. Khim.*, 1993, vol. 66, no. 10, pp. 2101–2105.
4. Storonkin, A.V., *Termodinamika geterogennykh sistem* (Thermodynamics of Heterogeneous Systems), Leningrad: Len. Gos. Univ., 1967, parts 1 and 2.
5. Pitzer, K.S., *J. Phys. Chem.*, 1973, vol. 77, no. 2, pp. 268.
6. Charykova, M.V., *Zh. Prikl. Khim.*, 1991, vol. 64, no. 7, pp. 1393–1397.
7. Filippov, V.K., Charykova, M.V., and Trofimov, Yu.M., *Zh. Prikl. Khim.*, 1985, vol. 58, no. 9, pp. 1961–1965.
8. Filippov, V.K., Charykov, N.A., and Solechnik, N.D., *Zh. Prikl. Khim.*, 1985, vol. 58, no. 9, pp. 1966–1970.
9. Mikulin, G.I., *Rastvory elektrolitov* (Electrolyte Solutions), Leningrad: Nauka, 1972.
10. *Spravochnik po rastvorimosti vodno-solevykh sistem*, (Reference Book of Solubilities of Aqueous-Salt Systems), Pel'sh, A.D., Ed., Leningrad: Nauka, 1963, vols. 1 and 2.
11. Kogan, V.B. and Ogorodnikov, S.E., *Spravochnik po rastvorimosti* (Reference Book of Solubilities), Leningrad: Nauka, 1967, vol. 2.
12. Charykov, N.A., Shakhmatkin, B.A., Charykova, M.V., and Ruzaev, S.V., *Zh. Fiz. Khim.*, 2000, vol. 74, no. 9, pp. 1562–1569.
13. Charykov, N.A., Rumyantsev, A.V., and Charykova, M.V., *Zh. Fiz. Khim.*, 1998, vol. 72, no. 10, pp. 1746–1750.

Russian Journal of Applied Chemistry, Vol. 77, No. 6, 2004, pp. 887–890. Translated from Zhurnal Prikladnoi Khimii, Vol. 77, No. 6, 2004, pp. 900–903.

PHYSICOCHEMICAL STUDIES OF SYSTEMS AND PROCESSES

Calculation of Conditional Equilibrium Constants of Reactions of Reduction of Titanium, Zirconium, and Hafnium Chlorides with Alkali Metals in a Melt of Their Chlorides

V. A. Oleinikova, N. A. Loginov, and V. V. Chebykin

Institute of High-Temperature Electrochemistry, Ural Division, Russian Academy of Sciences, Yekaterinburg, Russia

Received November 19, 2003

Abstract—Equilibrium constants of the reactions of reduction of Ti, Zr, and Hf chlorides with metallic Li, Na, K, Rb, and Cs in their molten chlorides were calculated from published data.

Metallic sodium finds use as a reducing agent in manufacture of some metals, and primarily titanium. Both in the domestic and in the foreign literature there exhibit monographs devoted to production, properties, and use of alkali metals [1–8], and also to description of the method based on reduction with sodium for manufacture of titanium. Sodium and titanium are virtually mutually insoluble [1–12]. Rather extensive studies have been performed in order to analyze the behavior of alkali metals, determine the redox potentials, and measure the vapor pressure of alkali metals [13–19].

$TiCl_4$ is reduced by sodium in accordance with the equation

$$TiCl_4 + 4Na = Ti + 4NaCl.$$

Theoretically, obtaining 1 kg of titanium requires 1.92 kg of sodium, and the theoretical consumption of magnesium in production of titanium is 1.01 kg [1]. The reduction occurs in the range 1074–1156 K, which is delimited by the melting point of sodium chloride (1074 K) and the boiling point of sodium (1156.3 K). The melting point of sodium is 370.98 K (97.83°C). The working range of the reduction of titanium chlorides with sodium to the metal is 1123–1193 K. $TiCl_4$ can be reduced in a single- or double-stage mode. In the single-stage scheme, titanium tetrachloride is reduced directly to the metal.

In manufacture of spongy titanium, sodium has a number of advantages as a reducing agent over magnesium. It is more active and the ?extent of its utilization is as high as 98–99.5% at high reaction rates and lower temperatures; below 880°C it does not react with iron. However, the power consumption for manufacture of sodium exceeds by 25% that for magnesium. The amount of reduction products formed exceeds that in the case of reduction with magnesium. During the process, reactions of incomplete reduction also occur, i.e., $TiCl_3$ and $TiCl_2$ are formed and dissolve in molten chlorides of alkali metals to give compounds of the types $MTiCl_4$, $MTiCl_3$, M_2TiCl_4, and M_3TiCl_6. This makes necessary the double-stage method, in which a melt of lower titanium chlorides is obtained in the first stage, and these chlorides are reduced to titanium in the second stage. The initial stage is performed in the first reactor and then the melt with lower chlorides is transferred to the second reactor. The final stage consists in reduction of $TiCl_2$ and $TiCl_3$ to metal.

Large-scale use of sodium requires serious safety precautions and a high production efficiency. Several characteristic features of reduction with sodium should be pointed out. The considerably stronger heat release in reduction reactions complicates heat removal from the reactor. Magnesium chloride formed reduction with magnesium can serve as a raw material for manufacture of metallic magnesium. In a production process combining manufacture of titanium with electrolysis of magnesium, the latter is recycled, whereas obtaining sodium by electrolysis of its chloride is a more complicated task. However, a simple charging and additional charging in the course of reduction and the quality of titanium obtained eliminate these disadvantages [1–12].

In this communication, a procedure for calculating conditional equilibrium constants of reactions in which

1070-4272/04/7706-0887 © 2004 MAIK "Nauka/Interperiodica"

Table 1. Standard potentials of metals in molten chlorides of alkali metals relative to a chloride reference electrode [20]

System	$E^*_{M^{n+}/M}$, V, in a melt
	LiCl
Ti(II)/Ti	$-2.25 + 4.4 \times 10^{-4} T \pm 0.01$
Ti(III)/Ti	$-2.04 + 3.0 \times 10^{-4} T \pm 0.01$
Ti(IV)/Ti	–
Zr(II)/Zr	$-2.36 + 6.3 \times 10^{-4} T \pm 0.01$
Zr(IV)/Zr	$-2.4 + 6.0 \times 10^{-4} T \pm 0.02$
Hf(II)/Hf	$-2.43 + 6.2 \times 10^{-4} T \pm 0.01$
Hf(IV)/Hf	–
	NaCl
Ti(II)/Ti	$-2.42 + 5.1 \times 10^{-4} T \pm 0.01$
Ti(III)/Ti	$-2.19 + 3.4 \times 10^{-4} T \pm 0.01$
Ti(IV)/Ti	$-2.02 + 4.6 \times 10^{-4} T \pm 0.01$
Zr(II)/Zr	$-2.54 + 7.1 \times 10^{-4} T \pm 0.01$
Zr(IV)/Zr	$-2.58 + 6.7 \times 10^{-4} T \pm 0.01$
Hf(II)/Hf	$-2.55 + 6.6 \times 10^{-4} T \pm 0.01$
Hf(IV)/Hf	$-2.67 + 7.3 \times 10^{-4} T \pm 0.02$
	KCl
Ti(II)/Ti	$-2.60 + 6.0 \times 10^{-4} T \pm 0.01$
Ti(III)/Ti	$-2.33 + 3.7 \times 10^{-4} T \pm 0.01$
Ti(IV)/Ti	$-2.09 + 3.8 \times 10^{-4} T \pm 0.01$
Zr(II)/Zr	$-2.77 + 8.1 \times 10^{-4} T \pm 0.02$
Zr(IV)/Zr	$-2.82 + 7.7 \times 10^{-4} T \pm 0.02$
Hf(II)/Hf	$-2.77 + 7.9 \times 10^{-4} T \pm 0.01$
Hf(IV)/Hf	$-2.9 + 8.1 \times 10^{-4} T \pm 0.02$
	RbCl
Ti(II)/Ti	$-2.64 + 6.1 \times 10^{-4} T \pm 0.01$
Ti(III)/Ti	$-2.39 + 3.9 \times 10^{-4} T \pm 0.01$
Ti(IV)/Ti	$-2.11 + 4.7 \times 10^{-4} T \pm 0.02$
Zr(II)/Zr	$-2.80 + 8.1 \times 10^{-4} T \pm 0.01$
Zr(IV)/Zr	$-2.86 + 7.7 \times 10^{-4} T \pm 0.02$
Hf(II)/Hf	$-2.82 + 8.1 \times 10^{-4} T \pm 0.01$
Hf(IV)/Hf	$-3.01 + 8.6 \times 10^{-4} T \pm 0.02$
	CsCl
Ti(II)/Ti	$-2.67 + 6.2 \times 10^{-4} T \pm 0.01$
Ti(III)/Ti	$-2.43 + 3.9 \times 10^{-4} T \pm 0.01$
Ti(IV)/Ti	$-2.12 + 3.5 \times 10^{-4} T \pm 0.02$
Zr(II)/Zr	$-2.83 + 8.2 \times 10^{-4} T \pm 0.01$
Zr(IV)/Zr	$-2.88 + 7.7 \times 10^{-4} T \pm 0.02$
Hf(II)/Hf	$-2.84 + 8.0 \times 10^{-4} T \pm 0.01$
Hf(IV)/Hf	$-2.99 + 8.3 \times 10^{-4} T \pm 0.02$

Table 2. Published values of the decomposition voltage of molten chlorides of alkali metals

Salt medium	mp, K	ε^0_{decomp}, V	Reference
LiCl	883	$3.962–5.43 \times 10^{-4} T$	[21]
NaCl	1074	$4.247–8.9 \times 10^{-4} T$	[16]
KCl	1043	$4.507–9.0 \times 10^{-4} T$	[16]
RbCl	992	$4.194–6.66 \times 10^{-4} T$	[21]
CsCl	918	$4.247–6.40 \times 10^{-4} T$	[21]

titanium, zirconium, and hafnium chlorides are reduced by metallic lithium, sodium, potassium, rubidium, and cesium in molten chlorides of these alkali metals. The equations describing how the conditional values of the standard electrode potentials of the metals depend on temperature, taken from [20], are listed in Table 1. Table 2 presents temperature dependences of the decomposition voltages of lithium, sodium, potassium, rubidium, and cesium chlorides. The data in Tables 1, 2 were used to calculate temperature dependences of the conditional equilibrium constants $\log K_n^*$ for the processes represented in Table 3. The calculation procedure was described in detail in [22, 23].

Of particular interest are reactions in which titanium, zirconium, and hafnium chlorides are reduced by sodium and potassium. The conditional equilibrium constants K_n^* of reactions (1)–(7) for different temperatures in NaCl and KCl melts, which are of practical interest, are listed in Table 4. Table 4 also gives for reactions (1)–(7) the values of K_n^* at 1150 K in relation to the nature of a metal and a cation of the solvent-salt. Reduction of $TiCl_2$, $ZrCl_2$, and $HfCl_2$ by alkali metals [reactions (1), (4), (6)] occurs less intensively than that of the tetrachlorides $TiCl_4$, $ZrCl_4$, and $HfCl_4$ [reactions (3), (5), (7)]. The conditional constant K_n^* increases by approximately 44–50 orders of magnitude (Tables 3, 4).

It should be noted that the final stage of titanium reduction in a NaCl melt occurs by reactions (1)–(3) (Table 3). At 1150 K, the conditional equilibrium constant of these reactions (Table 4) has the following values: $K_1^* = 2.13 \times 10^{44}$, $K_2^* = 1.10 \times 10^{66}$, and $K_3^* = 4.49 \times 10^{82}$. The equlibrium of these reactions is deeply sheefteed to the target products. Titanium tetrachloride forms complexes of the types $TiCl_5^{2-}$ and $TiCl_4^{2-}$ [20]. K_2 exceeds K_1 by 22 orders of magnitude.

The values of K_n^* for reactions (1)–(3), (6), and (7) at 1150 K in a potassium chloride melt are listed in Table 4. It is of interest to compare the values of the conditional equilibrium constants for the processes in which titanium and hafnium chlorides are reduced by molten magnesium, which are 1.1×10^6, 9.7×10^{19}, and 5.4×10^{17}, respectively for reactions (1)–(3) at 1150 K in a KCl melt [24], and 1.09×10^7 and 1.6×10^{12} for processes (6) and (7) under the same conditions [25]. The difference in the values of K_n^* is 40 to 80 orders of magnitude.

Use of metallic lithium, rubidium, and cesium as reducing agents is economically unfeasible.

Table 3. Conditional equilibrium constants log K_n of reactions (1)–(7) in molten chlorides of alkaline metals in the temperature range 1000–1250 K

Reaction no.	Reaction	Salt medium	log K_n^*
(1)	$TiCl_{2(melt)} + 2M_{(l)} = 2MCl_{(melt)} + Ti_{(s)}$	LiCl	$-9.909 + 62621/T$
		NaCl	$-14.113 + 67208/T$
	$\log K^* = [2 \times 10^4/(1.984T)][\varepsilon^0_{decomp} - E^*_{Ti(II)/Ti}]$	KCl	$-15.121 + 71643/T$
		RbCl	$-12.863 + 68891/T$
		CsCl	$-12.702 + 69728/T$
(2)	$TiCl_{3(melt)} + 3M_{(l)} = 3MCl_{(melt)} + Ti_{(s)}$	LiCl	$-12.747 + 90756/T$
		NaCl	$-18.599 + 97334/T$
	$\log K^* = [3 \times 10^4/(1.984T)][\varepsilon^0_{decomp} - E^*_{Ti(III)/Ti}]$	KCl	$-19.204 + 103382/T$
		RbCl	$-15.968 + 99557/T$
		CsCl	$-15.575 + 100963/T$
(3)	$TiCl_{4(melt)} + 4M_{(l)} = 4MCl_{(melt)} + Ti_{(s)}$	NaCl	$-27.218 + 126351/T$
		KCl	$-25.806 + 133004/T$
	$\log K^* = [4 \times 10^4/(1.984T)][\varepsilon^0_{decomp} - E^*_{Ti(IV)/Ti}]$	RbCl	$-22.903 + 127097/T$
		CsCl	$-19.960 + 128367/T$
(4)	$ZrCl_{2(melt)} + 2M_{(l)} = 2MCl_{(melt)} + Zr_{(s)}$	LiCl	$-11.825 + 63730/T$
		NaCl	$-16.129 + 68417/T$
	$\log K^* = [(2 \times 10^4/(1.984T)][\varepsilon^0_{decomp} - E^*_{Zr(II)/Zr}]$	KCl	$-17.238 + 73357/T$
		RbCl	$-14.879 + 70504/T$
		CsCl	$-14.718 + 71341/T$
(5)	$ZrCl_{4(melt)} + 4M_{(l)} = 4MCl_{(melt)} + Zr_{(s)}$	LiCl	$-23.044 + 128266/T$
		NaCl	$-31.452 + 137641/T$
	$\log K^* = [4 \times 10^4/(1.984T)][\varepsilon^0_{decomp} - E^*_{Zr(IV)/Zr}]$	KCl	$-33.669 + 147722/T$
		RbCl	$-28.952 + 142218/T$
		CsCl	$-28.427 + 143690/T$
(6)	$2HfCl_{2(melt)} + 2M_{(l)} = 2MCl_{(melt)} + Hf_{(s)}$	LiCl	$-11.724 + 64436/T$
		NaCl	$-15.625 + 68518/T$
	$\log K^* = [2 \times 10^4/(1.984T)][\varepsilon^0_{decomp} - E^*_{Hf(II)/Hf}]$	KCl	$-17.036 + 73357/T$
		RbCl	$-14.879 + 70706/T$
		CsCl	$-14.516 + 71442/T$
(7)	$2HfCl_{4(melt)} + 4M_{(l)} = 4MCl_{(melt)} + Hf_{(s)}$	NaCl	$-32.661 + 139456/T$
		KCl	$-34.476 + 149335/T$
	$\log K^* = [4 \times 10^4/(1.984T)][\varepsilon^0_{decomp} - E^*_{Hf(IV)/Hf}]$	RbCl	$-30.766 + 145242/T$
		CsCl	$-29.637 + 145907/T$

Table 4. Conditional equilibrium constants K_n^* of reactions (1)–(7) in molten chlorides of alkaline metals at different temperatures

Salt medium	T, K	K_1^*	K_2^*	K_3^*	K_4^*	K_5^*	K_6^*	K_7^*
LiCl	1150	3.5×10^{44}	1.48×10^{66}	–	3.91×10^{43}	3.1×10^{88}	2.03×10^{44}	–
NaCl	1100	9.66×10^{46}	7.699×10^{69}	4.43×10^{87}	1.17×10^{46}	4.74×10^{93}	4.61×10^{46}	1.31×10^{94}
	1150	2.13×10^{44}	1.095×10^{66}	4.49×10^{82}	2.31×10^{43}	1.72×10^{88}	9.03×10^{43}	4.03×10^{88}
	1200	7.828×10^{41}	3.26×10^{62}	1.19×10^{78}	7.68×10^{40}	1.77×10^{83}	2.97×10^{41}	3.57×10^{83}
KCl	1100	1.02×10^{50}	6.02×10^{74}	1.28×10^{95}	2.82×10^{49}	4.2×10^{100}	4.49×10^{49}	1.92×10^{101}
	1150	1.50×10^{47}	4.94×10^{70}	7.07×10^{89}	3.55×10^{46}	6.09×10^{94}	5.66×10^{46}	2.40×10^{95}
	1200	3.82×10^{44}	8.87×10^{66}	1.07×10^{85}	7.81×10^{43}	2.71×10^{89}	1.24×10^{44}	9.33×10^{89}
RbCl	1150	1.10×10^{47}	4.01×10^{70}	4.13×10^{87}	2.68×10^{46}	5.20×10^{94}	4.02×10^{46}	3.40×10^{95}
CsCl	1150	8.53×10^{47}	1.66×10^{72}	4.61×10^{91}	2.08×10^{47}	3.32×10^{96}	4.05×10^{47}	1.73×10^{97}

CONCLUSIONS

(1) Conditional equilibrium constants of the reactions of titanium, zirconium, and hafnium chlorides with molten metallic lithium, sodium, potassium, rubidium, and cesium in molten chlorides of these alkali metals were calculated using published data. Their values of these constants are rather high.

(2) Titanium, zirconium, and hafnium tetrachlorides react with alkaline metals more vigorously than dichlorides of the same metals do. The value of K_n^* increases by approximately 44–50 orders of magnitude.

(3) Use of metallic lithium, rubidium, and cesium as reducing agents is economically unfeasible.

REFERENCES

1. Gulyanitskii, B.S., *Poluchenie titana natrietermicheskim sposobom: Obzor zarubezhnoi literatury* (Production of Titanium by Reduction with Sodium: Review of Foreign Publications). Moscow: TsIINtsvetmet, 1959.
2. Garmata, V.A., Gulyanitskii, B.S., Kramnik, V.Yu., *et al.*, in *Metallurgiya titana* (Metallurgy of Titanium), Moscow: Metallurgiya, 1968, pp. 287–232.
3. Sergeev V.V., Galitskii, N.V., and Kiselev, V.P., in *Metallurgiya titana* (Metallurgy of Titanium), Moscow: Metallurgiya, 1964, pp. 152–180.
4. Musienko, V.T., *Metallotermiya titana* (Metallothermy of Titanium), Moscow: TsIINtsvetmet, 1958.
5. Reznichenko, V.A., Ustinov, V.S., Karyazin, I.A., and Khalimov, F.B., *Khimicheskaya tekhnologiya titana* (Chemical Technology of Titanium), Moscow: Nauka, 1983.
6. *Osnovy metallurgii* (Fundamentals of Metallurgy), vol. 3, Belyaev, A.I. and Greiver, N.S., Eds., Moscow: Metallurgizdat, 1963.
7. *Khimiya i tekhnologiya redkikh i rasseyannykh elementov* (Chemistry and Technology of Rare and Trace Elements), vol. 2, Bol'shakov, K.A., Ed., Moscow: Vysshaya Shkola, 1969.
8. Savin, V.D., Ogurtsov, S.V., Nikitin, A.V., and Ogorodnikova-Zakharova, N.V., *Issledovaniya v oblasti khlornoi metallurgii titana* (Research in Chlorine Metallurgy of Titanium), Moscow: Metallurgiya, 1969, pp. 216–221.
9. Alabyshev, A.F., Grachev, K.Ya., Zaretskii, S.A., and Lantratov, M.F., *Natrii i kalii* (Sodium and Potassium), Leningrad: Goskhimizdat, 1959.
10. Sittig, M., *Sodium: Its Manufacture, Properties, and Uses*, New York: Reinhold, 1956.
11. *Natrii: Svoistva. Proizvodstvo. Primenenie* (Sodium: Properties, Manufacture, and Use), Morachevskii, A.G., Ed., St. Petersburg: Khimiya, 1992.
12. Morachevskii, A.G., Beloglazov, I.N., and Kasynbekov, B.A., *Kalii: Svoistva, proizvodstvo, primenenie* (Potassium: Properties, Manufacture, and Use), Moscow: Ruda i metally, 2000.
13. Ivenko, V.M. and Tsiovkina, L.A., *Rasplavy*, 1998, no. 3, pp. 48–52.
14. Tsiovkina, L.A., Ivenko, V.M., Chebykin, V.V., *et al.*, *Zh. Prikl. Khim.*, 1987, vol. 60, no. 10, pp. 2365–2368.
15. Smirnov, M.V., Tsiovkina, L.A., and Chebykin, V.V., *Zh. Prikl. Khim.*, 1978, vol. 51, no. 10, pp. 2186–2190.
16. Smirnov, M.V., Chebykin, V.V., and Tsiovkina, L.A., *Electrochim. Acta*, 1981, vol. 26, no. 9, pp. 1275–1288.
17. Serebryakov, S.A., Chebykin, V.V., Ivenko, V.M., *et al.*, Abstracts of Papers, *Vsesoyuznaya konferentsiya po fizicheskoi khimii i elektrokhimii ionnykh rasplavov i tverdykh elektrolitov, Sverdlovsk, 20–22 oktyabrya 1987 g.* (All-Union Conf. on Physical Chemistry and Electrochemistry of Ionic Melts and Solid Electrolytes, Sverdlovsk, October 20–22, 1987), Sverdlovsk, 1987, vol. 1, pp. 73–74.
18. Ivenko, V.M., Chebykin, V.V., and Tsiovkina, L.A., Abstracts of Papers, *VIII Vsesoyuznaya konferentsiya po fizicheskoi khimii i elektrokhimii ionnykh rasplavov i tverdykh elektrolitov, Leningrad, 11–13 oktyabrya 1983 g.* (All-Union Conf. on Physical Chemistry and Electrochemistry of Ionic Melts and Solid Electrolytes, Leningrad, October 11–13, 1983), Leningrad, 1987, vol. 3, pp. 227–228.
19. Tsiovkina, L.A., Lyubimtseva, I.Ya., and Chebykin, V.V., *Trudy In–ta elektrokhimii* (Col. of Works of the Institute of Electrochemistry), Sverdlovsk, 1977, issue 25, pp. 15–17.
20. Smirnov, M.V., *Elektrodnye potentsialy v rasplavlennykh khloridakh* (Electrode Potentials in Moten Chlorides), Moscow: Nauka, 1973.
21. Kulik, N.P., Smirnov, M.V., and Stepanov, V.P., *Elektrokhimiya*, 1982, vol. 18, no. 5, pp. 665–667.
22. Oleinikova, V.A., Loginov, N.A., Smirnov, M.V., *et al.*, *Rasplavy*, 2001, no. 6, pp. 34–39.
23. Loginov, N.A. and Oleinikova, V.A., *Rasplavy*, 2002, no. 6, pp. 34–38.
24. Oleinikova, V.A. and Loginov, N.A., *Zh. Prikl. Khim.*, 2001, vol. 74, no. 6, pp. 1031–1033.
25. Loginov, N.A. and Oleinikova, V.A., *Zh. Prikl. Khim.*, 2001, vol. 74, no. 11, pp. 1745–1748.

Russian Journal of Applied Chemistry, Vol. 77, No. 6, 2004, pp. 891–895. Translated from Zhurnal Prikladnoi Khimii, Vol. 77, No. 6, 2004, pp. 904–908.

PHYSICOCHEMICAL STUDIES OF SYSTEMS AND PROCESSES

On Assessment of the Thermodynamic Consistency of Data on Liquid–Vapor Equilibrium

A. N. Marinichev

St. Petersburg State University, St. Petersburg, Russia

Received November 6, 2003

Abstract—A new method for assessment of the thermodynamic consistency of binary isothermal data on the liquid–vapor equilibrium by calculating the Redlich–Kiester integral with account of how the pressure of phase coexistence depends on the vapor composition is suggested. The Maple 8 software is used to compare the values of the integral and other characteristics calculated for systems with varied nature of departures from the Raoult law.

The thermodynamic consistency of experimental data on the liquid–vapor equilibrium in binary systems is frequently assessed using the value of the Redlich–Kiester integral I defined by

$$I = \int_0^1 \ln \frac{\gamma_1}{\gamma_2} \, dx, \qquad (1)$$

in which γ_1 and γ_2 are the activity coefficients of components 1 and 2, and x is the mole fraction of a component (let, for definiteness, this be the first component) in solution.

Strictly speaking, the equality $I = 0$, as also the Gibbs–Duheme equation used to establish it, are valid under isothermal–isobaric conditions (see, e.g., [1]). As a rule, the experimental data presented in reference books of the type [2, 3] refer to isothermal or isobaric conditions. In discussing isothermal data (and just this type of data is considered in the present study), it is commonly believed that the effect of pressure on the state of the condensed phase can be disregarded. In other words, the contribution from the "nonisobaricity" of isothermal data, which is due to the small (but still nonzero) excess molar volume of the solution, transforms the equality $I = 0$ into an expression $I \approx 0.0001$. A conclusion has been made on the basis of the results of measurements for a number of binary systems that the accuracy of data is satisfactory if $I < 0.02$ and that the deviations in composition by 3–5 mol % strongly affect the value of the integral [1]. It is recommended by the manual [3] that the dimensional (J mol^{-1}) criterion $RTI \equiv |RTI|$, where R is the universal gas constant and T is temperature (K), should be used to assess the thermodynamic consistency of isothermal data. It is also stated that data show a very good thermodynamic consistency at $RTI \leq 12$, good consistency at $RTI \leq 40$, and lack of consistency at $RTI > 40$.

The value of I can be found from different data sets. This is commonly done by calculating the activity coefficients, determining the concentration dependence of the logarithm of their ratio, $\ln(\gamma_1/\gamma_2)$, and performing "direct" integration over the entire range of solution compositions [1]. The limiting values of this ratio (for $x = 0$ and $x = 1$) cannot be calculated from experimental data. These values are different if different parametric approximating equations (like Redlich–Kiester, Margules, Van Laar, Wilson, *NRTL*, etc. equations) are used for the concentration dependence of the activity coefficients of a component. Moreover, in the case of such a "direct" calculation of integral I, only the compositions of the coexisting liquid and vapor phases are analyzed for thermodynamic consistency, whereas the question as to whether or not experimental data are consistent as regards the concentration dependence of the phase coexistence pressure remains unsolved. The known Van Ness method [1, 5] is aimed to study the thermodynamic consistency of complete data (x–y–T–P) on phase equilibria. An opinion has been expressed that, even if the composition of the vapor phase is known, it is possible to do without these data and it is only necessary that the dependence of the pressure P on the so-

1070-4272/04/7706-0891 © 2004 MAIK "Nauka/Interperiodica"

lution composition x should be known. Then, the composition of the vapor phase can be calculated after the parameters of the concentration dependences of the activity coefficients of the components are found by minimizing the discrepancy between the calculated and experimental data on pressure and using thermodynamically compatible equations for the above dependences [5].

Presently, various kinds of new equipment have become available (various vapor-phase analyzing attachments to gas chromatographs) and the composition of the vapor phase can be determined with a sufficiently high accuracy. Therefore, it is well justified to verify the thermodynamic consistency of incomplete data on phase equilibria and, in particular, of isothermal data on saturated vapor pressure and composition of the vapor phase. It turns out in this case that information about the composition of the liquid phase (which may be even heterogeneous) is not quite necessary. If integral (I) is transformed in such a way that the mole fraction y of the first component in the vapor phase is under the differential sign, then, as shown below, it becomes possible to analyze this issue too. It should be noted that, for thermodynamically consistent data (compositions and coexistence pressure of phases), the values of integral I and *RTI* criterion should be independent of the set of data used to calculate the integral. However, the thermodynamic consistency of the phase compositions does not mean yet in practice that they are consistent with the values of pressure. Hence follows the known statement that the closeness of integral I to zero is a necessary, but not sufficient condition for consistency of data. To establish the sufficiency, it is, apparently, necessary to use some additional equation that is a consequence of the conditions for isothermal interphase equilibrium. As an equation of this kind can serve the previously obtained expression [6], which relates the pressure P and the compositions of the coexisting solution (x) and ideal vapor (y):

$$x = y\left[1 - \beta(1 - y)\frac{\mathrm{d}\ln P}{\mathrm{d}y}\right], \qquad (2)$$

where β is the ratio of the difference between the molar volumes of the vapor and liquid phases to the molar volume of the vapor phase at the temperature of the experiment (at $\beta = 1$, this expression can also be derived from the conventional form of the Duheme–Margules equation [1]).

Let us introduce the following designations

$$\varphi(y) = \frac{\mathrm{d}\ln P}{\mathrm{d}y}, \quad \alpha = \frac{y(1 - x)}{x(1 - y)}$$

and use the apparent identity

$$\frac{x}{y} = x + \frac{1 - x}{\alpha}$$

to bring the relative volatility α to the form

$$\alpha = \frac{1 + y\varphi(y)}{1 - \beta(1 - y)\varphi(y)}. \qquad (3)$$

As $(\gamma_1/\gamma_2) = \alpha(P_2^0/P_1^0)$, the Redlich–Kiester integral I can be expressed as

$$I = \int_0^1 \left(\ln\alpha + \ln\frac{P_2^0}{P_1^0}\right)\frac{\mathrm{d}x}{\mathrm{d}y}\,\mathrm{d}y, \qquad (4)$$

where P_2^0 and P_1^0 are the vapor pressures of the individual components 1 and 2 at the phase coexistence temperature under study.

Using relations (2)–(4) and taking into account that $\beta = 1$, we can write the following calculation formula for integral I:

$$I = \int_0^1 \ln\left\{\frac{[1 + y\varphi(y)]P_2^0}{[1 - (1 - y)\varphi(y)]P_2^0}\right\} \times\left\{1 - (1 - y)\varphi(y) + y\left[\varphi(y) - (1 - y)\left(\frac{\mathrm{d}[\varphi(y)]}{\mathrm{d}y}\right)\right]\right\}\mathrm{d}y. \qquad (5)$$

If the dependence of $\ln P$ on y is, e.g., a third-order polynomial

$$\ln P = a + by + cy^2 + dy^3, \qquad (6)$$

then the functions $\varphi(y)$ and $\mathrm{d}[\varphi(y)]/\mathrm{d}y$ in the right-hand part of relation (5), expressed in terms of the coefficients b, c, and d, will apparently have the form

$$\varphi(y) = b + 2cy + 3dy^3,$$
$$\mathrm{d}[\varphi(y)]/\mathrm{d}y = 2c + 6dy.$$

On substituting the last two expressions with the coefficients b, c, and d found by the least-squares procedure into (5), we can calculate the values of integral I and *RTI* criterion. The basic equations were derived [and, in particular, Eq. (5)], their adequacy was verified, and all the calculations [determining the polynomial coefficients in relation (6), with subsequent integration] were carried out using Maple 8 software, which is applicable both to symbol transformations and to mathematical calculations. The dis-

crepancy between the calculated and experimental data was evaluated by the quantity

$$\Delta_z = \frac{1}{(n - k)} \Sigma |\hat{z}_i - z_i|,$$

in which the pressure P_i and mole fraction x_i of ith experimental point are regarded as a property z_i; n is the total number of (points) sets (x, y, P); k, the number of parameters (k = 4 in this study) in the polynomial regression equation $\ln P(y)$; and $\hat{z}_i$, the value of the property z_i for ith experimental point, calculated using a regression equation of the type (6) for the value of $\hat{P}_i$ or expression (2) for the value of $\hat{x}_i$ at a value y_i.

Let us present as an example the calculation of the Redlich–Kiester integral for the acetone–benzene system with the use of data on the liquid–vapor equilibrium at a temperature of 50°C. Let us consider the main stages of a calculation using Maple 8 software. The lines with sign > are commands, and those without this symbol, comments (ignored in the course of calculation).

(1) Pre-starting procedure, calling of necessary procedures.

```
> restart:
> with(stats):with(student):
```

(2) Input of experimental data {x_1, y_1, P} and their transformation to the necessary form. The figures in square brackets, with a sign := on the left and designated as P, x_1, and y_1 are, respectively, ordered "lists" of values of pressure and mole fractions of the first component in solution and in vapor. They are easily replaced in passing from one system to another.

```
>x1:=[0,.1564,.1787,.1975,.2218,.2358,.2536,.2732,.3553,
.4183,.4552,.4714,.4924,.5388,.5546,.5976,.6635,.7174,
.7446,.7564,.7811,.7987,.817,.8402,1]:y1:=[0,.3535,.3847,
.409,.4391,.4557,.4785,.4963,.5725,.6224,.6512,.6606,
.6765,.7084,.7197,.7467,.7899,.8234,.84,.8483,.8621,
.8727,.8841,.899,1]:n:=describe[count](x1):P:=[271.238,
362.131,373.059,381.16,391.571,397.991,405.964,413.18,
443.408,464.192,476.11,480.131,486.709,500.06,504.8,
516.299,534.638,547.509,553.622,557.702,563.62,567.468,
572.194,578.119,613.815]:P02:=P[1]:P01:=P[n]:
lP:=map(x->ln(x),P):T:=50+273.2:
```

(3) As approximating dependence of $\ln P$ on y_1 was taken a third-order polynomial,

```
>fit[leastsquare[[y,z],z=a+b*y+c*y^2+d*y^3,{a,b,c,d}]]
([y1,lP]):f(y):=unapply(exp(rhs(%)),y):g(y):=exp(rhs
(%%)):dg(y):=diff(ln(g(y)),y):h(y):=unapply(dg(y),y):
k:=4:
```

(4) Calculation of numerical characteristics.

(a) Average deviation (in magnitude) of the calculated pressure from its experimental value.

```
>Pcalc:=map(f(y),y1):zip((x,y)->abs(x-y),Pcalc,P):
Digits:=2:Delta['P']:=sqrt(add(i^2,i=%%)/(n-k));
```

$$\Delta_P = 0.36$$

(b) Average deviation (in absolute value) of the calculated mole fraction of the first component in solution from the experimental value.

```
>Digits:=10:phi:=map(h(y),y1):xc:=zip((x,y)->x*(1-(1-
x)*y),y1,phi):zip((x,y)->abs(x-y),x1,xc):Digits:=2:
Delta['x']:=sqrt(add(i^2,i=%%)/(n-k));
```

$$\Delta_x = 0.0069$$

(c) Values of the Redlich–Kiester integral, dimensional *RTI* criterion, and azeotropic compositions.

```
>middlesum(ln((dg(y)*y+1)/(1-dg(y)+dg(y)*y)*
P02/P01)*(1-(1-y)*dg(y)+y*(dg(y)-(1-y)*diff(dg(y),y))),
y=0..1,100): Digits:=2:'Redlich-Kister integral':=evalf
(%%);'RTI':=abs(%)*8.314472*T;
Redlich–Kister integral := –0.000045
```

$$RTI = 0.12$$

The above "listing" of the main stages is to be regarded as a finished template for calculating Δ_P, Δ_x, Redlich–Kiester integral I, and *RTI* criterion; the results of calculations, presented below, can serve as "test examples."

Table 1 compares the procedure suggested for assessment of the thermodynamic consistency of data with the previously known method for some systems represented in the monograph [1]. Data on phase equilibria in the systems represented in Table 1, taken from the known reference book [2], were obtained in studies published before 1965. On the whole, the new method for calculating the Redlich–Kiester integral is in an agreement with the results obtained using the conventional technique. However, these systems are characterized by noticeable errors in determining the composition of the vapor phase. There is good reason to believe that these errors are smaller in more recent data because of the use of modernized equipment for experimental studies of phase equilibria. Therefore, it was worthwhile to used data published after 1965. An information of this kind for vapor–liquid equilibria in binary mixtures can be found in the reference book [3].

Table 2 lists the results of data processing for some systems represented in this reference book by the method we suggested. In particular, it was found by comparing different-order polynomials that the depen-

Table 1. Results of calculation of the Redlich–Kiester integral I and a number of accompanying characteristics by the conventional method and that suggested in this study

System, number of points	T, °C	Data of [1]		Data of this study		
		I	Δy^*_{av}	Δ_P	Δ_x	L
n-C_3H_8–i-C_5H_{10}, 9–10	0	0.043	0.014	0.14	0.093	–0.057
	25	0.030	0.011	0.17	0.066	–0.29
	50	–0.018	0.003	0.15	0.077	–0.016
	75	0.036	0.003	0.13	0.11	0.0063
n-C_6H_{14}–n-C_7H_{16}, 10	30	0.066	0.012	1.2	0.013	–0.0052
	50	0.001	0.008	3.6	0.018	0.0013
CH_3OH–n-C_6H_{14}, 11	45	0.002	0.004	5.2		0.00065
n-C_6H_{14}–C_2H_5OH, 21	–10	0.033	0.012	1.0		–0.040
	10	–0.010	0.006	4.6		–0.036
	20	0.003	0.007	8.4		–0.016
C_2H_5OH–C_6H_6, 13–15	20	0.070	0.021	2.6		0.0092
	40	–0.010	0.008**	8.6		0.043
	60	0.147	0.032	20		0.0084

* Δy_{av} is the average modulus of the difference between the experimental and calculated values of y.

** Systematic errors in the data are observed; values considerably exceeding 0.15 are not presented.

Table 2. Results of calculation of Δ_P, Δ_x, Redlich–Kiester integral I, and RTI criterion for a number of systems mentioned in the reference book [2]

System*	T, °C	System no.	Number of points	Δ_P	Δ_x	I	RTI
HCl–N_2O	–90.83	1	11	1.2	0.0033	0.00076	1.2
H_2O–CH_3COOH	80	36	12	3.3	0.022	–0.0025	7.3
CCl_4–1,2-$C_2H_4Cl_2$	30	144	12	0.69	0.010	0.0032	8.0
CCl_4–n-C_6H_{14}	25	155	12	0.15	0.0015	0.00057	1.4
CCl_4–n-C_7H_{16}	25	156	14	0.30	0.0047	0.0033	8.2
$CHCl_3$–n-C_6H_{14}	25	170	14	0.54	0.0042	–0.0016	4.2
C_2H_5OH–$CH_3COC_2H_5$	55	332	7	2.8	0.022	0.0013	3.6
C_2H_5OH–C_6H_6	55	339	8	7.2	0.076	–0.0067	20
CH_3COCH_3–C_6H_6	50	441	25	0.36	0.0069	–0.000045	0.12
i-C_3H_7OH–C_5H_5N	40	477	14	0.30	0.0041	–0.0014	3.6
$CH_3COC_2H_5$–C_6H_6	50	544	35	0.13	0.0024	–0.00071	2.0
C_4H_9Br–C_6H_6	70	576	29	0.28	0.0039	–0.0012	3.4
$(C_2H_5)_2O$–C_6F_6	24.981	597	31	2.0	0.010	0.013	32
C_6H_6–C_6F_6	50	699	13	0.76	0.0054	0.0027	7.1
C_6H_6–C_6H_{12}	39.95	702	19	0.15	0.0026	–0.00059	1.5

* For all the systems, the dimension of pressure is mm Hg.

dence $\ln P(y)$ is, as a rule, well described by a third-order interpolation polynomial.

The results listed in Table 2 suggest that, at a number of experimental points of no less than 10, the cubic dependence of the logarithm of the pressure on the vapor composition well describes the experimental data, and small deviations (0.01 mole fraction and less) of the calculated solution composition from that found experimentally are in a full agreement with the small value of the Redlich–Kiester integral. This indicates the thermodynamic consistency of the experimental data. It is more difficult to analyze data with a number of points less than 10; in these cases, the deviation Δ_x may be frequently rather pronounced, whereas the value of integral I may indicate a thermodynamic consistency of the data on $P(y)$.

The benzene–cyclohexane system has an azeotrope of an equimolar composition, which corresponds to the highest pressure. If the range of the vapor phase compositions is represented as two concentration

intervals, before and after the azeotrope, and, e.g., second-order interpolation dependences are found, we obtain the following equations:

$$\ln P = 5.200 + 0.50641y - 0.503y^2 \quad (7)$$

for the interval $y \in [0-0.4979]$ and, with the coefficient of determination equal to 0.9997,

$$\ln P = 5.211 + 0.48641y - 0.500y^2 \quad (8)$$

for $y \in [0.5239–1]$, with the coefficient of determination equal to 0.99994. Let us represent expression (5), which is the Redlich–Kiester integral, as a sum of two integrals with changes in the composition of the vapor phases before and after the azeotrope. With account of Eqs. (7) and (8), their values are 0.1289 and –0.1300, and the integral itself, which is a sum of these two values, equals –0.0011, which points to a good thermodynamic consistency of the experimental data on the pressure and composition of the vapor phase. Calculation of the liquid phase composition with the use of equations of the type (2) and expressions (7) and (8) for the equimolar composition (0.5) of the vapor phase gives values of 0.4993 and 0.5035, which indicates the coincidence, within the experimental error, of the compositions of the liquid and vapor phases. The above example shows that the approach of this kind can be also extended to systems with limited mutual solubility of components. Similarly performed calculations for systems of this kind make it possible both to assess the thermodynamic consistency of data and to specify the compositions of the liquid phases into which decomposes in condensation the vapor phase of a heteroazeotropic composition.

CONCLUSION

It was shown that the Redlich–Kiester integral expressed in terms of pressure and vapor phase composition, combined with additional parameters, can characterize the thermodynamic consistency of data on phase equilibria and can be applied to systems with a heteroazeotrope.

REFERENCES

1. Morachevskii, A.G., Smirnova, N.A., Piotrovskaya, E.M., *et al.*, *Termodinamika ravnovesiya zhidkost'–par* (Thermodynamics of the Liquid–Vapor Equilibrium), Leningrad: Khimiya, 1989.
2. Kogan, V.B., Fridman, V.M., and Kafarov, V.V., *Ravnovesie mezhdu zhidkost'yu i parom* (Liquid–Vapor Equilibrium), Moscow: Nauka, 1966, vol. 1.
3. Lyudmirskaya, G.S., Barsukova, T.A., and Bogomol'nyi, A.M., *Ravnovesie zhidkost'–par* (Liquid–Vapor Equilibrium), Leningrad: Khimiya, 1987.
4. Lempe, D., Elsner, N., Schneider, F., and Kalz, G., *Thermodynamik der Mischphasen II*, Leipzig: VEB, 1974.
5. Reid, R.G., Prausnitz, J.M., and Sherwood, T.K., *The Properties of Gases and Liquids*, New York: McGraw-Hill Book Company, 1977.
6. Marinichev, A.N., *Zh. Prikl. Khim.*, 1995, vol. 68, no. 4, pp. 542–546.

Russian Journal of Applied Chemistry, Vol. 77, No. 6, 2004, pp. 896–900. Translated from Zhurnal Prikladnoi Khimii, Vol. 77, No. 6, 2004, pp. 909–913.

SORPTION AND ION-EXCHANGE PROCESSES

Preparation and Properties of Spherically Granulated Titanium Phosphate Modified with Fe(III) Hexacyanoferrate(II)

V. K. Mardanenko, V. V. Strelko, V. A. Kanibolotskii, and N. M. Patrilyak

Institute of Sorption and Endoecological Problems, National Academy of Sciences of the Ukraine, Kiev, Ukraine

Received August 12, 2003; in the final form, April 2004

Abstract—Spherically granulated titanium(IV) phosphate modified with Fe(III) hexacyanoferrate(II) was prepared by the improved sol–gel procedure, and its physicochemical and sorption characteristics were studied in comparison with those of the unmodified Ti(IV) phosphate.

This paper continues the series of publications [1–4] aimed at preparing radionuclide sorbents by depositing ferrocyanides(II) of heavy metals onto various supports.

It is known, owing to their structural features, that several poorly soluble heavy metal hexacyanoferrates(II) exhibit high affinity for toxic metals and especially for ^{137}Cs radionuclide [5–19].

Preparation of granulated hexacyanoferrates(II) suitable for sorption of metals from aqueous solutions under dynamic conditions is power-consuming. The sorbents based on finely dispersed hexacyanoferrate(II) are more available, but, due to their high hydrodinamic resistance, they are unsuitable for purification of contaminated solutions. Depending on the kind of problem, either granulated or gel-like hexacyanoferrate(II) sorbents are used [20]. Numerous attempts have been made to develop effective sorbent convenient for use and suitable for sorption of radionuclides, in particular ^{137}Cs. These attempts involved application of heavy metal hexacyanoferrate(II) to various supports: ion-exchange resins [5], fibrous activated carbon [12], cellulose [14–16], silica gel [18], aluminum oxide [19], natural aluminosilicates [15, 16, 21], sawdust [22], etc. In order to develop a new effective sorbent of this kind, an appropriate inexpensive support must be found.

Our approach to preparation of improved hexacyanoferrate(II) sorbents is based on the use of spherically granulated Fe(III)-containing titanium(IV) phosphate as support. This kind of titanium(IV) phosphate can be prepared by a sol–gel technique from aqueous solution of $TiOSO_4$ used for production of commercial TiO_2. The use of granulated support with required grain size in preparing the sorbent modified with hexacyanoferrate(II) is very advantageous, since in this case the granulometric composition of the modified sorbent is determined by the grain size of the initial titanium(IV) phosphate. Under these conditions, a nearly 100% yield of the desired modified sorbent is achieved.

As a rule, in all studies except [21], a support is sequentially treated in preparing sorbents modified with hexacyanoferrate(II), with aqueous solutions of an appropriate heavy metal salt and potassium hexacyanoferrate(II) $K_4[Fe(CN)_6]$ (K–HCF). In preparing our modified sorbent, a spherically granulated titanium phosphate (TiP) containing 2.0 to 3.2 wt % Fe(III) [23] was used as a support. By modification of these grains with aqueous potassium hexacyanoferrate(II), spherically granulated sorbents [24] containing from 40 to 120 mg g^{-1} Fe(III) hexacyanoferrate(II) $Fe_4[Fe(CN)_6]_3$ (Fe(III)–HCF) were prepared; these sorbents were used in our experiments.

The procedures used for titanium phosphate modification were optimized by varying the Fe(III) content in the initial TiP, pH, the modifier (K–HCF) concentration at constant TiP : K–HCF solution ratio, TiP grain size, and impregnation time. The sorption power of the initial TiP and its modified forms for radionuclide ions ^{137}Cs, ^{90}Sr, and some ions of heavy metals (Cu^{2+}, Cd^{2+}) was studied.

EXPERIMENTAL

A fresh spherically granulated titanium phosphate hydrogel in the H forms prepared by a sol–gel technique, was modified with Fe(III) hexacyanoferrate(II) under static conditions as follows. A granulated

1070-4272/04/7706-0896 © 2004 MAIK "Nauka/Interperiodica"

Table 1. Physicochemical characteristics of the initial granulated titanium phosphate

Content, wt %					P/Ti	S_{sp}, $m^2 g^{-1}$	V_s, $cm^3 g^{-1}$	
Fe_2O_3	TiO_2	P_2O_5	SO_3	H_2O			for H_2O	for C_6H_6
3.7	21.2	20.7	0.09	49.8	1.0	230.1	0.28	0.73
3.1	33.2	30.4	0.15	26.5	1.0	165.7	0.23	0.41
1.8	11.2	10.5	0.05	73.6	1.1	205.3	0.58	0.69

Table 2. Influence of pH of aqueous modifying solution on fixation of Fe(III)–HCF by titanium phosphate

pH of aqueous K–HCF		Fe(III)–HCF content in MTiP, mg g^{-1}	Fe(III) bound to modifier, %	pH of aqueous K–HCF		Fe(III)–HCF content in MTiP, mg g^{-1}	Fe(III) bound to modifier, %
initial	equilibrium			initial	equilibrium		
1.2	1.2	49.6	44.7	3.0	2.4	42.2	40.6
2.2	2.2	57.2	55.0	4.2	2.7	41.8	40.2

TiP hydrogel (5–20 g) was kept in 0.2 M aqueous $K_4[Fe(CN)_6]$ (7–67 cm^3) at pH 1.2–4.2 with stirring for 24 h at 19–20°C. Upon contact, the solid phase was separated and washed with distilled water to remove $K_4[Fe(CN)_6]$. The resulting modified TiP was airdried for 2 days and analyzed for $[Fe(CN)_6]^{4-}$. The initial TiP was analyzed for phosphorus, titanium, and iron. All the analyses were carried out by the conventional techniques [25, 26].

The sorption power of modified titanium phosphate for metal ions was determined upon its contact with a solution of the metal nitrate in 0.1 M $NaNO_3$ (supporting electrolyte) or in water. In the case of sorption of radionuclides, the Ringer solution (mM: NaCl 136.9, KCl 5.6, $CaCl_2$ 2.2 and $NaHCO_3$ 1.2) [27] was used as a supporting electrolyte. This supporting electrolyte was chosen taking into account that the deactivation of biological liquid media is a problem of current interest.

The static sorption experiments were carried out at the ratio of solid and liquid phases, s : l = 1 : (200–1000) with their stirring for 24 h. Under these conditions, the sorption equilibrium was attained upon contact for 10–24 h. The sorption of heavy metals was determined as the difference between their concentrations in the initial and equilibrium solutions. Similarly, the sorption of ^{137}Cs was determined as the difference between its activity in the initial and equilibrium solutions. The sorption kinetics of ^{137}Cs was studied under limited-volume conditions [28]. The specific surface area S_{sp} of sorbents was determined by gas–chromatography from the thermal desorption of argon. The volume of the sorptive pores V_s was determined with a desiccator technique [29] by sorption of benzene and water vapors.

The physicochemical characteristics of the initial granulated titanium phosphate are listed in Table 1.

Table 2 shows that, all other factors being the same, the maximal Fe(III) HCF fixation by titanium phosphate is reached at pH 2.2 of aqueous K–HCF. We found that deviation from this pH deteriorates the modifier accumulation in TiP. Therefore, all further experiments were carried out at pH 2.2.

It should be noted that, in the course of modification of titanium phosphate with Fe(III)–HCF, the pH of aqueous solutions of K–HCF somewhat decreases (from 2.9–3.0 to 1.2–2.7). We found that, in dilution of aqueous modifier, its fixation by titanium phosphate decreases. For example, at pH 2.2 and identical weighed portions and aqueous phase volumes, the content of Fe(III)–HCF in titanium phosphate decreases from 78.8 to 65.6 mg g^{-1} with the initial modifier concentration decreasing from 0.168 to 0.038 M.

It was found (Table 3) that, although the degree of modification somewhat grows with increasing Fe(III)

Table 3. Influence of Fe_{tot} content in TiP on the degree of Fe(III) fixation

Fe_{tot} content in TiP, mg g^{-1}	Fe(III)–HCF content in MTiP, mg g^{-1}		Fe(III), bound to modifier, %
	analysis	calculated from Fe_{tot}	
36.1	57.2	139.0	41.2
53.5	80.5	206.0	39.2
64.0	121.2	246.4	49.2

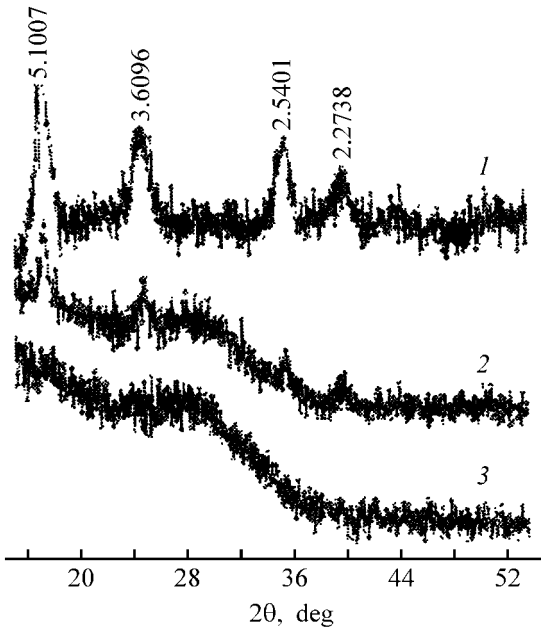

Fig. 1. X-ray diffraction pattern of (*1*) Fe(III) hexacyanoferrate(II), (*2*) titanium phosphate modified with Fe(III) hexacyanoferrate(II), and (*3*) initial titanium phosphate. (2θ) Bragg angle.

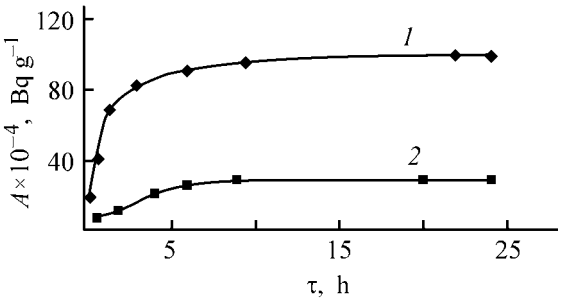

Fig. 2. Kinetic curves of ^{137}Cs sorption *A* on (*1*) MTiP and (*2*) TiP from a Ringer solution containing 59.6 Bq cm^{-3} ^{137}Cs. (τ) time.

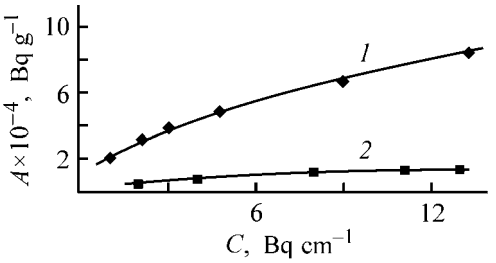

Fig. 3. Sorption *A* of ^{137}Cs from the Ringer solution on (*1*) MTiP and (*2*) initial TiP vs. activity of the equilibrium liquid phase *C*.

content in the initial TiP, the fraction of Fe(III) bound to K–HCF does not exceed 50%. We believe that the low efficiency of Fe(III) binding with the modifier is caused by formation of a dense Fe(III)–HCF surface film on the surface of TiP granules, hindering the penetration of $[Fe(CN)_6]^{4-}$ into the grain bulk. This effect was confirmed by a decrease in the intenity of the Fe(III)–HCF color from the grain surface to the center, observed visually in crushing coarse grains (2 mm).

The effect of grain size on the efficiency of titanium phosphate modification was studied with granulaed titanium phosphate hydrogel containing 2.56 wt % Fe(III). In these experiments, 0.1–0.3, 0.3–0.5, 0.5–1.0, and 1.0–2.0 mm fractions of TiP grains were used. With the grain size increasing in this series, the specific content of $Fe_4[Fe(CN)_6]_3$ in MTiP (mg g^{-1}) decreases: 50.5, 41.2, 30.0 and 15.6, mg g^{-1}, respectively. These data are consistent with our hypothesis about formation of a $Fe_4[Fe(CN)_6]_3$ surface layer hindering the penetration of hexacyanoferrate(II) anions into the grain bulk.

Our kinetic experiments showed that TiP grains became saturated with the modifier after no less than 2 days, i.e. the modification is a slow process. Data on the kinetics of Fe(III)–HCF accumulation in TiP grains (0.3–0.5 mm) are given below.

Fe(III)–HCF, mg g^{-1}	30.1	58.7	79.7	80.5
τ, h	5	10	24	48

The X-ray diffraction pattern in (Fig. 1) shows that modified TiP contains the Fe(III)–HCF phase with the interlayer spacings identical to those of the individual Fe(III)–HCF. This means that Fe(III)–HCF is not chemically bound to the TiP matrix. Figure 2 shows kinetic curves of ^{137}Cs sorption from the Ringer solution on the initial and modified TiP. In going from the initial TiP to its modified form MTiP, all other factors being the same, the degree of ^{137}Cs sorption increases from 28 to 98%. The sorption rate of ^{137}Cs on the modified sor bent also substantially increases. For example, within the first 0.5 h, radiocesium is sorbed by MTiP and TiP to 38% and 4% of the equilibrium amount, respectively. These data show that the sorbents based on granulated titanium phosphate are characterized by slow sorption kinetics; the sorption equilibrium is attained within 22–24 h. Therefore, all the sorption experiments were carried out for 24 h.

The comparison of sorption isotherms of ^{137}Cs on the initial and modified titanium phosphate (Fig. 3) shows that introduction of Fe(III)–HCF into the sorbent raises the cesium sorption by a factor of 5–6. However, there is no proportionality between the modifier content in the sorbent and its sorption power; the increase in the sorption power is substantially

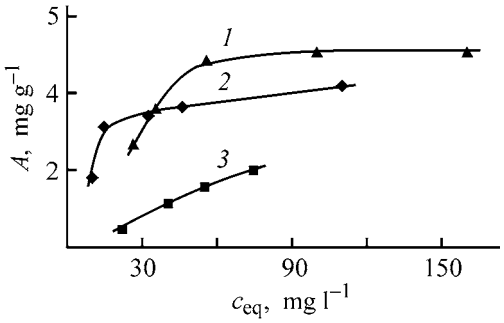

Fig. 4. Sorption isotherms of (*1*) Cu^{2+} and (*2*) Cd^{2+} on MTiP and (*3*) Cu^{2+} on the initial TiP from aqueous chloride solutions. (*A*) Sorption and (c_{eq}) equilibrium metal concentration.

weaker than that in the modifier content. A similar effect was found by us in [4]. The distribution factor K_d of ^{137}Cs between modified titanium phosphates and the Ringer solution, calculated from the sorption isotherms, is $(20-60) \times 10^3$ $cm^3\ g^{-1}$.

We found that the sorption of ^{90}Sr on titanium phosphate modified with Fe(III) hexacyanoferrate(II) is significantly lower than that of ^{137}Cs (K_d = 30–40 $cm^3\ g^{-1}$). These results are consistent with the data reported in [30, 31].

We also studied the sorption power of MTiP for several heavy metals. Figure 4 shows the sorption isotherms of copper and cadmium on the initial and modified titanium phosphate from their aqueous chloride solutions. These data show that, in going from the initial titanium phosphate to its modified form, the sorption of the heavy metals increases, but this effect is smaller than for radiocesium. Our experimental results show that titanium phosphate modified with Fe(III) hexacyanoferrate(II) is an effective sorbent for radiocesium and can be used for decontamination of aqueous solutions to remove this radionuclide under both dynamic and static conditions. These results can also be used for optimization of procedures for preparing titanium phosphate modified with metal hexacyanoferrate(II).

CONCLUSIONS

(1) Granulated titanium phosphate modified with Fe(III) hexacyanoferrate(II) (40–120 $mg\ g^{-1}$) was prepared from an initial granulated titanium phosphate containing 2–3.2 wt % Fe(III).

(2) The distribution factors of ^{137}Cs and ^{90}Sr between titanium phosphate modified with Fe(III) hexacyanoferrate(II) and aqueous solution are $(20-60) \times 10^3$ and 30–40 $cm^3\ g^{-1}$, respectively.

(3) Granulated titanium phosphate modified with Fe(III) hexacyanoferrate(II) can be used for efficient decontamination of aqueous solutions to remove radiocesium.

REFERENCES

1. Strelko, V.V., Mardanenko, V.K., Yatsenko, V.A., and Patrilyak, N.M., *Zh. Prikl. Khim.*, 1998, vol. 71, no. 10, pp. 1642–1645.
2. Strelko, V.V., Yatsenko, V.V., Mardanenko, V.K. and Mil'grandt, V.G., *Zh. Prikl. Khim.*, 1998, vol. 71, no. 8, pp. 1295–1297.
3. Mil'grandt, V.G., Mardanenko, V.K., Strelko, V.V., and Yatsenko, V.V., *Zh. Neorg. Khim.*, 1994, vol. 39, no. 9, pp. 1456–1459.
4. Strelko, V.V., Yatsenko, V.V., Mardanenko, V.K. and Mil'grandt, V.G., *Zh. Prikl. Khim.*, 1995, vol. 68, no. 9, pp. 1456–1460.
5. Karpova, I.F. and Kazakov, E.V., *Vestn. Leningr. Gos. Univ.*, 1966, no. 4, pp. 159–160.
6. *Khimiya ferrotsianidov* (Chemistry of Ferrocyanides), Tananaev, I.V., Seifer, G.B., Kharitonov, Yu.Ya., *et al.*, Eds., Moscow: Nauka, 1971.
7. Calabrese, A. and Hayses, R.G., *J. Am. Chem. Soc.*, 1974, vol. 96, pp. 50–54.
8. Watari, K., Imai, K., Ohmomo, Y., *et al., J. Nucl. Sci. Technol.*, 1988, vol. 25, no. 5, pp. 495–499.
9. Krylov, V.N., Borisov, S.M., and Burov, A.G., *Radiokhimiya*, 1988, vol. 30, no. 5, pp. 644–649.
10. Tamhara, K., *Radianal. Nucl. Chem. Lett.*, 1991, vol. 153, no. 6, pp. 399–408.
11. Segal, M.G. and Moris, K., *Chem. Brit.*, 1991, vol. 27, no. 10, p. 908.
12. Morozova, A.A., Shashkova, I.L., and Prodan, E.A., *Khim. Farm. Zh.*, 1994, vol. 28, no. 2, pp. 16–19.
13. Zheng, Z., Philip, C.V., Anthony, R.G., *et al., Ind. Eng. Chem. Res.*, 1996, vol. 35, pp. 4246–4256.
14. Demidov, V.V., Remez, V.P., and Shubin, A.S., *Zh. Prikl. Khim.*, 1991, vol. 64, no. 8, pp. 1769–1771.
15. Loos-Neskovic, C., Fedoroff, M., Garniek, E., and Gravereau, H., *Talanta*, 1984, vol. 31, no. 12, pp. 1133–1147.
16. Vakulevskii, S.M., Lishevskaya, M.O., Nikitin, A.I., *et al., Tr. Gos. Okeanogr. Inst.*, Study of Processes at Waste Discharge into Sea, 1985, issue 174, pp. 83–88.
17. USSR Inventor's Certificate, no. 322954.
18. JPN Patent no. 136044.
19. Homs, N., Piscina, P.R., and Bovvull, F., *J. Chem. Soc., Chem. Commun.*, 1988, no. 16, pp. 1075–1076.
20. Pechenyuk, S.I., *Usp. Khim.*, 1992, vol. 61, no. 4, pp. 711–733.
21. USSR Inventor's Certificate, no. 1774884.

22. Chistyakov, V.P., Gorshtanskaya, O.S., and Nemchinova, O.A., *Zh. Prikl. Khim.*, 1992, vol. 65, no. 12, pp. 2816–2818.
23. Ukrainian Application Patent 40389A.
24. Ukrainian Application Patent 39755A.
25. *Analiz mineral'nogo syr'ya* (Analysis of Mineral Raw Materials), Knipovich, Yu.N. and Morachevskii, Yu.V., Eds., Leningrad: Goskhimizdat, 1959.
26. Novikov, Yu.V., Lastochkina, K.O., and Boyazina, Z.N., *Metody issledovaniya kachestva vody vodoemov* (Methods for Determination of Pond Water Quality), Moscow: Meditsina, 1990.
27. *Bol'shaya meditsinskaya entsiklopediya* (Big Medical Encyclopedia), Bakulev, A.N., Ed., Moscow: Sovetskaya Entsiklopediya, 1960 vol. 14.
28. Rieman, W. and Walton, H.F., *Ion Exchange in Analytical Chemistry*, New York: Pergamon, 1970.
29. Kel'tsev, N.V., *Osnovy adsorbtsionnoi techniki* (Fundamentals of Sorption Technique), Moscow: Khimiya, 1984, 2nd ed.
30. Panasyugin, A.S., Trofimenko, N.E., Masherova, N.P., *et al.*, *Zh. Prikl. Khim.*, 1993, vol. 66, no. 9, pp. 2119–2122.
31. Milyutin, V.V., Gelis, V.M., and Leonov, N.B., *Radiokhimiya*, 1998, vol. 40, no. 3, pp. 418–420.

Russian Journal of Applied Chemistry, Vol. 77, No. 6, 2004, pp. 901–904. Translated from Zhurnal Prikladnoi Khimii, Vol. 77, No. 6, 2004, pp. 914–918.

SORPTION AND ION-EXCHANGE PROCESSES

Properties of Monocarboxy Cellulose Containing Sorbed Fe(III), Al(III), and Cr(III) Cations

N. K. Yurkshtovich, N. V. Golub, F. N. Kaputskii, T. L. Yurkshtovich, and R. I. Kosterova

Research Institute of Physicochemical Problems, Belarussian State University, Minsk, Belarus

Received November 28, 2003; in final form, March 2004

Abstract—Sorption of Fe(III), Al(III), and Cr(III) on monocarboxy cellulose at various pH, concentrations of metal chloride or sulfate in solution, and time was studied. The effect of type and amount of the cation sorbed on the physicomechanical properties, swelling, and stability in phosphate buffer of monocarboxy cellulose fibers was considered.

Multicharged Fe(III), Al(III), or Cr(III) cations introduced into carboxyl-containing cation exchangers form intermolecular bonds, which affect the exchanger properties: swelling decreases, mechanical strength and stability with respect to chemical reagents increase, etc. [1, 2].

Among medical polymers that can coordinate with the above cations, monocarboxy cellulose (MCC), which is the product of cellulose oxidation with nitrogen(IV) oxide, is of special interest. Monocarboxy cellulose is biocompatible with a living body, exhibits hemostatic effect, and can resolve in the organism without toxic reaction. These properties of MCC threads and the physicomechanical parameters of the initial cellulose fibers make them applicable as a resolving surgical sutures. However, along with the positive properties, MCC has substantial disadvantages: high swelling, low stability in alkaline media, and high rate of biodegradation.

In this study, we examined effect of Fe(III), Al(III), and Cr(III) sorption conditions on the content of cation sorbed, swelling, mechanical properties, and stability *in vitro* of MCC salt forms.

EXPERIMENTAL

Viscose cord threads (184 tex) oxidized with a 5% solution of nitrogen(IV) oxide in carbon tetrachloride [3] were used. The content of carboxy groups (CC) in MCC samples, determined by the Ca acetate method, [4] was 0.3–1.4 mmol g^{-1}. Sorption of Fe(III), Al(III), and Cr(III) with H form of MCC was performed under static conditions at $20 \pm 1°C$ from chloride and sulfate solutions for various times (from 1 min to 24 h). The cation exchanger sample weight was 1 g, and the solution volume, 40 ml. In the initial solutions, the salt concentration was 0.07–0.11 (Cr^{3+}), 0.02–0.17 (Fe^{3+}), and 0.02–0.14 M (Al^{3+}), pH of Cr(III) and Al(III) sulfate solutions was varied by addition of $Ba(OH)_2$. The relationship between pH and the amount of $Ba(OH)_2$ added is shown in Fig. 1. The pH limits are determined by instability of chromium and aluminum salts in alkaline media. The degree of swelling, Q, of MCC salt in water was determined by centrifugation [5]. The mechanical strength of fibers in dry and wet state and as a knot: P_d, P_w, and P_k, respectively, was determined by the method described in [6].

The Al(III), Cr(III), and Fe(III) content in the MCC phase was determined (after breakdown of an MCC sample in sulfuric acid, with hydrogen peroxide added)

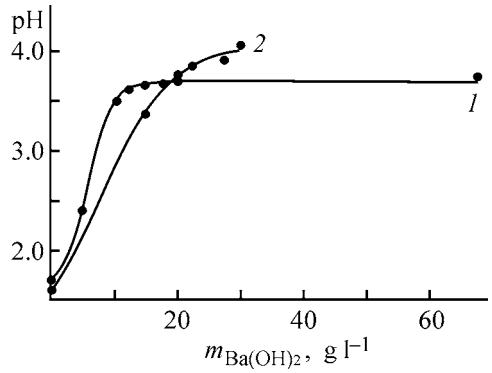

Fig. 1. pH of freshly prepared 0.1 M solutions of (1) aluminum sulfate and (*2*) chromium sulfate solutions vs. the amount of hydroxide added barium, $m_{Ba(OH)_2}$.

1070-4272/04/7706-0901 © 2004 MAIK "Nauka/Interperiodica"

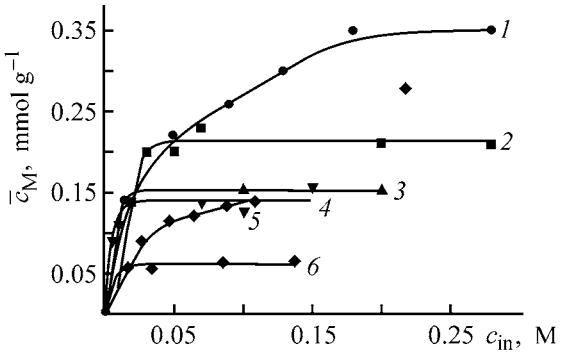

Fig. 2. Isotherms of sorption of cations (*1*, *2*, *6*) Fe^{3+}, (*3*) Al^{3+}, and (*4*, *5*) Cr^{3+} with MCC with EC_{COOH} (*2*–*6*) 0.7 and (*1*) 1.4 mmol g^{-1} from (*1*, *2*, *5*) chloride and (*3*, *4*, *6*) sulfate solutions. Sorption time 24 h. ($\bar{c}_M$) Metal cation concentration in MCC and (c_{in}) initial metal cation concentration.

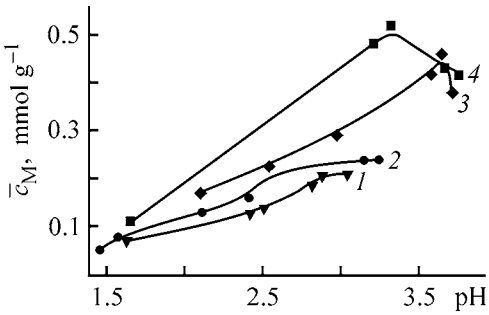

Fig. 3. Effect of pH on the amount of (*1*, *2*) Cr^{3+} and (*3*, *4*) Al^{3+} sorbed from 0.1 M metal(III) sulfate solution with cellulose threads. Content of carboxy groups in MCC (mmol g^{-1}): (*1*) 0.5, (*2*, *4*) 0.8, and (*3*) 0.7.

complexometrically with Dithizone as an indicator, chromatometrically, and colorimetrically in the presence of sulfosalicylic acid, respectively [7].

The isotherms of Fe^{3+}, Cr^{3+}, and Al^{3+} sorption from chloride and sulfate solutions on MCC samples with various contents of carboxy groups are shown in Fig. 2. It can be seen that the maximum exchange capacity (EC) of the cation exchanger at the equilibrium cation concentration of 0.03–0.1 M amounts to 0.21 (Fe^{3+}), 0.15 (Al^{3+}), and 0.12 mmol g^{-1} (Cr^{3+}), i.e., with respect to the maximal sorption, the metal ions are ranked in the order $Fe^{3+} > Al^{3+} > Cr^{3+}$.

Probably, the observed differences in the filling of the MCC phase with cations Fe^{3+}, Al^{3+}, and Cr^{3+} depend on the energy of their coordination interaction with fixed carboxy groups and denticity of ligands with respect to various cations. It was shown by potentiometric titration that complexes with the M : COO ratio of 1 : 2 prevail in the Fe(III)–MCC and Cr(III)–MCC systems, and 1 : 1 complexes, in the Al(III)–MCC system [8]. These results show that the fraction of carboxy groups that can be involved in formation of polymeric complexes is 51–57% (Fe^{3+}–MCC system with EC = 0.7 and 1.4 mmol g^{-1}), 20–28% (Cr^{3+}–MCC system with EC = 0.5 and 0.8 mmol g^{-1}), and 19% (Al^{3+}–MCC system with EC = 0.8 mmol g^{-1}). It should be noted that the degree of MCC filling with metal cations somewhat increases with decreasing exchange capacity of the cation exchanger.

It is well known that the degree of MCC filling with cations strongly depends of pH.

Figure 3 shows that Al(III) sorption with MCC fibers increases with pH and reaches a maximum at pH 3.2–3.7. The chromium(III) sorption is substantially lower and becomes the strongest at pH 2.6–2.8; it remains unchanged as the pH grows further.

The rise in metal sorption with MCC with increasing pH can be caused by the following factors: an increase in the content of chromium(III) and aluminum(III) hydroxo complexes, which form with carboxy groups stable six-membered rings [2]

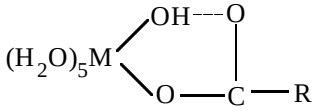

where R is the cellulose radical; an increase in the content of dissociated carboxy groups in the MCC phase; and an increase in the size of chromium(III) and aluminum(III) complexes because of their olation.

A well-defined maximum of Al(III) sorption is characteristic not only of the system studied but also of aluminum fixation on collagen [2]. In accordance with published data, a decrease in aluminum(III) sorption at pH > 3.7 is caused by substitution of carboxy groups in the inner coordination sphere of aluminum-containing complexes by OH groups and formation of aluminum hydroxide, which can precipitate in the sorbent phase. The absence of a similar maximum in the Cr^{3+}–MCC system at pH ≤ 3.5 indicates that the bonds between this cation and carboxy group are more stable in this case [2].

Figure 3 shows that maximum content of Al^{3+} ions fixed on MCC exceeds by more than a factor of two the content of Cr^{3+} ions. However, the degrees of binding of MCC carboxy groups with Al^{3+} and Cr^{3+} ions are similar, amounting to 60% of the total exchange capacity at the maximum sorption.

Influence of the amount of metal cations on mechanical properties and stability with respect to phosphate buffer of oxidized viscose threads with various exchange capacities

Thread type and treatment conditions	P_d	P_k	P_w	Q, g g^{-1}	$\bar{c}_M$, mmol g^{-1}	pH_{eq}	Loss of strength, %, in indicated time, days		
	kg cm^2						3	10	14
Viscose cord thread (d = 0.62 ± 0.02 mm)	2390	1260	1450	–	–	–	17	18	20
EC = 0.3 mmol g^{-1}									
MCC	2300	1240	1360	0.75	–	–	30	44	49
MCC + $FeCl_3$	2080	1260	1130	0.76	0.14	1.73	29	61	57
MCC + $CrCl_3$	2140	1150	1440	0.73	0.10	2.44	31	44	50
MCC + $Cr_2(SO_4)_3$	1880	1270	1340	0.67	0.18	2.85	14	36	45
MCC + $AlCl_3$	2180	1220	1350	0.77	0.16	3.18	33	48	49
MCC + $Al_2(SO_4)_3$	2140	1210	1130	0.81	0.20	3.64	37	53	58
EC = 0.4 mmol g^{-1}									
MCC	2120	1210	1460	0.75	–	–	31	42	50
MCC + $FeCl_3$	2190	1220	710	0.68	0.16	1.75	47	61	71
MCC + $CrCl_3$	2050	1240	1500	0.74	0.11	2.45	29	46	42
MCC + $Cr_2(SO_4)_3$	1950	1180	1510	0.70	0.18	2.89	20	37	42
MCC + $AlCl_3$	2180	1220	1350	0.76	0.17	3.22	35	64	68
MCC + $Al_2(SO_4)_3$	2250	1230	1380	0.77	0.21	3.66	33	52	40
EC = 0.5 mmol g^{-1}									
MCC	2180	1310	1300	0.77	–	–	40	60	71
MCC + $FeCl_3$	2110	1190	1250	0.71	0.21	1.71	42	59	65
MCC + $CrCl_3$	2140	1140	1420	0.65	0.14	2.44	32	56	56
MCC + $Cr_2(SO_4)_3$	1958	1060	1430	0.62	0.266	3.06	36	58	52
MCC + $AlCl_3$	2280	1200	1360	0.80	0.20	2.73	50	77	80
MCC + $Al_2(SO_4)_3$	2140	1110	1440	0.79	0.385	3.65	42	65	68

It follows from Fig. 4 that the sorption equilibrium is attained within 60 min for Fe^{3+} and Al^{3+} and within 10 min for Cr^{3+}.

Figure 5 and the table illustrate the effect of cation sorption on MCC thread swelling and mechanical properties. As seen, swelling decreases from 0.75 g g^{-1} for oxidized MCC fibers containing no metal to 0.62 g g^{-1} (by approximately 20%) for iron- and chromium-containing MCC, which can be a measure of increased cross-linking. By contrast, the water sorption with

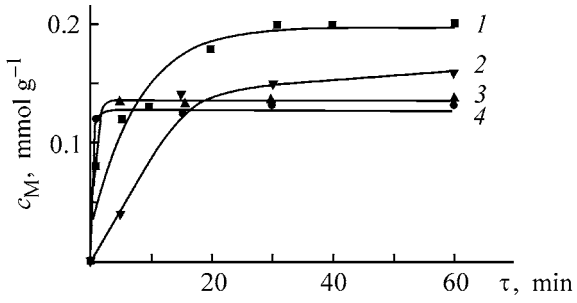

Fig. 4. Amount of cations c_M sorbed with MCC (EC_{COOH} = 0.7 mmol g^{-1}) vs. time τ. Cation: (*1*) Fe^{3+}, (*2*) Al^{3+}, and (*3*, *4*) Cr^{3+}. Solution, c_{in} = 0.1 M: (*1*, *3*) chloride and (*2*, *4*) sulfate.

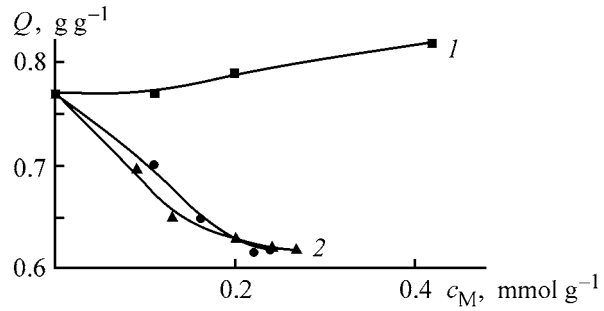

Fig. 5. Dependence of the degree of swelling, Q, of MCC salt species (EC_{COOH} = 0.7 mmol g^{-1}) on the amount of cation sorbed c_M. Cation: (*1*) Al^{3+} and (*2*) Cr^{3+}, Fe^{3+}.

aluminum-containing MCC increases relative to sorption with the initial oxidized cellulose. These results agree with published data that swelling depends on the composition and density of the complexes formed [1].

It follows from Fig. 5 that the minimum swelling of MCC with the 0.7 mmol g^{-1} content of carboxy groups is observed for samples containing 0.15–0.20 mmol g^{-1} metal salt sorbed and then remains unchanged with the further metal sorption. This can be accounted for by the fact that the further increase in the metal sorption is achieved by raising pH. In this case, the hydrolysis products are formed in the cation exchanger bulk. As a result, each cross-link involves several metal cations, which increases the metal consumption for formation of the network of the same density.

The table shows that a decrease in swelling of chromium-containing MCC is accompanied by preservation of the thread strength *in vitro* for a longer time. At the same time, we can see that the lowest stability toward the action of a phosphate buffer is characteristic of iron-containing MCC fibers. This effect can be accounted for by catalysis of the alkaline-oxidative degradation of carboxyl-containing cellulose with iron salts [9]. We can suggest that this property of iron(III) salts in preparing Occelon resolving retention sutures (MCC–Fe–tannin complex) [10] is masked by cation complex formation not only with oxidized cellulose but also with tannin.

It should be noted that there is no correlation between the composition, concentration, and stability of polycomplexes and mechanical properties of the salt forms of low-substituted MCC. The table shows that the value of sorption of multicharged cations does not affect noticeably the thread in both dry and wet states and as a knot. In accordance with published data [11], this can be caused by two reasons. Firstly, bridging bonds formed by metal ions are rigid and do not provide a sufficient segmental mobility of macromolecules. Secondly, the formation of small amounts of cross-links between macromolecules of oxidized cellulose is accompanied by partial rupture of H bonds that existed before metal sorption.

CONCLUSION

Iron(III), aluminum(III), and chromium(III) cations sorbed with monocarboxy cellulose from chloride and sulfate solutions do not affect noticeably the cellulose mechanical properties. The degree of swelling of monocarboxy cellulose salt form, compared to its H form, depends on the type and content of the metal cation and, at the same composition of the polycomplex, is independent of preparation conditions (pH of the initial solution 1.6–4.0; salt concentration 0.02–0.17 M; sorption time no more than 24 h).

REFERENCES

1. Saldadze, K.M. and Kopylova-Valova, V.D., *Kompleksoobrazuyushchie ionity (kompleksity)* [Complex-Forming Ion Exchangers (Complexites)], Moscow: Khimiya, 1980.
2. Mikhailov, A.N., *Khimiya dubyashchikh veshchestv i protsessov dubleniya* (Chemistry of Hardeners and Tanning), Moscow: Gizlegprom, 1953.
3. Yurkshtovich, N.K., Chekhovskii, A.K., Kaputskii, V.E., and Golub, N.V., *Vestn. Bel. Gos. Univ., Ser. Khim.*, 2000, no. 3, pp. 29–30.
4. Kaputskii, V.E., Yurkshtovich, T.L., and Balabaeva, M.D., *Vestn. Bel. Gos. Univ., Ser. II*, 1978, no. 1, pp. 15–18.
5. Kaputskii, V.E., Study of Physicochemical Properties of Monokcarboxy Cellulose, *Cand. Sci. Dissertation*, Minsk, 1971.
6. *Trikotazhnye issledovaniya: Gosudarstvennye standarty SSSR* (Tricot Studies: State Standards of the USSR), Moscow: Khimiya, 1965.
7. Charlot, G., *Les Methods de la Chemie Analytique., Analyse quantitative Minerale*, Quatrieme Edition, Paris: Masson, 1961.
8. Kosterova, R.I., Yurkshtovich, N.K., Golub, N.V., and Chekhovskii, A.K., Abstracts of Papers, *Mezhdunarodnaya nauchnaya konferentsiya "Novye lekarstvennye sredstva: sintez, tekhnologiya, farmakologiya, klinika"* (Int. Scientific Conf. "New Drugs: Synthesis, Technology, Pharmacology, and Applications"), 2001, p. 74.
9. Tsnesova, L.E., Gorodnov, V.D., and Kuptsova, L.P., *Izv. Vyssh. Uchebn. Zaved., Khim. Khim. Technol.*, 1986, vol. 29, no. 12, pp. 75–78.
10. Kuz'mina, N.L., Biber, B.L., Abakumova, G.L., *et al.*, *Khimicheskie i natural'nye niti dlya khirurgicheskikh shovnykh materialov* (Chemical and Natural Threads for Surgical Suture Materials), Moscow: NIITEKhIM, 1988.
11. Petropavlovskii, G.A., *Gidrofil'nye chastichno-zameshchennye efiry tsellyulozy i ikh modifikatsiya putem khimicheskogo sshivaniya* (Hydrophilic Partially Substituted Cellulose Ethers and Esters and Their Modification by Chemical Cross-Linking), Leningrad: Nauka, 1988.

Russian Journal of Applied Chemistry, Vol. 77, No. 6, 2004, pp. 905–914. Translated from Zhurnal Prikladnoi Khimii, Vol. 77, No. 6, 2004, pp. 919–928.

SORPTION AND ION-EXCHANGE PROCESSES

Planar Chromatography for Quantitative Analysis of Amino Acids in Fermentation Solutions of Industrial Producer Cultures

V. D. Krasikov and I. I. Malakhova

Lenkhrom Scientific and Technical Center, St. Petersburg, Russia

Received December 25, 2003; in final form, February 2004

Abstract—Proximate procedures for quantitative analysis of amino acids using high-performance thin-layer chromatography were developed.

Amino acids (hereinafter, natural *L*-amino acids) are the main building material in synthesis of specific tissue proteins, enzymes, peptide hormones, and other physiologically active compounds [1–5].

Analysis of amino acids in medicine, biochemistry, molecular genetics, etc. is problem of current unterest. Modern procedures for analysis of amino acid derivatives in albumin hydrolyzates, peptides, and biomedical samples are based on high-performance liquid chromatography. However, data on application of high-performance quantitative thin-layer chromatography (HPTLC) to separation of multicomponent mixtures of free amino acids (including 20 natural acids) are lacking.

In this study we developed chromatographic procedures for separation and quantitative determination of free amino acids in culture broths (CBs) of certain producer cultures. The main analytical method was HPTLC, and high-performance liquid chromatography (HPLC) was used for comparison [6–8]. In some specific cases, an amino acid analyzer (AA) was used.

It should be noted that the requirements to the reliability and adequacy of chromatographic procedures in biochemistry and biotechnology are essentially different. For example, procedures providing experimental error of no more than 15% and reproducibility of 90% are acceptable in biochemistry [9].

Similar requirements are imposed upon analytical chromatographic procedures in biotechnology at the stage of development of the producer cultures of amino acids. However, at the stage of optimization of the fermentation procedure the analysis error should not exceed 5%. The same requirement is imposed upon the chromatographic analysis in recovery and purification of the desired amino acid, because the error of 10–15% may cause either production of the preparation of insufficient purity or a significant loss unacceptable in the large-scale production.

EXPERIMENTAL

In our study we used densitometers (Shimadzu, Japan), a High Speed TLC Scanner CS-920 (Shimadzu, Japan), a TLC-Scanner-II (Camag, Switzerland), a DenSkan-01 video system (Lenkhrom, Russia), a DenSkan-04 video system (Lenkhrom, Russia), and a Delta Prep 3000 liquid chromatograph equipped with a Lambda Max 481 spectrophotometric detector and a 4.6×250-mm stainless steel column packed with μ-Bondapak C18 sorbent (5 μm, Waters, USA). The eluent was 10^{-3} M solution of copper(II) sulfate in 20% aqueous acetonitrile (0.5 ml min^{-1} flow rate, λ 235 nm).

The concentrations of some amino acids in CBs were measured using a Biocal amino acid analyzer (USA).

The tests were carried out using the following chromatographic plates: Sorbfil PTSKh-P-V (Institute of Macromolecular Compounds, Russian Academy of Sciences, Sorbpolymer Company, St. Petersburg, Russia) and Kieselgel 60 (Merck, Germany).

Mixtures of 1-propanol, 2-propanol, ethanol, ethyl acetate, chloroform, acetone, acetic acid, 25% aqueous ammonia, and water were taken as mobile phases.

1070-4272/04/7706-0905 © 2004 MAIK "Nauka/Interperiodica"

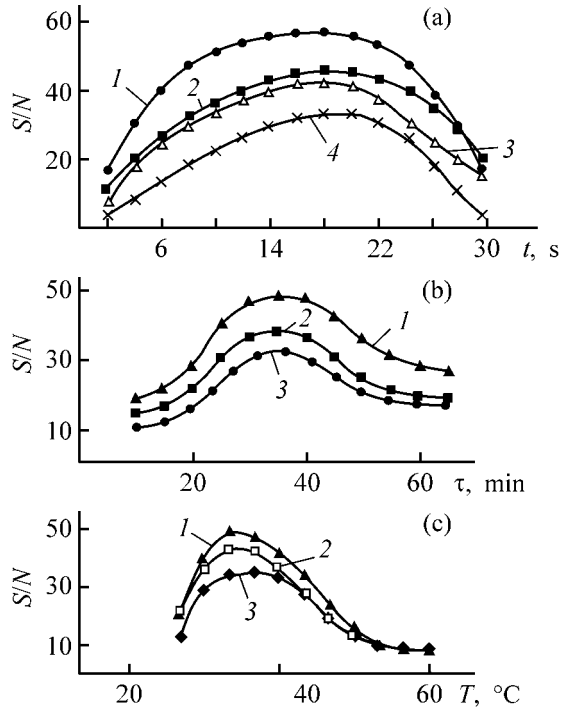

Fig. 1. Ratios *S*/*N* as influenced by (a) time *t* of the chromatogram exposure to the NH solution, (b) time τ of the color reaction, and (c) temperature *T* of the color reaction; system B as eluent. (a) Conditions of the color reaction: *T* = 50°C, τ = 30 min. (*1*) Lysine, (*2*) serine and valine, (*3*) glutamic acid, and (*4*) phenylalanine. (b) Exposure of the chromatogram to the NH solution for 20 s, *T* = 50°C. (*1*) Lysine; (*2*) serine, valine, and glutamic acid; and (*3*) phenylalanine. (c) Exposure of the chromatogram to the NH solution for 20 s, τ = 30 min. (*1*) Lysine; (*2*) serine, valine, and glutamic acid; and (*3*) phenylalanine.

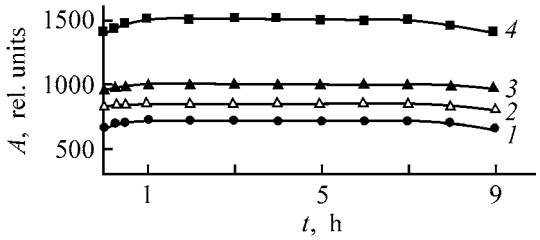

Fig. 2. Densimetric signal *A* of the spots of amino acids vs. time after completion of the color reaction on the chromatographic plate; system B as eluent, *T* = 21°C. (*1*) Lysine, (*2*) serine and valine, (*3*) glutamic acid, and (*4*) phenylalanine.

Organic solvents of ultrapure and chemically pure grades were used without additional treatment; water for analysis was prepared on a Super Q apparatus (Millipore, USA).

Free amino acids were separated on Sorbfil-P-V HPTLC plates based on silica gel with silica sol binder, which is an essential distinction of this chromatographic material from Silufol and Kieselgel 60 plates used previously in separation of free amino acids; this, in most cases hinders direct use of available data concerning mobile phases. Therefore, it was necessary to modify these mobile phases or develop new elution systems.

Amino acids (excluding tryptophan) were visualized in the chromatograms with ninhydrin (NH) solution, which was deposited on a chromatographic plate not by common spraying, but by immersion of the plate in a solution. This is due to the fact that the metrological characteristics of the results of quantitative analysis of some compounds (densitometry) with immersion were better than those obtained using the spraying procedure [12–15]. There are no data on the conditions for applying the ninhydrin reagent (immersion method) and performing the color reaction for amino acids. Therefore, we made special experiments to determine the optimal conditions of the color reaction on the chromatograms after their immersion in the ninhydrin solution (0.3% solution of ninhydrin in acetone containing 3% glacial acetic acid).

Using model mixtures of amino acids belonging to various classes (phenylalanine, lysine, glutamic acid, serine, and valine), we studied the dependences of the densimetric signal[1]/noise ratio (*S*/*N*) on the time of the exposure of a chromatogram to the NG solution (Fig. 1a), time of the color reaction (Fig. 1b), and temperature at which the color reaction was performed (Fig 1c).

These data showed that the optimal conditions for visualization of the spots of amino acid belonging to various classes are as follows: exposure of the chromatogram to the NH solution for 17–20 s; color reaction for 30–40 min at 45–50°C. Above 50°C, a light crimson background appears on the chromatogram surface owing to the thermal oxidation or condensation of the NH molecules.

In accordance with validation regulations of the planar chromatography (PC) [16] and for quantitative densimetric analysis, it was advisable to evaluate the coloration stability of the spots of the ninhydrin complexes on the chromatograms after completion of the color reaction.

We studied changes in the densimetric signals of some amino acids with time (Fig. 2). It can be seen

[1] The "densimetric signal" is the difference between the intensities of light of a certain wavelength reflected from the plate surface without and with a spot of a compound to be determined.

Table 1. Content of serine, homoserine, and threonine in the CB samples determined by HPTLC (DenSkan-01) and HPLC* procedures

Sample no.	HPLC			HPTLC	Sample no.	HPLC			HPTLC
	X, g l^{-1}	$\pm\Delta X$, g l^{-1}	ε, %	X, g l^{-1}		X, g l^{-1}	$\pm\Delta X$, g l^{-1}	ε, %	X, g l^{-1}
Serine n = 5, P = 0.95, r = 0.9949					Homoserine n = 5, P = 0.95, r = 0.9843				
1	9.8	0.32	3.3	10.8	1	23.5	0.71	3.0	22.8
2	6.8	0.31	4.6	5.8	2	40.1	1.72	4.3	40.0
3	12.8	0.24	1.9	12.8	3	43.2	1.21	2.8	44.0
4	11.4	0.52	4.6	9.3	4	35.7	1.03	2.9	36.0
5	12.0	0.26	2.2	12.1	5	31.9	1.18	3.7	32.6
6	12.4	0.62	5.0	12.5	Threonine n = 5, P = 0.95, r = 0.9831				
7	12.2	0.48	3.9	12.4	1	9.8	0.32	3.3	10.8
8	11,0	0.29	2.6	10.3	2	6.8	0.31	4.6	5.8
9	13.6	0.64	4.7	13.8	3	12.8	0.24	1.9	12.8
10	18.4	0.66	3.6	18.9	4	11.4	0.52	4.6	9.3
					5	12.0	0.26	2.2	12.1

* X is the average value; $\pm\Delta X$, standard deviation; ε, variation coefficient; n, number of independent measurement; P, confidence level; and r, correlation coefficient.

that the coloration of the spots of amino acids is stable in 0.5–7.0-h storage of the chromatograms in the dark at 21°C. These results were used in our experiments on visualization and quantitative analysis of amino acids.

Quantitative determination of serine, homoserine, and threonine. The CB of the serine producer culture often contains proline, glutamic acid, glycine, alanine, threonine, lysine, and, in rare cases, γ-aminobutyric acid. This mixture was separated using mobile phase A (designed with a PRIZMA model [17]): 2-propanol–acetone–ethyl acetate–25% aqueous ammonia–water (20 : 15 : 7 : 9 : 5 volume ratio); binary elution, l_1 = 75 and l_2 = 85 mm); R_f[2] of the serine spot was 0.40 (Fig. 3).

As a rule, the CB of the homoserine producer culture contains alanine, glutamic acid, lysine, glycine, isoleucine, and threonine. These amino acids were separated from homoserine using the same mobile phase A (binary elution, l_1 = 70 and l_2 = 80 mm); R_f of homoserine, alanine, and valine was 0.31, 0.25, and 0.38, respectively. Under these experimental conditions, threonine had R_f = 0.75 (Fig. 3).

As for CB of the threonine producer culture, it was treated using system B (2-propanol–ethyl acetate–25% aqueous ammonia–water, 20 : 20 : 1.5 : 25 volume ratio), which provided separation of threonine (R_f = 0.40) from the concomitant glutamic acid, lysine, glycine, and alanine. The content of the target amino acids in CB was determined on a DenSkan-01 video densitometer (Table 1). It was found that the concentration dependence of the densimetric signals of serine, homoserine, and threonine is linear in the 0.03–0.3 μg range, and the detection limit of these amino acids is 0.015 μg [18–22].

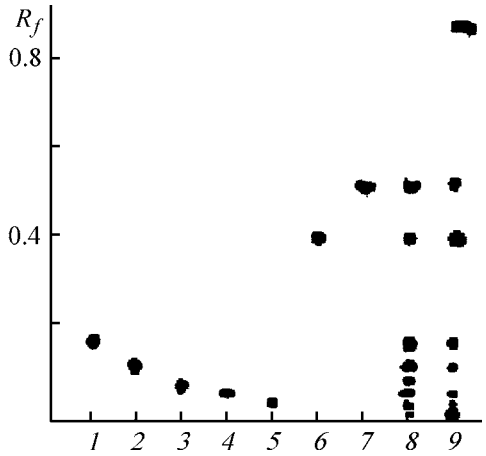

Fig. 3. Separation of amino acids in the CB of the serine producer culture; system A eluent, T = 20°C. (*1*) γ-Aminobutyric acid, (*2*) alanine, (*3*) glycine, (*4*) glutamic acid, (*5*) lysine, (*6*) serine, (*7*) threonine, (*8*) mixture of the above amino acids, and (*9*) CB of the serine producer culture.

[2] The retention factor R_f characterizes the spot location on the plate and is determined as the ratio of the distances from the start to the center of the spot and from the start to the eluent front.

Table 2. Response factor *a* of amino acids present in the CB of the serine producer (λ = 500 nm, Sorbfil HPTLC plates, Shimadzu CS-920 densitometer, $n = 5$, $P = 0.95$)

Amino acid	*a*	ε, %	Amino acid	*a*	ε, %
Serine	1.0	2.9	Alanine	0.96	1.0
Proline	0.49	1.8	Threonine	1.10	4.3
Glutamic acid	0.87	1.7	Lysine	2.02	2.4
Glycine	0.43	2.0			

Table 3. Metrological characteristics of the chromatographic densimetric analysis of tryptophan in reference solutions and CB samples

Sample	Tryptophan concentration X, g l^{-1}	Shimadzu CS-920, direct densimetric measurement of Kieselgel 60 plates		Shimadzu CS-920				DenSkan-01			
				method of spot detection on Sorbfil plates							
				II		I		II		I	
		$\pm\Delta X$, g l^{-1}	ε, %	$\pm\Delta X$, g l^{-1}	ε, %	$\pm\Delta X$, g l^{-1}	ε, %	$\pm\Delta X$, g l^{-1}	ε, %	$\pm\Delta X$, g l^{-1}	ε, %
Reference solutions	1.0	0.051	5.1	0.08	8.0	0.051	5.1	0.051	5.1	0.028	2.8
	2.0	0.146	7.6	0.17	8.5	0.090	4.5	0.080	4.0	0.096	4.8
	3.0	0.117	3.9	0.22	7.3	0.190	6.3	0.160	5.5	0.110	3.8
CB samples (AA)	9.8	0.490	5.0	0.92	9.4	0.600	6.1	0.410	4.2	0.340	3.5
	11.4	0.710	6.2	0.83	7.3	0.460	4.0	0.440	3.9	0.380	3.3
	13.6	0.770	5.7	1.33	9.8	0.760	5.3	0.860	6.3	0.370	2.7
	5.6	0.460	8.3	0.43	7.7	0.270	4.9	0.300	5.4	0.170	3.0

We determined the densimetric signals of the spots of amino acids accompanying serine (λ = 500 nm, content of each amino acid in the sample was 0.2 μg) and evaluated the correcting normalization coefficients (response factor); the magnitude of the densimetric signal of the serine spot was taken as unity (Table 2) [18–22].

Working with the serine producer culture required data not only on the content of the desired product, but also on the content of amino acids present in CB. This problem was solved with the use of the response factor; this parameter is widely used in liquid chromatography with spectrophotometric detection.

Quantitative determination of aromatic amino acids. Analysis of a tryptophan-containing CB, performed on the amino acid analyzer, showed that it also contained phenylalanine, tyrosine, leucine, isoleucine, threonine, valine, histidine, serine, lysine, glutamic acid, and asparagine. Such an amount of impurities significantly hindered complete separation of four aromatic amino acids: phenylalanine, tryptophan, and leucine-isoleucine mixture. Mobile system C (2-propanol–25% aqueous ammonia, 7 : 3 volume ratio) provided formation of compact tryptophan spots suitable for scanning ($R_f = 0.54$) and their separation from the spots of phenylalanine ($R_f = 0.65$) and valine ($R_f = 0.47$); however, the retention factors of leucine and isoleucine were very close ($R_f = 0.57$).

The selective quantitative determination of tryptophan in CB was provided using the modified Ehrlich reagent (0.5% ethanolic solution of *p*-dimethylaminobenzaldehyde containing 5% concentrated sulfuric acid) [19–21]. The quantitative analysis of chromatograms was performed by two procedures: (1) direct densimetric measurements of the tryptophan spots at λ = 276 nm and (2) immersion of the chromatograms in the detecting solution (I) and their spraying according to the Waldi procedure (II) [23], with subsequent heating at 110°C for 7–10 min (Table 3).

It was found that the spot color on the chromatograms is stable for at least a year of storage in the dark, and the concentration dependence of the densimetric signal magnitude is linear at the tryptophan content of 0.1 to 0.6 μg; the detection limit is 0.05 μg.

Table 4. Content of tryptophan in the CB, determined using DenSkan-01 unit and amino acid analyzer*

Sample no.	X, g l^{-1}		Sample no.	X, g l^{-1}	
	DenSkan-01	AA		DenSkan-01	AA
1	7.5	7.4	9	4.5	4.7
2	12.7	12.1	10	6.2	6.0
3	11.2	11.2	11	15.0	14.7
4	14.4	14.3	12	2.6	2.9
5	13.6	14.0	13	1.8	1.5
6	5.5	5.1	14	1.7	2.4
7	5.6	5.2	15	6.6	7.2
8	5.0	5.4	16	9.8	11.0
			17	6.6	6.2

* $r = 0.9920$, $y = 0.98x + 0.15$.

Table 5. Content of phenylalanine in various CB samples and metrological characteristics of the HPTLC (DenSkan-01) and HPLC* procedures

Sample no.	HPTLC			HPLC X, g l^{-1}
	X, g l^{-1}	$\pm\Delta X$, g l^{-1}	ε, %	
1	6.1	0.15	2.5	6.9
2	5.2	0.17	3.3	4.8
3	6.5	0.19	3.1	6.4
4	3.7	0.07	2.1	4.0
5	6.0	0.14	2.4	5.8
6	4.4	0.12	2.7	4.6
7	5.9	0.23	3.9	6.2

* $n = 5$, $P = 0.95$, $r = 0.9910$, $y = 0.96x - 0.21$.

The quantitative analysis was performed simultaneously on Shimadzu CS-920 and DenSkan-01 densitometers. A comparison of the metrological characteristics of Shimadzu CS-920 (ε = 8–9%) and DenSkan-01 (ε = 3–5%) showed that the latter is preferable for immersion procedures [24, 25] (Table 3).

The reliability of the tryptophan CB analysis performed by procedure I (DenSkan-01 unit) was additionally checked using the amino acid analyzer (Table 4) [26–28].

An analysis of a series of CBs on the amino acid analyzer showed that phenylalanine is often accompanied by the following by-products: glycine, alanine, glutamic acid, threonine, valine, leucine, tyrosine, tryptophan, tyramine, and tryptamine. Phenylalanine was separated from the mixture of amino acids occurring in CB using mobile phase D (designed with a PRIZMA model [29]): chloroform–ethanol (96%)–glacial acetic acid–water, (19.0–27.0) : (20.0–26.0) : (13.5–16.0) : (1.3–3.5) volume ratio [28]. This system allowed separation of phenylalanine from concomitant amino acids and gave individual chromatograms of valine, leucine, tryptophan, and tyrosine. Thus, the problem of separation of the "critical triad" of phenylalanine, tyrosine, and tryptophan was solved for the first time using domestic Sorbfil plates in the onedimensional mode [28]. The chromatogram development (treatment with ninhydrin reagent and color reaction) was performed similarly to the case of serine; phenylalanine had $R_f = 0.73 \pm 0.03$ (Fig. 4).

It was found that the output signal of the densitometer is a linear function in the 0.1–1.0 μg concentration range of phenylalanine; the detection limit is 0.05 μg.

The results of phenylalanine analysis in various CB series with the DenSkan-01 densitometer well agree with HPLC data ($r = 0.991$; Table 5) [28, 30, 31].

Quantitative determination of the main amino acids (lysine, ornithine, and arginine). In CB, lysine is accompanied by glutamic acid, alanine, valine, leucine (isoleucine), and homoserine. These amino acids were separated with eluent E (2-propanol–25% aqueous ammonia, 55 : 45 volume ratio), which provides separation of lysine ($R_f = 0.40$) from the concomitant amino acids. The content of lysine in the CB samples was measured on a DenSkan-01 densitometer (the concentration dependence of the densimetric signal intensity is linear in the 0.015–0.2 μg range; de-

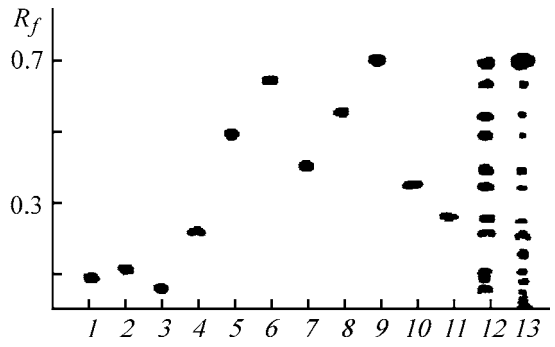

Fig. 4. Separation of amino acids in the CB of the phenylalanine producer culture; binary elution, $l_1 = 60$ and $l_2 = 65$ mm, system D as eluent, $T = 22$°C. (*1*) Glycine, (*2*) alanine, (*3*) glutamic acid, (*4*) threonine, (*5*) valine, (*6*) leucine, (*7*) tyrosine, (*8*) tryptophan, (*9*) phenylalanine, (*10*) phenylethylamine, (*11*) tyramine, (*12*) mixture of the above amino acids, and (*13*) CB of the phenylalanine producer culture.

Table 6. Content of lysine in the CB samples, determined by chromatographic densitometry and HPLC*

Sample no.	Chromatographic densitometry (DenSkan-01)			HPLC, X, g l^{-1}	Sample no.	Chromatographic densitometry (DenSkan-01)			HPLC, X, g l^{-1}
	X, g l^{-1}	$\pm\Delta X$, g l^{-1}	ε, %			X, g l^{-1}	$\pm\Delta X$, g l^{-1}	ε, %	
1	44.3	1.20	2.7	46.2	4	66.0	1.58	2.4	66.2
2	51.3	1.07	2.1	52.1	5	32.3	1.19	3.7	33.6
3	59.9	2.04	3.4	60.5					

* $n = 5$, $P = 0.95$, $r = 0.9907$, $y = 0.88x - 0.19$.

Table 7. Content of arginine and ornithine in various CB samples determined by HPTLC (DenSkan-04) and HPLC procedures

Sample no.	Chromatographic densitometry			HPLC X, g l^{-1}	Sample no.	Chromatographic densitometry			HPLC X, g l^{-1}
	X, g l^{-1}	$\pm\Delta X$, g l^{-1}	ε, %			X, g l^{-1}	$\pm\Delta X$, g l^{-1}	ε, %	
Arginine $n = 5$, $P = 0.95$, $r = 0.9795$, $y = 0.76x - 0.13$					Ornithine $n = 5$, $P = 0.95$, $r = 0.9807$, $y = 0.82x \pm 0.04$				
1	12.3	0.39	3.2	12.5	1	5.2	0.08	1.6	5.4
2	14.5	0.46	3.2	14.7	2	3.8	0.095	2.5	3.5
3	11.4	0.21	1.8	11.4	3	4.4	0.088	2.0	4.1
4	13.3	0.54	4.1	13.0	4	6.3	0.18	2.9	6.4
5	16.0	0.72	4.5	16.2	5	6.0	0.22	3.7	5.7
6	11.9	0.44	3.7	11.6	6	5.8	0.18	3.2	5.9
7	10.3	0.26	2.5	10.0	7	4.1	0.18	4.4	4.3

tection limit 0.009 μg) and using an HPLC device (Table 6, $r = 0.9907$).

The CBs of arginine and ornithine contain lysine, citrulline (arginine precursor), glutamic acid, alanine, valine, and leucine. Arginine ($R_f = 0.40$) and ornithine ($R_f = 0.62$) were separated from the above amino acids, using mobile phase G: 2-propanol–25% aqueous ammonia–water, (3.5–4.1) : (0.9–1.5) : (7.5–9.0) volume ratio [28] (Fig. 5). The quantitative analysis of the chromatograms was carried out on a DenSkan-04 densitometer.

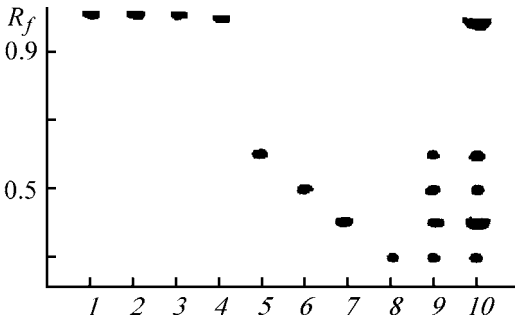

Fig. 5. Separation of amino acids in the CB of the arginine producer culture; system G as eluent, $T = 20°C$. (*1*) Glycine, (*2*) alanine, (*3*) glutamic acid, (*4*) valine, (*5*) ornithine, (*6*) lysine, (*7*) arginine, (*8*) citrulline, (*9*) mixture of the above amino acids, and (*10*) CB of the arginine producer culture.

It was found that the concentration dependences of the magnitudes of the densimetric signals of arginine and ornithine are linear in the 0.05–0.4 and 0.02–0.25 μg ranges for arginine and ornithine, respectively. The data on the content of these amino acids in various CB batches in comparison with HPLC results are listed in Table 7.

Quantitative determination of saturated amino acids (valine and leucine). The CB samples of the industrial valine and leucine producer cultures often contain homoleucine, lysine, glycine, alanine, glutamic acid, and isoleucine. Among these compounds, homoleucine is an especially undesirable impurity, because it significantly complicates purification of valine and leucine, cocrystallizing with them in the course of their recovery [32, 34]. The homoleucine content should not exceed 0.1%. At such a low content of this

Table 8. Content of valine and homoleucine in CB samples, determined by chromatographic densitometry (DenSkan-04) and HPLC

Sample no.	Valine,* chromatographic densitometry			HPLC	Homoleucine,** chromatographic densitometry			HPLC
	X, g l^{-1}	$\pm\Delta X$, g l^{-1}	ε, %	X, g l^{-1}	X, mg l^{-1}	$\pm\Delta X$, mg l^{-1}	ε, %	X, mg l^{-1}
1	57.3	1.48	2.6	58.6	4.8	0.21	4.4	4.6
2	49.4	1.18	2.4	48.4	5.2	0.2	3.9	5.0
3	51.5	0.57	1.1	50.8	4.5	0.21	4.6	4.7
4	64.0	1.21	1.9	65.7	5.0	0.26	5.2	5.0
5	73.5	2.49	3.4	75.1	4.4	0.22	4.9	4.6
6	61.3	2.72	4.3	60.2	3.8	0.18	3.1	4.0
7	54.5	1.69	3.1	53.9	6.2	0.29	4.6	6.5

* $n = 5$, $P = 0.95$.

** $n = 5$, $P = 0.95$, $r = 0.9818$, $y = 0.90x - 0.07$.

Table 9. Content of leucine* and homoleucine** in CB samples determined by chromatographic densitometry (DenSkan-04) and HPLC

Sample no.	Leucine, chromatographic densitometry			Homoleucine			
				chromatographic densitometry			HPLC,
	X, g l^{-1}	$\pm\Delta X$, g l^{-1}	ε, %	X, mg l^{-1}	$\pm\Delta X$, mg l^{-1}	ε, %	X, mg l^{-1}
1	12.6	0.31	2.5	2.7	0.11	3.9	2.6
2	15.2	0.29	1.9	2.0	0.09	4.6	2.4
3	11.4	0.35	3.1	1.0	0.03	2.9	1.1
4	20.3	0.37	1.8	1.3	0.025	1.9	1.5
5	13.4	0.31	1.6	2.2	0.06	2.7	2.0
6	18.1	0.43	2.4	2.9	0.07	2.3	3.1
7	13.2	0.26	2.0	3.3	0.1	2.9	3.4

* $n = 5$, $P = 0.95$.

** $n = 5$, $P = 0.95$, $r = 0.9854$, $y = 0.79x + 0.09$.

impurity, whose properties are similar to those of the desired products, only expensive amino acid analysis is an alternative to the planar chromatography.

Amino acids were separated with eluent D (binary elution, $l_1 = 60$ and $l_2 = 65$ mm). After elution, we observed round compact spots of valine ($R_f = 0.49$), leucine ($R_f = 0.64$), and homoleucine ($R_f = 0.71$) in the chromatograms. The concentration range of the linear dependence of the densimetric signal is 0.04–0.4 μg (detection limit 0.02 μg).

The results of valine + homoleucine and leucine + homoleucine analysis are listed in Tables 8 and 9, respectively.

As can be seen from these data, only in six out of 14 CB samples the content of homoleucine is less than 0.1% with respect to the desired product.

This example confirms once again that planar chromatography allows a fast and reliable analysis of the content of impurities in the final product even when the impurity/product ratio is less than 1/1000. In this case, the time of the analysis is a decisive factor, because the accumulation of homoleucine (to 0.1% with respect to valine and leucine) proceeds, as a rule, in 3–5 h and prompt detection of this impurity indicates that the fermentation process should be terminated, which is especially important in the large-scale industrial production.

To suppress the biosynthesis of homoleucine, new producer cultures with greater degrees of leucine accumulation due to transaminase activation were designed by genetic engineering. However, an analysis of the fermentation solutions of these producer cultures indicated the presence of an unknown compound

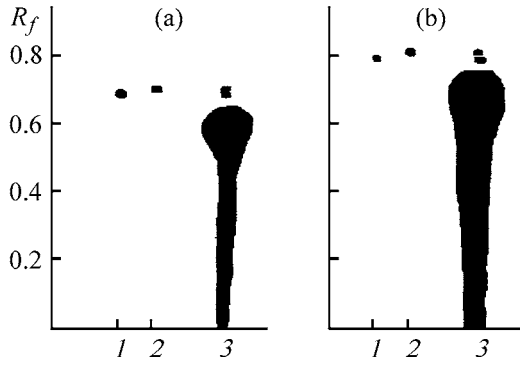

Fig. 6. Chromatogram of the CB of the leucine recombinant producer culture. (a) Keiselgel 60 HPTLC plates, system D as eluent, T = 20°C, single-step elution l = 55 mm; (b) ten-step elution (l_1 = 55, :, l_{10} = 85 mm, Δl = 3.0 mm). (*1*) Phenylalanine, (*2*) homoleucine, and (*3*) CB of the leucine produce culture.

whose R_f was greater than that of leucine, but smaller than that of homoleucine (Fig. 6a), and its mobility was similar to that of phenylalanine. Since accumulation of phenylalanine is untypical of the producer cultures used previously, this compound required additional identification. Homoleucine and unknown compound were separated by multiple elution under the isocratic conditions. They were separated after 10 elution steps (l_1 = 55, …, l_{10} = 85 mm, Δl = 3.0 mm) (Fig. 6b). The separation was performed on the Kieselgel 60 HPTLC plates with *in situ* spectrophotometric detection of the absorption spectra of the unknown compound and phenylalanine reference (Camag TLC Scanner II densitometer). It was found that the UV spectrum of this compound is similar to that of phenylalanine.

For additional identification, we recovered this compound from the CB by column chromatography and recorded its ^{1}H NMR spectrum, which was similar to that of the phenylalanine reference [35].

This example shows that the chromatographic procedures provide not only identification and quantitative analysis of the desired products and impurities, but also allow determination of the ways for improvement of the producer cultures and the conditions of their cultivation.

Quantitative determination of Schiff bases in CBs of industrial amino acid producer cultures. Schiff bases may cause loss in industrial biosynthesis of amino acids. At biosynthesis the pH of the fermentation solutions varies within 6.3–7.2. These conditions are favorable for formation of Schiff bases, i.e., the condensation products of amino groups in amino acidswith carbonyl groups of sugars, which are present in CBs and act as sources of carbon. It is known that Schiff bases are stable in aqueous solutions at pH 5.5–7.5 [36]; therefore, acidification of CB and use of eluents and detecting solutions containing acid or base reagents should cause decomposition of Schiff bases both in CBs and on the chromatographic plates. To verify this assumption, model solutions (equimolar mixtures) containing *D*-glucose and four amino acids (valine, phenylalanine, lysine, and serine) were incubated in a fermenter for 3 days at 35–37°C. Then, aliquot samples were deposited on plates (in the presence of references of *D*-glucose and amino acids, two replicate samples) and eluted using elution systems H (propanol–water, 70 : 30 volume ratio). The resulting chromatograms were treated with 1-butanol saturated with hydrochloric acid, dried, and then treated with a solution of ninhydrin and phosphomolybdic acid.

The ninhydrin reagent revealed the presence of a free amino acid and the same amino acid in the unknown product, and phosphomolybdic acid provided visualization of free glucose and glucose in the unknown product. To confirm the fact that this compound is the condensation product of amino acid and glucose, we determined the glucose:amino acid ratio in the unidentified products occurring after incubation in the four model systems. It was found that the glucose : amino acid ratio was 0.95 : 1.03 (except lysine), which confirmed the occurrence of condensation. Moreover, it was found that certain fractions of valine (6.3 ± 0.4%), phenylalanine (6.4 ± 0.4%), serine (5.8 ± 0.5%), and lysine (10.6 ± 0.4%) (n = 6, P = 0.95) were bound with sugar after incubation.

Based on the data for several drained CBs of the valine producer cultures grown on the media containing glucose, we found that 3.5 to 6.5% of the target product occurred in the form of Schiff bases by the end of the fermentation process (n = 5, P = 0.95) [37, 38].

Sample no.	Content of Schiff Base, %
1	4.3 ± 0.4
2	3.5 ± 0.4
3	6.5 ± 0.3
4	6.3 ± 0.4
5	4.1 ± 0.4

These results indicate that the drained CBs of the amino acid producer cultures should be acidified before recovery. We recommended to include acidification in the flowsheets of the amino acid production.

CONCLUSIONS

(1) The optimal conditions of the color reaction on the chromatograms in the course of the quantitative analysis of amino acids were determined. Chromatograms were immersed in the ninhydrin solution for 17–20 s, the color reaction was performed for 30–40 min at 45–50°C. The color of the spots of the reaction products of ninhydrin and amino acids is stable at 21°C for 0.5–7.0 h in the dark.

(2) Procedures were developed for quantitative analysis of aromatic, basic, saturated, and hydroxy amino acids in culture broths of the producer cultures: serine, threonine, homoserine, tryptophan, phenylalanine, lysine, ornithine, arginine, valine, and leucine. The undesirable admixtures of homoleucine and phenylalanine in the cultural broths of the valine and leucine producer cultures can be determined at their content less than 0.1% with respect to the desired products.

(3) The possibility of formation of the condensation products of amino acids with carbohydrates (Schiff bases) was confirmed experimentally. It was found for the example of the drained cultural broth of the valine producer culture that the content of Schiff base may be as high as 6% with respect to the target product. It is recommended to include in the flowsheet the stage of acidifying of the cultural broth of the amino acid producer cultures before recovery in order to improve the yield of the desired product.

REFERENCES

1. Mashkovskii, M.D., *Lekarstvennye sredstva* (Drugs), Moscow: Novaya Volna, 2000, vol. 1.
2. Debabov, V.G., *Biotekhnologiya* (Biotechnology), Moscow: Nauka, 1994.
3. Markov, V.L. and Varshavskii, A.E., *Nauka i vysokie tekhnologii v Rossii an rubezhe tret'ego tysyacheletiya* (Science and High Tech in Russia on the Eve of the Third Millenium), Moscow: Nauka, 2000.
4. Daveni, T., and Grei, Ya., *Aminokisloty i belki* (Amino Acids and Protein), Moscow: Mir, 1976.
5. Klenova, I.F. and Yaremenko, N.A., *Veterinarnye preparaty v Rossii* (Veterinary Drugs in Russia), Moscow: Sel'khozizdat, 2000.
6. Gruska, E., Levin, S., and Gilon, C.J., *J. Chromatogr.*, 1982, vol. 235, pp. 401–413.
7. Burikov, E.A., Kuznetsov, E.V., Tarasov, A.P., *et al.*, *Biotechnologiya*, 1996, no. 9, pp. 51–57.
8. Demina, N.G., Rumyantseva, N.F., Polanuer, B.M., and Sholin, A.F., *Biotechnologiya*, 1992, no. 5, pp. 53–55.
9. *Camag. Modern Thin-Layer Chromatography*, Muttenz, 2002.
10. *TU* (Technical Specifications) *26-11-17–89: Plates for Thin-Layer Chromatography on a Polymeric Support.*
11. RF Patent 1736541.
12. Postaire, E., Sarbach, C., and Deivarde, P., *J. Planar Chromatogr.*, 1990, vol. 3, pp. 247–250.
13. Pachaly, P., *Dunnschicht-Chromatographie der Apotheka*, Stuttgart: Wissenschafilich, 1996.
14. Renger, B., *J. Assoc. Off. Anal. Chem.*, 1993, vol. 76, pp. 7–15.
15. Sizova, I.A., Tyaglov, B.V., and Zvenigorodskii, V.I., *J. Planar Chromatogr.*, 1997, vol. 10, pp. 200–205.
16. Ferencz-Fodor, K., Vegh, Z., and Renger, B., *J. Assoc. Off. Anal. Chem.*, 2001, vol. 84, pp. 1265–1276.
17. Nytredy, S.Z., Erdelmeier, C.A., and Meier, B., *Planta Med.*, 1985, pp. 241–254.
18. Abilev, S.K., Vaisburg, A.F., Degtyar', V.G., *et al.*, *Biotechnologiya*, 1993, no. 5, pp. 44–47.
19. Degtiar, W.G., Tyaglov, B.V., Degterev, E.V., *et al.*, *J. Planar Chromatogr.*, 1994, vol. 7, pp. 54–57.
20. Malakhova, I.I., Krasikov, V.D., Degterev, E.V., *et al.*, *Biotechnologiya*, 1996, no. 11, pp. 27–32.
21. Malakhova, I.I., Tyaglov, B.V., Degterev, E.V., and Krasikov, V.D., *J. Planar Chromatogr.*, 1996, vol. 9, pp. 357–378.
22. Degterev, E.V., Tyaglov, B.V., Malakhova, I.I., and Krasikov, V.D., *Coll. of Papers, Planar Chromatography*, Hungary, May 11–13, 2002, pp. 197–204.
23. Bolliger, H.R., Brenner, M., und Ganshirt, H., *Dunnschicht Chromatographie. Ein Laboratoriumshandbuch*, Stahl, E., Hrsg., Berlin: Springer, 1962.
24. Kirchner, J.G., *Thin-Layer Chromatography*, New York: Wiley, 1978. 2d ed.
25. Jork, H., Funk, W., and Fisher, W., *Thin-Layer Chromatography: Reagents and Detection Methods*, Weinheim: VCH, 1990.
26. Degterev, E.B., Degtyar', V.G., Vaisburg, A.F., *et al.*, *Khim.-Farm. Zh.*, 1994, nos. 8–9, pp. 52–55.
27. Degterev, E.V., Degtiar, W.G., Tyaglov, B.V., *et al.*, *J. Planar Chromatogr.*, 2000, vol. 13, pp. 191–194.
28. Malakhova, I.I., Tyaglov, B.V., Degterev, E.V., and Krasikov, V.D., Abstracts of Papers, *8 Int. Symp. on Instrumental Planar Chromatography, Interlaken* (Switzerland), April 5–7, 1995, 1995, report Q9.
29. Niyredy, Sz. and Falter, Zs., *J. Planar Chromatogr.*, 1995, vol. 8, pp. 341–346.
30. RF Patent 2078342.
31. RF Patent 2095808.
32. Popova, T.E., *Razvitie biotekhnologii v SSSR* (Development of Biotechnology in USSR), Moscow: Nauka, 1989.

33. Lehninger, A.L., *Biochemistry*, New York: Worth, 1972.

34. Sarwar, G. and Botting, H.G., *J. Chromatogr.*, 1993, vol. 615, p. 1–22.

35. Malakhova, I.I, Quantitative High-Performance Thin-Layer Chromatography of Amino Acids, *Cand. Sci. Dissertation*, St. Petersburg, 2003.

36. Roberts, J.D. and Caserio, M.C., *Basic Principles of Organic Chemistry*, Amsterdam: Benjamin, 1964.

37. Malakhova, I.I., Krasikov, V.D., Tyaglov, B.V., and Degterev, E.V., Abstracts of papers, *Rossiiskaya nauchno-proizvodstvennaya konferentsiya "Sovremennoe sostoyanie teorii i prakticheskoe primenenie Metoda TSKh"* (Russian Scientific and Industrial Conference "Modern State of Theory and Practical Use of TLC"), Moscow, 1996, p. 24.

38. Tyaglov, B.V., Tarasov, A.P., Degterev, E.V. *et al.*, *Abstracts of Papers, Mezhdunarodnyi simpozium "Khromatografiya i spektroskopiya v analize ob"ektov okruzhayushchei sredy i toksikologii"* (Int. Symp. "Chromatography and Spectroscopy in Analysis of Environmental Objects and Toxicology"), St. Petersburg, June 18–21, 1996, pp. 2v–17.

Russian Journal of Applied Chemistry, Vol. 77, No. 6, 2004, pp. 915–920. Translated from Zhurnal Prikladnoi Khimii, Vol. 77, No. 6, 2004, pp. 929–934.

APPLIED ELECTROCHEMISTRY AND CORROSION PROTECTION OF METALS

Synthesis and Ionic Conductivity of Lithium-conducting Titanium Phosphate Solid Electrolytes

G. B. Kunshina, O. G. Gromov, A. P. Kuz'min, E. B. Seitenova, E. P. Lokshin, and V. T. Kalinnikov

Tananaev Institute of Chemistry and Technology of Rare Elements and Mineral Raw Materials, Kola Scientific Center, Russian Academy of Sciences, Apatity, Russia

Received March 28, 2003; in final form, September 2003

Abstract—Solid electrolytes were synthesized in the systems Li_2O–Al_2O_3–TiO_2–P_2O_5 and Li_2O–Al_2O_3–TiO_2–P_2O_5–H_2O–H_2O_2. Their ionic conductivities were studied and compared. The possibility of obtaining a film of $Li_{1.3}Al_{0.3}Ti_{1.7}(PO_4)_3$ solid electrolyte on a sapphire substrate from an aqueous peroxide solution of a precursor was analyzed.

To be suitable for practical application in chemical power cells or secondary batteries, a solid electrolyte must primarily have the maximum ionic conductivity, so that potential drop across the internal resistance of a cell be much lower than its working voltage. Presently, only few lithium-based solid electrolytes with a room-temperature ionic conductivity on the order of 10^{-3} Cm cm^{-1} are known [1]. These are, in the first place, lithium analogues of nasicons, compounds based on double lithium and titanium phosphates, in which some Ti^{4+} cations are replaced with In^{3+}, Sc^{3+} or Al^{3+} cations.

An important requirement to the solid electrolytes of lithium power cells is their high chemical stability when in contact with cathode and anode materials. In this case, it is necessary to take into account that metallic lithium or lithium alloys used as anode are rather chemically active. The known solid electrolytes based on double lithium and titanium phosphates are chemically unstable at elevated temperatures because of the interaction of metallic lithium with titanium phosphate [2]. Hence follows that, to enhance the chemical stability of this type of solid electrolytes, it is necessary to decrease the content of titanium and phosphate groups in them.

Previously [3], $Li_{1.3}Al_{0.3}Ti_{1.7}(PO_4)_3$ solid electrolytes have been synthesized by the ceramic method. However, this technique has some drawbacks limiting its application in the cases of increased requirements to the stability and reproducibility of properties of the materials. These drawbacks are due to the mechanism of solid-state reactions, which occur originally at the interface and then continue owing to the diffusion of atoms across a layer of the products formed. In the course of a reaction, the diffusion length increases and the reaction rate decreases. The ceramic process can commonly come to sufficiently full completion only in the case of an intermediate multiple grinding of the reaction mass. But even then, the required chemical and structural homogeneity of the product cannot be always achieved. To overcome the above difficulties, various modifications of the ceramic method, based on a number of procedures for preliminary homogenization down to the molecular level of the solid-phase reaction mixture, have been suggested. These are coprecipitation of components from solutions, drying of solutions by spraying, pulverization of the solutions into liquid nitrogen (cryochemical method), or sol–gel procedure. The sol–gel method shows promise for synthesis of lithium-based solid electrolytes [4].

The goal of this study was to search for ways to raise the ionic conductivity and chemical stability of phosphate lithium-conducting solid electrolytes in the solid-phase and sol–gel syntheses.

EXPERIMENTAL

As starting reagents were used Li_2CO_3 (special purity); $LiNO_3$ (analytically pure); $Al(NO)_3 \cdot 9H_2O$,

1070-4272/04/7706-0915 © 2004 MAIK "Nauka/Interperiodica"

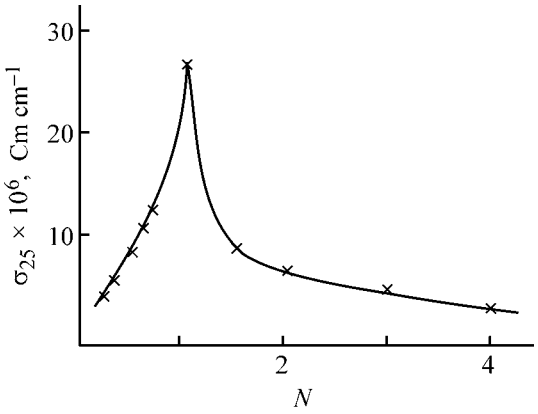

Fig. 1. Ionic conductivity σ_{25} of double lithium and titanium phosphates vs. Li_2O : TiO_2 molar ratio *N*.

Al_2O_3, and $(NH_4)_2HPO_4$ (all chemically pure); TiO_2 (special purity); and $(NH_4)_2TiO(SO_4)_2 \cdot H_2O$ (chemically pure). Freshly precipitated titanium(IV) hydroxide was obtained by dissolving a weighed portion of titanium(IV) oxide of the anatase modification in hydrofluoric acid. The resulting acid fluoride solution was heated to 50–60°C and added in small portions to a 25% solution of ammonium hydroxide under vigorous agitation. The precipitated amorphous titanium(IV) hydroxide was washed with a 5% NH_4OH solution to remove fluoride ions by repulping. The content of the F^{-1} ions was controlled potentiometrically using a Kh-F-001 fluoride-selective electrode. The content of the F^{-1} ions in the washing water from the final repulping was 10 mg l^{-1} and less.

The method for determining the ionic conductivity σ_{25} (at 25°C) of the samples of lithium-conducting solid electrolytes has been described in detail previously [5]. The measurements were done on an E7-12 digital LCR-meter at a frequency of 1 MHz in a cell with graphite electrodes on several pellets of different heights. For samples of the same composition, the σ_{25} values were reproduced to within ±5%.

Table 1. Ionic conductivity of $Li_{2+x}Al_xTi_{1-x}(PO_4)_2$ and $Li_{2-3x}Al_xTi_{1-x}(PO_4)_2$ solid solutions

Solution	Composition	σ_{25}, Cm cm^{-1}
(I)	$Li_2Ti(PO_4)_2$	2.7×10^{-5}
	$Li_{2.1}Al_{0.1}Ti_{0.9}(PO_4)_2$	1.3×10^{-4}
	$Li_{2.2}Al_{0.2}Ti_{0.8}(PO_4)_2$	3×10^{-5}
	$Li_{2.3}Al_{0.3}Ti_{0.7}(PO_4)_2$	2.3×10^{-5}
(II)	$Li_2Ti(PO_4)_2$	2.7×10^{-5}
	$Li_{1.7}Al_{0.1}Ti(PO_4)_2$	2.7×10^{-4}
	$Li_{1.4}Al_{0.2}Ti(PO_4)_2$	5.4×10^{-4}
	$Li_{1.1}Al_{0.3}Ti(PO_4)_2$	5.6×10^{-4}
	$Li_{0.8}Al_{0.4}Ti(PO_4)_2$	2.5×10^{-4}

The electronic conductivity σ_e was determined by the polarization Wagner method in a cell with irreversible graphite electrodes. A voltage lower than the voltage of electrolyte decomposition was applied to the measuring cell and the current in the circuit was measured with a U5-11 charge amplifier [6].

The phase composition of the products synthesized was studied by X-ray phase analysis (DRON-2 diffractometer, Cu_{K_α} radiation, graphite monochromator).

The base component of the known lithium-conducting solid electrolyte $Li_{1.3}Al_{0.3}Ti_{1.7}(PO_4)_3$ is double phosphate $LiTi_2(PO_4)_3$ with the molar ratio Li_2O : TiO_2 = 1 : 4. No data for double lithium and titanium(IV) phosphates with other molar ratios are available.

The synthesis of double lithium and titanium(IV) phosphates and the measurement of their ionic conductivity were performed at the Li_2O : TiO_2 ratio in the range from 1 : 4 to 4 : 1. These compounds were synthesized by the ceramic method [3] at the temperature of the final sintering stage equal to 800–1000°C, depending on composition. The results obtained in a study of σ_{25} of the samples obtained are presented in Fig. 1. It can be seen that the optimal composition is obtained at Li_2O : TiO_2 = 1 : 1 and corresponds to chemical formula $Li_2Ti(PO_4)_2$. The generally accepted composition $LiTi_2(PO_4)_3$ is unremarkable.

To study the influence exerted on the ionic conductivity by the $Ti^{4+} \rightarrow Al^{3+} + Li^+$ heterocharge substitution, experiments on the synthesis of $Li_{2+x}Al_xTi_{1-x}(PO_4)_2$ solid solutions were performed. The results presented in Table 1 show that such a substitution results in an increase in the ionic conductivity only at $x = 0.1$.

Because the composition $Li_2Ti(PO_4)_2$ is characterized by relatively high concentration of lithium ions, it was appropriate to perform the heterocharge substitution $3Li^+ \rightarrow Al^{3+}$. The data of Table 1 show that this type of heterocharge substitution considerably increases the ionic conductivity in the range $0.1 \le x \le 0.4$, with the ionic conductivity of the composition $Li_{1.1}Al_{0.3}Ti(PO_4)_2$ being the highest.

The results of experiments with mixed heterocharge substitution, i.e, with joint occurrence of $Ti^{4+} \rightarrow Al^{3+} +$

Li^+ and $3Li^+ \rightarrow Al^{3+}$ processes, are listed in Table 2. It can be seen that the composition $Li_{1.4}Al_{0.2}Ti(PO_4)_2$, in which the Ti : Li and PO_4^{-3} ratios are 0.71 and 1.43, respectively, is the most promising from the standpoint of chemical stability. At the same time, for the generally accepted composition $Li_{1.3}Al_{0.3}Ti(PO_4)_2$, these ratios are 1.3 and 2.31.

The room-temperature electronic conductivity of $Li_{1.4}Al_{0.2}Ti(PO_4)_2$ is 3×10^{-8} Cm cm^{-1}. Its ionic conductivity linearly increases in the range 25–100°C from 5.4×10^{-4} to 8.1×10^{-4} Cm cm^{-1}.

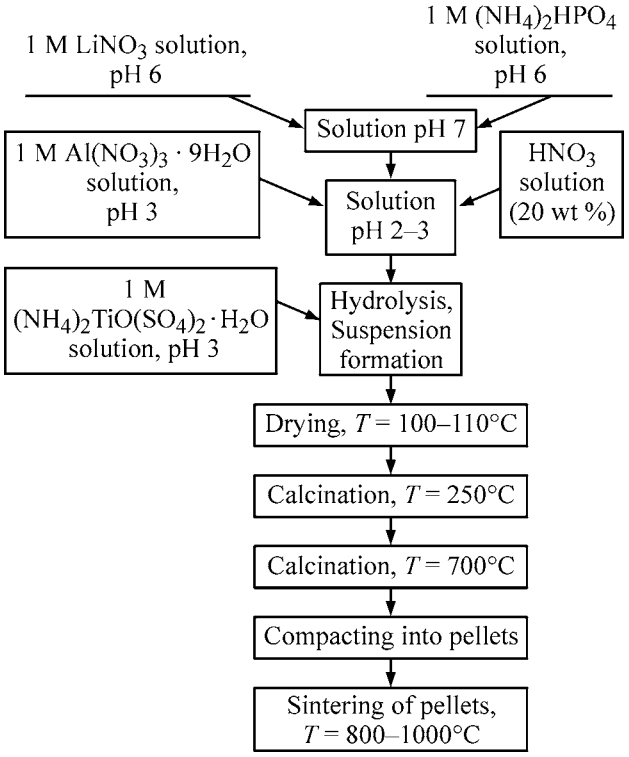

Scheme of the sol–gel process.

The sol–gel synthesis of lithium-conducting phosphate solid electrolytes was performed using 1 M aqueous solutions of the starting reagents, $LiNO_3$, $Al(NO_3)_3$, $(NH_4)_2HPO_4$, and $(NH_4)_2TiO(SO_4)_2 \cdot H_2O$, taken in stoichiometric amounts in accordance with the formula $Li_{1.3}Al_{0.3}Ti_{1.7}(PO_4)_3$. The process by which the solid electrolyte was synthesized is illustrated by the scheme. A neutral solution of $LiNO_3$ (pH 6) and a weakly alkaline solution of $(NH_4)_2HPO_4$ (pH 8) were poured together, and the acidity of the resulting solution was adjusted to pH 2–3 with a 20% solution of HNO_3. Then, $Al(NO_3)_3$ (pH 3) and $(NH_4)_2TiO(SO_4)_2$ (pH 1) solutions were successively poured-in under vigorous agitation. As a result, a white suspension was formed. The necessary condition was that the pH value was preliminarily adjusted to pH 2–3. Otherwise, crystalline quick-settling precipitate appeared in the solution instead of a suspension. The suspension obtained was poured onto a fluoroplastic pan, evaporated, and dried at 100–110°C for 8 h. As a result, a precursor of the solid electrolyte was formed as a loose bulky powder.

Table 2. Ionic conductivity of $Li_2Ti(PO_4)_2$-based solid solutions with a mixed heterocharge substitution

Composition	σ_{25}, Cm cm^{-1}
$Li_{0.9}Al_{0.1}Ti_{1.2}(PO_4)_2$	1.4×10^{-4}
$Li_{1.0}Al_{0.2}Ti_{1.1}(PO_4)_2$	6.2×10^{-4}
$Li_{1.1}Al_{0.3}Ti(PO_4)_2$	5.6×10^{-4}
$Li_{1.2}Al_{0.4}Ti_{0.9}(PO_4)_2$	2.4×10^{-4}
$Li_{1.3}Al_{0.1}Ti_{1.1}(PO_4)_2$	4.2×10^{-4}
$Li_{1.4}Al_{0.2}Ti(PO_4)_2$	5.4×10^{-4}
$Li_{1.5}Al_{0.3}Ti_{0.9}(PO_4)_2$	1.4×10^{-4}
$Li_{1.8}Al_{0.2}Ti_{0.9}(PO_4)_2$	1.1×10^{-4}

To obtain the final product, the precursor was calcined. The temperature mode and calcination time were determined from the results of thermal and X-ray phase analyses. According to the thermal analysis, the weak endothermic effects exhibited by the electrolyte precursor (Fig. 2) at temperatures of up to 158°C are due to removal of water. The exothermic effect at 254–293°C is associated with the interaction of $LiNO_3$ and $(NH_4)_2HPO_4$, with evolution of nitrogen oxides and $NH_3 \cdot (NH_4)_2TiO(SO_4)_2$ decomposes within the range 400–700°C. At higher temperatures, no thermal effects or mass loss was observed. There-

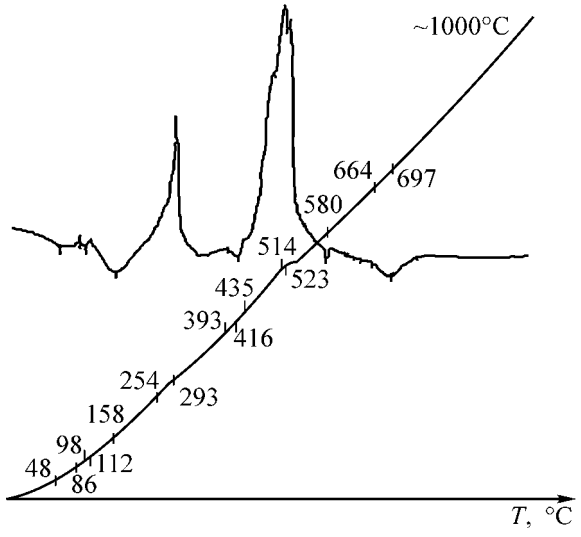

Fig 2. Thermogram for a precursor of lithium-conducting solid electrolyte $Li_{1.3}Al_{0.3}Ti_{1.7}(PO_4)_3$. ($T$) Temperature.

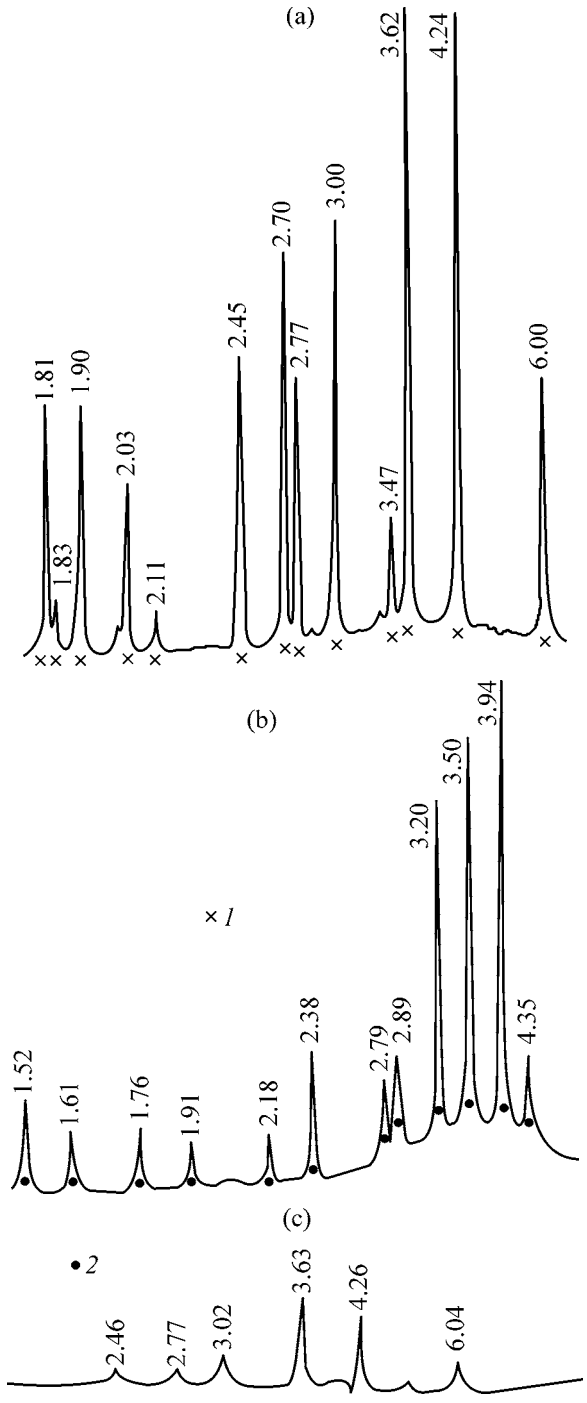

Fig. 3. Diffraction patterns of (a) lithium-conducting solid electrolyte $Li_{1.3}Al_{0.3}Ti_{1.7}(PO_4)_3$, (b) product of a synthesis of solid electrolyte with a 1.5-fold excess of H_3PO_4, and (c) $Li_{1.3}Al_{0.3}Ti_{1.7}(PO_4)_3$ film on a sapphire substrate. (*1*) $LiTi_2(PO_4)_3$ and (*2*) TiP_2O_7.

fore, the temperature was raised stepwise to 700°C. The precursor powder was kept at 250°C for 1 h (till gas evolution stopped) in the first stage and at 700°C for 2 h in the second. The product obtained (bulky, loose, and easily disintegrating) was compacted into pellets 12 mm in diameter and 2–3 mm thick and sintered at 800–1000°C. The sintered pellets frequently separated into layers, cracked, and deformed. To improve sintering and avoid deformation of the pellets, a C_2H_5OH binder was introduced into the powder before compaction. The diffraction patterns of the electrolyte samples sintered at $T > 800$°C contain only reflections associated with $LiTi_2(PO_4)_3$ (Fig. 3a). As follows from Table 3, the highest ionic conductivity $\sigma_{25} = 5 \times 10^{-4}$ Cm cm^{-1} is observed for the electrolyte sample sintered at 1000°C for a long time (7h).

In preliminary studies, we established that freshly precipitated titanium(IV) hydroxide satisfactorily dissolves in the form of a peroxide complex in an acid medium. To synthesize lithium-conducting solid electrolyte $Li_{1.3}Al_{0.3}Ti_{1.7}(PO_4)_3$, a freshly precipitated titanium(IV) hydroxide was dissolved in initial experiments in a mixture containing 40 vol % H_3PO_4 (acid concentration 85 wt %) and 60 vol % H_2O_2 (peroxide concentration 30 wt %). After stoichiometric amounts of aqueous solutions of $LiNO_3$ and $Al(NO_3)_3$ were added to the resulting titanium(IV) peroxide solution, a transparent solution (pH 0.7) of intense ruby color was formed. After evaporation of this solution at 150–160°C and subsequent drying of the precipitate at 300°C, a white powder was formed. The powder was compacted into pellets and sintered at 900°C for 1 h, with a mass loss of 35%. The sintered pellets were porous and could be easily broken. To obtain high-density pellets, sintering was performed at 1000°C for 1 h. It was found that the ionic conductivity is about 1×10^{-7} Cm cm^{-1}, i.e., is lower by three orders of magnitude than the predicted value. Additional sintering at 1200°C did not affect σ. According to XPA, the diffraction pattern of the product synthesized contains no reflections corresponding to $Li_{1.3}Al_{0.3}Ti_{1.7}(PO_4)_3$ (Fig. 3b), with the main reflections belonging to titanium diphosphate TiP_2O_7. Apparently, titanium(IV) polyphosphates, which do not decompose even at high temperature, are formed owing to excess content of H_3PO_4 in the initial solution.

In this connection, HNO_3 was used for obtaining an acid medium in dissolution of a freshly precipitated titanium(IV) hydroxide. The freshly precipitated titanium(IV) hydroxide was dissolved in a mixture containing 70 vol % HNO_3 (65 wt % concentration) and 30 vol % H_2O_2 (30 wt % concentration). To the resulting solution, stoichiometric amounts of aqueous solutions of $LiNO_3$, $Al(NO_3)_3$, and H_3PO_4 were added under agitation. The resulting aqueous peroxide solution of ruby color was transparent and contained 160–170 g l^{-1} of the final product. Evaporating the solution

in a desiccator at 150–160°C yielded a white powder, which was sintered at 900°C for 1 h with a mass loss of 31%. The powder was compacted into pellets and sintered at 1000°C for 1 h. The ionic conductivity of the sintered pellets was 6×10^{-4} Cm cm^{-1}, which coincides with the conductivity of $Li_{1.3}Al_{0.3}Ti_{1.7}(PO_4)_3$ samples obtained by the solid-phase synthesis. The electronic conductivity did not exceed 2×10^{-8} Cm cm^{-1}.

The scheme described was used to synthesize $Li_2Ti(PO_4)_2$ solid electrolyte and a number of electrolytes on its basis. The ionic conductivities of the samples synthesized are listed in Table 4.

It can be seen that the ionic conductivities of the samples obtained by two methods are virtually the same.

The main advantage of the method developed for preparing stable aqueous peroxide solutions in the Li_2O–Al_2O_3–TiO_2–P_2O_5–H_2O–H_2O_2 system consists in the possibility of using such solutions for obtaining thin films of solid electrolytes. Aqueous peroxide solution of a precursor of the $Li_{1.3}Al_{0.3}Ti_{1.7}(PO_4)_3$ electrolyte, which contained glycerol as a film-forming agent, was used to deposit films onto substrates by "dipping" method.

A solution containing (per 100 ml) 12 g of a precursor of the $Li_{1.3}Al_{0.3}Ti_{1.7}(PO_4)_3$ solid electrolyte and 5 ml of glycerol was stable (i.e., retained transparency and homogeneity) for seven days. To apply a film, the substrate was dipped into a solution and then withdrawn at a rate of 0.6 cm min^{-1}, dried in air, annealed at 450°C for 15 min, and cooled to room temperature. Then the solution was applied to the substrate again, only with the sample annealed at 850°C for 30 min this time. The existence of the film was confirmed by visual observation under a Neophot-2 microscope (magnification 200). An X-ray phase analysis showed that four relatively weak reflections (6.04, 4.26, 3.63, and 3.02 Å), which are characteristic of a powder-like electrolyte, are present in the diffraction pattern of the film obtained (Fig. 3c). The study performed demonstrated that dipping is a suitable method for obtaining on appropriate substrates films of lithium-conducting titanium phosphate solid electrolytes, which are promising for fabrication of thin-film chemical power cells.

CONCLUSIONS

(1) A study of the ionic conductivity of solid electrolytes obtained by the solid-phase method in the Li_3PO_4–$Ti_3(PO_4)_4$ system established that the maximum conductivity ($\sigma_{25} = 2.7 \times 10^{-5}$ Cm cm^{-1}) is observed for the composition $Li_2Ti(PO_4)_2$. The $Li_{1.4}Al_{0.2}Ti(PO_4)_2$ solid electrolyte with $\sigma_{25} = 5.4 \times 10^{-4}$ Cm cm^{-1} and the Ti : Li and PO_4^{3-} : Li molar ratios of 0.71 and 1.43, respectively, was obtained upon heterocharge substitution of some Li^+ ions for Al^{3+} ions in this compound. The same ratios for the generally accepted composition $Li_{1.3}Al_{0.3}Ti_{1.7}(PO_4)_3$ are 1.3 and 2.31.

Table 3. Ionic conductivity of $Li_{1.3}Al_{0.3}Ti_{1.7}(PO_4)_3$ at different conditions of pellet sintering

T_{sin}, °C	τ_{sin}, h	h_{tab}, cm	σ_{25}, Cm cm^{-1}
800	2	0.227	4×10^{-5}
	4	0.181	1.1×10^{-4}
900	2	0.130	3.9×10^{-4}
	7	0.118	3.8×10^{-4}
1000	2	0.428	3.8×10^{-4}
	7	0.427	5.0×10^{-4}

Table 4. Ionic conductivity of $Li_2Ti(PO_4)_2$-based solid electrolytes

Composition	σ_{25},* Cm cm^{-1}
$Li_{1.1}Al_{0.3}Ti(PO_4)_2$	4.8×10^{-4} (5.6×10^{-4})*
$Li_{1.4}Al_{0.2}Ti(PO_4)_2$	4.5×10^{-4} (5.4×10^{-4})
$Li_{1.6}Al_{0.2}Ti(PO_4)_2$	2×10^{-4}
$Li_2Ti(PO_4)_2$	1×10^{-4} (1×10^{-4})

* The σ_{25} values for samples obtained by solid-phase method are given in parentheses.

(2) A method for obtaining stable aqueous peroxide solutions of precursors of solid electrolytes in the Li_2O–Al_2O_3–TiO_2–P_2O_5–H_2O–H_2O_2 system was developed. It was established that the solid electrolytes obtained from these solutions compare well in the ionic conductivity with electrolytes synthesized by the solid-phase method.

(3) It was shown that aqueous peroxide solutions of precursors are suitable for obtaining films of lithium-conducting titanium phosphate solid electrolytes on appropriate supports, which are promising for fabrication of thin-film chemical power cells.

ACKNOWLEDGMENTS

The study was financially supported in part by the "New Principles and Methods of the Development and Directional Synthesis of Substances with Prescribed Properties" Integrated Program of the Presidium of the Russian Academy of Sciences.

REFERENCES

1. Vashman, A.A., and Petrov, K.I., *Funktsional'nye neorganicheskie soedineniya litiya* (Functional Inorganic Lithium Compounds), Moscow: Energoatomizdat, 1996.
2. Thangadurai, V., Shukla Ashok, K., and Gopalakrishnan, Ja., *J. Mater. Chem.*, 1999, vol. 9, no. 3, pp. 739–741.
3. Gromov, O.G., Kunshina, G.B., Kuz'min, A.P., and Kalinnikov, V.T., *Zh. Prikl. Khim.*, 1996, vol. 69, no. 3, pp. 433–436.
4. Livage, J., *Solid State Ionics*, 1992, vol. 50, no. 3–4, pp. 307–313.
5. Kunshina, G.B., Kuz'min, A.P., and Gromov, O.G., *Tekhnologiya mineral'nogo syr'ya i fiziko-khimicheskie issledovaniya produktov ego pererabotki* (Technology of Mineral Raw and Physicochemical Study of the Products of Its Processing), Apatity, 1994, pp. 39–44.
6. Kunshina, G.B., Kuz'min, A.P., Gromov, O.G., and Prokopets, V.E., *Tekhnologiya mineral'nogo syr'ya i fiziko-khimicheskie issledovaniya produktov ego pererabotki* (Technology of Mineral Raw and Physicochemical Study of the Products of Its Processing), Apatity, 1994, pp. 45–49.

Russian Journal of Applied Chemistry, Vol. 77, No. 6, 2004, pp. 921–924. Translated from Zhurnal Prikladnoi Khimii, Vol. 77, No. 6, 2004, pp. 935–938.

APPLIED ELECTROCHEMISTRY AND CORROSION PROTECTION OF METALS

Electrochemical Oxidation of Galenite in Carbonate Solutions

D. V. Makarov, W. Forsling, V. N. Makarov, and A. T. Belyaevskii

Tananaev Institute of Chemistry and Technology of Rare Elements and Mineral Raw Materials, Kola Scientific Center, Russian Academy of Sciences, Apatity, Russia

Luleo Technical University, Luleo, Sweden

Received June 10, 2003; in final form, April 2004

Abstract—Linear voltammetry, X-ray phase and differential thermal analyses, diffuse reflection IR Fourier spectroscopy, Raman spectroscopy, and scanning electron microscopy (SEM) were used to study the electrochemical oxidation of galenite in carbonate electrolytes.

The current interest in studying the oxidation of sulfides contained in wastes formed in extraction and concentration of ores stems from the fact that this process gives environmentally hazardous water-soluble salts of non-ferrous metals and changes the technological properties of mining wastes, part of which is presently regarded as deposits of technological origin [1–4].

The part played by a particular mechanism of oxidation of sulfides is determined by the climatic, hydrologic, and geochemical conditions of storage of mining wastes [5–7]. Frequently, electrochemical processes govern the kinetics of oxidation of sulfide mixtures both during storage of mining wastes and in flotation [8–13].

In this study, we examined the electrochemical oxidation of PbS in a 0.7 g l^{-1} solution of K_2CO_3 (pH 10.2). As shown previously [7], carbonate solutions are formed in weathering of chemically active nonmetalliferous minerals, such as dolomite, calcite, and others. Therefore, a solution of K_2CO_3 was chosen as a model solution. The results of the study could also be useful for better understanding of flotation processes. This study proceeds with investigation [14–16] of the electrochemical oxidation of the surface of sulfide minerals in carbonate solutions.

The electrochemical properties of PbS have been described in a number of publications, mostly for the case of flotation [8, 9, 17–24]. Anodic polarization of PbS at pH 6.8–11 results in the formation of a layer of PbO and S^0, which inhibits further oxidation [9]. The authors emphasize that, in opinion of a number of researchers, the thiosulfate ion is a major product of PbS oxidation in alkaline solutions. The formation of $S_2O_3^{2-}$ was established in [18, 19]. The IR Fourier spectroscopy of disturbed total internal reflection was used to identify *in situ* the compounds formed on the surface of galenite in the case of anodic polarization at potentials of –0.5…+0.7 V relative to a standard hydrogen electrode in a deoxygenated $Na_2B_4O_7$ solution (pH 9.18) [21]. It was concluded that lead hydroxide is formed on the surface of PbS by the "salt-film" mechanism. In the next stage of oxidation, PbS_2O_3 and $PbSO_3$ are formed [21]. In [22], the surface of PbS was studied electrochemically in solutions of various acids, and it was shown that the passivation is not associated with shielding of the electrode surface with sulfur, and lead salts and oxides, as well as acid anions, are directly involved in the electrochemical reactions. It was of interest to verify this assumption in the case carbonate alkaline solutions.

The following methods were used in the study: linear voltammetry with fast and slow potential sweeping, potentiostatic electrolysis, X-ray phase and differential thermal analyses, diffuse reflection IR Fourier spectroscopy, Raman spectroscopy and SEM. Natural galenite (Rudnyi Altai) was used, from which an edge electrode with area of about 10 mm^2, embedded in epoxy resin, was fabricated. An insulated copper wire served as a current lead. The electrode surface was polished and washed with distilled water and ethanol before each experiment. Silver chloride electrode was used as reference, and a platinum mesh (surface area of about 15 cm^2), as auxiliary electrode.

1070-4272/04/7706-0921 © 2004 MAIK "Nauka/Interperiodica"

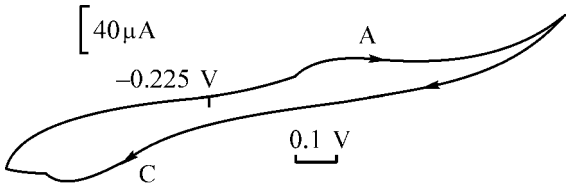

Fig. 1. Cyclic voltammogram of galenite at a potential sweep rate of 0.2 V s^{-1}.

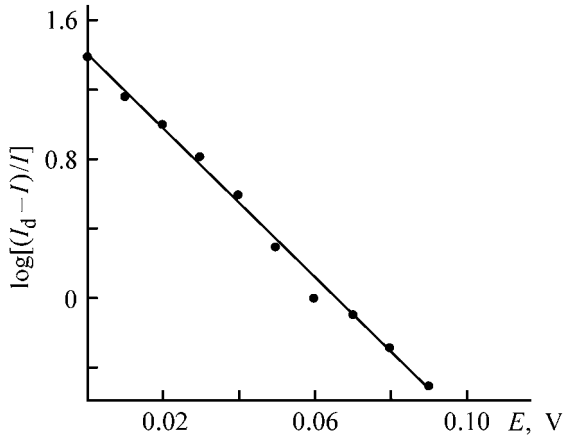

Fig. 2. $\log[(I_d - I)/I]$–E dependence. Potential sweep rate 0.001 V s^{-1}.

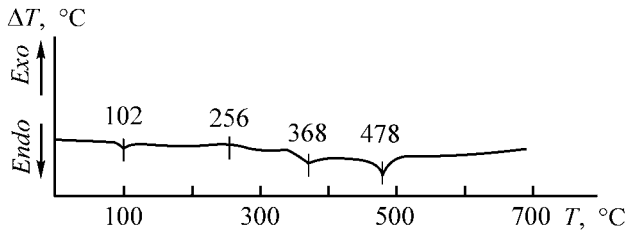

Fig. 3. Thermogram of the anodic products. Sample mass 6 mg, heating rate 15 deg min^{-1}. (T) Temperature.

The study was performed in argon atmosphere. The electrodes were polarized using a PI-50.1 potentiostatand a PR-8 programming unit. Voltammetric curves were recorded with a PDA-1 potentiometer.

An X-ray phase analysis of the products of the electrode reactions was done using an RKU-114 Debye chamber (Cu_{K_α} radiation). An IR spectroscopic analysis of the electrolysis products was performed with a Perkin-Elmer 2000 IR Fourier spectrometer. Raman spectra were recorded on a Renishaw 2000 Raman microscope.

A microscopic study was done on a Hitachi-405 electron microscope, and the differential thermal analysis, on an installation described in [25].

The electrode was polarized starting from the stationary potential of galenite, which is equal to –0.225 V relative to a silver chloride reference electrode. A typical cyclic voltammogram measured at a potential sweep rate of 0.2 V s^{-1} is shown in Fig. 1. It can be seen that the anodic polarization is characterized by a current peak A, to which corresponds a cathodic peak C. At potentials of +0.23…+0.54 V the voltammetric curve shows a plateau. The manner in which the potential of peak A depends on the rate of electrode polarization suggests that the anodic process is controlled by charge-transfer (the potential is shifted into the anodic region as the polarization rate increases).

For a voltammogram with fast potential sweep rate, the product βn_β can be calculated using the Matsuda–Ayabe equation [26]:

$$E_p - E_{p/2} = 1.857RT/\beta n_\beta F, \quad (1)$$

where β is the transfer coefficient; n_β, the number of electrons; and E_p and $E_{p/2}$, the peak and half-peak potentials, respectively.

Estimating the number of electrons involved in the anode reaction at polarization rates in the range 0.2–2 V s^{-1} yields an average value of 2.45 at β = 0.5.

For a steady-state voltammetric curve, the βn_β product can be calculated using the Frumkin–Bagotskii equation [26]:

$$E = E_{1/2} + 2.303RT/(\beta n_\beta F)\log[(I_d - I)/I], \quad (2)$$

where E is potential (V); I, the current density; and I_d, the limiting current density (A m^{-2}).

The $\log[(I_d - I)/I]$–E dependence measured for process A at a potential sweep rate of 0.001 V c^{-1} is shown in Fig. 2. The value obtained using Eq. (2) is n_β = 2.48 at β = 0.5.

Potentiostatic electrolyses at A-wave potentials of +0.14 and +0.5 V were performed. The phases newly formed on the surface of the mineral were carefully detached and studied by X-ray phase analysis, IR and Raman spectroscopies, differential thermal analysis, crystal-optical method, and SEM.

The X-ray phase analysis revealed the formation of basic lead carbonate $Pb_3(OH)_2(CO_3)_2$. The DTA curve for the new formations shows endothermic peaks at 102, 368, and 478°C and an exothermic peak at 256°C (Fig. 3). Probably, the first endothermic effect corresponds to melting of sulfur, and the exothermic effect, to its oxidation [27]. The second and third endothermic effects can be assigned to dissociation of $Pb_3(OH)_2(CO_3)_2$ to give $PbCO_3$ and nPbO · $PbCO_3$

[27, 28]. Figure 4a shows a diffuse reflection IR Fourier spectrum of the anodic products after the electrolysis in the range of the A-wave potentials. It contains bands at 680, 1046, 1104, 1435, 1734, 2413, and 2922 cm^{-1}. These bands are typical of basic lead carbonate $Pb_3(OH)_2(CO_3)_2$ [29–31]. Figure 5 shows the Raman spectrum of these products. The peaks at 146, 216, 427, and 464 cm^{-1} are characteristic of elementary sulfur [32]. The surface morphology of the galenite electrode after the electrolysis is shown in Fig. 6.

With account of the aforesaid, the electrode reaction can be hypothetically represented as

$$3PbS + 2H_2O + 2K_2CO_3 = Pb_2(OH)_2(CO_3)_2 + 3S + 4K^+ + 2H^+ + 6e. \quad (3)$$

Upon further polarization, S^{2-} is oxidized to oxidation numbers higher than S^0. The anodic products formed upon electrolysis at +0.5 V were studied by IR Fourier spectroscopy of diffuse reflection. Their typical spectrum is shown in Fig. 4b. Along with the bands characteristic of basic lead carbonate, the spectrum contains bands at 982 and 1118 cm^{-1}, probably associated with lead thiosulfate [29–31]. Thus, at potentials corresponding to the plateau, the sulfide sulfur is oxidized to thiosulfate ions $S_2O_3^{2-}$. The reaction can be represented as:

$$6PbS + 14H_2O + CO_3^{2-} = 3PbS_2O_3 + Pb_3(OH)_2(CO_3)_2 + 26H^+ + 28e. \quad (4)$$

After grinding of the mineral in an alkaline medium in air, $Pb_3(OH)_2(CO_3)_2$ and PbS_2O_3 are formed on the surface of galenite [31]. In [33], a similar mechanism of PbS oxidation was suggested to describe the surface processes that occur on galenite in flotation.

$$2PbS + 2H_2O + CO_3^{2-} = Pb(OH)_2 + PbCO_3 + 2S + 2H^+ + 4e. \quad (5)$$

CONCLUSION

The study of the electrochemical oxidation of galenite in a carbonate solution showed that the carbonate ion affects the formation of new phases on the surface of the mineral. It was established that $Pb_3(OH)_2(CO_3)_2$, PbS_2O_3, and S^0 are formed.

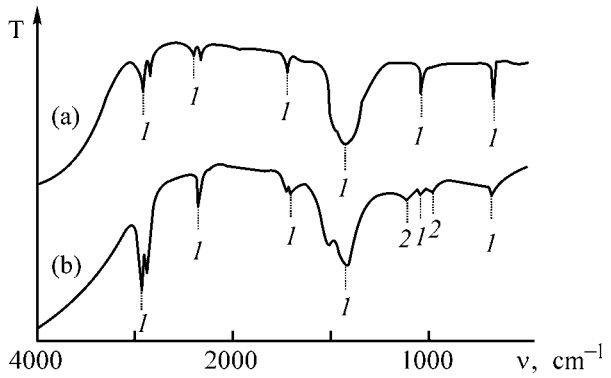

Fig. 4. IR fourier spectra of the anodic products after the electrolysis at a wave potential of (a) +0.14 V and (b) +0.5 V. (T) Transmission and (ν) wave number. (*1*) $Pb_3(OH)_2(CO_3)_2$ and (*2*) PbS_2O_3.

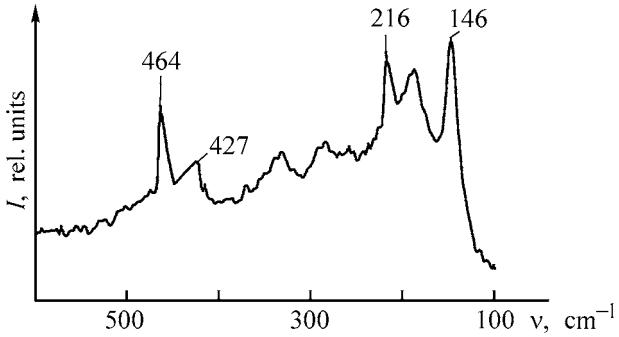

Fig. 5. Raman spectrum of the anodic products after electrolysis at a potential of +0.14 V. (*I*) Intensity and (ν) wave number.

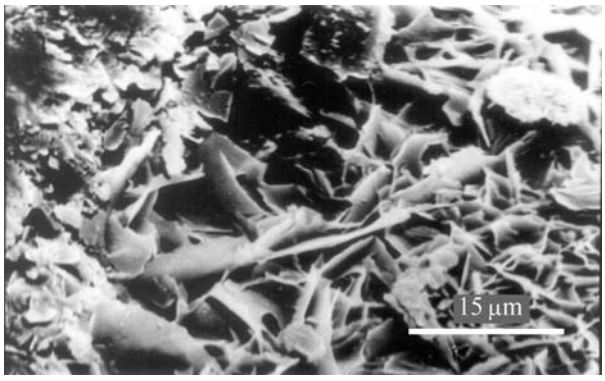

Fig. 6. SEM micrograph of the surface of the galenite electrode after the electrolysis at a potential of +0.14 V.

ACKNOWLEDGMENTS

The study was supported by a grant of the Swedish Institute. The authors are grateful to A.A. Bogdanova for performing X-ray phase analysis and M. Ranheimer for assistance in spectroscopic analyses.

REFERENCES

1. Trubetskoi, K.N., *Gorn. Zh.*, 1995, no. 1, pp. 3–8.
2. Doyle, F.M., *Sulfide Deposits–Their Origin and Processing*, London: The Inst. of Mining and Metallurgy, 1990, pp. 301–310.
3. Chanturiya, V.A., *Gorn. Zh.*, 1995, no. 1, pp. 50–55.
4. Vigdergauz, V.E., Danil'chenko, L.M., and Sarkisova, L.M., *Tsvetn. Met.*, 1999, no. 1, pp. 25–31.
5. Chanturiya, V.A., Makarov, V.N., Vasil'eva, T.N., *et al.*, *Tsvetn. Met.*, 1998, no. 8, pp. 14–18.
6. Chanturiya, V.A., Makarov, V.N., and Makarov, D.V., *Inzh. Ekol.*, 1999, no. 4, pp. 2–9.
7. Chanturiya, V.A., Makarov, V.N., and Makarov, D.V., *Geoekologiya*, 2000, no. 2, pp. 136–143.
8. Woods, R., and Richardson, P.E., *Advances in Mineral Processing*, Littleton, 1986, pp. 154–170.
9. Chanturiya, V.A., and Vigdergauz, V.E., *Elektrokhimiya sul'fidov: teoriya i praktika flotatsii* (Electrochemistry of Sulfides: Theory and Practice of Flotation), Moscow: Nauka, 1993.
10. Baev, A.V., and Orlov, A.I., *Izv. Vyssh. Uchebn. Zaved., Tsvetn. Met.*, 1975, no. 5, pp. 18–22.
11. Sveshnikov, G.B., *Elektrokhimicheskie protsessy na sul'fidnykh mestorozhdeniyakh* (Electrochemical Processes at Sulfide Deposits), Leningrad: Len. Gos. Univ., 1967.
12. Listova, L.P., and Bondarenko, G.P., *Rastvorenie sul'fidov svintsa, tsinka i medi v okislitel'nykh usloviyakh* (Dissolution of Lead, Zinc, and Copper Sulfides in Oxidative Conditions), Moscow: Nauka, 1969.
13. Lowson, R.T., *Chem. Rev.*, 1982, no. 5, pp. 461–497.
14. Makarov, D.V., Vasil'eva, T.N., and Makarov, V.N., *Zh. Prikl. Khim.*, 1999, vol. 72, no. 3, pp. 406–409.
15. Chanturiya, V.A., Makarov, V.N., Makarov, D.V., *et al.*, *Elektrokhimiya*, 1999, vol. 35, no. 7, pp. 852–857.
16. Makarov, D.V., Makarov, V.N., and Vasil'eva, T.N., *Zh. Prikl. Khim.*, 2000, vol. 73, no. 3, pp. 425–430.
17. Gardner, J.R., and Woods, R., *J. Electroanal. Chem.*, 1979, vol. 100, pp. 447–459.
18. Pritzker, M.D., and Yoon, R.H., *Int. J. Min. Proc.*, 1987, vol. 20, pp. 267–290.
19. Paul, R.L., Nicol, M.J., Diggle, J.W., and Saunders, A.P., *Electrochim. Acta*, 1978, vol. 23, no. 7, pp. 625–633.
20. Nicol, M.J., Paul, R.L., Diggle, J.W., and Saunders, A.P., *Electrochim. Acta*, 1978, vol. 23, no. 7, pp. 635–639.
21. Chernyshova, I.V., *Elektrokhimiya*, 2000, vol. 37, no. 6, pp. 679–685.
22. Mikhlin, Yu. L., Galkin, P.S., and Kopteva, N.A., *Izv. Akad. Nauk SSSR, Sib. Otd., Ser. Khim.*, 1988, no. 2, no. 1, pp. 11–17.
23. Ahlberg, E., Elfstrom Broo, A., *Int. J. Min. Proc.*, 1997, vol. 33, pp. 135–144.
24. Cisneros-Gonzalez, I., Oropeza-Guzman, M.T., and Gonzalez, I., *Hydrometallurgy*, 1999, vol. 53, no. 2, pp. 133–144.
25. Skiba, V.I., Makarov, D.V., and Shishaev, V.A., *Zavod. Lab.*, 2000, vol. 66, no. 4, pp. 39–40.
26. Galus, Zb., *Teoretyczne podstawy elektroanalisy chemicznej*, Warsaw: Naukowe, 1971.
27. Ivanova, V.P., Kasatov, Yu. K., Krasavina, T.N., and Rozanova, E.L., *Termicheskii analiz mineralov i gornykh porod* (Thermal Analysis of Minerals and Rocks), Leningrad: Nedra, 1974.
28. Bulakhova, V.I., Ben'yash, E.Ya., Shokarev, M.M., and Vershinina, F.I., *Zh. Neorg. Khim.*, 1972, vol. 17, no. 1, pp. 23–28.
29. Cases, J.M., Kongolo, M., De Donato, P., *et al.*, *Int. J. Min. Proc.*, 1990, vol. 28, pp. 313–337.
30. Cases, J.M., and De Donato, P., *Int. J. Min. Proc.*, 1991, vol. 33, pp. 49–65.
31. De Donato, P., Kongolo, M., Barres, O., *et al.*, Powder Technol., 1999, vol. 105, pp. 141–148.
32. Mycroft, J.R., Bancroft, G.M., McIntyre, N.C., *et al.*, *J. Electroanal. Chem.*, 1990, vol. 292, pp. 139–152.
33. Revnivtsev, V.I., Mashevsky, G.N., Kokorin, A.M., *et al.*, *XVII Int. Mineral Processing Congr.*, Dresden, 1991, vol. 2, pp. 295–305.

Russian Journal of Applied Chemistry, Vol. 77, No. 6, 2004, pp. 925–929. Translated from Zhurnal Prikladnoi Khimii, Vol. 77, No. 6, 2004, pp. 939–943.

APPLIED ELECTROCHEMISTRY AND CORROSION PROTECTION OF METALS

Corrosion-Electrochemical Behavior of Special-Purity Aluminum and Its AK1 Alloy Alloyed with Scandium

I. N. Ganiev

Nikitin Institute of Chemistry, Academy of Sciences of Tajikistan, Tajikistan

Received October 21, 2003

Abstract—The anodic behavior of aluminum of varied purity and the effect of scandium on the corrosion resistance of AK1 alloy based on special-purity aluminum in NaCl electrolyte solutions was studied.

Aluminum and its alloys are used as construction materials in a wide variety of fields of technology [1]. In a certain state and under severe working conditions, aluminum alloys may suffer dangerous types of corrosive destruction. Of particular interest is the corrosion of aluminum is nearly neutral solutions ($6 < pH < 8$). This is corrosion in natural media, such as seawater and water in lakes and rivers, potable water, and atmospheric precipitation. Under these conditions at ordinary temperatures, the rate of aluminum reaction with H^+ ions or H_2O molecules with evolution of hydrogen is negligible [2].

In this study, experiments were carried out in neutral solutions that contained NaCl in various concentrations, in accordance with the recommendations of GOST (State Standard) 9.017–74, i.e., in solutions imitating seawater, in order to reveal the influence exerted by chloride ions on the corrosion-electrochemical behavior of aluminum of varied purity and of AK1 alloy.

As is known, AK1 alloy is manufactured on the basis of special-purity aluminum and used in microelectronics to obtain epitaxial layers in integrated circuits [1]. Together with having a number of advantages, alloying of special-purity aluminum with single-crystal silicon is characterized by disadvantages, the main of which is a certain decrease in the corrosion resistance of the metal. Hence, an extremely important goal of modern materials science is to improve the corrosion resistance of AK1 alloy.

To solve this problem, AK1 alloy was alloyed in the present study with scandium, a metal of the same group as aluminum. However, scandium differs from aluminum in a lower electronegativity [3], standard potential E^0 [4], and high affinity for oxygen. The choice of scandium as the alloying element was also based on previous studies carried out by the author with pure aluminum [5] and on results of other researchers [6].

EXPERIMENTAL

Alloys were prepared using aluminum of varied purity (Table 1), single-crystal silicon, and (Al + 2.5% Sc) alloying additive with a total content of impurities of 0.13% (0.017% Fe, 0.11% Si, 7×10^{-4}% Cu, and 3.7×10^{-3}% Ti).

Table 1. Content of impurities in aluminum of various brands

Brand	Total content of impurities, wt %	Content of indicated impurity, wt %				
		Fe	Cu	Si	Zn	Ti
A6NO	1×10^{-4}	1×10^{-5}	5×10^{-4}	1×10^{-4}	1×10^{-6}	–
A995	5×10^{-4}	1.5×10^{-3}	1×10^{-3}	1.5×10^{-3}	1×10^{-3}	1×10^{-3}
A6	0.4	0.25	0.03	0.20	0.06	0.03

1070-4272/04/7706-0925 © 2004 MAIK "Nauka/Interperiodica"

Table 2. Corrosion-electrochemical parameters of aluminum of varied purity in a NaCl solution

Al brand	c_{NaCl}, %	$-E_{fr.cor}$	$-E_{pt}$	$-E_{rp}$	$-E_{cor}$	ΔE_{pr}	Corrosion rate	
		V					A m^{-2}	g m^{-2} h^{-1}
A6 (99.6% Al)	3	0.730	0.625	0.700	0.760	0.105	0.024	8.04×10^{-3}
A995 (99.9995% Al)	3	0.950	0.680	0.750	0.960	0.270	0.003	1.01×10^{-3}
	0.3	0.850	0.620	0.680	1.120	0.230	0.006	2.01×10^{-3}
	0.03	0.760	0.540	0.600	1.160	0.220	0.009	3.01×10^{-3}
A6NO (99.9999% Al)	3	0.955	0.740	–	1.180	0.215	0.00048	1.65×10^{-4}

The content of scandium in AK1 alloy was 0.005, 0.05, and 0.1 wt %. AK1 and aluminum–scandium alloys were obtained in an SNV vacuum resistance furnace in graphite crucibles. The alloy was alloyed with the alloying additive in SShOL open shaft laboratory furnaces. The resulting alloys and aluminum were cast in graphite molds to obtain cylindrical rods 8–10 mm in diameter and 80–100 mm long. The lateral surfaces of these rods were covered with a lacquer and the working edge was ground and polished with fine emery paper, washed with distilled water and ethanol, and, on being dried in a desiccator, used as the working electrode.

The study was carried out with a PI-50-1.1 potentiostat and LKD-4-002 recorder in a 3% NaCl solution. Some experiments were performed in 0.3 and 0.03% NaCl solutions. A silver chloride electrode served as reference, and platinum, as an auxiliary electrode. The potential sweep rate was 1 mV s^{-1}.

The electrodes were potentiodynamically anodically polarized from the stationary potential till a steep rise in current (to a constant value of 2 A) and then in the opposite direction to a potential of –1.5…–1.6 V, at which the oxide film is reduced. Then the samples were again polarized in the positive direction to the pitting potential. The thus obtained potentiodynamic curves were used to determine the basic electrochemical characteristics of the alloys: corrosion potential E_{cor}, corrosion current i_{cor}, and pitting (E_{pt}) and repassivation (E_{rp}) potentials.

The value of E_{rp} was found graphically as the potential at which a first inflection is observed in the back run of the anodic curve, or as the potential at which the forward and back runs of the anodic polarization curve intersect [7]. The interval of potentials E_{pas} of the passive region was determined as the difference between the potential at which passivation begins (after cathodic polarization) and the pitting potential. The corrosion current, the main electrochemical characteristic of the corrosion process, was calculated from the cathodic curve with account of the Tafel constant b_c = 0.12 V, because the pitting corrosion of aluminum and its alloys in neutral media is governed by the cathodic reaction of oxygen ionization. The rate of corrosion was found from the corrosion current by the formula

$$K = i_{cor} K^1,$$

where K^1 = 0.335 g A^{-1} h^{-1} for aluminum.

The results of a corrosion-electrochemical study of aluminum of varied purity are summarized in Table 2. The influence exerted by chloride ions on the corrosion rate was studied for the example of aluminum of A995 brand. It can be seen that the corrosion rate grows as the dilution of the NaCl solution becomes higher. The pitting and repassivation potentials are shifted to more positive values. The free corrosion potential $E_{fr.cor}$ is also shifted in the positive direction with dilution of the electrolyte. In this case, the corrosion potential of the activated electrode is shifted to more negative values. All the above-mentioned changes in the electrochemical parameters of aluminum in a NaCl solutions of various concentrations point to different dynamics of formation of a protective oxide film.

A study of the behavior of aluminum of varied purity in a 3% NaCl solution demonstrated the following. Such electrochemical parameters as E_{pt}, E_{rp}, and E_{cor} depend on the purity of the metal rather strongly, with their values widely varying (e.g., E_{pt} varies from –0.625 for aluminum of A6 brand to –0.740 for A6NO, and E_{cor}, from –0.760 to –1.180 V, respectively) and can be used to roughly estimate the purity of the metal. The free corrosion potential was the least sensitive to changes in metal purity. Of primary importance in corrosion of aluminum is, irrespective of the purity of the metal, the structure and

state of the initial surface oxide film, and it is this film that determines the further behavior of the metal.

As is known [8], the difference between the pitting potential and the free corrosion potential of the metal (pitting-resistance base ΔE_{pr}) is used as a comparative criterion of its susceptibility to pitting corrosion in a given medium. If the experimental data obtained are analyzed with regard to this parameter, it can be seen that the pitting-resistance base ΔE_{pr} grows to the greatest extent on passing from aluminum of A6 brand to A995, whereas further increase in metal purity to A6NO has virtually no effect on the E_{pr}. The corrosion rate of aluminum in a neutral medium containing chloride ions strongly depends on the purity of the metal. For example, on passing from technical-grade aluminum to special-purity aluminum, the corrosion current decreases by approximately a factor of 200 (from 0.024 to 0.00048 A m^{-2}), and on passing from aluminum of A995 brand to A6, the corrosion rate increases 8-fold. This is in an agreement with the data of [1], where it was shown that the corrosion rate in a 5% HCl solution increases by a factor of 3–15 in the above case. Analysis of the impurity composition of aluminum and the available published data indicates that the corrosion rate is strongly affected by such impurities as iron and copper, and to a lesser extent, by silicon.

According to [2], the passivation oxide formed on aluminum in neutral media has a low electrical conductivity. It hinders virtually completely not only the anodic reaction of metal dissolution, but also the conjugated cathodic reduction of oxygen dissolved in the electrolyte. The conductivity of oxide films formed on technical-grade aluminum and its alloys is higher. This accounts for the pronounced increase in the rate of oxygen reduction and, consequently, that of corrosion of technical-grade aluminum, too, compared with its high- and special-purity brands. In neutral solutions, oxide films formed on special-purity aluminum exhibit strongly protective properties and the corrosion occurs uniformly, at a minimum rate, and mainly at separate defects of the oxide film. In technical-grade aluminum, in which the total impurities (especially iron and silicon) amount to 1.0–1.5%, and the impurities are mainly contained in the form of anodic inclusions of intermetallic compounds, the corrosion occurs by the pitting mechanism and the rate of corrosion in a 3% NaCl solution occasionally reaches catastrophic values.

Thus, one of efficient methods to improve the corrosion resistance of aluminum is to raise its purity (which primarily refers to more electropositive impurities).

Table 3. Variation of the free-corrosion potential of A6NO aluminum and AK1 alloy alloyed with scandium with time of keeping in a 3% NaCl solution

τ, min	$-E_{fr.cor}$, V				
	A6NO	AK1 + Sc, wt %			
		0	0.005	0.05	0.1
0.15	1.360	1.145	0.920	0.900	0.890
0.25	1.320	1.135	0.905	0.890	0.885
0.5	1.285	1.130	0.895	0.880	0.870
0.75	1.245	1.125	0.885	0.870	0.865
1	1.235	1.115	0.880	0.860	0.850
2	1.210	1.095	0.870	0.850	0.845
3	1.195	1.080	0.865	0.845	0.840
4	1.180	1.060	0.860	0.840	0.840
5	1.160	1.040	0.855	0.840	0.830
10	1.125	1.025	0.850	0.825	0.820
15	1.095	1.005	0.840	0.815	0.800
20	1.050	0.985	0.840	0.800	0.785
30	1.015	0.975	0.835	0.785	0.775
40	0.975	0.950	0.835	0.780	0.765
50	0.960	0.940	0.830	0.775	0.765
60	0.955	0.935	0.830	0.775	0.765

The results of a study of AK1 alloy alloyed with scandium are presented in Tables 3, 4. The dynamics of variation of the free-corrosion potential with the time of keeping in a 3% NaCl solution characterizes the rate of formation of a protective oxide layer on the alloy surface. For example, for special-purity aluminum and scandium-free AK1 alloy, $E_{fr.cor}$ stabilizes in 1 h, whereas for alloys with scandium, this process is complete in 30–40 min, which indicates that a protective oxide layer is formed on alloys with scandium faster than on the scandium-free alloy. With special-purity aluminum, AK1 alloy, and alloys with scandium, the free-corrosion potential is shifted to more positive values when the time of keeping increases. The most positive potential (–0.765 V) is observed for AK1 alloy with 0.1% Sc. Addition of scandium increases, irrespective of the amount of scandium, the free-corrosion potential. In this case, the shift of the potential to more positive values is 160–190 mV as compared with the scandium-free aluminum and AK1 alloy. According to how the potential varies with time, the protective oxide film is formed on the electrode surface at the highest rate during the first 3–5 min after the electrode is submerged in the solution (Table 3).

Table 4. Corrosion and electrochemical parameters of A6NO aluminum and AK1 alloy with scandium in a 3% NaCl solution

Brand	Sc, wt %	$-E_{fr.cor}$	$-E_{cor}$	$-E_{pt}$	ΔE_{pas}	i_{cor}, A m^{-2}	$K \times 10^{-4}$, g m^{-2} h^{-1}
		V					
A6N0	–	0.955	1.180	0.740	0.440	0.00048	1.61
AK1	–	0.935	1.170	0.750	0.420	0.00060	2.0
AK1	0.005	0.830	1.160	0.680	0.480	0.00036	1.21
AK1	0.05	0.775	1.150	0.660	0.490	0.00033	1.11
AK1	0.10	0.765	1.080	0.650	0.330	0.00029	0.97

The corrosion and electrochemical characteristics of the alloys studied, which are listed in Table 4, indicate that alloying of special-purity aluminum with silicon and of AK1 alloy with scandium shifts the free-corrosion, pitting, and corrosion potentials in the positive direction. The free-corrosion potentials of all the alloys studied lie in the passive region, i.e., between the corrosion and pitting potentials. Alloying of aluminum with silicon somewhat narrows the passivation region ΔE_{pas} (from 440 to 420 mV), whereas introduction of scandium into AK1 alloy, especially that in an amount of 0.005–0.05%, markedly expands it (from 420 to 490 mV) (Table 4). On the whole, ternary alloys surpass the initial AK1 alloy both in electrochemical characteristics and in corrosion resistance. For example, alloys with 0.05 and 0.1% scandium surpass the initial, scandium-free AK1 alloy in corrosion resistance by a factor of 2.

The mechanism of corrosion of pure aluminum in neutral media is described by the equations [2]

$$Al + 3OH^- = Al(OH)_3 + 3e, \quad (1)$$

$$Al(OH)_3 + OH^- = Al(OH)_4^-. \quad (2)$$

The process is limited by the rate of supply of OH^- ions to the electrode surface. The role of a depolarizer in aerated neutral solutions is played by oxygen. Its reduction at the metal–solution interface proceeds in accordance with the equation

$$O_2 + 2H_2O + 4e = 4OH^-. \quad (3)$$

The process is limited by diffusion of oxygen dissolved in the electrolyte to the electrode, which, in the end, determines the corrosion rate of the metal. Hydrated oxide of general formula $Al_2O_3 \cdot nH_2O$ is deposited onto the surface as an intermediate formed in the interaction of the metal with OH^- ions. Various modifications of aluminum oxide and hydroxide are well soluble in alkaline and acid media, being virtually insoluble in neutral solutions. For this reason, the application domain of aluminum and its alloys in liquid media covers only nearly neutral solutions. In solutions of this kind, oxide films on aluminum exhibit good protective properties, and uniform corrosion of aluminum and its alloys is, as rule, weak and proceeds at separate defects of the oxide film [2]. The dissolution mechanism of AK1 alloy alloyed with scandium can be understood as follows [6]. When the alloys are brought in contact with the solution, scandium, being an electrochemically active component [4], is in part selectively dissolved from the solid solution and from finely dispersed particles of the intermetallic compound Al_3Sc, which leads to an increase in the vacancy concentration in the surface layer, and in part reacts with oxygen to give Sc_2O_3 accumulating on the surface. The thermodynamic activity of aluminum increases in the defective surface layer, which favors formation of a dense and less defective layer of aluminum oxyhydroxides with good protective properties [reactions (1), (2)]. The oxide Sc_2O_3 is accumulated in the upper part of this layer, whose density exceeds that of Al_2O_3 [4]. The corrosion potential of an alloy coated with a dense, only slightly defective layer of aluminum oxyhydroxides and with scandium oxide increases, whereas the reduction rate of the depolarizer and, accordingly, the corrosion rate of the scandium-containing alloy decrease. Sc_2O_3, which is insoluble in aqueous solutions and forms no mixed oxides with aluminum because of the lattice mismatch, accumulates on the surface and blocks it mechanically, thereby hindering both the dissolution of the alloy in anodic polarization and the pitting formation.

Thus, the studies performed resulted in that an alloying element was chosen, whose small additives can substantially improve the corrosion resistance

of AK1 alloy. The corrosion resistance of the alloy developed exceeds in corrosion resistance special-purity aluminum presently used as the main material for current leads in integrated circuits by nearly a factor of 2.

CONCLUSIONS

(1) It is shown that passing from technical-grade to special-purity aluminum diminishes the corrosion rate by approximately a factor of 200.

(2) Addition of scandium to AK1 alloy improves its corrosion resistance by nearly a factor of 2.

REFERENCES

1. Belyaev, A.I., Bochvar, O.S., Buinov, N.N., *et al.*, *Metallovedenie alyuminiya i ego splavov: Spravochnik* (Physical Metallurgy of Aluminum and Its Alloys: Reference Book), Moscow: Metallurgiya, 1983.
2. Pauling, L. C., *General Chemistry*, San Francisco: Freeman, 1954.
3. *Kratkii spravochnik fiziko-khimicheskikh velichin* (Concise Reference Book of Physicochemical Quantities), Ravdel', A.A. and Ponomareva, A.M., Eds., Leningrad: Khimiya, 1983.
4. Ganiev, I.N., Yunusov, I., and Krasnoyarskii, V.V., *Zh. Prikl. Khim.*, 1987, vol. 60, no. 6, pp. 190–195.
5. Vyazovkina, N.V., *Zashch. Met.*, 1999, vol. 35, no. 5, pp. 493–499.
6. Karimova, T .M., Ganiev, I.N., and Krasnoyarskii, V.V., *Zh. Prikl. Khim.*, 1988, vol. 61, no. 7, pp. 51–54.
7. Kaesche, H., *Die Korrosion der Metalle. Physikalisch-chemische Prinzipien und aktuelle Probleme*, Berlin: Springer, 1979.
8. Barkov, A.A., *Zashch. Met.*, 1999, vol. 35, no. 5, pp. 463–467.

Russian Journal of Applied Chemistry, Vol. 77, No. 6, 2004, pp. 930–933. Translated from Zhurnal Prikladnoi Khimii, Vol. 77, No. 6, 2004, pp. 944–947.

APPLIED ELECTROCHEMISTRY AND CORROSION PROTECTION OF METALS

Improvement of the Corrosion Resistance of Compressor Blades with Ion-Plasma-Deposited Titanium Nitride Coatings

D. A. Myshlyaev, I. N. Tsareva, E. A. Fedorova, and E. A. Motova

Blagonravov Institute of Engineering Science, Nizhni Novgorod Branch, Russian Academy of Sciences, Nizhni Novgorod, Russia

Received December 10, 2002; in final form, January 2004

Abstract—The effect of various technological procedures for reconditioning with the use of ion-plasma-deposited titanium nitride coatings on the resistance of steel compressor blades to pitting corrosion was studied.

The main type of surface damage to compressor blades of gas-turbine engines for gas-pumping units and aircraft is the erosion- and corrosion-related wear. The problem of improving the corrosion resistance of the working surface of blades is presently solved by using high-alloy steels and titanium alloys as the substrate material and by depositing various protective coatings. In this case, a coating must possess, together with a high corrosion and erosion resistance, also a high resistance to cyclic thermomechanical loads, sufficient plasticity and crack resistance, and good adhesion to the substrate. Promising in this regard are titanium nitride coatings deposited by the ion-plasma technique.

The present study is concerned with the corrosion properties of these coatings. The aim of the investigations of applied nature was to tackle with a concrete problem, i.e., to make longer the total service life of blades of a Nuovo Pignone GTK25I axial-flow compressor, which had exhausted their original durability (~60 000 h) and were subjected to reconditioning by ion-plasma deposition of titanium nitride coatings.

In the course of their operation, steel compressor blades are subjected to a strong attack by air flow at elevated temperatures (up to 350°C). The presence of noxious impurities in the industrial atmosphere, and primarily that of activating chloride ions, leads to nonuniform corrosion [1]. In the initial stage, pinpoint corrosion is observed, and semispherical pittings of depth 50–150 μm with deposits of iron oxides, from which pits are later formed, appear on the working surface of blades. The action of varying thermal and mechanical stresses leads to the formation of corrosion-fatigue cracks. A physicochemical modeling of the corrosion process, which was carried out on 12Kh13 steel samples (in a 10% solution of $FeCl_3$), using the method described in [2], established that corrosion occurs by the pitting mechanism and made it possible to reproduce the patterns of corrosion damage in different stages of the corrosion process [1].

EXPERIMENTAL

In the reconditioning cycle, the following procedures were employed: mechanical treatment (MT), spark-discharge polishing (SDP), reconditioning thermal treatment (TT) at 700°C for 2 h, deposition of ion-plasma TiN coatings by the method of condensation with ion bombardment on a VU-2MBS installation at a base voltage U = 180 V, arc current I = 160 A and a pressure P of the reaction gas in the chamber varied within the range 0.04–0.1 Pa.

The corrosion resistance of materials was determined electrochemically from their resistance to pitting corrosion in accordance with GOST (State Standard) 9.912–89 [3]. The experiments were performed with a P 5848 potentiostat in a 0.5 M aqueous solution of NaCl by measuring cyclic potentiodynamic curves at a potential sweep rate of 0.4 mV s^{-1}, with the pitting-resistance parameters determined after that: free-corrosion potential E_{cor}, pitting potential E_{pt}, repassivation potential E_{rep}, and additional bases of pitting resistance, ΔE_{pt} and ΔE_{rep}. The tests were performed with samples cut directly from the working

1070-4272/04/7706-0930 © 2004 MAIK "Nauka/Interperiodica"

Table 1. Parameters of pitting resistance of 12Kh13 steel in the initial state and after various technological procedures for reconditioning treatment

Type of treatment	E_{cor}	E_{pt}	E_{rep}	ΔE_{pt}	ΔE_{rep}
	V				
Initial state					
MT	–0.21	–0.096	–0.348	0.114	–0.138
MT + SDP	–0.119	0.043	–0.313	0.163	–0.193
After operation					
MT + SDP	–0.162	0.003	–0.324	0.165	–0.162
MT + SDP + TT + SDP	–0.150	0.030	–0.146	0.180	0.004
MT + SDP + TT + SDP + TiN coating at P, Pa:					
0.04	–0.010	0.069	0.010	0.070	0.011
0.06	–0.138	0.025	–0.090	0.163	0.152
0.08	–0.076	0.180	–0.067	0.256	0.010
0.1	–0.360	0.533	–0.300	0.893	0.060

blades of the GTK-25I axial-flow compressor in their initial state (before putting into operation) and after exploitation for 60 000 h.

In the initial state, after a mechanical polishing of the blade surface to a roughness $R_a < 63$ μm, the samples exhibited stable negative values of the potentials of pitting (E_{pt}) and repassivation (E_{rep}) (Table 1).

After treatment of the blade surface by spark-discharge polishing, the pitting and repassivation potentials shifted in the positive direction (Fig. 1, curve *2*) and the pitting-resistance base ΔE_{pt} of the material increased both in the initial and in the post-operation states (Table 1). It is known [3] that, when the microprofile of the surface is smoothed and the surface heterogeneity is diminished by fine polishing, the susceptibility of stainless steel to pitting corrosion becomes lower. Therefore, the improvement of the pitting-resistance parameters after spark-discharge polishing is mainly due to better surface uniformity of the samples because of the decrease in their surface roughness (from 0.55 to 0.44 μm for R_a).

The reconditioning thermal treatment used in the technological cycle to relieve the accumulated microstresses [4, 5] leads to a further improvement of all the pitting-resistance parameters (Table 1). The pitting-resistance base ΔE_{rep} increases and becomes positive. It may be assumed that, after the formation of stable pittings, the repassivation state is reached faster. The improvement of the corrosion resistance is probably due to a more uniform distribution of the carbide phase under the action of TT and to the resulting increase in the structural homogeneity. Photographs of the microstructure of blades before and after exploitation (Figs. 2a, 2b) and after reconditioning thermal treatment (Fig. 2c) confirm this assumption. Moreover, thermal treatment may lead to leveling of the concentrations of the alloying elements and to the resulting decrease in the number of chromium-deficient zones.

It is known that the properties of ion-plasma-deposited coatings are determined by a set of technological parameters (arc current, base voltage, substrate temperature, etc.), the main of which is the partial pres-

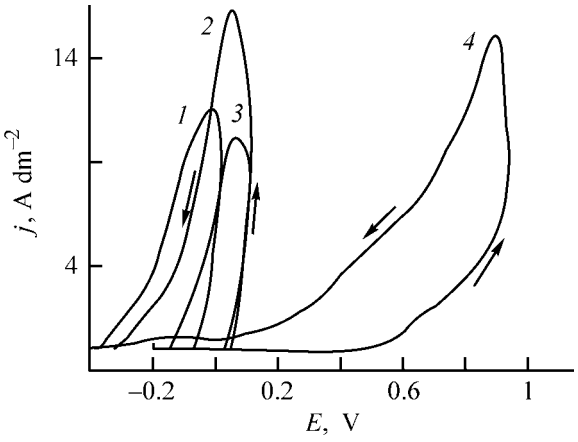

Fig. 1. Anodic potentiodynamic curves obtained on 12Kh13 steel on applying various technological procedures for reconditioning treatment of compressor blades. 293 K, 0.5 NaCl solution, V_{sw} = 0.4 mV s^{-1}. (j) Current density and (E) potential; the same for Fig. 3. (*1*) Initial state (MT); state after operation: (*2*) MT + SDP, (*3*) MT + SDP + TT + MT, and (*4*) MT + SDP + TT + SDP + TiN coating.

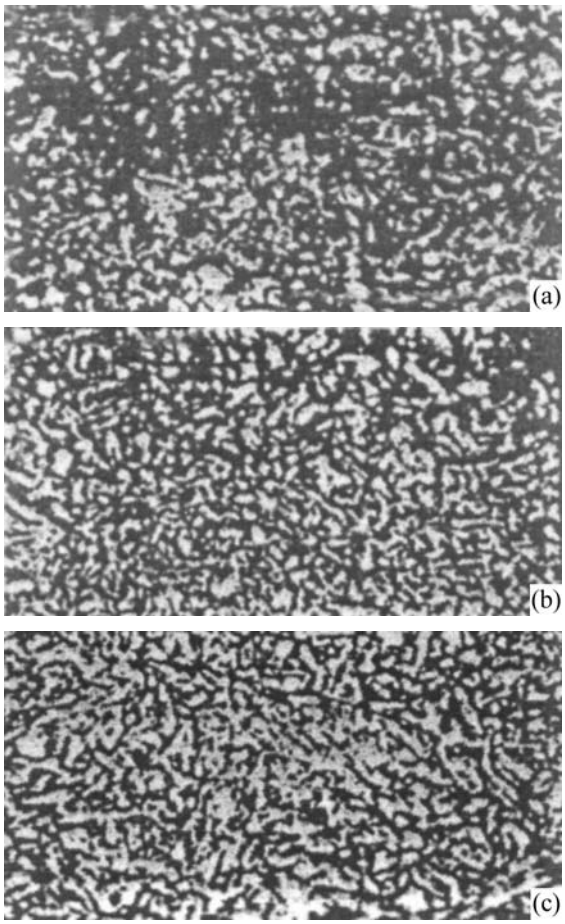

Fig. 2. Surface microstructure of 12Kh13 steel (a) in the initial state, (b) after exploitation, and (c) after reconditioning thermal treatment (700°C, 2h).

sure of the reaction gas in the chamber. In order to optimize the mode of formation of the anticorrosion coating, the properties of titanium nitride obtained at different gas pressures were studied. The phase composition and substructural parameters (microstrain ε, subgrain block size *D*) of TiN were determined by means of X-ray diffraction analysis ("grazing beam" method, probed depth of about 1 μm, Cu_{K_α} radiation). The mechanical properties of the coatings were studied by measuring the microhardness H_μ at a variable load on the indenter. The experimental values of microhardness of the 12Kh13 steel + TiN compositions were used to find the hardness of titanium nitride by a method taking into account the influence of the substrate [6]. On the basis of the resulting values of hardness, the plasticity coefficient δ_H of the coatings was calculated [7]. Table 2 lists the substructural parameters and mechanical characteristics of titanium nitride coatings obtained at different gas pressures in the chamber.

Table 2. Substructural parameters and mechanical characteristics of titanium nitride coatings obtained at different partial pressures P of the reaction gas in the chamber

P, Pa	ε ± 0.00001	*D* ± 2, nm	H_μ ± 0.3, GPa	δ_H
0.04	0.00034	27	16.6	0.67
0.06	0.00008	27	8.2	0.84
0.08	0.00002	28	9.6	0.81
0.10	0.00002	25	8.4	0.83

It was established that the coatings deposited in the pressure range under study have a phase composition δ-TiN + α-Ti. As the gas pressure decreases, an axial texture of the (001) type tends to appear. In this case, the subgrain block size remains virtually unchanged with pressure and equal to 25–28 nm (Table 2). At a lower pressure of the reaction gas, the coatings formed are characterized by a high level of microstrain in TiN grains and, as a consequence, have a higher microhardness (Table 2). In this case, the coatings show no microbrittleness under indentation and have a high plasticity coefficient δ_H = 0.81–0.84 in the pressure range 0.06–0.1 Pa. This favorably distinguishes these coatings from electroplated protective coatings composed of hard chromium (δ_H = 0.77 at the same hardness), which tend to undergo cracking under alternating-sign load. Tests for abrasive wear (with quartz sand used as eroding substance at a particle velocity of 200 m s^{-1}) demonstrated that depositing a titanium nitride coating improves the erosion resistance of the steel surface of compressor blades by 25%, on the average.

As regards the anticorrosion protection, the optimal pressure for depositing a coating is 0.1 Pa. Ion-plasma-deposition of a TiN coating onto the surface of steel samples in this mode leads to a pronounced increase in the pitting potential E_{pt} and in the pitting-resistance bases ΔE_{pt} and ΔE_{rep} (Table 1). Titanium nitride deposited onto a steel substrate serves as a cathodic coating.

Thus, application of an integrated reconditioning technology with the use of ion-plasma TiN coatings leads to a pronounced increase in the corrosion resistance of the working surface of steel compressor blades. The reconditioning treatment leads to a stable increase in the pitting potential E_{pt} and in the pitting-resistance bases ΔE_{pt} and ΔE_{rep} (Table 1), even with respect to the values in the initial state of the material (before exploitation), and to a more pronounced hysteresis in the forward and reverse runs of the polarization curves (Fig. 1).

Additionally, comparative studies of the behavior of 12Kh18N10T stainless steel without a coating and with Ti and TiN coatings in a 5% HCl solution were carried out (Fig. 3). It can be seen that (i) the corrosion potentials of the systems constituted by steel and a Ti coating and by steel and TiN coating are shifted in the positive direction and (ii) the corrosion currents j_{cor} found by extrapolation of the Tafel portions to their intersection become lower. The most pronounced decrease in j_{cor} was observed on depositing a titanium nitride layer onto the surface of the samples (curve *3*), which reflects the higher corrosion resistance of this coating, compared with that composed of titanium [8].

To determine the corrosion resistance of optimized titanium nitride coatings under conditions close to those in which aircraft compressor blades are working, tests were carried out in a salt-spray chamber (using the ISO 9227 procedure: 35°C, NaCl solution with a concentration of 47 g l^{-1}) with finished articles made of EP 866 alloy (15Kh16K5N2MVFAB). It was found that no pitting corrosion developed during 2060 h under an undamaged TiN coating. At the same time, blades without a coating showed corrosion defects already after 94 h.

Thus, the results of climatic tests also demonstrated the effectiveness of anticorrosion ion-plasma-deposited titanium nitride coatings.

The reconditioning technology with the use of ion-plasma-deposited TiN coatings, developed by the authors, was introduced into practice at the Volgotransgaz Ltd. in order to prolong the service life of compressor blades of a GTK-25I gas-pumping unit. The reconditioned blades have worked for more than 20000 h and are still in service now.

CONCLUSIONS

(1) A technology for reconditioning of steel compressor blades of gas-pumping units was developed. The application of this technology improves the corrosion resistance of the working surface of the blades.

(2) It was established that, of all the procedures for reconditioning treatment, the strongest positive influence, with the most pronounced increase in the resistance to pitting corrosion of 12Kh13 steel, is exerted by titanium nitride coatings obtained by the ion-plasma technique in certain modes.

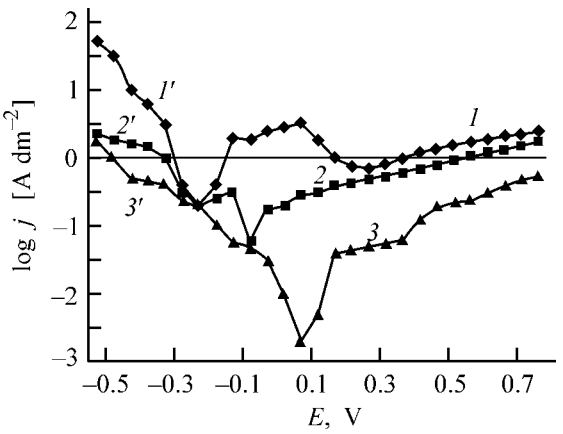

Fig. 3. (*1*–*3*) Anodic and (*1*′–*3*′) cathodic polarization curves obtained on 12Kh18N10T steel (*1*, *1*′) without a coating and with (*2*, *2*′) Ti and (*3*, *3*′) TiN coatings in a 5% HCl solution at 293 K.

(3) Titanium nitride coatings are recommended for anticorrosion protection of compressor blades in aircraft engines and gas-pumping units.

REFERENCES

1. Tsareva, I.N., Trenin, V.F., Sorokina, S.A., and Panchenko, A.V., *Fizicheskie tekhnologii v mashinovedenii: Sbornik nauchnykh trudov* (Physical Technologies in Engineering Science: Coll. of Sci. Works), Nizhni Novgorod, 2001, issue 2, pp. 92–98.
2. Sokol, I.Ya., *Struktura i korroziya metallov i splavov* (Structure and Corrosion of Metals and Alloys), Moscow: Metallurgiya, 1989.
3. *GOST* (State Standard) *9.912–89. Corrosion-Resistant Steels and Alloys*, Moscow: Izd. Standartov, 1990.
4. Tarasenko, Yu.P., Tsareva, I.N., and Trenin, V.F., *Gazoturbinn. Tekhnol., 2001, July–August*, 2001, pp. 40–42.
5. Tarasenko, Yu.P., Tsareva, I.N., Trenin, V.F., and Krivina, L.A., *Materialovedenie i vysokotemperaturnye tekhnologii: Sbornik nauchnykh trudov* (Materials Science and High-Temperature Techniques: Coll. Sci. Works), Nizhni Novgorod, 2000, issue 2, pp. 159–162.
6. Tsareva, I.N., Romanov, I.G., and Tarasenko, Yu.P., *Izv. Akad. Nauk, Ser. Fiz.*, 2002, vol. 66, no. 8, pp. 1223–1225.
7. Mil'man, Yu.V., Golanov, B.A., and Chugunova, S.I., *Kharakteristika plastichnosti, poluchaemaya pri izmerenii tverdosti* (Plasticity Coefficient Obtained in Hardness Measurements), Kiev: Naukova Dumka, 1992.
8. Tomashov, N.D. and Chernova, G.P., *Passivnost' i zashchita ot korrozii* (Passivity and Corrosion Protection), Moscow: Nauka, 1965.

Russian Journal of Applied Chemistry, Vol. 77, No. 6, 2004, pp. 934–937. Translated from Zhurnal Prikladnoi Khimii, Vol. 77, No. 6, 2004, pp. 948–951.

APPLIED ELECTROCHEMISTRY AND CORROSION PROTECTION OF METALS

Composition and Structure of Films Formed in Etching of Nickel in a $Ni(NO_3)_2$ Solution with $NiCl_2$ and $NaNO_2$ Additives

A. A. Bachaev, T. E. Kuzina, and L. A. Oshurina

Nizhni Novgorod State Technical University, Nizhni Novgorod, Russia

Received January 23, 2004

Abstract—The composition and structure of films formed in etching of nickel in a $Ni(NO_3)_2$ solution in the presence of Cl^- and NO_2^- ions was studied.

In fabrication of nickel oxide electrodes (NOE) on a metal-ceramic (MC) support, the impregnation in a solution of a nickel salt, mostly a $Ni(NO_3)_2$ solution, is the longest stage [1]. The impregnation time necessary for obtaining a required amount of the active substance in the pores is mainly determined by the rate of the electrochemical process in which nickel of the MC support is etched in the $Ni(NO_3)_2$ solution [2], and is associated with the hindrance to the cathodic process [3]. In dissolution of nickel, a film of the products is formed on its surface [4, 5], which, shielding the surface, impedes the supply of the oxidant. This makes the etching rate lower, and the impregnation time necessary for producing the active substance, longer.

In [5], the composition of the basic salts formed in $Ni(NO_3)_2$ solution at 60°C under an external cathodic polarization was determined to be $7.2Ni(OH)_2 \cdot Ni(NO_3)_2$. The impregnation of MC supports with a $Ni(NO_3)_2$ solution without external polarization results in the formation of basic salts of the type $Ni(OH)NO_3$ [4], which corresponds to the composition $Ni(OH)_2 \cdot Ni(NO_3)_2$.

In [3, 6], it was recommended to add $NiCl_2$ to a $Ni(NO_3)_2$ solution, and $NaNO_2$ to a $NiCl_2$ solution in order to raise the rate of nickel etching, but the composition of the films formed was not analyzed.

In this study, we determined the structure and composition of films formed by products of nickel etching in a $Ni(NO_3)_2$ solution with $NiCl_2$ and $NaNO_2$ additives.

EXPERIMENTAL

With account of the electrochemical nature of the process of nickel etching, its characteristics were determined in a model galvanic cell with relatively large (S = 14 cm^2) platinum cathode and anode made of nickel foil. The cathode and an anode compartments were separated by a diaphragm. To localize the cathodic process on Pt to a greater extent, a solution containing an oxidant (NO_3^-, NO_2^- ions) was poured into the cathode compartment, and a $NiSO_4$ ($c_{Ni^{2+}}$ = 200 g l^{-1}) or $NiCl_2$ solution ($c_{Ni^{2+}}$ = 320 g l^{-1}), into the anode compartment. The solutions were equal with respect to the ionic strength. It was assumed that the cathodic process is mainly localized on platinum, and the anodic process, on nickel. The results obtained on a model short-circuited galvanic cell Pt|solution|Ni are mainly of qualitative nature. This is because the cathodic process partly occurs on nickel, and, moreover, platinum can have some other electrocatalytic effect on the reduction of the oxidant, compared with nickel. The adequacy of the Pt–Ni model system suggested in impregnating solutions was confirmed by comparing the nickel etching process with that in a model system Ni | solution | Ni. The study was performed at 80°C.

A film of sparingly soluble products intended for X-ray diffraction analysis was formed on platinum. For this purpose, platinum electrode was short-circuited with a nickel electrode and kept in a solution for 1 h and then in air till the crystallization of the products on the electrode surface was complete. The X-ray diffraction patterns were measured on a sample with crystals of salts formed on its surface

1070-4272/04/7706-0934 © 2004 MAIK "Nauka/Interperiodica"

and on the same sample upon dissolution of the products in distilled water to give a monomolecular layer [7].

The X-ray diffraction analysis was performed on a DRON-2 diffractometer (Ag-radiation, λ_α = 0.58 Å, U = 32 kV, I_a = 0.8 mA, entrance and exit slits 1.8 mm). The composition was determined qualitatively by comparng the interplanar spacings of the substance studied and the substances whose presence in the film formed is expected [7]. The amount of the solid phase was judged from the relative intensities I of lines in an X-ray diffraction pattern. The lattice constants were determined by the procedure described in [2].

As reference served the X-ray diffraction pattern of the film formed on platinum in a $Ni(NO_3)_2$ solution without additives.

Only reflections corresponding to the $Ni(NO_3)_2 \cdot 6H_2O \cdot Ni(OH)_2$ complex (Table 1) are present in the diffraction pattern, with the content of $Ni(OH)_2$ in the compound exceeding that of $Ni(NO_3)_2 \cdot 6H_2O$ [7]. The film has a cubic crystal structure. Qualitatively, the composition of the film is similar to that of basic salts formed in a $Ni(NO_3)_2$ solution under the external cathodic polarization [5]. Basic salts are commonly unstable, their chemical composition and structure may change in recovery from solution and in washing, drying, and storage. In addition, the polarization potential, the density and amount of electricity passed in operation of a Pt–Ni macrocouple in a $Ni(NO_3)_2$ solution, differed from the data of [4], and this circumstance could be responsible for a certain discrepancy between the composition of the basic nickel(II) compounds and the data reported in [4].

It should be noted that the interplanar spacings for virtually all the compounds differ from the values for individual substances [7], which indicates that complexation is probable. The presence of the Ni and Pt reflections with a changed interplanar spacing shows that there occurs chemisorption of nickel ions on the platinum surface [8].

It is known [9] that Cl^- ions prevent formation of a passivation film on nickel anodes in nickel plating. The introduction of $NiCl_2$ into the $Ni(NO_3)_2$ solution did not affect the cubic structure of the film formed on platinum.

The X-ray diffraction analysis showed that a film of composition $Ni(NO_3)_2 \cdot NiCl_2 \cdot Ni(OH)_2 \cdot 6H_2O$ is formed on the surface of platinum kept under current in a mixture of $Ni(NO_3)_2$ and $NiCl_2$ solutions (volume ratio 1 : 1) (Table 2). The intensities of reflection

Table 1. Results of an X-ray diffraction analysis of a film formed on Pt in a $Ni(NO_3)_2$ solution ($c_{Ni^{2+}}$ = 320 g l^{-1})

Reflection no.	θ, deg	d/n, Å	Composition	I
1	6.3	2.96	$Ni(NO_3)_2 \cdot 6H_2O$	29
2	7.05	2.64	$Ni(NO_3)_2 \cdot 6H_2O \cdot Ni(OH)_2$	100
3	8.17	2.26	$Ni(NO_3)_2 \cdot 6H_2O \cdot Ni(OH)_2$	57.6
4	10.3	1.8	$Ni(NO_3)_2 \cdot 6H_2O$, Ni	29
5	11.62	1.6	$Ni(NO_3)_2 \cdot 6H_2O \cdot Ni(OH)_2$	50
6	12.02	1.55	$Ni(OH)_2$, Ni	26.3
7	13.72	1.35	Ni–Pt	71
8	14.2	1.31	Ni–Pt	18
9	16.1	1.16	Pt	16
10	16.5	1.13	Pt	23.7
11	18.12	1.03	Ni–Pt	23.6
12	18.65	1.01	Pt–Ni	31.5
13	20.47	0.92	Pt–Ni	26.3
14	21.75	0.86	Pt–Ni	21
15	24.95	0.76	Pt–Ni	23.6

Table 2. Results of an X-ray diffraction analysis of a film formed on Pt in a $Ni(NO_3)_2$ solution containing $NiCl_2$ ($c_{Ni^{2+}}$ = 193 g l^{-1})

Reflection no.	θ, deg	d/n, Å	Composition	I
1	6.25	2.96	$Ni(NO_3)_2 \cdot NiCl_2 \cdot 6H_2O$	16
2	7.12	2.61	$Ni(NO_3)_2 \cdot NiCl_2 \cdot Ni(OH)_2 \cdot 6H_2O$	100
3	8.12	2.28	$Ni(NO_3)_2 \cdot NiCl_2 \cdot Ni(OH)_2 \cdot 6H_2O$	53
4	10.25	1.81	$Ni(NO_3)_2 \cdot 6H_2O$, Ni	26.3
5	11.62	1.6	$Ni(NO_3)_2 \cdot NiCl_2 \cdot Ni(OH)_2 \cdot 6H_2O$	47
6	12.05	1.54	$NiCl_2 \cdot Ni(OH)_2 \cdot 6H_2O$	16
7	13.75	1.35	Ni–Pt	63
8	14.25	1.31	Ni–Pt	23.6
9	16.55	1.13	Pt	21
10	18.2	1.03	Ni–Pt	26.3
11	18.62	1.01	Pt–Ni	29
12	20.37	0.92	Pt–Ni	18
13	21.25	0.886	Pt–Ni	16
14	25.27	0.75	Pt–Ni	17

Table 3. Lattice constant *a* of a film formed on platinum in various solutions

Solution	*a*, Å	$(\eta \approx a^{-3}) \cdot 10$, Å [7]
$Ni(NO_3)_2$	5	8
$Ni(NO_3)_2$ containing:		
$NiCl_2$ (c_{Cl^-} = 193 g l^{-1})	5.6	5.7
$NaNO_2$		1.9

Table 4. Results of an X-ray diffraction analysis of a film formed on Pt in a $Ni(NO_3)_2$ solution containing 10 g l^{-1} $NaNO_2$

Reflection no.	θ, deg	*d*/*n*, Å	Composition	*I*
1	6.25	2.5	$Ni(NO_3)_2 \cdot 6H_2O \cdot$ β-NiOOH	28.3
2	7.1	2.28	$Ni(NO_3)_2 \cdot 6H_2O \cdot Ni(OH)_2 \cdot$ β-NiOOH	84
3	8.1	2	$NaNO_2$	41.5
4	10.25	1.55	$NaNO_2 \cdot Ni(OH)_2$	12.7
5	11.26	1.39	$NaNO_2$–Pt	56.5
6	12.1	1.33	Ni–Pt	25.2
7	13.25	1.22	Ni–Pt	47.1
8	16.5	0.98	Pt	12.7
9	18.1	0.9	Pt	22
10	18.5	0.88	Pt–Ni	22
11	20.5	0.8	Ni–Pt	23
12	21.9	0.75	Pt	16
13	23.9	0.69	Ni–Pt	12.7

nos. 2, 3, and 5 show that $Ni(OH)_2$ is also present in the film as a major component, but its crystal structure is changed. The intensities of virtually all the reflections in the X-ray diffraction pattern are lower than those for a film formed from a $Ni(NO_3)_2$ solution, which indicates that the amount of the solid phase is lower. The X-ray diffraction pattern of a film obtained from a mixture of $Ni(NO_3)_2$ and $NiCl_2$ solutions contains an additional reflection corresponding to the composition $NiCl_2 \cdot Ni(OH)_2 \cdot 6H_2O$.

The deposit formed in a $Ni(NO_3)_2$ solution containing a $NiCl_2$ additive has a larger lattice constant (Table 3), which indicates that its structure is less densely packed. The theoretically calculated density of a deposit formed in a mixture of solutions is lower by 40% than that of the deposit formed in a $Ni(NO_3)_2$ solution [7].

The results obtained made it possible to explain the fact that, after keeping a Pt–Ni short-circuited pair in a mixture of $Ni(NO_3)_2$ and $NiCl_2$ solutions, the current density in the system remained virtually unchanged and the etching process did not decay in time.

In [6], a method for MC NOE fabrication was suggested, which makes shorter the time necessary for impregnation of MC supports when a $NiCl_2$ solution with a $NaNO_2$ additive is used for impregnation.

Nitrite ions may undergo disproportionation at elevated temperatures in an acid medium [8], which may yield nitrogen(IV) oxide, a stronger oxidant than nitrite and nitrate ions [10]. This must, undoubtedly, change the structure and composition of a solid film also in a $Ni(NO_3)_2$ solution.

The introduction of $NaNO_2$ resulted in the appearance of reflections corresponding to a complex of Pt with $NaNO_2$ and to the $Ni(OH)_2 \cdot NaNO_2$ complex (Table 4). The film formed in a $Ni(NO_3)_2$ solution containing $NaNO_2$ has a composition $Ni(NO_3)_2 \cdot 6H_2O \cdot Ni(OH)_2 \cdot$ β-NiOOH and a cubic structure with a lattice constant of 8Å (Table 3). Nitrogen(IV) oxide can oxidize the components of the film ($E^0_{NiO_2/N_2}$ = 1.35, $E^0_{NO_2/Ni^{2+}}$ = 0.6–1 V, depending on the structure of higher oxides [2]). Therefore, reflections corresponding to β-NiOOH are present in the X-ray diffraction pattern (Table 4). The intensity of virtually all reflections decreases (Tables 1, 4), which points to a lower amount of the solid phase. The theoretically calculated density is four times lower than that of the deposit formed in a $Ni(NO_3)_2$ solution (Table 3), which is due to the less densely packed structure of the deposit formed in a $Ni(NO_3)_2$ solution with a $NaNO_2$ additive.

The film formed on platinum in a $Ni(NO_3)_2$ solution with a $NaNO_2$ additive is nonuniform across its thickness, which is indicated by the difference in the reflection intensities measured on a sample with salt crystals and that after their dissolution (Tables 4, 5). According to the reflection intensities (Tables 4, 5), the amount of $Ni(OH)_2 \cdot NaNO_2$ on the surface of platinum covered with a monomolecular solid layer is approximately twice that inside the film. This indicates that NO_2^- ions are consumed in the course of time in a $Ni(NO_3)_2$ solution with a $NaNO_2$ additive. The amount of nickel(III) oxide decreases across the thickness of the solid film, since the reflection intensity corresponding to β-NiOOH is higher by 30% on Pt covered with a monomolecular film, compared with Pt with salt crystals (Tables 4, 5). This shows that the oxidizing capacity of the solution de-

Table 5. Results of an X-ray diffraction analysis of a monomolecular layer on the film formed on Pt in $Ni(NO_3)_2$ solution containing 10 g l^{-1} $NaNO_2$

Reflection no.	θ, deg	d/n, Å	Composition	I	Reflection no.	θ, deg	d/n, Å	Composition	I
1	6.25	2.5	$Ni(NO_3)_2 \cdot 6H_2O \cdot \beta$-NiOOH	31.5	9	16	1.02	Ni–Pt	19
2	7.1	2.28	$Ni(NO_3)_2 \cdot 6H_2O \cdot Ni(OH)_2 \cdot \beta$-NiOOH	84	10	16.5	0.98	Pt	16
3	8.25	1.94	$NaNO_2$–Pt	62.75	11	18.1	0.9	Pt–Ni	22
4	10.4	1.55	$NaNO_2 \cdot Ni(OH)_2$	25.2	12	18.6	0.875	Pt	19
5	11.6	1.39	$NaNO_2$–Pt	59.6	13	20.5	0.8	Pt–Ni	19
6	12.15	1.32	Ni–Pt	12.7	14	21.9	0.75	Pt	19
7	12.75	1.27	Ni–Pt	15.8	15	23.9	0.69	Ni–Pt	11.5
8	13.7	1.18	Pt–Ni	75.2	16	25.25	0.65	Pt–Ni	12.7

creases with time (E_{NO_2/N_2} = 1.1 and 0.7 V before and after the solution is kept for 1 h, respectively).

The results of an X-ray diffraction analysis of the films formed in a $Ni(NO_3)_2$ solution with and without $NaNO_2$ suggest that the basic salts formed in etching of the metal undergo oxidation.

CONCLUSIONS

(1) The chemical composition and lattice constants of the films formed by etching products depend on the solution composition: Cl^- ions decrease the density of the deposit, the composition of the film is $Ni(NO_3)_2 \cdot NiCl_2 \cdot Ni(OH)_2 \cdot 6H_2O$ (cubic structure, lattice constant 5.6 Å); NO_2^- ions oxidize the components of a solid film to higher nickel oxides (oxidation state Ni^{3+}) and cause a decrease in the deposit density, the composition of the film is $Ni(NO_3)_2 \cdot 6H_2O \cdot Ni(OH)_2 \cdot \beta$-NiOOH (cubic structure, lattice constant 8 Å).

(2) The presence of a $NaNO_2$ additive in a $Ni(NO_3)_2$ solution makes solid films nonuniform across their thickness.

REFERENCES

1. Dasoyan, M.A., and Novoderezhkin, V.V., *Proizvodstvo elektricheskikh akkumulyatorov* (Manufacture of Electric Batteries), Moscow: Vysshaya Shkola, 1970.
2. Levinzon, L.M., Pozin, Yu.M., and Shtertser, N.I., *Tekhnologiya proizvodstva khimicheskikh istochnikov toka* (Manufacture of Chemical Power Cells), Moscow: Energoizdat, 1985.
3. Kuzina, T.E., and Bachaev, A.A., Abstracts of Papers, *V nauchno-tekhnicheskaya konferentsiya "Matematika i estestvoznanie"* (V Sci.-Techn. Conf. "Mathematics and Natural Sciences"), Nizhni Novgorod, 2003.
4. Pozin, Yu.M., and Shtertser, N.I., *Zh. Prikl. Khim.*, 1970, vol. 43, no. 7, pp. 1482–1486.
5. Pozin, Yu.M., Shtertser, N.I., and Grilikhes, N.E., *Sbornik rabot po KhIT* (Coll. of Works on Chemical Power Cells), Nikol'skii, V.A., Ed., Leningrad: Energiya, 1974, issue 9.
6. Pozin, Yu.M., *Zh. Prikl. Khim.*, 1982, vol. 55, no. 6, pp. 1367–1370.
7. Mirkin, L.I., *Spravochnik po rentgenostrukturnomu analizu polikristallov* (Handbook of X-Ray Diffraction Analysis of Polycrystals), Moscow: Fizmatgiz, 1961.
8. Ugai, Ya.A., *Obshchaya i neorganicheskaya khimiya* (General and Inorganic Chemistry), Moscow: Vysshaya Shkola, 2000.
9. Dasoyan, M.A., Pal'mskaya, I.Ya., and Sakharova, E.V., *Tekhnologiya elektrokhimicheskikh pokrytii* (Technology of Electroplating), Leningrad: Mashinostroenie, 1989.
10. Gur'yan, L.I., *Okislitel'no-vosstanovitel'nye reaktsii i potentsialy v analiticheskoi khimii* (Redox Reactions and Potentials in Analytical Chemistry), Moscow: Khimiya, 1989.

Russian Journal of Applied Chemistry, Vol. 77, No. 6, 2004, pp. 938–941. Translated from Zhurnal Prikladnoi Khimii, Vol. 77, No. 6, 2004, pp. 952–955.

ENVIRONMENTAL PROBLEMS OF CHEMISTRY AND TECHNOLOGY

Influence of Chlorination on the Composition of Partly Volatile Organic Contaminants of Water

M. Yu. Vozhdaeva, L. G. Tsypysheva, L. I. Kantor, and E. A. Kantor

Ufavodokanal Municipal Unitary Enterprise, Ufa, Bashkortostan, Russia
Ufa State Technical Petroleum University, Ufa, Bashkortostan, Russia

Received February 5, 2004

Abstract—The total content of carbon, chlorine, bromine, and oxygen in partly volatile organic impurities in potable water was determined by gas chromatography with atomic emission detection.

Disinfection of potable water with chlorine yields halogenated organic compounds, including those whose concentration in water is subject to hygienic regulations [1, 2]. In particular, chlorination of water containing natural humic compounds yields a large amount of the so-called volatile halohydrocarbons mostly composed of mixtures of chloro- and bromomethanes [3–5]. Halogenated organic compounds with higher molecular weights were studied less extensively. Nevertheless, it is known [6–8] that they can contain haloacetic acids, aldehydes, and aliphatic hydrocarbons. Supposedly, water contaminants of technologicalorigin can also be chlorinated [9, 10] to yield a broader spectrum of compounds. Thus, the mixtures of organic compounds in water from different water sources significantly differ, which makes identification of the chlorination products in each specific case a matter of current interest.

In this regard, much promise is offered by gas chromatography with atomic emission detection (AED) [11–13]. Although unsuitable for identification of all the compounds subjected to chromatographic analysis, this method yields information about the effect of chlorination from variation of the total elemental composition of the impurities.

In this study, we examined how the integrated indices of the elemental composition of partly volatile organic compounds (PVOCs) in water from various water sources are influenced by chlorination.

We studied water samples taken from two large water intakes in the city of Ufa, namely, the Northern open (NO) and Southern infiltration (SI) water intakes. The water source for the former intake is the Ufa river, and for the latter, water from wells situated on bank of the Ufa river.

EXPERIMENTAL

The impurities from the initial and chlorinated water were isolated by extraction with methylene chloride at pH 2, whereupon they were concentrated on a Kuderna-Danish apparatus and analyzed on an HP 6890 (HP G2350A AED) chromatograph (a 30 m × 0.25 mm column coated with 0.32 μm of DV-5; with the column heated at a rate of 20 deg min^{-1} from 35 to 60°C and at a rate of 6 deg min^{-1} from 60 to 280°C). This made it possible to determine the content in water of PVOCs with a molecular weight of up to 500, boiling away within 150–500°C. Using the chromatograms recorded at the carbon emission wavelength of 193 nm, we determined the total carbon content in the components eluted from the chromatographic column under the actual conditions, which is referred to as the organic carbon of technological origin (OCT) [14]. Based on the chromatograms recorded at 181, 178, 174, 479, and 478 nm, we estimated the total content of hydrogen H, phosphorus P, nitrogen N, oxygen O, chlorine Cl, and bromine Br in the PVOC components. Also, for all the samples we determined the total content of dissolved organic carbon (DOC) [15] characterizing the carbon content in organic compounds of primarily natural origin. Although not manifested in chromatograms recorded under the actual conditions, these com-

1070-4272/04/7706-0938 © 2004 MAIK "Nauka/Interperiodica"

Table 1. Annual average total content of the elements in PVOCs for the water from the water sources and for potable water

Element	NO				SI			
	water from the Ufa river		CWR*		well water		CWR*	
	mg dm^{-3}	%	mg dm^{-3}	%	mg dm^{-3}	%	mg dm^{-3}	%
C	0.006400	80.59	0.009400	22.26	0.004172	66.59	0.009900	44.28
H	0.000550	6.93	0.001700	4.03	0.001002	15.99	0.001600	7.16
Cl	0.000011	0.14	0.013400	31.73	0.000078	1.24	0.002500	11.18
Br	0.000002	0.03	0.015700	37.18	0.000021	0.33	0.003900	17.44
O	0.000880	11.08	0.001900	4.49	0.000573	9.15	0.003900	17.44
P	0.000011	0.14	0.000006	0.01	0.000006	0.09	0.000010	0.04
N	0.000005	0.06	–	–	0.000006	0.09	–	–
S	0.000080	1.00	0.000110	0.26	0.000379	6.04	0.000510	2.28
Σ	0.007941	100	0.042217	100	0.006265	100	0.022360	100
DOC	3.07		3.14		1.55		1.99	

* Clean water reservoir.

pounds are responsible for the formation of additional impurities in water being disinfected with chlorine.

Table 1 presents the previously determined annual average elemental composition of PVOCs for water samples from the Ufa river and SI wells.

Notably, the well water contains, on the whole, a smaller amount of organic substances from the group of interest. For example, the total content of impurities in the river water exceeds that in the well water by a factor of nearly 1.3. The PVOC components of the river water exhibit increased content, of OCT and oxygen while chlorine and bromine are virtually lacking in the PVOC components of the initial water.

The fact that the PVOC content in the well water is lower by a factor of ca. 1.3 than that in the river water is, evidently, due to removal of high-molecular-weight humic compounds (which can form side chlorination products) from the river water upon passing the filtration layers. This is indirectly evidenced by the fact that the DOC content in the well water is also smaller (by a factor of nearly 2) than that in the river water (Table 1).

The total PVOC content in the potable water originating from both water intakes tends to increase upon chlorination, namely, by factors of 5.3 and 3.6 for NO and SI, respectively. Along with a major increase in the content of chlorine and bromine in PVOCs, this is also accompanied by an increase in the content of carbon and oxygen by factors of 1.5, 2.4 and 2.2, 6.8, respectively (Table 1). Notably, bromine is the heaviest element in chlorinated water, and its relative content reaches 37% of the total concentration of the elements in the NO water.

Published data suggest that brominated organic compounds can originate both from inorganic bromides activated by water treatment with chlorine and from bromine impurities in the initial chlorine [8, 16, 17]. Also, a certain role is played by the differences in the process parameters of chlorination at NO and SI, namely, the contact time and number of chlorination runs (two runs at NO).

We carried out a comparative study of impurities in the initial water and in water chlorinated at the laboratory (Table 2). As initial water served that supplied from the river (NO) and that from the collecting reservoir of wells (SI). These experiments were carried out during a period of time when the river water was rather heavily contaminated, as evidenced by an enhanced DOC content of 4.8 mg dm^{-3}. We applied different chlorine doses; the chlorine–water contact time was close to that under the process conditions, namely, 4 h for the river water and 2 h for the well water. The fact that the total content of carbon, chlorine, bromine, and oxygen in the components tend to grow with increasing chlorine dose is, evidently, due to

Table 2. Elemental composition of PVOCs in the initial and chlorinated water from the Ufa river (NO) and wells (SI)

Element	Water				Element	Water			
	initial		chlorinated			initial		chlorinated	
	mg dm^{-3}	%	mg dm^{-3}	%		mg dm^{-3}	%	mg dm^{-3}	%
	Ufa river water					SI well water			
C	0.01400	67.80	0.02275	36.72	C	0.00880	69.24	0.02300	20.57
H	0.00367	17.77	0.00454	7.33	H	0.00220	17.31	0.00540	4.83
Cl	0.000087	0.42	0.00870	14.04	Cl	0.00013	1.02	0.002500	22.36
Br	0.00008	0.39	0.01495	24.13	Br	–	–	0.04500	40.24
O	0.00245	11.87	0.01078	17.40	O	0.00110	8.65	0.01300	11.62
P	0.00002	0.10	0.00001	0.02	P	0.00002	0.16	0.00002	0.02
S	0.00034	1.65	0.00022	0.36	S	0.00046	3.62	0.00041	0.37
Σ	0.02065	100	0.06195	100	Σ	0.01271	100	0.11183	100

oxidative degradation of high-molecular-weight natural contaminants of water into PVOCs, on the one hand, and by direct halogenation of the available and newly formed impurities, on the other (Figs. 1a and 1b). Interestingly, the content of the major elements in PVOCs passes through a maximum, as clearly demonstrated for the well water. The same pattern is, most probably, characteristic of the river water, but the necessary amount of chlorine is never used in the actual water treatment processes both for the river and well waters.

Table 2 compares the elemental compositions of the organic compounds eluted in chromatographic analysis at the chlorine dose of 2.5 mg dm^{-3}. The residual chlorine concentration was estimated by GOST (State Standard) 18190–72 at 0.8 and 1.9 mg dm^{-3} for the NO and SI water, respectively, which corresponds to 1.7 and 0.6 mg dm^{-3} of spent chlorine. This is a conditional parameter which does not incorporate the amount of the chlorine spent in the formation of volatile compounds, chlorination of humus into compounds heavier than PVOCs, and other possible reactions.

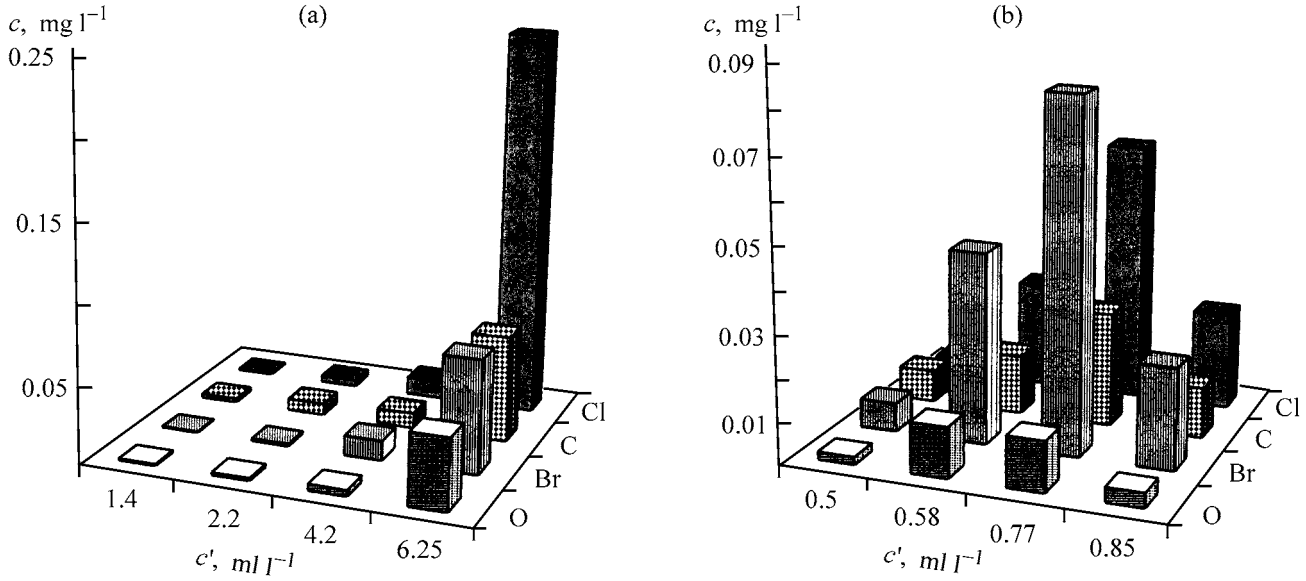

Variation of the content c of elements in partly volatile components under chlorination of the river water at (a) NO and (b) SI water intakes (c') Content of spent chlorine.

A common finding of all our experiments is the sharply increased content of chlorine and bromine in PVOCs contained in the chlorinated water. However, the distributions of these compounds in water from the two water intakes are different. For example, the proportion of chlorine increases from 0.4 to 14% for the river water and from 1 to 22% for the well water. This increase in the proportion of chlorine can be accounted for by degradative chlorination of humic compounds, and primarily of their low-molecular-weight fragments [18]. An increase in the proportion of bromine in PVOCs is even more prominent. For example, the proportion of bromine in the river water and the well water increased from 0.4 to 24 and to 40%, respectively. This is, evidently, due to a higher content of bromides in the well water, compared to the river water. This is accounted for, in turn, by the local hydrochemical features, namely, by the occurrence of halogen-containing rocks (rock salt, anhydrites, gypsums). Bromine contained in these rocks as an impurity can be activated during chlorination and be converted to organic compounds [8].

Water chlorination leads to an increase in the oxygen content in the PVOCs in NO and SI water by factors of 4.4 and 12, respectively. The increase in the concentration of oxygen-containing compounds after chlorination of water from both water intakes suggests that high-molecular-weight compounds degrade into low-molecular-weight compounds, in agreement with published data [19].

The percentage of chlorine spent was estimated at 68 and 24 for the river water and well water, respectively. However, the PVOC content in the well water increases upon chlorination by a factor of 8.8, which almost threefold exceeds the factor of 3 in the case of the river water. This suggests that formation of PVOCs in the case of SI water intake is a more rapid process requiring less chlorine, compared to NO water intake, which is accounted for by the difference in the initial water matrices for these water intakes.

CONCLUSIONS

(1) Water chlorination is a complex multifactor process requiring adjustment of the chlorine dose to the initial water quality.

(2) In the context of the increasingly stringent regulations concerning the content of halogenated organic compounds in water, it is essential to estimate by express analysis such integrated indices as the total carbon, total chlorine, bromine, and oxygen contents in partly volatile organic compounds contained in water.

REFERENCES

1. *SanPiN* (Sanitary Rules and Regulations) *2.1.4.1074-01: Potable Water: Hygienic Water Quality Norms for Central Potable Water Intake Systems.*
2. *GN* (Hygienic Regulations) *2.1.5.1093-02: Maximum Permissible Concentrations (MPCs) of Chemical Substances in Potable and Domestic Water.*
3. Richardson, S.D., *Anal. Chem.*, 1999, vol. 71, no. 12, pp. 181–215.
4. Alekseeva, L.P., *Povyshenie sanitarnogo kachestva vodoprovodnoi vody: issledovanie i opyt v Sovetskom Soyuze i Finlyandii* (Improvement of the Hygienic Quality of Tap Water: Investigation and Experience in the Soviet Union and Finland), Helsinki, 1990, pp. 7–38.
5. Alawi, M.A., Khalill, F., and Sashili, I., *Arch. Environ. Contam. Toxicol.*, 1994, vol. 26, pp. 381–386.
6. Stevens, A.A., Moore, L.A., and Miltner, R.J., *J. AWWA*, 1989, August, p. 45–60.
7. Pomes, M.L., Green, W.R., Thurman, E.M., *et al.*, *J. AWWA*, March, pp. 103–115.
8. Nawrocki, J. and Bilozor, S., *J. Water SRT-Aqua*, 1997, vol. 46, no. 6, pp. 304–323.
9. Kuzubova, L.I. and Kobrina, V.N., *Analiticheskii Obzor* (Analytical Review), *Ser.: Ekologiya* (Ecology), Novosibirsk, 1996.
10. Zholdakova, Z.I., Kharchevnikova, N.V., Polyakova, E.E., *et al.*, *Gig. Sanit.*, 2002, no. 5, p. 26–29.
11. Gurka, F.D., Pyle S., and Titus, R., *Anal. Chem.*, 1997, vol. 69, no. 13, pp. 2411–2417.
12. Vozhdaeva, M.Yu., Tsypysheva, L.G., Kantor, L.I., and Kantor, E.A., *Anal. Kontr.*, 2001, vol. 5, no. 2, pp. 171–185.
13. Anderson, J.T., *Anal. Bioanal. Chem.*, 2002, vol. 373, pp. 344–355.
14. Vozhdaeva, M.Yu., Tsypysheva, L.G., Kantor, L.I., *et al.*, *Khim. Tekhnol. Vody*, 2000, vol. 22, no. 6, p. 626.
15. *ISO 8245 International Standard: Water Quality: Guide on Total Organic Carbon (TOC) Determination.*
16. Vasil'eva, A.I., Kireeva, E.N., Vozhdaeva, M.Yu., *et al.*, Abstracts of Papers, *IV Mezhdunarodnyi kongress "Voda: Ekologiya i tekhnologiya"* (IV Int. Congr. "Water: Ecology and Technology"), EKVATEK-2000, Moscow, May 30–June 2, 2000, pp. 311–312.
17. Vasil'eva, A.I., Vozhdaeva, M.Yu., Gagarina, L.N., *et al.*, Abstracts of Papers, *IV Vserossiiskaya konferentsiya "Ekoanalitika-2000" s mezhdunarodnym uchastiem* (IV Russian Conf. "Ekoanalitika-2000" with Participation of Foreign Specialists), Krasnodar, September 17–23, 2000, pp. 282–284.
18. Pomes, M.L., Green, W.R., Thurman, M.E., *et al.*, *J. AWWA*, 1999, vol. 91, no. 3, pp. 103–115.
19. Kholodkevich, S.V., Viktorovskii, I.V., and Zyuzin, I.A., *Ekol. Khim.*, 1997, vol. 6, no. 4, pp. 230–240.

Russian Journal of Applied Chemistry, Vol. 77, No. 6, 2004, pp. 942–946. Translated from Zhurnal Prikladnoi Khimii, Vol. 77, No. 6, 2004, pp. 956–960.

PROCESSES AND EQUIPMENT OF CHEMICAL INDUSTRY

A Study of New Designs of Impact-Centrifugal Mills

A. E. Levdanskii

Belarussian State Technological University, Belarus, Minsk

Received December 3, 2003

Abstract—Main ways to diminish the power consumption in grinding of materials are considered, and their practical implementation in newly developed designs of impact-centrifugal mills with flow-through classification is suggested. Data obtained in experimental studies and industrial tests of the developed designs are presented.

The process of fine grinding of materials is widely used not only in chemical industry, but also in a wide variety of other industries, and, at the same time, is rather power consuming. Therefore, much attention is being paid to a search for ways to diminish the power consumption in grinding. For this purpose, many specialists in grinding suggest [1–3]: (a) to carry out grinding mainly via impact load, (b) to prevent accumulation of a ground material in the working chamber of a grinding apparatus by continuously removing the product from this zone, and (c) to perform classification when removing the ground products from the grinding zone in order to separate the coarse fraction and return it into the mill for additional grinding.

All these requirements can be satisfied with the highest probability in impact-centrifugal mills with a flow-through classification. Three designs of impact-centrifugal mills, which are the most widely used in the industry, are shown in Figs. 1a–1c [4–6].

All the three mills comprise a vertical cylindrical casing *1* with a flat bottom *2* and a removable cover *3*. Within the casing *1* rotates a working disc *4* with blades *5*. In the first two variants of mills (Figs. 1a, 1b) the disc is mounted directly on the shaft of the electric motor *6*, and in the third design, there is a shaft *7* at the center of the vessel *1*, on which two discs *4* with blades *5* are mounted; the shaft is driven by the electric motor *6* by means of a V-belt drive *8*.

In all the three designs, baffle rods *9* are mounted annularly at a small distance from the outer edges of blades *5*. In all the designs, the material is ground by its impact loading. For this purpose, the starting material is fed, through a pipe *10*, into the central part of the mill, wherefrom it is transported by the air flow to blades *5* and further, moving along these blades, is accelerated to high velocities. The particles of the material break loose from the blades *5*, strike the baffle rods *9*, and are ground by this impact. It should be noted that, in all the mills, the continuous medium is set in motion in a similar way, by a centrifugal ventilator, which makes it possible to use the motion of the air flow to transport the material.

The difference in the designs is in the following. In the first design (Fig. 1a), the baffle rods *9* have a rectangular cross-section and are mounted with a certain spacing in between. After the material strikes the rods, ground particles pass through the clearings under the action of a centrifugal force and the air flow and then, moving together with air in the space between the rods and the apparatus casing, arrive via a tangential discharging pipe *11* into a cyclone and filter for separation. Because of the swirling motion of air in the chamber and an oblique impact of the material against the rods, the ground particles approach the slits at a certain angle. Consequently, only particles that are much smaller than the slits between the rods can pass through these slits, which rules out slit clogging. Calculations and experimental studies demonstrated that only particles whose size is 2–3 times smaller than the slit width can pass through the clearings. By selecting a necessary rotation rate of the disc with blades and mounting rods with a certain clearing width, it is possible to achieve the required grinding fineness.

In the second mill design (Fig. 1b), the baffle rods have a circular cross-section and are mounted close to one another. In this case, grinding products are

1070-4272/04/7706-0942 © 2004 MAIK "Nauka/Interperiodica"

carried away from the working zone by the ascending air flow and pass through an annular window of the cover into the spiral channel and further, through the discharging pipe *11*, into the cyclone and filter for separation. Baffle plates *12* mounted obliquely form a flow-through classifier. The flow of a gas and solid particles, which ascends from the grinding zone, passes through the clearing between the classifier blades and executes a zigzag motion. In the process, coarser particles, which have higher inertia, strike the oblique blades, rebound, and fall down on the blades, to be again ground there. Fine particles, which have lower inertia, pass together with air through the clearings and are removed from the mill. In this mill design, the material being ground may suffer multiple impact and, consequently, this mill can be used to ground harder materials.

The third mill design (Fig. 1c) has two stages, with two discs with blades mounted on the common shaft. The material is initially ground in the first stage of the mill, with insufficiently ground coarse particles finally milled in the second stage. The design of the first stage is similar to that of the first variant of the mill (Fig. 1a), and the design of the second stage, to that of the second variant (Fig. 1b). In this mill design, the material does not stay long in the grinding zone, but passes successively both stages and is discharged into the cyclone through an annular window in the bottom part and a tangential pipe. The mill can operate successfully in grinding of medium-strength materials.

The main grinding efficiency criteria for any mill design are the specific power consumption and the quality of the product obtained. The energy consumption is most commonly evaluated by the ratio of the energy expenditure to the amount of ground material (kW h ton^{-1}). The most comprehensive characteristic of the quality of the product obtained is its granulometric (fraction) composition (particle size distribution).

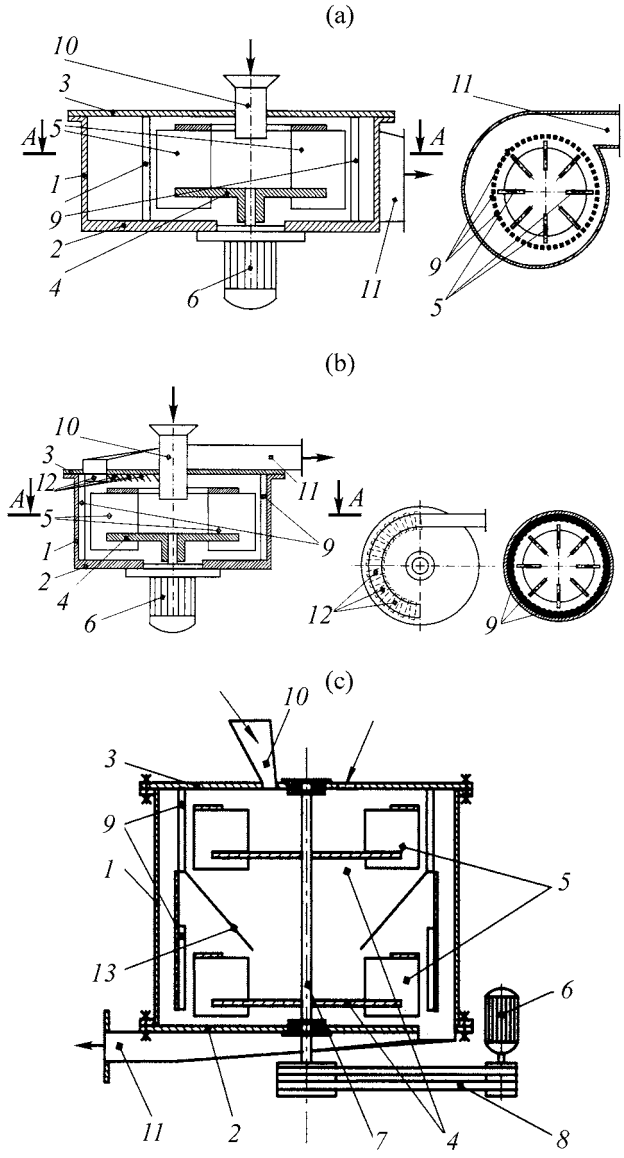

Fig. 1. Schematic of impact-centrifugal mills. Design: (a) with a tangential discharge, (b) with a top discharge, and (c) two-stage with a bottom discharge of a ground material. (*13*) cone, for other explanations, see text.

The power consumption and the grinding quality are affected both by parameters of the grinding process itself and by characteristics of a material being ground. The parameters of impact grinding are the following: impact velocity, number of impacts, impact angle, specific load, geometric dimensions of mill units and elements. To the characteristics of the material being ground should be referred its geometric dimensions, physicochemical parameters (hardness, elasticity modulus, ultimate strength), and moisture content. It is virtually impossible to take into account all the parameters of the grinding process and of the material being ground in constructing the theoretical model of the impact disintegration of the material. Therefore, the efficiency of grinding in mills of the designs developed was determined experimentally. First, the extent of impact grinding of the material upon its single pass through the mill was studied for the mill design (Fig. 1b) in which baffle rods *9* with circular or rectangular cross-section are mounted close to one another (without any clearing). In order to exclude a repeated grinding of the material, the ground material was discharged through an annular window and a tangential pipe in the bottom part, as

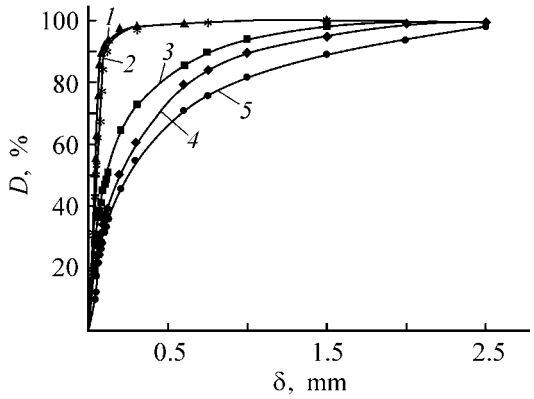

Fig. 2. Fraction composition of the products formed in impact grinding of various materials. (*D*) of the mass of particles (smaller than δ in size) to the total mass of particles and (δ) particle size; the same for Figs. 3–5. Substance being ground: (*1*) lime (grain size 4–8 mm), (*2*) chalk (particle size 4–8 mm), (*3*) gypsum stone, (*4*) sylvinite (particle size 3–10 mm), and (*5*) barley grain.

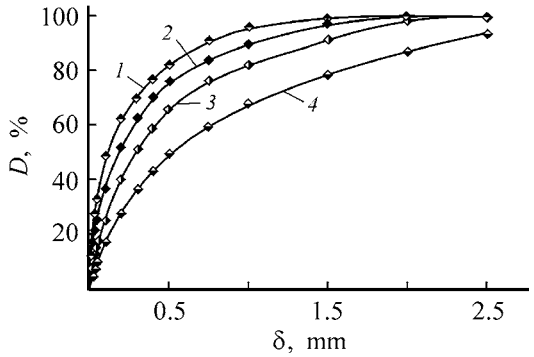

Fig. 3. Fraction composition of the products formed in impact grinding of sylvinite at different output capacities *G*. *G* (kg s^{-1}): (*1*) 0.061 (220 kg h^{-1}), (*2*) 0.133 (480 kg h^{-1}), (*3*) 0.211 (760 kg h^{-1}), and (*4*) 0.333 (1200 kg h^{-1}).

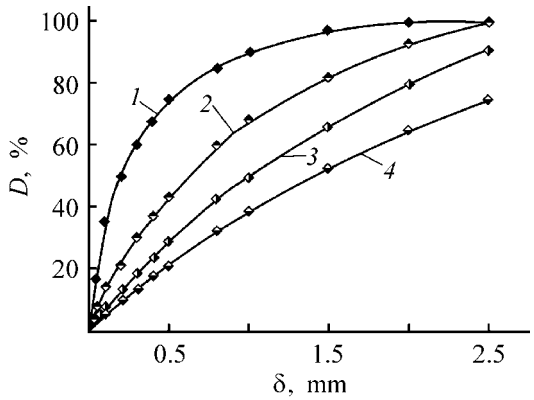

Fig. 4. Fraction composition of the products formed in impact grinding of sylvinite at different rates of rotor rotation (*n*) and linear velocities of the tips of the rotor blades (*w*). *w* (m s^{-1}): (*1*) 62.8, (*2*) 33, (*3*) 21, and (*4*) 16. *n* (rpm): (*1*) 3000, (*2*) 1500, (*3*) 1000, and (*4*) 750.

it is dome in the mill of design shown in Fig. 1c, rather than through the cover. The study was carried out on a mill with a rotor diameter of 400 mm (at blade tips), with the rate of rotation varied from 750 to 2900 rpm.

The results obtained in studying a single-pass impact grinding of materials are shown in Figs. 2–4 in the form of distribution functions in which the particle size δ is plotted along the abscissa axis, and the ratio *D* of the mass of particles with diameter less than δ to the total mass of the grinding product, along the ordinate axis. The curves of the fraction distribution of the products formed in impact grinding (Fig. 2) were obtained at a rotor rotation rate of 2900 rpm for various materials (lime, chalk, gypsum stone, sylvinite, barley grain). In all the experiments, the rate of substance supply was 460–520 kg h^{-1}, and the initial particle size, 4–8 mm. It can be seen that the finest grinding is achieved in the single-pass impact grinding for grains of lime and particles of chalk. As shown by analysis of the grinding products under a microscope, these grains and particles virtually disintegrate into fine crystallites. The worst results are obtained for barley grain, and primarily for its elastic sheath.

Figure 3 shows the fraction composition of products formed in grinding of sylvinite at a load by the starting material varied from 0.061 to 0.333 kg s^{-1} (220–1200 kg h^{-1}), and Fig. 4, the fraction composition of the products of its grinding at different rotor rotation rates.

A mathematical processing of the experimental data with the use of the Rosin–Rammler formula made it possible to obtain an empirical relation for describing the fraction composition of products formed in a single-pass impact grinding of materials in impact-centrifugal mills (Figs. 1a–1c):

$$D = 100\{1 - \exp[-0.68(\delta/\delta_{50})^{0.75}]\}, \qquad (1)$$

where *D* is the ratio of the mass of particles (smaller than δ in size) to the total mass of particles (%); δ, the particle size (*m*); and δ_{50}, the particle size for which the mass of smaller particles is 50%.

For determining the δ_{50} particle size, an empirical relation was obtained that took into account the characteristics of a material being ground, the load on the mill by the material being ground, and the linear velocity of the tips of the rotor blades:

$$\delta_{50} = 2.71cw^{-1.42}G, \qquad (2)$$

where *c* is a coefficient that takes into account the physicomechanical properties of the material and

the size of its initial particles (c = 0.05 for lime and chalk, 0.12 for gypsum stone, 0.2 for sylvinite and 0.25 for barley grain); w, the linear velocity of the tips of the rotor blades (m s^{-1}); and G, the amount of material fed into the mill (kg s^{-1}).

Analysis of the coarsest particles in grinding products shows that, even in grinding of barley grain and gypsum stone, their size is smaller than that in the starting materials by a factor of 2.5–3. When baffle rods with rectangular or circular cross-section were used in experiments, no noticeable influence of the rod shape on the fraction composition of the grinding products was observed. The process of grinding with a simultaneous classification was studied with a mill of the design shown in Fig. 1a. In this case, the baffle rods had a rectangular (14 × 14 mm) cross-section and the distance between the rods was varied from 0.5 to 4 mm. First, sylvinite and then other materials were ground at a rotor rotation rates of 2300 and 1450 rpm and load by material of 0.133 kg s^{-1}. In the course of the experiments, the fraction composition of the grinding products that passed through slits between the rods was constantly monitored. The experiments, whose results are shown in Fig. 5, demonstrated that the main factor that determines the fraction composition of grinding products is the width of the slits between the rods. The maximum size of the particles that passed through the slits was, in all the experiments with various materials, as follows:

$$\delta_{max} = (0.5 - 0.75)b, \quad (3)$$

where b is the width of the slits between the rods.

The fraction composition of the grinding products that passed through the slits between the baffle rods can also be described, with an accuracy sufficient for engineering calculations, using the Rosin–Rammler formula

$$D = 100[1 - \exp(-45.38\, b^{-2.3}\, \delta^{2.5})]. \quad (4)$$

In all the experiments, the power consumption by the mill drive was measured. Figure 6 shows how the power consumed by the mill depends on the load by material. It can be seen from the plot that, even in an idle run, the mills consume 1.8 to 3 kW of electric power. Most part of this energy goes to operation of a mill as a ventilator. Curves *1–3* in Fig. 6 were obtained in studying a mill of design shown in Fig. 1a, in which a continuous flow-through classification is effected by baffle rods mounted at a distance of 1 mm from one another. In grinding of lime (curve *1*), grains are disintegrated by the impact into fine crystals of size less than 0.5 mm (which is well seen in Fig. 2) and these crystals are carried by the air flow and easily pass through the slits between the rods, leaving the grinding zone without delay. Therefore, energy is consumed in this case only for acceleration of particles. Curves *2* and *3* were obtained in grinding gypsum stone and barley grain in the same mill. These materials do not completely ground upon impact into particles of less than 0.5 mm in size and accumulate in the grinding zone. Therefore, additional grinding occurs because of the wear in this zone, and, consequently, the loss of power substantially increases, especially at high loads.

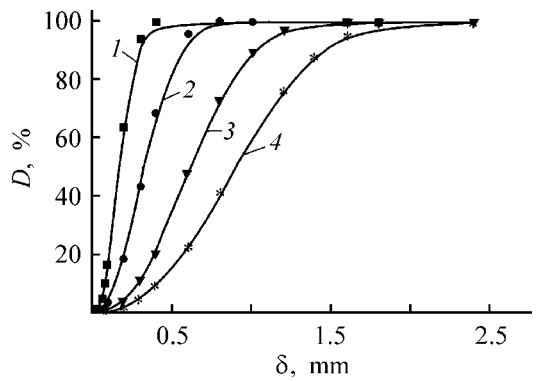

Fig. 5. Fraction composition of the products formed in grinding of sylvinite in the mill of design shown in Fig. 1a at different slit widths b. b (mm): (*1*) 0.5, (*2*) 1, (*3*) 2, and (*4*) 3.

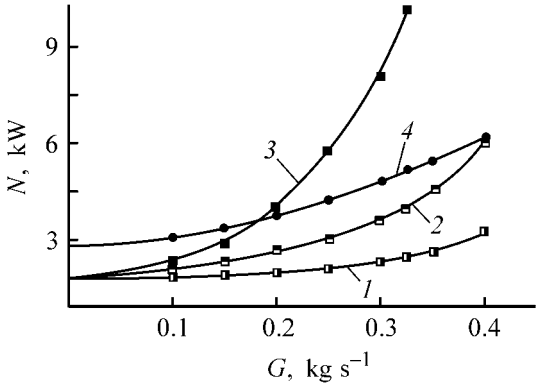

Fig. 6. Consumed power N vs. the load G by material. Ground substance: (*1*) lime, (*2*) gypsum stone, and (*3, 4*) barley grain. Mill design: (*1–3*) first (Fig. 1a) and (*4*) third (Fig. 1c).

Consequently, mills of the first and second designs (Figs. 1a, 1b) can be recommended for grinding of such materials as lime, chalk, lumps of dry clay, grains and crystals of salts. At small loads of up to 200 kg h^{-1} and mill rotor diameter of 400 mm, mills can be used to grind harder materials. For example, several mills

of second design (Fig. 1b) have long been used to grind roots and herbs in production of medicines and food additives.

Curve *4* shows an increase in the power consumption in grinding of barley grain in a mill of the third design (Fig. 1c). There are no dead zones in this mill and the material is ground under two-stage impact load; therefore, the power consumption gradually grows as the load on the mill increases.

CONCLUSION

The quality of grinding of materials with low and medium strength in impact-centrifugal mills substantially exceeds that in hammer mills, which are widely used for this purpose. At the same time, the specific electric power consumption by the impact-centrifugal mills is 20–30% lower. It is advisable to replace hammer mills with impact-centrifugal mills.

REFERENCES

1. Revnivtsev, V.I., Gaponov, G.V. Zarogatskii, L.P., *et al.*, *Selektivnoe razrushenie mineralov* (Selective Disintegration of Minerals), Moscow: Nedra, 1982, pp. 135–162.
2. Andreev, S.E., Perov, V.A., and Zverevich, V.V., *Droblenie, izmel'chenie i grokhochenie poleznykh iskopaemykh* (Crushing, Grinding, and Screening of Minerals), Moscow: Nedra, 1980, pp. 110–134.
3. Sidenko, P.M., *Izmel'chenie v khimicheskoi promyshlennosti* (Grinding in Chemical Industry), Moscow: Khimiya, 1977.
4. Belarussian Patent 4707.
5. Belarussian Patent 3011.
6. Belarussian Patent 4706.

Russian Journal of Applied Chemistry, Vol. 77, No. 6, 2004, pp. 947–956. Translated from Zhurnal Prikladnoi Khimii, Vol. 77, No. 6, 2004, pp. 961–970.

PROCESSES AND EQUIPMENT OF CHEMICAL INDUSTRY

Convective Mass Exchange between Flows of Finely Dispersed Media in a Valve-Pulsatory Mass-Exchange Apparatus

R. Z. Aliev, M. R. Aliev, and A. R. Aliev

Daghestan Research Institute of Food Industry, Makhachkala, Daghestan, Russia

Received March 26, 2003; in final form, November 2003

Abstract—A mathematical model of convective mass exchange between flows of finely dispersed media in a valve-pulsatory apparatus is developed with account of the mass exchange between the dispersed and continuous phase at $\mathrm{Sh} \cdot \mathrm{Fo} \geq 1$.

The rate of technological processes carried out in solid–liquid and solid–gas systems increases as the size of dispersed particles of the solid phase becomes smaller, and the relative velocity of counterflowing phases, higher. However, in the known methods of phase interaction, the maximum possible velocity of counterflowing phases is limited and becomes slower as the particle size and the difference of phase densities decrease.

These limitations are overcome in the new method of phase interaction, suggested by the authors. In this method, a dispersed solid phase is mixed with a part of the liquid (or gas) phase to form a suspension (or an aerosol) and a counterflow convective mass exchange between the flows of the resulting suspension and the liquid is carried out in an apparatus with long channels separated by a convectively permeable partition, by creating multiple alternating-sign pressure differences between the channels [1–3].

The new method of phase interaction is used to perform mass and heat exchange between flows of hydro- and gas-dispersed systems in technological processes of extraction and sorption, chemical reactions that yield a solid dispersed phase, phase-selective heating, and cooling of dispersed media [4–7].

In [8], the authors of the present study analyzed the convective mass exchange between flows of finely dispersed media with an inert solid phase in a valve-pulsatory mass-exchange apparatus (VPMEA) [1–3], which is used to carry out effective processes of heat and mass exchange in hydro- and gas-dispersed systems [4–7].

The aim of this study was to construct a mathematical model of the convective mass exchange in VPMEA with account of the interphase mass transfer for the case when the intensity of this mass transfer is so high that the continuous and dispersed phases can be considered to be in equilibrium at any point of the VPMEA at any instant of time. This is the case for a number of the above-mentioned processes, which are carried out effectively in the kinetically advantageous conditions of finely dispersed media, when the characteristic time of the interphase mass exchange is negligible as compared with the residence time t_R of a suspension in the VPME apparatus. Moreover, this situation, being a limiting case, makes it possible to estimate the maximum possible result of a convective mass exchange in a VPMEA and, in this sense, is of a certain practical importance.

First, let us describe in brief the design and operation mode of a VPMEA [8]. The finely dispersed medium is composed of a continuous and a dispersed phases; VPMEA contains two neighboring channels separated by a partition that is permeable to the continuous phases and impermeable to the dispersed phases of the flows (Fig. 1). Each phase contains a component that can pass from one phase into the other as a result of sorption, extraction, etc. The finely dispersed media move within the VPMEA channels in a counterflow. The operation of the VPMEA consists

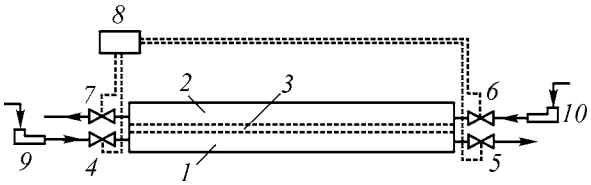

Fig. 1. Schematic of a valve-pulsatory mass-exchange apparatus: (*1*, *2*) VPMEA channels, (*3*) permeable partition, (*4–7*) valves, (*8*) valve control unit, and (*9*, *10*) pumps.

1070-4272/04/7706-0947 © 2004 MAIK "Nauka/Interperiodica"

in two alternating time steps of length t_{ts}, determined by the positions of valves at channel inlets and outlets.

In the first time step, the inlet valve of the first channel and the outlet valve of the second are open, whereas the inlet valve of the second channel and the outlet valve of the first are closed. The first finely dispersed medium with an initial concentration of the component $c_1(0, t) = c_{1\,in}$ and porosity $\varepsilon_1(0, t) = \varepsilon_{1\,in}$ is fed into the first channel and filtered through the permeable partition. This creates a flow in the second channel, which exits the second channel with a concentration $c_2(0, t) = c_{2\,out}(t)$ and porosity $\varepsilon_2(0, t) = \varepsilon_{2\,out}(t)$.

In the second time step, the inlet valve of the first channel and the outlet valve of the second are closed, whereas the inlet valve of the second channel and the outlet valve of the first are open. The second finely dispersed medium with an initial concentration $c_2(l_0, t) = c_{2\,in}$ and porosity $\varepsilon_2(l_0, t) = \varepsilon_{2\,in}$ is fed into the second channel and filtered through the partition to create in the first channel a flow with a concentration $c_1(l_0, t) = c_{1\,out}(t)$ and porosity $\varepsilon_1(l_0, t) = \varepsilon_{1\,out}(t)$ leaves the first channel. Here t is time, and l_0, the channel length. Thus, sign-alternating pressure differences are created between the channel spaces. During their residence within a VPMEA in the case of such a pulsatory motion, the first and second finely dispersed phases repeatedly exchange portions of continuous phases, without mixing of their dispersed phases. Owing to this circumstance, there occurs a counter flow convective mass exchange between the flows of the first and second media. As a result, the concentration $c_{2\,out}(t)$ at the outlet of the second channel becomes close to the initial concentration $c_{1\,in}$, and the concentration $c_{1\,out}(t)$ approaches the concentration $c_{2\,in}$ at the inlet of the second channel. As the dispersed phase cannot pass from one channel into the other, $\varepsilon_{1\,out}(t) = \varepsilon_{1\,in}$ and $\varepsilon_{2\,out}(t) = \varepsilon_{2\,in}$ in the stationary case of VPMEA operation.

In [8], it was assumed that the mass exchange between the solid and liquid phases within a VPMEA is low as compared with the convective transfer of the component in the flows. However, in many solid–liquid and solid–gas systems used in industrially important technological processes, there occurs an interphase mass transfer, and, therefore, it is a matter of current interest to determine the influence exerted by this process on the convective mass exchange in VPMEA.

If the interphase transfer of the component is taken into account, then terms responsible the interphase mass transfer appear in the equations that describe the convective mass exchange in VPMEA, derived in [8]. Let us consider the case when the interphase equilibrium in both channels of a VPMEA is described by the equation $c_S = Hc_L^*$, where c_S is the concentration of the component being transferred in the particles of the dispersed phase; c_L^*, the corresponding equilibrium concentration of the component being transferred in the continuous phase; and H, the interphase equilibrium constant, which is common to both the VPMEA channels. Then the system of equations describing the mass exchange in VPMEA can be written as follows {see system (5) in [8]}:

$$\frac{dU_1}{dX} + \frac{s_2}{s_1}\frac{dU_2}{dX} = 0, \tag{1}$$

$$\frac{dU_1}{dX} + \frac{l_0}{d_{e1}}\frac{Re_{01}}{R_{ef1}} = 0, \tag{2}$$

$$\frac{dEu}{dX} + \frac{d}{dX}\left(\rho_1\gamma_1 U_1^2 - \rho_2\gamma_2 U_2^2\right) + \frac{e_{u1}l_0}{2d_{e1}}\rho_1\xi_1 U_1^2 - \frac{e_{u2}l_0}{2d_{e2}}\rho_2\xi_2 U_2^2 = 0, \tag{3}$$

$$\frac{\partial\varepsilon_i}{\partial T} + U_i\frac{\partial\varepsilon_i}{\partial X} - \frac{dU_i}{dX}(1 - \varepsilon_i) = 0, \tag{4}$$

$$\varepsilon_i\frac{\partial C_{Li}}{\partial T} + \varepsilon_i U_i\frac{\partial C_{Li}}{\partial X} - \frac{\partial U_i}{\partial X}(C_{Lj} - C_{Li}) + \frac{l_0}{u_{01}}\beta_i f_i(1 - \varepsilon_i)(C_{Li} - C_{Si}) = 0, \tag{5}$$

$$\frac{\partial C_{Si}}{\partial T} + U_i\frac{\partial C_{Si}}{\partial X} - \frac{l_0}{u_{01}}\frac{\beta_i f_i}{H}(C_{Li} - C_{Si}) = 0, \tag{6}$$

where the index i takes the values 1 or 2 (channel number); $X = x/l_0$; $U_i(X) = u_i(x)/u_{01}$; $T = t/t_0$; $t_0 = l_0/u_{01}$; $C_{Li}(X, T) = [c_{Li}(x, t) - c_{L\min}]/(c_{L\max} - c_{L\min})$ and $C_{Si}(X, T) = [c_{Si}(x, t) - c_{S\min}]/(c_{S\max} - c_{S\min})$ are the dimensionless concentrations of the component in the continuous and dispersed phases; $c_{Li}(x, t)$ and $c_{Si}(x, t)$, the component concentrations in the continuous and dispersed phases; $c_{L\min}$ and $c_{L\max}$, the minimum and maximum concentrations among $c_{L1\,in}$, $c_{S1\,in}/H$, $c_{L2\,in}$, and $c_{S2\,in}/H$; $c_{S\min}$, $c_{S\max}$, the minimum and maximum concentrations among $c_{S1\,in}$, $Hc_{L1\,in}$, $c_{S2\,in}$ and $Hc_{L2\,in}$; $c_{L1\,in}$, $c_{S1\,in}$, $c_{L2\,in}$, $c_{S2\,in}$, the concentrations at the inlet of the first and second channels of VPMEA; l_0, the length of VPMEA; $Eu(X) = [p_1(x) - p_2(x)]/(\rho_L u_{01}^2)$; $\rho_i = \varepsilon_i + (1 - \varepsilon_i)\rho_{Si}/\rho_{Li}$; ρ_{Li}, and ρ_{Si}, the densities of the continuous and dispersed phases; $R_{ef} = s_1 r_{ef}/\pi_{v1}$; $e_{ui} = u_i/|u_i|$; x, the longi-

tudinal coordinate; t, time; $\mathrm{Re}_{01} = u_{01}d_{e1}\rho_{L1}/\mu_1$; π_{vi}, the permeable part of the perimeter of ith channel; $u_i(x)$, the average, over the cross-section of ith channel, longitudinal velocity; $u_{01} = u_1(0)$; $\varepsilon_i(X, T)$, the porosity in ith channel; $p_i(x)$, the pressure in ith channel; s_i, the cross-section of ith channel; r_{ef}, the filtration resistance; d_{ei}, the equivalent diameter of ith channel; ξ_i and γ_i, the coefficients of friction and momentum flux in ith channel; β_i, the interphase mass-transfer coefficient in ith channel; f_i, the ratio between the area of the outer surface of a particle belonging to the dispersed phase and its volume in ith channel; μ_i, the viscosity of the continuous phase; and $\mathrm{Sr} = t_{ts}/t_0$.

The value of j depends on the direction of filtration of the continuous phase in the VPMEA. In the case of filtration from the first channel of the VPMEA into the second (first time step), $j = 1$, and in back filtration (second time step), $j = 2$. The dimensionless concentrations $C_{Li}(X, T)$ and $C_{Si}(X, T)$ are chosen in such a way that $C_{Li}(X, T) = C_{Si}(X, T)$ under the conditions of interphase equilibrium.

Exact calculation of the change in the concentration of the component being transferred in the dispersed phase in a VPMEA is rather difficult. However, this change can be roughly estimated on the basis of the relative values of the characteristic time $t_D \sim d_S^2/D_L$ of molecular diffusion of the component in the continuous phase [9], characteristic time $t_\beta \sim 1/(\beta f) \sim d_S/\beta$ of a change in the concentration of the component being transferred in particles of the dispersed phase through interphase mass transfer, and time step duration t_{ts}. Here, D_L is the diffusion coefficient of the component within particles of the dispersed phase, and d_S is the equivalent diameter of these particles. Let us consider the following ratios: $t_D/t_\beta \sim \beta d_S/D_L = \mathrm{Sh}$, the Sherwood number; $t_{ts}/t_D \sim D_L t_{ts}/d_S^2 = \mathrm{Fo}$, the Fourier number; and $t_{ts}/t\beta \sim \beta t_{ts}/d_S = \mathrm{Sh}\cdot\mathrm{Fo}$. Let $t_{ts} \sim 1$ s. Then we obtain for aqueous suspensions ($D_L \sim 10^{-9}$ m^2 s^{-1}) at $d_S \sim 10^{-5}$ m Fo ~ 10, and, because Sh ≥ 2, then $t_{ts}/t_\beta \sim \mathrm{Sh}\cdot\mathrm{Fo} >> 1$. Similarly, for air aerosols ($D_L \sim 10^{-6}$ m^2 s^{-1}) at $d_S \sim 10^{-4}$ m, we have Fo ~ 100 and $t_{ts}/t_\beta \sim \mathrm{Sh}\cdot\mathrm{Fo} >> 1$.

Thus, for technological mass-exchange processes (sorption, extraction) in finely dispersed media ($d_S \sim 10^{-5}$–10^{-4} m), the time t_β of interphase exchange is negligible as compared with the time step duration t_{ts}, and the more so, compared with the residence time t_R of the suspension in the VPMEA. In this case, the dispersed and continuous phases in the VPMEA can be considered, to a first approximation, to be in equilibrium, and the dimensionless concentrations of the component being transferred in the respective phases, to be equal to each other: $C_{Li}(X, T) = C_{Si}(X, T) = C_i(X, T)$. This equilibrium is itself different at different points of the VPMEA and time-dependent. Then, Eqs. (5) and (6) can be transformed to the form

$$\frac{\partial C_i}{\partial T} + U_i\frac{\partial C_i}{\partial X} - \frac{\Delta_m C_i^L}{\Delta_m C_i^D}\frac{dU_i}{dX}(C_j - C_i) = 0, \qquad (7)$$

where $\Delta_m C_i^L/\Delta_m C_i^D = 1/[\varepsilon_i + (1 - \varepsilon_i)H] = (c_{L\max} - c_{L\min})/[\varepsilon_i(c_{L\max} - c_{L\min}) + (1 - \varepsilon_i)(c_{S\max} - c_{S\min})]$ is the ratio of the maximum possible change in the concentration of the component being transferred in the continuous phase to the maximum possible change in the concentration of the component being transferred in the finely dispersed phase in ith channel of the VPMEA.

Equation (7) is transformed into the corresponding equations of the system (5) from [8] in the case when $(1 - \varepsilon_i)H/\varepsilon_i >> 1$, i.e., the maximum possible change of the component being transferred in the dispersed phase is considerably smaller in both channels of the VPMEA than the maximum possible change in the concentration of the component being transferred in the continuous phase. This circumstance can be regarded as inertness of the dispersed phase.

In what follows, we consider the case when a continuous phase ($\varepsilon_{1in} = 1$) is fed into the first channel of the VPMEA, and a dispersed medium ($\varepsilon_{2in} < 1$), into the second.

If a VPMEA is used for sorption, then, commonly, $c_{L\max} = c_{L1in}$, $c_{L\min} = c_{L2in} = c_{S2in}/H$, $c_{S\max} = Hc_{L1in}$, $c_{S\min} = c_{S2in} = Hc_{L2in}$. Then, the boundary conditions in the dimensionless form are the following:

$$C_1(0, T) = C_{1in} = [c_{L1}(0, t) - c_{L\min}]/(c_{L\max} - c_{L\min}) = [c_{L1in} - c_{L2in}]/(c_{L1in} - c_{L2in}) = 1, \qquad (8)$$

$$C_2(1, T) = C_{2in} = [c_{L2}(l_0, t) - c_{L\min}]/(c_{L\max} - c_{L\min}) = [c_{L2in} - c_{L2in}]/(c_{L1in} - c_{L2in}) = 0 \qquad (9)$$

or

$$C_2(1, T) = C_{2in} = [c_{S2}(l_0, t) - c_{S\min}]/(c_{S\max} - c_{S\min}) = [c_{S2in} - c_{S2in}]/(Hc_{L1in} - c_{S2in}) = 0. \qquad (10)$$

If a VPMEA is used for extraction, then, commonly, $c_{L\max} = c_{L2in} = c_{S2in}/H$, $c_{L\min} = c_{L1in}$, $c_{S\max} = c_{S2in} = Hc_{L2in}$, $c_{S\min} = Hc_{L1in}$. Then, the boundary conditions in the dimensionless form are the following:

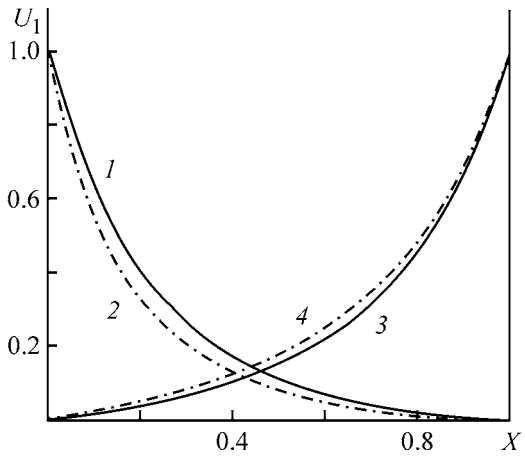

Fig. 2. Calculated dependences $U_1(X)$ of the velocity along the length of the first channel in the (*1*, *2*) first and (*3*, *4*) second time steps. $Re_{01} = 5000$, $l_0/d_e = 500$, $R_{ef1} = 10^6$, $R_{ef2}/R_{ef1} = 1.5$, $\delta_w/d_e = 10^{-2}$, $\varepsilon_{2in} = 0.97$. ρ_S/ρ_L: (*1*, *3*) 0.1 and (*2*, *4*) 10.

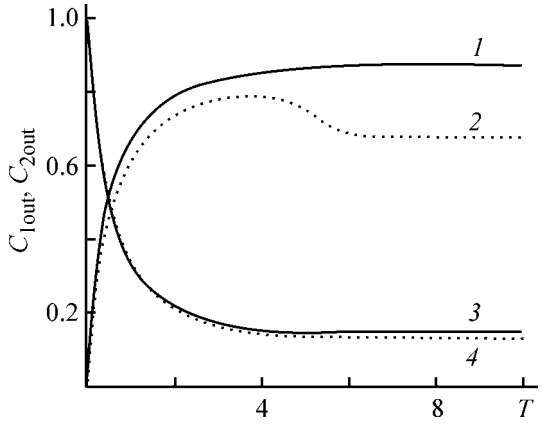

Fig. 3. Calculated dependences of the period-average dimensionless concentrations (*3*, *4*) $C_{1out}(T)$ and (*1*, *2*) $C_{2out}(T)$ on dimensionless time T at the outlets of the first and second VPMEA channels. $Re_{01} = 5000$, $l_0/d_e = 500$, $R_{ef1} = 10^6$, $R_{ef2}/R_{ef1} = 1$, $\delta_w/d_e = 10^{-5}$, $\varepsilon_{2in} = 0.97$, $\rho_S/\rho_L = 1$. H: (*1*, *3*) 0 and (*2*, *4*) 10.

$$C_1(0, T) = C_{1in} = [c_{L1}(0, t) - c_{Lmin}]/(c_{Lmax} - c_{Lmin}) = [c_{L1in} - c_{L1in}]/(c_{L2in} - c_{L1in}) = 0, \quad (11)$$

$$C_2(1, T) = C_{2in} = [c_{L2}(l_0, t) - c_{Lmin}]/(c_{Lmax} - c_{Lmin}) = [c_{L2in} - c_{L1in}]/(c_{L2in} - c_{L1in}) = 1 \quad (12)$$

or

$$C_2(1, T) = C_{2in} = [c_{S2}(l_0, t) - c_{Smin}]/(c_{Smax} - c_{Smin}) = [c_{S2in} - Hc_{L1in}]/(c_{S2in} - Hc_{L1in}) = 1. \quad (13)$$

Thus, the whole spectrum of boundary conditions for the concentrations $c_{L1}(0, t) = c_{L1in}$, $c_{L2}(l_0, t) = c_{L2in}$, $c_{S1}(0, t) = c_{S1in}$, $c_{S2}(l_0, t) = c_{S2in}$ is reduced in the case in question to two variants of dimensionless boundary conditions: $C_{1in} = C_1(0, T) = 1$, $C_{2in} = C_2(1, T) = 0$ or $C_{1in} = 0$, $C_{2in} = 1$. Together with Eqs. (7), these conditions form two possible boundary-value problems. It turns out that, with one of these boundary-value problems solved, the solution to the other can be readily obtained.

Let the functions $C_1(X, T)$ and $C_2(X, T)$ be a solution to the first boundary-value problem with boundary conditions $C_{1in} = 1$, $C_{2in} = 0$. Let us consider the functions $C^1(X, T) = 1 - C_1(X, T)$ and $C^2(X, T) = 1 - C_2(X, T)$. Hence we can express $C_1 = 1 - C^1$ and $C_2 = 1 - C^2$. Substituting the resulting expressions in Eq. (7), we make certain that C^1 and C^2 are solution to Eqs. (7). In addition, $C^1(0, T) = C^{1in} = 1 - C_{1in} = 0$ and $C^2(1, T) = C^{2in} = 1 - C_{2in} = 1$. Thus, we found the functions $C^1(X, T)$ and $C^2(X, T)$, which are the solution to the second boundary-value problem with boundary conditions $C^{1in} = 0$, $C^{2in} = 1$. The solution to the first boundary-value problem can be found similarly if the solution to the second problem is known.

In the calculations, the distributions $U_1(X)$, $U_2(X)$, and $Eu(X)$ are first calculated using Eqs. (1)–(3). Then $\varepsilon_2(X, T)$ is calculated using Eq. (4). Further, $C_1(X, T)$ and $C_2(X, T)$ are calculated by Eqs. (7). The calculations begin from $T = 0$ and continue till the end of the first time step $T = Sr$ with the boundary conditions of the first time step. Then the calculations are continued from $T = Sr$ till the end of the second time step $T = 2Sr$ with the boundary conditions of the second time step. This completes the first period of pulsations. Then, the calculation is performed with the boundary conditions of the first time step in the time interval from $T = 2Sr$ to $T = 3Sr$, with the boundary conditions of the second time step in the range from $T = 3Sr$ to $T = 4Sr$, and so on. After a certain time, the operation of the VPMEA reaches the steady state. The steady operation mode is such a mode at which the period-average concentrations $C_{1out}(T)$ and $C_{2out}(T)$ at VPMEA outlets do not vary between the periods: $C_{1out}(T) = C_{1outst}$ and $C_{2out}(T) = C_{2outst}$. Typical calculated dependences $U_1(X)$, $C_{1out}(T)$, $C_{2out}(T)$ are shown in Figs. 2, 3. The corresponding boundary conditions are described below.

The efficiency of the convective mass exchange between the flows in the VPMEA is the higher, the greater the average amount of the component transferred across the permeable partition during a period (two time steps) of pulsations in the steady mode of

VPMEA operation. The mass of the component transferred from one channel of the VPMEA into the other can be characterized by the difference between the concentrations $c_{\mathrm{L}\,in}$ and $c_{\mathrm{L}outst}$ at the inlet and outlet of one of the VPMEA channels. In the second channel, the concentration of the component in the continuous phase changes not only because of the flow between the VPMEA channels, but also as a result of the interphase transfer of the component. Therefore, the efficiency of the convective mass exchange between the flows in the VPMEA should be determined from the absolute value of the difference between the concentrations $c_{\mathrm{L}1\,in}$ and $c_{\mathrm{L}1outst}$ at the inlet and outlet of the first VPMEA channel. This difference is to be related to the maximum possible difference $c_{\mathrm{L}max} - c_{\mathrm{L}min}$:

$$E = |c_{\mathrm{L}1outst} - c_{\mathrm{L}1in}|/(c_{\mathrm{L}max} - c_{\mathrm{L}min}) = |C_{\mathrm{L}1outst} - C_{\mathrm{L}1in}| = |C_{1outst} - C_{1in}|. \quad (14)$$

The quantity E is named the degree of mass exchange between the VPMEA channels. It is independent of boundary conditions and determines the efficiency of the convective mass exchange between the flows in the VPMEA [8].

The hydrodynamic and mass-exchange characteristics of the VPMEA were calculated using Eqs. (1)–(4), (7) with the following boundary conditions. In the first time step, $U_1(0) = 1$, $U_2(0) = -1$, $U_1(1) = U_2(1) = 0$, $C_1(0, T) = C_{1in}$, $\varepsilon_1(0, T) = \varepsilon_{1in}$. In the second time step, $U_1(1) = 1$, $U_2(1) = -1$, $U_2(0) = U_1(0) = 0$, $C_2(1, T) = C_{2in}$, $\varepsilon_2(1, T) = \varepsilon_{2in}$. Initial conditions: $C_1(X, 0) = C_{01}$, $\varepsilon_1(X, 0) = \varepsilon_{01}$, $C_2(X,0) = C_{02}$, $\varepsilon_2(X, 0) = \varepsilon_{02}$. Here, $C_{j\mathrm{in}}$ is the dimensionless concentration of the component in the finely dispersed medium at the inlet of jth VPMEA channel, and C_{0j} and ε_{0j} are the dimensionless concentration and the porosity at the initial instant of time in the jth VPMEA channel. The parameters of the system being calculated are the following: $\varepsilon_{1in} = 1$; $\varepsilon_{2in} = 0.97$, 0.98, 0.99; $C_{1in} = 1$; $C_{2in} = 0$; $\varepsilon_{01} = \varepsilon_{1in}$; $\varepsilon_{02} = \varepsilon_{2in}$; $C_{01} = C_{1in}$; $C_{02} = C_{2in}$; $\rho_{L1} = \rho_{L2} = \rho_L$; $\rho_{S2} = \rho_S$; $\rho_S/\rho_L = 0.1$, 1, 10; $\mu_1 = \mu_2 = \mu$; $c_{L1} = c_{L2} = c_L$; $c_{S2} = c_S$; $c_S/c_L = 0$, 1, 10, 100, 1000; $t_{ts1} = t_{ts2} = t_{ts}$; $d_{e1} = d_{e2} = d_e$; $s_1 = s_2 = s$; $u_{01} = u_{02} = u_0$; $\pi_{v1} = \pi_{v2} = \pi_v$; $\mathrm{Sr} = t_{ts}/t_0 = 0.05$; $\mathrm{Re}_{01} = 200$, 400, 600, 800, 1000, 2000, 4000, 5000, 6000, 8000, 10 000; $l_0/d_e = 100$, 200, 300, 400, 500, 600, 700; $R_{ef1} = 10^6$, 10^7, 10^8; $R_{ef2}/R_{ef1} = 1.0$, 1.5; $\delta_w/d_e = 10^{-5}$, 10^{-2}; R_{ef1} and R_{ef2} are the effective dimensionless resistances to filtration in the first and second time steps; and δ_w is the thickness of the permeable partition in the VPMEA. Because $\varepsilon_{1in} = 1$, we have $\Delta_m C_1^L/\Delta_m C_1^D = 1$ and $\Delta_m C_2^L/\Delta_m C_2^D(X, T) = \{\varepsilon_2(X, T) + [1 - \varepsilon_2(X, T)]\mathrm{H}\}^{-1}$ for the first and second channels, respectively.

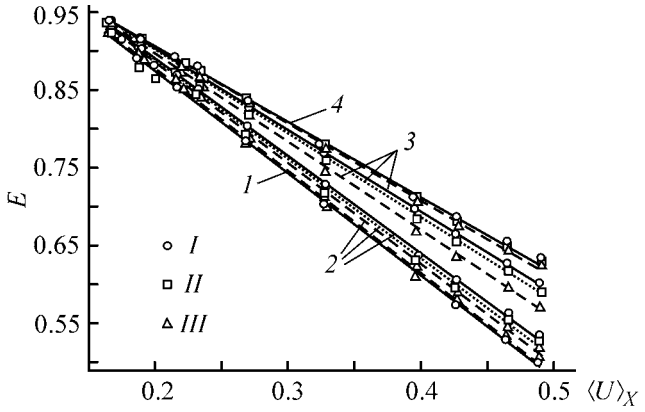

Fig. 4. Calculated dependences of the degree E of mass exchange between the flows in the VPMEA channels on $\langle U\rangle_X$. $R_{ef2}/R_{ef1} = 1$, $\delta_w/d_e = 10^{-5}$, $\rho_S/\rho_L = 1$. H: (*1*) 0, (*2*) 10, (*3*) 100, (*4*) 1000. ε_{2in}: (*I*) 0.97, (*II*) 0.98, (*III*) 0.99; the same for Fig. 5. Different values of $\langle U\rangle_X$ are set by varying Re_{01}, l_0/d_e, and R_{ef1} (Table 1).

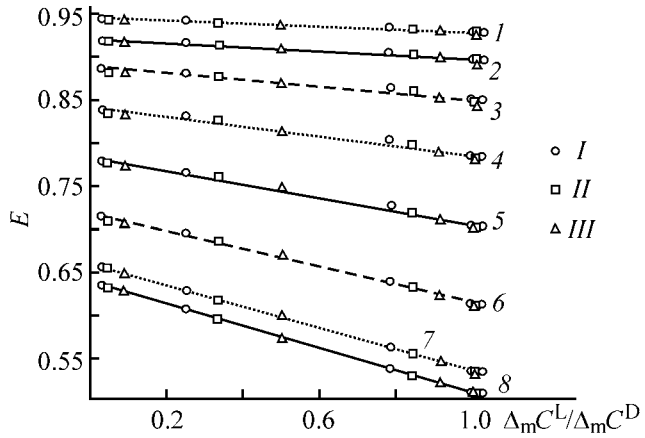

Fig. 5. Calculated dependences of the degree E of mass exchange between the flows in the VPMEA channels on $\Delta_m C^L/\Delta_m C^D = 1/[\varepsilon_{2in} + (1 - \varepsilon_{2in})H]$. $\mathrm{Re}_{01} = 5000$, $R_{ef2}/R_{ef1} = 1$, $\delta_w/d_e = 10^{-5}$, $\rho_S/\rho_L = 1$. R_{ef1}: (*1–7*) 10^6 and (*8*) 10^8. l_0/d_e: (*1*) 700; (*2*) 600; (*3, 8*) 500; (*4*) 400; (*5*) 300, (*6*) 200; and (*7*) 100. Different values of $\Delta_m C^L/\Delta_m C^D$ are set by varying H (Table 2).

The procedure for calculation of the hydrodynamic and mass-exchange characteristics of the VPMEA was described in detail in [8–18]. The results of calculations are presented in Figs. 2–6.

As can be seen from the above-mentioned calculation conditions, a continuous medium (continuous

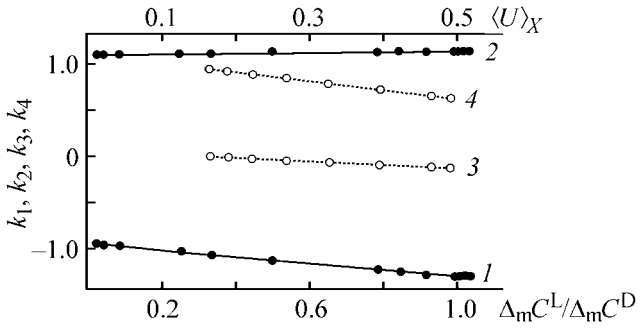

Fig. 6. Calculated dependences (*1*) $k_1(\Delta_m C^L/\Delta_m C^D)$, (*2*) $k_2(\Delta_m C^L/\Delta_m C^D)$ and (*3*) $k_3(\langle U\rangle_X)$, (*4*) $k_4(\langle U\rangle_X)$. $R_{ef2}/R_{ef1} = 1$, $\delta_w/d_e = 10^{-5}$, $\rho_S/\rho_L = 1$. Different values of $\langle U\rangle_X$ are set by varying Re_{01}, l_0/d_e, and R_{ef1} (Table 1); and those of $\Delta_m C^L/\Delta_m C^D$, by varying ε_{2in} and H (Table 2).

phase with a dimensionless concentration equal to unity) is delivered at the inlet of the first channel, and a finely dispersed medium with a dimensionless concentration equal to zero, at the inlet of the second channel.

In operation of a VPMEA, a continuous phase with high concentration flows from the first channel into the second during the first time step, and a continuous phase with low concentration flows from the second channel into the first during the second time step. Because of the flow of portions of the continuous phase between the VPMEA channels, the dimensionless concentration decreases in the first channel, and increases in the second. The changes in concentration in the VPMEA channels, which are caused by the flow, are described by the third term in Eq. (7). This term contains the factors $\Delta_m C_i^L/\Delta_m C_i^D$ and dU_i/dX. From Eqs. (1), (2) follows that $|Eu| \sim |dU_i/dX|$. The quantity $|Eu|$ determines the rate of flow between the channels (filtration rate). The efficient work of the VPMEA can be ensured in the following operation mode of the VPMEA: in the first time step, $|Eu|$ should be large in the input part of the VPMEA and small in its output part; in the second time step, by contrast, $|Eu|$ should be small in the input part of the VPMEA and large in its output part. During the first time step, the flow of the continuous phase with a high concentration between the channels occurs mainly in the input part of the VPMEA near the outlet of the second channel, whereas in the second time step, the flow of the continuous phase with a low concentration between the channels occurs mainly in the output part of the VPMEA near the outlet of the first channel. In this way, a high concentration of the component in the flow at the outlet of the second channel is ensured in the first time step, and a low concentration of the component in the flow at the outlet of the first channel, in the second time step.

Consequently, the efficient operation of a VPMEA requires that $|dU_i/dX|$ should be large at small X and small at large X in the first time step, and large at large X and small at small X in the second time step. This can be achieved at a large curvature of the curve describing the dependence $U_i(X)$ (Fig. 2). The larger the curvature of the $U_i(X)$ curve, the higher the efficiency of VPMEA operation. It has been shown [8, 13–18] that the efficiency of VPMEA operation is the higher, the greater Re_{01} and l_0/d_e and the smaller R_{ef1}. It is these three parameters that mainly determine the hydrodynamic situation in the VPMEA channels. In order to find out which combination of these three parameters is the most advantageous, it is necessary to determine, using Eqs. (1)–(3) the $U_i(X)$ distributions and to compare the curvatures of the $U_i(X)$ curves. The most advantageous is that combination of the parameters Re_{01}, l_0/d_e, R_{ef1} at which the curvature of the $U_i(X)$ is the largest. However, the notions "larger" and "smaller" curvature are insufficiently exact. Instead, it is necessary to use a clearly defined and readily calculable quantity that varies with the curvature of the $U_i(X)$ curve. As a parameter of this kind can serve the dimensionless longitudinal flow velocity averaged over the length of *i*th channel, $\langle U_i\rangle X$.

It is noteworthy that the extreme points of the dependence $U_i(X)$ are always fixed (Fig. 2). This follows from the boundary conditions presented above. It can be seen from Fig. 2 that the larger the curvature of the $U_i(X)$ dependence, the lower the dimensionless longitudinal flow velocity averaged over the length of *i*th channel $\langle U_i\rangle X$:

$$\langle U_i\rangle_X = \frac{1}{2}\left(\langle U_i\rangle_{1X} + \langle U_i\rangle_{2X}\right) = \frac{1}{2}\left(\int_0^1 U_i^{(1)}(X)\,dX + \int_0^1 U_i^{(2)}(X)\,dX\right), \quad (15)$$

where $U_i^{(1)}(X)$, $U_i^{(2)}(X)$, $\langle U_i\rangle_{1X}$, $\langle U_i\rangle_{2X}$ are dimensionless longitudinal velocities and their values averaged over the length of *i*th channel in the first and second time steps.

In the case of a counterflow, the absolute value of $\langle U_i\rangle_X$ coincides for the first and second channels, because $U_1(X) = -U_2(X)$ at any instant of time. Therefore:

$$\langle U\rangle_X = |\langle U_1\rangle_X| = |\langle U_2\rangle_X|. \quad (16)$$

The smaller $\langle U\rangle_X$, the larger the value of $|dEu/dX|$. Therefore, we can analyze, instead of the dependence

Table 1. Dimensionless longitudinal flow velocity averaged over the VPMEA length, $\langle U\rangle_X$, in relation to the characteristics of the VPMEA (R_{ef1}, l_0/d_e, Re_{01}) and to the porosity ε_{2in} of the finely dispersed medium $R_{ef2}/R_{ef1} = 1$, $\rho_S/\rho_L = 1$, $\delta_w/d_e = 10^{-5}$, $Re_{01} = 5000$, $l_0/d_e = 500$, $R_{ef1} = 10^6$

Parameter*	$\langle U\rangle_X$			
	$\varepsilon_{2in} = 0.97$	$\varepsilon_{2in} = 0.98$	$\varepsilon_{2in} = 0.99$	average
$R_{ef1} = 10^8$	0.49039	0.49041	0.49042	0.4904
$l_0/d_e = 100$	0.46542	0.46555	0.46563	0.4655
$R_{ef1} = 10^7$	0.4262	0.4266	0.4270	0.4266
$l_0/d_e = 200$	0.3959	0.3965	0.3971	0.3965
$l_0/d_e = 300$	0.326	0.327	0.329	0.3275
$l_0/d_e = 400$	0.269	0.270	0.271	0.2698
$Re_{01} = 200$	0.233	0.235	0.237	0.235
$Re_{01} = 400$	0.233	0.235	0.237	0.235
$Re_{01} = 600$	0.233	0.235	0.237	0.235
$Re_{01} = 800$	0.233	0.235	0.237	0.235
$Re_{01} = 1000$	0.233	0.235	0.237	0.235
$Re_{01} = 2000$	0.233	0.235	0.237	0.235
$Re_{01} = 4000$	0.230	0.232	0.234	0.232
$l_0/d_e = 500$	0.224	0.225	0.227	0.2253
$Re_{01} = 6000$	0.216	0.217	0.218	0.217
$Re_{01} = 8000$	0.200	0.201	0.202	0.201
$l_0/d_e = 600$	0.190	0.192	0.193	0.1915
$Re_{01} = 10000$	0.1877	0.1882	0.1886	0.1882
$l_0/d_e = 700$	0.165	0.166	0.167	0.1659

* For each particular calculation, those parameters are given, which differ from the prescribed conditions.

of E on $|dEu/dX|$, that of E on $\langle U\rangle_X$. Thus, the value of $\langle U\rangle_X$ is a parameter that determines the efficiency of the convective mass exchange between the flows in a VPMEA, and, in this regard, it replaces the quantity $|dEu/dX|$. The advantage of the parameter $\langle U\rangle_X$ over $|dEu/dX|$ consists in that it is more rigorously defined and can be more easily calculated. Table 1 lists values of $\langle U\rangle_X$ for different parameters of the VPMEA. The value of $\langle U\rangle_X$ decreases as Re_{01} and l_0/d_e increase and R_{ef1} decreases. The data in Table 1 indicate that, at Re_{01} 200–2000, $\langle U\rangle_X$ remains invariable. This circumstance can be readily understood if Eu is expressed in terms of Eq. (2) and substituted in Eq. (3), and account is taken of the fact that, in the case of a laminar flow, $\xi_i \sim \text{const}_i/[Re_{01}U_i(X)]$ and $\gamma_1 = \gamma_2$. At $\rho_S/\rho_L = 1$, we have $\rho_1 = \rho_2$ because $U_1^2 = U_2^2$ for a counterflow. The remaining three terms in Eq. (3) contain Re_{01} in their denominators. Therefore, Re_{01} can be canceled, with Eq. (3) brought to a form that is independent of Re_{01}. Consequently, the distributions of the x components of the dimensionless flow velocities along the VPMEA channels are independent of the Reynolds numbers at the cannel inlets in the case of a laminar flow.

Another parameter determining the value of E is the ratio $\Delta_m C_2^L/\Delta_m C_2^D$. The convenience of using the parameters $\langle U\rangle_X$ and $\Delta_m C_2^L/\Delta_m C_2^D$ consists, among other things, in that they have limited variation limits. At $H \to \infty$ we have $\Delta_m C_2^L/\Delta_m C_2^D \to 0$, and at $H = 0$, $\Delta_m C_2^L/\Delta_m C_2^D = 1/\varepsilon_2$. The data in Table 1 demonstrate that $\langle U\rangle_X$ varies from 0 to 1/2.

Figure 3 shows the calculated dimensionless concentrations $C_{1out}(T)$ and $C_{2out}(T)$ at the outlet of the first and second channels of the VPMEA at different values of H. It can be seen that, as the value of H increases (in this case, the $\Delta_m C_2^L/\Delta_m C_2^D$ ratio decreases), the stationary values C_{1outst} and C_{2outst} of the dimensioness concentrations C_{1out} and C_{2out} decrease. This fact is accounted for as follows. The concentration of the component being transferred in the second channel of the VPMEA increases because of the inflow of a continuous phase with a high concentration of this component from the first channel. The higher H, the larger the mass of the component that passes into the dispersed phase for an equilibrium to be established and the lower equilibrium concentration is attained in the second channel. This directly

Table 2. $\Delta_m C^L/\Delta_m C^D$ ratio of the maximum possible change in the concentration of the component being transferred in the continuous medium, averaged over the length of the second channel, to the similarly averaged maximum possible change in the concentration of the component being transferred in the finely dispersed medium at different interphase equilibrium constants H and porosities ε_{2in} of the finely dispersed medium at the inlet of the second channel of the VPMEA

H	$\Delta_m C^L/\Delta_m C^D$ at ε_{2in}		
	0.97	0.98	0.99
0	1.03	1.02	1.01
1	1.0	1.0	1.0
10	0.787	0.847	0.917
100	0.252	0.336	0.503
1000	0.032	0.048	0.091

follows from Eq. (7). The increase in the mass of the component being transferred in the second channel of the VPMEA as a result of the inflow of a continuous phase from the first channel is described by the last (third) term in Eq. (7). As H increases, this term becomes less important ($\Delta_m C_2^L/\Delta_m C_2^D$ ratio decreases), and the concentration in the second channel increases to a lesser extent. The concentration in the first channel decreases to a greater extent.

The dependence of the calculated degree $E = 1 - C_{1outst}$ of mass exchange between the VPMEA channel on the parameters $\langle U\rangle_X$ and $\Delta_m C_2^L/\Delta_m C_2^D$ for $R_{ef2}/R_{ef1} = 1$, $\delta_w/d_e = 10^{-5}$, $\rho_S/\rho_L = 1$ is generalized in Figs. 4, 5. The calculations were carried out at porosities $\varepsilon_{2in} = 0.97, 0.98, 0.99$ and interphase equilibrium constants $H = 0, 1, 10, 100, 1000$. For each pair of ε_{2in} and H, 19 calculations (19 values of $\langle U\rangle_X$; Table 1) were performed by varying Re_{01}, l_0/d_e, and R_{ef1}. Thus, a total of 285 calculations were performed to give 285 values of E.

Figure 4 shows the dependence of E on $\langle U\rangle_X$. It was found that the points for $H = 1$ differ only slightly from the corresponding points for $H = 0$, and, therefore, the points for $H = 1$ are not shown in the figure. Thus, Fig. 4 reflects the results of 228 calculations. It can be seen that the 19 points calculated at different VPMEA parameters (different $\langle U\rangle_X$), but at constant ε_{2in} and H fall approximately on the same straight line. Thus, there are 12 straight lines in Fig. 4, each of which is plotted using the least-squares method for 19 calculated points. As also can be seen from Fig. 4, the smaller the parameter $\langle U\rangle_X$ and the greater the constant H, the larger the calculated value of E, i.e., the higher the efficiency of the convective mass transfer between the flows in the VPMEA. In the absence of an interphase transfer ($H = 0$), the efficiency of the convective mass exchange between the flows in the VPMEA is at a minimum.

Figure 5 shows the dependence of E on the ratio $\Delta_m C^L/\Delta_m C^D$ of $\Delta_m C_2^L$ and $\Delta_m C_2^D$, averaged over the length of the second channel: $\Delta_m C^L/\Delta_m C^D = [\langle\varepsilon_2\rangle_X + (1 - \langle\varepsilon_2\rangle_X)H]^{-1}$, where $\langle\varepsilon_2\rangle_X$ is the porosity averaged over the length of the second channel. The use of the $\Delta_m C^L/\Delta_m C^D$ ratio is due to the fact that the variation of the porosity along the channel was insignificant in all the calculations [8]. Therefore, it was approximately taken that $\langle\varepsilon_2\rangle_X = \varepsilon_{2in}$. The values of the parameter $\Delta_m C^L/\Delta_m C^D$ at different ε_{2in} and H are listed in Table 2. In order not to overcharge Fig. 5, it shows the results of calculations only for 8 out of 19 different variants of the characteristics R_{ef1}, l_0/d_e, Re_{01} of the VPMEA. Thus, Fig. 5 reflects the results of 120 calculations. Because the quantity H does not appear in the hydrodynamic equations (1)–(3), 24 different values of $\langle U\rangle_X$ correspond to these 120 calculations (Table 1). The data of Table 1 indicate that changing ε_{2in} from 0.97 to 0.99 results in that the value of $\langle U\rangle_X$ changes by less than 2%. At the same time, changing the characteristics of the VPMEA leads to a significant change in $\langle U\rangle_X$. Therefore, the calculations performed at different ε_{2in} and H, but constant VPMEA characteristics show how E varies with $\Delta_m C^L/\Delta_m C^D$ at a constant $\langle U\rangle_X$. Figure 5 shows that the 15 points calculated at constant VPMEA characteristics for three different values of ε_{2in} and five different values of H fall approximately on the same straight line. Thus, Fig. 5 shows eight straight lines, each of which is plotted by the least-squares method for 15 calculated points. Each of these eight straight lines corresponds to a certain set of VPMEA characteristics and, accordingly, to a certain value of $\langle U\rangle_X$. The $\langle U\rangle_X$ averaged over three values of porosity are listed in Table 1. As can be seen in Fig. 5, the smaller the parameter $\Delta_m C^L/\Delta_m C^D$, the higher the value of E, i.e., the higher the efficiency of the convective mass exchange between the flows in the VPMEA.

According to Eqs. (7), the parameter $\Delta_m C^L/\Delta_m C^D$ directly affects the change in the concentration C_2 in channel *2* of VPMEA when the continuous phase flows from channel *1* into channel *2* (first time step). When the continuous phase flows from channel *2* into channel *1* (second time step), the last term in Eq. (7) for C_2 is zero. In Eq. (7) for C_1, the last term is zero during the first time step, and in the second, the coefficient of this term is unity. Therefore, the smaller

the parameter $\Delta_m C^L/\Delta_m C^D$, the weaker the influence exerted by the flow of the component from channel *1* into channel *2* on the change in the concentration C_2 in channel *2*, i.e., the lower C_2. Then, a continuous phase with a lower dimensionless concentration arrives at channel *1* in the second time step, and we obtain a lower $C_{1\,outst}$ at the outlet of channel *1* of the VPMEA and, accordingly, a higher degree E of mass exchange between the flows in the VPMEA channels.

Let us now discuss the influence exerted by the parameter $\Delta_m C^L/\Delta_m C^D$ on the efficiency of a VPMEA in terms of common dimensional concentrations. The parameter $\Delta_m C^L/\Delta_m C^D$ decreases when the constant H becomes larger (Table 2). A higher value of H means that, in passing from one equilibrium to another, the change in the concentration c_{L2} of the component in the continuous phase is considerably smaller than the change in the concentration c_{S2} of the component in the dispersed phase. The greater H, the smaller the change in c_{L2} and the greater the change in c_{L1}. In the case of adsorption, a considerable change in c_{L1} means that the initial continuous phase with a high concentration of the component is delivered to the inlet of channel *1*, whereas at the outlet of this channel we have a continuous phase with a low concentration of the component. In this case, a suspension with small c_{L2} and c_{S2} is delivered to the inlet of channel *2*. In the case of desorption, a substantial change in c_{L1} means that the initial continuous phase with a low concentration of the component is delivered to the inlet of channel *1*, and a continuous phase with a high concentration of the component is obtained at the outlet of channel *1*. In this case, a suspension with large c_{L2} and c_{S2} is delivered to the inlet of channel *2*. Thus, both in the case of adsorption and in desorption, the greater H, the higher E, i.e., the better the efficiency of the convective mass exchange between the flows in the VPMEA.

Each straight line in Fig. 4 is plotted at a certain value of $\Delta_m C^L/\Delta_m C^D$, and each straight line in Fig. 5, at a certain value of $\langle U\rangle_X$. Therefore, the family of straight lines in Fig. 4 can be described as

$$E\left(\langle U\rangle_X, \frac{\Delta_m C^L}{\Delta_m C^D}\right) = k_1\left(\frac{\Delta_m C^L}{\Delta_m C^D}\right)\langle U\rangle_X + k_2\left(\frac{\Delta_m C^L}{\Delta_m C^D}\right), \quad (17)$$

and the family of straight lines in Fig. 5, as

$$E\left(\langle U\rangle_X, \frac{\Delta_m C^L}{\Delta_m C^D}\right) = k_3(\langle U\rangle_X)\frac{\Delta_m C^L}{\Delta_m C^D} + k_4(\langle U\rangle_X). \quad (18)$$

The coefficients k_1, k_2 and k_3, k_4 were calculated for each straight line in Figs. 4, 5 by the least-squares method.

The dependences $k_1(\Delta_m C^L/\Delta_m C^D)$, $k_2(\Delta_m C^L/\Delta_m C^D)$, $k_3(\langle U\rangle_X)$, and $k_4(\langle U\rangle_X)$ are shown in Fig. 6. It can be seen that these dependences are linear. Each straight line in Fig. 6 is plotted on the basis of the calculated points, using the least-squares method:

$$k_1\left(\frac{\Delta_m C^L}{\Delta_m C^D}\right) = k_{11}\frac{\Delta_m C^L}{\Delta_m C^D} + k_{12}, \quad (19)$$

$$k_2\left(\frac{\Delta_m C^L}{\Delta_m C^D}\right) = k_{21}\frac{\Delta_m C^L}{\Delta_m C^D} + k_{22},$$

$$k_3(\langle U\rangle_X) = k_{31}\langle U\rangle_X + k_{32}, \quad (20)$$

$$k_4(\langle U\rangle_X) = k_{41}\langle U\rangle_X + k_{42},$$

where $k_{11} = -0.3521$, $k_{12} = -0.9529$, $k_{21} = 4.0394 \times 10^{-2}$, $k_{22} = 1.0998$, $k_{31} = -0.3539$, $k_{32} = 4.140 \times 10^{-2}$, $k_{41} = -0.9592$, $k_{42} = 1.1027$.

Substituting Eq. (19) into (17) and Eq. (20) into (18), we obtain

$$E\left(\langle U\rangle_X, \frac{\Delta_m C^L}{\Delta_m C^D}\right) = k_{11}\frac{\Delta_m C^L}{\Delta_m C^D}\langle U\rangle_X + k_{12}\langle U\rangle_X + k_{21}\frac{\Delta_m C^L}{\Delta_m C^D} + k_{22}, \quad (21)$$

$$E\left(\langle U\rangle_X, \frac{\Delta_m C^L}{\Delta_m C^D}\right) = k_{31}\langle U\rangle_X\frac{\Delta_m C^L}{\Delta_m C^D} + k_{32}\frac{\Delta_m C^L}{\Delta_m C^D} + k_{41}\langle U\rangle_X + k_{42}. \quad (22)$$

Thus, the dependence $E(\langle U\rangle_X, \Delta_m C^L/\Delta_m C^D)$ can be represented as

$$E\left(\langle U\rangle_X, \frac{\Delta_m C^L}{\Delta_m C^D}\right) = a_1\langle U\rangle_X\frac{\Delta_m C^L}{\Delta_m C^D} + a_2\frac{\Delta_m C^L}{\Delta_m C^D} + a_3\langle U\rangle_X + a_4, \quad (23)$$

where the coefficients $a_1 = (k_{11} + k_{31})/2 = -0.3530$, $a_2 = (k_{21} + k_{32})/2 = 4.090 \times 10^{-2}$, $a_3 = (k_{12} + k_{41})/2 = -0.9560$, $a_4 = (k_{22} + k_{42})/2 = 1.1012$.

An important temporal characteristic of the convective mass exchange between the flows in the VPMEA is the residence time $t_R \sim V/G \sim l_0/u_{01}$ of the finely dispersed phase in the VPMEA. Here, $V = l_0(s_1 + s_2)$ is the volume of the VPMEA; $G = (u_{01}s_1t_{ts1} + u_{02}s_2t_{ts2})/(t_{ts1} + t_{ts2})$, the average (in two time steps) flow rate of dispersed flows; and t_{ts1} and t_{ts2}, the durations of the first and second time steps. The residence

time is directly related to the time in which a steady-state operation of the VPMEA is attained. An exact calculation of the residence time is only possible for the dispersed phase. As particles of the dispersed phase do not pass from one channel into the other, the residence time of these particles in the VPMEA is the time of their motion within a certain channel, from inlet to outlet. A displacement dx along the channel takes a time d$x/u(x)$. Then, the residence time is found by integration along the channel length

$$t_R = \int_0^{l_0} \frac{dx}{u(x)} \quad \text{or} \quad T_R = \frac{t_R}{l_0} = \int_0^1 \frac{dX}{U(X)}. \qquad (24)$$

Exact calculation of the residence time for the continuous phase is impossible, because its different portions may move within a channel from inlet to outlet or may flow from one channel into the other, and such an interchanell flow may occur at any point of the permeable partition. At the same time, there is no doubt that the characteristic time of flow motion within the VPMEA is the l_0/u_{01} ratio, and the residence time will be of the same order of magnitude as this parameter. Therefore, if we are only interested in the order of magnitude of the residence time, we can use the l_0/u_{01} ratio. A more reliable estimate of the residence time is given by the V/G ratio. For the system being calculated, $V/G = 2l_0/u_{01}$. The corresponding value of the dimensionless time $T = 2$. It should also be noted that the parameter $1/\langle U\rangle_X$ can be regarded as the dimensionless residence time. This assumption is confirmed by the results of calculations. In Fig. 3, curves *1* and *2* level off (reach the stationary concentrations) at $T \approx 4$, with $1/\langle U\rangle_X = 4.221$. The discrepancy between these values does not exceed 5–6%.

CONCLUSIONS

(1) Integral parameters determining the efficiency of the convective mass exchange (degree of mass exchange) between flows of finely dispersed media in a valve-pulsatory mass-exchange apparatus were found for the case when the intensity of interphase mass transfer is so high that the continuous and dispersed phases can be considered to be in equilibrium ($\mathrm{Sh}\cdot\mathrm{Fo} = \beta t_{ts}/d_S >> 1$) at any point of the apparatus at any instant of time. These parameters are the following: (1) ratio $\langle U\rangle_X$ of the longitudinal flow velocity averaged over the channel length to the flow velocity at the channel inlet and (2) ratio $\Delta_m C^L/\Delta_m C^D = 1/[\varepsilon + (1 - \varepsilon)H]$ of the maximum possible change in the concentration of the component being transferred in the continuous phase to the maximum possible change in the concentration of the component being transferred in the dispersed phase. Here ε is the porosity of the finely dispersed phase and H is the constant characterizing the interphase equilibrium in the finely dispersed phase.

(2) It was established that the efficiency of the convective mass exchange (degree of mass exchange) between the flows of the finely dispersed and continuous media is the higher, the smaller the values of $\langle U\rangle_X$ and $\Delta_m C^L/\Delta_m C^D = 1/[\varepsilon + (1 - \varepsilon)H]$.

(3) It was shown that the parameters $\langle U\rangle_X$ and $\Delta_m C^L/\Delta_m C^D = 1/[\varepsilon + (1 - \varepsilon)H]$ can be used in optimization of the design and operation modes of a valve-pulsatory mass-exchange apparatus in the case of a very strong interphase mass transfer ($\mathrm{Sh}\cdot\mathrm{Fo} = \beta t_{ts}/d_S >> 1$).

REFERENCES

1. USSR Inventor's Certificate, no. 548290.
2. RF Patent 1337133.
3. RF Patent 1182722.
4. Aliev, M.R., Aliev, R.Z., and Aliev, A.R., *Teor. Osn. Khim. Tekhnol.*, 2001, vol. 35, no. 3, pp. 288–297.
5. Aliev, R.Z., Aliev, M.R., and Aliev, A.R., *Zh. Prikl. Khim.*, 2002, vol. 75, no. 12, pp. 2021–2025.
6. Aliev, M.R., Aliev, R.Z., and Aliev, A.R., *Teor. Osn. Khim. Tekhnol.*, 2003, vol. 37, no. 1, pp. 27–33.
7. Aliev, R.Z., Aliev, M.R., Aliev, A.R., and Bolshakov, O.V., *J. Food Eng.*, 2003, vol. 56, no. 4, pp. 377–385.
8. Aliev, R.Z., Aliev, M.R., and Aliev, A.R., *Zh. Prikl. Khim.*, 2001, vol. 74, no. 12, pp. 2006–2012.
9. Romankov, P.G., Rashkovskaya, N.B., and Frolov, V.F., *Massoobmennye protsessy khimicheskoi tekhnologii* (Mass-Exchange Processes in Chemical Technology), Leningrad: Khimiya, 1975.
10. Aliev, M.R. and Aliev, R.Z., *Teor. Osn. Khim. Tekhnol.*, 1997, vol. 31, no. 1, pp. 102–104.
11. Aliev, M.R., Aliev, R.Z., and Aliev, A.R., *Teor. Osn. Khim. Tekhnol.*, 1999, vol. 33, no. 1, pp. 23–29.
12. Aliev, M.R., Aliev, R.Z., and Aliev, A.R., *Chem. Eng. Technol.*, 2002, vol. 25, no. 7, pp. 735–737.
13. Aliev, M.R., Aliev, R.Z., and Aliev, A.R., *Mat. Model.*, 1998, vol. 10, no. 7, pp. 48–60.
14. Aliev, R.Z., Aliev, M.R., and Aliev, A.R., *Khim. Prom–st.*, 2000, no. 5, pp. 22–33.
15. Aliev, A.R., Aliev, M.R., and Aliev, R.Z., *Teploenergetika*, 2002, vol. 49, no. 6, pp. 64–69.
16. Aliev, A.R., Aliev, M.R., and Aliev, R.Z., *Teploenergetika*, 2003, vol. 50, no. 12, pp. 57–64.
17. Aliev, M.R., Aliev, R.Z., and Aliev, A.R., *Teor. Osn. Khim. Tekhnol.*, 2004, vol. 38, no. 2.
18. Aliev, A.R., Aliev, M.R., and Aliev, R.Z., *Teplofiz. Vys. Temp.*, 2004, vol. 42, no. 2.

Russian Journal of Applied Chemistry, Vol. 77, No. 6, 2004, pp. 957–963. Translated from Zhurnal Prikladnoi Khimii, Vol. 77, No. 6, 2004, pp. 971–977.

PROCESSES AND EQUIPMENT OF CHEMICAL INDUSTRY

Flow Hydrodynamics of non-Newtonian Fluid in a Cylindrical-Conical Hydrocyclone

V. O. Yablonskii

Volgograd State University, Volgograd, Russia

Received October 1, 2003

Abstract—A system of equations of rheodynamics that describes the flow of a non-Newtonian fluid with a free surface in a cylindrical-conical hydrocyclone was solved numerically. The fields of velocities and pressure, as well as the dependence of the thickness of the fluid film on the axial coordinate, were calculated. The influence exerted by the rheological properties of the fluid and by the defining similarity criteria on the flow hydrodynamics was studied.

Cylindrical-conical hydrocyclones are the most widely used industrial apparatus for separating inhomogeneous dispersed systems. The simplicity of their design, small size, and high separation efficiency ensure their preferential use as compared with centrifuges and separators.

Suspensions separated in chemical industry are in many cases non-Newtonian fluids whose effective vscosity depends on the deformation rates. Suspensions of this kind are separated in manufacture of protein–vitamin concentrates (paprin, haprin, meprin), in production of suspensions of biomass, glaze, and SiC_3, and in purification of wastewater to remove oil, fats, and other substances. The lack of any adequate model of the hydrodynamics of non-Newtonian fluids in a cylindrical-conical hydrocyclone is still the main obstacle on the way to development of a general procedure for calculating these apparatus.

The known studies devoted to a theoretical analysis of the hydrodynamics of cylindrical-conical hydrocyclones [1–4] cannot be used in developing a procedure for an engineering calculation of a hydrocyclone because of the fact that the mathematical models of the flow in a hydrocyclone most frequently do not reflect the real process and lead to deviation of calculated separation parameters from their true values. In particular, the studies mentioned did not consider the fluid flow in a hydrocyclone with a free surface, which impairs the accuracy and applicability of calculation formulas derived in these studies.

It was mentioned in [1] that, to construct an adequate model of the flow in a cylindrical-conical hydrocyclone, it is necessary to use complete Navier–Stokes equations, which are transformed into equations of rheodynamics in the case of separation of non-Newtonian media. In [5, 6], a conclusion was made that the rheological equation of state of a non-Newtonian fluid, which is commonly written in the form of a power-law Ostwald de Veille equation, is applicable to suspensions.

In [7, 8], the author modeled the hydrodynamics of a non-Newtonian fluid in a cylindrical straight-flow hydrocyclone used to classify particles of the solid phase of the suspension into fractions and to separate and purify suspensions in a centrifugal field. However, no solution of the complete equations of rheodynamics of a non-Newtonian fluid for a swirling flow in a cylindrical-conical hydrocyclone has been reported in the literature.

The mathematical model of the process of development of a rotatory flow of a film of a non-New tonian fluid in a cylindrical-conical hydrocyclone is a set of equations of rheodynamics, a continuity equation, boundary conditions, and an equation that expresses the constancy of the fluid flow rate along the axis of the hydrocyclone. The flow pattern is shown schematically in Fig. 1.

The hydrocyclone comprises a cylindrical chamber, into which a fluid is tangentially fed, and a conical part. The fluid fed into the casing of the hydrocyclone

1070-4272/04/7706-0957 © 2004 MAIK "Nauka/Interperiodica"

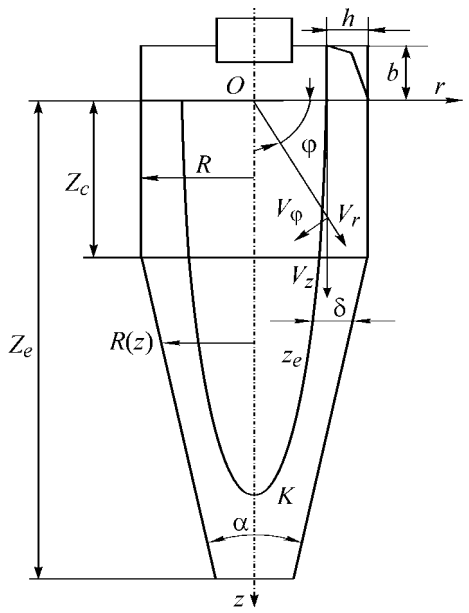

Fig. 1. Scheme of the flow in a cylindrical-conical hydrocyclone.

flows down, swirling, along the walls under the action of the gravity force and the pressure, being characterized by radial (V_r), circumferential (V_φ), and axial (V_z) velocity components. It is assumed that the velocity distribution is independent of the angular coordinate and the flow has a rotation symmetry. This assumption is well justified in practice [9], when the centrifugal acceleration exceeds the gravitational acceleration, which is characteristic of hydrocyclones of any design. It is also assumed that the flow is laminar, the surface tension force and that of friction of the film against the gas medium are negligible, the fluid is incompressible, and the flow is wave-free. The air pressure within the hydrocyclone casing is constant and equal to the atmospheric pressure P_0.

It is assumed that the rheological properties of the suspension are described by the generalized Ostwald de Veille law

$$\tau_{ij} = kA^{n-1}\gamma_{ij}, \qquad (1)$$

$$A = \sqrt{2\left(\frac{\partial V_r}{\partial r}\right)^2 + 2\left(\frac{V_r}{r}\right)^2 + 2\left(\frac{\partial V_z}{\partial z}\right)^2 + \left(\frac{\partial V_\varphi}{\partial r} + \frac{V_\varphi}{r}\right)^2 + \left(\frac{\partial V_\varphi}{\partial z}\right)^2 + \left(\frac{\partial V_z}{\partial r} + \frac{\partial V_r}{\partial z}\right)^2},$$

where τ_{ij} are components of the stress tensor (Pa); γ_{ij}, components of the deformation rate tensor (s^{-1}); A, the intensity of the deformation rates (s^{-1}); n the nonlinearity indicator for the flow curve; k, the consistency index (Pa s^n); and r, φ, z, the radial, circumferential, and axial coordinates, respectively.

The Navier–Stokes equations in terms of the components of the stress tensor and the continuity equation, written in a cylindrical system of coordinates [11], will have for the flow under consideration the following form

$$V_r\frac{\partial V_r}{\partial r} + V_z\frac{\partial V_z}{\partial z} - \frac{V_\varphi^2}{r} = -\frac{1}{\rho}\frac{\partial P}{\partial r} + \frac{1}{\rho}\left(\frac{\partial \tau_{rr}}{\partial r} + \frac{\partial \tau_{rz}}{\partial z} + \frac{\tau_{rr} - \tau_{\varphi\varphi}}{r}\right), \qquad (2)$$

$$V_r\frac{\partial V_z}{\partial r} + V_z\frac{\partial V_z}{\partial z} - \frac{V_\varphi^2}{r} = -\frac{1}{\rho}\frac{\partial P}{\partial z} + \frac{1}{\rho}\left(\frac{\partial \tau_{rz}}{\partial r} + \frac{\tau_{rz}}{r} + \frac{\partial \tau_{zz}}{\partial z}\right) + g, \qquad (3)$$

$$V_r\frac{\partial V_\varphi}{\partial r} + \frac{V_r V_\varphi}{r} + V_z\frac{\partial V_\varphi}{\partial z} = \frac{1}{\rho}\left(\frac{\partial \tau_{r\varphi}}{\partial r} + 2\frac{\tau_{r\varphi}}{r} + \frac{\partial \tau_{\varphi z}}{\partial z}\right), \qquad (4)$$

$$\frac{\partial V_r}{\partial r} + \frac{\partial V_r}{\partial z} + \frac{V_r}{r} = 0, \qquad (5)$$

where P is the pressure in the fluid (Pa); ρ, the average fluid density (kg m^{-3}); and g, the free fall acceleration (m s^{-2}).

The system of equations (2)–(5) should be solved with the following boundary conditions

$$z \le z_c,$$

$$r = R,\ V_r = 0,\ V_\varphi = 0,\ V_z = 0,$$

$$r = R - w,\ \tau_{r\varphi} = 0,\ \tau_{rz} = 0,\ V_r = V_z(\partial w/\partial z),\ P + \tau_{rr} = P_0;$$

$$z > z_c,$$

$$r = R - (z - z_c)\tan(\alpha/2),\ V_r = 0,\ V_\varphi = 0,\ V_z = 0,$$

$$r = R - (z - z_c)\tan(\alpha/2) - w,\ \tau_{r\varphi} = 0,\ \tau_{rz} = 0,$$

$$V_r = V_z(\partial w/\partial z),\ P + \tau_{rr} = P_0;$$

$$z = 0,$$

$$V_\varphi = (2/h)U_0(R - r),$$

$$V_z = [2U_0(R - r)b]/[\pi h(2R - h)],\ V_r = 0,\ P = P_b(r);$$

$$z = z_c,$$

$$\frac{\partial V_z}{\partial z} = \frac{\partial V_\varphi}{\partial z} = \frac{\partial V_r}{\partial z} = 0, \qquad (6)$$

where z_c and R are the axial size and the radius of the cylindrical chamber of the hydrocyclone casing (m); α, the cone angle of the conical part of the hydrocyclone casing (deg); $P_b(r)$ the pressure distribution function over the radial cross-section at $z = 0$ (Pa); z_e, the coordinate of the discharge opening in the conical part of the hydrocyclone casing (m); w, the thickness of the fluid film (m); and h and b, the width and height of the inlet pipe (m).

At the exit from the conical part of the hydrocyclone casing, a "soft" boundary condition is set [12]: the derivatives of the velocity components along the axial coordinates should be zero.

Substitution of the values of the stress tensor components found using the rheological relation (1) into the system of the Navier–Stokes and continuity equations (2)–(5) yields a system of rheodynamic equations for the non-Newtonian fluid in the dimensionless form:

$$f\frac{\partial f}{\partial \bar r} + H\frac{\partial f}{\partial \bar z} - \frac{\theta^2}{\bar r} = -\frac{\partial F}{\partial \bar r} + \frac{1}{\mathrm{Re}_n}\left[2\frac{\partial A_0^{n-1}}{\partial \bar r}\frac{\partial F}{\partial \bar r} + 2A_0^{n-1}\frac{\partial^2 F}{\partial \bar r^2} + \frac{\partial A_0^{n-1}}{\partial \bar z}\left(\frac{\partial H}{\partial \bar r} + \frac{\partial f}{\partial \bar z}\right) + A_0^{n-1}\frac{\partial^2 H}{\partial \bar z \partial \bar r} + A_0^{n-1}\frac{\partial^2 F}{\partial \bar z^2} + 2A_0^{n-1}\frac{1}{\bar r}\frac{\partial F}{\partial \bar r} - 2A_0^{n-1}\frac{f}{\bar r^2}\right], \quad (7)$$

$$f\frac{\partial H}{\partial \bar\tau} + H\frac{\partial H}{\partial \bar z} = -\frac{\partial F}{\partial \bar r} + \frac{1}{\mathrm{Re}_n}\left[\frac{\partial A_0^{n-1}}{\partial \bar r}\left(\frac{\partial H}{\partial \bar r} + \frac{\partial f}{\partial \bar z}\right) + A_0^{n-1}\left(\frac{\partial^2 H}{\partial \bar r^2} + \frac{\partial^2 f}{\partial \bar r \partial \bar z}\right) + 2A_0^{n-1}\frac{\partial^2 H}{\partial \bar z^2} + 2A_0^{n-1}\frac{\partial A_0^{n-1}}{\partial \bar z}\frac{\partial H}{\partial \bar z}\right] + \frac{1}{\mathrm{Fr}}, \quad (8)$$

$$f\frac{\partial \theta}{\partial \bar r} + \frac{\theta f}{\bar r} + H\frac{\partial \theta}{\partial \bar z} = \frac{1}{\mathrm{Re}_n}\left[\frac{\partial A_0^{n-1}}{\partial \bar r}\left(\frac{\partial \theta}{\partial \bar r} - \frac{\theta}{\bar r}\right) + A_0^{n-1}\left(\frac{1}{\bar r}\frac{\partial \theta}{\partial \bar r} - \frac{\theta}{\bar r^2} + \frac{\partial^2 \theta}{\partial \bar r^2}\right) + \frac{\partial A_0^{n-1}}{\partial \bar z}\frac{\partial \theta}{\partial \bar z} + A_0^{n-1}\frac{\partial^2 \theta}{\partial \bar z^2}\right], \quad (9)$$

$$\frac{\partial f}{\partial \bar r} + \frac{\partial H}{\partial \bar z} + \frac{f}{\bar r} = 0. \quad (10)$$

After a transformation to the dimensionless form, the boundary conditions (6) will look like

$$\bar z \le \bar z_c,$$

$$\bar r = 1,\ f = 0,\ \theta = 0,\ H = 0,$$

$$r = 1 - \bar w,\ \partial\theta/\partial\bar r - \theta/\bar r = 0,\ \partial H/\partial\bar r + \partial f/\partial\bar z = 0,$$

$$f = H\partial\bar w/\partial\bar z,\ F = -(2kU_0^{n-2}/\rho R^n)(A_0^{n-1}\partial f/\partial\bar r);$$

$$\bar z > \bar z_c,$$

$$\bar r = 1 - (\bar z - \bar z_c)\tan(\alpha/2),\ f = 0,\ \theta = 0,\ H = 0,$$

$$\bar r = 1 - (\bar z - \bar z_c)\tan(\alpha/2) - \bar w,$$

$$\partial\theta/\partial\bar r - \theta/\bar r = 0,\ \partial H/\partial\bar r + \partial f/\partial\bar z = 0;$$

$$z = 0,$$

$$\theta = (2/\bar h)(1 - \bar r),$$

$$H = [2\bar b(1 - \bar r)/(\pi\bar h(2 - \bar h),\ f = 0,\ F = F_b(\bar r);$$

$$z = z_e,$$

$$\frac{\partial H}{\partial \bar z} = \frac{\partial \theta}{\partial \bar z} = \frac{\partial f}{\partial \bar z} = 0, \quad (11)$$

where

$$\mathrm{Fr} = \frac{U_0^2}{gR},\ \mathrm{Re}_n = \frac{\rho R^n U_0^{2-n}}{k},\ \bar Q = \frac{Q}{\pi R^2 U_0} = \frac{bh}{\pi R^2}.$$

Fr is the centrifugal Froude number (separation factor); Re_n, an analogue of the Reynolds number for power-law fluids; $\bar Q$, the dimensionless flow rate; and

$$A_0 = \sqrt{2\left(\frac{\partial f}{\partial \bar r}\right)^2 + 2\left(\frac{f}{\bar r}\right)^2 + 2\left(\frac{\partial H}{\partial \bar z}\right)^2 + \left(\frac{\partial \theta}{\partial \bar r} - \frac{\theta}{\bar r}\right)^2 + \left(\frac{\partial \theta}{\partial \bar z}\right)^2 + \left(\frac{\partial H}{\partial \bar z} + \frac{\partial f}{\partial \bar r}\right)^2}.$$

A_0 is the dimensionless intensity of the deformation rate.

The dimensionless and dimensional variables are related by

$$\bar z = \bar z/R,\ \bar r = r/R,\ H(\bar r, \bar z) = V_r/U_0,\ f(\bar r, \bar z) = V_z/U_0,$$
$$\theta(\bar r, \bar z) = V_\varphi/U_0,\ F(\bar r, \bar z) = (P - P_0)/(\rho U_0^2),\ \bar w = w/R,$$
$$\bar h = h/R,\ \bar b = b/R,\ U_0 = Q/bh,$$

where $\bar z$, $\bar r$ are the dimensionless axial and radial coordinates, respectively; $H(\bar r, \bar z)$, $f(\bar r, \bar z)$, and $\theta(\bar r, \bar z)$, the dimensionless axial, radial, and circumferential components of the flow velocity; $F(\bar r, \bar z)$, the dimen-

sionless pressure; $F_b(\bar{r})$, the distribution function of dimensionless pressure over the radial cross-section at $\bar{z} = 0$ $\bar{w}$, the dimensionless thickness of the fluid film; $\bar{h}$, $\bar{b}$, the dimensionless width and height of the inlet pipe; $\bar{z}_c$, the dimensionless axial size of the cylindrical chamber of the hydrocyclone; $\bar{z}_e$, the dimensionless coordinate of the discharge opening in the conical part of the hydrocyclone casing; U_0, the average flow velocity in the inlet pipe of the hydrocyclone (m s^{-1}); and Q, the flow rate of the fluid (m^3 s^{-1}).

To determine the hydrodynamic parameters of the flow, it is necessary to numerically integrate the system of differential equations (7)–(10) in partial derivatives at appropriate boundary conditions (11) with account of the geometry of the working space of a hydrocyclone. The integration of the system of differential equations in partial derivatives was performed by the finite-difference method. The finite-difference analogue of the rheodynamic and continuity equations served as a basis for developing a calculation program written in the Compaq Visual Fortran language. The software developed performed calculations by formulas constructed on the basis of a finite-difference analogue of the mathematical model (7)–(11), which is an implicit finite-difference scheme. The solution was obtained on a computer by means of a sequential (over grid nodes) cyclic procedure based on the Zeidel method. At a grid node, the pressure P was found from the finite-difference analogue of Eq. (7); the axial component H of the flow velocity, from an analogue of Eq. (8); the circumferential component θ of the flow velocity, from an analogue of (9); and the radial component f of the flow velocity, from an analogue of the continuity equation (10). The calculated flow region was divided using a nonuniform grid with 50×50 cells along the radial and axial coordinates. The shape of the grid cells was determined by the profile of the free surface of the film and by the cone angle of the conical part of the hydrocyclone casing.

The thickness of the fluid film was found from the integral continuity equation

$$\bar{Q} = 2\int_{\bar{R}(\bar{z})-\bar{w}}^{\bar{R}(\bar{z})} \bar{r}H(\bar{r}, \bar{z})\mathrm{d}\bar{r} = \text{const}, \qquad (12)$$

where $\bar{R}(\bar{z}) = R(z)/R$ is the nondimensional radius of the hydrocyclone casing.

Equation (12) expresses the condition of a constant flow rate in a hydrocyclone in the axial direction. In expression (12), the profile of the axial component of the velocity was integrated across the fluid film thickness at a running value of the dimensionless radius $\bar{R}(\bar{z})$ of the apparatus casing, which is a piecewise-linear function of $\bar{z}$ and can be found from the relation $\bar{R}(\bar{z}) = 1$ for the cylindrical chamber of the hydrocyclone at $\bar{z} \le \bar{z}_c$ and from the formula

$$\bar{R}(\bar{z}) = 1 - (\bar{z} - \bar{z}_c)\tan(\alpha/2).$$

for the conical part of the casing at $z > z_c$.

The film thickness was calculated using the expression derived from Eq. (12):

$$\bar{w} = \bar{R}(\bar{z}) - \sqrt{\bar{R}(\bar{z}) - \bar{Q}/H_{\mathrm{av}}(\bar{z})}, \qquad (13)$$

where $H_{\mathrm{av}}(\bar{z})$ is the average value of the axial component of the velocity in the radial cross-section at $z = \text{const}$.

The value of $H_{\mathrm{av}}(\bar{z})$ was found by numerical integration of the resulting profile of the axial component of the velocity, $H(\bar{r}, \bar{z})$, in each radial cross-section at $\bar{z} = \text{const}$.

The film thickness was found using Eq. (13) in the direction of the $\bar{z}$ axis as far as the point of confluence of the fluid film into a continuous flow in the bottom zone of the conical part of the hydrocyclone casing (Fig. 1, point K). This point was named the critical point, on reaching which the calculation was terminated and the control was transferred to the loop operator for calculating the next approximation. In the case when no flow confluence occurred, the calculation was performed as far as the discharge opening in the conical part of the hydrocyclone casing.

The flow of a non-Newtonian fluid in a hydrocyclone is characterized by the nonlinearity indicator n for the flow curve, centrifugal Froude number Fr (separation factor), analogue of the Reynolds number for non-Newtonian fluids Re_n, and dimensionless flow rate $\bar{Q}$.

The numerical modeling was carried out at the nonlinearity indicator for the flow curve varying in the range $n = 0.6$–1.3, which corresponds to pseudoplastic ($n < 1.0$) and dilatant ($n > 1.0$) fluids, and also to a Newtonian fluid at $n = 1.0$, for a cylindrical-conical hydrocyclone in which the height of the cylindrical chamber is equal to the apparatus diameter ($z_c = 2$) and the cone angle of the conical part of the apparatus $\alpha = 10°$.

Figure 2 shows calculated dependences of the dimensionless thickness $\bar{w}$ of the film on the axial coordinate $\bar{z}$ at different nonlinearity indicators n for the flow curve. Analysis of the dependences shows that the dimensionless thickness of a film of a non-Newtonian fluid in a cylindrical-conical hydrocyclone first decreases and then starts to increase in the direction of the $\bar{z}$ axis of the apparatus. This is due to an steep rise in the axial component of the flow velocity in the initial region because of the influence exerted on the flow by the gravity force and pressure and to a decrease in the perimeter of the flow section of the conical part of the apparatus casing in the direction of the $\bar{z}$ axis. As the nonlinearity factor n for the flow curve increases, the dimensionless thickness $\bar{w}$ of the film grows, and this rise is the most pronounced near the discharge opening in the conical part of the hydrocyclone casing, which is caused by an increase in the effective viscosity of the non-Newtonian fluid.

The calculated dependences of the dimensionless thickness $\bar{w}$ of a film of a pseudoplastic liquid (n = 0.6) on the axial coordinate $\bar{z}$ for different values of the Froude number (separation factor) Fr are shown in Fig. 3a, and the same dependences for a Newtonian fluid (n = 1.0), in Fig. 3b. Analysis of the dependences in Figs. 3a and 3b shows that, as the Fr number increases, the thickness of the film of a pseudoplastic fluid grows, which is accounted for by the increasing influence of centrifugal forces on the flow and by the decreasing influence of gravity, especially in the bottom zone of the conical part of the cylindrical-conical hydrocyclone casing, where the circumferential component of the flow velocity increases dramatically. For the Newtonian fluid, the film thickness grows with increasing Froude number Fr more steeply, because at high shear rates the effective viscosity of a pseudoplastic fluid decreases, and that of Newtonian fluid remains constant.

The obtained dependences of the axial and circumferential components of the flow velocity on the radial coordinate can be approximated by the expressions

$$H(\bar{r},\bar{z}) = H_{\max}(\bar{z})\left[1 - \left(1 - \frac{1-\bar{r}}{\bar{w}}\right)^{M}\right],$$
$$\theta(\bar{r},\bar{z}) = \theta_{\max}(\bar{z})\left[1 - \left(1 - \frac{1-\bar{r}}{\bar{w}}\right)^{L}\right], \quad (14)$$

where $H_{\max}(\bar{z})$ is the maximum value of the axial component of the flow velocity at the surface of the fluid film; M, the filling factor of the profile of the axial component of the flow velocity; $\theta_{\max}(\bar{z})$, the maximum value of the circumferential component of the flow velocity on the surface of the fluid film; and L, the filling factor of the profile of the circumferential component of the flow velocity.

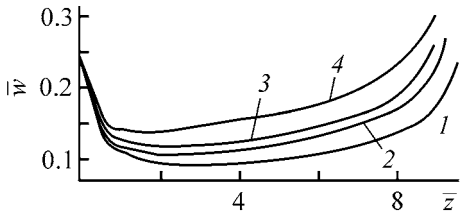

Fig. 2. Dimensionless thickness $\bar{w}$ of the fluid film vs. the axial coordinate $\bar{z}$ at different nonlinearity indicators n for the flow curve. Fr = 73.4, Re_n = 4000.0, $\bar{Q}$ = 0.04, α = 10°; the same for Figs. 4, 6. n: (*1*) 0.6, (*2*) 0.8, (*3*) 1.0, and (*4*) 1.2.

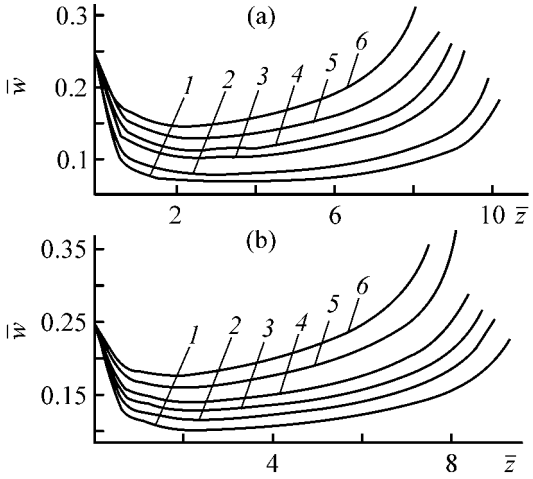

Fig. 3. Dimensionless thickness $\bar{w}$ of the fluid film vs. the axial coordinate $\bar{z}$ at different Froude numbers Fr. Re_n = 4000.0, $\bar{Q}$ = 0.04, α = 10°; the same for Fig. 5. n: (a) 0.6 and (b) 1.0. Fr: (*1*) 32.6, (*2*) 50.0, (*3*) 100.0, (*4*) 130.5, (*5*) 203.9, and (*6*) 293.6.

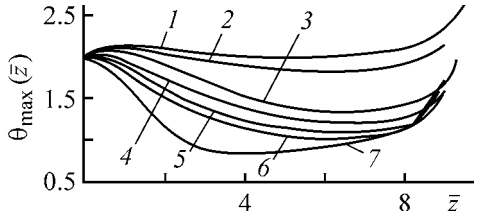

Fig. 4. Maximum circumferential component of velocity at the film surface, $\theta_{\max}(\bar{z})$, vs. the axial component $\bar{z}$ at different nonlinearity indicators n for the flow curve. n: (*1*) 0.6, (*2*) 0.7, (*3*) 0.8–0.9, (*4*) 1.0, (*5*) 1.1, (*6*) 1.2, and (*7*) 1.3.

Figure 4 shows how the maximum circumferential component of the flow velocity on the surface of a film of a non-Newtonian fluid, $\theta_{\max}(\bar{z})$, depends on the axial coordinate $\bar{z}$ at different nonlinearity indicators n for the flow curve. It was established that the cir-

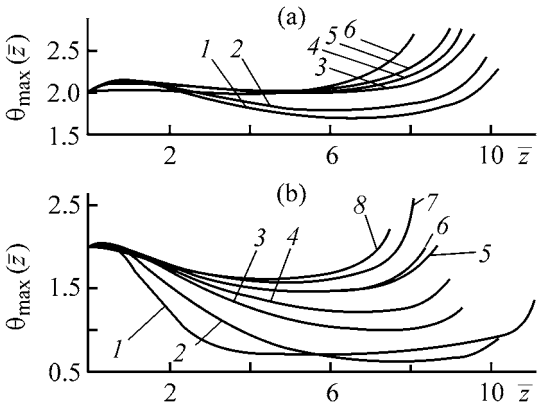

Fig. 5. Maximum circumferential component of velocity at the film surface, $\theta_{max}(\bar{z})$, vs. the axial component $\bar{z}$ at different Froude numbers Fr. *n*: (a) 0.6 and (b) 1.0. Fr: (a) (*1*) 32.6, (*2*) 50.0, (*3*) 73.4, (*4*) 100.0, (*5*) 130.5, and (*6*) 293.6; (b) (*1*) 8.2, (*2*) 18.4, (*3*) 50.0, (*4*) 73.4, (*5*) 100.0, (*6*) 130.5, (*7*) 203.9, and (*8*) 293.6.

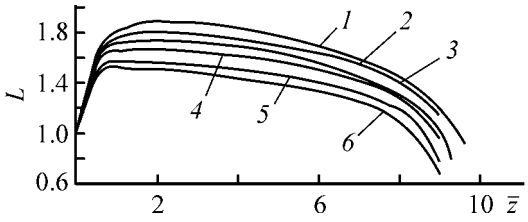

Fig. 6. Filing factor *L* of the profile of the circumferential component of the flow velocity vs. the axial component $\bar{z}$ at different nonlinearity indicators *n* for the flow curve. *n*: (*1*) 0.6, (*2*) 0.7, (*3*) 0.8–0.9, (*4*) 1.0, (*5*) 1.1, and (*6*) 1.2.

cumferential component of the flow velocity at the film surface first decays in the direction of the hydrocyclone axis and then, as the conical part of the casing becomes narrower, again increases, with this increase being the most pronounced in regions close to the film surface. The increase in the circumferential component of the velocity at the film surface is due to the conservation of the initial angular momentum of the swirling fluid. Analysis of the calculated dependences presented shows that the rate at which the maximum circumferential component of the flow velocity decays for pseudoplastic fluids ($n < 1.0$) decreases as the anomaly of non-Newtonian properties becomes more pronounced (as *n* decreases) because of a decrease in the effective viscosity in zones with high shear rates. For dilatant fluids, the rate at which the maximum circumferential component of the flow velocity grows as the anomaly of non-Newtonian properties becomes more pronounced (as *n* increases) because the effective viscosity of dilatant fluids increases with *n*.

Figure 5a shows how the maximum circumferential component of the flow velocity, $\theta_{max}(\bar{z})$, depends on the axial coordinate $\bar{z}$ for different values of the Froude number Fr for a pseudoplastic liquid ($n = 0.6$); similar dependences for a Newtonian fluid ($n = 1.0$) are presented in Fig. 5b. Analysis of the dependences in Fig. 5a shows that, as the Fr number increases, the maximum circumferential component of the flow velocity grows, especially near the discharge opening in the conical part of the hydrocyclone casing, which is accounted for by the increasing thickness of the fluid film. Analysis of the dependences in Fig. 5b shows that the decay of the circumferential component of the flow velocity in the direction of the hydrocyclone's axis decreases as the Froude number Fr grows, and does so to a greater extent than in the case of a pseudoplastic fluid, because the effective viscosity of the Newtonian fluid is independent of the shear rate.

Figure 6 shows how the filling factor of the profile of the circumferential component of the flow velocity of a non-Newtonian fluid, *L*, depends on the axial coordinate $\bar{z}$ for different nonlinearity indicators for the flow curve. Analysis of the dependences shows that the filling factor of the profile of the circumferential component of the flow velocity increases in the initial part of the flow and then decreases in the conical part of the hydrocyclone casing, especially near the discharge opening, which is due to the conservation of angular momentum of the swirling flow. As *n* becomes higher, the filling factor of the profile decreases, which corresponds to a decrease in the anomaly of the non-Newtonian properties of a pseudoplastic fluid or to an increase in the anomaly of the non-Newtonian properties of a dilatant medium.

According to the results of calculations, the thickness of the fluid film becomes lower as Re_n increases, which is due to a decrease in the effective viscosity of the fluid. As a result, as Re_n becomes higher, the maximum value of the circumferential component of the flow velocity at the film surface, $\theta_{max}(\bar{z})$, increases, and the rate at which $\theta_{max}(\bar{z})$ decays along the axial coordinate becomes lower, which is due to a decrease in the effective viscosity of the fluid and an increase in the axial component of the flow velocity because of the diminishing thickness of the film. As Re_n becomes higher, the filling factor of the profile of the circumferential component of the flow velocity grows, which is also accounted for by a decrease in the effective viscosity of the fluid.

CONCLUSIONS

(1) The influence exerted by the anomaly of the non-Newtonian properties of a fluid and by the defin-

ing similarity criteria on the hydrodynamics of flow in a cylindrical-conical hydrocyclone was analyzed by means of a numerical modeling. It was established that the circumferential component of the flow velocity at the film surface first decays in the direction of the hydrocyclone's axis, but then, as the conical part of the casing becomes narrower, again increases, with this increase being the steepest near the film surface.

(2) For pseudoplastic fluids, the rate at which the circumferential component of the flow velocity decays in the direction of the hydrocyclone's axis decreases as the anomaly of the non-Newtonian properties becomes more pronounced. The circumferential component of the flow velocity increases with Fr and Re_n numbers, and this increase is the most pronounced near the discharge opening in the conical part of the hydrocyclone casing and for Newtonian fluids.

(3) The dependences obtained can be used in modeling the concentration field in a cylindrical-conical hydrocyclone.

REFERENCES

1. Dik, I.G., Matvienko, O.V., and Neesse, T., *Teor. Osn. Khim. Tekhnol.*, 2000, vol. 34, no. 5, pp. 478–488.
2. Kutepov, A.M., Lagutkin, M.G., Pavlovskii, G.V., *et al.*, *Teor. Osn. Khim. Tekhnol.*, 1999, vol. 33, no. 5, pp. 571–577.
3. Ivanov, A.A., Ruzanov, S.R., and Lunyushkina, S.A., *Zh. Prikl. Khim.*, 1987, vol. 60, no. 5, pp. 1047–1051.
4. Kutepov, A.M., Ternovskii, I.G., and Kuznetsov, A.A., *Zh. Prikl. Khim.*, 1980, vol. 53, no. 12, pp. 2676–2681.
5. Romankov, P.G., *Teor. Osn. Khim. Tekhnol.*, 1972, vol. 6, no. 6, pp. 855–871.
6. Vainshtein, I.A., *Inzh.-Fiz. Zh.*, 1983, vol. 45, no. 4, pp. 602–608.
7. Yablonskii, V.O., *Zh. Prikl. Khim.*, 2000, vol. 73, no. 1, pp. 95–99.
8. Yablonskii, V.O. and Ryabchuk, G.V., *Teor. Osn. Khim. Tekhnol.*, 2001, vol. 35, no. 5, pp. 479–484.
9. Radin, S.I., Budkin, V.V., and Cherkez, G.S., *Teor. Osn. Khim. Tekhnol.*, 1978, vol. 12, no. 4, pp. 571–575.
10. Dyakowski, T. and Hornung, G., *Chem. Eng. Res. Des. A*, 1994, vol. 72, no. 4, pp. 523–520.
11. Bird, R.B. Stewart, W.E., and Lighfoot, E.N., *Transport Phenomena*, New York: Wiley & Sons, 1965.
12. Roache, P.J., *Computational Fluid Dynamics*, Albuquerque: Hermosa, 1976.

Russian Journal of Applied Chemistry, Vol. 77, No. 6, 2004, pp. 964–967. Translated from Zhurnal Prikladnoi Khimii, Vol. 77, No. 6, 2004, pp. 978–980.

ORGANIC SYNTHESIS AND INDUSTRIAL ORGANIC CHEMISTRY

Use of 1-Halo Derivatives of the 2,2,6,6-Tetramethylpiperidine Series as Oxidants and Halogenating Agents

V. P. Kashparova, E. Sh. Kagan, I. Yu. Zhukova, and E. P. Ivakhnenko

South-Russian State Technical University, Novocherkassk, Rostov oblast, Russia
Research Institute of Physical and Organic Chemistry, Rostov-on-Don, Russia

Received February 3, 2004

Abstract—1-Halo derivatives of the 2,2,6,6-tetramethylpiperidine series oxidize sterically hindered phenols to form dimers and *p*-quinones.

The capability of sterically shielded phenols to undergo oxidation is well known [1] and is one of the main characteristic properties of this class of compounds, allowing their use as effective antioxidants [2]. Diverse oxidation products are formed (phenoxyl radicals, quinoid compounds, quinones), depending on the structure of the phenols being oxidized and on the oxidant chosen. For example, oxidation of 2,4,6-tri-*tert*-butylphenol with PbO_2 or MnO_2 yields a stable phenoxyl radical, whereas oxidation with $NaNO_2$ yields quinones [1].

In this context, it seemed of interest to study the oxidation of shielded phenols with 1-halo derivatives of the 2,2,6,6-tetramethylpiperidine (TMP) series. These agents have apparent advantages over other *N*-haloalkylamines in that they show relatively high stability and low nucleophilicity; these compounds can be prepared in high yield from the available 2,2,6,6-TMP derivatives [3–5].

The oxidation of sterically hindered phenols with halo derivatives of the 2,2,6,6-TMP series is usually performed in an organic solvent, e.g., benzene or methylene chloride. 2,6-di-*tert*-butyl-4-methylphenol **I** and 2,6-di-*tert*-butylphenol **II** are oxidized with 1-halo derivatives of the 2,2,6,6-TMP series to form dimers: 3,3',5,5'-tetra-*tert*-butylstilbenoquinone **III** and 3,3',5,5'-tetra-*tert*-butyldiphenoquinone **IV**, respectively:

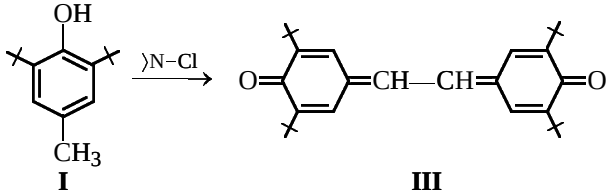

I **III**

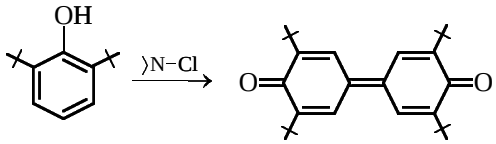

II **IV**

In an organic solvent, the dimerization apparently occurs by the radical mechanism [1]. The reaction rate depends on the rate of protonation of the 1-halo derivative. The possible pathway of dimer formation in the oxidation of phenols with chloramines of the 2,2,6,6-TMP series is shown in the scheme:

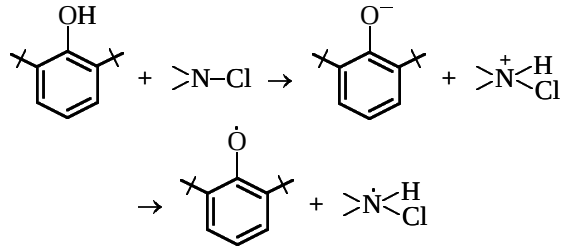

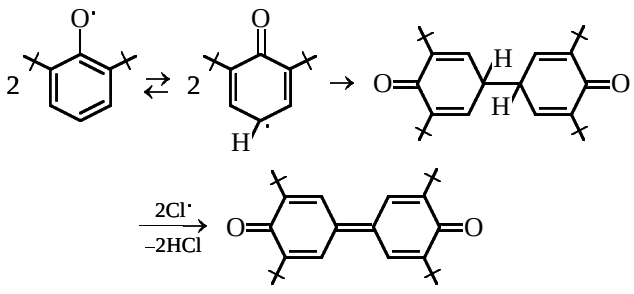

1070-4272/04/7706-0964 © 2004 MAIK "Nauka/Interperiodica"

The stability of the forming phenoxyl radical is determined by the structural features of the initial phenol molecule. For example, in oxidation of 2,4,6-tri-*tert*-butylphenol **V**, we obtained 2,6-di-*tert*-butylbenzoquinone **VI**. 2,4,6-Tri-*tert*-butylphenol does not undergo noticeable dimerization because of the high stability of the forming 2,4,6-tri-*tert*-butylphenoxyl radical [6]:

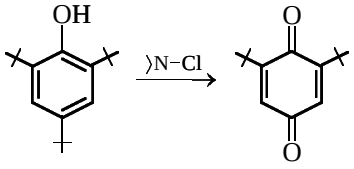

V **VI**

1-Chloro-2,2,6,6-TMP oxidizes hydroquinone **VII** in an organic solvent to *p*-benzoquinone **VIII** in quantitative yield:

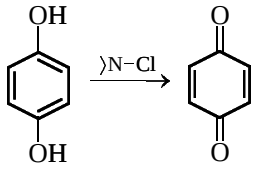

VII **VIII**

Phenol **IX** in organic solvent reacts with 1-chloro derivatives of the 2,2,6,6-TMP series to form 2,4,6-trichlorophenol **Xa** and with 1-bromo derivatives to form 2,4,6-tribromophenol **Xb**:

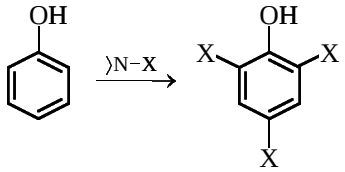

IX **Xa**, **Xb**

where X = Cl (**Xa**), Br (**Xb**).

In acidic solutions, the reactions apparently occur by the electrophilic mechanism, which is confirmed by the formation of *p*-chloroacetanilide **XII** as the only product in the reaction of acetanilide **XI** with 1-chloro-2,2,6,6-TMP:

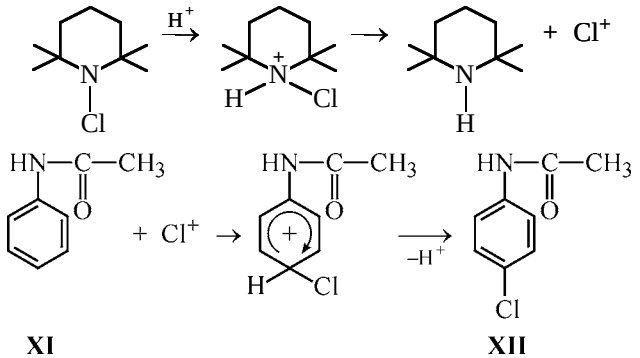

XI **XII**

1-Bromo-4-hydroxy-2,2,6,6-TMP reacts with dimethylphenylamine and diethylphenylamine in a weakly acidic solution (pH 4–5) also to form the corresponding *p*-bromo derivatives **XIIIa** and **XIIIb**:

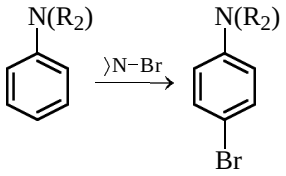

XIIIa, **XIIIb**

where R = CH_3 (**XIIIa**), C_2H_5 (**XIIIb**).

EXPERIMENTAL

3,3',5,5'-Tetra-*tert*-butylstilbenoquinone III. 2,6-Di-*tert*-butyl-4-methylphenol (Ionol), 4.4 g (0.02 mol), and 1-bromo-4-hydroxy-2,2,6,6-tetramethylpiperidine, 9.2 g (0.04 mol), were dissolved in 50 ml of benzene, and the mixture was allowed to stand at 25°C for 4–5 days. After the disappearance of the starting Ionol (TLC monitoring), the precipitate of 4-hydroxy-2,2,6,6-tetramethylpiperidinium bromide was separated. The solvent was distilled off under reduced pressure; 3.9 g (90%) of 3,3',5,5'-tetra-*tert*-butylstilbenoquinone was obtained; mp 304–305°C (from benzene).

The reaction with 1-chloro-4-hydroxy-2,2,6,6-tetramethylpiperidine was performed similarly. The reaction was slower, being complete in 6–7 days. Yield of **III** 3.6 g (85%).

3, 3', 5, 5'-Tetra-*tert*-butyldiphenoquinone IV. A mixture of 1 g (0.005 mol) of 2,6-di-*tert*-butylphenol and 1.7 g (0.01 mol) of 1-chloro-4-hydroxy-2,2,6,6-tetramethylpiperidine in 50 ml of benzene was allowed to stand for 2 days. After the disappearance of the starting phenol (TLC monitoring), the precipitate of 4-hydroxy-2,2,6,6-tetramethylpiperidinium chloride was separated. The solvent was distilled off under reduced pressure; 0.9 g (90%) of 3',3,5',5-tetra-*tert*-butyldiphenoquinone was obtained; mp 240–242°C. The isolated product was identified by comparison with an authentic sample [5].

2,6-Di-*tert*-butyl-*p*-benzoquinone VI. A mixture of 2.6 g (0.01 mol) of 2,4,6-tri-*tert*-butylphenol and 3.4 g (0.02 mol) of 1-chloro-2,2,6,6-tetramethylpiperidine in 50 ml of benzene was placed in a flask equipped with a reflux condenser and heated for 20 h on a water bath kept at 60°C. The mixture was cooled, the precipitated crystals of 2,2,6,6-tetramethylpiperi-

dinium chloride were filtered off, the solvent was evaporated, and the residue was chromatographed on a column (Al_2O_3, Brockmann grade II l = 20 cm, d = 3 cm, eluent hexane). The yellow fraction was collected. The solvent was removed under reduced pressure; 1.15 g (55%) of 2,6-di-*tert*-butyl-*p*-benzoquinone **VI** was obtained; mp 78–79°C (from hexane); published data [6]: mp 78–80°C.

***p*-Benzoquinone VIII.** A mixture of 2.2 g (0.02 mol) of hydroquinone and 3.6 g (0.02 mol) of 1-chloro-2,2,6,6-tetramethylpiperidine in 20 ml of methylene chloride was allowed to stand for 12 h. The precipitate of 2,2,6,6-tetramethylpiperidinium ch loride (3.5 g) was filtered off, and the solvent was distilled off on a rotary evaporator; 1.72 g (80%) of *p*-benzoquinone **VIII** was obtained, mp 116°C (from water). The product was identified by comparison with an authentic sample [7].

2,4,6-Trichlorophenol Xa. A mixture of 0.94 g (0.01 mol) of phenol and 5.66 g (0.03 mol) of 1-chloro-4-hydroxy-2,2,6,6-tetramethylpiperidine in 50 ml of benzene was allowed to stand for 24 h at room temperature. The benzene solution was extracted with 10% NaOH, the organic layer was separated, and the aqueous layer was acidified with HCl to pH 1. 2,4,6-Trichlorophenol precipitated from the aqueous phase; it was separated, washed with water, and dried in air. Yield 1.78 g (91%); mp 63–65°C (from ethanol–water, 1 : 1); published data [8]: mp 64–65°C. 4-Hydroxy-2,2,6,6-tetramethylpiperidine was isolated from the benzene layer; yield 4.2 g (90%), mp 130–132—C (from ethyl acetate) [9].

2,4,6-Tribromophenol Xb was prepared similarly, by the reaction of phenol with 1-bromo-4-hydroxy-2,2,6,6-tetramethylpiperidine. Yield 82%, mp 96–98°C (from ethanol–water, 1 : 1). Mixing with an authentic sample gave no depression of the melting point [8].

***p*-Chloroacetanilide XII.** Acetanilide, 2.7 g (0.02 mol), and 1-chloro-2,2,6,6-tetramethylpiperidine, 3.7 g (0.021 mol), were dissolved in 30 ml of benzene, and 25 ml of 1 M HCl was added. The mixture was stirred and heated on a water bath at 50–60°C for 15–20 min. The reaction progress was monitored by TLC. After the reaction was complete, the mixture was cooled, the organic layer was separated, and the solvent was evaporated under reduced pressure. The crystals of 4-chloroacetanilide were filtered off. Yield of **XII** 3.2 g (92%); rhombic needles, mp 175–177°C; published data [10]: mp 177–178°C.

***p*-Bromoacetanilide** was prepared similarly by the reaction with 1-bromo-2,2,6,6-tetramethylpiperidine; mp 167–168°C (from ethanol–water, 1 : 1). The product was identified by comparison with an authentic sample [10].

***p*-Bromo-*N*,*N*-diethylaniline XIIIb**. *N*,*N*-Diethylaniline, 1.49 g (0.01 mol), was dissolved in 20 ml of benzene, and a solution of 2.5 g (0.01 mol) of 1-bromo-4-hydroxy-2,2,6,6-tetramethylpiperidine in 20 ml of benzene was gradually added. The mixture was heated on a water bath at 60°C for 40–45 min. Then the mixture was cooled, and white crystals of 4-hydroxy-2,2,6,6-tetramethylpiperidine were filtered off. The solvent was evaporated, and 2.1 g (90%) of *p*-bromo-*N*,*N*-diethylaniline (white oily crystals) was obtained; mp 31–33°C (from ethanol–water, 1 : 1). Mixing with an authentic sample gave no depression of the melting point [10].

***p*-Bromo-*N*,*N*-dimethylaniline XIIIa** was prepared similarly. Yield 85%; mp 54–56°C (from ethanol–water, 1 : 1); published data [10]: mp 55–56°C.

CONCLUSIONS

(1) 2,6-Di-*tert*-butyl-4-methylphenol and 2,6-di-*tert*-butylphenol in an organic solvent are oxidized by 1-halo derivatives of 2,2,6,6-tetramethylpiperidine to form dimers.

(2) 1-Chloro-2,2,6,6-tetramethylpiperidine oxidizes in an organic solvent 2,4,6-tri-*tert*-butylphenol and hydroquinone to 2,6-di-*tert*-butylbenzoquinone and *p*-benzoquinone, respectively.

(2) Phenol in an organic solvent and aromatic amines in an acidic solution in the presence of 1-halo derivatives of the 2,2,6,6-tetramethylpiperidine series undergo halogenation.

REFERENCES

1. Ershov, V.V., Nikiforov, G.A., and Volod'kin, A.A., *Prostranstvenno-zatrudnennye fenoly* (Sterically Hindered Phenols), Moscow: Khimiya, 1972.
2. Roginskii, V.A., *Fenoksil'nye antioksidanty* (Phenoxyl Antioxidants), Moscow: Nauka, 1988.
3. Zhukova, I.Yu., Pozhidaeva, S.A., Kagan, E.Sh., and

Smirnov, V.A., *Zh. Org. Khim.*, 1993, vol. 29, no. 4, pp. 751–757.

4. Zhukova, I.Yu., Kashparova, V.P., and Kagan, E.Sh., *Izv. Vyssh. Uchebn. Zaved., Sev.-Kavk. Region, Estestv. Nauki*, 2001, no. 2, pp. 44–45.
5. Neale, R.S., *Synthesis*, 1971, no. 1, pp. 1–15.
6. *Condensation Monomers*, Stille, J.K. and Campbell, T.W., Eds., New York: Interscince, 1972.
7. Tolstikov, G.A., *Reaktsii gidroperekisnogo okisleniya* (Hydroperoxide Oxidations), Moscow: Nauka, 1976.
8. Rodionov, V.M., Bogoslovskii, B.M., and Fedorova, A.M., *Laboratornoe rukovodstvo po khimii promezhutochnykh produktov i krasitelei* (Laboratory Manual on Chemistry of Intermediates and Dyes), Moscow: Goskhimizdat, 1948.
9. Rozantsev, E.G., *Svobodnye iminoksil'nye radikaly* (Free Iminoxyl Radicals), Moscow: Khimiya, 1970.
10. Hickinbottom, W.J., *Reaction of Organic Compounds*, London: Longmans, Green and co., 1936.

Russian Journal of Applied Chemistry, Vol. 77, No. 6, 2004, pp. 968–971. Translated from Zhurnal Prikladnoi Khimii, Vol. 77, No. 6, 2004, pp. 981–984.

ORGANIC SYNTHESIS AND INDUSTRIAL ORGANIC CHEMISTRY

Influence of Ionic Surfactants on Tetrabromophenylfluorone Ionic Associates

S. A. Shapovalov, E. S. Gladkov, and T. A. Chernaya

Research Institute of Chemistry, Karazin Kharkov National University, Kharkov, Ukraine

Received December 9, 2003; in final form, March 2004

Abstract—Stability constants of ionic associates of a hydroxyxanthene dye, tetrabromophenylfluorone, with a series of organic cations were determined spectrophotometrically. The possibility of quantitative determination of anionic surfactants (alkyl sulfates) in an aqueous solution in the form of a dye anion associate with tetrabutylammonium cation was considered.

Ionic association of organic dyes substantially changes the optical properties of the medium and is studied in connection with a search for novel photosensitive materials [1, 2] and optically transparent polymers [3], and with biochemical research [4].

Dye ionic associates have been used for quantitative estimation of the content of surfactants in aqueous solutions [5]. Along with the dye ion, the associate contains an oppositely charged organic ion. Ionic associates can be more "sensitive" with respect to the content of ionic surfactants as compared to dye ions, because the spectral changes in the associate + surfactant system [6] occur at substantially lower concentrations of surfactant than in the dye + surfactant system [7].

Hydroxyxantene dye anions are of special interest as components of the associate. They have intense color and exhibit bright luminescence in aqueous solutions. Tetrabromophenylfluorone (TBPF), which is a structural analogue of eosin devoid of carboxy group, is one of such dyes. It has been found that the $TBPF^-$ anion

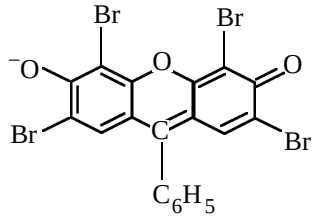

forms ionic associates with an organometallic complex of copper(I). This fact was used as a basis of an extractive procedure for the spectrophotometric determination of the metal in aqueous solutions [8]. Intensely colored hydroxyxantene anion in the associate provides a high sensitivity of the quantitative determination of copper.

It has been found previously [9] that associates decompose under the action of ionic surfactants. The color intensity of the solution directly depends on the surfactant concentration. This phenomenon is of interest as a basis of a sensitive method for determination of anionic surfactants. In this study, association of the $TBPF^-$ anion with tetrabutylammonium cation (TBA^+) and reaction of the TBA^+–$TBPF^-$ associate with anionic surfactants, alkyl sulfates, were examined to develop a procedure for quantitative determination of these surfactants in aqueous solutions.

EXPERIMENTAL

A sodium salt of TBPF was used [8]. The dye purity was monitored spectrophotometrically using the known extinction coefficients ε_{max} of protolytic species (aqueous solution) at absorption band peaks λ_{max}. Analytically pure tetrabutylammonium iodide [TU (Technical Specifications) 6-09-05-410–75] was used without additional purification. An anionic surfactant, sodium dodecyl sulfate (SDS), and a cationic surfactant, cetylpyridinium bromide (CPB), contained $98 \pm 1\%$ main substance. The other chemicals were of analytically pure grade. The pH of the solution was adjusted with acetate, phosphate, and borate buffers [10] and was monitored potentiometrically with a glass electrode. Absorption spectra were recorded on Hitachi-U3210 and SF-46 spectrophotometers at room temperature.

1070-4272/04/7706-0968 © 2004 MAIK "Nauka/Interperiodica"

TBPF is a monobasic acid with pK_a 3.0 [8]. At pH 5–9, it actually exists as a single-charged anion $TBPF^-$; its hydrolysis becomes noticeable at pH > 9.5. It was found experimentally that TBPF association occurs at fairly low (approximately 1×10^{-6} M and more) concentrations. The characteristic feature of TBPF association with organic counterions in aqueous solution is a decrease in the intensity of hydroxyxanthene absorption band. This is clearly observed in the case of colorless cations, e.g., TBA^+ (Fig. 1, spectra *1*, *4*). The extinction coefficient of the associate is almost half that of TBFF (see table). Similar spectral changes were observed when anions of the other hydroxyxanthenes (fluorescein, eosin, Rose Bengal B, erythrosine [6, 11]) associate with certain organic cations and when TBA^+ associates with other organic anions (anionic cyanines [12, 13]).

We found that, at dye concentrations of 1×10^{-6}–5×10^{-5} M, association follows the scheme $TBA^+ + TBPF^- \rightleftarrows TBA^+ \cdot TBPF^-$.

The stoichiometric ratio of the components in the associate, found by Adamovich's method [14], is 1 : 1. A similar scheme of association was determined for reaction of $TBPF^-$ with a cyanine dye, pinacyanol (PNC^+):

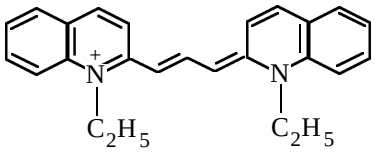

The logarithm of the association thermodynamical constant $\log K_{as}^T$ (calculated by analogy with data of [12]) for the $TBA^+ \cdot TBPF$ associate (see table) is lower than that for the $PNC^+ \cdot TBPF^-$ associate (6.38 ± 0.11) [11].

The $TBPF^-$ anion is more planar as compared to other hydroxyxanthenes containing carboxy group. The dihedral angle between the phenyl ring plane and the xanthene fragment, equal to 57°, is smaller than that in eosin (65°) and other xanthenes (results of RM3 geometric optimization [15]). As known [12, 16–18], the planar structure of the molecule favors ionic association between organic ions. Therefore, the $TBPF^-$ anion forms more stable associate with the more planar PNC^+ cation (the ethylquinolinium fragments are turned about the polymethine chain by only 15°) as compared to nonplanar TBA^+ cation.

Addition of an ionic surfactant to the $TBA^+ \cdot TBPF^-$ associate causes changes in the solution spectra. The experimental data show that, in the submicellar range of surfactant concentrations, the associate reacts with dodecyl sulfate anion (DS^-) or with cetylpyridinium cation (CP^+) in the substitution fasion:

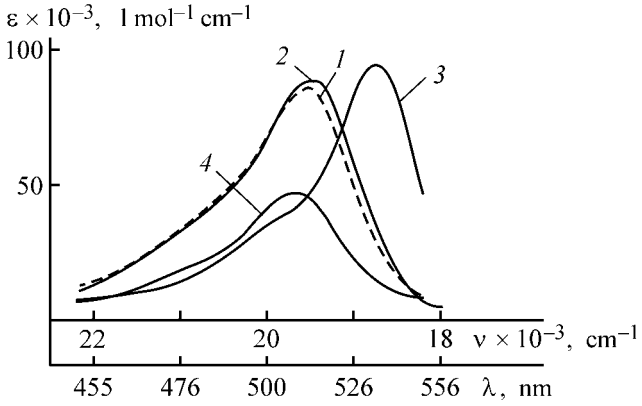

Fig. 1. Absorption spectra of $TBPF^-$ anion in (*1*) water, (*2*) SDS micelles, (*3*) CPB micelles, and (*4*) $TBA^+ \cdot TBPF^-$ associate. (ε) Extinction coefficient, (ν) wave number, and (λ) wavelength.

$$TBA^+ \cdot TBPF^- + DS^- \rightleftarrows TBA^+ \cdot DS^- + TBPF^-, \quad (1)$$

$$TBA^+ \cdot TBPF^- + CP^+ \rightleftarrows TBA^+ + CP^+ \cdot TBPF^-, \quad (2)$$

In the range of micellar concentrations (8.1×10^{-3} M SDS and 6.6×10^{-4} M CPB [19]), the associate reacts with the surfactant by another pathway. This interaction leads to solubilization of each counterion in the Stern layer of the corresponding micelles [7]:

$$TBA^+ \cdot TBPF^- + (x + y)DS^- \rightleftarrows (TBA^+)_{xDS^-} + (TBPF^-)_{yDS^-}, \quad (3)$$

$$TBA^+ \cdot TBPF^- + (x + y)CP^+ \rightleftarrows (TBA^+)_{xCP^+} + (TBPF^-)_{yCP^+}, \quad (4)$$

where x and y take integer values.

The spectral changes in the $TBA^+ \cdot TBPF^-$ + surfactant systems confirm the above schemes. For instance, in the case of SDS, the $TBPF^-$ anion is

Characteristics of $TBPF^-$ anion and $TBA^+ \cdot TBPF^-$ associate

Characteristics	$TBPF^-$	$TBA^+ \cdot TBPF^-$
λ_{max}, nm	515–516 [8]	508
$\varepsilon_{max} \times 10^{-3}$, l mol^{-1} cm^{-1}	86.0 [8]	43.0
$\log K_{as}^T$	–	4.87 ± 0.15

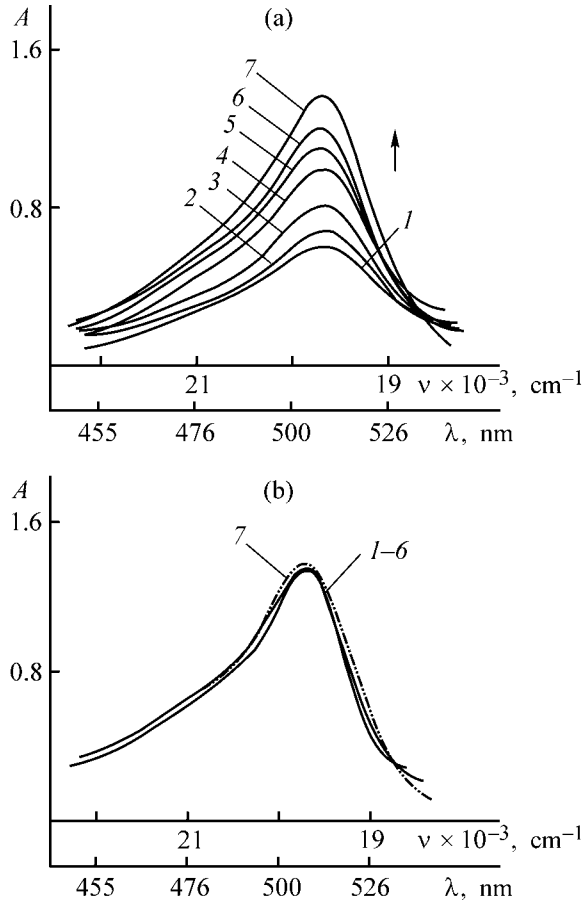

Fig. 2. Absorption spectra of aqueous solutions containing (a) $TBA^+ \cdot TBPF^-$ associate, (b) $TBPF^-$ anion, and SDS additives. Reference solution is water; absorbing layer thickness 1.00 cm; pH 6.9; $c_{TBPF} = 1.5 \times 10^{-5}$, $c_{TBA} = 6 \times 10^{-5}$ (M). (*A*) Optical density, (ν) wave number, and (λ) wavelength. c_{SDDS} (M): (*1*) 0; (*2*) 5×10^{-6}, (*3*) 1×10^{-5}, (*4*) 5×10^{-5}, (*5*) 1×10^{-4}, (*6*) 3×10^{-4}, and (*7*) 1.5×10^{-3}.

a product of associate decomposition in the submicellar range [scheme (1)]. At the constant initial $TBPF^-$ and TBA^+ concentrations and increase in SDS content (Fig. 2a, spectra *2*–*7*), the optical density of the solution increases due to increase in the resulting $TBPF^-$ concentration. The associate $TBA^+ \cdot DS^-$ formed does not absorb in the visible region, because it contains no colored ions.

At the same time, due to electrostatic repulsion, $TBPF^-$ does not form any associate with DS^-. This follows from invariability of the $TBPF^-$ spectrum in the presence of various concentrations of DS^- (Fig. 2b, spectra *2*–*7*). This fact indicates that the behavior of the anionic surfactant with respect to the dye anion and associate differs substantially: only in the second case the system is sensitive to the presence of the anionic surfactant in aqueous solution.

In the case of CPB, the associate decomposition is noticeable only in the micellar medium [scheme (4)], while at the submicellar concentrations the associate $CP^+ \cdot TBPF^-$ [scheme (2)] is formed. Its spectrum is similar to the spectrum of $TBA^+ \cdot TBPF^-$ associate (Fig. 1, spectrum *4*). It is important that the competitive character of the $TBA^+ \cdot TBPF^-$ reaction with CP^+ [scheme (2)] is confirmed by the fact that the stability of the $CP^+ \cdot TBPF^-$ associate is approximately the same ($\log K_{as}^T = 5.3 \pm 0.11$) as that of the $TBA^+ \cdot TBPF^-$ associate.

In the micellar region, the surfactants studied behave with respect to the associate components as a micromedium: the counterions are separated by surfactant micelles [schemes (3) and (4)]. Thus, $TBPF^-$ anions are released from the associate. This is confirmed by the spectra, which are similar in the shape and intensity to the spectra of $TBPF^-$ in micelles of anionic (Fig. 1, spectrum *2*) and cationic (Fig. 1, spectrum *3*) surfactants. This fact agrees with the reference data [7] on the influence of ionic surfactant micelles on the protolytic species of hydroxyxanthene dyes.

The sensitivity of the associate to the surfactant content in the solution is connected with the associate stability, since, at constant $TBPF^-$ and TBA^+ concentrations, changes in the associate + surfactant system appear at the lower surfactant content [schemes (1) and (2)]. It is found that the optical density of solutions with fixed $TBFF^-$ and TBA^+ concentrations increases in proportion to the concentration of alkyl sulfates (AS), anionic surfactants of the general formula $C_nH_{2n+1}OSO_3H$ (n = 8 and more). The optical density of the solution at λ 515 nm, A_{515}, and concentrations of $TBPF^-$ of 1.5×10^{-5} M and TBA^+ of 6×10^{-5}, within the AS concentration range 5×10^{-6}–8×10^{-5} M, is described by the equation

$$A_{515} = (0.07 \pm 0.01) + (2.09 \pm 0.12) \times 10^4 c_{AS},$$

where c_{AS} is AS molar concentration in the solution.

Similar dependences underlie spectrophotometric determination of AS, characterized by insignificant influence of pH. As mentioned above, both $TBPF^-$ and TBA^+ undergo no protolytic transformations within the pH 4.5–9.5 range. Therefore, AS determination can be performed within this pH range. The main characteristics of the proposed method of AS deter-

mination (DS^- standard) in aqueous solutions using $TBA^+ \cdot TBPF^-$ associate are presented below:

AS detection limit, M:	
by 3σ criterion [20]	2.5×10^{-6}
practical [21]	6.5×10^{-6}
Interval of AC concentrations determined, M	6.5×10^{-6}–2.0×10^{-3}
pH range	4.5–9.5

The properties of $TBA^+ \cdot TBPF^-$ associate can also be used for development of a method for semiquantitative estimation (test control) of the AS concentration. The procedure is as follows. A series of solutions containing the constant concentrations of TBPF and TBA (e.g., TBFF concentration is 1.5×10^{-6} M and TBA concentration is by a factor of 4–6 higher) and various AS concentrations (from 6.5×10^{-6} to 2×10^{-3} M with respect to SDS reference) are prepared. Each solution will have a specific color in accordance with the degree of the associate decomposition. To estimate the AS content, an aliquot of the solution to be analyzed is added to the TBPF and TBA mixture, and the resulting color is compared to that of reference solutions containing known AS concentration. The AS concentration is determined by interpolation using the reference solutions having the closest color.

CONCLUSIONS

(1) In aqueous solutions, tetrabromophenylfluorone anion forms 1 : 1 ionic associates with single-charged organic cations.

(2) Specific features of associate decomposition at various concentrations of anionic and cationic surfactants were determined. The associate decomposition in submicellar solutions is due to a competitive action of surfactant ions on ions forming the associates, while in micellar solutions, ionic surfactants impede association.

(3) The properties of tethabromophenylfluorone associates were used to develop a new method for determination of alkyl sulfate content in aqueous solutions. The proportional relationship between optical density of the associate solution and the content of anionic surfactant introduced is the basis of the quantitative determination. The method is characterized by a low detection limit (6.5×10^{-6} M for sodium dodecyl sulfate) and wide ranges of pH and surfactant concentrations.

REFERENCES

1. Ishchenko, A.A., *Teor. Eksp. Khim.*, 1988, vol. 34, no. 4, pp. 214–232.
2. Shapiro, B.I., *Teoreticheskie nachala fotograficheskogo protsessa* (Theoretical Principles of Photographic Process), Moscow: Editorial URSS, 2000.
3. Grinev, B.V., Sakhno, T.V, and Senchishin, V.G., *Opticheski prozrachnye i fluorestsiruyushchie polimery* (Optically Tranparent and Fluorescent Polymers), Kharkov: Inst. Monokristallov, 2003.
4. Uversky, V.N., Winter, S., and Loeber, G., *Biochim. Biophys. Acta*, 1998, vol. 1388, no. 1, pp. 133–142.
5. Shapovalov, S.A. and Svishcheva, Ya.A., *Zh. Prikl. Khim.*, 2002, vol. 75, no. 3, pp. 463–467.
6. Shapovalov, S.A., Svishcheva, Ya.A., and Larin, V.I., *Izv. Vyssh. Uchebn. Zaved., Khim. Khim. Tekhnol.*, 2002, vol. 45, no. 4, pp. 37–42.
7. Savvin, S.B., Chernova, R.K., and Shtykov, S.N., *Poverkhnostno-aktivnye veshchestva (Surfactants)*, Moscow: Nauka, 1991.
8. Shapovalov, S.A., *Vestn. Khar'kov. Univ., Khim.*, 1997, no. 1, pp. 203–208.
9. Shapovalov, S.A., Chernaya, T.A., and Samoilov, E.A., *Vestn. Kharkov. Univ., Khim.*, 2000, no. 6, pp. 110–112.
10. Lur'e, Yu.Yu., *Spravochnik po analiticheskoi khimii* (Handbook on Analytical Chemistry), Moscow: Khimiya, 1979.
11. Shapovalov, S.A., Svishcheva, Ya.A., and Larin, V.I., *Ukr. Khim. Zh.*, 2002, vol. 68, no. 4, pp. 107–110.
12. Ishchenko, A.A., Derevyanko, N.A., Popov, S.V., *et al., Izv. Ross. Akad. Nauk, Ser. Khim.*, 1997, no. 5, pp. 950–955.
13. Ishchenko, A.A., Derevyanko, N.A., Popov, S.V., *et al., Zh. Nauchn. Prikl. Fotogr. Kinematogr.*, 1997, vol. 42, no. 3, pp. 70–76.
14. Bershtein, I.Ya. and Kaminskii, Yu.L., *Spectrofotometricheskii analiz v organicheskoi khimii* (Spectrophotometric Analysis in Organic Chemistry), Leningrad: Khimiya, 1986.
15. Stewart, J.J.P., *J. Comput. Chem.*, 1989, vol. 10, no. 2, pp. 209–220.
16. Kessler, Yu.M., and Zaitsev, A.L., *Sol'vofobnye effekty. Teoriya, eksperiment, praktika* (Solvofobic Effects. Theory, Experiment, and Practice), Leningrad: Khimiya, 1989.
17. Reihard, K., Reichardt, Ch., *Solvents and Solvent Effects in Organic Chemistry*, Weinheim: VCH Verlagsgesellschaft, 1988.
18. Shapovalov, S.A., Koval', V.L., Mchedlov-Petrosyan, N.O., *et al., Dokl. Nats. Akad. Nauk Ukr.*, 1999, no. 2, pp. 156–161.
19. Abramzon, A.A., Bocharov, V.V., and Gaevoi, G.M., *Poverkhnostno-aktivnye veshchestva: Spravochnik* (Surfactants: Handbook), Leningrad: Khimiya, 1979.
20. Doerfel, K., *Statistic in der analytischen Chemie*, Leipzig: Leuna-Merseburg, 1966.
21. Blank, A.B., *Zh. Anal. Khim.*, 1962, vol. 17, no. 9, pp. 1040–1044.

Russian Journal of Applied Chemistry, Vol. 77, No. 6, 2004, pp. 972–975. Translated from Zhurnal Prikladnoi Khimii, Vol. 77, No. 6, 2004, pp. 985–988.

MACROMOLECULAR CHEMISTRY AND POLYMERIC MATERIALS

Synthesis of Epoxy–Oxazolidone Oligomers

V. V. Mikheev and R. R. Ivanova

Kazan State Technological University, Kazan, Tatarstan, Russia

Received December 22, 2003

Abstract—A procedure was developed for preparing oligomers containing terminal epoxy groups and 2-oxazolidone rings in the backbone.

One of the ways to improve the performance of epoxy polymeric materials is their modification with urethanes. The best developed modification procedure is preparation of epoxy–urethane oligomers containing urethane bonds in the backbone and terminal epoxy groups [1, 2]. The urethane fragments in such oligomers have a linear structure. It is known, however, that urethane groups in the 2-oxazolidone ring

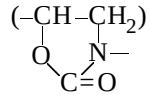

surpass linear urethane fragments in the resistance to base hydrolysis [3] and heat [4, 5].

In this study, we examined the possibility of preparing epoxy–oxazolidone oligomers (EOOs) containing 2-oxazolidone rings in the backbone and terminal epoxy groups by reactions of low-molecular-weight epoxy–4,4'-isopropylidenediphenol oligomers (EOs) with urethanes containing no substituents at the N atom:

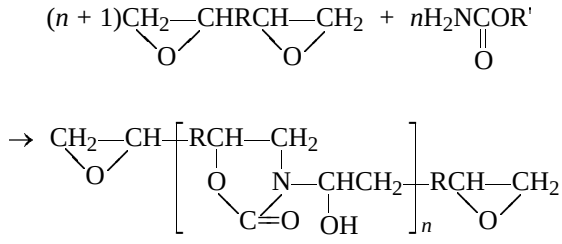

+ nR'OH

It is known [6] that reactions of equimolar amounts of diepoxides and ethyl urethane in the presence of triethylamine catalyst yield polyoxazolidones:

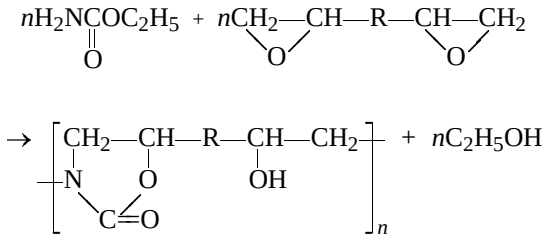

We expected that reactions of urethanes containing no substituents at the N atom with excess EO would yield EOOs. To examine this possibility, we used commercially available low-molecular-weight EOs of the ED-20 and E-40 brands, and also diphenylolpropane diglycidyl ether (DGE). As urethanes we chose *n*-butyl urethane (BU) and 1-hydroxy-2-propyl urethane (HU)

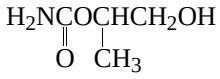

We found that EOs reacted with BU or HU (molar ratio 2 : 1) in the presence of catalytic amounts of tertiary amines (triethylamine, tributylamine) at 120–160°C. The reaction is accompanied by the release of by-products (butanol with BU and 1,2-propylene glycol with HU) but yields a gel. The gelation may be due to the fact that tertiary amines apparently catalyze not only the formation of the 2-oxazolidone ring but also the polymerization of excess epoxy groups. It is well known [7] that epoxides tend to polymerize in the presence of tertiary amines.

We found that EOOs could be prepared with dibutyltin dilaurate (DBTDL) used as a catalyst. This substance does not cause any decrease in the content of epoxy groups in EOs on heating to 200°C. The EOOs were prepared as follows. A mixture of urethane with

1070-4272/04/7706-0972 © 2004 MAIK "Nauka/Interperiodica"

Characteristics of EOOs

EOO	Starting substance		EO : urethane molar ratio	T_m, °C	E, wt %	M_n	η_{rel}
	EO	urethane					
EOO-1	ED-20	BU	2 : 1	44–48	10.3	840	1.55
EOO-1	ED-20	HU	2 : 1	45–50	10.2	840	1.54
EOO-2	ED-20	BU	3 : 2	55–60	7.2	1280	1.79
EOO-2	ED-20	HU	3 : 2	55–60	7.3	1280	1.76
EOO-3	ED-20	HU	4 : 3	60–65	5.5	1720	1.90
EOO-4	E-40	HU	2 : 1	70–75	6.9	1240	1.80
EOO-5	E-40	HU	3 : 2	73–78	4.7	1880	2.20
EOO-6	DGE	HU	2 : 1	41–45	12.2	720	1.58
EOO-7	DGE	HU	3 : 2	47–52	7.9	1100	1.61
EOO-8	DGE	HU	4 : 3	62–66	5.8	1480	1.75
EOO-9	E-40	HU	4 : 3	75–80	3.5	2520	2.40
EOO-10	ED-20	HU	5 : 4	70–75	4.2	2160	2.12

excess EO was heated in the presence of DBTDL first at 130–140°C under atmospheric pressure and then at 170–180°C in a vacuum until the release of the by-product was complete.

Epoxy–oxazolidone oligomers are solids soluble in polar organic solvents (ketones, acetates, Cellosolves). The products were characterized by the melting points T_m, epoxy group content E, molecular weight M_n, and relative viscosity η_{rel}. The structure of EOOs was confirmed by IR spectroscopy. The spectra contain absorption bands of epoxy groups (860, 920 cm^{-1}) and a band at 1740 cm^{-1}, characteristic of the urethane C=O group in the 2-oxazolidone ring [8]. The characteristics of EOOs are listed in the table.

We found that the mechanism of EOO formation involves three consecutive reactions. First, the epoxy groups in the starting EO are opened under the action of urethane to form an addition product. This was confirmed by the reaction of ED-20 with HU (1 : 2 molar ratio) at 130°C. Figure 1 shows that, in the absence of DBTDL, the epoxy groups remain virtually unchanged. The reaction noticeably accelerates in the presence of 1 wt % DBTDL, being complete in 4 h, with full conversion of the epoxy groups. No low-molecular-weight impurities were detected. According to IR data, the product contains no primary urethane groups present in the starting HU. The reaction follows the scheme

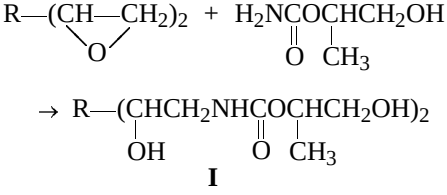

I

The reaction product is a highly viscous substance. Analysis for the content of OH groups (found 10.5, calculated 10.9%) confirms the suggested structure.

The next step of EOO synthesis is the elimination of the low-molecular-weight product (butanol or 1,2-propylene glycol) and the formation of oxazolidone structures. This was confirmed by conversion of addition product **I** at 170–180°C in a vacuum:

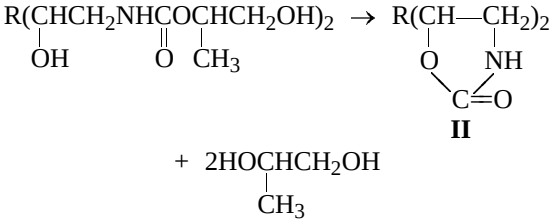

II

The structure of the resulting dioxazolidone **II** was confirmed by IR spectroscopy and analysis for the nitrogen content (found 5.53, calculated 5.70%), and 1,2-propylene glycol was identified by comparison of

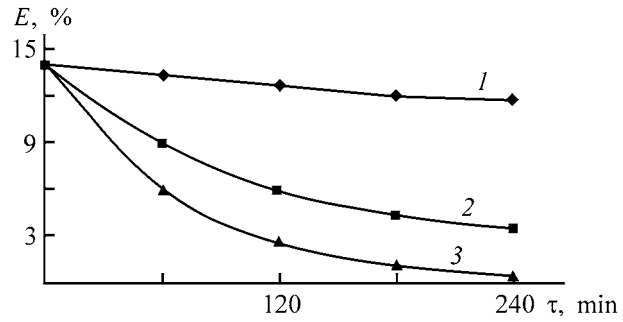

Fig. 1. Kinetic curves of the reaction of ED-20 with HU (molar ratio 1 : 2) at 130°C: (*E*) epoxy group content and (τ) time. DBTDL content, %: (*1*) 0, (*2*) 0.5, and (*3*) 1.0.

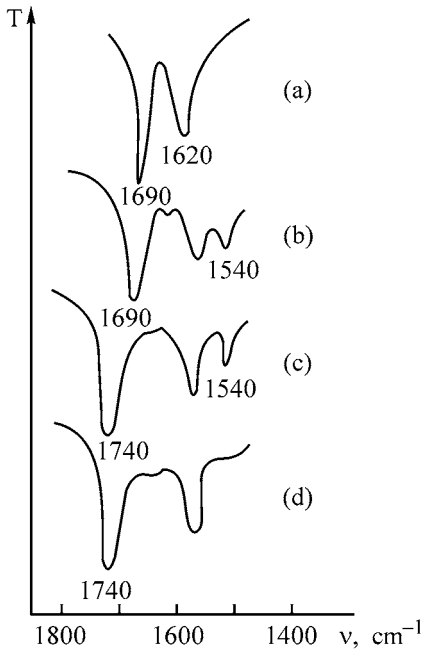

Fig. 2. Fragments of the IR spectra of (a) HU, (b) product of its addition to ED-20, (c) dioxazolidone, and (d) EOO derived from ED-20 and HU. (T) Transmission and (ν) wave number.

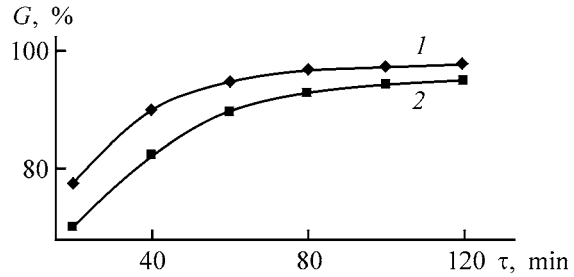

Fig. 3. Gel fraction content *G* in curing of mixtures of EOO-1 with (*1*) diethylenetriamine and (*2*) hexamethylenediamine at 120°C. (τ) Time; the same for Fig. 4.

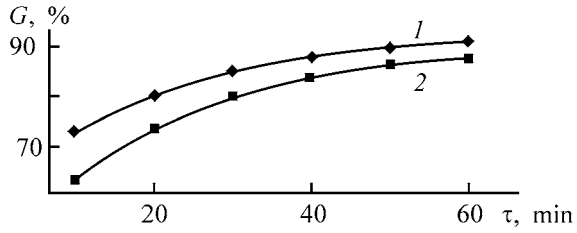

Fig. 4. Gel fraction content G in curing of mixtures of EOO-3 with (*1*) maleic and (*2*) phthalic anhydrides at 170°C.

its physical constants with reference data. Dioxazolidone **II** is a solid, T_m 92–96°C.

The final step of EOO formation is the reaction of excess epoxy groups of EO with the N–H bond in oxazolidone rings:

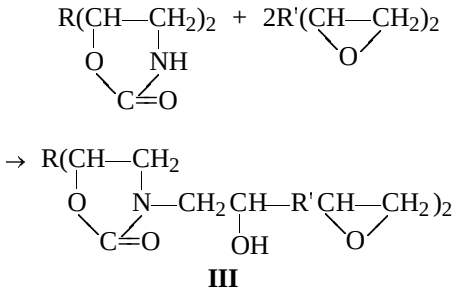

III

The possibility of this reaction was confirmed by the example of the reaction of **II** with ED-20 (molar ratio 1 : 2) at 170–180°C, which yielded EOO-2.

The above transformations are confirmed by the IR spectra. Figure 2 shows the fragments of the IR spectra (1500–1800cm^{-1}) of HU, product of its addition to ED-20 (molar ratio 2 : 1), dioxazolidone, and EOO derived from ED-20 and HU. Comparison of the spectra confirms the transformation of the NH_2 group in the starting HU (band at 1620 cm^{-1}) into the NH group in **I** and **II** (band at 1540 cm^{-1}).

EOO (compound **III**) exhibits no absorption in these regions. The band of the urethane C=O group shifts from 1690 (HU, compound **I**) to 1740 cm^{-1} (**II**, **III**); the latter frequency is typical of the oxazolidone ring. The spectrum of EOO also contains the absorption bands of the epoxy group (860, 915 cm^{-1}).

The EOOs are readily cured via epoxy groups with hardeners traditionally used for EOs. This is illustrated by Figs. 3 and 4. It is seen that network polymers are formed at high rates from mixtures of EOOs with the calculated amounts of aliphatic polyamines (Fig. 3) or anhydrides of dibasic acids (Fig. 4).

EXPERIMENTAL

n-Butyl urethanes were prepared by refluxing a mixture of butanol and urea in the presence of catalytic amounts of zinc acetate [9, 10]. 1-Hydroxy-2-propyl urethane was prepared by the reaction of 1,2-propylene carbonate with ammonia [11]. Diphenylolpropane diglycidyl ether (DGE) was isolated by vacuum distillation of ED-20 [12].

EOOs were prepared as follows (described for EOO-1 as example). A three-necked flask equipped with a stirrer, a thermometer, and a descending condenser with a condensate receiver was charged with 34 g (0.1 mol) of DGE, 6 g (0.05 mol) of HU, and 0.4 g of DBTDL. The mixture was heated with stirring to 130–140°C and kept at this temperature for 2 h at atmospheric pressure. Then the temperature was raised to 170–180°C, and the flask was evacuated to 0.7–0.8 kPa. Under these conditions, 1,2-propylene

glycol was distilled off into the receiver. The reaction was completed at a residual pressure of 0.2–0.25 kPa. The melt of the resulting EOO-1 was cooled to 120–130°C and cast onto a fluoroplastic plate on which it solidified.

The nitrogen content was determined by the Kjeldahl method [13]; the content of hydroxy groups, by acetylation [13]; and the content of epoxy groups, using a solution of HCl in acetone [14]. The molecular weight was determined from the content of epoxy groups, and the relative viscosity, viscometrically using 10% EOO solutions in butyl Cellosolve. The content of the gel fraction in curing of mixtures of EOOs with hardeners was determined by extraction of mixture samples with acetone in a Soxhlet apparatus for 6 h [15].

CONCLUSION

Urethanes react with excess low-molecular-weight epoxy oligomers in the presence of catalytic amounts of dibutyltin dilaurate to form epoxy–oxazolidone oligomers.

REFERENCES

1. Omel'chenko, S.I. and Kadurina, T.I., *Modifitsirovannye poliuretany* (Modified Polyurethanes), Kiev: Naukova Dumka, 1983.
2. Kadurina, T.I., Omel'chenko, S.I., and Stroganov, V.F., *Epoksiuretanovye sistemy: Obzornaya informatsiya. Epoksidnye smoly i materialy na ikh osnove* (Epoxy–Urethane Systems: Review. Epoxy Resins and Materials Based on Them), Moscow: NIITEKhIM, 1982.
3. *Heterocyclic Compounds*, Elderfield, R.C., Ed., New York: Wiley and Sons, 1957, vol. 5.
4. Gershanova, E.L., Trubnikova, N.A., and Sorokin, M.F., *Lakokras. Mater. Ikh Primen.*, 1982, no. 3, pp. 5–6.
5. Buhler, K.-U., *Spezialplaste*, Berlin: Verlag, 1978.
6. Fedorchenko, E.I., Pazenko, Z.N., and Kornev, K.A., in *Sintez i fizikokhimiya polimerov (Poliuretany)* (Synthesis and Physical Chemistry of Polymers (Polyurethanes)), Kiev: Naukova Dumka, 1970, vol. 6, pp. 66–69.
7. Sorokin, M.F., Kochnova, Z.A., and Shode, L.G., *Khimiya i tekhnologiya plenkoobrazuyushchikh veshchestv* (Chemistry and Technology of Film-Forming Substances), Moscow: Khimiya, 1989.
8. Rinchas, S. and Ben-Jshai, D., *J. Am. Chem. Soc.*, 1957, vol. 79, p. 4099.
9. Wirpsza, Z. and Brzezinzki, J., *Aminoplasty*, Warsaw: Naukowo-Techniczne, 1970.
10. Adams, P., and Baron, F.A., *Chem. Rev.*, 1965, vol. 65, no. 5, pp. 567–602.
11. Mikheev, V.V. and Zainullina, L.T., *Zh. Prikl. Khim.*, 2000, vol. 73, no. 12, pp. 2022–2025.
12. Kochetov, D.P., Grishchenko, F.R., and Spirin, Yu.L., *Vysokomol. Soedin., Ser. A*, 1979, vol. 21, no. 10, pp. 2171–2176.
13. Kalinina, L.S., Motorina, M.A., Nikitina, N.I., *et al.*, *Analiz kondensatsionnykh polimerov* (Analysis of Condensation Polymers), Moscow: Khimiya, 1984.
14. Toroptseva, A.M., Belogorodskaya, K.V., and Bondarenko, V.M., *Laboratornyi praktikum po khimii i tekhnologii vysokomolekulyarnykh soedinenii* (Practical Laboratory Course of Chemistry and Technology of Macromolecular Compounds), Leningrad: Khimiya, 1972.
15. Karyakina, M.I., *Laboratornyi praktikum po ispytaniyu lakokrasochnykh materialov i pokrytii* (Practical Laboratory Course of Testing Paint-and-Varnish Materials and Coatings), Moscow: Khimiya, 1977.

Russian Journal of Applied Chemistry, Vol. 77, No. 6, 2004, pp. 976–982. Translated from Zhurnal Prikladnoi Khimii, Vol. 77, No. 6, 2004, pp. 989–995.

MACROMOLECULAR CHEMISTRY AND POLYMERIC MATERIALS

Functionalization of Polyethylene with Peroxy-containing Formulations Derived from Resins Modified with Maleic Anhydride. Properties of Blends of Functionalized Polyethylene with Polyamide 6

Yu. M. Krivoguz, A. P. Yuvchenko, S. S. Pesetskii, and M. P. Bei

Belyi Institute of Mechanics of Metal–Polymer Systems, Belarussian National Academy of Sciences, Gomel, Belarus

Institute of Chemistry of New Materials, Belarussian National Academy of Sciences, Minsk, Belarus

Received March 1, 2004

Abstract—Peroxy-containing rosin–maleic and rosin–terpene–maleic resins were prepared and grafted to low-density polyethylene macromolecules by reactive extrusion. The morphology and mechanical properties of blends of functionalized polyethylene with polyamide 6 were determined.

One of the most versatile and economically feasible ways to improve the performance of plastics for machine-building and general technical purposes is the use of polymer blends. However, the applicability of polymer blends is restricted by the fact that many polymers are incompatible with each other, which results in phase segregation on blending [1, 2]. One of the main procedures eliminating or reducing the negative effect of the incompatibility of polymeric components is reactive mixing in which the mixing proper is accompanied by physicochemical transformations of reactive functional groups, which are present in macromolecules of the components or are introduced specially [1–3]. Functionalized (reactive) polymers based on polyolefins (POs) are prepared by grafting functional monomers to their macromolecules in polymer melts [3].

A convenient and efficient procedure for functionalization of POs is grafting of unsaturated monomers in a polymer melt using special extrusion reactors [4–7]. To initiate grafting in a reactive extrusion (RE) process, radical initiators are added to the reaction mixture along with the unsaturated monomers. The most widely used radical initiators are dialkyl peroxides [7].

In preping functionalized POs (FPOs), the functional groups and initiating peroxy groups can be combined in one substance, i.e., functional peroxy initiators (FPIs) can be used [7, 8]. It is suggested that decomposition of FPIs in the course of RE will yield fragments that contain functional groups and can be grafted to the polymer chain.

Apparently, the course of grafting and properties of the resulting FPOs will largely depend on the chemical structure of functional peroxides. For example, experiments on grafting of carboxyl-containing peroxides to polypropylene have shown that the degree of grafting of functional groups and degradation of polypropylene macromolecules could be controlled by varying the molecular structure of the peroxide [8].

The range of the available FPIs studied is limited, which makes it urgent to develop FPIs, optimize conditions of their grafting to PO macromolecules, and study properties of FPOs and blends based on them.

In this study, we prepared peroxy-containing formulations (PFs) based on rosin–maleic (RMR) and rosin–terpene–maleic (RTMR) resins and examined the fundamental aspects of grafting of these resins to polyethylene by RE and the properties of the resulting grafted products and their blends with polyamide 6 (PA6).

EXPERIMENTAL

In our study we used low-density polyethylene [LDPE, 15803-020 grade, GOST (State Standard)

1070-4272/04/7706-0976 © 2004 MAIK "Nauka/Interperiodica"

16337–77, density 0.92 g cm^{-3}, melting point 105°C), functional peroxides derived from RMR and RTMR, and dicumyl peroxide (DCP). Blends were prepared with PA6 of 210/310 grade.

The functionalization of LDPE was performed by grafting of a PF to its macromolecules in a single-screw extrusion reactor (screw diameter 25 mm, L/D = 25) equipped with a static mixer [9], under the following conditions: screw rotation rate 27 rpm (shear rate about 30 s^{-1}), temperature in the reaction zone 185°C, PF concentration in the reaction system 1.5 wt %.

Blends of PA-6 with functionalized LDPE (LDPE-*graft*-FPI) were prepared by extrusion mixing of a blend of the corresponding granulates in a single-screw plasticator (screw diameter 45 mm, L/D = 20); the melt temperature in the extrusion zone was 180–240°C. The LDPE-*graft*-FPI content in the blends was 15 wt %.

The grafting was characterized by the grafting efficiency α: the ratio of the weight of the grafted resin to the total weight of the resin introduced into the polymer. This quantity was determined by IR absorption spectroscopy, namely, from the content of PF in LDPE-*graft*-FPI before and after extraction with ethanol at 70°C [9].

The viscosity of polymer melts was evaluated by the melt flow index, which was determined at 190°C and 10-kg load with an IIRT-AM device.

The morphology of polymer blends was studied by scanning electron microscopy (JSM 50 Å electron microscope, Jeol, Japan) on chips of samples cooled with liquid nitrogen (notched bars for determining the impact resilience) and decorated with gold.

The mechanical properties of blends were determined by extension and impact failure methods using the standard procedures; samples were prepared by pressure casting.

FPIs were prepared from RMR and RTMR. Rosin–maleic resin was prepared from rosin and maleic anhydride at 180–190°C. It consisted of 75% maleopimaric acid **1** and 25% resin acids **2**–**6** [10]. Rosin–terpene–maleic resin was prepared by treatment of turpentine with maleic anhydride at 180–190°C. It contained 40% maleopimaric acid **1**, 40% mixture of adducts **7** and **8** and diadduct **9**, and 20% resin acids **2**–**6** [11, 12].

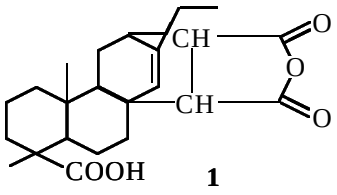

1

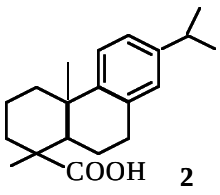

2

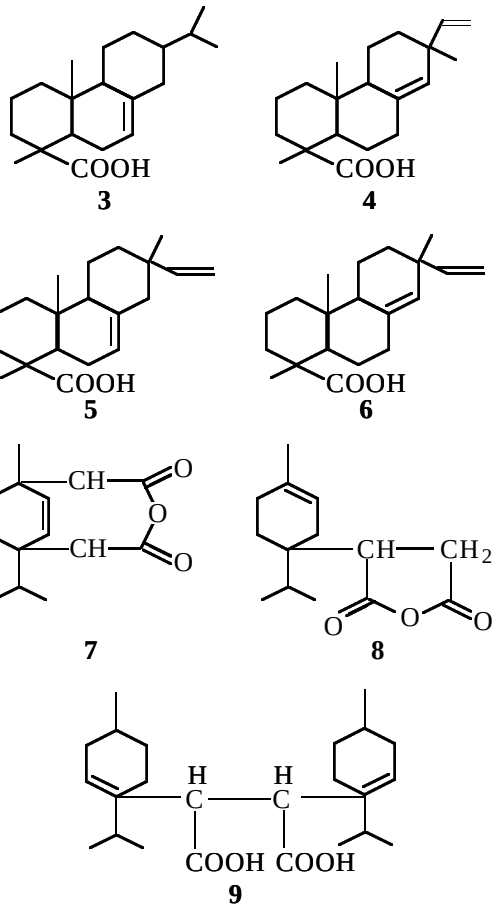

3 **4** **5** **6** **7** **8** **9**

FPIs were prepared by treatment of RMR and RTMR with hydroperoxides: *tert*-butyl hydroperoxide (TBHP) and acetylenic hydroperoxide, 3-methyl-3-hydroperoxy-1-butyne (HP-1), in chloroform in the presence of pyridine:

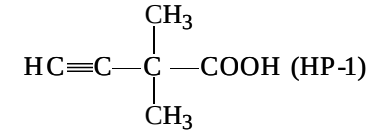

For this purpose, a solution of calculated amounts of resin, peroxide, and pyridine in chloroform was allowed to stand at room temperature for 7 days, after which the reaction mixture was diluted with ether and washed with 18% HCl and water to neutral reaction, and the organic layer was dried over $CaCl_2$. The solvent was distilled off, and the residue was dried in a vacuum at 40°C. The compositions of the reaction systems for preparing PFs are listed in Table 1. As seen from Table 1, the content of available oxygen in the PFs obtained was from 1.53 to 2.48%.

One of FPI samples based on RTMR (Table 1, sample C.40) was prepared by the process involving lithium orthophosphate instead of pyridine. According to

Table 1. Conditions of synthesis of various FPIs and physicochemical properties of the products (synthesis time 7 days, 25°C)

PF	Starting components					mp, °C	Yield based on starting resin, %	Concentration of available oxygen, %	
	RMR, RTMR, g	TBHP, mol	pyridine, mol	lithium orthophosphate, g	chloroform, ml			found	calculated
RMR–TBHP	10	0.0375	0.0625	–	50	55–85	76	2.27	2.54
RTMR–TBHP	10	0.075	0.125	–	50	50–75	70	2.48	2.34
RTMR–TBHP (C.40)	100		–	6	200	70–115	75	1.91	2.34
RMR–HP-1	8	0.02	0.05	–	40	50–105	84	1.58	2.50
RTMR–HP-1	8	0.025	0.075	–	40	40–70	80	1.53	2.24

this process, 6 g of lithium orthophosphate was added to a solution of 100 g of RTMR and 37.5 ml of TBHP in 200 ml of chloroform. The mixture was stirred for 7 days, 5 g of activated carbon was added to coagulate lithium orthophosphate, the catalyst was removed, the solvent was distilled off, and the residue was dried at 40°C/1 mm Hg. We obtained 84 g of a product with mp 70–115°C and available oxygen content of 2.34%. We found that replacement of pyridine with lithium orthophosphate makes FPI preparation considerably simpler and cheaper, since volatile dangerously inflammable solvents are eliminated from the process, as well as the steps of washing with HCl solution and water and drying over $CaCl_2$. With lithium orthophosphate, the target products are isolated immediately after the removal of the catalyst and solvent.

The reaction of RMR and RTMR with hydroperoxides apparently involves opening of the anhydride groups of the adducts to form the corresponding peroxy esters **10**–**12**:

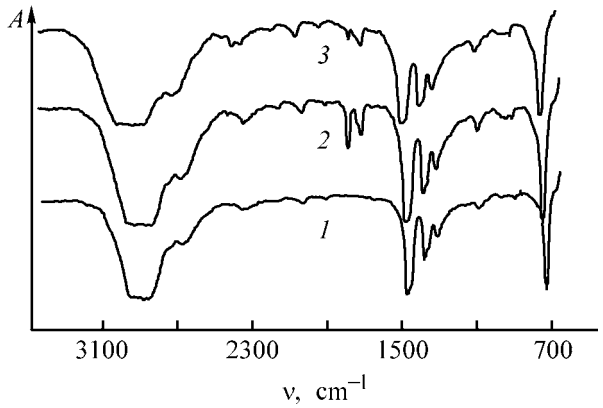

Fig. 1. IR spectra of (*1*) starting LDPE and (*2, 3*) LDPE functionalized with RMR–TBHP, before and after extraction with ethanol, respectively. (*A*) Transmission and (ν) wave number.

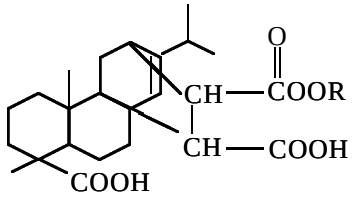

10a, 10b

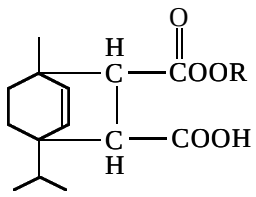

11a, 11b

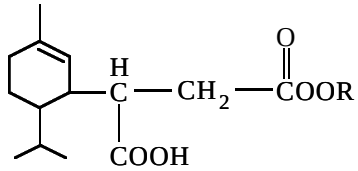

12a, 12b

where R = $C(CH_3)_3$ (**a**), $C(CH_3)_2C{\equiv}CH$ (**b**).

The PF based on RMR contains peroxy ester **10a**, a part of unchanged maleopimaric acid **1**, and resin acids **2**–**6** from the starting RMR.

With RTMR, TBHP and HP-1 react at the anhydride groups of both maleopimaric acid **1** and adducts **7** and **8**. Functional peroxy initiators derived from RTMR contain peroxy esters **10b**–**12b**, resin acids **2**–**6**, and diadduct **9**. Some properties of the PFs obtained are listed in Table 1.

The chemical structure of the FPIs prepared suggests that these compounds can be used in LDPE functionalization both as components of an initiating system (owing to the presence of peroxy ester groups) and as functional monomers (owing to the presence of fragments of resin acids: pimaric **4**, isopimaric **5**, and sandaracopimaric **6**, containing vinyl groups).

Comparison of the IR spectra of the starting LDPE and LDPE-*graft*-FPI shows that coextrusion of the reaction mixture of LDPE with FPI is accompanied by grafting of fragments of peroxide molecules to the LDPE macromolecules (Fig. 1). The IR spectra of modified LDPE contain a complex absorption band at 1700–1790 cm^{-1}, characteristic of stretching vibrations of

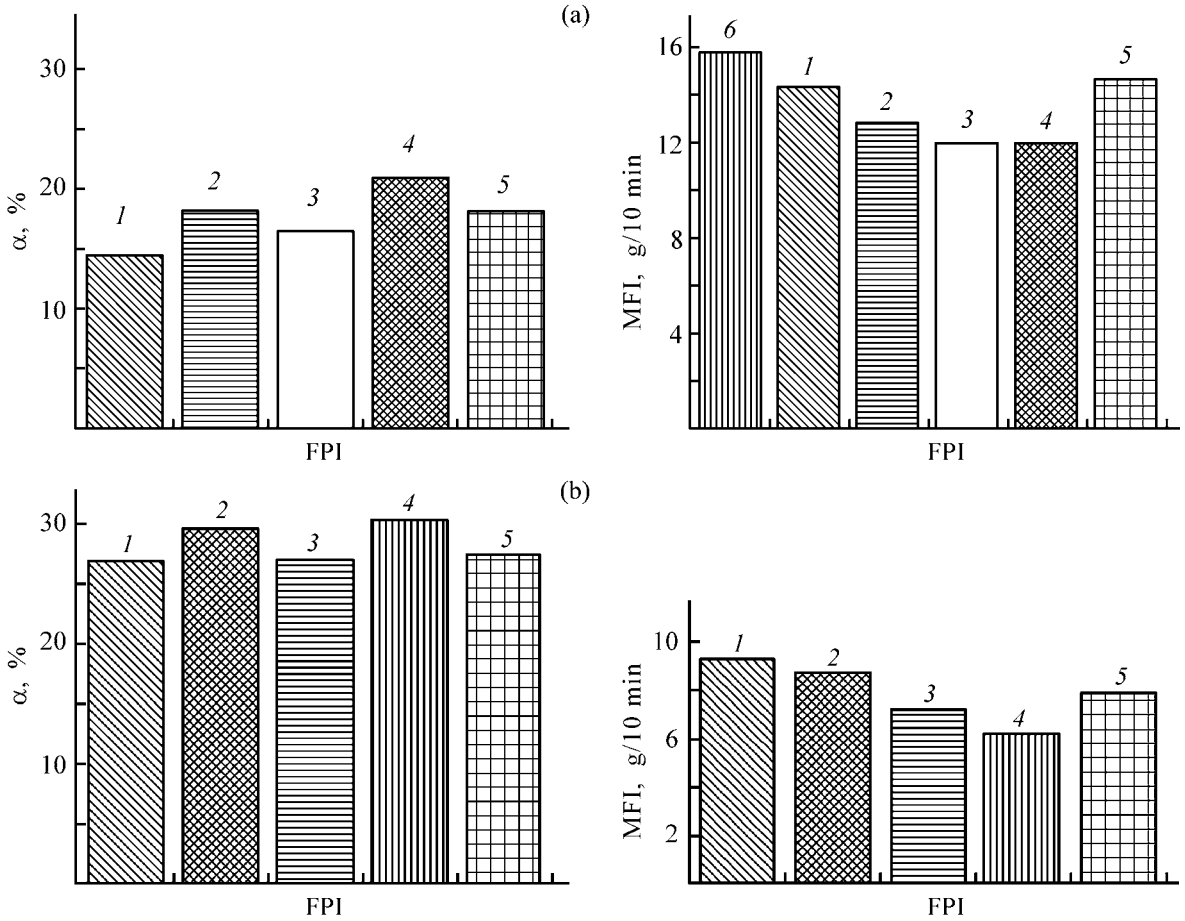

Fig. 2. Influence of (a) the kind of FPI and (b) DCP addition to FPI (0.2 wt %) on the efficiency α of grafting of peroxy fragments to LDPE and on the melt flow index MFI of LDPE-*graft*-FPI. Modifier concentration 1.5 wt %. (*1*) RMR–TBHP, (*2*) RTMR–TBHP, (*3*) RMR–HP-1, (*4*) RTMR–HP-1, (*5*) C.40, and (*6*) no modifier.

the C=O bond in ester, carboxy, aldehyde, and other carbonyl-containing groups. The fact that the C=O absorption is preserved upon extraction of modified LDPE samples with ethanol confirms the chemical binding ot PF molecules with LDPE. However, the intensity of absorption at 1700–1790 cm^{-1} noticeably decreases after the extraction. This fact was used to determine the grafting efficiency. Since the spectra of LDPE modified by PF grafting are characterized by a set of several overlapping bands in the range 1700–1790 cm^{-1}, the grafting efficiency was determined as the ratio between the total peak areas (per unit thickness of the film) in this range after and before extraction of LDPE-*graft*-FPI film samples with ethanol at 70°C.

The values of α for LDPE-*graft*-FPI obtained with vairous kinds of FPI and of the melt flow index (MFI) of LDPE–*graft*-FPI samples are given in Fig. 2a. The efficiency of grafting of FPI fragments to macromolecules varies within 15–21%, depending on the modifier composition. As shown by MFI, the viscosity of LDPE-*graft*-FPI increases only slightly relative to the starting polymer. The MFI values for the starting and modified LDPE differ by no more than 16%. Several factors may be responsible for the relatively low grafting efficiency; the main of these is, apparently, the low concentration of available oxygen. Therefore, the concentration of radicals generated in thermolysis is too low to give rise to a sufficient amount of polyethylene macroradicals to which the FPI fragments are grafted [8].

In this context, we performed a series of experiments on functionalization of LDPE with peroxy-containing formulations in the presence of DCP, which effectively initiates grafting of functional monomers to PO macromolecules [9]. We found that introduction of dicumyl peroxide (0.2 wt %) into the initiating system along with FPI appreciably increases the grafting efficiency (to 31% with FPI based on RTMR and HP-1, Fig. 2b). The rais in the grafting efficiency is accompanied by a decrease in MFI by a factor of 1.8–2.5.

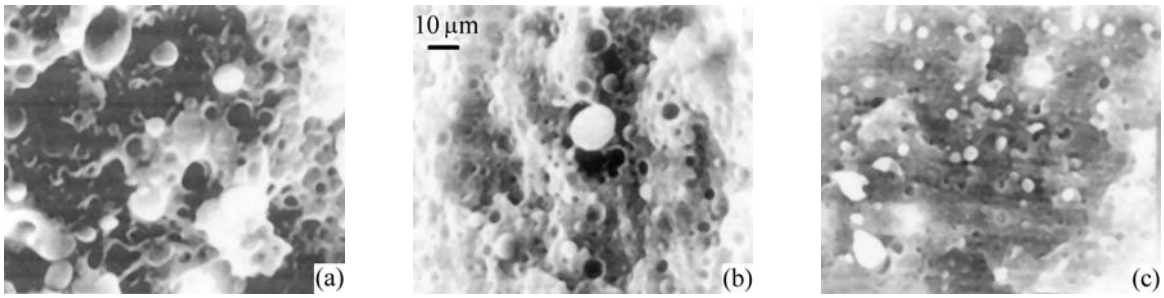

Fig. 3. Electron micrographs of (a) PA6/LDPE blend and (b, c) PA6/LDPE-*graft*-FPI (RMR–TBHP) blends prepared without and with addition of DCP, respectively. LDPE and LDPE-*graft*-FPI concentration in blends 15 wt %.

This is apparently due to an increase in the available oxygen concentration in the initiating system on adding DCP (the available oxygen content in DCP is 5.92%).

The most effective modifiers, from the viewpoint of the grafting efficiency attained under the experimental conditions, are those based on RTMR and HP-1, both in the presence and in the absence of DCP (Figs. 2a, 2b). As for the C.40 sample, which was prepared by a procedure differing from that used with the other FPIs, α and MFI of LDPE-*graft*-FPI obtained with this sample were similar to those of the product obtained with RTMR–TBHP (Figs. 2a, 2b).

Numerous papers [13–15] show that the presence in POs of functional oxygen-containing groups (aldehyde, carboxy, etc.) improves the compatibility of POs with many other polymers and, in particular, with aliphatic polyamides. In this context, it was interesting to assess the prospects for blending LDPE-*graft*-FPI with PA-6 with the aim to prepare composite materials of enhanced performance. In our study, we gave the major attention to the morphological features and physicomechanical properties of the blends.

Figure 3 shows the electron micrographs of chips obtained in liquid nitrogen from 80 × 10 × 4-mm bars of blends of PA6 with the starting LDPE and with LDPE-*graft*-FPI. It is seen that all the blends are two-phase. The polyethylene disperse phase is aggregated and forms droplets varying in size from ≤1 to 10 μm.

Table 2. Mechanical properties of blends*

Sample	σ_f, MPa	ε_t, %	*K*, %	*a*, kJ m^{-2}	
				acute notch	rectangular notch
PA6	61 ± 4	265 ± 17	99.2 ± 5.0	8.0 ± 0.4	6.0 ± 0.4
PA6/LDPE, 15%	42 ± 3	40 ± 3	70.0 ± 3.5	12.0 ± 0.6	11.0 ± 0.5
PA6/LDPE-*graft*-FPI, 15%; LDPE-*graft*-FPI, prepared with:					
RMR–TBHP	51 ± 3	77 ± 5	98.4 ± 5.0	16.0 ± 0.8	19.0 ± 0.9
RTMR–TBHP	47 ± 2	78 ± 5	92.0 ± 4.6	15.0 ± 0.7	18.0 ± 0.7
RMR–HP-1	51 ± 3	127 ± 8	95.7 ± 4.6	16.0 ± 0.8	20.0 ± 0.9
RTMR–HP-1	50 ± 3	114 ± 6	95.2 ± 5.0	18.0 ± 0.9	24.0 ± 0.8
RTMR–TBHP (C.40)]	49 ± 3	89 ± 5	91.0 ± 5.0	18.0 ± 0.9	24.0 ± 1.0
(RMR–TBHP) + DCP	54 ± 4	138 ± 7	99.0 ± 5.0	16.0 ± 0.8	24.0 ± 1.0
(RTMR–TBHP) + DCP	55 ± 4	108 ± 5	98.2 ± 4.2	17.0 ± 0.9	23.0 ± 1.0
(RMR–HP-1) + DCP	53 ± 3	88 ± 6	98.5 ± 4.3	18.0 ± 0.9	23.0 ± 0.9
(RTMR–HP-1) + DCP	52 ± 3	78 ± 6	96.2 ± 4.0	17.0 ± 0.7	23.0 ± 0.8
[RTMR–TBHP (C.40)] + DCP	51 ± 2	186 ± 11	94.7 ± 5.0	18.0 ± 0.7	25.0 ± 1.2

* (α_f) Upper yield point in extension of samples prepared by one-side injection from the end; (ε_t) relative elongation of samples prepared by one-side injection from the end; (*K*) seam strength coefficient in pressure casting, equal to the ratio of the yield point of the sample prepared by two-side injection of the melt from the blade ends to that of the sample prepared by one-side injection from the end; and (*a*) Charpy impact resilience.

A specific feature of the morphology of blends of PA6 with LDPE-*graft*-FPI prepared without adding DCP is the decreased size of spherical aggregates of the PO disperse phase in the blend and the decreased concentration of coarse aggregates as compared to the PA6/LDPE blend (Figs. 3a, 3b). At the same time, the smooth surface of the agglomerates suggests a relatively low interphase adhesion between the polyamide matrix and the disperse phase formed by LDPE-*graft*-FPI. Introduction of DCP into the reaction mixture in preparation of LDPE-*graft*-FPI increases the efficiency of grafting of FPI polar fragments, which, in turn, is reflected in the morphology of blends with PA6: The agglomerates become still smaller (≤1–2 μm), and the interphase zones in some cases become less sharp (Fig. 3c). Apparently, the decrease in the size of spherical agglomerates is due to intensification of interphase interactions and an increase in adhesion between the blend components owing to the growth of the concentration of polar FPI fragments grafted to LDPE macromolecules [16].

The yield point and relative elongation of the blends prepared show that the mechanical properties of systems of this kind are determined by the intensity of interaction between the components and, hence, depend on the content of polar fragments grafted to LDPE macromolecules (Table 2). In particular, blends with LDPE modified in the presence of DCP show a higher yield point and a larger relative elongation than the blends with LDPE functionalized in the absence of DCP. Blends of PA6 with LDPE-*graft*-FPI prepared both in the absence and in the presence of DCP exhibit considerably higher (by a factor of 2–3) impact resilience compared to the starting PA6 and to the PA6/LDPE blend (Table 2). The blends with LDPE-*graft*-FPI prepared in the presence of DCP show, on the whole, appreciably higher strength coefficient of the seams of melt flows in pressure casting of various items (blades) (Table 2). This fact indirectly confirms the stronger interphase adhesion in blends of PA6 with LDPE-*graft*-FPI characterized by higher grafting efficiency.

The increased impact resilience and the simplicity and environmental safety of production of PA6/LDPE-*graft*-FPI blends make them promising for practice.

CONCLUSIONS

(1) Reactive extrusion of low-density polyethylene with resins modified with maleic anhydride and peroxy compounds results in grafting to polyethylene macromolecules of polar fragments formed by thermolysis of functional peroxy initiators. The efficiency of grafting of functional peroxy initiators is 15–21%. The viscosity of the polymer melt, evaluated by the melt flow index, slightly grows upon grafting, suggesting loose cross-linking in the graft product.

(2) Additional introduction of cumyl peroxide (0.2 wt %) into the reaction mixture increases the efficiency of grafting of polar fragments of functional peroxy initiators by a factor of 2. The cross-linking of macromolecules is also intensified, causing an increase in the viscosity of the polymer melt by a factor of 2.5.

(3) The most effective modifiers from the viewpoint of ensuring the maximum grafting efficiency, both in the presence and in the absence of dicumyl peroxide, are functional peroxy initiators derived from rosin–terpene–maleic resin.

(4) Blends of polyamide 6 with both functionalized and initial polyethylene are heterogeneous. The disperse polyethylene phase occurs as droplets. A specific feature of the morphology of blends of polyamide 6 with functionalized polyethylene, compared to blends with the initial low-density polyethylene, is the smaller size of the disperse phase particles (the maximum particle size decreases from 10 to 2 μm), and also decreased concentration of coarse aggregates. Therefore, the blends exhibit higher impact resistance.

REFERENCES

1. Baranov, A.O., Kotova, A.V., Zelenetskii, A.N., and Prut, E.V., *Usp. Khim.*, 1997, vol. 66, no. 10, pp. 972–984.
2. Koning, C., Duing, M. von, Pagnoulle, C., and Jerome, R., *Prog. Polym. Sci.*, 1998, vol. 23, pp. 707–757.
3. Liu, N.C. and Baker, W.E., *Adv. Polym. Technol.*, 1992, vol. 11, pp. 249–262.
4. Xanthos, M., *Reactive Extrusion: Principles and Practice*, Munich: Hanser, 1992.
5. Prut, E.V. and Zelenetskii, A.N., *Usp. Khim.*, 2001, vol. 70, no. 1, pp. 72–87.
6. Lambla, M., *Macromol. Symp.*, 1994, vol. 83, pp. 37–58.
7. Moad, G., *Prog. Polym. Sci.*, 1999, vol. 24, pp. 81–142.
8. Assou, L., Manning, S.C., and Moore, R.B., *Polymer*, 1998, vol. 39, pp. 2571–2577.
9. Pesetskii, S.S., Jurkowski, B., Krivoguz, Y.M., and Urbanowicz, R., *J. Appl. Polym. Sci.*, 1997, vol. 65, pp. 1493–1502.
10. *Sinteticheskie produkty iz kanifoli i skipidara: Trudy*

Vsesoyuznogo nauchno-tekhnicheskogo soveshchaniya po voprosam sinteza novykh produktov na osnove kanifoli i skipidara (Synthetic Products from Rosin and Turpentine: Proc. All-Union Scientific and Technical Meet. on Synthesis of New Products from Rosin and Turpentine), Minsk: Nauka i Tekhnika, 1964.

11. Klyuev, A.Yu., Shlyashinskii, R.G., and Stromskii, A.S., *Vestsi Akad. Navuk Bel., Ser. Khim. Navuk*, 1995, no. 3, pp. 101–106.
12. Klyuev, A.Yu., Shlyashinskii, R.G., Titov, A.I., and Antonovich, I.V., *Zh. Prikl. Khim.*, vol. 70, no. 12, pp. 2056–2060.
13. Pesetskii, S.S. and Bogoslavskii, A.A., *Mater. Tekhnol. Instr.*, 1999, no. 2, pp. 27–38.
14. Dedecker, K. and Groeninckx, G., *Polymer*, 2001, vol. 39, pp. 4985–4992.
15. Bohn, C.C., Manning, S.C., and Moore, R.B., *J. Appl. Polym. Sci.*, 2001, vol. 79, pp. 2398–2407.
16. Willis, J.M. and Favis, B.D., *Polym. Eng. Sci.*, 1988, vol. 28, no. 21, pp. 1416–1426.

Russian Journal of Applied Chemistry, Vol. 77, No. 6, 2004, pp. 983–987. Translated from Zhurnal Prikladnoi Khimii, Vol. 77, No. 6, 2004, pp. 996–1000.

MACROMOLECULAR CHEMISTRY AND POLYMERIC MATERIALS

Coagulation of Butadiene–Styrene Latex with Poly-*N*,*N*-dimethyl-2-hydroxypropylenammonium Chloride

S. S. Nikulin, T. N. Poyarkova, and V. M. Misin

Voronezh State Academy of Forestry Engineering, Voronezh, Russia

Voronezh State University, Voronezh, Russia

Institute of Biochemical Physics, Russian Academy of Sciences, Moscow, Russia

Received March 22, 2004

Abstract—The flocculating performance of a cationic polyelectrolyte, poly-*N*,*N*-dimethyl-2-hydroxypropylenammonium chloride, in recovery of butadiene–styrene rubber in the presence of sulfuric acid at various temperatures was studied. The kinetic curves of flocculation of SKS-30 ARK latex at various amounts of the flocculant added were obtained.

Emulsion rubbers occupy one of the leading positions in production of synthetic rubbers. The absence of harmful substances and of dangerously explosive and inflammable organic solvents creates favorable prerequisites for further development of emulsion rubber production and improvement of the production process. An important step in production of emulsion rubbers is their recovery from latexes by coagulation. On the one hand, sodium chloride widely used for this purpose today is cheap and readily available, but, on the other, it gives rise to environmental problems because of large consumption (180–250 kg t^{-1} rubber [1]). Thus, an enterprise producing about 100 000 t $year^{-1}$ of butadiene–styrene rubbers discharges up to 25 000 t $year^{-1}$ of NaCl to water treatment facilities. Since sodium chloride is not subject to biodegradation at the water treatment facilities, this amount is further discharged into natural water reservoirs, causing environmental pollution with mineral salts and irretrievable harm to the nature. Therefore, active efforts are being made in Russia and other countries to develop new coagulating agents that would be adsorbed on the rubber during coagulation and would be recovered together with the rubber crumb. This would reduce the water consumption by rubber recovery shops, the amount of discharged aqueous phase, and the content of harmful and toxic products in it, with an increase in the productive capacity of the process as a whole.

Much attention has been given recently to the use of cationic organic coagulants with both low and high molecular weight [2–4]. With cationic agents, the consumption of coagulants used in recovery of synthetic rubbers from latexes can be considerably reduced.

In this study, we examined the flocculating performance of poly-*N*,*N*-dimethyl-2-hydroxypropylenammonium chloride (PDMHPAC) in recovery of synthetic butadiene–styrene rubber from SKS-30 ARK latex at various temperatures and additions of the acidifying agent.

EXPERIMENTAL

Experiments were performed with SKS-30 ARK commercial latex of butadiene–styrene rubber (content of bound styrene in the copolymer 21.9%). The polymer content in the latex was 190 g l^{-1}; surface tension, 56.4 mN m^{-1}; and mean size of latex globules, 29 nm.

The PDMHPAC sample used as flocculant had the following characteristics: main substance concentration 50%, viscosity 23.85 cP, pH 8.3, concentration of chloride ions 11.2%. The structural formula of PDMHPAC is as follows:

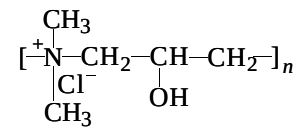

Rubber was recovered from the latex in a coagulation unit, namely, in a vessel equipped with a stirrer

1070-4272/04/7706-0983 © 2004 MAIK "Nauka/Interperiodica"

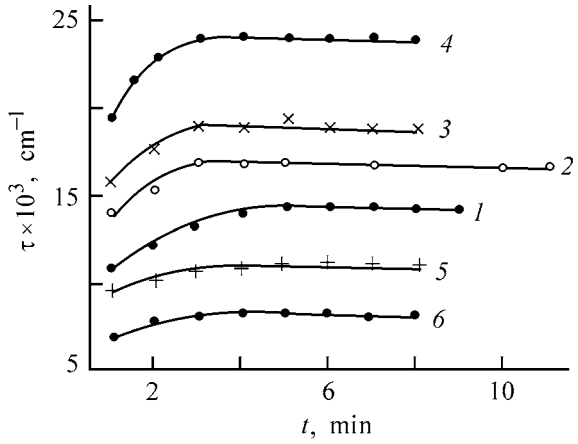

Fig. 1. Kinetic curves of flocculation of SKS-30 ARK latex with PDMHPAC solutions of various concentrations: (τ) turbidity and (t) time. Concentration $c \times 10^6$, M (in terms of monomeric units): (*1*) 1, (*2*) 2, (*3*) 3, (*4*) 4, (*5*) 5, and (*6*) 6.

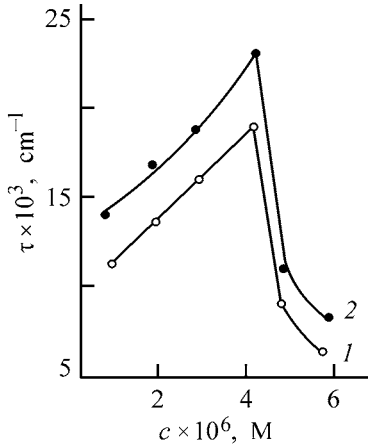

Fig. 2. (*1*) 1-min turbidity τ_1 and (*2*) limiting turbidity τ_∞ vs. PDMHPAC concentration c (in terms of monomeric units).

and placed in a thermostat. The completeness of coagulation was evaluated by the weight of the coagulum formed and visually, by the serum transparency (the serum transparency is an evidence of complete coagulation).

The kinetic curves of flocculation of SKS-30 ARK latex at various of the flocculant added were taken at room temperature with an NFM nephelometer. The procedures for nephelometric monitoring of the kinetics and for determination of the initial flocculation rate are described elsewhere [5].

Variation with time of the turbidity τ of a dilute ($1 : 10^4$) SKS-30 ARK latex in the presence of various amounts of PDMHPAC is shown in Fig. 1. As with other cationic agents (poly-*N*,*N*-dimethyl-*N*,*N*-diallylammonium chloride, PDMDAAC [6]; 2-methylimidazole [7]; 2,2,4-trimethyl-1,2-dihydroquinoline [8]), the turbidity initially grows, after which a constant limiting value, τ_∞, is attained, corresponding to the formation of coarse floccules stable in time [9]. The curve of the 1-min turbidity, characterizing the initial flocculation rate, vs. PDMHPAC concentration passes through a pronounced maximum (flocculation optimum) typical of polyelectrolytes (Fig. 2). The polyelectrolyte concentration corresponding to the maximum flocculation rate can be a measure of the flocculating performance [10]. The optimum is due to neutralization of the surface electric charge of particles as a result of binding of emulsifier anions into an insoluble nondissociating complex, which can be followed by recharging and restabilization of the sol through adsorption of excess polymer and build-up of the positive charge of the particles, and also to formation of relatively thick layers of the hydrophilic polymer (Fig. 2). Similar trends have been observed previously in flocculation of polystyrene latex [11, 12] and of butadiene–styrene and butadiene–acrylonitrile latexes [5] with PDMHPAC; in all cases, the occurrence of recharging was confirmed by measuring the electrokinetic potential of the latex particles.

The interaction of PDMHPAC with emulsifiers (potassium soap derived from tall oil, sodium paraffinate, Leukanol) can be schematically described by exchange reactions occurring in latex coagulation:

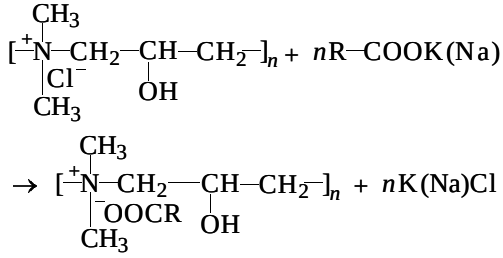

On acidification, the product can react with sulfuric acid, with the release of free organic acids:

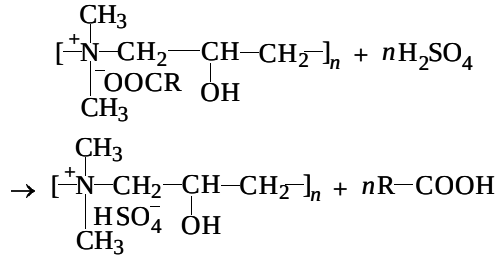

We examined the influence exerted on the coagulation of SKS-30 ARK butadiene–styrene latex by such an important parameter as the concentration of the disperse phase. In real industrial processes, the polymer

content in the latex can vary from 10 to 22%. Such significant fluctuations of the concentration can affect the amount of PDMHPAC required for complete recovery of the rubber from the latex. To examine the influence exerted by the concentration of the disperse phase on the completenes of coagulation with PDMHPAC, we prepared latexes with 50, 100, and 150 g l^{-1} of the disperse phase.

The dependences of the degree of the rubber coagulation φ on the PDMHPAC concentration at 20°C and various concentrations c_{dp} of the disperse phase are shown in Fig. 3. As the concentration of the disperse phase is increased, the curves of coagulum recovery steadily shift to higher flocculant concentrations. In the curves of the degree of rubber recovery vs. flocculant concentration, the initial ascent is followed by a plateau corresponding to complete recovery of the rubber from the latex. In [13], we described the specific features of the flocculating effect of polymeric agents at various concentrations of the disperse phase. Flocculation of sols by oppositely charged polymers was attributed to two destabilization factors: neutralization of the surface charge of the sol particles and bridging mechanism of particle agglomeration. This is followed by restabilization through surface recharging and formation of a dense polymolecular adsorption layer of a hydrophilic polymer on the particle surface. When the concentration of the disperse phase in SKS-30 ARK latex is as high as 50–150 g l^{-1}, the restabilization effect is lost, which may be due to relaxation processes occurring in adsorption layers of macromolecules on the particle surface [14]. It should be noted that the PDMHPAC consumption is virtually independent of the concentration of the disperse phase (in the examined range), amounting to 4–5 kg t^{-1} rubber.

Another important process parameter of rubber recovery from a latex is the consumption of an acidifying agent, an aqueous solution of sulfuric acid. As the H_2SO_4 consumption is increased, the coagulating power of PDMHPAC grows significantly (Fig. 4). This may be due to contraction of the diffuse electrical double layer and decrease in the electrostatic repulsion forces preventing agglutination of latex globules upon collisions. However, the effect of this factor is restricted to relatively low consumptions of H_2SO_4. Apparently, the major effect should be exerted by a nonelectrostatic stability factor, associated with the presence of a hydrated adsorption layer of the emulsifier on the surface of latex globules [15]. The overlapping of these layers determines the structural component of the wedging pressure [16, 17]. It is well known [18, 19] that the thickness of protective hydration

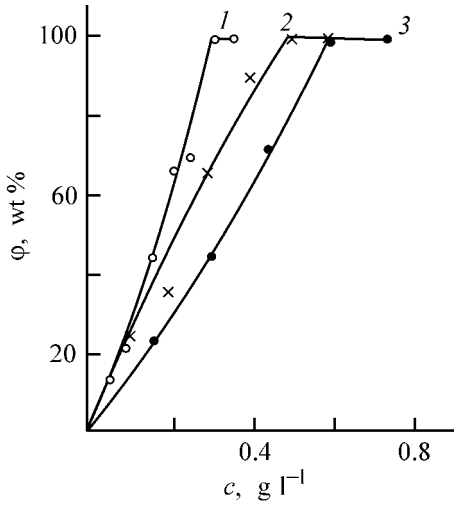

Fig. 3. Degree of coagulation φ of SKS-30 ARK latex vs. PDMHPAC concentration c at various concentrations c_{dp} of the disperse phase. H_2SO_4 amount 15 kg t^{-1} rubber. c_{dp}, g l^{-1}: (*1*) 50, (*2*) 100, and (*3*) 150.

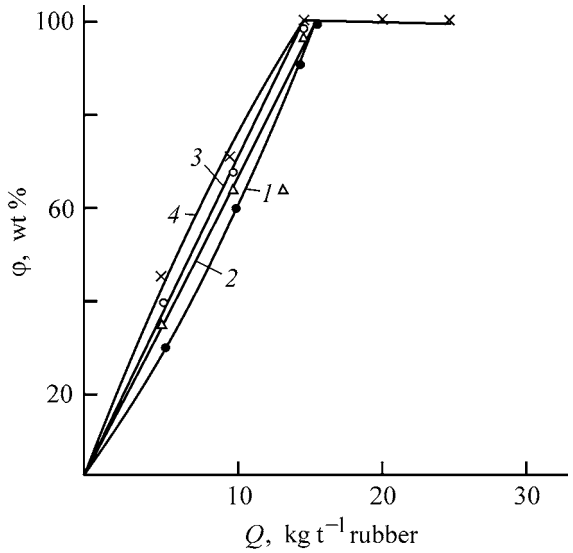

Fig. 4. Degree of coagulation φ of SKS-30 ARK latex vs. sulfuric acid consumption Q at various temperatures. Concentration of the disperse phase c_{dp} = 100 g l^{-1}; PDMHPAC consumption 4 kg t^{-1} rubber. T, °C: (*1*) 20, (*2*) 40, (*3*) 60, and (*4*) 80; the same for Fig. 5.

shells of latex particles decreases as the electrolyte concentration is increased. Hence, the observed increase in the flocculation efficiency in the presence of sulfuric acid, which is a strong dehydrating agent, is also attributable to breakdown and thinning of hydration shells of latex globules. The particles can come in this case closer to each other, making the bridging flocculation mechanism more probable.

Our experiments show that the consumption of the acidifying agent affects the coagulation more strongly

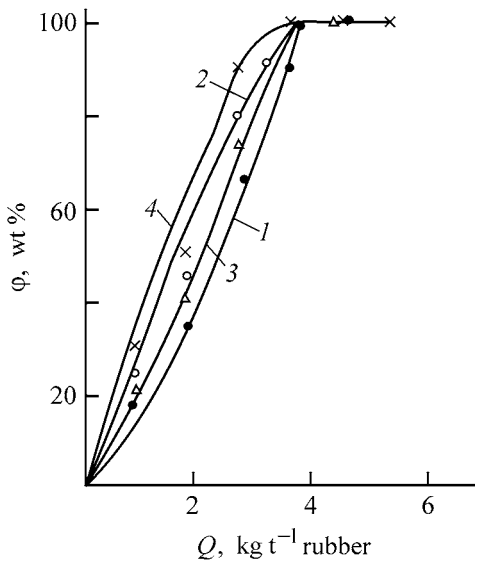

Fig. 5. Degree of coagulum recovery φ from SKS-30 ARK latex vs. PDMHPAC consumption Q at various temperatures. Disperse phase concentration c_{dp} = 100 g l^{-1}, H_2SO_4 consumption 15 kg t^{-1} rubber.

than does the concentration of the disperse phase (in the ranges examined). For example, at a PDMHPAC consumption of about 4 kg t^{-1} rubber (Fig. 4), the coagulum weight regularly grows with increasing amount of added sulfuric acid, reaching 100% at the H_2SO_4 consumption of 15 kg t^{-1} rubber. Further increase in the consumption of the acidifying agent (above 15 kg t^{-1} rubber) at this PDMHPAC consumption is not appropriate, as resulting in an excessive consumption of sulfuric acid and pollution of wastewater.

Our experiments show that, at large consumptions of the flocculant (4 kg t^{-1} rubber) and sulfuric acid (15 kg t^{-1} rubber), the influence of temperature on the degree of rubber recovery from the latex is insignificant. A similar result has been obtained previously [20] in studying the influence of temperature on the degree of rubber recovery from butadiene–acrylonitrile latex with a cationic polyelectrolyte at high latex concentrations, when the restabilization effect is lost.

At the same time, when the amount of PDMHPAC added was below the optimum, the degree of rubber recovery in a wide range of H_2SO_4 consumptions showed an appreciable temperature dependence. In the initial steps of recovery (at low PDMHPAC consumptions), the coagulum weight grew as the temperature increased from 20 to 80°C (Fig. 5). At the PDMHPAC consumption decreased from 4 to 3 kg t^{-1} rubber, the complete coagulation of SKS-30 ARK latex could be attained only at elevated temperatures (80–95°C) and the consumption of sulfuric acid increased to 30 kg t^{-1} rubber, and, at the PDMHPAC consumption decreased to 2 kg t^{-1}, even these conditions were insufficient to recover the rubber completely.

Thus, our studies show that the following reagent consumptions are optimal for coagulation of SKS-30 ARK rubber at the concentration of the disperse phase of 100 g l^{-1} and 60 ± 10°C: PDMHPAC 4 and H_2SO_4 15 kg t^{-1} rubber.

Properties of rubber stocks and vulcanizates based on SKS-30 ARK rubber

Parameter	Sample	
	control	experimental
Mooney viscosity	53	42.5
Karrer plasticity, arb. units	0.30	0.28
Recovery, mm	1.86	1.84
Vulcanization optimum at 143°C, min	80	60
Nominal stress at 300% elongation, MPa	8.4	14.0
Nominal tensile strength, MPa	27.0	27.6
Relative elongation at break, %	600	540
Deformation set, %	16	15
Rebound elasticity, %		
at 20°C	37	32
at 100°C	50	46
Shore hardness, arb. units	59	65
Schopper–Schlobach abrasion, $A \times 10^{-3}$, $cm^3\ m^{-1}$	1.80	1.31
Resistance to cutting propagation to 12 mm with puncture, thousands of cycles	39200	115200
Nominal tensile strength after aging (100°C, 72 h)	18.0	20.0
Relative elongation after aging (100°C, 72 h)	242	257

Under the optimal conditions, we obtained an experimental batch of the coagulum of SKS-30 ARK rubber for subsequent preparation of the standard rubber stock and vulcanizates. We assessed the effect of the coagulant on their properties as compared to the control sample recovered from the latex with NaCl (see table).

It is seen that the rubber stocks and vulcanizates based on the experimental batch of SKS-30 ARK rubber are not inferior in all the main parameters to the control samples obtained using sodium chloride and surpass the control samples in resistance to cutting propagation, aging, and tear.

CONCLUSIONS

(1) The 1-min (τ_1) and limiting (τ_∞) turbidities of SKS-30 ARK latex as functions of the poly-*N*,*N*-dimethyl-2-hydroxypropylenammonium chloride concentration pass through a pronounced maximum (flocculation optimum) typical of the flocculating effect of polyelectrolytes.

(2) The consumption of the acidifying agent exerts a stronger effect on coagulation than the temperature and the concentration of the disperse phase.

(3) Rubber stocks and vulcanizates based on the experimental SKS-30 ARK rubber are not inferior in the main parameters to the control sample obtained using sodium chloride for the rubber recovery and even surpass the control sample in some parameters.

REFERENCES

1. Kirpichnikov, P.A., Averko-Antonovich, L.A., and Averko-Antonovich, Yu.O., *Khimiya i tekh nologiya sinteticheskogo kauchuka* (Chemistry and Technology of Synthetic Rubber), Leningrad: Khimiya, 1987.
2. Verezhnikov, V.N., Nikulin, S.S., Poyarkova, T.N., and Misin, V.M., *Zh. Prikl. Khim.*, 2001, vol. 74, no. 7, pp. 1191–1194.
3. Nikulin, S.S., Verezhnikov, V.N., Poyarkova, T.N., and Dankovtsev, V.A., *Zh. Prikl. Khim.*, 2000, vol. 73, no. 5, pp. 833–836.
4. Verezhnikov, V.N., Nikulin, S.S., Poyarkova, T.N., and Garshin, A.P., *Vestn. Tambov. Univ.*, 1997, vol. 2, no. 1, pp. 47–52.
5. Verezhnikov, V.N., Nikulin, S.S., Poyarkova, T.N., and Vostrikova, G.Yu., *Zh. Prikl. Khim.*, 2000, vol. 73, no. 10, pp. 1720–1724.
6. Verezhnikov, V.N., Nikulin, S.S., Misin, B.M., and Poyarkova, T.N., *Russ. Polym. News*, 1999, vol. 4, no. 4, pp. 36–41.
7. Verezhnikov, V.N., Nikulin, S.S., and Garshin, A.P., *Zh. Prikl. Khim.*, 1997, vol. 70, no. 12, pp. 2052–2055.
8. Nikulin, S.S., Verezhnikov, V.N., Poyarkova, T.N., and Shmyreva, Zh.V., *Zh. Prikl. Khim.*, 2000, vol. 73, no. 1, pp. 144–148.
9. Baran, A.A., Tusupbaev, N.K., Solomentseva, I.M., *et al.*, *Kolloidn. Zh.*, 1980, vol. 42, no. 1, pp. 11–15.
10. Kudryavtseva, N.M., Muller, V.M., and Vapaev, S.F., *Kolloidn. Zh.*, 1978, vol. 40, no. 4, pp. 463–469.
11. Verezhnikov, V.N., Nikulin, S.S., Krutikov, M.Yu., and Poyarkova, T.N., *Kolloidn. Zh.*, 1999, vol. 61, no. 1, pp. 37–40.
12. Verezhnikov, V.N., Poyarkova, T.N., Nikulin, S.S., and Kurbatova, N.A., *Kolloidn. Zh.*, 2000, vol. 62, no. 1, pp. 26–30.
13. Verezhnikov, V.N., Nikulin, S.S., Poyarkova, T.N., and Vostrikova, G.Yu., *Zh. Prikl. Khim.*, 2002, vol. 75, no. 3, pp. 472–475.
14. Pelssers, E., Cohen, S., and Fleer, G., *J. Chem. Soc., Faraday Trans.*, 1990, vol. 86, no. 9, pp. 1355–1361.
15. Pashley, R.M., *Adv. Colloid Interface Sci.*, 1982, vol. 16, p. 57.
16. Derjaguin, B.V. and Churaev, N.V., *J. Colloid Interface Sci.*, 1974, vol. 49, pp. 249–251.
17. Churaev, N.V., *Kolloidn. Zh.*, 1984, vol. 46, no. 2, pp. 302–304.
18. Lebedev, A.V., *Kolloidnaya khimiya sinteticheskikh lateksov* (Colloid Chemistry of Synthetic Latexes), Leningrad: Khimiya, 1976.
19. Kiseleva, O.G. and Neiman, R.E., *Kolloidn. Zh.*, 1985, vol. 47, no. 4, pp. 799–801.
20. Verezhnikov, V.N., Vostrikova, G.Yu., and Poyarkova, T.N., *Zh. Prikl. Khim.*, 2003, vol. 76, no. 8, pp. 1359–1362.

Russian Journal of Applied Chemistry, Vol. 77, No. 6, 2004, pp. 988–993. Translated from Zhurnal Prikladnoi Khimii, Vol. 77, No. 6, 2004, pp. 1001–1006.

MACROMOLECULAR CHEMISTRY AND POLYMERIC MATERIALS

Redox Ion Exchangers Based on Pyridinecarbonitriles

E. E. Ergozhin, B. A. Mukhitdinova, V. V. Shalygina, B. Zh. Shekeeva, and K. M. Sartbaeva

Bekturov Institute of Chemical Sciences, Ministry of Education and Science of Kazakhstan Republic, Almaty, Kazakhstan

Received December 3, 2003; in final form, March 2004

Abstract—Thermal polymerization of *o*-, *m*-, and *p*-pyridinecarbonitriles and their derivatives under the action of Friedel–Crafts catalysts and binary catalysts was studied. The characteristics of the resulting polymers were determined.

In production of polymeric materials, not only the characteristics of functional groups, but also the structural features of macromolecule skeleton are very important. From this standpoint, macromolecular compounds with a system of conjugated bonds, with the backbone containing functional groups capable of ion exchange, complexation, and reversible redox reactions are of interest. These compounds combine high thermal and chemical stability, and radiation resistance, increased electrical conductivity, and capability for electron exchange, characteristic of conjugated polymers. The presence of functional ionogenic and/or redox groups opens up prospects for using these polymers as new redox ion exchangers.

In this context, pyridinecarbonitriles produced by oxidative ammonolysis of alkylpyridines [1–6] and used previously for preparing various ion exchangers [7–15] show considerable promise. Redox ion exchangers based on pyridinecarbonitriles have not been adequately studied [16–18]. The aim of this study was to prepare these polymers and to examine their characteristics.

Contrary to readily polymerizing vinyl monomers and dienes, nitriles of aromatic and heterocyclic acids polymerize only under rigorous conditions with a low yield of target polymers [19, 20].

EXPERIMENTAL

Pyridinecarbonitriles [2-, 3-, and 4-cyanopyridines (2-, 3-, and 4-CP); 2,5-, 3,5-, 2,3-, and 2,6-dicyanopyridines (2,5-, 3,5-, 2,3, and 2,6-diCP); 5-cyano-2-pyridinecarboxamide (A-5-C-2-PC) and 4-hydroxybenzonitrile (4-HBN)] were prepared at the Bekturov Institute of Chemical Sciences [1–6]. 3-Pyridinecarbonyl chloride hydrochloride (3-PCC-HC) was synthesized by the procedure described in [21]. The distillable substances were purified by distillation, and undistillable substances, by recrystallization (Table 1). The majority of the monomers are soluble in benzene, acetone, and ethanol.

The polymers were prepared by thermal polymerization of monomers (Table 1) in the bulk in the presence of stoichiometric amounts of the catalyst in am-

Table 1. Melting (boiling) points and data of elemental analysis of pyridinecarbonitriles and their derivatives

Monomer	mp, bp, °C (*P*, mm Hg)	Found, %					Formula	Calculated, %				
		C	H	N	O	Cl		C	H	N	O	Cl
2-CP	26/118(30)	69.01	4.00	26.81	–	–	$C_6H_4N_2$	69.23	3.83	26.88	–	–
3-CP	49/102(25)	69.20	3.84	26.76	–	–	〃	69.23	3.83	26.88	–	–
4-CP	79/145(5)	69.24	3.92	27.10	–	–	〃	69.23	3.83	26.88	–	–
2,5-diCP	112/–	65.33	2.39	32.56	–	–	$C_7H_3N_3$	65.12	2.33	32.54	–	–
3,5-diCP	113/–	65.11	2.33	32.55	–	–	〃	65.12	2.33	32.54	–	–
2,3-diCP-	80/–	65.12	2.37	32.57	–	–	〃	65.12	2.33	32.54	–	–
A-5-C-2-PC	254/–	57.20	3.60	28.32	10.92	–	$C_7H_5N_3O$	57.14	3.40	28.57	10.88	–
4-HBN	112/–	70.57	4.37	11.32	13.74	–	C_7H_5NO	70.59	4.20	11.76	13.45	–
3-PCC-HC	153/–	40.20	3.00	7.71	9.25	39.84	C_6H_4ClNO	40.49	2.80	7.87	8.99	39.85

1070-4272/04/7706-0988 © 2004 MAIK "Nauka/Interperiodica"

pules in a vacuum, under argon, or in air at the melting point of the nitrile–catalyst complex. The process catalysts were chlorides of coordination-unsaturated metals (Zn, Ti, Sn, Cr, Co, and Fe) of chemically pure or pure grade, produced by Aldrich. After reaction completion, the polymer was ground, purified by repeated precipitation from sulfuric acid to acetone, and washed with distilled water to neutral reaction for the corresponding cations and anions, after which it was dried in a vacuum at 150–200°C to constant weight.

The concentration of metal cations (Cu^{2+}, Co^{2+}, Zn^{2+}, Fe^{3+}, Mg^{2+}, and Hg^{2+}) for estimation of the sorption power of the ion exchangers was determined by titration with Na_2EDTA [22]; Ag^+, by the procedure described in [23]; and Os^{8+}, by the atomic absorption analysis.

Acid–base titration of the samples was carried out by the method of individual weighed portions [24] on a Mettler Toledo MP-220 pH meter. Redox potentiometric titration was carried out in a temperature-controlled cell in an argon flow in the presence of a calomel electrode coupled with a polished platinum electrode in 100 ml of a $K_2SO_4 + H_2SO_4$ buffer solution (pH 0.3–0.7) at 25°C. As an oxidizing agent was used a solution of $Ce(SO_4)_2$ in sulfuric acid, standardized with 0.1 N $Na_2S_2O_3$. To improve the titration efficiency, we used 0.03 N solution of Fe^{3+} as a mediator.[1] Using the titration data, we plotted the dependences of the potential E (mV) on the concentration of the added oxidizing agent. The standard oxidation potential of the polymer E_0 was evaluated by the Nernst equation [18].

Viscometric studies of the polymers synthesized were carried out by the procedure described in [25]. The swellability and moisture content of the ion exchangers, and also their chemical and thermal stability in water, mechanical strength, and bulk weight were determined according to GOSTs (State Standards).[2] The thermal stability of polymers in air was studied on an MOM derivatograph (Hungary). The heating rate was 4.50 deg min^{-1}. The IR spectra of the initial, intermediate, and final products were recorded on a Specord M-80 spectrophotometer.

The lower limiting temperatures of polymerization were found to be 230 (3-CP), 240–250 (2,3-diCP), approximately ~180 (2,5-diCP), approximately ~180 (A-5-C-2-CP), 150–160 (3,5-diCP), 200 (3-PCC-HC), and approximately ~240°C (4-HBN). We established

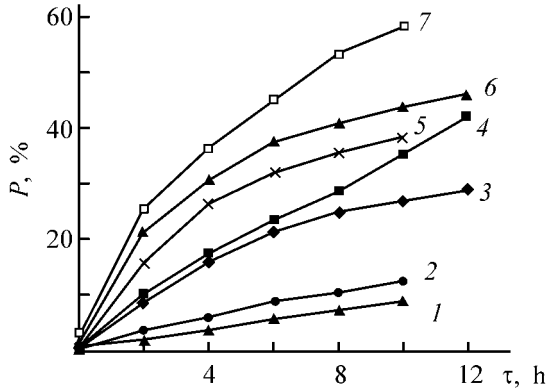

Fig. 1. Kinetic curves of 3-CP polymerization in the presence of anhydrous halides of (*1*) Sn^{2+}, (*2*) Cu^{2+}, (*3*) Ti^{4+}, (*4*) Fe^{3+}, (*5*) Zn^{2+}, (*6*) Co^{2+}, and (*7*) Cr^{2+}. Polymerization temperature 260°C; the same for Fig. 3. (*P*) Monomer conversion and (τ) reaction duration; the same for Figs. 2 and 3.

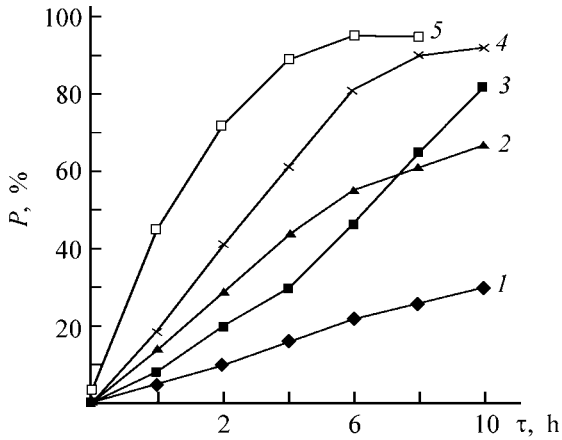

Fig. 2. Kinetic curves of 3-CP polymerization in the presence of binary catalysts: (*1*) Fe^{2+}, Cr^{6+}; (*2*) Co^{3+}, Zn^{2+}; (*3*) Cu^{2+}, Fe^{3+}; (*4*) Fe^{2+}, Co^{3+}; and (*5*) Co^{3+}, Sn^{2+}. Polymerization temperature 240°C.

that only *meta* derivatives of the nitriles studied polymerized under the chosen conditions; with respect to their activity, the nitriles are ranked in the order 3,5-diCP > 2,5-diCP ~ A-5-C-2-CP > 3-CP >> 2,3-diCP. In all cases, the optimal concentration of the catalyst is approximately 0.25 mol %. Its increase decelerates the reaction and causes formation of the products of low molecular weight with low concentration of paramagnetic centers (PMCs). A decrease in the catalyst concentration to 0.1 mol % does not affect the reaction rate and polymer characteristics, but significantly reduces the polymer yield. This is in good agreement with data that pyridine and its derivatives form predominantly complexes with the ratio metal ion : ligand = 1 : 4 [26].

With 3-CP as an example (Figs. 1–3), it is seen that the minimum possible synthesis temperature is

[1] A compound accelerating electron exchange between an insoluble polymer and electrodes [18].

[2] GOST 1897–74, 108981–74, 108984–74, 10899–64, 10900–64, 13504–68.

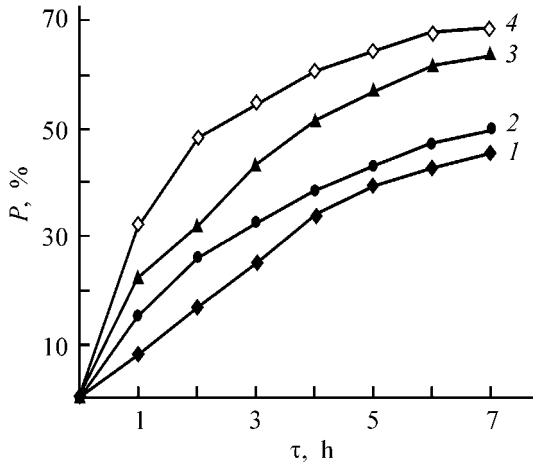

Fig. 3. Kinetic curves of 3-CP polymerization in the presence of 0.1 mol % H_2O in the reaction system with (*1*) Fe^{3+}, (*2*) Zn^{2+}, (*3*) Co^{3+}, and (*4*) Co^{2+}.

governed by the catalyst nature; the binary catalysts (Fig. 2) capable to form with the initial monomer compounds with various reactivities have the highest catalytic activity.

Table 2. Influence of the nature and amount of the catalyst and duration of polymerization of 3-PCC-HC and 4-HBN on the yield of the polymers (270°C)

Catalyst	Molar ratio 3-PCC-HC : 4-HBN : catalyst	τ, h	Yield, %
Co^{2+}	1 : 1 : 0.50	6	58.3
	1 : 1 : 0.25	6	70.4
	1 : 1 : 0.10	6	13.0
Fe^{2+}	1 : 1 : 0.50	6	17.3
	1 : 1 : 0.25	6	18.7
	1 : 1 : 0.10	6	8.1
Sn^{2+}	1 : 1 : 0.50	6	50.0
	1 : 1 : 0.25	6	56.8
Ti^{2+}	1 : 1 : 0.50	6	26.1
	1 : 1 : 0.25	6	33.0
Zn^{2+}	1 : 1 : 0.50	6	16.3
	1 : 1 : 0.25	6	19.1
Co^{2+}	1 : 1 : 0.25	12	78.2
	1 : 1 : 0.25	6	70.4
	1 : 1 : 0.25	2	38.6
Fe^{2+}	1 : 1 : 0.25	12	21.4
	1 : 1 : 0.25	6	18.2
	1 : 1 : 0.25	2	9.7
Sn^{2+}	1 : 1 : 0.25	12	69.6
	1 : 1 : 0.25	6	58.7
	1 : 1 : 0.25	2	39.0

A comparative study showed that, for polymerization of 4-HBN, the most effective is a combination of two Lewis acids, and the activity series of the polymerization catalysts is as follows: Lewis acid < Lewis acid + organic additive < Lewis acid + metal < Lewis acid + Lewis acid. In the presence of $ZnCl_2$, $ZnCl_2$ + epichlorohydrin, $ZnCl_2$ + Zn, and $ZnCl_2$ + $FeCl_3$, the polymer yield is 24.0, 56.8, 62.3, and 86.9%, respectively. In the presence of only Lewis acids, polymerization proceeds with extremely low conversion. The activity of metal chlorides decreases in the order Mg = Zn > Ni (Co) > Ti > Sn > Al > Fe.

In this case, the monomer : catalyst ratio equal to 1 : 4 is not observed. The maximum yield of the polymer is reached on addition of the catalyst in an amount of 10%. The presence of promoter strongly increases the yield of the polynitrile.

In the case of thermal polymerization of pyridine derivative 3-PCC-HC with 4-HBN, the polymer yield is the highest at the catalyst concentration of 0.25 mol % with respect to the monomer (as in the case of heterocyclic nitriles). This confirms once again the probability of formation of 1 : 4 complexes of the catalyst with pyridinecarbonitrile monomers. An increase in the amount of the catalyst to above 0.25 mol % decreases the yield of the polymer (Table 2). For example, in the presence of 0.1, 0.25, and 0.50 mol % Co^{2+}, the yield of the polymers is 58.3, 70.4, and 13.0%, respectively. Similar trends are observed in the other catalytic systems. When using the catalyst, in an amount exceeding 0.25 mol %, the reaction products contain excess metal irrespective of the process duration τ and polymerization temperature T_{pol}. The series of the activity of the Friedel-Crafts catalyst for 4-HBN is Co > Sn > Ti > Zn > Fe.

The medium affects the process kinetics and characteristics of the reaction products: in passing from vacuum or argon to relatively dry air, as in the case of presence of water traces (compare Figs. 1 and 2 with Fig. 3), the reaction rate and conversion of the monomer in some systems increase, but oxygen-containing structures –C(O)N= appear in the macromolecules.

For all the nitriles, the intrinsic viscosity of the resulting polymers [η] slightly increases with the synthesis duration and more significantly, with T_{pol}. In this case, the reaction temperature affects significantly not only the molecular weight of polymers but also the content of PMCs in the polymers. This is illustrated by polymerization of 3-CP, 2,5-diCP, and 3,5-

Table 3. Influence of temperature and reaction duration on the yield and intrinsic viscosity of the polymers based on CPs and on the content of PMCs

Monomer	Catalyst	T_{pol}, °C	τ, h	Yield, %	[η]	PMC, spin g^{-1}
2,5-diCP	Ti^{3+}, Cr^{2+}	220	4	99.0	2.01	4.12×10^{19}
	The same	200	4	92.0	1.86	4.00×10^{18}
	″	170	14	75.0	0.95	0.60×10^{17}
3-CP	Cr^{6+}, Fe^{2+}	240	6	98.0	1.92	0.51×10^{18}
	The same	220	6	84.5	0.78	6.10×10^{17}
	Fe^{3+}	280	6	92.4	1.25	3.87×10^{18}
	The same	270	6	86.5	1.01	2.46×10^{18}
	″	260	20	78.4	0.62	0.24×10^{17}
3,5-diCP	Co^{3+}, Cr^{2+}	210	3	99.5	2.01	4.00×10^{15}
	The same	180	4	98.4	1.92	1.20×10^{15}

Table 4. Characteristics of some syntheses with 2,5-, 3,5-diCP, and 3-CP

Run no.*	Monomer	Catalyst, mol %	T_{pol}, °C	τ, h	Catalyst after reaction	Yield, %
1	2,5-, 3,5-diCP	Fe^{3+}, Cu^{2+}, 0.25	240	4	Fe^{2+}, Cu^{2+}, Cu^{+}	89.6
2	The same	Sn^{2+}, Co^{3+}, 0.23	240	4	Co^{2+}, Sn^{4+}	99.7
3	″	Co^{3+}, Cr^{2+}, 0.24	210	3	Co^{2+}, Cr^{3+}	99.5
4	″	Co^{3+}, Zn^{2+}, 0.25	220	5	Co^{3+}, Co^{2+}, Zn^{2+}	88.4
5	″	Zn^{2+}, 0.25	240	6	–	73.0
6	3-CP	Fe^{3+}, 0.25	280	10	Fe^{2+}	92.0**
7	The same	Sn^{4+}, 0.25	270	10	Sn^{2+}, Sn^{4+}	63.2***
8	″	Fe^{3+}, Cu^{2+}, 0.25	240	6	Fe^{2+}, Cu^{2+}	77.8**
9	″	Cr^{6+}, Fe^{2+}, 0.25	190	6		48.0

* Run nos. 1 and 5 were performed in O_2; no. 4, in O_2 and H_2O; and nos. 2, 3, 6–9, in a vacuum.

** The reaction is accompanied by vigorous release of HCl.

*** Release of HCl is insignificant.

diCP as examples (Table 3): in polymerization of 2,5-diCP (170°C) and 3-CP (260°C) for 14 and 20 h, polynitriles with the intrinsic viscosity [η] of 0.95 and 0.62 and PMC content of 0.60×10^{17} and 0.24×10^{17} spin g^{-1}, respectively, are formed. Raising the polymerization temperature to 200°C and 280°C allows the process duration to be reduced to 4 and 6 h, respectively. In this case, [η] of the samples (1.86 and 1.25), the PMC content (4.00×10^{18} and 3.87×10^{18} spin g^{-1}), and the yield of the polymers increase.

Thus, we can conclude that polymerization of *meta*-substituted nitriles proceeds by scission of triple bonds of the cyano groups of the initial monomers. The process is provided by a combination of chemical transformations of monomers coordinated through the heterocyclic nitrogen atom in the initial complex, which results in significant weakening of the C≡N bond. The process is not complicated by side reactions. The yield of the polymers increases with time and approaches the quantitative yield with heating.

A significant difference in the lower limits of polymerization temperatures for various monomer–catalyst pairs suggests that one of the factors shifting the equilibrium to the formation of the polymer in the absence of a promoter is, apparently, chemical transformation of the monomer (pyridine–hydropyridine) [18], preceding polymerization and caused by a redox reaction of the coordinated monomer with the central metal atom. This corresponds to an increase in the activity of the catalysts with a rise in their standard redox potentials and is also confirmed by degradation of the catalyst in the course of the reaction with release of gaseous HCl and changes in the oxidation state of the metal cation (Table 4).

Elemental analysis shows that the composition of the polymeric products formed in an inert medium on

anhydrous catalysts is in good agreement with the elemental composition of the initial monomers. In the IR spectra of all the samples, there are no absorption bands in the range 2240–2260 cm^{-1}, corresponding to vibrations of the C≡N bond, whereas the absorption in the range 1590–1650 cm^{-1}, characteristic of double bonds, is more pronounced. The bands of stretching modes of the pyridine ring ($\nu_{C=C, C=N}$ approximately 1590, 1560–1570, 1470, and 1400 cm^{-1}) are presented, undergoing some changes. The spectra are characterized by noticeable background which becomes more pronounced with increasing color depth, i.e., with increasing molecular weight and PMC content.

Dynamic thermal gravimetric analysis shows that the temperature of the onset of thermal oxidative degradation of the polymers is 340–360°C. The polymers give a strong ESR signal, symmetrical singlet with a width of 1–3 Oe, whose *g*-factor corresponds to that of a free electron. The integral intensity of the signal is 10^{15}–10^{19} paramagnetic species per gram.

The final products are bifunctional weak bases with $pK_{\alpha 1}$ = 0.95–0.48 and $pK_{\alpha 2}$ = 0.67–0.54. These values significantly differ from those of the initial monomers, which is apparently caused by a strong influence of delocalization and electron-acceptor power of the polynitrile skeleton.

Based on the data of elemental analysis, IR and ESR spectroscopy, and data obtained in studying the characteristics of the resulting polymers (without considering the substitution type and possible migration of bonds), the following structure can be assigned to these polymers:

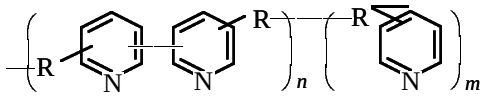

R = >C=N–C(=O)–N=.

The results of a study of the thermal, chemical, and radiation resistance of the resins synthesized suggest the possibility of their use in sorption and ion exchange from highly acidic radioactive solutions at elevated temperatures. The thermal stability of the samples is 98–99% at 100°C in corrosive media, the resistance to the action of oxidizing agents is 98–99% in the systems with redox potential of up to 2 V, and the resistance to alkalis, 98–99%. These samples withstand irradiation up to 10^9 rad.

The polymers with a system of conjugated bonds and functional redox groups in the conjugation chain have in some cases more pronounced redox characteristics in comparison with the analogues having localized bonds. In passing from oxidized to reduced form, the redox resins based on nitriles of heterocyclic acids change the color from bright red-brown to black. The standard redox potentials E_0 are fairly high (722–724, 730, 730, and 670 mV for 3-CP, 2,5-, 3,5-diCP, and A-5-C-2-CP, respectively) and suggest that electron-exchange characteristics of the macromolecules are provided by fragments significantly larger than isolated pyridine rings. The electron-exchange capacity of the polymers based on 3-CP, 2,5-, 3,5-diCP, and A-5-C-2-CP is 8.1, 8.8, 8.9, and 6.2 mg-equiv g^{-1}, respectively. The polymers have abnormally high capacity with respect to silver ions: 8.3–27.9 (pH 6.4–7.2) and 17.1–32.7 mg-equiv g^{-1} (pH 1.2–2.2), which is characteristic of polynitriles with the C=N bond. The static exchange capacity with respect to copper, cobalt, zinc, iron, osmium, palladium, and uranyl ions is 13.8, 2.9, 7.2, 4.7, 0.9–2.2, 1.6–2.4, and 4.4–6.7 mg-equiv g^{-1}, respectively.

CONCLUSIONS

(1) The possibility of a single-stage production of new polymers based on pyridinecarbonitriles, exhibiting along with high redox and sorption characteristics also a high thermal stability and chemical and radiation resistance was demonstrated.

(2) The resulting pyridinecarbonitriles are suitable for synthesis of ion-exchange, complexing, and redox polymers.

ACKNOWLEDGMENTS

This study was financially supported by the ISTC (project no. K604).

REFERENCES

1. Suvorov, B.V., *Okislitel'nyi ammonoliz organicheskikh soedinenii* (Oxidative Ammonolysis of Organic Compounds), Alma-Ata: Nauka, 1971.
2. USSR Inventors' Certificate, no. 676590.
3. USSR Inventors' Certificate, no. 548602.
4. USSR Inventors' Certificate, no. 311914.
5. USSR Inventors' Certificate, no. 197591.
6. USSR Inventors' Certificate, no. 298163.
7. Ergozhin, E.E., Mukhitdinova, B.A., Bakirova, K.Kh., *et al.*, *React. Polym.*, 1991/1992, vol. 16, pp. 321–334.
8. Ergozhin, E.E., Mukhitdinova, B.A., and Dusenbenova, Z.K., *React. Polym.*, 1992, vol. 18, pp. 15–23.
9. Ergozhin, E.E., Mukhitdinova, B.A., Dusenbeno-

va, Z.K., *et al.*, *Polymers*, 1993, vol. 34, no. 14, pp. 3096–3104.

10. Sartbaeva, K.M., Shalygina, V.V., Mukhitdinova, B.A., and Ergozhin, E.E., Abstracts of Papers, *XVII Mendeleevskii s"ezd po obshchei i prikladnoi khimii. Sektsiya B. Materialy i nanotekhnologii* (XVII Mendeleev Congr. on General and Applied Chemistry. Section B: Materials and Nanotechnologies), Kazan, September 21–26, 2003, p. 376.
11. Ergozhin, E.E., Mukhitdinova, B.A., Shalygina, V.V., *et al.*, Abstracts of Papers, *Vserossiiskaya konferentsiya "Sovremennye problemy khimii vysokomolekulyarnykh soedinenii: vysokoeffektivnye i ekologicheski bezopasnye protsessy sinteza prirodnykh i sinteticheskikh polimerov i materialov na ikh osnove"* (Russian Conf. "Modern Problems of Chemistry of Macromolecular Compounds: Efficient and Environmentally Safe Processes of Synthesis of Natural and Synthetic Polymers and Materials Based on These"), Ulan-Ude, August 20–27, 2002, Ulan-Ude: Buryat. Nauchn. Tsentr Sib. Otd. Ross. Akad. Nauk, 2002, p. 57.
12. Ergozhin, E.E., Mukhitdinova, B.A., Shalygina, V.V., and Sartbaeva, K.M., Abstracts of Papers, *VIII Mezhdunarodnaya konferentsiya po khimii i fizikokhimii oligomerov "Oligomery VIII." Sektsiya 3.20* (VIII Int. Conf. on Chemistry and Physical Chem. of Oligomers "Oligomers VIII," Section 3.20), Chernogolovka, September 10–14, 2002, p. 41.
13. Ergozhin, E.E., Mukhitdinova, B.A., Shalygina, V.V., and Sartbaeva, K.M., Abstracts of Papers, *Respublikanskaya nauchno-tekhnicheskaya konferentsiya "Akademik Sh. Esenov – ego rol' v razvitii nauki i tekhniki i v osvoenii prirodnykh resursov Kazakhstana"* (Republican Scientific and Technical Conf. "Academician Sh. Esenov and His Role in Development of Science and Technology and in Acceptance of Natural Resources of Kazakhstan"), Aktau, June 14–16, 2002, Almaty, 2002, pp. 21–22.
14. Ergozhin, E.E., Mukhitdinova, B.A., and Sarbaeva, K.M., Abstracts of Papers, *Respublikanskaya konferentsiya "Okislitel'nyi ammonoliz organicheskikh soedinenii"* (Republican Conf. "Oxidative Ammonolysis of Organic Compounds"), Almaty, October 2–3, 2003, pp. 63–64.
15. Ergozhin, E.E., Mukhitdinova, B.A., Shalygina, V.V., and Sartbaeva, K.M., Abstracts of Papers, *Regional'naya nauchno-prakticheskaya konferentsiya "Tekhnologiya organicheskikh veshchestv i vysokomolekulyarnykh soedinenii." Sektsiya III. Khimiya i tekhnologiya vysokomolekulyarnykh soedinenii* (Regional Scientific and Practical Conf. "Production of Organic Substances and Macromolecular Compounds." Section III: Chemistry and Technology of Macromolecular Compounds), Tomsk, October 8–10, 2003, pp. 150–151.
16. Cassidy, H.G. and Kun, K.A., *Oxidation-Reduction Polymers (redox Polymers)*, New York: Interscience, 1965.
17. Ergozhin, E.E. and Mukhitdinova, B.A., *Redoksionity* (Redox Ion Exchangers), Alma-Ata: Nauka, 1983.
18. Ergozhin, E.E. and Mukhitdinova, B.A., *Okislitel'novosstanovitel'nye ionoobmenniki* (Redox Ion Exchangers), Almaty: RIO VAK RK, 2000.
19. Kargin, V.A., Kabanov, V.A., Zubov, V.P., and Zezin, A.B., *Dokl. Akad. Nauk SSSR*, 1961, vol. 139, no. 3, pp. 605–607.
20. Zubov, V.P., Terekhina, I.P., Kabanov, V.A., and Kargin, V.A., *Vysokomol Soedin.*, 1966, vol. 8, no. 5, pp. 795–799.
21. Bohm, J. and Michalski, J., *Roczn. Chem.*, 1954, vol. 28, no. 3, pp. 501–503.
22. Pribil, R., *Komplexony v chemicke analyse*, Prague: Nakl. Ceskoslovenske akad., 1957.
23. Schwarzenbach, G. and Flaschka, H., *Die komplexometrische Titration*, Berlin: Ferdinand Enke, 1965.
24. Saldadze, K.M., Pashkov, A.P., and Titov, V.S., *Ionoobmennye vysokomolekulyarnye soedineniya* (Ion-Exchange Macromolecular Compounds), Moscow: Goskhimizdat, 1960, pp. 152–157.
25. Rafikov, S.R., Budtov, V.P., and Monakov, Yu.B., *Vvedenie v fizikokhimiyu rastvorov polimerov* (Introduction to Physical Chemistry of Polymer Solutions), Moscow: Nauka, 1978.
26. Bel'skii, I.F., *Geterotsikly v organicheskom sinteze* (Heterocyclic Compounds in Organic Synthesis), Kiev: Tekhnika, 1970.

Russian Journal of Applied Chemistry, Vol. 77, No. 6, 2004, pp. 994–997. Translated from Zhurnal Prikladnoi Khimii, Vol. 77, No. 6, 2004, pp. 1007–1010.

MACROMOLECULAR CHEMISTRY AND POLYMERIC MATERIALS

Use of Allylbenzene and Allyl Phenyl Ether as Chain-Transfer Agents in Radical Polymerization

V. O. Kudyshkin, N. R. Vokhidova, N. I. Bozorov, O. E. Sidorenko, I. N. Ruban, N. L. Voropaeva, and S. Sh. Rashidova

Institute of Polymer Chemistry and Physics, Academy of Sciences of Uzbekistan Republic, Tashkent, Uzbekistan

Received October 22, 2003; in final form, March 2004

Abstract—The performance of allylbenzene and allyl phenyl ether as chain-transfer agents in radical polymerization of styrene, methyl acrylate, butyl methacrylate, vinylpyrrolidone, and vinylcaprolactam was evaluated.

Chain-transfer agents are used in radical polymerization to control the molecular weight (MW) of the product. Allyl compounds are effective chain-transfer agents owing to the presence of a labile C–H bond in the methylene group at the α-position relative to the double bond (α-CH bond). Previously, we have reported on the possibility of preparing polyvinylcaprolactam (PVCL) of relatively low MW in the presence of a series of allyl compounds, among which allylbenzene (AB) appeared to be the most effective chain-transfer agent [1]. Allyl compounds can be used to control radical polymerization of a wide range of monomers.

In this study, we examined the performance of AB and allyl phenyl ether (APE) as chain-transfer agents in polymerization of a series of monomers differing in the reactivity.

EXPERIMENTAL

We studied polymerization of styrene (S), butyl methacrylate (BMA), methyl acrylate (MA), vinylpyrrolidone (VP), and vinylcaprolactam (VCL) in the presence of AB and APE. Methyl acrylate was double-distilled at atmospheric pressure, and the other monomers were double-distilled in a vacuum. The densities and refractive indices of the compounds coincided with reference data. The polymers were prepared under similar conditions by the radical mechanism at an AIBN (initiator) concentration of 1×10^{-2} M in dioxane at 50°C. The experiments were performed in ampules. The mixtures were degassed by freeze–pump–thaw cycles to a residual pressure of 0.13 Pa. The synthesis time was chosen so as to ensure the polymer yield of no less than 10%. Polyvinylpyrrolidone (PVP) and PVCL were reprecipitated into diethyl ether; poly(methyl acrylate) (PMA) and poly(butyl methacrylate) (PBMA), into ethanol; and polystyrene (PS), into hexane.

The polymerization rate was measured dilatometrically. The initiation rate was determined from the dependence of the induction period on the concentration of a stable radical, 2,2,6,6-tetramethylpiperidine-1-oxyl (TEMPO). In all the systems, the induction period showed a linear dependence on the TEMPO concentration. The intrinsic viscosities of PS, PVP, PBMA, and PMA were determined under the conditions given in Table 1. To determine [η], the experimental data were processed in the coordinates of the Huggins and Kraemer equations. For all the samples, the sum of the Huggins and Kraemer constants was close to 0.5. To calculate the MW of these polymers, we used the Mark–Kuhn–Houwink equations relating [η] to the number-average MW [2, 3]. Since these equations were deduced for fractionated polymer samples, we recalculated the constants K in the Mark–Kuhn–Houwink equations:

$$K^* = K\Gamma(2 + \alpha).$$

The correction $\Gamma(2 + \alpha)$ is characteristic of polymers whose MW is controlled by chain transfer or disproportionation [4]. To calculate the Γ-function, we used the asymptotic Stirling expansion. The MWs were calculated by the formula

$$[\eta] = K^* M_n^{\alpha}.$$

1070-4272/04/7706-0994 © 2004 MAIK "Nauka/Interperiodica"

The constants K^* are listed in Table 1. For PVCL, [η] was determined in DMF at 25°C. The MW was calculated by the equation

$$[\eta] = 7.43 \times 10^{-4} M^{0.53}.$$

The parameters of this equation were determined from the logarithmic dependence of [η] on the number-average MW increment, which was calculated from the integral MWD curves obtained by fast sedimentation method for PVCL samples prepared in the presence of AB [5].

The kinetic characteristics of polymerization are listed in Table 2. In all the systems studied, the polymerization rate and the MW of the polymers decrease as the concentration of AB and APE in the reaction mixture is increased. In all the cases, AB diminishes the rate and degree of polymerization more efficiently than APE does. The chain-transfer constants C_x were determined with the equation

$$P^{-1} = V_p[M]^{-2}K_t K_p^{-2} + C_x[X][M]^{-1}, \qquad (1)$$

where P is the degree of polymerization; [M], monomer concentration; [X], concentration of AB or APE; V_p, polymerization rate; $K_t K_p^{-2}$, ratio of the chain termination and chain propagation rate constants [4].

The dependences in the coordinates of Eq. (1) are plotted in Figs. 1a and 1b. The chain-transfer constants C_x calculated by the least-squares method are listed in Table 2.

The reactivity of monomers in the radical-chain process can be characterized by the Alfrey–Price parameters Q (characterizing the resonance stabilization factor) and e (characterizing the polarity of the double bond in the monomer). The monomers studied exhibit different reactivities. The parameters Q and e listed in Table 2 were taken from [6]. Notably, the chain-transfer constant with AB is higher than that with APE, irrespective of a particular monomer.

The chain transfer to allyl compounds involves reaction of the propagating radical with the labile hydrogen atom of the α-CH bond:

$$R^{\bullet} + B = RH + B^{\sim},$$

where $R^{\bullet}$ is the propagating radical; B, AB or APE; and $B^{\sim}$, the allyl radical stabilized by conjugation.

The activity of $B^{\sim}$ radical generated in this reaction is relatively low because of the electron delocalization over the allyl group. In this context, its reaction with the propagating macroradical seems the most probable:

$$R^{\bullet} + B^{\sim} = RB.$$

In accordance with the above reaction schemes, one molecule of allyl compounds terminates two macroradicals. Obviously, copolymerization of allyl compounds cannot be ruled out, but, owing to the presence of the labile α-CH bond, chain transfer competes with addition of the allyl compound to the macroradical, with opening of the double bond. The reinitiation of the double bond with the $B^{\sim}$ radical and recombination of allyl radicals are also possible theoretically, but the probability of these reactions is low because of the low activity of $B^{\sim}$ radical. It should be noted

Table 1. Parameters of the Mark–Kuhn–Houwink equations [2, 3] for calculating M_n and conditions for determining the intrinsic viscosity

Polymer	$K \times 10^4$	α	$K^* \times 10^4$	Solvent	T, °C
PVP	1.4	0.7	2.16	Water	25
PS	1.1	0.725	1.73	Toluene	30
PMA	0.459	0.795	0.766	Benzene	30
PBMA	0.115	0.89	0.208	Butanone	30

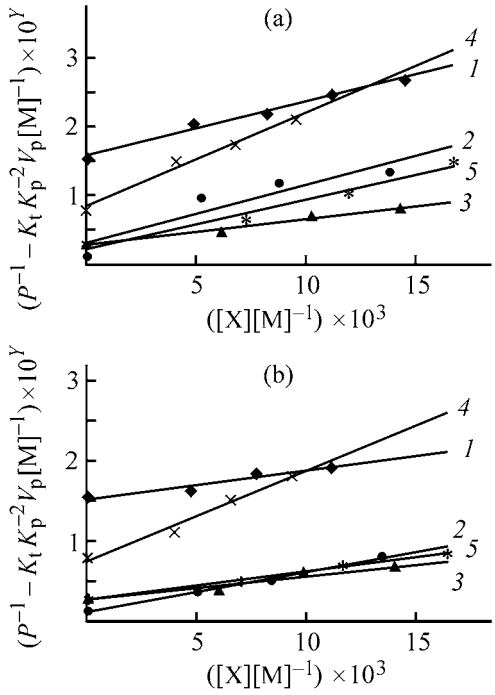

Fig. 1. Plot of $P^{-1} - K_t K_p^{-2} V_p[M]^{-1}$ vs. ratio of chain-terminating agent to the monomer [X] : [M] in polymerization of (*1*) VP, (*2*) S, (*3*) VCL, (*4*) MA, and (*5*) BMA. X: (a) AB and (b) APE. *Y*: (*1*, *2*, *5*) 3, (*3*) 2, and (*4*) 4.

Table 2. Kinetics of polymerization of monomers in the presence of allyl compounds

Monomer	X, M	C_x	Reaction rate, mol l^{-1} s^{-1}		$K_p K_t^{-0.5}$	[η], dl g^{-1}	$M \times 10^{-3}$
			$V_{in} \times 10^8$	$V_p \times 10^5$			
VP,	EB:						
[M] = 5.51 M,	0	0.078	2.83	12.24	0.132	0.49	62.4
Q = 0.088,	0.027			5.91		0.43	51.7
e = –1.62	0.045			5.70		0.41	48.4
	0.062			4.60		0.38	43.4
	0.080			3.62		0.36	40.2
	APE:						
	0.026	0.036		11.63		0.48	60.6
	0.043			8.78		0.45	55.2
	0.061			8.34		0.44	53.5
S,	EB:						
[M] = 5.12 M,	0	0.084	3.02	2.66	0.030	0.63	81.7
Q = 1.00,	0.027			0.88		0.60	76.4
e = –0.8	0.045			0.68		0.57	71.2
	0.071			0.52		0.55	67.7
	APE:						
	0.026	0.048		2.13		0.62	79.9
	0.043			1.90		0.61	78.1
	0.069			1.49		0.58	72.8
VCL,	EB:						
[M] = 4.35 M,	0	0.370	0.93	2.70	0.064	0.21	42.2
Q = 0.14,	0.027			1.20		0.17	28.3
e = –1.18	0.045			0.81		0.14	19.6
	0.062			0.62		0.13	17.1
	APE:						
	0.026	0.295		2.41		0.19	34.9
	0.043			1.75		0.15	22.3
	0.061			1.52		0.14	19.6
MA,	EB:						
[M] = 6.52 M,	0	0.014	3.63	27.2	0.219	2.20	405.3
Q = 0.45,	0.027			20.7		1.94	346.0
e = 0.64	0.045			18.1		1.85	325.9
	0.062			16.0		1.72	297.4
	APE:						
	0.026	0.011		25.0		2.05	370.9
	0.043			21.2		1.90	337.0
	0.061			20.0		1.77	308.3
BMA,	EB:						
[M] = 3.72 M,	0	0.073	2.42	1.76	0.031	0.53	89.2
Q = 0.82,	0.027			1.47		0.49	81.7
e = 0.28	0.045			1.03		0.48	79.8
	0.062			0.47		0.46	76.1
	APE:						
	0.026	0.035		1.60		0.50	83.5
	0.043			1.43		0.49	80.8
	0.061			1.27		0.48	79.8

that the substituent at the allyl bond exerts a decisive effect on the stability of the allyl radical.

To estimate the dissociation energy (DE) of the α-CH bond, we optimized the geometry and calculated the electronic structures of allyl compounds and their radicals. The calculation was performed by the PM3 semiempirical method, using the restricted Hartree–Fock method for molecules with closed electronic shells and the unrestricted Hartree–Fock method for radicals. The DE of the bond was calculated as the difference between the energy of the dissociation products and that of the starting allyl compound. The geometry was fully optimized for both the allyl compound and its radical. All calculations were performed with the HyperChem program [7]. The DE of the α-CH bond (kcal mol^{-1}) was 65.23 for AB and 67.12 for APE.

Below are the molecular diagrams of APE and AB radicals, showing the spin density on atoms:

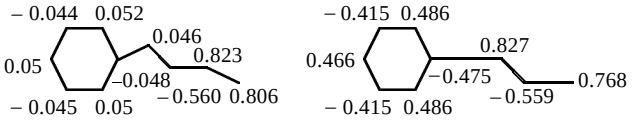

APE radical

AB radical

The molecular diagrams show that, in the AB radical, the unpaired electron is delocalized over all the carbon atoms, including the benzene ring. In the APE radical, only the carbon atoms of the allyl group participate in the delocalization to a significant extent. Thus, the AB radical has a longer conjugation chain and is hence more stable than the APE radical. It is known that the bond dissociation energy is the difference between the energy of the forming radical and hydrogen atom and that of the starting compound [8]. Therefore, any factor stabilizing the forming allyl radical should decrease the dissociation energy of the α-CH bond. Hence, a compound that forms a more stable radical upon hydrogen abstraction should be a more effective chain-transfer agent; the less active radical cannot initiate chain propagation but can recombine with the active propagating macroradical. In this case, such a compound is AB.

It seems appropriate to use for controlling MW such compounds in which the allyl group is directly bonded to the molecular fragment with a conjugation system (e.g., AB). The use of allyl ethers or allyl alcohols for controlling the radical polymerization is appropriate in cases when it is necessary not only to control MW, but also to prepare copolymers in which single allyl units are separated by blocks of the major monomer. Such copolymers may be of interest from the viewpoint of their subsequent modification aimed to prepare materials with special properties, e.g., chemodegradable polymers [9].

CONCLUSIONS

(1) The kinetics of radical polymerization of certain monomers in the presence of allylbenzene and allyl phenyl ether were studied, and the parameters of the reactivity of these allyl compounds in chain transfer from various macroradicals were evaluated.

(2) Allylbenzene is a more effective chain-transfer agent, which is due to the higher stability of its radical, compared to the allyl phenyl ether radical.

(3) It is appropriate to use allylbenzene to control the molecular weight of polymers prepared by the radical mechanism.

REFERENCES

1. Kudyshkin, V.O. and Mukhitdinova, N.A., *Zh. Prikl. Khim.*, 1999, vol. 72, no. 10, pp. 1742–1744.
2. Lipatov, Yu.S., Nesterov, A.E., Gritsenko, T.M., and Veselovskii, R.A., *Spravochnik po khimii polimerov* (Handbook of Polymer Chemistry), Kiev: Naukova Dumka, 1971.
3. Brandrup, J. and Immergut, E.H., *Polymer Handbook*, New York: Wiley, 1975, 2nd ed.
4. Bagdasar'yan, Kh.S., *Teoriya radikal'noi polimerizatsii* (Theory of Radical Polymerization), Moscow: Akad. Nauk SSSR, 1959.
5. Kudyshkin, V.O., Abdurakhmanova, T.R., and Kadyrkhanov, M.R., *Zh. Prikl. Khim.*, 2000, vol. 73, no. 9, pp. 1522–1525.
6. Greenly, R., *J. Macromol. Sci. Chem.*, 1980, vol. A14, no. 4, pp. 427–443.
7. *HyperChem 5.0 User Manuals*, Florida: Hypercube, 1996.
8. Grishin, D.F., Ignatov, S.K., Razuvaev, A.G., *et al.*, *Vysokomol. Soedin., Ser. A*, 2001, vol. 43, no. 10, pp. 1742–1749.
9. Solovskii, M.V., Nikol'skaya, N.V., Korneeva, E.V., *et al.*, *Zh. Prikl. Khim.*, 2001, vol. 74, no. 4, pp. 643–648.

Russian Journal of Applied Chemistry, Vol. 77, No. 6, 2004, pp. 998–1001. Translated from Zhurnal Prikladnoi Khimii, Vol. 77, No. 6, 2004, pp. 1011–1015.

MACROMOLECULAR CHEMISTRY AND POLYMERIC MATERIALS

Role of Peroxy Compounds in Oxidation of Crotonaldehyde with Molecular Oxygen

O. E. Fedevich, S. S. Levush, E. V. Fedevich, and Yu. V. Kit

L'vivs'ka Politekhnika National University, Lviv, Ukraine
Lviv State Agricultural University, Lviv, Ukraine

Received November 19, 2003; in final form, March 2004

Abstract—Oxidation of crotonaldehyde with molecular oxygen and the role of percrotonic acid accumulating in the process were studied.

Crotonic acid (CAc) and its derivatives are used as comonomers in production of rubbers, latexes, adhesives, and plastics. Some crotonic acid esters exhibit insecticidal or herbicidal properties.

The main synthetic route to CAc is oxidation of crotonaldehyde (CAl). In oxidation of CAl with molecular oxygen at atmospheric [1, 2] or elevated [3] pressure, peroxy compounds accumulate in concentrations comparable with that of the forming CAc.

Our goal was to examine the possibility of using peroxides accumulating in the oxidate to raise the yield of CAc.

EXPERIMENTAL

Pure-grade CAl was distilled before use on a laboratory column (10 TP, reflux ratio 2); the fraction with bp 375–376 K was collected. Crotonaldehyde was kept under argon at 253 K. An additional purification was performed by steam distillation, with the collection of the azeotrope (75.7 wt % CAl, 24.3 wt % H_2O), from which water was frozen out at 223 K, and CAl was dried over $MgSO_4$ and distilled on a column. A chromatographically pure CAl was thus obtained (bp 375 K, d_4^{20} 0.853 g cm^{-3}). The optimal medium for CAl oxidation, from the viewpoint of CAc yield, is ethyl acetate [1]. We used ethyl acetate of analytically pure grade ; it was dried over $CaCl_2$ and distilled before use.

Qualitative and quantitative analyses were performed by chemical methods [4], gas chromatography, and IR spectroscopy. Chromatographic analyses were carried out on a Tsvet-100 chromatograph (2000 × 3-mm column; sorbent Polysorb-1, 0.1–0.25 mm; column and vaporizer temperatures 423 and 463 K, respectively; thermal conductivity detector). In the oxidate, we determined the content of CAl and CAc. The total content of carbonyl compounds was determined by the hydroxylamine method [4], and the total content of acids, by titration with 0.1 N NaOH in the presence of phenolphthalein. The content of peroxides was determined by iodometric titration in glacial acetic acid.

The gas–chromatographic analysis gives the total content of crotonic and percrotonic (PCAc) acids, because PCAc transforms into CAc in the vaporizer. To confirm this conclusion, we performed absolute calibration with respect to CAc in the system CAc–ethyl acetate. Percrotonic acid was prepared by oxidation of CAc in ethyl acetate at a low temperature. For example, in oxidation of CAl at 12°C to 15% conversion, the content of PCAc in the sum of acids reaches 93%. Such an oxidate gives a chromatographic peak of CAc, whose area corresponds to the total calculated amount of PCAc and CAc and is consistent with the total acid content determined by chemical analysis.

In oxidation of CAl under various conditions, the oxidate always contains PCAc and CAc (Table 1). The PCAc : CAc ratio decreases with increasing temperature, oxidation time, and partial oxygen pressure. Peroxy compounds disappear from the oxidate upon prolonged storage (100–150 h). The approximate composition of the oxidate stored for 150 h at 20°C is as follows (wt %): ethyl acetate 75.04, CAl 8.97, CAc 12.46, propionaldehyde 0.40, propionic acid 0.50, formic acid 1.20, propenyl formate 0.60, and 1,2-epoxypropenyl formate 0.60.

1070-4272/04/7706-0998 © 2004 MAIK "Nauka/Interperiodica"

Table 1. Influence of the oxygen pressure and temperature on oxidation of CAl in ethyl acetate* (c^0_{CAl} = 2.46 M)

p_{O_2}, atm	τ, min	c_{CAl}, M	X_{CAl}, %	c_{PCAc}	c_{CAc}	S_{PCAc}	S_{CAc}	$S_{\Sigma CAc + PCAc}$
				M		%		
				T = 300 K				
1	35	2.09	15.0	0.25	0.06	67.6	14.8	82.4
	60	1.99	19.1	0.32	0.08	67.9	17.6	85.5
	120	1.60	35.0	0.55	0.18	65.1	19.9	85.0
	180	1.23	50.0	0.70	0.33	56.9	27.1	84.0
4	30	1.95	20.7	0.33	0.08	64.7	15.7	80.4
	60	1.83	25.6	0.40	0.12	63.5	19.0	82.5
	120	1.12	54.5	0.78	0.33	58.2	24.6	82.8
	180	0.61	75.2	0.96	0.54	51.9	29.2	81.1
				T = 309 K				
1	30	1.93	21.5	0.33	0.09	62.2	17.0	79.2
	60	1.64	33.3	0.53	0.17	64.6	19.9	84.5
	120	1.17	52.4	0.75	0.33	58.1	25.7	83.8
	180	0.68	72.4	0.95	0.53	53.3	29.8	83.1
16	30	1.66	32.5	0.42	0.18	52.5	22.5	75.0
	60	1.07	56.5	0.81	0.34	59.0	23.7	82.7
	120	0.59	76.0	1.07	0.47	57.7	24.8	82.5
	180	0.38	84.6	1.00	0.66	49.0	31.0	80.0

* (p_{O_2}) O_2 pressure, (τ) time from the start of the reaction, (c) concentration, (X) conversion, and (S) selectivity.

According to [5], CAc is formed by a parallel-consecutive mechanism directly from CAl and via PCAc. Table 1 shows that the selectivity of CAc formation grows with conversion, and the selectivity of PCAc formation decreases. Apparently, the consecutive formation CAc via PCAc is the major pathway.

According to the classical autooxidation scheme, peroxy compounds accumulating in oxidation of unsaturated aldehydes are mainly the corresponding per acids. As shown by Boboleva *et al.* [6], the poor selectivity of CAc formation in autooxidation of CAl at elevated temperature is due to consumption of PCAc in side processes, rather than to cleavage of the C=C bond in the course of oxidation. They believe that PCAc not only transforms into CAc, but also undergoes a radical decomposition:

$$RC(O)OOH \rightarrow RC(O)O^{\cdot} + {}^{\cdot}OH,$$
$$RC(O)O^{\cdot} \rightarrow CO_2 + R^{\cdot}.$$

With decreasing temperature, the decomposition decelerates [6], and the selectivity with respect to the sum of CAc and PCAc increases. Thus, by-products formed in CA oxidation mainly arise from radical decomposition of PCAc. There are also indications [7] that H_2O_2, diacyl peroxides, and polyperoxides are also formed in oxidation of unsaturated aldehydes along with per acids. Quantitative data on the composition of peroxy compounds in oxidation of CAl are lacking. This stimulated us to evaluate the content of undesirable stable peroxides in oxidation of CAl. For this purpose, after completion of the experiments and determination in oxidates of CAc and sum of peroxy compounds, the oxidates were stored for a long time at room temperature, after which the content of peroxides, CAc, and CAl was determined. The results are listed in Table 2.

It is seen that 95–98% of peroxides accumulated by the end of experiments are unstable and undergo consecutive transformations at room temperature. This means that thermally stable peroxides incapable of reacting with CAl are formed in oxidation of CAl in very low amounts (≤0.04 M). Presumably, the peroxides in the oxidate are mainly PCAc and certain amount of H_2O_2. The content of H_2O_2 in the oxidate must not be significant, since, as seen from Table 2, in some experiments (nos. 8, 10, 12, 13, 15), when the content of CAl exceeds that of peroxides, CAl transforms into CAc within the storage time in the amount equivalent to the content of peroxy compounds in the oxidate. This means that all the peroxides in the oxidate oxidize CAl to CAc. At the same time, hydrogen peroxide oxidizes CAl to CAc only in the presence of catalysts, Se^{4+} compounds [7]. Hence, hydroperoxides accumulating in oxidation of CAl with molecular

Table 2. Composition of CAl oxidate before and after storage at 293–295 K*

Run no.	Storage time, days	c^0_{CAl}	$c^0_{\Sigma CAc + PCAc}$	c^0_{HP}	c^τ_{CAl}	$c^\tau_{\Sigma CAc + PCAc}$	c^τ_{HP}
		M					
1	90	0.52	1.84	1.09	0.02	2.34	0.04
2	88	0.34	1.98	1.31	0.01	2.28	0.05
3	88	0.17	2.04	1.20	0.03	2.18	0.03
4	86	0.48	1.84	1.23	0.02	2.28	0.03
5	82	0.59	1.65	0.85	0.04	2.20	0.02
6	79	0.90	1.35	0.79	0.10	2.10	0.02
7	51	0.94	1.38	0.84	0.06	2.10	0.03
8	49	1.12	1.21	0.63	0.52	1.80	0.02
9	44	0.69	1.71	1.18	0.01	2.36	0.05
10	41	1.13	1.20	0.63	0.54	1.75	0.03
11	37	0.33	1.86	1.02	0.01	2.18	0.04
12	37	1.63	0.84	0.67	0.95	1.52	0.02
13	37	1.23	1.14	0.86	0.43	1.92	0.03
14	35	0.74	1.50	0.84	0.01	2.20	0.04
15	35	3.30	1.30	0.57	2.75	1.83	0.02

* (c^0) Content after oxidation, (c^τ) content after storage, (ΣCAc + PCAc) sum of acids, and (HP) hydroperoxides.

oxygen under the experimental conditions consist mainly of PCAc, which oxidizes CAl to CAc in the course of storage of the oxidate at room temperature, transforming itself into CAc. In the absence of a sufficient amount of CAl in the oxidate, PCAc also transforms into CAc (Table 2, run nos. 1, 2, 4, 9, 11, 14), but less selectively.

The fact that PCAc, one of the major products of CAl oxidation, virtually quantitatively transforms into CAc on keeping the oxidate at room temperature and oxidizes in the process an equimolar amount of CAl can be used to achieve the maximum yield of CAc. Oxidation of CAl with molecular oxygen should be performed up to accumulation of the maximum concentration of PCAc in the oxidate. In so doing, the concentration of unchanged CAl should only slightly exceed the PCAc concentration (Table 2, run nos. 6, 7). In the course of storage, CAl virtually quantitatively transforms into CAc in the reaction with PCAc.

For practical synthesis of CAc, it is necessary to find the optimal temperature for decomposition of PCAc in the oxidate, because at room temperature the reaction is too slow. The kinetics of PCAc and CAl consumption and CAc accumulation in the oxidate was studied at 318 and 333 K. After oxidation for 100 min at 309 K, the oxygen supply was stopped, the system was purged with argon and then heated to the required temperature, and the oxidate composition was monitored. The results of some experiments are shown as example in Fig. 1. As seen from Fig. 1a,

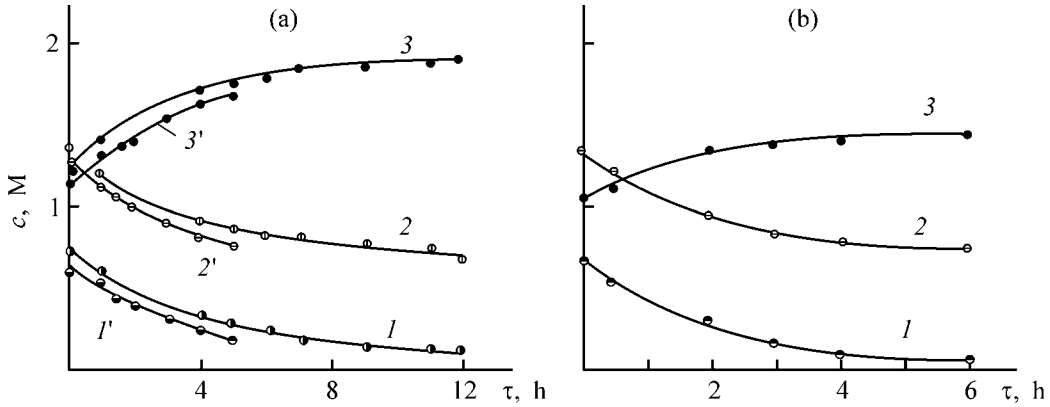

Fig. 1. Kinetic curves of (*1*, *1*') consumption of PCAc, (*2*, *2*') consumption of CAl, and (*3*, *3*') accumulation of the sum of CAc and PCAc at (a) 318 and (b) 333 K. (c) Concentration and (τ) time. (*1*, *1*', *2*, *2*', *3*, *3*') Results of replicate runs.

Table 3. Characteristics of the oxidate after oxidation and storage (CAl content at the beginning of experiments 2.46 M, oxidation time 180 min, storage for 7 h at 318 K)

T,* K	p_{O_2}, atm	c^0_{CAl}	c^0_{PCAc}	c^0_{CAc}	x_{CAl}	$S_{\Sigma CAc + PCAc}$	c^τ_{CAl}	c^τ_{PCAc}	c^τ_{CAc}	x_{CAl}	S_{CAc}
		M			%		M			%	
300	1	1.23	0.70	0.33	50.0	84.0	0.52	0.02	1.69	79.7	87.1
300	2	0.96	1.03	0.47	61.0	83.0	0.05	0.03	2.28	98.0	94.6
300	4	0.61	0.96	0.54	75.2	81.1	0.02	0.02	2.05	99.1	84.0
309	1	0.68	0.95	0.53	72.4	83.1	0.03	0.03	2.09	98.8	86.0
309	16	0.38	1.00	0.66	84.6	80.0	0.01	0.03	1.99	99.6	81.2

* (T) Oxidation temperature.

the concentrations of CAl and PCAc decrease to a similar extent, with the total concentration of CAc and PCAc growing simultaneously. For example, in 7 h, the PCAc concentration decreased by 0.61 M; that of CAl, by 0.59 M; and that of the sum of CAc and PCAc increased by 0.6 M. Within the same time, 9.6 ml of CO_2 and 2.4 ml of CO evolved from the oxidate (30 ml). Hence, at 318 K only 1–2% of PCAc is spent for side reactions (initiated radical decomposition), whereas 98–99% of PCAc reacts with CAl to form CAc.

At 333 K (Fig. 1b), PCAc is consumed considerably faster, and the process is complete within approximately 4 h. However, the relative contribution of PCAc decomposition grows. For example, 15 ml of CO_2 and 5.4 ml of CO evolved from the reactor in 4 h. Percrotonic acid is consumed noticeably faster than CAl: in 4 h, the PCAc concentration decreased by 0.62 M, and that of CAl, by 0.56 M. The total concentration of CAc and PCAc grew by only 0.54 M (87% of the consumed PCAc).

Apparently, to ensure the most efficient utilization of PCAc and maximum yield of CAc, the oxidate should be kept at relatively low temperatures. Table 3 illustrates the variation of the oxidate composition at 318 K in the course of 7 h. It is seen that oxidation of CAl to CAc with PCAc occurs more selectively than oxidation with molecular oxygen to CAc and PCAc. Table 3 shows that the maximum efficiency is reached when the concentrations of the accumulated PCAc and unchanged CAl in the oxidate by the end of autooxidation are approximately equal. This situation is attained at ~60% conversion of CAl. In the course of storage, unchanged CAl is oxidized with PCAc, and the total selectivity with respect to CAc reaches 94%.

The results of these studies allowed development of an efficient procedure for preparing CAc [8].

CONCLUSION

To achieve the maximum yield of crotonic acid, it is appropriate to perform oxidation of crotonaldehyde with molecular oxygen at 300–310 K to 55–65% conversion of crotonaldehyde, when the concentrations of perctoronic acid and unchanged crotonaldehyde in the oxidate become approximately equal. The unchanged crotonaldehyde is subsequently oxidized with percrotonic acid at 315–320 K within 7.0–7.5 h.

REFERENCES

1. Fedevich, O.E., Levush, S.S., and Kit, Yu.V., *Visn. Derzh. Univ. "L'vivs'ka Politekh.," Khim., Tekhnol. Rech. Ikh Zastosuv.*, 1998, no. 339, pp. 165–167.
2. Fedevich, O.E., Levush, S.S., and Kit, Yu.V., *Teor. Eksp. Khim.*, 1999, vol. 35, no. 5, pp. 332–337.
3. Fedevich, O.E., Levush, S.S., Fedevich, E.V., and Kit, Yu.V., *Zh. Prikl. Khim.*, 2002, vol. 75, no. 7, pp. 1146–1150.
4. Houben–Weyl, *Methoden der organischen Chemie*, vol. 2: *Analytische Methoden*, Stuttgart: Thieme, 1953.
5. Fedevich, O.E., Levush, S.S., Fedevich, E.V., and Kit, Yu.V., *Zh. Org. Khim.*, 2003, vol. 39, no. 1, pp. 41–43.
6. Boboleva, S.P., Bulygin, M.V., Valov, P.I., and Blyumberg, E.A., *Neftekhimiya*, 1990, vol. 30, no. 2, pp. 239–243.
7. Pikh, Z.G., Selective Oxidation of Unsaturated Compounds with Bound Oxygen, *Doctoral Dissertation*, Lviv, 1994.
8. Ukrainian Patent, Method for Preparing Crotonic Acid, *Promysl. Vlasp.*, 2002, no. 6.

Russian Journal of Applied Chemistry, Vol. 77, No. 6, 2004, pp. 1002–1006. Translated from Zhurnal Prikladnoi Khimii, Vol. 77, No. 6, 2004, pp. 1016–1020.

CHEMISTRY OF FOSSIL FUEL

Effect of Various High-Octane Additives on Antiknock Quality of Gasolines

A. M. Syroezhko, O. Yu. Begak, and G. S. Makurina

St. Petersburg State Technological Institute, St. Petersburg, Russia

Mendeleev Russian Research Institute of Metrology, Federal State Unitary Enterprise, St. Petersburg, Russia

Received April 7, 2004

Abstract—The possibility of manufacturing AI-92 and AI-95 high-octane blended gasolines using reformer naphthas[1], methyl *tert*-butyl ether, and an additive based on *N*-methylaniline and (methylcyclopentadienyl)-manganese tricarbonyl is studied.

The most important problem in oil refining is to improve the performance and environmental characteristics of gasolines. The increased aromaticity of domestic (Russian) high-octane gasolines is caused by the fact that their base component is reformer naphtha containing up to 5–6% benzene and up to 68% other arenes [1]. The use of oxygenates (methyl *tert*-butyl and methyl *tert*-pentyl ethers) and other environment-friendly high-octane antiknock compounds at Russian refineries is rather limited [2].

The goal of this study is to examine the effect of high-octane additives on the quality of gasolines manufactured by the Ukhta Refinery, and also to optimize formulations of AI-92 and AI-95 blended gasolines based on mixtures of straight-run naphthas and stable reformer naphthas taken in various proportions.

EXPERIMENTAL

Straight-run naphtha (ρ_4^{20} = 0.6689 g cm^{-3}) was taken from an AT-1 preliminary distillation plant; it had an octane number (ON) of 66.4 as determined by the engine method (EM). Its fractional composition was as follows [bp, °C (content, wt %)]: initial boiling (IB) 39; 52 (10); 63 (50); 85 (90); dry point (DP) 94.

Stable reformer naphtha [ρ_4^{20} = 0.7700 g cm^{-3}; ON 83.2 (EM); ON 92.1 (theoretical method, TM)] was taken from an L-35/11-300 plant. Fractional composition: IB 41; 78 (10); 117 (50); 153 (90); DP 178.

Base components were prepared by mixing straight-run naphtha with reformer naphtha (Table 1). As high-octane additives was used BVD containing 65 wt %

Table 1. Physicochemical characteristics of base components and blends

Base component	ρ_4^{20}, g cm^{-3}	Fractional composition, °C					Yield, vol %	ON	
		IB	10%	50%	90%	DP		EM	TM
A-76	0.7278	36	56	92	144	171	96	77.2	–
AI-92	0.7698	37	68	114	155	174	96	83.0	92.0
Reforming naphtha	0.7700	41	78	117	153	178	97	83.2	92.1
Straight-run naphtha	0.6689	39	52	63	85	94	97	66.4	–
Reforming naphtha/straight-run naphtha, wt %:									
10/90	0.6809	39	54	66	118	151	96	68	82.2
50/50	0.7230	41	58	86	144	169	96	75.1	86.6
70/30	0.7408	41	63	99	148	174	97	78.5	88.1
90/10	0.7628	41	72	111	142	178	98	81.2	91.0

[1] Lukoil-Ukhta-Neftepererabotka, Joint-Stock Company.

1070-4272/04/7706-1002 © 2004 MAIK "Nauka/Interperiodica"

Table 2. ON benefit of base components gained due to addition of BVD and MTBE

Base component	Initial ON		ON of a blend with 15 wt % MTBE		ΔON (MTBE)		ON of a blend with 1.9 wt % BVD		ΔON (BVD)	
	MM	TM	MM	TM	MM	TM	MM	TM	MM	TM
AI-92	83.0	92.0	86.8	95.2	3.8	3.2	86.7	94.5	3.7	2.5
A-76	76.2	85.1	80.2	91.0	4.0	5.9	79.8	91.0	3.6	5.9
Reforming naphtha	83.2	92.1	86.7	85.1	3.5	3.0	86.8	95.4	3.6	3.3
Reforming naphtha/straight-run naphtha, wt %:										
10/90	68.0	76.2	74.9	83.8	6.9	7.6	74.0	84.6	6.0	8.4
50/50	76.0	85.0	81.8	90.2	5.8	5.2	81.7	91.4	5.7	6.4
70/30	78.5	88.1	83.5	92.0	5.0	3.9	83.6	92.8	5.1	4.7
90/10	81.2	91.0	85.4	95.2	4.2	4.2	85.5	93.8	4.3	2.8

N-methylaniline [TU (Technical Specifications) 38.401-58-228–99] from Flagman Closed Corporation (Moscow); B-grade methyl *tert*-butyl ether (MTBE) (TU 38.103.704–90) from Ekros Closed Corporation (St. Petersburg); *N*-methylaniline (NMA) (TU 2471-269-00 204 168–96) from Volzhskii Orgsintez Joint-Stock Company (Volgograd oblast); and Hitec-3000 containing 24.4 wt % Mn (Ethyl Corporation, the United States). The active component of the latter additive is (methylcyclopentadienyl)manganese tricarbonyl (MMT).

The density of the base blends was determined according to GOST (State Standard) 3900–85 [3]; the fractional composition, to GOST 2177–99 [4]; NO, to GOST 511–82 (EM) [5] and GOST 8226–82 (TM) [6]. Benzene and total arenes in naphthas were determined according to GOST 29 040–91 on an LKhM-80 gas chromatograph.

In their fractional composition, the base components and blends used met the regulatory requirements to AI-92 and AI-95 gasolines (Table 1), but not in the octane number. A mixture containing 90 wt % reformer naphtha and 10 wt % straight-run naphtha has ON 91 (EM). Therefore, manufacture of AI-92 and AI-95 gasolines from this base blend requires a lower amount of high-octane additives.

It is seen from the figure that, even on adding the maximum amount (1.9 wt %) of the additive to the 10/90 and 50/50 base blends, the octane number required for AI-92 gasoline [ON 83 (EM) and 92 (TM)] is not obtained. At the same time, for the 90/10 and 70/30 blends, the required ON is attained at a BVD additive concentration of 1.5 and 1 wt %, respectively. With the BVD concentration increasing to 1.9 wt %, AI-92 and AI-95 gasolines can be obtained from both the reformer naphtha and mixtures of 10–30 wt % straight-run naphtha with reforming naphtha.

The ON benefit (ΔON) at a BVD concentration of 1.9 wt % is 3.6–6 points (EM) (Table 2). Addition of 15 wt % MTBE to the same base components provides ΔON of 3.5–6.9 points (EM) or 3–7.6 points (TM) (Table 2). The largest benefit [5.8–6.9 points (EM)] was obtained with blends containing 10 and 50 wt % reforming naphtha. However, even addition of the maximum amount (15 wt %) of MTBE to the base blends indicated does not provide ON required for AI-92 gasoline. At the same time, addition of the indicated amount of MTBE to AI-92 gasoline and to blends of 70–90 wt % reforming naphtha with straight-run naphtha (10–30 wt %) makes it possible to obtain AI-92 and AI-95 gasolines (Table 2).

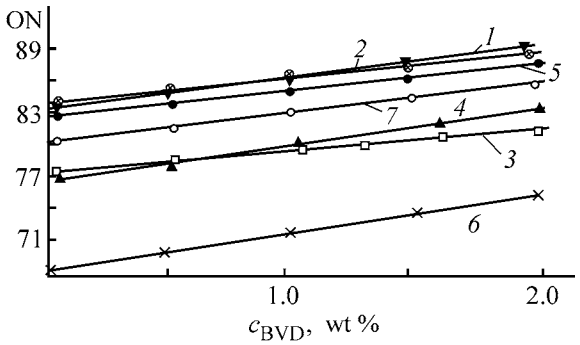

Effect of BVD addition on the ON of the base fuel components: (*1*) AI-92, (*2*) stable reforming naphtha, and (*3*) A-76. Reforming naptha/straight-run naphtha (wt %): (*4*) 50/50, (*5*) 90/10, (*6*) 10/90, and (*7*) 70/30. (c_{BVD}) Additive concentration.

Table 3. Performance of BVD/MTBE blend additives

Base component	ON (EM) at indicated MTBE/BVD mass ratio				
	0	5/0.5	10/0.5	5/1.9	10/1.9
AI-92	83.0	83.9	85.4	86.1	87.9 (95.1)*
A-76	76.2	78.2	79.9	81.0	81.5 (90.4)
Reforming naptha	83.2	85.0	86.8	87.0	89.7 (96.4)
Reforming naphtha/straight-run naphtha, wt %:					
10/90	68.0	71.8	75.0	76.1	78.6 (85.0)
50/50	76.0	77.6	80.1	81.6	83.4 (91.4)
70/30	78.5	80.4	82.2	83.5	84.4 (92.6)
90/10	81.2	82.8	84.3	85.7	86.4 (95.0)

* ON (TM) is given in parentheses.

Table 4. ON benefit of base blends on adding 0.5 and 1.3 wt % NMA additive

Base component	Initial ON		ON of a blend with 0.5 wt % NMA		ON of a blend with 1.3 wt % NMA		ΔON (0.5 wt % NMA)		ΔON (1.3 wt % NMA)	
	EM	TM	EM	TM	EM	TM	EM	TM	EM	TM
A-76	76.2	85.1	77.5	86.4	80.6	88.6	1.3	1.3	4.4	3.5
AI-92	83.0	92.0	83.5	92.8	84.6	93.4	0.5	0.8	1.6	1.4
Reforming naphtha	83.2	92.1	83.6	92.6	86.1	94.0	0.4	0.5	2.9	1.9
Reforming naphtha/straight-run naphtha, wt %:										
70/30	78.5	88.1	79.5	89.0	81.8	91.2	1.0	0.9	3.3	3.1
90/10	81.2	91.0	82.6	92.6	84.9	93.8	1.4	1.6	3.7	2.8

The combined action of MTBE and BVD is demonstrated in Table 3. Addition of 10 wt % MTBE + 1.9 wt % BVD to a base blend consisting of 70 wt % reforming naphtha and 30 wt % straight-run naphtha allows preparation of AI-92 gasoline. In the case of a 90/10 base blend, it is sufficient to add 10 wt % MTBE + 0.5 wt % BVD, while addition of 10 wt % MTBE + 1.9 wt % BVD gives AI-95 gasoline. Depending on the composition of the base blend, addition of 10 wt % MTBE + 1.9 wt % BVD provides an ON (EM) benefit from 4.9 to 10.6 points or ON (TM) benefit from 3.1 to 8.8 points.

The largest ON benefit was observed when the additives were taken in combination (Table 3). However, simultaneous addition of BVD and MTBE is inadvisable, because of the lack of a synergistic effect, and the expenses per a benefit ON point are larger compared to the use of individual additives.

The effect of NMA is demonstrated in Table 4 (*N*-methylaniline is a component of BVD additive).

According to the regulatory requirements, the NMA concentration in gasoline must be below 1.3 wt %. As seen, the effect of NMA is weaker than that of BVD [ON (EM) benefit is only 2.9–3.7 and ON (TM) benefit, 1.9–3.1 points].

Table 5 shows the effect of Hitec-3000 additive taken in concentration of 0.005–0.028 wt % (9–50 mg l^{-1} recalculated to Mn).

According to GOST R 51105–97, the maximum Mn concentration in Normal-80, Regulyator-91, Premium-95, and Super-98 grade gasolines is 50, 18, 0, and 0 mg l^{-1}, respectively. Table 5 shows that Hitec-3000 is an inefficient additive even if added to the maximum permissible concentration.

Table 5. Effect of Hitec-3000 additive on octane numbers (MM) of base components

Base component	ON at indicated additive concentration, wt %				
	0 (0)*	0.005(9)	0.01(18)	0.017(30)	0.028(50)
AI-92	83.0	83.4	83.8	84.6	85.3
A-76	76.2	76.6	78.1	78.4	80.8
Reforming naphtha	83.2	83.5	83.7	85.2	86.1
Reforming naphtha/straight-run naphtha, wt %:					
10/90	68.0	69.1	69.8	70.2	70.8
50/50	76.0	76.8	77.2	78.8	79.1
70/30	78.5	79.2	79.6	80.4	81.8
90/10	81.2	82.8	83.4	84.0	84.6

* Mn content (mg l^{-1}) is given in parentheses.

Table 6. Fabrication of Lukoil AI-92 and Premium-95 gasolines

Base component	Additive, wt %	ON (EM)	
		initial	additized
Lukoil AI-92			
A-76	MTBE/BVD = 15/1.9	76.2	84.5 (92.0)*
Reforming naphtha/straight-run naphtha = 70/30, wt %	BVD, 1.5	78.5	83.1 (92.5)
	MTBE/BVD = 10/1.9	78.5	84.4 (92.6)
Premium-95			
AI-92	MTBE, 10	83.0	85.7 (95.1)
Reforming naphtha	BVD, 1.9	83.2	86.8 (95.4)
	MTBE, 10	83.2	85.9 (95.0)
Reforming naphtha/straight-run naphtha = 90/10, wt %	MTBE, 15	81.2	85.4 (95.2)

* OM (TM) is given in parentheses.

Our results allow optimization of base blends and additives for manufacture of high-octane gasolines meeting the requirements of the operative Technical Specifications and State Standards (Table 6).

There are no catalytic cracking and hydrocracking, alkylation, isomerization, and isoselectoforming plants at the Ukhta Refinery, which limits the possibility of manufacture of high-octane base components. Therefore, blank AI-95 reformer gasoline manufactured at this refinery contains 4.17 wt % benzene and 57.07 wt % total arenes, which deteriorates its environmental characteristics. AI-95 gasoline with MTBE additive manufactured at the Lukoil–UNP contains 3.93 wt % benzene and 60.71 wt % total arenes.

As a conclusion, to manufacture AI-92 gasoline at the Lukoil-UNP, we suggest to add 15 wt % MTBE + 1.9 wt % BVD to A-76 unleaded gasoline. Now the Ukhta Refinery manufactures Premium-95 gasoline from AI-92 unleaded gasoline (Table 6).

Production of high-octane gasolines using MTBE and BVD additives and, in particular, of Lukoil AI-92 gasoline from A-76 and of Premium-95 from AI-92 unleaded gasoline is cost efficient, because the reformer naphtha is less expensive than AI-92 gasoline, and straight-run naphtha is cheaper than A-76.

CONCLUSIONS

(1) BVD and methyl *tert*-butyl ether additives demonstrate high antiknock efficiency, providing an octane number benefit from 3.6 to 6 points (engine method) and from 2.8 to 4 points (theoretical method) with BVD; and from 3.5 to 6.9 points (EM) and

from 3.0 to 7.6 points (TM) with methyl *tert*-butyl ether.

(2) With BVD additive (1.9 wt %), the formula of AI-92 gasoline is as follows: reformer naphtha 60–65% and straight-run naphtha the rest. For AI-95: reformer naphtha >90%, straight-run naphtha the rest.

(3) Simultaneous use of different additives is less efficient as compared to their individual introduction. Processes of fabrication of AI-92 and AI-95 gasolines can be multivariant. The formula of AI-92 gasoline may include from 60 to 99 wt % reforming naphtha, from 0 to 35 wt % straight-run naphtha, up to 15 wt % MTBE, and up to 1.9 wt % BVD; and that of AI-95, from 90 to 75 wt % reforming naphtha, up to 10 wt % straight-run naphtha, up to 15 wt % MTBE, and up to 1.9 wt % BVD.

(4) *N*-Methylaniline and Hitec-3000 additives are less efficient than methyl *tert*-butyl ether and BVD with regard to the base blends of the Ukhta Refinery.

REFERENCES

1. Begak, O.Yu. and Syroezhko, A.M., *Khim. Tekhnol. Topl. Masel*, 2001, no. 1 (505), pp. 37–38.
2. Zalishchevskii, G.D., Manufacture of High-Octane Gasoline with Decreased Content of Aromatic Hydrocarbons by Distillation of Reformer Naphthas, *Cand. Sci. Dissertation*, St. Petersburg, 2000.
3. *GOST* (State Standard) *3900–85 [ST SEV* (COMECON Standard) *6754–89]: Oil and Petroleum Products: Methods for Determination of the Density*, Moscow: Izd. Standartov, 1991.
4. *GOST 2177–99: Petroleum Products: Methods for Determination of the Fraction Composition*, Moscow: Izd. Standartov, 2000.
5. *GOST 511–82: Motor Fuel: Engine Method for Determination of the Octane Number*, Moscow: Izd. Standartov, 1982.
6. *GOST 8226–82: Motor Fuel: Theoretical Method for Determination of the Octane Number*, Moscow: Izd. Standartov, 1983.

Russian Journal of Applied Chemistry, Vol. 77, No. 6, 2004, pp. 1007–1009. Translated from Zhurnal Prikladnoi Khimii, Vol. 77, No. 6, 2004, pp. 1021–1023.

CHEMISTRY OF FOSSIL FUEL

Volatile Products of Temperature-Programmed Pyrolysis of Oil Shales

Kh. M. Kerimov

Azerbaijan State Petroleum Akademy, Baku, Azerbaijan

Received February 26, 2004

Abstract—Temperature-programmed pyrolysis of oil shales was studied. The composition of pyrolysis products was analyzed by the chromatographic technique.

The rise in thepower consumption in the world, with exhaustion of the traditional fuel resources, requires a search for alternative sources for power production and alternative raw materials for petrochemical synthesis. Among such raw materials are oil shales [1], i.e., organomineral sedimentary rocks containing concentrated sapropelic or humus-sapropelic organic substances of various origins. The main organic substance of oil shales is kerogen, which is inert to chemical reagents and practically insoluble in organic solvents. The main industrial procedure for kerogen recovery is pyrolysis. Other procedures, such as extraction with solvents and biochemical methods, are not yet widely used [2].

Oil shales are distinguished by the type of kerogen: (1) oil shales of sea origin, (2) oil shales formed in semi-closed sea reservoirs and in lakes and bogs, and (3) oil shales of continental genesis. A certain relationship between the type of kerogen and the distribution of alkanes in volatile products of pyrolysis of oil shales was noted in [2, 3].

In this study, we examined temperature-programmed pyrolysis of oil shales of the Dzhangichai deposit and determined the optimum temperature at which the yield of the products is the highest. The distribution of alkanes in the volatile products at various pyrolysis temperatures was also analyzed.

EXPERIMENTAL

The samples of oil shales subjected to pyrolysis were ground in a laboratory mill. A <0.1-mm fraction was selected for the study. This fraction was dried to constant weight at 105°C under nitrogen. The pyrolysis reactor consisted of a steel jacket (400 mm × 15 mm) and a quartz reaction tube with an inner diameter of 10 mm. A weighed portion of the oil shale was mixed with 5 ml of quartz sand (particle size 0.1–0.25 mm) and placed in the reaction tube. A thermocouple for measuring the temperature in the pyrolysis area was placed in the center of the sample bed.

The reaction tube with a sample was placed in a steel jacket of the temperature programmed furnace (electric heating). The temperature in the pyrolysis area was monitored by three thermocouples in the reaction tube. The temperatures measured during the process were recorded with a multichannel unit. The temperature variation along the reaction area did not exceed 1°C. The process was carried out in an argon flow (80 ml min^{-1}) at a heating rate of 2 deg min^{-1}. The reference substance, 0.507% neopentane in N_2, was introduced into the flow of the products released from the pyrolysis area at a rate of 20 ml min^{-1}. Samples were withdrawn from the flow of the products leaving the reactor into evacuated glass ampules. The procedures of sampling and chromatographic analysis of a multicomponent vapor–gas mixture have been described previously [5]. The pyrolysis products were analyzed in a Hewlett Packard HP-6890 capillary gas chromatograph. A 100 m × 0.25 mm column was coated with methylsilicone OV-1. Hydrogen was used as a carrier gas. The detector temperature (FID) was 350°C, and the injector temperature, 290°C. The qualitative identification of the components of the mixtures was carried out by comparison of the retention time with reference data stored in the computer (CHEMSTATION software for recording and processing of chromatographic data).

The quantitative interpretation of the chromatograms was carried out using an internal reference.

1070-4272/04/7706-1007 © 2004 MAIK "Nauka/Interperiodica"

Elemental composition and the results of Fischer analysis of oil shales

Products	Content, %*	Products	Content, %*	Products	Content, %*	Products	Content, %*
		Fischer analysis		Elemental analysis of tar		Elemental analysis of residue	
Total carbon	21.93	Tar	14.75				
		Decomposition water	2.62	C	77.46	C	17.76
Organic carbon	20.7	Solid residue	71.54	H	11.31	H	1.07
		Gas + loss including:	11.09	N	1.24	N	0.86
Hydrogen	2.56	CO	3.43	S	1.53	S	4.48
Nitrogen	0.92	CO_2	14.51				
Total sulfur	3.24	CH_4	45.46				
		C_2–C_4	36.6				

* The composition determined from the results of elemental analysis and Fischer analysis is given in weight percent, and the gas composition, in volume percent.

The content of *i*th component c_i (%) in the mixture being analyzed (yield, wt %) was evaluated by the formula

$$c_i = \frac{k_i Q_i}{k_{\text{ref}} Q_{\text{ref}}} \times 100r, \quad (1)$$

where k_i and k_{ref} are the correction coefficients for peak areas of the component and reference, Q_i and Q_{ref} are the peak areas of the component being analyzed and the reference (mm^2), and r is the ratio of the weight of the reference to the weight of the mixture being analyzed.

The rate of formation of the products v ($mg\ min^{-1}$) was evaluated by the formula

$$v = \frac{\Sigma Q - Q_{\text{ref}}}{Q_{\text{ref}}} m_{\text{C}}, \quad (2)$$

where m_{C} is the gravimetric flow rate of carbon in the flow of internal reference ($mg\ min^{-1}$), evaluated from the relationship

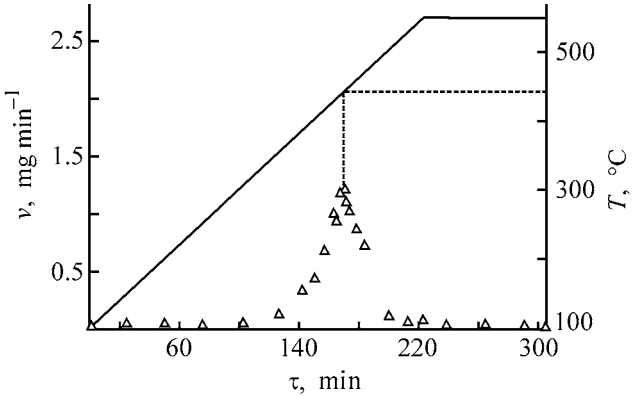

Fig. 1. Rate of formation of aliphatic hydrocarbons v vs. time τ and temperature T.

$$m_{\text{C}} = nN_{\text{C}}M_{\text{C}}/1000. \quad (3)$$

Here n is the molar flow rate of neopentane ($mol\ min^{-1}$); M_{C}, atomic weight of carbon ($12\ g\ mol^{-1}$); N_{C}, the number of carbon atoms in neopentane (5); and ΣQ, the sum of the peak areas in the chromatogram (mm^2).

Average characteristics of oil shales: moisture content 2.84 wt %, ash content 79.45 wt %, and heat of combustion 3880 $kJ\ kg^{-1}$. The following components were found in the ash (wt %): SiO_2 36.94, Fe_2O_3 17.34, CaO 22.95, MgO 0.68, K_2O 1.08, TiO_2 0.88, MnO 0.45, CuO 0.31, ZnO 0.14, SO_3 18.08, and P_2O_5 1.12. The results of elemental analysis and Fischer analysis are listed in the table.

As can be seen from Fig. 1, the rate of formation of pyrolysis products passes through a maximum at 440°C. With increasing pyrolysis temperature, along with increase in the concentration of hydrocarbons C_1–C_4 and C_5–C_{15}, hydrocarbons that are solids under standard conditions ($C_{>15}$) appeared in the pyrolysis products. This is caused by decomposition of kerogen in two consecutive steps.

At fairly low temperatures, the primary decomposition reactions yield gaseous and liquid hydrocarbons, and, beginning from 400°C, macromolecular fragments of kerogen, containing more than 15 carbon atoms, are formed. With further heating, the secondary decomposition begins, and the primary products decompose to form compounds of lower molecular weight. The temperature dependence of the yield of *n*-paraffins in the pyrolysis products is shown in

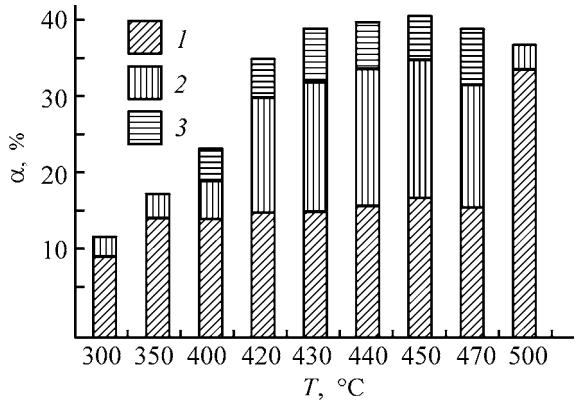

Fig. 2. Yield α and composition of *n*-paraffins vs. pyrolysis temperature *T* (°C): (*1*) C_1–C_4, (*2*) C_5–C_{15}, and (*3*) $C_{>15}$.

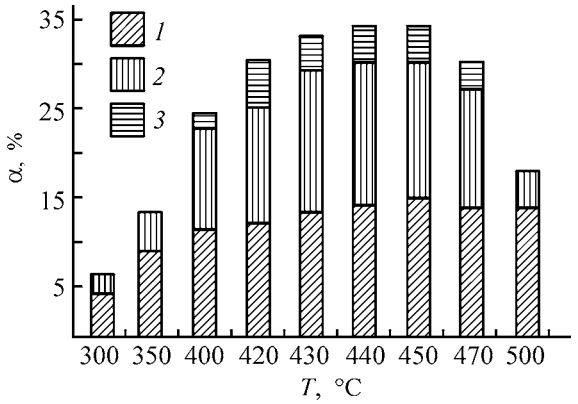

Fig. 3. Yield α and composition of α-olefins vs. pyrolysis temperature *T* (°C): (*1*) C_2–C_4, (*2*) C_5–C_{15}, and (*3*) $C_{>15}$.

Fig. 2. At relatively low temperatures, the composition of *n*-paraffins is characterized by a high content of gaseous products. For example, 12% *n*-paraffins (C_1–C_4 83%) was found in the pyrolysis products at 350°C. With heating, the products get enriched with liquid hydrocarbons. At the optimal temperature of pyrolysis (440°C), 41% *n*-paraffins (C_1–C_4 41%, C_5–C_{15} 44%, and $C_{>15}$ 15%) were found.

The content and distribution of α-olefins in the products at various pyrolysis temperatures are shown in Fig. 3. At 350°C, mainly low-molecular-weight α-olefins were found in the pyrolysis products. For example, in the 14% α-olefins found in the products at 350°C, the content of C_2–C_4 hydrocarbons was 71%. At 440°C 35% of the pyrolysis products were α-olefins (C_2–C_4 42%, C_5–C_{15} 45%, and $C_{>15}$ 13%).

CONCLUSIONS

(1) In temperature-controlled pyrolysis of Dzhangichai oil shales, the maximum yield of the products is reached at 440°C. At lower temperatures, the pyrolysis products are characterized by a high content of *n*-paraffins C_1–C_4 and at 440°C (the optimal pyrolysis temperature) the yield of C_5–C_{15} hydrocarbons is at a maximum, being considerably higher than the yield of $C_{>15}$. In addition, at the optimal temperature of pyrolysis the concentration of C_5–C_{15} alkenes in α-olefins is higher than that of $C_{>15}$.

(2) The distribution of *n*-alkenes and α-olefins in the pyrolysis products is in good agreement with the distribution characteristic of kerogen II.

ACKNOWLEDGMENTS

The author is grateful to the NATO-PC and TUBITAK foundations for financial support and also to the Engineering Department of the EGE University (Izmir, Turkey) for help in this study.

REFERENCES

1. Kuznetsov, D.T., *Goryuchie slantsy mira* (Oil Shales in the World), Moscow: Nedra, 1975.
2. Ballice, L., Yuksel, M., Saglam, M., and Schulz, H., *Fuel*, 1996, vol. 75, no. 4, pp. 453–455.
3. Arutyunova, Zh.E. and Zhuze, B.I., *Geologiya mesto-rozhdenii uglya i goryuchikh slantsev SSSR* (Geology of Deposits of Coal and Oil Shales in the USSR), Pogrebnov, N.I., Ed., Moscow: Nedra, 1976, vol. 11, pp. 399–414.
4. Miknis, F.P. and Conn, P.J., *Fuel*, 1992, vol. 71, no. 5, pp. 731–738.
5. Schulz, H., Bohringer, W., Kohl, C.P., *et al., Entwicklung und Anwendung der Kapillar GC Gesamtprobentechnik fur Gas/Dampf Veielschtoffegemische*, Hamburg: Deutsche Gesellschaft Mineralolwissenschaft und Kohlenchemie, 1984, pp. 4–20.

Russian Journal of Applied Chemistry, Vol. 77, No. 6, 2004, pp. 1010–1012. Translated from Zhurnal Prikladnoi Khimii, Vol. 77, No. 6, 2004, pp. 1024–1026.

CHEMISTRY OF FOSSIL FUEL

A Versatile Formulation Inhibiting Thermal Polymerization of Pyrocondensates and Styrene

A. F. Gogotov and A. V. Ivanova

Angarsk Petrochemical Company, Open Joint-Stock Company, Angarsk, Irkutsk oblast, Russia

Received November 20, 2003; in final form, April 2004

Abstract—A formulation composed of *tert*-butylpyrocatechol with copper diethyldithiocarbamate was developed for inhibiting thermal polymerization of styrene and liquid pyrolysis products of 30–180°C benzine fractions, and its performance was studied.

Reduction of loss associated with thermal polymerization of monomers in the course of their distillation is one of the most challenging and currently pressing problems of petrochemical industry [1]. It is known that unsaturated compounds (styrene, divinylbenzene, vinylpyridines, acrylic compounds, vinyl chloride, cyclopentadiene and/or dicyclopentadiene) are thermally unstable and intensely polymerize when heated to above 100°C. Therefore, in the course of their processing aimed to concentrate or purify the target product, it is necessary to add thermal polymerization inhibitors, since polymerization adversely affects the yield of the target product and the state of the equipment. Numerous inhibitors and inhibiting formulations have been suggested, but the actual choice is governed by the availability of compounds and feasibility of their use. Fairly widely used are phenolic inhibitors: Ionol, *tert*-butylpyrocatechol (TBPC), etc. [2, 3].

However, the assortment of antioxidants is not restricted to phenols. Dialkyldithiocarbamates of various metals (sodium, zinc, nickel, etc.) and thiurams also show high inhibiting performance in oxidation processes [4–9]. In petrochemical industry, the most widely used inhibitor of thermal polymerization of pyrocondensates and individual monomers is TBPC [10, 11]. The practice shows that the highest inhibiting performance in processing of pyrocondensates is exhibited by individual compounds, such as, e.g., TBPC, whereas in production of individual monomers (styrene, butadiene, etc.), formulations consisting of two or three components are more effective in inhibiting the undesirable polymerization.

The mechanism and efficiency of the action of metal dialkyldithiocarbamates as oxidation inhibitors have been described in detail [4–9]. In their use as inhibitors of radical processes and, in particular, of radical polymerization, the presence of oxygen as initiator of radical processes is necessary. For example, a high performance of inhibiting formulations consisting of TBPC, copper diethyldithiocarbamate, and oxygen was shown in [12, 13]. However, in processing of pyrocondensates, styrene, and other vinyl monomers, even small amounts of oxygen should be excluded because of the extremely high fire and explosion hazard. It should also be noted that dialkyldithiocarbamates of various metals essentially differ in the solubility. Ammonium, sodium, and potassium salts are soluble in water and insoluble in organic solvents, whereas zinc, nickel(II), and copper(II) salts, by contrast, are readily soluble in organic solvents and show different solubilities in water [14].

In this study, we continued a search for effective inhibiting formulations for processing of liquid pyrolysis products (pyrocondensates) and for production of styrene.

EXPERIMENTAL

We have developed a new inhibiting formulation based on TBPC, effective in production of both ethylene–propylene (EP) and styrene [15]. The results of testing of the inhibiting formulation we suggested in thermal processing of pyrocondensates (liquid pyrolysis products of benzine fractions, EP-300 unit) and styrene at the Angarsk Polymer Plant are listed in Tables 1 and 2.

1070-4272/04/7706-1010 © 2004 MAIK "Nauka/Interperiodica"

Table 1. Efficiency of polymerization inhibition in pyrocondensates

Run no.	Inhibitor or formulation, wt %	Resin yield, mg/100 cm^3	Inhibiting effect, %	Presence (+) or absence (–) of precipitate
1	–	420	–	
2	CuDTC (0.025)	33.2	92.1	+
3	TBPC (0.025)	75.6	85.0	–
4	CuDTC (0.010)	147	65.0	″
5	CuDTC (0.020)	53.3	87.3	+
6	TBPC (0.010)	163.8	61.0	–
7	CuDTC (0.015)	96.6	77.0	+
8	CuDTC (0.010) + TBPC (0.010)	30.7	92.7	–
9	CuDTC (0.010) + TBPC (0.015)	25.2	94.0	″
10	CuDTC (0.005) + TBPC (0.015)	50.4	88.0	″
11	CuDTC (0.005) + TBPC (0.020)	40.7	90.3	″

Table 2. Polymer yield in heating of styrene (120°C) in the presence of inhibitors

Run no.	Inhibiting system, % of styrene weight	Polymer yield, %, in indicated heating time, h					
		2	3	4	5	6	7
12	CuDTC (0.005)	11.0	21.7	33.2	–	–	–
13	TBPC (0.025)	18.7	29.4	54.3	–	–	–
14	CuDTC (0.025) + TBPC (0.025)	0.23	7.01	15.1	29.1	–	–
15	CuDTC (0.01) + TBPC (0.025)	0.21	0.36	0.61	0.63	0.70	1.07
16	CuDTC (0.0025) + TBPC (0.025)	4.21	19.3	21.5	–	–	–
17	CuDTC (0.005) + TBPC (0.025)	0.19	0.42	0.54	0.55	0.57	0.61
18	CuDTC (0.005) + TBPC (0.02)	0.32	0.61	0.67	0.70	0.72	0.78
19	CuDTC (0.0045) + TBPC (0.0255)	0.33	0.35	0.42	0.50	0.52	0.68
20	CuDTC (0.006) + TBPC (0.024)	0.23	0.32	0.44	0.52	0.57	0.73
21	CuDTC (0.007) + TBPC (0.023)	0.19	0.30	0.35	0.44	0.60	0.65
22	CuDTC (0.0075) + TBPC (0.0225)	0.25	0.35	0.42	0.48	0.68	0.87

The inhibiting formulation suggested: copper(II) diethyldithiocarbamate (CuDTC) + TBPC, was tested under laboratory conditions with pyrocondensates sampled from the bottoms of the K-27 column of the EP-300 unit at the Angarsk Polymer Plant.

The pyrocondensates were heat-treated at 130 ± 1°C for 1 h, with subsequent analysis for the total resin content in pyrocondensates with a POS-77 device [steam distillation at 160°C according to standard procedure, GOST (State Standard) 25336–82]. The results are listed in Table 1.

Table 1 shows that heat treatment at 130°C for 1 h of the pyrocondensate containing various unsaturated compounds (styrene, α-methylstyrene, vinyltoluene, cyclopentadiene, dicyclopentadiene, butadiene, isoprene, 1-butene), with the initial resin content of 10.5 mg/100 cm^3, raises the resin content to 420 mg/100 cm^3. The polymerization is inhibited by CuDTC and TBPC, taken both separately and in combination. With CuDTC, the strongest inhibiting effect is observed at its content of 0.025 wt %: polymer formation decreases by 92.1% (run no. 2). However, the copper salt loses in this case its solubility and precipitates in the course of heat treatment of the pyrocondensate, which is extremely undesirable for the technology. Precipitation was also observed at CuDTC content of 0.020 (run no. 5) and 0.015 wt % (run no. 7). No precipitate was formed only at the CuDTC content decreased to 0.010 wt % (run no. 4), but the inhibiting effect in this case also decreased significantly (to 65%).

tert-Butylpyrocatechol taken alone is also a fairly effective inhibitor of polymerization in pyrocondensates (run nos. 3, 6), though less effective than CuDTC taken in the same amount.

The above-noted shortcoming of CuDTC, precipitation after the heat treatment, can be eliminated by using CuDTC in combination with TBPC. The high

inhibition efficiency (>90%) is preserved at the total content of the inhibitors of 0.020–0.025 wt %, with the CuDTC content being as low as 0.005–0.010 wt % (run nos. 8–11).

The ratio of the coinhibitors in the formulation suggested is determined by physicochemical properties of TBPC and CuDTC.

The formulation suggested (with somewhat other component ratios) was also tested as inhibitor of styrene polymerization in the course of its heat treatment at 120°C for 2–7 h. The results (Table 2) show that this formulation is also effective with respect to styrene.

The results of run nos. 12 and 13 show that the components taken alone do not inhibit polymerization of styrene. Furthermore, the inhibiting performance is low at the maximum content of TBPC (0.025 wt % relative to styrene) and minimum (0.0025 wt % relative to styrene, run no. 16) and maximum (0.025 wt % relative to styrene, run no. 14) contents of CuDTC. The optimal CuDTC : TBPC ratio for inhibition of styrene polymerization is 1 : (3.3–5.7) at a total content of the components of 0.03% relative to styrene (run nos. 15, 17–22).

It should be noted that such a coincidence of the optimal compositions of inhibiting formulations for different substrates is extremely seldom in chemical technology.

CONCLUSION

A formulation composed of *tert*-butylpyrocatechol with copper(II) diethyldithiocarbamate shows high performance in inhibition of thermal polymerization of styrene and of a mixture of various unsaturated compounds from liquid pyrolysis products of benzine fractions in production of ethylene and propylene.

REFERENCES

1. Pavlov, S.Yu., *Vydelenie i ochistka monomerov dlya sinteticheskogo kauchuka* (Recovery and Purification of Monomers for Synthetic Rubber), Leningrad: Khimiya, 1987.
2. Kurbatov, V.A., Liakumovich, A.G., and Kirpichnikov, P.A., *Neftekhimiya*, 1983, vol. 23, no. 1, pp. 118–120.
3. Kirpichnikov, P.A., Liakumovich, A.G., Pobedimskii, D.G., and Popova, L.M., *Khimiya i tekhnologiya monomerov dlya sinteticheskikh kauchukov* (Chemistry and Technology of Monomers for Synthetic Rubbers), Leningrad: Khimiya, 1981.
4. Emanuel', N.M., Denisov, E.T., and Maizus, Z.K., *Tsepnye reaktsii okisleniya uglevodorodov v zhidkoi faze* (Chain Reactions of Liquid-Phase Oxidation of Hydrocarbons), Moscow: Nauka, 1965.
5. Shelkova, R.G., Kuz'mina, G.R., Dzyubina, M.A., *et al.*, *Neftekhimiya*, 1990, vol. 30, no. 2, pp. 244–251.
6. Shelkova, R.G., Kuz'mina, G.R., Sanin, P.I., *et al.*, *Kinet. Katal.*, 1990, vol. 31, no. 5, pp. 1246–1250.
7. Shkhiyants, I.V., Sher, V.V., Nechitailo, N.A., *et al.*, *Neftekhimiya*, 1969, vol. 9, no. 4, pp. 616–619.
8. Brooks, L.A., *Rubber Chem. Technol.*, 1963, vol. 36, no. 6, pp. 887–898.
9. Korenevskaya, R.G., Kuz'mina, G.N., Dzyubina, M.A., *et al.*, *Neftekhimiya*, 1986, vol. 26, no. 5, pp. 685–692.
10. RF Patent 2154048.
11. Gogotov, A.F., Amosov, V.V., Tayurskii, V.A., *et al.*, *Proizv. Ispol'z. Elastom.*, 2002, no. 1, pp. 3–9.
12. EPW Application 0485169.
13. JPN Patent 52-34606.
14. *Khimicheskii entsiklopedicheskii slovar'* (Chemical Encyclopedic Dictionary), Knunyants, I.L., Ed., Moscow: Sov. Entsiklopediya, 1983.
15. RF Patent 2196125.

Russian Journal of Applied Chemistry, Vol. 77, No. 6, 2004, pp. 1013–1018. Translated from Zhurnal Prikladnoi Khimii, Vol. 77, No. 6, 2004, pp. 1027–1032.

CHEMISTRY OF FOSSIL FUEL

Solubility and Binding of Water in Toluene Solutions of Asphaltenes

D. S. Khvostichenko, S. I. Andersen, and A. I. Viktorov

St. Petersburg State University, St. Petersburg, Russia

Technical University of Denmark, Lyngby, Denmark

Received January 21, 2004

Abstract—The solubility of water in toluene solutions of asphaltenes is determined, and the state of water molecules in these solutions is studied spectroscopically. A number of water molecules bound to an asphaltene molecule is estimated from the experimental data. Aggregation in the system asphaltene–water–toluene is simulated using the pseudophase approximation, and the Flory–Huggins parameters are estimated for the pair asphaltene–water. The potentiality of this model for simulation of mixed aggregates in the asphaltene–water–toluene systems is discussed.

Asphaltenes are heavy polyaromatic compounds contained in high-boiling oil fractions. They are prepared by precipitation from crude oil by adding a nonpolar solvent, mostly *n*-pentane or *n*-heptane. The increased interest in properties of asphaltenes is due to the fact that, under certain conditions, they can precipitate to form solid deposits, giving rise to serious problems in oil production and refining. Precipitation of asphaltenes can be also initiated by the impact of CO_2, mixing of different crude oils, and pressure variation.

Asphaltene-containing petroleum fluids are an example of complex fluid systems with aggregation, whose structure and thermodynamics are regarded as important fundamental problems. Like surfactants, asphaltenes demonstrate critical micelle concentration (CMC), as shown by various methods, such as determination of the surface tension [1, 2], calorimetric titration [3], and small-angle X-ray scattering [4].

Recently Andersen *et al*. have shown that water takes an important part in the colloidal behavior of asphaltenes [5]. In particular, micellization was not observed in toluene solutions of asphaltenes in the absence of trace amounts of water (~0.11 wt %), and that the concentration of water in a solvent (0.001–0.047 wt %) influences CMC of asphaltenes, as determined by the calorimetric method. It has also been shown that the solubility of water in toluene solutions of asphaltenes is higher than that in straight toluene [5]. Such an increase in the solubility can be attributed to the salting-in effect [6] and solubilization of water by asphaltene aggregates.

The state of water in inverse micelles and in organic solvents is commonly studied by IR spectroscopy as a method sensitive to hydrogen bonding [7–16]. The IR spectra of such systems show a set of absorption bands at 3800–3100 cm^{-1} due to stretching vibrations of the OH groups, which are strongly influenced by hydrogen bonding.

In this study, we examined the solubility of water and subjected to infrared analysis its state in toluene solutions of asphaltenes.

EXPERIMENTAL

The working asphaltene solutions were prepared by dilution of a concentrated stock solution (20 g l^{-1} toluene). The working solution was poured over distilled water, avoiding mixing with it, and allowed to stand for at least 72 h in the dark (according to Andersen *et al*. [5], this is the time required for saturation of the organic phase with water). Then a small sample of the organic phase was taken for analysis. The concentration of water s_w^{sat} was determined by Karl Fischer titration using RH 34836 reagent with a 30% toluene content (Hyrdanal coulamat AG). The instrument (652-KF Coulometer) was calibrated against reference solutions with the water concentrations covering the

1070-4272/04/7706-1013 © 2004 MAIK "Nauka/Interperiodica"

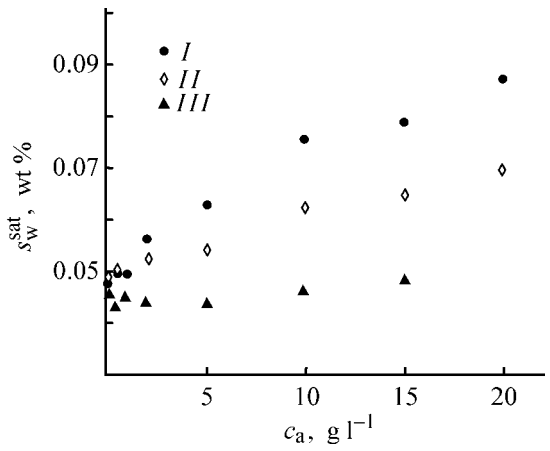

Fig. 1. Solubility of water in toluene s_w^{sat} vs. the asphaltene concentration c_a: (*I*) OMV, (*II*) NM1, and (*III*) A95.

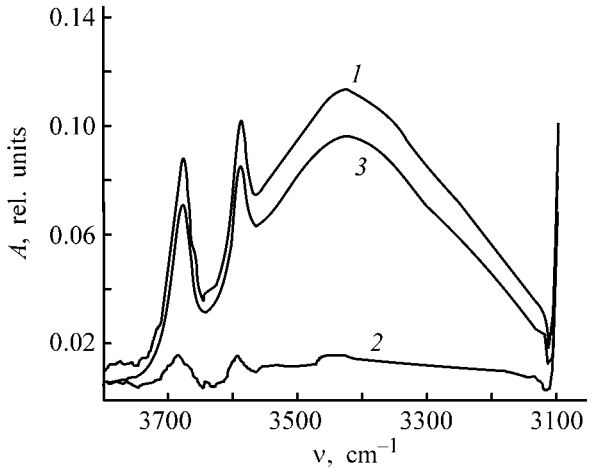

Fig. 2. IR spectra: (*1*) asphaltene–water–toluene, (*2*) asphaltene–toluene, and (*3*) differential spectrum. (*A*) Absorbance and (ν) wave number.

concentration range investigated. The relative error of determination was within 5%.

The IR spectra of the samples were recorded on a Perkin-Elmer PARAGON 1000 FTIR spectrometer using a Specac cell (NaCl windows, path length 0.5 mm). For each sample, 256 scans were made over the range 3800–3100 cm^{-1} with a 4-cm^{-1} resolution. The spectra were recorded against dry toluene as a reference. The absorption bands due to OH stretching vibrations was analytically divided into three Gaussian peaks using Microcal Origin program pack.

Asphaltene OMV was a purified precipitate from crude oil (Austria).

Asphaltenes A95 (Alaska) and NM1 (Venezuela) were prepared by precipitation with *n*-heptane from crude oil at room temperature, according to the modified IP-143 procedure [17]. *n*-Heptane was added to crude oil (30 ml g^{-1} crude oil), and the resulting mixture was allowed to stand in the dark for about 18 h. The precipitate was filtered off and dissolved in toluene, to separate toluene insolubles. Then toluene was removed by evaporation, and dry asphaltenes were washed several times with *n*-heptane as follows. Asphaltene was agitated with *n*-heptane on an ultrasonic bath and then centrifuged. The supernatant was poured out, and the washing was repeated with a fresh portion of heptane. Asphaltene was accepted pure when *n*-heptane after washing remained colorless or became only slightly yellow. Finally, the precipitate was vacuum-dried at 60°C, to remove residual heptane.

Toluene was dried over molecular sieves prior to use. Water-saturated toluene was prepared by mixing with excess water for at least three days. Unsaturated toluene samples were prepared by mixing water-saturated samples with dry toluene taken in desired volume ratios. The water concentration in unsaturated samples was determined by Karl Fischer titration.

The solubility of water in the organic phase was studied with asphaltene samples OMV, A95, and NM1. The solubility grows with increasing asphaltene concentration (Fig. 1), which is consistent with the data obtained by Andersen *et al*. [5]. The water content in the saturated sample was found to be 0.046 ± 0.002 wt % at 295 K, which is well consistent with published data (0.042 and 0.046 wt % at 293 K and 298 K, respectively [18]).

The state of water molecules in the system asphaltene–water–toluene was studied by IR spectroscopy. We studied three series of OMV asphaltene solutions in toluene with a constant total water content s_w (0.013, 0.019, and 0.027 wt %) and variable asphaltene concentration.

Figure 2 shows examples of the IR spectra of asphaltene solutions in dry toluene and in the presence of water and also the difference between these spectra over the range 3800–3100 cm^{-1}. According to published data [9, 14, 16], two sharp absorption bands at 3680 and 3592 cm^{-1} are due to vibrations of the OH groups in monomeric water molecules, not involved in hydrogen bonding. The appearance of a third, broad band is assigned to the presence in the system of hydrogen-bonded water. Since we observed a weak absorption in the systems with dry toluene also, we analyzed the difference spectra obtained by subtraction of the spectra of the corresponding asphaltenes in dry toluene from those of asphaltenes in the presence of water. This weak absorption in the systems with

dry toluene can be attributed to the presence of hydroxy and amino groups in asphaltenes and also to the fact that even dried toluene contains trace amounts of water (<0.001 wt %).

It was demonstrated that, at relatively low concentrations of water in toluene (0.013–0.027 wt %), the area of peak *1* is a linear function of the water concentration. Assuming that water in toluene totally occurs in the unbound monomeric state, we used this linear dependence as a calibration curve for determining the weight concentration of free water in asphaltene solutions in toluene. The results obtained with water-unsaturated toluene are given in Fig. 3.

From the concentration of free water, we estimated the amount of bound water molecules per asphaltene molecule in organic phase R_{wa}^{bound} (Fig. 4). In this case, the molar weight of the monomeric asphaltene was accepted to be 1000 g mol^{-1} [19, 20]. The R_{wa}^{bound} value is high in dilute asphaltene solutions, becoming below unity at higher concentrations. Since, above CMC, the systems contains both asphaltene aggregates and monomers, the amount of water molecules per asphaltene molecule in an aggregate should be somewhat different from the estimated values.

An interesting feature of all the curves shown in Fig. 3 is the local minimum in the concentration of free water at an asphaltene concentration near 0.1 g l^{-1}. The indicated concentration is remarkably lower than the critical concentration of formation of asphaltene aggregates [5], suggesting that water is bound to monomeric asphaltene molecules. With increasing asphaltene concentration to 0.5–2.0 g l^{-1}, micellization is observed, which is accompanied by an increase in the free water concentration. With further increase in the asphaltene concentration, s_w^{free} monotonically decreases.

In extremely dilute solutions, the dependence of the content of bound water on the asphaltene concentration should be linear, i.e., the amount of water molecules per asphaltene molecule should be constant. Assuming that, at an asphaltene concentration of 0.1 g l^{-1}, this dependence is still linear and accepting the mean experimental R_{wa}^{bound} for the three systems at c_a = 0.1 g l^{-1} as the limiting number of water molecules bound to an asphaltene molecule, one can estimate the amount of water bound to an asphaltene molecule at higher c_a (strictly speaking, the limiting R_{wa}^{bound} should be the same in solutions with different total water content; the mean R_{wa}^{bound} for the three systems at c_a = 0.1 g l^{-1} is about 20). However, this calculation gives a concentration of bound water that is

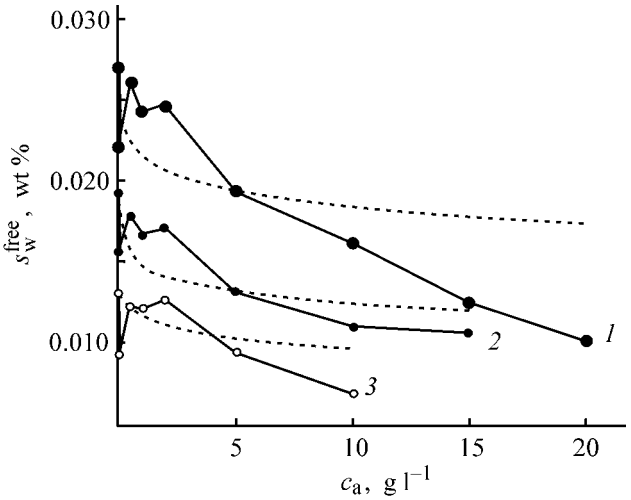

Fig. 3. Free water content s_w^{free} (wt %) vs. the asphaltene concentration c_a in the systems asphaltene–water–toluene at various initial water concentrations s_w (wt %): (*1*) 0.027, (*2*) 0.019, and (*3*) 0.013; the same for Fig. (4). Calculated data are presented by the *dotted lines*.

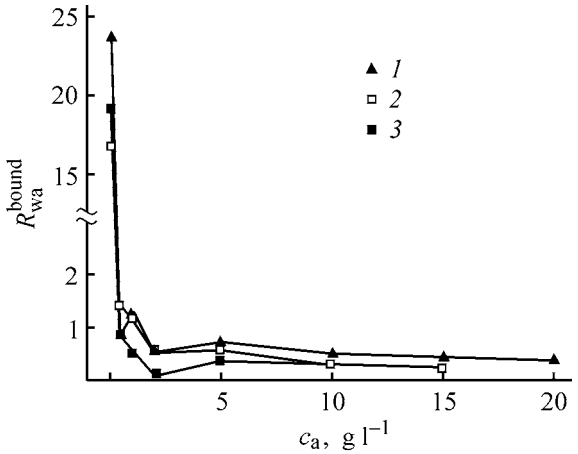

Fig. 4. Amount of bound water molecules per asphaltene molecule R_{wa}^{bound} in the system asphaltene–water–toluene. (c_a) Asphaltene concentration.

considerably higher than the total water concentration s_w in all the three systems even at an asphaltene concentration of 0.5–1.0 g l^{-1}, i.e., at higher c_a, water should be totally bound, which contradicts the experimental data. In this case, it may be suggested that, thanks to the onset of aggregation, only a part of asphaltene molecules is involved in interaction with water.

With further increase in s_a above CMC (at c_a = 10–15 g l^{-1}), the water to asphaltene molar ratio X_w/X_a becomes below unity, and, despite the fact that not all of the asphaltene molecules can participate in bonding with water, s_w^{free} decreases. The observed decrease

in R_{wa}^{bound} is probably due to increase in the asphaltene concentration also, since this parameter is defined as the ratio between the bound water concentration to the total asphaltene concentration, so that, at higher total asphaltene concentrations, this ratio is small. The available experimental data do not allow more detailed conclusions on the structure of the system, i.e., on what part of asphaltenes occurs in aggregated forms, and what is the ratio of the bound water molecules to the amount of aggregated asphaltene molecules.

The pseudophase approach widely used for characterization of surfactant solutions [21] is based on regarding the micelle formation as formation of a new phase. Therefore, the totality of the micelles is considered to be separate phase (pseudophase), and the equilibrium condition in the system is written as

$$\mu_i^M = \mu_i^\beta, \quad (1)$$

where μ_i^M and μ_i^β are the chemical potentials of a component in the micellar pseudophase and solution pseudophase, respectively.

For the dilute solution pseudophase (water and asphaltene mole fractions do not exceed 3×10^{-3}), the chemical potentials of the solutes (asphaltene and water) can be written, using the asymmetrical method of normalization of the activity coefficients, as

$$\mu_i^\beta = \mu_i^{*\beta} + kT \ln x_i^\beta, \quad i = a, w. \quad (2)$$

Assuming that the micellar pseudophase is composed by only the asphaltene and water, and using the symmetrical method of normalization for this pseudophase, we obtain

$$\mu_i^M = \mu_i^{0M} + kT \ln x_i^M \gamma_i^M, \quad i = a, w, \quad (3)$$

where μ is the chemical potential of a component in the pseudophase; μ^* and μ^0 are its standard terms for an infinitely dilute solution and the straight liquid as standard states, respectively; x is the mole fraction of a component in the pseudophase; and γ, the activity coefficient of the component in the pseudophase. Here the indices β and M refer to the solution and micellar pseudophases, and a and w, to asphaltenes and water, respectively.

The μ^* and μ^0 values for the solution pseudophase are related to each other through the limiting activity coefficients $\gamma_i^{\infty\beta}$:

$$\mu_i^* = \mu_i^0 + RT \ln \gamma_i^{\infty\beta}.$$

To determine the compositions of the pseudophase, it is necessary to add the material balance equations (4) to the set of Eqs. (1)–(3).

$$X_i = X_i^\beta + X_i^{aggr}, \quad i = a, w, \quad (4)$$

where X_a^{aggr} and X_w^{aggr} are the total mole fractions of asphaltenes and water occurring in the aggregates; X_{a1}^β and X_{w1}^β, total mole fractions of asphaltenes and water in the solution pseudophase; and X_a and X_w, total mole fractions of asphaltenes and water in the system.

The compositions of the pseudophase can be expressed via the total mole fractions of the components:

$$x_i^M = \frac{X_i^{aggr}}{\sum_i X_i^{aggr}}, \quad i = a, w; \quad (5a)$$

$$x_i^\beta = \frac{X_i^\beta}{X_{tol} + \sum_i X_i^\beta}, \quad i = a, w; \quad (5b)$$

where X_{tol} is the total toluene concentration.

The weight concentration of free water can be expressed in terms of X_w^β, X_w, and the total water concentration in the system s_w (wt %):

$$s_w^{free} = s_w \frac{X_w^\beta}{X_w}. \quad (6)$$

Expanding the equilibrium condition (1) for asphaltenes and water using Eqs. (2) and (3) and fixing the interrelation between μ^* and μ^0, the material balance conditions (4), and Eq. (5) at given total concentrations of the components X_a^{aggr}, X_w^{aggr}, and X_{tol}, s_w^{free} can be determined if the activity coefficients of asphaltenes and water in the micellar and solution pseudophases are known.

The activity coefficients of the components in the micellar pseudophase were estimated on the basis of the Flory–Huggins theory [22]:

$$\ln \gamma_{a1}^M = \ln \frac{\varphi_{a1}^M}{x_{a1}^M} + (1 - m^{a/w})\varphi_{w1}^M + m^{a/w}\chi^{a/w}(\varphi_{w1}^M)^2, \quad (7a)$$

$$\ln \gamma_{w1}^M = \ln \frac{\varphi_{w1}^M}{x_{w1}^M} + \left(1 - \frac{1}{m^{a/w}}\right)\varphi_{a1}^M + \chi^{a/w}(\varphi_{a1}^M)^2, \quad (7b)$$

where φ_{a1}^M and φ_{w1}^M are the volume fractions of asphaltenes and water in the aggregate; $m^{a/w} = \nu_{a1}/\nu_{w1}$

is the ratio of the molar volumes of asphaltene and water; and $\chi^{a/w}$, asphaltene–water interaction parameter.

In addition to the parameters of Eq. (7), for calculation it is also needed to determine the limiting activity coefficients of asphaltene and water in toluene, which relate μ^* and μ^0 to each other. There is no available experimental data for estimating the limiting activity coefficient of asphaltene in toluene $\gamma_{a1}^{\infty\beta}$, and we used the Flory–Huggins model for this purpose:

$$\ln\gamma_{a1}^{\infty\beta} = \ln\frac{v_{a1}}{v_{tol}} + (1 - m^{a/tol}) + m^{a/tol}\chi^{a/tol}, \quad (8)$$

where $m^{a/tol} = v_{a1}/v_{tol}$ is the ratio of the molar volumes of asphaltene and toluene; and $\chi^{a/tol}$, asphaltene–toluene interaction parameter.

The latter parameter (Table 1) was estimated as [22]

$$\chi^{a/tol} = \frac{v_{tol}}{RT}(\delta_a - \delta_{tol})^2, \quad (9)$$

where δ_a and δ_{tol} are the solubility parameters of asphaltenes and toluene, respectively (Table 2).

We estimated δ_a using the empirical relationship between the solubility parameter of asphaltene and its molecular weight [23]. The limiting activity coefficient of water in toluene (Table 2) was estimated using UNIQUAC model [24], since it is the model that has been recommended for representation of experimental data for the system in hand in DECHEMA database (Table 3) [18].

The asphaltene–water interaction parameters $\chi^{a/w}$ (Table 1) were estimated from the experimental free water concentration in asphaltene solutions. It was demonstrated that the effect of the composition (total water concentration in the system) on the Flory–Huggins parameter for the pair asphaltene–water should be taken into account ($\chi^{a/w}$ becomes less negative as the water content increases). Such a necessity has been reported previously for a series of systems [24]. The estimated results are given in Fig. 3 along with the experimental data on the free water concentration. At asphaltene concentrations below CMC, when water is bound to essentially asphaltene monomers, the theory fails to reproduce the distribution of water among free and bound states. At higher asphaltene concentrations (>2.0 g l^{-1}), the theory provides rather adequate qualitative fit to the experimental curves. Above CMC, asphaltenes occur essentially in the aggregated state, and water is bound, most likely, just to the asphaltene aggregates. Our result that the Flory–Huggins theory only qualitatively reproduces the experimental data obtained in this study is probably due to the fact that this theory was developed for flexible chain polymers and, therefore, it is not applicable to the full measure to asphaltenes (even though it was used for simulating phase separation in the systems asphaltene–organic solvent [26]).

Table 1. Flory–Huggins parameters

System	χ	m^*
Asphaltene–toluene (a/tol)	0.141	8.5
Asphaltene–water (a/w)	–0.915(0.013)**	
	–0.612(0.019)**	50.4
	–0.127(0.027)**	

* Estimated from data of Table 2.

** Total water content in the system (wt %) for which the parameter was estimated is given in parentheses.

Table 2. Parameters of Eqs. (7)–(9)

Component	Molar weight, g mol^{-1}	Density, g ml^{-1}	v, l mol^{-1}	δ, $MPa^{1/2}$	$\gamma^{\infty\beta}$
Asphaltene	1000	1.1 [5]	0.9091	20.06 [23]	0.015
Water	18	0.997	0.0181		455
Toluene	92	0.865	0.1064	18.25 [25]	

Table 3. Parameters of UNIQUAC model for the pair water–toluene [18]*

Component	r	q	a_{nm}	
			Water (1)	Toluene (2)
Water (1)	0.9200	1.400	0	1030.4
Toluene (2)	3.9228	2.968	289.19	0

* (r) Reduced van der Waals volume, (q) surface of the molecule, and (a_{nm}) interaction parameters.

CONCLUSIONS

(1) Both free and bound water occur in the asphaltene–toluene–water systems. With increasing asphaltene concentration, the free water concentration changes nonmonotonically, and a local minimum s_w^{free} is found at low asphaltene concentrations. Presumably, such an irregular shape of the experimental curves is caused by aggregation of asphaltenes.

(2) The use of the Flory–Huggins theory (preudophase approximation) for predicting the activity coefficients in the asphaltene–water–toluene systems provided the best fit to the experimental curves s_w^{free} vs. c_a at the asphaltene concentrations above the critical micelle concentration.

ACKNOWLEDGMENTS

The study was financially supported by the Russian Foundation for Basic Research (project 02-03-32 709).

REFERENCES

1. Sheu, E.Y. and Storm, D.A., *1Asphaltenes: Fundamentals and Applications*, Sheu, E.Y. and Mullins, O.C., Eds., New York: Plenum, 1995.
2. Rogel, E., Leon, O., Torres, G., and Espidel, J., *Fuel*, 2000, vol. 79, pp. 1389–1394.
3. Andersen, S.I. and Birdi, K.S., *J. Colloid Interface Sci.*, 1994, vol. 142, no. 2, pp. 497–502.
4. Sheu, E.Y., DeTar, M.M., Storm, D.A., and DeCanio, S.J., *Fuel*, 1992, vol. 71, pp. 299–302.
5. Ansersen, S.I., Rio, J.M. del, Khvostitchenko, D., *et al.*, *Langmuir*, 2001, vol. 17, pp. 307–313.
6. Ni, N., Et-Sayed, M.M., Sangmvi, T., and Yalkowsky, S.H., *J. Pharm. Sci.*, 2000, vol. 89, pp. 1620–1625.
7. Bey Temsamani, M., Maeck, M., El Hassani, I., and Hurwitz, H.D., *J. Phys. Chem., Ser. B*, 1998, vol. 102, pp. 3335–3340.
8. D'Angelo, M., Fuccello, A., Onori, G., and Santucci, A., *Prog. Colloid Polym. Sci.*, 1993, vol. 93, pp. 350–352.
9. D'Angelo, M., Onori, G., and Santucci, A., *J. Phys. Chem.*, 1994, vol. 98, pp. 3189–3193.
10. Jain, T.K., Varshey, M., and Maitra, A., *J. Phys. Chem.*, 1989, vol. 93, pp. 7409–7416.
11. Li, Q., Weng, Sh., Wu, J., and Zhou, N., *J. Phys. Chem., Ser. B*, 1998, vol. 102, pp. 3168–3174.
12. Novaki, L.P., Pires, P.A.R., and El Seoud, O.A., *Colloid Polym. Sci.*, 2000, vol. 278, no. 2, pp. 143–149.
13. Onori, G. and Santucci, A., *J. Phys. Chem.*, 1993, vol. 97, pp. 5430–5434.
14. Tassaing, T., *Vibr. Spectroscopy*, 2000, vol. 24, pp. 15–28.
15. Zeng, H.-X. and Li, Zhi-P., *J. Dispers. Sci. Tech.*, 1999, vol. 20, no. 6, pp. 1595–1607.
16. Zoidis, E., Yarwood, J., Tassaing, T., *et al.*, *J. Mol. Liq.*, 1995, vol. 64, pp. 197–220.
17. *Asphaltenes (n-Heptane Insolubles) in Petroleum Products: Standards for Petroleum and Its Products, Standard no. IP 143/90, Inst. of Petroleum*, London (UK), 143.1–143.7, 1985.
18. Sorensen, J.M. and Arlt, W., *Liquid-Liquid Equilibrium Data Collection*, DECHEMA Data Ser., 1979, vol. 5, part 1, p. 448.
19. Groenzin, H. and Mullins, O.C., *Energy Fuels*, 2000, vol. 14, pp. 677–684.
20. Sheu, E.Y., *Energy Fuels*, 2002, vol. 16, pp. 74–82.
21. Rusanov, A.I., *Mitselloobrazovanie v rastvorakh poverkhnostno-aktivnykh veshchestv* (Micelle Formation in Surfactant Solutions), St. Petersburg: Khimiya, 1992.
22. Prausnitz, J.M., Lichtenthaler, R.N., and Gomez de Azevedo, E., *Molecular Thermodynamics of Fluid-Phase Equilibria*, Englewood Cliffs: Prentice-Hall, 1986.
23. Mannistu, K.D., Yarranton, H.W., and Masliyah, J.H., *Energy Fuels*, 1997, vol. 11, pp. 615–622.
24. Smirnova, N.A., *Molekulyarnye teorii rastvorov* (Molecular Theories of Solutions), Leningrad: Khimiya, 1987.
25. Barton, A.M.F., *CRC Handbook of Solubility Parameters and Other Cohesion Parameters*, Boca Raton: CRC, 1983.
26. Wang, J.X. and Buckley, J.S., *Energy Fuels*, 2001, vol. 15, pp. 1004–1012.

Russian Journal of Applied Chemistry, Vol. 77, No. 6, 2004, pp. 1019–1021. Translated from Zhurnal Prikladnoi Khimii, Vol. 77, No. 6, 2004, pp. 1033–1035.

BRIEF COMMUNICATIONS

On the Possibility of Using Lithium-doped Copper Oxide in Lithium Cells

S. P. Kuksenko

Vernadskii Institute of General and Inorganic Chemistry, Ukrainian National Academy of Sciences, Kiev, Ukraine

Received January 28, 2004

Abstract—Lithium cells with cathodes based on lithium-doped copper oxide were studied.

Lithium cells with solid cathodes based on MnO_2, $(CF)_n$, FeS_2, and CuO are manufactured industrially [1]. Copper oxide–lithium cells (COL) are of special interest because of their being interchangeable with silver- and mercury-zinc cells as regards the working voltage and its stability. Copper oxide has the highest specific capacity of 4.26 A h cm^{-3}, which considerably exceeds that of MnO_2 (1.55 A h cm^{-3}). As the electrical conductivity of copper oxide is low (1×10^{-6} Ω^{-1} cm^{-1} [2]), we can assume that, after it is made higher, the capacity of COL cells can be increased, with the required pulsed power preserved, by lowering the content of electrically conducting additives and binder in the positive electrode. It has been reported previously that the electrical conductivity of copper oxide increases on introducing various metal ions (lithium, potassium, aluminum [2], and iron [3]) in its structure. The electrical conductivity of copper oxide increases to the greatest extent, to $(1–2) \times 10^{-1}$ Ω^{-1} cm^{-1}, upon doping with lithium [2]. In fabricating electrodes based on iron-doped copper oxide, it is necessary to introduce 3 wt % graphite and 2 wt % polytetrafluoroethylene as a binder [3].

It is known that, in the discharge of COL cells, lithium cations penetrate into appropriate interatomic spaces in the monoclinic lattice of copper oxide to give $Cu^{II}_{1-x}Cu^{I}_{x}Li_xO$ [4]. Moreover, it was demonstrated in [5] that copper oxide electrodes can be subjected to repeated reduction-oxidation without loss of capacity. Hence, a question arises as to what is the nature of lithium-doped copper oxide.

In the present study, we examined ^{7}Li NMR spectra of lithium-doped copper oxide and the discharge characteristics of lithium cells with cathodes based on this material. The study was carried out at varied content of the electrically conducting additive under continuous and pulsed loads in comparison with undoped copper oxide.

EXPERIMENTAL

Lithium-doped copper oxide was obtained as follows: (1) spherical copper particles were oxidized in pure oxygen at 1000°C, the resulting CuO was mixed with Li_2CO_3 in the ratio 100 : 1 [mol %] and annealed in air at 800°C for 8 h; (2) Cu_2O was mixed with Li_2CO_3 in the ratio 100 : 2 [mol %] and annealed under the same conditions. Copper oxide obtained by oxidation of spherical copper particles in pure oxygen at 1000°C with an additional thermal treatment in air at 800°C for 8 h was used as reference.

The completeness of conversion of the starting substances was verified by X-ray diffraction analysis on a DRON-2 X-ray installation with monochromatic Cu_{K_α} radiation. The ^{7}Li NMR spectra were recorded on a CXP-200 Brucker spectrometer in the single-pulse accumulation mode at a frequency of 77.78 MHz. To measure the electrical conductivity of lithium-doped copper oxide, the samples were compacted into pellets and a silver layer was deposited on both sides of a pellet in a vacuum. The conductivity was measured using an R5021 ac bridge.

In fabricating copper oxide electrodes, the copper oxide samples under study were mixed with graphite powder of C1 brand in various ratios and compacted into pellets under a pressure of 2300 kg cm^{-2}.

The thickness of the electrode pellets was selected so that the lithium cells produced remained within the allowed overall dimensions in the course of discharge. The pellets were placed in an evacuated cell, which was kept at 300°C for 1 h and then filled with

1070-4272/04/7706-1019 © 2004 MAIK "Nauka/Interperiodica"

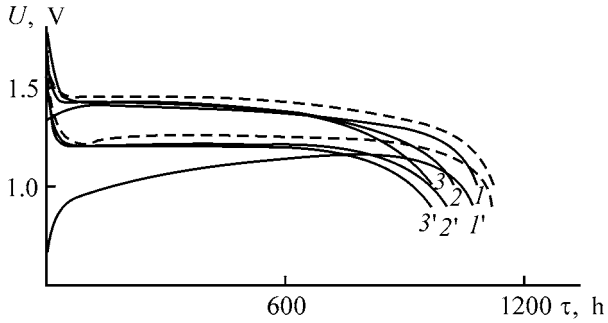

(*1*–*3*) Discharge curves of lithium cells with a cathode based on lithium-doped copper oxide with varied content of graphite and (*1*'–*3*') dependences of the voltage *U* of these cells by the end of a pulsed load on the duration τ of the continuos discharge. Cell dimension index 921, constant load 30 kΩ, pulsed load 1 kΩ s. Content of graphite (wt %): (*1*, *1*') 0, (*2*, *2*') 3, and (*3*, *3*') 5. *Dashed lines*: discharge curve of a cell with a cathode based on undoped copper oxide containing 3 wt % graphite (top); dependence of the voltage of this cell by the end of a pulsed load on the duration of continuos discharge (bottom).

dry argon. Disc-shaped anodes were fabricated from rolled lithium, and a Li–Zn–Al alloy was formed on their surface facing the cathode. A $LiClO_4$ 1.4 M solution in a PC (propylene carbonate) : DME = 42 : 58 mixture (by weight) containing less than 30 ppm of water was used as the electrolyte. The electrolyte was additionally dried with a lithium-enriched Li–Al alloy and blown through with dry argon. The cells were assembled in a glove box filled with dry argon. The cells with diameter of 9.5 mm and height of 2.10 mm were used in the measurements. Discharge curves were measured after 1 month of technological storage of the cells. A continuous load of 30 kΩ and a parallel pulsed load of 1 kΩ (1 s once in 24 h) were used to discharge the cells.

The electrical conductivities of the samples of lithium-doped copper oxide obtained by both techniques were the same and equal to $(5–6) \times 10^{-1}$ Ω^{-1} cm^{-1}. The X-ray diffraction patterns of doped and undoped copper oxide were almost identical. However, on raising the $CuO : Li_2CO_3$ ratio to 100 : 5 (wt %) in the first mixture, Li_2O peaks were observed in the X-ray diffraction pattern, which indicates that lithium is introduced into the structure of copper oxide by this technique in a very limited amount. The ^7Li NMR spectra appeared to be more informative in studying the nature of lithium-doped copper oxide. Since the ^7Li nucleus has a quadrupole moment *eQ* in addition to the magnetic moment, the ^7Li NMR line is split into a triplet if ^7Li nuclei experience an electric field with a symmetry lower than cubic. The triplet consists of a central line and two satellites with the intensity ratio of 3 : 4 : 3. The value of the quadrupole splitting is proportional to the electric field gradient (EFG) created by the nearest environment, i.e., the greater the distortion of the environment, the stronger the splitting. We determined the quadrupole coupling constant e^2qQ/h (*eq* is EFG; *eQ*, the quadrupole moment; and *h*, the Plank constant) from the splitting of the ^7Li NMR line of lithium-doped copper oxide samples. This constant was found to be 0.36 MHz, which is rather high for the ^7Li nuclei and points to a significant electric field gradient at the lithium site. A ^7Li atom at the copper site in the CuO lattice can have such a constant, and this may be responsible for the stability of lithium-doped copper oxide samples under common atmospheric conditions.

The discharge curves measured under continuos load and the dependences of the pulse voltage on the duration of continuos discharge of COL cells with cathodes based on lithium-doped copper oxide produced by technique 1 and with cathodes based on undoped copper oxide containing 3 wt % graphite are shown in the figure. Discharge curve *1* shows a dip in the cell voltage after connecting a continuos load and the following stabilization of this voltage. Curve *1*' exhibits a pronounced dip in the pulsed voltage at the beginning of discharge and a slow stabilization of the voltage after approximately 3/4 of the total discharge duration. It is likely that, in the absence of an electrically conducting additive, the reduction of the electrode at places of contact with the current lead begins directly in the stage of formation of metallic copper. The capacity of this cell in discharge to a final voltage of 1.2 V was 45 mA h. As can be seen in the figure (curves *2* and *2*'), introduction of 3 wt % graphite into the cathode results in a stabilization of both the discharge curve measured under a constant load and the curve describing how pulsed voltage varies in the course of the continuos discharge. However, the cell capacity decreased to 43 mA h. Curves *2* and *2*' also reflect the behavior of the cell with doped copper oxide produced by technique 2, mixed with 3 wt % graphite. Consequently, the nature of the starting copper oxide doped with lithium does not affect the discharge parameters of COL cells. Raising the content of graphite in the cathode from 3 to 5 wt % did not affect the run of the curves and the stability of the cell voltage under the continuos and pulsed loads (figure, curves *3* and *3*'), and only resulted in a decrease in the cell capacity to 39 mA h.

Under the same testing conditions, a cell with a mixture of undoped copper oxide and 3 wt % graphite had a higher average values of the voltage under a constant load and of the pulsed voltage, and also

a higher capacity of 50 mA h in discharge to 1.2 V. A small dip in the pulsed voltage in the initial stage of the continuous discharge, which is characteristic of the cell with undoped copper oxide, was absent in the case of the cell with doped copper oxide. This may be due to changes in the state of the surface of copper oxide particles upon doping.

CONCLUSIONS

(1) High-temperature doping of copper oxide with lithium increases its electrical conductivity to (5–6) × 10^{-1} Ω^{-1} cm^{-1}. In this case, lithium occupies copper sites in the CuO structure.

(2) In fabricating electrodes based on lithium-doped copper oxide, 3 wt % graphite without a binder is required to ensure stable voltages under continuous and pulsed loads.

(3) Discharge parameters of cells with lithium-doped copper oxide are independent of the prehistory of copper oxide. The doping makes lower the cell capacity, but eliminates the dip in the pulsed voltage in the initial stage of discharge under a continuous load.

REFERENCES

1. Skundin, A.M. and Nizhnikovskii, E.A., *Elektron. Komponenty*, 2001, no. 4, pp. 27–31.
2. Iijima, T., Toyoguchi, Y., Nishimura, J., and Ogawa, H., *J. Power Sources*, 1980, vol. 5, pp. 99–109.
3. Chmilenko, N.A., Prisyazhny, V.D., Tkalenko, D.A., *et al.*, *Materialy IV Mezhdunarodnoi Konferentsii "Fundamental'nye problemy elektrokhimicheskoi energetiki"* (Proc. IV Int. Conf. "Fundamental Problems of Electrochemical Power Engineering"), Saratov, 1999, pp. 136–138.
4. Novak, P. and Podhajecky, P., *J. Power Sources*, 1991, vol. 35, pp. 235–247.
5. Grugeon, S., Laruelle, S., Herrera-Urbina, R., *et al.*, *J. Electrochem. Soc.*, 2001, vol. 148, no. 4, pp. A285–A292.

Russian Journal of Applied Chemistry, Vol. 77, No. 6, 2004, pp. 1022–1024. Translated from Zhurnal Prikladnoi Khimii, Vol. 77, No. 6, 2004, pp. 1036–1037.

BRIEF COMMUNICATIONS

Behavior of Antimony in Desulfation of the Active Paste from Lead Battery Scrap with the Use of Potassium Carbonate or Hydroxide

A. G. Morachevskii, O. A. Kal'ko, and Yu. S. Kuznetsova

St. Petersburg State Polytechnical University, St. Petersburg, Russia

Cherepovets State University, Cherepovets, Russia

Received May 11, 2004

Abstract—The results obtained in a study of the behavior of antimony in desulfation of the active paste from lead battery scrap with the use of potassium carbonate or hydroxide are discussed.

At present, the lead battery scrap is the main type of secondary lead raw materials. Thus far, there have been no serious alternative to application of lead batteries in vehicles, whose number, and in particular that in our country, steadily grows. Now, the world's annual production of lead exceeds six million tons, with secondary lead constituting 55 to 60% of the total amount of the metal smelted.

The most efficient way to utilize worked-out batteries (battery scrap) is to crop them, with the metal (plate grids and connectors), sulfate-oxide (active paste of positive and negative plates), and organic (cases and separators) fractions recovered. The sulfate-oxide fraction is the most difficult for further processing. According to an X-ray diffraction analysis, its main components are $PbSO_4$ (anglesite) and lead oxide PbO_2 (plattnerite, tetragonal modification), which are present in comparable amounts [1]. Antimony and its compounds are the main impurities in the active paste. Antimony is introduced into plate grids of lead batteries to increase their mechanical strength. During operation of batteries, antimony tends to dissolve preferentially from positive plates via corrosion electrochemical processes [2–5]. The following reaction can occur on the positive electrodes

$$5PbO_2 + 2Sb + 5H_2SO_4 + 2H^+ \rightarrow 2SbO_2^+ + 5PbSO_4 + 6H_2O.$$

The most probable process on the negative electrodes is

$$2Sb + 2H^+ + H_2O \rightarrow 2SbO_2^+ + 5H_2.$$

Dissolved antimony is strongly adsorbed by lead dioxide, and only to a minor degree, by lead sulfate [5]. The total content of antimony in the sulfate-oxide fraction, which includes the active pastes of positive and negative plates, may be as high as 1.2–1.4 wt %.

The high content of lead sulfate in the components of the sulfate-oxide fraction makes difficult their direct reduction by carbon, requires rather high temperatures (up to 1000°C), and makes it necessary to catch the evolving sulfur dioxide. To utilize sulfur, the reduction stage is to be preceded by desulfation (desulfuration), which is based on the reaction of lead(II) sulfate with sodium or potassium carbonate or hydroxide [6–8]. The physicochemical and technological characteristics of desulfation with sodium carbonate have been studied in most detail [9, 10]. As demonstrated by X-ray diffraction analysis, the main components of the desulfated paste are cerussite $PbCO_3$, plattnerite PbO_2, and a minor amount of hydrocerussite $Pb_3(CO_3)_2(OH)_2$ [7]. Compounds with a more complex composition, such as $NaPb_2(CO_3)_2OH$ [8], may also be formed. Cerussite, plattnerite, and a minor amount of hydrocerussite are also main components in the case of desulfation with potassium carbonate [1].

An important issue is the extent to which the admixture of antimony in the active paste passes into the aqueous phase in the course of desulfation, because the resulting sodium and potassium sulfates are marketable products, and their purity is essential. It has been shown previously that a minor part of antimony contained in the sulfate-oxide fraction passes

1070-4272/04/7706-1022 © 2004 MAIK "Nauka/Interperiodica"

into the aqueous phase in desulfation with sodium carbonate [11, 12]. Under the common conditions of desulfation (50°C, 20% excess of Na_2CO_3 relative to the amount required for the complete conversion of $PbSO_4$ to $PbCO_3$), up to 1.7% of antimony contained in the paste to be desulfated passes into solution. When the content of lead sulfate in the starting solid phase is raised and temperature is elevated, up to 6% of antimony contained in the material being desulfated passes into the aqueous phase. In the case of desulfation with sodium hydroxide solutions, no antimony was found in the aqueous phase within the limits of experimental accuracy [13]. The detection limit of the method was 0.005 mg of Sb in 10 ml of a solution. An atomic-absorption analysis of anhydrous sodium sulfate obtained from the aqueous phase after desulfation with sodium hydroxide demonstrated that the content of antimony is less than 1×10^{-4}%.

The behavior of antimony in desulfation with potassium carbonate or hydroxide was studied at 50°C in the course of 45 min, with the solid-to-liquid ratio (s : l) varied from 1 : 4 to 1 : 5. The excess of the desulfating reagent was 20%. It has been shown previously that the desulfation proceeds rather effectively under these conditions, with the degree of extraction of sulfate ions from the active paste as high as 99.5%, on the average [1].

The photocolorimetric method with Violet Crystalline reagent, which forms an insoluble salt with antimony(V) if antimony is present in solution as $SbCl_6^-$ anions, was used to determine the content of antimony [12]. The compound formed by antimony(V) with Violet Crystalline is easily extracted with toluene; in this case, the organic layer is colored dark blue with a lilac tint, and the intensity of this color is used to determine the amount of antimony. The choice of techniques for monitoring the content of antimony in the products formed in processing of secondary lead raw materials was considered in detail in [12, 14], with a metrological comparison of the existing methods carried out.

According to a weight analysis, the starting sulfate-oxide fraction contained 45.0 wt % $PbSO_4$ (14.3% SO_4^{2-}), and the results of its X-ray analysis were reported earlier in [1]. The content of antimony was 1.17%, the average and maximum grain size of the material was 0.17 and 0.40 mm, respectively. In each experiment, 50 g of the active paste was desulfated.

In the case of desulfation with potassium carbonate at s : l = 1 : 4, the concentration of antimony in the aqueous phase was 0.050–0.065 g dm^{-3} in six parallel experiments; at s : l = 1 : 5, the content of antimony in the filtrate was 0.039–0.045 g dm^{-3}. The amount of antimony passing into solution was 1.6 to 2.1% (relative to its total amount contained in the material being desulfated) in the first case, and 1.6 to 1.8% in the second case.

In the case of desulfation with potassium hydroxide under the same conditions, the content of antimony in the aqueous phase did not exceed 5×10^{-4} g dm^{-3}.

Thus, the amount of antimony passing into the aqueous phase in desulfation of the active paste with sodium or potassium carbonate remains at the same level. In desulfation with sodium and potassium hydroxides, antimony virtually does not pass into the aqueous phase. These circumstances should be taken into account when selecting a desulfating reagent and developing a technology for production of sodium or potassium sulfate of a required purity.

CONCLUSION

When the active paste from lead battery scrap is desulfated with potassium carbonate, up to 2% of antimony contained in the solid phase passes into solution, whereas in the case of desulfation with potassium hydroxide, antimony virtually does not pass into solution.

ACKNOWLEDGMENTS

This study was financially supported by the foundation “Basic Research in Chemical Technologies” of the Ministry of Education of the Russian Federation, grant no. T02-9.4-3298.

REFERENCES

1. Morachevskii, A.G., Bochagina, E.V., and Habachev, M.N., *Zh. Prikl. Khim.*, 2003, vol. 76, no. 10, pp. 1748–1750.
2. Herrmann, W. and Props, G., *Z. Elektrochem.*, 1957, vol. 61, no. 9, pp. 1154–1158.
3. Jenkins, A.A. and Maskell, W.C., *J. Power Sources*, 1985, vol. 16, no. 3, pp. 171–178.
4. Jenkins, A.A., Maskell, W.C., and Tye F.L., *J. Appl. Electrochem.*, 1986, vol. 16, pp. 879–884.
5. Jenkins, A.A., Maskell, W.C., and Tye, F.L., *J. Power Sources*, 1987, vol. 19, no. 1, pp. 75–80.
6. Morachevskii, A.G., Vaisgant, Z.I., and Korelyakov, A.V., *Zh. Prikl. Khim.*, 2000, vol. 73, no. 7, pp. 1125–1130.
7. Morachevskii, A.G., Vaisgant, Z.I., Rusin, A.I., and

Habachev, M.N., *Zh. Prikl. Khim.*, 2001, vol. 74, no. 7, pp. 1075–1077.

8. Morachevskii, A.G., Vaisgant, Z.I., Bochagina, E.V., and Habachev, M.I., *Tsvet. Metal.*, 2002, no. 8, pp. 34–37.
9. Morachevskii, A.G., *Zh. Prikl. Khim.*, 1998, vol. 71, no. 6, pp. 881–890.
10. Morachevskii, A.G., *Pererabotka vtorichnogo svintsovogo syr'ya: Sovremennoe sostoyanie issledovanii i annotirovannyi ukazatel' literatyry za 1997–2001 g.* (Processing of Secondary Lead Raw Materials: Current State of Research and the Annotated Bibliographic Index for 1997–2001), St. Petersburg: SPb Gos. Univ., 2003.
11. Morachevskii, A.G., Kal'ko, O.A., and Vaisgant, Z.I., *Zh. Prikl. Khim.*, 1995, vol. 68, no. 1, pp. 127–128.
12. Kal'ko, O.A., Behaviour of Antimony in Processing of the Active Paste from Lead Battery Scrap, *Cand. Sci. (Chem.) Dissertation*, St. Petersburg, 1996.
13. Morachevskii, A.G., Vaisgant, Z.I., Kal'ko, O.A., *et al.*, *Zh. Prikl. Khim.*, 1997, vol. 70, no. 1, pp. 167–168.
14. Kal'ko'O.A. and Nadezhdina, L.S., *Zh. Prikl. Khim.*, 1994, vol. 67, no. 7, pp. 1104–1106.

Russian Journal of Applied Chemistry, Vol. 77, No. 6, 2004, pp. 1025–1027. Translated from Zhurnal Prikladnoi Khimii, Vol. 77, No. 6, 2004, pp. 1038–1040.

BRIEF COMMUNICATIONS

Fusibility Diagram of Cyclohexane–Tetradecane–Docosane Ternary System

I. P. Kalinina, A. Yu. Kopnina, and I. K. Garkushin

Samara State Technical University, Samara, Russia

Received July 23, 2003; in the final form, April 2004

Abstract—The fusibility diagram of the cyclohexane–tetradecane–docosane ternary system was obtained by low-temperature differential thermal analysis.

The functioning of heat exchangers is based on heat accumulation by working fluids due to their heat capacity [1–3]. The working fluids in these devices should ensure efficient heat accumulation and meet some other requirements, in particular, they should have low crystallization temperature [4].

Among organic substances meeting these requirements are *n*-alkanes, cyclic and aromatic hydrocarbons, and their mixtures [5].

It has also been found that cyclohexane [6], tetradecane [7], and their mixtures [8] are promising heat accumulators and heat-carriers.

In this study we obtained the melting diagram of the cyclohexane–tetradecane–docosane ternary system.

In our experiments, the heating and cooling curves of organic mixtures were obtained on a low-temperature differential thermal analyzer (LDTA) equipped with a Chromel–Copel thermocouple and a TZ 4620 flatbed *XY* recorder. One of the thermocouple junctions was immersed in an organic mixture being tested and the other was placed in a test tube filled with calcined aluminum oxide powder as reference. The cold thermocouple junction was placed in a Dewar flask filled with water–ice mixture at 0°C. The thermal electromotive force was amplified with a F116/1 photoamplifier. The sensitivity of recording of the thermo-emf was controlled with an MCP-33 resistance box. The baseline was controlled with an IRN-64 voltage source. The temperature was determined with an accuracy of ±0.2°C. In studies of phase transitions, the organic mixtures were cooled and heated in a TK-1 thermal chamber within the temperature range from –40 to +60°C at a temperature variation rate of 1–2 deg min^{-1}. The starting components were weighed on a VLR-200 analytical balance with an accuracy of up to 0.3 mg.

Cyclohexane, tetradecane, and docosane used in our experiments were of pure grade. Their characteristics coincided with reference data [9, 10]. The purity of these reagents was checked by gas–liquid chromatography (a Tsvet-00 gas chromatograph; 50 m × 0.25 mm and 25 m × 0.25 mm capillary columns, vaporizer temperature 350°C; tetradecane and dodecane were injected as toluene solutions).

The fusibility diagram of cyclohexane-tetradecane binary system has an eutectic point (cyclohexane

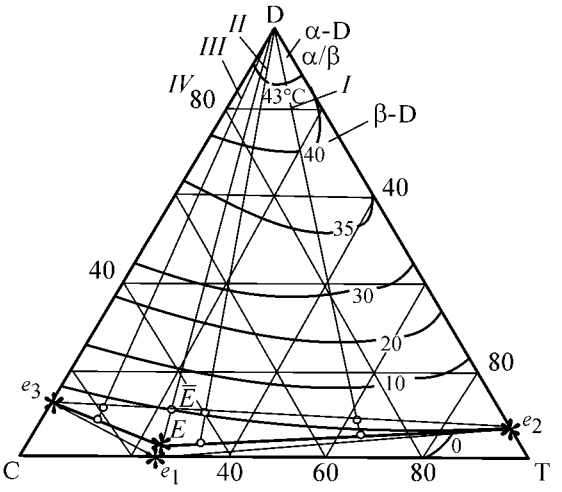

Fig. 1. Phase diagram of the cyclohexane–tetradecane–docosane system with projection of crystallization isotherms. (e_1, e_2, e_3) Binary eutectic mixtures and (E) ternary eutectic mixture. Sections: (*I*) Docosane–(cyclohexane 33.7%, tetradecane 66.3%); (*II*) Docosane–(cyclohexane 54.1%, tetradecane 45.9%); (*III*) Docosane–(cyclohexane 87.9%, tetradecane 12.1%); and (*IV*) Docosane–$\bar{E}\rightarrow E$ eutectic section.

1070-4272/04/7706-1025 © 2004 MAIK "Nauka/Interperiodica"

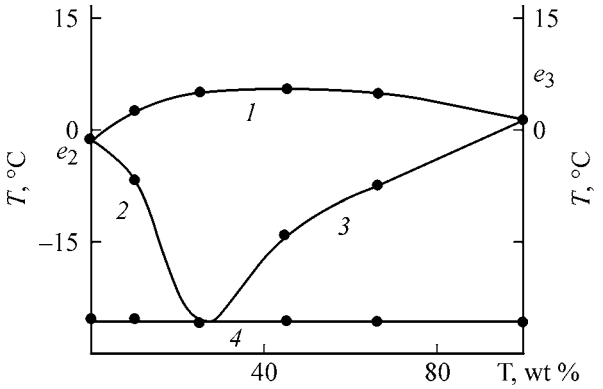

Fig. 2. Fields of joint crystallization of different phases in the cyclohexane–tetradecane–docosane system along the e_2–e_3 section in the plot of the tetradecane content against the crystallization temperature *T*. Crystallizing phases: (*1*) docosane, (*2*) cyclohexane, (*3*) tetradecane + docosane, and (*4*) cyclohexane + tetradecane + docosane.

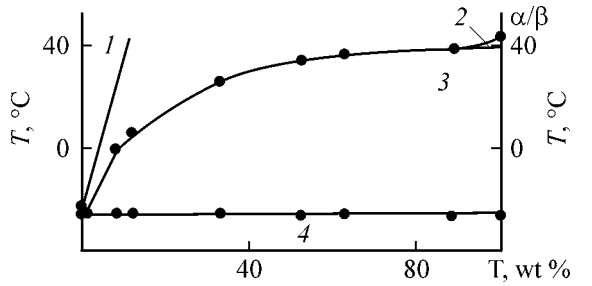

Fig. 3. Fields of joint crystallization of different phases in the cyclohexane–tetradecane–docosane system along the docosane–$E\rightarrow\bar{E}$ section in the plot of the docosane content against the crystallization temperature *T*. Crystallizing phases: (*1*) cyclohexane + tetradecane, (*2*) α-docosane, (*3*) β-docosane, and (*4*) cyclohexane + tetradecane + docosane.

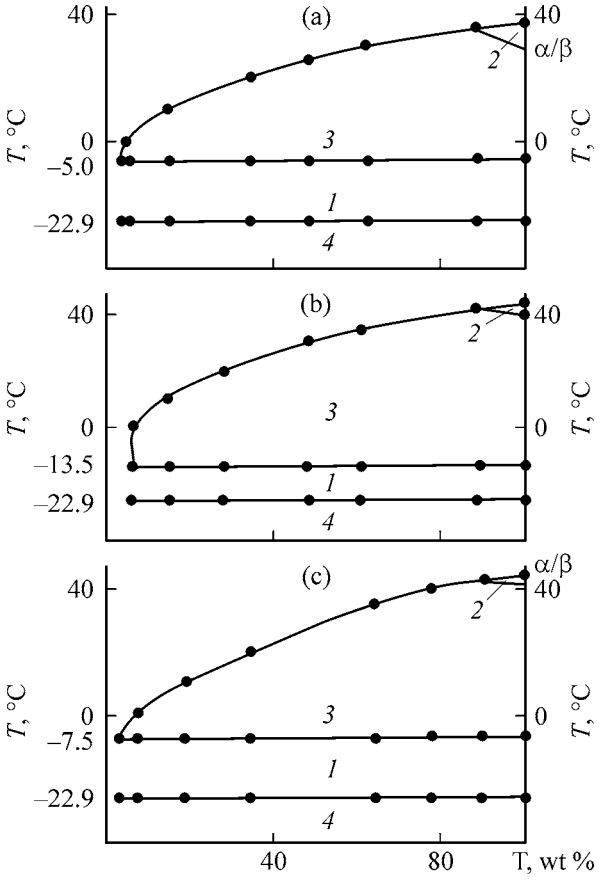

Fig. 4. Fields of joint crystallization of different phases in the cyclohexane–tetradecane–docosane system along sections (a) *I*, (b) *II* and (c) *III* in the plots of the crystallization temperature *T* against the docosane content. Crystallizing phases: (*1*) cyclohexane + tetradecane, (*2*) α-docosane, (*3*) β-docosane, and (*4*) cyclohexane + tetradecane + docosane.

75.03 wt %, tetradecane 24.97 wt %; melting point –22.5°C [7]).

The cyclohexane–docosane and tetradecane–docosane binary systems also form eutctic mixtures. In the cyclohexane–docosane system, the eutectic mixture contains 94.3% cyclohexane and 5.7% docosane (melting point is –4.6°C). The fusibility diagram of this binary system shows polymorphic transition (docosane content 95.2 wt %, mp 43°C) [8].

In the tetradecane–docosane system the eutectic mixture contains 2.3% docosane, mp 4.0°C. In this system, docosane also shows polymorphic transition (docosane content 97.0 wt %, mp 43°C) [11].

Figure 1 shows the phase diagram of the cyclohexane–tetradecane–docosane ternary system constructed as a series of projections on the diagram plane of the crystallization isotherms including the melting points of the corresponding binary systems. The cyclohexane : tetradecane ratio in the ternary eutectic mixture *E* and its melting point (–25.9°C) were determined from the polythermal section e_2–$\bar{E}$–e_3 passing through the field of docosane crystallization (Fig. 2).

The composition of the ternary eutectic was determined from the docosane–$\bar{E}\rightarrow E$ section (Fig. 1). This eutectic mixture contains (wt %) cyclohexane 74.9, tetradecane 24.1, and docosane 1.0 (Fig. 3).

The crystallization temperatures were determined for mixtures belonging to following sections: (*I*) docosane–(cyclohexane 33.7%, tetradecane 66.3%); (*II*) docosane–(cyclohexane 54.1%, tetradecane 45.9%), and (*III*) docosane–(cyclohexane 87.9%, tetradecane 12.1%) (Figs. 4a–4c).

Based on the whole set of the data obtained in our experiments, the series of crystallization isotherms

were constructed in the range 0–40°C and projected on the plane of the fusibility diagram plane. The crystallization isotherm at 43°C divides the triangle into the crystallization field of docosane α-modification, adjacent to the docosane triangle apex, and the field of docosane β-modification. The polythermal section shows that the field of docosane crystallization predominates.

The ternary system under consideration includes the following phase equilibria (see table).

Based on our experimental and calculated data, the specific enthalpy of melting of the ternary eutectic was calculated by the additive equation

$$\Delta H_{me} = x_1 \Delta H_{m1} + x_2 \Delta H_{m2} + x_3 \Delta H_{m3}, \quad (1)$$

where x_1, x_2 and x_3 are the contents of the individual components in the ternary eutectic (wt %).

We found that the specific melting enthalpy of the ternary eutectic is 146 J g^{-1}.

The experimental enthalpy of melting of the ternary eutectic mixture was determined by the equation

$$\Delta H_{me} = \frac{\Delta H_{m1} T_e S m_1}{T_{m1} S_1 m}, \quad (2)$$

where ΔH_{m1} is the specific entalphy of melting of a reference substance (undecane) (J g^{-1}) whose melting point is close to that of the ternary eutectic; T_{m1} is the melting point (K) of the reference substance; S_1 and S are half-areas (mm^2) of the peaks in cooling curve related to a reference substance and the ternary eutectic, respectively; m_1 and m are the weights (g) of the reference substance and the eutectic, respectively; and T_e is the ternary eutectic melting point (K).

The specific enthalpy of melting of the ternary eutectic was found to be 91 J g^{-1}.

CONCLUSION

The cyclohexane–tetradecane–docosane ternary system belongs to an eutectic type (mp –25.9°C, specific melting enthalpy 91 J g^{-1}). The ternary mixtures under consideration can be used as heat-accumulators and thermal-carriers.

Phase equilibria in the cyclohexane (C)–tetradecane (T)–docosane (D) system

Phase diagram elements	Equilibrium
Eutectic *E*, mp = –25.9°C	Nonvariant liq $\rightleftarrows$ solid (C + T + D)
	Monovariant:
e_1E	liq $\rightleftarrows$ solid (C + D)
e_2E	liq $\rightleftarrows$ solid (T + D)
e_3E	liq $\rightleftarrows$ solid (C + T)

REFERENCE

1. Levitskij, E.A., Aristov, Yu.I., Tokarev, M.M., and Parmon, V.N., *Solar Energ. Mater. Solar Cells*, 1996, vol. 44, no. 3, pp. 219–235.
2. Danilin, V.N. and Shabalina, S.G., *Izv. Vyssh. Uchebn. Zaved., Pishch. Tekhnol.*, 1996, nos. 1–2, pp. 47–48.
3. Danilin, V.N., *Tekhnol., Ser.: "Konstr. Kompozits. Mater.,"* 1995, nos. 3–4, pp. 3–6.
4. Saborio Savador Aceres, Nakamura Hajime, and Reistand Goldon, *J. Chem. Eng. Jpn.*, 1994, vol. 27, no. 6, pp. 779–784.
5. Danilin, V.N., Dotsenko, S.P., Borovskaya, L.V., *et al., Tekhnol. Ser.: "Konstr. Kompozits. Mater.,"* 1995, nos. 3–4, pp. 16–20.
6. Kopnina, A.Yu., Agafonov, I.A., Garkushin, I.K., and Nazmutdinov, A.G., *Zh. Obshch. Khim.*, 2001, vol. 71, no. 11, pp. 1921–1922.
7. Kopnina, A.Yu., Agafonov, I.A., Garkushin, I.K., and Miftakhov, T.T., in *Trudy respublikanskoi nauchno-tekhnicheskoi konferentsii molodykh uchenykh "Khimicheskie nauki. Khimicheskie tekhnologii"* (Proc. Republican Scientific and Technical Conf. of Young Scientists "Chemical Sciences. Chemical Technologies"), Samara, 1999, p. 14.
8. Kopnina, A.Yu., Agafonov, and I.A., Garkushin, I.K., *Izv. Vyssh. Uchebn. Zaved., Khim. Khim. Tekhnol.*, 2001, vol. 44, no. 5, pp. 84–85.
9. Tatevskii, V. M., *Fiziko-khimicheskie svoistva individual'nykh uglevodorodov* (Physicochemical Properties of Individual Hydrocarbons), Moscow; Gostoptekhizdat, 1959.
10. *Svoistva organicheskikh soedinenii: Spravochnik* (Properties of Organic Compounds: Handbook), Potekhin, A.A., Ed., Leningrad: Khimiya, 1984.
11. Agafonov, I.A., Garkushin, I.K., and Miftakhov, T.T., *Fazovye ravnovesiya v dvukhkomponentnykh sistemakh iz n-alkanov* (Phase Equilibria of *n*-Alkane Binary Systems), Samara: Samar. Gos. Tekh. Univ., 1997.

Russian Journal of Applied Chemistry, Vol. 77, No. 6, 2004, pp. 1028–1030. Translated from Zhurnal Prikladnoi Khimii, Vol. 77, No. 6, 2004, pp. 1041–1043.

BRIEF COMMUNICATIONS

Influence of Filler on Elastic-Relaxation Properties of Vulcanized Rubbers Based on Binary Blends of Diene Rubbers

N. I. Kurbanova

Institute of Polymeric Materials, Azerbaijan National Academy of Sciences, Sumgait, Azerbaijan

Received February 10, 2004

Abstract—The strength and elastic-relaxation properties of vulcanized rubbers based on binary blends of diene rubbers were studied as influenced by a filler, carbon black no. 330.

The progress achieved in the development of polymer-based multicomponent systems offers virtually unlimited scope for this line of modification of polymeric materials to impart to them the desired properties [1–3]. The conditions of preparation and processing of blends, as well as introduction of various additives, also significantly affect the structure and properties of the resulting materials [4–6]. Polymer blends and materials thereof hold much promise and can find other applications than their constituent polymers [7, 8].

Most of commercial rubber stocks are composed of an elastomer, a vulcanizing system, and a filler. Fillers favorably affect the process and physicomechanical characteristics, as well as the cost, of the compositions, which makes their use essential for polymeric materials [2, 5].

In this study, we analyzed how a filler modifies the properties of binary blends of divinyl (SKD) and styrene-butadiene (SKS) rubbers with polyisoprene (SKI).

We used Carifleks IR 309 (Shell) polyisoprene, cis-132 (96% cis) SKD, SKS incorporating 23% SRB-1500 styrene (BSL Olefinverbund GmbH Schkopau), and carbon black no. 330.

The component ratio (mass fraction) in the compositions was as follows: SKD(SKS) : SKI : carbon black = 50 : 50 : 50; vulcanizing system (mass fraction): sulfur 2.0, stearic acid 2.0, ZnO 3.0, thiuram 0.65, Altax 1.0, Captax 1.25 for SKD/SKI blend and sulfur 2.0, stearic acid 2.0, ZnO 5.0, Altax 2.75 for SKS/SKI blend.

The initial components were mixed in a Banbury mixer for 6 min in the case of unfilled systems, and for 7, 10, and 15 min, in the case of filled compositions.

The time, s, of introduction of the components into the mixer was as follows: SKD (SKS) 0, SKI 60, carbon black 90 (in three portions), sulfur + stearic acid + ZnO + accelerators 180.

The mixing mode was as follows: T_{in} = 50, T_{fin} = 60–65°C; n = 60 rpm. The vulcanization conditions and modes were specific to each composition.

We studied the physicomechanical properties of filled and unfilled vulcanizates of the prepared compositions under quasistatic and dynamic loading conditions.

The dynamic mechanical properties of the compositions were studied on a low-frequency (ν = 1 Hz) installation in the sinusoidal oscillation mode at temperatures from –120 to 70°C, and quasistatic properties, at room temperature at a strain rate of 200 mm min^{-1}.

Table lists the formulations and properties of the diene rubber-based binary blends (average of five measurements).

The most important and widely used filler for vulcanized rubbers is carbon black. Active fillers tend to increase the modulus of elasticity, tensile strength, tear resistance, and wear resistance of vulcanized rubbers.

Carbon blacks used for rubber filling contain appreciable amounts of chemically bound hydrogen (0.1–4%), oxygen (0.2–1%), and sometimes sulfur (up to 1%). Carbon black no. 330 or HAF used by us has a relative strengthening power of 100 at the specific surface area of 80 $m^2 g^{-1}$ [5].

1070-4272/04/7706-1028 © 2004 MAIK "Nauka/Interperiodica"

Formulations and properties of the compositions based on binary blends of diene rubbers*

Composition	σ_t, MPa	ε, %	M_{100}	M_{200}	M_{300}	τ_v^{143}, min
			MPa			
SKD/SKI	0.9	980.6	0.2	0.3	0.3	11.7
SKD/SKI/Carbon black (15, 10, 7 min)	11.5, 10.7, 10.1	158, 173, 128	6.2, 7.3, 7.8	0, 0, 0	0, 0, 0	7.1, 7.9, 11
SKS/SKI	4.7	995	0.5	0.7	1.0	22.5
SKS/SKI/Carbon black (15, 10, 7 min)	20.3, 21.1, 21.9	640, 512, 432	2.0, 3.3, 4.0	4.3, 7.1, 8.9	7.6, 11.7, 14.5	14.1, 15.7, 28

* σ_t is tensile strength; ε, relative elongation at break; M_{100}, M_{200}, and M_{300}, stresses at 100, 200, and 300% elongation, respectively; and τ_v^{143}, vulcanization time at 143°C.

The degree of mechanical dispersion of the carbon black particles throughout the elastomer substantially affects the structure of the strengthened system and its physicomechanical properties.

Optical spectroscopic studies showed that, in filled compositions prepared by 7-min mixing, carbon black is poorly dispersed in the system, which is responsible for the relatively poor properties of the resulting vulcanizates. A 10-min mixing affords better properties of the vulcanizates, compared to the blends prepared by 7- and 15-min mixing. Ten minutes can be regarded as the optimal mixing time.

Table shows that, upon introduction of the filler into the SKD/SKI blend, the strength σ_t increases 12-fold, but the relative elongation at break ε decreases 5-fold, and the stress at 300% elongation M_{300} decreases to zero, i.e., the system becomes rigid. Upon introduction of the filler into the SKS/SKI blend, σ_t increases by a factor of 4.5, ε decreases by a factor of 1.9, and M_{300} increases from 1.0 to 11.7 MPa. The vulcanization rate for the filled compositions exceeds by a factor of 1.5 that for unfilled composition. Evidently, carbon black promotes reactions involved in vulcanization of rubbers.

It is known [4] that the properties of filled polymeric materials are governed by the properties of the polymer matrix and filler, as well as by the filler dispersion and the nature of interaction at the polymer–filler interface.

Our study of the physicomechanical properties of vulcanizates of the resulting compositions under quasistatic loading showed that the filler (carbon black) increases the strength of the system. This can be accounted for by enhanced intermolecular interaction in the blends owing to formation of chemical bonds and adsorption bonding.

The results of our dynamic studies of the compositions obtained are presented in Figs. 1a and 1b. Our studies of the vulcanizates of the binary blends of diene rubbers in the range from –120 to 70°C revealed two glass transition points T_g [T_g(SKD) = –94 and T_g(SKI) = –54°C for SKD/SKI system; T_g(SKS) = –44 and T_g(SKI) = –54°C for SKS/SKI system] specific to each polymer; this means that these are two-phase systems. The temperature dependence of the modulus of elasticity E' of the compositions exhibited a two-step pattern, and the curve describing the variation of the mechanical loss indices $\tan\delta$ has two peaks. For the SKS/SKI system, the glass transition points are close for both polymers, which is responsible for the overlapping and broadening of the mechanical loss curve near the peak.

Figures 1a and 1b show that the glass transition points of the polymers remain unchanged upon introduction of active carbon black. This means that the mobility of the chain segments is independent of the presence of the filler particles; otherwise, T_g should shift owing to changes in the mobility of the macromolecules [9]. This suggests that the mechanical properties of vulcanized rubbers containing active filler are improved predominantly by physical forces; chemical bonds seem to be of minor importance.

Figure 1a shows that, in the initial binary blend of diene rubbers SKS/SKI, the modulus of elasticity E' can be estimated at 0 MPa at T = 30°C; upon intro-

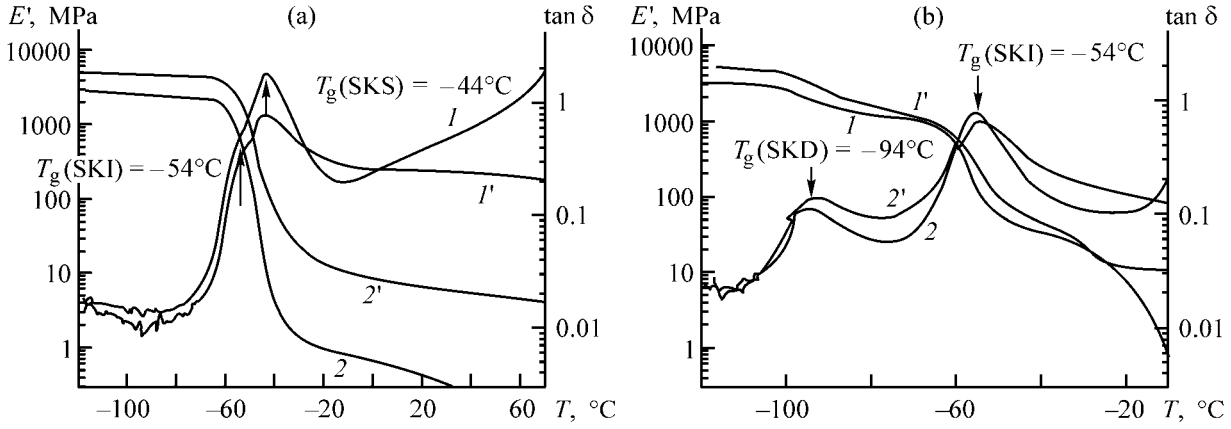

Fig. 1. Temperature dependences of the dynamic modulus of elasticity E', and tangent of mechanical loss tan δ of (a) SKS/SKI and (b) SKD/SKI compositions (ν = 1 Hz). Composition: (*1*, *2*) unfilled and (*1'*, *2'*) filled with carbon black no. 330.

duction of the filler it increases to 4 MPa at T = 30°C and remains unchanged to 70°C, which makes the composition applicable within a broader temperature range.

The tangent of mechanical loss tan δ (Fig. 1a) for the initial blend was estimated at 0.15 for T = 30°C and at 1.1 for T = 70°C, i.e., the mechanical loss increases with rising temperature. Upon introduction of the filler, the mechanical loss tangent decreases by an order of magnitude, namely, from 1.1 to 0.2, remaining virtually unchanged with temperature increasing from –20 to 70°C.

Figure 1b shows that, for the initial SKD/SKI blend at T = –10°C, the modulus of elasticity can be estimated at 1 MPa, and the mechanical loss tangent, at 0.2. Upon introduction of the filler, E' increases to 11 MPa, and tan δ decreases by an order of magnitude, from 0.2 to 0.03 (T = –10°C).

Thus, we showed that, upon introduction of the filler into compositions based on a binary blend of diene rubbers, the modulus of elasticity significantly increases and the mechanical loss tangent decreases by an order of magnitude. This is, evidently, due to enhanced degree of crystallinity or a higher degree of cross-linking of the resulting vulcanizates.

Carbon black no. 330 improves the properties of vulcanized rubbers based on a blend of rubbers, which is essential for preparation of various vulcanized rubbers.

ACKNOWLEDGMENTS

The author is grateful to H.-J. Radusch (Institute of Materials Science of the Martin-Luther University, Halle-Wittenberg, Germany) for assistance in preparation of compositions from binary blends of diene rubbers and in investigation of their properties.

REFERENCES

1. Pomogailo, A.D., *Usp. Khim.*, 2002, vol. 71, no. 1, p. 5.
2. Manson, J.A. and Sperling, L.H., *Polymer Blends and Composites*, New York: Plenum, 1976.
3. Bespalov, Yu.A. and Konovalenko, N.G., *Mnogokomponentnye sistemy na osnove polimerov* (Polymer-Based Multicomponent Systems), Leningrad: Khimiya, 1981.
4. Lezhnev, N.N., Kurylev, V.V., and Tsygankov, E.I., *Structure Characteristics and Elastic-Relaxation Properties of Filled Vulcanized Rubbers*, Moscow: TsNIITEneftekhim, 1981.
5. Studebeiker, M.Kh., *Reinforcement of Elastomers*, Kraus, G., Ed., New York: Interscience, 1965, p. 263.
6. Perer, J., *Vysokomol. Soedin., Ser. B*, 1998, vol. 40, no. 1, p. 102.
7. Zaikin, A.E., Galikhanov, M.F., and Arkhireev, V.P., *Vysokomol. Soedin., Ser. B*, 1997, vol. 39, no. 6, p. 1060.
8. Devikina, L.I., Makarenko, S.V., and Korsakov, V.G., *Zh. Prikl. Khim.*, 1990, vol. 63, no. 3, pp. 718–729.
9. Pein, A., *Reinforcement of Elastomers*, Kraus, G., Ed., New York: Interscience, 1965, p. 73.

Russian Journal of Applied Chemistry, Vol. 77, No. 6, 2004, pp. 1031–1033. Translated from Zhurnal Prikladnoi Khimii, Vol. 77, No. 6, 2004, pp. 1044–1046.

Professor Pavel Pavlovich Fedot'ev (1864–1934)

P.P. Fedot'ev, a professor of the Emperor Peter the Great Polytechnic Institute in St. Petersburg, is the founder of Russia's scientific school of applied electrochemistry and electrometallurgy of nonferrous metals. Together with numerous pupils, he made an outstanding contribution to the organization of the manufacture of aluminum and magnesium in our country and to the creation and development of quite a number of other electrochemical industries.

Pavel Pavlovich Fedot'ev was born on June 21, 1864, in Blagoveshchensk in Amur province into the family of a senior medical attendant. He spent his childhood at this town, and received his secondary education at Siberian Military Gymnasium in Omsk. On leaving the gymnasium, he entered Nikolai Engineering College in St. Petersburg. However, already in a year, he went to St. Petersburg Technological Institute, from whose chemical department he graduated in 1888.

P.P. Fedot'ev commenced his engineering activities at Bondyuzha chemical plant situated near the Kama River, not far from Yelabuga, Vyatka province. By 1890, the plant founded in 1868 occupied the leading position among chemical plants of Russia as regards the diversity and quality of the products it manufactured. The plant even possessed laboratories with newest, by that time, equipment. In 1891, P.P. Fedot'ev moved to Minsk and headed there the laboratory for materials testing at the railroad department. Beginning in December 1893, the young engineer worked at plants in St. Petersburg: he headed ammonia departments at gas plants and, beginning in 1894, supervised the production of nitric and sulfuric acids at Okhta state gunpowder plants. During these same years, P.P. Fedot'ev wrote quite a number of monographs devoted to most important chemical industries. These include: *Proizvodstvo sernoi kisloty* (Manufacture of Sulfuric Acid, 1896), *Dobyvanie potasha iz zoly* (Manufacture of Potash from Ash, 1896), *Sovremennoe sostoyanie khimicheskoi promyshlennosti v Rossii* (Modern State of Chemical Industry in Russia, 1897), *Sodovoe delo i svyzannye s nim proizvodstva* (Manufacture of Soda and the Related Industries, 1898), *Azotnaya kislota i ee soli* (Nitric Acid and Its Salts, 1900), and *Fiziko-khimicheskie tablitsy* (Physicochemical Tables, 1901).

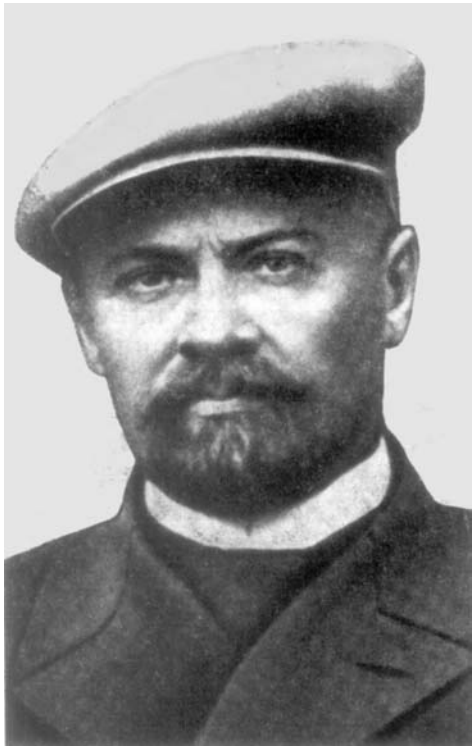

In the autumn of 1902, P.P. Fedot'ev, who had already become known to the scientific community and was experienced in practical work, was invited to the newly organized St. Petersburg Polytechnic Institute to organize the laboratory of mineral technology and technical electrochemistry and deliver the corresponding courses of lectures. To be prepared for occupying the position of a professor, P.P. Fedot'ev was sent to a business trip abroad. He chose Leipzig (Germany), where an international school of electrochemists had formed at the University and at the Institute of Physical Chemistry headed by W. Ostwald (1853–1932, 1909 Nobel Prize in Chemistry). Having returned to St. Petersburg on June 1, 1903, P.P. Fedot'ev presented a dissertation "Ammonia Soda Process from the Standpoint of the Theory of Phases." During his stay in Leipzig, he studied in detail works by J.W. Gibbs (1839–1903) and J.H. Van't Hoff (1852–1911, 1901 Nobel Prize in Chemistry), carried

1070-4272/04/7706-1031 © 2004 MAIK "Nauka/Interperiodica"

out numerous experimental studies, and analyzed above-mentioned complex technological process in terms of the phase rule. Among Russian scientists, only A.A. Yakovkin (1860–1936) applied, earlier than P.P. Fedot'ev, the phase rule to analysis of equilibria in his master's dissertation (1896). Having become an associate professor, P.P. Fedot'ev was elected an extraordinary professor at the chair of mineral technology and technical electrochemistry and his appointment was confirmed. On September 1, 1904, P.P. Fedot'ev started to organize at his chair a laboratory for studies of students and his own research work. At that time, the course of lectures on mineral technology covered basic chemical industries (manufacture of sulfuric and other acids, alkalis, salts, and silicates, such as ceramics, cement, and glass), and the course of lectures on technical electrochemistry, the electrochemical industries and electrometallurgy [1]. For that time, the laboratories were very well equipped; in 1912, undergraduate students started to carry out their graduation works at the chair. P.P. Fedot'ev himself delivered lectures on technology of mineral substances, technical electrochemistry, and electrometallurgy.

In 1906, P.P. Fedot'ev again went to a business trip abroad and visited a number of plants. His trip resulted in his publication of 1907: *"Modern State of Chemical and Electrochemical Industry in Continental Europe."* P.P. Fedot'ev paid much attention to textbooks. In 1906, were published *Tekhnicheskii analiz mineral'nykh veshchestv* (Technical Analysis of Mineral Substances) and *Uchebnik tovarovedeniya* (Manual of Commodity Research). In 1910, P.P. Fedot'ev was elected an ordinary professor of the Polytechnic Institute, and in 1911, he was sent to business trip abroad for familiarization with industrial electric furnaces. Based on the material collected during this business trip, he published a book *Elektricheskie pechi v metallurgii stali* (Electric Furnaces in Metallurgy of Steel, 1912).

The scientific investigations by P.P. Fedot'ev cover a wide range of problems. He paid much attention to the electrolytic method for manufacture of alkali and chlorine and maintained close relationships with plants for manufacture of these compounds. Simultaneously, he studied problems associated with electrochemical production of metals with the use of both aqueous and molten electrolytes. In 1911, P.P. Fedot'ev and his pupil, V.P. Il'inskii (1885–1964), performed an *"Experimental Study of the Electrometallurgy of Aluminum."* They analyzed the binary system AlF_3–NaF, solubility of Al_2O_3 in cryolite, the interaction of aluminum with cryolite-alumina melts, and the decomposition potential of the electrolyte. The authors gave recommendations concerning the choice of the optimal electrolyte composition and studied all the main phenomena accompanying the process of electrolysis [2, 3]. The importance of this publication for the understanding of the physicochemical fundamentals of the electrolyte based on cryolite-alumina melts was analyzed in detail in a monograph by A.I. Belyaev and O.I. Pavlova [4].

In 1915, another P.P. Fedot'ev's pupil, N.N. Voronin (1892–1956), developed methods for dehydration of carnallite and magnesium chloride and studied the electrolysis of molten carnallite. In 1916–1917, production of magnesium was organized under P.P. Fedot'ev's supervision on a large-laboratory scale at workshops of the Military Chemical Committee in Petrograd.

During World War I (1914–1918), P.P. Fedot'ev was actively engaged in works aimed to build-up Russia's military potential and raised the manufacture of chlorine and soda at plants of Southern Russia. The importance of this problems and ways to solve it were considered by V.N. Ipat'ev, head of the Chemical Committee at Chief Artillery Directorate [5, 6].

During the difficult period of 1918–1921, P.P. Fedot'ev was in Petrograd. In 1919, a chemical department was opened at the Polytechnic Institute on his initiative. This department incorporated all the chemical chairs, including the chair of mineral substances and technical electrochemistry. In 1921–1923, P.P. Fedot'ev was dean of the chemical department. In 1920, he also became a professor of the Technological Institute, where he delivered a course of lectures on technical electrochemistry till 1930, when the system of higher education in the country was reorganized.

On July 1, 1930, the Polytechnic Institute was reorganized into a number of separate specialized higher school institutions. The chemical department was included in the Technological Institute, and the metallurgical department was transformed into the Metallurgical Institute. P.P. Fedot'ev headed the chair of the electrometallurgy of nonferrous metals at the latter institute, and stopped lecturing at other places.

The intensive scientific activities at the Polytechnic Institute were resumed in the post-revolution time only in 1924, when the first post-graduate students appeared. Studies by P.P. Fedot'ev and his pupils were closely associated with the demands of industry. In Leningrad, electrolytic refining of silver was organized and problems associated with production of nickel and zinc were studied under P.P. Fedot'ev's

supervision. Much attention was given to preparation for industrial manufacture of aluminum and magnesium in Russia.

In 1929, pilot production of aluminum from entirely domestic raw materials was organized at Krasnyi Vyborzhets plant in Leningrad under P.P. Fedot'ev's supervision with the participation of P.P. Fedot'ev's son N.P. Fedot'ev (1897–1969) and the chief metallurgist of the plant Yu.V. Baimakov (1894–1980). Alumina was obtained at the Pilot Plant of the State Institute of Applied Chemistry (GIPKh) from low-grade Tikhvin bauxites, using the technology developed by Yakovkin. Cryolite and carbon materials were of domestic manufacture too. The first 8-kg batch of aluminum was produced on March 27, 1929. The participants of this work, N.P. Fedot'ev and Baimakov, were graduates from the Polytechnic Institute and P.P. Fedot'ev's pupils. Later, N.P. Fedot'ev headed the chair of technology of electrochemical industries at Leningrad Technological Institute, and Baimakov superceded his teacher at the chair of electrometallurgy of nonferrous metals at the Polytechnic Institute. The works by P.P. Fedot'ev and his pupils were exceedingly important for the creation of the domestic industry of aluminum and magnesium.

In 1933, P.P. Fedot'ev was elected a corresponding member of the Academy of Sciences of the USSR. On March 20, 1934, Pavel Pavlovich Fedot'ev died of a short severe illness. His life and scientific and pedagogical activities are reflected in recollections of those who were intimate with him [7–10] and other authors [4, 11, 12]. The contribution made by P.P. Fedot'ev and his pupils to the creation of the domestic aluminum industry was considered in [13, 14]. Not long before his death, P.P. Fedot'ev prepared for publication the textbook *Elektroliz v metallurgii* (Electrolysis in Metallurgy), whose first part is devoted to electrolysis of aqueous solutions, and the second, to electrolysis of molten salts. The book was published in 1935 [3].During many years, this book was the best manual of the electrometallurgy. A full list of P.P. Fedot'ev's scientific works can be found in [4, 9].

REFERENCES

1. *Sankt-Peterburgskii politekhnicheskii institut Imperatora Petra Velikogo: Metallurgicheskoe otdelenie* (Peter the Great Polytechnic Institute in St. Petersburg: Metallurgical Department), St. Petersburg, 1914.
2. Fedot'ev, P.P. and Il'inskii, V.P., *Izv. S.-Peterb. Politekhn. In–ta*, 1912, vol. 18, no. 1, *Otd. Tekhn. Estestvozn. Matem.*, pp. 147–196.
3. Fedot'ev, P.P., *Elektroliz v metallurgii* (Electrolysis in Metallurgy), Leningrad: ONTI, Khimteoret, 1935.
4. Belyaev, A.I. and Pavlova, O.I., *Pavel Pavlovich Fedot'ev*, Moscow: Metallurgiya, 1965.
5. Ipat'ev, V.N., *Rabota khimicheskoi promyshlennosti na oboronu vo vremya voiny* (The Work of Chemical Industry for Defense during the War), Petrograd, 1920.
6. Ipat'ev, V.N., *Khimicheskii komitet pri Glavnom artilleriiskom upravlenii i ego deyatel'nost' dlya razvitiya otechestvennoi khimicheskoi promyshlennosti* (Chemical Committee at Chief Artillery Directorate and Its Activities Aimed To Develop the Domestic Chemical Industry), Petrograd, 1921, part 1.
7. Menshutkin, B.N., *Priroda*, 1934, no. 5, pp. 89–91.
8. Baimakov, Yu.V., *Tr. Len. Politekhn. In–ta*, 1948, no. 1, pp. 133–139.
9. Baimakov, Yu.V., *Tr. Len. Politekhn. In–ta*, 1964, no. 239, pp. 5–15.
10. Sass-Tisovskii, B.A., *Tr. Len. Politekh. In–ta*, 1964, no. 239, pp. 16–21.
11. Belyaev, A.I. and Pavlova, O.I., *Izv. Vyssh. Uchebn. Zaved., Tsv. Metall.*, 1964, no. 3, pp. 166–171.
12. Belyaev, A.I., *Izv. Akad. Nauk SSSR, Metall. Gorn. Delo*, 1964, no. 3, pp. 12–16.
13. Kaluzhskii, N.A. and Taits, A.Yu., *Otechestvennaya metallurgiya alyuminiya – ot pervykh shagov do promyshlennogo proizvodstva* (Domestic Metallurgy of Aluminum: from First Steps to Industrial Manufacture), Moscow: Metallurgiya, 1991.
14. Morachevskii, A.G., *Ocherki ob uchenykh-khimikakh SanktPeterburgskogo politekhnicheskogo instituta* (An Outline of Scientists-Chemists of St. Petersburg Polytechnic Institute), St. Petersburg: SPb. Gos. Politekhn. Univ., 2002.

A. G. Morachevskii

Russian Journal of Applied Chemistry, Vol. 77, No. 6, 2004, pp. 1034–1035. Translated from Zhurnal Prikladnoi Khimii, Vol. 77, No. 6, 2004, pp. 1047–1048.

ANNIVERSARIES

Vladimir Aleksandrovich Proskuryakov (To 85th Anniversary of His Birthday)

On June 21, 2004, Vladimir Aleksandrovich Proskuryakov, an excellent person, pedagogue, and a real scientist is 85. The youth of Vladimir Aleksandrovich was scorched by the Great Patriotic War of 1941–1945. A fourth-year student of the Lensovet Technological Institute in Leningrad, V.A. Proskuryakov volunteered to go to the frontline, was badly wounded at Nevskii pyatyachok (foothold), then continued his field-duty, and finished his military service in the Far East in Kharbin. After demobilization, he continued his education at the Technological Institute. Having graduated as an engineer from the chair of pyrogenetic processes, he became a candidate of technical science for solving the problem of shale dressing and was appointed a lecturer at the chair of organic chemistry at the Lensovet Technological Institute in Leningrad.

The persistence, benevolence to people, and the skill to unite like-minded persons around him allowed Proskuryakov to create in 1964 a chair of petroleum- and coal-chemical industries on the basis of the chair of pyrogenetic processes. The chair successfully trains specialists in chemical technology of natural fuels and carbon materials and in basic organic synthesis.

While improving the scientific potentialities of the chair, Proskuryakov created an efficient system of training of highly skilled specialists. More than 200 candidate dissertations have been defended under Proskuryakov's supervision, and 20 doctors of science were trained with his participation.

Proskuryakov is the author of more than 600 scientific publications, including 100 inventor's certificates, patents, and monographs.

In 1967, the degree of a doctor of technical science was conferred on Proskuryakov and he acquired the rank of professor.

In 1965, Proskuryakov was appointed pro-rector of the Institute for educational work. In 1974, he was elected a corresponding member of the Academy of Pedagogical Sciences of the USSR for his important services in the organization of higher education. From 1975 till 1985, Proskuryakov was rector of the Lensovet Technological Institute in Leningrad. In this position, he continued in every possible way to develop new areas of science and technology and did his best to lay the material foundation for the development and implementation of new designs.

In addition to his administrative, educational, and scientific activities, Proskuryakov devoted considerable efforts and energy to popularization of science and to public activities. He headed for 15 years a division of the All-Russia Society Znanie (Knowledge), was deputy chairman and chairman of Leningrad Council of rectors, worked for a long time as an expert and a member of presidium of the Higher Attestation Commission, was chairman of specialized council for doctoral dissertations, and headed the Scientific Council of the Institute.

Proskuryakov has been awarded six Orders and numerous medals for his scientific, pedagogical, and administrative services, and also for feat of arms during the Great Patriotic War.

Proskuryakov is an honorary doctor of Merzburg and Vesprem Technical Universities, he has been awarded orders and medals of the Democratic People's Republic of Korea, Czechia, and Bulgaria.

Vladimir Aleksandrovich is a very well-wishing and kindly man, a good friend, and a patriot.

Many generations of students, post-graduate students, lecturers, and research workers have been and still are aware of his support and help.

1070-4272/04/7706-1034 © 2004 MAIK "Nauka/Interperiodica"

In his 85, Vladimir Aleksandrovich is vigorous and energetic, delivers lectures to students, and is actively engaged in problems of processing of shale and coal. He directs considerable effort to publishing activities as a member of the Editorial boards of the journals *Zhurnal Prikladnoi Khimii* (this journal), *Khimiya tverdogo topliva* (Chemistry of Solid Fuels, Russian Academy of Sciences), and *Goryuchie slantsy* (Oil Shale, Academy of Sciences of Estonia). During the last 10 years he has written and published more than 100 scientific papers.

We congratulate Vladimir Aleksandrovich Proskuryakov on his jubilee and wish him sound health and every success for the benefit of the homeland.

Chair of technology of petroleum- and coal-chemical industries, St. Petersburg State Technical University

Editorial board and editorial staff of Zhurnal Prikladnoi Khimii

Russian Journal of Applied Chemistry, Vol. 77, No. 6, 2004, pp. 1036–1037. Translated from Zhurnal Prikladnoi Khimii, Vol. 77, No. 6, 2004, pp. 1049–1050.

INFORMATION

XII Enikolopov Readings

The XII Enikolopov Readings were held on March 12, 2004, at the Enikolopov Institute of Synthetic Polymeric Materials (ISPM). On March 13, 2004, Academician N.E. Enikolopov could be 80.

The Readings were organized by the Department of Chemistry and Materials Sciences, Russian Academy of Sciences (RAS); ISPM; Scientific Council for Macromolecular Compounds, RAS; Semenov Institute of Chemical Physics (ICP); Institute of Chemical Physics Problems (ICPP); and Moscow Physicotechnical Institute.

The agenda of the Readings included six presentations. A presentation by A.A. Berlin and A.Yu. Shaulov from ICP was concerned with inorganic-organic materials, including various structural materials and their advantages and disadvantages from the viewpoint of the ease of processing, heat resistance, combustibility, strength, brittleness, etc. Particular interest of the audience was aroused by the information about inorganic polyoxides exhibiting a wide range of softening points, incombustibility, and high heat and radiation resistance. These are virtually not oxidizable and often readily available natural polymers. Unfortunately, these materials are brittle and often prone to hydrolysis. A.A. Berlin and A.Yu. Shaulov suggested a number of procedures to modify polyoxides, including that of boron, with various organic and inorganic compounds, in particular, linear polymers, and also discussed some important properties of materials and composites thereof.

The report by A.N. Ozerinskii from ISPM was devoted to nanostructured objects. In particular, he presented the general views on formation, structure, and selected properties of nanosized structural elements in polymers and polymeric materials. Also, A.N. Ozerinskii discussed examples of fabrication of elements of nanotechnologies underlain by development of nanostructures in amorphous and crystalline polymers, copolymers, block copolymers, and molecular composites. The presentation considered various procedures for preparation of polymeric nanostructures via synthesis of polymers with desired spatial architecture, as well as procedures based on molecular recognition, self-assembly, and self-organization of nanostructures in polymeric materials.

A presentation prepared by a group of researchers from ICP and ISPM (E.F. Oleinik, A.D. Kalashnikov, I.A. Karmilov, and N.K. Balabaev) concerned the structure and molecular dynamics of a polymer crystal containing $-CH_3$ branches in chains. It was N.S. Enikolopov who, late in his life, expressed active interest in the chemical and physical processes occurring in the solid phase and attempted establishing a correlation of the structural and defect features of various solids with their chemical reactivity. The presentation by E.F. Oleinik and coworkers showed that, at low concentrations of branchings, the crystal preserves its three-dimensional structure, but, with increasing branching concentration, loses its stability and is amorphisized anisotropically, losing initially the order along the *b* axis and later, along the *a* axis. Also, the presentation covered the variation of the chain dynamics near branchings of various structures and possible changes in the properties of polymers due to branching.

A presentation by A.D. Pomogailo and G.I. Dzhardimalieva (both from ICPP, RAS) was focused on the frontal polymerization of metal-containing monomers, which was recommended for designing of nanocomposites. Based on a study of the thermolysis kinetics of the complexes of interest and evolutionary transformations of the released gaseous products, A.D. Pomogailo and G.I. Dzhardimalieva identified the nature of the initiating particles in such systems. They showed that the structural and the chemical, as well as the thermophysical, characteristics of polymerizing systems are of key importance in frontal polymerization of metal-containing monomers studied by them.

The controlled polymerization of olefins was discussed in a presentation by P.E. Matkovskii (ICPP) who participated in developing the scientific principles and designing the process implementation for preparation of 1-butene, 1,4-hexadiene, C_4–C_{30} higher linear α-olefins, 5-decene, 6-dodecene, 7-tetradecene, waxy polyethylene, higher mono- and polyakylaromatic hydrocarbons, oligomeric bases of unsaturated, hydrogenated, and aromatized synthetic oils of various designation, as well as of synthetic polyethylene composites.

1070-4272/04/7706-1036 © 2004 MAIK "Nauka/Interperiodica"

Lastly, S.L. Bazhenov from ISPM made a report devoted to mechanical failure of filled composites containing a polymer matrix, namely, upon stretching of composites based on a thermoplastic matrix and vulcanized rubber particles. In the case of plastic matrix-based composites, introduction of rubbers typically decreases the elongation at break. S.L. Bazhenov found that the failure of large vulcanized rubber particles yields so-called rhomboid fractures whose propagation is responsible for early failure of composites.

The Enikolopov Readings showed that the ideas advanced by Academician N.S. Enikolopov are being further developed and successfully implemented by his disciples and his disciples' disciples. The scientific school created by Nikolai Sergeevich has been working successfully in the field of preparation of new polymeric materials and composites, study of their properties, and application.

G.E. Zaikov and M.I. Artsis

Russian Journal of Applied Chemistry, Vol. 77, No. 6, 2004, p. 1038. Translated from Zhurnal Prikladnoi Khimii, Vol. 77, No. 6, 2004, p. 1051.

BOOK REVIEWS

V.M. Mukhin, V.V. Chebykin, E.A. Galkin, N.P. Vasil'ev, V.S. Medyanik, and A.N. Tamam'yan, *Aktivnye ugli. Elastichnye sorbenty. Katalizatory, osushiteli i khimicheskie poglotiteli na ikh osnove: katalog* (Active Carbons. Elastic Sorbents, Catalysts, Desiccants, and Chemical Adsorbents Thereof: Catalog), Mukhin, V.M., Ed., Moscow: Ruda i Metally, 2003, 280 pp.

Sorption technologies permit high degrees of purification and high quality of products under minimum energy and capital expenditures. By the present time, sorption materials have significantly grown in importance in industrial pollution abatement. Recent developments in the production of sorption-active materials are successfully applied in industrial and hygienic purification of gases; potable water purification and production of filters for exhaustive treatment of potable water; wastewater treatment; soil protection against residual pesticides and crop yield enhancement; and recovery of precious and rare metals from dilute solutions.

We brought to readers' notice a catalog summarizing the information about the major sorption-active materials commercially produced in Russia. The catalog has five sections, of which Section 1 (pp. 17–152) holds the central position. It is focused on active carbons and has the following subsections: active carbons for gas and vapor adsorption; active carbons for adsorption from liquid media; active carbons for soil treatment; and medical active carbons. Each brand of these active carbons is characterized by its specific preparation procedure, application field, physicochemical properties (as specified by the acting technical specifications), and manufacturer. On the whole, Section 1 covers 79 brands of active carbons.

Section 2 (pp. 153–168) concerns commercial elastic adsorbents and catalysts thereof. Elastic adsorbents rank among the today's most promising technically important materials. Fibrous structure of elastic adsorbents makes them suitable for manufacturing of tapes, fabrics, threads, and fibers. This offers a wide scope for diversified implementation of the corresponding processes. Fibrous materials can be additionally endowed with chemisorptive and catalytic powers.

Section 3 (pp. 169–248) is focused on active carbons suitable as supports for catalysts, desiccants, and chemical adsorbents; these are active carbons with developed macro- and mesopores. Catalysts, most often metal oxides, are fixed on the carbon surface by impregnation with appropriate salts, followed by heat treatment at 110–150°C. Desiccants are active carbons impregnated with hydrophilic salts such as calcium chloride, lithium chloride, or lithium bromide. Presently, three brands of desiccants are manufactured; they are most widely used in facilities for respiratory tract protection against carbon monoxide. Active carbon-based chemical adsorbents (23 brands) are used for removal of aggressive or toxic substances from air; the adsorption is accompanied by a chemical reaction. Adsorbents are used in apparatus for treatment of air and gases without regeneration of the substances sorbed.

Small Section 4 (pp. 249–253) is devoted to reactivation of spent active carbons. Active carbons are produced in the largest volume among sorption-active materials, and their reactivation is of great interest. Presently, two brands of reactivated carbons are manufactured commercially.

Lastly, Section 5 (pp. 254–269) contains information about carbon materials used in production of active carbons or those prepared from raw materials for production of active carbons.

This well-designed catalog comprises both Russian and English versions. This handbook will certainly be of use for those specializing in various applications of sorption-active materials.

A.G. Morachevskii and I.N. Beloglazov

1070-4272/04/7706-1038 © 2004 MAIK "Nauka/Interperiodica"

Russian Journal of Applied Chemistry, Vol. 77, No. 6, 2004, p. 1039. Translated from Zhurnal Prikladnoi Khimii, Vol. 77, No. 6, 2004, p. 1052.

BOOK REVIEWS

V. D. Risovannyi, A. V. Zakharov, E. P. Klochkov, and T. M. Guseva, *Bor v yadernoi tekhnike* (Boron in Nuclear Engineering) Dimitrovgrad: Nauchno-Issled. Inst. Atomnykh Reaktorov, 2003.

The monograph *Bor v yadernoi tekhnike* (Boron in Nuclear Engineering) prepared by a group of scientists from the Research Institute of Atomic Reactors, State Scientific Center, Federal State Unitary Enterprise, is the first attempt in the Russian-language literature to analyze in detail the physicomechanical, nuclear, and radiation properties of boron carbide, metal borides, boron-based dispersion materials, and boron steels and alloys, i.e., all boron-containing materials used in manufacturing of atomic reactors. Among these materials, the most widely used in the world practice of reactor engineering is boron carbide with different degrees of enrichment in ^{10}B. Also, some other ^{10}B-containing materials are used as neutron absorbers, namely, boron steels and alloys and boric acid introduced into heat carriers.

Boron steels (with 2–3 wt % boron) are used in nuclear shields for storage and transportation of spent fuel assemblies from atomic reactors and in biological protecting shields. The monograph emphasizes the promise of refractory boron compounds like europium haxaboride EuB_6 and hafnium diboride HfB_2, which contain several absorbing isotopes.

The monograph consists of an introduction, eight chapters, and bibliography with 235 items from Russian and foreign literature.

The Introduction (pp. 6–10) briefly summarizes the problems associated with the use of boron and its compounds in nuclear engineering. A small Chapter 1 (pp. 11–29) presents evidence concerning various absorbing materials, as well as the selection criteria and the extent of their use. Chapter 2 (pp. 30–176), which holds the central position in the monograph, is focused on boron carbide and, in particular, on preparation of boron carbide and articles thereof, as well as on the physical, chemical, and mechanical properties of boron carbide, its structure and compatibility with other structural materials. Special attention is given to radiation resistance of boron carbide. Chapters 3 (pp. 177–192), 4 (pp. 193–211), and 5 (pp. 212–219) concern other boron-containing compositions, namely, boron steels, metal borides, and boron-containing dispersion absorbers. Chapter 6 (pp. 220–281) describes the major designs of control facilities manufactured from the above-mentioned materials and applied in Russian and foreign atomic reactor engineering. It should be emphasized that this monograph is the first attempt to summarise this kind of information. Chapter 7 (pp. 282–297) discusses an important problem of regeneration and reuse of boron carbide. Lastly, Chapter 8 (pp. 298–320) briefly summarizes a wide range of problems concerned with boron applications in other fields of nuclear engineering.

This monograph is intended, above all, for scientists and technical engineers engaged in designing and exploitation of atomic reactors. However, it will be also of interest for those specializing in inorganic materials science and chemistry of boron and its compounds. The monograph is written in a good language, without excessive use of special terminology, which increases the number of its potential readers.

A. G. Morachevskii

1070-4272/04/7706-1039 © 2004 MAIK "Nauka/Interperiodica"

Russian Journal of Applied Chemistry, Vol. 77, No. 7, 2004, pp. 1041–1049. Translated from Zhurnal Prikladnoi Khimii, Vol. 77, No. 7, 2004, pp. 1057–1065.

INORGANIC SYNTHESIS AND INDUSTRIAL INORGANIC CHEMISTRY

Preparation of Titanium-Containing Sulfuric Acid Solutions

E. P. Lokshin, T. A. Sedneva, and I. A. Tikhomirova

Tananaev Institute of Chemistry and Technology of Rare Elements and Mineral Raw Materials, Kola Scientific Center, Russian Academy of Sciences, Apatity, Murmansk oblast, Russia

Received July 1, 2003; in final form, February 2004

Abstract—The influence exerted by fluorine-containing agents introduced into nitric acid in leaching of calcium oxide from the sphene concentrate on the possibility of performing the process under atmospheric pressure to obtain titanium dioxide of anatase structure in the solid residue was examined. The sulfatization of the titanium–silica product obtained in nitric acid breakdown of the sphene concentrate and aqueous leaching of titanium sulfates from the forming cakes were studied.

The sphene concentrate manufactured on a semicommercial scale [TU (Technical Specification) 1715-069-00 203 938–2000] in dressing of complex ores from the Khibiny deposit[1] contains no less than 37 wt % TiO_2. Its industrial manufacture is hindered by the lack of an efficient technology for manufacturing titanium products of commercial value.

Sulfuric acid methods considered in detail in [1] gave no way of developing an efficient technology that could be used to produce pigment-grade TiO_2 from the sphene concentrate because of a number of inherent disadvantages. The most important of these are the high acid number (mass ratio of H_2SO_4 to TiO_2) of the resulting sulfate solutions of titanium(IV), which makes impossible direct hydrolytic precipitation of metatitanic acid, and the complexity of the necessary equipment. The increased content of TiO_2 (3–5 wt %) in the calcium silicate cake obtained in sulfuric acid treatment of the sphene concentrate predetermines the low recovery of titanium(IV) into a sulfate solution [1]. Despite many years' efforts, the titanium–calcium and titanium–silicate pigments produced by this technology failed to find use, and their semicommercial manufacture was terminated.

As the production of the sphene concentrate can be raised manyfold, it is of interest to develop an efficient technology for manufacture of high-quality titanium products from the concentrate.

One of the reasons for such a low recovery of titanium(IV) into a sulfate solution is the formation of $CaSO_4$, which forms with SiO_2 a composite that blocks the access of H_2SO_4 to sphene particles. Attempts have been made to tackle with this difficulty by preliminary leaching of CaO with nitric acid solutions.

It has been assumed [2] that sphene can be decomposed only with concentrated HNO_3 taken in a considerable excess with respect to the stoichiometrically necessary amount at a temperature of no less than 130°C, which made necessary, as seen from Table 1, use of an autoclave equipment [3]. In this case, the titanium–silica product obtained, as shown by the studies, consisted of a mixture of TiO_2 of mainly rutile modification with SiO_2 and, in fact, was artificial leucoxene, whose TiO_2 very difficultly reacts with H_2SO_4 [4].

As is known [5], HNO_3 salts-out $Ca(NO_3)_2$, which has been disregarded in previous studies of the nitric acid decomposition of the sphene concentrate [2]. Using an excess amount of concentrated HNO_3 created a situation when the concentration of the forming $Ca(NO_3)_2$ exceeded its solubility in a nitric acid solution. This made impossible complete decomposition of the sphene concentrate. Raising the temperature leads to an increase in the solubility of $Ca(NO_3)_2$ in HNO_3 solutions [5]. Therefore, when an excess amount of concentrated HNO_3 was used, it was necessary to carry out the process at an elevated temperature and, as a result, at a higher pressure.

It was of interest to study how the sphene concentrate reacts with nitric acid solutions of medium concentrations.

The sulfating of the titanium–silica product obtained in nitric acid breakdown of the sphene concentrate has not been studied yet. The titanium–silica

[1] Apatit Open Joint-Stock Company (Kirovsk, Murmansk oblast).

1070-4272/04/7707-1041 © 2004 MAIK "Nauka/Interperiodica"

Table 1. Equilibrium vapor pressure over HNO_3 solutions*

c_{HNO_3}, wt %	*A*	*B*	*T*, °C, at *p* = 0.1 MPa (1 atm)	*p*, MPa, at indicated *T*, °C				
				110	120	130	135	150
25	5.0108	2196.5	105	0.120	0.167	0.229	0.267	0.658
30	4.9000	2239.1	106.5	0.114	0.160	0.221	0.258	0.404
35	4.9908	2282.5	108	0.108	0.152	0.212	0.249	0.393
40	4.8750	2261.9	112	0.093	0.132	0.183	0.214	0.337
50	5.0727	2362.3	116	0.081	0.115	0.163	0.192	0.308
56	5.1273	2401.9	119	0.072	0.104	0.147	0.174	0.281
65	4.7527	2268.9	121	0.068	0.095	0.133	0.155	0.245
70	4.8782	2324.8	122.5	0.065	0.092	0.129	0.151	0.241

* Calculated from the data of [3] by the equation $\log p = A - B/T$, *p* (MPa).

product has a composition close to that of the natural leucoxene concentrate. However, TiO_2 of rutile modification, which is contained in the leucoxene concentrate, reacts sufficiently completely only with a large excess of concentrated H_2SO_4 at high temperatures of 250–300°C [6] close to the boiling point of the acid. Therefore, sulfuric acid technologies for its processing proved to be inefficient and it was of interest to study the possibility of obtaining TiO_2 in more readily broken down modifications, rather than in the rutile modification, and to analyze conditions for conversion of TiO_2 into a sulfate solution that can be used to manufacture pigment-grade TiO_2. As is known, solutions of this kind must have an acid number *K* not exceeding 2.0–2.2, contain no less than 220–240 g l^{-1} TiO_2, and be stable against hydrolytic decomposition (characterized by the stability factor K_s, which should be no less than 500) [7].

EXPERIMENTAL

The following chemicals were used in the study: purified sphene concentrate containing (wt %): 38.5 TiO_2, 27.3 CaO, 25.0 SiO_2, 1.18 Ln_2O_3, 1.21 Fe_2O_3, and 0.27 Al_2O_3; concentrated acids of pure grade: HNO_3 (68.1 wt %), HF (44 wt %), or H_2SiF_6 (45 wt %). The consumption of HNO_3 was determined from the equation

$$CaTiSiO_5 + 2HNO_3 \rightarrow Ca(NO_3)_2 + TiO_2(H_2O)SiO_2. \quad (1)$$

In addition to calcium ions, ions of lanthanides, iron, and aluminum may also pass into solution:

$$Ln_2O_3 + 6HNO_3 \rightarrow 2Ln(NO_3)_3 + 3H_2O, \quad (2)$$

$$Fe_2O_3 + 6HNO_3 \rightarrow 2Fe(NO_3)_3 + 3H_2O, \quad (3)$$

$$Al_2O_3 + 6HNO_3 \rightarrow 2Al(NO_3)_3 + 3H_2O. \quad (4)$$

The mineral was decomposed using HNO_3 taken in a 20% excess with respect to the amount stoichiometrically necessary for reaction (1), which was also sufficient for transferring into solution the concomitant compounds of lanthanides, iron, and aluminum. The expenditure of fluorine-containing acids in the experiments was varied from 0 to 1.0 mol F^-/mol TiO_2.

The concentrate was decomposed at 105–150°C in hermetically sealed containers placed, during the experiment, in a rotating furnace (autoclave breakdown) or in a temperature-controlled laboratory reactor with a reflux (breakdown under atmospheric pressure). The time of thermal treatment was 6 h. After cooling to 20–30°C, the slurry was filtered on a Büchner funnel, and the precipitate was washed with distilled water at s : l = 1 : (3–5) and dried at 100°C. The efficiency of the process was evaluated by the average rate of leaching of CaO into solution, V_{CaO} (M s^{-1}), and the extent of its recovery into solution, Q_{CaO} (wt %). The kinetics of leaching was monitored by sampling the solution and analyzing the samples taken at regular intervals of time.

The distribution of calcium, titanium, lanthanide, iron, aluminum, and fluorine atoms among the solution and precipitate, as well as the relative amounts of the rutile and anatase forms of titanium oxide in the titanium–silica products, were studied. The content of the elements (in terms of the corresponding oxides) was determined by the known methods of chemical and spectral analyses, and also by flame photometry. Solid precipitates were additionally subjected to X-ray phase analysis on a DRON-2 diffractometer.

Table 2 shows that the rate of CaO leaching from

sphene in the autoclave process grows as temperature is increased and the content of HNO_3 decreased in the range 68–25 wt %.

For example, reaching 89.6% recovery of CaO into solution with 68% HNO_3 requires that the temperature should be 150°C. In this case, the rate of CaO leaching from the concentrate into a nitric acid solution increases from 0.42×10^{-4} to 2.54×10^{-4} mol l^{-1} s^{-1}. At the same time, a deeper recovery of 96.2 wt % at a comparable rate of 2.32×10^{-4} mol l^{-1} s^{-1} can be achieved with 25% HNO_3 at 120°C. In this case, the pressure in the apparatus decreases from 0.243 to 0.167 MPa. The residual content of HNO_3 in the corresponding mother liquor does not exceed 4 wt %, which leads to a high solubility of $Ca(NO_3)_2$ in this solution [5]. The dependence of the CaO recovery on the HNO_3 concentration has an extremum, which is due to a decrease in the activity of the acid at its concentrations lower than 25 wt %.

An X-ray phase analysis of the solid residues demonstrated that both the rutile and anatase phases may exist in the titanium–silica product. Their relative amounts depend on the process temperature. As the content of HNO_3 is lowered from 50 to 25 wt %, which, simultaneously, makes it possible to lower the temperature of sphene decomposition from 150 to 120°C, the fraction of the anatase TiO_2 phase in the titanium–silica product increases from 26 to 60 wt % [8].

The formation of crystalline phases of TiO_2 (in contrast to amorphous SiO_2) in the titanium–silica product strongly suggests that, in the course of nitric acid decomposition of the sphene concentrate, there occurs not only substitution of the calcium cation with the hydroxonium cation, but also dissolution of TiO_2 to form a rather unstable nitrate compound of titanium that is readily hydrolyzed under these conditions. The precipitation of titanium(IV) from solution gives rise to growth of TiO_2 crystals of various modifications. The possibility of obtaining TiO_2 directly in the form of rutile or anatase by hydrolysis of nitrate solutions of titanium(IV) has been reported previously [9].

Introduction of fluoride ions into the nitric acid solutions used in leaching intensifies the decomposition of the sphene concentrate to an even greater extent. When 68% HNO_3 was used at 120°C, the introduction of 0.2 mol F^-/mol TiO_2 leads to a more than threefold increase in the degree of decomposition, but was insufficient. However, raising the amount of fluoride ions added to 0.8 mol F^-/mol TiO_2 had no effect, because further decomposition was made impossible by the saturation of the $Ca(NO_3)_2$ solution. The introduction of fluorine compounds in an amount equal to, or exceeding 0.2 mol F^-/mol TiO_2 into a solution containing 26 wt % HNO_3 ensured >92.5% recovery of CaO at 105°C and an average rate of the process of 2.23×10^{-4} mol l^{-1} s^{-1}. Hence followed that the process can be performed under atmospheric pressure, and this conclusion was confirmed in experiments on decomposition of the sphene concentrate in a reactor with a reflux (Table 3).

Table 2. Average rate of CaO leaching and recovery into solution at different initial concentrations of HNO_3, flow rates of fluoride ions, and temperatures of the process

c_{HNO_3}, wt %	F^-, mol mol^{-1} TiO_2	T, °C	$V_{CaO} \times 10^4$, mol l^{-1} s^{-1}	Q_{CaO}, wt %
68	0	110	0.42	14.1
68	0	120	0.64	21.9
68	0	130	1.30	44.3
68	0	140	2.00	67.9
68	0	150	2.54	89.6
68	0.2	120	2.42	68.4
68	0.4	120	2.42	68.6
68	0.8	120	2.43	68.8
52	0	130	1.44	55.4
35	0	130	1.56	70.5
25	0	130	2.33	96.9
25	0	120	2.32	96.2
25	0	110	1.87	77.6
25	0.2	105	2.23	92.5
25	0.4	105	2.27	94.2
25	0.8	105	2.32	96.5
15	0	130	1.04	91.9

It was found that raising the concentration of fluorine compounds leads not only to an increase in the efficiency of the decomposition process (Table 2), but also to preferential formation of the anatase form of TiO_2, which is virtually complete upon introduction of >0.4 mol F^-/mol TiO_2 (this follows from the X-ray diffraction patterns in Fig. 1). Comparison of the intensities of the characteristic peaks corresponding to the interplanar spacings of rutile and anatase (3.24 and 3.52 Å, respectively) shows that formation of the anatase modification of TiO_2 is favored by lower temperatures and higher concentrations of fluoride ions.

The absence of any differences in the course of the process between the cases when HF and H_2SiF_6 with comparable amounts of fluoride ions are used indirectly points to the following. In nitric acid solutions at a high temperature (>105°C), the hydrolysis of SiF_6^{2-}

Table 3. Recovery of concomitant elements into a nitric acid solution in decomposition of the sphene concentrate under atmospheric pressure (T = 105°C, c_{HNO_3} = 25 wt %)

F^-, mol mol^{-1} TiO_2	Recovery into solution, %						
	CaO	Ln_2O_3	Fe_2O_3	Al_2O_3	TiO_2	SiO_2	F^-
0	69.8	94.1	89.6	–	0.05	0.07	Not determined
0.2	92.5	86.3	72.3	–	0.12	0.17	4.62
0.3	93.6	80.2	62.4	43.2	0.14	0.42	6.21
0.5	95.2	65.1	49.7	–	0.42	1.77	11.5
1.0	97.3	48.6	36.4	–	2.66	4.85	19.2

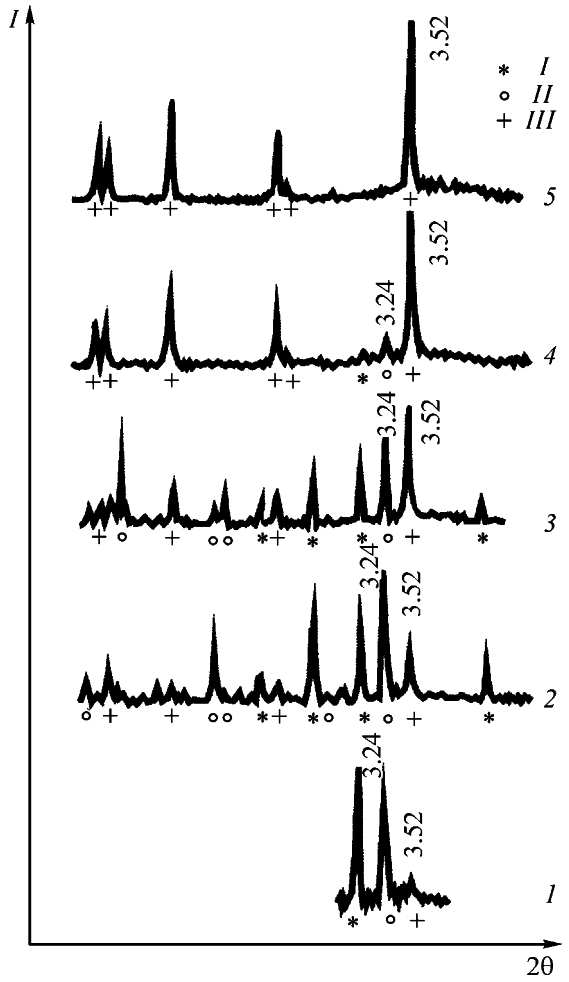

Fig. 1. Sequence of formation of the rutile and anatase phases in decomposition of the sphene concentrate with 25% HNO_3 in the presence of fluoride ions. (*I*) Intensity and (2θ) Bragg angle; the same for Fig. 6. (*I*) $TiCaSiO_5$, (*II*) TiO_2 (rutile), and (*III*) TiO_2 (anatase). T (°C), F^- (mol mol^{-1} TiO_2): (*1*) 110, 0 (autoclave); (*2*) 110, 0.5 (autoclave); (*3*) 110, 1.0 (autoclave); (*4*) 105, 0.2; and (*5*) 105, 0.5. Interplanar spacings are given in Å.

and TiF_6^{2-} ions by overall reaction (5) is stronger than at lower temperatures:

$$MF_6^{2-} + (2 + n)H_2O \rightarrow MO_2 \cdot nH_2O + 4H^+ + 6F^-. \quad (5)$$

The room-temperature equilibrium constant of this reaction for the SiF_6^{2-} ion, found to be 10^{-27}–10^{-28} [10], indicates that fluoride ions are formed via hydrolysis of SiF_6^{2-} in nitric acid solutions at room temperature in noticeable concentrations [11]. Raising the temperature must shift the equilibrium of reaction (5) to the right to an even greater extent.

Fluoride ions from solutions react with hydrated SiO_2 and, possibly, with titanium(IV) of the titanium–silica product after leaching of calcium(II); the forming complex fluoride anions pass into solution. At elevated temperatures, they are hydrolyzed in a nitric acid solution of medium concentration, with fluoride ions released in the process continuing to disintegrate the titanium–silica framework. When the breakdown process is complete and the solution is cooled, the main part of fluoride ions is captured by the titanium–silica product, with less than 7% of the introduced fluoride ions remaining in solution.

The kinetic curve that describes the rate of transfer of CaO into solution at 105°C is linear in the coordinates of the following first-order reaction (Fig. 2):

$$\ln c_{CaO} = \ln c_{CaO}^0 - k\tau, \quad (6)$$

where c_{CaO} and c_{CaO}^0 are the initial and running concentrations of the starting substance, and k is the effective rate constant of dissolution by reaction (1) (mol l^{-1} s^{-1}).

The slope of this straight line is equal to the rate constant of reaction (1):

$$k = \tan\alpha = 1.63 \times 10^{-4}. \quad (7)$$

Nitrates of lanthanides, iron, and, to a lesser extent, aluminum pass into a nitric acid solution together with calcium(II). The insufficiently good recovery of aluminum into solution is presumably due to the presence in solution of admixtures of accessory feldspars, and primarily albite, which are stable in nitric acid media. In the absence of fluoride ions, lanthanides(III) as well as iron(III) pass into solution to a greater extent, but their recovery falls as the content of fluoride ions in solution increases (Table 3). In the case of lanthanides(III), the possible reason is the formation of their sparingly soluble fluorides in the presence of an excess amount of fluoride ions.

Under the conditions of nitric acid decomposition of the sphene concentrate, compounds of titanium and silicon remain virtually completely in the solid phase: their concentration in the nitric acid solution does not exceed 0.08 and 0.07 g l^{-1} for TiO_2 and SiO_2, respectively. Their recovery into the liquid phase free of fluorine-containing additives does not exceed 0.05–0.07%. Upon introduction of fluoride ions, compounds of titanium and silicon pass into solution in greater amounts (wt %): 0.42 TiO_2 and 1.77 SiO_2 at 0.5 mol F^-/mol TiO_2. The probable reason is that the forming fluorine-containing complex anions of silicon(IV) and titanium(IV) are preserved in solution. The complexes are more soluble in nitric acid solutions than TiO_2 and SiO_2.

The experimental results show that using 25% HNO_3 with the optimal addition of fluorine compounds in an amount of 0.3 mol F^-/mol TiO_2 ensures recovery of ions of calcium, rare-earth elements, and iron into solution. The high recovery of lanthanides gives reason to believe that they can be concentrated by using in breakdown procedures recovered HNO_3, which can be obtained by treating $Ca(NO_3)_2$ solutions with concentrated H_2SO_4. The recovery of the most part of iron ions into solution simplifies the subsequent manufacture of high-quality titanium compounds from the titanium–silica product.

Nitric acid decomposition of the sphene concentrate under the optimal conditions gives nitrate solutions of $Ca(NO_3)_2$ that contain, in terms of oxides, (g l^{-1}): 120 CaO, <0.5 TiO_2, <0.5 SiO_2, <5.30 Ln_2O_3, <1.5 Fe_2O_3, <0.70 Al_2O_3, <1.2 F, and 20–40 HNO_3, and also a titanium–silica product containing (wt %): 48 TiO_2, 37 SiO_2, 0.56–3.00 CaO, <0.018 Ln_2O_3, <0.64 Fe_2O_3, <0.25 Al_2O_3, <2.2 F^-, and 3.60 NO_3^-. The main part of fluoride ions find way into the titanium–silica product. The calcination loss of the titanium–silica product is about 15 wt %, which somewhat exceeds the value calculated on the assumption that

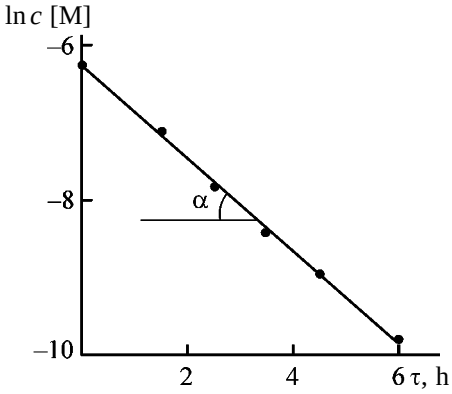

Fig. 2. CaO concentration in the sphene concentrate vs. the time τ of leaching at 105°C.

the amount of chemically bound water in the product is determined by reaction (1). The possible reason is that titanium(IV) is present in the titanium–silica product not only as anatase and(or) rutile, but, in part, also in the amorphous hydrated form.

The sulfatization was studied for the titanium–silica product obtained by leaching of the sphene concentrate with HNO_3 solutions with addition of fluorine-containing compounds (HF, H_2SiF_6) in an amount of 0.25 mol F^-/mol TiO_2. In the product, TiO_2 was present, according to X-ray phase analysis, in the anatase form. Such a product contained (wt %): 46.9–48.8 TiO_2, 34.5–37.4 SiO_2, 0.56–3.30 CaO, 0.003–0.180 TR_2O_3, 0.64 Fe_2O_3, 0.25 Al_2O_3, <2.20 F^-, and <3.69 NO_3^-. The calcination loss was 15–18 wt %. For comparison, some experiments were performed with a product obtained by nitric acid decomposition of the sphene concentrate at 120–130°C without addition of fluorine compounds. The product differed only in that it contained a part of TiO_2 in the rutile modification.

The titanium–silica product was decomposed with concentrated H_2SO_4 of pure grade [GOST (State Standard) 2184–77], from which the working solutions were prepared by dilution with distilled water.

The sulfatization (sintering of a weighed portion of the titanium–silica product with H_2SO_4) was performed by heating the reaction mixture to a prescribed temperature in sealed fluoroplastic containers for 1–5 h. The concentration of H_2SO_4 was varied from 22 to 94%, and the expenditure of the acid was within the range 1.6–2.2 kg kg^{-1} TiO_2. The cake was leached with water under continuous agitation. The sulfatization temperature was varied from 105 to 180°C; the leaching was performed at 50°C. The cooled slurry was filtered, and the precipitate (silica cake) was washed with distilled water.

The content of titanium, silicon, calcium, fluorine,

Table 4. Residual content of titanium(IV) in the precipitate and its recovery Q from the titanium–silica product into an aqueous solution at different initial concentrations of H_2SO_4 and its expenditure

Run no.	$c_{H_2SO_4}$, wt %	Expenditure of H_2SO_4, kg kg^{-1} TiO_2	T, °C	Content of TiO_2 in the silica cake, wt %	Q_{Ti}, %
1	22	2.0	105	46.4	10.6
2	38	2.0	112	46.1	13.6
3	40	2.0	114	46.3	13.2
4	45	2.0	118	47.9	16.8
5	50	2.0	124	40.1	30.4
6	54	2.0	130	21.3	60.1
7	57	2.0	135	13.5	81.7
8	80	1.6	150*	7.61	91.7
9	80	1.8	170*	5.72	93.7
10	80	1.8	170*	2.49	94.6
11	80	2.0	170*	4.80	95.0
12	80	2.0	170*	2.95	96.4
13	80	1.6	180*	5.17	93.3
14	80	1.8	180*	3.70	95.4
15	80	2.0	180*	2.33	95.4
16	94	2.0	170*	2.64	96.7
17	94	2.0	180*	3.50	96.7
18	94	1.8	150*	2.60	98.2
19	94	1.6	150*	2.30	98.0

* Below the boiling point of an acid of the corresponding concentration.

and iron in the solutions and dry residues was determined. The amount of titanium(IV) that passed into the aqueous phase (filtrate, washing water) and(or) its residual content in the silica cake was used to calculate the recovery of titanium(IV), Q (%), from the titanium–silica product, which served as a measure of the efficiency of the processes under study.

The efficiency of sulfatization was evaluated by the extent to which titanium(IV) passed into an aqueous solution after 3 h of leaching of a sample. As established in preliminary experiments, this time is sufficient for the transfer of the most part of titanium(IV). Figure 3 shows the kinetics of sulfatization at 150°C of a titanium–silica product containing 40% of TiO_2 in the anatase modification, and 60%, in the rutile modification (curve *1*) and of precipitates containing only the anatase phase of TiO_2 (curves *2*, *3*). The sulfatization was carried out with 56 and 77% solutions of H_2SO_4 at its expenditure of 2 kg kg^{-1} TiO_2.

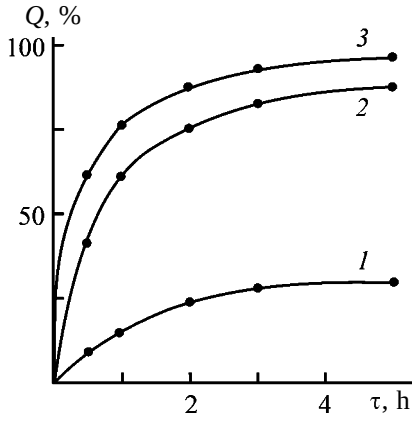

Fig. 3. Recovery Q of titanium(IV) from the titanium–silica product at 150°C vs. the duration τ of sulfatization of the titanium–silica product. Content of rutile in the titanium–silica product (wt %): (*1*) 60 and (*2*, *3*) 0. Content of H_2SO_4 (wt %): (*1*, *3*) 77 and (*2*) 56.

Figure 3 shows that the efficiency of the process depends on the concentration of H_2SO_4 and on the crystal structure of TiO_2. The amount of titanium(IV) that passed into solution from a titanium–silica product containing TiO_2 of anatase structure in 5 h was 87 and 96% depending on H_2SO_4 concentration, whereas the recovery of titanium(IV) from a rutile-containing product did not exceed 30% relative to its initial content. An X-ray phase analysis of the residue obtained after leaching of a sulfatized rutile-containing titanium–silica product revealed only TiO_2 of rutile structure, which, as demonstrated by further investigation, reacted with H_2SO_4 only at temperatures not lower than 180°C.

Thus, a study of the sulfatization kinetics of a titanium–silica product that contained TiO_2 in the anatase phase revealed the following process advantages over

the known methods [4, 6, 12, 13]: relatively low sulfatization temperature, lower expenditure of H_2SO_4, and shorter duration of the process.

The dependence of the recovery of titanium from the titanium–silica product on the concentration and expenditure of H_2SO_4 was studied (Table 4). The range in which the expenditure of the acid was varied was chosen in such a way that an acid factor close to 2 was obtained in leaching of titanium(IV) into an aqueous solution. The reaction mass (liquid suspension at H_2SO_4 concentrations lower than 57% and increasingly thick paste at higher concentration) was heated at required temperature in closed vessels to diminish evaporation of water in the course of sulfatization. The duration of heat treatment was 5 h; the sulfatization temperature was equal to, or lower than the boiling point of H_2SO_4 of a concentration used.

Also noteworthy is a steep rise in the efficiency of the process on raising the concentration of H_2SO_4 within the range 50–60 wt % (Table 4, run nos. 10, 11; 13, 14; 18, 19; Fig. 4). The most efficient is 80–94 wt % H_2SO_4, because it is within this concentration range that water-soluble $TiOSO_4 \cdot H_2O$ is formed [1]. The expenditure of H_2SO_4 within the limits studied does not affect significantly the completeness of the sulfatization process.

The sulfatized cake, which is mainly a mixture of titanium(IV) sulfates and hydrated SiO_2, was studied by thermal analysis and methods of crystal optics.

Figure 5 shows thermograms of cakes obtained at expenditure of 94% H_2SO_4 equal to 1.4, 1.6, and 1.8 kg kg^{-1} TiO_2.

The absence of exothermic effects at 540 and 590°C, which are commonly attributed [14] to thermal decomposition of $TiOSO_4 \cdot 2H_2O$, suggests that it is not contained in noticeable amounts in the cakes obtained. The endothermic effects at 380 and 426°C can be attributed to removal of water from $TiOSO_4 \cdot 2H_2O$, which, according to [9, 14], begins above 300°C. The endothermic effects at 600 and 683–700°C are associated with elimination of SO_3 to give TiO_2. The endothermic effects at 164–202°C are presumably due to removal of water from hydrated SiO_2 present in the cake.

Crystal-optic studies of the cakes demonstrated that they are composed of a finely dispersed amorphous powder (hydrated SiO_2) and crystalline phases. The main part of the crystalline phase consists of birefringent crystals with refractive indices N_g = 1.839 and N_p = 1.702, $TiOSO_4 \cdot 2H_2O$. Also, a minor amount of rhombic $TiOSO_4$ crystals with refractive indices N_g = 1.709 and N_p = 1.628 is observed.

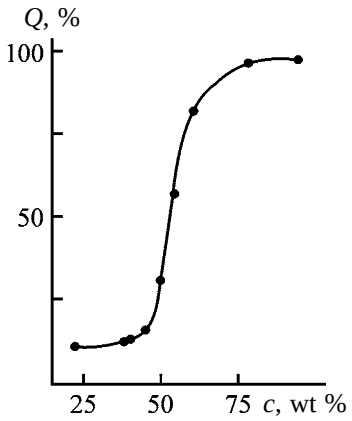

Fig. 4. Recovery Q of titanium(IV) from the titanium–silica product vs. the concentration c of sulfuric acid.

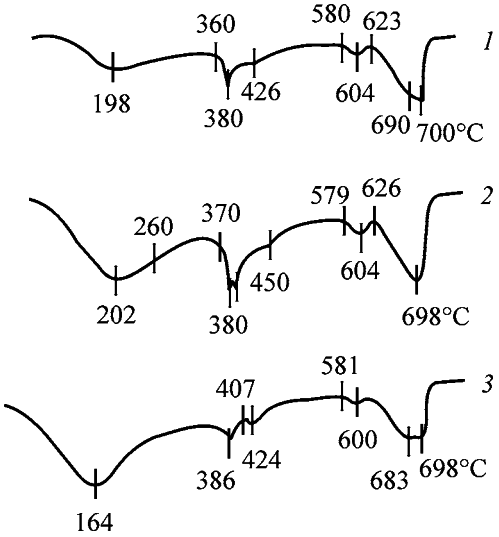

Fig. 5. Thermograms of products formed in sulfatization of the titanium–silica product. Expenditure of H_2SO_4 (kg kg^{-1} TiO_2): (*1*) 1.4, (*2*) 1.6, and (*3*) 1.8.

When the concentration of H_2SO_4 was lowered and its expenditure raised to more than 1.6 kg kg^{-1} TiO_2, the stock was flowing and thermal treatment yielded monolithic, very strong cakes, which virtually could not be removed mechanically from the reaction vessel. The reason for such a morphology of the cakes was presumably that $TiOSO_4 \cdot 2H_2O$ forming in the course of synthesis first dissolved in the excess amount of water contained in the stock and then crystallized to give a very strong composite with hydrated SiO_2. It was established that, when 80–94% H_2SO_4 was used and the acid number was, respectively, 1.6 and 1.8, the starting stock could be prepared in the form of briquettes which retained their shape even in the course of thermal treatment. The cake formed in this case was fragile and could be readily removed from the apparatus. To achieve a high degree of sulfatization of titani-

Table 5. Composition and properties of products formed in sulfatization–leaching of titanium(IV) from the titanium–silica product

Product	Content						K	K_s
	TiO_2	SiO_2	CaO	F^-	Fe_2O_3	H_2SO_4		
Titanium–silica product, wt %	46.9–48.8	34.5–37.4	0.56–3.30	1.9–2.4	0.64–1.00	–	–	–
Sulfuric acid solutions of $TiOSO_4$, g l^{-1}:								
filtrates	161	<0.05	1.62	4.40	1.74	282	1.75	800
	188	<0.05	2.34	5.40	1.82	368	1.95	950
	206	<0.05	2.07	6.14	2.50	380	1.84	850
	240*	<0.05	4.32	6.93	3.82	445	1.85	1500
	315*	<0.05	4.21	7.62	4.93	500	1.58	1000
	342*	<0.05	5.60	7.70	7.40	570	1.66	900
washing water	25.4	–	–	0.78	0.50	44.0	1.76	–
	48.3	–	–	1.24	0.71	95.6	1.97	–
	61.1	–	–	1.76	1.16	115	2.00	–
Silica cake, wt %	5.70	78.6	1.12	1.34	0.064	–	–	–
	4.80	80.0	1.08	1.06	0.050	–	–	–
	3.40	79.8	1.10	1.21	0.052	–	–	–

* Obtained in counterflow leaching.

um(IV), the stock was preliminarily thoroughly mixed. Otherwise, the recovery of TiO_2 into solution decreased to 92.0% when working with heavier weighed portions.

Table 5 lists typical compositions of the products obtained in leaching of titanium(IV) from a sulfatized titanium–silica product, as well as the values of K and K_s for sulfuric acid titanium-containing solutions. The concentration of titanium(IV) in an aqueous solution depends on the relationship between the mass of the cake and the volume of water. After the first stage of leaching, the moist precipitate contained about 20% titanium(IV), which was extracted by subsequent washing by repulpation on a filter. When a larger volume of water was taken in the stage of leaching, the concentration of titanium(IV) decreased, and when, by contrast, this volume was made smaller, the recovery of titanium(IV) declined. For example, when the s : l ratio was changed from 1 : 2 to 1 : 1.5 and 1 : 1.0, the recovery of titanium into the aqueous phase decreased, all other conditions being the same, from 86.7 to 81.2 and 75.8%, respectively. With water and s : l ≈ 1 : 1.5, solutions with 160–206 g l^{-1} of TiO_2 were obtained. A counterflow leaching (three stages) made it even possible to raise the concentration of titanium(IV) to 342 g l^{-1} of TiO_2 without performing the commonly used vacuum evaporation. The values of K in the solutions were in the range 1.6–2.0, and those of K_s, 850–1500, which well satisfies the requirements to thermohydrolysis conditions.

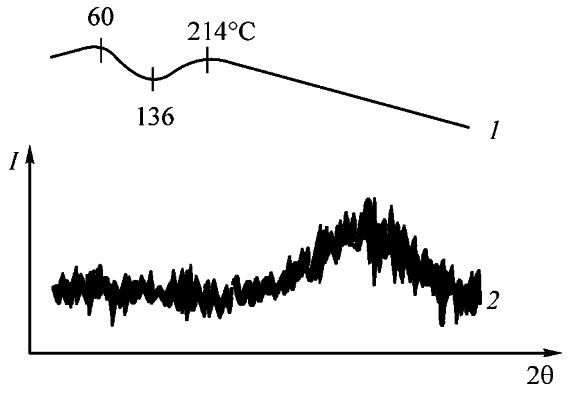

Fig. 6. (*1*) Thermogram and (*2*) X-ray diffraction pattern of a silica cake obtained by leaching of titanium(IV) from a sulfatized titanium–silica product.

Virtually 100% of SiO_2, about 20% of fluoride ions, and less than 5% of iron ions (all relative to the initial amount) remain in the silica cake after sulfatization and leaching. The X-ray diffraction pattern and thermogram shown in Fig. 6 indicate that the product is amorphous and contains SiO_2 as the main phase. 92–98% of titanium(IV) and 90–95% of iron(III) contained in the titanium–silica product are accumulated in the titanium solution.

Compared to the data of [4, 9, 12–15], where the mass ratio Fe_2O_3/TiO_2 in sulfuric acid titanium-containing solutions further subjected to thermohydrolysis was 0.07–0.10, processing of the sphene concentrate yields solution with a smaller ratio, equal to 0.012–0.022.

Thus, the technology being developed can yield sufficiently pure intermediate products, sulfuric acid solutions of $TiOSO_4$ and silica cake.

Under the optimal conditions, the silica cake contains (wt %): 75–80 SiO_2, 3.4 TiO_2, 1.0–1.2 CaO, 1.0–2.0 F, 0.05–0.08 Fe_2O_3, <0.007 TR_2O_3, and water the rest.

The sulfuric acid solutions of $TiOSO_4$, which are distinguished by high stability, contain (g l^{-1}): 160–340 TiO_2, 280–570 H_2SO_4, 1.6–5.6 CaO, 4.4–7.7 F, 1.7–7.4 Fe_2O_3, <0.05 SiO_2, and <0.20 TR_2O_3.

A study of thermohydrolytic precipitation of titanium(IV) from solutions of this kind demonstrated that fluoride ions present in the solutions have no effect on the course of the process and mainly remain in the hydrolytic H_2SO_4. The amount of titanium(IV) that passed into solution was 95.3–95.4%. If reduction of Fe^{3+} to Fe^{2+} was not carried out, the content of Fe_2O_3 in calcined TiO_2 was 0.09–0.11 wt %.

CONCLUSIONS

(1) It was established that HNO_3 solutions with a concentration of 25 wt %, which contain fluorine compounds (HF or H_2SiF_6), effectively leach CaO from the sphene concentrate at 105°C under atmospheric pressure. The titanium–silica product obtained in the process may contain TiO_2 of only anatase structure.

(2) In nitric acid decomposition of the sphene concentrate, up to 98 wt % of CaO, 86 wt % of Ln_2O_3, and 72 wt % of Fe_2O_3 are concentrated in the nitric acid solution, and no less than 99.5 wt % of titanium and silicon oxides find their way into the titanium–silica product, which contains about 48 wt % TiO_2 and 37 wt % SiO_2.

(3) The optimal mode of sulfatization of the titanium–silica product obtained in decomposition of the sphene concentrate with 25% HNO_3 containing fluorine compounds is as follows: process temperature 150°C and expenditure of concentrated (93.5 wt %) H_2SO_4 1.6–1.8 kg kg^{-1} of TiO_2 in the titanium–silica product. In leaching with water of the resulting brittle cake, the recovery of TiO_2 into the leaching solutions is 98%.

(4) To obtain concentrated solutions of $TiOSO_4$, which require no vacuum evaporation before performing the thermohydrolysis, it is necessary to carry out leaching with water in the counterflow mode. The resulting sulfate solutions are characterized by an acid number of 1.6–1.8 and a stability factor of 850–1500 and contain up to 340 g l^{-1} of TiO_2 at a mass ratio Fe_2O_3/TiO_2 = 0.012–0.022. Solutions of this kind can be used to obtain pigment-grade titanium dioxide and for other purposes.

ACKNOWLEDGMENTS

The study was financially supported by the Leading Scientific Schools Program (project no. NSh-1616-2003.3).

REFERENCES

1. Motov, D.L., *Fizikokhimiya i sul'fatnaya tekhnologiya titano-redkometall'nogo syr'ya* (Physical Chemistry and Sulfate Technology of Titanium–Rare-Earth Metal Raw Materials), Apatity: Kol'sk. Nauchn. Tsentr Ross. Akad. Nauk, 2002, part 1.
2. Brusilovskii, A.M., *Khibinskie redkie elementy i pirrotiny* (Khibiny Rare Elements and Pyrrhotines), Leningrad: Goskhimizdat, 1933, vol. 5, pp. 131–139.
3. Mel'nik, B.D., *Inzhenernyi spravochnik po tekhnologii neorganicheskikh veshchestv* (Engineer's Handbook of the Technology of Inorganic Substances), Moscow: Khimiya, 1975.
4. RF Patent 2090509.
5. Protsenko, P.I., Razumovskaya, O.N., and Brykova, N.A., *Spravochnik po rastvorimosti nitritnykh i nitratnykh sistem* (Reference Book of Solubilities of Nitrite and Nitrate Systems), Leningrad: Khimiya, 1971.
6. USSR Inventor's Certificate no. 235883.
7. Khazin, L.G., *Dvuokis' titana* (Titanium Dioxide), Leningrad: Khimiya, 1970.
8. RF Patent 2196736.
9. Goroshchenko, Ya.G., *Khimiya titana* (Chemistry of Titanium), Kiev: Naukova Dumka, 1970.
10. Ryss, I.G., *Khimiya ftora i ego neorganicheskikh soedinenii* (Chemistry of Fluorine and Its Inorganic Compounds), Moscow: Goskhimizdat, 1956.
11. Lokshin, E.P., Vershkova, Yu.A., Vershkov, A.V., and Tareeva, O.A., *Zh. Prikl. Khim.*, 2002, vol. 75, no. 11, pp. 1789–1795.
12. UK Patent 1135787.
13. USSR Inventor's Certificate no. 929566.
14. Popova, R.A., Frolova, M.I., Kuznetsov, V.Ya., and Goroshchenko, Ya.G., *Zh. Neorg. Khim.*, 1982, vol. 27, no. 8, pp. 1967–1971.
15. Dobrovol'skii, I.P., *Khimiya i tekhnologiya oksidnykh soedinenii titana* (Chemistry and Technology of Oxide Compounds of Titanium), Sverdlovsk: Ural'sk. Otd. Akad. Nauk SSSR, 1988.

Russian Journal of Applied Chemistry, Vol. 77, No. 7, 2004, pp. 1050–1055. Translated from Zhurnal Prikladnoi Khimii, Vol. 77, No. 7, 2004, pp. 1066–1071.

INORGANIC SYNTHESIS AND INDUSTRIAL INORGANIC CHEMISTRY

Recovery of Nitric Acid To Obtain a Gypsum Binder

E. P. Lokshin, B. I. Gurevich, T. A. Sedneva, I. A. Tikhomirova, and V. V. Tyukavkina

Tananaev Institute of Chemistry and Technology of Rare Elements and Mineral Raw Materials, Kola Scientific Center, Russian Academy of Sciences, Apatity, Murmansk oblast, Russia

Received July 1, 2003; in final form, February 2004

Abstract—The possibility of processing nitric acid leaching solutions to obtain recovered nitric acid and gypsum with good binding properties was studied in order to develop a new technology for processing of the sphene concentrate.

Nitric acid breakdown of the sphene concentrate yields nitric acid solutions of calcium nitrate, in which up to 97% of the spent HNO_3 is concentrated [1].

In order to develop a technology for their processing, it is of interest to study the possibility of recovery of HNO_3 bound to calcium nitrate, for further use of the acid, by sulfuric acid precipitation of sparingly soluble calcium sulfates. Despite that the process of production of $CaSO_4$, including that from sulfuric acid solutions, has been described, it is impossible to predict the degree of hydration of $CaSO_4$ being precipitated in the process under study on the basis of published data. The composition, structure, dimensions, and shape of crystals, number of molecules of the crystallization water, and properties of the compounds depend in a complicated way on numerous factors: temperature conditions, medium, and presence and type of impurities [2–8], whereas the development of a new technology requires that the process parameters and characteristics of the products obtained should be specified.

Therefore, we studied stoichiometric [with respect to Ca(II)] processing of nitrate solutions obtained in breakdown of the sphene concentrate with concentrated H_2SO_4.

In this work we studied the solid phases isolated under comparable conditions from model and process nitric acid solutions of $Ca(NO_3)_2$ and analyzed the composition of solutions of recovered HNO_3. In addition, we examined the conditions under which high-quality binders can be obtained from $CaSO_4$-based precipitates.

No published data are available on the issues mentioned above, although such data would be of practical and theoretical interest.

EXPERIMENTAL

Calcium sulfate was precipitated with concentrated sulfuric acid (94 wt % H_2SO_4) of pure grade. The model solutions contained 300–900 g l^{-1} of $Ca(NO_3)_2$ and 0–250 g l^{-1} of HNO_3 in various relative amounts; the process solutions contained (g l^{-1}): $Ca(NO_3)_2$, 40 HNO_3, 2.9 TR_2O_3, less than 0.15 TiO_2 and SiO_2, 1.5 Fe_2O_3, 0.5 Al_2O_3, and 1.25 F^-.

To the initial model solution was added with stirring, under temperature control (50°C), H_2SO_4 in a stoichiometric [with respect to Ca(II)] amount in accordance with the reaction

$$Ca(NO_3)_2 + H_2SO_4 = CaSO_4 + 2HNO_3.$$

After 15 min (which was sufficient for the precipitation to be complete), the stirring and heating were terminated. The resulting suspension was filtered in a vacuum at 15–20°C, and the humid precipitate obtained was dehydrated in a desiccator. The precipitate of $CaSO_4$, obtained from process solutions by their treatment with 94% H_2SO_4 at acid expenditure close (90–95%) to the stoichiometric amount, was additionally washed on a filter with distilled water at s : l = 1 : (5–10).

The precipitates kept in a desiccator or dried in a vacuum oven at 54°C or in a drying oven at 60–104°C were subjected to thermogravimetric (TGA), chemical, and X-ray phase (XPA) analyses. The content of HNO_3 and calcium and sulfate ions in the filtrates and precipitates was determined. The mass of the dry salt

1070-4272/04/7707-1050 © 2004 MAIK "Nauka/Interperiodica"

Table 1. Composition of the solid phase and recovery Q_{Ca} of Ca(II) into the precipitate at different contents of $Ca(NO_3)_2$ and HNO_3 in the starting solution, after its stoichiometric treatment with H_2SO_4

Run no.	Concentration, g l^{-1}		Composition of precipitate according to		Q_{Ca}, %
	$Ca(NO_3)_2$	HNO_3	TGA	XPA	
1	286	0	**$CaSO_4$**,* $CaSO_4 \cdot 2H_2O$	**$CaSO_4$**, $CaSO_4 \cdot 2H_2O$	96.8
2	286	25.0	**$CaSO_4$**, $CaSO_4 \cdot 2H_2O$	**$CaSO_4$**, $CaSO_4 \cdot 2H_2O$	96.5
3	286	50.0	**$CaSO_4$**, $CaSO_4 \cdot 2H_2O$	**$CaSO_4$**, $CaSO_4 \cdot 2H_2O$	96.6
4	286	100.4	**$CaSO_4$**, **$CaSO_4 \cdot 0.5H_2O$**, $CaSO_4 \cdot 2H_2O$	**$CaSO_4$**, $CaSO_4 \cdot 0.5H_2O$, γ-$CaSO_4$	94.4
5	286	249.0	**$CaSO_4 \cdot 0.5H_2O$**, $CaSO_4 \cdot 2H_2O$	**$CaSO_4 \cdot 0.5H_2O$**, $CaSO_4 \cdot 2H_2O$	93.7
6	561	99.8	β-**$CaSO_4 \cdot 0.5H_2O$**, $CaSO_4 \cdot 2H_2O$	**$CaSO_4 \cdot 0.67H_2O$**, $CaSO_4 \cdot 2H_2O$	94.1
7	714	100.3	**$CaSO_4 \cdot 2H_2O$**	**$CaSO_4 \cdot 2H_2O$**	94.3
8	857	99.6	**$CaSO_4 \cdot 2H_2O$**	**$CaSO_4 \cdot 2H_2O$**	95.0

* Major phases are printed bold.

was used to calculate, on the basis of the established composition of the solid phase, the recovery Q_{Ca} (%) of Ca(II) into the precipitate. Similar calculations were carried out on the basis of a chemical analysis for Ca(II) and sulfate ions in the liquid phase. The discrepancy did not exceed 3%.

$CaSO_4$ samples obtained from process solutions with varied degree of washing (s : l), which were dried in a drying oven in a vacuum or under atmospheric pressure at temperatures of 100–104°C and contained $CaSO_4 \cdot 0.5H_2O$ with admixture of NO_3^-, were tested for conformity to the requirements of GOST (State Standard) 125 (Gypsum Binders. Technical Specifications). The normal thickness of the gypsum paste corresponded in all cases to a water–gypsum ratio (w/g) of 0.9, at which the setting time τ (min) and compression strength P (MPa) were determined.

A study of model systems demonstrated that the degree of hydration of $CaSO_4$ depends on the content of the main components in a solution being processed (Table 1).

The results of TGA and XPA (Table 1, Fig. 1), which are in rather good agreement, indicate that the degree of hydration of $CaSO_4$ being precipitated depends on the concentrations of both free HNO_3 and calcium ions. In all cases, the deposits have the form of a finely crystalline snow-white product. At low or initially zero acid concentrations, mainly anhydrite (anhydrous $CaSO_4$) crystallizes, which is indicated by the presence in the thermograms (Fig. 1, thermograms *1, 2*) of an endothermic effect at 92–95°C and by a set of basic characteristic reflections at 3.50,

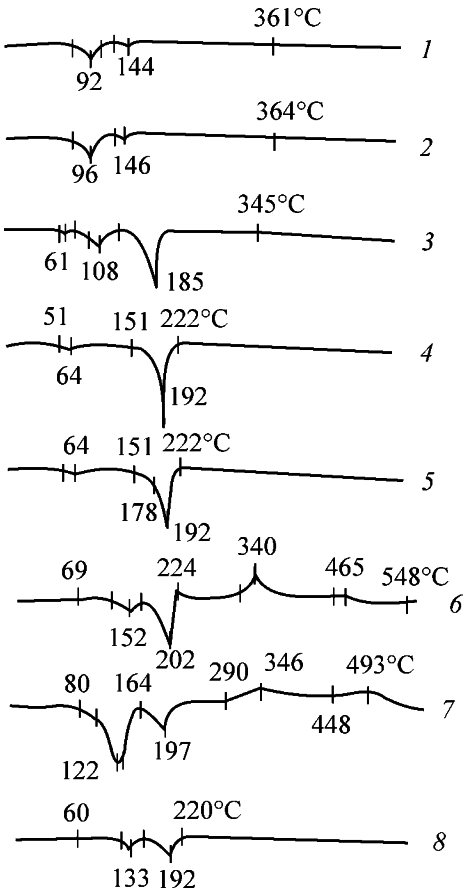

Fig. 1. Thermograms of calcium sulfate products precipitated from nitrate solutions obtained in decomposition of the sphene concentrate. Digits *1–8* correspond to run nos. in Table 1.

Table 2. Efficiency of $CaSO_4$ precipitation, Q, and concentration of recovered HNO_3, c_r, in relation to precipitation conditions and composition of calcium sulfates, depending on drying modes*

Initial concentration, g l^{-1}		T_{pr}, °C	c_r, g l^{-1}	T_{dr}, °C	Composition of precipitate according to XPA	Q_{Ca}, %
$Ca(NO_3)_2$	HNO_3					
360	21	40 → 15	190.3	100	$CaSO_4 \cdot 0.5H_2O$	95.5
360	21	40 → –10	283.5	100	″	95.9
240	10.5	40 → –10	138.6	100	″	93.2
360	21	40 → –10	283.5	100	″	96.7
340	59.5	40 → 15	346.5	100	″	96.4
360	21	40 → 15	283.5	54**	$CaSO_4 \cdot 2H_2O$	96.6
360	21	40 → 20	283.5	60	$CaSO_4 \cdot 0.5H_2O$	96.5
320	21	40 → 20	181.3	54**	$CaSO_4 \cdot 2H_2O$	90.7
120	10.5	40 → 20	99.5	54**	″	92.1
90	5	40 → 20	50.8	54**	″	84.1
330	46	50 → 15	289.5	104**	$CaSO_4 \cdot 0.67H_2O$	96.1
340	34	50 → 15	266.0	105	$CaSO_4 \cdot 0.5H_2O$	94.3

* T_{pr}, T_{dr} are the temperatures of precipitation and drying, respectively.
** Drying in a vacuum.

2.85, 2.33, and 2.21 Å in the X-ray diffraction pattern. The second endothermic effect at 144–146°C suggests a certain low content of gypsum $CaSO_4 \cdot 2H_2O$ in the precipitate, which is not revealed by XPA because of insufficient sensitivity. As the acidity increases, γ-$CaSO_4$ becomes the main modification of the anhydrite according to XPA. The solid phase becomes also enriched in hemihydrate $CaSO_4 \cdot 0.5H_2O$, bassanite, which is evidenced by the second endothermic effect (Fig. 1, thermograms *4*, *5*) shifted to higher temperatures (185 and 192°C). XPA also reveals this compound (characteristic reflections at 6.00, 3.46, 3.00, 2.80, and 2.19 Å). It should be noted that the hemihydrate is formed in solutions with an initial acid number K [mol HNO_3/mol $Ca(NO_3)_2$] exceeding 0.5 (Table 1). The results obtained are in agreement with published data [6, 8].

In the system under study, gypsum $CaSO_4 \cdot 2H_2O$ precipitates as the predominant phase from concentrated solutions that contain more than 364 g l^{-1} of $Ca(NO_3)_2$. Thermogram *8* in Fig. 1 takes the canonical form [9].

Thus, products with different properties can be obtained by varying the composition of nitric acid solutions of $Ca(NO_3)_2$. When the acidity and(or) concentration of Ca(II) in solution was raised, a transition from formation of anhydrite $CaSO_4$, poorly soluble in aqueous solutions, to a more soluble hemihydrate $CaSO_4 \cdot 0.5H_2O$ and then to gypsum $CaSO_4 \cdot 2H_2O$, which is again poorly soluble, was observed. The presence of insignificant amounts of gypsum in the anhydrite phase, in contradiction with the observed tendency toward a rise in the degree of $CaSO_4$ hydration with the acidity and Ca(II) concentration increasing ($CaSO_4 \rightarrow CaSO_4 \cdot 0.5H_2O \rightarrow CaSO_4 \cdot 2H_2O$), can be attributed to high hygroscopicity of the compounds, which results in that they rapidly absorb atmospheric moisture and are hydrated [6, 8].

The process solutions differ in the content of $Ca(NO_3)_2$, HNO_3, and concomitant elements, depending on the conditions under which the sphene concentrate is leached and the titanium–silica product is washed. $CaSO_4$ was precipitated (Table 2) from these solutions also with concentrated H_2SO_4 (94 wt %) with an expenditure close (90–95%) to that required by the stoichiometry. Calcium sulfates obtained from these solutions also have the form of snow-white finely dispersed clotting precipitates. It should be noted that the main part of $CaSO_4$ crystallizes fast (in the course of approximately 10 min); however, the solutions separated from the precipitate are supersaturated with $CaSO_4$ and become turbid upon subsequent keeping because of the continuing precipitation of $CaSO_4$. In this case, the dilution of the starting solution because of the use of concentrated HNO_3 does not exceed 11%, and the $CaSO_4$ precipitate crystallizes in a nitric acid solution containing 266 to 366 g l^{-1} (23–31 wt %) HNO_3. It is known that it is at this concentration of HNO_3 that the solubility of $CaSO_4$ is the highest (2.0 wt % at room temperature), which may pose difficulties in recycling of the recovered acid.

In order to recover Ca(II) into the precipitate to the maximum possible extent, experiments with freezing out of the suspensions obtained and their filtration at –10°C were carried out. In this case, the residual concentration of Ca(II) in solution decreased from 10 to approximately 6 g l^{-1} of CaO, which affected the recovery of Ca(II) into the precipitate: it increased from 93.2 to 96.7%.

The filtrates obtained contain up to 346 g l^{-1} HNO_3. The concentration of impurity elements (titanium, silicon, iron, aluminum) was less than 1 g l^{-1} from the very beginning, and that of Ca(II) and sulfate ions can be minimized. The recovered HNO_3 contains (g l^{-1}): 266–346 HNO_3, 3.6–6.0 CaO, 6.0–10.0 SO_4^{2-}, 2.5 Ln_2O_3, <1.3 Fe_2O_3, <1.0 F, and <0.4 Al_2O_3. In the acid, ions of rare-earth elements, iron, and fluorine concentrate in amounts, relative to the initial content in the nitric acid solution, of up to (%): 95–98 Ln_2O_3, 96–99 Fe_2O_3, and 99.4 F^-.

Thus, stoichiometric precipitation of calcium sulfates from solutions obtained in breakdown of the sphene concentrate can yield HNO_3 solutions (~25 wt %) whose recycling into the stage of decomposition of the sphene concentrate is rather efficient, but leads to accumulation of ions of rare-earth elements, thorium, and iron in the liquid phase, and Ca(II) in the titanium-silica precipitate. Even though the recovered HNO_3 contains ions of iron, aluminum, lanthanides, and radionuclides in low concentrations, its repeated recycling may lead to their accumulation, which requires an additional purification stage.

It should be noted that the composition of the precipitates obtained from the process solutions differs from that of the precipitates formed in the model solutions under similar conditions. In stoichiometric sulfuric acid precipitation of Ca(II) at temperatures lower than 50°C, mainly $CaSO_4 \cdot 2H_2O$ is formed, which, in contrast to the model systems, contains no anhydrite $CaSO_4$. It may be assumed that impurity elements destabilize the anhydrite and catalyze it fast hydration.

Gypsum preserves its composition $CaSO_4 \cdot 2H_2O$ upon drying in a desiccator or in a vacuum oven at temperatures of up to 60°C. Precipitates kept in a drying oven at temperatures exceeding 100°C have the form of a hemihydrate of the composition $CaSO_4 \cdot 0.67H_2O$ or bassanite $CaSO_4 \cdot 0.5H_2O$ (Figs. 2, 3).

The results obtained in TGA of the resulting $CaSO_4 \cdot 2H_2O$ (20.83% loss of mass virtually coincides with the calculated value) indicate (Fig. 2) that, when temperature is elevated at a rate of 9 deg min^{-1}, loss of water starts to be observed at temperatures

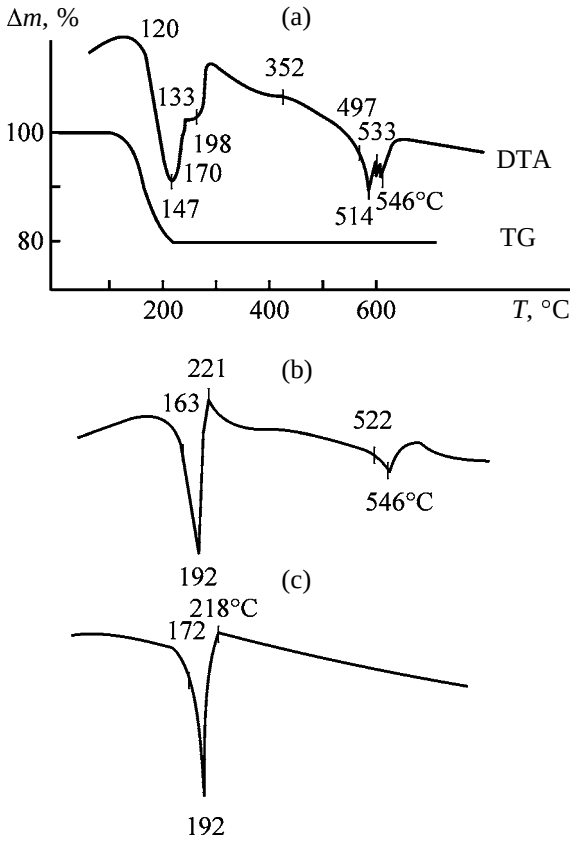

Fig. 2. Thermograms of samples precipitated from nitrate solutions obtained in decomposition of the sphene concentrate. (Δ*m*) Change in mass and (*T*) temperature. Sample: (a) $CaSO_4 \cdot 2H_2O$, (b) $CaSO_4 \cdot 2H_2O$ + $CaSO_4 \cdot 0.5H_2O$, and (c) $CaSO_4 \cdot 0.5H_2O$.

higher than 120°C. However, when subjected to prolonged thermostating, freshly precipitated $CaSO_4 \cdot 2H_2O$ starts to release water even at drying temperatures $T_{dr} \geq 60$°C, to be transformed into the hemihydrate $CaSO_4 \cdot 0.5H_2O$. A modification $CaSO_4 \cdot 0.67H_2O$ close to bassanite was also recorded.

The content of the main and impurity elements in the bassanite $CaSO_4 \cdot 0.5H_2O$ obtained is approximately as follows (wt %): 36.3 CaO, 65.5 SO_4^{2-}, 0.85 NO_3^-, 0.06 F^-, <0.04 Fe_2O_3, <0.20 Al_2O_3, 0.02–0.04 TR_2O_3, <0.01 $Nb(Ta)_2O_5$, <0.1 SiO_2, and 0.041 TiO_2. It should be noted that the recovery of iron and fluorine ions into the precipitate is low (1–3 and <0.55%, respectively), whereas aluminum(III) is distributed among the phases evenly. The low, on the whole, concentration (g l^{-1}) of impurity elements in the starting solution (1.5 Fe_2O_3, 0.5 Al_2O_3, 1.25 F^-) and washing of precipitates with water at s : l = 1 : (5–10) predetermine the high purity of the products obtained.

Table 3. Properties of dried gypsum precipitates based on $CaSO_4 \cdot 0.67H_2O$ and $CaSO_4 \cdot 0.5H_2O$

NO_3^-, wt %	Setting time, min		*P*, MPa			GOST 125	
	onset	end	2 h	1 day	7 days	brand	group
0.78*	1.0	3.0	1.7	4.8	5.0	None	None
0.85	9.0	17.0	4.2	–	–	G-4AIII	B
0.92	2.5	6.5	2.8	6.0	6.3	G-2AIII	A
2.8	3.0	7.5	2.9	6.5	6.7	G-2AIII	A
5.8	8.5	19.0	5.1	8.3	13.3	G-5AIII	B

* Drying under atmospheric pressure.

Because $CaSO_4 \cdot 2H_2O$ is unsuitable for production of building articles, it was dried to obtain precipitates of $CaSO_4 \cdot 0.67H_2O$ and $CaSO_4 \cdot 0.5H_2O$, and the possibility of their use to manufacture gypsum binders was studied.

It was established that the precipitates (gypsums) studied can be divided into fast-hardening (A) and normally hardening (B) (Table 3). An increase in the content of NO_3^- in the starting precipitate leads to an improvement of the quality of the building plaster. A similar behavior is observed upon introduction of the above impurity into gypsums obtained from natural raw materials [9, 10]. The optimum content of nitrate ions is 0.9–2.8 wt %, which remains in the sulfates upon washing at s : l = 1 : (5–10). This gives fast-hardening gypsums of white color, which belong to group A. As the content of NO_3^- ions is raised further, the setting time increases and samples become cream-colored. It should be noted that a gypsum sample obtained upon dehydration of the starting $CaSO_4 \cdot 2H_2O$ in a drying oven under atmospheric pressure was found to be substandard because of its exceedingly short setting time and low strength.

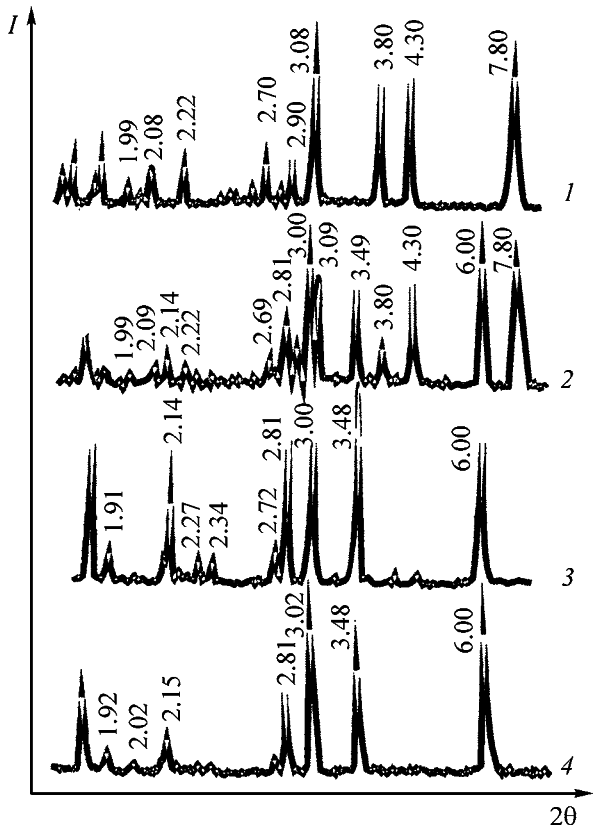

Fig. 3. X-ray diffraction patterns of samples precipitated from nitrate solutions obtained in decomposition of the sphene concentrate. (*I*) Intensity and (2θ) Bragg angle. Sample: (*1*) $CaSO_4 \cdot 2H_2O$, (*2*) $CaSO_4 \cdot 2H_2O$ + $CaSO_4 \cdot 0.5H_2O$, (*3*) $CaSO_4 \cdot 0.67H_2O$, and (*4*) $CaSO_4 \cdot 0.5H_2O$. Interplanar spacing are given in Å.

In their compression strength, setting times, and fineness of grinding, the gypsums correspond to brands G-2AIII, G-4BIII, and G-5BIII. The additionally measured strength of samples dried at 60°C to constant weight after 1 and 7 days of hardening demonstrated that their strength increased upon drying, which is particularly important in fabrication of gypsum articles [10]. As regards the whole set of their properties, gypsums manufactured from precipitates can be used for plastering and manufacture of building articles of any type.

CONCLUSIONS

(1) It was established that mainly $CaSO_4 \cdot 2H_2O$, which, in contrast to the case of model systems, contains no anhydrite $CaSO_4$, is formed in stoichiometric precipitation of calcium(II) from nitric acid solutions formed in nitric acid–fluoride breakdown of the sphene concentrate.

(2) Gypsums obtained on the basis of $CaSO_4 \cdot 0.67H_2O$ and $CaSO_4 \cdot 0.5H_2O$, products formed in vacuum drying of $CaSO_4 \cdot 2H_2O$, correspond to brands G-2AIII, G-2BIII, and G-5BIII and can find wide use in the building industry.

(3) Recovered nitric acid contains 266–346 g l^{-1} of the main substance (HNO_3) and concentrates rare-earth elements to 98% of their initial content, which may lead in repeated recycling to their pronounced accumulation for subsequent recovery into a separate product.

ACKNOWLEDGMENTS

The study was financially supported by the Leading Scientific Schools Program (project no. NSh-1616-2003.3).

REFERENCES

1. RF Patent 2 196 736.
2. Nenitescu, C.D., *Chimie Generala*, Bucharest: Tehnica, 1963.
3. Rudin, V.N., Voskresenskii, S.K., Novikov, A.A., *et al*., *Tr. Nauchno-Issled. Inst. Udobr. Insektofung*., 1982, issue 241, pp. 45–54.
4. Khamskii, E.V., *Kristallizatsiya v khimicheskoi promyshlennosti* (Crystallization in Chemical Industry), Moscow: Khimiya, 1979.
5. Lasis, A.Yu., *Stroit. Mater*., 1971, no. 1, pp. 38–39.
6. Abramyan, R.M., Grigoryan, G.O., Grigoryan, O.V., *et al*., *Zh. Neorg. Khim*., 1977, vol. 22, no. 3, pp. 622–625.
7. Vil'nits, E.L., Pozin, M.E., Kopylev, B.A., *et al*., *Novye issledovaniya po tekhnologii mineral'nykh udobrenii* (New Research in the Field of Technology of Mineral Fertilizers), Leningrad: Khimiya, 1970, pp. 67–73.
8. Podozerskaya, E.A., Tsikaeva, D.V., and Dvegubskii, N.S., Available from VINITI, 1978, Apatity, no. 872–79.
9. Gurevich, B.I., *Vyazhushchie veshchestva iz tekhnogennogo syr'ya Kol'skogo poluostrova* (Binders Manufactured from Raw Materials of Technological Origin from the Kola Peninsula), Apatity: Kol'sk. Nauchn. Tsentr Ross. Akad. Nauk, 1996.
10. Volzhenskii, A.V. and Ferronskaya, A.V., *Gipsovye vyazhushchie izdeliya (tekhnologiya, svoistva, primenenie)* (Gypsum-Based Binders (Technology, Properties, and Use)), Moscow: Stroiizdat, 1974.

Russian Journal of Applied Chemistry, Vol. 77, No. 7, 2004, pp. 1056–1060. Translated from Zhurnal Prikladnoi Khimii, Vol. 77, No. 7, 2004, pp. 1072–1076.

INORGANIC SYNTHESIS AND INDUSTRIAL INORGANIC CHEMISTRY

Electrohydraulic Treatment in Dressing of Gold-Containing Ores

N. P. Potsyapun, A. S. Buinovskii, and V. V. Bordunov

Seversk State Technological Institute, Seversk, Tomsk oblast, Russia
Institute of Petrochemistry, Siberian Division, Russian Academy of Sciences, Tomsk, Russia

Received January 28, 2004

Abstract—The influence exerted by electrohydraulic treatment of mineral samples of various compositions on the weakening of the ore material and redistribution of gold into finer classes was studied.

In some cases, the conventional processes of crushing and grinding in screw crushers and ball mills fail to improve the breakdown of minerals. By contrast, raising the fineness of grinding (to ~10 μm) leads to overgrinding and sludging of productive solutions and mineral slurries. At the same time, crushing and grinding consumes about 70% of energy expended for the entire process of dressing of mineral raw materials [1].

The failure to break down minerals leads to loss of the valuable component with final tailings. Analysis of the main loss in primary dressing shows [1] that 35–40% of the loss is associated with concretions, and 30–35%, with particles less than 10 μm in size. To diminish this loss in processing of finely disseminated ores and to ensure breakdown of concretions without excessive overgrinding, it is necessary to pass from the conventional nonselective methods of ore treatment to selective disintegration based on energy impact.

The electrohydraulic effect, which arises in electric breakdown of liquid media, may become an effective method of selective disintegration of mineral components. The electrohydraulic impact causes simultaneously a powerful shock pulse and ultrasonic and electromagnetic emission, changes the chemical composition of the medium through erosion of the material of the electrode and destruction of water molecules in the discharge channel. However, the main factors that affect the whole material are shock waves: primary, secondary, and reflected, and also microexplosions of bulk cavitation. Originally, a network of microcracks appears in mineral products under the action of the compression shock wave. The action of a pulse train on minerals enables multiple emission of secondary compression waves, which creates defective zones and strained states in the minerals being processed. Therefore, it is the most appropriate to use electrohydraulic treatment for preliminary disordering of the ore and selective breakdown of minerals [2–4].

EXPERIMENTAL

The efficiency of electrohydraulic treatment was studied on two objects: old tailings of Artemovskaya gold-extracting factory (sample I) and gold-containing ores from Zoloto Joint-Stock Company (sample II).

When choosing the mode of ore treatment and the dressing scheme, it is necessary to take into account the granulometric composition and morphological features of gold itself and gold-bearing phases. The mineral composition of the samples studied is listed in Table 1, and the results of chemical analysis of the samples, in Table 2.

A mineralogical analysis of sample I demonstrated [5] that the nonmetallic minerals contained in the

Table 1. Mineral composition of samples I and II

Mineral	Content, %, in indicated sample	
	I	II
Quartz	40	48.7
Feldspar	25	47.4
Carbonates (calcite)	15–20	1.6
Chlorites (magnesial-auric)	20	10
Pyrite	1–2	0.3
Arsenopyrite	1.0	1.2
Bistite (mica)	10–15	0.5
Magnesite	1–2	0.3

1070-4272/04/7707-1056 © 2004 MAIK "Nauka/Interperiodica"

sample are mostly represented by quartz in the form of grains of irregular angular shape, which is frequently impregnated with iron hydroxides and, as a result, has reddish color. Sulfides are represented by pyrite, pyrrhotine, chalcopyrite, arsenopyrite, sphalerite, and galenite.

The ore bodies of samples I and II are represented by quartz-vein low-sulfide formations and the embedding hydrothermally modified (quartz-containing, sulfidized) shale.

According to the results of a phase analysis, 14.5% of gold in sample I [5] is the native (amalgamable) phase, 76.8% of the metal is associated with sulfides, and 8.7%, with silicates. In sample II, about 72.9% of gold is in the free state, 4.6% is associated with sulfides, and 0.8%, with quartz and other minerals.

Table 3 lists the granulometric composition of the starting materials and the distribution of gold among fractions.

The results of a sieve analysis of the starting material of sample I demonstrate that the content of gold increases when the grain size becomes smaller, reaching the maximum value (19.4 and 33 g ton^{-1}) for the fractions –0.063+0.050 and –0.050 mm, respectively. However, the yield of these fractions, which are, in fact, concentrates, is extremely low, 4.9%. The amount of gold in coarser fractions decreases to 1–2 g ton^{-1}, but, at the same time, the amount of gold in these fractions is 60% of its total content. This is due to the increased (80%) yield of +0.1-mm fractions, compared with finer fractions. The finely dispersed gold (–1 μm) contained in these fractions is commonly extracted to only an insignificant extent. The main mass of this gold remains embedded in minerals, and more frequently in pyrite (the content of finely dispersed gold in pyrite may be as high as several hundred grams per ton). In the course of flotation dressing, this gold is extracted together with the carrier minerals.

The distribution of gold in the starting sample II is somewhat different. It can be seen from Table 3 that the distribution of gold among fractions is relatively even (10 to 20%). In the –0.1+0.05-mm fraction, the amount of gold is the largest (33.8%), which is accounted for by the low yield of these fractions (13.2%). In a finer (sludge) –0.05-mm fraction, the content of gold decreases, compared with that in the –0.1+0.05-mm fraction, by a factor of 4.7. However, the amount of gold in this fraction does not decrease significantly (9.6%) because of the simultaneous increase in its yield. Most part of gold is distributed among +0.63-mm fractions, which constitute 34% of the whole sample under study. Therefore, subsequent dressing without preliminary weakening or grinding of this fraction will lead to a considerable loss of the valuable component into the dressing tailings.

Table 2. Chemical composition of samples I and II

Element and compound	Content, %, in indicated sample	
	I	II
SiO_2	35.89	66.46
Al_2O_3	7.22	13.8
Fe_2O_3	15.47	5.94
Sb	0.028	<0.01
CaO	6.06	1.12
Zn	0.214	<0.01
Cd	0.0015	<0.01
Bi	0.0144	<0.01
Pb	0.75	0.01
S	13.49	0.97
As	0.28	0.62
Cu	0.925	0.03

The aim of this study was, first, to develop a process of ore treatment that would raise the yield of fine fractions containing gold of emulsion-type dissemination and, second, to simultaneously weaken to the maximum possible extent the binding between the mineral, carrier, and metal. The latter will intensify the subsequent procedures for recovery of gold into a commercial product.

The influence exerted by the electrohydraulic impact on the processing properties of particles of gold-containing samples was studied as follows: Mineral slurry with a certain concentration of the solid component (s : l = 1 : 10) and known geochemical properties of the mineral raw material was poured into a discharge chamber of certain volume and treated in various modes of the electrohydraulic impact.

In the course of electrohydraulic treatment, only the number of pulses applied to the slurry was varied, whereas all other parameters remained the same during the experiment: weighed portion being treated, 100 g; treatment duration, 20, 30, and 60 pulses; pulse repetition frequency, 2–3 pulses per second; pulse energy, 80 J; grain size of the starting product, ≤ 2 mm; and working liquid, water. After the electrohydraulic treatment, a sample was extracted from the reactor, and the mineral slurry was subjected to separation. The influence exerted by the electrohydraulic impact was evaluated on the basis of a sieve

Table 3. Granulometric composition* and distribution of gold among fractions in starting samples**

Fraction, mm	Sample I			Sample II		
	α, %	β, g ton^{-1}	γ, %	α, %	β, g ton^{-1}	γ, %
+0.630	7.90	0.5	7.60	34.00	2.05	17.80
–0.630 + 0.400	15.00	0.73	7.52	} 16.60	1.7	12.75
–0.400 + 0.315	16.50	0.45	7.20			
–0.315 + 0.200	20.30	0.02	8.00	12.60	1.5	11.70
–0.200 + 0.160	16.70	1.2	10.15	} 10.20	1.43	14.40
–0.160 + 0.100	12.10	1.85	11.58			
–0.100 + 0.063	6.60	1.96	10.80	6.10	2.33	18.60
–0.063 + 0.050	2.40	19.4	15.20	7.10	0.57	15.15
–0.050	2.50	33.0	21.95	13.40	0.5	9.60
Total	100.00	2.5	100.00	100.00	2.3	100.00

* Determined by dry sieving; the same for Table 4.
** α is yield; β, Au content; and γ, Au distribution.

Table 4. Granulometric composition and distribution of gold among fractions in samples I and II after electrohydraulic treatment

Fraction, mm	20 pulses			30 pulses			60 pulses		
	α, %	β, g ton^{-1}	γ, %	α, %	β, g ton^{-1}	γ, %	α, %	β, g ton^{-1}	γ, %
+0.630	8.3	3.43	5.3	8.1	0.13	4.8	7.8	0.05	1.8
–0.630 + 0.400	14.3	0.84	5.1	12.6	0.1	4.3	11.9	0.12	0.8
–0.400 + 0.315	15.8	0.5	6.1	16.1	0.12	5.1	14.8	0.17	4.1
–0.315 + 0.200	17.8	1.9	7.3	17.0	0.26	2.5	17.1	1.5	4.8
–0.200 + 0.160	15.9	2.54	6.5	16.4	0.44	7.2	15.0	0.07	4.2
–0.160 + 0.100	12.6	3.4	8.5	12.6	0.09	10.2	13.1	0.4	5.0
–0.100 + 0.063	8.7	9.4	16.3	9.5	6.16	11.9	10.4	3.55	15.6
–0.063 + 0.050	} 6.6 {	<0.5	19.5	} 7.7 {	15.87	21.8	} 9.9 {	0.71	25.3
–0.050		9.2	25.4		17.6	32.2		7.85	38.4
Total	100.0	2.53	100.0	100.0	2.37	100.0	100.0	2.28	100.0
+1.600	12.5	–	–	–	–	–	9.8	–	–
–1.600 + 0.630	15.2	0.13	11.3	–	–	–	12.0	0.25	5.1
–0.630 + 0.315	14.9	0.2	6.2	–	–	–	12.1	0.2	4.3
–0.315 + 0.200	11.1	0.3	10.1	–	–	–	9.7	0.03	7.2
–0.200 + 0.100	7.8	0.14	15.8	–	–	–	7.5	0.12	17.0
–0.100 + 0.063	7.6	0.3	23.9	–	–	–	8.5	0.3	24.5
–0.063 + 0.050	11.2	0.09	19.9	–	–	–	13.6	0.1	25.4
–0.050	19.7	0.05	12.8	–	–	–	26.8	0.18	16.5
Total	100.0	2.34	100.0	–	–	–	100.0	2.38	100.0

analysis and an analysis for the content of gold in the samples before and after the treatment. The content of gold in solid residues was determined by X-ray fluorescence analysis [6]. Each result was obtained for a minimum of three parallel runs. The results of an analysis performed five times for each sample were subjected to statistical processing and are presented here with account of errors.

For more clarity in describing the results of the study, the experimental data in Table 4 are plotted graphically.

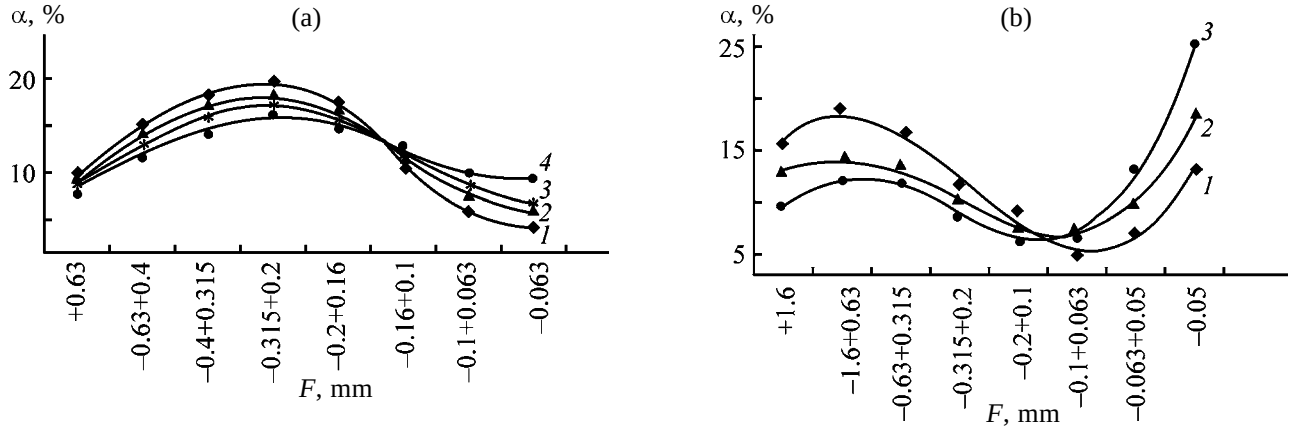

Fig. 1. Granulometric composition of samples (a) I and (b) II before and after electrohydraulic treatment. (α) Yield and (*F*) fraction. Sample: (*1*) untreated and (*2, 3, 4*) treated with 20, 30, and 60 pulses, respectively; the same for Fig. 2.

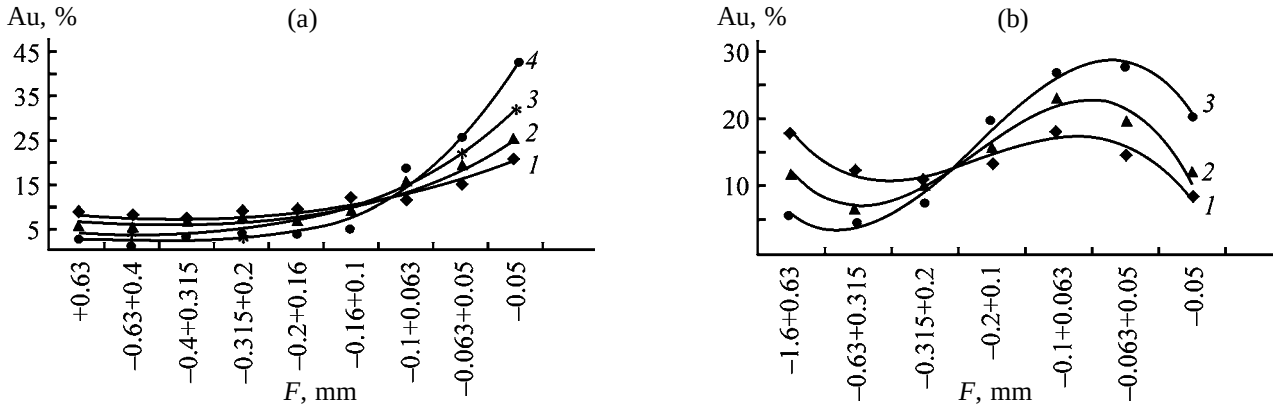

Fig. 2. Distribution of gold among fractions *F* in samples (a) I and (b) II before and after electrohydraulic treatment. (Au) Recovery of gold.

Figures 1a and 1b show how ground ore is distributed among fractions at different intensities of the electrohydraulic treatment. Figures 2a and 2b show how the distribution of gold among fractions depends on the intensity of electrohydraulic treatment.

Electrohydraulic treatment of samples I leads to an insignificant rise in the content of finer fractions in proportion to the increase in the treatment intensity (by 1%, on the average). After treatment with 60 pulses, the content of –0.63+0.16-mm fractions decreases by 12%, and that of –0.1-mm fractions increases by 12%. The coarser +0.63-mm fractions are virtually not ground at all under the action of the electrohydraulic effect. This can be explained as follows: the compression waves formed under the given experimental conditions, as well as the resulting secondary effects, which favor disintegration, have no significant effect on ore particles that belong to the +0.63-mm fraction. In addition, the influence exerted by grinding of the given type of samples is "masked" by the presence of compounds of iron and oxygen on the surface of gold grains. This indicates that the surface of gold grains is covered with films of oxides (hydroxides) of iron (film thickness not exceeding 2 μm). The last statement is clearly illustrated by Fig. 2a.

Figure 2a shows that gold is distributed in proportion to the yields, whose value depends on the intensity of electrohydraulic treatment. As the yield of finer fractions increases, the amount of gold in these fractions grows simultaneously. The richest in gold are –0.10-mm fractions. Similarly to the initial sample, the –0.1-mm fractions in samples treated with 20, 30, and 60 pulses are concentrates containing 61, 66, and 79% of the total amount of gold, respectively. Compared with the initial sample, the yield of these fractions in treated samples increases by factors of 1.5, 1.7, and 2, respectively.

Electrohydraulic treatment of samples II affects the granulometric composition considerably more strongly, compared with samples I. The content of coarser fractions decreases in proportion to the treatment intensity, and the yield of fine fractions, accordingly, increases. The +0.1-mm fractions are ground satisfactorily and their total decreases by 20%, whereas the yield of +0.1-mm fractions increases proportionally.

The type of gold distribution in samples II is similar to that in samples I. The only difference is that gold in samples I is distributed evenly over all fractions coarser than +0.1 mm, whereas the content of gold in samples II decreases when the treatment intensity increases, being redistributed into finer –0.2-mm fractions. This points to a weaker binding between the mineral, carrier, and metal in samples of the gold-containing ore. As a result of electrohydraulic treatment, 22% of gold passes from the +0.2-mm fraction to finer fractions. The content of gold in the –0.063-mm fraction increases twofold.

An analysis of the efficiency of the electrohydraulic treatment of samples I and II demonstrated that the treatment can produce microcracks in mineral products, which, in turn, facilitates the access of the leaching agent to the surface of gold grains. The weakening of concretions makes higher the recovery of Au into productive solutions. The efficiency of activation with electric discharges in a liquid makes it possible to regard the given process as a promising technique for pretreatment of mineral raw materials in ore dressing and recovery of gold by cyanidation or using other leaching agents.

CONCLUSIONS

(1) Electrohydraulic treatment changes the granulometric composition of mineral products. Secondary raw materials (old tailings) are ground to a lesser extent because of the formation of high-strength oxidation products on the surface of particles in a sample.

(2) Electrohydraulic treatment leads to disintegration and weakening of binding between the mineral and the metal, which leads to redistribution of gold from coarser to finer fractions.

(3) Electrohydraulic treatment is more preferable for gold-containing unyielding ores, because a stronger influence on the granulometric composition and gold recovery is observed in this case. This fact is accounted for by the presence of iron hydroxide films on the surface of gold in samples of old tailings, which creates an additional barrier for the electrohydraulic effect.

(4) The ore treatment process studied can be regarded as promising for processing of gold-containing unyielding ores, which are characterized by nonuniform distribution and fine dissemination of gold in the rock-forming minerals.

REFERENCES

1. Chanturiya, V.A., *Tsvetn. Met.*, 2002, no. 2, pp. 15–21.
2. Kassir, G.A., Shperling, V.I., Temnikov, E.M., *et al.*, *Novye fizicheskie metody razrusheniya mineral'nykh sred* (New Physical Methods for Disintegration of Mineral Media), Leningrad: Nedra, 1970, pp. 304–309.
3. Kulebakin, V.G., Terekhova, O.G., Molchanov, V.I., and Zhizhaev, A.M., *Aktivatsiya vskrytiya mineral'nogo syr'ya* (Activation of the Breakdown of Mineral Raw Materials), Novosibirsk: Nauka, 1999.
4. *Oborudovanie i tekhnologicheskie protsessy s ispol'zovaniem elektrogidravlicheskogo effekta* (Apparatus and Processes Using the Electrohydraulic Effect), Gulyi, G.A., Ed., Moscow: Mashinostroenie, 1997.
5. Algebraistova, N.K., Alekseeva, E.A., and Nikiforova, S.A., *Tsvetn. Met.*, 2001, no. 11, pp. 20–22.
6. Ageeva, L.D., Buinovskii, A.S., Kolpakova, N.A., and Kovyrkina, T.V., *Sovmestnoe opredelenie v rudakh i kontsentratakh zolota, serebra i metallov platinovoi gruppy rentgenofluorestsentnym metodom* (Joint Determination of Gold, Silver, and Platinum Metals in Ores and Concentrates by X-ray Fluorescence Analysis), Seversk: Seversk. Gos. Tekhnol. Inst., 2003.

Russian Journal of Applied Chemistry, Vol. 77, No. 7, 2004, pp. 1061–1065. Translated from Zhurnal Prikladnoi Khimii, Vol. 77, No. 7, 2004, pp. 1077–1081.

INORGANIC SYNTHESIS AND INDUSTRIAL INORGANIC CHEMISTRY

Damping of the Growth of Titanium Oxide Nanolayer Formed by Molecular Layer Deposition Technique on Oxidized Silicon Surface

V. P. Dorofeev, A. A. Malygin, and S. I. Kol'tsov

St. Petersburg State Technological Institute, St. Petersburg, Russia

Received October 28, 2003, in final form, February 2004

Abstract—Ellipsometric data on titanium oxide nanolayers synthesized by molecular layer deposition technique on oxidized Si(100) surface are discussed.

Numerous works [1–12] concern molecular layer deposition (MLD) of titanium oxide nanolayers on the surfaces of dispersed materials and flat supports in a vacuum and in flow systems under atmospheric pressure. Many works on the preparation of titanium oxide layers by ALD (atomic layer deposition) and ALE (atomic layer epitaxy), which are based on the same principles as the MLD technique, have been published recently [13–16]. Nanometer titanium oxide layers can be used in microelectronics for the formation of capacitors and undergate dielectrics for apparatus with minimal component sizes of 90 nm and less, and also for the production of catalytically active materials and sorbents [15, 17–19].

When titanium oxide layers were synthesized by the MLD technique on flat silicon and quartz supports, the dependence of the layer thickness on the number of MLD cycles was linear when the deposition was performed both under atmospheric pressure and in a vacuum [4–7, 9]. According to [5–7, 9], the thickness growth per one MLD cycle was 0.24–0.33 nm, which is close to the size of a titanium oxide octahedron.

The experiments have shown that, at temperatures higher than 200°C, damping of the growth of titanium oxide nanolayer takes place on the surface of single-crystal silicon coated by a layer of silicon oxide. The phenomenon was not described earlier in the literature. In this work we made an ellipsometric study of this process.

Titanium oxide layers were synthesized on single-crystal silicon (KDB-7.5 grade) plates with the (100) orientation. Their surface was coated with a film of silicon oxide of 2–3 nm thickness, which was obtained by silicon oxidation with concentrated nitric acid. It should be noted that the oxide film on silicon was formed in the presence of water without high-temperature treatment of the supports; therefore, maximal hydroxylation of the surface could be expected.

The synthesis was carried out in a vacuum glass installation with a volume of about 400 ml [6]. An MLD cycle included treatment of the plates by $TiCl_4$ vapor, pumping out of the forming hydrogen chloride and excess of $TiCl_4$ vapor, treatment with water vapor, and pumping out of hydrogen chloride and water vapor excess at 160–260°C. The contact time after the addition of $TiCl_4$ vapor was 1 min, and the evacuation time, 2 min. A two–threefold increase in these parameters did not change the thickness of the titanium oxide layers synthesized. The residual gas pressure after 2-min evacuation was about 0.3 Pa. The temperature in the reactor was maintained with an accuracy of ±3°C. The main inner parts of the installation being in contact with the reagents were heated to no less than 120°C.

The formation of titanium oxide layers was monitored by ellipsometry. A null-ellipsometer with a helium–neon laser (λ = 632.8 nm) assembled by a PCSA scheme with a fixed compensator [20] was used. The measurements were carried out by a four-zone technique, which eliminated most of the errors arising from imperfection of the ellipsometer optical scheme [20]. The ellipsometric measurements were carried out in air before and after synthesis of the samples; the incidence angle was 70°.

According to the ellipsometric data, the thickness of a titanium oxide nanolayer depended linearly on the number of MLD cycles at synthesis temperatures

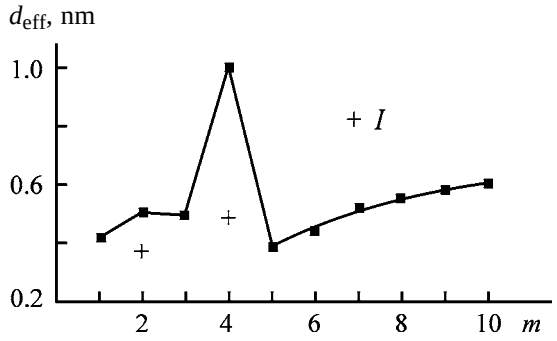

Fig. 1. Effective thickness of titanium oxide film d_{eff} as a function of the number of MLD cycles m on oxidized silicon surface. (*I*) After heating; the same for Fig. 2.

of 160–200°C. The refractive indices of the films were 2.4–2.5, which corresponds to the refractive index of anatase [21].

We have found that, in the range 200–235°C, the ellipsometric parameters of the sample surface remain practically constant after 10 and more (up to 20) MLD cycles. The parameter Δ decreased by 1°45′–2°10′, and the parameter ψ increased on the average by 1′.

According to the ellipsometric data, the increase in the synthesis temperature above 240°C resulted a in significant decrease in the thickness of titanium oxide nanolayers.

The change in the ellipsometric parameter Δ in the range 200–235°C corresponds to the thickness of a titanium oxide layer less than 1 nm; its refractive index can be determined exactly only by immersion ellipsometry [20]. Therefore, we calculated the effective thickness of the films using a preset refractive index n = 2.5 corresponding to anatase [21], which agrees well with an average increase in the ellipsometric parameter ψ by 1′. The maximal effective thickness of a titanium oxide film which was attained in ten and more MLD cycles was 0.60–0.67 nm. According to our calculations, a small error in the determination of the refractive index only slightly affects the calculated film thickness. For example, if we accept n = 2, the calculated film thickness decreases by 10% as compared to n = 2.5.

The effective thickness d_{eff} of a titanium oxide nanolayer synthesized at 225°C, determined by ellipsometry, is shown in Fig. 1 as a function of the number of MLD cycles m. It is seen from Fig. 1 that, in the initial stages of the nanolayer formation (m < 5), its effective thickness is abnormally high and increases nonmonotonically with the number of MLD cycles. The observed abnormally high values of the effective thickness are in agreement with the published data [8, 11, 12] on abnormally large changes in the ellipsometric parameter Δ in the initial stages of the formation of titanium oxide nanolayers. After five MLD cycles, the shape of the function $d_{eff} = f(m)$ changes, probably owing to compaction of the nanolayer.

The effects described are attributable to crystallization of titanium oxide nanolayers. It is mentioned in the monograph [22] that titanium dioxide starts to crystallize in the presence of water even at 60–100°C. The nanolayer effective thickness after five treatment cycles is 0.39 nm, which agrees well with the parameter a = 0.373 nm of the anatase unit cell [23]. It is likely that after five MLD cycles a dense crystalline film is formed, whereas after a smaller number of cycles the crystallization is incomplete. Amorphous and partially crystalline layers have lower density in comparison with crystalline films, and hence they have a larger thickness. In addition, because of the simultaneous presence of dense regions of the crystalline phase and loose regions of the amorphous phase in a film, its structure cannot be adequately described by a model of ideally smooth film with a constant refractive index throughout the surface. Consequently, the calculated effective thickness may be significantly increased, which seems to take place for m = 4, i.e., immediately before the complete crystallization.

To study the compaction of titanium oxide nanolayers, we have carried out experiments on annealing of the samples. We found that, on annealing the samples with m = 2 and m = 4 in a vacuum (300°C, 1 h) the effective thickness of nanolayers decreased to 0.37 and 0.48 nm, respectively (Fig. 1), and remained unchanged on further annealing. No thickness changes were observed on annealing of the other samples. It is likely that the annealing accelerates crystallization, which results not only in compaction of the film, but also in its greater uniformity, which causes a decrease in the effective thickness.

One of reasons for damping of the formation of a titanium oxide nanolayer can be formation of surface groups of the ≡Ti–Cl type, which results in formation of one titanium hydroxide group upon hydrolysis, instead of three groups used for its creation. The dehydroxylation of the sample surface can be another reason.

According to the chemical analysis [1, 3, 10, 16], formation of the ≡Ti–Cl groups is unlikely. At the same time, most of hydroxy groups are removed at 160°C from the titanium oxide surface [22], and at 200°C the main part of coordinated water is desorbed

(however, hydroxy groups and water are not removed completely by evacuation even at 300°C). We can expect that, in the course of formation of a titanium oxide nanolayer, the properties of the modified surface would gradually approach the properties of the surface of bulk titanium dioxide. Therefore, a more probable reason for damping of the growth of titanium oxide nanolayer is low thermal stability of the centers of $TiCl_4$ chemisorption. Special experiments confirmed this assumption. When a titanium oxide layer is synthesized at 225°C on a titanium oxide film with a thickness of 1.1 nm obtained at 185°C, no changes in the ellipsometric parameters are observed. On the contrary, on the titanium oxide layer obtained by ten MLD cycles at 225°C, the thickness of the film linearly depends on the number of cycles at 185°C.

It should be noted that the damping of molecular layer deposition process was found [1, 10] when studying the formation of a titanium oxide nanolayer on the silica gel surface. The authors explained this damping by obliteration of the matrix pore space in the course of the synthesis. It is of interest that, according to [1], the formation of a titanium oxide nanolayer practically ceases after ten MLD cycles, which corresponds to the results of this work.

As the properties of oxidized silicon surface are similar to the properties of amorphous silica, and its pretreatment did not involve heating to high temperatures, we can expect that the properties of this surface are similar to the properties of the silica gel surface. According to monograph [24], silica samples obtained without severe thermal treatment (particularly, silica gels) have significantly higher surface concentration of hydroxy groups (7–8 nm^{-2}) compared to the average concentration of 4–5 nm^{-2} for silica.

Therefore, it is of interest to compare the data on the formation of titanium oxide nanolayers on the oxidized silicon surface and the data obtained for silica gel in [1]. The interrelation between the amount of titanium on silica gel and the effective thickness of titanium oxide nanolayer on silicon is shown in Fig. 2a in the coordinates d_{eff}–$[Ti]_m$, where $[Ti]_m$ is the content of titanium on silica gel after m treatment cycles related to 1 g of anhydrous silica [1] (see table). It is seen from Fig. 2a that the points corresponding to $m \geq 5$ belong to the straight line outgoing from the origin. Thus, the effective thickness of a titanium oxide nanolayer on the silicon surface and the titanium content on the silica gel surface are proportional to each other at $m \geq 5$. The absence of proportionality at $m < 5$ is attributable to a smaller density of these

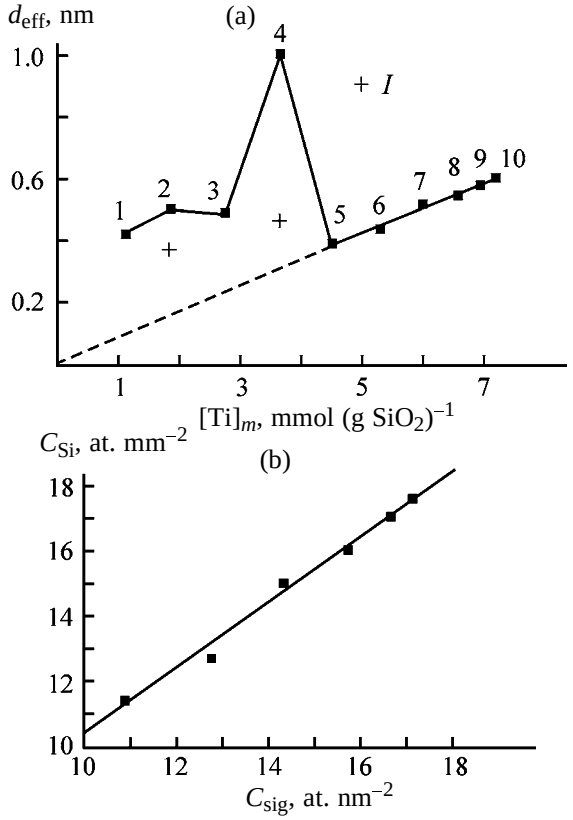

Fig. 2. Correlation of the (a) effective thickness of titanium oxide layer d_{eff} on the silicon surface with titanium content $[Ti]_m$ on the silica gel surface and (b) calculated amounts of titanium atoms per unit surface area of silicon C_{Si} and of silica gel C_{sig} for equal numbers of MLD cycles. (a) Figures at points denote cycle numbers.

layers compared to the density of the layers formed at $m \geq 5$.

As we have found that the thickness of a titanium oxide nanolayer on the silicon surface is proportional to the titanium content on the silica gel surface, it was of interest to compare the amounts of titanium per unit surface area on silicon and silica gel for an equal number of MLD cycles.

The number of titanium atoms per unit surface area of silicon C_{Si} can be calculated by the formula

$$C_{Si} = \frac{d_{eff}\rho}{M_{TiO_2}} N_A, \quad (1)$$

where d_{eff} is the effective film thickness; ρ, film density (which was taken at $m \geq 5$ to be equal to the anatase density of 3.83 g cm^{-3} [21]); N_A, Avogadro constant; and M_{TiO_2} = 79.90 g mol^{-1}, molar weight of TiO_2.

The number of titanium atoms per unit surface area of silica gel can be estimated from the data on the

Chemical composition and specific surface area of titanium-containing silica gel

m	$[Ti]_m$, mmol g^{-1} [1]	S_{sp}, $m^2\ g^{-1}$ [2]	Fraction of SiO_2 in product [1]	$[Ti]_m$, mmol $(g\ SiO_2)^{-1}$ [1]	S_{sp}, $m^2\ g^{-1}$ $(g\ SiO_2)^{-1}$ (our calculation)
0	0	270	0.969	0	279
1	0.97	239	0.893	1.09	268
2	1.52	224	0.835	1.82	268
3	2.16	200	0.784	2.76	255
4	2.73	195	0.744	3.67	262
5	3.21	160	0.710	4.53	225
6	3.63	–	0.683	5.31	–
7	3.95	–	0.659	6.00	–
8	4.21	–	0.641	6.57	–
9	4.41	140	0.633	6.96	221
10	4.51	–	0.629	7.17	–

chemical composition and specific surface area of titanium-containing silica gels [1, 2] (see table). The specific surface area of titanium-containing silica gels significantly decreases during the synthesis [2] (see table). However, the decrease in the sample specific surface area is caused not only by a change in the porous space geometry, but also by the weight gain upon layer deposition [25, 26]. For example, if a film grows on a sample with a flat surface, its surface area will not change; however, the specific surface area will decrease because the surface area would be related not to the initial sample weight, but to the total weight of the starting sample and the film. For this reason, to find true relations of surface areas of titanium-containing silica gels, they were related to the weight of anhydrous silica gel, which remains unchanged during the synthesis (similarly to the values of $[Ti]_m$ referred to 1 g of SiO_2 in [1, 2, 10]). The recalculation was fulfilled by dividing S_{sp} of samples by the fraction of anhydrous silica in them (see table). The resulting S_{sp} values $[m^2\ (g\ SiO_2)^{-1}]$ are given in the table. It is seen that the surface areas of titanium-containing samples referred to the weight of anhydrous silica change upon layer deposition only slightly. For approximate calculations, the average value $S_{av} = 250\ m^2\ (g\ SiO_2)^{-1}$ can be used. In this case, the number of Ti atoms per unit surface area of silica gel C_{sig} can be calculated by the formula

$$C_{sig} = \frac{[Ti]_m N_A}{S_{sp}}, \qquad (2)$$

where $[Ti]_m$ values are expressed in moles per gram of SiO_2.

The relationship between the numbers of titanium atoms per unit surface area of silica gel and silicon is shown in Fig. 2b in the coordinates C_{Si}–C_{sig}. These numbers were calculated by formulas (1) and (2) for equal numbers of MLD cycles starting from $m = 5$. The relationship is reasonably described by the equation $C_{Si} = 0.4 + 1.0C_{sig}$ (rms deviation $\sigma = 0.26$ at. nm^{-2}). Hence, the numbers of titanium atoms per unit surface area of silicon and silica gel for the same number of MLD cycles are virtually the same, which suggests that there is a certain similarity in molecular layer deposition of titanium oxide nanolayer on the oxidized silicon surface and on silica gel.

Earlier [27] we have drawn similar conclusions when comparing the amounts of Cr per unit surface area of chromium oxides synthesized by MLD technique on the silica gel surface and on silicon carbide particles. Silicon carbide is known to be coated with an SiO_2 film with a thickness of up to 10 nm. After the first MLD cycle, the chromium concentrations per unit surface area on silicon carbide and silica gel were almost equal.

CONCLUSIONS

(1) According to the ellipsometric data, the molecular layer deposition of a titanium oxide nanolayer damps in the range 200–235°C. After ten molecular layer deposition cycles, the formation of the nanolayer practically stops. In this case, the nanolayer thickness attains 0.60–0.67 nm.

(2) The initial stage of formation of titanium oxide nanolayer was studied ellipsometrically. An assumption was made that the layer was compacted after five molecular layer deposition cycles.

(3) Taking into account previous data on the synthesis of titanium oxide nanolayers on the silica sur-

face, it was proposed that the processes of molecular layer deposoition on the oxidized surface of single-crystal silicon and silica gel are similar.

ACKNOWLEDGMENTS

This work was financially supported by the RF President's grant "Leading Scientific Schools of Russia," project NSh-2236.2003.3 "The Chemistry of Highly Organized Substances."

REFERENCES

1. Kol'tsov, S.I., *Zh. Prikl. Khim.*, 1969, vol. 42, no. 5, pp. 1023–1028.
2. Kol'tsov, S.I., *Zh. Prikl. Khim.*, 1970, vol. 43, no. 9, pp. 1956–1959.
3. Kol'tsov, S.I., Sveshnikova, G.V., and Aleskovskii, V.B., *Izv. Vyssh. Uchebn. Zaved., Khim. Khim. Tekhnol.*, 1969, vol. 12, no. 5, pp. 562–564.
4. Sveshnikova, G.V., Kol'tsov, S.I., and Aleskovskii, V.B., *Sovremennye problemy ellipsometrii* (Modern Problems of Ellipsometry), Rzhanov, A.V., Ed., Novosibirsk: Nauka, 1980, pp. 141–145.
5. Drozd, V.E., Kol'tsov, S.I., and Redrova, T.A., *Sovremennye problemy ellipsometrii* (Modern Problems of Ellipsometry), Rzhanov, A.V., Ed., Novosibirsk: Nauka, 1980, pp. 134–141.
6. Kol'tsov, S.I., Drozd, V.E., and Aleskovskii, V.B., *Dokl. Akad. Nauk SSSR*, 1976, vol. 229, no. 5, pp. 1145–1147.
7. Kol'tsov, S.I., Gromov, V.K., and Aleskovskii, V.B., *Ellipsometriya – metod issledovaniya poverkhnosti* (Ellipsometry: A Method of Studying Surface), Rzhanov, A.V., Ed., Novosibirsk: Nauka, 1983, pp. 70–73.
8. Gromov, V.K. and Kol'tsov, S.I., *Ellipsometriya – metod issledovaniya poverkhnosti* (Ellipsometry: A Method of Studying Surface), Rzhanov, A.V., Ed., Novosibirsk: Nauka, 1983, pp. 73–76.
9. Kol'tsov, S.I., Kriul'kin, A.N., and Gromov, V.K., *Zh. Prikl. Khim.*, 1987, vol. 60, no. 1, pp. 181–183.
10. Malkov, A.A., Sosnov, E.A., and Malygin, A.A., in *Napravlennyi sintez tverdykh veshchestv* (Directed Synthesis of Solids), St. Petersburg: Sankt-Peterb. Gos. Univ., 1992, issue 3, pp. 10–29.
11. Kol'tsov, S.I., Yakovlev, A.S., and Bukhalov, L.L., *Poverkhn.: Fiz., Khim., Tekh.*, 1992, no. 5, pp. 75–81.
12. Kol'tsov, S.I., Yakovlev, A.S., and Bukhalov, L.L., *Poverkhn.: Fiz., Khim., Tekh.*, 1993, no. 4. pp. 92–99.
13. Aarik, J., Aidla, A., Uustare, T., *et al.*, *Appl. Surf. Sci.*, 2002, vol. 193, pp. 277–286.
14. Finnie, K.S., Triani, G., Short, K.T., *et al.*, *Thin Solid Films*, 2003, vol. 440, pp. 109–116.
15. Lindblad, M., Haukka, S., Kytökivi, F., *et al.*, *Appl. Surf. Sci.*, 1997, vols. 121/122, pp. 286–291.
16. Haukka, S., Lakomaa, E.-L., and Root, A., *J. Phys. Chem.*, 1993, vol. 97, pp. 5085–5094.
17. Gelatos, J., Chen L., Chung, H., *et al.*, *Solid State Technol.*, 2003, no. 2, pp. 44–48.
18. Seidel, T., Londergan, A., Winkler, J., *et al.*, *Solid State Technol.*, 2003, no. 5, pp. 67–71.
19. Aleskovskii, V.B., *Khimiya nadmolekulyarnykh soedinenii* (The Chemistry of Supramolecular Compounds), St. Petersburg: Sankt-Peterb. Gos. Univ., 1996.
20. Azzam, R.M. and Bashara, N.M., *Ellipsometry and Polarized Light*, Amsterdam: North-Holland, 1977.
21. *Fiziko-khimicheskie svoistva okislov* (Physicochemical Properties of Oxides: Handbook), Samsonov, G.V., Ed., Moscow: Metallurgiya, 1978.
22. Pletnev, R.N., Ivakhin, A.A., Kleshchev, D.G., *et al.*, *Gidratirovannye oksidy elementov IV i V grupp* (Hydrated Oxides of Group IV and V Elements), Moscow: Nauka, 1986.
23. Ormont, B.F., *Struktury neorganicheskikh veshchestv* (Structures of Inorgamic Substances), Moscow: Izd. Nauchno-Tekhnicheskoi Literatury, 1950.
24. Iler, R.K., *The Chemistry of Silica*, New York: Wiley–Interscience, 1979.
25. *Modifitsirovannye kremnezemy v sorbtsii, katalize i khromatografii* (Modified Silicas in Sorption, Catalysis, and Chromatography), Lisichkin, G.V., Ed., Moscow: Khimiya, 1986.
26. *Khimiya poverkhnosti kremnezema* (The Chemistry of Silica Surface), Chuiko, A.A., Ed., Kiev: Naukova Dumka, 2001, part 1.
27. Kol'tsov, S.I., Garshin, A.P., Malygin, A.A., *et al.*, *Izv. Vyssh. Uchebn. Zaved., Khim. Khim. Tekhnol.*, 1978, vol. 21, no. 2, pp. 168–171.

Russian Journal of Applied Chemistry, Vol. 77, No. 7, 2004, pp. 1066–1069. Translated from Zhurnal Prikladnoi Khimii, Vol. 77, No. 7, 2004, pp. 1082–1085.

INORGANIC SYNTHESIS AND INDUSTRIAL INORGANIC CHEMISTRY

X-ray Phase Analysis of Structure of Water–Salt Systems: NaCl–H_2O and KCl–H_2O

O. N. Pestova, Yu. P. Kostikov, and M. K. Khripun

St. Petersburg State University, St. Petersburg, Russia

Received May 27, 2004

Abstract—Aqueous solutions of sodium and potassium chlorides were studied by a diffraction method. The effect of cations on the structure of water was considered from the viewpoint of this method. The size of supramolecular structures and the number of water molecules per salt formula unit in solution were estimated.

The choice of aqueous solutions of sodium and potassium chlorides as objects of our study was caused by an important role of these systems in natural physicochemical, physiological, and biological processes, in geological research, and also by their wide industrial use [1–3].

It is known that even slight amounts of an electrolyte added to water change its physical and physicochemical properties because of changes in its structure. Presently Frank–Ibsen–Wen model [4] based on a dominating role of free water is used to describe structural changes in moderately concentrated solutions. Influence of electrolyte ions on water is accounted for from the viewpoint of the hydration theory.

In going to concentrated solutions, this approach becomes inapplicable, as the reasoning concerning the intrinsic structure of water in such solutions loses sense. Apparently, to study structures of concentrated solutions, alternative approach and model representations are required, and previously we have developed such a model [5–8]. This approach is based on the comparison of changes in the physical and chemical properties with the shape of the solubility polytherm of a salt. This approach allows us to divide the entire concentration range of the solution existence into zones with various dominating structures (cybotactic groups) corresponding to structures of solid phases crystallizing from the solution upon decreasing temperature: water, a crystal hydrate with a definite composition, or an anhydrous salt.

Results of cryoscopic, Raman-spectroscopic, viscometric, and calorimetric studies of solutions in wide concentration ranges provide indirect information on their structure; they point to structural reorganizations in systems occurring as concentrations of components change. According to the developed theory, such results allow us to make assumptions on the interconversions in a solution. To obtain more comprehensive information about a solution structure and to develop further the model views, we have proposed to use a modification of the X-ray diffraction method. The feature of this experiment consists in the fact that the measurements are carried out in a wide range of 2θ angles and that the result is the dependence of the dispersion intensity on the dispersion angle $I(2\theta)$, whereas when liquid systems are studied by the usual X-ray diffraction method, the scattering under small angles ($2\theta < 6°$) is considered and the diffraction patterns are presented as radial distribution curves $dI(2\theta)$ [9]. In so doing, average distances between particles are estimated.

We pursued different aims when studying solutions by the diffraction method. The method used in this work furnishes new information on the structure of a system as a whole. The X-ray phase experiments have been carried out earlier for several electrolyte solutions [10]. The results of these experiments have shown that this method is sensitive to structural changes in solutions and makes it possible to follow the effect of an electrolyte (as its concentration increases) on the structure of water.

EXPERIMENTAL

To prepare solutions, we used chemically pure grade salts and distilled water. The titration with a solution of mercury nitrate with diphenylcarbazone indicator was used to determine the concentration of chloride ions. Dilute solutions were prepared by volumetric dilution of saturated solutions.

1070-4272/04/7707-1066 © 2004 MAIK "Nauka/Interperiodica"

Diffraction patterns were measured on a DRON-2.0 difractometer with an Ni filter and CuK_α radiation. Mode of the tube operation: I = 8 mA, U = 18 kV, sweep rate 1 deg min^{-1}. A sample was transferred with a syringe into an 1 ml duralumin cell, equipped with a window made of 0.2-mm beryllium foil. The spectra were measured in the range of angles θ from 4° to 24° at room temperature.

The diffraction patterns of pure water and solutions of alkali metal chlorides with various salt concentrations are shown in Figs. 1–3. Narrow lines (five lines) in the region of large angles (2.45, 2.19, 2.07, 1.99, and 1.92 Å) belong to beryllium. In the diffraction pattern of pure water (Fig. 1), a wide and strong peak (halo) is observed at 3.14 Å, and a less intensive halo, at 2.32 Å. Their positions coincide with the positions of maxima of lines in the diffraction pattern of ice of tetragonal symmetry, i.e., the spectrum of water consists of wide lines of ice, which points to the absence of long-range order and the presence of short-range order in the structure of pure water.

The obtained diffraction patterns of solutions of sodium and potassium chlorides show certain regular trends.

An increase in the electrolyte concentration results in a reduction of the intensity of the water halo, its broadening, and shift of its maximum toward larger angles θ. It is indicative of gradual break of the intrinsic structure of water and increasing disorder in solution. The reduction of the halo intensity occurs up to a certain salt concentration, after which the intensity remains practically unchanged.

The data on sodium chloride solutions are shown in Fig. 2.

When the salt concentration increases from 0.35 to 1.97 M, the intensity of water halo decreases fairly sharply; with the further increase in the molarity of sodium chloride, the dependence becomes smoother, and in solutions close to saturation the intensity changes insignificantly. It seems to be indicative of a temporary structural constancy. Despite the sharp decrease in the intensity in dilute solutions, the half-width of the peak (30–31 mm) remains virtually unchanged (compared to that in pure water) up to ~5 M concentration of the salt. This indicates that no appreciable structure break takes place in the sodium chloride solution up to its ~5 M concentration, i.e., the structure existing at that moment appears to be no less ordered than that of pure water. Only at the salt concentration of 4.61 M the half-width of the halo increases (to 34 mm); this concentration corresponds

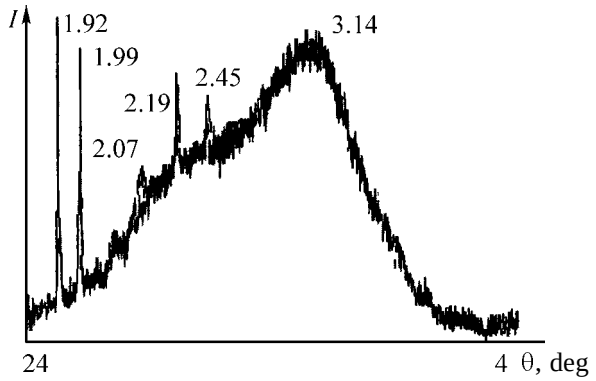

Fig. 1. Diffraction pattern of liquid water: (*I*) intensity and (θ) scattering angle. Spacings are given in Å.

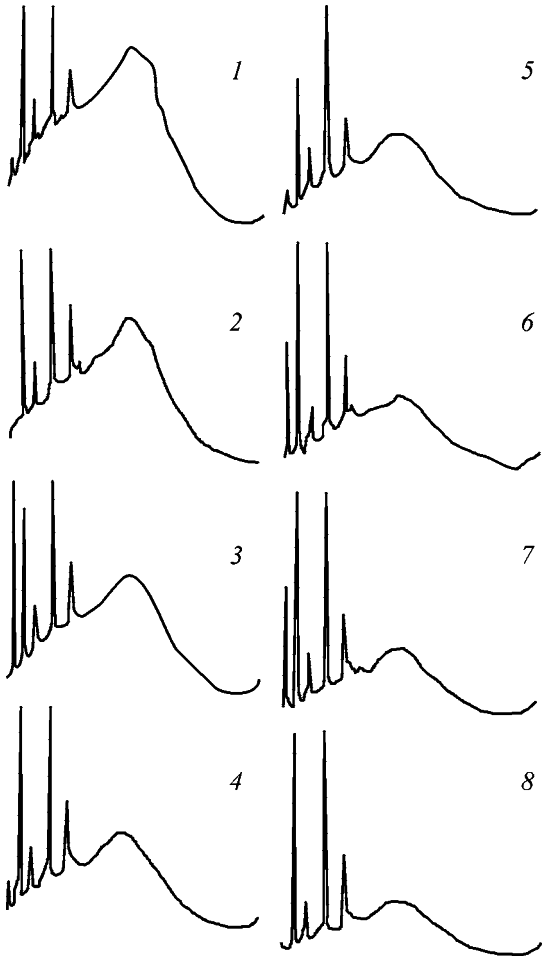

Fig. 2. Diffraction pattern of sodium chloride solutions. Solution concentration (M): (*1*) 0, (*2*) 0.35, (*3*) 1.07, (*4*) 1.90, (*5*) 3.00, (*6*) 3.8, (*7*) 4.61, and (*8*) 5.32.

to the eutectic concentration of sodium chloride (4.7 M [11]).

The decrease in the intensity of water halo with increasing concentration of potassium chloride in solu-

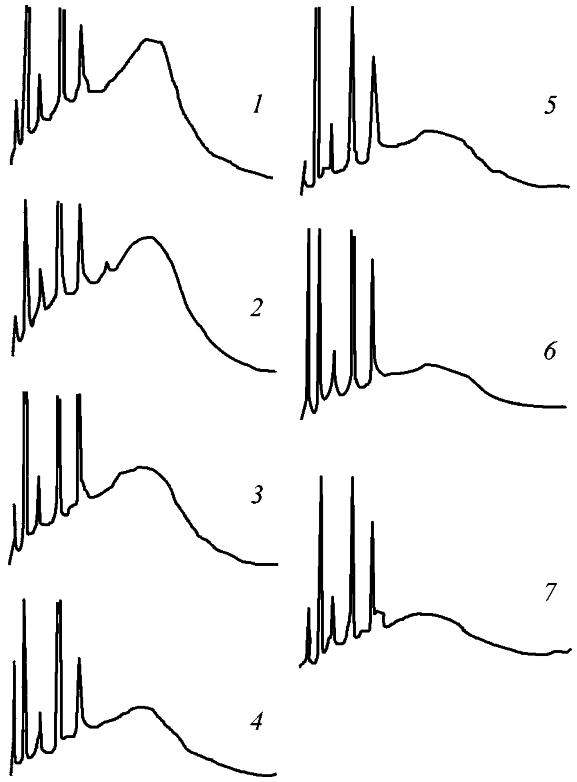

Fig. 3. Diffractoin patterns of potassium chloride solutions. Solution concentration (M): (*1*) 0, (*2*) 0.71, (*3*) 1.07, (*4*) 1.97, (*5*) 2.83, (*6*) 3.63, and (*7*) 4.41.

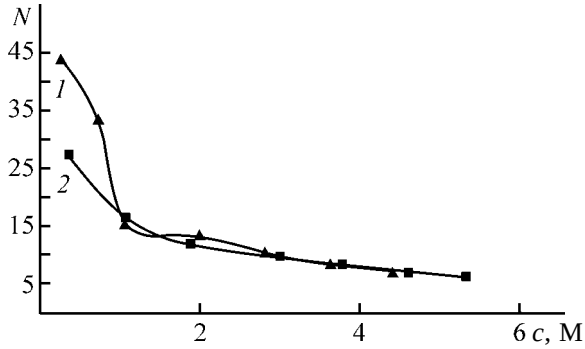

Fig. 4. Variaiton of the number of water molecules *N* per formula unit of (*1*) KCl and (*2*) NaCl with the molar concentration of the salts in solution *c*.

tions is not so sharp as in the case of sodium chloride. However, broadening of the halo is observed already at a minimal salt concentration (Fig. 3). Thus, potassium chloride starts to break the water structure at once.

We have calculated approximate sizes of supramolecular structures dominating in solution from the X-ray diffraction patterns using the Debye–Scherrer formula [12]

$$L = \lambda(B\cos\theta),$$

where λ is wavelength, Å; *B*, half-width of halo, rad; and θ, scattering angle, deg.

The size of associates in pure water is approximately 30 Å.

The size of structures in solutions with posteutectic concentrations can be estimated similarly. For example, the size of structures existing in the 5.32 M solution of sodium chloride is 26 Å, and in the 3.63 M solution of potassium chloride L = 33 Å. We believe that these values are quite reasonable but rather approximate, as the wider the halo and the lower its intensity (which, as a rule, is observed in concentrated solutions), the higher is the error in the *B* determination.

We believe that the composition of such structures (cybotactic groups) determines the composition of crystal unit cells of a substance, i.e., a cybotactic group in a solution is a combined modular structure containing many molecules. To form a crystal unit cell, a suitable environment is necessary, which arises even in a concentrated solution when structurally induced processes become to prevail. However, conditions for the formation of the corresponding environment are realized within fractions of seconds as we deal with a liquid system where chaotic thermal, translation, and rotation motions take place. Therefore, a cybotactic group is an associate having a short lifetime, which is insufficient for congestion of similar groups in the same place and thus for the formation of a solid phase.

The analysis of diffraction patterns allowed us to determine the number of water molecules per salt formula unit in solution according to the formula

$$[(I_w - I_i) \times 55.56/I_w]/c,$$

where I_w is the intensity of scattering in water (in a halo maximum), mm; I_i, intensity of scattering in a sample (in solution), mm; $(I_w - I_i) \times 55.56/I_w$, number of water moles from the water structure consumed for the salt hydration; and *c*, molar concentration of the solution.

The dependence of the number of water molecules per salt formula unit on its molar concentration is given in Fig. 4.

It should be noted that the dependence is not monotonic: the number of water molecules changes more sharply at low concentrations, and at higher concentrations it is smooth, gradually approaching a constant number. This points to the prevalence of the corresponding structure in solution. Figure 4 shows that

there are approximately seven water molecules per formula unit of sodium chloride in the saturated solution. Practically the same value (7–8) was also found for potassium chloride in saturated solution (at 25°C). It should also be noted that in the region of low concentrations the effect of K^+ cations on the water structure is pronounced much more strongly, which is attributable to the negative hydration power of these ions, whereas Na^+ cations are on the border between positive and negative hydration and do not exert pronounced structure-making or structure-breaking effect on water.

CONCLUSIONS

(1) X-ray diffraction patterns show how cations affect the water structure as an electrolyte is concentrated and allow estimation of the number of water molecules per formula unit of a solute and the size of cybotactic groups dominating in the solution.

(2) X-ray diffraction once again revealed a difference in the nature of Na^+ and K^+ ions in the region of dilute solutions, caused by their different hydration power. It is very important that, within the framework of a single experiment, we were able to observe all features of changes in the structure of solutions of such simple salts. It is clearly seen that the distinction in the nature of sodium and potassium ions is completely leveled off in going to high concentrations owing to the M^+–Cl^- ion–ion association and to the origination of microheterogeneity in solutions.

(3) X-ray diffraction is one more tool for studying liquid systems; it furnishes qualitatively new information on the structure of a solution as a whole.

REFERENCES

1. McManus, M.L., *New Engl. J. Med*., 1995, no. 9, pp. 1260–1264.
2. Pavlov, O.B. and Smirnov, V.M., *Narushenie vodno-elektrolitnogo obmena i kislotno-osnovnogo sostoyaniya. Infuzionnaya terapiya: Uchebno-metodicheskoe posobie* (Disturbance of Water–Electrolyte Exchange and of Acid–Base State. Infusion Therapy: A Textbook), Minsk: Bel. Med. Gos. Univ., 2003.
3. Charykova, M.V. and Charykov, N.A., *Termodinamicheskoe modelirovanie protsessov evaporitovoi sedimentatsii* (Thermodynamic Simulation of the Processes of Evaporite Sedimentation), St. Petersburg: Nauka, 2003.
4. Lilich, L.S. and Khripun, M.K., *Rastvory kak khimicheskie sistemy* (Solutions as Chemical Systems), St. Petersburg: Sankt-Peterb. Gos. Univ., 1994.
5. Khripun, M.K., Myund, L.A., Baranova, G.I., *et al*., *Zh. Obshch. Khim*., 1998, vol. 68, no. 4, pp. 550–555.
6. Khripun, M.K., Chervonenko, K.Yu., Kiselev, A.A., and Khripun, A.V., *Zh. Obshch. Khim*., 2001, vol. 71, no. 1, pp. 25–35.
7. Khripun, M.K., Chervonenko, K.Yu., Kiselev, A.A., and Petranovskii, V.P., *Zh. Obshch. Khim*., 2002, vol. 72, no. 6, pp. 932–937.
8. Kiselev, A.A., Zubtsov, M.K., and Khripun, M.K., *Vestn. Sankt-Peterb. Gos. Univ., Ser. 4*, 2002, no. 3. pp. 51–54.
9. Petrun'kin, S.P., Trostin, V.N., and Krestov, G.A., *Izv. Vyssh. Uchebn. Zaved., Khim. Khim. Tekhnol*., 1986, vol. 29, no. 6, pp. 15–19.
10. Khripun, M.K., Kostikov, Yu.P., Kiselev, A.A., and Pestova, O.N., *Zh. Obshch. Khim*., 2004, vol. 74, no. 2, pp. 190–193.
11. Kirgintsev, A.N., Trushnikova, L.N., and Lavrent'eva, V.G., *Rastvorimost' neorganicheskikh veshchestv v vode* (Solubility of Inorganic Substances in Water), Leningrad: Khimiya, 1972.
12. Kitaigorodskii, A.I., *Rentgenostrukturnyi analiz mikrokristallicheskikh i amorfnykh tel* (X-ray Structural Analysis of Microcrystalline and Amorphous Substances), Moscow: Gostekhizdat, 1952.

Russian Journal of Applied Chemistry, Vol. 77, No. 7, 2004, pp. 1070–1073. Translated from Zhurnal Prikladnoi Khimii, Vol. 77, No. 7, 2004, pp. 1086–1089.

INORGANIC SYNTHESIS AND INDUSTRIAL INORGANIC CHEMISTRY

Complexing Properties of Scandium(III) in Alkaline Medium

L. A. Pasechnik, A. G. Shirokova, O. V. Koryakova, N. A. Sabirzyanov, and S. P. Yatsenko

Institute of Chemistry of Solids, Ural Division, Russian Academy of Sciences, Yekaterinburg, Russia
Institute of Organic Synthesis, Ural Division, Russian Academy of Sciences, Yekaterinburg, Russia

Received December 2, 2003

Abstract—The behavior of scandium compounds in going from alkaline solutions to carbonate and hydrocarbonate solutions was studied. The possibility of coprecipitation of scandium(III) complex carbonate with zinc oxide was examined.

Integrated use of mineral raw material and development of low-waste processes become urgent in view of environmental protection. The possibility of scandium recovery from large-volume technogenic deposits from aluminum production is of particular interest. Such valuable components of bauxites as scandium, titanium, zirconium, yttrium, and lanthanides are almost completely concentrated in waste products after pressure leaching. A chemomineralogical analysis supported by laboratory studies has shown that the technology of recovery of scandium compounds from bauxite processing products and of scandium separation from concomitant components is largely simplified when scandium(III), which is weakly bound to macrocomponents, is converted to a carbonate complex. To find the optimal process conditions, we have studied scandium-containing alkaline carbonate and carbonate–hydrocarbonate systems.

Published data on the solubility of scandium(III) hydroxide in alkaline solutions are contradictory, probably owing to distinctions in experimental conditions [1, 2]. The behavior of scandium(III) in solutions of alkali metal carbonates and hydrocarbonates has been studied in more detail [3, 4]. We found no published data on the solubility of scandium(III) compounds in hydrocarbonate–carbonate ($NaHCO_3$–Na_2CO_3) solutions with low content of free alkali, which are required for understanding the scandium(III) behavior in processing of red mud by a soda–alkaline technology.

EXPERIMENTAL

When studying solubility of scandium(III) hydroxide in the above systems, we used chemically and analytically pure grade $NaHCO_3$, Na_2CO_3, NaOH, and ZnO as starting chemicals. Scandium(III) hydroxide was prepared from scandium oxide of the OS-99.0 grade. The scandium content was determined by EDTA titraiton or by photometry with Xylenol Orange as indicator. Zinc was determined quantitatively by complexometric titration with Eriochrome Black T as indicator. The concentrations of carbonates and hydrocarbonates were determined by volumetric titration with Methyl Red and phenolphthalein indicators, and that of free alkali, with phenolphthalein in the presence of barium chloride.

An alkaline solution of Sc(III) was obtained by heating a mixture of Sc_2O_3 and sodium hydroxide in a platinum cup on a sand bath with a minimal amount of water to homogenize the mixture and to increase the reaction surface area, and then the mixture was sintered at 400°C for 6–8 h. The cake was leached with double-distilled water, transferred into hermetically sealed polyethylene vessels, and kept at 18–20°C to reach the equilibrium. The liquid phase was sampled using a centrifuge. Carbonate systems were prepared by mixing scandium(III) hydroxide and the corresponding amount of sodium carbonate in 100 ml of a solution in a glass vessel and keeping it at room temperature to reach the equilibrium.

The IR absorption spectra were taken from samples prepared as mulls in mineral oil. We also used a diffuse reflection attachment. The spectra were obtained on a Perkin–Elmer Fourier IR spectrometer (450–3000 cm^{-1}). The thermal stability of the scandium complex compound was evaluated by differential thermal and thermogravimetric analyses on a Q-1500 derivatograph at a heating rate of 10 deg min^{-1}.

1070-4272/04/7707-1070 © 2004 MAIK "Nauka/Interperiodica"

The curve of scandium(III) solubility in alkaline solutions can have one or two maxima at quite different concentrations of sodium hydroxide, and the maximal solubility also varies over a wide range. The experimental solubility curve largely reproduces the initial branch of the curve given in [1]. We studied the saturation of alkali liquors with scandium(III) for 3 months. Probably, the saturation curve in Fig. 1, which was obtained after 3-month keeping of the solutions, is not equilibrium. Our experiments confirm the published data that the equilibrium between a solution and a solid phase at 18–20°C is attained very slowly (in 3 months and more) and that scandium(III) can form stable colloidal solutions, which complicates the experiment. According to Ivanov-Emin *et al*. [1], the autoclave treatment of a mixture of scandium oxide and sodium hydroxide at 160–180°C results in the reduction of the time required to reach an equilibrium to 20–40 days.

In going from alkaline to carbonate and then to hydrocarbonate solutions, the solubility of scandium(III) hydroxide grows singnificantly. It also grows as the concentration of the hydrocarbonate solutions increases (Fig. 1). The equilibrium in the systems was reached within two weeks. The resulting solubility curves are located somewhat lower than the curves described in the literature; however, in general, they agree well with each other.

As the concentration of hydroxide ions in solution increases, the content of scandium(III) considerably decreases. The influence of the concentration of OH^- ions on the solubility of scandium hydroxide was demonstrated with sodium carbonate solutions containing various amounts of $NaHCO_3$, Na_2CO_3, and NaOH [3]. The solubility sharply decreasesd (approximately from 5 to 2.2×10^{-3} g l^{-1} Sc_2O_3) as the molar ratio Na^+/CO_3^{2-} increased from 1.5 to 3.0. The further increase in the concentration of OH^- ions only slightly increased the solubility: to 5.8×10^{-3} g l^{-1} at Na^+/CO_3^{2-} = 3.5 [3, 4]. These data show that the content of scandium(III) oxide can reach 3 g l^{-1} in carbonate solutions in the presence of OH^- ions (at Na^+/CO_3^{2-} = 2.0–3.0).

Our experiments gave somewhat different results. Solutions were prepared by adding sodium hydroxide to the starting concentrated solution (solution A) containing 80 g l^{-1} of $NaHCO_3$ and 12.8 g l^{-1} of Sc_2O_3 and keeping the solutions at room temperature for 2 weeks. The scandium solubility regularly decreased and reached the minimal value of 7×10^{-3} g l^{-1} of Sc_2O_3 at $Na^+ : CO_3^{2-} = 2$ (Fig. 2). At the molar ratio

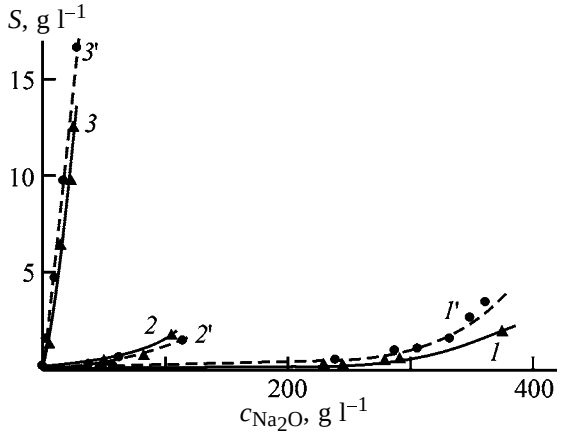

Fig. 1. Soluibility *S* of scandium oxide as a function of Na_2O concentration c_{Na_2O} in solutions of (*1*, *1*') NaOH, (*2*, *2*') Na_2CO_3, and (*3*, *3*') $NaHCO_3$. Data: (*1*–*3*) our experiments, (*1*') form [1], and (*2*', *3*') from [3].

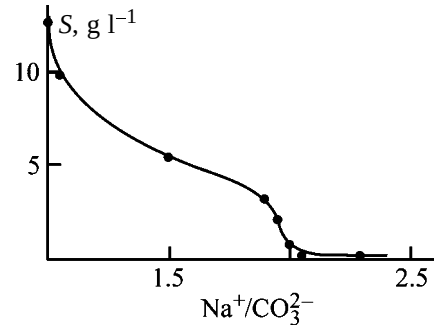

Fig. 2. Solubility of Sc_2O_3 as a function of the molar ratio Na^+/CO_3^{2-} in $NaHCO_3$–Na_2CO_3–NaOH solutions.

$Na^+/CO_3^{2-} < 2$, the solubility of scandium hydroxide grew as the concentration of CO_3^{2-} ions increased owing to the ability of scandium to form complexes. In the presence of even insignificant amount of alkali in the carbonate solution at $Na^+/CO_3^{2-} \geq 2$, scandium carbonate complexes are unstable, whereas scandium hydroxo compounds are poorly soluble and are stable only in the presence of a large excess of NaOH. We note that the scandium(III) concentration in $NaHCO_3$ solutions is much higher than in the carbonate solution with the same concentration of CO_3^{2-}.

We have isolated transparent crystals of the complex scandium carbonate $Na_5Sc(CO_3)_4 \cdot 18H_2O$ as prisms of up to 2 mm length from solution A cooled to 3–5°C and kept for 5–7 days. In time, the crystals grew together to form druses. The structure of this compound was proved by X-ray phase analysis.

We studied the thermal stability of the resulting crystal hydrate using differential thermal and thermogravimetric analyses. The decomposition occurs in several stages; first, 10 mol of water of crystallization is removed on heating to ~150°C, which corresponds

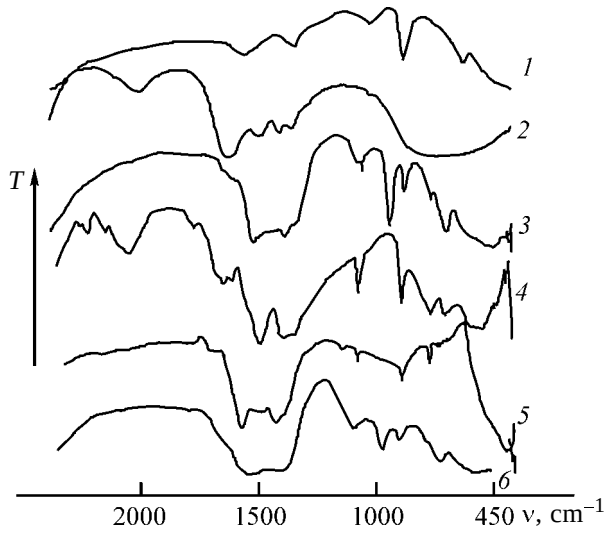

Fig. 3. IR spectra of (*1*) $Sc(OH)_3$ prepared from OS-99.0-grade Sc_2O_3, (*2*) solution A, (*3*) precipitate in equilibrium with solution A, (*4*) $Na_5Sc(CO_3)_4 \cdot 11H_2O$, (*5*) precipitated Zn–Sc concentrate, and (*6*) Zn–Sc concentrate treated with 10% NaOH solution. (*T*) Transmission and (ν) wave number.

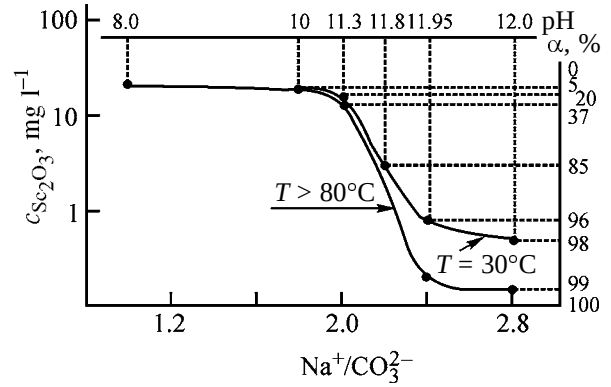

Fig. 4. Precipitation of scandium from solutions as influenced by the Na^+/CO_3^{2-} raito, temperature, and solution pH. Starting solution 1 M $NaHCO_3$, 20 mg l^{-1} of Sc_2O_3, time 2 h. ($c_{Sc_2O_3}$) Sc_2O_3 content and (α) degree of precipitation.

to the weight loss of 10.1%. In the range 230–340°C, the weight loss is 7.1%, and further, up to 430°C, it is 10.7%. Water and CO_2 are lost in these stages simultaneously, and the complex anion is destroyed.

The existence of a complex compound in solutions under study was proved by the IR spectra of solution A and of the precipitate in equilibrium with it. We also carried out potentiometric titration of 1 M solution of $NaHCO_3$ containing 0.87 g l^{-1} of Sc_2O_3. It was shown that scandium(III) ion coordinates four carbonate ligands. Some of these ligands are monodentate and the others are bidentate bridging. In the IR spectra of the hydrocarbonate solution of scandium(III), of the corresponding precipitate, and also of scandium(III) coprecipitated with zinc oxide from the hydrocarbonate solution (Fig. 3), we can distinguish sets of frequencies characteristic for coordinated carbonate groups OCO_2 with the symmetry reduced from D_{3h} to C_{2v}. The band ν_3 (D_{3h}) at 1420–1470 cm^{-1} is split to ν_1 and ν_5 (C_{2v}), with the strongest absorption bands being ν_5 (monodentate) = 1400–1419 and ν_1 (bidentate) = 1506–1558 cm^{-1}. The band ν_5 (bidentate) = 1347–1366 cm^{-1} corresponding to the bidentate coordination of OCO_2 groups is better pronounced in solution. In the lower-frequency region, there is the ν_2 band (C_{2v}) at 1020–1090 cm^{-1} and the ν_1 band, which is inactive in the IR spectra at the D_{3h} symmetry. A broad absorption band of water bending vibrations at ~1640 cm^{-1} is observed in the spectrum of the solution of the complex; it is also well resolved in the spectrum of the crystal hydrate.

Weak absorption bands at 665–675 and 705 cm^{-1} in the spectra of the solid products can correspond to the vibrations of the Sc–O and O–Sc–O bonds, including vibrations that involve oxygen atoms participating in the coordination bond of scandium with water molecules or carbonate groups. It is assumed that a part of carbonate groups in the scandium(III) complex carbonate act as bridging ligands participating in the construction of reticular structures with voids, which can be occupied by water molecules.

By varying the concentration and temperature (taking into account the kinetic factor), we found that the optimal temperature for the complex formation in the saturated hydrocarbonate solution is 40–50°C. We studied the precipitation of scandium from a carbonate–hydrocarbonate solution at various Na^+/CO_3^{2-} molar ratios, solution temperatures, and lower starting concentrations of scandium in solution. As the scandium(III) content in the starting solution and temperature decrease, the pH at which the Sc(III) compound starts to hydrolyze grows, i.e., a somewhat greater consumption of alkali is required and the degree of scandium(III) precipitation from the solution in the time of the experiment slightly decreases (Fig. 4).

To precipitate scandium(III) from carbonate solutions faster and more exhaustively, we suggested to coprecipitate its compounds with basic zinc carbonate. The precipitation was carried out under conditions of complete conversion of the hydrocarbonate solution to the carbonate solution, in the presence of a small excess of alkali. The solubility of the zincate in such solution is insignificant, and scandium(III) is captured by the forming precipitate. It is recommended to carry out the precipitation up to the excess NaOH concen-

tration of 10–25 g l^{-1} at 70–80°C. These conditions allow the residual scandium concentration in the mother solution to be decreased 0.2 mg l^{-1} of Sc_2O_3 [5].

The IR data suggest that scandium(III) is precipitated as a mixture of basic scandium(III) carbonate and the complex $Na_5Sc(CO_3)_4$; no heteronuclear zinc(II)–scandium(III) complexes are detected (Fig. 3). The bands corresponding to the basic carbonate disappear from the spectra of the zinc–scandium concentrate after washing it with a 10% solution of alkali to remove zinc, and the intensity of the bands of the complex decreases, but new bands appear, corresponding to $Sc(OH)_3$ which is insoluble in weakly alkaline solutions. These data show that scandium carbonate complexes do not exist in alkaline medium.

Based on the ability of scandium to form a soluble complex compound with carbonate ions, we developed a scheme of recovering scandium(III) from red mud, which is a waste product of alumina production. The complex formation of scandium(III) with carbonate anions makes it possible to use the equipment of the basic production, which makes the method economically and technologically attractive.

CONCLUSIONS

(1) The solubility of scandium(III) compounds in pure and mixed solutions of sodium hydroxide, carbonate, and hydrocarbonate was studied. It was shown that the solubility of scandium oxide decreases as the content of hydrocarbonate decreases, and when the free alkali appears, it falls down to 2.2×10^{-3} g l^{-1} of Sc_2O_3.

(2) The existence of the scandium complex compound $Na_5Sc(CO_3)_4 \cdot nH_2O$ in the hydrocarbonate solution, in the solid phase in equilibrium with it, and in the precipitate obtained by the coprecipitation of scandium with zinc oxide was proved by IR spectroscopy.

REFERENCES

1. Ivanov-Emin, B.N., Nisel'son, L.A., and Ivolgina, A.T., *Zh. Neorg. Khim.*, 1960, vol. 5, no. 12, pp. 2841–2842.
2. Favorskaya, L.N., *Khimicheskaya tekhnologiya skandiya* (Chemical Technology of Scandium), Alma-Ata: Kazakh. Inst. Mineral'nogo Syr'ya, 1969.
3. Komissarova, L.N., Krasnoyarskaya, A.A., and Shatskii, V.M., *Zh. Neorg. Khim.*, 1971, vol. 16, no. 7, pp. 1985–1988.
4. Komissarova, L.N., *Neorganicheskaya i analiticheskaya khimiya skandiya* (Inorganic and Analytical Chemistry of Scandium), Moscow: Editorial URSS, 2001.
5. Sabirzyanov, N.A., Yatsenko, S.P., Pasechnik, I.A., and Diev, V.N., *J. Int. Res. Publ.*, 2003, vol. 4, no. 1, pp. 78–87.

Russian Journal of Applied Chemistry, Vol. 77, No. 7, 2004, pp. 1074–1078. Translated from Zhurnal Prikladnoi Khimii, Vol. 77, No. 7, 2004, pp. 1090–1093.

INORGANIC SYNTHESIS AND INDUSTRIAL INORGANIC CHEMISTRY

Precipitation of Copper(II) with 1,2-Dibenzoylhydrazine from Aqueous Ammonia Solution

L. G. Chekanova, A. V. Radushev, Yu. B. El'chishcheva, and Yu. V. Kazakova

Institute of Technical Chemistry, Ural Division, Russian Academy of Sciences, Perm, Russia
Perm State University, Perm, Russia

Received July 8, 2003; in the final form, December 2003

Abstract—The physicochemical characteristics of 1,2-dibenzoylhydrazine relevant to precipitation of copper(II) with this reagent were studied.

Symmetrical aliphatic 1,2-diacylhydrazines (DAHs) of the general formula RC(O)NHNHC(O)R (R is C_3H_7–C_5H_{11}) are potentially tetradentate complexing agents suitable for concentration and separation of metals and for wastewater decontamination from nonferrous metals (NMs) by flotation [1] and from Cu(II) by precipitation [2]. DAHs are easily prepared and are characterized by low toxicity and strong complexation with NMs. However, these reagents are coordinated with NMs at pH 9–11 considerably exceeding pH of wastewater (5.5–8.7). It is reasonable to suggest that replacement of an electron-donor alkyl radical in a DAH molecule by an electron-acceptor radical, e.g., phenyl radical, can increase the acidity of this reagent and hence shift its complexation with NMs to lower pH.

In this work we studied the physicochemical characteristics of 1,2-dibenzoylhydrazine (DBH) and its complexation with copper(II).

EXPERIMENTAL

1,2-Dibenzoylhydrazine was prepared by thermal decomposition of the salt $2C_6H_5COOH \cdot N_2H_4 \cdot H_2O$ [3]. The main substance content in DBH prepared by this procedure was no less than 97% as determined by conductometric titration on an OK-102/1 conductometer (Hungary) equipped with an OK-0902P bell-shaped electrode [4]. The optical density of solutions was measured on an SF-26 spectrophotometer and a KFK-2 photocolorimeter; pH was measured on an EV-74 ionometer equipped with glass and silver chloride electrodes. The voltammetric curves of DBH ethanol solutions were obtained in the dc mode on a PU-1 polarograph with a three-electrode cell at room temperature without deaeration. A platinum electrode was used as an indicator electrode, and a platinum plate, as an auxiliary electrode. The potentials were measured relative to a saturated silver chloride electrode. The IR spectra (mulls in Vaseline oil) were recorded on a Specord M-80 IR spectrometer. The thermogravimetric curves were recorded on an MOM (Model Q-1500, Hungary) derivatograph. The copper(II) content in solutions was determined by the extraction-photometric technique using extractable Cu(II) complex with zinc diethyldithiocarbamate [5].

The DBH solubility in water and several other solvents was determined as follows. A portion of DBH was contacted with a solvent for 24 h at 20 ± 0.5°C. An aliquot of the liquid phase saturated with DBH was sampled and dried in a drying oven at 105–110°C, and the resulting dry residue was weighed. In the case of 0.1 M aqueous KOH as solvent, the DBH concentration in saturated solution was determined from its optical density (λ = 240 nm, 1-cm optical cell) using a calibration curve. The DBH solubility in the solvents used was as follows (g l^{-1}): water 0.22, 2-methylbutanol 1.34, ethanol 5.22, *p*-xylene 0.48, chloroform 0.02, and 0.1 M aqueous KOH 9.6. These results show that the DBH solutions in both ethanol and aqueous alkali can be used for precipitation of Cu(II) and as collectors in Cu(II) recovery by flotation.

The first and second DBH ionization constants were determined spectrophotometrically [6]. Figure 1 shows the electronic absorption spectra of aqueous DBH at different pH. The absorption bands of nonionized DBH molecules in water (spectrum *1*) and their ionized species in alkaline solutions (curves *2* and *3*) in the range 300–320 nm considerably differ. In order to calculate pK_{a_1} and pK_{a_2} of DBH, the de-

pendence of the optical density D on pH_{eq} at 325 nm was studied (Fig. 2). Figure 2 shows that the plot of D vs. pH has two inflection points. The inflection points corresponding to the first and second steps of DBH ionization are located within pH ranges 9–9.5 and 10.5–11.0, respectively [see Eq. (1)]:

$$C_6H_5{-}\underset{\underset{O}{\|}}{C}{-}NH{-}NH{-}\underset{\underset{O}{\|}}{C}{-}C_6H_5 \quad (H_2L)$$

$$\overset{K_{a_1}}{\rightleftharpoons} C_6H_5{-}\underset{\underset{O^-}{|}}{C}{=}NH{-}NH{-}\underset{\underset{O}{\|}}{C}{-}C_6H_5 \quad (HL^-)$$

$$\overset{K_{a_2}}{\rightleftharpoons} C_6H_5{-}\underset{\underset{O^-}{|}}{C}{=}NH{-}NH{=}\underset{\underset{O^-}{|}}{C}{-}C_6H_5. \quad (L^{2-}) \qquad (1)$$

The pK_{a_1} and pK_{a_2} calculated by the formulas published in [6] are 9.22 ± 0.04 and 10.8 ± 0.3, respectively. The comparison of these ionization constants with those of aliphatic 1,2-diacylhydrazines, e.g., 1,2-dipentanoylhydrazine (DPH) ($pK_{a_1} = 11.21 \pm 0.04$, $pK_{a_2} = 12.0 \pm 0.3$) shows that DBH is a stronger acid than DPH.

In order to determine the resistance of DBH to hydrolysis, a portion of DBH (0.05–0.08 mmol) was dissolved in 1 M aqueous KOH (50 ml) at 60 ± 0.1°C. At intervals of 1, 2, 3, and 4 h, aliquots (5.0 ml) of the reaction mixture were sampled, and their optical densities were determined at λ = 325 nm in a 1-cm optical cell. We found that the optical density of the DBH alkaline solutions does not change in the first 2 h and then gradually increases (for example, after a lapse of 3 h, the optical density increases by 25%). The DBH hydrolysis was monitored spectrophotometrically at λ = 325 nm, which corresponds to the maximal difference between the optical densities of dibenzoylhydrazine (DBH) and the main expected hydrolysis products: benzoylhydrazine (BH) and potassium benzoate (PB) (Fig. 3). These species were chosen assuming that DBH is hydrolyzed in an alkaline solution by a mechanism identical to that of aliphatic DAH, involving formation of benzoate and hydrazine hydrate as the main products and benzoic acid hydrazide as intermediate [7]. Figure 3 shows that, if DBH were hydrolyzed by the above hypothetical mechanism, the optical density would decrease. However, our experiments showed that base hydrolysis of DBH is accompanied by an increase in the optical density. We believe that this opposite trend is caused, at least in the first stage of hydrolysis, by the redox reaction producing azo compounds:

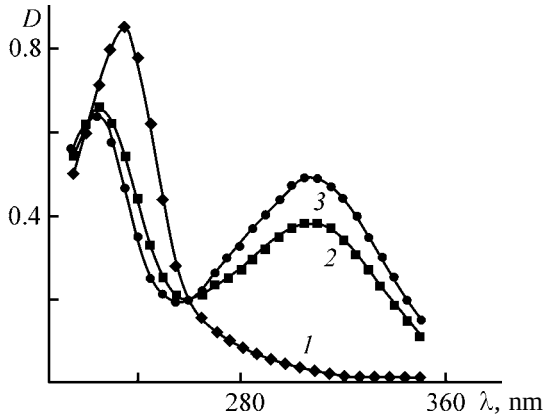

Fig. 1. Electronic spectra of 4×10^{-5} M aqueous DBH at different pH. (*D*) Optical density and (λ) wavelength; the same for Fig. 3. pH: (*1*) 6.35, (*2*) 9.9, and (*3*) 10.45.

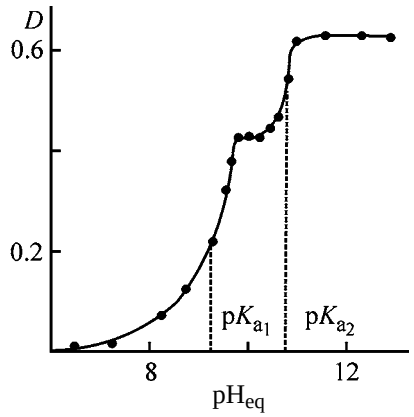

Fig. 2. Optical density of 4×10^{-5} M aqueous DBH vs. pH. λ = 325 nm and l = 1 cm.

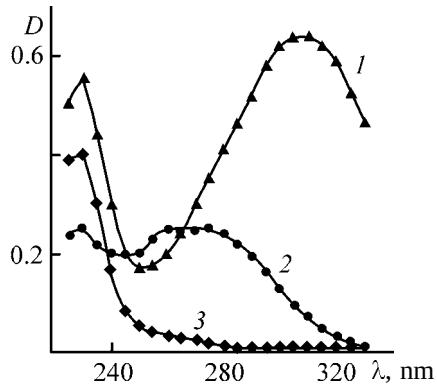

Fig. 3. Electronic spectra of (*1*) DBH, (*2*) benzoylhydrazine, and (*3*) potassium benzoate (4.5×10^{-5} M in 1 M aqueous KOH).

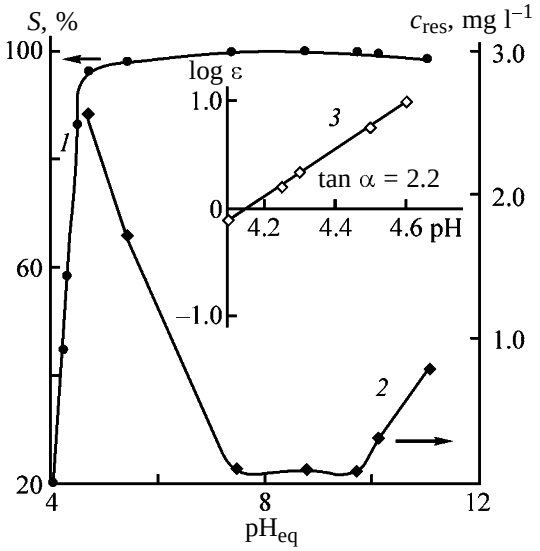

Fig. 4. (*1*) Degree of Cu(II) precipitation with DBH *S* and (*2*) residual Cu(II) concentration c_{res} vs. equilibrium pH. (*3*) Curve *1* after treatment with the technique of shifting the solubility. Content: Cu(II) 63.5 mg l^{-1}, ethanol solution of DBH 10^{-2} M; ammonia buffer solution: $(NH_4)_2SO_4$ 0.125 M + NH_4OH 0.25 M, V 25 ml, and τ 5 min.

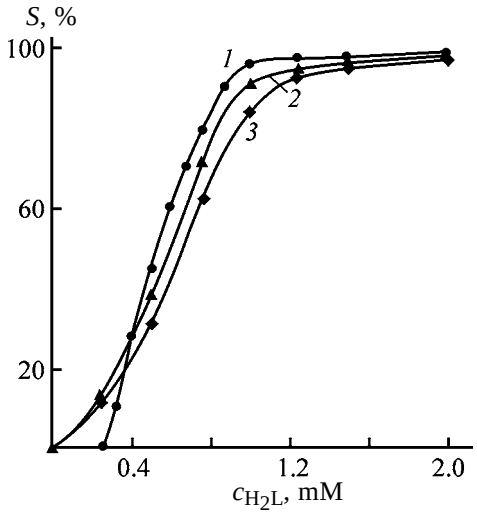

Fig. 5. Degree of precipitation of Cu(II) *S* as a function of DBH and DAH concentration c_{H_2L}. Cu(II) concentration 63.5 mg l^{-1}; ammonia buffer solution: $(NH_4)_2SO_4$ 0.125 M + NH_4OH 0.25 M, *V* 25 ml, and τ 5 min. H_2L: (*1*) DBH, (*2*) DPH and (*3*) dibutanoylhydrazine in ethanol.

$$2C_6H_5\text{–}\underset{\underset{O}{\|}}{C}\text{–NH–NH–}\underset{\underset{O}{\|}}{C}\text{–}C_6H_5 + O_2$$

$$\rightleftarrows 2C_6H_5\text{–}\underset{\underset{O}{\|}}{C}\text{–N=N–}\underset{\underset{O}{\|}}{C}\text{–}C_6H_5 + 2H_2O. \qquad (2)$$

Although the products of this reaction were not identified by us and its true mechanism is unknown, nevertheless, we established that DBH is chemically stable in 1 M aqueous KOH at 60°C for at least the first 2 h. At the same time, DPH under identical conditions decomposes to 40% in the first 3 h [6].

The voltammetric curves of DBH (10^{-2} M) in 1 M aqueous KOH were registered at the cathodic polarization at intervals of 1, 2, 3, 4 and 5 h. We found that the height of polarographic waves decreases with time due to electrochemical oxidation of DBH. The comparison of the voltammetric curves of DBH and DPH [6] shows that these compounds have approximately equal stability to electrochemical oxidation in 1 M aqueous KOH.

Since the poorly soluble complexes of Cu(II) with DBH are floatable only in the persence of a frother, the DBH complexation with Cu(II) was studied by a precipitation technique. Figure 4 shows that DBH precipitates Cu(II) within the wide pH range and the most complete precipitation (up to of 99.8%) is reached within pH 6–10. With increasing ammonia content to 0.5 M (pH ~11), the degree of recovery of Cu(II) decreases to 96% due to the competing formation of soluble Cu(II) ammonia complexes. Addition of $(NH_4)_2SO_4$ to 0.125 M does not noticeably affect the precipitation of Cu(II).

Figure 5 shows the degree of precipitation of Cu(II) as influenced by the content of DBH and aliphatic DAH. The curve obtained with DBH has an inflection point corresponding to Cu(II) : DBH ratio in the precipitate equal to unity. The plot of $\log \varepsilon$ [$\varepsilon = S_i(1 - S_i)$] vs. pH_{eq} shows that the precipitation of copper(II) with DBH in the form of 1 : 1 complex is accompanied by liberation of two moles of [H^+] per mole of DBH, i.e., the precipitated complex contains L^{2-} anions.

The comparison of the precipitation curves presented in Fig. 5 shows that at equal pH DBH (curve *1*) more efficiently precipitates Cu(II) than do aliphatic DAHs (curves *2* and *3*). The efficiency of precipitation of Cu(II) with DAHs from NH_4OH + $(NH_4)_2SO_4$ buffer mixture at pH 9–10 can be increased by adding KOH to increase the degree of DBH ionization [2]. DBH, owing to its high acidity, precipitates 96% of Cu(II) even at pH 5.

Thus, the precipitation of Cu(II) in the form of its complex with DBH can be described by the equation

$$[Cu(NH_3)_4]^{2+} + H_2L \rightleftarrows CuL\downarrow + 2NH_3 + 2NH_4^+. \qquad (3)$$

The residual Cu(II) concentration in the filtered solution (pH 9.4), determined 5, 15, 30, and 60 min after precipitation at Cu : DBH = 1 : 1, was constant. These data show that 5 min is sufficient for ripening of the CuDBH precipitate.

The Cu : DBH ratio in the precipitate was determined by conductometric titration as follows. 10^{-2} M aqueous $CuSO_4$ (5 ml) and distilled water (60 ml) were poured into a 100-ml beaker, and then the ammonia buffer solution was added dropwise until a blue color of Cu(II) ammonia complex appeared. This solution was titrated by adding 0.2-ml portions of 10^{-2} M DBH in alcohol. The curve of conductometric titration has three inflection points corresponding to formation of complexes with Cu : DBH ratios of 2 : 1, 1 : 1, and 1 : 2.

We attempted to isolate the complexes of Cu(II) with DBH from ammonia solutions at Cu : DBH ratios of 1 : 1 and 1 : 2. In these experiments, 10^{-2} or 5×10^{-3} M aqueous $CuSO_4$ (50 ml) was placed in a 250-ml beaker, and 10 M aqueous NaOH (2.8 ml) and 2.5 M aqueous $(NH_4)_2SO_4$ (5.2 ml) were added. Thereafter, while stirring this mixture, 10^{-2} M DBH in ethanol (50 ml) was added to each of these solutions, and the resulting suspensions were allowed to stand for 30 min. The precipitates were filtered off, successively washed on the filter with hot water and ethanol, and then air-dried.

The complexes precipitated at Cu : DBH ratios of 1 : 1 and 1 : 2 have green color and are poorly soluble in water and common organic solvents. Their IR spectra and thermogravimetric curves are identical. In the IR spectra, instead of the absorption bands of NH (3160 cm^{-1}) and C=O (1670, 1635 cm^{-1}) stretching vibrations in the DBH molecule, the absorption bands of the C=N (1520 cm^{-1}) and C–O (1400 cm^{-1}) vibrations appear. These spectroscopic data confirm that Cu(II) in the complexes under consideration coordinates with double-deprotonated DBH molecule (L^{2-}).

The thermogravimetric analysis shows that both 1 : 1 and 1 : 2 complexes are thermally stable up to 325°C. The elemental analysis shows that these complexes have identical copper content. The complexes prepared at Cu(II) : DBH = 1 : 1 and 1 : 2 contain 20.85% and 20.73% Cu(II), respectively, which is close to the calculated copper content in $Cu(C_6H_5OCNNCOC_6H_5)$, 21.06%.

Thus, although conductometric titration shows that in aqueous ammonia the 2 : 1, 1 : 1, and 1 : 2 complexes are formed, only the 1 : 1 complex was isolated. The precipitation of Cu(II) in the form of this poorly soluble complex can be used for quantitative gravimetric determination of Cu(II).

In industrial flotation and precipitation of metals, both the froth products and precipitates are commonly dried and ashed. Therefore, the development of procedures for reuse of the reagents is an important problem [8]. We found that, on treatment of the filtered poorly soluble complex of Cu(II) with DBH with 0.25–2.0 M aqueous H_2SO_4, this complex is readily broken down to give a white crystalline precipitate of DBH and a filtered solution of $CuSO_4$. This solution was collected in a 25-ml volumetric flask, and water was added the mark. A 5-ml aliquot of the filtered solution was sampled, and the Cu(II) content was determined by complexometric titration with EDTA [9]. It was established that the complete DBH regeneration with aqueous H_2SO_4 is reached at H_2SO_4 concentration not lower than 0.5 M.

CONCLUSIONS

(1) Introduction of phenyl radicals into 1,2-diacylhydrazines increases their acidity by two orders of magnitude and enhances their chemical stability in alkaline solutions.

(2) The complexes of 1,2-dibenzoylhydrazine with Cu(II) are formed in ammonia solutions at pH within 5–8 without adding alkali, whereas aliphatic 1,2-diacylhydrazines are coordinated with Cu(II) at pH 9–10.

(3) Owing to low solubility of 1,2-dibenzoylhydrazine in water and aqueous acids, this reagent can be recovered from its complexes with Cu(II) by treatment with 0.5 M aqueous H_2SO_4.

REFERENCES

1. Radushev, A.V., Zubareva, G.I., and Chekanova, L.G., *Izv. Vyssh. Uchebn. Zaved., Tsvetn. Metall.*, 1999, no. 1, pp. 3–6.
2. Chekanova, L.G., Radushev, A.V., and Shabalina, L.S., *Khimiya i tekhnologiya ekstraktsii* (Chemistry and Technology of Extraction), *Tr. Ross. Khim.-Tekhnol. Univ. im. D.I. Mendeleeva*, 2001, pp. 111–115.
3. Drozdetskii, A.G., Radushev, A.V., Turbin, A.S., *et al.*, *Zh. Prikl. Khim.*, 1998, vol. 71, no. 2, pp. 288–293.
4. Radushev, A.V., Chekanova, L.G., Gusev, V.Yu., and Sazonova, E.A., *Zh. Anal. Chem.*, 2000, vol. 55, no. 5, pp. 496–499.

5. Podchainova, V.N. and Simonova, L.N., *Analiticheskaya khimiya elementov: Med'* (Analytical Chemistry of Elements: Copper), Moscow: Nauka, 1990.
6. Chekanova, L.G., Radushev, A.V., Lesnov, A.E., and Sazonova, E.A., *Zh. Obshch. Khim.*, 2002, vol. 59, no. 8, pp. 1315–1319.
7. Chekanova, L.G., Equilibria in Solutions in Complexation of Symmetrical 1,2-Diacylhydrazines with Copper(II) and Several *d*-Element Cations, *Cand. Sci. Dissertation*, Perm, 2002.
8. Gol'man, A.I., *Ionnaya flotatsiya* (Ionic Flotation), Moscow: Nedra, 1982.
9. Korostelev, P.P., *Fotometricheskii i kompleksonometricheskii analiz v metallurgii* (Photometric and Complexometric Analysis in Metallurgy), Moscow: Metallurgiya, 1984.

Russian Journal of Applied Chemistry, Vol. 77, No. 7, 2004, pp. 1079–1082. Translated from Zhurnal Prikladnoi Khimii, Vol. 77, No. 7, 2004, pp. 1094–1097.

PHYSICOCHEMICAL STUDIES OF SYSTEMS AND PROCESSES

Thermodynamic Properties of Dimethylaminoarglabin Methyl Iodide $C_{18}H_{28}O_3NI$ and Its Analogs

Sh. B. Kasenova, Zh. K. Tukhmetova, A. Zh. Abil'daeva, S. M. Adekenov, B. K. Kasenov, and R. I. Dzhalmakhanbetova

Institute of Phytochemistry, Ministry of Education and Science of the Kazakhstan Republic, Karaganda, Kazakhstan

Received February 11, 2004

Abstract—The heat of solution of dimethylaminoarglabin methyl iodide $C_{18}H_{28}O_3NI$ at dilutions (mole of salt/mole of water) of 1 : 75000, 1 : 100000, and 1 : 150000 was determined by isothermal calorimetry. The data obtained were used to calculate the standard heat of solution of the compound in an infinitely dilute (standard) aqueous solution. The heats of combustion, melting, and formation of $C_{18}H_{28}O_3NI$ and 33 its analogs were estimated by approximate methods of chemical thermodynamics.

Calorimetric methods, which are the primary source of information in physical chemistry of solutions, are the most commonly used in biochemical thermodynamics [1]. A study of thermochemical and thermodynamic properties of terpenoids is of certain theoretical and practical significance for their controlled synthesis. In this respect, natural sesquiterpene lactones, most of which possess a wide spectrum of biological activity, are of interest [2]. Various pharmaceuticals based on sesquiterpene lactones have been and are being developed. For example, original antitumor preparation Arglabin based on sesquiterpene lactone derived from *Artemisia glabella* Kar. et Kir., growing solely in Central Kazakhstan, was developed and applied in medicine [3]. The Arglabin drug was registered in the Kazakhstan Republic, and its registration in the Russian Federation is in progress.

Thermochemical and thermodynamic properties of sesquiterpene lactones of the general formula $C_{15}H_{18}O_3$ (including Arglabin) and its derivatives have been studied previously [4].

EXPERIMENTAL

In this work, we studied experimentally the enthalpy of solution of dimethylaminoarglabin methyl iodide $C_{18}H_{28}O_3NI$ in water.[1] The structural formula of dimethylaminoarglabin methyl iodide is presented below:

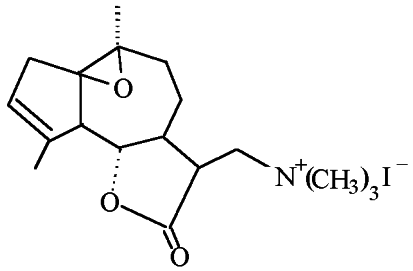

The enthalpy of solution of the compound was studied on a DAK-1-1A automated differential calorimeter at 25°C at dilutions (mole of substance/mole of water) of 1 : 75000, 1 : 100000, and 1 : 150000. The heat of solution was determined in the automatic heat compensation mode. The thermal effects were recorded with a KSP-4 self-recorder and IP-4 precision integrator. The time of the preliminary thermostating of the substance was 2 h. The integrator drift did not exceed three units of the last digit in 100 s. Prior to the experiment, the instrument was calibrated by Joulean heat. To do this, a calibrated voltage was supplied to a built-in heater of the instrument, and the released power was measured. The calibration of the instrument was checked by measuring the heat of solution of triply recrystallized potassium chloride at dilutions (mole of salt/mole of water) of 1 : 1600, 1 : 2400, and 1 : 3200. The average heat of the KCl solution in water (17860 ± 283 J mol^{-1}) agrees well (to within 1.6–2.0%) with the known values of 17577 ± 34 [5] and 17489 ± 371 J mol^{-1} [6].

[1] The compound of the pharmacopoeia purity was prepared at the Laboratory of Terpenoid Chemistry of the Institute of Phytochemistry.

1070-4272/04/7707-1079 © 2004 MAIK "Nauka/Interperiodica"

Table 1. Enthalpy of solution of dimethylaminoarglabin methyl iodide in water at various dilutions

$C_{18}H_{28}O_3NI$ weight, g	Q_s, J	ΔH_s^m, kJ mol^{-1}
Dilution 1:75 000		
0.0016	0.100	27.06
0.0017	0.106	26.99
0.0018	0.113	27.17
0.0015	0.093	26.84
0.0015	0.094	27.13
Average ΔH_s^m (1) = 27.04 ± 0.16		
Dilution 1 : 100 000		
0.0011	0.087	34.24
0.0012	0.094	33.91
0.0011	0.086	33.84
0.0012	0.096	34.63
0.0013	0.104	34.29
Average ΔH_s^m (2) = 34.18 ± 0.51		
Dilution 1 : 150 000		
0.0008	0.085	45.99
0.0008	0.084	45.45
0.0009	0.092	44.25
0.0007	0.074	45.76
0.0007	0.074	45.76
Average ΔH_s^m (3) = 45.44 ± 0.86		

The experimental errors and uniformity of their variance were calculated by the methods of mathematical statistics using the Student and Bartlett tests [7]. The results of the calorimetric study are presented in Table 1.

Then, the experimentally obtained enthalpies of dimethylaminoarglabin methyl iodide solution at various dilutions were extrapolated to infinite dilution, and the standard enthalpies of solution of the compound in an infinitely dilute (standard) aqueous solution were calculated. Based on the equation $\Delta H_s^m = fm^{1/2}$ (m is molal concentration), it was established [8] that the dependence of the enthalpy of $C_{18}H_{28}O_3NI$ solution, ΔH_s^m (kJ mol^{-1}), on the molal concentration is described by the relationship

$$\Delta H_s^m = 86.8 - 2206.0m^{1/2}, \quad (1)$$

from which the standard enthalpy of solution of dimethylaminoarglabin methyl iodide in an infinitely dilute (standard) aqueous solution was determined as 86.8 ± 1.2 kJ mol^{-1}.

To calculate the standard enthalpy of formation of $C_{18}H_{28}O_3NI$, its standard heat of combustion was estimated using the Karash and Frost methods [9], which are the most suitable procedures for taking into account contributions of various groups in the molecule to the heat of combustion.

The average enthalpy of combustion of $C_{18}H_{28}O_3 \cdot NI$ in liquid state, calculated by these two methods, is –10 792 ± 134 kJ mol^{-1}.

The $\Delta_f H^0_{298.15}$ of $C_{18}H_{28}O_3NI$(l) was calculated using the average ΔH^0_{comb} value by the Hess cycle based on the reaction

$$2C_{18}H_{28}O_3NI(l) + 47O_2(g) = 36CO_2(g) + 28H_2O(l) + N_2(g) + I_2(g) - \Delta H^0_{comb} \quad (2)$$

to be –300.3 kJ mol^{-1}.

It should be noted that the Karash and Frost methods can be applied solely to calculating the enthalpy of combustion ΔH^0 of liquid hydrocarbons. The required values of $\Delta_f H^0_{298.15}$ of CO_2(g) and H_2O(l) were taken from [10].

Since at standard temperature (298.15 K) the compound studied is in the crystalline state, a need arises to calculate $\Delta_f H^0_{298.15}$ of its solid modification. To do this, the ΔH^0_m values of the compounds were estimated by the empirical equation [11]

$$\Delta H^0_m = 44.4T_m - 4400. \quad (3)$$

The ΔH^0_m value of $C_{18}H_{28}O_3NI$, calculated by Eq. (3), is 16.7 kJ mol^{-1}. From the equation

$$\Delta_f H^0_{298.15}[C_{18}H_{28}O_3NI(s)] = \Delta_f H^0_{298.15}[C_{18}H_{28}O_3NI(l)] - \Delta H^0_m, \quad (4)$$

the standard enthalpy of formation of dimethylaminoarglabin methyl iodide in the crystalline state was calculated as –317.0 kJ mol^{-1}.

The standard enthalpy of formation of $C_{18}H_{28}O_3NI$ in aqueous solution was determined using the standard enthalpy of solution of dimethylaminoarglabin methyl iodide in standard (infinitely dilute) aqueous solution by the equation

$$\Delta_f H^0_{298.15}[C_{18}H_{28}O_3NI(sol., H_2O, stand. state)] = \Delta_f H^0_{298.15}[C_{18}H_{28}O_3NI(s)] + \Delta H^0_s; \quad (5)$$

it was found to be –230.2 kJ mol^{-1}.

Table 2. Standard heats of formation of $C_{18}H_{28}O_3NI$ and its analogs

Compound	$-\Delta_f H^0_{298.15}$, kJ mol^{-1}	Compound	$-\Delta_f H^0_{298.15}$, kJ mol^{-1}
$C_{18}H_{28}O_3NF$	497	$C_{18}H_{28}O_3NNO_2$	283
$C_{18}H_{28}O_3NBr$	294	$[C_{18}H_{28}O_3N]_3PO_4$	1760
$C_{18}H_{28}O_3NCl$	334	$[C_{18}H_{28}O_3N]_4P_2O_7$	2925
$C_{18}H_{28}O_3NClO_4$	309	$[C_{18}H_{28}O_3N]_2CO_3$	1009
$C_{18}H_{28}O_3NClO_3$	288	$[C_{18}H_{28}O_3N]_2C_2O_4$	1172
$C_{18}H_{28}O_3NBrO_3$	276	$C_{18}H_{28}O_3NAlO_2$	1080
$C_{18}H_{28}O_3NIO_3$	431	$C_{18}H_{28}O_3NBO_2$	908
$[C_{18}H_{28}O_3N]_2SO_4$	1251	$C_{18}H_{28}O_3NReO_4$	1016
$[C_{18}H_{28}O_3N]_2SO_3$	970	$C_{18}H_{28}O_3NMnO_4$	752
$[C_{18}H_{28}O_3N]_2SeO_4$	931	$[C_{18}H_{28}O_3N]_2Cr_2O_7$	1890
$[C_{18}H_{28}O_3N]_2TeO_4$	1115	$[C_{18}H_{28}O_3N]_2CrO_4$	1233
$[C_{18}H_{28}O_3N]_2S_2O_3$	1019	$[C_{18}H_{28}O_3N]_2WO_4$	1433
$[C_{18}H_{28}O_3N]_2SeO_3$	829	$[C_{18}H_{28}O_3N]_2MoO_4$	1259
$[C_{18}H_{28}O_3N]_2TeO_3$	859	$C_{18}H_{28}O_3NVO_3$	1083
$[C_{18}H_{28}O_3N]_2S$	319	$C_{18}H_{28}O_3NNbO_3$	1262
$[C_{18}H_{28}O_3N]_2Se$	360	$[C_{18}H_{28}O_3N]_3AsO_4$	1389
$C_{18}H_{28}O_3NNO_3$	388		

The equation

$$\Delta_f H^0_{298.15}[C_{18}H_{28}O_3N^+(\text{sol., } H_2O, \text{ stand. state})] = \Delta_f H^0_{298.15}[C_{18}H_{28}O_3NI(\text{sol., } H_2O, \text{ stand. state})] - \Delta_f H^0_{298.15}[I^-(\text{sol., } H_2O, \text{ stand. state})] \quad (6)$$

was used to calculate the standard enthalpy of formation of the $[C_{18}H_{28}O_3N]^+$ ion in a standard aqueous solution (–174.9 kJ mol^{-1}). The $\Delta_f H^0_{298.15}[I^-(\text{sol., } H_2O, \text{ stand. state})]$ value necessary for calculation was taken from a reference book [10].

The found $\Delta_f H^0_{298.15}[C_{18}H_{28}O_3N]^+$ value in aqueous solution made it possible to calculate the standard heats of formation of the $C_{18}H_{28}O_3NI$ analogs.

A method using the enthalpy increments, $\Delta_f H^i_{298.15}$, for calculating $\Delta_f H^0_{298.15}$ of inorganic salts has been proposed in [12, 13]. The increments, or standard constituents, are convenient for the calculation of thermodynamic properties assuming their additivity. In this case, the thermodynamic property of a substance is determined as the sum of the standard thermodynamic constants of its constituents (in the given case, ions). The standard enthalpy of formation of the crystalline salt was calculated by the formula [12, 13]

$$\Delta_f H^0_{298.15}[Me_m(X_\alpha O_\beta)_n] = m\Delta_f H^0_{298.15}[Me^{n+}(\text{sol., } H_2O, \text{ stand. state})]K + n\Delta_f H^i_{298.15}(X_\alpha O_\beta)^{m-}. \quad (7)$$

To use the given formula, it is sufficient to know the $\Delta_f H^0_{298.15}[Me^{n+}(\text{sol., } H_2O, \text{ stand. state})]$ values. The values of the K parameters (proportionality coefficients) and $\Delta_f H^i_{298.15}(X_\alpha O_\beta)^{m-}$ (the enthalpy increments of the anions) are tabulated in [12, 13]. For the compound $C_{18}H_{28}O_3NI$, scheme (7) can be presented as follows:

$$\Delta_f H^0_{298.15}[C_{18}H_{28}O_3NI(s)] = \Delta_f H^0_{298.15}[C_{18}H_{28}O_3N^+(\text{sol., } H_2O, \text{ stand. state})]K + \Delta_f H^i_{298.15}(I^-). \quad (8)$$

The calculated $\Delta_f H^0$ values for $C_{18}H_{28}O_3NI$ and 33 its analogs are presented in Table 2.

CONCLUSIONS

(1) The standard enthalpy of solution of dimethylaminoarglabin methyl iodide in water was determined by isothermal calorimetry.

(2) Its enthalpies of combustion and melting were calculated. The standard heat of formation of the cation $[C_{18}H_{28}O_3N]^+$ in aqueous solution was determined using the calculated and experimental enthalpies of solution of dimethylaminoarglabin methyl iodide in standard aqueous solution.

(3) The standard heats of formation of $C_{18}H_{28}O_3NI$ and 33 related compounds were calculated using the method of ionic increments.

REFERENCES

1. Abrosimov, V.K., Agafonov, A.V., Chumakova, R.V., *et al*., *Biologicheski aktivnye veshchestva v rastvorakh: Struktura, termodinamika i reaktsionnaya sposobnost'* (Biologically Active Substances in Solutions: Structure, Thermodynamics, and Reactivity), Moscow: Nauka, 2001.
2. Kagarlitskii, A.D., Adekenov, S.M., and Kupriyanov, A.N., *Seskviterpenovye laktony rastenii Tsentral'nogo Kazakhstana* (Sesquiterpene Lactones Derived from Plants of Central Kazakhstan), Alma-Ata: Nauka, 1987.
3. Adekenov, S.M., Sesquiterpene Lactones Derived from Kazakhstan Plants: Structure, Properties, and Use, *Doctoral Dissertation*, Moscow, 1992.
4. Kasenov, B.K., Adekenov, S.M., Mustafin, E.S., *et al*., *Zh. Fiz. Khim*., 2002, vol. 76, no. 2, pp. 206–209.
5. Mishchenko, K.P., and Poltoratskii, G.M., *Termodinamika i stroenie vodnykh i nevodnykh rastvorov elektrolitov* (Thermodynamics and Structure of Aqueous and Nonaqueous Electrolyte Solutions), Leningrad: Khimiya, 1977.
6. *Termicheskie konstanty veshchestv: Spravochnik* (Thermal Constants of Substances: Reference Book), Glushko, V.P., Ed., Moscow: Nauka, 1982, issue 10, part 2.
7. Spiridonov, V.P. and Lopatkin, A.A., *Matematicheskaya obrabotka eksperimental'nykh dannykh* (Mathematical Treatment of Experimental Data), Moscow: Mosk. Gos. Univ., 1970.
8. Krestov, G.A., *Termodinamika ionnykh protsessov v rastvorakh* (Thermodynamics of Ionic Processes in Solutions), Leningrad: Khimiya, 1984.
9. Kazanskaya, A.S., and Skoblo, V.A., *Raschety khimicheskikh ravnovesii* (Calculations of Chemical Equilibria), Moscow: Vysshaya Shkola, 1974.
10. Ryabin, V.A., Ostroumov, M.A., and Svit, T.F., *Termodinamicheskie svoistva veshchestv: Spravochnik* (Thermodynamic Properties of Substances: Reference Book), Leningrad: Khimiya, 1977.
11. Morachevskii, A.G., and Sladkov, I.B., *Termodinamicheskie raschety v metallurgii: Spravochnik* (Thermodynamic Calculations in Metallurgy: Reference Book), Moscow: Metallurgiya, 1985.
12. Kasenov, B.K., Abishev, D.N, and Bukharitsyn, V.O., *Termokhimiya shchelochnykh metallov* (Thermochemistry of Alkali Metals), Alma-Ata: Nauka, 1988.
13. Kasenov, B.K., Aldabergenov, M.K, and Pashinkin, A.S., *Termodinamicheskie metody v khimii i metallurgii* (Thermodynamic Methods in Chemistry and Metallurgy), Almaty: Rauan, 1994.

Russian Journal of Applied Chemistry, Vol. 77, No. 7, 2004, pp. 1083–1091. Translated from Zhurnal Prikladnoi Khimii, Vol. 77, No. 7, 2004, pp. 1098–1106.

PHYSICOCHEMICAL STUDIES OF SYSTEMS AND PROCESSES

Kinetics and Mechanism of Thermal Decomposition of Guanidinium Nitrate and Its Mixtures with Ammonium Nitrate

Yu. I. Rubtsov, A. I. Kazakov, D. B. Lempert, and G. B. Manelis

Institute of Problems of Chemical Physics, Russian Academy of Sciences, Chernogolovka, Moscow oblast, Russia

Received December 15, 2003; in final form, April 2004

Abstract—The kinetics of heat release in thermal decomposition of guanidinium and ammonium nitrates and their mixtures in the liquid phase in a calorimeter was studied. The kinetic equations of these processes and temperature dependences of the kinetic constants in these equations were evaluated. The oxidation rate constants of guanidinium and ammonium cations with molecular nitric acid in aqueous nitric acid solutions were found; these constants were calculated by solution of the reverse problem for salt melts. The temperatures and ΔH values of melting of the initial salts and their eutectic mixture were determined.

Ammonium nitrate (AN) is widely used in agriculture as nitrogen fertilizer and as oxidant in production of explosives and gas-generating fuel compositions. Modification of AN using various additives to provide the required physicochemical and energy properties of the resulting compositions is urgent, especially for fuels. One of possible ways of modification is addition to AN of other onium nitrates with negative oxygen balance, which thus can act as fuels. Unfortunately, many onium nitrates (hydrazinium, hydoxylammonium, urea, etc.) have poor thermal stability, which hinders their practical use. One of the most stable onium nitrates is, probably, guanidinium nitrate (GN); the mixture of 2 mol AN and 1 mol GN has zero oxygen balance. Initially, all the onium nitrates thermally degrade through equilibrium dissociation to form the initial base and nitric acid. As a rule, the rate of decomposition is determined by the equilibrium constant of dissociation of the nitrate into the base and nitric acid and by the rate of oxidation of the corresponding cation with a nitric acid molecule or by the rate of thermal transformation of the base [1].

In aqueous solution, guanidine is a stronger base (pK 13.6) than ammonia (pK 9.27) [2]. The pK values can strongly change on passing from aqueous solutions to the ionic nitrate melt. However, since the difference in pK in aqueous solutions is very large, we assumed that it cannot be completely leveled off in the melt, and thus the concentration of nitric acid in GN should be significantly smaller than in AN. Data on the rate of oxidation of $CN_3H_6^+$ ion with HNO_3 molecule are lacking. Theoretically, this constant may be noticeably higher than the rate constant of oxidation of NH_4^+ ion, which should significantly increase the rate of GN thermal decomposition. Relatively high melting point of guanidinium nitrate (214°C) indicates that the rate of NG decomposition is lower as compared with AN. Since at relatively high decomposition rate determination of the melting point is virtually impossible, the rate of GN decomposition at 214°C is small. Some data on the rate of hydrolysis of $CN_3H_6^+$ ion at 240–300°C are given in [3]. It was found that the nitrate ion does not participate in transformations at water excess, whereas $CN_3H_6^+$ ion undergoes autocatalytic hydrolysis to form CO_2 and NH_3 with urea intermediate. From the rates of heat release from liquid mixtures of AN and GN, it will be possible to assess the feasibility of their processing, in particular, the feasibility of granulation of these mixtures through the melt, as it is often used for technical AN (fertilizer).

EXPERIMENTAL

In this work we used analytically pure grade guanidinium and ammonium nitrates. The kinetics of heat release in thermal decomposition of GN and AN was studied with a DAK-1-2 differential dynamic calorimeter [4] using sealed glass ampules (2 cm^3 volume) completely accommodated in the working cell of the

1070-4272/04/7707-1083 © 2004 MAIK "Nauka/Interperiodica"

calorimeter and thus having no cold sections. The data on the rate of heat release at thermal decomposition of NA commercially produced as agricultural fertilizer [1] showed that the process rate strongly depends on the free volume of the system, due to the transfer into the gas phase at elevated temperatures of certain fraction of NH_3 formed at reversible dissociation of the nitrate into NH_3 and HNO_3. With NH_3 removal from the melt, the content of HNO_3 in the melt and the rate of thermal decomposition increase. To determine the decomposition rate of the salt with the composition closest to the stoichiometry, the process should be performed at the smallest possible free volume to exclude evaporation of NH_3. However, under these conditions, gaseous products formed by the salt decomposition sharply increase the internal pressure and the ampule can be broken. At 200–230°C, the glass ampule (internal diameter 7–8 mm and wall thickness 1–1.15 mm) withstands internal pressure of up to 2 MPa and is broken at higher pressures. Owing to this reason, our experiments on thermal decomposition of AN were interrupted in the initial stage of the process, and the amount of the released gaseous products and pressure in the ampule were evaluated from the amount of the heat released. For comparison, the kinetics of heat release in decomposition of GN and its mixtures with AN were studied under the same conditions, though the equilibrium guanidine pressure over GN at the experimental temperatures is low and the decomposition rate of pure salt is almost independent of the free ampule volume. As for AN + NG mixtures, this dependence becomes more pronounced with increasing AN content in the mixture.

The phase transition temperatures required to evaluate the possibility of granulation of the AN + NG mixtures through the melt (melting point of the eutectic mixture T_e and temperature of the complete melting of the mixture T_f) were determined from the thermograms recorded on a DAK-1-1 differential calorimeter in the linear heating mode. The experiments began at temperatures lower than T_e, when the mixture components are solid, and finished at T_f, when the heat absorption due to the salt melting was terminated. The temperatures T_e and T_f were determined from the beginning and end of the heat absorption. The rate of heat absorption in these steps changed rapidly; the temperatures of the beginning and end of the process could be determined with ±1% accuracy. The thermal effects of the phase transitions were calculated by integration of the curves of heat absorption registered during melting of the mixture.

The kinetics of the heat release in thermal decomposition of pure GN and AN were studied in the ranges 216.8–247.6 (Fig. 1a) and 201.0–230.7°C, respectively. Comparison of the rates showed that, at 200–230°C, the initial rate of heat release in GN decomposition is lower, compared to AN, by a factor of 2.0–3.5. But this difference is not so large as it should be expected if the difference in pK of CN_3H_5 and NH_3 remained constant on passing to the salt melts and the oxidation rate constants of the corresponding cations were similar. Decomposition of AN proceeds with self-acceleration determined by accumulation of nitric acid in the course of the process. The effect of HNO_3 and H_2O on the AN decomposition was studied previously [5]. The initial decomposition rate of reagent grade AN (W mol^{-1}) is close to that of granulated AN produced as fertilizer, but the degree of self-acceleration is significantly smaller. The resulting rate curves can be described by the following kinetic equation:

$$dQ/dt = k_1 + k_2Q. \quad (1)$$

A similar equation was used previously [5] to describe the kinetics of heat release in AN decomposition, but in this case the self-acceleration began only after release of 400–800 J mol^{-1} because of the presence of organic impurities in the sample oxidizable with HNO_3. The k_1 values from Eq. (1) are given below:

T, °C	201	209.6	216.8	223.6	230.7
$k_1 \times 10^2$, W mol^{-1}	3.5	9.8	18	36	78
$k_2 \times 10^5$, s^{-1}	6.4	8.1	8.9	9.4	10.5

The temperature dependences of the constants k_1 and k_2 are as follows:

$$k_1 = 8.4 \times 10^{20} \exp(-203 \times 10^3/RT),$$

$$k_2 = 0.21 \exp(331.8 \times 10^3/RT).$$

We should note slower self-acceleration and low activation energy of this process. The difference from AN produced as fertilizer is probably due to the impurities, which decrease the hygroscopicity and hinder phase transitions in AN. Moreover, the content of water in the AN samples in question is probably higher than in the fertilizer. We failed to remove water without loss of NH_3 by drying in air of small samples at temperatures ≥100°C; as a result, the content of HNO_3 in the sample and the initial decomposition rate increase. After drying of the sample for 3 h at 105°C, the initial decomposition rate increases by a factor of 4; no acceleration of the process was observed,

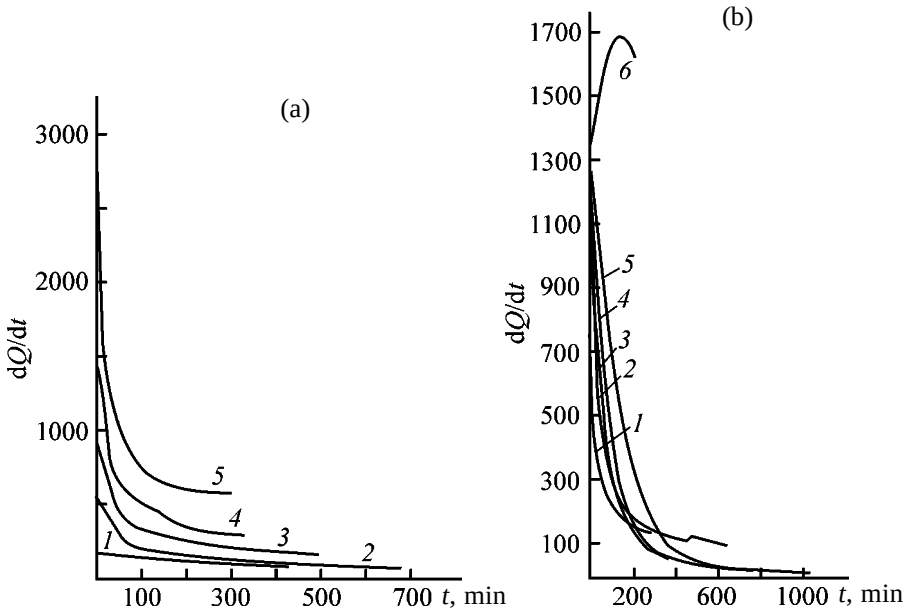

Fig. 1. Kinetic curves of heat release dQ/dt in thermal decomposition of (a) GN and (b) GN + AN mixtures at 223.6°C. (t) Time. (a) Decomposition temperature, °C: (*1*) 216.8, (*2*) 223.6, (*3*) 230.7, (*4*) 239.8, and (*5*) 247.6. (b) Mole fraction N_{AN}: (*1*) 0.147, (*2*) 0.356, (*3*) 0.690, (*4*) 0.810, (*5*) 0.905, and (*6*) 0.955.

because at relatively high initial concentration the acid is not further accumulated. Our results confirmed strong dependence of the rate of AN decomposition on the salt stoichiometry, content of impurities, and experimental conditions, found previously in [1].

The kinetics of heat release in GN thermal decomposition differs from that in AN decomposition; no self-acceleration is observed and the process rate sharply decreases in the course of experiments. This is obviously due to a change in the oxygen balance in GN as compared to AN, with the corresponding changes in the reaction pathways and products of oxidative decomposition. Since one HNO_3 molecule cannot oxidize all the three amino groups and the carbon atom in the $CN_3H_6^+$ molecule, GN is the oxidant-deficient compound. As a result, various bases, including probably NH_3 and CN_3H_5, are accumulated in thermal decomposition and not HNO_3 as in the case of AN. The equilibrium content of HNO_3 will decrease due to the shift in the equilibrium of salt dissociation to the acid and base with increasing total content of bases. As a result, the rate of oxidation with HNO_3 will also decrease. The amount of heat released during the experiments (Fig. 1a) is rather small and comprises 4–12 kJ mol^{-1}. This is significantly smaller than the theoretical heat of GN decomposition (460 kJ mol^{-1}) at complete consumption of oxygen in oxidation and formation of liquid water. The greater fraction of GN remains unchanged, and the rate of its decomposition is very small. This confirms that accumulation of bases (and not GN loss) is the decisive factor responsible for the process deceleration.

Taking into account the above reasons concerning the effect of the reaction products on the process rate, the resulting rate curves of the heat release can be described by the following kinetic equation:

$$\mathrm{d}Q/\mathrm{d}t = k/(b + fQ). \qquad (2)$$

The k/b value determines the initial decomposition rate. The parameters of this equation obtained by linearization of the experimental kinetic curves are given below:

T, °C	216.8	223.6	230.7	239.8	247.6
$k/b \times 10^2$, W mol^{-1}	5.4	16.4	20.4	36.7	79.0
k/f, J mol^{-2} s^{-1}	9.9	17.6	32.2	64.4	143

Their temperature dependences are as follows:

$$k/b = 4.2 \times 10^{16} \exp(-167.2 \times 10^3/RT),$$

$$k/f = 7.9 \times 10^{20} \exp(-179.7 \times 10^3/RT),$$

where k is the rate constant, dimensionless parameter b, the initial content of CN_3H_5 (mole) formed in the reverse dissociation of GN into base and acid; and f, amount of base (mole) formed at release of 1 J heat

due to decomposition of GN (mol J^{-1}); fQ is the dimensionless quantity.

Since in thermal decomposition of AN and GN the salt consumption affects the process rate only in the late stages, it was not taken into account in the kinetic equation. Due to the features of the evaluation procedure, we studied only the initial stages of the process, when the degree of decomposition was lower than 10%.

The rate of AN decomposition sharply increases during the process, whereas the rate of GN decomposition decreases by virtually the same factor. As a result, the difference in the decomposition rates of these salts rapidly increases in the course of the experiment, despite rather small difference in the initial decomposition rates. The period required to attain similar conversion for GN is significantly lower than for AN. For example, after heat release from both salts of 2000 J mol^{-1} at 230.7°C, their decomposition rates differ by a factor of 20, whereas the initial rates differ by a factor of only 3.5.

We studied the kinetics of heat release in thermal decomposition of AN + GN mixtures of various compositions at 223.6°C; at this and the other temperatures studied, all the mixtures are homogeneous liquid solutions. Since the decomposition rate in the salt mixture is determined by the equilibrium dissociation of these salts and all the equilibrium reactions in solutions are often expressed through the mole fractions of components N, the experimental rates of heat release were calculated per mole of solution, i.e., for a mixture with sum of the amounts of components equal to 1 mol. In such a solution, the mole fraction of a certain component equals to its amount in moles. The rate constants for pure AN and GN were also calculated per mole of the compound. The kinetic curves of heat release for AN + GN mixtures are shown in Fig, 1b. As seen, in contrast to the self-acceleration of decomposition of pure AN, the process rate gradually decreases on passing to the mixtures even at mole fraction of GN of 0.1, with a sharper decrease at higher GN content.

For the AN + GN mixture with 2 : 1 molar ratio, the initial rate of heat release (W mol^{-1}) in the 209.6–247.6°C range was measured:

T, °C	$(dQ/dt)_{t=0}$
209.6	0.16
216.8	0.20
223.6	0.86
230.7	0.54
239.8	1.1
247.6	1.7

and its temperature dependence was evaluated:

$$(dQ/dt)_{t=0} = 1.9 \times 10^{13} \exp(-130.0 \times 10^3/RT).$$

As will be shown below, the rate of heat release in the salt mixture is determined by sum of the oxidation rates of NH_4^+ and $CN_3H_6^+$, and its temperature dependence is given by the sum of the two corresponding exponents. Therefore, the temperature dependence presented is obviously formal and correct only in a narrow temperature range; in other temperature ranges, this dependence should change.

In the general form, the initial rate of heat release in decomposition of pure NH_4NO_3 and $CN_3H_6NO_3$ is determined by the salt content and by the rate constant and heat of salt decomposition. If the two salts in the mixture decomposed independently, the initial rate of heat release in the AN + GN mixture (per mole of the mixture) would be determined by the sum of contributions of each salt component to the total heat release, taking into account its content:

$$dQ/dt = k_{AN} Q_{AN} N_{AN} + k_{GN} Q_{GN} N_{GN} = k_{GN} Q_{GN} + N_{AN}(k_{AN} Q_{AN} - k_{GN} Q_{GN}), \quad (3)$$

where k_{AN} and k_{GN}, Q_{AN} and Q_{GN}, and N_{AN} and N_{GN} are the rate constants of decomposition, total heats of decomposition, and mole fractions of the corresponding salts in the mixture.

Thus, constants in Eqs. (1) and (2) can be given as follows:

$$k_1 = k_{AN} Q_{AN}, \qquad k/b = k_{GN} Q_{GN}.$$

The dependence of the rate of the heat release on the AN mole fraction should be linear, and the extreme points should correspond to the initial rates for the pure compounds. The dependence of the initial rate of the heat release in the AN + GN mixtures on the AN mole fraction is shown in Fig. 2. As seen, all the experimental points lie above the straight line connecting the initial rates of the heat release in decomposition of the pure salts. The salts interact with each other in the melt, but the deviations from the straight line are not very large, and the rates of the heat release in the AN + GN mixtures are fairly close from that in AN. These results suggest that the safety in treatment of liquid AN + GN mixtures (e.g., their granulation through the melt) under similar conditions is similar; at least, the difference is smaller than the differences in the rates of heat release for various

batches of commercial AN, differing by an order of magnitude and more. If we take into account that no self-acceleration is observed in the AN + GN mixtures at $N_{GN} > 0.1$ and the rate of heat release gradually decreases, the probability of the runaway should be smaller. At the same time, the specific conditions of the process require specific calculations of its thermal stability.

The data on the kinetics of AN thermal decomposition [1] showed that, at fairly high temperatures and low concentrations of nitric acid (as in the AN melt), this reaction proceeds through oxidation of NH_4^+ with molecular HNO_3 and the kinetic equation can be presented as follows:

$$dQ/dt = k_{NH_4^+} Q_{AN} c_{NH_4^+} c_{HA} V^0_{AN}, \quad (4)$$

where $k_{NH_4^+}$ is the oxidation rate constant of NH_4^+ ($cm^3\ mol^{-1}\ s^{-1}$), Q_{AN} is the heat of AN decomposition ($J\ mol^{-1}$), $c_{NH_4^+}$ and c_{HA} are the concentrations of NH_4^+ ions and HNO_3 molecules (M), and V^0_{AN} is the AN molar volume ($cm^3\ mol^{-1}$).

If we denote the initial concentrations of NH_4^+ ions and HNO_3 molecules as $c^0_{NH_4^+}$ and c^0_{HA}, then

$$k_1 = k_{NH_4^+} Q_{AN} c^0_{NH_4^+} c^0_{HA} V^0_{AN}.$$

Since at the process start $c^0_{NH_4^+} V^0_{AN} = 1$, then

$$k_1 = k_{NH_4^+} Q_{AN} c^0_{HA}.$$

Three series of experiments were performed to determine the $k_{NH_4^+} Q_{AN}$ product. We measured the initial rate of heat release in oxidation of NH_4^+ ions with solutions of nitric acid of various concentrations at 198°C; the initial rates ($W\ mol^{-1}$) obtained are given below:

HNO_3, wt %	20	25	30	32.5
$(dQ/dt)_{t=0}$	3.1	5.9	12.4	10.6

In these experiments, the concentration of NH_4^+ ions in the mixture was much lower than the concentration of HNO_3 molecules; the concentration of nitric acid did not noticeably change during the process. Due to the decrease in the NH_4^+ concentration, the first reaction order was observed. The concentration of nondissociated HNO_3 molecules in the nitric acid solutions was determined from the data given in [6]. Analysis of experimental data showed that the oxidation of NH_4^+ with HNO_3 solutions in the given concentration range proceeds as the first-order reaction with respect to the concentration of HNO_3 molecules. Using the oxidation rates of NH_4^+ ions with 32.5% nitric acid solution at various temperatures

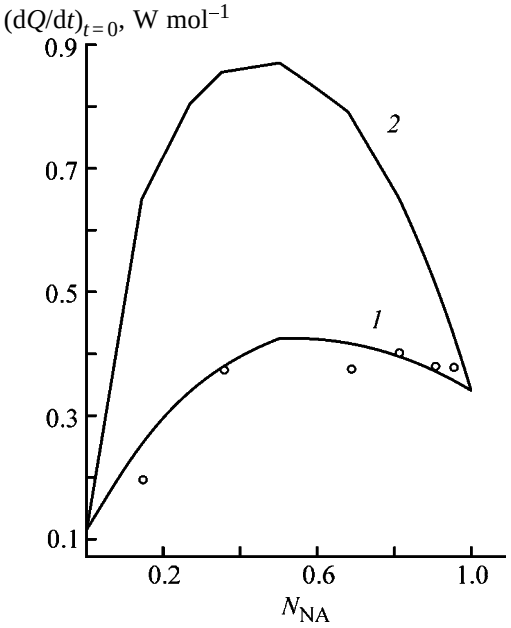

Fig. 2. Initial rate of heat release $(dQ/dt)_{t=0}$ in the AN + GN mixture as a function of the AN mole fraction N_{AN} at 223.6°C. (*1*) Experimental and (*2*) calculated from Eq. (7) using $k_{NH_4^+} Q_{AN}$ and $k_{GN^+} Q_{GN}$ determined for aqueous HNO_3 solutions.

T, °C	183.0	188.0	193.0	198.0
$(dQ/dt)_{t=0}$	1.5	4.7	7.5	10.6

and the data on concentrations of nondissociated HNO_3 molecules [6], we determined the temperature dependence of $k_{NH_4^+} Q_{AN}$ ($W\ cm^3\ mol^{-2}$):

$$k_{NH_4^+} Q_{AN} = 1.0 \times 10^{22} \exp(-150 \times 10^3/RT).$$

It was found [7] that, at lower temperatures, another oxidation mechanism involving N_2O_5 as oxidizing agent is realized.

It could be expected that the mechanism of $CN_3H_6NO_3$ decomposition would be similar and the rate of heat release in its decomposition would be determined by the rate of $CN_3H_6^+$ oxidation with HNO_3 molecule. In the temperature range studied, no thermal transformations of $CN_3H_6^+$ ion are observed in the absence of water. This is confirmed by higher stability of GN in comparison with AN. In this case, the kinetic equation of the process rate ($W\ mol^{-1}$) can be given as follows:

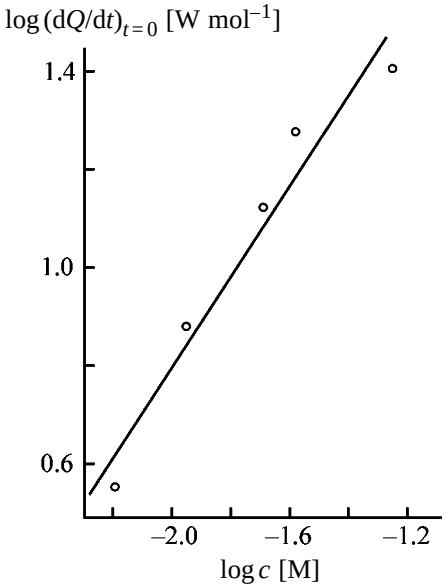

Fig. 3. Logarithm of the initial rate of the heat release $(dQ/dt)_{t=0}$ in oxidation of the $CN_3H_6^+$ ion as a function of the concentration of nondissociated HNO_3 molecules c at 172.4°C.

$$dQ/dt = k_{GH^+} Q_{GN} c_{GH^+} c_{HA} V^0_{GN}. \quad (5)$$

Correspondingly,

$$k/b = k_{GH^+} Q_{GN} c^0_{GH^+} c^0_{HA} V^0_{GN};$$

since at the process start $c^0_{GH^+} V^0_{GN} = 1$,

$$k/b = k_{GH^+} Q_{GN} c^0_{HA}.$$

The symbols and dimensions are similar to those used in Eq. (4), but they refer to guanidinium ion (GH^+) and guanidinium nitrate (GN).

To check this assumption, we studied the kinetic dependences of oxidation of $CN_3H_6^+$ ions with HNO_3 molecules. About 0.01 g (8.3×10^{-5} mol) of GN was placed in an ampule containing about 1.1 g of 20.01–39.03 wt % HNO_3 [$(3.5–6.8) \times 10^{-3}$ mol]. At such a large excess, the loss of HNO_3 in the oxidation does not noticeably alter the initial concentration, and the oxidation is described as a first-order reaction due to the consumption of $CN_3H_6^+$ ions. The concentration of nondissociated HNO_3 molecules in solutions were determined using the data given in [6]. The dependence of the initial rate of heat release (W mol^{-1}) on the concentration of HNO_3 molecules at 172.4°C is shown in Fig. 3; it corresponds to the first-order reaction with respect to molecular HNO_3. We also studied the dependence of the process rate on the concentration of $CN_3H_6^+$ ions in solutions (mol cm^{-3}) at 182.4°C:

$c_{GH^+} \times 10^5$	4.4	8.3	13.6	17.2
$(dQ/dt)_{t=0}$	76.8	73.1	68.4	67.5

In this case, the reaction is also first-order with respect to c_{GH^+} within the experimental error.

We studied the temperature dependence of the initial rate of heat release (W mol^{-1}) in oxidation of GH^+ in the 159.3–182.4°C range at HNO_3 concentration of 39.03 wt %.

T, °C	159.3	164.0	172.4	177.8	182.4
$(dQ/dt)_{t=0}$	17.2	23.4	25.6	50.2	73.1

Using these data and taking into account the concentrations of nondissociated HNO_3 molecules in solution, we obtained the temperature dependence of $k_{GH^+} Q_{GN}$ (W cm^3 mol^{-2}):

$$k_{GH^+} Q_{GN} = 8.4 \times 10^{18} \exp(-112 \times 10^3/RT).$$

Comparison of the independently determined rate constants of heat release in oxidation of NH_4^+ and $CN_3H_6^+$ ions in aqueous nitric acid solutions showed that, at 223.6°C, the rate of $CN_3H_6^+$ oxidation is higher by a factor of 8 than that of NH_4^+ oxidation, and this difference increases with decreasing temperature.

In the AN + GN melt, the rate of heat release can be evaluated as a sum of the oxidation rates of NH_4^+ and $GN_3H_6^+$ ions with molecular HNO_3. The interaction of AN and GN is obviously determined by common salt anion, changes in the equilibrium content of HNO_3 in the mixture in comparison with the initial components, and difference in the oxidation rate constants of NH_4^+ and $CN_3H_6^+$ ions. In this case, the increase in the content of HNO_3 molecules in the mixture in comparison with pure GN, at higher oxidation rate constant of $CN_3H_6^+$, is probably decisive.

If we denote the equilibrium mole fractions of NH_3, HNO_3, and CN_3H_5 as N_{NH_3}, N_{AN}, and N_{GN} and the constants of salt dissociation into base and acid as K_{AN} and K_{GN} and neglect the variations in the mole fractions of salt ions due to dissociation, because the degree of salt dissociation into base and acid is low, then the system of reactions of the reversible dissociation in the salt mixture can be presented as follows:

$$NH_4NO_3 \rightleftarrows NH_3 + HNO_3,$$

$$K_{AN} = N_{NH_3} N_{HA} / N_{AN};$$

$$CN_3H_6NO_3 \rightleftarrows CN_3H_5 + HNO_3,$$

$$K_{GN} = N_G N_{HA}/N_{GN}.$$

Since $b = N_G$ (i.e., mole fraction of the base in the system) and for pure salt $N_G = N_{HA}$ and $N_{GN} \sim 1$ due to small degree of salt dissociation into base and acid, then $b = (K_{GN})^{0.5}$.

Solution of this system for the initial moment in the absence of the reaction products gives the equilibrium mole fraction of HNO_3 in the system:

$$N_{HA} = [K_{AN}N_{AN}/(1 + a)]^{0.5} + [K_{GN}N_{GN}/(1 + a^{-1})]^{0.5},$$

$$a = K_{GN}N_{GN}/K_{AN}N_{AN}. \quad (6)$$

Since $c_{HA} = N_{HA}/V^0$, where V^0 is the molar volume of the salt mixture, and similar expressions can be given for all the system components, the final expression [based on Eqs. (4)–(6)] for the dependence of the initial rate of heat release in the AN + GN mixture on its composition is as follows:

$$dQ/dt = \{[K_{AN}N_{AN}/(1 + a)]^{0.5} + [K_{GN}N_{GN}/(1 + a^{-1})]^{0.5}\}$$

$$\times (k_{NH_4^+}Q_{AN}N_{AN} + k_{GH^+}Q_{GN}N_{GN})/V^0. \quad (7)$$

For pure salts, the mole fraction of salt is 1 and the initial rate of the process can be given as

$$(dQ/dt)_{AN} = k_{NH_4^+}Q_{AN}K_{AN}^{0.5}/V_{AN}^0,$$

$$(dQ/dt)_{GN} = k_{GH^+}Q_{GN}K_{GN}^{0.5}/V_{GN}^0. \quad (8)$$

To a first approximation, considering it as the additive value, the molar volume of the mixture can be calculated as the sum of the molar volumes of the initial salts:

$$V^0 = N_{AN}V_{AN}^0 + N_{GN}V_{GN}^0 = V_{AN}^0 + (V_{GN}^0 - V_{AN}^0)N_{GN}.$$

Using the temperature dependence of the density of liquid AN [8], we calculated $V_{AN}^0 = 56.7$ cm^3 mol^{-1} at 220°C. Since data on the density of liquid GN are lacking, we assumed the densities of AN and GN to be equal, and thus $V_{GN}^0 = 86.5$ cm^3 mol^{-1}.

The K_{GN} and K_{AN} values were calculated from the initial rates of heat release in decomposition of pure AN and GN using the experimental values of $k_{NH_4^+}Q_{AN}$ and $k_{GH^+}Q_{GN}$ (obtained in studying cation oxidation in HNO_3). Now, using all the above data and Eq. (7), we can evaluate the dependence of the rate of heat release in the AN + GN mixture on the AN mole fraction; this dependence is shown in Fig. 2 (curve *2*). As seen, the real rates of heat release are significantly lower than the calculated dependence. Such a difference can be only due to the changes in the oxidation rate constants of NH_4^+ and $CN_3H_6^+$ ions as compared to the values determined in this work for aqueous HNO_3 solutions.

The properties of the melt and aqueous solution of nitric acid are strongly different; the melt is composed virtually exclusively of the ions and has a low dielectric constant (2–4), whereas the aqueous solution contains many HNO_3 and H_2O molecules and its dielectric constant is higher by at least an order of magnitude.Probably, the solvation of cations in these media is different, which, in turn, should affect the rate constants of their oxidation. Changes in $k_{NH_4^+}Q_{AN}$ and $k_{GH^+}Q_{GN}$ should change the constants K_{AN} and K_{GN} [see Eq. (8)], but the initial rates of heat release in the salts are determined with relatively high accuracy. Unfortunately, we failed to determine experimentally the oxidation rate constants directly in the salt melts in question due to the difficulties with dosed supply of 100% nitric acid in the melt and, especially, due to the lack of procedures for quantitative analysis of nitric acid content in these melts. At the temperatures studied, nitric acid can form complexes with the other molten components and partially pass into the gas phase. Hence, the reverse problem was solved: we determined the $k_{NH_4^+}Q_{AN}$ and $k_{GH^+}Q_{GN}$ values (W cm^3 mol^{-2}) from the calculated dependence of the rates of heat release taking into account Eq. (8) provided that all the temperature dependences obtained were preserved:

$$k_{NH_4^+}Q_{AN} = 5.0 \times 10^{22} \exp(-150 \times 10^3/RT),$$

$$k_{GH^+}Q_{GN} = 1.0 \times 10^{19} \exp(-112 \times 10^3/RT).$$

For AN, these values are greater by a factor of 4.7 than those determined experimentally in aqueous acidic solutions, and for GN, by a factor of 1.2. The $k_{NH_4^+}Q_{AN}$ and $k_{GH^+}Q_{GN}$ values obtained by solving the reverse problem should be used to calculate the process rates in the melts, whereas the experimental data obtained previously are correct for aqueous acid solutions.

Using the calculated rate constants of heat release and the initial rates of heat release in pure salts, we obtained the following equilibrium constants of salt

dissociation into base and acid:

$$K_{AN} = 0.89\exp(-107\times10^3/RT),$$

$$K_{GN} = 0.13\exp(-111\times10^3/RT).$$

At 200°C, K_{AN} is greater by a factor of 20 than K_{GN}, which corresponds to the difference in the basicities of NH_3 and CN_3H_5 in the melts of the corresponding salts. Taking into account the fact that in Eq. (2) $b = (K_{GN})^{0.5}$, from the temperature dependences of k/b and k/f for NG decomposition we evaluated the following temperature dependences

$$b = 036\exp(-55.6\times10^3/RT),$$

$$f = 1.9\times10^{-5}\exp(-43\times10^3/RT)\ \ (\text{mol J}^{-1}).$$

To assess the feasibility of granulation or other treatment procedures of the AN + GN mixture through the melt, we determined the melting temperature of the eutectic mixture T_e and the temperature of complete melting of the AN + GN mixture (2 : 1 molar ratio) T_f on a DAK-1-1 calorimeter in the linear heating mode at a heating rate of 5×10^{-3} deg s^{-1}. The sample weights of the AN + GN mixture (2 : 1 molar ratio) were 1.5 and 0.15 g. The experimental temperatures (average of 5 measurements) were independent of the sample weight: $T_e = 126.0\pm1$ and $T_f = 132.5\pm1$°C.

Unfortunately, experimental T_e is close to the temperature of the phase transition AN II → AN I (125–126°C). The rate dependence of the heat release passes through two very closely located maxima; i.e., the phase transition and eutectic melting overlap. Though melting probably begins at temperatures higher than the phase transition by 1–1.5°C, their separation is virtually impossible. To evaluate the possibility of using the AN + GN mixture, it is important that the mixture begins to melt at 126°C, and at lower temperatures it is solid. The total amount of heat absorbed upon melting of the mixture was determined by numerical integration of the experimental curve of heat absorption. The heat of the process per mole of the mixture is independent of the sample weight, and its average value is 10.0±0.4 kJ per mole of the AN + GN mixture. According to published data [9], the enthalpy changes comprise $\Delta H_{pt} = 4.43\pm0.42$ and $\Delta H_m = 5.64\pm0.63$ kJ mol^{-1} for phase transition and melting, respectively.

Since the enthalpy of melting of AN, 6.40 kJ mol^{-1}, was determined long ago [9] and could be inaccurate and for GN such value was unknown, we evaluated the enthalpies of melting of AN and GN on a DAK-1-1 calorimeter using the procedure similar to those used for salt mixtures. We determined that AN melts at 169±1°C, with the enthalpy of melting $\Delta H = 6.35\pm0.63$ kJ mol^{-1}; and these results well agree with published data. For NG, the melting point was 215±1°C, which is close to the value from [10], with $\Delta H = 18.4\pm1.3$ kJ mol^{-1}. To evaluate the possibility of the phase transitions, the GN sample was heated in a DAK-1-2 calorimeter in the temperature range from 25°C to the melting point. Since no peaks of heat release or absorption were found, there are no phase transitions of the first kind in the temperature range studied. The enthalpies of melting of the two similar salts strongly differ, but AN undergoes three phase transitions with heat absorption in the temperature range from 25°C to the melting point; their total effect is 7.14 kJ mol^{-1}, and the total heat absorption (with melting) reaches 13.5 kJ mol^{-1}. Taking into account the differences in the structure and weight of the cations, this value well agrees with the enthalpy of melting of GN, for which the melting is not preceded by phase transitions.

Using the enthalpies of melting of AN and GN determined and considering the enthalpy of melting of the AN + GN mixture to be the additive value, we calculated for this mixture $\Delta H_m = 10.0$ kJ mol^{-1}. Probably, the difference with the experimental value of 4.4 kJ mol^{-1} is due to the changes in the enthalpy of the liquid phase as compared to the initial liquid salts; it is probably the heat of mixing.

Based on the Schroeder equation [1] describing changes in the melting temperature of one component upon addition of another one, assuming that the solution of these components is ideal, and using the above ΔH values of the salts studied, we calculated the melting diagram of the AN + GN mixture, but it poorly agrees with the experimental T_e and T_f. This fact suggests strong deviation of our system from the ideal solution. Since for ideal solution the heat of mixing is zero, our experimental results indicate strong interaction of ions in the molten salt mixture, which is greater than that in the melts of the pure components.

Our experimental data show that granules of the eutectic AN + GN mixture can be prepared though the melt using any known procedure of granulation of AN and fertilizers on its basis with sufficient safety level, because the rates of heat release in thermal decomposition of these mixtures are close to that observed with AN.

CONCLUSIONS

(1) The rate of heat release in thermal decomposition of $CN_3H_6^+$ and NH_4^+ nitrates and their mixtures in the liquid phase is determined by the oxidation rate of the corresponding cations with molecular HNO_3.

(2) The rate constant of $CN_3H_6^+$ oxidation is greater than that of NH_4^+ both in aqueous solutions of nitric acid and in molten salts. This difference decreases on passing from aqueous solutions with high dielectric constants to the melts with small dielectric constants.

(3) The difference in the basicity of NH_3 and CN_3H_5 strongly decreases on passing from aqueous solutions of nitric acid to melts, and the equilibrium constant of guanidinium nitrate dissociation in the melt is smaller than that of ammonium nitrate by a factor of only 20.

(4) The rates of heat release in thermal decomposition of the mixtures of ammonium and guanidinium nitrates are close to those observed with ammonium nitrate. At guanidinium nitrate content of 10 wt % and greater, no self-acceleration of the process is observed, and thus the known procedure of granulation of AN and fertilizers on its basis with sufficient safety level can be used to prepare solid granules from the molten salt mixture.

ACKNOWLEDGMENTS

This work was financially supported by the International Science and Technology Center (project no. 1882-2001).

REFERENCES

1. Manelis, G.B., Nazin, G.M., Rubtsov, Yu.I., and Strunin, V.A., *Termicheskoe razlozhenie i gorenie vzryvchatykh veshchestv i porokhov* (Thermal Decomposition and Combustion of Explosives and Gunpowders), Moscow: Nauka, 1996.
2. Albert, A. and Serjeant, E., *Ionization Constants of Acids and Bases. A Laboratory Manual*, New York: Wiley, 1962.
3. Schoppelrei, J.W., Kieke, M.L., Wang, X., *et al*., *J. Phys. Chem*., 1996, vol. 100, no. 34, pp. 14 343–14 351.
4. Galyuk, O.S., Rubtsov, Yu.I., Malinovskaya, G.F., *et al*., *Zh. Fiz. Khim*., 1965, vol. 39, no. 9, pp. 2319–2322.
5. Rubtsov, Yu.I., Kazakov, A.I., Morozkin, S.Yu., *et al*., *Zh. Prikl. Khim.*, 1984, vol. 57, no. 9, pp. 1926–1929.
6. Chedin, J., Feneant, S., and Vandoni, R., *J. Chim. Phys*., 1952, vol. 49, p. 109–125.
7. Kazakov, A.I., Andrienko, L.P., and Rubtsov, Yu.I., *Izv. Akad. Nauk SSSR, Ser. Khim.*, 1980, no. 5, pp. 972–977.
8. *Tekhnologiya ammiachnoi selitry* (Production of Ammonium Nitrate), Olevskii, R.M., Ed., Moscow: Khimiya, 1978.
9. *Termicheskie konstanty veshchestv* (Thermal Constants of Substances), Glushko, V.P., Ed., Moscow: VINITI, 1968, issue 3.
10. *Sprovochnik khimika* (Chemist's Handbook), Nikol'skii, B.P., Ed., Moscow: Goskhimizdat, 1951, vol. 2.
11. *Kurs fizicheskoi khimii* (Course of Physical Chemistry), Gerasimov, Ya.I., Ed., Moscow: Khimiya, 1969, vol. 1.

Russian Journal of Applied Chemistry, Vol. 77, No. 7, 2004, pp. 1092–1096. Translated from Zhurnal Prikladnoi Khimii, Vol. 77, No. 7, 2004, pp. 1107–1111.

PHYSICOCHEMICAL STUDIES OF SYSTEMS AND PROCESSES

Aging of Whey Gels in the Presence of Organic Colloids

S. G. Kozlov, A. Yu. Prosekov, and A. S. Sorochkina

Kemerovo Technological Institute of Food Industry, Kemerovo, Russia

Received December 22, 2003; in final form, April 2004

Abstract—Effects of organic colloids on gelation of curds and aging of whey gels are studied. The influence of some physicochemical factors on the predicted macrokinetic characteristics of whey gels is revealed.

The questions of structurization in disperse systems, as applied to various branches of industry, were considered in works of many leading research schools [1–4]. The theoretical concepts developed by them can find use in technology of structured foodstuffs of desired consistency. Agents supporting the consistency are used primarily in production of foodstuffs with unstable structure, which should remain homogeneous throughout the storage period [5, 6]. There are diverse agents modifying the rheological characteristics of such foodstuffs, including natural, synthetic, and bacterial ones.

Gels represent highly dispersed systems with a liquid dispersion medium, consisting of a fluid-filled framework forming a structure from dispersed solids. Gels are classified with two-phase systems with highly developed interface between a continuous or finely dispersed phase of a suspended solid and an aqueous (or aqueous-organic) phase, which also can be continuous or partially dispersed. A solid is commonly regarded as a fibrous structure. It can consist of poorly soluble compounds, for example, proteins, or thread-like crystals, like the silica or crystalline cellulose gels. The structural stability depends on the structure of the continuous phase network, so that the system as a whole exhibits many properties of a solid, regardless of the state of aggregation of the dispersion medium and dispersed phase themselves.

Aging results in degradation of the gel structure, which is accompanied by irreversible deterioration of the rheological characteristics (molecules of a gelator flocculate, providing immobilization of the dispersion medium). In aging, a monodisperse gel passes into a quasicontinuous body formed as a result of broken dispersity. The main cause of this transition is break of the structural stability, accompanied by mutual approach of the colloid particles.

In analysis of this phenomenon, it is advisable, first, to determine the kinetic parameters of the yield stress and the amount of the liberated functional groups, and, second, to evaluate the effect of process factors on the evolution of the strength of the gels formed.

The composition of the samples studied in this work was as follows (%): gelator [agar 1.2, or pectin 0.8, or agaroid 2.5, or gelatin 2.5, or methyl cellulose (MC) 1.5, or starch 2.5], sucrose 30, and whey as the rest. The acidity was adjusted to pH 4.0–4.2 with citric acid.

EXPERIMENTAL

The rheological behavior of the gels was studied on a Rheotest-2 instrument (GDR) [7] at 20°C. The shear stress τ (Pa) was estimated by Eq. (1):

$$\tau = z\alpha, \quad (1)$$

where z is the cell constant (Pa) and α, scale reading.

The effective viscosity η (Pa s) was determined by Eq. (2):

$$\eta = \tau/j, \quad (2)$$

where j is the shear rate (s^{-1}).

The flow curves were reproduced by the Herschel–Bulkley equation (3):

$$\tau = \tau_0 + kj^n, \quad (3)$$

where τ_0 is the yield stress (Pa) at a given shear rate gradient; k, the consistency factor (Pa s) characterizing the viscosity of the material at $j = 1\ s^{-1}$; and n, flow index characterizing the flow behavior.

The molecular weight of the gelators was determined by HPLC with Hewlett–Packard columns. In

1070-4272/04/7707-1092 © 2004 MAIK "Nauka/Interperiodica"

the first columns, the exhaust rate was 0.008, and in the second column, 0.0166 ml s^{-1}. Calibration was performed on a Dawn F laser nephelometer.

The relative content of functional groups (carboxy, methoxy, aldehyde, hydroxy, and amine) was determined using standard procedures. The initial content was accepted in all the cases to be 100%.

The relative content of free carboxy groups C_f (%) was determined by titration of a weighed portion of the gel with 0.1 N NaOH in the presence of Hinton reagent until development of red coloration [8]. Then C_f was estimated by Eq. (4):

$$C_f = \{(0.45a/G)_S[(0.45a/G)_N]^{-1}\} \times 100, \quad (4)$$

where a is the volume of the titrant consumed (ml); G, sample weight (g); and 0.45, conversion rate (1 ml of 0.1 N NaOH corresponds to 0.0045 g of COOH). The indices S and N refer to the sample after storage and the reference sample, respectively.

The relative content of the ether groups C_e (%) was determined by Eq. (5):

$$C_e = \{(0.45b/G)_S[(0.45b/G)_N]^{-1}\} \times 100, \quad (5)$$

where b is the volume of the titrant consumed for the second titration (ml).

The relative content of the acetyl groups C_{Ac} (%) was determined according to the procedure described in [8] using Eq. (6):

$$C_{Ac} = \{(43.04C/100G)_S[(43.04C/100G)_N]^{-1}\} \times 100, \quad (6)$$

where C is the difference between the titrant volume consumed for titration of the sample and that in the blank experiment (ml); and 43.04 is the equivalent weight of the acetyl groups.

The relative content of the methoxylated carboxy groups C_m (%) was estimated with correction for the acetyl groups by Eq. (7).

$$C_m = C_e + C_{Ac}. \quad (7)$$

The total content of the carboxy groups C_o (%) was estimated as

$$C_o = C_m + C_f. \quad (8)$$

The relative content of the amino groups C_a (%) was determined by titration according to Dudenkov's method [9] using Eq. (9):

$$C_a = [(mP)_S/(mP)_N] \times 100, \quad (9)$$

where m is the volume of 0.1 N NaOH consumed for titration (ml) and P, conversion factor.

The aldehyde groups was determined by the method based on the reaction with fuchsinsulfurous acid with formation of a colored product [10]. The hydroxy groups were determined by the neutralization method [11].

The samples were stored for 15 days under temperature- and humidity-controlled conditions.

Table 1 shows how the aging influences the mechanical characteristics of the gel structures, which is significant for the systems studied.

The results show that the trends in evolution of the yield stress do not depend on the gelator used. In the initial period (data printed bold), the gel structure strengthened. For agar, agaroid, pectin, MC, and

Table 1. Dynamics of evolution of the yield stress of whey gels ($X \pm m$; $m \leq 0.05$)

t,* h	Yield stress, Pa					
	agar	agaroid	pectin	gelatin	MC	starch
0	**220**	**241**	**230**	**267**	**92**	**77**
1	**228**	**250**	**250**	**270**	**112**	**83**
2	**235**	**256**	**276**	**279**	**123**	**90**
3	**240**	**263**	**299**	**288**	130	**99**
4	**246**	**270**	**318**	**299**	130	120
5	**252**	**278**	**329**	**306**	132	120
10	**270**	**282**	**330**	**311**	115	120
15	**278**	**290**	**335**	**320**	114	120
20	**294**	**295**	325	**325**	110	108
24	**300**	**300**	320	325	108	117
48	**313**	**309**	318	325	102	175
72	**320**	**315**	315	325	97	110
96	**335**	300	315	317	97	104
120	**349**	285	315	305	90	89
144	314	277	315	300	90	80
168	280	270	312	289	85	75
192	261	262	310	277	–	–
216	229	255	310	269	–	–
240	213	249	300	260	–	–
264	210	220	292	254	–	–
288	208	208	280	245	–	–
312	205	203	271	239	–	–
336	200	190	264	230	–	–
360	196	185	250	215	–	–

* (t) Storage time.

Table 2. Effect of temperature on the dynamics of aging in whey gels

T, °C	Time,* h					
	agar	agaroid	pectin	gelatin	MC	starch
0–5	120/144*	72/96	15/240	20/144	3/10	4/96
5–10	48/96	24/48	15/216	20/96	3/3	4/48
10–15	48/48	24/48	10/144	5/96	0/3	4/48
15–20	24/24	24/15	5/96	5/72	0/3	4/48
20–25	20/20	10/10	5/24	0/48	0/3	3/24
25–30	5/10	5/5	0/10	0/10	0/3	3/15
30–35	5/10	0/5	0/5	0/10	0/3	2/10
35–40	0/5	0/2	0/2	0/10	0/3	1/10
40–45	0/5	0/1	0/1	0/10	0/3	1/10

* Period of time in which the gel reaches its maximal strength/onset of aging.

starch, this period was 120, 72, 15, 20, 3, and 4 h, respectively. In this period, the strength increased by 58.5, 30.7, 45.6, 19.5, 33.6, and 28.5%, respectively, as compared to the initial sample. Evidently, the relative increase in the strength is controlled by the nature of interaction between the compounds composing the dispersion medium and the hydrated gelator.

The effect of structurization is promoted by the polymeric compounds of whey (for example, whey proteins promote cross-linking). Such a structurization is accompanied by transition of the thixotropic gel into a nonthixotropic structure and, finally, results in formation of a 3D matrix with infinitesimal number of "free nodes" containing the dispersion medium weakly bound to the gelator.

The structurization period in whey gels was followed by their aging. Two competitive processes were observed during aging. They were reflected in an elastic strain slowly decayed in time and also in a steady-rate plastic viscous flow. In this period, the number of broken bonds was higher than the number of newly formed bonds, as demonstrated by the rheological data.

For agar and agaroid, we observed a distinctly pronounced transition from the state characterized by the maximal strength to the state of degradation. This was not the case for pectin, gelatin, MC, and starch. In particular, the transition period in the systems with the indicated gelators was 24–216, 10–120, 3–5, and 2–96 h, respectively, depending on the nature of intermolecular interactions in these systems.

It is well known that the properties of gels strongly depend on the temperature. Therefore, we studied the temperature effect on aging of whey gels. As parameters characterizing this effect we selected the time in which the gel reaches its maximal strength and the time until the onset of degradation (aging). The results are given in Table 2.

In all the systems, we observed a decrease in the strength of whey gels with increasing temperature. For agar, agaroid, pectin, gelatin, and MC, the transitions were not observed at all at temperatures of 35–40, 30–35, 25–30, 20–25, and 10–15°C, respectively. This is due to increasing thermal motion of molecules, which have rotational radius insufficient for the system to acquire more stable state. Increasing temperature reduced the time to the onset of aging of the gel, caused by increase in the kinetic energy of the system as a result of heating.

It is significant that some of the organic colloids allowed preparation of the dispersions only at definite temperatures.

For example, methyl cellulose at 5–10°C after 3 h, in which structurization was completed, started to change its rheological behavior so that the process could be referred to as aging.

For some of the gels, after completion of the process we observed no structurization stage at all. In this case, aging started in a rather short time (shorter than after 1 day of storage).

The observed trends are caused by several factors, change in the relative molecular weight of the organic colloids being one of the most significant (Table 3). The results show that increase in the relative molecular weight is typical of the gelators in the initial hours of storage of whey gels. The longest time in which the relative molecular weight increased was observed with agaroid. This is due to the fact that agaroid had the minimal relative molecular weight, which increased in

the course of the sol–gel transition as a result of completion of the formation of adsorption layers at the organic colloid–dispersion medium interface.

The shortest period of time in which the relative molecular weight changed was observed for gelatin (~2 h). This fact can be attributed to the specific features of formation of the solvation shells in gelatin: potential sites of cross-linking in the polymer chain of gelatin were blocked because of a larger number of the interfacial layers. Thus, the maximal increase in the relative molecular weight of about 50% was found in agaroid, and the minimal increase (only 0.8%), in gelatin.

Analysis of the results obtained revealed the following general trends:

(1) The stabilizer is experienced to hydrolysis under the effect of certain internal and external factors;

(2) the integrity of the solvation shells is broken as a result of formation of structural defects under the effect of components of the gels;

(3) the activation barrier of aging is overcome at elevated temperatures.

Generally, aging of a gel is an irreversible process whose rate is controlled by the composition, temperature, and other factors.

The aging is described by Eq. (10):

$$\tau = \tau_0 \exp[(U_0 - \nu P)/k_B T], \quad (10)$$

where τ is the bond breakdown stress in the gel; τ_0, preexponential factor; U_0, true (initial) activation energy of degradation; ν, structural factor; k_B, Boltzmann constant; P, breaking stress; and T, temperature (K).

According to Eq. (10), degradation of a gel is a temperature-dependent process. With increasing temperature, the energy barrier U_0 of breaking of the bonds is overcome, as demonstrated by the liberation of functional groups of the gelators, which were directly involved in the sol–gel transition (Table 4).

The results obtained allowed evaluation of the relative contributions of different functional groups of the gelators to formation of whey-based dispersions. However, it should be pointed out that, in this case, they can be involved in formation of new types of bonds, as was demonstrated, for example, by data on the relative contents of functional groups in the gelatin-based gel.

Generally, gelatinous systems based on curds are classified with quasistable systems. In storage, the particles composing a 3D structure are reoriented, and the liquid phase is liberated (most of gels tend to break the structure). In such multicomponent systems as whey, aging proceeds less intensively as a result of partial absorption of the dispersed phase by other components of the gel through physicochemical interactions leading to formation of new bonds, thus preventing the transition into an absolutely stable state with separation into several individual phases.

Table 3. Variation in the relative molecular weight of gelators in storage ($X \pm m$; $m \leq 0.05$)

t, h	Relative molecular weight $M \times 10^{-2}$					
	agar	agaroid	pectin	gelatin	MC	starch
0	234	42	283	653	343	587
1	238	43	286	654	350	589
2	241	45	289	658	360	593
3	249	48	291	654	368	599
4	256	49	294	650	371	591
5	270	51	299	641	378	584
10	274	53	305	635	372	580
15	274	58	304	631	365	572
20	274	59	300	628	359	568
24	274	62	299	627	354	564
48	274	65	298	623	350	560
72	274	65	298	620	348	556
96	270	61	297	615	345	551
120	261	60	297	610	340	543
144	252	57	297	603	340	538
168	247	54	297	599	336	531
192	246	53	297	594	331	524
216	242	51	297	592	328	520
240	239	48	297	588	324	514
264	235	46	296	583	320	508
288	231	44	295	581	314	499
312	229	43	295	574	310	491
336	228	41	295	570	308	487
360	227	40	295	566	300	483

CONCLUSIONS

(1) Addition of organic colloids enhances the stability of whey gels.

(2) Structural stability of the gels decreases with increasing temperature of the process.

(3) In storage, the relative molecular weight of the hydrocolloids changes as a result of hydrolysis, distortion of the solvation shells, and overcoming of the energy barrier of degradation.

Table 4. Relative content of functional groups in the gel in the course of its aging ($X \pm m$; $m \leq 0.05$)

Functional group	Relative content, %, after indicated storage time, h							
	0	48	96	144	192	240	288	336
Pectin:								
–COOH	100.0	100.0	106.2	113.5	118.3	127.0	134.8	140.2
$-COOCH_3$	100.0	100.0	100.0	100.0	100.0	100.0	100.0	100.0
–CHO	100.0	100.0	105.0	109.8	114.2	119.5	122.8	126.4
Agar, –CHO	100.0	100.0	105.6	109.8	114.5	117.0	120.8	127.4
Agaroid, –CHO	100.0	108.2	115.3	123.0	129.6	131.7	145.8	156.4
Gelatin:								
$-CH_2OH$	100.0	100.0	100.0	100.0	100.0	96.2	92.1	90.4
–COOH	100.0	100.0	98.2	94.3	91.0	89.6	88.7	84.9
$-NH_2$	100.0	102.8	107.3	110.0	114.2	119.1	121.6	124.3
Methyl cellulose, $-COOCH_3$	100.0	100.0	100.0	107.0	111.5	114.8	129.6	131.8
Starch, –CHO	100.0	100.0	102.3	105.8	108.2	114.0	119.5	120.9

REFERENCES

1. Rebinder, P.A., *Izbrannye trudy* (Selected Works), Moscow: Nauka, 1978–1979, vols. 1–2.
2. Vlodavets, I.N., in *Materialy V Vsesoyuznoi konferentsii po fiziko-khimicheskoi mekhanike* (Proc. V All-Union Conf. on Physicochemical Mechanics), Ufa, 1971, pp. 115–116.
3. Deryagin, B.V., *Teoriya ustoichivosti kolloidov i tonkikh plenok* (Theory of Stability of Colloids and Thin Films), Moscow: Nauka, 1986.
4. Izmailova, V.N. and Rebinder, P.A., *Strukturoobrazovanie v belkovykh sistemakh* (Structurization in Protein Systems), Moscow: Nauka, 1974.
5. Dunchenko, N.I., *Strukturirovannye molochnye produkty* (Structured Dairy Products), Moscow: Kolos, 2002.
6. Khramtsov, A.G., *Molochnaya syvorotka* (Whey), Moscow: Agropromizdat, 1990.
7. Machikhin, Yu.A. and Machikhin, S.A., *Inzhenernaya reologiya pishchevykh materialov* (Engineering Rheology of Edible Materials), Moscow: Legkaya i Pishchevaya Prom–st., 1981.
8. Donchenko, L.V., *Tekhnologiya pektina i pektinoproduktov* (Technology of Pectin and Pectin Products), Moscow: DeLi, 2000.
9. Dudenkov, A.Ya., *Spravochnoe rukovodstvo dlya laborantov maslosyrodel'nykh zavodov* (Reference Guide for Analysts at Butter-Dairies), Moscow: Pishchevaya Prom–st., 1967.
10. Bazarova, V.I., Borovikova, L.A., and Dorofeev, A.L., *Issledovanie prodovol'stvennykh tovarov* (Characterization of Foodstuffs), Moscow: Ekonomika, 1986.
11. Zhvanko, Yu.N., Ponkratova, G.V., and Mamedova, Z.I., *Analiticheskaya khimiya i tekhnokhimicheskii kontrol' v obshchestvennom pitanii* (Analytical Chemistry and Technical and Chemical Control in Public Catering), Moscow: Visshaya Shkola, 1989.

Russian Journal of Applied Chemistry, Vol. 77, No. 7, 2004, pp. 1097–1099. Translated from Zhurnal Prikladnoi Khimii, Vol. 77, No. 7, 2004, pp. 1112–1115.

SORPTION AND ION-EXCHANGE PROCESSES

Mercury(II) Sorption on Nickel(II) Hydroxide: Influence of Halide Ion Concentration and pH of the Solutions

O. V. Nagornyi, A. S. Kolyshkin, and V. V. Vol'khin

Perm State Technical University, Perm, Russia

Received November 25, 2003

Abstract—Sorption of Hg(II) on β-$Ni(OH)_2$ was studied as influenced by chloride ion concentration and pH of the solutions, affecting the Hg(II) speciation. The sorption mechanism was considered.

Mercury(II) compounds are biologically hazardous. Mercury and its compounds are concentrated naturally by soil particles and mineral suspension and are accumulated in bottom sediments. Accumulation and transfer of mercury in the nature is largely controlled by adsorption [1].

Sorption is used to remove mercury compounds from aqueous solutions. Leikin *et al*. [2] used organic anion-exchangers as sorbents for negatively charged mercury halide complexes. Sorption of mercury(II) on natural minerals, kaolinite [3], goethite [4], and quartz [5], was studied.

Although many minerals can adsorb mercury compounds, only synthetic inorganic sorbents are efficiently used at present to remove mercury compounds from aqueous solutions. More than 90% of Hg(II) is removed with freshly prepared hydrated iron(III) oxide from aqueous solutions with pH from 5 to 8.6 [6]. A number of new inorganic sorbents including those for anionic complexes have been developed to date [7]. Nickel(II) hydroxide [8] and double nickel hydroxides with other metals [9] have relatively high anion-exchange capacity for Hg(II) complexes. Therefore, the study of synthetic inorganic sorbents for Hg(II) is an urgent problem.

The diversity of mercury species present in aqueous solutions complicates selection of inorganic sorbents for Hg(II). For example, in aqueous solutions containing Cl^- anions, Hg(II) exists in the form of the following aqua, hydroxoaqua, and mixed hydroxoaquachloride or chloride complexes: Hg^{2+}, $HgOH^+$, $Hg(OH)_{2(aq)}$, $Hg(OH)_3^-$, $HgCl^+$, $HgCl_{2(aq)}$, $HgOHCl_{(aq)}$, $HgCl_3^-$, $HgCl_4^{2-}$ [1, 4, 10, 11]. Formation of cationic, neutral, and anionic mercury(II) species can result in incomplete mercury sorption from aqueous solutions. Neutral and anionic Hg(II) species are stable mainly at pH close to that of natural waters [1]. In this case, anion exchangers can be used as the sorbents. However, to determine the mechanism of Hg(II) sorption on metal hydroxides exhibiting anion-exchange properties, additional studies are required.

The aim of this work was to determine the influence of Cl^- concentration and pH of the solution on Hg(II) sorption on nickel(II) hydroxide and to propose the sorption mechanism.

Nickel(II) hydroxide exists in α- and β-modifications. In this work we studied β-$Ni(OH)_2$. Both modifications have the layered brucite structure. The interlayer spacings in β-$Ni(OH)_2$ lattice are broadened owing to incorporation of H_2O molecules (c = 0.80 nm); the brucite layers in β-$Ni(OH)_2$ lattice are closer (c = 0.46 nm) [12]. The α-modification is unstable and is unsuitable as a sorbent.

β-$Ni(OH)_2$ was prepared by exchange reaction of aqueous solution of $Ni(NO_3)_2$ with NaOH taken in a 5% excess. The resulting precipitate was washed with distilled water and granulated by freezing. To remove NO_3^- impurity, the granulated material was treated with 0.1 M NaOH for a long time. The NO_3^- content in the solid phase was determined by IR spectroscopy.

The sorption experiments under dynamic conditions were performed by the conventional methods [13].

Aqueous Hg(II) solutions were prepared from $Hg(NO_3)_2 \cdot H_2O$. Mercury halide complexes were synthesized by addition of aqueous solutions of KCl, KBr, and KI. All the salts were of analytically pure grade. The Hg(II) content in the solution was determined by absorption of the mercury complex with Crystalline Violet at λ = 605 nm using a KFK-2MP photocolorimeter [14].

The relative content of different Hg(II) species formed at various concentrations of free Cl^- was cal-

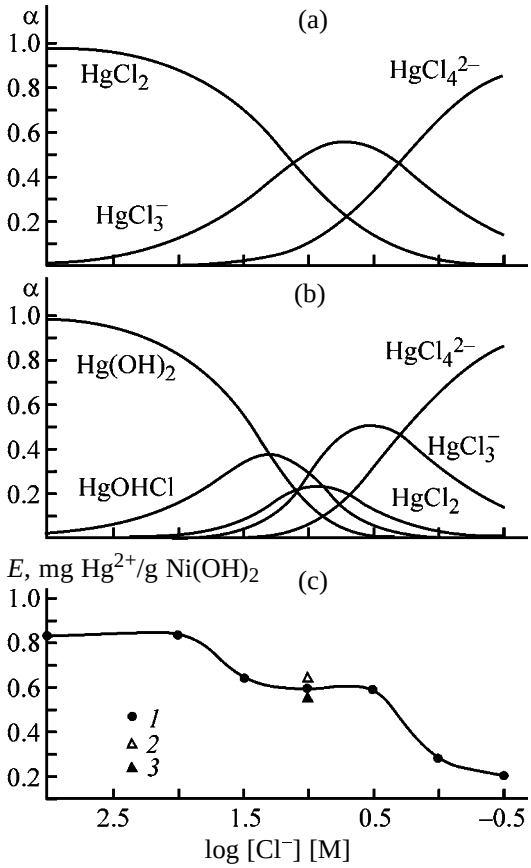

Fig. 1. (a, b) Mole fractions of Hg(II) species in solutions α and (c) sorption capacity of β-$Ni(OH)_2$ for Hg(II) *E* as functions of $[Cl^-]$. pH: (a) 5; (b) 9; (c) (*1*) ~5; (*2*) 7.8, kept for more than 24 h; and (*3*) 8.3, kept for more than 24 h.

culated from the equilibrium constants of the following reactions [15]:

$$Hg^{2+} + OH^- \rightleftarrows HgOH^+, \quad \log K = 10.6;$$

$$Hg^{2+} + 2OH^- \rightleftarrows Hg(OH)^0_{2(aq)}, \quad \log K = 21.8;$$

$$Hg^{2+} + Cl^- \rightleftarrows HgCl^+, \quad \log K = 7.2;$$

$$Hg^{2+} + 2Cl^- \rightleftarrows HgCl^0_{2(aq)}, \quad \log K = 14.0;$$

$$Hg^{2+} + 3Cl^- \rightleftarrows HgCl_3^-, \quad \log K = 15.1;$$

$$Hg^{2+} + 4Cl^- \rightleftarrows HgCl_4^{2-}, \quad \log K = 15.4;$$

$$Hg^{2+} + Cl^- + OH^- \rightleftarrows HgClOH^0_{(aq)}, \quad \log K = 18.1.$$

The results of these calculations for a solution with pH 5 are shown in Fig 1a. The dependence of the sorption capacity of β-$Ni(OH)_2$ for Hg, *E* [mg Hg^{2+}/g $Ni(OH)_2$], on the Cl^- concentration varied in the same range is shown in Fig. 1c. The total Hg(II) concentration in each solution was 10^{-3} M.

The dependence of the relative concentration of Hg(II) species in the solution on $[Cl^-]$ does not correlate with the dependence of the sorption capacity of β-$Ni(OH)_2$ for Hg(II) on $[Cl^-]$. This was due to the difference in the pH of solutions used for the calculation and the experimental pH of the working solutions. When the initial solution passed through a sorbent bed, its pH increased to 8.5–9.0. We recalculated the dependence of the relative concentrations of Hg(II) species on $[Cl^-]$ at pH 9. The results are presented in Fig. 1b.

Comparison of the calculated and experimental dependences allows the following conclusions. The maximal sorption capacity *E* was observed in the $[Cl^-]$ range from 10^{-3} to 10^{-2} M, when $Hg(OH)_2$ and HgOHCl were formed. When these complexes started to transform into $HgCl_3^-$ and $HgCl_4^{2-}$, the first drop of *E* [from 20 to 15 mg Hg^{2+}/g $Ni(OH)_2$] occurred. At $[Cl^-]$ higher than $10^{-0.5}$ M, the sorption capacity *E* decreased again from 15 to 7–6 mg Hg^{2+}/g $Ni(OH)_2$. Under these conditions, hydroxo complexes $Hg(OH)_2$ and HgOHCl disappeared completely. Then *E* remained constant at the level of 5.0–5.5 mg Hg^{2+}/g $Ni(OH)_2$.

To explain these results, let us consider possible mechanisms of Hg(II) sorption by metal hydroxides.

Anionic complexes $HgCl_3^-$ and $HgCl_4^{2-}$ can be adsorbed by the ion-exchange mechanism:

$$\equiv Ni{-}OH + HgCl_3^- \rightleftarrows \equiv Ni{-}ClHgCl_2 + OH^-.$$

Halide anions Cl^-, Br^-, and I^-, being in equilibrium with $HgHal_3^-$ and $HgHal_4^{2-}$, are absorbed by the same mechanism. Previously we showed that chloride ions are exchanged with equivalent amount of OH groups of metal hydroxides. This process, however, makes an insignificant contribution. The sorption in the absence of Hg hydroxo complexes occurs by the anion-exchange mechanism.

An increased sorption capacity for hydrolyzed Hg(II) species is due to the different sorption mechanism. Sarkar *et al*. [3] showed that M–O–Hg bridges (where M is metal ion of the metal hydroxide) are formed in this case. Sorption of Hg(II) hydroxo complexes involves formation of surface intraspheric complexes ≡MOHgCl or $MOHgOHCl^-$, with the formation of the latter complex being more thermodynamically favorable. For example, log *K* of formation of ≡AlOHgCl and $\equiv AlOHgOHCl^-$ complexes in adsorption of Hg(II) on gibbsite is 6.64 and –0.50, respectively.

Thus, hydrolyzed Hg(II) species such as HgOHCl are sorbed on nickel(II) hydroxide owing to formation

Sorption of Hg(II) on Ni(II) hydroxide from solutions containing Cl^-, Br^-, and I^-

Anion	E, mg Hg^{2+}/g $Ni(OH)_2$	Hg(II) desorption, %
Cl^-	17.8	31
Br^-	10.1	51
I^-	2.42	98

of the surface intraspheric complex ≡NiOHgCl. At the same time, HgOHCl is not the major mercury species at almost any concentrations of chloride ions in the solution. We suggest that the concentration of this complex remains approximately constant during the sorption (buffer effect). The only question is the rate of this process. We found that formation of HgOHCl is completed during passage of the solution through an ion-exchange column. The sorption capacity did not noticeably change after an Hg(II) solution was allowed to stand at pH 7.8 and 8.3 prior to sorption for additional time (see Fig 1b, points *2* and *3*, respectively).

The decrease in E at $[Cl^-] > 10^{-2}$ M remains unclear. We suggest that the presence of different anionic species in the solution interferes with the sorption via formation of Ni–O–Hg bonds. A change in the composition of the Hg(II) complex and a decrease in the equilibrium constant of its formation are also possible.

The results of this work show that Hg(II) sorption on Ni(II) hydroxide from solutions containing Br^- and I^- should decrease owing to formation of $HgHal_3^-$ and $HgHal_4^{2-}$ complexes. This assumption is confirmed by the experimental data presented in the table. The working solutions contained 10^{-3} M Hg(II) and 10^{-1} M Hal^-. Mercury was desorbed with 0.1 M NaOH. The data on Hg(II) sorption from a chloride solution are included in the table for comparison.

In the presence of Br^- and I^- in the solution, the probability of the ion-exchange sorption of Hg(II) increases and formation of intraspheric surface complexes is suppressed owing to stabilization of $HgBr_3^-$ and $HgBr_4^{2-}$ (pK 19.7 and 21.0, respectively) and especially HgI_3^- and HgI_4^{2-} (pK 27.6 and 29.8, respectively). As the contribution of ion-exchange sorption of Hg(II) by nickel(II) hydroxide increases, the fraction of desorbed mercury increases. In the experiments with chloride and bromide solutions, the Hg(II) desorption is 4.9–5.2 mg Hg^{2+}/g $Ni(OH)_2$, which correlates with the E vs. $[Cl^-]$ dependence (Fig. 1c). Chloride and bromide anions can be involved in the ion exchange. The equilibrium Hal^- concentrations in the solutions in the course of the sorption decrease in the following order: $Cl^- > Br^- > I^-$. Our experimental results show that the surface intraspheric Hg(II) complexes are stable in 0.1 M NaOH.

CONCLUSIONS

(1) The dependence of Hg(II) speciation in solutions with pH 5.0 and 9.0 on the Cl^- concentration was calculated.

(2) The dependence of the sorption capacity of β-$Ni(OH)_2$ for Hg(II) on $[Cl^-]$ was measured experimentally.

(3) The sorption capacity of β-$Ni(OH)_2$ for Hg(II) correlates with that calculated for solutions with pH 9.

(4) Ionic Hg(II) complexes can be absorbed by β-$Ni(OH)_2$ owing to exchange with OH groups of the hydroxide. The sorption mechanism of hydroxo Hg(II) complexes involves formation of surface intraspheric complexes like MOHgHal.

REFERENCES

1. Stumm, W. and Morgan, J.J., *Aquatic Chemistry*, New York: Wiley, 1996.
2. Leikin, Yu.A., Tarasova, T.I., Tikhonova, L.A., and Musa, N., *Zh. Fiz. Khim.*, 1997, vol. 71, no. 2, pp. 321–323.
3. Sarkar, D., Essington, M.E., and Misra, K.C., *Soil Sci. Soc. Am. J.*, 2000, vol. 64, pp. 1968–1975.
4. Barrow, N.J. and Cox, V.C., *J. Soil Sci*, 1992, vol. 43, pp. 295–304.
5. MacNaughton, M.G. and James R.O., *J. Colloid Interface Sci.*, 1974, vol. 47, pp. 434–440.
6. Kinniburgh, D.G. and Jackson, M.L., *Soil Sci Soc. Am. J.*, 1978, vol. 42, pp. 45–47.
7. Kapustin, A.E., *Usp. Khim.*, 1991, vol. 60, no. 12, p. 2685.
8. Vol'khin, V.V., Tomchuk, T.K., and Leont'eva, G.V., *Zh. Prikl. Khim.*, 1983, vol. 56, no. 4, pp. 767–772.
9. Sokolova, M.M. and Vol'khin, V.V., *Zh. Neorg. Khim.*, 1997, vol. 42, no. 7, pp. 1091–1093.
10. Newton, D.W., Ellis, R., Jr., and Paulsen, G.M., *J. Environ. Qual.*, 1976, vol. 5, pp. 251–254.
11. Barnum, D.W., *Inorg. Chem.*, 1983, vol. 22, p. 2297.
12. Scheinost, A.C. and Sparks, D.L., *J. Colloid Interface Sci.*, 1999, vol. 223, p. 170.
13. Polyanskii, N.G., Gorbunov, G.V., and Polyanskaya, N.L., *Metody issledovaniya ionitov* (Methods for Studying Ion Exchangers), Moscow: Khimiya, 1976.
14. Tarayan, V.M., Ovsepyan, E.N., and Lebedeva, S.P., *Arm. Khim. Zh.*, 1970, vol. 23, no. 12, pp. 1085–1090.
15. Morel, F.M.M., Kraepiel, A.M.L., and Amyot, M., *Ann. Rev. Ecol. Systemat.*, 1998, vol. 29, p. 551.
16. Sokolova, M.M. and Vol'khin, V.V., *Zh. Neorg. Khim.*, 1997, vol. 42, no. 10, pp. 1631–1635.

Russian Journal of Applied Chemistry, Vol. 77, No. 7, 2004, pp. 1100–1103. Translated from Zhurnal Prikladnoi Khimii, Vol. 77, No. 7, 2004, pp. 1116–1119.

SORPTION AND ION-EXCHANGE PROCESSES

Recovery of Cadmium(II) Ions with a Sulfur-Containing Carbon Sorbent

L. A. Zemskova, V. A. Avramenko, V. V. Chernykh, V. N. Kustov, and Yu. M. Nikolenko

Institute of Chemistry, Far Eastern Division, Russian Academy of Sciences, Vladivostok, Russia

Received May 14, 2003; in final form, March 2004

Abstract—The sorptive properties of a sulfur-containing sorbent, selective with respect to cadmium(II) ions in extraction from aqueous solutions, including process solutions, were studied.

Heavy metal ions (mercury, chromium, cadmium, zinc, lead, copper, and nickel ions) are usually removed from wastewater using reagent treatment methods involving precipitation with hydroxides or sulfides. In the latter case, a more profound purification is attained, since the solubility of heavy metal sulfides is considerably lower than that of hydroxides and carbonates [1]. An alternative, rather efficient method of the removal of heavy metal ions from solutions, especially at their low concentrations, is sorption on, e.g., activated carbon (AC) [2]. Therefore, a possibility can be considered of using sorption on activated carbon materials (ACMs) to remove cadmium and cobalt ions whose concentration in wastewater is very low compared to other heavy metal ions [1]. In addition, sorption on ACMs can be the final stage of the purification of industrial wastewater. For example, use of AC after sulfide precipitation decreases the residual concentration of zinc and cadmium ions by approximately 50% [2].

Fibrous carbon materials (FCMs) show promise for extraction of heavy metal ions, since they combine filtering and sorptive properties, high specific surface area, and developed porosity. However, FCMs are rather expensive. In addition, their sorption capacity with respect to heavy metal ions is relatively low. Therefore, treatment of large volumes of industrial wastewater containing heavy metal ions requires a large number of relatively cheap and readily available sorbents. In this connection, using technogenic wastes as sorbents is of particular interest. They should exhibit selectivity with respect to heavy metal ions, being group reagents of a sort with respect to the given class of metals. Among sorbents intended, e.g., for concentrating mercury ions the most promising are S,N-containing sorbents, whose selectivity is higher than that of their N,O-containing analogs [3]. In this connection, spent activated carbons containing both elemental sulfur and surface sulfides, which are used as sorbents, e.g., for treatment of natural gas or gases in cellulose production, may be of interest [4].

In this work, modified sulfur-containing fibrous carbon sorbents obtained from waste of textile production and a commercial carbon fiber were studied and tested for recovery of cadmium ions from solutions of various concentrations and compositions.

EXPERIMENTAL

Sulfur-containing carbon fibers were prepared by treating activated carbon fiber, obtained from natural fibers, at 600°C in a mixture of an inert gas (nitrogen), hydrogen sulfide, and water vapor (sorbent I), or in a mixture of an inert gas and hydrogen sulfide (sorbent II) [5]; alternatively, they were prepared by impregnating an activated fiber with a sulfur solution in turpentine with subsequent drying (sorbent III). The Aktilen-V commercial carbon fiber (sorbent IV) with a specific surface area of 700 $m^2 g^{-1}$ and a pore volume of 0.400 $cm^3 g^{-1}$ was also used for comparison.

The sorption was performed in the static mode at continuous agitation for 2 days (a Type 357 shaker with a water bath, ELPAN plant, Poland, 150 rockings per minute) from the initial solutions containing 100, 80, 60, 40, and 20 mg l^{-1} Cd(II). The solutions were prepared by volumetric dilution of the stock solution containing 100 mg l^{-1} Cd(II) and 700 mg l^{-1} Ca(II). $CdCl_2 \cdot 2.5H_2O$ (analytically pure grade) and anhydrous $CaCl_2$ (pure grade) were used as the starting compounds for preparing the stock solution. The volume of the solutions studied was 25 ml, and the

1070-4272/04/7707-1100 © 2004 MAIK "Nauka/Interperiodica"

weight of the fiber portions, 0.025 g. The content of Cd(II) in the solutions after sorption was determined by atomic absorption spectroscopy (AA-780 spectrometer, Nippon Jarrell Ash). The amount of sorbed Cd(II) was calculated from the difference in its content in the solutions before and after sorption. The sorption kinetics was studied with sorbent I having the maximal sorption capacity (SC) from the solutions containing 10 and 4.3 mg l^{-1} Cd(II), prepared by dilution of stock solution, and with sorbent III.

The spectra of core electrons were measured on an ES-2401 commercial X-ray photoelectron spectrometer (AlK_α radiation). The chamber of the analyzer was evacuated to 7×10^{-8} mm Hg. The energy scale of the spectrometer was calibrated by the Au4$f_{7/2}$ peak (binding energy E_b 84.0 eV). Gold was sputtered in the sample pretreatment chamber of the spectrometer. Experimental spectra were treated by the method described in [6, 7]. The measured binding energies were reproduced to within 0.2 eV, and the error of determination of the relative concentrations of the elements was no more than 20%.

The isotherms of the Cd(II) sorption on sulfur-containing carbon sorbents I–III are shown in Fig. 1 in comparison with those on Aktilen-B (IV). The sorption capacities of sorbents I and II, obtained in different series of the experiments, fall within the area between curves *1* and *2*. Curve *1* reflects the Cd(II) sorption on the samples of sorbents I and II having the highest sorption capacity. The graphs show that, despite scatter of values, sulfur-containing carbon sorbents I and II have the higher sorption capacity compared to sorbent III containing elemental sulfur and to commercial activated fiber IV.

The isotherms are described by the Freundlich equation:

$$a = bc^{1/n}, \quad (1)$$

where a is the equilibrium concentration of Cd(II) in the sorbent (sorbent capacity SC) (mg g^{-1}); c, equilibrium concentration of Cd(II) in the solution (mg l^{-1}); and b and n, constants.

The values of b and n for the sorbents, as calculated from data in Fig. 1, are presented below:

Sorbent	b	n
I	19.2	5.7
II	12.5	6.3
III	0.52	1.4
IV	0.82	1.8

Comparinson of the capacities for Cd(II) in aqueous solutions, exhibited by sulfur-containing sorbents I and II and by oxidized carbons [8], shows that these values are comparable. At the same time, in sorption of ions from multicomponent mixtures, the sorption capacities differ considerably. Therefore, the sorption capacity was determined from the solutions containing a mixture of cadmium and calcium salts to confirm the selectivity.

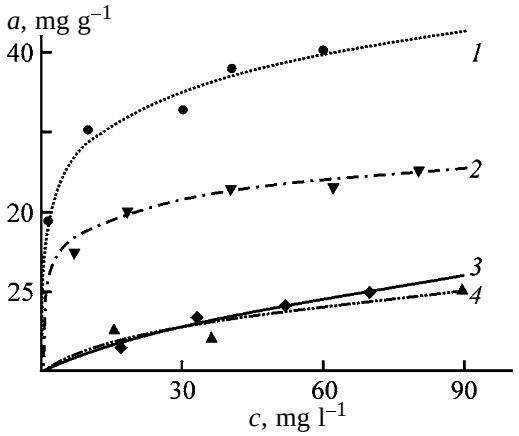

Fig. 1. Isotherms of the Cd(II) sorption from aqueous solutions in the presence of excess Ca(II) ions. (*a*) Equilibrium concentration of Cd(II) on the sorbent and (*c*) equilibrium concentration of cadmium in the solution. Sorbent: (*1*) I, (*2*) II, (*3*) III, and (*4*) IV.

As known, a certain correlation exists between sulfide and oxohydrate sorbents. The role of aqua, OH groups, and O atoms in sulfides can be played, respectively, by H_2S and HS groups and S atoms. In the general case, numerous kinds of sorption events are possible with sulfides; however, these are surface processes determining the colloidal and chemical properties of sulfides [9].

Assuming that the selectivity by Cd(II) of carbon-containing sorbents I and II is due to the nature of the sulfur-containing groups on the sorbent surface, we studied the sorbent samples by X-ray photoelectron spectroscopy (XPES).

Examples of the C1*s* and S2*p* experimental photoelectron spectra for sorbent I are shown in Fig. 2. In the S2*p* electron range, two peaks with binding energies E_b of 164.1 ± 0.2 and 168.3 ± 0.2 eV are present. The E_b values allow peaks to be assigned to bridging sulfur (C–S–H, C–S–C, or C–S–S–C) and to SO_2 groups, respectively [10, 11]. It was found that the S content in the sorbents studied is 1–3%, and most of it is incorporated in bridging groups (Fig. 2b).

The difference in the sorption capacities of sorbents I and II, on the one hand, and sorbent III, on the other

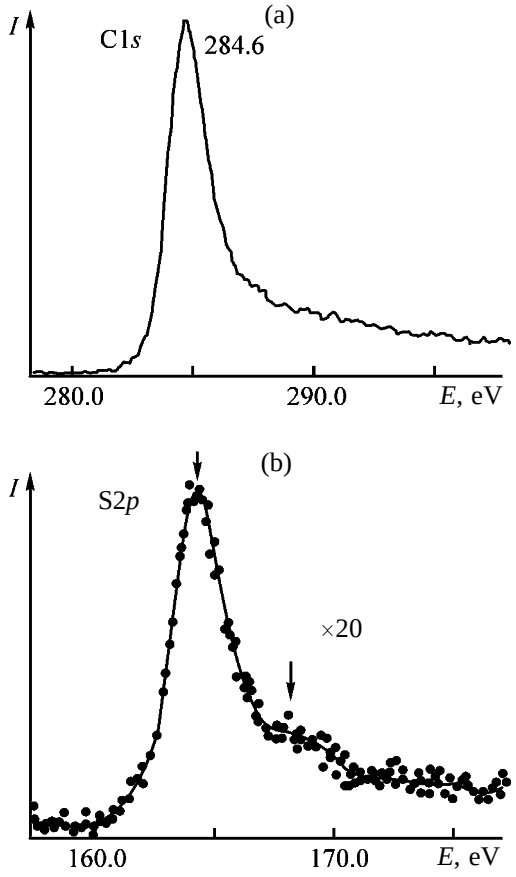

Fig. 2. C1*s* and S2*p* X-ray photoelectron spectra of sorbent I. (*I*) Intensity and (*E*) binding energy. Spectrum: (a) experimental and (b) experimental and after smoothing.

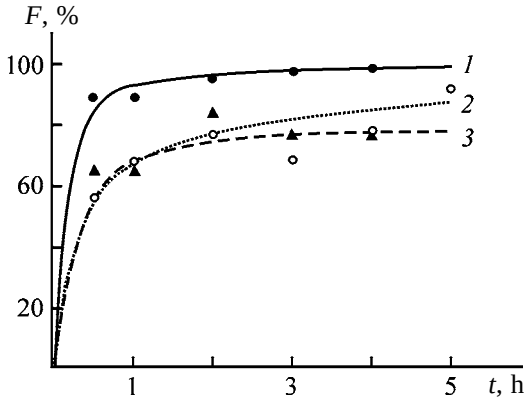

Fig. 3. Cd(II) sorption vs. time of contact with the sorbent *t*. (*F*) Ratio of the sorbed Cd(II) amount to the maximum amount sorbed in 24 h. Sorbent: (*1*, *2*) I and (*3*) III. c_0, mg l^{-1}: (*1*, *3*) 4.3 and (*2*) 10.

hand, indirectly confirms that sorbents I and II do not contain elemental S (Fig. 1).

For sorbent I, whose capacity under the static conditions is the highest, we studied the kinetics of Cd(II) sorption. Figure 3 shows that sulfur-containing carbon sorbent I sorbs more than 50% of the maximum value (attained during 24 h of sorption) in the first 0.5 h and more than 90–98% of Cd(II), within 5 h.

The rate constant k was calculated from the slope of the straight line in the $\log c$–t coordinates, in accordance with the equation of the first-order irreversible reaction transformed into the form

$$\log c = \log c_0 - 0.434tk, \quad (2)$$

where c_0 and c are the initial and current concentrations of Cd(II) in the solution (mg l^{-1}) and t is time (s) [12].

The obtained rate constant of the Cd(II) sorption by sorbents I and III are as follows.

Sorbent	c_0, mg l^{-1}	$k \times 10^{-4}$, s^{-1}
I	4.3	1.273
	10	0.480
III	4.3	0.510

Sulfur-containing carbon sorbents I and II were used under the laboratory and pilot-plant conditions for the purification of industrial water containing 0.6 mg l^{-1} Cd(II). The total salt content in the water was 2.5 g l^{-1}, and the content of hardness salts, 10 mg-equiv l^{-1}. In industrial water treatment, we used a radial filter containing 1 kg of fibrous sorbent (a mixture of sorbents I and II). The flow rate was 200 l h^{-1}. 180 m^3 of industrial water was purified during the test. The residual concentration of Cd(II) in the purified water was less than 0.001 mg l^{-1}.

CONCLUSIONS

(1) The study of fibrous carbon sorbents containing 1–3% sulfur showed that the selective properties of sorbents I and II are due to the presence of sulfide and hydrosulfide groups and C–S–C and C–S–S–C bridging groups.

(2) Treatment of multicomponent process solutions containing 0.6 mg l^{-1} Cd(II) with sorbents I and II decreases the cadmium concentration in the purified water to less than 0.001 mg l^{-1}.

REFERENCES

1. Rodionov, A.I., Klushin, V.N., and Sister, V.G., *Tekhnologicheskie protsessy ekologicheskoi bezopasnosti: Osnovy envaironmentalistiki* (Processes of Environ-

mental Safety. Fundamentals of Environmentalistics), Kaluga: Izd. Bochkarevoi, 2000.

2. Young, Ku, and Peters, R.W., *Environ. Prog.*, 1987, vol. 6, no. 2, pp. 119–124.
3. Simonova, L.N., Bruskina, I.M., and Ivanov, V.M., *Zh. Anal. Khim.*, 1989, vol. 44, no. 4, pp. 581–596.
4. Kienle, H. von and Bader, E., *Aktivkohle und ihre industrielle Anwendung*, Stuttgart, 1980.
5. RF Patent 2187362.
6. Yudin, D.V., and Zelenskii, Yu.V., *Zh. Prikl. Spektrosk.*, 1990, vol. 52, no. 3, pp. 445–451.
7. Zelenskii, Yu.V., and Yudin, D.V., *Zh. Prikl. Spektrosk.*, 1991, vol. 54, no. 1, pp. 40–45.
8. Tarkovskaya, A.I., *Okislennyi ugol'* (Oxidized Coal), Kiev: Naukova Dumka, 1981.
9. Vol'khin, V.V., Egorov, Yu.V., Belinskaya, F.A., *et al.*, *Ionnyi obmen* (Ion Exchange), Senyavin, M.M., Ed., Moscow: Nauka, 1981, pp. 25–44.
10. Nefedov, V.I., *Rentgenoelektronnaya spektroskopiya khimicheskikh soedinenii: Spravochnik* (X-ray Photoelectron Spectroscopy of Chemical Compounds: Reference Book), Moscow: Khimiya, 1984.
11. Siegbahn, K., Nordling, G., Fahlman, A., *et al.*, *Atomic, Molecular, and Solid State Structure Studied by Means of Electron Spectroscopy*, Uppsala, 1967.
12. *Kurs fizicheskoi khimii* (Course of Physical Chemistry), Gerasimov, Ya.I., Ed., Moscow: Khimiya, 1973, vol. 2.

Russian Journal of Applied Chemistry, Vol. 77, No. 7, 2004, pp. 1104–1107. Translated from Zhurnal Prikladnoi Khimii, Vol. 77, No. 7, 2004, pp. 1120–1122.

APPLIED ELECTROCHEMISTRY AND CORROSION PROTECTION OF METALS

Electrodeposition of Copper–Tin Alloy from Sulfate Electrolyte

G. I. Medvedev, N. A. Makrushin, and O. V. Ivanova

Novomoskovsk Institute, Mendeleev Russian University of Chemical Engineering, Novomoskovsk, Tula oblast, Russia

Received December 22, 2003

Abstract—The electrodeposition of copper–tin alloy from a sulfate electrolyte containing $CuSO_4 \cdot 5H_2O$, $SnSO_4$, H_2SO_4, and benzyl alcohol was studied.

The Cu–Sn alloy containing 10–20 wt % Sn (yellow bronze) is applied as protective, protective-decorative, and antifriction coating [1, 2]. Numerous electrolytes were proposed for the electrodeposition of Cu–Sn alloy, among which cyanide–stannate electrolytes have found the widest industrial application [1, 2]. At the same time, these electrolytes have a number of drawbacks such as toxicity and high working temperature.

Sulfate bronzing electrolytes, which more completely meet the process requirements, being less toxic, comparatively cheap, and simple in preparation and service and operating at room temperature, are considered today to be the most promising. Of specific interest are sulfate electrolytes for obtaining lustrous Cu–Sn coatings. However, the electrolytes developed for obtaining lustrous coatings operate at low current densities i_c and require pretreatment [3–5].

In this work we studied the electrodeposition of Cu–Sn alloy from a sulfate electrolyte in the presence of benzyl alcohol (BA). This additive is used in electrolytes to obtain Sn, Sn–Sb, and Sn–Bi lustrous coatings [6–8].

The study was performed in an electrolyte containing $CuSO_4 \cdot 5H_2O$ 30–50 g l^{-1}, $SnSO_4$ 30–50 g l^{-1}, H_2SO_4 70–120 g l^{-1}, and BA 1–10 ml l^{-1}. Copper foil was used as material for cathodes, on which a 9–15-μm-thick alloy layer was deposited. Anodes were made of bronze (85 wt % Cu and 15 wt % Sn), copper, and tin. The alloy was analyzed by the method described in [2]. The content of Sn^{2+} in the electrolyte was determined by iodometric titration [9]. The Sn^{4+} content in the electrolyte was calculated by the difference between the total content of tin and the Sn^{2+} content [9]. The copper(II) content in the electrolyte and that in the alloy were determined electrogravimetrically at direct current [2]. The X-ray diffraction analysis of Cu–Sn deposits was done on a DRON-2 diffractometer (CuK_α radiation). The polarization curves were recorded on a P-5827 potentiostat in the potentiodynamic mode at a linear potential sweep rate of 2 mV s^{-1}. A mercury sulfate electrode was the reference. In this study, all potentials are given relative to standard hydrogen electrode. The current efficiency by the Cu–Sn alloy was determined by the electrogravimetric method from the results of the electrolysis in the galvanostatic mode. The electrodeposition was performed at 18–20°C with and without stirring the electrolyte.

Data on how the BA concentration affects the outward appearance of the coatings depending on the current density (electrolyte composition, g l^{-1}): $CuSO_4 \cdot 5H_2O$ 30–50, $SnSO_4$ 30–50, and H_2SO_4 90) showed that the widest i_c interval (3–5 A dm^{-2}) for obtaining lustrous coatings is attained at an alcohol concentration of 2–4 ml l^{-1}. Outside this concentration range, dull or semilustrous coatings were obtained. It was established that the outward appearance of the coatings was also affected by the H_2SO_4 concentration in the electrolyte. At an H_2SO_4 concentration of 70–80 g l^{-1}, the coatings obtained were semilustrous (i_c = 3–5 A dm^{-2}), and the electrolyte operation was unstable. With acid concentration increased to 90–120 g l^{-1}, lustrous coatings were obtained at i_c = 3–5 A dm^{-2}. It should be noted that only stirring ensured formation of quality lustrous coatings in all the electrolytes studied. The coatings obtained without stirring were dull and rough.

The chemical analysis of the lustrous coatings obtained showed that, in this case, the Cu–Sn electrolytic alloy is formed. The influence of i_c on alloy the composition was studied. It was found that, with in-

1070-4272/04/7707-1104 © 2004 MAIK "Nauka/Interperiodica"

creasing current density, the Cu content in the alloy decreased (Fig. 1, curve *1*), with the current efficiency by the alloy being as high as 95.0–96.8% (Fig. 1, curve *2*).

We studied the influence of $CuSO_4 \cdot 5H_2O$ and $SnSO_4$ concentrations on the alloy composition. The table shows that the Cu content in the alloy increases with increasing $CuSO_4 \cdot 5H_2O$ concentration (at a constant $SnSO_4$ concentration) and decreases with increasing $SnSO_4$ concentration (at a constant $CuSO_4 \cdot 5H_2O$ concentration).

Variation of the H_2SO_4 concentration within 90–100 g l^{-1} does not affect the alloy composition. At higher acid concentrations (110–120 g l^{-1}), the Cu content in the alloy increases by 1–2%.

The polarization measurements were performed in the electrolytes for Cu, Sn, and Cu–Sn electrodeposition. We found that BA inhibits electrodeposition. Figure 2 shows that, in a BA-containing electrolyte, the cathodic polarization curve of the Cu–Sn deposition lies between the polarization curves of the Cu and Sn deposition at i_c = 1–3.8 A dm^{-2} and at more positive potentials at higher current densities (i_c > 3.8 A dm^{-2}) (Fig. 2, curves *1–3*).

To determine the rate of the Cu and Sn electrodeposition, we calculated in this study the partial polarization curves. The calculation was performed taking into account the alloy compositions at various i_c values, current efficiencies by the alloy, and electrochemical equivalents of Cu, Sn, and Cu–Sn [10]. As seen, the rate of the Cu deposition into the alloy is considerably higher than that of the Sn deposition (Fig. 2, curves *1*', *2*').

The analysis of the cathodic polarization curves of the individual metal deposition and of the partial curves shows that, as compared to separate deposition, Cu is deposited into the alloy with an overpolarization, and Sn, with a considerable depolarization (Fig. 2, curves *1*, *1*' and *2*, *2*').

The overpolarization in deposition of ions of a more electropositive metal cannot be explained in terms of the thermodynamics [1], since the maximal work spent for the alloy formation upon the deposition of both electropositive and electronegative metals is positive. Evidently, the overpolarization at Cu electrodeposition into the alloy is associated with the presence of BA in electrolyte, which decreases the process rate owing to adsorption on the electrode. Apparently, the depolarization in the Sn deposition into the alloy results from a decrease in its partial

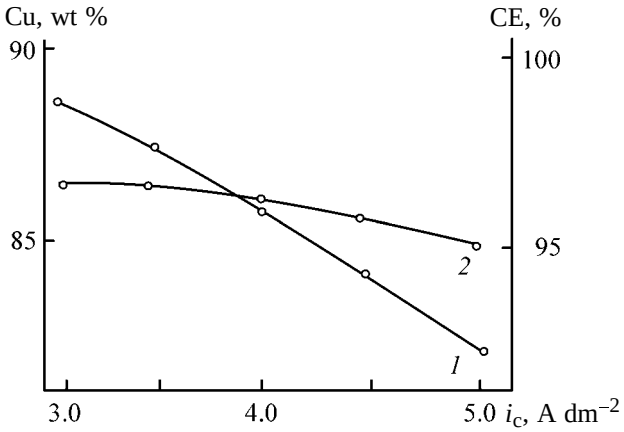

Fig. 1. (*1*) Copper content Cu and (*2*) current efficiency CE by the Cu–Sn alloy vs. cathodic current density i_c. Electrolyte: $CuSO_4 \cdot 5H_2O$ 30 g l^{-1}, $SnSO_4$ 30 g l^{-1}, H_2SO_4 90 g l^{-1}, and BA 3 ml l^{-1}; mechanical stirring; the same for Figs. 2 and 3.

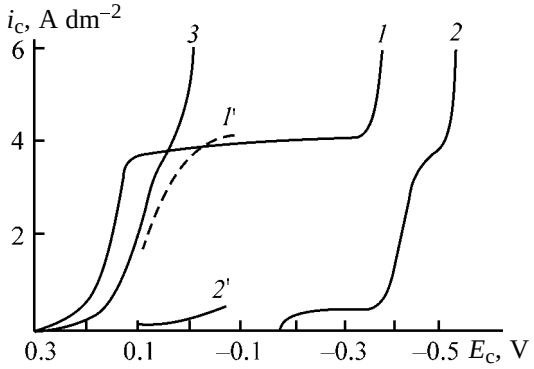

Fig. 2. Cathodic polarization curves for electrodeposition of (*1*) copper, (*2*) tin, and (*3*) Cu–Sn alloy. (i_c) Current density and (E_c) potential (vs. standard hydrogen electrode). (*1*', *2*') Partial polarization curves of copper and tin deposition.

energy released upon formation of intermetallic compounds in bronzes [1]. This is confirmed by the analysis of the alloy phase composition. It was found that the alloy formed in formation of yellow bronze con-

Composition of the Cu–Sn alloy at various concentrations of $CuSO_4 \cdot 5H_2O$ and $SnSO_4$. i_c = 3 A dm^{-2}, mechanical stirring

$SnSO_4$, g l^{-1}	Cu content in alloy, wt %, at indicated $CuSO_4 \cdot 5H_2O$ concentration, g l^{-1}		
	30	40	50
30	85.8	87.6	89.0
40	84.3	86.3	88.4
50	82.7	84.5	86.6

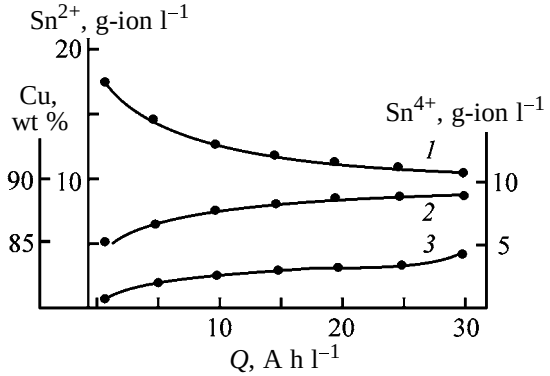

Fig. 3. Influence of the amount of passed electricity *Q* on the content of (*1*) Sn^{2+} and (*2*) Sn^{4+} ions in the bronzing electrolyte and (*3*) on the copper content Cu in the alloy at i_c = 3 A dm^{-2} and bronze anodes (85 wt % Cu and 15 wt % Sn).

sisted of CuSn and $Cu_{31}Sn_8$ intermetallic compounds.

The electrochemical stability of a bronzing electrolyte was studied in the course of prolonged electrolysis with bronze and copper anodes. It was found that, with increasing amount of the passed electricity, the concentration of the Sn^{2+} ions in the electrolyte decreases, whereas the Sn^{4+} concentration increases (Fig. 3, curves *1*, *2*). The Cu^{2+} content in the electrolyte varies insignificantly, and the Cu content in the alloy increases (Fig. 3, curve *3*). It should be noted that, in the course of the electrolysis with bronze anodes, the Sn^{2+} concentration in the electrolyte and the alloy composition vary to a lesser extent than in the course of the electrolysis with Cu anodes.

To ascertain why the content of Sn^{2+} ions in the electrolyte decreases considerably and the Sn^{4+} content increases, we took the anodic polarization curves. It was found that the potential of a bronze anode at i_a = 1–5 A dm^{-2} lies in the range of potentials from 0.36 to 0.38 V, and that of a copper anode, in the range from 0.32 to 0.47 V, i.e., they both are more positive than the standard potential of the oxidation of Sn^{2+} to Sn^{4+} (0.16 V) [11]. The data presented show that the oxidation of Sn^{2+} to Sn^{4+} with subsequent hydrolysis and precipitation of metastannic acid suspension are responsible for the low electrochemical stability of the bronzing electrolyte with respect to Sn^{2+}, with both bronze and copper anodes. With tin anodes, the dissolution potential at i_a = 1–5 A dm^{-2} varies from –0.18 to –0.10 V, i.e., the potential of the Sn anode acquires more negative values than the potential of the Sn^{2+} oxidation to Sn^{4+}, which makes this oxidation on the anode infeasible. At the same time, it is not reasonable to use tin anodes for the electrodeposition of yellow bronze, since in this case the Sn^{2+} concentration in the electrolyte increases considerably and the Cu^{2+} concentration decreases. A decrease in the Sn^{2+} concentration in the electrolyte is due to its contact deposition onto tin anodes when switching off the current. The Sn anodes can be used for adjusting the composition of the sulfate electrolyte both to increase the Sn^{2+} concentration in the electrolyte and to decrease the concentration of Cu^{2+} if its excessive amount is accumulated.

Thus, we developed a sulfate electrolyte for obtaining lustrous Cu–Sn coatings (yellow bronze). The electrolyte contains $CuSO_4 \cdot 5H_2O$ 30–50 g l^{-1}, $SnSO_4$ 30–50 g l^{-1}, H_2SO_4 90–100 g l^{-1}, and BA 2–4 ml l^{-1}; i_c = 3–5 A dm^{-2}.

The current efficiency is 95–98%. The tin content in the alloy is 11–18 wt %. Anodes are made of bronze (85 wt % Cu and 15 wt % Sn). The process is performed at 18–20°C at stirring and continuous filtration of the electrolyte. After passing 25–30 A h l^{-1} of electricity, the Sn^{2+} and Cu^{2+} concentrations require correction. Adjustment of the BA concentration is performed on the basis of spectrophotometric analysis data [6].

CONCLUSIONS

Electrodeposition of Cu–Sn alloy is performed at 18–20°C with stirring and continuous filtration of the electrolyte containing $CuSO_4 \cdot 5H_2O$ 30–50 g l^{-1}, $SnSO_4$ 30–50 g l^{-1}, H_2SO_4 90–100 g l^{-1}, and benzyl alcohol 2–4 ml l^{-1}.

REFERENCES

1. *Elektrokhimicheskie splavy* (Electrochemical Alloys), Fedot'ev, N.P., Ed., Moscow: Mashgiz, 1962.
2. Vyacheslavov, P.M., *Novye elektrokhimicheskie pokrytiya* (New Electrochemical Coatings), Leningrad: Lenizdat, 1972.
3. Galdekiene, O.K. and Motskus, Z.I., Extended Abstracts, *Kongress "Zashchita-92"* (Congr. "Protection-92"), Moscow, 1992, vol. 1, part 2, p. 373.
4. Medvedev, G.I. and Tkachenko, N.N., *Zashch. Met.*, 1994, vol. 20, no. 3, pp. 484–486.
5. Noyanova, G.A., Kosmodamianskaya, L.V., Tyutina, K.L., and Kudryavtsev, V.N., *Gal'vanotekh. Obrab. Poverkh.*, 1999, vol. 7, no. 3, pp. 9–13.
6. Medvedev, G.I. and Makrushin, N.A., *Zh. Prikl. Khim.*, 2001, vol. 74, no. 11, pp. 1787–1790.

7. Medvedev, G.I. and Fursova, N.Yu., *Zashch. Met.*, 2000, vol. 36, no. 4, pp. 425–428.
8. Medvedev, G.I., Makrushin, N.A., and Dubenkov, A.N., *Zashch. Met.*, 2003, vol. 39, no. 4, pp. 414–424.
9. Spivakovskii, V.B., *Analiticheskaya khimiya olova* (Analytical Chemistry of Tin), Ser.: *Analiticheskaya khimiya elementov* (Analytical Chemistry of Elements), Moscow: Nauka, 1975, p. 250.
10. Kudryavtsev, N.G., *Osnovnye zakonomernosti elektroliticheskikh protsessov polucheniya metallov i splavov* (Principles of Electrolytic Deposition of Metals and Alloys), Moscow: Mosk. Khim.-Tekhnol. Inst., 1973.
11. *Spravochnik po elektrokhimii* (Reference Book on Electrochemistry), Sukhotin, A.M., Ed., Leningrad: Khimiya, 1981.

Russian Journal of Applied Chemistry, Vol. 77, No. 7, 2004, pp. 1108–1116. Translated from Zhurnal Prikladnoi Khimii, Vol. 77, No. 7, 2004, pp. 1123–1131.

APPLIED ELECTROCHEMISTRY AND CORROSION PROTECTION OF METALS

Preparation of High-Purity Lithium Hydroxide Monohydrate from Technical-Grade Lithium Carbonate by Membrane Electrolysis

A. D. Ryabtsev, N. M. Nemkov, N. P. Kotsupalo, and L. A. Serikova

Ekostar-Nautekh Private Company, Novosibirsk, Russia

Received September 2, 2003; in final form, February 2004

Abstract—A scheme for preparing high-purity lithium hydroxide monohydrate from technical-grade lithium carbonate is suggested.

The basic stage in preparation of $LiOH \cdot H_2O$ from Li_2CO_3 is transformation of solid Li_2CO_3 into a LiOH solution. In this case, the throughput of the conversion process and its energy consumption, as well as the concentration and purity of the resulting LiOH solution largely determine the quality of the product obtained, its production cost, and the efficiency of the method as a whole.

Of the known techniques for preparing LiOH from Li_2CO_3, the method based on the reaction of Li_2CO_3 with lime milk $Ca(OH)_2$ is mainly used in practice [1, 2]. Despite the simplicity of this method and use of low-cost and readily available raw materials, it has a number of important disadvantages. For example, to obtain high-quality $LiOH \cdot H_2O$, it is necessary to impose stringent requirements on the purity of the starting components. In view of the low solubility of $Ca(OH)_2$, the technique in question is also characterized by low yield of LiOH into solution and large loss of Li^+, associated with the necessity for washing and settling of voluminous precipitates of $CaCO_3$.

To raise the yield of LiOH and improve the purity of the $LiOH \cdot H_2O$ obtained, it has been suggested to use, instead of $Ca(OH)_2$, a more soluble compound, $Ba(OH)_2$ [2]. However, the given method is also largely characterized by the same disadvantages. Moreover, $Ba(OH)_2$ is more expensive than $Ca(OH)_2$.

A method for obtaining LiOH by hydration of its oxide formed in thermochemical dissociation of Li_2CO_3 in a vacuum was suggested in [2]. However, the low rate of Li_2CO_3 decomposition gives no way of using this technique in the industry.

In recent years, electrochemical methods using ion-exchange membranes have found wide use in manufacture of high-purity alkali metal hydroxides [3–9].

For example, a method is known for preparing LiOH from Li_2CO_3 in a two-chamber electrolyzer with a cation-exchange membrane, lead anode, and iron cathode [8].

In [9], it was suggested to prepare LiOH from solid Li_2CO_3-containing wastes by bringing them in contact with water and subsequent separation of the clarified liquid phase. A lithium-containing solution is passed through the central chamber of a three-chamber electrolyzer, and a LiOH solution is obtained in the cathode chambe, and a solution of a mixture of acids, in the anode chamber. The circulation of the starting solution leads to desalting of the liquid in the central chamber, and this liquid is recycled into the dissolution stage.

The above-mentioned electrochemical methods for conversion of Li_2CO_3 into LiOH exhibit important advantages over chemical production techniques, because they make it possible to directly obtain high-purity LiOH at lower loss of Li^+. Therefore, development of a process for obtaining high-purity $LiOH \cdot H_2O$ by membrane electrolysis shows promise. However, the low output capacity and high energy consumption by electrochemical conversion, which is due to low solubility of Li_2CO_3 in water, is an important disadvantage in setting up a large-scale production.

The above disadvantages can be eliminated by preliminarily converting Li_2CO_3 into a well-soluble lithium salt. In this case, the solubility of the salt in water, electrical conductivity of its solution, and the nature of anodic reactions and products formed will

1070-4272/04/7707-1108 © 2004 MAIK "Nauka/Interperiodica"

largely determine the efficiency of membrane electrolysis.

The most suitable salt is Li_2SO_4, which is due not only to its high solubility, but, to a considerable extent, also to specificity of the anodic processes that occur in electrolysis of a Li_2SO_4 solution.

The main anodic reaction in electrolysis of the sulfate solution proceeds to give O_2 and H_2SO_4 as products, which makes it possible to use readily available and inexpensive lead anodes. In addition, the evolving O_2 presents no problems with its utilization, and H_2SO_4 generated in the anolyte is easily neutralized with Li_2CO_3, with its conversion into Li_2SO_4.

In addition to the electromembrane conversion of Li_2CO_3 into a LiOH solution, it is necessary to solve, in developing a process for production of high-purity $LiOH \cdot H_2O$, the problem of removal of Na, Ca, Mg, Al (halides and sulfates) impurities, and also SiO_3^{2-} ions, contained in Li_2CO_3. Solving this problem required a number of experimental studies and predetermined the goals of this work. Among the issues studied were the following: electrochemical conversion $Li_2SO_4 \rightarrow LiOH$ with determining the main technical and economical characteristics of the process and factors affecting the yield and qualitative composition of the conversion-produced LiOH; evaporation of the conversion-produced LiOH solution, crystallization of $LiOH \cdot H_2O$ from this solution, distribution of impurities among the liquid and solid phases, and washing of the resulting $LiOH \cdot H_2O$ crystals to remove mother liquor; and carbonation of mother liquors after evaporation as applied to utilization of Li^+ from these solutions.

EXPERIMENTAL

In the study was used technical-grade Li_2CO_3 manufactured by the SQM company (Chile) and containing about 1% impurities. The starting Li_2CO_3 solution was prepared from chemically pure grade crystalline lithium sulfate and distilled water.

The electrochemical conversion was studied in a galvanostatic mode on a laboratory setup whose main part is a membrane electrolyzer in the form of a filter-press apparatus with a stainless steel cathode and lead anode. The interelectrode space of the electrolyzer is separated by an MK-40 cation-exchange membrane into the anode and cathode chambers. The working area of the membrane and electrodes was the same and equal to 0.78 dm^2.

The rate of solution circulation in all the experiments was 0.15 l min^{-1}. The thickness of the electrode chambers was varied from 2 to 16 min, and the concentration of H_2SO_4 in the anolyte, from 0 to 87 g l^{-1}. The concentration of the resulting LiOH was in the range from 10 to 85 g l^{-1}, and the current density, from 5.2 to 15.4 A dm^{-2}. The process temperature depended on the current load and varied in the range 30–40°C.

In the experiments, the main parameters of the electrolysis process (transfer of Li^+ ions into the cathode chamber, current efficiency, electrolyzer voltage, and specific electric power consumption) were determined. In addition, the qualitative and quantitative composition of the conversion-produced LiOH and the influence exerted on these parameters by the anolyte composition were found.

The rate of transfer of Li^+ ions into the cathode chamber, ΔP_{Li^+}, (g Li h^{-1} dm^{-2}), was determined from changes in the concentration of Li^+ ions, or in the equivalent concentration of OH^- ions in the catholyte (the negligible content of impurity ions in the catholyte was disregarded), and from changes in its volume in unit time, using the formula

$$\Delta P_{Li^+} = \frac{\Delta V_c \Delta c_{Li^+}}{\tau S_m} \times 0.292,$$

where ΔV_c is the change in the catholyte volume in a time τ (l); Δc_{Li^+}, the change in the concentration of LiOH in the time τ (g l^{-1}); τ, the time of electrolysis (h); S_m, the membrane area (dm^2); and 0.292, the recalculation factor.

The current efficiency η (%) was calculated by the formula

$$\eta = \frac{\Delta P_{Li^+} F}{j E_{Li^+}} \times 100,$$

where j is the current density (A dm^{-2}); F = 26.8, the Faraday constant (A h); and E_{Li^+} = 7, the chemical equivalent of lithium (g).

The specific energy expenditure was determined using the formula

$$W = \frac{Uj}{\Delta P_{Li^+}},$$

where W is the specific expenditure of electric power (W h g^{-1} Li), and U is the electrolyzer voltage (V).

The crystallization of $LiOH \cdot H_2O$, including the stage of its washing, was studied with conversion

solutions of LiOH. A solution was evaporated to a LiOH concentration in solution of 170–180 g l^{-1}. Then, the evaporated solution was cooled in a closed flask to room temperature and the crystals formed were rapidly filtered off. The product was dried in a desiccator at room temperature and then analyzed for the content of impurities and subjected to washing.

The mother liquor, which is a saturated solution of LiOH with impurities, was recycled into the stage of evaporation and crystallization, and so on. This yielded, each time, crystals and mother liquors increasingly contaminated with impurities. A total of five different samples were obtained.

The resulting $LiOH \cdot H_2O$ samples were, each separately, washed to remove impurities with a pure saturated solution of LiOH in accordance with a scheme of three-stage batch washing with phase mixing; the l : s ratio was 1 : 1 for each stage.

The washed $LiOH \cdot H_2O$ samples were dried, and the residual content of impurities in them was determined.

A mother liquor formed after crystallization, which is a saturated LiOH solution contaminated with Na, K, and Ca ions, was placed in a vessel for carbonation, into which CO_2 was fed from a cylinder at a rate of 0.3 l min^{-1} through a gas-distribution unit. The carbonation was performed in the bubbling mode to pH 12.3 to prevent formation of lithium hydrocarbonate.

The resulting suspension was separated by filtration, after which the precipitate was washed on the filter with a threefold volume of distilled water, dried in a desiccator, and analyzed for the content of impurities.

The conventional analytical techniques were used in the study. The concentration of Li, K, and Na ions was determined by the spectral method on a Philips AAS-SP-9 atomic-absorption spectrophotometer [10]; that of calcium and magnesium ions, by EDTA titration [11]; that of OH^- and H^+ ions, by titration with a 0.1 N solution of HCl or KOH, respectively [12]; and that of chloride ions, by mercurimetric titration, with nitroprusside as indicator [13]. Sulfate ions were determined in solutions with their concentration exceeding 1 g l^{-1} by volumetric EDTA titration [14], and in cases when the concentration of these ions was lower than 1 g l^{-1}, by the nephelometric method on a KFK-1 photocolorimeter [12]. The accuracy of determination was 5%. The formation of PbO_2 in the system under study was monitored as follows. The precipitate was filtered off and then boiled, together with the filter, in a mixture of HNO_3 with H_2O_2, with the whole amount of PbO_2 quantitatively dissolved. The concentration of lead in solution was determined by EDTA titration, with Xylenol Orange as indicator, at pH 5.5 [15]. The concentrations of Cl_2 and O_3 in the gas phase were determined by photocolorimetry on a KFK-2MP instrument [16].

The procedure for obtaining high-purity $LiOH \cdot H_2O$ from technical-grade Li_2CO_3 is shown in Scheme 1.

According to the scheme suggested, a Li_2SO_4 solution is obtained from H_2SO_4 and Li_2CO_3 [reactions (1), (2)]. In the process, impurities of Na^+, K^+, Ca^{2+}, Mg^{2+}, Al^{3+}, Fe^{3+}, SiO_3^{2-}, and Cl^- ions will also pass into solution from technical-grade Li_2CO_3. Some of these impurities can impair the quality of the resulting LiOH solution and disturb the course of electrolysis to the point of its complete termination. This primarily refers to cations that tend to form poorly soluble compounds on coming in contact with alkali formed in the cathode chamber. Therefore, prior to delivering the Li_2SO_4 solution to electrochemical conversion, it should be alkalized to pH 11–12 in order to precipitate these impurities in the form of poorly soluble compounds [reactions (4)–(9)]. The purified Li_2SO_4 solution is fed into the anode chamber of the electrolyzer. In the course of electrolysis, water is oxidized electrochemically at the anode to give gaseous O_2 and H^+ ions by reaction (10).

The cathode space is filled with a dilute LiOH solution, with the electrochemical reduction of water occurring at the cathode to give gaseous H_2 and OH^- ions by reaction (12). The cation-exchange membrane separating the cathode and anode spaces of the electrolyzer ensures free transfer of cations (mainly Li^+) from the anode space of the electrolyzer into its cathode space under the action of an electric field and precludes transfer of anions. As a result, a fairly pure LiOH solution concentrates in the cathode chamber [reaction (13)]. The main ingredients that contaminate LiOH will be Na^+ and K^+, which are present in the anolyte and cannot be removed from the anolyte in the stage of its alkaline purification preceding the electrolysis. Therefore, these cations will also freely pass, together with Li^+ cations, into the cathode chamber and thereby contaminate the product [reactions (14), (15)].

The thus obtained LiOH solution containing a certain amount of Ba^+ and K^+ impurities is delivered to the stage of evaporation and crystallization of $LiOH \cdot H_2O$ and is, in part, used to alkalize the Li_2SO_4 solution before the electrochemical conversion.

Scheme 1

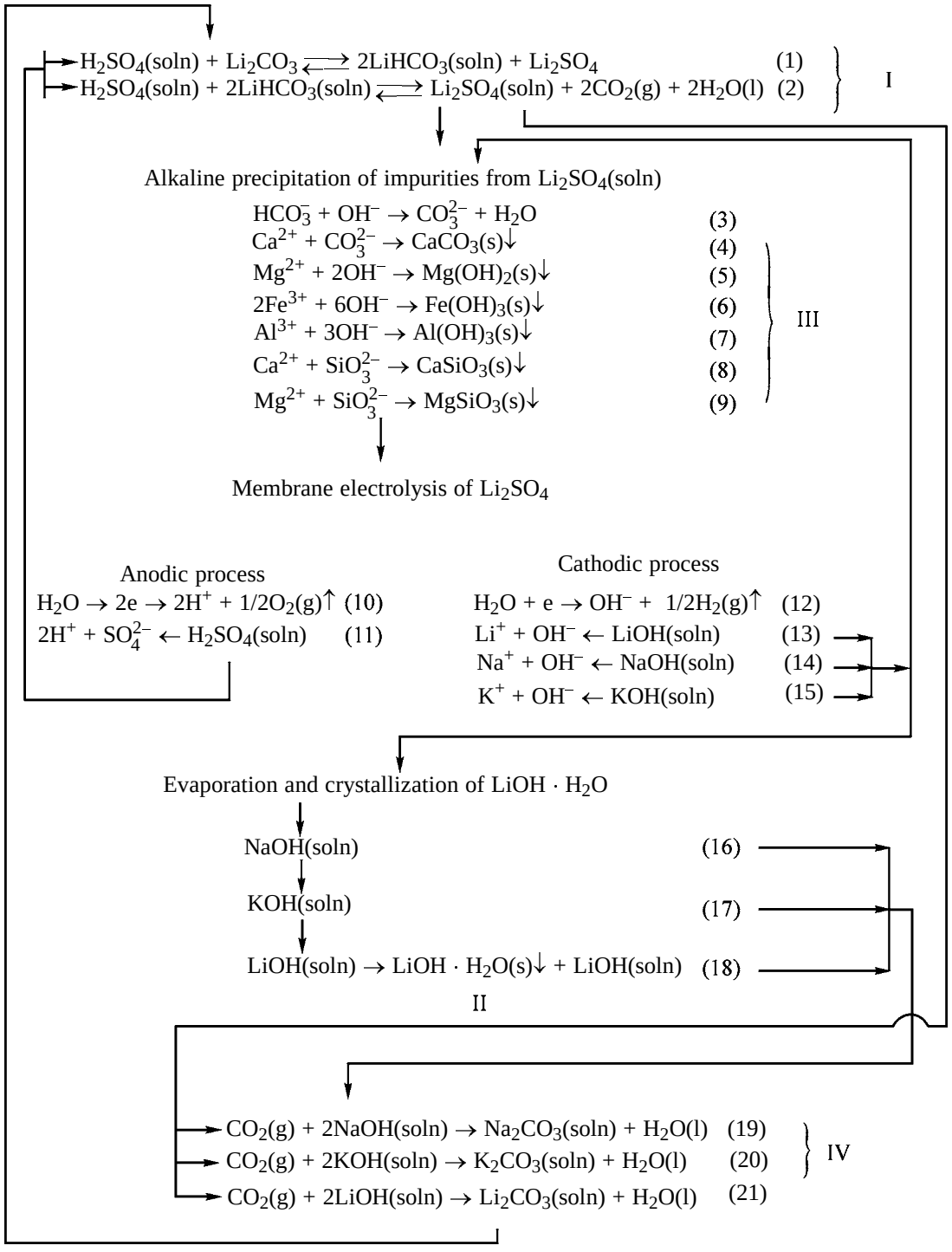

Chemical reactions that occur in preparing high-purity $LiOH \cdot H_2O$ from technical-grade lithium carbonate.

The required degree of purification of the final product to remove Na^+ and K^+ can be achieved by crystallization of $LiOH \cdot H_2O$ from an evaporated LiOH solution [reactions (16)–(18)]. In the crystallization of $LiOH \cdot H_2O$, Na^+ and K^+ ions must mainly remain in the mother liquor because of the higher solubility of NaOH and KOH and, up to their certain content in the solution being evaporated, must not affect the purity of the $LiOH \cdot H_2O$ crystals obtained. In this case, the resulting $LiOH \cdot H_2O$ crystals should

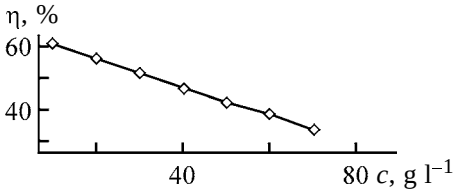

Fig. 1. Current efficiency η vs. LiOH concentration *c*.

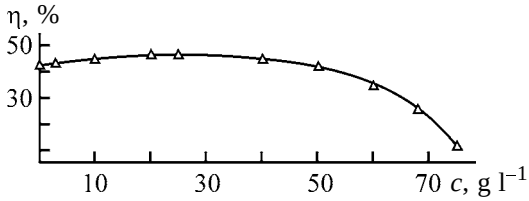

Fig. 2. Current efficiency η by conversion LiOH vs. the H_2SO_4 concentration *c* in the analyte.

be washed with the condensate for more complete removal of the mother liquor from their surface.

In order to prevent the loss of Li^+, it is advisable to treat spent washing solutions and mother liquors with carbon dioxide evolved in reaction (2). It is necessary to separate the poorly soluble Li_2CO_3 from the liquid phase, which contains mostly Na_2CO_3 and K_2CO_3 [reactions (19)–(21)]. The carbonate mother liquors formed after separation of Li_2CO_3 can be used in the industry, e.g., for neutralization of wastewater, or in installations for water softening.

The main characteristic of any process is the specific energy expenditure necessary for obtaining the target product. The specific energy expenditure in electrolysis is determined by the electrolyzer voltage and current efficiency by the target product. The electrolyzer voltage is largely determined by the electrical conductivity of the electrolyte, which, as a rule, depends on its concentration. In studying the electrochemical conversion of Li_2SO_4 into LiOH, the optimal Li_2SO_4 concentration in the solution delivered to the conversion stage was determined to be 180–230 g l^{-1} [17]. To this concentration corresponds the maximum electrical conductivity of approximately 0.09 S cm^{-1}, which, combined with the relatively low viscosity, ensures the minimum energy expenditure for overcoming the ohmic and hydrodynamic resistances in the given process. It was established experimentally that changing the thickness of chambers of the electrolysis cell in the range 2–8 mm has virtually no effect on the loss of voltage in electrolysis of a Li_2SO_4 solution with a concentration of 200 g l^{-1} in the current density range studied. In the elementary cell, the chamber thickness was taken to be 4 mm, which enables one, on the one hand, to simplify to the maximum possible extent the fabrication of an electrolyzer of the filter-press type, and, on the other, to construct apparatus with a high output capacity and relatively small dimensions.

The concentration of LiOH in the cathode chamber affects the loss of voltage in an elementary cell of the electrolyzer only at LiOH concentrations of up to 40–45 g l^{-1}.

A much stronger influence is exerted by the concentration of LiOH obtained on the current efficiency by LiOH, whose value directly determines the specific energy expenditure.

The dependence of the current efficiency on the concentration of the LiOH being obtained, shown in Fig. 1, indicates that the transfer of Li^+ ions linearly decreases as the content of Li^+ ions in the catholyte becomes higher. This leads to a proportional rise in the specific expenditure of electric power. The minimum specific expenditure of electric power for electrochemical conversion corresponds to concentrations of LiOH obtained equal to 20–25 g l^{-1}. However, obtaining a more concentrated LiOH solution is advantageous as regards energy saving in evaporation of a solution of conversion LiOH in production of $LiOH \cdot H_2O$.

Rough feasibility studies demonstrated that, as regards lowering to the maximum possible extent the total energy expenditure for obtaining $LiOH \cdot H_2O$ as a commercial product, the optimal concentration of conversion LiOH is 40–50 g l^{-1}. In this case, the concentration of the acid in the anolyte does not exert, in a rather wide range (up to 50 g l^{-1} of H_2SO_4), any noticeable influence on the cathode current efficiency by LiOH (Fig. 2). A moderate increase in the acidity even improves the process parameters because of a certain enhancement of the transfer of Li^+ ions and the corresponding increase in the current efficiency (by approximately 5%). The possible reason is that, when the acidity of the anolyte increases, H^+ ions neutralize OH^- ions in the membrane or in the near-membrane layer on the anode side to give water. The reaction between H^+ and OH^- ions, which are charge carriers, is compensated for by an increase in the fraction of current transported by Li^+ ions. The optimal concentration of H_2SO_4 in the anolyte in production of LiOH is in the range 15–40 g l^{-1}. Impurity ions constantly delivered into the anolyte with Li_2CO_3 in the neutralization of the acid cannot affect the process parameters to any noticeable extent because of their insignificant content in the anolyte.

In addition to the parameters described above,

those affecting the feasibility of electrolysis include the current density, which determines the specific output capacity of the process. The dependences in Figs. 3 and 4 clearly demonstrate that raising the current density leads to an increase in the electrolyzer voltage (Figs. 3, 4) and to the corresponding rise in the specific energy expenditure (Fig. 4, straight line *2*). At the same time, raising the current density leads to a proportional increase in the rate of transfer of Li^+ ions, ΔP_{Li^+}, i.e., in the specific output capacity of the process (Fig. 4, straight line *1*). For example, a threefold increase in the current density leads to an identical increase in the specific output capacity of the process, whereas the energy expenditures grows by only 36.6%. It was also established that the current density does not affect significantly the qualitative composition of the LiOH obtained. The electrolysis is more efficient at higher current densities, because the component of the production cost, associated with the capital cost and running expenses, decreases in this case. This conclusion is also supported by the fact that the concentration polarization of the electrodes and membranes, which makes shorter their service life, is not observed at the current densities studied. This is indicated by the stable current efficiency by LiOH and by the sufficiently high chemical and corrosion resistance of the membranes and electrodes, observed in the course of the study.

The main disadvantage of MK-40 membranes is their high permeability to OH^- ions, which leads to low current efficiency. At the same time, these membranes enable production of LiOH that is virtually free of any foreign anions. The main impurities that pass from Li_2CO_3 into a LiOH solution in electrochemical conversion are Na^+ and Ca^{2+} ions, whose concentrations in the 2 M LiOH solution obtained in a stationary electrolysis mode are 35–40 and 12–15 mg l^{-1}, respectively. A decrease or increase in the concentration of LiOH does not affect their relative concentration in solution. The study performed demonstrated that, as expected, the concentration of Ca^{2+} ions in alkali can be diminished to 2–4 mg l^{-1} by purifying the anolyte by the carbonate–alkaline method. No transfer of lead ions into the LiOH solution was observed in the course of electrolysis.

The parameters characterizing the purification of $LiOH \cdot H_2O$ by evaporation, crystallization, and washing of the crystals obtained to remove the remainder of contaminated mother liquor are listed in Tables 1 and 2.

Table 2 shows that the maximum content of Na^+ ions in the $LiOH \cdot H_2O$ samples obtained, at which high-purity $LiOH \cdot H_2O$ can be obtained by their washing to remove mother liquor (residual content of $Na^+ \le 0.002$ wt %), is about 0.06 wt %. As seen from Table 1, the concentration of Na^+ ions in a LiOH solution from which $LiOH \cdot H_2O$ with a residual sodium content $c \le 0.06$ wt % can be obtained should not exceed 1.4 g l^{-1}.

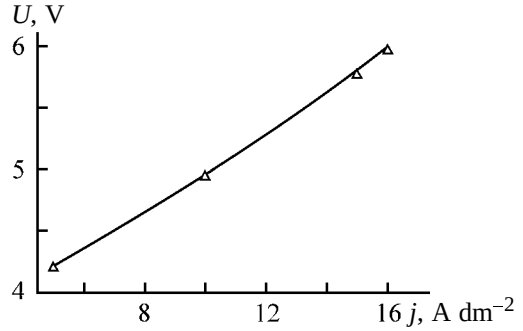

Fig. 3. Voltage U vs. the current density j in production of LiOH.

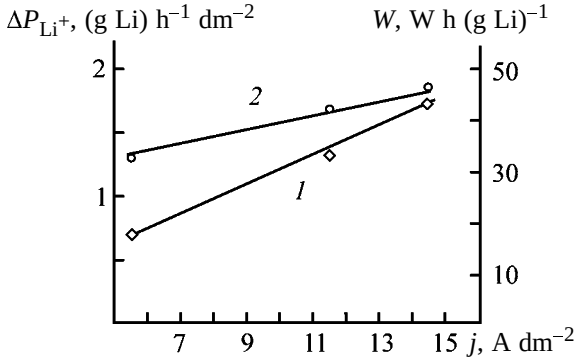

Fig. 4. (*1*) Rate of transfer of Li^+ ions and (*2*) specific energy expenditure W vs. the current density j in production of a LiOH solution. (ΔP_{Li^+}) Specific transfer of Li^+ ions to the cathode chamber.

As expected, Ca^{2+} is removed by washing to a considerably lesser extent than Na^+, and, therefore, the maximum content of Ca^{2+} impurity in the $LiOH \cdot H_2O$ samples delivered to the washing stage should not exceed 0.003 wt % for $LiOH \cdot H_2O$ of required purity as regards Ca^{2+} ions (residual content of Ca^{2+} $c \le 0.001$ wt %) to be obtained. In this case, the concentration of Ca^{2+} in a LiOH solution from which $LiOH \cdot H_2O$ with a residual content of Ca^{2+} $c \le 0.003$ wt % can be obtained should not exceed 0.05 g l^{-1}. Provided that the concentration of Ca^{2+} in the starting solution of conversion LiOH is lowered to 2–4 mg l^{-1} by its alkaline–carbonate removal from the anolyte delivered to electrolysis, it may be stated that Ca^{2+} is not an impurity component that determines the quality of $LiOH \cdot H_2O$ produced by the technique suggested.

Table 1. Characteristics of starting solutions and crystalline $LiOH \cdot H_2O$ samples obtained from these solutions

Sample no.	LiOH solution	Solution volume, l	c_{LiOH} in solution, g l^{-1}	Na^+ content		Ca^{2+} content	
				in solution, g l^{-1}	in $LiOH \cdot H_2O$, wt %	in solution, g l^{-1}	in $LiOH \cdot H_2O$, wt %
1	Starting	7.00	45.5	0.070	0.008	0.015	0.003
2	Mother liquor after crystallization: first	1.25	Saturated solution, ~120 g l^{-1}	0.520	0.017	0.051	0.004
3	second	0.75	″	0.784	0.057	0.056	0.006
4	third	0.42	″	1.435	0.061	0.078	0.012
5	fourth	0.23	″	2.200	0.092	0.088	0.036
6	fifth	0.11	″	3.560	–	0.084	–

Note: The concentration of K^+ ions in all the samples and solutions studied is an order of magnitude lower than that of Na^+ ions.

Table 2. Results of a comparative analysis of $LiOH \cdot H_2O$ samples for the content of impurities after washing to remove mother liquor

Sample no.	Content of Na^+, wt %		Content of Ca^{2+}, wt %	
	before washing	after washing	before washing	after washing
1	0.008	0.0006	<0.003	<0.001
2	0.017	0.0020	<0.004	<0.002
3	0.057	0.0024	<0.006	<0.003
4	0.061	0.0022	0.012	<0.006
5	0.092	0.0103	0.036	0.020

In order to test the process on an enlarged scale, a pilot batch of the product was prepared from lithium carbonate of Chilean manufacture.

In the process, 8.5 l of a conversion solution of LiOH with an average concentration of 45 g l^{-1} was obtained. The average concentrations of the main impurities in the resulting solution are as follows (mg l^{-1}): Na^+ 70, Ca^{2+} 15, CO_3^{2-} 300. The contents of other impurities (Pb, Fe^{2+}, Mg^{2+}, SO_4^{2-}, Cl^-) were either an order of magnitude lower than that of Na^+ and Ca^{2+}, or these impurities could not be detected at all by the analytical methods used.

Table 3. Composition of Li_2CO_3 manufactured by SQM (Chile) and of $LiOH \cdot H_2O$ obtained

Main substance and impurities	Content, wt %	
	Li_2CO_3	$LiOH \cdot H_2O$
Li_2CO_3	99.0	0.6*
Cl^-	0.02	0.1×10^{-3}
Na^+	0.12	2×10^{-3}
K^+	0.05	0.2×10^{-3}
Ca^{2+}	0.04	$\leq 4 \times 10^{-3}$
Mg^{2+}	0.011	$\leq 1 \times 10^{-3}$
SO_4^{2-}	0.1	$\leq 0.1 \times 10^{-3}$
Fe_2O_3	0.03	$\leq 1 \times 10^{-3}$
Insolubles	0.02	–
Pb	–	–

* The product contains a CO_3^{2-} impurity because of its storage conditions.

It follows from Table 3 that the quality of $LiOH \cdot H_2O$ satisfies the requirements of GOST (State Standard) 8595–83 (LGO-1 brand) in all the parameters except the content of Ca^{2+}.

The increased content of Ca^{2+} (~0.004 wt % against 0.001 wt % required by GOST) can be brought to satisfactory values by preliminary alkaline–carbonate purification of the anolyte delivered to electrolysis.

A study of the carbonation of alkaline mother liquors obtained after evaporation and crystallization, which cannot be used to produce commercial $LiOH \cdot H_2O$ because of the high content of impurities, demonstrated sufficiently high efficiency of this process for utilization of Li^+. Li_2CO_3 obtained by carbonation

Scheme 2

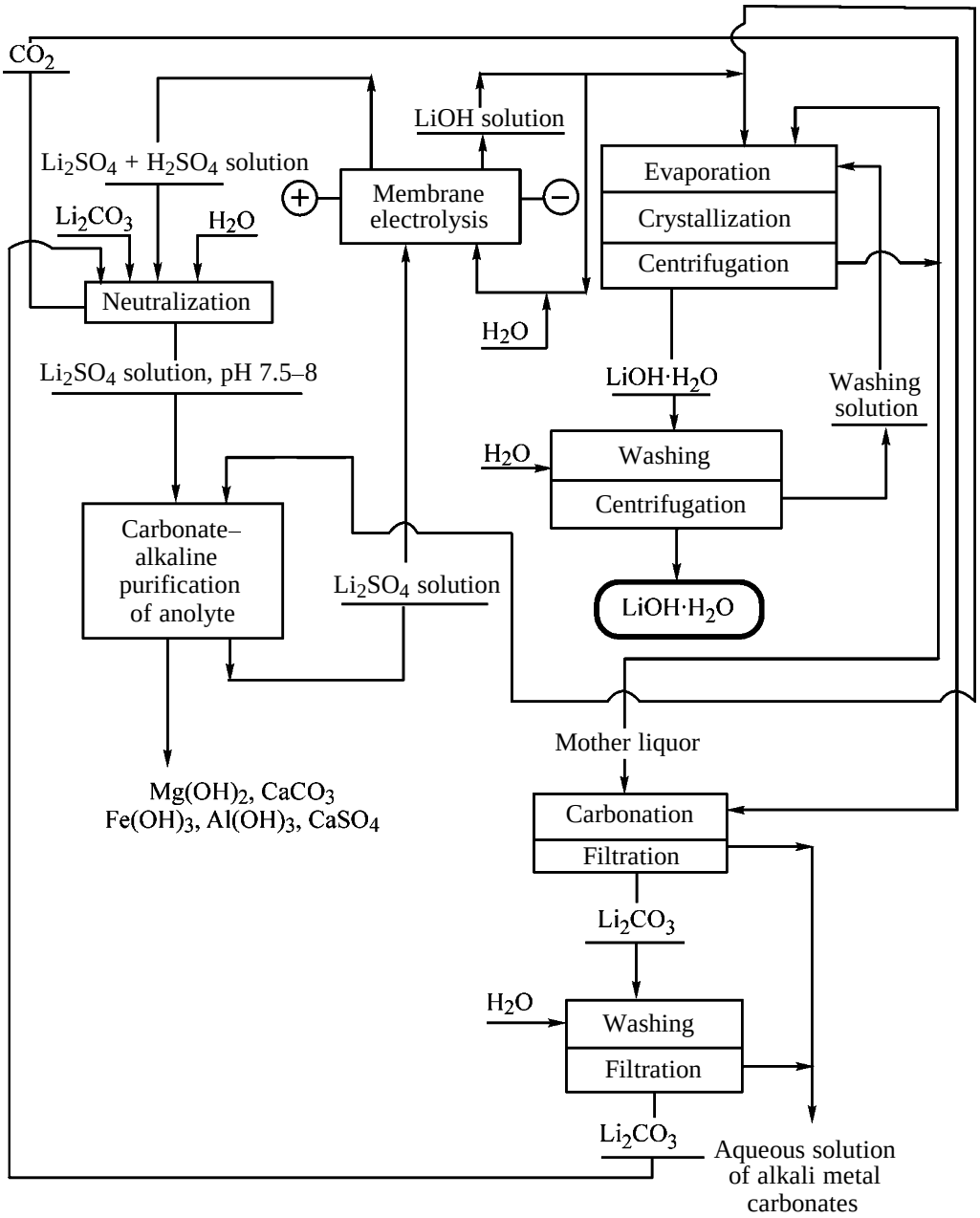

Flowsheet for production of high-purity $LiOH \cdot H_2O$.

contains only 0.007 wt % Na^+ and 0.043 wt % Ca^{2+}, which allows its recycling into the stage of electrochemical conversion. It was established that the main part of Ca^{2+} passes into the solid phase of Li_2CO_3 and cannot be removed by subsequent washing. Part of Na^+ ions (88%) remains in solution, and 12% Na^+ coprecipitates with Li_2CO_3, and this Na^+ can be completely removed by washing.

A calculation of the conversion of Li_2CO_3 into $LiOH \cdot H_2O$ of LGO-1 brand demonstrated that the loss of Li^+ without utilization from mother liquors formed in crystallization of $LiOH \cdot H_2O$ is 5.4%. With utilization of Li^+ from mother liquors by their carbonation and recycling of Li_2CO_3, the loss of Li^+ is about 1%.

The results obtained were used to develop a technique for manufacture of high-purity $LiOH \cdot H_2O$ from Li_2CO_3 by membrane electrolysis (Scheme 2). The technique was patented in the Russian Federation [18].

CONCLUSIONS

(1) The experimental study of production of $LiOH \cdot H_2O$ from technical-grade Li_2CO_3 by membrane electrolysis via Li_2SO_4 demonstrated that the use of a sulfate solution of Li^+ makes it possible to perform the process in an intensive mode at high current densities and allows use of lead anodes and MK-40 cation-exchange membranes of domestic manufacture.

(2) The use of these materials in a practical implementation of the process of electrochemical conversion demonstrated their high stability and efficiency. The technique is distinguished by an integrated approach to solution of the problem of use of technical-grade Li_2CO_3 and, in particular, that of Chilean manufacture. It yields high-purity $LiOH \cdot H_2O$ with a minimum amount of reagents used and does not produce any toxic waste.

REFERENCES

1. Ostroushko, Yu.I., Buchikhin, P.I., Alekseeva, V.V., *et al*., *Litii, ego khimiya i tekhnologii* (Lithium: Chemistry and Technology), Moscow: Atomizdat, 1960.
2. Plyushchev, V.E. and Stepin, B.A., *Khimiya i tekhnologiya soedinenii litiya, rubidiya i tseziya* (Chemistry and Technology of Lithium, Rubidium, and Cesium Compounds), Moscow: Khimiya, 1970.
3. *Prikladnaya elektrokhimiya* (Applied Electrochemistry), Rotinyan, A.L., Ed., Leningrad: Khimiya, 1974.
4. Mazanko, A.F., Kamar'yan, G.M., and Romashin, O.P., *Promyshlennyi membrannyi elektroliz* (Industrial Membrane Electrolysis), Moscow: Khimiya, 1989.
5. FRG Patent Appl. 2 700 748.
6. RF Patent 2 090 503.
7. Ryabtsev, A.D., Kishkan', L.N., Kotsupalo, N.P., and Menzheres, L.T., *Khim. Inter. Ustoich. Razv*., 2001, no. 9, pp. 61–69.
8. Grebenyuk, V.D., *Elektrodializ* (Electrodialysis), Kiev: Tekhnika, 1976.
9. RF Patent 2 071 819.
10. Poluektov, N.S., *Metody analiza po fotometrii plameni* (Flame Photometry Analysis), Moscow: Khimiya, 1967.
11. *Metody analiza rassolov i solei* (Methods for Analysis of Brines and Salts), Morachevskii, Yu.V. and Petrova, E.M., Eds., Moscow: Khimiya, 1964.
12. Charlot, G., *Les Methods de la chimie analytique. Analyse quantitative Minerale*, Paris: Masson, 1961, 4th ed.
13. Williams, W.J., *Handbook of Anion Determination*, London: Butterworths, 1979.
14. Schwarzenbach, G. und Flaschka, H., *Die komplexometrische Titration*, Stuttgart: Ferdinand Enke, 1965.
15. Polyanskii, N.G., *Svinets* (Lead), Moscow: Nauka, 1986.
16. Peregud, E.A.. and Chernet, E.V., *Khimicheskii analiz vozdukha promyshlennykh predpriyatii* (Chemical Analysis of Air at Industrial Plants), Leningrad: Khimiya, 1973.
17. *Svoistva elektrolitov: Spravochnik* (Properties of Electrolytes: Reference Book), Maksimova, I.N., Ed., Moscow: Metallurgiya, 1987.
18. RF Patent 2 196 735.

Russian Journal of Applied Chemistry, Vol. 77, No. 7, 2004, pp. 1117–1120. Translated from Zhurnal Prikladnoi Khimii, Vol. 77, No. 7, 2004, pp. 1132–1135.

APPLIED ELECTROCHEMISTRY AND CORROSION PROTECTION OF METALS

N-Phenacylpyridinium Bromides as Acid Corrosion Inhibitors

R. I. Yurchenko, I. S. Pogrebova, T. N. Pilipenko, and T. E. Shubina

Kiev Polytechnic Institute, National Technical University of Ukraine, Kiev, Ukraine

Received March 11, 2004

Abstract—The inhibiting effect of *N*-phenacylpyridinium bromides with the amide group in the pyridine ring on corrosion of carbon steel in 3 M sulfuric acid is studied. A relationship between the nature of substituents at the amide group and the corrosion-protective properties of the compounds studied is revealed. Compounds demonstrating high protection efficiency in acid solutions at elevated temperatures are found.

In the previous work [1] we demonstrated that the corrosion-protective efficiency of *N*-phenacylpyridinium bromides (**I**)

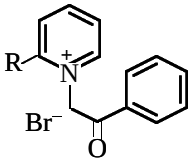

at 20 and 40°C can be characterized as the correlation between the inhibiting factor γ and σ_c^0 constants of the substituent R. At higher temperatures (60 and 80°C), they demonstrate considerably higher inhibiting efficiency, depending on the nature of the substituent. As the temperature increased from 20 to 60°C, the inhibiting factor of the compound with the NH_2 group increased by a factor of 8 (from 23.7 to 200.3), while that of the compound with the acetyl group, by a factor of 35 (from 7.6 to 262.8). Such a difference in the increase of the inhibiting efficiency between these compounds is due to the fact that, at the elevated temperature, the metal surface more actively interacts with the $COCH_3$ group as compared to the amino group under the same conditions. Therefore, for further study of the relationship between the structure of *N*-phenacylpyridinium bromides and their corrosion-protective properties, we selected compounds bearing carbonyl substituents at the position 2 of the pyridine ring. These are the amides 2-benzoylamino-1-(2-oxo-2-phenylethyl)pyridinium bromide (**II**), 2-(3-phenylacryloyl)amino-1-(2-oxo-2-phenylethyl)-pyridinium bromide (**III**), 2-(4-methoxybenzoyl)amino-1-(2-oxo-2-phenylethyl)pyridinium bromide (**IV**), 2-(2-furylcarbonyl)amino-1-(2-oxo-2-phenylethyl)pyridinium bromide (**V**), 2-(2-tetrahydrofurylcarbonyl)-amino-1-(2-oxo-2-phenylethyl)pyridinium bromide (**VI**), 2-(thienylcarbonyl)amino-1-(2-oxo-2phenylethyl)pyridinium bromide (**VII**), 2-(3-(2-furyl)-acryloyl]amino-1-(2-oxo-2-phenylethyl)pyridinium bromide (**VIII**), 2-(1-adamantoyl)amino-1-(2-oxo-2-phenylethyl)pyridinium bromide (**IX**), and 2-octadecanoylamino-1-(2-oxo-2-phenylethyl)pyridinium bromide (**X**).

These compounds bearing three and, in some cases, even four reactive centers capable of interacting with the metal surface are of particular interest for further investigation of the effect of intramolecular synergism in corrosion-protective action of organic compounds. They were synthesized by the reaction of 2-aminopyridine with the corresponding acid chlorides, followed by alkylation of the resulting amides with ω-bromoacetophenone:

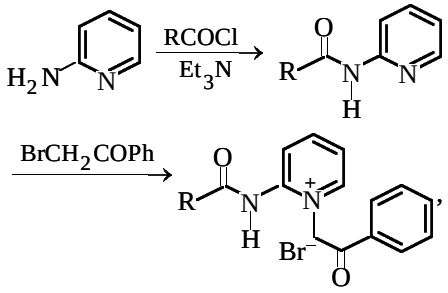

where R = C_6H_5 (**II**), $C_6H_5CH{=}CH$ (**III**), 4-$CH_3C_6H_4$ (**IV**),

 (**V**),  (**VI**),  (**VII**),

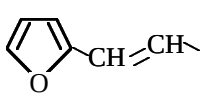 (**VIII**), 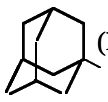 (**IX**), $CH_3(CH_2)_{16}$ (**X**).

The structures of the products were confirmed by IR and ^1H NMR spectra.

1070-4272/04/7707-1117 © 2004 MAIK "Nauka/Interperiodica"

Table 1. Inhibiting factors γ of phenacylpyridinium bromides **II**–**X** and protection rates *Z* of 0.8KP steel in 3 M H_2SO_4

Compound	R	20°C		40°C		60°C		80°C	
		γ	*Z*, %	γ	*Z*, %	γ	*Z*, %	γ	*Z*, %
II	C_6H_5	2.60	61.54	4.78	79.08	17.20	94.19	12.00	91.66
III	$C_6H_5CH=CH$	32.10	96.88	43.45	97.70	365.90	99.73	360.10	99.72
IV	4-$CH_3OC_6H_4$	33.30	96.99	47.80	97.91	731.85	99.86	595.00	99.83
V	2-Furyl	24.30	95.88	33.70	97.03	317.15	99.68	220.20	99.55
VI	2-Tetrahydrofuryl	30.00	96.66	43.45	97.70	365.90	99.73	333.80	99.70
VII	2-Thienyl	28.10	96.44	43.45	97.70	456.16	99.78	453.00	99.78
VIII	2-Furyl–CH=CH–	36.00	97.22	45.52	97.80	475.70	99.79	360.10	99.72
IX	1-Adamantyl	26.60	96.24	28.80	96.53	432.45	99.77	318.26	99.69
X	1-Octadecyl	24.30	95.88	43.45	97.70	365.90	99.73	325.80	99.69

EXPERIMENTAL

A mixture of 0.02 mol of appropriate acid chloride, prepared from the acid and thionyl chloride, 0.02 mol of 2-aminopyridine, 0.22 mol of triethylamine, and 20 ml of anhydrous benzene was refluxed for 3 h. Then benzene was removed in a vacuum (water-jet pump), and the residue was treated with water. Solid amides were separated, and oily amides were extracted with benzene. The resulting benzene solutions were dried over anhydrous sodium sulfate, and benzene was removed in a vacuum (water-jet pump). Equimolar amounts (0.0015 mol) of the amides thus obtained and ω-bromoacetophenone were refluxed with 15 ml of ethyl acetate for 3 h. The reaction mixture was treated with diethyl ether, and a solid (**II**, **V**, **VIII**, or **IX**) was separated. In the case of oily products, the solvent was removed by decantation, and the residue was washed with ether and dried in a vacuum (water-jet pump). The yields (%) and melting points (°C) of compounds **II**, **V**, **VIII**, and **IX** are as follows: **II** 80, 176–179; **V** 75, 210–212; **VIII** 72, 180–181; and **IX** 82, 237–240.

The corrosion-protective properties of compounds **II**–**X** were studied at their concentration of 1×10^{-2} M by determining the inhibiting factor γ and protection rate *Z* of 08KP steel in 3 M H_2SO_4 at 20, 40, 60, and 80°C using the gravimetric method. The results are summarized in Table 1.

Since substitution of the hydrogen atom of the amino group by an acyl residue is accompanied by a decrease in the electron-donating power of this group, it could be expected that the compounds in hand would demonstrate lower protective efficiency at room temperature as compared to their unsubstituted analogs. Indeed, we found that, on passing from **I** (R = NH_2) to amide **II**, the inhibiting factor considerably decreases not only at 20 or 40°C, but also at higher temperatures. Evidently, in this case, the processes blocking the negative electron induction of the benzamide group and promoting protective action do not occur.

Different behavior was observed for the other amides, whose acyl residue contains (in addition to the phenyl group or in its place) such substituents as an ethylene bridge (compound **III**), *p*-methoxy group (**IV**), heterocyclic systems: furan, tetrahydrofuran, and thiophene rings (compounds **V**–**VII**), or a vinyl group and a furan ring (**VIII**). The inhibiting factor of these compounds at all the temperatures studied was considerably higher as compared not only to amide **II**, but also to the compound with an NH_2 group. Increase in the protective rate was observed also with substitution of the phenyl group in **II** by a bulky adamantyl group (compound **IX**) or stearic acid residue (**X**). Following [1–4], enhancement of the inhibiting action in compounds **II**–**VIII** is caused to a considerable extent by immediate participation of the substituents R in adsorption, and, in amides **IX** and **X**, by either the shielding effect of the adamantyl and octadecyl groups or small electron-donating effects characteristic of these groups [2–5].

For compounds **I**, **II**, and **V**–**VII** we have made quantum-chemical calculations of the charge distribution in the molecules (Table 2). The geometry was optimized by the B3LYP method [6] with the standard basis 6-31G using the GAUSSIAN program pack [7]. All the stationary points were fixed on the basis of full analysis of normal modes of harmonic vibrations, where NIMAG = 0 corresponds to the minima on the potential energy surfaces for all the optimized structures. The results showed that, on passing from **I** (R =

Table 2. Effective charges q on the heteroatoms of the compounds

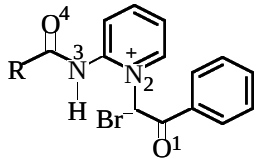

R*	q				
	O^1	N^2	N^3	O^4	$O(S)^5$
C_6H_5	–0.54580	–0.29956	–0.66758	–0.58872	–
	–0.54576	–0.32251	–0.65968	–0.55209	–0.50162
	–0.53863	–0.32422	–0.65884	–0.55516	–0.64280
	–0.56683	–0.34702	–0.65833	–0.56042	0.46288

* Effective charges q in **I** (R = NH_2): –0.57072 (O^1), –0.35093 (N^2), and –0.80152 (N^3).

NH_2) to compounds **II** and **V**–**VIII**, the negative charge on the nitrogen atom N^3 at the pyridine ring decreases to about the same level (somewhat higher value was obtained for **II**). This fact and also practically equal charges on the oxygen atoms of the acyl groups in these compounds suggest that the value of the negative charges on the amide nitrogen and oxygen atoms is not the factor determining the inhibiting factor of the compounds studied, and the observed differences in their protective characteristics are caused, without question, by the nature of substituents R.

The calculation data showed that, in amides **V**–**VII**, the oxygen atoms of the furan and tetrahydrofuran rings bear negative charges, and the sulfur atom of the thiophene ring, a positive charge, which is responsible for different mechanisms of interaction of the heterocyclic fragments in the indicated compounds with the metal surface. Adsorption of the oxygen-containing heterocyclic structures on the metal proceeds via the nucleophilic oxygen atoms. Therefore, the larger negative charge localized on the oxygen atom of the tetrahydrofuran ring is responsible for somewhat higher protective performance of **VI** as compared to amide **V**. In compound **VII** containing a thiophene ring, specific adsorption on the steel surface can occur by virtue of formation of back coordination bond with electron transfer from the metal to the sulfur atom, thanks to its ability to accept electrons on *d* orbitals.

The electrocapillary curves obtained on mercury in 3 M H_2SO_4 at 20°C in the presence of some of the compounds studied showed that these compounds are readily adsorbed on both negatively and positively charged electrode surfaces (maximum in the electrocapillary curve slightly shifted toward positive values). This suggests the possibility that oppositely charged reactive centers of the compounds participate in the adsorption and that their presence induces a positive adsorption jump of the potential.

The voltammetric measurements made in the presence of compounds **V** and **IX** revealed that they are corrosion inhibitors of a mixed type. Being adsorbed on a negatively charged surface of corroded steel, these compounds inhibit both the anodic and cathodic corrosion processes. Comparison of the experimental and theoretical (calculated from the kinetic equations [8]) inhibiting factors showed that, in the presence of some of the compounds, inhibition of acid corrosion of steel at 40 and 60°C proceeds by the coupled energy-blocking mechanism. However, making such calculations at 20°C is complicated by the occurrence of a mixed hydrogen–oxygen depolarization in their presence.

As the temperature increased from 20 to 60°C, the inhibiting factor of amide **II** increased by a factor of 6, and that of compounds **II**–**X**, by a factor of 11–22, which is higher by a factor of 1.5–3.6 than the inhibiting factor of the unsubstituted compound at the

same temperature. Such an enhancement of the protective properties of the indicated compounds is due to increase in the contribution of the specific adsorption via the carbonyl group of the phenyl residue, and also to more effective participation of the acylamide groups in adsorption. With further increase in the temperature, the protective activity of the most of these compounds slightly decreases, which, as known, is a result of a high renewal rate of the surface of corroded steel, retarding adsorption of the inhibitor.

It should be pointed out that the inhibiting factors of the compounds in hand at 20 and 40°C only slightly differ from each other, suggesting that the effect of substituents in the acyl groups is leveled off under these conditions. As the temperature rises to 60–80°C, interaction of these compounds with the metal surface considerably increases, and the differences in their inhibiting activity become more pronounced. For example, at 20°C, the inhibiting factors of compounds **III** and **IV** differ by about unity (or by a factor of 1.04), while at 60°C, this difference becomes equal to 366 (or by a factor of 2). The difference between **IV** and **V** is 6 (1.37) at 20°C and 414 (2.31) at 60°C. The reason is that, at low temperatures, the same reactive centers are responsible for adsorption of all the amides studied, and the substituents R have only insignificant effect. At higher temperatures, more favorable conditions for effective participation of the substituents are realized, whose different structure provides their different contributions to the corrosion-inhibiting activity of the molecule as a whole.

CONCLUSIONS

(1) *N*-Phenacylpyridinium bromides bearing an amide group in the pyridine ring are highly efficient acid corrosion inhibitors. The inhibiting factor of these compounds depends on the nature of substituents in the acyl group, insofar as they can directly participate in the interaction with the metal surface.

(2) High inhibiting value of *N*-phenacylpyridinium bromides is a result of a combined action of all the reactive centers of the molecules, which is particularly pronounced at elevated temperatures. The inhibiting factor of the compounds is as high as 300–700, and the protective rate of steel, 99.7–99.9%.

REFERENCES

1. Yurchenko, R.I., Pogrebova, I.S., Pilipenko, T.N., and Kras'ko, E.M., *Zh. Prikl. Khim*., 2003, vol. 76, no. 11, pp. 1814–1818.
2. Zhdanov, Yu.A. and Minkin, V.I., *Korrelyatsionnyi analiz v organicheskoi khimii* (Correlation Analysis in Organic Chemistry), Rostov-on-Don: Rostov. Univ., 1966.
3. Grigor'ev, V.P. and Ekilik, V.V., *Khimicheskaya struktura i zashchitnoe deistvie ingibitorov korrozii* (Chemical Structure and Protective Action of Corrosion Inhibitors), Rostov-on-Don: Rostov. Univ., 1978.
4. Reshetnikov, S.M., *Ingibitory kislotnoi korrozii metallov* (Acid Corrosion Inhibitors), Leningrad: Khimiya, 1986.
5. Yurchenko, R.I., Klepa, T.I., Voitsekhovskaya, O.M., *et al*., *Zh. Obshch. Khim*., 1990, vol. 60, no. 10, pp. 2280–2282.
6. Becke, A.D., *J. Chem. Phys*., 1993, vol. 98, p. 5648.
7. Frisch, M.J., Trucks, G.W., Schlegel, H.B., *et al*., GAUSSIAN 98, Pittsburgh, PA: Gaussian, 1999.
8. Antropov, L.I. and Pogrebova, I.S., *Itogi Nauki Tekh., Ser.: Korroz. Zashch. Korroz*., 1973, vol. 2, pp. 27–112.

Russian Journal of Applied Chemistry, Vol. 77, No. 7, 2004, pp. 1121–1129. Translated from Zhurnal Prikladnoi Khimii, Vol. 77, No. 7, 2004, pp. 1136–1143.

CATALYSIS

Oxidation of Carbon in the Presence of Catalysts Based on Cesium Lanthanum Vanadate

A. A. Ostroushko, A. M. Makarov, and V. I. Minyaev

Research Institute of Physics and Applied Mathematics, Ural State University, Yekaterinburg, Russia
Institute of Solid-State Chemistry, Ural Division, Russian Academy of Sciences, Yekaterinburg, Russia

Received May 6, 2003; in final form, February 2004

Abstract—Some kinetic aspects of the catalytic oxidation of carbon with atmospheric oxygen and nitrogen oxide NO in the presence of catalysts based of cesium lanthanum vanadate were studied. The influence exerted by a promoter, cesium sulfate, and its content on the course of catalytic reactions was analyzed.

Recently, the interest of researchers has been attracted by catalytic oxidation of carbonaceous substances (carbon black) with oxygen and with nitrogen oxides. These reactions are of practical importance for treatment of effluent gases in thermal power engineering, metallurgy, building, and at garbage incineration plants. The interest is due to the fact that fume gases contain, in addition to other toxic components, carbon black, nitrogen oxides, and residual oxygen. These reactions can be used to neutralize exhausts of diesel engines and to decrease the exhaust smoke emission. Discharges of carbon black are dangerous because of the carcinogenic compounds it contains. Deposits of carbonaceous substances impair the efficiency of thermocatalytic neutralizers. There exist complex oxide catalysts that markedly accelerate the oxidation of carbon black with the residual oxygen, and some of these can be used to oxidize carbonaceous substances via reduction of nitrogen oxides to molecular nitrogen.

Carbon can be oxidized in the presence of solid or partly molten catalysts [1–7], with complex compounds of vanadium distinguished by their high catalytic activity. The activity of, e.g., lanthanum vanadate increases dramatically when alkali metal ions are incorporated into its structure, with the catalytic activity the higher, the larger the atomic mass of a metal [2, 3]. In addition, the promoting effect is exhibited by alkali metal salts and, in particular, Cs_2SO_4 introduced into the catalyst composition. The mechanism of catalysis of the reactions mentioned above is rather complicated; to similar types of interactions can be referred processes occurring in catalytic gasification of coal and other carbonaceous substances [8]. Steam–oxygen gasification is catalyzed by compounds of alkali metals, e.g., by their carbonates. The activity of alkali metal compounds also increases in going from lithium to cesium. A similar behavior has been observed for carbon oxidation with nitrogen oxide N_2O [9].

Thermocatalytic devices for neutralization of waste gases [10], working in the continuous or batch mode, should ensure a virtually complete burning-out of the carbon black absorbed. Carbon black substances of different origins have different structure and composition [11]. However, finer structures are stronger than more complex ones, and, therefore, deposits of diesel carbon black are mainly composed of formations not larger than 5–10 μm in size. The particles may contain incompletely burnt oils, mineral components of additives to combustive-lubricating materials, products formed in wear of the piston and cylinder, etc. [10]. Impurities of this kind diminish the effective oxidation surface of carbon black and hinder access of oxidizing agents into pores, so that the particles are only oxidized on their surface.

The kinetic parameters of combustion of various carbonaceous substances strongly differ [12]. For dust-like particles of various coals, the overall activation energy E of combustion in air varies from 75 to 170 kJ mol^{-1}. Very strongly (by several orders of magnitude) differ the pre-exponential factors K_0 in the Arrhenius equation, obtained for these reactions. Determining the kinetic parameters is experimentally difficult. The individual specific features of materials lead to a wide scatter of points in experimental dependences. However, despite this circumstance, empirical equations relating E and K_0 have been derived. To higher activation energies correspond greater values of K_0. There exists an opinion that K_0 is proportional to the number of active centers on the carbon surface [12]. As their number grows, the energy of each center

1070-4272/04/7707-1121 © 2004 MAIK "Nauka/Interperiodica"

decreases, which leads to an increase in the activation energy. It has been suggested to use as a parameter describing the process the specific surface rate of reaction with carbon, K_S^C [12]. This quantity depends on whether the process is kinetically or diffusion-controlled. It is related to the concentration of O_2 in the gas medium, relative amounts of the forming oxides CO and CO_2, etc. It is commonly believed that, for carbonaceous particles of size not exceeding 10 μm, reactions at their internal surfaces at low temperatures are not important, and the overall combustion rate is determined by the kinetics of the chemical reaction between O_2 and carbon. If carbon combustion occurs within a bed, the key importance is acquired by diffusion processes, and E decreases severalfold [12].

For the properties of samples in modeling of reactions with gases to be reproducible, a certain type of a carbonaceous material is chosen [9, 12], e.g., activated carbon. In this study, experiments were performed with activated carbon ground to 10 μm, which makes the samples similar in particle size and specific surface area of particles to carbon black. The presence of mineral substances in the carbon makes the experimental conditions close to reality. An attempt was made to carry out a comparative analysis of kinetic features of the process of carbon oxidation by atmospheric oxygen and nitrogen oxide NO in the presence of a cesium lanthanum vanadate catalyst with a monazite structure, promoted with various amounts of Cs_2SO_4.

EXPERIMENTAL

Powder catalysts were synthesized using $La(NO_3)_3 \cdot 6H_2O$, $CsNO_3$, KNO_3, and $AgNO_3$ (all of chemically pure grade), NH_4VO_3 of pure grade, $Cu(NO_3)_2 \cdot 3H_2O$, and polyvinyl alcohol of 11/2 brand. $Cs_xLa_{1-x}VO_{4\pm y}$ ($x = 0-0.5$) was synthesized by pyrolysis of polymer–salt formulations [13, 14]. A 5–10% solution of polyvinyl alcohol in distilled water was prepared on a water bath and prescribed amounts of $La(NO_3)_3 \cdot 6H_2O$ and $CsNO_3$ were dissolved in this solution. Ammonium vanadate was dissolved in water under heating, and the resulting solution was mixed with a separate portion of the aqueous solution of polyvinyl alcohol and with an aqueous-polymeric solution of the nitrates. A gel prepared using the methods described in [15, 16] was dried in a thin layer under an infrared lamp and subjected to pyrolysis and then to calcination (4 h at 600°C). The product obtained was analyzed on a DRON-1.5 diffractometer with CoK_α radiation using the JCPDS file. To introduce the promoter, cesium sulfate Cs_2SO_4, an aqueous–alcoholic solution of a technical-grade reagent was prepared, and the catalyst powder was impregnated with a prescribed volume of this solution and then dried at 90°C. Other samples were also prepared by pyrolysis of polymer–salt compositions from the appropriate salts [13, 17].

The catalyst (S_{sp} = 8–15 $m^2\ g^{-1}$) was ground in an agate mortar and mixed in a mass ratio of 4 : 1 with a preliminarily ground activated carbon of BAU brand [18] ($S_{sp} \approx 100\ m^2\ g^{-1}$, ash content 4 wt %). The ash contained oxides of aluminum, iron, silicon, and other metals (microimpurities). The catalytic activity in carbon oxidation by atmospheric oxygen was determined gravimetrically in an open reactor, with the layer of a mixture of a powdered catalyst with carbon placed in ceramic boats. Oxidation of carbon with nitrogen oxide NO was studied in a similar manner in a flow-through quartz reactor through which NO obtained in a reaction of a concentrated solution of $NaNO_2$ or KNO_2 and a solution of $FeSO_4$ acidified with hydrochloric acid (all reagents of chemically pure grade) was passed at a flow rate of 30 ml min^{-1}. The first solution was added dropwise to the second.

To determine the optimal composition of the catalyst, $Cs_xLa_{1-x}VO_{4\pm y}$ (x = 0 to 0.5; monazite structure), and $M_{0.1}La_{1.9}Cu_{0.95}V_{0.05}O_{4\pm y}$ (M = K, Cs), which belong to the K_2NiF_4 structural type, were synthesized as single-phase samples. The introduction of alkali metals changed the constants of the crystal lattice of the K_2NiF_4 type. On introducing the larger cesium ion, these constants were 0.2% greater than those upon substitution of lanthanum with potassium. The activity of multicomponent compounds was evaluated in carbon oxidation with atmospheric oxygen, with step-by-step isothermal (20 min) exposures of the reaction mixtures in the temperature range from 100 to 600°C. As a reference sample served carbon without a catalyst or with addition of indifferent substances of mass equal to that of the catalyst. The nominal reaction ignition temperature T_{ig} was determined from the temperature dependences of the degree of carbon burning-out. The activity of $Cs_xLa_{1-x} \cdot VO_{4\pm y}$ exceeded (T_{ig} = 300–310°C) that of $M_{0.1}La_{1.9}Cu_{0.95}V_{0.05}O_{4\pm y}$. An analysis of the activity of catalysts of the last type confirmed its relationship with the atomic mass of the alkali metal ion incorporated into the structure. For the composition containing Cs^+ or K^+, the ignition temperatures were 330 and 340°C, respectively. For samples without a catalyst, the ignition temperature was 410°C. It was found that the optimal catalyst composition is

$Cs_{0.3}La_{0.7}VO_{4\pm y}$, and just this composition was used in further experiments. A higher content of Cs^+ commonly gives no additional increase in the catalytic activity. A heterogeneous catalyst [17, 19, 20] of the empirical formula $Ag_{0.25}La_{0.75}MnO_{3\pm y}$ (T_{ig} = 360°C), which exhibits high activity in oxidation of CO and organic compounds, was also inferior in activity to $Cs_{0.3}La_{0.7}VO_{4\pm y}$.

In studying the kinetics of carbon oxidation, isothermal experiments were performed in the practically important working temperature range of catalysts, 300–400°C. As promoter for $Cs_{0.3}La_{0.7}VO_{4\pm y}$ served Cs_2SO_4. The conversion was determined at exposures ranging from 5 min to 1–1.5 h. At a relatively short duration of an experiment, the time of heating of the samples exerts a noticeable influence, and there is an induction period of the reaction, associated with the sorption of O_2 on the carbon surface. It was confirmed in the course of the study that addition of Cs_2SO_4 to the catalyst markedly raises the rate of carbon oxidation with oxygen and lowers the ignition temperature of the reaction (Table 1, Fig. 1). In carbon oxidation in the kinetic mode at the external surfaces of grains, the dependences of the conversion α on time τ at isothermal exposures must be described by the equation of a "collapsing sphere"

$$[1 - (1 - \alpha)^{1/3}] = k\tau, \quad (1)$$

where k is the rate constant.

On the whole, the experimental data can be described, within the experimental error, by the above equation, which is confirmed by data processing in the coordinates of reduced time. However, deviations from this dependence are observed in some cases at relatively high conversions, with the conversion found to be somewhat lower than the calculated value. This may be due to existence in the final stage of residues of the coarsest or difficultly oxidizable particles, because the carbon powders used were not exactly monodisperse and homogeneous: they were produced from raw materials of natural origin. Moreover, a certain contribution may come from carbon particles with nonspherical shape. Such particles are similar to stable chains in carbon black. For formations of this kind, the time dependence of the conversion is described by the equation of a "collapsing cylinder," which also leads to a certain decrease in the rate of the overall oxidation process:

$$[1 - (1 - \alpha)^{1/2}] = k\tau. \quad (2)$$

For practical implementation of oxidation of carbonaceous particles in gas flows, it is advisable to bring them in contact with solid surfaces at a sufficiently high velocity, e.g., with a special baffler for disintegration of ensembles of particles. Further, to determine the kinetics of carbon oxidation in more detail, it would be appropriate to perform experiments with monodisperse powders. The carbon combustion observed could also be described using the equation of a first-order reaction with respect to carbon

$$\ln[1/(1 - \alpha)] = k\tau. \quad (3)$$

A calculation of the rate constants of the combustion reaction by Eqs. (1) and (3) gave similar results.

Table 1. Ignition temperature of carbon oxidation

Sample no.	Sample composition	Ignition temperature T_{ig}, °C	
		air	NO
1	Carbon	410	500
2	Carbon + catalyst	300–310	380
3	Carbon + catalyst + promoter, wt %:		
	1	350	480
4	5	290	440
5	10	270	360

In the presence of catalysts based on cesium lanthanum vanadate, the overall rate constant of carbon oxidation, K, was higher (Table 2), compared with the case of their absence. The values of E for carbon oxidation in the presence of catalysts for sample nos. 2–5 are in good agreement with the data obtained by other authors [12]. Consequently, it may be considered that the oxidation mode is close to that of burning of separate particles in a gas medium; the preexponential factors also conform to this model.

Introduction of 1 wt % Cs_2SO_4 dramatically changes the properties of the catalyst: E and T_{ig} increase (Tables 1, 2; Figs. 2, 3). Also strongly grows the pre-exponential factor, with the result that the rate of carbon oxidation, on the whole, increases. The phenomenon observed can be attributed to changes in the nature of the phases present in the catalyst and the extent of contact with carbon particles at the boundary of the catalyst. As the content of Cs_2SO_4 in the catalyst increases, the activation energy of combustion becomes lower, as also does the ignition temperature. In the presence of 10 wt % Cs_2SO_4 (Table 2), E has a value characteristic of burning in a bed. For noncatalytic carbon oxidation, the E obtained has

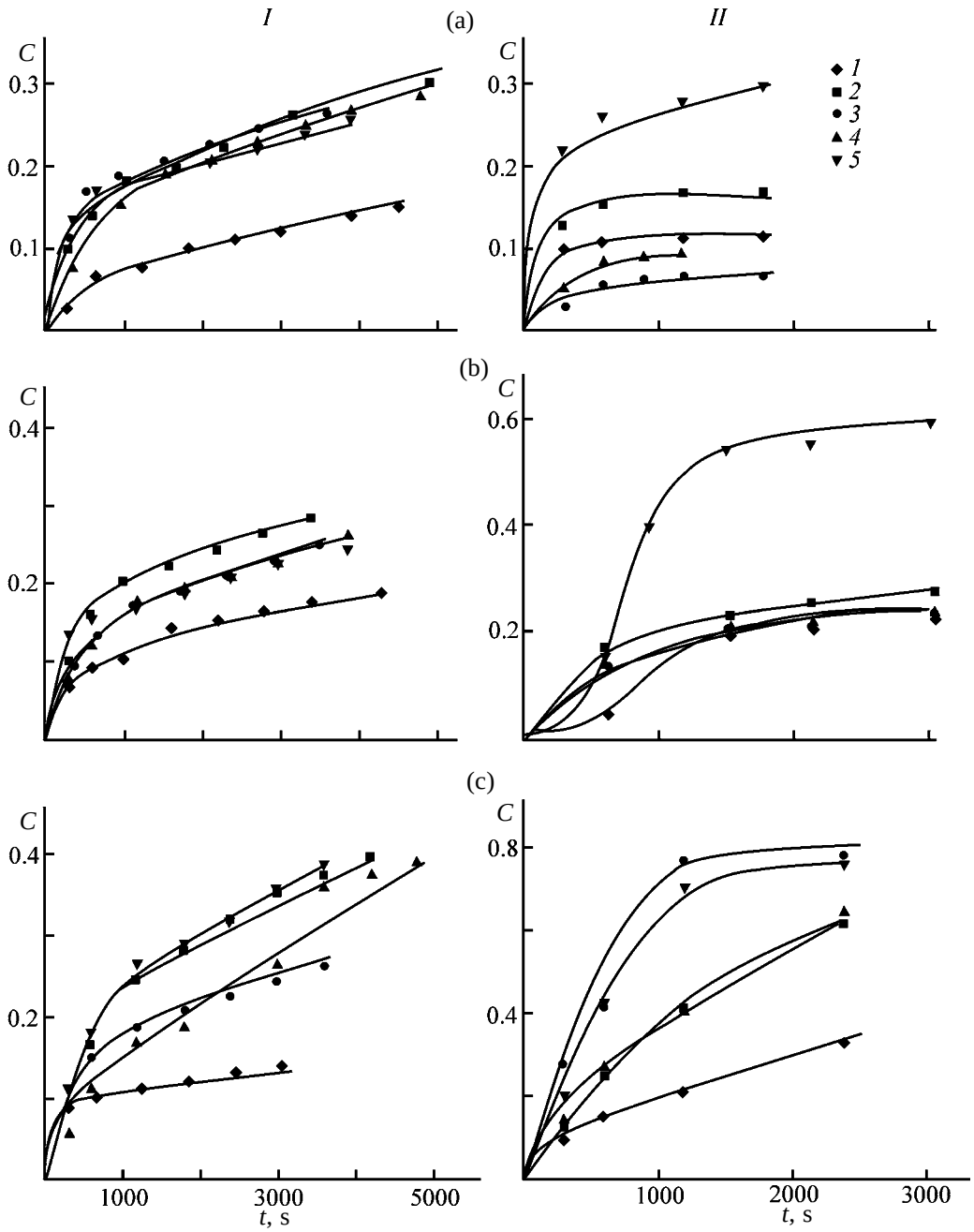

Fig. 1. Examples of the dependences of the extent of carbon removal, *C*, on the process duration *t* in oxidation with (*I*) nitrogen oxide and (*II*) atmospheric oxygen. Temperature (°C): (a) 300, (b) 350, and (c) 400. Sample: (*1*) without catalyst, (*2*) carbon with catalyst without promoter, (*3*) carbon with catalyst containing 1 wt % promoter, (*4*) the same with 5 wt % promoter, and (*5*) the same with 10 wt % promoter.

an intermediate value between the cases of particle burning and carbon oxidation in a bed [12]. In this case, the values of K_0 (Table 2) do not correspond to those calculated using the particle burning equations. Because the rate of noncatalytic oxidation of carbon is, on the whole, lower, the combustion parameters are strongly affected by reactions that occur at the internal surface of particles, which require an internal diffusion of oxygen and back transport of oxidation products, in accordance with the equation derived by L.N. Khitrin [12]:

$$K_S^C = \beta c_0 (1/K_1 + R/D)^{-1}, \quad (4)$$

where c_0 is the ambient oxygen concentration; *D*, the

Table 2. Kinetic parameters of catalytic oxidation of carbon with oxygen

Sample no.	Sample composition	E, kJ mol^{-1}	Pre-exponential factor $\log K_0$ (K_0, s^{-1})			
			experiment	1*	2*	3*
1	Carbon	55	0.52	1.80	1.69	3.10
2	Carbon + catalyst	70	1.93	2.42	2.05	3.40
	Carbon + catalyst + promoter, wt %:					
3	1	88	3.64	3.18	2.48	3.76
4	5	80	3.30	2.84	2.29	3.60
5	10	25	–1.40	0.54	0.99	2.50
6	Carbon + $Ag_{0.25}La_{0.75}MnO_{3\pm y}$	88	3.53	3.18	2.48	3.76

* Calculated by equations [16] suggested by (*1*) L.A. Vulis, $\log K_0 = 1.75 \times 10^{-4}E - 0.5$; (*2*) G.F. Knorre, I.I. Paleev, and K.M. Aref'ev, $\log K_0 = 0.991 \times 10^{-4}E + 0.398$; and (*3*) S.M. Shestakov, $\log K_0 = 0.838 \times 10^{-4}E + 2$.

diffusion coefficient; K_1, the overall reaction rate constant; and R, the particle radius.

Here, we should take into account the factor β, which is the stoichiometric coefficient (mass ratio of reacted carbon to spent oxygen) determined by relative yields of CO and CO_2 in oxidation of carbon:

$$\beta = \frac{12}{32}(1 - \xi), \quad (5)$$

where $\xi = 1$ for yield of only CO, $\xi = 0$ for yield of CO_2, and $\xi = 0.33$ at $CO/CO_2 = 1$; 12 and 32 are the molecular weights of carbon and oxygen.

The value of β in the presence of catalysts is, probably, substantially higher. The catalysts can affect both the reaction of carbon with atmospheric oxygen [reaction (6)] and the oxidation of CO formed in the process [reaction (7)]:

$$C + 1/2O_2 \rightarrow CO, \quad (6)$$

$$CO + 1/2O_2 \rightarrow CO_2. \quad (7)$$

Both the reactions are rather complex. Depending on the influence exerted by a catalyst on processes (6) and (7), the overall oxidation mechanism may also vary. In the absence of a promoter or at its low content, it may be assumed, by virtue of the limited area of contact between carbon and the catalyst, that CO oxidation (7) predominates. This leads to a higher value of factor β. In the presence of a catalyst, reaction (7) is, probably, localized at the surface of the complex oxide. In this case, the effective activation energy is comparable with the values of E for CO oxidation on complex oxide catalysts (64 to 132 kJ mol^{-1}) [17], which confirms the assumption made. Estimating the specific rate of oxidation at the catalyst surface

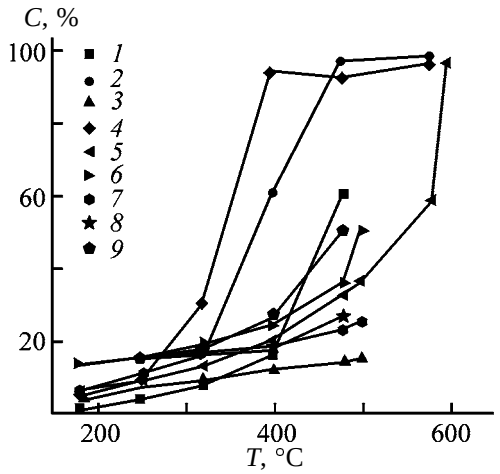

Fig. 2. Extent C of carbon removal at a 20-min exposure in oxidation with (*1, 2, 4*) atmospheric oxygen and (*3, 5–9*) nitrogen oxide vs. temperature T. Sample: (*1* [9], *3*) carbon without catalyst, (*6*) carbon with catalyst without promoter, (*7*) carbon with catalyst containing 1 wt % promoter, (*8*) the same with 5 wt % promoter, (*4, 9*) the same with 10 wt % promoter, and (*2, 5*) carbon with promoter.

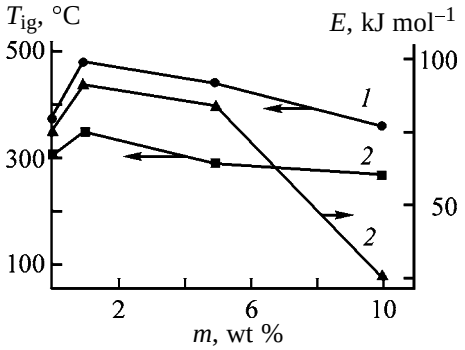

Fig. 3. Nominal ignition temperature T_{ig} and effective activation energy E vs. the amount of promoter introduced, m, in carbon oxidation with (*1*) nitrogen oxide and (*2*) atmospheric oxygen.

of CO formed in the combustion of carbon gives values that are close to the rate of catalytic CO oxidation proper [17]. In oxidation of carbon in the presence of catalysts in the temperature interval 300–400°C, the amount of burning CO is within the range $(1.3–6.1) \times 10^{17}$ molecules/(m^2 s). According to [17], $2.12 \times 10^{17}–3.44 \times 10^{18}$ CO molecules/(m^2 s) burns at 240°C on complex oxide catalysts. This also confirms the hypothesis formulated here. The possible elementary event determining the rate of the overall process is interaction of adsorbed CO with dissociatively adsorbed oxygen at the surface of the complex oxide. Intermediate species of the carbonate type are formed in the course of the reaction, and decomposition of these species is facilitated by transfer of an electron from a cation of the *d* metal of the complex oxide to the oxygen molecule. Thus, a local reduction of the surface of the catalyst, which contains ions with variable oxidation state, occurs in the course of the reaction. Vanadium can change its oxidation state as follows: $V^{5+} \rightleftarrows V^{4+}$. In addition, an intrinsic nonstoichiometry may exist in the compound $Cs_xLa_{1-x} \cdot VO_{4 \pm y}$, and, therefore, oxygen incorporated into the structure of the vanadate may be partly involved in the reactions at elevated temperatures. It can be seen from the previously obtained gravimetric curves [21] that reversible changes in the mass of complex oxide samples occur at the working temperatures in the presence of a carbon residue. After local reduction, the catalyst surface is again oxidized with oxygen, and the next cycle of CO oxidation occurs. However, the described factor affecting the oxidation is hardly the only factor, because catalysts based on manganites (Table 2) and cuprates are somewhat inferior to vanadate catalysts in their activity in oxidation of carbon, although the bonding energy of oxygen, which commonly determines the catalytic activity in CO oxidation [22, 23], is substantially lower than that in the vanadium compounds.

The aforesaid suggests that there should exist a direct influence of the catalyst on the primary oxidation reaction (6) in the zone of contact with carbon, which may be particularly strongly manifested in the presence of a considerable amount of a promoter. This is confirmed by the fact that the catalytic activity of the compounds under study in the given reaction depends on the atomic mass of the dopant cation. At places of contact between the catalyst and carbon, the alkali metal ion can form surface salt complexes of the carbonate type [8]. In addition, raising the amount of promoter makes lower the melting point of the catalytic formulation, and it gains the capacity to envelop carbon particles, thereby increasing the extent of contact. In this case, it becomes understandable why the effective *E* for sample no. 5 (Table 2) strongly decreases and the process passes into the diffusion-controlled mode, in which the overall rate of carbon oxidation is limited by the supply of the oxidizing agent from air into the reaction zone or by removal of gaseous products. Here, as also for sample no. 1, a discrepancy is observed between the experimental values of K_0 and those calculated using the particle combustion equations. It was shown in special-purpose experiments (Fig. 2) that the promoter itself also affects the carbon oxidation. Technical-grade Cs_2SO_4 shows an acid reaction and contains $CsHSO_4$ impurities. It may be assumed that the oxidation reaction is initiated by interaction with this impurity contained in the promoter, e.g.:

$$4CsHSO_4 + C \rightarrow 2H_2O + CO_2 + 2Cs_2SO_4 + 2SO_2, \quad (8)$$

or

$$2CsHSO_4 + C \rightarrow Cs_2CO_3 + H_2O + 2SO_2, \quad (9)$$

$$2CsHSO_4 + C \rightarrow Cs_2SO_4 + H_2O + SO_2 + CO. \quad (10)$$

Reactions of this kind give rise to carbon burning, and they are complete after the acid part of the promoter is exhausted and no considerable amounts of SO_2 are evolved. A thermodynamic estimation of reactions of this type, with compounds of alkali metals involved, demonstrated that they can be performed at low temperatures. The probability of occurrence of reaction (8) is the highest, and that of reaction (10), the lowest. Some promoter samples contained admixtures of $CsNO_3$, which has a melting point of 417°C and can act as a carbon-oxidizing agent, especially in a melt. However, when a promoter containing no impurities of the above kind was used, the type of its influence on the carbon oxidation remained unchanged. It should be assumed in this case that the promoter has a catalytic effect, which is determined by the fact that Cs_2SO_4 is an alkali metal salt. As already mentioned, alkali metal compounds exhibit a catalytic activity in heterogeneous reactions with carbon [8]. It may be stated that cesium lanthanum vanadate and, if present in a considerable amount, Cs_2SO_4 are cocatalysts.

The carbon oxidation with nitrogen oxide NO is also accelerated in the presence of a catalyst. At relatively low temperatures (Figs. 1, 2), the rates of oxidation with nitrogen oxides and atmospheric oxygen are comparable or the rate of the former process is somewhat higher. On raising the temperature, the oxi-

Table 3. Exponent b in the kinetic equation $k\tau = a\alpha^b$ for carbon oxidation with nitrogen oxide

Sample no.	Sample composition	b at indicated temperature, °C		
		300	350	400
1	Carbon	0.50	0.36	0.20
2	Carbon+ catalyst	0.37	0.36	0.45
	Carbon + catalyst +promoter, wt %:			
3	1	0.34	0.39	0.33
4	5	0.43	0.41	0.69
5	10	0.24	0.23	0.44

dation with nitrogen oxides is slower than that with O_2. The complete oxidation of carbon includes two main stages:

$$C + NO \rightarrow CO + 1/2N_2, \quad (11)$$

$$CO + NO \rightarrow CO_2 + 1/2N_2. \quad (12)$$

There is published evidence that the oxidizing capacity of nitrogen oxides NO [23] and N_2O [9] toward CO is lower than that of O_2. This is accounted for, in particular, by the strong difference between the sorption properties of nitrogen oxides and O_2 on the surface of complex oxide catalysts. A possible rate-determining stage of the overall process of carbon oxidation with nitrogen oxide is reaction (12), which is localized at the surface of the complex oxide. To verify this assumption, it is important to study the influence exerted by the promoter on the interaction of carbon with NO. Addition of Cs_2SO_4 plays a less positive role in reactions with NO, compared with the effect of the promoter Cs_2SO_4 on the carbon oxidation with oxygen (Figs. 1, 2). This, probably, occurs because of the change in the sorption capacity of the catalyst surface in the presence of Cs_2SO_4. To evaluate the nominal ignition temperatures, experiments were performed with catalyst–carbon mixtures kept at prescribed temperatures for 20 min (Table 1; Figs. 2, 3). As also in the case of carbon oxidation with O_2, introduction of 1 wt % Cs_2SO_4 markedly changes the properties of the catalyst.

In the temperature range studied, it was more difficult to estimate the effective activation energy of carbon oxidation with nitrogen oxide NO, compared to oxidation with atmospheric oxygen, because the activation energy is temperature-dependent. This points to a significant change in the reaction mechanism with increasing temperature. It is known for carbon that the mechanism of formation of a surface oxide changes in the range 300–550°C [18]. Processing of experimental data by Eqs. (1)–(3) failed to produce any satisfactory result. It was established using the Table Curve 2D v2.0 program by AISN Software Inc. that the experimental data are better described by power-law equations. This software made it possible to find the exponent b in an equation of the type $k\tau = a\alpha^b$ (Table 3). The most pronounced change in the reaction mechanism is observed for noncatalytic oxidation and for catalysts containing 5 and 10 wt % Cs_2SO_4. The trends exhibited by the exponent b for different samples are the opposite. For sample no. 1, E increases as the temperature is raised, and for sample nos. 4 and 5, contrariwise, decreases.

These facts may point to an oxidation mechanism in which direct chemical interaction is not the key factor. It is known [9] that carbon oxidation with nitrogen oxide NO can be hindered at relatively low temperatures by formation of N_2O, whose catalytic decomposition rate is low. In the temperature range studied, formation of N_2O is hardly possible. This is also indicated by effective values of E for samples with the weakest temperature dependence of the exponent b. These values are markedly lower than those for the carbon oxidation with O_2 and N_2O (146 kJ mol^{-1}) [9], being equal to 6–20 kJ mol^{-1}, which is characteristic of sorption or diffusion processes. The decrease in the activation energy for the reaction of carbon oxidation with nitrogen oxide NO, compared to that with atmospheric oxygen, can be attributed to differences between the heats of O_2 and NO sorption on the catalyst surface. Moreover, the oxidation of carbon with nitrogen oxide is more thermodynamically feasible than that with oxygen: the enthalpy of formation of nitrogen oxides is positive. The low effective activation energy of carbon oxidation with nitrogen oxide results in that the oxidation can occur in this case at lower temperatures, compared to the reaction in air (Fig. 2), with only stage (11) probable. At the same time, oxidation of CO with nitrogen oxide NO [reac-

tion (12)] occurs at the catalyst surface. The rate of reaction (12) is considerably lower than that of the CO oxidation with oxygen [reaction (7)], even in the presence of catalysts.

Thus, specific features of the course of practically important reactions were studied. The results obtained in testing of pilot neutralizers of exhaust gases produced by the engine of a ChMZ-3 diesel locomotive and engine of a ZIL-157K truck, operating on natural gas, demonstrated the high performance of combined complex oxide catalysts, including afterburners of carbon black [21, 25, 26]. Catalysts of the composition $Cs_{0.3}La_{0.7}VO_{4+y}$ (with a promoter) and $Ag_{0.25} \cdot La_{0.75}MnO_{3\pm y}$ were fabricated on foamed-nickel supports with an intermediate layer of aluminum oxide stabilized with lanthanum oxide. Catalytic elements of different compositions were assembled in a single unit. The exhaust smoke emission (content of carbon black particles) by the diesel locomotive decreased, on the average, by 50–60%, the decrease in the level of nitrogen oxides was also as large as 60%. As carbon black accumulated in the neutralizer of the ZIL-157K engine because of the burning of oil entrained by pistons, the degree of exhaust purification to remove nitrogen oxides increased by 30–40%. The total decrease in the concentration of CO was 60–80%. Consequently, the reactions studied can, indeed, be carried out under real conditions.

CONCLUSION

A study of some kinetic features of the reactions of carbon oxidation with nitrogen oxide NO and atmospheric oxygen demonstrated that lanthanum–cesium vanadate $Cs_xLa_{1-x}VO_{4\pm y}$ is an effective catalyst in the temperature range studied. Its activity in the reaction with oxygen increases in the presence of a promoting additive Cs_2SO_4, whose effect on the reaction with NO is considerably weaker. The carbon oxidation occurs in the working temperature range of the catalysts by different mechanisms, whose changeover is associated with, e.g., such a factor as the quantitative content of the promoter.

ACKNOWLEDGMENTS

The authors thank for support the Russian Foundation for Basic Research (project nos. 02-03-32777 and Urals 02-03-96443), American Civil Research and Development Foundation (project REC-005), and the Ministry of Education of the Russian Federation.

REFERENCES

1. *Khimiya redkikh elementov: Silikaty. Germanaty. Fosfaty. Arsenaty. Vanadaty* (Chemistry of Rare Elements: Silicates, Germanates, Phosphates, Arsenates, and Vanadates), Moscow: Nauka, 1983.
2. Teraoka, Y., Nakano, K., Kagawa, S., and Shangguan, W.F., *Appl. Catal. B: Environ.*, 1995, vol. 5, pp. L181–L185.
3. Teraoka, Y., Nakano, K., Shangguan, W., and Kagawa, Sh., *Catal. Today*, 1996, vol. 27, pp. 107–113.
4. Krijnsen, H.C., Bertin, S.S., Makkee, M., *et al.*, Abstracts of Papers, *5th Eur. Congr. on Catalysis*, Limeric (Ireland), September 2–7, 2001, book 4, report 7-P-18.
5. Van Setten, B.A.A.L., Makkee, M., and Moulijn, J.A., Abstracts of Papers, *5th Eur. Congr. on Catalysis*, Limeric (Ireland), September 2–7, 2001, book 4, report 7-P-19.
6. Fino, D., Russo, N., Badini, C., *et al.*, Abstracts of Papers, *5th Eur. Congr. on Catalysis*, Limeric (Ireland), September 2–7, 2001, book 4, report 7-P-07.
7. Van Setten, B.A.A.L., Bremmer, J., Jelles, S.J., *et al.*, *Catal. Today*, 1999, vol. 53, no. 4, pp. 613–621.
8. Ostashkova, I.V. and Kosinets, N.I., *Zh. Vses. Khim. O–va. im. D.I. Mendeleeva*, 1984, vol. 29, no. 4, pp. 434–436.
9. Babenko, V.S. and Buyanov, R.A., *Kinet. Katal.*, 1995, vol. 36, no. 4, pp. 571–574.
10. Morozov, K.A., *Toksichnost' avtomobil'nykh dvigatelei* (Toxicity of Automobile Engines), Moscow: Legion-Avtodata, 2001.
11. Machul'skii, F.F., *Doklady uchastnikov simpoziuma s uchastiem spetsialistov stran SEV: Toksichnost' dvigatelei vnutrennego sgoraniya i puti ee snizheniya, 6–10 dekabrya 1966* (Reports by Participants of a Symposium of Specialists from COMECON Countries: Toxicity of Internal Combustion Engines and Ways To Decrease It, December 6–10, 1966), Moscow: Nauka, 1966, pp. 206–219.
12. Vilenskii, T.V. and Khzmalyan, D.M., *Dinamika goreniya pylevidnogo topliva* (Dynamics of Combustion of Dust-Like Fuel), Moscow: Energiya, 1977.
13. Ostroushko, A.A., *Ross. Khim. Zh.*, 1998, vol. 42, no. 1–2, pp. 123–133.
14. Ostroushko, A.A., Mogil'nikov, Yu.V., and Ostroushko, I.P., *Izv. Ross. Akad. Nauk, Neorg. Mater.*, 2000, vol. 36, no. 12, pp. 1490–1498.
15. Ostroushko, A.A., Mikhalev, D.S., and Reshetnikova, N.V., *Zh. Prikl. Khim.*, 2002, vol. 75, no. 8, pp. 1245–1248.
16. Ostroushko, A.A., Abstracts of Papers, *Vserossiiskaya konferentsiya "Khimiya tverdogo tela i funktsional'-*

nye materialy", Ekaterinburg, 24–26 okt. 2000 g. (Russian Conf. "Solid-State Chemistry and Functional Materials," Yekaterinburg, October 24–26, 2000), Yekaterinburg: Inst. Khim. Tverd. Tela, 2000, pp. 280–281.

17. Ostroushko, A.A., Shubert, E., Zhuravleva, L.I., *et al.*, *Zh. Prikl. Khim.*, 2000, vol. 73, no. 8, pp. 1311–1320.
18. Kolyshkin, D.A. and Mikhailov, K.K., *Aktivnye ugli: Svoistva i metody ispytanii: Spravochnik* (Active Carbon: Properties and Methods for Testing: Reference Book), Leningrad: Khimiya, 1972.
19. Udilov, A.E. and Ostroushko, A.A. Abstracts of Papers, *7-e Vserossiiskoe soveshchanie "Vysokotemperaturnaya khimiya silikatov i oksidov", Sankt-Peterburg, 19–21 noyabrya 2002 g.* (7th Russian Meet. "High-Temperature Chemistry of Silicates and Oxides," St. Petersburg, November 19–21, 2002), St. Petersburg: Inst. Khim. Silikatov, Ross. Akad. Nauk, 2002, p. 175.
20. Ostroushko, A.A., Shubert, E., Makarov, A.M., *et al.*, *Zh. Prikl. Khim.*, 2003, vol. 76, no. 8, pp. 1292–1297.
21. Ostroushko, A.A., Udilov, A.E., Makarov, A.M., *et al.*, *II Int. Conf. "Automobiles & Technosphere" (ICATS'01)*, Kazan, June 13–15, 2001, Kazan: Tupolev Kazan State Technical Univ., 2001, pp. 175–176.
22. Golodets, G.I., *Geterogenno-kataliticheskoe okislenie organicheskikh veshchestv* (Heterogeneous-Catalytic Oxidation of Organic Substances), Kiev: Naukova Dumka, 1978.
23. Popova, N.M., *Katalizatory ochistki gazovykh vybrosov promyshlennykh proizvodstv* (Catalysts for Treatment of Industrial Gas Wastes), Moscow: Khimiya, 1991.
24. Ostroushko, A.A., Zhuravleva, L.I., Pirogov, A.N., and Mogil'nikov, Yu.V., *Zh. Neorg. Khim.*, 1997, vol. 42, no. 6, pp. 932–937.
25. Ostroushko, A.A., Makarov, A.M., Budnikov, V.I., *et al.*, *Trudy regional'nogo nauchno-prakticheskogo seminara RFFI "Puti kommertsializatsii fundamental'nykh issledovanii v oblasti khimii dlya otechestvennoi promyshlennosti", Kazan', 26–28 noyabrya 2002 g.* (Proc. Regional Scientific and Practical Workshop of the Russian Foundation for Basic Research "Ways of Commercialization of Basic Research in Chemistry for Domestic Industries," Kazan, November 26–28, 2002), Kazan: Unipress, 2002, pp. 107–108.
26. Ostroushko, A.A., *Tekhnologiya izgotovleniya katalizatorov: Termokataliticheskaya ochistka otkhodyashchikh gazov v promyshlennosti, energetike, na transporte: Nauchno-prakticheskoe izdanie* (Technology for Fabrication of Catalysts: Thermocatalytic Purification of Waste Gases in Industry, Power Engineering, and Transport: Scientific and Practical Publication), Yekaterinburg: Ural. Univ., 2002.

Russian Journal of Applied Chemistry, Vol. 77, No. 7, 2004, pp. 1130–1135. Translated from Zhurnal Prikladnoi Khimii, Vol. 77, No. 7, 2004, pp. 1144–1149.

CATALYSIS

Transformations of Cyclohexane under the Action of *in situ* Generated Aluminum Halides

R. A. Sadykov, M. G. Samokhina, P. N. Petrov, E. A. Paramonov, and U. M. Dzhemilev

Institute of Petrochemistry and Catalysis, Academy of Sciences of Bashkortostan Republic and Ufa Scientific Center, Russian Academy of Sciences, Ufa, Bashkortostan, Russia
Bashkir Republican Ecological Center, Ufa, Bashkortostan, Russia

Received January 9, 2004

Abstract—Transformations of inert cyclohexane into dimethyldecalins under mild conditions in the presence of a simple catalytic system consisting of aluminum metal and halomethanes were studied.

The catalytic activation of C–H bonds in cyclic and acyclic alkanes with transition metal complexes or electrophilic agents such as Friedel–Crafts catalysts is a promising field of research. As a rule, the catalysts used for activating hydrocarbons are aprotic Lewis acids based on salts of transition and main-group metals in combination with active additives.

Superelectrophilic complexes $RCOX \cdot 2AlX_3$ and $CX_4 \cdot 2AlX_3$ (X = Cl, Br) are the most effective in transformations of saturated hydrocarbons under mild conditions [1–3]. It was shown recently [4] that the reaction system consisting of an organoaluminum compound (OAC) and halomethane in the presence of catalytic amounts of transition metal complexes exhibits similar activity toward cycloalkanes. The activity of this system was tentatively explained by generation of $AlCl_3$ in the reaction of OAC with halomethane, catalyzed with a transition metal, which is followed by formation of a superelectrophilic complex with the starting halomethane, similar to $CX_4 \cdot 2AlX_3$. If this is true, then it will be possible to generate a similar complex *in situ* using a simpler and more available agent, aluminum metal [5]:

$$2Al + 6CCl_4 \rightarrow 2AlCl_3 + 3C_2Cl_6. \quad (1)$$

This work is the first study of chemical transformations of cyclohexane under the action of aluminum halides generated *in situ* by the reaction of halomethanes (CCl_4, $CHCl_3$, $CHBr_3$, CH_2Cl_2, CH_2Br_2) with aluminum metal preliminarily activated with iodine or AlR_3.

The choice of cyclohexane as investigation object was governed by the large body of data available on the effect of aluminum halides in combination with various promoters on cyclohexane.

Pure anhydrous $AlCl_3$ is virtually inert toward cyclohexane [6]. However, in the presence of water [6], HCl, and acetyl chloride [7] $AlCl_3$ effects isomerization of cyclohexane into methylcyclopentane. The reaction of cyclohexane with cyclohexyl bromide [8] in the presence of $AlCl_3$ yields a mixture of dimethyldecalins. A similar mixture of dimethyldecalins is formed by dimerization of methylcyclopentane, effect by the reaction system $AlCl_3$ + *t*-BuCl in the HCl [9]. Dimethyldecalins were detected in the reaction of chlorocamphor with $AlBr_3$ in cyclohexane [9]. Heating of cyclohexane with $AlCl_3$ and HCl in an autoclave for 1 day to 140–150°C results not only in isomerization into methylcyclopentane but also in formation of dicyclohexyl and di(methylcyclopentyl) [10]. At 180°C, methylcyclopentane, 1,3-dimethylcyclohexane, dicyclohexyl, and di(methylcyclopentyl) $C_{12}H_{22}$ were detected together with a small amount of isobutane [11]. Formation of dimethyldecalins was also reported in [12]. Transformation of cyclohexane into alkyladamantanes was noted in [13].

Under the action of superelectrophilic systems $RCOX \cdot 2AlBr_3$ [2] and $CH_nX_{4-n} \cdot AlX_3$ (X = Cl, Br) [3], cyclohexane transforms into dimethyldecalins at room temperature or 40°C with 22 and 10% yield based on cyclohexane, respectively. With excess cyclohexane, dimethyldecalins are formed selectively in low yields.

Aluminum metal was activated by a common procedure by heating under argon in the presence of several iodine crystals until iodine sublimed virtually completely and was removed from the reaction vessel. In some cases, to accelerate the start of the reaction of aluminum with halomethane, a small amount (~0.1 ml) of *i*-Bu_3Al and Et_3Al was added to the reaction mixture.

1070-4272/04/7707-1130 © 2004 MAIK "Nauka/Interperiodica"

Yields of major products of cyclohexane transformations under the action of the reaction system Al–halomethane*

Run no.	CX_nH_{4-n}	$C_6H_{12} : CX_nH_{4-n} : Al$	C_6H_{12} conversion, %	Product yield,** mol %		
				alkylcyclohexanes	dimethyldecalin	tricyclanes
1	CCl_4	100 : 22 : 8	20	–	27	–
2	CCl_4	100 : 32 : 20	62	4	47	13
3	CCl_4	100 : 45 : 28	74	13	49	25
4	CCl_4	100 : 45 : 28	80	19	40	28
5	CCl_4	100 : 160 : 23	56	4	46	21
6	$CHCl_3$	100 : 34 : 25	48	6	35	13
7	$CHCl_3$	100 : 54 : 27	51	6	38	11
8	$CHCl_3$	100 : 100 : 49	47	4	50	14
9	$CHCl_3$	100 : 108 : 30	52	4	23	9
10	$CHBr_3$	100 : 74 : 31	49	9	48	13
11	CH_2Br_2	100 : 154 : 40	21	29	33	–
12	CH_2I_2	100 : 80 : 31	42	14	17	–
13	BuCl	100 : 57 : 27	47	24	22	13

* Some other products (see text for details) were detected in insignificant amounts.
** Yield based on converted cyclohexane.

Transformations of the hydrocarbon start simultaneously with the onset of the reaction of aluminum with halomethane. The exothermic reaction is accompanied by the release of HCl and tarring. The major chlorinated reaction products in the case of CCl_4 are $CHCl_3$ and CH_2Cl_2. In contrast to the reaction of Al with CCl_4 without a solvent, in which the yield of hexachloroethane is virtually quantitative, in the presence of the hydrocarbon the yield of C_2Cl_6 is low. Among other chlorinated prodcts, trace amounts of tetrachloroethylene and tetrachloroethane were detected.

According to GLC and GC/MS, the major products of cyclohexane transformation are isomeric dimethyldecalins (see table). The figure shows as example the

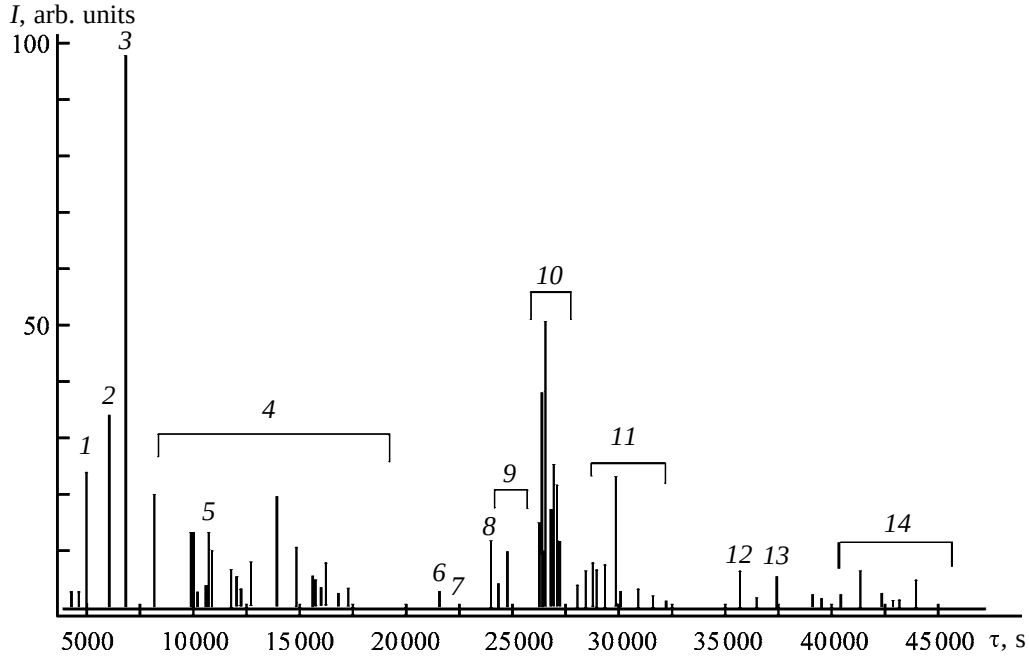

Chromatogram of a mixture of products obtained in run no. 4 (see table) and their identification. (*I*) Intensity and (τ) retention time. (*1*) Methylene chloride, (*2*) methylcyclopentane, (*3*) cyclohexane, (*4*) alkylcyclohexanes, (*5*) perchloroethylene, (*6*) decalin, (*7*) hexachloroethane, (*8*) methyldecalin, (*9*) methyl-substituted adamantanes, (*10*) isomeric dimethyldecalins, (*11*) trimethyldecalins, (*12*, *13*) tricyclanes with $[M]^+$ 192, and (*14*) tricyclanes with $[M]^+$ 248.

chromatogram of a mixture of products obtained in run no. 4 (see table). The mass spectrum of each isomer contains a fairly strong molecular peak ($[M]^+$ 166) and the same set of fragment peaks characteristic of dimethyldecalins (*m*/*z* 151, 137, 124, 123, 110, 109, 96, 82, etc.), corresponding to elimination of alkyl radicals [14] from CH_3 to C_6H_{12} from the moleclar ion. The isomeric mixture mainly consists of the most thermodynamically stable [15] *E*3,*E*8-dimethyl-*trans*-bicyclo[4.4.0]decane and *E*3,*E*9-dimethyl-*trans*-bicyclo[4.4.0]decane. The structures of these isomers were determined from the ^{13}C NMR spectra by comparison with the reference data [16] after isolation of the group of compounds corresponding to *M* 166 from the product mixture by preparative chromatography. As seen from the chromatogram (see figure), other isomers of dimethyldecalin are also present.

Among other products, we detected alkyl-substituted cyclohexanes whose total yields are also given in the table. For example, in run no. 4 we detected methylcyclohexane ($[M]^+$ 98, 2.5%), dimethyl- ($[M]^+$ 112, 4%), trimethyl- ($[M]^+$ 126, 2.4%), tetramethyl- ($[M]^+$ 140, 5.8%), ethyl- ($[M]^+$ 112, traces), methylethyl- ($[M]^+$ 126, 0.15%), and dimethylethylcyclohexanes ($[M]^+$ 140, 1.5%). Also, in the same experiment we detected methylcyclopentane ($[M]^+$ 84, 5%), decalin ($[M]^+$ 138, 0.3%), methyldecalin ($[M]^+$ 152, 1.3%), and trimethyldecalin ($[M]^+$ 180, 5.5%). These compounds were identified by GC/MS. The mass spectra obtained by us coincided with the reference data (NBS library) to 90–96%.

In the mixture of products, we also detected small amounts of methyl-substituted adamantanes: dimethyladamantane ($[M]^+$ 164, 0.5%), trimethyladamantane ($[M]^+$ 178, 1.4%), and tetramethyladamantane ($[M]^+$ 192, 1,1%). The assignment was based on comparison with published data [17].

Peaks *12* and *13* in the chromatogram (see figure) correspond to hydrocarbons with $[M]^+$ 192 and 206, respectively. Group of peaks *14* mainly belongs to hydrocarbons with $[M]^+$ 248. The mass spectra of compounds giving the strongest chromatographic peaks in this group are characterized by the base peak at *m*/*z* 233 [$M^+ - CH_3$] and medium-intensity peaks at *m*/*z* 177, 163, 123, and 109. Some of them contain ions with *m*/*z* 219 [$M^+ - C_2H_5$]. The products of oxidative dimerization of cyclohexane formed under the action of the superelectrophilic complex [3] $CBr_4 \cdot 2AlBr_3$ contain hydrocarbons with $[M]^+$ 248 giving similar mass spectra. Apparently, in our case these compounds can also be identified as alkylated tricyclanes $C_{18}H_{32}$ with methyl and, possibly, ethyl substituents. In addition, compounds with molecular weights of 206, 220, 234, and 262 were identified in trace amounts:

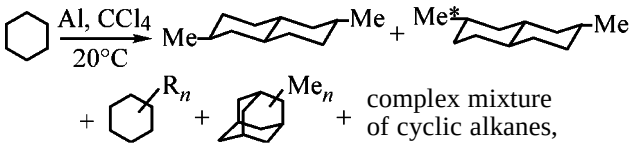

where R = Me, Et; *n* = 1, 2, 3, 4.

The relative yields of all the heavy products are listed in the table.

As in [2], in experiments with excess cyclohexane alkylcyclohexanes and tricyclanes are not formed, and the reaction products contain dimethyldecalins and methylcyclopentane. As the content of halomethane and aluminum in the starting mixture is increased, the content of methylcyclopentane in the reaction products decreases simultaneously with an increase in the content of dimethyldecalin, alkylcyclohexanes, and tricyclanes. Analysis of the reaction products in various steps showed a similar dependence of the product concentrations on the reaction time. The content of methylcyclopentane grows in the initial steps and then decreases. This fact indicates that cyclohexane first isomerizes into methylcyclopentane, transforming then into dimethyldecalin and other products. This result is consistent with the available data [6, 7] on equilibrium isomerization of cyclohexane into methylcyclopentane under the action of $AlCl_3$ with additions of various promoters and on dimerization of methylcyclopentane under the action of $AlCl_3$ and *t*-BuCl [9].

Cyclohexane is successfully involved in transformations also on replacement of CCl_4 by other halomethanes. Data obtained with chloroform, bromoform, methylene bromide, methylene iodide, and butyl chloride are given in the table.

It should be noted that the order of adding reagents [successively (see table, run no. 4), with CCl_4 added to activated Al first and cyclohexane added after the reaction completion, or simultaneously (run no. 3)] have no noticeable effect on the yield of the major products.

As it is difficult to isolate $AlCl_3$ from the reaction mixture and determine its content, we determined the residual content of active aluminum in the reaction mixture after the reaction completion. We found that, after activation of Al with iodine, the amount of Al^{3+} did not exceed 0.5% of the initial amount; after treatment with CCl_4, it was ~42%, and after the reaction

with cyclohexane, ~64%. Carbon tetrachloride was taken in 3 : 1 ratio relative to Al. A noticeable increase in the Al^{3+} content in the presence of cyclohexane can be accounted for as follows. In the reaction of Al with CCl_4 in the absence of the hydrocarbon, the main reaction products are C_2Cl_6 and $AlCl_3$ in the complex with CCl_4, and also tars. On adding cyclohexane, the complex $AlCl_4^- \cdot CCl_3^+$ reacts with the hydrocarbon to form $CHCl_3$ and cyclohexyl carbocation. Chloroform subsequently reacts with a new portion of Al to give $AlCl_3$. $AlCl_3$ effects transformations of cyclohexane. Thus, $AlCl_3$ is formed not only in the initial step of the reaction, but also directly in the course of transformations of the hydrocarbon.

It should be noted that oxidative dimerization of cyclohexane to dimethyldecalin under the action of the system Al–CCl_4 occurs selectively when cyclohexane is in excess.

Our results and published data suggest the following reaction mechanism. In the first step, aluminum metal reacts with CCl_4 to give $AlCl_3$ which forms the complex $AlCl_4^- \cdot CCl_3^+$ with the starting halomethane:

$$AlCl_3 + CCl_4 \rightarrow AlCl_4^- \cdot CCl_3^+. \quad (2)$$

Then formation of dimethyldecalins follows the known scheme [9] according to which CCl_3^+ abstracts the hydride ion from a cyclohexane molecule to give cyclohexyl cation and chloroform. Cyclohexyl carbenium ion isomerizes into more stable methylcyclopentyl carbenium ion:

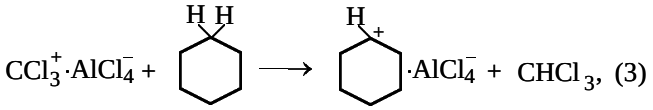

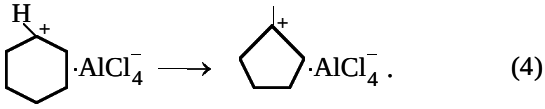

The latter transfers the charge to the cyclohexane molecule to give methylcyclopentane:

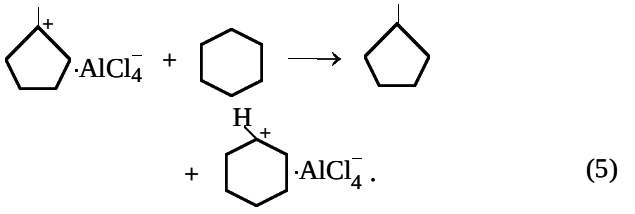

Alternatively, proton abstraction yields methylcyclopentene, $AlCl_3$, and HCl (HCl evolution is indeed observed in the course of the reaction):

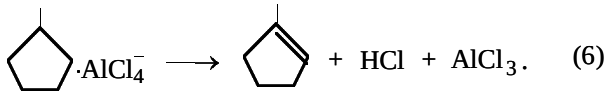

Addition of the olefin to methylcyclopentyl carbenium ion yields dicycloalkylcarbenium ion, whose rearrangement yields thermodynamically stable dimethyldecalinium ion. The subsequent charge transfer from the cyclohexane molecule to the dimethyldecalinium ion results in formation of dimethyldecalin and generation of cyclohexyl cation:

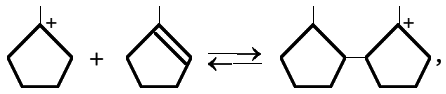

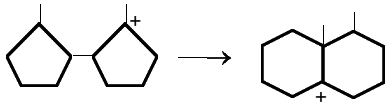

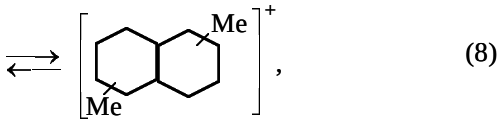

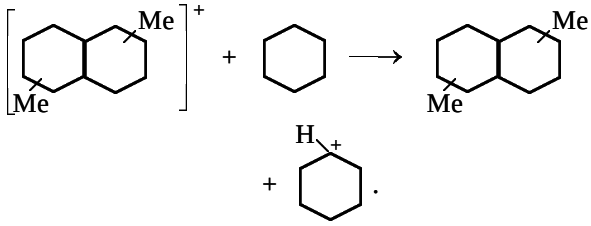

According to [3], the activity of the complex $CCl_4 \cdot 2AlBr_3$ toward cyclohexane is noticeably higher than that of the complex $CCl_4 \cdot 2AlCl_3$. In our case, the complex based on *in situ* generated $AlCl_3$ shows high activity, comparable with that of the superelectrophilic complex $CCl_4 \cdot 2AlBr_3$ which is today one of the most effective initiators of alkane activation under mild conditions, along with the system $RCOX \cdot 2AlBr_3$.

EXPERIMENTAL

CCl_4, $CHCl_3$, $CHBr_3$, CH_2Br_2, CH_2I_2, *t*-BuBr, and cyclohexane (chemically pure grade) were dried and distilled from P_2O_5. Aluminum (chemically pure grade) was used as powder. For comparison, we tested preliminarily ground granulated aluminum (analytically pure grade) and aluminum wire. The results were identical. The ^{13}C NMR spectra were recorded on a JEOL-FX90Q spectrometer. The products were analyzed on a Chrom-5 chromatograph with a capillary column (25 m, SE-30). The GC/MS analysis was performed on a VG TRIO 1000 device (the United King-

dom). We used a JZW Scientific DB-5 capillary column (60 m × 0.25 mm × 0.2 μm) (the Unted States) in the linear heating mode and the NBS library of mass spectra (the United States) containing 75000 mass spectra.

To perform the reaction of cyclohexane with the system Al–CCl_4, a 50-ml glass reactor was charged under Ar with 0.348 g (13 g-at) of Al and several crystals of iodine. The mixture was heated on an alcohol burner until the iodine completely sublimed and was removed from the reactor. The reactor was placed on a magnetic stirrer, and 7 ml (65 mmol) of cyclohexane and 2 ml (19 mmol) of CCl_4 were added. Stirring was continued at room temperature for 2 h. The reaction was accompanied by HCl evolution. After reaction completion, two layers formed: a transparent upper layer and a dark brown viscous lower layer containing aluminum chloride and residual aluminum metal. The upper layer was separated and filtered through Al_2O_3. Determination of the bromine number showed the absence of unsaturated bonds in the products. A GLC analysis of the resulting transparent liquid revealed the presence of dimethyldecalins (39%) nd unchanged cyclohexane (19.6%). The products giving a group of peaks with $[M]^+$ 166 (GC/MS) were isolated by preparative chromatography. Their ^{13}C NMR analysis showed that the samples contained 45% *E*3,*E*8-dimethyl-*trans*-bicyclo-[4.4.0]decane, 41% *E*3,*E*9-dimethyl-*trans*-bicyclo-[4.4.0]decane, four unidentified isomers of dimethyldecalin with $[M]^+$ 166 (2–3% each), and five other isomers with $[M]^+$ 166 (0.2–0.3% each).

***E*3,*E*8-Dimethyl-*trans*-bicyclo[4.4.0]decane.** ^{13}C NMR spectrum ($CDCl_3$), δ, ppm (in parentheses are published data [16]): C^1, C^2, C^6, C^7 43.0, (43.0); C^3, C^8 33.1 (33.1); C^4, C^9 35.6 (35.6); C^5, C^{10} 34.3 (34.2); C^3 CH_3, C^8 CH_3 22.8 (22.8); $[M]^+$ 166.

***E*3,*E*9-Dimethyl-*trans*-bicyclo[4.4.0]decane.** ^{13}C NMR spectrum: C^1, C^2, C^{10} 43.3 (43.3); C^3, C^9 33.1 (33.1); C^4, C^8 35.7 (35.7); C^5, C^7 34.0 (34.0); C^6 42.9 (42.9); C^3 CH_3, C^9 CH_3 22.9 (22.8); $[M]^+$ 166.

Mass spectra. Methylcyclopentane. Experiment: *rt* [retention time (min)] 5.98; *m*/*z* (I_{rel}, %): 84 $[M]^+$ (17), 69 (59), 57 (5), 56 (100), 55 (28), 42 (24), 41 (51); published data [18]: 84 $[M]^+$ (16), 69 (32), 57 (5), 56 (100), 55 (26), 42 (28), 41 (64).

Methylcyclohexane. Experiment: *rt* 8.13; 98 $[M]^+$ (51), 84 (7), 83 (100), 82 (18), 70 (20), 69 (20), 67 (5), 56 (21), 55 (59), 42 (19), 41 (31); published data [18]: 98 $[M]^+$ (41), 84 (7), 83 (100), 82 (17), 70 (20), 69 (21), 67 (4), 56 (28), 55 (83), 42 (30), 41 (46).

Ethylcyclohexane. Experiment: *rt* 11.85; 112 $[M]^+$ (25), 84 (7), 83 (100), 82 (47), 69 (7), 67 (13), 57 (1), 56 (10), 55 (77), 42 (8), 41 (33); published data [18]: 112 $[M]^+$ (19), 84 (6), 83 (100), 82 (41), 69 (9), 67 (11), 57 (5), 56 (12), 55 (75), 42 (8), 41 (34).

Dimethylcyclohexane. Experiment: *rt* 9.83; 112 $[M]^+$ (29), 97 (100), 84 (2), 83 (5), 70 (8), 69 (17), 56 (15), 55 (63), 43 (6), 41 (19); published data [18] (1,3-dimethylcyclohexane): 112 $[M]^+$ (28), 97 (100), 84 (3), 83 (5), 70 (10), 69 (19), 56 (21), 55 (88), 43 (9), 41 (27).

Methylethylcyclohexane. Experiment: *rt* 14.03; 126 $[M]^+$ (19), 111 (2), 97 (100), 96 (14), 83 (2), 81 (7), 70 (3), 69 (19), 56 (9), 55 (86), 43 (7), 41 (21); published data [18] (*cis*-1-methyl-3-ethylcyclohexane): 126 $[M]^+$ (15), 111 (2), 97 (100), 96 (14), 83 (2), 81 (5), 70 (3), 69 (20), 56 (10), 55 (91), 43 (8), 41 (23).

Trimethylcyclohexane. Experiment: *rt* 11.75; 126 $[M]^+$ (26), 111 (97), 97 (3), 84 (2), 83 (4), 70 (10), 69 (100), 56 (12), 55 (51), 43 (8), 42 (9), 41 (26); published data [18] (*cis*,*cis*-1,3-trimethylcyclohexane): 126 $[M]^+$ (23), 111 (95), 97 (2), 84 (2), 83 (4), 70 (10), 69 (100), 56 (12), 55 (56), 43 (10), 42 (5), 41 (30).

Tetramethylcyclohexane. Experiment: *rt* 14.82; 140 $[M]^+$ (2), 125 (100), 97 (1), 84 (7), 83 (40), 70 (12), 69 (99), 57 (14), 56 (9), 55 (33), 43 (12), 41 (26); published data [18] (1,1,3,5-tetramethylcyclohexane): 125 (92), 97 (3), 84 (7), 83 (53), 70 (6), 69 (100), 57 (15), 56 (11), 55 (34), 43 (13), 41 (27).

Decalin. Experiment: *rt* 21.55; 138 $[M]^+$ (99), 110 (9), 108 (18), 96 (71), 95 (60), 82 (71), 81 (61), 69 (41), 68 (87), 67 (100), 55 (34), 41 (51); published data [18] (*trans*-decalin): 138 $[M]^+$ (100), 110 (7), 109 (17), 96 (58), 95 (63), 82 (60), 81 (54), 69 (45), 68 (91), 67 (91), 55 (41), 41 (82).

Trimethyldecalin. Experiment: *rt* 29.25; 180 $[M]^+$ (74), 165 (98), 138 (3), 137 (4), 123 (15), 109 (94), 95 (100), 83 (34), 82 (18), 81 (67), 69 (30), 67 (37), 55 (55); published data [18] (3,4,8-trimethyldecalin): 180 $[M]^+$ (74), 165 (97), 138 (5), 137 (6), 123 (21), 109 (94), 95 (100), 83 (40), 82 (21), 81 (70), 69 (30), 67 (39), 55 (68).

Dimethyladamantane. Experiment: *rt* 24.30; 164 $[M]^+$ (10), 150 (13), 149 (100), 107 (18), 95 (6), 93 (31), 91 (9), 81 (7), 79 (9), 77 (7), 67 (6), 55 (6); published data [17] (1,4-dimethyladamantane): 164 $[M]^+$ (14), 150 (13), 149 (100), 107 (18), 95 (11), 93 (35), 91 (11), 81 (17), 79 (16), 77 (11), 67 (13), 55 (14).

Trimethyladamantane. Experiment: *rt* 24.67; 178

$[M]^+$ (8), 164 (13), 163 (100), 150 (1), 149 (2), 135 (3), 121 (8), 107 (48), 93 (10), 91 (9), 79 (7), 77 (6), 55 (8); published data [17] (1,3,5-trimethyladamantane): 178 $[M]^+$ (8), 164 (12), 163 (100), 150 (11), 121 (16), 107 (62), 93 (17), 91 (12), 81 (8), 79 (10), 77 (8), 67 (6), 55 (8).

Tetramethyladamantane. Experiment: *rt* 24.80; 192 $[M]^+$ (5), 178 (14), 177 (100), 163 (2), 135 (3), 121 (42), 107 (13), 95 (6), 93 (5), 91 (7), 81 (3), 79 (5), 77 (5), 67 (4), 55 (9); published data [17] (1,3,5,6-tetramethyladamantane): 192 $[M]^+$ (7), 178 (16), 177 (100), 163 (4), 135 (5), 121 (37), 107 (25), 95 (9), 93 (8), 91 (10), 81 (6), 79 (7), 77 (6), 67 (6), 55 (13).

Tricyclane (see figure, peak *12*). Experiment: *rt* 35.59; 192 $[M]^+$ (100), 177 (62), 151 (33), 149 (22), 135 (27), 121 (22), 109 (20), 107 (16), 95 (85), 93 (25), 81 (49), 79 (29), 77 (13), 67 (35), 55 (24).

Tricyclane (see figure, peak *13*). Experiment: *rt* 37.32; 206 $[M]^+$ (100), 191 (70), 165 (15), 149 (18), 135 (44), 121 (19), 109 (61), 107 (17), 95 (72), 91 (16), 81 (43), 79 (26), 67 (34), 55 (33).

To determine active aluminum, a three-necked flask was charged under Ar with 100 mg of Al. Several crystals of iodine were added, and the flask was heated until the iodine completely sublimed and was removed from the vessel. To the resulting activated Al, 50 ml of distilled water was added, and the mixture was analyzed according to [19].

Two three-necked flasks were charged under Ar with 100 mg of Al each. After actvation with iodine, the reaction with 2 ml of CCl_4 was performed in both flasks, and then the reaction with 5 ml of cyclohexane was performed in one of them. After the reaction completion, the resulting mixtures were hydrolyzed with 50 ml of water. The subsequent analysis was performed similarly.

CONCLUSION

The readily available reaction system consisting of activated aluminum metal and halomethane efficiently induces chemical transformations of cyclohexane at 20–60°C and atmospheric pressure. The major product is an equilibrium mixture of dimethyldecalin isomers; methyl-substituted cyclohexanes and tricyclic compounds are formed in smaller amounts.

REFERENCES

1. Akhrem, I.S. and Orlinkov, A.V., *Izv. Ross. Akad. Nauk, Ser. Khim.*, 1998, no. 5, pp. 771–794.
2. Akhrem, I.S., Orlinkov, A.V., Mysov, E.I., and Vol'pin, M.E., *Tetrahedron Lett.*, 1981, vol. 22, no. 39, pp. 3891–3894.
3. Akhrem, I.S., Churilova, I.M., and Vitt, S.V., *Izv. Ross. Akad. Nauk, Ser. Khim.*, 2001, no. 1, pp. 78–84.
4. Sadykov, R.A., Samokhina, M.G., and Dzhemilev, U.M., *Izv. Ross. Akad. Nauk, Ser. Khim.*, 2001, no. 7, pp. 1262–1265.
5. Furman, A.A. and Rabovskii, B.G., *Osnovy khimii i tekhnologii bezvodnykh khloridov* (Fundamentals of Chemistry and Technology of Anhydrous Chlorides), Moscow: Khimiya, 1970.
6. Nenitescu, C.D., *Chimie generala*, Bucharest: Technic, 1963.
7. Zelinsky, N.D. and Tarasova, E.M., *Lieb. Ann.*, 1934, no. 508, pp. 115–118.
8. Doering, W.E. and Schoenewaldt, E.F., *J. Am. Chem. Soc.*, 1951, vol. 73, no. 11, pp. 4578–4580.
9. Conn, W.K. and Schneider, A., *J. Am. Chem. Soc.*, 1954, vol. 76, pp. 4578–4580.
10. Komarewsky, V.I. and Ipatieff, V.N., *J. Am. Chem. Soc.*, 1934, vol. 56, no. 9, pp. 1926–1928.
11. Zelinskii, N.D. and Arbuzov, Yu.A., *Dokl. Akad. Nauk SSSR*, 1941, vol. 30, no. 8, pp. 717–717.
12. Thoret-Bauchet, J.P., Mortreux, A., and Petit, F., *J. Mol. Catal.*, 1993, vol. 83, pp. 323–327.
13. Gavrilov, B.T., Luksha, V.G., Slobodin, Ya.M., and Kovyazin, V.E., *Zh. Org. Khim.*, 1975, no. 11, pp. 597–600.
14. Brodskii, E.S., Lukashenko, I.M., Musaev, I.A., *et al.*, *Neftekhimiya*, 1976, vol. 16, no. 1, pp. 13–15.
15. Berman, S.S., Stukanova, L.N., and Petrov, A.A., *Neftekhimiya*, 1970, vol. 10, no. 5, pp. 635–641.
16. Whitesell, J.K. and Minton, M.A., *Stereochemical Analysis of Alicyclic Compounds by ^{13}C NMR Spectroscopy*, London: Chapman and Hall, 1987.
17. Polyakova, A.A., Khramova, E.V., Bagrii, E.I., *et al.*, *Neftekhimiya*, 1973, vol. 13, no. 1, pp. 9–16.
18. Petrov, A.A., Golovkina, L.S., and Rusinova, G.V., *Mass-spektry neftyanykh uglevodorodov* (Mass Spectra of Petroleum Hydrocarbons), Moscow: Nedra, 1975.
19. Charlot, G., *Les methods de la chimie analytique. Analyse quantitative minerale*, Paris: Masson, 1961, 4th ed.

Russian Journal of Applied Chemistry, Vol. 77, No. 7, 2004, pp. 1136–1141. Translated from Zhurnal Prikladnoi Khimii, Vol. 77, No. 7, 2004, pp. 1150–1155.

CATALYSIS

Influence of Activation (Reduction) Conditions on the Catalytic Activity of Copper–Zinc Catalysts of NTK-10 Series

P. D. Androsov, I. A. Mamaeva, and E. Z. Golosman

Novomoskovsk Institute of Nitrogen Industries, Open Joint-Stock Company, Novomoskovsk, Tula oblast, Russia

Received December 26, 2003

Abstract—X-ray phase analysis and the temperature-programmed reduction method were applied to study the activation (reduction) of copper–zinc catalysts of the NTK-10 series. The catalytic activity of catalysts reduced under various conditions in steam conversion of carbon monoxide was determined.

Copper–zinc catalysts are widely used in various processes of chemical, petrochemical, and metallurgical industries. To these belong, in particular, the following: steam conversion of carbon monoxide; synthesis of methanol, butyl alcohols, and aniline; and purification of waste gases to remove organic compounds. In recent years, copper–zinc–alumina–calcium catalysts, which are distinguished by high service parameters, such as activity and mechanical strength, have exhibited good performance. The main distinctive feature of catalysts of the NTK-10 series from most of analogs is that they are manufactured in an uncalcined form [1, 2].

The active surface of both calcined and uncalcined catalysts is formed in the course of activation, i.e., heating in a reducing atmosphere. Activation of calcined copper–zinc catalysts (NTK-4) is sufficiently well understood, and it is noted that lowering the activation temperature affects positively the formation of the active surface of the catalysts and their catalytic activity [3–5].

The activation of NTK-10 catalysts is accompanied by two parallel processes: decomposition of copper-containing compounds contained in the catalyst and reduction of copper. The decomposition of copper-containing compounds is accompanied by heat absorption, whereas the reduction of copper is characterized by an exothermic effect; thus, the overall heat effect of activation is virtually zero. This makes it possible to prevent undesirable overheating in the course of reduction of the catalyst and, thereby, to use a gas with a higher content of a reducing agent, which markedly shortens the activation time. According to the recommendations developed for charging and activation of catalysts of the NTK-10 series, a catalyst is to be heated to 210–230°C and then a gas with the content of the reducing agent increasing from 0 to 20–30% is to be supplied [2]. However, the equipment used in some processes, such as synthesis of aniline and conversion of carbon monoxide on installation for obtaining hydrogen in metallurgical and electrochemical industries does not allow activation at temperatures higher than 200°C, which makes markedly narrower the field of application of NTK-10 catalysts. In this context, it was necessary to study the activation of NTK-10 catalysts in order to assess the possibility of their activation at lowered temperatures and reveal the influence exerted by various parameters of the activation process on the catalytic activity of these catalysts.

For this purpose, the following samples of NTK-10 catalysts were studied: NTK-10-2FM catalyst for low-temperature conversion of CO; NTK-10-7F catalyst, containing manganese oxide, for treatment of waste gases to remove organic compounds; and NTK-10-2FA catalyst for synthesis of aniline.

For comparison was studied NTK-4 catalyst, which is also used in synthesis of aniline [6].

X-ray studies were performed on a DRON-2 diffractometer with monochromatized copper radiation (graphite monochromator in the path of the diffracted beam). The data obtained were used to identify the phase composition of catalysts and determine the dispersity (size of coherent domains) of copper.

The catalyst activation was studied by the method of temperature-programmed reduction. A sample was heated in a flow of H_2, with the temperature raised

1070-4272/04/7707-1136 © 2004 MAIK "Nauka/Interperiodica"

Table 1. Chemical and phase composition of catalysts

Catalyst	Chemical composition, wt %						Phase composition
	CuO	ZnO	Al_2O_3	CaO	MnO	Cr_2O_3	
NTK-10-2FM	49.5	20.3	18.2	12	–	–	A, R, HA, CuO, calcite, CA_2,* gibbsite, aragonite
NTK-10-7F	48.5	19.8	18.9	12	0.8	–	HA, A, calcite, R, CA_2, CuO, $MnCO_3$, gibbsite, aragonite, $Cu(OH)_2$
NTK-10-2FA	44.6	20.3	21.6	13.5	–	–	CuO, HA, R, A, calcite, CA_2, gibbsite, aragonite
NTK-4	54.5	10.5	20.5	–	–	14.5	CuO, $ZnCr_2O_4$, boehmite, graphite

* $CaO \cdot 2Al_2O_3$.

linearly at the prescribed rate of 2.5 deg min^{-1}. The amount of products released in activation was determined with a katharometer.

The activities of the catalysts were determined in the steam conversion of CO. The test were performed on a flow-through laboratory installation under the following conditions: gas composition 10.9% CO, 89.1% He; steam/gas ratio 0.2–0.25; space velocity 15000 h^{-1}. The activity of a catalyst was judged from the reaction rate constant calculated using the first-order equation with respect to carbon monoxide:

$$k_v = \ln[1/(1 - x)]W(1 + S/G),$$

where k_v is the reaction rate constant (s^{-1}); x, average CO conversion; W, space velocity of dry gas (s^{-1}); and S/G, steam/gas ratio.

Prior to a test, a sample was activated.

The chemical and phase compositions of the samples studied are listed in Table 1. The catalysts of the NTK-10 series contain copper in the form of various compounds that are precursors of the active component of the catalyst. The main phases are the following: rosasite (R), which is a solid solution of zinc ions in the structure of $(CuOH)_2CO_3$; aurichalcite (A), a solid solution of copper(II) ions in the structure of $(ZnOH)_2CO_3$; and hydroxoaluminate (HA) of copper and zinc.

The catalyst activation leads to thermal decomposition and reduction of these compounds to form a solid solution of copper in an anion-modified zinc oxide; and it is this solid solution that ensures the high activity of a catalyst [2].

The profiles of temperature-programmed reduction of NTK-10-series and NTK-4 catalysts are shown in Fig. 1.

The activation of NTK-10 catalysts is accompanied by two processes: decomposition of copper-containing compounds and reduction of copper. The first stage in the range 170–175°C refers to the process of decomposition–reduction of a copper-containing compound with a rosasite structure, reduction of copper oxide, and removal of interlayer water from hydroxoaluminate of copper and zinc. At 195–205°C, copper from a compound with a structure of aurichalcite and from hydroxoaluminate of copper and zinc is reduced [2, 7] (Fig. 1).

The sample activation is accompanied by release of considerable amounts of H_2O and CO_2. The temperatures at which their release has the maximum intensity coincide with the reduction temperatures of copper-containing compounds contained in catalysts of the NTK-10 series (Fig. 2). The total weight loss in activation is approximately 25%, of which 60–70% is H_2O and 30–40% CO_2.

In contrast to uncalcined NTK-10 catalysts, the activation of a calcined NTK-4 sample occurs in a single stage, and the activation profile of this sample contains the only peak at 160–170°C. The activation consists in this case in reduction of copper from its oxide [3–5].

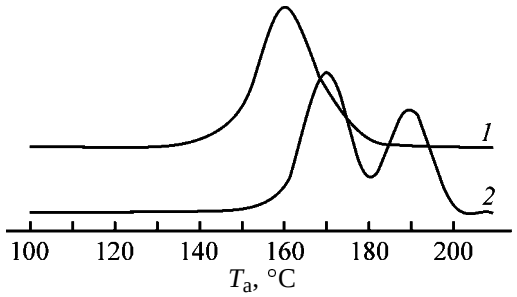

Fig. 1. Activation profiles of (*1*) NTK-4 and (*2*) NTK-10 series catalysts. (T_a) Activation temperature; the same for Fig. 2.

Table 2. Phase composition of catalysts at different activation temperatures T_a

Catalyst	Phase composition at indicated T_a, °C			
	160	170	180	250
NTK-10-2FM	Cu, ZnO, $CaCO_3$, A, HA, CA_2, gibbsite, aragonite, R	Cu, ZnO, $CaCO_3$, A, HA, CA_2, gibbsite, aragonite	Cu, ZnO, $CaCO_3$, A, HA, CA_2, gibbsite, aragonite	Cu, ZnO, $CaCO_3$, CA_2, gibbsite, aragonite
NTK-10-2FA	Cu, ZnO, $CaCO_3$, A, HA, R, CA_2, gibbsite, aragonite	Cu, ZnO, $CaCO_3$, A, HA, CA_2, gibbsite, aragonite	Cu, ZnO, $CaCO_3$, A, HA, CA_2, gibbsite, aragonite	Cu, ZnO, $CaCO_3$, CA_2, gibbsite, aragonite
NTK-10-7F	Cu, ZnO, $CaCO_3$, CA_2, A, HA, gibbsite, aragonite, R, $MnCO_3$	Cu, ZnO, $CaCO_3$, CA_2, A, HA, gibbsite, aragonite, $MnCO_3$	Cu, ZnO, $CaCO_3$, CA_2 A, HA, gibbsite, aragonite, $MnCO_3$	Cu, ZnO, $CaCO_3$, CA_2, $MnCO_3$, aragonite, boehmite, CA
NTK-4	Cu, $ZnCr_2O_4$, boehmite, ZnO, Cu_2O	Cu, $ZnCr_2O_4$, boehmite, ZnO, Cu_2O	Cu, $ZnCr_2O_4$, boehmite, ZnO, Cu_2O	Cu, $ZnCr_2O_4$, boehmite, ZnO, Cu_2O

In the first set of experiments, the catalysts were activated in a flow of 100% H_2 at temperatures of 160, 170, 180, and 250°C for 1.5 h.

The completeness of reduction of the samples was judged from the decrease in the intensity of the lines in the X-ray diffraction patterns, associated with the initial copper-containing compounds. The results of an X-ray phase analysis of samples activated under these conditions are listed in Table 2. Figure 3 shows how the intensity of the aurichalcite lines in the X-ray diffraction patterns depends on the temperature T_r at which the sample was reduced.

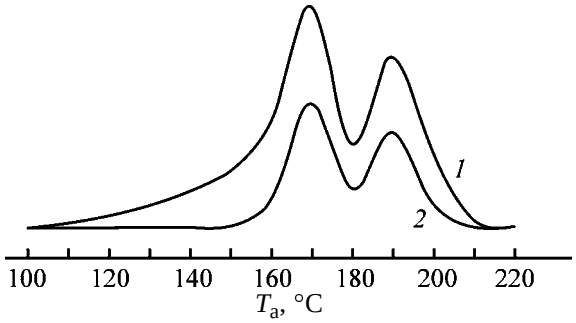

Fig. 2. Intensity of release of (*1*) water and (*2*) CO_2 in activation of catalysts of NTK-10 series.

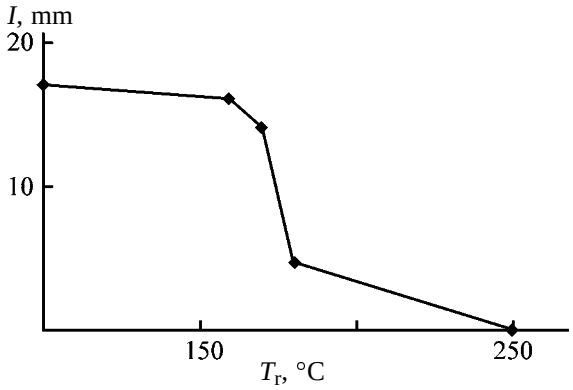

Fig. 3. Intensity *I* of the line associated with aurichalcite in X-ray diffraction patterns vs. the reduction temperature T_r.

Table 2 and Fig. 3 show that the reduction of copper-containing compounds contained in catalysts of the NTK-10 series at 160°C is incomplete. The phase composition of the sample contains insignificant amounts of rosasite. The intensity of the aurichalcite lines remained virtually unchanged, compared to the initial sample. Activation with hydrogen at 170°C leads to complete reduction of copper contained in the structure of rosasite, whereas aurichalcite is reduced only partly (the intensity of lines in the X-ray diffraction patterns decreases only slightly). As the activation temperature is raised to 180°C, there occurs intensive reduction of copper from the aurichalcite structure, which is indicated by a pronounced decrease in the intensity of its lines in the X-ray diffraction patterns. And finally, reduction at 250°C leads to complete reduction of copper from its compounds.

Figures 4a and 4b show how the dispersity of reduced copper (judged from the results of an X-ray phase analysis) and intensities of copper lines vary with the activation temperature.

The intensity of copper lines increases dramatically as the activation temperature increases from 160 to 180°C, which points to intensive reduction of copper in this temperature range. When the temperature is elevated further from 180 to 250°C, the intensity of copper lines increases only slightly, i.e., additional

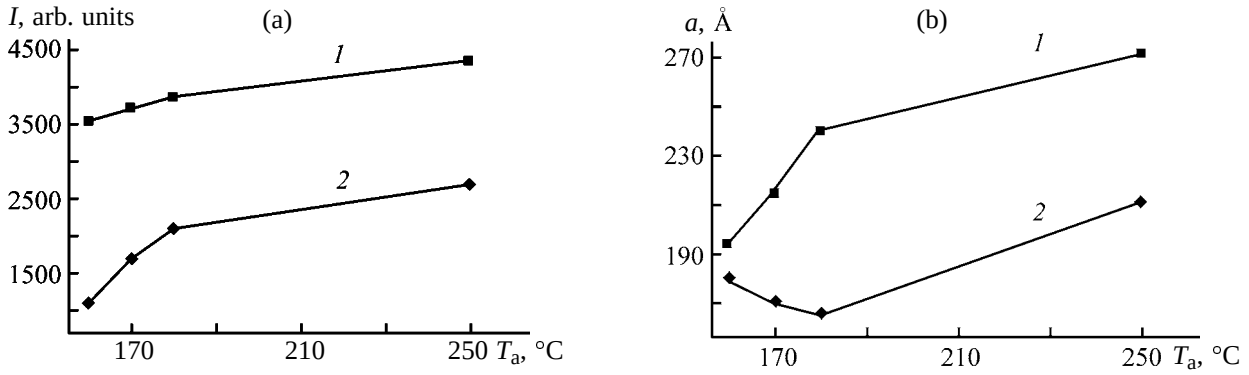

Fig. 4. (a) Intensity *I* of copper lines in X-ray diffraction patterns and (b) sizes a of crystallites of reduced copper vs. the activation temperature T_a. (*1*) NTK-4 and (*2*) NTK-10.

reduction of copper compounds and crystallization of X-ray amorphous copper occurs at these temperatures.

The dependence of the dispersity of reduced copper on the activation temperature shows an extremum. Raising the reduction temperature from 160 to 180°C leads to a gradual decrease in the size of copper crystallites from 180 to 165 Å, because the most finely dispersed part of copper is reduced just from the structure of aurichalcite, which is mostly reduced just in this temperature range, As the activation temperature is elevated to 250°C, the size of copper crystallites increases to 210°C, which is due to agglomeration of copper.

The activities of the samples were determined at three temperatures: 160, 180, and 200°C. The results obtained (Table 3) are in good agreement with the data furnished by X-ray phase analysis.

The activity of samples reduced at 160°C is low, because considerable part of copper remains unreduced. Raising the activation temperature to 170°C leads to a certain increase in the activity of the samples; however, as the copper-containing compounds are reduced to an insignificant extent, the reaction rate constant grows only slightly. When the reduction temperature is elevated to 180°C, copper is reduced virtually completely, which leads to a high activity of the samples. Further increase in the activation temperature to 250°C makes the activity lower, which can be attributed to agglomeration of copper in the course of reduction.

With NTK-4 catalyst, the influence of the activation temperature on formation of the active surface and on the activity is somewhat different.

It can be seen that complete reduction of the copper component of this catalysts occurs even at 160°C. Raising the activation temperature (Figs. 4a, 4b) leads to a minor increase in the intensity of copper lines in the X-ray diffraction patterns, which is due to crystallization of X-ray amorphous copper. The size of crystallites of metallic copper increases in this case from 195 to 270 Å because of copper agglomeration. Accordingly, the activity of the samples decreases as the activation temperature is elevated.

A clearly observable feature is that the thermal stability of NTK-4 catalyst is considerably lower than that of NTK-10 catalysts: the size of copper crystallites in NTK-4 increases by more than 40% as the activation temperature is elevated to 250°C, with the resulting substantial loss of activity.

Thus, the study performed shows that an activation temperature of 180°C not only ensures sufficient reduction of NTK-10 catalysts, but also leads to an

Table 3. Activities of catalysts reduced at different temperatures

T_a	T_r	Activity, s^{-1}			
°C		NTK-10-2FM	NTK-10-7F	NTK-10-2FA	NTK-4
160	160	2.2	2.5	2.1	3.4
	180	4.3	4.7	4.2	6.2
	200	7.9	8.1	7.9	10.1
180	160	2.7	2.7	2.8	3.0
	180	5.3	5.4	5.5	5.8
	200	9.1	9.2	9.2	9.7
180	160	3.9	3.9	3.7	2.6
	180	7.0	6.8	6.9	5.4
	200	11.2	10.9	11.5	9.4
250	160	3.5	3.2	3.4	2.2
	180	6.5	6.4	6.4	4.7
	200	10.6	10.4	10.5	8.5

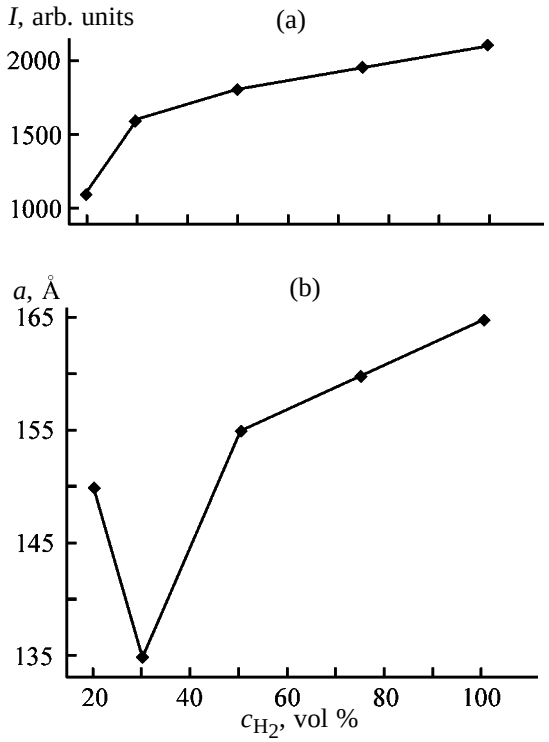

Fig. 5. (a) Intensity I of copper lines in X-ray diffraction patterns and (b) size a of crystallites of reduced copper vs. the content of H_2 in the reducing gas.

increase in their initial activity because of the formation of a more finely dispersed copper.

In the next stage of the study, it was necessary to evaluate the influence exerted by the concentration of H_2 in the reducing gas on the activity of NTK-10 catalysts, obtained at an activation temperature of 180°C.

Table 4. Activities of catalysts reduced at different contents of H_2 in the reducing gas

c_{H_2}, vol %	T_r, °C	Activity, s^{-1}		
		NTK-10-2FM	NTK-10-7F	NTK-10-2FA
20	160	1.2	1.5	1.2
	180	4.3	4.7	4.2
	200	6.9	7.1	6.9
30	160	4.2	4.3	4.2
	180	7.1	7.2	7.2
	200	11.8	11.9	11.8
50	160	4.0	4.1	4.0
	180	7.0	7.0	7.0
	200	11.5	11.4	11.6
75	160	3.9	3.9	3.7
	180	6.9	6.8	6.8
	200	11.3	11.0	11.4

Figures 5a and 5b show how the intensities of lines of reduced copper and the dispersity of copper depend on the content of H_2.

It can be seen that the intensity of copper lines in the X-ray diffraction patterns grows as the content of H_2 in the gas becomes higher. The steepest increase is observed in the range from 20 to 30 vol %. This is due to intensive reduction of copper from the aurichalcite structure, which is also indicated by the decrease in the size of copper crystallites in this range of H_2 contents. As the content of H_2 in the gas increases further, the intensity of copper lines increases only slightly, i.e., the hydrogen content of 30 vol % ensures virtually complete reduction of copper.

The copper particle size grows from 135 to 165 Å as the content of H_2 in the reducing gas becomes higher than 30 vol %.

The highest activity was observed (Table 4) for samples reduced with a gas containing 30 vol % hydrogen. Thus, the hydrogen content of 20–25 vol % is insufficient for complete reduction of copper compounds. Further increase in the content of H_2 in the gas leads to formation of coarser copper crystallites, which adversely affects the activity of the catalysts.

Thus, lowering the activation temperature to 180°C at a sufficient content of the reducing agent in the gas positively affects the formation of the active surface in NTK-120 catalysts, which leads to an increase in their activity, compared with the initial value. At the same time, the activation conditions should ensure complete reduction of copper from its compounds. It is critically important for NTK-10 catalysts that aurichalcite, which contains the most active copper, should be completely reduced. Therefore, lowering the reduction temperature to an even greater extent and diminishing the content of hydrogen are undesirable.

ACKNOWLEDGMENTS

The authors thank A.I. Nechugovskii, Z.A. Tertichnik, and G.M. Tesakova (Novomoskovsk Institute of Nitrogen Industry) for help in carrying out the study.

REFERENCES

1. Golosman, E.Z. and Yakerson, V.I., *Proizvodstvo i ekspluatatsiya promyshlennykh tsementsoderzhashchikh katalizatorov* (Manufacture and Use of Industrial Cement-Containing Catalysts), Available from NII-

TEKhIM, Cherkassy, September 1, 1992, no. 287-khp–92.

2. Golosman, E.Z., Nechugovskii, A.I., Kreindel', A.I., *et al*., *Khim. Prom-st*., 1999, no. 1, pp. 36–39.
3. Pavlov, Yu.L., Activation of Low-Temperature Catalysts for Conversion of Carbon Monoxide, *Cand. Sci. Dissertation*, Moscow, 1998.
4. Shchibrya, G.G., Pavlov, Yu.L., Vasilevich, A.A., *et al*., in *Voprosy kinetiki i kataliza: Mezhvuzoskii sbornik* (Problems of Kinetics and Catalysis: Intercollegiate Coll. of Works), Ivanovo, 1986, p. 53.
5. Smirnov, V.A., Study of Formation of Supported Copper-Containing Catalysts in the Stage of Their Activation, *Cand. Sci. Dissertation*, Ivanovo, 1978.
6. Batrin, Yu.D., Scientific Foundations of Synthesis of *N*-Methylaniline on NTK-4 Catalyst, *Cand. Sci. Dissertation*, Volgograd, 2000.
7. Golosman, E.Z., *Kinet. Katal*., 2001, vol. 42, no. 3, pp. 383–393.

Russian Journal of Applied Chemistry, Vol. 77, No. 7, 2004, pp. 1142–1146. Translated from Zhurnal Prikladnoi Khimii, Vol. 77, No. 7, 2004, pp. 1156–1160.

ENVIRONMENTAL PROBLEMS OF CHEMISTRY AND TECHNOLOGY

Neutralization and Clarification of Strongly Alkaline Wastewater from Silicate Production, Based on Microflotation with Chemical Agents

N. B. Mel'nikova, V. G. Sokolov, and L. I. Molvina

Nizhni Novgorod State Technical University, Nizhni Novgorod, Russia

Received December 2, 2003; in final form, April 2004

Abstract—A study was made of neutralization and clarification of wastewater from silicate production, which exhibits buffer properties. The promise of a two-stage procedure involving the primary thickening of the dispersed phase, followed by separation of the dispersed phase and water by flotation, was elucidated. The choice of the polymeric reagent and its concentration was substantiated.

Wastewater from production of silicate building materials, including cement, brick, etc., cause significant damage to soils via cementation, alkalization, and pollution with gypsum. Huge areas allocated for burial of wastes from silicate production virtually lose their fertility. This is especially pressing for cities consuming large amounts of building materials. Nowadays, silicate-producing enterprises have settlers for separation of coarse fractions, whereupon wastewater is neutralized with sulfuric acid and then removed from the production process. Such procedures pose environmental problems and are cost-ineffective because of large amounts of sulfuric acid and water they require. This makes urgent water reuse at silicate-producing enterprises.

In this work we studied neutralization of strongly alkaline wastewater from silicate production and developed a procedure for reuse of the purified water.

The subjects of our study were cement suspensions comprising calcium silicates, aluminosilicates, ferrites, and aluminoferrites, as well as various additions [1]. Wastewater from cement production contains not only cement components but also their hydration and hydrolysis products formed by the reactions [1, 2]

$$3CaO \cdot SiO_2 + mH_2O \rightarrow xCaO \cdot SiO_2 \cdot nH_2O + (3 - x)Ca(OH)_2, \quad (1)$$

$$2CaO \cdot SiO_2 + nH_2O \rightarrow 2CaO \cdot SiO_2 \cdot nH_2O, \quad (2)$$

$$3CaO \cdot Al_2O_3 + 6H_2O \rightarrow 3CaO \cdot Al_2O_3 \cdot 6H_2O, \quad (3)$$

$$4CaO \cdot Al_2O_3 \cdot Fe_2O_3 + mH_2O \rightarrow 3CaO \cdot Al_2O_3 \cdot 6H_2O + CaO \cdot Fe_2O_3 \cdot nH_2O, \quad (4)$$

$$3CaO \cdot Al_2O_3 \cdot 6H_2O + 3(CaSO_4 \cdot 2H_2O) + 19H_2O \rightarrow 3CaO \cdot Al_2O_3 \cdot 3CaSO_4 \cdot 31H_2O. \quad (5)$$

Analysis of the products of hydrolysis and hydration of the initial ingredients of cement shows that the dispersion medium for the suspensions is, essentially, a solution of calcium hydroxide in equilibrium with the dispersion of solid $Ca(OH)_2$ particles. This strongly complicates sedimentation of the suspension in settlers, as well as neutralization of the wastewater. In this connection, we paid much attention to the choice of flocculants able of efficiently binding the suspended particles at pH above 11, as well as to isolation of the solid dispersed phase by flotation to enable extraction of colloidal impurities from the wastewaters within a not very long time [3].

EXPERIMENTAL

We used M-400 D 20 [GOST (State Standard) 10178–85] Portland cement, pure grade sulfuric acid H_2SO_4 (GOST 4204–77), and pure grade orthophosphoric acid H_3PO_4 (GOST 6552-80).

Polyelectrolytes (flocculants) were prepared from cationic polymers: Praestol 644BC, Praestol 650BC (Moscow–Stockhausen–Perm Closed Joint-Stock Company); Polymin SK, Katiofast SF, Polymin KP (BASF, Germany); Kat-flok-487F (KEM-TRON Inc., Germany).

1070-4272/04/7707-1142 © 2004 MAIK "Nauka/Interperiodica"

The efficiency of thickening and compaction of the sediments was assessed from the velocity of displacement of the interface between the clarified and nonclarified parts of the solution in a volumetric flask with a working volume of 2000 cm^3. The sedimentation was assessed quantitatively using the dimensionless parameter D [4]:

$$D = \gamma/\gamma_0 - 1,$$

where γ and γ_0 are the sedimentation rates of the cement suspension with and without cationic flocculant, respectively.

In all the experiments we estimated γ from attainment of a fixed degree of clarification at identical concentration of the flocculant in the thickening solution (c_f = 0.5%).

The acidity of the medium and of the buffer solutions was monitored with a pH 320 SET (Wissenschaftlich-Technische-Werkstätten GmbH) microprocessor-based pH meter.

The charge density of the cationic flocculants, mg-equiv g^{-1}, was determined by colloidal-chemical titration with a 0.01% solution of the polymer with aqueous potassium polyvinyl sulfate (molecular weight M = 132 000, 60 mg l^{-1}) in the presence of Toluidine Blue as indicator [5]. Flotation isolation of the cement suspension sediment was carried out on a pilot pressure installation. The experiments were run in a cylindrical flotator equipped with a facility providing for tangential motion of the flow. The air pressure in the saturator was 3.5 MPa. In the course of the process, we monitored the size of the air bubbles at the outlet of the reducing valve, as well as the degree of clarification of water and the concentration of the ions of pollutant remaining in water. The size of the bubbles was estimated optically, in an MBP-2 horizontal microscope.

Neutralization of a 1% cement suspension (pH 11.8) was studied under the static (a 5-s single stirring run at the beginning of the process) and dynamic (continuous stirring) conditions.

Under static conditions, upon addition of 60 ml l^{-1} of a 5% H_2SO_4 solution to 1 l of 1% cement suspension, pH of the suspension initially decreased to 7.0 and then slowly increased, virtually regaining the initial value. The experiments under dynamic conditions showed that, upon neutralization, stirring accelerates the growth of pH. In this connection, we studied the dynamics of variation of pH of the cement suspension during its neutralization with a 5% solution of H_2SO_4

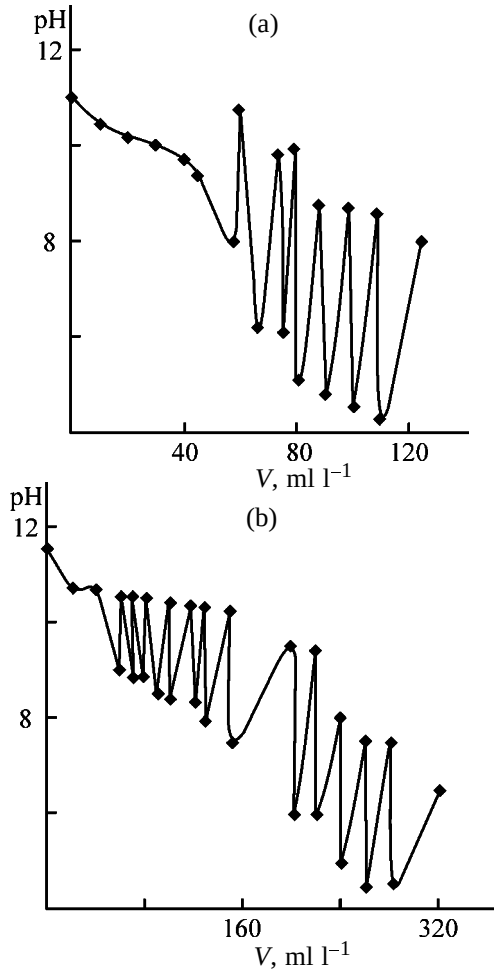

Fig. 1. Variation of pH of a 1% aqueous cement suspension upon introduction of 5% solutions of (a) H_2SO_4 and (b) H_3PO_4 in amount V in portions under stirring.

under continuous stirring. The first 60 ml of the H_2SO_4 solution was introduced into the suspension under stirring in 10-ml portions at 30-s intervals. Next, the acid solution was added in 10-ml portions at 30-min intervals. Figure 1a shows how the acidity varied with the volume of the acid solution introduced; it is seen that pH of the suspension, which strongly decreased under the action of the acid, increased again several minutes later, virtually regaining its initial value. Upon introduction of additional portions of the acid into the solution, this process was reproduced, resulting in a gradual final decrease in the acidity of the solution. The amount of the acid spent is very significant. For example, decreasing pH of the suspension from 11 to 8 requires adding 110 ml of 5% H_2SO_4 to 1 l of the suspension. This also holds for 5% H_3PO_4 (Fig. 1b); neutralization requires a much greater amount of H_3PO_4 and is much slower. Neutralization to pH 6.5 is achieved by introducing

Table 1. Main properties of polymeric cationic flocculants

Flocculant	pH of 0.5% polymer solution	Charge density, mg-equiv g^{-1}	Test	
			for thickening*	for clarification**
Praestol***:				
611BC	4.91	1.43	3	3
644BC	4.58	2.72	1	1
650BC	4.34	1.94	3	3
Polymin SK	7.17	5.5	0	0
Katiofast SK	6.85	13.9	0	0
Polymin KP	4.64	1.0	3	3
Kat-floc-487F	4.85	2.85	3	3

* Three-point scale: 0 means no thickening, and 3, efficient thickening (D = 10) yielding strong floccules.
** Three-point scale: 0 means turbid water, and 3, exhaustive clarification within 5 min.
*** Polymer with a molecular weight above 500 000.

320 ml of 5% H_3PO_4 solution per liter of suspension. Notably, in both cases the solid dispersed phase did not disappear: Instead of solid cement particles, we observed appearance of poorly soluble sulfates, phosphates, and other products of solid-phase reactions and topochemical processes. This is most probably due to the buffer action of the suspended $Ca(OH)_2$ particles.

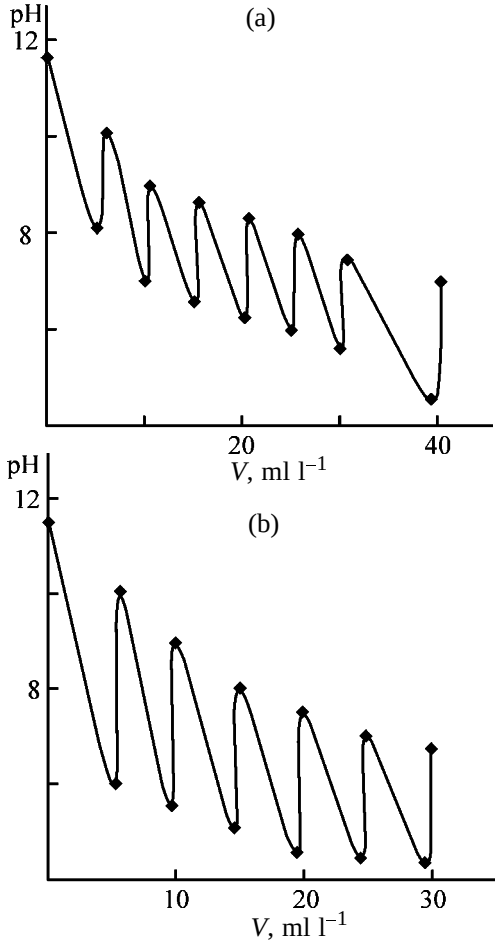

Fig. 2. Variation of pH of a 1% aqueous cement suspension upon introduction of combined flocculants based on Katfloc-487F polymer and (a) H_2SO_4 and (b) H_3PO_4 in amount V in portions under stirring.

Since solutions of acids proved to be inefficient in neutralization of cement suspensions, we studied neutralization of suspensions with combined acid solutions containing a polymeric flocculant.

A preliminary study showed that nonionic polyacylamide (PAA) exerts a very weak flocculation effect on cement suspensions. The same is true of anionic polyelectrolytes like hydrolyzed PAA. Since cement suspensions contain negatively charged particles with a fairly high negative electrokinetic ε potential, it is most probable that, along with "bridging," neutralization of the surface charge by macromolecular compounds is important in flocculation.

In view of the above-said, we studied in this work cationic polyelectrolytes, namely, cationic polymeric flocculants (Table 1). When choosing a polyelectrolyte, we estimated the flocculation effect from the results of the qualitative tests on clarification of the suspension and thickening (compaction) of the sediment. In tests, we added 7 ml of a 0.5% solution of a flocculant to 1 l of a 1% aqueous cement suspension. Among the polymeric flocculants studied, satisfactory results were obtained with Praestol 611BC, Praestol 650BC, Polymin KP, and Kat-floc-487F with a cationic charge of 1–3 mg-equiv g^{-1}.

Neutralization of the suspension with compositions combining aqueous solutions of the above-mentioned flocculants and acids showed that these are more efficient than solutions of acids traditionally used for neutralization. Figures 2a and 2b show how pH varies during neutralization of a suspension with a combined

Table 2. Formulations of combined flocculants and the main characteristics of the two-stage purification of wastewater from cement production

Version no.	Stage 1 (thickening)			
	formulation no. 1		amount spent, ml l^{-1}	pH of suspension upon adding the formulation
	Kat-flok-487F, g l^{-1}	H_3PO_4 (30 wt %), ml l^{-1}		
1	4.0	10	7.0	11.6
2	4.0	20	7.0	11.2
3	4.0	30	7.0	11.0
4	2.5	no. 3*	7.0	6.7

Version no.	Stage 2 (flotation)						Amount of dry polymer spent in two stages, mg l^{-1}
	formulation no. 2**		amount spent, ml l^{-1}	pH of composition	pH of aqueous phase upon flotation	diameter of flotation bubbles, μm	
	Kat-flok-487F, g l^{-1}	Na_2CO_3, g l^{-1}					
1	2.0	20	3.0	1.0	7.0	450	34.0
2	2.0	20	6.0	2.0	7.3	800	40.0
3	2.0	20	3.0	1.0	6.9	400	34.0
4	–	–	–	1.5	6.6	170	17.5

* Composition no. 3 was prepared according to version no. 2; concentration of Na_2CO_3 was 20 g l^{-1}.

** The composition was prepared by adding concentrated HCl into an aqueous solution of Na_2CO_3 to pH 1.5 (pH 1.5 corresponds to the concentration of excess HCl; concentration of H_2CO_3 is 3.8×10^{-2} M; there are no carbonate ions).

composition based on Kat-floc-487F. In this case, the required amount of the chemicals decreases to 30–40 ml l^{-1}; compositions containing phosphoric acid (Fig. 2b) are more efficient. On the whole, however, the acidity of the suspensions remains unstable during neutralization.

In this connection, we tested neutralization involving removal of the Ca^{2+} ions from solution by converting them into a poorly soluble form. One way of binding Ca^{2+} ions in an alkaline medium is converting them to a poorly soluble carbonate, $CaCO_3$, by the scheme

$$Ca^{2+} + CO_3^{2-} \rightarrow CaCO_3, \quad (6)$$

$$Ca(OH)_2 + CO_2 \rightarrow CaCO_3 + H_2O. \quad (7)$$

Simultaneously, soluble hydrocarbonate can be formed in an acid medium:

$$Ca(OH)_2 + 2HCO_3^- \rightarrow Ca(HCO_3)_2 \rightleftarrows Ca^{2+} + 2HCO_3^-. \quad (8)$$

This assumption was verified experimentally; we found that passing CO_2 through the cement suspension upon isolation of coarse fractions leads to a sharp and, what is essential, irreversible decrease in pH and clarification of the solution.

Our results allowed us to propose compositions including cationic polyelectrolyte and a solution yielded by the reaction of Na_2CO_3 with excess HCl (to pH 1.5) [6].

Figure 3 shows how the flocculation effect *D* varies with the concentration of the combined flocculant

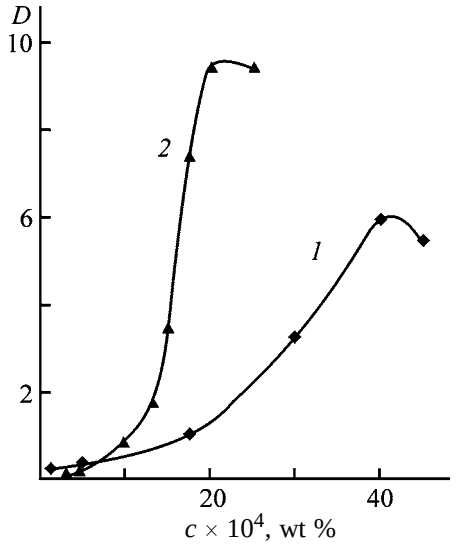

Fig. 3. Flocculation effect *D* as a function of the concentration of the combined flocculant *c*. Formulation no. 1 (Table 2): (*1*) version 3 and (*2*) version 4.

proposed. Curve *2* in Fig. 3 shows that the composition proposed is much more efficient. Thus, the combined flocculants can be regarded as agents favoring neutralization in a strongly alkaline medium containing $Ca(OH)_2$, which makes such compositions suitable for separation of complex dispersed systems.

We separated the suspension into fractions by pressure flotation at the air pressure in the saturator of 3.5 MPa, using a pilot installation proposed in [7, 8]. Table 2 summarizes the results of two-stage purification of the wastewater from cement production, based on separation of the solid and liquid phases by flotation. Stage 1 of removal of the suspension from water involved thickening of the dispersion by combined flocculants (versions 1–4). Neutralization of the wastewater was achieved only with a combined flocculant (version 4). Stage 2 involved flotation with (versions 1–3) and without (version 4) additionally introduced agents. Table 2 suggests high efficiency of purification and neutralization of strongly alkaline wastewater from cement production in a two-stage process involving flotation separation. Water purification was the most efficient in the case of version 4, when a combined flocculant was used in stage 1 of the process (thickening).

CONCLUISONS

(1) Neutralization of strongly alkaline wastewater with H_2SO_4 and H_3PO_4 solutions occurs as an unstable and reversible process, as shown by the example of a 1% cement suspension containing silicates, aluminosilicates, and ferrites.

(2) Efficient neutralizing compositions for wastewater from silicate productions are combined flocculants based on cationic polymers with a cationic charge of 1–33 mg-equiv g^{-1}, including polymers with a molecular weight above 500 000 and the solution yielded by the reaction of sodium carbonate with excess HCl (to pH 1.5).

(3) The combined flocculants proposed allow highly efficient flotation treatment of strongly alkaline wastewater from silicate production.

REFERENCES

1. Butt, Yu.M., *Tekhnologiya tsementa i drugikh vyazhushchikh veshchestv* (Technology of Cement and Other Binders), Moscow: Vysshaya Shkola, 1964.
2. *Kratkaya khimicheskaya entsiklopediya* (Concise Chemical Encyclopedia), Moscow: Sovetskaya Entsiklopediya, 1965.
3. Deryagin, B.V., Dukhin, S.S., and Rulev, N.N., *Mikroflotatsiya: vodoochistka, obogashchenie* (Microflotation: Water Treatment, Enrichment), Moscow: Khimiya, 1986.
4. Myagchenkov, V.A., Baran, A.A., Benturov, V.A., and Bulidorova, G.V., *Poliakrilamidnye flokulyanty* (Poliamide Flocculants), Kazan: Tekhnol. Univ., 1998.
5. Baran', Sh. and Gregory D., *Kolloidn. Zh.*, 1996, vol. 58, no. 1, pp. 13–18.
6. RF Patent 2 114 068.
7. RF Patent 2 118 294.
8. RF Patent 2 129 528.

Russian Journal of Applied Chemistry, Vol. 77, No. 7, 2004, pp. 1147–1149. Translated from Zhurnal Prikladnoi Khimii, Vol. 77, No. 7, 2004, pp. 1161–1163.

ORGANIC SYNTHESIS AND INDUSTRIAL ORGANIC CHEMISTRY

Acylation of Aromatic Amines with Carboxymethyl Dextran in the Presence of Small Amounts of Water

O. V. Sibikina, A. A. Iozep, and B. V. Passet

St. Petersburg State Academy of Pharmaceutical Chemistry, St. Petersburg, Russia

Received February 13, 2004

Abstract—Acylation of aromatic amines with carboxymethyl dextran and its ethyl ester in dioxane, ethanol, 1-propanol, and 2-propanol in the presence of small amounts of water was studied.

It was shown previously that esters of polysaccharidecarboxylic acids are convenient agents for acylation of amines in synthesis of physiologically active polymers (PAPs) [1–3]. They can be used for fixation on a polysaccharide matrix of such biologically active substances as antibiotics and enzymes. In this connection, we developed simple procedures for synthesis and analysis of carboxymethyl polysaccharide (CMP) esters and determined conditions of their reactions with various amines in water, dioxane, and DMSO [1–5]. However, difficult isolation of CMP esters from the reaction mixture after their synthesis is a significant drawback of this procedure for PAP preparation. Therefore, we studied the reaction of carboxymethyl dextran (CMD) with aromatic amines in lower alcohols with the aim to eliminate the step of CMD ester isolation and make the modification of dextran less time- and labor-consuming.

Chemical modification of polysaccharides was performed by the following scheme:

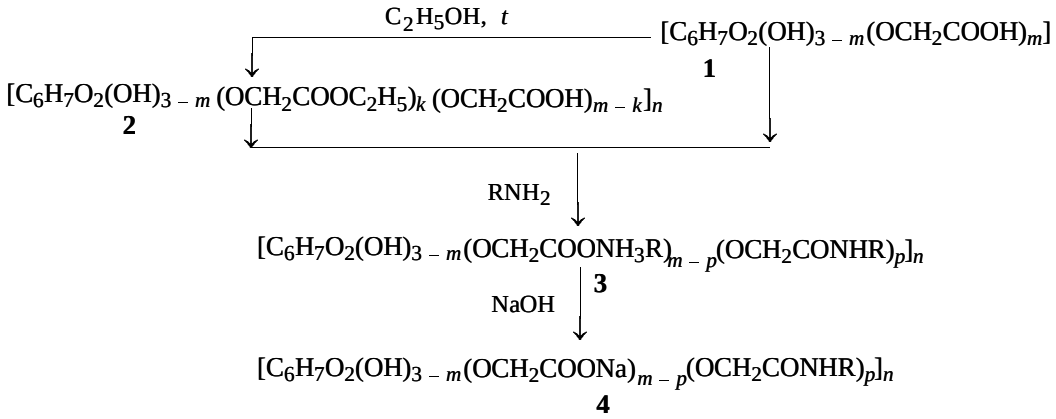

Carboxymethyl dextran **1** and its ethyl ester (CMDEE) **2** were prepared as described in [4–6]. The resulting CMD and CMDEE samples were characterized by the degree of carboxymethylation C_{cm} and degree of alkoxycarbonylmethylation C_{acm} (number of carboxymethyl or ester groups per polysaccharide monomeric unit). Acylation of amines with CMD and CMDEE was performed in dioxane [3]. The reaction of CMD with amines in ethanol was performed similarly to the reaction of CMDEE with amines in dioxane but by two procedures: with preliminary esterification of poly acid (procedure 1) and without it (procedure 2). In procedure 1, the H^+ form of CMD was refluxed in excess ethanol for 4–6 h, after which an amine was added to the resulting CMDEE-containing mixture, and refluxing was continued for an additional 4 h. In procedure 2, the reaction mixture containing the H^+ form of CMD, amine, and excess alcohol was refluxed for 4 h. In so doing, it was suggested that first the CMD ester is formed, which is followed by

1070-4272/04/7707-1147 © 2004 MAIK "Nauka/Interperiodica"

Table 1. Results of acylation of amines with CMD (C_{cm} = 0.9) and its ethyl ester (C_{cm} = 0.94, C_{acm} = 0.41) in anhydrous dioxane at 100°C [3] and with CMD in ethanol at 78°C. Reaction time 4 h, 5 mol of amine per mole of carboxy groups

Amine	pK_a of amine	C_{am} in dioxane, %		C_{am} of CMD in ethanol, %	
		CMD	CMDEE	procedure 1	procedure 2
p-Nitroaniline	1.02	2	0	0	7
p-Bromoaniline	3.93	–	–	18	32
Aniline	4.61	24	21	29	41
p-Toluidine	5.12	29	26	35	46
p-Phenetidine	5.25	29	27	35	49

acylation, since aromatic amines are not noticeably acylated with the poly acid at 78°C in dioxane [3].

Products **3** were isolated, purified, and analyzed as described in [3].

The number of amide groups in samples of polysaccharides **4** was determined by elemental analysis and UV spectroscopy. Acylation was characterized by the degree of amidation C_{am} (percentage of polysaccharide acyl groups involved in the reaction). The results are given in Table 1.

We found that acylation of aromatic amines in ethanol at 78°C by the suggested procedures gives better results than acylation with CMD and its ethyl ester in dioxane at 100°C. In acylation of amines in dioxane, C_{am} is lower than in acylation of amines in alcohol, on the average, by 20–30 (in procedure 1) and 65–85% (in procedure 2).

With the aim to increase the conversion of CMD carboxy groups into amide groups, we studied the reactions of CMD with aromatic amines in 1- and 2-propanol whose boiling points are higher than that of ethanol (97 and 82°C, respectively). However, despite higher reaction temperature, C_{am} of CMD in these alcohols appeared to be lower than in ethanol.

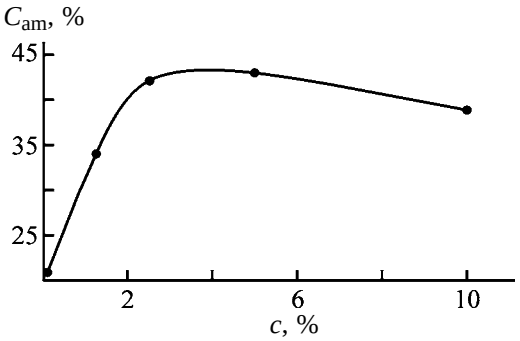

Fig. 1. Degree of amidation C_{am} of CMD (C_{cm} = 1.45) in reaction with aniline as a function of water content *c* in dioxane. Reaction time 4 h, 70°C, 10 ml of amine per mole of monosaccharide units.

This may be due to steric effects associated with longer carbon chain in the alcohol molecule or its branching. A similar trend was observed in acylation of benzylamine with CMD esters in water [4]. However, more detailed examination of the reaction conditions and reagent purity showed that dioxane, 1-propanol, and 2-propanol (chemically pure or pure grade) contained no more than 1% water, whereas rectified ethanol contained 4% water. Therefore, we suggested that water could exert a certain effect on the reaction. Under the conditions of procedure 2, when the H^+ form of CMD and amine are added to the alcohol simultaneously, the carboxylic acid (CMD) rather than CMD ester reacts with the amine, and the acid is a stronger acylating agent. This accounts for the fact that acylation of amines in ethanol by procedure 2 gives the target product in a higher yield compared to preliminary esterification of carboxy groups.

A study of the reaction of CMD with aniline in dioxane containing small amounts of water showed that the efect of water on the reaction is maximal at a water concentration of 2.5–5% (Fig. 1) [7].

In this connection, we suggested that addition of this amount of water to dioxane and 1-propanol will increase the yield of the target product in reactions with the other amines also. The boiling points of dioxane and 1-propanol are approximately equal and higher than that of ethanol; therefore, we expected that the degrees of CMD amidation in acylation of aromatic amines in 1-propanol or dioxane containing 4% water will be the same or even greater, compared to the reaction in ethanol.

Indeed, addition of 4% water to dioxane and 1-propanol increased C_{am} relative to the anhydrous solvent, in some cases by a factor of more than 2 (Table 2). As expected, the yield of CMD amide in 1-propanol was higher than in ethanol (by approximately 30%). Comparison of C_{am} of CMD in water-containing 1-propanol and dioxane is difficult, since

Table 2. Results of acylation of amines with CMD (C_{cm} = 0.9–1.1) in solvents containing 4% water. Reaction temperature 100°C, 4 h, 5 mol of amine per mole of carboxy groups

Amine	C_{am} of CMD, %			
	anhydrous dioxane	dioxane	1-propanol	ethanol*
p-Bromoaniline	26	42	32	
Aniline	24	47	55	41
p-Toluidine	29	57	59	46
p-Phenetidine	29	65	65	49

* At 75°C.

the dependences of the product yield on pK_a of the amine in these solvents are essentially different (Fig. 2).

Thus, addition of 2.5–5% water to dioxane and lower alcohols at temperatures above 70°C allows efficient acylation of aromatic amines with CMD used instead of its ethyl ester, which considerably simplifies the modification of the polysaccharide and increases the yield of the target product by a factor of more than 2.

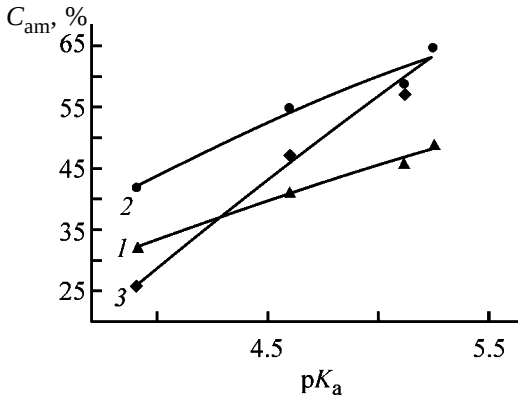

Fig. 2. Degree of amidation C_{am} of CMD in reactions with aromatic amines in (*1*) ethanol, (*2*) propanol, and (*3*) dioxane, containing 4% water, vs. pK_a of the amine. Boiling point of the solvent, 4 h, fivefold excess of the amine.

CONCLUSION

Experiments on acylation of aromatic amines with carboxymethyl dextran and its ethyl ester in wet dioxane, ethanol, 1-propanol, and 2-propanol show that addition of 2.5–3% water to dioxane and lower alcohols allows acylation of aromatic amines at temperatures above 70°C to be performed with carboxymethyl dextran instead of its ethyl ester, which considerably simplifies the modification of the polysaccharide and increases the yield of the target product by a factor of more than 2.

REFERENCES

1. Iozep, A.A., Il'ina, T.Yu., and Passet, B.V., *Zh. Prikl. Khim.*, 1994, vol. 67, no. 3, pp. 470–474.
2. Iozep, A.A., Il'ina, T.Yu., and Passet, B.V., *Zh. Prikl. Khim.*, 1995, vol. 68, no. 1, pp. 106–109.
3. Iozep, A.A., Sibikina, O.V., Kuznetsova, T.E., and Passet, B.V., *Zh. Prikl. Khim.*, 1995, vol. 68, no. 2, pp. 307–311.
4. Iozep, A.A., Il'ina, T.Yu., and Passet, B.V., *Zh. Prikl. Khim.*, 1993, vol. 66, no. 5, pp. 1106–1110.
5. Iozep, A.A., Il'ina, T.Yu., Kuznetsova, T.E., and Passet, B.V., *Zh. Prikl. Khim.*, 1994, vol. 67, no. 6, pp. 1012–1016.
6. *Methods in Carbohydrate Chemistry*, Whistler, R.L. and Wolfrom, M.L., Eds., New York: Academic, 1962–1965.
7. Sokolov, V.B., Synthesis and Study of Lactones Derived from Polysaccharidecarboxylic Acids and Their Use for Acylation of Low-Molecular-Weight Biologically Active Substances, *Cand. Sci. Dissertation*, St. Petersburg, 1999.

Russian Journal of Applied Chemistry, Vol. 77, No. 7, 2004, pp. 1150–1155. Translated from Zhurnal Prikladnoi Khimii, Vol. 77, No. 7, 2004, pp. 1164–1169.

ORGANIC SYNTHESIS AND INDUSTRIAL ORGANIC CHEMISTRY

Determination of Catecholamines by Capillary Electrophoresis–Mass Spectrometry

L. A. Kartsova, E. A. Bessonova, A. A. Sidorova, V. A. Kazakov, I. A. Tver'yanovich, and L. I. Velikanova

St. Petersburg State University, St. Petersburg, Russia
St. Petersburg Medical Academy of Postgraduate Studies, St. Petersburg, Russia
Analytical Spectrometry, Shared Center, Limited Liability Company, St. Petersburg, Russia

Received August 13, 2003; in final form, May 2004

Abstract—A method for determination of catecholamines (adrenaline, noradrenaline, and dopamine) by capillary electrophoresis–electrospray ionization–mass spectrometry is described. The electrospray operating mode is optimized as well as the system for capillary electrophoresis.

Quantitative analysis for the most important neurotransmitters such as adrenaline (A), noradrenaline (NA), and dopamine (DA) is of great significance for diagnostics and treatment of various brain diseases. In this case it is required to determine individual catecholamines, but not their total. Since the concentration of catecholamines in actual objects is extremely low (nano- and picograms), the methods for their determination should be highly sensitive and selective. In recent years, a novel method for separating complex mixtures, capillary electrophoresis (CE), is being actively developed. Its doubtless advantages are very high performance, surpassing that of the chromatographic methods by several orders of magnitude; very small sample volume required for analysis (several nanoliters); small consumption of reagent solutions; and a shorter analysis time than in HPLC.

The most of published works deal with capillary zone electrophoresis with UV detection, which is characterized by insufficient concentration sensitivity. The zone CE–mass spectrometry (MS) combines the high efficiency of separation of components with highly sensitive and selective detection. A great advantage of an MS detector is the possibility of identifying unknown components in matrices of complex samples.

A liquid chromatograph or a CE system can be connected to a MS detector via ESI (electrospray ionization) interface. In the case of CE, such a hybrid mode of determination is known as CE–ESI–MS (capillary electrophoresis–electrospray ionization–mass spectrometry). The method is based on separation of components of a sample in a quartz capillary under the action of an applied potential, electrospray of an electrolyte and the sample followed by ionization in an electrosprayer of a mass analyzer, and recording of an analytical signal from ions in a quadrupole MS detector. Electrospray is electrokinetic injection of the solution to be analyzed to a mass spectrometer under the action of a high potential difference applied to the ends of the quartz capillary, and under a voltage applied between the capillary outlet and MS inlet.

Three major engineering solutions of the ESI interface, to connect a CE block to a mass analyzer are currently used: employment of a quartz capillary with a metal sputtered on its pointed end through which spraying occurs; the use of a gold wire microelectrode arranged into the capillary outlet; and the use of a three-layer metallic needle.

The study was carried out on an Agilent instrument with an ESI interface using a three-layer metallic needle. Three flows are coaxially fed into the needle serving as an electrosprayer: a drying gas (external coating) ensuring transfer of the solvent into the vapor phase; coating liquid [through a high-pressure isocratic pump used in HPLC to ensure liquid contact of the needle (serving also as an electrode) with the liquid flowing from the capillary]; and, finally, a flow of a liquid from the quartz capillary. Particles of the aerosol, formed in the electrosprayer cell under the action of high voltage applied between the needle and the electrode of the inlet capillary of the mass spectrometer (~3000–4000 V), start to crush down. As

1070-4272/04/7707-1150 © 2004 MAIK "Nauka/Interperiodica"

a result, the initially high charge density on their surface decreases, and ions, having no solvation shell, i.e., solvent molecules in the gaseous state, are formed.

The goal of this study is to develop a method for determination of the most important catecholamines by capillary electrophoresis–mass spectrometry. In the work we used an Agilent 1100 CE–MS system, Tsvet Yauza liquid chromatograph with an amperometric detector, and MALDI TOF Voyager DE mass spectrometer. The inner and outer diameters of the capillary were 50 and 375 μm, respectively, and the effective length, 80–90 cm. The inner capillary wall was coated with a polymer. The capillary projected from the ESI needle by 0.3 mm. The voltage applied to the capillary ends was 30 kV. A sample was taken from a sampler wheel (hydraulic input 900 mbar s^{-1}). The capillary was conditioned with water (5 min), 10% ammonia (5–10 min), and again with water (5 min) under a pressure of 1 atm. After completion of the analysis, the capillary was washed with a buffer electrolyte for 4 min.

In detecting positive ions in the mass spectrometer, we used an ESI interface with a three-layer metallic needle. Into the needle serving as an electrosprayer, flows of a drying gas and coating liquid were coaxially fed. The ESI voltage was +4 kV. The coating liquid flow rate was 4 μl min^{-1}, and that of the drying gas (nitrogen), 5 l min^{-1}; temperature 200°C. The objects to be analyzed were dry adrenaline, dopamine, and noradrenaline hydrotartrates (Fluka).

Stock buffer solutions were prepared from standard titrants [$Na_2B_2O_4 \cdot 10H_2O$ (pH 9.18), HCl, CH_3COOH, aq. NH_3, diethylamine hydrochloride $(C_2H_5)_2NH \cdot HCl$, and Na_2EDTA]. The effect of an organic solvent as a component of the electrolyte on the parameters of separation of the mixtures was studied with 2-propanol. All the chemicals used were of chemically pure grade. All the solutions were prepared with double-distilled water. The buffer electrolyte was 0.05–0.1 M acetate buffer containing 5×10^{-3} M $(C_2H_5)_2NH \cdot HCl$; pH was adjusted to 4.5 by adding 10% aq. NH_3. The resulting solutions were filtered through a membrane filter (pore size 1.2 μm) and then degassed under vacuum (water-jet pump).

Stock solutions of the catecholamines (1000 mg l^{-1}) were prepared in 0.1 M HCl and stored at –20°C. Under these conditions, the solutions were stable for a year. Working solutions of catecholamines were prepared by dilution of the stock solutions with water. The coating liquid was prepared from a mixture of methanol or 2-propanol and water (40 : 60–95 : 5 v/v) with addition of 0.5 vol % acetic acid.

Table 1. Relative contribution of protonated molecular ions $[M + H]^+$ and daughter ions in the mass spectra of catecholamines

Major species formed in MS	A	NA	DA
$[M + H]^+$, *m*/*e*	184 (100)	170 (100)	154 (100)
Fragment, *m*/*e*	166 (10)	152 (12)	137 (11)
Neutral fragment, *m*	–18 (H_2O)	–17 (NH_3)	–17 (NH_3)
SIM, *m*/*e*	184	170	154

Solid-phase extraction of catecholamines was performed with active alumina. CE separation of components improves the sensitivity of the MS quadrupole detector, which is caused primarily by the fact that, in this case, operation in the SIM mode becomes possible. We have found only a few versions of determination of catecholamines by CE–MS with electrospray ionization [1–3], and about ten versions, by CE [4–7]. It appeared promising to use capillary electrophoresis with MS detection. Prior to CE–MS analysis, we recorded the MS spectra of standard catecholamines. They show two types of ions: a molecular ion and a daughter ion formed by elimination of the H_2O or NH_3 molecule from the protonated molecular ion. By varying the drying gas temperature and pressure under which it is fed to the needle, we made it possible that the mass spectrometer recorded molecular peaks of the components with practically no fragmentation (Table 1). Above 250°C, the catecholamine molecules are fragmented with the loss of NH_3. Therefore, detection of catecholamines is based, primarily, on the corresponding signals of molecular ions.

There are two modes of MS detector. In the SCAN mode, ions from a selected mass range (*m*/*e*) are detected, and the total ion current is recorded as a function of the time. In the SIM mode, signals from the only ion with a fixed mass are integrated. Signals from other ions are not recorded, and that is why it becomes so important to separate components of the sample prior to input into the mass analyzer. In operating in this mode, the sensitivity of analysis increases by several times. In this case, it is important to attain a good reproducibility in the migration time of components (time in which a component passes through the quartz capillary). Therefore, the quality of preparation of the capillary for analysis is of a great significance in the CE–MS method. We registered the MS spectra under the following conditions: SCAN

mode: *m*/*e* 150–185 and SIM mode: *m*/*e* 154 (0–11.25 min), 170 (11.25–11.8 min), and 184 (11.8–12.0 min).

In capillary zone electrophoresis, components of a sample are separated as cations or anions, depending on pH.

At pH >10, catecholamines occur in the anionic form [3], and at pH <8, in the cationic form (pK_a of catecholamines ~8.5) [2, 6]:

Anionic and cationic forms of catecholamines

Anionic form

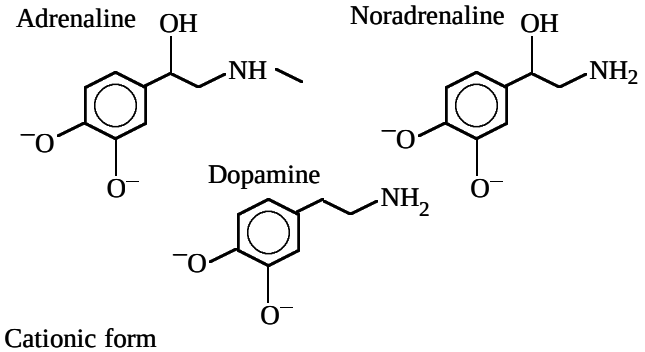

Cationic form

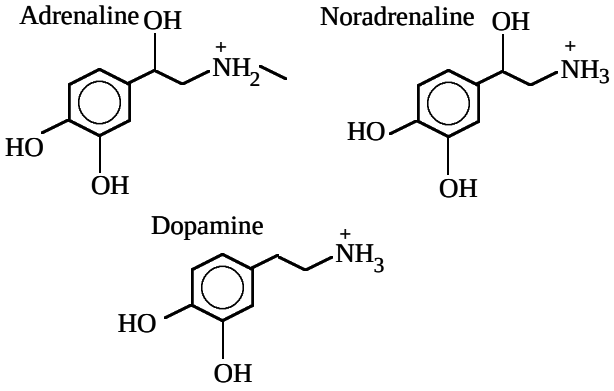

We tested both alternatives. We optimized the composition of the sample and buffer electrolyte by varying the concentration, pH, salt additives, and organic modifiers (Table 2). It was demonstrated that the use of buffer solutions with pH > 7 provides better separation, but, in this case, oxidation of catecholamines can occur. Here the requirements to the MS detector should also be taken into account. For example, the use of low-volatile borate buffer makes it impossible to attain stable spraying of the components to be analyzed. Therefore, in the subsequent, all the experiments were carried out in a buffer solution with pH < 7. To increase the solution viscosity and improve the separation, we added 10–20% 2-propanol. However, this resulted in broadening of the peaks and decreased resolution. To overcome these effects through preventing adsorption of the analytes on the capillary wall, we added $(C_2H_5)_2NH \cdot HCl$ in the buffer electrolyte. The optimal conditions were found to be as follows: 0.05 M acetate buffer containing 5×10^{-3} M diethylamine hydrochloride (pH 4.5) and separating voltage +30 kV. Note that, in the CE–MS analysis, the voltage should be higher than in CE–UV, since the ESI voltage applied to the end of the capillary decreases the total electric field in it.

An important step in carrying out this study was optimization of the MS detection conditions. It was necessary to select the ratio of the rates of the drying gas and coating liquid and the coating liquid composition so as to maximize the analytical peaks.

Taking the published data [2, 6, 8] into account, we tested the systems methanol–water and 2-propanol–water (50 : 50 v/v) with addition of an acid. Since acetate buffer was used in separating catecholamines in CE, we selected acetic acid, so as to introduce no additional ions into the system. The maximal intensity of signals of the analytes was observed in the system with 2-propanol, which is consistent with the results of Peterson *et al*. [2] who demonstrated that 2-propanol is the best suited solvent for the coating liquid. Nevertheless, the authors have preferred to use methanol, since, in this case, the signal/noise (S/N) ratio appeared to be higher. Under our experimental conditions, the noise level was higher with methanol. After optimization of the solvent, we selected the system 2-propanol–water (50 : 50 v/v). Additionally, it should be pointed out that the stability of electrospraying decreases as the fraction of the organic solvent in the coating liquid increases. The acetic acid concentration was varied from 0.1 to 1.0%, which had only slight effect on the signal intensity. Thus, the optimal composition of the coating liquid is 2-propanol–water (50 : 50 v/v) + 0.5% acetic acid.

Another significant parameter influencing the response is the coating liquid flow rate. This parameter was optimized over the range of flow rates at which electrospraying is stable (2–8 μl min^{-1}).

According to [8], the coating liquid, being around the capillary and mixing with the outflowing sample, dilutes by half the sample zone when flowing out from the capillary with increasing flow rate from 2 to 8 μl min^{-1}. The highest response and the best separation efficiency were obtained at a flow rate of 4 μl min^{-1}.

To realize stable spraying, it is important to optimize the position of the capillary end relative to the coating liquid outlet. If the end of the capillary projects too much from the ESI needle, there is no way to realize stable spraying. In turn, spraying is also

Table 2. Parameters of separation of catecholamines optimized with standard solutions

Run no.	Sample composition	Supporting electrolyte	Electrospray operation mode		
			flow rate, l min^{-1}	*T*, °C	*P*, kPa
1	20 mg l^{-1} A, NA; 0.01 M ammonia buffer (pH 9.4)	0.01 M*	2	150	69
2	″	0.01 M, 7×10^{-3} M NaCl*	2	150	69
3	″	0.01 M; 0.015 M NaCl*	0.3	60	55
4	20 mg l^{-1} A, NA; 0.05 M ammonia buffer (pH 9.4); 1×10^{-3} M Na_2EDTA; 3×10^{-3} M Na_2SO_3	0.05 M, 1×10^{-3} M Na_2EDTA*	10	55	55
5	″	0.05 M; 1×10^{-3} M Na_2EDTA; 20% 2-propanol*	10	55	55
6	20 mg l^{-1} A, NA; 0.07 M ammonia buffer (pH 9.4); 1×10^{-3} M Na_2EDTA; 3×10^{-3} M Na_2SO_3; 20% 2-propanol	0.07 M; 1×10^{-3} M Na_2EDTA; 20% 2-propanol*	10	55	55
7	20 mg l^{-1} A, NA; 2% CH_3COOH (pH 2.8)	0.09 M; 10% 2-propanol	6	130	117
8	″	0.1 M; 10% 2-propanol**	6	130	117
9	″	0.05 M	3	300	7
10	10 mg l^{-1} A, NA; 2×10^{-3} M diethylamine hydrochloride	0.1 M; 2×10^{-3} M diethylamine hydrochloride**	5	200	14
11	10 mg l^{-1} A, NA in water	0.1 M**	5	200	14
12	″	0.05 M; 5×10^{-3} M diethyl amine hydrochloride**	5	200	14

* Ammonia buffer (pH 9.4).
** Acetate buffer (pH 4.5).

Table 3. Detection limits of catecholamines, as determined by CE–MS, CE–UV, and HPLC–amperometry

Compound	*m*/*e* [M + 1]	Normal catecholamine concentration range	Detection limit, nM		
			CE–MS	CE–UV	HPLC–amperometry
DA	154.1	649–4930	110 ± 3	650 ± 2	1.87 ± 0.04
A	184.1	81.5–200	90 ± 2	540 ± 1	0.15 ± 0.03
NA	170.1	58.8–230	100 ± 1	590 ± 3	0.27 ± 0.03

unstable if the end of the capillary is arranged inside the needle. In this case, the eluent is diluted, and the sample can be broken. The best results were obtained in the case when the capillary projected from the ESI needle by 0.3 mm, which is consistent with data of [9].

Under the optimal conditions, using MS detection in the SIM mode, detection limits of 110, 100, and 90 nM were achieved for dopamine, noradrenaline, and adrenaline, respectively (at S/N = 3).

It should be pointed out that an ESI–MS detector is highly sensitive to the sample salinity. At high salt content, the stability of spraying decreases. Therefore, samples should be purified prior to analysis.

Sample preparation procedure was optimized with a model system using solid-phase extraction (SPE) on alumina pretreated with an acid.

Preparation of a sample (2 ml) was carried out as follows. The solution pH was adjusted to 8.5 by adding Na_2CO_3. Alumina (20 mg) was added, and the mixture was stirred for 3 min. After filtration, alumina was washed with water (3 × 2 ml), and the catecholamines were then eluted with 300 μl of 1 M CH_3COOH. Finally, the eluate was analyzed by CE–MS, CE–UV, or reversed-phase HPLC–amperometry.

As eluents we tested 0.6 and 0.1 M $HClO_4$ [7], 0.3 M HCl [6], 0.3 and 1 M CH_3COOH [8], and a mixture of 0.6 M $HClO_4$ with 1 M CH_3COOH

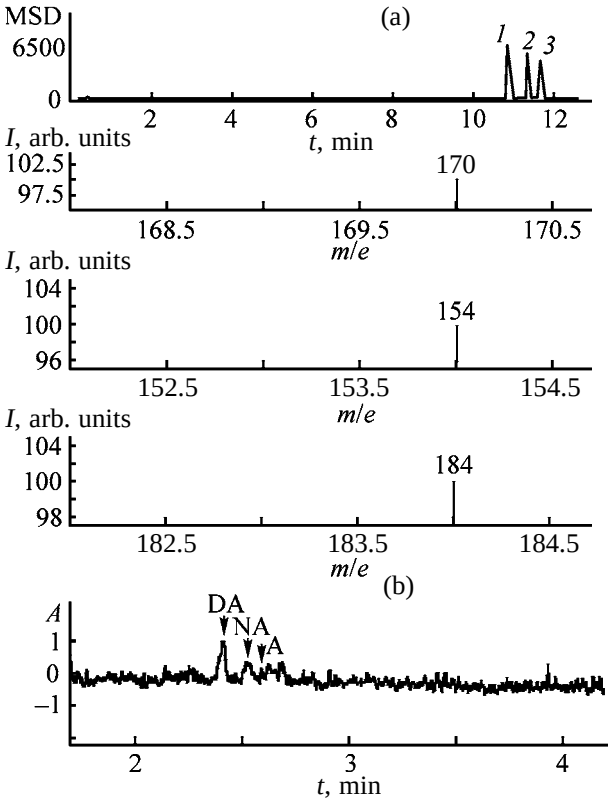

Fig. 1. Electrophoregram of standard samples: (*1*) dopamine, (*2*) noradrenaline, and (*3*) adrenaline. Agilent instrument; sample: 1 mg l^{-1} catecholamine in 1×10^{-2} M HCl; CE conditions: supporting electrolyte acetate buffer (pH 4.45), 0.005 M diethylamine hydrochloride; hydrodynamic injection: 50 mbar × 10 s; separation: 27 kV, 10.5 μA; MS detection: SIM, *m*/*e* 154 (0–11.25 min), 170 (11.25–11.8 min), and 184 (11.8–12.2 min). (*I*) Intensity of MS signal, (*A*) absorbance, (*m*/*e*) mass to charge ratio, and (*t*) migration time. (a) SIM mode (MS detector) and (b) UV detector.

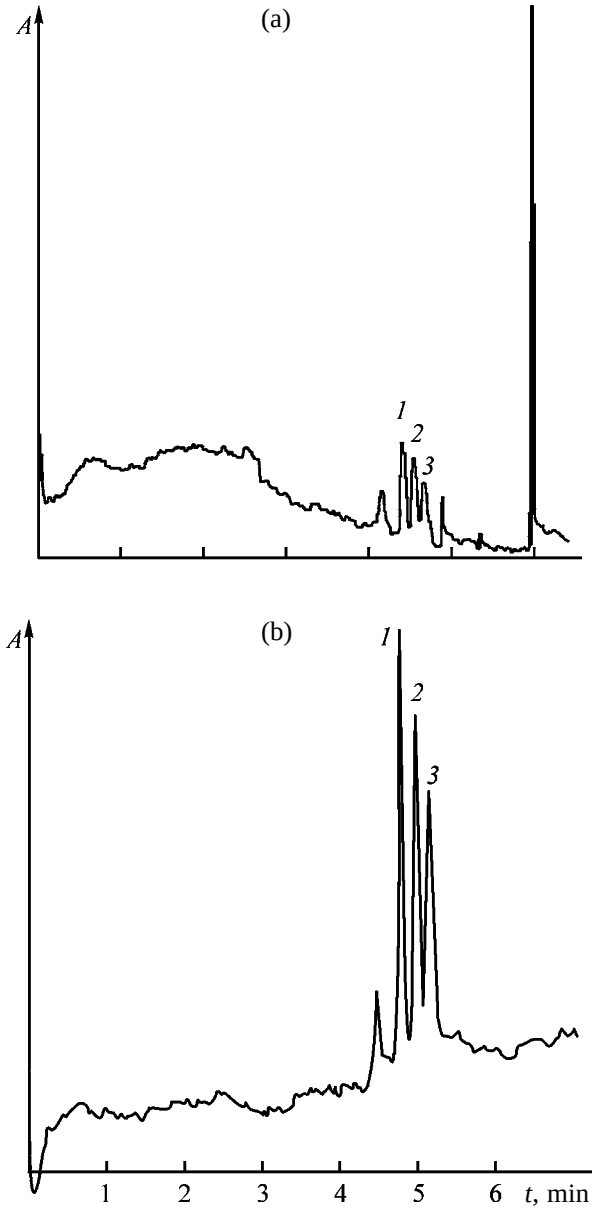

Fig. 2. Electrophoregram of a model mixture of catecholamines after purification by SPE on alumina. (*A*) Absorbance and (*t*) migration time. Kapel' 103 RE instrument; hydrodynamic injection: 10 mbar × 10 s; separation: 25 kV; UV detection at 254 nm. Model mixture: (*1*) dopamine, (*2*) noradrenaline, and (*3*) adrenaline (2 mg l^{-1}). Sample volume (ml): (a) 2 and (b) 5.

(20 : 80). When optimizing the SPE conditions, we varied the amount of alumina from 10 to 100 mg and the eluent concentration from 0.3 to 5 M. The most efficient extraction was obtained with 20 mg of alumina as a sorbent and 1 M CH_3COOH as an eluent. The extract was then analyzed by CE–MS. The recoveries of dopamine, noradrenaline, and adrenaline with 1 M CH_3COOH were 90 ± 2, 104 ± 2, and 82 ± 2%, respectively. The results of analysis of the model mixtures by CE with MS detection (SIM) are presented in Fig. 1, and with UV detection, in Fig. 2 (10- and 25-fold preconcentration).

Table 3 shows that the CE–MS method is inferior to HPLC–amperometry in the sensitivity, the total analysis time being well comparable for both methods. As a conclusion, thanks to the high efficiency of CE and versatility of MS detection, CE–MS can be used also for determination of neurotransmitters other than those described in this work as well as of various organic compounds with an amino group in complex mixtures.

CONCLUSIONS

(1) A method for electrophoretic determination of catecholamines (adrenaline, noradrenaline, and dop-

amine) with mass-spectrometric detection wss developed on simulated mixtures, and the detection limits for the analytes were determined. The supporting electrolyte was 0.05 M acetate buffer containing 0.05 M diethylamine hydrochloride. The electrospray operation mode was optimized to improve the sensitivity of mass-spectrometric detection. The optimal conditions are as follows: drying gas flow rate 5 l min^{-1}, temperature 200°C, pressure 14 kPa, composition of the coating liquid for the inner capillary 2-propanol–H_2O = 1 :1 + 0.5% CH_3COOH, and flow rate 4 μl min^{-1}.

(2) A comparative study was made of the methods of capillary electrophoresis–UV spectrometry, capillary electrophoresis–mass spectrometry, and reversed-phase HPLC–amperometry, as applied to determination of catecholamines. It was demonstrated that adrenaline, noradrenaline, and dopamine can be determined in a biological object by capillary electrophoresis–UV spectrometry and HPLC–amperometry without preconcentration. Capillary electrophoresis surpasses HPLC–amperometry in the performance by an order of magnitude, being inferior to it in the sensitivity.

REFERENCES

1. Vuorensola, K., Kokkonen, J., Siren, H., and Ketola, R.A., *Electrophoresis*, 2001, vol. 22, pp. 4347–4354.
2. Peterson, Z.D., Collins, D.C., Bowerbank, C.R., *et al*., *J. Chromatogr., Ser. B*, 2002, vol. 776, pp. 221–229.
3. Kirby, D.P., Thorne, J.M., Gotzinger, W.K., and Karger, B.L., *Anal. Chem*., 1996, vol. 68, pp. 4451–4457.
4. Vuorensola, K. and Siren, H., *J. Chromatogr., Ser. A*, 2000, vol. 895, pp. 317–327.
5. McKibin, P.B. and Chen, D.D.J., *Anal. Chem*., 2000, vol. 72, pp. 1242–1252.
6. Chen, D.-C., Zhan, D.-Z., Cheng, C.-W., *et al*., *J. Chromatogr., Ser. B*, 2001, vol. 750, pp. 33–39.
7. Paquette, D.M., Sing, R., Banks, P.R., and Waldron, K.C., *J. Chromatogr., Ser. B*, 1998, vol. 714, pp. 47–57.
8. Banks, J.F., Jr., *J. Chromatogr., Ser. A*, 1995, vol. 712, pp. 245–252.
9. Riggin, R.M. and Kissinger, P.T., *Anal. Chem*., 1977, vol. 49, no. 13, pp. 2109–2111.

Russian Journal of Applied Chemistry, Vol. 77, No. 7, 2004, pp. 1156–1159. Translated from Zhurnal Prikladnoi Khimii, Vol. 77, No. 7, 2004, pp. 1170–1173.

MACROMOLECULAR CHEMISTRY AND POLYMERIC MATERIALS

Specific Features of Synthesis of Poly(Methyl Methacrylate) in the Presence of Bis(isopropylcyclopentadienyl)tungsten Dichloride

E. V. Telegina, L. L. Semenycheva, and D. F. Grishin

Research Institute of Chemistry, Lobachevsky Nizhni Novgorod State University, Nizhni Novgorod, Russia

Received January 26, 2004

Abstract—Synthesis of poly(methyl methacrylate) in the bulk and in dimethylformamide under conditions of radical initiation in the presence of bis(isopropylcyclopentadienyl)tungsten dichloride was studied.

Radical polymerization of methyl methacrylate (MMA), initiated with azobis(isobutyronitrile) (AIBN) in the presence of bis(isopropylcyclopentadienyl)tungsten dichloride (**I**) in the bulk and in dimethylformamide (DMF), is characterized by uniform course with significant reduction of the gel effect and its shift toward higher conversions; the viscosity-average and number-average molecular weights (MW) of the resulting polymer linearly grow with conversion, and the molecular-weight distribution (MWD) curves shift toward higher molecular weights.

Radical polymerization by the mechanism involving a change in the metal atom valence (atom transfer radical polymerization, ATRP) with participation of organometallic compounds as chain-transfer agents is a promising line in controlled polymerization under conditions of radical initiation [1, 2].

A specific feature of ATRP is its applicability to a wide range of monomers, including acrylic monomers [1]. In particular, poly(methyl methacrylate) (PMMA), one of the most important large-tonnage polymeric products, was prepared by the ATRP mechanism in the presence of various complexes of transition metals, in particular, Mo(III) [3], Cu(I) [1, 4, 5], Ru(II) [6, 7], Fe(II) [1, 8–11], etc. It was shown [3] that oxidation of a transition metal by the reversible Kharasch reaction [12] with alkyl halide RX in the medium of a vinyl monomer allows fragment-by-fragment chain propagation:

$$RX + M^nY_mL_x \rightleftarrows R^{\cdot} + X\text{–}M^{n+1}Y_mL_x, \quad (1)$$

$$R^{\cdot} + M \rightarrow RM^{\cdot}, \quad (2)$$

where M^n is the metal atom in oxidation state n; L, ligand; Y and X, halogen atoms; and M, monomer.

This method, however, has signficant drawbacks: toxicity of some organic halides RX, instability of many organometallic compounds in air [10], and relatively low reaction rate. To solve this problem, so-called "reverse" or "alternative" polymerization by the ATRP mechanism was suggested [4, 8, 10, 11]; in the process, standard radical initiators, e.g., azo compounds [4, 10], are used in combination with organic compounds of transition metals in higher oxidation state. In this case, after decomposition of the initiator into radicals, the reversible Kharasch reaction formally "starts" from the left side of Eq. (1) (Reverse Atom Transfer Radical Polymerization, RATRP).

In this study, we examined the prospects for using compound **I** [hereinafter, $W(IV)L_2X_2$, L = *i*-PrC_5H_4] for controlled synthesis of PMMA under conditions of radical initiation in the bulk and in DMF.

EXPERIMENTAL

$W(IV)L_2X_2$ was purchased from Aldrich. AIBN (polymerization initiator) [13], MMA (monomer) [14], and organic solvents [15] were purified by standard procedures.

The calculated amounts of $W(IV)L_2X_2$ and AIBN were dissolved in MMA and DMF (for the process in the solvent), and PMMA was prepared in evacuated ampules at a residual pressure of 1.3 Pa. The kinetics of MMA polymerization in solution was studied gravimetrically and thermographically [16]. The molecular-weight characteristics of PMMA were determined viscometrically [17] and by gel permeation chromatography (GPC) on an installation equipped with a set of five Styrogel columns with pore diameters of 10^5, 3×10^4, 10^4, 10^3, and 250 Å (Waters, the United

1070-4272/04/7707-1156 © 2004 MAIK "Nauka/Interperiodica"

Molecular-weight characteristics of PMMA synthesized in the presence of 0.1 mol % AIBN in DMF*

$W(IV)L_2X_2$: AIBN weight ratio	γ, %	$M_\eta \times 10^{-3}$	$M_n \times 10^{-3}$	$M_w \times 10^{-3}$	M_w/M_n
0 : 1	11.6	218	–	–	–
	22.0	239	189	365	1.9
	43.8	365	233	603	2.6
	58.0	545	319	908	2.8
	61.3	697	–	–	–
	78.2	737	–	–	–
	86.7	658	403	1121	2.8
5 : 1	6.3	156	–	–	–
	13.7	181	155	301	1.9
	21.0	185	–	–	–
	27.5	217	188	376	2.0
	37.0	233	–	–	–
	52.0	295	219	548	2.5
	61.3	383	–	–	–
	69.7	322	–	–	–
	78.2	369	274	663	2.4

* (M_w) Weight-average MW.

States). An R-403 differential refractometer (Waters) was used as detector. The eluent was THF. Calibration was done with close-cut polystyrene references [18].

The kinetic data on MMA polymerization initiated with AIBN in the presence of 0.1 mol % $W(IV)L_2X_2$ in the bulk at 70°C show that the gel effect at the equimolar content of $W(IV)L_2X_2$ relative to AIBN (0.1 mol %) considerably decreases. Figure 1a shows typical kinetic curves for MMA polymerization with the W(IV) complex as the chain-transfer agent. The possible concentration of the organometallic complex for the reaction in the bulk is restricted by its solubility in MMA. Therefore, radical polymerization of MMA with additions of $W(IV)L_2X_2$ was performed in a solvent, DMF. The kinetic data on polymerization of MMA at 70°C in the presence of $W(IV)L_2X_2$ dissolved in DMF ([MMA] : [DMF] = 5 : 1, [AIBN] = 0.1 mol %) indicate that the autoacceleration is suppressed to a significantly greater extent compared to the process in the bulk; with increasing concentration of $W(IV)L_2X_2$, the controlling effect becomes more pronounced (Fig. 1b).

Study of the molecular-weight characteristics of the polymers prepared in the presence of $W(IV)L_2X_2$ confirms a significant effect of the organotungsten compound on the chain propagation step in MMA polymerization both in the bulk and in DMF (see table). As seen from the table, and also from Figs. 2a and 2b, the viscosity-average (M_η) and number-average (M_n) molecular weights linearly grow with the monomer conversion γ in MMA polymerization both in the bulk and in the solvent. The MWD curves of PMMA samples show a shift toward higher MW, typical of controlled polymerization (Fig. 3). The polydispersity coefficients M_w/M_n (see table) of the polymers prepared in polymerization of MMA in DMF are considerably lower as compared to the polymer prepared in the bulk, although in this case the growth of M_w/M_n at high conversions is observed also. Such a phenom-

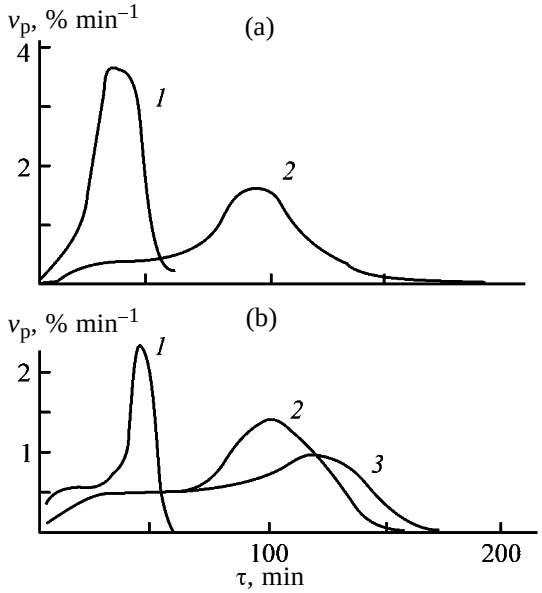

Fig. 1. Differential kinetic curves of MMA polymerization, initiated with AIBN (0.1 mol %) and $W(IV)L_2X_2$ (a) in the bulk and (b) in DMF at 70°C. (v_p) Polymerization rate and (τ) time. $W(IV)L_2X_2$ concentration relative to MMA, mol %: (a) (*1*) 0 and (*2*) 0.1; (b) (*1*) 0, (*2*) 0.3, and (*3*) 0.5.

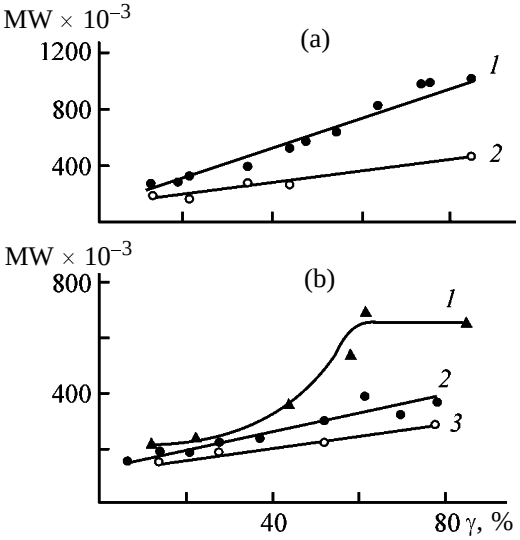

Fig. 2. Molecular weight (MW) of PMMA as a function of convesion γ (0.1 mol % AIBN, 70°C) (a) in the presence of $W(IV)L_2X_2$ (0.1 mol %) and (b) in DMF (*1*) in the absence and (*2*, *3*) in the presence of $W(IV)L_2X_2$ (0.5 mol %). Molecular weight: (a) (*1*) viscosity-average and (*2*) number-average; (b) (*1*, *2*) viscosity-average and (*3*) number-average.

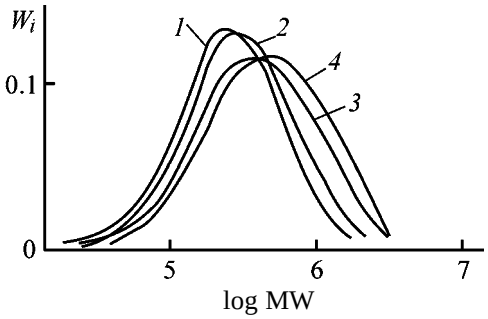

Fig. 3. Molecular-weight distribution of PMMA samples prepared in the presence of 0.5 mol % $W(IV)L_2X_2$ and 0.1 mol % AIBN in DMF. (W_i) Weight proportion of given fraction. Conversion, %: (*1*) 13.7, (*2*) 27.5, (*3*) 52, and (*4*) 78.2.

enon is observed fairly frequently in polymerization in the presence of other organometallic compounds as chain-transfer agents [4, 5, 11]. The growth of the polydispersity coefficients is apparently due to simultaneous occurrence both of the controlled synthesis and of common radical polymerization with bimolecular chain termination, and also of other side reactions [2]. In particular, in the presence of organometallic compounds the growth of the polydispersity coefficients is often associated with the catalytic chain transfer [3].

Thus, polymerization of MMA in the presence of $W(IV)L_2X_2$ in the amount comparable with that of the initiator has features of a controlled process. The strongest controlling effect is observed at the 1 : 5 ratio of the initiator and additive (polymerization in a solvent). In particular, at the 0.5 mol % concentration of the organometallic compound, the gel effect is virtually suppressed, the number-average molecular weight linearly grows with conversion, and M_w/M_n is considerably lower than in the case of the polymer prepared under comparable conditions but without additive.

By analogy with data on polymerization of vinyl monomers in the presence of organomolybdenum complexes $[C_5H_5Mo(PH_3)_2BrCl_2$ and $C_5H_5MoCl_3L$, where L = $P(CH_3)_3$, PCH_3Ph_2, etc.] by the ATRP mechanism [3], we can assume that, in the case of $W(IV)L_2X_2$, whose electronic structure is similar to that of the Mo(IV) complex, the control of the polymeric chain is also accomplished by the ATRP mechanism. Since in the system under consideration the source of primary initiating radicals is AIBN and not the organic halide, the overall reaction scheme will somewhat differ from the usual ATRP mechanism [4, 8, 10, 11]. In particular, in contrast to the ATRP mechanism [reactions (1), (2)], in our case the initiating radicals R$^\bullet$ are generated by homolytic cleavage of AIBN:

$$\text{AIBN} \rightarrow 2R^\bullet, \quad (3)$$

$$R^\bullet + n\text{M} \rightarrow \text{RM}_n^\bullet. \quad (4)$$

Then the arising propagation radicals $RM_n^\bullet$ react with the organometallic compound to give the adduct RM_nX with chlorine abstraction from $W(IV)L_2X_2$. In the process, the oxidation state of the metal decreases:

$$\text{RM}_n^\bullet + W(IV)L_2X_2 \rightleftarrows \text{RM}_n\text{X} + W(III)L_2X, \quad (5)$$

where X is the halogen atom.

The organic halide formed in the reaction can reversibly react with $W(III)L_2X$ [schemes (1), (5)]. This results in regeneration of radicals which can react with the monomer to form propagating chains [scheme (2)]. Taking into account the kinetic features of MMA polymerization in the presence of $W(IV)L_2X_2$ in DMF, and also the molecular-weight characteristics of the synthesized polymers, we can conclude that this chain-transfer agent takes a direct part in the step of chain propagation by the RATRP mechanism.

CONCLUSIONS

(1) Bis(isopropylcyclopentadienyl)tungsten dichloride exerts a significant effect on the kinetic param-

eters of methyl methacrylate polymerization and molecular-weight characteristics of polymethyl methacrylate at temperatures similar to those of commercial synthesis of this polymer (70°C).

(2) The controlling effect of the organotungsten compound is associated with a reversible change in the oxidation state of the metal in the course of the polymer synthesis.

ACKNOWLEDGMENTS

The study was financially supported by the Russian Foundation for Basic Research (project no. 02-03-32427) and by the Competitive Center for Basic Natural Science (project no. A03-2.11-506).

REFERENCES

1. Matyjaszewski, K. and Xia, J., *Chem. Rev.*, 2001, vol. 101, pp. 2921–2990.
2. Grishin, D.F. and Semenycheva, L.L., *Usp. Khim.*, 2001, vol. 70, pp. 486–510.
3. Grognes, E. Le, Claverie, J., and Poli, R., *J. Am. Chem. Soc.*, 2001, vol. 123, pp. 9513–9524.
4. Xia, J. and Matyjaszewski, K., *Macromolecules*, 1997, vol. 30, pp. 7692–7696.
5. Xia, J. and Matyjaszewski, K., *Macromolecules*, 1999, vol. 32, pp. 5199–5202.
6. Watanabe, Y., Ando, T., Kamigaito, M., and Sawamoto, M., *Macromolecules*, 2001, vol. 34, pp. 4370–4374.
7. Ando, T., Kamigaito, M., and Sawamoto, M., *Macromolecules*, 2000, vol. 33, pp. 5825–5829.
8. Qin, D.-Q., Qin, S.-H., Chen, X.-P., and Qiu, K.-Y., *Polymer*, 2000, vol. 41, pp. 7347–7353.
9. Matyjaszewski, K., Wei, M., Xia, J., and McDerwott, N.E., *Macromolecules*, 1997, vol. 30, pp. 8161–8164.
10. Moineau, G., Dubois, Ph., Jérôme, R., Senninger, T., and Teyssié, Ph., *Macromolecules*, 1998, vol. 31, pp. 545–547.
11. Teodorescu, M., Gaynor, S., and Matyjaszewski, K., *Macromolecules*, 2000, vol. 33, pp. 2335–2339.
12. Kharasch, M.S. and Fields, E.K., *J. Am. Chem. Soc.*, 1941, vol. 63, pp. 2316–2320.
13. *Organic Synthesis*, New York: Wiley, 1946–1952, vols. 26–32.
14. *Entsiklopediya polimerov* (Polymer Encyclopedia), Kargin, V.A., Ed., Moscow: Sov. Entsiklopediya, 1972, vol. 1.
15. Weissberger, A. and Proskauer, E.S., *Organic Solvents. Physical Properties and Methods of Purification*, Riddick, J.A. and Toops, E.E., Eds., New York: Interscience, 1955.
16. Arulin, V.I. and Efimov, L.I., in *Trudy po khimii i khimicheskoi tekhnologii* (Papers on Chemistry and Chemical Technology), Gor'kii: Gor'k. Gos. Univ., 1970, pp. 74–76.
17. Shatenshtein, A.I., Vyrskii, Yu.P., Pravikova, N.A., *et al.*, *Prakticheskoe rukovodstvo po opredeleniyu molekulyarnykh vesov i molekulyarno-vesovogo raspredeleniya polimerov* (Manual on Determination of Molecular Weights and Molecular-Weight Distribution of Polymers), Moscow: Khimiya, 1964.
18. Moris, S., *J. Liq. Chromatogr.*, 1990, vol. 13, no. 9, p. 1719.

Russian Journal of Applied Chemistry, Vol. 77, No. 7, 2004, pp. 1160–1164. Translated from Zhurnal Prikladnoi Khimii, Vol. 77, No. 7, 2004, pp. 1174–1178.

MACROMOLECULAR CHEMISTRY AND POLYMERIC MATERIALS

Copolymers Based on Diallylhydrazines

A. I. Vorob'eva, M. N. Gorbunova, V. Yu. Gusev, R. R. Muslukhov, S. V. Kolesov, and A. G. Tolstikov

Institute of Technical Chemistry, Perm Scientific Center, Russian Academy of Sciences, Perm, Russia
Institute of Organic Chemistry, Ufa Scientific Center, Russian Academy of Sciences, Ufa, Bashkorkostan, Russia

Received March 12, 2004

Abstract—The possibility of preparing polymers based on *N*,*N*-diallylhydrazine derivatives by allylation of carboxylic acid hydrazides was considered.

The range of nitrogen-containing allyl compounds from which linear macromolecular polymers can be produced by radical homo- and copolymerization is very limited. Actually, only quaternary diallylammonium salts are widely used as monomers for synthesis of polyfunctional polymers [1–3]. At the same time, such polymers exhibit unique properties [4–6], which makes it urgent to search for and study nitrogen-containing allyl monomers of new structural types. In this respect, promising monomers are *N*-allylated derivatives of carboxylic acid hydrazides. Hydrazides of aliphatic acids have flotation properties [7], and hydrazides of naphthenic acids are selective extracting agents for copper [8, 9].

Preparation of derivatives of *N*,*N*-diallylhydrazines (DAHs) is the way not only to produce new polyfunctional polymers but also to impart to them certain physicochemical and biological characteristics typical for the initial compounds. The first stage on this way is to establish the possibility of involving these derivatives in radical polymerization.

Here we attempted to prepare polymers based on DAHs, in particular, *N*,*N*-diallyl-*N*′-acylhydrazine (DAAH), *N*,*N*-diallyl-*N*′-propanoylhydrazine (DAPH), and *N*,*N*-diallyl-*N*′-benzoylhydrazine (DABH).

EXPERIMENTAL

N,*N*-Diallylhydrazines were synthesized by the reaction of hydrazides of aliphatic and aromatic acids with allyl halides (AllHlg):

$$R–CO–NH–NH_2 + 2AllHlg \rightarrow R–CO–NH–N(All)_2 + 2HHlg,$$

where R is CH_3, C_3H_7, or C_6H_5.

The monomers used for the synthesis of copolymers were acrylonitrile (AN), acrylamide (AA), methyl methacrylate (MMA), vinyl acetate (VA), *N*-vinylpyrrolidone (VP); the initiators were azobis(isobutyronitrile) (AIBN), potassium persulfate (PP), and benzoyl peroxide (BP); the solvents were methanol, chloroform, and dimethyl sulfoxide. After purification by common procedures, the characteristics of all chemicals were in good agreement with published data. Sulfur dioxide was dried by passing through concentrated H_2SO_4 and freshly calcined $CaCl_2$.

Copolymerization of DAHs with vinyl monomers (VMs) was carried out in a vacuum in the bulk and in a solution in the presence of radical initiators (for polymerization conditions, see Table 1).

Copolymerization of DAHs with sulfur dioxide was carried out in a glass reactor by the procedure described in [10] (for polymerization conditions, see Table 2). The polymers were dried by twofold reprecipitation from a solvent to a precipitant chosen individually for each system. The purified polymers were dried in a vacuum at 50°C to constant weight. The compositions of copolymers were evaluated from the results of elemental analysis. The ^{13}C NMR spectra were recorded on a Bruker AM-300 spectrometer operating at 75.46 MHz. DMSO-d_6 and D_2O were used as solvents, and tetramethylsilane and DSS, respectively, as internal references. The UV spectra were recorded on a Shimadzu UV-VIS-NIR 3100 spectrophotometer. The composition of the complex was determined by the method of isomolar series [11].

Under usual conditions, DAHs practically do not enter into homopolymerization by a free-radical mech-

1070-4272/04/7707-1160 © 2004 MAIK "Nauka/Interperiodica"

Table 1. Copolymerization of diallylhydrazine derivatives (M_1) with VMs (M_2) [AIBN] = 3.0 wt %, T = 90°C

M_1	M_2	Composition of initial mixture, mol %		Medium	Yield, %	Copolymer composition, mol %		Solvent for copolymers
		M_1	M_2			m_1	m_2	
DAAH	MMA	50.0	50.0	In the bulk	31.5	18.3	81.7	DMSO, methanol, acetone,
		66.6	33.4	″	12.8	23.0	73.0	benzene, THF, chloroform
DAAH	AN	50.0	50.0	″	18.0	14.2	85.8	DMSO, DMF, pyridine
		57.9	42.1	″	12.8	25.0	75.0	
DAAH	AA	50.0	50.0	H_2O*	41.0	20.3	79.7	DMSO, H_2O
		64.4	35.6	Methanol	21.0	28.0	72.0	
DAAH	VA	50.0	50.0	In the bulk	11.0	38.0	62.0	DMSO, methanol, acetone
		65.7	34.3	″	3.0	–	–	
DAAH	VP	50.0	50.0	″	28.2	19.0	81.0	H_2O, methanol, acetone
		55.0	45.0	″	10.0	–	–	
DAAH	Acrylic acid	50	50	″	27.2	15.0	85.0	DMSO
DABH	AN	34	66	Methanol	29.3	10.2	89.8	DMSO, DMF, pyridine, acetone
DABH	AA	33	37	″	38.2	10.5	89.5	Insoluble

* Potassium persulfate initiator.

Table 2. Copolymerization of diallylhydrazine derivatives (M_1) with SO_2. Composition of the initial mixture: $M_1 : M_2 = 1 : 1$; [In] = 3.0 wt %, T = 90°C

M_1	Medium	Initiator	Yield, %	Copolymer composition, %		Solvent for copolymer
				m_1	m_2	
DAAH	In the bulk	AIBN	41.7	48.0	52.0	DMSO, water
		AIBN*	48.2	49.0	51.0	
	″	BP	5.6	47.0	53.0	
	Aqueous	PP	38.5	47.0	53.0	
	Acetone	AIBN	50.2	53.0	47.0	
	Chloroform	AIBN	60.0	48.0	52.0	
DAPH	In the bulk	AIBN	50.0	49.0	51.0	DMSO, methanol
	Chloroform	AIBN	70.4	48.0	52.0	
	Methanol	AIBN**	34.3	49.0	51.0	
	DMSO	AIBN**	44.4	50.0	50.0	
	Chloroform	AIBN**	57.4	48.0	52.0	
DABH	In the bulk	AIBN	23.1	49.0	51.0	DMSO, DMF
	Methanol	AIBN	35.5	50.0	50.0	

* In the presence of HCl.
** Polymerization duration 1 h.

anism. The activity of DAHs somewhat increases on adding protic and aprotic acids, which is a well-known procedure for activation of allyl monomers. However, in this case, e.g., in polymerization of DAAH in the presence of HCl, H_3PO_4, and $ZnCl_2$ at the ratio DAH : acid = 1 : 1.2 (T = 90°C, initiator AIBN, 30 h), the yield of the homopolymer did not exceed 6–10%.

The use of DAHs in radical copolymerization with VMs containing both electron-acceptor (AA, AN, and methacrylic acid) and electron-donor (VA and VP) substituents is significantly more efficient. Copolymerization of DAHs (M_1) with vinyl monomers (M_2) proceeds at a noticeable rate at a temperature above 80°C and initiator concentration of no less than 2.5 wt %. DAHs are less active than vinyl monomers.

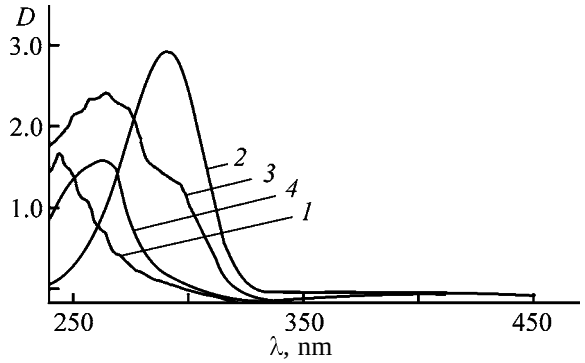

Electronic absorption spectra of solutions in chloroform. (*D*) Optical density and (λ) wavelength. (*1*) DAAH ([DAAH] 1×10^{-1} M), (*2*) SO_2 ([SO_2] 1×10^{-3} M), (*3*) a mixture of DAAH and SO_2 ([DAAH] 5×10^{-3} M, [SO_2] 5×10^{-4} M), and (*4*) difference of spectrum *3* and half-sum of spectra *1* and *2*.

Copolymers of all the monomer pairs are enriched with VM units as compared to the composition of the initial mixture (Table 1). At the equimolar ratio of the monomers in the initial mixture, the content of DAHs in the copolymers (excluding the copolymer with VA) does not exceed 20 mol %.

In spite of high temperature (90°C) and high initiator concentration (3 wt %), the rate of copolymerization of DAHs with VM is low, especially at the content of M_1 in the reaction mixture exceeding 50 mol %.

DAHs are significantly more active in copolymerization with sulfur dioxide having high electron-acceptor power. All the DAHs copolymerize with SO_2 to form alternating copolymers with equimolar composition, irrespective of the ratio of the monomers in the initial mixture, solvent and initiator nature, and reaction temperature (Table 2). The constancy of the composition of the copolymers, irrespective of the ratio of the monomers in the reaction mixture, suggests that copolymerization of DAHs with SO_2 proceeds with formation of complexes [DAH···SO_2]. The UV spectra of a mixture of DAAH with SO_2 in chloroform contain a new band of charge transfer with λ_{max} = 263 nm (for SO_2, λ_{max} = 275.9 nm), suggesting formation of a donor–acceptor complex (see figure).

The reaction conditions do not affect the composition of copolymers but significantly affect the copolymer yield (Table 2). In particular, higher yields of copolymers of DAH with SO_2 were obtained with AIBN and PP as an initiator; with BP, there was virtually no copolymerization.

In the systems under consideration, the yields of polymers in copolymerization in the bulk do not exceed 50% even at extremely long reaction time (up to 10 h). In copolymerization in a solution, the yield of copolymer depends on the solvent. In particular, in chloroform the yields of DAPH copolymers are higher than those in the bulk and can reach 70%.

The structure of the copolymers was determined by ^{13}C NMR. In the spectra of copolymers (Table 3) of derivatives of DAHs with SO_2 (nos. 6–8), along with the signals of substituent atoms at the –NHR group, where R is CH_3, C_3H_7, and C_6H_5, there are only three pairs of signals corresponding to two methylene and one methine groups of the polymer chain, which are stereoisomeric. This suggests the structural homogeneity of the copolymers. Two pairs of low-field triplets correspond to *cis*/*trans* stereoisomeric carbon atoms $C^1C^{1'}$ and $C^3C^{3'}$; two doublet signals correspond to stereoisomeric C^2 and $C^{2'}$ atoms of the heterocycle. The relative content of *cis*/*trans* stereoisomeric units of DAH was estimated from the ^{13}C NMR spectrum to be approximately 4/1. The chemical shifts of the above carbon atoms, considering the additive effect of substituents, $–SO_2–$ and NH–R groups, are close to the chemical shifts of the corresponding atoms of the copolymer of *N*,*N*-dimethyl-*N*,*N*-diallylammonium chloride with SO_2 [10]. The chemical shifts of VM units in the spectra of the copolymers are practically the same as those for the corresponding carbon atoms of their homopolymers [12–16]. In the spectra of the copolymers with broad-band proton decoupling, similarly to the spectra of VM homopolymers, there are configuration multiplets belonging to pseudo-asymmetric C^7 atom and adjacent α and β carbon nuclei. These data suggest that the copolymer contains VM blocks alternating with separate DAH units.

The resulting copolymers are soluble in polar solvents such as DMSO and DMF. Copolymers of DAAH with SO_2, AA, and VP are also soluble in water. Preliminary tests showed that copolymers of DAAH with SO_2 have flocculation properties, in particular, in precipitation of $Cu(OH)_2$.

CONCLUSIONS

(1) Derivatives of diallylhydrazines are a new structural type of *N*-allylated monomers promising for production of polyfunctional polymers, among them water-soluble, in radical polymerization.

(2) Diallylhydrazines enter into copolymerization reactions with participation of both double bonds to

Table 3. Chemical shifts and multiplicity of the signals in the ^{13}C NMR spectra of copolymers

Copolymer no.	Stereoisomer	C^1, $C^{1'}$	C^2, $C^{2'}$	C^3, $C^{3'}$	C^4	C^5	C^6	C^7	C^8	C^9	C^{10}	C^{11}
1	*cis*	62.20	40.19	28.09	175.04	21.69	36.19	44.40	182.09			
	trans	62.35	40.88	28.41	174.75	q	37.14	44.18	183.05			
		t	d	t	s		36.82	43.82	s			
							t	d				
2	*cis*	58.96	39.69	25.44	173.71	21.17	32.56	27.86	120.28			
	trans	60.08	41.53	28.73	173.58	19.62	32.88	27.38	120.83			
		t	d	t	s	q	t	26.72	121.94			
								d	s			
3	*cis*	58.76	34.80	29.76	176.74	21.16	43.85	44.38	19.47	177.15	51.60	
	trans	59.32	36.05	32.77	s	q	t	s	18.45	176.17	q	
		t	d	t					q	s		
4	*cis*	59.98	40.25	27.30	178.30	20.40	32.80	66.51	170.15	21.12		
	trans	62.81	43.41	29.94	s	q	31.94	69.31	169.87	19.48		
		t	d	t			t	72.19	s	q		
			34.91	32.77				d				
			35.63	35.44								
			d	t								
5	*cis*	62.25	35.08	29.14	173.54	21.45	31.85	46.25	179.78	33.67	19.95	44.76
	trans	64.85	40.63	32.14	s	q	t	48.06	s	t	t	t
		t	d	t				d				
	cis		38.13									
	trans		41.05									
			d									
6	*cis*	61.90	35.41	54.01	177.13	22.42						
	trans	61.33	37.82	57.02	s	q						
		t	d	t								
7	*cis*	57.80	33.53	52.19	165.51	133.09	127.45	128.55	131.83			
	trans	58.35	36.51	55.45	s	s	d	d	d			
		t	d	t								
8	*cis*	57.41	33.27	52.09	170.73	35.58	18.50	13.45				
	trans	58.04	33.27	55.26	s	t	t	q				
		t	d	t								

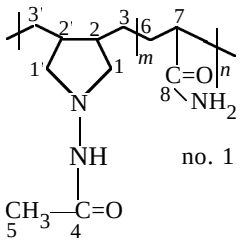

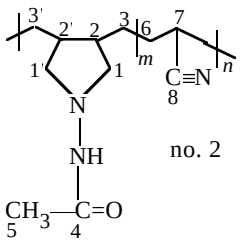

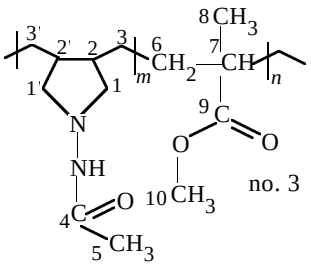

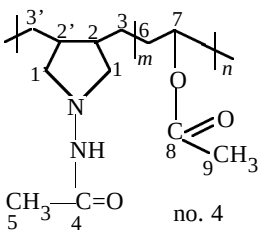

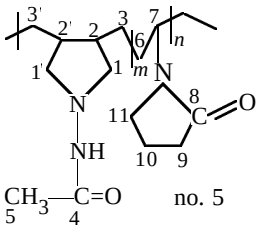

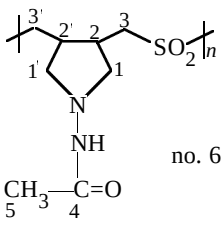

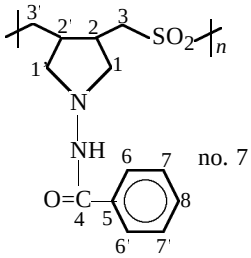

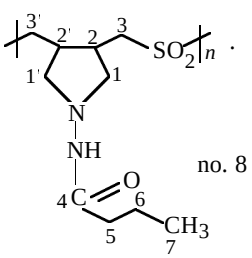

form soluble cyclolinear polymers of pyrrolidone structures.

(3) Copolymerization of diallylhydrazines with vinyl monomers yields random copolymers, and that with sulfur dioxide, alternating copolymers of equimolar composition.

REFERENCES

1. Topchiev, D.A., Bikasheva, G.T., Martynenko, A.I., *et al.*, *Vysokomol. Soedin., Ser. B*, 1980, vol. 22, no. 4, pp. 269–273.
2. Wandrey, Ch. and Jaeger, W., *Acta Polym.*, 1985, vol. 36, no. 2, pp. 100–102.
3. Vorob'eva, A.I., Kartusheva, E.R., Leplyanin, G.V., *et al.*, *Vysokomol. Soedin., Ser. B*, 2000, vol. 44, no. 5, pp. 868–871.
4. USSR Inventor's Certificate no. 1514759.
5. USSR Inventor's Certificate no. 1744797.
6. RF Patent no. 2095056.
7. Teterina, N.N., Radushev, A.V., Adeev, M.S., and Gusev, V.Yu., *Zh. Prikl. Khim.*, 1995, vol. 68, no. 1, pp. 3–8.
8. Radushev, A.V., Gusev, V.Yu., Bogomazova, V.S., *et al.*, *Zh. Prikl. Khim.*, 1996, vol. 69, no. 8, pp. 1283–1289.
9. Radushev, A.V., Gusev, V.Yu., Bogomazova, V.S., and Kichichin, V.I., *Izv. Vyssh. Uchebn. Zaved., Tsvetn. Metall.*, 1999, no. 6, pp. 28–30.
10. Vorob'eva, A.I., Vasil'eva, E.V., Gaisina, Kh.A., *et al.*, *Vysokomol. Soedin., Ser. A*, 1996, vol. 38, no. 10, pp. 1663–1667.
11. Gur'yanova, E.N., Gol'dshtein, I.P., and Romm, I.P., *Donoro-aktseptornaya svyaz'* (Donor–Acceptor Bond), Moscow: Khimiya, 1973.
12. Bajaj, P., Padmanaban, M., and Gandhi, R.P., *Polymer*, 1985, vol. 26, no. 3, pp. 391–396.
13. Berestova, S.S., Shchirets, V.A., Selikhova, V.I., *et al.*, *Vysokomol. Soedin., Ser. B*, 1996, vol. 38, nos. 9–10, pp. 1612–1613.
14. Lancaster, J.E. and O'Connor, M.N., *J. Polym. Sci., Polym. Lett. Ed.*, 1982, vol. 20, no. 10, pp. 547–550.
15. Moad, G., Solomon, D.H., Spurling, T.H., *et al.*, *Aust. J. Chem.*, 1986, vol. 39, no. 1, pp. 43–50.
16. Cheg, H.N., Smith, T.E., and Virtus, D.M., *J. Polym. Sci., Polym. Lett. Ed.*, 1981, vol. 19, pp. 29–31.

Russian Journal of Applied Chemistry, Vol. 77, No. 7, 2004, pp. 1165–1168. Translated from Zhurnal Prikladnoi Khimii, Vol. 77, No. 7, 2004, pp. 1179–1182.

MACROMOLECULAR CHEMISTRY AND POLYMERIC MATERIALS

Thermal Properties of Copolymers of Sodium 2-Acrylamido-2-methylpropanesulfonate with *N*-Vinylpyrrolidone

V. F. Kurenkov, T. A. Zhelonkina, S. S. Galibeev, and F. I. Lobanov

Kazan State Technological University, Kazan, Tatarstan, Russia
Degussa Evraziya Open Joint-Stock Company, Moscow, Russia

Received March 22, 2004

Abstract—Thermal transformations of sodium 2-acrylamido-2-methylpropanesulfonate–*N*-vinylpyrrolidone copolymers of various chemical compositions were studied by thermogravimetric, differential thermal, and thermomechanical analyses within 20–600°C in air. The thermal degradation parameters in various temperature ranges were estimated, as well as the heat resistance of the copolymers.

Random copolymers of sodium 2-acrylamido-2-methylpropanesulfonate (Na-AMS) with *N*-vinylpyrrolidone (VP) are of great technical and medical importance owing to high flocculation [1] and adhesion and antistatic [2], as well as thickening and complexing powers. During preparation, dissolution, and application, these copolymers can be subjected to various thermal impacts, but thermal properties of the copolymers are studied inadequately. Only thermal degradation of poly-2-acrylamido-2-methylpropanesulfonic acid (H-PAMS) [3, 4] and its salts with single- and double-charged cations [5], as well as of poly-*N*-vinylpyrrolidone (PVP) [6, 7], was reported.

In this work, we characterize the thermal properties of Na-AMS–VP copolymers of various compositions in the temperature range 20–600°C and compare them with those for homopolymers, Na-PAMS and PVP.

EXPERIMENTAL

Copolymers of Na-AMS with VP, as well as Na-PAMS, were prepared by radical (co)polymerization in aqueous solutions at pH 9 and 50°C, initiated with potassium persulfonate, and PVP, by bulk polymerization at 60°C, initiated with azobis(isobutyronitrile). The procedure of synthesis of (co)polymers was identical to that described in [8]. The resulting (co)polymers were precipitated into acetone, washed with acetone, and vacuum-dried at 50°C to constant weight. Table 1 presents the molecular characteristics of the (co)polymers.

The content of the Na-AMS units in the Na-AMS–VP copolymers was estimated from the sulfur content determined by elemental analysis [9]. The molecular weight MW of the copolymers was estimated from the intrinsic viscosity [η], for which the Mark–Houwink equation [η] ~ MW holds. The intrinsic viscosity [η] was measured in 0.5 M NaCl at 25°C in a VPZh-3 capillary viscometer (capillary diameter 0.56 mm). The intrinsic viscosity [η] was determined from the

Table 1. Molecular characteristics of the (co)polymers

(Co)polymer	Sample no.	Content of units, mol %		[η], $cm^3\ g^{-1}$
		Na-AMS	VP	
Na-PAMS	1	100	0	180
Na-AMS–VP	2	52.8	47.2	230
	3	44.1	55.9	120
	4	21.4	78.6	172
	5	8.9	91.1	37
PVP	6	0	100	30

* (Co)polymer:

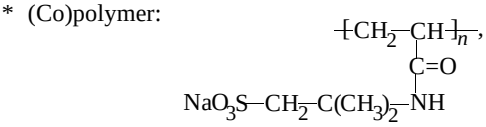

Sample no. 1

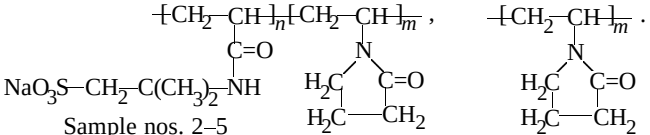

Sample nos. 2–5

Sample no. 6

1070-4272/04/7707-1165 © 2004 MAIK "Nauka/Interperiodica"

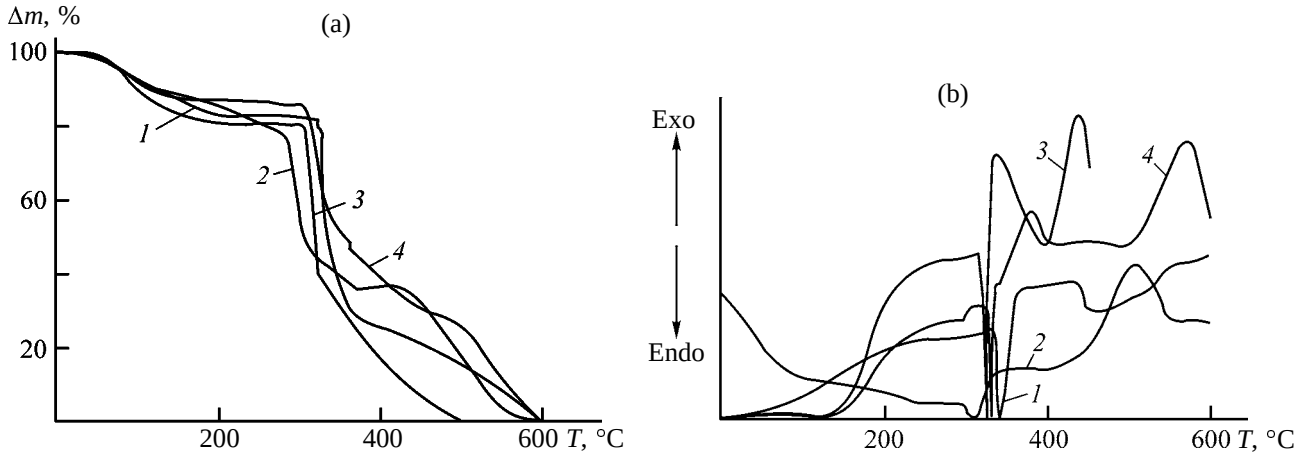

Fig. 1. (a) TG and (b) DTA curves for Na-AMS–VP copolymers. (Δ*m*) Mass loss and (*T*) temperature; the same for Fig. 2. Sample no.: (*1*) 2, (*2*) 3, (*3*) 4, and (*4*) 5.

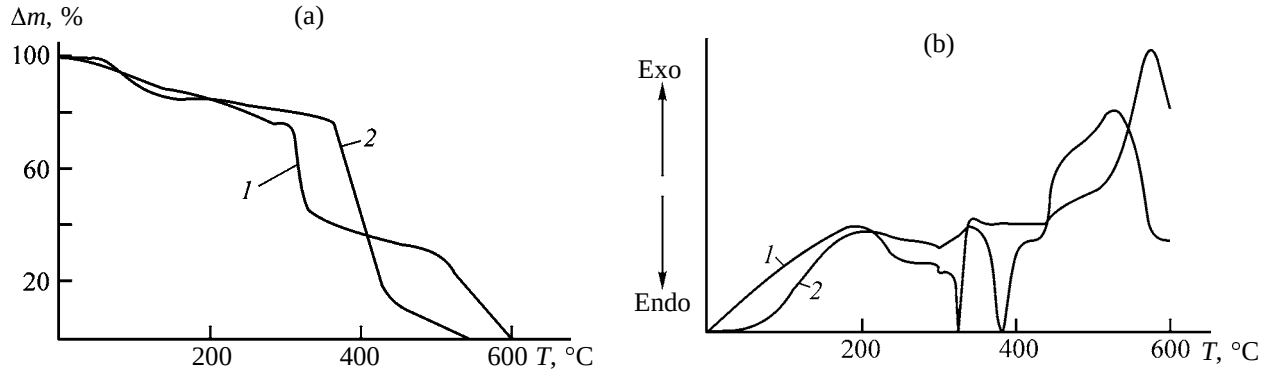

Fig. 2. (a) TG and (b) DTA curves for (*1*) Na-PAMS and (*2*) PVP. Sample no.: (*1*) 2 and (*2*) 6.

linear plot of (η_{sp}/c_p) vs. c_p, where c_p is the copolymer concentration, and $[\eta] = \lim(\eta_{sp}/c_p)$ at $c_p \to 0$.

The differential thermal (DTA) and thermogravimetric (TG) analyses were carried out on an MOM derivatograph (heating rate 3 deg min^{-1} in air; 20-mg weighed portion).

Thermomechanical analysis (TMA) was carried out on a modified Kargin balance at a load of 100 g mm^{-2} and a heating rate of 3 deg min^{-1} in air. The (co)polymer samples were 2-mm-thick films.

The qualitative and quantitative transformations of the (co)polymers in air at 20–600°C were determined from analysis of the DTA and TG curves (see Figs. 1a and 1b for copolymers of Na-AMS with VP and Figs. 2a and 2b for Na-PAMS and VP homopolymers). Table 2 presents the temperature ranges and the mass loss percentages for thermal degradation of the polymer samples. Figures 1 and 2 and Table 2 suggest that thermal transformations of Na-AMS–VP copolymers and PVP include two, and those of Na-PAMS, three stages. According to the TG curves (Figs. 1a and 2a) and to Table 2, heating of the polymer and copolymer samples is accompanied by gradual mass loss from 40–50 to 150°C, followed by a plateau extending to 295–350°C, depending on the specific polymer sample.

The mass loss recorded in the first stage of degradation for all the polymer samples can, evidently, be due to release of water and volatiles, as well as to partial thermal and (possible in air) thermooxidative degradation of the (co)copolymers. These assumptions were confirmed by identification of the products of thermal degradation of H-PAMS [3, 4] and of depolymerization of PVP within 230–270°C [6]. Also, we did not rule out release of ammonia, yielded by imidization, in the first stage of degradation. This assumption was confirmed by identification of the products of thermal degradation of H-PAMS [3] and polyacrylamide [10].

Further heating leads to the second stage of degradation, when the DTA curves for all the copoly-

Table 2. Temperature characteristics of the (co)polymers*

(Co)polymer	Sample no.	DTA			TG		TMA, T_{soft}
		degradation stage	T, °C	Δm, %	T_{10}	T_{50}	
					°C		
Na-PAMS	1	1	40–307	26	110	320	55
		2	307–500	70			
		3	500–600	100			
Na-AMS–VP	2	1	50–322	18	125	340	57
		2	322–600	100			
	3	1	40–295	25	125	310	61
		2	295–600	100			
	4	1	50–307	19	115	318	60
		2	307–500	100			
	5	1	50–307	15	115	360	–
		2	307–600	100			
PVP	6	1	40–350	21	115	400	57
		2	350–560	100			

* T_{10}, T_{50} are temperatures corresponding to 10 and 50% mass loss, respectively; T_{soft} is the softening point.

meric (Fig. 1b) and polymeric samples (Fig. 2b) exhibit clear endothermic peaks with maxima at various temperatures within 300–405°C, depending on the specific sample. This results in substantial acceleration of the mass loss by copolymers (Fig. 1a) and polymers (Fig. 2a). Above 310–435°C, depending on the specific sample, the mass loss by Na-AMS–VP copolymers and PVP tends to decelerate. At the same time, for Na-PAMS, the third stage of degradation began above 500°C, and the mass loss accelerated again.

More profound, compared to the first stage, transformations of the (co)polymers in the second stage of thermal degradation suggest intensified thermal and thermooxidative degradation, as seen from the DTA and TG curves. This process involves cleavage of the main chains of the macromolecules and imide rings formed in the first stage of degradation. This is accompanied by release of various liquid and gaseous products, in accordance with the published data on thermal degradation of H-PAMS [3, 4] and its salts [5], as well as of PVP [6, 7]. At 500–600°C we observed formation of an insoluble carbon-like powder in all cases.

From the TG curves (Figs. 1a and 2a), we determined the temperatures corresponding to 10 (T_{10}) and 50% (T_{50}) mass loss as the characteristics of the heat resistance of the (co)polymers. The T_{10} and T_{50} parameters are listed in Table 2. Comparison of the T_{10} parameters shows that, at low degradation temperatures, sample nos. 2 and 3 of Na-AMS–3VP copolymers are the most thermally stable among the (co)polymer samples studied by us. Evidently, enhanced thermal stability of sample nos. 2 and 3 having approximately equimolar composition is due to the donor–acceptor interactions between the Na-AMS and VP units in the macromolecules (Na-AMS has a medium electron-acceptor, and VP, a medium electron-donor power). At higher temperatures, as judged from the T_{50} parameters (Table 2), the copolymers become less stable than the homopolymers [except for sample no. 2 having the highest MW among the samples studied by us (Table 1), which is responsible for its slightly higher T_{50} compared to Na-PAMS]. A decrease in the thermal stability of the copolymers at high temperatures is, evidently, due to degradation of the donor–acceptor complexes between the Na-AMS and VP units in the macromolecules.

Figure 3 shows the TMA curves recorded at 20–200°C. It is seen that the strain tends to increase in the course of heating for all the samples. This is due to "defrosting" of the segmental activity of the macromolecules, when softening occurs at the softening point and co(polymer) converts from the glassy to hyperelastic state. Further heating does not change the strain, and the polymer degradation temperature corresponds to the upper limit of the hyperelastic state. Based on Fig. 3, we estimated the softening points (Table 2), which proved to be slightly higher for the copolymers than for the polymers. The highest

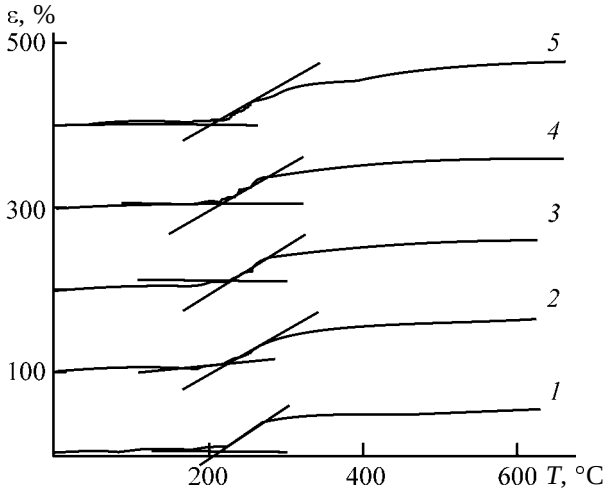

Fig. 3. TMA curves for (*1*) Na-PAMS, (*2*–*4*) Na-AMS–VP copolymers, and (*5*) PVP. (ε) Strain and (*T*) temperature. Sample no.: (*1*) 1, (*2*) 2, (*3*) 3, (*4*) 4, and (*5*) 6.

softening points were recorded for copolymeric sample no. 2. This can be due to formation of donor–acceptor complexes between the Na-AMS and VP units in the macromolecules. However, it is difficult to derive a correlation between the softening point and the chemical composition of the copolymer macromolecules because of the difference in the MWs of the samples (Table 1).

CONCLUSION

The differential thermal, thermogravimetric, and thermomechanical analyses of the copolymers of sodium 2-acrylamido-2-methylpropanesulfonate with *N*-vinylpyrrolidone and of the corresponding polymers in air at 20–600°C showed that, at low temperatures, the thermal stabilities and softening points of the copolymers with approximately equimolar compositions are higher than for the other samples studied, but at high temperatures this trend is lost.

REFERENCES

1. Kurenkov, V.F., Sharapova, Z.F., and Khairullin, M.P., *Zh. Prikl. Khim.*, 1999, vol. 72, no. 8, pp. 1374–1378.
2. Shevtsova, S.A., Borkhanova, T.A., Zhelonkina, T.A., and Kurenkov, V.F., *Materialy konferentsii "Tret'i Kirpichnikovskie chteniya"* (Proc. Conf. "Third Kirpichnikov Readings"), Kazan, March 25–27, 2003, pp. 308–311.
3. Frolov, M.I., Oshmarina, L.A., Chervyakova, V.I., *et al.*, *Vysokomol. Soedin., Ser. B*, 1990, vol. 32, no. 1, pp. 16–19.
4. Aggour, Y.A., *Acta Polym.*, 1993, vol. 14, no. 2, pp. 97–99.
5. Kurenkov, V.F. and Safin, A.G., *Zh. Prikl. Khim.*, 1998, vol. 71, no. 11, pp. 1927–1929.
6. Smith, S., *J. Polym. Sci.*, 1958, vol. 30, pp. 459–465.
7. Gibbert, J.B., Kipling, J.J., McEnaney, B., and Sherwood, J.N., *Polymer*, 1962, vol. 3, no. 1, pp. 1–10.
8. Kurenkov, V.F. and Zhelonkina, T.A., *Zh. Prikl. Khim.*, 2004, vol. 77, no. 2, pp. 310–315.
9. Charlot, G., *Les methods de la chimie analytique. Analyse quantitative minerale*, Paris: Masson, 1961, 4th ed.
10. Leung, W.M., Axelson, D.E., and Van Dyke, J.D., *J. Polym. Sci., Polym. Chem.*, 1987, vol. 25, no. 7, pp. 1825–1846.

Russian Journal of Applied Chemistry, Vol. 77, No. 7, 2004, pp. 1169–1171. Translated from Zhurnal Prikladnoi Khimii, Vol. 77, No. 7, 2004, pp. 1183–1185.

MACROMOLECULAR CHEMISTRY AND POLYMERIC MATERIALS

Optimization of Polymer-Analogous Transformations in Grafted Chains of Polycaproamide–Polyglycidyl Methacrylate Copolymers

I. V. Lavnikova, V. F. Zheltobryukhov, and A. E. Godenko

Volgograd State Technical University, Volgograd, Russia

Received December 17, 2003; in final form, April 2004

Abstract—Mathematical simulation and optimization of graft polymerization and polymer-analogous transformations in grafted chains of polycaproamide–polyglycidyl methacrylate copolymers were carried out.

A great number of ion-exchange fibers based on graft polycaproamide–glycidyl methacrylate (PCA–GMA) copolymers were developed. Preparation of ion-exchange fibers involves two stages: (1) graft polymerization of PCA and PGMA and (2) polymer-analogous transformations (namely, phosphorylation) of grafted polyglycidyl methacrylate (PGMA) chains.

Polymer-analogous transformations in grafted chains of PGMA are an efficient way to introduce new functional groups into the side chain. In particular, phosphorylation of graft copolymers of PCA with introduction of phosphorus into the side chains of the macromolecule not only improves the characteristics of the initial fiber but also makes the polymer materials capable of ion exchange and sorption of transition metal ions from solutions [1–3].

Previous studies [4, 5] allowed determination of the main kinetic parameters affecting the yield of grafted PGMA and the efficiency of heterophase graft polymerization and polymer-analogous transformations of grafted PGMA chains with 1-hydroxyethylidenediphosphonic acid (HEDP) $C_2H_3(OH)_5(P{=}O)_2$. The kinetic parameters affecting the phosphorus content in the graft copolymer and transformation of α-oxide groups were found.

The aim of this work was to develop a mathematical model of synthesis of PCA–PGMA graft copolymers and subsequent polymer-analogous transformations in grafted chains of a certain composition (PGMA content 43–48%, phosphorus content in PCA–PGMA 2.8–3%). For this purpose, a mathematical model of the process was developed from the experimental data. This model was used for determination of the process parameters to obtain the required amount of PGMA and phosphorus in the graft copolymer. It was found that the main parameters affecting the yield of the graft polymer are concentration of Cu^{2+} X_1, concentration of H_2O_2 X_2, initiation time X_3, temperature of PCA initiation X_4, concentration of GMA X_5, concentration of emulsifying agent X_6, grafting temperature X_7, and duration of graft polymerization X_8. The process was evaluated by such an output parameter as the amount of grafted PGMA Y_1, since this parameter governs the content of α-oxide groups. Among the main parameters characterizing the second stage of the process in hand are concentration of HEDP in the solution X_9, reaction temperature X_{10}, and reaction duration X_{11}. The output parameter for the second stage of the process was the amount of phosphorus in graft copolymer Y_2, since this parameter governs the amount of sorption-active groups in the fiber.

To develop a mathematical model, we used the experimental data on the process. The initial data were brought to the dimensionless form using the parameter values averaged over the sample. In the subsequent discussion, by the process parameters X_i we will mean the normalized values of the variables.

We suggest to describe graft polymerization process by the product of polynomials and exponential functions of the above process parameters:

$$Y_1 = a_2 \exp(b_0 X_{11}^b)(b_2 X_2^2 + b_{21} X_2 + b_{31}) \exp(b_{30} X_3^b) \times (b_4 X_4^2 + b_{41} X_4 + b_{42})(b_5 X_5^2 + b_{51} X_5 + b_{52})(b_6 X_6^2 + b_{61} X_6 + b_{62})(b_7 X_7^2 + b_{71} X_7 + b_{72})[1 - \exp(d_1 X_8^2 + d_2 X_8)]. \quad (1)$$

The coefficients a_j, b_j, and d_j were selected so as to attain the best agreement between the calculated and

1070-4272/04/7707-1169 © 2004 MAIK "Nauka/Interperiodica"

Process parameters, Q = 0.972

Parameter	X_i^0	$X_i^{\#}$	X_i^{opt}	q
Concentration of copper ions X_1, M	0.018	0.01	0.015	0.91
Concentration of hydrogen peroxide X_2, M	0.12	0.075	0.08	0.1
Initiation duration X_3, s	90	60	66	0.99
Initiation temperature X_4, °C	90	75	77	0.99
GMA concentration X_5, M	3	1	2.2	0.94
PVA (polyvinyl alcohol) concentration X_6, M	0.15	0.09	0.12	0.93
Grafting temperature X_7, °C	80	69	73	0.99
Grafting duration X_8, s	900	55	75	0.96
Amount of grafted PGMA Y_1, M	47	47	47	47
HEDP concentration X_9, M		2.4	2.3	1
Phosphorylation temperature X_{10}, °C	100	90	89	1
Phosphorylation duration X_{11}, s	300	220	259	0.98
Phosphorus amount in graft copolymer Y_2, %	2.8	2.8	2.8	2.8

experimental data. For this purpose we minimized by the modified Newton method the standard deviation $(Y_1^{exp} - Y_1^{calc})^2$, where Y_1^{exp} are experimental data and Y_1^{calc} are the corresponding estimated parameters [formula (1)].

In a similar manner, for phosphorylation of graft chains of PGMA, the dependence was searched for in the form

$$Y_2 = a_0(a_1X_9^2 + a_2X_9 + a_3)(b_1X_{10}^2 + b_2X_{10} + b_3) \times [1 - \exp(d_1X_{11}^2 + d_2X_{11})]. \quad (2)$$

The same procedure was used for choosing the coefficients.

It should be noted that the standard deviation obeys the Gauss law and does not exceed 20%. This fact allows conclusion that data obtained by formulas (1) and (2) are in satisfactory agreement with experimental data.

The best quality of modified PCA is obtained at the amount of the grafted component of 43–48% and phosphorus amount in the graft copolymer of 2.8–3%. In this case, it is evident that material and power consumption will be characterized by the process parameters X_i, i = 1, 11, and a decrease in these parameters will result in a decrease in the above expenditures in production of modified PCA. Thus, the problem of optimization involves choice of the process parameters so that

$$X_i \rightarrow \min(i = 1, 11),$$
$$Y_i \rightarrow \max(i = 1, 2). \quad (3)$$

To realize the computation procedure of choosing the optimal process parameters, we introduced Q-criterion of quality, which is an integral parameter characterizing to what extent the specific set of parameters and the results obtained correspond to our views on the process quality. The maximum value of the quality criterion is obtained when all parameters reach maximum and minimum, respectively [formula (3)]. If one of the parameters lies out of the tolerable interval $[X_i^0, X_j^{\#}]$, the quality criterion Q abruptly decreases.

For each of the parameters (3), in turn, we determined the local quality criterion g_i, where i = 1, 13 (partial qualities) are numerical characteristics, which increase to 1 when conditions (3) are obeyed and decrease to 0 when these conditions are not obeyed.

The total quality of the process is defined as the exponential mean of its partial qualities [6]:

$$Q = -\ln\left\{\left[\sum_{i=1}^{13}\exp(-g_i)\right]/13\right\}. \quad (4)$$

Thus, the optimization problem is reduced to the search for the maximum of the function Q, which depends only on the process parameters X_i (i = 1, 11), since the parameters Y_i (i = 1, 2) are related to X_i by (1) and (2).

Let us consider that partial qualities g_i (i = 1, 11) are polynomial functions of the corresponding process parameters:

$$g_i = 1 - \left(\frac{X_i - X_i^{\#}}{X_i^{\#} - X_i^0}\right)^k, \quad (5)$$

where X_i^0 and $X_i^\#$ are so-called "mediocre" and "excellent" values of parameter X_i, governing the interval of desirable values.

For qualities corresponding to the amount of the resulting product in the first and in the second stage, respectively, we take the following functions of partial qualities:

$$g_{12} = \frac{X_{12} - X_0}{X_{12}^\# - X_0},$$

$$g_{13} = \frac{X_{13} - X_0}{X_{13}^\# - X_0}. \quad (6)$$

The "mediocre" and "excellent" values taken for optimization of the process are listed in the table.

The problem of searching the maximum of the target function Q is by far extremal in the range specified by the boundaries of possible values of process parameters. To solve the extremal task, we used the method of gradient descent.

As a result of the calculations we obtained the optimal values of process parameters in the framework of the considered model (see table), which provide preparation of high-quality product with the minimal expenditures.

EXPERIMENTAL

PCA was modified by graft polymerization in GMA monomer emulsion (2.35 M) for 60 min at 70°C with the Cu^{2+}–H_2O_2 redox initiating system. The graft copolymer was modified by treatment with HEDP (4.86 M) in a flask with a reflux condenser for 300 min at 90°C.

CONCLUSIONS

(1) The constructed mathematical model provides good agreement between the calculated and experimental data.

(2) The mathematical model allows determination of the process parameters providing preparation of polycaproamide–polyglycidyl methacrylate graft copolymers with specified characteristics.

(3) The optimization of the process allows determination of the process parameters providing the value of the target function close to 1 (0.972).

REFERENCES

1. Druzhinina, T.V. and Nazar'ina, L.A., *Khim. Volokna*, 1999, no. 4, pp. 8–16.
2. Druzhinina, T.V., Tvorogova, M.M., and Mosina, N.Yu., *Khim. Volokna*, 1997, no. 3, pp. 13–16.
3. Druzhinina, T.V., Emel'yanova, A.N., Nazar'ina, L.A., *et al*., *Khim. Volokna*, 1998, no. 3, pp. 13–15.
4. Lavnikova, I.V. and Zheltobryukhov, V.F., *Zh. Prikl. Khim*., 2001, vol. 74, no. 4, pp. 657–659.
5. Lavnikova, I.V. and Zheltobryukhov, V.F., *Zh. Prikl. Khim*., 2001, vol. 74, no. 12, pp. 2062–2064.
6. Bryzgalin, G.I., *Proektirovanie detalei iz kompozitsionnykh materialov voloknistoi struktury* (Design of Parts from Composite Materials with Fibrous Structure), Moscow: Mashinostroenie, 1982.

Russian Journal of Applied Chemistry, Vol. 77, No. 7, 2004, pp. 1172–1177. Translated from Zhurnal Prikladnoi Khimii, Vol. 77, No. 7, 2004, pp. 1186–1191.

MACROMOLECULAR CHEMISTRY AND POLYMERIC MATERIALS

Influence of Thermal Aging Conditions on the Molecular Characteristics of Cellulose and Mechanical Properties of Paper Thereof

S. I. Ganicheva, E. S. Bystrova, and E. M. Lotsmanova

Russian National Library, St. Petersburg, Russia

Received January 12, 2004

Abstract—Molecular characteristics of cellulose during accelerated aging were studied over wide temperature and time ranges. Also studied were mechanical properties of model samples of paper made of cotton, sulfate, and sulfite cellulose. Interrelation of the molecular characteristics of cellulose and strength properties of paper was investigated.

In the recent 20 years, nonpaper information carriers such as compact disks and microfilms found wide use in storage and use of reference, information, and bibliographical literature in libraries and archives. At the same time, there are contradictory published data concerning the lifetime of the information stored on these carriers (from 5 to 100 years). Thus, preparation of high-strength acid-free paper suitable for long-term (up to 500 years) storage of information is still urgent.

In this work, we studied the trends in variation of the molecular characteristics of cellulose and strength properties of paper thereof under accelerated thermal aging.

EXPERIMENTAL

We studied model paper samples manufactured under pilot conditions at the Goznak factory on a 38-cm-wide planar-grid paper-making machine. Cotton (C), sulfate (SFA), and sulfite (SFI) celluloses served as semifinished products. The paper was made without use of sizing and bleaching substances and fillers; therefore, model paper samples were all-cellulose (sulfate bleached, sulfite bleached, or cotton) fiber compositions. After conditioning, the paper samples were placed into hermetically sealed glass tubes and kept in an air thermostat at 80, 100, 120, 150, and 180°C for 3, 9, 12, 18, and 30 days.

The molecular weight M of cellulose was determined from the intrinsic viscosity $[\eta]$ measured in a Cadoxen solution at 25°C, by the formula [1]

$$[\eta] = 3.85 \times 10^{-4} M^{0.76}.$$

The functional groups in the cellulose samples before and after accelerated aging were determined photocolorimetrically (carbonyl groups, by the Subolx technique, and carboxy groups, by the Weber technique) [2]. The mechanical characteristics of paper were determined according to appropriate GOSTs (State Standards), namely, the folding resistance at a tension of 4.9 N according to GOST 13525–80, and the breaking force according to GOST 13525.1–79.

It is essential to study how molecular characteristics of cellulose paper vary during aging, since the molecular weight M and the chemical composition of cellulose affect the process characteristics of the resulting paper.

Table 1 presents the calculated intrinsic viscosities $[\eta]$ and molecular weights M of the cellulose samples, calculated from the relative viscosities of solutions η_{rel} measured in the chosen modes of accelerated thermal aging of the paper samples in the tubes. In the case of the SFI samples, we failed to measure the relative viscosity under accelerated aging because of a low velocity of the solution outflow, close to that of the solvent outflow. Table 1 suggests that the initial molecular weights M of the cellulose samples tend to decrease during accelerated aging, most rapidly in the case of C cellulose. As known, polymers with high molecular weights degrade more rapidly that those with lower molecular weights under identical conditions, which is true of cellulose as well. The specific pattern of decrease in the molecular weight of the samples studied was explained by the fact that the supramolecular structure of cellulose comprises various ordered domains (amorphous and crystalline).

1070-4272/04/7707-1172 © 2004 MAIK "Nauka/Interperiodica"

Table 1. Variation of the molecular characteristics of cellulose during accelerated thermal aging

τ,* days	Aging temperature									
	80		100		120		150		180	
	[η], dl g^{-1}	*M*, kDa	[η], dl g^{-1}	*M*, kDa	[η], dl g^{-1}	*M*, kDa	[η], dl g^{-1}	*M*, kDa	[η], dl g^{-1}	*M*, kDa
Cotton cellulose										
0	8.8	543	8.8	543	8.8	543	8.8	543	8.8	543
3	7.4	433	7.3	425	5.0	257	2.0	79	1.3	44
9	3.7	175	4.3	213	1.8	75	1.9	74	1.0	32
18	2.2	88	3.6	166	2.0	79	1.6	59	0.9	28
30	0.7	19	3.4	153	2.0	79	1.4	51	0.6	15
SFA cellulose										
0	8.1	488	8.1	488	8.1	488	8.1	488	8.1	488
3	3.8	180	3.6	167	3.6	167	2.1	84	1.2	58
9	3.5	163	2.8	121	1.9	74	1.1	33	0.8	23
18	3.3	146	2.7	88	2.8	124	1.1	33	0.6	17
30	3.4	156	2.9	92	2.2	88	1.2	43	0.6	17
SFI cellulose										
0	4.4	221	4.4	221	4.4	221	4.4	221	4.4	221
3	4.2	203	3.6	169	3.4	156	1.1	35	–	–
9	3.8	177	3.7	174	2.9	126	1.0	32	–	–
18	3.9	188	3.0	132	2.6	108	0.9	29	–	–
30	4.2	203	2.6	112	1.8	69	0.7	19	–	–

* τ is aging time.

For example, a sharp decrease in *M* in the initial stage of depolymerization occurs initially in amorphous domains, which are more sensitive to thermal impact than crystalline domains.

Using the data from Table 1, we constructed the log[η] vs. log*M* plots (Fig. 1). For cellulose types studied in this work (C, SFA, and SFI), these plots are linear for *M* within 15–540 kDa (for the relative viscosity determined accurately to within 10%). The viscometrically estimated molecular weights of cellulose agree well with the published data. For example, a number of researchers [3–5] reported similar [η] vs. *M* dependences recorded in Cadoxen for both nonfractionated samples of cellulose and their close-cut fractions; these plots were also linear for molecular weights of up to ~600 kDa. However, for cotton cellulose and cotton linter samples with higher molecular weights ($M \approx 1000$ kDa) the log[η] vs. log*M* plot tended to deviate from linearity, which was explained in [5] by deteriorated thermodynamic quality of the solvent.

As known, natural aging of paper in air involves slow oxidation with oxygen, which somewhat weakens the 1–4 glycoside bonds without rapid degradation and significant decrease in the molecular weight of cellulose. Accelerated thermal aging can be run in several ways: in air thermostats under natural air circulation at 102°C (TAPPI standard), at 100°C [6, 7], in hermetically sealed glass tubes (sealed am-

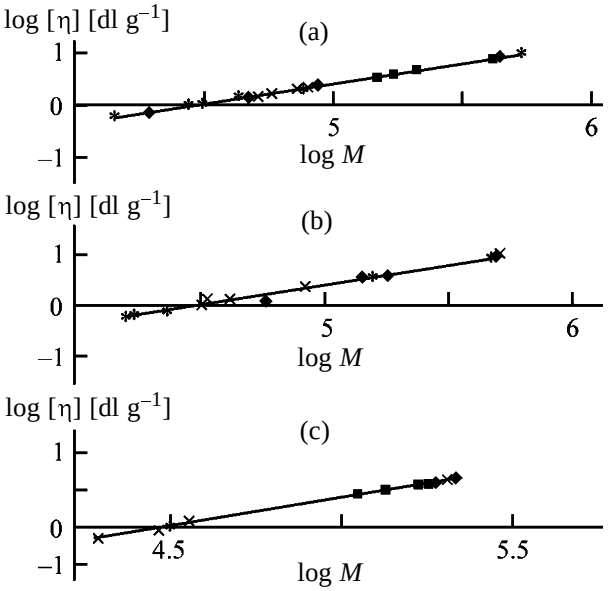

Fig. 1. Intrinsic viscosity [η] as a function of the viscosity-average molecular weight *M* of solutions of (a) C, (b) SFA, and (c) SFI cellulose in Cadoxen.

Table 2. Average degree of polymerization of cellulose during aging at 100°C

τ, days	Degree of polymerization *P* of cellulose								
	cotton			SFA			SFI		
	[11]	[10]	experiment*	[11]	[10]	experiment*	[12]	[10]	experiment*
0	2900	2950	3351	1200	1054	3017	1073	935	1364
3	–	2750	2623	1100	1030	1037	881	1043	
5	–	–	–	–	–	–	828	–	–
6	2500	–	–	1100	–	–	–	–	–
9	–	–	1025	–	–	744	–	–	1074
10	2200	2470	–	1000	1000	–	690	737	–
15	–	–	–	–	–	–	690	–	–
18	–	–	1315	–	–	525	–	–	815
20	1600	2165	–	900	980	–	690	660	–
30	1100	1960	944	–	890	568	–	–	691

* The degrees of polymerization *P* determined in this work during aging in tubes.

pules) [8], and in climatic chambers with controllable temperature and relative air humidity [9].

Paper aging conditions predetermine the physicochemical reactions of degradation of cellulose macromolecules. When the temperature in an air thermostat exceeds 100°C, the paper rapidly loses moisture. Therefore, this procedure is regarded as "dry" aging, and degradation mechanism is conventionallytreated as thermoooxidative. In a climatic chamber, the material is exposed simultaneously to two factors, heat and moisture (modern chambers are additionally supplied with UV radiation sources). Under these conditions, aging follows two mechanisms, thermooxidative and hydrolytic. From the chemical viewpoint, thermal degradation involves cleavage of the 1–4 glycoside bonds and oxidation of the hydroxy groups in the cellulose macrochains. Both reactions proceed simultaneously and are accelerated with rising temperature and increasing exposure time, thus decreasing *M* (or the degree of polymerization *P*).

Various authors showed that the extent of degradation depends not only on the temperature, time of heat treatment, and initial degree of polymerization of cellulose, but also on the composition and nature of the medium in which degradation occurs. Aging of paper made of C, SFA, and SFI cellulose, which is free from fillers and sizing agents, was studied by Belen'kaya and Alekseeva [10] and by Perl'shtein [11, 12] by the dry aging technique at 100°C in thermostats under natural air circulation.

Table 2 compares the data on variation of the degree of polymerization *P* of the samples in air, reported in [10–12], and during aging in tubes at identical temperatures (100°C). It is seen that *P* tends to decrease more rapidly under thermal aging in tubes than in air. The extent of degradation of C and SFA cellulose is greater (see the limiting *P* for 30-day aging). Therefore, paper in tubes ages (or suffers damage) more rapidly than in air. A possible reason is a decrease in the free oxygen concentration and simultaneous accumulation of thermal degradation products in the reaction medium in a closed space of tubes, which accelerates oxidative and hydrolytic degradation of the macromolecules. This effect is less pronounced in the case of SFI cellulose having a lower molecular weight; the limiting $P = 690$ for SFI cellulose agrees well with the published data.

Three hydroxy groups in the unit of cellulose make it very susceptible to oxidation, which modifies the chemical composition of the macromolecules via formation of carbonyl CHO– and carboxy COOH– groups at the C1, C2, C3, C4, and C6 atoms during natural aging of cellulose materials in air [13]. Oxidation is significantly accelerated under artificial thermal aging, which increases the content of the above-mentioned groups in the samples [7–14]. It should be noted that the contents of the CHO– and COOH– groups, reported by different authors, differ significantly depending on the specific analytical method [10, 13–15].

Table 3 lists the contents of the CHO– groups in cellulose for the samples of paper made of C, SFA, and SFI cellulose after thermal aging in tubes. The content of CHO– groups in the samples before and

after heat treatment tends to vary as C < SFA < SFI. These data agree with the available published data [7, 10, 13, 14, 16]. For example, Alekseeva and Belen'kaya [16] found a minimal content of the CHO– groups in cotton cellulose samples, and a maximal, in SFI cellulose samples. As the temperature increases to 100–120°C, oxidation is accelerated due to accumulation of the degradation products in tubes. This increases the content of the CHO– groups in cellulose for each aging time fixed. The scatter of data is the greatest for high temperatures (150–180°C), possibly due to release and accumulation of volatile degradation products. On the whole, our results agree with the published evidence of increase in the content of the functional groups in cellulose macromolecules under thermal aging.

Because of easy oxidation, virtually all cellulose materials contain a small amount of carboxy groups, along with the carbonyl groups. For example, C, SFA, and SFI celluloses contain 0.005, 0.047, and 0.053 mg g^{-1} COOH– groups, respectively [13]. Table 4 lists the contents of the COOH– groups of cellulose for the paper samples subjected to accelerated thermal aging in tubes. These results still remain to be interpreted, but it is seen that the content of the COOH groups of cellulose in the paper samples before and after aging is the lowest for the cotton paper and tends to vary as C < SFA < SFI. As the heating time increased from 3 to 30 days, the content of the COOH– groups either decreased or remained unchanged at all the temperatures.

A similar trend was revealed by Belen'kaya and Alekseeva [10], who attributed it to deceleration of oxidation and domination of decarboxylation reactions at high temperatures (above 100°C). Thus, our data suggest a change in the molecular characteristics and chemical composition (*M* and content of the functional groups) in macromolecules of C, SFA, and SFI cellulose upon degradation. In view of the fact that no other chemicals were applied in preparation of the model samples, we could trace the trends in variation of the estimated strength properties of the paper with the molecular weight *M* of cellulose. In this work, we estimated two indicators of the mechanical strength, namely, folding resistance *N* (*N* is the number of double folds at a load of 4.9 N) and breaking force *F*, N. Our mechanical tests showed the following. For the samples of paper from the C cellulose, *N* remained within 2400–2700 as the initial *M* decreased from 543 to 175 kDa. Similarly, as *M* decreased from 543 to 66 kDa, *F* remained virtually unchanged (75–80 N). Further decrease of *M* from 175 to 57 kDa caused *N* to sharply decrease to 1; *F* also decreased (from 80 to 15 N) as *M* decreased from 66 to 30 kDa.

Table 3. Content of the carbonyl groups of cellulose in paper samples under thermal aging in tubes*

τ, days	Content of the CHO– groups, %, at indicated aging temperature, °C				
	80	100	120	150	180
	Cotton cellulose				
3	0.074	0.075	0.126	0.237	0.231
6	0.072	0.059	0.118	0.213	0.319
9	0.058	0.079	0.099	0.322	0.270
12	0.049	0.089	0.114	0.245	0.357
15	0.046	0.081	0.095	0.216	0.479
18	0.088	0.048	0.119	0.307	0.351
21	0.060	0.086	0.185	0.324	0.573
24	0.045	0.083	0.179	0.358	0.411
27	0.073	0.126	0.278	0.453	0.374
30	0.061	0.087	0.147	0.307	0.387
	SFA cellulose				
3	0.103	0.113	0.144	0.451	0.514
6	0.168	0.170	0.241	0.470	0.545
9	0.154	0.222	0.241	0.573	0.588
12	0.145	0.225	0.219	0.563	0.684
15	0.103	0.222	0.159	0.553	0.680
18	0.137	0.204	0.188	0.520	0.621
21	0.161	0.175	0.219	0.402	0.585
24	0.165	0.198	0.299	0.596	0.662
27	0.119	0.194	0.324	0.583	0.701
30	0.128	0.194	0.229	0.569	0.845
	SFI cellulose				
3	0.204	0.259	0.274	0.669	0.496
6	0.237	0.286	0.359	0.556	0.612
9	0.254	0.285	0.318	0.551	0.593
12	0.256	0.321	0.424	0.486	0.566
15	0.258	0.320	0.334	0.580	0.643
18	0.286	0.318	0.296	0.508	0.417
21	0.232	0.304	0.488	0.568	0.664
24	0.260	0.237	0.439	0.482	0.684
27	0.275	0.310	0.426	0.575	0.769
30	0.212	0.292	0.364	0.629	0.542

* Content of the carbonyl groups before aging, %: 0.045 for C, 0.058 for SFA, and 0.215 for SFI cellulose.

In the case of the samples of paper made of SFA cellulose, *N* remained virtually unchanged (900–1000) as the molecular weight decreased from 488 to 140 kDa. The parameter *F* also remained at a level of 93–95 N as *M* decreased from 488 to 120 kDa. Further decrease of *M* from 140 to 70 kDa caused *N* to

Table 4. Content of carboxy groups of cellulose in the paper samples upon thermal aging in tubes*

T, °C	Cotton cellulose			SFA cellulose			SFI cellulose		
	content of COOH– groups, %, at indicated aging time, days								
	3	18	30	3	18	30	3	18	30
80	0.020	0.006	0.005	0.043	0.030	0.031	0.063	0.062	0.037
100	0.014	0.005	0.008	0.044	0.043	0.013	0.065	0.043	0.038
120	0.006	0.005	0.010	0.038	0.029	0.035	0.041	0.036	0.039
150	0.016	0.008	0.008	0.038	0.032	0.038	0.043	0.028	0.015
180	0.020	0.043	0.028	0.048	0.083	0.020	0.022	0.009	0.017

* Content of carboxy groups before aging, mg g^{-1}: 0.005 for C, 0.034 for SFA, and 0.065 for SFI cellulose.

sharply decrease to 1; *F* also decreased from 95 to 38 N as *M* decreased from 120 to 33 kDa.

In the case of the samples of paper made of SFI cellulose with a lower molecular weight, a decrease in *M* from 220 to 70 kDa resulted in regular decreases in both strength indicators, namely, from 170 to 1 for *N* and from 75 to 56 N for *F*.

Figures 2 and 3 represent our results as the $\log N = f(\log M)$ and $F = f(\log M)$ plots. It is seen that, with decreasing molecular weight of cellulose due to degradation, the strength of the paper tends to decrease. For the C and SFA cellulose samples, whose molecular weights exceed that of SFI cellulose, we revealed the ranges of the molecular weights *M* within which *N* and *F* remained virtually unchanged. For example, the "limiting" molecular weight above which the mechanical strength was independent of *M* was estimated at ca. 175 kDa ($P \approx 1100$) for C cellulose and at ca. 140 kDa ($P \approx 860$) for SFA cellulose. An inflection in the $\log N$ vs. $\log M$ and *F* vs. $\log M$ plots can be due to degradation of various types of structural bonds (intra- and interfibrillar) during mechanical tests of the samples and to the morphological differences in their structure (length and flexibility of fibers). Belen'kaya *et al.* [6] and Sadovskaya and Blank [8] carried out a comparative study of the

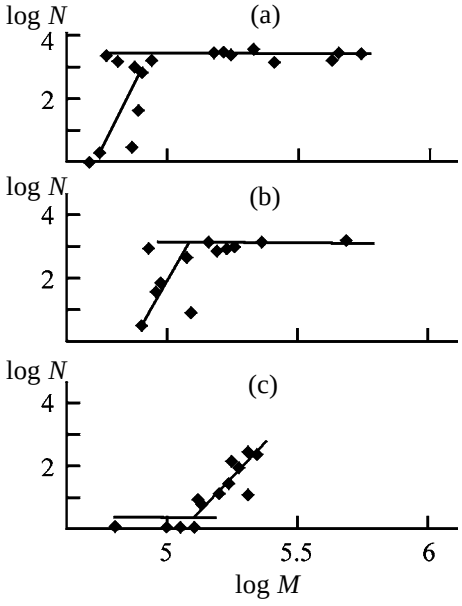

Fig. 2. Variation of the number of double folds *N* with the viscosity-average molecular weight *M* for model samples of paper made of (a) C, (b) SFA, and (c) SFI cellulose under thermal aging in tubes.

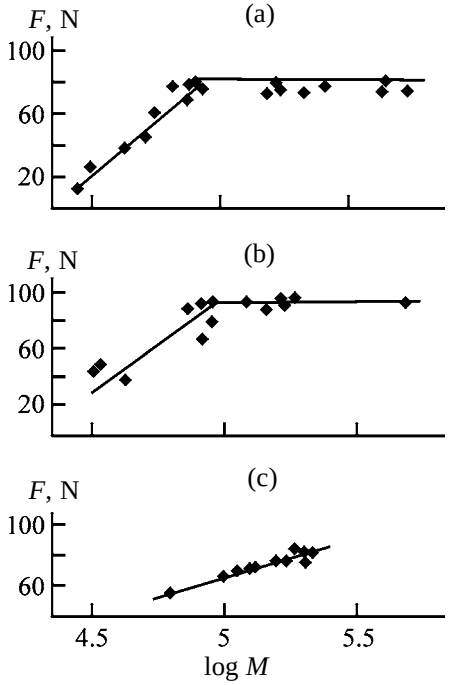

Fig. 3. Variation of the breaking force *F* with the viscosity-average molecular weight *M* for model samples of paper made of (a) C, (b) SFA, and (c) SFI cellulose under chemical aging in tubes.

mechanical properties of the paper made of C, SFA, and SFI cellulose under pilot conditions when subjected to accelerated thermal aging in closed tubes and in air. Despite certain differences in the procedures for determining the molecular weight of cellulose and strength of paper, we can also postulate, on the whole, a similar trend, namely, a thermal degradation-induced decrease in the mechanical strength of the paper samples; this trend is the most pronounced in the case of aging in tubes. Thus, our results supplement the previously revealed trends in variations of the chemical composition and the degree of polymerization of cellulose, as well as of the mechanical properties of paper, upon heat treatment.

CONCLUSIONS

(1) Accelerated thermal aging decreases the molecular weight M and modifies the chemical composition of the macromolecules of cotton, sulfate, and sulfite cellulose. Thermal degradation of the samples in tubes is faster than in air.

(2) At molecular weights above 100 kDa, the strength properties of the paper made of cotton and sulfate cellulose remain unchanged and tend to decrease with decreasing molecular weight of cellulose below this limit.

REFERENCES

1. Brown, W., *Eur. Polym. J.*, 1965, vol. 1, pp. 1–10.
2. Obolenskaya, A.V., El'nitskaya, Z.P., and Leonovich, A.A., *Laboratornye raboty po khimii drevesiny i tsellyulozy* (Laboratory Works on Chemistry of Wood and Cellulose), Moscow: Ekologiya, 1991.
3. Bolotnikova, L.S. and Samsonova, T.S., *Zh. Prikl. Khim.*, 1961, vol. 34, no. 4, pp. 659–662.
4. Bolotnikova, L.S. and Samsonova, T.S., *Vysokomol. Soedin.*, 1964, vol. 6, no. 3, pp. 533–537.
5. Lyubina, S.Ya., Klenin, S.I., Strelina, I.A., *et al.*, *Vysokomol. Soedin., Ser. A*, 1977, vol. 19, no. 2, pp. 176–180.
6. Belen'kaya, N.G., Istrubtsina, T.V., and Smirnova, V.A., in *K voprosu o starenii bumagi* (On Paper Aging), Moscow: Nauka, 1964, pp. 15–35.
7. Ivanov, G.A., in *Voprosy sokhraneniya dokumenta* (Document Preservation Problems), Leningrad, 1973, pp. 40–45.
8. Sadovskaya, O.I. and Blank, M.G., in *Khimiya i tekhnologiya tsellyulozy: Mezhvuzovskii sbornik nauchnykh trudov* (Chemistry and Technology of Cellulose: Intercollegiate Collection of Scientific Works), Leningrad, 1976, issue 3, pp. 15–55.
9. Lotsmanova, E.M., Dobrusina, S.A., and Anokhin, Yu.A., *Materialy mezhdunarodnoi nauchnoi konferentsii "BAN: 10 let posle pozhara"* (Proc. Int. Scientific Conf. "Library of the Academy of Sciences: 10 Years since the Fire"), St. Petersburg, February 16–18, 1998, pp. 140–148.
10. Belen'kaya, N.G. and Alekseeva, T.V., in *Dolgovechnost' dokumenta* (Life of a Document), Leningrad: Nauka, 1981, pp. 5–12.
11. Perl'shtein, E.Ya., in *Voprosy dolgovechnosti dokumenta* (Problems of the Document Life), Leningrad: Nauka, 1973, pp. 13–18.
12. Perl'shtein. E.Ya., in *Voprosy dolgovechnosti dokumenta* (Problems of the Document Life), Leningrad: Nauka, 1973, pp. 46–48.
13. Nikitin, N.I., *Khimiya tsellyulozy i drevesiny* (Chemistry of Cellulose and Wood), Moscow: Akad. Nauk SSSR, 1962.
14. Rozmarin, G.M., *Usp. Khim.*, 1965, vol. 34, no. 11, pp. 1365–1386.
15. Rogovin, Z.A., *Khimiya tsellyulozy* (Chemistry of Cellulose), Moscow: Khimiya, 1972.
16. Alekseeva, T.V. and Belen'kaya, N.G., in *Prichiny razrusheniya pamyatnikov pis'mennosti i pechati* (Factors Responsible for Degradation of Written and Printed Monuments), Leningrad: Nauka, 1967, pp. 36–47.

Russian Journal of Applied Chemistry, Vol. 77, No. 7, 2004, pp. 1178–1181. Translated from Zhurnal Prikladnoi Khimii, Vol. 77, No. 7, 2004, pp. 1192–1196.

MACROMOLECULAR CHEMISTRY AND POLYMERIC MATERIALS

Polysaccharides from Buckwheat Production Wastes

L. A. Zemnukhova, S. V. Tomshich, E. D. Shkorina, and A. G. Klykov

Institute of Chemistry, Far Eastern Division, Russian Academy of Sciences, Vladivostok, Russia
Pacific Institute of Bioorganic Chemistry, Far Eastern Division, Russian Academy of Sciences, Vladivostok, Russia
Primor'e Research Institute of Agriculture, Russian Academy of Agricultural Sciences, Timiryazevskii, Primorskii krai, Russia

Received March 1, 2004

Abstract—The content, structure, and monosaccharide composition of polysaccharides recovered by sequential extraction with water, ammonium oxalate solution, and sodium hydroxide solution from wastes from production of a series of buckwheat strains were studied. Data characterizing the raw material (ash residue), aqueous, oxalate, and alkaline extracts (list of metals and their concentration in solution), polysaccharides (structure, content of metals absorbed from solution), and insoluble residue of the raw material (weight of the residue) are presented.

In the course of growing and cleaning buckwheat grains, large amounts of wastes are formed (straw, husk, fine particles of grains). These wastes can be considered as valuable renewable raw materials for chemical, food, and pharmacological industries, suitable for production of polysaccharides [1–3], cellulose [4], dyes and food additives [5, 6], furfural [1], and drugs [7]. To develop a scheme for integrated processing of buckwheat production wastes, it is necessary to know the compositions of the raw materials depending on the plant strain and on the site of its growth. Available data on this matter are insufficient.

In this work, we studied the composition and content of carbohydrates from husk and straw of a series of buckwheat strains grown in Primorskii and Krasnoyarsk krais.

EXPERIMENTAL

Polysaccharides (PSs) were recovered from buckwheat husk (BH) and straw (BS) by sequential extraction with water, ammonium oxalate solution, and sodium hydroxide solution; their qualitative and quantitative monosaccharide compositions were determined. Husk and straw samples (particle size ≥2 and ≤10 mm, respectively) were washed with water and dried in air to constant weight.

Samples (70 g) of BH and BS were sequentially treated with water and 0.5 N solutions of ammonium oxalate and sodium hydroxide. Water was added to a raw material sample to S : L = 1 : 10 by weight, and the mixture was heated on a boiling water bath for 3 h. The solution was filtered, concentrated on a rotary evaporator, and centrifuged (4500–5000 rpm, 20–25 min) to remove the residual raw material; polysaccharides were precipitated with a fourfold volume of acetone. The resulting precipitate was separated by centrifugation, dissolved in water, and lyophilically dried to obtain water-extractable PSs.

To the solid residue after extraction with water, a 0.5 N solution of ammonium oxalate was added to S : L = 1 : 10, and the mixture was heated on a water bath under the same conditions as described above. The solution was filtered and dialyzed against running water for 2–3 days and against distilled water for 1–2 days, after which it was concentrated on a rotary evaporator, and a fourfold volume of acetone was added. The precipitate was separated by centrifugation, dissolved in water, and lyophilically dried to obtained oxalate-extractable PSs.

The solid residue after extraction with water and ammonium oxalate was suspended in a 0.5 N NaOH solution and heated on a water bath for 2 h. The solution was separated by centrifugation and worked up as described above to obtain alkali-extractable PSs.

The qualitative and quantitative monosaccharide compositions of the isolated PSs were determined after their acid hydrolysis, which was performed with 1 N trifluoroacetic acid (TFA) at 100°C for 4–5 h. Analysis was performed by paper chromatography

1070-4272/04/7707-1178 © 2004 MAIK "Nauka/Interperiodica"

Table 1. Content, structure, and monosaccharide composition of PSs from extracts of buckwheat husk and straw. Extractant: (1) H_2O, (2) $(NH_4)_2C_2O_4$, and (3) NaOH

Raw material	Extractant	PS characteristics			Monosaccharide composition,* mol %							Presence of uronic acids	
		yield based on raw material, wt %	color	structure	Rha	Ara	Xyl	Man	Glc	Gal	Int	GalA	GlcA
BH-6	1	2.63	Light brown	a	3	4	Traces	8	64	21	Traces	+	Traces
	2	1.40	Light brown	c + a	8	21	5	9	39	18	″	+	–
	3	4.4**	Black	a	10	18	25	7	22	18	–	+	+
BH-8	1	2.76	Light brown	a	Traces	Traces	Traces	13	72	15	Traces	Traces	–
	2	1.52	Light brown	c + a	–	18	Traces	Traces	61	21	Traces	+	Traces
	3	1.31**	Black	a	8	13	17	10	33	19	–	+	+
BH-10	1	2.14	Brown	a	Traces	6	Traces	7	73	14	–	+	–
	2	0.52	Light brown	a	4	13	8	7	60	8	–	+	–
	3	1.1**	Black	a	8	24	25	6	19	18	–	+	+
BS-4	1	4.84	Yellow-brown	c	4	4	2	5	59	9	17	+	–
	2	2.71	White	c + a	12	21	4	7	32	24	–	+	–
	3	0.32**	Black	a	14	23	6	Traces	31	26	Traces	+	–
BS-7	1	9.28**	Brown	a	9	19	8	8	16	4	31	+	–
	2	1.60	Light brown	c	17	41	8	Traces	11	22	–	+	–
	3	1.37	″	a	7	36	23	3	11	20	–	+	+

* Monosaccharides: (Rha) rhamnose, (Ara) arabinose, (Xyl) xylose, (Man) mannose, (Glc) glycose, (Gal) galactose, and (Int) inositol; uronic acids: (GalA) galacturonic and (GlcA) glucuronic; structure: (a) amorphous and (c) crystalline.
** Soluble + insoluble PS.

(PC), gas–liquid chromatography (GLC), and gas chromatography–mass spectrometry (GC–MS), after conversion of the polyols to acetates. The descending PC was performed on Filtrak FN-12 paper in the solvent system 2-butanol–pyridine–water (6 : 4 : 3 by volume). The monosaccharides were detected by treatment with an alkaline solution of silver. Uronic acids were detected by GLC in the form of methyl glycoside acetates after methanolysis of PSs (acetyl chloride : methanol 1 : 10 by volume, 100°C, 7–8 h) followed by acetylation. Gas–liquid chromatography was performed with an Agilent 6850 chromatograph (the United States) equipped with a flame-ionization detector; an HP 5MS capillary column (30 m × 250 μm) was coated with 0.25 μm of 5% phenylmethylsiloxane; the temperature schedule was as follows: 150°C, 1 min; heating to 230°C, 3 deg min^{-1}; 230°C, 10 min. The GC–MS analysis was performed with a Hewlett–Packard 6890 chromatograph (the United States) connected to a Hewlett–Packard 5973 mass spectrometer (the United States). The column and temperature schedule were the same as in the GLC analysis.

Data on the PS structure were obtained by X-ray phase analysis (XPA) on a DRON-2.0 diffractometer (CuK_a radiation) by the standard procedure.

Data on PSs recovered by sequential extraction in stepwise hydrolysis of the raw material from buckwheat production wastes are listed in Table 1.

It should be noted that, when recovering alkali-extractable PSs from the raw mateiral and water-extractable PSs from BS-7, the PS precipitate formed on adding a fourfold volume of acetone to the extract did not fully dissolve in water again; therefore, the soluble PSs (supernatant) and PSs insoluble in water (precipitate) were lyophilically dried separately. The total yield of these polysaccharides is given in Table 1, with the monosaccharide composition given only for the soluble fraction.

The PS content depends on the raw material (husk or straw) and plant strain. The total yield of PSs from buckwheat husk varies from 3.2 (BH-10) to 6.3 wt % (BH-6) based on the raw material, and that from buckwheat straw, from 7.6 (BS-4) to 12.2 wt % (BS-7).

The highest yield of PSs from buckwheat wastes in all the cases is attained in the first extraction (with water) (Table 1). The product color depends on the raw material and extractant, being white, light brown,

Table 2. Ash residue, yields of soluble substances sequentially extracted from buckwheat husk and straw with water, 0.5 N ammonium oxalate, and 0.5 N NaOH, and weight of insoluble residue M_{res}

Raw material	Ash residue, wt %	Content of soluble substances, %, extracted with			M_{res}, %
		H_2O	$(NH_4)_2C_2O_4$	NaOH	
BH-6	2.3	14.3	2.6	19.2	63.9
BH-8	2.1	14.7	2.8	23.7	58.7
BH-10	1.8	14.4	2.6	18.7	64.3
BS-4	6.3	21.3	3.8	14.4	60.4
BS-7	11.1	18.6	1.7	24.3	55.4

Table 3. Content of metal cations in aqueous and oxalate extracts from buckwheat husk and straw and in polysaccharides

M^{n+}	Content			
	in extract, g l^{-1}		in PSs, %	
	BH-6, 8, 10	BS-4, 7	BH-6, 8, 10	BS-4, 7
K^+	$(1.2–1.8)\times10^{-1}$	$(2.0–10.6)\times10^{-1}$	$(1.5–3.4)\times10^{-1}$	2.8×10^{-1}–1.6
Na^+	$(1.0–2.0)\times10^{-2}$	$(0.7–1.5)\times10^{-2}$	8.5×10^{-3}–1×10^{-1}	3.5×10^{-3}–1.5×10^{-1}
Ca^{2+}	$(0.2–1.2)\times10^{-2}$	$(0.2–1.0)\times10^{-2}$	6.5×10^{-3}–2.2×10^{-2}	6.5×10^{-3}–1×10^{-1}
Mg^{2+}	$(2.0–7.0)\times10^{-2}$	$(2.5–6.7)\times10^{-2}$	5.5×10^{-2}–1.1×10^{-1}	7.5×10^{-2}–1.3×10^{-1}
Zn^{2+}	$(0.5–4.5)\times10^{-3}$	$(0.9–1.5)\times10^{-3}$	4.6×10^{-4}–2.4×10^{-3}	6.1×10^{-4}–1.8×10^{-3}
Mn^{2+}	$(0.7–8.5)\times10^{-3}$	$(0.7–1.7)\times10^{-3}$	8.5×10^{-4}–2.5×10^{-3}	$(1–1.9)\times10^{-3}$
Fe^{3+}	$(0.5–6.2)\times10^{-3}$	$(0.2–1.3)\times10^{-3}$	1×10^{-4}–1.5×10^{-3}	$(1–4.5)\times10^{-3}$
Cu^{2+}	$(0.4–2.8)\times10^{-4}$	$(0.2–0.5)\times10^{-4}$	3.5×10^{-5}–4.1×10^{-4}	$(3.1–5.1)\times10^{-5}$

or dark. According to XPA, the polysaccharides have an amorphous or crystalline structure, and the majority of PSs extractable with oxalate have mixed amorphous-crystalline structure.

Polysaccharides extractable with water and oxalate from all the BH samples and from BS-4 have increased glucose content. All the PSs extractable with alkali have a more complex monosaccharide composition and contain residues of rhamnose, arabinose, xylose, mannose, glucose, and galactose. Water-extractable straw PSs (BS-4 and BS-7) contain a significant amount of inositol (17 and 31 mol %, respectively). In some other polysaccharides studied, it was detected on the trace level.

All the recovered PSs were analyzed for the presence of uronic acids (Table 1). The major component among uronic acids is galacturonic acid (GalA). Glucuronic acid (GlcA) was detected in trace amounts and not in all the PSs studied. All the water-extractable PSs, from both husk and straw, have a low content of uronic acid, except BS-7 in which the content of galacturonic acid is comparable with that of hexoses. On the contrary, oxalate-extractable PSs from buckwheat husk and straw are characterized by a high content of uronic acids, and in BH-6, BS-4, and BS-7 polysaccharides the GalA content substantially (by a factor of 2–4) exceeds the total content of hexoses. In soluble alkali-extractable PSs, as in water-extractable PSs, the content of uronic acids (GalA and GlcA, with GalA apparently prevailing) is lower than in the oxalate-extractable PSs from the same sources. Insoluble alkali-extractable PSs, like oxalate-extractable PSs, contain a large amount of galacturonic acid, especially straw PSs.

Available data on properties of PSs from buckwheat processing wastes are extremely scarce. Dudkin and Ozolina [2] reported on synthesis of carboxymethyl cellulose from buckwheat husk; this product has already found use in medicine [7]. It is also known that many PSs from higher plants exhibit a wide spectrum of biological activity: immunomodulating, antiphlogistic, antiviral, antitumor, anticomplementary, and wound-healing [8].

The insoluble BH and BS residue after three successive extractions is cellolignin, which can be used as a secondary raw material for production of various materials from plant fibers [9–13].

Data on the content of soluble substances recovered by sequential extraction from buckwheat husk and straw, on the weight of the insoluble residue, and on the ash residue after oxidative calcination of the raw material at 600°C are listed in Table 2. Oxidative calcination of the raw material and analysis of elements in the ash and extracts were performed according to [13].

The results show that the ash residue from BH is lower than from BS. The ash contained K, Ca, Mg, Na, Si, Zn, Mn, Fe, Al, Cu, Ni, Cr, and Ag; their content depended on the plant strain and kind of the waste (husk or straw). Potassium, magnesium, and calcium compounds prevailed in all the ash samples.

In extraction, metals are recovered to some extent along with organic substances. The list of the metals detected in the extracts and their concentrations are given in Table 3. The polysaccharides recovered from the extracts in the solid state take up some metals present in solution, as seen from Table 3. The insoluble residue after the extraction gives virtually no ash.

CONCLUSIONS

(1) The content of polysaccharides recovered from buckwheat processing wastes and their monosaccharide composition (qualitative and quantitative) depend on the kind of the raw material (husk or straw) and recovery procedure. The total yield of polysaccharides from buckwheat husk varies within 3.2–6.3 wt % based on the dry raw material, and that from buckwheat straw, within 7.6–12.2%.

(2) Polysaccharides extractable with water and oxalate from buckwheat husk and straw have increased glucose content. Polysaccharides extractable with alkali have a more complex monosaccharide composition and contain residues of rhamnose, arabinose, xylose, mannose, glucose, and galactose in different ratios depending on the raw material source.

(3) The inositol content in aqueous extracts from buckwheat straw is substantially higher (17–31 mol %) than in those from buckwheat husk, in which inositol was detected in trace amounts.

(4) Uronic acids are present in all the polysaccharides obtained, and their content is the highest in oxalate-extractable and insoluble alkali-extractable polysaccharides, especially in those recovered from buckwheat straw. The major component among uronic acids is galacturonic acid.

(5) In extraction of buckwheat husk and straw, metals are also recovered into solution and are then taken up by polysaccharides; the insoluble residue of the raw material gives virtually no ash.

REFERENCES

1. Sharkov, V.I. and Kuibina, N.I., *Khimiya gemitsellyuloz* (Chemistry of Hemicelluloses), Moscow: Lesn. Prom–st., 1972.
2. Dudkin, M.S. and Ozolina, S.A., *Khim. Prirodn. Soedin.*, 1976, no. 4, pp. 417–419.
3. Ozolina, S.A. and Darman'yan, P.M., *Pishch. Prom–st.*, 1977, no. 23, pp. 40–42.
4. Dudkin, M.S., Ozolina, S.A., and Shkantova, N.G., *Khim. Drev.*, 1980, no. 4, pp. 18–22.
5. Aleinikov, I.N., Sergeev, V.N., Rusakov, A.V., and Aganyan, V.E., *Pishch. Ingred.: Syr'e Dobavki*, 2001, no. 1, pp. 30–31.
6. Aleinikov, I.N. and Sergeev, V.N., *Pishch. Prom–st.*, 1998, no. 8, p. 43.
7. Kaputskii, F.N. and Yurkshtovich, T.L., *Lekarstvennye preparaty na osnove proizvodnykh tsellyulozy* (Medicinals Based on Cellulose Derivatives), Minsk: Universitetskoe, 1989.
8. Ovodov, Yu.S., *Bioorg. Khim.*, 1998, vol. 24, no. 7, pp. 483–501.
9. *TU* (Technical Specifications) *2164-003-02 698 192–69: RShMS Sorbents*, Moscow: Izd. Standartov, 1998, section L91, p. 193.
10. RF Patent 2 117 527.
11. Marshall, W.E., Champaque, E.T., and Evans, W.J., *J. Environ. Sci. Health*, 1993, vol. 28A, no. 9, pp. 1977–1992.
12. Dudkin, M.S., Ozolina, S.A., and Darman'yan, P.M., *Khim. Drev.*, 1976, no. 3, pp. 33–35.
13. Zemnukhova, L.A., Sergienko, V.I., Davidovich, R.L., *et al., Vestn. Dal'nevost. Otd. Ross. Akad. Nauk*, 1996, no. 3, pp. 82–85.

Russian Journal of Applied Chemistry, Vol. 77, No. 7, 2004, pp. 1182–1189. Translated from Zhurnal Prikladnoi Khimii, Vol. 77, No. 7, 2004, pp. 1197–1204.

CHEMISTRY OF FOSSIL FUEL

A Study of the Composition of Water Vapor Saturated Natural Gas, as Applied to Elucidation of the Nature of Vapor–Gas Thermal Phenomena

G. R. Anpilogova, R. A. Khisamutdinov, Yu. I. Murinov, R. M. Kharasov, I. Sh. Khuramshin, and E. G. Galkin

Institute of Organic Chemistry, Ufa Scientific Center, Russian Academy of Sciences, Ufa, Bashkortostan, Russia

Received January 9, 2004

Abstract—The composition of water vapor saturated gases of various temperatures from reserve wells of Yangantau health resort was studied. The dependence of the concentration and composition of organic substances from the vapor condensate and of the extent of thermal oxidative degradation of the shale organic matter on the rock temperature in the heating zone was examined.

Unique vapor–gas thermal phenomena of the Yangantau mountain attract researchers' attention for more than two centuries. A number of hypotheses associating the origin of the thermal anomaly with exo- and endogenic factors were put forward; however, there is still no common opinion on the origin and evolution of this phenomenon [1, 2]. The component composition of the organic matter (OM) of Yangantau bituminous shales has not been studied. According to the elemental composition {C 78.35, H 6.84, (S + N + O) 14.51% [3]}, the OM of shales can be classed with asphaltites [4].

In this work, we studied the composition of water vapor saturated gas from wells by a set of spectral methods to elucidate the physicochemical processes occurring in the bulk of bituminous rocks of the mountain; also, we examined how the temperature conditions in a well affect the composition of the organic components of the vapor condensate (VC).

EXPERIMENTAL

We studied the gas and vapor (vapor condensate) components of water vapor saturated gases from reserve wells 22 and 27 (Yangantau health resort, Yangantau mountain, Salavat raion, Bashkortostan, Russia), differing in the maximal temperature of rocks along the well shaft (temperature in the heating zone T_{max} 81–86 and 140–150°C at a depth of 70.0 and 65.7 m, respectively [1, 5]). The gas phase was studied with a Varian MAT CH-5 mass spectrometer.

The concentration of nonferrous and ferrous metal ions in VC was determined by atomic absorption spectrophotometry on a Hitachi 508 device (acetylene–air flame). The pH values of the condensate were measured on an OP-211/1 pH meter with a combined glass electrode.

Moderately and slightly volatile organic components of the vapor condensates were isolated by sequential extraction from acidic (concentrate I), alkaline (concentrate II), and neutral (concentrate III) solutions [6]. The isolated extracts of organic substances are greasy yellow-brown substances with specific odor. Each concentrate was examined by spectroscopy and elemental analysis. The gas chromatographic–mass spectrometric (GC–MS) analysis of the concentrates was performed with an HP 5890 chromatograph equipped with an HP 5972A mass-selective detector and a 50 m × 0.20 mm capillary column with the grafted phase 5% methylphenylsilicone–95% methylsilicone rubber. The column was heated from 40 to 250°C at a rate of 10 deg min^{-1}. The data were processed on an HP ChemStation computer. The solvent was CCl_4. The spectra were identified using the artificial intellect program included in the HP ChemStation software. The index of agreement between the experimental mass spectra and published data in most cases was no less than 75%. At lower indices, the methods of spectrum–structure correlations [7] were used. The presence of the main classes of compounds identified by GC–MS was confirmed by the electronic absorption (Specord M40, acetonitrile, cell thickness

1070-4272/04/7707-1182 © 2004 MAIK "Nauka/Interperiodica"

0.2 cm) and IR (300–4000 cm^{-1}, Specord M80, liquid film, KRS5 windows, assignment according to [8–10]) spectra.

The gas phase of water vapor saturated gases from wells 22 and 27 contains, along with air components, also methane + ethane (>0.5 vol % relative to the total gas sample volume) and increased amount of CO_2. The gas sample from well no. 27 also contained small amounts of CO and H_2 (0.052 and 0.028 vol %, respectively [5]). According to the observations, the content of CO_2, CO, and O_2 and the temperature of the water vapor saturated gas appreciably vary depending on the season and wind rose. In summer, the concentration of CO_2 grows, and that of O_2 decreases [11]. The increased content of CO_2 in water vapor saturated gases cannot be attributed to thermal decomposition of the inorganic components of bituminous rocks, $CaCO_3$ and $MgCO_3$ [3], since the maximal temperature of the heated rocks, 380°C [5], is considerably lower than the decomposition temperatures of $CaCO_3$ and $MgCO_3$ (825 and 500°C, respectively [12]). It is known that oxidation of petroleum residues with atmospheric oxygen is characterized by an increase in the oxygen uptake with temperature and by formation of CO_2 in the amount exceeding that of the forming CO [13]. Thus, the presence of CO and of increased amounts of CO_2 and the absence of hydrogen in the sample of the burned out rock (results of elemental analysis), taken on the southern slope of the mountain at the site of the outcrop of thermally altered rocks to the diurnal surface, confirms the hypothesis about thermal oxidative degradation of the organic matter of shale. On the southern steep slope of the Yangantau mountain, there are a lot of cracks arising from slope deformations and providing natural ventilation of the mountain with prevailing SW winds [11]. This provides the oxygen access to the heating sites to sustain the exothermic thermal oxidative reactions of the organic matter of shales.

The vapor condensates from wells 22 and 27 have pH 7.43 and 7.34, respectively. We found that, as T_{max} grows, the total content of organic matter in VC (46.3 and >124.5 mg l^{-1} for wells 22 and 27, respectively) and the content of phenols (0.8 and 25 mg l^{-1} for wells 22 and 27, respectively) increases. The unsuitability of vapor from well 27 for balneological purposes [14] is due to the high content of phenols.

The C : H atomic ratio in concentrates I (1 : 1.84 and 1 : 1.03 in wells 22 and 27, respectively), obtained under the conditions of predominant concentration of neutral substances, acids, and phenols [6], suggests lower content of aromatic substances in the concentrate from well 22.

The results of GC–MS analysis of concentrate I from well 27 show that its major organic component is phenol (21.2%); the other components are thiobenzoic acid (6.91%), *o*-, *p*-, and *m*-cresols (1.8%), 3-ethylphenol (<1%), and benzoic (0.6%), α-naphthoic (<1%), and octenoic acids (<1%). The IR spectrum of the concentrate confirms the presence of aromatic compounds [ν(CH) 3080 cm^{-1}; ν(C=C) 1600, 1580, 1496 cm^{-1}; δ(CH) 1176 cm^{-1} for mono- and 1,3-disubstituted rings, 808 cm^{-1} for 1,3- and 1,4-disubstituted rings and α-naphthoic acid] and thiobenzoic acid [ν(C=S) 1324 cm^{-1}]. The spectrum contains the bands ν(OH) at 3360, 3180 cm^{-1} of phenols and carboxylic acids; strong ν(C=O) bands of aliphatic carboxylic acids (1704 cm^{-1}) and carbonyl groups conjugated with an aromatic ring (1690 cm^{-1}, benzoic acid, aryl alkyl ketones); ν(COC) at 1288 and 1128 cm^{-1} belonging to carboxylic acid esters; δ(CH) at 936 cm^{-1} of unsaturated compounds of the type *trans*-$R^1CH{=}CHR^2$. The electronic absorption spectrum of this substance contains bands at 228 (s, sh) and 277 nm (w), assignable to the $\pi \rightarrow \pi^*$ electronic transitions in phenol and cresols (E_2 and *B* bands, respectively) and in benzoic acid (bands *K* and *B*, respectively) [8]. The presence of weak bands at 302 (sh) and 310 nm (sh) suggests the presence of compounds with a thiocarbonyl group ($\pi \rightarrow \pi^*$ and $n \rightarrow \sigma^*$ in the range 250–320 nm [8]) and of the naphthalene core (221, 286, 312 nm [8]).

The previous [5] study of the composition of organic microimpurities in VC from well 27 revealed also the presence of aliphatic (29 kinds) and aromatic carboxylic acids, nitrogen bases (quinolines, benzothiazoles, indoles, carbazoles), sulfur compounds (benzothiophenes, dibenzothiophenes), and hydrocarbons of the naphthalene and anthracene series. Among volatile organic compounds, toluene, ethylbenzene, chlorobenzene, xylene, carbon disulfide, and thiophene were detected in the vapor condensate.

In the organic matter isolated from vapor condensate from well 22 in the form of three concentrates, we identified by GC–MS the following compounds (% of total organics): *n*-alkanes C_{10}–C_{25} 7.20 (with even C_{16} and C_{18} homologs prevailing, odd/even coefficient 0.54); branched alkanes 3.51 (including isoprenanes 2.37); naphthenes 1.41; alkenes 2.19; aliphatic saturated (13.45) and unsaturated (13.28) carboxylic acids; phenols 1.71; aromatic ketones 2.98; α-hydroxyphenylacetic acid and/or 2-hydroxy-1,2-diphenylethanone 12.84; aliphatic and aromatic alde-

Table 1. Alkanes and aliphatic acids detected by gas chromatography–mass spectrometry in the vapor condensate from well 22

Compound	Formula	Content, % of OM of vapor condensate	T_m	T_b
			°C [12, 15, 16]	
n-Alkanes:				
decane	$C_{10}H_{22}$	0.02	–29.8	174.0
undecane	$C_{11}H_{24}$	0.12	–25.7	195.8
dodecane	$C_{12}H_{26}$	0.42	–9.7	216.2
tridecane	$C_{13}H_{28}$	0.18	–6.2	234.0
tetradecane	$C_{14}H_{30}$	0.65	5.5	252.5
pentadecane	$C_{15}H_{32}$	0.18	10.0	270.5
hexadecane	$C_{16}H_{34}$	0.82	18.2	287.5
heptadecane	$C_{17}H_{36}$	0.66	22.5	303.0
octadecane	$C_{18}H_{38}$	1.03	28.0	317.0
nonadecane	$C_{19}H_{40}$	0.58	32.0	330.0
eicosane	$C_{20}H_{42}$	0.64	36.4	344.0
heneicosane	$C_{21}H_{44}$	0.49	40.4	356.0
docosane	$C_{22}H_{46}$	0.57	44.4	368.0
tricosane	$C_{23}H_{48}$	0.37	47.7	380.0
tetracosane	$C_{24}H_{50}$	0.53	50.9	389.2
pentacosane	$C_{25}H_{52}$	0.06	54.0	405.0
Branched alkanes:				
2-methyltridecane	$C_{14}H_{30}$	0.08		
3-methyltridecane	$C_{14}H_{30}$	0.49		
5-methyltetradecane	$C_{15}H_{32}$	0.01		
7-methylhexadecane	$C_{17}H_{36}$	0.10		
8-methylheptadecane	$C_{18}H_{38}$	0.18		
6-propyltridecane	$C_{16}H_{34}$	0.06		
4,5-dimethylnonane	$C_{11}H_{24}$	0.02		
2,3-dimethylundecane	$C_{13}H_{28}$	0.02		
3,6-dimethylundecane	$C_{13}H_{28}$	0.06		
3-methyl-3-ethyldecane	$C_{13}H_{28}$	0.02		
2-methyl-6-propyldodecane	$C_{16}H_{34}$	0.11		
Isoprenanes:				
2,6,10-trimethylpentadecane	$C_{18}H_{38}$	0.15	<–70	300.0
2,6,10,14-tetramethylpentadecane (pristane)	$C_{19}H_{40}$	0.95	<–70	331.2–332.5
2,6,10,14-tetramethylhexadecane (phytane)	$C_{20}H_{42}$	1.14	<–70	352.5–353.0
2,6,10,14-tetramethylheptadecane	$C_{21}H_{44}$	0.14		
Alkanoic acids:				
hexanoic	$C_5H_{11}COOH$	0.71	–1.5	205.3
heptanoic	$C_6H_{13}COOH$	0.28	–10.5	223
2-ethylhexanoic	$C_7H_{15}COOH$	0.11		
octanoic	$C_7H_{15}COOH$	0.05	16.2	237.5
nonanoic	$C_8H_{17}COOH$	1.07	12.5	254
decanoic	$C_9H_{19}COOH$	0.26	31.5	268.4
dodecanoic	$C_{11}H_{23}COOH$	0.26	44.2	298.9
tetradecanoic	$C_{13}H_{27}COOH$	0.79	54.1	330
hexadecanoic	$C_{15}H_{31}COOH$	8.21	62.6	340–356
octadecanoic	$C_{17}H_{35}COOH$	1.68	69.3	360–383
3,7,11,15-tetramethylhexadecanoic	$C_{20}H_{41}COOH$	0.03		
2-hydroxydecanoic	$C_8H_{17}CH(OH)COOH$	0.05		
Unsaturated aliphatic acids:				
hexadec-9-enoic	$C_{15}H_{29}COOH$	0.90		
octadec-9-enoic (oleic)	$C_{17}H_{33}COOH$	12.22	16.0	
eicosa-8,11,14-trienoic	$C_{19}H_{33}COOH$	0.16		

hydes 0.58; aliphatic primary alcohols 0.46 and ketones 0.20; unsaturated oxidized cyclohexane derivatives 1.34; carboxylic acid esters 2.25; oxidized compounds of the naphthalene series 0.17; furan derivatives (isobenzofuran-1,3-dione, 2-pentylfuran) 0.12; S,N-containing compounds (4-methylthiazole, 4-methylisothiazole, benzothiazole) 0.60; nitrogen compounds (3-benzylquinoline, quinoline *N*-oxide, 2,5-diphenyloxazole) 0.50 (Tables 1, 2).

The electronic absorption spectra of the concentrates contain three absorption bands at 222 (s, sh), 272–273 (m), and 278 nm (m, sh) of the substituted aromatic ring. The intensity ratio of these bands in the spectrum of concentrate I A_{222}/A_{272} = 4.6 and A_{222}/A_{278} = 3.9 allows their assignment to the $\pi \rightarrow \pi^*$ electronic transitions in phenols and substituted phenols (for phenol, $\varepsilon_{210}/\varepsilon_{270}$ = 4.3). The *R* band ($n \rightarrow \pi^*$) makes, apparently, a certain contribution to the band at 278 nm. In the spectra of concentrates II and III, the band at 222 nm is considerably more intense, probably owing to the contribution from nonconjugated alkenes. The presence of a very weak broad band at 370–455 and 382–434 nm in the spectra of concentrates II and III, respectively, suggests the presence of small amounts of compounds of the anthracene and naphthacene series [8].

The IR spectra of the concentrates contain the absorption bands of the following structures (cm^{-1}): alkanes and cycloalkanes [ν(CH) 3008–3010; $\nu(CH)_{as}$ 2960 (CH_3), 2928 (CH_2); $\nu(CH)_s$ 2856 (CH_2, CH_3); $\delta(CH_3)_{as}$, $\delta(CH_2)_s$ 1464–1456; $\delta(CH_3)_s$ 1376; $\rho(CH_2)$ 720–736]; alkenes $R^1HC{=}CHR^2$ of the *cis* [ν(C=C) 1660] and *trans* configurations [ν(C=C) 1680, δ(CH) 960–965], $RHC{=}CH_2$ [ν(C=C) 1645–1648, δ(CH) 908–916]; substituted aromatics [ν(CH) 3072–3080; ν(C=C) 1600–1624, 1576, 1500–1495]. Also present are vibration bands of oxygen-containing compounds (cm^{-1}): ν(OH) 3472–3336, 3220 of carboxylic acids, phenols, alcohols; ν(C=O) of alkanoic acid esters and aliphatic aldehydes at 1740–1744, of carboxylic acids and ketones at 1720–1728, of conjugated aromatic acids and aryl alkyl ketones at 1696, of diaryl ketones at 1680; ν_{as}(COC) 1272–1288 and ν_s(COC) 1120 of esters; ν(C–O) 1145 of phenols and aliphatic ethers.

The C (70.4%) and H (10.9%) content in OM recovered from well 22 suggests lower content of aromatic compounds, compared to OM from shales, and the C : H ratio of 1 : 1.85 is close to that in nonoxidized bitumenoids [17].

Among branched alkanes, biomarkers of the isoprenoid structure (Table 1), in particular, phytane and pristane, prevail. The detected naphthenes are mainly monocyclic. On the whole, the composition of alkanes and naphthenes suggests that they belong to nonoxidized bitumenoids or oil component of OM of shales [15, 18–20].

The detected olefins are mainly *n*-alkenes corresponding to the prevailing *n*-alkanes (Tables 1, 2). The presence of olefins is untypical of OM of shales [20]. It is known that intrastratal burning of bituminous shales is accompanied by thermal, catalytic, and oxidative cracking of OM of shales, with formation of unsaturated hydrocarbons [20, 21]. Inorganic components of the rocks (clay, silica, minerals containing oxides and salts of transition metals Cu, Ni, Co, Mn, Fe, REE) catalyze this process [15, 21, 22]. The bituminous rocks of Yangantau contain clay, quartz sand, and fairly large amount of pyrite (up to 2–3%) [3]. The increased H_2 concentration in the vapor from Yangantau [5] suggests that the presence of alkanes in the vapor from well 22 is due to thermocatalytic dehydrogenation of oil alkanes.

Among the eleven fatty acids detected (Table 1), hexadecanoic acid prevails; also present, in smaller amounts, are C_{18}, C_{14}, and C_9 acids, and one isoprenoid C_{20} acid. The composition of the acids and the prevalence of the even homologs are typical of bitumenoids from shales of the algal origin [18, 23]. The maximal temperature of the rocks along well 22 T_{max} is insufficient for efficient and intense thermocatalytic oxidation of paraffins and alkanoic acids of oil in the presence of transition metal compounds from the rock (100–120°C [16, 24]).

Therefore, all the fatty alkanoic and unsaturated acids are mainly oil acids and acids released by hydrolysis. As T_{max} increases (well 27), the composition of the alkanoic acids changes substantially: the number of the detected acids and the total content of low-molecular-weight acids C_5–C_{10} increase. Among fatty acids, isopentanoic acid prevails [5]. This suggests higher extent of thermal oxidative degradation of oil alkanes and acids, and also of eliminated side alkane and acid groups of asphaltenes. Oxidation of saturated monocarboxylic acids in the presence of initiators (oxidizable oil hydrocarbons and eliminated side alkane groups of resin–asphaltene substances of OM of shales) mainly occurs at the α- or β-CH_2 group and is accompanied by conjugated decarboxylation [24]:

$$RCH_2CH_2COOH \xrightarrow{O_2} \begin{cases} \rightarrow RCH_2COOH + CO_2 + H_2O, \\ \rightarrow RC(=O)CH_3 + CO_2 + H_2O. \end{cases}$$

Table 2. Naphthenes, olefins, and oxygen-containing and aromatic compounds detected in the vapor condensate from well 22 by gas chromatography–mass spectrometry

Compound	Formula	Content, % of OM of vapor condensate
Cycloalkanes:		
cyclododecane	$C_{12}H_{24}$	0.32
cyclotetradecane	$C_{14}H_{28}$	0.55
decylcyclopentane	$C_{15}H_{30}$	0.06
heneicosylcyclopentane	$C_{26}H_{52}$	0.13
1,2-dimethylcyclooctane	$C_{10}H_{20}$	0.07
1-methyl-1-ethylcylcohexane	C_9H_{18}	0.05
1,2,3-trimethylcyclopentane	C_8H_{16}	0.21
(3-methylbutyl)cyclopentane	$C_{10}H_{20}$	0.02
Olefins:		
3,3-dimethyl-1-butene	C_6H_{12}	0.14
2-octene	C_8H_{16}	0.32
1-dodecene	$C_{12}H_{24}$	0.02
1-tetradecene	$C_{14}H_{28}$	1.28
(*E*)-3-tetradecene	$C_{14}H_{28}$	0.07
(*E*)-5-tetradecene	$C_{14}H_{28}$	0.04
(*Z*)-7-tetradecene	$C_{14}H_{28}$	0.02
1-hexadecene	$C_{16}H_{32}$	0.08
(*E*)-5-octadecene	$C_{18}H_{36}$	0.17
9-eicosene	$C_{20}H_{40}$	0.05
Aliphatic and cyclic alcohols, aldehydes, ketones, ethers:		
2-ethyl-1-butanol	$C_6H_{13}OH$	0.17
4-methyl-1-hexanol	$C_7H_{15}OH$	0.03
2-ethyl-1-hexanol	$C_8H_{17}OH$	0.01
1-octanol	$C_8H_{17}OH$	0.10
1-nonanol	$C_9H_{19}OH$	0.01
2,2-dimethyl-1-octanol	$C_{10}H_{21}OH$	0.02
tetradecanol	$C_{14}H_{29}OH$	0.05
1-hexadecanol	$C_{16}H_{33}OH$	0.07
cyclohex-2-enol	C_6H_9OH	0.01
2,2-dimethylpropanal	$C_5H_{10}O$	0.41
3-methylhexanal	$C_7H_{14}O$	0.03
nonanal	$C_9H_{18}O$	0.06
7-hydroxy-3,7-dimethyloctanal	$C_{10}H_{20}O_2$	0.05
6-methyl-3-heptanone	$C_8H_{16}O$	0.12
5-methyl-3-heptanone	$C_8H_{16}O$	0.02
3-octanone	$C_8H_{16}O$	0.06
2,6-di-*tert*-butylcyclohexa-2,5-diene-1,4-dione	$C_{14}H_{20}O_2$	1.32
4-methyl-4-phenylcyclohex-2-enone	$(CH_3)(C_6H_5)C_6H_6O$	0.09
1-ethoxyhexane	$C_2H_5OC_6H_{13}$	0.92
Carboxylic acid esters:		
hexyl hexanoate	$C_6H_{13}O_2C_6H_{11}$	0.04
3-methylbutyl octanoate	$C_5H_{11}O_2C_{18}H_{35}$	0.12
isopropyl tetradecanoate	$C_3H_7O_2C_{14}H_{27}$	0.56
methyl hydrogen butanedioate	$CH_3O_2C_3H_4COOH$	0.08
didecyl decanedioate	$(C_{10}H_{21})_2O_4C_{10}H_{16}$	0.64
methyl tetracos-15-enoate	$CH_3O_2C_{24}H_{45}$	0.23
3-methylbutyl benzoate	$C_5H_{11}O_2CC_6H_5$	0.58
Aromatic compounds:		
phenol	C_6H_5OH	0.11
2,4-dimethylphenol	$(CH_3)_2C_6H_3OH$	0.16

Table 2. (Contd.)

Compound	Formula	Content, % of OM of vapor condensate
2,6-di-*tert*-butylphenol	$(C_4H_9)_2C_6H_3OH$	1.20
3-methyl-4-ethylphenol	$(CH_3)(C_2H_5)C_6H_3OH$	0.15
1-naphthol	$C_{10}H_7OH$	0.09
1-(3-methylphenyl)-1-ethanone	$CH_3C_6H_4C(O)CH_3$	0.74
1-(4-ethylphenyl)-1-ethanone	$C_2H_5C_6H_4C(O)CH_3$	0.07
diphenylmethanone	$(C_6H_5)_2CO$	1.72
2-hydroxy-1,2-diphenylethanone and/or α-hydroxyphenylacetic acid	$C_6H_5C(O)CH(OH)\cdot C_6H_5$ $C_6H_5CH(OH)COOH$	12.84
3-methylbenzophenone	$CH_3C_6H_4C(O)C_6H_5$	0.36
1-naphthyl-1-ethanone	$C_{10}H_7C(O)CH_3$	0.08
benzaldehyde	C_6H_5CHO	0.03

The rate of the conjugated decarboxylation grows with an increase in the molecular weight of the monocarboxylic acid and temperature (from 120 to 145°C). Under similar conditions, C_6–C_9 fatty acids are more resistant to oxidation than C_{10}–C_{20} acids [24].

In VC from well 22, we identified two monounsaturated and one trienoic acids, among which oleic acid prevailed (Table 1). The high content of natural unsaturated acids C_{18} and C_{16} suggests the algal origin of OM os Yangantgau shales [18]. Thermocatalytic oxidation of oleic acid is possible at 70–100°C. The process yields aldehydes and aldehydo acids with 6–12 carbon atoms, which are readily oxidized to the corresponding carboxylic and dicarboxylic acids at temperatures less than 60°C [24]. Therefore, decanedioic acid (present as ester), nonanal (Table 2), and a part of C_6–C_{11} alkanoic acids can be considered as products of thermocatalytic oxidation of oleic acid.

Primary alkanols present in small amounts (Table 2) may originate from elimination of side groups of resins and asphaltenes by hydrolytic cleavage of ether and ester bonds; they may also be components of oil (*n*-alcohols) [18]. Aliphatic esters, ketones, phenols, furan derivatives, S,N-containing compounds, and nitrogen bases have the composition typical of bitumenoids [15, 18, 23] or are oxidized bitumenoids (isobenzofuran-1,3-dione, quinoline *N*-oxide). Unsaturated oxidized cyclohexane derivatives are probably products of thermal oxidative elimination of cyclohexane cores from resins and asphaltenes. The presence of metal ions (Pb [5], Fe 0.4, Cu 0.5, Zn 2.1–6.3 mg l^{-1}) in the vapor condensates is due to steam distillation of their complexes with methylthiazoles, benzothiazole, benzoquinoline, and other low-molecular-weight complexing agents from OM of shales [15, 20].

Identified (alkylphenyl)ethanones, benzophenones, and 2-hydroxy-1,2-diphenylethanone are apparently products of thermocatalytic oxidation of the corresponding aromatic components of bitumen oil: (alkylphenyl)ethanes and bridged diphenylalkanes [15] which are less resistant to oxidation than alkanes [24]. Significant content of 2-hydroxy-1,2-diphenylethanone (or α-hydroxyphenylacetic acid) in VC from well 22 is probably due to oxiative elimination of peripheral groups from bitumen resins. Bitumen resins are unstable to oxidation with atmospheric oxygen even at low temperature [15]. It is known that, in oxidation of hydrocarbons, the hydroperoxy radical attacks the least stable C–H bond. In the aromatic bitumenoids under consideration, this is the C–H bond in the methylene group in the α-position to the benzene ring [24]. Oxidation of a part of 2-hydroxy-1,2-diphenylethanone yields benzaldehyde and benzoic acid. Benzaldehyde is oxidized to benzoic acid even at moderate temperatures (<60°C) [24].

Oxidation of asphaltenes with atmospheric oxygen is accompanied by formation of arenes, ketones, and acids (mainly benzenecarboxylic) and by a decrease in the number of aromatic and aliphatic rings and long alkyl chains [15]. Therefore, high content of aromatic compounds in vapor condensate from well 27 is attributable to thermal oxidative degradation of resin–asphaltene components of OM of shales. Relatively high content of phenol in VC from well 27 may be due to thermocatalytic oxidation of benzoic acid in the presence of atmospheric oxygen, water vapor, $MgCO_3$, and transition metal ions (Cu [3]) from the rock at a relatively high temperature. It is known that catalytic decarboxylation of aromatic acids (benzoic, toluic) in the liquid phase in the presence of Cu(II) compounds or Mg(II) and Cu(II) benzoates at 200–300°C, conjugated with oxidation with atmospheric oxygen, yields phenols with the release of CO_2 [15,

24]. Thus, an increase in the total content of organic impurities and phenols in the vapor condensate with increasing T_{max} suggests greater extent of thermal oxidative degradation of OM of shales, involving oxidation of condensed compounds of resins and asphaltenes.

The bulk of bituminous shales of the Yangantau mountain is considerably heated above and below the heating sites. Regions heated to 50°C sometimes reach the external surface and groundwater [2]. The melting points of oil alkanes, fatty acids, phenols, and unsaturated acids detected in VC from well 22 do not exceed 70°C (Table 1) [12]. Hence, the majority of components of bitumen oils and unsaturated acids occur in the molten state in a wide region of heated rocks and can migrate in the bulk of the mountain as melts, solutions, and colloids under the influence of temperature, concentration, and pressure gradients; in the regions of elevated temperatures, they can also be steam-distilled in the native form or as products of thermal oxidative degradation. The mobile components of OM, when appearing in heating sites with temperatures $T \geq 100$°C, undergo intense exothermic thermocatalytic oxidation with atmospheric oxygen [16, 24]. This provides supply of hydrocarbons to the heating sites and maintenance of high temperatures required for thermal oxidative degradation of resin–asphaltene components of bitumen. Thermal oxidative degradation of polymeric components of bitumen is also exothermic [20, 23]. Local accumulation of heat and slow progress of the combustion front to the depth of the mountain are favored by the low thermal conductivity of the rocks [21] (~1 $W\,m^{-1}\,K^{-1}$ for Green River dolomite marls [18]).

The presence of methane and ethane in water vapor saturated gases from Yangantau suggests supply of the combustion sites with light oil and gas hydrocarbons migrating along natural cracks from deep oil- and gas-bearing strata. The Yangantau mountain is located on the Yuryuzan–Aya depression of the Yuryuzan–Sylva region of South Cis-Ural oil and gas fields [25, 26]; it is located in the zone of oil and gas collectors widely occurring in carbonate deposites of early Carboniferous–early Permian periods [27]. The seismic and tectonic activity in the region of the Yangantau mountain [2] may facilitate distortion of rocks covering deep oil- and gas-bearing strata [28].

CONCLUSIONS

(1) Water vapor saturated gases of the Yangantau mountain contain products of therma oxidative degradation of organic matter of shales, unsaturated hydrocarbons, CO, and increased amounts of CO_2 and H_2, which suggests the occurrence of thermal and thermocatalytic degradation of the organic matter of shales with atmospheric oxygen in the presence of inorganic components of the rock [pyrite, Cu(II), silica].

(2) With increasing T_{max}, the extent of thermal oxidative degradation of the organic matter of shales and the concentration of organic matter (and, in particular, phenol) in the vapor condensate increase.

(3) The presence of moderately and slightly volatile organic (in particular, resin) substances and of metal ions in water vapor saturated gases is due to steam distillation of mobile components and products of thermal oxidative degradation of the organic matter of shales, and also of complexes of rock metal ions with complexing compounds of the organic matter of shales.

(4) The heat release in the Yangantau mountain is due to the occurrence of exothermic thermal and thermocatalytic oxidation of the organic matter of shales with atmospheric oxygen. The local accumulation of heat is favored by low thermal conductivity of the carbonate rocks. The supply of organic matter to the combustion sites and slow progress of the combustion front to the depth of the mountain are provided by migration of molten components of the organic matter of shales from the heated adjacent rocks and, possibly, of light hydrocarbons of oil and gas from deep oil- and gas-bearing strata along natural cracks.

REFERENCES

1. Akbashev, R.Sh., *Kurort Yangantau* (Yangantau Health Resort), Ufa: Bashkirskoe Knizhnoe, 1986.
2. Nigmatulin, R.I., Kazantseva, T.T., Kamaletdinov, M.A., *et al.*, *Geologiya i genezis teplovykh anomalii gory Yangantau* (Geology and Genesis of Thermal Anomalies of the Yangantau Mountain), Ufa: Akad. Nauk Resp. Bashkortostan, Otd. Nauk o Zemle i Ekologii, 1998.
3. Strakhov, N.M. and Osipov, S.S., *Byull. Mosk. O–va. Isp. Prir.: Otd. Geol.*, 1935, vol. 13, no. 1, pp. 3–39.
4. Gol'dberg, I.S., *Prirodnye bitumy SSSR (Zakonomernosti formirovaniya i razmeshcheniya)* (Natural Bitumens of the USSR (Regular Trends in Formation and Location)), Leningrad: Nedra, 1981.
5. Khuramshin, I.Sh., Kharasov, R.M., and Korzhova, L.F., in *Trudy Mezhdunarodnogo foruma po problemam nauki, tekhniki i obrazovaniya* (Proc. Int. Forum on Problems of Sciences, Engineering, and Education), Moscow: Akad. Nauk o Zemle, 2000, vol. 2, pp. 105–106.
6. Lur'e, Yu.Yu. and Rybnikova, A.I., *Khimicheskii ana-*

liz proizvodstvennykh stochnykh vod (Chemical Analysis of Industrial Wastewaters), Moscow: Khimiya, 1974.

7. Takhistov, V.V., *Organicheskaya mass-spektrometriya* (Organic Mass Spectrometry), Leningrad: Nauka, 1989.
8. Silverstein, R.M., Bassler, G.C., and Morrill, T.C., *Spectrometric Identification of Organic Compounds*, New York: Wiley, 1974.
9. Svehla, D., *Comprehensive Analytical Chemistry*, Amsterdam: Elsevier, 1976, vol. 6.
10. Shriner, R.L., Fuson, R.C., Curtin, D.Y., and Morrill, T.C., *The Systematic Identification of Organic Compounds. A Laboratory Manual*, New York: Wiley, 1980, 6th ed.
11. Pilipenko, G.F., in *Informatsionno-metodicheskie materialy po voprosam gidrogeologii i bal'neotekhniki lechebnykh vod i gryazei* (Information and Methodical Materials on Hydrogeology and Balneology of Curative Waters and Muds), Moscow: Geominvod, 1961, issue 3, pp. 50–60.
12. Rabinovich, V.A. and Khavin, Z.Ya., *Kratkii khimicheskii spravochnik* (Concise Chemical Handbook), St. Petersburg: Khimiya, 1994.
13. Gimaev, R.N., Gandalipov, F.A., Kudasheva, F.Kh., *et al.*, in *Neftebituminoznye porody: Dostizheniya i perspektivy: Materialy Vtorogo Vsesoyuznogo soveshchaniya po kompleksnoi pererabotke i ispol'zovaniyu neftebituminoznykh porod* (Oil-Bearing and Bituminous Rocks: Achievements and Prospects: Proc. Second All-Union Meet. on Integrated Processing and Use of Oil-Bearing and Bituminous Rocks), Alma-Ata: Nauka, 1988, pp. 211–214.
14. Maksimov, G.G., in *Aktual'nye voprosy kurortologii i fizioterapii: Materialy k mezhregional'noi nauchno-prakticheskoi konferenrtsii, posvyashchennoi 60-letiyu kurorta Yangantau* (Urgent Problems of Spa Science and Physical Therapy: Proc. Interregional Scientific and Practical Conf. Dedicated to 60th Anniversary of Yangantau Health Resort), Ufa: Poligrafkombinat, 1997, pp. 32–35.
15. Proskuryakov, V.A. and Drabkin, A.E., *Khimiya nefti i gaza* (Oil and Gas Chemistry), Leningrad: Khimiya, 1981.
16. Alaev, B.S., *Proizvodstvo sinteticheskikh zhirnykh kislot* (Production of Synthetic Fatty Acids), Moscow: Pishchepromizdat, 1952.
17. Vyshemirskii, V.S. and Doil'tsyn, E.F., in *Metody issledovaniya prirodnykh organicheskikh veshchestv* (Methods for Studying Natural Organic Substances), Novosibirsk: Nauka, 1985, pp. 6–9.
18. Ien, T.F. and Chilingaryan, D.V., *Goryuchie slantsy* (Oil Shales), Leningrad: Nedra, 1980.
19. Beskrovnyi, N.S. and Krasnov, S.G., *Neftegazonosnost', geokhimicheskaya kharakteristika i usloviya obrazovaniya bituminoznykh slantsev* (Oil and Gas Content, Geochemical Characteristics, and Conditions of Formation of Bituminous Shales), Moscow: VIEMS, 1979.
20. Kayukova, G.P., Romanov, G.V., Muslimov, R.Kh., *et al.*, *Khimiya i geokhimiya permskikh bitumov Tatarstana* (Chemistry and Geochemistry of Permian Bitumens of Tatarstan), Moscow: Nauka, 1999.
21. Mukhametzyanov, U.K., Kleev, A.M., and Gibadullin, K.G., in *Neftebituminoznye porody: Dostizheniya i perspektivy: Materialy Vtorogo Vsesoyuznogo soveshchaniya po kompleksnoi pererabotke i ispol'zovaniyu neftebituminoznykh porod* (Oil-Bearing and Bituminous Rocks: Achievements and Prospects: Proc. Second All-Union Meet. on Integrated Processing and Use of Oil-Bearing and Bituminous Rocks), Alma-Ata: Nauka, 1988, pp. 117–121.
22. Musaev, G.A., Trokhimenko, M.S., and Lykova, L.F., in *Neftebituminoznye porody: Dostizheniya i perspektivy: Materialy Vtorogo Vsesoyuznogo soveshchaniya po kompleksnoi pererabotke i ispol'zovaniyu neftebituminoznykh porod* (Oil-Bearing and Bituminous Rocks: Achievements and Prospects: Proc. Second All-Union Meet. on Integrated Processing and Use of Oil-Bearing and Bituminous Rocks), Alma-Ata: Nauka, 1988, pp. 270–272.
23. *Goryuchie slantsy evropeiskogo Severa SSSR* (Oil Shales of the European North of the USSR), Dedeev, V.A. and Yudovich, Ya.E., Eds., Syktyvkar: Komi Nauchn. Tsentr Ural'sk. Otd. Akad. Nauk SSSR, 1989.
24. Denisov, E.T., Mitskevich, N.I., and Agabekov, V.E., *Mekhanizm zhidkofaznogo okisleniya kislorodsoderzhashchikh soedinenii* (Mechanism of Liquid-Phase Oxidation of Oxygen-Containing Compounds), Minsk: Nauka i Tekhnika, 1975.
25. Ogarinov, I.S., Alekseev, A.A., Arslanbekova, L.B., *et al.*, Division of the South-Eastern Periphery of the Russian Platform and Western Slope of the South Urals into Districts Based on Oil-and-Gas Geological and Metallogenic Criteria and Directions of Geological Prospecting, *Preprint of the Bashkir Branch of the USSR Acad. Sci.*, Ufa, 1981.
26. Sidorov, A.D., Oil- and Gas-Bearing Characteristics of the Russian Platform and Adjacent Foredeeps, *Nauchn. Tr. Inst. Geol. Razrab. Goryuch. Iskop.*, 1979, no. 20, pp. 121–129.
27. Chepikov, K.R., Burovoi, A.M., Melamud, E.L., *et al.*, Oil- and Gas-Bearing Characteristics of the Russian Platform and Adjacent Foredeeps, *Nauchn. Tr. Inst. Geol. Razrab. Goryuch. Iskop.*, 1979, no. 20, pp. 107–120.
28. Mikhailov, I.M., Bagdasarova, M.V., Afanas'ev, Yu.G., *et al.*, Oil- and Gas-Bearing Characteristics of the Russian Platform and Adjacent Foredeeps, *Nauchn. Tr. Inst. Geol. Razrab. Goryuch. Iskop.*, 1979, no. 20, pp. 90–98.

Russian Journal of Applied Chemistry, Vol. 77, No. 7, 2004, pp. 1190–1194. Translated from Zhurnal Prikladnoi Khimii, Vol. 77, No. 7, 2004, pp. 1205–1209.

CHEMISTRY OF FOSSIL FUEL

A Mathematical Model of Catalytic Decomposition of Cyclohexyl Hydroperoxide in the Presence of 3*d*-Metal Acetylacetonates

A. M. Syroezhko and O. Yu. Begak

St. Petersburg State Technological Institute, St. Petersburg, Russia
Mendeleev Russian Research Institute of Metrology, Federal State Unitary Enterprise, St. Petersburg, Russia

Received May 14, 2003; in final form, March 2004

Abstract—Decomposition of cyclohexyl hydroperoxide in the presence of 3*d*-metal acetylacetonates was studied by mathematical simulation.

Previously [1] we considered the kinetic features of the catalytic decomposition of secondary and tertiary naphthene hydrocarbon hydroperoxides and showed that the complexing power of 3*d* metal acetylacetonates with respect to cyclohexyl hydroperoxide (CHP) correlates with the metal electronegativity and increases in the order V(II) ≈ Cr(III) < Mn(III) ≈ Fe(III) < Co(III) < Ni(II) < Cu(II). The activation energy of hydroperoxide decomposition increases in the same order.

CHP decomposes homolytically at the 3*d*-metal acetylacetonate concentrations of 6×10^{-5}–6×10^{-4} M and, in addition, heterolytically at 8.8×10^{-4}–8.8×10^{-3} M [1]; the catalysts studied and CHP [2] exist not only as monomers but also as self-associates. 3*d*-Metal acetylacetonates catalyzing CHP decomposition can be subdivided into three groups. Compounds of first group do not change the metal oxidation state in the reaction event [$Fe(acac)_3$, $Zn(acac)_2$]; compounds of the second group undergo one-electron transition and alternately transfer during the reaction with CHP into oxidized and reduced states (Co, Mn, Cu); and in compounds of the third group the metal oxidation state partially changes (V, Cr).

In this work, we developed a mathematical model of the CHP catalytic decomposition in the presence of 3*d*-metal acetylacetonates. The methods were described previously [1, 3].

The typical kinetic curves of CHP (ROOH) decomposition (Fig. 1a) in the presence of the catalysts studied and of accumulation of the reaction products [cyclohexanol (ROH), cyclohexanone (R=O), isomeric decanols] show that, in the overall process of CHP decomposition, these products are formed in comparable amounts and that catalyst occurs in the free state (in the heterogeneous form) and as a complex with CHP. The content of the catalyst heterogeneous form monotonically increases with time from the start of the CHP decomposition, whereas the contents of the free and complexed forms decrease. The whole set of our experimental and published data [1, 2] suggests the following scheme of the CHP decomposition, where HS is decane (diluent); SOH, isomeric decanols; ROH, cyclohexanol; $RO^{\bullet}$, cyclohexylalkoxy radical; $S^{\bullet}$, secondary isomeric alkyl radicals; k_h, constant of catalyst heterogenization; and k_d, constant of CHP dimerization.

(a) Catalysts in which the metal oxidation state is preserved [$Fe(acac)_3$, $Zn(acac)_2$]:

$$m\mathrm{M(acac)}_n \underset{}{\overset{K_1 = 38.5\ \mathrm{M}^{-1}}{\rightleftharpoons}} [\mathrm{M(acac)}_n]_m, \quad (1)$$

$$\mathrm{M(acac)}_n + \mathrm{ROOH} \overset{K_2 = 4.6\ \mathrm{M}^{-1}}{\rightleftharpoons} \mathrm{ROOH \cdot M(acac)}_n, \quad (2)$$

$$\mathrm{ROOH \cdot M(acac)}_n \xrightarrow[k_1 = 5\ \mathrm{min}^{-1}]{} \begin{cases} \xrightarrow{\alpha = 0.41} \mathrm{RO^{\bullet} + {\cdot}OH + M(acac)}_n, \\ \xrightarrow{\beta = 0.59} \mathrm{H_2O + R{=}O + M(acac)}_n, \end{cases} \quad (3)$$

$$\mathrm{HS^{\bullet} + {\cdot}OH} \xrightarrow{k_2} \mathrm{H_2O + S^{\bullet}}, \quad (4)$$

$$\mathrm{S^{\bullet} + {\cdot}OH} \xrightarrow{k_3} \mathrm{SOH}, \quad (5)$$

$$\mathrm{RO^{\bullet} + HS} \xrightarrow{k_4} \mathrm{ROH + S^{\bullet}}, \quad (6)$$

1070-4272/04/7707-1190 © 2004 MAIK "Nauka/Interperiodica"

$$M(acac)_n \cdot ROOH + HS \xrightleftharpoons{k_5 = 0.06\ l\ mol^{-1}\ min^{-1}} HOS + ROH + M(acac)_n, \quad (7)$$

$$ROH + M(acac)_n \xrightleftharpoons{K_3 = 20.3\ M^{-1}} M(acac)_n \cdot ROH, \quad (8)$$

$$M(acac)_n + H_2O \xrightleftharpoons{K_4 = 163\ M^{-1}} M(acac)_n \cdot H_2O, \quad (9)$$

$$2ROOH \xrightleftharpoons{K_d = 0.26\ M^{-1}} (ROOH)_2, \quad (10)$$

$$(ROOH)_2^* \xrightarrow{k_6 = 0.425\ min^{-1}} \begin{cases} \xrightarrow{\gamma} ROH + RO_2^{\cdot} + OH, \\ \xrightarrow{\delta} RO^{\cdot} + RO_2^{\cdot} + H_2O, \end{cases} \quad (11)$$

$$RO_2^{\cdot} + RO_2^{\cdot} \longrightarrow O_2 + ROH + R{=}O, \quad (12)$$

$$M(acac)_n(hom) \xrightarrow{k_h = 0.01\ min^{-1}} M(acac)_n(het), \quad (13)$$

$$M(acac)_n(het) + ROOH \xrightarrow{k_8 = 0.2\ M^{-1}} R{=}O + H_2O. \quad (14)$$

Let us consider the above scheme of the CHP decomposition in the presence of $Fe(acac)_3$ quantitatively. The rate of the overall process of CHP decomposition v is described by the equation

$$v = (1.95 \pm 0.2)[ROOH]^{1 \pm 0.08}[(Fe(acac)_3)_0]^{0.6 \pm 0.02}. \quad (I)$$

At [ROOH] = 0.1 M and $[Fe(acac)_3] = 8.8 \times 10^{-3}$ M, $v = 12.5 \times 10^{-3}$ mol l^{-1} min^{-1}.

The following system of differential equations corresponds to the above mechanism:

$$-d[ROOH]/d\tau = (k_1 + k_5[HS])K_2[Fe(acac)_3]_{fr}[ROOH]_{fr} + 2k_6K_d[ROOH]^2 + k_8[ROOH][Fe(acac)_3](het), \quad (II)$$

$$Fe(acac)_3(het) = [Fe(acac)_3]_{fr}(hom)(e^{k\tau} - 1), \quad (III)$$

$$d[R{=}O]/d\tau = d[H_2O]/d\tau = \beta k_1K_2[Fe(acac)_3)]_{fr}[ROOH]_{fr} + k_6K_d[ROOH]^2 + k_8[ROOH][Fe(acac)_3)](het), \quad (IV)$$

$$d[ROH]/d\tau = (\alpha k_1 + k_5[HS])K_2[ROOH]_{fr}[Fe(acac)_3]_{fr} + 2k_6K_d[ROOH]^2, \quad (V)$$

$$d[SOH]/d\tau = (\alpha k_1 + K_5[HS])K_2[Fe(acac)_3]_{fr}[ROOH]_{fr} + k_6K_d[ROOH]^2. \quad (VI)$$

* Association via α- and β-oxygen atoms of CHP is presumed.

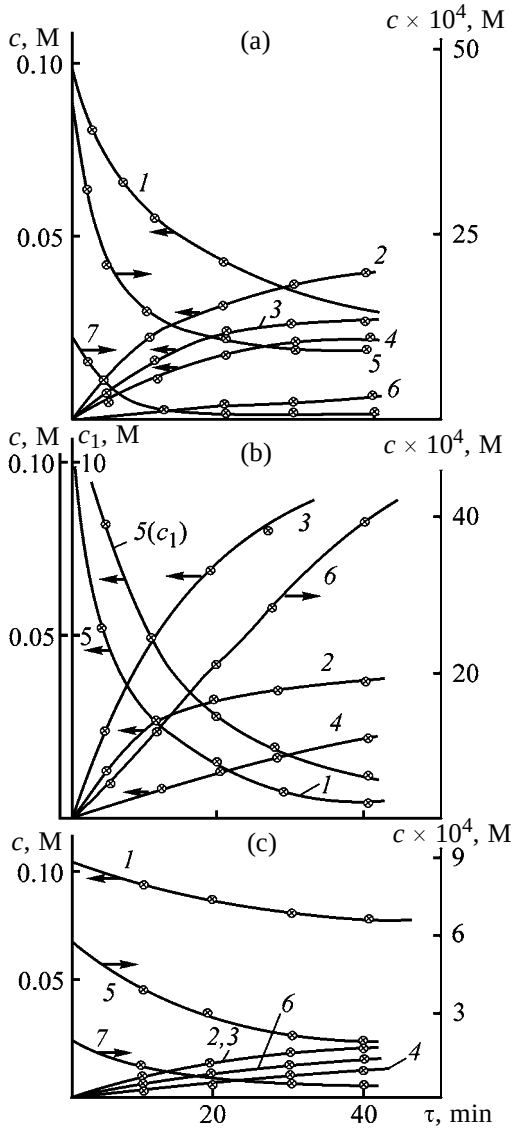

Fig. 1. Consumption and accumulation of (*1*) CHP, (*2*) cyclohexanone, (*3*) cyclohexanol, (*4*) isomeric decanols, (*5*) (a, b) $[Fe(acac)_3]_{fr}$ and (c) $[Co(acac)_2]_{fr}$, (*6*) (a, b) $[Fe(acac)_3]$(het) and (c) $Co(acac)_2$(het), and (*7*) (a, b) $[Fe(acac)_3 \cdot ROOH]$ and (c) $Co(acac)_2OH$ at 95°C. $[Fe(acac)_3]_0$: (a) 8.8×10^{-3} and (b) 8.8×10^{-4} M; $[Co(acac)_2]_0$: (c) 8.8×10^{-3} M. (c, c_1) concentration and (τ) time. Points; experiment; curves: calculation.

The initial concentrations of free CHP and catalyst ([ROH] = $[H_2O]$ = 0) were found from the material balance:

$$[ROOH]_0 = [ROOH]_{fr} = [ROOH][Fe(acac)_3] + [(ROOH)_2] \approx [(ROOH)]_{fr}, \quad (VII)$$

$$[Fe(acac)_3]_0 = [Fe(acac)_3]_{fr} + [Fe(acac)_3]_m + [Fe(acac)_3] \cdot ROOH. \quad (VIII)$$

The stoichiometric coefficient in Eq. (1) allows calculation of the concentration of the free catalyst $[Fe(acac)_3]_{fr} = 5.3 \times 10^{-3}$ M at $[Fe(acac)_3]_0 = 8.8 \times 10^{-3}$ M.

The equilibrium constant of $ROOH \cdot Fe(acac)_3$ complex formation was found from the CHP decomposition kinetics as a slope of the $1/K_{eff}$–1/[ROOH] dependence; it is equal to 4.6 l mol^{-1} (95°C). Knowing K_2, $[ROOH]_{fr}$, and $[M(acac)_3]$, we can calculate K_1 from Eq. (VII). $K_1 = 38.5$ l mol^{-1} for $Fe(acac)_3$ dimer and 0.54×10^4 l^2 mol^{-2} for the trimer. Taking into account the ratio of the yields and initial rates of formation of alcohol, ketone, and isomeric decanols (Fig. 1) and assuming dimerization of the catalyst, we can find k_1, k_5, and k_6 from the above system of differential equations.

The CHP dimerization constant k_d and the constant of $RO_2^{\bullet}$ recombination were taken from the literature [4, 5]. Calculations show that the initial rates of the CHP consumption and of accumulation of the reaction products in the whole range of ROOH (0.02–0.1 M) and catalyst (8.8×10^{-4}–8.8×10^{-3} M) concentrations are satisfactorily described by the system of differential equations with the found values of the corresponding rate constants. However, during the CHP decomposition, heterogenization of the catalyst occurs concurrently with formation of complexes with the reaction products (alcohol and water). At the further optimization of the CHP decomposition, we refined the equilibrium constants K_3 and K_4 and determined k_5 and k_8. The concentration of the free catalyst with regard to formation of all the above complexes and partial transformation into heterogeneous form was found from the condition of the material balance

$$[Fe(acac)_3]_0 = [Fe(acac)_3]_{fr} + [Fe(acac)_3](het) + [Fe(acac)_3]_m + [Fe(acac)_3] \cdot ROOH + [Fe(acac)_3 \cdot ROH] + [Fe(acac)_3 \cdot H_2O. \quad (IX)$$

(b) Catalysts in the lower oxidation state $[Co(acac)_2]$, in which the metal oxidation state changes during the hydroperoxide decomposition:

$$2Co(acac)_2 \xrightleftharpoons{K_1 = 226\ M^{-1}} (Co(acac)_2)_2, \quad (15)$$

$$2Co(acac)_2 + ROOH \xrightleftharpoons{K_2 = 8.62\ M^{-1}} Co(acac)_2 \cdot ROOH, \quad (16)$$

$$Co(acac)_2 \cdot ROOH + ROOH \xrightleftharpoons{k_1 = 67\ l\ mol\ min^{-1}} ROOH + H_2O + Co(acac)_2OH, \quad (17)$$

$$Co(acac)_2OH + ROOH \xrightarrow{k_2 = 36.9\ l\ mol\ min^{-1}} RO_2^{\bullet} + H_2O + Co(acac)_2, \quad (18)$$

$$Co(acac)_2 \cdot ROOH + HS \xrightarrow{k_3 = 0.07\ l\ mol\ min^{-1}} SOH + ROH + Co(acac)_2, \quad (19)$$

$$RO_2^{\bullet} + RO_2^{\bullet} \xrightarrow{k_4} ROH + R{=}O + O_2, \quad (20)$$

$$ROH + Co(acac)_2 \xrightleftharpoons{K_3 = 80.3\ M^{-1}} ROH \cdot Co(acac)_2, \quad (21)$$

$$H_2O + Co(acac)_2 \xrightleftharpoons{K_4 = 363\ M^{-1}} H_2O \cdot Co(acac)_2, \quad (22)$$

$$Co(acac)_2 + RO_2^{\bullet} \xrightarrow{k_5} Co(acac)_2OH + R{=}O, \quad (23)$$

$$ROH + Co(acac)_2OH \xrightarrow{k_6 = 7.55 \times 10^{-4}\ l\ mol\ min^{-1}} Co(acac)_2 + R{=}O + H_2O, \quad (24)$$

$$RO_2^{\bullet} + Co(acac)_2 \xrightarrow{k_7} ROO \cdot Co(acac)_2, \quad (25)$$

$$ROO \cdot Co(acac)_2 \xrightarrow{k_8} RO^{\bullet} + O^{\bullet}Co(acac)_2, \quad (26)$$

$$O^{\bullet}Co(acac)_2 + SH \xrightarrow{k_9} S^{\bullet} + Co(acac)_2OH, \quad (27)$$

$$RO^{\bullet} + SH \xrightarrow{k_{10}} ROH + S^{\bullet}, \quad (28)$$

$$S^{\bullet} + OH \xrightarrow{k_{11}} SOH, \quad (29)$$

$$Co(acac)_2(hom) \xrightarrow{k_{12} = k_h = 0.02\ M^{-1}} Co(acac)_2(het), \quad (30)$$

$$Co(acac)_2(het) + ROOH \xrightleftharpoons{K_5 = 9.1\ M^{-1}} ROOH \cdot Co(acac)_2(het), \quad (31)$$

$$ROOH \cdot Co(acac)_2(het) \xrightleftharpoons{k_{13} = 5\ M^{-1}} Co(acac)_2(het) + HO^{\bullet} + RO^{\bullet}, \quad (32)$$

$$2\mathrm{ROOH} \xrightleftharpoons[]{K_d = 0.26\ \mathrm{M}^{-1}} (\mathrm{ROOH})_2, \quad (33)$$

$$(\mathrm{ROOH})_2^* \xrightarrow{k_{14} = 0.425\ \mathrm{min}^{-1}} \begin{cases} \xrightarrow{\alpha = 0.95} \mathrm{ROH} + \mathrm{RO}_2^{\bullet} + \mathrm{OH}^{\bullet}\ \text{(a)}, \\ \xrightarrow{\beta = 0.05} \mathrm{RO}^{\bullet} + \mathrm{RO}_2^{\bullet} + \mathrm{H_2O}\ \text{(b)}. \end{cases} \quad (34)$$

The scheme of the above mechanism of CHP decomposition considers dimerization of both CHP and catalyst, formation of complexes of the catalyst with CHP and reaction products (alcohols, water), and the observed heterogenization of the catalyst proceeding as a first-order reaction. This scheme corresponds to the total order of approximately 2 with respect to CHP and 0.5 with respect to the catalyst. The reactions of formation of the alcohol and ketone from CHP radical reacting with the reduced form of the catalyst [6] and oxidation of the alcohol with cobalt(III) were also considered. It is known that the rate constants of reactions (9) and (11) in the case of the Co catalyst differ by a factor of 2.

The following system of differential equations corresponds to the mechanism considered:

$$-\mathrm{d[ROOH]}/\mathrm{d}\tau = 2k_1[\mathrm{Co(acac)_2 \cdot ROOH}][\mathrm{ROOH}] + k_2[\mathrm{Co(acac)_2OH}][\mathrm{ROOH}] + k_3[\mathrm{HS}][\mathrm{Co(acac)_2 \cdot ROOH}] + k_{13}[\mathrm{ROOH \cdot Co(acac)_2(het)}] + k_{14}[(\mathrm{ROOH})_2], \quad (X)$$

$$\mathrm{d[ROH]}/\mathrm{d}\tau = 2k_1[\mathrm{ROOH}][\mathrm{Co(acac)_2 \cdot ROOH}] + k_3[\mathrm{HS}] \times [\mathrm{Co(acac)_2 \cdot ROOH}] + k_{13}[\mathrm{ROOH \cdot Co(acac)_2(het)}] - k_6[\mathrm{ROH}][\mathrm{Co(acac)_2OH}] + (1.5 + 0.5\alpha - 0.5\beta)k_{14}[(\mathrm{ROOH})_2], \quad (XI)$$

$$\mathrm{d[R{=}O]}/\mathrm{d}\tau = k_1[\mathrm{ROOH}][\mathrm{Co(acac)_2 \cdot ROOH}] + 0.25(2 + \alpha - \beta)k_{14}[(\mathrm{ROOH})_2] + k_6[\mathrm{ROH}][\mathrm{Co(acac)_2OH}], \quad (XII)$$

$$\mathrm{d[H_2O]}/\mathrm{d}\tau = k_2[\mathrm{ROOH}][\mathrm{Co(acac)_2OH}] + k_6[\mathrm{ROH}][\mathrm{Co(acac)_2OH}] + \beta k_{14}[(\mathrm{ROOH})_2], \quad (XIII)$$

$$\mathrm{d[SOH]}/\mathrm{d}\tau = k_3[\mathrm{HS}][\mathrm{Co(acac)_2 \cdot ROOH}] + k_{13}[\mathrm{ROOH \cdot Co(acac)_2(het)}] + \alpha k_{14}[(\mathrm{ROOH})_2], \quad (XIV)$$

$$[\mathrm{Co(acac)_2}]_{fr} = [(B_2 + 4K_1C - B)/2K_1]^{0.5}, \quad (XV)$$

$$B = K_2[\mathrm{ROOH}] + k_1/k_2K_2[\mathrm{ROOH}] + K_3[\mathrm{ROH}] + K_4[\mathrm{H_2O}] + (e^{k\tau} - 1)(1 + K_5[\mathrm{ROOH}]), \quad (XVI)$$

$$C = [\mathrm{Co(acac)_2}]_0 - 0.5D/k_8 - 0.5D/k_9[\mathrm{SH}] - 0.75D/k_2[\mathrm{ROOH}] \approx [\mathrm{Co(acac)_2}]_0, \quad (XVII)$$

$$D = (\alpha - \beta)k_{14}[(\mathrm{ROOH})_2],$$

$$[\mathrm{Co(acac)_2}](\mathrm{het}) = [\mathrm{Co(acac)_2}]_{fr}(e^{k\tau} - 1), \quad (XVIII)$$

$$[\mathrm{RO_2}] = \{k_1[\mathrm{ROOH}][\mathrm{Co(acac)_2 \cdot ROOH}] + 0.5k_{14}[(\mathrm{ROOH})_2]/k_4]^{0.5}, \quad (XIX)$$

$$[\mathrm{Co(acac)_2OH}] = (k_1[\mathrm{ROOH}][\mathrm{Co(acac)_2 \cdot ROOH}] + 0.75D)/(k_2[\mathrm{ROOH}] + k_6[\mathrm{ROH}] \approx (k_1[\mathrm{ROOH}][\mathrm{Co(acac)_2 \cdot ROOH}] + 0.75D)/k_2[\mathrm{ROOH}]. \quad (XX)$$

The rate of the overall process of CHP decomposition v in the presence of $\mathrm{Co(acac)_2}$, expressed by the equation $v = 32.5[\mathrm{ROOH}]_0^{1.8\pm0.15}[\mathrm{MeL}_n]_0^{0.5\pm0.35}$, is equal to 5×10^{-2} mol l^{-1} min^{-1}. At [ROOH] = 0.1 M and $[\mathrm{Co(acac)_2}] = 8.8 \times 10^{-3}$ M, we found K_1 = 226 l mol^{-1} (95°C) from the equation of the material balance with respect to the catalyst at the initial time of the reaction (Fig. 1b). Taking into account that the initial process is steady-state with respect to $\mathrm{RO_2^{\bullet}}$, $\mathrm{S^{\bullet}}$, $^{\bullet}\mathrm{OH}$, $^{\bullet}\mathrm{OCo(acac)_2}$, and $\mathrm{Co(acac)_2OH}$, from the content of Co(II) and Co(III) (in the absence of the heterogeneous form of the catalysts) and of complexes with alcohol and water, we calculated k_1–k_3 and coefficients α and β from the system of differential equations (X)–(XX). The equilibrium constant was determined previously [1]; the constants k_4–k_7 are given in [5, 7–9]. The initial stage of the decomposition is well described with the rate constants found [scheme (15)–(34)]. In the developed reaction, the concurrent formation of the CHP complexes with reaction products (alcohol and water) and the catalyst heterogenization should be considered. The subsequent optimization allows selection of the equilibrium constants K_3–K_5 and determination of k_{13}. The constant of the catalyst heterogenization k_h was determined in the special experiments. The system of differential equations (X)–(XX) integrated with the rate constants obtained adequately describes the CHP decomposition (Fig. 1c) {[ROOH] = 0.02–0.1 M, $[\mathrm{Co(acac)_2}]_0 = 8.8 \times 10^{-4}$–$8.8 \times 10^{-3}$ M}.

* Association via α- and β-oxygen atoms of CHP is presumed.

In accordance with the calculated coefficients α and β, the association with respect to β-atom of CHP is preferable, which agrees with data of [10] and contradicts the results of [4]. The contribution of this reaction to the overall process of the CHP decomposition is small.

(c) For catalysts in which the metal is in the higher oxidation state [$Co(acac)_3$, $Cu(acac)_2$, $Mn(acac)_3$] and is partially reduced during the CHP decomposition, the scheme of the reaction mechanism should be supplemented by the reactions of one-electron transfer and substitution of acetylacetone with CHP in the coordination sphere of the metal ion. The observed high order of the reaction with respect to ROOH [in the presence of $Co(acac)_2$] indirectly suggests the possibility of two-sphere coordination of CHP.

From the data obtained, we can conclude that the lower catalytic activity of 3*d*-metal acetylacetonates as compared to 3*d*-metal stearates is caused by the different electron density on the metal ion, which affects the strength of the CHP O–O bond because of the change in the degree of delocalization of the unpaired electron to the ligand. The system of conjugated atoms in the chelates provides the enhanced stability of the complex. Increase in the ligand bonding with 3*d*-metal ion decreases its acceptor power; as a result, the rate constant is lower than with the corresponding carboxylates [11, 12].

The catalytic power of 3*d*-metal acetylacetonates and carboxylates in decomposition of hydroperoxides depends on a number of factors: catalyst tendency to self-association and heterogenization, hydroperoxide association, and catalyst complexing power with respect to hydroperoxides and products of their transformation ($RO_2^{\bullet}$, alcohol, water). As a rule, the equilibrium constants of the catalyst complex formation with hydroxyperoxides and alcohols and the relative contribution of the ROOH radical decomposition increase as the 3*d*-metal electronegativity increases.

CONCLUSIONS

(1) A mathematical model of cyclohexyl hydroperoxide decomposition in the presence of 3*d*-metal acetylacetonates was developed.

(2) Along with the mechanism involving one-electron transfer (change in the metal oxidation state in the catalyst), cyclohexyl hydroperoxide can decompose without changes in the oxidation state of the 3*d* metal [Fe(III), Zn(II) acetylacetonates], as it takes place in the presence of alkali and alkaline-earth (*s* metals) metal ions. The catalyst controlling function is manifested in the step of the cyclohexyl hydroperoxide decomposition.

REFERENCES

1. Syroezhko, A.M. and Begak, O.Yu., *Zh. Prikl. Khim.*, 2004, vol. 77, no. 1, pp. 54–59.
2. Syroezhko, A.M., Liquid-Phase Oxidation of Alkanes, Cycloalkanes, and Their Oxygen-Containing Derivatives with Oxygen and Ozone in the Presence of Compounds of *s* and 3*d* Elements, *Doctoral Dissertation*, Leningrad, 1985.
3. Proskuryakov, V.A., Syroezhko, A.M. and Smirnov, P.A., *Zh. Prikl. Khim.*, 1976, vol. 49, no. 7, pp. 1588–1592.
4. Yablonskii, O.P., Complex Formation and Its Role in Oxidation and Separation of Hydrocarbons, *Doctoral Dissertation*, Ivanovo, 1979.
5. Denisov, E.T., *Konstanty skorosti gomoliticheskikh zhidkofaznykh reaktsii* (Rate Constants of Homolytic Liquid-Phase Reactions), Moscow: Nauka, 1971.
6. Denisov, E.T. and Kovalev, G.I., *Okislenie i stabilizatsiya reaktivnykh topliv* (Oxidation and Stabilization of Jet Fuels), Moscow: Khimiya, 1983.
7. Emanuel', N.M., Denisov, E.T., and Maizus, Z.K., *Tsepnye reaktsii okisleniya uglevodorodov v zhidkoi faze* (Chain Reactions of Liquid-Phase Oxidation of Hydrocarbons), Moscow: Nauka, 1965.
8. Denisov, E.T., Mitskevich, N.I., and Agabekov, V.E., *Mekhanizm zhidkofaznogo okisleniya kislorodsoderzhashchikh soedinenii* (Mechanism of Liquid-Phase Oxidation of Oxygen-Containing Compounds), Minsk: Nauka i Tekhnika, 1975.
9. Emanuel', N.M., Zaikov, G.E., and Maizus, Z.K., *Rol' sredy v radikal'no-tsepnykh reaktsiyakh okisleniya organicheskikh soedinenii* (Role of the Medium in Radical-Chain Oxidation of Organic Compounds), Moscow: Nauka, 1973.
10. Sapunov, V.N., Kudryavtsev, A.B., Litvintsev, I.Yu, and Diall, Kh.M., *Tr. Mosk. Khim.-Tekhnol. Inst. im. D.I. Mendeleeva*, 1978, issue 99, p. 123.
11. Azhikova, R.M., Syroezhko, A.M., and Proskuryakov, V.A., *Zh. Prikl. Khim.*, 1984, vol. 57, no. 8, pp. 1792–1797.
12. Azhikova, R.M., Oxidation and Epoxidation of Cycloolefins, *Cand. Sci. Dissertation*, Leningrad, 1980.

Russian Journal of Applied Chemistry, Vol. 77, No. 7, 2004, pp. 1195–1197. Translated from Zhurnal Prikladnoi Khimii, Vol. 77, No. 7, 2004, pp. 1210–1212.

BRIEF COMMUNICATIONS

Solubility of Iodine in the System Water–Nitric Acid

A. I. Lutsyk, S. Yu. Suikov, V. S. Chuprina, and V. Yu. Portnyanskii

Litvinenko Insitute of Physical Organic and Coal Chemistry, National Academy of Sciences of Ukraine, Donetsk, Ukraine

Received October 29, 2002; in final form, November 2003

Abstract—The solubility of iodine in 30–55% nitric acid at 25°C was measured. Particular attention was given to the control of equilibration in the system. An equation was suggested for estimating the iodine solubility in nitric acid in the concentration range 0–70 wt % HNO_3.

Iodine solutions in concentrated nitric acid are of great practical importance. They found wide application as relatively cheap strong oxidants. Recently, the interest in solubility of iodine in nitric acid increased in the context of utilization of substandard concentrated solutions of nitric acid.

Experimental measurement of the iodine solubility in nitric acid and data interpretation is a complex problem, despite availability of high-sensitivity methods and pronounced absorption of iodine solutions in the visible and UV ranges. Iodine is relatively poorly soluble in polar solvents and forms solutions with considerable deviation from ideality [1]. In oxidative systems, iodine can enter numerous reactions. For example, in concentrated fuming nitric acid it can be oxidized to iodates in preparative yield [2].

Carter [3] measured the iodine solubility in 3.3–72.6% HNO_3 at 10, 25, and 35°C. According to these data, at all the temperatures studied the iodine solubility grows over the entire examined range of the acid concentrations.

Sozontov *et al*. [4] measured the iodine solubility in 20–100% HNO_3 in the range 0–80°C. They found that, at all the temperatures studied, the iodine solubility decreased as the acid concentration increased to 60–80 wt % (depending on temperature), reached a minimum (lower by a factor of 4–5 compared to water), and then, at higher concentrations up to 100% HNO_3, increased slowly to the value remaining, however, lower than that in water. Sozontov *et al*. [4] explained a decrease in the I_2 solubility with HNO_3 concentration increasing from 0 to 60% by binding of water molecules to the molecules of nitric acid, and the subsequent growth of the solubility, by the reaction of iodine with HNO_3 to form more soluble iodic acid. However, it seems incorrect to consider this process in terms of the solubility (and the solubility models), since formation of iodic acid in concentrated nitric acid is irreversible. The iodine compound formed in 100% HNO_3 is also sparingly soluble, as can be observed visually as transformation of violet iodine crystals into the orange precipitate.

The experimental data [3, 4] at 25°C are compared in Fig. 1. As seen, the difference in the numerical solubility values reaches an order of magnitude and more. It should be noted that, according to [4], the iodine solubility in 100% nitric acid is lower than that in water, which is rather unusual for a nonelectrolyte.

Carter's results [3] were obtained by iodometric titration of saturated iodine solutions, whereas Sozontov *et al*. [4] used the dynamic method with gravimetric determination of the solute amount. In these studies, the mechanism by which the equilibrium was attained was not considered.

Here we tried to reveal the causes of the discrepancy of the iodine solubility values reported by various authors and to determine the values suitable for practical use.

EXPERIMENTAL

The equilibration in the system in the course of the iodine dissolution was monitored spectrophotometrically. The iodine electronic spectrum in acid (H_2SO_4) solutions was described in [5], and a long-wave shift (by 50 nm in going from 0 to 94.9% H_2SO_4) of the absorption maximum and slight variation of the extinction with increasing acid concentration were reported.

In this study, the total spectra of iodine in nitric acid were obtained with a Specord-2000 spectropho-

1070-4272/04/7707-1195 © 2004 MAIK "Nauka/Interperiodica"

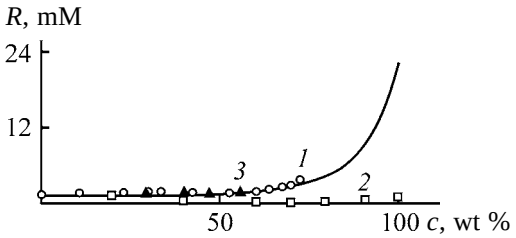

Fig. 1. Iodine solubility R in the H_2O–HNO_3 system vs. HNO_3 concentration c at 25°C. Data from (*1*) [3], (*2*) [4], and (*3*) this study; (line) calculation by model (1).

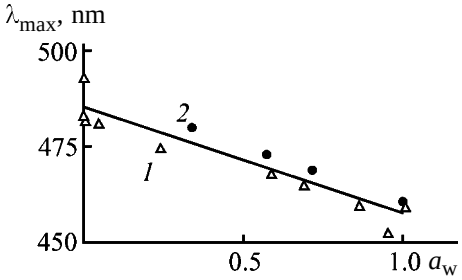

Fig. 2. Position of the absorption maximum λ_{max} for the iodine solutions in (*1*) H_2SO_4 [5] and (*2*) HNO_3 vs. water activity a_w [6] at 25°C.

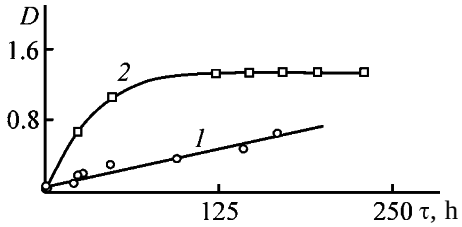

Fig. 3. Solution optical density D vs. time τ for the system I_2–30% HNO_3 (*1*) kept without stirring and (*2*) stirred 3–5 times daily. λ = 465 nm (SF-46), 25°C.

tometer (Fig. 2). As in the case of H_2SO_4, the maximum shifts to the long-wave region with decreasing water activity, without changes in the line shape. In this case, the data for both sulfuric and nitric acids are fitted by the same straight line (Fig. 2).

As seen from Fig. 3, without stirring the equilibrium in the iodine–water–nitric acid system is not attained even in more than 160 h (line *1*). If the vessel for dissolving iodine is shaken at regular intervals (3–5 times daily), then the equilibrium can be attained in 5–6 days (line *2*). Therefore, the solutions were prepared by saturating nitric acid with iodine for 7–8 days in an air thermostat at 25°C with regular shaking. The dissolved iodine was extracted with carbon tetrachloride, and its concentration was determined by iodometric titration. The titer of the thiosulfate solution was determined using chemically pure grade $K_2Cr_2O_7$ and ultrapure grade KI. The reproducibility was within 0.3%.

Unfortunately, none of the methods considered is suitable for measuring the iodine solubility in concentrated nitric acid, since observations at 25°C show that, under these conditions, iodine is completely oxidized within several minutes.

It was found previously [7] that, over the entire composition range, from 0 to 100%, the solubility of saturated hydrocarbons in the water–nitric acid system is adequately described by the equation

$$(\log\alpha)^E \equiv \log\alpha - x_w\log\alpha_w - x_a\log\alpha_a = L(V^E/V), \quad (1)$$

which relates the excess $(\log\alpha)^E$ value, expressed in terms of mole fractions of water and acid, x_w and x_a, to the excess volume $V^E = V - x_wV_w - x_aV_a$ (compression) of a water–acid two-component solvent; α_w, α_a, V_w, and V_a refer to pure components; α is the equilibrium coefficient of distribution of the substrate between the gas phase and the solution, $\alpha = \lim(c_{gas}/c_{liq})$ at $c_{gas} \to 0$; α^{-1} is equal to the substrate solubility (M etc.) at its given concentration in the gas phase. Among the forms accepted in the literature for describing the solubility of gases and volatile compounds (molarity, mole and weight fractions and percents, Henry and Bunsen constants, solvomolality, etc.), it is reasonable to use just the distribution coefficient, because it is equal to the activity coefficient of the substrate in a solution if ideal gas is chosen as the standard system [8].

Taking into account that Eq. (1) quantitatively describes the salting-out effects in concentrated electrolyte solutions, including water–acid (sulfuric, nitric, phosphoric, and other acids) systems, and in a variety of nonelectrolytes [9–11], we suggest that the solubility of such a typical nonelectrolyte as iodine in the water–nitric acid system can be adequately described by this equation. In calculation by Eq. (1), we used the value of 1.32×10^{-3} M for iodine solubility in water [5]. The solubility in M was converted to α using the value of 0.309 mm Hg for the iodine saturated vapor pressure at 25°C from [12], according to which the concentration of saturated iodine vapor is equal to 1.66×10^{-5} M: $\alpha = (1.66\times10^{-5}\ \text{M})/(1.32\times10^{-3}\ \text{M}) = 1.3\times10^{-2}$.

The α coefficient for the iodine solution in 100% HNO_3 (α_a = 0.00073) and the L (L = –2.2) parameter were calculated from the dependences presented in [7]:

$$L = -5.2 + 0.054\bar{V}_s^0,$$

$$\log(\alpha_a/\alpha_w) = 0.37 - 0.029\bar{V}_s^0,$$

where $\bar{V}_s^0$ is the partial molal volume of the nonelectrolyte in water.

We used the value $\bar{V}_{iod}^0 = 56$ cm^3 mol^{-1}, as estimated from data of [13]. The excess volume of the solvent V^E was calculated using the density of HNO_3 solutions [14]. The calculated curve of the iodine solubility in the water–nitric acid system (line in Fig. 1) at $[HNO_3] < 70$ wt % adequately describes the experimental data of [3] and those obtained in this study. The fact that the experimentally measured solubility exceeded the calculated value at $[HNO_3] > 70$ wt % may be due to the contribution of iodine oxidation under these conditions.

REFERENCES

1. Hildebrand, J.H. and Jenks, C.A., *J. Am. Chem. Soc*., 1920, vol. 42, no. 11, pp. 2180–2189.
2. *The Synthesis and Characterization of Inorganic Compounds*, Brauer, G., Ed., Stuttgart: Enke, 1981.
3. Carter, J.S., *J. Chem. Soc*., 1925, vol. 127, pp. 2861–2865.
4. Sozontov, V.G., Karamzin, I.G., Mitronov, O.P., and Salomakhina, S.O., *Khim. Prom–st. Ukr*., 2000, no. 3(38), pp. 24–27.
5. Bower, J.G. and Scott, R.L., *J. Am. Chem. Soc*., 1953, vol. 75, no. 14, pp. 3583–3585.
6. *Voprosy fizicheskoi khimii rastvorov elektrolitov* (Problems of Physical Chemistry of Electrolyte Solutions), Mikulin, G.I., Ed., Leningrad: Khimiya, 1968.
7. Lutsyk, A.I., Rudakov, E.S., and Gundilovich, G.G., *Ukr. Khim. Zh*., 1992, vol. 58, no. 8, pp. 646–650.
8. Ben-Naim, A. and Mazo, R., *J. Phys. Chem. B*., 1997, vol. 101, no. 51, pp. 11221–11225.
9. Rudakov, E.S., Lutsyk, A.I., and Suikov, S.Yu., *Zh. Fiz. Khim*., 1987, vol. 61, no. 5, pp. 1153–1164.
10. Rudakov, E.S., Lutsyk, A.I., and Gundilovich, G.G., *Mendeleev Commun*., 1994, no. 1, pp. 27–28.
11. Lutsyk, A.I., Rudakov, E.S., Akopov, A.V., and Mochalin, V.N., *Zh. Fiz. Khim*., 2002, vol. 76, no. 12, pp. 2194–2199.
12. Gillespie, L.J. and Fraser, L.H.D., *J. Am. Chem. Soc*., 1936, vol. 58, no. 11, pp. 2260–2263.
13. Shinoda, K. and Hildebrand, J.H., *J. Phys. Chem*., 1958, vol. 62, no. 3, pp. 295–296.
14. *Chemical Engineers' Handbook*, Perry, J.H., Ed., New York: McGraw-Hill, 1963.

Russian Journal of Applied Chemistry, Vol. 77, No. 7, 2004, pp. 1198–1199. Translated from Zhurnal Prikladnoi Khimii, Vol. 77, No. 7, 2004, pp. 1213–1214.

BRIEF COMMUNICATIONS

Quantitative Representation of Tananaev's Effect

A. Pigaga and O. Timofeeva

Institute of Chemistry, Vilnius, Lithuania

Received February 25, 2004

Abstract—Average concentrations of Ni(II) in suspended hydroxide and basic salts precipitated with NaOH from $NiSO_4$ solutions and the degree of concentration of Ni(II) as functions of the initial concentration of Ni(II) salt in solution were studied.

Precipitation methods have long been in use in chemical technology and chemical analysis for concentrating, separating, and purifying various substances.

Much attention is given now to secondary use of both precious and non-ferrous metals (zinc, chromium, nickel, and copper), which are lost in electroplating industry when washing workpieces. A reliable method of nickel regeneration is its precipitation as poorly soluble salts and hydroxide using such cheap precipitants as NaOH and Na_2CO_3.

The precipitates obtained should have favorable technological characteristics: high filtration factor, high sedimentation rate, and small volume of the final sediment.

The kinetics of precipitation of poorly soluble nickel(II) compounds with sodium hydroxide and sodium carbonate solutions from dilute Limed NB-I electrolyte with nickel(II) concentration of 0.2–20 g l^{-1} was studied previously. It is believed that, when nickel(II) is precipitated with sodium hydroxide from $NiSO_4$ solutions (of concentration less than 1 M), two basic salts, $NiSO_4 \cdot 9Ni(OH)_2$ and $NiSO_4 \cdot 4Ni(OH)_2$, or $Ni(OH)_2$ is precipitated depending on the concentration [1]. The self-compaction of the precipitates practically stopped after the lapse of 1.5–4 h, though a slight volume reduction was observed within a few days.

The results obtained show that the average concentration c_{Ni} of nickel in the precipitate depends on its initial concentration c^0_{Ni}.

It is known that, when some metals hydroxides are precipitated from solutions of their salts, the density of pseudo-amorphous precipitates increases with increasing concentrations of the salts (Tananaev's effect) [2]. There are no quantitative relationships for this effect; therefore, we decided to study this phenomenon in more detail.

EXPERIMENTAL

The experiments were carried out at room temperature (17–20°C) with solutions of $NiSO_4$ in which the nickel(II) concentration was varied from 0.1 to 20.0 g l^{-1}. The solutions were prepared by dilution of the starting solution with c^0_{Ni} = 30 g l^{-1}. The precipitant (20% aqueous solution of NaOH) was added dropwise with stirring to 25 ml of the starting solution until the required pH was reached (8.0, 9.0, 10.0, and 11.0), as monitored with a pH-340 pH-meter. After the precipitation, the resulting suspensions of insoluble compounds were poured in calibrated test tubes and allowed to settle for 24 h.

The average concentration of nickel(II) in suspensions c_{Ni} (g l^{-1}) was calculated by the formula

$$c_{Ni} = c^0_{Ni} V_0 / V_n,$$

where V^0 is the initial volume of $NiSO_4$ solution (ml), and V_n, the volume of the precipitate (ml).

The degree of concentration ε was expressed as

$$\varepsilon = c_{Ni} / c^0_{Ni}.$$

In the calculations, we did not take into account the concentration of nickel(II) in an aqueous phase above a precipitate, as it is less than the initial concentration by more than two orders of magnitude and thus can be neglected. The pH of solutions above the precipitate gradually decreases (after four days, ΔpH is 0.2–1.5 depending on initial pH and c^0_{Ni}), which seems to be due to the hydrolysis of Ni(II) basic salts [1, 2].

It should be noted that the results obtained are well reproducible. In two series of five parallel experi-

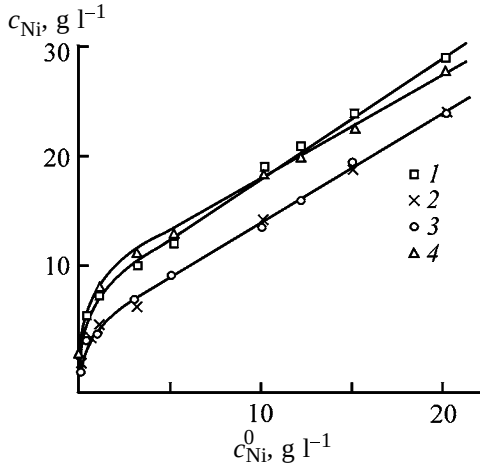

Fig. 1. Average nickel(II) concentration in the precipitate c_{Ni} as a function of its initial concentration in solution c^0_{Ni}. Precipitation with 20% NaOH solution up to the following final pH values: (*1*) 8.0, (*2*) 9.0, (*3*) 10.0, and (*4*) 11.0; the same for Fig. 2.

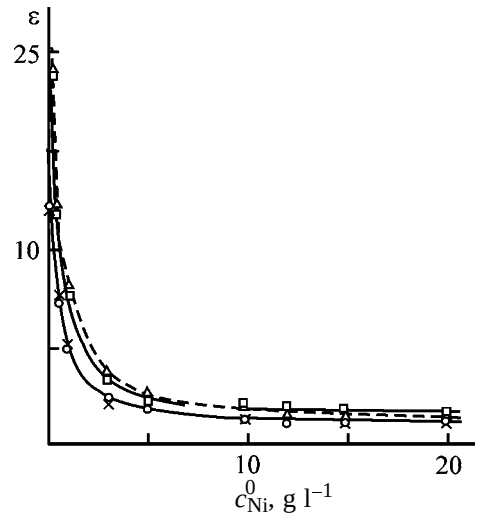

Fig. 2. Degree of concentration ε as a function of the initial nickel(II) concentration c^0_{Ni}.

ments, the deviation from the average c_{Ni} and ε values does not exceed 5%.

The experimental results are given in Fig. 1, which shows that the dependences of c_{Ni} on c^0_{Ni} in the pH range under study are similar and can be described by the equation

$$c_{Ni} = c^0_{Ni}/(ac_{Ni} + b) + cc_{Ni}, \quad (1)$$

where *a*, *b*, and *c* are empirical coefficients. At pH 8.0, $a = 0.14$, $b = 0.02$, and $c = 1.14$; at pH 9.0 and 10.0, $a = 0.24$, $b = 0.06$, and $c = 1.00$; and at pH 11.0, $a = 0.098$, $b = 0.09$, and $c = 0.98$. It is interesting that the curves obtained at pH 9.0 and 10.0 practically coincide (all the three coefficients are identical), and the curves obtained at pH 8.0 and 11.0 are close to each other. At pH 8.0 and 11.0, c_{Ni} is much higher than that at pH 9.0 and 10.0.

The initial steep ascent of the curves is attributable to the fact that, as c^0_{Ni} increases, the composition of the precipitate changes from less dense $Ni(OH)_2$ to more dense basic salts. The further increase in the density of the precipitates is explained by the effect of coagulating ions [nickel(II)] at their increased concentration [2].

Furthermore, we have found that the volume of the precipitate is independent of the concentration of sodium hydroxide used for the precipitation (concentration range 2–20% NaOH).

The density of the forming precipitates is important for the technology. Denser precipitates have more perfect structure; they are better filtered and contain less impurities.

The degree of concentration of Ni(II) is plotted in Fig. 2 vs. the initial nickel(II) concentration in solution. It is seen that the precipitation of nickel(II) as poorly soluble compounds with an NaOH solution is an efficient concentrating method at moderate initial concentrations ($c^0_{Ni} \le 3$ g l^{-1}). At higher nickel concentrations ($c^0_{Ni} > 3$ g l^{-1}), the degree of concentration approaches unity, i.e. the volume of the precipitate approaches the volume of the initial solution. In the industry such precipitates are subsequently compacted (dehydrated) using press-filters, vacuum filters, or centrifuges.

CONCLUSIONS

(1) At pH 8–11, the dependence of the average nickel(II) concentration c_{Ni} in the precipitate on its initial concentration c^0_{Ni} in the solution can be described by Eq. (1) with empirical coefficients *a*, *b*, and *c*.

(2) The precipitation of nickel(II) as poorly soluble compounds with NaOH solutions as an efficient concentrating method at moderate initial concentrations ($c^0_{Ni} \le 3$ g l^{-1}).

REFERENCES

1. Chalyi, V.P., *Gidrookisi metallov* (Metal Hydroxides), Kiev: Naukova Dumka, 1972.
2. Vasserman, I.M., *Khimicheskoe osazhdenie iz rastvorov* (Electroless Precipitation from Solutions), Leningrad: Khimiya, 1980.

Russian Journal of Applied Chemistry, Vol. 77, No. 7, 2004, pp. 1200–1202. Translated from Zhurnal Prikladnoi Khimii, Vol. 77, No. 7, 2004, pp. 1215–1217.

BRIEF COMMUNICATIONS

Bismuth(V) Oxide and Silver Bismuthate as Oxidizing Agents for Gas-Chromatographic Elemental Microanalysis

A. Yu. Shvykin, V. V. Platonov, V. P. Proskuryakov, K. B. Chilachava, E. M. Khmarin, and I. V. Kovtun

Tolstoy State Pedagogical University, Tula, Russia
St. Petersburg State Technological Institute, St. Petersburg, Russia

Received June 24, 2003; in final form, April 2004

Abstract—Bismuth(V) oxide, silver bismuthate, and a mixture of bismuth(V) oxide with fine silver powder were studied as oxidizing additives in gas-chromatographic elemental microanalysis of readily combustible organic substances and coal.

Gas-chromatographic elemental analysis (GCEA) is one of fast and automated methods for analyzing organic compounds. The accuracy and reproducibility of this method are comparable with, and sometimes, exceed those of conventional elemental analysis.

One of serious problems of GCEA is efficient and almost instantaneous oxidative thermolysis of an organic sample to form products suitable for chromatographic analysis. To provide compete oxidation of a sample, appropriate oxidizing agents or their mixtures with combustion catalysts are added to the sample, and oxidation is performed in a carrier gas (usually helium) containing oxygen. A wide range of oxidizing agents and combustion catalysts providing reliable and complete oxidation of a sample are used in modern GCEA. However, frequently samples of organoboron, organosilicon, and organogermanium compounds, salts of polybasic carboxylic acids, salts of sulfonic acids, various solid caustobioliths, and their derivatives (lignite, coal, peat, sapropels, humic acids, and their extracts) are incompletely burnt in the presence of these oxidizing agents. This is due to high content of mineral fraction (up to 95%) in these materials. Therefore, a search for new effective oxidizing agents and combustion catalysts for difficultly oxidizable organoelemental compounds and solid caustobioliths is an urgent problem.

Diverse inorganic compounds and their mixtures were studied as oxidizing additives to samples to be burnt up [1–4]. Some of them such as PbO_2 and MnO_2 are oxygen donors. Other compounds, e.g., NiO, Cr_2O_3, WO_3, and CeO_2 are surface combustion catalysts. Compounds of the third groups (V_2O_5, Ag_2O, $AgMnO_4$, $AgVO_3$, $Ag_2Cr_2O_7$, and Ag_2O_2) are both oxygen donors and oxidation catalysts. Among compounds of the third group, silver-containing substances $AgMnO_4$ and Ag_2O_2 are the most effective. Metallic silver formed in their thermolysis is a very active catalyst for surface oxidation of the organic component of organoelemental compounds as well as high-ash and high-carbon caustobioliths. These oxidizing agents are suitable for highly effective and complete combustion of difficultly combustible samples in GCEA. The procedure of GCEA of solid caustobioliths, with coals as example, using a Carlo Erba-1100 elemental analyzer was developed and optimized in [4]. $AgMnO_4$, PbO_2, $Ar_2Cr_2O_7$, and Ag_2O_2 were studied as oxidizing catalysts for sample combustion. The most effective were $AgMnO_4$, PbO_2, and Ag_2O_2. In addition, the procedures for weighing and pretreatment of the samples were substantially modified, and mathematical treatment of the chromatrograpms was improved. As a result, the accuracy and reproducibility of the analysis sharply increased.

Bismuth(V) compounds, Bi_2O_5, and $AgBiO_3$, have not been used as oxidizing agents for GCEA. We suggest that bismuth(V) oxide should be an active oxygen donor; $AgBiO_3$ should be both an oxygen donor and a catalyst of surface oxidation owing to the presence of silver in its composition. The influence of catalytic additives of fine metallic silver powder on the oxidizing power of inorganic compounds that are used in modern GCEA as oxygen donors but are not oxidation catalysts was not fully understood. In this work we studied synthesis of bismuth(V) oxide and silver bismuthate and tested these compounds as oxidizing agents for GCEA. We

1070-4272/04/7707-1200 © 2004 MAIK "Nauka/Interperiodica"

Average results of elemental analysis of *p*-nitrophenol and coal of Yakutiya basin in the presence of the oxidizing agents

Oxidizing agent	*p*-Nitrophenol, %			Coal, %		
	C	H	N	C	H	N
$AgMnO_4$	51.83	3.58	10.05	68.37	5.18	0.20
Bi_2O_5	51.79	3.55	10.05	54.01	5.06	0.23
Bi_2O_5 + Ag	51.81	3.57	10.06	68.24	5.21	0.21
$AgBiO_3$	51.82	3.63	10.08	57.08	5.17	0.21
Calculated data	51.80	3.60	10.07	68.38*	5.19	0.20

* Determineded by conventional elemental analysis

also studied the influence of catalytic additives of fine metallic silver powder on the oxidizing properties of these compounds in combustion of microamounts of difficultly combustible samples.

EXPERIMENTAL

γ-Bi_2O_5 was prepared by treatment of $NaBiO_3 \cdot 2H_2O$ with a large excess of 68% HNO_3 at –15°C for 1 h [5–7]:

$$2NaBiO_3 \cdot 2H_2O + 2HNO_3 + (n - 5)H_2O \rightarrow Bi_2O_5 \cdot nH_2O\downarrow + 2NaNO_3.$$

After reaction completion, excess HNO_3 was neutralized to pH 7 with an $NaHCO_3$ solution cooled to 0°C. The $Bi_2O_5 \cdot nH_2O$ precipitate was filtered off, washed many times with water, and predried at 20°C for 48 h over freshly calcined $CaCl_2$. Anhydrous bismuth(V) oxide was prepared by drying $Bi_2O_5 \cdot nH_2O$ at 105°C for 10 h in a drying oven:

$$Bi_2O_5 \cdot nH_2O \rightarrow Bi_2O_5 + nH_2O.$$

$AgBiO_3$ was prepared by reaction of 28-fold excess of $AgNO_3$ with $NaBiO_3 \cdot 2H_2O$ in an aqueous solution at 20°C for 1 h [5]:

$$NaBiO_3 \cdot 2H_2O + AgNO_3 \rightarrow AgBiO_3\downarrow + NaNO_3 + 2H_2O.$$

The $AgBiO_3$ precipitate was filtered off, washed many times with distilled water, and predried at 20°C for 48 h over freshly calcined $CaCl_2$. Anhydrous $AgBiO_3$ was obtained by heating at 60°C for 24 h in a drying oven.

To study the influence of catalytic amounts of silver on the oxidation power of Bi_2O_5, bismuth oxide was mixed with fine silver powder prepared by reduction of $[Ag(NH_3)_2]Cl$ with $N_2H_4 \cdot HCl$ in excess NH_4OH. The resulting mixture was thoroughly ground in an agate mortar and stored without air access. The weight fraction of Ag(0) in the mixture was 22.56 wt %.

Bi_2O_5, $AgBiO_3$, and Bi_2O_5 + Ag(0) were studied as oxidizing additives to samples for GCEA. We also studied $AgMnO_4$ as reference effective oxidizing agent. The organic compound to be analyzed was *p*-nitrophenol. Coal of Yakutiya basin was used as the sample of difficultly combustible high-carbon caustobiolith. The average rounded weight (mg) of Bi_2O_5, $AgBiO_3$, Bi_2O_5 + Ag(0), and $AgMnO_4$ added to the sample was 9.6, 11.4, 28.5, and 43.7, respectively, with their volume being approximately the same. The chromatographic analysis and mathematical treatment of the results were performed by the procedure in [4]. The results of the elemental analysis are summarized in the table.

Since Bi_2O_5 and $AgBiO_3$ are loose powders, their bulk density is minimal among the examined oxidizing agents. $AgMnO_4$ has the highest bulk density. The bulk density of Bi_2O_5 increases by a factor of approximately 3 after addition of Ag(0), i.e., addition of Ag(0) increases the Bi_2O_5 amount in the sample, on the average, by a factor of 2.3. Hence, the amount of "active" oxygen liberated in thermolysis of Bi_2O_5 increases by the same factor, which should make oxidation of the sample more complete. Thus, the increase in the bulk density of Bi_2O_5 after grinding with fine Ag(0) powder should increase the completeness of sample combustion owing to an increase in the amount of the oxidizing agent added to the sample, even if there were no catalytic effect of Ag(0).

As seen from the table, the results of elemental analysis of *p*-nitrophenol, performed with all the tested oxidizing agents, agree with each other and with the calculated values. Hence, all these oxidizing agents can be used in GCEA of readily combustible organic compounds like *p*-nitrophenol (or their mix-

tures). On the contrary, the carbon contents in coal determined in the presence of these compounds strongly differ. Only nitrogen and hydrogen contents are consistent. The carbon content determined with Bi_2O_5 (54.01% C) is lower by 14.36% than that determined with $AgMnO_4$ (68.37% C). The carbon content determined in the presence of $AgBiO_3$ (57.08% C) is underestimated by 11.29%. The results obtained with a Bi_2O_5 + Ag (68.24% C) mixture are close to those obtained with $AgMnO_4$. Hence, addition of fine Ag(0) powder sharply increases the oxidizing power of Bi_2O_5 under GCEA conditions. This mixture can be used to analyze difficultly combustible materials like caustobioliths. Probably, Ag(0) can also enhance the oxidizing power of $AgBiO_3$ and other compounds.

CONCLUSIONS

(1) Bismuth(V) oxide, its mixture with fine silver powder, and sliver bismuthate can be used as effective oxidizing agents for combustion of readily combustible organic compounds in chromatographic elemental microanalysis.

(2) The nitrogen and hydrogen contents determined in coal samples by gas-chromatographic elemental microanalysis in the presence of the tested Bi(V) compounds and their mixtures are consistent. The carbon content in coal, determined with bismuth(V) oxide and silver bismuthate, is lower than that determined in the presence of $AgMnO_4$. The carbon content determined with Bi_2O_5 + Ag(0) mixture is close to that determined with $AgMnO_4$. This mixture can be used as oxidizing additive in gas-chromatographic analysis of solid caustobioliths.

REFERENCES

1. *Metody kolichestvennogo organicheskogo elementnogo mikroanaliza* (Methods of Quantitative Organic Elemental Microanalysis), Gel'man, N.E., Ed., Moscow: Khimiya, 1987.
2. Berezkin, V.G., *Khimicheskie metody v gazovoi khromatografii* (Chemical Methods in Gas Chromatography), Moscow: Khimiya, 1980.
3. Childs, C.E. and Henner, E.B., *Microchem. J.*, 1966, vol. 10, no. 3, pp. 402.
4. Platonov, V.V., Shvykin, A.Yu., Proskuryakov, V.A., *et al.*, *Zh. Prikl. Khim.*, 2002, vol. 75, no. 5, pp. 852–857.
5. Sholder, R. and Stobbe, H., *Z. Anorg. Chem.*, 1941, vol. 247, no. 3, pp. 392–414.
6. Martin-Frere, H., *Chem. Rev.*, 1941, vol. 213, no. 4, pp. 436–437.
7. Gattow, G. and Klippel, W., *Z. Anorg. Allg. Chem.*, 1980, vol. 470, no. 1, pp. 25–34.

Russian Journal of Applied Chemistry, Vol. 77, No. 7, 2004, pp. 1203–1205. Translated from Zhurnal Prikladnoi Khimii, Vol. 77, No. 7, 2004, pp. 1218–1220.

BRIEF COMMUNICATIONS

Combinatorial-Multiplicative Method of Calculating the Limiting Filling of Composites with Solid Dispersed Components

A. S. Ermilov and A. M. Fedoseev

Perm State Technical University, Perm, Russia

Received October 21, 2003

Abstract—A new method for engineering calculation of the limiting volume filling of various composites with particles of solid components with arbitrary granulometric composition is presented. A calculation of the density of random packing of dispersed fillers is described, including an algorithm for calculating the porosity of two fractions. The precision of the method is evaluated.

The limiting degree of volume filling, φ_m, with dispersed components of binder matrices of various composites (asphalts, concretes, polymeric composites, blended solid propellants) is the most important characteristic of the aggregate parameter φ/φ_m (φ is the volume fraction of the filler). It has been shown for rubbers that φ_m depends on the shape and granulometric composition of filler particles, as well as on their physicochemical interaction with binders [1]. The parameter φ/φ_m invariantly determines the strengthening of composites in, e.g., the dynamic viscosity coefficient or the initial modulus of viscoelasticity. The strongest influence on the strengthening of composites (at φ = const) is exerted by the density of random packing of filler particles in the original bulk form.

This communication suggests, in contrast to [2, 3], a more precise combinatorial-multiplicative method for engineering calculations of the limiting volume filling of composites with solid dispersed fillers with an arbitrary number of fractions and particle size distribution by determining the density of random packing of particles of a loose material.

The algorithm for calculating φ_m is based on determining the porosity of, first, a mixture of two fractions and then replacing this mixture with a single fraction with equivalent particle size. After that, the porosity is calculated for a mixture of the equivalent and next fraction and so on to *n*th fraction (*n* is the number of fractions in the filler). The $(n - 1)$th iteration yields the volume fraction of pores in a mixture of *n* fractions, equal to φ_p, with the density of random packing equal to $\varphi_m = 1 - \varphi_p$. A method for calculating the porosity of a mixture of two fractions from the known porosity and mass-average particle size (diameter) is described below. The input information for calculating φ_p for an arbitrary mixture of filler fractions are the factor vector $\mathbf{D} = (d_1, d_2, d_3,..., d_n)$, with fraction particle sizes arranged in increasing (or decreasing) order, and the corresponding vectors of fraction porosities $\mathbf{Q} = (q_1, q_2, q_3,..., q_n)$ and volume shares of fractions $\Phi = (\varphi_1, \varphi_2, \varphi_3,..., \varphi_n)$. Then follows a calculation of φ_p by the algorithm. Let the porosity of a mixture of *i*th ($i = 1, 2, 3,..., n - 1$) and *j*th ($j = i + 1$) fractions be q_z (for the last iteration, the porosity $q_z = \varphi_p$). Then the result of the first iteration ($i = 1$) is a fraction that is equivalent to a mixture of the first and second fractions, whose characteristics are the following:

$$q^{(i+1)} = q_z = F_z(d^{(i)}, d_j, q^{(i)}, q_j, \varphi^{(i)}, \varphi_j), \quad (1)$$

$$d^{(i+1)} = (\varphi^{(i)} + \varphi_j)/(\varphi^{(i)}/d^{(i)} + \varphi_j/d_j), \quad (2)$$

$$\varphi^{(i+1)} = (\varphi^{(i)} + \varphi_j), \quad (3)$$

where $q^{(i+1)}$, $d^{(i+1)}$, $\varphi^{(i+1)}$ are the porosity, particle size, and volume share of the equivalent fraction, which are calculated as a result of $(i + 1)$th iteration; F_z, the function determining the dependence of the porosity of a mixture of two fractions on their characteristic parameters and volume shares; $q^{(i)}$, $d^{(i)}$, $\varphi^{(i)}$, the porosity, particle size, and volume share of the equivalent fraction in the *i*th iteration ($q^{(1)} = q_1$, $d^{(1)} = d_1$, $\varphi^{(1)} = \varphi_1$); and q_j, d_j, φ_j, the porosity, particle size, and volume share of *j*th fraction.

1070-4272/04/7707-1203 © 2004 MAIK "Nauka/Interperiodica"

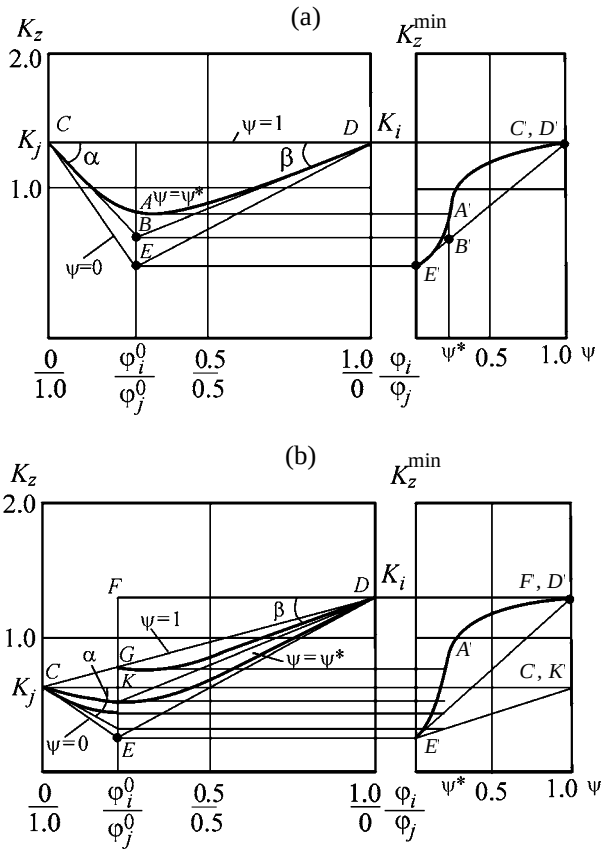

Fig. 1. Dependence $K_z(\varphi_{i(j)}, \psi_{ij})$ at (a) $K_i = K_j$ and (b) $K_i \neq K_j$.

In the second iteration ($i = 2$), the equivalent fraction is "mixed" with the third ($j = 3$). As a result, the parameters of a fraction equivalent to a mixture of the first, second, and third fractions are calculated, with the characteristics determined by formulas (1)–(3), etc.

The particle size ratio ψ_{ij} ($i < j$), the porosity coefficients K_i and K_j of ith and jth fractions, their additive porosity coefficient K_a, and the optimal volume share φ_i^0 of ith fraction in a mixture ($\varphi_j^0 = 1 - \varphi_i^0$) are given by the expressions

$$\psi_{ij} = d_i/d_j \text{ at } d_i < d_j; \quad (4)$$

$$K_i = q_i/(1 - q_i),\ K_j = q_j/(1 - q_j); \quad (5)$$

$$K_a = K_i\varphi_{zi} + K_j\varphi_{zj} \text{ at } \varphi_{zi} = \varphi_i/(\varphi_i + \varphi_j) \text{ and } \varphi_{zj} = \varphi_j/(\varphi_i + \varphi_j); \quad (6)$$

$$\varphi_i^0 = K_j/(1 + K_i + K_j),\quad \varphi_j^0 = (1 + K_i)/(1 + K_i + K_j). \quad (7)$$

These expressions are derived from the obvious relation

$$\varphi_i^0/\varphi_j^0 = \varphi_i^0/(1 - \varphi_i^0) = [(1 - \varphi_{mj})\varphi_{mi}]/\varphi_{mj}, \quad (8)$$

which is valid at $\psi \to 0$. Here φ_{mi} and φ_{mj} are the packing densities of ith and jth fractions. The geometric interpretation of the algorithm for identifying how the porosity coefficient of a mixture depends on volume shares of fractions for known porosity coefficients of the fractions and a prescribed particle size ratio is shown in Fig. 1a for $K_i = K_j$ and Fig. 1b for $K_i \neq K_j$. The dependence $K_z(\varphi_{i(j)})$ is determined by two branches (*CA* and *AD*), each of which is described by a third-degree polynomial (Fig. 1a):

$$K_z = a_i + b_i\varphi_i + c_i\varphi_i^2/2 + d_i\varphi_i^3/3 \quad \text{at } \varphi_i \le \varphi_i^0, \quad (9)$$

$$K_z = a_j + b_j\varphi_j + c_j\varphi_j^2/2 + d_i\varphi_i^3/3 \quad \text{at } \varphi_i \ge \varphi_i^0. \quad (10)$$

The polynomial coefficients $a_{i(j)}$, $b_{i(j)}$, $c_{i(j)}$, $d_{i(j)}$ are found by solving a system of four equations written with account of the boundary conditions and the key dependence $W(\psi)$ (e.g., curve E', B', K', C', D' in Fig. 1a) of the minimum normalized porosity coefficient $K_z^{min}(\psi)$ on the particle size ratio ($\psi = \psi^*$ is an arbitrary value):

$$W(\psi) = [K_z^{min}(\psi) - K_z^{min}(0)]/[K_z^{min}(1) - K_z^{min}(0)] = \exp(-1.818\log^2\psi), \quad (11)$$

which is obtained by summarizing experimental data obtained by different authors. The system of equations has the form

$$K_z = a_{i(j)} + b_{i(j)}\times 0 + c_{i(j)}\times 0/2 + d_{i(j)}\times 0/3 = K_{j(i)} \quad \text{at } \varphi_{i(j)} = 0, \quad (12)$$

$$K_z = a_{i(j)} + b_{i(j)}\varphi_{i(j)}^0 + c_{i(j)}(\varphi_{i(j)}^0)^2/2 + d_{i(j)}(\varphi_{i(j)}^0)^3/3 = K_{j(i)}^4 \quad \text{at } \varphi_{i(j)} = \varphi_{i(j)}^0, \quad (13)$$

$$dK_z/d\varphi_{i(j)} = b_{i(j)} + c_{i(j)}\times 0 + d_{i(j)}\times 0 = \tan\alpha(\beta) = (K_{i(j)} - K_{i(j)}^B)/\varphi_{i(j)}^0 \text{ at } \varphi_{i(j)} = 0, \quad (14)$$

$$dK_z/d\varphi_{i(j)} = b_{i(j)} + c_{i(j)}\varphi_{i(j)}^0 + d_{i(j)}(\varphi_{i(j)}^0)^2 = 0 \quad \text{at } \varphi_{i(j)} = \varphi_{i(j)}^0. \quad (15)$$

At $K_i \neq K_j$ (see Fig. 1b), e.g., for a mixture of particles of spherical and arbitrary shape, the scheme of calculation for each branch of the sought-for dependence is first similar to that in the case $K_i = K_j$, i.e., the parameters of the left and right branches are found to be imaginary. Further, the branches (equations) are matched to form a common smooth curve *CD* via a transformation performed in accordance with the

Porosity coefficients of four-fraction mixtures

Volume share of fractions				Porosity coefficient		
φ_1	φ_2	φ_3	φ_4	experiment	calculation by	
					MCM	MWS
0.375	0.125	0.375	0.125	0.432	0.432	0.468
0.143	0.429	0.286	0.143	0.481	0.473	0.514
0.333	0.333	0.222	0.111	0.445	0.450	0.473
0.273	0.182	0.273	0.273	0.429	0.425	0.465
0.250	0.250	0.250	0.250	0.440	0.429	0.472
0.200	0.300	0.200	0.300	0.424	0.429	0.473
0.222	0.222	0.222	0.333	0.430	0.428	0.464
0.250	0.125	0.250	0.375	0.432	0.432	0.455
0.167	0.167	0.167	0.500	0.457	0.452	0.456
0.300	0.300	0.300	0.100	0.380	0.457	0.484

congruence rule (ΔCKE is extended to ΔCGE, and ΔDFE is contracted to ΔDGE; the line CGD corresponds to the additive porosity coefficient of the mixture).

The table lists experimental values of the porosity coefficients for four-fraction mixtures of packing elements of a catalyst for reactions columns, which have different shapes and sizes [3], and values of K_z, calculated using a software for the method suggested here (MCM), in comparison with those furnished by the method developed by Polish engineers Wienckowsky and Strek (MWS) [2, 3]. The sizes of fraction elements, arranged in decreasing order, are as follows: d_1 = 25.4, d_2 = 12.7, d_3 = 6.35, d_4 = 3.18 mm. The porosity coefficients of the fractions: K_1 = 0.765, K_2 = 0.680, K_3 = 0.623, K_4 = 0.610. Comparison of the results obtained shows better, on the average, agreement of the calculated and experimental data for the method suggested here, compared to the MWS method. This is due to taking into account the nonlinearity of the dependence $K_z(\varphi_{i(j)})$ in the optimal range of volume ratios of the fractions in the calculation by MCM. The precision of this method for calculation of the porosity or density of random packing of particles of granulated materials is about 7%.

A transition from a loose state of the filler to a composite is done by using as input data the porosity coefficients of the fractions determined via $\varphi_{m\,i}$ viscometrically, with account taken of the physicochemical interaction at the filler–binder interface [1]. The MCM technique is recommended for optimization of the granulometric composition of a solid dispersed filler by the criterion of the limiting volume filling of a binder in a composite.

CONCLUSIONS

(1) A procedure for calculating the density of random packing of particles in loose form is described. This procedure employs the combinatorial-multiplicative method, suggested by the authors, for calculating the limiting filling of composites with solid dispersed components.

(2) The algorithm for calculating the porosity of a mixture of two fractions of a solid dispersed filler is described and the approach used is illustrated graphically.

(3) Comparison of the calculated and experimental data shows that the precision of the method suggested is about 7%.

REFERENCES

1. Ermilov, A.S. and Zyryanov, K.A., *Zavod. Lab.*, 2001, vol. 67, no. 9, pp. 62–64.
2. Wienckowsky, A. and Strek, F., *Chem. Stosow.*, 1966, vol. 1B, pp. 95–127.
3. Wienckowsky, A. and Strek, F., *Chem. Stosow.*, 1966, vol. 4B, pp. 431–447.

Russian Journal of Applied Chemistry, Vol. 77, No. 7, 2004, pp. 1206–1207. Translated from Zhurnal Prikladnoi Khimii, Vol. 77, No. 7, 2004, pp. 1221–1222.

BRIEF COMMUNICATIONS

Inhibition of Polymerization of Poly-bis-maleimides in Solution

D. M. Mognonov and V. V. Khakhinov

Baikal Institute of Nature Management, Siberian Division, Russian Academy of Sciences, Ulan-Ude, Buryatia, Russia
Buryat State University, Ulan-Ude, Buryatia, Russia

Received April 8, 2004

Abstract—The influence of inhibitors on the rate of polymerization of poly-bis-maleimide in organic solvents at various temperatures was studied.

One of the most important problems of applied chemistry of macromolecular compounds is production of thermostable composite polymeric materials reinforced with continuous fibers [1, 2]. In this case, the main requirement to the binder is high stability of viscous characteristics of polymer solutions for a long time; in so doing, the impregnation solution is usually heated to decrease its viscosity. This problem can be solved using appropriate inhibitors of thermal polymerization. The criterion for the choice of these inhibitors is high solubility in organic solvents and high performance in a wide temperature range.

Polymerization of unsaturated monomers and oligomers can be decelerated or inhibited almost completely with relatively small amounts of an inhibitor. Previous studies of inhibition of polymerization with molybdenum, tungsten, and vanadium compounds by the example of poly-bis-maleimide (PBMI) [3, 4] showed their high performance.

In this work we studied the inhibiting effect of heteropoly compounds (HPCs) in thermal polymerization of PBMI in organic solvents. The specific viscosity of oligomer in a solvent (η_{sp}), which increases in high-temperature impregnation of the filler or in prolonged storage, was selected as a parameter defining the inhibition efficiency. The specific viscosity was determined on an Ostwald–Pinkevich viscometer in the range 25–140°C. The temperature gradient in the heat-carrier bulk did not exceed ±0.5°C.

As inhibitors we took HPCs recrystallized from aqueous solutions and readily soluble in organic media: $H_3PMo_{12}O_{40}\cdot nH_2O$ (PMO_{12}) and $H_3PW_{12}O_{40}\cdot nH_2O$ (PW_{12}), where n = 6–14. Poly-bis-maleimide produced by the Karbolit RPA [TU (Technical Specifications) 00-06-173–73] was used without additional purification. The UV spectra of aqueous solutions were recorded on an SF-46 spectrophotometer. Typical dependences of the specific viscosity of PBMI in DMF and *N*-methylpyrrolidone (*N*-MP) solutions with added HPCs on time at various temperatures and inhibitor concentrations are shown in Figs. 1a and 1b. With increasing temperature, the viscosity of the solutions regularly increases. The curves of variation of the specific viscosity of PBMI solution in the presence of the inhibitor show that the polymerization rate significantly decreases. As seen from Fig. 1, the dependence of the specific viscosity on time is characteristic of a zero-order reaction independent of the concentration of the initial reactants. The curves of viscosity variation in time, obtained at various temperatures, are unambiguously related to the presence of multiple bonds, since polymerization of PBMI though double bonds results in gelation and an increase in the solution viscosity. Therefore, the polymerization rates obtained are relative quantities, and in this stage they allow us to choose only an inhibitor and its concentration.

The time dependences of the viscosity of PBMI solutions and also the relative rates of PBMI polymerization in the presence of various HPCs confirm higher inhibiting power of PMo_{12}, whose oxidation potential is higher than that of PW_{12}. The assumption that the mechanism of inhibition with HPCs is caused by reduction of heteropoly anion is confirmed by the electronic spectrum of an aqueous extract of a mixture of PBMI and HPC, preheated at 200°C for 30 min, considering this fact that the polymer is insoluble in water. A broad absorption band in the range 660–750 nm, characteristic of transitions in reduced HPC species, appears in the spectrum. Preservation of the band with a maximum at 750 nm suggests that the structure of the heteropoly anion remains the same

1070-4272/04/7707-1206 © 2004 MAIK "Nauka/Interperiodica"

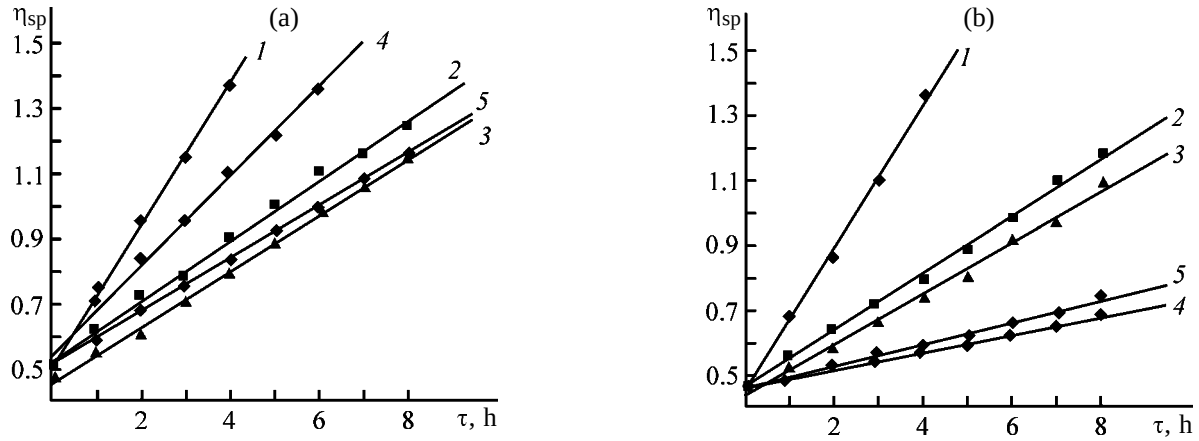

Fig. 1. Specific viscosity η_{sp} of PBMI solutions containing inhibitors as a function of time τ at (a) 140 and (b) 120°C. (a) Inhibitor concentration 2 wt %; (*1*) PBMI in DMF (no inhibitor), (*2*) PBMI with PW_{12} in N-MP, (*3*) PBMI with PMo_{12} in N-MP, (*4*) PBMOI with PW_{12} in DMF, and (*5*) PBMI with PMo_{12} in DMF. (b) PBMI solution in *N*-MP, inhibitor PMo_{12}; inhibitor concentration, wt %: (*1*) 0, (*2*) 2, (*3*) 5, (*4*) 10, and (*5*) 20.

[5, 6]. The relative rate of thermal polymerization of PBMI decreases with increase in concentration from 2 to 10 wt % (Fig. 1b); however, further increase in the HPC content in the solution does not significantly affect the inhibition process but deteriorates the final technical characteristics of polymer.

Since inhibition of the polymerization was monitored by variation of the specific viscosity of the polymer solution, the effective activation energy of the process was determined from the coefficients of transformation of the kinetic curves. This made it unnecessary to determine the absolute values of the reaction rate and know of the analytical equation of the kinetic curve. The effective activation energy of thermal polymerization of PMBI in the *N*-MP solution is 12.2 kJ mol^{-1}, and in the presence of 10 wt % PMo_{12}, 44.9 kJ mol^{-1}, which suggests that addition of HPC significantly increases the activation barrier of PBMI polymerization.

Thus, HPCs can be used as polymerization inhibitors in organic solvents. The process mechanism involves reduction of the heteropoly anion and is in good agreement with previous data on inhibition of polymerization in melt.

REFERENCES

1. Babaevskii, P.G., *Plastiki konstruktsionnogo naznacheniya* (Structural Plastics), Moscow: Khimiya, 1974.
2. Plate, N.A. and Slivinskii, E.V., *Osnovy khimii i tekhnologii monomerov* (Principles of Chemistry and Technology of Monomers), Moscow: Nauka, 2002.
3. Khakhinov, V.V., Mognonov, D.M., Tumurova, L.V., and Mokhosoev, M.V., *J. Therm. Anal.*, 1988, vol. 34, pp. 99–104.
4. Mognonov, D.M., Khankhasaeva, S.Ts., Khakhinov, V.V., *et al.*, *Zh. Prikl. Khim.*, 1998, vol. 71, no. 11, pp. 1925–1927.
5. Alimarin, I.P., Kazanskii, L.P., Dorokhova, E.N., and Prokhorova, G.V., *Zh. Anal. Khim.*, 1980, vol. 53, no. 10, pp. 2000–2025.
6. Emmanuel', N.M. and Knorre, D., *Kurs khimicheskoi kinetiki* (Course of Chemical Kinetics), Moscow: Vysshaya Shkola, 1962.

Russian Journal of Applied Chemistry, Vol. 77, No. 7, 2004, pp. 1208–1209. Translated from Zhurnal Prikladnoi Khimii, Vol. 77, No. 7, 2004, pp. 1223–1224.

ANNIVERSARIES

Mikhail Mikhailovich Shul'ts (to 85th Anniversary of His Birthday)

On July 1, 2004, Mikhail Mikhailovich Shul'ts, Academician of the Russian Academy of Sciences, Hero of Socialist Labor, and a known Russian scientist in the field of physical chemistry, thermodynamics, chemistry and electrochemistry of glass, and membrane electrochemistry, was 85.

M.M. Shul'ts is the head of one of the best known Russian scientific schools. Under his supervision, 45 scientists defended their candidate's dissertations and five scientists became doctors of science (and one of these, a corresponding member of the Russian Academy of Sciences).

Shul'ts entered the chemical department of the Leningrad State University in 1937, volunteered to the front line in the Great Patriotic War, and graduated from the University in 1947, to become a postgraduate student. His supervisor was an outstanding scientist, later an academician, Boris Petrovich Nikol'skii. In his scientific activities, Shul'ts became the main continuer of Nikol'skii's researches.

Most part of the scientific life and activities of Shul'ts was associated with the St. Petersburg (Leningrad) University, where he successively occupied positions of an assistant researcher, docent, head of a laboratory at the Research Institute of Chemistry, and professor of the Chair of Physical Chemistry. In 1967–1972, he was dean of the Chemical Department. The main scientific achievements of Shul'ts are associated with investigations of the electrode properties of glasses, solution of a wide variety of theoretical and applied problems of ionometry, and especially pH-metry. Shul'ts suggested a rigorous proof of the metallic function of a glass electrode and studied the mechanism of ion transport in membranes of varied nature. Under his supervision, a set of glasses for pH-metry, glasses with metallic electrode functions, and glass redox-metric electrodes were developed. The results of studies in this area found exceedingly wide use in many fields of industry, in agriculture, in medicine, and in research.

Another important study by Shul'ts at the University is that of fundamental problems of the thermodynamic theory of heterogeneous systems, performed together with Professor A.V. Storonkin. Here, a separate mention should be made of the following: the Le Chatelier–Braun principle was refined, fundamental thermodynamic aspects of phase and chemical transformations in closed systems were established, and methods for investigation of complex systems forming solid solutions were developed.

In 1972, after he started to work at the Grebenshchikov Institute of Silicate Chemistry as director of this institute (till 1998), Shul'ts continued intensive research work in a third field: he studied the structure and thermodynamic properties of glasses and oxide melts. He created a leading scientific school "Thermodynamics and Chemical Structure of Glasses and Oxide Melts," which now efficiently works under his supervision. Papers by Shul'ts and co-workers, devoted to this subject and published in *Fizika i Khimiya Stekla* (Glass Physics and Chemistry) journal, were distinguished in 1996 and 2000 by an award established by Interperiodica publishing house. Shul'ts was twice awarded for his studies State Prizes of the USSR (1973 and 1986), twice he received the First University Prize. He was awarded the Grebenshchikov Prize of the Russian Academy of Sciences (1999). In 2003, he received Mendeleev Prize in

1070-4272/04/7707-1208 © 2004 MAIK "Nauka/Interperiodica"

Chemical Sciences, established by the Government of St. Petersburg and by the St. Petersburg Scientific Center of the Russian Academy of Sciences.

Shul'ts combined intensive research with pedagogical activities: he delivered a general course of lectures "Physical Chemistry" and special courses of lectures. At St. Petersburg State University and Institute of Silicate Chemistry, he supervised the work of postgraduate students and consulted those who prepared doctoral dissertations. His disciples include known scientists and doctors and candidates of science. The list of his scientific works contains more than 350 titles, including four monographs, textbooks, and subject collections of works, edited by him.

Shul'ts is engaged in intensive scientific-organizational activities, being a member of many interbranch and academic councils, chairman of the scientific council of the Russian Academy of Sciences for ceramic materials, and a member of scientific and dissertation councils at St. Petersburg State University and Institute of Silicate Chemistry, and a chairman or member of organizing committees of Russian and international conferences.

During the days of the remarkable jubilee, 85th birthday, numerous disciples, friends, and colleagues of Mikhail Mikhailovich wish him sound health, preservation of his inherent good spirits, creative activity, and joy of life.

A. G. Morachevskii, N. A. Smirnova, A. A. Belyustin, and I. S. Ivanovskaya

Editorial Board and Editorial Staff of *Zhurnal Prikladnoi Khimii*

Russian Journal of Applied Chemistry, Vol. 77, No. 7, 2004, pp. 1210–1212. Translated from Zhurnal Prikladnoi Khimii, Vol. 77, No. 7, 2004, pp. 1125–1127.

HISTORY OF CHEMISTRY AND CHEMICAL TECHNOLOGY

Professor Nikolai Ivanovich Stepanov (to 125th Anniversary of His Birthday)

At the very beginning of the XX century, a scientific school of inorganic chemistry, the largest in Russia and known worldwide, was formed on the basis of chemical laboratories of three higher-school institutions of St. Petersburg, Mining, Polytechnic, and Electrotechnical Institutes, under the supervision of N.S. Kurnakov (1860–1941, Academician since 1913). One of its most prominent representatives was N.I. Stepanov, Corresponding Member of the USSR Academy of Sciences and Professor of the Mining Institute.

Nikolai Ivanovich Stepanov was born on July 6, 1879, in the town of Tara, uezd center of Tobol'sk province (now Omsk oblast), into the family of a doctor at Altai okrug. In spring of 1888, the family moved to Tomsk, where Stepanov, owing to his good home training and natural abilities, was accepted directly in IV form. He finished his secondary education at one of the best nonclassical secondary schools of St. Petersburg, where the Stepanov family moved in 1895. In 1897, he successfully passed a competition and entered the Mining Institute. Founded in 1773 by the empress Catherine II, the Mining Institute was one of the oldest and best higher-school institutes of Russia at the end of the XX century. Its lecturers included in those years such known scientists as chemists I.F. Schroeder (1858–1918) and Kurnakov, crystallographer E.S. Fedorov (1853–1919), mathematicians I.P. Dolbnya (1853–1912) and G.A. Thieme (1831–1910), and electrical engineer M.A. Shatelen (1866–1957). Already when being a fifth-year student, Stepanov carried out, under Kurnakov's supervision, a complex experimental study: he analyzed the phase diagrams of the magnesium–tin and magnesium–lead systems and found intermetallic compounds in these systems. In 1903, he finished, the best among the graduates of that year, the Mining Institute and was left as assistant researcher at the Chair of Analytical Chemistry. Simultaneously, he continued his investigations of metallic alloys with strong interaction between the components and intermetallic compounds formed. Together with using thermal analysis as a method for studying the nature of alloys in the solid state, Stepanov employed the method of measurement

of the electrical conductivity, having improved the experimental procedure. The investigations of the young scientist were honored by a minor Mendeleev Prize, awarded by the Russian Physicochemical Society in February 1910.

The whole set of experimental studies, whose results were published in *Zhurnal Russkogo Fiziko-Khimicheskogo Obshchestva* in 1905–1910 under the general title "On Electrical Conductivity of Metal Alloys in the Context of the Electronic Theory," was submitted by Stepanov as a dissertation for the degree of an associate professor at the Chair of Chemistry. The author, in particular, noted that the method of electrical conductivity measurements proved to be very sensitive to the boundaries of formation of solid solutions. All the results were explained in terms of the electronic theory existing at that time. The study was highly appreciated by Kurnakov and P.I. Walden (1863–1957, academician since 1910). The dissertation was successfully defended at the Mining Institute on December 11, 1911. In accordance with the regulations existing at that time, Stepanov delivered on December 14 of the same year two trial lectures: "On the Rule of Phases" and "Extraction of Salts from

1070-4272/04/7707-1210 © 2004 MAIK "Nauka/Interperiodica"

Seawater, According to Studies by van't Hoff." After the degree of an associate professor was conferred on him, Stepanov was sent to a business trip to Germany and Switzerland to familiarize himself with the methodology of teaching of chemistry and to visit laboratories of higher-school institutions. The scientist had a perfect command of German and French from childhood. During the trip, Stepanov made acquaintance with the following prominent chemists of that time; G. Tammann (1861–1938), who left Russia in 1903 and occupied the position of a professor at Goettingen University (Germany); S.A. Arrhenius (1859–1927), Swedish physical chemist and 1903 Nobel Prize winner; and Swiss chemist A. Werner (1866–1919, 1913 Nobel Prize in chemistry), founder of the coordination chemistry.

In 1912–1914, Stepanov published a series of papers devoted to electrochemistry of aqueous solutions. Beginning in 1913, he studied, on a commission from the Mining Department, together with a professor of the Mining Institute A.A. Skochinskii (1876–1960), the explosive properties of the coal dust at mines of the Donets basin. This work continued for a number of years. In 1916, Stepanov was elected an extraordinary professor at the Chair of Chemistry. In 1918, he was charged with delivery of all the main chemical courses of lectures at the Mining Institute. Stepanov's lectures enjoyed a considerable and well-deserved success with students.

In 1918, Stepanov commenced, simultaneously with his pedagogical activities, work at the Institute for Studies of Platinum and Other Noble Metals, organized on the initiative of Professor L.A. Chugaev (1873–1922). However, already in 1920 he went to the Institute of Physicochemical Analysis, headed by Kurnakov. Stepanov carried out interesting studies in the field of kinetics of transformations in metals and alloys. The main results of these studies were reported at the III Mendeleev Congress in May 1922. In those same years, the scientist started a series of his most important studies devoted to the theory of physicochemical analysis. This new research area was named the chemical metrics of equilibrium systems. The success in this area was achieved because Stepanov showed great abilities in mathematics and had a perfect command of the necessary mathematical apparatus. Spacious publications by Stepanov in *Izvestiya Instituta Fiziko-Khimicheskogo Analiza* in 1928–1933 and in *Uspekhi Khimii* journal (1936, vol. 5, nos. 7–8) were devoted to the new field of physicochemical analysis.

In October 1933, at the First All-Union Conference

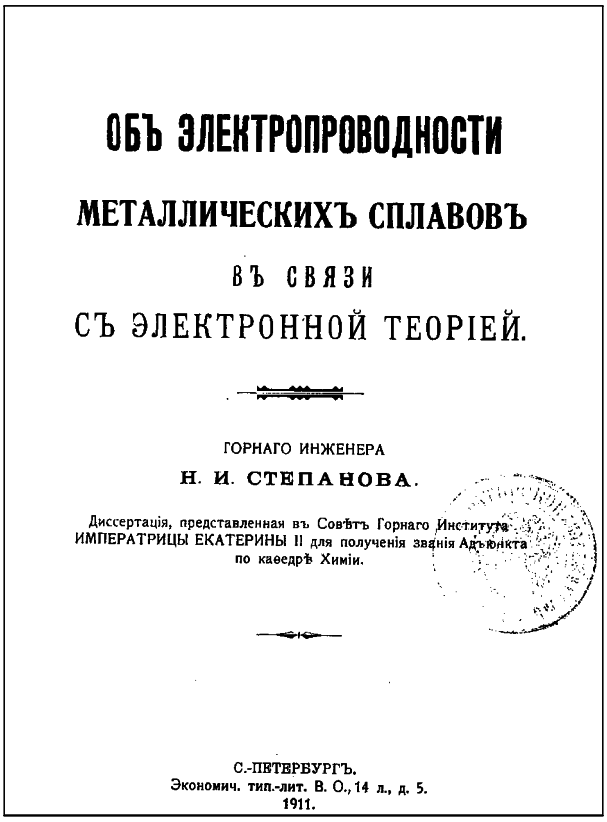
ОБЪ ЭЛЕКТРОПРОВОДНОСТИ

МЕТАЛЛИЧЕСКИХЪ СПЛАВОВЪ

ВЪ СВЯЗИ

СЪ ЭЛЕКТРОННОЙ ТЕОРІЕЙ.

ГОРНАГО ИНЖЕНЕРА

Н. И. СТЕПАНОВА.

Диссертація, представленная въ Совѣтъ Горнаго Института ИМПЕРАТРИЦЫ ЕКАТЕРИНЫ II для полученія званія Адъюнкта по каѳедрѣ Химіи.

С.-ПЕТЕРБУРГЪ.
Экономич. тип.-лит. В. О., 14 л., д. 5.
1911.

Stepanov's dissertation "On Electrical Conductivity of Metal Alloys in the Context of the Electronic Theory."

of Physicochemical Analysis, Stepanov made three reports at plenary sessions. One of these considered the relationship between the law of mass action and the equilibrium composition–property diagram, and the two others discussed the run of the solubility isotherm in ternary systems. At the Jubilee Mendeleev Congress in Leningrad, in September 1934, Stepanov summarized the main results of the series of his investigations in the report "The Critical Points of Mendeleev's Theory of Solutions and the Metrics of a Chemical Diagram."

On March 28, 1934, the general meeting of the USSR Academy of Sciences made a decision to unite the Institute of Physicochemical Analysis, Institute for Study of Platinum and Other Noble Metals, and Laboratory of General Chemistry into the Institute of General and Inorganic Chemistry, Academy of Sciences of the USSR. Academician Kurnakov was elected director of the Institute. On June 14, 1934, the Government of the country included the institute into the list of institutions transferred from Leningrad to Moscow [1]. As a closest Kurnakov's associate and aide, Stepanov took a rather active part in the organization of a new scientific institution, in which the

basic areas of inorganic chemistry were to be represented. In 1936, Stepanov headed the sector of physicochemical analysis at this institute.

The scientific interests of Stepanov were rather diverse; a complete list of his scientific works can be found in [2]. Two scientist's publications were devoted to the history of chemistry: "Biographic Evidence Concerning Some Personalities in the Field of Russian Platinum Industries" (*Izv. Inst. Platiny*, 1927, vol. 5) and "Chemistry at the Mining Institute during the Last 150 Years" (*Izv. Inst. Fiz.-Khim. Anal*., 1927, vol. 3). Professors A.T. Grigor'ev [2] and S.V. Lipin, who were closely acquainted with Stepanov, noted in the articles devoted to the life and scientific activities of their colleague the breadth of his interests, his intimate knowledge of literature, painting, and sculpture, and his talent for music.

In the last years of his life, Stepanov suffered from a heart illness, but continued intensive work. Nikolai Ivanovich Stepanov died on May 19, 1938. Kurnakov characterized his disciple as follows: "Nikolai Ivanovich Stepanov is one of the most prominent and outstanding alumni of the Mining Institute, who studied at our chemical laboratory. He combined the capacity for a fine experimental study and a profound mathematical erudition... The studies of dear Nikolai Ivanovich Stepanov will erect an eternal monument to him, which will serve as a guiding source in the wide world of the chemical metrics of equilibrium systems" [4].

REFERENCES

1. Solov'ev, Yu.I., *Inst. obshchei i neorganicheskoi khimii im. N.S.Kurnakova Rossiiskoi Akademii nauk: Istoricheskii ocherk* (Kurnakov Inst. of General and Inorganic Chemistry, Russian Acad. Sci.: A Historical Outline), Moscow: Nauka, 1993.
2. Grigor'ev, A.T., *Izv. Sekt. Fiz.-Khim. Anal., Inst. Obshch. Neorg. Khim., Akad. Nauk SSSR, Otd*. I, 1940, vol. 13, pp. 7–12.
3. Lipin, S.V., *Vydayushchiesya uchenye Gornogo instituta: 1773–1948. Sbornik statei, posvyashchennykh 175-letiyu Gornogo instituta* (Outstanding Scientists of the Mining Inst.: 1773–1948, Coll. of Articles Devoted to 175th Anniversary of Foundation of the Mining Inst.), Moscow: Metallurgizdat, 1951, issue 2, pp. 97–105.
4. Solov'ev, Yu.I., *Nikolai Semenovich Kurnakov: 1860–1941*, Moscow: Nauka, 1986.

A. G. Morachevskii

Russian Journal of Applied Chemistry, Vol. 77, No. 7, 2004, p. 1213. Translated from Zhurnal Prikladnoi Khimii, Vol. 77, No. 7, 2004, p. 1228.

BOOK REVIEWS

Kovenskii, I.M. and Povetkin, V.V., *Elektrolitricheskie splavy* (Electrolytic Alloys)

Moscow: Internet Inzhiniring, 2003, 288 pp.

Electroplated coatings find exceedingly wide use in various fields of technology. Coatings composed of individual metals are the subject of a vast body of industrial-technological and reference literature, textbooks, and scientific monographs. A much smaller number of publications and lesser evidence are devoted to electrolytic alloys. At the same time, use of electrolytic alloys makes it possible to obtain coatings more completely satisfying the necessary operational requirements. The monograph by I.M. Kovenskii and V.V. Povetkin summarizes the presently available results of investigations of electrolytic alloys, carried out by the authors and devoted to preparation, properties, thermal treatment, and amorphization of these alloys. The primary attention is given by the authors to electrolytic alloys in the form of single-phase solid solutions. The book comprises six chapters, each with its own bibliographic list.

Chapter 1 (pp. 3–19) describes methods for determining the properties of electrolytic coatings. The whole set of techniques for evaluating the mechanical, physical, and chemical properties and service characteristics is briefly considered. Microscopic and X-ray diffraction analyses, electron spectroscopy, and resonance methods are described.

Chapter 2 (pp. 20–44) is devoted to thermodynamic and kinetic aspects of alloy formation processes. Also considered are the influence exerted by electrolysis parameters on the chemical composition of alloys and the mechanism by which impurities pass into the deposit. Chapter 3 (pp. 45–136), which occupies the central position in the monograph, discusses how the structure of alloys is formed in the course of electrocrystallization.

Chapter 4 (pp. 137–179) considers the whole set of the properties of the alloys: hardness; internal stresses; electrical, magnetic, and optical properties; wear resistance; solderability; corrosion resistance; and catalytic activity. The application fields of electrolytic alloys are briefly discussed. Chapter 5 (pp. 180–243) is devoted to various kinds of thermal treatment of electrolytic deposits. Chapter 6 (pp. 244–286) presents evidence concerning amorphous alloys: amorphization conditions, structure, thermal stability, and properties.

The monograph contains a total of 281 references, and many of these, to publications by the authors themselves. A rather positive impression is created by the section in which the structure of the alloys and its formation are considered (Chapter 3). Chapter 1 is written too concisely, the physical methods of investigation could be described in more detail. There are debatable critical remarks concerning the description of the thermodynamic characteristics of alloying processes.

The monograph is intended for researchers, engineers, and technicians working in the field of deposition of coatings with special properties and corrosion protection of metals; it can also be of use for post- and undergraduate students specialized in the corresponding branches of chemical technology and metallurgy.

A. G. Morachevskii

1070-4272/04/7707-1213 © 2004 MAIK "Nauka/Interperiodica"

Russian Journal of Applied Chemistry, Vol. 77, No. 8, 2004, pp. 1215–1218. Translated from Zhurnal Prikladnoi Khimii, Vol. 77, No. 8, 2004, pp. 1233–1236.

INORGANIC SYNTHESIS AND INDUSTRIAL INORGANIC CHEMISTRY

A Study of the Kinetics of Conversion of Natural Langbeinit Mixed with Carnallite

I. Yu. Kostiv and O. M. Khatsevich

Precarpathian Vasyl Stefanyk University, Ivano-Frankivsk, Ukraine
State Research Institute of Mineral-Salt Technology, Kalush, Ukraine

Received March 22, 2004

Abstract—The dependence of the process of conversion of natural langbeinite with carnallite in the presence of a carnallite solution on the process duration, temperature, and particle size was studied. The mechanism and kinetics of the process were analyzed.

The most valuable component of Precarpathian polymineral potassium ores is a sulfate mineral, langbeinite, whose content in the ore may be as high as 20–30%. In the mineral-salt technology of ore processing, used in practice, only 20–23% of the difficultly soluble langbeinite passes into solution, with the rest remaining in the halitelangbeinite residue, which is the waste. Because of the low solubility of langbeinite, the recovery of K^+ into fertilizer does not exceed 60%, and the content of chloride ions in the finished product is not higher than 25% [1]. Therefore, a study of how the solubility of langbeinite components can be raised is a matter of current interest.

A method for processing of langbeinite ores is known. This method consists in washing-out with water of well-soluble salts to give a langbeinite concentrate. Drying of the concentrate yields a compound that contains 18 wt % MgO, 22 wt % K_2O, and ≤2.5 wt % Cl^- [2]. Polymineral ores are also processed using electrostatic separation [3]. However, these methods are not applicable to processing of Precarpathian polymineral ores because of the high content of readily soluble potassium–magnesium minerals kainite, sylvine (20–30%), and clayey admixtures (up to 20%) [2].

Also known is a method for processing of polymineral ores with preliminary conversion of langbeinite into schoenite [4] by the reaction

$$K_2SO_4 \cdot 2MgSO_4 + 13H_2O \rightleftarrows K_2SO_4 \cdot MgSO_4 \cdot 6H_2O + MgSO_4 \cdot 7H_2O. \quad (1)$$

The recovery of components of the polymineral ore into fertilizer is 80–82%. This technique cannot provide a >85% conversion of langbeinite into solution, because an increase in the concentration of the reaction product, $MgSO_4$, in the liquid phase leads to a shift of the point corresponding to the solution composition into the region of langbeinite crystallization. Kainite present in the polymineral potassium ore also enters into the conversion reaction to give schoenite [3]:

$$2[KCl \cdot MgSO_4 \cdot 3H_2O] \rightleftarrows K_2SO_4 \cdot MgSO_4 \cdot 6H_2O + MgCl_2. \quad (2)$$

The forming $MgCl_2$ hinders the course of reaction (2). The negative effect of kainite on the conversion of langbeinite into schoenite was noted in [5]. In addition, conversion of langbeinite into schoenite requires a large amount of water, which is bound into crystal hydrates, and soluble salts crystallize entrapping particles of the ore. In dissolution of a schoenite-containing ore, there occurs crystallization of secondary leonite, which gives no way of achieving a high saturation of the solution with sulfate potassium–magnesium salts.

Also, a method for conversion of langbeinite with a magnesium chloride solution into kainite has been developed [1]. The process occurs in a suspension and can be represented as

$$K_2SO_4 \cdot 2MgSO_4 + 9H_2O + MgCl_2 + KCl \rightleftarrows 3[KCl \cdot MgSO_4 \cdot 3H_2O]. \quad (3)$$

The reaction of $MgCl_2$ with langbeinite terminates already at its concentration in solution equal to 16 wt %. The figurative point of the system shifts from the field of kainite into the field of crystallization of langbeinite, where the conversion terminates.

1070-4272/04/7708-1215 © 2004 MAIK "Nauka/Interperiodica"

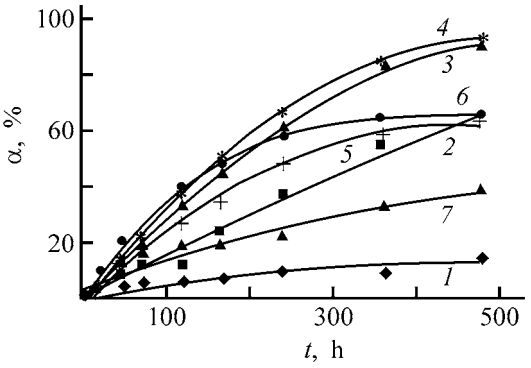

Fig. 1. Langbeinite conversion α vs. the process duration *t*. *T* (°C): (*1*) 20, (*2*) 30, (*3*) 40, (*4*) 50, (*5*) 60, (*6*) 70, and (*7*) 80.

A complete conversion of langbeinite into kainite requires an excess amount of $MgCl_2$. In the subsequent dissolution of the converted ore, the excess $MgCl_2$ makes lower the dissolution rate and solubility of potassium–magnesium minerals.

A method for conversion of langbeinite into kainite with the use of carnalite is suggested. The process can be described by the equation

$$K_2SO_4 \cdot 2MgSO_4 + 3H_2O + KCl \cdot MgCl_2 \cdot 6H_2O \rightleftarrows 3[KCl \cdot MgSO_4 \cdot 3H_2O]. \quad (4)$$

The process occurs at the interface between solid phases and the minimum amount of a liquid phase; $MgCl_2$ passes from carnallite crystals into the liquid phase on their surface and, simultaneously, enters into the reaction with langbeinite. A limited amount of the liquid phase acts as a transport medium for transfer of $MgCl_2$ and as a source of water necessary for the reaction to occur. By the end of the process, the reaction mass becomes nearly dry, and, consequently, the remaining amount of free $MgCl_2$ is small. Therefore, the dissolution of potassium–magnesium minerals is not decelerated in the stage of ore dissolution.

EXPERIMENTAL

The influence exerted by various factors on the conversion of langbeinite mixed with carnallite into kainite was studied under laboratory conditions. A langbeinite rock from the presently used potassium mine was crushed to particle size of less than 3 mm, washed to remove admixtures of soluble salts with a plentiful of tap water under stirring, and filtered. The remaining intercrystallite moisture was removed with acetone. The washed langbeinite was dried at 50°C for three days and the 1–3-mm fraction was separated by sieving on wire sieves. The resulting product had the following composition (wt %): K^+ 19.12, Mg^{2+} 11.44, Ca^{2+} 0.16, Na^+ 0.05, Cl^- 0.12, SO_4^{2-} 69.01 (or 97.3% langbeinite, 0.1 anhydrite, 0.9 polyhalite, 0.12 halite, 0.08 sylvine, 1.4 arcanite).

Carnallite was prepared from chloride–magnesium solutions formed in processing of polymineral potassium ores by synthesis with crystalline KCl. The composition of the solid phase of carnallite was as follows (wt %): K^+ 13.04, Mg^{2+} 8.15, Ca^{2+} 0.16, Na^+ 1.5, Cl^- 38.28, SO_4^{2-} 0.2, H_2O 38.67. Also, a carnallite solution obtained by filtering-off carnallite was used (wt %): K^+ 0.33, Mg^{2+} 7.52, Ca^{2+} 0.45, Na^+ 0.26, Cl^- 23.42, SO_4^{2-} 0.02, H_2O 68.0.

The prepared weighed portions of langbeinite, carnallite, and carnallite solution were kept separately in thermostats for 24 h for heating to the temperature of the experiment. Then they were mixed together and a sample was taken for a blank run. The langbeinite samples and the carnallite solution contain soluble sulfate impurities, which leads to experimental errors.

The reaction mixtures were kept under isothermal conditions for 480 h, with agitation and sampling at regular intervals. Samples of mass 100 g were dissolved in 400 g of distilled water at 20 ± 1.0°C in the course of 10 min in a thermostated reactor. The resulting suspension was filtered on a preliminarily weighed Buchner funnel under reduced pressure. The filtrate was weighed and analyzed for the content of K^+ and Na^+ by flame photometry, Mg^{2+} and Ca^{2+} by complexonometry, Cl^- by mercurimetry, and SO_4^{2-} by gravimetry [6]. The conversion of langbeinite, α, was calculated by the formula

$$\alpha = [m(SO_4^{2-})_{sol} - m_0(SO_4^{2-})]/[m(SO_4^{2-})_{lang} - m_0(SO_4^{2-})],$$

where $m(SO_4^{2-})_{sol}$ is the mass of sulfate ions in the resulting solution; $m_0(SO_4^{2-})$, the mass of sulfate ions in the solution from the blank run; and $m(SO_4^{2-})_{lang}$, the mass of sulfate ions in the weighed portion of the ore.

Also, the effect of temperature on the conversion process was studied. The conversion of langbeinite into kainite is accompanied by heat release and warming-up of the reaction mass. In addition, the carnallite used for the conversion is formed in evaporation of solutions obtained in ore processing and has a temperature of 40–70°C. Therefore, the temperature of the conversion process can be varied.

The results of the study show (Fig. 1) that the reaction is the slowest at 20°C, with the conversion in

20 days being as low as 15%. The conversion is also low at 80°C, which can be attributed to stabilization of langbeinite at elevated temperatures. At 40°C, the conversion in 20 days is 89.7%. The maximum conversion of langbeinite into kainite is achieved at 50°C (93% in 20 days).

The conversion of langbeinite into kainite is a topochemical reaction, whose kinetics is commonly studied using the Erofeev equations [7, 8]

$$\alpha = 1 - \exp(-kt^n), \quad (5)$$

where α is the conversion; k, the reaction rate constant; t, time; and n, the reaction order.

The correctness of choosing Eq. (5) for describing the kinetics of langbeinite conversion into kainite is confirmed by the plot of the dependence $\alpha = f(t)$ in the coordinates $[1 - (1 - \alpha)^{1/3}]$–t (Fig. 2). The kinetic dependences of the conversion α on the process duration t are plotted as straight lines in these coordinates, which indicates that the zone of the conversion reaction is close to the surface of spherical langbeinite particles. A rearrangement of Eq. (5) yielded

$$n\log t = \log(1/k) + \log[-\ln(1 - \alpha)]. \quad (6)$$

Figure 3 shows the dependence of the conversion of langbeinite into kainite, which is linear when plotted in the coordinates $\log[-\ln(1 - \alpha)]$–$\log t$. The rate constant of the reaction can be determined graphically from the condition

$$k = -\ln(1 - \alpha_{t=1}). \quad (7)$$

The results obtained are listed in the table.

The plot of the rate constant of the reaction of langbeinite conversion into kainite against temperature in the coordinates $1/T$–$\ln k$ (Fig. 4) was used to determine the activation energy, which was equal to 39.08 kJ mol^{-1} in the temperature range 40–70°C. This means that the heterogeneous reaction is governed both by diffusion and by the chemical process at the interface. The activation energy of langbeinite conversion at 20–40°C is 53.2 kJ mol^{-1}, which corresponds to the kinetic region of the heterogeneous process. The temperature at which the conversion rate is the highest was determined graphically (Fig. 4) to be 39.5°C.

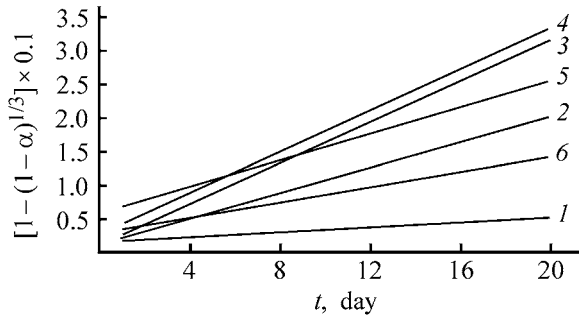

Fig. 2. Graphical verification of the occurrence of langbeinite conversion into kainite by the mechanism of a contracting sphere. (*t*) Time. *T* (°S): (*1*) 20, (*2*) 30, (*3*) 40, (*4*) 50, (*5*) 70, and (*6*) 80.

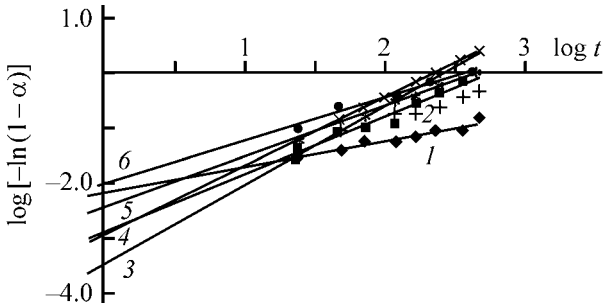

Fig. 3. Graphical determination of the reaction rate constants by the Erofeev equation. *T* (°C): (*1*) 20, (*2*) 30, (*3*) 40, (*4*) 50, (*5*) 60, and (*6*) 70.

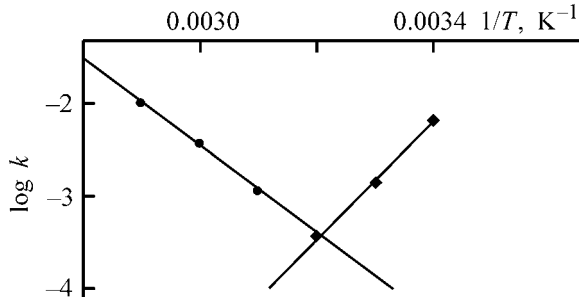

Fig. 4. Rate constants *k* vs. temperature *T*.

Equation (6) was used to find the reaction order *n*: 1.418 at 40°C, 1.25 at 50°C, and 0.65 at 80°C, which

Reaction rate constants at different temperatures

T, K	log *k*	*k*	*T*, K	log *k*	*k*
293	–2.17	0.0068	323	–2.76	0.0017
303	–2.57	0.0027	333	–2.39	0.0041
313	–3.48	0.0003	343	–1.72	0.0191
			353	–2.08	0.0083

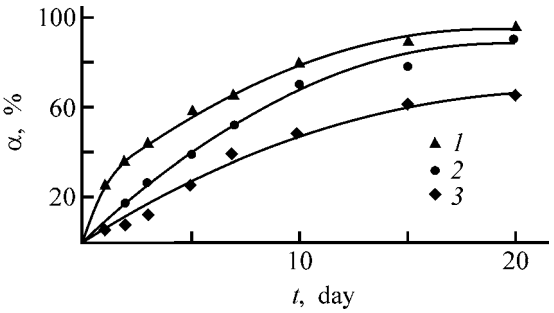

Fig. 5. Conversion α vs. the process duration for different langbeinite fractions. Fraction (mm): (*1*) 0.5–1, (*2*) 1–3, and (*3*) 3–5.

points to a complex nature of the processes accompanied by formation of intermediate compounds.

The conversion of langbeinite mixed with carnallite into kainite in a carnallite solution is a heterogeneous process whose kinetics is affected by the area of the phase boundary. Therefore, the influence exerted by the particle size of langbeinite on the conversion was studied at 50°C with 3–5-, 1–3-, and 0.5–1-mm langbeinite fractions. The results obtained are shown in Fig. 5. It can be seen that the conversion in 10 days is 48.9% for the 3–5-mm fraction and 70.4% for the 1–3-mm fraction. For the 0.5–1-mm fraction, the conversion in 10 days is 79.6%. Consequently, the smaller the langbeinite particles, the faster and the more complete its conversion into kainite. For the 0.5–1-mm fraction, a 96.8% conversion was achieved in 20 days.

The data obtained can be used in developing a technique for processing of polymineral potassium ores. The conversion of langbeinite mixed with carnallite into kainite in a carnallite solution makes it possible to raise the recovery of K^+ into a fertilizer to 85% and diminish the content of Cl^- ions in the fertilizer to 3%.

This method can be applied not only to Precarpathian polymineral potassium ores, but also to langbeinite ores from the United States by adding KCl, which forms with $MgCl_2$, in the course of solution evaporation, carnallite necessary for the reaction of conversion with langbeinite.

CONCLUSIONS

(1) The highest conversion of langbeinite into kainite in the temperature range 20–70°C is achieved at 50°C, and the fastest reaction rate, at 39.5°C.

(2) The activation energy is 53.2 kJ mol^{-1} in the temperature range 20–39.5°C, which points to the kinetic region, and 39.08 kJ mol^{-1} at 40–70°C, which corresponds to the transition region of the heterogeneous process.

(3) The reaction order *n* is 1.41 at 40°C, 1.25 at 50°C, and 0.65 at 80°C. As the langbeinite particles become smaller, the conversion grows and exceeds 96.8% in 20 days at a particle size of less than 1–0.5 mm.

REFERENCES

1. Mazur, T.V., Kostiv, I.Yu., and Yavorskii, V.T., *Zh. Prikl. Khim.*, 2001, vol. 74, no. 5, pp. 705–708.
2. Grabovenko, V.A., *Proizvodstvo beskhlornykh kaliinykh udobrenii* (Manufacture of Chlorine-free Potassium Fertilizers), Leningrad: Khimiya, 1980.
3. Kashkarov, O.D. and Sokolov, I.D., *Tekhnologiya kaliinykh udobrenii* (Technology of Potassium Fertilizers), Leningrad: Khimiya, 1987.
4. Grebenyuk, D.V., Processing of Langbeinite Ores To Obtain Chlorine-free Potassium Fertilizers, *Cand. Sci. Dissertation*, Minsk, 1986.
5. Grebenyuk, V.D., Opanasik, N.P., Podobailo, N.N., *et al.*, *Zh. Prikl. Khim.*, 1985, vol. 58, no. 9, pp. 2118–2120.
6. *Metody analiza rassolov i solei* (Methods for Analysis of Brines and Salts), Morachevskii, Yu.V. and Petrova, E.M., Eds., Moscow: Khimiya, 1964.
7. Pozin, M.E. and Zinyuk, R.Yu., *Fiziko-khimicheskie osnovy neorganicheskoi tekhnologii* (Physicochemical Foundations of Inorganic Technology), Leningrad: Khimiya, 1989.
8. Stromberg, A.G. and Semchenko, D.P., *Fizicheskaya khimiya* (Physical Chemistry), Moscow: Vysshaya Shkola, 1988.

Russian Journal of Applied Chemistry, Vol. 77, No. 8, 2004, pp. 1219–1222. Translated from Zhurnal Prikladnoi Khimii, Vol. 77, No. 8, 2004, pp. 1237–1240.

INORGANIC SYNTHESIS AND INDUSTRIAL INORGANIC CHEMISTRY

Distribution of Natural Radionuclides

N. A. Mel'nik, E. P. Lokshin, and T. A. Sedneva

Tananaev Institute of Chemistry and Technology of Rare Elements and Mineral Raw Materials, Kola Scientific Center, Russian Academy of Sciences, Apatity, Russia

Received July 1, 2003; in final form, February 2004

Abstract—The distribution of natural nuclides and of the effective specific radioactivity in processing of the sphene concentrate was studied.

The total specific radioactivity ΣA of the sphene concentrate obtained in dressing of Khibiny ores varies within the range 10–15 kBq kg^{-1} [1]. In conformity with the regulations concerning the radiation safety [2–4], the content of natural radionuclides and the effective specific radioactivity A_{eff} (Bq kg^{-1}) in the starting concentrate and in the products obtained from this concentrate in three main process stages [5] was determined in developing a technology for processing of the sphene concentrate: titanium-silica product, nitric acid solution of $Ca(NO_3)_2$, meta-titanic acid $TiO_2 \cdot nH_2O$, hydrolytic H_2SO_4, silica cake, $CaSO_4 \cdot 2H_2O$, and recovered HNO_3.

EXPERIMENTAL

The study was carried out on the certified equipment of an accredited laboratory for radiation monitoring: Progress-AG gamma spectrometer with a 63 × 63 mm NaJ/Tl scintillation detector and a Sputnik alpha-beta radiometer. Freshly prepared technological products (see Scheme), kept for 1–45 days for restoration of the radioactive equilibrium in the uranium-238 and thorium-232 series, were analyzed by two methods under different conditions. It was necessary to use different methods because of the possible disturbance of the radioactive equilibrium in radioactive series in chemical treatment of the concentrate.

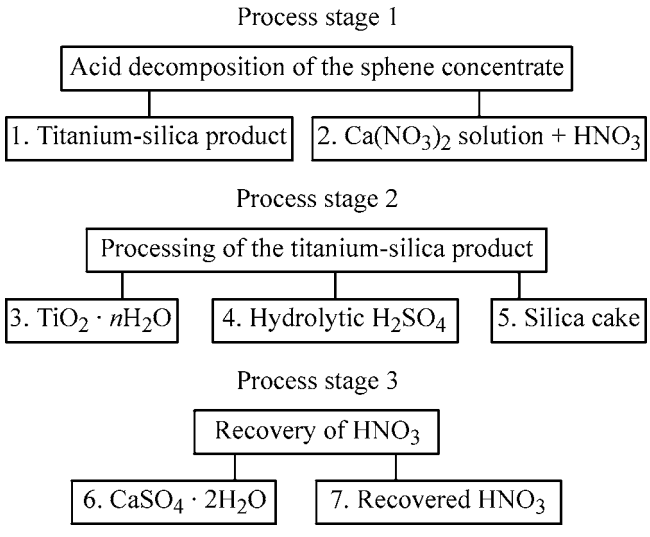

Scheme of the main process stages in processing of the sphene concentrate.

Gamma spectrometry was applied to analysis of solid and liquid products. The measurements were performed in the "Marinelli" (volume 1 l) and "Petri dish" (80 × 35 and 90 × 90 mm) configurations at an exposure duration of 1800–5400 s. Radiometry was used to analyze powder samples with weighed portions of 3–15 g and exposure duration of 3 × 600 s.

The significance of the results was confirmed by using control and reference sources of ionizing radiation (OSGI, ^{90}Sr, ^{238}Pu), a reference source of natural radionuclides (bulk measure of activity), State standard samples SG-1, SVT-16, OSO-6, and other references certified for the content of uranium and thorium in the range 2×10^{-4}–9×10^{-1} wt % (with varied U/Th ratio and chemical composition). Control sources were used to calibrate the gamma spectrometer in energy and to verify the invariability of parameters of the spectrometric installation and radiometers. The determination error for a confidence probability of 0.95 was 19–25 rel. % for ^{238}U and ^{226}Ra and 15–18 rel. % for ^{232}Th. A good agreement between the results obtained by different methods was observed. The precision and sensitivity of analysis ensured that the radionuclides could be determined at the level required by NRB-99 (Radiation Safety Standard) and GOST (State Standard) 30 108–94.

1070-4272/04/7708-1219 © 2004 MAIK "Nauka/Interperiodica"

Table 1. Radiation-hygienic characteristics of the main technological products

Product	Specific radioactivity of indicated radionuclides, Bq kg^{-1}			A_{eff}, Bq kg^{-1}	Activity, Bq kg^{-1}			α/β
	^{40}K	^{226}Ra	^{232}Th		α-	β-	$\Sigma A(\alpha, \beta, \gamma)$	
Sphene concentrate	<450	190	510	880	4070	5010	9500	0.8
Titanium-silica product	<290	86	246	410	2240	2500	5030	0.9
Silica cake	<310	90	148	290	850	1850	3010	0.5
Metatitanic acid	<270	80	94	105	1760	610	2640	2.9
Gypsum	160	80	86	210	–	–	–	–

Table 2. Distribution of uranium-238 and thorium-232 in processing of the sphene concentrate

Product	Amount, kg	Uranium-238		Q, %	Thorium-232		Q, %	Th/U
		wt %	g (g l^{-1})*		wt %	g (g l^{-1})*		
Process stage 1								
Sphene concentrate	1.0	0.0015	0.015	100	0.0126	0.126	100	8.4
Titanium-silica product	0.8	0.0007	0.0056	37.3	0.0600	0.0480	38.1	68.6
$Ca(NO_3)_2$ solution + HNO_3	2.1	0.0045	0.0094	62.7	0.0400	0.0840	66.7	9.0
Total				100.0			104.8	
Unbalance				0			+4.8	
Process stage 2								
Metatitanic acid	0.42	0.0006	0.0025	16.8	0.0023	0.0097	7.7	3.8
Hydrolytic H_2SO_4	0.6	0.0015	0.0009	6.0	0.0246	0.0148	11.7	16.4
Silica cake	0.4	0.0007	0.0028	18.7	0.0036	0.0144	11.4	5.1
Total				41.5			30.8	
Unbalance				+4.2			–7.3	
Process stage 3								
Gypsum	0.5	0.0006	0.0030	20.0	0.0021	0.0105	8.3	3.4
Recovered HNO_3	2 l	0.0008	0.0032	21.4	0.0371	0.0742	58.9	46.4
Total				41.4			67.2	
Unbalance				–21.3			+0.5	
Sum total for the scheme				82.7			104.3	
Unbalance				–17.3			+4.3	

* For liquid products.

Table 1 lists the average results of gamma-spectrometric and radiometric analyses of the main technological products.

The distribution Q of the radionuclides relative to their content in the sphene concentrate (taken to be 100%) is given in Table 2 for uranium and thorium and in Table 3 for radium and effective specific activity.

As can be seen from Table 2, the radioactivity of the sphene concentrate under study is due to

Table 3. Distribution of radium-226 and A_{eff} for the scheme

Product	Amount, kg	Radium-226		Q, %	A_{eff}		Q, %
		Bq kg^{-1}	Bq		Bq kg^{-1}	Bq	
Process stage 1							
Sphene concentrate	1.0	190	190	100	880	880	100
Titanium-silica product	0.8	86	68.8	36.2	410	328.0	37.3
$Ca(NO_3)_2$ solution + HNO_3	2.1	43	116.5	61.3	210	564.5	64.1
Total				97.5			101.4
Unbalance				–2.5			+1.4
Process stage 2							
Metatitanic acid	0.42	77	33.34	17.0	105	44.1	5.0
Hydrolytic H_2SO_4	0.6	15	10.95	5.8	126	92.0	10.5
Silica cake	0.4	89	35.6	18.7	290	116.0	13.2
Total				41.5			25.4
Unbalance				+5.3			–11.9
Process stage 3							
Gypsum	0.5	80	40	38.6	210	105.0	11.9
Recovered HNO_3	2.0	8.3	19.42	10.2	178	416.5	47.3
Total				48.8			58.2
Unbalance				–12.5			–5.9
Sum total for the scheme				90.3			83.6
Unbalance				–9.7			–16.4

0.013 wt % ^{232}Th and 0.002 wt % ^{238}U. The experiments performed demonstrated that the radioactive equilibrium in the processing products is disturbed only slightly. The disturbed equilibrium, especially that in liquid products, was restored during the time of the experiments, specified above, and was taken into account when calculating the content of uranium and thorium.

The ratios of the amounts of alpha- and beta-emitting substances (α/β) in the final products are close to those in sphene. In the intermediate titanium-silica product, α/β increases to 2.9 because of the redistribution of radionuclides (Th/U = 68.6).

In leaching of the sphene concentrate with a HNO_3 solution, with addition of fluorine compounds, most part of the radioactivity (up to 65–70%, process stage 1) passes into the nitric acid solution, which contains 0.06 g l^{-1} of ^{232}Th and 0.007 g l^{-1} of ^{238}U (Tables 2, 3). In process stage 1, the distribution of ^{238}U, ^{226}Ra, and ^{232}Th among the solid and liquid phases is the same and approximately equal to 1 : 2.

In separating titanium from silicon in process stage 2, there occurs partial separation of the radionuclides. Uranium-238, radium-226, and thorium-232 are virtually evenly distributed among TiO_2 and SiO_2, with approximately 15% of these radionuclides remaining in the filtrate. A greater amount of uranium and radium, compared with that of thorium, coprecipitates with TiO_2. SiO_2 contains the largest amount of radioactivity: 35% relative to that in the titanium-silica precipitate. The amount of thorium in the filtrate after hydrolysis is 46.5% relative to that in TiO_2 + SiO_2, which is 2.8 times the amount of uranium and radium.

In precipitation of $CaSO_4$ in process stage 3, 84% of radium and 15% of thorium passes into solution. Up to 60–88% of thorium and 16% of uranium and radium [relative to the intermediate product, $Ca(NO_3)_2$

solution] passes into the filtrate containing nitrates of rare-earth elements. Thus, partial separation of radionuclides occurs in this stage, too.

On the whole, the unbalance of radioactivity in the process stages and in the entire scheme is within the errors of the methods used.

It follows from the results obtained that the effective specific activity of the sphene concentrate, $A_{eff} = 880 \pm 140$ Bq kg^{-1}, i.e., the concentrate belongs to Class-II materials with increased content of natural radionuclides ($0.74 < A_{eff} < 1.5$ Bq kg^{-1}) [2].

The processing of the concentrate by the technique developed yields products, both intermediate and final, whose total specific radioactivity is a factor of 1.6–3.6 lower than the initial radioactivity; no concentration of radioactivity in a separate product occurs. The effective specific activity of natural radionuclides in the titanium-silica product, silica cake, gypsum, and metatitanic acid is within 50–420 Bq kg^{-1}. According to NRB-99 and OSPORB-99 (Basic Sanitary Regulations Concerning Radiation Safety), working with the products under study is radiation-safe and the products are not radioactive. The effective specific activity of TiO_2 and SiO_2, as well as that of $CaSO_4 \cdot 2H_2O$, is less than 370 Bq kg^{-1}. According to NRB-99 [2], these products belong to Class-I building materials and can be used in manufacture of building materials without any radiation-related restrictions.

The filtrate obtained after separation of TiO_2, which contains 300 g l^{-1} of H_2SO_4, is used, upon an approximately 3-fold dilution, for chemical purification of the sphene concentrate and after that can be discharged into a tailing dump [6]. Recovered HNO_3 is recycled into the stage of decomposition of further batches of the sphene concentrate.

CONCLUSIONS

(1) In radioecological studies, the distribution of natural radionuclides in products formed in processing of the sphene concentrate was examined and it was shown that the total specific radioactivity of both intermediate and final products is a factor of 1.6–3.6 lower than its initial value and no concentration of radioactivity in a separate product occurs.

(2) It was established that the effective specific activity of natural radionuclides in the final products of processing: metatitanic acid, gypsum, and silica cake, is less than 370 Bq kg^{-1}. These products belong to Class-I building materials and can be used without any radiation-related restrictions.

ACKNOWLEDGMENTS

The study was financially supported by the "Leading Scientific Schools" Program (project no. NSh-1616-2003.3).

REFERENCES

1. Mel'nik, N.A., Radiation-Safe Use of Wastes from the Kola Mining Complex in Manufacture of Buiolding Materials, *Cand. Sci. Dissertation*, Apatity, 2001.
2. *Normy radiatsionnoi bezopasnosti (NRB-99): Sanitarnye priavila SP 2.6.1.758–99* [Radiation Safety Standard (NRB-99): Sanitary Regulations SP 2.6.1.758–99], Moscow: Minzdrav Rossii, 1999.
3. *Obrashchenie s mineral'nym syr'em i materialami s povyshennym soderzhaniem prirodnykh radionuklidov: Sanitarnye pravila SP 2.6.1.798–99* (Working with Mineral Raw Materials and Substances with Increased Content of Natural Radionuclides: Sanitary Regulations 2.6.1.798–99), Moscow: Minzdrav Rossii, 2000.
4. *Osnovnye sanitarnye pravila obespecheniya radiatsionnoi bezopasnosti (OSPORB–99): 2.6.1. Ioniziruyushchee izluchenie, radiatsionnaya bezopasnost': SP 2.6.1.799–99* [Basic Sanitary Regulations Concerning the Radiation Safety (OSPORB–99): 2.6.1, Ionizing Radiation, Radiation Safety: SP 2.6.1.799–99], Moscow: Minzdrav Rossii, 2000.
5. RF Patent 2 196 736.
6. *Sanitarnye pravila obrashcheniya s radioaktivnymi otkhodami (SPORO–2002): SP 2.6.6.1168–02* [Sanitary Regulations Concerning Working with Radioactive Waste (SPORO–2002): SP 2.6.6.1168–02], Moscow: Fed. Tsentr Gossanepidnadzora Minzdrava Rossii, 2003.

Russian Journal of Applied Chemistry, Vol. 77, No. 8, 2004, pp. 1223–1226. Translated from Zhurnal Prikladnoi Khimii, Vol. 77, No. 8, 2004, pp. 1241–1244.

INORGANIC SYNTHESIS AND INDUSTRIAL INORGANIC CHEMISTRY

Methods for $MgSiN_2$ Synthesis

F. F. Grekov and B. V. Chernovets

State Polytechnic University, St. Petersburg, Russia

Received June 8, 2004

Abstract—Direct synthesis of $MgSiN_2$ from simple substances was performed in a flow-through system. The sequence of transformations that occur on heating mixed magnesium and silicon powders in flow of nitrogen was determined by X-ray phase analysis.

Owing to the increasing interest in semiconductor nitrides, works on synthesis and study of $A^2B^4N_2$ compounds (A^2, Mg or Zn; B^4, Si or Ge) have been resumed recently [1–4]. These compounds inherit the structure of a double prototype compound A^3B^5 (wurtzite or a derivative orthorhombic structure) and, as established by approximate calculations and experiments, must have electronic and optical characteristics closely similar to those of double nitrides.

Aluminum nitride can not only be used as a wide-bandgap semiconductor, but is also regarded now as one of the best materials for substrates of integrated circuits. It has a higher thermal conductivity than the traditionally used aluminum oxide, which makes it possible to raise substantially the degree of integration and speed of response of integrated circuits. Similar applications are possible for a direct analogue of aluminum nitride, $MgSiN_2$.

The best known methods for synthesis of $MgSiN_2$ in the form of a powder are based on sintering of mixtures of double nitrides or on nitration of magnesium silicide [4]. The necessity for a preliminary synthesis of double half-products makes process more complex and is a potential source of impurities. This is especially true for the insufficiently chemically stable magnesium nitride.

This study was aimed to carry out a direct synthesis of $MgSiN_2$ from simple substances: Mg, Si, and N_2. The second goal was to perform a gas-phase synthesis of $MgSiN_2$, using volatile Si compounds as a source and relying upon the volatility of Mg.

The direct synthesis was performed in a tubular porcelain reactor connected to a gas-distributing system in such a way that a rarefaction, a flow of N_2 or Ar, or a static atmosphere of N_2 could be obtained in it. We used containers made of sintered corundum and inserts for collection of sublimates. The heating was performed in a resistance furnace. The temperature was monitored and controlled using platinum to platinum–rhodium thermocouples. The flow rates of high-purity gases {nitrogen [GOST (State Standard) 9293–74] and argon (GOST 101 157–79)} was dosed and monitored using valve floating rotameters.

The starting mixture was prepared by a thorough dry mixing of powders obtained by mechanical grinding of high-purity ingots of Mg (GOST 6001–79) and Si (semiconductor-grade purity, GOST 19 658–81). The particle size was 100–200 μm for the magnesium powder and <10 μm for the silicon powder.

The mass of the starting substances, reaction products, and, in some cases, sublimates was measured on an analytical balance. X-ray diffraction patterns were obtained with Fe_{K_α} radiation at angles $2\theta = 20$–$120°C$. The processing of the results relied upon the PDF-2 database [5].

The Mg : Si ratio in the starting mixture was varied within the range 1–1.8 to compensate for the unavoidable loss of Mg in the flow-through system. The process was performed with an excess of N_2 delivered from an external source, with the temperature gradually elevated. To reveal the sequence of the occurring transformations, the experiment was interrupted at one or another stage, the products were cooled in a flow of N_2 and subjected to analysis.

The results of the experiments are presented in Fig. 1. The phase composition is shown in the form of a diagram constructed on the basis the results of a qualitative XPA of the products formed in the course

1070-4272/04/7708-1223 © 2004 MAIK "Nauka/Interperiodica"

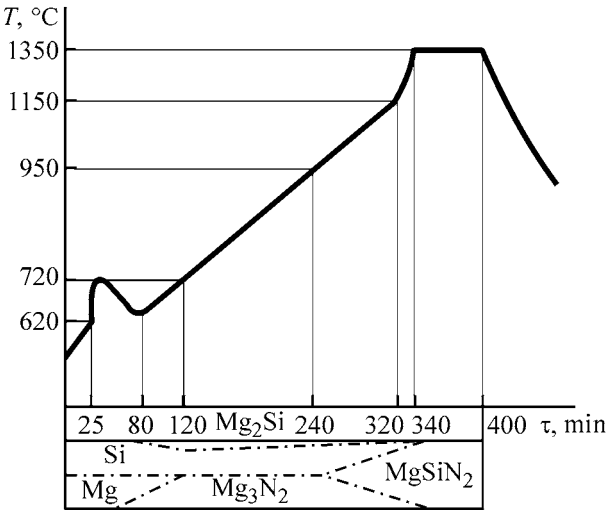

Fig. 1. Direct synthesis of $MgSiN_2$ and variation of the phase composition of the mixture in the course of the reaction. (T) Temperature and (τ) time.

of the experiments interrupted at different stages of synthesis. When constructing the diagram, points of appearance or disappearance of the reflections of the corresponding phase were used. Connecting these points, we obtained the conditional boundaries of phase coexistence at different stages of the process, which gives notion of the most probable scheme of the transformations resulting in the synthesis of a single-phase product.

After a temperature of 620°C is reached, indications of a reaction appear. Magnesium starts to be transformed into nitride:

$$3Mg + N_2 = Mg_3N_2,\ \Delta H^0_{298} = -461.8\ \text{kJ mol}^{-1}.$$

Simultaneously, a minor part of magnesium is bound with silicon into a silicide:

$$2Mg + Si = Mg_2Si,\ \Delta H^0_{298} = -79.5\ \text{kJ mol}^{-1}.$$

The first reaction is strongly exothermic, and for a certain time the synthesis proceeds in the self-ignition mode, which is manifested, in particular, in a dramatic increase in the N_2 absorption at the inlet of the reactor, at its outlet closed and the heater switched off. During this period of time, local warming-up leads to difficultly controllable loss of Mg, indicated by the appearance of sublimates. After this stage is complete, i.e., intense absorption of N_2 stops, the amount of free Mg in the reaction mixture is insignificant.

On further heating, $MgSiN_2$ starts to be formed, probably, with partly dissociating Mg_3N_2 involved. The appearance of $MgSiN_2$ was observed at those same temperatures (>900°C) at which the sublimation of Mg_3N_2 in a flow-through reactor was intensified. Since no indications of silicon nitration were observed, the most probable schemes of the final transformations do not involve Si_3N_4 and can be presumably represented as

$$Mg_3N_2 + Si = MgSiN_2 + 2Mg\uparrow,$$
$$Mg_2Si + N_2 = MgSiN_2 + Mg\uparrow.$$

The equations of these reactions include magnesium compounds, which are unstable with respect to dissociation at the experimental temperatures, on the left-hand side, and a volatile product (Mg vapor), which facilitates both the thermodynamic and kinetic aspects of the process, on the right-hand side.

The final annealing at about 1350°C ensures the completion of the reaction and improves the crystallinity of the product. The excess amount of Mg condenses in the cool part of the reactor in the form of Mg_3N_2.

The material obtained is a light gray powder, which is, according to X-ray analysis, a single-phase $MgSiN_2$ [6].

The reaction yield by silicon approaches 100%. In the preliminary experiments, compaction of the powder synthesized under RF heating in a mixture N_2–H_2 produced compact ceramic samples. However, the sintering process was sufficiently successful only with oxide additives introduced.

The possibility of codeposition of $MgSiN_2$ from the gas phase is not reflected in the literature, although this process has been performed previously in a chloride system for an analogue of this compound, $ZnGeN_2$ [7]. The fact that $MgCl_2$ has a relatively low volatility (T_{boil} = 1420°C) and readily undergoes hydrolysis gives no way of applying the above method directly to the system studied.

To make control of the process simpler and to diminish the possible contamination, the following reaction of hydride synthesis was chosen as the main reaction

$$Mg + SiH_4 + 2NH_3 = MgSiN_2 + 5H_2.$$

The involvement of two metastable hydrides in the process ensures a complete irreversibility of the deposition of the ternary nitride. At the same time, there appears a risk of development of a side reaction, pyrolysis of silane. Magnesium (T_{boil} = 1120°C)

is considerably more volatile than its chloride $MgCl_2$, but certain difficulties are caused by the corrosiveness of the Mg vapor with respect to the container materials.

We used an axially symmetric vertical reactor with a graphite reactor unit (Fig. 2). Graphite was covered with a Si_3N_4 layer from the inside. A uniaxial feeding of the reagents and the upper, with respect to the gas-flow inlet, position of the substrate were used. The position of the substrate was adjusted in the vertical direction. The design of the reactor unit ensured the minimum time of contact between SiH_4 and heated surfaces to prevent its decomposition. The Mg vaporizer was fabricated in the form of an annular cavity connected with the main channel via effusion orifices. Within a vaporizer of this type, the Mg vapor pressure is mainly temperature-controlled and the rate of vapor outflow from it is rather stable. As the carrier gas served Ar, the silane–argon mixture or NH_3 was fed through separate pipes. The sealing was ensured by ground-quartz joints and an upper annular ring-shaped seal. A two-zone resistance furnace allowed independent variation, within certain limits, of the temperatures of the substrate and Mg vaporizer.

Magnesium with less than 0.08 wt % impurities, a silane–argon mixture containing 96 vol % high-purity Ar and 4 vol % SiH_4, and NH_3 with a content of H_2O vapor less than 0.04 vol % were used as starting substances. The consumption of Mg was controlled by varying the temperature within the zone of its evaporation and monitored by the change in its mass during the experiment. The partial pressures in the deposition zone were calculated from the molar consumption of the reagents.

The deposition was done onto polished leucosapphire substrates etched in a mixture of H_2SO_4 and H_3PO_4. The duration of the experiment was about 60 min, and the deposition rate did not exceed 3 $\mu m\ h^{-1}$.

All the experiments were performed at a deposition temperature of 1050°C. At higher temperatures, the process is complicated by pyrolysis of SiH_4, and at lower temperature, it is difficul to ensure a sufficient flow rate of Mg vapor. The ratio of the partial pressures of Mg and SiH_4 in the mixture was maintained close to equimolar value, whereas the excess of NH_3 was overwhelming (about 200).

The position of a substrate in the gas flow is an important parameter [8], because homogeneous transformations, which dramatically affect the result of deposition, may develop in a thermodynamically unstable gas mixture. At different total flow rates in the

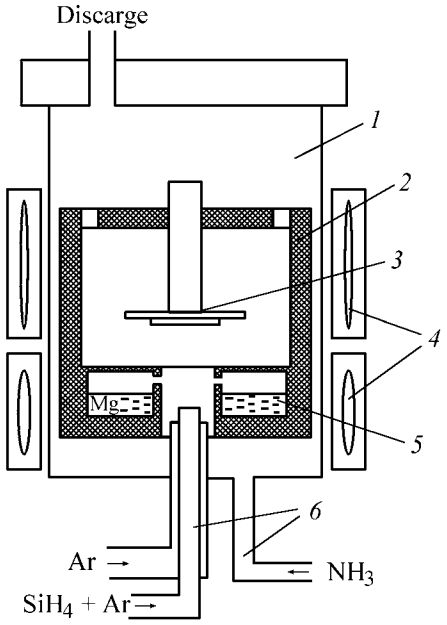

Fig. 2. Reactor for synthesis of $MgSiN_2$ in the hydride system. (*1*) Reactor shell (quartz) (*2*) reactor unit (graphite), (*3*) substrate holder, (*4*) two-zone furnace, (*5*) effusion vaporizer of magnesium, and (*6*) gas-feeding pipes.

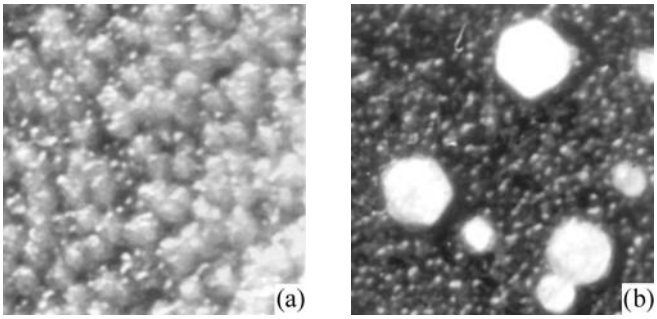

Fig. 3. $MgSiN_2$ layers obtained in different zones of the reaction volume. (a) Spherulitic structure of $MgSiN_2$, (b) spherulitic structure of $MgSiN_2$ in combination with Mg_3N_2 crystals.

reactor, zonal patterns of the same type were observed for the variation of the composition of the layers being deposited with the distance between the nozzle end and the substrate.

In the first, nearest to the nozzle, position on the substrate, Mg_3Ni_2 is formed as druses of well-faceted crystals, which constitute a solid layer at a sufficiently long duration of the experiment. At longer distances, a mixture of Mg_3N_2 and spherulitic $MgSiN_2$ is formed on the substrate (Fig. 3b). A dense $MgSiN_2$ layer composed of white spherulitic grains 100–200 μm in size can be obtained as the distance from the mixing zone increases further (Fig. 3a). When the distance from the substrate to the nozzle is too long, the rate

of layer growth decreases considerably and the film losses its crystalline structure.

At the optimal position of the substrate, found under the above conditions, deviations of the vapor composition from the magnesium-to-silane equimolar ratio strongly change the deposit properties. In these experiments, the molar consumption of Mg with respect to SiH_4 was varied from 0.5 to 2.0 (at a constant consumption of SiH_4). At a deficit of Mg, the growth rate of the layer decreases, but its morphology and phase composition correspond to the pattern shown in Fig. 3a. At an excess of Mg, the mass of the deposit increases and the growth pattern corresponds to a two-phase mixture $MgSiN_2$ + Mg_3N_2.

In some experiments, the $MgSiN_2$ film peeled-off in storage of samples under laboratory conditions. Most probably, this is due to formation of a Mg_3N_2 sublayer at the interface with the substrate. Probably, this phenomenon can be used as a method for separating thick layers of the ternary nitride. At the same time, it is necessary to have an opportunity to ensure a sufficient adhesion of the film to the substrate.

A transition mode precluding formation of a Mg_3N_2 sublayer may consist in such a sequence of reagent supply at which the interaction of Mg and NH_3 vapors would be impossible in the first stage of growth. Special experiments performed under the same conditions, but in the absence of NH_3, showed that the growth rate of Mg_2Si films is negligible, compared with that of $MgSiN_2$ films. This circumstance was used as follows. Delay in the delivery of NH_3 by 180–200 s (time in which a silicide sublayer can be formed, but its thickness is apparently negligible) with respect to that of Mg and SiH_4 did eliminate the peeling-off even in the case of a subsequent storage in a water vapor of the sample obtained.

An X-ray analysis of the $MgSiN_2$ deposits obtained did not reveal any reproducible texture. This may be due to the presence of a sublayer, which eliminates the orienting influence of the substrate. The reflections observed were identified using published data [6], which yielded, after processing with a UNITCELL software [9], the following constants of the rhombic lattice (Å): $a = 5.26 \pm 0.03$, $b = 6.52 \pm 0.02$, and $c = 5.04 \pm 0.01$.

CONCLUSIONS

(1) On heating mixtures of Mg and Si powders in a flow of N_2, there occurs an exothermic reaction of Mg_3N_2 formation, which makes it difficult to control the process. By choosing the composition of the starting mixture, the rate at which the temperature is elevated, and the rate of the N_2 flow, it is possible to optimize the process mode and perform a direct synthesis of $MgSiN_2$.

(2) $MgSiN_2$ is deposited in the hydride system at 1050°C onto sapphire substrates in the form of spherulitic polycrystalline layers at the equimolar ratio of Mg and SiH_4 vapors and an overwhelming excess of NH_3.

REFERENCES

1. Uheda, K., Takizawa, H., Endo, T., *et al., J. Mat. Sci. Lett.*, 2001, vol. 20, pp. 1753–1755.
2. Misaki, T., Wu, X., Wakahara, A., and Yoshida, A., *IPAP Conf. Ser. 1*, 2000, pp. 685–688.
3. Huang, J.U., Tang, L-C., and Lee, M.H., *J. Condens. Matter*, 2001, vol. 13, pp. 10 417–10 431.
4. Bruls, R.J., *The Thermal Conductivity of Magnesium Silicon Nitride $MgSiN_2$ Ceramics and Related Materials*, Eindhoven: Eindhoven Tech. Univ., 2000.
5. *PCPDFWIN, version 1.30*, 1997, *JCPDC–ICDD.*
6. David, J., Laurent, Y., and Lang, J., *Bull. Soc. Fr. Miner. Crystallogr.*, 1970, vol. 93, pp. 153–157.
7. Zykov, A.M., Grekov, F.F., and Zykov, V.A., *Zh. Prikl. Khim.*, 1974, vol. 47, no. 1, pp. 201–205.
8. Grekov, F.F., Zykov, A.M., and Savvin, G.S., *Zh. Prikl. Khim.*, 1987, vol. 60, no. 9, pp. 1944–1948.
9. Holland, T.J.B., and Redfern, S.A.T., *J. Appl. Cryst.*, 1997, vol. 30, p. 84.

Russian Journal of Applied Chemistry, Vol. 77, No. 8, 2004, pp. 1227–1231. Translated from Zhurnal Prikladnoi Khimii, Vol. 77, No. 8, 2004, pp. 1245–1248.

INORGANIC SYNTHESIS AND INDUSTRIAL INORGANIC CHEMISTRY

Synthesis and *in situ* Gravimetric Monitoring of Formation of Titanium-Oxide Layer on Silica Surface

A. A. Malkov, E. A. Sosnov, and A. A. Malygin

St. Petersburg Technological Institute, St. Petersburg, Russia

Received April 9, 2004

Abstract—Stages of formation of a titanium oxide monolayer in a flow reactor combined with a McBain balance were studied *in situ* in successive treatment of porous silica with a $TiCl_4$ vapor, dried inert gas, water vapor, and again dried inert gas. The chemical composition of the resulting products, calculated using the data obtained in gravimetric monitoring, is in agreement with the results of a chemical analysis.

Gravimetric methods for studying heterogeneous processes find wide application owing to the possibility of *in situ* monitoring of separate stages of synthesis, high precision of measurements, and conveniently obtained kinetic dependences in varied technological modes [1–7]. Synthesis of element-oxide surface structures by molecular layering (ML) is based on performing chemical reactions between active reagents, e.g., between chlorides of an element and functional groups on the surface of oxide solid matrices [8–9]

$$m(\equiv M\text{–}OH) + ECl_n \rightarrow (\equiv M\text{–}O\text{–})_m ECl_{n-m} + m HCl, \quad (1)$$

followed by a vapor-phase hydrolysis of element-oxide groups

$$(\equiv M\text{–}O\text{–})_m ECl_{n-m} + (n - m)H_2O \rightarrow (\equiv M\text{–}O\text{–})_m E(OH)_{n-m} + (n - m)HCl. \quad (2)$$

The sample weight may change in the course of reaction (1) because of the replacement of, first, OH groups with element-oxochloride groups and then chloride groups with hydroxide groups [reaction (2)]. Comparing the observed weight changes with the chemical composition of surface groups, we can gain insight into the nature of the occurring conversions on the basis of the material balance. However, only a linear weight change in relation to the number of ML cycles has been established and discussed in the available reports on gravimetric studies of ML reactions [10–12]. This weight change is determined after the completion of a separate synthesis cycle, which gives no way of regarding the thermogravimetric method as a tool for an *in situ* study of separate synthesis stages and mechanisms of reactions occurring on the matrix surface.

The purpose of this study was to examine separate ML stages for the example of synthesis of a titanium oxide monolayer on the surface of porous silica on a thermogravimetric installation equipped with a McBain balance.

The experiments were carried out with a silica gel of ShSKG brand, purified to remove admixtures (0.2–0.4-mm fraction, average pore diameter 15.6 nm, specific surface area by BET [13] 235 $m^2 g^{-1}$) [14]. The thermogravimetric installation used in the study (Fig. 1) includes a flow reactor *1* with an indirect

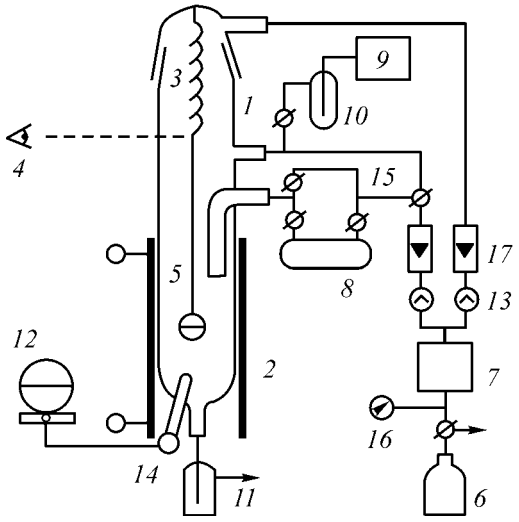

Fig. 1. Schematic of the thermogravimetric installation with a flow reactor and a McBain balance. (*1*) Quartz flow reactor, (*2*) indirect-heating furnace, (*3*) quartz spring, (*4*) cathetometer, (*5*) container for a matrix, (*6*) source of carrier gas, (*7*) gas-drying unit, (*8*) container with a reagent, (*9*) microcompressor, (*10*) bubbler with H_2O, (*11*) absorber, (*12*) potentiometer, (*13*) fine-tuning valves, (*14*) thermocouple, (*15*) cocks, (*16*) manometer, and (*17*) rotameters.

1070-4272/04/7708-1227 © 2004 MAIK "Nauka/Interperiodica"

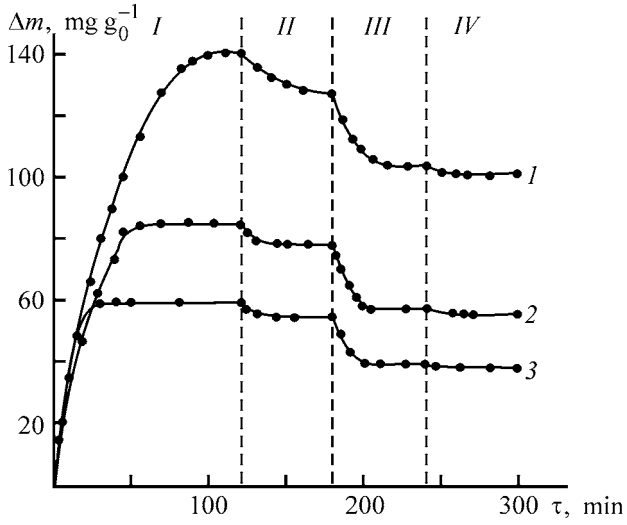

Fig. 2. Change in the sample weight, Δm, during ML synthesis of a titanium oxide monolayer on ShSKG silica ($T_0 = T_{chs} = T_h$) at (*1*) 200, (*2*) 400, and (*3*) 600°C. (τ) Time. (*I*) $TiCl_4$ chemisorption, (*II*) removal of the excess amount of the reagent, (*III*) vapor-phase hydrolysis, (*IV*) drying of the sample.

electric heater *2* and a spring balance in the reactor. A quartz spring *3* with a constant of 3.25 mg mm^{-1} was used in the experiments. Estimating the relative spring extension with a KM-6 cathetometer *4* ensured that changes in the sample weight were measured with an accuracy of ±0.03 mg. With a weighed sample of about 0.1 g, placed in pan *5*, the change in the sample weight was measured with an accuracy of ±(0.3–0.4) mg g^{-1}. Reagents were transported by an inert gas, air or high-purity nitrogen from a cylinder *6*, with a residual oxygen content less than 0.0001 vol %. After being passed through a unit *7*, which ensured a residual moisture content corresponding to a dew-point temperature not higher than –60°C (4.5 mg H_2O/m^3), the dry gas was saturated with $TiCl_4$ vapors in batcher *8* at room temperature and fed into the reactor. The vapor-phase hydrolysis of titanium chloride surface groups was carried out with a humid air passed through a bubbler *10* with distilled water at room temperature and fed into the reactor by a microcompressor *9*. The excess amount of reactants and gaseous reaction products was absorbed in the bubbler *11*. The temperature in the reaction zone was maintained constant to within ±5°C by a potentiometer *12*. The products synthesized were analyzed for the content of titanium(IV) and chloride ions [15, 16]. To compare the chemical compositions of samples obtained at different temperature, the concentrations of Ti(IV) and chloride ions in these samples were recalculated to 1 g of an anhydrous matrix (g_0) [17–19].

Based on the assumed schemes of occurrence of the surface chemical reactions (1) and (2), we can estimate changes in the product weight in the synthesis of, first, titanium oxochloride and, further, a titanium chloride monolayer. The increase in the sample weight, Δm_{chs} (mg g_0^{-1}), as a result of $TiCl_4$ chemisorption accompanied only by the replacement of the hydrogen ions of the surface OH groups with titanium chloride groups [scheme (1)] can be calculated by the formula

$$\Delta m_{chs} = [Ti]M_{Ti} + [Cl]M_{Cl} - [OH_{used}]M_H. \quad (3)$$

Here [Ti] and [Cl] are the contents of Ti(IV) and Cl^- in the chemisorption product; $[OH_{used}]$, the amount of OH groups (mmol g^{-1} of anhydrous matrix) consumed in the reaction; M_{Ti}, M_{Cl}, and M_H, the atomic weights of titanium, chlorine, and hydrogen, respectively.

The amount of hydroxide groups consumed in the reaction is given by

$$[OH_{used}] = (4 - [Cl]/[Ti])[Ti] = 4[Ti] - [Cl]. \quad (4)$$

Transforming expression (3) and taking (4) into account, we obtain

$$\Delta m_{chs} = (M_{Ti} - 4M_H)[Ti] + (M_{Cl} + M_H)[Cl]. \quad (5)$$

Then the concentration of Ti(IV) in the product of chemisorption can be calculated by the formula

$$[Ti] = \frac{\Delta m_{chs} - (M_{Cl} + M_H)[Cl]}{M_{Ti} - 4M_H}. \quad (6)$$

To determine the number of Cl^- ions in the titanium oxochloride groups, we used the thermogravimetric data obtained in the stage of the vapor-phase hydrolysis and subsequent treatment with a dry gas at the temperature of synthesis. According to reaction (2), the weight change Δm_h (mg g_0^{-1}) in hydrolysis with an equivalent exchange of Cl^- for OH groups can be represented as

$$\Delta m_h = (M_{OH} - M_{Cl})[Cl]. \quad (7)$$

Then we can calculate the amount of chlorine:

$$[Cl] = \frac{\Delta m_h}{M_{OH} - M_{Cl}}. \quad (8)$$

Typical thermogravimetric curves obtained in different stages of synthesis of a titanium oxide monolayer are shown in Fig. 2: (*I*) $TiCl_4$ chemisorption,

Table 1. Reproducibility of the synthesis of a titanium oxide monolayer

Curve in Fig. 2	Determination error, %		Weight change, mg g_0^{-1}	
	$\varepsilon_{\Delta m_{chs}}$	$\varepsilon_{\Delta m_h}$	Δm_{chs}	$-\Delta m_h$
1	3.5	6.8	129.8 ± 4.6	47.7 ± 3.2
2	3.3	3.9	81.4 ± 2.7	25.5 ± 1.0
3	3.8	3.0	55.0 ± 2.1	16.5 ± 0.5

Table 2. Chemical (calc.) and gravimetric (exp.) analyses in synthesis of titanium oxide structures

Curve in Fig. 2	Content, mmol g_0^{-1}		Δm_{chs} (calc.)	$-\Delta m_h$ (calc.)	Δm_{chs} (exp.)	$-\Delta m_h$ (exp.)	$\frac{\Delta m_{chs}\ (exp.)}{\Delta m_{chs}\ (calc.)}$	$\frac{\Delta m_h\ (exp.)}{\Delta m_h\ (calc.)}$
	Ti	Cl	mg g_0^{-1}					
1	1.08	2.35	133.2	43.4	132.6	46.9	0.996	1.081
2	0.79	1.29	81.8	23.9	80.6	27.1	0.985	1.134
3	0.49	0.84	52.1	15.5	53.5	16.7	1.027	1.077

(*II*) removal of the excess amount of a reagent with a flow of a carrier gas, (*III*) vapor-phase hydrolysis, and (*IV*) drying of the product in a carrier-gas flow at the temperature of synthesis. The reproducibility of the experimental data after the completion of stage *IV* of synthesis at different temperatures (according to the results of 3–5 experiments) is illustrated in Table 1.

The results of a chemical analysis and sample weight changes in synthesis on a thermogravimetric installation are listed in Table 2. It can be seen that the experimental weight changes in chemisorption and desorption (stages *I* and *II*) coincide, within the experimental error (Table 1), with similar values calculated from the chemical analysis data. At the same time, the weight changes for samples (Fig. 2) after hydrolysis of titanium chloride structures (stage *III*) and after removal of the excess amount of the low-molecular reagent (stage *IV*) are greater than those calculated from the chemical analysis data by 8–13%, which exceeds the corresponding errors of determination (Table 1). These differences can be associated with occurrence of additional, with respect to reaction (2), transformations in the composition of titanium-containing groups in stages *III* and *IV*.

It is known that OH groups are present on the surface of TiO_2, with their maximum content being as high as 6.6 and 15.4–15.6 μmol m^{-2} for crystalline and amorphous TiO_2, respectively [20]. The heat treatment of TiO_2 at $T_0 > 15$°C is accompanied by a significant dehydroxylation of the surface, with the complete removal of OH groups from a surface attained, according to different publications, even at $T_0 = 450-600$°C [21]. As follows from Fig. 2, a significant amount of silanols (7.1 μmol m^{-2} [22]) that can enter into chemical reactions still remains on the silica gel surface under the same conditions ($T_0 = 600$°C). As the thermal stability of titanols is much lower than that of Si–OH groups, the most probable reason for the discrepancies indicated in Table 2 may be partial dehydroxylation of Ti–OH groups formed in the stage of the vapor-phase hydrolysis, which is accompanied by the formation of bridging Ti–O–Ti bonds. This should result in an additional decrease in weight in the hydrolysis stage and in the subsequent drying:

$$\Delta m_{\Sigma h} = \Delta m_h + \Delta m_{dh}. \quad (9)$$

Here Δm_{dh} is the weight change associated with the dehydroxylation of surface groups.

$$\Delta m_{dh} = \frac{M_{H_2O}}{2}[OH_{dh}], \quad (10)$$

where $[OH_{dh}]$ is the amount of dehydroxylated titanols.

Then, with account of (7), we obtain

$$[OH_{dh}] = \frac{\Delta m_{\Sigma h} - (M_{Cl} - M_{OH})[Cl]}{M_{H_2O}/2}. \quad (11)$$

Using the derived expression (11) and thermogravimetric data obtained in the stage of hydrolysis and subsequent thermal treatment, we can estimate the

Table 3. Composition of titanium oxide structures on silica

Curve in Fig. 2	Content, mmol g_0^{-1}				$\frac{[OH_{res}]}{[OH_{calc}]}$	Distance l_{Ti-Ti}, nm
	Ti	OH_{calc}	OH_{dh}	OH_{res}		
1	1.08	2.35	0.39	1.96	0.83	0.60
2	0.79	1.29	0.36	0.93	0.72	0.70
3	0.49	0.84	0.13	0.71	0.84	0.89

thermal stability of titanium hydroxide groups on the surface of the dispersed support. The calculations for the samples represented in Fig. 2 demonstrated that, in the synthesis conditions under consideration, Ti–OH groups are partly dehydroxylated in the stages of hydrolysis and drying immediately after their formation, with the degree of dehydroxylation equal to 0.39, 0.36, and 0.13 mmol g_0^{-1} at 200, 400, and 600°C, respectively (Table 3). In this case, 70 to 85% of the hydroxo groups forming by reaction (2) in vapor-phase hydrolysis of titanium chloride groups remains on the surface of the samples (Table 3). This is in a good agreement with the results of a chemical analysis of multilayer titanium oxide coatings synthesized at the same temperatures, because the remaining amount of hydroxide groups is sufficient for further growth of the titanium oxide layer [18].

At the same time, no complete dehydroxylation of surface titanium-containing structures on silica at 600°C (as differentiated from the surface of pure TiO_2) is observed. The enhanced thermal stability of titanols on silica may be due to the stabilizing effect of the silica matrix [23]. By contrast, the amount of removed hydroxo groups even decreases in comparison with the samples synthesized at 200 and 400°C, which is presumably due to the topography of active sites on the surface of the starting matrix. The rise in the T_0 of silica results in a substantial increase in the average distance between the groups synthesized (Table 3), which hinders interfunction interactions because of the spatial remoteness of the structures synthesized on the matrix surface.

CONCLUSION

The use of gravimetric measurements makes it possible to monitor *in situ* separate stages of molecular layering of element-oxide surface structures, to calculate the chemical composition of the groups synthesized, and to analyze the possible processes of dehydroxylation of the newly formed hydroxyl groups.

ACKNOWLEDGMENTS

This study was carried out within the framework of the grant of the President of Russian Federation "Leading Scientific Schools of Russia," "Chemistry of Highly Organized Substances" Program (project NSh 2236.2003.3) and was financially supported in part by the Russian Foundation for Basic Research (project no. 04-03-32048) and Programs of the Ministry of Education of the Russian Federation.

REFERENCES

1. Barret, P., *Cinetique Heterogene*, Paris: Ganthier-Villars, 1973.
2. Krashennikova, A.A., Syrkina, I.G., and Ul'yankina, G.S., *Zh. Fiz. Khim.*, 1978, vol. 52, no. 9, pp. 2255–2258.
3. Sharygin, L.M. and Tret'yakov, S.J., *Available from VINITI*, 1973, Moscow, no. 6597-73.
4. Tret'yakov, S.J. and Sharygin, L.M., *Available from VINITI*, 1976, Moscow, no. 433-76.
5. Riis, T., Dahl, J.M., and Ellestad, O.H., *J. Molec. Catal.*, 1983, vol. 18, no. 2, pp. 203–214.
6. Kovaleva, N.Yu., Gavrilov, Yu.A., Morozov, M.V., *et al.*, *Kompleksnye metallorganicheskie katalizatory polimerizatsii olefinov* (Complex Organometallic Catalysts for Polymerization of Olefins), 1986, no. 10, pp. 164–170.
7. Sosnov, E.A., Malkov, A.A., and Malygin, A.A., *Zh. Prikl. Khim.*, 1988, vol. 61, no. 1, pp. 29–34.
8. Koltsov, S.I., *Reaktsii molekulyarnogo naslaivaniya: Tekst lektsii* (Molecular Layering Reactions: Text of Lectures), St. Petersburg: StPbTI (Technical University), 1992.
9. Aleskovskii, V.B., *Khimiya nadmolekulyarnykh soedinenii* (Chemistry of Supramolecular Compounds), St. Petersburg: Izd. SPbGU, 1996.
10. Tolmachev, V.A., *Zh. Prikl. Khim.*, 1982, vol. 55, no. 6, pp. 1410–1412.
11. Romanychev A.I., *Napravlennyi sintez tverdykh veshchestv* (Directed Synthesis of Solids), 1992, issue 3, pp. 110–116.

12. Romanychev, A.I., *Zh. Prikl. Khim.*, 1992, vol. 65, no. 12, pp. 2672–2676.
13. Klyachko-Gurvich, L.A., *Izv. Akad, Nauk SSSR, Otd. Khim. Nauk*, 1968, vol. 26, no. 10, pp. 1884–1891.
14. Koltsov, S.I. and Aleskovskii, V.B., *Silikagel', stroenie i khimicheskie svoistva* (Silica Gel, Structure and Chemical Properties), Leningrad: Goskhimizdat, 1963.
15. Bulatov, M.I. and Kalinkin, I.P., *Prakticheskoe rukovodstvo po fotokolorimetricheskim metodam analiza* (Manual of Photocolorimetric Methods for Analysis), Leningrad: Khimiya, 1986.
16. Charlot, G., *Les Methods de la Chemie Analytique. Analyse quantitative Minerale, Quatrieme Edition*, Paris: Masson, 1961.
17. Koltsov, S.I. and Aleskovskii, V.B., *Zh. Fiz. Khim.*, 1968, vol. 42, no. 5, pp. 1210–1214.
18. Malkov, A.A., Sosnov, E.A., and Malygin, A.A., *Napravlennyi sintez tverdykh veshchestv* (Directed Synthesis of Solids), 1992, no. 3, pp. 10–29.
19. Sosnov, E.A., Malkov, A.A., and Malygin, A.A., *Zh. Prikl. Khim.*, 2000, vol. 73, no. 7, pp. 1074–1079.
20. Doremieux-Morin, C., Enriquez, M.A., Sanz, J., *et al.*, *J. Colloid Interface Sci.*, 1983, vol. 95, no. 2, pp. 502–512.
21. Pletnev, R.N., Ivakin A.A., Kleshchev, D.G., *et al.*, *Gidratirovannye oksidy elementov IV i V grupp* (Hydrated Oxides of Elements of IV and V Groups), Moscow: Nauka, 1986.
22. Koltsov, S.I., Volkova, A.N., and Aleskovskii, V.B., *Zh. Fiz. Khim.*, 1970, vol. 44, no. 9, pp. 2246–2249.
23. Koltsov, S.I. and Tuz, T.V., *Izv. Vyssh. Uchebn. Zaved., Khim. Khim. Tekhnol.*, 1991, vol. 34, no. 2, pp. 90–94.

Russian Journal of Applied Chemistry, Vol. 77, No. 8, 2004, pp. 1232–1238. Translated from Zhurnal Prikladnoi Khimii, Vol. 77, No. 8, 2004, pp. 1249–1255.

INORGANIC SYNTHESIS AND INDUSTRIAL INORGANIC CHEMISTRY

Scientific Foundations of Development of New Chemically and Radiation-Resistant Cd-containing Crystalline Materials

A. A. Lukuttsov, M. L. Spiridonova, N. A. Kulagina, A. I. Orlova, V. I. Pet'kov, and I. A. Kulikov

Lobachevskii State University, Nizhni Novgorod, Russia

Federal State Unitary Enterprise (FGUP), State Scientific Center of the Russian Federation "Vsesoyuznyi nauchno-issledovatel'skii institut neorganicheskikh materialov" (All-Union Research Institute of Inorganic Materials), Moscow, Russia

Received April 12, 2004

Abstract—Cadmium phosphate $Cd_{0.5}Zr_2(PO_4)_3$ was obtained by precipitation from aqueous solutions and studied by means of X-ray phase analysis and IR spectroscopy. The behavior of powdered and ceramic samples in water, aqueous ammonia solutions, nitric acid, EDTA, and also in gamma-radiation fields (^{60}Co source), was examined. Experimental characteristics of the chemical and radiation stability are presented.

Cadmium compounds are a dangerous component of wastes formed in some industries [1]. At present, methods for conversion of cadmium-containing wastes into an environmentally safe stable form by their solidification are being developed. For this purpose, it has been suggested to use polymers and resins [2], cements [3, 4], glasses, and glassy ceramic [5, 6] and ceramic materials [7]. The method of incorporation of waste products into crystalline (mineral-like) forms is ecologically expedient. These forms can find application for detoxication of highly toxic waste products and for their insulation from the biosphere, and also as new materials with special and practically important properties. One of approaches to the solution of this problem is to convert soluble cadmium compounds into a crystalline phosphate, which is temperature- and radiation-resistant and chemically stable and can be further used as a sorbent in various media, including application in ion-exchange chromatography. When creating such a material, it is necessary to take into account the stability of the phosphate brought in contact with a liquid medium, the rate at which ions pass into solution, and, when in a contact with a radioactive medium, also its radiation stability.

The goal of this study was to obtain cadmium phosphate $Cd_{0.5}Zr_2(PO_4)_3$, characterize it by X-ray phase analysis (XPA) and IR spectroscopy, examine its behavior in chemically aggressive media in the presence of complexing substances, and assess its radiation stability. This compound belongs to the structural type of sodium-dizirconium triphosphate $NaZr_2(PO_4)_3$ [8], or the cosnarite mineral [9], and has a skeleton structure (Fig. 1). The skeleton is built from ZrO_6 octahedra and PO_4^{3-} tetrahedra jointed by

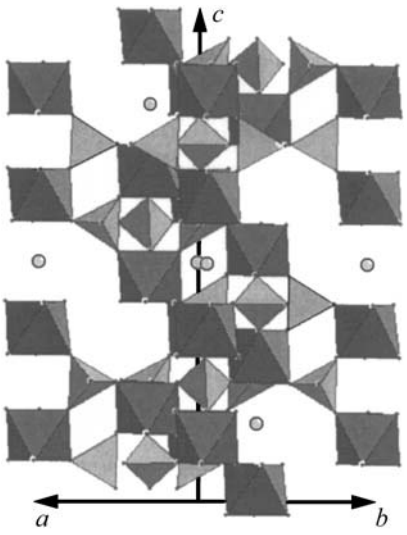

Fig. 1. Structure of the phosphate $Cd_{0.5}Zr_2(PO_4)_3$ (a fragment of the structure is constructed using the data of [10]).

1070-4272/04/7708-1232 © 2004 MAIK "Nauka/Interperiodica"

common vertices. Representatives of this family are known to have a high thermal and hydrolytic stability [11, 12]. Some of these, including Cd^{2+} phosphates, have low thermal expansion and ability to withstand multiple thermal shocks [13–16]. The structure of the compounds is favorable for performing an ionic diffusion.

EXPERIMENTAL

Phosphate $Cd_{0.5}Zr_2(PO_4)_3$ was prepared by the sol–gel technique [16, 17]. Chemically pure reagents $Cd(NO_3)_2 \cdot 4H_2O$, $ZrOCl_2 \cdot 8H_2O$, and H_3PO_4 served as starting substances for the synthesis. Stoichiometric amounts of aqueous solutions of $Cd(NO_3)_2$ and $ZrOCl_2$ were poured together at room temperature and then a solution of H_3PO_4 was added dropwise with stirring. The resulting gel was dried at 80°C and subjected to a heat treatment at 600, 800, 1000, and 1100°C for no less than 24 h in each stage. Step-by-step heating was alternated with dispersion.

Ceramic samples were also prepared. For this purpose, a powder of the phosphate was compacted (at a pressure of about 10 MPa) into pellets and annealed at 800–1100°C for 24 h.

A ceramic sample of the phosphate $Cd_{0.5}Zr_2(PO_4)_3$ (diameter 1.13 cm, height 0.45 cm) was subjected to hydrothermal tests.

The hydrolytic stability was studied under dynamic conditions in a Soxhlet apparatus at 95°C, with distilled water (MSS-1 test) as a solvent. The volume of the solvent was 300 ml, the cycle duration of the apparatus was 100–120 min. The experiment duration was 28 days.

The solvent was changed after certain time intervals. The Cd^{2+} content in these solvent portions was determined by inversion voltammetry on a TA-1 analyzer equipped with an IBM-compatible computer.

The rate of Cd^{2+} leaching was calculated by the equation

$$R = m/(c_{sp} S \tau).$$

Here R is the rate of leaching of an element (g cm^{-2} day^{-1}) in a time τ; m, the mass (g) of an element that passed into a solution during a time τ; c_{sp}, the specific concentration of an element in the solid phase (g g^{-1} of a solid phase); S, the surface area of a ceramic sample (cm^2); and τ, the time of leaching (days).

The behavior of the phosphate in aggressive chemical media in the presence of complexing compounds was studied as follows. A weighed portion of a powdered cadmium-zirconium phosphate (0.1 g) was poured over with a solution under study (2 ml) and kept for a certain time.

Aqueous solutions of HNO_3 (10 and 65%), NH_4OH (25%), and EDTA (0.1 M) were used as contacting solutions.

Similar studies were carried out with a phosphate of the same composition in the form of a ceramic pellet (diameter 1.11 cm, height 0.13 cm). In this case, 10% HNO_3 served as a contacting solution.

The analysis of samples (of volume 10 μl) for the content of Cd^{2+} and PO_4^{3-} was carried out on a Tsvet 306 liquid chromatograph in a flow-through-injection mode without a separation column. As detector served an SF-00 spectrophotometer. An ammonia solution (5×10^{-4} M) of cadion-IREA and NH_4OH_{conc} in the ratio 1 : 1 was used as a mobile phase.

Preliminarily, absorption spectra of ammonia solutions of cadion and its complexes with Cd^{2+}, ZrO^{2+}, and PO_4^{3-} were recorded using the detector and wavelengths were selected at which Cd^{2+} and PO_4^{3-} ions do not interfere with determination of each other: 625 nm for Cd^{2+} and 400 nm for PO_4^{3-}. At these wavelengths the spectrum of a ZrO^{2+} complex with the cadion coincides with that of the mobile phase and does not interfere with the determination of Cd^{2+} and PO_4^{3-}.

We have found that the calibration plots of peak areas in output curves vs. weights of ions, used to Cd^{2+} and PO_4^{3-} ions with cadion ammonia solutions, are described by the equations $y_1 = 9.947x_1$ ($R^2 = 0.995$) and $y_2 = 0.1355x_2$ ($R^2 = 0.992$), respectively. Here y_1 and y_2 are the areas under the output curves (mm^2) for Cd^{2+} and PO_4^{3-} ions, and x_1 and x_2 are the weights of Cd^{2+} and PO_4^{3-} ions (μg).

To study the behavior of cadmium-zirconium phosphate under the action of gamma-radiation, we used a ^{60}Co source ($\tau_{1/2} = 5.272$ year, $E_\gamma = 1.17$, 1.33 MeV). The dose rate p at a sample was determined by a Fricke dosimeter, i.e., a ferrosulfate system consisting of a 0.001 M solution of Mohr's salt $(NH_4)_2Fe(SO_4)_2 \cdot 6H_2O$ in 0.4 M H_2SO_4. The p (Gr s^{-1}) was calculated by the formula

$$p = CN_A/(G\tau \times 6.25 \times 10^{15}).$$

Here c is the experimental concentration of Fe^{3+} ions (M); G, the yield of Fe^{3+}, equal to 15.6 ion/100 eV for ^{60}Co gamma-radiation; N_A, the Avogadro number; and τ, the irradiation time (s).

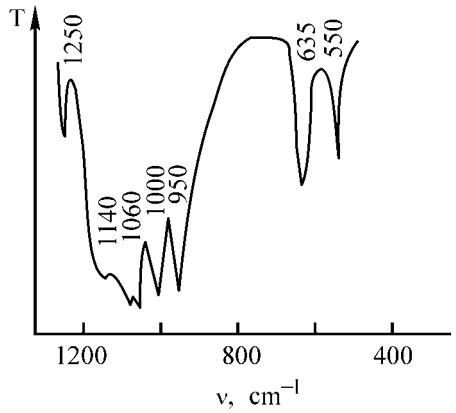

Fig. 2. IR spectrum of the phosphate $Cd_{0.5}Zr_2(PO_4)_3$. (T) Transmittance and (ν) wave number.

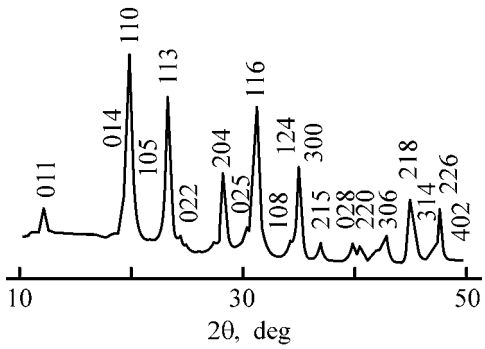

Fig. 3. X-ray diffraction pattern of the phosphate $Cd_{0.5}Zr_2(PO_4)_3$. (2θ) Bragg angle.

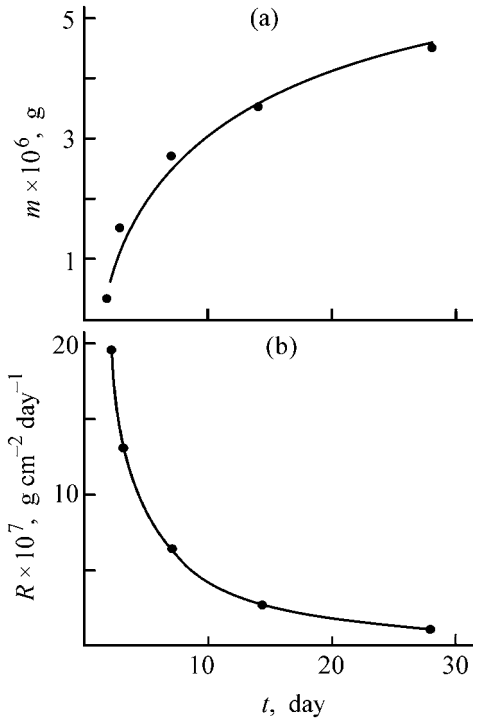

Fig. 4. (a) Mass of Cd^{2+} m that passed into distilled water from the phosphate $Cd_{0.5}Zr_2(PO_4)_3$ and (b) leaching rate R of cadmium vs. time t.

The concentration c of Fe^{3+} ions formed in radiolysis was determined by spectrophotometry on an SF-4A instrument.

The irradiated sample was studied by X-ray phase analysis and IR spectroscopy and compared with an unirradiated control sample.

The gas evolution from a gamma-irradiated sample (powder, $m \approx 30$ g) placed in an ampoule was judged from the composition of the gas and the rate of its evolution. The composition of the gas was determined by chromatography on Shimadzu 3G-AH and LKhM-8M instruments.

The X-ray phase analysis of the phosphates was carried out on a DRON-2.0 diffractometer with filtered Cu_{K_α} radiation. The lattice constants were determined from X-ray diffraction patterns analyzed at $2\theta = 10°–50°$ and refined by the least-squares method.

The IR absorption spectra of samples prepared as finely dispersed films on a KBr substrate were recorded on a Specord-75 IR spectrophotometer at frequencies of 1800–400 cm^{-1}.

The ESR spectra of powdered unirradiated and gamma-irradiated samples were recorded on a Bruker EMX-113 spectrometer (wavelength $\lambda = 3$ cm) at room temperature. The working frequency of the device was 9.5 GHz.

Several samples synthesized were in the form of a white polycrystalline powders.

We found that the synthesis of the phosphates was complete at 800°C. A slight increase in the intensity of diffraction reflections was observed in the X-ray diffraction patterns of substances heated to 1100°C.

The IR spectral data indicate that the phases obtained belong to the class of orthophosphates (Fig. 2). On the whole, the IR spectrum is characteristic of phases with an *NZP* structure and $R\bar{3}$ space group: the bands at 1250–1000 cm^{-1} correspond to the stretching asymmetrical vibrations ν_3; that at ~950 cm^{-1}, to the stretching symmetrical vibrations ν_1; and the bands at 630 and 550 cm^{-1}, to bending vibrations ν_4 of PO_4^{3-} ions. Five bands out of the six allowed by selection rules are observed in the range of stretching asymmetrical vibrations.

In the X-ray diffraction pattern, there were reflections characteristic of $Cd_{0.5}Zr_2(PO_4)_3$ (Fig. 3). The set of the interplanar distances obtained was compared with the data of [18]. The calculated parameters of the rhombohedral cell of the compound

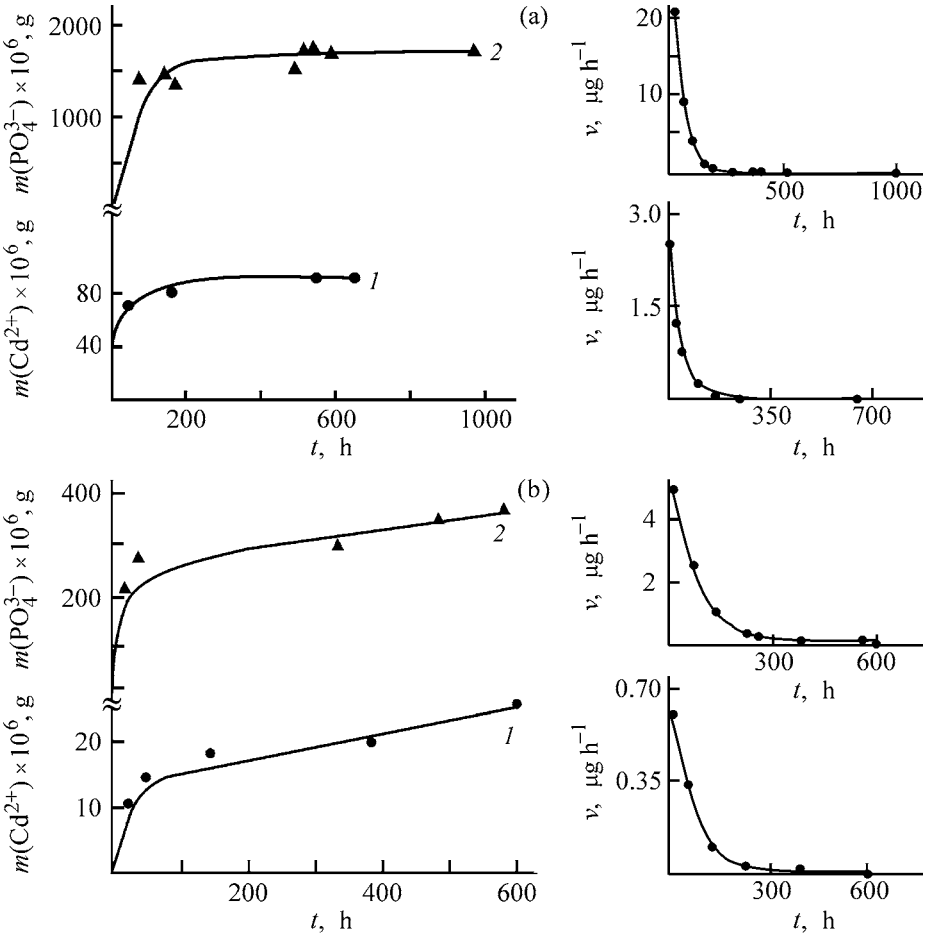

Fig. 5. Mass m of (*1*) Cd^{2+} ions and (*2*) PO_4^{3-}-ions that passed into HNO_3 solutions during the time t of contact and rates v at which these ions passed into solution vs. time t. (a) 65% solution of HNO_3, powdered sample; (b) 10% solution of HNO_3, ceramic sample.

(space group $R\bar{3}$) in a hexagonal positioning were as follows: a = 8.822 Å (1), c = 22.28 Å (1), and V = 1502 Å^3.

The time dependences of the mass of Cd^{2+} that passed into distilled water from the phosphate $Cd_{0.5}Zr_2(PO_4)_3$ and of the leaching rate of Cd^{2+} are shown in Fig. 4.

Within the first three days of contact with water, the leaching rate rapidly decreased with time. The minimum experimental leaching rate was 1.1×10^{-7} g cm^{-2} day^{-1} (by the 28th day).

According to the XPA data, the phase composition of the sample after tests remained unchanged.

The time dependences of the mass of Cd^{2+} and PO_4^{3-}-ions that passed into 10 and 65% HNO_3 solutions and of the rates at which they pass into the solutions are shown in Fig. 5. It can be seen that, when powdered samples are brought in contact with a 65% HNO_3 solution, a quasi-equilibrium state is attained after 200–250 h for both Cd^{2+} and PO_4^{3-}-ions. When ceramic samples are brought in contact with a 10% HNO_3 solution, no equilibrium was attained within more than 600 h of the experiment.

The data obtained allowed us to determine the quasi-equilibrium degree of extraction of Cd^{2+} and PO_4^{3-}-ions from a powdered sample and the degree of extraction of these ions from a ceramic sample in 600 h of contact, and also to calculate the minimum rate D of their transfer from a pellet sample into the contacting medium (Table 1).

The value of D was calculated for a cylindrical sample with a fixed height l from the slope of the linear dependence of M_t/M_∞ on $\sqrt{t}$ [19]:

$$\frac{M_t}{M_\infty} = \frac{4}{\sqrt{\pi}}\sqrt{\frac{D}{l^2}}\sqrt{t}.$$

Here M_t is the mass of ions (Cd^{2+} and PO_4^{3-}) that passed from a pellet into a solution by the instant of

Table 1. Degree of extraction, *c*, and rate *D* at which ions pass into nitric acid

HNO_3, %	*c*, wt %		*D*, $cm^2\ s^{-1}$	
	Cd^{2+}	PO_4^{3-}	Cd^{2+}	PO_4^{3-}
10	0.25	0.7	3×10^{-11}	5×10^{-12}
65	0.82	3.12	–	–

time *t*; M_∞, the masses of Cd^{2+} and PO_4^{3-}-ions that passed into a 65% HNO_3 solution from a powdered sample until an equilibrium was attained (Fig. 5a); *t*, the time of the contact of a pellet with a 10% HNO_3 solution (s); *l*, the height of a pellet (cm); *D*, the rate at which the ions under control pass from a pellet into a 10% HNO_3 solution ($cm^2\ s^{-1}$).

The data listed in Table 1 indicate that Cd^{2+} and PO_4^{3-}-ions pass into nitric acid at rates approaching the rates of diffusion in solids.

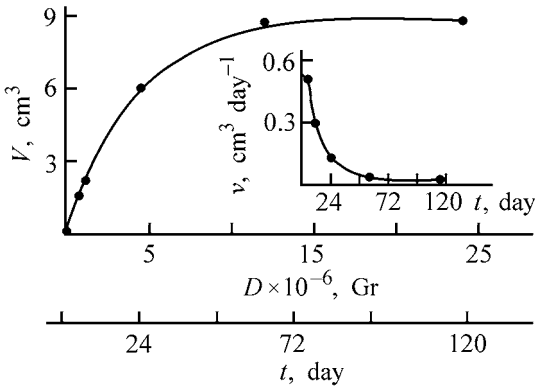

Fig. 6. Volume *V* of the gas evolved in gamma-irradiation of the phosphate $Cd_{0.5}Zr_2(PO_4)_3$ vs. time *t* and absorbed dose *D*. Inset: gas evolution rate *v* vs. time *t*.

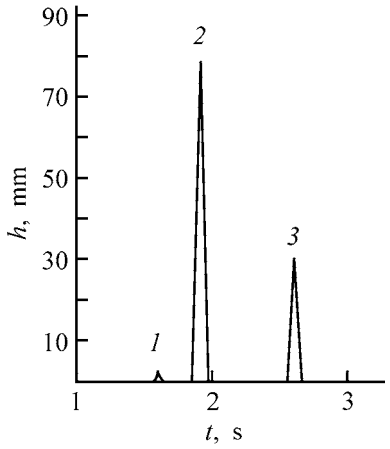

Fig. 7. Chromatogram of the gas mixture. (*h*) Peak height and (*t*) elution time. (*1*) H_2, (*2*) O_2, (*3*) N_2.

It also follows from these data that ratios between Cd^{2+} and PO_4^{3-}-ions in the solid phase and in solution differ from each other. The solution is enriched with Cd^{2+} ions. This seems to be due to different positions of these ions in the phosphate structure: PO_4^{3-} is a skeleton-forming group, whereas Cd^{2+} ions occupy extra-skeleton positions, in which the contribution of the ionic component is more important. This circumstance results in a selective dissolution (leaching).

We also studied the behavior of a powdered $Cd_{0.5}Zr_2(PO_4)_3$ sample in a 0.1 M EDTA solution and a 25% NH_4OH solution. The degree of Cd^{2+} extraction in 600 h is given below:

Contact solution	*c*, wt %
Water	0.003
10% HNO_3	0.2
65% HNO_3	0.8
25% NH_4OH	0.03
0.1 M EDTA	0.01

These values are an order of magnitude higher than those for a sample brought in contact with water and an order of magnitude lower than those for 10 and 65% HNO_3 solutions.

Thus, complexing compounds NH_4OH and EDTA, which form stable complexes with Cd^{2+} ions [20, 21], lead to an only slight disintegration of the structure of the Cd–Zr phosphate.

To assess the radiation resistance, we irradiated a $Cd_{0.5}Zr_2(PO_4)_3$ sample for 4 months, using a ^{60}Co-source. The maximum accumulated dose was $D = 2.5 \times 10^7$ Gr (dose rate $p = 2.4$ Gr s^{-1}). A comparison of the X-ray diffraction patterns of the samples before and after irradiation demonstrated that the structure remains virtually unchanged upon irradiation. An IR spectral analysis of an irradiated sample revealed no changes in the structure of Cd–Zr phosphate, either.

The radiation resistance of the phosphate was also judged from the amount and composition of the gas evolved under the action of gamma-radiation. The dependence of its volume on the irradiation time *t* and on the accordingly accumulated dose of gamma-radiation, *D*, is shown in Fig. 6.

A total of 9 ml of the gas evolved during the test. It was found by chromatography that the main component of the mixture was O_2, with minor amounts of N_2 and H_2 and trace amounts of CO_2 also detected (Fig. 7).

The compositions of the gas mixtures at various doses of irradiation of a $Cd_{0.5}Zr_2(PO_4)_3$ sample are listed in Table 2.

The calculated radiative-chemical yield was 0.058 ± 0.005 molecules/100 eV. The fraction of O_2 evolved from Cd–Zr-phosphate as a result of its radiative-chemical destruction was about 0.0009 of its calculated content in a sample with the formula $Cd_{0.5}Zr_2(PO_4)_3$.

To describe qualitatively the radiation resistance of Cd–Zr phosphate, we also used ESR data, which make it possible to establish the fact of formation of paramagnetic centers in the phosphate structure under the action of radiation. As follows from the experimental data, the ESR spectra of unirradiated and irradiated samples do not differ significantly. In the spectrum of the irradiated phosphate, the signal of Zr^{3+} ions becomes somewhat stronger, and very weak signals of PO_3^- groups appear. These radical anions are presumably formed due to bond rupture in the phosphate structure, which results in the observed evolution of oxygen.

On the whole, the results of XPA of irradiated and unirradiated samples, the low radiative-chemical yield of the gas mixture, and the insignificant difference between the ESR spectra of unirradiated and irradiated samples indicate a high radiation resistance of Cd–Zr phosphate. The rate of gas evolution, which reaches a constant value in approximately 48 days, remains virtually unchanged in further irradiation, even in a long-term test (Fig. 6), and does not exceed the values obtained.

CONCLUSIONS

(1) The possibility of utilization of cadmium(II) from crystalline (ceramic) Cd-containing zirconium phosphate, which belongs to structural analogues of $NaZr_2(PO_4)_3$ and has a skeleton structure, was demonstrated.

(2) An all-round study of the behavior of the phosphate $Cd_{0.5}Zr_2(PO_4)_3$ in water and aqueous solutions of NH_3, HNO_3, and EDTA was carried out, and the parameters of leaching of cadmium(II) and phosphate ions in these media were determined.

(3) It was shown experimentally that the Cd-containing zirconium phosphate $Cd_{0.5}Zr_2(PO_4)_3$ is stable in water and aggressive chemical media, including those containing complexing substances. The occurring radiation-stimulated destruction is insignificant.

Table 2. Composition of gas mixture evolved in gamma-irradiation of a Cd-containing zirconium phosphate at doses $D \le 2.4 \times 10^7$ Gr

D, Gr	Gas mixture component, %			
	H_2	O_2	N_2	CO_2
6.8×10^5	0.8 ± 0.1	88.3 ± 1.5	9.9 ± 1.3	Trace
1.08×10^6	1.4 ± 0.2	92.3 ± 0.9	7.3 ± 0.9	〃
4.5×10^6	1.2 ± 0.4	88.3 ± 1.1	9.1 ± 0.8	1.4
1.2×10^7	1.7 ± 0.3	87.1 ± 1.5	8.8 ± 1.5	1.7
2.4×10^7	1.3 ± 0.2	90.2 ± 1.3	7.9 ± 1.3	0.9

(4) The data obtained and the specific structural features of zirconium-cadmium phosphate make it possible to regard this compound as a form of immobilization of cadmium(II) and a basis for development of new sorbents resistant to aggressive chemical media and radiation. They can be used in ion-exchange chromatography and, taking into account the nuclear properties of cadmium(II), as a basis for neutron-absorbing ceramics.

ACKNOWLEDGMENTS

This study was financially supported by the Russian Foundation for Basic Research (project no. 02-03-32181).

REFERENCES

1. *Lehrbuch der Ekologischen Chemie: Grundlagen und Konzepte fur Ekologische Beurteilung von Chemikalien*, Korte, F., Ed., Stuttgart: Thieme, 1992.
2. German Patent Application 4439173.
3. Diez, J-M., Madrid, J., and Macias, A., *Cem. Concr. Res.*, 1997, vol. 27, no. 4, pp. 479–492.
4. Ubbriaco, P., Bruno, P., and Traini, A., *Ann. Chim.* (Italia), 2000, vol. 90, no. 1–2, pp. 137–143.
5. US Patent 5573564.
6. Orru, R., Sannia, M., Cincotti, A., and Cao, G., *Chem. Eng. Sci.*, 1999, vol. 54, no. 15–16, pp. 3053–3061.
7. US Patent 5860908.
8. Hagman, L.O. and Kierkegaard, P., *Acta Chem. Scand.*, 1968, vol. 22, no. 6, pp. 1822–1832.
9. Brownfield, M.E., Foord, E.E., Sutlex, S.J., and Botinelly, T., *Am. Mineral.*, 1993, vol. 78, pp. 653–656.
10. ßrochu, R., El-Yacoubi, M., Louer, M., *et al.*, *Mat. Res. Bull.*, 1996, vol. 32, no. 1, pp. 15–23.
11. Agrawal, D.K., Huang, C.-Y., and McKinstry, H.A., *Int. J. Thermophys.*, 1991, vol. 12, no. 4, pp. 697–710.
12. Orlova, A.I., Zyryanov, V.N., Egor'kova, O.V., and

Demarin, V.T., *Radiokhimiya*, 1996, vol. 38, no. 1, pp. 28–32.

13. Samoilov, S.G., Kryukova, A.I., Kazantsev, G.N., *et al.*, *Neorg. Mater.*, 1993, vol. 28, nos. 10/11, pp. 2197–2202.
14. Orlova, A.I., Kemenov, D.V., Pet'kov, V.I., *et al.*, *High Temperatures—High Pressures*, 1999, vol. 31, pp. 105–111.
15. Orlova, A.I., Kemenov, D.V., Samoilov, S.G., *et al.*, *Neorg. Mater.*, 2000, vol. 36, no. 8, pp. 995–1000.
16. Pet'kov, V.I., Orlova, A.I., Kazantsev, G.N., *et al.*, *J. Therm. Anal. Cal.*, 2001, vol. 66, no. 2, pp. 623–632.
17. Pet'kov, V.I., Orlova, A.I., and Kapranov, D.A., *Zh. Neorg. Khim.*, 1998, vol. 43, no. 9, pp. 1534–1540.
18. Pet'kov, V.I., Kurazhkovskaya, V.S., Orlova, A.I., and Spiridonova, M.L., *Kristallografiya*, 2002, vol. 47, no. 5, pp. 802–809.
19. Malkin, A.Ya. and Chalykh, A.E., *Diffuziya i vyazkost' polimerov: Metody izmereniya* (Diffusion and Viscosity of Polymers: Measurement Techniques), Moscow: Khimiya, 1979.
20. Shcherbov, D.P. and Matveets, M.A., *Analiticheskaya khimiya kadmiya* (Analytical Chemistry of Cadmium), Moscow: Nauka, 1973.
21. Lazarev, A.I., *Organicheskie reaktivy v analize metallov* (Organic Reagents in Analysis for Metals), Moscow: Metallurgiya, 1980.

Russian Journal of Applied Chemistry, Vol. 77, No. 8, 2004, pp. 1239–1244. Translated from Zhurnal Prikladnoi Khimii, Vol. 77, No. 8, 2004, pp. 1256–1261.

INORGANIC SYNTHESIS AND INDUSTRIAL INORGANIC CHEMISTRY

Synthesis of Nanocomposites by Abrasive-Reactive Wear of Grinding Bodies in a Mechanochemical Reactor

F. H. Urakaev

Institute of Mineralogy and Petrography, Siberian Division, Russian Academy of Sciences, Novosibirsk, Russia
Novosibirsk State University, Novosibirsk, Russia

Received November 28, 2003

Abstract—The possibility of synthesis of various nanocomposites and processing of mineral and technological raw materials with the use of abrasives and the material of grinding bodies of mechanochemical reactors was studied.

As a rule, only the possibility of contamination of mechanical activation (MA) products with substances of frictional wear of the grinding bodies [1–3] is taken into account when considering the direct influence of the material of grinding bodies on the course of mechanochemical processes. As it is impossible to eliminate the wear phenomenon, it is suggested to consider the material of grinding bodies subjected to abrasive wear as one of inherent components of the MA system, the abrasive amorphous substances being the most convenient component as regards interpretation of the results of an X-ray phase analysis (XPA).

In this study, the influence exerted by wear of grinding bodies on the course of mechanical activation of reagent–abrasive systems in a mill with steel accessories is analyzed.

At the same time, finding, studying, and obtaining nanoparticles in natural and model systems with the use of various methods are of primary interest [4]. For example, it has been found that the abrasive-reactive wear of the steel material of grinding bodies in a mechanochemical reactor can be used to modify the surface of quartz particles with an amorphous nanolayer of iron silicates, which have magnetic properties [5]. Of specific interest for extending the potentialities of this method is the use of carbon (in particular, graphite) and sulfur, which have unique physicochemical and mechanical properties [6, 7]. Also of interest is the processing of mineral and technological raw materials.

The use of carbon and sulfur in the method of abrasive-reactive wear can give a new impetus to the development of carbide or sulfide functional nanocomposite materials. This method can also be successfully used in utilization of dust formed in decarbonization and desulfurization of the coke-oven gas formed in cake and by-product industries [8, 9]. The accumulation of sulfur at oil refineries and plants processing natural gas also makes its utilization a matter of current interest.

Analysis, breakdown, enrichment, and processing of mineral and technological raw materials (in particular, complex oxides and sulfides) by mechanochemical methods have also found wide application in recent years [10–19]. This is primarily due to the possibility of directly obtaining metal components and various composite nanocrystalline materials from geological and technological materials by, mechanothermal methods [12, 13], both in progressive [12, 14, 17, 18] and in explosive [12, 13, 16, 19] modes of the exothermic reaction.

EXPERIMENTAL

The mechanical activation was carried out in an AGO-2 double-drum steel-ball water-cooled planetary-centrifugal mill (mill volume 140 cm^3, 400 balls of radius 0.2 cm) at a relative impact veocity of grinding bodies of 11 m s^{-1} [13]. For more effective processing of samples, all the four possible orientations of the mill axis were used: vertical, horizontal and ±15° to the horizontal. The duration of MA was varied from 5 up to 240 min.

MA products were studied by the standard XPA method. Mechanically activated amorphous samples

1070-4272/04/7708-1239 © 2004 MAIK "Nauka/Interperiodica"

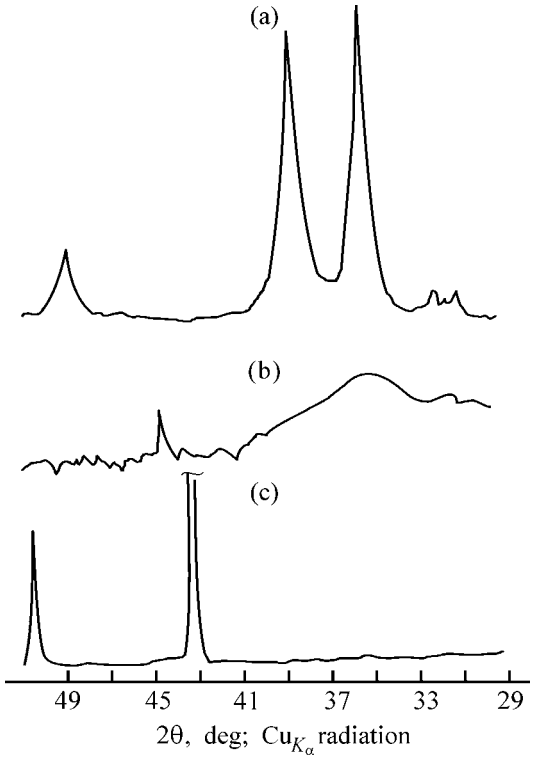

Fig. 1. XPA spectra of the system constituted by fused silica (3 g) and tenorite (1.5 g). (2θ) Bragg angle; the same for Figs. 2–4. (a) Initial tenorite (cf. PDF 48-1548 and 80-1917); (b) MA duration 60 min; and (c) MA duration 60 min, annealing for 2 h in argon at 700°C (PDF 4-836 for copper).

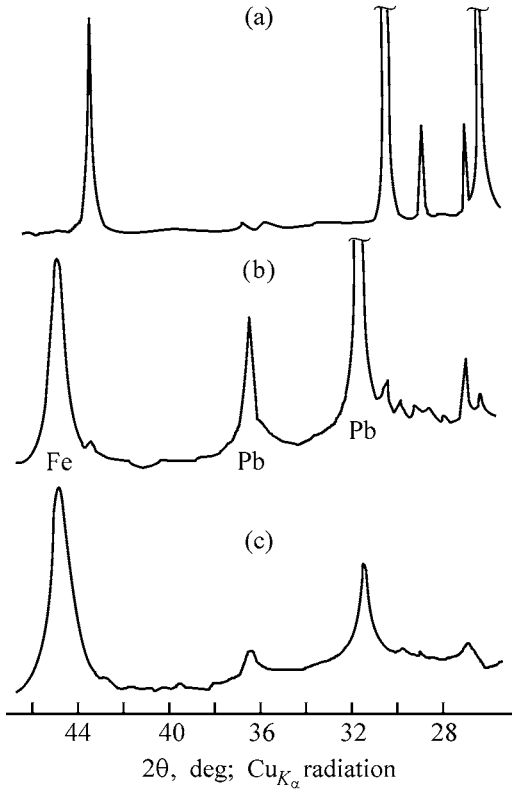

Fig. 2. XPA spectra of the system constituted by fused silica (3 g) and galenite (1.5 g). (a) Initial mixture (PDF 1-880); (b) MA duration 60 min (PDF 4-686 and 6-696); (c) MA duration 210 min.

were also isothermally annealed (2 h) in a flow of argon (~1 cm^3 s^{-1}) in alundum crucibles with graphite plugs and titanium sponge placed before the crucibles in the heated area of the quartz tube to remove the possible oxygen impurity from argon. The chosen annealing temperatures were certainly lower than the temperature of formation of the target products and corresponded to the maximum temperatures used for crystallization of MA products [20].

Graphite, sulfur, galena (PbS), or tenorite (CuO) were introduced in amounts of 0.3–1.6 g into a crushed amorphous (microscopic slide or fused silica) or crystalline (natural α-quartz) abrasive taken in an amount of 3.0 g. The initial tenorite was obtained by thermal decomposition of malachite at ~250°C in the course of 7 h. XPA spectra of this black powder are shown in Fig. 1a. The samples were preliminary crushed and homogenized for 1 h in a Fritsch Pulverisette mill equipped with steel accessories (mortar diameter 9.45 cm + 1 ball of diameter 5.16 cm). The XPA spectrum of a sample of this kind, based on natural galena, is shown in Fig. 2a. It indicates the presence of not only galena, but also some admixtures (mainly crystalline quartz) commonly contained in this mineral. The XPA results for the initial graphite-based samples correspond to PDF 1-640 for graphite in mixtures with an amorphous abrasive. In a mixture with α-quartz, a superposition of reflections (PDF 1-640 and, e.g., PDF 75-443 for α-SiO_2) was observed. The XPA results for the initial sulfur-based samples in mixtures with an amorphous abrasive also point to the presence of only orthorhombic sulfur crystals (PDF 83-2285). According to the data of optical microscopy, the initial average size of abrasive particles was 0.015–0.025 cm for the initial homogenized samples.

Preliminary experiments demonstrated that the mechanochemical processes involving tenorite and galena show both similarity and significant differences. In both the systems, there occurs abrasive wear of steel grinding bodies, which is more pronounced in the system with galena. Even a short-term (5–15 min) MA of the system with tenorite (Fig. 1) results in a self-lining of the grinding bodies with the material being processed. Tenorite starts to change color for green after 1 h of MA, and this color, as well as the

self-lining, is preserved and becomes more intense in the course of MA. By contrast, the self-lining phenomenon is completely absent in the system with galena (Fig. 2), and, after a short time of MA, a black homogeneous "oily" powder of a composite material is formed.

The results obtained in studying the products of MA of the systems under study by XPA and isothermal annealing methods point to the occurrence of various processes. These are the abrasive wear of steel grinding bodies, amorphization, and reduction of copper from tenorite and lead from galena. There are no crystalline phases of other products (iron oxides and halides) of reduction reactions, e.g., CuO + Fe = Cu + FeO ($\Delta_r G^0$ = –28.0 kcal mol^{-1}).

Figure 1b indicates that an X-ray-amorphous product is formed in the system with tenorite and iron wear occurs (peak at 44°–45°). The degree of amorphization increases as the processing duration becomes longer, even the Fe peak is broadened. Metallic copper is the only product formed in annealing of this sample at ~700°C: reflections of all other products that can be formed in the exchange reaction, iron oxides, are completely absent (Fig. 1c).

Figure 2b illustrates a similar phenomenon of abrasive wear of Fe and reduction of galena by this iron, which occur, in this case, directly in the course of MA. It should be noted here that there are no reflections of other possible products of the reduction-exchange reaction, namely iron sulfides. If the MA duration is raised to 120 min, the spectrum remains virtually unchanged: only the reflections of the α-SiO_2 admixture in natural galena disappear (because of amorphization). Annealing of these products also does not change the situation: only the relative intensities change insignificantly and the corresponding reflections become considerably narrower. If the MA duration is increased further, abrasive wear of Fe starts to prevail over all other processes (Fig. 2c).

The data obtained confirm that the self-lining of grinding bodies prevents their abrasive wear and, as a consequence, hinders the reduction reaction of tenorite with the material of grinding bodies in the course of MA. By contrast, the full absence of self-lining of grinding bodies in the system with galena results in a fast breakdown of galena by iron formed in the abrasive wearing of grinding bodies.

It is difficult to give an unambiguous interpretation of the fact that reflections of iron oxides (sulfides) disappear after reductive breakdown of tenorite (galena) without thoroughly studying the MA of natural quartz with the material of steel grinding bodies [5]. The results of [5] suggest that the surface of quartz particles can be modified not only by amorphous iron silicates (after annealing of mechanically activated tenorite samples), but also by iron sulfides after MA of galena together with amorphous quartz particles. In the case of galena, a nanosize surface layer on quartz particles must be formed of a certain amorphous compound of the system Fe_xS_y–SiO_2. An even more complex compound of green color, which is formed upon MA of tenorite and contains nanosize particles produced by abrasive wear of the steel accessories (Fig. 1b), is the amorphous compound $Cu_xFe_yO_z$–SiO_2 on the surface of quartz particles.

The following aspect is associated with dimensional effects. In the case of the conventional mechanochemical reduction of, e.g., copper sulfides [18] with metallic Fe powders with an initial particles size of about 50 μm, the duration of MA is tens of hours. In the new abrasive-reactive method of breakdown of, e.g., galena, suggested here, the size of initial particles formed in abrasive wear of Fe is close to 10 nm, which is orders of magnitude shorter than that in the conventional mechanochemical exchange reaction. Therefore the rate of the breakdown reaction involving the material of steel grinding bodies is also higher and, as a consequence, the time of MA breakdown of minerals becomes shorter.

The XPA data were used to calculate by the known method [2, 10, 17, 18] the structure of crystalline blocks in metal particles obtained in the course of MA in the system with galena. The parameters of the fine crystal structure were calculated from the halfwidth of diffraction peaks (Figs. 2b and 2c) for MA duration of 60, 210, and 120 min (XPA spectrum is not shown). To determine the instrumental broadening of the lines, we used the profiles of the corresponding reflections after the annealing of these samples. The resulting size of Pb blocks was (nm): 83 (60 min MA), 61 (120 min MA), and 46 (210 min MA); the corresponding data for particles formed in wear of Fe were 24, 19, and 12 nm.

Thus, we obtained metal-oxide–sulfide nanocomposite powders based on the quartz matrix in the course of MA of natural minerals (tenorite and galena) mixed with an abrasive (fused silica) in an AGO-2 mill with steel accessories.

Cementite (Fe_3C) is commonly obtained by MA of mixtures of iron and carbon powders, with subsequent thermal or arc-plasma processing of the MA products [21–23]. Sulfides are, as a rule, obtained from elements on heating. However, the morphology

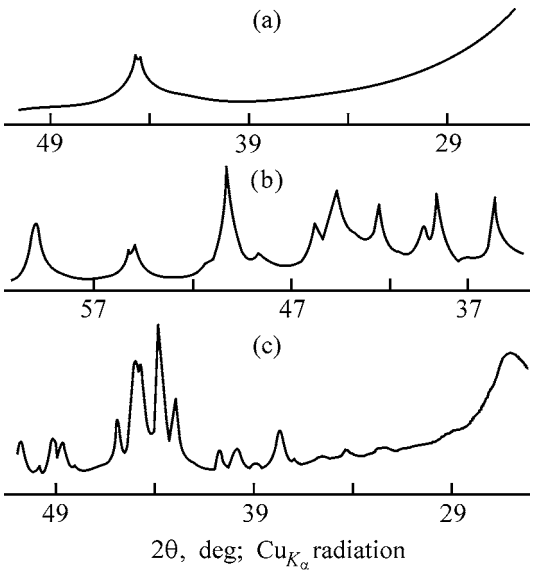

Fig. 3. XPA spectra of the system constituted by quartz (3 g) and graphite (1.5 g). (a) Amorphous quartz, MA duration 90 min; (b) α-quartz, MA duration 90 min; (c) annealing of MA sample (a) for 2 h in argon at 960°C.

and the homogeneity of the target products are not always of the required level. It depends on a number of factors and, in particular, on the area and state of the surface of the starting reagents. The use of a mechanochemical reactor eliminates these drawbacks. At present, iron sulfides, especially those of nanosize [17], are applied in power cells with a high energy density, in photoelectrolysis and solar power engineering, and in synthesis of superconducting, diagnostic, and luminescent materials and chalcogenide glasses.

The results of simulation of mechanochemical reactions involving sulfur [7] show that the most important process for the synthesis of sulfides, e.g., ZnS, is the plastic flow of sulfur. The heat pulse in the shock displacement of molten sulfur is determined by the thickness of layers on the surface of Zn particles lined with softer sulfur. The thinner this layer, the higher the temperature and the faster the amorphization of sulfur (polymerization with a transition to the glassy state). However, the occurrence of this process has not been confirmed experimentally. Therefore, to substantiate the theory [7, 19], it was necessary to choose for MA a system that would contain an inert amorphous component, alongside with crystalline sulfur. Ordinary glass and fused silica are suitable for this purpose. To confirm the mechanochemical amorphization of sulfur, is also the goal of this study.

The XPA spectrum of the system constituted by amorphous quartz and graphite after MA is shown in Fig. 3a. It indicates an amorphization of graphite and wear of steel grinding bodies (α-Fe reflection at $2\theta = 44.68°$ or PDF 6-696).

In the course of MA of the system with α-SiO_2, quartz reflections are preserved, but with significant broadening and decrease in intensity, compared with the initial homogenized sample (cf., e.g., PDF 75-443). Wear of steel grinding bodies also occurs (see a fragment of the spectrum in Fig. 3b at $2\theta = 44°–45°$).

As already noted, MA samples were annealed under the conditions that ruled out thermal synthesis of cementite [24]. In both low (660°C) and high-temperature (960°C, Fig. 3c) annealing, cementite crystallizes (PDF 75-910) from the amorphous phase. However the degree of cementite crystallization from the amorphous phase for samples annealed at 660°C is lower than that for the samples annealed at 960°C. The presence of residual nanosize iron particles in the samples [5] is confirmed by the following: the peak of cementite at $2\theta = 44.72°$ overlaps the base reflection of α-Fe, but not its reflection at $2\theta = 82.4°–82.5°$. In annealing, a partial crystallization of graphite also occurs (halo at $2\theta \approx 26°$ in Fig. 3b). Similar results were obtained for the system with crystalline quartz. It can be stated that the nanocomposite Fe–Fe_3C–C–SiO_2 is formed in the course of MA of quartz–graphite systems.

Experiments on MA of only sulfur crystals (weighed portion 2 g) were carried out under identical conditions. The XPA data for samples of mechanically activated sulfur (MA duration of up to 180 min) show that no structural transformations in sulfur takes place. All the reflections are preserved without any appreciable change in their shape and relative intensity (PDF 83-2285), except for the absence of a halo associated with the presence of amorphous particles of quartz or glass. The situation changes (Fig. 4a) when sulfur is treated in the presence of inert glass particles.

According to the results of a simulation [7], the structural changes in sulfur are due to the attainment of the necessary *t–P–T* conditions in the impact-frictional contact of sulfur-lined glass particles. Although the hardness of glass particles somewhat exceeds that of steel, the abrasive wear of steel accessories is small. Furthermore, the heat pulse in the impact-frictional contact of grinding bodies and particles being processed cannot exceed the glass softening point (~700 K), which also does not favor synthesis of iron sulfides within the activation time specified. We note that the synthesis of iron sulfides

in MA of Fe and S powders [17] requires tens and hundreds of hours of MA.

Fundamental changes occur in activation of samples based on amorphous quartz: pyrite is formed (FeS_2, PDF 71-2219; Fig. 4b). The hardness of quartz particles is considerably higher than that of steel, and its softening point substantially exceeds that of glass. In this case, amorphization of sulfur (absence of reflections of excess sulfur in Fig. 4b) and its chemical reaction with iron nanoparticles (which have already appeared in a significant amount as a result of abrasive-reactive wear of steel accessories) to form pyrite FeS_2 occur simultaneously. The formation of just FeS_2 is due to the excess of sulfur in MA samples.

Using the above-described method and the XPA data, we also calculated the sizes of crystal blocks and the extents of distortion in the structure of the resulting FeS_2 (and Fe particles). The parameters of fine crystal structure were calculated from the half-widths of the diffraction peaks (220) and (440), which are commonly associated with FeS_2 [10]. To determine the instrumental broadening, we used the profile of lines of crystalline FeS_2. The resulting size of blocks in FeS_2 was about 24 nm (~10 nm for iron particles [5]), and the extent of distortion, 1%. Similar results were obtained in [17], but after more than 110 h of MA of a 1 : 2 mixture of powders of Fe (particle size of about 50 μm) and S.

We determined gravimetrically the following absolute and relative values of wear of the material of steel grinding bodies—drum (D) and balls (B), for the systems under study: (1) amorphous quartz (3 g) and graphite (1.5 g), MA duration 90 min, D (0.63 g or 0.077%) and B (0.52 g or 0.50%), total wear 1.15 g; (2) α-quartz (3 g) and graphite (1.5 g), 60 min, D (0.23 g or 0.028%) and B (0.25 g or 0.26%), total wear 0.48 g; (3) amorphous quartz (3 g) and sulfur (1.6 g), 135 min, D (0.21 g or 0.077%) and B (0.47 g or 0.50%), total wear 0.68 g; and (4) glass (3 g) and sulfur (1.6 g), 135 min, D (0.03 g or 0.077%) and B (0.43 g or 0.50%), total wear 0.073 g.

We note that the experiment gives higher abrasive characteristics for fused silica, compared with crystalline α-quartz.

Let us assume that the nanosize particles formed upon abrasive wear of steel grinding bodies are completely consumed for formation of the phase Fe_3C (FeS_2) by the reaction $3Fe + C = Fe_3C$ ($Fe + 2S = FeS_2$). Then we would have the following composition of nanosize MA products: Fe_3C (1.23 g), C (1.42 g), and amorphous quartz (3 g); Fe_3C (0.51 g), C (1.46 g), and α-quartz (3 g); and FeS_2 (1.46 g), S (0.82 g), and amorphous quartz (3 g).

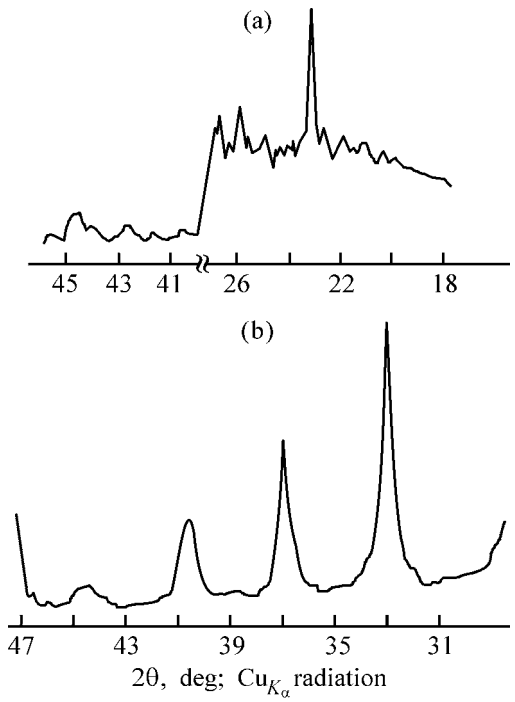

Fig. 4. XPA spectra of systems with sulfur. (a) Glass (3 g) and sulfur (0.4 g), MA duration 135 min; (b) amorphous quartz (3 g) and sulfur (1.6 g), MA duration 135 min.

However, the structure of composites formed may be considerably more complex [5].

CONCLUSIONS

(1) The study performed demonstrated that the steel material of grinding bodies can be involved in direct mechanochemical breakdown of minerals and synthesis of nanocomposites with the use of the abrasive properties of quartz varieties. The mechanical activation of mixtures of quartz and reagents (galena, tenorite, graphite, or sulfur) yielded nanocomposites in a time one to two orders of magnitude shorter than that in the case of activation of mixtures of iron powders with the reagents.

(2) Abrasive-reactive wear of the material of steel grinding bodies in an AGO-2 planetary mill was measured quantitatively under fixed conditions of mechanical activation.

(3) A scrap of any metal and ceramic products can be used as grinding bodies, which makes it possible to extend considerably the potentialities of the method suggested, based on abrasive-reactive wear of the material of grinding bodies in mechanochemical reactors and substances being processed.

REFERENCES

1. Natarajan, K.A., *Int. J. Mineral Proc.*, 1996, vol. 46, nos. 3–4, pp. 205–213.
2. Suryanarayana, C., *Progress Materials Sci.*, 2001, vol. 46, nos. 1–2, pp. 1–184.
3. Konygin, G.N., Stevulova, N., Dorofeev, G.A., *et al., Khim. Interes. Ustoich. Razv.*, 2002, vol. 10, nos. 1–2, pp. 119–126.
4. *Vestn. Ross. Akad. Nauk*, 2003, vol. 73, no. 5.
5. Ketegenov, T.A., Urakaev, F.Kh., Tyumentseva, O.A., *et al., Dokl. Nats. Akad. Nauk Resp. Kazakhstan*, 2003, no. 2, pp. 66–72.
6. Kurdyumov, A.V., Malogolovets, V.G., Novikov, N.V., *et al., Polimorfnye modifikatsii ugleroda i nitrida bora: Spravochnoe izdanie* (Polymorphic Modifications of Carbon and Boron Nitride: Reference Book), Moscow: Metallurgiya, 1994.
7. Urakaev, F.Kh., Takach, L., Soika, V., *et al., Zh. Fiz. Khim.*, 2001, vol. 75, no. 12, pp. 2174–2179.
8. Stepanov, Yu.V., Berkutov, N.A., Kruglov, V.N., *et al., Koks Khim.*, 2001, no. 8, pp. 18–26.
9. Dement'eva, N.V., Nazarov, V.G., Glyanchenko, V.D., *et al., Koks Khim.*, 1999, no. 2, pp. 23–27.
10. Kulebakin, V.G., Terekhova, V.I., Molchanov, V.I., *et al., Aktivatsiya vskrytiya mineral'nogo syr'ya* (Activation of Breakdown of Mineral Raw Materials), Novosibirsk: Nauka, 1999.
11. Balaz, P., *Extractive Metallurgy of Activated Minerals*, Amsterdam: Elsev. Sci., 2000.
12. Urakaev, F.Kh., Shevchenko, V.S., Chupakhin, A.P., *et al., Fiz.-Tekhn. Probl. Razrab. Polezn. Iskop.*, 2001, no. 6, pp. 78–88.
13. Urakaev, F.Kh., Shevchenko, V.S., Nartikoev, V.D., *et al., Khim. Interes. Ustoich. Razv.*, 2002, vol. 10, no. 3, pp. 365–373.
14. Welham, N.J., *Mineral Eng.*, 2001, vol. 14, no. 3, pp. 341–347.
15. Ficeriova, J., Balaz, P., Boldizarova, E., *et al., Hydrometallurgy*, 2002, vol. 67, nos. 1–3, pp. 37–43.
16. Bakhshai, A., Pragani, R., and Takacs L., *Metall. Mater. Trans. A.*, 2002, vol. 33, no. 11, pp. 3521–3526.
17. Jiang, J.Z., Larsen, R.K., Lin, R., *et al., J. Solid State Chem.*, 1998, vol. 138, no. 1, pp. 114–125.
18. Balaz, P., Takacs, L., Jiang, J.Z., *et al., Kovove Materialy*, 2002, vol. 40, no. 4, pp. 268–280.
19. Urakaev, F.Kh., Takach, L., Shevchenko, V.S., *et al., Zh. Fiz. Khim.*, 2002, vol. 76, no. 6, pp. 1052–1058.
20. Urakaev, F.H., Avvakumov, E.G., Chumachenko, J.V., *et al., Izv. Sib. Otd. Akad. Nauk SSSR, Ser. Khim. Nauk*, 1985, no. 15, issue 5, pp. 59–65.
21. Elsukov, E.P., Dorofeev, G.A., and Boldyrev, V.V., *Dokl. Akad. Nauk*, 2003, vol. 391, no. 5, pp. 640–645.
22. Umemoto, M., Liu, Z.G., Liu, D.Y., *et al., Materials Sci, Forum.*, 2001, vol. 386–388, pp. 199–204.
23. Vasil'ev, L.S. and Lomaeva, S.F., *Kolloid. Zh.*, 2003, vol. 65, no. 5, pp. 697–705.
24. Rzhevskaya, S.V., *Materialovedenie* (Materials Science), Moscow: Mos. Gos. Geol. Univ., 2003.

Russian Journal of Applied Chemistry, Vol. 77, No. 8, 2004, pp. 1245–1248. Translated from Zhurnal Prikladnoi Khimii, Vol. 77, No. 8, 2004, pp. 1262–1265.

INORGANIC SYNTHESIS AND INDUSTRIAL INORGANIC CHEMISTRY

Magneto-optic and Luminescent Properties of Tellurite Glass TeO_2–$ZnCl_2$ Doped with Rare-Earth Elements

I. A. Grishin, V. A. Gur'ev, E. B. Intyushin, Yu. E. Elliev, O. V. Pavlova, and A. P. Savikin

Lobachevskii State University, Nizhni Novgorod, Russia

Research Physicotechnical Institute, Nizhni Novgorod State University, Nizhni Novgorod, Russia

Received June 2, 2003; in final form, May 2004

Abstract—Tellurite glasses were synthesized on the basis of the binary system composed of 70 mol % TeO_2 and 30 mol % $ZnCl_2$ and doped with Nd^{3+}, Pr^{3+}, Tb^{3+}, Er^{3+}, Yb^{3+}, Ho^{3+}. The physicochemical, luminescent, and magneto-optic properties of these glasses were studied.

Tellurite glasses based on TeO_2 have a wide optical transmission range (0.35–5.5 μm) and good chemical and crystallization resistance. Tellurite glasses doped with ions of rare-earth elements (REE) exhibit interesting magneto-optic and luminescent properties [1–7].

Tellurite glasses of the following composition were synthesized: (1) (100 – *x*)(70 mol % TeO_2–30 mol % $ZnCl_2$)–*x*Ln_2O_3, where *x* = 0.1–3.0 wt %, Ln = Nd^{3+}, Pr^{3+}, Tb^{3+}, Er^{3+}, and Yb^{3+}; (2) 96 wt % (70 mol % TeO_2–30 mol % $ZnCl_2$)–1 wt % Er^{3+}–3 wt % Yb^{3+}; (3) (100 – *x*)(70 mol % TeO_2–30 mol % $ZnCl_2$)–*x*R'F_3, where *x* = 0.1–2.0 wt %, R' = Pr^{3+}, Tb^{3+}, Ho^{3+}; (4) 96 wt % (70 mol % TeO_2–30 mol % $ZnCl_2$)–1 wt % Er^{3+}–3 wt % Yb^{3+}, in order to study their magneto-optic and luminescent properties (Table 1).

EXPERIMENTAL

The glasses were synthesized from analytically pure (TeO_2, $ZnCl_2$) and special-purity (Nd_2O_3, Pr_2O_3, Tb_2O_3, Er_2O_3, Yb_2O_3, PrF_3, TbF_3, HoF_3) reagents in porcelain crucibles in two stages. First, a two-component glass composed of 70 mol % TeO_2 and 30 mol % $ZnCl_2$ was synthesized at 650°C. The glass obtained was cooled and ground, and xenon difluoride XeF_2 was added to the resulting powder. The mixture was kept at 200–250°C for 30 min. Then, weighed portions of oxides and fluorides of the above-mentioned REE were added and the resulting mass was fused at

Table 1. Compositions of tellurite glasses

Composition no.	Content							
	TeO_2	$ZnCl_2$	Er_2O_3	YbF_3	Nd_2O_3	HoF_3	TbF_3	PrF_3
	mol %		wt %					
1	69.2	30.4	0.4	–	–	–	–	–
2	68.7	30.1	1.2	–	–	–	–	–
3	67.8	29.8	0.4	2.0	–	–	–	–
4	69.7	29.8	–	–	0.5	–	–	–
5	68.4	30.2	–	–	–	1.4	–	–
6	69.0	30.3	–	–	–	–	0.7	–
7	68.7	30.1	–	–	–	–	1.4	–
8	68.9	30.3	–	–	–	–	–	0.8

1070-4272/04/7708-1245 © 2004 MAIK "Nauka/Interperiodica"

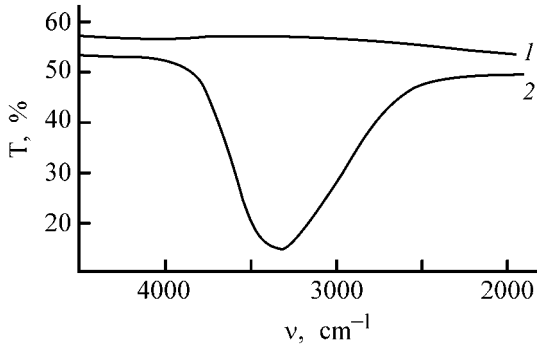

Fig. 1. Transmission spectra of tellurite glasses synthesized (*1*) with and (*2*) without XeF_2. (T) Transmission and (ν) wave number.

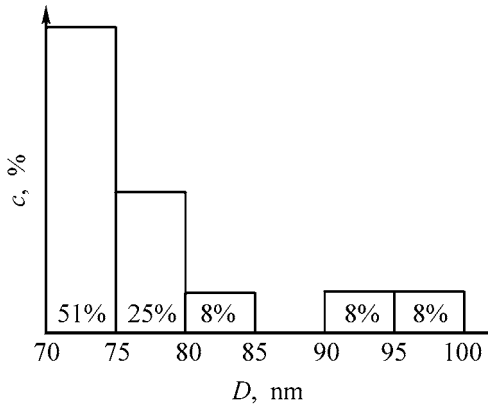

Fig. 2. Histogram of particle distributions over sizes and numeric concentrations for a tellurite glass with 3 wt % erbium(III). (*c*) Relative concentration and (*D*) particle diameter. Total particle concentration 3.21×10^4 cm^{-3}.

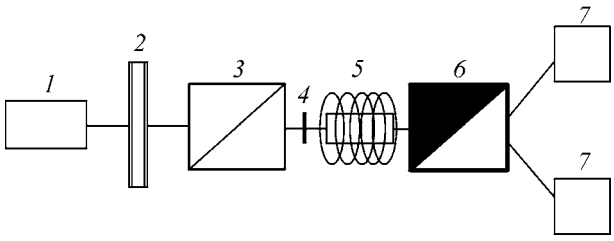

Fig. 3. Schematic of the setup for studying the Faraday effect. (*1*) Laser, (*2*) modulator, (*3*) polarizer, (*4*) sample, (*5*) solenoid, (*6*) beam-splitting prism, and (*7*) photodiodes.

700–750°C. After the muffle furnace was switched off, the crucible was left inside for 30 min for a homogenization of the melt to occur. The glass obtained was annealed at 250°C. The glass was successively cut, ground, and polished. Glass samples had the shape of 15×30 mm planar polished plates of thickness 3 mm.

To make smaller the content of water, XeF_2 was introduced into the stock. Previously [8], the fluoride method has been specially developed to obtain tellurite glasses with a low content of water. Photoluminescence (PL) spectra of the glasses were recorded on a Jobin–Yvon HR-640 spectrometer. As PL excitation source was used a semiconductor LED (~1 W, 980 nm). Transmission spectra were recorded on a Specord 75 M spectrophotometer in the spectral range 4600–1600 cm^{-1}. The optical quality of the glasses obtained was assessed by means of laser ultramicroscopy.

The IR spectrum of a tellurite glass synthesized in air contains a broad absorption band at 2.8–3.6 μm (3600–2800 cm^{-1}), which is due to the high content of water. Synthesis in the atmosphere of dry nitrogen did not lead to any significant changes in the spectrum, because the glass is inevitably contaminated with water owing to the hygroscopicity of the starting $ZnCl_2$ and it is impossible to obtain a tellurite glass containing no trace amounts of water without taking special measures (use of anhydrous $ZnCl_2$). Therefore, it was decided to remove water from the tellurite glass with the use of dehydrating reagents. As reagent of this kind, which produced a positive effect, was used XeF_2 added to a powdered tellurite glass. A crucible with its contents was placed in a quartz vessel blown-through with nitrogen from a Dewar flask. After a short-term fusion and subsequent cooling to room temperature, the glass was extracted from the crucible and its transmission spectrum was recorded. Figure 1 shows transmission spectra of tellurite glasses synthesized (*1*) with and (*2*) without XeF_2. In the former case, the band associated with H_2O vibration completely disappears. For some of the glasses, optical heterogeneities were analyzed by means of laser ultramicroscopy. Figure 2 shows a typical histogram of particle distributions over sizes and numeric concentrations for a sample of a tellurite glass containing 3 wt % erbium(III). The total content of particles is 3.21×10^4 cm^{-3}. A large fraction of impurity particles (~75%) are 0.07–0.08 μm in size.

The magneto-optic properties of tellurite glasses doped with Nd(III), Pr(III), Tb(III), Er(III), Yb(III), and Ho(III) were studied for compositions with 70 mol % TeO_2, 30 mol % $ZnCl_2$, and 0.1–3.0 wt % dopant. The setup for studying the rotation of the polarization plane of linearly polarized light is shown schematically in Fig. 3. As source of light served helium–neon (λ = 632 nm) and neodymium (λ 534 and 1060 nm) lasers. The exciting light passed through a modulator *2* to eliminate noise and a polarizer *3*. The linearly polarized light was incident onto a polarization beam splitter *6*. The orientation of the incident light determines the relative intensities of the resulting two beams. The beam intensities in both

channels of the double-beam polarizer become equal when the polarization plane of the incident light makes a 45° angle with the polarizing directions of the prism. When the polarization plane is rotated, the intensities of the two beams change in opposite directions; an increase in the intensity of one of these beams leads to an automatic decrease in the intensity of the other. Further, the signals were recorded with two photodiodes *7* and fed into the inputs of a differential amplifier. The difference signal was recorded at the output. This is convenient because the excess noise signals are subtracted simultaneously.

The Verdet constants were measured at three wavelengths: 1060, 632, and 532 nm. The results obtained in studying the effect of rotation of the polarization plane of linearly polarized light are listed in Tables 2, 3.

The rare-earth elements neodymium, praseodymium, erbium, ytterbium, and holmium, which were used as dopants in the tellurite glasses synthesized, exhibit a paramagnetic rotation in the polarization plane. Their Verdet constants are negative. It can be seen from Table 2 that the Verdet constants increase as the wavelength of the probing light decreases. The Verdet constants also grow as the concentration of the doping ion in the glass becomes higher. Fluorine-zirconate glasses also exhibit a rotation effect, but it is very weak. Their Verdet constants are three times smaller than those for tellurite glasses. Phosphate glasses surpass tellurite glasses in the efficiency of the rotation effect when doped with ions of such REE as terbium and praseodymium and are inferior to the tellurite glass in this regard when doped with ions of neodymium and erbium (Table 3).

The luminescent properties were studied for tellurite glasses doped with ions of erbium and neodymium or with the pair erbium–ytterbium. The ions of erbium and ytterbium were excited with a semiconductor laser (emission wavelength 980 nm). The mechanism of pumping of Er^{3+} consists in successive absorption of two exciting photons by an erbium ion, with the result that Er^{3+} is excited to the $^4F_{7/2}$ level. After thermal relaxation to the $^4S_{3/2}$ level there occurs the transition $^4S_{3/2} \rightarrow {}^4I_{15/2}$ (to the ground level), to which corresponds the band peaked at 545 nm. Erbium ions also can give rise to a green ($^2H_{11/2} \rightarrow {}^4I_{15/2}$ transition) and red ($^4F_{7/2} \rightarrow {}^4I_{15/2}$ transition) emission, which is characteristic of, e.g., the fluorine-zirconate glass. However, these peaks are not observed in the PL spectrum of Er^{3+} in the tellurite matrix. This circumstance is associated with the properties of the tellurite matrix and is manifested in the kinetics of the Er^{3+} luminescence. The PL of a tellurite glass doped with a donor–acceptor pair Er^{3+}–Yb^{3+} is markedly different. The ion–ion interaction leads to energy transfer from Yb^{3+} to Er^{3+}. As a result of a cascade transition, an excited ion Er^{3+} goes to the $^4F_{7/2}$ level. As in the case of Er^{3+}, relaxation to the $^4S_{3/2}$ level is followed by the $^4S_{3/2} \rightarrow {}^4I_{15/2}$ transition corresponding to the band peaked at 545 nm (green emission). However, green emission is also observed in this case in the $^2H_{11/2} \rightarrow {}^4I_{15/2}$ transition (PL band peaked at 530 nm). Occupation of the $^4F_{9/2}$ level with depletion of the $^4S_{3/2}$ level (thermal relaxation) leads to a $^4F_{9/2} \rightarrow {}^4I_{15/2}$ transition corresponding to a band peaked at 651 nm, i.e., red emission from Er^{3+} is observed. The intensity of red PL is very low as compared with that of the green emission (545 nm). The intensities of all the above-mentioned transitions in the tellurite glass are lower than that of similar transitions in the fluoride glass. This is due to a higher probability on nonradiative transitions in the tellurite glass. The energy of phonons is ~800 cm^{-1} in the tellurite glass and 600 cm^{-1} in the fluoride glass. For the same reason, the probability of the $^4I_{13/2} \rightarrow {}^4I_{15/2}$ transition, to which corresponds a band peaked at 1.536 μm, is lower in the tellurite glass, compared with the fluoride glass.

Table 2. Verdet constants V of tellurite glasses

Component, wt %	V (min Oe^{-1} cm^{-1}) at indicated λ, nm		
	1060	632	534
TeO_2–$ZnCl_2$	0.020	0.086	0.115
Nd^{3+}, 1	0.022	0.092	0.134
Er^{3+}, 1	0.021	0.088	0.127
Er^{3+}, 3	–	–	0.150
Tb^{3+}, 1	–	0.1023	–
Pr^{3+}, 1	–	0.095	–

Table 3. Verdet constants V of phosphate glasses

Component, 1 wt %	V (min Oe^{-1} cm^{-1}) at indicated λ, nm		
	405	500	635
Ce^{3+}	0.672	0.326	0.173
Pr^{3+}	0.447	0.261	0.150
Nd^{3+}	0.250	0.155	0.080
Tb^{3+}	0.560	0.323	0.190
Dy^{3+}	0.540	0.331	0.098
Er^{3+}	0.139	0.111	0.051

Exposure of a tellurite glass doped with Nd^{3+} to light of a mercury lamp gives rise to a green luminescence with λ = 510–540 nm. The Nd^{3+} ion absorbs light with a wavelength of 432 nm, which is present in the spectrum of the mercury lamp. The light with λ = 432 nm, absorbed by the neodymium ion, is reemitted with a wavelength characteristic of the green emission. The UV part of the spectrum (up to λ = 440 nm) was cut off with a UFS-1 filter. In this case, no green luminescence was observed.

CONCLUSIONS

(1) Tellurite glasses with a concentration of impurity particles of 3.21×10^4 cm^{-3} and particle size of 0.07–0.08 μm, doped with neodymium, praseodymium, terbium, erbium, ytterbium, and holmium ions, were synthesized.

(2) A method for lowering the content of water in the tellurite glass is recommended.

ACKNOWLEDGMENTS

The study was supported by the Competition Center for Basic Natural Science (grant no. E 00-3.4-312).

REFERENCES

1. Yakhkind, A.K., Physicochemical Properties of Tellurite Glasses and Synthesis of New Optical Superheavy Flint Glasses on Their Basis, *Doctoral Dissertation*, Leningrad, 1972.
2. Yakhkind, A.K. and Chebotarev, S.A., *Fiz. Khim. Stekla*, 1980, vol. 6, no. 4, pp. 485–492.
3. Chebotarev, S.A., *Fiz. Khim. Stekla*, 1986, vol. 12, no. 4, pp. 493–494.
4. Brachkovskaya, I.B., Volkova, V.V., Dymnikov, A.A., *et al.*, *Fiz. Khim. Stekla*, 1990, vol. 16, no. 6, pp. 916–922.
5. *Struktura i fiziko-khimicheskie svoistva neorganicheskikh stekol* (Structure and Physicochemical Properties of Inorganic Glasses), Vlasov, A.G. and Florinskaya, V.A., Eds., Leningrad: Khimiya, 1974.
6. Kovaleva, I.V., Kolobkov, V.P., and Yakhkind, A.K., *Fiz. Khim. Stekla*, 1975, vol. 1, no. 4, pp. 308–313.
7. Kolobkov, V.P., Ovcharenko, N.V., Morozova, I.N., *et al.*, *Fiz. Khim. Stekla*, 1987, vol. 13, no. 5, pp. 771–774.
8. Tatarintsev, B.V. and Yakhkind, A.K., *Fiz. Khim. Stekla*, 1976, vol. 2, no. 4, pp. 356–361.

Russian Journal of Applied Chemistry, Vol. 77, No. 8, 2004, pp. 1249–1254. Translated from Zhurnal Prikladnoi Khimii, Vol. 77, No. 8, 2004, pp. 1266–1270.

INORGANIC SYNTHESIS AND INDUSTRIAL INORGANIC CHEMISTRY

A Study of Complexation in the System Constituted by Water, Carbamide, and Sulfur Dioxide at 293 K

R. E. Khoma, M. I. Gavrilenko, and V. I. Nikitin

Mechnikov National University, Odessa, Ukraine

Received October 7, 2003; in final form, March 2004

Abstract—Electronic absorption spectroscopy and potentiometry were applied to study complexation at 293 K in a system constituted by water, carbamide, and sulfur dioxide. The composition and stability of the molecular and ionic complexes formed was determined in relation to the concentration of components in solution.

A study of the complexation of sulfur dioxide with carbamide in water is of theoretical and practical importance [1]. Carbamide, which exhibits properties of a weak base, reacts with mineral acids to give products of salt nature [2–5]; however, only a limited number of publications have been concerned with the chemistry of compounds formed by this ligand and SO_2. Potentiometry has been used to study the reaction of sulfur dioxide with aqueous solutions of carbamide at temperatures in the range from 273 to 313 K [1, 6, 7]. In [8], the interaction in the system constituted by water, carbamide, and sulfur dioxide was studied by means of conductometry at 298–353 K. However, the presently existing interpretations of the mechanism of interaction between SO_2 and aqueous solutions of carbamide are contradictory.

The aim of this study was to examine equilibrium processes in the systems H_2O–SO_2 and H_2O–$CO(NH_2)_2$–SO_2 at 293 K by spectrophotometry and potentiometry.

EXPERIMENTAL

As starting substances were used gaseous sulfur dioxide and analytically pure carbamide (Ur). The water used to prepare all solutions was distilled and deoxygenated by bubbling with nitrogen for 4–6 h. The concentration of Ur in the systems studied was monitored photometrically [9].

Aqueous solutions of SO_2 were prepared by saturating deoxygenated water with gaseous sulfur dioxide purified by the method described in [10] and by diluting the resulting solution to required concentrations. The concentration of sulfur(IV) was determined by iodometry [11] and by Scheniger's procedure [12]. The values yielded by these methods coincided. No sulfate ions were found in the system under study, which contradicts the model suggested in [8].

Electronic absorption spectra were recorded on Specord M400 (230 to 310 nm) and SF-18 (256 and 276 nm) spectrophotometers in 1-cm-thick quartz cuvettes. The potentiometric measurements were performed with a pH-150M pH-meter with an ESK-10601 combined glass electrode.

Published data on physicochemical properties of sulfur(IV) anions [13–15] suggest that sulfur dioxide dissolved in water exists as equilibrium forms $H_2O \cdot SO_2$, HSO_3^-, $S_2O_5^{2-}$, and SO_3^{2-}:

$$H_2O \cdot SO_2 \overset{K_1}{\rightleftarrows} H^+ + HSO_3^-, \quad (1)$$

$$2HSO_3^- \overset{K^*}{\rightleftarrows} S_2O_5^{2-} + H_2O, \quad (2)$$

$$HSO_3^- \overset{K_2}{\rightleftarrows} H^+ + SO_3^{2-}. \quad (3)$$

It is known that the electronic spectra of aqueous solutions of SO_2 show three absorption peaks at λ 276 (A_{276}), 256 (A_{256}), and 210 nm. The peak at 276 nm corresponds to sulfur dioxide hydrate; light absorption at about 256 nm, to the pyrosulfite ion; and the peak at about 210 nm, to the disulfite ion [13, 16, 17].

Published data on ion-molecular equilibria in the H_2O–SO_2 system at 293 K are obtained with account of only reactions (1) and (3), with reaction (2) disregarded [18].

1070-4272/04/7708-1249 © 2004 MAIK "Nauka/Interperiodica"

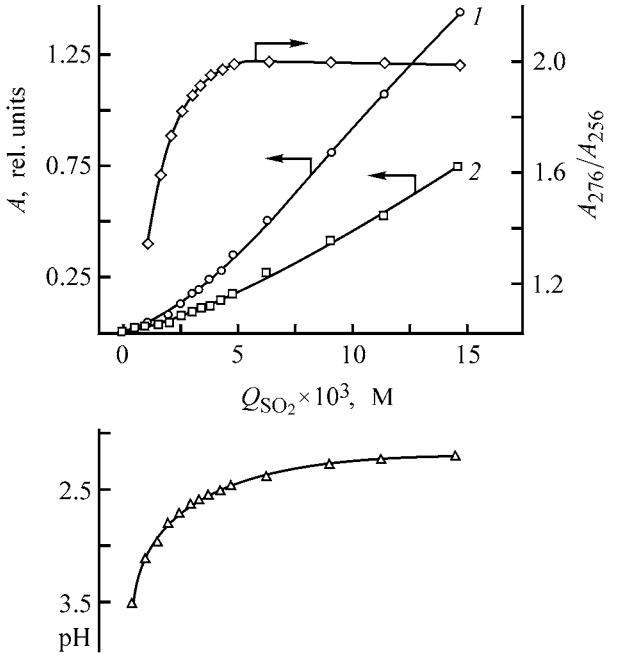

Fig. 1. Spectrophotometric and potentiometric characteristics of aqueous solutions of sulfur dioxide at 293 K. (*A*) Optical density and (Q_{SO_2}) concentration of SO_2 in solution. λ (nm): (*1*) 276 and (*2*) 256.

Spectrophotometric studies of the equilibrium system H_2O–SO_2 at 293 K (Fig. 1) demonstrated that the optical densities A_{276} and A_{256} increase virtually in direct proportion to the total content of SO_2 in the solutions under study (at $Q_{SO_2} \geq 2.5 \times 10^{-3}$ M, where Q_{SO_2} is the total content of SO_2 in solution, M). Consequently, the solutions analyzed are described by the Bouguer–Lambert–Beer law in the concentration range $Q_{SO_2} = (2.5–15.0) \times 10^{-3}$ M. However, $A_{276}/A_{256} \neq \varepsilon_{276}/\varepsilon_{256}$ in this range. This indicates that A_{256} is an additive quantity. Analysis of the data in Fig. 1 shows that, as the total content of sulfur dioxide in water increases, the $A_{276} : A_{256}$ ratio grows and reaches a constant value at $Q_{SO_2} = 4.0 \times 10^{-3}$ M.

Table 1. Comparison of published and experimental data obtained by analysis of electronic absorption spectra of aqueous solutions of sulfur dioxide

Equilibrium form	λ, nm	ε, M^{-1} cm^{-1}
$SO_2 \cdot H_2O$	276	~500 [16, 19], 500*
$S_2O_5^{2-}$	256	2217 [13], 5790 [20], 1940*
$HOSO_2^-$	256	3.8 [13], 2.5*

* Data obtained in the present study.

To find the quantitative relationships between the concentrations of oxo compounds of sulfur in an aqueous solution of SO_2, it is necessary to determine the constants K_1 and K^*, since equilibrium (3) can be disregarded at pH < 4. To calculate the dimerization constant of hydrosulfite ions, K^*, the molar absorption coefficients ε of hydrosulfite and disulfite ions were preliminarily determined. The molar absorption coefficients of HSO_3^- and $S_2O_5^{2-}$ at 256 nm were found by extrapolation of the dependences $A_{256}/Q_{SO_2} = f(Q_{SO_2})$ and $A_{256}/Q_{SO_2} = f(1/\sqrt{Q_{SO_2}})$ to intersection with the ordinate axis [13].

The molar absorption coefficient of sulfur dioxide hydrate was determined at λ = 276 nm in a similar way. Comparison of the resulting values of $\varepsilon_{H_2O \cdot SO_2}$, $\varepsilon_{HSO_3^-}$, and $\varepsilon_{S_2O_5^{2-}}$ with those previosly known (Table 1) shows a good coincidence of these values with the calculated data.

The concentration constants K_1 and K^* were calculated with account of Eqs. (4) and (5) (which reflect the mass action law), the additivity rule (6) and (7), and material balance and electroneutrality conditions (8) and (9):

$$K_1 = \frac{[H^+][HSO_3^-]}{[H_2O \cdot SO_2]}, \quad (4)$$

$$K^* = \frac{[S_2O_5^{2-}]}{[HSO_3^-]^2}, \quad (5)$$

$$A_{276} = \varepsilon^{276}_{H_2O \cdot SO_2}[H_2O \cdot SO_2], \quad (6)$$

$$A_{256} = \varepsilon^{256}_{S_2O_5^{2-}}[S_2O_5^{2-}] + \varepsilon^{256}_{HSO_3^-}[HSO_3^-], \quad (7)$$

$$Q_{SO_2} = [H_2O \cdot SO_2] + 2[S_2O_5^{2-}] + [HSO_3^-], \quad (8)$$

$$[H^+] = 2[S_2O_5^{2-}] + [HSO_3^-]. \quad (9)$$

In processing of the experimental data, a linear dependence of the ionic strength I of the aqueous solutions on the amount of sulfur dioxide dissolved in these solutions was established ($2.5 \times 10^{-3} \leq Q_{SO_2} \leq 15.0 \times 10^{-3}$ M):

$$I = 0.8113Q_{SO_2} + 0.0002, \quad R^2 = 0.99, \quad (10)$$

where R^2 is the statistical significance of approximation.

The dependences of the concentration constants K_1 and K^* on the total concentration of SO_2 ($2.5 \times 10^{-3} \leq$

$Q_{SO_2} \le 15.0 \times 10^{-3}$ M) are shown in Fig. 2. These dependences can also be described by the equation whose parameters are listed in Table 2:

$$pK = A_0 + A_1\sqrt{Q_{SO_2}} + A_2 Q_{SO_2}, \quad (11)$$

where $pK = -\log K$.

Ur can react with sulfur dioxide in water in several ways: (i) via direct addition [Eq. (12)] and (ii) via protonation of Ur [Eq. (13)] [7]:

$$mH_2O \cdot SO_2 + nCO(NH_2)_2 + (h - m)H_2O \rightleftarrows mSO_2 \cdot nCO(NH_2)_2 \cdot hH_2O, \quad (12)$$

$$CO(NH_2)_2 + H^+ \rightleftarrows \{CO(NH_2)_2H\}^+. \quad (13)$$

The equilibrium processes in the system H_2O–Ur–SO_2 were studied spectrophotometrically in the spectral range 230–310 nm. For this purpose, light absorption of 30 solutions was recorded at 16 wavelengths. The number of light-absorbing species was determined by analyzing a matrix with orthogonal rows by the Mark method [21].

Analysis of how the matrix rank depends on the prescribed experimental error (Fig. 3) shows that the number of types of light-absorbing species in the system under study is, in all probability, four. In this case, the error in determining the optical density must fall within the range $0.0018 \le S_A \le 0.004$ units of light absorption. If, however, the error is lowered to 0.00016, and further to 0.00006, the results of calculations point to five forms; if, by contrast, the error is increased to 0.0042–0.0046 light-absorption units, the number obtained is three. A similar tendency was observed in [22] when analyzing the matrix rank for a system constituted by hafnium(IV), perchloric acid, and chloranilic acid.

It should also be noted that the number of different types of light-absorbing species in the system H_2O–SO_2 is three. Then, it is highly probable that the number of types of light-absorbing species in the system H_2O–Ur–SO_2 is greater than three.

It was established that the absorption peaks are not shifted upon complexation, whereas the optical densities of the peaks change significantly. Therefore, all further studies were carried out by analyzing the light absorption at 276 and 256 nm.

The composition of the complexes in solution was determined using the method of molar ratios [22].

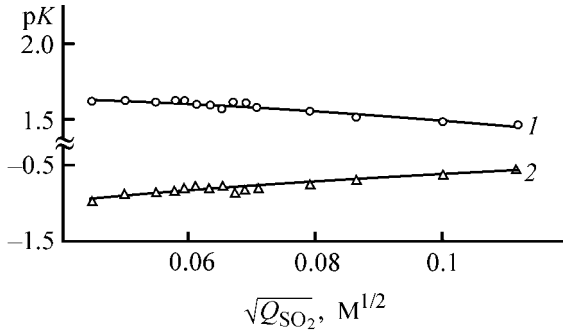

Fig. 2. (*1*) pK_1 and (*2*) pK^* vs. the total content of SO_2, Q_{SO_2}.

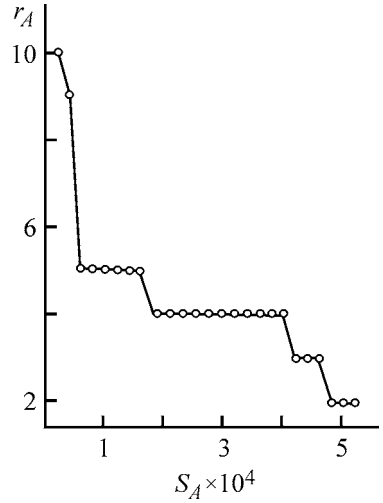

Fig. 3. Matrix rank r_A vs. the prescribed experimental error S_A for the system H_2O–Ur–SO_2.

The calculations were based on deviations of the optical densities from additivity, ΔA ($\Delta A = A_\Sigma - A_{SO_2} - A_{Ur}$, where A_Σ is the total optical density of all the components of a solution; and A_{SO_2} and A_{Ur} are the optical densities of solutions of the components SO_2 and Ur at concentrations equal to those in the series under study). The resulting values of ΔA were used to construct ΔA–composition diagrams for the solution series under study (Fig. 4).

When analyzing the data in Fig. 4 (curves *1*, *2*), it should be noted that compounds of composition

Table 2. Values of parameters in Eq. (11) ($R^2 = 0.91$)

pK	A_0	A_1	A_2
pK_1	1.7917	0.7902	–37.652
pK^*	–1.2925	8.7247	–19.152

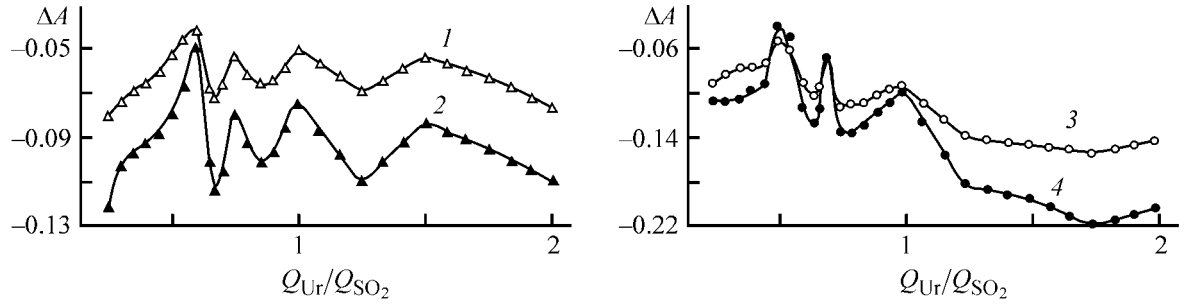

Fig. 4. ΔA vs. the composition of the system constituted by water, carbamide, and sulfur dioxide at 293 K. Q_{SO_2} (M): (*1*, *2*) 5.0×10^{-3} and (*3*, *4*) 7.5×10^{-3}. pH: (*1*, *2*) 2.66 ± 0.02 and (*3*, *4*) 2.42 ± 0.02. λ (nm): (*1*, *3*) 256 and (*2*, *4*) 276.

$[mSO_2 \cdot nCO(NH_2)_2 \cdot hH_2O]$, in which $m : n$ = 5 : 3, 3 : 2, 4 : 3, 6 : 5, 1 : 1, 4 : 5, and 2 : 3, exist in the 5.0×10^{-3} M solution of sulfur dioxide. A 7.5×10^{-3} M solution of SO_2 is characterized by the ratios $m : n$ = 2 : 1, 3 : 2, 4 : 3, 1 : 1, and 4 : 7 (Fig. 4, curves *3* and *4*). Similarly, it was also established that complexes of composition $[SO_2 \cdot CO(NH_2)_2 \cdot hH_2O]$ (I) and $[2SO_2 \cdot CO(NH_2)_2 \cdot hH_2O]$ (II) exist in a 2.5×10^{-3} M solution of sulfur dioxide.

With account of Eqs. (4), (5), (14), and (15) (which reflect the mass action law), the material balance and electroneutrality conditions (16)–(18), the numerical values of the arbitrary complexation constants β_1 and β_2 were calculated for compounds (I) and (II), respectively (Table 3):

$$\beta = \frac{[[mSO_2 \cdot nCO(NH_2)_2 \cdot hH_2O]]}{[H_2O \cdot SO_2]^m [CO(NH_2)_2]^n}, \quad (14)$$

$$K_a = \frac{[CO(NH_2)_2][H^+]}{[\{CO(NH_2)_2H\}^+]}, \quad (15)$$

$$Q_{SO_2} = [H_2O \cdot SO_2] + 2[S_2O_5^{2-}] + [HSO_3^-] + mc_K, \quad (16)$$

$$Q_{Ur} = [CO(NH_2)_2] + [\{CO(NH_2)_2H^+\}] + nc_K, \quad (17)$$

$$[\{CO(NH_2)_2H^+\}] + [H^+] = [HSO_3^-] + 2[S_2O_5^{2-}] + [OH^-], \quad (18)$$

where $c_K = [[mSO_2 \cdot nCO(NH_2)_2 \cdot hH_2O]]$; Q_{SO_2} and Q_{Ur}, the total content of sulfur dioxide and Ur, respectively, in the system under study; $p\beta = -\log \beta$.

In the calculations, the value of pK_a was taken to be 0.18 [23].

The arbitrary constants β_3 and β_4 characterize the acid–base interaction of uronium cations with hydrosulfite and disulfite ions, respectively:

Table 3. Results obtained in spectrophotometric studies of the system H_2O–$CO(NH_2)_2$–SO_2 at 293 K

Parameter	Concentration $Q_{SO_2} \times 10^3$, M		
	2.5	5.0	7.5
$Q_{Ur} \times 10^3$, M	1.85–2.50	4.50–5.00	6.00–7.50
pH	2.90	2.66	2.42
$p\beta_1 \pm \Delta p\beta_1$	-4.03 ± 0.051	-3.74 ± 0.057	-3.28 ± 0.065
$p\beta_3 \pm \Delta p\beta_3$	-5.98 ± 0.051	-5.62 ± 0.057	-5.02 ± 0.065
$p\beta_4 \pm \Delta p\beta_4$	-11.8 ± 0.10	-10.4 ± 0.12	-9.37 ± 0.13
$\log \varepsilon_{K(I)}^{276}$	2.04	1.91	1.95
$\log \varepsilon_{K(I)}^{256}$	1.80	1.56	1.51
$Q_{Ur} \times 10^3$, M	1.25	1.50–2.50	2.25–3.75
pH	2.91	2.66	2.42
$p\beta_2 \pm \Delta p\beta_2$	-8.06 ± 0.042	-7.67 ± 0.268	-6.74 ± 0.182
$\log \varepsilon_{K(II)}^{276}$	2.40	2.20	2.33
$\log \varepsilon_{K(II)}^{256}$	1.98	1.86	1.95

$$\{CO(NH_2)_2H^+\} + HSO_3^- + (h - 1)H_2O \rightleftarrows [SO_2 \cdot CO(NH_2)_2 \cdot hH_2O], \quad (19)$$

$$\beta_3 = \frac{[[SO_2 \cdot CO(NH_2)_2 \cdot hH_2O]]}{[HSO_3^-][\{CO(NH_2)_2H\}^+]}, \quad (20)$$

$$2\{CO(NH_2)_2H^+\} + S_2O_5^{2-} + (2h - 2)H_2O \rightleftarrows 2[SO_2 \cdot CO(NH_2)_2 \cdot hH_2O], \quad (21)$$

$$\beta_4 = \frac{[[SO_2 \cdot CO(NH_2)_2 \cdot hH_2O]]}{[S_2O_5^{2-}][\{CO(NH_2)_2H\}^+]^2}. \quad (22)$$

It was established in the study that compounds (I) and (II) absorb in the UV spectral range:

$$A_{276} = \varepsilon^{276}_{H_2O \cdot SO_2}[H_2O \cdot SO_2] + \varepsilon^{276}_K c_K, \quad (23)$$

$$A_{256} = \varepsilon^{256}_{S_2O_5^{2-}}[S_2O_5^{2-}] + \varepsilon^{256}_{HSO_3^-}[HSO_3^-] + \varepsilon^{256}_K c_K, \quad (24)$$

where ε^{276}_K and ε^{256}_K are the molar absorption coefficients of the forming complexes at 276 and 256 nm, respectively.

The fact that the values of $\varepsilon^{276}_{K(I)}$, $\varepsilon^{256}_{K(I)}$ and $\varepsilon^{276}_{K(II)}$, $\varepsilon^{256}_{K(II)}$ for compounds (I) and (II), respectively (Table 3) depend on the total content of sulfur dioxide and Ur in solution presumably indicates that the composition of complexes (I) and (II) also depends on the concentrations of these components in solution.

Analysis of the data in Table 3 shows that, as the solutions are diluted, the stability of the compounds increases, which would be impossible if hydrolysis dominated over complexation. Hence follows that the complexes are hydrated from the very beginning and a further increase in the concentration of water does not lead to displacement of other species from the compounds.

In all probability, the effects described above are due to selective solvation in aqueous-carbamide solutions of sulfur dioxide.

CONCLUSION

Joint application of spectrophotometric and potentiometric methods enables a conclusion that both molecular and ion complexes can be formed in the system H_2O–$CO(NH_2)_2$–SO_2. The composition and stability of the forming compounds strongly depend on the concentration of components in solution. It is established that the hydration of the complexes dominates over their hydrolysis in the system under study.

REFERENCES

1. Khoma, R.E., Nikitin, V.I., and Gavrilenko, M.I., *Zh. Prikl. Khim.*, 2003, vol. 76, no. 4, p. 533.
2. Nurakhmetov, N.N. and Beremzhanov, B.A., *Zh. Neorg. Khim.*, 1978, vol. 23, no. 2, pp. 504–514.
3. Beremzhanov, B.A., Nurakhmetov, N.N., Tashenov, A., and Suyundikova, F.O., *Zh. Neorg. Khim.*, 1987, vol. 32, no. 1, pp. 256–259.
4. Gubin, A.I., Buranbaev, M.Zh., Nurakhmetov, N.N., *et al., Kristallografiya*, 1988, vol. 33, no. 2, pp. 509–510.
5. Gel'mbol'dt, V.O., Ostapchuk, L.V., Ganin, E.V., and Ennan, A.A., *Koord. Khim.*, 1998, vol. 24, no. 8, pp. 571–574.
6. Nikitin, V.I., Khoma, R.E., and Gavrilenko, M.I., *Izv. Vyssh. Uchebn. Zaved., Khim. Khim. Tekhnol.*, 2000, vol. 43, no. 2, pp. 14–16.
7. Khoma, R.E., Nikitin, V.I.,and Gavrilenko, M.I., *Izv. Vyssh. Uchebn. Zaved., Khim. Khim. Tekhnol.*, 2001, vol. 44, no. 6, pp. 42–44.
8. Okhotnikova, O.P., Kostoglod, O.B., Astrelin, I.M., and Knyazev, Yu.V., *Sbornik nauchnykh trudov Mezhdunarodnoi nauchno-tekhnicheskoi konferentsii "Sovremennye problemy khimicheskoi tekhnologii neorganicheskikh veshchestv"* (Proc. Int. Sci.-Pract. Conf. "Modern Problems of the Chemical Technology of Inorganic Substances"), Odessa, 2001, vol. 2, p. 156.
9. Crocker, C.L., *Am. J. Med. Technol.*, 1967, vol. 33, p. 361.
10. Voskresenskii, P.I., *Tekhnika laboratornykh rabot* (Technology of Laboratorty Studies), Moscow: Khimiya, 1973.
11. Charlot, G., *Les Methods de la Chemie Analytique. Analyse quantitative Minerale, Quatrieme Edition*, Paris: Masson, 1961.
12. Klimova, V.A., *Osnovnye metody analiza organicheskikh soedinenii* (Main Methods for Analysis of Organic Compounds), Moscow: Khimiya, 1975.
13. Romanenko, S.A., Component Composition of Aqueous Solutions ofSulfur(IV) Oxide, *Cand. Sci. Dissertation*, Leningrad, 1986.
14. Labutin, N.A., Batikha, M.M., Groshev, G.L., and Korotaevskii, K.N., *Izv. Vyssh. Uchebn. Zaved., Khim. Khim. Tekhnol.*, 1997, vol. 40, no. 4, p. 55.

15. Pereda, S., Thomsen, K., and Rasmussen, P., *Chem. Eng. Sci.*, 2000, vol. 55, pp. 2663–2671.
16. Huss, A.J. and Eckert, C.A., *J. Phys. Chem.*, 1977, vol. 81, no. 24, pp. 2268–2270.
17. Deister, U., Neeb, R., Helas, G., and Warneck, P., *J. Phys. Chem.*, 1986, vol. 90, no. 14, pp. 3213–3217.
18. Khoma, R.E., Nikitin, V.I., Sokhranenko, G.P., and Gavrilenko, M.I., *Visnik Odessk. Nats. Univ., Ser. Khim.*, 2002, vol. 6, no. 8, p. 176.
19. Ermakov, A.N., Poskrebyshev, G.A., and Purmal', A.P., *Kinet. Kataliz*, 1997, vol. 38, no. 3, pp. 325–338.
20. Connick, R.E., Tam, T.M., and von Deuster, E., *Inorg. Chem.*, 1982, vol. 21, no. 1, pp. 103–107.
21. Bershtein, I.Ya. and Kaminskii, Yu.L., *Spektrofotometricheskii analiz v organicheskoi khimii* (Spectrophotometric Analysis in Organic Chemistry), Leningrad: Khimiya, 1986.
22. Hartley, F.R., Burgess, C., and Alcock, R.M., *Solution Equilibria*, Chichester: Ellis Horwood, 1980.
23. Albert, A. and Serjeant, E., *Ionization Constants of Acids and Bases. A Laboratory Manual*, New York: Wiley, Methuen, 1962.

Russian Journal of Applied Chemistry, Vol. 77, No. 8, 2004, pp. 1255–1258. Translated from Zhurnal Prikladnoi Khimii, Vol. 77, No. 8, 2004, pp. 1271–1274.

PHYSICOCHEMICAL STUDIES OF SYSTEMS AND PROCESSES

Thermodynamic Calculation of the Solubility of Solid Hydroxides $M(OH)_2$ in Water and Alkaline Media

E. V. Shkol'nikov

St. Petersburg State Forestry Academy, St. Petersburg, Russia

Received April 15, 2004

Abstract—The influence exerted by the pH value on the molar solubility of a number of amorphous and crystalline hydroxides of Group-II elements in an aqueous alkaline medium was calculated thermodynamically with account of the formation of hydroxo complexes.

Previously, the thermodynamic method has been used to establish the limits of applicability of crystalline sensor membranes in a strongly acidic medium [1]. However, as the hydrogen index of the medium increases, binding of free cations into hydroxo complexes changes the response of Cd- (Hg, Ca, Cu, Pb)-ion-selective electrodes by making narrower the range of admissible pH values in a potentiometric analysis for cations. At the same time, the effect of the pH value on the solubility of metal hydroxides in an aqueous-alkaline medium is of interest in itself in determining the conditions of hydrolysis, virtually complete precipitation, or effective masking of cations in the form of soluble hydroxo complexes [2]. In addition, the amphoteric behavior and the effect of structural-chemical specific features of te hydroxides on their solubility in water have been studied insufficiently [2, 3].

A thermodynamic calculation of the solubility of a number of hydroxides in pure water and in an aqueous-alkaline medium (with addition of NaOH or $HClO_4$) at pH 7–15 and 25°C was performed. As objects of study were chosen hydroxides of Group-II elements, which are used in chemical processing of wood and vegetable waste, forestry and agriculture, medicine, and analytical chemistry.

In an aqueous solution saturated with a sparingly soluble hydroxide $M(OH)_2$, a heterogeneous chemical equilibrium

$$M(OH)_2(\text{cryst}) \rightleftarrows M^{2+}(\text{sol}) + 2OH^-(\text{sol}), \qquad (1)$$

is attained, whose thermodynamic constant is given by the expression

$$K_s^0 = \text{SP}^{\text{th}} = a_{M^{2+}} a_{OH^-}^2 = \text{const}(T), \qquad (2)$$

where $a_{M^{2+}}$ and a_{OH^-} are the activities of the ions M^{2+} and OH^-.

The constant K_s^0 was calculated using the thermodynamic relation [1]

$$\log K_s^0 = -0.175\Delta G_{s,298}^0, \qquad (3)$$

where $\Delta G_{s,298}^0$ is the standard change in the Gibbs energy (kJ mol^{-1}), which was calculated for the dissolution process (1) by the equation

$$\Delta G_s^0 = \Delta G_{f,M^{2+}}^0 + 2\Delta G_{f,OH^-}^0 - \Delta G_{f,M(OH)_2}^0; \qquad (4)$$

The values of ΔG_f^0 for ion formation in aqueous solutions were taken from [4]; those for Zn^{2+}, from the reference book [5]; and values of ΔG_f^0 for formation of amorphous or crystalline modifications of hydroxides at 298 K, from the reference books [5–7] or found by calculation [8]. In the calculation for mercury(II) in a saturated aqueous solution, the following chemical equilibria were taken into account

$$HgO(\text{cryst}) + H_2O(\text{l}) \Leftrightarrow Hg(OH)_2(\text{sol}) \Leftrightarrow Hg^{2+}(\text{sol}) + 2OH^-(\text{sol}). \qquad (5)$$

The molar solubility of $M(OH)_2$ in pure water and in aqueous NaOH solutions was calculated taking into account the ionic strength of the solution and the formation of mononuclear hydroxo complexes [2], using the generalized equation

$$s = c_M \frac{K_s^0}{f_{M^{2+}} + f_{OH^-}^2} \sum_{i=0}^{n} \beta_i [OH^-]^{i-2}, \qquad (6)$$

1070-4272/04/7708-1255 © 2004 MAIK "Nauka/Interperiodica"

Ionicity and thermodynamic parameters of dissolution of crystalline hydroxides in water and alkali at 25°C

Composition	P_i, %	ΔG_s^0, kJ mol^{-1}	pK_s^0		s, M		A	$\bar{n}$
			calculation	[2]	in H_2O	in 1 M NaOH		
$Be(OH)_2^*$	64	121.8	21.32	21.31	6×10^{-7}	5×10^{-3}	2×10^4	3.87
α-$Be(OH)_2$		125.4	21.94	–	3×10^{-7}	1×10^{-3}	1×10^4	
β-$Be(OH)_2$		128.0	22.39	–	1.4×10^{-7}	4×10^{-4}	8×10^3	
β-$Be(OH)_2^*$		126.9	22.20	–	1.8×10^{-7}	6×10^{-4}	9×10^3	
$Mg(OH)_2^*$	74	(52.7)	–	9.22	7×10^{-4}	2×10^{-7}	6×10^{-5}	0.1
$Mg(OH)_2$		63.4	11.10	11.15	2×10^{-4}	4×10^{-9}	4×10^{-6}	
$Ca(OH)_2$	78	29.1	5.10	5.19	2×10^{-2}	2×10^{-3}	0.1	1.99
$Sr(OH)_2^{**}$	79	18.0	3.15	3.50	8×10^{-2}	2×10^{-3}	4×10^{-3}	0.98
β-$Ba(OH)_2^{**}$	81	15.1	2.65	2.30	0.28	0.046	0.1	1.1
α-$Zn(OH)_2$	64	90.4	15.81	–	5×10^{-5}	0.10	5×10^4	3.99
β-$Zn(OH)_2$		92.1	16.12	–	1.9×10^{-5}	0.051	7×10^4	
γ-$Zn(OH)_2$		92.3	16.14	–	1.8×10^{-5}	0.048	7×10^4	
δ-$Zn(OH)_2$		92.5	16.18	–	1.7×10^{-5}	0.044	6×10^4	
ε-$Zn(OH)_2$		94.1	16.48	16.86	1.5×10^{-5}	0.022	4×10^4	
α-$Cd(OH)_2^*$	65	77.8	13.62	13.66	2.2×10^{-5}	2.5×10^{-5}	15	3.90
β-$Cd(OH)_2$		81.6	14.27	14.23	1.3×10^{-5}	6×10^{-6}	6	
α-HgO	47	145.6	25.49	25.52	2.0×10^{-4}	2.4×10^{-4}	1.6	2.54
β-HgO		146.0	25.55	–	1.9×10^{-4}	2.3×10^{-4}	1.6	

* Freshly precipitated amorphous.

** Octahydrate.

where c_M is the total molality of all the chemical forms of M(II) in a saturated solution; $f_{M^{2+}}$ and f_{OH^-}, the molar activity coefficients of the ions M^{2+} and OH^-; $\beta_0 = 1$; and β_1, β_2, β_3, and β_4, the total stability constants of the hydroxo complexes MOH^+, $M(OH)_2$, $M(OH)_3^-$, and $M(OH)_4^{2-}$.

The concentration of free anions OH^- and the pH value of saturated hydroxide solutions in pure water were found by solving the system of three equations

$$[M^{2+}][OH^-]^2 = K_s^0, \quad \frac{[MOH^+]}{[M^{2+}][OH^-]} = \beta_1,$$

$$[M^{2+}] + [MOH^+] = [OH^-] \qquad (7)$$

with the use of the Cardano method for a cubic equation.

The results of the calculations are listed in the table ($pK_s^0 = -\log K_s^0$; P_i, the ionicity of the chemical bond M–O in a hydroxide, evaluated using the Pauling curve in relation to the difference of the electronegativities of the elements M and O; A, the amphoterism parameter; and $\bar{n}$, the ligand number).

It can be seen from the table that there is a satisfactory agreement between the pK_s^0 values calculated by Eq. (3) and those taken from the reference book [2]. For a number of hydroxide modifications, K_s^0 was calculated for the first time. For strontium and barium hydroxides, the parameters of dissolution of octahydrates, which are stable in saturated aqueous solutions, were determined.

As the ionicity of the M–O bond increases in the order $Be \rightarrow Mg \rightarrow Ca \rightarrow Sr \rightarrow Ba$, the solubility of the hydroxides $M(OH)_2$ in pure water grows dramatically (see table). The solubility of freshly precipitated amorphous hydroxides of beryllium, magnesium, zinc, and cadmium exceeds that of their crystalline modifications. The solubility of these latter strongly depends on structure and decreases on passing to the stable modifications β-$Be(OH)_2$, ε-$Zn(OH)_2$, and β-HgO.

It can be seen from the table and the figure (curves *2*, *3*) that, as the pH or the active alkalinity of the medium (a_{OH^-}) increases, the molar solubility of the bases $Mg(OH)_2$, $Ca(OH)_2$, $Sr(OH)_2$, and $Ba(OH)_2$ steadily decreases, following the approximate equation $s = K_s/[OH^-]^2$. The effect of a strong decrease in solubility in the presence of the likely charged OH^- ions is not compensated for by a weak positive effect of formation of the unstable hydroxo complexes

MOH^+ and $M(OH)_2$. The solubility of the yellow (α) and red (β) modifications of HgO is nearly independent of pH in the range 7–13, and only at pH ≥ 14 starts to increase noticeably [see table and figure (curve *6*)]. The solubility of amphoteric hydroxides of beryllium, zinc, and cadmium passes through a minimum as the pH value of the medium increases (see figure, curves *1*, *4*, and *5*). Analysis of Eq. (6) shows that the lowest solubility of $M(OH)_2$ precipitates is observed at the optimal concentration of OH^- ions, when neutral complexes $M(OH)_2$ are predominant among the equilibrium species in solution. From the condition for the maximum mole fraction $x_{M(OH)_2}$, the following equation was obtained

$$2\beta_4[OH^-]^4 + \beta_3[OH^-]^3 - \beta_1[OH^-] - 2 = 0. \quad (8)$$

Solving this equation approximately with the use of the Newton method and the constants β_i from the reference book [2] yielded the $[OH^-]_{opt}$ at $x_{M(OH)_2} = \max$ and then s_{min} (see figure). The values of s_{min} (M) at 25°C are 1.5×10^{-7} and 1.3×10^{-8} for freshly precipitated amorphous and β-$Be(OH)_2$, respectively, at pH 8.9; 2×10^{-5} and 5×10^{-6} for α- and ε-$Zn(OH)_2$ at pH 10.2; and 2×10^{-6} and 4×10^{-7} for α- and β-$Cd(OH)_2$ at pH 11.6.

The mole fraction of free cations M^{2+} in saturated aqueous solutions of $M(OH)_2$ was calculated using the equation

$$x_{M^{2+}} = [M^{2+}]/c_M = \left(1 + \sum_{i=0}^{n} \beta_i [OH^-]^i\right)^{-1}, \quad (9)$$

where $n = 1$ for Mg^{2+} and Sr^{2+}; $n = 2$ for Ca^{2+} and Ba^{2+}, $n = 3$ for Hg^{2+}; and $n = 4$ for Be^{2+}, Zn^{2+}, and Cd^{2+} [2].

Doubly charged cations not bound into hydroxo complexes can be determined potentiometrically in pure aqueous solutions at pH less than 1.5 (Hg), 3.5 (Be), 5.5 (Zn, Cu, Pb), 8.0 (Cd), 9.5 (Mg), and 10.5 (Ca, Sr, Ba).

In purely aqueous saturated solutions of the hydroxides (shown by the arrows in the figure), $BeOH^+$, Mg^{2+}, Ca^{2+}, Sr^{2+}, Ba^{2+}, $ZnOH^+$, Cd^{2+}, and $Hg(OH)_2$ predominate. The complexation is the strongest for cations of mercury(II), beryllium, and zinc, which form the least stable and least water-soluble hydroxides.

It can be suggested to evaluate the amphoterism of the hydroxides by ratio ($A > 1$) of their molar solubilities in an alkaline medium with pH 14.7 (5 M NaOH solution) and in pure water. As follows from the table, the amphoterism of the hydroxides decreases in the order $Zn(OH)_2 \rightarrow Be(OH)_2 \rightarrow Cd(OH)_2 \rightarrow HgO$. In approximately the same order decreases the mean ligand number $\bar{n}$ in the hydroxo complexes (Bjorrum function) at $[OH^-] = 10$ M (see table). Hydroxides of magnesium, calcium, strontium, and barium show no amphoterism ($A < 1$, $n < 2$).

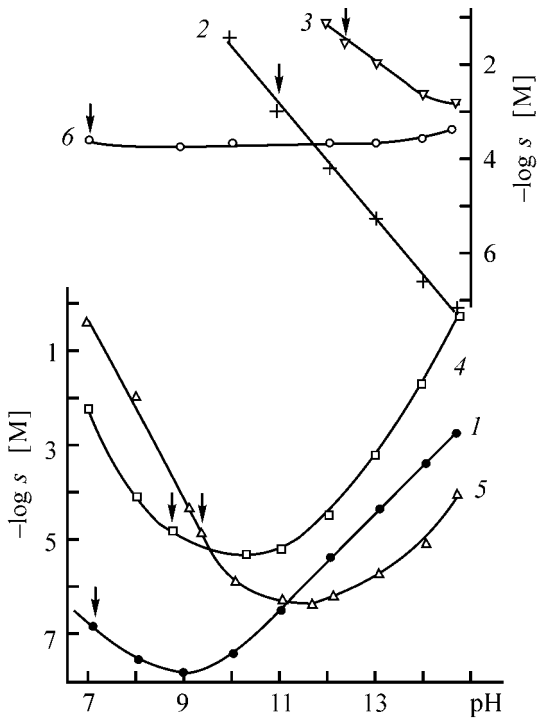

Solubility *s* of solid hydroxides vs. the pH value of the aqueous-alkaline medium at 25°C. (*1*) (β-$Be(OH)_2$, (*2*) freshly precipitated $Mg(OH)_2$, (*3*) $Ca(OH)_2$, (*4*) (ε-$Zn(OH)_2$, (*5*) (β-$Cd(OH)_2$, and (*6*) (α-HgO.

CONCLUSIONS

(1) The molar solubility of $M(OH)_2$ hydroxides in water grows as the ionicity of the chemical bond M–O increases in the order $Be \rightarrow Mg \rightarrow Ca \rightarrow Sr \rightarrow Ba$ and depends on their structure, decreasing on passing from the amorphous to the stable crystalline modification.

(2) The thermodynamic method is used to calculate the effect of the pH value on the solubility of the hydroxides $M(OH)_2$ in an aqueous-alkaline medium. A condition for existence of amphoterism in $M(OH)_2$ (mean ligand number in the hydroxo complexes $\bar{n} > 2$) and its estimate (parameter $A > 1$) increasing in the order $HgO \rightarrow Cd(OH)_2 \rightarrow Be(OH)_2 \rightarrow Zn(OH)_2$ are suggested. The pH intervals in which cations of Group-II metals are not bound into hydroxo complexes are determined.

(3) The minimum solubility and the pH values at which the precipitation of amphoteric hydroxides of beryllium, zinc, and cadmium is the most complete are calculated with account of the formation of hydroxo complexes.

REFERENCES

1. Shkol'nikov, E.V., *Zh. Prilk. Khim.*, 2003, vol. 76, no. 11, pp. 1785–1787.
2. Lur'e, Yu.Yu., *Spravochnik po analiticheskoi khimii* (Handbook of Analytical Chemistry), Moscow: Khimiya, 1989.
3. Kumok, V.N., Kuleshova, O.M., and Karabin, L.A., *Proizvedeniya rastvorimosti* (Solubility Products), Novosibirsk: Nauka, 1983.
4. Vasil'ev, V.P., *Termodinamicheskie svoistva rastvorov elektrolitov* (Thermodynamic Properties of Electrolyte Solutions), Moscow: Vysshaya shkola, 1982.
5. *Kratkii spravochnik fiziko-khimicheskikh velichin* (Concise Reference Book of Physicochemical Quantities), Ravdel', A.A. and Ponomareva, A.M., Eds., Leningrad: Khimiya, 1983.
6. Karapet'yants, M.Kh. and Karapet'yants, M.L., *Osnovnye termodinamicheskie konstanty neorganicheskikh i organicheskikh veshchestv* (Basic Thermodynamic Constants of Inorganic and Organic Substances), Moscow: Khimiya, 1968.
7. *Termodinamicheskie svoistva individual'nykh veshchestv* (Thermodynamic Properties of Individual Substances), Glushko, V.P., Ed., Moscow: Nauka, 1979–1981, vols. 1–4.
8. Shkol'nikov, E.V., Naraev, V.N., and Fomicheva, T.I., *Osnovy khimicheskoi termodinamiki* (Fundamentals of Chemical Thermodynamics), St. Petersburg: SPb. Gos. Lesotekhn. Akad., 2002.
9. Ormont, B.F., *Vvedenie v fizicheskuyu khimiyu i kristallokhimiyu poluprovodnikov* (Introduction into Physical Chemistry and Crystal Chemistry of Semiconductors), Moscow: Vysshaya shkola, 1973.

Russian Journal of Applied Chemistry, Vol. 77, No. 8, 2004, pp. 1259–1262. Translated from Zhurnal Prikladnoi Khimii, Vol. 77, No. 8, 2004, pp. 1275–1278.

SORPTION AND ION-EXCHANGE PROCESSES

Selective Ion-Exchange Sorption of K^+ from Aqueous Solutions Containing Na^+–K^+ Mixture on Sn(IV) Hydrophosphate

G. I. Smirnov, L. M. Dimova, and A. A. Redchenko

Irkutsk State University, Irkutsk, Russia

Received December 23, 2003; in the final form, April 2004

Abstract—Ion-exchange sorption of K^+ and Na^+ from their mixture on X-ray-amorphous and crystalline Sn(IV) hydrophosphates was studied. These sorbents exhibit a high selectivity for K^+. Amorphous Sn(IV) hydrophosphate can be used for efficient purification of aqueous sodium salt solutions to remove potassium impurity.

It is known that metal(IV) hydrophosphates show a high selectivity in the ion-exchange sorption of various metal cations, including chemical analogues. However, the most part of data on this subject concern the sorption of metals from aqueous solutions containing only one kind of cations. Data on ion-exchange sorption of metals from their binary mixtures on Zr(IV) hydrophosphate are scarce [1–3]. A procedure has been developed for purification of sodium iodide to remove potassium cations by sorption treatment of aqueous NaI–KI mixture with Sn(IV) hydrophosphate [4]. However, the physicochemical reasons for the selectivity of sorbents based on Sn(IV) hydrophosphate for K^+ and the effect of their crystalline ordering on selectivity for alkali metals are poorly understood.

In this study, we examined the selectivity of ion-exchange sorption of Na^+ and K^+ from their binary mixture on X-ray-amorphous and crystalline samples of Sn(IV) hydrophosphate.

EXPERIMENTAL

X-ray-amorphous Sn(IV) hydrophosphate was prepared by recrystallization of crude Sn(IV) hydrophosphate (P : Sn ratio 1.4) in 0.5 M aqueous H_3PO_4 for 48 h [5]. Crystalline Sn(IV) hydrophosphate was prepared by precipitation from refluxing 12 M aqueous H_3PO_4 (reaction time 175 h) [6]. The ion-exchange characteristics of both amorphous and crystalline Sn(IV) hydrophosphates were determined by potentiometric titration of their weighed portions with a multicomponent alkaline titrant containing 0.1 M KCl and 0.1 M NaCl, or 0.1 M KOH and 0.1 M NaOH [7].

The content of K^+ and Na^+ ions in solution before and after sorption was determined using the atomic-absorption method. The relevative standard deviation was 0.002.

It has been reported [5, 6] that both crystalline and amorphous ion-exchangers based on Sn(IV) phosphate are composed of Sn(IV) hydrophosphate $Sn(HPO_4)_2$ containing the hydrophosphate anions as the cation-exchange sites. Figure 1 shows the curves of potentiometric titration of amorphous and crystalline Sn(IV) hydrophosphates with the alkaline multicomponent titrant, plotted as pH vs. the amount of hydroxide added. We found that, on addition of the titrant to the initial sorbent–water suspension to pH 9, the concentration of phosphate anions in the liquid phase remains constant (3×10^{-2} g l^{-1}), i.e., the ion-exchange sorption of alkali metals does affect the solubility of Sn(IV) hydrophosphate. Figure 1 shows that, on adding the alkaline titrant to an aqueous suspension of amorphous Sn(IV) hydrophosphate, the pH gradually increases. Such a shape of the sorption titration curve shows that, in sorption of alkali metal cations under consideration, a continuous series of their solid solutions in the amorphous sorbent is formed. By contrast, for crystalline Sn(IV) hydrophosphate, the slope of the titration curve sharply decreases at pH 6.2 due to fundamental changes in the sorption mechanism.

At pH < 6.2, the sorption capacity of the amorphous sorbent for K^+ and Na^+ exceeds that of the crys-

1070-4272/04/7708-1259 © 2004 MAIK "Nauka/Interperiodica"

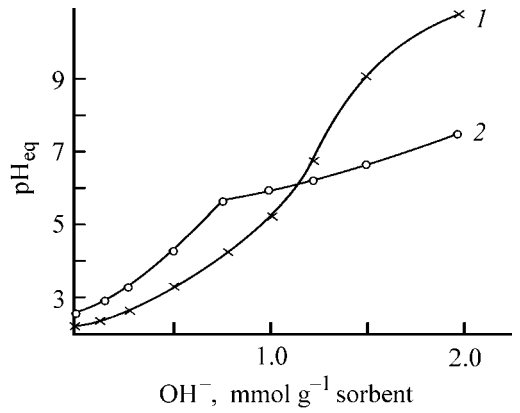

Fig. 1. Curves of potentiometric titration of Sn(IV) hydrophosphate with an alkaline titrant containing $K^+$and Na^+. (OH^-) Amount of hydroxide anions added. Sorbent type: (*1*) X-ray-amorphous (recrystallized from 0.5 M H_3PO_4 for 48 h) and (*2*) crystalline (prepared by boiling in 12 M H_3PO_4 for 175 h).

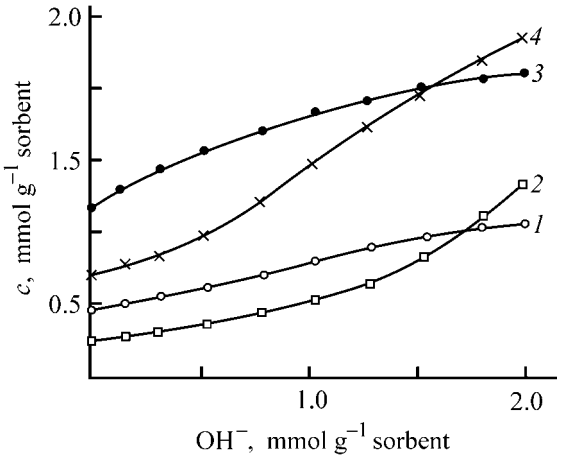

Fig, 2. Sorption of K^+ and Na^+ from their mixtures on Sn(IV) hydrophosphate vs. the amount of hydroxide anions added. Sorbent type: (*1, 3*) X-ray-amorphous and (*2, 4*) crystalline. (*1, 2*) Na^+ and (*3, 4*) K^+.

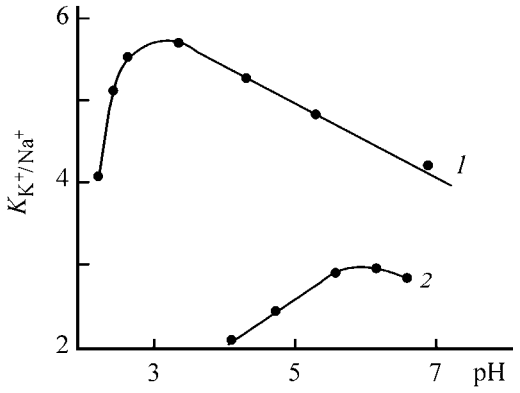

Fig. 3. K^+/Na^+ separation factor for sorption on Sn(IV) hydrophosphate as influenced by pH. Sn(IV) hydrophosphate: (*1*) X-ray-amorphous and (*2*) crystalline.

talline sorbent. At the same time, the crystalline Sn(IV) hydrophosphate becomes a stronger sorbent for alkali metal cations at pH > 6.2 (Fig. 1). This difference is caused by features of the amorphous and crystalline sorbents. The amorphous Sn(IV) hydrophosphate (interplanar spacing 0.874 nm) has a more disordered structure than the crystalline sorbent (interplanar spacing 0.785 nm) [5, 6]. Therefore, at pH < 6.2 the sorbing sites of the amorphous sorbent are more accessible to alkali metal cations. As the alkaline titrant is added, the content of protons in Sn(IV) hydrophosphate decreases and excess hydroxide anions are sorbed. As a result, the sorbent matrix becomes negatively charged and the sorbent capacity for charge-compensating alkali cations increases [7, 8]. It is also believed [9] that the sorption of Na^+ on crystalline Sn(IV) hydrophoshate facilitates the sorption of K^+ owing to broadening of the channels and cavities in the sorbent structure and decrease in the sterical hindrance to sorption. Therefore, at pH > 6.2 the total sorption capacity of the crystalline sorbent for K^+ and Na^+ exceeds that of the amorphous sorbent.

The curves in Fig. 2 demonstrate the contribution of $K^+$and Na^+ cations to the total sorption capacity of the sorbents for these cations. These curves show that the sorption capacity of both crystalline and amorphous Sn(IV) hydrophosphates grows with increasing amount of hydroxide anions added. These correlations are consistent with the well-known effect of acidity on the concentration of ionized sorbent sites in the cation exchanger [8]. When the amount of added hydroxide anions exceeds 0.75 mmol g^{-1} of sorbent, the curves describing sorption of K^+ and Na^+ on the crystalline sorbent becomes steeper than the curves for sorption these cations on the amorphous sorbent and, ultimately, both alkali metal cations become more sorbable on the crystalline sorbent.

Figure 2 shows that, in sorption of K^+ and Na^+ from their mixtures on X-ray-amorphous Sn(IV) hydrophosphate, the sorption of K^+ prevails. The stronger sorption of K^+ than Na^+ on Sn(IV) hydrophosphate was also observed in sorption of these cations from aqueous solutions containing only one kind of these cations [5]. Thus, our data show that K^+ and Na^+ do not interfere with each other in their simultaneous sorption on the sorbents under consideration.

It was reported in [6] that, in sorption of K^+ and Na^+ from their aqueous solutions containing either Na^+ or K^+ on crystalline Sn(IV) hydrophosphate, Na^+ cations are more sorbable than K^+. At the same time, Fig. 2 shows that the sorption of K^+ prevails in sorption of K^+ and Na^+ from their binary mixture on the crystalline sorbent. We believe that, in sorp-

tion of K^+ and Na^+ from their mixture on crystalline Sn(IV) hydrophosphate, the sorption of relatively small Na^+ cations facilitates that of larger K^+ cations owing to broadening of the channels and cavities in the sorbent. Similar effects have been reported for crystalline zirconium and titanium hydrophosphates [9].

Figure 3 shows that the plots of the K^+/Na^+ separation factor against pH for crystalline and amorphous Sn(IV) hydrophosphate have similar shapes with a maximum. The greatest K^+/Na^+ separation factors for amorphous and crystalline sorbents, equal to 5.7 and 3.0, are observed at pH 3.2 and 5.8, respectively. Thus, the X-ray-amorphous sorbent is more selective for K^+ than the crystalline sorbent.

The data reported in [5, 6] show that amorphous Sn(IV) hydrophosphate exhibits a higher chemical stability than crystalline Sn(IV) hydrophosphate. For example, in sorption of Na^+ from aqueous NaI on amorphous and crystalline sorbents, the phosphate concentration in the equilibrium sorbate was 13.0 and 20.2 mg l^{-1}, respectively. Since amorphous Sn(IV) hydrophosphate is more chemically stable and more selective to K^+ than the crystalline sorbent, the former is more suitable for practical separation of K^+ from Na^+.

The separation of microamounts of K^+ from similar amounts of Na^+ microamounts is one of important problems in analytical chemistry. In this context, the sorption of K^+ and Na^+ from their mixture on amorphous Sn(IV) hydrophosphate was studied in relation to pH (see table). The sorption was carried out under static conditions from an aqueous NaCl–KCl mixture containing 1 mg l^{-1} of each cation.

The table shows that, with the pH increasing to 3.2, the distribution and separation factors of K^+ first grow and then remain constant. By contrast, the sorption of Na^+ begins at pH 3.2. These data show that the best separation of K^+ from Na^+ is achieved in the case of sorption on amorphous Sn(IV) hydrophosphate at low pH.

Owing to the high selectivity of amorphous Sn(IV) hydrophosphate for K^+, this sorbent can be used for efficient purification of sodium salts to remove K^+. Taking into account that this procedure must ensure efficient separation of potassium from both micro and macroamounts of sodium, the sorption of K^+ on amorphous Sn(IV) hydrophosphate from aqueous solutions containing various NaI amounts was studied at pH 3 (Fig. 4). The K^+ content in all the K^+–Na^+ mixtures tested was 5×10^{-3} wt %.

Figure 4 shows that, with increasing NaI concentration, the efficiency of NaI purification to remove

Sorption of microamounts of K^+ and Na^+ from their mixture on X-ray-amorphous Sn(IV) hydrophosphate*

pH_{eq}	E, %		K_d		K_{K^+/Na^+}
	K^+	Na^+	K^+	Na^+	
1.0	68	0	110	0	–
2.0	94	0	780	0	–
2.9	96	0	1200	0	–
3.2	99	22	4950	14	350
3.2	99	33	4950	25	200

* (E) Degree of sorption (%) and (K_d) distribution factor.

K^+ decreases. Therefore, in order to ensure a high efficiency of NaI purification to remove K^+, the NaI concentration in the NaI–KI mixture should be low. However, we found that even at a NaI content as high as 300–400 g l^{-1}, the separation of potassium from sodium was quite acceptable to ensure an efficient purification of NaI to remove KI under dynamic conditions. The sorptive separation of K^+ from Na^+ on amorphous Sn(IV) hydrophosphate ensures preparation of sodium salts of ultrapure grade, which contain less than 2×10^{-4}% K^+.

CONCLUSIONS

(1) In the pH range below 6.2, the total cation-exchange capacity of X-ray-amorphous Sn(IV) hydrophosphate for a K^+–Na^+ mixture exceeds that of crystalline Sn(IV) hydrophosphate but, at pH > 6.2, the crystalline sorbent becomes more efficient than its amorphous modification.

(2) Owing to its higher selectivity for K^+ and higher chemical stability as compared to the crystal-

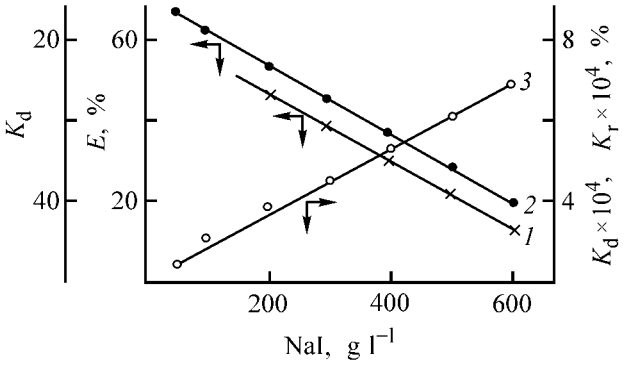

Fig. 4. Characteristics of K^+ sorption on amorphous Sn(IV) hydrophosphate vs. NaI concentration. (*1*) Distribution factor K_d, (*2*) degree of sorption E, and (*3*) residual K^+ content in aqueous solution K_r.

line modification, amorphous Sn(IV) hydrophosphate is more suitable for separation of K^+ from Na^+. The optimal separation is achieved at pH lower than 3.2. Amorphous Sn(IV) hydrophosphate can also be used for efficient purification of concentrated Na-containing solutions to remove K^+ microimpurities.

REFERENCES

1. Kullberg, L. and Clearfild, A.J., *Inorg. Nucl. Chem.*, 1981, vol. 43, no. 10, pp. 2543–2548.
2. Kullberg, L. and Clearfild, A., *Solent Extr. Ion Exch.*, 1983, vol. 1, no. 1, pp. 77–96.
3. Clearfild, A. and Madina, A.S., *J. Inorg. Nucl. Chem.*, 1973, vol. 35, no. 18, pp. 2985–2992.
4. USSR Inventor's Certificate, no. 814865.
5. Smirnov, G.I., Redchenko, A.A., Kachur, N.Ya., *et al., Zh. Prikl. Khim.*, 2000, vol. 73, no. 12, pp. 1945–1950.
6. Smirnov, G.I., Redchenko, A.A., Dimova, L.M., *et al., Izv. Vyssh. Uchebn. Zaved., Khim. Khim. Tekhnol.*, 2000, vol. 43, no. 5, pp. 43–47.
7. *Teoreticheskoe i prakticheskoe rukovodstvo k laboratornym rabotam po fizicheskoi khimii* (Theoretical and Practical Laboratory Manual on Physical Chemistry), Nikol'ski, B.P., Ed., Leningrad: Goskhimizdat, 1951.
8. Yaroslavtsev, A.B., *Usp. Khim.*, 1977, vol. 46, no. 7, pp. 641–659.
9. Alberti, G., Costanantino, U., and Gupta, J.P., *J. Inorg. Nucl., Chem.*, 1974, vol. 36, no. 9, pp. 2109–2114.
10. Smirnova, O.M., Smirnov, G.I., Chernyak, A.S., *et al.*, in *Materialy dlya opticheskikh ustroistv i stsintillyatorov: Sbornik nauchnikh trudov VNII monokristallov* (Materials for Optical Devices and Scintillators: Transactions of All-Union Research Inst.of Singlecrystals), Kharkov: 1986, no. 18.

Russian Journal of Applied Chemistry, Vol. 77, No. 8, 2004, pp. 1263–1267. Translated from Zhurnal Prikladnoi Khimii, Vol. 77, No. 8, 2004, pp. 1279–1283.

SORPTION AND ION-EXCHANGE PROCESSES

Acid–Base Characteristics of Carbon Adsorbents, Determined by Potentiometric Titration

A. M. Puzii, O. I. Poddubnaya, and S. S. Stavitskaya

Institute of Sorption and Endoecological Problems, National Academy of Sciences of the Ukraine, Kiev, Ukraine

Received May 12, 2003; in final form, March 2004

Abstract—For initial carbons of varied origin and carbons oxidized with various oxidizing agents, the continuous distribution function of surface groups with respect to the protonation constants was determined by acid–base potentiometric titration.

The surface chemistry of carbon materials is of great importance for their use as adsorbents, catalysts, or supports of catalytically active substances [1–3]. The surface characteristics of carbon adsorbents are governed by heteroatoms, which can substitute carbon atoms in the carbon structure or occur in the form of surface groups.

To determine the surface groups of carbon materials, various methods have been used [3]. The best known and rather simple method is selective neutralization of surface groups with alkaline ($NaHCO_3$, Na_2CO_3, NaOH, NaOEt) or acidic (HCl) solutions [4]. According to this method, the surface groups are classified into several discrete types of acidic (carboxy, lactonic, phenolic, carbonyl) and basic (pyrone, chromene) nature depending on their ability to add or eliminate proton. However, assignment of individual types of surface groups to definite chemical structures is arbitrary. For example, neutralization of carboxy groups with sodium hydrogen carbonate or phenolic groups with sodium hydroxide has been reported to be incomplete [5].

One of the methods for determining acid–base surface groups is potentiometric titration. It was shown that the titration curve of carbon black oxidized with nitric acid suggests the presence of surface groups with the acidity close to that of carboxy groups [6]. Later, a more perfect method was suggested, in which the titration curves obtained in the experiments (dependence of equilibrium solution pH on the volume of titrant added) are transformed into the isotherms of proton sorption (dependence of the amount of sorbed protons on pH) [7]. However, the isotherms are usually characterized in the case of carbon adsorbents by smooth variation of the amount of sorbed protons throughout the entire pH range without any plateaus or inflections. This shape of the isotherm gives no way of distinguishing individual surface groups without using complicated calculation procedures.

A significant progress in the analysis of acid–base characteristics of carbon adsorbents was achieved with the nonuniformity of surface groups analyzed by solving the integral equation of adsorption by approximation of the local isotherm (the Rudzinskii–Jagiello method) [8]. This method allows evaluation of continuous distribution of surface groups with respect to protonation constants. Later the resolution of peaks in the distribution curve was improved by numerical solution of the integral adsorption equation by the SAIEUS method [9, 10]. However, this method disregards the electrostatic interaction of the charged adsorbent surface with ions of the nearsurface layer is not considered.

For carbon adsorbents, the difference in the proton concentrations in the solution and near the surface may be as large as two to three orders of magnitude. Therefore, the constants calculated without taking into account the influence of the charged adsorbent surface on the concentration of ions near surface groups are only apparent.

In this study, we applied the method of a continuous distribution of surface groups with respect to the protonation constants, with account taken of the electrostatic interaction, to analysis of the surface groups of carbon adsorbents on the basis of potentiomentric titration data [11, 12].

1070-4272/04/7708-1263 © 2004 MAIK "Nauka/Interperiodica"

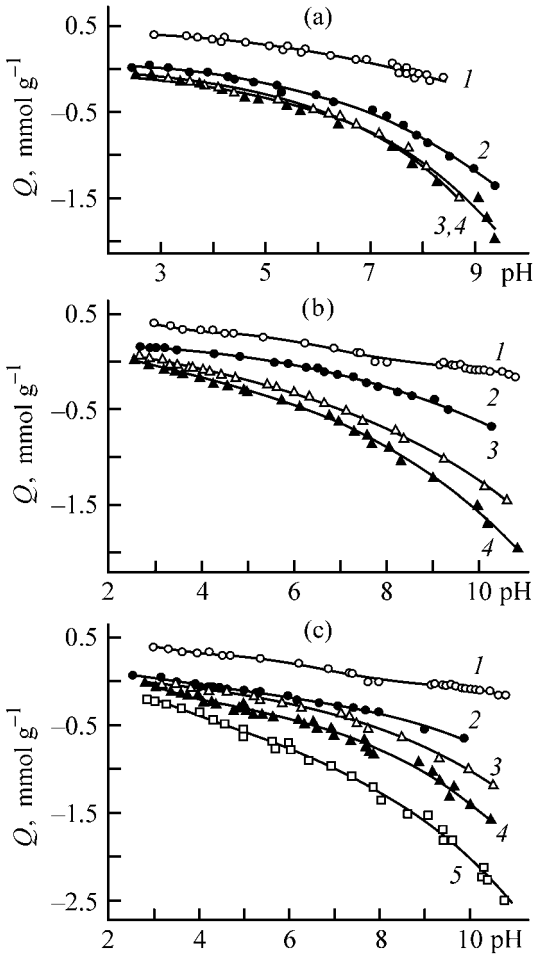

Fig. 1. Proton sorption Q by (a) SKN synthetic carbons oxidized with air and KAU pit carbons oxidized with (b) air and (c) HNO_3, vs. pH. (a) (*1*) SKN, (*2*) SKNo-1.6, (*3*) SKN0-2.0, and (*4*) SKNo-2.2; (b) (*1*) KAU, (*2*) KAUo-1.0, (*3*) KAUo-1.7, and (*4*) KAUo-2.2; (c) (*1*) KAU, (*2*) KAUo-0.8, (*3*) KAUo-1.2, (*4*) KAUo-1.8, and (*5*) KAUo-2.6; the same for Fig. 2.

EXPERIMENTAL

Synthetic carbon SKN from vinylpyridine copolymer [13] and carbon KAU from apricot pit [14] with progressive increase in the degree of oxidation were used. The synthetic (SKN) and pit (KAU) carbons were oxidized by hot humid air (300 ml min^{-1}) at 430°C for 2, 6, and 10 h. Pit carbon KAU was also oxidized with boiling 25% nitric acid (carbon : acid = 1 : 3) for 0.5, 2.5, 10, and 15 h.

Potentiometric titration was carried out by the method of separate weighed portions at constant ionic strength (0.1 M NaCl) [11]. The sorption isotherms of protons were calculated from the potentiometric titration data by the formula

$$Q = \frac{V_0 + V_{tit}}{m}\left([H^+]_{in} - [OH^-]_{in} - [H^+]_{eq} + [OH^-]_{eq}\right), \quad (1)$$

where V_0 and V_{tit} are the volumes of the supporting electrolyte and added titrant, respectively; m is the adsorbent weight; $[H^+]$ and $[OH^-]$ are the concentrations of protons and hydroxyl ions, respectively; subscripts "in" and "eq" refer to the initial and equilibrium concentrations.

The distribution functions of surface groups with respect to the protonation constants were calculated by solving the integral adsorption equation by means of the CONTIN procedure [11, 12]:

$$Q_t(\mathrm{pH}) = \int_{\mathrm{p}K_{min}}^{\mathrm{p}K_{max}} Q_l(\mathrm{pH}, \mathrm{p}K)\, f(\mathrm{p}K)\,\mathrm{d}\,\mathrm{p}K + Q_0, \quad (2)$$

where Q_t is the experimental isotherm, Q_l is the local isotherm (Langmuir type) describing the adsorption on a uniform surface group, $f(\mathrm{p}K)$ is unknown distribution function, and Q_0 is a constant that accounts for the adsorption of protons by surface groups with pK values outside the limits of the experimentally determined range.

The distribution function describes the concentration of surface groups as a function of the protonation constant and is a unique characteristic of the adsorbent surface groups. The electrostatic interaction of the charged surface with adsorbed ions was considered in terms of the diffusion model of electric double layer [11, 12].

The isotherms of proton sorption by carbon adsorbents can have both positive and negative values of adsorption Q (Fig. 1). The positive values of sorption mean proton association, and the negative values correspond to passing of protons into solution via dissociation of acidic surface groups. The intersection point of the isotherm with the pH axis corresponds to the zero-charge potential (ZCP) at which the adsorption values of potential-determining ions (protons and hydroxyls) are the same.

The isotherms of proton sorption by unoxidized and weakly oxidized carbons have both positive and negative values of adsorption, and strongly oxidized carbons show negative proton sorption only (Fig. 1). With increasing degree of oxidation, the carbon surface becomes more acidic, which is manifested in an increasing cation-exchange power, decreasing ZCP, and shift of the isotherm to negative values of proton sorption (Fig. 1). The most significant variation of acid–base characteristics of carbons is observed in the initial stages of oxidation; the amount of surface

groups responsible for proton association significantly decreases and the content of acidic groups increases (see table). This effect is the most pronounced for SKN synthetic carbon.

The gradual increase in the degree of oxidation of both SKN synthetic carbon and KAU pit carbon results in an increase in the amount of all types of surface acidic groups. At the same duration of oxidation with air, SKNo synthetic carbon has a more acidic surface than KAUo pit carbon. In addition, at all degrees of oxidation, the surface of KAUo carbon oxidized with air contains a noticeable amount of basic surface groups capable of proton adsorption (see table, Q_0).

The distribution of surface groups with respect to the protonation constants (Fig. 2) suggests that the acid–base characteristics of the carbons studied are nonuniform. The peaks in the distribution curves are relatively broad, the peak width at half-maximum is approximately 2.0 pK units, which suggests a high nonuniformity of individual types of surface groups. The distribution of surface groups with respect to the protonation constants suggests the presence of three types of groups at the surface of weakly oxidized carbons KAUo-1.0 and KAUo-0.8 with pK 3.6–4.3, 7.0, and 9.6–10.5. The pK values of the first two groups are lower than ZCP and therefore correspond to proton association. These groups can be assigned to sorption of protons with by surface groups, or they result from electrochemical reduction of oxygen by the reaction

$$\equiv C + O_2 + 4H^+ \rightarrow \equiv C^+ + 2H_2O. \qquad (3)$$

The release of protons with pK 9.6–10.5 corresponds to dissociation of phenolic groups. It should be noted that unoxidized carbons SKN and KAU have only one group capable of releasing protons, while in oxidized carbons there are two (SKN) or even three (KAU) groups releasing protons into a solution (Fig. 2).

The distribution function of surface groups with respect to the protonation constants for synthetic oxidized carbons SKNo shows the presence of only two types of surface groups capable of releasing protons (Fig. 2a). Contrastingly, oxidized pit carbons KAU contain, irrespective of the oxidation procedure, three types of acidic surface groups (Figs. 2b, 2c). Most likely, the difference in the amount of the types of functional groups at the surface of SKN synthetic carbon and KAU pit carbon is due to the difference in the structure and characteristics of these carbons. In particular, it is well known [13] that synthetic carbons of the SKN type, produced from nitrogen-containing polymeric raw materials (vinylpyridine copolymer), contain 3–5% nitrogen and give in carbonization

Parameters of the distribution function of the surface groups with respect to protonation constants

Carbon*	Q_0	Q_{in}	pK_{in}	ZCP
SKN carbons oxidized with air				
SKN	0.445	0.098	4.30	7.9
		0.452	7.00	
		0.553	9.61	
SKNo-1.6	0.058	0.257	3.85	3.3
		1.412	6.52	
SKNo-2.0	0.044	0.396	3.08	~2.4
		1.667	6.10	
SKNo-2.2	–0.022	0.394	3.46	~2.0
		1.793	6.23	
KAU carbons oxidized with air				
KAU	0.513	0.216	3.56	8.6
		0.311	7.00	
		0.302	10.51	
KAUo-1.0	0.171	0.148	4.09	5.6
		0.376	6.73	
		0.657	8.72	
KAUo-1.7	0.229	0.371	2.85	3.1
		0.528	5.49	
		1.032	7.65	
KAUo-2.2	0.183	0.511	2.91	2.5
		0.853	5.87	
		1.028	7.74	
KAU carbons oxidized with HNO_3				
KAU	0.513	0.216	3.56	8.6
		0.311	7.00	
		0.302	10.51	
KAUo-0.8	0.124	0.243	3.34	3.5
		0.114	5.32	
		0.555	7.62	
KAUo-1.2	0.052	0.172	2.97	2.7
		0.245	5.13	
		0.852	7.34	
KAUo-1.8	0.073	0.433	3.09	~2.4
		0.394	5.44	
		1.074	7.57	
KAUo-2.6	–0.108	0.617	3.02	~1.9
		0.554	5.00	
		1.416	7.26	

* The index in the carbon name denotes the cation-exchange capacity determined from the adsorption of NaOH [4].

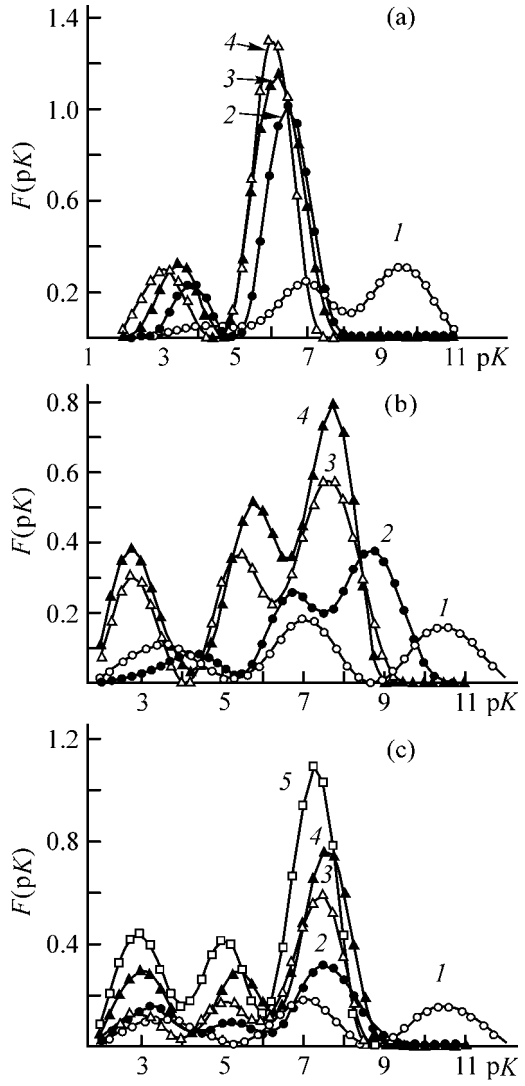

Fig. 2. Distribution of surface groups $F(pK)$ with respect to the protonation constants pK in (a) KAU synthetic carbons oxidized with air and KAU pit carbons oxidized with (b) air and (c) HNO_3.

a fairly dense carbon (d = 1.92–1.96 g cm^{-3}), while the raw material for production of pit carbon is a natural polysaccharide, cellulose, with a high oxygen content. Therefore, carbon with a density lower than that of SKN synthetic carbon (d = 1.83–1.85 g cm^{-3}) is formed in carbonization of fruit pits. This carbon is more active in oxidation.

The nature of surface groups of oxidized carbons can be considered in the framework of the commonly accepted scheme based on the analogy of the dissociation constants of surface groups and the known chemical compounds [3]. When comparing the experimental protonation constants of oxidized carbons with reference data, it should be taken into account that the pK values obtained in this study were measured in a solution with the ionic strength of 0.1 and, therefore, they are only apparent. The thermodynamic pK values of surface groups, corrected for the salt effect, are greater by 0.12–0.60 pK units than the apparent values, depending on the stage of dissociation [11].

According to the above scheme, the most acidic surface groups with pK 2.9–3.6 for oxidized SKNo synthetic carbons and with pK 3.1–3.9 for oxidized KAUo pit carbons can be assigned to carboxy groups. It should be noted that surface carboxy groups are more active than the isolated carboxy group, e.g., in acetic (pK 4.75) or benzoic (pK 4.18) acid. This is accounted for by the mutual influence of two or more adjacent functional groups due to the inductive effect. For example, addition of a hydroxy or a second carboxy group to benzoic acid results in a decrease in pK to 3.0 in salicylic acid and to 2.95 in *o*-phthalic acid. The carboxy group surrounded by two substituents with negative inductive effect, e.g., in 2,6-dihydroxybenzoic acid (pK 1.22) is still more acidic. The nature of the carbon skeleton also affects the characteristics of acidic groups via the resonance effect.

According to the scheme from [3], the less acidic surface groups with pK 6.1–6.5 for oxidized SKNo synthetic carbons and with pK 5.0–6.7 for oxidized KAUo pit carbons can be identified as second carboxy groups in dibasic acid fragments or lactonic groups.

The least acidic surface groups are observed at the surface of oxidized KAUo pit carbons (pK 7.3–8.7); these can be identified, in all probability, as phenolic groups.

CONCLUSIONS

(1) Calculation of the continuous distribution function of surface groups with respect to the protonation constants from the potentiometric titration data shows that unoxidized carbons have two types of surface groups capable of proton adsorption and one type of acidic surface groups. Oxidized SKNo synthetic carbons have two types of acidic surface groups (carboxy and phenolic), and pit carbons, three types of acidic surface groups (carboxy, lactonic, and phenolic).

(2) The composition of the surface groups is affected most significantly by the origin of the initial carbon and, to a lesser extent, by the procedure of oxidation of the carbon surface.

REFERENCES

1. Radovic, L.R., Morena-Castilla, C., and Rivera-Utrilla, J., in *Chemistry and Physics of Carbon*, New York: Marcel Dekker, 2000, vol. 27, pp. 227–405.

2. Radovic, L.R. and Rodriguez-Reinoso, F., in *Chemistry and Physics of Carbon*, New York: Marcel Dekker, 1997, vol. 25, pp. 243–358.
3. Leon y Leon, C.A. and Radovic, L.R., in *Chemistry and Physics of Carbon*, New York: Marcel Dekker, 1994, vol. 24, pp. 213–310.
4. Boehm, H.P., *Advances in Catalysis*, New York: Academic, 1966, vol. 16, pp. 179–274.
5. Zavadzki, J., in *Chemistry and Physics of Carbon*, New York: Marcel Dekker, 1989, vol. 21, pp. 147–386.
6. Puri, B.R. and Bansal, R.C., *Carbon*, 1964, vol. 1, no. 4, pp. 457–464.
7. Arico, A.S., Antonucci, V., Minutoli, M., and Giordano, N., *Carbon*, 1989, vol. 27, no. 3, pp. 337–347.
8. Bandosz, T.J., Jagiello, J., Contescu, C., and Schwarz, J.A., *Carbon*, 1993, vol. 31, no. 7, pp. 1193–1202.
9. Jagiello, J., Bandosz, T.J., and Schwarz, J.A., *Carbon*, 1994, vol. 32, no. 7, pp. 1026–1028.
10. Jagiello, J., *Langmuir*, 1994, no. 10, pp. 2778–2785.
11. Puziy, A.M., Poddubnaya, O.I., Ritter, J.A., *et al.*, *Carbon*, 2001, vol. 39, no. 15, pp. 2313–2324.
12. Puziy, A.M., Poddubnaya, O.I., Martinez-Alonso, A., *et al.*, *Carbon*, 2002, vol. 40, no. 9, pp. 1493–1505.
13. Kartel, N.T., Puziy, A.M., and Strelko, S.S., in *Characterization of Porous Solids*, Amsterdam: Elsevier, 1991, pp. 439–447.
14. Stavitskaya, S.S., Kartel', N.T., and Petrenko, T.P., *Zh. Prikl. Khim.*, 1999, vol. 72, no. 9, pp. 1451–1455.

Russian Journal of Applied Chemistry, Vol. 77, No. 8, 2004, pp. 1268–1272. Translated from Zhurnal Prikladnoi Khimii, Vol. 77, No. 8, 2004, pp. 1284–1288.

APPLIED ELECTROCHEMISTRY AND CORROSION PROTECTION OF METALS

Electrodeposition of Lustrous Zinc Coatings from Sulfate Electrolyte

G. I. Medvedev and N.A. Makrushin

Novomoskovsk Institute, Mendeleev Russian University of Chemical Engineering, Novomoskovsk, Tula oblast, Russia

Received November 25, 2003

Abstract—The electrodeposition of lustrous zinc coatings from a sulfate electrolyte containing $ZnSO_4$, Na_2SO_4, buffer additives, and 2-butyne-1,4 diol was studied.

Sulfate zinc-plating electrolytes are now used for coating of articles of a simple shape. To obtain high-quality coatings, various organic substances, such as dextrin, condensation products, and various mixtures, are added to the electrolyte [1]. At present, zinc is electrodeposited using electrolytes with luster-forming additives, which are organic substances of a rather complex composition [2–4].

In this communication, we report the results obtained in a study of Zn electrodeposition from a sulfate electrolyte in the presence of 2-butyne-1,4-diol (BD), which is widely used in deposition of lustrous nickel and zinc coatings [3, 5]. The electrolyte contained (g l^{-1}): $ZnSO_4 \cdot 7H_2O$ 200–250, $Na_2SO_4 \cdot 10H_2O$ 50–100, $Al_2(SO_4)_3 \cdot 18H_2O$, H_3BO_3, and aminoacetic acid 25–30; 2-BD (35 wt % solution) 1–70 ml l^{-1}. A 10–12-μm-thick zinc layer was deposited onto unpolished St.3 steel. The polarization curves were measured in the potentiodynamic mode with a P-5828 potentiostat. The leveling power P of the electrolytes was determined by a direct method involving a profilographic measurement of the sample surface with a sine-shaped microprofile and calculation by the formula [6]

$$P = 2.3\frac{a}{2}\pi h_{av}\log\left(\frac{H_0}{H_i}\right),$$

where a is the amplitude of the wave of the sine-shaped microprofile; h_{av}, the average thickness of the coatings (10 μm); and H_0 and H_i, the initial and final wave amplitudes of the sine-shaped profile, respectively.

The capacitance of a double electric layer was measured in the course of electrolysis with a P-5021 ac bridge at a frequency of 30 kHz in a series equivalent circuit. As the working electrode served a zinc-coated platinum wire situated at the center of a platinum-plated cylinder. The pH value of the near-electrode layer was measured by the method described in [7]. The electrodeposition was performed at 18–25°C with and without agitation of electrolytes with a magnetic stirrer.

The influence exerted by the BD concentration, nature of the buffer solution, and current density i_c on the outward appearance of the coatings is illustrated in Table 1. As can be seen, lustrous coatings are obtained in H_3BO_3- and $Al_2(SO_4)_3$-containing electrolytes at a BD concentration of 30–45 ml l^{-1}, and in an electrolyte containing aminoacetic acid, at 60–70 ml l^{-1}. The i_c range in which lustrous coatings are formed varies with the nature of the buffer solution. It is the widest in a $Al_2(SO_4)_3$-containing electrolyte (i_c = 1–6 A dm^{-2}). It should be noted that high-quality lustrous coatings are obtained solely in an agitated electrolyte, and lusterless and rough coating are formed without agitation.

The pH value of the electrolytes should be within 3–4. At pH < 3, the i_c range in which lustrous coatings are formed is narrower and the current efficiency (CE) is lower. At pH > 4, semilustrous coatings are formed, and the electrolyte operation is unstable. The current efficiency was studied in the electrolytes ensuring formation of lustrous coatings. It was found that, in electrolytes containing BD, $Al_2(SO_4)_3$, and H_3BO_3, CE varies at i_c = 1–6 A dm^{-2} within 93–95%. At the same time, in an electrolyte containing BD and aminoacetic acid at i_c = 4–8 A dm^{-2}, CE decreases from 94 to 89%.

1070-4272/04/7708-1268 © 2004 MAIK "Nauka/Interperiodica"

Table 1. Influence of the BD concentration, nature of a buffer additive, and current density on the outward appearance of the coatings [electrolyte (g l^{-1}): $ZnSO_4 \cdot 7H_2O$ 200, $Na_2SO_4 \cdot 10H_2O$ 50; pH 3.5; mechanical agitation]

Buffer solution, 30 g l^{-1}	BD, (35 wt % solution, ml l^{-1})	i, A dm^{-2}	Outward appearance of coating
$Al_2(SO_4)_3$	1–5	1–8	Lusterless
	6–10	1–8	Silvery
	11–29	1–4	"
		5–8	Silvery with luster at edges
	30–40	1–6	Lusterous
		7–8	Lustrous with burnt ports
	41–45	1–4	Lusterous
		5–7	Lustrous with lusterless stripes
		8	Lustrous with overheating
H_3BO_3	1–5	1–8	Lusterless
	6–10	1–8	Silvery
	11–29	1–5	"
		6–8	Silvery with overheating
	30–40	1–5	Lusterous
		6–7	Lustrous with lusterless stripes
		8	Lusterous with burnt ports
Aminoacetic acid	1–5	1–8	Lusterless
	6–30	1–8	Silvery
	40–50	1–8	"
			Silvery with luster at edges
	60–70	1	Silvery
		2–3	Semilustrous
		4–8	Lusterous
		9	Lustrous with burnt ports

In the zinc-plating electrolytes, cathodic polarization curves were measured on a rotating-disc electrode. It can be seen from Fig. 1 that BD leads to an increase in the cathodic polarization ΔE_c (curves *1*, *2*). As the rate of rotation of the disc electrode is raised from 200 to 2000 rpm in a BD-containing electrolyte, ΔE_c increases (curves *2–4*).

The inhibiting influence exerted by BD on the Zn electrodeposition is due to its adsorption on the electrode surface. This is confirmed by measurements of the capacitance of the double electric layer. In an electrolyte without BD, the dependence of the capacitance on the potential has a minimum (20 μF cm^{-2}) at $E = -0.8$ V (Fig. 1, curve *5*). In the presence of BD, the capacitance of the double electric layer decreases to 9 μF cm^{-2} at $E = -0.8$ V (curve *6*). At more electronegative potentials, an increase in the capacitance is observed owing to desorption of a part of luster-forming additive from the electrode surface [8].

Analysis of the cathodic polarization curves shows that the extent to which the Zn electrodeposition is hindered depends on the rate at which BD is delivered to the cathode surface: the higher the rate of delivery of the additive to the cathode surface, the stronger the hindrance to the process. As is known [6], such a dependence of the polarization curves on the rotation rate of a disc electrode is adopted as a basis for classification of additives with respect to their leveling power. If the polarization increases with rotation rate, then it would be expected that the additive will produce a leveling effect under the given conditions

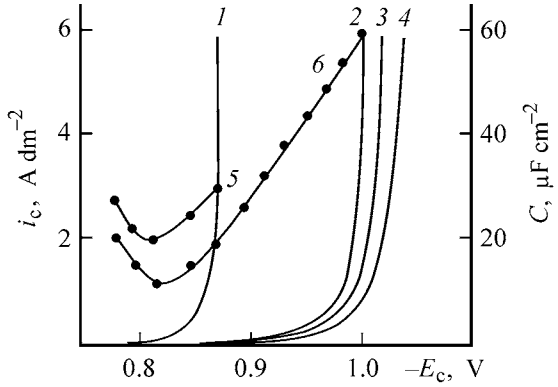

Fig. 1. Current density i_c and capacitance C of the double electric layer vs. the electrode potential relative to a standard hydrogen electrode E in the zinc-plating electrolyte. Electrolyte (g l^{-1}): $ZnSO_4 \cdot 7H_2O$ 200, $Na_2SO_4 \cdot 10H_2O$ 50, $Al_2(SO_4)_3 \cdot 18H_2O$ 30; pH 3; the same for Fig. 2; (*1, 5*) Electrolyte, (*2–4, 6*) electrolyte + BD (35 wt % solution) 35 ml l^{-1}. Curves *1–4* were obtained on the rotating-disc electrode at a rotation rate (rpm): (*1, 2*) 0, (*3*) 200, and (*4*) 2000.

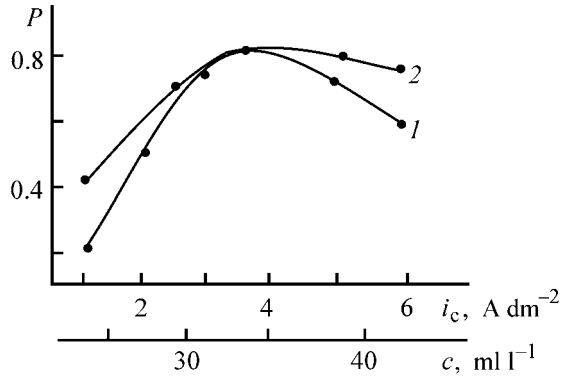

Fig. 2. Leveling power P of the zinc-plating electrolyte vs. (*1*) current density i_c and (*2*) BD concentration c (35 wt % solution). Mechanical agitation: (*1*) c_{BD} = 35 ml l^{-1} and (*2*) i_c = 4 A dm^{-2}.

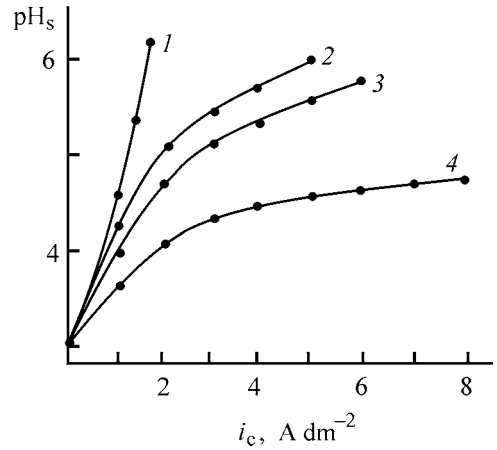

Fig. 3. pH in the near-cathode layer vs. the current density i_c in the zinc-plating electrolyte. Electrolyte (g l^{-1}): $ZnSO_4 \cdot 7H_2O$ 200, $Na_2SO_4 \cdot 10H_2O$ 50, and BD (35 wt % solution) 35 ml l^{-1}. (*1*) Electrolyte; (*2*, *3*, *4*) 1 + H_3BO_3, $Al_2(SO_4)_3 \cdot 18H_2O$. Aminoacetic acid 30 g l^{-1}, respectively.

[6]. Profilographic measurements on a gently sloping sine-shaped profile showed that surface leveling does occur in the course of Zn electrodeposition.

The dependences of P on i_c and BD concentration are shown in Fig. 2. It can be seen that the P–i_c and P–C dependences pass through a maximum at i_c = 4 A dm^{-2} (curves *1*, *2*). The run of these dependences can be understood in terms of the adsorption-diffusion leveling theory [6]. Raising i_c first leads to an increase in the leveling power. Then, at relatively high current densities, the concentration of the additive on the surface and its inhibition effect will decrease even at microprojections owing to the high rate of surface renewal, which must diminish the efficiency of leveling. At a too low concentration of the additive in the electrolyte, when the Zn electrodeposition is inhibited only slightly, the leveling effect cannot be stronger. At the same time, at too high concentrations of the additive, the leveling power decreases because of the termination of the diffusion control over the rate of delivery of the additive and its inhibition effect. Thus, it was established that a luster-forming additive BD to a zinc-plating electrolyte provides a leveling effect because of its being simultaneously a leveling additive.

As is known [3], the formation of lustrous coatings is due to the leveling of submicrometer irregularities on the surface. In this case, it is sufficient that the additive should be adsorbed on the cathode surface, with the overvoltage of electrocrystallization increased, for a lusterless coating to be formed. At the same time, it is necessary that, for lustrous coatings to be obtained, an adsorption layer of a certain composition should be present on the cathode surface. Layers of this kind can be formed from organic substances and products of secondary reactions in the near-cathode layer. In the case of a simultaneous deposition of metal and evolution of hydrogen, the adsorption layer may consist of hydroxides and other basic compounds [3].

The assumption that hydroxo compounds of zinc are formed in the near-cathode space is confirmed by measurements of pH_s in the near-cathode layer. As can be seen from Fig. 3, the pH value varies from 3.5 to 6 at i_c = 1–8 A dm^{-2} (depending on the type of a buffer solution). The pH_s varies to the smallest extent in an electrolyte containing aminoacetic acid (curve *4*). It should be noted that hydrates are formed in a zinc-plating electrolyte at pH 6.4. All these facts suggest that the presence of hydroxo compounds of zinc in the near-cathode layer is not a necessary condition for obtaining lustrous deposits. Apparently, lustrous coatings are formed in the case when a highly dispersed adsorption layer is formed on the electrode surface [3].

Evidently, the dispersity of the adsorption layer is controlled by buffer solutions. In their presence, the adsorption layer can change because of the formation of both $Al(OH)_3$ and sparingly soluble zinc borates in the near-cathode layer. It is not improbable that complex compounds are formed by orthoboric and aminoacetic acids with zinc ions, and intracomplex chelate compounds, by H_3BO_3 with BD and products of its reduction [3].

Of high importance in obtaining lustrous coatings is the hydrodynamic mode in which a luster-forming additive is delivered to the cathode surface and decomposition products are removed from the near-cathode space, as also noted in [9].

It has been shown [10] that, in the course of electrolysis, the luster-forming additive BD undergoes complex transformations, which strongly affects the quality of the coatings obtained. A gas-chromatographic analysis of the BD-containing electrolyte showed that, as the electrolysis duration increases, 2-butene-1,4-diol, 2-butane-1,4-diol, 2.6-octene-1,8-diol, 2-butenol, and butanol are accumulated owing to diol reduction. The influence exerted by luster-forming additives in acid electrolytes may be associated with their reduction in the near-cathode layer [11]. This is accompanied by a deceleration of the hydrogen evolution and the corresponding change in the structure of the adsorption layer, as well as by a decrease in the degree of hydrogen saturation of the metal [12].

To elucidate the mechanism of the influence exerted by BD on the Zn electrodeposition, the system consisting of hydrated ions present in the electrolyte and BD molecules was subjected to a quantum-chemical analysis. The calculation was performed using the semiempirical chemical method PM3 [13, 14]. We calculated the coordination numbers of hydration for ions and BD molecules. According to the calculation performed, these numbers are 5 for Zn^{2+}, 3 for H_3O^+, 8 for SO_4^{2-}, and 9 for BD. Introduction of H_3O^+ and SO_4^{2-} ions into a Zn^{2+}-containing aqueous solution results in their additional interaction. It was shown that each BD molecule displaces two H_2O molecules from the hydration sheaths of Zn^{2+} ions, thus forming stable complexes with the ions. It was established that the interaction of Zn^{2+} ions with BD molecules is energetically more favorable than the formation of the hydration sheath of an ion. It is the most probable, with account of the composition of the zinc-plating sulfate electrolyte, that complex ions $[Zn(H_2O)_x(BD)_y]^{2+}$ (x = 1–5 and y = 1–3) exist in the bulk of the electrolyte.

In the following stage, the structure of BD at the electrode–solution interface was analyzed by the quantum-chemical method. In doing so, the surface of the zinc electrode was modeled by a negatively charged cluster consisting of 49 atoms situated in two layers having a hexagonal shape. The cluster was chosen with account of the recommendations made in [15]. To model the process of Zn^{2+} reduction on the surface of the zinc electrode, a system constituted by a zinc cluster Zn_{49}, Zn^{2+}, and BD was calculated. It was shown that, when approaching the cluster, the BD molecules contained in the complex form a stable system at a distance of 310 pm from the cluster. In this case, the interaction energy is 353 kJ mol^{-1}, which considerably exceeds the energy of interaction of the cluster with a hydrated zinc ion (200 kJ mol^{-1}). It is noteworthy that the BD molecule forms no stable system with the cluster without Zn^{2+} ions.

Table 2. Change in the total energy of the products in comparison with the total energy of the starting substances

Reaction	Reaction equation	ΔE, kJ mol^{-1}
(1)	$Zn(OH)_2 + e = ZnOH + OH^-$	271
(2)	$ZnOH^+ + e = ZnOH$	–897
(3)	$[ZnBD]^{2+} + e = Zn^+ + BD$	–1051
(4)	$[Zn(OH)BD]^+ + e = ZnOH + BD$	–579
(5)	$[Zn(OH)_2BD] + e = ZnOH + OH^- + BD$	337

Alkalization may result in that mixed aqua hydroxo complexes of varied composition with BD are formed in the near-cathode layer. With account taken of the fact that BD molecules displace H_2O molecules from the aqua complexes with Zn^{2+}, the most probable is the formation in the near-cathode layer of the following species: $Zn(OH)_2$, $Zn(OH)^+$, $[ZnBD]^{2+}$, $[Zn(OH)BD]^+$, and $[Zn(OH)_2BD]$. The highest energy of interaction with a Zn_{49} cluster is observed for $Zn(OH)^+$ species. The presence of a BD molecule in a complex species somewhat decreases the energy of such an interaction and increases the distance between the Zn^{2+} ion and the cluster surface. One of the reasons for such a behavior may be the spatial structure of the complexes being formed, which creates steric hindrance to approach of Zn^{2+} ions to the cluster.

The rather wide diversity of complex species in the near-cathode layer suggests a mechanism of their discharge (Table 2). To qualitatively estimate the probabilities of the occurring processes, we calculated the change in the total energy of the presumed reactions in comparison with the total energy of the initial substances (ΔE, Table 2). In doing so, we took into account that the energy necessary for an electron to be involved in each of the above processes is a constant value. In the given case, the reaction was considered with and without BD.

It follows from the data in Table 2 that the most energetically probable are reactions (2)–(4), which yield a ZnOH species and a Zn^+ ion. Apparently, reaction (3) is the first of these three to occur. The Zn^+ ions formed in this case enter into the electrochemical reaction

$$Zn^+ + e \rightarrow Zn,$$

and BD molecules may be reduced electrochemically to give various products [10].

Table 3. Composition of zinc-plating sulfate electrolytes yielding lustrous coatings with leveled surface (T = 18–25°C, pH 3–4, mechanical agitation)

Components and working mode of electrolyte	Component concentration, g l^{-1}		
	1	2	3
$ZnSO_4 \cdot 7H_2O$	200–250		
$Na_2SO_4 \cdot 10H_2O$	50–100		
$Al_2(SO_4)_3 \cdot 18H_2O$	25–30		
H_3BO_3		25–30	
Aminoacetic acid			25–30
BD (35 wt % solution)	30–40	30–40	60–70
Current density, A dm^{-2}	1–6	1–5	4–8
Current efficiency, %	92–95	93–95	89–94

Thus, the quantum-chemical calculation showed that it is the most probable that, in a sulfate zinc-plating electrolyte containing BD, the complex ions $[Zn(H_2O)_x(BD)_y]^{2+}$ are present in the electrolyte bulk and $Zn(OH)^+$, $[ZnBD]^{2+}$, and $[Zn(OH)BD]^+$ are electroactive species in the near-cathode space owing to alkalization.

As a result of the study performed, electrolytes of simple composition were developed for obtaining lustrous zinc coatings with a leveled surface (Table 3). To diminish the contamination of the electrolyte with sludge, it is necessary to place the anodes (of Ts0 or Ts1 brand) into jackets made of a polypropylene fabric. The electrolyte is to be adjusted with respect to the main components on the basis of chemical analysis data [16].

CONCLUSIONS

(1) The study of the electrodeposition of zinc from a sulfate electrolyte containing 2-butyne-1,4-diol and buffer additives $Al_2(SO_4)_3 \cdot 18H_2O$, H_3BO_3, and aminoacetic acid showed that, depending on the type of additive, lustrous coatings are formed in an agitated electrolyte at i_c = 1–8 A dm^{-2}.

(2) The system constituted by hydrated Zn^{2+} ions and 2-butyne-1,4-diol molecules was studied by the quantum-chemical method. It was shown that presence of complexes of the type $[Zn(H_2O)_x(BD)_y]^{2+}$ in the electrolyte bulk is the most probable. In the near-cathode layer, $Zn(OH)^+$, $[ZnBD]^{2+}$, and $[Zn(OH)BD]^+$ are electroactive species owing to alkalization. Sulfate electrolytes for obtaining lustrous zinc coatings with a leveled surface were developed.

REFERENCES

1. Kudryavtsev, N.G., *Elektroliticheskie pokrytiya metallami* (Electroplating of Metals), Moscow: Khimiya, 1979.
2. Zhilenene, B.M., *Patentnaya literatura po elektroosazhdeniyu zinka iz netsianistykh rastvorov za 1960–1972 gg.* (Patent Literature Devoted to Electrodeposition of Zinc from Cyanide-free Solutions, Published in 1960–1972), Vilnius: Inst. Khim. Khim. Tekhn., 1972.
3. *Blestyashchie elektroliticheskie pokrytiya* (Lustrous Electrolytic Coatings), Matulis, Yu.Yu., Ed., Vilnius, Mintis, 1969.
4. Proskurin, E.V., Popovich, V.A., and Moroz, T.M., *Zinkovanie: Spravochnoe izdanie* (Handbook of Zinc Plating), Moscow: Metallurgiya, 1988.
5. Medvedev, G.I. and Gorbunova, I.M., *Zh. Prikl. Khim.*, 1990, vol. 63, no. 4, pp. 807–812.
6. Kruglikov, S.S., *Itogi nauki i tekhniki: Khimiya. Elektrokhimiya* (Advances in Science and Technology: Chemistry, Electrochemistry), Moscow: VINITI, 1965, pp. 117–147.
7. Gershov, V.M., Purin, B.A., and Ozol'-Kalnin', G.A., *Elektrokhimiya*, 1972, vol. 8, no. 5, pp. 673–675.
8. Damaskin, B.B., Petrii, O.A., and Batrakov V.V., *Adsorbtsiya organicheskikh soedinenii ne elektrodakh* (Adosrption of Organic Substances on Electrodes), Moscow: Nauka, 1968.
9. Gorbunova, K.M., Ivanovskaya, T.V., and Shishakov, M.A., *Zh. Fiz. Khim.*, 1951, vol. 25, no. 8, pp. 981–987.
10. Nivinskene, O.Yu., *Zashch. Met.*, 1992, vol. 28, no. 6, pp. 1028–1031.
11. Makrushin, N.A., Medvedev, G.I., Fursova, N.Yu., *et al., Izv. Tul'sk. Gos. Univ.: Khimiya. Elektrokhimicheskie vozdeistviya na materialy*, Tula, 2000, pp. 9–12.
12. Gamburg, Yu.D., *Elektrokhimicheskaya kristallizatsiya metallov i splavov* (Eletrochemical Crystallization of Metals and Alloys), Moscow: Yanus-K, 1997.
13. Stewart, J.J.P., *J. Comput. Chem.*, 1989, vol. 10, no. 2, pp. 209–220.
14. Stewart, J.J.P., *J. Comput. Chem.*, 1991, vol. 12, no. 3, pp. 320–341.
15. Shapnik, M.S., *Elektrokhimiya*, 1994, vol. 30, no. 2, pp. 143–149.
16. Vyacheslavov, P.M. and Shmeleva, N.M., *Kontrol' elektrolitov i pokrytii* (Control of Electrolytes and Coatings), Leningrad: Mashinostroenie, 1965.

Russian Journal of Applied Chemistry, Vol. 77, No. 8, 2004, pp. 1273–1278. Translated from Zhurnal Prikladnoi Khimii, Vol. 77, No. 8, 2004, pp. 1289–1294.

APPLIED ELECTROCHEMISTRY AND CORROSION PROTECTION OF METALS

Electrodeposition of $CuSe_x$ Compounds onto Carbon-containing Electrodes

M. B. Dergacheva, V. V. Chaikin, V. P. Grigor'eva, and E. P. Pantileeva

Sokol'skii Institute of Organic Catalysis and Electrochemistry, Ministry of Education and Science of the Republic of Kazakhstan, Alma-Ata, Kazakhstan

Received December 26, 2003; in final form, May 2004

Abstract—The electrodeposition of copper(II) and selenium(IV) onto pyrographite and carbon-pyroceramic electrodes in sulfate solutions was studied. The optimal conditions for obtaining a compound of composition Cu_2Se were found.

Copper–indium double selenide $CuInSe_2$ is of interest as a material for high-efficiency solar cells [1]. The possibility of electrodeposition of a thin film of copper-indium double selenide is even more interesting because this compound can be obtained in the polycrystalline state by joint deposition of three components. This procedure for film fabrication is the least expensive among the known methods. The main factor determining the photoelectric properties of semiconductor films is their composition. In crystallization from a melt, $CuInSe_2$ is formed by the solid-phase reaction between Cu_2Se and In_2Se_3 [2].

In electrochemical codeposition under nonequilibrium conditions, another process can take place. Therefore, it is important to study the electrodeposition of each pair of components, especially for such systems as Cu–Se and In–Se, which are distinguished by strong interaction and formation of intermediate phases. Preliminary studies [3] have shown that the electrodeposition of Cu^{2+} and H_2SeO_3 is a diffusion-limited process. Therefore, the relative concentrations of components in the electrolyte will affect the composition of the forming deposit and depend on diffusion coefficients.

The goal of this study was to demonstrate, for the example of the copper–selenium system, how the stoichiometric composition of the forming compounds can be determined from the change in the cathodic and anodic portions of the voltammetric curves upon gradual variation of the concentration of copper(II) or selenium(IV).

EXPERIMENTAL

As working electrodes were used pyrographite and carbon-pyroceramic disc electrodes with a geometric surface area of 0.12 and 0.07 cm^2, respectively. A three-electrode cell contained the electrode under study, an auxiliary platinum electrode with a surface area of 1.5 cm^2, and a silver chloride reference electrode. All the potentials are given relative to this electrode. Prior to each experiment, the working electrodes were trimmed with an Al_2O_3 fine powder and washed with alcohol and water. We used the salts $CuSO_4 \cdot 7H_2O$ and Na_2SeO_3 (both analytically pure). As the supporting electrolyte served a solution 0.05 M H_2SO_4 + 0.45 M Na_2SO_4. The voltammetric curves were measured without agitation. The accumulation of a deposit on the electrode occurred in an electrolyte agitated with a magnetic stirrer. The study was performed at room temperature. An X-ray phase analysis of the copper selenide deposits on 1×1-cm glassy carbon plates was made on a DRON-4 diffractometer (Co_{K_α} radiation). Simultaneously with the X-ray analysis, an electron-microscopic study of the deposits was performed on an EM-125-K instrument, using the method of singlestep replicas.

The reduction of the Cu(II) ions was studied on a pyrographite electrode.

Figure 1 shows reduction voltammograms measured at various potential sweep rates. In reduction of Cu(II) ions, one wave with a peak at a potential of –0.130 V is observed (Fig. 1a). The oxidation of copper in the reverse run of the voltammetric curve

1070-4272/04/7708-1273 © 2004 MAIK "Nauka/Interperiodica"

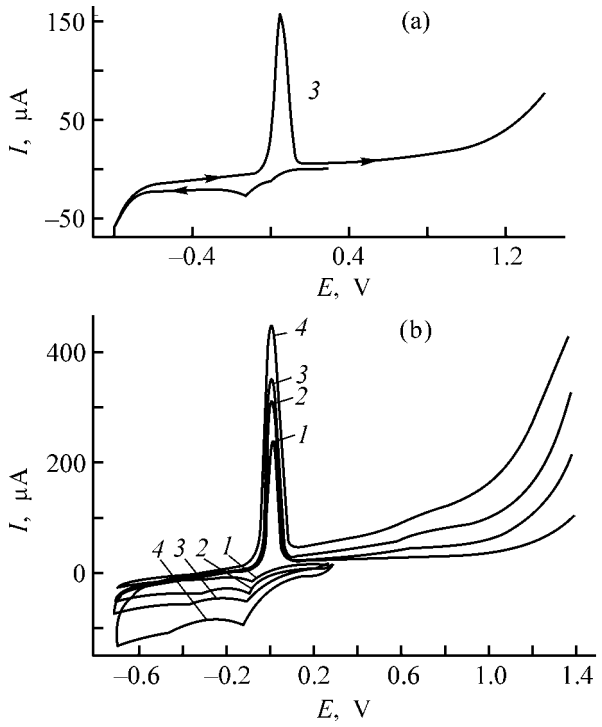

Fig. 1. Voltammetric curves measured in Cu(II) deposition on a pyrographite electrode in a solution containing $c_{Cu(II)} = 1 \times 10^{-3}$ M at various potential sweep rates. (*I*) Current and (*E*) potential; the same for Figs. 2, 3, 5–7. Sweep rate (mV s^{-1}): (*1*) 2, (*2*) 10, (*3*) 20, and (*4*) 50.

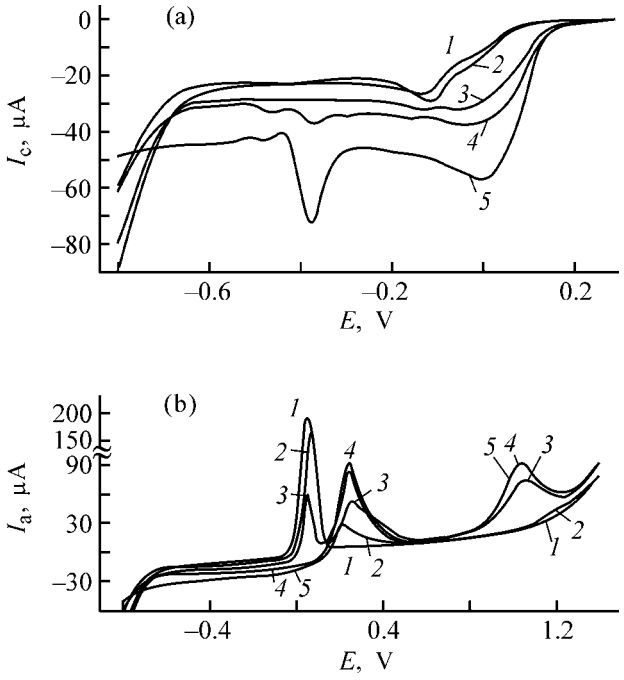

Fig. 2. (a) Cathodic and (b) anodic portions of the voltammetric curves measured in codeposition of Cu(II) and Se(IV) ions on a pyrographite electrode at $c_{Cu(II)} = 1 \times 10^{-3}$ M. Supporting solution 0.05 M H_2SO_4 + 0.45 M Na_2SO_4, V = 20 mV s^{-1}; the same for Figs. 6, 7. $c_{Se(IV)}$ (M): (*1*) 0, (*2*) 1×10^{-4}, (*3*) 3×10^{-4}, (*4*) 5×10^{-4}, and (*5*) 1×10^{-3}.

is accompanied by the appearance of a peak of the anodic current at $E_{ox} = 0.04$ V.

The reduction of Cu(II) is diffusion-controlled and can be described as a classical behavior determined by the mass-transfer rate. The reduction starts at +0.1 V and occurs in accordance with the scheme:

$$Cu^{2+} + 2e \rightarrow Cu^0. \quad (1)$$

When copper(II) and selenium(IV) ions are simultaneously reduced from an electrolyte containing $CuSO_4$ and an excess amount of H_2SeO_3, the reduction onset potential shifts to positive region. In the reduction voltammograms, two, and occasionally three waves are observed in the potential range +0.3… –0.85 V, depending on the relative concentrations of the components.

According to [4, 5], the shift of the first reduction wave in the positive direction may be due to enhanced adsorption of copper and selenium adatoms on the electrode surface. It is necessary to note that desorption of HSO_4^- and SO_4^{2-} anions from the electrode surface occurs in the same range of potentials [6].

The main cathodic wave is observed at potentials of +0.15…–0.2 V. The limiting current of this wave increases in proportion to the Se(IV) concentration (Fig. 2a). At a constant concentration of selenium(IV), the limiting current of this wave does not remain constant, but increases with the Cu(II) concentration. At potentials of +0.15…–0.2 V, the main process of copper and selenium codeposition occurs to give a compound $CuSe_x$:

$$Cu^{2+} + xH_2SeO_3 + 4xH^+ + (2 + 4x)e \rightarrow CuSe_x + 3xH_2O. \quad (2)$$

According to the phase diagram, the compounds Cu_2Se, CuSe, and Cu_3Se_2 can be formed in the system Cu–Se [7].

The higher the Se(IV) concentration, the stronger the shift of the first reduction wave in the positive direction. Thus, it should be concluded that the codeposition of selenium(IV) and copper(II) is facilitated in the presence of large amounts of H_2SeO_3 and proceeds at more positive potentials (Fig. 2a).

At –0.4 V and more negative potentials, one clearly pronounced and one weak peak of cathodic cur-

rent appear in the cathodic curve. The current peak at –0.4 V is the most characteristic feature of the cathodic process of joint reduction of copper and selenium at copper concentrations in the electrolyte lower than selenium concentration, and up to a 1 : 1 ratio. This peak appears even upon addition of a minor amount of copper(II) ions to a 10^{-3} M Se(IV) solution (Fig. 3a).

Comparison of curves *2* and *3* (Fig. 3a) shows that this peak can be assigned to formation of selenide ions. In accordance with the suggestion of [5, 8], curve *3* reflects the occurrence of an electron-addition reaction in which $CuSe_x$ is transformed into a compound Cu_2Se, which is the most stable in this system and has an enthalpy of formation equal to –61 kJ mol^{-1}:

$$2CuSe_x + 2xH^+ + 2xe \rightarrow Cu_2Se + xH_2Se. \quad (3)$$

The appearance of a weakly pronounced current peak in the more negative range of potentials may be due to further reduction elementary selenium formed by reaction (4) or to formation of Cu_2Se by reaction (5) and its further reduction:

$$2H_2Se + H_2SeO_3 \rightarrow 3Se + 3H_2O, \quad (4)$$

$$2Cu^{2+} + H_2Se + 2H^+ + 2e \rightarrow Cu_2Se + 2H_2. \quad (5)$$

Copper selenide Cu_2Se can also be reduced in the region of negative potentials that are close to the potential of hydrogen evolution by the reaction

$$Cu_2Se + 2H^+ + 2e \rightarrow 2Cu + H_2Se. \quad (6)$$

The chemical composition of the compound $CuSe_x$ strongly depends on the delivery of a substance to the electrode. Without agitation of the electrolyte, the mass-transfer process is controlled by the relative concentrations of substances in the electrolyte and by their diffusion coefficients.

According to [5, 9, 10], the diffusion coefficient of Cu^{2+} ions in a 10^{-3} M $CuSO_4$ solution is $D_{Cu(II)} = (6.5 \pm 0.6) \times 10^{-6}$ cm^2 s^{-1}, $D_{Se(IV)} = (9.2 \pm 0.6) \times 10^{-6}$.

The composition parameter x characterizing the compound $CuSe_x$ is determined by the relative concentrations of the components by formula

$$x = \left(\frac{D_{Se}}{D_{Cu}}\right)\frac{c_{H_2SeO_3}}{c_{CuSO_4}} = 1.41\frac{c_{H_2SeO_3}}{c_{CuSO_4}}. \quad (7)$$

To verify the assumptions concerning the composition of copper selenide forming in the joint electrodeposition, the anodic portions of the voltammetric curves were analyzed. As can be seen from Fig. 2b, introduction of a minor amount of Se(IV) (curve *2*) into the 10^{-3} M Cu^{2+} solution does not result in any considerable change in the cathodic portion of the voltammetric curve. An additional peak of anodic current peak appears in the anodic portion. The additional current peak is observed at potentials that are 200 mV more positive than the potential of the current peak of copper oxidation. It is determined by dissolution of copper from copper selenide $CuSe_x$. The current peak becomes the highest at an ion concentration ratio $c_{Cu^{2+}} : c_{Se^{4+}} = 2.2 : 1$, and the potential of the current peak shifts in the positive direction to +0.25 V. Immediately after a peak of cathodic current appears at –0.4 V in the cathodic portion of the voltammetric curve, the current peak corresponding to oxidation of copper selenide starts to decrease in height, which reflects a decrease in its amount on the electrode. This suggests that the decrease in the amount of the deposit is due to its partial decomposition and to evolution of hydrogen selenide by reaction (3). When the greatest amount of the deposit is formed on the electrode, which is indicated by the maximum current of its oxidation, the current peak corresponding to oxidation of free copper (present in an excess

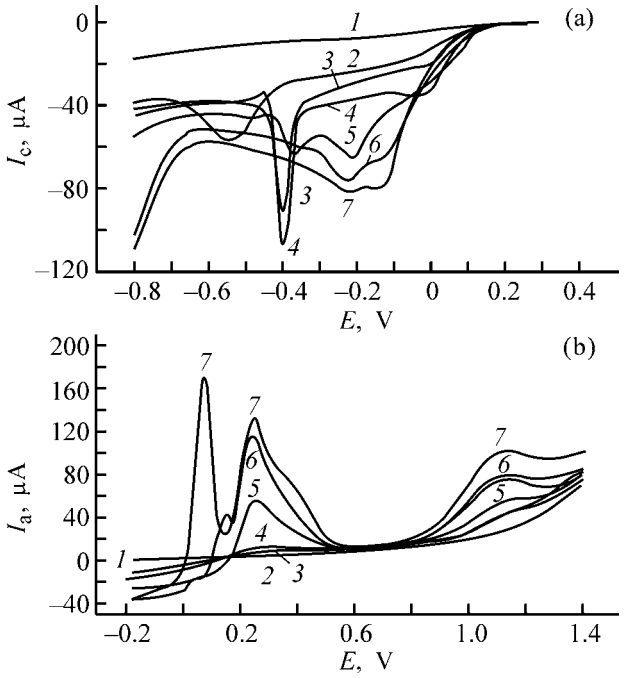

Fig. 3. (a) Cathodic and (b) anodic portions of the voltammetric curves in codeposition of Cu(II) and Se(IV) ions on a pyrographite electrode at $c_{Se(IV)} = 1 \times 10^{-3}$ M. V = 20 mV s^{-1}; Supporting solution 0.05 M H_2SO_4 + 0.45 M Na_2SO_4 (*1*). $c_{Cu(II)}$ (M): (*2*) 0, (*3*) 1×10^{-4}, (*4*) 3×10^{-4}, (*5*) 1×10^{-3}, (*6*) 2×10^{-3}, and (*7*) 3×10^{-3}.

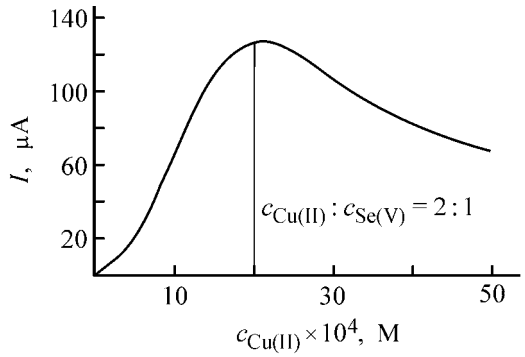

Fig. 4. Peak anodic current I at E_{ox} = 0.25 V vs. the concentration of copper ions, $c_{Cu(II)}$. $c_{Se(IV)} = 1 \times 10^{-3}$ M.

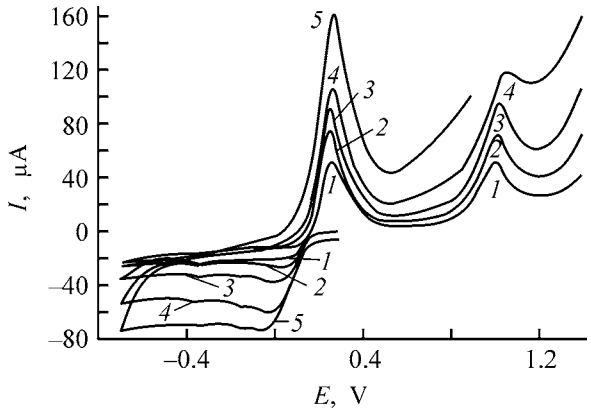

Fig. 5. Voltammetric curves measured in joint electrodeposition of copper and selenium and in electrooxidation of the deposit on a carbon-pyroceramic electrode at various potential sweep rates. $c_{Cu(II)} = 1 \times 10^{-3}$ and $c_{Se(IV)} = 5 \times 10^{-4}$ M. Sweep rate (mV s^{-1}): (*1*) 5, (*2*) 10, (*3*) 20, (*4*) 50, and (*5*) 100.

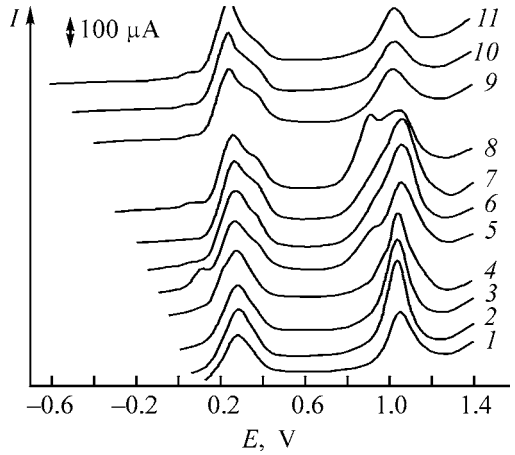

Fig. 6. Anodic portions of the voltammetric curves obtained after keeping the electrode was at various potentials, at $c_{Cu(II)} = 2 \times 10^{-3}$ M. $c_{Se(IV)} = 1 \times 10^{-3}$ M, τ_{keep} = 30 s; the same for Fig. 7. Potential (mV): (*1*) +100, (*2*) +50, (*3*) 0, (*4*) –50, (*5*) –100, (*6*) –150, (*7*) –200, (*8*) –300, (*9*) –400, (*10*) –500, and (*11*) –600.

with respect to the stoichiometric composition Cu_2Se) disappears, whereas that corresponding to oxidation of Se(0) is not shifted markedly and its height increases with the Se(IV) concentration in the electrolyte. When the current peak of oxidation of the compound decreases in height, that corresponding to oxidation of selenium remains unchanged.

It can be seen from Fig. 3a that the first cathodic wave shifts in the positive direction with increasing concentration of copper(II) ions. This may be due to reduction of Se(IV) ions on copper. As already noted, the maximum anodic current of oxidation of the compound is observed at a Cu(II) : Se(IV) concentration ratio in the electrolyte greater than unity. We analyzed how the current peak of oxidation of the compound varies with concentration of a component added. In all cases, the maximum corresponded to the composition with Cu : Se ≈ 2 : 1 (Fig. 4).

In the study, we analyzed the influence exerted by the potential sweep rate on the oxidation potential of a compound. It was found that, as the potential sweep rate increases, the potential of the current peak observed on the carbon-pyroceramic electrode shifts only slightly (by about 30 mV) in the positive direction (Fig. 5).

To analyze in more detail the anodic portions of the voltammetric curves measured in oxidation of the compound $CuSe_x$ in an electrolyte with ion concentrations (M): $c_{Cu^{2+}} = 2 \times 10^{-3}$ and $c_{Se^{4+}} = 1 \times 10^{-3}$, the deposit was accumulated with the electrode kept at different potentials (Fig. 6).

It can be seen that the compound Cu_2Se is formed even at a potential of +0.1 V. The probable mechanism is the reduction of Se(IV) on copper. In codeposition of selenium and copper, only the current peaks corresponding to oxidation of the compound Cu_2Se (E_{ox} = 0.25 V) and of selenium (E_{ox} = 1.1 V) are observed in the anodic curve at all potentials. The additional shoulder observed both at the first and at the second current peaks of oxidation after the deposition in the potential range –0.15…–0.4 V (Fig. 6, curves *6*–*9*) may indicate that different forms of the compound are present and that this is the transition region between two of these. When the deposition is performed at potentials corresponding to the limiting current of reduction (at –0.5 and –0.6 V), only a single form of the compound is present, which is, probably, the most stable Cu_2Se. The voltammetric curve of Cu(II) and Se(IV) codeposition, measured at 80°C and a 2 : 1 concentration ratio, repeats the main features of the curve measured at room temperature. In particular, a partial reduction of copper selenide

occurs at –0.4 V to give H_2Se in accordance with Eq. (3).

The results obtained show that codeposition of copper and selenium occurs even at a potential of +0.10 V via reduction of selenium(IV) on copper, which is confirmed by the rise in the current of the first wave upon gradual addition of selenium (IV) to a solution with a constant Cu^{2+} concentration of 10^{-3} M (Fig. 2a).

If a solution containing a large excess of copper ions ($c_{Cu^{2+}} : c_{Se^{4+}} = 4 : 1$) is taken as the starting solution, then the accumulation of copper deposit at any potential results in the deposition of free copper, which is in excess with respect to the stoichiometric composition Cu_2Se (Fig. 7).

Figure 7 shows voltammetric curves measured in oxidation of a deposit accumulated at various deposition potentials under the conditions of an excess amount of copper ions in the electrolyte. The peak corresponding to oxidation of the excess copper is present in all the curves, along with the peak of oxidation of the compound. This result confirms the conclusion that the copper-to-selenium concentration ratio in the electrolyte not exceeding 2.2 : 1 is the optimal for obtaining a compound of composition Cu_2Se.

The structural properties of the surface of films electrodeposited onto glassy carbon plates at a chosen composition of the electrolyte showed that the structure of the deposit formed at a potential of –0.6 V corresponds to the composition of the compound $Cu_{2-x}Se$.

The main reflections in the X-ray diffraction pattern measured after annealing the film at 300°C correspond to this compound (Fig. 8a). According to the ASTM File, the composition parameter x for the compound is 0.15. An electron-microscopic study with analysis of microdiffraction patterns demonstrated that the structure of the compound Cu_2Se manifests itself in the form of separate reflections related to the coarsely crystalline phase (>200 Å). The clearly pronounced rings correspond to the finely crystalline phase of the same compound (crystallite size 15–25 Å). A micrograph of crystals of this compound, whose size corresponds to the finely crystalline phase, is shown in Fig.8b. For all the samples, the preferred reflections correspond to the [111] directions in the cubic lattice.

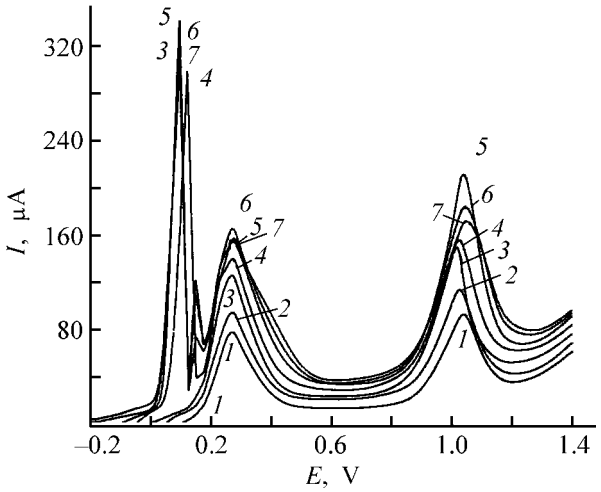

Fig. 7. Anodic portions of the voltammetric curves measured after keeping the electrode at various potentials at $c_{Cu(II)} = 4 \times 10^{-3}$ M. Potential (mV): (*1*) +100, (*2*) +50, (*3*) 0, (*4*) –50, (*5*) –100, (*6*) –200, and (*7*) –300.

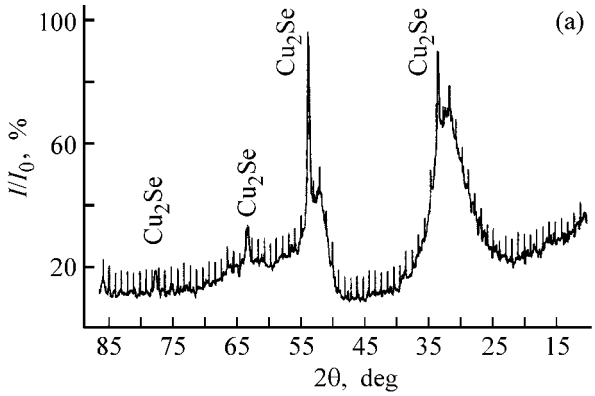

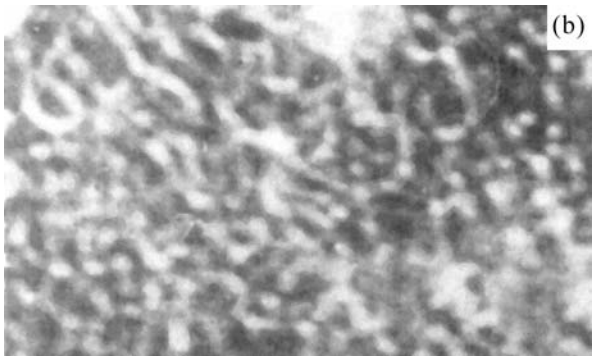

Fig. 8. (a) X-ray diffraction pattern of an electrodeposited Cu_2Se film and (b) a micrograph of the film surface. Magnification ×120 000. (I/I_0) Relative intensity and (2θ) Bragg angle.

CONCLUSIONS

(1) Compounds of various composition are formed in the electrodeposition of copper(II) and selenium(IV), depending on the relative amounts of the components in the electrolyte and on the deposition potential.

(2) The condition for the formation of the compound Cu_2Se is that the Cu(II) : Se(IV) concentration ratio should be 2.2 : 1.

(3) Copper and selenium compounds of any composition give a peak of oxidation current at a potential of $+0.25 \pm 0.02$ V. The peak potential shifts only slightly in the positive direction as the content of copper ions increases.

REFERENCES

1. Contreras, M.A., Egaas, B., King, D., *et al.*, *Thin Solid Films*, 2000, vol. 361, pp. 167–172.
2. Bachmann, K.J., Fearheiley, M., Shing, Y.H., and Tran, N., *Appl. Phys. Lett.*, 1984, vol. 44, pp. 407–408.
3. Dergacheva, M.B. and Chaikin, V.V., *Khimiya: nauka, promyshlennost': Materialy Mezhdunarodnoi naucho-prakticheskoi konferentsii, Pavlodar, 15–16 noyabrya 2001 g.* (Chemistry: Science and Industry, Proc. Int. Sci.-Pract. Conf., Pavlodar, November 15–16, 2001), Pavlodar, 2001, pp. 279–286.
4. Carbonnelle, R., and Lamberts, L., *J. Electroanal. Chem.*, 1992, vol. 340, pp. 53–57.
5. Marlot, A. and Vedel, J., *J. Electrochem. Soc.*, 1999, vol. 146, no. 1, pp. 178–183.
6. Danilov, A.I., Molodkina, E.B., and Polukarov, Yu.M., *Elektrokhimiya*, 1997, vol. 33, no. 3, pp. 313–319.
7. Rau, M. and Ralenau, A., *J. Solid State Chem.*, 1970, vol. 1, pp. 515–519.
8. Thouin, L., Rouquette-Sanchez, S., and Vedel, J., *Electrochim. Acta*, 1993, vol. 38, pp. 2383–2389.
9. Massaccesi, S., Sanchez, S., and Vedel, J., *J. Electrochem. Soc.*, 1993, vol. 140, pp. 2540–2545.
10. Quickenden, T.J., and Xu, Q., *J. Electrochem. Soc.*, 1996, vol. 143, pp. 1248–1251.

Russian Journal of Applied Chemistry, Vol. 77, No. 8, 2004, pp. 1279–1282. Translated from Zhurnal Prikladnoi Khimii, Vol. 77, No. 8, 2004, pp. 1295–1298.

APPLIED ELECTROCHEMISTRY AND CORROSION PROTECTION OF METALS

Anodic Behavior of Aluminum–Zirconium Alloys Microalloyed with Strontium and Cerium

I. N. Ganiev, R. O. Barotov, and M. B. Inoyatov

Nikitin Institute of Chemistry, Academy of Sciences of the Republic of Tajikistan, Dushanbe, Tajikistan

Received October 21, 2004

Abstract—The potentiodynamic method was used to study in solutions of 3% NaCl and 0.01 N NaOH the corrosion-electrochemical behavior of aluminum alloyed with zirconium, strontium, and cerium.

In choosing alloying elements in the development of aluminum-based conductor alloys and alloys for cable sheaths it is necessary to take into account not only the strength, technological, and electrical properties, but also the corrosion resistance. This refers in full measure to transition, alkaline-earth, and rare-earth metals, which are increasingly used for these purposes. There is published evidence concerning the positive influence of these metals on the corrosion resistance of aluminum [1–6].

The present communication reports the results of a study of the influence exerted by small additions of zirconium, strontium, and cerium on the corrosion resistance of technical-grade aluminum.

EXPERIMENTAL

As the starting material for preparing the alloys under study served aluminum of 99.6% purity, as well as strontium and cerium with a purity of no less than 99.8%. All the alloying components were introduced in the form of the corresponding alloys at a melt temperature of 800–850°C. From each melting, cylindrical samples 8 mm in diameter and 100 mm long were cast into a heated graphite mold.

The study was performed electrochemically in a neutral (3% NaCl) or alkaline (0.01 N NaOH) medium. The electrode potentials were measured with a PI-50-1 potentiostat relative to a silver chloride reference electrode during a month at 1-day intervals. The potentials are given relative to this electrode. The free-corrosion potential was determined from the potential–time dependence. The classical, well-reproducible polarization curves were obtained in the neutral medium by using the potentiodynamic method in combination with a preliminary deep cathodic polarization at a potential of –2.0 V for 5 min [7]. The current corresponding to each potential was recorded with an LKD-4 *X*–*Y* recorder in the potential–current coordinates. In the alkaline medium, polarization curves were measured, after the free-corrosion potential was attained, at a potential sweep rate of 2 mV s^{-1}.

In neutral solutions containing halogen ions, the passive oxide film on aluminum and its alloys ceases to be solid and pitting corrosion occurs. To assess the resistance of the alloys to pitting corrosion, the pitting potential and the corrosion potential under the identical testing conditions were compared.

Tables 1–3 list the results of an electrochemical study of the aluminum alloys. The dependences of the electrode potentials of aluminum–zirconium alloys on the time of keeping demonstrated that addition of zirconium shifts the free-corrosion potential of aluminum to a more negative region (Table 1). When

Table 1. Free-corrosion potential E_{fc} of alloys of the system Al–Zr in relation to the time τ of keeping in a 3% NaCl solution

Zr, wt %	$-E_{fc}$ (V) at indicated τ, min					
	without keeping	1	5	30	60	steady value
0.0	1.09	1.05	0.93	0.81	0.75	0.73
0.01	1.02	0.92	0.82	0.78	0.72	0.71
0.05	1.02	0.86	0.80	0.75	0.75	0.75
0.1	1.16	1.10	0.109	0.96	0.91	0.87
0.3	1.14	1.12	0.109	0.96	0.92	0.89
0.5	1.04	1.02	0.98	0.94	0.92	0.89

1070-4272/04/7708-1279 © 2004 MAIK "Nauka/Interperiodica"

Table 2. Electrochemical parameters of alloys of the systems Al–Zr, and Al–Zr–Sr(Ce) in a 3% NaCl solution*

Alloy component,** wt %			$-E_{fc}$	$-E_{po}$	$-E_{cp}$	$-E_{pt}$	i_{po}	i_{cp}	v_c, g m^{-2} h^{-1}
Zr	Sr	Ce	V				mA cm^{-2}		
0.0	0.0	0.0	0.760	1.42	1.32	0.68	2.10	0.37	0.0185
0.01	–	–	0.710	1.45	1.30	0.68	1.60	0.35	
0.05	–	–	0.750	1.46	1.37	0.67	1.60	0.30	
0.10	–	–	0.870	1.45	1.38	0.65	1.65	0.30	
0.30	–	–	0.890	1.45	1.31	0.65	1.70	0.35	
0.50	–	–	0.890	1.45	1.25	0.64	2.10	0.45	
0.01	0.05	–	0.745	1.42	1.32	0.64	1.8	0.34	0.0152
0.05	0.05	–	0.755	1.42	1.32	0.63	1.5	0.30	
0.10	0.05	–	0.790	1.44	1.32	0.65	1.6	0.30	
0.30	0.05	–	0.820	1.45	1.32	0.65	2.2	0.36	
0.50	0.05	–	0.830	1.45	1.35	0.65	2.5	0.46	
0.01	–	0.05	0.750	1.43	1.38	0.68	1.70	0.23	0.0172
0.05	–	0.05	0.770	1.42	1.38	0.66	1.60	0.32	
0.10	–	0.05	0.815	1.43	1.35	0.65	1.60	0.30	
0.50	–	0.05	0.825	1.44	1.35	0.64	1.85	0.35	
0.01	–	0.10	0.745	1.41	1.36	0.65	2.30	0.29	
0.05	–	0.10	0.825	1.45	1.35	0.64	2.00	0.21	
0.10	–	0.10	0.840	1.45	1.36	0.65	2.00	0.23	
0.05	0.05	0.05	0.680	–	–	0.60	–	0.15	
0.05	0.05	0.10	0.675	–	–	0.61	–	0.12	
0.05	0.10	0.05	0.685	–	–	0.64	–	0.18	

* E_{po}, E_{cp}, and E_{pt} are the potentials of passivation onset, complete passivation, and pitting, respectively; v_c, the corrosion rate.
** Aluminum the rest.

Table 3. Free-corrosion potential E_{fc} and passivation current density for alloys of the system Al–Zr–Sr(Ce) in relation to the time τ of keeping in an alkaline medium

Alloy no.	Alloy component,* wt %			$-E_{fc}$ (V) at indicated τ, days					i_{cp}, mA cm^{-2}
	Zr	Sr	Ce	without keeping	1	3	10	20	
1	0.05	–	–	1.58	1.22	1.13	1.02	0.99	0.44
2	0.05	0.05	–	1.52	1.12	1.10	0.97	0.99	0.40
3	0.05	0.10	–	1.45	1.10	1.08	0.97	0.95	0.40
4	0.05	0.15	–	1.54	1.09	1.06	0.96	0.96	0.46
5	0.05	–	0.05	1.47	1.13	1.08	0.97	0.93	0.39
6	0.05	–	0.10	1.53	1.15	1.09	0.96	0.96	0.45
7	0.05	–	0.15	1.55	1.18	1.09	0.95	0.94	0.50
8	0.05	0.05	0.05	1.51	1.08	1.02	0.93	0.93	0.35
9	0.05	0.10	0.05	1.51	1.12	1.06	0.96	0.93	0.36
10	0.05	0.05	0.10	1.51	1.11	1.09	0.96	0.94	0.40

* Aluminum the rest.

the electrodes are submerged in a 3% NaCl solution, the corrosion potentials of the alloys have a higher negative value, but are shifted in the positive direction during the first 5–10 min. Further keeping for 1 h results in that a virtually stationary potential is attained, which is due to the formation of oxide films on the surfaces under study.

Table 2 lists electrochemical parameters of alloys of the system Al–Zr. Raising the content of zirconium in the alloys shifts the potentials of complete passivation and pitting to more positive values, with the passivation region extended by 40–100 mV. Introduction of up to 0.3% zirconium makes somewhat lower the current densities

of passivation onset (i_{po}) and complete passivation (i_{cp}).

The influence exerted by the alloying of the starting Al + (0.01–0.5%) Zr alloy with strontium or cerium was analyzed using the data for the binary alloys. The alloying shifts the free-corrosion potential to more positive values to –0.675…–0.680 V, and the pitting potential by 40–60 mV. The strongest shift of the potential in the positive direction is observed upon joint introduction of strontium and cerium. Analysis of the potentiodynamic curves measured in a 3% solution of NaCl shows that the free-corrosion potential of the alloys under study lies within the passive region. The irreversibility of the process of formation of passivating layers is confirmed by the hysteresis loop observed when measuring the curve in the reverse sweep. The potentiodynamic curves for the alloys are similar to those for pure aluminum, but the passivation current densities for the alloys with strontium and cerium are lower than those for the starting alloy and pure aluminum, which indicates that the dissolution rate of the alloys under study in a neutral medium is lower (Table 3).

The corrosion resistance of aluminum is largely determined by the nature of a corrosive medium and by the possibility of formation or dissolution of a protective film. It is believed that the medium with pH > 8.5 is the most corrosive for aluminum. According to [8], the process of dissolution of aluminum can be understood as follows. First, after aluminum is submerged in an alkali solution, the natural thin oxide film is chemically dissolved under the action of OH^- ions, and then, after the film is partly removed, there begins the electrochemical dissolution of the metal. The anodic dissolution process is described by the equation

$$Al + 3OH^- = AlOOH + H_2O + 3e.$$

In an alkaline medium, the thickness of the boehmite film increases with time, which leads to partial passivation, shifts the electrode potentials in the positive direction, and makes slower the corrosion rate of aluminum and alloys under study. A pronounced shift of the potentials in the positive direction occurs during the first 10 days. The cathodic and anodic curves for the alloys under study are similar to those for pure aluminum, and the passivation current densities indicate that the corrosion resistance of aluminum alloys containing up to 0.1% strontium and cerium increases. The lowest passivation current density is observed for the alloys with both strontium and cerium. The high corrosion resistance of these alloys is confirmed by gravimetric measurements of the corrosion rate in the same NaOH medium (pH ≈ 11.6).

Table 4. Effect of annealing on the electrochemical parameters of the system Al–Zr–Sr(Ce) in various media

Alloy no. (the same as in Table 3)	Electrolyte				
	3% NaCl*			0.01 N NaOH**	
	$-E_c$, V	$-E_{pt}$, V	$-i_{cp}$, mA cm^{-2}	i_{cp}, mA cm^{-2}	v_c, g m^{-2} h^{-1}
1	0.865 / 0.855	0.620 / 0.700	0.32 / 0.43	0.38	1.06
2	0.815 / 0.865	0.670 / 0.700	0.30 / 0.30	0.28	1.01
3	0.810 / 0.870	0.650 / 0.670	0.20 / 0.30	0.24	0.96
4	0.765 / 0.875	0.670 / 0.670	0.18 / 0.25	0.25	0.94
5	0.775 / 0.800	0.630 / 0.650	0.22 / 0.17	0.23	1.02
6	0.735 / 0.795	0.630 / 0.680	0.22 / 0.19	0.27	1.14
7	0.720 / 0.860	0.620 / 0.690	0.26 / 0.20	0.26	1.09
8	0.680 / 0.790	0.600 / 0.640	0.15 / 0.13	0.20	0.81
9	0.685 / 0.835	0.640 / 0.660	0.18 / 0.20	0.22	1.05
10	0.675 / 0.785	0.610 / 0.645	0.12 / 0.17	0.21	0.93
Al	0.735 / 0.760	0.680 / 0.680	0.37 / 0.37	0.32	1.23

* Numerator, data for cast alloys; denominator, for annealed alloys.

** Data for annealed alloys.

The nature and amount of the second phase in the alloys affect the pitting potential only slightly, which was demonstrated by tests of the alloys under study before and after thermal treatment (Table 4).

The alloys were homogenized at 500°C for 6 h, with subsequent quenching in cold water. The pitting potentials of these alloys are in the range –600… –700 mV. It can be seen that the thermal treatment strongly affected the passivation current density and the corrosion potential. It follows from the data in Table 4 that a homogenizing thermal treatment can

improve the corrosion resistance of aluminum alloys with strontium and cerium in an alkaline medium, which is indicated by the decrease in the passivation current density.

CONCLUSION

A study by the potentiodynamic method demonstrated the possibility of improving the corrosion resistance of technical-grade aluminum by its microalloying with zirconium, strontium, and cerium.

REFERENCES

1. Drits, M.E. and Kadaner, E.S., *Fizikokhimiya redkikh metallov* (Physical Chemistry of Rare Metals), Moscow: Nauka, 1972, pp. 162–174.
2. Raman Aravamudhan, *Z. Metallkunde*, 1997, vol. 68, no. 3, pp. 163–172.
3. Elagin, V.I., Zakharov, V.V., and Rostova, T.D., *Tsvetn. Met.*, 1982, no. 12, pp. 96–99.
4. Ganiev, I.N., Yunusov, I., and Krasnoyarskii, V.V., *Zh. Prikl. Khim.*, 1987, vol. 60, no. 9, pp. 2119–2123.
5. Ganiev, I.N. and Trubnyakova, E.D., *Zh. Prikl. Khim.*, 1996, vol. 69, no. 11, pp. 2545–2548.
6. Ganiev, I.N. and Shukroev, M.Sh., *Zh. Prikl. Khim.*, 1998, vol. 71, no. 8, pp. 1916–1919.
7. Rozenfel'd, I.L., Persiantseva, V.V., and Zorina, V.E., *Zashch. Met.*, 1979, vol. 15, no. 1, pp. 89–94.
8. Fateev, Yu.F., Vrzhosek, G.G., and Antropov, L.I., *Trudy 2-i Ukrainskoi respublikanskoi konferentsii po elektrokhimii* (Proc. 2nd Ukr. Republ. Conf. on Electrochemistry), Kiev, 1998, pp. 134–137.

Russian Journal of Applied Chemistry, Vol. 77, No. 8, 2004, pp. 1283–1286. Translated from Zhurnal Prikladnoi Khimii, Vol. 77, No. 8, 2004, pp. 1299–1302.

APPLIED ELECTROCHEMISTRY AND CORROSION PROTECTION OF METALS

Fundamental Aspects of Film Formation in Electrochemical Polishing of Silver and Silver–Copper Alloys in Thiosulfate Solutions

E. P. Grishina, S. I. Galanin, and O. A. Ivanova

Institute of Chemistry of Solutions, Russian Academy of Sciences, Ivanovo, Russia
Kostroma State Technological University, Kostroma, Russia

Received April 15, 2004

Abstract—The anodic behavior of silver and its alloys with copper in thiosulfate solutions was studied by cycling voltammetry. A scheme of an electrochemical polishing process including the stage of formation of a resistive layer of silver thiosulfate and the chemical stage of its dissolution is suggested.

Electrochemical polishing has found fairly wide use for finishing treatment of plated silver coatings and silver articles [1, 2]. The variety of electrolytes used for this purpose is limited to few solutions with high concentrations of CN^- [3, 4], CNS^- [5], $S_2O_3^{2-}$ [6, 7], and NH_4^+ [8] ions. All these anions form with the Ag^+ cation highly stable complex compounds [9], which ensure that the products of the anodic reactions exist in a soluble form. At the same time, it is known that the electrochemical polishing of silver is accompanied by periodic formation and dissolution of the surface passivating salts films of the corresponding sparingly soluble compounds. The chemical stability of these films in concentrated solutions of like anions is low, which is presumably due to the occurrence of fast reactions of film dissolution to give complex salts.

A nontoxic thiosulfate solution, in which passivating films [7] of sparingly soluble silver thiosulfate [10] can also be formed, is rather promising for electrochemical polishing of silver. The fundamental aspects of the film-forming process in anodic oxidation of silver have been little studied. This leads to higher labor expenditure in choosing the optimal polishing conditions.

The main difficulty in working with thiosulfate solutions is the strong influence exerted by the acidity of the medium on the stability of the $S_2O_3^{2-}$ ion. In an acid medium, this ion decomposes by reaction [11]

$$S_2O_3^{2-} + 2H^+ \rightarrow SO_2 + S\downarrow + H_2O. \quad (1)$$

In addition, the cathodic reduction of the anion to the S^{2-} ion is facilitated [11]:

$$S_2O_3^{2-} + 6H^+ + 8e \rightarrow 2S^{2-} + 3H_2O. \quad (2)$$

In this context, it is appropriate to use in the study a sodium thiosulfate solution combined with an acetate buffer system [6], which maintains the neutral pH value both in the near-electrode layers and in the electrolyte bulk. According to [12], the silver electrode interacts with $S_2O_3^{2-}$ ions at considerably less positive potentials than those in the case of acetate ions [12]. Therefore, acetate ions will not affect the anodic oxidation of the metal under study at the potentials considered.

The aim of this study was to examine the kinetic aspects of the anodic dissolution of silver and silver–copper alloys in a thiosulfate solution for the case of electrochemical polishing.

EXPERIMENTAL

The study is concerned with the electrochemical oxidation of silver (Sr999 brand) and binary single-phase silver–copper alloys (SrM940 and SrM910 brand, containing 94% and 91% silver, respectively, and copper the rest) in 320 g l^{-1} $Na_2S_2O_3$ solutions (in acetate buffer system, pH 6.5) [6] using the methods described in [13] (PI 50-1 potentiostat). Prior to the polarization measurements, the samples of silver and silver alloys were mechanically polished,

1070-4272/04/7708-1283 © 2004 MAIK "Nauka/Interperiodica"

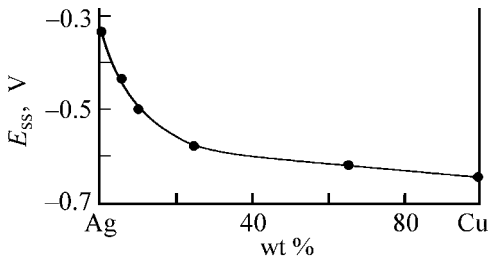

Fig. 1. Steady-state potential E_{ss} of the alloys of the Ag–Cu system vs. their composition in a solution containing 320 g l^{-1} $Na_2S_2O_3$ at 20°C.

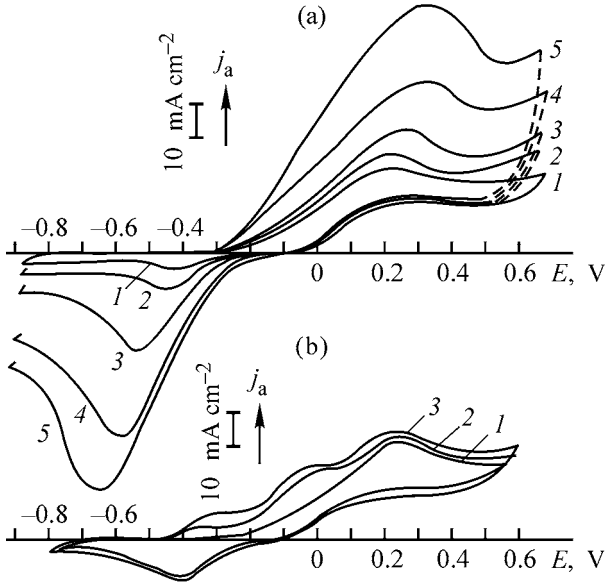

Fig. 2. Cyclic voltammograms measured in a thiosulfate solution at 20°C on (a) Sr999 silver at various potential sweep rates and (b) on silver and Ag–Cu alloys at V = 10 mV s^{-1}. (j_a) Anodic current density and (E) potential (V, relative to a silver chloride reference). (a) Potential sweep rate (mV s^{-1}): (*1*) 5, (*2*) 10, (*3*) 20, (*4*) 50, and (*5*) 100. (b) (*1*) Sr999, (*2*) SrM940, and (*3*) SrM910.

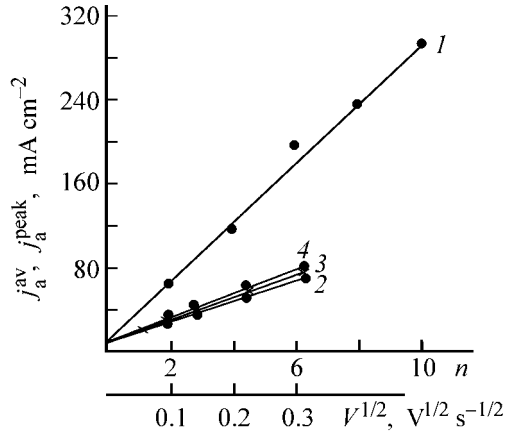

Fig. 3. (*1*) Average anodic current density in a pulse, j_a^{av} vs. the on-off time ratio n and (*2–4*) the peak anodic current density j_a^{peak} vs. $V^{1/2}$. (V) Potential sweep rate. (*1*) SrM925, (*2*) Sr999, (*3*) SrM940, and (*4*) SrM910.

degreased, and washed. In some cases, silver was subjected to chemical polishing in a 1 : 1 aqueous solution of HNO_3 for 1 min, instead of mechanical polishing, which made the silver surface white matte, similarly to a plated silver coating. The polarization measurements were performed in the temperature range 20–40°C, with temperature maintained constant to within ±0.1°C, at a potential sweep rate in the interval 5–100 mV s^{-1}.

The quality of the surface was judged from the fractal dimension and the reflectivity of the electrode surface. The fractal dimension D_f, related to the surface roughness, was calculated from a frequency dependence of the electrode impedance, measured with a P5021 ac bridge by the method described in [14, 15]. The surface reflectivity was measured on a specially designed setup [16].

The steady-state potentials of Sr999 silver and silver–copper alloys in thiosulfate solutions strongly depend on the alloy composition and concentration of sodium thiosulfate (Fig. 1). Owing to the high complexing ability of Ag^+ with respect to the $S_2O_3^{2-}$ ion and the low solubility product of $Ag_2S_2O_3$ [10], the steady-state potential of the silver electrode in the solution studied is rather negative and lies within the range –0.360…–0.340 V relative to a saturated silver chloride reference electrode.

The anodic behavior of silver in this solution is described by a polarization curve with a clearly defined peak of the anodic current (Fig. 2a). The height of this peak linearly depends on the square root of the potential sweep rate V (Fig. 3). This is due to the formation, by the electrochemical mechanism, of a resistive porous layer of sparingly soluble products of silver oxidation [17]. The most probable is formation of a salt layer of $Ag_2S_2O_3$, since the potential of the redox process under study, measured as the half-sum of potentials of the anodic and cathodic current peaks, is –0.220 to –0.150 V.

The experimental data in Fig. 2a show the following. As the time of anodic polarization decreases (i.e., the potential sweep rate increases), a peak of cathodic current, gradually increasing in height, is observed in the cathodic portion of the cyclic voltammogram. This peak is conjugate to the anodic peak and reflects the reduction of the salt layer. The electrolyte used shows a high chemical activity with respect to the resistive layer and dissolves it, apparently owing to the occurring complexation. The dissolution rate of the primary product of the electrode process at 20°C, expressed in current density units and determined as the intercept on the current-density axis (Fig. 3) [13],

is 10 mA cm^{-2} and is diffusion-limited (the effective energy of activation of this process, determined by the temperature-kinetic method, is A_{eff} = 12 kJ mol^{-1}). Based on the aforesaid and taking into account the known forms of complex ions [9, 10], we can represent the electrochemical dissolution of silver in a thiosulfate solution as

$$\begin{array}{l} 2Ag + S_2O_3^{2-} \rightarrow Ag_2S_2O_{3(s)} + 2e \\ \qquad\qquad \downarrow +nS_2O_3^{2-} \\ \qquad\qquad Ag(S_2O_3)_{2(sol)}^{3-}, \\ \qquad\qquad Ag(S_2O_3)_{3(sol)}^{5-} \end{array} \qquad (3)$$

The electrochemical polishing of silver was performed in a solution of the above composition in the ac mode, which ensures anodic formation, partial chemical removal, and cathodic reduction of the residual amount of the film substance. The alternation of such actions at a certain frequency results in a pronounced leveling of the surface [fractal dimension D_f decreases, luster appears or is enhanced for both mechanically and chemically treated surfaces (see table)].

The anodic polarization curves of SrM940 and SrM910 alloys, compared with those of silver, show two additional electrochemical responses recorded in the form of waves (Fig. 2b). Such changes in the polarization curve are due to the electrochemical oxidation of the more electronegative component of the alloy, i.e., copper, which proceeds in two single-electron stages [18]. In the process, the half-wave potentials $E_{1/2}$ of Cu $\rightarrow$ Cu(I) and Cu(I) $\rightarrow$ Cu(II) oxidation are strongly different. It may be suggested that, in all probability, the forming compounds of Cu(I) are sparingly soluble, similarly to Ag(I) compounds. Therefore, if the potentials corresponding to the Cu(I) $\rightarrow$ Cu(II) transition, which enables formation of soluble thiosulfate complexes of Cu(II), are not attained in the electrochemical treatment of the alloy, no surface polishing will occur.

A study of the electrochemical polishing of the alloys in a thiosulfate solution with short current pulses (pulse width $t_p = 3.0 \times 10^{-3}$ s at the on-off time ratio g = 2–10) showed that polishing takes place at the electrode polarization in the range ΔE = 0.4–0.75 V, i.e., after the potential of ionization of copper to Cu(II) and that of silver are attained. Another reason why the ΔE interval in which the polishing process occurs is so narrow is that the potentials of processes involving copper

$$2Cu + H_2O = Cu_2O + 2H^+ + 2e, \qquad (4)$$

Characterization of the surface of a silver electrode before and after electrochemical polishing in a thiosulfate solution

Sample preparation	Surface	D_f	Luster, cd m^{-2}
Mechanical	Initial	2.3–2.4	400–450
	Electrochemically polished	2.3–2.4	585–615
Chemical	Initial	2.7–2.75	300–330
	Electrochemically polished	2.3–2.4	400–450

$$Cu_2O + H_2O = 2CuO + 2H^+ + 2e \qquad (5)$$

are attained at a stronger polarization [18].

The reaction of copper oxides with the $S_2O_3^{2-}$ ion is rather slow. Apparently, this is the reason why the optimization of the polishing conditions for silver–copper alloys is very difficult and why copper and alloys containing >9% copper cannot be polished in thiosulfate solutions.

In polarization of silver alloys in the pulsed mode, the kinetic component of the anodic current can be also distinguished (Fig. 3). Extrapolation of the dependence of the average pulsed current density j on the on-off time ratio n to $n \rightarrow 0$ gives the same j_0 value as that found in the potentiodynamic study (Fig. 3). This value is 10 mA cm^{-2} and corresponds to the anodic current density at which the rate of film formation is close to the rate of its dissolution via chemical reaction with thiosulfate ions. The coincidence of the j_0 values obtained in different experiments confirms the physical meaning of this parameter, as well as its effect on the kinetics of anodic dissolution of silver and silver alloys.

CONCLUSIONS

(1) The electrochemical polishing of silver in a thiosulfate solution is accompanied by the formation of a resistive porous layer of silver thiosulfate, whose dissolution rate is 10 mA cm^{-2} under the given conditions. This current density is the optimal for polishing of silver and the alloys studied with short current pulses.

(2) The complex polarization dependence for silver–copper alloys in thiosulfate solutions, which indicates the formation of a number of sparingly soluble copper(I, II) compounds, along with silver oxidation,

predetermines the rather narrow interval of alloy polarization in which electrochemical polishing occurs. To obtain a polishing effect, it is necessary to perform the anodic process at the potentials of occurrence of the reactions $Cu(I) \rightarrow Cu(II)$ and $Ag_2S_2O_{3\,(sol)}$.

REFERENCES

1. Tegart, W.J.McG., *The Electrolytic and Chemical Polishing of Metals in Research and Industry*, London: Pergamon, 1956.
2. Grilikhes, S.Ya., *Elektrokhimicheskoe polirovanie metallov* (Electrochemical Polishing of Metals), Moscow: Mashinostroenie, 1976.
3. Fedot'ev, N.P. and Grilikhes, S.Ya., *Elektrokhimicheskoe travlenie, polirovanie i oksidirovanie metallov* (Electrochemical Etching, Polishing, and Oxidation of Metals), Moscow: Mashinostroenie, 1957.
4. FRG Patent 2 249 249.
5. USSR Inventor's Certificate, no. 497 357.
6. Cabane-Brouty, F. and Ruze, B., *Metaux (Corros.-Inds.)*, 1964, vol. 39, no. 469, pp. 343–345.
7. Nukulin, V.N. and Tsypin, M.Z., *Zh. Prikl. Khim.*, 1960, vol. 33, no. 2, pp. 469–471.
8. Yuzikis, P.A., Yankauskas, T.Yu., Buchinskas, D.A., and Yankauskene, E.K., *Zh. Prikl. Khim.*, vol. 52, no. 7, pp. 1659–1661.
9. *Spravochnik khimika* (Chemist's Handbook), Nikol'skii, B.P., Ed., Leningrad: Khimiya, 1964, vol. 3.
10. Von Remy, H., *Lehrbuch der anorganischen Chemie*, Leipzig: Akad. Verlag-Geest und Portig, 1960.
11. Karapet'yants, M.Kh. and Drakin, S.I., *Obshchaya i neorganicheskaya khimiya* (General and Inorganic Chemistry), Moscow: Khimiya, 1981.
12. *Spravochnik po elektrokhimii* (Handbook of Electrochemistry), Sukhotin, A.M., Ed., Leningrad: Khimiya, 1981.
13. Grishina, E.P. and Rumyantsev, E.M., *Elektrokhimiya*, 2001, vol. 37, no. 4, pp. 474–478.
14. Grishina, E.P., and Noskov, A.V., *Izv. Vyssh. Uchebn. Zaved., Khim. Khim. Tekhnol.*, 2003, vol. 46, no. 3, pp. 104–107.
15. Noskov, A.V., Balmasov, A.V., Kozlova, N.B., and Lilin, S.A., *Zh. Fiz. Khim.*, 2003, vol. 77, no. 11, pp. 2081–2083.
16. Galanin, S.I., Chekotin, A.V., and Nikonova, M.V., *Zh. Prikl. Khim.*, 2001, vol. 74, no. 10, pp. 1633–1635.
17. Calandra, A.J., de Tacconi, R.N., Pereiro, R., and Arvia, A.J., *Electrochim. Acta*, 1974, vol. 19, no. 12, pp. 901–905.
18. Grishina, E.P., Udalova, A.M., and Rumyantsev, E.M., *Elektrokhimiya*, 2003, vol. 39, no. 8, pp. 1003–1007.

Russian Journal of Applied Chemistry, Vol. 77, No. 8, 2004, pp. 1287–1291. Translated from Zhurnal Prikladnoi Khimii, Vol. 77, No. 8, 2004, pp. 1303–1307.

APPLIED ELECTROCHEMISTRY AND CORROSION PROTECTION OF METALS

Corrosion-Electrochemical Behavior of Aluminum Alloys Low-Alloyed with Magnesium and Alkaline-Earth Metals

I. N. Ganiev, R. O. Barotov, and M. B. Inoyatov

Nikitin Institute of Chemistry, Academy of Sciences of the Republic of Tajikistan, Dushanbe, Tajikistan

Received March 2, 2004

Abstract—In connection with the development of low-alloyed aluminum alloys, their corrosion-electrochemical behavior was studied in various media.

The positive effect of magnesium on the physicochemical properties and corrosion resistance of aluminum is known. Taking into account this fact, series of industrial alloys of AMg6 and AMg8 brands, which contain increased amounts of the alloying element, have been developed [1, 2]. Data on the influence exerted by small amounts of magnesium are contradictory and require refinement. In view of the development of low-alloyed aluminum alloys for electrical engineering purposes, the influence exerted by addition of magnesium in an amount of 0.01–1.0% and of alkaline-earth metals (AEM) on the corrosion-electrochemical behavior of aluminum of A6 brand in a 3% NaCl solution was studied.

EXPERIMENTAL

To obtain classical polarization curves with all the three kinetic regions of active dissolution, active-passive transition, and repassivation, the potentiodynamic method was used in combination with a preliminary deep cathodic polarization at a potential of –2.0 V for 2 min [2]. This technique yields well-reproducible dependences in the case when a potentiodynamic polarization curve is measured at a potential sweep rate of 10–20 mV s^{-1} immediately after the cathodic polarization. The study was carried out with a PI-50-1 potentiostat and an LKD-4 X-Y recorder. The potentials are given relative to a silver chloride reference electrode.

The alloys studied were obtained on a shaft resistance furnace from aluminum, magnesium, and Al + 10% AEM alloys. The melt was cast to give cylindrical samples 10 mm in diameter and 100 mm long. The rods were pressed in Teflon tubes, sand-papered, polished, degreased, etched in a 10% NaOH solution, thoroughly washed with water, and placed in the working solution. The measurements were performed at a temperature of 20°C and potential sweep rate of 10 mV s^{-1}. The main electrochemical parameters of binary alloys of the system Al–Mg, deduced from potentiodynamic polarization curves, are listed in Table 1.

It can be seen that addition of magnesium positively affects the electrochemical parameters of aluminum. For example, a shift of the free-corrosion potential to the negative region has virtually no effect on the potentials of pitting and passivation onset, which, on the whole, extends the passivation interval.

The free-corrosion potentials of all the alloys studied, as well as that of aluminum, lie in the passivation region, which points to their high capacity for spontaneous passivation. Alloying of aluminum with mag-

Table 1. Electrochemical parameters of aluminum–magnesium alloys in a 3% NaCl solution*

Mg, wt %	$-E_{fc}$	$-E_{po}$	$-E_{cp}$	$-E_{pt}$	$-E_{rp}$	i_{po}	i_{cp}
	V					mA cm^{-2}	
0.0	0.760	1.42	1.32	0.680	0.730	2.10	0.37
0.1	0.900	1.42	1.32	0.660	0.750	1.70	0.25
0.3	0.907	1.42	1.35	0.670	0.750	1.75	0.28
0.5	0.910	1.42	1.37	0.670	0.750	1.75	0.28
0.7	0.920	1.45	1.38	0.670	0.750	1.78	0.28
1.0	0.930	1.45	1.38	0.670	0.750	1.78	0.30

* E_{fc}, E_{po}, E_{cp}, E_{pt}, and E_{rp} are the potentials of free corrosion, passivation onset, complete passivation, pitting, and repassivation, respectively; i_{po} and i_{cp}, the current densities of passivation onset and complete passivation, respectively.

1070-4272/04/7708-1287 © 2004 MAIK "Nauka/Interperiodica"

Table 2. Electrochemical parameters of alloys of the systems Al–Sr and Al–Ba in a 3% NaCl solution

Alloy component, wt %		$-E_{po}$	$-E_{cp}$	$-E_{pt}$	i_{po}	i_{cp}
Sr	Ba	V			mA cm^{-2}	
0.00	0.00	1.420	1.320	0.690	2.10	0.48
0.01	–	1.410	1.320	0.640	0.92	0.30
0.01	–	1.400	1.320	0.650	0.86	0.31
0.10	–	1.390	1.320	0.650	1.00	0.34
0.50	–	1.300	1.320	0.640	2.20	0.34
–	0.01	1.410	1.320	0.680	0.98	0.29
–	0.1	1.410	1.320	0.680	0.98	0.25
–	0.15	1.410	1.330	0.670	1.05	0.30
–	0.30	1.380	1.270	0.700	1.75	0.36
–	0.50	1.370	1.270	0.700	1.85	0.36

nesium leads to a decrease in the passivation current density in the entire range of the concentrations studied, especially for the alloy with 0.1% Mg. The resistance to pitting corrosion can be evaluated by a characteristic of the pitting resistance, pitting-resistance basis ΔE_{pt} [4]:

$$\Delta E_{pt} = \Delta E_{pt} - \Delta E_{k}.$$

In this parameter, the alloys markedly surpass pure aluminum, which is indicated by an increase in ΔE_{pt} from 80 mV for aluminum to 260 mV for the alloy containing 1% magnesium.

Table 2 lists the results of an electrochemical study of binary alloys of aluminum with small additions of strontium and barium. Alloying of aluminum with these metals als0 leads to a decrease in the current densities of complete passivation and passivation onset in the potentiodynamic curves. Introduction of strontium and barium in amount of 0.10–0.15 wt % has virtually no effect on the main electrochemical parameters of aluminum. As the content of the alloying element is raised further, the passivation region somewhat narrows and the current densities of passivation onset and complete passivation increase.

With account of previous studies [5, 6], the following concentration ranges were chosen in developing the composition of complex alloys based on ternary systems aluminum–magnesium–AEM (wt %): 0.01–1.0 for magnesium and 0.01–0.05 for AEM.

The results obtained in a study of ternary alloys are listed in Tables 3 and 4. The variation with time of the free-corrosion potential of alloys of the optimal composition in a 0.1 N NaOH solution shows that the corrosion potential in an alkaline medium reaches a constant value in 2–3 h. A strong shift of the potential into the positive region is observed in the first 30 min, and then only a minor shift of the potential is observed till its complete stabilization (Table 3).

At a constant content of AEM and increasing concentration of magnesium, the corrosion potential of the alloys are shifted, as also in the case of binary alloys of the system Al–Mg, into the negative region (Table 4). However, addition of up to 0.5 wt % magnesium has virtually no effect on the electrochemical parameters of aluminum: E_{pt} and E_{rp} change only slightly. The free-corrosion potential lies in the passive region, which points to good passivation characteristics of the ternary alloys. Virtually all of the alloys studied have a lower current density of complete passivation than pure aluminum (Table 4).

The best corrosion resistance is observed for alloys that contain (wt %): magnesium 0.05–0.020, AEM 0.05. The electrochemical data are confirmed by gravimetric measurements of the corrosion rate of a number of alloys in a 3% NaCl solution containing 0.1% H_2O_2 (Table 4). Alloying of aluminum with magnesium and AEM simultaneously can raise its corrosion resistance by 30–50%.

The effect of plastic deformation at an extent of deformation equal to 80% on the corrosion-electrochemical behavior of the alloys was studied for the example

Table 3. Variation of the free-corrosion potential E_{fc} for aluminum alloys with magnesium and AEM in a 0.1 N NaOH solution at 20°C

Alloy component, wt %				$-E_{fc}$, V, at indicated keeping time, min					
Mg	Sr	Ca	Ba	without keeping	5	30	60	120	steady-state value
Al(A6)	–	–	–	1.520	1.485	1.465	1.455	1.453	1.453
0.1	0.02	–	–	1.510	1.385	1.355	1.345	1.323	1.318
0.1	0.03	–	–	1.550	1.472	1.440	1.420	1.387	1.387
–	–	0.05	–	1.515	1.430	1.405	1.398	1.390	1.387
–	–	–	0.05	1.500	1.428	1.388	1.385	1.383	1.383

Table 4. Electrochemical parameters of aluminum alloys with magnesium and AEM in a 3% NaCl solution

Alloy component, wt %				$-E_c$	$-E_{cp}$	$-E_{pt}$	i_{cp}, mA cm^{-2}	v_c, g m^{-2} h^{-1}
Mg	Ca	Sr	Ba	V				
0.01	0.01	–	–	0.765	1.340	0.680	0.27	–
0.01	0.05	–	–	0.780	1.325	0.680	0.22	–
0.05	0.05	–	–	0.790	1.325	0.680	0.20	0.0174
0.10	0.05	–	–	0.800	1.320	0.670	0.25	0.0132
0.20	0.05	–	–	0.850	1.320	0.670	0.27	0.0122
0.50	0.05	–	–	0.875	1.280	0.700	0.35	–
0.01	–	0.01	–	0.760	1.360	0.680	0.24	–
0.05	–	0.05	–	0.770	1.360	0.670	0.20	0.0150
0.10	–	0.05	–	0.780	1.360	0.630	0.18	–
0.30	–	0.05	–	0.780	1.300	0.630	0.22	–
0.60	–	0.05	–	0.790	1.320	0.640	0.19	–
1.00	–	0.05	–	0.810	1.250	0.640	0.19	–
0.01	–	–	0.01	0.750	1.340	0.650	0.22	–
0.05	–	–	0.05	0.750	1.320	0.640	0.20	0.0107
0.10	–	–	0.05	0.760	1.320	0.635	0.22	–
0.30	–	–	0.05	0.775	1.300	0.630	0.19	–
0.60	–	–	0.05	0.780	1.300	0.630	0.19	–
1.00	–	–	0.05	0.810	1.280	0.650	0.18	–
A1(A6)	–	–	–	0.760	1.320	0.680	0.35	0.0185

Table 5. Effect of deformation on the corrosion-electrochemical parameters of aluminum alloys in a 3% NaCl solution

Alloy component, wt %				$-E_{fc}$,	$-E_{pt}$,	$-i_{cp}$, mA cm^{-2}	v_c, g m^{-2} h^{-1}
Mg	Ba	Ca	Sr	V			
2.0	0.05	–	–	0.810* 0.980	0.710 0.650	0.22 0.20	–
1.0	0.05	–	–	0.780 0.790	0.650 0.685	0.18 0.17	–
0.5	0.05	–	–	0.795 0.840	0.660 0.680	0.11 0.09	0.0164 0.0110
0.5	–	0.05	–	0.765 0.960	0.620 0.680	0.17 0.12	0.0170 0.0094
0.15	–	–	0.05	0.750 0.890	0.660 0.675	0.15 0.11	0.0127 0.0105
A1(A6)	–	–	–	0.735 0.815	0.660 0.695	0.24 0.18	0.0185 0.0158

* Numerator, data for cast alloys; denominator, for deformed alloys.

of alloys with varied content of magnesium and constant content of AEM, equal to 0.05% (Table 5).

The electrochemical studies were carried out in a 3% NaCl solution, and gravimetric studies, in a solution of 3% NaCl + 0.1% H_2O_2.

The technological procedure used to fabricate compacted samples consisted in forging of rectangular $20 \times 30 \times 100$-mm cast samples preliminarily heated to 500°C on planar blocks, with their thickness decreasing by 80%, i.e., to 4 mm. Further, the samples were cut to required dimensions.

Comparison of the parameters of the alloys and the starting aluminum before and after deformation shows that the corrosion potential shifts to a more negative region after the deformation. This, on the whole, makes greater the pitting-resistance basis of the alloys. The decrease in the current density of complete passivation leads to an increase in the corrosion resistance of alloys of the optimal composition after their deformation, which is confirmed by gravimetric data. The corrosion rate v_c of the alloys subjected to deformation is 30–50% lower than that of the starting aluminum under the same conditions. This is due to the following: in the case of an oriented structure, the corrosion mainly develops along the surface, i.e., in parallel with the vector of the maximum deformation (compaction) in the fabrication of a semifinished product [7]. In addition, the dissolution rate is also affected by the formation on the surface of a protective passivating film on the defects of the crystal lattice of the surface layer of the metal [8].

According to the phase diagram of ternary alloys of the systems Al–Mg–AEM, all the alloys studied, which contain up to 1% magnesium, form solid solutions, i.e., have a single-phase structure [9]. The anodic potentiodynamic curves of the alloys show only a single peak of the anodic current, which characterizes the active dissolution of the given phase. The presence a peak of this kind in potentiodynamic curves and its nature is explained differently by different authors. All the existing hypotheses consist in the following.

(1) The peak is due to active dissolution of aluminum (or its solid solution) with the subsequent formation of aluminum oxide [3]. The role of the cathodic polarization consists in alkalization of the near-electrode layer, which results in chemical dissolution of the oxide film that passivates aluminum.

(2) Because of the existence of aluminum hydride in aqueous solutions, the presence of an anodic peak in a potentiodynamic curve can be attributed to the decomposition of this compound. The formation of the hydride is favored by the cathodic polarization of the electrode [11]. Timonov *et al*. [10] observed an anodic current peak after keeping the electrode at potentials of –2.5 and –3.0 V, i.e., at those potentials at which Al is stable according to thermodynamic data and no hydride should be formed.

(3) The adherents of the theory of cathodic introduction of an alkaline metal into aluminum to give an intermetallic compound in solutions of alkali metal chlorides attribute the presence of a current peak in the potentiodynamic curve to decomposition of this intermetallic compound, which is formed in the cathodic polarization of the electrode. A study performed in LiCl, NaCl, KCl, NH_4Cl, and $CaCl_2$ [10] demonstrated that the current peak is present in solutions of alkali metal chlorides and absent in solutions of NH_4Cl and $CaCl_2$.

However, analysis of the phase diagrams of the systems Li–Al, Na–Al, K–Al, and Ca–Al shows that intermetallic compounds are formed in the systems Li–Al and Ca–Al. The systems Na–Al and K–Al are characterized by complete absence of interaction between the components and by formation of a monotectic system [14].

Thus, it is possibly necessary to agree with the authors of the theories that attribute the existence of the peak to active dissolution of aluminum with the subsequent formation of aluminum oxide passivating the metal [3].

CONCLUSION

The possibility of improving the corrosion resistance of technical-grade aluminum by its microalloying with magnesium and alkaline-earth metals was demonstrated by means of the potentiodynamic method.

REFERENCES

1. Postnikov, N.S., *Korrozionnostoikie alyuminievye splavy* (Corrosion-resistant Aluminum Alloys), Moscow: Metallurgiya, 1976.
2. Tomashov, N.D. and Chernova, G.P., *Teoriya korrozii i korrozionnostoikie konstruktsionnye splavy* (Theory of Corrosion and Corrosion-resistant Construction Alloys), Moscow: Metallurgiya, 1986.
3. Rezenfel'd, I.L., Persiantseva, V.V., and Zorina, V.E., *Zashch. Met.*, 1979, no. 1, pp. 89–94.
4. Freiman, L.I., *Novye dostizheniya v oblasti teorii i praktiki protivokorrozionnoi zashchity materialov: Sbornik dokladov seminara po korrozii* (New Achievements in Theory and Practice of Corrosion Protection

of Materials. Proc. of Symp. On Corrosion), Moscow: Nauka, 1981, pp. 51–54.

5. Ganiev, I.N. and Shukroev, M.Sh., *Dokl. Akad. Nauk TadzhSSR*, 1984, vol. 27, no. 11, pp. 652–654.
6. Ganiev, I.N., Krasnoyarskii, V.V., and Zhukova, T.I., *Zh. Prilk. Khim.*, 1995, no. 7, pp. 1146–1149.
7. Sinyavskii, V.S., Val'kov, V.D., and Kalinin, V.D., *Korroziya i zashchita alyuminievykh splavov* (Corrosion and Protection of Aluminum Alloys), Moscow: Metallurgiya, 1986.
8. Gurskii, L.I. and Zelenin V.A., *Struktura i kinetika vzaimodeistviya metalla s okislyayushchimi sredami* (Structure and Kinetic of Interaction of a Metal with Oxidizing Media), Minsk: Nauka i tekhnika, 1982.
9. Vakhobov, A.V. and Ganiev, I.N., *Diagrammy sostoyaniya dvoinykh i troinykh sistem s uchastiem bariya i strontsiya* (Phase Diagrams of Binary and Ternary Systems Containing Barium and Strontium), Dushanbe: Donish, 1992.
10. Timonov, A.M., Sysoeva, V.V., and Berkman, E.A., *Zh. Prilk. Khim.*, 1980, vol. 53, no. 1, pp. 231–233.
11. Antropov, L.I., Vrzhosek, G.G., and Fateev, Yu.F., *Zashch. Met.*, 1975, no. 3, pp. 300–303.
12. Kabanov, B.N., Astakhov, I.I., Kiseleva, I.G., and Tomasheva, N.N., *Zashch. Met.*, 1975, no. 11, pp. 131–133.
13. Tomashova, N.N., Kiseleva, I.G., and Kabanov, B.N., *Elektrokhimiya*, 1972, no. 8, pp. 112–115.
14. Vol, A.E., *Stroenie i svoistva dvoinykh metallicheskikh sistem* (Structure and Properties of Binary Metallic Systems), Moscow: Nauka, 1979, vol. 1.

Russian Journal of Applied Chemistry, Vol. 77, No. 8, 2004, pp. 1292–1300. Translated from Zhurnal Prikladnoi Khimii, Vol. 77, No. 8, 2004, pp. 1308–1315.

APPLIED ELECTROCHEMISTRY AND CORROSION PROTECTION OF METALS

Finding an Effective Way to Inhibit Carbon Dioxide Corrosion of Ferrous Metals in Oil-and-Gas Production Media

L. S. Moiseeva

Scientific-Engineering Center of Lukoil Company, Moscow, Russia

Received December 22, 2003; in final form, June 2004

Abstract—Main ways to control the carbon dioxide corrosion, type of inhibitors employed, reasons for choice of the inhibitors, and various factors determining the efficiency of inhibitors of different types in carbon dioxide oil-and-gas production media are considered.

When solving problems related to carbon dioxide corrosion, which are encountered in oil and gas fields, it is particularly important to determine the most effective protective method [1, 2]. Inhibition is an efficient and, in many cases, rational protection technique [1–5]. Previously, mechanisms of carbon dioxide corrosion in single- and double-phase oil-and-gas production media at various pH values have been analyzed [6, 7].

The aim of this study was to continue investigations aimed to choose the most promising ways to control the carbon dioxide corrosion and to consider main types of inhibitors and factors determining their efficiency.

An analysis of the mechanism of action of CO_2 revealed its main specific features (Scheme 1). Primarily, the accelerating effect of CO_2 is due to en-

Scheme 1.
Effect of CO_2 on the corrosion of steel*

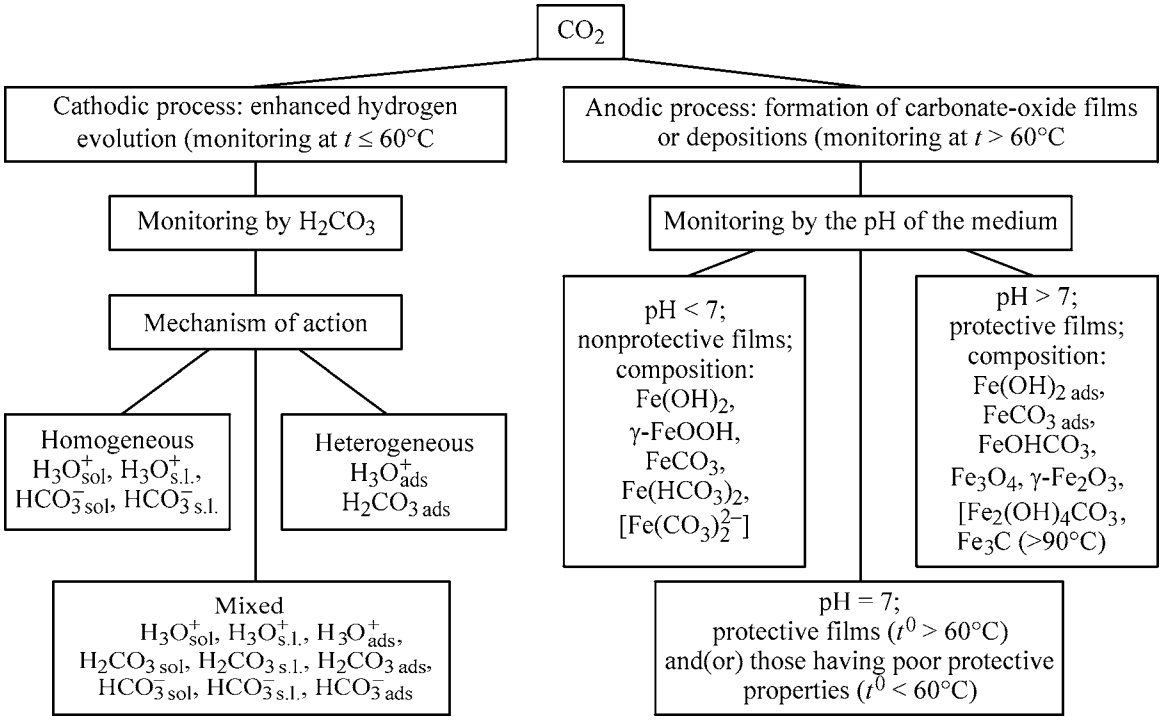

* Content of depolarizer in the surface layer (s.l.) and is solution (sol).

1070-4272/04/7708-1292 © 2004 MAIK "Nauka/Interperiodica"

hanced evolution of hydrogen and formation of carbonate-oxide films on the metal surface (which may have good or poor protective properties) [8–16]. Hence follows that an effective protection can be achieved, first, by hindering the cathodic process and, second, by forming protective carbonate films on the steel surface [12–14]. These films preclude penetration of depolarizers (H_3O^+, HCO_3^-, H_2CO_3) and activators (Cl^-, SO_4^{2-}) to the metal surface and(or) migration of iron ions across the film [16–19].

The cathodic process can be effectively hindered (1) by lowering the concentration of depolarizers in solution and in the surface layer by their chemical binding with derivatives of aminoformic acid: amides, carbamates, hydrazides, organic carbonates, neutral acyclic carbonates, and carbonic acid esters [20]; (2) by displacing depolarizers with ions or molecules of inhibitors (competing adsorption) with the use of ethylene imine, and ethers or esters (PIK 12, SNPKh-6302, Minkor-2) [20, 21]; and (3) by forming protective oxide-carbonate, inhibiting, or mixed films that preclude migration of depolarizers and activators to the metal surface or that of Fe^{2+} ions across the film by using compounds with an active adsorption group or a long hydrocarbon radical, such as SZhK, OR-2K, GIPKh-3A, SNPKh-6011B, Neftegaz, Tarin, KRTs-3G, or organophosphorus compounds: FAN-403M, F-741, etc. [1–3, 22–24].

In the last case, films or deposits formed on the metal surface can affect both the anodic and cathodic processes. The extent of this influence is determined by the composition and structure of the films and by presence and size of pores in them [12–19]. When a carbonate-oxide film or deposit with poor protective properties is formed on the metal surface, its hindering action can be enhanced by introducing into the medium a specially selected inhibitor, which is not only adsorbed but also can penetrate into the pores in the film.

The hindrance of the anodic process in carbon dioxide corrosion, which is closely associated with the formation of protective siderite films or deposits, can be achieved by raising the pH of the medium (by shifting the pH to the alkaline region) or elevating the temperature (to 40–60°C) [8–19, 23–27].

The pH of the medium can be adjusted by using inhibitors that shift the pH to the alkaline region to 8–10, which favors formation of a protective siderite layer on the metal surface, the so-called neutralization method [12, 15, 18, 28–31].

It should be noted that the pH of water can change with temperature and strength of an external electromagnetic field [32, 33]; thermochemical reactions can be used to maintain the temperature of the medium in a prescribed temperature interval. In particular, the possibility of a thermohydrodynamic adjustment of the pH of water in the range 5.7–8.6 was demonstrated in [32]. It was established that the pH of water grows as the number of cycles of hydrodynamic cavitation becomes greater. After 9 to 10 cycles, pH = 8.6. Adjusting *t* thermochemically and pH by physical methods in systems for production, gathering, and transportation of oil and gas is, presumably, possible only in separate localities.

The main ways to control the carbon dioxide corrosion, including that with the use of inhibitors, are shown in Scheme 2.

Scheme 2.
Main ways to control the carbon dioxide corrosion of steel

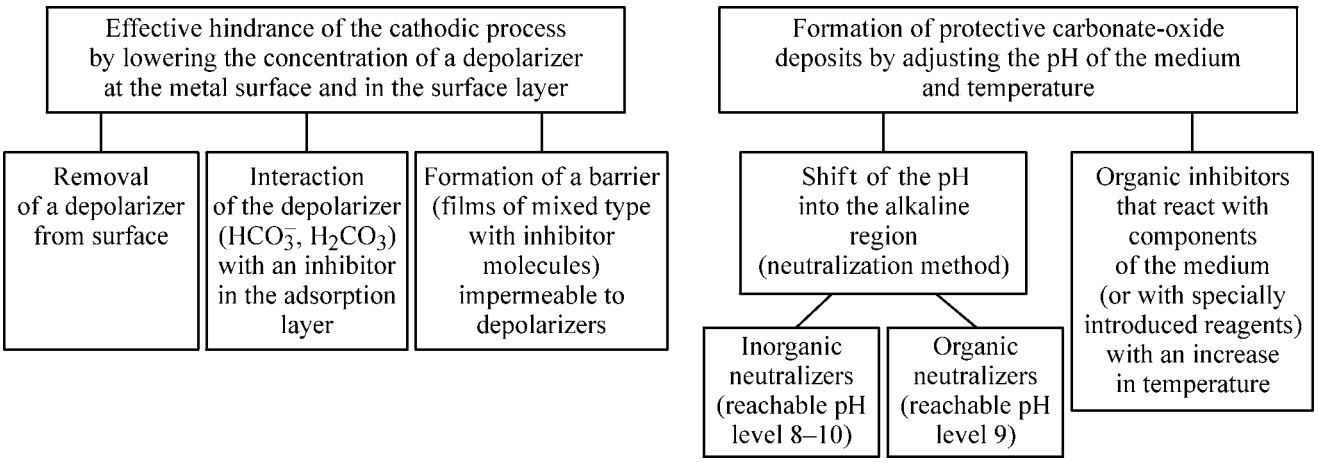

Table 1. Effect of the chemical structure of molecules of quaternary ammonium salts on the protection of St.80 steel in a 50 mg l^{-1} NaCl + 250 mg l^{-1} CH_3COOH solution saturated with CO_2 or H_2S

Inhibitor	Z (%) at indicated inhibitor concentration, mg l^{-1}			
	10	100	10	100
	CO_2		H_2S	
I	10	50	62	85
II	44	62	71	99
III	40	76	94	99
IV	29	84	96	99
V	83	84	98	98
VI	15	22	15	36
VII	17	31	17	62
VIII	68	80	68	96

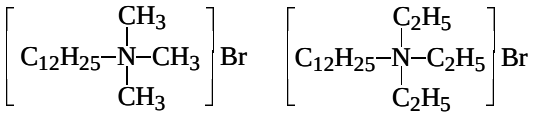

I

II

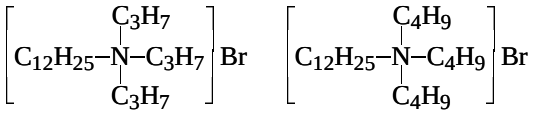

III

IV

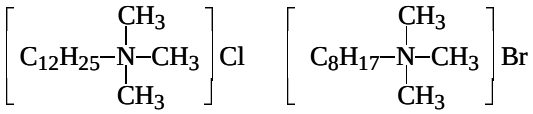

V

VI

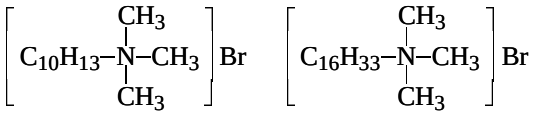

VII

VIII

As is known, inhibitors are classified by the mechanism of action (anodic, cathodic, or mixed) [4], chemical nature (in accordance with classes of organic and inorganic compounds) [3, 4, 22–24], and the principle of action (neutralizers and film-forming agents) [31, 34]. According to the presently developed concepts concerning the mechanisms of carbon dioxide corrosion, the effective inhibiting effect can be produced by inhibitors of the cathodic or mixed type, with predominant hindrance of the cathodic process [35, 36]. At the same time, inhibitors of the anodic type (KhOSP, OR-2K, GIPKh-3, etc.) are frequently used in practice to control the carbon dioxide corrosion [1, 2, 23].

Traditionally, ferrous metals are protected from the carbon dioxide corrosion at oil and gas fields using N-containing compounds and, in particular, amines, imidazolines, and nitrogen heterocycles (Olazol, Sepacorr 5120, Sepacorr ES-3201, Corexit 7755 and 7798, Norust-9M, Norust RA 23D, XC-320, KW-10, etc.) [1–5, 30, 35–39] despite numerous failures of the equipment. These compounds can act both as neutralizers and as film-forming agents. As is known [4, 5], amines and imidazolines are effective in protection from carbon dioxide corrosion in the presence of hydrogen sulfide. It was shown in [40, 41] that lower primary and secondary amines hinder the carbon dioxide corrosion of steel in the aqueous and gaseous phases at their considerable concentration in solution (20–80 g l^{-1}). Despite their higher, compared with primary amines, basicity, tertiary amines are ineffective in protection from the carbon dioxide corrosion.

In [42], results of a comparative study of the influence exerted by quaternary ammonium salts with alkyl radicals of length from C_1 to C_{16} on the carbon dioxide and hydrogen sulfide corrosion of steel in NaCl solutions were reported, which confirm, to a certain extent, the validity of the concepts described above (Table 1). In particular, it was established that, in a CO_2-containing medium, they are inhibitors of the cathodic type, which shift the corrosion potential into the negative region and lead to a noticeable increase in the Taffel slopes $b_c \approx 300$ mV and $b_a \approx 100$ mV. This is due to the formation on the metal surface of a film that is poorly permeable to the depolarizer. In the presence of H_2S in the medium, these same quaternary ammonium salts act as inhibitors of the anodic type. The observed differences in the shift of the corrosion potentials are due to the formation of corrosion products of some other composition and to their influence on the adsorption of inhibitor molecules. In the case of hydrogen sulfide corrosion, quaternary ammonium compounds are adsorbed on the layer of earlier adsorbed HS^-_{ads} species, i.e., at anodic areas. In CO_2-containing media, no layer of adsorbed $HCO^-_{3(ads)}$ species is formed on the steel surface and quaternary ammonium cations are adsorbed directly at the cathodic areas on the metal surface.

Taking into account the chemical nature of the depolarizers, carbonic acid and hydrocrabonate ions, and the related adsorption activity toward iron, which is due to the presence of both a carboxyl and a carbonyl group in the molecule, it would be expected

that organic substances that contain these groups (carboxylic acids, ketones, and esters) are effective inhibitors of the carbon dioxide corrosion because they can compete for adsorption sites and displace depolarizers from the metal surface. Presumably, it was not a mere chance that the first inhibitors of the carbon dioxide corrosion were the calcium salt of acid tar (IKSG-1), synthetic fatty acids, and wastes containing a mixture of high-molecular-weight carboxylic acids and their salts [4]. Until now, vegetable oils (palm "copra," coconut, burdock, soybean), tall oil, and resin acids (abietic acid derivatives of general formula $C_{20}H_{30}O_2$: levopimaric, neoabietic, dehydrobithienic, and palustric) are used to manufacture many foreing inhibitors [3, 42–4]. It should be noted that publications concerned with the influence exerted by this group of substances on the carbon dioxide corrosion of ferrous metals in oil-and-gas production media are scarce [6, 7, 18, 20, 45], and inhibitors containing these compounds a virtually not used at all in domestic oil and gas fields.

Apart from the organic substances mentioned above, possible effective inhibitors of the carbon dioxide corrosion may be compounds that have, in addition to a high adsorption activity, an ability to create on the metal surface a protective film, the so-called film-forming agents [3, 5, 29, 31, 45–48]. In these compounds, the excess electron density on the heteroatom (N, S, P) or at the unsaturated bond is the prerequisite of their chemisorption [5, 49, 50].

The choice of one or another type of inhibitor of the carbon dioxide corrosion is also governed by the initial state of the metal surface [presence or absence of films and(or) deposits on the surface of a metal being protected and their type] [8, 15].

In media with pH $\geq$ 7, in the presence of films or deposits, it is preferable to use oxygen-containing organic inhibitors {salts of carboxylic acids, some derivatives of carbamic acid (carbamates, amides, hydrazides), and organic derivatives of carbonic acid [19]}, which can, first, be adsorbed on this layer and, second, shift the corrosion potential into the negative region, with the result that the general and local corrosion is hindered.

The inhibitors should be able to penetrate into pores of deposits that are stable in the medium (according to the classification presented in [51]) and reach the metal surface or to enhance the protective properties of deposits unstable in the medium. This ability is determined by the correspondence between the size of inhibitor molecules and that of pores in the film. In the second case, an important role in the effective protection is played by the correspondence between the spatial structure of inhibitor molecules and the crystal structure of the deposit.

By contrast, Crolet [51] related the protective properties of corrosion deposits to the internal mechanism of their control and to the structure of the corresponding diffusion model, rather than to their chemical composition and morphology. In this study, films or deposits composed of siderite, amorphous phase of corrosite $FeCO_3 \cdot FeO$, Fe_3C matrix filled with siderite were classified with stable deposits, and films or deposits composed of oxyhydroxides $FeO_x(OH)_{3-2x}$, intermediate phase of α-FeOOH and lepidocrocite γ-FeOOH, and $Fe_2(OH)_4CO_3$ and $FeOHCO_3$ complexes, with unstable deposits.

In the same pH range, and with unstable deposits that tend to grow intensively, it is preferable to use inhibitors that can bind cations (Ca^{2+}, Fe^{2+}) or exhibit the so-called crystal-disintegration effect [52].

In media with pH < 7, in the absence of films or deposits, it is preferable to use neutralizers that favor a shift of the pH into the alkaline region and formation of deposits on the metal surface. In this case, the choice of a neutralizer is determined by the pH.

The neutralization can be achieved by using both contact-type and volatile corrosion inhibitors (inorganic and organic bases or their salts). With account of the characteristic features of the carbon dioxide corrosion in oil-and-gas production media and the necessity for simultaneous protection of the equipment in liquid and gaseous phases, use of volatile inhibitors-neutralizers is a matter of current interest.

The first attempts to use ammonia and carbonates to adjust the pH failed [31, 53]. With these compounds, the pH value widely fluctuated (8–1). This adversely affected the protective properties of the forming film, and the danger of intensive growth of carbonate deposits was preserved. At present, nitrogen-containing organic compounds and their salts (dimethylamine, ethylenediamine, methoxypropylamine, morpholine, sodium salt of merkaptobenzothiazole MBTNa, etc.) are used to control the pH in CO_2-containing media.

The mechanism of protective action of organic nitrogen-containing bases in media with a large content of dissolved CO_2 is not reduced to only neutralization of a weak acid H_2CO_3, whose solutions have a large buffer capacity. Reacting with dissolved carbon dioxide, nitrogen-containing organic bases maintain the pH value at 9, which favors formation of HCO_3^- [53]:

$$R_2N\text{–}H + H_2CO_3 \rightarrow HCO_3^- + R_2NH_2^+. \quad (1)$$

Further, this leads to formation of CO_3^{2-} ions and protective carbonate films. Reaction (1), which occurs in solution and in a thin electrolyte film, is slow, irreversible, and going to completion [16, 53].

Standard amines (A) used to control the pH are, as a rule, volatile, with an ionization constant on the order of 10^{-11}. A part of amine, as well of that of CO_2 present in the gas, dissolves in drops of the condensation moisture. Two compounds react with each other, with the result that the following equilibrium is established [54]:

$$A + H^+ = AH^+ \quad (2)$$

$$CO_2 + H_2O = HCO_3^- + H^+ \quad (3)$$

$$A + CO_2 + H_2O = AH^+ + HCO_3^- \quad (4)$$

The concentration of the free amine in solution under real conditions can be calculated using the equilibrium constants of reactions (2) and (3), K_A and K^* [54]:

$$K_A = [AH^+]/([A][H^+]),$$

$$K^* = [HCO_3^-][H^+]/P_{CO_2}.$$

The partial pressure of amine over solution, P_A, and the concentration of amine in solution, [A], are related by

$$P_A/P_A^0 = [A]/[A_{sat}], \quad (5)$$

where P_A^0 is the partial pressure over pure amine, and $[A_{sat}]$, the concentration of a saturated amine solution.

According to [54], use of Eq. (5) makes it possible to monitor the efficiency of the corrosion protection with inhibitors of the neutralizing type in the gaseous and aqueous phases.

In [40, 41], the influence exerted by the partial pressure of amine, P_A, in a single reaction series of organic substances on the corrosion of steel was prognosticated. It was established that introduction of minor amounts of such bases as monoethanolamine, cyclohexylamine, and diallylamine into a 0.5% NaCl solution containing 250 mg l^{-1} of acetic acid and saturated with CO_2 (1 atm) stimulates corrosion of carbon steel. The protective effect is observed at considerable concentrations of amines in solution (32–48 g l^{-1}). The stimulating action of these amines is attributed to an increase in the content of carbonate ions in the electrolyte, because the solubility of CO_2 at a constant pressure grows as pH becomes higher.

The efficiency of neutralizers is determined by their neutralizing capacity, which can be evaluated by the basicity (K_b) or acidity (K_a, or pK_a [31]) constants. As a rule, the greater pK_a, the higher the efficiency of a neutralizer. The inhibiting efficiency of organic bases is affected by the length of the hydrocarbon chain and the degree of its branching, configuration of a molecule, and position and number of adsorption centers in the molecule [3, 4].

The efficiency of neutralization is affected to a certain extent by the buffer capacity of the solution [31]. For example, the amount of methoxypropylamine necessary for neutralization of a solution considerably exceeds that of ethylenediamine, and the buffer capacity of the former is negligible compared with that of the latter, so that even a minor decrease in the concentration of methoxypropylamine leads to a considerable change in the pH value and strongly raises the corrosion rate [54, 55].

Another factor determining the efficiency of neutralizers, the distribution of neutralizing amines, is characterized by the distribution factor $K_d = c_g/c_a$, where c_g and c_a are the equilibrium concentrations of amine in the gaseous and aqueous phases under the conditions of a phase transition (in evaporation and condensation). Amine exhibits the strongest neutralizing properties in both the gaseous and aqueous phases at $K_b > 100 \times 10^{-6}$ and $K_d = 1.0$ [31].

An important issue is the correspondence between the chemical types of a neutralizer and an acidic agent present in the corrosive medium [55]. In the general case, the following should be noted: (1) presence, together with H_2CO_3 ($CO_2 \cdot H_2O$), of a strong inorganic acid in the medium requires that a strong, mostly inorganic base ($K_b \times 10^6 > 500$) should be used as a neutralizer; (2) presence of a weak inorganic acid with a high buffer capacity (of the carbonic type) requires that organic neutralizers with a high buffer capacity should be used; and (3) presence, together with H_2CO_3, of corrosive carboxylic acids (lower carboxylic, naphthenic) requires use of organic bases with a high adsorption capacity for the metal, whose molecules can compete for adsorption sites and, in the end, displace molecules of the acid from the metal surface, which favors formation of a protective film.

The state of the metal surface is one more factor determining the efficiency of an inhibitor-neutralizer. In particular, morpholine is more efficient in the case of a clean steel surface, and cyclohexylamine, in the case of steel covered with oxides [54, 55].

It should be noted that some of organic corrosion inhibitors protect a relatively clean steel surface to

a lesser extent, compared with that covered with corrosion products. Such an action, determined by the difference between the adsorption properties of inhibitors on a clean metal surface and on corrosion products, depends on their concentration in the corrosive medium [56, 57]. It was shown in [9, 10, 35, 36] that film-forming inhibitors with a cathodic type of action, which contain a carbonyl or carboxyl group, are universal as applied to the carbon dioxide corrosion. They can be used both on a clean metal surface and on that covered with a carbonate-oxide film or a layer of deposits.

As shown by practical experience, choosing inhibitors among the reagents conventionally used to control the hydrogen sulfide corrosion without taking into account the specific features of the carbon dioxide corrosion frequently yields unsatisfactory results.

A set of corrosion inhibitors of the KRTs brand have been developed specially for inhibition of the carbon dioxide corrosion in oil-and-gas production media. These inhibitors include organic substances containing a carboxyl and a carbonyl groups (cyclic ketones, ethers, and esters) [47, 35, 36]. The efficiency of inhibitors with respect to the carbon dioxide corrosion was studied in a wide range of pH values, 2–10. The behaviors of anodically and cathodically polarized steels in a two-phase medium (pH 2) saturated with CO_2 were compared and the influence exerted on these processes by inhibitors of various types was studied: Neftekhim-3, a product of reaction between fatty acids of light tall oil and polyethylepolyamine with dispersed additives; SNPKh-6302 A and B, a mixture of alkylpyridinium bromide of aminoparaffin, fatty acid, and anionogenic surfactant; OR-2K, a mixture of rhodanic benzylquinolinium and still bottoms produced in monoethanolamine purification of natural gas; and Korreksit, a formulation containing imidazolines, oxyalkylated resins, and esters in a hydrocarbon solvent.

Potentiodynamic polarization curves were measured using the standard procedure [36].

On introducing inhibitors KRTs-3G, KRTs-2, Neftekhim-3, and SNPKh-6302, the stationary potential E_{st} is shifted in the negative direction, and the hindrance to the anodic process dominates over that of the cathodic process (Table 2).

In the presence of inhibitors KRTs-2 and KRTs-3G, the maximum shift of E_{st} is observed. The inhibitors in which the hindrance to the anodic process predominates over that to the cathodic process were found to be inefficient (Table 2).

Table 2. Hindrance factors for the corrosion rate (γ_{cor}) and the cathodic (γ_c) and anodic (γ_a) processes occurring on St.3 steel in a two-phase medium 0.1 N NaCl + kerosene (10 : 1), pH 2, saturated with CO_2, in the presence of 1 g l^{-1} of inhibitors

Inhibitor	E_{st}, V	Hindrance factor		
		γ_c	γ_a	γ_{cor}
Fon	–0.24	–	–	–
KRTs-3	–0.26	5.6	1.4	6.3
KRTs-2	–0.27	22	5.0	25
KRTs-8	–0.19	4.0	6.3	3.2
KRTs-3G	–0.26	5.5	1.3	6.4
Neftekhim-3	–0.25	4.4	2.5	5.1
Corexit 7798	–0.20	3.9	5.8	2.9
SNPKh-6302	–0.24	3.8	4.0	3.8
OR-2K	–0.25	4.3	2.9	4.8

It was established that the adsorption of components of the inhibiting formulations KRTs on the steel surface leads to an increase in the slope of the Taffel portion of the cathodic polarization curve to 130–190 mV, which indicates that the cathodic process is hindered. At the optimal, from the standpoint of adsorption, relative contents of components, the strongest increase in b_c was observed. It has been established that the KRTs reagents are inhibitors of the blocking type [35, 36, 45]. Presumably, the reaction between the components of the formulation in the adsorption layer yields molecular compounds forming a protective film that precludes penetration of depolarizers (HCO_3^-, $CO_2 \cdot H_2O$) to the metal surface. In media with pH > 8, the inhibitors of the KRTs series hinder both the cathodic and anodic process, with the hindrance to the former predominating. Inhibitor-bactericide CNPKh-1002, taken as reference, even stimulates the overall corrosion of steel when present in a low concentration. The effect becomes weaker as the concentration of the inhibitor is raised. This confirms the previously established fact that inhibitors of the anodic type are dangerous when present in solution in an insufficient concentration.

The efficiency of inhibitors of the blocking type, Corexit 7798 and Corexit 6350 (manufactured by Nalco-Exxon) was demonstrated by industrial tests in oil and gas fields of Western Siberia, where the carbon dioxide corrosion is predominant (CO_2 in a water–oil emulsion, 200 mg l^{-1}). The corrosion rate was monitored gravimetrically using witness samples and by the electrostatic method on the basis of the polarization resistance in pipe sections suffering from cor-

Table 3. Efficiency of the protective action of inhibitors in a water-oil emulsion of varied composition*

Inhibitor	Concentration, g m^{-3}	Test duration, months (number of shutdowns)	*Z* (%) in an emulsion of indicated composition	
			I	**II**
Emulsion of composition:				
I	0	12 (300)	–	–
II	0	7 (22)	–	–
Corexit 7798	100 (in the first 4 h, then 15–35)	12 (0)	69/94**	–
	100	5 (14)	–	63/61
Corexit 6350	100 (in the first 24 h, then 25–35)	12 (1)	98/25	–
Neftekhim-3	25	6 h	77/30	–
	50	6 h	91/68	–
	100	6 h (**I**); 5 (12) (**II**)	91/80	81/79
Norust RA 2D	25–30	12 (12)	–	90/89
KRTs-3	100	6 (0)	–	85/83
KRTs-3G	100	6 (0)	–	89/87
SNPKh-6302	100	5 (9)	–	82/81

* Emulsion composition: (**I**) [CO_2] = 200 mg l^{-1}, mineralization 93 g l^{-1}, pH 6.4 (Samotlor field); (**II**) [CO_2] = 99 mg l^{-1}, [H_2S] = 55 mg l^{-1}, mineralization 78 mg l^{-1}, pH 6.2 (Chutyra field).

** Numerator, determined by gravimetry; denominator, found electrochemically (from the polarization resistance).

rosion to the greatest extent and subject to replacement once in seven months. Both the inhibitors led to a decrease in the corrosion rate and in the number of pipe accidents (Table 3). The electrostatically determined efficiency of the inhibitors was somewhat lower than that furnished by the gravimetric method.

As regards the end result, lowering the number of accidents and making longer the interrepair life of pipes, the most efficient inhibitors are KRTs-3 and KRTs-3G (Table 3). At the same time, when the efficiency of corrosion inhibitors is evaluated gravimetrically on witness samples placed in a flow of a water-oil emulsion, the most efficient was the Norust RA 2D inhibitor, which diminished the pipe accident rate (monitored during a longer time: a year and more) to a lesser extent. These facts indicates that caution is necessary in evaluating the efficiency of inhibitors by a single method.

Thus, the results of industrial tests of oxygen-containing inhibitors of the cathodic type of action (KRTs) in systems for oil gathering and utilization of wastewater and formation water, in pumping oil, gas-lift, and gas-condensate wells with CO_2 concentration in the product in the range from 43 to 230 g m^{-3} revealed the efficiency of these inhibitors both on a relatively clean metal surface and on that covered with a significant amount of carbonate-oxide deposits and demonstrated that development of efficient inhibitors of the carbon dioxide corrosion on the basis of compounds that contain a carbonyl group is possible and shows promise.

CONCLUSIONS

(1) It is shown that the following inhibitors ensure an effective protection from the carbon dioxide corrosion in oil-and-gas production media: organic compounds containing a carboxyl and a carbonyl groups; nitrogen containing neutralizers, both of contact type and volatile; film-forming agents favoring formation of protective siderite films or forming protective films themselves; all with the cathodic type of action.

(2) The choice of the type of an inhibitor of the carbon dioxide corrosion is governed by the pH of the medium, temperature, partial pressure of CO_2 in the system, and initial state of the metal surface [presence or absence of films and(or) deposits on the metal surface, and their type and structure].

REFERENCES

1. Saakiyan, L.S. and Efremov, A.P., *Zashchita neftegazopromyslovogo oborudovaniya ot korrozii* (Corrosion Protection of Oil-and-Gas Production Equipment), Moscow: Nedra, 1982.

2. Gonik, A.A., *Korroziya neftepromyslovogo oborudovaniya i mery ee preduprezhdeniya* (Corrosion of Oil-and-Gas Production Equipment and Measures for Its Prevention), Moscow: Nedra, 1976.
3. Bregman, J.I., *Corrosion Inhibitors*, New York: Macmillan, 1963.
4. Rozenfel'd, I.L., *Ingibitory korrozii* (Corrosion Inhibitors), Moscow: Khimiya, 1977.
5. Lahogny-Sarc, O., *6th Eur. Symp. on Corrosion Inhibitors*, Ferrara, Itaky, 1985, p. 1313.
6. Moiseeva, L.S. and Rashevskaya, N.S., *Zh. Prilk. Khim.*, 2002, vol. 75, no. 10, pp. 1659–1667.
7. Moiseeva, L.S. and Kuznetsov, Yu.I., *Zh. Prilk. Khim.*, 1998, vol. 71, no. 6, pp. 950–955.
8. De Waard, C. and Lotz, U., *Corrosion NACE*, 1993, Paper no. 69.
9. Markin, A.N., *Zashch. Met.*, 1996, vol. 32, no. 5, pp. 497–501.
10. Moiseeva, L.S. and Kuznetsov, Yu.I., *Zashch. Met.*, 1996, vol. 32, no. 6, pp. 565–572.
11. Schmitt, G., *Advances on CO_2 Corrosion*, Houston, NACE, 1984, vol. 1, pp. 1–6, 10–15.
12. De Waard, C., Lotz, U., and Milliams, D.E., *Corrosion NACE*, 1991, vol. 47, no. 12, pp. 976–981.
13. Videm, K. and Dugstaad, A., *Corrosion NACE*, 1988, Paper no. 186.
14. Videm, K. and Dugstaad, A., *Materials Performance*, 1989, vol. 28, no. 3, pp. 63–72.
15. Videm, K. and Dugstaad, A., *Materials Performance*, 1989, vol. 28, no. 4, pp. 46–51.
16. Videm, K., *Corrosion NACE*, 1993, Paper no. 83.
17. Videm, K., *Corrosion NACE*, 1987, Paper no. 42.
18. De Waard, C. and Milliams, D.E., *Corrosion NACE*, 1975, vol. 31, no. 5, pp. 177–183.
19. Hausler, R.H., *Advances in CO_2 Corrosion*, Houston: NACE, 1984, pp. 72–78.
20. Crolet, J.-L., *10th Eur. Corrosion Congress*, Barcelona, Spain, 5–8 July, 1993, Paper no. 270.
21. *Khimicheskaya entsiklopediya* (Chemical Encyclopedia), Zefirov, N.S., Ed., Moscow: Sovetskaya Entsiklopediya, 1990, vols. 2 and 5.
22. Markin, A.N., *Zashch. Met.*, 1994, vol. 30, no. 1, pp. 51–55.
23. Gabitov, A.I., *Itogi i perspektivy v teorii i praktike bor'by s korroziei* (Theory and Practice of Corrosion Control: Advances and Promises), Ufa: Reaktiv, 1998.
24. Rakhmankulov, D.L. and Bugai, D.E., *Ingibitory korrozii* (Corrosion Inhibitors), Ufa: Reaktiv, 1997, vol. 1.
25. Wieckowski, A., Ghali, E., Szklarczuk, M., and Sobkowski, J., *Electrochim. Acta*, 1983, vol. 28, pp. 1619–1624.
26. Valand, T., *Proc. 6th Eur. Symp. on Corrosion Inhibitors, Ann. Univ. Ferrara, N.S. Ser. V, Suppl.*, 1985, pp. 1401–1407.
27. Valand, T. and Sjowall, P.A., *Electrochim. Acta*, 1989, vol. 34, no. 2, pp. 273–278.
28. Videm, K., *Progress in the Understanding and Prevention of Corrosion*, Costa, J.M. and Mercer, A.D., Eds., Publ. Institute of Materials, 1993, Book 550, vol. 1.
29. Valand, T., *Corrosion NACE*, 1993, no. 3, pp. 4–8.
30. Dugstad, A., *Corrosion NACE*, 1993, no. 3, pp. 15–19.
31. Iovchev, M., *Korroziya teploenergeticheskogo oborudovaniya* (Corrosion of Heat-and-Power Equipment), Transl. From Bulgarian, Moscow: Energoatomizdat, 1988.
32. Zaporozhets, E.P. and Zibert, G.K., *Khim. Neftegaz. Mashinostr.*, 1999, no. 10, pp. 43–45.
33. Reid, K.F., *Properties and Reactions of Bonds in Organic Molecules*, London: Longmans, Green and Co Ltd., 1968.
34. Rozenfel'd, I.L. and Persiantseva, V.P., *Ingibitory atmosfernoi korrozii* (Inhibitors of Atmospheric Corrosion), Moscow: Nauka, 1986.
35. Moiseeva, L.S. and Tereshina, R.M., *Zashch. Met.*, 1994, vol. 30, no. 4, pp. 410–414.
36. Moiseeva, L.S. and Pushina, O.I., *Zashch. Met.*, 1996, vol. 32, no. 3, pp. 277–281.
37. Buchan, R.C., *Corrosion NACE*, 1950, vol. 6, no. 6, pp. 178–181.
38. Rogers, W.F., *World Oil*, 1948, vol. 128, no. 6, pp. 154–160.
39. Nestle, Al., *Corrosion Inhibitors*, Nathan, C.C., Ed., Houston, TX, 1973, pp. 61–65.
40. Kuznetsov, Yu.I., Andreev, N.N., and Ibatulin, K.A., *Zashch. Met.*, 1999, vol. 35, no. 6, pp. 586–593.
41. Andreev, N.N. and Kusnetsov, Yu.I., *Corrosion NACE*, 1998, Paper no. 2, pp. 41–47.
42. Boden, P.J. and Richardson, J., *6th Eur. Symp. on Corrosion Inhibitors, Ann. Univ. Ferrara*, 1985, no. 8, pp. 1283–1286.
43. *Katalog normativnykh materialov po ingibitoram korrozii i bakteritsidam* (Catalogue of Standards Concerning Corrosion Inhibitors and Bactericides), Kazan: VNIPInefteprom khim, NPO Soyuzneftepromkhim, 1989.
44. Robinson, J.S., *Corrosion Inhibitors: Recent Developments*, Park Bridge, N.J., Noyes Data Corp., 1979.
45. Moiseeva, L.S. and Fedorov, Yu.V., Abstracts of Papers, *V Respublikanskaya konferentsiya "Korroziya metallov pod napryazheniem i metody zashchity"* (V Republ. Conf. "Corrosion of Metals under Stress and Protection Methods"), Lvov, 1989, p. 273.
46. Moiseeva, L.S. and Komarnitskii, N.V., *Zashch. Met.*, 1998, vol. 34, no. 4, pp. 427–431.
47. Lorenz, W.J. and Mansfeld, F., *Electrochim. Acta*, 1986, vol. 31, no. 4, pp. 467–472.
48. Getmanskii, M.D., Gonik, A.A., Nizamov, K.R., and Khudyakova, L.P., *Korroziya i zashchita v neftegazo-*

voi promyshlennosti: Obzor informtsii (Corrosion and Corrosion Protection in Oil-and-Gas Industry: Review), Moscow: VNIIOENG, 1979.

49. Krylov, O.V. and Kiselev, V.F., *Adsorbtsiya i kataliz na perekhodnykh metallakh i ikh oksidakh* (Adsorption and Catalysis on Transition Metals and Their Oxides), Moscow: Khimiya, 1981.
50. Gregg, S.J. and Sing, K.S.W., *Adsorption, Surface Area and Porosity*, London: Academic, 1982.
51. Crolet, J.-L., *J. Mater. Sci.*, 1993, vol. 28, p. 17.
52. Dyatlova, N.M., Dytyuk, L.T., Samakaev, R.Kh., *et al.*, *Primenenie kompleksonov v neftedobyvayushchei promyshlennosti* (Use of Complexons in Oil Production Industry), Moscow: NIITEKhIM, 1983.
53. Crolet, J.-L. and Samaran, J.-P., *Corrosion NACE*, 1993, Paper no. 102.
54. Forsen, O., Aromaa, J., Rintamaki, K., and Tavi, M., *Progress in the Understanding and Prevention of Corrosion: 10th Eur. Corrosion Congress*, Barcelona; London, July 1993, vol. 1, pp. 590.
55. Moiseeva, L.S. and Pashevskaya, N.S., *Prakt. Protivokorr. Zashch.*, 2002, no. 1, pp. 30–35.
56. Gutman, E.M., Markin, A.N., Sivokon', I.S., *et al.*, *Zashch. Met.*, 1991, vol. 27, no. 5, pp. 767–772.
57. Markin, A.N., *Zashch. Met.*, 1993, vol. 30, no. 1, pp. 51–55.

Russian Journal of Applied Chemistry, Vol. 77, No. 8, 2004, pp. 1301–1307. Translated from Zhurnal Prikladnoi Khimii, Vol. 77, No. 8, 2004, pp. 1316–1322.

CATALYSIS

Kinetic Features of Catalytic Decomposition of Cyclohexyl Hydroperoxide and 1-Methylcyclohexyl hydroperoxide

A. M. Syroezhko and O. Yu. Begak

St. Petersburg State Technological Institute, St. Petersburg, Russia

Mendeleev Russian Research Institute of Metrology, Federal State Unitary Enterprise, St. Petersburg, Russia

Received June 25, 2003; in final form, April 2004

Abstract—Catalytic decomposition of cyclohexyl and 1-methylcyclohexyl peroxides in the presence of 3*d*-metal acetylacetonates was studied.

A cyclohexanol–cyclohexanone mixture is commercially produced on a large scale by oxidation of cyclohexane with atmospheric oxygen on a cobalt catalyst [1]. Cyclohexyl hydroperoxide (CHP, ROOH) is formed in the first step of this process. Kinetic features of the oxidation and the composition of the oxidation products are mainly determined by the course of catalytic decomposition of this intermediate. Previously, we have shown that the selectivity of cyclohexanone formation in the presence of chromium-containing catalysts is higher than that in the presence of industrial cobalt-containing catalysts [2].

The oxidation of methylcyclohexane depends on the catalyst present in the system. The reaction yields either a tertiary alcohol (1-methylcyclohexanol) or a mixture of methylcyclohexanols and methylcyclohexanones, formed by reaction of the secondary C–H bonds with oxygen and peroxy radicals [3]. In the latter case, the reaction kinetics and composition of the oxidation products are determined by the course of transformation of tertiary 1-methylcyclohexyl hydroperoxide (MCHP, ROOH) into secondary methylcyclohexyl hydroperoxides.

In this study, we examined the catalytic decomposition of CHP and MCHP in the presence of 3*d*-metal compounds.

As shown previously [4, 5], *s*- and 3*d*-metal carboxylates form with MCHP complexes $ML_n \times m$ROOH (n, m = 1, 2). This is due to the fact that intermolecular hydrogen bonds in the complexes of *s* elements and the coordination bond between 3*d* metals and the α-O atom of hydroperoxide are stronger than the hydrogen bonds in peroxide self-associates. These complexes catalyze decomposition of the hydroperoxide into radicals and molecular products. The catalytic activity of *s*-metal carboxylates [e.g., stearates (St)] in MCHP decomposition decreases with a decrease in the cation radius in the following order: CsSt > $BaSt_2$ > NaSt ~ Na^1_{pel} > $CaSt_2$ > LiSt [6].

EXPERIMENTAL

Cyclohexyl hydroperoxide was prepared via intermediate trialkyl borates [7] at –78°C, which were oxidized with H_2O_2. MCHP was prepared by the procedure described in [8]. The content of the available oxygen in the hydroperoxides was 100%.

3*d*-Metal acetylacetonates were prepared by the procedure described in [9].

Decomposition of CHP and MCHP at 85–105°C in the presence of catalysts listed in Table 1 was studied in decane and methylcyclohexane solutions, respectively. The catalyst concentration ranged from 3×10^{-5} to 3×10^{-4} and from 6×10^{-4} to 8.8×10^{-3} M; and the concentration of hydroperoxides, from 0.01 to 0.1 M. The first concentration range of the catalysts was chosen so as to minimize their association at 85–105°C.

The representative kinetic curves of overall CHP decomposition are shown in Fig. 1. The fast decomposition in the first steps decelerates with time owing to catalyst deactivation. The limiting degrees of CHP decomposition are determined by the nature and con-

[1] Na pelargonate.

1070-4272/04/7708-1301 © 2004 MAIK "Nauka/Interperiodica"

Table 1. Activation energy of CHP decomposition in the presence of 3*d*-metal carboxylates and 3*d*-metal acetylacetonates* ([ROOH] = 0.1 M)

Catalyst	$[ML_n] \times 10^4$, M	Conversion,** %	$v \times 10^3$, mol l^{-1} min^{-1}	E_{ef}, kJ mol^{-1}	Ketone/alcohol, mol/mol	$(v_r/v_\Sigma) \times 10^2$, %
$Co(acac)_2$	8.8	up to 72	16.08	65.0 ± 2.4	0.67	17.5
	10.0	up to 62	17.50		–	
	60.0	up to 95	44.20		0.58	
	88.0	up to 78	50.00		0.45	
$Co(acac)_3$	8.8	up to 45	6.90	79.1 ± 2.0	–	21.5
	10.0	up to 50	7.55		0.58	
	60.0	up to 60	–		0.65	
	88.0	up to 75	34.50		0.81	
$Mn(acac)_3$	8.8	up to 20	6.02	76.0 ± 2.0	0.82	33.0
	60.0	up to 60	–		0.70	
	88.0	up to 51	18.46		0.60	
$Cu(acac)_2$	8.8	up to 17	3.00	76.4 ± 2.5	–	
	10.0	up to 50	3.60		0.60	
	60.0	up to 82	16.10		0.80	
	88.0	up to 90	22.11		0.54	44.0
$Fe(acac)_3$	8.8	up to 15	2.61	79.4 ± 3.1	1.00	36.0
	10.0	up to 12	2.80		0.99	
	88.0	up to 50	12.50		1.38	
$Ni(acac)_2$	8.8	up to 9	1.44	92.2 ± 1.8		
	10.0	up to 20	1.85			
	88.0	up to 26	8.52		0.88	50.3
$Cr(acac)_3$	6.0	up to 80	8.20	82.0 ± 1.5	5.0	
	8.8	up to 65	10.01		7.2	
	10.0	up to 55	10.60		–	
	60.0	up to 80	12.72		–	
	88.0	up to 84	13.75		2.7	27.0
$Zn(acac)_2$	60.0	up to 20	4.20	107.0 ± 3.5	0.95	–
$VO(acac)_2$	8.8	up to 80	13.8	70.0 ± 1.8	1.5	–
$Cr(ac)_3$	8.8	up to 13	2.34	–	2.7	–
	10.0	up to 15	2.51		2.1	
	88.0	up to 20	9.21		3.5	
$CrSt_3$	6.0	up to 90	8.70	82.5 ± 4.0	–	
	8.8	up to 55	9.20		8.65	11.0
	10.0	up to 75	10.00		6.70	
	88.0	up to 76	16.37		3.80	
$Cr(CO)_6$	8.8	up to 25	4.82	79.1 ± 4.0	–	8.3
	10.0	up to 25	6.10		4.40	
	88.0	up to 42	18.50		3.60	
$Co(ac)_2$–$Cr(ac)_3$	8.8	up to 14	–	–	2.15	–
$CuSt_2$	60.0	up to 80	32.0	78.6 ± 2.8	–	–
No catalyst	–	up to 35	0.62	110.1 ± 4.5	0.5–0.6	

* v_r and v_Σ are the rates of radical and overall decomposition, respectively.

** The hydroperoxide decomposition sharply decelerates at the indicated conversion.

centration of the catalyst (Table 1). The dependence of the initial rate of overall CHP decomposition on the catalyst concentration in the range $(0.3–3) \times 10^{-4}$ M is linear, and that on $[ROOH]_0$ tends to level off (Figs. 2a, 2b). This suggests the of intermediate $ML_n \cdot ROOH$ (n = 2–3) is formed:

$$ROOH + ML_n \overset{K_1}{\rightleftarrows} ML_n \cdot ROOH \overset{k_0}{\rightarrow} \text{decomposition products.}$$

The initial rate of hydroxoperoxide decomposition can be described by the following equation:

$$v_0 = \frac{k_0 K_1 [\mathrm{ML}_n]_0 [\mathrm{ROOH}]^{n_1}}{1 + K_1 [\mathrm{ROOH}]}. \quad (1)$$

3*d*-Metal acetylacetonates react with one ROOH molecule [10]. The rate constants of the decomposition and the equilibrium constants of complexation of these catalysts with the hydroxoperoxide were obtained (Fig. 1, Table 2) by graphical solution of Eq. (2) at $n_1 = 1$ in the coordinates $1/v$-vs.-$1/[\mathrm{ROOH}]$ (Fig. 3)

$$1/v_0 = 1/k_0 K_1 [\mathrm{ML}_n][\mathrm{ROOH}] + 1/k_0 [\mathrm{ML}_n]_0. \quad (2)$$

The catalytic activity estimated from the product $k_0 K_1$ increases in the following order: Ni(II) < Cr(III) < Fe(III) < Mn(III) < Cu(II) < Co(III) < Co(II). The complexing power of 3*d*-metal acetylacetonates grows in the series VO(II) ≈ Cr(III) < Mn(III) ≈ Fe(III) < Co(III) < Ni(II) < Cu(II) and correlates with the electronegativity of the metals [10]. Both oxidized and reduced catalyst species are present in the solution in the course of CHP decomposition. The stability of the complexes of the reduced form with most of oxygen-containing ligands increases in the following order [11]: $Mn^{2+} < Fe^{2+} < Co^{2+} < Ni^{2+} < Cu^{2+} < Zn^{2+}$.

The hydroperoxide decomposition in the presence of $Cr(CO)_6$, $Cr(acac)_3$ and at certain concentrations of $Ni(acac)_2$ and $Fe(acac)_3$ occurs with an induction period (Fig. 1). This is due to the relatively slow formation of the catalytically active complex at 85–95°C.

The kinetic data obtained at $[\mathrm{ML}_n] = 8.8 \times 10^{-4}$–$8.8 \times 10^{-3}$ M suggest a complex mechanism of the hydroperoxide decomposition. The dependence of the overall reaction rate on [ROOH] and $[\mathrm{ML}_n]$ cannot be adequately described if only the complexation of the initial reagents is taken into account. The fractional reaction orders with respect to [ROOH] and $[\mathrm{ML}_n]$ (Table 2) suggest that the homogeneous complexation of the hydroxoperoxide with the oxidized form of the catalyst and heterogeneous complexation with the reduced form can be accompanied by reactions of the hydroxoperoxide with the solvent. The formation of isomeric decanols supports this assumption. The fractional reaction orders with respect to the catalyst (from 0.14 to 0.865) are probably due to self-association of the catalysts (Table 3). The com-

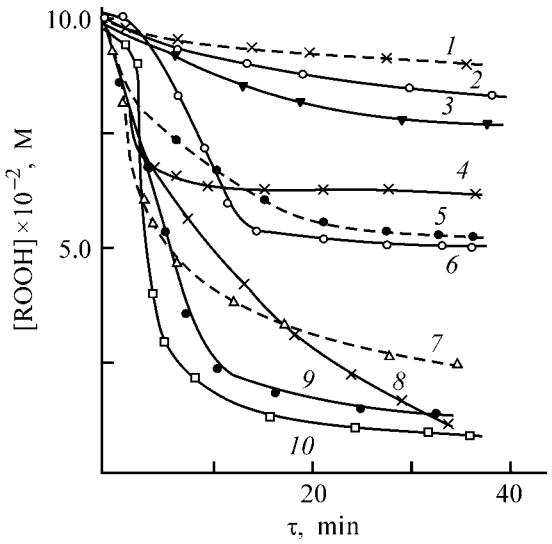

Fig. 1. Kinetic curves of cyclohexyl peroxide decomposition [ROOH] at T = 95°C, $[\mathrm{ML}_n]_0 = 8.8 \times 10^{-4}$ M in the presence of (*1*) $Ni(acac)_2$, (*2*) $Cr(acac)_3$, (*3*) $Fe(acac)_3$, (*4*) $Mn(acac)_3$, (*5*) $Co(acac)_3$, (*6*) $Cr(CO)_6$, (*7*) $Co(acac)_2$, (*8*) $Cu(acac)_2$, (*9*) $Cr(St)_3$, and (*10*) $Cr(acac)_3$ (τ) Time.

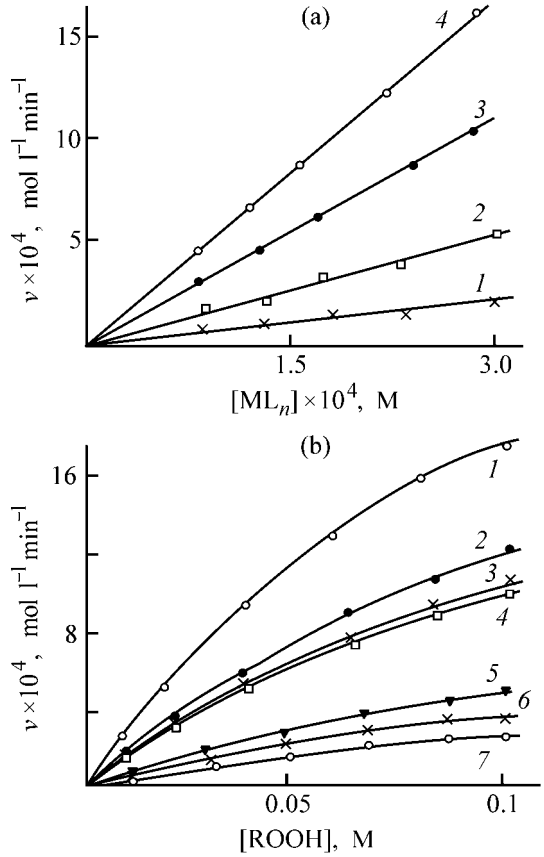

Fig. 2. Initial rate of the overall cyclohexyl hydroperoxide decomposition, v, vs. (a) $[\mathrm{ML}_n]$ and (b) [ROOH]. (a) (*1*) $Fe(acac)_3$ ([ROOH] = 0.02 M); and (*2*–*4*) $Co(acac)_2$ ([ROOH] = 0.02, 0.05, 0.1 M, respectively); (b) (*1*) $Co(acac)_2$, (*2*) $Co(acac)_3$, (*3*) $Mn(acac)_3$, (*4*) $Cu(acac)_2$, (*5*) $Fe(acac)_3$, (*6*) $Cr(acac)_3$, and (*7*) $Ni(acac)_2$.

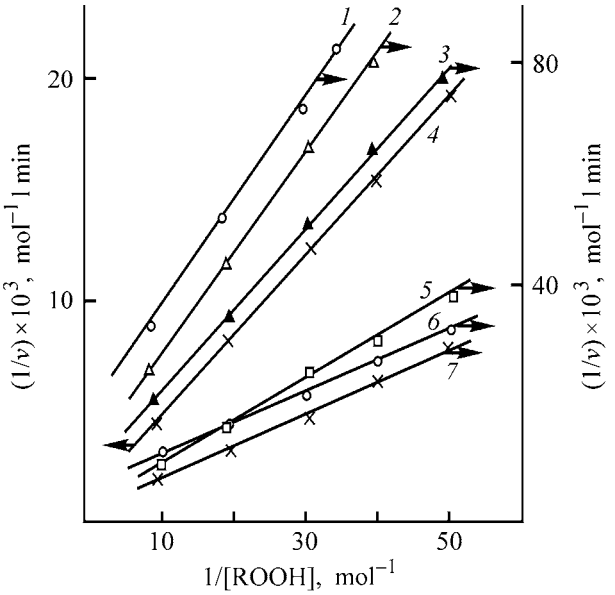

Fig. 3. Curves $1/v$ vs. 1/[ROOH] for CHP decomposition at 95°C in the presence of 3×10^{-5} M. (*1*) $Ni(acac)_2$, (*2*) $Cr(acac)_3$, (*3*) $Fe(acac)_3$, (*4*) $Co(acac)_3$, (*5*) $Mn(acac)_3$, (*6*) $Cu(acac)_2$, and (*7*) $Co(acac)_3$.

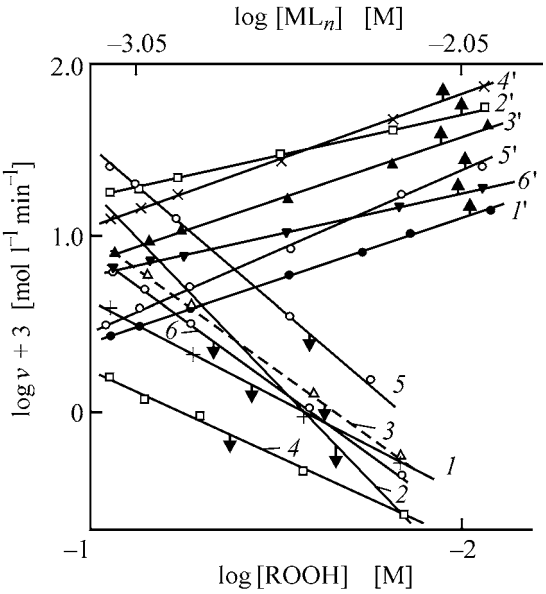

Fig. 4. Rate of overall CHP decomposition v vs. (*1*–6) CHP concentration and (*1*'–6') catalyst concentration, (*1*, *1*') $Fe(acac)_3$, (*2*, *2*') $Co(acac)_2$, (*3*, *3*') $Co(acac)_3$, (*4*, *4*') $Ni(acac)_2$, (*5*, *5*') $Cu(acac)_2$, and (*6*, *6*') $Mn(acac)_3$.

petition of the reaction products (ROH and H_2O) with ROOH for complexation with ML_n makes lower the content of the catalytically active species, thus decelerating the decomposition. The dependences of the rate of overall CHP decomposition on the catalyst concentration and on the initial CHP concentration are linearized in the log–log coordinates (Fig. 4). The overall rate of CHP decomposition in the examined range of the initial CHP and catalyst concentrations is described by the equation

$$v_0 = k_i[\mathrm{ROOH}]_0^{n_{i1}}[\mathrm{ML}_n]_0^{n_{i2}}, \quad (3)$$

where n_{i1} and n_{i2} are the partial reaction orders with respect to the hydroxoperoxide and catalyst, respectively.

The parameters of this equation are listed in Table 3.

The dependence of the activation enthalpy of CHP decomposition on the nature of 3*d*-metal acetylacetonate complexes passes through two extrema, which is characteristic of the stability constants of these complexes. The stability of these complexes depends both on the M(II)/M(III) redox potential and on the number of *d* electrons of the central metal. The dependence of the size of 3*d*-metal cations on the atomic number is not smooth. The dependence of E_{eff} measured in the presence of d^0, d^5, and d^{10} systems having spherical distribution of the electron density is smooth (crystal

Table 2. Rate constants k_0 and K_1 of CHP decomposition at 95°C and [ROOH] = 0.01–0.1 M

ML_n	k_0, min^{-1}	K_1, l mol^{-1}
$Co(acac)_2$	12.4	8.6 ± 0.3
$Co(acac)_3$	9.5	6.6 ± 0.2
$Fe(acac)_3$	5.0	4.6 ± 0.25
$Mn(acac)_3$	10.6	4.7 ± 0.3
$Ni(acac)_2$	1.87	8.9 ± 0.4
$Cu(acac)_2$	6.4	9.2 ± 0.3
$Cr(acac)_3$	4.1	4.4 ± 0.4
$Cr(CO)_6$	35.8	1.7 ± 0.2
$VO(acac)_2$	23.6	4.6 ± 0.2

Table 3. Partial reaction orders with respect to the initial components in catalytic decomposition of CHP

Catalyst	k_i,* mol l^{-1} min^{-1}	n_{i1}	n_{i2}
$Cr(ac)_3$	1.53 ± 0.02	1.0 ± 0.07	0.595 ± 0.05
$Cr(CO)_6$	2.1 ± 0.1	0.84 ± 0.16	0.59 ± 0.04
$Cr(acac)_3$	0.520 ± 0.045	1.25 ± 0.25	0.14 ± 0.02
$CrSt_3$	1.67 ± 0.03	1.5 ± 0.15	0.25 ± 0.05
$Co(acac)_2$	32.5 ± 0.5	1.8 ± 0.15	0.50 ± 0.035
$Co(acac)_3$	31.0 ± 0.1	1.5 ± 0.15	0.705 ± 0.04
$Fe(acac)_3$	1.95 ± 0.2	1.0 ± 0.08	0.60 ± 0.02
$Mn(acac)_3$	5.60 ± 0.05	1.5 ± 0.2	0.48 ± 0.03
$Ni(acac)_2$	2.10 ± 0.01	0.96 ± 0.045	0.70 ± 0.025
$Cu(acac)_2$	42.0 ± 1.0	1.5 ± 0.1	0.865 ± 0.035

* (k_i) Rate constant of overall hydroperoxide decomposition.

field stabilization energy CFSE = 0 [10]). Theoretically, two maxima should be observed in the case of octahedral complexes for d^4 [Cr(III)] and d^9 [Cr(II)] ions. A regular octahedral coordination environment of these ions is impossible. The Jahn–Teller effect results, as a rule, in an underestimation, compared to the experimental values, of the theoretical stabilization energy due to occupation of low-lying *d*-orbitals (CFSE). This is the case when the coordination number of these ions is 4. If the Jahn–Teller stabilization is low and the coordination number is 6, Ni(II) and Cr(III) complexes should be more stable than the Cu(II) and Mn(III) analogs. The enthalpy of complexation of $Cr(acac)_3$ with 1-methylcyclohexane is lower than that of the $Ni(acac)_2$. Since all the acetylacetonate complexes in question are of high-spin type [12], the presence of two maxima in the dependence of E_a on the atomic number of the 3*d* metal indirectly suggests that the CFSE contribution is no less than 5–10% of the total metal–ligand bond energy. Subtraction of the parameter proportional to CFSE from the experimental E_{eff} (taking the *d* configuration of the metal into account) gives a linear dependence of E_a on the number of *d* electrons in the 3*d* metal atom. A similar dependence has been observed for ethylbenzene decomposition [13].

Since the enthalpy of formation of the hydroperoxide–catalyst complex is low (Table 1), E_{eff} characterizes both the decomposition of this complex and other pathways of hydroperoxide decomposition. As determined by NMR spectroscopy, only one hydroperoxide molecule is present in the complexes with 3*d*-metal acetylacetonates. Hydroxoperoxide does not substitute acetlyacetonate ligands in the complexes of Cr(III), Mn(III), Fe(III), and Co(III). In the initial steps of this reaction, only "anisotropic" complexes with intermediate intra-outerspheric coordination of hydroperoxide are formed. The hydroperoxide ligand expands (inflates) the coordination sphere and changes the electronic structure of the catalyst, which affects the reactivity of the catalyst with respect to the substrate. In the case of square planar complexes, the hydroperoxide ligand attacks in the direction normal to the plane of the complex. In the further steps, the acetylacetonate ligand can be substituted by two monodentate or one bidentate ligand. In the case of substitution in $Cu(acac)_2$ and $Co(acac)_2$, octahedral complexes can be formed only after coordination of two ligands.

Catalytic decomposition of CHP and MCHP was studied by UV spectroscopy in the range 240–700 nm. Oxidation of V(III) to V(V) and a partial change in the oxidation state of Co(II), Cr(III), Mn(III), and Cu(II) were observed. Solutions of 3*d*-metal acetylacetonates in ethanol and chloroform absorb in the range 240–400 nm. The absorption bands and the extinction coefficients of these compounds were measured in [14]. The electronic absorption spectra of methylcyclohexane solutions of Mn(II) and Cu(II) stearates and Mn(III), Co(IIII), Cr(III), Cu(II) acetylacetonates have a broad band at 330–350 nm; $Ni(acac)_2$ absorbs at 300 nm; $Fe(acac)_3$ has two bands at 350 and 440 nm. The high-frequency bands in the UV spectra of 3*d* metal acetylacetonates are due to $\pi \rightarrow \pi^*$ transition in the ligand [14]. The weaker band in the visible region (550–700 nm) is assigned to the *d–d* transition in the metal.

The UV spectra of methylcyclohexane solutions of $Co(acac)_2$, $CoSt_2$, $Co(acac)_3$, $Mn(acac)_3$, and $Co(Nf)_3$ (St = stearate and Nf = naphthenate) substantially change upon addition of MCHP. The UV absorption of a $CoSt_2$ solution in methylcyclohexane, initially characterized by a weak band with λ_{max} = 275 nm, substantially increases upon addition of hydroxoperoxide. The spectrum of the mixture is a monotonically decreasing curve with an inflection at 330 nm. This long-wavelength band is due to a charge transfer from the metal to hydroperoxide ligand in the donor–acceptor complex. This pattern cannot be attributed to oxidation of Co(II) in the presence of the hydroperoxide, since Co(III) absorbs in the long-wavelength range. Uncoordinated MCHP has a weak band at 260 nm, which is not overlapped with the spectrum of the complex.

When cobalt(II) acetylacetonate is added to an MCHP solution, a strong band of the $Co(acac)_2$–MHCHP complex appears. The solution color changes from pink [Co(II)] to green [Co(III)]. The *d–d* transition band appears in the visible range. The electronic absorption spectra of reactions mixtures of $Mn(acac)_3$, $Co(acac)_3$, and Co(Nf)3 with the hydroxoperoxide contain the bands of the donor–acceptor complexes of the catalysts with the hydroxoperoxide. Clearly, both the oxidized and reduced forms of the catalyst form these complexes. It should be noted that the band of $Mn(acac)_3$–ROOH complex is weaker than that of free $Mn(acac)_3$, whereas the bands of the complexes $CoSt_2$–ROOH, $Co(acac)_2$–ROOH, $Co(acac)_3$–ROOH, and $Co(Nf)_3$–ROOH are stronger than those of the initial salts. The color of solutions of $Co(acac)_3$ and $Co(Nf)_3$ changes after mixing with the hydroxoperoxide, which suggests the occurrence of the Co(III) $\rightleftarrows$ Co(II) equilibrium. In the spectrum recorded immediately after reagent mixing, the band of free acetylacetone (275 nm) is absent. This band appears in the course of the reaction.

The coordination sphere of Co in anisotropic complexes [$(Co(acac)_3 \cdot ROOH$, $Co(Nf)_3 \cdot ROOH$] rear-

ranges owing to a change in the oxidation state of the central metal in the course of the reaction. The hydroxoperoxide can be coordinated to both Co(II) and Co(III).

It is known that 3*d*-metal stearates are associated in hydrocarbon solvents [15]. We recorded IR spectra of *s*- and 3*d*-metal acetates, stearates, and acetylacetonates in decane. The upper concentration limit of the analyzed solutions was determined by the solubility of these compounds in decane at 25°C. It was possible to obtain 10^{-3} M solutions of all the catalysts examined. The spectra of $CoSt_2$, $CuSt_2$, $Cu(acac)_2$, $VO(acac)_2$, $Zn(acac)_2$ and $Ni(acac)_2$ solutions contained only the bands on nonassociated species (1700–1710 cm^{-1}). In the spectra of 10^{-3} M solutions of $Co(acac)_2$, $Co(acac)_3$, $Mg(acac)_2$, $Fe(acac)_3$, $Cr(acac)_3$, and $Mn(acac)_3$ in decane, the band of associated species (1580 cm^{-1}) are observed along with the bands of the monomeric complexes (1705 cm^{-1}). Addition of ROOH, which exhibits surfactant properties increases the solubility of the catalysts. However, both monomeric and associated complexes are present in 8.8×10^{-4}–8.8×10^{-3} M solutions of acetylacetonates in decane and methylcyclohexane containing CHP and MCHP. The fractional reaction orders with respect to catalysts in CHP decomposition (Table 3) are apparently caused by partial association of the catalysts.

The yield of free radicals released into the bulk of the solution upon homolytic rupture of O–O bonds in the course of thermolysis of CHP at 150°C was found [16] to be 12%. In the presence of chromium-containing catalysts, this yield is 8.3–27.0%. Chromium-containing compounds catalyze the conversion of CHP into cyclohexanone. The solvent is involved in the radical decomposition (isomeric decanols were detected in the reaction mixture). The oxidation state of the central metal atom (Co, Mn, V, Cr, and Cu) changes alternately in the course of reaction with the hydroperoxide. The reaction rate is determined by the difference between the energies of the oxidized and reduced metal species. The heaviest metals of the 3*d* series have a single stable oxidation state [Co(III), Cu(II), Ni(II)]. Hence, the catalytic cycle requires a higher activation enthalpy with an increase in the atomic number of the central metal atom [17]. This assumption was confirmed experimentally. As the electronegativity of metals increases, the stability of their complexes grows.

CONCLUSIONS

(1) The complexing power of 3*d*-metal acetylacetonates with respect to cyclohexyl hydroperoxide correlates with the metal electronegativity and increases in the order: VO(II) ≈ Cr(III) < Mn(III) ≈ Fe(III) < Co(III) < Ni(II) < Cu(II). The activation energy of hydroperoxide decomposition increases in the same order.

(2) Kinetic parameters of cyclohexyl hydroperoxide decomposition (overall rate constants, reaction orders with respect to the hydroperoxide and catalyst) via formation of intermediate complexes with 3*d*-metal acetylacetonates were determined at the catalyst concentration ranging from 8.8×10^{-4} to 8.8×10^{-3} M.

(3) Cyclohexyl hydroxoperoxide decomposition is a homogeneous reaction proceeding by radical and molecular pathways to form not only $ML_n \cdot ROOH$ intermediate at low concentrations of nonassociated catalysts, but also associated and partially heterogeneous catalytic species.

(4) *s*- and 3*d*-Metal carboxylates form $ML_n \times m$ROOH (m = 1, 2) complexes with 1-methylcyclohexyl hydroperoxide, which is due to the fact that the intermolecular hydrogen bonds (*s* metals) and bonds of the metal with α-oxygen atom of hydroperoxide (3*d* metals) are stronger than the hydrogen bonds in associated hydroperoxides. The formation of these complexes catalyzes decomposition of tertiary hydroperoxide into radicals and molecular products.

REFERENCES

1. Badrian, A.S., Kokoulin, F.G., Ovchinnikov, V.I., *et al.*, *Proizvodstvo kaprolaktama* (Production of Caprolactam), Moscow: Khimiya, 1977.
2. Syroezhko, A.M. and Proskuryakov, V.A., Abstracts of Papers, *IV Mezhdunarodnyi simpozium po gomogennomu katalizu* (IV Int. Symp. on Homogeneous Catalysis), Leningrad, June 12, 1984, pp. 177–178.
3. Syroezhko, A.M. and Proskuryakov, V.A., *Zh. Prikl. Khim.*, 1976, vol. 49, no. 4, pp. 1125–1131.
4. Smirnov, P.A., Timofeeva, T.N., Syroezhko, A.M., *et al.*, *Zh. Org. Khim.*, 1974, vol. 10, no. 9, pp. 1892–1896.
5. Proskuryakov, V.A., Syroezhko, A.M., Yakovlev, A.S., *et al.*, Abstacts of Papers, *7-ya Vsesoyuznaya konferentsiya po khimii organicheskikh peroksidov* (7th All-Union Conf. on Chemistry of Organic Peroxides), Volgograd, September 16, 1980, pp. 166–167.
6. Syroezhko, A.M., Liquid Phase Oxidation of Alkanes, Cycloalkanes, and Their Oxygen-Containing Derivatives with Oxygen and Ozone in the Presence of Compounds of *s* and 3*d* Metals, *Doctoral Dissertation*, Leningrad, 1985.
7. Wilke, G. and Heimbach, P., *Lieb. Ann.*, 1962, vol. 652, no. 2, pp. 7–21.

8. Crigee, R. and Dietruch, H., *Ann.*, 1948, vol. 560, no. 1, p. 135.
9. Gribov, A.A., Zolotov, Yu.A., and Noskova, M.N., *Zh. Strukt. Khim.*, 1968, vol. 9, no. 3, pp. 448–457.
10. Day, M.C and Selbin, J., *Theoretical Inorganic Chemistry*, New York: Reinhold, 1969, 2nd ed.
11. Jorgensen, C.K., *Inorganic Complexes*, New York: Academie, 1963, pp. 11–17.
12. Yablonskii, O.P., Complexation and Its Role in Oxidation and Separation of Hydrocarbons, *Doctoral Dissertation*, Ivanovo, 1979.
13. Sapunov, V.N., Hydroperoxide Epoxidation of Olefins, *Doctoral Dissertation*, Moscow, 1980.
14. Krylov, I.A., Oxidation of Cyclohexane with Molecular Oxygen in the Presence of Variable-Valence Metal Complexes as Catalysts, *Cand. Sci. Dissertation*, Moscow, 1979
15. Dial Khomadi Modi, Comparative Study of the Catalytic Activity of Variable Valence Metals in Reactions of Hydroperoxides, *Cand. Sci. Dissertation*, Moscow, 1977.
16. Kudryashov, V.M., Kinetics of Liquid-Phase Catalytic Oxidation of nPentadecane and Composition of the Oxidation Products, *Cand. Sci. Dissertation*, Moscow, 1979.
17. Itskovich, V.A., Homogeneous Catalytic Oxidation and Autooxidation of Cycloparaffins in the Presence of Boron-Containing Compounds, *Doctoral Dissertation*, Leningrad, 1980.

Russian Journal of Applied Chemistry, Vol. 77, No. 8, 2004, pp. 1308–1311. Translated from Zhurnal Prikladnoi Khimii, Vol. 77, No. 8, 2004, pp. 1323–1326.

CATALYSIS

Features of Claus Treatment of Acid Gases with Low Content of Hydrogen Sulfide

O. I. Platonov, A. G. Ryabko, and L. Sh. Tsemekhman

Gipronikel Institute Joint-Stock Company, St. Petersburg, Russia

Received April 5, 2004

Abstract—Changes in the activity of industrial alumina catalysts CR-31 and AO-MK-2, which occur under the real industrial conditions in the last catalytic stage of the Claus process in the coke-oven gas treatment shop of the Magnitogorsk Metallurgical Plant, are analyzed.

More than 30 million tons of sulfur is produced in the world in the course of treatment of natural gas and petroleum products by the procedure described in [1]. This procedure involves partial oxidation of hydrogen sulfide with subsequent catalytic conversion of the reduction products by the Claus reaction:

$$2H_2S + SO_2 = 2H_2O + 3/nS_n, \quad n = 1–8. \quad (1)$$

The known and newly developed procedures for utilization of metallurgical off-gases from melting of sulfide raw materials to obtain elemental sulfur [2] also involve treatment of the products of sulfur dioxide reduction by the Claus procedure (1). Since the efficiency of the multistage Claus treatment is determined by the residual concentrations of sulfur-containing components in the tail gases, optimization of the operation parameters in the last catalytic stage of industrial Claus installations is a problem of current interest.

In this study, we analyzed changes in the activity of alumina catalysts CR-31 (La Roche Chemicals) and AO-MK-2 [GRES-24 (State Regional Power Station)] in a two-sectional Claus reactor at the coke-oven gas treatment shop of the Magnitogorsk Metallurgical Plant (MMP) [3].

The gas treated at 230–270°C contained, vol %: 1.15 ± 0.33 H_2S, 0.47 ± 1.6 SO_2, 0.51 ± 0.08 COS, 4.6 ± 0.8 CO, 26.6 ± 3.3 CO_2, 3.6 ± 1.1 H_2, 62.5 ± 3.5 N_2, elemental sulfur (10–30 g m^{-3}), and water (120 g m^{-3}), which corresponds to the typical gas composition in the last catalytic stage of the Claus process.

The catalyst activity was evaluated from the conversion η_i (where i is the component index) of the main sulfur-containing products (H_2S, COS, and SO_2), using the chromatographic method. For this purpose, the volume concentrations of N_2, O_2, H_2, CH_4, CO_2, CO, H_2S, COS, and SO_2 were determined [4] in dried samples of the process gas at the inlet and outlet of certain stages of the Claus reactor, which were synchronized with an accuracy of 2–5 min by the sampling procedure. For example, the conversion of H_2S was calculated from the initial ($c_0 \equiv [H_2S])_{in}$) and final ($c \equiv [H_2S]_{out}$) concentrations in the process gas at the inlet and outlet of given stage of the Claus reactor as follows

$$\eta_{H_2S} = 1 - [H_2S]_{out}[N_2]_{in}/([H_2S]_{in}[N_2]_{out}) = \{[N_2]_{in} \approx [N_2]_{out}\} \approx 1 - c/c_0. \quad (2)$$

Measurements were carried out twice a day at a 2–3-h interval for the available gas of variable composition [3], which ensured independence of the resulting η_i values.

To reveal the factors of activity and the effects of aging and regeneration, the dynamics of the catalyst activity was studied separately for hydrogen sulfide and carbonyl sulfide. In this case, the conversion η_i for each component was determined as its daily mean value found by averaging two pairs of η_i values, i.e., from four paired measurements timed with an accuracy of no less than ±1.5 h. To determine the general dependences $\eta_i = \eta_i(\tau)$, the experimental η_i values were additionally averaged over the nearest points, which is equivalent to digital filtration [5].

The experimental dependence of the conversion of the sulfur-containing components in the course of treatment, plotted using the daily conversion values η_{H_2S} and η_{COS} recorded during 3 years of operation of the CR-31 catalyst in the first stage of the Claus re-

1070-4272/04/7708-1308 © 2004 MAIK "Nauka/Interperiodica"

actor, are shown in Fig. 1 (points). The corresponding empirical dependences η_i–τ calculated by averaging nine nearest η_i values are represented by curves. Although the first two η_{COS} values are absent[1] in Fig. 1, the generally monotonic empirical dependence of η_{COS} on time τ strongly suggests that the carbonyl sulfide conversion η_{COS} at the beginning of the CR-31 catalyst operation tends to 100%.

As can be seen from Fig. 1, the conversion of hydrogen sulfide on a fresh CR-31 catalyst under given operation conditions (space velocity $W \sim 1000$ h^{-1} and average temperature $T \sim 250.5$°C) is characterized by significant negative values ($\eta_{H_2S} \to -40$ rel %), which suggests generation of H_2S in the initial period of CR-31 catalyst operation. With time, the conversion of H_2S increases and reaches $\eta_{H_2S} = 40-45$% by the second month of operation, and then it gradually decreases to approximately 30% in the subsequent two years (Fig. 1). It should be noted that the current deviations of the empirical daily values of η_{H_2S} and η_{COS} from the general dependences η_{H_2S}–τ and η_{COS}–τ (due to changes in the temperature and composition of the process gas) correlate in antiphase.

The revealed $\eta_{H_2S} = f(\tau)$ and $\eta_{COS} = f(\tau)$ dependences were verified in industrial tests of the AO-MK-2 alumina catalyst supplied by GRES-24 (Mosenergo Joint-Stock Company, Moscow, Russia). For this purpose, 12 m^3 of the CR-31 catalyst after ~2.5 year operation in the first section of the Claus reactor were replaced with 5 t (~7 m^3) of AO-MK-2 catalyst, and its activity characteristics were studied by the procedure given above.

The variation of the conversion of hydrogen sulfide (η_{H_2S}) and carbonyl sulfide (η_{COS}) and of the total conversion η_S during nearly one year of operation of the AO-MK-2 catalyst in the first stage of the Claus reactor is shown in Fig. 2. Since the first values were recorded on heating the reactor to the temperature of the catalyst bed of 189°C, which is lower by 50°C than the working temperature, the conversion η_{COS} is underestimated, whereas η_{H_2S} and η_S are overestimated relative to the values typical of the fresh catalyst.

The empirical dependence of the carbonyl sulfide conversion h_{COS} on AOMK-2 catalyst is qualitatively similar to the kinetic dependence $\eta_{COS} = f(\tau)$ found previously; it gradually decreases in first 6–7 months of operation from the initial $\eta_{COS}(0) = 98$% to minimal $\eta_{COS}(0.3) \sim 40-45$% (Fig. 2). At the same time, the conversion of hydrogen sulfide [$\eta_{H_2S} = f(\tau)$] and the total conversion of sulfur-containing gases [$\eta_S = f(\tau)$] monotonically increase (to a first approximation) up to the maximal values at $\tau = 0.05$ year ($\eta_{H_2S\,max} \sim 60$ and $\eta_{S\,max} \geq 50$ rel %) and then decrease to $\eta_{H_2S\,min} \sim 30$ and $\eta_{S\,min} \sim 40$ rel %, respectively.

The experiment on regeneration of the AO-MK-2 catalyst after 7-month operation consisted in heating of the catalyst bed in the first stage of the Claus reac-

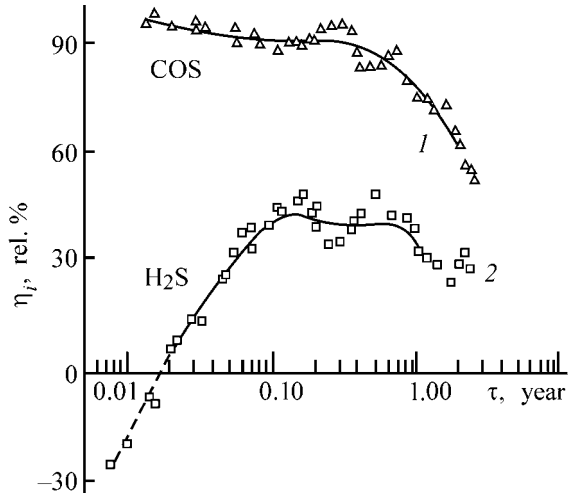

Fig. 1. Conversion η_i of (*1*) carbonyl sulfide and (*2*) hydrogen sulfide on CR-31 alumina catalyst vs. the operation time. Space velocity 1000 h^{-1} and temperature 250.5 ± 5.9°C.

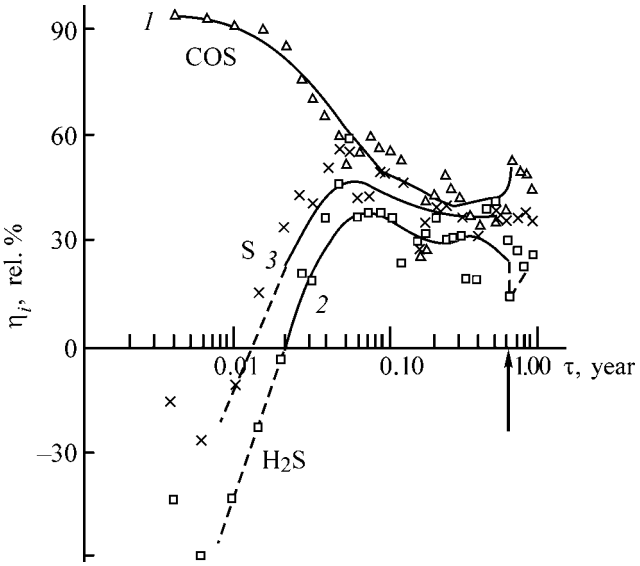

Fig. 2. Conversion η_i of (*1*) carbonyl sulfide, (*2*) hydrogen sulfide, and (*3*) sulfur-containing gases on AO-MK-2 alumina catalyst vs. the operation time (year). Space velocity 2000 h^{-1} and temperature 253 ± 6°C.

[1] Due to the delay in calibration with respect to COS, the content of carbonyl sulfide at the new MMP Claus line put in operation on September 1, 2000 was not recorded till August 4, 2000.

tor to 300°C, which was performed using the in-line bypass of a primary boiler-utilizer without interruption of the line operation and changes in the operation schedule of hydrogen sulfide oxidation in the Claus reactor. As can be seen from Fig. 2, the conversion of carbonyl sulfide η_{COS} first increased at the beginning of the catalyst regeneration (marked by an arrow in Fig. 2) from 39 to 53% and then monotonically decreased; and vice versa, the conversion of hydrogen sulfide η_{H_2S} first sharply decreased and then increased to the initial value.

The qualitative similarity of the dynamic dependences $\eta_{COS} = f(\tau)$, and $\eta_{H_2S} = f(\tau)$ found for different catalysts and space velocities differing by a factor of 2 (Figs. 1 and 2), suggests that the features of conversion of the "depleted" gases (with low content of hydrogen sulfide) on alumina catalysts are similar. Fresh industrial alumina catalysts are characterized by high negative conversion (i.e., generation) of H_2S at a complete (up to 98 rel %) consumption of COS. After the beginning of operation, the COS conversion decreases, whereas the observed conversion of H_2S increases, reaches a maximum in several weeks, and then monotonically decreases with the catalyst aging. The opposite trends are observed in the conversion of H_2S and COS at varying catalyst activity: with an increase in the COS conversion, the conversion of H_2S decreases, and *vice versa*.

Using the Tekhnolog program [6], we performed a thermodynamic analysis of the acid gas of given composition at 250°C and found that the equilibrium concentrations of the gas components ($[H_2S]^{eq}$ = 3.07, $[COS]^{eq}$ = 0.005, $[H_2O]^{eq}$ = 9.6, $[H_2]^{eq}$ = 4.6, $[CO]^{eq}$ = 0.15, $[CO_2]^{eq}$ = 27.6, and $[S]^{eq} \approx 0.0001$ vol %) correspond to a negative conversion of hydrogen sulfide, $\eta_{H_2S}^{eq}$ = –233%, at nearly complete consumption of COS (η_{COS}^{eq} = 99.3%). Thus, the equilibrium conversion of depleted gas is characterized by hydrogen sulfide generation, which is accompanied by hydrolysis and hydrogenation of elemental sulfur and carbonyl sulfide, described by the following reactions

$$2COS + SO_2 = 2CO_2 + 3/nS_n \quad (n = 1–8), \quad (3.1)$$

$$COS + H_2O = H_2S + CO_2, \quad (3.2)$$

$$1/nS_n + H_2 = H_2S. \quad (3.3)$$

The formation of H_2S by reactions (3.2) and (3.3) is opposite to its conversion by the Claus reaction (1). Therefore, the resulting process can be described as a competition of reactions (1) and (3). In this case, negative conversion of hydrogen sulfide on fresh alumina catalysts is thermodynamically expectable. With the catalyst activity decreasing in the course of operation, the conversion of carbonyl sulfide also decreases (Figs. 1 and 2), which, in turn, causes deceleration of the slow hydrolysis reactions (3.2), and, in the course of time, the conversion of hydrogen sulfide by reaction (1) becomes predominant.

Similarly, the effects of nonmonotonic changes (fluctuations) in the catalyst activity under various operation conditions on the conversion of H_2S and COS are also different. For example, a sharp decrease in the activity of the CR-31 catalyst due to its overheating ($T > 500$°C) at the end of the second year of operation was accompanied by a strong decrease in the COS conversion, whereas the hydrogen sulfide conversion increased (Fig. 1).

Along with the hydrolysis of COS and/or elemental sulfur by reaction (3.2), hydrolysis of carbon sulfide is also observed:

$$CS_2 + 2H_2O = 2H_2S + CO_2, \quad (4)$$

providing an increase in the hydrogen sulfide concentration in the initial period of operation of a fresh catalyst.

Our experimental data suggest that the difference between the $\eta_{H_2S} = f(\tau)$ and $\eta_{COS} = f(\tau)$ dependences is due to the difference in the mechanisms of H_2S and COS conversion on the active surface and at the active centers of the catalyst.

The deceleration of hydrolysis and hydrogenation on alumina catalysts can probably account for the increase in the equilibrium yield of elemental sulfur in the course of the Claus conversion [1].

The results of industrial tests show that the conversion of sulfur-containing components of depleted gas is due to the hydrolysis and hydrogenation, causing negative conversion of H_2S with complete consumption of COS at the start of operation of a fresh alumina catalyst. Since the conversion of H_2S in depleted gases on industrial alumina catalysts is provided at the expense of deceleration of carbonyl sulfide hydrolysis, it is necessary to reliably determine the kinetic mode of the catalyst operation in the last stage of the Claus treatment of acid gases.

Our results show that the use of similar-type (even highly active) catalysts in different stages of the Claus process is inefficient. The high total activity of the catalyst bed, frequently determined from the content of products formed in hydrolysis of sulfur-containing

organic compounds (COS, CS_2) [7], in the last conversion stage does not ensure a low residual content of hydrogen sulfide in the tail gases. As we know, this obvious conclusion is frequently ignored in designing and running Claus process lines.

CONCLUSION

Based on experimental data, the thermodynamic principles of treatment of depleted acid gases are refined and ways to optimize kinetic modes of the catalyst operation in the last treatment stage are suggested.

REFERENCES

1. Grunval'd, V.R., *Tekhnologiya gazovoi sery* (Technology of Gas Sulfur), Moscow: Khimiya, 1992.
2. Platonov, O.I., Vasil'ev, Yu.V., Ryabko, A.G., *et al.*, *Tsvetn. Met.*, 2004, no. 2, pp. 68–72.
3. Egorov, V.N., Krinitsyn, E.N., Mel'nikov, I.I., *et al.*, *Koks Khim.*, 2001, no. 12, pp. 14–19.
4. Mel'nikova, I.I., Reprintseva, L.I., Bakhareva, V.P., *et al.*, *Koks Khim.*, 2001, no. 12, pp. 20–23.
5. Hamming, R.W., *Digital Filters*, Englwood Cliffs: Prentice-Hall, 1977.
6. *Tekhnolog: Kreslo tekhnologa & teplotekhnika: Spravochno-reshayushchaya sistema: Versiya 1.5 1990, 1991: Rukovodstvo pol'zovatelya* (Production Engineer: Work Station of Production Engineer & Heating Engineer: Reference Database and Computation System; Version 1.5 1990, 1991: User's Manual), Moscow: Tekhnosoft, 1990.
7. Connock, L., *Sulphur*, 2004, no. 291, pp. 35–41.

Russian Journal of Applied Chemistry, Vol. 77, No. 8, 2004, pp. 1312–1315. Translated from Zhurnal Prikladnoi Khimii, Vol. 77, No. 8, 2004, pp. 1327–1330.

ENVIRONMENTAL PROBLEMS OF CHEMISTRY AND TECHNOLOGY

Removal of Ni(II) with Sodium Ferrate(VI) from EDTA-containing Aqueous Solutions

D. Yu. Stupin and M. I. Ozernoi

St. Petersburg State Agricultural University, St. Petersburg, Russia

Received April 26, 2004

Abstract—A procedure was developed for removal of Ni(II) from EDTA-containing aqueous solutions with sodium ferrate(VI) Na_4FeO_5.

Any treatment procedure to remove heavy metal ions from wastewater involves precipitation and coagulation [i.e., addition of Fe(II), Fe(III), or Al(III) salts] at a given pH, with the subsequent removal of hydroxide precipitates. However, precipitation is hindered by complexation of heavy metal ions with organic ligands. This process is frequently used in separation of metal ions by extraction or ion exchange, in metal electroplating, in cleaning of metal surfaces, in antiscale treatment, etc. The resulting complexes can be decomposed with strong oxidants.

For this purpose, alkali metal ferrates(VI) are rather promising. The ferrate ion FeO_4^{2-} acts as an oxidant and coagulant, and no harmful by-products are formed in its reduction to Fe(III) oxides and hydroxides [1]. Its coagulation efficiency is greater as compared with the most widely used inorganic coagulants, such as Fe(II), Fe(III), and Al(III) salts [2].

Ferrates efficiently remove heavy metals from natural and waste water [2–6]. However, such a treatment is occasionally inefficient in the presence of some complexing agents. For example, the results of treatment of a low-level wastewater containing Am and Pu and complexing agents that form chelates with these radionuclides were unsatisfactory. These chelating agents were ethanolamine, 2-butoxyethanol, Triton X100, and of dipropylene glycol methyl ether. As the amount of potassium ferrate added was raised, the degree of radionuclide removal increased to some constant value (about 40%); i.e., removal of radionuclides was incomplete. Moreover, a similar removal of radionuclides from solutions was found upon addition of Fe^{3+} ions to the solutions at the same pH. Obviously, ferrate ions act under given experimental conditions as only a source of iron hydroxide $Fe(OH)_3$ without any oxidizing effect [Fe(VI) → Fe(III)].

In this case, apparently, the rate of water oxidation (decomposition of ferrate ions) strongly exceeds the oxidation rate of chelating ligands. As in the case of the other oxidants, this is probably due to a sharp decrease in the redox potential of the ferrate ion in alkaline medium under the experimental conditions studied (pH 7.2–10.0). At pH < 5, the oxidation rate of ferrate ions should be extremely high.

It is known that Fe(VI) is reduced to Fe(III) step-by-step via short-lived Fe(IV) and Fe(V), which are also rather strong oxidants [7, 8].

Only ozone is a stronger oxidant than the ferrate ion FeO_4^{2-}. Its redox potential depends on pH and varies from 2.07 (pH 0) to 0.9 (alkaline medium) [9]. The stability of ferrate ions is also determined by pH and grows with increasing pH to a maximum at pH ~ 10. At pH < 7, ferrate ions are unstable and are involved in water oxidation with liberation of oxygen. In most cases, Fe(VI) was studied in the form of potassium ferrate K_2FeO_4.

In this study, we used specially prepared sodium ferrate Na_4FeO_5. Upon dissolution in water, the FeO_5^{4-} ion apparently immediately transforms into FeO_4^{2-}; as a result, the absorption spectra of purple potassium and sodium ferrate solutions are identical and exhibit absorption bands at ~515 and ~318 nm, respectively.

EXPERIMENTAL

We used analytically pure reagents. Sodium ferrate(VI) was prepared by the solid-phase reaction $Fe_2O_3 + Na_2O_2$ in an oxygen flow [10]. An X-ray diffraction (XRD) analysis of 20 samples prepared showed the set of reflections similar to those found for Na_4FeO_5 [10]. No additional reflections belong-

1070-4272/04/7708–1312 © 2004 MAIK "Nauka/Interperiodica"

ing to the initial compounds (Fe_2O_3 and Na_2O_2), ferrate(IV), ferrate(III), and Na_2CO_3, which can be formed in the presence of air, were observed. Since the sensitivity of the conventional XRD analysis is about 5%, we believe that the content of Fe(VI) in the sample was no less than 95%.

The reference $[NiEDTA]^{2-}$ solution with pH 3.9 and 2×10^{-4} M concentration was prepared by mixing the corresponding amounts of 0.1 M $Ni(NO_3)_2$ and 0.01 M Na_2EDTA solutions. This reference solution (50 ml) was poured into a three-electrode Teflon cell with a glass electrode for pH measurements of the buffer solutions, a standard reference electrode, and a platinum working electrode for redox measurements. The required amount of iron ions was added to the sample with constant stirring either as a weighed portion of powdered sodium ferrate(VI) or as an aliquot of 0.1 M $Fe(NO_3)_3$ solution. Since the breakdown of Na_4FeO_5 in water with liberation of oxygen is accompanied by the formation of NaOH [pH ~ 12 upon dissolution of a 20–mg portion of sodium ferrate in water (20 ml)], its required amount (30–220 mg) was added in small portions (5–10 mg), and the required solution pH was adjusted using 1 M HNO_3. After the breakdown of ferrate ions in solution, the pH was brought to 6–8 by adding crystalline Na_2CO_3 to provide the optimal conditions for precipitation of Fe(III) compounds. The resulting flakes of iron(III) oxides and hydroxides were allowed to precipitate for 1 h, after which a 5-ml portion of the solution in equilibrium with the precipitate was sampled and filtered through a "blue ribbon" filter.

The residual content of nickel(II) in the solution was determined by measuring its X-ray fluorescence with a spectrophotometer recording the energy dispersion with an accuracy of 210 eV (Mn $K_{\alpha 1}$ line). The sample for X-ray fluorescence measurements was prepared as follows. The sample was evaporated to 0.5 ml, and the residue was placed on a porous disc of chromatographic cardboard (8 mm in diameter) and dried at 343–353 K. The X-ray fluorescence spectrum of nickel(II) was excited by primary gamma-radiation (^{109}Cd source). The content of Ni(II) in the calibration samples was varied within 2–100 μg. The peak area ($K_{\alpha 1}$) was a linear function of the nickel(II) content (μg); the analysis accuracy was ±5%.

In some experiments, we added to the initial sample of the reference $[NiEDTA]^{2-}$ solution before addition of sodium ferrate one of the reagents NaCl, HCl, K_2SO_4, or H_2O_2 + HCl mixture to the 10^{-4}–10^{-2} M concentration in order to study the possibility of promoting the EDTA oxidation.

In the experiments with Fe(III) coagulant, the required amount of 0.1 M solution of $Fe(NO_3)_3$ was added to the solution, the solution pH was adjusted to 1.5 (1 M HNO_3), and the resulting solution was allowed to stand for 20 min; then Na_2CO_3 was added in order to precipitate metal hydroxides. Further procedure of preparation of the solution sample over the precipitate for X-ray fluorescence analysis was similar to those given above.

The data on the effect of Fe(III) and Fe(VI) coagulants on aqueous solutions of $[NiEDTA]^{2-}$ are listed in the table.

Since the difference in the molecular weights of Na_4FeO_5 and $Fe(NO_3)_3$ is relatively small (227.85 and 241.85, respectively), similar portions of these salts contain similar amounts of Fe(III). Our results showed that, with decreasing solution pH, the degree of Ni(II) removal increases simultaneously with an increase in the redox potential of the solution. Upon addition of sodium ferrate (40–50 mg), the removal of nickel(II) changed from 5 at pH 5 to 50–55% at pH 2. The sulfate ions did not affect the removal of nickel from the sample.

However, on replacing HNO_3 with HCl or on adding NaCl to the sample acidified with HNO_3 to pH ~ 2, the degree of Ni(II) removal sharply increased up to 85% at 65-mg portion of sodium ferrate. At pH < 4.5, water immediately decomposed Fe(VI) and chloride ions occurring in solution were partially oxidized to free chlorine Cl_2; the decrease in the Cl^- ions concentration was recorded with a silver chloride electrode. It is apparent that rapid reduction of Fe(VI) in solution yields highly reactive species, which are then involved in oxidation of chloride ions and EDTA.

It should be noted that the complexes of *d* elements with EDTA are very strong, and one of the strongest complexes is $[NiEDTA]^{2-}$. Just in this connection, we studied the possibility of its breakdown with ferrate ions. The reduction of $Fe^{VI}O_4^{2-}$ in aqueous solution to Fe(III) hydroxo compounds occurs via formation of short-lived $Fe^{V}O_4^{3-}$ and $Fe^{IV}O_4^{4-}$ species, which are highly aggressive oxidants. Sharma *et al.* [8] studied the oxidation of CN^- ions with potassium ferrate(VI) in alkaline solutions and found that the rate of this oxidation with Fe(V) and Fe(IV) species is greater by four and two orders of magnitude, respectively, as compared to Fe(VI).

Thus, Cl^- ions are probably also oxidized by ferrate(VI) ions via intermediate species, which oxidize EDTA and cause liberation of gaseous Cl_2 even at a concentration of chloride ions smaller than 10^{-3} M at

Evaluation of the optimal conditions of Ni(II) removal from aqueous solutions in the presence of EDTA ($[NiEDTA]^{2-}$ concentration 8.2×10^{-5} M, solution volume 50 ml)

pH	Reagent for pH adjustment	Na_4FeO_5 or $Fe(NO_3)_3$, mg	Additional reagent, M	Degree of Ni(II) removal, %	Maximal redox potential in solution, mV
4.0	–	42	–	5	+280
3.8	HNO_3	56	–	35	+650
3.4	HNO_3	45	–	35	+650
2.5	HNO_3	18	–	40	+520
2.8	HNO_3	70	–	55	+590
2.0	HNO_3	53	–	55	–
1.9	HNO_3	51	HCl	50	+750
1.95		49	HCl	60	+760
1.9	HNO_3	65	NaCl, 10^{-2}	85	+780
1.9		72	H_2O_2, 2×10^{-2} HCl, 10^{-2}	65	–
1.9–6.3	Na_2CO_3	26	H_2O_2, 1.6×10^{-3} HCl, 10^{-2}	25	–
1.4–9.0	Na_2CO_3	221	–	100	+700
1.5–9.0	Na_2CO_3	$Fe(NO_3)_3$ 242	–	77	+730
1.5–6.8	Na_2CO_3	$Fe(NO_3)_3$ 121	–	60	–
1.5	HNO_3	186	–	100	–
1.4	HNO_3	157	–	95	–
1.4	HNO_3	123	–	100	–
1.7	HNO_3	95	–	90	–
2.2	HNO_3	78	–	82–85	–
2.3	HNO_3	54	–	55	–
2.1	HNO_3	48	K_2SO_4, 10^{-3}	55	–
2.2	HNO_3	44	K_2SO_4, 10^{-2}	50	–

pH ~ 2. The formation of $Fe^{IV}O_4^{4-}$ and hypochlorous acid can proceed by the following scheme.

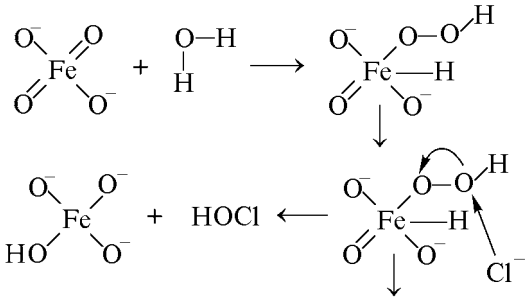

These reactions are similar to the scheme of formation of $Fe^{IV}O_4^{4-}$ and H_2O_2, suggested in [7]. The other oxidants probably are involved in further processes, including HClO reduction to Cl_2.

The liberation of Cl_2 from the sample was monitored by decrease in the chloride ion concentration. The redox potential observed in a series of solutions (see table) was the highest (+780 mV) in the sample with the concentration of chloride ions of 10^{-2} M. Just in this case the removal of nickel(II) from the sample was the most efficient (85%) upon addition of an "average" (65 mg) weighed portion of sodium ferrate. Separate series of experiments were performed to study the oxidation of Cl^- ions.

Aliquots of a 10^{-3} M NaCl solution were acidified with 1 M HNO_3 to attain the pH values from 1.5 to 4.0. Sodium ferrate Na_4FeO_5 (27–40 mg) was added in small portions to the sample; the solution pH was maintained constant by adding 0.1 M HNO_3. After complete decomposition of Fe(VI), the solution pH was brought to 5–7 by introducing crystalline Na_2CO_3. The concentration of the residual chloride ions was determined with a selective chloride electrode. Under the given experimental conditions, the maximum removal of chloride ions (about 80%) was observed at

pH ~ 2; the analysis accuracy was ±20%. These results and the data listed in the table indicate that the optimal conditions for removing Ni(II) from aqueous solutions containing EDTA are as follows: pH 1.5–2.0 and 100 mg of sodium ferrate per 50 ml. In the presence of 10^{-2} M chloride ions, the removal of Ni(II) becomes more efficient.

In aqueous solutions containing EDTA and metal ions, the degree of their complexation depends on pH. At pH 10, EDTA is completely ionized and, if $c_{Ni^{2+}} = c_{EDTA} = 1 \times 10^{-4}$ M, the NiY^{2-} complex is formed in a concentration of 1×10^{-4} M. With decreasing pH, other EDTA species are formed, namely HY^{3-}, H_2Y^{2-}, H_3Y^{-}, and H_4Y, and, as a result, NiY^{2-} decomposes partially or completely with liberation of Ni^{2+} ions. Calculations based on the stability constant of Ni(II) complex with EDTA ($K_{EDTA} = 4.2 \times 10^{18}$) and the fraction of nondissociated EDTA at a given pH [11] showed that, at pH 2 or 1.5, 22.4 or 82.5% of nickel, respectively, occurs in solution as Ni^{2+} ions. As a result, a certain fraction of nondissociated EDTA (H_4Y) is oxidized under the above optimal conditions for ferrate(VI) reduction at pH < 2. Mediators (chloride ions) promote the oxidation and the amount of ferrate ions to be added can be decreased [removal of Ni(II) is complete upon addition of 100 mg of Na_4FeO_5 per 50 ml of solution]. Addition of $Fe(NO_3)_3$ coagulant did not provide any quantitative removal of nickel(II); even when the portion of Fe(III) was greater than that of Fe(VI) by a factor of 2.5 (other conditions being equal), only 77% of Ni(II) was removed.

CONCLUSION

Complete breakdown of the $[NiEDTA]^{2-}$ complex [~5 mg Ni(II) per liter] with the subsequent removal of Ni(II) from aqueous solution is ensured by treatment of the initial solution with sodium ferrate(VI): 2 g l^{-1} at pH ~ 2. Chloride ions added to the solution decrease the required amount of sodium ferrate.

REFERENCES

1. Stoupine, D., Osmolovski, M., Lachkova, D., *et al.*, *Extended Abstracts, Int. Conf. "Advances in Environmental Engineering and Chemical Engineering,"* Guangzhou (China), October 8–11, 1997, pp. 29–32.
2. De Luca, S.J., Cantinelli, M., and De Luca, M.A., *Water Sci. Technol.*, 1992, vol. 26, nos. 9–11, pp. 2077–2080.
3. Potts, M.E. and Churchwell, D.R., *Water Environ. Res.*, 1994, vol. 66, no. 2, pp. 107–109.
4. Stupin, D.Yu. and Ozernoi, M.I., *Radiokhimiya*, 1995, vol. 37, np. 4, pp. 359–362.
5. Murmann, R.K. and Robinson, P.R., *Water Res.*, 1974, vol. 8, pp. 543–547.
6. Waite, T.D., *J. Environ. Eng. Div., ASCE*, 1979, vol. 105, no. EE6, pp. 1023–1034.
7. Lee, D.G. and Gai, H., *Can. J. Chem.*, 1993, vol. 71, pp. 1394–1400.
8. Sharma, V.K., Rivera, W., Smith, J.O., *et al.*, *Environ. Sci. Technol.*, 1998, vol. 32, no. 17, pp. 2608–2613.
9. Read, J.F., Boucher, K.D., Mehiman, S.A., *et al.*, *Inorg. Chim. Acta*, 1998, vol. 267, no. 3, pp. 159–163.
10. Kiselev, Yu.M., Kopelev, N.S., Zav'yalova, N.A., *et al.*, *Zh. Neorg. Khim.*, 1989, vol. 34, no. 9, pp. 2199–2202.
11. Skoog, D.A. and West, D.M., *Fundamentals of Analytical Chemistry*, New York: Rinehart and Winston, 1976. Translated under the title *Osnovy analiticheskoi khimii*, Moscow: Mir, 1979, vol. 1, pp. 304–306.

Russian Journal of Applied Chemistry, Vol. 77, No. 8, 2004, pp. 1316–1320. Translated from Zhurnal Prikladnoi Khimii, Vol. 77, No. 8, 2004, pp. 1331–1335.

ORGANIC SYNTHESIS AND INDUSTRIAL ORGANIC CHEMISTRY

Synthesis and Corrosion-Protective Properties of Acetylenic Esters of Bicyclo[2.2.1]hept-5-ene-2-carboxylic Acid

E. G. Mamedov

Institute of Petrochemical Processes, National Academy of Sciences of Azerbaijan, Baku, Azerbaijan

Received March 5, 2004

Abstract—A procedure was developed for preparing acetylenic esters of bicyclo[2.2.1]hept-5-ene-2-carboxylic acid. The structures of the compounds were confirmed by IR and ^{1}H NMR spectroscopy. The Kovats indices of the compounds were determined, and their boiling points were estimated by gas–liquid chromatography. The protective properties of the esters against acid corrosion of steel were studied.

Norbornene derivatives exhibit various useful properties. Thanks to their rigid framework structure, these compounds with fixed substituents are promising models for studying structure–property relationships [1]. Some norbornene derivatives exhibit analgetic, antiseptic, and antiphlogistic properties [2, 3]. Of particular interest are acetylenic esters of norbornenecarboxylic acid. On the one hand, they have valuable properties themselves; on the other hand, they are promising as synthetic precursors of diverse valuable compounds owing to the combination of reactive norbornene and acetylenic fragments [4].

The synthesis of propargyl norbornenecarboxylate by esterification of norbornenecarboxylic acid with propargyl alcohol in the presence of Brønsted acid catalysts was described in [5]. However, the yield (30%) and purity (88%) of the target product were poor.

Proceeding with studies concerned with synthesis of acetylenic esters of norbornenecarboxylic acids [6–8], we developed a convenient synthetic route to these compounds and examined their protective properties against acid corrosion of metals. The compounds were prepared by reactions of bicyclo[2.2.1]hept-5-ene-2-carboxylic acid chloride **I** with acetylenic alcohols **II**–**IV**:

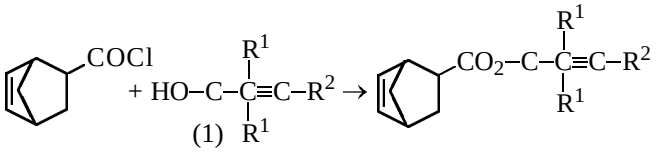

(1)

I **II**–**IV** **V**–**VII**

where $R^1 = R^2 = H$ (**II**, **V**); $R^1 = Me$, $R^2 = H$ (**III**, **VI**); $R^1 = Me$, $R^2 = CH{=}CH_2$ (**IV**, **VII**).

The reaction with primary alcohol **II** occurs at room temperature with heat liberation and is complete in 0.5 h. With tertiary alcohols **III** and **IV**, the reaction is less facile, and the corresponding esters **VI** and **VII** were obtained by heating at 80°C for 5 h. The yield of the target products was 90–96%.

The structure of esters **V**–**VII** was confirmed by independent synthesis. First, we prepared acetylenic acrylates **IX**–**XI** by a reaction of acryloyl chloride with acetylenic alcohols **II**–**IV**. This was followed by the Diels–Alder addition of cyclopentadiene **VII** to acrylates **IX**–**XI** to obtain compounds **V**–**VII**:

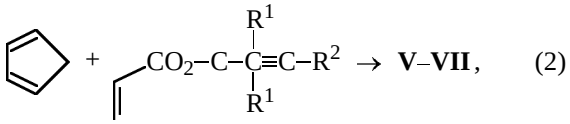

(2)

VIII **IX**–**XI**

where $R^1 = R^2 = H$ (**IX**); $R^1 = Me$, $R^2 = H$ (**X**); $R^1 = Me$, $R^2 = CH{=}CH_2$ (**XI**).

The constants of compounds **IV**–**VII** prepared by both procedures are identical; they are listed in Table 1. The compositions and structures of the compounds were also confirmed by elemental analysis and by IR (Table 1) and ^{1}H NMR spectroscopy.

The IR spectra of **V**–**VII** contain the stretching vibration bands (cm^{-1}) of C=O (1730–1740), C–O (1225–1240) and C≡C (2160–2165) groups. The band at 3290 cm^{-1} in the spectrum of **V** is characteristic of the ≡C–H bond. The stereoisomers of **V** and **VII** have similar IR spectra, with the absorption bands of the double bond in the norbornene moiety at 1580–1555 [ν(C=C)] and 730–710 [δ(=C–H)] cm^{-1}. The unusual

1070-4272/04/7708-1316 © 2004 MAIK "Nauka/Interperiodica"

Table 1. Properties of acetyenic esters **V**–**VII** of norbornenecarboxylic acid

Compound	Yield, %	bp, °C / *P*, mm Hg	n_D^{20}	d_4^{20}	Found, % / Calculated, %		Formula	IR spectrum, ν, cm^{-1}
V	96	100/5	1.4936	1.0836	74.61/75.0	6.73/6.81	$C_{11}H_{12}O_2$	1740 (C=O), 1110 (C–C), 1620 (C=C), 3290 (≡C–H)
VI	92	78/2	1.4810	1.0318	75.01/74.45	7.11/7.84	$C_{13}H_{16}O_2$	1735 (C=O), 1020 (C–C), 1620 (C=C), 2160 (C≡C)
VII	90	98/2	1.5011	1.0269	77.21/78.26	7.12/7.82	$C_{15}H_{18}O_2$	1730 (C=O), 1040 (C–C), 1615 (C=C), 2165 (C≡C)

Table 2. Retention volumes V_r, relative retention volumes V_r^{rel} (menthol as reference), Kovats indices I_K, and boiling points of compounds **V**–**VII** and reference substances

Compound	V_r^{rel}		V_r		log V_r (on Apiezon)	I_K	bp, °C
	PEGS	Apiezon	PEGS	Apiezon			
Menthol	1	1	228	446	–	–	–
exo-**V**	4.21	1.46	730	730	2.86	1128	221.3
endo-**V**	4.91	1.52	880	780	2.89	1240	223.9
exo-**VI**	4.15	1.45	440	860	2.93	1256	227
endo-**VI**	4.85	1.50	560	910	2.96	1268	229.3
exo-**VII**	5.02	2.45	810	2310	3.36	1243	257.1
endo-**VII**	6.92	2.65	1000	2500	3.40	1438	259.7
Octane	–	–	–	60	1.78	800	125
Nonane	–	–	–	99	1.99	900	157
Decane	–	–	–	168	2.23	1000	174
Undecane	–	–	–	266	2.43	1100	196
Dodecane	–	–	–	528	2.72	1200	216
Tridecane	–	–	–	888	2.95	1300	235
Tetradecane	–	–	–	1668	3.22	1400	253
Pentadecane	–	–	–	2600	3.56	1459	263.7

position of the first band may be due to the strained state of the ethylene bond in the bicyclo[2.2.1]heptene moiety [9]. The position of the δ(=C–H) band depends on the orientation of the substituent in the carbon skeleton of **V** (705–700 and 735–720 cm^{-1} for *exo* and *endo* isomers, respectively).

In the ^{1}H NMR spectra, the major differences between stereoisomeric propargyl esters of bicyclo-[2.2.1]hept-5-ene-2-carboxylic acid consist in the positions of the signals of the protons at the C^2, C^5, and C^6 atoms.

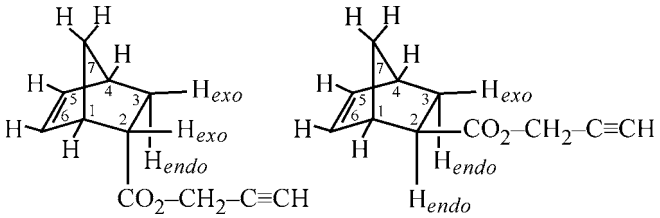

The olefinic protons (at C^5, C^6) in the *endo* isomer of **V** are nonequivalent because of the steric proximity of the substituent situated in the rear part of the bicyclic core. Therefore, these protons give relatively widely separated signals: at 6.12 (5-H) and 6.24 (6-H) ppm. The 5-H and 6-H protons in the *exo* isomer of **V**, more weakly influenced by the remote substituent, give closely situated signals. The 2-H proton in *exo*-**V** has an *endo* orientation and gives a signal at 2.97 ppm, whereas the 2-H proton in *endo*-**V** has an *exo* orientation and gives a multiplet at 2.17 ppm.

The coupling constants are as follows (Hz): *endo*-**V**, $^3J_{5,6}$ = 5.62, $^3J_{1,6}$ = 3.66, $^3J_{4,5}$ = 3.00; *exo*-**V**, $^3J_{5,6}$ = 5.60, $^3J_{1,6}$ = $^3J_{4,5}$ = 2.93.

The stereoisomers of **V** were separated by preparative gas–liquid chromatography. The isomeric composition of esters **V**–**VII** was determined by GLC anal-

Table 3. Inhibiting effect of acetylenic esters **V**–**VII** of bicyclo[2.2.1]hept-5-ene-2-carboxylic acid in HCl solutions*

Inhibitor	c_{HCl}, N	c_{inh}, mM	25°C			60°C			80°C		
			K, g m^{-2} h^{-1}	Z, %	γ	K, g m^{-2} h^{-1}	Z, %	γ	K, g m^{-2} h^{-1}	Z, %	γ
No inhibitor	1	–	1.64	–	–	94.3	–	–	474	–	–
V	1	3	0.28	82.9	5.7	2.4	97.6	39.3	14.2	36.8	33.4
	1	6	0.27	83.5	6.1	1.3	98.6	72.5	7.3	96.3	64.8
	1	12	0.36	78	4.4	1.5	98.4	63	5.2	98.8	91.2
No inhibitor	3	–	2.67	–	–	141	–	–	776	–	–
V	3	3	0.3	89.8	8.9	1.9	98.7	74.2	35.1	95.5	22.1
	3	6	0.22	91.8	12.1	0.97	99.3	145.4	21.7	97.2	35.8
	3	12	0.22	91.8	12.1	0.79	99.4	178.5	3.4	99.6	228.2
No inhibitor	5	–	8.27	–	–	287	–	–	1334	–	–
V	5	3	1.23	85.1	6.7	18.0	98.7	15.9	255	80.9	5.2
	5	6	0.67	91.9	12.4	8.4	97.1	34.2	109	91.8	12.2
	5	12	0.23	97.2	35	3.9	98.6	73.6	25	98.1	53.5
VI	1	3	0.31	80.1	4.3	2.8	94.4	34.3	13.21	34.7	31.2
	1	6	0.29	81.2	5.7	1.6	94.2	66.4	7.1	93.5	60.0
	1	12	0.28	82.9	5.9	1.4	94.1	57	4.9	95.4	81.02
	3	3	0.4	79.8	7.9	2.8	96.7	71.2	34.1	92.5	21.1
	3	6	0.3	81.9	11.1	1.42	97.3	139.4	20.7	94.2	34.8
	3	12	0.39	81.8	11.02	1.44	97.4	165.3	13.4	96.5	210.1
	5	3	1.27	83.1	5.9	1.93	97.8	165.4	25.4	78.8	51.0
	5	6	0.69	91.1	11.3	1.89	96.1	34.2	106.5	90.1	12.1
	5	12	0.39	94.2	13.3	1.97	92.2	69.6	21.7	92.1	51.5
VII	1	3	0.21	91.8	5.9	2.1	98.8	41.3	12.2	38.8	35.4
	1	6	0.20	93.8	6.3	0.94	99.5	74.5	5.3	99.3	66.8
	1	12	0.19	93.1	4.7	0.71	99.6	65	4.2	99.8	93.2
	3	3	0.27	86.2	9.1	1.4	99.8	76.2	33.1	97.5	24.1
	3	6	0.24	93.1	12.7	0.91	99.7	147.4	19.7	99.3	37.7
	3	12	0.23	96.2	12.8	0.71	99.9	180.5	2.4	81.9	7.2
	5	3	1.1	89.9	19.1	1.71	96.5	171.5	2.51	93.6	13.1
	5	6	0.57	91.3	13.1	8.2	97.2	34.2	104.5	99.8	53.5
	5	12	0.18	90.8	4.9	3.7	99.1	75.6	23	98.9	53.7
Prop-2-ynyl benzoate (reference)	3	30	1.36	87.26	7.9**	21.0	90.56	10.56**	No data		

* (K) Corrosion rate, (Z) degree of protection, and (γ) inhibition coefficient.

** Calculated from data for the reference.

ysis. It was found that the isomeric composition fully coincided with that of the starting acid chloride **I**. The fraction of the *exo* isomer in adducts **V**–**VII** is 10%.

The compounds synthesized were studied chromatographically on two stationary liquid phases: polar [5% polyethylene glycol succinate (PEGS) in Dinokhrom P] and nonpolar (5% Apiezon N on Dinokhrom P). The polar PEGS phase appeared to be the best for separation of the *endo* and *exo* isomers of **V**–**VII**. The retention parameters, Kovats indices (procedure from [10]), and boiling points (procedure from [11]) of the compounds were determined (Table 2).

Compounds **V**–**VII** were tested as inhibitors of the acid corrosion of steel. The inhibiting activity was studied in relation to the structure of the alcoholic moiety; the temperature was varied within 25–80°C; the HCl concentration was 1, 3, and 5 N; and the inhibitor concentration was 3, 6, and 12 mM. The results are listed in Table 3.

As can be seen from Table 3, all the compounds **V**–**VII** are effective inhibitors of the acid corrosion of steel. They surpass in inhibiting power the known

structurally related inhibitor, propargyl benzoate. This fact suggests that the certain contribution to the inhibiting effect of **V**–**VII** is made by the norbornene moiety, along with the acetylenic fragment.

Table 3 shows that all the three compounds **V**–**VII** show a better performance than the reference, propargyl benzoate, when added in lower concentrations (3, 6, and 12 mM, against 30 mM for the reference).

The best performance is shown by **V**. This may be due to the steric hindrance produced by two geminal methyl groups in the position adjacent to the triple bond in **VI** and **VII**.

EXPERIMENTAL

The IR spectra were recorded on a UR-20 spectrophotometer (4000 – 400 cm^{-1}, thin films or KBr pellets), and the ^1H NMR spectra, on a Tesla BS-487C spectrometer (80 MHz, CCl_4, internal references HMDS and TMS). The preparative separation was performed on a Varian-Aerograph chromatograph [900 × 0.8-cm column, 5% polyethylene glycol adipate on porous support (Porovina), vaporizer temperature 250°C, column temperature 175°C, carrier gas nitrogen (flow rate 200 $cm^3\ min^{-1}$), sample volume 100 μl, flame ionization detector]. The chromatographic analysis of the compounds, with determination of their purity, was performed on an LKhM-8MD chromatograph [thermal conductivity detector, 300 × 0.3-cm columns, 5% Apiezon or PEGS on Dinokhrom P, carrier gas helium (40 $cm^3\ min^{-1}$, column temperature 150°C, vaporizer temperature 250°C).

The compounds were tested as corrosion inhibitors in HCl solutions with 50 × 20 × 3-mm St.3 steel plates; the test time was 2 h. The HCl concentration was 1, 3, or 5 N, and the temperature was varied within 25–80°C. The corrosion rate and the degree of protection, *Z*, were determined as described in [12].

Acryloyl chloride was prepared by refluxing benzoyl chloride with acrylic acid [13] in a 2 : 1 ratio; bp 75–76°C. Bicyclo[2.2.1]hept-5-ene-2-carboxylic acid chloride **I** was prepared by condensation of acryloyl chloride with freshly distilled cyclopentadiene.

2-(Prop-2-ynyloxycarbonyl)bicyclo[2.2.1]hept-5-ene V. To a stirred solution of 5.6 g (0.1 mol) of prop-2-yn-1-ol **II** (propargyl alcohol) and 10.1 g (0.1 mol) of triethylamine in 30 ml of absolute diethyl ether, we added dropwise 15.5 g of chloride **I**. The reaction was exothermic. The precipitate of triethylammonium chloride was filtered off. The ether from the filtrate was evaporated, and the residue was distilled in a vacuum to give 20 g of **V**; bp 100°C (5 mm Hg), n_D^{20} = 1.4936, d_4^{20} = 1.0836. Published data [2]: bp 72–80°C (0.7 mm Hg).

2-(1,1-Dimethylprop-2-ynyloxycarbonyl)bicyclo-[2.2.1]hept-5-ene VI. To a stirred solution of 8.4 g (0.1 mol) of 1,1-dimethylprop-2-yn-1-ol **III** and 10.1 g (0.1 mol) of triethylamine in 30 ml of absolute benzene, we addded dropwise 15.5 g (0.1 mol) of chloride **I**. The mixture was refluxed with stirring for 5 h. The salt precipitate was filtered off, the solvent was evaporated, and the residue was distilled in a vacuum to give 18.76 g of **VI**. The physicochemical characteristics of **VI** are listed in Table 1.

2-(1,1-Dimethylpent-2-yn-4-enyloxycarbonyl)bicyclo[2.2.1]hept-5-ene VII. To a solution of 11 g (0.1 mol) of 1,1-dimethylpent-2-yn-4-en-1-ol **IV** and 10.1 g (0.1 mol) of triethylamine in 30 ml of absolute benzene, we added dropwise with stirring 15.5 g (0.1 mol) of chloride **I**. The mixture was refluxed with stirring for 5 h and worked up as described above. Yield of **VII** 20.7 g; for constants, see Table 1.

CONCLUSIONS

(1) Acetylenic esters of norbornenecarboxylic acid of high purity were prepared in good yields by reactions of primary and tertiary acetylenic alcohols with norbornenecarboxylic acid chloride in the presence of tertiary amines (pyridine, triethylamine). The primary alcohol reacts with the chloride at room temperature, whereas in the case of tertiary alcohols, elevated temperatures (80°C) and longer reaction times (5 h against 0.5 h) are required.

(2) Chromatographic procedures were developed for separation and analysis of acetylenic esters of norbornenecarboxylic acid; their Kovats indices and boiling points were determined. The esters are mainly *endo* isomers; the content of the *exo* isomer is 10%.

(3) Acetylenic esters of norbornenecarboxylic acid were tested as inhibitors of metal corrosion and showed a good protective performance.

REFERENCES

1. Tarabara, I.N., Kas'yan, A.O., Krishchik, O.V., *et al.*, *Zh. Org. Khim.*, 2002, vol. 38, no. 9, pp. 1354–1363.
2. Kas'yan, A.O., Golodaeva, E.A., Tsygankov, A.V., *et al.*, *Zh. Org. Khim.*, 2002, vol. 38, no. 11, pp. 1661–1667.
3. Kas'yan, A.O., Tarabara, I.N., Zlenko, E.T., *et al.*, *Zh. Org. Khim.*, 1999, vol. 35, no. 7, pp. 1042–1055.

4. Veliev, M.G., Chalabaeva, A.Z., Shatirova, M.I., *et al.*, *Zh. Org. Khim.*, 2003, vol. 39, no. 6, pp. 847–879.
5. US Patent 3 341 108.
6. Akhmedov, I.M., Mamedov, E.G., and Kyazimov, E.A., *Azerb. Khim. Zh.*, 1980, no. 5, pp. 51–54.
7. Mamedov, E.G., Abstracts of Papers, *III Bakinskaya mezhdunarodnaya Mamedalievskaya neftekhimicheskaya konferentsiya* (III Baku Int. Mamedaliev Petrochemical Conf.), Baku, 1998, p. 109.
8. Mamedov, E.G., *Azerb. Khim. Zh.*, 2001, no. 2, pp. 60 – 64.
9. Zefirov, N.S. and Sokolov, V.I., *Usp. Khim.*, 1967, vol. 36, no. 2, pp. 243–268.
10. Kovatsh, E., *Helv. Chim. Acta*, 1958, vol. 41, pp. 1915–1932.
11. Sakharov, V.M., Leont'eva, S.A., and Lulova, N.I., *Khim. Tekhnol. Topl. Masel*, 1967, vol. 6, no. 1, pp. 58– 60.
12. Rezenfel'd, I.L. and Zhigalova, K.A., *Uskorennye metody korrozionnykh ispytanii metallov* (Accelerated Methods for Corrosion Tests of Materials), Moscow: Metallurgiya, 1966.
13. Weygand–Hilgetag, *Organisch-Chemische Experimentierkunst*, Leipzig: Barth, 1964, 3rd ed.

Russian Journal of Applied Chemistry, Vol. 77, No. 8, 2004, pp. 1321–1324. Translated from Zhurnal Prikladnoi Khimii, Vol. 77, No. 8, 2004, pp. 1336–1339.

ORGANIC SYNTHESIS AND INDUSTRIAL ORGANIC CHEMISTRY

Reactions of Dithiocarbamic Acids Derived from Alkaloids, Morpholine, and Piperidine with Acrylic Acid and Its Derivatices

T. S. Zhivotova, A. M. Gazaliev, M. K. Ibraev, S. D. Fazylov, and R. Z. Kasenov

Institute of Organic Synthesis and Coal Chemistry of the Republic of Kazakhstan, Limited Liability Company, Karaganda, Kazakhstan

Received April 20, 2004

Abstract—β-(Thiocarbamoylthio)propionic acids derived from alkaloids, morpholine, and piperidine and their esters, amides, and nitriles were prepared by reactions of the corresponding dithiocarbamic acids with acrylic acid and its derivatives. Some of the compounds were tested for insecticidal activity.

Dithiocarbamic acids are important synthetic precursors of various antimicrobial [1], fungicidal [2], pesticidal [3], bactericidal [4], and other biologically active agents.

Dithiocarbamic acid esters containing various functional groups in the mercaptan residue can be prepared by reactions of dithiocarbamic acids with unsaturated electrophilic compounds in which the double bond is activated with electron-withdrawing substituents, such as unsaturated acids, their esters and anhydrides, unsaturated ketones, and related compounds.

Proceeding with a search for new biologically active dithiocarbamate derivative of alkaloids and their synthetic structural analogs [5], we performed reactions of dithiocarbamic acids prepared *in situ* from amines **I**–**IV** and CS_2 (with or without the base catalyst, triethylamine) with acrylic acid and its derivatives:

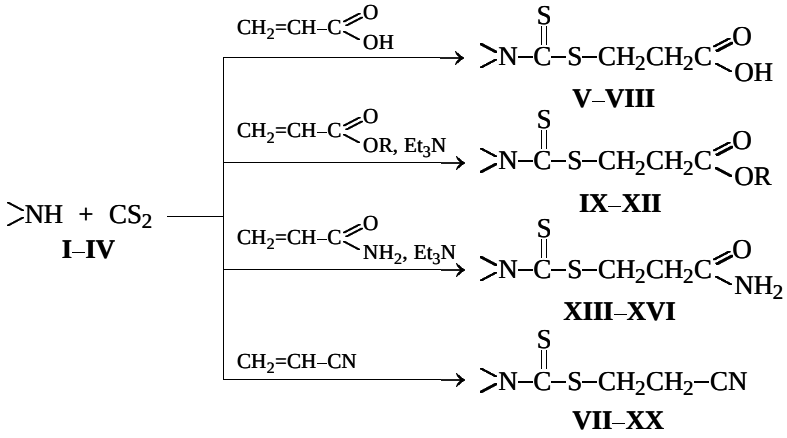

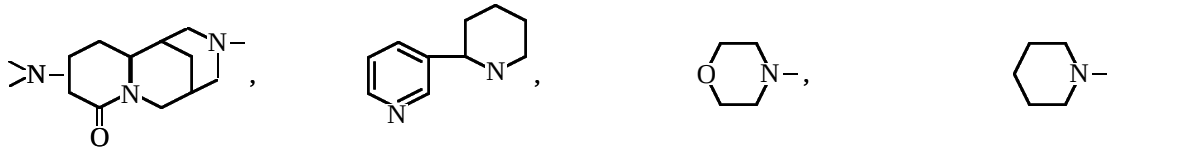

I, V, IX, XIII, XVII **II, VI, X, XIV, XVIII** **III, VII, XI, XV, XIX** **IV, VIII, XII, XVI, XX**

R = CH_3 (**a**), *i*-C_3H_7 (**b**), and C_4H_9 (**c**).

1070-4272/04/7708-1321 © 2004 MAIK "Nauka/Interperiodica"

Table 1. Yields, physicochemical constants, and elemental analyses of **V**–**VIII**

Compound	Yield, %	mp, °C	R_f^*	Found, %			Formula	Calculated, %		
				C	H	N		C	H	N
V	89	252–253	0.58	52.61	6.46	8.32	$C_{15}H_{22}N_2O_3S_2$	52.63	6.43	8.19
VI	86	Oil	0.53	54.24	5.86	9.02	$C_{14}H_{18}N_2O_2S_2$	54.19	5.81	9.03
VII	92	120–121	0.76	40.79	5.52	6.00	$C_8H_{13}NO_3S_2$	40.85	5.53	5.96
VIII	93	106-107	0.69	46.38	6.43	6.05	$C_9H_{15}NO_2S_2$	46.35	6.44	6.01

* Eluent 2-propanol–ammonia–water, 7 : 2 : 1.

Table 2. Yields, physicochemical constants, and elemental analyses of **IX**–**XII**

Compound	Yield, %	n_D^{20} (mp, °C)	R_f^*	Found, %			Formula	Calculated, %		
				C	H	N		C	H	N
IXa	70	(94–95)	0.65	53.96	6.70	7.90	$C_{16}H_{24}N_2O_3S_2$	53.93	6.74	7.87
IXb	65	1.5359	0.58	55.59	6.21	8.68	$C_{15}H_{20}N_2O_2S_2$	55.55	6.17	8.64
IXc	73	(59–60)	0.71	43.41	6.00	5.59	$C_9H_{15}NO_3S_2$	43.37	6.02	5.62
Xa	77	1.5468	0.69	48.55	7.03	5.71	$C_{10}H_{17}NO_2S_2$	48.58	6.88	5.67
Xb	66	1.5518	0.62	56.22	7.32	7.27	$C_{18}H_{28}N_2O_3S_2$	56.25	7.29	7.29
Xc	61	1.5423	0.61	57.97	6.87	7.93	$C_{17}H_{24}N_2O_2S_2$	57.95	6.82	7.95
XIa	70	1.5585	0.75	47.70	6.83	5.01	$C_{11}H_{19}NO_3S_2$	47.65	6.86	5.05
XIb	68	1.5510	0.66	52.38	7.62	6.01	$C_{12}H_{21}NO_2S_2$	52.36	7.64	5.09
XIc	63	1.5138	0.49	57.30	7.56	7.01	$C_{19}H_{30}N_2O_3S_2$	57.29	7.54	7.04
XIIa	57	1.5265	0.36	59.03	7.13	7.68	$C_{18}H_{26}N_2O_2S_2$	59.02	7.10	7.65
XIIb	71	1.5172	0.60	51.54	6.96	4.66	$C_{13}H_{21}NO_3S_2$	51.49	6.93	4.62
XIIc	74	1.5157	0.55	54.14	7.68	4.90	$C_{13}H_{22}NO_2S_2$	54.17	7.64	4.86

* Eluent benzene–acetone, 1 : 1.

In view of the high physiological activity of dithiocarbamates and alkaloids, it seemed interesting to combine, in a single molecule, alkaloid and dithiocarbamate fragments and to study the biological properties of such compounds.

Acrylic acid contains a double bond conjugated with the carboxy group. The withdrawing effect of the carbonyl oxygen on the π electrons of the double bond facilitates its attack by nucleophilic agents. Therefore, dithiocarbamic acids react with acrylic acid under mild conditions to form the corresponding β-[alkaloido(amino)thiocarbonylthio]propionic acids **V**–**VIII** in high yields, 86–93% (Table 1).

The alkyl groups in alkyl acrylate exhibit a positive inductive effect and noticeably decrease the conjugation between the carbonyl oxygen atom and C=C bond of the acrylate; as a result, the rate of reaction of dithiocarbamic acids with alkyl acrylates somewhat decreases. Compounds **I**–**IV** react with alkyl acrylates under more severe conditions, in the presence of triethylamine, apparently via formation of an ammonium salt. The length of the carbon chain and the degree of substitution of the α-C atom in the alcoholic residue exert no significant effect on the yield of β-[alkaloido(amino)thiocarbonylthio]propionic acid esters **IX**–**XII**. The yield of esters **IX**–**XII** derived from methyl (**a**), isopropyl (**b**) and butyl (**c**) acrylates ranges from 57 to 77% (Table 2).

The reaction with acrylamide also occurs in the presence of triethylamine; the yields of β-[alkaloido(amino)thiocarbonylthio]propionic acid amides **XIII**–**XVI** range from 74 to 91% (Table 3). In the absence of triethylamine, the reaction takes somewhat more time and requires heating; the yield of amides **XIII**–**XVI** appreciably decreases. This may be caused by thermal instability of dithiocarbamates and by consumption of the amine or alkaloid as a base for the salt formation. The product of direct

Table 3. Yields, physicochemical constants, and elemental analyses of **XIII**–**XVI**

Compound	Yield, %	mp, °C	R_f^*	Found, %			Formula	Calculated, %		
				C	H	N		C	H	N
XIII	87	148–150	0.50	52.81	6.70	12.38	$C_{15}H_{23}N_3O_2S_2$	52.79	6.74	12.32
XIV	74	115–116	0.43	54.34	6.19	13.55	$C_{14}H_{19}N_3OS_2$	54.37	6.15	13.59
XV	91	140–141	0.51	40.06	6.02	12.01	$C_8H_{14}N_2O_2S_2$	41.03	5.98	11.97
XVI	78	106–107	0.54	46.51	6.87	12.11	$C_9H_{16}N_2OS_2$	46.55	6.90	12.07

* Eluent benzene–acetone, 1 : 1.

Table 4. Yields, physicochemical constants, and elemental analyses of **XVII**–**XX**

Compound	Yield, %	mp, °C	R_f^*	Found, %			Formula	Calculated, %		
				C	H	N		C	H	N
XVII	85	41–42	0.79	55.77	6.46	13.02	$C_{15}H_{21}N_3OS_2$	55.73	6.50	13.00
XVIII	79	Oil	0.78	57.70	5.88	14.48	$C_{14}H_{17}N_3S_2$	57.73	5.84	14.43
XIX	87	88–89	0.81	44.40	5.52	13.01	$C_8H_{12}N_2OS_2$	44.44	5.56	12.96
XX	90	78–79	0.75	50.50	6.58	13.12	$C_9H_{14}N_2S_2$	50.47	6.54	13.08

* Eluent benzene–acetone, 1 : 1.

addition of the amine to acrylamide is formed as a by-product.

The reactivity of acrylonitrile toward **I**–**IV** is similar to the reactivity of acrylic acid, which is due to the high electron-withdrawing power of the nitrile group, facilitating nucleophilic attack of the C=C bond by the carbamate anion. The reactions of *in situ* prepared diethyldithiocarbamic acids with acrylonitrile are performed with a small excess of CS_2; β-[alkaloido(amino)thiocarbonylthio]propionitriles **XVII**–**XX** are obtained in high yields, 78–91% (Table 4).

The nucleophilic addition of the dithiocarbamates to acrylic acid and its derivatives occurs against the Markownikoff rule [scheme (1)].

β-[Alkaloido(amino)thiocarbonylthio]propionic acids **V**–**VIII** are crystalline substances insoluble in organic solvents, but readily soluble in alkalis with the formation of the corresponding salts. Esters **IX**–**XII**, amides **XIII**–**XVI**, and nitriles **XVII**–**XX** were isolated as crystalline substances or light yellow oils, soluble in the majority of organic solvents.

Some of compounds **V**–**XX** and alkali metal salts of **V**–**VIII** were tested for insecticidal activity with respect to *Lepidosaphes ulmi* (Diaspididae family), *Capitophorus ribis* (Aphididae family), and *Abrahas grossulariata* (Geometridae family). The insecticidal activity was compared to that of a reference agent, Sumi-alpha (Sumito Chemical Co., Ltd, Japan).

We found that salts of **V** and **VIII**, sodium β-[cytisinothiocarbonylthio]propionate and potassium β-[cytisinothiocarbonylthio]propionate, exhibit pronounced insecticidal activity with respect to all of the examined pests, exceeding that of Sumi-alpha by a factor of 1.5–2.

The results were confirmed by the results of biological tests; compounds **V** and **VIII** were recommended for further comprehensive studies with the aim to assess the possibility of their use in agriculture as pesticides.

EXPERIMENTAL

The compositions and structures of the compounds were confirmed by elemental analysis and IR spectroscopy.

The IR spectra were recorded on a UR-20 spectrometer (KBr pellets, mulls in mineral oil, or solutions in $CHCl_3$ and CCl_4).

β-(Cytisinothiocarbonylthio)propionic acid V. A solution of 1.90 g (0.01 mol) of cytisine in ethanol was added to a solution of 0.76 g (0.01 mol) of CS_2 and 0.72 g (0.01 mol) of acrylic acid in ethanol.

The mixture was stirred for 5–6 h. After the removal of the solvent, a white precipitate formed. Recrystallization from alcohol gave 3.04 g (89.0%) of **V**, mp 252–253°C. IR spectrum, ν, cm^{-1}: 700–600 (C–S), 1500–1470 (N–C=S), 1320–1210 (COOH).

Found, %: C 52.61, H 6.46, N 8.32.

$C_{15}H_{22}N_2O_3S_2$.

Calculated, %: C 52.63, H 6.43, N 8.19.

Compounds **VI**–**VIII** were prepared similarly.

Methyl β-(cytisinothiocarbonylthio)propionate IXa. A solution of 1.90 g (0.01 mol) of cytisine and 1.01 g (0.01 mol) of triethylamine in ethanol was slowly added dropwise with stirring to a solution of 0.86 g (0.01 mol) of methyl acrylate and 0.76 g (0.01 mol) of CS_2 in ethanol. The mixture was heated for 1 h at 60–70°C. After the removal of the solvent, a white precipitate formed. Its recrystallization from alcohol gave 2.5 g (70.0%) of **IXa**, mp 94–95°C. IR spectrum, ν, cm^{-1}: 700–610 (C–S), 1500–1470 (N–C=S), 1410–1300 (COO^-).

Found, %: C 53.96, H 6.70, N 7.90.

$C_{16}H_{24}N_2O_3S_2$.

Calculated, %: C 53.93, H 6.74, N 7.87.

Compounds **Xa**–**XIIa**, **IXb**–**XIIb**, and **IXc**–**XIIc** were prepared similarly.

β-(Cytisinothiocarbonylthio)propionamide XIII. A solution of 1.9 g (0.01 mol) of cytisine and 1.01 g (0.01 mol) of triethylamine in ethanol was slowly added dropwise with stirring to a solution of 0.71 g (0.01 mol) of acrylamide and 0.76 g (0.01 mol) of CS_2 in absolute ethanol. The mixture was heated for 4–5 h. After the removal of the solvent, a white precipitate formed. Its recrystallization from alcohol gave 2.9 g (87.0%) of **XIII**, mp 148–150°C. IR spectrum, ν, cm^{-1}: 710–610 (C–S), 1520–1480 (N–C=S), 1140–1070 ($CONH_2$).

Found, %: C 52.81, H 6.70, N 12.38.

$C_{15}H_{23}N_3O_2S_2$.

Calculated, %: C 52.79, H 6.74, N 12.32.

Compounds **XIV**–**XVI** were prepared similarly.

β-(Cytisinothiocarbonylthio)propionitrile XVII. A solution of 1.9 g (0.01 mol) of cytisine in ethanol was slowly added dropwise to a solution of 0.53 g (0.01 mol) of acrylonitrile and 1.14 g (0.015 mol) of CS_2 in ethanol. The mixture was stirred at 40–50°C for 2–3 h. After the removal of the solvent, a light yellow oil crystallizing on storage was obtained. Its recrystallization from alcohol gave 2.75 g (85.0%) of **XVII**, mp 41–42°C. IR spectrum, ν, cm^{-1}: 700–610 (C–S), 1510–1460 (N–C=S), 2260–2240 (C≡N).

Found, %: C 55.77, H 6.46, N 13.02.

$C_{15}H_{21}N_3OS_2$.

Calculated, %: C 55.73, H 6.50, N 13.00.

Compounds **XVIII**–**XX** were prepared similarly.

CONCLUSIONS

(1) β-[Alkaloido(amino)thiocarbonylthio]propionic acids and their esters, amides, and nitriles were prepared by reactions of dithiocarbamic acids derived from alkaloids, morpholine, and piperidine with acrylic acid and its derivatives.

(2) Alkali metal β-(aminothiocarbonylthio)propionates derived from cytisine and piperidine exhibit a pronounced insecticidal activity.

REFERENCES

1. Desai, N.C., *Indian J. Chem.*, 1993, vol. 32, no. 3, pp. 343–346.
2. Gazaliev, A.M., Zhurinov, M.Zh., and Fazylov, S.D., *Novye bioaktivnye proizvodnye alkaloidov* (New Biologically Active Alkaloid Derivatives), Almaty: Gylym, 1992.
3. Mel'nikov, N.N., Volkov, A.I., and Korotkova, O.A., *Pestitsidy i okruzhayushchaya sreda* (Pesticides and the Environment), Moscow: Khimiya, 1977.
4. Dolin, P.J., Raviglione, M.C., and Kochi, A., *Bull. World Health Organ.*, 1994, vol. 72, pp. 213–220.
5. Fazylov, S.D., Gazaliev, A.M., Kudaibergenova, S., *et al., Zh. Obshch. Khim.*, 2002, vol. 72, no. 2, p. 349.

Russian Journal of Applied Chemistry, Vol. 77, No. 8, 2004, pp. 1325–1330. Translated from Zhurnal Prikladnoi Khimii, Vol. 77, No. 8, 2004, pp. 1340–1345.

ORGANIC SYNTHESIS AND INDUSTRIAL ORGANIC CHEMISTRY

Spectral-Luminescent and Generation Properties of Rhodamine Dyes in Thin Polymer Films under Optical Excitation

V. A. Vaitulevich, N. S. Eremina, T. N. Kopylova, G. M. Mokrousov, L. G. Samsonova, and V. A. Svetlichnyi

Tomsk State University, Tomsk, Russia

Siberian Physicotechnical Institute, Tomsk State University, Tomsk, Russia

Received March 1, 2004

Abstract—A study was made of the absorption, fluorescence, and emission spectra of organic dyes Rhodamine 6Zh and Rhodamine C in thin (0.6–1.0 μm) layers based on methyl methacrylate–methacrylic acid copolymers formed by centrifugation on optically transparent glasses. The influence of a terbium salt on the properties of laser dyes in acrylic films was elucidated.

Xanthene dyes rhodamine 6Zh (R6Zh) and rhodamine C (RC), classic representatives of laser dyes, have unique optical properties and find wide application as laser-active substances operating in liquid and solid polymer solutions. The spectral-luminescent properties of these dyes in liquid media and, in particular, in methyl methacrylate (MMA), and in a solid medium based on poly(methyl methacrylate) and a copolymer of MMA with methacrylic acid (MAA) were studied in [1, 2]. Solid solutions of dyes in polymer matrices are mainly prepared by bulk radical polymerization of solutions of dyes in a monomer in the presence of initiator in special molds. At the same time, the preparation of such solutions as thin polymer films and, especially, the energy transformations by rhodamine dyes in them are little studied, despite great scientific and technical importance of these processes.

In this study, we examined the spectral-luminescent properties (absorption and fluorescence spectra) of rhodamine dyes (R6Zh and RC), as influenced by their chemical structure in thin polymer layers based on MMA–MAA copolymers under optical excitation. We determined the generation power of the dyes and their photostability in polymer films. Also, we studied how the characteristics of rhodamines in acrylic films are influenced by addition of terbium trifluoroacetate and analyzed theoretically the processes occurring in the polymer–dye–salt system.

EXPERIMENTAL

Xanthene dyes R6Zh and RC exhibit luminescent properties and, thus, are promising for application in luminescent devices. The chemical structure of rhodamines can be varied within one structural type of the dyes, which makes them suitable for studies of the photoluminescent properties of dyed polymers. The substances studied in the form of films have the following structural formulas:

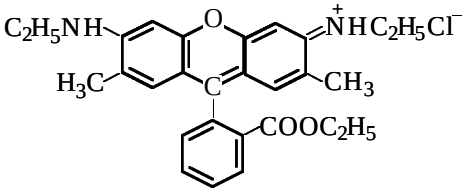

R6Zh

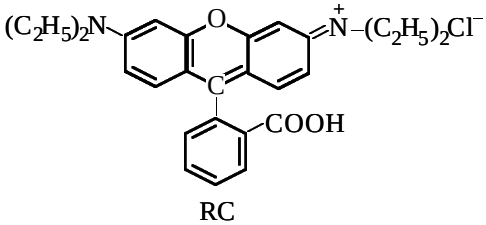

RC

As polymer base we used commercial solutions of MMA–MAA copolymers in organic solvents, known as electronic resists ELP-9 and ERP-40. The content

1070-4272/04/7708-1325 © 2004 MAIK "Nauka/Interperiodica"

Table 1. Spectral properties of R6Zh and RC dyes in films based on ELP-9 resist (Tb(III) salt concentration 2.5×10^{-2} M)

Dye	Tb(III) salt	ν_{ads}, cm^{-1}	D_{max}	γ_{fl}, nm	Film thickness, μm	ε, $l\ cm^{-1}\ mol^{-1}$
R6Zh:						
thin film	–	18700	0.18	554	0.55	6.5×10^5
	Tb(III)	18800	0.28	564	0.64	8.7×10^5
thick film	–	18700	0.26	554	0.82	6.3×10^5
	Tb(III)	18850	0.46	564	1.0	9.2×10^5
RC:						
thin film	–	18000	0.019	567	–	
	Tb(III)	18000	0.085	593	–	
thick film	–	18000	0.065	567	–	
	Tb(III)	18000	0.32	593	–	

of carboxy groups in the copolymers and their structural features were determined by IR spectroscopy. The films for IR-spectroscopic studies were prepared by applying a polymer solution onto transparent KBr plates. The IR spectra were recorded on a Specord M80 spectrophotometer at 4000–400 cm^{-1}. The spectra were interpreted using the reference data from [3–5]. The modifying additives were introduced into the resists by homogeneous dissolution. The content of the dyes in the initial solutions was 1×10^{-3} M. In parallel, we studied solutions of the xanthene dyes in the resists with terbium(III) trifluoroacetate (TFA-Tb) added in the amount of 2.5×10^{-2} M. A more complete dissolution of the modifying additives was achieved via stirring on a WU-4 vibrating mixer and ultrasonic treatment. Mechanical inclusions were removed from the solutions by filtration through a polyamide filter with a pore diameter of 0.5 μm. The polymer films were formed by centrifugation (at 2500–3000 rpm) on preliminarily degreased substrates made of an optically transparent glass, with diameters of 20 and 35 mm. After application, the films were dried for 30 min at 165 ± 5°C. The thickness of the films, mostly under 1 μm, was determined with an MII-4 interference microscope. To measure the film thickness more precisely (to improve the reflection), a 0.1-μm aluminum layer was deposited on their surface in a UVN-71P3 vacuum sputtering setup. To prepare thicker (≥1 μm) films, we increased the viscosity of the initial solutions by evaporating the solvents at room temperature. Next, we studied the spectral-luminescent characteristics, generation properties, and photostability of the resulting samples. The electronic spectra were recorded on a Specord M40 (200–900 nm) spectrophotometer. The luminescent properties were studied on an upgraded KSVU-23 spectral complex and on a Hitachi 850 spectrofluorimeter. Laser-induced fluorescence excited by $XeCl^-$ or YAG–Nd^{3+} lasers was recorded by a Real spectrometer.

The generation powers of the rhodamines in films were studied in a transverse excitation scheme. Laser radiation was focused into a 18 × 0.8 mm band, at which the radiation intensity was about 30 MW cm^{-2}. The induced radiation was formed without an external resonator.

The generation photostability $P_{0.5}$ was estimated as the number of excitation pulses upon which the generation efficiency decreased by half due to degradation of the dye.

The molecular photostability of the dyes was studied by irradiating the films with unfocused radiation from a YAG–Nd^{3+} laser (532 nm). The quantum yield of degradation was determined by the formula $\gamma = N_{phot}/N_{abs}$, where N_{phot} is the number of the molecules that underwent phototransformations in the irradiation zone, and N_{abs}, the number of the photons absorbed. We estimated N_{phot} spectrophotometrically, from the variation of the optical density at the absorption band maximum during irradiation.

We found that the compositions with dye additives exhibited good film-forming power and adhesion to the substrate surface. The films based on these compositions have no defects and are equal in thickness, except at the substrate edge, where a thicker polymer layer (compaction) was formed. The initial polymer compositions without modifiers had a high light transmission (up to 97%) at wavelengths over 280–300 nm. Upon introduction of the dyes into the polymer formulations, the corresponding absorption bands appeared in the electronic absorption spectra. In the spectra of the rhodamines in the MMA–MAA copolymer, the absorption peak is observed at the same wavelength as in solutions in MMA, this peak being almost identical in position to that of the dyes in ethanol. Table 1 presents the spectral properties of the dyes studied. The optical density D_{max} of R6Zh is

Table 2. Generation power of R6Zh and RC dyes in films based on ELP-9 resist (dye concentration 1×10^{-3}, and Tb(III) salt concentration, 2.5×10^{-2} M)

Dye	Tb(III) salt	D_{max}	λ_{gen}, nm	Efficiency, %	$P_{0.5}$, pulses
R6Zh:					
thin film	–	0.18	574 (532)*	10 (532)	2060 (532)
					60 (308)
	Tb(III)	0.28	589 (532)	17 (532)	2020 (532)
					190 (308)
thick film	–	0.26	574 (532)	15 (532)	<1 (308)
				2050 (532)	60 (308)
	Tb(III)	0.46	589 (532)	13 (532)	2000 (532)
				<1 (308)	120 (308)
RC:					
thin film	–	0.019	No generation		
	Tb(III)	0.085			
thick film	–	0.065			
	Tb(III)	0.32	595 (308)	22 (532)	15 (308)
					5000 (532)

* (532) and (308) mean that these data were obtained under pumping with YAG–Nd^{3+} and $XeCl^{-}$ lasers, respectively.

several times that of RC in identically prepared films, while the molar extinction coefficients ε of these dyes in ethanol are close (~10^5 l cm^{-1} mol^{-1}). When calculating the molar extinction of the rhodamines in films, we assumed that the content of the dye after removal of the solvent in the course of drying increased to 5×10^{-3} M.

Introduction of a terbium(III) salt into the initial compositions increases the absorption band intensities of the dyes in films by 30–45% (Table 1). The spectral properties of the rhodamines are intensified due to an increase in polarity of the polymer solutions upon introduction of trifluoroacetate and terbium ions and to the reaction of the dye molecules with the metal salt. In the case of RC, stronger bonds (hydrogen, donor–acceptor) can be formed via the carboxy groups occurring in its structure. The strengthening of the cohesion forces in the polymeric medium upon introduction of a terbium salt is also suggested by the measured thicknesses of the films of various compositions. The films with TFA-Tb are, on the average, 15–20% thicker than those without the Tb(III) salt. In the case of R6Zh, the thin and thick films differed in thickness (as estimated from the optical densities and measured microscopically) by 40–50%, and those in the case of RC, by 300–400% (as estimated from the optical densities).

The luminescence spectra of the dyed films contained one band; the contour of the fluorescence curve was the mirror image of that of the absorption band. In the presence of the Tb(III) ions, the luminescence intensity of the rhodamines substantially increases due to a rise in the intensity of the absorption bands. The fluorescence spectra of the rhodamine dyes in methacrylic films and in ethanolic solutions are virtually identical, probably due to the influence of polar (carboxy) groups of the polymer chain. The luminescence intensity of R6Zh in methacrylic films is 6–9 times that of RC, which is also due to a higher optical density of R6Zh in films (Table 1).

The generation properties of the xanthene dyes in films are presented in Table 2. In the case of R6Zh, lasing was observed in all the samples studied, excited both by $XeCl^{-}$ and YAG–Nd^{3+} lasers. Under excitation at λ = 308 nm, generation is recorded spectrally; the generation energy is small; the efficiency is under 1%. Under excitation at 532 nm, the efficiency is 10–17%. Lasing develops in the long-wave branch of the fluorescence band (Fig. 1a). The emission band is separated by ca. 20 nm from the fluorescence band maximum. Such a large shift is due to the loss caused by the reabsorption of emitted light by the dye. Notably, the generation photostability $P_{0.5}$ of R6Zh in film is fairly high. At the pumping power density of ca. 30 MW cm^{-2} for the YAG–Nd^{3+} laser, the working life of the active medium is about 2000 pulses. Terbium(III) salt noticeably affects the photostability of the active medium, predominantly under UV irradiation. Table 2 shows that the working life $P_{0.5}$ remained virtually unchanged upon introduction of

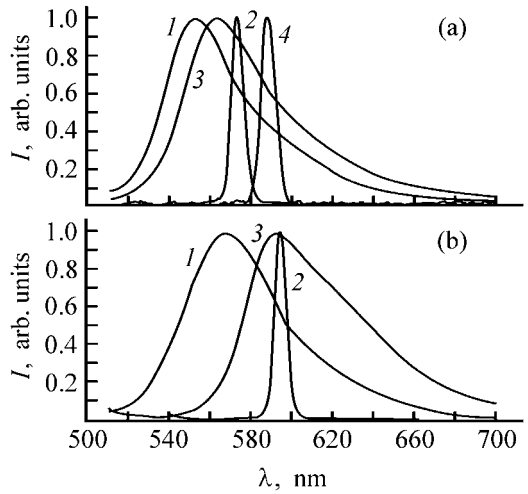

Fig. 1. Emission spectra of (a) R6Zh and (b) RC in films (*1*, *2*) with and (*3*, *4*) without Tb(III). (*I*) Intensity and (λ) wavelength.

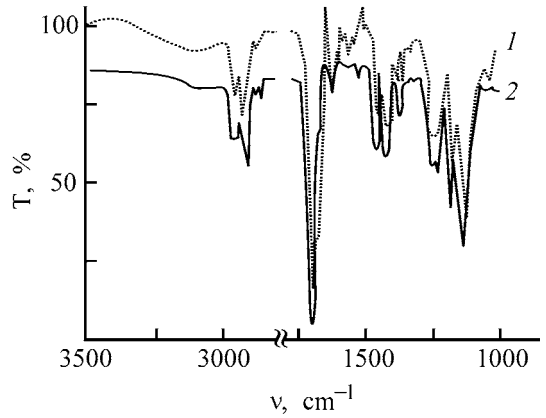

Fig. 2. IR spectra of the films based on (*1*) ERP-40 and (*2*) ELP-9 resists. (T) Transmission and (ν) wave number.

a Tb(III) salt under excitation at λ = 532 nm and increased 2–3-fold under excitation at λ = 308 nm.

In the case of RC, generation was observed only in one sample whose optical density was 0.32 in the absorption band maximum under pumping with both $XeCl^-$ and YAG–Nd^{3+} lasers (Fig. 2). Under excitation at λ = 308 nm, the generation efficiency was low, while under pumping at λ = 532 nm, the generation efficiency for this sample was 22%, and the working life, over 5000 pulses. In the case of other samples with thinner films, no generation developed because of the very low optical density, which was probably due to chemical binding of the dye to the polymer molecules via carboxy groups in the course of drying of the samples:

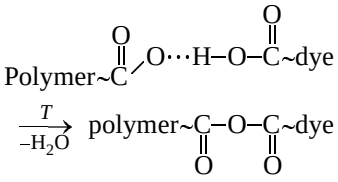

As is known, the generation efficiency of RC chemically bound to the polymer is lower that of the dye in a free state [6]. Upon dissolution of the dye and the metal salt in the copolymer, the modifier competes with the dye for formation with the MAA molecules of hydrogen or other, e.g., donor–acceptor, bonds, and these compositions exhibit in thick layers generation of RC unbound with the polymer.

We estimated the molecular photostability of the rhodamine molecules in films, γ, at ca. 10^{-6} and 5×10^{-6} for R6Zh and RC, respectively. These data agree with those for ethanolic solutions of the dyes under excitation at λ = 532 nm. Thus, the photostability of the rhodamines in films is not poorer than that in solutions.

In the presence of the ions of rare-earth elements in the films, the effect exerted on the luminescence intensity by external factors, namely, light, UV radiation, moisture, and low temperature, was significantly weaker. The samples were irradiated with the full spectrum of a DRL-400 mercury lamp for 120 h, kept for 30 days in the light, in a moisture chamber (relative humidity 95%), and in a freezing chamber (–15°C). As a criterion of resistance to radiation, light, and moisture, we took the relative change in the luminescence intensity $I_{rel} = (I_0 - I_t)/I_0 \times 100\%$ after exposure (Table 1).

Table 3. Influence of various factors on the luminescence intensity of R6Zh and RC in acrylic films

Film composition	I_{rel}, %, after effect of			
	UV radiation	light	moisture	temperature
ELP-9 + RC	49	61	34	30
ELP-9 + RC + TFA-Tb	28	36	18	13
ELP-9 + R6Zh	27	48	23	17
ELP-9 + R6Zh + TFA-Tb	14	22	9	2

Table 3 shows that the terbium salt noticeably improves the resistance of the dyes to all the external factors. The fact that the Tb(III) salt containing active groups enhances the resistance of the dye to irradiation and illumination is, evidently, due to formation of intermolecular bonds (hydrogen, van der Waals, etc.)

with polymer macromolecules, yielding a three-dimensional network in the polymer. Dyes are known to exhibit enhanced photostability in a more photostable (modified) matrix characterized by a smaller number of macrochain breaks [7]. Also, metal ions in the system can diminish the concentration of free radicals forming in the polymer during irradiation (illumination). This decreases the probability of reactions between the radicals and the dye molecules, which are accompanied by photoinduced degradation of the dye. The decelerating effect of terbium(III) ions on the degradation of a dye molecule may also be due to deactivation of the excited states via increasing dye–cation coordination. The moisture-protecting action of terbium trifluoroacetate is evidently due to the presence of highly active centers (metal cation, fluoride ions, carbonyl oxygen) able to form fairly strong bonds with water molecules, thus preventing the diffusion of water molecules deep inside the polymer film. The intermolecular attraction due to forces of varied nature in the polymer–dye–salt system can exert another favorable effect, namely, prevent the diffusion of the dye dissolved in the polymer and, in particular, the transfer of dye molecules into the environment (the so-called exudation).

A change from the ELP-9 to ERP-40 polymer matrix does not significantly affect the position of the absorption and fluorescence bands, but their intensities in the case of EPR-40 are 1.5–2 times lower than those in the case of ELP-9, whatever the composition. This can be due to the high content of carboxy groups in ERP-40, which interact with reactive groups in R6Zh and RC molecules during film preparation, thus deteriorating the spectral-luminescent characteristics of the dyes. The content of the carboxy groups in the polymers was estimated from the optical density ratio of the absorption band at 3400–3100 cm^{-1}, I_1, corresponding to stretching vibrations of OH groups, to that near 1300–1100 cm^{-1}, I_0, which are characteristic of the 3CO–O– acrylate moiety. In the IR spectra of the films with ERP-40, the intensity of the bands near 3400–3100 cm^{-1} is more than 2 times that of the films with ELP-9 (Fig. 2). The optical density was estimated by plotting the baseline [8]. As the I_1/I_0 ratio served the ratio of the areas confined in the IR spectrum by the baseline and the corresponding absorption band. A larger content of methacrylic acid in the case of the films with ERP-40 is also evidenced by a broader, compared to ELP-9, absorption band with a fine structure at 1730 cm^{-1}, corresponding to vibrations of the C=O group.

The higher content of carboxy groups in the case of the films with ERP-40 is also evidenced by lithographic data, namely, by the fact that the exposure time in which elements with identical size can be formed in the polymer films of equal thickness is 10–15 s longer in the case of the films with ERP-40 compared to those based on ELP-9. This can be caused by a denser three-dimensional network in the film with ERP-40 due to formation of hydrogen bonds between the COOH groups, whose cleavage requires more energy. The lithographic studies employed the procedure described in [9].

CONCLUSIONS

(1) The feasibility of preparing thin luminescent layers of organic molecules (film thickness $\leq 1\mu m$) was demonstrated.

(2) The absorption and emission intensity of the xanthene dyes in films can be raised by introducing a terbium(III) salt into copolymers: In the case of R6Zh, the absorption band intensity increases by 30–40%, and in the case of RC, the increment is an order of magnitude larger. The luminescence intensity of R6Zh in the films increases 6–9-fold. This is accompanied by an increase in the resistance of the material to aggressive external factors, namely, moisture, temperature, and UV radiation.

(3) The molecular photostability of the xanthene dyes in films is comparable with that in ethanolic solutions.

(4) Generation of laser radiation in the xanthene dyes in films under excitation with an YAG–Nd^{3+} laser is efficient (up to 22%) and photostable (working life up to 5000 pulses), which makes the materials prepared suitable for creation of microlasers.

ACKNOWLEDGMENTS

This study was financially supported by the Russian Foundation for Basic Research (RFFI-inno, project no. 02-02-08104).

REFERENCES

1. Vaitulevich, E.A., *Cand. Sci. Dissertation*, Tomsk, 2003.
2. Serova, V.N., Shmakova, O.P., Chirkov, V.V., *et al.*, *Vysokomol. Soedin., Ser. A*, 1999, vol. 41, no. 6, pp. 970–976.

3. Kuptsov, A.Kh. and Zhizhin, G.N., *Fur'e spektry kombinatsionnogo rasseyaniya i infrakrasnogo pogloshcheniya polimerov: Spravochnik* (Fourier Raman and Infrared Absorption Spectra of Polymers: Reference Book), Moscow: Fizmatlit, 2001.
4. Haslam, J. and Wills, H.A., *Identification and Analysis of Plastics*, London: Iliffe, 1965.
5. Poluektov, N.S. and Kononenko, L.I., *Spektrofotometricheskie metody opredeleniya individual'nykh redkozemel'nykh elementov* (Spectrophotometric Methods of Determination of Individual Rare-Earth Elements), Kiev: Khimiya, 1968.
6. Alekseev, N.N., Gorelenko, A.Ya., Kalosha, I.I., and Serova, V.N., *Zh. Prikl. Spektrosk.*, 1988, vol. 49, no. 6, pp. 912–915.
7. Serova, V.N., Vasil'ev, A.A., Cherkasova, O.A., *et al.*, *Opt. Atmosf. Okeana*, 1993, vol. 6, no. 3, pp. 269–273.
8. Dechant, J., Danz, R., and Kimmer, W., *Ultrarotspektroskopieshe Untersuchungen an Polymeren*, Berlin: Akademie, 1972.
9. Eremina, N.S., Mokrousov, G.M., Deniskina, O.I., and Gavrilenko, N.A., *Zh. Prikl. Khim.*, 1995, vol. 68, no. 3, pp. 520–522.

Russian Journal of Applied Chemistry, Vol. 77, No. 8, 2004, pp. 1331–1335. Translated from Zhurnal Prikladnoi Khimii, Vol. 77, No. 8, 2004, pp. 1346–1350.

ORGANIC SYNTHESIS AND INDUSTRIAL ORGANIC CHEMISTRY

Determination of the Deuterium Content in Organic Compounds by Gas Chromatography

A. M. Egorov, S. A. Matyukhova, I. S. Demidova, V. V. Platonov, and V. A. Proskuryakov

Tula State University, Tula, Russia
Lomonosov State University, Moscow, Russia
Leo Tolstoy State Pedagogical University, Tula, Russia
St. Petersburg State Technological Institute, St. Petersburg, Russia

Received December 4, 2003; in final form, April 2004

Abstract—A gas-chromatographic method was developed for determining deuterium in organic compounds at its atomic fraction of 1 to 99%. The accuracy of the method is 0.1–0.5%.

Deuterium-labeled organic compounds are widely used in various branches of science and technology [1, 2]. As a rule, the isotopic composition of hydrogen in such compounds is determined by ^{1}H NMR spectroscopy [1] and mass spectrometry [2, 3]. The choice of the analytical method depends on the structure and properties of a compound to be studied. The cheapest and the most versatile is the method for determining the isotope composition of hydrogen directly in organic compounds using commercial class-II mass spectrometers [2]. The method involves solution of a system of 2m equations with $m + 1$ unknowns, taking into account the probability of formation of all the possible molecular fragments. The method can be used for proximate analysis of the isotopic composition of hydrogen in simple organic compounds, e.g., in deuteroacetone. The atomic fraction of deuterium is determined in the range 1–99% with an accuracy of 0.2–3%. With compounds exhibiting a complex fragmentation pattern under electron impact, it is necessary to take into account various empirical factors and to use a computer, which considerably complicates the analysis and impairs its accuracy [2].

We developed a procedure for determining the isotope composition of hydrogen in organic compounds of various classes, using elemental analysis on standard equipment. The accuracy of determination of the deuterium atomic fraction is 0.1–0.5%.

The elemental analysis of deuterated organic compounds was performed on a Carlo Erba 1100 gas-chromatographic elemental analyzer as follows. The organic compound being analyzed was subjected to oxidative pyrolysis. After separation of water and its deuterium analogues, a mixture of gaseous N_2 and CO_2 was analyzed by chromatography, and desorbed water containing the deuterium label was converted to a mixture of H_2, HD, and D_2; its composition was determined by gas-adsorption chromatography. The oxidative pyrolysis was performed in the C,H,N channel of the device by the standard procedure at 1050°C. The charge of the combustion reactor, recommended by the producer, was changed: Over a bed of CuO wire (10 cm), we placed a bed of Cr_2O_3 (9 cm) and then a bed of quartz crumb (1 cm). This allowed efficient after-oxidation of the pyrolysis products and fully eliminated the danger of reactor plugging with fused reduced metallic copper.

The analysis was performed in the dynamic mode. The flow rate of the carrier gas (Ar containing 80 vol % O_2) was 30 ml min^{-1} in the C,H,N channel and 20 ml min^{-1} in the reference channel. A sample (0.5 mg) was placed in an aluminum container. The oxidant was $AgMnO_4$, which showed high performance in previous studies [4]. As references we used both cyclohexanone 2,4-dinitrophenylhydrazone (recommended by the producer of the device) and nonlabeled analogs of the organic compounds to be analyzed. For example, in analysis of toluene-α-*D*, we used toluene as reference. Samples were fed into the combustion reactor from a ring-shaped automatic

1070-4272/04/7708-1331 © 2004 MAIK "Nauka/Interperiodica"

dosing unit with 23 sample cells in the manual or automatic mode. Samples were arranged in this unit in the following order: container with reference sample and oxidant, container with oxidant, three containers with the compound being analyzed and oxidant, again container with the reference sample and oxidant, container with oxidant, three containers with the compound being analyzed and oxidant, container with reference sample and oxidant, container with oxidant, and four containers with the compound being analyzed. Such an arrangement allows accurate determination of the zero signal for the given element and ensures the best reproducibility of the results.

The mixture obtained by oxidative pyrolysis was analyzed for the content of N_2, CO_2, H_2O, HOD, and D_2O.

No direct method is known today for analysis of this gas mixture. Determination of N_2 and CO_2 by gas chromatography involves no problems; numerous sorbents are suitable for this purpose [5, 6]. Water is determined by this method relatively poorly and, as a rule, is converted with appropriate reagents into other chemical forms convenient for chromatographic determination [6, 7]. Therefore, the mixture was analyzed after separation of water and its deuterium analogues. For this purpose, the gas mixture was passed at room temperature through two columns made of transparent quartz (l = 0.2 m, d = 6 mm), packed with the water absorbent and appropriate reagent, after which the mixture of N_2 and CO_2 was analyzed using an aluminum column (l = 4 m, d = 3 mm) packed with alumina-supported Chromosorb-102. The column temperature was 120°C. A thermal conductivity detector was used. After determination of N_2 and CO_2 in the gas mixture, a tubular furnace preheated to 120°C was moved on the column with the water absorbent.

Commercial units for adsorption drying of gases use silica gels ASK and ASKM [8]. However, silanol groups present on the surface of these adsorbents distort the results of analysis because of the isotope exchange. It is known that silanol groups transform into siloxane groups on heating [9]. Therefore, for qualitative and semiquantitative analysis, we calcined the silica gels of the above brands for 3 h at 400°C in a vacuum (1 mm Hg) and then modified them with trimethylchlorosilane [9]. In this case, however, the error was relatively large and the reproducibility was poor, which does not allow use of silica gel for determining deuterium in organic compounds by our procedure. With Carbowax-550 (methoxy polyethylene glycol) supported (30%) on quartz crumb (0.25–0.5 mm) as water sorbent, it appeared possible to decrease the temperature of water desorption to 120°C and considerably accelerate its release. At 120°C, water was desorbed rapidly and quantitatively; the amount and isotopic composition of the desorbed water were determined by reaction gas chromatography.

This method is widely used for quantitative determination of nonlabeled water [6, 7, 10, 11]. In this method, water vapor in a carrier gas flow is fed into a column with an appropriate reagent that quantitatively converts water into another chemical form convenient for gas-chromatographic determination. To convert nonlabeled water into H_2, the following reagents meeting the requirements of reaction gas chromatography are used: CaH_2 [12, 13], $LiAlH_4$ [14], $NaAlH_4$ [15], and sodium metal [13]. These reagents, however, are unsuitable for quantitative determination of the isotope composition of deuterium-labeled water, because the hydrogen formed in the reaction will differ in the isotope composition from the initial water sample.

To convert deuterium-labeled water into a mixture of H_2, HD, and D_2, we performed its reaction with activated magnesium (Khlorvinil Production Association, Ukraine, MRSh-1 brand, 0.25–0.5-mm fraction) at 500°C [16]. Magnesium was activated with iodine directly in the column (l = 0.2 m, d = 6 mm) or in a quartz test tube at 500°C [16]. Five grams of activated magnesium is sufficient for more than 100 experiments on water conversion. The absence of the chromatographic peak of water and its deuterium analogues confirms the 100% conversion. The detection of water indicates that the reagent has lost its activity and requires replacement. Similar results have been obtained in water conversion with reduced iron powder (Reakhim Production Association, Russia) at 650°C [17].

Determination of the isotope composition of the released hydrogen by gas-adsorption chromatography involves no problems; the procedure has been well developed [5, 6].

In the present study, the isotope composition of the released hydrogen was determined with a Tsvet-570 gas chromatograph [18] following the procedure suggested in [19], which allows determination of the content of HD, D_2, and H_2 within 3 min with a <1% error on a column (l = 4 m, d = 3 mm) packed with zeolite 13X at 40°C, using a thermal conductivity detector. Isimura and Kaetsu [19] used high-purity helium as carrier gas. However, the thermal conductivity detector has a low sensitivity to hydrogen with this carrier gas

because of the small difference in the thermal conductivities of these gases [10]. With zeolite 5A, which separates hydrogen isotopes more efficiently than to 13X, used as adsorbent and with dry argon as carrier gas [5, 10], we were able to decrease the determination error to 0.1–0.2%.

Since there were no reference gas mixtures containing deuterium among the reference samples produced in Russia, we tested our installation with D_2O reference samples produced by Aldrich (the United States).

A reference sample of D_2O was analyzed as described above with the only difference that the D_2O sample (0.25 μl) was introduced directly into the absorption column preliminarily purged with dry argon. The error of determination of the isotope composition of hydrogen was calculated from the results of ten analyses of D_2O reference samples. The results are listed in Table 1.

From the results of the analysis, we calculated the following characteristics: content of elements x (%); arithmetic mean content of elements; standard deviation of single determination for each element, s (%); estimated variance of the mean content of each element, s^2; and confidence intervals $\langle x\rangle \pm st_{0.95,9}$, where $t_{0.95,9}$ is the Student coefficient for the con-

Table 1. Results of elemental analysis of deuterium-labeled water samples with different atomic fractions of deuterium

Sample no.	D, at. %	Calculated, wt %		Found		Found D, at %
		D, wt %	H, wt %	D, at. %	H, wt %	
1*	0.10	0.022	11.189	0.0220 ± 0.0002	11.190 ± 0.030	0.098 ± 0.001
2*	0.50	0.112	11.128	0.1120 ± 0.0006	11.130 ± 0.030	0.501 ± 0.007
3*	1.00	0.223	11.066	0.2230 ± 0.0005	11.070 ± 0.030	0.998 ± 0.002
4*	10.00	2.212	9.960	2.212 ± 0.002	9.960 ± 0.010	10.000 ± 0.010
5*	50.00	10.593	5.299	10.590 ± 0.020	5.300 ± 0.010	50.00 ± 0.10
6	90.00	18.292	1.017	18.290 ± 0.040	1.017 ± 0.003	90.00 ± 0.20
7	99.00	19.939	0.101	19.940 ± 0.030	0.100 ± 0.001	99.00 ± 0.17
8**	99.00	19.939	0.101	19.940 ± 0.030	0.102 ± 0.001	99.00 ± 0.20
9***	99.92 ± 0.01	20.106 ± 0.002	0.008 ± 0.001	20.110 ± 0.050	0.0080 ± 0.0002	99.90 ± 0.10
10***	99.98 ± 0.01	20.117 ± 0.002	0.002 ± 0.001	20.120 ± 0.010	0.0020 ± 0.0001	99.99 – 0.07 + 0.001

* The sample was obtained by dilution of sample no. 7 (Aldrich) with distilled water.

** D_2O conversion was performed by reaction with iron powder at 650°C.

*** Reference samples produced by Aldrich.

Table 2. Results of elemental analysis of oxygen-containing compounds with different atomic fractions of deuterium

Compound	D, at. %	Content, wt %				
		C	H	D	O	N
Dimethylformamide-d_7, C_3D_7ON**	99.5*	44.980	0.044	17.519	19.972	17.485
	99.50 ± 0.12	44.980 ± 0.050	0.0450 ± 0.0001	17.520 ± 0.020	19.975 ± 0.050	17.490 ± 0.020
	70	46.179	2.713	12.654	20.503	17.951
	70.00 ± 0.18	46.200 ± 0.120	2.710 ± 0.006	12.650 ± 0.030	20.510 ± 0.050	17.950 ± 0.050
	50	47.029	4.605	9.204	20.881	18.281
	50.00 ± 0.15	47.000 ± 0.140	4.610 ± 0.013	9.200 ± 0.027	20.890 ± 0.050	18.270 ± 0.050
	20	48.364	7.576	3.786	21.474	18.800
	19.97 ± 0.05	48.360 ± 0.120	7.580 ± 0.020	3.780 ± 0.010	21.480 ± 0.060	18.800 ± 0.050
	1	49.249	9.547	0.193	21.867	19.144
	0.99 ± 0.01	49.240 ± 0.100	9.550 ± 0.030	0.190 ± 0.002	21.870 ± 0.060	19.150 ± 0.050

Table 2. (Contd.)

Compound	D, at. %	Content, wt %				
		C	H	D	O	N
2-Propan-one-D (acetone-d_6)	99.5	56.221	0.047	18.769	24.963	–
	99.50 ± 0.12	56.220 ± 0.070	0.050 ± 0.0002	18.770 ± 0.020	24.960 ± 0.030	–
	70	57.829	2.912	13.582	25.677	–
	70.00 ± 0.13	57.830 ± 0.100	2.910 ± 0.006	13.580 ± 0.025	25.680 ± 0.050	–
	50	58.973	4.949	9.893	26.185	–
	50.00 ± 0.11	59.000 ± 0.120	4.950 ± 0.010	9.900 ± 0.020	26.190 ± 0.052	–
	20	60.776	8.161	4.078	26.985	–
	20.00 ± 0.05	60.800 ± 0.150	8.160 ± 0.020	4.080 ± 0.010	27.000 ± 0.067	–
	1	61.976	10.298	0.208	27.518	–
	1.01 ± 0.01	62.000 ± 0.130	10.300 ± 0.030	0.210 ± 0.002	27.520 ± 0.050	–
2-Methyl-2-propanol-d_{10} (*tert*-butanol-d_{10})	99	57.132	0.120	23.722	19.026	–
	99.00 ± 0.12	57.130 ± 0.080	0.1200 ± 0.0002	23.720 ± 0.025	19.030 ± 0.040	–
	70	59.188	3.725	17.377	19.710	–
	70.00 ± 0.14	59.190 ± 0.090	3.720 ± 0.007	17.380 ± 0.030	19.710 ± 0.040	–
	50	60.694	6.367	12.728	20.211	–
	50.00 ± 0.10	60.700 ± 0.100	6.370 ± 0.013	12.730 ± 0.025	20.200 ± 0.040	–
	20	63.102	10.591	5.293	21.014	–
	19.99 ± 0.04	63.100 ± 0.150	10.590 ± 0.020	5.290 ± 0.010	21.020 ± 0.050	–
	1	64.729	13.445	0.271	21.555	–
	0.995 ± 0.005	64.730 ± 0.150	13.450 ± 0.020	0.270 ± 0.002	21.550 ± 0.050	–
Toluene-α-D	99	90.271	7.587	2.142	–	–
	98.92 ± 0.13	90.270 ± 0.130	7.590 ± 0.010	2.140 ± 0.003	–	–
	70	90.555	7.925	1.520	–	–
	70.04 ± 0.18	90.550 ± 0.270	7.930 ± 0.023	1.520 ± 0.004	–	–
	50	90.752	8.160	1.088	–	–
	50.11 ± 0.09	90.760 ± 0.180	8.150 ± 0.016	1.090 ± 0.002	–	–
	20	91.050	8.514	0.436	–	–
	19.94 ± 0.05	91.050 ± 0.220	8.520 ± 0.018	0.435 ± 0.001	–	–
	1	91.238	8.740	0.022	–	–
	1.006 ± 0.005	91.220 ± 0.080	8.745 ± 0.025	0.0220 ± 0.0001	–	–
Toluene-d_8	99.5	83.946	0.040	16.014	–	–
	99.47 ± 0.10	83.950 ± 0.080	0.0400 ± 0.0001	16.010 ± 0.016	–	–
Benzene-d_6	99.6	85.658	0.029	14.313	–	–
	99.58 ± 0.15	85.660 ± 0.090	0.0300 ± 0.0001	14.310 ± 0.020	–	–
1-Phenyl-ethane-1-D	99	89.664	8.475	1.861	–	–
	98.92 ± 0.11	89.660 ± 0.180	8.480 ± 0.010	1.860 ± 0.010	–	–
2-Methyl-2-propan(ol-D)	98	63.965	12.105	2.630	21.300	–
	98.00 ± 0.11	63.960 ± 0.160	12.110 ± 0.030	2.630 ± 0.008	21.300 ± 0.060	–
Acetonitrile-d_3	99.6	54.519	0.027	13.665	–	31.789
	99.64 ± 0.16	54.520 ± 0.110	0.0300 ± 0.0001	13.670 ± 0.020	–	31.780 ± 0.060
Ethan(oic-D) acid (acetic acid O–D)	98	39.355	4.987	3.235	52.423	–
	98.15 ± 0.27	39.350 ± 0.110	4.990 ± 0.014	3.240 ± 0.009	52.420 ± 0.130	–

* Numerator: calculated; denominator: found.

** Oxygen was determined in the O channel of the Carlo Erba 1100 gas-chromatographic elemental analyzer.

fidence level $P = 0.95$ and significance level $f = 0$, $l = 9$, which is equal to 2.26.

An independent determination of oxygen was performed in the O channel of the Carlo Erba 1100 gas-chromatographic elemental analyzer in the form of CO, after reductive pyrolysis of the sample over activated carbon. The pyrolysis was performed in a quartz tube with the following packing (cm): quartz wool, 1; thin twisted silver wire, 4; activated carbon, 15; and quartz crumb, 1. The temperature of the quartz tube in the pyrolysis zone and in the upper part of the reduction zone was 1120 ± 5°C. The carrier gas was He or Ar. The flow rate of the carrier gas in the O channel was 20 ml min^{-1}. Pyrolysis of organic compounds yields oxygen in the form of CO, CO_2, H_2O, D_2O, HOD, and molecular oxygen. After passing through a bed of activated carbon, the gas mixture mainly consists of He (or Ar), CO, and CO_2, with minor impurities of H_2 and CH_4. The mixture was analyzed by gas-adsorption chromatography on a column (l = 2.5 m, d = 3 mm) packed with zeolite 5A at 118 ± 2°C, using a thermal-conductivity detector (carrier gas He or Ar). As reference channel we used the C, H channel of the same device.

The results of elemental analysis of samples of organic compounds with different atomic fractions of deuterium are listed in Table 2.

Our results show that, in contrast to the results of [2], the atomic fraction of deuterium can be determined in the range 1–99% with a 0.1–0.5% accuracy. Furthermore, the method suggested in [2] involves additional problems (determination of empirical coefficients) and is applicable to a limited group of organic compounds.

CONCLUSION

The developed gas-chromatographic method for quantitative determination of deuterium has no limitations with respect to structure of organic compounds and ensures a high accuracy (0.1–0.5%) in a wide range of deuterium content (1–99%).

ACKNOWLEDGMENTS

The study was financially supported by the Ministry of Education of the Russian Federation, scientific program "Basic Research of Higher School in the Field of Natural Sciences and Humanities. Universities of Russia," project no. UR.05.01.012.

REFERENCES

1. Gunter, H., *NMR spectroscopy: Basic Principles, Concepts and Applications in Chemistry*, Chichester: Wiley, 1995, 2nd ed.
2. Ordzhonikidze, K.G., Parulava, L.P., Vakhaniya, G.V., and Tarielashvili, V.O., *Zavod. Lab.*, 1989, vol. 55, no. 8, pp. 48–51.
3. Polyakova, A.A., *Molekulyarnyi mass-spektral'nyi analiz organicheskikh soedinenii* (Molecular Mass-Spectrometric Analysis of Organic Compounds), Moscow: Khimiya, 1983.
4. Platonov, V.V., Shvykin, A.Yu., Proskuryakov, V.A., *et al.*, *Zh. Prikl. Khim.*, 2002, vol. 75, no. 5, pp. 852–857.
5. Drugov, Yu.S. and Konopel'ko, L.A., *Gazokhromatograficheskii analiz gazov* (Gas-Chromatographic Analysis of Gases), Moscow: Moimpeks, 1995.
6. Anvaer, B.I. and Drugov, Yu.S., *Gazovaya khromatografiya neorganicheskikh veshchestv* (Gas Chromatography of Inorganic Substances), Moscow: Khimiya, 1976.
7. Nichunovskii, G.F., *Opredelenie vlazhnosti khimicheskikh veshchestv* (Determination of Moisture Content of Chemical Substances), Leningrad: Khimiya, 1977.
8. Zhdanova, N.V. and Khalif, A.L., *Osushka uglevodorodnykh gazov* (Drying of Hydrocarbon Gases), Moscow: Khimiya, 1984.
9. *Handbuch der Gaschromatographie*, Leibnitz, E. and Struppe, H.G., Eds., Leipzig: Geest & Portig, 1984.
10. Jeffery, P.G. and Kipping, P.J., *Gas Analysis by Gas Chromatography*, Oxford: Pergamon, 1972.
11. Berezkin, V.G., *Analiticheskaya reaktsionnaya gazovaya khromatografiya* (Analytical Reaction Gas Chromatography), Moscow: Nauka, 1998.
12. Drawert, F., Felgenhaner, K., and Kupfer, G., *Angew. Chem.*, 1968, vol. 72, p. 385.
13. Starshov, N.M., Voevodkin, Yu.P., and Khalimov, A.A., in *Gazovaya khromatografiya: Sbornik statei* (Gas Chromatography: Coll. of Papers), Moscow: NIITEKhIM, 1965, no. 3, pp. 103–106.
14. Yajima, S., Shiba, K., Handa, M., and Takahashi, Y., *Bull. Chem. Soc. Jpn.*, 1964, vol. 37, no. 6, pp. 800–804.
15. Berezkin, V.G., Mysak, A.E., and Polak, L.S., *Neftekhimiya*, 1964, vol. 4, no. 1, p. 156.
16. Fedoseev, P.M. and Baidulina, G.O., *Zavod. Lab.*, 1971, vol. 37, pp. 1424–1425.
17. Vecera, M., *Z. Anal. Chem.*, 1962, vol. 191, p. 293.
18. Yashin, Ya.I., *Zavod. Lab.*, 1989, vol. 55, no. 6, pp. 14–17.
19. Isimura, S. and Kaetsu, H., *Rep. Inst. Phys. Chem. Res.*, 1981, vol. 51, no. 1, pp. 1–6.

Russian Journal of Applied Chemistry, Vol. 77, No. 8, 2004, pp. 1336–1340. Translated from Zhurnal Prikladnoi Khimii, Vol. 77, No. 8, 2004, pp. 1351–1355.

ORGANIC SYNTHESIS AND INDUSTRIAL ORGANIC CHEMISTRY

Chemiluminescence in the Course of Inhibited Oxidation of Vegetable Oil

N. I. Belaya, T. A. Filippenko, A. N. Nikolaevskii, and V. A. Zaets

Donetsk National University, Donetsk, Ukraine

Received February 5, 2004

Abstract—A study was made of the chemiluminescence in the course of initiated oxidation of sunflower oil with a luminescence activator in the presence of natural phenols. The kinetic parameters $k_2/\sqrt{k_1}$ were determined, which take into account the appearance of chemiluminescence and characterize the antioxidative activity of the phenols.

Antioxidative stabilization of fats, oils, fat-containing foodstuff, and pharmaceuticals is practical problem of current interest, which can be solved by using natural phenolic antioxidants [1]. Application of plant phenols as inhibitors of radical-chain oxidation in vegetable oils requires that the antioxidative activity (AOA) of these phenols should be estimated and their action in complex substrates be taken into account.

In this study, we examined the antioxidative activity of natural phenols in sunflower oil and revealed the specific features of chemiluminescence (CL) in the course of inhibited oxidation of the oil.

EXPERIMENTAL

Commercial oil produced from sunflower seeds, whose initial physicochemical characteristics were specified by GOST (State Standard) 1129–93, was used without further purification. Pure-grade ethylbenzene (ETB) and chlorobenzene were purified by the standard procedure [2]. As the source of free radicals served pure-grade azobis(isobutyronitrile) (AIBN) double-recrystallized from absolute ethanol and benzoyl peroxide purified by the procedure from [3]. We used 9,10-dibromoanthracene (DBA) and 1,10-phenanthroline complex of europium thenoyltrifluoroacetonate (Eu chelate) as CL activators. Synthesis and purification of DBA and Eu chelate were described in [4, 5]. Plant phenols and p.a.-grade Ionol (Merck) were used without further purification. The CL kinetics in the course of inhibited oxidation was followed using a setup whose schematic was described in [6]. The formulas of the phenols studied are presented below:

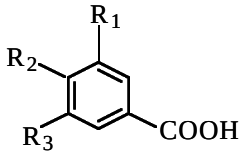

$R_1 = R_2 = R_3 = OH$, gallic acid
$R_1 = R_2 = OH$, $R_3 = H$, pyrocatechic acid
$R_1 = R_3 = OCH_3$, $R_2 = OH$, syringic acid
$R_1 = OCH_3$, $R_2 = OH$, $R_3 = H$, vanillic acid
$R_2 = OH$, $R_1 = R_3 = H$, *p*-hydroxybenzoic acid

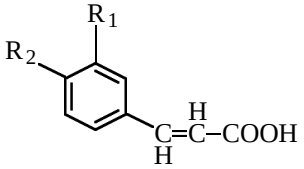

$R_1 = R_2 = OH$, caffeic acid
$R_1 = OCH_3$, $R_2 = OH$, ferulic acid

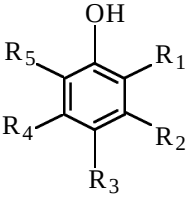

$R_2 = R_4 = OH$, $R_1 = R_3 = R_5 = H$, phloroglucinol
$R_3 = CH_3$, $R_1 = R_5 = C(CH_3)_3$, $R_2 = R_4 = H$, Ionol
$R_2 = OH$, $R_1 = R_3 = R_4 = R_5 = H$, resorcinol

1070-4272/04/7708-1336 © 2004 MAIK "Nauka/Interperiodica"

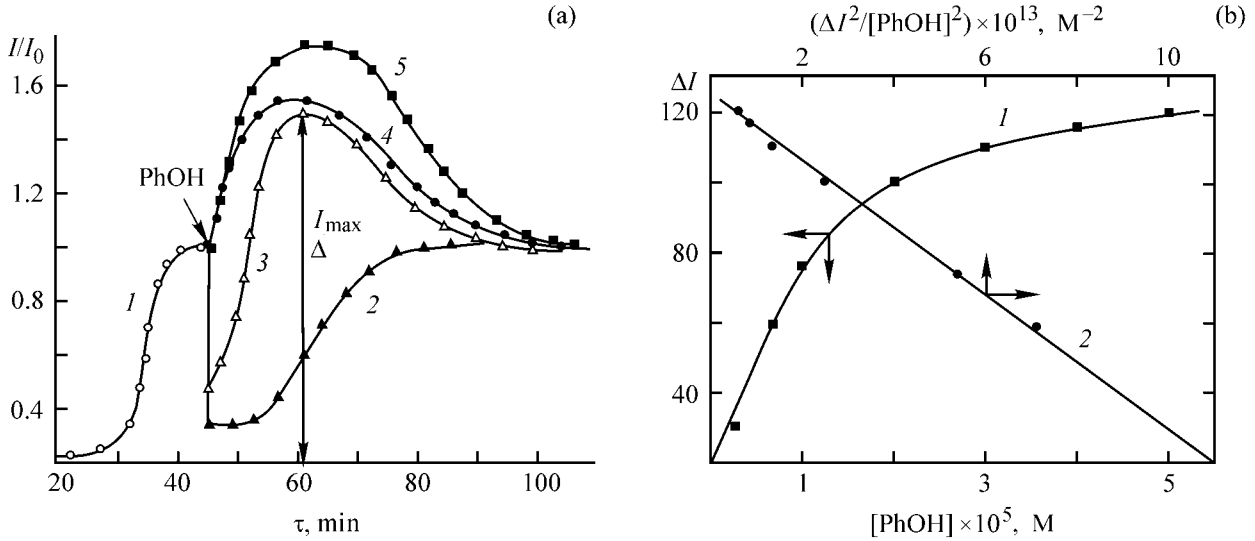

Fig. 1. (a) Kinetics of variation of I/I_0 in the course of initiated oxidation of the oil (*1*) in a 1 : 1 oil : chlorobenzene mixture and (*2*–*5*) in the presence of phenols ($c = 5 \times 10^{-4}$ M) and (b) the dependence of ΔI on (*1*) the concentration of gallic acid, [PhOH], and (*2*) $\Delta I^2/[PhOH]^2$ in the course of initiated oxidation of oil in a 1 : 1 oil : chlorobenzene mixture. (a) [DBA] = 2×10^{-3} M, T = 343 K, [AIBN] = 2×10^{-2} M; (b) $V_i = 2.2 \times 10^{-6}$ M. (*I*) CL intensity and (τ) time. (a): (*2*) Ionol, (*3*) ferulic acid, (*4*) phloroglucinol, and (*5*) pyrocatechic acid.

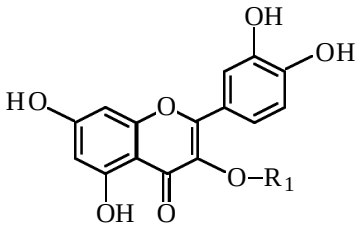

R_1 = H, quercetin; R_1 = $C_{12}H_{20}O_9$, rutin

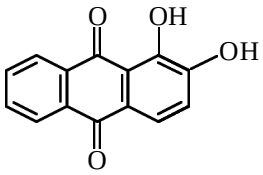

alizarine

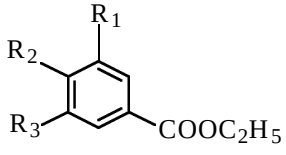

ethyl gallate

We estimated the kinetic parameters of the antioxidative action of phenols PhOH in the course of oxidation of the oil by the CL method based on measuring the luminescence (I_0) arising during homolytic oxidation of organic substances with oxygen [7]. Electronically excited products of this reaction are typically yielded by recombination of peroxy radicals ROO•:

$$ROO^{\bullet} + ROO^{\bullet} \xrightarrow{k_1} [ROOOOR] \rightarrow R{=}O^{*} \rightarrow R{=}O + h\nu. \quad (1)$$

In the presence of inhibitors, the reaction between peroxy radicals is suppressed, and the CL decays (*I*) or completely disappears:

$$ROO^{\bullet} + PhOH \xrightarrow{k_2} ROOH + PhO^{\bullet}. \quad (2)$$

AIBN-initiated oxidation of sunflower oil with or without DBA activator was carried out in a 1 : 1 oil : chlorobenzene mixture. The phenolic antioxidant was introduced into the system after all the natural antixodants of oil, tocoferols, were spent and the CL intensity attained saturation, I_0. Figure 1a shows three types of kinetic curves describing variation of I/I_0 upon introduction of the phenols into the oil. It is seen that only Ionol and syringic acid exhibit classical patterns [the luminescence intensity decreases upon introduction of inhibitor (*I*), whereupon it regains the initial value of I_0 as the antioxidant is consumed]. The second type of kinetic curves is characteristic of phloroglucinol, resorcinol, pyrocatechic acid, gallic acid, and ethyl gallate: Upon introducing these phenols into the oil, the luminescence intensity increases, rather than decreases. On introducing into the oil the remaining phenols (quercetin, caffeic, syringic, ferulic, vanillic, and *p*-hydroxybenzoic acids, rutin, and alizarine) the CL intensity initially decreases and then increases, exceeding I_0 (Fig. 1a). Evidently, the final products of transformation of the phenols do not affect the CL, since all the kinetic curves of CL tend to $I/I_0 - 1$, which corresponds to the time at which the phenolic antioxidant is fully exhausted.

The nonclassical influence of the phenols on the CL of the oil being oxidized could seemingly be accounted for by the lack of antioxidative properties of these

Table 1. Induction periods for initiated oxidation and high-temperature autooxidation of ethylbenzene and sunflower oil in the presence of the phenols*

Compound	τ, min, 343 K		τ, min, 393 K	
	ETB, [AIBN] = 1.1×10^{-2}, M	oil, [AIBN] = 2.0×10^{-2} M	ETB	oil
Ethyl gallate	35	30	570	125
Gallic acid	31	22	240	105
Caffeic acid	28	26	250	85
Pyrocatechic acid	30	18	500	45
Syringic acid	23	5	140	35
Ferulic acid	19	5	145	30
Rutin	18	7	70	25
Vanillic acid	11	3	90	35
Alizarine	10	3	30	25
Phloroglucinlol	29	4	110	15
p-Hydroxybenzoic acid	7	3	90	25

* The phenol concentration is 5×10^{-4} in initiated oxidation and 5×10^{-5} M in high-temperature autooxidation.

substances in oil. However, a parallel gas-volumetric study showed that all the phenols inhibit to a certain extent the oxidation of the oil, by reacting with peroxy radicals with chain termination (Table 1). We compared the induction periods τ for initiated oxidation of the oil and a model hydrocarbon substrate ethylbenzene and found that, on going from saturated (ethylbenzene) to a more complex unsaturated (oil) substrate, the phenols preserved the AOA. Also preserved were the trends in variation of this activity along the series of phenols differing in the structure. The most efficient inhibitors of the oil oxidation are *ortho* polyphenols: gallic acid and ethyl gallate, caffeic acid, and quercetin. Notably, the AOA of the phenols in the oils most prominently decreases relative to ethylbenzene in the case of high-temperature oxidation (Table 1). A decrease in the activity of the phenols in the oil may be due to a number of factors, among which the chain propagation via phenoxy radicals seems to be the most essential.

Special experiments on the CL in phenol-inhibited oxidation of the oil showed that the phenols and their transformation products are not common photosensitizers. Without luminescence activators, the CL intensity during the oil oxidation is very weak and lies below the detection limit of the CL setup. Therefore, we studied CL in the oil in the presence of activators only. We found that, on going from DBA activator to Eu chelate, the degree of enhancement of CL by the phenols remains unchanged during the induction period of oxidation; the enhancement of luminescence on introducing the phenols into the oil is preserved upon changing to another initiator; without initiator and upon termination of the oxygen supply no CL is observed. With increasing initiation rate V_i (at [PhOH] = const), I_{max} tends to linearly grow, and at a constant AIBN concentration I_{max} tends to increase with increasing phenol concentration and reaches a constant value at a certain concentration of the phenol. These data agree with our earlier conclusions [8] that the factor responsible for the additional luminescence in the substrates being oxidized (ethylbenzene, cumene, methyl ethyl ketone) is the reaction between the phenoxy $PhO^\bullet$ and peroxy radicals, yielding a phenol transformation product (quinone) in an electronically excited state, capable of light emission during transition to the ground state:

$$PhO^\bullet + ROO^\bullet \xrightarrow{k_3} \text{products}. \qquad (3)$$

Thus, the CL intensity in the induction period in inhibited oxidation of the oil will depend on the contributions from all the reactions giving rise to [reactions (1) and (3)] and quenching [reaction (2)] the luminescence and will be described by the expression

$$I = k_1\varphi_1[ROO^\bullet]^2 + k_3\varphi_3[ROO^\bullet][PhO^\bullet]. \qquad (4)$$

Here, k_1, k_3, φ_1, and φ_3 are the rate constants and quantum yields of reactions (1) and (3), respectively.

If [PhOH] = 0, $[PhO^\bullet] = 0$, then $I = I_0 = k_1\varphi_1[ROO^\bullet]^2 = \varphi_1 V_i$. With increasing [PhOH], $[PhO^\bullet]$ tends to grow, and at a high phenol concentration $[PhP^\bullet] \gg [ROO^\bullet]$; hence, $I = I_{max} = k_3\varphi_3[ROO^\bullet][PhO^\bullet] = \text{const}$.

In contrast to the case of ethylbenzene [8], the CL in the oil is enhanced during the induction period of inhibited oxidation in the presence of activator. This can be associated with the influence exerted by the polarity of the substrate on the CL in reaction (3). To elucidate how the polarity of the medium affects I_{max}, we studied CL of the oil in the presence of the phenols upon introduction into the oil of a nonpolar solvent, benzene. The results are presented in Fig. 2a; it is seen that I_{max} tends to decrease with increasing benzene content in the system. This supports our earlier conclusions [8] that, in polar media, the energy levels of the forming excited product get higher; also, the probability of transition of quinone from the excited singlet state Q_{S_1} to the excited triplet state Q_{T_1} increases. A portion of the excited triplet molecules have time to transfer the excitation energy to the activator A:

$$ROO^{\cdot} + PhO^{\cdot} \xrightarrow{k_3} Q_{S_1} \xrightarrow{\text{Polar nolecule}} Q_{T_1} \xrightarrow{A} Q + A^{*}. \quad (5)$$

The intensity of CL in reaction (3) in the oil varies with the structure of the phenol and activity of the corresponding radical. This luminescence is characteristic only of the phenols capable of forming quinones by reaction (3). We characterized the activity of the phenoxy radicals in this reaction by the electron affinity E_A, which was calculated by the AM1 quantum-chemical semiempirical method in the software package [9] by the formula

$$E_A = H^0_{Ph^{\cdot}} - H^0_{PhO^{\cdot}}.$$

Here, E_A is the adiabatic electron affinity, and $H^0_{Ph^{\cdot}}$ and $H^0_{PhO^{\cdot}}$, the standard heats of formation of phenoxy radical anion and radical, respectively.

Figure 2b shows that, with increasing electron affinity of the phenoxy radical, CL in the induction period of oil oxidation inhibited by the corresponding phenol tends to increase in intensity. This supports the suggested mechanism of occurrence of an additional luminescence in the reaction involving phenoxy radical.

Since the introduction of the phenols into the oil being oxidized enhances CL, the rate constants k_2 of the reactions of these phenols with peroxy radicals of the oil cannot be calculated by the conventional procedure [7]. We calculated these constants by the procedure taking into account the CL by reaction (5) as well [10]. According to this procedure, the luminescence intensity in the presence of a phenol is described by Eq. (4). Based on the kinetic scheme of inhibited oxidation [1] and taking into account the steady-state

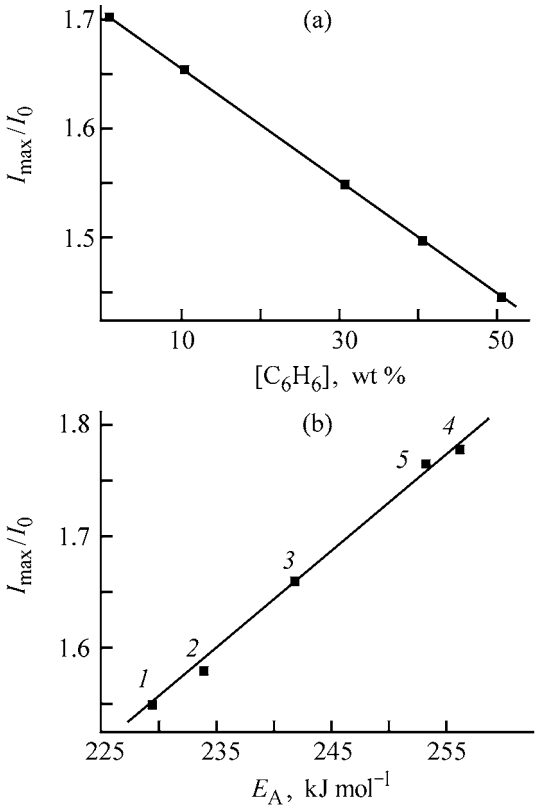

Fig. 2. I_{max}/I_0 vs. (a) benzene concentration $[C_6H_6]$ in a 1 : 1 oil : chlorobenzene mixture in the presence of pyrocatechic acid ($c = 4 \times 10^{-4}$ M) and (b) calculated electron affinity E_A of phenoxy radicals. (a) [AIBN] = 2×10^{-2}, [DBA] = 2×10^{-3} M, T = 343 K; (b) [PhOH] = 5×10^{-4} M. (*1*) phloroglucinol, (*2*) ethyl gallate, (*3*) gallic acid, (*4*) pyrocatechic acid, and (*5*) resorcinol.

concentration in the system of $ROO^{\cdot}$ and $PhO^{\cdot}$ radicals, we can write

$$\frac{d[ROO^{\cdot}]}{dt} = V_i - k_1[ROO^{\cdot}]^2 - k_2[ROO^{\cdot}][PhOH] = 0,$$

$$\frac{d[PhO^{\cdot}]}{dt} = k_2[ROO^{\cdot}][PhOH] - k_3[ROO^{\cdot}][PhO^{\cdot}] = 0.$$

By substituting $[ROO^{\cdot}]$ and $[PhO^{\cdot}]$ into Eq. (4), we obtain

$$\Delta I = (\eta_3 - 2\eta_1)\frac{k_2^2[PhOH]^2}{k_1}\left[\left(1 + \frac{V_i k_1}{k_2^2[PhOH]^2}\right)^{1/2} - 1\right]. \quad (6)$$

Equation (6) is mathematically transformed into

$$\Delta I = \frac{\varphi_3 - 2\varphi_1}{2} V_i - \frac{k_1}{2(\varphi_3 - 2\varphi_1)k_2^2}\frac{\Delta I^2}{[PhOH]^2}, \quad (7)$$

where $\Delta I = I_{max} - I_0$ and φ_1 and φ_3 are the quantum yields of CL for reactions (1) and (3), respectively.

Table 2. Calculated parameters $k_2/\sqrt{k_1}$ of selected phenols in initiated (AIBN) oxidation of ethylbenzene ($V_i = 4.9 \times 10^{-7}$ mol l^{-1} s^{-1}) at $T = 343$ K

Phenol	$k_2/\sqrt{k_1}$, l$^{1/2}$ mol$^{-1/2}$ s$^{-1/2}$		Phenol	$k_2/\sqrt{k_1}$, l$^{1/2}$ mol$^{-1/2}$ s$^{-1/2}$	
	oil : chlorobenzene = 1 : 1	ethylbenzene		oil : chlorobenzene = 1 : 1	ethylbenzene
Ethyl gallate	$(9.9 \pm 0.2) \times 10^1$	$(1.5 \pm 0.1) \times 10^2$	Pyrocatechic acid	8.0 ± 0.2	$(2.0 \pm 0.1) \times 10^1$
Gallic acid	$(6.9 \pm 0.2) \times 10^1$	$(1.30 \pm 0.09) \times 10^2$	Phloroglucinol	1.10 ± 0.04	2.6 ± 0.1

* The initiation rate V_i for sunflower oil was estimated as $V_i = f[\mathrm{PhOH}]/\tau$ with Ionol (inhibition coefficient $f = 2$ [11]) as reference inhibitor.

To calculate $k_2/\sqrt{k_1}$, we constructed the ΔI-vs.-[PhOH] plots (Fig. 1b), which were then linearized in the coordinates of Eq. (7). The $\eta_1 - 2\eta_2$ parameters were estimated from the intercepts on the ordinate, and $k_2/\sqrt{k_1}$, from the slope of the corresponding straight lines (Fig. 1b). Table 2 lists the $k_2/\sqrt{k_1}$ parameters calculated by this procedure for selected phenols in the oil against those in ethylbenzene. It is seen that these parameters exhibit similar trends in the series of the phenols studied and that the $k_2/\sqrt{k_1}$ parameters for the oil are lower, which is also a reason for the decrease in AOAs of the phenols in the oil.

CONCLUSION

In the course of inhibited oxidation of sunflower oil with luminescence activator in the presence of natural phenols, chemiluminescence is prominently enhanced in the induction period due to the influence exerted by the substrate (oil) on the luminescence arising in the reaction between phenoxy and peroxy radicals. The chemiluminescence intensity measured depends on the total contribution from the reactions responsible for the generation and quenching of luminescence in the system. The kinetic parameters for the oil oxidation, characterizing the antioxidative activity of the phenols, suggest a higher reactivity of natural *ortho* polyphenols (gallic acid and ethyl gallate, caffeic acid, and quercetin), compared to other phenols studied. At the same time, the antioxidative activity of the phenols in the oil is, on the whole, much lower than that in the case of ethylbenzene.

REFERENCES

1. Roginskii, V.A., *Fenol'nye antioksidanty* (Phenolic Antioxidants), Moscow: Nauka, 1988.
2. Weissberger, A. and Proskauer, E.S., *Organic Solvents. Physical properties and methods of purification*, Riddig, J.A. and Toops, E.E., Eds., New York: Interscience, 1955.
3. Toroptseva, A.M., Belgorodskaya, K.V., and Bondarenko, V.M., *Laboratornyi praktikum po khimii i tekhnologii vysokomolekulyarnykh soedinenii* (Laboratory Practical Guide on Chemistry and Technology of Macromolecular Compounds), Leningrad: Khimiya, 1972.
4. *Sintezy organicheskikh preparatov* (Syntheses of Organic Chemicals), Kazanskii, B.A., Ed., Collection of works 1, Moscow: Inostrannaya Literatura, 1949. Translated under the titles *Organic Synthesis. Collective Volume I. Being a revised edition of annual volumes I–IX*, Blatt, A.H., Ed., New York: Wiley, 1944, second ed.
5. Konenko, L.I., Tishchenko, M.A., Vitkun, R.A., *et al.*, *Zh. Neorg. Khim.*, 1987, vol. 10, no. 11, pp. 123–128.
6. Emanuel', N.M. and Denisov, E.T., *Neftekhimiya*, 1976, vol. 16, no. 3, pp. 366–375.
7. Shlyapintokh, V.Ya., Karpukhin, O.N., Postnikova, L.M., *et al.*, *Khemilyuminestsentnye metody issledovaniya medlennykh khimicheskikh protsessov* (Chemiluminescent Methods of Investigation of Slow Chemical Processes), Moscow: Nauka, 1966.
8. Belaya, N.I., Filippenko, T.A., Nikolaevskii, A.N., *et al.*, *Teor. Eksp. Khim.*, 2003, vol. 39, no. 3, pp. 161–166.
9. Steward, J.J.P., *MOPAC-93 Manual*, Oxford, 1993.
10. Vardanyan, R.L., *Kinet. Katal.*, 1974, vol. 15, no. 3, pp. 794–796.
11. Gol'denberg, V.I. and Shmulovich, V.G., *Neftekhimiya*, 1979, vol. 19, no. 2, pp. 208–213.

Russian Journal of Applied Chemistry, Vol. 77, No. 8, 2004, pp. 1341–1344. Translated from Zhurnal Prikladnoi Khimii, Vol. 77, No. 8, 2004, pp. 1356–1359.

MACROMOLECULAR CHEMISTRY AND POLYMERIC MATERIALS

Grafting of Poly-*N*-methacryloylaminodeoxyglucose on Poly-*N*-vinylpyrrolidone

O. V. Nazarova, G. M. Pavlov, E. E. Kever, E. V. Afanas'eva, and E. F. Panarin

Institute of Macromolecular Compounds, Russian Academy of Sciences, St. Petersburg, Russia
Institute of Physics, St. Petersburg State University, St. Petersburg, Russia

Received April 29, 2004

Abstract—A graft copolymer simulating glycoprotein was prepared by reaction of poly-*N*-methacryloylaminodeoxyglucose containing terminal amino group with a copolymer of *N*-vinylpyrrolidone and acrylic acid *N*-hydroxysuccinimide ester.

Synthetic glycopolymers attract growing researchers' interest as polymeric carriers for biologically active substances, immunomodulators, and as objects for studying molecular biorecognition mechanisms [1–5]. The molecular recognition is based on a specific interaction of macromolecular systems containing, in particular, carbohydrate and peptide fragments. Detailed understanding of the mechanisms of this interaction in natural polymeric systems is difficult because of their complex chemical and supramolecular structure. In this context, it is appropriate to study model systems with controllable chemical structures. Suitable objects are synthetic water-soluble polymers that contain recognizing fragments: carbohydrates, oligosaccharides, oligopeptides, or proteins. In this study, we developed a method for preparing a model system, graft copolymer with poly-*N*-vinylpyrrolidone (PVP) backbone (a model of peptide chains) and polyvinyl saccharide (namely, poly-*N*-methacryloylaminodeoxyglucose, PMAG) side chains.

Linear and cross-linked random copolymers of *N*-vinylpyrrolidone (VP) and other vinylamides with vinyl saccharides were described in [6–8]. Graft copolymers based on these monomers have been unknown previously.

The desired graft copolymers were prepared by reaction of a copolymer of *N*-vinylpyrrolidone and acrylic acid *N*-hydroxysuccinimide ester (VP–AA HSIE) with PMAG containing terminal primary amino group (PMAG-NH_2):

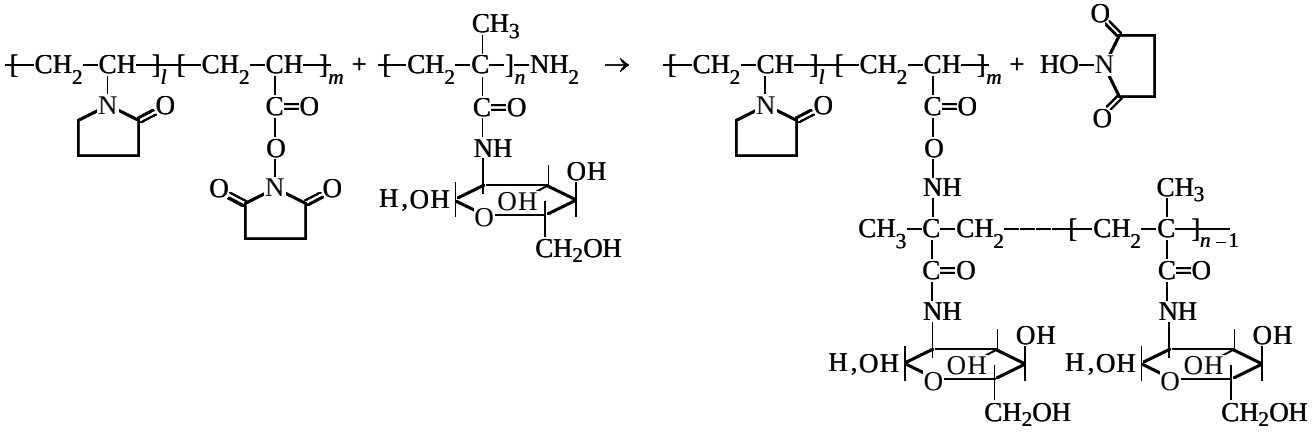

1070-4272/04/7708-1341 © 2004 MAIK "Nauka/Interperiodica"

Hydrodynamic characteristics and molecular weights of polymers

Polymer	*s*, Svedberg units	Fraction, %	$M_s \times 10^{-3}$	[η], dl g^{-1}	$M_\eta \times 10^{-3}$
VP–AA HSIE copolymer	1.5	>90	25	0.12	19
PMAG-NH_2	1.7	56	7	0.06	30
	3.2	37	27		
Reaction product	2.3	60	–	Not determined	–
	$3.9 < s < 5.0$	40			

EXPERIMENTAL

The procedures for purifying *N*-vinylpyrrolidone and preparing AA HSIE were described in [9]. The VP–AA HSIE copolymer (88 : 12 mol %) was prepared by radical copolymerization of the corresponding monomers; after isolation, its composition was determined [9, 10]. PMAG-NH_2 was prepared by radical polymerization of the monomer in the presence of a chain-transfer agent, amino-containing mercaptan; it was characterized according to [11, 12]. To study the hydrodynamic characteristics of VP–AA HSIE copolymer and of a mechanical blend of the starting polymers with VP–AA HSIE copolymer, the reactive groups were removed with *n*-butylamine.

Exclusion chromatography of the polymers was performed on a KhZh-1309 gel microchromatograph (Scientific and Technical Society, USSR Academy of Sciences) equipped with a refractometric detector [13]. A 0.5 × 367-mm column was packed with TSK G3000PW sorbent (Japan); the eluent was 0.05 M sodium trifluoroacetate in water.

The centrifugal sedimentation of polymers was studied in 0.2 M NaCl on a Beckman XLI analytical ultracentrifuge in two-sector cells (12 mm) with titanium inserts at 57000 rpm. Rayleigh interference optics served as an optical recording system. Solutions of a concentration $c = 0.15 \times 10^{-2}$ g cm^{-3}, corresponding to strong dilution ($c[\eta] \ll 1$), were studied. The sedimentograms were processed using the Sedfit program [14]. The program allows the choice of the best numerical solution of the general Lamm sedimentation equation [14] for a set of noninteracting particles (molecules). The set of such solutions gives the total calculated interferograms that fit the experimental interferograms to the maximum possible extent. By this procedure we obtain the sample distribution with respect to sedimentation coefficients, which may be multimodal (multipeak) in the general case. The program allows determination of the weight fraction of each distribution; the sum of all the fractions is unity. The floatability factor $1 - \nu\rho_0$ of the system was determined from the measured densities of solutions of various concentrations (DMA Kratky densimeter [15], Anton Paar, Graz, Austria).

The high reactivity of polymeric AA HSIE [16] allows its reaction with amines to be performed at room temperature. The reaction between the starting polymers was performed in dimethylformamide for 24 h at room temperature. Then *n*-butylamine was added to remove unchanged AA HSIE groups. The reaction product was isolated by precipitation into ethanol, in which PMAG is insoluble [12], but PVP is soluble.

The molecular weights M_η of the starting polymers, PMAG-NH_2 and VP–AA HSIE copolymer containing 12.0 mol % AA HSIE units, were calculated from the intrinsic viscosity, using the Kuhn–Mark–Houwink–Sakurada (KMHS) relationships [10, 12] (see table). Since the content of AA HSIE units was low, M_η of VP–AA HSIE copolymer was calculated with the equation obtained for PVP [10].

A sedimentation analysis showed that the starting VP–AA HSIE copolymer has a unimodal distribution, whereas PMAG-NH_2 is bimodal. When estimating M_s from the sedimentation coefficients, we used the following relationships: $s_0 = 3.55 \times 10^{-15} M^{0.44}$ (for PMAG) [12] and $s_0 = 1.28 \times 10^{-15} M^{0.47}$ (for PBP) [10]. The *M* values calculated from the intrinsic viscosity and sedimentation coefficient are reasonably consistent (see table).

In the distribution of the reaction product with respect to the sedimentation coefficient, there is a fraction with the sedimentation coefficient of 2.3 Svedberg units, close to that found for the starting polymers (see table). At the same time, another fraction appears, with the sedimentation coefficients distributed in a wider range: $3.9 < s < 5.0$ Svedberg units. This fact suggests the presence of heavier macromolecules of the graft copolymer. It is known that the sedimentation coefficient *s* is directly proportional to *M* and inversely proportional to the size of a moving molecule [17]. Therefore, we can generally determine from the sedimentation coefficient only the ratio *M*/*R*,

where R is the hydrodynamic size of the molecule in friction. Estimation of the molecular weight of the graft copolymer from a single hydrodynamic characteristic seems to be impossible, because KMHS-type correlations for it are unknown.

Comparison of the chromatograms (see figure) of the starting VP–AA HSIE and PMAG–NH_2 copolymers, their mechanical blend, and reaction product shows that, in contrast to the blend of the starting polymers, the chromatogram of the reaction product contains new peaks with small retention volumes. These peaks suggest the formation of graft copolymers of higher molecular weight, compared to the starting polymers, which is consistent with centrifugal sedimentation data.

In independent experiments, we obtained the density increment $\Delta\rho/\Delta c$ of the reaction product, from which we determined its specific partial volume: $\nu = 0.707$ cm^3 g^{-1}. From this value, it is possible to estimate, to a first approximation, the composition of the reaction product. This was done as follows. First, we determined [10, 12] ν for PVP and PMAG: $\nu_{PVP} = 0.778$ and $\nu_{PMAG} = 0.669$ cm^3 g^{-1}. The reaction product was isolated by precipitation into ethanol, in which PVP is soluble, but PMAG is not and precipitates. If the low-molecular-weight peak in the sedimentogram is due to the presence in the unchanged form of only one of the starting polymers, PMAG, then the specific partial volume corresponding to the graft copolymer can be calculated from the following relationship (assuming the additivity of the specific partial volumes):

$$\nu_{product} = \nu_{graft} x + \nu_{PMAG}(1 - x),$$

where x is the fraction of the graft copolymer in the reaction product.

We obtain $\nu_{graft} = 0.764$ cm^3 g^{-1}, which can be used for estimating the composition of the graft copolymer:

$$\nu_{graft} = \nu_{PVP} y + \nu_{PMAG}(1 - y),$$

where y is the PVP fraction in the graft copolymer; we obtained $y = 0.35$.

Thus, using two independent methods, we proved the possibility of preparing graft copolymers by the reaction of two polymers containing mutually reactive activated ester and amino groups in the side chain and at the end of the macromolecule, respectively.

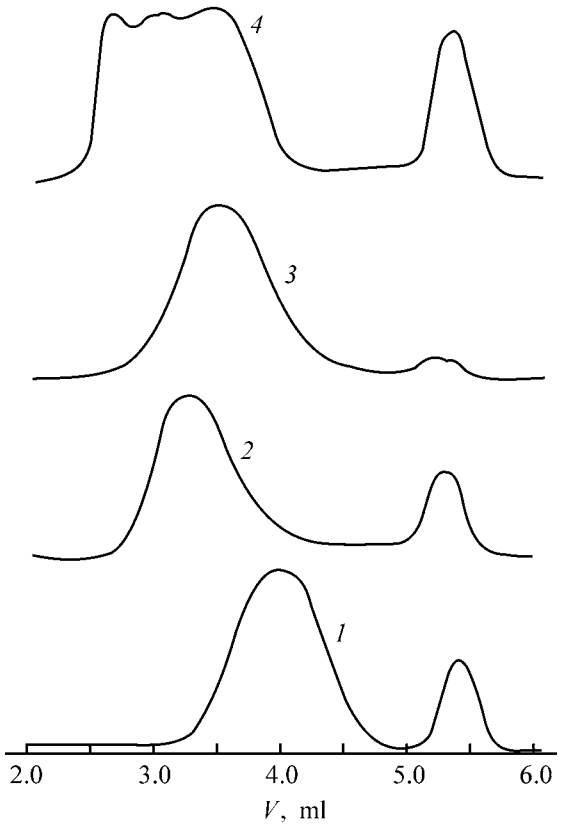

Chromatograms of the polymers. Eluent 0.05 M sodium trifluoroacetate in water, elution rate 3 μl min^{-1}, 25°C. (V) Retention volume. (*1*) PMAG-NH_2, (*2*) VP–AA HSIE copolymer, (*3*) mechanical blend of the starting polymers, and (*4*) reaction product.

CONCLUSIONS

(1) A graft copolymer with polyvinylpyrrolidone backbone and poly-*N*-methacryloylaminodeoxyglucose side chains was prepared by the reaction of poly-*N*-methacryloylaminodeoxyglucose with a copolymer of *N*-vinylpyrrolidone and acrylic acid *N*-hydroxysuccinimide ester.

(2) The hydrodynamic parameters of the copolymer obtained were calculated.

ACKNOWLEDGMENTS

The authors are grateful to Dr. H.Cölfen (Max-Planck-Institut für Kolloid- und Grenzflächenforschung, Potsdam, Germany) for the opportunity to perform sedimentation experiments at his laboratory.

The study was financially supported by the Russian Foundation for Basic Research (project no. 02-03-33110a) and by grant NSh-1823.2003.3.

REFERENCES

1. Garcia-Martin, M.G., Jimenez-Hidalgo, C., Al-Kass, S.S.J.V., *et al.*, *Polymer*, 2000, vol. 41, no. 3, pp. 821–826.
2. Panarin, E.F., Ivanova, N.P., Belokhvostova, A.T., and Potapenkova, L.S., *Immunologiya*, 1999, no. 2, pp. 26–28.
3. Panarin, E.F., Ivanova, N.P., Belokhvostova, A.T., and Potapenkova, L.S., *Khim.-Farm. Zh.*, 2002, vol. 36, no. 4, pp. 19–22.
4. Yamada, K., Minoda, M., and Miyamoto, T., *Macromolecules*, 1999, vol. 32, no. 11, pp. 3553–3558.
5. You, L.-Ch., Lu, F.-Zh., Li, Z-Ch., *et al.*, *Macromolecules*, 2003, vol. 36, no. 1, pp. 1–4.
6. Ivanova, N.P., Panarin, E.F., and Denisov, V.M., *Zh. Prikl. Khim.*, 1998, vol. 71, no. 1, pp. 1872–1875.
7. Shantha, K.L. and Harding, D.R.K., *Eur. Polym. J.*, 2003, vol. 39, no. 1, pp. 63–68.
8. Panarin, E.F., Ershov, A.Yu., and Ivanova, N.P., *Zh. Prikl. Khim.*, 2000, vol. 73, no. 12, pp. 1998–2001.
9. Nazarova, O.V., Solovskij, M.V., Panarin, E.F., *et al.*, *Eur. Polym. J.*, 1992, vol. 28, no. 1, pp. 97–100.
10. Pavlov, G.M., Panarin, E.F., Korneeva, E.V., *et al.*, *Vysokomol. Soedin., Ser. A*, 1990, vol. 32, no. 6, pp. 1190–1196.
11. Nazarova, O.V., Afanas'eva, E.V., Panarin, E.F., and Ivanova, N.P., *Zh. Prikl. Khim.*, 2000, vol. 73, no. 12, pp. 2060–2062.
12. Pavlov, G.M., Korneeva, E.V., Mikhailova, N.A., *et al.*, *Vysokomol. Soedin., Ser. A*, 1993, vol. 35, no. 10, pp. 1647–1650.
13. Belen'kii, B.G., Gotlib, V.A., and Kever, E.E., *Nauchn. Priborostr.*, 1991, vol. 1, no. 1, pp. 9–31.
14. Schuck, P., *Biophys. J.*, 2000, vol. 78, no. 3, pp. 606–619.
15. Kratky, O., Leopold, H., and Stabinger, H., *Meth. Enzymol.*, 1973, vol. 27, pp. 98–110.
16. Nazarova, O.V. and Panarin, E.F., *Zh. Prikl. Khim.*, 1999, vol. 72, no. 4, pp. 529–541.
17. Tsvetkov, V.N., Eskin, V.E., and Frenkel', S.Ya., *Struktura makromolekul v rastvorakh* (Structure of Macromolecules in Solutions), Moscow: Nauka, 1964.

Russian Journal of Applied Chemistry, Vol. 77, No. 8, 2004, pp. 1345–1350. Translated from Zhurnal Prikladnoi Khimii, Vol. 77, No. 8, 2004, pp. 1360–1365.

MACROMOLECULAR CHEMISTRY AND POLYMERIC MATERIALS

Behavior of Binary and Ternary Systems Based on Poly(Vinyl Chloride), Poly(Methyl Methacrylate), and Their Copolymers

N. A. Bichuch, V. A. Izvozchikova, S. D. Zaitsev, A. G. Kronman, and Yu. D. Semchikov

Research Institute for Radio Engineering, Nizhni Novgorod, Russia

Research Institute of Chemistry, Lobachevsky State University, Nizhni Novgorod, Russia

Lobachevsky State University, Nizhni Novgorod, Russia

Sibur-Neftekhim Joint-Stock Company, Dzerzhinsk, Nizhni Novgorod oblast, Russia

Received April 15, 2004

Abstract—Mechanical properties, optical transmission, surface topography, and dielectric loss are studied for films formed by blends of polymers of vinyl chloride and methyl methacrylate with their copolymers.

The development of new polymeric materials based on blends of large-scale polymers is one of the most promising areas of research on the way to modification of properties of polymers. In this context, a major interest was focused on the system poly(methyl methacrylate) (PMMA)–poly(vinyl chloride) (PVC), which has been studied in detail by 2D NMR spectroscopy, differential scanning calorimetry, X-ray diffraction [1], electron microscopy [2], and microcalorimetry [3, 4]. It was concluded in most studies that PMMA and PVC are incompatible [1, 5–7]. In particular, Li *et al.* [7] have drawn such a conclusion on the basis of the fact that two glass transition temperatures were found over the entire composition range of the blends. Our thought is that the compatibility of this pair of polymers can be improved by introducing a third component, vinyl chloride (VC)/methyl methacrylate (MMA) copolymer, into the system. Therefore, the goal of this study was to examine in detail blends of VC and MMA homopolymers with VC/MMA copolymer.

EXPERIMENTAL

Homopolymerization of VC and MMA and copolymerization of these monomers were carried out by the suspension method in a specially designed 3.5-l laboratory autoclave equipped with a 200-rpm impeller agitator, a doser, a sampler, and a cooling jacket. The MMA and VC monomers met the requirements of GOST (State Standard) 20 370–74 and TU (Technical Specifications) 6-01-14–90. The content of the main component in both cases was no less than 99.9%. In synthesis of PVC and VC-rich copolymers, we used as an emulsifier F-50 hydroxypropyl methyl cellulose (HPMC) containing 28.5 wt % methoxy groups and 7.0 wt % hydroxypropyl groups. In preparation of PMMA and MMA-rich copolymers, we used the saponification product of the copolymer of methacrylic acid (78.8 wt %) and MMA (21.2 wt %). As initiators we used di-2-ethylhexyl peroxydicarbonate (EHPC) and lauryl peroxide (LP), and as chain-terminating agents, 0.2 wt % lauryl mercaptans (in preparation of MMA-rich copolymers) and 0.75 wt % trichloroethylene (TCE) (in preparation of VC-rich copolymers). The liquor ratio (water to monomer ratio) was 2 : 1 and 5 : 1 in VC- and MMA-rich systems, respectively. The synthesis of PMMA with low (<10 wt %) VC content was carried out at 80°C. In this case, the reaction mass was rapidly cooled after 1–3 h. The synthesis of PVC and VC-rich copolymers was performed at 66°C until the pressure in the autoclave decreased by 0.5 atm, which corresponded to a 75% consumption of VC. Copolymers with increased degree of homogeneity (DH) were obtained by stepwise addition of the more reactive monomer, MMA, under nitrogen pressure. To the initial mixture of VC (800 g) and MMA (40 g), three 40-g portions of MMA were added at 3.5-h intervals. The polymers were separated from the mother liquor on a Buchner funnel, washed with distilled water, and dried in an oven at 60°C. The conversion was determined gravimetrically. The composition of the VC/MMA copolymers was determined

1070-4272/04/7708-1345 © 2004 MAIK "Nauka/Interperiodica"

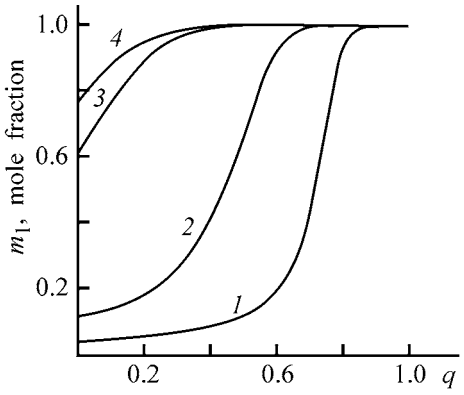

Fig. 1. Instantaneous composition of VC/MMA copolymer vs. the molar conversion q. (m_1) Mole fraction of VC units in the copolymer. Mole fraction of VC in the monomer mixture M_{10}: (*1*) 0.348, (*2*) 0.615, (*3*) 0.941, and (*4*) 0.969.

from the chlorine content according to GOST 25303–92. The method is based on complete burning of a sample in an oxygen flow, followed by chlorine determination by titration with mercury nitrate. The molecular weight (MW) of PVC and VC-rich copolymers was determined viscometrically in cyclohexanone at 25°C, using the Mark–Kuhn–Houwink equation:

$$[\eta] = KM^{\alpha} \quad (K = 1.37 \times 10^{-4},\ \alpha = 0.78).$$

For PMMA and MMA-rich copolymers, $K = 5.91 \times 10^{-4}$ and $\alpha = 0.57$ (solvent methyl ethyl ketone; temperature 30°C) [8]. The films were obtained by casting organic solutions of the mixtures in hand onto a glass support. The film thickness ranged within 0.15 ± 0.01 mm. The transmittance was determined using a KF-77 photoelectric colorimeter. The films with a transmittance of 100–80, 80–30, and <30% were classified as transparent, semitransparent, and opaque, respectively. The mechanical tests were performed on an RMI-5 tensile-testing machine.

Table 1. Characteristics of VC–MMA copolymerization products (75–90% conversion)

Product no.	VC content		$M_\eta \times 10^{-3}$
	wt %	mol %	
1	0	0	42.0 and 116.0
2	4.5	7.0	33.0
3	10.1	13.2	35.0
4	29.5	40.1	–
5	46.5	58.2	–
6*	57.7	68.6	–
7	68.1	77.4	–
8**	74.0	82.0	35.0
9	78.9	85.7	46.0
10	84.9	90.0	42.0
11	89.0	92.8	42.0
12	94.1	96.2	42.4
13	100	100	47.0 and 90.0

* Conversion 36.5%.

** Copolymer with increased compositional homogeneity.

Copolymerization of VC with MMA is complicated by the more rapid exhaustion of the more reactive monomer. Figure 1 shows the conversion dependences of the instantaneous composition of the copolymer, estimated from the relative reactivity of the monomers $r_1 = 0.11$ and $r_2 = 12.73$ (here and hereinafter, indices 1 and 2 refer to VC and MMA, respectively). It is significant that these values were obtained from data on copolymerization [9]. It is seen from Fig. 1 that, in copolymerization of the mixtures enriched with VC to a considerable extent, PVC homopolymer is formed even at intermediate conversions. Therefore, to obtain the copolymer as the only product, the process should be completed on reaching relatively low (30–40%) conversions. This is cost-inefficient, and, moreover, makes no sense if the goal is to prepare PVC–PMMA copolymer blends. Therefore, copolymerization of VC-rich VC–MMA mixtures was performed until reaching the maximal conversions. In this case, the product was a blend of PVC with VC/MMA copolymer. The composition of such blends was determined as follows. First, the conversion corresponding to the onset of PVC formation (conventionally defined as that corresponding to 99 mol % VC + 1 mol % MMA) was estimated from the theoretical dependence of the instantaneous composition of the copolymer on the conversion. Second, the bulk composition of the copolymer was determined as

$$q_o' \bar{m}_1 = M_{10} - M_1(1 - q_o'),$$

where q_o' is the conversion corresponding to the onset of PVC formation (wt %); $\bar{m}_1$, bulk composition of the copolymer; and M_{10} and M_1 are the initial and instantaneous mole fractions of the monomer in the mixtures.

Then we determined the PVC content (wt %) in the copolymerization product:

$$\text{PVC} = q_{\text{lim}} - q_o',$$

where q_{lim} is the experimental limiting conversion (wt %).

Characteristics of the copolymerization products are listed in Table 1. At [VC]/[MMA] < 1, they are copolymers, and at [VC]/[MMA] > 1, a blend of the

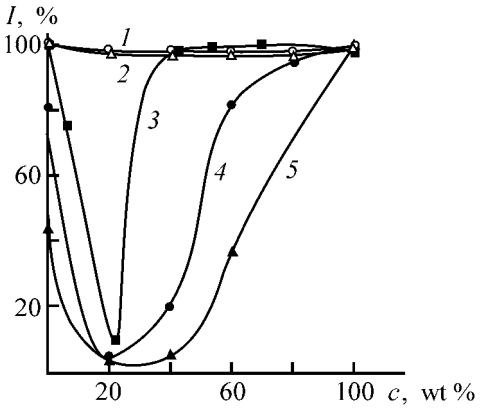

Fig. 2. Optical transmission of mixed films from PMMA blends: (*1*) PMMA–MMA/VC copolymer (46.5 wt % VC), (*2*) PMMA–MMA/VC copolymer of high compositional homogeneity (74 wt % VC), (*3*) PMMA–MMA/VC copolymer (78.9 wt % VC), (*4*) PMMA–PVC, and (*5*) PMMA–copolymerization product (89% VC–11% MMA). (*I*) Optical transmission and (*c*) PMMA content; the same for Fig. 3.

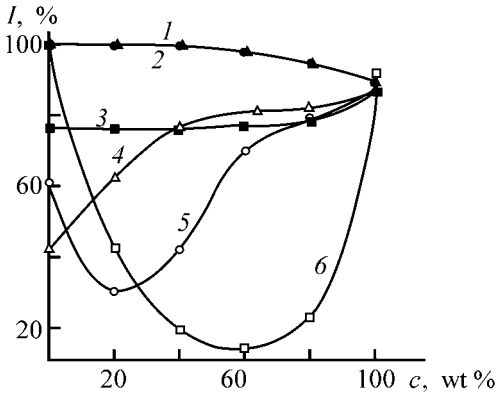

Fig. 3. Optical transmission of mixed films from PVC blends: (*1*) PVC1–MMA/VC copolymer (10.1 wt % VC); (*2*) PVC1–MMA/VC copolymer of high compositional homogeneity (74 wt % VC); (*3*, *4*, *5*) PVC1–MMA/PC copolymerization products containing (*3*) 94.1, (*4*) 89, and (*5*) 84 wt % VC; and (*6*) PVC2–MMA/VC copolymer (10.1 wt % VC). Molecular weight: PVC1 4.7×10^4 and PVC2 9.0×10^4.

copolymer with PVC is formed. The relative contents of the products, estimated by the above-described procedure, are listed in Table 2.

Figures 2 and 3 show the most typical dependences illustrating how the composition of blends of MMA and VC homopolymers with products of their copolymerization affects the optical transmission of the resulting films. The films from PVC–PMMA (Fig. 2, curve *4*) and PMMA–MMA/VC copolymer (curve *3*) blends are opaque at a low MMA contents (minimal optical transmission is observed for the compositions with 20–30 wt % MMA).

The copolymers with a considerable MMA content (4.5, 10.1, 29.5, and 46.5 wt % VC) form transparent films when taken in combination with both PMMA and PVC over the entire composition ranges. Typical examples are given in Figs. 2 and 3 (curves *1*). This is also true for the copolymer with a lower MMA content (26 wt %), but with increased compositional homogeneity (Figs. 2 and 3, curves *2*).

The blends of the VC-rich copolymerization products (78.9, 84.9, 89.0, and 94.1 wt % VC) form opaque films with PMMA and semitransparent films with PVC (Fig. 2, curve *5*; Fig. 3, curves *3*–*5*).

For the blends containing VC/MMA copolymer (10.1 wt % VC, 89.9 wt % MMA), the changing molecular weight of PMMA from 4.2×10^4 to 1.16×10^5 had no effect on the optical transmission of the film, which was close to 100%, while increasing the molecular weight of PVC from 4.7×10^4 to 9.0×10^4 resulted in that the films became opaque (Fig. 3, curves *1* and *6*).

PVC–PMMA–copolymer (or copolymerization product) ternary blends were characterized by the Gibbs diagrams. We measured the optical transmission of the films over the entire composition range. The optical transmission of ternary films mostly correlated with that of the binary films containing common components. If some copolymer or VC/MMA copolymer-

Table 2. PVC content in VC–MMA copolymerization products

Product no.	VC content in monomer mixture	VC content in copolymer	q_1^*	q_2^*, wt %	PVC weight fraction in blends with the copolymer
1	0.969** / 0.952	0.925 / 0.885	0.410 / 0.421	81.5	0.451
2	0.941 / 0.909	0.873 / 0.791	0.465 / 0.483	74.7	0.264
3	0.914 / 0.870	0.829 / 0.752	0.500 / 0.524	79.9	0.216
4	0.889 / 0.833	0.680 / 0.570	0.328 / 0.365	36.5	–
5	0.615 / 0.500	0.465 / 0.352	0.720 / 0.775	79.0	–

* (q_1, q_2) Conversions corresponding to completion of copolymerization and of the whole process, respectively.

** The mole fraction is given in the numerator, and the weight fraction, in the denominator.

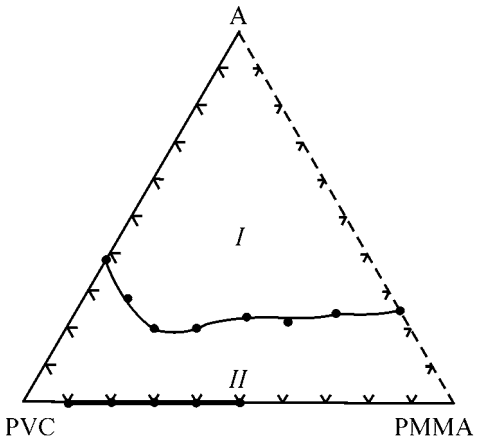

Fig. 4. Fields of compositions forming (*I*) opaque and (*II*) transparent films in the system PVC–PMMA–copolymerization product (89 wt % VC, 11 wt % MMA), composed by PVC and copolymer A (79.1 wt % VC, 20.9 wt % MMA).

ization product forms transparent films, being taken in combination with both PVC and PMMA, then, with rare exception, ternary films are transparent also. For example, the ternary films containing MMA-rich copolymers are mostly transparent. The ternary films with copolymerization products with high VC content form both transparent and opaque films. Let us consider, for example, copolymerization product no. 11 (89 wt % VC–11 wt % MMA) (Table 1). It follows from the results of a theoretical estimation by the above-described procedure that this product is a mixture of PVC (26.4 wt %) and VC/MMA copolymer (79.1 wt % VC). Figure 4 shows the Gibbs diagram with this copolymer as a separate component, but not the copolymerization product as a whole. Its another fraction, PVC, is summed with the corresponding component added to the mixture.

Field *II* corresponds to the compositions of transparent films, and field *I*, of opaque films. Binary blends copolymer–PMMA cannot be obtained, as the copolymer is initially mixed with PVC, and, therefore, the corresponding axis is given as a dashed line. In the PVC–PMMA axis, we distinguish a segment corresponding to PVC–PMMA blends forming opaque films.

The use of VC/MMA copolymers with comparable VC and MMA contents (31.9% MMA–68.1% VC; 42.3% MMA–57.7% VC) as the third component provides formation of films with an optical transmission of 80%. In both cases, the most transparent films are formed from blends containing 20% of the copolymer, PVC (70–50%), and PMMA (10–30%). It was interesting to analyze the correlations between the optical transmission of the films and their structural and mechanical characteristics. Data for films of close compositions, containing from 80 to 83.6% VC, are listed in Table 3. The lowest strength was observed for opaque PMMA– PVC binary films, and the highest strength, for transparent PMMA–PVC–copolymer ternary films. With close total relative content of the monomeric units, the increase in the strength appeared to be rather significant (by a factor of about 2), with the relative elongation remaining practically unchanged (within 16–20%). The compositions selected for comparison contain large amounts of the VC units. Such a decision was made taking into account such factors as the low cost of the base monomer and the incombustibility of PVC and PVC-based materials, which is significant from the practical standpoint.

To elucidate the features characteristic of the transparent and opaque films formed by PVC–PMMA blend compositions, we performed dielcometric and scanning electron microscopic experiments. Figure 5 shows the surface topography at side illumination of the opaque film composed by a blend of 80% PVC and 20% PMMA and also of the transparent film (*I* = 80%, Fig. 3) consisting of 70% PVC and 30% copolymer (89% VC, 11% MMA). As seen, the surface of the opaque film is more developed, with grains 2,5–3 μm in size. On the surface of the opaque film, the intergrain boundaries are more diffuse, and the grains are considerably smaller, being about 1 μm in size. Data on the surface topography of the films at normal illumination show considerable differences in the surface roughness (1.66 and 0.14 μm for opaque and transparent films, respectively), also suggesting that the surface of the opaque films is more developed.

Since formation of a highly developed rough surface is thermodynamically unfavorable because of

Table 3. Strength and optical transmission of binary and ternary mixtures of MMA and VC copolymers

Composition, wt %	Total VC and MMA contents, wt %	σ, MPa	*I*, %
20 PMMA–80 PVC	20 PMMA–80 PVC	1.34	5
20 copolymer (89.9 MMA–10.1 VC)–80 PVC	18 PMMA–82 PVC	2.08	100
20 copolymer (31.9 MMA–68.1 VC)–10 PMMA–70 PVC	16.4 PMMA–83.6 PVC	2.90	80
20 copolymer (42.3 MMA–57.7 VC)–10 PMMA–70 PVC	18.5 PMMA–81.5 PVC	2.46	80

the higher surface free energy as compared to a smooth surface, it may be concluded that formation of a smooth surface is impeded by the incompatibility of the components. The surface of the transparent film is considerably less rough, suggesting better compatibility of the components in this case.

Figure 6 shows the temperature dependence of the dielectric loss tangent for the films formed by PVC, PMMA, a blend of 80% PVC and 20% PMMA, and binary and ternary blends containing the copolymerization product (89% VC, 11% MMA). For the blend polymer (curve *1*), a characteristic plateau is observed, while the curves of the homopolymers pass through a maximum corresponding to the glass transition (75 and 110°C for PVC and PMMA, respectively). It may be suggested that the weakly pronounced plateau in curve *3* (Fig. 6) is a result of superposition of the peaks characteristic of the components of an incompatible or partly compatible polymer blend. In all the cases of the binary and ternary blends of the copolymers with the homopolymers, only one peak is observed.

The results show that the properties of the films formed by blends of PVC and PMMA and VC/MMA copolymers depend on the extent of compatibility of the components. The dielcometric data obtained for the blends containing the copolymers suggest a higher level of compatibility of the components as compared to PMMA–PVC blends, which is also supported by the SEM data. Therefore, it may be concluded that the effect of interpenetration of the polymer networks in PVC–PMMA mixtures is considerably enhanced in the presence of VC/MMA copolymers. As a result, the polymer blend becomes more homogeneous, which is reflected, in particular, in erosion of the phase boundaries as a result of formation of a transition layer consisting of segments of all the components.

CONCLUSIONS

(1) Suspension copolymerization of vinyl chloride with methyl methacrylate can be performed to high conversions over a wide range of compositions of monomer mixtures. In PVC-rich systems, poly(vinyl chloride) is formed in the final stage of the process, as a result of strongly different copolymerization constants.

(2) Poly(vinyl chloride)–poly(methyl methacrylate) blends enriched in PVC form opaque films. The use of PVC/MMA copolymers as a component of the blends allows preparation of transparent films from blends of any composition.

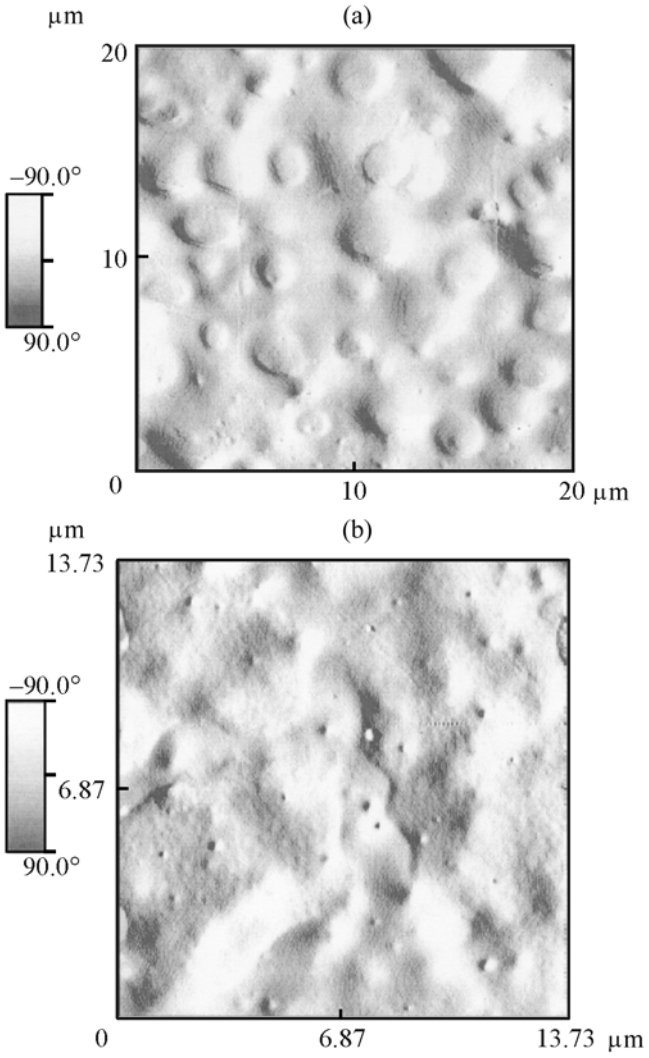

Fig. 5. Surface topography of the films: (a) 80% PVC–20% PMMA and (b) 70% PVC–30% copolymerization product (89% VC, 11% MMA).

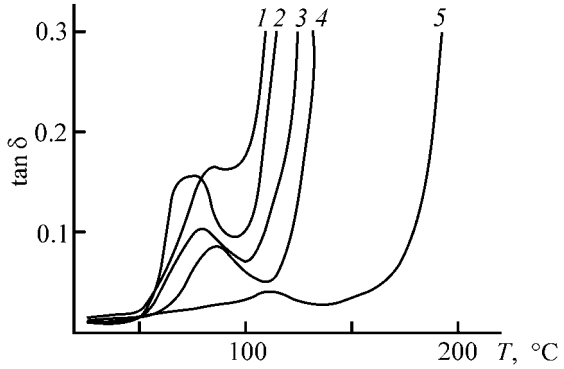

Fig. 6. Dielectric loss tangent tan δ vs. the temperature *T*. Film composition (%): (*1*) PVC + PMMA, (*2*) PVC, (*3*) 70 PVC–30 copolymerization product (89 VC), (*4*) 20 copolymerization product 89 VC–60 PVC–20 PMMA, and (*5*) PMMA.

(3) Transparent films formed by blends of the polymers and PVC/MMA copolymers demonstrate a higher strength as compared to opaque films of similar compositions. This can be attributed to better compatibility of components, as demonstrated by the dielcometric and scanning electron microscopic data.

ACKNOWLEDGMENTS

The study was financially supported by the Scientific and Technological Program "High School Research on the Priority Leads in Science and Technology" (Subprogram no. 203: "Chemical Technology," project no. 02.01.009).

REFERENCES

1. Wlochowicz, A. and Janicki, J., *J. Appl. Polym. Sci.*, 1989, vol. 38, no. 8, pp. 1469–1472.
2. Vesely, D. and Finch, D.S., *Makromol. Chem., Makromol. Symp.*, 1988, vol. 16, pp. 329–340.
3. Bosma, M., Brinke, G., and Ellis, T.S., *Macromolecules*, 1988, vol. 21, no. 5, pp. 1465–1470.
4. Parmer, J.F., Dickinson, L.C., Chein, J.C.W., and Porter, R.S., *Macromolecules*, 1989, vol. 22, no. 3, pp. 1078–1083.
5. Chalykh, A.E., Sapozhnikova, I.N., and Medvedeva, L.I., *Dokl. Akad. Nauk SSSR*, 1986, vol. 288, no. 4, pp. 939–943.
6. Kolesov, S.V., Kulish, E.I., and Minsker, K.S., *Vysokomol. Soedin., Ser. A*, 2000, vol. 42, no. 2, pp. 306–311.
7. Li, W., Shi, L., Shen, D., and Zheng, *J., Polym. Int.*, 1992, vol. 27, no. 1, pp. 57–62.
8. Rafikov, S.R., Pavlova, S.A., and Tverdokhlebova, I.I., *Metody opredeleniya molekulyarnykh vesov i polidispersnosti vysokomolekulyarnykh soedinenii* (Methods for Determination of Molecular Weights and Polydispersity of Macromolecular Compounds), Moscow: Akad. Nauk SSSR, 1963.
9. Bichuch, N.A., Malyshev, A.S., Kronman, A.G., *et al.*, *Vysokomol. Soedin., Ser. B*, 2003, vol. 45, no. 5, pp. 851–855.

Russian Journal of Applied Chemistry, Vol. 77, No. 8, 2004, pp. 1351–1354. Translated from Zhurnal Prikladnoi Khimii, Vol. 77, No. 8, 2004, pp. 1366–1369.

MACROMOLECULAR CHEMISTRY AND POLYMERIC MATERIALS

Carbonization of Some Cellulose Ethers and Their Graft Copolymers with Polyacrylonitrile

Yu. N. Sazanov, L. A. Nud'ga, V. A. Petrova, A. V. Novoselova, V. L. Ugolkov, G. N. Fedorova, E. M. Kulikova, and A. V. Gribanov

Institute of Macromolecular Compounds, Russian Academy of Sciences, St. Petersburg, Russia

Institute of Silicate Chemistry, Russian Academy of Sciences, St. Petersburg, Russia

Received June 8, 2004

Abstract—Low-temperature carbonization of hydroxyethyl, allyloxyethyl, and allylcarboxymethyl cellulose ethers and their copolymers with polyacrylonitrile was studied. The quantitative relationships between the degree of carbonization, on the one hand, and the degree of substitution of cellulose hydroxy groups and chemical structure of the substituents, on the other, were established. The dependence of the carbon residue on the amount of grafted polyacrylonitrile chains tends to a certain limit. The carbon residue depends on the atmosphere in which the carbonization is performed.

Graft copolymers of cellulose and polyacrylonitrile (PAN) simulate the structure of precarbonizates obtained by joint thermolysis of cellulose and its nitrogen-containing derivatives with PAN [1].

In this study, we examined the behavior of cellulose ethers (hydroxyethyl, HOEC; allyloxyethyl, AOEC; allylcarboxymethyl, ACMC) and their graft copolymers with PAN (AOEC–PAN, ACMC–PAN) at heating in the range 20–900°C in a vacuum, in a self-generated atmosphere (SGA) and in CO_2. Our goal was to find synthetic routes to carbon compounds based on cellulose derivatives and to elucidate the influence of nitrogen-containing polymers on the yield of the forming carbonizates.

EXPERIMENTAL

The cellulose ethers and PAN were prepared by published procedures (see references in [1]).

The kinetics of thermochemical transformations in various gas media were studied by thermovolumetric analysis (TVA) with manometric recording [2]. The behavior of the samples in SGA was studied on an MOM C derivatograph [3] with recording of the weight loss and thermal effects. Carbonization of the compounds in a CO_2 atmosphere was studied with an STA 429 device (Netzsch), with recording of the same parameters [4].

In accordance with the principal goal of our study, determination of carbonization conditions ensuring the maximal carbon residue (CR), we performed express analysis of the samples in SGA. As noted previously, carbonization of cellulose ethers and some other cellulose derivatives occurs mainly in three steps; their kinetic features were considered in [1, 5–9]. The most interesting for us, in the context of this study, were the quantitative and specific qualitative characteristics directly related to the carbonization step occurring, as a rule, above 400–500°C.

Comparison of the main parameters characterizing degradation and cross-linking (carbonization) of our samples (Table 1) reveals the following facts. The ethers in hand show relatively poor heat resistance, compared to PAN (the weight loss due to dehydration up to the temperature T_0 is 10–15%), and CR at 800°C is within 0–13%. Thermal degradation and cross-linking, according to TGA (Fig. 1a), occur in two steps. For cellulose ethers, in the first step in the range 200–350°C, degradation occurs with the release of a large amount of volatiles (up to 70% weight loss, depending on the structure of substituents). As seen from the DTA curves (Fig. 1b), degradation is exothermic; it involves several reactions: dehydration, decarboxylation, and formation and release of levoglucosan. The peaks of these reactions lie in the same range, 250 ± 20°C. The sharp exothermic peak

1070-4272/04/7708-1351 © 2004 MAIK "Nauka/Interperiodica"

Table 1. Thermal characteristics of degradation and cross-linking of cellulose ethers and their copolymers with PAN in SGA*

Sample**	T_0	T_5	T_{10}	T_{50}	T_I	T_{II}	T_{III}	T_{IV}	E_a, kcal mol^{-1}	CR, % of sample weight, 800°C
	°C				°C					
PAN	270	287	304	730	282(+)	–	471(–)	550(–)	155.6	42.4
HOEC	192	244	263	305	234(+)	311(+)	367(+)	540(+)	65.1	0.0
AOEC, γ:										
8	193	240	250	310	232(+)	273(+)	448(+)	542(+)	77.7	5.6
30	203	235	266	315	270(+)	–	476(+)	–	121.5	4.1
ACMC, γ = 6	260	268	272	285	258(+)	350(+)	–	546(+)	66.4	12.8
AOEC–PAN, *C*:										
52	231	274	295	441	294(+)	–	410(–)	477(–)	30.8	25.4
112	252	285	315	501	271(+)	–	417(–)	508(–)	55.7	33.0
239	237	277	352	716	247(+)	–	444(–)	484(–)	62.3	43.7
315	254	293	342	737	255(+)	–	454(–)	535(–)	74.4	44.4
400	232	277	322	716	270(+)	–	444(–)	532(–)	78.3	43.0
480	252	283	351	736	257(+)	–	441(–)	535(–)	77.9	44.0
ACMC–PAN, *C*:										
130	190	220	281	405	256(+)	–	432(–)	475(–)	169.5	20.0
370	222	238	272	600	241(+)	–	448(–)	–	138.6	36.1
670	260	300	407	>800	226(+)	–	454(–)	518(–)	142.1	50.2

* (T_5, T_{10}, T_{50}) Temperatures of 5, 10, and 50% weight loss, respectively (determined with the weight loss in the initial step of heating disregarded); (T_I–T_{IV}) temperatures of the exo- (+) and endothermic (–) peaks corresponding to steps I–IV of thermal degradation and cross-linking; (E_a) activation energy of sample degradation in the range 200–350°C.

** (γ) Degree of substitution and (*C*) degree of PAN grafting.

in the DTA curve of PAN, corresponding to the onset of its cyclization [10] (Fig. 1b, curve *4*), lies in the same range. These facts suggest that, in joint thermolysis of cellulose ethers and PAN in the range 200–350°C, reactions involving the reactive products can shift the degradation–cross-linking balance toward cross-linking. To substantiate this assumption, we considered the thermal characteristics of graft AOEC and ACMC copolymers with various degrees of substitution, γ, and various degrees of PAN grafting, *C*. Table 1 shows that grafting of small amounts of PAN to both ethers increases CR by a factor of 3–4 and noticeably enhances the overall heat resistance of the cellulose ethers. As *C* for AOEC–PAN grows, CR increases to 44.5%. For ACMC–PAN samples, the highest CR value was obtained at the highest *C* value, *C* = 670.

The enhancement of the heat resistance and the increase in the carbon residue in carbonization of graft copolymers are apparently due to formation of cross-

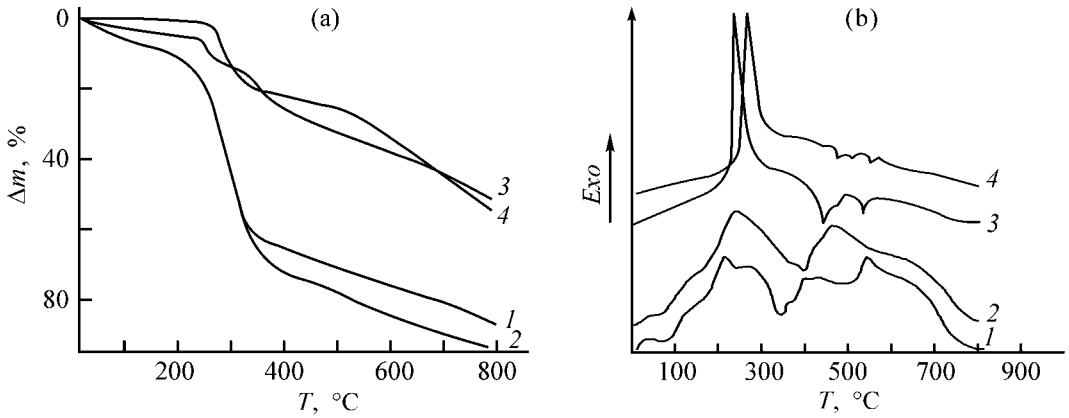

Fig. 1. (a) TG and (b) DTA curves of thermal degradation and carbonization under SGA conditions. Heating rate 10 deg min^{-1}, sample weight 50 mg. (Δ*m*) Weight loss and (*T*) temperature. Ether: (*1*) AOEC, γ = 8; (*2*) AOEC, γ = 30; (*3*) AOEC–PAN, *C* = 480; and (*4*) PAN.

Table 2. Thermal characteristics of degradation and cross-linking in CO_2 of samples of cellulose ethers and their copolymers with PAN

Sample	T_0	T_5	T_{10}	T_{50}	T_{max}, °C	CR, % of sample weight, 800°C
	°C					
HOEC	230	272	281	319	332	19.2
AOEC, γ = 8	263	278	282	760	325	47.3
ACMC, γ = 6	264	270	278	720	292	43.8
AOEC–PAN, C = 480	261	290	324	>800	262	55.7
ACMC–PAN, C = 500	271	282	311	>800	274	59.5

* (T_{max}) Temperature of the exothermic peak.

linked structures by reactions of allyl groups with nitrile nitrogen or reactions involving the degradation products (radicals, intermediates). With ACMC–PAN, the first steps of degradation may be accompanied by condensation of carboxy groups with amino groups arising in the course of PAN degradation.

The increased CR of the graft copolymers, compared to CR of pure PAN, indicates that the cellulose ethers are involved in cocarbonization with PAN. This fact shows that it is promising to use PAN for modification of carbonizates of cellulose derivatives under appropriate cocarbonization conditions differing from dynamic heating in SGA.

It is known that the carbon residue in carbonization of cellulose materials in some cases appreciably increases when the carbonization is performed in CO_2 [11]. To find whether this is the case for our system, we performed a combined TG–DSC analysis of the samples under dynamic conditions in a CO_2 atmosphere at temperatures of up to 800°C (Table 2).

Comparison of the thermal characteristics of the samples heat-treated in SGA and CO_2 shows that the balance of thermochemical degradation and cross-linking shifts toward formation of cross-linked carbonized products. Saturation of the surrounding atmosphere with degradation products causes an appreciable increase in CR; this parameter reaches 60% for the copolymers. The heat resistance, especially T_{50}, increases also. Presumably, the changes mainly concern thermolysis of cellulose ethers; their CR increases by almost an order of magnitude when the samples are heat-treated in CO_2. The heat resistance parameters and CR of the graft copolymers increase also, but this trend is less pronounced, compared to the ethers.

Thus, we confirmed once more the previous data [12] that the rate of PAN cyclization in the initial heating steps (250–300°C) is independent of the ambient atmosphere.

Similar features are observed in thermolysis of graft copolymers of PAN with AOEC and ACMC in a vacuum. At any degree of grafting, the TVA curve, similarly to the DTA and DSC curves, contains a very sharp, "bursting" peak corresponding to the onset of PAN cyclization. Even at small C, this peak appears at the same temperature; only its area proportionally changes. At higher temperatures, the effect of PAN on the formation of the cocarbonizate with cellulose ethers varies, depending on the composition of the surrounding gas phase and on the temperature mode. As shown by our experiments, the CR varied under dynamic heating conditions in opposite direction with the heating rate and depended also on the chemical structure of the cellulose ether, values of γ and C, and temperature range of heating; the dependence for all the samples is proportional. For example, the CR of the PAN–AOEC samples, compared to PAN–ACMC samples, is higher if the thermolysis in the range 150–300°C is performed faster. This may be due to competition of degradation through the hydroxy and carboxy groups of the ethers with cross-linking through the allyl groups. Above 300°C, the difference is less pronounced, but the PAN fragments play a more significant role in the thermolysis under these conditions.

In the case of isothermal carbonization mode (expected to be favorable for attaining maximal CR), there are no clear correlations with the temperature and time of the process. Experiments on isothermal heating of the samples at 200°C in a vacuum for 10 h and at 300°C in SGA for 4 h revealed only the expected dependence of the CR on the ambient gas medium. In thermolysis in a vacuum, i.e., under conditions of continuous removal of degradation products, the CR is approximately 10–15% lower, compared to the heat treatment in SGA. As for the time of heat treatment and temperature, the CR of cellulose ethers and copolymers shows no direct correlation with these parameters. As in experiments on dynamic heating,

the competition of degradation and cross-linking should be taken into account in some cases; the development of these processes is closely associated with the chemical structure of the polymers. For example, the CR of an AOEC sample with $\gamma = 8$ after heating for 10 h in a vacuum at 200°C is 40.7%, whereas the copolymer with PAN under the same conditions gives a CR of 27.6%. Furthermore, there is no direct correlation even with the PAN content: As the PAN content increases, the CR varies from 49 to 38%, passing through a minimum (27%).

One more interesting feature of the carbonization of the examined cellulose ethers and their copolymers with PAN in SGA is the appearance of endothermic peaks at 450–600°C in the DTA curves (Fig. 1b, curves *3* and *4*). It is clearly seen that, when a sample of PAN–AOEC copolymer ($C = 480$) is heated at a constant rate, endothermic peaks appear at 441 and 535°C. Similar, but weaker peaks at 471 and 553°C are seen in the DTA curve of PAN. Related peaks, slightly differing in the position and differing in the area, are also observed in the DTA curves of the other copolymers with different degrees of PAN grafting. These endothermic peaks are apparently associated with the formation of ordered areas in the carbonizate structure. The shapes and intensities of these peaks suggest that the initiator of the formation of the ordered crystallite-like structures is PAN, but carbonizates of cellulose ethers are also involved in the processes, increasing the degree of orientation of the ordered areas. Special spectroscopic studies are required to gain insight into this phenomenon; here we can tentatively suggest formation of primary turbostratic structures with various degrees of ordering in this temperature range of precarbonization. Depending on the concentration and mutual orientation of the cyclic products of the reaction of PAN and AOEC, intermediate polycyclic compounds with a crystalline structure can form, and their melting is detected by DTA. Similar effects have also been observed with PAN–ACMC copolymers, with the only difference that the endothermic effect was the most pronounced in the range 440–460°C [1].

Both the carbonization and degradation are influenced by the ambient atmosphere. For example, when thermolysis is performed in CO_2, changes occur only in the carbonizate structure originating from cellulose ethers, and no ordered structures are formed. No structural rearrangements are observed in the copolymers in the range from 400 to 800°C. As for carbonization in a vacuum, a noticeable weight loss below 500°C and a certain release of hydrogen above 650°C cause loosening and amorphization of the carbonizate.

CONCLUSIONS

(1) Hydroxyethyl, allyloxyethyl, and allylcarboxymethyl cellulose ethers and their graft copolymers with acrylonitrile show promise for preparation of carbon compounds.

(2) The composition of the surrounding atmosphere in carbonization exerts a decisive influence on the carbon residue, which reaches 30–40% for some ethers.

(3) In carbonization of graft copolymers in CO_2, the carbon residue reaches 55–60%.

REFERENCES

1. Sazanov, Yu.N., Nud'ga, L.A., Novoselova, A.V., *et al.*, *Zh. Prikl. Khim.*, 2004, vol. 77, no. 4, pp. 643–648.
2. Sazanov, Yu.N. and Sysoev, V.A., *Eur. Polym. J.*, 1974, vol. 10, pp. 867–869.
3. Gribanov, A.V., Sazanov, Yu.N., Beloborodova, E.V., *et al.*, *Zh. Prikl. Khim.*, 1999, vol. 72, no. 3, pp. 467–473.
4. Sazanov, Yu.N., Ugolkov, V.A., Prasolova, O.E., *et al.*, *Zh. Prikl. Khim.*, 2003, vol. 76, no. 7, pp. 1167–1171.
5. Plisko, E.A., Sazanov, Yu.N., Baulin, A.A., *et al.*, *Zh. Prikl. Khim.*, 1974, vol. 47, no. 7, pp. 1617–1621.
6. Sazanov, Yu.N., Fedorova, G.N., Plisko, E.A., and Nud'ga, L.A., *Zh. Prikl. Khim.*, 1980, vol. 53, no. 9, pp. 2143–2146.
7. Sazanov, Yu.N., Plisko, E.A., Nud'ga, L.A., *et al.*, *Zh. Prikl. Khim.*, 1981, vol. 54, no. 3, pp. 691–697.
8. Vasil'eva, G.G., Petropavlovskii, G.A., Fedorova, G.N., and Sazanov, Yu.N., *Zh. Prikl. Khim.*, 1982, vol. 55, no. 3, pp. 677–681.
9. Nud'ga, L.A., Petrova, V.A., Petropavlovskii, G.A., and Sazanov, Yu.N., *Zh. Prikl. Khim.*, 1991, vol. 64, no. 7, pp. 1523–1526.
10. Sazanov, Yu.N., Shirokov, N.A., and Goltsin, B.E., *Thermo-chim. Acta*, 1978, vol. 24, pp. 81–88.
11. Nikitin, N.I., *Khimiya drevesiny i tsellyulozy* (Chemistry of Wood and Cellulose), Moscow: Akad. Nauk SSSR, 1962.
12. Gribanov, A.V. and Sazanov, Yu.N., *Zh. Prikl. Khim.*, 2000, vol. 73, no. 3, pp. 465–469.

Russian Journal of Applied Chemistry, Vol. 77, No. 8, 2004, pp. 1355–1358. Translated from Zhurnal Prikladnoi Khimii, Vol. 77, No. 8, 2004, pp. 1370–1373.

MACROMOLECULAR CHEMISTRY AND POLYMERIC MATERIALS

Controlling the Viscosity of Melts of Partially Crystalline Polyimides Used for Preparing Carbon-Reinforced Plastics

T. A. Kostereva, Yu. N. Panov, A. L. Didenko, I. G. Silinskaya, V. M. Svetlichnyi, V. E. Yudin, and V. V. Kudryavtsev

Institute of Macromolecular Compounds, Russian Academy of Sciences, St. Petersburg, Russia

Received February 13, 2004

Abstract—The influence exerted by the molecular weight of partially crystalline polyimide derived from 4,4'-bis(4-aminophenoxy)diphenyl and 1,3-bis(3,4-dicarboxyphenoxy)benzene on the viscosity of its melt was studied.

Composites with a partially crystalline polyimide (PI) matrix are promising structural materials. This matrix exhibits high mechanical and adhesion parameters, enhanced resistance to solvents, and high resistance to heat and thermal oxidation. Composite materials based on such a polymer exhibit an increased interlayer failure viscosity in combination with a high softening point, determined not by glass transition but by the melting of the binder [1]. An important property of the PI binder is its capability to crystallize after melting and subsequent cooling. The crystallizability of the polymer increases with a decrease in the molecular weight of PI and on addition of a bisimide structurally related to the macromolecule unit or diamine moiety [2]. The film-forming properties of the binder are preserved when the molecular weight of the polymer compounded with a bisimide is decreased only to a strictly definite level.

Apparently, the melting point and viscosity of PI depend on its molecular weight and on the bisimide added. When preparing a composite from a prepreg, it is necessary to know the behavior of the melt of the polymeric matrix (polymeric compound).

Our goals were to determine how the viscosity of the melt of a PI compound varies with time, depending on the molecular weight of the starting PI and on the bisimide content, and to find a formulation with a stable and relatively low melt viscosity.

EXPERIMENTAL

The polyimide derived from 1,3-bis(3,4-dicarboxyphenoxy)benzene dianhydride (R, mp 163–164°C) and 4,4'-bis(4-aminophenoxy)diphenyl (OP_2O, mp 193–194°C) was prepared in two stages [3]. In the first stage, we prepared a solution of the polyamido acid (PAA), which was applied to a glass support and dried. In the second stage, the resulting film was subjected to thermal imidization with step heating to 280°C. The chemical structure of PI is as follows:

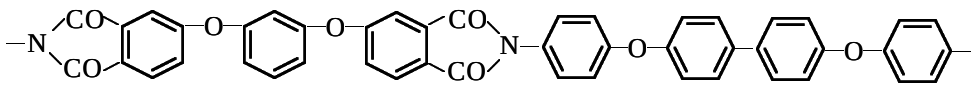

R OP_2O

The molecular weight of PAA was decreased by varying the stoichiometric ratio of the monomers. In the first procedure, the dianhydride was taken for preparing PAA in a 3 or 5 mol % excess relative to the stoichiometry, and in the second procedure, the dianhydride was taken in a 3, 5, or 10 mol % deficiency relative to the diamine, with phthalic anhydride (PA) added in the final stage in the amount equivalent to the content of the remaining amino groups (6, 10, and 20 mol %, respectively).

1070-4272/04/7708-1355 © 2004 MAIK "Nauka/Interperiodica"

Table 1. Intrinsic viscosities and molecular weights of PAA

Sample no.	Dianhydride : diamine molar ratio	PA, mole	$[\eta]_{DMF}$, dl g^{-1}	$M_w \times 10^{-4}$	Sample no.	Dianhydride : diamine molar ratio	PA, mole	$[\eta]_{DMF}$, dl g^{-1}	$M_w \times 10^{-4}$
1	1.05 : 1	–	0.61	2.0	4	0.97 : 1	0.06	0.67	2.4
2	1.03 : 1	–	0.74	2.9	5	0.95 : 1	0.1	0.50	1.3
3	1 : 1	–	1.67	15.0	6	0.90 : 1	0.2	0.38	0.8

Bisimides 1 and 2 were prepared by thermal imidization of bisphthalamido acids prepared by the reaction of OP_2O and 4,4'-bis(p-aminophenoxy)diphenyl sulfone, respectively, with PA in 1 : 2 molar ratio in *N*-methylpyrrolidone (MP):

Bisimide 1

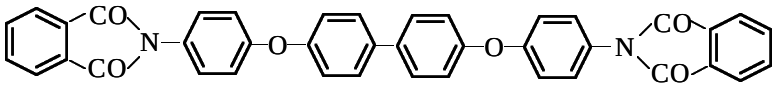

Bisimide 2

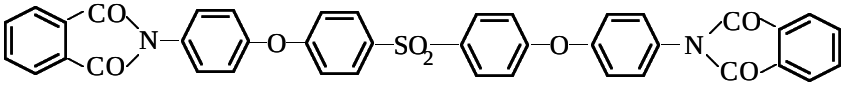

Bisimide 1 or 2 was added to a PAA solution in an amount of 1, 3, 5, or 10 wt %.

Oligoimide 3 was prepared by three-step synthesis. Reaction of a twofold excess of OP_2O with 1,3-bis-(3,4-dicarboxyphenoxy)benzene in MP gave the corresponding oligomeric diamino amido acid, to which we subsequently added phthalic anhydride in the amount equivalent to the amount of amino groups. The solution was imidized thermally, with azeotropic distillation of water with toluene, to obtain the oligoimide:

Oligoimide 3

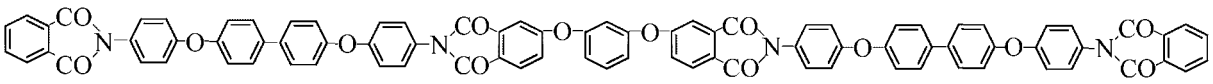

The intrinsic viscosity of PAA [η] was measured with an Ubbelohde viscometer at 25°C in DMF. The molecular weight of the samples was determined by measuring the light scattering. The characteristics of the polymers are listed in Table 1.

The viscosities of PI solutions were measured on a PIRSP cone–plate rheogoniometer [4] (angle at the cone apex 1°, diameter 40 mm, shear rate 0.02 s^{-1}, 350°C).

Among samples prepared by the first procedure, only the polymer with MW 2.0×10^4 (sample no. 1) melts; higher-molecular-weight sample nos. 2 and 3 do not melt at 350°C. The initial viscosity of sample no. 1 was 1.4×10^4 Pa s; the viscosity rapidly grew in time, reaching 10^6 Pa s in 30 min.

To decrease the viscosity of melts, we added to PI 10 wt % bisimide 1, containing the same diamine fragment as the PI and acting as plasticizer [5]. However, sample no. 3 (MW 1.5×10^5) did not melt even at 350°C. For the other two samples, addition of bisimide 1 decreased the initial viscosity of the melt; the effect was more pronounced with PI of lower molecular weight (Fig. 1, curves *4*, *5*). Similarly to the sample without bisimide addition, the melt viscosity grew

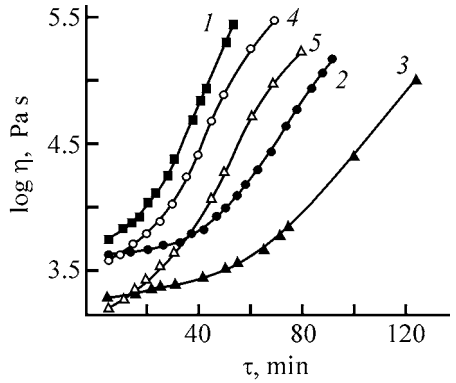

Fig. 1. Viscosity η of melts of sample nos. 1–3 with addition of (*1–3*) 10% bisimide 2 and (*4, 5*) 10% bisimide 1 vs. time τ. 350°C; $\gamma = 0.02\ s^{-1}$; the same for Fig. 2. R : OP_2O molar ratio: (*1*) 1 : 1, (*2, 4*) 1.03 : 1, and (*3, 5*) 1.05 : 1.

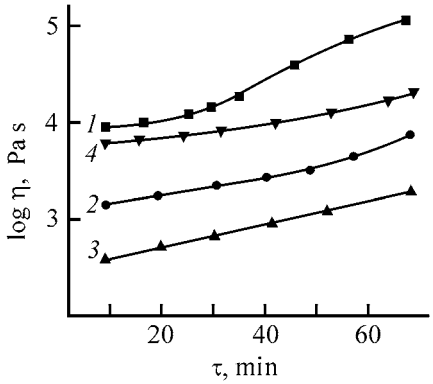

Fig. 2. Viscosity η of sample nos. 4–6 vs. time τ. R : OP_2O PA molar ratio: (*1*) 0.97 : 1 : 0.06, (*2*) 0.95 : 1 : 0.1, (*3*) 0.9 : 1 : 0.2, and (*4*) 0.97 : 1 : 0.06 with addition of 10 wt % bisimide 2.

fairly rapidly. The viscosity grows in two steps. The rates of these steps are equal for both samples (Table 2, sample nos. 4 and 5, b_1 and b_2).

Bisimide i is insoluble in amide solvents. Therefore, the system formed upon its mixing with PAA in MP is heterogeneous, and the performance of bisimide 1 as plasticizer for high-molecular-weight PI is poor. In the subsequent experiments, bisimide 1 was replaced with bisimide 2, which is soluble in MP owing to the introduction of an SO_2 bridge between the phenylene groups in the amine fragment. With this plasticizer, all the mixed systems melted at 350°C. The initial viscosities of melts of sample nos. 1 and 2 were the same as those of the samples with bisimide 1; the viscosity also grew in two steps (Fig. 1, curves *1–3*). However, the rate of viscosity growth in this case depends on the molecular weight of the PI. With lower-molecular-weight PI samples, the second step began later and at lower viscosities, and the viscosity growth was slower.

The viscosity growth with time was described by the relationship $\log \eta = a + bt$. Its parameters were determined from the slopes of the tangents to the experimental curve. The interception point of the tangents is the point of transition from the slow to the fast step (Table 2).

Thus, we found that only a compound of the lowest-molecular-weight PI with 10% bisimide 2 has the low initial viscosity of the melt and the viscosity grows slowly during relatively long time; however, the viscosity grows more steeply in the second step, probably owing to mutual linking of macromolecules through terminal groups at high temperature.

To eliminate this process, we used samples with PI of decreased molecular weight, obtained by the second procedure (endcapping with PA). The effect was demonstrated for the example of a compound modeling the chemical structure of PI (oligoimide 3). This oligoimide is crystalline, but its melting point is lower than that of PI. Therefore, its viscosity was measured at 330°C, and it remained virtually unchanged over a period of 2 h.

Figure 2 (curves *1–3*) shows how the viscosities of melts of sample nos. 4–6 (Table 1) vary with time. A decrease in MW by endcapping with PA resulted in a significant stabilization of the viscosity. However, only sample no. 4 with MW 2.4×10^4 showed satisfactory film-forming properties, necessary for obtaining composite PI materials with the required properties. This sample showed an insignificant growth of the viscosity with time. To further decelerate the viscosity growth, we compounded this polymer with 10% bisimide 2. As a result, we not only ensured the slowest growth of the melt viscosity (Fig. 2, curve *4*), but also decreased the initial viscosity of the melt.

Table 2. Coefficients of the equation $\log \eta = a + bt$ for the slow (1) and fast (2) steps of viscosity growth; time and viscosity corresponding to the transition from the slow to fast step

Sample no.*	a_1, Pa s	$b_1 \times 10^2$, Pa s min^{-1}	a_2, Pa s	$b_2 \times 10^2$, Pa s min^{-1}	t, min	log η (η, Pa s)
1	3.7	1.5	2.9	4.7	24	4.0
2	3.6	0.6	2.4	3.1	47	3.8
3	3.2	0.5	2.0	2.4	65	3.5
4	3.5	1.5	2.7	4.2	27	3.9
5	3.1	1.4	2.1	4.3	35	3.6

* Sample nos. correspond to curve nos. in Fig. 1.

CONCLUSIONS

(1) The viscosity of melts of partially crystalline polyimide prepared from 1,3-bis(3,4-dicarboxyphenoxy)benzene dianhydride and 4,4'-bis(4-aminophenoxy)diphenyl and of its compounds with bisimides 1 and 2 rapidly grows with time.

(2) The initial viscosity of the melt decreases on compounding of the polyimide with 10 wt % bisimide 1 or 2. The viscosity growth decelerates with bisimide 2, soluble in *N*-methylpyrrolidone; the effect is the more pronounced, the lower the molecular weight of the initial polyimide.

(3) To obtain a polyimide whose melt would exhibit the viscosity most stable in time, the macromolecule ends can be capped with phthalimide groups. The viscosity characteristics of a compound of such polyimide with soluble bisimide 2 is the optimal for preparing composites.

REFERENCES

1. Strong, C.E., *Prog. Polym. Sci.*, 1991, vol. 16, pp. 561–694.
2. Yudin, V.E., Svetlichnyi, V.M., Gubanova, G.N., *et al.*, *Vysokomol. Soedin., Ser. A*, 2002, vol. 44, no. 2, pp. 257–267.
3. Bessonov, M.I., Koton, M.M., Kudryavtsev, V.V., and Laius, L.A., *Polyimides—Thermally Stable Polymers*, New York: Consultants Bureau, 1987.
4. Vinogradov, G.V., Malkin, A.Ya., Plotnikova, E.P., *et al.*, *Vysokomol. Soedin., Ser. A*, 1978, vol. 20, no. 2, pp. 226–230.
5. Yudin, V.E., Svetlichnyi, V.M., Gubanova, G.N., *et al.*, *J. Appl. Polym. Sci.*, 2002, vol. 83, pp. 2873–2882.

Russian Journal of Applied Chemistry, Vol. 77, No. 8, 2004, pp. 1359–1363. Translated from Zhurnal Prikladnoi Khimii, Vol. 77, No. 8, 2004, pp. 1374–1377.

MACROMOLECULAR CHEMISTRY AND POLYMERIC MATERIALS

Influence of Molecular Weight of Polyacrylic Acid on the Rate of Copper Dissolution

V. N. Kislenko and R. M. Verlinskaya

L'vovskaya Politekhnika National University, Lviv, Ukraine

Received October 16, 2003; in final form, April 2004

Abstract—The weight of polyacrylic acid adsorbed on copper from an aqueous solution and the rate of copper dissolution in the presence of hydrogen peroxide as functions of molecular weight of the polymer were studied.

Dispersions and solutions of acrylic polymers containing carboxy groups find growing use in metal-protection paints and adhesives. In this context, a need arises to study the processes on the metal surface being in contact with solutions of carboxyl-containing polymers. Numerous papers are devoted to the mechanism of adsorption of polymers from solutions [1–5], which is caused by the wide industrial use of this process. In the majority of publications, the conditions of adsorption equilibrium and kinetics of polymer adsorption were studied. A study of competitive adsorption of polymers from dilute and semidilute solutions of polymers [6–8] showed that, in a number of cases, one polymer is substituted for another polymer in the adsorption layer. Desorption of polymers has not been adequately studied. A study of polystyrene desorption under conditions of varied solvent flow upon the adsorbed polymer layer [9, 10] showed that, with increasing velocity gradient, the amount of the adsorbed polymer decreases, reaching a minimum. The thickness of the adsorption layer of polyacrylamide and polystyrene [11, 12] decreases with increasing velocity of the solvent flow over the layer.

A study of the kinetics of dissolution of copper(II) oxide in polyethylenimine [10] and polyacrylic acid (PAA) [11], dissolution of zinc oxide in PAA [12], and also adsorption of polymer at their surfaces showed that the rate at which the metal concentration in the solution grows depends on the amount of adsorbed polymer.

Here we studied the influence of molecular weight of PAA on the adsorption of the polymer at the copper surface and the rate of copper dissolution in aqueous solution of PAA and hydrogen peroxide [13–15].

As seen from Fig. 1 (curve *1*) and data listed in the table, the weight of PAA adsorbed on 1 m^2 of copper surface increases with increasing molecular weight of polymer and is virtually independent of the initial concentration of the polymer in the solution at its concentration above 10 g l^{-1}. The latter suggests that the saturation of the adsorption layer is reached in this range of PAA concentration.

The copper surface area occupied with one macromolecule in the saturated adsorption layer was evaluated by the formula

$$S_b = M/(AN_A), \quad (1)$$

where M is molecular weight of PAA, A is the weight of PAA adsorbed at the unit surface area, and N_A is the Avogadro number.

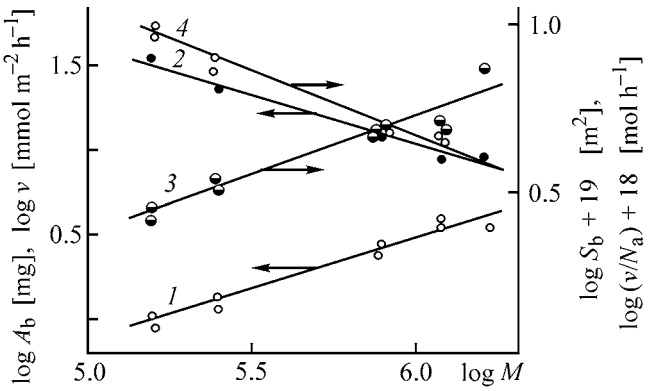

Fig. 1. (*1*) Weight of PAA adsorbed on 1 m^2 of copper surface A, (*2*) dissolution rate v, (*3*) surface area of copper occupied by one macromolecule S_b, and (*4*) ratio of the rate of copper dissolution to the amount of PAA macromolecules adsorbed on 1 m^2 of copper surface, v/N_a, vs. the molecular weight of PAA, M.

1070-4272/04/7708-1359 © 2004 MAIK "Nauka/Interperiodica"

Influence of the molecular weight of PAA on the weight of PAA adsorbed on 1 m^2 of copper surface occupied by one macromolecule in the adsorption layer and on the rate of copper dissolution in PAA and H_2O_2 solutions

$M \times 10^{-5}$	MWD*	[PAA], g l^{-1}	A, mg m^{-2}	$S_b \times 10^{19}$, m^2	v, mmol m^{-2} h^{-1}
16.0	1.22	20	3.5	7.55	9.9
11.5	1.18	20	4.1	4.61	9.5
11.5	1.18	10	3.9	4.88	9.5
7.60	1.21	20	2.7	4.61	12.9
7.60	1.21	10	2.6	4.75	12.9
2.43	1.16	20	1.2	3.32	22.3
2.43	1.16	10	1.3	3.19	22.3
1.54	1.25	20	0.9	2.77	33.1
1.54	1.25	10	1.0	2.56	33.1

* Molecular-weight distribution.

As seen from the table, the surface area occupied by one macromolecule in the adsorption layer of the copper surface increases with increasing molecular weight of PAA.

The dependence of the surface area occupied by a macromolecule in the absorption layer on the molecular weight of the polymer is linear in the logarithmic coordinates. The correlation coefficient of the straight line is 0.949, and the slope, 0.35 ± 0.07. Hence, the dependence of the surface area occupied by a PAA macromolecule on its molecular weight can be written as

$$S_b = 10^{-17.4} M^{0.35}. \quad (2)$$

The H_2O_2 concentration in dissolution of copper in PAA was chosen so that the rate of copper oxidation to copper(II) ions was significantly lower than the rate of formation of polyacrylates and the rate of their desorption. During the experiment, the copper plate was not coated with a copper(II) oxide layer. The PAA concentration in the solution was chosen so that it corresponded to a plateau in the adsorption isotherm, which is suggested by the close weights of PAA adsorbed on the unit copper surface area at various initial PAA concentrations in the solution (see table). This allowed us to determine the influence of the degree of filling of the plate surface with the polymer and to reveal the influence exerted by the molecular weight of the polymer on the rate of copper dissolution.

A study of the rate of copper dissolution in aqueous PAA showed that, in the examined concentration range, it does not noticeably depend on the initial concentration of the polymer in the solution (Fig. 2). The linear dependence of the amount of dissolved copper on time in the initial stage of the process suggests an insignificant influence of the copper ion concentration on the process rate. At the same time, an increase in the molecular weight of PAA results in a noticeable increase in the process rate (Fig. 1, curve *2*). The rate of copper dissolution varies regularly with variation of the weight of PAA adsorbed on the unit copper surface area (see table). This suggests that the rate of accumulation of copper(II) ions in the solution is proportional to the rate of desorption of copper(II) polyacrylates from the adsorption layer:

$$v = d[Cu^{2+}]/dt = \gamma k_d N_a, \quad (3)$$

where γ is the coefficient of proportionality between the rate of copper dissolution and the rate of polymer desorption, k_d is the rate constant of PAA desorption, and N_a is the amount of PAA macromolecules adsorbed on the unit copper surface area,

$$N_a = AN_A/M. \quad (4)$$

To elucidate the influence of PAA molecular weight on the rate constant of its desorption, we rearranged expression (3) to obtain the equation

$$\log (v/N_a) = B + b \log M. \quad (5)$$

As seen from Fig. 1, curve *4*, the dependence of the experimental data in the coordinates of Eq. (5) is linear. The correlation coefficient of the straight line

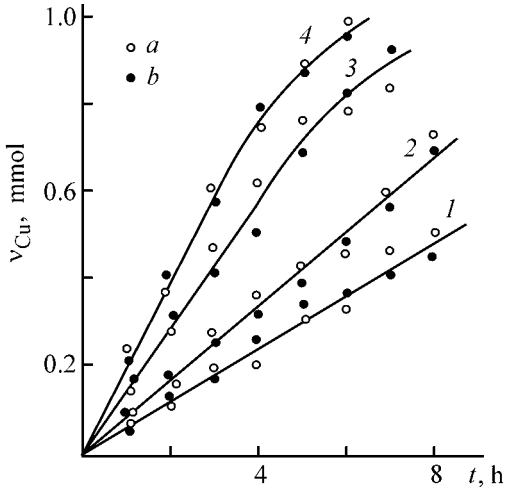

Fig. 2. Variation of the amount of dissolved copper, v_{Cu}, in time t at PAA concentration of (*a*) 10 and (*b*) 20 g l^{-1}. H_2O_2 concentration 12 mmol l^{-1}, 70°C. Molecular weight of PAA, $M \times 10^{-5}$: (*1*) 11.5, (*2*) 7.6, (*3*) 2.43, and (*4*) 1.54.

is 0.944. The parameter b is -0.29 ± 0.8. Thus, expression (3) can be written in the form

$$v = 10^{-15.5} N_a / M^{0.29}. \quad (6)$$

A comparison of the exponents at molecular weights in Eqs. (2) and (6) shows that, to a first approximation, the rate of desorption of macromolecules from the adsorption layer is proportional to the amount of macromolecules adsorbed on the unit copper surface area and is in inverse proportion to the surface area occupied by one macromolecule:

$$v = \gamma k_d N_a / S_b \approx \gamma k_d N_a / M^{0.35}. \quad (7)$$

Our attempt to linearize dependence (7) in the logarithmic coordinates failed. The correlation coefficient was less than 0.4, and the errors in determination of the slope and the intercept on the ordinate axis were significantly greater than the value itself. This can be accounted for by the fact that the rate of polymer desorption is affected by the number of bonds between the macromolecule in the adsorption layer and active centers of the surface. In general case, this effect is not proportional to the surface area occupied by a macromolecule in the adsorption layer.

It is well known that formation of copper salts with PAA results in variation of the hydrodynamic cross section of the macromolecule globule in the solution [16, 17], and reaction of PAA with H_2O_2 results in degradation of macromolecule. Monitoring of the variation of the relative viscosity of PAA solution, which can characterize the variation of the state of the polymer macromolecule, showed that, in dissolution of copper at high H_2O_2 concentration (0.12 M), this value noticeably decreases (Fig. 3, curve *1*). It should be noted that copper(II) oxide is formed in this case at the plate surface even within the first minutes after the beginning of the process. The rate of copper dissolution is an order of magnitude higher than that in the above studies. The insignificant decrease in the solution viscosity in time suggests that the degradation of the polymer in reaction of H_2O_2 with PAA in the absence of copper ions is slow (Fig. 3, curve *2*). An increase in the concentration of copper ions in the solution (Fig. 3, curves *3* and *4*) accelerates the PAA degradation under the experimental conditions.

An increase in the concentration of copper ions in PAA solution results in a decrease in the relative viscosity of the PAA solution (Fig. 4, curve *1*). However, this dependence is less pronounced that the dependence of the relative viscosity of the solution on the molecular weight of PAA (Fig. 4, curve *2*).

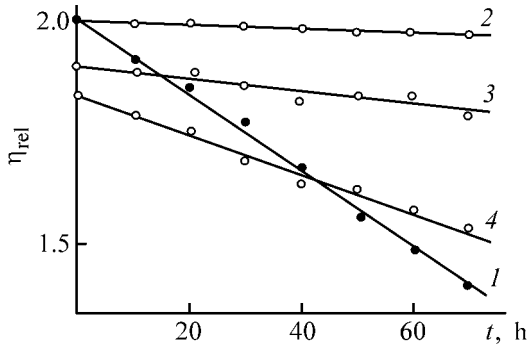

Fig. 3. Variation of the relative viscosity of PAA solution η_{rel} with time t (*1*) in dissolution of copper, and in reaction of PAA with H_2O_2 (*2*) in the absence of copper ions and in the presence of (*3*) 5.7 and (*4*) 21.4 mmol l^{-1} of copper(II) sulfate at 70°C. Molecular weight of PAA 11.5×10^5, PAA concentration 20 g l^{-1}, H_2O_2 concentration 120 mmol l^{-1}.

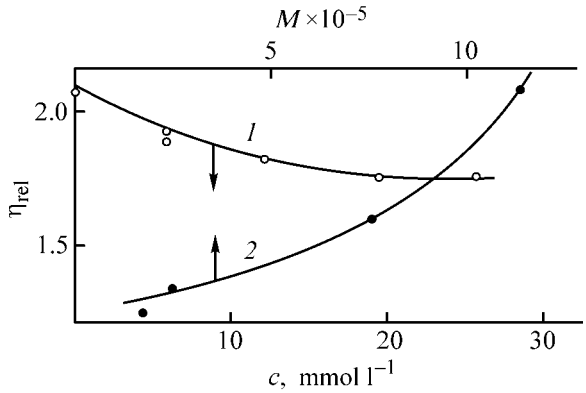

Fig. 4. Relative viscosity η_{rel} of solution with a PAA concentration of 21 g l^{-1} vs. the (*1*) concentration of copper(II) sulfate in solution c and (*2*) molecular weight of PAA M.

Thus, in the initial stage of copper dissolution in PAA solution in the presence of H_2O_2, the polymer degradation and, accordingly, the variation of the hydrodynamic characteristics of the macromolecule due to formation of copper salts with PAA insignificantly affect the rate of the polymer desorption.

EXPERIMENTAL

We used PAA samples with various molecular weights, prepared by radical polymerization in an aqueous solution. We used acrylic acid distilled at 140°C (freezing point 13°C), potassium persulfate recrystallized from aqueous solution, and hydroquinone of chemically pure grade. The purity of acrylic acid, determined from the content of double bonds by the bromide-bromate method [18], was 99.6%, and that determined from the content of carboxy groups (titra-

tion with 0.05 N NaOH) was 99.8%. The polymerization was carried out at 80–90°C; the concentrations of acrylic acid, sodium persulfate, and hydroquinone were 180–230, 5–10, and 0–6 g l^{-1}, respectively. The molecular weight was adjusted by addition of various amounts of hydroquinone to the reaction mixture. The PAA samples were recrystallized with hydrochloric acid and dried at room temperature. The molecular weights evaluated from the intrinsic viscosity of PAA solution in dioxane at 30°C and the molecular-weight distribution of PAA samples, determined by fractional dissolution, are listed in the table. The rate of copper dissolution in PAA was studied using a copper plate (purity 99.9%, total surface area 65×10^{-4} m^2). The adsorption of PAA was studied on a copper powder produced electrochemically with average particle size of 3×10^{-6} m. Before experiments, the copper plate and copper powder were washed with acetone to remove organic impurities and with hydrochloric acid to remove copper oxide from the surface.

Preliminary studies showed that the rate of copper dissolution in PAA at room temperature is very low both in the absence and in the presence of the oxidizing agent, H_2O_2. Therefore, further studies were carried out at 70°C with continuous rotation of the metallic plate in the solution of the polymer and the oxidizing agent. To determine the copper concentration in the solution upon the plate, 10-ml samples of the polymer solution were taken at certain intervals and an excess of concentrated ammonia solution was added to this sample.

The concentration of copper salts in the samples was determined from the spectrum of the ammonia complex of copper at 448 nm (Specord 40 spectrophotometer, cell thickness from 0.2 to 10 mm, depending on the concentration of the copper complex). The amount of copper was evaluated by the formula

$$v(t_n) = c_r(t_n)V_r(t_n)(1000M) + \sum_{j=1}^{n} c_s(t_j)V_s(t_j)/(1000M),$$

where $v(t_n)$ is the amount of copper (mole) released by the instant of time t_n; $c_r(t_n)$, $c_s(t_j)$, $V_r(t_n)$, and $V_s(t_j)$ are the concentrations (g l^{-1}) and volumes (ml) of the solution in the reactor and in the samples at the instants of time t_n and t_j, respectively; M = 63.5 is the atomic weight of copper.

The adsorption of PAA on copper powder was studied in the absence of H_2O_2 at 70°C. A study of the process kinetics showed that the equilibrium concentration of polymer in the adsorption layer is reached within 1–5 min after the beginning of the process. Therefore, to study the adsorption isotherm, a copper suspension in a PAA solution was stirred for 0.5 h and centrifuged for 15 min at a rate of 8000 rpm. The PAA concentrations in the initial solution and in the solution after centrifuging were determined by potentiometric titration with 0.01 N NaOH on a pH-646 pH-meter. The concentration of adsorbed PAA in the mixture was determined from the difference between these concentrations. The PAA adsorption was evaluated by division of the concentration of adsorbed PAA by the concentration of the dispersed phase.

CONCLUSIONS

(1) Adsorption of polyacrylic acid on the copper surface increases with increasing molecular weight of the polymer.

(2) A decrease in the molecular weight of the polymer results in a higher rate of copper dissolution in polyacrylic acid solution in the presence of hydrogen peroxide.

(3) The rate of copper dissolution is governed by the rate of desorption of polyacrylates; it is proportional to the amount of polymer macromolecules adsorbed on the unit surface area and is in inverse proportion to the surface area occupied by the macromolecule in the adsorption layer.

REFERENCES

1. Fleer, G.J., Cohen Stuart, M.A., Scheutjens, J.M.H.M., *et al.*, *Polymers at Interfaces*, London: Chapman, 1993.
2. Cohen Stuart, M.A., Cosgrove, Y., and Vincent, B., *Adv. Colloid Interface Sci.*, 1986, vol. 24, nos. 2–3, pp. 143–239.
3. Fleer, G.J., Scheutjens, J.M.H.M., and Cohen Stuart, M.A., *Colloids Surf.*, 1988, vol. 31, no. 1, pp. 1–14.
4. Kislenko, V.N., *Adsorption Theory, Modelling, and Analysis*, Toth, J., Ed., New York: Marcel Dekker, 2002, pp. 743–802.
5. Kislenko, V.N., *Encyclopedia of Surface and Colloid Scince*, Hubbard, A., Ed., New York: Marcel Dekker, 2002, pp. 5269–5282.
6. Lipatov, Yu.S., Todosiichyuk, T.T., and Chornaya, V.N., *Usp. Khim.*, 1995, vol. 64, issue 5, pp. 497–504.
7. Lipatov, Yu.S., Finerman, A.E., Todosiichyuk, T.T., *et al.*, *J. Colloid Interface Sci.*, 2000, vol. 228, pp. 114–120.
8. Lipatov, Yu.S., Finerman, A.E., Todosiichyuk, T.T.,

and Chornaya, V.N., *J. Colloid Interface Sci.*, 1999, vol. 215, pp. 290–295.

9. Lee, J.J. and Fuller, G.G., *Macromolecules*, 1984, vol. 17, no. 1, pp. 375–379.
10. Besio, G.J., Prudhomme, R.K., and Benziger, J.B., *Macromolecules*, 1988, vol. 21, no. 3, pp. 1070–1076.
11. Cohen, Y. and Metzner, A.B., *Macromolecules*, 1982, vol. 15, no. 5, pp. 1425–1431.
12. Cohen, Y., *Macromolecules*, 1988, vol. 21, no. 2, pp. 494–501.
13. Kislenko, V.N. and Verlinskaya, R.M., *J. Colloid Interface Sci.*, 2000, vol. 231, pp. 332–327.
14. Kislenko, V.N. and Verlinskaya, R.M., *Kolloidn. Zh.*, 2001, vol. 63, no. 6, pp. 558–562.
15. Kislenko, V.N. and Verlinskaya, R.M., *Kolloidn. Zh.*, 2002, vol. 64, no. 4, pp. 447–452.
16. Kolawole, E.G. and Mathieson, S.M., *J. Polym. Sci., Polym. Chem. Ed.*, 1977, vol. 15, no. 10, pp. 2291–2302.
17. Kolawole, E.G. and Mathieson, S.M., *J. Polym. Sci., Polym. Chem. Ed.*, 1979, vol. 17, no. 9, pp. 573–578.
18. Cheronis, N.D. and Ma, T.S., *Organic and Functional Group Analysis by Micro and Semimicro Methods*, New York: Wiley, 1964.

Russian Journal of Applied Chemistry, Vol. 77, No. 8, 2004, pp. 1364–1367. Translated from Zhurnal Prikladnoi Khimii, Vol. 77, No. 8, 2004, pp. 1378–1381.

MACROMOLECULAR CHEMISTRY AND POLYMERIC MATERIALS

Variation of the Parameters of Inhibited Oxidation of Polyethylene in the Region of Phase Transition

Yu. A. Shlyapnikov and N. N. Kolesnikova

Emanuel' Institute of Biochemical Physics, Russian Academy of Sciences, Moscow, Russia

Received February 10, 2004

Abstract—Parameters of oxidation of polyethylene with molecular oxygen in the presence of a phenolic antioxidant, 2,2'-methylenebis(4-methyl-6-methylcyclohexylphenol), at 80–210°C were studied. The possible mechanism of interaction of the polymer with the antioxidant near the melting point was considered theoretically. The suggested theoretical relationships are consistent with experimental data.

Polymeric materials are usually intended for long-term service. However, tests performed in the course of their development are limited in time, and it is difficult to reliably estimate from their results the service life of the materials under real conditions. Accelerated tests are performed at elevated temperatures at which the polymer exists as a melt, and it is important to know to what extent the results of accelerated tests can be extrapolated to the real service conditions. One of the factors complicating the extrapolation is the phase transition (melting) of the polymer.

A polymeric substance differs from its low-molecular-weight analogues in a number of characteristics, among which the most significant for studies of oxidation processes are the virtually zero vapor pressure in the entire temperature range of existence of the polymer and the extremely low translation mobility of polymer macromolecules in combination with the high the vibration mobility of the segments.

In this study, we examined the inhibited oxidation of the simplest polymer, polyethylene (PE), with molecular oxygen in the temperature range 80–210°C including the range of melting of this "crystalline" polymer (108°C). As inhibitor we used 2,2'-methylenebis(4-methyl-6-methylcyclohexylphenol) (MCHP). The relatively high molecular weight of this antioxidant, M = 400, decreased its volatilization in the course of the reaction, but, at the same time, made us to use an indirect method for monitoring its consumption: a study of the dependence of the induction period on the initial antioxidant concentration.

In going from a low-molecular-weight substance to its high-molecular-weight analogue, the role of the cage effect substantially increases. As a result, the yield of hydroperoxides decreases from approximately 100% in hydrocarbons to 5–20% in hydrocarbon polymers (polyolefins) [1, 2], and stable nonuniformities in the macromolecular packing play the role of a second component dissolved in a polymeric substance [3]. In crystalline polymers, crystalline formations appear below the melting points; their content increases with lowering temperature, and in some cases they behave as radical (or, more precisely, free-valence) scavengers. It was interesting to understand to what extent the properties of the intercrystallite amorphous substance differ from the properties of a melt of the same polymer.

The main steps of oxidation of hydrocarbon polymers are similar to the related steps of oxidation of low-molecular-weight hydrocarbons:

$$R^{\bullet} + O_2 \rightarrow RO_2^{\bullet}, \quad (1)$$

but the differences become significant in the step

$$RO_2^{\bullet} + RH \rightarrow ROOH + R^{\bullet}. \quad (2)$$

In polymers, the primary products are located close to each other, and their reaction, e.g., by the scheme

$$ROOH + R^{\bullet} \rightarrow RO^{\bullet} + ROH. \quad (3a)$$

is highly probable. As a result, the yield of the hydroperoxide per mole of uptaken oxygen (α) is considerably lower than unity (or 100%) and depends on the oxygen concentration [1, 2]. Therefore, the process can be described by the overall reaction

1070-4272/04/7708-1364 © 2004 MAIK "Nauka/Interperiodica"

$$RO_2^{\bullet} + RH \rightarrow \alpha ROOH + R^{\bullet}. \quad (3b)$$

Common antioxidants (IH), phenols and aromatic amines, react with oxygen more readily than do monomeric units of the polymer [1, 4]; therefore, the initiating step of the oxidation is the reaction of the antioxidant with oxygen. Since the majority of the radicals generated in the process decays in the reaction with the same antioxidant, the process can be described by the scheme [5]

$$IH + O_2 \rightarrow I^{\bullet} + HO_2^{\bullet} \quad (4)$$

(rate constant k_0),

$$HO_2^{\bullet} + IH \rightarrow H_2O_2 + I^{\bullet} \quad (5)$$

with the subsequent reaction of hydrogen peroxide with the antioxidant:

$$H_2O_2 + 2IH \rightarrow H_2O + 2I^{\bullet}. \quad (6)$$

Thus, one event of antioxidant oxidation [reaction (4)] leads to consumption of $f = 4$ antioxidant molecules. A minor part of radicals generated in the process reacts with monomeric units of the polymer RH, initiating the oxidation:

$$HO_2^{\bullet} + RH \rightarrow H_2O_2 + R^{\bullet}. \quad (7)$$

However, the chains initiated by these radicals are subsequently terminated by the same antioxidant. Therefore, reaction (7) does not affect f.

The chain termination occurs in reaction of IH with $RO_2^{\bullet}$ radicals involved in the polymer oxidation:

$$RO_2^{\bullet} + IH \xrightarrow{k_t} ROOH + I^{\bullet}. \quad (8)$$

The $I^{\bullet}$ radicals can also recombine with $R^{\bullet}$, i.e., they can inhibit oxidation, but the major fraction of $I^{\bullet}$ radicals finally transforms into a nonvolatile colored product inhibiting the oxidation in the absence of the starting antioxidant species [1, 6].

The reaction of hydroperoxy groups with adjacent monomeric unitgs RH results in chain branching. In all the steps of branching, the cage effect preventing the escape of free radicals plays an important role:

$$ROOH + RH \rightarrow RO^{\bullet} + R^{\bullet} + H_2O$$
$$\rightarrow \ldots \rightarrow \sigma R^{\bullet} + \text{products}. \quad (9)$$

In a developed chain reaction, free radicals mainly arise in chain branching processes (formation and decomposition of hydroperoxy groups). If the chain branching rate is higher than the chain termination rate, the reaction is autoaccelerating; otherwise the reaction occurs in the steady-state mode, i.e., the reaction rate is a single-valued function of the concentrations of the reactants: monomeric units of the polymer [RH], oxygen, and antioxidant. The antioxidant concentration corresponding to the point of transition from the steady-state to autoaccelerating mode is termed the critical concentration. As shown in [1, 7], it is determined as follows:

$$[IH]_{cr} = \frac{\alpha\sigma k_2 [RH]}{(1 - \sigma)k_t}. \quad (10)$$

Thus, the expression for $[IH]_{cr}$ contains the ratio of two rate constants and the product of two coefficients, each of which may be temperature-dependent.

Above the critical concentration, the antioxidant is mainly consumed for oxidation [steps (4)–(6)]; the process is first-order with respect to the antioxidant. Then

$$-\frac{d[RH]}{dt} = k_{app}[IH], \quad (11)$$

where the constant k_{app} is equal to the rate constant of the reaction IH + O_2, k_0, multiplied by f. The first order of consumption of strong antioxidants in oxidation of polyolefins has been observed repeatedly [1, 3].

When the antioxidant concentration decreases to the critical level in the course of its consumption, the reaction rate steeply increases, and the residual amount of the antioxidant is consumed in a short time τ_{cr}. The dependence of the induction period on the initial antioxidant concentration $[IH]_0$, calculated with this assumption, can be described by the formula [1, 7]

$$\tau = \tau_0 + \frac{1}{k_{app}} \ln \frac{[IH]_0}{[IH]_{cr}}. \quad (12)$$

Formula (12) can be used to determine the parameters of inhibited oxidation: critical antioxidant concentration and apparent rate of its consumption. In particular, the rate constant k_{app} (s^{-1}) is

$$k_{app} = \frac{\Delta \ln [IH]_0}{\Delta \tau}, \quad (13)$$

and the well-defined inflection in the curve of induction period τ vs. the initial antioxidant concentration $[IH]_0$ corresponds to the critical antioxidant concentration.

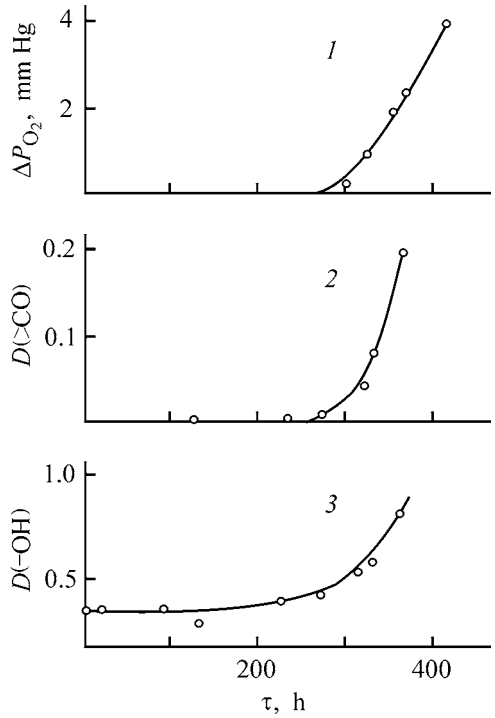

Fig. 1. (*1*) Oxygen uptake and accumulation of (*2*) carbonyl and (*3*) hydroxy groups [monitored by the optical density at 1700 (>CO) and 3600 cm^{-1} (–OH)] in oxidation of PE containing 1.25×10^{-4} mol kg^{-1} MCHP. 100°C, O_2 pressure 150 mm Hg. (ΔP_{O_2}) Change in the oxygen pressure, (*D*) optical density, and (τ) reaction time.

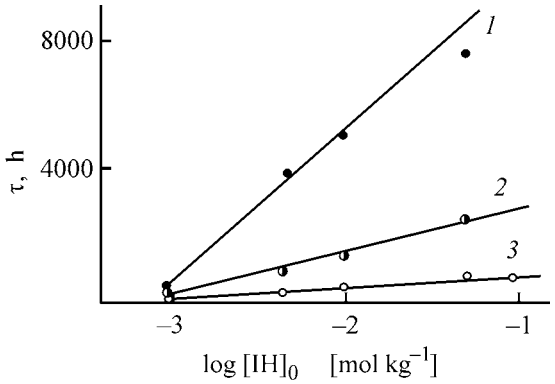

Fig. 2. Induction period τ of PE oxidation vs. the initial antioxidant concentration $[IH]_0$. Temperature, °C: (*1*) 80, (*2*) 90, and (*3*) 100.

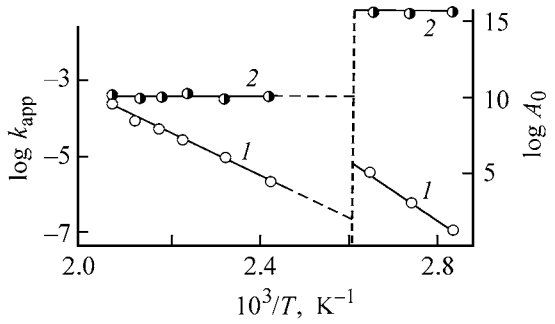

Fig. 3. (*1*) Apparent rate constant k_{app} of antioxidant consumption and (*2*) preexponential factor A_0 vs. temperature *T* in the Arrhenius coordinates. *Dashed line* denotes the melting point of the polymer.

EXPERIMENTAL

We used low-density PE (molecular weight M_w = 55700) and MCHP antioxidant. Polyethylene was reprecipitated from *m*-xylene and washed with alcohol; MCHP (mp 140°C) was recrystallized from alcohol. Samples were prepared by blending the polymer and antioxidant powders with addition of a small amount of alcohol, which subsequently vaporized. Samples of 0.05 g weight were oxidized in a static vacuum unit [1] at an oxygen pressure of 150 mm Hg (which approximately corresponds to the partial pressure of oxygen in the atmosphere).

Figure 1 shows the kinetic curves of the O_2 uptake and accumulation of the –OH and >CO groups in oxidation of a sample containing 1.25×10^{-4} mol kg^{-1} MCHP at 100°C. Oxidation under these conditions occurs with a significant induction period; all the three curves start to ascend at the same temperature. According to the theory [1, 7], the onset of the ascent corresponds to the instant of time at which the antioxidant concentration decreases to the critical value.

In accordance with formula (12), the induction periods of PE oxidation at all the temperatures vary with the initial antioxidant concentration, following the logarithmic law (Fig. 2). This allowed is to obtain the temperature dependences of the rate constants k_{app}. In the portions above and below the melting point, k_{app} varies according to the Arrhenius law with the apparent activation energy of 153 and 126 kJ mol^{-1} below and above the melting point, respectively (Fig. 3). An unexpected result was a strong variation of the preexponential factor; its common logarithm decreased from 15.6 to 10.0 [s^{-1}] on melting of the polymer.

The critical MCHP concentration also varied differently above and below the melting point. It is more convenient to determine this concentration from the nontransformed curves of the induction period vs. the initial antioxidant concentration. In contrast to k_{app}, the apparent activation energy of variation of $[IH]_{cr}$ in the solid polymer was lower than that in the melt: 12.6 and 48.2 kJ mol^{-1}, respectively (Fig. 4). The expression for the critical concentration contains several rate constants, and we cannot assign the observed jump to any of them.

According to Eqs. (4)–(6), the direct reaction of IH with O_2 is followed by a series of secondary reactions, and the constant k_{app} can be expressed as $k_0[O_2]f$. Variation of the local IH concentration in the phase transition should not affect the value of the constant, which is first-order with respect to [IH]. The quantity f, equal to 3 according to (5)–(7), should not significantly change either, even if the actual reaction mechanism is different.

The higher activation energy of the antioxidant oxidation below the melting point can be readily explained as follows. According to the sorption mechanism suggested in [3, 8], molecules dissolved in a polymer are mainly concentrated at the sorption centers Z_a (sites of distorted short-range order) matching most closely the dissolved molecules (MCHP in our case) in size and shape. Below the melting point of a polymer, crystalline formations arise, preventing migration of macromolecules and their segments, and rearrangement of a sorption center required for formation of a reaction complex requires more energy. The increased (by five orders of magnitude) preexponential factor below the melting point is more difficult to explain.

CONCLUSIONS

(1) An experimental study of polyethylene oxidation with molecular oxygen in the presence of a dipolar antioxidant revealed breaks in the temperature dependences of kinetic parameters near the melting point polyethylene (180°C). This fact indicates that the completely molten polymer essentially differs in properties and structure from the amorphous substance remaining below the melting point.

(2) Extrapolation of data on inhibited oxidation of polyethylene beyond the melting point with the simple Arrhenius law is incorrect.

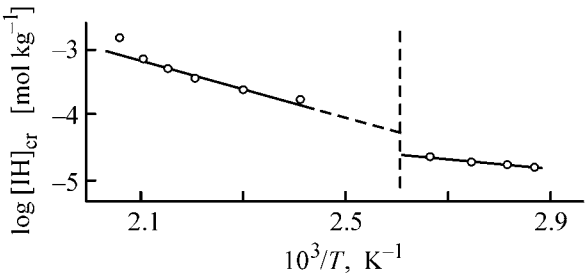

Fig. 4. Variation of the critical concentration of the antioxidant $[IH]_{cr}$ with temperature T in the Arrhenius coordinates.

REFERENCES

1. Shlyapnikov, Yu.A., Kiryushkin, S.G., and Mar'in, A.P., *Antiokislitel'naya stabilizatsiya polimerov* (Stabilization of Polymers against Oxidation), Moscow: Khimiya, 1986.
2. Monakhova, T.V., Bogaevskaya, T.A., Gromov, B.A., and Shlyapnikov, Yu.A., *Vysokomol. Soedin., Ser. B*, 1974, vol. 16, no. 2, pp. 91–94.
3. Shlyapnikov, Yu.A., *Usp. Khim.*, 1997, vol. 66, no. 11, pp. 1064–1076.
4. Shlyapnikov, Yu.A., Miller, V.B., and Torsueva, E.S., *Izv. Akad. Nauk SSSR, Ser. Khim.*, 1961, no. 11, pp. 1966–1970.
5. Tyuleneva, N.K. and Shlyapnikov, Yu.A., *Polym. Degrad. Stab.*, 1995, vol. 47, pp. 257–260.
6. Shlyapnikov, Yu.A., Miller, V.B., Neiman, M.B., and Torsueva, E.S., *Vysokomol. Soedin.*, 1963, vol. 5, no. 12, pp. 1507–1512.
7. Shlyapnikov, Yu.A., *Developments in Polymer Stabilisation*, Scott, G., Ed., London: Applied Science, 1982, vol. 5, pp. 1–22.
8. Shlyapnikov, Yu.A., *Kinet. Katal.*, 1978, vol. 19, pp. 503–506.

Russian Journal of Applied Chemistry, Vol. 77, No. 8, 2004, pp. 1368–1375. Translated from Zhurnal Prikladnoi Khimii, Vol. 77, No. 8, 2004, pp. 1382–1388.

MACROMOLECULAR CHEMISTRY AND POLYMERIC MATERIALS

Cluster Structure of Epoxy-Phenolic Polymer Prepared by Curing a Mixture of Epoxy-4,4'-Isopropylidenediphenyl and Phenol-Formaldehyde Oligomers

A. N. Krasovskii, D. V. Novikov, and V. N. Filippov

Pigment Research and Production Company, St. Petersburg, Russia

Received July 16, 2003; in final form, May 2004.

Abstract— The kinetics of viscosity variation and the concentration and kinetic modes of precondensation of a mixture of epoxy-4,4'-isopropylidenediphenyl and phenol-formaldehyde oligomers in Cellosolve solutions in the presence of phosphoric acid at 333 K were studied. The cluster structure parameters of the chemical network of epoxy-phenolic polymeric coating on a tin plate, obtained by thermal curing of precondensates of an oligomer mixture, were determined using the silver chloride sputtering method.

In studying the structure of cross-linked epoxy-phenolic polymers we have demonstrated previously [1, 2] that a uniform chemical network is formed on the surface of polymeric coatings at an epoxydiane (EO) to phenol-formaldehyde (PO) oligomer molecular weight ratio close to 4 : 1, the optimal molecular weight of EO (M_n) being about 3500. To improve the compatibility of EO and PO in solutions and to obtain an epoxy-phenolic polymer by thermal curing of the oligomers, precondensation of EO and PO is carried out in the presence of phosphoric acid [3, 4]. On adding H_3PO_4 to a solution of the oligomers, mono-, di-, and triphosphates of EO are formed [5]. In the course of thermal curing of a mixture of the oligomers, the methylol (butoxy) groups of PO react with the epoxy (hydroxy) groups of EO, and the methylol groups of PO form etheric cross-linking bonds [6, 7].

In [1, 2, 8], we suggested a cluster mechanism of aggregation of oligomeric molecules in solutions in the course of thermal precondensation of EO/PO mixtures. Following the cluster model [9, 10], one can distinguish three major kinetic stages of precondensation of the oligomers, as well as the corresponding topological types of the chemical network structure of cross-linked epoxy-phenolic polymer. The precondensation mechanism in EO–PO mixed solutions, i.e., the structural evolution of aggregates of the oligomers, involves disaggregation of EO and PO aggregates and formation of mixed EO–PO aggregates and then of an infinite cluster of these macromolecules. Such an approach is useful for optimization of the molecular, concentration, and kinetic parameters of precondensation of the oligomers in solutions [2]. Previously we have shown [8] that the oligomer molar ratio $N_1(EO)/N_2(PO)$ and the phosphoric acid concentration N_3 predetermine the shape of the kinetic curves characterizing the viscosity dynamics in EO–PO mixed solutions.

A uniform chemical network of the epoxy-phenolic polymer is formed in curing of the oligomer mixture, provided that the density of EO and PO aggregates approaches that of the infinite cluster in the vicinity of the threshold concentration of the particles in the solution [2]. Such a network is not formed in the initial and intermediate stages of precondensation of the oligomers. In this case, the correlation radius ξ of clusters representing the network junctions initially decreases from ~250 to ~50 nm and then increases to ~500 nm with precondensation time, which is consistent with data on the Rayleigh light scattering in EO and PO solutions [11].

The topology of the points of the chemical network on the surface of the epoxy-phenolic polymer depends on the molecular weight M_n and concentration of EO and PO [1]. At $M_n(EO) = 2100$ and $M_n(PO) = 850$, some extended discrete clusters ("lattice monsters" [1, 9]) are found, which have a low lattice density and constitute an inhomogeneous chemical network of the crosslinked polymer. A uniform and homogeneous network of the epoxy-phenolic polymer is formed at $M_n(EO) = 2800–3500$ [1, 2]. At the same time, it

1070-4272/04/7708-1368 © 2004 MAIK "Nauka/Interperiodica"

should be noted that the structure of the points of the chemical network in the epoxy-phenolic polymer obtained by curing the oligomers in the presence of phosphoric acid remains to be understood [4, 12].

In this study, we examined the kinetics of viscosity variation in mixed solutions of EO and PO oligomers in the course of precondensation in the presence of phosphoric acid. The distribution of the points of the chemical network on the epoxy-phenolic polymeric coatings on a tin plate, prepared by curing of precondensates of oligomer mixtures containing various phosphoric acid concentrations, was also determined.

EXPERIMENTAL

Samples of E-05 epoxy-4,4'-isopropylidenediphenyl resin and DFFr phenol-formaldehyde resin (based on diphenylolpropane and formaldehyde) (Pigment holding company) were characterized by capillary viscometry and gel chromatography [13, 14]. The number-average molecular weight M_n and the M_w/M_n ratio (M_w is the weight-average molecular weight) of the oligomers are listed in Table 1. The intrinsic viscosity [η] of the oligomers was determined in Cellosolve (C).

The dependences of the viscosity η of mixtures of E-05 and DFFr in Cellosolve on the precondensation time t were obtained at c(E-05) = 26.7 g dl^{-1} and c(DFFr) = 9.12 g dl^{-1}, which corresponds to N_1(E-05)/N_2(DFFr) = 1 [2]. Precondensation and viscosity measurements in E-05 and DFFr mixed solutions in C in the presence of H_3PO_4 were carried out directly in a cylinder–cylinder cell of a Rheotest-2 rotary viscometer at 333 K. The results are presented in Fig. 1 and Table 2. The viscosity was measured at a shear rate g = 81 s^{-1} to within 3 mPa s.

Table 1. Characteristics of oligomers at 298 K*

Oligomer	EN, %	[η], dl g^{-1}, ±5%	DP ±10%	M_n ±10%	M_w/M_n ±10%
E-05	1.8	0.134	10–17	2850	2.70
DFFr	–	0.061	2–5	1030	3.85

* (EN) Epoxide number and (DP) degree of polymerization.

Table 2. Time of reaching the limiting viscosity η in precondensation of E-05–DFFr mixture in EC (N_1/N_2 = 1, g = 81 s^{-1}, T = 333 K)

Sample no.	$c(H_3PO_4)$ %	$N_3/(N+N_2)$* ±5%	η, Pa s, ±0.03	t, min
1	0	0	1.54 (1.42)**	180
2	14.3	0.02	1.47 (1.28)	150
3	30	0.04	1.42 (1.43)	120
4	50	0.07	1.50 (1.51)	120
5	75	0.09	1.47 (1.49)	120
6	100	0.13	1.38 (1.47)	90
7	125	0.17	1.59	150
8	150	0.20	1.56 (1.56)	>180
9	490	0.66	1.53 (1.40)	>240

* (N_1, N_2, N_3) Moles of E-05, DFFr, and H_3PO_4, respectively.

** Given in the parentheses is the viscosity η of E-05–DFFr mixture in solution, corresponding to the extremum in the η(t) curve in the course of precondensation of the oligomers.

Phosphoric acid was added to the E-05–DFFr mixture in the initial stage of precondensation of the olig-

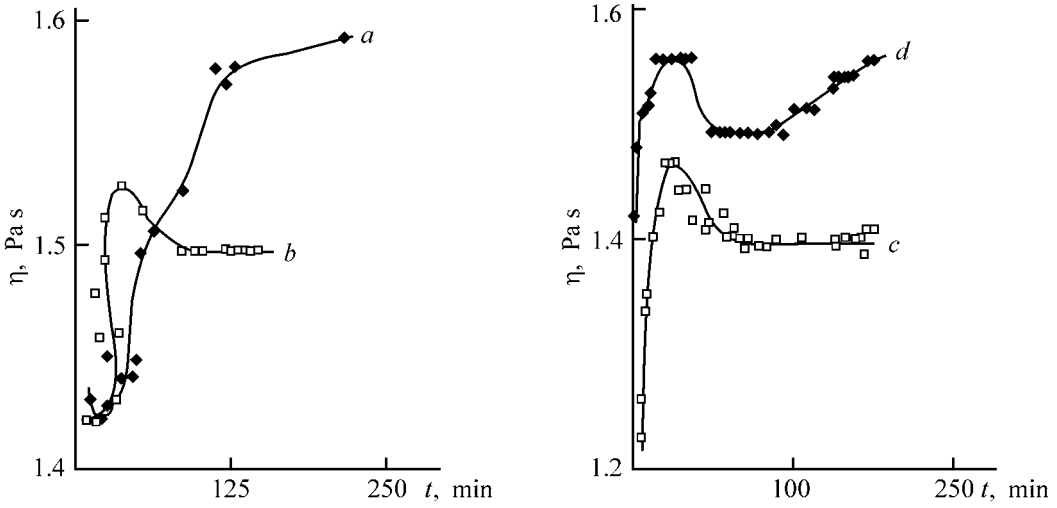

Fig. 1. Kinetic curves of the viscosity η of a mixture of E-05 and DFFr resins in C solutions in the presence of phosphoric acid. $c(H_3PO_4)$ (rel %): (*a*) 0, (*b*) 75, (*c*) 100, and (*d*) 150. Shear rate g = 81 s^{-1}; T = 333 K. (*t*) Precondensation time.

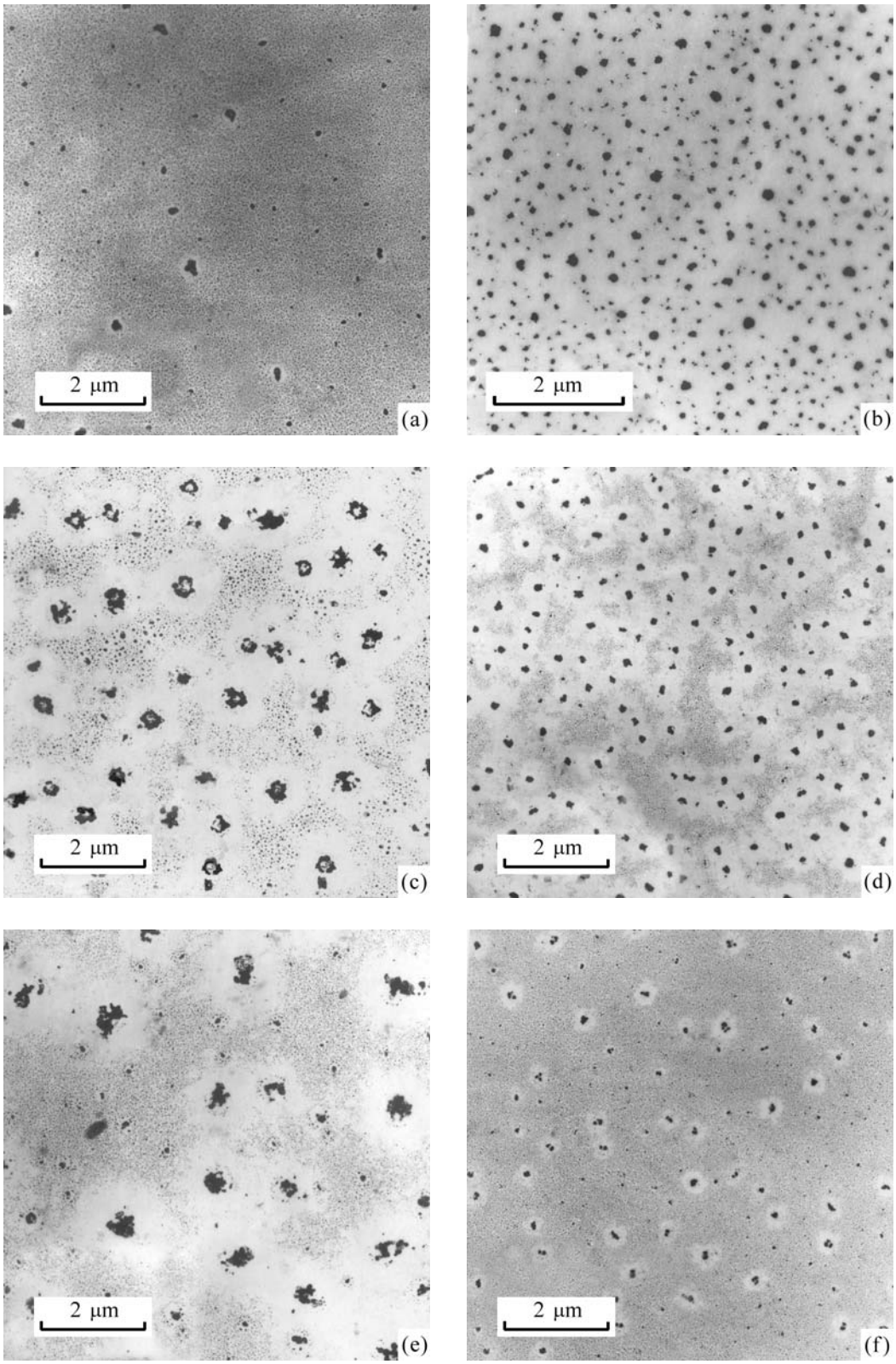

Fig. 2. Microdecorographs of epoxy-phenolic coatings on food tin. (a, b) Fragments of the coating surface; H_3PO_4 concentration in mixed oligomer solution (rel %): (c) 30, (d) 75, (e) 100, and (f) 150. Magnification: (a, c–f) 8000 and (b) 10 000.

Table 3. Parameters of the cluster structure of the chemical network of the epoxy-phenolic polymer, obtained from the electron microscopic data (coatings on tin were prepared by curing precondensates of a mixture of oligomers)

Sample no.	$\rho_1 \pm 0.03$	ξ_1, ξ_2, nm	$D \pm 7\%$	$m \pm 0.2$	R, nm, ±5%	$\langle R \rangle$, nm
1	0.93	430	1.97	6.8	41	–
	0.91**	560**	1.89**	4.1**	(280)***	
2	0.94	450	1.93	4.1	46	450
	0.73**	1200**	1.78**		(1000)	
3	0.59	350	1.82	4.5	50	315
	0.30**	2000**	1.68**		(1250)	
4	0.54	260	1.85	5.3	26	177
	0.34**	1490**	1.66**		(900)	
5	0.60	270	1.81	5.8	31	105
	0.48**	810**	1.62**		(800)	
6	0.55	590	1.93	4.1	31	308
	0.34**	2600**	1.74*		(2000)	
7	0.47	400	1.85	5.0	31	378
	0.25**	1500**	1.3 **		(1000)	
8	0.96	520	1.94	7.0	36	478
					(800)	
9	0.98	560	1.95	7.1	37	–
					(1200)	

* Lattice density ρ_1 of the fine fraction of AgCl particles (ρ_1) corresponds to the correlation radius ξ_1. ($\langle R \rangle$) Mean radius of the aggregates meeting the condition $R < \xi_1$ [9].

** Parameters related to coarse AgCl particles or to the DFFr phase.

*** Given in the parentheses is the minimum average distance between coarse AgCl particles.

omers. The H_3PO_4 concentration in the mixed oligomer solution was varied from 14.3 to 490 rel % (a quantity of 0.25 g of H_3PO_4 per 36 g of the E-05–DFFr mixture was taken as 100% [3]) (Table 2, sample nos. 1–9). Polymeric coatings 4 to 6 μm thick were prepared by casting 20% solution of the precondensate in C onto electrolytic tin plate, followed by air-curing for 15 min at 483 K [15, 16] (Table 3, sample nos. 1–9).

The cluster structure of the epoxy-phenolic polymer was studied by depositing silver chloride by thermal evaporation onto the coating surfaces in a vacuum (1.33×10^{-3} Pa) to an effective thickness of the layer of 0.4 nm. Carbon replicas with decorating AgCl nanoparticles were obtained using the procedure described in [1] and then studied with an EVM 100 L electron microscope. The electron micrographs of the surface of polymer films on food tin were improved by digital image processing [2] (Figs. 2a–2f).

The kinetic curves characterizing the variation of the viscosity in the course of precondensation of an E-05–DFFr mixture in the presence of H_3PO_4 show extrema (Fig. 1). Previously, it has been demonstrated [8] that the position of the extrema in the viscosity curves as well as that of the ascending and descending portions and those of saturation depend on the parameter $N_3/(N_1 + N_2)$. The dip in the curves corresponds to $N_3/(N_1 + N_2) < 0.04$, and the peak was observed at $N_3/(N_1 + N_2) = 0.09 - 0.13$ (Table 2, sample nos. 5, 6). With increasing phosphoric acid concentration at $N_3/(N_1 + N_2) > 0.17$, the viscosity of the mixed oligomer solution does not approach the saturation in a finite time interval (Fig. 1*d*; Table 2, sample nos. 8, 9).

The observed different shapes of the viscosity curves can be interpreted in terms of the cluster mechanism of precondensation of the EO–PO mixture [2]. This mechanism predicts that the density of the aggregates of oligomeric molecules changes in the course of precondensation with the H_3PO_4 concentration [8]. We have demonstrated previously [2] that the dip in the viscosity curves is caused by the formation of mixed elementary aggregates of the oligomers, having high packing density, and the peak in the curves can be attributed to the formation of aggregates with a relatively lower density of molecular packing.

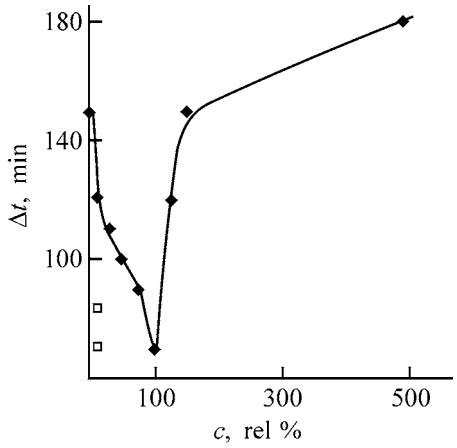

Fig. 3. Relative time Δt of precondensation of the oligomer mixture in C vs. the concentration c of phosphoric acid.

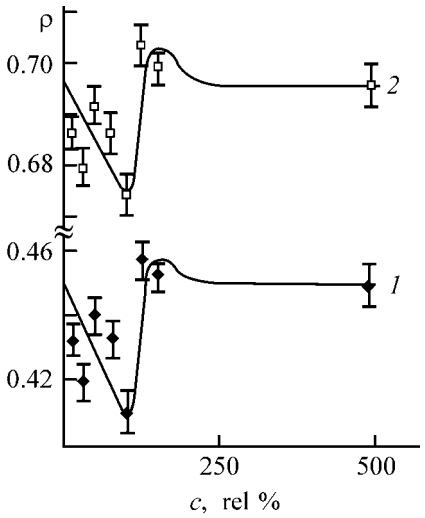

Fig. 4. Density ρ of aggregates of the oligomeric molecules vs. the concentration c of phosphoric acid. Fractal dimension D of aggregates: (*1*) 1.7 and (*2*) 2.

Table 2 allows us to derive a correlation between the limiting viscosity η of the mixture and the time t in which it is attained in the course of precondensation of the oligomers in the solution. From these data one can estimate the optimal H_3PO_4 concentration and the parameter $N_3/(N_1 + N_2)$ corresponding to the minimum viscosity of the oligomeric mixture. The time t in which the limiting viscosity η of the mixed oligomeric solution is attained, estimated relative to the position of the extremum in the η-vs.-t curve, is the shortest at $N_3/(N_1 + N_2) \approx 0.1$, like that for η (Fig. 3). If the parameter $N_3/(N_1 + N_2)$ deviates from this optimal value, the time of precondensation increases (Table 2, sample nos. 1–4, 7–9).

Using the cluster model, the density ρ of the aggregates of E-05 and DFFr molecules can be expressed in terms of the relative viscosity η_{rel} of the oligomer mixture in the solution [8]:

$$\rho \sim w^{(3-D)/D}([\eta]c/\ln \eta_{rel})^{(3-D)/(3-2D)},$$

where $w = 0.637$ is the factor of random packing of hard spheres; D, the fractal dimension of the aggregates in the solution [9]; and $\eta_{rel} = \eta/\eta_0$ (η and η_0 are the viscosities of the solution and the solvent, respectively) [14].

The density of the aggregates of the oligomeric molecules in the solution was estimated for the precondensates of the E-05–DFFr mixture in Cellosolve at $[\eta]c = 5.0$ (dimensionless parameter) and the intrinsic viscosity of the precondensates $[\eta] = 0.15$ dl g^{-1} (Table 2, sample nos. 1–9). The fractal dimension D of the aggregates of the oligomeric molecules was taken to be 1.7 and 2 (Fig. 4).

Figure 4 shows that the density ρ of aggregates of the oligomers changes in parallel with the limiting viscosity of the oligomer mixture in the solution in the course of precondensation. The density is the lowest near $c(H_3PO_4) = 100\%$, which corresponds to $N_3/(N_1 + N_2) \approx 0.1$ and to $N_3/N_1 \sim 0.3$ (Table 2, sample no. 6). In this case, the observed relatively low density of aggregates of the oligomers is caused by the fact that EO monophosphates are preferentially formed in the solution [5]. The increase in the limiting viscosity η of the oligomer mixture and in the density ρ of aggregates of the oligomeric molecules within the range $N_3/(N_1 + N_2) = 0.17–0.66$ is probably due to the formation of di- and triphosphates [7].

The patterns of distribution of decorating particles on the surface of the epoxy-phenolic polymer reveal an inhomogeneous structure of the coatings, which is represented by regions of localization of fine (20–30 nm) and coarse (150–500 nm) AgCl particles (Fig. 2). The inhomogeneous energy microprofile of the polymeric coating, i.e., different strengths of binding of the adsorbed AgCl particles to the support, is caused by the parameters of distribution of the reactive functional groups of E-05 and DFFr on the surface. Clusters of fine AgCl particles firmly bound to the polymer surface primarily reflect the distribution of EO functional groups [1, 2]. Clusters of coarse AgCl particles on the surface of the epoxy-phenolic coatings are formed, as demonstrated previously [1, 2], via coalescence of fine particles and topologically correspond to the distribution of the functional groups of PO.

The mechanism of interaction of silver chloride with the functional groups of PO involves partial

reduction of AgCl to metallic silver by quinonemethide groups of the epoxy-phenolic polymer formed in thermal curing of the oligomer mixture [7]. In the next stage, nucleation of Ag nanoparticles starts, providing growth of coarse decorating particles of AgCl. Reduction of silver chloride by hydroxybenzenes, which, taken as a mixture with hydroquinone, are effective reducing agents for silver halides, are widely used in chemical photographic processing of silver halide materials [17]. This mechanism of interaction of AgCl with the functional groups of PO is additionally supported by the fact that the amount of coarse AgCl particles on the surface of the epoxy-phenolic polymer falls with decreasing PO concentration in the oligomer mixture [1, 2].

Spatially correlated groups of fine and coarse decorating particles can be regarded as lattice clusters [9] differing in the fractal dimension D, coordination number m, density of the quasilattice points, and correlation radius ξ. These parameters control the short-range distribution of particles on the surface of polymeric films on the scale $R < \xi$ [18], and they can be estimated from the radial distribution function [1, 2] (Table 3).

On the surface of the film prepared by thermal curing of the precondensate of the oligomer mixture in the absence of phosphoric acid (Tables 2 and 3, sample no. 1), we found a two-phase macroinhomogeneous structure of the resulting polymer (Figs. 2a, 2b). The fine and coarse AgCl fractions are localized separately. These fractions are represented by extended domains hundreds of micrometers in size. In this case, a uniform chemical network is not formed on the polymer surface on the scale close to the correlation radius ξ of AgCl clusters as a result of the poor compatibility of the oligomers in the solution.

In the presence of phosphoric acid, thermal curing of the precondensates gives a more uniform chemical network of the epoxy-phenolic polymer (Tables 2 and 3, sample nos. 2–9). Generally, two types of fractal clusters of fine and coarse AgCl particles are distinguished on the polymer surface, which form two chemical networks whose points contain either E-05 or DFFr (Figs.2c–2f). The size and lattice density distribution of these clusters on the polymer surface depend on the phosphoric acid concentration in the mixed oligomer solution.

The mean cluster lattice density ρ_l, estimated by the method described in [1], varies as a function of the radius R of the circle with a center at the lattice point occupied by a particle by the law $\rho_l(R) \sim (R)^{D-2}$

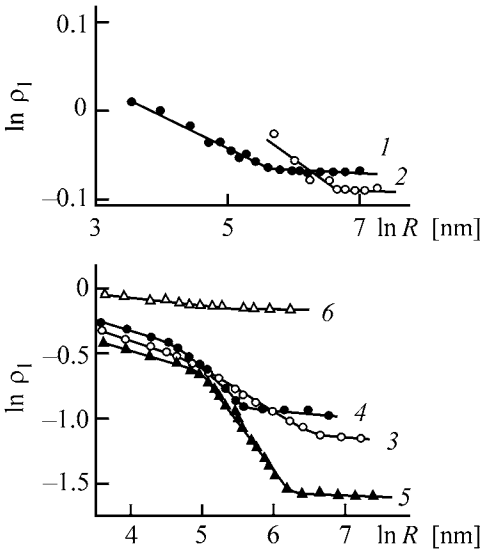

Fig. 5. Lattice density ρ_l of the clusters of decorating AgCl particles vs. the radius R of the circle surrounding a cluster of the particles. Coatings on tin plate. H_3PO_4 concentration (rel %): (*1*, *2*) 0 (curves *1* and *2* correspond to the fragments of the surface of sample no. 1, Table 3), (*3*) 30, (*4*) 100, (*5*) 125, and (*6*) 150.

[9]. Transition to the network is controlled by changing D on the scale $R = \xi$ [18].

Table 3 summarizes parameters of the cluster structure of the polymer prepared by curing the precondensates at various H_3PO_4 concentrations. In the absence and at a large excess of phosphoric acid in the precondensate, the cluster lattice density ρ_l on the polymer surface is higher than that at $c(H_3PO_4)$ = 30–125%.

For coatings prepared by curing the precondensates in the absence of phosphoric acid and also for those obtained at a large excess of the acid in the oligomer mixture, the dependences $\rho_l(R)$ plotted in the logarithmic coordinates are represented by of two linear portions (Fig. 5). For the coating obtained in the absence of the acid, two dependences $\rho_l(R)$ were obtained, corresponding to polymeric phases enriched with either E-05 or DFFr (Fig. 5, curves *1*, *2*). At $c(H_3PO_4)$ = 14–125 rel %, the $\rho_l(R)$ curves consist of three portions (Table 3, sample nos. 2–6). At $c(H_3PO_4) \geq$ 150 rel %, the chemical network of the epoxy-phenolic polymer is characterized by a unique correlation radius ξ, and within the range 14–125 rel %, by two values ξ_1 and ξ_2 corresponding to the short- and long-range order in the AgCl particle density distribution on the surface (Fig. 5, curves *3*–*6*).

The mean radius of the clusters, $\langle R \rangle$, which characterizes the average distance between the chemical network points on the scale $R \leq \xi_1$ [9], reaches the

minimum value at $c(H_3PO_4)$ = 75 rel % (Table 3, sample no. 5). Here the particle size and the distance between coarse AgCl particles on the surface are at a minimum, and their concentration is at a maximum. In this case, the coordination number $m \approx 6$ corresponds to a triangular quasilattice [8], and the lattice density $\rho_l(\xi_1)$ of the clusters reaches a local maximum (correlation radius ξ_2 reaches a local minimum). It is significant that, in this case, a uniform network of the infinite cluster is formed from coarse and fine AgCl particles, and the localization regions can be imagined as two fractal (infinite) clusters nested within each other, the coverages of the surface with these clusters being approximately equal.

According to the percolation theory [9], the threshold of percolation in microinhomogeneous systems for two types of points on a triangular lattice corresponds to the critical percolation probability $p_{cr} = 0.5$. In our case, points of such a lattice are occupied by coarse and fine AgCl particles, and the lattice density ρ_l of fractal clusters of fine and coarse particles is close to the critical value corresponding to an infinite cluster [9, 18]. Therefore, it may be suggested that, at $c(H_3PO_4)$ = 75 rel %, the chemical network of the epoxy-phenolic polymer is the most uniform, which is confirmed by high protective characteristics of the polymeric coatings in simulated media [8].

At small deviations from $c(H_3PO_4)$ = 75 rel %, less uniform networks are formed on the surface, and the coordination number *m* of the quasilattice decreases from 6 to 4–5 (Table 3, sample nos. 4, 6). At $c(H_3PO_4)$ = 50 rel. %, the infinite cluster consists of only coarse AgCl particles with inclusions of discrete domains of localization of fine particles. At $c(H_3PO_4)$ = 100 rel %, the uniform network is formed by only fine AgCl particles (no uniform network of coarse particles).

In the range $c(H_3PO_4)$ = 100–125 rel %, the fractal structure of the chemical network is represented by an infinite cluster of fine AgCl particles and extended discrete domains of localization of coarse particles. The cluster structure of these extended regions of localization of coarse AgCl particles is similar to lattice monsters on a square lattice ($m = 4$) [19], since an extended cluster of coarse particles does not spread throughout the lattice, but only partially covers the surface [1, 9]. Such a cluster has a branched structure. However, its lattice density ρ_l on the scales $R < \xi$ and $R > \xi$ is lower than the critical lattice density ($\rho_{cr} \approx 0.59$) at which an infinite cluster starts to form on a square lattice [19].

At $c(H_3PO_4)$ = 50, 100, and 125 rel % (Table 3, sample nos. 4, 6, and 7), the chemical network of epoxy-phenolic coatings is characterized by noticeable fluctuations of the lattice density ρ_l in the vicinity of ξ_1 and ξ_2 corresponding to the short- and long-range orders of AgCl particle distribution on the surface. Such coatings demonstrate worse protective properties as compared to those obtained at $c(H_3PO_4)$ = 75 rel % [8].

At a considerable excess of phosphoric acid in the precondensate, the coordination number *m* of the lattice on the coating surface grows with increasing acid concentration in parallel with the lattice density ρ_l of clusters, and also in parallel with the limiting viscosity of the oligomer mixture in the solution in the final stage of precondensation (Tables 2 and 3, sample nos. 8, 9). In these cases, a highly cross-linked chemical network of the epoxy-phenolic polymer is formed on the coating surface.

CONCLUSIONS

(1) The minimum values of the limiting viscosity of the oligomer mixture and the density of aggregates of the oligomers in the final stage of precondensation, and also the preferential formation of monophosphates of the epoxy-4,4'-isopropylidenediphenyl oligomer in solution, were observed at the orthophosphoric acid to oligomer molar ratio $N_3/(N_1 + N_2) \approx 0.1$.

(2) The most uniform cluster structure of the chemical network of the epoxy-phenolic polymer is formed on the coating surface at $N_3/(N_1 + N_2) \approx 0.1$. In this case, the lattice density of infinite clusters of AgCl particles, which represent points of the chemical network formed in thermal curing of a mixture of the epoxy-4,4'-isopropylidenediphenyl and phenol-formaldehyde oligomers is close to the threshold of percolation on a triangular lattice, and the coverages of the surface with these clusters are nearly equal.

REFERENCES

1. Krasovskii, A.N., Novikov, D.V., Krasheninnikov, V.A., *et al., Zh. Prikl. Khim.*, 2001, vol. 74, no. 1, pp. 124–134.
2. Krasovskii, A.N., Novikov, D.V., Filippov, V.N., *et al., Zh. Prikl. Khim.*, 2003, vol. 76, no. 2, pp. 304–312.
3. *Lakokrasochnye materially dlya konservnoi tary* (Paintwork Materials for Canning Package), Lyalyushenko, S.M., Ed., Moscow: NIITEKhim, 1981.
4. Markevich, M.A., Kuzaev, A.I., Vladimirov, L.V.,

et al., *Vysokomol. Soedin., Ser. A*, 1985, vol. 27, no. 5, pp. 1000–1008.

5. Sorokin, M.F., Kochnova, Z.A., Nikolaev, L.P., *et al.*, *Tr. Mosk. Khim.-Tekhnol. Inst. im. D.I. Mendeleeva*, 1980, issue 110, pp. 63–67.
6. Aleksandrov, V.N., Tarasov, A.N., and Rozenberg, B.A., *Lakokras. Mater. Ikh Primen.*, 1986, no. 2, pp. 16–19.
7. Kochnova, Z.A., Khrisanova, T.A., and Sorokin, M.F., *Lakokras. Mater. Ikh Primen.*, 1989, no. 2, pp. 82–89.
8. Krasovskii, A.N. and Filippov, V.N., *Zh. Prikl. Khim.*, 2003, vol. 76, no. 6, pp. 1000–1005.
9. Feder, J., *Fractals*, New York: Plenum, 1988.
10. Krasovsky, A.N., Novikov, D.V., Filippov, V.N., *et al.*, Abstracts of Papers, *4th Int. Symp. "Molecular Order and Mobility in Polymer Systems,"* St. Petersburg, 2002, p. 257.
11. Sukhareva, L.A., Sorokin, M.F., Kochnova, Z.A., *et al., Lakokras. Mater. Ikh Primen.*, 1982, no. 4 pp. 30–31.
12. Markevich, M.A., Structural and Kinetic Aspects of Formation of Epoxy-4,4'-Isopropylidenediphenyl Oligomers and 3*D* Polymers on Their Basis, *Doctoral Dissertation*, Chernogolovka, 1986.
13. Gorshkov, A.V., Verenish, S.S., Evreinov, V.V., and Entelis, S.G., *Chromatographia*, 1988, vol. 26, pp. 338–342.
14. Tsvetkov, V.N., Eskin, V.E., and Frenkel', S.Ya., *Struktura makromolekul v rastvorakh* (Structure of Macromolecules in Solutions), Moscow: Nauka, 1964.
15. Tarasov, A.I., Shuvarin, N.A., Aleksashina, M.V., and Eselev, A.D., *Lakokras. Mater. Ikh Primen.*, 1979, no. 6 pp. 30–32.
16. Aleksandrov, V.N., Tarasov, A.N., and Rozenberg, B.A., *Lakokras. Mater. Ikh Primen.*, 1985, no. 6, pp. 35–38.
17. Betcher, H.G.O. und Epperlein, J., *Moderne photographische Systeme*, Leipzig: Grundstoffindustrie, 1990.
18. Ziman, J.M., *Models of Disorder: The Theoretical Physics of Homogeneously Disordered Systems*, Cambridge: Cambridge Univ., 1979.
19. El'yashevich, A.M., Modern Theory of Flowing and Potentialities for Its Application to the Theory of Polymers in Solid Phase, *Preprint of Inst. of Chemical Physics, USSR Acad. Sci.*, Chernogolovka: Inst. Khim. Fiz. Akad. Nauk SSSR, 1985.

Russian Journal of Applied Chemistry, Vol. 77, No. 8, 2004, pp. 1376–1378. Translated from Zhurnal Prikladnoi Khimii, Vol. 77, No. 8, 2004, pp. 1389–1391.

MACROMOLECULAR CHEMISTRY AND POLYMERIC MATERIALS

Radical Polymerization of the Quinone Derived from Monoethanolamine Vinyl Ether and Chloranil

E. E. Ergozhin, B. A. Mukhitdinova, S. A. Shoinbekova, A. I. Nikitina, and G. N. Zhunusova

Bekturov Institute of Chemical Sciences, Ministry of Education and Science of the Republic of Kazakhstan, Almaty, Kazakhstan

Received March 19, 2004

Abstract—Radical polymerization of the quinone derived from monoethanolamine vinyl ether and 2,3,5,6-tetrachloro-1,4-benzoquinone (chloranil) was studied by classical polarography. The conditions of preparation of the redox polymer were optimized. The kinetic characteristics of the process were calculated.

One of the main lines of the Kazakhstan-2030 strategic development program is the use of domestic raw materials and their processing into materials useful for industry and agriculture, with the aim to replace imported materials. The use of redox polymers (or redox ion exchangers) in research and practice is restricted by the lack of starting monomers for their synthesis.

Systematic studies are made to develop procedures for preparing new unsaturated monomers based on monoethanolamine vinyl ether (MEAVE) produced in Kazakhstan. Previous studies have been concerned with the preparation of new redox polymers derived from MEAVE and suitable for production of redox ion exchangers [1], conditions of radical homopolymerization of some compounds derived from MEAVE and quinones, kinetic characteristics of the process [2–4], and copolymerization of these compounds with acrylic acid, styrene, 4-vinylpyridine, and *N*-vinylpyrrolidone. For these reaction systems, the relative activity constants, resonance stabilization factors *Q*, and polarities *e* have been calculated [5, 6].

In this study, we analyzed polarographically the radical polymerization of the disubstituted derivative of chloranil and MEAVE, MEAVE–CA–MEAVE.

EXPERIMENTAL

Azobis(isobutyronitrile) (AIBN) was recrystallized from absolute methanol, mp 102–103°C.

2,5-Bis[*N*-(2-vinyloxy)ethyl]amino-3,6-dichloro-1,4-benzoquinone ($C_{14}H_{16}N_2O_4Cl_2$) (MEAVE–CA–MEAVE) was prepared according to [1].

The radical polymerization was performed as described in [2–4]. The optimal conditions were determined polarographically: 80°C, initiator concentration 6 wt %, monomer concentration in DMF 20 g l^{-1}, polymerization time 5 h. The polymer yield under these conditions is 80.47%. The reaction kinetics was monitored polarographically (by the amount of unchanged monomer) and gravimetrically (by the polymer yield).

The polarograms were recorded in a temperature-controlled cell of a PU-1 polarograph at 25 ± 0.5°C, using a mercury dropping electrode with the open-circuit capillary characteristic $m^{2/3} t^{1/6} = 4.38$ mg$^{2/3}$ s$^{-1/2}$, vs. saturated calomel electrode. The supporting electrolyte was phosphate buffer solution (pH 7.4) in 25% DMF. Prior to polarographic measurements, the solutions were bubbled with argon to remove oxygen.

The IR spectra were measured on a Specord M-80 spectrophotometer using KBr pellets (200 mg KBr + 1 mg sample). In the spectra of the polymers, the vinyl C–H band at 2928 cm^{-1} disappears, but the NH stretching (3248 cm^{-1}) and bending (1592 cm^{-1}) bands are preserved, as well as the bands of the ring C=C bonds at 1504 cm^{-1}, =C–N bond at 1328 cm^{-1}, ether group at 1208 cm^{-1}, and C–Cl bonds at 712 and 752 cm^{-1}. The quinone carbonyl band is broadened

1070-4272/04/7708-1376 © 2004 MAIK "Nauka/Interperiodica"

Table 1. Elemental composition and some physicochemical properties of the disubstituted monomer derived from chloranil and MEAVE and of its polymer

Compound	Calculated, % / found, %				Yield, %	mp, °C	[η], dl g^{-1}	ρ, g cm^{-3}	SEC	RC
	C	H	N	Cl					mg-equiv g^{-1}	
Monomer	48.43 / 48.55	4.64 / 4.64	8.06 / 8.18	20.42 / 20.36	86.20	103–105	–	0.2385	–	–
Polymer	48.43 / 48.55	4.64 / 4.64	8.06 / 8.18	20.42 / 20.36	80.47	190	0.16–0.18	1.0424	1.45	2.12

and shifted to higher frequencies (1688 cm^{-1}, against 1660 cm^{-1} for the monomer), which is typical of quinone polymers.

Viscometric studies were performed in Ubbelohde capillary viscometers in a temperature-controlled cell at 25°C in DMF; the density, static exchange capacity (SEC), and redox capacity (RC) were determined as described in [2–4].

The reaction of chloranil with MEAVE yielded an unsaturated redox monomer capable, in contrast to the starting ether, of radical polymerization. The chemical composition and some physicochemical characteristics of the MEAVE-substiututed quinone and its polymer are listed in Table 1.

From the measured content of the unchanged monomer, we determined the degree of its conversion and constructed the kinetic curves of polymerization (FIg. 1).

To calculate the rate constants of the overall polymerization process, we determined the reaction order. From the linear dependence of log c of the monomer on the reaction time (Fig. 2), we found that the process is monomolecular with respect to the monomer (m = 0.74) and is described by first-order reaction relationships.

The rate constants of MEAVE–CA–MEAVE polymerization, calculated from the first-order kinetic equation, and the preexponential factors k_0, calculated from the Arrhenius equation $k = k_0 e^{-E/RT}$, are listed in Table 2.

The plot of ln k vs. 1/T (Fig. 3) is a straight line; from its slope, we determined the activation energy:

$$E = 4.571 \,|\tan\alpha\,|\,\xi,$$

where α is the slope of the straight line relative to the abscissa, and ξ is the ratio of scales along the abscissa and ordinate.

In the chosen scales, $\tan\alpha = \tan 30° = 0.5774$, $\xi = 10^3$, and the activation energy $E = 4.571 \times 0.5774 \times 10^3 = 26.393$ kcal mol^{-1} (110.35 kJ mol^{-1}).

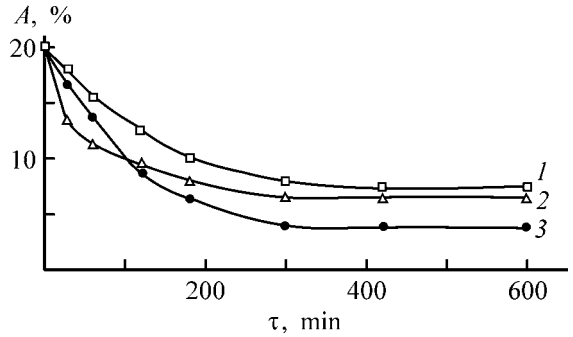

Fig. 1. Kinetic curves of MEAVE–CA–MEAVE polymerization. (*A*) Polymer yield and (τ) time. Temperature, K: (*1*) 346, (*2*) 360, and (*3*) 353.

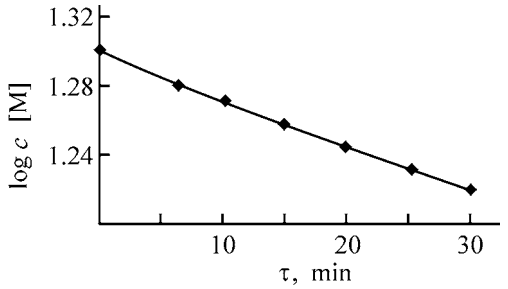

Fig. 2. Concentration c of the monomer vs. the time τ of MEAVE–CA–MEAVE polymerization.

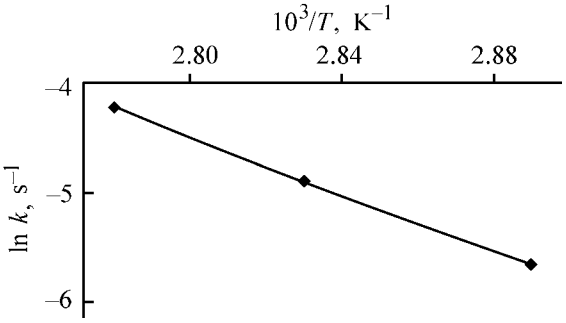

Fig. 3. Rate constant k of MEAVE–CA–MEAVE polymerization vs. temperature T.

The redox monomer prepared from MEAVE and chloranil is capable of polymerization, whereas MEAVE does not form homopolymers in the presence of radical initiators [2–4]. It should be noted, however, that the reactivity of MEAVE–CA–MEAVE in homopolymerization is considerably lower than that of other MEAVE-substituted quinones:

Redox monomer	E, kJ mol^{-1}
MEAVE–1,4-benzoquinone–MEAVE	11.95
MEAVE–2,3-dichloro-5,6-dicyano-1,4-benzoquinone	47.34
MEAVE–1,2-naphthoquinone	62.50
MEAVE–1,4-benzoquinone	76.71
MEAVE–1,4-naphthoquinone	82.84
MEAVE–chloranil–MEAVE	110.35

Comparison of the activation energies of polymerization of structurally related disubstituted 1,4-benzoquinone and chloranil derivatives shows that the monomer based on 1,4-benzoquinone is considerably more reactive than the chloranil derivative. Apparently, the two symmetrically situated chlorine atoms cause redistribution of the electron density, leading to a certain decrease in the polarization of the double bond. As a result, the activity of the radical and hence the homopolymerization rate decrease.

CONCLUSIONS

(1) The conditions of radical polymerization of a new disubstituted quinone derivative obtained from monoethanolamine vinyl ether and 2,3,5,6-tetrachloro-1,4-benzoquinone (chloranil) were optimized.

Table 2. Kinetic characteristics of polymerization of the disubstituted monomer derived from MEAVE and chloranil

T, K	$10^{-3}/T$	$k \times 10^{-4}$, s^{-1}	$\ln k$	$k_0 \times 10^{12}$, s^{-1}
346	2.89	0.58	–5.65	2.71
353	2.83	1.23	–4.90	2.69
360	2.78	2.42	–4.22	2.54

(2) The kinetic of radical homopolymerization was studied, and the rate constants of the process, activation energies, and preexponential factors of the Arrhenius equation were determined. The presence of two chlorine atoms in the monomer affects the activity of the radical and considerably decreases the reactivity of the monomer in radical polymerization.

REFERENCES

1. Kazakhstan Patent 8813.
2. Ergozhin, E.E., Mukhitdinova, B.A., Shoinbekova, S.A., and Nikitina, A.I., *Zh. Prikl. Khim.*, 2001, vol. 74, no. 11, pp. 1847–1849.
3. Ergozhin, E.E., Mukhitdinova, B.A., Shoinbekova, S.A., *et al.*, *Zh. Prikl. Khim.*, 2003, vol. 76, no. 3, pp. 475–478.
4. Shoinbekova, S.A., Nuranbaeva, B.M., Nikitina, A.I., *et al.*, *Izv. Minist. Obraz. Nauki Resp. Kaz., Ser. Khim.*, 2002, no. 3, pp. 111–115.
5. Shoinbekova, S.A., Nuranbaeva, B.M., Nikitina, A.I., *et al.*, *Izv. Minist. Obraz. Nauki Resp. Kaz., Ser. Khim.*, 2002, no. 4, pp. 91–99.
6. Shoinbekova, S.A., Nuranbaeva, B.M., Nikitina, A.I., *et al.*, *Izv. Minist. Obraz. Nauki Resp. Kaz., Ser. Khim.*, 2002, no. 5, pp. 51–58.

Russian Journal of Applied Chemistry, Vol. 77, No. 8, 2004, pp. 1379–1381. Translated from Zhurnal Prikladnoi Khimii, Vol. 77, No. 8, 2004, pp. 1392–1394.

MACROMOLECULAR CHEMISTRY AND POLYMERIC MATERIALS

Sample Pretreatment and Chromatographic Determination of Benz[*a*]pyrene in Wastewater

N. I. Kayutkina, I. A. Platonov, and A. V. Bulanova

Samara State University, Samara, Russia

Received September 16, 2003

Abstract—A procedure was developed for gas-chromatographic determination of benz[*a*]pyrene in wastewater, with similar pretreatment of reference solutions used for plotting the calibration diagrams and of real wastewater.

The environmental monitoring becomes an increasingly topical problem, because the development of industrial production gives rise to a greater number of pollution sources.

Among the known toxic agents, polyaromatic hydrocarbons (PAHs) require the most stringent control in environmental objects due to their carcinogenic activity.

Polycyclic aromatic hydrocarbons are formed in incomplete combustion of organic compounds; they appear in air, soil, and water from various cultural and natural sources, such as combustion of fuels, smoking, oil refining, forest fires, volcanic activity, etc. In the atmosphere, PAHs are transferred with air masses to long distances and their fall-outs contaminate the environment. One of the known PAHs exhibiting high carcinogenic activity is benz[*a*]pyrene (3,4-benzpyrene, BP); its maximum permissible concentration (MPC) in the atmosphere and in air in working areas of industrial plants is 0.1×10^{-5} and 1.5×10^{-4} mg m^{-3}, respectively; MPC for water and soil is 5×10^{-6} mg l^{-1} and 0.02 mg kg^{-1} [1], respectively.

Analysis of PAHs occurring in the environmental objects in so small concentrations requires that rather stringent requirements should be satisfied at any stage of the procedures used and, thus, very selective and sensitive analytical methods should be developed. The procedures devised in [2, 3] for analysis of PAHs in water are based on capillary gas chromatography with mass-spectrometric detection. Due to simplicity of experimental equipment and availability of modern methods for data recording and treatment, these procedures can be used in both routine and proximate analyses. However, these procedures are based on the quantitative treatment of the gas-chromatographic data and do not take into account experimental errors originating from the sample preparation.

Since monitoring of water samples for the content of BP impurities involves its determination at concentrations not higher than MPC, this problem cannot be solved without preconcentration. Small amounts of PAHs (including BP) are recovered using extraction and sorption methods, supercritical fluid extraction, etc. Despite the significant number of studies devoted to optimization and use of various procedures for sample pretreatment, no one can be considered preferable. However, the main stage in almost all the known procedures of sample pretreatment is still liquid-liquid extraction [4], with benzene as extractant providing the best recovery of PAHs from water. It should be noted that only thoroughly purified solvents and freshly prepared references should be used in the analysis.

EXPERIMENTAL

In this study, wastewater samples were treated using liquid–liquid extraction with benzene as extractant.

The chromatographic tests were performed on a GALS-311 gas chromatograph (LYuMEKS company, Russia) equipped with a flame-ionization detector and a capillary quartz column (3000×0.025 cm) with a low-polarity stationary phase; ultrapure nitrogen carrier gas was used.

The following hydrocarbon impurities occurring in water (aliphatic hydrocarbons C_1–C_{10}, benzene, tolu-

1070-4272/04/7708-1379 © 2004 MAIK "Nauka/Interperiodica"

Quantitative analysis of BP

Procedure	c_{BP}*, mg dm^{-3} (added)	Found $x \pm 1\Delta x$, mg dm^{-3}	Δ, %
		Absolute calibration procedure	
(A)	0.0049	$0.0007 \pm 11.2 \times 10^{-4}$	85.7
	0.0096	$0.0026 \pm 13.9 \times 10^{-4}$	72.9
	0.0489	$0.0155 \pm 11.9 \times 10^{-3}$	68.3
	0.0976	$0.0563 \pm 15.1 \times 10^{-3}$	42.3
	0.8957	$0.6438 \pm 14.5 \times 10^{-2}$	28.1
(B)	0.0049	$0.0043 \pm 7.1 \times 10^{-4}$	12.2
	0.0096	$0.0089 \pm 11.4 \times 10^{-3}$	7.3
	0.0489	$0.0448 \pm 15.8 \times 10^{-3}$	8.4
	0.0976	$0.0921 \pm 19.2 \times 10^{-3}$	5.6
	0.8957	$0.8425 \pm 15.9 \times 10^{-2}$	5.9
		Analysis with calibration curve	
(A)	–	$1.52 \times 10^{-3} \pm 12.6 \times 10^{-4}$	
		$2.63 \times 10^{-3} \pm 13.4 \times 10^{-4}$	
		$4.44 \times 10^{-3} \pm 13.6 \times 10^{-4}$	
(B)	–	$2.48 \times 10^{-3} \pm 14.2 \times 10^{-4}$	
		$3.68 \times 10^{-3} \pm 15.2 \times 10^{-4}$	
		$6.55 \times 10^{-3} \pm 15.9 \times 10^{-4}$	

* (c_{BP}) concentration of BP and (Δ) relative error.

ene, ethylbenzene, xylene isomers, acetone, carbon tetrachloride, chloroform, 1,2-dichloroethane, 1,2-dibromoethane, chloroethane, bromoethane, naphthalene, 2-methylnaphthalene, 1-methylnaphthalene, biphenyl, acenaphthene, etc.) do not interfere with the chromatographic determination of BP, because these compounds are efficiently separated on the column used. Benz[*a*]pyrene was identified by the retention time of the reference (t_{Rsr} = 17.2 min).

In this study, we employed the published procedure [5] in which the reference solutions with known contents of compounds in question is used for constructing calibration diagrams, being subjected to the same pretreatment as the samples to be analyzed. The effect of the sample pretreatment on the results of qualitative gas-chromatographic determination of BP was studied using model systems.

In procedure A, we prepared a series of reference solutions in benzene with known concentrations of BP and then plotted the chromatographic peak areas vs. the BP concentration [6].

In procedure B, the calibration curve was plotted using the data of chromatographic analysis of reference solutions subjected to the same pretreatment as real water. We prepared five model mixtures with known BP concentration; for this purpose, the required weighed portions of the State Reference Sample (benzene solution with BP concentration of 1 mg cm^{-3}) were added to distilled water (1 dm^3). The resulting solution was thoroughly mixed, sodium chloride was added, and the system was extracted with three portions of benzene. The benzene solutions were combined and passed through anhydrous Na_2SO_4, which was then twice washed with benzene. Then, the combined extracts were evaporated to nearly 1 cm^3 volume. The whole procedure B is shown in the scheme.

Preparation of the calibration by procedure B.

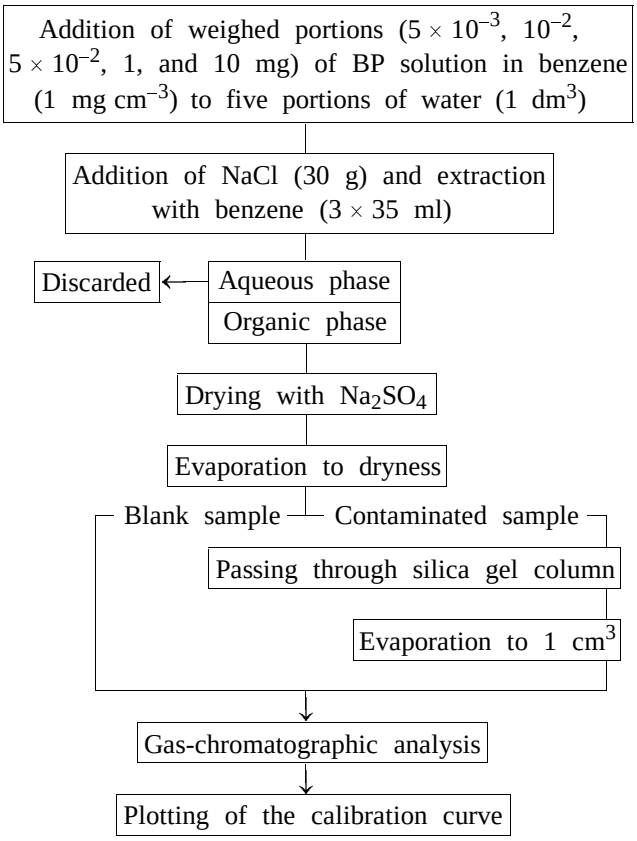

As indicated by the experimental results (see table), the relative error in determining BP in water by procedure A at its low content is 86%, and it does not exceed 12% in procedure B.

The results of a quantitative gas chromatographic analysis of real wastewater are also listed in the table.

CONCLUSIONS

(1) Chromatographic analysis of benz[a]pyrene is based on comparison with the calibration curves for reference solutions subjected to the same treatment as real wastewater in question.

(2) In contrast to the procedure involving solutions subjected to the same pretreatment as the samples to be analyzed, the straight use of reference solutions of known concentration can cause underestimation of the benz[*a*]pyrene content in real systems by up to an order of magnitude.

REFERENCES

1. Drugov, Yu.S., *Ekologicheskaya analiticheskaya khimiya* (Environmental Analytical Chemistry, Moscow: Anatoliya, 2000.
2. Soniassy, R., Sandra, P., and Schlett, C., *Water Analysis: Organic Micropoluttants*, Hewlett-Packard, 1994.
3. Vlasova, I.V., Vershinin, V.I., Smirnov, Yu.N., *et al.*, *Zh. Anal. Khim.*, 1998, vol. 43, no. 3, pp. 516–522.
4. Yanysheva, N.Ya., Chernichenko, I.A., Balenko, N.V., *et al.*, *Gigiena Sanit.*, 2001, no. 2, pp. 67–70.
5. Kayutkina, N.I., Platonov, I.A., and Bulanova, A.V., *Zavod. Lab.*, 2004, vol. 72, no. 2, pp. 3–6.
6. Gol'bert, K.A. and Vigdergauz, M.S., *Vvedenie v gasovuyu chromatografiyu* (Introduction in Gas Chromatography), Moscow: Khimiya, 1990.

Russian Journal of Applied Chemistry, Vol. 77, No. 8, 2004, pp. 1382–1385. Translated from Zhurnal Prikladnoi Khimii, Vol. 77, No. 8, 2004, pp. 1395–1397.

MACROMOLECULAR CHEMISTRY AND POLYMERIC MATERIALS

Preparation and Vulcanizing Properties of 1,3,5-Trinitrosobenzene

O. R. Klyuchnikov, F. G. Khairutdinov, and Ya. O. Klyuchnikov

Kazan State Technological University, Kazan, Tatarstan, Russia

Received May 11, 2004

Abstract—A procedure was developed for preparing a new trifunctional vulcanizing agent for unsaturated rubber composites, 1,3,5-trinitrosobenzene; its suitability as an additive to rubber–substrate adhesive formulations was examined.

Dinitrosoarenes are used as highly active vulcanizing agents for unsaturated rubbers and composites thereof [1]; *p*-dinitrosobenzene (DNB) is widely used in rubber–substrate adhesive formulations [2]. The curing power of dinitrosoarenes is based on their bifunctional structure allowing cross-linking of two unsaturated rubber molecules. Calculations predict [3] that 1,3,5-trinitrosobenzene (TNB) should be more reactive in vulcanization than DNB. Therefore, synthesis of trifunctional TNB is of theoretical and applied interest.

The goal of this study was to develop a facile procedure for preparing TNB and to evaluate its vulcanizing properties and adhesive power in rubber–substrate formulations.

The initial attempts to prepare TNB by reduction of 1,3,5-trinitrobenzene to 1,3,5-tri(hydroxylamino)benzene, followed by oxidation, failed because of side reactions yielding azo and azoxy derivatives. Another route led to success: oxidation of cyclohexane-1,3,5-trione trioxime (CTO) with 30–35% HNO_3 in the presence of minor amounts (~0.1%) of nitrogen oxides. In the course of the reaction, TNB is formed as a hydrophobic foam:

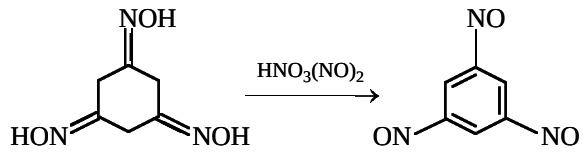

In dilute nitric acid free of nitrogen oxides, CTO readily dissolves to form a brown solution, without oxidation to TNB. Addition of a small amount of sodium nitrite as a source of nitrogen oxides initiates oxidation of CTO to TNB; thus, NO_2 and N_2O_4 are key compounds in the reaction.

EXPERIMENTAL

Cyclohexane-1,3,5-trione trioxime was prepared as described in [4].

1,3,5-Trinitrosobenzene. Dilute nitric acid was prepared by adding 16 ml of 98% HNO_3 containing 0.2–0.4% nitrogen oxides to 50 g of ice. To the resulting 35% HNO_3 solution containing dissolved nitrogen oxides (~0.1%), 1.0 g of CTO was added with vigorous stirring at 12–15°C. Virtually immediately after the dissolution of CTO, TNB was formed as a hydrophobic foam. The product was filtered off, washed with water to neutral reaction and then with acetone, and dried. Yield 0.32 g (34%); light turquoise powder, mp 170°C with decomposition. No tarring was observed. Analytical data:

Found, %: C 43.90, N 25.20, H 1.65.

$C_6H_3N_3O_3$.

Calculated, %: C 43.65, N 25.45, H 1.83.

The mass spectrum (EI, 70 eV) recorded on a Finnigan MAT-212 device showed that the sample completely sublimed on being introduced into the ion source. Mass spectrum, m/z (I_{rel}, %): 165.1 $[M]^+$ (59), 135 $[M–NO]^+$ (42), 105.1 $[M–NO–NO]^+$ (8), 75.1 $[M–NO–NO–NO]^+$ (100). The fragmenta-

1070-4272/04/7708-1382 © 2004 MAIK "Nauka/Interperiodica"

tion pattern involves the loss of NO groups characteristic of nitrosoarenes [5] and can be described by the scheme

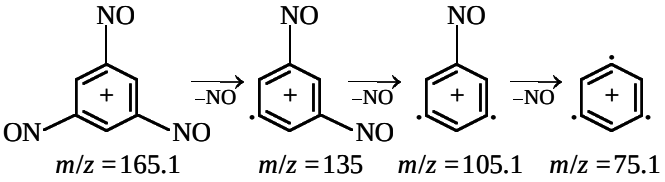

At room temperature, TNB is virtually insoluble in organic solvents and sparingly soluble in hot (100°C) toluene or xylene with the formation of an unstable green solution.

Oxidation of TNB yields 1,3,5-trinitrobenzene, similarly to oxidation of nitrosoarenes [2]. In particular, addition of 1 g of TNB to 20 ml of hot (80°C) 98% nitric acid, followed by keeping at this temperature for 2–3 min and dilution with 100 ml of water, yields 0.9 g (70%) of 1,3,5-trinitrobenzene, mp 121–122°C; its spectral (IR, ^{1}H NMR) and TLC (R_f) characteristics coincide with those of an authentic sample.

The IR spectrum of TNB (KBr), recorded on a Bruker Vector-22 spectrometer (Fig. 1), contains a strong band at 1272 cm^{-1}, characteristic of nitroso-arene *trans* dimers [5]; the band at 3119 cm^{-1} is assigned to stretching vibrations of the aromatic C–H bonds. The spectrum suggests that solid TNB has a polymeric structure with *trans*-dimerized nitroso groups, which makes this compound difficultly soluble and relatively stable, comparable in properties with polymeric *p*-dinitrosobenzene having similar *trans*-azo-*N,N*'-dioxide structure [6–8]:

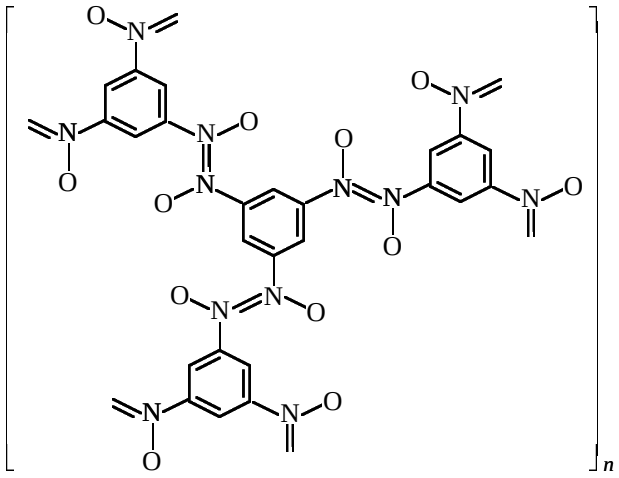

In agreement with the theoretical predictions [3], TNB surpasses DNB in the vulcanizing activity and is of interest as a high-rate curing agent for composite systems based on unsaturated rubbers.

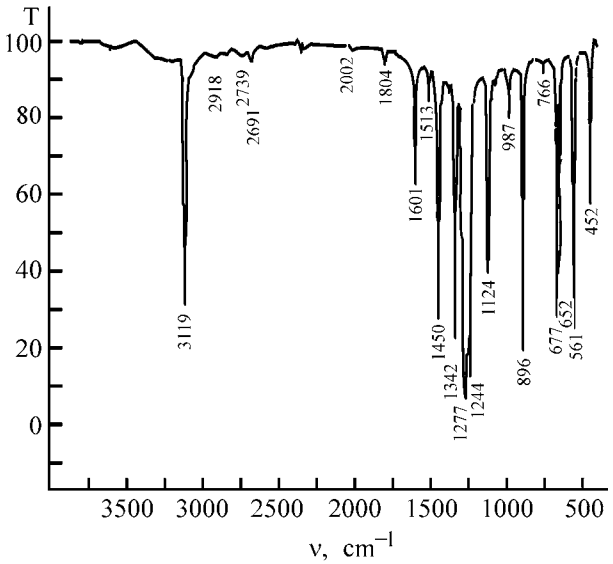

Fig. 1. IR spectrum of TNB in KBr. (T) Transmission and (ν) wave number.

We compared the physicomechanical properties of vulcanized products obtained under "cold" (25°C) vulcanization conditions with TNB and its structural analogue applied in the same field, DNB. The stock compounding was performed on cold rollers; the weight proportions of the components were as follows: butyl rubber 100, DG-100 channel black (filler) 50, stearic acid (plasticizer) 2, and DNB or TNB (vulcanizing agent) 1.

Vulcanization of rubber stocks was performed with 1–1.2-mm-thick plate samples at room temperature for 24 h, after which the physicomechanical characteristics of the vulcanizates were studied with an RMI-250 tensile testing machine (Table 1).

As seen from Table 1, cold vulcanization of a model formulation with TNB ensures better physicomechanical characteristics.

We also examined the possibility of using TNB as a component of a rubber–substrate adhesive formulation. The impregnating compound was prepared by mixing 100 wt parts of *o*-xylene, 10 wt parts of SKN-

Table 1. Physicomechanical characteristics of vulcanizates

Vulcanizing agent	Tensile strength, MPa cm^{-2}	Elongation at break, %
DNB	7.5	320
TNB	9.3	380

Table 2. Results of tests by the H method

Cord thread	Strength H with indicated agent	
	DNB	TNB
25KNTS	175	195
13ATL-VU	103	128

40 butadiene–acrylonitrile rubber, 5 wt parts of chlorinated Nairit (chloroprene rubber), and 5 wt parts of DNB or TNB. The resulting compound was used to treat 25KNTS polycaprolactam cord threads and 13ATL-VU Anid (nylon) threads by their short dipping into a tank with the impregnating compound. After drying, the impregnated cord threads were placed in a mold for vulcanization with a standard rubber stock based on SKI-3 isoprene rubber, with subsequent determination of the rubber–cord binding strength by the H method [9]. The results are listed in Table 2.

As seen from Table 2, TNB used as component of a rubber–substrate adhesive formulation ensures higher adhesive characteristics, compared to the formulation with DNB.

An ESR study of the vulcanization mechanism with TNB (Radiopan SE/X 2544 spectrometer) revealed, in the initial steps of the reaction of SKDK divinyl rubber (toluene solution) with TNB, the signals of nitroxyl radicals (Fig. 2; a_N = 1.06, a_H = 0.28 mT; g = 2.0057).

The mechanism of unsaturated rubber vulcanization with TNB presumably involves depolymerization of TNB to the monomer and subsequent reactions similar to those of DNB with olefins [10, 11]: pseudo-Diels–Alder addition to the alkene unit, formation and oxidation of the hydroxylamine derivative to nitroxyl, and reactions yielding a three-dimensional network:

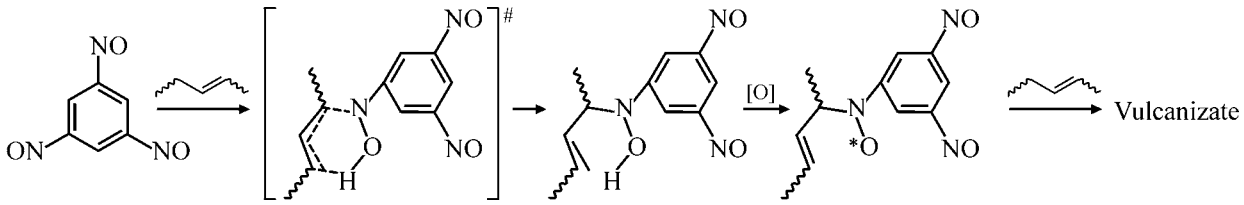

Owing to the presence of three reactive nitroso groups, TNB shows advantages over dinitrosoarenes.

CONCLUSIONS

(1) A procedure was developed for preparing 1,3,5-trinitrosobenzene by oxidation of cyclohexane-1,3,5-trione trioxime with dilute nitric acid in the presence of nitrogen oxides.

(2) Solid 1,3,5-trinitrosobenzene is a polymer owing to the intermolecular dimerization of the nitroso groups and formation of *trans*-azo-*N*,*N*'-dioxide fragments.

(3) The trifunctional structure of 1,3,5-trinitrosobenzene ensures higher physicomechanical characteristics of vulcanizates and higher adhesive characteristics of rubber–substrate adhesive formulations prepared with this agent.

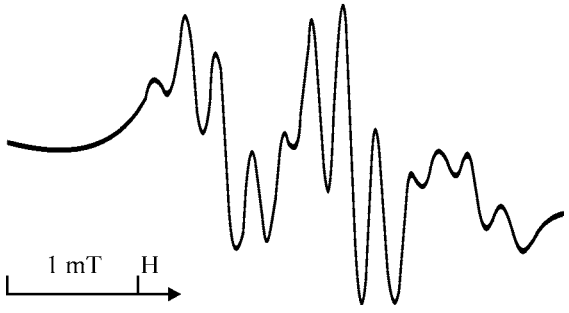

Fig. 2. ESR spectrum of the nitroxyl radical in the initial step of the reaction of TNB with SKDK.

REFERENCES

1. Hofmann, W., *Vulkanisation und Vulkanisationshilfsmittel unter besonderer Berücksichtigung der Bayer-Produkte*, Stuttgart: Berliner Union, 1965.
2. Tikhonova, N.P., Ginzburg, L.V., and Dontsov, A.A., *Kauchuk Rezina*, 1987, no. 3, pp. 13–15.
3. Klyuchnikov, O.R., *Energeticheskie kondensirovannye sistemy: Materialy Vserossiiskoi konferentsii 28–31 oktyabrya 2002 g.* (Chernogolovka, IPKhF RAN)

(High-Energy-Capacity Condensed Systems: Proc. Russian Conf., October 28–31, 2002 (Chernogolovka, Inst. of Problems of Chemical Physics, Russian Acad. Sci.)), Moscow: Yanus-K, 2002, pp. 94–95.

4. Baeyer, E., *Ber. Deutsch. Chem. Ges.*, 1886, vol. 19, p. 159.
5. *Comprehensive Organic Chemistry. The Synthesis and Reactions of Organic Compounds*, Barton, D. and Ollis, W.D., Eds., vol. 2: *Nitrogen Compounds*, Oxford: Pergamon, 1979.
6. Klyuchnikov, O.R., Thermal Decomposition of *N*-Oxides and Aromatic *C*-Nitroso Compounds, *Cand. Sci. Dissertation*, Kazan, 1990.
7. Hacker, N.P., *Macromolecules*, 1993, vol. 26, pp. 5937–5942.
8. Klyuchnikov, O.R., Makarov, T.V., Vol'fson, S.I., *et al.*, *Izv. Vyssh. Uchebn. Zaved., Khim. Khim. Tekhnol.*, 2004, vol. 47, no. 2, pp. 22–27.
9. *GOST* (State Standard) *14863–69: Vulcanized Rubber: Procedure for Determining the Rubber–Cord Binding Strength (H Method).*
10. Zhuzhgov, E.L., Strunina, N.V., Komarov, V.F., *et al.*, *Kinet. Katal.*, 1972, vol. 13, pp. 1405–1408.
11. Gan, L.M. and Chew, C.H., *Rubber Chem. Technol.*, 1983, vol. 56, no. 5, pp. 883–891.

Russian Journal of Applied Chemistry, Vol. 77, No. 8, 2004, pp. 1386–1387. Translated from Zhurnal Prikladnoi Khimii, Vol. 77, No. 8, 2004, pp. 1398–1400.

BRIEF COMMUNICATIONS

Influence of Fulleroid Nanoparticles (Astralenes) on Absorption of Water by Epoxy Resin

D. V. Kositskii, V. M. Yudovich, M. E. Yudovich, and A. N. Ponomarev

Astrin-Kholding Private Company, St. Petersburg, Russia

Received April 29, 2004

Abstract—Water absorption by ED-20 epoxy resin modified with fullerid nanoparticles, astralenes, was studied as influenced by the modifier content.

Epoxy resins, epoxy-acrylic copolymers, and their composites are used in electrical engineering and radioelectronic industry, aircraft construction, shipbuilding, and mechanical engineering. These materials are also used in building industry as components of potting and impregnation compounds, adhesives, sealants, and binders of reinforced plastics. The adhesion of epoxy resins to most of fillers, supports, and reinforcing fibers is high. Epoxy adhesives are among the best known polymers in the adhesive strength. Cured epoxy resins have good mechanical properties, low shrinkage, and high chemical resistance.

Since polymeric epoxy composites are used in large (usually multilayer) power and insulating structures, water absorption of the epoxy matrix should be estimated. It should be noted that the strength and elastic modulus decrease by 15–20% and the glass transition point substantially decreases at water absorption of 5–8 wt % [1]. The dielectric properties of polymeric composites used for electrical and radio engineering purposes are strongly deteriorated by water absorption.

Epoxy matrices with water absorption of no higher than 1% are the most promising for preparing modern polymeric and composite structures [1].

In this study, we examined the modification of ED-20 epoxy-4,4'-isopropylidenediphenol resin with astralene carbon nanoparticles to decrease its water absorption.

EXPERIMENTAL

We used astalenes, carbon fulleroid nanoparticles, [2] as the modifier.

A typical polyhedral multilayer particle 150 nm long with internal slit capillary is shown in Fig. 1. Similar particles are shown in Fig. 2. Their

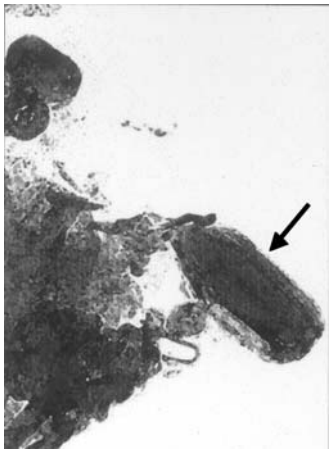

Fig. 1. Typical polyhedral multi-layer particle 150 nm long with internal slit capillary. Scale 1 : 1; the same for Fig. 2.

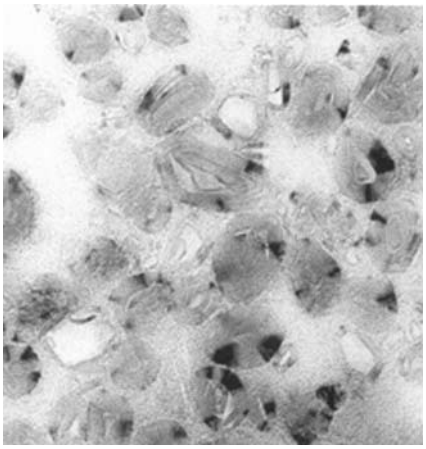

Fig. 2. General view of dispersed astralenes.

1070-4272/04/7708-1386 © 2004 MAIK "Nauka/Interperiodica"

shape and the configuration of the slit capillary are clearly seen.

We used ED-20 epoxy resin [GOST (State Standard) 10587–84], PEPA curing agent [TU (Technical Specification) 2413-357-00203447–99], and carbon nanomodifier (TU 2166-001-13800624–2003). The experiments were performed using a VLR-200 analytical balance and an UZV2-1.6/18 ultrasonic bath with an UZG16-1.6/22 ultrasonic generator.

The epoxy resins were modified by two methods. The first method was developed in our laboratory. The nanomodifier was dispersed for 15 min in acetone in an ultrasonic bath, and then the acetone was removed. The epoxy resin was also treated in the ultrasonic bath for 15 min. Then a weighed portion of the modifier was added in small portions to the resin with stirring over a period of 20 min without interrupting the ultrasonic treatment. The curing agent was introduced with continuous vigorous stirring over a period of 5 min. The weight ratio of the curing agent to the resin was 1 : 10. The finished formulation was cast into a mold and cured at room temperature for 24 h. The completely cured sample was weighed and boiled in 0.2 wt % NaCl solution to remove the excess curing agent. Then the sample was weighed again and boiled in NaCl solution for 2 h. After that it was dried between pieces of filter paper and weighed to determine the water absorption.

The second procedure was performed in accordance with GOST 4650–80. Each point of the concentration dependence of water absorption was obtained with 10–15 samples of two different batches of the resin. The experimental dependences of the water absorption by the epoxy matrix on the nanomodifier concentration are shown in Figs. 3a and 3b.

The relative error for each point of the concentration dependences does not exceed 18 rel % at the confidence level of 0.95.

As seen from both figures, the water absorption is low. It is this fact that necessitates the use of the original procedure. The sample obtained by the procedure performed in accordance with GOST 4650–80 should be weighed within 3 min after its removal from the cooled solution. In this case, residual moisture is retained on its surface. The presence of surface water masks the actual water absorption in the bulk of the epoxy matrix. The almost constant (0.7 wt %) water

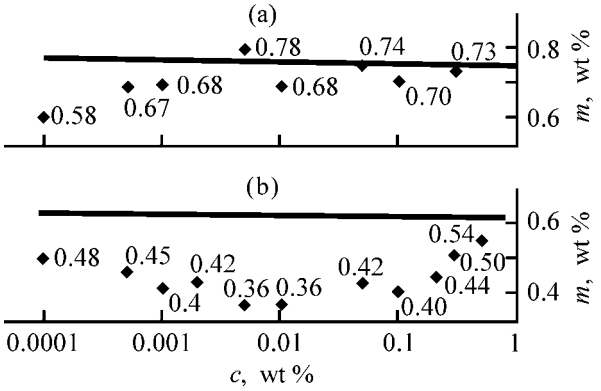

Fig. 3. Water absorption *m* by ED-20 epoxy resin, determined by (a) conventional and (b) original procedure, vs. the content *c* of nanomodifier (astralene) in the polymeric matrix. *Bold line* shows water absorption by the unmodified resin. *Figures at the points* denote water absorption (wt %).

absorption for all the samples prepared by the conventional procedure (Fig. 3a) is due just to this fact. The water absorption by the unmodified resin is shown by the bold line.

The water absorption determined by the original procedure, which involves removal of the surface water, strongly depends on the modifier content (Fig. 3b). It should be noted that the dependence passes through a minimum at the astralene concentration of 5×10^{-2} to 2×10^{-3} wt %. Probably, this concentration of fulleroid particles catalyzes formation of the polymeric matrix.

This is also the case for other astralene-containing composites.

CONCLUSION

The dependence of water absorption by ED-20 epoxy resin on the concentration of a fulleroid modifier was obtained. The water absorption decreases by a factor of 2 at the modifier concentration of 5×10^{-2}–2×10^{-3} wt %.

REFERENCES

1. Mikhailin, Yu.A., Miichenko, I.P., and Pervushin, Yu.S., *Trebovaniya k matritsam konstruktsionnykh polimernykh kompositsionnykh materialov: Uchebnoe posobie* (Requirements for Matrices of Structural Polymeric Composites: Handbook), Ufa: UGATU, 1996.
2. RF Patent 2196731.

Russian Journal of Applied Chemistry, Vol. 77, No. 8, 2004, pp. 1388–1391. Translated from Zhurnal Prikladnoi Khimii, Vol. 77, No. 8, 2004, pp. 1401–1403.

Jons Jakob Berzelius (To 225th Anniversary of His Birthday)

Professor Jons Jakob Berzelius, a member of the Royal Swedish Academy of Sciences (since 1808), its president (1810–1818) and permanent secretary (since 1818), an honorary foreign member of the Imperial Petersburg Academy of Sciences (since 1820), and a member of academies of sciences and scientific societies of many other countries occupies a rather honorary place in the history of chemistry.

Being one of the best experts on chemistry of his time, he made an outstanding contribution to the creation and development of quite a number of its most important fields.

J.J. Berzelius was born on August 20, 1779, in southern Sweden into a teacher's family. Having received his primary education at home, he entered the gymnasium at a small Swedish town of Linköping in 1793. Already at an early age, Berzelius was interested in natural science and studied the flora and fauna of the neighborhood. Having early lost his parents, he was obliged to earn his living already when studying at the gymnasium and gave lessons. In the end of September 1796, the seventeen-years-old youth entered the old-established university of the town of Uppsala. Founded in 1477, this educational institution was deservedly famed. When being an undergraduate medical student, Berzelius become interested in chemistry and gained an opportunity to use the facilities of the university's chemical laboratory. Berzelius was particularly attracted by the basic research conducted by a prominent French chemist A.L. Lavoisier (1743–1794) and by fundamentals of his oxygen theory explaining the processes of burning and oxidation. The young Swedish scientist took an active interest in the results of investigations carried out by an English physicist and chemist J. Dalton (1766–1844), which were published at the very beginning of the XIX century, and in studies of his Italian colleagues: physiologist L. Galvani (1737–1798) and physicist A. Volta (1745–1827).

In May 1801, the degree of a candidate of medicine was conferred on Berzelius for his studies of medicinal mineral water. Having completed his education, Berzelius obtained the place of supernumerary assistant at the Medical-Surgical Institute in Stockholm. During those same years, Berzelius managed, with assistance of W. Hisinger (1766–1852), a Swedish industrialist and scientist, to equip a laboratory and fabricate instruments necessary for investigations, in-luding a voltaic pile. Already in May 1802, he presented a paper devoted to the effect of electricity on living organisms and became a doctor of medicine and pharmacy. In that same year, at the age of 23, Berzelius was appointed an adjunct of medicine and pharmacy at the Medical-Surgical Institute in Stockholm. In 1807, he was appointed an ordinary professor of chemistry and pharmacy at the same institute. In 1807, Berzelius founded the Swedish Society of Physicians.

In 1808, the young scientist was inducted into the Royal Swedish Academy of Sciences, and was elected its president in 1810. Beginning in 1818, he was the permanent secretary of the Academy for thirty years. In 1818, Berzelius was ennobled; he became

1070-4272/04/7708-1388 © 2004 MAIK "Nauka/Interperiodica"

a baron in 1835. In 1832 he terminated his teaching activities and concentrated all his attention on scientific studies. As mentioned in the monograph [1], already by the end of the 1810s, Berzelius became the leading figure in world's chemical science and attracted the attention of scientists from many countries.

The scientific activities of Berzelius were diverse and successful, their scale is astonishing. Having started with an analysis of the influence exerted by electricity on organic bodies, Berzelius performed, together with Hisinger, a first study in the field of electrochemistry of solid solutions already in 1802. He subjected aqueous solutions of various salts of sulfuric acid to electrolysis. In the same year, he published in Swedish the book *Treatise on Galvanism*. The results of his experiments were described in more detail and more completely in an article published by Berzelius and Hisinger in German in 1803. Already this first publication presented new concepts of the behavior of chemical compounds in electrolysis. In the following years, these concepts were transformed into the electrochemical theory of affinity. Much attention was given to investigations by Berzelius and the closely related studies carried out by G. Davy (1778–1829) in the same years in a book by I.A. Kablukov [2]. According to Berzelius, any complex body can be separated into two parts, one electronegative and the other electropositive. In a comparatively finished form, the main concepts of the electrochemical theory developed by Berzelius were formulated in papers published in 1812 and 1815 [1].

In 1803, Berzelius and Hisinger discovered, virtually simultaneously with M.H. Klaproth (1743–1817), a German chemist analyst, a new element, cerium. In 1817, Berzelius discovered in the waste from sulfuric acid production one more new element, an analogue of tellurium. This element was named selenium. In 1828, Berzelius discovered and, in the next year, isolated in pure form a new element and named it thorium. In 1823, Berzelius obtained silicon in pure form for the first time.

In 1817, a Swedish chemist J.A. Arfwedson (1792–1841) discovered lithium at Berzelius's laboratory and under his supervision and described the properties of this element. In 1830, another pupil of Berzelius, N.G. Sefström (1787–1845), discovered vanadium. Berzelius studied the chemistry of vanadium compounds.

In addition to isolating thorium and silicon, Berzelius was the first to obtain zirconium and tantalum, which had been only known in compounds, in the form of individual metals. The Swedish scientist paid a considerable attention to ores and minerals, in which the nature of Scandinavia is so rich. Having done an enormous amount of work and performed a great number of analyses, Berzelius systematized, in fact, for the first time the available minerals and, based on the results of chemical analyses and on electrochemical concepts developed by the him, combined them in families and groups. Berzelius also improved the existing methods for qualitative analysis of minerals. Before the beginning of the XIX century, mineralogy had been a purely descriptive science. After Berzelius's works, the chemical composition of minerals became their basic classification characteristic. The investigations performed by the Swedish scientist laid the foundation of the chemical area in geology and mineralogy, which was further developed in the second half of the XIX century.

In 1811–1818, Berzelius analyzed and determined the percentage composition of about two thousand compounds, and determined the atomic weights of a great number of elements known by that time. This enormous work served as a confirmation and experimental substantiation of Dalton's atomistic concepts. Dalton introduced the notion of the atomic weight at the very beginning of the XIX century and compiled the first table of relative atomic weights of the most important elements, with the atomic weight of hydrogen taken to be unity, and formulated the law of multiple proportions. The standpoint of Berzelius in the field of atomism and its transformation were analyzed in detail in the monograph by Yu.I. Solov'ev and V.I. Kurinnoi [1]. In 1826, based on newly discovered laws and results of investigations (Dulong–Petit law, investigations of isomorphism), Berzelius composed a new system of atomic weights for 29 chemical elements, with the atomic weights of 23 of these being very close to their modern values.

Berzelius suggested a simple and understandable notation of chemical elements, which is used by chemists until now. This notation was first described by the author in 1813, and in a more complete form, in 1815. So the chemists got a unified chemical language.

In 1811, Berzelius commenced a study of organic compounds, having started with the fabrication of instruments for their elemental analysis. This made it possible to analyze with high precision quite a number of important organic compounds and to conclude that their composition can be described using chemical formulas. This aspect of Berzelius's activities was considered in detail in the monograph [3]. Berzelius him-

self wrote in 1839: "A chemical study of the organic nature have become one of the most interesting subject of natural science" [3]. By the end of Berzelius's life, organic chemistry occupied the leading position in chemistry.

During a number of years, Berzelius worked on a textbook of chemistry and was occupied with its reedition and improvement. The first volume was published in 1808, and the following four volumes, in 1812, 1818, 1827, and 1828. The textbook was translated into other languages. For example, in 1843–1848 a translation of the fifth edition was published in German in five large volumes; in 1845–1850, a French translation was published. The textbook written by Berzelius discussed for the first time such notions as isomerism, allotropy, and catalysis.

Berzelius was the first organizer of scientific information in the history of science. In 1821, *Annual Report of Advances in Physics and Chemistry* was published in Swedish. During the period of time from 1821 till 1847, 27 issues of *Annual Reports* were published, all of which were translated into German. During the first years of publication, the issues covered investigations in physics, chemistry, astronomy, zoology, botany, and technology. The issues published in 1825 to 1839 covered only physics and chemistry. Beginning in 1840, the issues were devoted to chemistry and mineralogy. Berzelius not only reviewed a great number of scientific publications, but also attempted to make an objective critical estimate of most of these works.

Berzelius maintained close scientific relationships with many leading scientists of his time. In the summer of 1812, he visited London and got acquainted with of Davy, whose works in electrochemistry had long been known to Berzelius. In 1818, the Swedish scientist made a long trip abroad, during which he visited England, France, Switzerland, and Germany. He became closely acquainted with C.L. Berthollet (1748–1822), P.L. Dulong (1785–1838), and German and Swiss chemists. Later, Berzelius repeatedly visited Germany and got acquainted with outstanding representatives of this country: poet, philosopher, and natural scientist J.W. Goethe (1749–1832); scientist, traveller, and public figure A. Humboldt (1769–1859); and well-known chemist J. Liebig (1803–1873). Such prominent and, later, well-known German chemists as Ch.G. Gmelin (1792–1860), H. Rose (1795–1864) and his brother G. Rose (1798–1873), F. Wöhler (1800–1882), and H.G. Magnus (1808–1871) were trained in different times at Berzelius's laboratory. Among the Russian chemists who improved their education at this laboratory were G.I. Gess (1802–1850), Yu.V. Fritsshe (1808–1871), G.V. Struve (1822–1908), and K. Shmidt (1822–1894). Later, Gess and Fritsshe were elected members of the St. Petersburg Academy of Sciences (in 1830 and 1852, respectively), and Struve and Shmidt, corresponding members (in 1876 and 1873). The scientific relationships between Berzelius and Russian scientists were analyzed in a monograph [1] and in [4, 5]. As already noted, Berzelius was elected for "outstanding achievements in chemistry" an honorary member of the St. Petersburg Academy of Sciences. A great number of his works were published in Russian translation in periodical [mostly in Gornyi zhurnal (Mining Journal)] and other publications. In turn, Berzelius paid a sufficient attention to works of Russian scientists and noted their high level and practical value [4]. Berzelius corresponded with a number of Russian scientists; the correspondence with Gess was especially intensive [5].

Jons Jakob Berzelius died of a continuous illness on August 7, 1848. His life and activities were described in detail in monographs [1, 6]. A vast literature: articles in journals [7] and reference publications [8–10], is devoted to the outstanding Swedish scientist. The achievements of Berzelius in chemistry of rare-earth metals were considered by D.N. Trifonov [11]. The contribution of the Swedish scientist to the theory of catalysis was discussed by V.I. Kuznetsov [12]. The known historian of chemistry B.N. Menshutkin (1874–1938) named Berzelius "the most outstanding chemist of the first half of the XIX century" [13].

REFERENCES

1. Solov'ev, Yu.I. Kurinnoi, V.I., *Yakob Bertselius: Zhizn' i deyatel'nost'* (Jakob Berzelius: Life and Activities), Moscow: Nauka, 1980.
2. Kablukov, I.A., *Ocherki po istorii elektrokhimii za XIX vek* (Outline of the History of Electrochemistry of the XIX Century), Moscow, 1901.
3. G'el't, E., *Istoriya organicheskoi khimii s drevneishikh vremen do nashego vremeni: Perevod s nemetskogo* (History of Organic Chemistry from Ancient Times till the Present Day), Kharkov; Kiev: Gos. Nauchn.-Tekhn. Izd. Ukrainy, 1937.
4. Kurinnoi, V.I., *Vopr. Ist. Estestvozn. Tekhn.*, 1960, no. 10, pp. 85–88.
5. Solov'ev, Yu.I., *Vopr. Ist. Estestvozn. Tekhn.*, 1958, no. 6, pp. 166–175.
6. Jorpes, J.E., *Jac Berzelius: His Life and Work*, Transl. from Swed., B. Steele, Stockholm, 1966.

7. Yaffe, B., *Usp. Khim.*, 1938, vol. 7, no. 4, pp. 620–630.
8. Blokh, M.A., *Biograficheskii spravochnik: Vydayushchiesya khimiki i uchenye XIX–XX stoletii, rabotavshie v smezhnykh s khimiei oblastyakh nauki* (Biographic Reference Book: Outstanding Chemists and Scientists of the XIX and XX Centuries, Who Worked in Fields of Science Adjacent to Chemistry), Leningrad: Nauch. Khim.-Tekhn., 1929, vol. 1.
9. Tuchs, G., Heinig, K., Kertscher, G. *et al.*, *Biographien bedeutender Chemiker*, Berlin: Volk und Wissen Volkseigener, 1977.
10. Leicester, H.M., *Dictionary of Scientific Biography*, Gillespie, Ch.C., Ed.,. New York: Charles Scribner's a. Sons, 1981, vol. 1, pp. 90–97.
11. Trifonov, D.N., *Tr. In–ta Ist. Estestvozn. Tekhn.*, 1962, vol. 39, pp. 77–86.
12. Kuznetsov, V.I., *Vopr. Ist. Estestvozn. Tekhn.*, 1961, no. 11, pp. 82–88.
13. Menshutkin, B.N., *Khimiya i puti ee razvitiya* (Chemistry and Ways of Its Development), Moscow: Akad. Nauk SSSR, 1937.

A. G. Morachevskii

Russian Journal of Applied Chemistry, Vol. 77, No. 8, 2004, pp. 1392–1393. Translated from Zhurnal Prikladnoi Khimii, Vol. 77, No. 8, 2004, pp. 1404–1405.

INFORMATION

Third International Scientific-Practical Conference "New Fuels with Additives"

III International Scientific-Practical Conference "New Fuels with Additives" was held in St. Petersburg on June 1–3, 2004. The conference was organized by the St. Petersburg Scientific Center of the Russian Academy of Sciences, Scientific Council for Combustion and Explosion of the Russian Academy of Sciences (Northwestern division), Administration of St. Petersburg (Committees for Transport and for Nature Management, Environment Protection, and Ecological Safety), Prikladnaya Khimiya Russian Scientific Center, a number of other institutes, and St. Petersburg fuel company. Among the participants of the conference were 136 institutions and associations from 9 countries, including 26 research institutions, 18 higher school institutions, 62 plants of oil-refining and fuel industry, and 5 plants for manufacture and repair of engines.

The conference was timed with the 95th birthday of V.S. Shpak, an outstanding scientist in the field of applied chemistry, Honored scientist and technologist of the Russian Federation, Honorary chemist, and academician of the Russian Academy of Sciences. Opening the conference, Shpak mentioned that the requirements to the quality of all kind of fuels have become increasingly stringent, primarily as regards the ecological conditions of their use. Also important is the energy resource saving. To significantly improve the ecological safety of fuels, raise their energy content, increase the reliability and service life of stationary and on-board power installations, it is necessary to use new chemical means of doping of the hydrocarbon raw materials. This leads to creation of a wide variety of chemical products, which are named fuel additives and are new to the chemical industry.

The widening of the variety of products and organization of their manufacture should be consistent with the development of petrochemical industries, because oils and base fuels may differ strongly and this circumstance complicates the doping of fuels and bringing their quality in conformity with the new international standards. Shpak urged the conference participants to actively discuss these problems.

The conference participants were also addressed by the deputy chairman of the St. Petersburg Scientific Center of the Russian Academy of Sciences, Academician G.F. Tereshchenko. He conveyed to them the greeting message of Zh.I. Alferov, Nobel Prize Laureate and academician of the Russian Academy of Sciences, and wished successful work.

More than 80 reports devoted to various aspects of manufacture and use of fuels with additives were delivered at the conference. Review reports were presented by leading specialists of our country: T.N. Mitusova (Volgograd), V.E. Emel'yanov (Moscow), A.M. Danilov (Moscow), F.V. Turovskii (Moscow), V.N. Lozhkin (St. Petersburg), V.V. Sokolov (Moscow), E.M. Mokhnatkin (St. Petersburg), A.L. Dmitriev (St. Petersburg), V.F. Bol'shakov (St. Petersburg), A.V. Nikolaenko (St. Petersburg), S.N. Volgin (Moscow), O.I. Shapovalenko (St. Petersburg), and many others. The reports were mostly devoted to development and manufacture of fuel additives in Russia. Production of cetane-improving additives based on nitrates and peroxides and octane-improving additives containing compounds of iron, nickel, and manganese, as well as amines and oxygenates, were discussed.

Problems associated with the use of oxygenate fuels from renewable sources of raw materials, and also liquefied natural gas, were considered. A lengthy discussion was aroused by reports devoted to methods for obtaining, storing, and using hydrogen in internal combustion engines.

As a result of the discussion of the reports, a conclusion was made that the quality of the most part of fuels manufactured in Russia fail to conform to the modern requirements.

The main achievement of the domestic oil-refining industry was the complete termination of the manufacture and use of leaded gasoline, beginning on July 1, 2003. The speakers noted the insufficiency of the material resources of testing centers and laboratories for carrying out certification, qualification, and validation tests of new and alternative fuels with additives. Until now there is no sufficient coordination of works in the field of manufacture of a variety of additives to motor fuels. At the same time, there exist domestic technologies for manufacture of additives that make

1070-4272/04/7708-1392 © 2004 MAIK "Nauka/Interperiodica"

it possible to obtain fuels on a level with the highest world's standards.

The conference participants noted the benefits of the exchange of views and familiarization with the newest developments in the field of production and use of new fuels and additives. It was found advisable to hold such scientific-practical conferences once in two years and a decision was made to hold the next conference in 2006.

One of the most promising ways to improve the quality of motor fuels and diminish noxious discharges into the atmosphere is to use oxygen-containing additives, combustion catalysts, and alternative fuels, such as liquefied natural gas and hydrogen.

In order to diminish the dependence of Russia on the import of additives, the conference found it appropriate to commission the Scientific council for combustion and explosion of the Russian Academy of Sciences with addressing the Government. A suggestion is to be made to create on the basis of the Council for combustion and explosion, with specialists from other organizations, a Center for coordination of development and manufacture of additives to fuels. The resolution of the conference makes quite a number of recommendations aimed to improve the production and quality evaluation of fuels, additives, and other petroleum products.

A. G. Morachevskii

Russian Journal of Applied Chemistry, Vol. 77, No. 8, 2004, pp. 1394–1395. Translated from Zhurnal Prikladnoi Khimii, Vol. 77, No. 8, 2004, pp. 1406–1407.

BOOK REVIEWS

Sergeev, G.B., *Nanokhimiya* (Nanochemistry), Moscow: Mos. Gos. Univ., 2003, 288 pp.

The book by G.B. Sergeev, a professor of Moscow State University, is the first domestic monograph devoted to the new and rapidly developing scientific area, nanochemistry. Nanosize particles have been actively studied in various fields of science in the recent 15–20 years. These investigations became particularly intensive in the 1990s, and the term nanochemistry appeared in those same years. Presently, such terms as "nanoparticles," "nanoclusters," "nanocomposites," and "nanotechnologies" are already in wide use.

The monograph comprises an introduction, eight chapters, a conclusion, and a bibliographic list. In the brief introduction (pp. 9–11), the author, in particular, notes that studies of nanoparticles composed of various elements of the periodic system open up new areas of chemical research, which cannot be understood in terms of the already developed concepts. The presently available experimental material makes it possible to define nanochemistry as a field of science that is concerned with production, properties, and reactivity of particles and ensembles of particles that have, at least in one direction, a size less than 10 nm. Determining how the particle size or the number of atoms in a particle affect its physicochemical properties and reactivity is one of the most fundamental problems of modern chemistry. The monograph being discussed gives primary attention to the specifics of obtaining and chemical transformations of atoms, clusters, and nanoparticles of metals belonging to various groups of the periodic system. A separate chapter is devoted to nanoparticles based on carbon and silicon.

The small first chapter (pp. 12–20) is devoted to a general characterization of the problem, presents the author's classification of nanoparticles, and formulates some important concepts. It is, in particular, noted that the particle size is an active variable, which determines, together with other variables, the state of the system and its reactivity. Reactions into which solid substances do not enter are possible for their nanoscale particles.

The second chapter (pp. 21–53) considers ways to obtain and stabilize nanoparticles. The high chemical activity characteristic of metal atoms is preserved in dimers, trimers, and in clusters formed from these atoms, as well as in nanoparticles with a great number of atoms. Studies of active particles of this kind are only possible if various stabilizing agents are used. The following methods are discussed: chemical reduction mainly in the liquid phase; reactions in micelles, emulsions, and dendrimers;, photo- and radiation-induced chemical reduction; cryochemical synthesis; and physical techniques. The material presented in the chapter is mainly based on publications of 2000 and 2001.

The third chapter (pp. 54–66) is devoted to methods for determining the size and studying some properties of nanoparticles in the gas phase, on a surface, in the bulk, or in a matrix. To methods of this kind belong transmission or scanning electron microscopy, electron-probe microscopy, diffraction techniques (X-ray and neutron diffraction analysis), and a number of other physical techniques. Despite the wide diversity of the existing methods for studying individual nanoparticles in the gas phase and in the bulk of nanostructures, the author notes the necessity for developing new techniques that should not only measure various parameters of nanoparticles, but also trace in detail how these parameters vary in the course of formation and subsequent self-organization of nanoparticles and upon fabrication of nanotechnological devices on their base.

The fourth chapter (pp. 67–135) presents the main concepts of the intensively developing new scientific area: cryochemistry of nanosize particles or cryonanochemistry.[1] The chapter is mainly constituted by results of experimental studies of processes involving nanoparticles of magnesium, silver, and rare-earth metals at low (77 K) and ultralow (4–7 K) temperatures. The final section of the chapter considers the possibility of modeling of the physicochemical properties and reactivity of metal nanoparticles.

The fifth chapter (pp. 136–191), named "Chemical nanoreactors" by the author, pays considerable attento application of the method of matrix isolation for

[1] G.B. Sergeev is a known specialist in cryochemistry and one of the authors of the monograph *Kriokhimiya* (Cryochemistry) (Moscow: Khimiya, 1978).

1070-4272/04/7708-1394 © 2004 MAIK "Nauka/Interperiodica"

stabilization of active particles. The method consists in that substances are accumulated under the conditions that hinder reactions. For example, the matrix in a solid inert substance at low temperature hinders diffusion, and active particles are virtually immobile (stable), frozen in the medium that cannot react with them. Inert gases can serve as matrices. A great number of examples of reactions involving various metals in inert and active matrices are given.

The rather small sixth chapter (pp. 192–200) contains evidence concerning the nanochemistry of carbon and silicon. The author emphasizes the importance of the discovery of fullerenes and, later, carbon nanotubes for development in the future of nanotechnologies applicable in actual practice.

The seventh chapter (pp. 201–219) is devoted to dimension effects in nanochemistry. By dimension effects in chemistry is understood the fundamental change in the physicochemical properties and reactivity, depending on the number of atoms or molecules in a substance particle, which occurs at particles sizes of less than 100 atomic-molecular diameters. The manifestation of dimension factors is one of the basic distinctions of nanochemistry from the chemistry of reactions that occur under ordinary conditions. It is emphasized at the end of the chapter that it is studying the dimension factors and establishing a relationship between the number of atoms involved in a reaction and the resulting fundamental chemical changes that is the main subject of nanochemistry. The size, shape, and organization of metal particles in the nanometer range directly affect the chemical activity of the resulting systems, stability and properties of the materials obtained and the possibility of their use in nanotechnology.

The eighth chapter (pp. 220–253) contains the most recent evidence (the years of 2000–2002) concerning various fields of application of nanoparticles in science and technology: development of new catalysts, use of highly active nanocrystalline metal oxides in various syntheses, use of semiconductor nanoparticles, and development of nanophotonics, which is a new area of research concerned with optical properties of objects with a size considerably smaller than the wavelength of light. A separate section of the chapter is devoted to application of carbon nanotubes.

In the conclusion (pp. 254–260), the author formulates, on the basis of an analysis of the experimental material described, some general conclusions and points out promising areas of investigations into the chemical properties and reactivity of various elements of the periodic system, depending on the particle size. The origination and development of nanoscience, and nanochemistry as its most important component, is in line with the modern development of natural science.

The bibliographic list (pp. 261–284) contains 606 references to publications by domestic and foreign authors. Noteworthy is the fact that more than 75% of references is to publications of the years of 1990 to 2002. Particularly great is the number of publications in the field of nanochemistry in 2000 and 2001. The monograph by G.B.Sergeev has a subject index (pp. 285–287).

Nanoscience has an interdisciplinary nature; it relies upon the approaches and investigation techniques used in physics, chemistry, biology, and materials science. The importance and role of this science will grow in the XXI century year by year. The very interestingly and rather simply written monograph by G.B.Sergeev may be undoubtedly of interest to a wide audience of specialists. The book will arouse interest in nanochemistry, its possibilities, fundamental aspects, and tasks.

A. G. Morachevskii

Russian Journal of Applied Chemistry, Vol. 77, No. 9, 2004, pp. 1397–1403. Translated from Zhurnal Prikladnoi Khimii, Vol. 77, No. 9, 2004, pp. 1409–1415.

INORGANIC SYNTHESIS AND INDUSTRIAL INORGANIC CHEMISTRY

Features of Oxidation of Titanium Group Metals in Air

V. I. D'yachkov

St. Petersburg State University, St. Petersburg, Russia

Received July, 9, 2004

Abstract—The kinetics and mechanism of oxidation of titanium, zirconium, and hafnium in air at 973–1473 K were studied in relation to the properties of the metals.

The kinetics and mechanism of oxidation of titanium, zirconium, and hafnium were extensively studied, but the behavior of these metals actually was not compared under identical conditions, except for certain data in [1]. At the same time, such data are of both practical and scientific interest, as they give insight into the features of oxidation of these metals.

The purpose of this work was to reveal how the properties of titanium, zirconium, and hafnium affect the kinetic parameters, temperature dependence of rate constants, and activation energy of the oxidation, the diffusion mechanism of scaling, and properties of the scale.

Experiments were carried out in air with controllable humidity at a pressure of 101.3 kPa in the range 973–1473 K. The materials under study were high-purity metals (99.93% Ti, 99.80% Zr, and 99.70% Hf) melted in a fluidized bed in an electromagnetic field in an atmosphere of purified argon [2]. The technique of the preparation of $1.0(1.5) \times 1.0 \times (0.2–0.5)$-cm samples with a grain size of about 50 μm and the experimental procedures in use are described in [3–5].

Comparison shows that the parameters of the oxidation of titanium, zirconium, and hafnium are essentially different. In particular (Table 1), the rate of Ti oxidation at 1073–1473 K is much lower than that of Zr, but much higher (at $T > 1073$ K) than that of Hf.

Processing of the oxidation curves (Fig. 1) shows that Evans equation (1) [6] and laws close to parabolic, cubic, and sometimes linear (2)–(4) are obeyed:

$$K_l q^2 + K_p q = K_l K_p \tau + C, \quad (1)$$

$$q^2 = K_p \tau + C, \quad (2)$$

$$q^3 = K_c \tau + C, \quad (3)$$

$$q = K_l \tau + C, \quad (4)$$

where q is the weight of absorbed gases; τ, time; C, a constant; K_l, K_p, and K_c, rate constants of the oxidation by linear, parabolic, and cubic laws, respectively.

In fact, laws (2)–(4) are not strictly fulfilled in the case of the Zr and Hf oxidation, and the experimental data can be formally described by expression (5) with various n values.

$$q^n = K\tau + C. \quad (5)$$

As follows from Table 2, the kinetics of Ti oxidation (3 h) at 1073–1373 K almost fully follows Evans equation (1) (Fig. 2), which suggests nonstationary character of this process and, hence, comparable control of its rate by diffusion and by interphase reactions [6, 7]. At $T < 1073$ K, the equation is obeyed only at the beginning of the test, being then replaced by another relationship with $2 < n < 3$ in expression (5). Above 1373 (1423) K, the Evans law is not obeyed owing to a considerable influence of a strong overheating of the sample surface on the kinetics of the oxidation in the initial period [8]. With Hf (3 h), the Evans law is obeyed only at 973–1023 K and, as opposed to Ti, above 1423 K, whereas in the range 1073–1423 K it is obeyed only at the beginning of the oxidation (Fig. 2), with the subsequent transition to dependence (2), which is close to parabolic. With

Table 1. Weight gain Δq oxidation of Ti, Zr, and Hf in air for 3 h

M	Δq, mg cm^{-2}, at indicated temperature, K						
	973	1073	1173	1273	1323	1373	1473
Ti	0.40	1.5	7.9	21.5	34.4	31.7	35.7
Zr	2.00	3.1	13.2	31.1	54.5	43.1	82.9
Hf	0.40	1.5	2.2	9.3	8.0	10.3	19.2

1070-4272/04/7709-1397 © 2004 MAIK "Nauka/Interperiodica"

Table 2. Influence of temperature T and time τ of oxidation of Ti, Zr, and Hf on the type of kinetic law*

Law of oxidation, temperature range, and time of its action		
Ti	Zr	Hf
Eq. (1): 973–1023 K, i.p.; 1073–1373 K, $\tau \geq 3$ h Eq. (5): 973–1023 K, a.i.p., $2 < n < 3$; 1373–1473 K, $\tau \geq 3$ h, $2.5 \leq n \leq 5.0$	Eqs. (2) and (5): 973–1373 K, i.p., $2.0 \leq n \leq 2.4$ Eqs. (3) and (5): 973–1473 K, a.i.p., $2.6 \leq n \leq 3.0$	Eq. (1): 973–1023, 1473 K, $\tau \geq 3$ h; 1073–1423 K, i.p. Eqs. (2) and (5): 1073–1423 K, a.i.p., $2.1 \leq n \leq 2.4$

* (i.p.) Initial period; (a.i.p.) after initial period.

Zr, the Evans equation is not obeyed at all, and the oxidation process is usually described by parabolic law (2) and subsequently by cubic law (3), or by laws close to them.

In some cases, the cubic law converts to almost linear law (4) with a noticeable increase in the oxidation rate, suggesting a decrease in the protective properties of the oxide film. It should be noted that almost all papers devoted to the kinetics of oxidation of Ti, Zr, and Hf in air at 973–1473 K [4, 9–11] contain evidences for the validity of laws (2)–(4) or those close to them. The nonstationary character of Ti and Hf oxidation under the same conditions was found for the first time in [3, 5].

Figure 3, in which $K_l^{(1)}$ and $K_p^{(1)}$ characterize the oxidation according to Evans equation (1) and $K_p^{(2)}$, the oxidation according to parabolic law (2), shows that the temperature coefficient $K_l^{(1)}$ for Ti increases on passing to the region $T > 1173$ K, whereas in the case of Hf oxidation, on the contrary, it decreases. The dependences $\log K_p^{(1)} = f(1/T)$ for both metals are similar and consist of three sections; however, the intermediate region in the case of Hf is longer compared to Ti and is shifted toward higher temperatures. The dependences $\log K_p^{(2)} = f(1/T)$ for Zr and Hf are also similar in shape and somewhat differ from each other in the inflection points and lengths of separate regions.

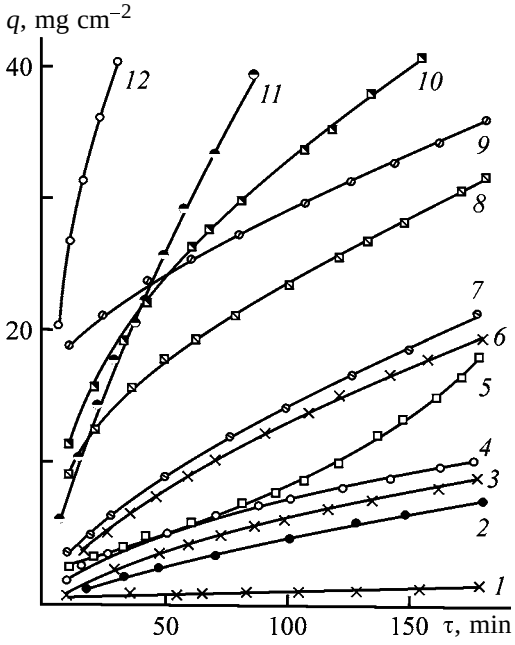

Fig. 1. Curves of the oxidation in air of (*2, 7, 9, 11*) titanium, (*5, 8, 10, 12*) zirconium, and (*1, 3, 4, 6*) hafnium. (q) weight gain and (τ) time; the same for Fig. 2. Temperature (K): (*1, 2, 5*) 1173, (*3, 7, 8*) 1273, (*10, 11*) 1373, and (*6, 9, 12*) 1473.

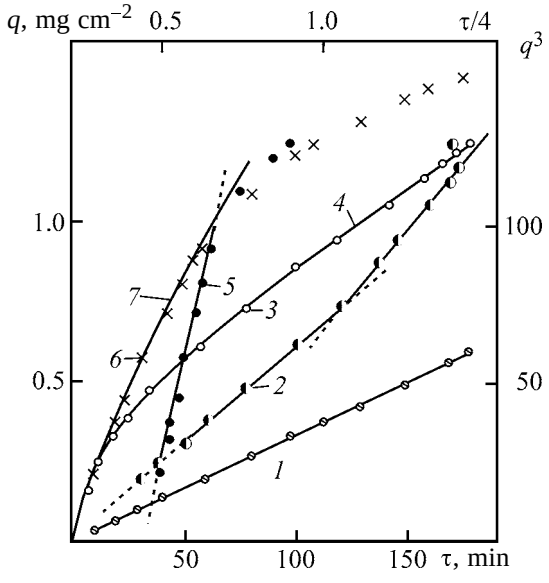

Fig. 2. Data on the of oxidation in air of (*1*) zirconium, (*2–4*) titanium, and (*5–7*) hafnium in the coordinates of (*2, 5*) Evans equation and (*1*) cubic law; position of (*3, 6*) experimental points relative to (*4, 7*) curves of Evans equation constructed with the values of $K_l^{(1)}$ and $K_p^{(1)}$ obtained.

Table 3. Apparent activation energy of oxidation of Ti, Zr, and Hf by linear [$E_l^{(1)}$], parabolic [$E_p^{(1)}$, $E_p^{(2)}$], and cubic (E_c) laws

M	$E_l^{(1)}$	$E_p^{(1)}$	$E_p^{(2)}$	E_c
	kJ mol^{-1}			
Ti	71 (973–1173)*	235 (973–1123)	–	–
	199 (1173–1423)	510 (1123–1223)	–	–
	–	159 (1223–1373)	–	–
Zr	–	–	125 (973–1173)	175 (973–1173)
	–	(1173–1323)	300 (1173–1323)	460 (1173–1273)
	–	–	–	235 (1273–1473)
Hf	150 (973–1173)	90 (973–1173)	95 (1073–1223)	–
	100 (1173–1473)	220 (1173–1373)	250 (1223–1423)	–
	–	98 (1373–1473)	–	–

* Temperature, K, is given in parentheses.

The apparent activation energies of the oxidation by the corresponding laws (Table 3) are determined with an error of ±(3–7)%. As compared to Hf, for Ti the apparent activation energy $E_l^{(1)}$ of interphase processes at T < 1173 K in Table 3 is lower, and at T > 1173 K, much higher. In the case of $E_p^{(1)}$, the relationship is inverse. The activation energy of oxidation of Zr by parabolic law, $E_p^{(2)}$, and by cubic law, E_c, is much greater than $E_p^{(1)}$ and $E_p^{(2)}$ for Hf in all the temperature ranges.

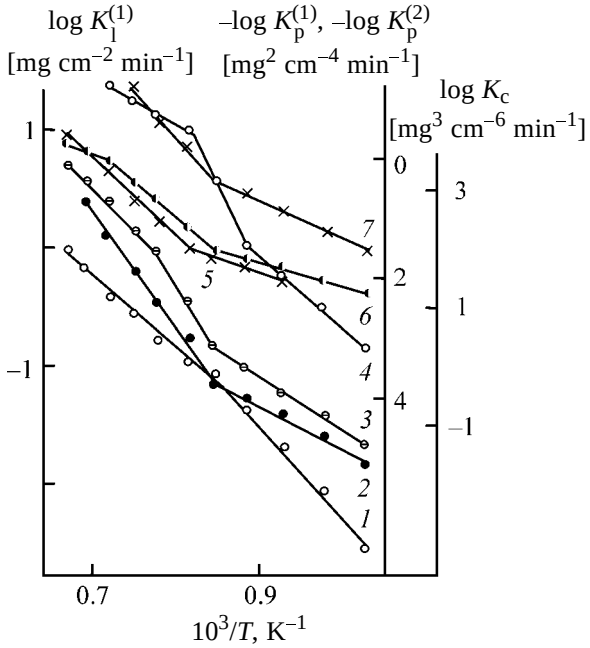

Fig. 3. Temperature dependence of (*1, 2*) $K_l^{(1)}$, (*4, 6*) $K_p^{(1)}$, (*5–7*) $K_p^{(2)}$, and (*3*) K_c for the oxidation in air of (*2, 4*) titanium, (*3, 7*) zirconium, and (*1, 5, 6*) hafnium. K_l, K_p, and K_c are constant of the oxidation by linear, parabolic, and cubic laws, respectively.

According to Table 4, the role of the formation of a diffusion oxygen layer (DOL) in the overall oxidation process sharply increases in going from Ti to Hf, whereas the rate of its growth by parabolic law (2) increases less significantly. This is caused, in particular, by higher protective properties of the scale on Hf. Indeed, on the replacement of titanium by hafnium the total oxidation rate decreases (Table 1) owing to a noticeable decrease in the scaling rate (Table 4).

In both cases, especially in the case of Ti, the oxygen fraction z in DOL decreases as the time of isothermal oxidation (1273 K) increases. This is attributable to the fact that the DOL increases by parabolic law (2), and the oxide layer, by Evans equation (1), i.e., the first process is retarded faster than the second one. As the temperature increases up to approximately 1273 K, the role of the DOL formation in the overall

Table 4. Influence of temperature T and time τ of Ti and Hf oxidation on the content q and fraction z of oxygen in the diffusion layer

T, K	τ, min	Ti		Hf	
		q, mg cm^{-2}	z, %	q, mg cm^{-2}	z, %
1073	180	0.3	24	–	–
1173	180	1.3	16	1.5	69
1273	15	1.0	24	1.0	71
	30	1.5	21	1.6	63
	60	2.0	16	2.6	61
	120	2.8	14	4.3	61
	180	3.4	13	5.4	60
1373	180	8.2	26	2.7	24
1473	180	10.4	29	3.6	18

Table 5. Influence of metal and temperature on the ratio $K_l^{(1)}/K_p^{(1)}$ in the initial period of oxidation

M	$K_l^{(1)}/K_p^{(1)}$, mg cm^{-2}, at indicated temperature, K							
	1073	1123	1173	1223	1273	1323	1373	1423
Ti	3.1	1.7	0.2	0.05	0.06	0.08	0.08	–
Hf	5.7	2.2	2.0	2.00	0.40	1.00	0.20	0.20

process of Ti oxidation noticeably decreases, but it sharply increases as the temperature increases to 1473 K. However, in the case of Hf, passing to the region of $T > 1273$ K is accompanied, on the contrary, by an essential decrease in both the DOL growth rate and the oxygen fraction in it.

According to the X-ray diffraction analysis, the scale formed in oxidation of Ti, Zr, and Hf at 973–1473 K consists of their dioxides: tetragonal TiO_2 (rutile), monoclinic (α-phase) and, above 1223 K, also tetragonal (β-phase) ZrO_2, and monoclinic HfO_2. A practically white oxide film is formed on Ti at 973–1473 K, whereas in the case of Zr and Hf the film is formed only at $1273 < T < 1373$ and $1173 < T < 1423$ K, respectively, which is usually accompanied by cracking of the sample along edges. Outside these regions the scale on Zr and Hf has an anthracitic color. Unlike Ti with a regular microlayered structure of the scale on edges ($T \le 1373$ K), a denser oxide layer of pillared crystals with pores arranged mainly perpendicularly to the sample surface is formed in oxidation of Zr and Hf at temperatures of up to 1473 K.

The scale on Ti obtained at $T > 1073$ K has a weak adhesion to the matrix surface after cooling, whereas in the case of Zr and Hf it is very strongly linked to the metal, which makes practically impossible its quantitative mechanical separation.

According to the experiments with "inert" labels, the oxide film on Zr and Hf grows up to 1473 K almost exclusively owing to diffusion of O_2 [4, 5]. In the case of Ti, the role of cationic diffusion in the formation of the oxide film becomes noticeable above 1373 K, and some authors believe [9] that it is dominating even at $T < 1273$ K.

It follows from Table 5 that the ratio $K_l^{(1)}/K_p^{(1)}$ noticeably increases in going from Ti to Hf, suggesting an increasing role of diffusion processes in the control over the rate of the nonstationary oxidation. As the temperature increases, at least within certain limits [up to 1273 (1323) K for Ti and up to 1273 K for Hf], the ratio $K_l^{(1)}/K_p^{(1)}$ decreases, suggesting an increasing role of interphase processes in the resulting oxidation rate according to the theoretical concept [12]. The increase in $K_l^{(1)}/K_p^{(1)}$ at $T > 1273$ (1323) K is associated with specific features of the temperature dependences of $K_l^{(1)}$ and $K_p^{(1)}$ (Fig. 3) and with a change in the mechanism of the nonstationary oxidation.

Thus, the data obtained show that, in going from Ti to its chemical analogs, the overall rate and the type of kinetic relationships of the oxidation considerably change, with Evans equation (1) not obeyed at all for Zr. The position and length of particular regions of the temperature dependence of the rate constants, its character in the case of K_l^1, and the activation energy of oxidation also change essentially.

Simultaneously the role of diffusion in the control over the rate of the nonstationary oxidation and the fraction of oxygen in DOL increase, the adhesion of the oxide film to the matrix surface strengthens, its color and morphology change, and the role of anionic diffusion in scaling grows. The behavior of Zr during the test especially strongly differs from that of Ti. As far as the type of oxidation relationships is concerned, hafnium is more similar to titanium, but with respect to the role of reacting components in the diffusion process of scaling and certain properties of the scale it is similar to zirconium.

The specific features of the oxidation of Ti-group metals in air are apparently associated with differences in their physical and chemical properties (Table 6). In particular, the similarity of a number of important characteristics of Zr and Hf and their dioxides, such as the electronic configuration of the outer shell, atomic and ionic radii, crystal structure, unit cell parameters, ionization potential, molar volume, and Pilling–Bedworth coefficient ($\nu MO_2/\nu M$), and the same type of point defects in the lattices of the dioxides determine similarity of their behavior in oxidation. It appears, for example, in the identity of the diffusion mechanism of scaling, the similarity of its morphology, color, and adhesion properties, in a common parabolic law of the oxidation, and in the same type of temperature dependences of $K_p^{(2)}$. At the same time, certain differ-

Table 6. Main properties of titanium-group metals and their dioxides [13–15]

Property	Ti	Zr	Hf	TiO_2	ZrO_2	HfO_2
Electronic configuration	$3d^24s^2$	$4d^25s^2$	$5d^26s^2$	–	–	–
Atomic radius, Å	1.46	1.59	1.58	–	–	–
Ionic radius, Å	0.61	0.74	0.75	–	–	–
Crystal structure	α, hcp β, bcc	α, hcp β, bcc	α, hcp β, bcc	Tetragonal Tetragonal	Monoclinic Tetragonal	Monoclinic Tetragonal
Unit cell parameters of α-phase, Å	c = 4.683 a = 2.950	c = 5.147 a = 3.231	c = 5.040 a = 3.188	a = 4.584 c = 2.963	Monoclinic a = 5.17 b = 5.26 c = 5.30	Monoclinic a = 5.12 b = 5.18 c = 5.25
$T_{\alpha\to\beta}$, K	1155	1135	1573	–	1273	1973
T_m, K	1938	2133	2503	2123	2970	3085
$-\Delta G^0_{298}$, kJ mol^{-1}	–	–	–	889	1037	1054
$m\theta^2 \times 10^{18}$, g deg^2	8.6	10.9	13.5	–	–	–
H_{273}, MPa	900	1600	1700	–	–	–
Ionization potential, eV	6.7	6.9	7.0	–	–	–
Solubility of oxygen in α-M, at. %	34	29	20.5	–	–	–
$V_{at(mol)}$, Å^3	10.8	14.0	13.4	18.8	21.9(α)	21.8(α)
$\nu MO_2/\nu M$	–	–	–	1.74	1.56	1.62
Type of defects in MO_2	–	–	–	$V_O^{\cdot\cdot} + Ti_j^{\cdot\cdot\cdot\cdot}$	$V_O^{\cdot\cdot}$	$V_O^{\cdot\cdot}$

ences in the properties of Zr and Hf and their dioxides (Table 6) cause the observed differences in the oxidation rate, type of kinetic relationship (Table 2), and also in apparent activation energy $E_p^{(2)}$, though sometimes this correlation is ill-defined.

However, many important characteristics for Ti and TiO_2 differ from those of Zr, Hf, and their dioxides more essentially, except for types of crystal lattices of the metals, TiO_2, ZrO_2 (T > 1273–1373 K), and HfO_2 (T > 1973 K). This is manifested, e.g., in substantial growth in the energy of interatomic bonds $m\theta^2$ in going from Ti to its analogs and in the strength of the lattices of their dioxides in going from TiO_2 to HfO_2, which favors the observed increase in the Hf resistance to oxidation (T > 1073 K). A decrease in the electronegativity in the same direction is accompanied, in particular, by a decrease in the solubility of oxygen in the α- and β-phases of the metals. This explains the observed decrease in the rate of DOL growth (T > 1273 K) in going from Ti to Hf (Table 4). Taking into account the opposite effect exerted on the DOL growth by oxygen dissolution in a metal proper and by transfer of the interface with scale into the depth of the matrix, we should expect a similar result in the range T < 1273 K. Furthermore, higher energy of interatomic bonds in Zr and Hf lattices, as compared to Ti, increases the relative role of intercrystallite boundaries as the most reactive surface regions in the oxidation process. As a result of the penetration of the oxide in these regions into the depth of the metal, the strength of the adhesion of the oxide film with the matrix sharply increases, which is proved experimentally. In the case of Ti, the role of this factor is much weaker.

Owing to the stronger bonding between scale crystallites on Zr and Hf and to high Pilling–Bedworth coefficients for monoclinic ZrO_2 (1.56) and HfO_2 (1.62), the stress arising in the scale results in its cracking along edges of the sample, and sometimes even in its deformation. When titanium is oxidized in air, owing to the even higher Pilling–Bedworth coefficient for rutile (1.74) and lower strength of adhesion between the scale and the matrix and between scale particles, as compared to Zr and Hf, the scale integrity gets disturbed, which results in increasing chemical potential of oxygen. This promotes formation of rutile with approximately stoichiometric composition. Virtual absence of this phenomenon in the case of Zr and Hf at a higher scale density is proved, in addition to other facts, by a considerable role of the near-parabolic and cubic laws in their oxidation. According to the existing concept [16], cubic law (3) of the growth of thick oxide films is a result of superposition on the diffusion process of secondary

phenomena in the scale such as the aging, retarding the oxidation.

These factors ultimately determine a number of morphological features of the scale and its phase boundary with the metal. However, an important circumstance, usually neglected in such studies, should be noted. Namely, structures of the forming scale and the scale after cooling the sample withdrawn from the hot zone can differ essentially owing to unequal coefficients of thermal expansion, plasticity, and cooling rates of the metal and the oxide film. In fact, the samples of refined and commercial titanium VT1-0 withdrawn from a hot zone (1273 K) had a regular microlayer structure of porous scale and a cavity on its boundary with the matrix, whereas the oxide film obtained by cooling the samples with the furnace to room temperature tightly adhered to the metal surface and showed no microlamination. In this case, pores were mainly arranged as chains parallel to the interface between the metal and oxide phases. These results show that the existing concept of the mechanism of formation of the microlayered scale [1, 9, 12] should be corrected.

The influence of the properties of Ti and Hf on the temperature dependence of $K_l^{(1)}$ is manifested as a decrease in its slope for Hf as compared to Ti in going to the range $T > 1173$ K. In the case of the $\log K_p^{(1)} = f(1/T)$ dependence, the inflection points are somewhat shifted toward higher temperatures, and the length of the middle region increases in going from Ti to Hf.

It is know that inflections in the temperature dependences of the rate constants suggest a change in the oxidation mechanism. The first bend (Fig. 3) is attributable to the fact that the allotropic $\alpha \rightarrow \beta$ transition in the metal phase starts to affect the oxidation process. This transformation, which takes place at 1155 and 1135 K for pure Ti and Zr [14], respectively, is accompanied by loosening of the metal lattice in excited states of the atoms. However, the fact that in the same temperature region there is also a bend for Hf, which is characterized by a change in the temperature coefficient $K_l^{(1)}$ different from that for Ti and by $T_{\alpha\rightarrow\beta} = 1973$ K (Table 6), suggests the action of another mechanism in this case. The effect of the $\alpha \rightarrow \beta$ transition on the oxidation appears not only at the equilibrium temperature, but also within a certain temperature range. It is caused, in particular, by the fact that the equilibrium temperatures of the $\alpha \rightarrow \beta$ transition on the surface and in the bulk of the metal are essentially different (80 K for Ti) [17]. The second bend is attributable to stabilization of the β-phase, and for Zr, also to the transformation of monoclinic ZrO_2 into the tetragonal form at $T \geq 1273$ K [14].

Because of the greater accepting power of Ti compared to Zr (owing to incomplete filling of its 3*d* shell, whereas in the case of Zr the 4*d* shell is filled completely), the metallic bonding predominates in Ti_6O and Ti_3O suboxides and covalent bonding, in Zr_6O and Zr_3O [14, 15]. As a result, the strength of the interatomic bonding in the titanium lattice increases as the concentration of oxygen in it grows, which enhances the scale resistance of Ti–O alloys, whereas the dissolution of oxygen in Zr is accompanied by a decrease in the strength of the interatomic bonding [14, 15]. In particular, this fact seems to be responsible for the observed increase in the oxidation rate in going from Ti to Zr.

The predominance of oxygen vacancies $V_O^{\cdot\cdot}$ in ZrO_2 and HfO_2 lattices [13] causes the observed scale growth up to 1473 K owing to anionic diffusion. At the same time, when Ti is oxidized in air at high temperatures ($T > 1373$ K), owing to the presence of interstitial $Ti_j^{""}$ cations in the rutile lattice along with $V_O^{\cdot\cdot}$ [13], the participation of the titanium cations in scaling becomes apparent.

As found earlier [18], the higher activity of oxygen in scale on its boundary with the metal, compared to the equilibrium activity, is a reason for the nonstationary oxidation of Ti in oxygen and in air. The results obtained in this work do not contradict the assumption that in the case of Hf nonequilibrium conditions of the oxidation in air are mainly localized on the scale–gas boundary. However, precise solution of this problem requires a special study.

CONCLUSIONS

(1) Many basic parameters of the oxidation essentially change in going from Ti to Zr and Hf, which is primarily caused by the fact that the strength of chemical bonds in the crystal lattices of the metals and their dioxides, accepting powers of these elements, types of point defects in the lattices of the dioxides, and Pilling–Bedworth coefficients are different.

(2) The similarity of the physical and chemical properties of Zr and Hf, and of their dioxides causes the similarity of the diffusion mechanism of scaling and of the scale characteristics. The behavior of Zr in the oxidation differs from that of Ti most sharply, whereas Hf is more similar to Ti than to Zr as far as the type of oxidation relationships is concerned.

REFERENCES

1. Wallwork, G.R. and Jenkins A.E., *J. Electrochem. Soc*., 1959, vol. 106, no. 1, pp. 10–14.
2. Fogel', A.A., *Izv. Akad. Nauk SSSR, Otd. Tekh. Nauk, Metall. Topl*., 1959, no. 2, pp. 24–29.
3. Tikhomirov, V.I. and D'yachkov, V.I., *Zh. Prikl. Khim*., 1967, vol. 40, no. 11, pp. 2405–2413.
4. D'yachkov, V.I. and Tikhomirov, V.I., *Zh. Prikl. Khim*., 1977, vol. 50, no. 12, pp. 2648–2652.
5. D'yachkov, V.I., *Zh. Prikl. Khim*., 1990, vol. 63, no. 4, pp. 758–762.
6. Evans, U.R., *Trans. Electrochem. Soc*., 1924, vol. 46, no. 1, pp. 247–274.
7. Tikhomirov, V.I. and D'yachkov, V.I., *Fiz. Met. Metalloved*., 1969, vol. 27, no. 3, pp. 459–465.
8. D'yachkov, V.I., and Tikhomirov, V.I., *Fiz. Met. Metalloved*., 1970, vol. 30, no. 1, pp. 97–104.
9. Bai, A.S., Lainer, D.I., Slesareva, E.N., and Tsypin, M.I., *Okislenie titana i ego splavov* (Oxidation of Titanium and Its Alloys), Moscow: Metallurgiya, 1970.
10. Pemsler, J.P., *J. Electrochem. Soc*., 1965, vol. 112, no. 2, pp. 477–486.
11. Smeltzer, W.W. and Simnad, M.T., *Acta Metallurg*., 1957, vol. 5, pp. 328–334.
12. Hauffe, K., *Reaktionen in und an festen Stoffen*, Berlin: Springer, 1955, vol. 2.
13. Kofstad, P., *Nonstoichiometry, Diffusion, and Electrical Conductivity in Binary Metal Oxides*, New York: Wiley–Interscience, 1972.
14. Kornilov, I.I. and Glazova, V.V., *Vzaimodeistvie tugoplavkikh metallov perekhodnykh grupp s kislorodom* (Reactions of Refractory Transition Metals with Oxygen), Moscow: Nauka, 1967.
15. Kornilov, I.I., *Titan* (Titanium), Moscow: Nauka, 1975.
16. Irwing, B.A., *Nature*, 1964, vol. 204, pp. 1082–1087.
17. Fukuda, Y., Lancaster, G.M., Honda, F., and Rabalais, W.J., *Phys. Rev*., 1978, vol. 18, no. 11, pp. 1691–1694.
18. D'yachkov, V.I. and Tikhomirov, V.I., *Fiz. Met. Metalloved*., 1969, vol. 27, no. 4, pp. 655–662.

Russian Journal of Applied Chemistry, Vol. 77, No. 9, 2004, pp. 1404–1408. Translated from Zhurnal Prikladnoi Khimii, Vol. 77, No. 9, 2004, pp. 1416–1420.

INORGANIC SYNTHESIS AND INDUSTRIAL INORGANIC CHEMISTRY

Preparation of α-Fe_2O_3 by Thermal Hydrolysis of Iron(III) Basic Sulfate

L. S. Eshchenko and V. A. Salonikov

Belarussian State Technological University, Minsk, Belarus

Received June 15, 2004

Abstract—Features of the hydrolytic transformation of iron(III) basic sulfate under hydrothermal conditions at 140–200°C were studied. The influence of the conditions of the hydrothermal treatment of iron(III) basic sulfate on the rate and degree of its hydrolysis was examined. The chemical and phase composition of metastable intermediates was ascertained, and conditions for the formation of the final product of thermal hydrolysis, hematite of high phase purity, were determined.

Hydrothermal technique plays a growing role in production of the α modification of superfine iron(III) oxide. This technique allows fine control of the particle sizes and shapes and preparation of virtually monodisperse products. The monodispersity ensures high physicochemical characteristic of pigments, whereas the variation of particle sizes and shapes makes it possible to vary color tints over a wide range [1].

Procedures for the production of α-Fe_2O_3 at elevated temperatures from aqueous suspensions of iron(III) α-, β-, and γ-oxyhydroxides have been described in the literature, and the influence of various factors on the transformation rate and product characteristics has been elucidated [2–4]. Data on the production of α-Fe_2O_3 by hydrothermal treatment of iron(III) basic salts, particularly of $FeOHSO_4$, are available [5, 6]. However, data on the phase and chemical transformations occurring during the process are limited, which prevents development of a method for the production of α-Fe_2O_3 from $FeOHSO_4$. Therefore, the aim of this work was to study chemical, phase, and disperse composition of the products of $FeOHSO_4$ hydrolysis in relation to the treatment conditions.

EXPERIMENTAL

Iron(III) basic sulfate was prepared by thermal treatment of pure grade iron(II) sulfate heptahydrate first at 105°C for 1.5 h and then at 250°C for 4–6 h [6]. The resulting iron(III) basic sulfate with the composition $Fe_2O_3 \cdot 2.01SO_3 \cdot 0.01FeO \cdot 1.19H_2O$ was suspended in water and then subjected to the hydrothermal treatment at 140–200°C. The treatment was performed in Teflon-lined steel autoclaves. The temperature was maintained with the accuracy of ±1°C. After the treatment, the autoclave was quickly cooled to room temperature, and the precipitate was separated from the liquid phase by filtration and dried at 105°C. The content of iron(III) and sulfate ions in the liquid and solid phases was determined by chemical analyses. The degree of hydrolysis was calculated from the content of Fe^{3+} and SO_4^{2-} ions in the solid phase. Products of the $FeOHSO_4$ hydrolysis were studied by X-ray phase analysis (DRON-2 installation, filtered CoK_α radiation), by a microscopic technique (a Cam Scan scanning electron microscope equipped with an AN-1000 EDS detector), by a stereologic method (a Mini-Magiscan automatic image analyzer, Jojce Loebl), and by thermogravimetry (a Paulik–Paulik–Erdey Q-1500 derivatograph, heating rate 5 deg min^{-1}).

Our study has shown that hematite, α-Fe_2O_3, is the final stable phase of the hydrothermal treatment of the aqueous suspension of iron(III) basic sulfate. Phase and chemical transformations occurring in the system iron(III) basic sulfate–water are manifested as significant changes in sizes and shapes of solid phase crystals, occurring during the hydrothermal treatment. The difference in the crystal habit (morphology) of the starting $FeOHSO_4$ and final hematite phase is clearly seen in the electron micrographs (Fig. 1). Particles of the starting $FeOHSO_4$ have a globular shape with a size of 10–30 μm. Particles of α-Fe_2O_3 have a pillared shape with an average length of 1 μm and average width of 0.5 μm. Such a significant change in

1070-4272/04/7709-1404 © 2004 MAIK "Nauka/Interperiodica"

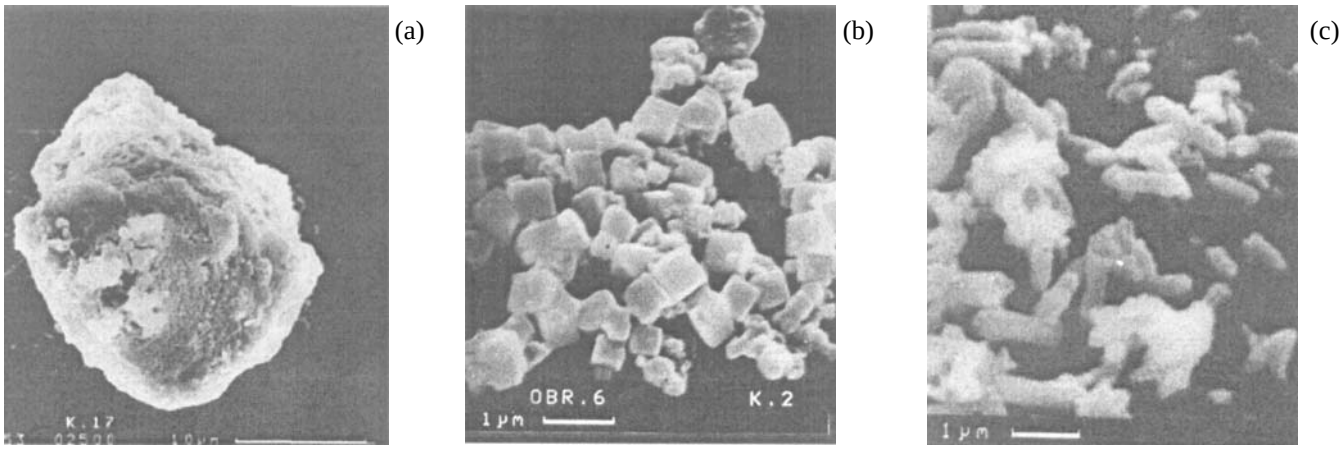

Fig. 1. Electron micrographs. Sample: (a) starting $FeOHSO_4$, (b) intermediate hydrolysis product, and (c) α-Fe_2O_3.

the crystal morphology suggests that the transformation of $FeOHSO_4$ into α-Fe_2O_3 occurs by the dissolution–precipitation mechanism.

It is known that one of the main synthesis parameters determining the habit of α-Fe_2O_3 crystals is pH of the medium. For example, according to [6], needle-shaped hematite crystals are formed in an acid medium and isometric crystals, in neutral and weakly basic media, but the crystals formed in a strongly basic medium have a platelike shape [4]. It is most likely that in our case the formation of pillared hematite crystals is determined by low pH of the medium produced by the hydrolysis of $FeOHSO_4$.

It should be noted that the distribution of hematite particles over both length and width is narrow (Fig. 2). Such a narrow distribution is attained owing to the uniformity of nucleation and crystal growth in the entire reaction volume.

Data on the composition of the forming solid and liquid phases as influenced by the conditions of $FeOHSO_4$ hydrolytic transformations are given in the table. According to these data, the rate of formation the α-Fe_2O_3 phase and the phase purity depend on temperature, duration of hydrothermal treatment, and the $FeOHSO_4 : H_2O$ ratio in the suspension. The rate of iron oxide formation significantly increases as the H_2O weight fraction in the suspension and treatment temperature increase. For example, according to the X-ray phase analysis, hematite is detected after 12-, 8-, 4-, and 2.5-h treatment of the $FeOHSO_4$ suspension at 140, 160, 180, and 200°C, respectively.

Single-phase α-Fe_2O_3 precipitates (according to the X-ray data) are formed at high degrees of hydrolysis when the residual content of sulfate ions is less than 3%.

The dependences of the degree of hydrolysis of the iron(III) salt on the $FeOHSO_4 : H_2O$ ratio, temperature, and hydrothermal treatment duration are shown in Fig. 3, which indicates that the highest degree of

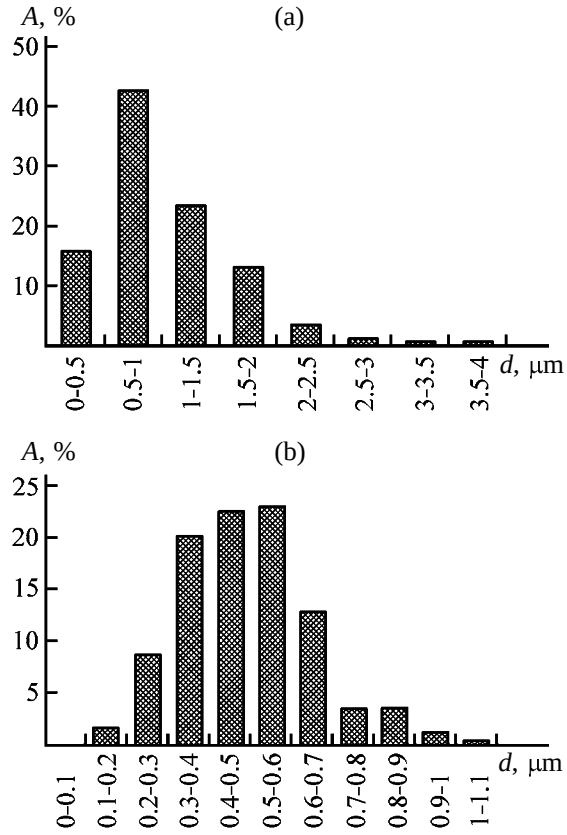

Fig. 2. Histograms of α-Fe_2O_3 particle distribution with respect to (a) length and (b) width. (*A*) Content and (*d*) particle size.

Influence of conditions of $FeOHSO_4$ hydrolytic transformations on the composition of the solid and liquid phases

Treatment conditions			Analytical data			
initial $FeOHSO_4 : H_2O$ weight ratio	T, °C	τ, h	pH of liquid phase	concentration of Fe(III) in liquid phase, g l^{-1}	content of SO_4^{2-} in solid phase, wt %	phase composition of product
1 : 15	160	1	2.0	14.3	46.1	$Fe(OH)_{3-2x}(SO_4)_x \cdot nH_2O$
1 : 5	160	25	0.57	24.8	20.0	α-Fe_2O_3 + $Fe(OH)_{3-2x}(SO_4)_x \cdot nH_2O$
1 : 10	160	25	0.46	11.2	17.6	α-Fe_2O_3 + $Fe(OH)_{3-2x}(SO_4)_x \cdot nH_2O$
1 : 15	160	25	0.81	9.6	7.6	α-Fe_2O_3 + $Fe(OH)_{3-2x}(SO_4)_x \cdot nH_2O$
1 : 25	160	25	0.79	3.6	4.3	α-Fe_2O_3 + $Fe(OH)_{3-2x}(SO_4)_x \cdot nH_2O$
1 : 15	140	25	0.91	4.0	16.2	α-Fe_2O_3 + $Fe(OH)_{3-2x}(SO_4)_x \cdot nH_2O$
1 : 15	180	25	0.78	9.3	0.6	α-Fe_2O_3
1 : 15	200	25	0.73	8.1	0.5	α-Fe_2O_3
1 : 15	160	40	0.76	9.4	2.9	α-Fe_2O_3

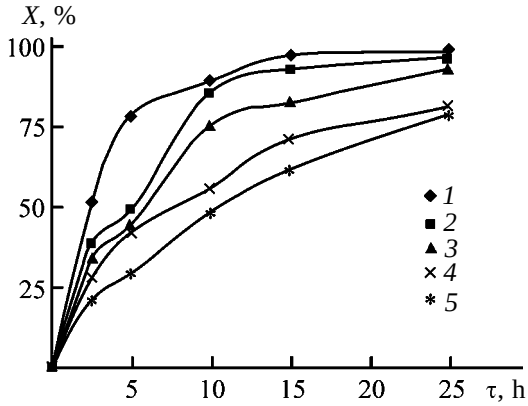

Fig. 3. Dependences of the degree of $FeOHSO_4$ hydrolysis X on the treatment duration τ at various temperature and $FeOHSO_4 : H_2O$ ratios. Temperature (°C): (*1*) 200, (*2–4*) 160, and (*5*) 140. $FeOHSO_4 : H_2O$: (*1, 3, 5*) 1 : 15, (*2*) 1 : 25, and (*6*) 1 : 5.

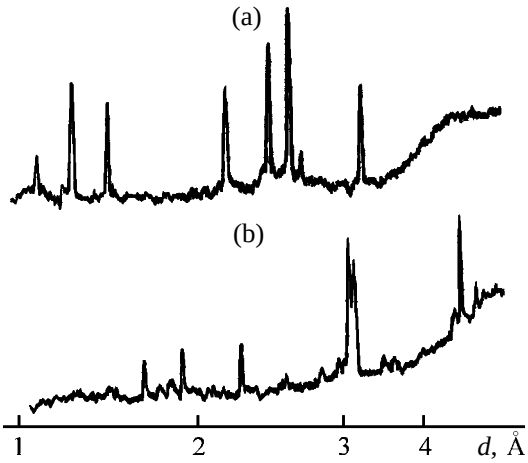

Fig. 4. X-ray diffraction pattern of hydrolysis products obtained at 160°C after a treatment for (a) 40 h and (b) 2 h. (*d*) Interplanar spacing.

$FeOHSO_4$ hydrolysis (98.5%) is attained at 200°C and an $FeOHSO_4 : H_2O$ ratio of 1 : 25. As the synthesis temperature decreases and the $FeOHSO_4 : H_2O$ ratio increases, the degree of hydrolysis decreases, with its value depending on the synthesis conditions. For example, the hydrothermal treatment of an $FeOHSO_4$ suspension at 140°C makes it possible to attain the degree of hydrolysis of 79.2%.

According to X-ray data (Fig. 4), the hydrolytic transformation of $FeOHSO_4$ occurs under the experimental conditions to give an intermediate phase of iron basic sulfates with the gross composition $Fe(OH)_{3-2x}(SO_4)_x \cdot nH_2O$ (x and n are variables depending on the solid : liquid ratio in suspension, temperature, and treatment duration; x = 0.5–0.9 and n = 0.6–1). When the degree of hydrolysis reaches 70%, in addition to the $Fe(OH)_{3-2x}(SO_4)_x \cdot nH_2O$ phase, the α-Fe_2O_3 phase appears, its amount increasing with the progress of the hydrolysis. Consequently, the formation of a series of iron hydroxysulfates of variable composition, which are stable within a wide temperature range, precedes the formation of hematite in the $FeOHSO_4$–H_2O system. The study of these hydrolysis products shows that they have a well-pronounced crystal structure and the crystals are of a regular cubic shape (Fig. 1b). According to the experimental data on this phase, the crystal size monotonically increases as the temperature and duration of the hydrothermal treatment increase. The maximal edge length attains 1.2–1.5 μm.

The derivatogram of the starting $FeOHSO_4$ appreciably differs from that of the intermediate product (Fig. 5). According to the structural data [7], water in the iron(III) basic sulfates $3Fe_2O_3 \cdot 4SO_3 \cdot 9H_2O$,

$Fe_2O_3 \cdot 2SO_3 \cdot H_2O$, and $Fe_2O_3 \cdot 2SO_3 \cdot 5H_2O$ can be in various forms. In particular, in $Fe_2O_3 \cdot 2SO_3 \cdot H_2O$ water is entirely in the form of OH^- groups and hence the endothermic effect in the range 500–550°C is caused by its removal. Apparently, $Fe(OH)_2(SO_4)_{0.5} \cdot 0.7H_2O$ contains water of crystallizatiopn, coordinated water, and bridging hydroxy groups, responsible for three endothermic effects in the sample thermogram (Fig. 5b). The removal of bridging hydroxy groups from iron(III) hydroxysulfate at 500°C is accompanied by the breakdown of the structure and formation of two phases: α-Fe_2O_3 and $Fe_2(SO_4)_3$. The deep endothermic effect in the range 680–750°C corresponds to the decomposition of iron(III) sulfate. Hematite is the final product of the thermal treatment of iron(III) basic sulfates.

In contrast to the thermal transformation, the hydrolytic transformation of the intermediate phase $Fe(OH)_{3-2x}(SO_4)_x \cdot nH_2O$ to hematite under hydrothermal conditions is more complicated. In this case, the formation of hematite follows the dissolution–precipitation mechanism involving formation of nuclei of a new phase and their further growth. The mechanism of the hydrolysis of iron(III) salts and of the formation of insoluble products with a composition strongly depending on the conditions of their formation is considered in [8–10]. It was shown [10] that possible products of the hydrolysis of iron(III) salts are goethite, lepidocrocite, hematite, and amorphous hydrogel. In the course of prolonged aging at a temperature below 90°C, amorphous hydrogel transforms into goethite, and at higher temperatures, into α-Fe_2O_3. Direct precursors of the forming solid phase of iron(III) oxides and hydroxides are polynuclear hydrolysis products containing from 3 to 13, from 13 to 33, and from 33 to 100 iron(III) atoms in a molecule [8–10]. The composition of the polymers affects significantly the structure and physicochemical properties of the precipitates. The oligomers (3–13) under certain conditions can transform both into a solid phase and into oligomers (13–33). In turn, these oligomers can participate in the aggregation of the goethite precipitate (α-FeOOH) or transform into stable hydroxylated polymers. As the polymer lifetime decreases with increasing temperature [8], the rate of the α-Fe_2O_3 phase formation grows. Thus, according to our experimental data, at 200°C this phase is formed within 2–4 h, and at 160°C, within 15–24 h.

It is known [10] that the nature of an anion appreciably affects the whole pattern of the hydrolysis of Fe^{3+} ions. Anions block one or more coordination sites of iron(III) in the stage of the formation of equilibrium hydrolysis products and thus significantly affect the structure and sizes of polymers by incorporation into their molecules, hindering formation of the solid phase. For example, in the presence of sulfate ions, goethite and hematite appear as additions to sulfate-containing solid phases. Therefore, it is quite natural that the intermediate phase of the variable composition $Fe(OH)_{3-2x}(SO_4)_x \cdot nH_2O$, which is stable within a wide temperature range, is formed in the course of the $FeOHSO_4$ hydrolysis.

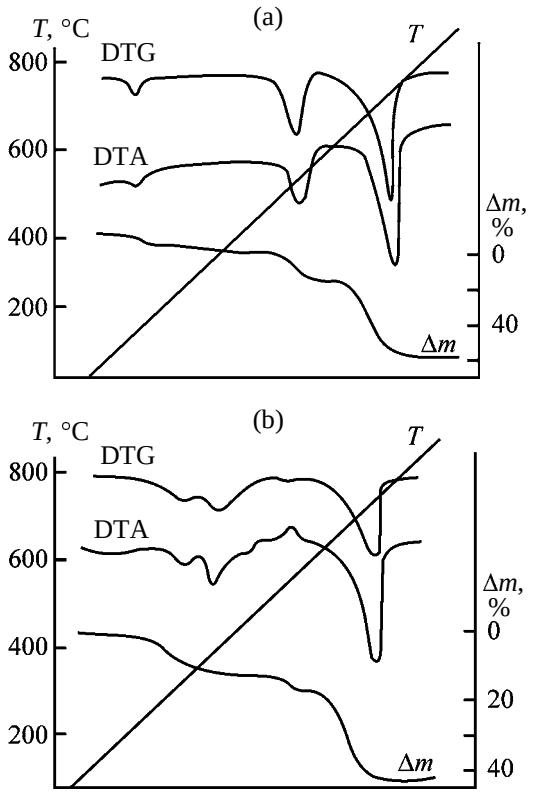

Fig. 5. Derivatograms of (a) initial iron(III) basic sulfate and (b) iron(III) basic sulfates obtained at 160°C and the $FeOHSO_4 : H_2O$ ratio of 1 : 15 after 5-h treatment. (*T*) Temperature and (Δ*m*) weight loss.

The experimental data on the effect of the $FeOHSO_4 : H_2O$ ratio on the degree and rate of the hydrolysis of Fe^{3+} ions can be explained as follows. As the $FeOHSO_4$–H_2O suspension is diluted, i.e., the water content in it increases, the equilibrium is shifted toward formation of hydrolysis products. The accumulation of H^+ ions in the liquid phase in the process leads to a decrease in pH, an increase in the degree of dissolution of hydrolysis intermediates, and the growth of iron(III) concentration in the liquid phase. In this case, the rate of hydrolytic transformations giving rise to stable insoluble hydrolysis products, hematite in particular, increases.

CONCLUSIONS

(1) The influence of the $FeOHSO_4 : H_2O$ ratio, temperature, and time of the hydrothermal treatment on the rate and degree of the hydrolysis of iron(III) basic sulfate was studied. The hydrolysis of $FeOHSO_4$ is accompanied by the formation of a metastable phase of iron(III) basic sulfates of variable composition, $Fe(OH)_{3-2x}(SO_4)_x \cdot nH_2O$.

(2) Hematite is the final hydrolysis product in the system $FeOHSO_4$–H_2O. The hematite crystals have a pillared shape and are characterized by a narrow size distribution.

REFERENCES

1. Agafonov, G.I., Kleshchev, D.G., Tolchev, A.V., *et al*., *Lakokras. Mater. Ikh Primen*., 1999, nos. 7–8, pp. 41–46.
2. Tolchev, A.V., Bagautdinova, R.R., Kleshchev, D.G., *et al*., *Izv. Ross. Akad. Nauk, Neorg. Mater*., 1996, vol. 32, no. 11, pp. 1377–1380.
3. Bagautdinova, R.R., Kleshchev, D.G., Pletnev, R.N., *et al*., *Izv. Ross. Akad. Nauk, Neorg. Mater*., 1998, vol. 34, no. 5, pp. 584–586.
4. Tolchev, A.V., Bagautdinova, R.R., and Kleshchev, D.G., *Zh. Prikl. Khim*., 2001, vol. 74, no. 3, pp. 353–356.
5. USSR Inventor's Certificate no. 1 809 833.
6. Klimenko, E.V., Hydrothermal Synthesis of Red Iron Oxide Pigmnents, *Cand. Sci. Dissertation*, Kiev, 1995.
7. Zvyagintsev, O.E., Ginzburg, S.I., and Lyakhmanov, S.B., *Zh. Neorg. Khim*., 1969, vol. 16, no. 6, pp. 1475–1477.
8. Pykhteev, O.Yu., Efimov, A.A., and Moskvin, L.N., *Zh. Obshch. Khim*., 1998, vol. 68, no. 6, pp. 905–911.
9. Pechenyuk, S.P., Rogachev, D.L., Kasikov, A.G., *et al*., *Zh. Neorg. Khim*., 1985, vol. 30, no. 2, pp. 311–315.
10. Pykhteev, O.Yu., Efimov, A.A., and Moskvin, L.N., *Zh. Prikl. Khim*., 1999, vol. 72, no. 1, pp. 11–21.

Russian Journal of Applied Chemistry, Vol. 77, No. 9, 2004, pp. 1409–1412. Translated from Zhurnal Prikladnoi Khimii, Vol. 77, No. 9, 2004, pp. 1421–1424.

INORGANIC SYNTHESIS AND INDUSTRIAL INORGANIC CHEMISTRY

Hydrated Cobalt(II) and Nickel(II) Ammine Diphosphates Isolated from Aqueous Solutions

L. V. Voitenko, I. D. Zhilyak, and V. A. Kopilevich

National Agricultural University, Kiev, Ukraine

Received May 12, 2004

Abstract—Hydrated amorphous cobalt and nickel(II) ammine diphosphates were prepared.

The chemistry of binary compounds of double-charged metal ions is fairly well studied, and the possibilities for development of new phosphate materials based on them are almost exhausted or require higher-level approaches [1, 2]. Amorphous phosphates having an increased reactivity owing to their thermodynamic instability are of special interest even among known compounds [3]. They are formed as aqua and hydroxo complexes in ammonia solutions [4]. In this context, it was interesting to isolate new phosphate compounds containing coordinated ammonia from ammonia solutions. Such compounds can exhibit a biological or catalytic activity [5–8] and also can be used as luminophores or their components [9].

Published procedures for preparing transition metal ammine complexes [10–14] can be subdivided into homogeneous and heterogeneous procedures. The homogeneous procedures are based on reactions of metal salt solutions with an aqueous ammonia solution, followed by precipitation of ammine complexes with an organic solvent, evaporation, or freezing of the solution. In the heterogeneous procedures, a solution or a solid metal salt is treated with gaseous ammonia.

The main problem of isolating solid diphosphates of double-charged metal ammine complexes from a homogeneous mixture is very high solubility of salts with complex $[M(NH_3)_n]^{2+}$ ions; therefore, it appears difficult to achieve the solubility product (SP) for precipitating complex phosphate salts.

EXPERIMENTAL

We prepared hydrated nickel(II) ammine diphosphate by salting it out from an ammonia solution with an organic solvent [14]. As the starting reagent we used $Ni_2P_2O_7 \cdot 6H_2O$ (37.0% NiO) synthesized according to [15]. We dissolved 1 g of this compound in 10 ml of 23% ammonia. We added 25 ml of acetone to the resulting solution. In so doing, a blue substance precipitated, which was then separated from the mother liquid and kept at 15–25°C in air until it completely solidified (to constant weight). Found, %: NiO 33.41; P_2O_5 32.56; NH_3 10.70; H_2O 23.34. Nickel(II) ammine diphosphate $Ni_2P_2O_7 \cdot 3NH_3 \cdot 6H_2O$. Calculated, %: NiO 32.41; P_2O_5 32.11; NH_3 11.24; H_2O 23.78.

The composition of the anionic component was determined by quantitative paper chromatography [1] (% of P_2O_5): $P_2O_7^{4-}$ 95.50, PO_4^{3-} 4.50. The starting nickel diphosphate contained 3.50% of P_2O_5 as PO_4^{3-}.

We prepared hydrated cobalt(II) ammine diphosphate by the procedure similar to that used for preparing cobalt(II) ammine monophosphate [7]. The starting cobalt diphosphate $Co_2P_2O_7 \cdot 6H_2O$ was prepared according to [16, 17]. The synthesis included saturation of $Co_2P_2O_7 \cdot 6H_2O$ powder with gaseous ammonia under static conditions at 15–25°C for 96 h, followed by keeping in air of the resulting powder at 15–25°C to a constant weight. Found, %: CoO 32.95; P_2O_5 32.01; NH_3 13.26; H_2O 21.69. Cobalt(II) ammine diphosphate $2Co_2P_2O_7 \cdot 7NH_3 \cdot 11H_2O$. Calculated, %: CoO 32.97; P_2O_5 32.11; NH_3 13.12; H_2O 21.80.

Composition of the anionic component (quantitative paper chromatography [1], % of P_2O_5): $P_2O_7^{4-}$ 93.80 and PO_4^{3-} 6.20. The starting cobalt(II) diphosphate contained 5.30% of P_2O_5 as PO_4^{3-}.

The content of Ni^{2+} and Co^{2+} was determined complexometrically, that of P_2O_5, gravimetrically [19], that of ammonia, by distilling it off on a Seren'ev apparatus [20], and that of water and ammonia (in total), by the weight loss on heating for 2 h at 650°C.

1070-4272/04/7709-1409 © 2004 MAIK "Nauka/Interperiodica"

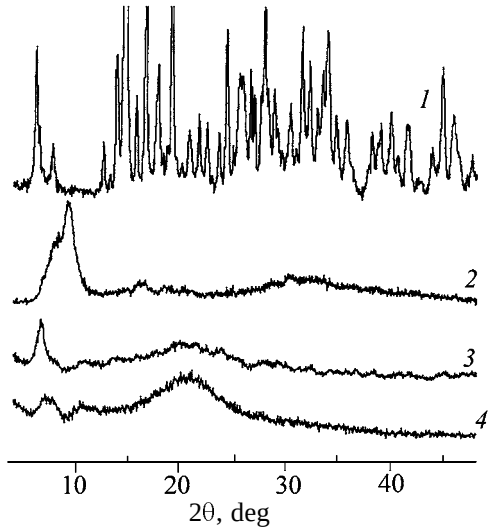

Fig. 1. X-ray patterns of the starting hydrated diphosphates and of nickel and cobalt ammine diphosphates (*1*) $Ni_2P_2O_7 \cdot 6H_2O$, (*2*) $Ni_2P_2O_7 \cdot 3NH_3 \cdot 6H_2O$, (*3*) $Co_2P_2O_7 \cdot 6H_2O$, and (*4*) $2Co_2P_2O_7 \cdot 7NH_3 \cdot 11H_2O$. (2θ) Bragg angle.

The X-ray analysis was carried out on a DRON-UM1 diffractometer (CuK_α radiation), with a graphite single crystal fixed in the diffracted beam as a monochromator. The X-ray patterns were recorded by step-by-step scanning over the angle range 2θ 4°–80°. The scanning step was 0.05°, and the exposure time in a point, 3–9 s. The measured diffraction maxima were approximated by the Voight pseudofunction, separating out the K_{α_1} component. The IR spectra were recorded with a Specord 75-IR spectrophotometer using KBr pellets (sample concentration 0.2–0.3 wt %). The electronic diffuse reflection spectra were taken on a Specord M-40 device in the range 30 000–12 000 cm^{-1}.

The results of the X-ray analysis show that the starting $Ni_2P_2O_7 \cdot 6H_2O$ is crystalline, whereas the starting $Co_2P_2O_7 \cdot 6H_2O$ as a whole is X-ray amorphous with a single distinct reflection maximum at 2θ = 6.5° and a broad band with a maximum at 2θ = 19°–20°. Their X-ray patterns agree with the published data [21, 22]. Ammine diphosphates of Ni(II) and Co(II) synthesized from these compounds were found to be X-ray amorphous. In the case of $Ni_2P_2O_7 \cdot 3NH_3 \cdot 6H_2O$, a reflection maximum is observed at 2θ = 9.5°, and $2Co_2P_2O_7 \cdot 7NH_3 \cdot 11H_2O$ has ill-defined maxima at 2θ = 7.0°, 11.0°, and 19°–21°, which may correspond to a proportional distance in the subsequent formation of the crystal structure in the compounds (Fig. 1).

The IR spectra of the starting nickel and cobalt hydrated diphosphates and of the ammine diphosphates obtained from them are given in the table. In the spectra of all the compounds, there is a strong

Frequencies of the absorption maxima in the IR spectra of the compounds

ν, cm^{-1}				
$Ni_2P_2O_7 \cdot 6H_2O$	$Co_2P_2O_7 \cdot 6H_2O$	$Ni_2P_2O_7 \cdot 3NH_3 \cdot 6H_2O$	$2Co_2P_2O_7 \cdot 7NH_3 \cdot 11H_2O$	Assignment
3600–3000 s, br	3500–3000 s, br	3400–3000 s, br	3400–3100 s, br	$\nu(H_2O)$, $\nu_{as}(NH_3)$
1640 m	1675 sh; 1620 m	1665 sh	1650 sh; 1600 m	
1510 w	1540 w	1610 m	1545 sh	$\nu(H_2O)$, $\delta_{as}(NH_3)$
		1465 sh	1445 w	$\delta_s(NH_3)$
		1430 m		
		1410 sh		
			1325 m	$\delta_s(NH_3)$
1110 s	1120 w	1140 w	1125 sh	$\nu_{as}(PO_3)[P_2O_7]$
	1110 s	1120 w	1100 s	
1070 s	1080 s	1095 s	1080 s	
1030 w	1025 w	1010 w	1010 w	
895 s	890 s; 800 sh	890 s	865 s	$\nu_s(PO_3)(PO)$
	700 w, sh		710 w	$\nu_{as}(POP)[P_2O_7]$
665 s, sh	680 w	670 w	680 sh	$\delta_{as}(OPO)$
		650 w		
		580 sh		
540 s	540 s	540 m	540 m	$\delta_s(OPO)$
		510 m	510 sh	M–N
480 sh	450 w	450 sh	440 sh	M–O

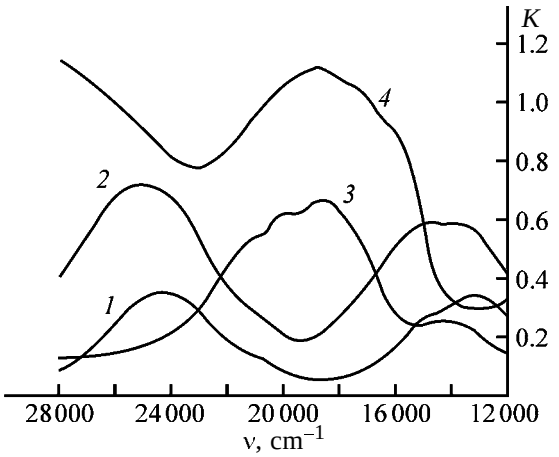

Fig. 2. Electronic diffuse reflection spectra of (*1*) $Ni_2P_2O_7 \cdot 6H_2O$, (*2*) $Ni_2P_2O_7 \cdot 3NH_3 \cdot 6H_2O$, (*3*) $Co_2P_2O_7 \cdot 6H_2O$, and (*4*) $2Co_2P_2O_7 \cdot 7NH_3 \cdot 11H_2O$. (ν) Wave number and (*K*) reflection coefficient.

broad absorption band in the range 3400–3000 cm^{-1}, corresponding to the stretching vibrations of NH and OH groups. In the range 1675–1540 cm^{-1}, there are absorption bands corresponding to the bending vibrations of H_2O and asymmetric bending vibrations of NH_3 in the ammine complexes. The vibrations of coordinated NH_3 and H_2O in these regions could not be distinguished. The range 1465–1410 cm^{-1} of the spectra of the ammine diphosphates suggests the presence of NH_3 involved in a stable hydrogen bond with proton transfer with the $P_2O_7^{4-}$ anion. It is accompanied by averaging of the electron density over the whole chain of atoms forming the hydrogen bond [23, 24]. These compounds have an absorption band in the range of 1325 cm^{-1}, assignable only to the symmetric bending vibrations of coordinated NH_3 molecules [25]. The asymmetric and symmetric stretching vibrations of the $P_2O_7^{4-}$ group are manifested in the range 1125–800 cm^{-1} as strong absorption bands. At 720–540 cm^{-1}, weak absorption bands assignable to the vibrations of P–O–P and O–P–O groups are observed. In the range 510–545 cm^{-1}, the stretching vibrations of M–N and M–O bonds are observed in the spectra of the ammine diphosphates [23, 26].

Thus, examination of the IR spectra suggests that two different types of NH_3 molecules are present in the composition of nickel(II) and cobalt(II) ammine diphosphates: the molecules interacting with metal ions by the donor–acceptor mechanism only and the molecules additionally involved in hydrogen bonding with charge transfer.

The electronic reflection spectra of the starting aqua and ammine diphosphates of nickel(II) and cobalt(II) are shown in Fig. 2. The long-wave reflection (absorption) maximum in the reflection spectra is known to shift to higher frequencies on successive substitution of ammine ligands for aqua ligands [27]. The comparison of the spectra of $Ni_2P_2O_7 \cdot 6H_2O$ (Fig. 2, curve *1*) and nickel(II) ammine diphosphate (Fig. 2, curve *2*) shows that the reflection maxima are shifted from 13200 to 14840 cm^{-1} and from 24360 to 25240 cm^{-1}, i.e., toward higher frequencies. The electronic reflection spectra of $Co_2P_2O_7 \cdot 6H_2O$ (curve *3*) and cobalt(II) ammine diphosphate (curve *4*) are also shown. In these spectra we also observe the shift of the reflection maxima from 18640 to 18880 cm^{-1}.

CONCLUSIONS

(1) Solid X-ray amorphous hydrated ammine diphosphates of nickel(II) and cobalt(II), $Ni_2P_2O_7 \cdot 3NH_3 \cdot 6H_2O$ and $2Co_2P_2O_7 \cdot 7NH_3 \cdot 11H_2O$, were prepared.

(2) The synthesized compounds were studied by IR and electronic spectroscopy, and their coordination structure was confirmed.

REFERENCES

1. Shchegrov, L.N., *Fosfaty dvukhvalentnykh metallov* (Bivalent Metal Phosphates), Kiev: Naukova Dumka, 1987.
2. Konstant, Z.A. and Dindune A.P., *Fosfaty dvukhvalentnykh metallov* (Bivalent Metal Phosphates), Riga: Zinatne, 1987.
3. Sinyaev, V.A., Levchenko, L.V., Shustikova, E.S., and Griggs, J., *Zh. Prikl. Khim.*, 2003, vol. 76, no. 4, pp. 529–532.
4. Eshchenko, L.S., Main Regular Trends in Formation of Trivalent Metal Phosphates and Development of Scientific Principles for Their Preparation, *Doctoral Dissertation*, St. Petersburg, 1992.
5. Corbridge, D.E., *Phosphorus. An Outline of Its Chemistry, Biochemistry and Technology*, Amsterdam: Elsevier, 1980.
6. Kopilevich, V.A., Kokhan, S.S., and Voitenko, L.V., *Proc. 11th World Fertilizer Congr. CIEC*, Ghent, 1997, vol. 2, p. 296.
7. Voitenko, L.V., *Cand. Sci. Dissertation*, Kiev, 1994.
8. RF Patent 2032615.
9. *Neorganicheskie fosfatnye materialy* (Inorganic Phosphate Materials), Kanazawa, T., Ed., Kiev: Naukova Dumka, 1998.
10. Ukrainian Patent 13102.
11. Spacu, P. and Vasilescu, C., *An. Univ. C.I. Parhon*,

Ser. Stiint. Natur., 1957, no. 13, pp. 79–83.

12. Acharyya, H. and Ropy, H., *Technology* (India), 1972, vol. 9, no. 4, pp. 273–277.
13. Voitenko, L.V., Shchegrov, L.N., and Kopilevich, V.A., *Ukr. Khim. Zh*., 1992, vol. 58, no. 3, pp. 223–226.
14. Ukrainian Patent 62782.
15. Lavrov, A.V., Bykanova, T.A., and Kessler, Yu.M., *Izv. Akad. Nauk SSSR, Neorg. Mater*., 1976, vol. 12, no. 3, pp. 491–494.
16. Basset, W.L., Bedwell, J.B., and Hutchinson, J.B., *J. Chem. Soc*., 1936, no. 10, pp. 2883–2885.
17. Ammar, I.A. and Saad, A., *Electrochim. Acta*, 1971, vol. 16, pp. 383–389.
18. Přibil, R., *Komplexony v chemicke analyse*, Prague: Ceskoslovenske Akad., 1957.
19. *GOST* (State Standard) *20851–75: Mineral Fertilizers: Methods of Analysis*, Moscow: Izd. Standartov, 1986.
20. *Sovremennye metody khimicheskogo analiza pochv i rastenii (metodicheskie ukazaniya)* (Modern Methods of Chemical Analysis of Soils and Plants (Methodical Instructions)), Kiev: Nauchno-Issled. Inst. Sakharnoi Svekly, 1984.
21. Lavrov, A.V. and Bykanova, T.A., *Izv. Akad. Nauk SSSR, Neorg. Mater*., 1979, vol. 15, no. 9, pp. 1653–1657.
22. Kokhanovskii V.V. and Prodan, E.A., *Zh. Neorg. Khim*., 1988, vol. 33, pp. 761–765.
23. Voitenko, L.V., Kopilevich, V.A., and Shchegrov, L.N., *Zh. Neorg. Khim*., 1992, vol. 37, no. 9, pp. 2055–2060.
24. Shevchenko, Yu.N., *Doctoral Dissertation*, Moscow, 1991.
25. Nakamoto, K., *Infrared Spectra of Inorganic and Coordination Compounds*, New York: Wiley, 1963.
26. *Atlas IK spektrov fosfatov: Dvoinye mono- i difosfaty* (Atlas of IR Spectra of Phosphates: Double Mono- and Diphosphates), Pechkovskii, V.V., Ed., Moscow: Nauka, 1990.
27. Cotton, F.A. and Wilkinson, G., *Advanced Inorganic Chemistry*, New York: Interscience, 1966.

Russian Journal of Applied Chemistry, Vol. 77, No. 9, 2004, pp. 1413–1417. Translated from Zhurnal Prikladnoi Khimii, Vol. 77, No. 9, 2004, pp. 1425–1429.

INORGANIC SYNTHESIS AND INDUSTRIAL INORGANIC CHEMISTRY

Identification of Impurities Accumulated in the Extractant in the Course of Purification of Wet-Process Phosphoric Acid with Tri-*n*-butyl Phosphate

V. M. Lembrikov, L. V. Konyakhina, V. V. Volkova, A. A. Perov, O. V. Kiseleva, and S. M. Ershova

Voskresensk Research Institute for Fertilizers and Phosphoric Acid, Joint-Stock Company, Voskresensk, Moscow oblast, Russia

Karpov Institute of Physical Chemistry, State Scientific Center of Russian Federation, Moscow, Russia

Received February 20, 2004

Abstract—Impurities accumulated in the extractant in the course of operation of the plant for purification of wet-process phosphoric acid, obtained from apatite concentrate, by extraction with tri-*n*-butyl phosphate are identified by IR and mass spectra.

According to [1], by 2000 the world output of pure phosphoric acid was about 2.3 million tons (recalculated on P_2O_5), including 1.7 million tons of purified phosphoric acid (PPA) from wet-process phosphoric acid (WPPA). At the Voskresensk Institute of Fertilizers and Phosphoric Acid, Joint-Stock Company, an experimental-industrial plant for production of PPA from WPPA by tributyl phosphate (TBP) extraction on pulsating columns operates since 1995. Its annual output capacity is above 15000 t of P_2O_5.

It should be pointed out that purification of WPPA is performed using crude TBP. In the recycling mode, TBP is rapidly contaminated with impurities contained in WPPA. This changes for worse the hydrodynamic parameters of the pulsating columns, resulting in reduction of their output capacity and even in flooding of the apparatuses. It was demonstrated in studying the phase separation rate in the emulsions H_3PO_4–TBP and H_3PO_4–actual extractant at various densities of the aqueous and organic phases that, over the entire density range, the settling rate of the emulsion in the system extractant–H_3PO_4 is considerably lower than that in the system TBP–H_3PO_4. The results are given in Table 1 and Fig. 1. The experiments were performed under practically identical conditions (viscosity, density, stirring rate) (see, for example, experiment nos. 6 and 18, 8 and 20, 11 and 23, etc.). Evidently, in the systems, some surfactants are gradually accumulated, acting as emulsifiers, emulsion stabilizers, and interfacial layer blockers.

The sedimentation rate of an actual emulsion in the gravitational field is described by Eq. (1) [2].

$$v = \frac{2gr^2(\rho_1 - \rho_2)}{3\mu_2}\frac{\mu_1 + \mu_2}{3\mu_1 + 2\mu_2}, \quad (1)$$

where ρ_1 and ρ_2 are the densities of the dispersed and continuous phases, respectively (determined experimentally); μ_1 and μ_2 are the viscosities of the dispersed (from [3]) and continuous (determined experimentally) phases; and r is the radius of dispersed particles.

The mean radii of the dispersed particles r (cm) in the H_3PO_4–TBP and H_3PO_4–extractant emulsions, estimated by Eq. (1), are given in Table 1. At identical densities and viscosities of the phases, the mean size of the dispersed particles in the H_3PO_4–extractant emulsions is lower by a factor of 1.5–3.5 than in the H_3PO_4–TBP emulsions.

To remove organic impurities from the extractant, we used the method described in [4]. The extractant was washed with 15% Na_2CO_3 ($V_o : V_w = 3 : 1$) at 50°C. The resulting aqueous solution containing sodium phosphates and some organic admixtures was treated with 40% phosphoric acid (recalculated on P_2O_5) at a 5 : 1 volume ratio with continuous stirring. At this stage we observed separation of either a powder-like deep brown substance (sample no. 1) or a resin also colored deep brown (sample no. 2). These substances were separated by filtration or decanting, washed with distilled water, and dried at about 60°C

1070-4272/04/7709-1413 © 2004 MAIK "Nauka/Interperiodica"

Table 1. Settling rates in H_3PO_4–TBP and H_3PO_4–extractant emulsions at 20°C

Experiment no.	Organic phase			Aqueous phase			v, cm s^{-1}	r, cm
	ρ, g cm^{-3}	P_2O_5, M	μ, cP	ρ, g cm^{-3}	P_2O_5, M	μ, cP		
Crude TBP–H_3PO_4								
1	1.031	0.66	10.46	1.236	3.43	3.83	0.0029	0.002
2	1.049	0.92	12.71	1.290	4.16	5.01	0.0092	0.004
3	1.055	1.01	13.57	1.297	4.26	5.20	0.0062	0.003
4	1.061	1.10	14.48	1.297	4.26	5.20	0.0040	0.003
5	1.078	1.35	17.40	1.352	5.07	6.85	0.0026	0.002
6	1.106	1.79	23.56	1.429	6.29	10.12	0.0101	0.005
7	1.115	1.94	25.97	1.470	6.98	12.45	0.0154	0.006
8	1.156	2.62	40.46	1.470	6.98	12.45	0.0129	0.007
9	1.100	1.69	22.08	1.441	6.48	10.74	0.0044	0.003
10	1.142	2.38	34.78	1.533	8.09	17.10	0.0151	0.007
11	1.156	2.62	40.46	1.561	8.60	19.66	0.0105	0.006
12	1.161	2.71	42.71	1.570	8.77	20.58	0.0096	0.006
Extractant–H_3PO_4								
13	1.027	0.61	10.02	1.202	2.99	3.23	0.0045	0.003
14	1.047	0.89	12.44	1.252	3.64	4.15	0.0055	0.003
15	1.052	0.96	13.13	1.265	3.81	4.42	0.0050	0.003
16	1.067	1.19	15.45	1.279	4.01	4.75	0.0020	0.002
17	1.070	1.22	15.87	1.312	4.49	5.62	0.0007	0.001
18	1.102	1.73	22.56	1.404	5.88	8.92	0.0020	0.002
19	1.109	1.83	24.31	1.466	6.91	12.19	0.0019	0.002
20	1.130	2.17	30.48	1.466	6.91	12.19	0.0017	0.002
21	1.091	1.55	20.03	1.414	6.05	9.39	0.0021	0.002
22	1.137	2.30	32.94	1.535	8.12	17.24	0.0013	0.002
23	1.152	2.55	38.54	1.563	8.65	19.90	0.0010	0.002
24	1.161	2.71	42.71	1.570	8.77	20.58	0.0012	0.002

in an oven. The chemical composition of sample no. 2 was as follows (wt %): C 30.6, H 5.6, N 1.05, S 1.4, P 14.31, F 2.17, Cl 0.3, Si 0, Na 0.59, Fe 0.16, and Ca 0.16.

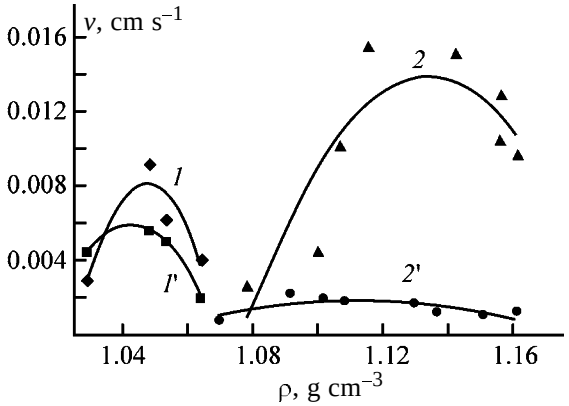

Fig. 1. Settling rate v in emulsions: (*1*, *2*) H_3PO_4–TBP and (*1'*, *2'*) H_3PO_4–extractant as a function of the viscosity of the organic phase ρ.

As seen, the product separated from the extractant has a complex composition. Presumably, in addition to organics it contains some inorganic compounds such as phosphoric acid, phosphogypsum, fluorides, and sodium and iron phosphates.

To identify compounds composing the products separated from the extractant, we measured the IR spectra of sample nos. 1 and 2 with a Perkin–Elmer 983 spectrometer (Fig. 2). The spectra show the bands due to C–H stretching vibrations at 2931 and 2955 cm^{-1}; CH bending vibrations at 1457 cm^{-1}; and C=O vibrations (1709, 1710 cm^{-1}) characteristic of saturated and unsaturated aliphatic acids [5]. Also the spectra show the band at 1606 cm^{-1} typical of C=C in-plane vibrations of aromatic compounds [5]. It should be pointed out that this band becomes more distinctly pronounced after recrystallization of sample no. 2 from acetone. For comparison, in Fig. 2 are presented the spectra of crude TBP [TU (Technical

Specifications) 2435-305-05763458–01], OP-4 emulsifier (TU 6-02-997–90), and crude oleic acid [GOST (State Standard) 7580–55].

We also studied the product separated from the extractant by mass spectrometry in the electron impact mode. The sample was placed into a gold crucible and heated in a vacuum (10^{-5} Pa) until a vapor appeared. The spectra were recorded at 150°C (Fig. 3).

The mass spectra of both samples are identical. Comparison with reference data reveal that the samples contain tri-*n*-butyl phosphates [6, 7]; oleic, abietic, and stearic acids; and, possibly, butanol, poly(acrylamide) [8], and naphthenic acids.

According to the reference data [7], the mass spectrum of TBP shows the following peaks (*m*/*e*) [relative intensity (%) is given in parentheses]: 237 (0.3), 211 (15), 183 (1), 181 (1.5), 167 (2), 156 (1), 155 (22), 154 (1.5), 153 (2), 137 (5), 127 (2), 125 (8), 113 (1), 112 (1), 111 (2), 100 (3), 99 (100), 83 (1), 82 (2), 81 (1), 57 (12), 56 (5), and 55 (4). To these values we can also add the peak *m*/*e* 41 [6]. All these peaks were found in the spectra of sample nos. 1 and 2.

According to [8], the mass spectrum of oleic acid is as follows (*m*/*e*): 41 (100), 55 (94.9), 43 (64.9), 83 (34.4), 67 (33.3), 57 (33.3), 54 (26.7), 56 (24.4), 81 (23.6), and 97 (23.1). All the ten peaks were found in sample no. 2 and nine of them, in sample no. 1.

In the spectrum of sample no. 1 we found the following peaks assigned to stearic acid (*m*/*e*): 43, 57, 41, 55, 71, 73, 60, and 69; and in sample no. 2: 43, 57, 41, 55, 71, 73, and 69. The peaks assigned to abietic acid are as follows (*m*/*e*): 91, 105, 77, 79, 121, 93, 67, and 81 (sample no. 2).

Furthermore, in the spectrum of sample no. 2 we found practically all the peaks reported in [8] for such naphthenic acids and esters as cyclopentyl acetate, cyclohexanecarboxylic acid, cyclohexyl acetate, and cyclohexylpropionic acid.

In addition to electron impact, the samples were also studied by such a mild mass-spectroscopic method as field desorption (Table 2).

In the field-desorption mass spectrum of sample no. 1 (powder), the most intensive peak corresponds to the sodium atom, suppressing all the other peaks. The next in the intensity is the peak corresponding to the potassium atom. The peaks found in the spectrum of sample no. 2 can be assigned to several individual compounds such as TBP (MW 266.3), dibutylphosphoric acid (MW 210), phosphate of oxyethylated alkylphenol $CH_3(CH_2)_8–C_6H_4O(CH_2–CH_2O)_3–CH_2CH_2O–P(OH)_2O$ (MW 476), its fragment $CH_3·(CH_2)_8–C_6H_4$ (MW 203), and also oxyethylated alkylphenol $CH_3(CH_2)_{10}C_6H_4O(CH_2–CH_2O)_4H$ (MW 424).

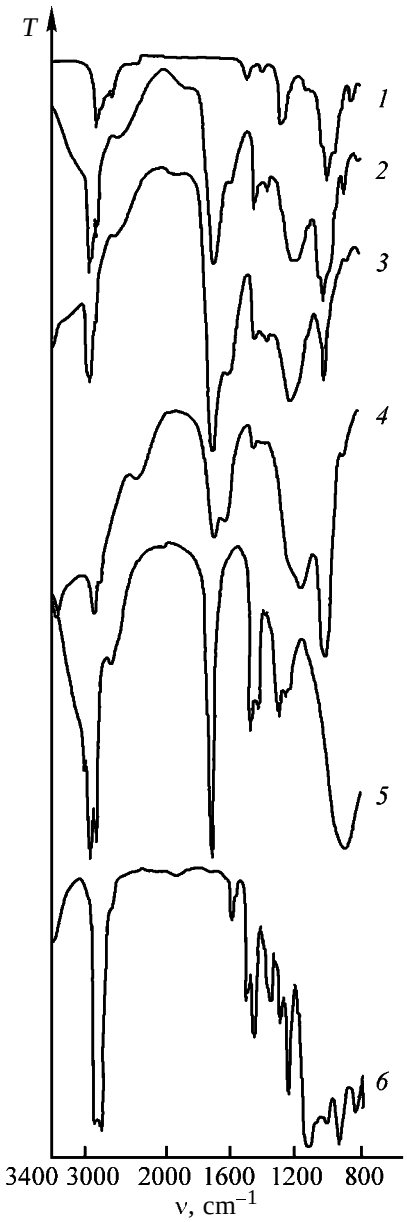

Fig. 2. Infrared spectra of organic compounds: (*1*) TBP, (*2*) sample no. 1, (*3*) sample no. 2, (*4*) sample no. 2 recrystallized from acetone, (*5*) oleic acid, and (*6*) OP-4 emulsifier. (*T*) Transmittance and (ν) wave number.

Thus, our results show that the extractant circulating in the system contains such impurities as dibutylphosphoric acid, oxyethylated alkylphenols and their phosphates, oleic, abietic, and stearic acids, butanol, amines, naphthenic acids, etc.

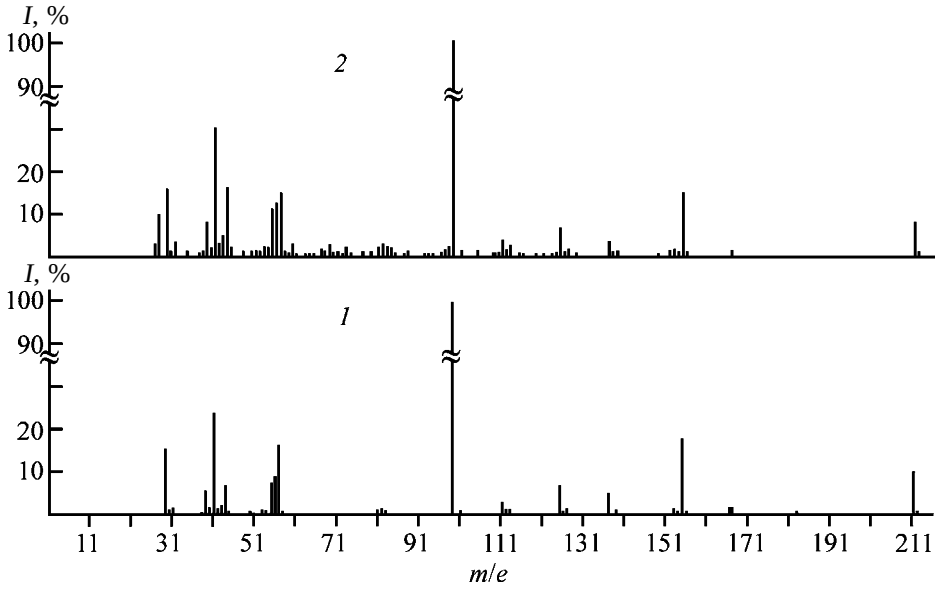

Fig. 3. Mass spectra of substances separated from the extractant: (*1*) sample no. 1 and (*2*) sample no. 2. (*I*) Intensity.

The product separated from the extractant by soda washing, being introduced into the process solutions, demonstrates the surfactant effect. It was found that introduction of 0.1% of this product into TBP decreases the phase separation rate in the system TBP–H_3PO_4 by a factor of 6.5.

The source of the indicated compounds is apatite concentrate containing some flotation agents such as oleic acid, tall oil, OP-4 emulsifier, and also compounds, e.g., poly(acrylamide), formed in the stage of sulfuric acid decomposition of the concentrate and in the course of clarification of H_3PO_4. OP-4 emulsifier is the source of oxyethylated alkylphenols with the general formula $C_nH_{n+1}C_6H_4O(CH_2–CH_2O)_mH$, where m = 3, 4. Tall oil is the source of resin acids (e.g., abietic acid) and unsaturated (oleic) and saturated (stearic) acids. Note also that crude oleic acid contains up to 10% of naphthenic acids. Furthermore, sulfuric acid decomposition of apatite is accompanied by sulfonation and phosphatization. Evidently, oxyethylated alkylphenols are involved in phosphatization with formation of phosphates.

Table 2. Field-desorption mass spectra with acetone as a solvent

Sample no.	I_{rel}, %	Mass
1	2.5	127
	2.8	99
	2.3	89
	9.0	58
	9.1	39
	100.0	23
2	17.6	477
	6.9	422
	27.9	421
	9.5	268
	61.6	267
	10.6	212
	100.0	211
	7.0	203
	9.9	189
	86.2	59
	19.0	57

The product separated has a complex composition, containing the major impurities from the extractant. Therefore, it is advisable to use it as a reference for photocolorimetric determination of the degree of contamination of the extractant. The applicability of this method is limited by the maximal content of organic impurities in the extractant at a level of 2 mg ml^{-1}. At higher contamination level, poorly separable systems are formed.

To conclude, surfactants accumulated in the system deteriorate extraction purification of WPPA with TBP. To keep the operating parameters of the system at a reasonable level (i.e., to avoid accumulation of surfactants), it is necessary to introduce the stage of soda washing of the extractant. Furthermore, it is necessary to avoid introduction of surfactants to the WPPA purification system and, as far as possible, at the stage of manufacture of WPPA.

CONCLUSION

The extractant (tri-*n*-butyl phosphate) circulating in the system of extraction purification of wet-process phosphoric acid, obtained from apatite concentrate, contains impurities of dibutylphosphoric acid, oxyethylated alkylphenols and their phosphates, oleic, abietic, stearic, and naphthenic acids, butanol, amines, etc.

REFERENCES

1. Grinevich, A.V., Korneva, Z.N., Moshkova, V.G., *et al*., *Mir Sery, N, P, K: Byull*., 2001, no. 6, pp. 7–13.
2. Abramzon, A.A., *Poverkhnostno-aktivnye veshchestva, svoistva i primenenie* (Surfactants: Properties and Applications), Leningrad: Khimiya, 1981.
3. Postnikov, N.N., *Termicheskaya fosfornaya kislota: Khimiya i tekhnologiya* (Thermal Phosphoric Acid: Chemistry and Technology), Moscow: Khimiya, 1970.
4. RF Patent 2 205 789.
5. Bellamy, L.J., *The Infrared Spectra of Complex Molecules*, London: Wiley, 1954.
6. Etinger, A.G., Poponova, R.V., Pilyugin, V.M., *et al*., *Vysokochist. Veshch*., 1987, no. 3, pp. 210–213.
7. *Advances in Mass Spectrometry*, London: Heyden & Son, 1959. Translated under the title *Uspekhi mass-spektrometrii*, Moscow: Inostrannaya Literatura, 1963, pp. 360–379.
8. *Katalog sokrashchennykh mass-spektrov* (Catalog of Truncated Mass Spectra), Novosibirsk: Nauka, 1981.

Russian Journal of Applied Chemistry, Vol. 77, No. 9, 2004, pp. 1418–1422. Translated from Zhurnal Prikladnoi Khimii, Vol. 77, No. 9, 2004, pp. 1430–1434.

INORGANIC SYNTHESIS AND INDUSTRIAL INORGANIC CHEMISTRY

Thermodynamic Study of Extraction of Cerium(III) and Yttrium(III) with Tributyl Phosphate

D. E. Chirkst, T. E. Litvinova, A. A. Chistyakov, and M. Yu. Ionova

St. Petersburg State Mining Institute, St. Petersburg, Russia

Received February 25, 2004

Abstract—To increase the efficiency of hydrometallurgical processing of lean rare-earth raw material, the effect of salt anion and metal cation on the characteristics of Ce(III) and Y(III) recovery from dilute aqueous solutions with tri-*n*-butyl phosphate was studied on the basis of the thermodynamic theory of extraction.

Modern hydrometallurgy of rare-earth metals (REM) is based on the extraction of their nitrates with tri-*n*-butyl phosphate (TBP). However, as lean rare-earth raw materials, for instance, eudialyte ores of the Kola peninsula, are involved in the process the efficiency of extraction recovery and separation of lanthanide salts should be increased. It becomes urgent to search for new, more efficient extractants and study the effect of the salt anion on the extractability. It is advisable to characterize the extraction by Gibbs constants and energies of extraction. Previously, we studied the thermodynamics of extraction of zirconium salts with TBP and solutions of trialkylbenzylammonium salts (TABA, alkyl: C_4H_9–$C_{10}H_{21}$) in *o*-xylene [1, 2] and extraction of cerium and yttrium sulfates with TABA sulfate in *o*-xylene [3, 4]. In this work, we compare the characteristics of extraction of Ce(III) and Y(III) salts with TBP and TABA.

The features of Ce(III) and Y(III) extraction with TBP were studied using model systems REM nitrate–$Mg(NO_3)_2$. The REM content was approximately preset by the weight of the metal nitrate taken and was then refined photometrically. All the reagents were of chemically pure grade. The metal ion concentration was similar to the REM content in solutions from leaching of eudialyte concentrates and was about 0.01 mol kg^{-1}.

The extraction and phase separation were performed in separating funnels. The stirring rate was 2000 rpm and was preset with an automatic stirrer. The duration of phase contact required for equilibration was determined experimentally and amounted to 30 min. The phases fully separated within 15 min.

The content of cerium(III) and yttrium(III) in the aqueous phase (initial and equilibrium) was determined photometrically (λ 670 nm) with Arsenazo III in the acetate buffer solution at pH 3 [5]. The chemicals used in the analysis were of analytically pure grade. The REM content in the organic phase was determined as the difference of the concentrations in the initial and equilibrium aqueous phases with regard to the difference in the phase volumes (weights):

$$c_{org} = (c_0 - c_{aq})\frac{m_{aq}}{m_{org}}, \quad (1)$$

where c_{org} is the equilibrium metal concentration in the organic phase (mol kg^{-1}); c_{aq}, REM concentration in the equilibrium aqueous phase (mol kg^{-1}); c_0, initial content of cerium or yttrium in the aqueous phase (mol kg^{-1}); and m_{aq}/m_{org}, ratio of weights of the aqueous and organic phases, respectively.

The experimental values of the metal distribution coefficients were determined as follows:

$$D = c_{org}/c_{aq}, \quad (2)$$

where D is the metal ion distribution coefficient; c_{aq}, c_{org}, equilibrium concentrations of the metal ion in the aqueous and organic phases, respectively (mol kg^{-1}).

The experimental data were obtained at pH 3. pH was monitored with a pH-150M pH-meter with a combined electrode.

To elucidate the mechanism of REM extraction with tributyl phosphate and calculate the extraction constants, we measured the dependences of the Ce(III) and Y(III) distribution coefficients between the aqueous and organic phases on the TBP concentration in *o*-xylene at a constant ionic strength supported by 2 M

$Mg(NO_3)_2$. The initial concentration of Ce(III) or Y(III) nitrates was 0.01 mol kg^{-1}. Thus, change in the concentration of REM nitrates during extraction should not noticeably affect the solution ionic strength, equal to 6 mol kg^{-1}. The measured ln–ln dependences of the Ce(III) and Y(III) distribution coefficients on the TBP mole fraction are shown in Figs. 1a and 1b. The TBP concentration was expressed in mole fractions, because the standard state of the extractant is the pure liquid with the mole fraction $X = 1$. Logarithmic coordinates were used to obtain linear dependences. The equation of the extraction reaction is

$$M^{3+}(aq) + 3NO_3^-(aq) + n\text{TBP(org)} \rightleftarrows Me(NO_3)_3 \cdot n\text{TBP(org)}, \quad (3)$$

where M is Ce or Y.

The law of mass action (for Ce) appears as

$$K = \frac{[Ce(NO_3)_3 \cdot n\text{TBP}]}{[Ce^{3+}][NO_3^-]^3 \gamma_{Ce^{3+}} \gamma_{NO_3^-}^3 [\text{TBP}]^n}, \quad (4)$$

where γ_i are activity coefficients of ions.

We replace the product of activity coefficients by the mean ionic activity coefficient of cerium(III) nitrate:

$$\gamma_\pm = (\gamma_{Ce^{3+}} \gamma_{NO_3^-})^{1/2}. \quad (5)$$

With regard to (2), Eq. (4) transforms into

$$K = \frac{D}{[NO_3^-]^3 \gamma_\pm^4 [\text{TBP}]^n}. \quad (6)$$

and, after taking the logarithm, into

$$\ln D = \ln K + 3\ln[NO_3^-] + 4\ln\gamma_\pm + n\ln[\text{TBP}]. \quad (7)$$

It follows from (7) that the dependence of $\ln D$ on $\ln[\text{TBP}]$ for Ce(III) or Y(III) should be linear at the constant ionic strength with the slope equal to the solvation number in the extractable complex. The dependences in Fig. 1 are approximated by straight lines with the confidence factors R^2 0.94 and 0.96 for Ce(III) and Y(III), respectively:

$$\ln D = 1.64\ln[\text{TBP}] + 2.25 \text{ for Ce(III)}, \quad (8)$$

$$\ln D = 1.93\ln[\text{TBP}] + 1.55 \text{ for Y(III)}. \quad (9)$$

It follows from Eq. (8) that about 36% of cerium

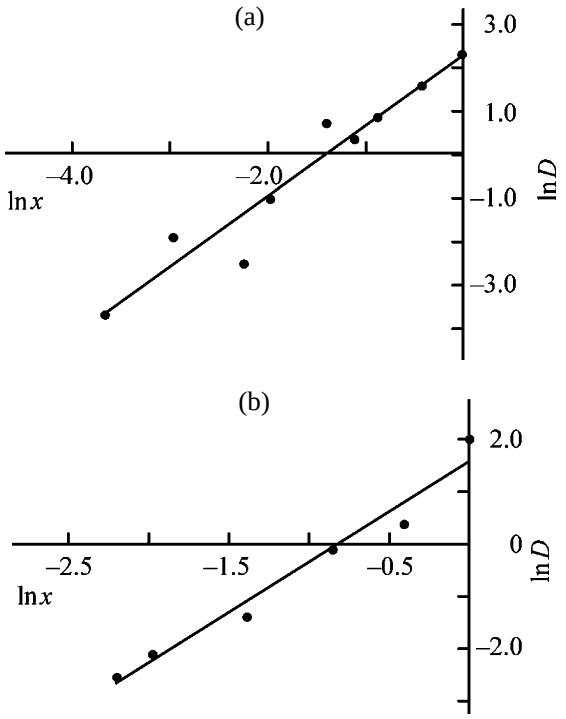

Fig. 1. Logarithm of distribution coefficient D of (a) cerium(III) nitrate and (b) yttrium(III) nitrate as a function of logarithm of TBP mole fraction x in *o*-xylene.

nitrate solvates contain one TBP molecule and 64%, two TBP molecules. According to Eq. (9), the solvation number of yttrium nitrate within the error limits is equal to 2. The extraction constants can be calculated from the absolute terms of the equations

$$\ln K = 2.25 - 3\ln[NO_3^-] - 4\ln\gamma_\pm \text{ for Ce(III)}, \quad (10)$$

$$\ln K = 1.55 - 3\ln[NO_3^-] - 4\ln\gamma_\pm \text{ for Y(III)}. \quad (11)$$

The concentration of nitrate ions in the experiments was 4 mol kg^{-1}. The value of the mean ionic activity coefficient was taken equal to that for $LaCl_3$ at the ionic strength of 6 mol kg^{-1}, $\gamma_\pm = 0.342$ [6]. From these values, we calculated the extraction constants $K_{Ce} = 10.8$ and $K_Y = 5.4$ and the Gibbs free energies $\Delta G^0_{298}(Ce) = -5.90$ and $\Delta G^0_{298}(Y) = -4.18$ kJ mol^{-1}.

We also studied the dependence of $\ln D$ on the concentration of the salting-out agent, $Mg(NO_3)_2$. Experiments were performed at the initial cerium concentration of 0.01 mol kg^{-1} without diluent. The results are shown in Figs. 2a and 2b.

The ln–ln dependences of the distribution coefficients of Ce(III) and Y(III) on the nitrate ion concentration are described by the following linear equations

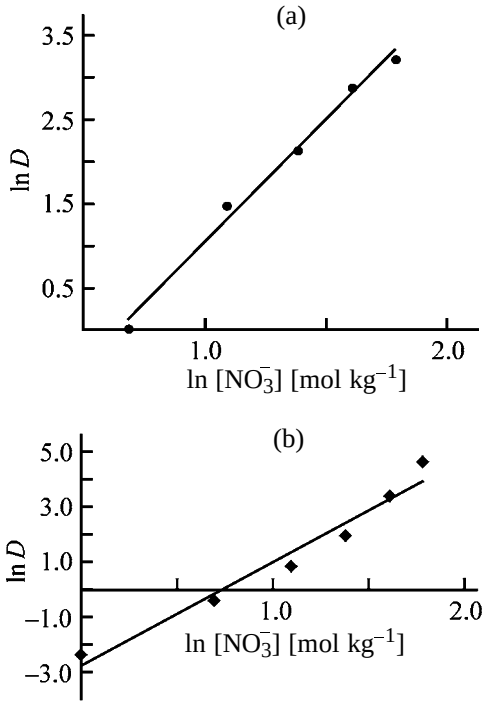

Fig. 2. Logarithm of distribution coefficient D of (a) cerium(III) nitrate and (b) yttrium(III) nitrate as a function of logarithm of nitrate ion concentration $[NO_3^-]$.

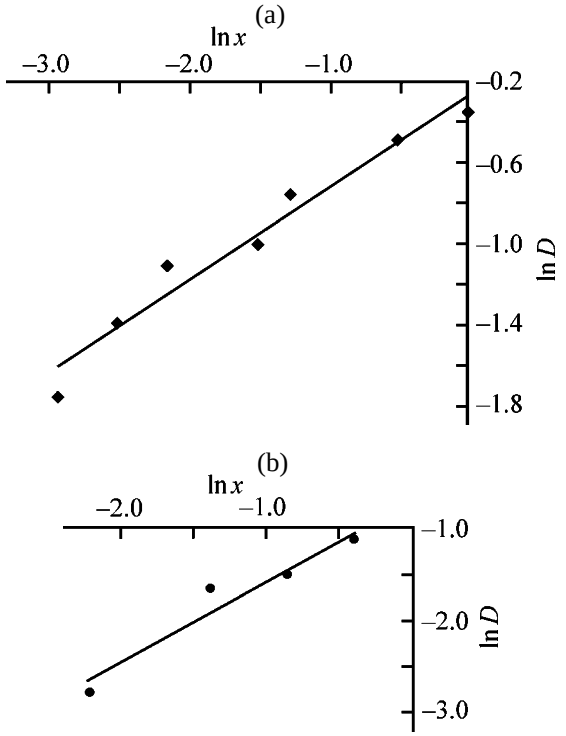

Fig. 3. Logarithm of distribution coefficient D of (a) cerium(III) chloride and (b) yttrium(III) chloride as a function of logarithm of TBP mole fraction x in *o*-xylene.

with the confidence factor R^2 0.92 and 0.99, respectively:

$$\ln D = 2.93\ln[NO_3^-] - 1.89 \quad \text{for Ce(III)}, \tag{12}$$

$$\ln D = 3.29\ln[NO_3^-] - 2.67 \quad \text{for Y(III)}. \tag{13}$$

The slopes of straights lines (12) and (13) within the error limits are close to 3, i.e., to the stoichiometric coefficient at nitrate ion in Eq. (3) (in other words, to the number of anions in the extractable complex). The extraction constants can be calculated from the absolute terms of Eqs. (12) and (13). Since neat TBP was used, its activity in the equation for the law of mass action is equal to 1. Then, Eq. (7) transforms into

$$\ln D = \ln K + 4\ln\gamma_{\pm} + 3\ln[NO_3^-]. \tag{14}$$

As above, the mean ionic activity coefficient is taken equal to 0.342. From (12) and (13) we obtain

$$\ln K = -1.89 - 4\ln\gamma_{\pm} = 2.40 \quad \text{for Ce(III)}, \tag{15}$$

$$\ln K = -2.67 - 4\ln\gamma_{\pm} = 1.62 \quad \text{for Y(III)} \tag{16}$$

and calculate the constants and Gibbs free energies K_{Ce} = 11.0 and K_Y = 5.0; ΔG^0_{298}(Ce) = –5.95 and ΔG^0_{298}(Y) = –4.02 kJ mol^{-1}. Thus, the consistent thermodynamic characteristics of the extraction were obtained by two independent methods. The averaged values are $K_{Ce} = 10.9 \pm 0.1$ and $K_Y = 5.2 \pm 0.2$; $\Delta G^0_{298}(Ce) = -5.92 \pm 0.03$ and $\Delta G^0_{298}(Y) = -4.10 \pm 0.08$ kJ mol^{-1}.

To study the effect of anion on REM extraction, we measured the ln–ln dependences of the distribution coefficients of $CeCl_3$ and YCl_3 on the TBP mole fraction in *o*-xylene at the concentration of the salting-out agent, $MgCl_2$, of 2 mol kg^{-1} (Figs. 3a, 3b). The logarithmic dependences are well described by straight lines with the confidence factor R^2 0.96 and 0.93, respectively:

$$\ln D = 0.5\ln[TBP] - 0.27 \quad \text{for Ce (III)}, \tag{17}$$

$$\ln D = 0.9\ln[TBP] - 0.69 \quad \text{for Y (III)}. \tag{18}$$

Their slopes give solvation numbers of 0.5 for $CeCl_3$ and approximately 1 for YCl_3 in the organic phase, and hence the extraction reactions are described by the following equations:

$$Ce^{3+}(aq) + 3Cl^-(aq) + 0.5TBP(org) \rightleftarrows CeCl_3 \cdot 0.5TBP(org), \tag{19}$$

$$Y^{3+}(aq) + 3Cl^-(aq) + TBP(org) \rightleftarrows YCl_3 \cdot TBP(org). \quad (20)$$

The extraction constants were calculated from the absolute terms of Eqs. (17) and (18). Here, the formula similar to (7) is also valid:

$$\ln D = \ln K + 3\ln[Cl^-] + 4\ln\gamma_\pm + n\ln[TBP]. \quad (21)$$

The mean ionic activity coefficient was taken equal to 0.342, similarly to nitrates. Hence,

$$\ln K_{Ce} = -0.27 - 3\ln[Cl^-] - 4\ln\gamma_\pm = -0.14, \quad (22)$$

$$\ln K_Y = -0.69 - 3\ln[Cl^-] - 4\ln\gamma_\pm = -0.56; \quad (23)$$

$K_{Ce} = 0.87$ and $K_Y = 0.57$; $\Delta G^0_{298}(Ce) = 0.35$ and $\Delta G^0_{298}(Y) = 1.39$ kJ mol^{-1}.

We also studied the dependence of the distribution coefficient of $Ce_2(SO_4)_3$ on the TBP concentration in *o*-xylene at a $MgSO_4$ concentration of 2 mol kg^{-1} (ionic strength 8 mol kg^{-1}) (Fig. 4). It is described by the equation

$$\ln D = 1.5\ln[TBP] - 2.40. \quad (24)$$

In accordance with the condition of electroneutrality, the equation of the extraction equilibrium is

$$2Ce^{3+}(aq) + 3SO_4^{2-}(aq) + n TBP(org) \rightleftarrows Ce_2(SO_4)_3 \cdot n TBP(org). \quad (25)$$

In this case, the law of mass action is

$$K = \frac{[Ce]_{org}}{2[Ce^{3+}]^2[SO_4^{2-}]^3\gamma_\pm^5[TBP]^n} = \frac{D}{[Ce^{3+}][SO_4^{2-}]^3\gamma_\pm^5[TBP]^n}. \quad (26)$$

The Ce concentration in the organic phase should be divided by two to take into account association of $Ce_2(SO_4)_3$ in the solvate [it follows from (24) that the solvation number in cerium sulfate extraction is equal to 1.5]. The extraction constant was calculated by the equation

$$\ln K = -2.40 - \ln[Ce^{3+}] - 3\ln[SO_4^{2-}] - \ln 2 - 5\ln\gamma_\pm = 2.90. \quad (27)$$

The cerium(III) concentration in the organic phase was, on the average, taken equal to 0.01 mol kg^{-1}, the concentration of sulfate ions, 2 mol kg^{-1}, and the mean ionic activity coefficient, 0.5, which is equal to that of lanthanum chloride at an ionic strength of 8 mol kg^{-1} [6]. For reaction (25), we obtain $K = 18.2$ and $\Delta G^0_{298} = -7.19$ kJ mol^{-1}. Per mole of Ce(III), the solvation number is 0.75, $K = 4.3$, and $\Delta G^0_{298} = -3.60$ kJ mol^{-1}.

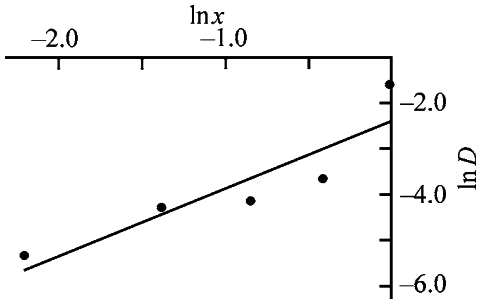

Fig. 4. Logarithm of distribution coefficient *D* of cerium(III) sulfate as a function of logarithm of TBP mole fraction *x* in *o*-xylene.

The characteristics of extraction of Ce(III) and Y(III) salts with TBP at the concentration of the corresponding magnesium salts of 2 mol kg^{-1} are listed in Table 1. All the values are given per mole of REM.

It follows from Table 1 that in the series chloride–sulfate–nitrate the solvation number and extraction constant increase and the Gibbs energy decreases. This is caused by a decrease in the charge on the terminal oxygen atoms in anions, *z*, which was calculated as a quotient of division of the anion charge by the number of terminal atoms. The *z* value characterizes the density of the negative charge on the anion. The lower the charge density, the more strongly the cation polarizes the phosphoryl group of TBP and binds TBP according to the scheme

$$An^{z-} \rightarrow Ce^{3+} \leftarrow O{=}P(OC_4H_9)_3.$$

Table 1. Molar characteristics of extraction of cerium(III) and yttrium(III) salts with TBP

Salt	[*z*]	Solvation number	*K*	ΔG^0_{298}, kJ mol^{-1}
Nitrate:				
Ce(III)	1/3	1.64	10.9 ± 0.1	–5.92 ± 0.03
Y(III)		2	5.2 ± 0.2	–4.10 ± 0.08
Sulfate:				
Ce(III)	1/2	0.75	4.3	–3.6
Chloride:				
Ce(III)	1	0.5	0.57	0.35
Y(III)		1	0.87	1.39

Table 2. Comparison of extraction characteristics of cerium(III) and yttrium(III) salts with TBP and TABA (100% TBP, extraction of nitrates; 0.5 M TABA, extraction of sulfates; pH 3; concentration of magnesium salts 2 mol kg^{-1}; REM concentration about 0.01 mol kg^{-1})

M^{3+}	TBP		TABA	
	D	ΔG^0_{298}, kJ mol^{-1}	D	ΔG^0_{298}, kJ mol^{-1}
Ce(III)	8.6	-5.92 ± 0.03	35 ± 4	-8.9 ± 0.3
Y(III)	7.3	-4.10 ± 0.08	10.2 ± 2.0	-7.5 ± 0.2
Separation coefficient	1.18		3.5	

The solvation numbers of yttrium(III) are higher than those of Ce(III), which can be explained by smaller ionic radius of yttrium. The smaller the cation radius, the higher is its ionic potential and the more strongly the cation polarizes the phosphoryl group. However, the extraction constants for yttrium(III) salts are lower and the Gibbs energies, higher than for the Ce(III) salts. This can be explained as follows. During extraction, TBP molecules substitute water from the first coordination sphere of the cation. In the process, the H-bonds with the second coordination sphere are ruptured. Water molecules, which are more polar than TBP molecules, are bound more strongly with Y(III) than with Ce(III) having lower ionic potential. Therefore, the energy consumption for dehydration of Y(III) cations is not compensated by the energy of solvation, and the thermodynamic characteristics of extraction of Y(III) salts are less favorable as compared to Ce(III).

Virtually no separation of yttrium and cerium in extraction with TBP is observed. The distribution coefficients of Ce(III) and Y(III) nitrates in extraction with neat TBP and those of their sulfates in extraction with 0.5 M TABA sulfate in *o*-xylene [3, 4] at pH 3 and magnesium salt concentration of 2 mol kg^{-1} are listed in Table 2. The initial REM concentrations were 0.01 mol kg^{-1}. As seen, the efficiency and selectivity of REM extraction with TABA is substantially higher than with TBP. This result is especially important in hydrometallurgical processing of lean rare-earth raw materials.

CONCLUSIONS

(1) The constants and Gibbs energies of cerium(III) and yttrium(III) extraction with TBP are determined. The extraction constants and solvation numbers increase and Gibbs energies decrease in the series chloride–sulfate–nitrate, which can be explained by a decrease in the charge density on the anion and the corresponding growth in polarization of the phosphoryl group. In going from cerium(III) to yttrium(III), the solvation number increases, but the extraction constants decrease.

(2) The extraction constants and distribution and separation coefficients of cerium(III) and yttrium(III) are higher in extraction with trialkylammonium salts than with TBP.

REFERENCES

1. Dibrov, I.A., Chirkst, D.E., and Litvinova, T.E., *Zh. Prikl. Khim.*, 1996, vol. 69, no. 3, pp. 397–403.
2. Dibrov, I.A., Chirkst, D.E., and Litvinova, T.E., *Zh. Prikl. Khim.*, 2002, vol. 75, no. 2, pp. 202–207.
3. Dibrov, I.A., Chirkst, D.E., and Litvinova, T.E., *Zh. Prikl. Khim.*, 2002, vol. 75, no. 2, pp. 197–201.
4. Dibrov, I.A., Chirkst, D.E., and Litvinova, T.E., *Tsvetn. Met.*, 2003, no. 7, pp. 112–115.
5. Savvin, S.B., *Arsenazo III* (Arsenazo III), Moscow: Atomizdat, 1966.
6. *Kratkii spravochnik fiziko-khimicheskikh velichin* (Brief Handbook of Physicochemical Quantities), Ravdel', A.A., Ed., Moscow: Vysshaya Shkola, 2001, p. 133.

Russian Journal of Applied Chemistry, Vol. 77, No. 9, 2004, pp. 1423–1425. Translated from Zhurnal Prikladnoi Khimii, Vol. 77, No. 9, 2004, pp. 1435–1437.

INORGANIC SYNTHESIS AND INDUSTRIAL INORGANIC CHEMISTRY

Effect of Heat Treatment on Thermal Stability of Limestone

A. A. Kabanov

Krasnoyarsk State Pedagogical University, Krasnoyarsk, Russia

Received April 15, 2004

Abstract—The nature of the anomalous effect exerted by the heat treatment of limestone at 500 and 600°C on its thermal stability at 825°C was studied.

The author's method involving preliminary heat treatment of limestone in air at 500 and 600°C to accelerate its thermal decomposition at high temperatures has been patented [1]. After the heat treatment at both temperatures, the positive effect was obtained; after treatment at 500°C, the effect was stronger, which seems to be abnormal. The nature of this effect could be discussed only after the composition and thermal stability of calcium carbonate and natural limestone were studied in detail [2–6]. In this study we supplemented and developed these studies with the aim to elucidate the nature of the effect discovered in [1].

After natural limestone was dispersed [1], its <0.08-mm fraction was sieved and heat-treated in air for 6 h at 200, 500, and 600°C. Then, the preparations were stabilized again by keeping over P_2O_5 for no less than 10 days. The preparation heat-treated at 200°C was considered as the starting sample.

The composition of the starting samples and results of the phase analysis are presented in [5, 6]. The minerals present in the starting samples from the Solomenskoe deposit are as follows (wt %): $CaCO_3$ (calcite) 96.20, α-$Fe_2O_3 \cdot 0.38H_2O$ (hydrohematite) 1.06, $(Fe^{III}, Al_4)[OH]_8(Si_4O_{10}) \cdot 1.74H_2O$ (ferrihalloysite) 1.47, and other impurities 1.17.

The kinetic curves of the limestone decomposition were taken at 825 ± 0.1°C with 0.100-g samples using the volumetric analysis [3]. The X-ray phase analysis (XPA) was done on a DRON-3 diffractometer. The magnetic susceptibility of the powdered samples (0.20 g) was measured on a pendular magnetic balance [6] at a heating rate of 2.0 ± 0.1 deg min^{-1}. The IR spectra were recorded on a UR-20 spectrophotometer using mulls in mineral oil. The Mössbauer spectrum was obtained on an electrodynamic spectrometer based on an AI-5006-3M-V100 analyzer operating in the constant acceleration mode. The spectra were processed on an ES-1022 computer. The ^{57}Co isotope with an activity of 0.5 GBq in a chromium matrix was the γ-radiation source.

The kinetic curves of the thermal decomposition of limestone show that, compared to heat treatment at 600°C, the heat treatment at 500°C produces an abnormal effect on the decomposition rate (Fig. 1). The thermal decomposition was performed till the first, metastable state [6] of the limestone samples was attained. The heatings decrease the time of attaining the final degree of the sample decomposition. The reason why the decomposition after heating to 500°C is accelerated to a greater extent can be suggested on the basis of the XPA data (Figs. 2a, 2b). The impurities formed in the limestone at 500°C are oxides α-Fe_2O_3 and Fe_3O_4, whereas at 600°C only the FeO impurity is formed. As compared to wüstite FeO,

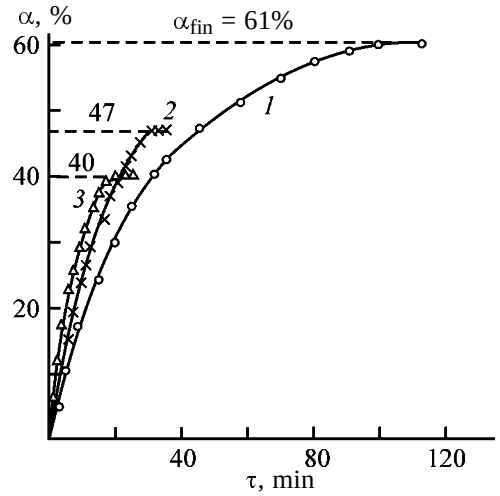

Fig. 1. Kinetic curves of the limestone decomposition at 825 ± 0.5°C. (α) Degree of decomposition and (τ) time. Sample: (*1*) Starting and (*2*, *3*) heat-treated at 600 and 500°C, respectively.

1070-4272/04/7709-1423 © 2004 MAIK "Nauka/Interperiodica"

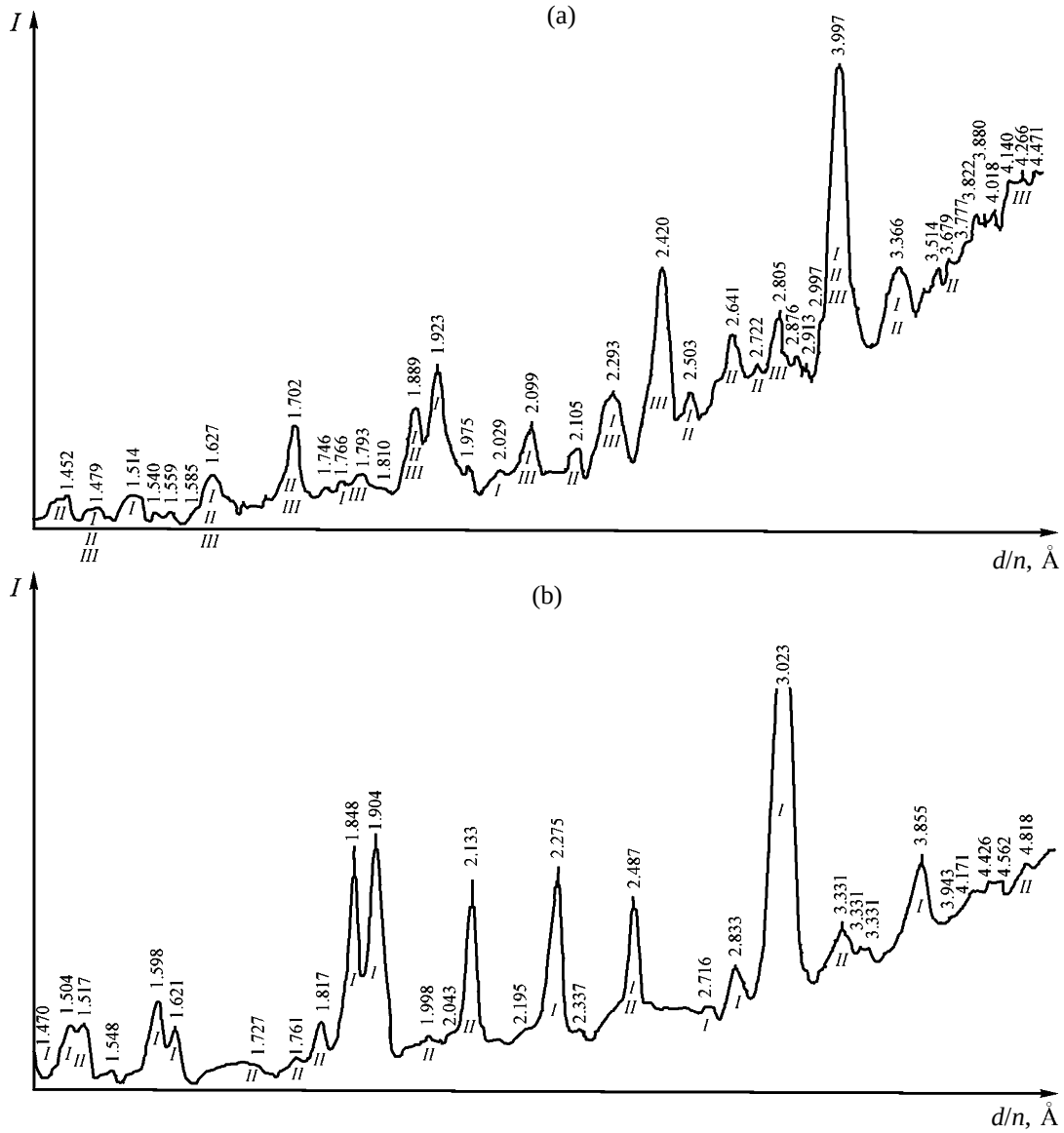

Fig. 2. X-ray diffraction patterns of the limestone heat-treated at (a) 500 and (b) 600°C. (*I*) Absorption intensity and (d/n) interplanar spacing. (a) (*I*) $CaCO_3 \cdot xH_2O$, (*II*) α-$Fe_2O_3 \cdot yH_2O$, and (*III*) Fe_3O_4; (b) (*I*) $CaCO_3 \cdot xH_2O$ and (*II*) FeO.

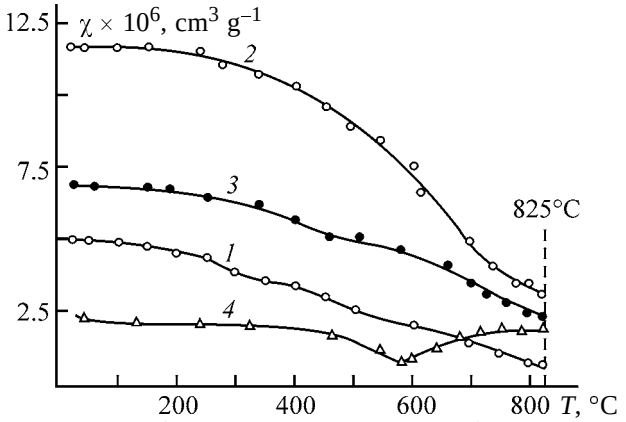

Fig. 3. Specific magnetic susceptibility χ of limestone vs. temperature T. Sample: (*1*) starting and (*2–4*) heat-treated at 500, 600, and 825°C, respectively.

hematite at 825°C is a stronger catalyst of the calcite decomposition. This is due to the fact that the magnetic susceptibility of hematite at a temperature of the limestone decomposition is higher than that of wüstite [4]. Magnetite Fe_3O_4 is a well-known ferromagnetic, and, owing to high magnetic susceptibility, its catalytic activity should be higher than that of hematite and wüstite.

The above hypothesis is confirmed by the results of the magnetic measurements (Fig. 3). Indeed, the magnetic susceptibility of the samples heated at 500°C is higher at all the temperatures, up to the temperature of limestone decomposition (825°C), than that of the samples heated at 600°C. In both cases, the magnetic

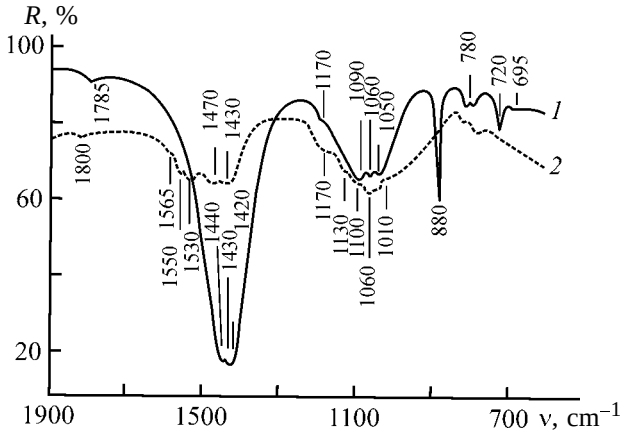

Fig. 4. IR spectra of the limestone heat-treated at (*1*) 200 and 500°C and (*2*) at 825°C. (*R*) Transmission and (*ν*) wave number.

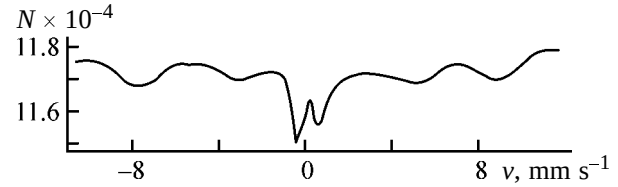

Fig. 5. Mössbauer spectrum of limestone. (*N*) Counts per channel and (*v*) velocity of the γ-ray source.

susceptibility of the samples is higher than that of the starting sample (curve *1*). The magnetic susceptibilities of the samples heat-treated at 825°C (curve *4*) show that both the main substance (calcite) and the impurities of iron compounds present in it undergo profound chemical transformations. The IR spectra of the samples heated at 200 and 500°C are similar (Fig. 4, curve *1*). Their assignment is given in [3]. The IR spectra taken after the heating at 825°C (curve *2*) revealed significant changes in the main substance, with a certain portion of calcite and water retained in the product, as in the case of reagent-grade calcium carbonate [3]. In other words, calcite does not fully decompose in this case either, and structural water stabilizes its lattice. The Mössbauer spectrum (Fig. 5) revealed hematite in the samples heated at 825°C. Comparison of this spectrum with that of the starting limestone [6] shows that, after heating at 825°C, the hematite particles are agglomerated, which accounts for the decrease in their magnetic susceptibility (Fig. 3, curve *4*).

CONCLUSIONS

(1) The limestone from the Solomenskoe deposit, heat-treated at 500°C for 6 h, shows lower thermal stability at 825°C than that heat-treated at 600°C.

(2) The abnormal temperature effect exerted by the limestone heat treatment on its thermal stability during the subsequent heating to 825°C is due to the different catalytic activities of iron oxides, which are formed in the limestone from impurities in the course of the heat treatments.

REFERENCES

1. USSR Inventor's Certificate no. 791 678.
2. Kabanov, A.A., *Zh. Fiz. Khim.*, 2001, vol. 75, no. 4, pp. 746–748.
3. Kabanov, A.A., *Zh. Fiz. Khim.*, 2002, vol. 76, no. 2, pp. 227–232.
4. Kabanov, A.A., *Zh. Fiz. Khim.*, 2002, vol. 76, no. 9, pp. 1719–1721.
5. Kabanov, A.A., *Zh. Fiz. Khim.*, 2003, vol. 77, no. 11, pp. 1961–1965.
6. Kabanov, A.A., *Zh. Prikl. Khim.*, 2003, vol. 76, no. 7, pp. 1077–1079.

Russian Journal of Applied Chemistry, Vol. 77, No. 9, 2004, pp. 1426–1429. Translated from Zhurnal Prikladnoi Khimii, Vol. 77, No. 9, 2004, pp. 1438–1441.

PHYSICOCHEMICAL STUDIES OF SYSTEMS AND PROCESSES

Activity of Copper in Liquid Nickel–Copper–Iron Alloys

A. G. Morachevskii, L. B. Tsymbulov, and E. Yu. Kolosova

St. Petersburg State Polytechnic Institute, St. Petersburg, Russia
Gipronikel' Institute, Open Joint-Stock Company, St. Petersburg, Russia

Received July 26, 2004

Abstract—The activities of copper in liquid nickel–copper–iron alloys at 1600°C were calculated along sections with constant $x_{Ni} : x_{Fe}$ ratios of 3 : 1, 1 : 1, and 1 : 3 (x_i is the mole fraction of a component in an alloy).

The integral molar excess Gibbs energies ΔG^{ex} and enthalpies ΔH of mixing of liquid Ni–Cu–Fe alloys at 1600°C, calculated from experimental data for binary boundary systems, have been reported previously [1, 2]. A number of geometric models and the polynomial Redlich–Kister method have been used in the calculations. Modern techniques for calculation of integral thermodynamic characteristics of liquid ternary metallic systems on the basis of the corresponding properties of binary systems were considered in detail in [3]. As a kind of a calculation reliability criterion in the absence of experimental data for a ternary system can serve the closeness of the results obtained using different geometric models and the analytical technique. For the Ni–Cu–Fe system, calculations of ΔG^{ex} and ΔH by different methods yield reasonably consistent results [1, 2].

The partial molar thermodynamic characteristics of copper in liquid alloys of the system Ni(1)–Co(2)–Fe(3) can be calculated using the known expressions relating the partial and integral parameters in ternary systems [3]. For example, the partial excess Gibbs energy for copper (component 2) along a path with a constant ratio of the other two components ($x_1 : x_3$) is given by

$$\Delta G_2^{ex} = \Delta G^{ex} + (1 - x_2)(\partial \Delta G^{ex}/\partial x_2)_{x_1/x_2}, \qquad (1)$$

where ΔG_2^{ex} is the partial molar excess Gibbs energy for the composition determined by the mole fractions x_1, x_2, and x_3 (or x_2, $x_1 : x_3$), and ΔG^{ex} is the integral molar excess Gibbs energy of the ternary system for the composition under consideration.

Another possibility of estimating the partial molar parameters of copper or any other component of the ternary system is to calculate them from the related quantities for binary boundary systems. This method is applied to liquid metallic systems rather rarely [4]. At the same time, it follows from the basic equation of the Toop method [3, 4], which is widely used for calculating the thermodynamic characteristics of ternary systems, that

$$\Delta G_2^{ex} = \left[\frac{x_1}{1 - x_2}\Delta G_{2(12)}^{ex} + \frac{x_3}{1 - x_2}\Delta G_{2(23)}^{ex}\right]_{x_2} - (1 - x_2)^2[\Delta G_{13}^{ex}]_{x_1/x_3}, \qquad (2)$$

where $\Delta G_{2(12)}^{ex}$ and $\Delta G_{2(23)}^{ex}$ are the excess partial molar Gibbs energies for component 2 in binary boundary systems 1–2 and 2–3 at a given x_2; and ΔG_{13}^{ex} is the excess integral molar Gibbs energy of the binary boundary system 1–3 at a given ratio $x_1 : x_3$.

The available data on the thermodynamic properties of liquid alloys in the binary boundary systems Ni–Cu, Cu–Fe, and Fe–Ni have been discussed in detail [1, 2]. The input data used in calculations for the system Ni–Cu were based on the results of [5–7], and the ΔG^{ex} and ΔH values recommended by Batalin [8, 9] were adopted for the systems Cu–Fe and Ni–Cu. The dependence of the integral thermodynamic functions on composition was expressed analytically with the use of Redlich–Kister polynomials [1, 2]. The table compares the activities of copper in liquid alloys of the ternary system Ni–Cu–Fe, calculated using Eqs. (1) and (2) for compositions that lie on secants of the concentration triangle with $x_{Ni} : x_{Fe}$ ratios of 3 : 1, 1 : 1, and 1 : 3. The agreement between the results obtained is quite satisfactory. If the only goal of a calculation of the thermodynamic properties of a ternary system from data on binary boundary systems is to obtain the partial molar parameters of a component of

Activity of copper in liquid nickel–copper–iron alloys at 1600°C, calculated using Eqs. (1) and (2)

x_{Cu}	$x_{Ni} : x_{Fe} = 3 : 1$		$x_{Ni} : x_{Fe} = 1 : 1$		$x_{Ni} : x_{Fe} = 1 : 3$	
	(1)	(2)	(1)	(2)	(1)	(2)
0.10	0.35	0.33	0.41	0.41	0.45	0.46
0.20	0.53	0.53	0.61	0.59	0.64	0.62
0.30	0.67	0.64	0.72	0.69	0.74	0.70
0.40	0.74	0.72	0.76	0.75	0.77	0.76
0.50	0.79	0.77	0.80	0.80	0.79	0.80
0.60	0.82	0.81	0.84	0.83	0.83	0.84
0.70	0.85	0.84	0.88	0.86	0.89	0.87
0.80	0.89	0.87	0.91	0.88	0.93	0.89
0.90	0.93	0.92	0.94	0.92	0.94	0.92

the ternary system, then calculation by Eq. (2) seems to be preferable, compared to that by Eq. (1). Figure 1 shows isoactivity lines for copper in Ni–Cu–Fe liquid alloys at 1600°C.

Equation (2) makes it possible to estimate, on the basis of data for binary boundary systems, the limiting activity coefficient for copper in Ni–Fe liquid alloys. At $x_2 = 0$ ($x_{Cu} = 0$), Eq. (2) takes the form

$$(\Delta G_2^{ex})^{\infty} = x_1[\Delta G_{2(12)}^{ex}]^{\infty} + x_3[\Delta G_{2(23)}^{ex}]^{\infty} - [\Delta G_{13}^{ex}]_{x_1/x_3}. \quad (3)$$

In turn, knowledge of the limiting excess Gibbs energy for component 2 enables calculation of the activity coefficient for this component at infinite dilution by considering liquid alloys 1–3 of various compositions as solvents:

$$(\Delta G_2^{ex})^{\infty} = RT\ln\gamma_{2(13)}^{\infty}. \quad (4)$$

The quantities $\Delta G_{2(12)}^{ex}$ and $\Delta G_{2(23)}^{ex}$, related to binary systems 1–2 and 2–3, can be calculated using the Redlich–Kister polynomial, which describes the concentration dependence of the integral excess Gibbs energy in these systems. For example, the following dependences were obtained for the Ni–Cu system (ΔG^{ex} is in kJ mol^{-1}, 1873 K):

$$\Delta G^{ex} = x_{Ni}(1 - x_{Ni})[18.8829 - 3.5732(2x_{Ni} - 1) - 0.3147(2x_{Ni} - 1)^2],$$

and for the Cu–Fe system

$$\Delta G^{ex} = x_{Cu}(1 - x_{Cu})[29.5990 + 0.2475(2x_{Cu} - 1) + 6.8151(2x_{Cu} - 1)^2].$$

As already reported [1], equations of this kind describe experimental data with high precision.

Now, a polynomial relation for the binary system 1–2 is considered in the general form:

$$\Delta G^{ex} = x_1(1 - x_1)[b_1 + c(2x_1 - 1) + d(2x_1 - 1)^2]. \quad (5)$$

For the binary system 1–2, Eq. (1) takes the form

$$\Delta G_1^{ex} = \Delta G^{ex} + (1 - x_1)(\partial\Delta G^{ex}/\partial x_1)_{P,T}, \quad (6)$$

$$\Delta G_2^{ex} = \Delta G^{ex} - x_1(\partial\Delta G^{ex}/\partial x_1)_{P,T}. \quad (7)$$

Differentiation of Eq. (5) and substitution of the appropriate values into Eqs. (6) and (7) yields

$$\Delta G_1^{ex} = (1 - x_1)^2[b + c(4x_1 - 1) + d(12x_1^2 - 8x_1 + 1)], \quad (8)$$

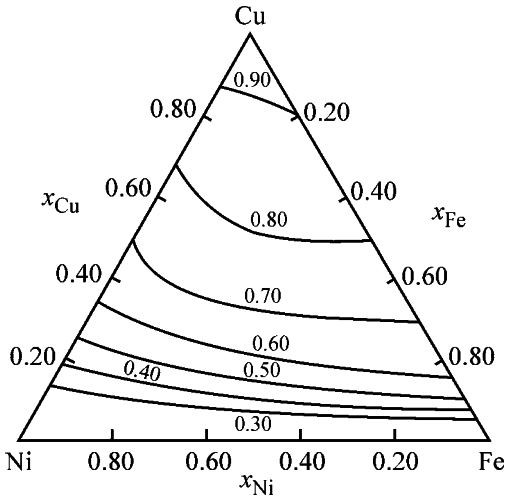

Fig. 1. Isoactivity lines for copper in liquid Ni–Cu–Fe alloys at 1873 K.

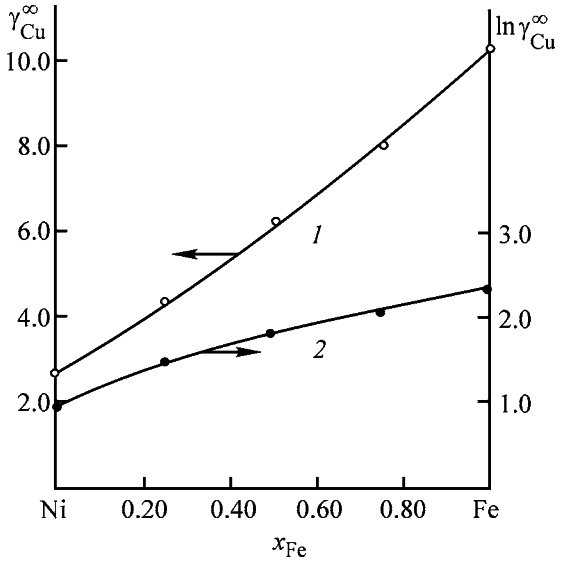

Fig. 2. (*1*) Limiting activity coefficient of copper, γ^{∞}_{Cu}, and (*2*) its logarithm vs. the composition x_{Fe} of the liquid Ni–Fe alloy at 1873 K.

$$\Delta G_2^{ex} = x_1^2[b + c(4x_1 - 3) + d(12x_1^2 - 16x_1 + 5)]. \quad (9)$$

At $x_1 \to 0$ or $x_1 \to 1$ ($x_2 \to 0$), accordingly,

$$(\Delta G_1^{ex})^{\infty} = b - c + d, \quad (10)$$

$$(\Delta G_2^{ex})^{\infty} = b + c + d. \quad (11)$$

In the boundary system Ni–Cu, copper is component 2 and Eqs. (9) and (11) are to be used for calculating ΔG^{ex}_{Cu} and $(\Delta G^{ex}_{Cu})^{\infty}$. At the same time, copper is component 1 in the boundary system Cu–Fe, and similar calculations require that Eqs. (8) and (10) should be used.

Thus,

$$[\Delta G^{ex}_{Cu(Ni)}]^{\infty} = 18.8829 - 3.5732 - 0.3147$$

$$= 14.995 \text{ kJ mol}^{-1},$$

$$\ln\gamma^{\infty}_{Cu(Ni)} = 0.963, \quad \gamma^{\infty}_{Cu(Ni)} = 2.619.$$

$$[\Delta G^{ex}_{Cu(Fe)}]^{\infty} = 29.5990 - 0.2475 + 6.8151$$

$$= 36.167 \text{ kJ mol}^{-1},$$

$$\ln\gamma^{\infty}_{Cu(Fe)} = 2.323, \quad \gamma^{\infty}_{Cu(Fe)} = 10.201.$$

The limiting values of the activity coefficients of copper in liquid alloys with nickel or iron are reasonably consistent with published experimental data [1].

For the iron–nickel system, the dependence of ΔG^{ex} on the alloy composition at 1873 K is described by the equation

$$\Delta G^{ex} = x_{Fe}(1 - x_{Fe})[-11.0909 + 6.1995(2x_{Fe} - 1)$$

$$- 0.9194(2x_{Fe} - 1)^2].$$

Data on ΔG^{ex} for the system Fe–Ni at $x_{Ni} : x_{Fe}$ of 3 : 1, 1 : 1, and 1 : 3 are required for substitution into Eq. (5). In other words, it is necessary to know ΔG^{ex} at $x_{Ni} = 0.75$, 0.50, and 0.25:

x_{Ni}	0.75	0.50	0.25
x_{Fe}	0.25	0.50	0.75
ΔG^{ex}_{Ni-Fe}, kJ mol^{-1}	–2.704	–2.770	–1.541

As a result, the following values of the limiting thermodynamic functions are obtained for copper in liquid Ni–Fe alloys of various compositions at a temperature of 1873 K:

x_{Ni}	0.75	0.50	0.25
$[\Delta G^{ex}_{Cu}]^{\infty}$, kJ mol^{-1}	22.992	28.351	32.414
$\ln\gamma^{\infty}_{Cu}$	1.476	1.821	2.082
γ^{∞}_{Cu}	4.378	6.176	8.016

Figure 2 shows that the dependence of $\ln\gamma^{\infty}_{Cu}$ and γ^{∞}_{Cu} on the composition of the liquid Ni–Fe alloys is very close to a linear dependence.

CONCLUSIONS

(1) Calculation of the activity of copper in liquid nickel–copper–iron alloys at 1600°C by two different methods yields consistent results.

(2) Estimates of the limiting values of the activity coefficients of copper in liquid Cu–Ni, Cu–Fe, and Cu–(Ni–Fe) alloys are presented. The dependence of γ^{∞}_{Cu} on the composition of the Ni–Fe alloy is nearly linear.

REFERENCES

1. Morachevskii, A.G., Fedorova, N.A., Tsymbulov, L.B., and Tsemekhman L.Sh., *Zh. Prikl. Khim.*, 2002, vol. 75, no. 11, pp. 1881–1885.
2. Morachevskii, A.G., Ryabko, A.G., and Tsemekhman, L.Sh., *Termodinamika zhidkikh splavov sistemy nikel'–med'–zhelezo* (Thermodynamics of Liquid Alloys in the System Nickel–Copper–Iron), St. Petersburg: Sankt-Peterb. Gos. Univ., 2002.

3. Morachevskii, A.G., Voronin, G.F., Geiderikh, V.A., and Kutsenok, I.B., *Elektrokhimicheskie metody issledovaniya v termodinamike metallicheskikh sistem* (Electrochemical Methods of Investigation in Thermodynamics of Metallic Systems), Moscow: Akademkniga, 2003.
4. Jakob, K.T. and Fitzner, K., *Thermochim. Acta*, 1977, vol. 18, pp. 197–206.
5. Berezutskii, V.V. and Lukashenko, G.M., *Ukr. Khim. Zh.*, 1987, vol. 53, no. 10, pp. 1029–1032.
6. Turchanin, M.A., Porokhnya, S.V., Belevtsov, L.V., and Kokhan, A.V., *Rasplavy*, 1994, no. 4, pp. 8–12.
7. Kulkarni, A.D. and Johnson, R.E., *Met. Trans*., 1973, vol. 4, pp. 1723–1727.
8. Batalin, G.I. and Sudavtsova, V.S., *Metally*, 1980, no. 2, pp. 45–49.
9. Batalin, G.I., *Termodinamika zhidkikh splavov na osnove zheleza* (Thermodynamics of Iron-Based Liquid Alloys), Kiev: Vyshcha Shkola, 1982.

Russian Journal of Applied Chemistry, Vol. 77, No. 9, 2004, pp. 1430–1433. Translated from Zhurnal Prikladnoi Khimii, Vol. 77, No. 9, 2004, pp. 1442–1445.

SORPTION AND ION-EXCHANGE PROCESSES

Synthesis of Magnesium Oxide with High Adsorptive Properties

N. N. Treushchenko, B. A. Dmitrevskii, D. R. Mishina, A. Yu. Popov, B. Ya. Galkin, and V. A. Treushchenko

Khlopin Radium Institute, St. Petersburg, Russia
St. Petersburg State Technological Institute, St. Petersburg, Russia

Received July 23, 2004

Abstract—The synthesis of magnesium oxide with high adsorptive properties by the sulfate–ammonia and sulfate–carbonate methods and the effect exerted by the conditions of synthesis of magnesium oxide and hydroxide on their adsorptive activity were studied. The thermograms of the synthesized samples are presented. The activity of the samples, evaluated by the iodine number, was determined in relation to the synthesis conditions.

Chemically synthesized magnesium oxide and hydroxide have large specific surface area and high mechanical strength, and therefore they have high catalytic activity and good adsorptive properties [1]. Magnesium hydroxide has high adsorption capacity with respect to the majority of Group III–VIII elements [2]. Also, magnesium compounds form cements of the type of hydroxy salts, crystallizing in mixing of magnesium oxide with various water-soluble magnesium salts [3, 4]. This study was aimed to develop an adsorbent of radioactive iodine for its utilization and disposal.

The sorption capacity of magnesia depends on the specific surface area and is characterized in industry by the iodine number N, i.e., by the amount of absorbed iodine (mg-equiv) per 100 g of MgO. The ability of magnesium compounds to take up iodine and form cements with various anions suggests the possibility of synthesis of magnesium hydroxide and oxide with high adsorptive properties and subsequent preparation of stone-like structures suitable for utilization and disposal of radioactive iodine.

The surface and adsorptive properties of synthetic magnesia strongly depend on both the kind of the starting compounds and the synthesis method [5].

The effect exerted by synthesis conditions on the chemical composition and surface properties of magnesium hydroxide and oxide has been determined previously by the example of the magnesia synthesis from pure solutions of analytically pure grade $MgSO_4$, which involved precipitation of $Mg(OH)_2$ with ammonia [6]. It was shown that the synthesis conditions, including temperature T, concentration of the initial solution c_{init}, amount of alkaline reagent, and process time τ, essentially affect the specific surface area S_{sp} of magnesium hydroxide and oxide.

In this study, we studied the properties and performed the qualitative analysis of magnesia obtained from natural caustic magnesite. The raw material was caustic magnesite from the Sadkinskoe deposit (Chelyabinsk oblast) containing (wt %) MgO 86, CaO 4.06, Fe_2O_3 1.46, CO_2 1.3, Al_2O_3 0.8, and the insoluble residue 0.8. Magnesia was prepared by the sulfate–ammonia and sulfate–carbonate processes. The bound magnesium was transferred into the solution using H_2SO_4 and $(NH_4)_2SO_4$ solutions.

The sulfate–ammonia process for production of magnesia from caustic magnesite involves treatment of the raw material with 10–15 wt % solutions of $(NH_4)_2SO_4$ (amount 100–110% of the stoichiometry), yielding $MgSO_4$ solutions and gaseous ammonia. After the precipitate is separated, the $MgSO_4$ solution is treated with ammonia to precipitate $Mg(OH)_2$, from which magnesium oxide is obtained by calcination. The process involves the reactions

$$MgO\downarrow + (NH_4)_2SO_4 = MgSO_4 + 2NH_3 + H_2O,$$

$$MgSO_4 + 2NH_3 + 2H_2O = Mg(OH)_2\downarrow + (NH_4)_2SO_4,$$

$$Mg(OH)_2 = MgO + H_2O.$$

The process time is 2 h; temperature interval, 80–100°C; and the concentration of the resulting $MgSO_4$ solution, 12–15 wt %. The $MgSO_4$ solutions contain the following impurities (wt %): CaO 0.12, SiO_2

0.01–0.02, and Al_2O_3 0.002. Solutions of such composition do not require additional purification. The solid phase consisting of undecomposed magnesite and impurities was filtered on a vacuum filter.

Magnesium hydroxide $Mg(OH)_2$ was precipitated from the $MgSO_4$ solution at 20–80°C for 2–10 min. The precipitate was filtered off, dried, and calcined at 250–900°C.

The chemical composition of the magnesium hydroxide precipitate prepared at different temperatures is given in the table.

Composition of the magnesium hydroxide precipitate

T, °C	Content in precipitate, wt %	
	$Mg(OH)_2$	$MgSO_4 \cdot 3Mg(OH)_2 \cdot 8H_2O$
20	66.6	33.4
30	70.4	29.6
40	81.4	18.6
60	82.5	17.5
80	92.4	7.6

The table shows that, along with magnesium hydroxide, $MgSO_4 \cdot 3Mg(OH)_2 \cdot 8H_2O$ is present in the precipitates at lower synthesis temperatures; the lower the temperature, the higher its mass fraction. The compound $MgSO_4 \cdot 3Mg(OH)_2 \cdot 8H_2O$ exhibits binding properties, and its presence in the cements will improve the quality of stone-like structures.

The sulfate–carbonate synthesis of magnesia included dissolution of caustic magnesite in sulfuric acid at pH 3–3.5 to prepare a magnesium sulfate solution, into which caustic magnesite was added to remove impurity calcium compounds and sesquioxides. The precipitate was separated on a vacuum filter, the resulting magnesium sulfate solution was neutralized with a solution of potassium carbonate, and magnesium subcarbonate was precipitated. To obtain magnesia, magnesium subcarbonate was calcined at 250–900°C. The process involves the reactions

$$MgO + H_2SO_4 = MgSO_4 + H_2O,$$

$$3MgSO_4 + 3K_2CO_3 + 5H_2O = 2MgCO_3 \cdot Mg(OH)_2 \cdot 4H_2O + 3K_2SO_4 + CO_2\uparrow,$$

$$2MgCO_3 \cdot Mg(OH)_2 \cdot 4H_2O = 3MgO + 2CO_2 + 5H_2O.$$

Magnesium subcarbonate synthesized by the above technology contains (wt %) MgO 40, CO_2 29, H_2O 24, and CaO 0.26.

The chemical analysis of the synthesis products was done by the methods presented in [7]. The surface properties of magnesium hydroxide and oxide were characterized by the iodine number *N*. The iodine number was determined according to [8].

The dependences of the iodine numbers of magnesium hydroxide on the temperature of its synthesis and of magnesium oxide on the calcination temperature are shown in Fig. 1 for the samples synthesized by the sulfate–ammonia method. The magnesium hydroxide samples were obtained by drying in air of wet hydroxide obtained at different temperatures of the synthesis.

The dependence of *N* on the synthesis temperature for the samples dried at 20°C shows that the lower the synthesis temperature, the higher the iodine number *N* of magnesium hydroxide (curve *3*). The sample synthesized at 20°C and dried in air has the highest adsorption activity (*N* = 155). With increasing synthesis temperature, *N* decreases to 124 at 40°C and to 70 at 80°C.

The adsorption activity of magnesium oxide samples depends on the calcination temperature. Among magnesium hydroxide samples calcined in the range 450–700°C, the samples calcined at 450°C have the highest *N* value; for example, the sample synthesized at 20°C (Fig. 1, curve *1*) has *N* = 340. With increasing synthesis temperature, *N* decreases markedly, to 275 at 40 and to 230 at 80°C. Increasing the calcination temperature to 500°C decreases *N* by a factor of 1.3 (curve *2*). Under these conditions, *N* of magnesium oxide is, however, larger than that of hydroxide

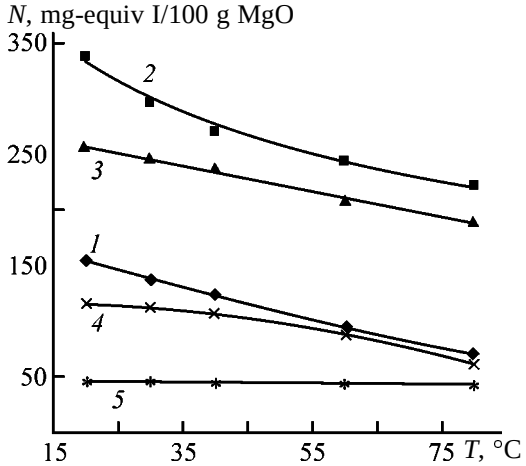

Fig. 1. Iodine number *N* vs. the synthesis temperature *T* of magnesium hydroxide. Temperature of calcination of magnesium oxide (°C): (*1*) 450, (*2*) 500, (*4*) 600, and (*5*) 700. Temperature of drying of magnesium hydroxide (°C): (*3*) 20.

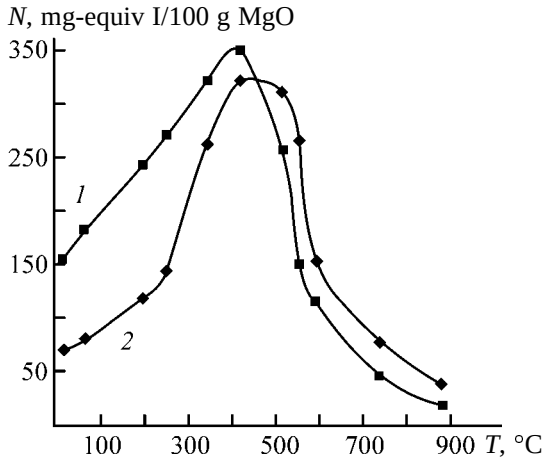

Fig. 2. Iodine number *N* vs. the calcination temperature *T* of magnesium hydroxide and magnesium subcarbonate. Sample: (*1*) no. 1 and (*2*) no. 2.

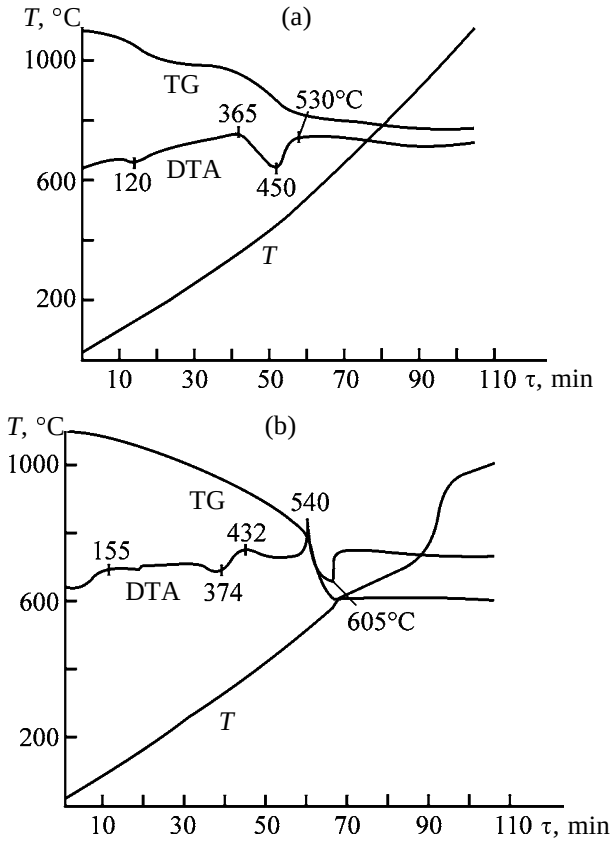

Fig. 3. DTA and TG curves of (a) magnesium hydroxide and (b) magnesium subcarbonate. (*T*) Temperature and (τ) time.

(curve *3*). As the calcination temperature is increased further to 600 and 700°C, *N* decreases drastically, irrespective of the temperature of the magnesium hydroxide synthesis.

Examination of the microstructure of the precipitates obtained under the different conditions shows that small particles with a more developed surface are formed at lower synthesis temperatures and coarser particles with a less developed surface, at higher temperatures. This accounts for the dependences characterizing the effect of temperature on the hydroxide surface properties.

The magnesium oxide samples synthesized by the sulfate–ammonia (sample no. 1) and sulfate–carbonate (sample no. 2) methods have different surface characteristics. The *N* value of the starting samples is 155 for sample no. 1 and 70 for sample no. 2. The dependence of the iodine number on the calcination temperature has a maximum (Fig. 2). At a calcination temperature of 450°C, the *N* value of the samples synthesized by the ammonia and carbonate methods is maximal (340 and 320, respectively). At lower calcination temperatures, the *N* values differ considerably: e.g., at 350°C *N* is 322 (sample no. 1) and 262 (sample no. 2).

As the calcination temperature is increased to 500–530°C, *N* remains fairly high, 250–260, for both the samples. At higher temperatures *N* drastically decreases, and at 700–900°C its value for the sample synthesized from magnesium hydroxide is lower than in that for the sample obtained using potassium carbonate.

Such a trend in variation of the surface properties of the calcined samples with temperature is due to the fact that, in the course of the calcination of sample no. 1 to 450°C, water of hydration is removed with formation of pores, with the magnesium hydroxide skeleton preserved. At higher temperatures, the structural rearrangement, agglomeration, and sintering take place.

For sample no. 2, the removal of water of hydration, which is complete at 450°C, is accompanied by decarbonation, with most of carbon dioxide being also removed in the range 400–500°C. Variation of the carbon content in the calcined magnesium subcarbonate (sample no. 2) confirms this result.

T, °C	CO_2, vol %
20	30.5
300	28.9
350	28.2
400	7.5
450	1.1

Heating to higher temperatures results in the agglomeration and sintering. This is also confirmed by the thermogravimetric analysis of the samples.

The thermogravimetric analysis of sample no. 1 (Fig. 3a) shows that, at 120–130°C, hygroscopic

moisture and a part of water of hydration are removed, which is associated with the presence in magnesium hydroxide of the impurity salt $MgSO_4 \cdot 3Mg(OH)_2 \cdot 8H_2O$. The removal of hygroscopic and hydration water from the above salt is confirmed by a diffuse endothermic effect at 130°C. Water of hydration is removed stepwise through hydrates of magnesium oxosulfate. The weight loss in the process is 12.8%. The dehydration of magnesium hydroxide is complete at 450°C, with the weight loss of 22.2%.

The thermogravimetric analysis of sample no. 2 (Fig. 3b) shows that its water of hydration is removed at 315°C, giving rise to an endothermic effect. The weight loss is 19.3%. The endothermic effect at 432°C corresponds to the magnesium carbonate dissociation. The weight loss is 8.3%. Magnesium hydroxide is dehydrated within 400–420°C. The decarbonation is complete at 580°C, with the weight loss of 31.7%.

The methods proposed make it possible to synthesize magnesium oxide surpassing in the surface properties the samples produced by the leading world companies.[1]

CONCLUSION

Highly active magnesia can be synthesized from natural material using sulfate reagents for the dissolution and ammonia and potassium carbonate for the precipitation of magnesium compounds.

REFERENCES

1. Neimark, I.E., *Sinteticheskie mineral'nye adsorbenty i nositeli katalizatorov* (Synthetic Mineral Adsorbents and Catalyst Supports), Kiev: Naukova Dumka, 1982.
2. Ruzankin, V.I., Sorption Processes in Magnesium and Iron Hydroxides, *Cand. Sci. Dissertation*, Dushanbe, 1978.
3. *Obshchaya tekhnologiya silikatov* (General Silicate Technology), Pashchenko, A.A., Ed., Kiev: Vishcha Shkola, 1983.
4. Vyrodov, I.P., Some Principles of the Hydration Theory of Mineral Binders, *Doctoral Dissertation*, Krasnodar, 1968.
5. Dzis'ko, V.A., *Ratsional'nye osnovy prigotovleniya nekotorykh oksidnykh katalizatorov. Doklad po opublikovannym rabotam* (Reasonable Principles of Preparation of Some Oxide Catalysts: A Report Based on the Published Papers), Novosibirsk: Inst. Katal., Sib. Otd., Akad Nauk SSSR, 1965.
6. Treushchenko, N.N., Dmitrevskii, B.A., Kebryakova, N.V., *et al.*, *Zh. Prikl. Khim.*, 1994, vol. 67, no. 4, pp. 550–553.
7. *Rukovodstvo po analizu i proizvodstvu fosfora, fosfornoi kisloty i fosfornykh udobrenii* (Manual on Production of Phosphorus, Phosphoric Acid, and Phosphorus Fertilizers), Moizhes, E.B., Ed., Leningrad: Khimiya, 1973.
8. *GOST* (State Standard) *844–79*.

[1] The iodine numbers of magnesium oxide produced by different companies are as follows: Dead Sea (Israel), 130–150; Lobel (the United States), 75; Perekop Bromine Plant, 70; Mikhailovsk Plant of Chemical Reagents, 60; the iodine number in our samples is higher by a factor of 1.5–4.

Russian Journal of Applied Chemistry, Vol. 77, No. 9, 2004, pp. 1434–1439. Translated from Zhurnal Prikladnoi Khimii, Vol. 77, No. 9, 2004, pp. 1446–1451.

SORPTION AND ION-EXCHANGE PROCESSES

Thermodynamic Parameters Characterizing Adsorption of Organic Compounds from Aqueous Solutions on Iron Oxide α-Fe_2O_3

B. N. Afanas'ev, E. A. Aleksandrova, and Yu. P. Akulova

St. Petersburg State Technological Institute, St. Petersburg, Russia

Received October 22, 2003

Abstract—Adsorption of a series of organic compounds on the surface of α-Fe_2O_3 is studied. The experimental data are analyzed using the Frumkin and Langmuir isotherms. The standard Gibbs energies of adsorption ΔG_A^0 and ΔG_{ads}^0 corresponding to different standard states are estimated.

Adsorption of organic compounds from aqueous solutions on iron and its oxides should be taken into account in studying inhibition of ferrous metal corrosion, flotation of ores, and electroplating [1, 2]. To control these processes, it is necessary to find parameters uniquely characterizing the binding of an organic molecule to the metal or oxide surface. In the works on adsorption of surfactants on metals or oxides, the common method is to obtain an adsorption isotherm describing the dependence of the coverage of the surface with adsorbed molecules (θ) on their molar concentration in the bulk of the solution c_{org} [1–3].

From the experimental adsorption isotherm

$$f(\theta) = Bc_{org}, \quad (1)$$

the constant B is determined, and then the standard Gibbs energy of adsorption ΔG_A^0, corresponding to asymmetric standard state, is calculated by well-known Eq. (2) [2, 3]:

$$\Delta G_A^0 = -RT\ln(55.5B). \quad (2)$$

In this case, the activity coefficient of the organic compound in the bulk of the solution $f_{org} \to 1$ if $c_{org} \to 0$.

In practice, the Langmuir isotherm [$f(\theta) = \theta/(1 - \theta)$] or the Frumkin isotherm is commonly used. In the latter case,

$$f(\theta) = [\theta/(1 - \theta)]\exp(-2a\theta).$$

If the adsorption isotherm is written in the form of Eq. (3),

$$f(\theta) = Ba_{org} = \exp(\Delta G_{ads}^0/RT)x_{org}\gamma_{org}, \quad (3)$$

where x_{org} and γ_{org} are the mole fraction and activity coefficient of the organic compound in the bulk of the surfactant-containing aqueous solution, the standard Gibbs energy of adsorption ΔG_{ads}^0 corresponds to the symmetrical standard state in the bulk of the solution [4]. In this case, the pure substance is taken to be the standard state, for which the condition $a_{org} = x_{org} = 1$ is valid.

From Eqs. (1) and (3), taking into account Eq. (2), we obtain the standard Gibbs energy of adsorption expressed via the activity coefficient of the organic compound at infinite dilution [4]:

$$\Delta G_A^0 = \Delta G_{ads}^0 - RT\ln\gamma_{org}^{\infty}. \quad (4)$$

In this case, the surfactant activity coefficient γ_{org}^{∞} corresponding to the symmetrical standard state at infinite dilution ($x_{org} \to 0$) includes all kinds of interactions occurring in the solution between the surfactant molecule and water. Depending on the nature of the organic molecule, the γ_{org}^{∞} value can range from 1 to 10^3–10^4 [5]. It follows from Eqs. (1), (2), and (4) that ΔG_A^0 depends on both the metal–surfactant binding energy and the properties of the aqueous surfactant solution. Therefore, the ΔG_A^0 value does not provide an unambiguous information on the surfactant–metal or surfactant–oxide binding energy, and this parameter cannot be used for characterization of the interaction between the surfactant molecule and the surface of a solid, as was made in [6, 7].

At the same time, it follows from Eq. (4) that the Gibbs energy ΔG_{ads}^0 characterizes the binding of an organic molecule to the metal or oxide surface, since

1070-4272/04/7709-1434 © 2004 MAIK "Nauka/Interperiodica"

Table 1. Physicochemical and adsorption properties of surfactants

Surfactant	I, eV	λ, nm	c_{org}^{sat}, M	$RT\ln\gamma_{org}^{\infty}$	$-\Delta G_A^0$	$-\Delta G_{ads}^0$	ν
				kJ mol^{-1}			
β-Naphthylamine	7.25	229 274 334	1.74×10^{-3}	25.2	24.5 ± 0.9 (26.3 ± 0.4)*	0.7 –0.8	2.5 ± 0.6
Aniline	7.7	230 280	3.52×10^{-1}	12.3	17 ± 0.5	–4.7	2.7 ± 0.2
β-Naphthol	7.8	226 270 323	4.3×10^{-3}	23.0	23.7 ± 0.4	–0.7	2.2 ± 0.1
Naphthalene	8.1	218 270 310	2×10^{-4}	30.7	28.1 ± 0.8	2.6	2.4 ± 0.3
Benzoic acid	9.6	230 280	2.2×10^{-2}	19.1	19.4 ± 0.5	–0.3	2.5 ± 0.2
Phthalic anhydride	10.1	205 280	3.5×10^{-2}	17.9	20.4 ± 0.6	–2.5	4.0 ± 0.1

* Estimated by Eqs. (8) and (2).

the bulk properties of the solution are taken into account through the parameter $RT\ln\gamma_{org}^{\infty}$ [4].

The goal of this work is experimental study of adsorption of a series of surfactants from aqueous solutions on the surface of α-Fe_2O_3 and estimation of ΔG_{ads}^0 using Eq. (4), to characterize the surfactant–oxide surface binding.

EXPERIMENTAL

As a subject matter we selected surfactants strongly different in their chemical and physicochemical properties. The difference between the first ionization energies of the organic molecules I, which, to a first approximation, reflect the energy of the highest occupied molecular orbitals, is about 3 eV (1 eV = 96.485 kJ mol^{-1}) (Table 1).

Organic compounds (analytically or chemically pure grade) were purified as follows. β-Naphthylamine was recrystallized from hot distilled water to obtain pearl white-pink flakes; β-naphthol, from hot distilled 90% ethanol, as white crystals; naphthalene, from hot distilled 90% ethanol, as white flakes; benzoic acid, from hot distilled water, as white crystals. Phthalic anhydride was purified by sublimation, to obtain white needles; and aniline, by distillation, to obtain a transparent liquid. The adsorbent was prepared as follows. Iron(III) oxide (analytically pure grade) was fired at 650°C for 3 h, furnace-cooled to 150–200°C, transferred into an desiccator with dry silica gel, and cooled to room temperature. This procedure provided removal of water and CO_2 molecules from the oxide surface, dehydration of iron(III) hydrous oxide occurring at 300–420°C, and finally, its conversion into reddish-brown α-Fe_2O_3 (hematite). All the aqueous solutions were prepared with double-distilled water. Initially, nearly saturated stock surfactant solutions were prepared (Table 1), which then were diluted to the desired concentrations. The oxide was contacted with a surfactant solution with intermittent stirring for 2 h at 19±1°C and then separated by centrifugation. The surfactant concentration in the solution after centrifugation was determined by the optical density D measured on an SF 2000 spectrophotometer in a 1-cm cell. This instrument provides reliable measurements over the optical density range from 0.3 to 1.0, so that the solutions should be diluted to obtain distinct UV spectra. The amount of the adsorbed surfactant Γ_{org} (mol m^{-2}) was estimated by Eq. (5).

$$\Gamma_{org} = \frac{(c_{org}^0 - c_{org})V}{A}, \qquad (5)$$

where A is the effective surface area (m^2) of the oxide sample (g); V, volume of the solution (l); and c_{org}^0 and c_{org} are the surfactant concentrations (M) in the solution before and after adsorption.

Table 2. Parameters of surfactant adsorption on α-Fe_2O_3

Surfactant	Frumkin isotherm					Langmuir isotherm			
	$\Gamma_{max} \times 10^6$, mol m^{-2}	$2a$	B, l mol^{-1}	Δ	K_r	$\Gamma_{max} \times 10^6$, mol m^{-2}	B, l mol^{-1}	Δ	K_r
β-Naphthylamine	5.2 ± 1.4	–2.4 ± 0.1	460 ± 160	1.93×10^{-9}	0.989	2.5 ± 0.2 2.35*	840 ± 100 950 ± 100*	2.1×10^{-9}	0.986 0.986
Aniline	4.4 ± 0.2	0.80 ± 0.13	18 ± 2	6×10^{-5}	0.95	5.0 ± 0.3 5.3*	22 ± 3 19 ± 3*	6×10^{-5}	0.948 0.944
β-Naphthol	5.5 ± 0.3	0.6 ± 0.1	330 ± 30	2.6×10^{-8}	0.978	6.8 ± 0.5 7.0*	300 ± 38 300 ± 72*	2.6×10^{-8}	0.979 0.951
Naphthalene	5.0 ± 0.7	0.95 ± 0.05	1680 ± 320	5.8×10^{-11}	0.982	5.0 ± 1.0 5.9*	2110 ± 550 1667 ± 810*	9.7×10^{-11}	0.969 0.891
Benzoic acid	4.8 ± 0.3	1.45 ± 0.1	50 ± 7	2×10^{-6}	0.928	7.3 ± 0.2 8.1*	49 ± 15 42 ± 16*	2.1×10^{-6}	0.923 0.857
Phthalic anhydride	3.0 ± 0.1	0.5 ± 0.2	81 ± 12	7.7×10^{-6}	0.929	3.1 ± 0.2 2.9*	100 ± 16 122 ± 23*	7.4×10^{-6}	0.928 0.890

* Parameters B and Γ_{max} were estimated by Eq. (8).

The concentrations of the surfactants in solutions were determined using the calibrating curves D–c_{org} at the corresponding wavelengths λ (Table 1). The optical density at these wavelengths was demonstrated to be proportional to the surfactant concentration.

The BET surface area of the α-Fe_2O_3 powder, determined by the low-temperature adsorption of nitrogen, was from 6.1 to 11.7 m^2 g^{-1}, depending on the sample, which is well consistent with the reference data for zirconium [8] and zinc [9] oxides.

For a given surfactant, adsorption was studied with the same oxide sample. The sample weight was 1 or 2 g. The surface area of the oxide powder was greater by a factor of at least 10^3 than the surface area of the cell and that of the air/solution interface. Therefore, the interfacial adsorption could be neglected.

For poorly soluble surfactants, the activity coefficient γ^0_{org} can be estimated by Eq. (6) [5].

$$RT \ln \gamma^{\infty}_{org} \cong -RT \ln x^{sat}_{org}, \quad (6)$$

where x^{sat}_{org} is the surfactant concentration in the saturated aqueous solution (mole fraction).

The solubilities of the organic compounds in water were taken from [10–12]. Since we found no published data for β-naphthylamine, its solubility was determined experimentally. A saturated solution of β-naphthylamine was prepared in distilled water saturated with Ar at 19°C with continuous stirring for 3 days in the dark. The solubility was estimated at 1.45×10^{-3} from the optical density by extrapolation of the calibrating curve.

The $RT \ln \gamma^0_{org}$ values estimated by Eq. (6) are given in Table 2.

The experimental Γ and c_{org} isotherms were analyzed by the Frumkin isotherm equation reduced to the form of Eq. (7), using the Origin program pack.

$$y = \left[\frac{x}{P_3(P_1 - x)}\right] \exp(-P_2 x), \quad (7)$$

where $y \equiv c^0_{org}$, $x \equiv \Gamma$ (mol m^{-2}), $P_1 \equiv \Gamma_{max}$, $P_2 \equiv 2a/\Gamma_{max}$ (a is the attraction constant in the Frumkin isotherm equation), and $P_3 \equiv B$. In so doing, we found the empirical coefficients P_1, P_2, and P_3, the variance Δ of c_{org}, correlation factor r, and standard deviations for P_1, P_2, and P_3.

Note that Eq. (7) includes dimensionless parameters $\Gamma/(\Gamma_{max} - \Gamma)$ and $2a(\Gamma/\Gamma_{max})$. Therefore, the true value of B was determined regardless of how reliable is the parameter A in Eq. (5). At $2a = 0$, the Frumkin isotherm is reduced to the Langmuir isotherm. To obtain reasonably reliable parameters of Eq. (7), the number of experimental Γ values estimated by Eq. (5) should be at least 15–20 (see figure).

Table 2 summarizes data on the parameters Γ_{max}, $2a$, and B, and also on the variance Δ for Eq. (7) and correlation factor r.

The Langmuir isotherm can be written as

$$\frac{1}{c_{org}} = B\frac{\Gamma_{max}}{\Gamma} - B. \quad (8)$$

Representation of the experimental data in the coordinates $1/c_{org}$–$1/\Gamma$ makes it easy to determine the parameters B and Γ_{max}. Table 2 shows these parameters estimated by Eq. (7) at $2a = 0$ using the Origin program pack, and also by Eq. (8). The results obtained by these two methods are well consistent. Changing the Frumkin isotherm for the Langmuir isotherm results in increasing Γ_{max} at $2a > 0.5$ or in decreasing Γ_{max} at considerably negative $2a$ values. It follows from Eq. (4) that ΔG^0_{ads} depends on the Gibbs energy ΔG^0_A, and the latter, in turn, on the equation of the adsorption isotherm. It also follows from Table 2 that, if $0 < 2a < 1.5$, changing one isotherm for another has practically no effect on B. Therefore, in this case, within the errors indicated in Table 1, the Gibbs energy ΔG^0_A estimated by Eq. (2) does not depend on the equation of the adsorption isotherm used for analysis of the experimental c_{org}–Γ curves.

Nikolenko *et al*. [8] studied adsorption of a series of surfactants on the surface of ZrO_2 in 0.1 M KCl. Addition of a strong electrolyte to water results in salting-out of the surfactant from the aqueous solution (Sechenov effect):

$$(\Delta G^0_A)_{sol} = \Delta G^0_A + \Delta G^0_{sol}, \quad (9)$$

where $(\Delta G^0_A)_{sol}$ is the Gibbs energy of adsorption of the surfactant in the aqueous electrolyte solution and ΔG^0_{sol}, difference of the Gibbs energy of adsorption caused by salting-out of the surfactant.

In 0.1 M KCl, $\Delta G^0_{sol} \approx -1$ kJ mol^{-1} [13]. The $(\Delta G^0_A)_{sol}$ values for benzoic acid and aniline are –23.3 and –17.6 kJ mol^{-1}, respectively [8]. Therefore, the ΔG^0_A values characterizing adsorption of these surfactants on ZrO_2 are –22.3 and –16.6 kJ mol^{-1}, respectively, which is consistent with the ΔG^0_A values from Table 1.

Table 1 also includes the standard Gibbs energy of adsorption ΔG^0_{ads} corresponding to the symmetrical standard state, estimated by Eq. (4). The values of this energy are small for all the surfactants studied except aniline. Table 1 shows that aniline is rather readily soluble in water, and, therefore, estimation of γ^∞_{org} by Eq. (6) can provide an error of 2 to 3 kJ mol^{-1} in determination of the parameter $RT\ln\gamma^\infty_{org}$. Since the error of determination of the surfactant solubilities is unknown, one cannot estimate the error of determination of ΔG^0_{ads}.

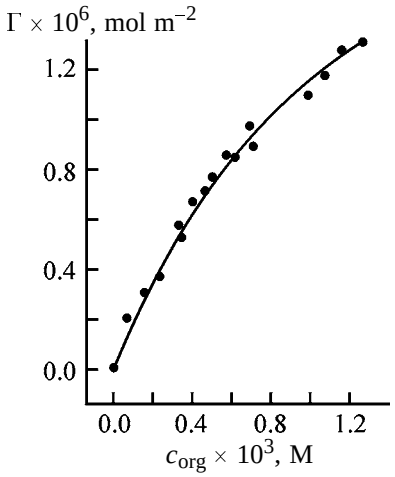

c_{org} vs. Γ plot for β-naphthylamine adsorbed on α-Fe_2O_3, estimated by Eq. (7) using the Origin program pack with the parameters given in Table 2. (Γ) Amount of adsorbed surfactant and (c_{org}) surfactant concentration in the solution.

Previously we demonstrated [4] that there is a distinct correlation between ΔG^0_{ads} and the first ionization potentials of the surfactant molecules adsorbed on bismuth. Table 1 shows, firstly, that such a correlation is lacking and, secondly, that $|\Delta G^0_{ads}| \ll |\Delta G^0_A|$. Except for aniline, one may accept ΔG^0_{ads} = const. Then, the arithmetic mean $\overline{\Delta G^0_{ads}} \approx 0$.

It follows from Eq. (4) that the observed high negative ΔG^0_A values and, correspondingly, high adsorbability of the surfactants on iron(III) oxide are controlled by the surfactant activity coefficients in the bulk of the solution. In other words, the adsorbability of the surfactants on α-Fe_2O_3 is controlled not by the interaction of the surfactant with the oxide surface, but by the bulk characteristics of the aqueous surfactant solution. Dissolution of the organic surfactant is accompanied by distortion of the structure of water, and the solvent tends to throw out the organic molecules to the interface layer.

In this context, it becomes clear why the adsorbability of carboxylic acids on ZrO_2 decreased with increasing pH [8]. At pH >7.5, readily soluble carboxylates are formed. Decreasing γ^∞_{org} results in increase in ΔG^0_A and, correspondingly, in decrease in the adsorption constants B and θ.

Table 2 shows that, in most cases, the Frumkin isotherm better fits the experimental Γ–c_{org} curves than does the Langmuir isotherm (Δ is lower, and r is

somewhat higher). It is seen also that, for all the surfactants except phthalic anhydride, Γ_{max} corresponds to the vertical orientation of the organic molecules on the surface. This is clear from the physical standpoint, since the solvent tends to push out as many surfactant molecules as possible to the interface layer.

Adsorption of a surfactant from a solution on the surface of a solid is always accompanied by replacement of water molecules from the surface to the bulk of the solution. It was demonstrated in [3, 4] that, in this case, the expression for ΔG^0_{ads} can be written as

$$\Delta G^0_{ads} = \Delta G^0_{org} - \nu \Delta G^0_{H_2O}, \quad (10)$$

where ΔG^0_{org} and $\Delta G^0_{H_2O}$ are the standard Gibbs energies characterizing the work of transfer of a mole of the pure substance (surfactant or water) from the bulk to the surface and ν is the number of moles of water replaced from the surface layer formed at the interface in adsorption of 1 mol of the surfactant.

Parameter ν is estimated by Eq. (11) [14]:

$$\nu = \Gamma_{max, H_2O}/\Gamma_{max}, \quad (11)$$

where Γ_{max, H_2O} is the maximal coverage of the surface with water (mol m^{-2}).

It is commonly accepted that $\Gamma_{max, H_2O} = 12 \times 10^{-6}$ mol m^{-2} [14]. The ν values estimated by Eq. (11) are given in Table 1.

The numerical values of parameters ΔG^0_{org} and $\Delta G^0_{H_2O}$ are resultants of the work that should be done for partial break of the bonds between the molecules and for their transfer to the surface, and the work spontaneously expended for the formation of a new bond between the adsorbed molecules and the oxide surface.

The work associated with the transfer of ν moles of water from the bulk to the surface is written as [4]

$$W = \nu \sigma_{H_2O} A_{H_2O}, \quad (12)$$

where σ_{H_2O} is the surface tension of water ($\sigma_{H_2O} = 71.96 \times 10^{-3}$ J m^{-2} [15]); A_{H_2O}, area occupied by 1 mol of water on the surface ($A_{H_2O} = 8.3 \times 10^4$ m^2 mol^{-1}). At $\nu = 2.5$ (Table 1), $W = 15$ kJ mol^{-1}. This value is well comparable with the dispersion interaction energy [16].

The result that $\Delta G^0_{ads} \approx 0$ is probably due to the fact that the water and surfactant molecules are bound to the oxide surface by the dispersion forces. In this case, ΔG^0_{org} and $\nu \Delta G^0_{H_2O}$ are small as a result of the compensating effects of different factors.

For the case of $\Delta G^0_{ads} \approx 0$, ΔG^0_A, B, and, correspondingly, θ can be estimated theoretically by Eqs. (1), (2), and (4) without performing laborious measurements on the adsorption of the surfactants.

CONCLUSIONS

(1) The adsorbability of organic surfactants from aqueous solutions on the surface of α-Fe_2O_3 is controlled not by the specific interaction of organic molecules with the oxide surface, as commonly believed, but by the surfactant activity coefficients γ^∞_{org} in the bulk of the solution.

(2) The γ^∞_{org} values depend only on the properties of the binary solution, and knowing γ^∞_{org} allows estimation of the adsorbability of surfactant on α-Fe_2O_3.

ACKNOWLEDGMENTS

The work was supported by the Ministry of Education of the Russian Federation (project E02-5.0-260).

REFERENCES

1. Rozenfel'd, I.L., *Ingibitory korrozii* (Corrosion Inhibitors), Moscow: Khimiya, 1977.
2. Reshetnikov, S.M., *Ingibitory kislotnoi korrozii metallov* (Acid Corrosion Inhibitors), Leningrad: Khimiya, 1977.
3. Damaskin, B.B., Petrii, O.A., and Batrakov, V.V., *Adsorbtsiya organicheskikh soedinenii na elektrodakh* (Adsorption of Organic Compounds on Electrodes), Moscow: Nauka, 1968.
4. Afanas'ev, B.N., Akulova, Yu.P., and Yakovleva, O.R., *Zh. Fiz. Khim.*, 2003, vol. 77, no. 4, pp. 727–731.
5. Morachevskii, A.G., Smirnova, N.A., Balasheva, I.M., and Pukinskii, I.B., *Termodinamika razbavlennykh rastvorov neelektrolitov* (Thermodynamics of Dilute Nonelectrolyte Solutions), Leningrad: Khimiya, 1982.
6. Kuprin, V.P., Ivanova, M.V., and Nikolenko, N.V., *Zh. Fiz. Khim.*, 2000, vol. 74, no. 7, pp. 1277–1283.
7. Kuprin, V.P. and Shcherbakov, A.G., *Adsorbtsiya organicheskikh soedinenii na tverdoi poverkhnosti* (Adsorption of Organic Compounds of Solid Surfaces), Kiev: Naukova Dumka, 1996.
8. Nikolenko, N.V., Vereshchak, V.G., and Grab-

chuk, A.D., *Zh. Fiz. Khim.*, 2000, vol. 74, no. 12, pp. 2230–2235.

9. Gregg, S.J. and Sing, K.S.W., *Adsorption, Surface Area and Porosity*, London: Academic, 1982.
10. *Spravochnik khimika* (Chemist's Handbook), Moscow: Goskhimizdat, 1963, vols. 1–2.
11. *CRC Handbook of Chemistry and Physics*, Lide, D.R., Ed., London, 1999.
12. *Khimicheskie reaktivy and preparaty* (Chemicals), Kuznetsov, V.I., Ed., Moscow: Goskhimizdat, 1953.
13. Afanas'ev, B.N., Akulova, Yu.P., and Eron'ko, O.N., *Elektrokhimiya*, 1995, vol. 31, no. 8, pp. 1049–1057.
14. Koppitz, F.D., Schultze, J.W., and Rolle, D., *J. Electroanal. Chem.*, 1969, vol. 20, pp. 297–301.
15. *Kratkii spravochnik fiziko-khimicheskikh velichin* (Concise Handbook of Physicochemical Quantities), Ravdel', A.A. and Ponomareva, A.M., Eds., Leningrad: Khimiya, 1983.
16. *Fizicheskaya khimiya* (Physical Chemistry), Krasnov, K.S., Ed., Mosocw: Vysshaaya Shkola, 1982.

Russian Journal of Applied Chemistry, Vol. 77, No. 9, 2004, pp. 1440–1443. Translated from Zhurnal Prikladnoi Khimii, Vol. 77, No. 9, 2004, pp. 1452–1455.

SORPTION AND ION-EXCHANGE PROCESSES

Development of the Specific Surface Areas of Natural Coal in the Course of Thermolysis in the Presence of Potassium Hydroxide

Yu. V. Tamarkina, V. A. Kucherenko, and T. G. Shendrik

Litvinenko Institute of Physical Organic Chemistry and Coal Chemistry, National Academy of Sciences of Ukraine, Donetsk, Ukraine

Received April 14, 2004

Abstract—The development of the surface of natural coal from Donets field in the course of thermolysis with KOH was studied. The dependences of the specific surface area of coal containing 90% carbon on the activation time, temperature (400–800°C), and KOH/coal ratio (0.75–4.5 g g^{-1}) were determined. The effect exerted on the development of the porous coal structure by low-temperature (20 ± 2°C) oxidative modification causing formation of oxygen functional groups and reorganization of the coal three-dimensional structure was studied.

Thermolysis in the presence of alkali metal hydroxides (chemical activation) is widely used for preparing activated carbons (ACs) with a high specific surface area and a developed system of nanopores (down to 2 nm) [1, 2]. Nanoporous ACs are of particular importance owing to their use in air and water treatment, metal sorption, etc., and also in storage of methane and hydrogen as fuels for internal-combustion engines [3]. As a rule, thermolysis in CO_2 or steam atmosphere (physical activation) does not yield nanoporous ACs, because in this case meso- (2–50 nm) and macropores (more than 50 nm) are mainly developed [1].

Various carbon materials, especially, biomass wastes or coals with low degree of metamorphization (DM) are used for preparing ACs by chemical activation [1]. However, data on conversion of highly metamorphized coals and anthracites into nanoporous ACs by chemical modification are virtually lacking, despite the fact that these carbons are very promising as AC precursors owing to high content of aromatic carbon and high strength, which can be retained in the final activation products. We studied the conversion of highly metamorphized coals from Donets field into materials with a high specific surface area by heat treatment in the presence of alkali metal hydroxides.

EXPERIMENTAL

In this work we used highly metamorphized coals with the carbon content from 90 (OS brand coal) to 95.2 wt % (anthracite) and particle size of 0.16–0.25 mm; the detailed characteristics of these coals are given in [4]. The chemical activation was performed in two stages: (1) mixing of carbon with 50% aqueous KOH solution, storage for 72 h at 20 ± 2°C, drying, and grinding (KOH/dry coal weight ratio was varied within R_{KOH} = 0.75–4.5 g g^{-1}); (2) heating of carbon with alkali in a horizontal quartz tubular reactor in an argon flow (2 dm^3 h^{-1}) at activation temperature T for time τ. The solid product was cooled, washed to remove alkali successively with water, HCl, and again water (to negative reaction for Cl^- ions), and dried at 105 ± 5°C. The yield of AC Y (wt %) was determined, and the specific surface area S_{BET} (m^2 g^{-1}) was measured by low-temperature adsorption of argon [5].

The structure of carbon samples was studied by X-ray diffraction (XRD) analysis on a DRON-3 UM diffractometer (CuK_α radiation) and by diffuse reflection Fourier IR spectroscopy on a Bio-Rad Win-IR spectrometer in the 4000–400 cm^{-1} range (5% carbon samples in KBr, 500 scans, 2 cm^{-1} resolution).

Thermolysis of the initial carbons in the absence of alkali at 800°C for 2 h gives products with a low specific surface area (Fig. 1, curve *1*); the S_{BET} values vary in the 11–16 m^2 g^{-1} range and are independent of the carbon content. In the presence of alkali, the specific surface area of carbons increases, but this increase strongly depends on DM (Fig. 1, curve *2*). This effect, being minimal for anthracite, approximately linearly increases with decreasing carbon content,

1070-4272/04/7709-1440 © 2004 MAIK "Nauka/Interperiodica"

being maximal for OS coal. The development of the specific surface area of this coal as influenced by the main factors of chemical activation (time, temperature, and alkali/coal weight ratio) was studied more comprehensively. As seen from the kinetic data, first S_{BET} sharply increases within 1 h of activation (T = 800°C), then nearly exponentially decreases, and remains constant within the experimental error at $\tau \geq$ 2 h. The AC yield changes in the opposite direction. Since our results are similar to those given previously in [6], the activation time in further experiments was 2 h.

The AC specific surface area remains unchanged in the 400–550°C temperature range and linearly increases with temperature from 550 to 800°C (Fig. 2, curve *1*). The S_{BET} values increase with increasing KOH content up to $R_{KOH} \leq 2$ g g^{-1}, whereas further increase in the alkali content does not affect the specific surface area (Fig. 2, curve *2*). These data show that the maximal specific surface area of AC prepared form OS coal using the activation procedure is $S_{BET} = 500 \pm 50$ m^2 g^{-1}. This value is relatively low for ACs prepared by chemical activation, because their specific surface area is usually higher than 1000 m^2 g^{-1} [1, 2].

In this work we also studied the influence exerted on the development of the specific surface area by low-temperature preactivation. This low-temperature chemical modification of the coal structure with oxidants can precede both chemical and physical activation. Atmospheric oxygen and perchloric and nitric acids are often used as oxidants; HNO_3 can be used as vapor, aqueous solution, and mixtures with $HClO_4$ or Ac_2O [7].

We studied modification of OS coal, whose chemical activation was the most efficient (Fig. 1). The activation was performed using the HNO_3–Ac_2O modifying system, which, according to [8], rapidly reacts with coals of various nature and DM at room temperature, and modification proceeds not only in the surface layer, but also in the coal matrix bulk.

In contact with HNO_3–Ac_2O mixture (50 mol kg^{-1} coal), the structure of the OS coal is completely reorganized within 6 h at 18 ± 2°C; as a result, the coal is converted into structurally modified coal (SMC) [4, 6]. This new material is characterized by higher content of oxygen (by a factor of 3.7) and nitrogen (by a factor of 3.6) and lower content of carbon (see table). In contrast to the initial coal, the main structural elements of SMC are polynuclear nitroarenes. The IR spectra of SMCs show the C=C skeleton vibrations at 1600 cm^{-1} and the stretching (1540 and 1350 cm^{-1}) and bending (750 cm^{-1}) vibrations of the aromatic nitro groups. The side substituents of nitroarenes are methyl (2955 and 2870 cm^{-1}) and methylene (2925, 2865, 1440 cm^{-1}) groups and oxygen-containing functional groups: carboxy (1720 cm^{-1}), phenolic (1280 cm^{-1}), ether (1270, 1230 cm^{-1}), and quinoid (1564 cm^{-1}).

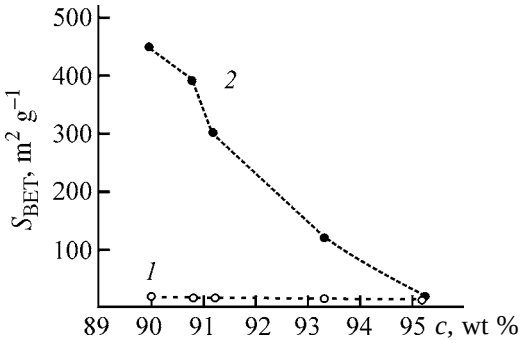

Fig. 1. Development of the specific surface area S_{BET} in thermolysis of coals (*1*) in the absence of alkali and (*2*) in the presence of KOH (R_{KOH} = 1.5 g g^{-1}, T = 800°C, and τ = 2 h). (*c*) Carbon content.

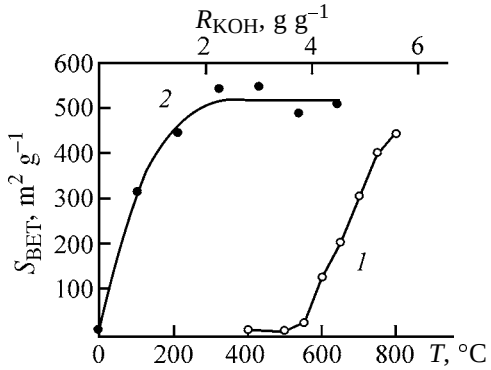

Fig. 2. Development of the specific surface area S_{BET} of OS coal as influenced by (*1*) activation temperature T (R_{KOH} = 1.5 g g^{-1}, τ = 2 h) and (*2*) alkali/coal weight ratio R_{KOH} (T = 800°C, τ = 2 h).

Composition of the initial and modified OS coal

Composition	Content in coal, %	
	initial	SMC
Ash	1.1	0.8
C	90.0	66.4
H	4.4	4.1
S	0.9	0.9
N	1.6	5.8
O	3.1	22.8

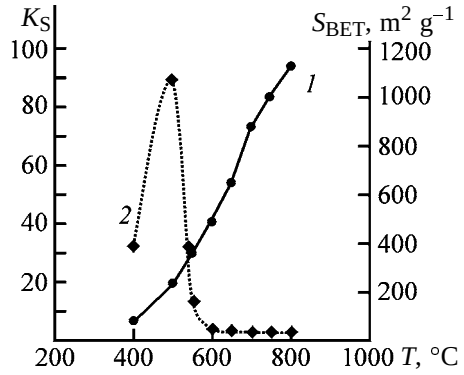

Fig. 3. (*1*) Specific surface area S_{BET} and (*2*) efficiency coefficient K_S as functions of temperature T at activation of SMC (R_{KOH} = 1.5 g g^{-1}, τ = 2 h).

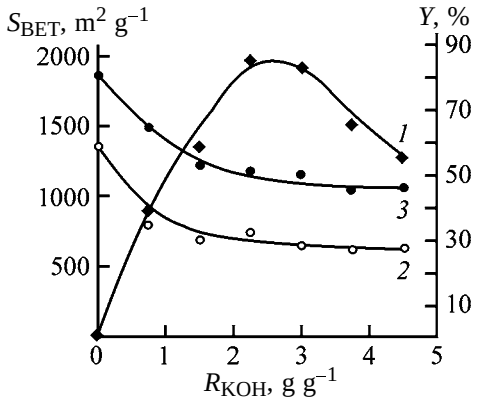

Fig. 4. (*1*) Specific surface area S_{BET} and (*2, 3*) yield Y as functions of the alkali/coal weight ratio R_{KOH} Coal: (*1, 2*) SMC and (*3*) initial OS coal.

Similarly to arenes in the initial coal, nitroarenes in SMCs are aggregated in "crystallites," but the parameters of the supramolecular structure are different. Owing to modification, the interlayer spacing d_{002} increases from 0.378 to 0.381 nm, whereas the height L_c and average diameter L_a of crystallites decrease from 1.05 to 0.9 and from 1.38 to 1.33 nm, respectively. As compared to the initial coal, SMC is more reactive to alkali even at stage of mixing (20 ± 2°C), due to reaction of KOH with OH-acidic functional groups. In the course of thermolysis, SMC is converted into AC with the best characteristics.

The temperature dependence of S_{BET} for SMC is shown in Fig. 3 (curve *1*). In contrast to the initial carbon (Fig. 2, curve *1*), the development of SMC surface begins at 400°C, and the specific surface area almost linearly increases to 1200 m^2 g^{-1} in the temperature range studied (400–800°C). The effect of structural modification can be illustrated by the efficiency coefficient K_S, which is the ratio of the specific surface area of ACs prepared from SMC and from the initial coal at similar T, τ, and R_{KOH}. The highest modification effect is observed at 400–600°C; in the 600–800°C range K_S varies within 2.5–3.8.

With increasing KOH/SMC ratio, the specific surface area passes through a maximum (Fig. 4, curve *1*). The maximal values are obtained at R_{KOH} = 2.5–3.0 g g^{-1} and reach 2000 m^2 g^{-1}. The yields of ACs from SMC and initial carbon decrease with increasing R_{KOH} (Fig. 4, curves *2, 3*). The shapes of the curves are similar, but the yields of ACs from SMCs are lower by a factor of 1.5–2.0. Thus, in the presence of KOH the specific surface area of the modified carbon develops more intensively as compared to the initial carbon. This effect is probably due to the presence of a significant amount of functional groups appearing in the carbon structure in the course of modification. At mixing, functional groups react with KOH with formation of potassium phenolates and carboxylates and cleavage of the ester groups. These reactions promote penetration of K^+ and OH^- ions and KOH molecules and their fixation in the carbon skeleton as separate ions, molecules, and molecular aggregates (clusters).

Occupation of the intermolecular space with ionic and molecular aggregates of alkali sterically hinders formation of the C–C bonds in the AC skeleton, which is formed at 400–800°C under the thermolysis conditions. Probably, the volume of the alkali cluster is the volume of the future pore, whose size and hence the internal surface area are determined by the cluster size.

At low content of functional groups in carbon, the content of incorporated alkali and the number of clusters is small, which causes small pore volume and low specific surface area of SCs. This explains low S_{BET} for the initial OS coal (Fig. 2); the content of oxygen in it is 3.1 wt %, compared to 22.8 wt % in the modified coal (see table). With increasing steric hindrance to penetration of alkali into the carbon matrix on passing from OS coal to anthracites, the efficiency of chemical modification decreases (Fig. 1, curve *2*) and treatment with KOH does not noticeably affect the development of the specific surface area of anthracites. However, the efficiency of chemical modification for anthracites is rather high and allows preparation of ACs with a specific surface area of up to 450 m^2 g^{-1} [9].

CONCLUSIONS

(1) Thermolysis of natural coals in the presence of KOH increases the specific surface area of activated

carbons. The effect decreases with increasing degree of metamorphization of the coal and increases with temperature in the 400–800°C range; it is determined by the alkali/coal weight ratio.

(2) Low-temperature oxidative modification significantly (by a factor of 2.5–3.8) promotes the development of the specific surface area at activation in the presence of KOH. Heating of modified carbon in the presence of KOH (2–3 g of KOH per gram of coal) at 700–800°C yields a carbon material with a highly developed surface area (1800–2000 $m^2 g^{-1}$) in a yield of 28–30%.

REFERENCES

1. *Introduction to Carbon Technologies*, Marsh, H., Heintz, E.A., and Rodroguez-Reinozo, F., Eds., Alicante: Universidad, 1997.
2. Lozano-Castello, D., Lillo-Rodenas, M.A., Cazorla-Amoros, D., *et al*., *Carbon*, 2001, vol. 39, pp. 741–749.
3. Lozano-Castello, D., Cazorla-Amoros, D., Lonares-Solano, A., *et al*., *Carbon*, 2002, vol. 40, pp. 989–1002.
4. Tamarkina, Yu.V. and Shendrik, T.G., *Uglekhim. Zh*., 2002, nos. 1–2, pp. 3–7.
5. *Okislenie i samovozgoranie tverdogo topliva* (Oxidation and Spontaneous Ignition of Solid Fuels), Sapunov, V.A., Ed., Kiev: Naukova Dumka, 1994.
6. Tamarkina, Yu.V. and Shendrik, T.G., *Khim. Tverd. Topl*., 2002, no. 6, pp. 3–10.
7. Tamarkina, Yu.V., Shendrik, T.G., and Kucherenko, V.A., *Khim. Tverd. Topl*., 2003, no. 5, pp. 38–50.
8. Tamarkina, Y.V., Shendrik, T.G., Krzton, A, *et al*., *Fuel Proc. Technol*., 2002, vols. 77–78, pp. 9–15.
9. Tamarkina, Yu.V., Khabarova, T.V., Shendrik, T.G., *et al*., *Extended Abstracts, Prospects for Coal Science in the 21st Century*, Taiyan: Shanxi Sci. Technol., 1999, vol. II, pp. 961–965.

Russian Journal of Applied Chemistry, Vol. 77, No. 9, 2004, pp. 1444–1449. Translated from Zhurnal Prikladnoi Khimii, Vol. 77, No. 9, 2004, pp. 1456–1461.

SORPTION AND ION-EXCHANGE PROCESSES

Sorption of Zinc Complex Ions from Chloride Solutions with Ion Exchangers

V. I. Skorokhodov, B. K. Radionov, and O. Yu. Goryaeva

Ural State Technical University, Yekaterinburg, Russia

Received March 17, 2004

Abstract—To characterize the reaction of zinc ions with anion exchangers of various types, the equilibrium compositions of all the components of the sorption system (zinc salt, hydrochloric acid, and water) and distribution of associated molecules in the resin phase were considered.

Anion exchangers are widely used in chemical analysis and in hydrometallurgy for concentration of zinc ions and their separation from concomitant elements in chloride solutions [1–3]. In analytical chemistry, a series of ion-exchange resins are recommended for separation of non-ferrous metals in the hydrochloric acid media [1, 2, 4, 5]. In hydrometallurgy, anion exchangers of various basicities (VP-1aP, AMP, VP-1P, AP, EDE-10P) and ampholytes Dowex-1, ANKB-35, etc. [1, 6, 7] are used for purification of nickel and cobalt-containing solutions. In spite of extensive data on sorbents for zinc(II) recovery, there is no common opinion on interaction between zinc chloride complexes and resin functional groups. The prevailing opinion is that zinc(II) exists in the solution and is sorbed by anion exchangers mainly in the form of negatively charged complexes $[ZnCl_3]^-$ and $[ZnCl_4]^{2-}$ [1–7]. Theoretically, sorption of neutral species $[ZnCl_2]^0$ by the nonexchange mechanism is not ruled out also [8]. The preferred adsorption of Zn(II) neutral complexes with anion exchangers because of weak hydration is suggested in [9]. Tremillon [10] explains sorption of Zn(II) from chloride solutions by participation of counterions of the fixed anion-exchange groups (in this case, chloride ions) in completion of the coordination sphere of the unsaturated zinc(II) acido complexes. Balakin *et al*. [11] studied the effect of the basicity and degree of hydration of amino groups on the zinc ion sorption and concluded that the selectivity with respect to zinc chloride complexes is caused by the "electroselectivity" phenomenon. All the above shows that, by now, the sorbed zinc species have not been identified reliably, and no criteria allowing selection of the most efficient sorbent for zinc(II) recovery from various process solutions have been formulated. In this work, the equilibria in the ion exchanger–HCl–KCl–$ZnCl_2$–H_2O system were studied to characterize the interaction of Zn(II) acido complexes with the ion exchanger ionogenic groups and the influence of amino group structure and other factors on this interaction, with the aim of predicting sorption properties of ion exchangers.

EXPERIMENTAL

The following ion exchangers of various types were used in the study: AV-17, VP-1P, VP-1aP, SN-3, SB-1, AN-18, AN-31, and ANKB-35.

Structure of the functional groups of the ion exchangers studied

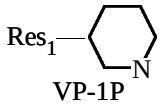

VP-1P

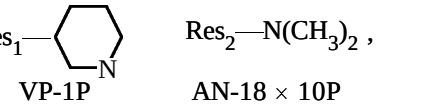

AN-18 × 10P

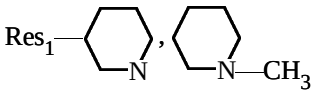

VP-1aP

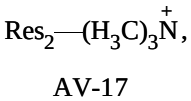

AV-17

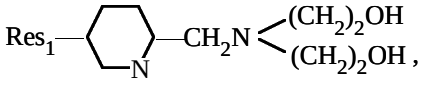

SN-3

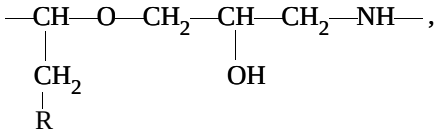

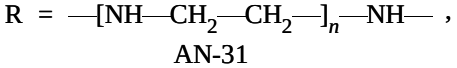

AN-31

1070-4272/04/7709-1444 © 2004 MAIK "Nauka/Interperiodica"

Table 1. Main physicochemical properties of ion exchangers studied*

Ion exchanger	Anion-exchange groups, mg-equiv g^{-1}	Capacity for Zn(II), mg-equiv g^{-1}	pK (pH at $\alpha = 0.5$)	$K_d^n(ZnCl_2)$
VP-1P	4.81	3.37	4.49	41.76
AN-18 × 10P	3.76	2.71	7.00	39.53
VP-1aP	3.93	5.50	8.9	64.06
AV-17	1.59	3.00	10.95	127.9
SN-3	4.13	2.47	3.31	29.07
AN-31	8.85	2.21	3.79	24.20
SB-1	8.15	1.83	3.55	17.55
ANKB-35	0.74	0.57	2.86	47.21

* The capacity for Zn(II) was determined as recalculated on $[ZnCl_4]^{2-}$ at c_{HCl} = 2.5 M; averaged values of $K_d^n(ZnCl_2)$ at $c_{eq}(Zn)$ = 0.01 mmol dm^{-3} are listed.

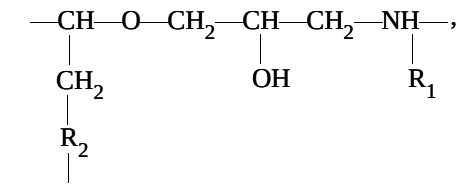

R_1 = —CH_2—CH_2—OH,

R_2 = —[NH—CH_2—CH(OH)—CH_2]$_n$—NH—, SB-1

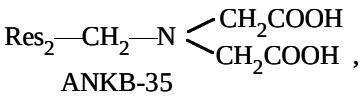

ANKB-35,

where Res_1 is copolymer of vinylpyridine and divinylbenzene (DVB); Res_2, copolymer of styrene and DVB.

Pretreatment of ion exchangers and determination of their anion-exchange capacity were performed as in [12, 13]. All the ion exchangers were transferred into the Cl^- form. The main properties of the ion exchangers used are listed in Table 1.

The acid–base properties of ion exchangers were determined potentiometrically [12] in 0.5 M KCl as supporting electrolyte. The pK was calculated by the Henderson–Hasselbach equation as pH of 50% neutralization (protonation) of amino groups. The ion-exchange equilibrium in the anion exchanger–electrolyte system was studied at the liquid-to-solid ratio of 50 : 1. The solutions were prepared using ultrapure grade HCl and analytically pure grade zinc chloride and KCl. The duration of ion exchanger contact with solution was 7 days, which is sufficient to attain the ion-exchange equilibrium. The capacity of ion exchangers for zinc was determined from the difference between the metal concentrations in the solution before and after sorption and from the results of regeneration of the anion exchanger with distilled water (l : s = 200 : 1). The amount of hydrochloric acid sorbed was monitored from its content in the eluate. The concentrations of the components were determined: HCl potentiometrically, Zn^{2+} complexometrically, and Cl^- conductometrically. The moisture content in ion exchangers was determined from thermograms [12] measured on a Q-1500 D derivatograph.

Ion exchangers differing in the acid–base properties of amino groups, matrix structure, functional composition, and synthesis method were taken (Table 1).

Ion exchangers SB-1 and AN-31 are epoxy–amine resins of polycondensation type; the other resins are of polymerization type and are based on copolymer of styrene with DVB (AV-17, AN-18, ANKB-35) or of vinylpyridine with DVB (VP-1aP, AN-31, SN-3).

Ion exchangers SB-1, AN-31, and AV-17 have the gel structure of the matrix, all the others have the porous structure.

Ion exchangers AV-17, AN-18, AN-31, SB-1, and ANKB-35 contain aliphatic amino groups of various compositions; anion exchangers VP-1aP, VP-1P, and SN-3 contain pyridine fragments.

Ion exchangers AV-17, AN-18, and VP-1P are virtually monofunctional, while all the other resins contain combinations of amino groups of various types (SN-3). Furthermore, anion exchangers SN-3, SB-1, and AN-31 additionally contain hydroxy groups and ampholyte ANKB-35, carboxy groups.

It is known [1, 8, 10] that the maximal capacity of highly basic anion exchangers with respect to zinc is attained at 2–3 M Cl^- in the solution. This is also true for sorbents considered in our study (Fig. 1). In spite

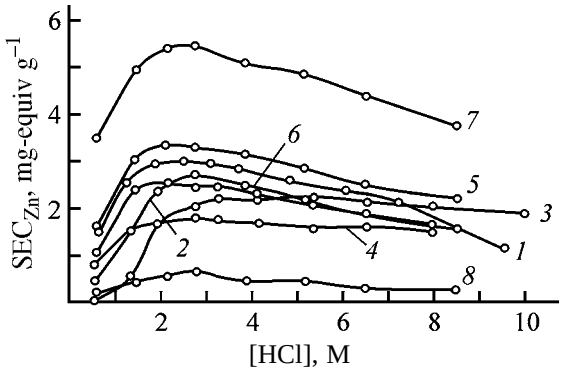

Fig. 1. Static exchange capacity of ion exchangers SEC_{Zn} as a function of hydrochloric acid concentration [HCl] in the equilibrium solution. (*1*) AV-17, (*2*) SN-3, (*3*) AN-31, (*4*) SB-3, (*5*) VP-1P, (*6*) AN-18, (*7*) VP-1aP, and (*8*) ANKB-35.

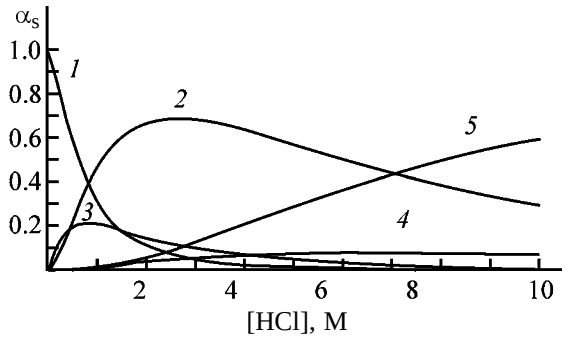

Fig. 2. Influence of the chloride ion concentration on zinc(II) speciation. (α_s) Fraction of the given zinc(II) species in the solution and ([HCl]) concentration of hydrochloric acid. (*1*) Zn^{2+}, (*2*) $[ZnCl_2]^0$, (*3*) $[ZnCl]^+$, (*4*) $[ZnCl_3]^-$, and (*5*) $[ZnCl_4]^{2-}$.

of the difference in the absolute values of the static exchange capacity for Zn(II) (SEC_{Zn}) apparently connected with physicochemical properties of the polymers, similar shape of the dependences for so different resins (Fig. 1) suggests similar mechanism of adsorption of zinc acido complexes.

The reaction of functional groups with zinc ions can be analyzed in detail from data on zinc(II) speciation in chloride solutions. Figure 2 shows that, at $[Cl^-]$ = 2–3 M, only 20% of zinc(II) exists as cationic species (Zn^{2+}, $ZnCl^+$) unsorbable by anion exchangers; 70% as the neutral complex $[ZnCl_2]^0$; and only 10%, as negatively charged ions $ZnCl_3^-$ and $ZnCl_4^{2-}$. Such a distribution and the above-indicated similar trends in the Zn(II) sorption (Fig. 1) suggest that the sorption equilibrium is determined by the concentration of the prevailing neutral complex $[ZnCl_2]^0$. The statistical treatment of zinc sorption with AV-17 anion exchanger (Table 2) confirms this suggestion, since SEC_{Zn} maximally correlates with the $ZnCl_2$ content in the solution (R^2 = 0.99), and the $ZnCl_2$ distribution coefficient between the solution and ion exchanger is virtually independent of the Cl^- concentration.

Similar pattern is shown by the other ion exchangers studied, except polyfunctional ion exchangers for which $K_d(ZnCl_2)^0$ tends to increase with the HCl concentration (Table 3). More pronounced influence of the acidity on the sorption of Zn(II) ions is demonstrated by Fig. 3, which shows the results obtained at different concentrations of HCl but constant concentration of Cl^- supported by KCl ([HCl] + [KCl] = const).

With increasing HCl concentration, the sorption capacity for Zn(II) is practically constant for AV-17 monofunctional anion exchanger and increases by 15–25% for SN-3 and SB-1, by 40% for AN-31, and by 60% for ANKB-35 within the 0–2.5 M HCl concentration range.

The increase in the sorption capacity, characteristic for anion exchangers with additional donor centers, is caused by the induction effect discussed in [14–16]. It was shown in these works that, in aminocarboxylic ampholytes, the basicity of amino groups substantially depends on the solution acidity due to positive charge on carboxy groups, which is transferred along the conjugated polymer chain to amino groups. Thus, when the concentration of the chloride ions is sufficient to form the neutral complex $[ZnCl_2]^0$ (total concentration of HCl + KCl 2.5 M) and this species predominates, the exchange capacity is maximal and constant for AV-17 monofunctional ion exchanger and somewhat increases with increasing HCl content for polyfunctional ion exchangers with additional active centers affecting the basicity of the sorbent amino groups.

It is interesting that the exchange capacity for Zn(II) of AV-17 and VP-1aP ion exchangers is by a factor of 1.5–3 higher than the exchange capacity of the functional groups themselves {similar effect was observed previously with highly basic anion exchanger Dowex 2×10 in sorption of mercury(II) chloride complexes [10]}. This excess is observed within virtually the whole interval of HCl concentrations studied (0.7–9 M). This phenomenon is in conflict with the exchange equivalence if we assume that zinc ions are sorbed as negatively charged ions, especially as $[ZnCl_4]^{2-}$, taking into account their small fraction among the other Zn(II) species in the chloride solution. This "anomaly" in the Zn(II) behavior can be explained assuming that the neutral zinc complexes

Table 2. Zinc(II) distribution between the solution and AV-17 anion exchanger as a function of hydrochloric acid concentration and zinc(II) speciation in the solution*

Composition of equilibrium solution		SEC_{Zn}, mmol g^{-1}	$K_d(\Sigma Zn)$	Zn^{2+}		$[ZnCl]^+$		$[ZnCl_2]^0$		$[ZnCl_3]^-$		$[ZnCl_4]^{2-}$	
c_{HCl}, M	$c_{eq}(\Sigma Zn)$, mM			c^{eq}, mM	K_d	c^{eq}, mM	K_d	c^{eq}, mM	K_d	c^{eq}, mM	K_d	c^{eq}, mM	K_d
0.65	21.02	0.743	35.36	10.12	73.4	4.25	174.7	6.48	114.67	0.11	6750	0.06	13 500
1.25	18.79	1.286	67.69	4.35	296.0	3.50	366.9	10.28	125.2	0.34	3782	0.32	4083
1.8	20.36	1.468	81.56	4.41	665.8	2.68	546.7	11.86	123.8	0.59	2488	0.82	1790
2.49	17.80	1.497	83.20	1.13	1144	2.10	711.6	12.29	121.9	0.80	1861	1.48	1009
3.1	17.91	1.478	82.07	0.64	1749	1.69	874.3	12.28	120.4	1.00	1478	2.30	642
3.7	18.00	1.422	78.97	0.57	2495	1.36	1046	11.79	120.7	1.14	1242	3.14	452
4.83	18.61	1.301	70.28	0.31	4195	0.97	1341	10.96	118.7	1.39	936	4.98	261
6.00	19.24	1.195	62.85	0.18	6636	0.70	1706	9.87	121.0	1.56	766	6.93	172
7.27	19.76	1.064	53.18	0.11	9668	0.50	2106	8.62	123.4	1.65	645	8.88	120
$R^2_{SEC_{Zn}/c(ZnCl_n)}$		0.540		0.366		0.097		0.990		0.032		0.019	

* $K_d(\Sigma Zn) = SEC_{Zn}/c_{eq}(\Sigma Zn)$, $K_d(ZnCl_n) = SEC_{Zn}/c_{eq}(ZnCl_n)$, where n is the number of coordinated chloride ions, $n = 0-4$.

Table 3. Distribution coefficients $K_d(ZnCl_2)^0$ for various ion exchangers as a function of acidity [$c_{eq}(\Sigma Zn) = 0.01$ mM]

c_{HCl}, M	$K_d(ZnCl_2)^0$							
	VP-1P	AN-18 × 10P	VP-1aP	AV-17	SN-3	AN-31	SB-1	ANKB-35
0.6	185.6	150.9	239.6	199.1	110.6	186.6	122.2	29.1
2.4	203.7	145.1	255.7	205.8	115.1	206.4	135.1	30.2
3.0	205.1	149.1	250.9	214.0	113.0	205.7	142.3	33.8
3.8	196.7	147.1	254.4	203.1	120.4	211.6	148.8	36.0
6.2	209.1	149.8	257.1	199.6	128.4	234.2	153.6	39.0
9.5	205.0	149.8	252.8	198.5	133.4	240.5	156.2	41.4
Average	200.9	148.6	251.8	203.4	120.1	214.2	143.0	34.9

are sorbed. It is believed in [9] that one of the causes of the sorption selectivity is solvation of both ionogenic group and sorbable species in the solution and in the ion exchanger phase, i.e., the selectivity is considered as competition between solvation of fixed active groups of the ion exchanger and solvation of the sorbable species in the solution and in the ion exchanger phase. If zinc(II) is sorbed from chloride solutions with anion exchangers in the form of neutral complexes, we can suggest that this process should be accompanied by the loss of neutral molecules forming the solvation shell around the ionogenic groups. The experimental data on distribution of the components of the system between the electrolyte and resin phase, listed in Table 4, confirm the above mechanism of the sorption.

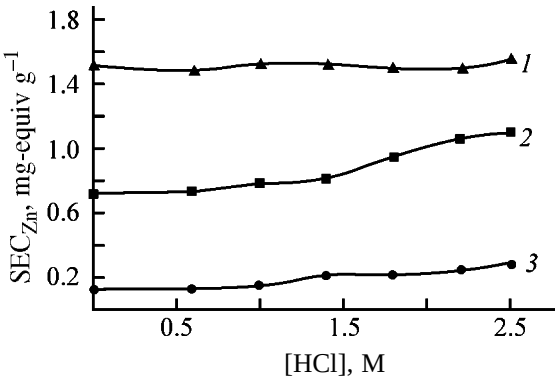

Fig. 3. Static exchange capacity of ion exchangers SEC_{Zn} as a function of concentration of free hydrochloric acid [HCl] at total KCl and HCl concentration of 2.5 M. (*1*) AV-17, (*2*) AN-31, and (*3*) ANKB-35.

Table 4. Influence of the electrolyte composition on sorption of solution components with AV-17 anion exchanger

Experiment no.	Composition of equilibrium solution, M			Composition of ion exchanger phase, mmol g^{-1}			
	HCl	$[ZnCl_2]^0$	KCl	HCl	$[ZnCl_2]^0$	KCl	H_2O
1	0	0	0	0	0	0	53.86
2	0.51	0	0	0.35	0	0	46.31
3	3.18	0	0	3.08	0	0	42.68
4	6.71	0	0	6.83	0	0	42.69
5	0	0	0.65	0	0	0.13	45.39
6	0	0	2.09	0	0	0.79	37.55
7	0	0	4.37	0	0	1.61	32.16
8	0.50	0.05	0	0.30	0.85	0	31.15
9	3.26	0.05	0	1.28	1.72	0	14.08
10	6.63	0.05	0	3.42	1.54	0	18.31
11	2.67	0.05	0	1.02	1.74	0	13.72
12	2.65	0.1	0	0.93	2.03	0	11.86
13	2.68	0.55	0	0.88	2.33	0	10.14
14	0	0.05	2.75	0	1.54	0.56	11.58
15	0	0.1	2.68	0	1.77	0.52	10.89
16	0	0.57	2.69	0	2.18	0.51	8.20

In particular, in accordance with run nos. 2–7 (Table 4), increase in HCl (or KCl) concentration in the electrolyte naturally increases the degree of their penetration into the ion exchanger due to Donnan effect [8, 9]. At the same time, this phenomenon is accompanied by substantial loss of hydration water from the sorbent. Even small amounts of Zn ions in the system (run nos. 10, 14) promote not only sorbent dehydration but also displacement of HCl and (or) KCl molecules. The higher the sorption of zinc complexes, the smaller amount of the competing molecules of the electrolyte components remains in the ion exchanger phase (run nos. 8, 10).

Table 1 reveals a correlation between the degree of sorption of zinc acido complexes and basicity of amino groups. This correlation becomes more obvious when the experimental data are graphically presented in the pK_d–$\log K_d^n$ coordinates, where K_d^n is the average distribution coefficient related to the concentration of ion exchanger amino groups.

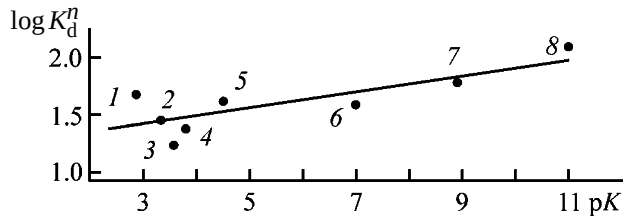

Fig. 4. $[ZnCl_2]^0$ distribution coefficient as a function of the basicity of amino groups: (*1*) ANKB-35, (*2*) SN-3, (*3*) SB-1, (*4*) AN-31, (*5*) VP-1P, (*6*) AN-18 × 10P, (*7*) VP-1aP, and (*8*) AV-17.

The linearity of this dependence (Fig. 4) shows that the basicity of amino groups, along with their content, is the governing factor in sorption of zinc acido complexes, except $K_d(ZnCl_2)^0$ for amino carboxylic ampholyte ANKB-35, which, as mentioned above, substantially depends on HCl concentration in the equilibrium solution. The results obtained suggest the following interpretation of the sorption process. Amino groups in the chloride solutions are surrounded by the solvation shell consisting of water and HCl molecules. Interaction of the neutral complexes $[ZnCl_2]^0$ with the resin functional groups results in substitution of HCl and H_2O molecules from the solvation shells of these groups. Thus, sorption of Zn(II) with anion exchangers from chloride solutions is due to competition of neutral molecules (HCl, H_2O, $ZnCl_2$) for solvation of the resin functional groups, rather than to ion exchange proper.

CONCLUSIONS

(1) The study of the equilibrium in the Zn^{2+}–HCl–KCl–H_2O system showed that sorption of zinc acido complexes with an ion exchanger proceeds not by the anion-exchange mechanism but by the solvation

mechanism, i.e., $[ZnCl_2]^0$ molecules exchange with neutral molecules forming the solvation shell of the resin amino groups.

(2) The main factors affecting Zn(II) sorption from solutions are the amount and basicity of anion exchanger amino groups; these factors should govern the choice of ion exchangers for practical tasks.

(3) The procedure of the synthesis, type of the matrix, porosity, and degree of monofunctionality (structure of ionogenic groups) of ion exchangers, the mutual position of nitrogen atoms in the chain of ionogenic groups, and other factors affect the zinc(II) sorption equilibrium insignificantly.

REFERENCES

1. Marhol, M., *Ion Exchangers in Analytical Chemistry. Their Properties and Use in Inorganic Chemistry*, Prague: Academia, 1982.
2. Zhivopistsev, V.P. and Selezneva, E.A., *Analiticheskaya khimiya tsinka* (Analytical Chemistry of Zinc), Moscow: Metallurgiya, 1975.
3. *Ionity v tsvetnoi metallurgii* (Ion Exchangers in Non-Ferrous Metallurgy), Lebedev, K.B., Ed., Moscow: Metallurgiya, 1975.
4. Stepin, V.V., Silaeva, E.V., Kurbatova, V.I., *et al*., *Analiz tsvetnykh metallov i splavov* (Analysis of Non-Ferrous Metals and Alloys), Moscow: Metallurgiya, 1974.
5. Bulatov, M.I. and Kalinkin, I.P., *Prakticheskoe rukovodstvo po kolorimetricheskim i spektrofotometricheskim metodam analiza* (Practical Guide on Colorimetric and Spectrophotometric Methods of Analysis), Leningrad: Khimiya, 1965.
6. *Gidrometallurgiya: Avtoklavnoe vyshchelachivanie. Sorbtsiya. Ekstraktsiya* (Hydrometallurgy: Autoclave Leaching. Sorption. Extraction), Laskorin, B.N., Ed., Moscow: Nauka, 1976.
7. Kazantsev, E.I., Khudyakov, I.F., Demidova, P.V., and Tolstoguzov, A.D., *Izv. Vyssh. Uchebn. Zaved., Tsvetn. Metall*., 1976, no. 1, pp. 24–28.
8. Helfferich, F., *Ionenaustauscher*, Weinheim: Chemie, 1959, vol. 1.
9. *Ion Exchange. A Series of Advances*, Marinsky, J.A., Ed., New York: Dekker, 1966, vol. 1.
10. Tremillon, B., *Les separations par les resines echangeuses d'ions*, Paris: Gauthier Villars, 1965.
11. Balakin, V.M. and Bazhenova, S.I., *Izv. Sib. Otd. Akad. Nauk SSSR, Ser. Khim. Nauk*, 1974, no. 14, issue 6, pp. 56–61.
12. Polyanskii, N.G., Gorbunov, G.V., and Polyanskaya N.A., *Metody issledovaniya ionitov* (Methods of Investigation of Ion Exchangers), Moscow: Khimiya, 1976.
13. Lur'e, Yu.Yu., *Spravochnik po analiticheskoi khimii* (Handbook of Analytical Chemistry), Moscow: Khimiya, 1979.
14. Saldadze, K.M. and Valova-Kopylova V.D., *Kompleksoobrazuyushchie ionity (kompleksity)* (Complexing Ion Exchangers (Complexites)), Moscow: Khimiya, 1980.
15. Gorokhovatskaya, N.V., Atamanenko, I.D., Korolenko, N.B., *et al*., *Ukr. Khim. Zh*., 1982, vol. 48, no. 11, pp. 1163–1168.
16. Gantman, A.I. and Veshev, S.A., *Zh. Fiz. Khim*., 1986, vol. 60, no. 2, pp. 463–465.

Russian Journal of Applied Chemistry, Vol. 77, No. 9, 2004, pp. 1450–1454. Translated from Zhurnal Prikladnoi Khimii, Vol. 77, No. 9, 2004, pp. 1462–1466.

SORPTION AND ION-EXCHANGE PROCESSES

Sorption Capture of Chlorine with Carbon Adsorbents from Waste Gases Yielded by Electrolysis of Chloride Solutions

S. S. Stavitskaya, A. N. Tomashevskaya, V. E. Goba, N. T. Kartel', and V. V. Strelko

Institute of Sorption and Problems of Endoecology, National Academy of Sciences of Ukraine, Kiev, Ukraine

Received December 3, 2003; in final form, April 2004

Abstract—The performance of various carbon materials in sorption capture of chlorine from waste gases yielded by electrolysis of nickel–manganese solutions was studied. A simple method was proposed for regeneration of carbons after sorption of chlorine, which makes them suitable for repeated use in sorption installations for chlorine capture.

Sorption methods are widely used for capture of toxic impurities such as ammonia, CO_2, SO_2, NO_x, H_2S, CS_2, methanol, chlorobenzene, ethyl acetate, *o*-xylene, diethylamine, acetic acid, and methane from waste gases yielded by various production processes. We found [1–7] that the capacity and selectivity of carbon sorbents can be significantly improved by modification with metal ions, their salts, and nitrogen, sulfur, and phosphorus heteroatoms; also, we elucidated the role played by surface complexing and by other factors affecting sorption of the above-mentioned substances.

In this work we tested the suitability of sorption for removal of one of the most toxic gases, chlorine, yielded by electrolysis of nickel–manganese solutions.

Activated carbons are known as fairly efficient sorbents of gaseous Cl_2; they were used in development of war gas masks since World War I [8–11]. More recent works [12–14] concerned interaction of carbon materials (CMs) with Cl_2 under various conditions. For example, activated carbons were suggested as sorbents for removal of dissolved molecular chlorine and its oxygen-containing compounds (so-called "active chlorine") from water after its disinfection, as well as from process solutions such as, e.g., anolyte after electrolysis of sodium chloride [15–17].

All these facts suggested that Cl_2 would be efficiently sorbed by CMs from waste gases yielded by electrolysis of nickel–manganese solutions. To quantitatively estimate the sorption efficiency, we studied here the sorption power of a number of CMs with respect to gaseous and dissolved chlorine generated on a laboratory electrolysis installation[1] and formulated recommendations on chlorine capture from waste gases.

To estimate the efficiency of binding Cl_2 by various CMs, we carried out experiments on a model sorption installation. The carbon under study was charged either into a vessel (column) with the desired volume (for room-temperature experiments) or into a quartz tube (for experiments at 200–650°C). In the latter case, the tube was placed into an oven with controlled temperature. The amount of carbon varied with the specific CM, depending on the volume of the column used (typically 30×3 cm) and the bulk weight of the carbon. The weighed portion was 40–60 g on the average. Gaseous Cl_2 was produced by reacting concentrated HCl with crystalline $KMnO_4$. In all the experiments, 100 ml of HCl was gradually added to 100 g of $KMnO_4$. The rate of supply of the Cl_2 being released (initial concentration 22 mg l^{-1}) was governed by the rate of its formation in the above-mentioned reaction. The chlorine that broke through was absorbed by an alkali solution.

We tested as sorbents commercial carbons BAU, AR-B, SKT, activated anthracite (AA), and carbon fabric (AUT). Selected structural characteristics of these carbons are listed in Table 1.

The amount of bound chlorine was estimated both from the sorbent mass increment and by chemical analysis (iodometric titration) of the solutions absorbing the chlorine that broke through or was desorbed [18].

The sorbed Cl_2 was washed out from the carbons with water both under static (by shaking a known amount of the sorbent with the required amount of water) and dynamic conditions. The amount of the desorbed chlorine and its concentration in other solu-

[1] This work was carried out jointly with the Institute of Superhard Materials, National Academy of Sciences of Ukraine.

1070-4272/04/7709-1450 © 2004 MAIK "Nauka/Interperiodica"

tions were determined similarly [18]. It should be noted that iodometric determination of active chlorine in the electrolyte is hindered by high concentrations of nickel and manganese salts.

We found that various CM samples take up significant amounts of Cl_2, namely, 300–600 mg g^{-1} and over (Table 2). The highest capacities for chlorine were exhibited by activated anthracite and SKT commercial carbon. These materials are also characterized by acceptable mechanical strength and are relatively inexpensive and readily available. AR-B carbon and carbon fabric (AUT) have considerably lower capacities; the BAU granules markedly break down after several runs. The capacity of the carbons for chlorine was increased by moistening, as well as by preheating at 200°C.

Table 2 shows that the amount of the Cl_2 sorbed tends to increase with temperature. This suggests a complex chemical interaction between this gas and carbon [19], which can involve adsorption and a substitution, addition, or another reaction. The nature of interaction can vary depending on the composition of the carbon material, the presence of reactive impurities promoting such interaction, chemical nature of the surface, pore structure characteristics (the presence of pores with a definite size), and other factors.

Probably, in the case of anthracite and SKT carbon these factors were favorably combined, making these materials the most efficient agents for capture of Cl_2 from waste gases yielded by electrolysis. For example, Table 1 shows that carbons with high capacities for chlorine contain significant amounts of micropores V_{micro} (cf. BAU, AR-B, and SKT).

To prevent release of toxic Cl_2 into the environment, it is essential to estimate not only the total capacity for chlorine but also the capacity of sorbents until breakthrough (or the related parameter, protective action time [5, 6, 9]). These parameters are typically different: The breakthrough occurs before the sorption power of an adsorbent is exhausted. Our experiments showed that this is the case for sorption of Cl_2 by the carbons. However, with activated anthracite and SKT the protective action time remains fairly long. Also, we observed the so-called "rest" of sorbent, i.e., resumption of sorption, evidently, after diffusion of the sorbed Cl_2 inside the sorbent grains. When the process is terminated, Cl_2 fills the internal space of the pores, the surface gets free, and the process continues. Similar effect was observed by Zelinskii and Sadikov [8].

Based on the sorption capacities and specific features of sorption of Cl_2 on CMs, revealed in model laboratory experiments, we calculated the characteristics of a sorption installation for sorption of Cl_2 from waste gases yielded by electrolysis of Ni–Mn solutions. This installation incorporates two vertical fixed-bed carbon adsorbers. One adsorber is placed directly at the bath outlet and operates until saturation with chlorine, and another adsorber serves for exhaustive capture of Cl_2 in cases of a possible breakthrough in the first adsorber and of possible fluctuations of the amount of chlorine released.

To estimate the amount of the sorbent required for Cl_2 capture, we determined the content of Cl_2 in waste gases from electrolysis on a laboratory electrochemical installation with the electrolyte volume of 500 l. We found that electrolysis of Ni–Mn-containing solutions in this installation at room temperature yields 35.5 mg l^{-1} of active chlorine, or 213 mg l^{-1} at elevated temperatures (60–70°C).

Table 1. Selected structural characteristics of carbon sorbents*

Carbon	W_s for C_6H_6, cm^3 g^{-1}	Pore volume, m^3 g^{-1}		S_{sp}, m^2 g^{-1}
		V_{meso}	V_{micro}	
BAU	0.35	0.25	0.10	750
AR-B	0.45	0.30	0.15	418
SKT	0.40	0.36	0.28	650
AUT	0.63	0.53	0.10	1200
AA	0.28	0.05	0.23	742

* W^s is the total volume of sorption pores for benzene [9], V_{meso}, volume of mesopores; V_{micro}, volume of micropores; and S_{sp}, specific surface area of the sorbent.

Table 2. Chlorine sorption by various carbon materials

Sample no.	Sorbent	Moisture content	T, °C	Capacity for chlorine, mg g^{-1}
1	AA	Air-dry	25	305
2	″	Dried at 200°C	25	358
3	″	Moistened	25	452
4	″	Air-dry	200	521
5	″	″	450	525
6	″	″	650	540
7	BAU	″	25	270
8	″	Dried at 200°C	>25	370
9	AUT	Air-dry	25	102
10	AR-B	″	25	260
11	SKT	″	25	610

Based on the capacity for chlorine, capacity until breakthrough, the amount of the Cl_2 released from the anode space of the electrolysis installation, and bulk density of the carbon, the amount of SKT or activated anthracite required for exhaustive capture of the Cl_2 released from a 500-l electrolysis bath within a month was estimated at 15–20 kg (50–60 l).

The sorption filter should be shaped as a cylindrical column manufactured from a chlorine-resistant material (polyvinyl chloride, fluoroplastic) with recommended diameter of 25 cm and height of 130–150 cm.

The nature and strength of chlorine binding under various sorption conditions differ substantially (Table 2). This is of deciding importance for the fate of the waste sorbent which can be suitable either for repeated use without discharging in the same process of Cl_2 sorption after regeneration or for use in other processes (after discharging) as a sorbent with different properties. The properties of the spent sorbent can actually be different, since the contact of Cl_2 with carbon under certain conditions can involve chemical interaction modifying the chemical nature of the carbon surface. We showed [19] that chlorinated carbons acquire new, e.g., bactericidal, properties. For example, we prepared a number of samples containing strongly bound chlorine, exerting a persistent disinfecting effect, which do not release chlorine into the environment or release it into water in amounts close to those specified by GOST (State Standard) 2874–82 "Potable Water" (0.3–0.5 mg l^{-1}).

In this work we focused on regeneration of carbon to make it suitable for repeated runs in adsorbers. Carbons are typically regenerated by thermal, eluent (desorption), and destructive methods [20, 21].

Clearly, the deciding factor in choosing the method is the nature and strength of Cl_2 binding. Therefore, we determined the sorption capacity of the carbons with respect to Cl_2 at different temperatures and also tested the possibility of washing out chlorine sorbed under different conditions. Table 2 shows that the carbons exhibit high sorption capacities for Cl_2 both at room temperature and upon heating to 200–650°C.

Below we characterize desorption of chlorine, sorbed under various conditions, with water.

It is seen that Cl_2 sorbed by the carbons at room temperature is easily and rapidly, virtually exhaustively, washed out with water in a single washing run (sample nos. 2–5, 10), and there is almost no desorption of Cl_2 sorbed at high temperatures (sample no. 6). This is, most probably, due to different characters of Cl_2 sorption. For example, despite fairly low capacity for chlorine at room temperature, AUT carbon exhibits no desorption of chlorine, probably because of its too strong binding by the fibrous sorbent. Desorption is enhanced by repeated water treatment of the carbon being regenerated.

Desorption of active chlorine from various carbons by single washing with distilled water. Weighed portion of carbon 1 g; water volume 100 ml; contact time 1.5 h; initial concentration c_0 of active chlorine (per gram of sorbent) ca. 6.0 mg l^{-1}

Table 2

Sample no.	2	3	4	5	6	9	10
c_d,* mg l^{-1}	5.39	5.04	5.39	3.69	0.14	0.00	4.54

* Active chlorine concentration in the desorbate.

Triple washing out of active chlorine from anthracite with distilled water. Weighed portion of carbon 15 g; water volume 200 ml; contact time 15 min; initial concentration c_0 of active chlorine (per gram of sorbent) ca. 5.4 mg l^{-1}

Washing	First	Second	Third
c_d, mg l^{-1}	4.20	0.40	0.05

After the first washing of activated anthracite, the chlorine concentration decreases from 5.4 to 4.2 mg l^{-1} (by 22%); after the second, by 92%; and the third washing affords 99% regeneration of AA.

Our data suggest that conventional thermal methods of carbon regeneration are unsuitable in our case. Evidently, regeneration is favored by weak binding of chlorine with carbon or reduction of chlorine into chloride ions directly in carbon pores [15–17].

We showed that, although the capacity for chlorine increases at high temperatures, regeneration of such spent sorbents is hindered. Therefore, it is reasonable to capture chlorine from waste gases without specially rising the temperature and to regenerate carbons by water treatment.

Our previous studies [17] on removal of active chlorine with activated carbons from spent anolyte (saturated NaCl solution) yielded by chlorine production revealed conditions suitable for regeneration of carbon sorbents saturated with chlorine. Indeed, we found (see figure) that chlorine is most efficiently removed by washing spent carbons with acidic solutions (pH 2–4).

We found that, upon contact with carbons, chlorine is removed from anolyte mostly via reduction of

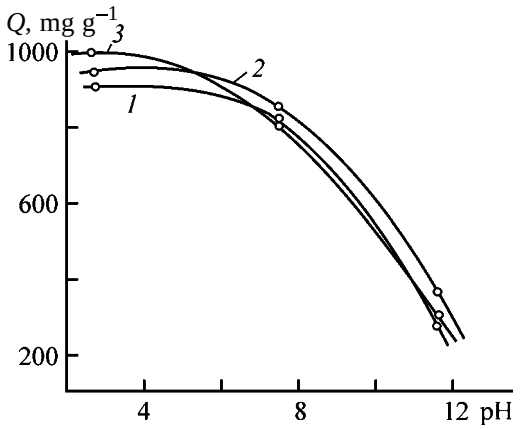

Amount Q of active chlorine removed from the anolyte with (*1*) AR-B, (*2*) AA, and (*3*) SKT carbons as influenced by pH of the medium.

HClO and molecular chlorine to chloride ions; carbon is oxidized to oxide compounds both on the surface and in the bulk.

The procedure for dechlorination in acidic medium, developed by us, was tested under process conditions at active chlorine concentrations of 100–300 ml l^{-1}. The experiments were run under dynamic conditions on two columns containing 20 kg of SKT each, at 80°C and the anolyte flow velocity of ca. 22 m h^{-1}. Both columns operated for over 75 days in total, and throughout this period there was no breakthrough of active chlorine.

Our results show that washing out of the sorbed chlorine from spent carbons with acidified water will involve not only desorption but also reduction of chlorine to chloride ions. Conversion of the sorbed chlorine into chloride ions, followed by washing of carbon, can be used for utilization of chlorine and regeneration of the sorbent.

The content of chlorine in wash waters can be reduced to MPC either by dilution or by dechlorination with carbon materials, involving reduction of active chlorine to chloride ions. The latter process can occur under certain conditions in carbon pores as well.

CONCLUSIONS

(1) Sorption capture of Cl_2 with various carbon sorbents was studied, and the capacities of the sorbents for chlorine were estimated at different temperatures and other experimental conditions; the best sorbents were selected.

(2) Specific features of Cl_2 sorption on carbon materials were revealed, namely, the sorbent "rest" phenomenon, i.e., resumption of sorption after diffusion of the sorbed Cl_2 inside the sorbent grains, and the required predominance of micropores.

(3) The amount of the sorbent required for exhaustive capture of chlorine within 1 month for a 500-l electrolysis bath was tentatively estimated from the capacity of the sorbent for chlorine, the capacity until breakthrough, the amount of the chlorine released in electrolysis of Cl_2, and the bulk density of the carbon. The dimensions of the sorption filter proposed were estimated.

(4) Spent sorbents can be regenerated by desorption of active chlorine by a single or repeated treatment with water, as well as under conditions favoring dechlorination via reduction of active chlorine to chloride ions at pH of wash waters of 2–4.

REFERENCES

1. Tomashevskaya, A.N., Tarkovskaya, I.A., and Baidenko, V.I., *Ukr. Khim. Zh.*, 1992, vol. 58, no. 2, pp. 156–161.
2. Tarkovskaya, I.A., Stavitskaya, S.S., and Tikhonova, L.P., *Zh. Prikl. Khim.*, 1996, vol. 69, no. 4, pp. 602–606.
3. Tarkovskaya, I.A., Stavitskaya, S.S., Larina, A.A., and Farberova, E.A., *Khim. Tekhnol.*, 1990, vol. 69, no. 4, pp. 47–51.
4. Tarkovskaya, I.A., Stavitskaya, S.S., Strelko, V.V., *et al.*, *Teor. Eksp. Khim.*, 2001, vol. 37, no. 2, pp. 118–124.
5. Tarkovskaya, I.A. and Stavitskaya, S.S., *Zh. Fiz. Khim.*, 2001, vol. 75, no. 9, pp. 1691–1696.
6. Tarkovskaya, I.A., Stavitskaya, S.S., Goba, V.E., and Tomashevskaya, A.N., *Khim. Tverd. Topl.*, 2001, no. 3, pp. 28–37.
7. Tarkovskaya, I.A., Stavitskaya, S.S., and Luk'yanchuk, V.M., *Zh. Prikl. Khim.*, 2001, vol. 74, no. 3, pp. 396–400.
8. Zelinskii, N.D. and Sadikov, V.S., *Ugol' kak sredstvo bor'by s udushayushchimi i yadovitymi gazami* (Carbon as a Control Agent for Suffocating and Toxic Gases), Moscow: Akad. Nauk SSSR, 1941.
9. Kel'tsev, N.V., *Osnovy sorbtsionnoi tekhniki* (Basics of Sorption Technique), Moscow: Khimiya, 1984.
10. Tarkovskaya, I.A., *Okislennyi ugol'* (Oxidized Carbon), Kiev: Naukova Dumka, 1981.
11. Tarkovskaya, I.A., *Sto "professii" uglya* (A Hundred "Jobs" of Carbon), Kiev: Naukova Dumka, 1983.
12. Siedlewski, G. and Szczesny, A., *Przem. Chem.*, 1974, vol. 53, no. 1, pp. 33–37.
13. Tetenov, V.V., Gavrilov, D.N., Ivakhnyuk, G.K.,

et al., Available from ONIITEKhIM, Cherkassy, 1981, no. 882 khp-D 81.

14. Ivakhnyuk, G.K., Fedorov, N.F., and Babkin, O.E., in *Poluchenie, struktura i svoistva sorbentov* (Preparation, Structure, and Properties of Sorbents), Leningrad: Khimiya, 1985, pp. 40–44.
15. Kul'skii. L.A., Savchuk, O.S., and Kayumova, G.Kh., *Intensifikatsiya protsessov obezzarazhivaniya vody* (Intensification of Water Disinfection Processes), Kiev: Naukova Dumka, 1978, pp. 5–9.
16. Tarkovskaya, I.A., Bondarenko, N.V., Kononchuk, T.I., and Kheifets, I.M., *Zh. Prikl. Khim.*, 1975, vol. 48, no. 5, pp. 966–970.
17. Tarkovskaya, I.A., Tomashevskaya, A.N., Goba, V.E., *et al.*, *Adsorb. Adsorb.*, 1974, no. 2, pp. 50–55.
18. Kul'skii, L.A., Levchenko, T.M., and Petrov, M.B., *Khimiya i mikrobiologiya vody* (Chemistry and Microbiology of Water), Kiev: Vishcha Shkola, 1976.
19. Stavitskaya, S.S., Goba, V.E., and Kartel', N.T., *Zh. Prikl. Khim.*, 2002, vol. 75, no. 12, pp. 1997–2001.
20. Tarkovskaya, I.A., Goba, V.E., and Atamanyuk, V.Yu., *Khim. Tekhnol.*, 1991, no. 3, pp. 38–41.
21. Stavitskaya, S.S., Goba, V.E., and Tsyba, N.N., *Zh. Prikl. Khim.*, 2002, vol. 75, no. 12, pp. 1993–1996.

Russian Journal of Applied Chemistry, Vol. 77, No. 9, 2004, pp. 1455–1459. Translated from Zhurnal Prikladnoi Khimii, Vol. 77, No. 9, 2004, pp. 1467–1471.

APPLIED ELECTROCHEMISTRY AND CORROSION PROTECTION OF METALS

Effect of Benzaldehyde Derivatives on the Rate of Hydrogen Evolution in a Sealed Lead–Acid Battery

Yu. B. Kamenev, A. V. Kiselevich, E. I. Ostapenko, and V. N. Varypaev

Elektrotyaga Scientific and Technological Center, Private Joint-Stock Company, St. Petersburg, Russia

Received March 5, 2004

Abstract—The influence exerted by a number of benzaldehyde derivatives on the rate of hydrogen evolution from a lead–acid battery was studied.

The market of sealed lead–acid batteries shows a steady rising tendency [1]. Use of batteries of this kind makes it possible to virtually rule out any gas evolution and to dramatically diminish the amount of maintenance work. The last factor is of primary importance, because, for some batteries, the maintenance cost during the service life is comparable with the initial price of the battery itself [2]. The possibility of sealing the lead–acid battery is based on the fact that virtually the whole amount of O_2 evolved at the positive electrode in charging is reduced at the negative electrode (closed oxygen cycle). Performing a similar hydrogen cycle is impossible without using additional catalytic systems because of the extremely low rate of H_2 oxidation at the positive electrode. According to [3], the rate of H_2 oxidation at the PbO_2 electrode is lower than that of O_2 reduction on Pb by a factor of 10^3. Thus, sealing the lead–acid battery requires that the rate of H_2 evolution should be minimized.

The scheme shows the sequence of operations carried out to diminish the rate of H_2 evolution in the sealed battery. It can be seen that the task of inhibiting H_2 formation in the battery is integrated and involves solutions related to the design and the composition of the components of the electrode block (1.1, 1.3, 2.1), to use of external, with respect to the block, devices (2.2, 2.3, 2.4), and to optimization of the charging mode (1.3).

Apparently, the most efficient are the operations intended to diminish the H_2 evolution rate, rather than those aimed to oxidize the gas that has already evolved within the battery, because the former operations control the causes, and the latter, the consequences of the negative phenomenon.

The rate of H_2 evolution can be markedly diminished by (i) excluding elements with low hydrogen overvoltage (Sb, Cu, Ag, As, Fe, Mn, Ni, Co) from the composition of the active paste and structural materials [4], (ii) using additives that make higher the overvoltage of H_2 evolution at the negative electrode, (iii) optimizing the relative amounts of the active pastes [5, 6], and (iv) optimizing the charging mode [7].

At present, neither catalytic electrodes made of platinum or carbon materials nor H_2 absorbents find use in the world practice. Their use, on the one hand, is inefficient and unreliable (catalyst poisoning, low absorption of H_2 because of its low partial pressure within the battery), and on the other, makes higher the cost of batteries.

Additives are widely used in lead batteries to improve their energy-storage and resource parameters. An important role of additives as expanders of negative active pastes, which slow down the rate of recrystallization of spongy lead and preserve its large specific surface area, is well known [8]. Additives are also used as inhibitors of self-discharge [9]. The mechanism of their action commonly consists in that the overvoltage of H_2 evolution on lead and phase impurities increases, which makes slower the rate of the conjugated reaction of Pb oxidation. Additives are also introduced into positive active pastes to improve their mechanical strength and preclude their sagging [10]. Additives of this kind can be introduced in the form of fibers, powders, or suspensions. A considerable progress has been made in all of these areas. However, the specific features of operation of a sealed battery, on the one hand, impose restrictions on additives used in ordinary batteries, and on the other, require that new types of additives should be developed.

The aim of this study was to examine additives that inhibit H_2 evolution in a lead–acid battery.

1070-4272/04/7709-1455 © 2004 MAIK "Nauka/Interperiodica"

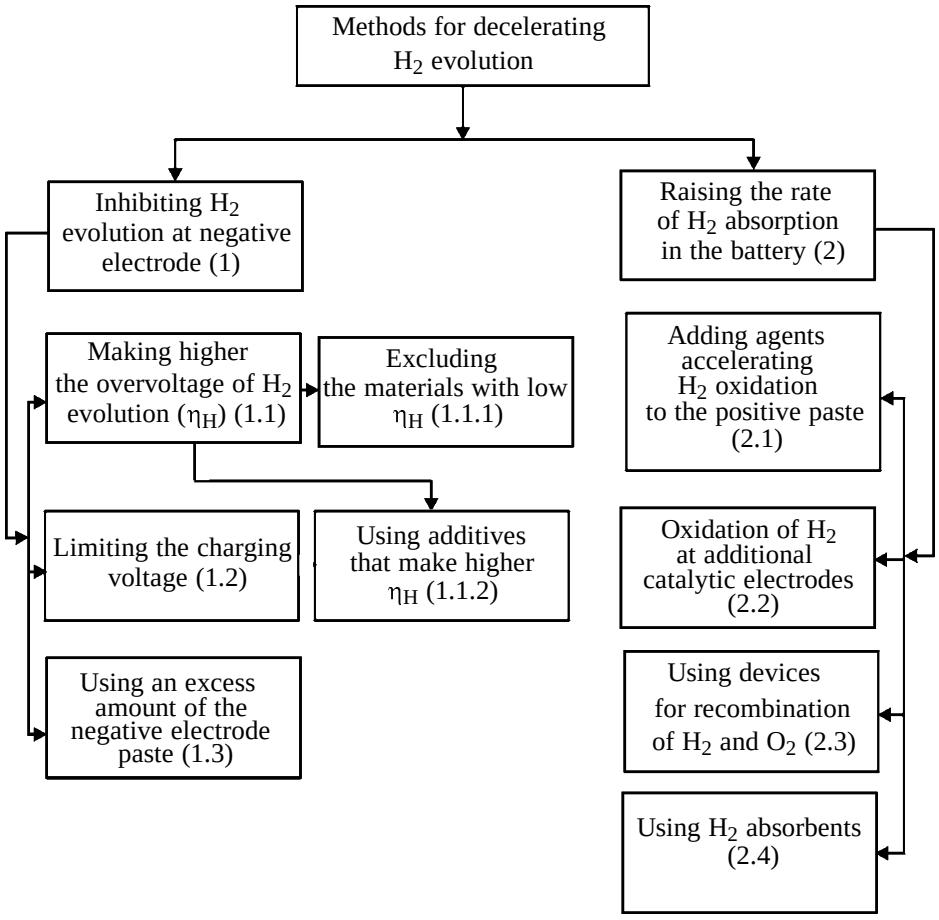

General scheme of operations aimed to diminish the rate of H_2 evolution in a sealed battery.

It is known that Pb belongs to metals with a high overvoltage of H_2 evolution. The constant *a* in the Tafel equation for lead is 1.52–1.56 V. However, phase impurities composed of metals with a low H_2 overvoltage can be formed in a working battery on the surface of the negative current lead. To elements of this kind primarily belong Sb and Cu, for which *a* is 0.9 and 0.8 V, respectively. Antimony finds its way to the negative electrode through corrosion of the current lead (made of lead–antimony alloys) of the positive electrode, and lead-plated copper current leads of the negative electrode serve as a source of Cu. During the service life of a battery, the protective properties of the lead coating are impaired and Cu appears on the surface of the negative active paste. Thus, an additive that would make higher the overvoltage of H_2 evolution on Sb and Cu but would not affect the course of the main current-producing processes at the negative and positive electrodes is necessary. With account of the fact that the mechanism by which the gas evolution is hindered is associated with adsorption of additives (surfactants) onto the metal surface, an efficient additive that would inhibit gas evolution must exhibit a high adsorption selectivity with respect to Cu and Sb, on the one hand, and Pb, on the other. As possible additives were studied benzaldehyde derivatives. In [11, 12], it was shown that aromatic aldehydes, which are characterized by clearly pronounced polarity with high dipole moment and, therefore, exhibit an increased adsorption capacity, exert an inhibiting influence on H_2 evolution. However, their adsorption capacity largely depends on a substituting group, which determines the electron distribution between the benzene ring and this group. The choice of an inhibitor is determined by the following: it should exhibit a selective adsorption on Sb and Cu impurities, without decelerating the current-producing reaction or O_2 reduction. The following benzaldehyde derivatives were examined in this study: 2-hydroxybenzaldehyde $C_7H_6O_2$ (2-HB) and 2-methoxybenzaldehyde $C_8H_8O_2$ (2-MB).

The study was carried out with Sb of SU1 brand, copper foil, and Pb of S1 brand in specially purified

5 M H_2SO_4. The performance of the additives was estimated by analyzing the polarization curves measured at current in the range 0.5–50 mA cm^{-2} at 25 ± 0.1°C.

Figure 1 shows the polarization curves obtained on Sb and Cu in an H_2SO_4 solution with addition of 0–1.30 g l^{-1} of 2-MB and 0–1.17 g l^{-1} of 2-HB. The table lists the efficiency factors K_{eff}, defined as the ratio of H_2 evolution rates at a potential of 0.6 V in solutions with and without an additive, for the additives studied.

Figure 1 shows that 2-MB and 2-HB are exceedingly efficient in hindering the H_2 evolution on both Sb and Cu. At their concentration in the electrolyte equal to 9.6×10^{-3} M, K_{eff} is 11.6–22.9 on Sb and 48–50 on Cu. It also follows from Fig. 1 that the inhibiting effect of 2-MB and 2-HB grows as their concentration in solution increases, to become the most pronounced at a concentration of 9.6×10^{-3} M. However, the results obtained give no reason, as yet, to recommend 2-MB and 2-HB as inhibitors of H_2 evolution for lead batteries. For this purpose, it is necessary to make sure that these additives do not affect simultaneously the current-producing reactions and the reactions of the closed oxygen cycle.

Figure 2 shows the polarization curves obtained on a porous lead cathode in a 5 M H_2SO_4 solution with addition of 0–0.9 g l^{-1} of 2-MB and 0–0.8 g l^{-1} of 2-HB. It can be seen that addition of 2-MB leads, in the entire range of concentrations, to an increase in the overvoltage of H_2 evolution. This indicates that the additive can be adsorbed on the Pb surface and can thereby affect the main current-producing processes. At the same time, addition of 2-HB affects the rate of H_2 evolution on Pb only slightly, suggesting its low adsorption capacity with respect to the Pb surface.

It is known that the zero-charge potentials for Pb, Cu, and Sb are –0.69, –0.04, and 0.0 V, respectively (relative to a standard hydrogen electrode). Thus, the surface of Pb is charged positively, and that of Cu and Sb, negatively, at potentials of the negative electrode. Therefore, the surface of Pb is covered in H_2SO_4 with an adsorption layer of HSO_4^- ions, and that of Sb and Cu, with H^+ ions [13]. It is also known that introduction of various substituent groups into the structure of benzaldehyde changes its electronic configuration and the dipole moment of the molecule [14].

The concept of moderate and strong inhibitors of H_2 evolution, which are derivatives of aromatic hydrocarbons [13], can be used to account for the experimental data obtained. It should be assumed that strong inhibitors hinder not only the H_2 evolution on Sb and Cu through their adsorption on the surface of these metals, but also the processes on the surface of Pb because of the ability of such inhibitors to displace HSO_4^- ions and be adsorbed on the surface. As a result, the current-producing reaction is hindered.

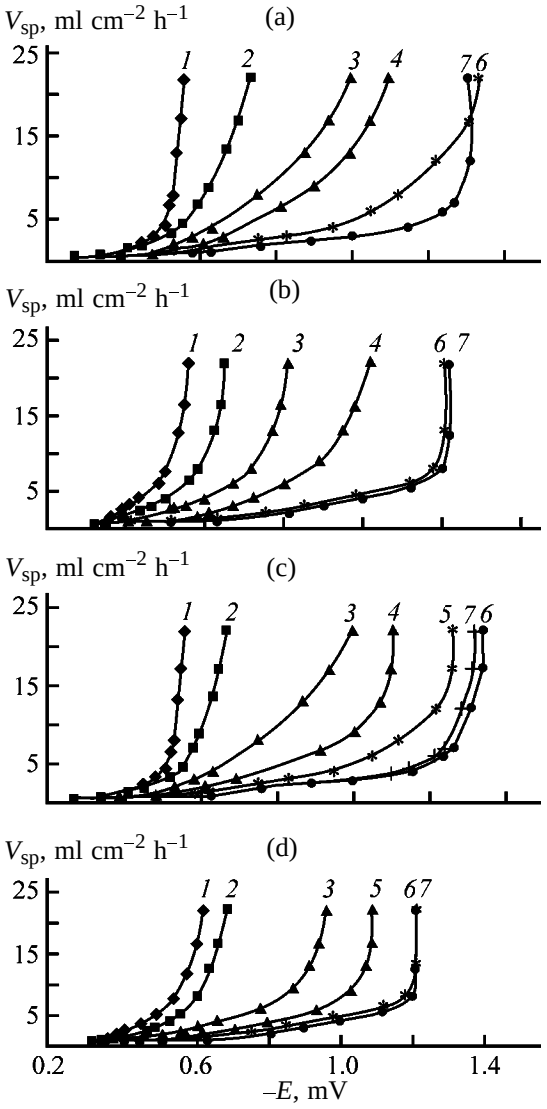

Fig. 1. Specific rate of hydrogen evolution, V_{sp}, on (a, b) antimony and (c, d) copper in a 5 M H_2SO_4 solution with addition of (a, c) 2-MB and (b, d) 2-HB vs. the polarization potential E. Concentration (g l^{-1}): 2-MB: (*1*) 0, (*2*) 0.05, (*3*) 0.17, (*4*) 0.34, (*5*) 0.65, (*6*) 0.83, and (*7*) 1.30; 2-HB: (*1*) 0, (*2*) 0.23, (*3*) 0.47, (*4*) 0.58, (*5*) 0.70, (*6*) 0.88, and (*7*) 1.17.

It was shown that the 2-MB additive has a high adsorbability not only on Sb and Cu, but also on Pb. The latter is strongly undesirable because of the de-

Efficiency factors of 2-MB and 2-HB additives

2-MB		2-HB	
c, g l^{-1} (M)	K_{eff}	c, g l^{-1} (M)	K_{eff}
Antimony cathode			
0.05 (3.7×10^{-4})	1.8	0.23 (1.9×10^{-3})	2.3
0.17 (1.2×10^{-3})	4.0	0.47 (3.8×10^{-3})	5.9
0.34 (2.5×10^{-3})	6.6	0.58 (4.7×10^{-3})	12.8
0.83 (6.1×10^{-3})	8.7	0.88 (7.2×10^{-3})	18.7
1.30 (9.6×10^{-3})	11.6	1.17 (9.6×10^{-3})	22.9
Copper cathode			
0.05 (3.7×10^{-4})	2.9	0.23 (1.9×10^{-3})	2.7
0.17 (1.2×10^{-3})	12.5	0.47 (3.8×10^{-3})	10.5
0.34 (2.5×10^{-3})	16.7	0.70 (4.7×10^{-3})	24.0
0.65 (4.8×10^{-3})	45.0	0.88 (7.2×10^{-3})	42.0
0.83 (6.1×10^{-3})	50.0	1.17 (9.6×10^{-3})	48.0
1.30 (9.6×10^{-3})	50.0	–	–

creasing rate of the main current-producing process at the negative electrode. Thus, the 2-MB inhibitor cannot be recommended for use in lead batteries despite its high performance. In the opinion of Böhnstedt and Radel [13], moderate inhibitors cannot displace HSO_4^- and be adsorbed on Pb, which predetermines the high degree of their selective adsorption. Inhibitors of this kind are mainly adsorbed on detrimental impurities (Sb, Cu) and suppress H_2 evolution on these elements. At the same time, they are not adsorbed on Pb and do not exert any negative influence on the processes that occur on this element. Consequently, the 2-HB inhibitor can be classed with moderate inhibitors and recommended for use in lead batteries.

However, prior to recommending 2-HB for use in lead batteries, it is necessary to find out whether or not it has an effect on the operation of the positive electrode and, primarily, on the rate of O_2 evolution, which characterizes the efficiency of utilization of the charging current, as well as on the kinetics of the current-producing reaction. An influence of this kind is, in principle, possible because of the contact between the inhibitor introduced into a solution with the positive active paste. For this purpose, polarization curves were measured on a PbO_2 electrode in the anodic potential range in a solution containing the 2-HB inhibitor (Fig. 3a). Figures 3a and 3b show that 2-HB has no effect on the rate of O_2 evolution at the PbO_2 electrode and on its discharge characteristics.

The performance of the 2-HB inhibitor was tested in stationary batteries with a rated capacity of 12000 A h. At the end of the service life of these batteries, the rate of H_2 evolution was 600 (battery no. 1) and 700 $cm^3\ min^{-1}$ (battery no. 2). A 2-HB

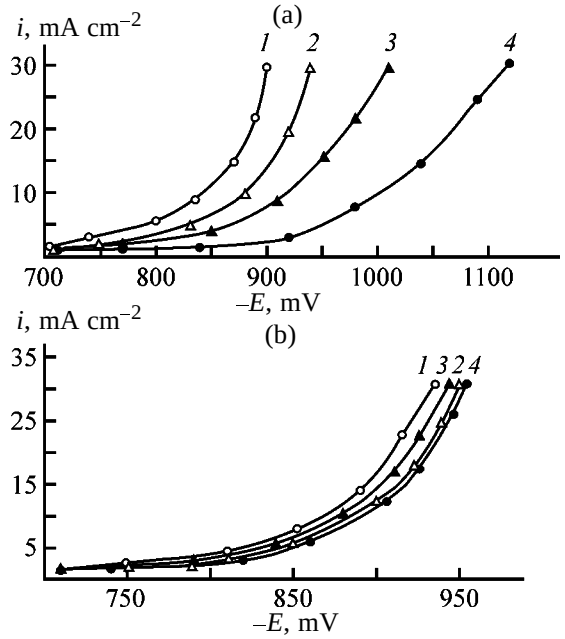

Fig. 2. Polarization curves obtained on a porous lead cathode in a 5 M H_2SO_4 solution with addition of (a) 2-MB and (b) 2-HB. (*i*) Current density and (*E*) potential. Concentration (g l^{-1}): 2-MB: (*1*) 0, (*2*) 0.01, (*3*) 0.09, and (*4*) 0.9; 2-HB: (*1*) 0, (*2*) 0.01, (*3*) 0.1, and (*4*) 0.8.

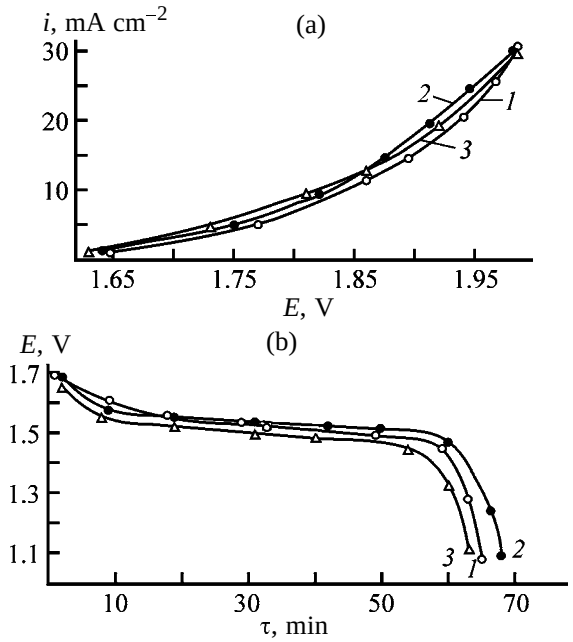

Fig. 3. (a) Polarization and (b) discharge curves obtained on a PbO_2 electrode in a 5 M H_2SO_4 solution (*1*) without additives and with addition of (*2*) 2-MB and (*3*) 2-HB. Concentration (g l^{-1}): 2-MB, 0.9; 2-HB, 0.8. (*i*) Current density, (*E*) potential, and (τ) time.

additive was introduced into battery no. 2, with the result that the rate of gas evolution decreased to 200 $cm^3 min^{-1}$ in the subsequent cycle. In battery no. 1, into which no additive was introduced, the gas evolution rate increased to 670 $cm^3 min^{-1}$.

CONCLUSIONS

(1) According to our results, 2-hydroxybenzaldehyde can be recommended as an additive effectively inhibiting the evolution of H_2 in sealed lead–acid batteries.

(2) This inhibitor can diminish the rate of H_2 evolution on Sb and Cu by factors of 10–12 and 15–29, respectively, with the discharge characteristics of the electrodes and the efficiency of the closed oxygen cycle remaining virtually unaffected.

REFERENCES

1. Winckel, J.W. and Rice, D.M., *J. Power Sources*, 1998, vol. 73, pp. 3–10.
2. Pesaran, A., *J. Batteries Int.*, 2001, issue 47, April, pp. 107–110.
3. Aguf, I.A., Tsenter, B.I., and Mrga, I., *Problema germetizatsii svintsovogo akkumulyatora: Elektrotekhnicheskaya promyshlennost', Ser. 22* (Problem of Sealing of Lead Battery: Electrical Industry, Ser. 22), Moscow: Informelektro, 1989.
4. Kamenev, Yu.B., Kiselevich, A.V., and Ostapenko, E.I., *Zh. Prikl. Khim.*, 2002, vol. 75, no. 4, pp. 562–565.
5. Kamenev, Y., Chunts, N., and Ostapenko, E., *J. Power Sources*, 2003, vol. 116, pp. 169–173.
6. Kamenev, Y., Chunts, N., and Ostapenko, E., *J. Power Sources*, 2002, vol. 108, pp. 58–63.
7. Kamenev, Yu.B., Chunts, N.I., and Ostapenko, E.I., *Elektrokhim. Energet.*, 2003, vol. 3, no. 3, pp. 139–146.
8. Pavlov, D. and Myrvold, B., in *Int. Conf. on Lead–Acid Batteries, LABAT'99*, Bulgaria, June 7–10, 1999, pp. 37–42.
9. Dietz, H. and Hoogestaat, G., *J. Power Sources*, 1995, vol. 53, pp. 359–365.
10. Babaeva, L.I. and Vasil'ev, V.G., in *Sbornik rabot po KhIT* (Coll. of Works on Chemical Power Sources), Leningrad: Energiya, 1975, issue 10, pp. 96–104.
11. Doring, H. and Radman, M., *J. Power Sources*, 1989, vol. 28, pp. 381–386.
12. Gust, S. and Hameenoja, E., *J. Power Sources*, 1990, vol. 30, pp. 189–192.
13. Böhnstedt, W. and Radel, C., *J. Power Sources*, 1987, vol. 19, pp. 301–309.
14. Ramsden, E.N., *A-Level Chemistry*, Stanley Thornes, 1985.

Russian Journal of Applied Chemistry, Vol. 77, No. 9, 2004, pp. 1460–1468. Translated from Zhurnal Prikladnoi Khimii, Vol. 77, No. 9, 2004, pp. 1472–1480.

APPLIED ELECTROCHEMISTRY AND CORROSION PROTECTION OF METALS

Anodic-Spark Layers on Aluminum and Titanium Alloys in Electrolytes with Sodium Phosphotungstate

I. V. Lukiyanchuk, V. S. Rudnev, V. G. Kuryavyi, and P. S. Gordienko

Institute of Chemistry, Far Eastern Division, Russian Academy of Sciences, Vladivostok, Russia

Received June 16, 2003; in final form, January 2004

Abstract—The influence exerted by the pH of an aqueous 0.0083 M solution of $Na_2H[PW_{12}O_{40}]$ on the composition and morphology of anodic coatings galvanostatically formed on aluminum and titanium alloys at sparking and breakdown voltages was studied.

Anodic treatment of rectifying metals in aqueous electrolytes in the sparking and microarc mode (henceforth, anodic-spark deposition) can give coatings that contain, in addition to oxides of a metal or alloy being treated, oxygen compounds of elements contained in the electrolyte. As a result, coatings that exhibit functions typical of anodic films and are promising for use in catalysis [1], as active elements of gas analyzers [2, 3], and bioinert compounds [4] can be obtained. As an example can serve the formation on titanium of layers that contain barium, strontium, or lead titanates and exhibit ferroelectric properties [5, 6].

One of the main processes that determine the composition of the forming anodic-spark layers is thermolysis of the electrolytic deposit around electric-breakdown channels. Use of electrolytes containing anionic complexes opens up additional opportunities for directed formation of oxide structures. Coatings of various compositions and purposes can be obtained in electrolytes of this kind. For example, wear-resistant coatings containing α-Al_2O_3 are obtained in solutions with hexafluoroaluminate complexes [7]; corrosion-resistant coatings with vanadium oxides, in electrolytes with phosphovanadate heteropolyanions [8, 9]; biocidal coatings with zinc phosphates, in solutions with zinc polyphosphate complexes [10]; bioinert coatings with hydrooxyapatite for implants, in electrolytes with calcium glycerophosphate complexes [4]; and light-reflecting coatings that contain ZrO_2 and are resistant to the action of hard ultraviolet, in solutions with alkali metal hexafluorozirconate complexes [11].

At the same time, the processes of coating formation in electrolytes with anionic complexes are now in the stage of research and accumulation of experimental data. Among such electrolytes, those containing iso- and heteropolyanions (IPA and HPA) are the least studied. The interest in these electrolytes is due to the following.

(a) The variety of IPA and HPA is rather wide. Only the position of the central atom in an HPA can be occupied by more than 60 elements [12]. Formation of coatings with diverse chemical compositions would be expected in electrolytes with HPA. These compositions must, apparently, reflect the scheme of thermal transformations of HPA or of products formed in their interaction with a metal being anodized.

(b) Conditions for formation of IPA and HPA are satisfied in many aqueous solutions that are used in anodic-spark oxidation and contain compounds of vanadium, molybdenum, and tungsten in higher oxidation states. Consequently, revealing the relationship between the presence or absence of HPA in electrolytes and the composition of the anodic-spark layers being formed is both practically and theoretically important.

(c) Thermal decomposition of heteropoly compounds is used to produce oxide catalysts [13]. It is quite possible that thermolysis of HPA or products of their interaction with a metal being anodized, which occurs near electric-breakdown channels, will make it possible to form on metals oxide structures promising as regards their possible catalytic activity.

(d) It has been shown previously that films formed in electrolytes with HPA show satisfactory protective properties [8, 14, 15].

Until now, fundamental aspects of how the elements contained in HPA are incorporated into coatings on rectifying metals have been studied in multicomponent electrolytes containing simultaneously

1070-4272/04/7709-1460 © 2004 MAIK "Nauka/Interperiodica"

Table 1. Characteristics of the electrolyte (0.0083 M $Na_2H[PW_{12}O_{40}]$ + NaOH) and phase composition of coatings according to XPA

Electrolyte				Coatings on aluminum		Phase composition of coatings on titanium
initial		after anodizing		i, A dm^{-2}	phase composition	
pH	æ × 10^3, S cm^{-1}	pH	æ × 10^3, S cm^{-1}			
2.0	4.5	1.8	4.8	1–10	$WO_{2.9}$	$WO_{2.9}$
4.1	3.1	6.8	3.3	1–10	〃	$Na_{0.1}WO_3$
6.5	3.8	7.0	4.0	1–10	$WO_{2.9}$ or $Na_{0.1}WO_3$	〃
7.1	6.0	7.3	6.0	1–10	$Na_{0.1}WO_3$	〃
7.8	12.0	10.9	12.0	1–2	Amorphous	?$Na_{0.1}WO_3$
				3–10	$Na_{0.1}WO_3$	
12.6	14.3	13.0	14.3	1	Amorphous	$Na_{0.1}WO_3$
				2–10	WO_3 or $Na_{0.1}WO_3$	

phosphate or borate anions and anions of transition metals [9, 16–18]. Publications that report use of commercial heteropoly compounds to form anodic-spark coatings are scarce [14, 15]. The functional properties and surface morphology of coatings formed in electrolytes of this kind remain virtually unstudied. Data on how coatings are formed in electrolytes with phosphate and tungstate ions and various concentrations of salts and pH values are contradictory [17].

It is known that the forms in which IPA and HPA are present in the electrolyte depend on its pH [12]. The aim of this study was to determine how the composition and morphology of anodic-spark layers on aluminum and titanium alloys depend on transformations of tungsten–phosphorus (phosphotungstate) HPA that occur when the pH value of the electrolyte is varied.

EXPERIMENTAL

The electrolytes were prepared from distilled water and commercial $Na_2H[PW_{12}O_{40}]\cdot 9H_2O$ and NaOH of chemically pure grade. All the electrolytes were produced by mixing the solutions at room temperature. The concentration of sodium hydrotungstophosphate in all the electrolytes was 0.0083 M, which corresponds to a total tungsten(VI) concentration in solution equal to 0.1 M. The electrochemical cell employed and the procedure for pretreatment of aluminum (AMtsM) and titanium (VT1-0) samples (40 × 10 × 1 mm) have been described previously [19, 20]. In each of the electrolytes, oxide layers were successively formed on the samples in the galvanostatic mode in the course of 10 min at current densities of 1 to 10 A dm^{-2} for the aluminum alloy and 10 A dm^{-2} for the titanium alloy (because it was impossible to reach the sparking mode for titanium in 10 min at lower i). The electrolyte temperature did not exceed 20°C in anodic-spark oxidation of aluminum and became as high as 30°C in anodic-spark treatment of titanium. After the treatment, samples with coatings were thoroughly washed first with tap water and then with distilled water and dried in air at room temperature.

The sparking voltage was estimated from the appearance of first visually observed sparks on the anode surface or by analyzing $U = f(t)$ curves (from the beginning of deviation of the dependence of the voltage U across the electrodes on time t from linear behavior). The phase composition of the coatings was studied by X-ray phase analysis (XPA) on a DRON-2.0 diffractometer (CuK_α radiation). The elemental composition of the coatings was determined with a JEDE JXA-5A X-ray fluorescence analyzer. ^{31}P NMR spectra of aqueous solutions were recorded on a Bruker WP-80SY high-resolution spectrometer at a frequency of 32.442 MHz. The chemical shifts are given in the δ scale (ppm) relative to 85% H_3PO_4. The surface morphology was studied with an LEO 430 scanning electron microscope (SEM).

The pH values and the electrical conductivities of tungstophosphate electrolytes before and after anodic-spark treatment, and also the phase compositions of the coatings formed, are listed in Table 1. It should be noted here that the pH strongly increases in the course of anodic-spark deposition from the initial values of 4.1 and 7.8 at an only slight change in the electrical conductivity of the solutions, and the electrical con-

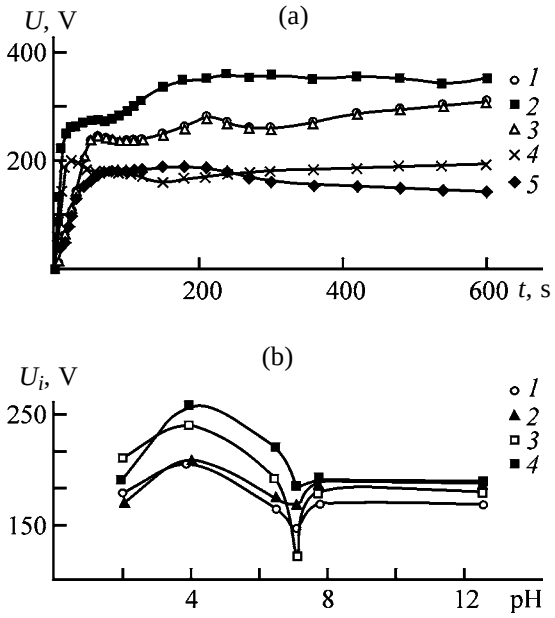

Fig. 1. Effect of pH of the electrolyte (a) on the dependence of the voltage U across the electrodes on time τ at i = 10 A dm^{-2} and (b) on the sparking voltage U_i in anodic-spark deposition on the aluminum alloy. (a) pH: (*1*) 2.0, (*2*) 4.1, (*3*) 6.5, (*4*) 7.8, and (*5*) 12.6. (b) i (A dm^{-2}): (*1*) 2, (*2*) 3, (*3*) 8, and (*4*) 10.

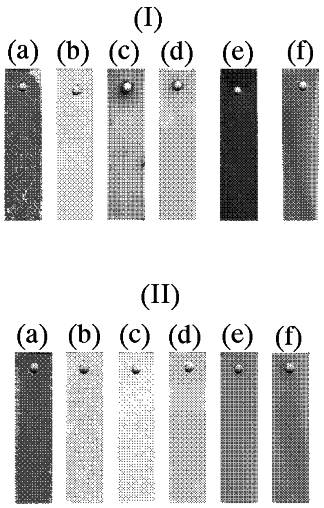

Fig. 2. Effect of pH of an electrolyte with 0.0083 M of $Na_2H[PW_{12}O_{40}]$ on the outward appearance of coatings on the aluminum and titanium alloys. Coating: (*I*) on the AMtsM alloy, i = 2 A dm^{-2}; (*II*) on the VT1-0 alloy, i = 10 A dm^{-2}. pH before/after coating formation: (a) 2.0/1.8, (b) 4.1/6.8, (c) 6.5/7.0. (d) 7.1/7.3, (e) 7.8/10.9, and (f) 12.6/13.0.

ductivity decreases on passing from an electrolyte with pH 2.0 to that with pH 4.1. The coatings formed on both aluminum and titanium alloys contain $WO_{2.9}$ or $Na_{0.1}WO_3$. The coatings formed on the aluminum alloy at low current densities at pH 7.8–13.0 are X-ray amorphous. The position of the curves describing the $U = f(t)$ dependences changes with the pH value and the electrical conductivity (Fig. 1a). All the pH dependences of the sparking voltage U_i show a maximum at pH 4.1 and a minimum at pH 7.1.

The outward appearance of the coatings formed on aluminum and titanium samples at various pH values of the electrolyte is shown in Fig. 2. The coatings formed on aluminum and titanium alloys in weakly acidic and neutral electrolytes are green (white in black-and-white photographs). In other cases, the coatings on titanium are gray-green, and those on aluminum are constituted by gray and green layers. The outer green layer of the coatings formed in an electrolyte with pH 6.5 show blue point-like inclusions (darker in the photograph). Despite the differences in the outward appearance, most of the coatings contain phases of nonstoichiometric tungsten oxide and sodium–tungsten bronze (Table 1). As green regions nucleate and grow on the surface of the aluminum samples, peaks of these phases appear in X-ray diffraction patterns and their intensity increases; in the absence of green regions, XPA shows that the coatings are amorphous. Thus, gray layers formed on the aluminum alloy in electrolytes with pH 2.0, 7.8, and 12.6 are amorphous, and green layers contain crystalline compounds of tungsten. The green regions may appear as separate points and grow in the radial direction, which is observed in electrolytes with pH 2.0 and 7.8–10.6. Crystalline tungsten-containing layers are formed in an electrolyte with pH 12.6. They appear at sample edges and expand as a whole front over the surface, with the surface coverage depending on the quantity Q of electricity passed. At Q = 6 C cm^{-2}, there are no green regions as yet; at Q = 12 C cm^{-2}, the area of the anode surface covered with green regions is small; and, beginning with Q = 60 C cm^{-2}, the layer of a new phase of green color occupies more than half of the anode surface, with the arrangement of green regions symmetrical for both sides of a sample.

The dependence of the content of the main elements in the coatings on pH is shown in Figs. 3a–3c. The content of tungsten in the surface layers of the coatings is maximal, and the content of aluminum or titanium, minimal at pH 4.1–7.3, i.e., in the range of formation of crystalline tungsten-containing oxide layers. The amorphous layers formed on the aluminum alloy at pH 2.0 and 7.8–10.9 have approximately the same elemental composition (Table 2), with the W/P atomic ratio for these layers close to 12.

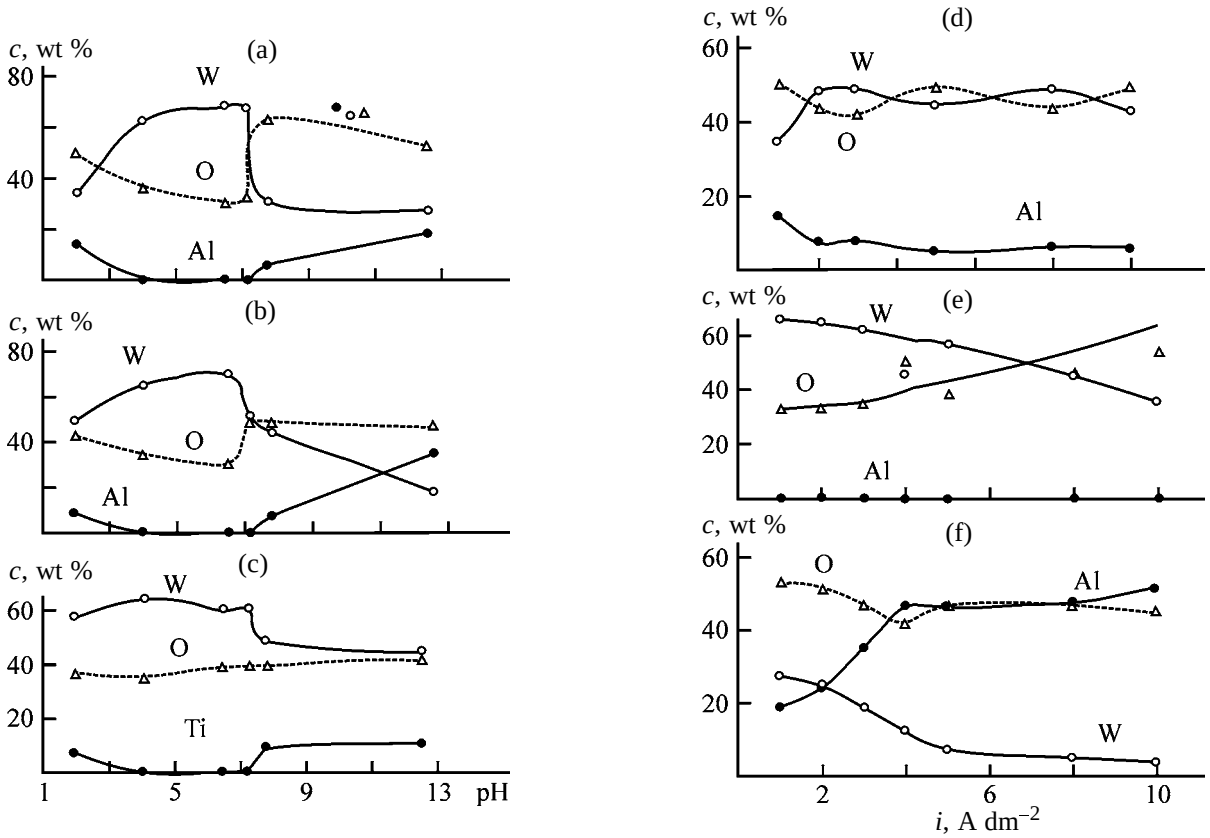

Fig. 3. Effect of pH of an electrolyte and of the current density i on the content c of the main elements in the coatings formed on (a, b, d–f) aluminum and (c) titanium alloys. Current density i (A dm^{-2}): (a) 1, (b) 3, and (c) 10. pH: (d) 2.0, (e) 4.1, and (f) 12.6.

SEM images of the surface of the coatings formed on the aluminum alloy in electrolytes with pH 2.0, 7.8–10.9, and 12.6–13.0 are shown in Fig. 4(I). Noteworthy is the similarity of the surface morphologies of amorphous layers [Figs. 4(I)b, 4(I)d] obtained in acid (pH 2.0) and alkaline (pH 12.6–13.0) electrolytes. The only difference consists in the size of depressions and partly fused raised formations, which are larger in the latter case [Fig. 4(I)d]. Amorphous layers deposited from an electrolyte with pH 7.8–10.9 [Fig. 4(I)c] are formed of threads or fibers 3–10 μm in diameter on a cellular partly melted surface. Cracks are present on the surface of the fibers. Spherical embedded particles (lighter in black-and-white photographs), which are crystalline inclusions of nonstoichiometric compounds of tungsten, are observed on the surface of the amorphous layer formed in an acid electrolyte [Fig. 4(I)b)] and mostly on the surface of fibers in the coatings formed in an electrolyte with pH 7.8–10.9. Of the same crystalline formations are composed more extended green regions, as shown in Fig. 4(I)a (projecting fragment in the photograph).

The influence exerted by the current density on the composition of coatings formed on the aluminum alloy is illustrated by Figs. 3d–3f. The content of the main elements (Al, W) in the amorphous layers of the coatings formed in an acid electrolyte (pH 2) is independent of current density in the range i = 2–10 A dm^{-2} (Fig. 3d). When anodic-spark coatings are formed in an alkaline electrolyte (pH 12.6), the concentration of aluminum grows and that of tungsten falls as the current density increases (Fig. 3f); the composition of the coatings is constant in the range i = 5–10 A dm^{-2}. The crystalline tungsten-containing green layers show a general tendency toward a decrease in the concentration of tungsten with increasing current density (Fig. 3e), despite that the phase composition is constant and aluminum is virtually absent. As can be seen in SEM images of the crystalline layers ([Fig. 4(II)], the fragments of the surface profile become coarser, and the distances between them, longer, as the current density increases.

The sparking voltage U_i is related to the electrical conductivity of the anodizing solution by the following expression [21]:

$$U_i = a - b\ln æ. \quad (1)$$

Table 2. Effect of pH of phosphotungstate electrolyte on the concentration *c* and atomic ratios *A* of the main elements in coatings

pH	*c*, wt %						*A*	
	Al(Ti)	W	P	Na	Mn	O*	W/Al(Ti)	W/P
Coatings on aluminum**								
Black regions								
2.0–1.9	6.7	44.7	0.64	0.16	0.04	42.6	1.1	12.1
4.1–6.8								
6.5–7.0	No black regions							
7.0–7.3								
7.8–10.9	6.41	43.6	0.65	0.26	0.08	49.0	1.0	11.3
12.6–13.0	38.5	14.1	0.16	0.11	0.3	33.8	0.1	15.7
Green regions								
2.0–1.9	0.11	56.9	0.26	0.16	0.04	42.6	–	39
4.1–6.8	0.16	53.6	0.4	0.15	0.26	45.5	–	24
6.5–7.0	0.03	59.7	0.41	0.15	0.03	39.7	–	27
7.0–7.3	–	56.8	0.25	0.16	–	42.8	–	33
7.8–10.9	0.02	55.5	0.36	0.31	–	43.8	–	40
12.6–13.0	0.14	59.2	0.15	0.18	0.06	40.3	–	65
Coatings on titanium								
2.0–1.9	6.29	57.0	0.37	0.22	–	35.55	2.4	26
4.1–6.8	0.04	64.0	0.07	0.36	–	35.22	–	154
6.5–7.0	–	60.3	0.14	0.28	–	39.07	–	73
7.0–7.3	–	60.3	0.22	0.3	–	39.01	–	46
7.8–10.9	8.97	48.6	1.05	0.88	–	39.23	1.4	7.8
12.6–13.0	11.1	44.6	0.55	1.04	–	41.73	1.0	13.7

* The content of the element is determined as difference.
** The contents of elements obtained in experiments at different current densities were averaged.

In the given case, æ depends on the amount of the alkali added (Fig. 5a). The curve describing the dependence of pH of a 0.0083 M solution of $Na_2H[PW_{12}O_{40}]$ on the volume of a 1 M NaOH solution (titration curve) shows two steps at pH 3–7 and 8–12 (Fig. 5b). The first step corresponds to neutralization of the acid salt (2), which leads to a smaller number of charge carriers and, consequently, to a decrease in æ (Fig. 5b):

$$Na_2H[PW_{12}O_{40}] + NaOH \rightarrow Na_3[PW_{12}O_{40}] + H_2O. \quad (2)$$

In accordance with Eq. (1), a decrease in the electrical conductivity leads to an increase in the sparking voltage [to the minimum value of æ in the æ = $f(V_{NaOH})$ plot corresponds the maximum value of U_i in the $U_i = f(\text{pH})$ plot, Fig. 1b]. At the same time, the minimum in the dependence $U_i = f(\text{pH})$ is not accompanied by changes in the type of the electrical conductivity of the solutions or steplike changes in pH. By contrast, it lies in the range of stable pH values (Fig. 5b).

The following scheme of mutual transformations at different pH values of an aqueous solution is known for tungsten–phosphorus HPA [12]:

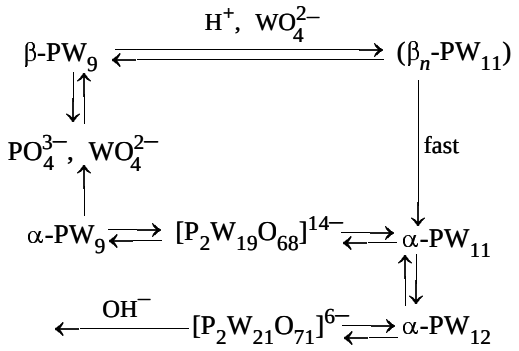

Already at pH 1–2, an equilibrium is established between PW_{12} and PW_{11}:

$$[PW_{12}O_{40}]^{3-} + (5 - x)OH^- \rightleftarrows [H_xPW_{11}O_{39}]^{(x-7)} + HWO_4^- + (2 - x)H_2O. \quad (3)$$

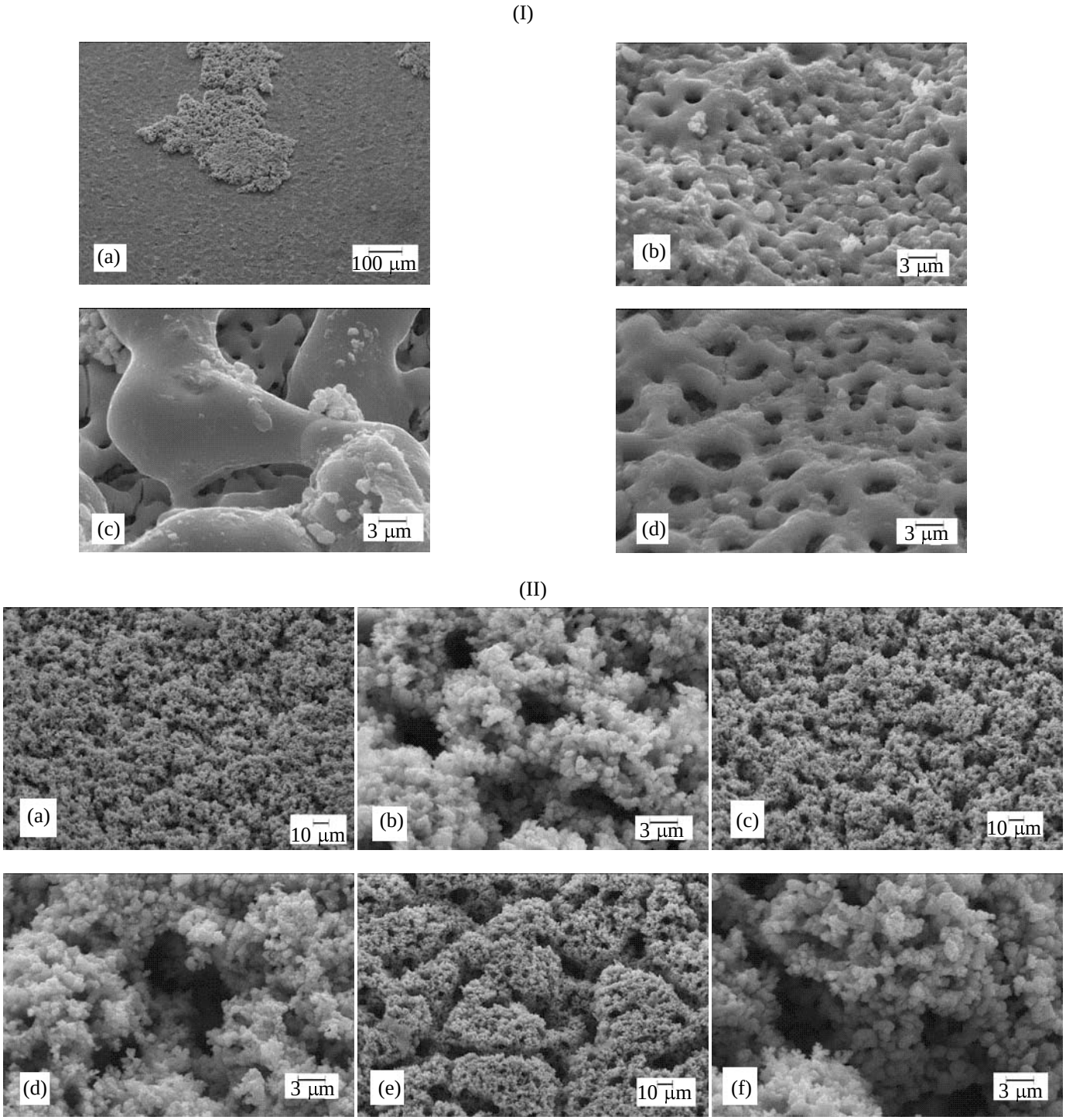

Fig. 4. SEM images (45° view) of the surface of coatings formed on aluminum (I) at i = 2 A dm^{-2} in electrolytes with pH (a, b) 2.0, (c) 7.8, and (d) 12.6 and (II) in electrolytes with pH 4.1 at i (A dm^{-2}): (a, b) 1, (c, d) 3, and (e, f) 8.

$[PW_{11}O_{39}]^{7-}$ solutions are stable in the range pH 2–6; however, PW_{11} anions are in equilibrium with PW_9 and PO_4^{3-} + WO_4^{2-} at pH > 5. Simultaneously with the appearance of lacunar HPA in solution, mono- or polytungstate will be present, depending on pH. At pH > 9, tungsten–phosphorus HPAs decompose. In the ^{31}P NMR spectra of a 0.0083 M $Na_2H[PW_{12}O_{40}]$ solution, this is accompanied by appearance of a peak at δ = +2.9 ppm. This peak corresponds to the phosphate anion [22] and is absent

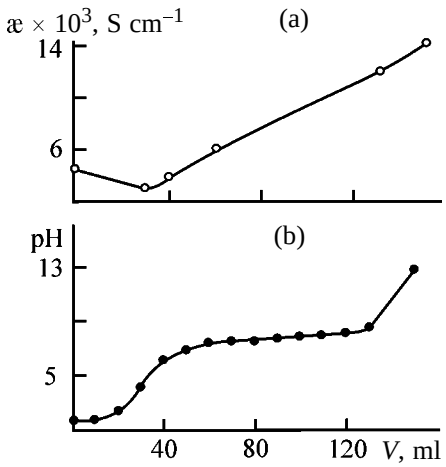

Fig. 5. Effect of the volume V of 1 M of NaOH in a 0.0083 M $Na_2H[PW_{12}O_{40}]$ solution on (a) electrical conductivity æ and (b) pH.

at lower pH. The complex transformations in the electrolyte correlate with the run of the curves describing the dependences $U = f(t)$ (higher or lower position in the plot depending on pH, Fig. 1a) and $U_i = f(\text{pH})$ (occurrence of maxima and minima, Fig. 1b) and with the outward appearance (Fig. 2) and composition of the coatings obtained (Fig. 3; Tables 1, 2). Analysis of the titration curve (Fig. 5b) and the data in Table 1 (comparison of the initial and final pH values) shows the following. In cases when the initial electrolyte has the pH corresponding to that portion of the curve for which the pH is nearly independent of the amount of the alkali added (range of buffer solution), the final pH value varies only slightly in the course of anodic-spark deposition. If, however, the initial pH value corresponds to the onset or middle of the titration step, the variation of pH in the course of the anodic-spark treatment will be pronounced. This is also observed in electrolytes with initial pH 4.1 and 7.8, i.e., the narrowest variation of the pH value in the course of anodic-spark deposition corresponds to the minimum U_i.

As also in the case of tungstate electrolytes [23], the electrical conductivity of solutions varies in the course of anodic-spark deposition only slightly even when pH changes considerably (Table 1). At high mobility of hydroxide ions, this fact can be attributed to a decrease in the number of charge carriers, e.g., as a result of discharge of tungstate ions to give WO_3.

The green layers must seemingly contain WO_3 (yellow) with a minor admixture of W(V) compounds (blue). According to [16], one of processes that lead to incorporation of the electrolyte components into the coatings obtained is thermolysis of compounds that are present on the anode near the electric-breakdown channels. It was established experimentally that crystalline WO_3 is a product formed upon annealing of $Na_2H[PW_{12}O_{40}]\cdot 9H_2O$ in a muffle furnace in air at 600°C for 2 h. In addition to thermal decomposition of the heteropoly compound in anodic-spark deposition, there occurs thermolysis of water [24]. In the breakdown channel and in regions adjacent to this channel, tungsten(VI) oxide is reduced in the presence of hydrogen formed in thermolysis of water, which is accompanied by the appearance of blue point regions in the green layer (Fig. 2, pH 6.5/7.0). The fact that XPA does not reveal WO_3 is presumably due to lower crystallinity of this phase. In all probability, the green layers of the coatings contain both WO_3 and phases of nonstoichiometric composition, which include W(V) (Table 1).

The dependence of the elemental composition of the coatings (Figs. 3a–3c) and of the atomic ratio W/P (Table 2) on pH is, apparently, associated with changes in the electrolyte composition. At pH 2.0, the same W/P ratios in the coatings formed on aluminum and in the electrolyte can be accounted for by involvement of PW_{12} HPA in the coating formation. Being adsorbed on the surface of aluminum oxide, HPA can favor transfer of Al^{3+} ions from the crystal lattice into solution in the form of soluble salts of aluminum [25] or as aluminum-substituted heteropolytungstates [26, 27]. The anionic complexes formed can be involved in coating formation. Presumably, these processes affect the content of aluminum in an anodic-spark layer.

The change in the ionic composition of the electrolyte at pH 4.1–7.3, which is associated with the formation of lacunar species of HPA and isopolytungstates, may favor growth of WO_3-containing oxide layers [23]. In this range of pH, aluminum and titanium oxides are virtually insoluble [28], so that the deposition of tungsten-containing oxide layers may occur at the minimum involvement of the substrate components.

At high pH values, hydrolysis of tungsten–phosphorus HPAs to monomeric anions leads to a decrease in the concentration of tungsten in amorphous layers and in the number of regions that contain crystalline compounds of tungsten. At the same time, raising the concentration of hydroxide ions in the electrolyte promotes chemical dissolution of aluminum and leads to a rise in the concentration of hydroxoaluminate or hydroxotitanate complexes in the electro-

lyte and to their involvement in coating formation. As a result, the content of aluminum or titanium in the coatings grows (Table 2). Despite the disintegration of HPA in alkaline electrolytes (according to the above scheme [12]), the atomic ratio W/P in coatings formed on aluminum in electrolytes with pH 7.8–13.0 is 11.3–15.7, i.e., is the same as that for coatings formed in acid electrolytes. The value of the W/P ratio can be understood in this case as follows. Amorphous insoluble aluminum phosphates and tungstates or compounds of composition $Al_2O_3 \cdot mP_2O_5 \cdot nWO_3$ are formed in the coatings, and phosphorus and tungsten atoms are incorporated into the anodic-spark layers in proportion to the concentrations of these atoms in the electrolyte. The formation of aluminum tungstates in electrolytes with pH 7.8–10.6, presumably in the amorphous form, is indicated by the closeness of the elemental composition and the morphology of the coatings to those formed in a 0.1 M solution of Na_2WO_4 [23, 29].

The fact that the dependences of the elemental composition of the anodic-spark layers on aluminum and titanium on the pH value of the electrolyte are the same confirms that HPAs are involved in their formation. However, it remains unclear why the W/P and W/Ti atomic ratios for coatings formed by anodic-spark deposition on aluminum in an acid electrolyte are nearly twice the W/P and W/Al ratios for coatings on aluminum (Table 2). It should be noted that not only the composition of HPAs, but also the solubility of aluminum and titanium compounds in aqueous electrolytes is a function of the solution pH. In acid and alkaline media, the processes of chemical dissolution of amphoteric oxides are enhanced, and those in neutral media are insignificant. These processes can affect formation, composition, and morphology of coatings.

Despite certain differences between the elemental compositions of amorphous layers formed on aluminum in acid and alkaline electrolytes (pH 2.0 and 12.6), their SEM images [Figs. 4(I)b, 4(I)d] are similar and the coatings resemble in the surface structure those obtained in an electrolyte with H_3PO_4 and Na_2WO_4 [30]. The coatings formed in electrolytes with pH 2.0 and 7.8 have close elemental compositions, but differ in surface morphology. The morphology of crystalline tungsten-containing layers depends on the current density or amount Q of electricity expended for their formation [Fig. 4(II)], rather than on pH of the electrolyte. As Q increases, both the projecting fragments or surface profile motives and depressions become larger, which is accompanied by an increase in the volume of voids. In the case of a microprobe analysis, the presence of voids leads to a decrease in the surface-averaged concentration of tungsten in the coatings, furnished by this method (Fig. 3e).

CONCLUSIONS

(1) The composition of coatings formed on aluminum and titanium alloys in electrolytes with sodium tungstophosphate reflects the pH dependence of the composition of heteropolyanions in an electrolyte solution.

(2) Multilayer coatings that contain in their outer layer oxides of elements constituting the ligand sphere of heteropolyanions are formed in weakly acidic, neutral, and weakly alkaline electrolytes. In acid and alkaline solutions, the components of heteropolyanions are incorporated into coatings formed on aluminum and titanium to a lesser extent.

(3) The surface layers formed in electrolytes with sodium phosphotungstate contain $WO_{2.9}$ or $Na_{0.1}WO_3$, products of thermolysis of tungsten-phosphorus heteropolyanions.

(4) The surface of coatings formed in a neutral medium is constituted by loose layers of crystalline tungsten oxide compounds. The size of fragments of these layers depends on the current density. The surface of coatings formed in an alkaline medium has a cellular structure.

(5) The data obtained confirm the direct relationship between the forms in which iso- and heteropolyanions are present in electrolytes and the composition of the layers being formed.

ACKNOWLEDGMENTS

The authors thank T.A. Kaidalova for performing the X-ray phase analysis, E.S. Pankina for performing microprobe X-ray fluorescence analysis of the coatings, L.M. Tyrina for carrying out experiments on thermal decomposition of sodium tungstophosphate, and V.V. Kon'shin for measuring the NMR spectra of solutions.

The study was supported in part by the Far-Eastern Division, Russian Academy of Sciences (grant no. 03-1-0-04-011).

REFERENCES

1. Gordienko, P.S., Rudnev, V.S., Gnedenkov, S.V., *et al.*, *Zh. Prikl. Khim.*, 1996, vol. 68, no. 6, pp. 971–974.

2. Efimenko, A.V. and Semenova, T.L., *Izv. Ross. Akad. Nauk, Neorg. Mater.*, 1999, vol. 35, no. 11, pp. 1327–1332.
3. Nogami, G., Maruyama, H., and Hongo, K., *J. Electrochem. Soc.*, 1993, vol. 140, no. 8, pp. 2370–2373.
4. Ishizawa, H. and Ogino, M., *J. Mater. Sci.*, 1996, vol. 31, no. 23, pp. 6279–6284.
5. Gordienko, P.S. and Gnedenkov, S.V., *Mikrodugovoe oksidirovanie titana i ego splavov* (Microarc Oxidation of Titanium and Its Alloys), Vladivostok: Dal'-nauka, 1997.
6. Schlottig, F., Dietrich, D., Schreckenbach, J., *et al.*, *Fresenius J. Anal. Chem.*, 1997, vol. 358, p. 105.
7. Gnedenkov, S.V., Khrisanfova, O.A., Zavidnaya, A.G., *et al.*, *Surf. Coat. Technol.*, 2000, vol. 123, no. 1, pp. 24–28.
8. Gordienko, P.S., Rudnev, V.S., Orlova, T.I., *et al.*, *Zashch. Met.*, 1993, vol. 29, no. 5, pp. 739–742.
9. Rudnev, V.S., Gordienko, P.S., Kon'shin, V.V., *et al.*, *Elektrokhimiya*, 1996, vol. 32, no. 10, pp. 1242–1246.
10. Rudnev, V.S., Tyrina, L.M., Nikitin, V.M., *et al.*, *Zashch. Met.*, 2003, vol. 39, no. 4, pp. 376–379.
11. Nedozorov, P.M., Kilin, K.N., Yarovaya, T.P., *et al.*, *Zh. Prikl. Spektrosk.*, 2001, vol. 68, no. 4, pp. 511.
12. Pope, M.T., *Heteropoly and Isopoly Oxometalates*, Berlin: Springer, 1983.
13. Obrubov, V.A., Zhdanova, S.A., and Shchukin, V.P., *Zh. Prikl. Khim.*, 1988, vol. 61, no. 5, pp. 1153–1155.
14. USSR Inventor's Certificate no. 964026.
15. US Patent 3834999.
16. Gordienko, P.S. and Rudnev, V.S., *Elektrokhimicheskoe formirovanie pokrytii na alyuminii i ego splavakh pri potentsialakh iskreniya i proboya* (Electrochemical Formation of Coatings on Aluminum and Its Alloys at Sparking and Breakdown Potentials), Vladivostok: Dal'nauka, 1999.
17. Rudnev, V.S., Lukiyanchuk, I.V., Kon'shin, V.V., and Gordienko, P.S., *Zh. Prikl. Khim.*, 2002, vol. 75, no. 7, pp. 1099–1103.
18. Lukiyanchuk, I.V., Rudnev, V.S., Tyrina, L.M., *et al.*, *Zh. Prikl. Khim.*, 2002, vol. 75, no. 12, pp. 2009–2015.
19. Lukiyanchuk, I.V., Rudnev, V.S., Kaidalova, T.A., *et al.*, *Zh. Prikl. Khim.*, 2000, vol. 73, no. 6, pp. 926–929.
20. Tyrina, L.M., Tyrin, V.I., Gordienko, P.S., *et al.*, *Zh. Prikl. Khim.*, 1995, vol. 68, no. 6, pp. 949–952.
21. Chernenko, V.I., Snezhko, L.A., and Papanova, I.I., *Poluchenie pokrytii anodno-iskrovym elektrolizom* (Deposition of Coatings by Anodic-Spark Electrolysis), Leningrad: Khimiya, 1991.
22. Emsley, J.W., Feeney, J., and Sutcliffe, L.H., *High Resolution Nuclear-Magnetic Resonance Spectroscopy*, Oxford: Pergamon, 1965. Translated under the title *Spektroskopiya YaMR vysokogo razresheniya*, Moscow: Mir, 1969, vol. 2, pp. 380–381.
23. Lukiyanchuk, I.V., Rudnev, V.S., Andenko, N.A., *et al.*, *Zh. Prikl. Khim.*, 2002, vol. 75, no. 4, pp. 587–592.
24. Ragaliavicius, R. and Jusis, Z., *Chemija* (Lithuania), 1992, no. 2, pp. 45–50.
25. Nikitina, E.A., *Geteropolisoedineniya* (Heteropoly Compounds), Moscow: Goskhimizdat, 1962.
26. Carrier, X., Lambert, J.-F., and Che, M., *J. Am. Chem. Soc.*, 1997, vol. 119, pp. 10137–10146.
27. Carrier, X., d'Espinose de la Caillerie, J.-B., Lambert, J.-F., and Che, M., *J. Am. Chem. Soc.*, 1999, vol. 121, pp. 3377–3381.
28. Lur'e, Yu.Yu., *Spravochnik po analiticheskoi khimii* (Handbook of Analytical Chemistry), Moscow: Khimiya, 1971.
29. Lukiyanchuk, I.V., Rudnev, V.S., Kuryavyi, V.G., *et al.*, *Thin Solid Films*, 2004, vol. 446, no. 1, pp. 54–64.
30. Kuang, Y.F., Liu, J.P., Hou, Z.H., and He, D.L., *J. Appl. Electrochem.*, 2001, vol. 31, no. 11, pp. 1267–1271.

Russian Journal of Applied Chemistry, Vol. 77, No. 9, 2004, pp. 1469–1475. Translated from Zhurnal Prikladnoi Khimii, Vol. 77, No. 9, 2004, pp. 1481–1486.

APPLIED ELECTROCHEMISTRY AND CORROSION PROTECTION OF METALS

Optimization of Electroplating Processes in Drum Baths To Obtain a More Uniform Coating

V. I. Karavaev and Yu. V. Litovka

Tambov State Technical University, Tambov, Russia

Received April 6, 2004

Abstract—The optimization of the electroplating process in drum electrolyzers to minimize the standard deviation of the coating thickness is considered.

The uniformity of a deposited metal layer is one of the main quality parameters of electroplated coatings obtained in baths with drums. The problems of achieving a prescribed or the minimum possible variance of the coating thickness arise both in design of electrochemical systems and in control of the processes. Solution of these problems is complicated by the lack of a well-developed theory of the process and by inconsistency of experimental data on how parameters of an electrochemical system affect the uniformity of a coating.

Technical specifications for fabrication of articles with electroplated coatings commonly give the minimum acceptable thickness of deposits, which predetermines the electrolysis duration. If the coatings deposited are nonuniform, then, on obtaining the minimum possible deposit thickness in some parts of an article, the thickness of deposits in other regions may exceed the minimum value severalfold. This leads to an unproductive increase in the expenditure of a metal deposited, electrolyte, and electric power, lowers the output capacity of the electroplating apparatus, and makes higher the production cost of the articles manufactured.

The choice of the electrolyte composition and electrolysis parameters, as well as of the design of the electroplating equipment and feeding units is governed by the necessity for obtaining articles with the highest possible thickness uniformity in their different parts.

As an optimization criterion is commonly used the root-mean-square deviation (also termed standard deviation) σ of the thickness of a coating on articles from its average value.

The main factors that affect the chosen criterion are the current I, drum filling C_t, drum rotation frequency ω, and drum parameters: diameter D and degree of wall perforation f_0. Let I, C_t, and D be variables. Then, to optimize the drum electrolyzer, it is necessary to find the current I, drum filling C_t, and drum diameter D at which the standard deviation of the coating thickness, $\sigma(I, C_t, D)$ is the smallest:

$$\sigma(I, C_t, D) \rightarrow \min,$$

at constraints determined by the equations of a mathematical model and by process limitations.

A particular case of the optimization problem to be solved is a search for process variables: current I and filling C_t for an available drum. In this case, it is necessary to find the current I and drum filling C_t at which the standard deviation of the coating thickness, $\sigma(I, C_t)$, is the smallest:

$$\sigma(I, C_t) \rightarrow \min.$$

To relate the chosen criterion to the variables, we construct a system of equations of the mathematical model. Theoretical concepts of the process and generalized experimental data formed a basis for the constraint equation suggested in [1], which relates the standard deviation of the thickness of a coating deposited onto articles in a rotating drum to the parameters of the system:

$$\sigma = K\bar{h}\Delta\tau^{-0.5}, \quad (1)$$

where K is the scatter factor; h, average coating thickness; and $\Delta\tau$, electrolysis duration.

The average coating thickness is found from the equation

$$\bar{h} = \frac{\sum_{i=1}^{n} h_i}{n},$$

1070-4272/04/7709-1469 © 2004 MAIK "Nauka/Interperiodica"

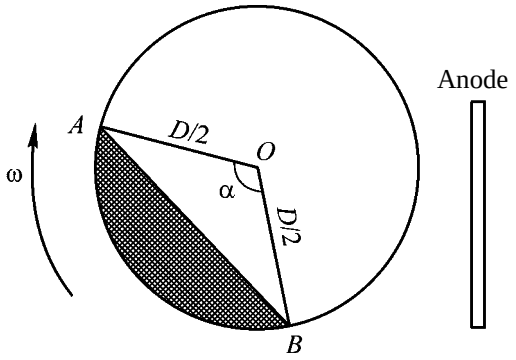

Fig. 1. Cross section of a drum electrolyzer.

where h_i is the deposit thickness on the surface of ith article, and n is the number of articles in the drum.

The scatter factor K is found using the formula

$$K = \left[(\gamma D f_e - 1)\frac{\alpha}{390\omega E_m}\left(1 + \frac{\omega D \sin(\alpha/2)}{V_t \alpha/360}\right)\right]^{0.5}, \quad (2)$$

where γ is the current distribution parameter; D, drum diameter; f_e, filling factor; α, central angle opposite to the charge surface; ω, drum rotation frequency; E_m, efficiency of stirring of the articles; and V_t, article falling velocity (V_t = 525 cm min^{-1} was recommended in [1]).

The parameter ψ is determined by the geometry of the articles being processed and by the electrolyte properties in accordance with the equation

$$\gamma = [(S/V_z)ZFi_0/(\chi RT)]^{0.5}, \quad (3)$$

where S/V_z is the ratio of the total area of the charge to its volume; i_0, exchange current density (the physical meaning of this quantity is the rate of the ion exchange between the metal and solution in equilibrium; it has a tabulated value determined by the type of the electrode and the composition of the electrolyte); χ, electrical conductivity of the solution; Z, number of electrons involved in the electrochemical reaction; F, Faraday number F = 96 484.56 C mol^{-1}; R, universal gas constant, R = 8.31433 J mol^{-1} K^{-1}; and T, absolute temperature of the solution.

Taking into account that $V_z = V_{ar}$ and $S = nS_{ar}$, where V_{ar} and S_{ar} are the volume and surface area of an article, respectively, we have

$$S/V_z = S_{ar}/V_{ar}.$$

Then formula (3) takes the form

$$\gamma = [(S_{ar}/V_{ar})ZFi_0/(\chi RT)]^{0.5}.$$

The feed factor f_e is calculated using the equation [2]

$$f_e = \frac{\alpha/360 - 1/(2\pi)\sin\alpha - V_d/V_b}{8[f_0\alpha/360 - 1/\pi \sin(\alpha/2)]}, \quad (4)$$

where V_d is the volume of the cathode contacts; V_b, drum volume; and f_0, degree of perforation of drum walls.

The drum filling C_t is the quantity found from the formula

$$C_t = V_z/V_b. \quad (5)$$

Let us consider a cross section of a round drum that is perpendicular to its axis (Fig. 1).

The hatched region is that part of the drum in which the articles are contained. Let L be the drum length. Then $V_b = S_bL$ and $V_z = S_zL$, where S_b is the cross-sectional area of the drum, and S_z is the area of the feeding cross section. Hence,

$$C_t = S_z/S_b. \quad (6)$$

The cross-sectional area of the drum is found as

$$S_b = \pi D^2/4,$$

and the area of the feeding cross section is defined as the difference of areas of sector AOB and triangle AOB:

$$S_z = \frac{\alpha}{2\pi}(\pi D^2/4) - 0.5(D^2/4)\sin\alpha.$$

Then Eq. (6) is brought to the form

$$C_tS_b = S_z,$$

$$C_t(\pi D^2/4) = \frac{\alpha}{2\pi}(\pi D^2/4) - 0.5(D^2/4)\sin\alpha,$$

$$C_t\pi = \alpha/2 - \sin(\alpha/2),$$

$$\alpha = \sin\alpha + 2C_t\pi. \quad (7)$$

If the drum filling is known, we can find from Eq. (7) the central angle α (rad) opposite to the charge surface.

In [1], the stirring efficiency E_m is defined as the number of random agitations of the charge, divided by the number of drum revolutions or, in other words,

the number of random agitations of the charge per revolution of the drum.

Let us assume that the drum electrolyzer has the form of a rotating smooth drum, within which a granular substance, loaded articles, moves. The substance in the drum moves in the rolling mode and circulates around point *C*, the circulation center (Fig. 2).

It has been shown that the average time τ_{av} of a cycle of circulation of the material around point *C* can be found as

$$\tau_{av} = \frac{2Q}{4\rho_{bl}\omega(R^2 - R_c^2)},$$

where $Q = 1/2L\rho R^2(2\delta_0 - \sin 2\delta_0)$ is the total amount of the material in the drum; *R*, drum radius; ρ_{bl}, bulk density of the material; δ_0, angles *AOC* and *COB* (Fig. 2); and R_c, distance from the drum axis to the circulation center *C*.

Then

$$\tau_{av} = \frac{LR^2(2\delta_0 - \sin 2\delta_0)}{4\omega(R^2 - R_c^2)}. \quad (8)$$

As $\tau_{av} \geq 0$ and $Q \geq 0$, it follows from (8) that $R^2 - R_c^2 > 0$, $R > R_c$ or $R_c < R$. This condition is satisfied when the drum is less than half-filled. Consequently, $C_t < 0.5$. The average number *N* of circulation cycles during the time $\Delta\tau$ spent by the material in the drum is given by

$$N = \Delta\tau/\tau_c. \quad (9)$$

Then, at $\Delta\tau$ equal to the time of a revolution, $N = E_m$. The time of a revolution

$$\tau_1 = 1/\omega. \quad (10)$$

Combining formulas (8)–(10) and taking into account that $2\delta_0 = \alpha$, we have

$$E_m = \frac{4}{L(\alpha - \sin\alpha)}[1 - (R_c/R)^2].$$

In [4], a procedure for calculating R_c was reported, whence follows that, as a rule, the circulation center *C* is situated at a distance equal to one third of the charge depth from the charge surface. Then

$$R_c = a + 1/3(R - a) = (2a + R)/3 = (2R\cos\delta_0 + R)/3$$

$$= R/3[2\cos(\alpha/2) + 1].$$

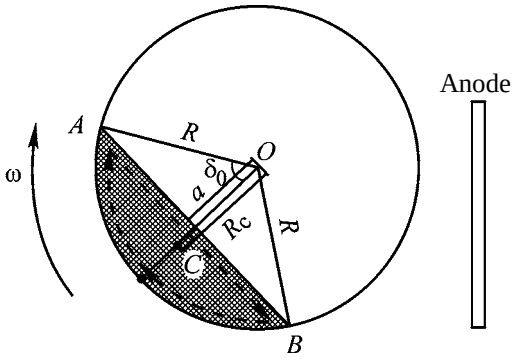

Fig. 2. Circulation of articles in the drum.

Hence,

$$E_m = \frac{4}{L(\alpha - \sin\alpha)}\left[1 - \left(\frac{2\cos(\alpha/2) + 1}{3}\right)^2\right]. \quad (11)$$

The average coating thickness $\bar{h}$ on articles from the same charge is determined from the Faraday law [5]:

$$\bar{h} = (E\eta/\rho_m)i\Delta\tau, \quad (12)$$

where η is the current efficiency; *E*, electrochemical equivalent of a metal being deposited (g A^{-1} h^{-1}); ρ_m, density of the metal being deposited (g cm^{-3}); and *i*, average current density (A cm^{-2}).

When the articles move within the drum, the charge is strongly agitated. As a result of the mechanical impact, the coatings being deposited are partly rubbed away, which is particularly pronounced in electrodeposition of soft metals (zinc, tin, etc.). In [6], the wear loss factor ξ was introduced, which has the following values: 20–40 and 40–60% for hard and soft metals, respectively. With account of the coefficient ξ, Eq. (12) takes the form

$$\bar{h} = [E\eta/\rho_m(1 + 0.01\xi)]i\Delta\tau. \quad (13)$$

The current density is the ratio of the current *I* to the area of that surface of the layer of articles, which faces the anode:

$$i = I/S_a. \quad (14)$$

Let us assume that the surface facing the anode is a rectangle with sides *AB* and *L* (Fig. 1). The side *AB* = $D\sin(\alpha/2)$. Then the area S_a is given by

$$S_a = LD\sin(\alpha/2). \quad (15)$$

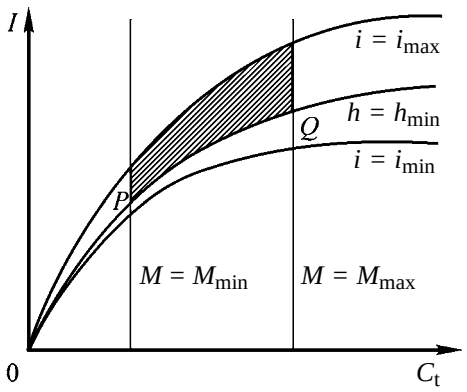

Fig. 3. Constrains and feasibility region for the optimization problem. (I) Current and (C_t) drum filling; the same for Figs. 4–6. $I = i_{min}$ and $i = i_{max}$ are the curves of constraints on the average current density i; $M = M_{min}$ and $M = M_{max}$, straight lines of constraints on the charge mass M; and $h = h_{min}$, curve of constraint on the thickness h of a coating being deposited.

With account of (14) and (15), Eq. (13) takes the form

$$\bar{h} = [E\eta/\rho_m(1 + 0.01\xi)][I/LD\sin(\alpha/2)]\Delta\tau. \quad (16)$$

Let us determine how the charge area S_z depends on the drum filling C_t.

Provided that identical articles are coated in the drum, we have for the charge area

$$S_z = nS_{ar}.$$

It follows from Eq. (5) that the charge volume $V_z = C_t V_b$. The bulk density can be defined as

$$\rho_{bl} = M/V_z,$$

where M is the mass of the charge.

Hence follows that $M = \rho_{bl} V_z = \rho_{bl} C_t V_b$. Then the number of articles in the drum

$$n = M/M_{ar} = \rho_{bl} C_t V_b/(\rho_{ar} V_{ar}),$$

where M_{ar} is the mass of an article, and ρ_{ar} is the density of its material.

The charge area

$$S_z = nS_{ar} = C_t V_b S_{ar}/V_{ar}\rho_{bl}/\rho_{ar}.$$

With account of the mathematical model we constructed, the mathematical formulation of the optimization problem is as follows: it is necessary to find the current I, drum filling C_t, and drum diameter D at which the standard deviation of the coating thickness, $\sigma(I, C_t, D)$, is at a minimum:

$$\sigma(I, C_t, D) \rightarrow \min.$$

The constraint equations are the following:

$$\sigma = K\bar{h}\Delta\tau^{-0.5},$$

$$\bar{h} = [E\eta/\rho_m(1 + 0.01\xi)][I/LD\sin(\alpha/2)]\Delta\tau,$$

$$K = \left[(\gamma D f_e - 1)\frac{\alpha}{390\omega E_m}\left(1 + \frac{\omega D\sin(\alpha/2)}{V_t\alpha/360}\right)\right]^{0.5},$$

$$E_m = \frac{4}{L(\alpha - \sin\alpha)}\left[1 - \left(\frac{2\cos(\alpha/2) + 1}{3}\right)^2\right],$$

$$f_e = \frac{\alpha/360 - 1/(2\pi)\sin\alpha - V_d/V_b}{8[f_0\alpha/360 - 1/\pi\sin(\alpha/2)]},$$

$$\gamma = [(S_{ar}/V_{ar})ZFi_0/(\chi RT)]^{0.5}, \quad (17)$$

$$\alpha = \sin\alpha + 2C_t\pi,$$

$$i = I/S_a,$$

$$M = C_t V_b \rho_{bl},$$

$$V_b = L\pi D^2/4.$$

Constraints:

$$\bar{h} \geq h_{min}, \quad (18)$$

$$\Delta\tau \leq \Delta\tau_{max}, \quad (19)$$

$$M_{min} \leq M \leq M_{max}, \quad (20)$$

$$i_{min} \leq i \leq i_{max}, \quad (21)$$

where h_{min} is the prescribed minimum coating thickness; $\Delta\tau_{max}$, maximum acceptable time of coating deposition; M_{min}, minimum mass of charge (determined by the prescribed output capacity): M_{max}, maximum acceptable mass of charge (determined by the drum design); i, average current density; i_{max}, maximum acceptable current density (exceeding this value leads to appearance of rejects); and i_{min}, minimum acceptable current density.

With i_{min} and i_{max} known, we can determine the constraints on the current: $I_{min} = S_a i_{min}$, $I_{max} = S_a i_{max}$ at a fixed surface area S_a of the layer of articles that faces the anode. We start solving the optimization problem from a particular, the simplest, case.

First, it is necessary to make analysis for existence of a solution to the optimization problem. The problem can be solved if there exists a feasibility region specified by constraints (18) and (20)–(21) (Fig. 3).

The plots of the functions $i = i_{min}$, $i = i_{max}$, and $h = h_{min}$ are curves emerging from the origin of coordinates. The slope of these curves is directly proportional to the current density i. For the first function, $i = i_{min}$; for the second, $i = i_{max}$; and for the third, $i = i_{hmin}$, where i_{hmin} is the current density at which the coating thickness is h_{min}. The value of i_{hmin} can be found from Eq. (13):

$$i_{hmin} = \frac{h_{min}(1 + 0.01\xi)\rho_m}{E\eta\Delta\tau}.$$

The condition for existence of a feasibility region and, consequently, of the solution itself is as follows: the plot of the function $h = h_{min}$ must run above the plot of the function $i = i_{min}$, but below that of the function $i = i_{max}$, which is possible if the following condition is satisfied:

$$i_{min} \le i_{hmin} \le i_{max}. \quad (22)$$

The optimization problem is two-dimensional (2D), because it has two sought-for variables. Let us consider Eq. (1). Let us assume that the scatter factor K is constant. Then, with account of $\Delta\tau$ = const, the standard deviation of the coating thickness, σ, will be at a minimum at the smallest average coating thickness h, i.e., the sought-for solution (C_t^*, I^*) will lie on the curve $h = h_{min}$ in the feasibility region (PQ portion).

The minimum standard deviation of the coating thickness $\sigma = Kh_{min}\Delta\tau^{-0.5}$. The scatter factor K is independent of $\Delta\tau$. Then $\sigma = \text{const}\,\Delta\tau^{-0.5}$. Consequently, the standard deviation of the coating thickness, σ, decreases as the time of coating deposition, $\Delta\tau$, becomes longer, and the minimum value of σ is observed at $\Delta\tau = \Delta\tau_{max}$. Therefore, inequality (19) is transformed into the equality $\Delta\tau$ = const = $\Delta\tau_{max}$.

The scatter factor function K is independent of the current I, being determined only by the drum filling C_t. Then, having found the value of C_t^* at which the scatter factor function $K(C_t)$ takes the minimum value, we can determine the precise position of the sought-for solution to the optimization problem on the $h = h_{min}$ curve in the feasibility region:

$$I^* = \text{Si}_{hmin} = LD\sin(\alpha/2)\,i_{hmin}. \quad (23)$$

Thus, the 2D optimization problem is reduced to a 1D problem that consists in a search for a minimum of the function $K(C_t)$ on the interval $[C_{t_P}, C_{t_Q}]$, where

$$C_{t_P} = M_{min}/(\rho_{bl}V_b),$$

$$C_{t_Q} = M_{max}/(\rho_{bl}V_b).$$

To solve the general optimization problem, which is of the 3D type, we considered particular cases at different diameters D of the drum electrolyzer.

The minimum standard deviation of the coating thickness $\sigma = Kh_{min}\Delta\tau^{-0.5} = K(D)$const. In formula (2) for the scatter factor K, the diameter D is in the numerator with a positive sign, and, therefore, the standard deviation of the coating thickness, σ, increases as D becomes larger. Thus, the minimum value of σ is achieved at the minimum possible values of the diameter D.

Then, the general optimization problem is solved as follows: D is raised, beginning with D_{min}, with a step ΔD until there exists the feasibility region [condition (22) is satisfied]. This diameter is taken to be the optimal diameter D^*. Further, the minimum of the function $K(C_t)$ is found on the interval $[C_{t_P}, C_{t_Q}]$ using a method for 1D optimization (e.g., the bisection method). The resulting optimal value of C_t^* is used to calculate by formula (23) the optimal current I^*.

Thus, a 1D algorithm is used in the final stage when solving the 3D optimization problem.

If constraint (18) is used, negative deviations of the coating thickness from the average value are possible for a large number of articles. It is more correct to use constraints of the following type:

$$\bar{h} - \sigma \ge h_{min},$$

$$\bar{h} \ge h_{min} + \sigma. \quad (24)$$

The standard deviation of the coating thickness, σ, will be at a minimum at the smallest h, i.e., at

$$\bar{h} = h_{min} + \sigma,$$

The coordinate C_t^* corresponds to the minimum of the function $K(C_t)$. I^* can be calculated from h and C_t^* by formulas (7) and (16).

It is necessary to satisfy condition (24). This is achieved as follows.

(1) The starting value $\sigma^{(0)} = 0$ is set. It is taken that $h_{min} = h_{min} + \sigma^{(0)}$. The optimization problem is solved with constraint (18). As a result, the optimal value $\sigma^{(1)}$ is obtained.

(2) It is taken that $h_{min} = h_{min} + \sigma^{(1)}$. The optimization problem is solved with constraint (18). As a result, the optimal value $\sigma^{(2)}$ is obtained, etc.

This procedure is continued until the condition

$$|\sigma^{(i+1)} - \sigma^{(i)}| \le \varepsilon,$$

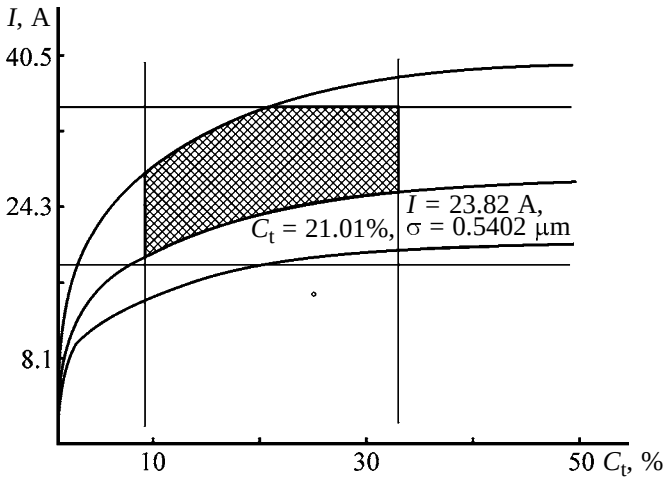

Fig. 4. Solution of the optimization problem for the operation mode of a drum electrolyzer for $10 \le M \le 40$ kg.

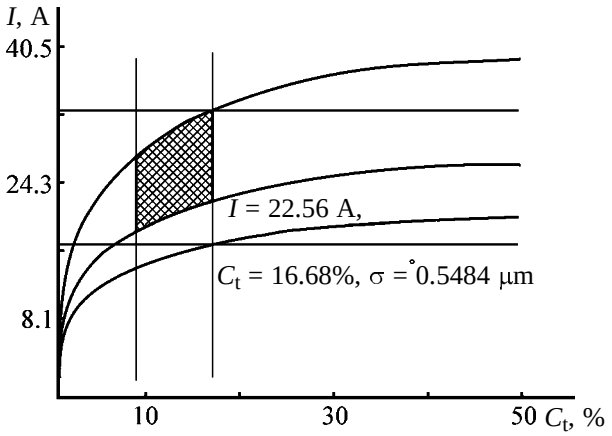

Fig. 5. Solution of the optimization problem for the operation mode of a drum electrolyzer for $10 \le M \le 20$ kg.

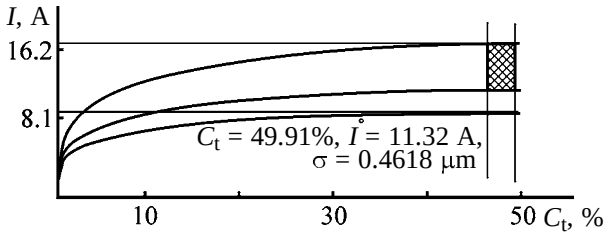

Fig. 6. Solution of the optimization problem in designing a drum electrolyzer.

where i is the number of iteration and ε is prescribed accuracy, is satisfied.

In the study, the problem of optimization of the operation mode of a drum-type nickel-plating bath is solved. As an example is taken a drum electrolyzer with the following parameters: diameter D = 22.5 cm, length L = 60 cm, rotation frequency ω = 8 rpm, and degree of wall perforation f_0 = 22%.

The parameters of the metal being deposited (nickel) and the electrolyte are as follows: electrochemical equivalent E = 1.095 g A^{-1} h^{-1}; current efficiency η = 0.97; wear coefficient ξ = 40%; number of electrons involved in electrolysis z = 2; exchange current density i_0 = 0.001 A cm^{-2}; electrical conductivity χ = 0.5 Ω^{-1} cm^{-1}; electrolyte temperature T = 313 K; and metal density ρ_m = 8.9 g cm^{-3}.

Articles with a total surface area S_{ar} = 6 cm^2 and volume V_{ar} = 1 cm^3 are to be nickel-plated. The density of the material of the articles ρ_{ar} = 7.8 g cm^{-3}, bulk density ρ_{bl} = 5 g cm^{-3}, time of coating deposition $\Delta\tau$ = 30 min. The minimum acceptable coating thickness h_{min} = 8 μm. The constraint on the charge mass M: $10 \le M \le 40$ kg; and the current density $1.5 < i < 3$ A dm^{-2}.

The solution of the problem produced the following result (Fig. 4): drum filling C_t = 21.01%, current I = 23.82 A, standard deviation σ = 0.5402 μm, average coating thickness $\bar{h}$ = 8.5402 μm, charge surface area S = 1.927 m^2, charge mass M = 25.06 kg, current density i = 2.004 A dm^{-2}, and constraint on the current I: $17.84 < I < 35.67$ A.

At another constraint on the charge mass ($10 \le M \le 20$ kg), the following result was obtained (Fig. 5): drum filling C_t = 16.68%, current I = 22.56 A, standard deviation σ = 0.5484 μm, average coating thickness $\bar{h}$ = 8.5484 μm, charge surface area S = 1.531 m^2, charge mass M = 19.91 kg, current density i = 2.006 A dm^{-2}, and constraint on the current I: $16.87 < I < 33.75$ A.

Solving the problem in designing a drum electrolyzer, when not only process, but also design parameters are sought for, yielded the following result (Fig. 6): drum diameter D = 9.5 cm, drum filling C_t = 49.91%, current I = 11.32 A, standard deviation σ = 0.4618 μm, average coating thickness $\bar{h}$ = 8.4618 μm, charge surface area S = 0.8163 m^2, charge mass M = 10.61 kg, current density i = 1.985 A dm^{-2}, and constraint on the current I: $8.55 < I < 17.1$ A.

CONCLUSION

The problem of optimization of a drum electrolyzer in order to minimize the standard deviation of the article coating thickness from the average value was formulated and solved. The definition domain of the optimization problem was analyzed. An algorithm for a search for the optimal parameters of a drum electrolyzer was developed.

REFERENCES

1. Craig, S.E., Harr, R.E., and Mathiessen, P., *Plating*, 1974, no. 12, pp. 1101–1110.
2. Zhuravlev, B.L., Kaidrikov, R.A., Nuriev, N.K., *et al*., in *Prikladnaya elektrokhimiya* (Applied Electrochemistry), Kazan, 1987, pp. 61–64.
3. Pershin, V.F., *Khim. Neft. Mashinostr*., 1986, no. 12, pp. 15–16.
4. Pershin, V.F., *Mashiny barabannogo tipa: osnovy teorii, rascheta i konstruirovaniya* (Drum-Type Apparatus: Fundamentals of Theory, Calculation, and Design), Voronezh: Voronezh. Gos. Univ., 1990.
5. Andreev, I.N., Ivshin, Ya.V., Kaidrikov, R.A., *et al*., in *Prikladnaya elektrokhimiya* (Applied Electrochemistry), Kazan, 1980, pp. 66–67.
6. Lobanov, S., *Prakticheskie sovety gal'vaniku* (Practical Recommendations for Galvanic Worker), Leningrad: Mashinostroenie, 1983.

Russian Journal of Applied Chemistry, Vol. 77, No. 9, 2004, pp. 1476–1480. Translated from Zhurnal Prikladnoi Khimii, Vol. 77, No. 9, 2004, pp. 1487–1490.

APPLIED ELECTROCHEMISTRY AND CORROSION PROTECTION OF METALS

Intensification of Impregnation of Metal–Ceramic Supports in Fabrication of Nickel Oxide Electrodes by the Nitrate Technique

T. E. Kuzina and A. A. Bachaev

Nizhni Novgorod State Technical University, Nizhni Novgorod, Russia

Received December 2, 2003; in final form, May 2004

Abstract—The possibility of making shorter the time of fabrication of a nickel oxide electrode by impregnation of a metal–ceramic support in a nickel nitrate solution with addition of sodium nitrite was studied.

The duration of multicycle procedures in fabrication of nickel oxide electrodes (NOE) on metal–ceramic (MC) supports is mainly determined by the time of impregnation of MC supports in a solution that contains nickel salts, most frequently $Ni(NO_3)_2$ (pH < 7) [1]. Up to 97–98% of the total impregnation time (up to 15 h) is necessary for obtaining the active substance via oxidation of nickel from the support, which occurs by the electrochemical mechanism [1, 2]. The fraction of the active substance obtained via oxidation of nickel from an MC support in a $Ni(NO_3)_2$ solution is about 30% [3]. To make shorter the time in which MC NOEs are fabricated and to diminish the power consumption and labor intensity of the process, it is necessary to accelerate the oxidation of nickel in the course of impregnation.

The influence exerted by $NaNO_2$ on impregnation of MC supports was studied by Zhdanov *et al.* [4]. However, in contrast to our study, Zhdanov *et al.* [4] used a chloride solution, which has a lower oxidation capacity and does not undergo disproportional self-regeneration.

The aim of this study was to examine the influence exerted by addition of $NaNO_2$ to $Ni(NO_3)_2$ solution on the rate of etching of nickel contained in MC supports and on the electrical characteristics of MC NOEs obtained.

EXPERIMENTAL

The electrodes studied were fabricated on $30 \times 10 \times 1.6$-mm MC nickel supports with a bulk porosity of 70–75%. The MC supports were filled with nickel(II) hydroxide by the following scheme: impregnation with an $Ni(NO_3)_2$ solution ($c_{Ni(II)}$ = 300–330 g l^{-1}) containing $NaNO_2$ (5–10 g l^{-1}), pH 1–5, temperature 60–80°C, τ = 1 h; crystallization in air (30 min); treatment in an alkali solution (c_{KOH} = 300–330 g l^{-1}, T = 60–80°C, τ = 1 h); washing to remove the alkali; and drying (T = 110°C). Changes in the mass of the MC supports were determined as the difference of masses before impregnation and after a full cycle of the procedures performed. The mass of nickel dissolved from the MC support was determined by complexometric titration [5]. The characteristics of the nickel etching process were found using the model described in [5]. The chemical composition of the active substance in NOE was determined by the procedure described in [6].

The composition of the corrosion products formed was identified by X-ray diffraction analysis on a DRON-2 diffractometer at an acceleration voltage of 32 kV, current of 0.8 mA, slit dimensions of $1 \times 8 \times 1$ mm, and filter wavelength of 0.58 Å. Qualitative analysis of the X-ray diffraction patterns was made using the procedure described in [7].

The rate-determining stage of reduction of NO_3^- and NO_2^- was identified using a potentiodynamic method in which polarization curves were measured with a linear potential sweep at a rate of 2–20 mV s^{-1}.

The capacity characteristics of the electrodes fabricated were determined by discharge in cells with auxiliary electrodes made of cut-through nickel foil with separators fabricated from perforated rigid PVC. As an electrolyte served a KOH solution (1.19–1.20 g cm^{-3}). In the course of charging, 150% of the theoretical capacity of the electrodes was imparted to them at a current density of 4.4 mA cm^{-2} [8]. The

1070-4272/04/7709-1476 © 2004 MAIK "Nauka/Interperiodica"

discharge was performed at the same current density until the working potential changed abruptly.

Analysis of the corrosion diagram obtained for the system under study (Fig. 1) shows that nickel is etched in a $Ni(NO_3)$ solution with a $NaNO_2$ additive by the electrochemical mechanism with a cathodic control. The rate of nickel dissolution in solutions with addition of sodium nitrite increases by a factor of approximately 5 as compared to that of nickel etching in a $Ni(NO_3)_2$ solution (Fig. 1).

The introduction of a $NaNO_2$ additive into a $Ni(NO_3)_2$ solution changed its oxidation power: the equilibrium potential of the redox system in solution was 1.1 V, and the shift of the potential, 0.13 V (Fig. 2). At first sight, this dependence seems to be anomalous: the product formed in cathodic reduction of nitrates, NO_2^- ions, has a higher oxidation power than the starting reagent, NO_3^-. Such an anomaly can be accounted for only by formation of an electrochemically active substance with a higher oxidation power.

According to [9], the following slow reaction of autocatalysis, which precedes the discharge, occurs in concentrated nitrate solutions:

$$HNO_3 + HNO_2 \rightleftarrows N_2O_4 + H_2O. \quad (1)$$

Nitrites are always present in nitrate solutions because of the partial decomposition of the $Ni(NO_3)_2$ solution at elevated temperatures (100–300°C) [6]:

$$2Ni(NO_3)_2 \rightarrow 2NiO + 4NO_2 + O_2. \quad (2)$$

Nitrogen oxide NO_2 reacts with water [10]:

$$2NO_2 + H_2O \rightarrow HNO_3 + HNO_2. \quad (3)$$

The presence of NO_2^- ions in a $Ni(NO_3)_2$ solution must facilitate formation of the active component N_2O_4 by shifting the equilibrium of reaction (1) to the right. The content of nitrite in the $Ni(NO_3)_2$ solution will be maintained constant, in the case of its low values, by disproportionation of HNO_2 in hot acid solutions [10]:

$$3HNO_2 \rightleftarrows HNO_3 + 2NO + H_2O. \quad (4)$$

Nitrogen(II) oxide being formed by reaction (4) can be oxidized in the presence of oxygen to NO_2 [10], which dimerizes to N_2O_4 [9, 11]. This dimer is a strong oxidizing agent (E^0 = 1.2 V [12]), which can convert basic salts of nickel(II), contained within

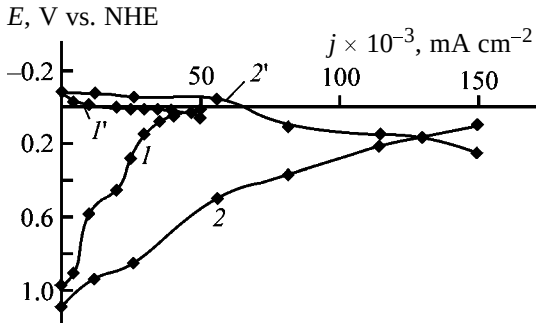

Fig. 1. Corrosion diagram obtained on nickel in a $Ni(NO_3)_2$ solution without an additive and with a $NaNO_2$ additive. T = 80°C, $c_{Ni(II)}$ = 320 g l^{-1}, pH 3; the same for Fig. 2. (*E*) Potential and (*j*) current density; the same for Fig. 2. $NaNO_2$ content (g l^{-1}): (*1*) 0 and (*2*) 10; the same for Fig. 2. Curves: (*1*, *2*) cathodic, obtained on Pt; (*1'*, *2'*) anodic, obtained on Ni.

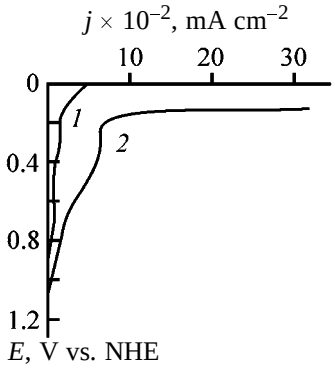

Fig. 2. Cathodic potentiodynamic polarization curves obtained on Pt. Potential sweep rate 2 mV s^{-1}.

pores of the MC supports, into NiOOH (E^0 = 0.6–1 V [8]).

The voltammetric curve obtained on Pt in a $Ni(NO_3)_2$ solution at a potential sweep rate of 2 mV s^{-1} shows at potentials of 0.35–0.1 V a region of the limiting current density, which is associated with reduction of NO_3^- ions to NO_2^- (Fig. 2). Upon addition of $NaNO_2$ to a $Ni(NO_3)_2$ solution, the limiting current density increases by a factor of approximately 5 (Fig. 2). This suggests the occurrence of joint reduction of NO_3^- and NO_2^- ions ($E^0_{NO_3^-/NO_2^-}$ = 0.83 V, $E^0_{NO_2^-/NH_4^+}$ = 0.86 V [12]) and increase in the total concentration of the depolarizing agent in solution.

At potential sweep rates of 5–10 mV s^{-1}, the voltammograms show a peak of the cathodic current. A $Ni(NO_3)_2$ solution without additives and with a $NaNO_2$ additive is characterized by a linear dependence of the current density on the square root of the

Table 1. Effect of the solution composition on the intensity of lines in the X-ray diffraction pattern

Solution	Film composition	*I*
$Ni(NO_3)_2$	$Ni(NO_3)_2 \cdot Ni(OH)_2$	100, 58, 50
$Ni(NO_3)_2$ + $NaNO_2$	$Ni(NO_3)_2 \cdot Ni(OH)_2 \cdot \beta$-NiOOH	84, 32

potential sweep rate, $j_p = f(V^{1/2})$. This dependence is extrapolated into the origin of coordinates, which is due to a slowed-down diffusion of the depolarizing agent to the electrode surface [13]. As the potential sweep rate is made faster, films of basic compounds of nickel, which appear when the pH of the near-electrode zone increases, have not enough time to be formed. The process passes into the quasi-reversible region: the dependence $j_p = f(V^{1/2})$ deviates from a linear behavior, which suggests occurrence of a slowed-down chemical reaction preceding the discharge.

The diffusion coefficient was calculated by the Randles–Shevchik equation [13]

$$j_p = 0.446 \frac{n^{3/2} F^{3/2}}{R^{1/2} T^{1/2}} D^{1/2} V^{1/2} c_{ox}^0, \quad (5)$$

where j_p is the peak current density (A cm^{-2}); c_{ox}, oxidant concentration (M); D, diffusion coefficient (cm^2 s^{-1}); V, potential sweep rate (V s^{-1}); n, number of electrons exchanged in an elementary event; T, process temperature (K); F, Faraday number (C mol^{-1}); and R, universal gas constant (J K^{-1} mol^{-1}).

For a $Ni(NO_3)_2$ solution with addition of $NaNO_2$, the diffusion coefficient of the oxidizing agent was 9.4×10^{-5} cm^2 s^{-1}, which exceeds by a factor of 6 its value in the $Ni(NO_3)_2$ solution (1.5×10^{-5} cm^2 s^{-1}). This indicates that the diffusion hindrance to the process is partly lifted in the case of joint reduction of NO_3^- and NO_2^- ions. The rate of the cathodic process in a $Ni(NO_3)_2$ solution with addition of $NaNO_2$ starts to be determined, to a greater extent than that in the $Ni(NO_3)_2$ solution, by the rate of the chemical reaction (1), in which nitrate ions react with nitrite ions.

The presence of a $NaNO_2$ additive in the $Ni(NO_3)_2$ solution makes higher the rate of the cathodic stage and the overall intensity of the process. In addition, impregnation of MC supports in a $Ni(NO_3)_2$ solution with a $NaNO_2$ additive leads to formation of higher nickel oxides of general formula $NiO_{1.5–1.6}$ within the pores of the electrode. The high electrochemical activity of the resulting compound is confirmed by the fact that electrodes subjected to a single act of impregnation in a $Ni(NO_3)_2$ solution with a $NaNO_2$ additive have a specific discharge capacity of 2.25 mA h cm^{-3} without any preliminary charging. The deep oxidation of nickel in the impregnation of MC supports was favored by the presence in solution of a strong oxidizing agent, formed in disproportionation of NO_2^- ions.

An X-ray diffraction analysis demonstrated (Table 1) that a smaller amount of the solid phase is formed in the presence of NO_2^- ions, compared to a $Ni(NO_3)_2$ solution without additives, as indicated by the lower intensity I of diffraction lines. In this case, higher nickel oxides with a structure of β-NiOOH are contained in the film formed on cathodic areas of nickel in a $Ni(NO_3)_2$ solution with a $NaNO_2$ additive.

The optimal conditions of impregnation of MC support in a $Ni(NO_3)_2$ solution with a $NaNO_2$ additive were determined taking into account that the equilibrium of reaction (4) must shift to the right as temperature is elevated and pH of the solution decreases [10]. It is inadvisable to raise the impregnation temperature to above 80°C for process reasons. The rate of nickel etching in a $Ni(NO_3)_2$ solution with a $NaNO_2$ additive does increase as the acidity of the solution is made higher. In this case, the oxidation state of nickel increases to $NiO_{1.8}$ at pH 1. This can be attributed to a shift of the equilibrium of reaction (4) to the right, which leads to an increase in the content of the oxidizing component N_2O_4 in solution.

The rate of nickel etching in a $Ni(NO_3)_2$ solution with a $NaNO_2$ additive grows during the first hour of the process and then decreases somewhat, which is due to the formation of difficultly soluble films of basic nickel compounds on the surface.

The greatest weight gain of the MC support and a fairly high nickel etching rate (0.1 g g^{-1} h^{-1}) were obtained at the following impregnation conditions: $c_{Ni(II)}$ = 300–330 g l^{-1}, c_{NaNO_2} = 5–10 g l^{-1}, pH 3, T = 60–80°C, τ = 1 h.

The results obtained in impregnation of MC supports and the electrical characteristics of the MC NOEs fabricated under the optimal impregnation conditions are listed in Table 2.

The rate of Ni dissolution in a $Ni(NO_3)_2$ solution with a $NaNO_2$ additive is by a factor of approximately 4 higher than that in the $Ni(NO_3)_2$ solution (Table 2). In the second cycle of impregnation, when higher nickel oxides are present in pores of the MC supports, the maximum rate of nickel oxidation is observed

Table 2. Parameters of the process and MC NOE after impregnation in a $Ni(NO_3)_2$ solution*

Parameter	Concentration of NO_2^- ions, g l^{-1}	
	0	10
Relative weight loss of the MC support, Δm, g g^{-1}:		
1st cycle	0.04	0.1
2nd cycle	0.03	0.12
Σ in 5 cycles	0.11	0.43
Weight change of MC supports upon impregnation, Δm, g cm^{-3} Σ in 5 cycles	0.74	0.97
Q, A h cm^{-3}	0.23	0.31
K_{util}, %	100	100

* Q, specific discharge capacity; K_{util}, coefficient of utilization of the active substance.

because of the operation of a Ni–NiO_x cell. The subsequent decrease in the oxidation rate in a $Ni(NO_3)_2$ solution with a $NaNO_2$ additive is due to partial exhaustion of the oxidizing agent, N_2O_4. The mass of the active substance, necessary for obtaining a specific discharge capacity of 0.3 A h cm^{-3} [2] of MC supports impregnated by the technique developed, is accumulated in 5 cycles of impregnation for 1 h (Table 2). At the same time, only 76% of the required mass is obtained in metal–ceramic supports impregnated under the same conditions in a $Ni(NO_3)_2$ solution without an additive. Up to 61% of the active substance is formed through etching of nickel contained in an MC support in the case of impregnation in a $Ni(NO_3)_2$ solution with a $NaNO_2$ additive, and only 35%, in impregnation of MC supports in a $Ni(NO_3)_2$ solution (Table 2). The stronger oxidation of the nickel support in nitrate–nitrite solutions does not impair the mechanical strength of the electrodes obtained, because only 15% of the total amount of nickel is oxidized (up to 20% is acceptable [8]).

The electrochemical activity of $Ni(OH)_2$ obtained from a $Ni(NO_3)_2$ solution with a $NaNO_2$ additive was tested in forming of MC NOE. The utilization coefficient of the active substance in electrodes of this kind is the same as that for electrodes impregnated in a $Ni(NO_3)_2$ solution (Table 2).

When a $NaNO_2$ additive was introduced into a $Ni(NO_3)_2$ solution, the total time of impregnation of MC supports decreased to 5 h, whereas in the case of the "nitrate" technique, the necessary amount of the active substance in an MC support is only accumulated after 18 h of impregnation in a $Ni(NO_3)_2$ solution [3]. As demonstrated by experiments on dissolution of nickel from an MC support, the influence exerted by the $NaNO_2$ additive is preserved during 5 to 6 cycles. Further, the rate of Ni oxidation in a $Ni(NO_3)_2$ solution with a $NaNO_2$ additive becomes the same as that in the $Ni(NO_3)_2$ solution.

CONCLUSIONS

(1) The time of impregnation of metal–ceramic supports of nickel oxide electrodes becomes 30–38% shorter, compared to an ordinary nitrate impregnation, upon introduction of 5–10 g l^{-1} $NaNO_2$ into a $Ni(NO_3)_2$ solution. A process for nitrate–nitrite impregnation is suggested.

(2) The effect of the nitrite additive is attributed to disproportionation of nitrites to give an electrochemically active dimer of nitrogen(IV) oxide.

ACKNOWLEDGMENTS

The authors thank V.N. Flerov for assistance and consulting in writing the article.

REFERENCES

1. Dasoyan, M.A. and Novoderezhkin, V.V., *Proizvodstvo elektricheskikh akkumulyatorov* (Manufacture of Electric Batteries), Moscow: Vysshaya Shkola, 1970.
2. Pozin, Yu.M. and Shtertser, N.I., *Zh. Prikl. Khim.*, 1970, vol. 43, no. 7, pp. 1482–1486.
3. Levinzon, L.M., Pozin, Yu.M., and Shtertser, N.I., *Tekhnologiya proizvodstva khimicheskikh istochnikov toka: Sbornik nauchnykh trudov* (Technology for Manufacture of Chemical Power Cells: Coll. of Works), Leningrad: Energoizdat, 1985.
4. Zhdanov, V.V., Poltavchenko, V.S., Tikhonov, K.I., and Pozin, Yu.M., *Zh. Prikl. Khim.*, 1982, vol. 55, no. 3, pp. 694–696.

5. Kuzina, T.E. and Bachaev, A.A., *Zh. Prikl. Khim.*, 2002, vol. 75, no. 11, pp. 1839–1842.
6. Sorokina, N.V., in *Sbornik rabot po KhIT* (Coll. of Works on Chemical Power Cells), Nikol'skii, V.A., Ed., Leningrad: Energiya, 1974, issue 9.
7. Gorelik, S.S., Skakov, Yu.A., and Rastorguev, L.N., *Rentgenograficheskii i elektronno-opticheskii analiz* (X-ray Diffraction and Electron-Optical Analyses), Moscow, 1994.
8. Pervushin, Yu.N., A Study in Technology of Fabrication of an MC NOE for Alkaline Battery, *Cand. Sci. Dissertation*, Novocherkassk, 1968.
9. Safonova, T.Ya. and Petrii, O.A., *Elektrokhimiya*, 1995, vol. 31, no. 12, pp. 1373–1377.
10. Cotton, F.A. and Wilkinson, G., *Advanced Inorganic Chemistry*, New York: Interscience, 1966.
11. Vetter, K.J., *Elektrochemische Kinetik*, Berlin: Springer, 1961.
12. Gur'yan, L.I., *Okislitel'no-vosstanovitel'nye reaktsii i potentsialy v analiticheskoi khimii* (Redox Reactions and Potentials in Analytical Chemistry), Moscow: Khimiya, 1989.
13. Galus, Zb., *Teoretyczne podstawy elektroanalisy chemicznej*, Warsaw: Naukowe, 1971.

Russian Journal of Applied Chemistry, Vol. 77, No. 9, 2004, pp. 1481–1486. Translated from Zhurnal Prikladnoi Khimii, Vol. 77, No. 9, 2004, pp. 1491–1496.

APPLIED ELECTROCHEMISTRY AND CORROSION PROTECTION OF METALS

Development of Processes for Utilization of By-Products from Production of Fluoropolymers

S. L. Fuks, S. V. Devyaterikova, S. V. Khitrin, and V. A. Samara

Vyatka State University, Kirov, Russia

Received March 22, 2004

Abstract—Recovery of zinc from solid wastes from production of fluoropolymers is studied. The processes of zinc utilization for preparation of zinc–graphite and zinc–phosphate–poly(tetrafluoroethylene) anticorrosion coatings are developed, including those using mother liquors from production of fluoropolymers.

Composite electrochemical coatings (CECs) are widely used today thanks to valuable properties of their metallic matrix and nonmetallic inclusions. In this work we developed processes for preparation of zinc–graphite and zinc–phosphate–poly(tetrafluoroethylene) (PTFE) coatings, including those using by-products from production of fluoropolymers.

EXPERIMENTAL

In zinc electroplating, large amounts of zinc salts and zinc anodes are expended. In this connection, a process has been developed for utilization of zinc catalyst waste from production of trifluorochloroethylene, which is used in manufacture of fluorocopolymers. Significant contents of zinc and its compounds in the sludge (12 wt % Zn, 10 $ZnCO_3$, 64 ZnO, and 8–14 $ZnCl_2$) allows electrochemical recovery of zinc on a cathode. To prepare the electrolyte (230–300 g l^{-1} $ZnSO_4$), zinc was leached with an estimated amount of sulfuric acid with heating and stirring. After filtration, pH was adjusted to 3–4, and the precipitated iron(III) hydroxide was filtered off.

Zinc was deposited onto aluminum cathodes (S = 0.36–0.45 dm^2) using lead anodes at various current densities and an electrolysis time of 1.5 h. The dependence of the current efficiency (CE) on the current density is parabolic (Fig. 1) with a maximum at I_c = 400–600 A m^{-2}. Visual observations showed that the grey grainy zinc deposit is formed with small dendrites at the edges of the cathode.

In full utilization of by-products from production of fluoropolymers (see scheme), the zinc-containing sludge goes from the storage tank to washing with deionized water and dissolution of salts. After settling, the solution is separated by decantation. The precipitate of Zn, ZnO, and $ZnCO_3$ goes to sulfuric acid dissolution to convert it into $ZnSO_4$. Simultaneously Zn^{2+} is recovered from the decanted $ZnCl_2$ solution by adding NaOH to pH 8–9 at which $Zn(OH)_2$ is formed [1] (pH 10.5 corresponding to dissolution of the precipitate [1] must not be reached). The resulting precipitate of $Zn(OH)_2$ is settled, separated from the solution, washed, and directed to sulfuric acid leaching. The solutions are mixed in a reactor. The resulting electrolyte goes to filtration, analysis, and conditioning. A conditioned solution should contain 70–120 g l^{-1} Zn(II) and 50–100 g l^{-1} sulfuric acid [2]. The electrolyte prepared for use is fed to a galvanic tank, representing a flow-through electrolyzer, where zinc is deposited onto aluminum cathodes using lead anodes. Spent electrolyte is depleted of zinc(II) and enriched with sulfuric acid according to the reaction

$$ZnSO_4 + H_2O \rightleftarrows Zn + H_2SO_4 + 0.5O_2.$$

The spent electrolyte is conditioned by adding zinc hydroxide.

In the next stage, zinc is mechanically removed from the cathodes and directed to fusing and manufacture of plates, and then, to fabrication of anodes and preparation of the electrolyte fed to a zinc-plating bath. Zinc anodes are also arranged in an electrolytic tank. Also electrochemically reduced zinc can be returned to the trifluorochloroethylene production cycle. Composite electrochemical coatings can be prepared by adding a disperse phase to the zinc electrolyte.

We studied the possibility of preparing Zn–graphite CEC. To prepare a suspension electrolyte we used ammonium chloride zinc solution with a composition

1070-4272/04/7709-1481 © 2004 MAIK "Nauka/Interperiodica"

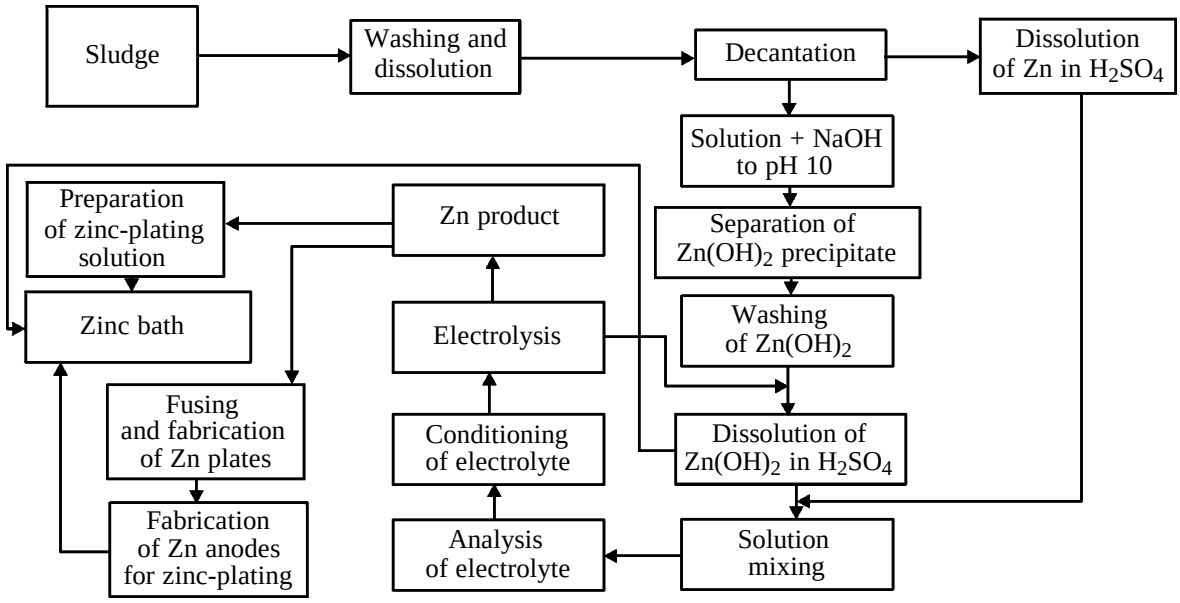

Flowsheet of utilization of zinc-containing wastes from production of monomer-3.

($g\ l^{-1}$): $ZnCl_2$ 40–120, NH_4Cl 180–220, Likonda A 30–70, Likonda B 3–5; pH 5.4–6.5; T = 15–30°C; i_c = 0.5–3.0 A dm^{-1}. The particle size in colloidal graphite was 0.5–1.0 μm. Coatings were applied onto heat-treated 08 kp steel.

The corrosion resistance of the coatings was studied using the procedure described in [3]. The free corrosion potentials were determined for 08 kp steel and the same steel but zinc-plated or coated with a CEC layer (graphite concentration 5–15 $g\ l^{-1}$). The contacting time of the samples with a drop of an electrolyte (1% NaCl) was 15 min at 20°C. The results are given in Table 1.

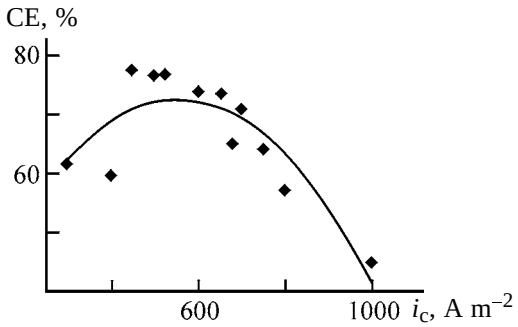

Fig. 1. Current efficiency CE as a function of the current density i_c in the electrolyte prepared from the zinc sludge.

Table 1. Free corrosion potential ε_{cor}

Graphite concentration, $g\ l^{-1}$	08 kp steel	$-\varepsilon_{cor}$, V
0	No coating	0.175
0	Zinc coating 10 μm thick	0.695
5	CEC coating 10 μm thick	0.680
10		0.680
15		0.690

As seen, the corrosion potential of Zn is more negative than that of steel, being close to the standard potential of the zinc electrode (–0.76 V [3]). As expected, inclusions of positively charged graphite particles only slightly shift the potential to the positive direction. Therefore, CEC, like the zinc coating, will be a protector for steel.

The observed insignificant positive shift of the potential is a result of the self-lubricating effect in the coating. Comparison of the emf values of the contacting pairs Zn–Fe, CEC–Fe, and CEC–Zn obtained under similar conditions at τ = 5 min showed the increase in the protective effect:

$$\Delta E = \mathrm{emf}^{CEC} - \mathrm{emf}^{0},$$

where emf^{CEC} is the contact potential in the pairs Fe–CEC or Zn–CEC; and emf^{0}, the contact potential in the pairs Fe–Zn or Zn–Zn.

The measured data are given in Table 2. Increasing graphite concentration in CEC provides a proportional increase in ΔE of the pair CEC (Zn–graphite)–iron. This is also the case for the pair CEC (Zn–graphite)–zinc.

The potential of the CEC–iron couple increases more significantly as compared to CEC–zinc. There-

Table 2. Contact potential of voltaic couples

Graphite concentration, g l^{-1}	Graphite content in CEC, vol %	Voltaic couple	emf $\times 10^3$	$\Delta E \times 10^3$
			V	
0	0	Zn–Fe	609 ± 13	–
0	0	Zn–Zn	0	–
5	21.7	CEC–Fe	626 ± 17	17
		CEC–Zn	15 ± 2	15
10	26.8	CEC–Fe	642 ± 21	33
		CEC–Zn	25 ± 4	25
15	35.6	CEC–Fe	660 ± 12	51
		CEC–Zn	35 ± 0	35

fore, CEC is more efficient protector for steel than zinc. If there is a need in more effective protection, it is recommended to apply a two-layer coating Zn/Zn–graphite.

The corrosion resistance of steel coated with zinc or CEC was studied in a corrosion cell under water vapor at 40°C for 900 h. The area of the samples was 15.2 cm^2; the coating thickness, 5, 8, and 10 μm. We determined the gravimetric corrosion index $K = \Delta m/(\tau S)$ (g h^{-1} cm^{-2}) and counted up the number of corrosion spots per 1 cm^2 of the coating.

Visual examination revealed that the marks of corrosion occur on all the samples studied (as a white thin film and multiple dark areas). However, the number of corrosion spots was smaller in the CEC-coated samples.

Data on the gravimetric corrosion index are presented in Table 3.

The gravimetric corrosion index of zinc-plated steel decreases by half with increasing coating thickness from 5 to 10 μm, but the corrosion rate is independent of the CEC thickness.

Thus, zinc–graphite coating effectively protects steel from corrosion in chloride solutions.

It appeared interesting to change the graphite disperse phase for a more inert, polymeric phase. For this purpose we used a PTFE suspension. It was found that the deposits formed in ammonium chloride zinc-plating solution with PTFE are inhomogeneous and show no corrosion resistance. Therefore, we modified the composition of the polymer-containing zinc coating.

Zinc coatings were obtained on flat and screw samples of 30KhGSA steel. To improve the adhesion, the zinc-plated surface was subjected to additional processing (phosphatization) in the solutions whose compositions are given in Table 4.

The selection criterion of a solution was the specific weight of the phosphate coating. To attain the optimal characteristics, it should be 2–10 g m^{-2}.

Visual examination revealed that the phosphate coatings formed on steel and zinc are quite homogeneous. Light-grey or dark-grey deposits consisting of fine or medium-sized crystals are formed. For differently shaped samples, at the same process time, the specific weight of the phosphate coatings was approximately the same, regardless of the solution composition.

Table 3. Gravimetric corrosion index K

Coating	Coating thickness δ, μm	$K \times 10^7$, g h^{-1} cm^{-2}
Zinc	5	11.7
	8	9.0
	10	5.8
CEC	5	6.1
	8	5.9
	10	5.8

Table 4. Solution compositions and phosphatization modes

Solution no.	Additive concentration	T, °C	τ, min
1	H_3PO_4, 9.5–13.5 $Zn(NO_3)_2 \cdot 6H_2O$, 42–58 $Zn(H_2PO_4)_2$, 28–36	85–95	3–12 4–6
2	$Zn(H_2PO_4)_2$, 8–12 $Zn(NO_3)_2 \cdot 6H_2O$, 10–12 $Ba(NO_3)_2$, 30–40	75–85	

Table. 5. Results of corrosion tests in the salt spray cell (phosphatization time 5 min)

Sample no.	Phosphatizing solution no.	Sample shape	Centrifugation time, min	Occurrence of corrosion spots
1	1	Flat	1	–
2			5	–
3			10	–
4	2		1	+
5			5	–
6			10	–
7	1	Screw	1	+
8			5	–
9			10	–
13	2		1	–
14			5	–
15			10	–

Modification of the phosphate coating with PTFE particles was performed by dipping in a stabilized suspension. The film was held in it for 1 min, after which the samples were air-dried. A phosphate layer with PTFE particles in the pores [phosphate–PTFE composite chemical coating (CCC)] was formed on the surface. With 25% PTFE suspension, we obtained a smooth, transparent CCC, but having insufficient adhesion to the surface. The formation of a metal–CCC friction couple resulted in exfoliation of the coating under a stress below 2 kg cm^{-2}. Presumably, this is due to insufficient penetration of the hydrophobic PTFE particles to the phosphate coating, which is caused by water occurring in the pores. In the subsequent experiments we used 50% aqueous PTFE suspension stabilized with OP-10 stabilizer. In this case, we attained reasonable adhesion, but the coating was inhomogeneous in the composition and thickness. To remove the excess of PTFE, the freshly coated samples were centrifuged for 1 min at 1000 rpm.

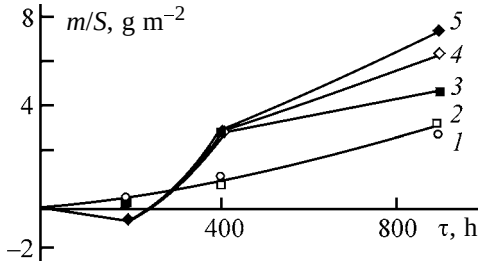

Fig. 2. Specific weight of the samples m/S as a function of the time τ of the corrosion tests in the salt spray cell with natural spraying. Sample shape: (*1, 2*) flat and (*3–5*) screw. Phosphatizing solution no.: (*1, 3, 4*) 1 and (*2, 5*) 2. Phosphatization time (min): (*1–3, 5*) 5 and (*4*) 10.

This operation provided dehydration of the coating, which became more uniform. The specific weight of CCC before centrifugation was 21 g m^{-2}. After centrifugation it became 2–3 times lower. To attain a desired weight, it was sufficient to centrifuge differently shaped samples for no more than 5 min.

Corrosion tests of the three-layered coating were carried out gravimetrically in a salt spray cell with artificial spraying for 200 h and also electrochemically in the galvanostatic mode.

After completion of gravimetric corrosion tests, the samples were analyzed for corrosion products. The results are summarized in Table 5.

Flat sample nos. 1 and 4 and screw sample no. 7 did not pass the corrosion tests after centrifugation for 1 min. Therefore, phosphatization of flat samples and screw joints can be performed with any of the solutions tested at a centrifugation time of no less than 5 min.

The samples were also tested in a cell with natural spraying for 900 h. The weighing results obtained after 200, 400, and 900 h are presented in Fig. 2. It is seen that, after 200 h, the specific weight is slightly decreased in the screw samples phosphatized in solution nos. 1 and 2 for 10 and 5 min, respectively. With increasing testing time to 400 h, the weight of all the samples studied increased, the effect being more pronounced in the screw samples. We observed no corrosion of the support throughout the 900-h test, i.e., the coatings and deposition modes could be recommended for practical use.

Electrochemical corrosion tests were carried our by measuring the free corrosion potential on the surface of 08 kp steel (30 × 50 mm) and also on the coated surfaces (Fig. 3). The corrosion potential of steel in 3% NaCl was found to be –0.3 V. Application of a Zn coating shifts the potential by 0.56 V to the negative region. Phosphatization of the surface shifts the free corrosion potential of the coating by 0.07 V to the positive direction. The subsequent modification of the coating by impregnation with PTFE shifts the potential to 0.62 V.

The results show that the multilayered metal–phosphate–polymer coating effectively protects steel against corrosion.

Finally, we recommend the process for preparation of multilayered coatings involving chemical degreasing, acid activation, zinc-plating, phosphatization, impregnation with PTFE, centrifugation, and drying.

In the dispersion method of PTFE production, large amounts of wastes, including liquid wastes, are

formed. Therefore, we made efforts to utilize them as solvents and surface-active additives in preparation of zinc solutions.

The mother liquor contains F 4D fluoroplastic (>0.1%) or SKF rubber (3.5–5%). The examination by gas–liquid chromatography–mass spectrometry (GC–MS) revealed the presence of oligomers, molecular weight stabilizers, polymerization initiators, and ammonium carboxylates used in the process as emulsifiers.

We performed a series of experiments with the aim to utilize the mother liquors for preparing composite electrochemical coatings containing zinc, fluoroplastic and fluoroelastomer particles, and oligomers. Previously [4, 5] we demonstrated that the stabilizers and initiators of polymerization are nonionic species, which are nonspecifically adsorbed in the cathode and anode spaces and can be used as surfactants increasing the overvoltage of the cathodic process.

To elucidate the contribution of the surfactants to the properties of the zinc–polymer coating, we examined perfluorinated quaternary ammonium salts of amido amines of hexafluoropropylene oxide oligomers (ChAS-T). Data on the electrophoretic mobility of polymeric species are presented in Fig. 4 with an example of PTFE.

Figure 4 shows that, at a PTFE concentration in the electrolyte suspension of 10 g l^{-1}, the electrophoretic potential passes through a maximum at a ChAS-T concentration of 2 g l^{-1}. In the absence of ChAS-T, the ζ potential is lower than the maximal value by a factor of 3.5. As the electrophoretic mobility of the PTFE particles increases in the presence of ChAS-T, their concentration in the coating should increase. It should be expected also that the current efficiency of zinc increases in the presence of PTFE in the cathode space, since PTFE serves as an additional carrier for the $[Zn(NH_3)_2]^{2+}$ ions. Data on the current efficiency of zinc are given in Table 6.

Introduction of PTFE into the solution, indeed, slightly increases the current efficiency of the coating, regardless of the current density used. With increasing PTFE concentration, the current efficiency decreases, i.e., the dependence of the current efficiency on the PTFE concentration is parabolic with a maximum at 5 g l^{-1} PTFE and 1 g l^{-1} ChAS-T.

To conclude, our results show that wastes from production of fluoropolymers can be utilized for preparing corrosion-resistant coatings.

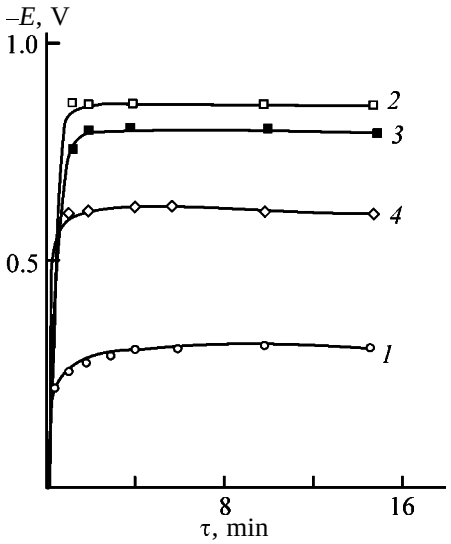

Fig. 3. Free corrosion potential E as a function of time τ: (*1*) steel, (*2*) steel–Zn, (*3*) steel–Zn–phosphate, and (*4*) steel–Zn–phosphate–PTFE.

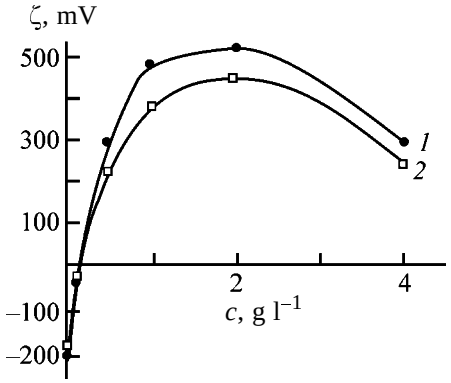

Fig. 4. The ζ potential as a function of the ChAS-T concentration c. PTFE concentration 10 g l^{-1}. τ (min); (*1*) 20 and (*2*) 30.

Table 6. Current efficiency at various PTFE concentrations

Concentration, g l^{-1}		CE, %, at indicated I, A dm^{-2}		
PTFE	ChAS-T	0.5	1.5	2.0
0	0	97.6	98.2	94.0
5	1	98.0	99.6	98.9
10	2	92.7	93.6	93.8

CONCLUSIONS

(1) A process is developed for preparing zinc coatings from zinc-containing sludge from production of trifluorochloroethylene.

(2) A zinc–graphite composite electrochemical coating is prepared from ammonium chloride zinc-plating solution.

(3) A zinc–phosphate–poly(tetrafluoroethylene) three-layered composite coating is prepared, which demonstrated anticorrosion properties.

(4) The mother liquors from production of fluoropolymers were suggested as a disperse phase in preparation of the coatings.

REFERENCES

1. Lur'e, Yu.Yu., *Spravochnik po analiticheskoi khimii* (A Handbook of Analytical Chemistry), Moscow: Khimiya, 1979.
2. Tararin, S.V., *Elektroliz vodnykh rastvorov v tsvetnoi metallurgii* (Electrolysis of Aqueous Solutions in Nonferrous Metallurgy), Moscow: Metallurgiya, 1990.
3. Mattsson E., *Elektrokemi och korrosionslara*, Stockholm: Korrosionsinstitutet, Bulletin no. 100, 1987.
4. Devyaterikova, S.V., Khitrin, S.V., and Fuks, S.L., Abstracts of Papers, *Yubileinaya nauchno-prakticheskaya konferentsiya "III Kirpichnikovskie chteniya"* (Memorial Scientific and Practical Conference "Third Kirpichnikov Symp."), Kazan (Russia), March 25–28, 2003, p. 450.
5. Khitrin, S.V., Fuks, S.L., Agalakova, N.V., *et al.*, Abstracts of Papers, *Vserossiiskaya nauchno-tekhnicheskaya konferentsiya "Nauka–proizvodstvo–tekhnologii–ekologiya"* (Russian Scientific and Technical Conf. "Science–Industry–Technology–Ecology"), Kirov: Vyatsk. Gos. Univ., 2003, vol. 3, p. 47.

Russian Journal of Applied Chemistry, Vol. 77, No. 9, 2004, pp. 1487–1490. Translated from Zhurnal Prikladnoi Khimii, Vol. 77, No. 9, 2004, pp. 1497–1500.

APPLIED ELECTROCHEMISTRY AND CORROSION PROTECTION OF METALS

A Study of Adsorption of Lead, Cadmium, and Zinc Ions on the Glass Surface by Stripping Voltammetry

I. E. Stas', B. P. Shipunov, I. N. Pautova, and Yu. V. Sankina

Altai State University, Barnaul, Russia

Received February 20, 2004

Abstract—Stripping voltammetry was applied to study the influence exerted by the brand of glass on the amount of adsorption of heavy metal ions from solution. The dependence of the amount of the adsorbed ions on their concentration in solution and on the concentration of the supporting electrolyte was analyzed.

The material from which laboratory glassware and vessels for storage of solutions are fabricated may be a source of contamination and a reason for a change in the concentration of solutions they contain [1]. The laboratory glassware is most frequently made of glass. Various brands of glass differ in the composition, chemical resistance, and sorption power [2]. It is known that the glass surface is charged negatively in aqueous solutions because of the surface dissociation of silanol groups [3]. Therefore, glass can adsorb cations.

To determine microscopic amounts of a substance, on the order of 10^{-7} M and less, stripping voltammetry (SVA) is widely used [4–6]. For this technique, changes in the concentration of elements to be determined, which occur as a result of adsorption–desorption processes, are important. This is so because, when working with concentrations of about $n \times 10^{-7}$ M, $n \times 10^{-9}$ mol of a substance is contained in a solution being analyzed (at a sample volume of 10–20 ml), whereas the adsorption of ions may be as high as $n \times 10^{-10}$ mol cm^{-2} [7]. However, no systematic studies of the adsorption of heavy metal ions, conventionally determined by SVA, on the glass surface and no comparative estimates of the adsorption capacity of various brands of glass have been performed.

The aim of this study was to examine the adsorption of lead, cadmium, and zinc ions on the glass surface by SVA at ion concentrations in solution of $n \times 10^{-7}$ M.

EXPERIMENTAL

The study was carried out using a PU-1 polarograph with two-electrode cells fabricated from various brands of glass. A needle-like mercury-film electrode on a silver substrate (S = 0.35 cm^2) served as indicator electrode, and a silver chloride electrode, as reference. Reference and supporting-electrolyte solutions were prepared using demineralized water and chemically pure reagents. As supporting electrolyte served 0.01 M KCl (pH 5.95). Reference solutions of the elements being studied were prepared by the known method [8]. The concentration of the elements to be determined in the solutions under study was $c_{Pb^{2+}} = c_{Cd^{2+}} = 4 \times 10^{-7}$, $c_{Zn^{2+}} = 9 \times 10^{-7}$ M. Dissolved oxygen was removed by bubbling preliminarily purified gaseous nitrogen through a solution. The same flow of nitrogen served to agitate ground glass (adsorbent).

Zinc, lead, and cadmium were accumulated on the electrode at a potential E_e = –1.3 V in the course of 60 s, after which the dissolution current of the resulting amalgam was recorded at a linear potential sweep at a rate of 60 mV s^{-1}. The interval of potential scanning was from –1.3 to 0.1 V. In the course of the experiment, reproducible analytical signals of the elements were recorded, and then a certain amount of ground glass was added and the solution was agitated for 5 min without recording any voltammograms. Then the agitation was terminated and the substances under study was again accumulated on the electrode. After reproducible voltammograms were recorded, a new portion of the adsorbent was introduced and the solution was again agitated for 5 min. The elements to be determined were accumulated and voltammograms were recorded from an unagitated solution, because recording with an agitated solution with an adsorbent yielded unsatisfactory results as a consequence of the irreproducibility of hydrodynamic conditions and adhesion of adsorbent particles to the electrode sur-

1070-4272/04/7709-1487 © 2004 MAIK "Nauka/Interperiodica"

Table 1. Chemical composition of laboratory glass of various brands

Glass	Content, wt %							
	SiO_2	B_2O_3	Al_2O_3	CaO	MgO	BaO	Na_2O	K_2O
Pyrex	80.64	12.0	2.0	0.36	–	–	4.0	1.0
MG	7.0	35.0	23.0	6.3	14.2	4.3	–	–
Glass no. 23	68.4	2.7	3.9	8.5	0.08	–	9.4	7.1

face. The extent to which the signal of the element being determined decreased was calculated by the formula

$$I_{rel} = \frac{\Delta I}{I} = \frac{I_0 - I_m}{I_0}, \quad (1)$$

where I_0 is the peak current measured without adsorbent addition, and I_m is the peak current in the presence of an adsorbent in an amount m (g).

The adsorption of ions was calculated by the equation

$$\Gamma = \frac{(c_{in} - c_f)}{1000m}, \quad (2)$$

where Γ is the adsorption (mol g^{-1}); c_{in}, initial concentration of metal ions in the starting solution (M): c_f, concentration of metal ions in solution in the presence of an adsorbent (M); V, solution volume (ml); and m, mass of the adsorbent (g).

The pretreatment of the glass included several stages: (1) glass grinding in an agate mortar and sieving with a mesh of 1.5 mm; (2) boiling of the resulting powders in triple-distilled water, with water replaced several times to remove adsorbed contaminants; and (3) drying of filtered-off glass powder in an oven at 150°C.

Table 2. Current I of anodic peaks of heavy metal ions for various brands of glass. Supporting electrolyte 0.01 M KCl; $c_{Cd^{2+}} = c_{Pb^{2+}} = 4 \times 10^{-7}$, $c_{Zn^{2+}} = 9 \times 10^{-7}$ M; $E_e = -1.3$ V; $t_e = 60$ s; $V_s = 60$ mV s^{-1}

Glass	I, μA		
	Zn^{2+}	Cd^{2+}	Pb^{2+}
Pyrex	14.0 ± 1.0	13.0 ± 1.1	17.0 ± 1.5
MG	14.6 ± 1.2	19.8 ± 2.3	19.0 ± 2.0
ChG no. 23	9.2 ± 0.5	9.6 ± 0.6	10.6 ± 1.0

Molybdenum glass (MG), chemical glass no. 23 (ChG), and Pyrex were used in the study. Table 1 lists the chemical compositions of the glasses. Their chemical resistance decreases in the order Pyrex > MG > ChG. In the same order vary the heat resistance, brittleness, and hardness.

It should be noted that the magnitudes of the analytical signals of the elements to be determined and their relative values depended on the brand of a glass used to fabricate electrochemical cells (Table 2). The weakest signals were recorded in a cell made of ChG, and the strongest signals, in an MG cell. The greatest difference was observed for the signal of cadmium: The peak current decreased twice in going from MG to ChG. The results obtained indicate that the adsorption of heavy metal ions on the glass surface is strong and selective.

To determine the optimal time of agitation of a solution with the adsorbent, we measured the kinetic curves. These curves demonstrate that the analytical signal decreases as a result of adsorption of an element to be determined during the first 5 min. Upon further agitation, the signals of lead and cadmium remained virtually unchanged, and that of zinc changed only slightly. The efficiency of suppression of the analytical signal (anodic current peak) of the metal ions under study was analyzed as a function of the mass of the glass added. The scatter of experimental data in parallel measurements did not exceed 10%.

Figure 1 shows the dependences of the extent to which the peak currents I_{rel} of heavy metal ions simultaneously present in solution decrease on the mass of Pyrex glass added. The analytical signals of the elements under study were suppressed on introducing this brand of glass into solution when its mass increased to 0.20 g. The extent of depression of the signal was the greatest for Pb^{2+} ions and decreased in order $Pb^{2+} > Zn^{2+} > Cd^{2+}$ (Fig. 1). A similar dependence was obtained with ChG. With MG used as adsorbent, the maximum depression of signals was observed even on introducing it into solution in an amount of 0.15 g. The extent to which the signal was

suppressed decreased in the order Zn^{2+} > Pb^{2+} > Cd^{2+}. It was established that the adsorption of the ions under study is the strongest on molybdenum glass and the weakest on Pyrex. The strongest difference was observed in the case of adsorption of Cd^{2+} ions. For example, the signal of cadmium decreased by 23% on introducing 0.24 g of powdered Pyrex and by 63% on introducing an MG powder of the same mass. The difference in the adsorbability of zinc and lead ions is considerably less pronounced. The peak current decreased, depending on the brand of glass, by 70–90% for Zn^{2+} and by 74–85% for Pb^{2+}. Thus, it was established that cadmium ions are adsorbed on the glass surface to the smallest extent, but the selectivity of their adsorption is the highest. Data on how the analytical signals of the elements under study decrease in the presence of powdered glass of various brands are presented in Fig. 2.

It should be noted that the adsorbability of the ions under study on glass powder differs from that on a flat surface. Table 2 shows that the adsorption of the ions is the weakest on the MG surface (peak currents are the highest), whereas the analytical signals of the ions are the lowest in the presence of a powdered glass of this brand, which indicates that their adsorption is the strongest. Possibly, grinding of MG gives rise to a greater number of active centers per unit surface, compared with other brands of glass. At the same time, grinding of different brands of glass may yield particles of unequal sizes because of the difference in hardness between these glasses, which affects the surface area of the adsorbent. This circumstance invites further analysis.

It is known that heavy metal ions are specifically adsorbed on solid surfaces [7]. However, competitive adsorption of Zn^{2+}, Pb^{2+}, and Cd^{2+} ions and indifferent cations of the supporting electrolyte, whose concentration is several orders of magnitude higher than that of heavy metal ions, must be observed in the presence of a large excess of a supporting electrolyte. Our experiments show that raising the concentration of the supporting electrolyte leads to a significant decrease in the adsorption of Zn^{2+}, Pb^{2+}, and Cd^{2+} ions. This is manifested in a decreased depression of the analytical signal. Table 3 illustrates the influence exerted by the concentration of the supporting electrolyte (KCl) on the degree of suppression of the peak current of heavy metal ions in the presence of powdered glass of various brands (m_g = 0.1 g). Table 3 shows that raising the concentration of the supporting electrolyte to 1 M minimizes the adsorption of the ions being determined. In this case, cadmium ions are virtually not adsorbed at all, and the

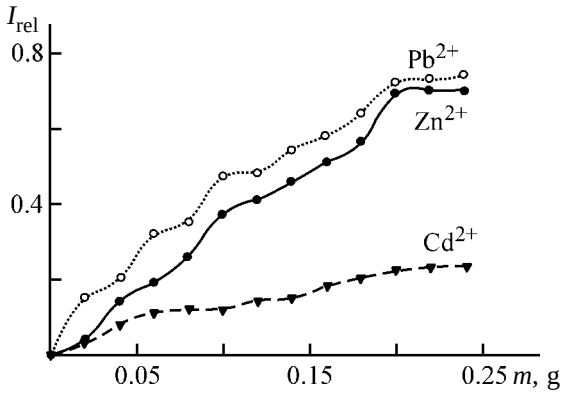

Fig. 1. Extent to which the currents of the anodic peaks of heavy metal ions are suppressred, I_{rel}, vs. the mass m of powdered Pyrex glass. Supporting electrolyte 0.01 M KCl; $c_{Cd^{2+}} = c_{Pb^{2+}} = 4 \times 10^{-7}$, $c_{Zn^{2+}} = 9 \times 10^{-7}$ M; E_e = –1.3 V; t_e = 60 s; V_s = 60 mV s^{-1}; the same for Fig. 2.

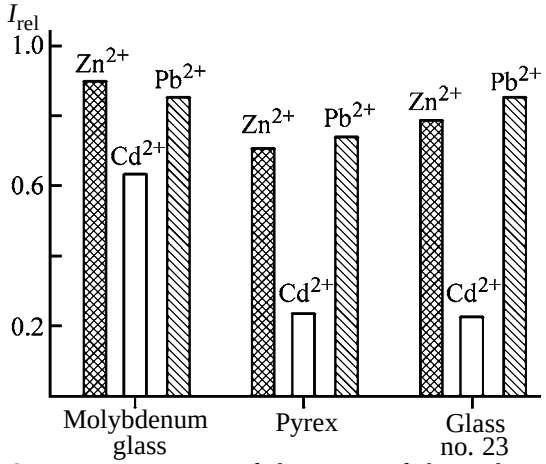

Fig. 2. Maximum extents of depression of the analytical signals I_{rel} of heavy metal ions in the presence of powdered glass of various brands (m_g = 0.24 g).

signals of zinc and lead are suppressed by less than 30%. Irrespective of the glass brand and concentration of the supporting electrolyte, the adsorbability of heavy metal ions decreases in order Pb^{2+} > Zn^{2+} > Cd^{2+}. Zn^{2+} ions are best adsorbed on the ChG surface, and Cd^{2+} ions, on the MG surface. The brand of a glass on whose surface Pb^{2+} ions are adsorbed to the greatest extent changes as the concentration of the supporting electrolyte increases.

The adsorption of ions also depends on the concentration of ions being adsorbed. On determining the concentrations of heavy metal ions before and after adsorption by the SVA method, their adsorption Γ on the surface of various brands of glass was calculated using Eq. (2). The results obtained with Zn^{2+}, Pb^{2+}, and Cd^{2+} at their concentrations in the range 10^{-7}–10^{-5} M are given in Table 4. An increase in the concentration of the ions in solution shifts the adsorption–

Table 3. Depression of the current of anodic peaks of heavy metal ions in the presence of a powder of various brands of glass at different concentrations of the supporting electrolyte. $c_{Cd^{2+}} = c_{Pb^{2+}} = 4 \times 10^{-7}$, $c_{Zn^{2+}} = 9 \times 10^{-7}$ M; $E_e = -1.3$ V; $t_e = 60$ s; $V_s = 60$ mV s^{-1}; $m_g = 0.1$ g

c_{KCl}, mol g^{-1}	$\Delta I/I_0$								
	Pyrex			MG			ChG no. 23		
	Zn^{2+}	Cd^{2+}	Pb^{2+}	Zn^{2+}	Cd^{2+}	Pb^{2+}	Zn^{2+}	Cd^{2+}	Pb^{2+}
0.001	0.35	0.14	0.45	0.38	0.32	0.63	0.53	0.33	0.70
0.01	0.29	0.12	0.42	0.35	0.27	0.52	0.35	0.16	0.49
0.1	0.20	0.09	0.35	0.27	0.13	0.42	0.26	0.09	0.27
1.0	0.14	0.05	0.26	0.17	0.09	0.30	0.21	0.04	0.15

Table 4. Adsorption Γ of heavy metal ions at their different concentrations in solution. Supporting electrolyte 0.01 M KCl, $T = 20$°C

$c_{M^{2+}}$, mol g^{-1}	$\Gamma \times 10^8$, mol g^{-1}								
	Pyrex			MG			ChG no. 23		
	Zn^{2+}	Cd^{2+}	Pb^{2+}	Zn^{2+}	Cd^{2+}	Pb^{2+}	Zn^{2+}	Cd^{2+}	Pb^{2+}
10^{-7}	1.5	0.48	0.70	1.7	0.69	0.79	1.9	0.46	0.78
10^{-6}	3.0	1.2	1.1	3.0	1.3	1.3	2.9	1.1	1.3
10^{-5}	14	10	–	17	10	–	14	10	–

desorption equilibrium toward the adsorption process. If the concentration of the ions being adsorbed increases by an order of magnitude, their adsorption becomes 1.5–2 times stronger. At a concentration of the ions in solution on the order of 10^{-5} M, the analytical signals of lead and cadmium are overlapped, which hinders their identification. Therefore, the adsorption of zinc and cadmium ions at their content in solution of 1×10^{-5} M was determined in the absence of lead ions. In this case, the amounts of adsorbed Zn^{2+} and Cd^{2+} ions became closer to each other. The data obtained suggest that the adsorption of heavy metal ions is competitive: adsorption of Pb^{2+} ions hinders adsorption of Cd^{2+} ions. In the absence of lead ions, the adsorption of cadmium ions is considerably stronger.

The study performed demonstrated the importance of adsorption processes at the glass–solution interface in determining low concentrations of ions, which may make incorrect the analytical results. The adsorption of heavy metal ions can be markedly diminished by an appropriate choice of the material of a storage vessel and electrochemical cell and also by use of sufficiently concentrated supporting-electrolyte solutions. To make smaller the determination error, it is recommended to prepare reference solutions in a supporting electrolyte rather than in pure water.

REFERENCES

1. Korenman, I.M., *Analiticheskaya khimiya malykh kontsentratsii* (Analytical Chemistry of Low Concentrations), Moscow: Khimiya, 1966.
2. Voskresenskii, P.I., *Tekhnika laboratornykh rabot* (Manual of Laboratory Works), Leningrad: Khimiya, 1970.
3. Fridrikhsberg, D.A., *Kurs kolloidnoi khimii* (A Course of Colloid Chemistry), Leningrad: Khimiya, 1974.
4. Bond, A.M., *Polyarograficheskie metody v analiticheskoi khimii* (Polarographic Methods in Analytical Chemistry), Moscow: Khimiya, 1983.
5. Brainina, Kh.Z., Neiman, E.Ya., and Slepushkin, V.V., *Inversionnye vol'tamperometricheskie metody* (Stripping Voltammetric Methods), Moscow: Khimiya, 1988.
6. Vydra, F., Štulik, K., and Julákova, E., *Rozpouštecí polarografie a voltametrie*, Prague: Nakl. Technicke Literatury, 1977.
7. *Adsorption from Solution at the Solid/Liquid Interface*, Parfitt, G.D. and Rochester, C.H., Eds., London: Academic, 1983.
8. Zakharova, E.A. and Pikula, N.P., *Inversionnaya vol't-amperometriya* (Stripping Voltammetry), Tomsk: Tomsk. Gos. Univ., 1995, p. 35.

Russian Journal of Applied Chemistry, Vol. 77, No. 9, 2004, pp. 1491–1499. Translated from Zhurnal Prikladnoi Khimii, Vol. 77, No. 9, 2004, pp. 1501–1509.

CATALYSIS

Ni–Cu Catalysts on Ceramic Supports

A. V. Dul'nev, V. N. Efremov, M. A. Obysov, E. Z. Golosman, and V. I. Yakerson

Novomoskovsk Institute of Nitrogen Industry, Open Joint-Stock Company, Novomoskovsk, Tula oblast, Russia
Zelinsky Institute of Organic Chemistry, Russian Academy of Sciences, Moscow, Russia

Received April 5, 2004

Abstract—The physicochemical and catalytic characteristics of catalysts fabricated on ceramic supports of various types was studied. The influence exerted by addition of cobalt and manganese on the catalytic activity of supported nickel–copper catalysts in high-temperature treatment of off-gases to remove nitrogen oxides was studied.

It is known that catalysts based on noble metals, such as platinum, palladium, ruthenium, rhodium, and iridium, exhibit unique catalytic properties, and primarily polyfunctionality, which is responsible for their wide use in various catalytic processes, especially those intended for treatment of off-gases to remove noxious impurities [1, 2]. However, despite all their advantages, these catalysts are exceedingly expensive and their operation leads to irrecoverable loss of noble metals. In this context, a ceaseless search for catalytic formulations that contain no noble metals is being conducted. One of formulations of this kind is the nickel–copper catalytic system, which is employed in quite a number of catalytic processes, because it also exhibits polyfunctionality [3–7]. There is evidence that nickel–copper systems are close in their catalytic properties to platinum [8].

Among the most widely used methods for fabrication of nickel–copper catalysts are fusion with subsequent leaching, mixing, coprecipitation of components, and deposition of the active component onto a support by impregnation. Since the requirements to a catalyst for treatment of off-gases demand that it should have a high activity, mechanical strength, and stability in operation at high temperatures and space velocities, as well as an invariably low hydraulic resistance, the last of the above-mentioned techniques seems to be the most promising, because the support can satisfy most of these requirements [9].

The aim of this study was to examine supported nickel–copper catalysts with addition of cobalt and manganese, which are fabricated using various supports and are intended for use in detoxication of off-gases and, in particular, for treating these gases to remove nitrogen oxides.

EXPERIMENTAL

Samples were prepared on ceramic supports used in fabrication of catalysts of NIAP-18[1] [10] and NIAP-03-01[2] [11] brands for conversion of natural gas with steam, which show good working characteristics, as well as on a cellular block support. An annular pelletized ceramic support of the NIAP-18 catalysts is fabricated by high-temperature calcination. The support of the NIAP-03-01 catalyst, which is produced by slip casting followed by high-temperature calcination, has an intricate geometric shape with seven apertures [13]. The cellular support is composed of a highly porous cellular material (HPCM) obtained by replication of cellular polymeric matrices (foamed polymers) by deposition of inorganic coatings on these matrices and their subsequent thermal treatment, during which the organic component burns out and the cellular structure of the block support is formed [14]. A structure of this kind has a developed geometric surface and low hydraulic resistance and provides an increased mass-exchange coefficient and the most efficient utilization of the deposited active component [15]. The basic characteristics of the supports used are listed in Table 1.

The catalysts were prepared by impregnation of supports with aqueous solutions of Ni(II), Cu(II), Co(II), and Mn(II) nitrates. As starting substances served $Ni(NO_3)_2 \cdot 6H_2O$, $Cu(NO_3)_2 \cdot 3H_2O$, $Co(NO_3)_2 \cdot 6H_2O$, and $Mn(NO_3)_2 \cdot 6H_2O$. The supports were submerged in an impregnating solution and kept there at 6°C for 1.5 h.

The impregnated samples were dried and then calcined at 400°C for 4 h. Depending on the goal of an

[1] Former name GIAP-18.
[2] Former name NIAP-22.

Table 1. Comparison of properties of the supports

Parameter	NIAP-18	NIAP-03-01	HPCM
Grain shape	Ring	Cylinder with seven apertures	Block
Dimensions $D \times d \times h$, mm	$15.08 \times 7.0 \times 12.5$	$16.5 \times (7)3.0 \times 14.0$	$50.0 \times (2–3)^* \times 45.0$
Bulk density, kg l^{-1}	1.05	0.93	0.30**
Bed porosity, $m^3\ m^{-3}$	0.50	0.54	0.85***
Water-absorption capacity, %	29.1	24.9	27.8
Phase composition	α-Al_2O_3, $CaO \cdot 6Al_2O_3$, $CaO \cdot 2Al_2O_3$	α-Al_2O_3	α-Al_2O_3, α-SiO_2, $3Al_2O_3 \cdot 2SiO_2$

* Cell dimensions.
** Apparent block density.
*** Block porosity.

experiment, one to four impregnations with intermediate calcination of the samples were carried out. Integrated thermal analysis was made in air on an OD-102 derivatograph with linear heating at a rate of 5 deg min^{-1}. X-ray phase analysis was made on a DRON-2 diffractometer with copper-filtered monochromated radiation. Temperature-programmed reduction (TPR) was done on a thermochromatographic installation with linear heating at a rate of 5 deg min^{-1}. The catalytic activity of the samples was studied in high-temperature reduction of nitrogen oxides contained in off-gases on a flow-through laboratory installation in the temperature range 500–800°C at a space velocity of 15000 h^{-1}. Composition of the working gas (vol %): O_2 3, NO_x 0.10–0.15, CH_4/O_2 = 0.6, N_2 the rest.

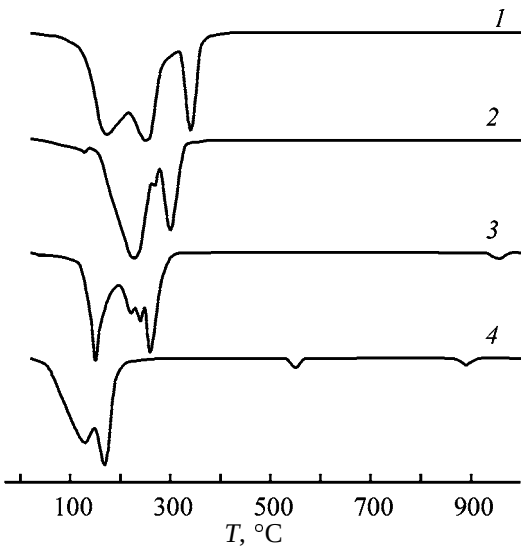

Fig. 1. DTG curves for decomposition of metal nitrates. (*T*) Temperature; the same for Figs. 2 and 4–6. (*1*) $Ni(NO_3)_2 \cdot 6H_2O$, (*2*) $Cu(NO_3)_2 \cdot 3H_2O$, (*3*) $Co(NO_3)_2 \cdot 6H_2O$, and (*4*) $Mn(NO_3)_2 \cdot 6H_2O$.

The temperature at which the impregnated samples were calcined (400°C) was chosen on the basis of data obtained by thermal analysis of the corresponding metals (Fig. 1). Thermolysis of these salts is accompanied by a number of endothermic effects of varied intensity, which correspond to removal of hydration water and stepwise decomposition of a salt. The lowest decomposition temperature is observed for $Mn(NO_3)_2$ (140–170°C). Water is removed in the first stage, which is accompanied by partial decomposition of the salt, and the remaining anhydrous $Mn(NO_3)_2$ decomposes in the second stage [16]. $Cu(NO_3)_2$ decomposes via formation of basic copper nitrate, which then decomposes to the oxide at 300°C [17–19]. The endothermic effect corresponding to $Co(NO_3)_2$ decomposition has a maximum at 260°C. It follows from [17, 18, 20] that thermolysis of $Co(NO_3)_2$ occurs via formation of basic salts. However, Kalinichenko *et al*. [19] did not record any intermediate formation of basic salts and suggested that $Co(NO_3)_2 \cdot 6H_2O$ dehydrates stepwise and then decomposes to the oxide. The highest decomposition temperature is characteristic of $Ni(NO_3)_2$ (340°C). The endothermic effects peaked at 550 and 890°C in the derivatogram of $Mn(NO_3)_2$ and at 960°C in the derivatogram of $Co(NO_3)_2$ can be assigned to conversion of manganese and copper oxides to less oxidized species.

To reveal the essence of the processes that occur when supported catalysts are formed, one-, two, and three-component systems were considered. In order to obtain catalysts with exactly the prescribed content of active components, it was of interest to study the competing capacity of metal nitrates in support impregnation. For this purpose, impregnating solutions of $Ni(NO_3)_2$, $Cu(NO_3)_2$, $Co(NO_3)_2$, and $Mn(NO_3)_2$ with a concentration of 75 g l^{-1} in terms of the metal were prepared. Four impregnations of supports were performed, with intermediate calcinations. The deriva-

tograms of the impregnated supports are shown in Fig. 2. The differential thermogravimetric (DTG) curves of the samples are similar to the DTG curves of the pure salts. It should be noted that the effects corresponding to decomposition of the deposited salts are somewhat broadened and their peaks are shifted to lower temperatures, compared to the pure salts. The presence of effects with characteristic temperatures of 310 and 450°C in the derivatograms of all the salts deposited on the support of the NIAP-18 catalyst can be attributed to stepwise dehydration of $3CaO \cdot Al_2O_3$ $6H_2O$, which is formed via hydration of $CaO \cdot 2Al_2O_3$ in support impregnation.

According to the results of X-ray phase analysis (Table 2), NiO and CuO are products of $Ni(NO_3)_2$ and $Cu(NO_3)_2$ decomposition at 400°C. Cobalt nitrate decomposes to Co_3O_4. The X-ray diffraction patterns of manganese-containing systems show the β-MnO_2 phase and a minor amount Mn_2O_3. The crystallite size L (Å) of the active components present in the oxide form is within 260–310 Å for all the systems studied. In manganese-containing systems, the size of MnO_2 crystallites could not be determined because of the low intensity of the diffraction lines of β-MnO_2 and the superposition of α-Al_2O_3 and β-MnO_2 lines.

The results of chemical analysis of the samples after each impregnation are presented in Fig. 3. It can be seen that the largest amount is contained in the support of NIAP-18, which can be attributed to its higher water absorption (Table 1). The difference in the concentrations of nickel, copper, cobalt, and manganese in this support at equal number of impregnations is slight. However, a similar trend is observed with all the supports tested: The content of cobalt is the greatest, and that of copper, the smallest, at equal number of impregnations. Under identical conditions, the impregnating capacity of nitrates decreases in the order $Co(NO_3)_2$ > $Mn(NO_3)_2$ > $Ni(NO_3)_2$ > $Cu(NO_3)_2$.

The reduction of nickel systems (Fig. 4a) begins at 280–300°C and reaches its maximum rate at 280–320°C. A slight effect in the TPR curves at 450–470°C is presumably due to reduction of nickel oxide more strongly bound to the support. This conclusion is confirmed by the results of [21], where the interaction of such an inert support as α-Al_2O_3 with the nickel component of the catalyst is substantiated. The deposited copper oxide is reduced (Fig. 4b) at lower temperatures (230–270°C), whereas CuO that is more strongly bound to the support is reduced at 330–360°C. The TPR curves of cobalt systems (Fig. 4c) also show two peaks at 360–380 and 480–490°C.

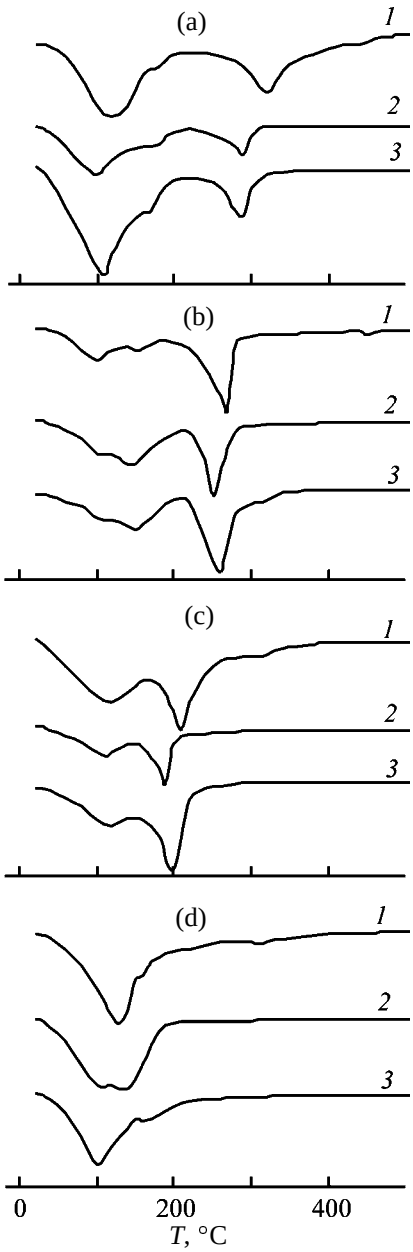

Fig. 2. DTG curves for decomposition of (a) nickel, (b) copper, (c) cobalt, and (d) manganese nitrates deposited on (*1*) NIAP-18, (*2*) NIAP-03-01, and (*3*) HPCM supports.

The activation in manganese systems (Fig. 4d) occurs in several stages, which is due to stepwise reduction of manganese oxides. The activation process can be represented [22] by the reactions

$$2MnO_2 + H_2 = Mn_2O_3 + H_2O, \quad (1)$$

$$3Mn_2O_3 + H_2 = 2Mn_3O_4 + H_2O, \quad (2)$$

$$Mn_3O_4 + H_2 = 3MnO + H_2O. \quad (3)$$

Table 2. Results of X-ray diffraction analysis of samples calcined at 400°C

Active component	Support	Phase composition	Crystallite size, *L*, Å
NiO	NIAP-18	α-Al_2O_3, $CaO \cdot 6Al_2O_3$, $CaO \cdot 2Al_2O_3$, NiO	270
	NIAP-03-01	α-Al_2O_3, NiO	310
	HPCM	α-Al_2O_3, α-SiO_2, $3Al_2O_3 \cdot 2SiO_2$, NiO	260
CuO	NIAP-18	α-Al_2O_3, $CaO \cdot 6Al_2O_3$, $CaO \cdot 2Al_2O_3$, CuO	280
	NIAP-03-01	α-Al_2O_3, CuO	270
	HPCM	α-Al_2O_3, α-SiO_2, $3Al_2O_3 \cdot 2SiO_2$, CuO	260
Co_3O_4	NIAP-18	α-Al_2O_3, $CaO \cdot 6Al_2O_3$, $CaO \cdot 2Al_2O_3$, Co_3O_4	300
	NIAP-03-01	α-Al_2O_3, Co_3O_4	300
	HPCM	α-Al_2O_3, α-SiO_2, $3Al_2O_3 \cdot 2SiO_2$, Co_3O_4	260
MnO_2	NIAP-18	α-Al_2O_3, $CaO \cdot 6Al_2O_3$, $CaO \cdot 2Al_2O_3$, β-MnO_2, Mn_2O_3	–
	NIAP-03-01	α-Al_2O_3, β-MnO_2, Mn_2O_3	–
	HPCM	α-Al_2O_3, α-SiO_2, $3Al_2O_3 \cdot 2SiO_2$, β-MnO_2, Mn_2O_3	

Table 3. Results of X-ray diffraction analysis of catalyst samples reduced at 600°C in a flow of H_2

Active component	Support	Phase composition	a_0*	*L*
			Å	
Ni	NIAP-18	α-Al_2O_3, $CaO \cdot 6Al_2O_3$, $CaO \cdot 2Al_2O_3$, Ni	3.526	270
	NIAP-03-01	α-Al_2O_3, Ni	3.525	310
	HPCM	α-Al_2O_3, α-SiO_2, $3Al_2O_3 \cdot 2SiO_2$, Ni	3.525	220
Cu	NIAP-18	α-Al_2O_3, $CaO \cdot 6Al_2O_3$, $CaO \cdot 2Al_2O_3$, Cu	3.618	600
	NIAP-03-01	α-Al_2O_3, Cu	3.617	600
	HPCM	α-Al_2O_3, α-SiO_2, $3Al_2O_3 \cdot 2SiO_2$, Cu	3.617	550
Co	NIAP-18	α-Al_2O_3, $CaO \cdot 6Al_2O_3$, $CaO \cdot 2Al_2O_3$, Co	3.546	360
	NIAP-03-01	α-Al_2O_3, Co	3.547	390
	HPCM	α-Al_2O_3, α-SiO_2,$3Al_2O_3 \cdot 2SiO_2$, Co	3.546	350
Mn	NIAP-18	α-Al_2O_3, $CaO \cdot 6Al_2O_3$, $CaO \cdot 2Al_2O_3$, MnO	4.448	200
	NIAP-03-01	α-Al_2O_3, MnO	4.447	130
	HPCM	α-Al_2O_3, α-SiO_2, $3Al_2O_3 \cdot 2SiO_2$, MnO	4.448	140

* Tabulated unit cell parameters a_0, Å: Ni 3.524, Cu 3.615, Co 3.544, and MnO 4.445.

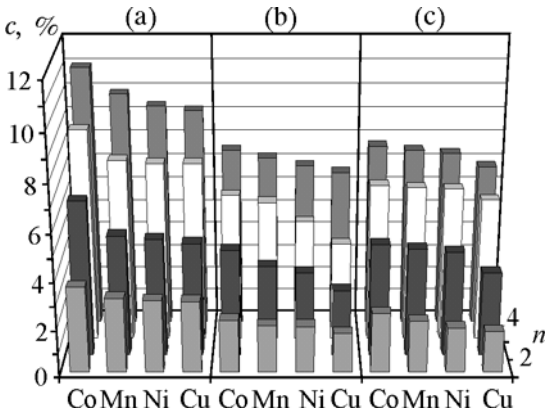

Fig. 3. Influence of the number *n* of impregnations on the content *c* of nickel, copper, cobalt, and manganese in the supports studied. Support: (a) NIAP-18, (b) NIAP-03-01, and (c) HPCM.

It should be noted that the temperatures of the reduction peaks in the TPR curves for all the active components increase in order HPCM < NIAP-03-01 < NIAP-18. This is presumably due to different strengths of binding of the active components to the supports. For example, the presence of calcium aluminates in the support of NIAP-18 favors stronger binding of the active component. In the support based on HPCM, the reduction temperature is strongly affected by the developed geometric surface of this support, which facilitates supply of reagents and removal of reduction products.

According to the results of X-ray phase analysis, all the oxides deposited on supports are reduced to metals upon heating in a flow of H_2 at 600°C (Table 3). The only exception are manganese-containing systems whose reduction under the given condi-

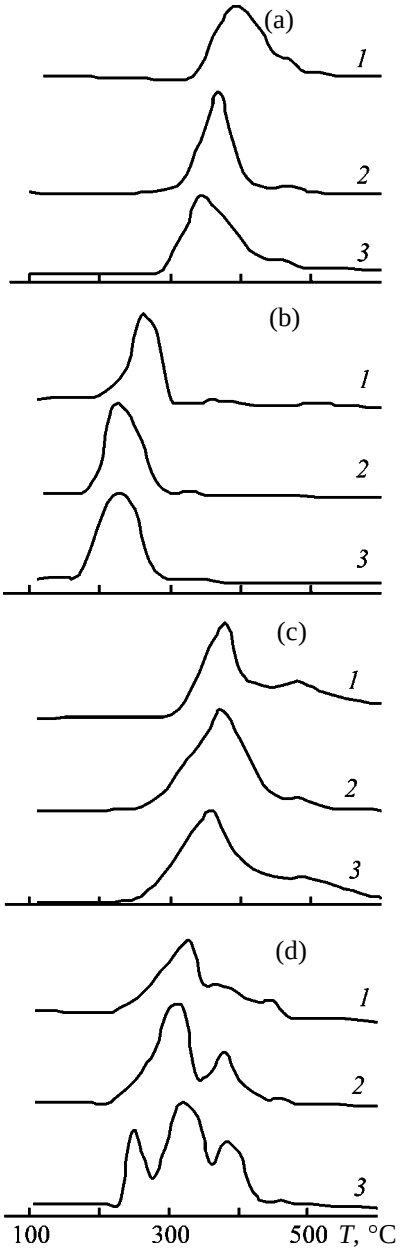

Fig. 4. TPR curves for (a) nickel, (b) copper, (c) cobalt, and (d) manganese systems on the supports studied. Support: (*1*) NIAP-18, (*2*) NIAP-03-01, and (*3*) HPCM; the same for Figs. 5 and 6.

tions ends in the formation of MnO. The calculated unit cell parameters a_0 of the active components are in good agreement with their tabulated values. In contrast to the oxide phases, the sizes of Cu and Ni crystallites formed upon reduction differ by a factor of 2: L = 550–600 Å for copper systems and 220–310 Å for those with nickel. The cobalt systems occupy an intermediate position. The dispersity of Co formed under the given conditions is within 350–390 Å.

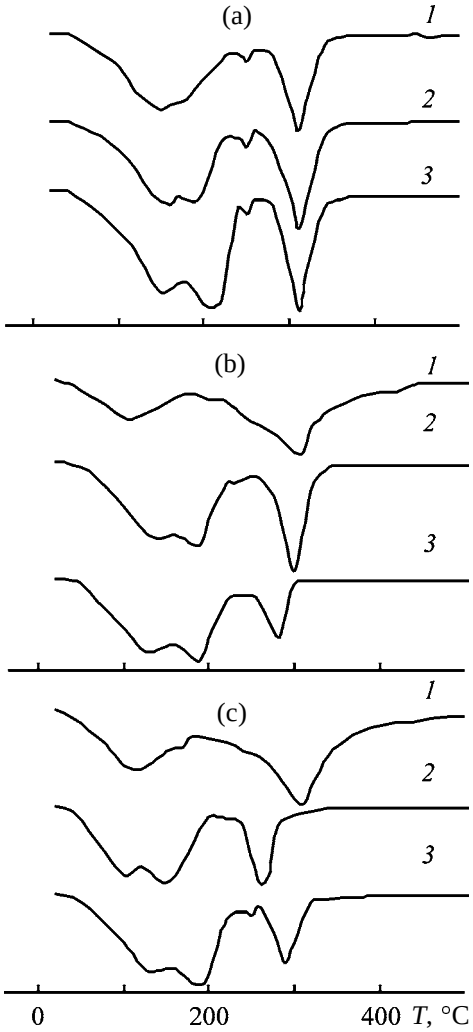

Fig. 5. DTG curves for decomposition of (a) Ni–Cu, (b) Ni–Cu–Co, and (c) Ni–Cu–Mn systems on the supports studied.

Thus, it may be concluded that Cu crystallites show an enhanced tendency toward sintering at high temperatures.

In preparing two-component nickel–copper and three-component nickel–copper–manganese systems, a NiO : CuO ratio of (2.3–3) : 1 was chosen. This ratio ensures the highest activity of the catalyst in high-temperature reduction of nitrogen oxides [23]. The content of cobalt and manganese oxides in samples of three-component catalysts was maintained within the range 1.0–1.5%.

The pattern of decomposition of nickel, copper, cobalt, and manganese nitrates in binary and ternary systems (Fig. 5) is virtually the same as that of decomposition of these nitrates in the single-component systems. The characteristic endothermic peaks are

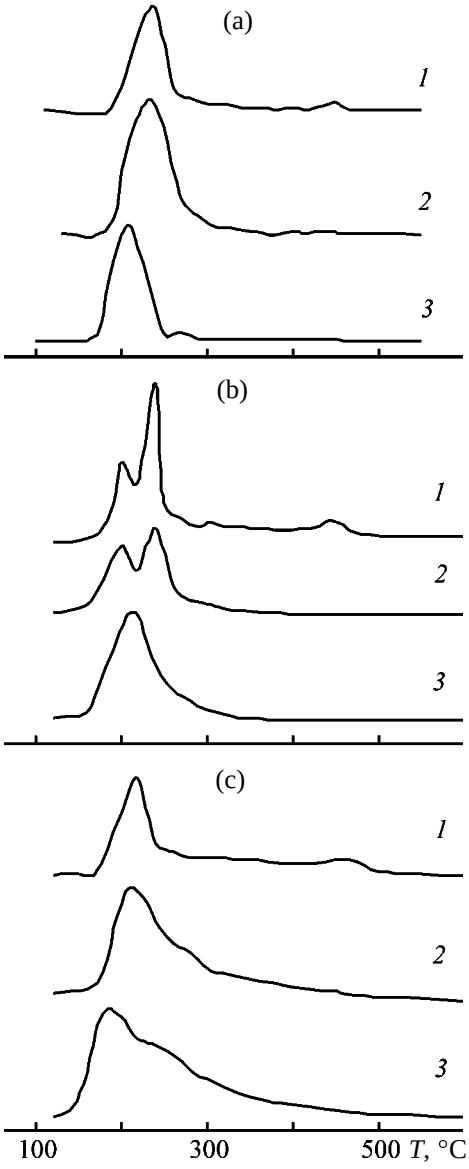

Fig. 6. TPR curves for (a) Ni–Cu, (b) Ni–Cu–Co, and (c) Ni–Cu–Mn systems on the supports studied.

observed at 130–140, 180–190, 250–260, and 280–310°C.

Figure 6 shows the results of TPR of two- and three-component systems in H_2. The difference between the characteristic reduction temperatures of samples prepared on different supports is to be noted. For example, a peak in the TPR curve is observed at 210°C for a nickel–copper sample on HPCM, at 230°C on NIAP-03-01, and at 240°C on NIAP-18 (Fig. 6a). The reduction curves of one-component nickel systems on the same supports show peaks in the range 340–390°C (Fig. 4a), and the reduction of one-component copper systems occurs at 230–260°C (Fig. 4b). Such a difference in the type of reduction of two- and one-component systems is due to the promoting effect of Cu on activation of Ni [24]. The final product of this process in two-component systems is a Ni–Cu solid solution. This conclusion is confirmed by the results of X-ray diffraction studies of reduced two- and three-component systems (Table 4). Ni and Cu phases were recorded in one-component nickel and copper samples. The diffraction lines of Cu are absent in the X-ray diffraction patterns of two- (Ni–Cu) and three-component (Ni–Cu–Mn) systems. For one-component samples, the unit cell parameters a_0 of Ni and Cu are close to the tabulated values. For two- and three-component samples, a_0 differs rather strongly from the tabulated crystal lattice parameters for Ni and Cu. The distortion of a_0 is due to incorporation of Cu atoms into the crystal lattice of Ni, resulting in the formation of a nickel–copper solid solution with $a_{0(Ni–Cu)}$ = 3.541–3.560 Å, which occupies an intermediate position between $a_{0(Ni)}$ = 3.524 and $a_{0(Cu)}$ = 3.615 Å [4]. A similar dependence is observed for unreduced calcined samples. The forming nickel–copper oxide solution has the unit cell parameter $a_{0(NiO–CuO)}$ = 4.186–4.194 Å (Table 4), which also occupies an intermediate position between $a_{0(NiO)}$ = 4.177 and $a_{0(CuO)}$ = 4.684 Å. The presence of a weak effect peaked at 440–450°C in the TPR curve of samples fabricated by impregnation of the NIAP-18 support can be accounted for by decomposition of products of hydration of $CaO \cdot 2Al_2O_3$, formed in the course of impregnation of the support.

A similar run of the TPR curves is observed for nickel–copper–manganese systems (Fig. 6c), but with peaks shifted to lower temperatures. The more complex nature of reduction of nickel–copper–cobalt systems (Fig. 6b) is presumably determined by partial displacement of copper by cobalt from the Ni–Cu solid solution and by separate reduction of free copper oxide to Cu and of the Ni–Cu–Co oxide solid solution. This assumption is confirmed by the results of X-ray diffraction analysis of these systems (Table 4).

The catalytic activity of the samples under study was evaluated by the conversion α of nitrogen oxides. Our studies show that one-component nickel, cobalt, and manganese systems exhibit no noticeable activity up to 800°C, with the conversion not exceeding 20–30%. The temperature at which a 50% conversion of nitrogen oxides on copper samples is reached is very high (730–750°C). This gives no way of recommending these catalysts for use in treatment of off-gases to remove nitrogen oxides. The results obtained in a study of the catalytic activity of nickel–copper,

Table 4. Results of X-ray diffraction analysis of Ni–Cu, Ni–Cu–Co, and Ni–Cu–Mn catalyst samples calcined at 400°C and reduced at 600°C in a flow of H_2

Active component	Support	Phase composition	a_0, Å		L, Å	
			NiO	Ni	NiO	Ni
		Calcined samples				
NiO–CuO	NIAP-18	α-Al_2O_3, $CaO \cdot 6Al_2O_3$, $CaO \cdot 2Al_2O_3$, NiO	4.194	–	200	–
	NIAP-03-01	α-Al_2O_3, NiO	4.190	–	250	–
	HPCM	α-Al_2O_3, α-SiO_2, $3Al_2O_3 \cdot 2SiO_2$, NiO	4.188	–	190	–
NiO–CuO–Co_3O_4	NIAP-18	α-Al_2O_3, $CaO \cdot 6Al_2O_3$, $CaO \cdot 2Al_2O_3$, NiO	4.194	–	180	–
	NIAP-03-01	α-Al_2O_3, NiO, CuO	4.192	–	215	–
	HPCM	α-Al_2O_3, α-SiO_2, $3Al_2O_3 \cdot 2SiO_2$, NiO	4.186	–	200	–
NiO–CuO–MnO_2	NIAP-18	α-Al_2O_3, $CaO \cdot 6Al_2O_3$, $CaO \cdot 2Al_2O_3$, NiO	4.190	–	150	–
	NIAP-03-01	α-Al_2O_3, NiO	4.186	–	220	–
	HPCM	α-Al_2O_3, α-SiO_2, $3Al_2O_3 \cdot 2SiO_2$, NiO	4.184	–	200	–
		Reduced samples				
Ni–Cu	NIAP-18	α-Al_2O_3, $CaO \cdot 6Al_2O_3$, $CaO \cdot 2Al_2O_3$, Ni	–	3.546	–	230
	NIAP-03-01	α-Al_2O_3, Ni	–	3.543	–	330
	HPCM	α-Al_2O_3, α-SiO_2, $3Al_2O_3 \cdot 2SiO_2$, Ni	–	3.541	–	230
Ni–Cu–Co	NIAP-18	α-Al_2O_3, $CaO \cdot 6Al_2O_3$, $CaO \cdot 2Al_2O_3$, Ni, Cu	–	3.548	–	190
	NIAP-03-01	α-Al_2O_3, Ni, Cu	–	3.544	–	180
	HPCM	α-Al_2O_3, α-SiO_2, $3Al_2O_3 \cdot 2SiO_2$, Ni, Cu	–	3.550	–	170
Ni–Cu–Mn	NIAP-18	α-Al_2O_3, $CaO \cdot 6Al_2O_3$, $CaO \cdot 2Al_2O_3$, Ni	–	3.556	–	150
	NIAP-03-01	α-Al_2O_3, Ni	–	3.550	–	160
	HPCM	α-Al_2O_3, α-SiO_2, $3Al_2O_3 \cdot 2SiO_2$, Ni	–	3.560	–	150

nickel–copper–cobalt, and nickel–copper–manganese systems are presented in Fig. 7. The catalytic activity tends to grow with increasing process temperature. The introduction of copper into the nickel system results in that the temperature at which 50% conversion is reached decreases to 620–630°C. The size of crystallites of the Ni–Cu solid solution in these samples is 230–330 Å (Table 4). At 680–750°C, the activity of all the samples is virtually the same. The residual content of nitrogen oxides in the purified gas is 0.004–0.005 vol %. These parameters are level with those obtained with an APK-2 palladium catalyst [25, 26], which is widely used in the industry. The strongest difference in the catalytic activity is observed at 550–650°C. The maximum activity is exhibited by nickel–copper–cobalt samples. It is noteworthy that the crystallite size in these samples is 40–150 Å smaller than that in nickel–copper samples. The activities of the nickel–copper and nickel–copper–cobalt systems are virtually the same. Thus, addition of Co makes it possible to enhance somewhat the activity of the nickel–copper catalysts under study, whereas Mn is not an effective promoting additive under the given conditions. The temperature at which 50% conversion is reached with all the samples under study is within the range 570–640°C, which somewhat exceeds the same parameter for the APK-2 catalyst. It was found that the most effective are catalysts on NIAP-18 support, which is due to the greater amount of active components because of its higher water-absorption capacity (Table 1), and on HPCM because of the network-cellular structure of this

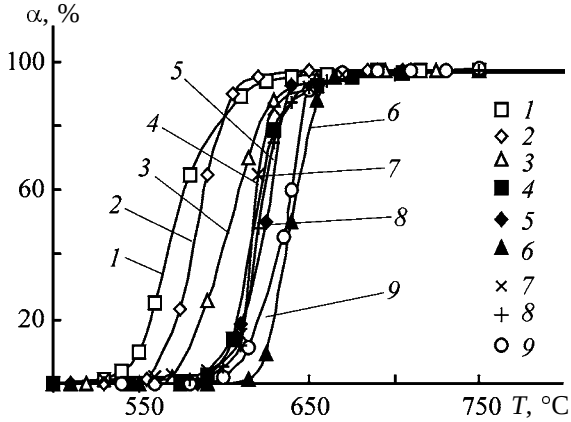

Fig. 7. Conversion α of nitrogen oxides vs. temperature T for various catalyst samples. Catalyst: (*1*) HPCM/NiCuCo, (*2*) NIAP-18/NiCuCo, (*3*) NIAP-03-01/NiCuCo, (*4*) HPCM/NiCuMn, (*5*) NIAP-18/NiCuMn, (6) NIAP-03-01/NiCuMn, (*7*) HPCM/NiCu, (*8*) NIAP-18/NiCu, and (*9*) NIAP-03-01/NiCu.

support, which ensures an increased mass-exchange coefficient and a developed geometric surface making it possible to utilize more efficiently the deposited active component.

Our experimental data were used to develop specifications for NIAP-15-12 and NIAP-15-13 catalysts [27] intended for performing the catalytic high-temperature treatment of off-gases to remove nitrogen oxides, deep oxidation of methane, and catalytic treatment of process gases to remove oxygen. The NIAP-15-12 catalyst is manufactured with NIAP-03-01 support, and NIAP-15-13, with NIAP-18 support.

To charge two reactors for catalytic treatment of gases to remove nitrogen oxides in UKL-7-76 installations at a shop for manufacture of aqueous nitric acid, 2 t of the NIAP-15-13 catalyst and 4 t of the NIAP-15-12 catalyst were fabricated.[3] The NIAP-15-12 catalyst was charged in an amount of 2 t on the grate of the first shelf of the reactor for catalytic treatment.[4] The bed of this catalyst was covered, through a separating Nichrome grid, with a mixture of the NIAP-15-13 and fresh APK-2 catalysts in amounts of 1 and 0.65 t, respectively. The addition of the APK-2 catalyst to the main catalytic mass made it possible to lower the "ignition" temperature of the process.

The tests were carried out at loads on the oxidation reactor of 4900 to 6000 $m^3 h^{-1}$ by ammonia and 45000 to 57000 $m^3 h^{-1}$ by air (recalculated to normal conditions). The CH_4/O_2 ratio was maintained in the range 0.4–0.6 in the course of the catalytic treatment. The content of nitrogen oxides at the inlet of the reactor for catalytic treatment was in the range 0.09–0.11 vol %. The gas temperature at the reactor inlet was 460–480°C. In the course of purification, the temperature increased to become 460–480°C at the outlet. The residual content of nitrogen oxides in gases leaving the reactor was 0.002–0.003 vol % (required ≤0.005 vol %), and that of CO, 0.01–0.04 vol % (required ≤0.10 vol %).

CONCLUSIONS

(1) Distinctive features of catalysts on various supports in the stages of impregnation, calcination, and reduction were revealed.

(2) The impregnating capacity of nitrates in impregnation of ceramic supports decreases in the order $Co(NO_3)_2 > Mn(NO_3)_2 > Ni(NO_3)_2 > Cu(NO_3)_2$.

(3) Cobalt is a promoting additive enhancing the activity of nickel–copper catalysts in treatment of off-gases to remove nitrogen oxides. Addition of manganese has virtually no effect on the catalytic activity.

(4) The industrial tests performed demonstrated high performance of the catalysts in high-temperature treatment of off-gases to remove nitrogen oxides in manufacture of aqueous nitric acid.

[3] Tatazot Open Joint-Stock Company, manufacture of nitric acid; Novomoskovsk Institute of Nitrogen Industry, Open Joint-Stock Company, manufacture of the catalysts.

[4] Performed by specialists from Tatazot Open Joint-Stock Company.

REFERENCES

1. Popova, N.M., *Katalizatory ochistki gazovykh vybrosov promyshlennykh proizvodstv* (Catalysts for Treatment of Industrial Off-Gases), Moscow: Khimiya, 1991.
2. Popova, N.M., *Katalizatory ochistki vykhlopnykh gazov avtotransporta* (Catalysts for Treatment of Automobile Exhaust Gases), Alma-Ata: Nauka, 1987.
3. Golosman, E.Z., Efremov, V.N., and Khilkova, A.A., *Khim. Prom–st.*, 1994, no. 11, pp. 20–26.
4. Efremov, V.N., Tesakova, G.M., Mamaeva, I.A., *et al.*, *Zh. Prikl. Khim.*, 1988, vol. 61, no. 11, pp. 2404–2409.
5. US Patent 6245709.
6. Wang Yaquan, *Cuihua Xuebao* (J. Catal.), 1998, vol. 19, no. 2, pp. 166–168.
7. Wainwright, M.S. and Young, D.J., *J. Catal.*, 1980, vol. 64, no. 1, pp. 116–123.
8. Ollis, David F. and Taheri, H., *J. Am. Chem. Soc.*, 1976, vol. 21, no. 2, pp. 368–374.
9. Stiles, A.B., *Catalyst Supports and Supported Catalysts. Theoretical and Applied Concepts*, Boston: Butterworths, 1987.
10. *TU* (Technical Specifications) *113-03-2010–93: Catalyst for Conversion of Natural Gas.*
11. *TU* (Technical Specifications) *113-03-00209510-93–2002: Nickel Catalyst.*
12. RF Patent 1790208.
13. RF Patent 2105604.
14. Antsiferov, V.N. and Porozova, S.E., *Vysokoporistye pronitsaemye materialy na osnove alyumosilikatov* (Highly Porous Permeable Materials Based on Aluminosilicates), Perm: Perm. Gos. Tekh. Univ., 1996.
15. Antsiferov, V.N. and Kalashnikova, M.Yu., *Ekol. Prom–st. Ross.*, 1997, no. 11, pp. 14–17.
16. De Bruijn, T.J., De Jong, W.A., and Van Den De Berg, P.J., *Thermochim. Acta*, 1981, vol. 45, no. 3, pp. 265–278.
17. Sirina, A.M., Kalinichenko, I.I., and Purtov, A.I., *Zh.*

Neorg. Khim., 1970, vol. 15, no. 9, pp. 2430–2433.

18. Kalinichenko, I.I., Sirina, A.M., and Purtov, A.I., *Zh. Neorg. Khim.*, 1974, vol. 19, no. 6, pp. 1547–1552.
19. Mu, J. and Perlmutter, D.D., *Thermochim. Acta*, 1982, vol. 56, no. 3, pp. 253–260.
20. Pribylov, K.P. and Valeev, R.R., *Zh. Neorg. Khim.*, 1981, vol. 26, no. 9, pp. 2350–2352.
21. Richardson, T. and Twigg, V., *Appl. Catal. A: Appl. Catal.*, 1998, vol. 167, no. 1, pp. 57–64.
22. Rode, E.Ya., *Kislorodnye soedineniya margantsa* (Oxygen Compounds of Manganese), Moscow: Akad. Nauk SSSR, 1952.
23. Efremov, V.N., Zinov'eva, T.A., Tesakova, G.M., *et al.*, *Zh. Prikl. Khim.*, 2000, vol. 73, no. 2, pp. 246–251.
24. Vass Mihai, J. and Contescu, Cr., *Rev. Roum. Chim.*, 1980, vol. 25, no. 1, pp. 55–56.
25. *Proizvodstvo azotnoi kisloty v agregatakh bol'shoi edinichnoi moshchnosti* (Manufacture of Nitric Acid in Apparatus with High Unit Capacity), Olevskii, V.M., Ed., Moscow: Khimiya, 1985.
26. *Spravochnik azotchika* (Handbook of Nitrogen Worker), Mel'nikov, E.Ya., Ed., Moscow: Khimiya, 1987, 2nd revised ed.
27. *TU* (Technical Specifications) *113-03-00 209 510-98–2003: Catalyst for Treatment of Process Gases.*

Russian Journal of Applied Chemistry, Vol. 77, No. 9, 2004, pp. 1500–1504. Translated from Zhurnal Prikladnoi Khimii, Vol. 77, No. 9, 2004, pp. 1510–1515.

CATALYSIS

Thermal Stability and Activity in Hydrogen Oxidation of Palladium Catalysts Supported on Fibrous Sulfonic Cation Exchanger in the Hydrogen and Magnesium Forms

Yu. G. Egiazarov, V. Z. Radkevich, L. S. Kravchuk, and A. A. Ivko

Institute of Physical Organic Chemistry, Belarussian National Academy of Science, Minsk, Belarus

Received August 6, 2003; in final form, May 2004

Abstract—The effect of reduced palladium on the thermal stability of the hydrogen and magnesium forms of FIBAN K-1 fibrous sulfonic cation exchanger was studied. The activity of palladium catalyst supported by the H and Mg forms of the cation exchanger in hydrogen oxidation was determined, as influenced by the temperature of treatment of the catalyst with the reaction mixture.

As shown previously [1–5], the thermal stability of sulfonic cation exchangers in the metal forms is higher than that of the H forms. In particular, a mass-spectrometric study (10^{-7} torr) of the physicochemical properties of FIBAN K-1 sulfonic cation exchanger in the alkali metal and alkaline-earth metal forms showed that the Mg form had the highest thermal stability [4, 5]. Hence, the Mg form can be used as a support for metal catalysts of redox reactions.

However, the effects exerted by the metal phase on the thermal stability of sulfonic cation exchanger and by the metal cation on the catalytic activity of the supported metal were not understood. In this work we studied the thermal stability of the H and Mg forms of FIBAN K-1 sulfonic cation exchanger containing reduced palladium, the palladium dispersity in these matrices as influenced by the exchangable cation, and the palladium activity in hydrogen reduction as influenced by the temperature of the treatment of the catalysts with the reaction mixture.

EXPERIMENTAL

The H form of FIBAN K-1 fibrous sulfonic cation exchanger was prepared by bulk radiation grafting of styrene (98%)–divinylbenzene (2%) copolymer to polypropylene staple fiber, followed by sulfonation of the poly(styrene–divinylbenzene) matrix with concentrated H_2SO_4 [6].

Pure Mg form was prepared by washing of a column packed with the H form (exchange capacity 3 mg-equiv g^{-1}) with excess 0.5 M $MgCl_2$ solution until pH of the solution at the outlet became neutral. Then the column was washed with distilled water until the absence of chloride ions in the wash waters and then was dried in air.

To prepare catalysts with 2.5 wt % Pd content, the H or Mg form of the cation exchanger was treated under static conditions with a solution of tetrammine-palladium(II) chloride $[Pd(NH_3)_4]Cl_2$ of a definite concentration at room temperature and pH 8–8.5. The Pd(II) concentration in the solutions before and after ion exchange was measured spectrophotometrically [7]. Then the samples were washed with distilled water until the absence of chloride anions in the wash waters, and the $[Pd(NH_3)_4]^{2+}$ cations were reduced with an aqueous solution of $N_2H_4 \cdot H_2O$ at 40°C for 30 min. After that, the samples were washed again with distilled water to neutral reaction and were dried at room temperature.

To determine the degree of Pd(II) reduction, the ion-exchangeable Pd(II) species were completely washed out from the samples with excess 1 M NaCl and then the palladium concentration in the solution was measured. In the course of reduction, the ion-exchange sites of the catalyst are converted to the H form after removal of $[Pd(NH_3)_4]^{2+}$ cations. To convert these sites into the Mg^{2+} form, the reduced samples were repeatedly treated with a $MgCl_2$ solution, washed, and dried.

X-ray phase analysis of the palladium catalysts was performed on a DRON-1 diffractometer using CuK_α radiation. Thermal gravimetric analysis of the supports and catalysts was performed on an MOM derivatograph (Hungary) in the temperature range 20–450°C.

The mass spectra of the gaseous thermolysis products of the samples were recorded on an MKh 1320

mass spectrometer interfaced with a computer. A ampule with a sample was placed in the inlet system of the mass-spectrometer. The sample was heated with a platinum wire used also as a temperature gage. The mass spectra of thermolysis products were recorded at an ionizing voltage of 50 V and an accelerating voltage of 2.5 kV.

The thermal stability of the initial sulfonic cation exchangers and the palladium catalysts was studied as follows. A weighed portion of a sample was placed in the reactor and heated in an inert gas flow. The temperature at which a $KMnO_4$ solution in a Drechsel vessel arranged at the outlet of the reactor was decolorized with thermolysis products of the sulfonic cation exchanger was recorded.

The dependence of the catalytic activity on the temperature of pretreatment of the catalysts with the reaction mixture was studied in a glass flow reactor with automatic electric heating. A weighed portion of the catalyst (1 g) was placed in the reactor. The height of the catalyst bed was about 40 mm. The sample was heated at 130°C in a helium flow for 1 h. Then the catalyst was treated with a reaction mixture (3 vol % H_2 in air) at a definite temperature from 100 to 250°C for 1 h. The flow rate of the reaction mixture was 250 $cm^3\ min^{-1}$. After that, the reactor was cooled to 100°C. Samples of the gas phase were taken at the reactor outlet in 15–20 min and were analyzed on a Gazokhrom 31 chromatograph. The hydrogen conversion was calculated as the difference between the hydrogen content at the inlet and outlet of the reactor.

The specific activity of Pd A ($cm^3\ g_{Pd}^{-1}\ s^{-1}$) at 100°C was calculated by the equation

$$A = V_{H_2}\,\alpha\, m_{Pd}^{-1} \times 100,$$

where V_{H_2} is the hydrogen feed rate ($cm^3\ g_{cat}^{-1}\ s^{-1}$), α is the hydrogen conversion (vol %), and m_{Pd} is the palladium content in the catalyst ($g_{Pd}\ g_{cat}^{-1}$).

The initial catalytic activity was determined by the above procedure without treatment of the samples with the reaction mixture. The composition of the reaction mixture in all the experiments was the same.

The weight loss Δm on heating of FIBAN K-1 in the H form and 2.Pd/H-K1 catalyst and FIBAN K-1 in the Mg form and 2.5Pd/Mg-K-1 catalyst is plotted in Figs. 1a and 1b, respectively. It should be noted that it is difficult to determine the onset temperature of thermolysis of the sulfonic cation exchanger by TG. Since the thermolysis starts before the H_2O molecules strongly bound by hydrogen bonds with the sulfo

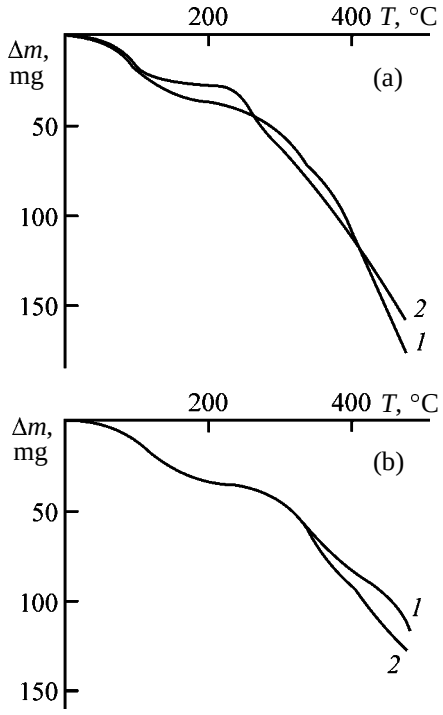

Fig. 1. Weight loss of FIBAN K-1 fibrous sulfonic cation exchangers not containing and containing palladium as a function of temperature. Sample weight 200 mg. Sample: (a) (*1*) H-K-1 and (*2*) 2.5Pd/H-K-1; (b) (*1*) Mg-K-1 and (*2*) 2.5Pd/Mg-K-1; the same for Fig. 2.

groups are completely desorbed from the sample, it is possible to determine only the temperature range of thermolysis of the ion exchanger. Nevertheless, as seen from Fig. 1a, the weight loss of 2.5Pd/H-K-1 in the range 110–215°C is substantially decelerated as compared to the initial H-K-1 resin.

Previous results of TG and chemical analysis show [8–11] that the H form of the sulfonic cation exchanger is desulfonated in air at 150–220°C. Thus, we suggest that the thermal stability of the sulfo groups of the sulfonic cation exchanger in the H form increases after introduction of Pd particles into the sample.

It should be noted that reduced Pd has virtually no effect on the thermal stability of the functional groups of the Mg form of the ion exchanger: the Δm vs. T dependences for Mg-K-1 and 2.5Pd/Mg-K-1 are similar up to 330°C. The differences in the thermal stability are observed only at higher temperatures (Fig. 1b).

It is known that palladium catalyzes a number of redox reactions including thermal oxidative degradation of organic compounds [12]. The fact that the thermal stability of 2.5Pd/Mg-K-1 at temperatures

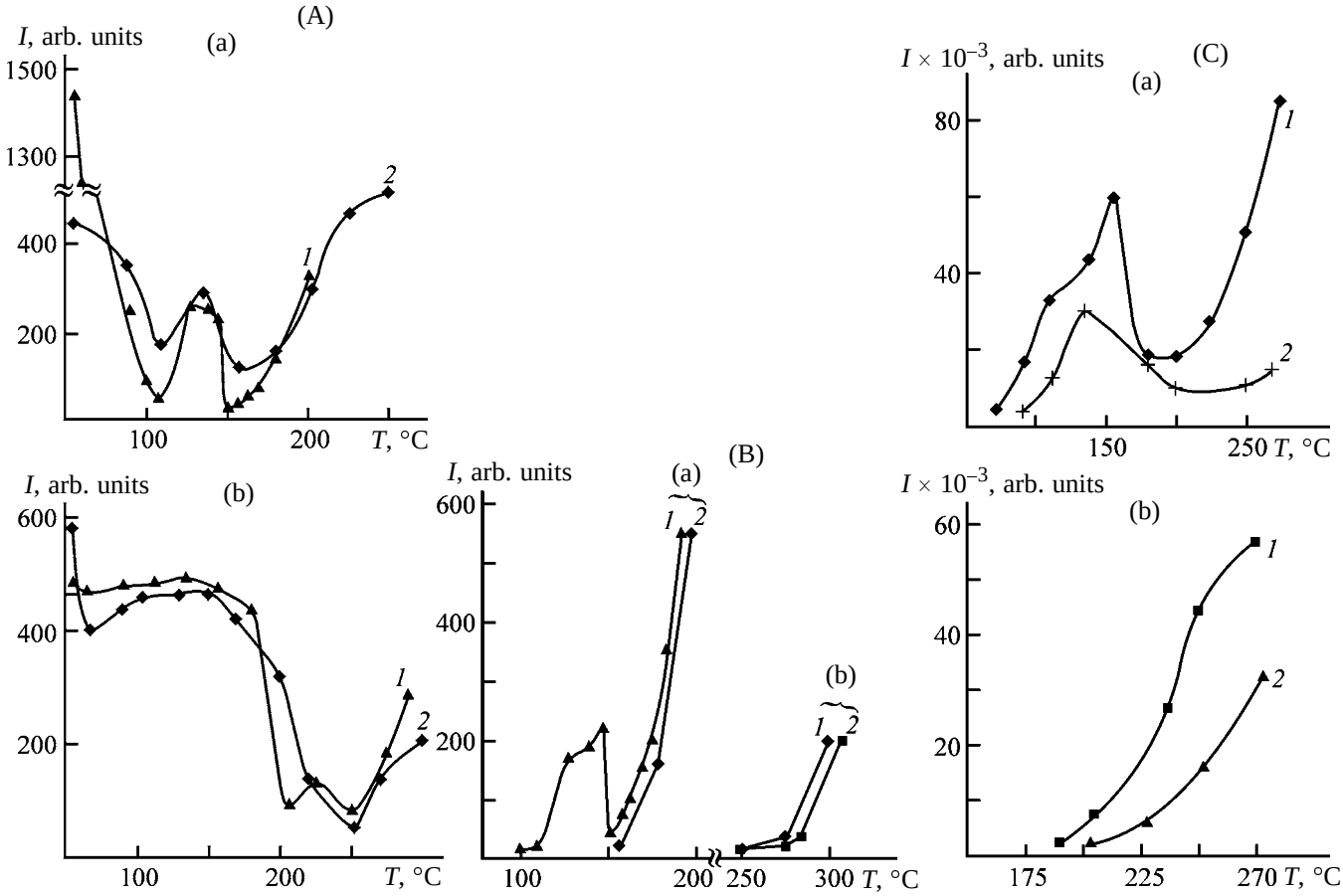

Fig. 2. Relative intensity of ion currents I of (A) H_2O^+, (B) SO_2^+, and (C) hydrocarbon fragments with m/e = 70–150 in the gas phase as a function of temperature T. For explanations, see text.

higher than 330°C is lower than that of Mg-K-1 can be due to the catalytic effect of palladium.

The volatile thermolysis products of H-K-1 and Mg-K-1 and palladium catalysts on their base were studied by mass spectrometry. The results are shown in Figs. 2A–2C. The temperature dependence of the relative content of H_2O^+ ions (m/z = 18) in the gas phase in thermolysis of H-K-1 (Fig. 2Aa, curve *1*) has three distinct sections: up to 110 (desorption of free and weakly bonded water), 110–150 (dehydration and decomposition of dissociated sulfo groups to form water), and above 150°C (thermolysis of nondissociated and associated sulfo groups to form water). The similar dependence was observed for 2.5Pd/H-K-1 (Fig. 2Aa, curve *2*). However, in this case water is liberated in greater amount and the onset temperature of decomposition of nondissociated and associated sulfo groups is higher by approximately 10°C. The onset temperature of thermolysis of dissociated and nondissociated sulfo groups of Mg-K-1 is 200 and 250°C, respectively (Fig. 2Ab, curve *1*). At the same time, the functional groups of 2.5Pd/H-K-1 start to decompose above 250°C (Fig. 2Ab, curve *2*).

The dependences of the intensity of SO_2^+ ion currents (m/z = 64) on the sample temperature (Fig. 2B) show that introduction of reduced Pd into H-K-1 increase the onset temperature of thermolysis of the sulfo groups from 100 to 155°C, whereas desulfonation of Mg-K-1 and 2.5Pd/Mg-K-1 starts at the same temperature (250°C).

Hydrocarbon fragments with m/z = 70–150 (cleavage of the C–C bond) are detected in the gas phase over the H form of the cation exchanger (Fig. 2Ca, curve *1*) at temperatures substantially lower than those in the case of the Mg form (Fig. 2Cb, curve *1*). Introduction of Pd particles enhances the thermal stability of the FIBAN K-1 matrix. The temperature at which hydrocarbon fragments are detected in the gas phase increases by 20–25°C for both 2.5Pd/H-K-1 (Fig. 2Ca, curve *2*) and 2.5Pd/Mg-K-1 (Fig. 2Cb, curve *2*). In addition, the amount of hydrocarbons liberated into

the gas phase on heating of the samples up to 275°C is substantially lower than that on heating of the initial H-K-1 and Mg-K-1 cation exchangers.

Thus, Pd particles enhance the thermal stability of FIBAN K-1 sulfonic cation exchanger in the H and Mg forms at moderate temperatures (up to 200–275°C).

Evaluation of the thermal stability of the ion exchangers by the temperature of decolorization of a $KMnO_4$ solution gave the similar results (see table). Introduction of reduced palladium enhances to a greater extent the thermal stability of the H form of the ion exchanger (growth form 130 to 180°C).

The degree of palladium reduction in 2.5Pd/H-K-1 and 2.5Pd/Mg-K-1 is 98 and 93%, respectively. The initial specific activity of Pd in the Mg form (8.7 $cm^3\ g_{Pd}^{-1}\ s^{-1}$) is substantially higher that in the H form (3.4 $cm^3\ g_{Pd}^{-1}\ s^{-1}$) (see table).

The X-ray pattern of 2.5Pd/H-K-1 contains sharp reflections with *d* 2.234, 1.958, and 1.166 Å assigned to crystals of metallic Pd. In the pattern of 2.5Pd/MgK-1, these reflections are broadened, suggesting lower crystallinity of Pd. Hence, the fact that the catalytic activity of 2.5Pd/Mg-K-1 in oxidation of H_2 is higher than that of 2.5Pd/H-K-1 is probably due to finer dispersity of Pd in 2.5Pd/Mg-K-1.

However, not only the dispersity of Pd but also its electronic state governed by strong metal–support interaction (SMSI) can affect the catalytic activity. As shown previously [13–18], the electronic state of metals supported by inorganic ion exchangers, zeolites, depends on the acid–base properties of the support. Metals on strongly acidic zeolites have low electron density, and metals supported by basic zeolites have excess electronic density. In this work we also studied the influence of the acid–base properties of the sulfonic ion exchangers on the activity of supported palladium catalysts.

These experiments were performed as follows. A sample of reduced catalyst 2.5Pd/H-K-1 was treated with 0.5 M $MgCl_2$ solution until H^+ ions were completely exchanged for Mg^{2+}. Then the sample was thoroughly washed with distilled water to the absence of chloride ions in the wash waters, dried, and heated in a helium flow as described above.

The palladium dispersity in this sample (2.5Pd/Mg-K-1) and in the initial catalyst (2.5Pd/H-K-1) is the same. The specific activity *A* of these catalysts is 5.7 and 3.4 $cm^3\ g_{Pd}^{-1}\ s^{-1}$, respectively (see table). This difference in the catalytic activity can only be due to the different cationic form of the support affecting the electronic state of Pd. Thus, the increased catalytic activity of 2.5Pd/MgK-1 compared to 2.5Pd/H-K-1 is caused not only by finer dispersity of metallic palladium but also by different effective charge of palladium particles (the absence of deficiency of the electron density).

Thermal stability and specific activity *A* in H_2 oxidation of palladium catalysts supported by the H and Mg forms of FIBAN K-1 sulfonic cation exchanger

Sample	Onset temperature of thermolysis, °C	*A*, $cm^3\ g_{Pd}^{-1}\ s^{-1}$
H-K-1	130	–
Mg-K-1	225	–
2.5Pd/H-K-1	180	3.4
2.5Pd/Mg-K-1	250	8.7
2.5Pd/Mg-K-1'	250	5.7

Thus, the effective charge of metal particles supported by both organic and inorganic ion exchangers depends on the acid–base properties (cationic form) of the support. In the case of an organic ion exchanger, the electron density is transferred along the polymeric chain over relatively long distances. This phenomenon, caused by the presence in the polymeric chain of atoms with different electronegativity, was discussed in our previous work [19] when we found that the degree of reduction of $[Pd(NH_3)_4]^{2+}$ cations introduced into sulfonic cation exchanger by the ion-exchange procedure depended on the salt form of the resin.

As seen from Fig. 3, the catalytic activity increases after treatment of the palladium catalysts with the reaction mixture at 100–180°C. Previous EXAFS spectroscopic studies showed that the active metal

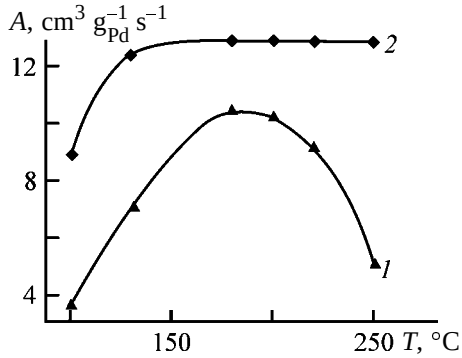

Fig. 3. Activity *A* of (*1*) 2.5Pd/H-K-1 and (*2*) 2.5Pd/Mg-K-1 as a function of temperature *T* of treatment of the catalysts with the reaction mixture.

oxide phase containing Pd–Pd and Pd–O bonds was formed after treatment of a palladium-containing zeolite with a mixture of 1% CO and air at 100–200°C. The activity of the palladium-containing zeolite was found to linearly increase with the ratio of O_2 and CO chemisorbed on the metal surface [21]. The fact that the catalytic activity of 2.5Pd/H-K-1 and 2.5Pd/Mg-K-1 in H_2 oxidation increases after high-temperature treatment of these catalysts with the reaction mixture is probably due to formation on Pd particles of a thin oxide layer which readily chemisorbs oxygen.

The activity of 2.5Pd/Mg-K-1 remains the same and the activity of 2.5Pd/H-K-1 sharply decreases after treatment at higher temperature (from 180 to 250°C). This decrease in the catalytic activity (see table) is clearly due to thermal degradation of the H form, which starts, as shown above, at temperatures higher than 180°C.

CONCLUSIONS

(1) The presence of reduced palladium in the H and Mg forms of FIBAN K-1 fibrous sulfonic cation exchanger enhances their thermal stability. The onset temperature of thermolysis of both the sulfo groups and the hydrocarbon matrix of the H form increases as well as the onset temperature of thermolysis of the hydrocarbon matrix of the Mg form.

(2) The activity of 2.5Pd/Mg-K-1 in H_2 oxidation is higher than that of 2.5Pd/H-K-1. This is due to different dispersities and electronic states of reduced palladium in these matrices.

(3) The catalytic activity in H_2 oxidation increases after treatment of the samples with the reaction mixture at temperatures from 100 to 180°C. After treatment at higher temperature (180–250°C), the activity of the catalyst based on the Mg form remains the same and the activity of the catalysts based on the H form of the ion exchanger sharply decreases owing to thermolysis of the support.

REFERENCES

1. Karpov, O.N., Tulupov, P.E., and Volkov, V.I., *Zh. Fiz. Khim.*, 1971, vol. 45, no. 7, pp. 1750–1763.
2. Uglyanskaya, V.A., Zav'yalova, T.A., Romanenko, E.F., *et al.*, *Zh. Fiz. Khim.*, 1981, vol. 35, no. 11, pp. 2868–2871.
3. Kurenkov, V.F. and Safin, A.G., *Zh. Prikl. Khim.*, 1998, vol. 71, no. 11, pp. 1927–1929.
4. Egiazarov, Yu.G., Kravchuk, L.S., Radkevich, V.Z., *et al.*, *Zh. Prikl. Khim.*, 2002, vol. 75, no. 1, pp. 34–38.
5. Kravchuk, L.S., Radkevich, V.Z., Lusenko, G.N., and Ivko, A.A., *Vysokomol. Soedin., Ser. A*, 2002, vol. 44, no. 4, pp. 648–654.
6. Soldatov, V.S., Pokrovskaya, A.I., and Martsinkevich, R.V., *Zh. Prikl. Khim.*, 1984, vol. 57, no. 9, pp. 2030–2034.
7. Veshtort, V.Z., Shingel', I.A., Savchits, M.F., and Egiazarov, Yu.G., *Zavod. Lab.*, 1989, vol. 55, no. 10, pp. 6–8.
8. Karpov, O.N., Tulupov, P.E., and Volkov, V.I., *Zh. Fiz. Khim.*, 1971, vol. 45, no. 7, pp. 1750–1763.
9. Polyanskii, N.G., Tulupov, P.E., Sadovskaya, G.K., and Slovokhotov, N.A., *Zh. Prikl. Khim.*, 1965, vol. 38, no. 4, pp. 910–918.
10. Saldadze, K.M., Polyanskii, N.G., and Pashkov, A.B., in *Khromatografiya, ee teoriya i primenenie* (Chromatography, Its Theory and Application), Moscow: Akad. Nauk SSSR, 1960, pp. 77–82.
11. Tulupov, P.E., *Stoikost' ionoobmennykh materialov* (Stability of Ion-Exchange Materials), Moscow: Khimiya, 1984.
12. *Kataliticheskie svoistva veshchestv* (Catalytic Properties of Substances), Roiter, V.A., Ed., Kiev: Naukova Dumka, 1968.
13. Egiazarov, Yu.G., Savchits, M.F., and Ustilovskaya, E.Ya., *Geterogenno-kataliticheskaya isomerizatsiya uglevodorodov* (Heterogeneous Catalytic Isomerization of Hydrocarbons), Minsk: Nauka i Tekhnika, 1989.
14. Savchits, M.F., Radkevich, V.Z., Ustilovskaya, E.Ya., *et al.*, *React. Kinet. Catal. Lett.*, 1994, vol. 52, no. 1, pp. 43–47.
15. Galezot, P., in *Proc. 6th Int. Zeolite Conf.*, Guildorf, 1984, pp. 352–367.
16. Ione, G.K., *Polifunktsional'nyi kataliz na tseolitakh* (Polyfunctional Catalysis with Zeolites), Novosibirsk: Nauka, 1982.
17. Samont, M.G. and Boudart, M., *J. Phys. Chem.*, 1991, vol. 95, no. 10, pp. 4070–4074.
18. Bredikhin, M.N. and Lochov, Yu.A., *J. Catal.*, 1989, vol. 115, no. 2, pp. 601–604.
19. Egiazarov, Yu.G. and Radkevich, V.Z., *Kinet. Katal.*, 2002, vol. 43, no. 6, pp. 1–6.
20. Radkevich, V.Z., Savchits, M.F., Novgorodov, B.N., *et al.*, *Zh. Prikl. Khim.*, 1998, vol. 71, no. 10, pp. 660–664.
21. Radkevich, V.Z., Ivko, A.A., and Egiazarov, Yu.G., *Kinet. Katal.*, 2001, vol. 42, no. 4, pp. 574–578.

Russian Journal of Applied Chemistry, Vol. 77, No. 9, 2004, pp. 1505–1509. Translated from Zhurnal Prikladnoi Khimii, Vol. 77, No. 9, 2004, pp. 1516–1519.

PRODUCTION AND USE OF NEW MATERIALS

New Materials for Sorption of Hydrogen

A. A. Ol'shanskaya, N. A. Sobgaida, and S. S. Popova

Engels Technological Institute, Saratov State Technical University, Engels, Saratov oblast, Russia

Received January 28, 2004

Abstract—The influence of temperature, duration of thermal treatment, and oxidation modes of the aluminum base on processes in which intermetallic compounds LiLaAl are formed by the method of electrochemical cathodic intercalation was studied. The optimal modes of formation of $LiLaAl_{ox}$ compounds exhibiting high sorption capacity for hydrogen were determined.

Hydrogen is a versatile and environmentally clean kind of fuel. One of the most important tasks of hydrogen power engineering is the development of efficient systems for hydrogen storage, because none of the existing systems for hydrogen storage under high pressure, in absorbed state at low temperature, in liquid state, and in the form of metal hydrides and intermetallic compounds satisfies the requirements to H_2 accumulators. In the case of mobile storage systems, the mass content of H_2 should be no less than 6.5 wt %, and the volume content, no less than 63 kg m^{-3} [1, 2]. According to the regulations by the International Energy Agency, an H_2 accumulator should contain no less than 5 wt % H_2 and release it at a temperature not higher than 373 K [1–3].

One of the most promising and presently widely studied ways to solve the above-mentioned problem is accumulation of H_2 by metals and alloys, based on reversible sorption of hydrogen.

The interaction of H_2 with metals or alloys commonly involves the following processes: physical adsorption on the surface, activated absorption in the bulk, diffusion, migration, and molecular absorption (occlusion), to form hydrides [2–10]. The nature of a metal or an alloy and presence of defects in their structure strongly affect the mechanism by which H_2 interacts with the base. Diffusion, or mass transfer, commonly leads to formation of interstitial or substitution solid solutions. The key factor in the sorption process is the defectiveness of the crystal lattice and existence of hydrogen dissolved in it in the form of protons [5–8]. The solubility of H_2 and its sorption by various matrices are affected by such factors as pressure, mechanical treatment of the surface, grain size of the metal, presence of impurity compounds on the metal surface, pH value of the solution, and electrolyte composition [1, 4–13]. Thus, the surface and volume properties of a material that sorbs H_2 and the number of defects (vacant places for hydrogen atoms) can be changed by means of various physicochemical or electrochemical methods.

The aim of this study was to examine the possibility of using the method of cathodic intercalation to obtain reversible H_2 sorbents based on lithium–aluminum–lanthanum (LiAlLa) alloys.

EXPERIMENTAL

Aluminum foil (A 99.95) was conditioned with synthetic corundum of M-28 brand, twice washed with double-distilled water, and dried. Then, electrodes with a geometric working surface area of 1 cm^2 were subjected to a 30-min preliminary thermal treatment (Al_{th}; T_{tr} = 200–500°C, step 50°C). After that, lanthanum was introduced into the Al_{th} matrix by cathodic intercalation from a 0.03 M solution of lanthanum sulfanilate in dimethylformamide (DMF) at the cathodic polarization potential E_{cp} = –2.7 V for 1 h. Then, lithium was introduced into the resulting $LaAl_{th}$ alloy from a 1 M solution of $LiClO_4$ in a mixture of propylene carbonate (PC) and dimethoxyethane (DME) taken in a 1 : 1 volume ratio at E_{cp} = –2.9 V for 1 h. $LiLaAl_{th}$ phases with the highest energy storage capacity are obtained after thermal treatment of the Al base at 400°C. In the next stage, the duration of the thermal treatment was varied: the starting Al samples were treated at 400°C for 15–120 min (step 15 min), and then Al_{th} samples were treated in nonaqueous solutions of La and Li salts as described above. In another set of experiments, the starting Al or Al_{th} was preliminarily oxidized, in order to "develop" the electrode surface, in a

1070-4272/04/7709-1505 © 2004 MAIK "Nauka/Interperiodica"

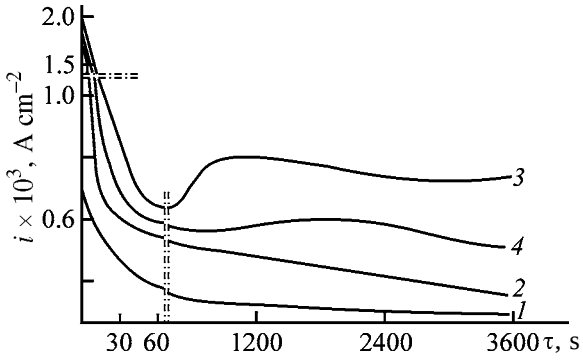

Fig. 1. Potentiostatic curves of cathodic intercalation of La into aluminum matrices from a 0.03 M solution of lanthanum sulfanilate in DMF. E_{cp} = –2.7 V (relative to a nonaqueous silver chloride electrode), 20°C. (*i*) Current density and (τ) time; the same for Figs. 2–5. Matrix: (*1*) Al, (*2*) Al_{th}, (*3*) Al_{ox}, and (*4*) $(Al_{th})_{ox}$.

mixture of acids (g l^{-1}): sulfuric 150, oxalic 30, citric 30, and nicotinic 10, at anode current densities i_a = 10–50 mA cm^{-2} (step 10 mA cm^{-2}) and oxidation time t_{ox} = 10–60 min (step 10 min). As counter electrodes in oxidation served lead plates (S = 10 cm^2). Al plates (S = 10 cm^2) were used in cathodic intercalation of La and Li. As reference electrode was used nonaqueous silver chloride electrode fabricated from an EVL-1 standard silver chloride electrode, placed in a working electrolyte solution, 1 M $LiClO_4$ in PC + DME (1 : 1). LiCl crystals were introduced into the electrolyte in order to eliminate the diffusion potential. The potential of the nonaqueous silver chloride electrode at 20°C is –0.06 V vs. standard silver chloride electrode, 0.163 V vs. hydrogen electrode, and 3.05 V vs. lithium electrode in the working electrolyte solution. In measurements in DMF-based solutions, an intermediate vessel with the working solution was used. The silver chloride electrode Ag^+/Ag is reversible and stable in the aprotic solvents used in the study [14]. In studying the sorption of H_2 by the formed LiLaAl, $LiLaAl_{ox}$, and $LiLa(Al_{th})_{ox}$, HCl and $HClO_4$ solutions with concentrations of 0.375, 0.750, 1.500, and 2.000 wt % were used. The sorption was performed at potentials E_{cp} from –1.0 to –2.2 V (step 0.1 V) in the course of 1 h. All the measurements in this study were carried out at 20°C on a P-5848 potentiostat with a KSP-4 recorder. The diffusion-kinetic parameters of the process were determined using the potentiostatic method. The initial portions of current decay in curves plotted in the coordinates i–$1/\tau^{1/2}$ were analyzed in terms of the Cottrell equation [15] for solid-state diffusion in thin films

$$K_i = \Delta i/\Delta(1/t^{1/2}) = zFc^*D^{1/2}/\pi^{1/2},$$

where K_i is the diffusion-kinetic parameter of intercalation (A s$^{1/2}$ cm^{-2}); i, current density (A cm^{-2}), F = 96 485 C mol^{-1}, Faraday number; and D, diffusion coefficient (cm^2 s$^{1/2}$).

Table 1. Diffusion-kinetic characteristics of intercalation of La into Al matrices and Li into Al–La matrices

Electrode	$K_i \times 10^4$, A s$^{1/2}$ cm^{-2}	$c^0D^{1/2} \times 10^{-9}$, mol cm^{-2} s$^{-1/2}$
LaAl	1.3	2.4
$LaAl_{th}$	2.7	4.9
$LaAl_{ox}$	3.4	6.2
$La(Al_{th})_{ox}$	5.2	9.5
LiLaAl	4.3	7.9
$LiLaAl_{th}$	7.6	13.9
$LiLaAl_{ox}$	9.7	17.8
$LiLa(Al_{th})_{ox}$	1.1	2.0

An oxide film with a structure that is looser than the natural structure can be formed on the surface of Al (A 99.95) by selecting the temperature (200–500°C) and time (15–120 min) of thermal treatment. It was found that the optimal mode is mode I: T_{tr} = 400°C and τ_{tr} = 60 min. Similarly, the optimal mode in the case of anodic oxidation in a mixture of acids (g l^{-1}): sulfuric 150, oxalic 30, citric 30, and nicotinic 10 is mode II: anode current density i_a = 20 mA cm^{-2}, τ_{ox} = 20 min (Fig. 1). Under the chosen conditions of thermal treatment and oxidation, the oxide film on the surface of Al has such properties and structure which, as shown previously [16, 17], favor introduction of La into the Al electrode from a lanthanum sulfanilate solution. Upon the introduction of lanthanum at E_{cp} = –2.7 V and τ_{cp} = 60 min, the negative potential of the formed electrode $(Al_{th})_{ox}La$ was about –2.0 V. The calculated diffusion-kinetic parameters of the processes of successive introduction of La and Li into the starting Al and aluminum and lanthanum–aluminum bases preliminarily formed in modes I and II are listed in Table 1.

Upon introduction of lithium into $La(Al_{th})_{ox}$ electrodes from a 1 M solution of LiCl in PC + DME (1 : 1) in the potentiostatic mode (Fig. 2), a classical curve of cathodic intercalation was obtained [18–20]. Incorporation of La and Li atoms into the structure of thermally treated and oxidized Al (Figs. 1, 2) leads to successive distortion of the initial crystal lattice of Al and to formation of additional vacancies and structural defects and zones with increased diffusion rate.

This must facilitate sorption of H_2 and its accommodation at the forming vacant sites. The study demonstrated that the best parameters of the processes are achieved for the $LiLaAl_{ox}$ electrode (Figs. 1, 2; Table 1).

The quantitative and qualitative pattern of the process of H_2 sorption by preliminarily formed $LiLaAl_{ox}$ electrodes depends on the nature of a hydrogen-containing agent (HCl and $HClO_4$), its concentration, and cathodic polarization potential E_{cp} (Figs. 3, 4).

According to Smith's classification [1, 3], all metals can be divided into three groups by their relation to hydrogen: the first comprises metals, including Li, that form with H_2 saltlike hydrides; the second, metals that form with H_2 chemical compounds with covalent bonding, covalent hydrides (Al); and the third, endo- and exothermic absorbers of hydrogen and, in particular, La [3]. Thus, the metal components of the $LiLaAl_{ox}$ alloy under study belong to different groups and, therefore, the variety of alloys formed with H_2 may be exceedingly wide. In cathodic polarization of the $LiLaAl_{ox}$ electrode in HCl solutions of various concentrations at a potential E_{cp} = –1.1 V, the rate of discharge of H^+ ions grows 3–4-fold when the HCl concentration increases from 0.375 to 1.5 wt % (Fig. 3). Analysis of the influence exerted by the cathode potential on the sorption of H_2 by the $LiLaAl_{ox}$ alloy shows (Fig. 4) that a shift of the potential in the negative direction accelerates saturation of the electrode surface with discharged hydrogen atoms and makes shorter the critical time in which the first nuclei of a new phase are formed, when prerequisites for their growth and formation of a layer of this phase are created. At E_{cp} = –1.1 V, this critical time is not reached under the given experimental conditions; at E_{cp} = –1.5 V, it is as long as 300 s, and at E_{cp} = –2.0 V, as short as 10 s.

In the initial stage of the current decay, the dependence i–$1/\tau^{1/2}$ is represented by straight lines with a sharp bend, which make intercepts i_∞ on the ordinate axis (Fig. 5). This may be due to parallel occurrence of two processes: introduction of H^+ ions into the oxide layer (i_{ox}) and intercalation of discharged hydrogen ions into the metal at the inner M | oxide interface (i_M). The resistance of the protonated oxide layer is so high that, at E_{cp} = –1.1 V, the electrode current remains constant during approximately 18 s. And only after that there appears a concentration gradient of hydrogen ions, dc_{H^+}/dx, that is sufficient for ensuring the diffusion of H^+ ions to the inner interface with the metal of the electrode, where the fol-

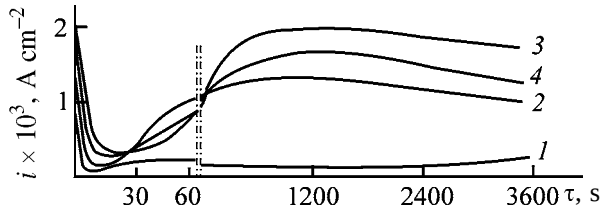

Fig. 2. Potentiostatic curves of cathodic intercalation of Li from a 1 M solution of $LiClO_4$ in PC + DME (1 : 1) into electrodes. E_{cp} = –2.9 V (relative to a nonaqueous silver chloride electrode), 20°C. Electrode: (*1*) LaAl, (*2*) $LaAl_{th}$, (*3*) $LaAl_{ox}$, and (*4*) $La(Al_{th})_{ox}$.

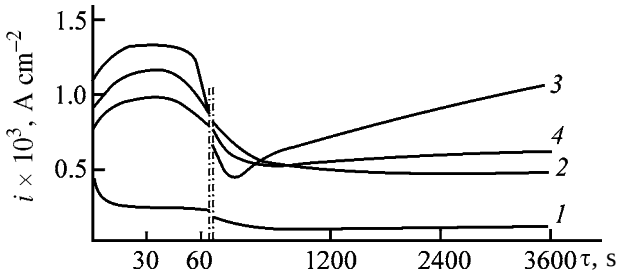

Fig. 3. Potentiostatic curves obtained in treatment of a $LiLaAl_{ox}$ electrode in HCl solutions at E_{cp} = –1.1 V. c_{HCl} (wt %): (*1*) 0.375, (*2*) 0.5, (*3*) 1.5, and (*4*) 2.0.

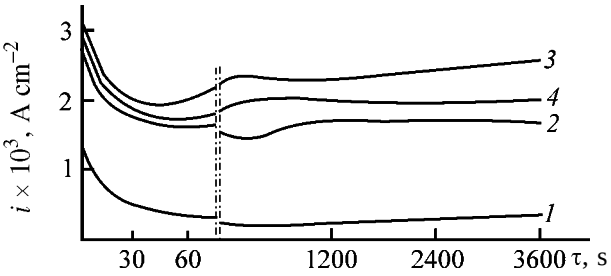

Fig. 4. Potentiostatic curves obtained in treatment of a $LiLaAl_{ox}$ electrode in a 1.5% HCl solution. Potential E_{cp} (V): (*1*) 1.1, (*2*) 1.5, (*3*) 2.0, and (*4*) 2.2.

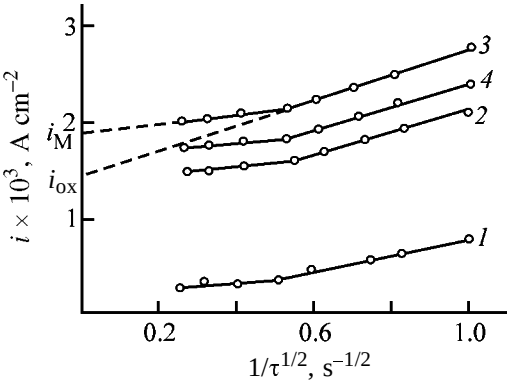

Fig. 5. i–$1/\tau^{1/2}$ dependence for a $LiLaAl_{ox}$ electrode (plotted using the data of Fig. 4).

Table 2. Constants of hydrogen sorption by $LiLaAl_{ox}$ electrode from a 1.5% HCl solution and $c^0D^{1/2}$ product at different cathodic polarization potentials

$-E_{cp}$, V	$K_i \times 10^3$ (ox), A $s^{1/2}$ cm^{-2}	$c^0D^{1/2} \times 10^8$ (ox), mol cm^{-2} $s^{-1/2}$	$K_i \times 10^3$ (M), A $s^{1/2}$ cm^{-2}	$c^0D^{1/2} \times 10^8$ (M), mol cm^{-2} $s^{-1/2}$
2.2	1.2	2.2	0.25	0.5
2.0	1.4	2.6	0.44	0.8
1.5	1.3	2.4	0.38	0.7
1.1	1.0	1.8	0.42	0.8

lowing exchange reactions are possible:

$$LiAl + xH^+ + xe = AlH_xLi_{1-x} + xLi$$

or

$$La + xH^+ + xe = LaH_x,$$

$$Li + xH^+ + xe = LiH_x.$$

It was established experimentally that hydrogen is sorbed from HCl solutions at a higher rate. In the case of $HClO_4$, adsorption of ClO_4^- anions on the alloy surface hinders introduction of H^+ ions into the structure of the electrode, and an additional energy is required for this process to begin. This is achieved, for example, at a significant shift of the cathodic polarization potential in the negative direction (to + 0.05 V relative to Li^+/Li and –3.0 V relative to the nonaqueous silver chloride electrode).

Raising the concentration of HCl from 0.375 to 1.5 wt % makes the rate of hydrogen intercalation 3–4 times faster. In this case, the electrochemical parameters of the process depend on E_{cp} (Table 2).

CONCLUSIONS

(1) In the chosen modes of preliminary thermal treatment and oxidation, an oxide film whose properties and structure favor cathodic intercalation of La and Li into an aluminum electrode is formed on the Al surface.

(2) Introduction of lithium and lanthanum is accompanied by successive distortion of the crystal lattice by La and Li and formation of additional vacancies and structural defects and of zones with an increased diffusion rate. This facilitates the subsequent sorption of hydrogen and its accommodation in the structure of the LiLaAl alloys formed.

(3) Hydrogen sorption is affected by the solution concentration and nature (anionic composition) of a hydrogen-containing agent.

REFERENCES

1. Gamburg, D.Yu., Semenov, V.P., Dubovkin, N.F., and Smirnova, L.N., *Vodorod: Svoistva, poluchenie, khranenie, transportirovanie, primenenie: Spravochnoe izdanie* (Hydrogen: Propeties, Manufacture, Storage, Transportation, and Use: Reference Book), Moscow: Khimiya, 1989.
2. Marshakov, A.I. and Mikhailovskii, Yu.N., *Elektrokhimiya*, 1994, vol. 30, no. 4, pp. 530–543.
3. Grilikhes, M.S. and Bozhevol'nov, V.B., *Zh. Prikl. Khim.*, 1995, vol. 68, no. 3, pp. 353–365.
4. Korovin, N.V., *Elektrokhimiya*, 1971, vol. 8, no. 2, pp. 172–179.
5. Kuznetsov, V.V., Khaldeev, G.V., and Kichigin, V.I., *Navodorozhivanie metallov v elektrolitakh* (Hydrogen Saturation of Metals in Electrolytes), Moscow: Mashinostroenie, 1993.
6. Skuratnik, L.B., *Elektrokhimiya*, 1977, vol. 13, no. 8, pp. 1122–1126.
7. Krapivnyi, N.G., *Elektrokhimiya*, 1981, vol. 17, no. 5, pp. 634–637.
8. Krapivnyi, N.G., *Elektrokhimiya*, 1981, vol. 17, no. 5, pp. 678–685.
9. Petrii, O.A. and Kolotyrkina, T.Ya., *Elektrokhimiya*, 1973, vol. 9, no. 2, pp. 254–257.
10. Korkashvili, T.Sh., Tsionskii, V.M., and Krishtalik, L.I., *Elektrokhimiya*, 1980, vol. 16, no. 6, pp. 886–888.
11. Batrakov, V.V., Dittrich, J., and Popova, A.N., *Elektrokhimiya*, 1972, vol. 8, no. 4, pp. 640–643.
12. Kudryashov, I.V. and Falin, L.A., *Elektrokhimiya*, 1971, vol. 7, no. 12, pp. 1770–1772.
13. Lavrenko, V.A., Yagupol'skaya, L.N., and Tikush, V.L., *Elektrokhimiya*, 1970, vol. 6, no. 6, pp. 887–890.
14. Butler, J., *Elektrokhimiya metallov v nevodnykh rastvorakh* (Electrochemistry of Metals in Nonaqueous Solutions), Moscow: Mir, 1974.
15. Vetter, K.J., *Electrochemische Kinetik*, Berlin: Springer, 1961.

16. Popova, S.S., Sobgaida, N.A., and Spiridonov, E.V., in *Litievye istochniki toka: Materialy 6-i Mezhdunarodnoi konferentsii, Novocherkassk, 19–21 sentyabrya 2000 goda* (Proc. 6th Int. Conf. on Lithium Power Sources, Novocherkassk, September 19–21, 2000), Novocherkassk: Nabla, 2000, pp. 104–105.
17. Politaeva, N.A. and Popova, S.S., in *Khimiya: sostoyanie i perspektivy nauchnykh issledovanii na poroge tret'ego tysyacheletiya: Sbornik statei molodykh uchenykh* (Chemistry: State and Promises of Research at the Turn of the Third Millenium: Coll. of Works of Young Scientists), Saratov: Saratov. Univ., 1999, pp. 106–107.
18. Popova, S.S., Kabanov, B.N., Alekseeva, L.A., and Ol'shanskaya, L.N., *Elektrokhimiya*, 1985, vol. 21, no. 1, pp. 38–45.
19. Kabanov, B.N., Kiseleva, I.G., and Astakhov, I.I., *Elektrokhimiya*, 1972, vol. 8, no. 7, pp. 955–972.
20. Alekseeva, L.A., Kiseleva, I.G., and Kabanov, B.N., *Elektrokhimiya*, 1980, vol. 16, no. 3, pp. 413–416.

Russian Journal of Applied Chemistry, Vol. 77, No. 9, 2004, pp. 1510–1514. Translated from Zhurnal Prikladnoi Khimii, Vol. 77, No. 9, 2004, pp. 1520–1524.

ENVIRONMENTAL PROBLEMS OF CHEMISTRY AND TECHNOLOGY

Mechanism and Products of Thermal Treatment of Slimes Obtained at Treatment of Wastewaters Using Ferroferrihydrosol

D. Budilovskis and L. S. Eshchenko

Gediminis Vilnius Technical University, Vilnius, Lithuania
Belarussian State Technological University, Minsk, Belarus

Received June 15, 2004

Abstract—Phase, dispersion, and chemical compositions of the products of thermal treatment of slimes obtained by treatment of model solutions and industrial wastewaters from electrochemical production using ferroferrihydrosol were studied. The dependence of the phase composition of the slime treatment products as influenced by the content and ratio of heavy metals in wastewaters was evaluated.

One of procedures for reagent treatment of electrochemical production wastewaters is based on the use of ferroferrihydrosol (FFH) [colloidal suspension of iron(II) and iron(III) oxyhydrates] exhibiting high sorption, coagulation, and reduction powers [1]; this agent is prepared by electrochemical treatment of steel cuttings. This treatment procedure provides simultaneous removal of a wide spectrum of heavy metals without separation into certain (e.g., zinc-containing, copper-containing) fractions. The resulting slime, being low-toxic, stable to aggressive media, and enriched with iron, can be a valuable secondary raw material.

Utilization of slimes from electrochemical production is of particular social and economical importance, because solution of this problem can decrease expenses for building of environmentally hazardous treatment fields and save natural resources owing to use of secondary raw materials. The procedures for treatment and utilization of electrochemical production slimes are analyzed in [2–7]. These data show that the slimes can be used as additives in bulk coloring of ceramics and in brick production to improve its strengths and frost resistance, as claydite-like light porous filters, pigments, and pigment-fillers. Published data suggest that the most advisable solution is preparation of inorganic pigments whose properties are not inferior to those of standard commercial samples. This is especially the case for pigments based on the slimes from treatment of the wastewaters with FFH, because the content of iron in them exceeds 50%.

The main stage of the slime treatment to prepare pigments and pigment-fillers is their thermal treatment, which allows formation of hexagonal or cubic structure of iron oxide (α-Fe_2O_3, γ-Fe_2O_3) providing color properties of the products. It should be noted that compounds of chromium, nickel, copper, zinc, and some other metals can strongly affect the chemical and phase transformations proceeding in the course of slime heating and thus the composition and color properties of the resulting products. The data on thermal transformations of iron, chromium, nickel, zinc, and copper compounds in precipitates, e.g., in the slimes from treatment of the electrochemical production wastewaters with FFH, are lacking, which hinders determination of the optimal conditions of their treatment to prepare pigments and pigment-fillers. Hence, in this work we studied the mechanism and products of thermal treatment of precipitates (slimes) obtained by treatment of model solutions and industrial wastewaters using an electrochemically prepared reagent, FFH.

EXPERIMENTAL

In our work we used the precipitates (slimes) from treatment of model solutions and industrial wastewaters from the following plants: Chermet (Grodno, Belarus) and Vilma and Vingis (Vilnius, Lithuania). The thermal transformations in the course of slime heating were studied by differential thermal analysis (DTA) using an OD-102 derivatograph (MOM, Hungary) at a heating rate of 10 deg min^{-1} (0.5–1.0 g

1070-4272/04/7709-1510 © 2004 MAIK "Nauka/Interperiodica"

Table 1. Composition of model solutions and precipitation conditions

Model solution no.	Content in solution (model wastewater), mg l^{-1}				FFH recalculated on Fe, mg l^{-1}	Weight ratio of the metal ions at precipitation	Precipitant
	Zn(II)	Cr(VI)	Ni(II)	Cu(II)			
1	10	10	10	10	500	Zn : Cr : Ni : Cu : Fe = 1 : 1 : 1 : 1 : 50	NaOH
2	10	10	10	10	500	Zn : Cr : Ni : Cu : Fe = 1 : 1 : 1 : 1 : 50	Degreasing solution (PO_4^{3-}, CO_3^{2-}, NaOH)
3	10	10	10	10	500	Zn : Cr : Ni : Cu : Fe = 1 : 1 : 1 : 1 : 50	$Ca(OH)_2$
4	200	10	10	10	500	Zn : Cr : Ni : Cu : Fe = 20 : 1 : 1 : 1 : 50	NaOH
5	10	10	200	10	500	Zn : Cr : Ni : Cu : Fe = 1 : 1 : 20 : 1 : 50	NaOH
6	10	10	10	200	500	Zn : Cr : Ni : Cu : Fe = 1 : 1 : 1 : 20 : 50	NaOH
7	10	200	10	10	900	Zn : Cr : Ni : Cu : Fe = 1 : 20 : 1 : 1 : 90	NaOH
8	600	10	10	10	600	Zn : Cr : Ni : Cu : Fe = 60 : 1 : 1 : 1 : 60	NaOH
9	10	10	600	10	600	Zn : Cr : Ni : Cu : Fe = 1 : 1 : 60 : 1 : 60	NaOH
10	10	10	10	600	600	Zn : Cr : Ni : Cu : Fe = 1 : 1 : 1 : 60 : 60	NaOH
11	10	600	10	10	900	Zn : Cr : Ni : Cu : Fe = 1 : 60 : 1 : 1 : 90	NaOH

sample weight). The phase compositions of the treatment products were determined on a DRON-2 diffractometer with an iron anode. The chemical compositions of the slimes and final products were determined by chemical analysis and X-ray spectral microanalysis. The dispersion composition was studied by transmission and scanning microscopy on a Mini-Magiscan certified automatic pattern analyzer using a Genias 26 program. For scanning microscopy, a layer of gold was preliminarily sputtered over the sample surface.

The compositions of the model solutions prepared from $ZnSO_4$, $NiSO_4$, $CuCl_2$, CrO_3, and tap water containing calcium and magnesium ions (5–7 mg-equiv l^{-1}) are listed in Table 1. Then, an aqueous suspension of FFH and alkaline reagents [NaOH, $Ca(OH)_2$, or degreasing solution] were added to pH 8.1–8.5. In FFH, the crystalline phase is Fe_3O_4, and the Fe(II) : Fe(III) ratio is (1–2) : 10.

The mechanism of FFH treatment of wastewaters containing simultaneously double- and triple-charged cations involves complex physicochemical transformations in the solid phase. The Cu(II), Zn(II), Cr(III), and Ni(II) ions occurring in the wastewaters can be sorbed with FFH and react with iron compounds. As a result, complex spinel-like crystalline structures can appear, as in the case of electrochemical wastewater treatment [8]:

$$n\mathrm{M}^{2+} + (3 - n)\mathrm{Fe}^{2+} + 6\mathrm{OH}^- \rightarrow \mathrm{M}_n\mathrm{Fe}_{3-n}(\mathrm{OH})_6,$$

$$\mathrm{M}_n\mathrm{Fe}_{3-n}(\mathrm{OH})_6 \xrightarrow{+0.5\mathrm{O}_2} \mathrm{M}_n\mathrm{Fe}_{3-n}\mathrm{O}_4 + 3\mathrm{H}_2\mathrm{O}.$$

Thus, the precipitates obtained by wastewater treatment with FFH are mixtures of iron oxyhydrates with sorbed compounds of heavy metals, magnetite Fe_3O_4 and ferrites $M_nFe_{3-n}O_4$. Moreover, formation of amorphous heteropoly compounds with molecular units containing Fe(M)(OH)–O– groups and of hydroxides of metals present in the purified water cannot be ruled out [9]. The chemical compositions of the dried precipitates obtained from the model solutions and industrial wastewaters are listed in Table 2. As seen, the content of metal and water in the precipitates depends on the composition of the initial wastewater.

The XRD analysis of the precipitate samples also showed certain differences in their phase composition. For example, there are no well-crystallized phases in the precipitates obtained by treatment of industrial wastewaters with FFH, whereas the XRD patterns of the samples precipitated from the model solutions exhibit the reflections typical for magnetite at predominant content of chromium or nickel ions in solution or belonging to an unidentified phase at predominant content of copper ions in solutions. It should be noted that the lattice parameters of the magnetite phase are slightly distorted, probably due to the formation of intercalation or substitution solid solutions.

As seen from the data of the transmission and scanning microscopy, the average particle size is 0.36–0.41 μm. As for industrial samples, the average size of the particles prepared at the Chermet and Vilma plants is slightly greater than those formed upon precipitation from the model solutions and wastewaters from the Vingis plant.

Table 2. Composition of precipitates obtained from model solutions and industrial wastewaters

Sample no.	Content of the main components recalculated on metal oxides						
	Fe_2O_3	FeO	Cr_2O_3	ZnO	NiO	CuO	H_2O
4	57.3	1.2	1.3	20.0	1.1	1.1	18.3
5	56.1	1.7	1.4	1.0	20.0	1.2	18.3
8	43.8	1.7	0.8	35.7	0.7	0.7	17.5
9	42.3	0.6	0.7	0.6	35.4	0.7	20.9
10	44.6	0.1	0.6	0.7	0.7	36.2	16.8
11	66.7	4.0	12.1	0.3	0.3	0.3	18.7
Chermet	52.9	–	6.1	3.7	1.9	4.3	19.3
Vilma	39.2	–	4.4	1.9	13.6	5.0	25.8
Vingis	48.5	–	3.3	14.3	0.9	0.8	22.1

* Sample no. corresponds to the number of the model solution treated with FFH.

The DTA curves of the slimes in question are shown in Fig. 1. The endothermic effects in the 100–400°C range are due to the slime dehydration. As seen, the water molecules are liberated stepwise on heating. This process is characterized by two and more endothermic peaks in the DTA curves; the first of them in the 100-210°C range is due to the loss of hydration water, whereas the second peak is due to liberation of crystallization water and probably cleavage of the bridging OH groups. The heating curves of sample nos. 2 and 3 obtained from the model solutions exhibit only two endothermic effects: the first peak with a minimum at 125°C and the second broad peak in the 200–400°C range. These curves correspond to the heating curves of iron(III) oxide hydrates

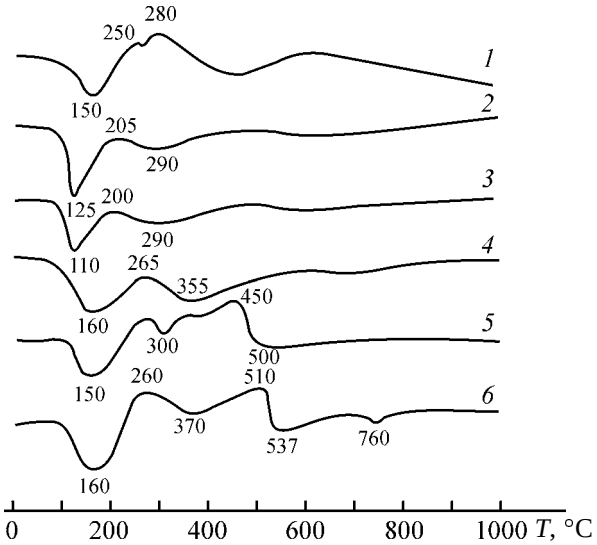

Fig. 1. DTA curves of (*1*) FFH and precipitates obtained from model solution (*2*) no. 4 and (*3*) no. 5 and from industrial wastewaters of the (*4*) Vilma, (*5*) Vingis, and (*6*) Chermet plants. (*T*) Temperature.

[10], in particular, of goethite FeOOH, but differ from the DTA curve of FFH (Fig. 1), which suggests chemical and phase transformations of FFH in the wastewaters. The heating curve of the slime prepared under the operation conditions at the Vilma plant is similar to curves *2* and *3*, but it is characterized by a more diffuse broad endothermic effect, probably due to the differences in the chemical composition, particle size, specific surface area, and thus the amounts of adsorbed and hydration water. The DTA curves of sample nos. 5 and 6 are characterized by ascending baseline in the 320–510°C range, which corresponds to the γ-$Fe_2O_3 \rightarrow \alpha$-$Fe_2O_3$ phase transition. The height and position of the endothermic peak at 510°C are determined by the degree of crystallinity of Fe_2O_3, amount of this phase, and its particle size [5]. It is known that the DTA peaks can shift toward lower temperatures with decreasing particle size.

The phase compositions of the products obtained by the slime thermal treatment at 800°C for 0.5 h was studied by XRD analysis. The XRD data (Figs. 2a, 2b) show that the products of the slime thermal treatment contain at least two crystalline phases, and one of them is hematite Fe_2O_3.

In accordance with the sets of the interplanar spacings, the XRD patterns can be divided in several groups. The first group includes the diffraction patterns with interplanar spacings corresponding to hematite. These patterns are typical for the products of thermal treatment of the samples prepared from model solutions with the concentrations of zinc, chromium, nickel, and copper of 10 mg l^{-1}, and with the concentrations of copper and zinc of 200 mg l^{-1}. The second group includes the patterns typical for Fe_2O_3 and Fe_3O_4 phases. These two crystalline phases are

formed at treatment of both model solutions containing chromium (200 and 600 mg l^{-1}) and copper (600 mg l^{-1}) ions and industrial wastewaters from the Vilma and Chermet plants. With increasing chromium concentration in the wastewater, the content of crystalline phase with the magnetite structure decreases (Fig. 2).

As the zinc concentration in wastewaters from the Vingis plant is high (Table 1), the precipitates heated at 800°C yield a mixture of α-Fe_2O_3 and ZnO, which is confirmed by interplanar spacings *d* 2.476, 2.816, and 2.602 Å in the XRD patterns. Similar phases are obtained from zinc-rich model solutions.

The products of annealing of the precipitates obtained from the model solutions containing 200 mg l^{-1} nickel give the XRD patterns exhibiting the reflections typical for α-Fe_2O_3 and γ-Fe_2O_3. With increasing nickel content to 600 mg l^{-1}, we obtained the precipitates whose thermal treatment yields a phase with a magnetite-type structure. Thus, our experimental data show certain dependence between the content of copper, zinc, and nickel ions in the wastewaters and phase composition of the products of the slime thermal treatment.

The phase transformations proceeding at thermal treatment of the slimes can be described as follows. The α-Fe_2O_3 phase is formed by dehydration of iron(III) oxide hydrates present in the precipitates and subsequent transformations of magnetite according to the following reaction:

$$2FeO \cdot Fe_2O_3 + 0.5O_2 \rightarrow 3\gamma\text{-}Fe_2O_3 \rightarrow 2\alpha\text{-}Fe_2O_3.$$

The other crystalline phases and, in particular, magnetite in the products of thermal treatment probably result from formation of intercalation and substitution solid solutions with participation of metal ions present in the wastewaters. For example, magnetite, as ferrite, has the structure of inverse spinel $Fe^{3+}[Fe^{2+}Fe^{3+}]O_4^{2-}$ with the random distribution of double- and triple-charged cations in the octahedral sites of the lattice containing both cationic and anionic vacancies. It is known that ferrites of several metals also have the inverse spinel structure. These structures can be formed both in treatment of the wastewaters and in annealing of the precipitates. Similarly, ferrite-type spinel can appear at filling of the vacancies in the structure of γ-Fe_2O_3 with crystallographic formula $Fe^{3+}[\square_{1/3}Fe^{3+}_{5/3}]O_4^{2-}$, where $\square$ is the cationic vacancy. In accordance with XRD data, the phases with the γ-Fe_2O_3 structure are formed by thermal treatment of precipitates obtained from the model solutions with

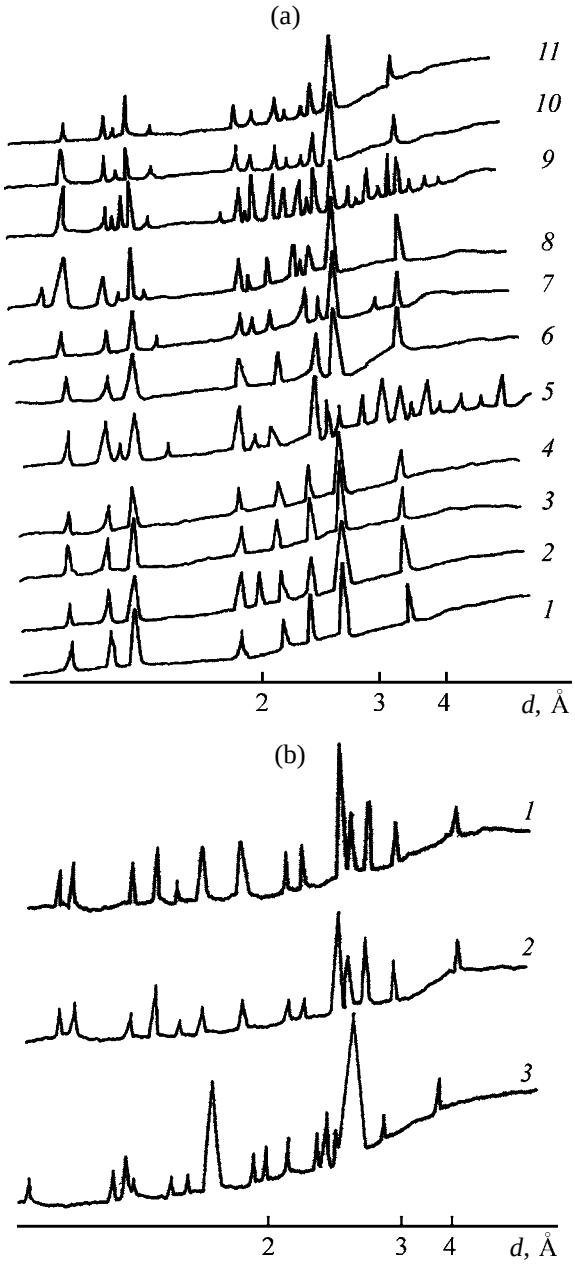

Fig. 2. XRD patterns of the products obtained by thermal treatment of precipitates (a) formed in model solution nos. 1–11 (respective curve numbers) and (b) formed by treatment of wastewaters from the (*1*) Vingis, (*2*) Vilma, and (*3*) Chermet plants. (*d*) Interplanar spacing.

the prevalence of nickel ions. At the same time, chromium ions promote formation of spinel with the magnetite structure. The effect of zinc and copper ions on the composition of the resulting crystalline phases is quite different from that of nickel and chromium. At a content of these metal in model solutions of 200 mg l^{-1}, after annealing we obtained only crystalline α-Fe_2O_3, and no spinels of magnetite of γ-Fe_2O_3

types were found. With increasing content of zinc in the model wastewater, zinc oxide appeared in the annealing products, whereas in the case of copper, the spinel-type crystalline phase was formed.

Similar phase transformations as influenced by the content of heavy metals in the wastewaters were detected in slimes obtained by FFH treatment at the Chermet, Vilma, and Vingis plants. The effect of chromium and nickel on the phase transformations in the course of thermal treatment becomes pronounced only at their high content in the wastewaters. For example, at 14.3% zinc content in the slime from the Vingis plant, the annealing product contains hematite and zinc oxide, whereas heating of the slimes obtained from the Chermet and Vilma plants at 800°C yields α-ferrite and ferrite with magnetite structure, due to high concentrations of nickel and chromium in the wastewaters.

The scanning microscopy data showed that the average particle size in the samples after heating at 800°C is similar to the average particle size of the samples dried at 105°C. For example, the average particle sizes of the precipitate obtained from model solution no. 11 (Table 1) and of the product of its thermal treatment is 0.36–0.37 μm. At the same time, the granulometric composition of the product changes as compared to the initial material at the expense of the finest fraction at thermal treatment.

CONCLUSION

The phase, dispersion, and chemical compositions of slimes obtained by treatment of model solutions and industrial wastewaters using FFH and of their annealing products were studied. Based on these dada, the dependence of the phase composition of the slime treatment products as influenced by the content of chromium, nickel, zinc, and copper was evaluated.

REFERENCES

1. Budilovskis, Yu., *Ekol. Prom–st. Ross.*, 1996, no. 8, pp. 12–15.
2. Voitov, I.V., Zhukov, N.N., Lysukha, N.A., and Sen'-ko, A.S., *Prirodn. Resursy*, 2000, no. 2, pp. 95–99.
3. Eshchenko, L.S. and Kordikov, V.D., *Zh. Prikl. Khim.*, 2000, vol. 73, no. 4, pp. 555.
4. Belarussian Patent 3949.
5. Makarov, V.M., Complex Utilization of Precipitates (Slimes) in the Wastewaters of Electrochemical Production, *Doctoral Dissertation*, Ivanovo, 2001.
6. Zubarev, G.I., *Khim. Prom–st.*, 1999, no. 5, pp. 22–26.
7. Lukachev, Yu.F., Development of a Process for Utilization of Slimes from Electrochemical Production, *Doctoral Dissertation*, Nizhni Novgorod, 1999.
8. Kovalev, V.V., *Intensifikatsiya elektrokhimicheskikh protsessov vodoochistki* (Intensification of Electrochemical Water Treatment Procedures), Chisinau, 1986.
9. Budilovskis, D., Extended Abstracts, *Mezhdunarodnaya nauchno-tekhnicheskaya konferentsiya "Noveishie dostizheniya v oblasti importozameshcheniya v khimicheskoi promyshlennosti i proizvodstve stroitel'nykh materialov"* (Int. Scientific Technical Conf. "Recent Progress in Replacement of Imported Products in Chemical Industry and Production of Building Materials"), Minsk, 2003, pp. 132–135.
10. Belen'kii, E.F. and Riskin, I.V., *Khimiya i tekhnologiya pigmentov* (Chemistry and Technology of Pigments), Leningrad: Khimiya, 1974.

Russian Journal of Applied Chemistry, Vol. 77, No. 9, 2004, pp. 1515–1517. Translated from Zhurnal Prikladnoi Khimii, Vol. 77, No. 9, 2004, pp. 1525–1527.

ENVIRONMENTAL PROBLEMS OF CHEMISTRY AND TECHNOLOGY

Wastewater Treatment with New Activated Charcoals To Remove Butanol

P. A. Krivosheev, L. F. Komarova, M. A. Poletaeva, I. A. Lebedev, and S. S. Lavrinenko

Polzunov Altai State Technical University, Barnaul, Russia

Received January 13, 2004

Abstract—Adsorption of butanol under static conditions on two types of activated charcoals, prepared from birch and a blend of oak and beech, was studied. The adsorption on birch charcoal was carried out under dynamic conditions. The limiting stage of the process was determined. The dependence of the purification efficiency on the fractional composition of activated charcoal and the feed rate of the contaminated solution was studied. The regeneration of birch charcoal with steam and by calcination was performed.

The efficient nature management is largely associated with recovery of individual components from wastes formed in reprocessing of the initial raw materials, in particular, from wastewater. This allows a decrease in consumption of natural resources and in detrimental impact on water objects.

Lower alcohols are widely used in industry and get into wastewater. Butanol, isobutanol, and *tert*-butanol contaminate paint-and-varnish industrial wastewater; ethanol and butanol, wastewater from production of photographic films and ascorbic acid, and also from other branches of organic synthesis and food industry [1].

During the main processes, alcohols form mixtures with water and should be separated before water recycling or discharge. In traditional processes, such as extraction or special distillation procedures (azeotropic, extractive, etc.), as a rule, alcohols are recovered from aqueous solutions at their high content and water purification is incomplete. Therefore, it is necessary to use additional purification procedures, one of which is adsorption [2, 3].

High cost of sorbents often hampers wide industrial use of adsorption. Therefore, it would be appropriate to use adsorbents produced from industrial wastes, such as activated charcoals prepared from a blend of oak and beech or from birch, produced by the ANITIM Joint-Stock Company.[1]

Previous studies [4] showed the advantages of birch activated charcoal. It has lower moisture content, greater pore volume, and high sorption capacity with respect to iodine. However, further experiments showed that birch charcoal has lower mechanical strength than charcoal produced from a blend of oak and beech. First we studied recovery of butanol from water on the above nonfractionated activated charcoals.

As a result of studying adsorption under static conditions, we obtained isotherms of adsorption of butanol on activated charcoals (Fig. 1). As seen from Fig. 1, the sorption curves in the range of low concentrations of butanol (less than 0.5 wt %) coincide, but with increasing concentration of butanol in water the sorption capacity of birch charcoal becomes significantly greater than that of mixed charcoal. Thus, at the equilibrium concentration of alcohol of 7.5 wt %, the sorption capacity of birch charcoal is 0.84 g g^{-1}, which is greater than that of mixed charcoal by a factor of 2 (0.42 g g^{-1}).

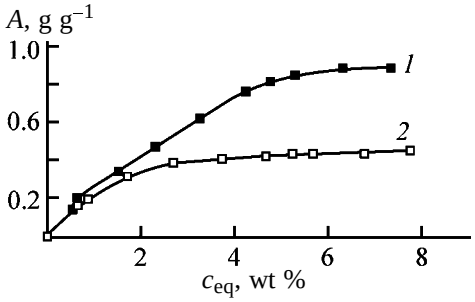

Fig. 1. Isotherms of adsorption of butanol on activated charcoals. (*A*) Adsorption capacity and (c_{eq}) equilibrium concentration. Charcoal: (*1*) birch and (*2*) produced from a blend of oak and beech.

[1] On the base of the Altai Research Institute of Precision Mechanical Engineering, Barnaul.

1070-4272/04/7709-1515 © 2004 MAIK "Nauka/Interperiodica"

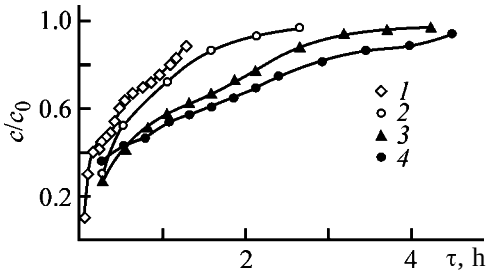

Fig. 2. Kinetics of adsorption under dynamic conditions. (c, c_0) Current and initial concentrations, respectively; (τ) time. Concentration of butanol in the initial solution (mg l^{-1}): (*1*) 4000, (*2*) 1500, (*3*) 800, and (*4*) 600.

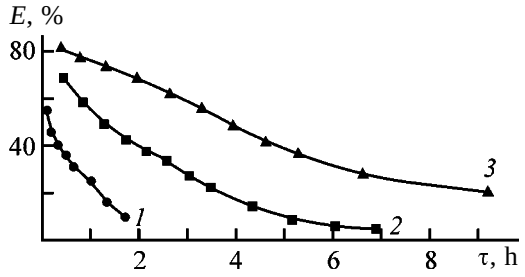

Fig. 3. Purification efficiency E as a function of time τ at various feed velocities of contaminated solution at c_0 = 800 mg l^{-1}. Feed velocity, m h^{-1}: (*1*) 4, (*2*) 2, and (*3*) 1.

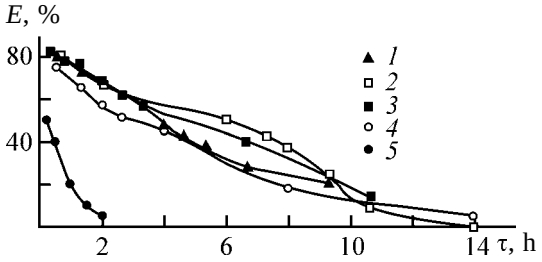

Fig. 4. Purification efficiency E as a function of time τ with charcoal of various fractional composition at c_0 = 800 mg l^{-1}. (*1*) Nonfractionated charcoal; fractional composition, d_{eff} (mm): (*2*) <1.5, (*3*) 1.5–3, (*4*) 3–6, and (*5*) >6.

We studied the dynamics and kinetics of adsorption for only birch charcoal, since studying the main characteristics of charcoals and sorption isotherms revealed apparent advantages of birch charcoal. The kinetic data (Fig. 2) show that the highest purification efficiency, i.e., the lowest ratio of the butanol concentration at the outlet from the adsorber c to its initial concentration c_0 is reached at low initial concentrations of butanol. With increasing concentration of butanol, the c/c_0 ratio increases and the purification efficiency decreases.

We studied the influence of the solution feed velocity on adsorption. We found that the purification efficiency noticeably increases with decreasing feed velocity of the contaminated solution, irrespective of the initial concentration of alcohol. The dependence of the purification efficiency on the feed velocity of the contaminated solution (Fig. 3) shows that, after 2 h of operation of activated charcoal at a feed velocity of the contaminated solution of 1 m h^{-1}, the purification efficiency is approximately 70%; at a feed velocity of 2 m h^{-1}, approximately 40%; and at a feed velocity of 4 m h^{-1}, 4–5%.

As a rule, in adsorption purification the charcoal with a definite fractional composition is used [5]; therefore, birch charcoal was subjected to sizing. The study of the dependences of the purification efficiency on time and fractional composition showed that the highest purification efficiency is reached with the fraction with d_{eff} < 1.5 mm (Fig. 4). However, this fraction has very high hydrodynamic resistance, which makes it unsuitable for adsorption purification. As for the other fractions, the purification efficiency decreases in the order: d_{eff} = 1.5–3 mm, nonfractionated charcoal, d_{eff} = 3–6 mm, and d_{eff} > 6 mm. The increase in the purification efficiency with decreasing grain size of adsorbent can be explained by the limiting role of the inner diffusion [6].

The dependence of the hydraulic resistance of the adsorption bed (lost head expressed in kPa) on the fractional composition is shown in Fig. 5. It is seen that the fraction with d_{eff} = 3–6 mm has the lowest hydraulic resistance, and the fraction with d_{eff} < 1.5 mm, the highest hydraulic resistance. In this case, with increasing velocity of solution filtration through the sorbent bed variation of resistance is insignificant for the coarsest fraction and is maximal for the finest fraction.

Purification on activated charcoals necessarily involves regeneration of the adsorbent with the aim to recover the adsorbed component (in regenerative purification) and reuse the sorbent [6]. Initially the regeneration was carried out by steam. The influence of regenerate volume on the alcohol concentration in the regenerate at various alcohol concentrations in the solution to be purified was established. The content of alcohol in the regenerate increases by a factor of no more than 3 in comparison with the initial solution, and the alcohol concentration in the regenerate decreases with increasing volume of steam condensate.

Regeneration with steam requires high power consumption for production of steam, and the alcohol concentration in the regenerate does not exceed 2 g l^{-1}, which makes it unsuitable for further use. We also attempted to regenerate activated charcoal by calcina-

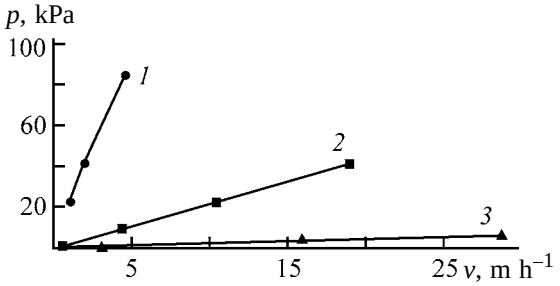

Fig. 5. Hydraulic resistance of charcoal bed p (H = 35 cm) as a function of solution velocity v for various fractional compositions. Fractional composition d_{eff} (mm): (*1*) <1.5, (*2*) 1.5–3, and (*3*) 3–6.

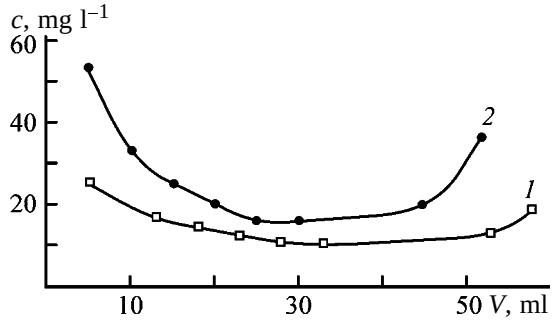

Fig. 6. Alcohol concentration c in the regenerate as a function of regenerate volume V in thermal regeneration of charcoal. c_0 (mg l^{-1}): (*1*) 800 and (*2*) 1500.

tion. The results of thermal regeneration of activated charcoal at 100–300°C at various initial concentrations of alcohol are presented in Fig. 6. For c_0 = 1500 mg l^{-1}, the alcohol concentration in the regenerate reached 53 g l^{-1}, and for c_0 = 800 mg l^{-1}, 25 g l^{-1}. The highest content of alcohol in the regenerate is reached at the beginning of charcoal calcination and at the process completion. This can be explained by the fact that, at the beginning of regeneration, water and alcohol molecules weakly bonded by sorption forces vaporize at approximately 100°C. By process completion at 300°C, molecules tightly bonded by adsorption interactions are released.

To compare the adsorption capacities of freshly prepared and regenerated charcoals, we studied adsorption of butanol on regenerated birch charcoal. The adsorption powers of freshly prepared and regenerated birch charcoals are shown in Fig. 6. As seen, the adsorption power of charcoal does not noticeably decrease upon regeneration.

CONCLUSIONS

(1) At equilibrium concentration of alcohol of 7.5 wt % the sorption capacity of birch charcoal is 0.84 g g^{-1}, which is greater by a factor of 2 than that of the charcoal prepared from a blend of oak and beech (0.42 g g^{-1}).

(2) The dependence of the purification efficiency on the solution feed velocity was elucidated: with increasing solution feed velocity from 1 to 4 m h^{-1}, the purification efficiency decreases from 70 to 4–5%.

(3) The purification efficiency decreases with increasing equivalent diameter of activated charcoal grains from d_{eff} < 1.5 to d_{eff} > 6 mm. The limiting stage of adsorption is inner diffusion.

(4) At 100–300°C, the alcohol concentration in the regenerate reaches 53 g l^{-1} at c_0 = 1500 mg l^{-1} and 25 g l^{-1} at c_0 = 800 mg l^{-1}. In this case, the adsorption characteristics of charcoal in its subsequent use do not appreciably vary.

REFERENCES

1. *Tekhnologiya spirta* (Process of Alcohol Production), Yarovenko, V.L., Ed., Moscow: Kolos, 1999.
2. Komarova, L.F. and Kormina, L.A., *Inzhenernye metody zashchity okruzhayushchei sredy: Tekhnika zashchity atmosfery i gidrosfery ot promyshlennykh zagryaznenii* (Engineering Approach to Environmental Protection: Protection of Atmosphere and Hydrosphere from Industrial Pollution), Barnaul, 2000.
3. Smirnov, A.D., *Sorbtsionnaya tekhnologiya ochstki vody* (Sorption Procedure of Water Treatment), Leningrad: Khimiya, 1982.
4. Blinov, E.M., Komarova, L.F., Polishchuk, S.A., *et al.*, *Zh. Prikl. Khim.*, 2002, vol. 75, no. 7, pp. 1215–1217.
5. *Adsorption from Solution at the Solid/Liquid Interface*, Parfitt, G.D. and Rochester, C.H., Eds., London: Academic, 1983.
6. Rodionov, A.I., Klushin, V.N., and Torocheshnikov, N.S., *Tekhnika zashchity okruzhayushchei sredy* (Technique of Environmental Protection), Moscow: Khimiya, 1989, 2nd ed.

Russian Journal of Applied Chemistry, Vol. 77, No. 9, 2004, pp. 1518–1522. Translated from Zhurnal Prikladnoi Khimii, Vol. 77, No. 9, 2004, pp. 1528–1532.

ORGANIC SYNTHESIS AND INDUSTRIAL ORGANIC CHEMISTRY

Thermolysis of Hexachlorocyclohexane in a Flow-Through Packed Reactor

A. M. Kut'in, N. V. Gubanova, A. D. Zorin, V. F. Zanozina, M. L. Markova, I. A. Suprunova, and E. A. Bykova

Lobachevsky State University, Nizhni Novgorod, Russia

Received March 12, 2004

Abstract—Thermolysis of hexachlorocyclohexane in a flow-through packed system in an inert gas atmosphere was studied.

The aim of the study is to analyze experimentally the thermolysis of hexachlorocyclohexane in a laboratory flow-through packed reactor, elucidate the mechanism of the process, and determine its kinetic parameters using a macrokinetic model that allows modification of the process from a laboratory reactor to an industrial installation.

EXPERIMENTAL

The thermal decomposition was studied under dynamic conditions by passing hexachlorocyclohexane through a heated U-shaped reactor made of Pyrex glass. A glass packing with a grain size of 0.4–0.63 mm served to increase the reaction surface area. The study was performed on a Tsvet-530 chromatograph. A heated reactor in a thermally insulated jacket was placed in the thermostat of the chromatograph, with the reactor inlet connected directly to the evaporator. Four packed reactors with lengths of 0.107, 0.215, 0.322, and 0.427 m were used.

The temperature mode of the reactor was controlled with a quartz furnace. The temperature was set and maintained in the range from 250 to 500°C, with a step of 50°C, using a Proterm-100 microprocessor temperature controller. The temperature fluctuated around the preset value in the course of thermostating within ±1°C.

A sample introduced was mixed and diluted with an inert gas (N_2) in the evaporator of the chromatograph. The carrier gas ensured that the reaction mixture flowed within the heated zone of the reactor in the plug mode. In the experimental regard, the study performed is similar to a pulsed version of the chromatographic method.

The results of a chromatographic–mass-spectrometric analysis (MD800/GC8060 instrument, HP 5MS column 60 m long and 0.32 mm in diameter) were used to identify the composition of products formed in thermolysis of hexachlorocyclohexane that was performed preliminarily under static conditions. Five components were recorded under the chosen chromatographic conditions: 1,2,4-trichlorobenzene, 1,2,4,5-tetrachlorobenzene, 1,2,3,4,5-pentachlorocyclohexene, and two of the possible eight stereoisomers of hexachlorocyclohexane, α-hexachlorocyclohexane and γ-hexachlorocyclohexane.

The starting substances and the thermolysis products were analyzed under the following chromatographic conditions: 100 × 0.4-cm glass column packed with Inerton AW-DMCS with grain size of 0.25–0.315 mm (impregnated with 5% SE-30); column temperature in the temperature-programmed mode varied from 100 (2 min) to 210°C (5 min) at a rate of 10 deg min^{-1}; temperature of the evaporator and detector (FID) 200°C; flow rate of the carrier gas (nitrogen) in the reactor and in the column 20 ml min^{-1}; flow rates of hydrogen and air equal to 26 and 300 ml min^{-1}, respectively; motion velocity of the chart paper 600 mm h^{-1}. The substance was introduced in the form of a melt on the needle of a microsyringe directly into the evaporator.

To construct a calibration dependence for the substrate, hexachlorocyclohexane solutions in acetone were prepared. The calibration was made under conditions similar to those in which products formed in thermal decomposition of hexachlorocyclohexane were analyzed, with the volume of a sample introduced equal to 1 μl.

The experimental dependences of the composition (mole fraction) of hexachlorocyclohexane and conver-

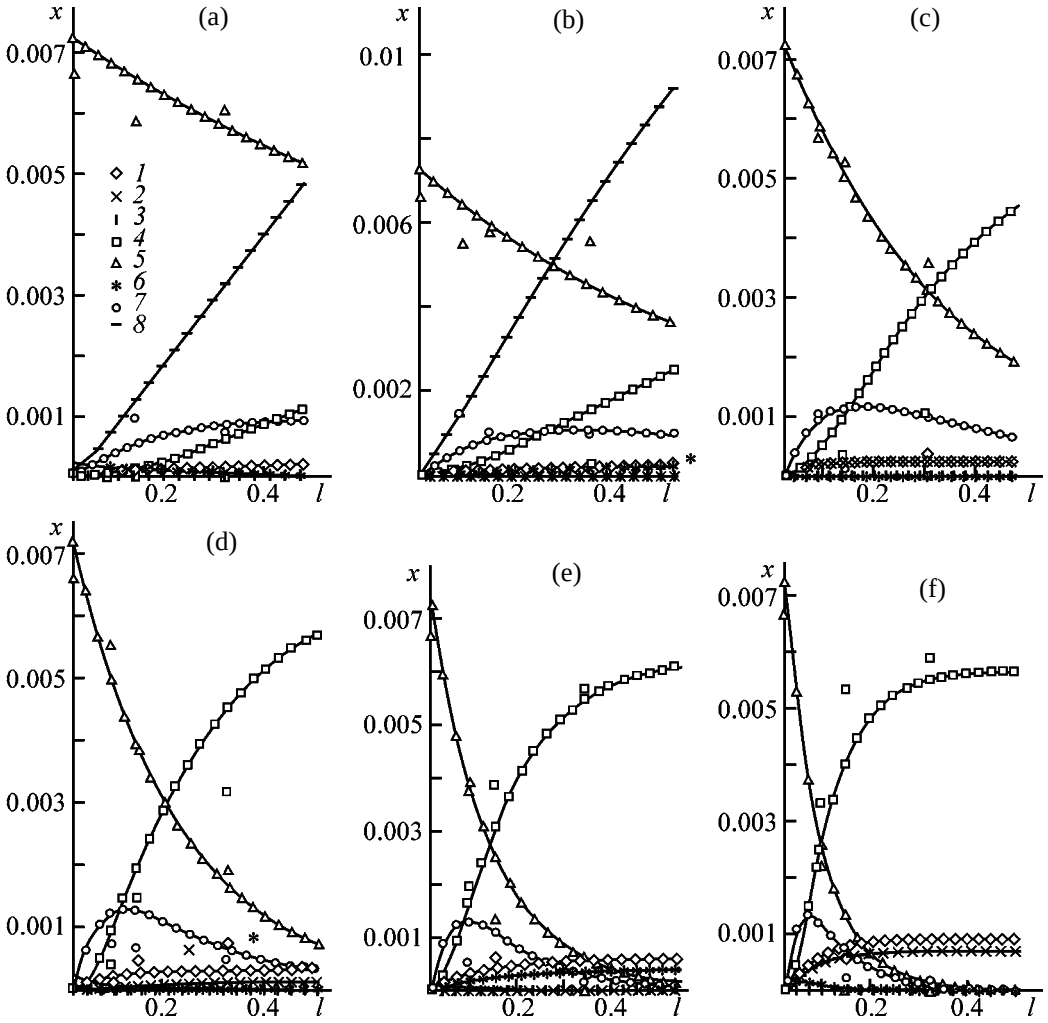

Fig. 1. Mole fractions x of products formed in thermolysis of hexachlorocyclohexane along the reactor length l at (a) 250, (b) 300, (c) 350, (d) 400, (e) 450, and (f) 500°C. Calculated values, symbols connected by lines; experimental data, the corresponding open symbols. (*1*) 1,2,4,5-$C_6H_2Cl_4$, (*2*) 1,1,2,3,4,5,6-$C_6H_5Cl_7$, (*3*) 1,2,3,4,5-$C_6H_7Cl_5$, (*4*) 1,2,4-$C_6H_3Cl_3$, (*5*) $C_6H_6Cl_6$, (*6*) 1,2- and 1,4-$C_6H_4Cl_2$, and (*7*) $C_6H_5Cl_5$; (*8*) HCl.

sion products on the reactor length are shown in Fig. 1.

For a steady-state mode of operation of a plug reactor, the material balance for ith component along a reactor length element dz can be represented as [1, 2]

$$d\dot{n}_i/dz = S_a\tilde{r}_i, \qquad (1)$$

where S_a is the surface area of the packing and reactor walls per unit reactor length; $\dot{n}_i$, component flow rate; and $\tilde{r}_i$, component velocities for the overall reaction.

The kinetic scheme of the process is constituted by J concurrent reactions:

$$0 = \sum_{i=1}^{I} \nu_{ji} A_i, \qquad 1 \le j \le J, \qquad (2)$$

where the stoichiometric coefficients of ith component in jth reaction $\nu_{ji} < 0$ for reactants and $\nu_{ji} > 0$ for reaction product, and I is number of components (substances) appearing in the equations of the chemical reactions [Eqs. (2)].

Instead of the component flow rates $\dot{n}_i$ (mol s^{-1}), reaction flow variables $\dot{\xi}_j$ (mol s^{-1}), reaction flow rates, can be used. In this case, the component flow rates $\dot{n}_i$ are expressed in terms of the reaction flow rates as

$$\dot{n}_i = \dot{n}_{0i} + \sum_{j=1}^{J} \nu_{ji}\dot{\xi}_j, \qquad 1 \le i \le I, \qquad (3)$$

where $\dot{n}_{0i}$ are the component flow rates at the reactor inlet ($z = 0$).

The component rates $\tilde{r}_i$ can be expressed in term of the reaction rates $\tilde{R}_j$ as

$$\tilde{r}_i = \sum_{j=1}^{J} \nu_{ji}\tilde{R}_j, \qquad 1 \le i \le I. \tag{4}$$

Substitution of (3), (4) into Eq. (1) gives another, equivalent to (1), form of material balance equations for J independent reactions:

$$d\dot{\xi}_j/dz = S_a\tilde{R}_j, \quad 1 \le j \le J, \tag{5}$$

The change in enthalpy of the components in the reactions, which is due to the flux of heat across the reactor walls along its length element dz [expression (6)] gives an additional, with respect to relation (5), differential equation (7) for the temperature of the reaction mixture:

$$\sum_{i=1}^{I} d(\dot{n}_i\bar{H}_i) = \alpha S_S(T_S - T)dz, \tag{6}$$

$$\frac{dT}{dz} = \frac{\alpha S_S(T_S - T) - S_a\sum_i \tilde{r}_i\bar{H}_i}{\sum_i \dot{n}_i C_{pi}}, \tag{7}$$

where $\bar{H}_i$ is the molar enthalpy of ith component; α, heat-transfer coefficient; S_S, lateral heat-exchange surface area per unit reactor length; T_S, temperature of the heat-carrying agent in the jacket; and C_{pi}, molar specific heats of the components.

In this case, the sum over the components in the numerator of (7) can be expressed in terms of the rates $\bar{R}_j$ and enthalpies $\Delta H_j = \sum_{i=1}^{I} \nu_{ji}\bar{H}_i$ of the reactions:

$$\sum_i \tilde{r}_i\bar{H}_i = \sum_j \tilde{R}_j\Delta H_j. \tag{8}$$

An equation similar to (7) describes the variation of the temperature of the heat-carrying agent in the temperature-control jacket:

$$\frac{dT}{dz} = \frac{\alpha S_S(T_S - T)}{\dot{n}_S C_{pS}}, \tag{9}$$

where the flow rate of the heat-carrying agent $\dot{n}_S > 0$ if its flow direction coincides with that of the flow in the reactor (forward flow) and $\dot{n}_S < 0$ otherwise (counterflow).

Additional expressions that relate and define the quantities used have, as functions of z, the form

$$y_i = \dot{n}_i/\dot{n}, \qquad \dot{n} = \Sigma\dot{n}_i, \tag{10}$$

$$\dot{V} = \dot{n}_i RT/\tilde{P}P^0, \qquad v = \dot{V}/S, \tag{11}$$

$$c_i = \dot{n}_i\dot{V}, \tag{12}$$

$$\tilde{P}_i = c_i RT/P^0, \qquad \tilde{P} = \sum_i \tilde{P}_i, \tag{13}$$

where y_i is the mole fraction; $\dot{n}_i$, total gas flow rate in the second of formulas (1); $\dot{V}$ and v, space velocity and linear flow velocity [formulas (11)]; S, cross-sectional area of the reactor; c_i, component concentrations in the flow; $\tilde{P}_i$ and $\tilde{P}$, partial and total pressures (atm) (P^0 = 101 325 Pa).

Pressure can also be a sought-for function of the coordinate, if the hydrodynamic resistance is taken into account. However, the pressure is considered in this study to be constant along the reactor.

The system of differential equations is supplemented with boundary conditions at the reactor inlet (z = 0)

$$T(0) = T_0, \quad T_S(0) = T_{S0} \quad \text{(for the forward flow)}, \qquad \dot{\xi}(0) = 0 \ (1 \le j \le J). \tag{14}$$

The coordinate at the outlet is equal to the reactor length ($z = L$).

It is noteworthy that, when solving the system numerically, its composition can be determined both from Eqs. (1) and from Eqs. (5). The software implementation of the method is preceded by a procedure in which a change to dimensionless variables is performed. The system of ordinary nonlinear differential equations was solved using the fourth-order Runge–Kutta method with automatic choice of the step interval.

In terms of the given model, a heterogeneous chemical process is considered to be defined if its following characteristics are defined and prescribed: kinetic scheme (2) of chemical reactions at the surface; block of thermodynamic data represented by quantities X_j, which determine the direction and extent of jth reaction:

$$\ln X_j = \Delta_r G/RT = \Delta_r g = \sum_i \nu_{ji}[g_i^0(T,P) + \ln x_i]$$

$$= -\ln K_j^{(x)} + \sum_i \nu_{ji}\ln x_i, \tag{15}$$

$$g_i^0(T,P) = g_i^0(T) + \delta_i \ln \tilde{P}, \quad (16)$$

where x_i is the mole fraction of ith component, and g_i^0 are the standard reduced chemical potentials of the components.

The chain of equalities (17), derived from (15) with account of expressions that relate the equilibrium constants, demonstrates the invariance of the quantities X_j expressed on different concentration scales:

$$X_j = \exp \Delta_r g_j = \prod_i x_i^{\nu_{ij}} / K_j^{(x)} = \prod_i \tilde{P}_i^{\nu_{ij}} / K_j^0 = \prod_i c_i^{\nu_{ij}} / K_j^{(c)}, \quad (17)$$

$$K_j^{(x)} = K_j^0 (\tilde{P})^{-\Delta\nu_j}, \qquad K_j^{(c)} = K_j^0 (RT/P^0)^{-\Delta\nu_j}, \quad (18)$$

where $\Delta\nu_j = \sum_i \nu_{ij}$ is the change in the number of moles in jth reaction, and $K_j^0 = \exp[-\sum g_i^0(T)]$ is the standard equilibrium constant.

The validity of Eqs. (17) and (18) is confirmed using the relations between the partial pressures $\tilde{P}_i$ (atm) of the components, mole fractions x_i, and volume concentrations c_i (mol m^{-3}) of ith components: $\tilde{P}_i = x_i \tilde{P} = c_i RT/P_0$.

The diffusion-kinetic model used in the study is based on the known law of summation of the diffusion and kinetic resistances [1]:

$$\frac{1}{\beta_{ij}^*} = \frac{1}{\beta_{ij}} + \frac{1}{k_j}, \qquad k_j = A_j \exp(-E_j/RT). \quad (19)$$

The effective coefficient β_{ij}^* of mass transfer of ith component to the reaction surface is determined by the smallest of the following two quantities: β_{ij}, the initial diffusion mass-transfer (mass-supply) coefficient for ith component, and k_j, the coefficient describing the "efficiency of a chemical event of transfer" of a component from the category of reactants to that of products of jth reaction. In the latter case, the actual rate constant k_j of the heterogeneous reaction is represented in expression (19) by an Arrhenius term with an activation energy E_j and a pre-exponential factor A_j, which also determines the dimension of the rate constant of the heterogeneous reaction (m s^{-1}).

The constant A_j can be conveniently redefined and expressed in terms of the known, and more illustrative parameter T_j^*, the temperature at which the reaction passes from the kinetic to the diffusion control. In doing so, a natural condition of its definition is the equality $k_j = \beta_{ij}$ of the diffusion and kinetic components in expression (19). Substitution of the formula $k_j = \beta_{ij}(T_j^*) \exp[(E_j/R)(1/T_j^* - 1/T)]$, which follows from this equality, into the first of expressions (19) yields, after obvious rearrangements, the relation

$$\frac{1}{\beta_{ij}^*} = \frac{1}{\beta_{ij}} \left\{ 1 + \frac{\beta_{ij}(T)}{\beta_{ij}(T_j^*)} \exp[-E_j R^{-1}(1/T - 1/T_j^*)] \right\}. \quad (20)$$

Neglecting the considerably weaker temperature dependence of the diffusion mass-transfer coefficient (which is commonly proportional to $T^{1/2}$), compared to the exponential dependence of the co-factor containing E_j, gives the following relations for the effective mass-transfer coefficient:

$$\beta_{ij}^* = \beta_{ij} w_j, \quad w_j = \frac{1}{1 + \exp[-E_j R^{-1}(1/T - 1/T_j^*)]}. \quad (21)$$

The resulting expression for the rate of jth heterogeneous reaction [2]

$$\tilde{R}_j = [(1 - X_j) w_j][\sum_i \nu_{ij} (\beta_{ij} c_i)^{-1} \sum_i \nu_{ij} + X_j \sum_i{}' \nu_{ij} (\beta_{ij} c_i)^{-1} \sum_i{}' \nu_{ij}]^{-1} \quad (22)$$

contains a factor $0 < w_j < 1$, which has the form of a switch that "turns on" the diffusion-controlled mode of the reaction at temperatures $T > T_j^*$ and "switches" it into the kinetically controlled mode at $T < T_j^*$. The range of temperatures close to the transition temperature T_j^* corresponds to a mixed diffusion-kinetic control, and at $T = T_j^*$ the shares of each of the limiting modes are equal ($w_j = 0.5$). The simultaneously high activation energy E_j (which exceeds its estimate based on bond dissociation energies) and T_j^* (above the temperature range under study) give $w_j \to 0$, which indicates that this equation is to be excluded from the kinetic scheme. Thus, the trial, but insignificant within the experimental error, equations were rejected in the stage of experimental data processing.

The information data block for solving the macrokinetic problem included the following factors: standard thermodynamic functions [3], which were evaluated for unstudied substances by the group contribution method [4]; transfer coefficients (viscosity, heat conductivity) calculated using the procedures described in [4]; and heat- and mass-transfer coefficients in the form of criterial relations for a grainy bed from [5–7].

Raw experimental data (areas of chromatographic peaks), converted to mole fractions, were subjected to a smoothing approximation processing. The kinetic

Activation energies E_j and characteristic temperatures T_j^* [formulas (19)–(21)] of the reactions that constitute the kinetic scheme [Eqs. (2)] of hexachlorocyclohexane thermolysis

Reaction no. (j)	Reaction equation	T_j^*, K	E_j, J mol^{-1}
1	$C_6H_6Cl_6 \rightleftarrows C_6H_5Cl_5 + HCl$	10 257.5	35 802.6
2	$C_6H_5Cl_5 \rightleftarrows C_6H_3Cl_3 + 2HCl$	16 118.2	28 240
3	$2C_6H_6Cl_6 \rightleftarrows C_6H_7Cl_5 + C_6H_5Cl_7$	822.729	151 652
4	$C_6H_6Cl_7 \rightleftarrows C_6H_2Cl_4 + 3HCl$	2136.06	34 282.2
5	$C_6H_7Cl_5 \rightleftarrows C_6H_4Cl_2 + 3HCl$	–	–

parameters of the reactions were found by solving the inverse problem (see table). The average relative deviation of the calculated curves from the experimental values was 5.7%.

In the mathematical processing, the concentrations of by-product components: 1,2,4,5-tetrachlorobenzene, 1,2-dichlorobenzene, and 1,4-dichlorobenzene, were taken into account in addition to the data for the main substances (loss of hexachlorocyclohexane and increase in the concentration of 1,2,4-trichlorobenzene). However, the available data gave no way of understanding in detail the mechanism of their formation. A numerical solution made it possible to specify the parameters of the corresponding overall reaction nos. 3–5, with the last of these occurring under purely diffusion control.

The kinetic scheme of thermal decomposition of hexachlorocyclohexane is oriented toward the observable products and comprises a set of overall reactions that only indirectly take into account a number of possible intermediate species, including radicals. For example, reaction no. 2, in which 1,2,4-trichlorobenzene is formed, actually includes two successive stages. As already mentioned, this refers to an even greater extent to the compound reaction nos. 4 and 5.

In the temperature range studied, products of deeper stages of thermolysis of hexachlorocyclohexane, which include breakdown of the benzene ring, were not observed, and, therefore, they are not reflected in the kinetic scheme.

CONCLUSIONS

(1) Thermolysis of hexachlorocyclohexane in its conversion into trichlorobenzene occurs by the commonly accepted mechanism of successive elimination of HCl in two stages, with an intermediate, pentachlorocyclohexene, formed in the first of these (which is rate-limiting).

(2) The formation of by-products, 1,2,4,5-tetrachlorobenzene, 1,2-dichlorobenzene, and 1,4-dichlorobenzene, is due to the concurrent bimolecular reaction of exchange of hydrogen and chlorine atoms in the substrate; dilution of the system with an inert component must make higher the yield of 1,2,4-trichlorobenzene.

(3) The mechanism of the process, established in the study, and the obtained kinetic parameters of the occurring reactions, which account for the properties of the packing and the heat-and-mass-exchange characteristics of the process, enable a scaling transition from a laboratory reactor to an industrial installation for processing of outdated and prohibited pesticides based on hexachlorocyclohexane.

REFERENCES

1. Frank-Kamenetskii, D.A., *Diffuziya i teploperedacha v khimicheskoi kinetike* (Diffusion and Heat Transfer in Chemical Kinetics), Moscow: Nauka, 1987.
2. Kut'in, A.M., Pyadushkin, D.V., Zorin, A.D., and Katsnel'son, K.M., *Matem. Model. Optim. Upravl.: Vestn. Nizhegor. Gos. Univ.*, 1998, no. 1(18), pp. 96–104.
3. *Termodinamicheskie svoistva individual'nykh veshchestv: Spravochnik* (Thermodynamic Properties of Individual Substances: Reference Book), Gurvich, L.V., Voits, I.V., Medvedev, V.A., *et al.*, Eds., Moscow: Khimiya, 1982.
4. Reid, R.G., Prausnitz, J.M., and Sherwood, T.K., *The Properties of Gases and Liquids*, New York: McGraw-Hill, 1977.
5. Kutateladze, S.S., *Teploperedacha i gidrodinamicheskoe soprotivlenie: Spravochnoe posobie* (Heat Transfer and Hydrodynamic Resistance: Reference Book), Moscow: Energoizdat, 1990.
6. Gol'dshtik, M.A., *Protsessy perenosa v zernistom sloe* (Transfer Processes in a Grainy Bed), Novosibirsk: Inst. Teplofiz. Sib. Otd. Akad. Nauk SSSR, 1984.
7. Bezobrazov, Yu.N. and Molchanov, A.V., *Geksakhloran* (Hexachlorocyclohexane), Moscow: Goskhimizdat, 1949.

Russian Journal of Applied Chemistry, Vol. 77, No. 9, 2004, pp. 1523–1527. Translated from Zhurnal Prikladnoi Khimii, Vol. 77, No. 9, 2004, pp. 1533–1538.

ORGANIC SYNTHESIS AND INDUSTRIAL ORGANIC CHEMISTRY

Reactivity of Congeners of Sovol Technical Mixture of Polychlorinated Biphenyls toward Sodium Methoxide

O. N. Zabelina, T. I. Gorbunova, M. G. Pervova, V. E. Kirichenko, A. Ya. Zapevalov, V. I. Saloutin, and O. N. Chupakhin

Institute of Organic Synthesis, Ural Division, Russian Academy of Sciences, Yekaterinburg, Russia

Received April 29, 2004

Abstract—The reaction of Sovol technical mixture of polychlorobiphenyls with sodium methoxide in bipolar aprotic solvents was studied. The reactivity of polychlorobiphenyls was evaluated using gas chromatography and gas chromatography–mass spectrometry.

With adoption in 2001 of the Stockholm Convention on Persistent Organic Pollutants, which prohibited the use of technical polychlorobiphenyls (PCBs), the number of papers concerning these pollutants increased. Primary attention is given to detection of PCBs in various natural objects and biological media, determination of pollution levels, and elucidation of pathways of PCB transformations and metabolism in living bodies. Considerably less attention was given to development of new procedures for rendering PCBs harmless, which is largely due to wide use of efficient methods involving complete breakdown of PCBs (e.g., thermolysis). Other possible procedures for PCB treatment are often considered to be of low promise, either because of incomplete conversion or because of possible formation of more toxic polychlorodibenzofurans and polychlorodibenzodioxins in side reactions.

The major drawback of alternative pathways of rendering PCBs harmless is that it is impossible to predict reliably the behavior of particular PCB congeners in the processes, since technical PCBs contain up to 50–70 congeners differing in the number of chlorine atoms and their mutual positions in aromatic structures [1, 2].

Previous studies of reagent (chemical) processing of PCBs showed that reactions of PCBs with various sodium or potassium alcoholates formally result in substitution of two aryl-bonded chlorine atoms by alkoxy groups [3]. These conclusions were confirmed by elemental analysis, IR spectroscopy, and some data on the solubility of the resulting derivatives. The reactivity of PCB congeners present in the mixture was not discussed.

In this context, our goal was to determine the chemical composition of mixtures obtained by reaction of Sovol PCB mixture with sodium methoxide, to evaluate the reactivity of PCB congeners in this mixture, and to find conditions ensuring the most complete conversion of the starting compounds.

Previously we determined the composition and content of PCB congeners in Sovol and identified more than 30 components; the total contents of tetra-, penta-, and hexachlorobiphenyls were found to be about 20, more than 50, and about 20%, respectively; minor amounts of trichloro- and heptachlorobiphenyls were also detected [2]. A typical chromatogram of Sovol is shown in Fig. 1. The IUPAC designations of all the possible PCB congeners are given in [1]; the components of Sovol are listed in Table 1.

Published data on nucleophilic substitutions in PCB aromatic systems **I** are virtually lacking. The reaction of technical PCB mixture **I** with sodium methoxide can formally be described by the scheme

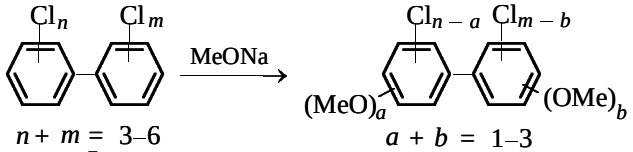

$n + m = 3–6$ (**I**) $\quad a + b = 1–3$ (**II**)

Our first goal was to find the optimal conditions for nucleophilic substitution of aryl-bonded chlorine atoms by methoxy group: solvent, reactant ratio, temperature, and time.

Mixtures **II** obtained from the reactions were analyzed by capillary gas–liquid chromatography with flame-ionization (GLC–FID) and mass-spectrometric (GLC–MSD) detectors. The trends in variation of the

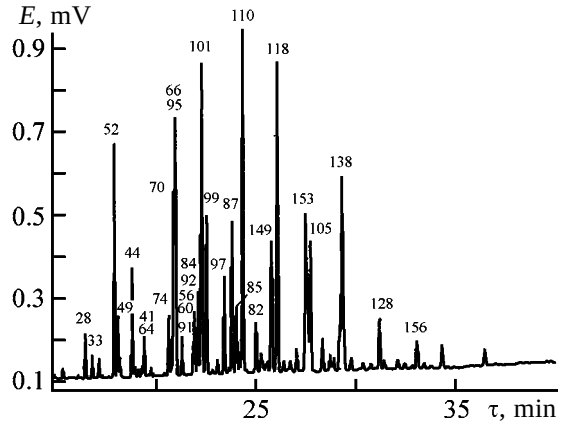

Fig. 1. Chromatogram of Sovol technical mixture of polychlorinated biphenyls: (*E*) potential and (τ) time; the same for Figs. 2.

retention times and the relative intensities of peaks were evaluated under optimal conditions of GLC–FID analysis.

EXPERIMENTAL

The reaction progress was monitored with a Shimadzu GC-17A gas chromatograph [flame-ionization detector; MDN 5S (30 000 × 0.25 mm) quartz capillary column coated with 0.25 μm of methylphenylsilicone stationary phase containing 5% grafted phenyl groups; carrier gas nitrogen; flow division ratio 1 : 30; column temperature: 100°C, 1 min; heating to 200°C, 10 deg min^{-1}; heating to 300°C, 2 deg min^{-1}; vaporizer temperature 250°C; detector temperature 280°C; solvent toluene; sample volume 0.2 μl].

Table 1. Major congeners of Sovol technical mixture of polychlorinated biphenyls

IUPAC no.	Positions of Cl atoms	IUPAC no.	Positions of Cl atoms
33	2', 3, 4	101	2, 2', 4, 5, 5'
28	2, 4, 4'	99	2, 2', 4, 4', 5
52	2, 2', 5, 5'	97	2, 2', 3', 4, 5
49	2, 2', 4, 5'	87	2, 2', 3, 4, 5'
47	2, 2', 4, 4'	85	2, 2', 3, 4, 4'
44	2, 2', 3, 5'	110	2, 3, 3', 4', 6
41	2, 2', 3, 4	82	2, 2', 3, 3', 4
64	2, 3, 4', 6	149	2, 2', 3, 4', 5', 6
74	2, 4, 4', 5	118	2, 3', 4, 4', 5
70	2, 3', 4', 5	153	2, 2', 4, 4', 5, 5'
66	2, 3', 4, 4'	132	2, 2', 3, 3', 4, 6'
95	2, 2', 3, 5', 6	105	2, 3, 3', 4, 4'
91	2, 2', 3, 4', 6	138	2, 2', 3, 4, 4', 5'
56	2, 3, 3', 4'	128	2, 2', 3, 3', 4, 4'
60	2, 3, 4, 4'	156	2, 3, 3', 4, 4', 5

The compounds were identified with a Fisons gas chromatograph–mass spectrometer [MD 800 detector; HP-5 (25 000 × 0.25 mm) quartz capillary column coated with 0.25 μm of stationary phase; carrier gas helium; flow division ratio 1 : 20; column temperature: 100°C, 1 min; heating to 200°C, 10 deg min^{-1}; heating to 300°C, 2 deg min^{-1}; vaporizer temperature 250°C; ionization by electron impact, 70 eV; scanning rate 1 mass spectrum per second; scanning of total ion current in the range 20–700 amu.

Quantitative calculations were performed by the internal normalization method.

Reaction of PCB I with sodium methoxide. A round-bottomed flask equipped with an air condenser and a $CaCl_2$ tube was charged with 5.4 g (0.1 mol) of freshly dried MeONa and 25 ml of dimethyl sulfoxide (DMSO) dried over molecular sieves. The flask was heated on a Wood's alloy bath for 5–10 min at 165–170°C with shaking. Then 8.2 g (0.025 mol) of PCB **I** was added, and the mixture was heated on a Wood's alloy bath at 170°C for 25 min with shaking. After cooling, the mixture was diluted with 100 ml of water and transferred into a separating funnel. The homogeneous mixture was extracted with toluene (2 × 20 ml); the toluene extracts were combined, washed with water (5 × 100 ml), filtered, and dried over $CaCl_2$; the solvent was evaporated, and the residue was kept in a vacuum. The resulting yellow oily mass was analyzed.

The reaction of PCB **I** with sodium methoxide was performed in bipolar aprotic solvents: DMSO, dimethylformamide (DMF), sulfolane, *N*-methyl-2-pyrrolidone, diglyme, and 1,4-dioxane. Under similar conditions [the same PCB concentration, PCB : MeONa ratio 1 : 4, 25 min, boiling point of the solvent], the best results were obtained in DMSO, DMF, sulfolane, and *N*-methyl-2-pyrrolidone.[1] In diglyme and 1,4-dioxane, no reaction of PCB **I** with MeONa was observed. Thus, the requirements to solvents for this process are high polarity and high electron density on the oxygen atom (ε > 15) [4]. Such properties ensure strong interaction of Na^+ ions with the solvent, enhancing the reactivity of MeO^-.

The degree of conversion was evaluated from a decrease in the areas of the peaks of the starting PCBs **I** and increase in the areas of the peaks of methoxy derivatives **II**. Figures 2a and 2b show chromatograms of mixtures obtained from the reactions.

[1] The reactions of PCB **I** with sodium methoxide in sulfolane and *N*-methyl-2-pyrrolidone were performed at 175–180°C.

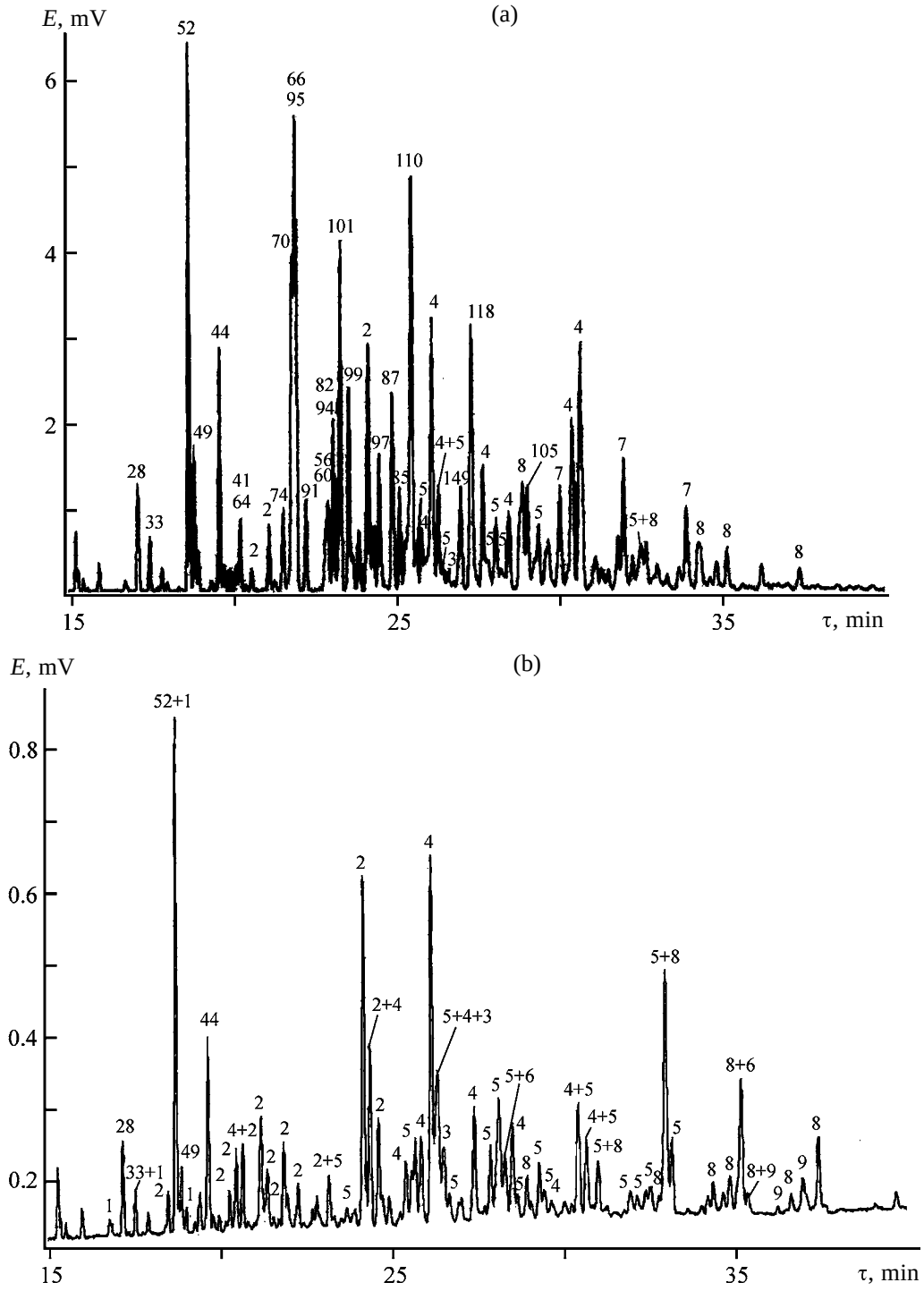

Fig. 2. Chromatogram of reaction products **II**. 170°C, DMSO, 25 min. **I** : MeONa: (a) 1 : 1 and (b) 1 : 4. Peak assignment: (1) $C_{12}H_7Cl_2OCH_3$, (2) $C_{12}H_6Cl_3OCH_3$, (3) $C_{12}H_6Cl_2(OCH_3)_2$, (4) $C_{12}H_5Cl_4OCH_3$, (5) $C_{12}H_5Cl_3(OCH_3)_2$, (6) $C_{12}H_5Cl_2 \cdot (OCH_3)_3$, (7) $C_{12}H_4Cl_5OCH_3$, (8) $C_{12}H_4Cl_4(OCH_3)_2$, and (9) $C_{12}H_4Cl_3(OCH_3)_3$; for other designations, see Table 1.

The reactions in DMSO, DMF, sulfolane, and *N*-methyl-2-pyrrolidone gave qualitatively and quantitatively similar results. The composition of mixtures **II** was complex, with increased number of chromatographic peaks. Under the optimal conditions, 8–15% of the starting PCBs **I** (mainly tri- and tetrachlorobiphenyls) remained unchanged.

The chemical composition of mixtures **II** and de-

gree of conversion of PCBs **I** were determined by GLC–MSD. To do this, we reconstructed the mass chromatograms for particular ions characteristic of the starting tri-, tetra-, penta-, and hexachlorobiphenyls and thus estimated the relative content of unchanged PCBs **I**. Then, as far as possible, we studied the mass spectra of all the detected products.

Synthesis of individual monomethoxypolychlorobiphenyls by cross coupling of the corresponding monoaromatic systems and the fragmentation patterns of these compounds under electron impact were reported in [5, 6]. A specific feature of the mass spectra of pure monomethoxypolychlorobiphenyls is the presence of strong molecular peaks. No such data are available in mass-spectrometric databases on di- and trimethoxypolychlorobiphenyls. We have revealed in the mass spectra of **II** strong molecular peaks belonging to monomethoxydi(tri-, tetra-)chlorobiphenyls, dimethoxydi(tri-, tetra-)chlorobiphenyls, and trimethoxydi(tri-)chlorobiphenyls.

Reconstruction of the mass chromatograms for the molecular peaks of PCB methoxy derivatives **II** allowed us to assign the peaks and reveal the cases of joint elution of the derivatives. Since the columns used in GLC–FID and GLC–MSD experiments were similar, we obtained similar chromatograms, which allowed peak assignment in the chromatograms obtained by GLC–FID (Fig. 2).

As described previously for monomethoxypolychlorobiphenyls [5, 6], the fragmentation pattern of such compounds under electron impact depends on the position of the methoxy groups. However, their position in components of **II** cannot be determined from the available data.

For example, *p*-monomethoxy derivatives of PCBs show the peaks $[M - 15]^+$ ($M - CH_3$) and $[M - 43]^+$ ($M - CH_3 - CO$); *o*-isomers, the peaks $[M - 35]^+$ ($M - Cl$) and strong peaks $[M - 50]^+$ ($M - CH_3Cl$); and *m*-isomers, medium-intensity peaks $[M - 43]^+$ and $[M - 50]^+$. All the three types of fragmentation were detected in our study.

The characteristic peaks of dimethoxy derivatives of PCBs were $[M - 65]^+$ ($M - CH_3 - CH_3Cl$), $[M - 93]^+$ ($M - CH_3Cl - CH_3 - CO$), and $[M - 156]^+$ ($M - CH_3Cl - CH_3 - CO - COCl$). In some cases, we also detected the peaks $[M - 15]^+$ and $[M - 43]^+$, and in other cases, the peaks $[M - 50]^+$ and $[M - 65]^+$, which may be associated with the location of the two methoxy groups.

The mass spectra of PCB trimethoxy derivatives contain peaks characteristic of monomethoxy ($[M - 15]^+$, $[M - 43]^+$, $[M - 50]^+$) and dimethoxy ($[M - 65]^+$, $[M - 93]^+$) derivatives.

To evaluate the reactivities of PCB congeners, we studied in more detail the reaction of **I** with sodium methoxide in DMSO; we varied the reaction temperature and time and the molar ratio of the reactants. The results are listed in Table 2.

Quantitative treatment of the chromatographic data for mixtures **II** shows that the reactivity of PCB congeners grows with increasing number of chlorine atoms.

Hexachlorobiphenyls (PCB 149, PCB 153, PCB 138, PCB 128) started to transform at a relatively low temperature (60°C), mainly into monomethoxy derivatives $C_{12}H_4Cl_5OCH_3$ (Figs. 2a, 2b, peak 7). Their reactivity increased with temperature, methoxylation proceeded further, and, starting from 150°C, monomethoxypentachlorobiphenyls were no longer detected; the reaction yielded dimethoxy [$C_{12}H_4Cl_4 \cdot (OCH_3)_2$, 8] and trimethoxy [$C_{12}H_4Cl_3(OCH_3)_3$, 9] derivatives, with dimethoxytetrachlorobiphenyls prevailing. The starting hexachlorobiphenyls were not detected in the reaction products. These results were obtained in all the four solvents: DMSO, DMF, sulfolane, and *N*-methyl-2-pyrrolidone.

Pentachlorobiphenyls started to react with sodium methoxide at 60°C, and their reactivity also increased with temperature. The major products were monomethoxy ($C_{12}H_5Cl_4OCH_3$, 4) and dimethoxy [$C_{12}H_5 \cdot Cl_3(OCH_3)_2$, 5] derivatives. Minor amounts of trimethoxy derivatives [$C_{12}H_5Cl_2(OCH_3)_3$, 6] were also detected by GLC–MSD. PCB 85, PCB 99, PCB 105, and PCB 118 containing chlorine atoms in both *p*-positions appeared to be more reactive. These congeners entered into the reaction earlier than the other pentachlorobiphenyls.

Tetrachlorobiphenyls were characterized by relatively low degree of reaction with sodium methoxide, with predominant formation of monomethoxytrichlorobiphenyls ($C_{12}H_6Cl_3OCH_3$, 2); minor amounts of dimethoxydichlorobiphenyls 3 also formed. PCB 47, PCB 60, PCB 66, and PCB 74 containing two chlorine atoms in the *p*-positions showed high reactivity; PCB 41, PCB 49, PCB 64, and PCB 70 containing one chlorine atom in the *p*-position appeared to be less reactive.

Tetrachlorobiphenyls PCB 52 and PCB 44 containing no chlorine in *p*-positions did not noticeably react under the experimental conditions. Trichlorobiphenyls PCB 28 and PCB 33 containing one chlorine in *p*-position under the optimal conditions partially trans-

Table 2. Conditions of the reaction of PCBs **I** with sodium methoxide in DMSO and transformation products

Reaction conditions				PCB transformations products			
T, °C	τ, min	PCB : NaOMe ratio	content of unchanged PCB congeners, %	trichloro- ($C_{12}H_7Cl_3$)	tetrachloro- ($C_{12}H_6Cl_4$)	pentachloro- ($C_{12}H_5Cl_5$)	hexachloro- ($C_{12}H_4Cl_6$)
60	25	1 : 4	87	Unchanged	Unchanged	$C_{12}H_5Cl_4OCH_3$	$C_{12}H_4Cl_5OCH_3$
80	25	1 : 4	62	〃	〃	$C_{12}H_5Cl_4OCH_3$ $C_{12}H_5Cl_3(OCH_3)_2$	$C_{12}H_4Cl_5OCH_3$ $C_{12}H_4Cl_4(OCH_3)_2$
100	25	1 : 4	28	〃	$C_{12}H_6Cl_3OCH_3$ $C_{12}H_6Cl_2(OCH_3)_2$	$C_{12}H_5Cl_4OCH_3$ $C_{12}H_5Cl_3(OCH_3)_2$	$C_{12}H_4Cl_5OCH_3$ $C_{12}H_4Cl_4(OCH_3)_2$
150	25	1 : 4	23	$C_{12}H_7Cl_2OCH_3$	$C_{12}H_6Cl_3OCH_3$ $C_{12}H_6Cl_2(OCH_3)_2$	$C_{12}H_5Cl_4OCH_3$ $C_{12}H_5Cl_3(OCH_3)_2$	$C_{12}H_4Cl_4(OCH_3)_2$ $C_{12}H_4Cl_3(OCH_3)_3$
170	10	1 : 4	40	Unchanged	$C_{12}H_6Cl_3OCH_3$ $C_{12}H_6Cl_2(OCH_3)_2$	$C_{12}H_5Cl_4OCH_3$ $C_{12}H_5Cl_3(OCH_3)_2$	$C_{12}H_4Cl_5OCH_3$ $C_{12}H_4Cl_4(OCH_3)_2$
170	25	1 : 4	13	$C_{12}H_7Cl_2OCH_3$	$C_{12}H_6Cl_3OCH_3$ $C_{12}H_6Cl_2(OCH_3)_2$	$C_{12}H_5Cl_4OCH_3$ $C_{12}H_5Cl_3(OCH_3)_2$ $C_{12}H_5Cl_2(OCH_3)_3$	$C_{12}H_4Cl_4(OCH_3)_2$ $C_{12}H_4Cl_3(OCH_3)_3$
170	25	1 : 6	11	$C_{12}H_7Cl_2OCH_3$	$C_{12}H_6Cl_3OCH_3$ $C_{12}H_6Cl_2(OCH_3)_2$	$C_{12}H_5Cl_4OCH_3$ $C_{12}H_5Cl_3(OCH_3)_2$ $C_{12}H_5Cl_2(OCH_3)_3$	$C_{12}H_4Cl_4(OCH_3)_2$ $C_{12}H_4Cl_3(OCH_3)_3$
170	25	1 : 1	59	Unchanged	$C_{12}H_6Cl_3OCH_3$ $C_{12}H_6Cl_2(OCH_3)_2$	$C_{12}H_5Cl_4OCH_3$ $C_{12}H_5Cl_3(OCH_3)_2$	$C_{12}H_4Cl_5OCH_3$ $C_{12}H_4Cl_4(OCH_3)_2$
170	120	1 : 4	10	$C_{12}H_7Cl_2OCH_3$	$C_{12}H_6Cl_3OCH_3$ $C_{12}H_6Cl_2(OCH_3)_2$	$C_{12}H_5Cl_4OCH_3$ $C_{12}H_5Cl_3(OCH_3)_2$ $C_{12}H_5Cl_2(OCH_3)_3$	$C_{12}H_4Cl_4(OCH_3)_2$ $C_{12}H_4Cl_3(OCH_3)_3$

formed into monomethoxydichlorobiphenyls $C_{12}H_7 \cdot Cl_2OCH_3$ (1).

Thus, we have revealed the features of chemical transformations of PCB (Sovol) congeners under the action of sodium methoxide, as influenced by the number of chlorine atoms in the molecule, their relative location, and reaction conditions.

CONCLUSIONS

(1) Reaction of Sovol mixture of polychlorobiphenyls with sodium methoxide is the most efficient in bipolar aprotic solvents (dimethyl sulfoxide, dimethylformamide, sulfolane, *N*-methyl-2-pyrrolidone).

(2) Among Sovol congeners, the most reactive toward sodium methoxide are hexa- and pentachlorobiphenyls; tetra- and trichlorobiphenyls are less reactive.

(3) Reaction of polychlorobiphenyls with sodium methoxide (170°C, 25–120 min, PCB : MeONa 1 : 4) in various solvents does not ensure complete conversion of the main pollutants.

REFERENCES

1. Frame, G.M., *Fresenius J. Anal. Chem.*, 1997, vol. 357, pp. 714–722.
2. Piterskikh, I.A., Kirichenko, V.E., Pervova, M.G., and Kandakova, V.V., *Zavod. Lab.*, 2001, vol. 67, no. 8, pp. 63–66.
3. Gorbunova, T.I., Zapevalov, A.Ya., Kirichenko, V.E., *et al.*, *Zh. Prikl. Khim.*, 2000, vol. 73, no. 4, pp. 610–614.
4. Reichardt, Ch., *Solvents and Solvent Effects in Organic Chemistry*, Weinheim: VCH, 1988.
5. Lehmler, H.-J. and Robertson, L.W., *Chemosphere*, 2001, vol. 45, no. 8, pp. 1119–1127.
6. Bergman, A., Klasson, W.E., Kuroki, H., and Nilsson, A., *Chemosphere*, 1995, vol. 30, no. 10, pp. 1921–1938.

Russian Journal of Applied Chemistry, Vol. 77, No. 9, 2004, pp. 1528–1531. Translated from Zhurnal Prikladnoi Khimii, Vol. 77, No. 9, 2004, pp. 1539–1542.

MACROMOLECULAR CHEMISTRY AND POLYMERIC MATERIALS

Influence of Copper Stearate on Oxidation of Polyethylene Stabilized with Neozon D

D. G. Lin, E. V. Vorob'eva, and N. V. Marchenko

Skorina State University, Gomel, Belarus

Received March 19, 2004

Abstract—Catalytic reaction of copper(II) stearate with Neozon D in a polyethylene melt was studied.

Maizus *et al*. [1] showed that decomposition of decyl hydroperoxide is catalyzed by a mixture of an aromatic amine (*N*-phenyl-2-naphthylamine) and copper(II) stearate. Based on this result, Maizus *et al*. suggested [1] that mixtures of variable-valence metal salts with inhibitors of free-radical reactions can be used to develop new antioxidants (AO). This possibility was extensively studied, in particular, in [2, 3]. It was found that a Neozon D–copper(II) stearate mixture is rapidly consumed in decane oxidation. Based on the fact that the induction period of hydrocarbon oxidation (IPO) lasted for a long time after complete consumption of the AO, Vetchinkina *et al*. suggested [2] formation of a new compound inhibiting the oxidation. Two pathways giving rise to a new, more effective AO were proposed [2]. The first is reaction of *N*-phenyl-2-naphthylamine with copper(II) stearate to form a copper(I) complex with $C_{10}H_7NC_6H_5$ radical and stearic acid. The second pathway involves reaction of the liberated stearic acid with the free AO to form a salt that cannot react with copper(II) stearate. Vetchinkina *et al*. [2, 3] believe that specifically copper(I) complexes effectively inhibit oxidation after consumption of amine-containing AO. Clearly, the antioxidative effect of the copper(I) complex will be maximal if free oxidation catalysts {copper(II) stearate [4, 5] and stearic acid [5]} will be absent in the system after the complex formation. If AO reacts only with copper(II) stearate and with liberated stearic acid, the molar ratio of Neozon D and copper(II) stearate should be 2 : 1. At other molar ratios of these components, some amount of either AO or copper(II) stearate and stearic acid will remain unchanged in the system.

To improve the antioxidative properties of Neozon D, we studied in this work the influence of copper(II) stearate on oxidation of a polyethylene (PE) melt stabilized with Neozon D.

EXPERIMENTAL

We used nonstabilized high-density PE [GOST (State Standard) 16338–85, base trademark 20308-005). Films to be studied were prepared from PE powder or form a composite of PE with a modifier. Copper(II) stearate [TU (Technical Specifications) 6-09-12-152–75] and Neozon D (*N*-phenyl-2-naphthylamine, GOST 39–79) were used as the modifiers. The composite was prepared as follows. Powders of copper stearate and Neozon D were dissolved in acetone (GOST 2603–79) and the resulting solution was stirred with a magnetic stirrer for 3 min. Polyethylene powder was impregnated with these solutions (or their mixture) and dried at room temperature. The PE films were oxidized by heating in an oven in air at 150°C. This temperature is higher than the melting point of the polymer.

The degree of PE oxidation was estimated form the optical density of the carbonyl band at 1720 cm^{-1}. The optical density was determined by the baseline method using the absorption band at 1460 cm^{-1} as an internal reference. The IR spectra were recorded on a Specord-75 IR spectrophotometer.

Neozon D-copper(II) stearate mixtures with molar ratios of 0.5 : 1, 1 : 1, 2 : 1, 4 : 1, 6 : 1, 8 : 1, and 10 : 1 (hereinafter, these mixtures will be referred to I–VII, respectively) were prepared. These mixtures were introduced in PE in the amount providing 0.1 wt % concentration of Neozon D in the resulting composite. The copper(II) concentration in samples I–VII decreased in the following order (wt %, $\times 10^3$): 147, 29, 14, 7, 5, 4, and 3, respectively.

The kinetic curves of accumulation of carbonyl groups in samples I, III, IV, and VII are shown in Fig. 1a. We expected that introduction of a Neozon D–copper(II) stearate mixture into the polymer would

1070-4272/04/7709-1528 © 2004 MAIK "Nauka/Interperiodica"

increase its IPO. However, we obtained the opposite result (accumulation of carbonyl groups in the reference film containing only 0.1 wt % Neozon D is described by curve *1*). The induction period of hydrocarbon oxidation is shortened when the copper(II) concentration increases from 3×10^{-3} (sample VII) to 7×10^{-3} wt % (sample IV) and slowly increases with increasing copper(II) concentration to 0.147 wt % (sample I), i.e., the dependence of IPO on the copper(II) stearate concentration passes through a minimum (Fig. 1b, curve *7*).

The abnormal behavior of PE containing Neozon D and copper(II) stearate is due to the fact that no copper(I) complexes exhibiting strong antioxidative power are formed in the molten polymer. In this case, the probability of formation of copper complexes is low owing to slow diffusion of the modifiers. Under these conditions, AO inhibits oxidation of the polymer and copper(II) stearate catalyzes this reaction. As a result, small additions of copper(II) stearate make the IPO shorter. We suggest that the experimental dependence of IPO on the copper concentration (Fig. 1b, curve *7*) is caused by specific features of the effect of copper(II) stearate on PE oxidation [5, 6].

We also studied oxidation of nonstabilized PE containing copper(II) stearate with concentrations from 0 to 0.020 wt % (this concentration range corresponds to that in samples I–VII). In this case, the dependence of IPO on the copper(II) concentration also passes through a minimum (Fig. 1b, curve *6*). This result confirms the known fact that small amounts of copper(II) stearate catalyze PE oxidation [5, 6]. When the modifier concentration increases, the oxidation is inhibited and the induction period increases (Fig. 1b, curve *6*).

Copper(II) stearate taken in an amount of approximately 7×10^{-3} wt % [in terms of copper(II)] has the strongest catalytic effect on oxidation of both nonstabilized PE and PE stabilized with Neozon D (Fig. 1b, curves *6* and *7*). Thus, introduction of copper(II) stearate in a PE melt stabilized with Neozon D does not significantly enhance the antioxidative power of the AO. Probably these modifiers do not react with each other and work independently.

At the same time, introduction of copper(II) compounds can enhance the inhibiting properties of the amine AO. Accumulation of carbonyl groups in PE films oxidized on reactive (copper) and inert (KBr) supports is shown in Fig. 2. Oxidation of nonstabilized PE on the copper support is faster and is characterized by shorter induction period than that on KBr supports (Fig. 2, curves *1*, *2*). Introduction of

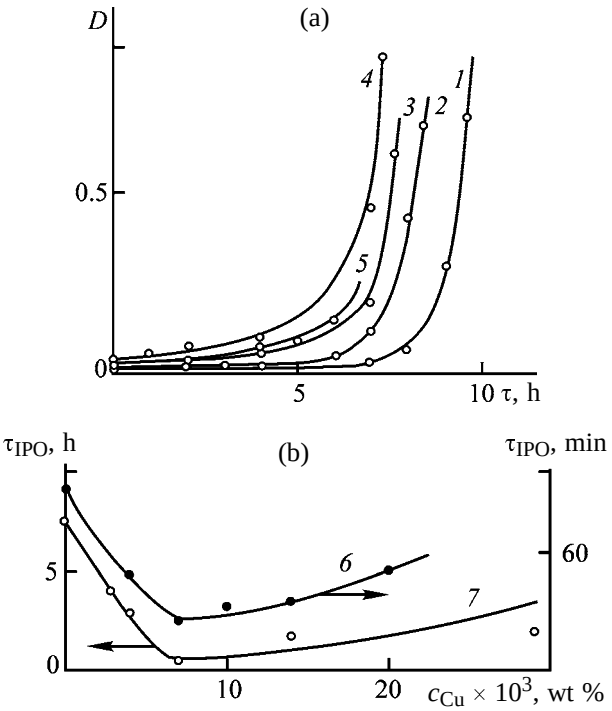

Fig. 1. (a) Accumulation of carbonyl groups in PE samples containing (*1*) 0.1 wt % Neozon D and mixtures (*2*) I, (*3*) III, (*4*) IV, and (*5*) VII; (b) IPO of PE (*6*) nonstabilized and (*7*) stabilized with 0.1 wt % Neozon D as a function of copper(II) stearate content in the samples. (a) (*D*) optical density and (τ) oxidation time; the same for Figs. 2 and 3. (b) (c_{Cu}) Copper(II) concentration and (τ_{IPO}) IPO duration.

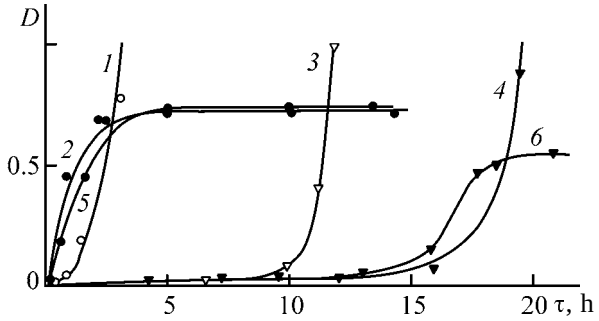

Fig. 2. Accumulation of carbonyl groups in PE films with a Cu powder content of (*1–4*) and (*5*, *6*) 10 wt % and Neozon D content of (*1*, *2*, *5*) and (*3*, *4*, *6*) 0.3 wt %, as a function of time of their oxidation τ (h) on (*2*, *4*) copper and (*1*, *3*, *5*, *6*) KBr supports.

Neozon D increases the IPO. Curiously, the IPO of PE on a copper support increases to a greater extent that that on KBr plates (Fig. 2, curves *3*, *4*). Apparently, Neozon D in PE films on copper supports is converted into a more effective AO.

To confirm these results, we studied oxidation of PE filled with copper powder. The oxidation was per-

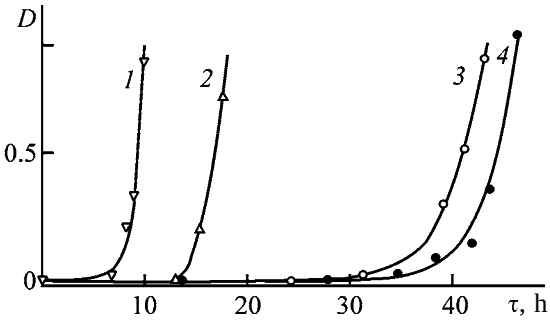

Fig. 3. Accumulation of carbonyl groups in the course of oxidation of PE films stabilized with 0.1 wt % of (*1*) initial AO, (*2*) AO thermally modified at 150°C for 10 h, and a mixture of copper(II) stearate and Neozon D taken in a ratio of (*3*) 1 : 24 and (*4*) 1 : 246, as a function of oxidation time τ.

formed on KBr plates. As in the case of oxidation on a copper support, IPO of the polymer stabilized with Neozon D increases, which indicates the enhanced performance of the amine AO.

We can give two possible explanations of modification of the AO after contact with a copper support. The first is penetration of the AO to the polymer–support interface and direct reaction with copper to form a more effective compound. The second mechanism is more complex. It is known [4, 6, 7] that copper carboxylates are formed in oxidation of PE on copper. These compounds can diffuse into the polymer matrix and react there with AO to form copper complexes with strong antioxidative power. The second mechanism, however, is improbable. First, no copper(I) complexes with Neozon D were found in a PE melt containing copper(II) stearate (analog of copper compound formed in PE oxidation). Second, the concentration of copper compounds that diffused in the polymer matrix by the end of IPO is negligible. Hence, the amount of copper(I, II) complexes with Neozon D, formed in the polymeric matrix, should be insufficient. We believe that the direct reaction of AO with the copper support is the most probable explanation.

To study direct reaction of AO with copper, we performed the following experiment. A thin (~1 mm) layer of Neozon D was applied to a copper support and was heated at 150°C in air for 10 h. Then 0.1 wt % of thermally modified AO was introduced into PE, and the IPO of the composite was measured. This treatment of AO substantially enhances its performance. The induction period of hydrocarbon oxidation of PE stabilized with thermally modified AO increases by a factor of more than 2 (Fig. 3, curves *1, 2*).

Similar experiments were performed with mixtures of the AO with copper(II) stearate. We studied two mixtures with Neozon D : copper(II) stearate molar ratios of 24 : 1 (mixture A) and 242 : 1 (mixture B). These ratios are substantially higher than the ratio optimal for complex formation (2 : 1). After the heat treatment, the mixtures were introduced into PE in the amount required to obtain 0.1 wt % AO in the polymer. The inhibiting power of AO substantially increased after the heat treatment. The IPO of samples containing mixtures A and B increased by factors of 5 and 6, respectively. The inhibiting power of the AO increased with decreasing the copper(II) amount in the mixture. If the properties of the initial AO changed due to the complexation, the pattern would be inverse. Since this is not the case, we believe that the inhibiting properties of the amine AO are enhanced in the course of its contact with copper and its compounds.

Probably, strong antioxidation stabilization of PE with Neozon D in the presence of copper (Fig. 2, curves *4, 6*) or its salts (Fig. 3, curves *3, 4*) is caused by copper-catalyzed oxidation of Neozon D to form stable nitroxyl radicals:

$$C_{10}H_7\text{–}NH\text{–}C_6H_5 \xrightarrow{Cu} C_{10}H_7\text{–}N^{\bullet}\text{–}C_6H_5$$

$$\xrightarrow{[O]} C_{10}H_7\text{–}NO^{\bullet}\text{–}C_6H_5.$$

Nitroxyl radicals (>NO$^{\bullet}$) terminate chain oxidation reactions of polymers, thus enhancing the performance of AO [9].

Since copper(II) stearate and Neozon D are separated by low-mobile PE macromolecules (Fig. 1), the modifiers work independently: copper stearate catalyzes polymer oxidation and Neozon D inhibits this reaction.

CONCLUSIONS

Inhibiting power of the amine AO can be enhanced by its catalytic reaction with copper or copper(II) stearate in the course of oxidation of a PE melt.

REFERENCES

1. Maizus, Z.K., Skibida, I.P., and Emanuel', N.M., *Zh. Fiz. Khim.*, 1966, vol. 40, no. 2, pp. 322–327.
2. Vetchinkina, V.N., Maizus, Z. K., Skibida, I.P., and

Emanuel', N.M., *Dokl. Akad. Nauk SSSR*, 1967, vol. 177, no. 3, pp. 625–628.

3. Vetchinkina, V.N., Skibida, I.P., and Maizus, Z.K., *Izv. Akad. Nauk SSSR, Ser. Khim.*, 1977, vol. 5, no. 1008–1013.
4. Chan, M.G. and Allara, D.L., *J. Colloid Interface Sci*., 1974, vol. 47, p. 697.
5. Denisov, E.T., *Okislenie i destruktsiya karbotsepnykh polimerov* (Oxidation and Degradation of Carbon-Chain Polymers), Leningrad: Khimiya, 1990.
6. Allara, D.L. and Roberts, R.F., *J. Catal.*, 1976, vol. 45, p. 54.
7. Lin, D.G., and Vorob'eva, E.V., *Zh. Prikl. Khim*., 2002, vol. 75, no. 5, pp. 836–839.
8. *Kataliticheskie svoistva veshchestv: Spravochnik* (Catalytic Properties of Substances: Handbook), Raiter, V.A., Ed., Kiev: Naukova Dumka, 1968.
9. Denisov, E.T., Sarkisov, O.M., and Likhtenshtein, G.I., *Khimicheskaya kinetika* (Chemical Kinetics), Moscow: Khimiya, 2000.

Russian Journal of Applied Chemistry, Vol. 77, No. 9, 2004, pp. 1532–1535. Translated from Zhurnal Prikladnoi Khimii, Vol. 77, No. 9, 2004, pp. 1543–1546.

MACROMOLECULAR CHEMISTRY AND POLYMERIC MATERIALS

Mechanism of Photostabilization of a Europium(III) Complex in Polyethylene with Tinuvin-622

A. M. Mirochnik, P. A. Zhikhareva, V. E. Karasev, and V. G. Kuryavyi

Institute of Chemistry, Far Eastern Division, Russian Academy of Sciences, Vladivostok, Russia

Received October 21, 2003; in final form, May 2004

Abstract—The mechanism by which selected photostabilizing sterically hindered amines (Tinuvin-622, Diacetam-5, Polyacetam-81) affect the photostability of the complex $Eu(Phen)_2(NO_3)_3$ in low-density polyethylene was studied by the luminescence, ESR, and ^1H NMR spectroscopy.

Light-transforming polymeric materials find wide application in agriculture (as plant growth stimulants), medicine, and electronics [1, 2]. As polymer base for such materials serve commercial polymers widely used in agriculture, in particular, low-density polyethylene (LDPE), and as luminescent additives efficiently stimulating plant growth, Eu(III) complexes [1, 2]. In processing, exploitation, and storage, polymers are exposed to numerous factors (heat, light, penetrating radiation, oxygen), which is responsible for their accelerated aging. Combined introduction into polymers of photostabilizers and agents inhibiting thermal oxidative degradation significantly improves such performance characteristics of films as weather and light stability. This makes it urgent to elucidate the mechanism by which the photostability of luminescent complexes is affected by sterically hindered amines (SHAs) and other types of photostabilizers (antioxidants, UV absorbers, etc. [3]).

Data on interaction of luminescent Eu(III) complexes and photostabilizers in LDPE are scarce. We [4, 5] and Raida *et al*. [6] found that, when introduced into luminescent compositions, Diacetam-5 and Polyacetam-81 photostabilizers decrease the photoluminescence intensity and accelerate photodegradation of the europium complex. At the same time, photostabilizer Tinuvin-622 enhances luminescence of the europium complex and inhibits its UV-induced photodegradation [5, 6].

This work, continuing our previous studies [4, 5], is aimed at elucidating the mechanism by which selected photostabilizing SHAs affect the luminescence intensity of the europium(III) complex and its photostability in photolysis. As luminophore to be introduced into LDPE we chose $Eu(Phen)_2(NO_3)_3$, where Phen is 1,10-phenanthroline. As SHA photostabilizers we used those commercially used for producing photoresistant LDPE articles: Diacetam-5 [3-(2,2,6,6-tetramethylpiperidin-4-yl)aminopropionic acid 2,2,6,6-tetramethylpiperidin-4-ylamide], Polyacetam-81, Tinuvin-622 [oligomeric photostabilizer derived from 1-(2-hydroxyethyl)-2,2,6,6-tetramethyl-4-hydroxypiperidine and dimethyl succinate; Ciba Geigy AG] [7]. Notably, Tinuvin-622 is the only SHA used in food industry as stabilizer for polymeric packaging materials. Unlike oligomeric Tinuvin-622, low-molecular-weight Diacetam-5 contains NH groups capable of complexing with metal atoms. The structural formulas of Diacetam-5 and Tinuvin-622 are presented below.

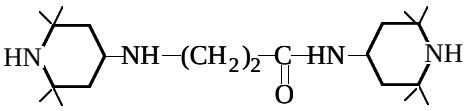

Diacetam-5

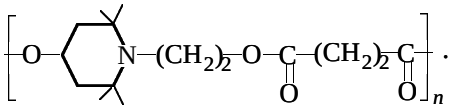

Tinuvin-622

EXPERIMENTAL

Film samples were prepared by introducing $Eu(Phen)_2(NO_3)_3$ (0.3 wt %) and a stabilizer (0.1–0.9 wt %) into LDPE. The components were thoroughly mixed, pressed on a hydraulic press at T = 150°C and p = 110 atm, and cooled to obtain films. Accelerated aging of the films was achieved by irradiating the samples with unfiltered light of a DRT-250 mercury lamp. The lamp–sample distance was 20 cm. The luminescence spectra were recorded on an SDL-1

1070-4272/04/7709-1532 © 2004 MAIK "Nauka/Interperiodica"

spectrometer (excitation by a DRSh-250 lamp; UFS-6 filter; λ_{exc} = 365 nm). The luminescence excitation spectra were recorded on a Shimadzu RF-5000 instrument (λ_{lum} = 612 nm, $^5D_0$–$^7F_2$ transition of Eu^{3+}). The ESR spectra were recorded in the *X* frequency range on an ESR-231 spectrometer (Germany). The sample was UV-irradiated in the spectrometer resonator with a DRSh-100 lamp. The ^1H NMR spectra were measured on a Bruker NMR AS-250 spectrometer (Germany) in $CDCl_3$ at 300 K with tetramethylsilane as internal reference.

Studies of the photodegradation rate of the Eu(III) complex in a polymer composition as influenced by the photostabilizers should take into account the fact that the complex can degrade both during irradiation and during preparation of the polymer luminescent composition (as a result of a chemical reaction between the complex and the stabilizer).

Indeed, our experiments showed that a combination of the europium complex and a photostabilizer in the composition affords even during primary processing a fourfold decrease in the fluorescence intensity of the composition relative to the composition without stabilizer in the case of Diacetam-5 and a 20% decrease in the case of Polyacetam-81. At the same time, during primary processing of the polymer composition containing Tinuvin-622 the luminescence intensity of the complex increases by a factor of 1.7.

Additional information about the processes of interest comes from analysis of the luminescence excitation spectra of the polymer compositions (Fig. 1). The spectrum of the initial composition (without photostabilizers) contains a broad intense band corresponding to the π–π* electronic transitions in the absorption spectrum of the phenanthroline molecule.

A fine-structured part of the spectrum (330–350 nm) corresponds to intraconfiguration *f*–*f* transitions of Eu(III). Introduction of Diacetam-5 into the composition substantially modifies the luminescence excitation spectrum: A new band appears in the shortwave region of the spectrum (210–250 nm), and the luminescence intensity of the composition decreases fourfold. The excitation spectrum of the luminescent composition with Tinuvin-622 is almost identical to that of the initial composition; however, the relative intensity of the band at 230–280 nm increases (with the luminescence intensity increasing by a factor of 1.7). This suggests a sensitizing effect of Tinuvin-622 on the excitation energy transfer to the energy levels of Eu(III).

Fig. 1. Luminescence excitation spectra of (*2*) $Eu(Phen)_2(NO_3)_3$ in LDPE and (*1*, *3*) $Eu(Phen)_2(NO_3)_3$ + photostabilizer composition in LDPE. (*I*) Intensity and (λ) wavelength. Stabilizer: (*1*) Tinuvin-622 and (*3*) Diacetam-5.

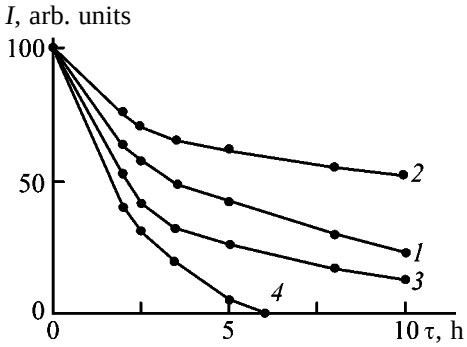

Fig. 2. Luminescence intensity *I* (λ_{lum} = 615 nm) of (*1*) $Eu(Phen)_2(NO_3)_3$ in LDPE and (*2*–*4*) $Eu(Phen)_2(NO_3)_3$ + photostabilizer composition in LDPE as a function of the UV irradiation time τ. Stabilizer: (*2*) Tinuvin-622, (*3*) Polyacetam-81, and (*4*) Diacetam-5.

We followed the photoinduced degradation of the fluorescent characteristics of the $Eu(Phen)_2(NO_3)_3$ + LDPE composition from the fluorescence spectra. UV irradiation weakens the luminescence in the band of Eu(III) with λ = 615 nm and enhances luminescence in the blue-green region (400–500 nm), due to luminescence of the photodegradation products of the compositions [8]. Figure 2 characterizes accelerated photoinduced aging of the compositions in LDPE under the laboratory conditions. It is seen that Diacetam-5 and Polyacetam-81 accelerate photodegradation of the Eu(III) complex: With Diacetam-5 as stabilizer the luminescence of the sample completely disappears already within 6 h of irradiation; at the same time, Tinuvin-622 markedly inhibits photodegradation.

As known, SHAs, whose photolysis yields nitroxyl radicals, act mostly as acceptors of peroxy radicals in

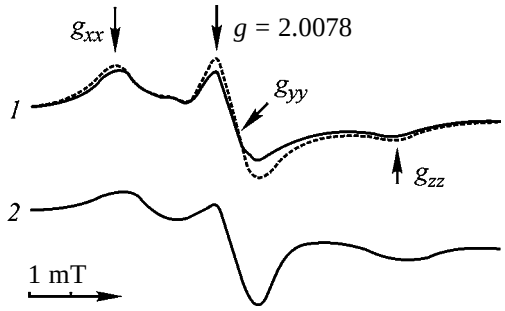

Fig. 3. ESR spectra of (*1*) Diacetam-5 before (solid line) and after (dashed line) UV irradiation for 10 min and (*2*) Tinuvin-622 before UV irradiation. *X*-frequency range, T = 300 K.

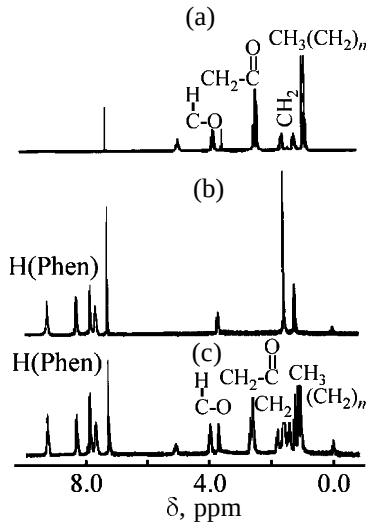

Fig. 4. ^{1}H NMR spectra of (a) Tinuvin-622, (b) $Eu(Phen)_2(NO_3)_3$, and (c) $Eu(Phen)_2(NO_3)_3$ + Tinuvin-622 composition in deuterochloroform (300 K). (δ) Chemical shift; the same for Fig. 5.

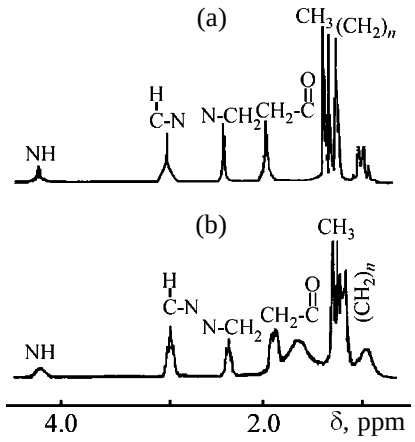

Fig. 5. ^{1}H NMR spectra of (a) Diacetam-5 and (b) $Eu(Phen)_2(NO_3)_3$ + Diacetam-5 composition in deuterochloroform (300 K).

photooxidation of polymers [3]. Additional information about the action mechanism of Diacetam-5 and Tinuvin-622 is furnished by their ESR spectra. They have a triplet structure identical to that of nitroxyl radical (Fig. 3) [9]. Figure 3 shows that irradiation of Diacetam-5 modifies the shape of the ESR spectrum, specifically, the spectral component ratio. We found that UV irradiation of the stabilizers enhances the intensity of all the spectral components, most profoundly in the case of the peak corresponding to the g-tensor component g_{yy}. The ESR data suggest efficient generation of nitroxyl radicals in photolysis of the photostabilizers, with low-molecular-weight Diacetam-5 accumulating the radicals more rapidly than oligomeric Tinuvin-622.

Thus, the NH groups in low-molecular-weight SHAs (Diacetam-5, Polyacetam-81), capable of complexing with metal atoms and exhibiting a greater, compared to oligomeric Tinuvin-622, power for generating nitroxyl radicals, seem to be responsible for the accelerating effect on the photodegradation of the europium complex in a polymeric composition.

We confirmed interaction between Diacetam-5 and the complex and the lack of such interaction in the case of the complex + Tinuvin-622 composition by ^{1}H NMR spectroscopy (Figs. 4, 5). We studied model systems [photostabilizer, Eu(III) complex, Eu(III) complex + photostabilizer] in deuterochloroform at 300 K.

Comparative analysis of the ^{1}H NMR spectra (Fig. 4) shows that the spectrum of the composition is a superposition of the spectra of the complex and the photostabilizer, which unambiguously suggests the lack of interaction in the system. At the same time, comparison of the ^{1}H NMR spectra of solutions of Diacetam-5, Eu(III) complex, and the complex + Diacetam-5 composition reveals broadening of the signals assigned to the protons from the Diacetam-5 molecule in the spectrum of the composition (Fig. 5). This suggests interaction between the photostabilizer and the complex.

CONCLUSIONS

(1) The mechanism by which sterically hindered amines (Tinuvin-622, Diacetam-5, Polyacetam-81) affect the photostability of the $Eu(Phen)_2(NO_3)_3$ complex in low-density polyethylene was studied by luminescence, ESR, and ^{1}H NMR spectroscopy. Tinuvin-622 enhances the luminescence intensity and photoresistance of the europium complex.

(2) A greater, compared to oligomeric Tinuvin-

622, rate of generation of nitroxyl radicals by low-molecular-weight sterically hindered amines under UV irradiation and the presence of NH groups able of complexing with metal ions are responsible for accelerated photodegradation of the europium complex in the polymer matrix.

ACKNOWLEDGMENTS

The authors are grateful to V.V. Isakov for measurement of the NMR spectra and assistance in interpretation of the experimental results.

REFERENCES

1. Karasev, V.E., *Vestn. Dal'nevost. Otd. Ross. Akad. Nauk*, 1995, no. 2, pp. 66–73.
2. Ostakhov, S.S., Kuznetsov, S.I., Murinov, Yu.I., *et al.*, *Vysokomol. Soedin., Ser. B*, 1995, vol. 37, no. 3, pp. 523–527.
3. Shlyapintokh, V.Ya., *Fotokhimicheskie prevrashcheniya i stabilizatsiya polimerov* (Photochemical Transformations and Stabilization of Polymers), Moscow: Khimiya, 1979.
4. Mirochnik, A.G., Karasev, V.E., Lifar, L.I., and Chernikova, A.V., *Zh. Prikl. Khim*., 1998, vol. 71, no. 6, pp. 1038–1040.
5. Mirochnik, A.G., Zhikhareva, P.A., Kuryavyi, V.G., and Karasev, V.E., *Issledovano v Rossii* electronic journal, http://zhurnal.ape.relarn.ru/articles/2002/096.pdf.
6. Raida, V.S., Dolmatova, S.G., Minich, A.S., and Tolstikov, G.A., *Plast. Massy*, 2002, no. 11, pp. 37–40.
7. Matisovarychla, L., Rychly, J., Fodor, Z., *et al.*, *Int. J. Polym. Mater*., 1990, vol. 13, nos. 1–4, pp. 227–235.
8. Ranby, B.J. and Rabek, J.F., *Photodegradation, Photo-Oxidation, and Photostabilzation of Polymers*, London: Wiley, 1975.
9. Kokorin, A.I., Parmon, V.N., and Shubin, A.A., *Atlas anizotropnykh spektrov EPR azotoksidnykh biradikalov* (Atlas of Anisotropic ESR Spectra of Nitroxyl Biradicals), Moscow: Nauka, 1984, p. 102.

Russian Journal of Applied Chemistry, Vol. 77, No. 9, 2004, pp. 1536–1539. Translated from Zhurnal Prikladnoi Khimii, Vol. 77, No. 9, 2004, pp. 1547–1550.

MACROMOLECULAR CHEMISTRY AND POLYMERIC MATERIALS

An IR Study of Organosolvent Lignin

T. E. Skrebets, K. G. Bogolitsyn, D. S. Kosyakov, and S. A. Verbitskaya

Arkhangelsk State Technical University, Arkhangelsk, Russia

Received November 11, 2003; in final form, April 2004

Abstract—The functional composition of lignin recovered from spruce wood and treated with alkali in aqueous and aqueous-ethanol medium and that of lignins recovered from alkaline cooking solutions in the presence of ethanol were studied by IR spectroscopy. The influence of ethanol on the content of the main functional groups in lignin was examinated.

IR spectroscopy is widely used for studying wood lignin for a long time. Numerous studies are devoted to identification of recovered lignin-containing samples, comparison of lignins recovered from wood by various procedures, establishment of differences between lignins recovered from various types of wood by the same procedure, quantitative determination of lignin in wood and cellulose, and structural studies of lignins produced in various procedures of cellulose cooking [1].

The IR spectra of industrial (soda and kraft) lignins and lignosulfonates are adequately studied, contrary to so-called organosolvent lignins. This is caused by the following factors. First, cooking with organic solvents was developed only recently in comparison with traditional delignification procedures, and practically none of these cooking procedures were brought to industrial use. Second, numerous organic solvents belonging to various types of organic compounds (alcohols, acids, aldehydes, and phenols) are used as agents of organosolvent cooking [2].

In this work we made an IR study of organosolvent lignins recovered from spent solution of aqueous-ethanol cooking of cellulose.

EXPERIMENTAL

For recording the IR spectra, lignin samples were prepared as mulls in Vaseline oil [3]. The spectra were recorded in potassium bromide and cesium iodide pellets on a Specord M80 spectrophotometer (Carl Zeiss, Jena) in the range 4000–400 cm^{-1} with the spectral resolution of 2 cm^{-1}; the monochromator was purged with dry air.

The data obtained were processed using the Softspectra 5.0 software (Etalon Joint-Stock Company, Moscow). The baseline was corrected using transmission maxima at ν 3700, 1800, 700, and 500 cm^{-1}. After that, the optical densities D in the main absorption maxima (except the range of vibrations of aliphatic C–H bonds obscured by absorption of Vaseline oil at 3000–2800, 1460, 1370, and 722 cm^{-1}) were determined. Assuming that the aromatic structures do not degrade under treatment, we selected the absorption band at 1512 cm^{-1} corresponding to the skeleton modes in the aromatic ring as an internal reference and evaluated the relative optical densities (ROD, %) of the other bands with respect to this band [4]:

$$\mathrm{ROD} = \frac{D_\nu}{D_{1512}} \times 100,$$

where D_{1512} is the optical density at 1512 cm^{-1} and D_ν is the optical density at wave number ν.

Since delignification of wood is a complicated process, first we recorded the IR spectra of the samples of spruce dioxane lignin recovered by the Pepper procedure [2] and subjected to treatment in alkaline (8 g l^{-1} NaOH), aqueous, and aqueous-ethanol media at 55, 70, 80, and 90°C. After treatment, the lignin was recovered by acidification of the solution with hydrochloric acid to pH 3.

Both the absorption spectrum of the initial lignin sample and the spectra of the samples subjected to treatment contain a set of absorption bands characteristic of dioxane lignins of coniferous wood. The results of assignment of the bands, based on published data [1, 5], are listed in Table 1.

The similarity of the spectra suggests principal preservation of the chemical structure of dioxane lignin and degree of its polydipersity, affecting spectrum

Table 1. Absorption bands of dioxane lignin samples

ν, cm^{-1}	Assignment
3420	Stretching modes of O–H bonds
1712	Stretching modes of C=O bonds in aldehydes, nonconjugated ketones, and COOH groups
1672	Stretching modes of C=O bonds in *para*-substituted aryl ketones
1592, 1512	Skeleton vibrations of aromatic ring
1268, 1220	Skeleton vibrations of guaiacyl ring
1140	In-plane bending modes of C–H bonds in guaiacyl ring
1080	Stretching modes of C–O bonds
970	Out-of-plane bending modes of =C–H bond (*trans*)
855	Out-of-plane bending modes of C–H bond in aromatic ring

Table 2. Relative optical densities in the absorption maxima of untreated dioxane lignin and the samples after treatment

ν, cm^{-1}	ROD, %					
	without treatment	treatment conditions				
		water, 55°C	aqueous ethanol, 55°C	water, 70°C	water, 80°C	water, 90°C
3420	56.0	60.0	57.0	55.0	54.0	62.0
1712	26.0	20.0	21.0	23.0	24.0	26.0
1672	25.0	20.0	19.0	21.0	22.0	24.0
1592	47.0	45.0	45.0	46.0	47.0	49.0
1512	100.0	100.0	100.0	100.0	100.0	100.0
1268	107.0	105.0	113.0	108.0	108.0	111.0
1220	78.0	75.0	83.0	79.0	80.0	84.0
1140	70.0	64.0	72.0	64.0	65.0	69.0
1080	52.0	44.0	51.0	46.0	47.0	48.0

diffuseness in the range 1600–800 cm^{-1}. Noticeable differences in the spectra of the samples studied are observed only in the range of stretching modes of carbonyl groups between 1750 and 1650 cm^{-1}. Treatment at a temperature above 55°C in aqueous medium results in disappearance of the absorption maximum at 1672 cm^{-1}, i.e., the ratio of the amounts of α-carbonyl groups conjugated with an aromatic ring and nonconjugated C=O bonds somewhat decreases.

A comparison of the relative intensities of the main absorption bands of the samples studied (Table 2) shows that, in all of the samples subjected to treatment, especially at low temperatures, the content of carbonyl groups somewhat decreases compared to the initial lignin. Some increase in the content of carbonyl structures at high treatment temperature is apparently caused by development of oxidation processes under the action of dissolved oxygen. Hydroxy groups in lignin remain essentially unchanged at a temperature below 80°C. At 90°C, the content of hydroxy groups increases by approximately 7–8% owing to developing degradation of aryl alkyl ether structures accompanied by release of phenolic and alcoholic groups. This conclusion is confirmed by variation of the optical density at 1080 cm^{-1} corresponding to the stretching modes of the C–O bonds, mainly of those in the C–O–C ether structures.

The similar results were obtained in chemical analysis of functional composition of the samples by the standard procedures [6] (Table 3). These results suggest that conversion of lignin in alkaline aqueous and aqueous-ethanol medium proceeds by the mechanism of oxidative degradation. Then, we studied lignins recovered from the solutions of alkaline (NaOH concentration 60 $g\,l^{-1}$) cooking of spruce wood in aqueous (soda cooking) and 25% aqueous-ethanol (organosolvent cooking) media at 170°C and 160°C, respectively (Table 4). Samples of the cooking solution were withdrawn in 5, 6, and 7 h in soda cooking (samples N/1–N/3, respectively) and every hour in organosolvent cooking (E/1–E/6, respectively). We analyzed the precipitates formed in the liquor

Table 3. Functional composition of untreated dioxane lignin and samples after treatment

Functional group	Content, %					
	without treatment	treatment conditions				
		water, 55°C	aqueous ethanol, 55°C	water, 70°C	water, 80°C	water, 90°C
Methoxy	16.00	14.90	15.33	14.82	14.65	14.83
Total acidic	3.37	2.83	2.93	4.01	4.41	4.42
Strongly acidic (carboxy)	0.75	0.56	0.87	0.91	1.07	1.00
Carbonyl	3.58	2.07	2.24	2.51	2.78	3.91
Phenolic hydroxy	2.98	2.27	2.06	3.10	3.34	3.42

Table 4. Relative optical density of the samples in the maxima of absorption bands for lignins recovered from soda cooking liquor (N/1-N/3) and organosolvent liquor (E/1-E/6)

ν, cm^{-1}	ROD, %, for indicated sample								
	N/1	N/2	N/3	E/1	E/2	E/3	E/4	E/5	E/6
3420	90.0	76.0	71.0	61.0	65.0	65.0	62.0	60.0	56.0
1712	45.0	35.0	35.0	65.0	30.0	29.0	30.0	29.0	27.0
1672	36.0	34.0	30.0	30.0	29.0	27.0	33.0	27.0	28.0
1592	58.0	54.0	51.0	46.0	48.0	45.0	49.0	44.0	45.0
1512	100.0	100.0	100.0	100.0	100.0	100.0	100.0	100.0	100.0
1268	112.0	119.0	110.0	117.0	113.0	110.0	115.0	112.0	108.0
1220	92.0	97.0	90.0	87.0	89.0	89.0	94.0	91.0	86.0
1140	104.0	99.0	84.0	88.0	88.0	84.0	93.0	83.0	79.0
1080	0.0	102.0	78.0	92.0	100.0	86.0	113.0	90.0	80.0
972	24.0	46.0	32.0	0.0	38.0	32.0	46.0	33.0	30.0
856	0.0	30.0	22.0	24.0	25.0	25.0	28.0	25.0	22.0

after its keeping for 1 day after cooking completion and the samples recovered immediately after cooking by acidification of the liquor with hydrochloric acid to pH 3. The latter procedure allows recovery of lignin from the cooking liquor practically quantitatively, whereas only high-molecular-weight fraction of lignin precipitates spontaneously. The absorption spectra of these precipitates (Figs. 1a, 1b) contain a strong broad band at approximately 1600 cm^{-1}, which can be assigned to asymmetric stretching vibrations of the carbon–oxygen bond in carboxylate anion. This is confirmed by significant absorption at 1400 cm^{-1}, partially overlapping with absorption bands of Vaseline oil and corresponding to $\nu_s(-COO^-)$. The absorption bands corresponding to the skeleton vibrations of the aromatic ring, bending vibrations of aromatic CH bonds, and vibrations of the ether bonds, characteristic of lignin samples, allow us to assign these samples to coniferous lignin samples in the salt form due to recovery from alkaline solution.

Normalization of the resulting spectra by referencing the optical densities to absorption of aromatic ring, which is a common procedure in IR spectroscopy of lignin, appeared to be impossible because of overlapping of absorption bands corresponding to the skeleton vibrations and those of carboxylate anion. In addition, the lignins recovered by this procedure are not representative samples. Therefore, we further analyzed the samples recovered from liquors by acidification with hydrochloric acid. The spectra of these samples are typical for coniferous lignins and have a set of absorption bands consistent with published data (Table 1).

Comparison of the series of samples N/1–N/3 with E/1–E/6 (Table 4) reveals the influence of alcohol on the functional composition of the resulting lignin. Samples N/1–N/3 prepared by soda delignification are characterized by increased content of hydroxy groups, decreasing in the course of cooking. This is apparently

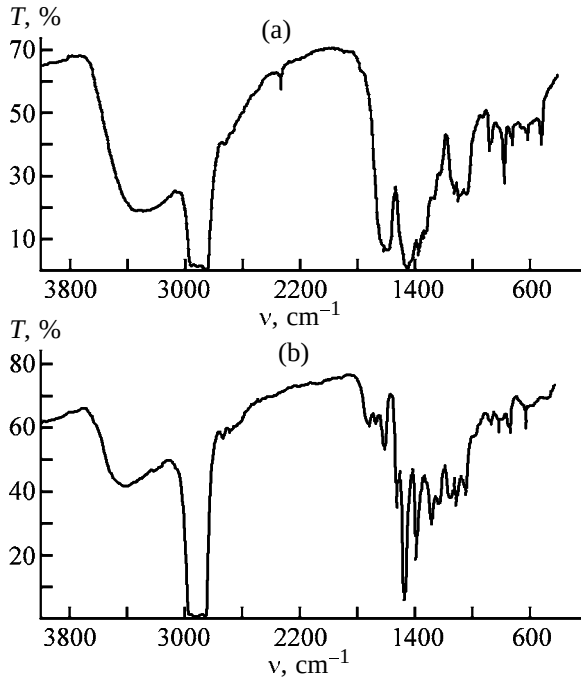

Fig. 1. IR spectra of (a) lignin obtained in keeping of solution of alkaline aqueous-ethanol cooking for 1 day and (b) lignin recovered from the solution of alkaline aqueous-ethanol cooking by acidification. (*T*) Transmission and (ν) wave number.

caused by ethoxylation of phenolic hydroxyls under conditions of alcoholic cookings. In the range of absorption of carbonyl structures, the most pronounced difference between the two series appears for the band at 1700 cm^{-1}: the content of C=O bonds nonconjugated with the aromatic ring in lignin produced by soda cooking is less by 20–50%, i.e., this lignin is significantly more oxidized in comparison with the samples obtained in the presence of ethanol. In the range of absorption of C–O single bonds, no significant differences between these series of samples were observed.

Comparison of the absorption intensity of the samples withdrawn at various instants of time shows some decrease in the relative content of the main functional groups of lignin. This is apparently caused by both elimination of various groups from aromatic ring and development of radical condensation of lignin. This effect is the most typical for soda cooking (N/1–N/3). In the case of alcohol cooking, lignin obtained at various instants of time in the last stage of the process has the smallest differences in the functional structure.

CONCLUSIONS

(1) The IR spectra of organosolvent lignins recovered by alkaline delignification in the presence of ethanol have the set of absorption bands typical for lignin of spruce wood.

(2) Comparison of the IR spectra of organosolvent and alkaline (soda) lignins shows that, in delignification in aqueous-ethanol medium, lignin passes into solution in less oxidized state than in cooking of wood in aqueous alkaline medium.

REFERENCES

1. *Lignins: Occurrence, Formation, Structure, and Reactions*, Sarkanen, K.V. and Ludwig, C.H., Eds., New York: Wiley, 1971.
2. Skrebets, T.E., Gur'ev, A.Yu., Ryabeva, N.V., and Bogolitsyn, K.G., *Izv. Vyssh. Uchebn. Zaved., Lesn. Zh.*, 1994, no. 1, pp. 103–110.
3. *Applied Infrared Spectroscopy*, Kendall, D., Ed., New York: Chapman and Hall, 1966.
4. Smith, A., *Applied Infrared Spectroscopy*, New York: Wiley, 1979.
5. Karklin', V.B., *Khim. Drev.*, 1981, no. 4, pp. 34–44.
6. Zakis, G.F., Mozheiko, L.N., and Telysheva, G.M., *Metody opredeleniya funktsional'nykh grupp lignina* (Methods of Determination of Functional Groups of Lignin), Riga: Zinatne, 1975.

Russian Journal of Applied Chemistry, Vol. 77, No. 9, 2004, pp. 1540–1543. Translated from Zhurnal Prikladnoi Khimii, Vol. 77, No. 9, 2004, pp. 1551–1554.

MACROMOLECULAR CHEMISTRY AND POLYMERIC MATERIALS

Nonadditive Effect of Components of a Binary Plasticizer on the Properties of Polyether–Urethane–Ureas

V. V. Tereshatov, V. V. Fedchenko, E. N. Tereshatova, and M. A. Makarova

Institute of Technical Chemistry, Ural Division, Russian Academy of Sciences, Perm, Russia

Received April 28, 2004

Abstract—The effect of a mixture of di(2-ethylhexyl) phthalate and tributyl phosphate on the properties of segmented polyether–urethane–ureas was examined. The data obtained for the elastomers with individual and mixed plasticizers were compared. The efficiency of using the binary plasticizer for controlling the properties of polyether–urethane–ureas was assessed.

One of the ways to control the rheological, thermal, and mechanical properties of polyurethane compounds is their plasticization with liquids of various chemical structures: ethers, esters, chloroparaffins, and other compounds [1–5]. The performance of certain liquids as plasticizers was demonstrated for many block (so-called segmented, SPU) polyurethanes [2–5].

The properties of microheterogeneous plasticized polyurethanes depend on the effect of the plasticizer on the miscibility of liquid and solid polymer blocks. As the solubility of rigid blocks in the flexible phase of the polymer changes, the amount of the rigid component in this phase and the content of the microdispersed filler (domains of rigid blocks) in the material increase or decrease; the SPU properties change correspondingly.

In plasticization of the same polyurethane with different liquids, samples of the material with a lower glass transition point of the flexible phase T_g^s may have higher elastic modulus and higher strength. On the contrary, less strong and softer SPU samples may have higher glass transition point of the flexible polymeric matrix [2]. All these data were obtained with microheterogeneous polyurethane compounds plasticized with individual liquids.

The possibility of controlling the SPU properties by plasticization with mixtures of low-molecular-weight liquids has not been examined. The use of mixed plasticizers instead of individual liquids may offer new opportunities. Of practical interest are mixtures of commercially available plasticizers.

Our goal was to assess the possibility of controlling the properties of segmented polyether–urethane–ureas (SPUUs) by using binary plasticizers consisting of tributyl phosphate (TBP) and di(2-ethylhexyl) phthalate (DEHP). These compounds affect the structure and properties of SPUUs differently. Depending on the structure of flexible polyether blocks, DEHP either does not noticeably affect the microphase segregation in the material or acts as a "precipitant" of rigid blocks, whereas TBP improves the miscibility of flexible polyether and rigid urethane–urea blocks [2].

EXPERIMENTAL

We used plasticized polyether–urethane–ureas based on oligoethers: SPUU-1 with polypropylene oxide flexible segments and SPUU-2 with polytetramethylene oxide flexible blocks. The SPUUs were prepared from oligo(propylene oxide)diol and oligo(tetramethylene oxide)diol prepolymers (Laprol-1052 and SKU-PFL-100, respectively) prepared by reactions of the corresponding oligomeric diols with toluene-2,4-diisocyanate (diisocyanate : diol molar ratio 2 : 1). The molecular weight of the oligomeric diols and prepolymers was ~1000 and ~1400, respectively (estimated from the content of functional groups).

The prepolymers were cured with methylenebis(*o*-chloroaniline) (Diamet Kh) preliminarily dissolved in DEHP, TBP, or their mixtures. The molar ratio of the prepolymers to Diamet Kh was 1.03. Samples were prepared as described in [5].

The plasticizer content in all the samples was 14 wt %. Such amount of the plasticizers ensures high relative strain (>600%) and high strength of the material (tensile strength of SPUU-1 and SPUU-2 no less than 25 and 30 MPa, respectively). The physicome-

1070-4272/04/7709-1540 © 2004 MAIK "Nauka/Interperiodica"

Properties of SPUU-1 derived from oligo(propylene oxide)diol (1) and SPUU-2 derived from oligo(tetramethylene oxide)diol (2)

x_2	σ_n, MPa		E_{100}, MPa		ε, %		T_g^s, °C		η, Pa s^{-1}	
	1	2	1	2	1	2	1	2	1	2
0	17.1	22.8	1.7	6.2	850	680	–24	–61	8	4
0.30	22.7	31.7	2.8	7.4	840	710	–32	–67	13	7
0.43	23.5	32.9	3.3	7.9	820	700	–35	–68	18	10
0.57	25	35.8	3.6	8.3	800	640	–38	–70	22	11
0.70	25.4	34.0	4.1	8.9	790	650	–41	–71	28	12
1.0	26.3	33.2	6.9	10.6	770	640	–45	–71	43	21

chanical characteristics of SPUUs {nominal tensile strength σ_n (maximal stress calculated per initial cross section of the sample), relative elongation at break ε_n (at σ_n), elastic modulus E_{100} (at ε_n = 100%), and breaking stress per actual sample cross section, $f_b = \sigma_n[(\varepsilon_n + 100)/100]$} were determined at an extension rate of 0.28 s^{-1} at 23°C.

The glass transition point of the flexible phase of SPUUs was determined with a DSM-2 differential scanning calorimeter at slow (~0.02 deg s^{-1}) heating.

The rheological properties of the reaction mixture were studied at the compounding and casting temperature of 55 ± 1°C on a Rheotest-2 cone–plate viscometer at a shear rate of 180 s^{-1}.

The IR spectra were recorded on a Bruker IFS 66/S Fourier spectrometer. Elastomer films were prepared without using volatile solvents [5].

The mechanical characteristics, glass transition points T_g^s of SPUUs, and shear viscosities η of the reaction mixtures 30 min after compounding at various contents x_2 of DEHP in the binary plasticizer are listed in the table.

Figure 1 shows the dependence of the breaking tensile stress of SPUU-1 and SPUU-2 on x_2. These data show that components of the mixed plasticizer affect the mechanical properties of the materials and the glass transition point of the flexible phase nonadditively. The effect of DEHP and TBP on the viscosity η of the reaction mixtures after compounding is also nonadditive.

In plasticization solely with TBP, the strength characteristics and elastic modulus of SPUUs are the lowest, and T_g^s, the highest, which is due to the negative effect of TBP on the microphase segregation of flexible polyether and rigid urethane–urea blocks. This is clearly seen, e.g., from the IR spectra of SPUU samples in the range of stretching vibrations of carbonyl groups in urethane and urea fragments (ν = 1620–1750 cm^{-1}) (Figs. 2a, 2b). According to [5–7], the microphase segregation of flexible and rigid blocks in the material can be judged from the intensity of the band at ν = 1640 cm^{-1} (carbonyl vibrations in self-associates of urea groups localized in domains of urethane–urea blocks).

An appreciable decrease in the intensity of this band in the IR spectra of SPUU-1 and SPUU-2 plasticized with TBP (Fig. 2a, curve *5*; Fig. 2b, curve *4*) suggests transition of a part of rigid blocks from the rigid to flexible phase of the elastomer; as a result, the amount of the microdispersed rigid phase acting as reinforcing filler decreases. Increased content of the rigid component in the flexible phase of the polymer in the presence of TBP results in a weaker effect of this plasticizer on the glass transition point T_g^s of SPUU, compared to plasticization with DEHP, despite the fact that the glass transition point T_g of TBP (–131°C) is lower than that of DEHP (–90°C). The T_g^s of nonplasticized SPUU-1 is –16°C. Similar pattern is observed with SPUU-2 (see table).

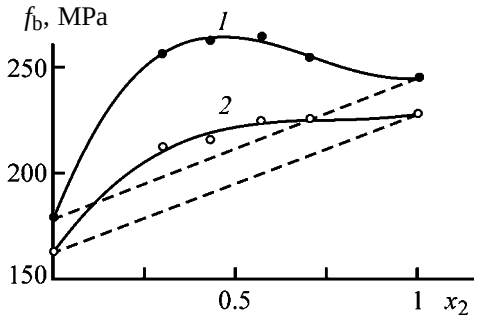

Fig. 1. Breaking tensile stress f_b of (*1*) SPUU-1 and (*2*) SPUU-2 as a function of DEHP content x_2 in the mixed plasticizer. Dashed lines correspond to the additive effect of the plasticizer components.

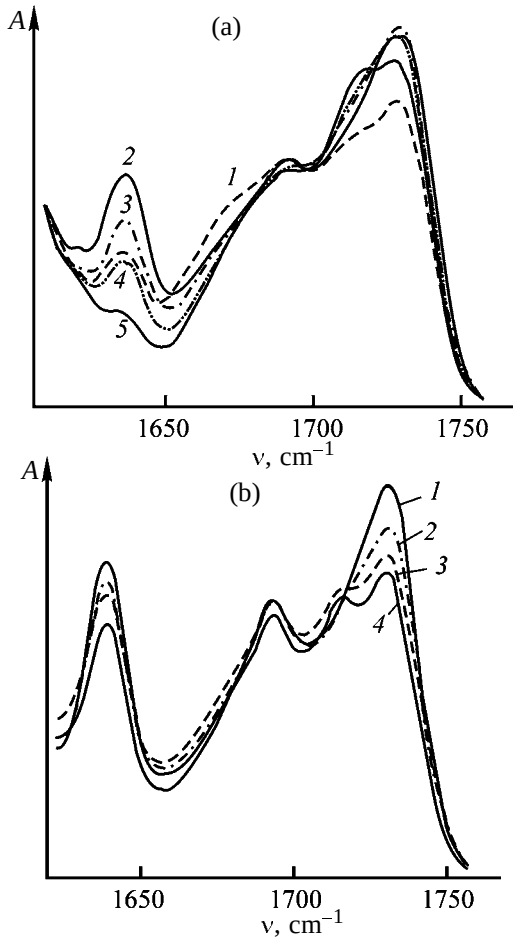

Fig. 2. IR spectra of (a) SPUU-1 and (b) SPUU-2 as influenced by the binary plasticizer composition. (*A*) Absorption and (ν) wave number. (a) (*1*) no plasticizer; DEHP content (wt %) in the binary plasticizer: (*2*) 100, (*3*) 70, (*4*) 30, and (*5*) 0. (b) DEHP content (wt %) in the binary plasticizer: (*1*) 100, (*2*) 70, (*3*) 30, and (*4*) 0.

The influence of individual plasticizers (including DEHP and TBP) on the structure and properties of SPUUs was described in detail in [2].

On replacement of 30 wt % of TBP (x_2 = 0.3) by DEHP, the amount of self-associates of urea groups in SPUU-1 becomes close to the content of these stable species in the nonplasticized material, which can be readily seen from changes in the intensity of the carbonyl absorption band at ν = 1640 cm^{-1} (Fig. 2a, curve *3*). The strength characteristics of the material, σ_n and f_b, sharply increase in going from the individual to mixed plasticizer, and the glass transition point T_g^s decreases because of a decrease in the amount of rigid blocks dissolved in the flexible phase of the polymer.

As the DEHP content in the mixture with TBP is increased further, the glass transition point of the flexible phase of SPUU decreases to a lesser extent. This is especially true for SPUU-2 containing poly(tetramethylene oxide) flexible segments. As already noted, di(2-ethylhexyl) phthalate has virtually no effect on the microphase segregation in the material. Increased DEHP content in the binary plasticizer has a weaker effect on T_g^s of SPUU-2, compared to T_g^s of SPUU-1, which could be expected from the IR data (band at ν = 1640 cm^{-1}, Figs. 2a, 2b).

It is known that the strength of segmented polyurethanes depends not only on the amount of the reinforcing filler but also on other factors, including intermolecular interaction in the flexible phase and orientation of polymeric chains in extension of the material [8]. An increase in the degree of microphase segregation with increasing DEHP content in the plasticizer is accompanied by a decrease in the content of urethane and urea groups capable of hydrogen bonding in the SPUU elastic matrix; this factor negatively affects the strength of the material. Apparently, the superposition of factors oppositely acting on the mechanical properties of SPUUs is responsible for the essentially nonlinear dependence of the material strength on the DEHP content in the binary plasticizer. Even at x_2 = 0.6, the tensile strength and breaking stress of SPUU-1 plasticized with the mixed plasticizer only slightly differ from ε_n and f_b of the elastomer plasticized with individual DEHP (see table, Fig. 1). The dependence of the SPUU-2 strength on the DEHP content in its mixture with TBP passes through a maximum at x_2 = 0.6. The elastic modulus E_{100} of this material is appreciably lower than that of the SPUU plasticized with individual DEHP. For example, at x_2 = 0.57, E_{100} of SPUU-2 decreases from 10.6 to 8.3 MPa. For SPUU-1, the decrease in E_{100} is still more pronounced: from 7.0 to 3.6 MPa.

Thus, the mechanical properties of SPUUs plasticized with the mixed plasticizer and one of its components differ essentially.

Another positive effect achieved on partial replacement of DEHP by TBP in SPUU is a sharp decrease in the viscosity of the reaction mixture, with the high strength of the cured material being preserved. For example, at the TBP weight fraction in the mixture of 0.43 (x_2 = 0.57), the viscosity of the SPUU-1 reaction mixture decreases from 21 to 12 Pa s. The viscosity of the uncured SPUU-2 reaction mixture 30 min after compounding at 50°C is 22 Pa s, whereas with a single plasticizer, DEHP, the viscosity under the same conditions is as high as 43 Pa s.

Preservation for a long time of the low viscosity of polyurethane compounds is necessary for obtaining

reinforced and unreinforced polyurethane items of complex shape without blisters.

For polyurethane items subjected to strong strains in service, it is important to ensure high strength with considerably decreased tension modulus E_{100}. At the same strain, the material with lower E_{100} will experience weaker mechanical load, which will enhance its performance.

It should be noted that, according to our experiments, a similar decrease in E_{100} of SPUU-1 can be attained by introducing 20 wt % DEHP instead of 14 wt % mixed plasticizer. In so doing, however, the material strength decreases from 25 to 17 MPa.

CONCLUSIONS

(1) In plasticization of segmented polyether–urethane–ureas with a mixture of tributyl phosphate with di(2-ethylhexyl) phthalate of various compositions, we revealed a pronounced nonadditive influence of the plasticizer components on the strength and elasticity of these materials, on the glass transition point of the flexible phase, and on the rheological properties of the reaction mixtures.

(2) According to IR data, the plasticizer composition significantly affects the microphase segregation in polyether–urethane–ureas. This is manifested particularly strongly in the material with poly(propylene oxide) flexible blocks.

(3) The strength and strain characteristics of segmented polyurethane–ureas plasticized with a 60 : 40 mixture of di(2-ethylhexyl) phthalate and tributyl phosphate are not inferior to those of the material plasticized solely with di(2-ethylhexyl) phthalate. At the same time, the compositions with the binary plasticizer have two times lower viscosity, with considerably smaller tension modulus E_{100} of the cured material. This is important for preparing high-quality items and ensuring their efficiency at significant strains.

REFERENCES

1. *Thinius. Chemie, Physik und Technologie der Weichmacher*, Leipzig, 1963.
2. Tereshatov, V.V., Senichev, V.Yu., Tereshatova, E.N., and Makarova, M.A., *Handbook of Plasticizers*, Toronto: ChemTec, 2003, pp. 74–83.
3. Lyamkin, D.I., Misyuk, K.G., Pasternak, V.Sh., *et al.*, *Vysokomol. Soedin., Ser. B*, 1997, vol. 39, no. 3, pp. 545–550.
4. Baoyan Zhang and Huimen Tan, *Eur. Polym. J.*, 1988, vol. 34, nos. 3–4, pp. 571–580.
5. Tereshatov, V.V., Tereshatova, E.N., Makarova, M.A., and Tereshatov, S.V., *Vysokomol. Soedin., Ser. A*, 2002, vol. 44, no. 3, pp. 443–449.
6. Zharkov, V.V., Kopusov, L.I., and Kozlova, T.V., *Plast. Massy*, 1981, no. 12, pp. 41–45.
7. Tereshatov, V.V., Tereshatova, E.N., Begishev, V.P., *et al.*, *Vysokomol. Soedin., Ser. A*, 1994, vol. 36, no. 12, pp. 1988–1995.
8. Speckhard, T.A. and Cooper, S.L., *Rubber Chem. Technol.*, 1986, vol. 59, no. 3, pp. 405–431.

Russian Journal of Applied Chemistry, Vol. 77, No. 9, 2004, pp. 1544–1546. Translated from Zhurnal Prikladnoi Khimii, Vol. 77, No. 9, 2004, pp. 1555–1557.

MACROMOLECULAR CHEMISTRY AND POLYMERIC MATERIALS

Synthesis of Urea–Formaldehyde Oligomers without a Solvent

T. V. Bezbozhnaya, V. V. Zamashchikov, and A. I. Lutsyk

Litvinenko Institute of Physical Organic and Coal Chemistry, National Academy of Sciences of Ukraine, Donetsk, Ukraine

Received February 5, 2004

Abstract—A urea–formaldehyde oligomer comparing well with commercially avaliable KF-MT and KF-M resins in the adhesive power was prepared from solid paraform and urea without a solvent.

Synthetic urea–formaldehyde oligomers (UFOs) are widely used in wood-working industry as binders and as a base for adhesives. However, UFOs tend to self-cure during prolonged storage and transportation. Furthermore, the modern industrial synthesis of UFOs in multistep [1–4] and involves water as a solvent, with its subsequent distillation.

In this study we examined the possibility of preparing highly stable UFO without a solvent. The starting compounds were paraform (F) and urea (U). The products were tested as binders in production of chip boards.

EXPERIMENTAL

A flask equipped with a power-driven stirrer and a thermometer was charged with urea [pure grade, GOST (State Standard) 6691–77] and paraform [TU (Technical Specifications) 6-09-3208–78] in a definite molar ratio (the U : F ratio was varied from 1 : 1 to 1 : 6), after which solid sodium hydroxide (up to 2% relative to the total weight of U and F) preliminarily ground with a small amount of urea was added. The mixture was heated with stirring at 333 K for 2.5–3 h.

Within 5–10 min after switching on the stirrer, the mixture started to liquefy, and within 15–20 min it fully transformed into a viscous sticky liquid. Upon further heating for 2.5 h, the products with U : F > 1 : 3 hardened, and those with U : F 1 : 3.25, 1 : 3.5, 1 : 4, and 1 : 6 remained liquid. At room temperature, the oligomers with U : F 1 : 3.25 and 1 : 3.5 hardened in several days, and that with U : F 1 : 4 remained a stable viscous sticky liquid for at least 12 months.

The mixture starts to liquefy earlier with increasing temperature, stirring intensity, degree of initial grinding of urea grains, and amount of sodium hydroxide added. In the absence of NaOH, the mixture does not become liquid at 333 K over a period of 2.5 h. The individual components (urea, paraform) separately mixed with NaOH do not form liquid systems under similar conditions.

The liquefaction is not associated with accumulation of water during the reaction. According to GLC data (LKhM-8MD chromatograph, catharometer, stationary phase 5% TSEP on Polysorb, internal reference *n*-PrOH), the water content in the resin (initial ratio U : F = 1 : 4) 3 h after the start of the reaction did not exceed 4%. The change in the aggregation state of the system is undoubtedly caused by the base-catalyzed reaction of urea with paraform: during the first 20 min, the formaldehyde concentration sharply decreases (see figure) with accumulation of methylol groups, and subsequent changes occur more smoothly (the concentration of free formaldehyde in the resin was determined according to GOST 14231–88, and the concentration of methylol groups, by iodometric titration [5]). The main reaction of formation of methylol groups from formaldehyde is accompanied by side Cannizzaro reaction. According to GLC data, the methanol content in the oligomer sample with the initial ratio U : F = 1 : 4 did not exceed 3%.

The solid products obtained at the initial molar ratio U : F > 1 : 3 are virtually insoluble in water. The oligomers obtained at a high initial content of formaldehyde are readily soluble in water, but at U : F = 1 : 6 dissolution in water is accompanied by the release of unchanged paraform.

As the oligomer with U : F = 1 : 4 showed high stability, high solubility in water, and apparent adhesive power, we chose this product for subsequent tests as binder in chip board production.

This product has a high content of methylol groups (up to 30%). The high degree of nitrogen functionali-

1070-4272/04/7709-1544 © 2004 MAIK "Nauka/Interperiodica"

zation is confirmed by IR spectroscopy (Specord 75-IR, film on KBr, ν, cm^{-1}; the bands were assigned according to data of [6]): 3350 vs, br [ν(NH)]; 1000 vs, br [δ(OH) in $–CH_2OH$]; 1655 vs (amide I); 1538 vs (amide II); 1260 s (amide III); 1455 w, 1380 s [ν(CH) in $–CH_2OH$]; 2910 m [ν_{as}(CH) in $–CH_2OH$]; 2960 m [ν_{sym}(CH) in CH_2 of ethers, $–CH_2OH$]; 1170 w, 1060 [ν(C–O) in –C–O–C–]; 970, 935, 845 m, 805 w, 775 m [ν(C–O) in –C–O–C–, symmetric ring].

In the range 3500–3100 cm^{-1}, there is only one very strong band at 3350 cm^{-1}. This means that the amount of NH groups in the resin considerably exceeds the amount of NH_2 groups. The resins with a lower initial formaldehyde content exhibit two bands in this range, 3430 and 3330 cm^{-1}, characterizing the presence of $–NH_2$ and NH groups, respectively. A strong band at 1000 cm^{-1} is consistent with the high content of methylol groups.

There as an apparent unbalance between the initial amount of formaldehyde and total amount of formaldehyde and methylol groups determined in the resin 3 h after the start of the reaction; the unbalance grows with decreasing U : F ratio:

U : F	F_{in}, wt %	F + $–CH_2OH$, wt % (3 h)
1 : 1	33.0	30.1
1 : 1.23	38.0	34.5
1 : 2	50.0	46.5
1 : 3	60.0	52.7
1:3.5	63.6	40.9
1 : 4	66.7	40.4

Comparison of these results with the IR data shows that the unbalance is caused by formation of ether fragments in the resin (condensation of methylol groups) or of cyclic fragments like uronic rings [intramolecular reaction of methylol groups, reaction (1)]:

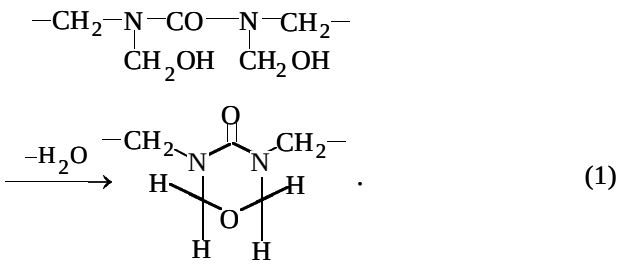

(1)

The bands at 845, 805, and 775 cm^{-1} can be apparently assigned to cyclic structures [6, 7], and the band at 1060 cm^{-1}, to linear ethers.

To check the binding power of the oligomer with U : F = 1 : 4, we prepared by standard procedures experimental chip board specimens. These specimens

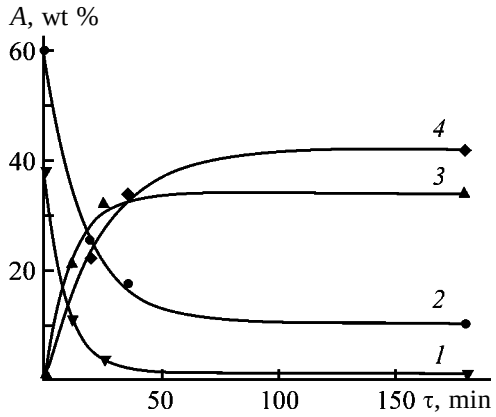

Kinetic curves of (*1*, *2*) consumption of free formaldehyde and (*3*, *4*) accumulation of methylol groups in condensation of urea with paraform. U : F (*1*, *3*) 1 : 1.23 and (*2*, *4*) 1 : 3; 333 K. (*A*) Content and (τ) time.

were prepared for tests according to GOST 10632–89 (COMECON Standard 5879–87). Pressing was performed at 433 K. The oligomer was added in an amount of 10 wt % relative to dry wood chips. The curing agent was NH_4Cl (1 wt % relative to the oligomer). As the oligomer with U : F = 1 : 4 is very viscous, it was taken as 40% aqueous solution.

To bring the U : F ratio to the level commonly used in commercial resins and to bind free formaldehyde whose content in the oligomer is 9–10%, we added urea to the oligomer just before use, so that the U : F ratio became 1 : 1.23.

For comparison, we also prepared chip board specimens with commercial resins KF-MT and KF-M, taken in the same amounts as the oligomer (as calculated for the dry matter). As seen from the table, the experimental chip board specimens prepared with our oligomer are not inferior in the bending strength to the specimens prepared with commercial resins KF-MT and KF-M and show lower water absorption and swelling in thickness.

Results of tests of experimental chip board specimens

Parameter	Oligomer*	KF-MT	KF-M
Density ρ, kg m^{-3}	704 ± 9	–	820
Ultimate bending strength σ_b, MPa	19.9 ± 0.4	22.0	21.0
Swelling in thickness in 2 h *h*, %	4.2 ± 0.6	10.0	10.0
Water absorption in 2 h *m*, %	32 ± 3	36.0	36.0

* Mean value for four chip board specimens.

The public-health tests of the experimental chip board specimens performed by the Sanitary-Epidemiological Station of Donetsk oblast showed the absence of formaldehyde emission.

CONCLUSIONS

(1) Urea–formaldehyde oligomers can be prepared without a solvent at the initial urea : formaldehyde ratio varied from 1 : 1 to 1 : 6.

(2) The oligomer with the initial molar ratio U : F = 1 : 4 can be used as a binder in production of chip boards.

REFERENCES

1. Doronin, Yu.G., Miroshnichenko, S.N., and Svitkina, M.M., *Sinteticheskie smoly v derevoobrabotke* (Synthetic Resins in Wood-Working), Moscow: Lesnaya Prom–st., 1987.
2. Siimer, K., Pehk, T., and Christjanson, P., *Macromol. Symp.*, 1999, vol. 148, pp. 149–156.
3. Kim, M.G., *J. Appl. Polym. Sci.*, 2000, vol. 75, no. 10, pp. 1243–1254.
4. Lisperguer, J. and Droguett, C., *Bol. Soc. Chil. Quim.*, 2002, vol. 47, no. 1, pp. 33–38.
5. Kalinina, L.S. and Kasterina, T.N., in *Khimicheskie metody issledovaniya sinteticheskikh smol i plastichеskikh mass* (Chemical Methods for Studying Synthetic Resins and Plastics), Moscow: Goskhimizdat, 1963, p. 159.
6. Jada, S.S., *J. Appl. Polym. Sci.*, 1988, vol. 35, pp. 1573–1592.
7. Pshenitsyna, V.P., Molotkova, N.N., and Pukhovitskaya, A.N., *Vysokomol. Soedin., Ser. A*, 1982, vol. 24, no. 8, pp. 1730–1734.

Russian Journal of Applied Chemistry, Vol. 77, No. 9, 2004, pp. 1547–1555. Translated from Zhurnal Prikladnoi Khimii, Vol. 77, No. 9, 2004, pp. 1558–1567.

CHEMISTRY OF FOSSIL FUEL

A Kinetic Model of Thermochemical Transformation of Solid Organic Fuels

E. A. Boiko and S. V. Pachkovskii

Krasnoyarsk State Technical University, Krasnoyarsk, Russia

Received February 17, 2004

Abstract—A kinetic model of thermochemical transformation of solid organic fuels was constructed. The mathematical model describes the kinetics of drying, release and combustion of volatiles, and combustion and gasification of the nonvolatile (coke) residue at linear heating. The kinetic curves of burn-out of Irsha–Borodino brown coal at various heating rates and model parameters were calculated.

The experience of using solid organic fuels at thermal power plants shows that there are still no pretreatment and combustion procedures ensuring high efficiency, reliability, and environmental safety of boiler operation [1].

To formulate recommendations concerning conditions and modes of combustion of solid organic fuels, it is necessary to elucidate an interrelation, based on kinetic parameters, between various steps and processes of thermochemical transformation of coals [2].

Description of heat and mass exchange and of aerodynamics in combustion chambers of boilers involves elucidation of the mechanism and construction of an adequate kinetic model of burn-out of a solid organic fuel [3–7]. The following questions should be answered [8]: What steps control the overall process kinetics? What steps are excessive in the kinetic scheme under consideration, and can this scheme be simplified? What kinetic mechanism (among several alternatives) is the most probable?

When a solid fuel is burnt as a dust, the degree of its thermochemical conversion is determined by a set of parameters of consecutive-parallel processes, in particular [9–13], by the rate of moisture evaporation, rate of release and combustion of volatiles, and rate of combustion of the nonvolatile residue. The scheme of burn-out of a coal substance is complicated in certain steps by such processes as low-temperature chemisorption of oxygen, gasification of the nonvolatile residue with carbon dioxide, steam, and hydrogen, transformations of chemical components of the mineral matter of the fuel, etc. [14].

As these processes strongly influence each other and their endo- and exothermic effects are significant, they should be taken into account in constructing the pattern of thermochemical transformation. The rates and parameters of the above processes are largely determined by the quality of the initial fuel. In this connection, to correctly describe and calculate the coal burn-out, it is necessary to elucidate the mechanism and construct a kinetic model of themochemical transformation of a solid organic fuel under conditions of a combustion chamber. This would allow proper choice of the process modes and conditions for pretreatment and combustion of solid organic fuels.

Analysis of the mechanism of complex physicochemical processes that occur in combustion of coals involves evaluation of the significance of particular process steps [15] and construction of a hierarchy of this steps following preset criteria [16]. To construct a mathematical model of thermochemical transformation of a solid organic fuel, we used the following process scheme. The process is subdivided into several relatively independent parallel-consecutive multistep stages (Fig. 1): drying and heating of a particle until release or ignition of volatiles; release of volatiles and their combustion near the particle; combustion of the nonvolatile (coke) residue consisting of organic and mineral matter [10].

The physicochemical model of thermal transformation of a solid organic fuel in a wide temperature range suggests that drying of a moist material is characterized by moisture evaporation from the bulk of a coal particle, with the evaporation front moving inside the particle as a phase transition front, under the influence of an increase in the temperature of the dry surface. Since the moisture present in fuel forms bonds

1070-4272/04/7709-1547 © 2004 MAIK "Nauka/Interperiodica"

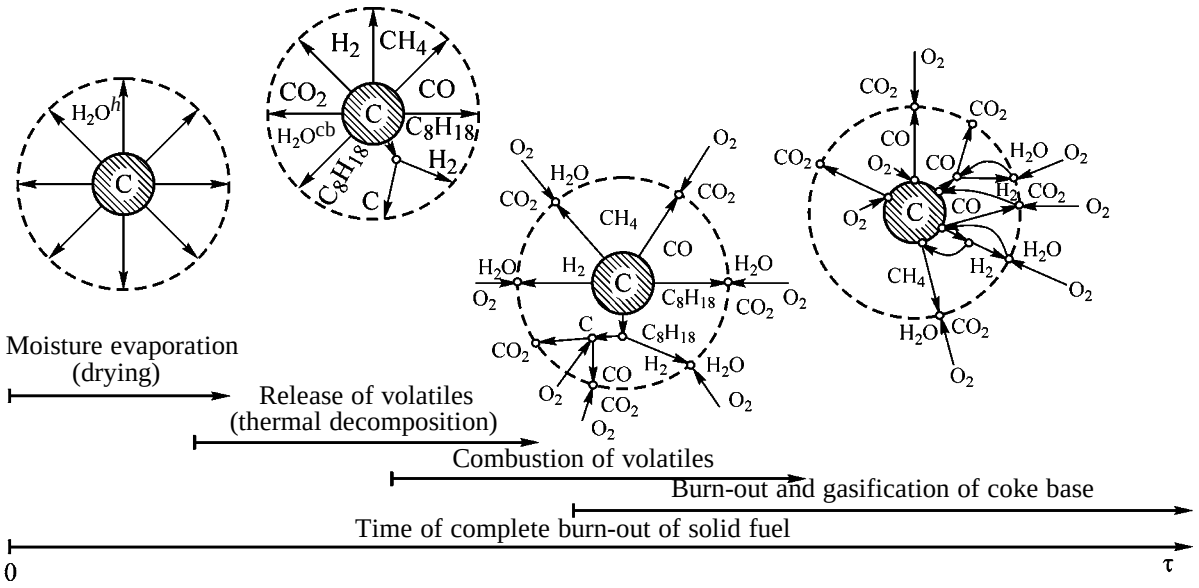

Fig. 1. Physicochemical model of thermochemical transformation of a solid fuel.

of different strength with the coal matter, it is appropriate to consider two independent fronts of evaporation of hygroscopic and chemically bound moisture [17], with the latter lagging behind the former.

As the temperature of the surface layer increases, the organic matter starts to thermally degrade, with the release of volatiles. The modern pyrolysis models consider the organic matter of coal as an ensemble of condensed aromatic, hydroaromatic, and heterocyclic structures (clusters) containing various functional groups as substituents [18]. As a fuel is heated, the bonds linking functional groups to ring clusters are cleaved, with the release of gaseous components (mainly CO_2, H_2, H_2O, CO, CH_4, HCN, aliphatic hydrocarbons). Simultaneously with the release of low-boiling gaseous components, the bridged structure of coal is cleaved, with the release of coarse molecular fragments (resins $C_8H_{18} \cdot 2H_2O$).

The released combustible gaseous compounds, on reaching certain concentration, start to react in the gas phase with atmospheric oxygen to give the final products: CO_2 and H_2O [19]. At deficiency of oxygen, the resins can degrade further to form secondary products, in particular, acetylene, benzene, hydrogen, and carbon black, which, in turn, can also react with oxygen to give products of complete (CO_2, H_2O) and incomplete (e.g., CO) combustion, with their subsequent afterburning [20].

The release of volatiles and their subsequent combustion are accompanied by heating of the coal particle, initiating combustion of its nonvolatile (coke) base. This reaction occurs on the surface of the coal particle and involves adsorption of oxygen from the gas phase on the carbon surface. Oxygen atoms react with the carbon surface to give complex carbon–oxygen species C_xO_y [11]. These species subsequently decay to give products of complete (CO_2) and incomplete (CO) combustion.

Water vapor and carbon dioxide formed by drying, evaporation of ballast volatiles, burning of combustible volatiles and of the coke base, and afterburning of incomplete combustion products can react with the solid phase to form CO and H_2. These reactions occur by the radical-chain mechanism and directly involve hydroxy groups as intermediates, with formation of HCOH molecules and then of donor–acceptor bonds with atomic carbon [21]. Collisions of atoms and molecules with vacant sites results in formation of intermediate complexes. These complexes stimulate electron transfer, providing chemisorption of gaseous components on the surface of the coke base.

The hydrogen formed by secondary reactions can react with carbon to form CH_4 and with oxygen to form H_2O [22]. Methane is oxidized in the gas phase to CO_2 and H_2O. The products of complete (H_2O) and incomplete (CO) combustion can react with each other to form CO_2 and H_2 [10].

The reactions that occur in the gas volume surrounding a particle and the heterogeneous reactions can be described by the following stoichiometric equations [7, 15, 17, 21, 23].

(1) Moisture evaporation: $W_0^h \rightarrow W^h$, where W_0^h is the initial moisture content of a fuel, and W^h is the amount of evaporated moisture in the gas volume.

(2) Release of volatiles: $V_{0i} \rightarrow V_{i,j}$, where V_{0i} is the initial concentration of volatiles in the solid phase of *i*th component, and $V_{i,j}$ is the concentration of volatiles in the gas phase of *i*th component in *j*th step.

(3) Secondary degradation of resins: $a_i V_{i,j,n} \rightarrow g_i V_{i,j,n+1}$, where $V_{i,j,n}$ are *i*th components of *j*th step of *n*th reaction of secondary degradation; $V_{i,j,n+1}$, *i*th components formed by $(n + 1)$st reaction of secondary degradation in *j*th step; and a_i and g_i, stoichiometric coefficients of degradation of *i*th component.

(4) Combustion of volatiles: $a_i V_i + b_i O_2 \rightarrow g_i P$, where $V_y i$ is the concentration of volatiles in the gas phase of *i*th component; O_2, oxygen concentration; *P*, concentration of combustion products of volatiles; and a_i, b_i, and g_i, stoichiometric coefficients in oxidation of *i*th component.

(5) Heterogeneous combustion of coke residue: $a_r c + b_r O_2 \rightarrow g_r P$, where *c* is the carbon concentration in the fuel (solid phase); *P*, concentration of products of complete and incomplete combustion of carbon; and a_r, b_r, and g_r, stoichiometric coefficients of combustion of the coke base.

(6) Homogeneous afterburning of incomplete combustion products: $a_m P_m + b_m O_2 \rightarrow g_m P$, where P_m is the concentration of incomplete combustion products; a_m, b_m, and g_m, stoichiometric coefficients for *m*th component of incomplete combustion products.

(7) Gasification of the coke residue: $a_s c + b_s P \rightarrow g_s P$, where a_s, b_s, and g_s are the stoichiometric coefficients of reactions involved in gasification of the coke base.

(8) Gasification of the products: $a_y P_m + b_y P_u = g_y P$, where P_u is the concentration of complete combustion products; a_y, b_y, and g_y, stoichiometric coefficients of reactions involving products of complete and incomplete combustion.

The suggested physicochemical formulation of the problem can be described by the following calculation scheme which allows construction of a mathematical model allowing control of material balances both for separate steps of coal combustion and for the overall process. In construction of a mathematical model, we assumed that multistep processes of thermochemical transformation of a solid fuel are additive, the functional groups in thermolysis of the fuel transform independently, the ratio of functional groups in the resin is the same as in the initial coal, and the volatiles released in pyrolysis of coal dust and the nonvolatile coke residue are ideally mixed with the oxidant (air) prior to the chemical reaction.

The mathematical model of kinetic processes of thermochemical transformation of a solid organic fuel, taking into account the above assumptions, is given in the differential form below (see scheme).

The kinetic equation of drying describes the kinetics of evaporation of hygroscopic moisture from the coal surface:

$$dH_2O_0^h/d\tau = -k_{0_{H_2O_0^h}} \exp[-E_{H_2O_0^h}/RT(\tau)]H_2O_0^h,$$

where $H_2O_0^h$ is the initial concentration of hygroscopic moisture in the fuel, kg kg^{-1}; k_0, preexponential factor, s^{-1}; *E*, activation energy, J mol^{-1}; *R*, universal gas constant, J mol^{-1} K^{-1}; *T*, process temperature, K; and τ, time, s.

The kinetic equation for the release of volatiles describes the content of residual volatiles in the fuel as a result of a multistep process of bond cleavage with the release of ballast (H_2O, CO_2) and combustible (H_2, CH_4, CO, resins $C_8H_{18} \cdot 2H_2O$) volatile vaporous and gaseous components during thermal decomposition of the coal organic matter [9]:

$$dV_0/d\tau = -\sum_{i=1}^{I}\sum_{j=1}^{J} k_{0_{V_{0i,j}}} \exp[-E_{V_{0i,j}}/RT(\tau)]V_{0i,j},$$

where V_0 is the initial concentration of volatiles in the fuel (solid phase), kg kg^{-1}; $i = 1, ..., I$, numbers of vaporous and gaseous components taken into account; and $j = 1, ..., J$, numbers of separate steps responsible for the release of *i*th component.

The kinetic equation of combustion of volatiles in the gas phase characterizes homogeneous combustion of the released volatiles and products of their secondary degradation in the absence of oxidant (O_2). The first and third terms in this equation describe the dynamics of accumulation of the released volatiles and their subsequent degradation. The second term describes formation of secondary volatile gaseous components by degradation of resins. The fourth term described homogeneous combustion of volatiles formed both by fuel degradation and by secondary degradation of particular vaporous and gaseous components (resins) [20]:

$$dV_0/d\tau = -\sum_{i=1}^{I}\left\{\left[\sum_{j_0=1}^{J_0} k_{0_{V_{0i,j_0}}} \exp[-E_{V_{0i,j_0}}/RT(\tau)]V_{0i,j_0}\phi_{V_{0i,j_0}}\right.\right.$$

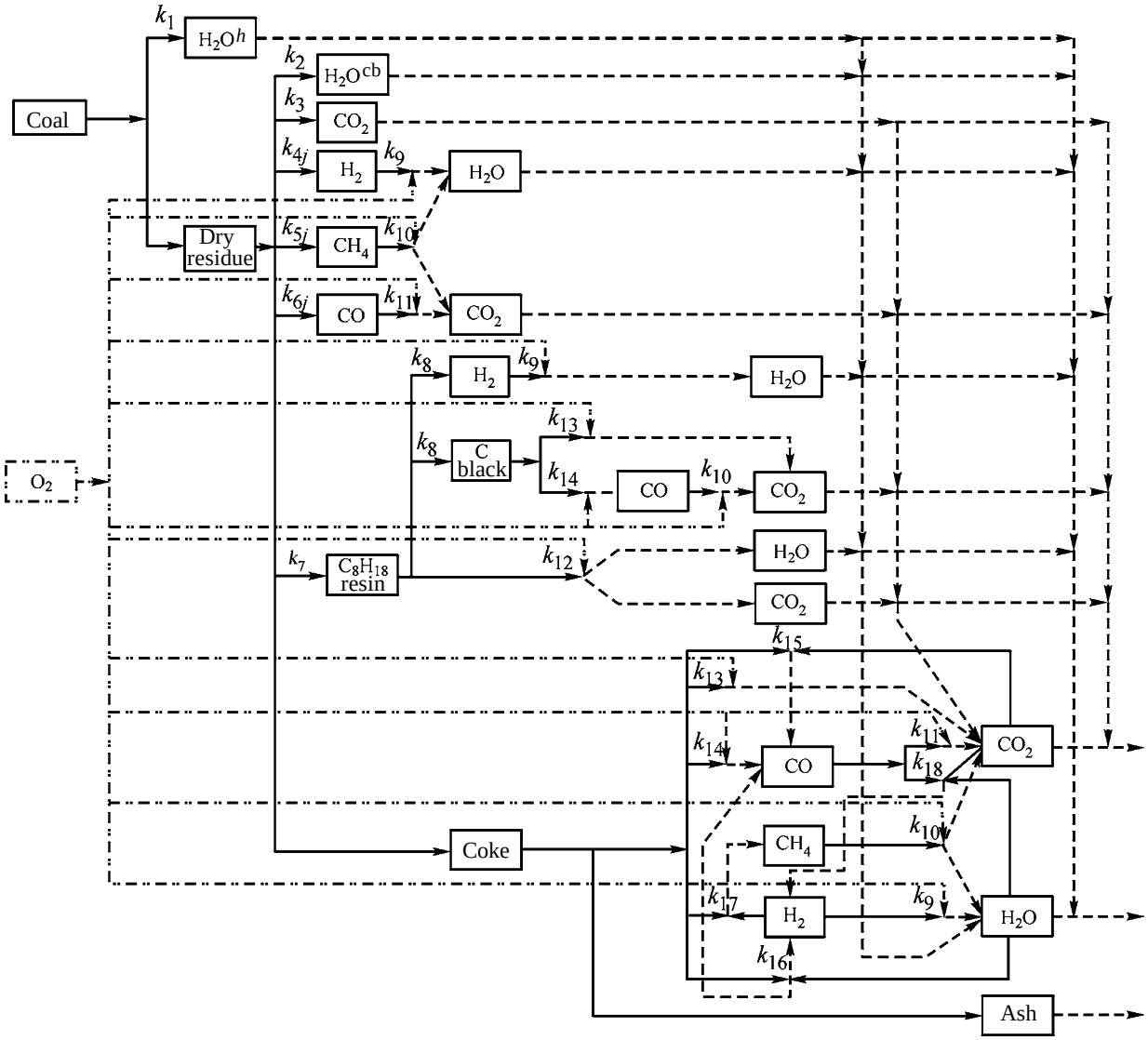

Scheme of calculating the kinetic parameters of thermochemical transformation of a solid fuel.

$$+ \sum_{i_d=1}^{I_d} \sum_{j_d=1}^{J_d} k_{0V_{i_d,j_d}} \exp[-E_{V_{i_d,j_d}}/RT(\tau)] V_{i_d,j_d} \phi_{i_d,j_d}$$

$$- \sum_{j=1}^{J} k_{0V_{i,j}} \exp[-E_{V_{i,j}}/RT(\tau)] V_{i,j} \phi_{i,j} \Big]$$

$$- k_{0V_i} \exp[-E_{V_i}/RT(\tau)] a_i V_i^{q_i} O_2^{b_i} \Big\},$$

where V is the concentration of volatiles in the gas phase, kg kg^{-1}; $j_0 = 1, ..., J_0$, numbers of separate steps responsible for the release of ith component from the fuel; $i_d = 1, ..., I_d$, numbers of volatile components whose degradation yielded ith substance; $j_d = 1, ..., J_d$, numbers of separate steps responsible for the release of ith component from an intermediate substance in the course of its degradation; a and b, stoichiometric coefficients; and ϕ_x, coefficient taking into account the mole fraction of component x in the gas phase.

The equation for the kinetics of burn-out and gasification of the coke base describes the consumption of carbon in oxidation of a fuel to CO and CO_2 and in reduction of products of compete and incomplete combustion (CO_2, H_2O, H_2, etc.). The first term describes the dynamics of burn-out of the coke base, and the second term, gasification of the combustion products [21]:

$$dc/d\tau = -\Big\{ \sum_{r=1}^{R} k_{0c,r} \exp[-E_{c,r}/RT(\tau)] a_r c^{a_r} O_2^{b_r}$$

$$+\sum_{s=1}^{S} k_{0_{c,s}} \exp[-E_{c,s}/RT(\tau)] a_s c^{a_s} P^{b_s}\Bigg\},$$

where c is the carbon concentration in the fuel (solid phase), kg kg^{-1}; O_2, oxygen concentration, kg kg^{-1}; P, concentration of fuel thermolysis products: evaporated moisture, released unburned volatiles, and products of complete and incomplete combustion of the nonvolatile residue (coke), kg kg^{-1}; r = 1, ..., R, numbers of groups of reactions taken into account when describing the burn-out of the coke base; and s = 1, ..., S, numbers of groups of reactions taken into account when describing the gasification.

In the equation describing the dynamics of variation of the oxygen concentration in homogeneous and heterogeneous combustion of volatiles and the coke base, the first, second, and third terms reflect consumption of O_2 in combustion of volatiles and the coke base and in homogeneous oxidation of incomplete combustion products, respectively:

$$dO_2/d\tau = -\Bigg\{\sum_{i=1}^{I} k_{0_{V_i}} \exp[-E_{V_i}/RT(\tau)] b_i V_i^{a_i} O_2^{b_i} + \sum_{r=1}^{R} k_{0_{c,r}} \exp[-E_{c,r}/RT(\tau)] b_r c^{a_r} O_2^{b_r} + \sum_{m=1}^{M} k_{0_{P_m}} \exp[-E_{P_m}/RT(\tau)] b_m P_m^{b_m} O_2^{b_m}\Bigg\},$$

where m = 1, ..., M are the numbers of incomplete combustion products of the coke base P_m.

The concentration of products of thermochemical transformation of a coal dust particle is taken into account by the equation describing the dynamics of moisture evaporation, release of ballast volatiles and of volatiles that remained unchanged in oxidation, complete and incomplete combustion of volatiles and the coke base, and gasification of the nonvolatile products [15]. The first term is related to moisture evaporation; the second term, to release or secondary degradation of ballast and unburned volatiles; the third term, to homogeneous combustion of volatiles; the fourth term, to heterogeneous burn-out of the coke base; the fifth and seventh terms, to gasification; the sixth term, to combustion of incomplete combustion products; and the eighth, ninth, and tenth terms, to consumption of components as a result of combustion and gasification of incomplete combustion products:

$$dP/d\tau = -k_{0_{H_2O_0^h}} \exp[-E_{H_2O_0^h}/RT(\tau)] H_2O_0^h + \sum_{i=1}^{I}\Bigg\{k_{0_{V_{0i,j_0}}} \exp[-E_{V_{0i,j_0}}/RT(\tau)] V_{0i,j_0} \phi_{V_{0i,j_0}} + \sum_{i_d=1}^{I_d}\sum_{j_d=1}^{J_d} k_{0_{V_{i_d,j_d}}} \exp[-E_{V_{i_d,j_d}}/RT(\tau)] V_{i_d,j_d} \phi_{V_{i_d,j_d}} - \sum_{j=1}^{J} k_{0_{V_{i,j}}} \exp[-E_{V_{i,j}}/RT(\tau)] V_{i,j} \phi_{V_{i,j}}\Bigg\} + \sum_{i=1}^{I} k_{0_{V_i}} \exp[-E_{V_i}/RT(\tau)] g_i V_i^{a_i} O_2^{b_i} \phi_{V_i} + \sum_{r=1}^{R} k_{0_{c,r}} \exp[-E_{c,r}/RT(\tau)] g_r c^{a_r} O_2^{b_r} \phi_{c,r} + \sum_{s=1}^{S} k_{0_{c,s}} \exp[-E_{c,s}/RT(\tau)] g_s c^{a_s} P^{b_s} \phi_{c,s} + \sum_{m=1}^{M} k_{0_{P_m}} \exp[-E_{P_m}/RT(\tau)] g_m P_m^{b_m} O_2^{b_m} \phi_{P_m} + \sum_{y=1}^{Y} k_{0_{P,y}} \exp[-E_{P,y}/RT(\tau)] g_y P_m^{a_y} P_u^{b_y} \phi_{P,y} + \sum_{s=1}^{S} k_{0_{c,s}} \exp[-E_{c,s}/RT(\tau)] b_s c^{a_s} P^{b_s} - \sum_{m=1}^{M} k_{0_{P_m}} \exp[-E_{P_m}/RT(\tau)] a_m P_m^{b_m} O_2^{b_m} - \sum_{y=1}^{Y} k_{0_{P,y}} \exp[-E_{P,y}/RT(\tau)] a_y P_m^{a_y} P_u^{b_y} - \sum_{y=1}^{Y} k_{0_{P,y}} \exp[-E_{P,y}/RT(\tau)] b_y P_m^{a_y} P_u^{b_y},$$

where y = 1, ..., Y are the number of groups of reactions involving products of complete P_u and incomplete P_m combustion of fuels; a, b, and g are stoichiometric coefficients.

The above system of differential kinetic equations was calculated with the following initial conditions: $H_2O_0^h = H_2O_{0in}^h$, $V_0 = V_{0in}$, $c = c_{in}$, $O_2 = O_{2in}$, $H_2O = 0$, $V = 0$, $P = 0$.

Along with the kinetic equations, this system ensures the law of mass preservation: $H_2O_0 + V_0 + c + O_2 + P = H_2O_{0in} + V_{0in} + c_{in} + O_{2in}$, because the following relationship is valid: $dH_2O_0^h/d\tau + dV_0/d\tau + dc/d\tau + dO_2/d\tau - dP/d\tau = 0$, where $P = P_u + P_m$.

This mathematical model describing the kinetics

Table 1. Mechanism and kinetic characteristics of various steps of thermochemical transformation of Irsha–Borodino brown coal

Step no.	Process	Reaction no.	Reaction	E, kJ mol^{-1}	k_0, s^{-1} (mol s^{-1})	References
1	Moisture evaporation (drying)	1	$H_2O_0^h \xrightarrow{k_1} H_2O$	14.4	4.01	[9]
2	Release of volatiles (thermolysis)	2	$H_2O_0^{cb} \xrightarrow{k_2} H_2O$	28.3	3.5×10^2	[9]
		3	$CO_{2_0} \xrightarrow{k_2} CO_2$	71.7	1.1×10^3	[9]
		4	$H_{2_0}^{(I)} \xrightarrow{k_{41}} H_2$	92.4	45.0	[9]
			$H_{2_0}^{(II)} \xrightarrow{k_{42}} H_2$	142.3	4.9×10^6	[9]
		5	$CH_{4_0}^{(I)} \xrightarrow{k_{51}} CH_4$	106.9	1.4×10^5	[9]
			$CH_{4_0}^{(II)} \xrightarrow{k_{52}} CH_4$	92.3	5.2×10^5	[9]
		6	$CO_0^{(I)} \xrightarrow{k_{61}} CO$	90.2	87.9	[9]
			$CO_0^{(II)} \xrightarrow{k_{62}} CO$	140.9	4.5×10^6	[9]
			$CO_0^{(III)} \xrightarrow{k_{63}} CO$	71.5	4.5×10^2	[9]
			$CO_0^{(IV)} \xrightarrow{k_{64}} CO$	43.2	0.3	[9]
		7	$C_8H_{18_0} \xrightarrow{k_7} C_8H_{18}$	75.9	2.5×10^2	[9]
		8	$C_8H_{18} \xrightarrow{k_9} 8C + 9H_2$	52.8	2.8×10^5	[9]
3	Combustion of volatiles	9	$2H_2 + O_2 \xrightarrow{k_9} 2H_2O$	41.1	250.0	[10]
		10	$CH_4 + 2O_2 \xrightarrow{k_{10}} CO_2 + 2H_2O$	50.3	230.0	[10]
		11	$2CO + O_2 \xrightarrow{k_{11}} 2CO_2$	42.7	222.0	[10]
		12	$2C_8H_{18} + 25O_2 \xrightarrow{k_{12}} 16CO_2 + 18H_2O$	55.3	306.0	[11]
4	Burn-out and gasification of coke base	13	$C + O_2 \xrightarrow{k_{13}} CO_2$	113.0	1.1×10^4	[9]
		14	$2C + O_2 \xrightarrow{k_{14}} 2CO$	118.0	1.2×10^4	[9]
		15	$C + CO_2 \xrightarrow{k_{15}} 2CO$	214.0	79.0×10^4	[9]
		16	$C + H_2O \xrightarrow{k_{16}} CO + H_2$	181.4	1.6×10^4	[9]
		17	$C + 2H_2 \xrightarrow{k_{17}} CH_4$	113.1	0.1×10^4	[11]
		18	$CO + H_2O \xrightarrow{k_{18}} CO_2 + H_2$	138.3	4.2×10^7	[10]

of thermochemical transformation of a solid fuel was used as the basis for an analytical experiment related to the burn-out of Irsha–Borodino brown coal (Kansk–Achinsk deposit) at various heating rates. The coal composition (per working mass) is as follows, %: moisture W^r 33, ash A^r 9.98, sulfur S^r 0.29, carbon C^r 41.2, hydrogen H^r 2.89, nitrogen N^r 0.57, and oxygen O^r 12.1, at Q_i^r = 15318 kJ kg^{-1}, V^{daf} = 48.2%. The mathematical model was based on the results of complex thermal analysis of the coal reactivity in various steps and on the evaluated kinetic parameters: numbers of separate steps i and j, activation energies E, probability factors k_0, fraction of the reacted substance, temperature ranges of reactions, etc. [24].

The types of the considered chemical reactions included in the calculation scheme and the kinetic parameters of various processes and steps of thermal transformation of Irsha–Borodino coal are given in Table 1.

To describe the nonisothermicity of themochemical transformation of coal, we supplemented the mathematical model with the linear heating law: $T = T_0 + b\tau$. It should be noted that, because of the large size

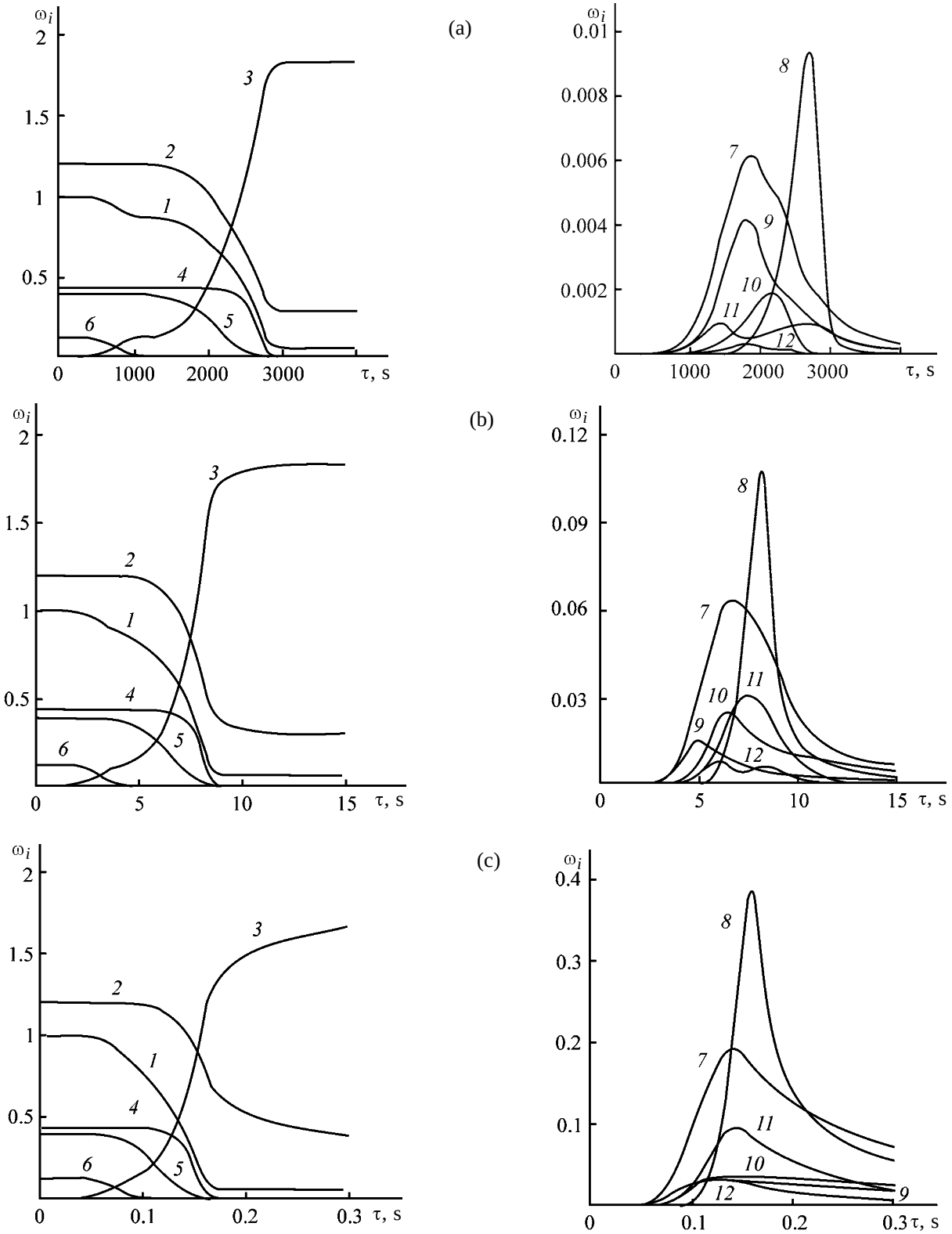

Fig. 2. Kinetics of thermochemical transformation of Irsha– Borodino coal at various heating rates ($b = dT/d\tau$, deg s^{-1}): (a) 0.167, (b) 10^2, and (c) 10^4. (*1*) Fuel weight loss, (*2*) oxygen concentration, (*3*) combustion products, (*4*) burn-out of the coke base, (*5*) release of volatiles, (*6*) moisture evaporation, (*7*) combustion of volatiles, (*8*) combustion of secondary degradation and gasification products, (*9*) combustion of CO, (*10*) combustion of H_2, (*11*) combustion of resin, and (*12*) combustion of CH_4; (ω_i) conversion and (τ) time.

Table 2. Relative duration of steps of thermochemical transformation of Irsha–Borodino coals at various heating rates

Step no.	Process	Heating rate, b, deg s^{-1}			
		0.167 (10 deg min^{-1})			
		onset, $\bar{\tau}_{i_o}$*	end, $\bar{\tau}_{i_e}$**	duration, $\bar{\tau}_{i_e} - \bar{\tau}_{i_o}$	superposition, $\bar{\tau}_{i_e} - \bar{\tau}_{i+1_o}$
1	Moisture evaporation (drying)	0	0.32	0.32	0.06
2	Release of volatiles	0.26	0.81	0.55	0.48
3	Combustion of volatiles	0.33	0.95	0.62	0.27
4	Burn-out and gasification of coke bae	0.68	1.0	0.32	–

Step no.	Heating rate, b, deg s^{-1}							
	100				10 000			
	onset, $\bar{\tau}_{i_o}$	end, $\bar{\tau}_{i_e}$	duration, $\bar{\tau}_{i_e} - \bar{\tau}_{i_o}$	superposition, $\bar{\tau}_{i_e} - \bar{\tau}_{i+1_o}$	onset, $\bar{\tau}_{i_o}$	end, $\bar{\tau}_{i_e}$	duration, $\bar{\tau}_{i_e} - \bar{\tau}_{i_o}$	superposition, $\bar{\tau}_{i_e} - \bar{\tau}_{i+1_o}$
1	0	0.42	0.42	0.17	0	0.55	0.55	0.31
2	0.25	0.80	0.55	0.51	0.24	0.78	0.54	0.51
3	0.29	0.90	0.61	0.38	0.27	0.88	0.61	0.42
4	0.52	1.0	0.48	–	0.46	1.0	0.54	–

* $\bar{\tau}_{i_o} = \tau_{i_o}/\tau_t$, where τ_t is the total burn-out time.
** $\bar{\tau}_{i_e} = \tau_{i_e}/\tau_t$.

and pronounced rigidity of the system of differential equations, the kinetic mechanism can be realized, as a rule, only within the framework of a unidimensional scheme [17]. The calculations were performed with a Pentium 4 computer in the Builder C++ 5.0 environment. The system of kinetic equations was solved numerically by the Runge–Kutta–Fehlberg method with automatic choice of the step and accuracy of 10^{-4}.

The results of calculating the dynamics of processes involved in combustion of Irsha–Borodino coal particles (both in separate steps and in total) are shown in Fig. 2 as degrees of thermochemical transformation ($\omega_i = m_i/m_0$, where m_i is the current weight of ith reacting component and m_0 is the initial weight of the fuel–air mixture) vs. time at various heating rates.

The computational experiment was performed at varied rates of linear heating of a coal particle, $b = dT/d\tau = 0.167$, 10^2, and 10^4 deg s^{-1}.

The results confirm the strong influence of the heating rate on the processes [23, 26]. Figure 2 shows that, as the vapor–gas medium is heated faster, the times characteristic of separate processes become shorter and are shifted relative to each other.

For example, the relative times in which the drying overlaps with the release of volatiles and the combustion overlaps with the gasification of the coke base are, respectively, 6 and 27% at $b = 0.167$ deg s^{-1}, 17 and 38% at $b = 10^2$ deg s^{-1}, and 31 and 42% at $b = 10^4$ deg s^{-1} (Table 2). As the heating rate is increased, the time of the onset of all types of reactions becomes shorter, and the relative times of the processes somewhat change. In particular, the time of moisture evaporation relative to the total burn-out time was 32% at $b = 0.167$ deg s^{-1}, 42% at $b = 10^2$ deg s^{-1}, and 55% at $b = 10^4$ deg s^{-1}; the relative time of the release of volatiles was 55, 55, and 54%; that of the combustion of volatiles, 62, 61, and 61%; and that of combustion and gasification of the nonvolatile (coke) residue, 32, 48, and 54%, respectively. Whereas at a heating rate of 0.167 deg min^{-1} superposition of the processes is insignificant, at 10^4 deg s^{-1} virtually all the processes occur in parallel, and the relative time of their superposition reaches 61%.

The heating rate affects the duration of separate steps of thermochemical transformation of the solid fuel and the rates and temperatures corresponding to the maxima of process steps. In particular, the total release of volatiles from Irsha–Borodino coal at a heating rate $b = 0.167$ deg s^{-1} is $W_{rv}^{max} = 5.66$ mg (g combustible matter)$^{-1}$ deg^{-1} and $T_{rv}^{max} = 340$°C, at

$b = 10^2$ deg s^{-1} $W_{rv}^{max} = 4.82$ mg (g combustible matter)$^{-1}$ deg^{-1} and $T_{rv}^{max} = 720$°C, and at $b = 10^4$ deg s^{-1} $W_{rv}^{max} = 3.56$ mg (g combustible matter)$^{-1}$ deg^{-1} and $T_{rv}^{max} = 830$°C. The burn-up of the coke base of Irsha–Borodino coal at a heating rate $b = 0.167$ deg s^{-1} is $W_{bc}^{max} = 2.95$ mg (g combustible matter)$^{-1}$ deg^{-1} and $T_{bc}^{max} = 460$°C, at $b = 10^2$ deg s^{-1} $W_{bc}^{max} = 2.1$ mg (g combustible matter)$^{-1}$ deg^{-1} and $T_{bc}^{max} = 950$°C, and at $b = 10^4$ deg s^{-1} $W_{bc}^{max} = 0.96$ mg (g combustible matter)$^{-1}$ deg^{-1} and $T_{bc}^{max} = 1750$°C. These data show that, at the coal heating rate increased to 10^2 deg s^{-1}, the burn-up of the nonvolatile residue (up to 50%) can be completed during the fuel heating, and the time of complete thermochemical transformation includes the nonisothermal and isothermal constituents.

CONCLUSION

The results of numerical experiments show that the suggested kinetic scheme and the corresponding mathematical model, on the one hand, allow analysis of the influence exerted by separate steps on the dynamics of the overall process and, on the other hand, are useful for calculating the degree of thermochemical transformation of solid organic fuels under actual industrial conditions.

REFERENCES

1. Pronin, M.S., Meshcheryakov, V.G., Kozlov, S.G., *et al.*, *Teploenergetika*, 1996, no. 9, pp. 7–12.
2. Kotler, V.R., *Teploenergetika*, 1992, no. 2, pp. 72–76.
3. Polyakov, A.A. and Shlenskii, O.F., *Khim. Tverd. Topl.*, 1994, no. 1, pp. 83–88.
4. Bykov, V.I., Vishnevskaya, T.M., and Tsirul'nichenko, N.M., *Fiz. Goren. Vzryva*, 1997, vol. 33, no. 4, pp. 39–45.
5. Starchenko, A.V., *Fiz. Goren. Vzryva*, 1998, vol. 34, no. 5, pp. 3–13.
6. Makarov, V.N. and Gerasimov, G.Ya., *Fiz. Goren. Vzryva*, 1999, vol. 35, no. 2, pp. 23–29.
7. Denisov, E.T., *Kinetika gomogennykh khimicheskikh reaktsii* (Kinetics of Homogeneous Chemical Reactions), Moscow: Vysshaya Shkola, 1978.
8. Panchenkov, G.M. and Lebedev, V.P., *Khimicheskaya kinetika i kataliz* (Chemical Kinetics and Catalysis), Moscow: Khimiya, 1974, 2nd ed.
9. Boiko, E.A., *Thermochim. Acta*, 2000, vol. 348, pp. 97–104.
10. *Osnovy prakticheskoi teorii goreniya* (Principles of the Practical Combustion Theory), Pomerantsev, V.V., Ed., Leningrad: Energoatomizdat, 1986.
11. Vilenskii, T.V. and Khzmalyan, D.M., *Dinamika goreniya pylevidnogo topliva* (Dynamics of Combustion of Pulverized Fuel), Moscow: Energiya, 1978.
12. Shatil', A.A., *Topochnye protsessy i ustroistva (issledovaniya i raschet)* (Combustion Processes and Devices (Studies and Calculation)), St. Petersburg: Tsentr. Kotloturb. Inst., 1997.
13. Babii, V.I. and Kuvaev, Yu.F., *Gorenie ugol'noi pyli i raschet pyleugol'nogo fakela* (Combustion of Coal Dust and Calculation of Coal-Dust Flare), Moscow: Energoatomizdat, 1986.
14. Boiko, E.A., Shishmarev, P.V., Didichin, D.G., and Zhadovets, E.M., *Khim. Tverd. Topl.*, 2003, no. 4, pp. 70–78.
15. Varfolomeev, S.D. and Gurevich, K.G., *Biokinetika* (Bioengineering), Moscow: FAIR, 1999.
16. *Eksperimental'nye metody khimicheskoi kinetiki* (Experimental Methods of Chemical Kinetics), Emanuel', N.M. and Sergeev, G.B., Eds., Moscow: Vysshaya Shkola, 1980.
17. Boiko, E.A., *Zh. Prikl. Khim.*, 1998, vol. 71, no. 10, pp. 1736–1741.
18. Boiko, E.A., Didichin, D.G., and Shishmarev, P.V., *Zh. Prikl. Khim.*, 2003, vol. 76, no. 4, pp. 605–610.
19. Yavorskii, I.A., *Fiziko-khimicheskie osnovy goreniya tverdykh goryuchikh iskopaemykh topliv i grafitov* (Physicochemical Principles of Combustion of Solid Fossil Fuels and Graphites), Novosibirsk: Nauka, 1973.
20. Warnatz, J., Maas, U., and Dibble, R.W., *Combustion: Physical and Chemical Fundamentals, Modeling and Simulation, Experiments, Pollutant Formation*, Berlin: Springer, 2001, 3rd ed.
21. Golovina, E.S., *Fiz. Goren. Vzryva*, 2002, vol. 38, no. 4, pp. 25–34.
22. Muller, M. and Pachaly, R., in *XXXII Kraftwerkstechnisches Kolloquium*, Dresden, 2000, pp. 99–108.
23. Maiboroda, V.D., Gergalov, V.I., and Petryaev, E.P., *Matematicheskoe modelirovanie khimicheskoi kinetiki* (Mathematical Simulation of Chemical Kinetics), Minsk: Universitetskoe, 1989.
24. Emanuel', N.M. and Knorre, D.G., *Kurs khimicheskoi kinetiki* (A Course of Chemical Kinetics), Moscow: Vysshaya Shkola, 1984, 4th ed.
25. Shemyakin, V.N., Mishina, K.I., and Kim, V.E., in *Sbornik nauchnykh trudov po problemam teplo- i massoperenosa v topochnykh ustroistvakh, gazogeneratorakh i khimicheskikh reaktorakh* (Coll. of Scientific Works on the Problems of Heat and Mass Transfer in Combustion Chambers, Gas Generators, and Chemical Reactors), Minsk, 1983, pp. 134–145.
26. Yablonskii, G.S. and Spivak, S.I., *Matematicheskie modeli khimicheskoi kinetiki* (Mathematical Models of Chemical Kinetics), Moscow: Znanie, 1977.

Russian Journal of Applied Chemistry, Vol. 77, No. 9, 2004, pp. 1556–1558. Translated from Zhurnal Prikladnoi Khimii, Vol. 77, No. 9, 2004, pp. 1568–1570.

BRIEF COMMUNICATIONS

Heterogeneous Equilibria in the Y–Mn–O and Tm–Mn–O Systems in Air

O. M. Fedorova, S. G. Titova, V. F. Balakirev, and Yu. V. Golikov

Institute of Metallurgy, Ural Division, Russian Academy of Sciences, Yekaterinburg, Russia

Received March 18, 2004

Abstract—The subsolidus phase diagrams of the systems Ln–Mn–O (Ln = Y, Tm) in air in the range 850–1400°C were constructed, based on the X-ray phase analysis of the homogeneous phases and heterogeneous mixtures of compositions $R = N_{Mn}/(N_{Mn} + N_{Ln})$ 1/5, 1/2 ($LnMnO_3$), 3/5, 2/3 ($LnMn_2O_5$), and 4/5. The boundaries of the phase areas were outlined.

The fact that oxides of systems Mn–M–O (M = Sc, Y, Ho, ..., Lu) exhibit ferromagnetic properties [1] makes it urgent to study the phase diagrams of these systems, as these data are necessary for directional synthesis of the compounds. In this study, the data of the X-ray phase analysis of the homogeneous phases and heterogeneous mixtures of compositions $R = N_{Mn}/(N_{Mn} + N_{Ln})$ 1/5, 1/2 ($LnMnO_3$), 3/5, 2/3 ($LnMn_2O_5$), and 4/5, obtained by the ceramic synthesis from the oxides in air at 850–1400°C, were used to construct the subsolidus phase diagrams of the systems Ln–Mn–O (Ln = Y, Tm) in air.

EXPERIMENTAL

The samples were synthesized by the ceramic technology, which was used in [2] for the Yb–Mn–O and Lu–Mn–O systems to construct the analogous phase diagrams, from the oxides Y_2O_3 (99.99% pure), TuO-2 grade Tm_2O_3 [TU (Technical Specification) 48-4-182–72], and ultrapure grade Mn_2O_3. It should be noted that, as in [2], two methods were used for cooling of the annealed samples to room temperature: quenching in air in a ceramic crucible and cooling with a furnace for 4 h. The X-ray phase analysis (DRON-2.0 diffractometer, CuK_α radiation) of the substances synthesized showed that the cooling procedure does not affect the phase composition of the system and only weakly affects the unit cell parameters of the solid phases.

The results of the performed analysis in the form of the phase diagrams of the systems Ln–Mn–O (Ln = Y, Tm) are presented in Fig. 1. To construct them, we used data on equilibria in the binary systems Ln–O [3] and Mn–O. For example, the temperatures of the α-Mn_2O_3–β-Mn_3O_4 (883.6°C) and β-Mn_3O_4–γ-Mn_3O_4 (1172°C) phase equilibria in air were taken from [4] and [5], respectively.

Area *1* in the diagrams shown in Fig. 1 describes coexistence in air of two phases, Ln_2O_3 (space group *Ia*3) and $LnMnO_3$ (hexagonal crystal structure, space group $P6_3cm$ [4]). $LnMnO_3$ and γ-Mn_3O_4 (spinel structure, space group Fd_3m) are in equilibrium in air in area *2*, and $LnMnO_3$ and β-Mn_3O_4 (hausmannite, space group *I*4/*amd*), in area *3*. Area *4* is the region of coexistence of $LnMn_2O_5$ ($DyMn_2O_5$-like

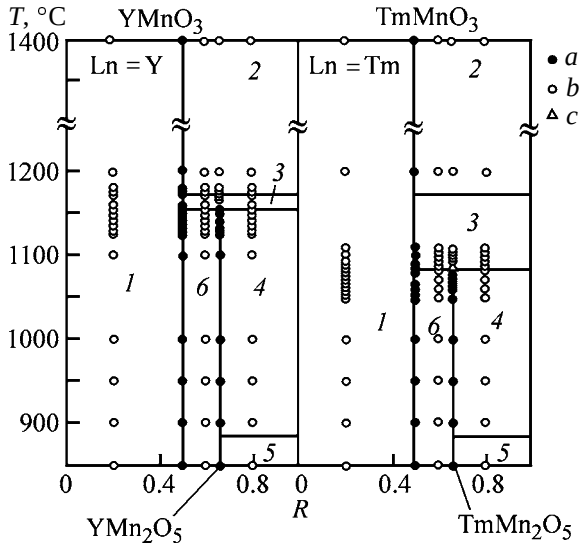

Fig. 1. Phase diagrams of the systems Mn–Ln–O (Ln = Y, Tm) in air. (*T*) Temperature; $R = N_{Mn}/(N_{Mn} + N_{Ln})$; (*N*) mole fraction of the element. Number of phases detected by X-ray analysis: (*a*) 1, (*b*) 2, and (*c*) 3; for the remaining explanations, see text.

1070-4272/04/7709-1556 © 2004 MAIK "Nauka/Interperiodica"

orthorhombic crystal structure, space group *Pbam* [4]) and β-Mn_3O_4, and area *5*, the region of coexistence of $LnMn_2O_5$ and α-Mn_2O_3. In area *6*, oxides $LnMnO_3$ and $LnMn_2O_5$ are in equilibrium.

The monovariant equilibria

$$LnMn_2O_5 = LnMnO_3 + 1/3Mn_3O_4 + 1/3O_2 \ (Ln = Y, Tm) \quad (1)$$

were revealed by X-ray phase analysis at 1155±5 (Ln = Y) and 1085±5°C (Ln = Tm). At temperatures higher and lower by 20°C than the equilibrium temperature, the samples for X-ray phase analysis were prepared at 5°C intervals to approach the equilibrium from the different sides [6]. The temperature at which all the three solid phases, $LnMnO_3$, $LnMn_2O_5$, and Mn_3O_4, were detected by X-ray phase analysis was accepted as the equilibrium temperature.

It should be noted that the unit cell parameters of manganese oxides in areas *2–5* are equal within the experimental error to those of the individual oxides annealed at the same temperatures. This is also true for yttrium and thulium oxides in area *1*. This result suggests no mutual solubility of yttrium and manganese oxides and of thulium and manganese oxides. On the contrary, the parameters and volumes of the unit cells of the chemical compounds $YMnO_3$ and YMn_2O_5 differ from the corresponding values of these compounds in the adjacent regions of the bivariant equilibria. This is illustrated by Fig. 2, where the volumes of the unit cells of the individual $YMnO_3$ and YMn_2O_5 are given along with the volumes of these substances in areas *1*, *4*, and *6* of the phase diagram (Fig. 1). The above difference is observed for all the parameters in all the areas of the phase diagrams of the Y–Mn–O system (Fig. 1). The $YMnO_3$ and YMn_2O_5 unit cell parameters as functions of the chemical composition of the systems *R* show that the regions of homogeneity of these systems with respect to metallic components are significant. Therefore, special studies of these regions including, e.g., positions of their boundaries as functions of chemical composition of the system and synthesis temperature should be performed. The dependence of the volume of the $TmMnO_3$ unit cell on the synthesis temperature is shown in Fig. 3. This dependence suggests with high probability the oxygen nonstoichiometry in this substance and its relation to the temperature, in agreement with the data of numerous studies [3, 7] devoted to the oxygen nonstoichiometry of rare-earth element manganites and to the effect exerted on it by the temperature and oxygen pressure.

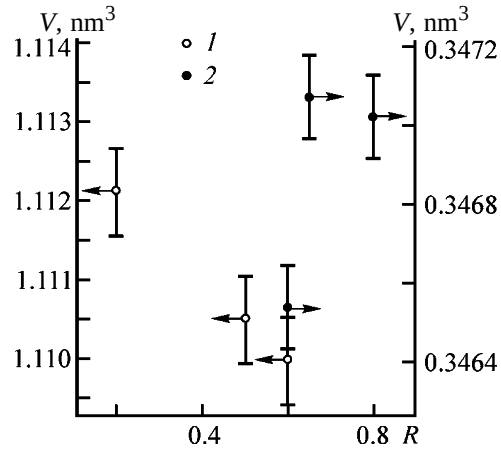

Fig. 2. Volumes *V* of the unit cells of (*1*) $YMnO_3$ and (*2*) YMn_2O_5 quenched from 1140°C vs. the chemical composition of the Y–Mn–O system. $R = N_{Mn}/(N_{Mn} + N_Y)$; (*N*) mole fraction of the element.

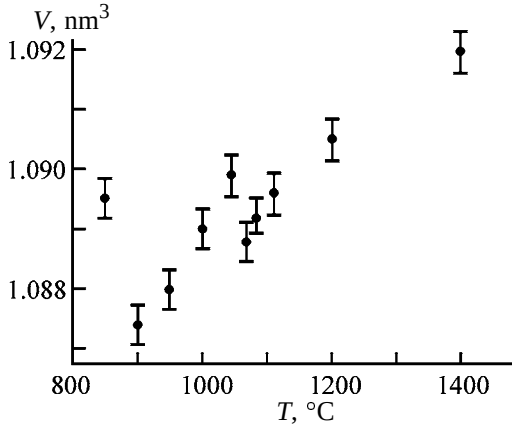

Fig. 3. Volume *V* of the $TmMnO_3$ unit cell vs. the quenching (annealing) temperature *T*.

The fact that the parameters and volumes of the unit cells of $YMnO_3$, YMn_2O_5, and $TmMn_2O_5$ are independent of the synthesis temperature does not rule out the oxygen nonstoichiometry of these compounds.

In the Tm–Mn–O system, the dependences of the $TmMnO_3$ and $TmMn_2O_5$ unit cell parameters on the chemical composition of the system (*R* parameter), similar to those presented in Fig. 2, were not observed. This shows that the regions of homogeneity of the above substances with respect to the metallic components are narrow.

CONCLUSIONS

(1) The thermodynamically stable chemical compounds in the systems Y–Mn–O and Tm–Mn–O at

subsolidus temperatures in air are $LnMnO_3$ and $LnMn_2O_5$ (Ln = Y, Tm).

(2) The double oxides $LnMn_2O_5$ dissociate in air at 1155 ± 5 (Ln = Y) and 1085 ± 5°C (Ln = Tm).

(3) In the system Y–Mn–O, the parameters and volumes of the unit cells of $YMnO_3$ and YMn_2O_5 depend on the chemical composition of the system, suggesting the nonstoiciometry of these substances with respect to metallic components.

(4) The parameters and volumes of the $TmMnO_3$ unit cells depend on synthesis temperature, suggesting the oxygen nonstoichiometry of this compound.

ACKNOWLEDGMENTS

The study was financially supported by the Russian Foundation for Basic Research (project no. 02-03-32877), Grant of the Russian Federation President for Young Russian Scientists, and the Foundation of the Leading Research Schools (project no. NSh-468.2003.3).

REFERENCES

1. Venevtsev, Yu.N., Gagulin, V.V., and Lyubimov, V.N., *Segnetomagnetiki* (Ferromagnetics), Moscow: Nauka, 1982.
2. Vedmid', L.B., Titova, S.G., and Golikov, Yu.V., *Zh. Fiz. Khim.*, 2001, vol. 75, no. 6, pp. 1122–1124.
3. Portnoi, K.I., and Timofeeva, N.I., *Kislorodnye soedineniya redkozemel'nykh elementov* (Oxygen Compounds of Rare-Earth Elements), Moscow: Metallurgiya, 1986.
4. Keller, M., and Dieckmann, R., *Ber. Bunsenges. Phys. Chem.*, 1985, vol. 89, no. 10, pp. 1095–1104.
5. Eliott, Y.E., and Gleiser, M., in *Thermochemistry for Steelmaking:* Reding, Mass.: Addison-Westley, 1960, vol. 1, p. 296.
6. Balakirev, V.F., Barkhatov, V.P., Golikov, Yu.V., and Maizel', S.G., *Manganity: Ravnovesnye i nestabil'nye sostoyaniya* (Manganites: Equilibrium and Unstable States), Yekaterinburg: Ural. Otd., Rus. Akad. Nauk, 2000.
7. Kamata, K., Nakajama, T., and Nakamura, T., *Mater. Res. Bull.*, 1979, vol. 14, pp. 1007–1012.

Russian Journal of Applied Chemistry, Vol. 77, No. 9, 2004, pp. 1559–1560. Translated from Zhurnal Prikladnoi Khimii, Vol. 77, No. 9, 2004, pp. 1571–1572.

BRIEF COMMUNICATIONS

Extaction of Lanthanide (III) Nitrates from Aqueous Solutions with *n*-Octanol

V. A. Keskinov, A. V. Kudrova, O. V. Valueva, and A. K. Pyartman

St. Petrsburg State Technological Institute, St. Petersburg, Russia

Received October 22, 2003; in final form, April 2004

Abstract—Extraction of lanthanide(III) nitrates (Ln–Gd) with *n*-octanol was studied at 298.15 K. The extraction isotherms were obtained and mathematically treated.

n-Octanol is widely used as an additive in industrial extraction of rare-earth metals to improve phase separation and increase the solubility of extractable complexes in the organic phase [1]. Published data on extraction of cerium-group lanthanide(III) nitrates with alcohols are virtually lacking. Extraction of lanthanum(III), praseodymium(III), and neodymium(III) from aqueous nitric acid solutions and those containing alkali and 3*d*-metal nitrates with butyl, amyl, and isoamyl alcohols was studied in a limited Ln(III) concentration range. For all the systems studied, the lanthanide(III) distribution coefficient was found to increase in going from lanthanum(III) to neodymium(III).

In this work we studied extraction of cerium-group lanthanide(III) (La–Nd, Sm–Gd) nitrates from aqueous solutions with *n*-octanol at 298.15 K.

The initial aqueous solutions of Ln(III) nitrates were prepared by dissolution of the corresponding Ln(III) oxide (ultrapure grade) in nitric acid (ultrapure grade). The Ln(III) concentration in the initial aqueous solution of Ln(III) nitrates and equilibrium aqueous and organic phases was determined complexometrically [3]. *n*-Octanol was of chemically pure grade (ρ = 0.8220 g dm^{-3} at 298.15 K).

We studied the extraction of lanthanide(III) nitrates (La–Gd) from their aqueous solutions with neat *n*-octanol (6.31 mol dm^{-3}). We found (see table) that Ln(III) were not extracted at their initial concentration in the aqueous phase below 0.6 mol dm^{-3}. Comparison of the extraction isotherms of Ln(III) of different types (see figure) shows that, at equal Ln(III) concentration in the aqueous phase, their content in the equilibrium organic phase increases in going from La(III) to Gd(III).

The extraction of Ln(III) from aqueous solution with *n*-octanol can be described by the reaction equation

$$Ln^{3+}(aq) + 3NO_3^-(aq) + i\text{ROH(o)} \rightleftarrows [Ln(NO_3)_3(ROH)_i](o). \quad (1)$$

The concentration extraction constant is expressed by the equation

$$K_{ex}^{i} = \frac{\{[Ln(NO_3)_3(ROH)_i](o)\}}{\{Ln^{3+}(aq)\}\{NO_3^-(aq)\}^3\{ROH(o)\}^i}, \quad (2)$$

where braces denote the equilibrium concentrations of species.

The correlation between the thermodynamic and concentration extraction constants is described by the equation

$$K_{ex}^{0,i} = K_{ex}^{i}\frac{Y_{[Ln(NO_3)_3(ROH)_i](o)}}{Y_{\pm}^{4}Y_{[ROH(o)]}^{i}}, \quad (3)$$

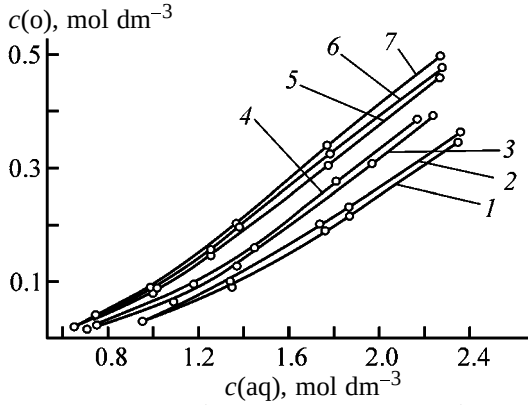

Extraction isotherms of lanthanide(III) nitrates from aqueous solutions with neat (6.31 mol dm^{-3}) *n*-octanol at 298.15 K. [*c*(o), *c*(aq)] Lanthanide(III) concentrations in the organic and aqueous phases, respectively. Ln(III): (*1*) La, (*2*) Ce, (*3*) Pr, (*4*) Nd, (*5*) Sm, (*6*) Eu, and (*7*) Gd.

1070-4272/04/7709-1559 © 2004 MAIK "Nauka/Interperiodica"

Thermodynamic extraction constants of lanthanide(III) nitrates with neat *n*-octanol at 298.15 K, calculated from our experimental extraction isotherns by Eq. (1) at $i = 6$

Ln	c(aq)	c(o)	[ROH]	$y_{\pm}$	$\log K_{ex}^{0,6}$
	M				
La	0.96	0.03	6.13	0.192	–4.74
	1.35	0.088	5.782	0.195	–4.74
	1.76	0.188	5.182	0.210	–4.72
	1.87	0.216	5.014	0.216	–4.72
	2.35	0.345	4.24	0.248	–4.72
				Mean	–4.73 ± 0.03
Pr	0.696	0.015	6.220	0.210	–4.68
	1.09	0.063	5.932	0.208	–4.69
	1.374	0.126	5.554	0.217	–4.70
	1.966	0.305	4.48	0.257	–4.67
	2.24	0.391	3.964	0.284	–4.64
				Mean	–4.68 ± 0.03
Nd	0.75	0.025	6.16	0.209	–4.55
	1.18	0.093	5.75	0.212	–4.61
	1.45	0.157	5.37	0.223	–4.65
	1.81	0.275	4.66	0.247	–4.60
	2.16	0.383	4.01	0.280	–4.59
				Mean	–4.60 ± 0.03
Eu	0.65	0.020	6.19	0.222	–4.52
	1.02	0.088	5.78	0.223	–4.48
	1.25	0.155	5.38	0.233	–4.49
	1.78	0.325	4.36	0.275	–4.51
	2.28	0.475	3.46	0.340	–4.54
				Mean	–4.51 ± 0.03
Ce				〃	–4.70 ± 0.03
Sm				〃	–4.53 ± 0.03
Gd				〃	–4.48 ± 0.03

where Y(o) are the molar activity coefficients of extractable complexes in the organic phase and $Y_{\pm}$ is the mean ionic activity coefficient of Ln(III) nitrate in the aqueous phase.

Taking into account that $Y_{[Ln(NO_3)_3(ROH)_i](o)} \times \{Y^i_{[ROH(o)]}\}^{-1} = \text{const} = 1$, Eq. (3) can be transformed into the form

$$K_{ex}^{0,i} = K_{ex}^{i}/Y_{\pm}^{4}. \quad (4)$$

The mean ionic activity coefficients of lanthanide(III) nitrates were calculated from the data reported in [4].

In calculation of the thermodynamic extraction constants of lanthanide(III) nitrates with neat octanol, the stoichiometric term i was varied from 0 to 6. The results of these calculations for $i = 6$ [formation of $Ln(NO_3)_3(ROH)_6$ extractable complex only] are listed in the table. It seen that $\log K_{ex}^{0,6}$ is virtually independent of lanthanide(III) concentration in the organic phase, which shows that our physicochemical model is suitable for description of extraction of Ln(III) nitrates with *n*-octanol. As seen from the table, the mean extraction constant is close for La(III), Ce(III), and Pr(III) and slightly increases in going from Pr(III) to Gd(III) within the examined lanthanide(III) concentration range.

Thus, the difference between the extraction isotherms of individual Ln(III) nitrates is mainly caused by variation in their activity coefficients in the aqueous phase (see table). To increase the selectivity of extraction of Ln(III) nitrates with *n*-octanol, their extraction should be performed from concentrated aqueous solution.

CONCLUSIONS

(1) The Ln(III) nitrates are not noticeably extracted with *n*-octanol at lanthanide(III) concentration in the aqueous phase below 0.6 mol dm^{-3}. At Ln(III) concentration in the aqueous phase above 0.6 mol dm^{-3}, the extraction increases in going from La(III) to Gd(III).

(2) The thermodynamic extraction constants calculated assuming the formation of the extractable complex $Ln(III)(NO_3)_3(ROH)_6$ as the only species are close for Ln(III), Ce(III), and Pr(III) and slightly increase in going to Gd(III). The difference in the extraction isotherms of Ln(III) nitrates with *n*-octanol is mainly caused by variations of Ln(III) nitrate activity coefficients in the aqueous phase. The selectivity of extraction of Ln(III) nitrates with *n*-octanol increases with increasing their concentration in the aqueous phase.

REFERENCES

1. Mikhailichenko, A.I., Mikhlin, E.B., and Patrikeev, Yu.B., *Redkozemel'nye metally* (Rare-Earth Metals), Moscow: Metallurgiya, 1987.
2. Panasenko, E.B., Belokoskov, V.I., and Ivanova, T.M., *Khimicheskaya tekhnologiya redkozemel'nogo syr'ya* (Chemical Technology of Rare-Earth Raw Materials), Moscow: Nauka, 1966.
3. Přibil, R., *Komplexometrie*, Prague: Chemapol, 1955.
4. Pyartman, A.K. and Kopyrin, A.A., *Radiokhimiya*, 1997, vol. 39, no. 2, pp. 149–154.

Russian Journal of Applied Chemistry, Vol. 77, No. 9, 2004, pp. 1561–1563. Translated from Zhurnal Prikladnoi Khimii, Vol. 77, No. 9, 2004, pp. 1573–1574.

BRIEF COMMUNICATIONS

Synthesis of Di(polyfluoroalkyl) Ethers

A. I. Rakhimov, A. V. Nalesnaya, and O. V. Vostrikova

Institute of Chemical Problems of Ecology, Volgograd State Technical University, Volgograd, Russia

Received July 6, 2004

Abstract—New procedures for preparing di(polyfluoroalkyl) ethers by reactions of polyfluoropropyl chlorosulfonites with polyfluorinated alcohols were tested.

Polyfluorinated dialkyl ethers are promising ozone-friendly and moderately toxic solvents [1]. In particular, tetrafluoroethyl difluoromethyl ether and its closest homolog, di(tetrafluoropropyl) ether can be used instead of perfluorohydrocarbons for dry etching in microelectronics [2], and, with subsequent electrochemical afterfluorination in anhydrous HF, these compounds can be recommended for cleaning of electronic circuits and as polymerization media [3–5]. Polyfluorinated ethers of higher molecular weight are used as compression, motor, and vacuum oils [6].

Alkyl polyfluoroalkyl ethers are prepared by addition of polyfluorinated alcohols to alkenes and fluoroalkenes [1, 7] and by alkylation of alcoholates derived from polyfluorinated alcohols with alkyl halides [8, 9].

We suggest a procedure for preparing polyfluorinated ethers from available raw materials, polyfluorinated alcohols and thionyl chloride, via intermediate polyfluoroalkyl chlorosulfonites [10]. This procedure is environmentally safe and economically attractive, as its cost is determined by the cost of polyfluorinated alcohols (some of them are production wastes) and thionyl choride and by small production expenditures.

With the aim to extend the homologous series of symmetrical and unsymmetrical di(polyfluoroalkyl) ethers, we suggested catalytic and noncatalytic procedures based on reactions of polyfluoroalkyl chlorosulfonites with polyfluorinated alcohols. The catalytic reaction (1) is performed in the presence of dimethylformamide (DMF) as catalyst, and the noncatalytic reaction (2), in the presence of triethylamine:

$$R_FCH_2OS(O)Cl + R'_FCH_2OH \xrightarrow{DMF} R_FCH_2OCH_2R'_F + SO_2 + HCl, \quad (1)$$

$$R_FCH_2OS(O)Cl + R'_FCH_2OH \xrightarrow{NEt_3} R_FCH_2OCH_2R'_F + SO_2 + NEt_3 \cdot HCl, \quad (2)$$

where $R_F = R'_F = H(CF_2CF_2)_2$ (**I**), HCF_2CF_2 (**II**), $H(CF_2CF_2)_3$ (**III**), $R_F = HCF_2CF_2$, $R'_F = H(CF_2CF_2)_2$ (**IV**), $R_F = HCF_2CF_2$, $R'_F = H(CF_2CF_2)_3$ (**V**), $R_F = HCF_2CF_2$, $R'_F = H(CF_2CF_2)_4$ (**VI**), $R_F = H(CF_2CF_2)_2$, $R'_F = H(CF_2CF_2)_3$ (**VII**).

In procedure (1), a solution of polyfluoroalkyl chlorosulfonite was added to appropriate alcohol containing DMF (molar ratio from 1 : 0.005 to 1 : 0.01) at –10°C; the mixture was allowed to stand for 24 h at room temperature. After distilling off the solvent (chloroform, diethyl ether), the product was distilled; yield 59–98%.

In procedure (2), a solution of polyfluoroalkyl chlorosulfonite was added at –10°C to a complex of alcohol with triethylamine, prepared in advance; the resulting mixture (solvent pentane or hexane) was allowed to stand for 24 h at room temperature. The triethylammonium chloride precipitate was filtered off, and the fluorinated ether was distilled; yield 52–85%.

Symmetrical ethers **I**–**III** were prepared by reactions of polyfluoroalkyl chlorosulfonites with the related alcohols. The highest yield (98%) was attained with the most reactive tetrafluoropropyl chlorosulfonite in the presence of DMF. With increasing length of the fluorocarbon chain, the yield of di(polyfluoroalkyl) ethers decreases. Tetrafluoropropyl octafluoropentyl ether was obtained in 85% yield, and the yields of the ethers with longer fluorocarbon chains were still lower.

Although both procedures allow preparation of the ethers in similar yields, the catalytic process is preferable because of lower production cost and higher purity of the target product; the triethylammonium salt formed in reaction (2) appreciably contaminates the resulting ether.

1070-4272/04/7709-1561 © 2004 MAIK "Nauka/Interperiodica"

EXPERIMENTAL

The structures of ethers **I**–**VII** were proved by IR and ^{1}H NMR spectroscopy. The IR spectra were recorded on a Specord-M82 spectrometer (thin films). The ^{1}H NMR spectra were taken on a Varian Mercury-300 spectrometer (working frequency 300 MHz, internal reference tetramethylsilane, solvent CCl_4).

Di(1,1,5-trihydroperfluoropentyl) ether I. (a) A 4.4-g portion of 1,1,5-trihydroperfluoro-1-pentanol was mixed with 0.015 ml of DMF in 15 ml of chloroform and cooled to –10°C; a solution of 5.9 g of 1,1,5-trihydroperfluoropentyl chlorosulfonite in 10 ml of chloroform was added with stirring, with the temperature maintained at –10°C. Then the mixture was allowed to warm up to 20°C and was kept at this temperature for 2 h, with bubbling of dry air to remove the released hydrogen chloride. After that, the mixture was allowed to stand for 24 h at room temperature. The solvent was distilled off, and the product was distilled in a vacuum. Yield of **I** 4.5 g (59%), bp 103°C (2 mm Hg), n_D^{20} 1.3385, d_4^{20} 1.7344. IR spectrum, ν, cm^{-1}: 1137 s (νC–O–C), 1176 s (νCF_2), 2860 w, 2946 m (νCH_2), 3016 w (νCHF_2).

(b) A 5.0-g portion of 1,1,5-trihydroperfluoro-1-pentanol was mixed with 2.1 of triethylamine in 15 ml of hexane and cooled to –10°C; a solution of 6.7 g of 1,1,5-trihydroperfluoropentyl chlorosulfonite in 10 ml of hexane was gradually added with stirring, with the temperature maintained at –10°C. Then the mixture was allowed to warm up to 20°C and to stand at this temperature for 24 h. The precipitated salt was filtered off, the solvent was distilled off, and the product was vacuum-distilled. Yield of **I** 5.2 g (52%).

Compounds **II**–**VII** were prepared similarly to **I** by procedure (a) or (b).

Di(1,1,3-trihydroperfluoropropyl) ether II. Procedure (a). Yield 98%, bp 65°C (1 mm Hg), n_D^{20} 1.3575, d_4^{20} 1.6251. IR spectrum, ν, cm^{-1}: 1111 s.br (νC–O–C), 1223 s (νCF_2), 2850 m, 2920 m, 2960 m (νCH_2), 3008 w (νCHF_2). ^{1}H NMR spectrum, δ, ppm (*J*, Hz): 5.803 t.d (H^1, H^6; *J* 52.8, 3.3), 4.274 q (H^3, H^4, *J* 13.2).

Di(1,1,7-trihydroperfluoroheptyl) ether III. Procedure (a). Yield 57%, bp 130°C (1 mm Hg), n_D^{20} 1.3370, d_4^{20} 1.8014. IR spectrum, ν, cm^{-1}: 1124 s (νC–O–C), 1249 s (νCF_2), 2860 w, 2980 m (νCH_2), 3024 w (νCHF_2).

1,1,5-Trihydroperfluoro-1-(1,1,3-trihydroperfluoropropyloxy)pentane IV. Procedure (b). Yield 85%, bp 83°C (2 mm Hg), n_D^{20} 1.3500, d_4^{20} 1.6790. IR spectrum, ν, cm^{-1}: 1116 s (νC–O–C), 1242 s (νCF_2), 2860 w, 2934 w, 2980 m (νCH_2), 3017 w (νCHF_2). ^{1}H NMR spectrum, δ, ppm (*J*, Hz): 5.966 t.t (H^8, *J* 51.6, 5.4), 5.810 t.t (H^1, *J* 52.1, 3.8), 4.432 t (H^3, *J* 13.2), 4.255 t (H^4, *J* 12.6).

1,1,7-Trihydroperfluoro-1-(1,1,3-trihydroperfluoropropyloxy)heptane V. Procedure (b). Yield 51%, bp 95°C (1 mm Hg), n_D^{20} 1.3450, d_4^{20} 1.7310. IR spectrum, ν, cm^{-1}: 1116 s (νC–O–C), 1223 s (νCF_2), 2868 w, 2937 w, 2968 m (νCH_2), 3014 w (νCHF_2).

1,1,9-Trihydroperfluoro-1-(1,1,3-trihydroperfluoropropyloxy)nonane VI. Procedure (a). Yield 34%, mp 49°C, bp 130°C (1 mm Hg). IR spectrum, ν, cm^{-1}: 1120 s (νC–O–C), 1216 s (νCF_2), 2856 m, 2894 w, 2932 m (νCH_2), 2954 w (νCHF_2). ^{1}H NMR spectrum, δ, ppm (*J*, Hz): 5.975 t.t (H^1, H^{12}, *J* 52, 5.1), 4.359 t (*J* 16.6) and 4.331 t (*J* 12.3) (H^3, H^4).

1,1,7-Trihydroperfluoro-1-(1,1,5-trihydroperfluoropentyloxy)heptane VII. Procedure (a). Yield 62%, bp 110°C (1 mm Hg), n_D^{20} 1.3380, d_4^{20} 1.7647. IR spectrum, ν, cm^{-1}: 1120 s (νC–O–C), 1220 s (νCF_2), 2864 w, 2932 m, 2961 m (νCH_2), 3009 w (νCHF_2).

CONCLUSION

A catalytic reaction of polyfluorinated alcohols with polyfluoroalkyl chlorosulfonites in the presence of DMF allows preparation of the corresponding di(polyfluoroalkyl) ethers in 59–98% yield.

REFERENCES

1. Il'in, A.A., Bakhmutov, Yu.L., Ivanova, L.M., *et al.*, *Zh. Prikl. Khim.*, 2004, vol. 77, no. 1, pp. 102–105.
2. Orlov, A.P., Shchavelev, V.B., and Korol'kov, D.N., Abstracts of Papers, *3-ya Mezhdunarodnaya konferentsiya "Khimiya, tekhnologiya i primenenie ftorsoedinenii"* (3rd Int. Conf. "Chemistry, Technology, and Applications of Fluoro Compounds"), St. Petersburg, June 6–9, 2001, R 1–34, p. 170.
3. US Patent 5474657.
4. US Patent 5516946.
5. Novicova, M., Zakharov, V., Denisov, A., and Jukova, V., *J. Fluorine Chem.*, 1992, vol. 58, nos. 2–3, p. 169.
6. Popova, L.M., Vinogradova, V.N., Prytkova, O.A., *et al.*, Abstracts of Papers, *2-ya Mezhdunarodnaya*

konferentsiya "Khimiya, tekhnologiya i primenenie ftorsoedinenii" (2nd Int. Conf. "Chemistry, Technology, and Applications of Fluoro Compounds"), St. Petersburg, September 23–26, 1997, R 3–9, p. 123.

7. Dear, R.E.A. and Gilbert, E.E., *J. Chem. Eng. Data*, 1969, vol. 14, no. 4, pp. 493–497.
8. Malichenko, B.F. and Tsypina, O.N., in *Sintez i fiziko-khimiya polimerov: Respublikanskii mezhvedomstvennyi sbornik* (Synthesis and Physical Chemistry of Polymers: Republican Interdepartmental Coll.), Kiev: Naukova Dumka, 1971, issue 9, pp. 7–10.
9. Krylov, A.I., Vakhlamova, L.Sh., Petrova, T.M., *et al.*, *Zh. Vses. Khim. O–va.*, 1977, vol. 22, no. 4, pp. 469–470.
10. Rakhimov, A.I. and Vostrikova, O.V., *Zh. Org. Khim.*, 1999, vol. 35, no. 5, pp. 815–816.

Russian Journal of Applied Chemistry, Vol. 77, No. 9, 2004, pp. 1564–1567. Translated from Zhurnal Prikladnoi Khimii, Vol. 77, No. 9, 2004, pp. 1575–1578.

HISTORY OF CHEMISTRY AND CHEMICAL TECHNOLOGY

Professor Oleg Alekseevich Esin (to Centennial Anniversary of His Birthday)

O.A. Esin, an honored scientist and technologist of the Russian Soviet Federative Socialist Republic and a professor of the Ural Polytechnic Institute, made a major contribution to studies of the physicochemical foundations of metallurgical processes, development of applied electrochemistry, and organization of the higher metallurgical education in the Urals and created a prominent scientific school.

Oleg Alekseevich Esin was born on September 7, 1904, in Yekaterinburg. In 1913, he entered a non-classical secondary school, but was forced to quit when studying in the sixth form by financial difficulties.

The youth of the scientist-to-be coincided with the early time of development of the higher education in the Middle Urals. The Mining Institute was opened in Yekaterinburg in October 1917, and a decision was taken in three years, in October 1920, to organize the Ural State University. It was intended that University is to include mining, polytechnic, and some other institutes, and also a worker's faculty. Esin was sent to this faculty to complete his secondary education and then became a student of the chemical-metallurgical department of the Polytechnic Institute at the Ural University. Among Esin's teachers were such prominent metallurgists of that time as V.E. Grum-Grzhimailo (1864–1928) and I.A. Sokolov (1867–1947), both of whom were well experienced in working at Ural's plants; A.E. Makovetskii, a many-sided chemist-technologist; and S.G. Mokrushin (1896–1986), who became a known specialist in physical chemistry of surface phenomena in the future. Esin recollected Grum-Grzhimailo's and Makovetskii's lectures in the warmest words [1, 2]. Esin performed his first scientific investigations together with Mokrushin. When still being a student, Esin worked as laboratory assistant at the electrochemical laboratory and also found time for scientific research.

In 1925, the Polytechnic Institute, as well as the other institutes that comprised the University, became an independent educational institution. In May 1925, Esin defended his graduation thesis devoted to electrochemistry of aqueous solutions and, as one of the most talented students, was left at the Polytechnic Institute for post-graduate education "to be prepared for professorship." The first Esin's investigations (carried out together with Mokrushin and I.G. Shcherbakov and published in 1926–1928) were concerned with processes for electrolytic production of ammonium persulfate, electrolysis of chromate solutions, and precipitation of metallic chromium from aqueous solutions. At the end of 1928, Esin successfully finished his post-graduate education and was sent to a one-year business trip to Germany to make acquaintance with higher-school institutions and industrial plants of this country. In particular, Esin minutely familiarized himself with the Higher Technical College in Dresden.

All Esin's further scientific and pedagogical activities were associated with the Ural Polytechnic Institute and research institutions of Yekaterinburg. Esin became a professor of the Ural Polytechnic Institute in 1934 and headed the Chair of the Theory of Metallurgical Processes at the same institute from 1943 till 1969. In 1971, he became a scientific consultant of the Institute of Metallurgy, Ural Scientific Center, Academy of Sciences of the USSR.

The first period of Esin's scientific investigations, which continued for 18 years, from 1926 till 1944, was devoted to electrochemistry of aqueous solutions, with both generally theoretical and practical problems tackled. Already in 1932–1933, Esin developed on the basis of a great number of experimental studies a quantitative theory of joint discharge of ions, including hydrogen ions, from solutions of simple and complex salts. Later, a spacious summary paper devoted to joint discharge of hydrogen ions and metal ions was published [3].

Of particular interest is Esin's study, together with B.F. Markov, of electrocapillary curves of a mercury electrode in various aqueous solutions (1939). The authors were first to discover the anomalously strong shift of the zero-charge potential, depending on the activity of an electrolyte. By suggestion of a known American electrochemist D. Grahame (1955) this phenomenon was named the "Esin–Markov effect." This Esin and Markov's study stimulated further

1070-4272/04/7709-1564 © 2004 MAIK "Nauka/Interperiodica"

investigations into the structure of the discrete double layer both by representatives of the school of Academician A.N. Frumkin in the Soviet Union [4] and by a number of foreign scientists.

In 1934, two Esin's monographs were published: *Electroliticheskoe rafinirovanie medi* (Electrolytic Refining of Copper) (written together with A.I. Gaev) and *Affinazh blagorodnykh metallov* (Refining of Noble Metals) (together with O.E. Zvyagintsev). Both these books were intended for a widest audience of engineers and technical workers. In 1937, Esin published already his third monograph *Elektroliz tsinka* (Electrolysis of Zinc) (together with Gaev).

In the severe war years. Esin was among those who initiated organization of assistance of scientists to industrial plants of the Ural region. In the context of the needs of Pyshma copper-electrolyte plant, the possibility of intensification of copper electrolysis was examined, the behavior of arsenic, antimony, and noble metals under these conditions was studied, and a method for manufacture of a copper powder was developed. In 1945–1947, the results of these investigations were published.

The second period of scientific investigations by Esin and the scientific school created by him, from 1945 till 1979, was mainly devoted to studies of the physicochemical foundations of the interaction of metals with slags in the molten state and to development of new processes involving metal–slag systems. Particularly important for the development of wide-scale investigations in this area was Esin's relatively brief, but very informative brochure *Elektroliticheskaya priroda zhidkikh shlakov* (Electrolytic Nature of Liquid Slags) (1946). This brochure formulated a fundamentally new approach to the nature of liquid slags. The author, in particular, noted: "The electrochemical theory of the equilibrium between a metal and a slag, outlined by Tammann, deserves a close attention and requires further development." The above-mentioned study by the outstanding physical chemist and metallographer G. Tammann (1861–1938, moved from Russia to Germany in 1903, an honorary member of the Academy of Sciences of the USSR since 1927) was published in 1931. Wide-scale studies of metals, slags, and metal–slag equilibria in the molten state by Esin and his numerous disciples (P.V. Gel'd, S.I. Popel', I.T. Sryvalin, B.M. Lepinskikh, S.K. Chukmarev, N.A. Vatolin, Yu.P. Nikitin, L.N. Barmin, V.N. Voronenkov, A.I. Sotnikov, *et al.*) developed in various areas. Together with silicate melts, oxide and sulfide systems were the object of considerable interest.

Metal and slag phases and their equilibria were examined using a wide variety of electrochemical techniques: measurement of the electromotive forces in various circuits with solid and molten electrolytes under equilibrium conditions; electrolysis of melts; polarization measurements; analysis of the kinetics of electrode processes; determination of the transport numbers of ions in melts; measurement of the electrocapillary curves and estimation of the capacitance of the double layer in metal–slag systems; determination of the exchange current in these systems; and study of the electrical conductivity of slags, electrotransport of impurities in liquid metals, and diffusion in molten metals and slags.

There is no escape from mentioning the high methodological level of experimental studies of compound high-temperature systems, carried out by Esin and co-workers. They were the first to use the chronopotentiometric method in studying cathodic and anodic processes at the metal–slag interface (1959–1962). This made it possible to estimate the diffusion coefficients of ions in the slag phase and of components of the metallic phase. Important conclusions concerning the oxidation state of ions involved in electrode reactions were made. A rotating disc electrode was used for the first time to study cathodic and anodic processes in molten slags at 1300–1500°C (1963–1965). Beginning in 1967, electrochemical relaxation methods (impedance measurements, coulostatic and potentiostatic studies) came into wide use. Esin and coworkers were the first to demonstrate experimentally the electrochemical nature of the interaction between liquid cast iron, steel, ferroalloys, and mattes with molten slags. The occurrence of all these most important phenomena at the interface between these phases was revealed.

Simultaneously, physicochemical studies were performed: the thermodynamic properties of metallic and slag melts were studied; their volume and surface properties and wetting phenomena were analyzed; the viscosity of slags of varied nature, their structure and conduction type were determined; and magnetic properties of metallic phases were examined. Considerable attention was given to studying the mechanism and kinetics of reduction and oxidation proceses in high-temperature systems, determining the solubility of gases and oxides of some metals in molten slags.

Esin and co-workers carried out quite a number of investigations devoted to solution of applied problems. To these belong development of methods for removing phosphorus and sulfur from liquid steels, electrochemical refining and alloying of ferrous metals, and recovery of valuable nonferrous methods from waste slags.

Based on a vast experimental material, Esing made quite a number of fundamental theoretical generalizations concerning the nature of metallic and slag melts and the interaction between these. For example, he put forward, experimentally substantiated, and confirmed by calculations the concept of microheterogeneity of molten slags, which results from the energetic nonequivalence of different ions. Esin more than once modified the polymeric model suggested by him for silicate solutions, improved the model of regular solutions as applied to description of the concentration dependence of thermodynamic functions in metallurgical melts with varied nature of interaction between components. Esin and Sotnikov substantiated the alternating-sign structure of the liquid plate of the double layer in molten electrolytes.

The development of research in the field of high-temperature physical chemistry in our country was strongly affected by the fundamental monograph by Esin and Gel'd. Its second edition [5, 6] was published, similarly to the first edition, in two parts, which cover a wide variety of problems related to pyrometallurgy. Of particular interest are Esin's large summarizing papers: Ionic Nature of Liquid Slags [7], On the Structure of Molten Silicates [8], Molten Slags and Their Interaction with Metals [9], Electrode Processes in Molten Slags [10], and Application of the Theory of Polymers to Molten Slags [11].

Esin's scientific legacy is vast. In 1974, a special collection of works *Elektrokhimiya i rasplavy* (Electrochemistry and Melts) was published in connection with Esin's 70th birthday. This collection contained papers by prominent domestic scientists, which described recent achievements in the field of electrochemistry of aqueous solutions and high-temperature systems and investigations of the physicochemical properties and structure of liquid metallic and slag systems. In addition to the introductory article by Academician N.V. Ageev, devoted to Esin's scientific activities, a list of Esin's works, which was limited to before the middle of 1973, but still contained 491 items, was presented [12]. Despite that Esin's scientific school was started to be created only during the postwar years, it has no rivals in the field of high-temperature physical chemistry. Esin's closest associates and disciples included such known scientists as Gel'd (1911–1993), corresponding member of the Russian Academy of Sciences; Vatolin, an academician of the Russian Academy of Sciences; E.A. Pastu-

khov, corresponding member of the Russian Academy of Sciences; G.P. Vyatkin, corresponding member of the Russian Academy of Sciences; professor Popel', and many others.

Esin's many-years' pedagogical and scientific activities were honored by high Governmental awards.

Oleg Alekseevich Esin died on February 13, 1979, at the age of 74.

In 1982, Esing and a group of his associates were awarded a State Prize of the USSR in science and technology for a series of investigations Studies of the Structure, Properties, and Interaction of Metallurgical Alloys, published in 1957–1980.

REFERENCES

1. Grum-Grzhimailo, V.E., *Khochu byt' poleznym Rodine* (I Want To Serve My Motherland), Yekaterinburg: Ural'skii Rabochii, 1996.
2. *Ural'skii gosudarstvennyi universitet v biografiyakh* (Ural State University in Biographies), Yekaterinburg: Ural'sk. Univ., 2000, 2nd revised ed.
3. Esin, O.A., *Tr. Ural'sk. Industr. Inst*., 1947, coll. 27, pp. 52–68.
4. Frumkin, A.N., Petrii, O.A., and Grigor'ev, N.B., in *Elektrokhimiya i rasplavy* (Electrochemistry and Melts), Moscow: Nauka, 1974, pp. 31–36.
5. Esin, O.A. and Gel'd, P.V., *Fizicheskaya khimiya pirometallurgicheskikh protsessov* (Physical Chemistry of Pyrometallurgical Processes), Moscow: Metallurgizdat, 1962, part 1.
6. Esin O.A. and Gel'd, P.V., *Fizicheskaya khimiya pirometallurgicheskikh protsessov* (Physical Chemistry of Pyrometallurgical Processes), Moscow: Metallurgiya, 1966, part 2.
7. Esin, O.A. and Gel'd, P.V., *Tr. Ural'sk. Politekh. Inst*., 1954, coll. 49, pp. 4–46.
8. Esin, O.A., *Usp. Khim*., 1957, vol. 26, no. 12, pp. 1374–1387.
9. Esin, O.A., in *Fizicheskaya khimiya i elektrokhimiya rasplavlennykh solei i shlakov* (Physical Chemistry and Electrochemistry of Molten Salts and Slags), Leningrad: Khimiya, 1968, pp. 17–29.
10. Esin, O.A., in *Fizicheskaya khimiya rasplavlennykh shlakov* (Physical Chemistry of Molten Slags), Kiev: Naukova Dumka, 1970, pp. 5–34.
11. Esin, O.A., in *Fiziko-khimicheskie issledovaniya metallurgicheskikh protsessov: Mezhvuzovskii sbornik* (Physicochemical Studies of Metallurgical Processes: Intercollegiate Coll. of Works), Sverdlovsk: Ural'sk. Politekh. Inst. im. S.M. Kirova, 1973, issue 1, pp. 5–17.
12. Ageev, N.V., in *Elektrokhimiya i rasplavy* (Electrochemistry and Melts), Moscow: Nauka, 1974, pp. 3–27.

A. G. Morachevskii

Russian Journal of Applied Chemistry, Vol. 77, No. 9, 2004, pp. 1568–1569. Translated from Zhurnal Prikladnoi Khimii, Vol. 77, No. 9, 2004, pp. 1579–1580.

BOOK REVIEWS

Karyakin, N.V., *Osnovy khimicheskoi termodinamiki: Uchebnoe posobie dlya vuzov* (Fundamentals of Chemical Thermodynamics: Textbook for Higher Institutions)

Nizhni Novgorod: Nizhegorodsk. Gos. Univ.; Moscow: Akademiya, 2003, 464 pp.

The book to which readers' attention is called is a somewhat extended presentation of various sections of chemical thermodynamics and theory of phase equilibria and solutions, which are conventionally included in courses of physical chemistry for chemical-technological and metallurgical specialties at higher school institutions.

The book comprises a foreword, introduction, ten chapters combined into three sections, conclusion, and appendix. The brief foreword (pp. 12–15) gives a general notion of the content of sections and chapters of the book. The introduction (pp. 16–19) formulates the object of study and goals of the thermodynamics as a whole and chemical thermodynamics, in particular. Chapters 1–4 are combined into the section named Thermodynamics, Basic Concepts, Phase Equilibria. Chapter 1 (pp. 20–41) discusses the basic concepts of chemical thermodynamics. Chapter 2 (pp. 42–115) presents the first law of thermodynamics and the related issues: application of the first law of thermodynamics to ideal gases, to chemical reactions, to methods for calculation of the enthalpies of chemical reactions, to the effect of pressure and temperature on the enthalpy, and to the specific heat and methods for its calculation.

Chapter 3 (pp. 116–184) contains evidence concerning the second law of thermodynamics. The author discusses in ample detail various formulations of the second law and pays considerable attention to the statistical interpretation of entropy and to calculation of changes in entropy in various processes. Chapter 4 (pp. 185–235) considers phase equilibria, the Gibbs phase rule, polymorphism, and second-order phase transitions.

The second section of the book, Thermodynamics of Solutions, Chemical Equilibrium, comprises five chapters, from 5 to 9. The whole Chapter 5 (pp. 236–296) is devoted to thermodynamic properties of solutions. The author introduces the notion of partial molar quantities, discusses the thermodynamic characteristics of ideal and infinitely dilute solutions, considers the properties of solutions and liquid–vapor equilibria for binary systems, and pays considerable attention to the notion of component activity in solution and to methods for determining the activity. Chapter 6 (pp. 297–321) includes evidence concerning the thermodynamic analysis of chemical reactions and the chemical equilibrium. The chapter considers homogeneous equilibria that involve only gaseous substances and heterogeneous equilibria that include a condensed phase containing a single component. The mass action law and various forms of expression of the equilibrium constant are discussed.

Chapter 7 (pp. 322–353) presents the third law of thermodynamics and considers methods for calculation of equilibria. Also devoted to various kinds of calculations of equilibria are Chapters 8 (pp. 354–365) and 9 (pp. 366–396).

The third section of the book, Foundations of Statistical Thermodynamics, comprises only single, comparatively short Chapter 10 (pp. 397–426), in which the basic terms associated with quantum-statistical calculations of chemical equilibria are explained. The book ends in a brief conclusion (pp. 427–432) and an appendix (pp. 433–455). The appendix presents thermodynamic data for elements and simple inorganic compounds (308 substances), as well as for organic compounds of various classes (114 substances). The appendix also gives solutions of the equation for the mass action law for various types of reactions.

The author included in the textbook 97 examples, frequently very simple, with detailed solutions. It seems not quite justified that the book combines a theoretical material and a collection of examples and problems. At the worst, the examples and problems could be placed in the appendix, without disturbing the compactness and wholeness of the main material. The number of digressions with various comments and explanations is too great (more than 50). The author covers a wide variety of issues, but, unfortunately, there are separate annoying inaccuracies. Here, only several examples will be given. The

1070-4272/04/7709-1568 © 2004 MAIK "Nauka/Interperiodica"

derivation of the phase rule (p. 187) should have been preceded by a proof of the equality of chemical potentials in coexisting equilibrium phases. However, no material of this kind is presented in Chapter 3. The chemical potential always refers to some component of a system, and such expressions as "chemical potential of a solution" and "chemical potential of a mechanical mixture" (pp. 226, 227) are incorrect. The thermodynamic interpretation of the Nernst distribution law (p. 254) seems to be unsatisfactory because it does not cover the choice of the standard state for a component distributed among the phases. It is hardly appropriate to divide components into a "solvent" and a "solute" in discussing the thermodynamic description of phases with a variable composition (p. 275). The expressions for the chemical potential of a component in ideal and real solutions, presented on the same page, need additional explanations. The term "Gibbs energy" is commonly accepted in the world literature, and, in the reviewer's opinion, there is no need to replace it with the term "Gibbs function."

Despite the existence of a sufficient number of textbooks on chemical thermodynamics, written on varied level by both domestic and foreign authors, the appearance of a new one is, undoubtedly, of interest. In the level and type of presentation, the material in Karyakin's book is close, except in some places, to that devoted to chemical thermodynamics and related issues in rather high-level textbooks on physical chemistry, e.g., in that for chemical specialties of chemical higher-school institutions, written by A.G. Stromberg and D.P. Semchenko [*Fizicheskaya khimiya* (Physical Chemistry), Moscow: Vysshaya Shkola, 1999]. Naturally, this fact does not minimize the merits of the book discussed here and its value.

Karyakin paid considerable attention in his textbook to scientific-biographic evidence concerning the scientists who made a major contribution to the development of thermodynamics. Unfortunately, they do not include van't Hoff (1852–1911), who received the first Nobel Prize in chemistry "in recognition of the extraordinary services he has rendered by the discovery of the laws of chemical dynamics and osmotic pressure in solutions." As far as the reviewer knows, biographic evidence has not been included in chemical textbooks since the time of the classical textbook on general chemistry, written by the know historian of chemistry, B.N. Menshutkin [*Kurs obshchei khimii* (A Course of General Chemistry), Leningrad: Goskhimizdat, 1933].

The reference material, presented by Karyakin in the appendix, would be of better use if the corresponding temperature intervals were specified for the temperature dependences of the specific heat and references to sources of these data were given.

A. G. Morachevskii

Russian Journal of Applied Chemistry, Vol. 77, No. 9, 2004, pp. 1570–1571. Translated from Zhurnal Prikladnoi Khimii, Vol. 77, No. 9, 2004, pp. 1581–1582.

INFORMATION

The 2nd International Conference on Times of Polymers

The 2nd International Conference on Times of Polymers (TOP) was held in Italy from June 20 to 23, 2004. The conference was organized by Italian groups on polymer science and sponsored by leading Italian and trans-European companies manufacturing and employing polymeric materials. The Conference Co-chairmen were Alberto D'Amore [Engineering Schools of II University of Naples (SUN), Department of Aerospace and Mechanical Engineering] and Domenico Acierno (Department of Materials and Production Engineering, University of Naples Federico II).

The International Scientific Committee included also Francesco Paolo La Mantia (Italy), Giuseppe Marrucci (Italy), Baltasar Mena (Mexico), Jovan Mijovic (the United States), Luidgi Nicolais (Italy), George Papanicolaou (Greece), and Guennadi E. Zaikov (Russia).

The conference program focused on the recent advances in the following topics: Viscoelasticity, Industrial Rheology, Durability of Polymers and Composites, Processing, Blends, Biomaterials, Nanocomposites, Cultural Heritage, and Fracture and Yielding. All the thirteen plenary lectures were made by invited lecturers. Additionally, there were 35 oral and 27 poster contributions.

About 150 scientists from 16 countries (Bulgaria, Canada, France, Germany, Greece, Israel, Italy, Japan, Mexico, Russia, Slovenia, South Korea, Sweden, Turkey, the United Kingdom, and the United States) participated in the Conference. They represented about 50 leading research centers in the field of chemistry and physics of polymers and polymer production and application.

D'Amore and Acierno in their opening remarks outlined topicality of the Conference for fundamental and applied polymer research.

The first plenary lecture [G.B. McKenna (the United States)] was dedicated to the effects of the molecular architecture on the rheology of polymer melts. In the lecture, a comparison was made of linear, long-chain branched, and ring molecules. The results were recommended for use in industrial rheology.

In the next lecture, G. Marrucci (Italy) also analyzed the rheological problems and proposed solutions for a series of tasks of the industrial rheology.

B. Mena (Mexico) in his lecture reported on the flow of non-Newtonian fluids around bubbles.

A lecture prepared by a group of scientists [J.M. Kenny, A. Terenzi, and S.E. Barbosa (Italy)] was devoted to rheology of polymers, polymer blends, and polymeric nanocomposites.

Considerable interest was aroused in the audience by the lecture prepared by G.C. Papanicolaou, Th.V. Kosmidou, N.K. Anifantis, and D.E. Mouzakis (Greece) in which they considered the effect of damage in macromolecules on the mechanical behavior of polymers.

M. Narkis (Israel) in his lecture reported on polymeric sensors for chemicals based on electrically conductive polymers and their applications in various branches of industry and in private life.

The next plenary lecture [D.E. Kranbuehl (the United States)] concerned the problems of preparation and characterization of hybrid nanoparticle metal polyimide films.

The lecture given by J. Mijovic was devoted to the study of the adhesion properties of a number of polymers, including network polymers. Particularly, the lecturer reported on water–network dynamics in adhesive joints, studied by experimental and computational methods.

Considerable interest has been expressed by the participants in the results reported by S. Simon in her lecture entitled Volume Recovery and the Tau-Effective Paradox: New Measurements on Polymeric Glass-Formers.

The lecture given by F.P. La Mantia (Italy) was devoted to degradation and stabilization of polymer blends and composite materials.

The durability of polymeric materials (fundamental and practical aspects) was the subject of the lecture given by J.L. Gardette (France).

H. Watanabe (Japan) in his lecture analyzed the dielectric and viscoelastic data of thermoelastoplastics in dynamic conditions.

The last plenary lecture was given by G.E. Zaikov (Russia) who reviewed the works concerning degradation of PVC and searching for the ways to its stabilization.

1070-4272/04/7709-1570 © 2004 MAIK "Nauka/Interperiodica"

Oral and poster presentations covered the problems of synthesis, characterization, and applications of a wide variety of polymers, polymer blends, and composites with a special emphasis made on nanocomposites. Several presentations included data on the processes for preparation of polymeric and composite materials.

The Conference revealed that the times of polymers have come long ago, and there are no grounds to expect that these times are soon over.

The next Conference "Times of Polymers"-III is planned to be held in 2006 at the same place.

Proceedings of the Conference will be published in 2005 as a special issue of the journals dedicated to the conference. The Program of the Conference and Abstracts of all the contributions are available from the library of the Institute of Chemical Physics, Russian Academy of Sciences (Moscow, Russia).

G. E. Zaikov, M. I. Artsis, and A. V. Zaikova

Russian Journal of Applied Chemistry, Vol. 77, No. 10, 2004, pp. 1573–1592. Translated from Zhurnal Prikladnoi Khimii, Vol. 77, No. 10, 2004, pp. 1585–1604.

REVIEW

Extraction of Gold From Ores and Concentrates by Leaching with the Use of Cyanides and Alternative Reagents

L. F. Kozin and V. T. Melekhin

Vernadskii Institute of General and Inorganic Chemistry, National Academy of Sciences of the Ukraine, Kiev, Ukraine

Ukrpolimetall State Corporation, Kiev, Ukraine

Received January 9, 2003; in final form, June 2004

Abstract—The problems associated with gold mining are considered from the standpoint of application of heap leaching, a method for gold recovery. Data on the kinetics and mechanism of gold dissolution in cyanide and alternative solvents [thiocarbamide solutions containing Fe(III) ions and hypochlorite-chloride bromine-bromide, iodine-iodide, and copper-thiosulfate solutions], which make it possible not only to improve the working efficiency in gold mining, but also to lessen the contamination of the environment with highly toxic compounds.

The method of heap leaching (HL) is a geotechnological method for processing of low-grade gold-containing ores and rejects of concentration plants. Alkaline solutions of cyanides are used in enormous amounts as solvents for gold [1, 2], which gives rise to quite a number of ecological problems. From the standpoint of environment protection [3], it is unsafe to use the HL technique in countries with fertile soils and high population density. Therefore, an exceedingly important problem of the HL technique is that alternative solvents for gold are to be developed [3].

In the HL of gold, special attention is given to taking into account the natural factors, absence of rifts, density of the surface layer of soil, presence of clay strata, and absence of compounds of such elements as arsenic, selenium, cadmium, thallium, lead, etc. in the ores. An exceedingly important specific feature of the HL technique is the possibility of processing of both moderate amounts of gold-containing ores and concentrates (tens and hundreds of thousands of tons) and enormous quantities of gold-containing raw materials of technological origin (tens and hundreds of millions of tons) [1, 2]. At present, the HL of gold is the most cost-effective method for leaching of low-grade gold-containing ores. However, despite the high economical efficiency of the HL of gold, proper attention is not, paradoxically, paid to the environment protection in gold-mining regions [3].

The rise in gold output in many countries all over the world is clearly seen from the data in Fig. 1. A steep rise in the output of gold has been noted in

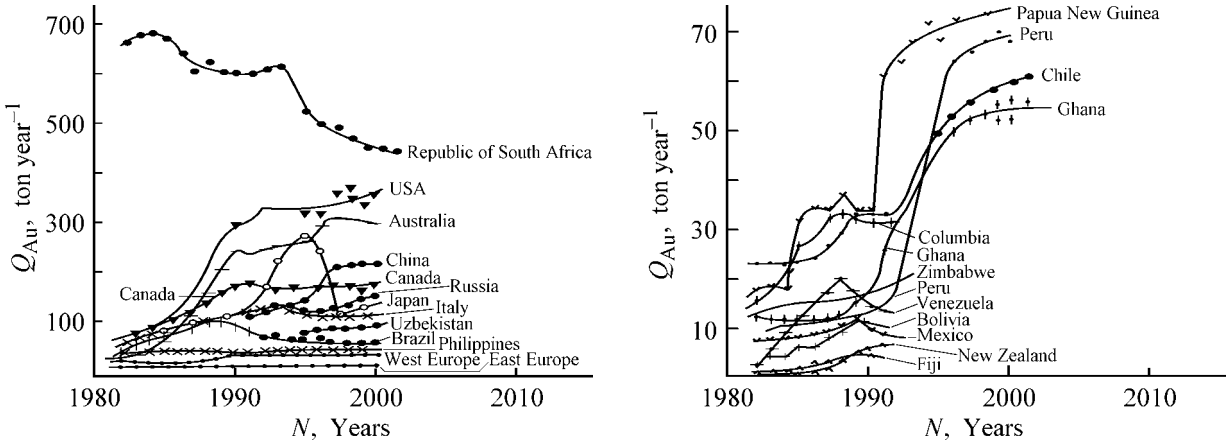

Fig. 1. Output of gold, Q_{Au} in some countries. (N) Years; the same for Fig. 2.

1070-4272/04/7710-1573 © 2004 MAIK "Nauka/Interperiodica"

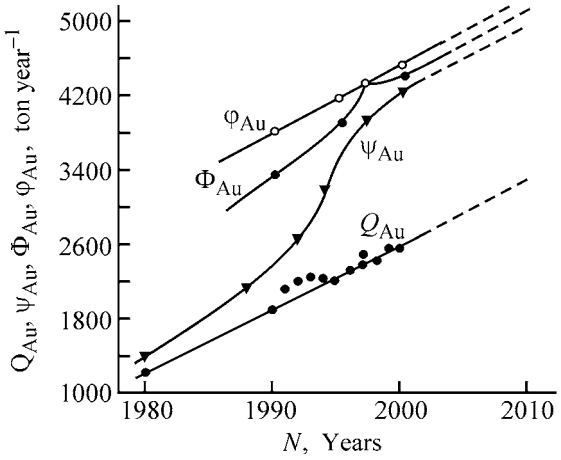

Fig. 2. Output Q_{Au}, consumption Ψ_{Au}, supply Φ_{Au}, and demand φ_{Au} for gold in the world.

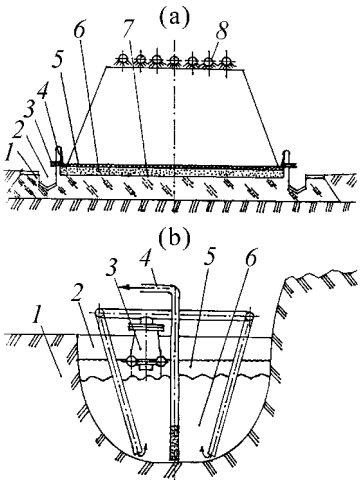

Fig. 3. Schematic of facilities for formation of blocks of gold-containing materials on (a) horizontal leaching pads and (b) landscape with a complex profile. (a) (*1*) Base of the leaching pad, (*2*) drainage trench with watertight liner, (*3*) discharge pipes for the leaching and product-containing solutions, (*4*) berm (0.6–0.8 m), (*5*) asphalt cover (0.1–0.2 m), (*6*) buffer layer (sand, 0.25–0.30 m), (*7*) all-welded polyethylene or PVC film (δ = 5–40 mm), and (*8*) system for sprinkling with the leaching solution. (b) (*1*) Natural base, (*2*) ravine or mountain rift, (*3*) supply of the leaching solution, (*4*) discharge pipe, (*5*) leaching solution, and (*6*) gold-containing starting product.

the United States, Australia, Canada, China, Russia, Japan, Italy (Fig. 1a), and also in the Philippines, Brazil, Papua New Guinea, Peru, Chile, Ghana, Venezuela and others (Fig. 1b) [4]. As can be seen, the 1980s, the years in which the HL of gold was mastered, are characterized by an explosive increase in the output of gold all over the world. The only exception is the South African Republic, which, although using the HL method for recovery of gold from gold-fields and raw materials of technological origin, obtains most part of its gold from ledge ores at large depths (1–3 km).

In the world as a whole, the output of gold has been growing linearly beginning in 1980 (Fig. 2).

Calculation shows that the 2010 world's output of gold will be 3320 ± 20 tons per year. The increase in the output of gold leads to higher demand for, and consumption of, gold [5]. However, as can be seen in Fig. 2, the supply of gold fails to satisfy the demand, which is quite understandable because mining of gold is very capital-intensive.

Analysis of the technologies for gold mining shows that the main contribution to the increase in the gold output is made by the heap leaching. The technological process of the HL of gold from gold-containing ores started to be developed in the second half of the 1960s by the US Mining Bureau. The development and fast implementation of the new technology for HL of gold from low-grade ores in the US industry were promoted by the special program devised by the US Mining Bureau and the preferential terms provided by the government, including reasonable taxation.

Already in the early 1980s, there were 110 HL installations with annual throughput of 100 thousand to 3.5 million tons of rock for recovery of gold and silver [1, 2, 6–9]. The steady increase in the annual output of gold in the US and many other countries (Fig. 1) is due to the involvement of low-grade ores in the production process and to recovery of gold and silver from these ores by heap cyanide leaching. The mastering of the method of heap leaching enabled some countries to raise the output of gold dramatically. As can be seen in Fig. 1a, the output of gold increased during the period of time from 1975 till 1992 by factors of 3, 10, and 15 in Canada, United States, and Australia, respectively [9]. Presently, the technology of heap leaching of gold and other noble metals is used at more than 150 plants, with some of these having an annual throughput capacity of 20–30 million tons of rock. Depending on the mineral composition of gold-containing ores and concentrates, the HL process makes it possible to recover 42 to 90% of gold and rapidly process hundreds of thousands and even millions of tons of raw materials, and, therefore, is being intensively developed [1, 2].

The method of heap leaching consists in the following. A certain amount (hundreds of thousands of tons and more) of an ore permeable to a reagent/solvent (commonly alkaline solutions of cyanides) and crushed to a size less than 20 mm is placed on a leaching pad with a concrete (or made of clay, clay with waste rock, etc.) base of a thickness of 0.5–1.0 m with a prescribed slope (frequently double-side). The device for heap leaching is shown schematically in Fig. 3. Such a device can be constructed on a hor-

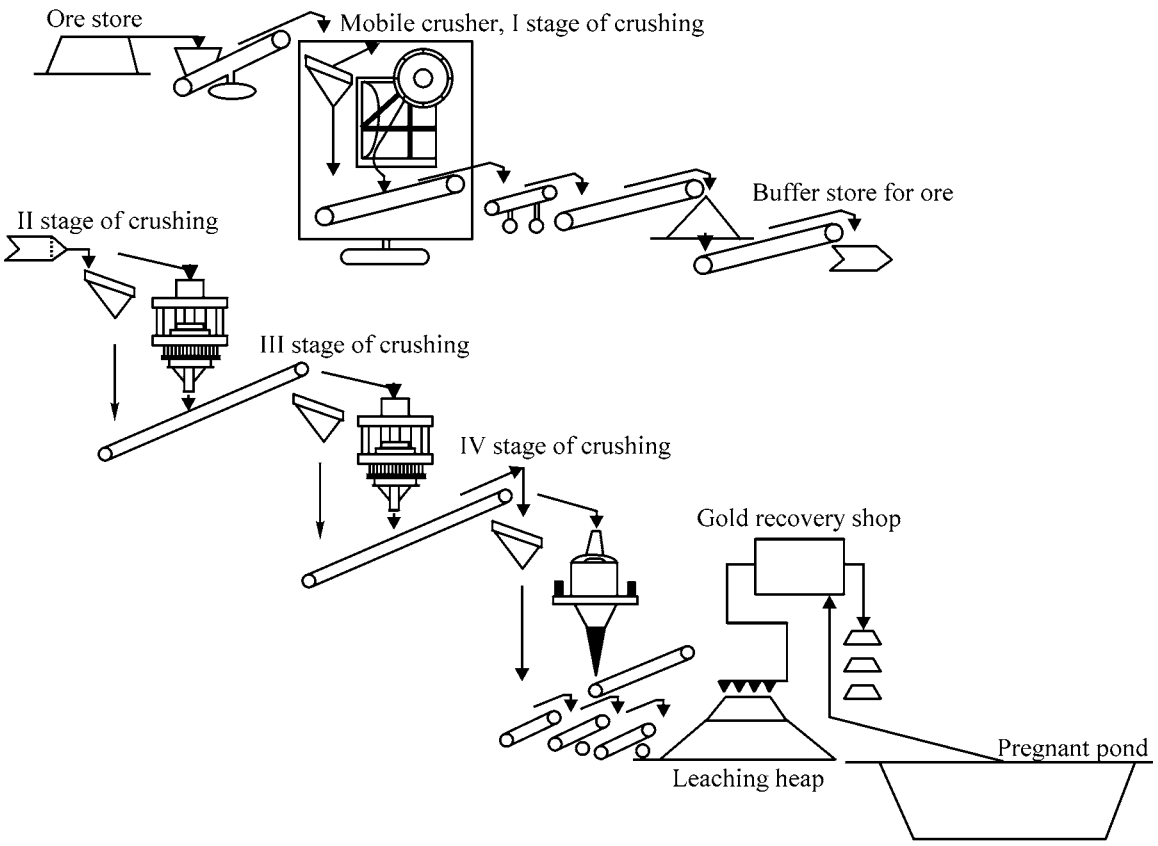

Fig. 4. Schematic of the production process at a plant of the Zarafshan-Newmont joint venture, supplemented with a "pregnant pond" [11].

izontal area (Fig. 3a) or on a landscape with a complex profile, with clay or rock walls and a liner impermeable to aqueous solutions (Fig. 3b). To provide a drain for the cyanide solutions, the leaching pad has a slope of 2°–7° toward the collectors of product-containing solutions. The pad of the HL installation may lie on a concrete or rammed-clay bed, on which a water-proofing layer is placed for protection from underground water. This layer has the form of two or three layers of all-welded polyethylene films with raised edges and a buffer sand-gravel layer of thickness 0.25–0.30 m. The total thickness of the base layer depends on its constituent components. In the case of a water-impermeable "pillow" of clay and screens made of concrete and one or two layers of asphalt, the total thickness of the base may exceed 1.2–1.5 m. Schematics of the pads for construction of heaps (or piles) with account of the landscape profile for bulk leaching of gold- and silver-containing materials were presented in [1]. The watertight base is the most important component of the installation for heap leaching, because it is intended to preclude loss of leaching and product-containing solutions. An important part of the leaching pad is the system for collection and removal of product-containing solutions. The ore is laid in bulk as a heap or pile 5–12 m (occasionally 30 m) high and 100–1500 m long. In gold leaching by the HL method, the surface of heaps (piles) is irrigated with cyanide solutions by means of perforated pipes, sprinkling nozzles, perforated outlet pipes in the bulk of the heaps, etc.

The general tendency in the development of the gold-mining industry in the world is the desire to involve in the industrial production in increasing amounts the low-grade and difficultly processable, the so-called stubborn and difficultly concentrated ores. Gold-containing ores, which include silicified and lime sedimentary rocks, hydrothermal rocks, quartzites, quartz-pyrites, sand dolomites, and shales of quartz and eruptive rocks (3–15 g of Au per ton of ore) can be readily dressed and are processed by gravitation or flotation methods [4, 10]. Ores of the same type, but with a low content of gold (0.2–1.8 g/ton), as well as rejects from concentration mills (including those stored in dumps), are a promising raw material for the HL technique. Figure 4 shows schematically how gold is recovered by the HL meth-

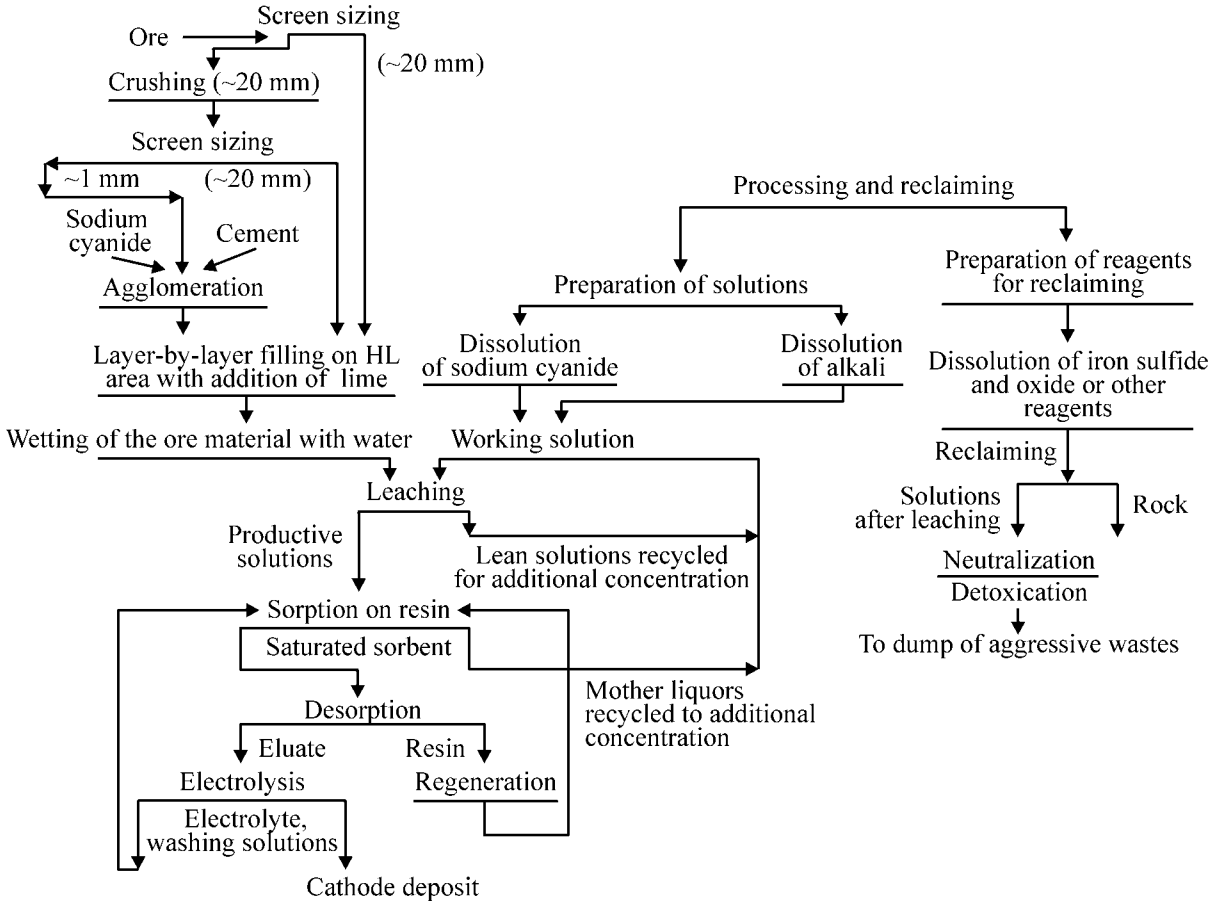

Technological scheme for ore processing by the HL with alkaline cyanide solutions [1].

od at a plant of the Zarafshan-Newmont joint venture [11]. The main expenditure in recovery of gold by leaching from resource ores (1.4 g of Au per ton) of the Muruntau deposit (Uzbekistan) is associated with ore pretreatment. The ore is subjected to four-stage crushing to obtain 94% of ore particles 3.25 mm in size. Further, the crushed ore is granulated by addition of cement, lime, and water. In the course of granulation, coarser and dust-like particles are bound into grains, which improves the permeability of the ore bed to the leaching solution. Lime is consumed in the course of granulation for raising the pH value of the cyanide leaching solution. The planned processing capacity of a heap for HL is 80 m (eight layers 10 m in height each). It can be seen from Fig. 4 that the HL process itself involves only a small number of technological procedures.

The simplicity of implementation of the HL process and low capital outlay and operation expenditure, which constitute, respectively, 25 and 35–40% of the expenditure for processing of gold-containing ore by the conventional techniques, make it possible to recover Au, Ag, and nonferrous and less-common metals from low-grade ores that are not economically viable for other technologies (0.2–0.6 g of Au per ton). The HL method is commonly used to process ores with 0.5–3.0 g/ton of gold and rejects from concentration mills (≥0.35 g/ton).

The amount of gold recovered in HL depends on the amount of the gold-containing material being processed. The concentration of Au(I) recovered from product-containing solutions depends on a number of factors: permeability of a material being leached to the solvent, porosity of the material, composition of the solvent, structure of ore materials being leached (gold-containing minerals and porous ore bodies scarred by crevasses, etc.), form in which gold is contained in the material (free, bound, dispersed, etc.), and length of the filtration path. Commonly, the permeability of the ore material and rejects is 0.5–10 cm h^{-1}. The admissible minimum permeability is 0.5–1.5 cm h^{-1}. To improve the permeability of heaps and to raise the rate of leaching and the recovery of gold, the ore is pelletized by treating the crushed ore material (or rejects)

Table 1. Standard potentials of gold in simple and complex-forming aqueous media [14, 15]

Half-reaction	$E^0_{Ox/Red}$, V	Half-reaction	$E^0_{Ox/Red}$, V
$Au(CN)_2^- + e = Au + 2CN^-$	–0.611	$AuBr_4^- + 2e = AuBr_2^- + 2Br^-$	0.802
$Au(S_2O_3)_2^{3-} + e = Au + 2S_2O_3^{2-}$	0.153	$AuBr_4^- + 2e = AuBr + 3Br^-$	0.820
$[Au(TC)_2]^+ + e = Au + 2TC^*$	0.380	$AuBr_4^- + 3e = Au + 4Br^-$	0.854
$AuI + e = Au + I^-$	0.530	$AuCl_4^- + 2e = AuCl_2^- + 2Cl^-$	0.926
$AuI_4^- + 2e = Au\ I_2^- + 2I^-$	0.550	$AuBr_2^- + e = Au + 2Br^-$	0.959
$AuI_4^- + 3e = Au + 4I^-$	0.560	$AuCl_4^- + 3e = Au + 4Cl^-$	1.002
$AuI_2^- + e = Au + 2I^-$	0.578	$AuCl + e = Au + Cl^-$	1.150
$[AuBr(OH)]^- + e = Au + Br^- + OH^-$	0.959	$AuCl_2^- + e = Au + 2Cl^-$	1.130
$Au(SCN)_4^- + 3e = Au + 4SCN^-$	0.636	$Au^{3+} + 2e = Au^+$	1.401
$Au(SCN)_4^- + 2e = Au(SCN)_2^- + 2SCN^-$	0.645	$Au^{3+} + 3e = Au$	1.498
$Au(SCN)_2^- + e = Au + 2SCN^-$	0.661	$Au^+ + e = Au$	1.692

* TC, thiocarbamide $[(NH_2)_2C=S]$.

with a binder, portland cement (2.5–3.0 kg/ton), set with an alkaline cyanide solution [1, 7–9]. The pelletization is carried out in special granulators or on a transporter delivering the mixture to the vertex of a cone. The granulation occurs when the ore material with a binder moves down the sloping wall of the cone. The porosity of the thus obtained grains may be as high as 15–30%.

Alkaline solutions of NaCN commonly serve as solutions for extraction of gold from ores by leaching. However, an intensive search is underway for alternative solutions that can be used for this purpose. These solutions must satisfy the requirements of "green" chemistry and allow creation of gold-recovering shops that would not affect adversely the environment.

Cyanides. The technological scheme for heap leaching of gold with the use of cyanides [1] comprises the whole cycle of the HL process: pretreatment of ore, including crushing, introduction of a granulating additive (mainly portland cement), and agglomeration; leaching with alkaline cyanide solutions of NaCN (1.2–1.5 g l^{-1} at pH 10–11.5; NaOH expenditure 2.2–2.5 kg per ton of ore); and subsequent processing of the solutions obtained [12]. The optimal pH of the solution, equal to 11–11.5, is controlled by introduction of CaO, NaOH, {or $Ca(OH)_2$ [1]}. The expenditure of reagents is as follows (kg/ton): NaCN 0.3–1.5, NaOH 0.15–3.0, CaO 2 [1, 2, 4–8, 12, 13]. The expenditure of reagents and materials for agglomeration is as follows (kg/ton): cement 10–15, NaCN 0.5–3.0, CaO 1–3; H_2O 12–14% [1]. The resulting pellets 15–30 mm in size are directed to HL. The total area of heaps in HL is as large as 200 thousand square meters. The extraction of gold and silver is performed using the standard scheme on a HL pad with the use of solvents in the system for sprinkling, collection, and removal of the solution obtained. Further follow the recovery of the metals from the solutions by sorption on ion-exchange resins or activated carbons, desorption of the metals (accompanied by regeneration of adsorbents) to give an eluate, and electrolysis of the eluate to give a cathode deposit containing gold and silver. Gold can also be recovered from the eluates by cementation on electronegative metals. The technological process of gold leaching includes the following stages: preparation of leaching solutions, construction of dumps for processed rock, and its delivery to utilization.

The dissolution rate of gold and time of its extraction from an ore depend on the structure of the ore, which determines its permeability and porosity, and on the composition of the leaching solvent.

The time of leaching also depends on the mass of the ore and the form in which gold is present in it (bound or free gold, coarsely crystalline or dispersed) and may be in the range from several weeks to a year. In the case of a preliminary pelletization of the ore, the rate of heap leaching commonly increases [1, 2]. The sprinkling density is maintained at the level of 10–15 l m^{-2} h^{-1} in the case of a uniform sprinkling of the heap with the leaching solvent, and at 6–8 l m^{-2} h^{-1} in the case of a low permeability.

The standard potential of the half-reaction in the system constituted by gold and dicyanoaurate(I) anion:

$$Au(CN)_2^- + e \rightarrow Au + 2CN^- \quad (1)$$

is, as can be seen from Table 1, the most electronegative, compared with other media, and equal to

Table 2. Standard potentials of a number of redox systems [14, 15]

Half-reaction	$E^0_{Ox/Red}$, V	Half-reaction	$E^0_{Ox/Red}$, V
$FAD^* + 2H^+ + 2e = 2TC$	0.420	$BrCl + 2e = Br^- + Cl^-$	1.20
$I_2 + 2e = 2I^-$	0.535	$2ICl_2^- + 2e = I_2 + 4Cl^-$	1.056
$I_3^- + 2e = 3I^-$	0.536	$2ICl + 2e = I_2 + 2Cl^-$	1.19
$I_{2(aq)} + 2e = 2I^-$	0.621	$2ICl_3 + 6e = I_2 + 6Cl^-$	1.28
$3I_2 + 2e = 2I_3^-$	0.789	$ICl_3 + 2e = ICl + 2Cl^-$	1.31
$HIO + H^+ + 2e = I^- + H_2O$	0.987	$2HClO + 2H^+ + 2e = Cl_2 + 2H_2O$	1.630
$2HIO + 2H^+ + 2e = I_2 + 2H_2O$	1.45	$HClO + H^+ + 2e = Cl^- + H_2O$	1.482
$IO_3^- + 6H^+ + 6e = I^- + 3H_2O$	1.085	$NaClO + H_2O + 2e = NaCl + 2OH^-$	0.890
$3IO_3^- + 18H^+ + 16e = I_3^- + 9H_2O$	1.1539	$Cl_{2(aq)} + 2e = 2Cl^-$	1.396
$2IBr_2^- + 2e = I_2 + 4Br^-$	0.87	$Cl_3^- + 2e = 3Cl^-$	1.415
$2IBr + 2e = I_2 + 2Br^-$	1.02	$HClO + 2H^+ + 2e = Cl_{(g)} + 2H_2O$	1.63
$HBrO + H^+ + 2e = Br^- + H_2O$	1.330	$O_2 + 2H^+ + 2e = H_2O_2$	0.682
$2HBrO + 2H^+ + 4e = Br_2 + 2H_2O$	1.596	$Fe^{3+} + e = Fe^{2+}$	0.771
$BrO^- + 2H^+ + 2e = Br^- + H_2O$	1.589	$O_2 + 4H^+ + 4e = 2H_2O$	1.229
$3Br_2 + 2e = 2Br_3^-$	1.145	$MnO_2 + 4H^+ + 2e = Mn^{2+} + 2H_2O$	1.23
$Br_{2(aq)} + 2e = 2Br^-$	1.087	$S_2O_8^{2-} + 2e = 2SO_4^{2-}$	2.01
$Br_3^- + 2e = 3Br^-$	1.051	$S_2O_8^{2-} + 2H^+ + 2e = 2HSO_4^-$	2.123
$Br_5^- + 4e = 5Br^-$	1.145		

* FAD, formamidine disulfide $(NH_2)_2(NH)_2C_2S_2$.

$E^0_{Au} = -0.611$ V [14, 15]. Therefore, the dissolution of gold can proceed, in the case of heap leaching with cyanide solutions, in the presence of a wide variety of oxidizing agents (electron acceptors): oxygen, hydrogen peroxide, or potassium peroxydisulfate, in accordance with the following equations [16]:

$$2Au + 4NaCN + O_2 + 2H_2O \rightarrow 2Na[Au(CN)_2] + 2NaOH + H_2O_2, \quad (2)$$

$$2Au + 4NaCN + H_2O_2 \rightarrow 2Na[Au(CN)_2] + 2NaOH, \quad (3)$$

$$2Au + 4NaCN + K_2S_2O_8 \rightarrow Na[Au(CN)_2] + 2Na_2SO_4. \quad (4)$$

Table 2 lists the standard potentials [14, 15] of a number of redox systems promising for dissolution (recovery) of gold, silver, and platinum metals from ores, concentrates, and other materials in which they are contained, with the requirements of "green" chemistry satisfied [3]. The same table presents the standard potentials (V, relative to standard hydrogen electrode) of half-reactions with oxygen-based oxidizing agents. However, despite the high potentials of the oxidizing agents and large difference between the potentials of gold, E^0_{Au}, and oxidizing agents, $E^0_{Ox/Red}$, in cyanide solutions, the dissolution rate of gold in cyanide solutions is low. For example, the rate constant of gold dissolution is $k_{Au} = 27$ μmol m^{-2} s^{-1} [17] or $k_{Au} = 2.7 \times 10^{-9}$ mol cm^{-2} s^{-1} even in the presence of hydrogen peroxide. The rate constant of gold dissolution by a first-order reaction to give $[Au(CN)_2]^-$ is $k_{[Au(CN)_2]^-} = 2.33 \times 10^{-7}$ s^{-1} at 298 K. At temperatures of 323, 333, and 353 K, the values of $k_{[Au(CN)_2]^-}$ are, respectively, 1.10×10^{-6}, 1.51×10^{-6}, and 4.7×10^{-6} s^{-1} [18]. Therefore, as can be seen from Fig. 5b, curve *1*, the concentration of gold(I) in the solution reaches, in leaching with cyanides, only 0.8–1.5 mg l^{-1} even after a long time.

To raise the rate of gold dissolution, it has been suggested [17] to introduce Tl(I) ions into the cyanide solutions. However, this leads to a higher load on the environment (MPC 0.1 μg l^{-1} [19, 20]). At a concentration of Tl(I) ions equal to 0.5 mmol, the rate of dissolution of a rotating disc electrode made of gold (ω = 400 rpm) in a solution containing (M): NaCN 0.01, H_2O_2 0.01 at pH 10, $P_{O_2} = 0.21$ atm, and 25°C, increases from 275 to 785 μmol m^{-2} s^{-1}. In the case of Au dissolution in the presence of H_2O_2, the optimal rate is observed at pH 10.5–12.0 and H_2O_2 concentration of 0.005–0.03 M. In the temperature range 20–35°C, the rate of gold dissolution is limited by kinetic factors (activation energy $E_A = 140.8$ kJ mol^{-1}), and

at temperatures higher than 40°C, it is controlled by diffusion (E_A = 4.8 kJ mol^{-1}).

Let us now consider the reasons for the low rate of gold dissolution and the mechanism of gold dissolution in cyanide solutions. In anodic dissolution of gold in a cyanide solution containing 0.1 M of KCN and 0.1 M of KOH, three clearly pronounced peaks are observed in the i_a–E_a curve at potentials of –0.4, 0.3, and 0.6 V (relative to a standard hydrogen electrode), with broad passivation regions resulting from the passivating influence of hydroxide ions being adsorbed [21, 22]. The limiting stage of the anodic process is the stage of detachment of the first electron

$$AuCN^-_{ads} \rightarrow AuCN_{ads} + e \qquad (5)$$

from an $AuCN^-_{ads}$ species formed in adsorption of a cyanide ion on gold. The activation energy of the rate-determining stage is 93 ± 8 kJ mol^{-1}. In view of the fact that the point of zero charge (PZC) of gold is positive: $E^{Au}_{PZC} = 0.19 \pm 0.01$ V (relative to a standard hydrogen electrode) [23], its surface is negatively charged in a cyanide electrolyte at potentials more negative than the PZC ($E^0_{Au(CN)_2^-/Au^0} = -0.61$ V). The adsorption of cyanide ions on the surface of gold is hindered by the electrostatic repulsion of negative charges. Mainly positively charged potassium ions K^+ are adsorbed on the negatively charged surface of gold, and adsorption of CN^- occurs in the form of a secondary layer by the scheme

$$Au^{\delta-} \,|\, {}^{\delta+}K^{(1-\delta+)\delta-}CN^{\delta-}$$

to give a multilayer adsorption system. The adsorbed species $AuCN^-_{ads}$ is formed in this system by the exchange reaction, and then gold is ionized by the redox reaction Au → Au(I) + e with the subsequent binding of gold into a poorly soluble compound AuCN (SP 6.3×10^{-32} [24]). The formation of a neutral poorly soluble compound AuCN is the reason why the surface of gold is passivated. As a result, the ohmic resistance at the interface Au | AuCN–electrolyte increases. The neutral species AuCN blocks active centers on the surface of gold. As a consequence, the second cyanide ion adds to the AuCN species by the donor–acceptor mechanism at a very slow rate to give a soluble anion, dicyanoaurate(I) $[Au(CN)_2]^-$, which, having a negative charge, is repelled from the negatively charged surface of gold. Therefore, the rate of gold dissolution in cyanide solutions is very low.

As an example of low rates in cyanide extraction of gold by the HL method can serve processing of a low-grade ore at the Muruntau deposit of the Zarafshan-

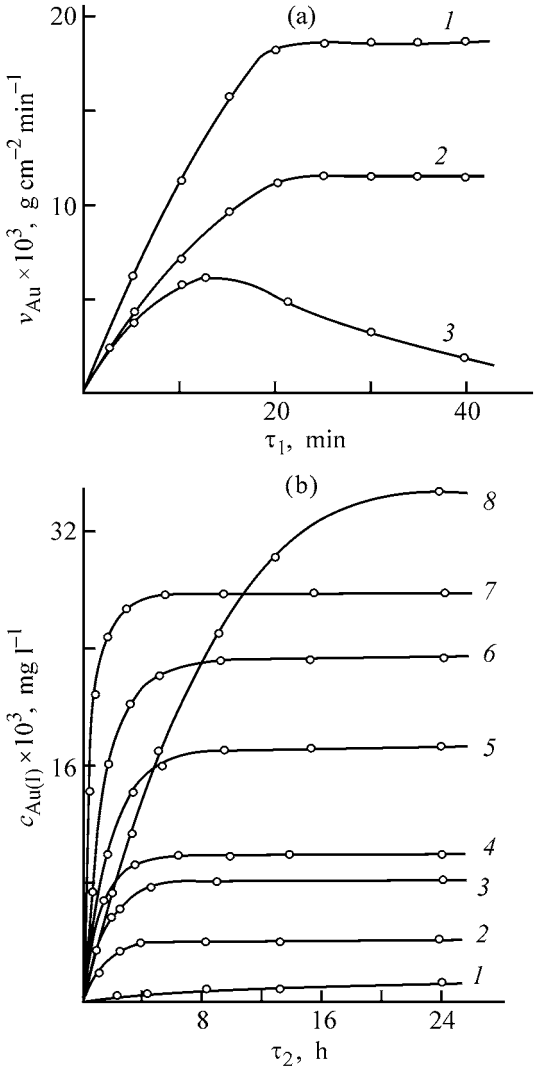

Fig. 5. (a) Rate of gold dissolution, v_{Au}, in a TC solution containing (*1*, *2*) iron(II) sulfate and (*3*) hypochlorite and (b) concentrations of gold ions, $c_{Au(I)}$, in various solutions vs. the time of contact τ_1, τ_2. For solution compositions, see text. (a) Temperature (K): (*1*, *2*) 298 and (*3*) 333. (b) Solution: (*1*) alkaline cyanide; (*2*, *3*) iodine-iodide at pH (*2*) 11.7 and (*3*) 10; (*4*) copper-thiosulfate, (*5*–*7*) thiocarbamide with (*5*) 0.01, (*6*) 0.1, and (*7*) 0.2 M of TC; and (*8*) hypochlorite.

Newmont joint venture [11, 19]. Multilayer piles of height 85 m are constructed for gold leaching [11, 19]. The leaching is carried out during a long period of time (up to 226 days). In this case, the variation of the concentration of gold(I) in the solution depends on the density of sprinkling with a leaching solvent and on the time of ore leaching. For example, in leaching of ore for 0–20 days (density of sprinkling with a leaching cyanide solution χ = 15 l h^{-1} m^{-2}), the concentration of gold slowly increases to 1.3–1.4 mg l^{-1} to reach the maximum of 6–6.3 mg of Au

per liter after τ = 24–50 days (χ = 12 l h^{-1} m^{-2}). Then, after τ = 51–70 days at χ = 10 l h^{-1} m^{-2}, the concentration of gold in solution decreases to 1.9 mg l^{-1}, and further, after τ = 71–100 days at χ = 8 l h^{-1} m^{-2}, falls to 1.2 mg l^{-1}. If the density of sprinkling with the leaching solution is not lowered, then, at τ = 240 days, the concentration of gold in the solution decreases to a level at which the processing of solutions becomes economically inexpedient. Therefore, the spraying density is chosen to be 8 l h^{-1} m^{-2} or less, so that the concentration of gold in the solution should be "maintained at a level of no less than 1.2 mg l^{-1}," [19]. This ensures effective recovery of gold from the solution obtained on a Merrill Crow installation [19]. To catch suspensions, the solution is passed through filtering units. The dissolved oxygen is removed by vacuum deaeration in two towers [11]. Then, zinc dust and lead nitrate are introduced into the solution to diminish the share of the parasitic reaction by raising the overvoltage of hydrogen evolution on lead. The cementate formed is separated on five pressure filters, and the spent solution is recycled into the HL process. The resulting precipitate is calcined in two furnaces at 650°C to oxidize zinc and metals coprecipitated in cementation of gold. The calcined precipitate is mixed with a flux based on borax, saltpeter, and silica and fused in an arc smelting furnace. The gold alloy produced by the smelting contains three main impurities (%): Ag 10, Cu 5, and Pb 2–3, and the total content of other impurities is 2%. The content of gold in the crude metal is 80–81%. After purification by refining, the content of gold in the commercial product is 99.99%. The manufacture of gold by the Zarafshan-Newmont joint venture was 13.683 and 11.724 ton $year^{-1}$ in, respectively, 1997 and 1998 [11], and 13.483–16.886 ton $year^{-1}$ in 1999–2001 [19].

Interesting results were obtained by the authors of [25] in HL of gold-rich grainy long-stored products formed in finishing treatment at a plant for processing of heavy concentrates, which contained mainly quartz and fragments of bearing strata: pyrite, arsenopyrite, and chalcopyrite. Gold was mainly present in the free form (grain size 2 mm) and was associated with quartz and sulfides. According to the results of assaying, the content of gold was 60–80 g of Au per ton. The gold-containing material was crushed (95% to grain size –4 mm and 5% to –0.074 mm). The prepared gold-containing materials were cyanated at a phase ratio l : s = 1 : 2, leaching duration of 72 h, and spraying density of 70–80 l h^{-1} m^{-2}. The recovery of gold into product-containing solutions somewhat exceeded 80%. After the recovery of gold and separation of the liquid phase, 8–16 g of Au per ton remained in the cakes. Only under the above conditions of cyanidation, the content of gold in the cyanide leaching solutions was as high as 10–100 mg l^{-1} [25]. It has been established that cementation on zinc shavings is efficient for recovery of gold from such rich productive solutions. The cemented precipitate of gold is extracted and fused into an alloy ingot of gold after acid treatment to remove zinc and some impurities. The solutions from which gold was extracted and washed cyanidation cakes were detoxicated with a solution of calcium hypochlorite prior to being delivered to special storage facilities [25].

It can be seen from the data presented that the rates of the cyanidation reaction are low both in [11, 19] and in [25].

However, the rate of the cyanidation reaction can be, in our opinion, raised manyfold if the charge of the gold surface is changed. It is known that positively charged ions: Pb^{2+}, Zn^{2+}, Cd^{2+}, Cu^{2+}, Cu^{+}, Ag^{+}, Tl^{+}, can be adsorbed on a negatively charged gold surface. For these ions, the point of zero potentials E_{PZC} of the metallic phase are considerably more negative then the PZC of gold (V): $E_{PZC}^{Pb} = -0.60$, $E_{PZC}^{Zn} = -0.60$, $E_{PZC}^{Cd} = -0.75$ [20], $E_{PZC}^{Cu} = -0.43$ [26], $E_{PZC}^{Ag} = -0.70$, $E_{PZC}^{Tl} = -0.71$. In dissolution of gold in the presence of redox components in solution, the adsorbed ions Pb^{2+}, Zn^{2+}, Cd^{2+}, Cu^{+}, Ag^{+}, Tl^{+} are reduced at more positive potentials (undervoltage effect) [27] to a metal, to form positively charged nanosize islands on the surface of gold. These islands may give rise to a positive, the so-called compromise potential of the gold surface. As a result, the reaction surface of gold acquires a more positive potential, which stimulates the adsorption of cyanide ions [18]. As a consequence, the rate of gold dissolution may increase by several orders of magnitude, by analogy with the anodic dissolution of gold in electrolytes with addition of Tl(I), Pb(II), and other ions [21].

The solutions formed in extraction of gold by leaching are directed into the so-called "pregnant pond" (see scheme). From this pond, solutions containing Au(I) in the form of the anion $[Au(CN)_2]^-$ with the accompanying silver(I) anion $[Ag(CN)_2]^-$ are commonly fed into columns packed with an ion-exchange resin (anionite) or activated carbon. Elution of gold from the anionite or activated carbon by various methods gives concentrated eluates, wherefrom gold is extracted by treatment with powdered zinc [11, 19] or zinc shavings [25], or by electrolysis. The authors of [28] believe that aluminum is to be preferred for recovery of gold from cyanide solutions by cementation. In contrast to zinc, aluminum forms no complex com-

pounds with cyanide ions. Therefore, regeneration of cyanide is observed in cementation of gold from eluates. Aluminum ions can be removed from solutions by simple liming. Aluminum can be used in the form of a dust, shavings, sheets, or alloys with silicon, grains of silumin Al–Si [28]. Gold and silver can also be recovered from solutions by electrolysis with graphitized fiber cathodes, with current efficiencies of 80–90 and 50–60%, respectively [29]. The payback period in industrial implementation of the HL processes described is in the range from several months to a year [30].

The technology of heap leaching of gold has been tested and mastered in Russia, Kazakhstan, and Uzbekistan on the industrial scale since the early 1990s [10, 13, 34].

As examples of use of cyanide solutions in gold mining in CIS countries can serve the following deposits: Muruntau [11] and Besapantau [31] (Uzbekistan); Vasil'kovskoe [32], Pustynnoe, Enbekshi, Ortasoi, Kar'ernoe, Zhanan [33] (Kazakhstan); Maiskoe, Kuznetskoe, Lopukhovskoe, Murtykty, Vorontsovskoe [34] (Russia). The factor that hinders use of the HL of gold for processing of gold-containing ores from the Muruntau and Besapantau deposits is the high sorption capacity (up to 91%) of carbonaceous shales contained in these ores [31].

Particular difficulties are encountered in recovery of gold by the HL and gravitational methods in the case of clayey gold-containing materials [35–37]. Clays form, in the course of gravitational concentration in wet media, colloid solutions and sludges whose particles sorb finely dispersed gold and carry it away to rejects, which results in its low recovery. At the same time, granulation of clayey gold-containing ores markedly raises their permeability to the leaching solutions and improves recovery of gold into leaching solutions.

Thiocarbamides. Rather promising, from the standpoint of "green" chemistry, reagents for gold leaching are thiocarbamides, thiosemicarbamides, thiocyanates, and derivatives of chlorine, bromine, iodine, etc., in which the rates of gold dissolution are higher than those in cyanide solutions [18, 38, 39]. One of properties of these reagents used for extraction of gold and silver by leaching is their capacity for spontaneous redox reactions involving atmospheric oxygen, water (hydrolysis), biota (plants and products of their decomposition, microorganisms), which convert spent (or spilled) solvents into acids (H_2SO_4 reacting with silicates, alumina, etc.) to give neutral salts, microfertilizers, or even food products for microorganisms.

The standard potential of the half-reaction of gold in a solution containing thiocarbamide [$SC(NH_2)_2$, TC] is $E^0_{Au\,TC_2^+}$ = 0.380–0.420 V (Table 1) [14]. Figure 5a shows kinetic curves of gold dissolution in a thiocarbamide solution containing iron sulfate of the following composition (M): $SC(NH_2)_2$ 0.4, $Fe_2(SO_4)_3$ 0.36; H_2SO_4 0.1 (to pH 1.0) at 298 and 333 K. The procedure for measuring kinetic curves was described in [18, 38, 39]. It can be seen that the rate of dissolution of metallic gold depends on the time of its contact with a thiocarbamide solution and on temperature. Gold dissolves in thiocarbamide solutions by the following first-order reaction

$$c = c_{max}(1 - e^{k}3\tau), \quad (6)$$

where c_{max} is the limiting concentration of gold in solution, equal to 1.47×10^{-4} M (28.96 mg l^{-1}); and k is the rate constant (s^{-1}) of gold dissolution, equal to 6.18×10^{-4} s^{-1} at 298 K [18].

The quantity $k_{Au\,TC_2^+}$ exceeds by a factor of 2500 $k_{[AuCN]_2^-} = 2.33 \times 10^{-7}$ s^{-1} at a given temperature. Reactions of the following set occur in solution in the course of gold dissolution:

$$SC(NH_2)_2 + FeSO_4 \rightleftarrows FeSO_4 \cdot SC(NH_2)_2^+, \quad (7)$$

$$2SC(NH_2)_2 + 2FeSO_4 \cdot SC(NH_2)_2^+ \rightleftarrows S_2C_2(NH)_2(NH_2)_2 + 2FeSC(NH_2)_2^{2+} + 2HSO_4^-, \quad (8)$$

$$2Au + S_2C_2(NH)_2(NH_2)_2 + 2SC(NH_2)_2 + 2H^+ \rightarrow 2Au[SC(NH_2)_2]_2^+, \quad (9)$$

$$Au + 2SC(NH_2)_2 + FeSO_4 \cdot SC(NH_2)_2^+ \rightarrow Au[SC(NH_2)_2]_2^+ + FeSO_4 \cdot SC(NH_2)_2. \quad (10)$$

The potential of the reaction

$$2SC(NH_2)_2 \rightleftarrows S_2C_2(NH)_2(NH_2)_2 + 2H^+ + 2e \quad (11)$$

of formation of formamidine disulfide (FAD) is E^0_{FAD} = 0.420 V (Table 2) and depends on the solution pH and concentration of thiocarbamide in accordance with the reaction

$$E_{eq} = 0.420 - 0.059\,pH + 0.0295 \log\{[S_2C_2(NH)_2(NH_2)_2]/[SC(NH_2)_2]^2\}. \quad (12)$$

The rate of gold dissolution in thiocarbamide solutions depends on many factors: rate of FAD formation by reaction (8), whose equilibrium constant is K^0_{eq} =

6.7×10^{10}; optimal Fe(III) : TC ratio, 1 : 2; pH 0.8–1.2; and temperature, 5–25°C [18]. The activation energy of the reaction of gold dissolution in TC solutions in the presence of complex ions formed by iron and thiocarbamide, $FeSO_4 \cdot SC(NH_2)_2^+$, in the temperature range 5–25°C is E_A 13.4 kJ mol^{-1}, i.e., the rate of gold dissolution in TC solutions is controlled by diffusion, and in the temperature range 25–60°C, E_A = 42.8 kJ mol^{-1}, i.e., the rate of dissolution is controlled kinetically. The equilibrium constant of reaction (9) is $K_{eq}^0 = 3.4 \times 10^{13}$. Reactions (7) and (8) are reversible, and reactions (9) and (10) of gold dissolution are irreversible. Interestingly, the standard potential of gold in a carbamide solution is 0.380 V (Table 1). The standard redox potential of formamidine disulfide $[(NH_2)_2(NH)_2C_2S_2]$ is only 0.420 V (Table 2). The difference of the standard potentials, equal to 0.040 V, is sufficient for the reaction of gold dissolution to occur.

It was found in leaching of ores from the Muzhievskoe deposit in laboratory conditions with TC solutions that the concentration of gold(I) in the product-containing solution depends on the TC concentration in solution, being equal to 17, 22.8, and 27.5 mg l^{-1} at [TC] = 0.05, 0.1, and 0.2 M, respectively (Fig. 5b, curves *5–7*). For ores that are richer in gold, the concentration of gold(I) in the leaching solution may be considerably higher. The equilibrium concentration of gold(I) in thiocarbamide solutions may be as high as several tens of grams per liter of solution. As can be seen in Fig. 5a, the kinetic curves of gold dissolution (curves *1, 2*) become parallel to the abscissa axis after the maximum dissolution rate is reached. This may be due to inhibition of the gold surface both by products formed in decomposition of TC (HS^-, S^0) via reactions of hydrolysis and oxidation

$$S{=}C(NH_2)_2 + 2H_2O \rightarrow O{=}C(NH_2)_2 + HS^- + H_3O^+, \quad (13)$$

$$S{=}C(NH_2)_2 + \frac{1}{2}O_2 \rightarrow O{=}C(NH_2)_2 + S^0, \quad (14)$$

$$HS^- + \frac{1}{2}O_2 \rightarrow S^0 + OH^-, \quad (15)$$

and by poorly soluble products {AuHS, AuS^-, $[Au(HS)_2]^-$, $[Au(H_2S)_2]^+$, $[Au_2(HS)_2S]^{2-}$, $[Au(H_2S)_2]^+$, $[Au(H_2S)_3]^+$}. The composition of the hydrosulfide complexes of gold and their solubility in aqueous solutions depend on the solution pH and temperature. It was established that the following complex species are formed in hydrosulfide solutions: $[Au(HS)_2]^-$, $[Au_2(HS)_2S]^{2-}$, $AuHS_2^{3-}$, AuHS, and AuS^-. Processing of experimental data demonstrated that the instability constants K_{ins} of the complex ions $[Au(HS)_2]^-$ and $[Au_2(HS)_2S]^{2-}$ at different temperatures are as follows: 1.0×10^{-36} and 4.0×10^{-70} at 298 K, 1.2×10^{-33} and 2.0×10^{-66} at 323 K, 7.9×10^{-24} and 1×10^{-53} at 448 K, and 3.2×10^{-20} and 1.2×10^{-48} at 523 K.

In the course of dissolution, positively charged species $FeSO_4 \cdot SC(NH_2)_2^+$, TC molecules, and positively charged hydrosulfide complexes $[Au(H_2S)_2]^+$, $[Au(H_2S)_3]^+$ and, as a result of multilayer adsorption, also negatively charged complexes $[Au(HS)_2]^-$, $[Au_2(HS)_2S]^{2-}$, and $AuHS_2^{3-}$ are adsorbed on the surface of gold. The source of sulfide ions in the thiocarbamide solution is its hydrolysis by reaction (13).

As a result of exchange reactions, poorly soluble sulfides (Au_2S) and hydrosulfides (AuHS) of gold are formed in the surface reaction layer of gold. The formation of poorly soluble sulfides in extraction of gold with thiocarbamide solutions is a major disadvantage of this reagent. A study of the surface films on gold by Auger spectroscopy confirmed these conclusions [38].

Figures 6a and 6b show micrographs of the adsorption film on the surface of gold, and Figs. 6c and 6d, electronic Auger spectra of these films. The surface adsorption films were obtained by dissolving a gold disc in a thiocarbamide solution of a composition (M) $SC(NH_2)_2$ 0.138 and Fe(III) 0.046 at pH 2.0 and disc rotation rate ω = 180 rpm in the course of 200 min. It can be seen that the surface film is constituted by dark particles ($\delta \leq 0.1$ μm), coarse conglomerates of particles ($\delta \leq 50 \pm 10$ μm) and light areas. The Auger spectra of the dark particles are shown in Figs. 6c and 6d. The composition of the particles was determined layer-by-layer by Auger spectroscopy, by etching the film with argon ions for τ = 10 (Fig. 6c) and 60 s (Fig. 6d). A layer of thickness 7.0 ± 0.2 Å was removed from the sample surface in 10 s, and 40.0 ± 0.5 Å, in 60 s. The total thickness of the adsorption film was $\delta = 260 \pm 10$ Å. An analysis of the adsorption film by means of Auger spectroscopy demonstrated that it contains gold, sulfur, carbon, and oxygen. The Au : S ratio in the film, equal to 54.5 : 44.7 = 1.21 (10 s) and 65.0 : 35.3 = 1.84 (60 s), indicates that hydrosulfides AuHS and sulfides Au_2S are formed in the adsorption film. The concentration of gold(I) in the thiocarbamide solutions reached a value of 6.156 g l^{-1} in 170 min at a TC : Fe(III) ratio of 0.337 : 0.305 = 1.04.

Hypochlorites. As oxidizing agent for gold can be used sodium [1, 40] or calcium hypochlorites [41]. When brought in contact with water or alkali solu-

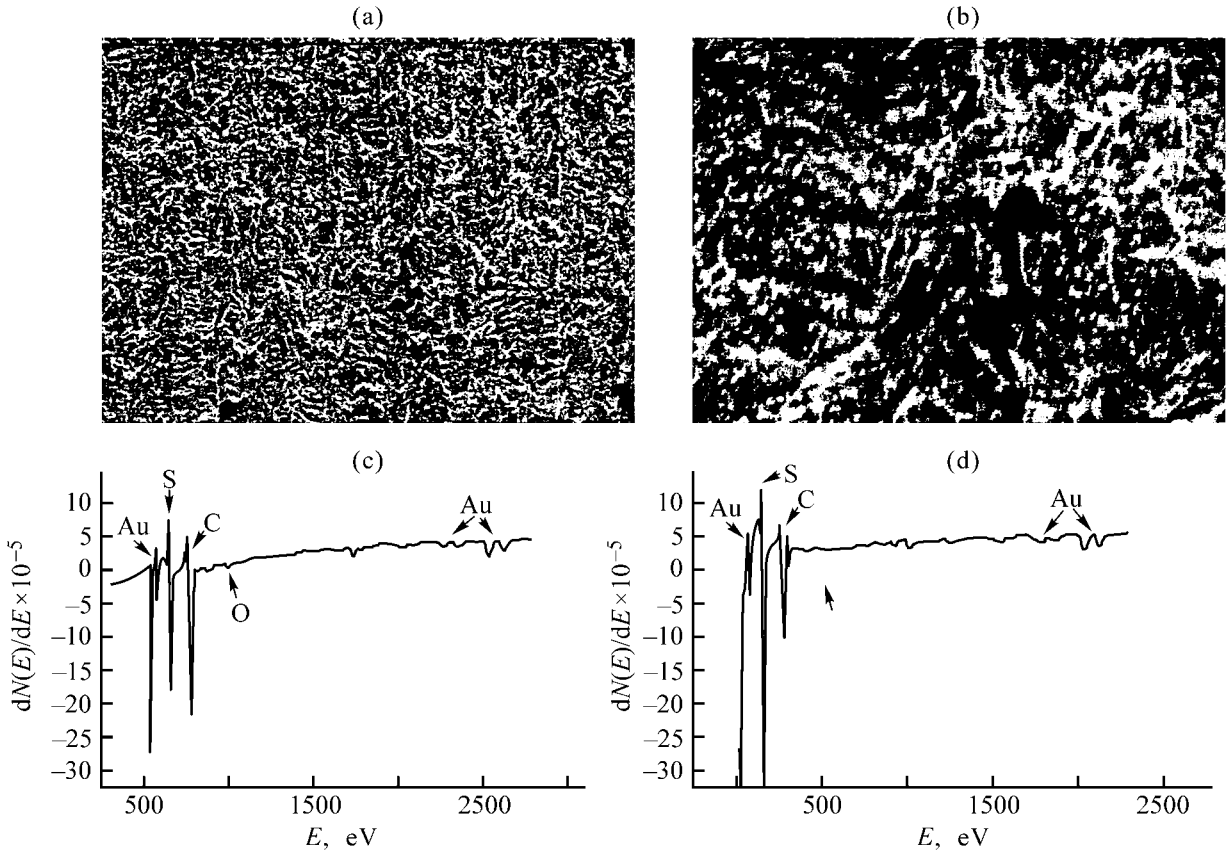

Fig. 6. (a, b) Micrographs of the adsorption film on the surface of gold and (c, d) electronic Auger spectra of (c) dark and (d) light parts of the film. Magnification: (a) 200 and (b) 3000.

tion, chlorine disporoportionates in accordance with the equations

$$Cl_2 + H_2O = HClO + HCl, \quad (16)$$

$$Cl_2 + NaOH = HClO + NaCl, \quad (17)$$

$$Cl_2 + 2NaOH = NaClO + NaCl + H_2O. \quad (18)$$

The equilibrium constant of reaction (16) is $K_{eq} = 4.2 \times 10^{-4}$, and the equilibrium concentration of HClO in water at 298 K is 0.030 M (1.06 g l^{-1}). The solubility of chlorine $Cl_{2\,(aq)}$ at 298 K is 0.0921 M (3.26 g l^{-1}). The equilibrium constant of the reaction of chlorine dissolution in aqueous solutions, $Cl_{2\,(g)}/Cl_{2\,(aq)} = 0.062$. The solubility of Cl_2 in solutions of hydrochloric acid and of the salts NaCl and NaClO markedly increases because of the formation of the anion Cl_3^-.

The equilibrium potential (V) of the redox reaction involving the hypochlorite ion in an alkaline medium:

$$ClO^- + H_2O + 2e \rightleftarrows Cl^- + 2OH^- \quad (19)$$

conforms to the equation [42]:

$$E_{19} = 0.890 + (2.303RT/2F)\log [ClO^-] - (2.303RT/2F)\log [Cl^-] - (2.303RT/2F)\text{pH}. \quad (20)$$

In an acid solution, the redox potential of the reaction

$$HClO + H_2O + 2e \rightleftarrows Cl^- + H^+ + 2OH^- \quad (21)$$

is more positive and conforms to the equation

$$E_{21} = 1.494 + (2.303RT/2F)\log [HClO] - (2.303RT/2F)\log [Cl^-] - (2.303RT/2F)\text{pH}. \quad (22)$$

The value of the potential of reaction (21) points to a high oxidizing capacity of hypochlorites.

The potential of the half-reaction of metallic gold in chloride solutions [43]

$$AuCl_2^- + e = Au + 2Cl^-, \quad (23)$$

$$E_{23} = 1.130 + (2.303RT/F)\log [AuCl_2^-] - 2(2.303RT/F)\log [Cl^-] \quad (24)$$

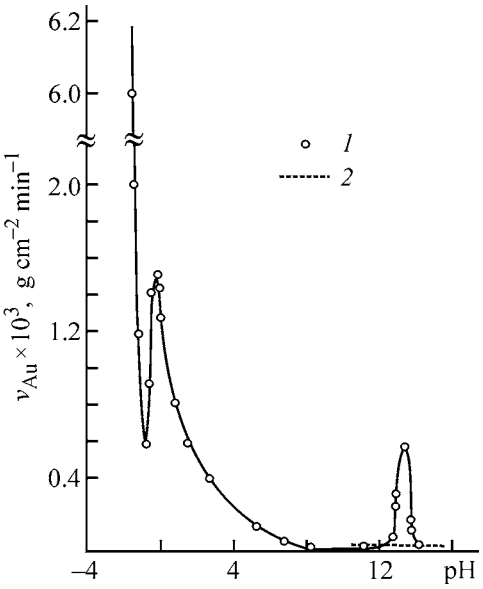

Fig. 7. Rate of gold dissolution, v_{Au}, vs. pH at 298 K in various solutions. Solution (*1*) hypochlorite, with 5.0% NaClO and 4.7% NaCl, pH 1.06; (*2*) alkaline cyanide, 10 g l^{-1} of NaCN and NaOH added to pH 12.2–14.8.

is more negative than the potential of hypochlorite in acid media. The difference of the equilibrium potentials of the redox reaction of gold dissolution

$$2Au + HClO + 3H^+ + 3Cl^- = 2AuCl_2^- + H_2O + 2H^+ \quad (25)$$

conforms to the equation

$$\Delta E_{25} = 0.364 + (2.303RT/2F)\log [HClO] - (2.303RT/F)\log [AuCl_2^-] + 3(2.303RT/F)\log [Cl^-] + 1.5(2.303RT/F)pH. \quad (26)$$

Equation (26) was used to calculate the equilibrium constant of reaction (25) at concentrations (M): [HClO] = 0.1, [HCl] = 0.3, $[AuCl_2^-]$ = 0.1. In this case, ΔE_{25} = 0.346 V and $K_{eq} = 7.15 \times 10^5$. The resulting value of K_{eq} indicates that a sufficiently complete dissolution of gold in acid hypochlorite solutions is thermodynamically possible.

In [40], a method for extraction of noble metals by leaching with in hypochlorite-chloride solutions was suggested. A solution containing >3% NaCl and <0.3% NaClO at pH 5–8 was recommended. However, hypochlorites exhibit in this pH range the minimum redox potential. Therefore, the influence exerted by the pH value (*x* moles of HCl) on the rate of gold dissolution in a wide range of acidities was studied. Figure 7 (curve *1*) shows the rate of gold dissolution in a hypochlorite-chloride (6% NaClO + 4.7% NaCl) solution in the course of 5 min. It can be seen that the rate of gold dissolution at low pH is as high as 6.0×10^{-3} g cm^{-2} min^{-1}. At higher pH, the rate of gold dissolution decreases and passes through a minimum at pH –1. Then, as the pH increases, the dissolution rate gradually becomes higher and passes through a maximum (1.54×10^{-3} g cm^{-2} min^{-1}) at pH –0.2. As the pH value increases further, the rate of gold dissolution gradually decreases to the minimum value of $(1.1–1.2) \times 10^{-4}$ g cm^{-2} min^{-1} at pH 9–12. At pH 12.5–14.5, the rate of gold dissolution again increases at reaches a maximum of 5.6×10^{-4} g cm^{-2} min^{-1} at pH 13.5.

The rate of gold dissolution in hypochlorite solutions substantially exceeds that in alkaline cyanide solutions (Fig. 7, curve *2*) [41]. The latter depends on the concentration of oxygen in the system under study. It has been established that the dissolution rate of gold, v_{Au}, at an oxygen concentration of 11.0, 21.0, and 99.0% in the oxygen–nitrogen mixture and a solution pH > 10.5 is 1.67×10^{-5}, 3.2×10^{-5}, and 1.3×10^{-4} g cm^{-2} min^{-1}, respectively.

The dissolution rate of gold linearly depends on the concentration of NaClO. The curves describing the dependence in the v_{Au}–[NaClO] coordinates at different pH values intersect at a single point on the ordinate axis, forming a fan. They are described by a linear equation that gives, depending on the solution pH, certain values of the slope ratio:

$$v_{Au} = –0.12 + \Psi[NaClO], \quad (27)$$

where Ψ are the slope ratios for hypochlorite solutions with pH 1.06, 4.15, and 6.65, equal to 0.267, 0.1067, and 0.025 g cm^{-2} min^{-1} mol^{-1}, respectively.

These data indicate that, as the solution pH increases from 1.06 to 6.65, the slope ratio decreases by more than an order of magnitude. At NaClO and NaCl content in solution equal to 6.0 and 4.7%, respectively, and the solution pH decreasing from 6.65 to 1.06, the dissolution rate of gold increases by a factor of 26.7. The dissolution rates of gold, v_{Au}, in solutions of TC and hypochlorite are compared in Fig. 5a. It can be seen that, in a hypochlorite solution containing 5.0% NaClO, 3.8% NaCl, and 0.1 M of HCl (at pH 1.08–1.12 and temperature of 298 K) (Fig. 5a, curve *3*) at τ = 20 and 40 min, v_{Au} is 2.2 and 6.3 times, respectively, lower than that in a thiocarbamide solution (Fig. 5a, curve *2*, solution composition is given above). The decrease in the dissolution rate of gold in hypochlorite solutions is due, as demonstrated below, to inhibition of the reaction surface of gold by reaction products.

In hypochlorite solutions, the surface has a positive potential at E_{PZC}. Therefore, hypochlorite ions are adsorbed on the surface of gold (hypochlorite ion adsorbed on an active center captures no less than two atoms of gold) and enter into a redox interaction with surface atoms of gold in accordance with the equations

$$Au^0 + HClO = AuClO^-_{ads} + H^+, \quad (28)$$

$$AuClO^-_{ads} \rightarrow AuCl^*O^-_{ads}, \quad (29)$$

$$AuCl^*O^-_{ads} + Au^0 + H_2O \rightarrow AuCl(OH)^- + AuOH \quad (30)$$

to give an intermediate, $AuCl^*O^-_{ads}$, with a zero charge of the chlorine atom ($Cl^* = Cl^0$) as a result of successive transfers of an electron in ionization of the first atom of gold to the positively charged atom of chlorine [by Eq. (29)], and then in ionization of the second atom of gold and addition of the electron to a neutral atom of chlorine (Cl^*) by Eq. (30). At high concentrations of ligands (e.g., chloride ions from NaCl, HCl) in solutions, negatively charged complex ions $AuCl^-_2$, $Au(OH)^-_2$, $AuCl(OH)^-$ are formed in accordance with the equations

$$AuCl^*O^-_{ads} + Au^0 + HCl \rightarrow AuCl + AuCl(OH)^-, \quad (31)$$

$$AuCl^*O^-_{ads} + Au^0 + 2HCl \rightarrow AuCl^-_2 + AuCl + H_2O, \quad (32)$$

$$AuCl^*O^-_{ads} + Au^0 + NaCl + H_2O \rightarrow AuCl^-_2 + AuOH + NaOH, \quad (33)$$

$$AuCl^*O^-_{ads} + Au^0 + Cl^- + H_2O \rightarrow AuCl^-_2 + Au(OH)^-_2. \quad (34)$$

These ions are adsorbed on the positively charged surface of gold and form adsorption layers. This makes lower the dissolution rate because of the inhibition of the surface. Gold monochloride AuCl is poorly soluble in aqueous solutions. Its solubility product SP_{AuCl} for water is 1.8×10^{-12} [44, 45]. Hence, the calculated concentration of gold(I) in a saturated aqueous solution is 1.34×10^{-6} m. [0.26 mg of Au(I) per liter]. In an excess amount of chlorides, AuCl forms a complex $AuCl^-_2$, which has a higher solubility than gold monochloride. In the hypochlorite-chloride solutions we studied, the concentration of NaCl was close to 1 M. Apparently, complexation of gold monochloride with the chloride ions of the hypochlorite-chloride solution resulted in that the concentration of gold(I) in the leaching solution was, as can be seen in Fig. 5b (curve *8*), 35.3 mg Au per liter.

The rate constants $k_{AuCl^-_2}$ of gold dissolution in a hypochlorite-chloride solution (5.3% NaClO + 0.1 M HCl + 4.06% NaCl) at 277, 289, and 304 K, calculated from the experimental data obtained, are 0.0790, 0.2695, and 0.4030 s^{-1}, respectively. The rate constant of gold dissolution in alkaline cyanide solutions to give complex ions $[Au(CN)_2]^-$, is lower than k_{Au} $AuCl^-_2$ at 304 K by a factor of 1.73×10^6 (k_{Au} $[AuCN]^-_2 = 2.33 \times 10^{-7}$ s^{-1} at 298 K). The activation energy E_A, calculated from the temperature dependence (277–304 K) of the rate constants obtained, $\log k_{Au}$–$1/T$, is 53.43 kJ mol^{-1}. This value of E_A indicates that the rate of gold dissolution in a hypochlorite-chloride solution is kinetically controlled. It is possible to overcome the kinetic limitations by raising the temperature and the concentration of chlorides in the hypochlorite solution and by eliminating the diffusion hindrance to delivery of the reagents to gold. In addition, the deceleration of gold dissolution by the hypochlorite solution because of the formation of adsorption layers composed of reaction products can be prevented if the process is carried out at low pH of the chloride-containing solutions.

Bromine-bromides. Gold(I, III) forms with bromide ions binary (AuBr, $AuBr_3$) and complex compounds ($M[AuBr_2]$, $M[AuBr_4]$). In aqueous solutions, gold(I) bromide disproportionates by the reaction

$$3AuBr^-_2 = 2Au + AuBr^-_4 + 2Br^-. \quad (35)$$

The equilibrium constant of the disproportionation (DPP) reaction is given by

$$K_{DPP} = [AuBr^-_4] \cdot [Br^-]^2/[AuBr^-_2]^3 \quad (36)$$

at an ionic strength $\mu = 1.0$ is $(6.5–8.1) \times 10^4$ (298 K) [45, 46] and 1.4×10^4 (323 K) [46]. The equilibrium constant of the reverse reaction, reaction of coproportionation, $K_{CPP} = 1/K_{DPP} = 1.54 \times 10^{-3}$ (298 K) [47].

The disproportionation of $AuBr^-_2$ is accompanied by changes in the Gibbs free energy, $\Delta G^0 = -28.87$ kJ mol^{-1}, enthalpy, $\Delta H = -61.1$ kJ mol^{-1} [46], and entropy, $\Delta S^0 = -90.79$ J mol^{-1} K^{-1}. The solubility products for AuBr and $AuBr_3$ for water are 5.0×10^{-17} and 4.0×10^{-36}, respectively. According to [48], the solubility product of gold(I) monobromide, $SP_{AuBr} = 7.9 \times 10^{-16}$, and the stability constant of $AuBr^-_2$, $\beta_2 = 1.3 \times 10^{15}$. In bromide solutions, gold ions form planar-square complexes $[AuBr_4]^-$ with a stability constant $K_{1-4} = 3.16 \times 10^{31}$. The standard potentials of half-reactions

$$AuBr^-_4 + 2e = AuBr^-_2 + 2Br^-, \quad E^0 = 0.820 \text{ V}, \quad (37)$$

$$AuBr^-_4 + 3e = Au + 4Br^-, \quad E^0 = 0.854 \text{ V} \quad (38)$$

are more negative than those for the chloride systems. This set of properties indicates that the process of gold extraction with bromine is more favorable than that with chlorine. The solubility of bromine in water is 35 g l^{-1} ($\log[Br_{2(hydr)}] = -0.643$). In solutions with a low concentration of bromides, bromine is present in the form of hydrated particles. In solutions of bromides, iodides, and chlorides, the solubility of bromine increases because of the formation of tribromide ions Br_3^- [49]

$$Br_2 + Br^- = Br_3^- \quad (39)$$

and interhalide compounds BrCl, $BrCl_2$, IBr_2^- [50, 51]. The Br_3^- ions predominate only in solutions with a concentration of bromide ions exceeding 0.89 M. The equilibrium constant of reaction (39) is K_{eq} = 16.3. At higher concentrations of bromides, pentabromide ions Br_5^- are formed

$$2Br_2 + Br^- = Br_5^- \quad (40)$$

with an equilibrium constant K_{eq} = 27.5 [42, 49].

The potential of the half-reaction

$$Br_2 + 2e = 2Br^- \quad (41)$$

is described by the equation

$$E_{41} = 1.0066 + (2.303RT/2F)\log[Br_2] - (2.303RT/F)\log[Br^-]. \quad (42)$$

It should be noted that the Br_3^- and Br_5^- ions can be formed in electrolysis in bromide electrochemical systems

$$3Br^- = Br_3^- + 2e, \quad (43)$$

$$5Br^- = Br_5^- + 4e. \quad (44)$$

The potential of reaction (43) under equilibrium conditions can be represented as

$$E_{43} = 1.0162 + (2.303RT/2F)\log[Br_3^-] - 3(2.303RT/2F)\log[Br^-], \quad (45)$$

and the standard potential of reaction (44) is 1.068 V (relative to a standard hydrogen electrode) [15]. The potential of the half-reaction involving the interhalide compound BrCl (Table 2) is 1.20 V. In water, molecules of bromine undergo a disproportionation reaction

$$Br_2 + H_2O = HBrO + Br^- + H^+ \quad (46)$$

with an equilibrium constant described by the equation

$$\log\{[HBrO][Br^-]/[Br_2]\} = pH - 8.17, \quad (47)$$

and the potential of the redox reaction

$$HBrO + H^+ + 2e = Br^- + H_2O \quad (48)$$

conforms to the equation

$$E_{48} = 1.331 + (2.303RT/2F)\log\{[HBrO^-]/[Br^-]\} - (2.303RT/F)[pH]. \quad (49)$$

Bromides and tribromides are readily oxidized in electrolysis to bromate ions [42, 43]

$$Br^- + 3H_2O = BrO_3^- + 6H^+ + 6e, \quad (50)$$

$$E_{50} = 1.4116 + (2.303RT/6F)\log\{[BrO_3^-]/[Br^-]\} - 6(2.303RT/6F)[pH], \quad (51)$$

$$Br_3^- + 9H_2O = 3BrO_3^- + 18H^+ + 16e, \quad (52)$$

$$E_{52} = 1.4523 + 3(2.303RT/16F)\log[BrO_3^-] - (2.303RT/16F)\log[Br_3^-] - 18(2.303RT/16F)[pH]. \quad (53)$$

Comparison of the standard potentials of the electrode half-reactions of gold in bromide solutions

$$AuBr_2^- + e \rightleftarrows Au + 2Br^-, \quad E^0 = 0.959\ V, \quad (54)$$

$$E_{54} = 0.959 + (2.303RT/F)\log[AuBr_2^-] - 2(2.303RT/F)\log[Br^-], \quad (55)$$

$$AuBr_4^- + 3e \rightleftarrows Au + 4Br^-, \quad (56)$$

$$E_{56} = 0.854 + (2.303RT/3F)\log[AuBr_2^-] - 4(2.303RT/3F)\log[Br^-] \quad (57)$$

with the standard potentials of redox reactions of bromine and its derivatives, (43), 50, and (52), shows that the difference of the standard potential (V) at n = 1 is $\Delta E_{(43)-(54)}$ = 0.0572, $\Delta E_{(50)-(54)}$ = 0.4526, $\Delta E_{(52)-(54)}$ = 0.4933. The difference of the potentials of half-reactions of the interhalide compound BrCl ($E^0_{BrCl/Br^-,\,Cl^-}$ = 1.20 V, Table 2) and of half-reaction (54) is ΔE = 0.241 V. The difference of the standard potentials of the half-reactions at n = 3 is $\Delta E_{(43)-(56)}$ = 0.1622, $\Delta E_{(50)-(56)}$ = 0.5576, $\Delta E_{(52)-(56)}$ = 0.5983. The equilibrium constants of the reactions considered are as follows: at n = 1: $K_{p(43)-(54)}$ = 9.28, $K_{p(50)-(54)}$ =

4.55×10^7, $K_{p(52)–(54)} = 2.22 \times 10^8$, $K_{p(BrCl)–(54)} = 1.22 \times 10^4$, and at $n = 3$: $K_{p(43)–(56)} = 1.7 \times 10^8$, $K_{p(50)–(56)} = 2.02 \times 10^{28}$, $K_{p(52)–(56)} = 2.35 \times 10^{30}$. Consequently, the pathways of the reactions of bromate ions with elementary gold are preferable in bromide solutions. The data obtained suggest that the HL of gold with bromide solutions that are continuously renewed by means of cyclic electrochemical oxidation of bromide ions in the circulating leaching solutions (in flow-through electrolyzers of special design) to molecular bromine Br_2, with the accompanying reactions of formation of tribromide (Br_3^-) and hypobromite ions (BrO^-), can ensure a complete recovery of gold even from a sulfide-containing ore. Commonly, the ore sulfur is removed in processing of sulfide-containing ores prior to recovery of gold by leaching by means of calcination [52, 53], oxidation under elevated pressure of oxygen [54, 55], or by bio-oxidation [56, 57]. The author of [58] suggested a two-stage technology for extraction of gold by bromine leaching. In the first stage, molecular bromine is synthesized in an acid medium with the use of pyrolusite by the reaction

$$2MBr + MnO_2 + 2H_2SO_4 = Br_2 + MnSO_4 + M_2SO_4 + 2H_2O, \quad (58)$$

where M = Na, K.

The standard potential of the redox system MnO_2 : $MnSO_4$ is 1.23 V, and that of the system Br_2/Br^-, 1.0066 V. The potentials of sulfides are, as a rule, negative, e.g. (V, relative to a standard hydrogen electrode): $E_{PtS_2/S^{2-}} = –0.64$, $E_{Ag_2S/S^{2-}} = –0.66$, $E_{HgS/S^{2-}} = –0.70$, $E_{CuS/S^{2-}} = –0.76$, $E_{PbS/S^{2-}} = –0.93$, $E_{FeS_2/S^{2-}} = –0.95$, $E_{CoS/S^{2-}} = –1.07$, etc. Therefore, sulfides are readily oxidized by molecular bromine, e.g., by the reactions

$$3Br_2 + 2FeS_2 = 2FeBr_3 + 4S^0, \quad (59)$$

$$Br_2 + MS = MBr_2 + 2S^0, \quad (60)$$

where M = Hg, Cu, Cd, Pb, Sn, Co, Ni, etc.

The bromide ions formed by reactions (59) and (60) are again oxidized by pyrolusite by reaction (58) to free bromine. The oxidation of the sulfides frees gold and makes the ore porous and permeable to reagents. Therefore, molecular bromine oxidizes gold to gold bromides by Eqs. (37), (38), (54), and (61):

$$2Au + 3Br_2 + 2Br^- \rightarrow 2AuBr_4^-. \quad (61)$$

Experiments have shown that the recovery of gold by the standard cyanide procedure is 56.8%, whereas that in the presence of potassium bromide and pyrolusite is 83.4% at a lower expenditure of reagents [58–61]. A higher efficiency of extraction of gold by leaching from ores has been achieved in a two-stage process that includes calcination of sulfide- and carbon-containing gold-rich ores and leaching of the resulting cake with bromine-containing (Br_3^-, Br_2, HBrO, NaBr) solutions [59]. In this case, the tribromide ion was synthesized by the following reactions:

$$NaBr + Br_2 = NaBr_3, \quad (62)$$

$$CaBr_2 + 2Br_2 = Ca(Br_3)_2. \quad (63)$$

Reactions (62) and (63) are reversible. For fast bromine-bromide leaching, it is suggested to prepare two types of concentrates. The first type, concentrate of tribromide ions is prepared from NaBr (or $CaBr_2$) and Br_2, Commonly, concentrate I contains (wt %): $NaBr_3$ 63–64, Br_2 20.5, and free NaBr 3.0–10.5. In concentrate I, molecular bromine partly undergoes disproportionation (46) to give hypobromous acid HBrO.

The content of hypobromite ions BrO^- in the concentrate was approximately 2–6%. A higher oxidizing capacity with respect to gold is exhibited by the bromate ion, which is formed in alkaline solutions in accordance with the equation

$$3Br_2 + 6OH^- = BrO_3^- + 5Br^- + 3H_2O \quad (64)$$

[compare with Eq. (53) in acid solutions]. Therefore, concentrate of type II, a hypobromite solution based on NaBr, Br_2, and NaOH (10–20%), is specially prepared. The concentrate contains 5–8% sodium hypobromite. Table 3 lists the contents of $NaBr_3$, Br_2, NaBrO,and NaBr in the tribromide (type I) and hypobromite (type II) concentrates.

In preparing a leaching solution, one part of a hypobromite solution was taken per four parts of a tribromide solution, and vice versa. Irrespective of the relative amounts in which type-I and -II concentrates are taken, the pH value of the "resulting" solution should be in the range 6.5–7.5. Table 3 also lists the equivalent concentrations of molecular bromine (ECMB), determined in molar units as a sum of the actual molar concentrations of bromine and tribromide ions, tripled molar concentration of the bromate ions, and concentrations of hypobromite ions and hypobromous acid (HBrO).

Table 3. Composition and properties of leaching solutions obtained at different relative amounts of the tribromide and hypobromite concentrates

Relative amounts of the concentrates, wt fraction		Content, wt %				Density, g cm^{-3}	pH	Content, wt %
I	II	$NaBr_3$	Br_2	$NaBrO_3$	NaBr			
1.0	0	63.64	4.28	–	2.76	2.029	1.0	Not determined
0.8	0.2	50.91	3.42	1.58	7.55	1.826	5.6	39.4
0.5	0.5	31.82	2.14	3.94	14.80	1.612	6.7	34.0
0.2	0.8	12.73	0.86	6.01	22.02	1.444	7.2	28.6
0	1.0	–	–	7.87	26.83	1.345	8.0	Not determined

In [59], a set of experiments on leaching of ores that are rich in gold (265–212 g ton^{-1}) and silver (190–205 g ton^{-1}) or poor in the same elements (5.5 and 61.9 g of Au and Ag, respectively, per ton) was described. Prior to leaching, the ores were calcined in a rotating (5 rpm) tubular furnace at a temperature of 650°C for 120 min in order to remove the sulfide sulfur (15.5 wt %) and carbon (12.5 wt %). The content of the sulfide sulfur in the calcined concentrate was 0.7%. The concentrates were used to prepare a leaching solution that contained type-I and -II concentrates in various relative amounts listed in Table 3. The concentrates taken in any relative amounts were diluted to a concentrate concentration of 2.0 to 6.0 g l^{-1} at pH 5–6. The time of leaching was 6 h. The recovery of gold was in the range from 94 to 96.3%, and that of silver exceeded 50%.

It should be noted that a specific feature of tribromide and bromate concentrates is that they have a lower pressure of bromine vapor, compared with molecular bromine. The concentrate containing about 34% ECMB has a total vapor pressure of only 23 mm Hg at 0°C and 112.5 mm Hg at 35°C. The vapor pressure of liquid bromine is 75 and 214 mm Hg at 0 and 35°C, respectively. Therefore, the concentrates can be used to prepare leaching solutions. The authors of [60] suggested, in order to lower the vapor pressure of bromine in extraction of gold from ores, a leaching solution that contains oxidizing agents: $FeCl_3$, H_2O_2, and NaClO. Investigations demonstrated that the dissolution rate of gold in a solutions containing bromides, $FeCl_3$, H_2O_2, and NaClO exceeds severalfold that in cyanide solutions.

Iodine-iodides. Gold(I, III) also forms with iodide ions binary (AuI, AuI_3) and complex compounds ($M[AuI_2]$, $M[AuI_4]$). The solubility product of gold(I) iodide AuI and gold(III) triiodide AuI_3 in water is 1.6×10^{-23} and 1×10^{-46}, respectively.

According to [48], the solubility product of gold(I) iodide, $SP_{AuI} = 4.0 \times 10^{-23}$, and the stability constant of AuI_2^-, $\beta_2 = 3.2 \times 10^{21}$. Gold(I) iodide is virtually insoluble in aqueous solutions (1.23×10^{-14} g of AuI per liter), and, therefore, it does not disproportionate when in solid state [15]. Upon introduction of potassium iodide (iodide ion) into a solution, the solubility of AuI increases because of the formation of a complex ion, AuI_2^-:

$$AuI + I^- = AuI_2^-. \quad (65)$$

The solubility of molecular iodine (I_2) in water is 0.3 g l^{-1}. The equilibrium constant of the reaction of disproportionation of molecular iodine in water

$$I_2 + H_2O = I^- + H^+ + HIO \quad (66)$$

has a small value $K_{DPP} = 5.32 \times 10^{-13}$ [60]. The solubility of iodine in aqueous solutions of KI and NaI increases manyfold because of the formation of the triiodide ion (I_3^-) or higher-molecular-weight polyiodides. The equilibrium constant of the reaction of formation of the triiodide ion

$$I_2 + I^- \rightleftarrows I_3^-, \quad (67)$$

equal to $K_{eq} = 697.9$, indicates that the equilibrium of the reaction is strongly shifted to the right. Iodide ions are more readily oxidized, compared with bromide ions:

$$3I^- = I_3^- + 2e, \quad (68)$$

$$E_{69} = 0.5364 + (2.303RT/2F)\log[I_3^-] - 3(2.303RT/2F)\log[I^-], \quad (69)$$

and the triiodide ion, to molecular iodine and iodate ions:

$$2I_3^- = 3I_2 + 2e, \quad (70)$$

$$E_{71} = 0.7892 + 3(2.303RT/2F)\log[I_2] - (2.303RT/F)\log[I_3^-], \quad (71)$$

$$I_3^- + 9H_2O \rightleftarrows IO_3^- + 18H^+ + 16e, \quad (72)$$

$$E_{73} = 1.1539 + 3(2.303RT/16F)\log[IO_3^-] - (2.303RT/16F)\log[I_3^-] - 18(2.303RT/16F)\text{pH}. \quad (73)$$

No oxidation of molecular iodine to iodic acid HIO_3 and iodate ion IO_3^- occurs in electrolysis in aqueous solutions, because the standard potentials of these reactions (E^0 = 2.9226 and 2.9454 V) are considerably more positive than that of the oxygen electrode (E^0 = 1.229 V). Therefore, evolution of oxygen from water at the anode is the preferable reaction.

As can be seen in Table 1, the standard potentials of the half-reactions of gold in iodide solutions are as follows (V): $E^0_{AuI/Au}$ = 0.530, $E^0_{AuI_2^-/Au}$ = 0.578, $E^0_{AuI_4^-/Au}$ = 0.550, $E^0_{AuI_4^-/Au}$ = 0.560 [14, 15]. The standard potentials of the oxidizing agents based on iodine are listed in Table 2 (V): $E^0_{I_2/I^-}$ = 0.535, $E^0_{I_3^-/I^-}$ = 0.536, $E^0_{I_2(aq)/I^-}$ = 0.621, $E^0_{I_2/I_3^-}$ = 0.789 [14, 15]. It can be seen that the most positive potential is observed for the system I_2/I_3^-. In this case, the difference of the standard potentials of the half-reactions of gold(I)

$$AuI_2^- + e = Au + 2I^-, \quad E^0 = 0.578 \text{ V}, \quad (74)$$

$$E_{75} = 0.578 + (2.303RT/F)\log[AuI_2^-] - 2(2.303RT/F)\log[I^-] \quad (75)$$

and that of formation of triiodide ions by reaction (68), $E^0_{I_2/I_3^-}$ = 0.789 V, is ΔE^0 = 0.211 V. Therefore, the following reaction is the best acceptable for dissolution of gold with triiodide ions as an oxidizing agent:

$$2Au + I_3^- + I^- = 2AuI_2^-. \quad (76)$$

The equilibrium constant of reaction (78) is $K_{eq} = 3.7 \times 10^3$. This indicates that gold can be extracted from ores with iodine-iodide solutions.

The standard potentials of the electrode reactions of gold in iodide electrolytes [14, 15]

$$AuI_4^- + 2e = AuI_2^- + 2I^-, \quad (77)$$

$$AuI_4^- + 3e = Au + 4I^- \quad (78)$$

are more negative than the potentials of gold in chloride and bromide solutions (Table 1). The dependence of the potentials on the concentrations of iodide and gold(III) ions in solution are described by the following equations [42, 43]:

$$E_{80} = 0.560 + (2.303RT/3F)\log[AuI_4^-] - 4(2.303RT/3F)\log[I^-]. \quad (79)$$

Analysis and comparison of the standard redox potentials of iodide systems and the potentials of gold show that the difference of the standard potentials in the case when triiodide ions are in equilibrium with iodide ions is close to zero. In the case when iodate ions are in equilibrium with triiodide ions in the system, the difference of the standard potentials of the reactions will be 0.5759 and 0.5939 V, respectively. The equilibrium constants of the overall reactions

$$5Au + 2IO_3^- + 12H^+ + 11I^- = 5AuI_2^- + I_3^- + 6H_2O, \quad (80)$$

$$10Au + 6IO_3^- + 36H^+ + 37I^- = 10AuI_4^- + I_3^- + 18H_2O \quad (81)$$

of dissolution of gold to give gold ions AuI_2^- and AuI_4^- in oxidation by iodate ions will be 5.4×10^9 and 1.3×10^{30}, respectively. Consequently, reactions of interaction of iodate ions with elementary gold are also preferable in iodide solutions. In this case, the electrochemical oxidation of triiodide ions to iodate ions in solutions will also favor a more complete recovery of gold from ores and gold-containing raw materials [61–63]. Thermodynamic analysis shows that a necessary condition in dissolution of gold with the use of elementary iodine is the presence of iodide ions, and especially iodide and chloride ions together, in solutions. Systems based on iodine and chlorine, which form interhalide compounds, have more positive potentials than the systems Au/Br_n and Au/I_n. Iodine-chlorine interhalide compounds are particularly promising for development of reagent solutions with a high reactivity toward gold and platinum metals.

The authors of this review used for extraction of gold from ores of the Muzhikhoevskoe deposit an iodine-iodide solution containing ($g\,l^{-1}$) 200 KI, 14 I_2, 5 KOH, and also some other depressants of dissolution of heavy metals and metals of the iron group. The results obtained are shown in Fig. 5b (curves *2*, *3*). It can be seen that the concentration of gold(I) increases as the solution pH decreases.

Copper-thiosulfate solutions. The standard potential of the half-reaction of gold in a thiosulfate solution:

$$Au(S_2O_3)_2^{3-} + e = Au + 2S_2O_3^{2-} \quad (82)$$

is 0.153 V [14]. In Eq. (82), the thiosulfate ion acts as a ligand. The standard potentials of the half-reactions of thiosulfate depend on the final product, which may be HS^-, H_2S, S^0, or S_5^{2-} [14, 15]:

$$S_2O_3^{2-} + 6H^+ + 8e = 2S^{2-} + 3H_2O, \quad E^0 = -0.006 \text{ V}; \quad (83)$$

$$S_2O_3^{2-} + 8H^+ + 8e = 2HS^- + 3H_2O, \quad E^0 = 0.200 \text{ V}; \quad (84)$$

$$5S_2O_3^{2-} + 30H^+ + 24e = 2S_5^{2-} + 15H_2O, \; E^0 = 0.331 \text{ V}; \quad (85)$$

$$S_2O_3^{2-} + 6H^+ + 4e = 2S + 3H_2O, \quad E^0 = 0.465 \text{ V}; \quad (86)$$

$$K_2S_2O_3 + 6H^+ + 4e = 2K^+ + 2S + 3H_2O, \quad E^0 = 0.452 \text{ V}; \quad (87)$$

$$Na_2S_2O_3 + 6H^+ + 4e = 2Na^+ + 2S + 3H_2O, \quad E^0 = 0.455 \text{ V}. \quad (88)$$

It can be seen from the data presented that certain thiosulfate-containing solutions behave as oxidizing agents with respect to gold. The most positive potential is observed for the redox system represented by Eq. (86). As oxidizing agent can be used copper(II) sulfate ($CuSO_4 \cdot 5H_2O$) and rhodanide. The potential of the half-reaction of copper

$$Cu^{2+} + SCN^- + e = CuSCN \quad (89)$$

is 0.96 V [14]. A study of the kinetics of leaching of gold and silver at pH 10 with ammonium-thiosulfate solutions containing $CuSO_4$ as an oxidizing agent demonstrated that the rate of silver dissolution is controlled by diffusion, and that of gold, kinetically [64].

As already noted, the efficiency of the HL of gold from stubborn sulfide-carbon and carbon gold-containing ores by cyanide leaching is, as a rule, very low. Commonly, the sulfide sulfur and carbon are removed in processing of these ores, prior to recovery of gold by leaching, by calcination [52, 53], treatment with nitric acid, or bio-oxidation [56, 57, 65]. Use of ammonium-thiosulfate solutions as leaching solvents markedly facilitates the HL processing of stubborn sulfide-carbon and carbon gold-containing ores [65, 66].

As a thiosulfate leaching solution is commonly used a mixture containing preferably 15 to 30 g l^{-1} of $(NH_4)_2S_2O_3$ and 8–16 g l^{-1} $CuSO_4$ or $Na_2S_2O_3$ + $CuSO_4$ (pH 9.2–10.0). It is believed that ammonium ions and ammonium thiosulfate stabilize copper(II), which acts as an oxidizing agent in accordance with the equation

$$2Au + (NH_4)_2S_2O_3 + 2CuSO_4 = Au_2SO_4 + Cu_2S_2O_3 + (NH_4)_2SO_4, \quad (90)$$

and also catalyze the reaction of dissolution of gold in the presence of oxygen

$$2Au + (NH_4)_2S_2O_3 + H_2O + 1/2\,O_2 = Au_2S_2O_3 + 2NH_4OH. \quad (91)$$

In the HL method, the thiosulfate leaching solution is used in a closed cycle [65–67]. A side reaction in extraction of gold is oxidation of thiosulfate by Cu(II) or dissolved oxygen to give ammonium tetrathionate $(NH_4)_2S_4O_6$ and trithionate $(NH_4)_2S_3O_6$. To improve the cost efficiency of the process of gold leaching, the reactions in which tetra- and trithionate are formed are commonly suppressed to the maximum possible extent [68]. After the thiosulfate leaching solution is saturated with gold, the solution, or its part, is continuously reduced, preferably by cementation, in a special device. Spent leaching solutions are regenerated by addition of sulfur or soluble sulfides [65, 67].

The authors of this review used for extraction of gold from ores of the Muzhikhoevskoe deposit a copper-containing solution of the following composition (g l^{-1}): $Na_2S_3O_3 \cdot 5H_2O$ 74, $CuSO_4 \cdot 5H_2O$ 12, $(NH_4)_2SO_4$ 100, NH_4OH 100 or 50 ml of a 25% ammonia solution per liter of the resulting solution. The results obtained are shown in Fig. 6b (curve *4*). It can be seen that copper-thiosulfate solutions are effective oxidizing agents for gold. In [69], to make lower the expenditure for extraction of gold by thiosulfate leaching, sodium thiosulfate was synthesized from the gold-containing sulfide ore itself by adding elementary sulfur to the raw material, sulfide ore. Such a method lowers the cost of leaching with thiosulfate solutions and makes this process competitive with that based on cyanides, which are, undoubtedly, more toxic by themselves [61–64, 67, 70, 71]. In [61–64, 67–69, 72–75], it was suggested to use bromine-bromide, iodine-iodide, and copper thiosulfate solutions for extraction of gold and silver directly from gold- and silver-containing sulfide ores.

On the whole, thiocarbamide, hypochlorite, and bromine-bromide solutions, as well as iodine-iodide solutions, are rather promising for extraction of gold from ores by leaching. Under natural conditions, these solvents spontaneously undergo conversion into harmless compounds: urea, ammonium sulfate, and halide salts.

Use of thiocarbamide, hypochlorite and halogen-halide solutions, which, in our opinion fully comply with the main requirement to the industry of the XXI century, "make no harm to the ecology," can not only raise the labor productivity in gold mining, but also eliminate the problem of environment contamination.

REFERENCES

1. Pakhtanov, B.A. and Chernykh, S.I., *Tsvetn. Metall.*, 1997, nos. 5–6, pp. 26–44.
2. Dement'ev, V.E., Tatarinov, A.P., and Gudkov, S.S., *Gorn. Zh.*, 2001, no. 5, pp. 53–55.
3. Pokhodenko, V.D. and Pavlishchuk, V.V., *Teor. Eksp. Khim.*, 2002, vol. 38, no. 2, pp. 67–83.
4. Sadykov, R.Kh., Fazlullin, M.I., and Rysev, V.P., *Gorn. Zh.*, 1994, no. 11, pp. 54–58.
5. Novoselov, V.A. and Bolotova, L.S., *Gorn. Zh.*, 2002, no. 2, pp. 53–56.
6. Telegina, L.E. and Kofman, V.Ya., *Tsvetn. Met.*, 1984, no. 7, pp. 44–47.
7. Pyzhov S.S., Makarova S.N. *Tsvetn. Met.*, 1984, no. 11, pp. 25–28.
8. Mineev, G.G., *Tsvetn. Met.*, 1985, no. 1, pp. 96–97.
9. Chamberlin, P.D., *Gold Forum Technol. and Pract. "World Gold–89": Proc. 1st Joint Int. Meet. between SME and Aus IMN, Reno, Nev., Nov. 5–8, 1989*, Littleton, 1989, pp. 225–232.
10. Mosinets, V.N., *Gorn. Zh.*, 1996, nos. 1–2, pp. 108–111.
11. Tolstov, E.A. and Prokhorenko, G.A., *Tsvetn. Met.*, 1999, no. 7, pp. 53–56.
12. Sycheva, M.N., Gorenkov, N.L., Turlichkin, V.M., and Tsarev, V.V., *Gorn. Zh.*, 2001, no. 5, pp. 59–60.
13. Sedel'nikova, G.V., *Gorn. Zh.*, 1996, nos. 1–2, pp. 122–124.
14. *Spravochnik po elektrokhimii* (Handbook of Electrochemistry), Sukhotin, A.M., Ed., Leningrad: Khimiya, 1981.
15. Milazzo, G. and Caroli, S., *Tables of Standard Potentials*, New York: J. Wiley and Sons, 1978.
16. Guzman, L., Chimenos, J.M., Fernandez, M.A., *et. al.*, *Hydrometallurgy*, 2000, no. 1, pp. 185–193.
17. Guzman, L., Segara, M., Chimenos, J.M., *et. al.*, *Hydrometallurgy*, 1999, no. 1, pp. 21–35.
18. Kozin, L.F., Berezhnoi, E.O., and Bogdanova, A.K., *Teor. Eksp. Khim.*, 2000, vol. 36, no. 5, pp. 296–300.
19. Nixon, G. and Tolstov, D.E., *Gorn. Zh., Special issue*, 2002, pp. 25–28.
20. Grushko, Ya.M., *Vrednye neorganicheskie soedineniya v promyshlennykh stochnykh vodakh* (Harmful Inorganic Compounds in Industrial Wastewater), Leningrad: Khimiya, 1979.
21. Turgood, C.P., Kirk, D.W., Foulker, F.R., and Graydon, W.F., *J. Elektrochem. Soc.*, 1981, vol. 128, no. 8, pp. 1980–1985.
22. Bek, R.Yu., Kosolapov, G.V., and Shuraeva, L.I., *Elektrokhimiya*, 2001, vol. 37, no. 3, pp. 294–299.
23. Khrushcheva, E.I. and Kazarinov, V.E., *Elektrokhimiya*, 1986, vol. 12, no. 9, pp. 1262–1263.
24. Kumok, V.N., Kuleshova, O.M., and Karabin, L.A., *Proizvedenie rastvorimosti* (Solubility Product), Novosibirsk: Nauka, 1983.
25. Byval'tsev, V.Ya., Emel'yanov, Yu.E., Stroganov, Yu.B., *et al.*, *Tsvetn. Met.*, 1996, no. 11, pp. 7–8.
26. Lazarova, E. and Nikolov, Ts., *Elektrokhimiya*, 1986, vol. 12, no. 9, pp. 1217–1220.
27. Herrero, E., Buller, J.L., and Abruna, H.D., *Chem. Rev.*, 2001, vol. 101, no. 7, pp. 1897–1930.
28. Tatarinov, A.P., Byval'tsev, V.Ya., Dement'ev, V.E., *et al.*, *Tsvetn. Met.*, 1999, no. 3, pp. 28–30.
29. Varentsov, V.K., *Izv. Sib. Otd. Akad. Nauk SSSR, Ser. Khim.*, 1984, no. 17/8, pp. 106–120.
30. Batwell, J.W., *Mining Eng.* (USA), 1990, vol. 42, no. 12, pp. 520.
31. Tedeev, M.N., Tolstov, E.A., and Kustova, L.A., *Tsvetn. Met.*, 1999, no. 7, pp. 56–58.
32. Lerman, B.D., Gabdullin, T.G., Absalyamov, Kh.K., *et al.*, *Gorn. Zh.*, 2001, no. 11, pp. 71–73.
33. Lizin, B.S., *Gorn. Zh.*, 2001, no. 11, pp. 78–79.
34. Rudoi, G.N., Golomzik, A.I., Bazheva, T.A., *et al.*, *Tsvetn. Met.*, 1999, no. 3, pp. 39–40.
35. Tarasova, T.B., Man'kov, V.M., Ivanov, A.Yu., *et al.*, *Gorn. Zh.*, 1996, no. 11–12, pp. 86–88.
36. RF Patent 2 122 593.
37. RF Patent 2 124 062.
38. Kozin, L.F. and Bogdanova, A.K., *Zh. Fiz. Khim.*, 2002, vol. 76, no. 4, pp. 711–718.
39. Kozin, L.F. and Bogdanova, A.K., *Teor. Eksp. Khim.*, 2000, vol. 37, no. 4, pp. 251–255.
40. US Patent 5 169 503.
41. Zyr'yanov, M.N. and Doshlov, O.I., *Tsvetn. Met.*, 1995, no. 9, pp. 34–37.
42. Kelsall, G.H., Welham, N.J., and Diaz, M.A., *J. Electroanal. Chem.*, 1993, vol. 361, no. 1, pp. 13–24.
43. Diaz, M.A., Kelsall, G.H., and Welham, N.J., *J. Electroanal. Chem.*, 1993, vol. 361, no. 1, pp. 25–38.
44. Edens, G.J., *Interfas.*, 1994, vol. 3, no. 2, pp. 45–46.
45. Busev, A.I. and Ivanov, V.M., *Analiticheskaya khimiya zolota* (Analytical Chemistry of Gold), Moscow: Nauka, 1973.
46. Nikolaeva, N.M., Erenburg, A.M., and Antipina, V.A., *Izv. Sib. Otd. Akad. Nauk SSSR*, 1972, no. 4, no. 9, pp. 126–128.
47. Kozin, L.F., *Elektroosazhdenie i rastvorenie mnogovalentnykh metallov* (Electrodeposition and Dissolu-

tion of Polyvalent Metals), Kiev: Naukova Dumka, 1989.

48. Shul'man, V.M., *Reaktsionnaya sposobnost' koordinatsionnykh soedinenii* (Reactivity of Coordination Compounds), Moscow: Nauka, 1976, pp. 20–43.
49. Liebhafsky, H.A., *J. Am. Chem. Soc.*, 1934, vol. 56, no. 7, pp. 1500–1505.
50. Fialkov, Ya.A., *Mezhgaloidnye soedineniya* (Interhalide Compounds), Kiev: Akad. Nauk USSR, 1958.
51. Karapet'yants, M.Kh. and Drakin, S.I., *Obshchaya i neorganicheskaya khimiya* (General and Inorganic Chemistry), Moscow: Khimiya, 1981.
52. Kolesnikov, N.A., Kazakov, V.N., Bakhtina, I.I., *et al.*, *Byul. Tsvetn. Metall. TsIIN*, 1968, no. 3 (344), pp. 21–26.
53. Marsden, J., *Int. Gold Mining Newslett.*, 1992, vol. 19, no. 9, pp. 138–141.
54. RF Patent 2119963.
55. Roman, M.G.S. and Weir, D.R., *Gold Forum Technol. and Pract. "Word Gold–89": Proc. 1st Joint Int. Meet. between SME and Aus IMM, Reno, Nev., Nov. 5–8, 1989*, Littleton, 1989, pp. 295–304.
56. Mineev, G.G., *Biometallurgiya zolota* (Biometallurgy of Gold), Moscow: Metallurgiya, 1989.
57. Barrett, J., Ewart, D.K., Hughes, M.N., and Poole, R.K., *J. Int. Biochem.*, 1991, vol. 43, no. 2–3, pp. 484.
58. RF Patent 2087568.
59. RF Patent 2102507.
60. Trindate, R.B., Araujo, R.V.V., and Barbosa, J.P., *Proc. 19th Int. Miner. Process Congr., San Francisco, Calif., 1995*, vol. 4, Littleton (Colo), 1995, pp. 83–86.
61. Dadgar, A., J. of Metals (JOM), 1989, vol. 41, no. 12, pp. 37–41.
62. US Patent 5137700.
63. Davis, A. and Tran, T., *Hydrometallurgy*, 1991, vol. 26, pp. 165–177.
64. Jeffrey, M.J., *Hydrometallurgy*, 2001, vol. 60, no. 1, pp. 7–16.
65. RF Patent 2125107.
66. Hemmati, M., Hendrix, J.L., Nelson, J.H., and Milosavlievic, E.B., *Extr. Met. 89: Pap. Symp., London, July 10–13*, 1989, London, 1989, pp. 665–678.
67. Meretukov, M.A. and Orlov, A.M., *Metallurgiya blagorodnykh metallov: Zarubezhnyi opyt* (Metallurgy of Noble Metals: Foreign Experience), Moscow: Metallurgiya, 1991.
68. Aylmore, M.G. and Muir, D.M., *Miner. and Met. Process.*, 2001, vol. 18, no. 4, pp. 221–227.
69. Vorob'ev, A.E. and Gladush, A.D., *Geokhimiya zolota: Resursy i tekhnologii Rossii* (Geochemistry of Gold: Resources and Technologies of Russia), Moscow: Ross. Univ. Druzhby Narodov, 2000.
70. Stryzhko, L.S., *Metallurgiya zolota i serebra* (Metallurgy of Gold and Silver), Moscow: Mosk. Inst. Stali Splavov, 2001.
71. *Austr. Mining*, 2000, vol. 92, no. 9, p. 44.
72. Randell, P.A. and Hendrix, J.L., *Extr. Met. 81 Symp., London, 21–23 Sept., 1981*, London, 1981, pp. 57–75.
73. Shen Jin, Jiang Tao, and Xu Shi, *Zhongnan kuangye xueyuan xuebao* (J. Cent.–S. Inst. Min. and Met.), 1993, vol. 24, no. 2, pp. 169–173.
74. Barbosa, O. and Monhemius, A.J., *Precious Metals' 89: Proc. Int. Symp. TMS Annu. Meet., Las Vegas, Nev., Febr. 27–March 2, 1988*, Warrendate (Pa), 1988, pp. 307–339.
75. Jiang Tao, Xu Shi, and Shen Jin, *Zhongnan kuangye xueyuan xuebao* (J. Cent.–S. Inst. Min. and Met.), 1993, vol. 24, no. 2, pp. 174–180.

Russian Journal of Applied Chemistry, Vol. 77, No. 10, 2004, pp. 1593–1597. Translated from Zhurnal Prikladnoi Khimii, Vol. 77, No. 10, 2004, pp. 1605–1609.

INORGANIC SYNTHESIS AND INDUSTRIAL INORGANIC CHEMISTRY

Synthesis of Willemite by Modified Sol–Gel Technique

A. G. Golovkin, F. F.Grekov, and B. V. Chernovets

State Polytechnic University, St. Petersburg, Russia

Received July 9, 2004

Abstract—Silicate luminophor Zn_2SiO_4 : Mn was synthesized using silica gel as an active form of silicon dioxide. Factors affecting the degree of crystallinity of the silicate obtained were studied. Willemite was doped with manganese(II) in the course of synthesis. The luminescence parameters of the resulting samples were estimated.

The synthesis of luminophors for various applications and the improvement of their working parameters constitute one of the most topical problems of the technology of functional materials.

Doped willemite Zn_2SiO_4 : Mn is one of the first photo-, cathodo-, and X-ray-luminophors. It has been extensively studied with the aim to elucidate the fundamental physical aspects of luminescence and to study the effect of conditions of luminophor formation on the intensity and spectral parameters of luminescence.

Although Zn_2SiO_4 exists in three modifications, α-Zn_2SiO_4 (rhombohedral structure of *R*3 space group) is usually formed under ordinary conditions. Luminophors based on zinc silicate are described in [1–5]. Willemite doped with manganese(II), which replaces Zn(II) in amounts of 0.5–5 wt %, emits light in the green spectral range. Industrial photoluminophors FL-530, FGI-520-1, FGI-528-1, and cathodoluminophors K-35, K-36, K-60, and KV-520-2 have been developed on its basis. To obtain a luminophor with orange-red luminescence, zinc silicate doped with Mn(II) should be formed in the presence of small amounts of beryllium and cadmium silicates, which are isomorphous to willemite [4]. Recently, willemite doped with rare-earth elements has been under investigation [6, 7].

Usually, doped willemite is synthesized by the solid-phase technique, by sintering a mixture of the appropriate oxides with silica at a temperature of about 1350°C for tens of hours [8]. It has been shown [4] that the degree of dispersion of the starting mixture strongly affects the reaction kinetics. This technique produces high-quality luminophors, being, however, rather power-consuming and sensitive to the difficultly controllable stock preparation process.

The crystal perfection of a luminophor governs its luminescence characteristics [1]. In a nonequilibrium (deformed) matrix, many of luminescence centers are involved in nonradiative transitions, which diminishes the quantum efficiency and, accordingly, the intensity of luminescence. The concentration of an activator affects the efficiency both directly (via the number of centers) and indirectly (via the number of structural defects) [4, 5].

Apparently, it is necessary to develop such synthesis methods that would ensure a complete and controlled mixing of components (including dopants) in the preliminary stage and, consequently, an ordering of the forming structure under relatively mild conditions.

The sol–gel technology finds increasing use for synthesis of luminophors. To synthesize doped willemite, oxides are transformed into nitrates. SiO_2 is obtained using a solution of tetraethoxysilane (TES) $(C_2H_5O)_4Si$, which hydrolyzes under heating to give SiO_2. Nitric acid and colloid solutions are mixed in certain proportions, and the mixture is subsequently dehydrated until a jelly-like mass is formed. This mass is dried in a thermostat at 120–140°C and then calcined at 1300°C for 10 h. In the finishing thermal treatment, the formation of the silicate is complete [9, 10].

The coprecipitation method, a modification of the sol–gel technique, is the most advanced. However, as shown by practical experience, this method is extremely sensitive to minute details of the TES hydro-

1070-4272/04/7710-1593 © 2004 MAIK "Nauka/Interperiodica"

lysis (order of component introduction, concentration, temperature, and mixing mode) and, thus, requires further improvement.

In this context, the already obtained active form of silicic acid, specifically, silica-gel, seems to be unappreciated. The chemistry of silica gel was described in detail in the monographs [11–14]. Silica gel in aqueous solutions shows all properties of monosilicic acid, and, consequently, can be regarded as polysilicic acid. At pH > 8, SiO_2 particles pass into solution to form silicate ions.

As is known, different types of silica gel have a wide variety of pore sizes (10–500 Å) and a developed internal surface area. Cations of appropriate sizes readily penetrate into silica gel particles. Heavy-metal ions react with active silica in ammonia solutions to form high-molecular-weight compounds of the type of basic salts. In acid solutions at pH < 6, reactions of metal ions with silica gel yield new functional groups capable of cationic exchange. Adsorption of cations may also occur on dehydrated parts of the silica surface.

The aim of this study was to develop a new method for synthesis of a silicate luminophor and to optimize it with respect to the degree of crystallinity, and also to assess the possibility of doping of the luminophor in the course of synthesis.

The central idea of the approach suggested is to modify the precipitation method (its sol–gel variant) so as to exclude the most difficultly controllable stage of formation of a homogeneous gel of silicic acid.

Partially dehydrated xerogel of silicic acid, with high specific surface area and sorption capacity, was used as an active reagent. Despite that silica gel has a great number of modifications and is widely used as a sorbent, we failed to find any information on its application as a starting reagent for synthesis of silicates in the available literature. This may be due to the fact that silica gel is traditionally regarded as a phase of uncertain composition in the SiO_2–H_2O system. However the amount of SiO_2 in the silica gel composition can be easily determined by gravimetry, and blending with SiO_2 is not difficult. It is convenient to introduce a cation (e.g., zinc or manganese) by saturating silica gel with an appropriate salt, preferably of an organic acid, because the salt should be water-soluble and thermally unstable. The saturation of the xerogel provides a thorough and uniform mixing of the components on the molecular level.

To raise the pH of the solution and to dissolve (partially) the gel, it is expedient to use ammonium hydroxide. At pH > 8, the gel passes into the solution as low-molecular-weight polysilicic acid, $kH_2O \cdot mSiO_2$ (where k and $m < 100$), and the cation precipitated as a hydroxide. This makes it possible to perform the "reverse" process, i.e., to saturate the freshly formed metal hydroxide with micellar particles $mSiO_2 \cdot kH_2O$ from the solution. The possibility of a simultaneous introduction of an activator within such a scheme is apparent.

EXPERIMENTAL

We used silica gel of three brands [GOST (State Standard) 3956–54]: ASK, KSK, and ShSM, differing in porosity and sorption capacity. The reagents were stored for a long time under laboratory conditions at narrowly varying temperature and humidity.

The content of the main substance SiO_2 (wt %) was determined by calcination at 1200°C in a muffle furnace to constant weight: ASK 94.25, KSK 93.2, ShSM 71.8.

It was found in control experiments that the humidity of these sorbents varies within ±0.03 wt % under usual storage conditions, which is comparable with the characteristics of other powders (zinc and manganese oxides) used in the experiments. Silica gel granules were reduced to a powder with particle size of less than 10 μm, using an LDI-65 grinder.

Other reagents (oxides; salts;, acetic, citric, and tartaric acids) were no less than analytically pure.

Weighed samples were prepared on a ZMP analytical balance. The pH values were measured using a standard indicator paper set. Pellets of semi-products were produced in a steel press mold under a pressure of about 21 000 atm. The calcination was carried out in air in an SUOL-0,25.2,5/14K-42 tube furnace at a temperature not exceeding 1250°C. An X-ray phase analysis (XPA) was performed on a TuR M-62 diffractometer with an HZG-4 goniometer with Cr_{K_α} radiation. A qualitative luminescent analysis was carried out on an LYuMAM R1 luminescent microscope (365 nm) and with the use of an LGI-21 (337 nm) nitrogen laser.

Cation-containing solutions were prepared by dissolving weighed samples of ZnO or other metal compounds in an excess amount of acetic, nitric, tartaric, or citric acid. In some experiments, appropriate nitrates were directly used. A weighed sample of silica gel was introduced into a solution, and silica gel was saturated (impregnated) with a cation-containing solution at room or elevated temperature for a specified

time (in some experiments up to several days). Solutions with impregnated gel were dehydrated by evaporation of the suspension in a wide quartz crucible until an air-dry amorphous powder was formed. The powder was calcined with stirring for additional 0.5 h until partial decomposition of thermally unstable salt, which was judged from gas evolution.

Pellets with a mass of about 2 g were produced by compaction without a binder. The pellets were calcined in air in a sinter-corundum container at a specified temperature for 3.5–28 h.

A phase analysis was carried out on the basis of X-ray diffraction patterns of the samples obtained, using the PDF-2 database [15] and the PowderCell for Windows software [16].

To assess the crystal perfection of the samples, we used such a parameter as the "degree of crystallinity." This parameter is not a physical quantity, but shows the extent to which the ideal crystal structure of a substance is attained (or the fraction of the crystalline component in a substance), estimated on the basis of a diffraction pattern. The degree of crystallinity may be approximately determined as [17]:

$$A = \sum_{i=1}^{n} \frac{I_{\text{ref},\,i}}{I_i}.$$

Here A is the degree of crystallinity; $I_{\text{ref},\,i}$, intensity (angular flux density) of a useful reflected signal at ith point; and I_i, intensity (angular flux density) of the total reflected signal at ith point.

All the reflections (X-ray peaks) corresponding to the phase under study were used.

Luminescent properties were examined by the conventional technique [18]. A luminescence spectrum was recorded, and the quantum efficiency was calculated. The quantum efficiency of a sample was determined by comparison with the quantum efficiency of a reference luminophor under the same excitation conditions.

To evaluate the effect of the solution pH on the phase composition and degree of crystallinity of a product synthesized, a series of experiments were carried out. Zinc(II) was added in the form of a freshly prepared acetate solution. Silica gel of ASK brand, taken in an amount necessary for the stoichiometric orthosilicate to be formed, was impregnated for 92 h at room temperature without stirring. A dried compacted mixture was calcined at 1240°C for 24 h. Only one crystalline phase of willemite was found by means of XPA in all the samples. Its lattice parameters somewhat varied between different experiments within the limits slightly exceeding the error of the experiment.

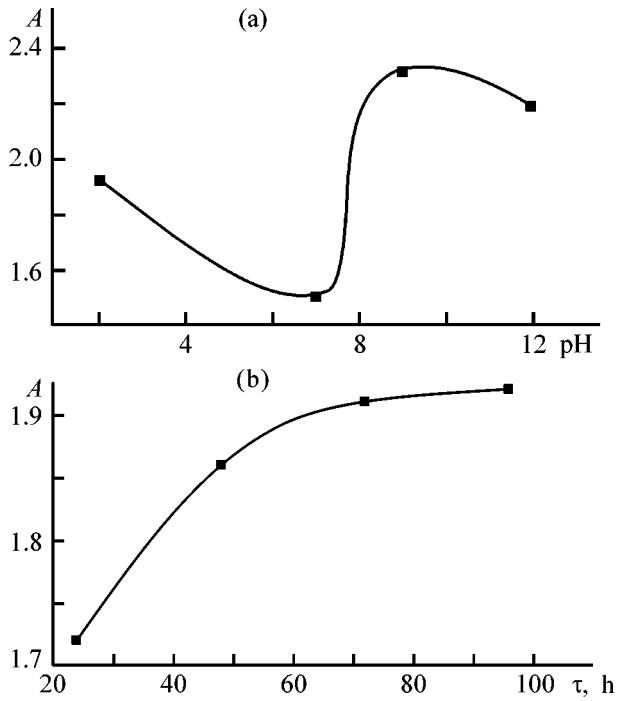

Fig. 1. Degree of crystallinity of willemite, A, vs. (a) pH of $(CH_3COO)_2Zn$ solution and (b) saturation time τ.

The dependence of the degree of crystallinity of willemite on the solution pH is shown in Fig. 1a.

The degree of crystallinity of the product depends on the pH of the impregnating solution of zinc salt nonmonotonically. If the solution is nearly neutral, the resulting product has the minimum degree of crystallinity. This fact is attributable to the saturation (blocking) of the silica gel surface mostly with water molecules. In acid solutions, the results are better because the silica gel surface is saturated with cations to form chemical bonds even at room temperature [13]. The impregnation in alkaline solutions also results in an appreciable tendency toward an increase in the degree of crystallinity of the resulting silicate. In alkaline solutions, the process can yield high-molecular-weight compounds [11] $(Si_2O_5H_2)_{n-p}[Si_2O_5(MOH)_2]_p$ which are close to basic salts, and this also leads to the desired result.

Further, it was of interest to estimate the influence exerted by the duration of saturation on the degree of crystallinity of the resulting Zn_2SiO_4. To avoid the hydrolysis of zinc acetate, the saturation was carried out in an acid medium at pH 2. Other experimental conditions were the same as in the preceding series.

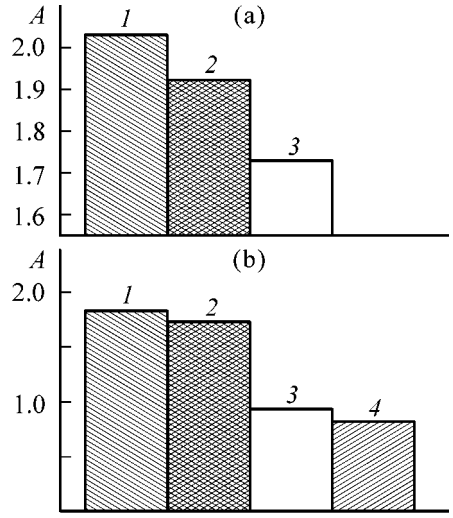

Fig. 2. Effect of (a) type of silica gel and (b) nature of the acid residue on the degree of crystallinity, *A*. Silica gel: (*1*) KSK, (*2*) ASK, (*3*) ShSM. Zinc salt: (*1*) nitrate, (*2*) acetate, (*3*) tartrate, (*4*) citrate.

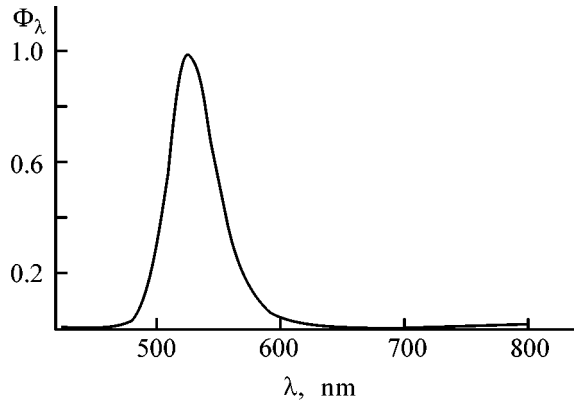

Fig. 3. Luminescence spectrum of Zn_2SiO_4 : Mn (see text). (Φ_λ) Relative intensity of luminescence and (λ) wavelength.

Regardless of the calcination time, only willemite with unchanged lattice parameters (a = 13.74 and c = 9.43 Å) corresponding to the data of [15] was found in the annealed product.

The dependence of the degree of crystallinity of willemite on the duration of saturation of dispersed silica gel is shown in Fig. 1b.

It is apparent that after about 3 days at room temperature the system comes to a steady state, and further increase in the time of treatment hardly affects the result. Similar results were obtained in impregnation with a hot (60–70°C) solution.

The effect of the type of silica gel on the degree of crystallinity of the resulting Zn_2SiO_4 was also studied. The saturation was carried out in an acid solution in the course of 96 h, compacted samples were calcined at 1200°C for 24 h. In all the samples, only a single crystalline phase of willemite was found by XPA. Its lattice parameters varied between the experiments within the limits slightly exceeding the error of the experiment. The results obtained are shown in Fig. 2a in the form of a histogram.

Comparison of the values of A shows that the best results are obtained with KSK and ASK silica gels. Probably, this is associated with the diffusion mechanism of impregnation, which is mainly affected by the sizes and relative volumes of pores. The pore sizes of the KSK and ASK silica gels are comparable (about 300–500 Å), whereas those of the ShSM slica gel are 100–350 Å [14]. Apparently, for a complete and uniform diffusion saturation to be obtained, the size of a solvated cation should be significantly less than that of pores in the silica gel.

The influence exerted by the acid residues of zinc salts on the phase composition of products and the crystallinity of the resulting Zn_2SiO_4 were studied. The impregnation was carried out in acid medium for 48 h, the pellets were calcined at 1200°C for 27 h. When $Zn(NO_3)_2$ and $(CH_3COO)_2Zn$ were used, a single-phase willemite was obtained, whereas the use of zinc tartrate and citrate led to incomplete reactions. In addition to the poorly crystallized willemite, a second phase of ZnO was detected in such samples by XPA.

The effect of the nature of acid residues is shown in Fig. 2b. It follows from the comparison of the values of A that the best results are obtained with $Zn(NO_3)_2$ and $(CH_3COO)_2Zn$. The extent of the reaction and the product quality are strongly impaired if larger anions of tartaric or citric acids are used. This is probably due to the above-mentioned steric hindrances arising upon the impregnation. Despite that the best results are obtained with $Zn(NO_3)_2$, zinc acetate should be preferably used because no toxic oxides are released in its pyrolysis.

Ground ASK silica gel was used to synthesize willemite doped with manganese. Acetate solutions were obtained by separate dissolution of weighed samples of ZnO and Mn_2O_3 in an excess amount of acetic acid. A Mn : Zn atomic ratio of 1 : 99 was obtained in the combined solution (pH ≈ 2). The impregnation and calcination conditions were selected with account of the data presented above. The lattice parameters of the willemite synthesized are as follows: a = 13.94, c = 9.36 Å.

A bright green luminescence which is typical of willemite doped with manganese(II) was observed upon excitation of the crushed product by the 365-nm line (Fig. 3). The relative intensity of luminescence

reaches a maximum at 525 nm. Obviously, manganese(III) is partially reduced in the course of synthesis to be incorporated in the solid solution, statistically occupying lattice sites of zinc(II).

The luminophor synthesized is, as yet, considerably exceeded by industrial specimens in quantum efficiency. The method of synthesis can be additionally optimized, in particular, as regards the purity of the silica gel and also the concentration and initial form of the activator.

CONCLUSIONS

(1) Willemite can be synthesized by a modified sol–gel method with the use of a xerogel of silicic acid as an active form of silica gel and an aqueous solution of a zinc salt (acetate or nitrate).

(2) The solution pH in the initial stage of the synthesis strongly affects the crystallinity of the resulting samples. A primary reaction of amorphous SiO_2 with the salt added seems to occur in acid and alkaline solutions, which leads to a more perfect (equilibrium) structure of the silicate produced by a subsequent calcination.

(3) The degree of crystallinity of the willemite synthesized depends on the size of pores in the starting silica gel and on the nature of acid residues. The primary reaction is facilitated in a macroporous gel and with salts forming compact solvates (nitrate and acetate).

(4) Introduction of manganese(II) in small amounts into the starting solution provides a green luminescence which is typical of a willemite luminophor.

REFERENCES

1. Kazankin, O.N., Markovskii, L.Ya., Mironov, I.A., *et al., Neorganicheskie lyuminofory* (Inorganic Luminophors), Leningrad: Khimiya, 1975.
2. Volotskoi, N.V., Zil'ber, D.A., and Knoring, G.M., *Lyuminestsentnoe osveshchenie* (Luminescent Lighting), Moscow: Gosenergoizdat, 1955.
3. *Khimiya i tekhnologiya lyuminoforov* (Chemistry and Technology of Luminophors), Markovskii, L.Ya., Ed., Leningrad: Khimiya, 1964, issue 51.
4. Konstantinova-Shlezenger, M.A., *Khimiya lampovykh geterodesmicheskikh lyuminoforov* (Chemistry of Heterodesmic Lamp Luminophors), Moscow: Nauka, 1970.
5. Levshin, V.L. and Levshin, L.V., *Lyuminescenciya i ee primenenie* (Luminescence and Its Application), Moscow: Nauka, 1972.
6. Zhang, H.X., Buddhudu, S., Kam, C.H., *et al., Mater. Chem. Phys.*, 2001, vol. 68, pp. 31–35.
7. Zhang, Q.Y., Pita, K., Ye,W., and Que, W.X., *Chem. Phys. Lett.*, 2000, vol. 351, pp. 163–170.
8. Sohn, K.-S., Cho, B., Dong Park, H., *et al., J. Eur. Ceram. Soc.*, 2000, vol. 20, pp. 1043–1051.
9. Khristov, C.I., Popovich, N.V., and Galaktionov, S.S., *Neorg. Mater.*, 1996, vol. 32, pp. 89–94.
10. Ahmadi, T.S., Haase, M., and Weller, H., *Mater. Res. Bull.*, 2000, vol. 35, pp. 1869–1879.
11. Kol'tsov, S.I. and Aleskovskii, V.B., *Silikagel', ego stroenie i khimicheskie svoistva* (Silica Gel, Its Structure and Chemical Properties), Leningrad: Goskhimizdat, 1963.
12. Terenin, A.N., *Poverkhnostnye khimicheskie soedineniya i ikh rol' v yavleniyakh adsorbtsii* (Surface Chemical Compounds and Their Role in Adsorption Phenomena), Moscow: Mos. Gos. Univ., 1955.
13. Neimark, I.E. and Shenfain, R.Yu., *Silikagel', ego poluchenie, svoistva i primenenie* (Silica Gel, Its Production, Properties, and Application), Kiev: Naukova dumka, 1973.
14. Laskorin, B.N., Strelko, V.V., Strazhesko, D.N., and Denisov, V.I., *Sorbenty na osnove silikagelya v radiokhimii: Khimicheskie svoistva: Primenenie* (Sorbents Based on Silica Gel in Radiochemistry: Chemical Properties: Application), Moscow: Atomizdat, 1977.
15. *PCPDFWIN*, version 1.30, 1997, JCPDC-ICDD.
16. Kraus, W. and Nolze, G., PowderCell for Windows, version 2.3, 1999, Berlin.
17. Vasil'ev, D.M., *Difraktsionnye metody issledovaniya struktur* (Diffraction Methods for Structural Studies), St. Petersburg: Spb. Gos. Tekhn. Univ., 1998.
18. Epshtein, M.I., *Spektral'nye izmereniya v elektrovakuumnoi tekhnike* (Spectral Measurements in Electrovacuum Technique), Moscow: Energiya, 1970.

Russian Journal of Applied Chemistry, Vol. 77, No. 10, 2004, pp. 1598–1605. Translated from Zhurnal Prikladnoi Khimii, Vol. 77, No. 10, 2004, pp. 1610–1617.

INORGANIC SYNTHESIS AND INDUSTRIAL INORGANIC CHEMISTRY

Effect of Mechanical Activation on the Reactivity of Oxides of Rare Earth Elements and Yttrium

A. M. Kalinkin, E. V. Kalinkina, O. A. Zalkind, and T. N. Vasiljeva

Tananaev Institute of Chemistry and Technology of Rare Elements and Mineral Raw Materials, Kola Scientific Center, Russian Academy of Sciences, Apatity, Russia

Received April 1, 2004

Abstract—Processes occurring in mechanical activation of pure and mixed La(III), Nd(III), Er(III), Yb(III), and Y(III) oxides in air were studied. The influence exerted by the mechanical activation and by the accompanying absorption of atmospheric carbon dioxide on the selectivity of dissolution of components of mixed oxides in acid treatment were studied.

It has been found previously [1–3] that such stable compounds as silicate minerals of calcium and magnesium undergo deep structural and chemical transformations under a prolonged mechanical treatment. The ability of silicates to absorb significant amounts of CO_2 from the ambient atmosphere in mechanical activation (MA) appeared to be one of the factors responsible for these transformations. Fine grinding in air or in atmosphere of CO_2 leads to a strong saturation of a silicate mineral with carbon dioxide, which "dissolves" in the amorphized mineral, being incorporated into a disordered silicate matrix in the form of carbonate ions. The content of CO_2 in the amorphized samples may be as high as 20–22 wt %. Such considerable changes in the chemical composition and structure of a substance must affect its physicochemical properties. The influence exerted by MA and the accompanying CO_2 absorption on the increase in the reactivity of some minerals toward acids have been studied earlier.

This study is a part of the investigation of the mechanical activation of silicates and composite oxides of varied composition and structure. The aim of the study was to examine processes that occur in mechanical activation of individual and mixed oxides of rare earth elements in air and to analyze the effect of MA on their reactivity.

It is known that, when stored in air, REE oxides absorb in noticeable amounts carbon dioxide and water from the atmosphere to form basic carbonates [4–6]. It is natural to assume that MA of REE oxides would accelerate their reactions with atmospheric moisture and carbon dioxide. As the atomic weight increases in the series of REE, their ionic radii and basic properties decrease owing to lanthanide contraction, and, therefore, we can expect that oxides of light REEs, e.g., lanthanum, will react in the course of MA in air with H_2O and CO_2 to a greater extent than oxides of heavy REEs, e.g., erbium. Therefore, when activated mixed oxides are treated with an acid, the newly formed basic carbonates of REEs must pass into solution before the starting oxides, owing to the removal of CO_2 from the reaction sphere.

In this study, we examined the influence exerted by preliminary MA of mixed REE oxides in air on the selectivity of their separation in dissolution in an acid and also on the crystallization of binary perovskite-like oxides $Ln^{(1)}Ln^{(2)}O_3$ in thermal treatment of the mixed oxides.

EXPERIMENTAL

Mixed oxides of REEs and yttrium were obtained by coprecipitation of hydroxides from solutions of chemically pure nitrates with ammonia and subsequent washing of the precipitates with water and their calcination at 1000°C for 2 h. According to the data furnished by chemical and thermal analyses and also by IR spectroscopy, a complete removal of residual nitrate ions, water, and CO_2 from the samples is achieved in this case [4, 5]. Individual oxides of La, Nd, Y, Er and Yb were obtained similarly from solutions of corresponding nitrates. The content of the main substance in the oxides was no less than 99.9%.

1070-4272/04/7710-1598 © 2004 MAIK "Nauka/Interperiodica"

According to the results of an X-ray phase analysis (XPA), the starting Ln_2O_3 and Nd_2O_3 were of the hexagonal A-form, and Y_2O_3, Er_2O_3, and Yb_2O_3, of the cubic C-form.

Freshly calcined oxides were mechanically activated in a Fritsch mechanical agate mortar (model 5) in air at 293 ± 2 K. The natural content of carbon dioxide in air [$P(CO_2)$ = 30 Pa] was virtually constant, which is confirmed by the reproducibility of the degrees of carbonization of samples in parallel experiments. The relative humidity of air during the experiments was 60–70%. The weight of a sample charged into the mortar was 5 g. After the MA, the samples were kept in a vacuum desiccator over silica gel. The content of CO_2 in the activated samples was determined by a gas-volumetric technique on an AN-7529 express analyzer. IR spectra were measured in pellets with KBr on a modified UR-20 spectrometer supplied with a device for obtaining spectra in the digital form. X-ray diffraction patterns were measured with a DRON-2.0 diffractometer with unfiltered Cu_{K_α} radiation. A differential thermal analysis was carried out on NTR-70 and PRT-1000 instruments with a Pt–Pt/Rh thermocouple in air. The rate of sample heating was 20 deg min^{-1}, calcined Al_2O_3 served as a reference. Thermogravimetric (TG) curves were obtained on a VT-1000 torsion balance. The specific surface areas of the samples were measured by the method of nitrogen thermal desorption (single-point method), using a Micromeritics FlowSorb II 2300 analyzer. Solutions obtained upon acid leaching of the activated samples were analyzed for the content of REE oxides by the atomic-emission method on a Perkin–Elmer Plasma 400 spectrometer. The content of REEs in the mixed oxides and precipitates was determined by the X-ray fluorescent method on a VRA-2 instrument with an external reference after calcination of the samples at 1000°C for 2 h.

The IR spectra of La, Nd, Y, Er, and Yb oxides after 12-h MA are shown in Fig. 1. They indicate that a noticeable hydration and carbonization of the samples occurs because of the absorption of atmospheric H_2O and CO_2. In the case of the oxide of lanthanum, which has the largest ionic radius, a narrow band at 3600 cm^{-1}, associated with stretching vibrations of an isolated hydroxy group, and a band at 643 cm^{-1}, corresponding to pendular bending vibrations of OH groups, indicate that lanthanum hydroxide is formed [7]. This is confirmed by XPA data (not shown), according to which La_2O_3 is completely converted into $La(OH)_3$ already after 3 h of abrasion. Further increase in the time of activation results only in a broadening of $La(OH)_3$ lines in the X-ray diffraction patterns and

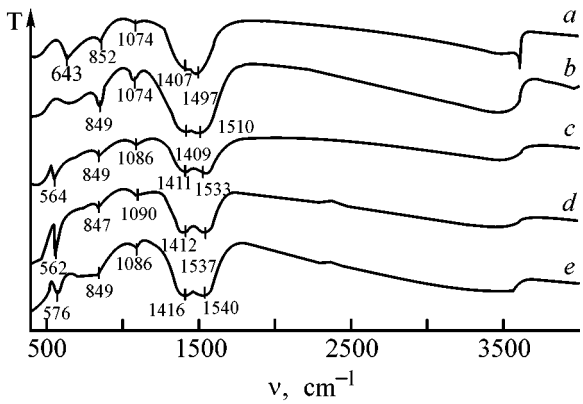

Fig. 1. IR spectra of samples of REEs and yttrium oxides after MA for 12 h. (T) Transmission and (ν) wave number. (*a*) La_2O_3, (*b*) Nd_2O_3, (*c*) Y_2O_3, (*d*) Er_2O_3, (*e*) Yb_2O_3.

in a decrease in their intensity, which indicates that the sample is amorphized and(or) the particles decrease in size. Reflections of $Nd(OH)_3$ also appear in the X-ray diffraction patterns of mechanically activated Nd_2O_3 (not shown) on the background of an appreciable decrease in the intensities of the lines associated with the oxide; however, their intensity is relatively low. After a 12-h abrasion treatment of oxides of yttrium-group elements (Y_2O_3, Er_2O_3, and Yb_2O_3), a diffuse halo appeared in their X-ray diffraction patterns, which points to the presence of a certain amount of an amorphous phase, and the intensities of reflections of the corresponding oxide somewhat decreased.

Broad bands associated with stretching vibrations of OH groups in the range 3300–3600 cm^{-1} are present in the IR spectra of all mechanically activated oxides (Fig. 1). The absence of bands of bending H–O–H vibrations at 1630–1670 cm^{-1} indicates that water is present in samples only in the form of OH groups. The broadening of the band of stretching OH vibrations is presumably due to a noticeable contribution of hydrogen bonds formed by protons of the hydroxy groups [8, 9]. Formation of bridging OH groups between two metal atoms is also not improbable [10]. The absorption bands at 564, 562, and 576 cm^{-1} in the IR spectra of Y_2O_3, Er_2O_3, and Yb_2O_3 (Fig. 1, curves *c*, *d*, and *e*, respectively) correspond to Ln–O stretching vibrations in the crystal lattices of the oxides [11, 12], in agreement with the XPA data.

The high-intensity double band at 1380–1550 cm^{-1}, which appears in the IR spectra of all the oxides under study as a result of their mechanical activation, corresponds to the ν_3 stretching vibrations of CO_3 groups. The splitting of this band, typical of basic carbonates of REEs, is due to lifting of the degeneration by the lowering symmetry of the carbonate group [13–21].

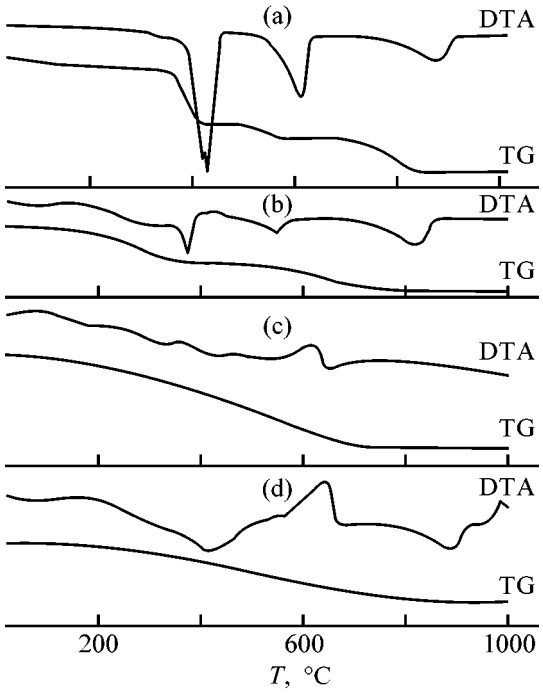

Fig. 2. DTA and TG curves of samples after MA. (*T*) Temperature. (*a*) La_2O_3, (*b*) Nd_2O_3, (*c*) Er_2O_3, (*d*) mixed oxide La_2O_3 and Er_2O_3. MA duration (h): (*a*) and (*b*) 3, (*c*) and (*d*) 12. For the TG curve of Er_2O_3 sample the scale of the ordinate axis is multiplied by a factor of 3.

The splitting $\Delta\nu_3(CO_3)$ equal to 90–125 cm^{-1} points to the monodentate coordination of carbonate groups, which is characterized by the appearance of absorption bands at 1380–1550, 1075, and 850 cm^{-1} [9, 13, 14, 22].

The processes that occur in La_2O_3, CeO_2, Sm_2O_3, Dy_2O_3, and Yb_2O_3 during their storage in air for 2–3 years have been studied by X-ray photoelectron spectroscopy (XPS) [5]. It was found that X-ray-amorphous basic carbonates are formed not only on the surface, but also in the bulk of all the samples under study. The peaks of the corresponding hydroxides appeared in the X-ray diffraction patterns of La and Sm oxides upon their exposure to air. For Dy_2O_3 and Yb_2O_3, only broadening of the reflections of the starting oxides was observed. As would be expected, the MA in our experiments considerably accelerates the reactions of oxides with atmospheric H_2O and CO_2, with the nature of the occurring processes being similar to that described in [5]. The oxide La_2O_3, and to a lesser extent Nd_2O_3, probably first react with moisture to form hydroxides, which are then converted into X-ray-amorphous basic hydroxides in reactions with CO_2. The exposure of $Ln(OH)_3$ to air is known to yield basic carbonates $Ln_2(CO_3)_x(OH)_{2(3-x)} \cdot nH_2O$ [6]. As already mentioned, the IR spectra of the samples subjected to MA contain no bands associated with bending vibrations of H–O–H. This suggests that basic carbonates formed in abrasion in air have the formula $Ln_2(CO_3)_x(OH)_{2(3-x)}$.

It is probable that X-ray-amorphous basic carbonates are also present in mechanically activated oxides of Y, Er, and Yb, which have smaller ionic radii, although the process of their formation is somewhat different. It should be noted that the peaks of the double band associated with stretching vibrations ν_3 of the CO_3 group (Fig. 1) are shifted to shorter wavelengths as the ionic radius of Ln^{3+} decreases:

Ionic radii of REEs by Goldschmidt [4]

Ion	La^{3+}	Nd^{3+}	Y^{3+}	Er^{3+}	Yb^{3+}
r, Å	1.22	1.15	1.06	1.04	1.00

In this case, the splitting $\Delta\nu_3(CO_3)$ for mechanically activated Y_2O_3, Er_2O_3, and Yb_2O_3 exceeds by 20–30 cm^{-1} that for samples of La and Nd oxides obtained under the same conditions. In view of the decrease in the basic properties in the order La > Nd > Y > Er > Yb, this result is somewhat unexpected because the shift of the ν_3 band and the increase in its splitting indicate a stronger binding of the CO_3 group [13, 22]. As formation of hydroxides was observed in MA of La_2O_3 and Nd_2O_3, we may assume that the OH group is a primary ligand in the resulting basic lanthanum and neodymium carbonates, and the CO_3 group is bound to it by hydrogen bonds [15, 18]. In the basic carbonates of Y, Er, and Yb, both the carbonate and hydroxyl groups are probably bound to the metal.

The DTA and TG curves of a lanthanum oxide sample subjected to a 3-h MA are shown in Fig. 2a. The shape of the DTA curve and the position of the peaks of effects are close to those in a similar curve for amorphous basic lanthanum carbonate obtained by precipitation of a hydroxide from a nitrate solution brought in contact with atmospheric CO_2 [5]. The endothermic effects at 400°C are probably associated with removal of water. Further increase in temperature results in the appearance of an endothermic peak at 584°C, which corresponds to the simultaneous removal of H_2O and CO_2 [5]. Carbon dioxide is completely removed at temperatures above 850°C. Three steps in the TG curve of the lanthanum oxide sample after 3 h of MA correspond to three main endothermic effects in the DTA curve (Fig. 2a). The loss of weight by this sample after calcination at 1000°C was

16.6 ± 0.4 wt %. The TG curve in Fig. 2a is similar to the curve of the same kind, obtained for lanthanum oxide after its exposure to air for 2 years, with the weight loss in calcination at 800°C equal to 13.4–14.0 wt % [5].

The DTA curve of neodymium oxide after MA for 3 h (Fig. 2b) is similar to the DTA curve for activated lanthanum oxide (Fig. 2a). The positions of the peaks of the effects for the neodymium oxide sample are shifted to lower temperatures, in agreement with published data [15, 16], which indicate that the decomposition temperatures of basic REE carbonates become lower as the ionic radius decreases. The results of a thermal analysis for an Er_2O_3 sample subjected to 12 h of MA, presented in Fig. 2c (for the TG curve the scale of ordinate axis for this sample is multiplied by a factor of 3), point to a noticeably smaller degree of H_2O and CO_2 absorption and to another nature of thermal decomposition, compared with activated lanthanum and neodymium oxides. As the atomic weight of a metal increases, the shape of the TG curves changes from a steplike for mechanically activated samples of lanthanum and neodymium oxides to almost monotonic for samples of erbium oxide (Fig. 2c). The same tendency was observed for REE oxides exposed to air [5] and for basic REE carbonates precipitated from solutions [21]. It is necessary to note that the thermolysis of basic REE carbonates is of a multistage complex nature. A number of intermediate phases are formed in the process, with the technique used to obtain the starting samples being of importance [5, 15, 16, 21].

The extents of carbonization, P (wt % CO_2), of individual oxides of REEs and yttrium subjected to MA are listed in Table 1. The data obtained indicate that, on the whole, the extent of carbon dioxide absorption in MA is in agreement with the basicity of the metals, which is determined by radii of their ions. Oxides of elements with larger ionic radii (lanthanum and neodymium) are carbonized to the greatest extent, whereas erbium and ytterbium oxides are carbonized to a lesser degree. Yttrium is an exception. Its ionic radius is intermediate between those of light and heavy REEs. At the same time, the CO_2 content in the sample of yttrium oxide after MA is comparable with that for lanthanum oxide (Table 1). It is necessary to note that specific surfaces areas of the starting La, Nd, Y, Er, and Yb oxides are 1.6, 1.7, 7.8, 2.3, and 1.0 $m^2 g^{-1}$, respectively. The relatively large initial specific surface area of yttrium oxide can be one of reasons for the increased content of the carbonate after MA. Another possible reason is the noticeably smaller molecular weight of yttrium oxide, compared with REE oxides. As the weight of the oxide charge in all the activation experiments was the same (5 g), the numbers of moles of the substances absorbing CO_2 were inversely proportional to their molecular weights. It is likely that, in the case of equal inputs of the mechanical energy per unit mass of a sample, a greater number of oxide moles will react with a greater amount of carbon dioxide, all other factors being the same. The extents of carbonization of REE oxides, which are normalized to their molecular weights (Table 1), show a clearly pronounced, although not absolutely strict, tendency toward a decrease in the absorption of CO_2 with decreasing ionic radius of a metal.

Table 1. Extent of carbonization of individual REE oxides after MA*

Oxide	P_3, wt % CO_2	$P_3 M$	P_{12}, wt % CO_2	$P_{12} M$
La_2O_3	3.3 ± 0.1	1075 ± 33	9.1 ± 0.3	2965 ± 98
Nd_2O_3	3.2 ± 0.1	1077 ± 34	7.6 ± 0.2	2557 ± 67
Y_2O_3	3.6 ± 0.1	813 ± 23	9.0 ± 0.3	2032 ± 68
Er_2O_3	1.6 ± 0.1	612 ± 38	3.2 ± 0.1	1224 ± 38
Yb_2O_3	1.8 ± 0.1	709 ± 39	4.7 ± 0.2	1852 ± 79

* P_3 and P_{12}, the extents of carbonization after MA for 3 and 12 h, respectively; M, the molecular weight of the corresponding REE oxide.

The aim of further experiments was to determine whether or not the REE oxides included in a mixed compound obtained by coprecipitation from a solution of their salts with ammonia, with the subsequent calcination, differ in their tendency to react with atmospheric CO_2 in a mechanical activation similarly to activated individual oxides, and whether or not it is possible to make one of the components (oxide) of such a mixed compound to be converted into a basic carbonate first. Then it would be possible to expect a selective dissolution of this same component when a mixed oxide reacts with an acid. To verify this assumption, we synthesized mixed oxides of the following metals: (1) lanthanum, neodymium, and yttrium; (2) lanthanum and erbium; and (3) neodymium and ytterbium. The first mixed oxide included elements rather close to each other in the susceptibility to carbonization. By contrast, the lanthanum–erbium and neodymium–ytterbium compositions involved the elements as distant as possible from each other in the series of REEs. The choice of elements for the compositions was determined, among other things, by the availability of compounds. The mixed oxides

Table 2. Relative amounts of lanthanum, neodymium, and yttrium oxides in solutions and solid phases after dissolution of a mixed oxide in 0.5 M HNO_3* (molar ratio $La_2O_3 : Nd_2O_3 : Y_2O_3$ in the starting sample 1 : 1.03 : 1.10)

τ, h	$La_2O_3 : Nd_2O_3 : Y_2O_3$, mol, after dissolution in acid		α($La_2O_3 + Nd_2O_3 + Y_2O_3$), wt %
	in solid phase	in solution	
–	1 : 1.50 : 1.70	191 : 16 : 1	5.2
–	1 : 1.73 : 1.88	19 : 6 : 1	17.1
3	1 : 1.05 : 1.12	1.16 : 0.88 : 1	12.9
3	1 : 1.04 : 1.11	1.08 : 0.95 : 1	34.5
6	1 : 1.04 : 1.11	1.06 : 1.00 : 1	13.2

* τ, the processing (MA) duration; α, the degree of dissolution.

Table 3. Relative amounts of lanthanum and erbium oxides in solutions and solid phases after dissolution of a mixed oxide in 0.1 M HNO_3 (molar ratio $La_2O_3 : Er_2O_3$ in the starting mixed oxide 1 : 1.04)

Sample	$La_2O_3 : Er_2O_3$, mol, after dissolution in acid		α($La_2O_3 + Er_2O_3$), wt %
	in solid phase	in solution	
Mixed oxide without MA	1 : 4.28	4.10 : 1	44.1
Mixed oxide, MA for 12 h	1 : 1.15	1.29 : 1	33.2
$LaErO_3$ without MA	1 : 1.14	1.12 : 1	36.1

Table 4. Relative concentrations of neodymium and ytterbium oxides in solutions and solid phases after dissolution of a mixed oxide in 0.1 M HNO_3 (molar ratio $Nd_2O_3 : Yb_2O_3$ in the starting sample 1 : 1.05)

τ, h	$Nd_2O_3 : Yb_2O_3$, mol, after dissolution in acid		α(Nd_2O_3+Yb_2O_3), wt %
	in solid phase	in solution	
–	1 : 2.52	1.55 : 1	49.7
12	1 : 1.11	1.07 : 1	33.3

Table 5. Extent of carbonization of mixed oxides of REEs and yttrium after MA

Sample	τ, h	CO_2, wt %	Sample	τ, h	CO_2, wt %
$La_2O_3 + Nd_2O_3 + Y_2O_3$	3	4.4 ± 0.1	$La_2O_3 + Er_2O_3$	12	7.3 ± 0.2
	6	5.1 ± 0.1	$Nd_2O_3 + Yb_2O_3$	12	6.9 ± 0.2

we synthesized contained approximately equimolar amounts of oxides of each metal, their compositions are listed in Tables 2–4.

To study the effect of MA on the selectivity of leaching of separate components, we dissolved the starting unactivated mixed oxides under identical conditions in dilute nitric acid with continuous stirring for 2 h, until complete neutralization of the acid. The dissolution of the mixed oxides subjected to preliminary mechanical activation and, therefore, carbonized to a considerable extent (Table 5) was carried out similarly. We used for dissolution 0.1 and 0.5 M nitric acid. After that, the solid phase remaining upon partial dissolution of the mixed oxides was separated from the solution by filtering, washed, dried at 100°C, and calcined to oxides at 1000°C for 2 h. To obtain data on the distribution of REEs and yttrium among the liquid and solid phases as a result of reactions of

the starting and activated samples of the mixed oxides with dilute solutions of nitric acid, we analyzed the solid phase and the filtrates for the content of REEs. The total content of REE oxides in the solid phase and in the filtrate always differed from their content in the starting mixed oxide by no more than 1–2%, i.e., the loss was at a minimum. The data on the distribution of REEs and yttrium among the liquid and solid phases after dissolution of mixed oxides in the acid are listed in Tables 2–4. The degree of dissolution of the mixed oxides is represented as the ratio of the amount of oxides that passed into solution and the amount of oxides in a sample before dissolution. For the ternary mixed oxide La–Nd–Y (Table 2), not subjected to preliminary MA, rather selective leaching-out of lanthanum is observed when 5.2% of the sample passes into solution. Its concentration in solution exceeds that of neodymium by more than a factor of 10 and that of yttrium by almost a factor of 200, whereas in the starting sample the oxides were present in approximately equimolar amounts. At higher expenditure of the acid, the selectivity of leaching-out of lanthanum upon dissolution of 17.1% of a sample of the ternary oxide essentially decreases: the concentration of lanthanum in solution exceeds that of neodymium by only a factor of 3, and that of yttrium by a factor of 19. It also follows from Table 2 that the MA leads to a dramatic decrease in the selectivity of leaching. Comparison of samples of the ternary oxide, activated for 3 and 6 h in the mechanical mortar, shows that, at the same extent of sample dissolution (about 13%), the relative concentrations in solution, $La_2O_3 : Nd_2O_3 : Y_2O_3$ are equalized to 1.16 : 0.88 : 1 and 1.06 : 1.00 : 1, respectively. A similar behavior in passing of REEs into solution is observed in dissolution of La–Er and Nd–Yb binary mixed oxides (Tables 3 and 4).

Thus, the experimental data show that the dissolution in an acid of starting mixed oxides not subjected to MA occurs in accordance with the basicity of elements, which is determined by their ionic radii. In the case of a mixed oxide of lanthanum, neodymium, and yttrium (Table 2), the extent to which a metal passes into a solution increases in the order Y < Nd < La, and hence the enrichment of the solid phase occurs in the reverse sequence. When the fraction of the dissolved sum of oxides increases, which occurs at a higher expenditure of the acid, the selectivity of separation falls. A similar trend is observed in reactions involving unactivated binary oxides of lanthanum and erbium, and also of neodymium and ytterbium: lanthanum and neodymium preferentially pass into solution, and heavy REEs are concentrated in the solid phase (Tables 3 and 4).

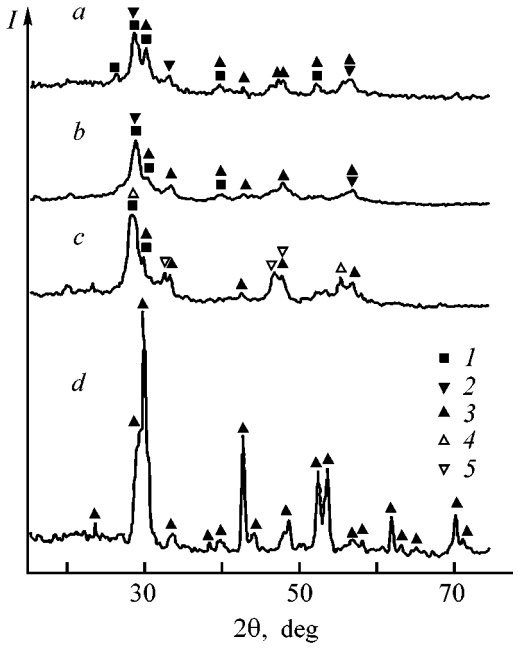

Fig. 3. X-ray diffraction patterns of the mixed oxide La_2O_3 + Er_2O_3. (*I*) intensity and (2θ) Bragg angle. (*a*) Starting oxide calcined at 1000°C; (*b*) sample *a* after MA for 12 h; (*c*) sample *b* after heating at 700°C; (*d*) sample *b* after heating at 1000°C. (*1*) La_2O_3, (*2*) Er_2O_3, (*3*) $LaErO_3$, (*4*) $La_2O_2CO_3$, (*5*) $Er_2O_2CO_3$.

Preliminary MA of the mixed oxides noticeably changes the distribution of elements among the liquid and solid phases in reaction with an acid, because REEs and yttrium pass into solution to approximately the same extent, i.e., virtually no selectivity is observed in dissolution. Thus, the experiments show that the MA of the mixed oxides adversely affects the selectivity of their separation.

The data obtained can be explained as follows. Presumably, several processes occur in MA of the mixed oxides. It is possible that, alongside with carbonization and hydration, a solid-phase reaction occurs to give precursors of binary perovskite-like oxides of REEs $Ln^{(1)}Ln^{(2)}O_3$, which dissolve in the acid congruently. To verify this assumption, we synthesized a mixed oxide of lanthanum and erbium and activated it in a mechanical mortar for 12 h, and then subjected it to a heat treatment. The results of XPA and thermal analysis show that the thermal relaxation of mechanically activated mixed oxide of La and Er results in the synthesis of the perovskite-like oxide $LaErO_3$. The X-ray diffraction patterns of the starting mixed oxide of La and Er and of the same sample after MA for 12 h with the subsequent heating at 700 and 1000°C are shown in Fig. 3. The degree of crystallinity of the starting mixed oxide sample is low

(Fig. 3, curve *a*), and the MA results in a certain broadening of the reflections and in a decrease in their intensity (Fig. 3, curve *b*). The fact that there are no reflections of $La(OH)_3$, which is formed in abrasion of pure La_2O_3, in the X-ray diffraction patterns of a mechanically activated sample (Fig. 3, curve *b*) indirectly shows that a reaction between La and Er oxides occurs in MA. This conclusion is also confirmed by the strong difference between the thermograms of mechanically activated mixed (Figs. 2a and 2d) and individual (Figs. 2a and 2c) oxides of La and Er. The endothermic peaks at 300–640°C in the DTA curve of the mixed oxide of lanthanum and erbium after 12-h MA probably correspond to removal of water and, in part, of CO_2 (Fig. 2d). The exothermic effect at 642°C apparently corresponds to formation of dioxomonocarbonate $Ln_2O_2CO_3$. According to published data [20], the appearance of such an exothermic peak precedes the formation of $La_2O_2CO_3$ in thermal decomposition of the mono-oxocarbonate $La_2O(CO_3)_2 \cdot 1.4H_2O$. This assumption is supported by the fact that reflections that can be assigned to $La_2O_2CO_3$ and $Er_2O_2CO_3$ [23, 24] appear in the X-ray diffraction pattern of the mechanically activated mixed oxide of La and Er heated to 700°C (Fig. 3, curve *c*). At the same time, no changes are observed in the X-ray diffraction pattern of the same sample heated to 500°C (not shown). The endothermic effect at 880°C in Fig. 2d probably corresponds to removal of carbon dioxide. The exothermic peak at 983°C corresponds to crystallization of the binary oxide $LaErO_3$ [25], which is confirmed by the XPA (Fig. 3, curve *d*). The TG curve of the mixed oxide after MA (Fig. 2d) is monotonic, as in the case of mechanically activated erbium oxide (Fig. 2c).

Table 3 lists the data on dissolution in dilute nitric acid of the binary mixed oxide of lanthanum and erbium and of $LaErO_3$ synthesized as described above. The congruence of the $LaErO_3$ dissolution in dilute HNO_3 confirms the assumption concerning the possible reason for the negative effect of the MA of the mixed oxides on the selectivity of REE separation.

It should be noted that a method for synthesis of $Ln^{(1)}Ln^{(2)}O_3$ compounds has been described in the literature [26]. This method consists in a prolonged (10–40 h) heating of coprecipitated hydroxides at 1400–1800°C [26]. The $Ln^{(1)}Ln^{(2)}O_3$ compounds activated with metal ions hold much promise as scintillators and materials for laser technology [27]. The mechanical activation of mixtures of solids finds increasing use in synthesis of complex oxides [28, 29]. The above-mentioned decrease in the temperature of $LaErO_3$ synthesis as a result of a preliminary MA of the stock may be of interest for improving the existing methods for preparation of perovskite-like binary REE oxides.

CONCLUSIONS

(1) The mechanical activation of individual oxides of lanthanum, neodymium, erbium, ytterbium, and yttrium strongly accelerates the absorption of CO_2 and moisture from air by these compounds. As the atomic weights of REEs increase, their ionic radii and also basic properties of the metals decrease owing to the lanthanide contraction. In the same direction decreases the extent of carbonization of the oxides in mechanical activation.

(2) The mechanical activation of individual lanthanum and neodymium oxides results in that they are converted into hydroxides via reaction with moisture contained in air, yielding hydroxides, which form amorphous basic carbonates, presumably of the composition $Ln_2(CO_3)_x(OH)_{2(3-x)}$, by reacting with atmospheric carbon dioxide. Individual oxides of the yttrium-group elements (Y_2O_3, Er_2O_3, and Yb_2O_3) are more stable against mechanical actions.

(3) The effect of the mechanical activation and of the accompanying absorption of atmospheric carbon dioxide on the selectivity of dissolution of components of mixed oxides was studied. The mechanical activation results in a decrease in the selectivity of separation of elements in treatment of the mixed oxides with nitric acid solutions. Presumably, this is due to formation of precursors of binary perovskite-like oxides in mechanical activation. It was established for the example of lanthanum and erbium oxides that a preliminary mechanical activation of a mixture of starting oxides noticeably lowers the temperature of $LaErO_3$ formation in heat treatment.

ACKNOWLEDGMENTS

The authors are grateful to V.V. Boldyreva and A.A. Politova for helpful discussions.

This study was financially supported by the Russian Foundation for Basic Research (project no. 03-03-32077a).

REFERENCES

1. Kalinkina, E.V., Kalinkin, A.M., Forsling, W., and Makarov, V.N., *Int. J. Miner. Process.*, 2001, vol. 61, no. 4, pp. 273–299.
2. Kalinkin, A.M., Politov, A.A., Boldyrev, V.V., *et al., Int. J. Miner. Process.*, 2001, vol. 378, no. 2, pp. 233–237.

3. Kalinkin, A.M., Kalinkina, E.V., and Makarov, V.N., *Int. J. Miner. Process.*, 2003, vol. 69, no. 1–4, pp. 143–155.
4. Serebrennikov, V.V. and Alekseenko, L.A., *Kurs khimii redkozemel'nykh elementov* (Course of the Chemistry of Rare-Earth Elements), Tomsk: Tomsk Univ., 1963.
5. Alvero, L., Odriozola, J.A., Trillo, J.M., and Bernal, S., *J. Chem. Soc. Dalton Trans.*, 1984, no. 1, pp. 87–91.
6. Caro, P. and Lemaitre-Blaise, M., *C. R. Acad. Sc. C.*, 1969, vol. 269, pp. 687–690.
7. Zubova, N.V., Makarov, V.M., Nikol'skii, V.D., *et al.*, *Zh. Neorg. Khim.*, 1968, vol. 13, no. 1, pp. 15–19.
8. Glushkova, V.B. and Suglobov, D.N., *Zh. Strukt. Khim.*, 1965, vol. 6, no. 6, pp. 837–842.
9. Little, L.H., *Infrared Spectra of Adsorbed Species*, London: Academic, 1966.
10. Nakamoto, K., *Infrared and Raman Spectra of Inorganic and Coordination Compounds*, New York: Wiley, 1986.
11. Urban, M.W. and Cornilsen, B.C., *J. Phys. Chem. Solids.*, 1987, vol. 48, no. 5, pp. 475–479.
12. Batsanov, S.S., Grigorjeva, G.N., and Sokolova, N.P., *Zh. Strukt. Khim.*, 1962, vol. 3, no. 3, pp. 339–342.
13. Nakamoto, K., Fujita, J., Tanaka, S., and Kobayashi, M., *J. Am. Chem. Soc.*, 1957, vol. 79, no. 18, pp. 4904–4908.
14. Filippova, A.A., Davydov, A.A., Shchekochikhin, Yu.M., *Kinet. Katal.*, 1973, vol. 14, no. 5, pp. 1333–1335.
15. Komissarova, L.N., Shatskii, V.M., Pushkina, G.J., *et al.*, *Soedineniya redkozemel'nykh elementov: Karbonaty, oksalaty, nitraty, titananty* (Compounds of Rare-Earth Elements: Carbonates, Oxalates, Nitrates, Titanates), Moscow: Nauka, 1984.
16. Charles, R.G., *J. Inorg. Nucl. Chem.*, 1965, vol. 27, no. 7, pp. 1489–1493.
17. Turcotte, R.P., Sawyer, J.O., and Eyring, L.R., *Inorg. Chem.*, 1969, vol. 8, no. 2, pp. 238–246.
18. Caro, P.E., Sawyer, J.O., and Eyring, L.R., *Spectrochim. Acta*, 1972, vol. 28A, no. 6, pp. 1167–1173.
19. Peterson, E.J., Onsott, E.I., and Bowman, M.G., *The Rare Earths in Modern Science and Technology*, McCarthy, G.J. and Rhyne, J.J., Eds., New York: Plenum, 1978, pp. 245–251.
20. Nagashima, K., Wakita, H., and Mochizuki, A., *Bull. Chem. Soc. Japan*, 1973, vol. 46, no. 1, pp. 152–156.
21. Luiz, J.M., Matos, J.R., and Ionashiro, M., *Thermochim. Acta*, 1995, vol. 254, pp. 209–218.
22. Busca, G. and Lorenzelli, V., *Materials Chem.*, 1982, vol. 7, no. 1, pp. 89–126.
23. Petru, F., Kutek, F., and Satava, J., *Collect. Czech. Chem. Comm.*, 1966, vol. 31, no. 11, pp. 4459–1462.
24. Loginova, V.E., Dvornikova, L.M., Loginov, V.I., and Bol'shakov, A.F., *Izv. Vyssh. Uchebn. Zaved., Khim. Khim. Tekhnol.*, 1972, vol. 15, no. 10, pp. 1441–1447.
25. Muller-Buschbaum, H. and Graebner, P.H., *Z. Anorg. Allg. Chem.*, 1971, vol. 386, no. 2, pp. 158–162.
26. Arsen'ev, P.A., Kovba, L.M., Bagdasarov, H.S., *et al.*, *Soedineniya redkozemel'nykh elementov: Sistemy s oksidami elementov I–III grupp* (Compounds of Rare-Earth Elements: Systems with Oxides of the Elements of I–III Groups), Moscow: Nauka, 1983.
27. Petrosyan, A.G., Pedrini, K., Shirinyan, G.O., *et al.*, *Neorg. Mater.*, 1999, vol. 35, no. 8, pp. 949–952.
28. Mi, G., Murakami, Y., Shindo, D., and Saito, F., *Powder Technol.*, 1999, vol. 104, no. 1, pp. 75–79.
29. Avvakumov, E.G. and Pushnyakova, V.A., *Khim. Tekhnol.*, 2002, no. 5, pp. 6–17.

Russian Journal of Applied Chemistry, Vol. 77, No. 10, 2004, pp. 1606–1608. Translated from Zhurnal Prikladnoi Khimii, Vol. 77, No. 10, 2004, pp. 1618–1620.

INORGANIC SYNTHESIS AND INDUSTRIAL INORGANIC CHEMISTRY

Interaction of Tri-*n*-butyl Phosphate, Water, and Phosphoric Acid in Purification of Wet-Process Phosphoric Acid

V. M. Lembrikov, L. V. Konyakhina, V. V. Volkova, M. V. Lobova, and O. V. Pokidova

Voskresensk Research Institute for Fertilizers and Phosphoric Acid, Joint-Stock Company, Voskresensk, Moscow oblast, Russia

Received April 22, 2004; in final form, August 4, 2004

Abstract—The material balance of water, phosphoric acid, and tri-*n*-butyl phosphate in the real process of purification of wet-process phosphoric acid by TBP extraction was studied. A process mechanism was suggested.

One of the methods for purification of wet-process phosphoric acid (WPPA) is extraction with tri-*n*-butyl phosphate (TBP). At the Voskresensk Institute of Fertilizers and Phosphoric Acid, Joint-Stock Company, a pilot plant for production of purified phosphoric acid PPA from WPPA by tributyl phosphate (TBP) extraction in pulse columns have been operating for more than eight years. Its daily output capacity was brought to 50–55 tons of P_2O_5 [2]. In this study, we examined the mechanism of water transfer with the extractant from the back-extraction column to the extraction stage. To our knowledge, there is no information on this mechanism in the literature. The process flowsheet is presented below. The material balance was determined from the process parameters measured during seven workdays. This balance appeared to be typical of extraction systems.

Comparison of the sums of the input (G_{WPPA} + G_{H_2O}) and output (G_{raf} + $G_{pur.\,acid}$) aqueous flow rates in the system reveals that the difference between them is 173.9 kg h^{-1}, the major part of the debalance (163 kg h^{-1}) being accounted for by water. It follows from an analysis of the operation of the unit that this amount of water is evaporated from the column in the course of back extraction, since this stage is performed at 52–55°C, which causes high water vapor pressure in the top part of the column.

Furthermore, measurements of the WPPA input flow and raffinate flow output from the bottom of the extraction column show that the amount of water input to the column with WPPA (1455.1 kg h^{-1}) is considerably smaller (by 321.7 kg h^{-1}) than that removed from the column with the raffinate. As a result, a more dilute raffinate (26.89% recalculated for P_2O_5) is formed instead of the estimated 30.3%.

At the same time, in determining the rate of the water flow fed into to the column for back extraction, it was found that the amount of water entering the top part of the column (G_{H_2O} = 2980 kg h^{-1}) exceeds by 484.7 kg h^{-1} that necessary for formation of 5447.3 kg h^{-1} of purified phosphoric acid. It was demonstrated that 163 kg h^{-1} is evaporated from the column. It is evident then that the remaining 321.7 kg h^{-1} should enter the first extraction column.

Therefore, it follows from the analysis of the material balance that about 5% of water entering the column is evaporated from it, and the rest (about 11%) passes to the extraction stage and then is removed from the system with the raffinate flow.

To verify this assumption, we analyzed the extract passing to back extraction, and also the extractant passing to the extraction column, for the content of water, using the Fischer titration method [GOST (State Standard) 14 870–77]. Additionally, we analyzed the extract and extractant for H_3PO_4 by potentiometric titration [3]. The results are listed in the table.

The results obtained allowed estimation of the amount of water circulating in the system with the extract and extractant flows: 968 kg h^{-1} passes to the column with the extractant and 739 kg h^{-1}, i.e., an amount smaller by 229 kg h^{-1}, is removed with the extract. According to our estimates (see table), the composition of the extract can be represented as $(C_4H_9O)_3PO \cdot 0.89H_2O \cdot$

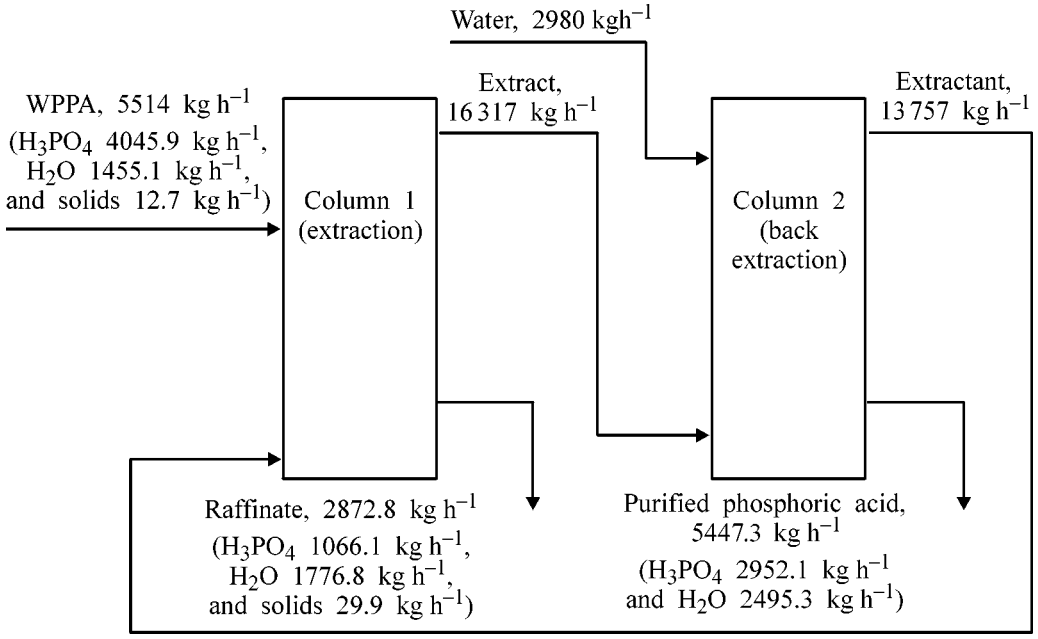

Flowsheet of the pilot plant for production of purified phosphoric acid from WPPA by TBP extraction.

$0.73H_3PO_4$, and that of the extractant, as $(C_4H_9O)_3PO \cdot 1.15H_2O \cdot 0.08H_3PO_4$. Therefore, the extraction/back extraction cycle can be described by Eq. (1).

$$100TBP \cdot 115H_2O \cdot 8H_3PO_4 + 65H_3PO_4 \rightleftarrows 100TBP \cdot 89H_2O \cdot 73H_3PO_4 + 26H_2O. \quad (1)$$

It is of interest to compare the results of our measurements with published data on interactions between TBP, H_3PO_4, and H_2O. According to Higgins and Baldwin [4], the water concentration in these phases is 5 and 9%, respectively, at an H_3PO_4 concentration in the extract and extractant of 20.22 and 2.75%.

Characteristics of the organic flows circulating in the process

Extract				Extractant				Molar ratio					
ρ, g cm^{-3}	content, wt %			ρ, g cm^{-3}	content, wt %			extract			extractant		
	H_3PO_4	H_2O	TBP		H_3PO_4	H_2O	TBP	TBP	H_2O	H_3PO_4	TBP	H_2O	H_3PO_4
1.087	19.28	4.14	76.58	0.996	2.90	6.27	90.83	1	0.80	0.68	1	1.02	0.09
1.0984	20.15	4.57	75.28	0.995	2.84	7.54	89.62	1	0.90	0.73	1	1.24	0.09
1.095	20.34	4.57	75.09	0.994	2.65	7.2	90.15	1	0.90	0.74	1	1.18	0.08
1.101	21.18	4.52	74.30	0.993	2.37	6.84	90.79	1	0.90	0.77	1	1.11	0.07
1.097	20.69	4.61	74.70	0.993	2.51	7.46	90.03	1	0.91	0.75	1	1.23	0.08
1.098	20.92	4.35	74.73	0.996	2.91	7.16	89.93	1	0.86	0.76	1	1.18	0.09
1.096	20.51	4.94	74.55	0.997	3.16	6.81	90.03	1	0.98	0.75	1	1.12	0.10
1.094	20.27	4.72	75.01	0.994	2.73	7.6	89.67	1	0.93	0.73	1	1.25	0.08
1.103	21.90	4.4	73.70	0.993	2.61	7.74	89.65	1	0.88	0.81	1	1.28	0.08
1.086	18.66	4.57	76.77	0.994	2.87	7.07	90.06	1	0.88	0.66	1	1.16	0.09
1.082	18.27	4.66	77.07	0.994	2.70	6.95	90.35	1	0.89	0.64	1	1.14	0.08
1.103	21.76	4.11	74.13	0.993	2.44	6.63	90.93	1	0.82	0.80	1	1.08	0.07
1.086	18.99	4.37	76.64	0.994	2.82	5.91	91.27	1	0.84	0.67	1	0.96	0.08
Mean values:													
1.094	20.22	4.53	75.26	0.994	2.75	7.04	90.21	1	0.89	0.73	1	1.15	0.08

Therefore, in the system TBP–H_2O–H_3PO_4 with the content of H_3PO_4 and water equal to 20.22 and 5% and 2.75 and 9%, the hydrosolvates $(C_4H_9O)_3PO \cdot 0.99H_2O \cdot 0.72H_3PO_4$ and $(C_4H_9O)_3PO \cdot 1.51H_2O \cdot 0.08H_3PO_4$ are, respectively, formed. Therefore, the interaction in the TBP–H_2O–H_3PO_4 system can be described by Eq. (2).

$$100\text{TBP} \cdot 151H_2O \cdot 8H_3PO_4 + 64H_3PO_4 \rightleftarrows 100\text{TBP} \cdot 99H_2O \cdot 72H_3PO_4 + 52H_2O. \quad (2)$$

According to [4], 440 kg h^{-1} of water should be transferred with the organic phase from the back-extraction column to the extraction column, which slightly exceeds the amount determined in our study. The cited data were obtained at 25°C, while our results correspond to the actual process temperature (40–50°C), which, most likely, causes the observed discrepancy.

In conclusion, our determinations of the water content in the organic phases by means of Fischer titration allowed a more precise estimation of the water balance in the system. The transfer of water from one column to another, i.e., from the organic phase to the raffinate, was interpreted in terms of the hydration-solvation mechanism.

REFERENCES

1. Lembrikov, V.M., Konyakhina, L.V., Nikitin, V.G., and Volkova, V.V., *Khim. Tekhnol.*, 2004, no. 8, pp. 4–8.
2. RF Patent 2075436.
3. Skornyakova, R.A., Konyakhina, L.V., and Tokmakova, T.V., *Otechestvennyi proizvodstvennyi opyt: Metody analiza i kontrolya proizvodstva: Ekspress-informatsiya* (Domestic Industrial Experience: Methods for Analysis and Control of Industrial Processes: Express Information): Moscow: NIITEKhim, 1985, no. 6, pp. 20–22.
4. Higgins, C.E. and Baldwin, W.H., *J. Inorg. Chem.*, 1962, vol. 24, pp. 415–427.

Russian Journal of Applied Chemistry, Vol. 77, No. 10, 2004, pp. 1609–1612. Translated from Zhurnal Prikladnoi Khimii, Vol. 77, No. 10, 2004, pp. 1621–1624.

INORGANIC SYNTHESIS AND INDUSTRIAL INORGANIC CHEMISTRY

Indium-Tin Oxide Films Obtained from Solutions Based on Acetylacetone

S. A. Kuznetsova, T. D. Malinovskaya, E. S. Zaitseva, and V. I. Sachkov

Tomsk State University, Tomsk, Russia

Siberian Physicotechnical Institute, Tomsk, Russia

Received July 21, 2003; in final form, August 2004

Abstract—The influence exerted by the composition of film-forming solutions based on acetylacetone on the electrical and optical properties of indium-tin oxide films obtained from these solutions by the dip-coating process was revealed.

Films composed of indium oxide with addition of tin(IV) have a high electrical conductivity and, at the same time, remain transparent in the visible spectral range [1]. Thanks to these properties, these films find wide use in optoelectronics and solar power engineering. One of promising methods for obtaining In_2O_3–Sn coatings, especially on large-area articles, is the dip-coating process (drawing from solution). However, the wide variety of film-forming solutions (FFS) and the scarcity of data on the influence of the FFS composition on the physicochemical characteristics of In_2O_3–Sn films make necessary research in this area.

EXPERIMENTAL

The aim of this study was to reveal the influence of the FFS composition on the electrical and optical properties of indium-tin oxide films.

The FFS were prepared by dissolving acetylacetone (Hacac) and a salt, $InCl_3$, $SnCl_2 \cdot 2H_2O$, or $SnCl_4$, in 96% ethanol. The solutions were kept in a thermostat at 333 K for 1 h. In order to analyze the effect of Hacac concentration and FFS acidity on the properties of the films obtained, a set of alcoholic solutions with c_{Hacac} in the range from 0 to 0.72 M and c_{HCl} of 0 to 0.2 M were prepared. The starting components of all the FFS are listed in Table 1.

The composition of all the FFS was studied by IR and UV spectroscopies. The IR spectra were measured on an IKS-29 spectrophotometer in the frequency range 400–4200 cm^{-1}, and the UV spectra, on an SF-20 instrument at 220–340 nm. The film-forming capacity of all the solutions was evaluated by their viscosity. The viscosity was measured at a temperature of 298 K on a VPZh-2 viscometer with a capillary diameter of 0.73 and 0.99 mm. The measurement error was 0.07 $mm^2\ s^{-1}$.

In_2O_3–Sn(II, IV) films were obtained on glass substrates by drawing from FFS at a rate of 2 $mm\ s^{-1}$. The thermal treatment of the samples was carried out in a muffle furnace at 873 K. The resistance and transparency of the films was determined with a VK7-9 voltmeter in a two-probe circuit and with an IKS-3 spectrophotometer, respectively.

The absorption bands in the IR spectra of FFS nos. 3 and 5 and of the initial Hacac are listed in Table 2. The IR spectrum of Hacac contains a set of

Table 1. Initial composition of alcoholic FFS

FFS no.	Composition	c_{HCl}/c_{Hacac}, M
1	$InCl_3$–$SnCl_2 \cdot 2H_2O$–Hacac–HCl	0.20/0.71
2	$InCl_3$–$SnCl_2 \cdot 2H_2O$–Hacac–HCl	0.25/0.71
3	$InCl_3$–$SnCl_4$–Hacac–HCl	0.00/0.71
4	$InCl_3$–$SnCl_4$–Hacac–HCl	0.01/0.71
5	$InCl_3$–$SnCl_4$–Hacac–HCl	0.03/0.71
6	$InCl_3$–$SnCl_4$–Hacac–HCl	0.05/0.71
7	$InCl_3$–$SnCl_4$–Hacac–HCl	0.10/0.71
8	$InCl_3$–$SnCl_4$–Hacac–HCl	0.20/0.71
9	$InCl_3$–$SnCl_2 \cdot 2H_2O$–Hacac–HCl	0.20/0.00
10	$InCl_3$–$SnCl_2 \cdot 2H_2O$–Hacac–HCl	0.20/0.18
11	$InCl_3$–$SnCl_2 \cdot 2H_2O$–Hacac–HCl	0.20/0.72
12	$InCl_3$–$SnCl_4$–Hacac	0.00/0.00
13	$InCl_3$–$SnCl_4$–Hacac	0.00/0.18
14	$InCl_3$–$SnCl_4$–Hacac	0.00/0.72

1070-4272/04/7710-1609 © 2004 MAIK "Nauka/Interperiodica"

Table 2. Absorption bands in IR spectra of Hacac, Hacac in an acidified solution of C_2H_5OH, FFS no. 3, and FFS no. 5

Assignment of frequencies	ν, cm^{-1}			
	Hacac	Hacac in C_2H_5OH	FFS no. 3	FFS no. 5
(O–H)	–	3560–2750	3315	3300
–CO–C=C–OH	–	–	–	–
(C=O)	1735	1680	1646	1652
(C–O) + (C–C) enol ring	1514	1560	1534	1543
(C–CH_3) + (C–C)	1310	1280	–	1254
(C–O–H), (CH_3)	1399	–	1091	1097, 1062
(C–C) + (C–O)	1197	937	1053	900
π(C–H)	812	845	891	795
Ring deformation	–	–	793, 658	667
In–O	–	–	510	510
(–C–CH_3)	–	–	461	466

absorption bands that is characteristic of β-diketones [2, 3]. The absorption band at 1735 cm^{-1} points to the presence of a ketone form of Hacac, and the absorption bands at 1514, 1399, and 812 cm^{-1} indicate the existence of a enolic form of Hacac. The IR spectra of FFS nos. 3 and 5 also contain a set of absorption bands that characterizes the keto–enol equilibrium of Hacac. However, these bands are shifted to lower frequencies, compared with the absorption bands of Hacac and Hacac in a 96% ethanol solution. This can be attributed to the influence of the solvent C_2H_5OH and formation of complex species by In(III) and Hacac. In contrast to the IR spectrum of Hacac, the IR spectra of FFS nos. 3 and 5 show absorption at around 510 cm^{-1}, which is associated with vibrations of the In–O bond [4]. It can be seen from Table 2 that an increase in acidity affects vibrations of the ketone and enol groups of Hacac. The absorption bands ν(C=O) and ν[(C–O) + (C–C)] are shifted to higher frequencies. In addition, the intensity of the ν(C=O) band increases. This fact indicates that the equilibrium is shifted toward ketolization of Hacac when the concentration of HCl in FFS becomes higher.

The UV transmission spectrum of FFS no. 5 contains one broad absorption band at λ = 270–275 nm, associated with π–π^* transitions in Hacac. According to published data [5], this region characterizes the keto–enol equilibrium in Hacac, with the enol form of Hacac being undissociated. To the dissociated enol form of Hacac corresponds the absorption band at 290 nm in the UV spectral range [6].

According to the whole set of experimental data, complex ions constituted by In(III) and of the ketone and undissociated enol forms Hacac exist in alcoholic FFS in $[In(Hacac)_3]^{3+}$. The existence of $[SnHacac]^{3+}$ in acidified solutions of ethanol has been established previously [7].

The values of the kinematic viscosity of all the FFS $(1.10–2.35) \pm 0.04$ $mm^2\ s^{-1}$ confirm their film-forming capacity [8]. During the first 15 days, the viscosity of FFS does not reach a constant value. The run of the viscosity-vs.-time curves is about the same for all the FFS, which indicates that similar processes (hydrolysis, polycondensation, changes in the orientation of solvent molecules) occur in alcoholic solutions of complex compounds of Sn(II, IV) and In(III). An increase in the acidity of FFS from pH 2 to pH 0.7 results in that the viscosity grows from 1.83 to 2.00 $mm^2\ s^{-1}$. This is, possibly, due to a rise in the rate of polycondensation of hydrolyzed complex ions of Sn(II, IV) and In(III). A more structured FFS is formed. An increase in the content of Hacac in FFS to 0.72 M results in that the viscosity of the solutions decreases from 2.35 to 1.83 $mm^2\ s^{-1}$. This fact can be accounted for by a decrease in the degree of hydrolysis of complex species of Sn(II, IV) and In(III), which occurs because the content of ethanol falls as the concentration of Hacac increases. As FFS with a higher acidity and lower content of Hacac have a relatively high viscosity, more porous films must be formed from these FFS under the same conditions because of the hindrance to removal of products of FFS decomposition from the oxide skeleton. Analysis of the surface resistance *R* and transmittance *T* of the films (Table 3) obtained from these FFS confirms

Table 3. Properties of In_2O_3–Sn(II, IV) films (12 at. %) obtained from FFS of various compositions

FFS no.	1		8		2		9		12		10		13	
Number of layers	*R*, kΩ	*T*, %	*R*, kΩ	*T*, %	*R*, kΩ	*T*, %	*R*, kΩ	*T*, %	*R*, kΩ	*T*, %	*R*, kΩ	*T*, %	*R*, kΩ	*T*, %
1	>10 000	–	>10 000	–	>10 000	–	80–100	–	>10 000	–	50–100	–	>10 000	–
2	50–20	–	10	–	500	–	10–100	–	>10 000	–	20–70	–	>10 000	–
3	0.1–0.5	86.9	1–1.5	81.4	0.03–0.6	81.4	11–12	86.4	>10 000	86.5	5–10	85.0	2000	86.7

Table 4. Physical properties of In_2O_3–Sn(II, IV) films (12 at. %) obtained from acetylacetone FFS

FFS no.	$InCl_3$–$SnCl_2$ thermostat		$In(NO_3)_3$–$SnCl_2$ thermostat/reflux		$InCl_3$–$SnCl_4$ thermostat/reflux		$In(NO_3)_3$–$SnCl_4$ thermostat	
	R, kΩ	*T*, %	*R*, kΩ	*T*, %	*R*, kΩ	*T*, %	*R*, kΩ	*T*, %
1	10–20	92	120/10–20	88/92	60–140/80–90	97/99	70–120	98
2	2.5–3	–	1.5–2/2.5–3	–	6–11/1.5–1.6	–	10–80	–
3	1–2	86	2/1–2	80/81	1.5–4/0.7–0.8	92/94	29/50	94
4	0.7–0.9	–	0.8–1.5/0.7–0.9	–	0.8–1/0.5–0.6	–	9–11	–
5	0.5–0.6	–	0.7–1.1/0.5–0.6	–	1/0.35–0.45	–	4–5	–
6	0.5–0.6	75	0.5–0.9/0.5–0.6	72/74	0.4–1/0.3–0.4	89/90	1.8–3	91

this assumption. As the acidity of FFS with Sn(II) or Sn(IV) increases, the resistance of the films obtained grows (the structure becomes more defective) and their transmittance decreases. In can also be seen from Table 3, that films obtained from FFS based on $SnCl_4$ are rather transparent (86.5 and 86.7%), but their resistance at this transparency exceeds 100 MΩ and 2000 kΩ, respectively. At the same time, films obtained from FFS based on $SnCl_2$ have a resistance of 11–12 and 5–10 kΩ at a transparence of 86.4 and 85.0%, respectively. This fact can be understood as follows: SnO is formed as an intermediate product in preparing oxide films from FFS based on Sn(II); this intermediate is involved at 380–1073 K in a disproportionation reaction, which yields SnO_2 and Sn [9]. An admixture of metallic Sn makes the conductivity of a film higher, and its transparence, lower. Because FFS with addition of Sn(IV) and high content of Hacac is to be used for obtaining films with lower resistance and high transparence, further study was aimed to prepare films from an FFS in which Hacac is both an organic ligand and a solvent.

The FFS was prepared by dissolving the salts $SnCl_2 \cdot 2H_2O$, or $SnCl_4$, $In(NO_3)_3 \cdot 4H_2O$, or $InCl_3$ in Hacac at 333 K in a thermostat or with a reflux condenser. The viscosity of these FFS reaches a constant value in 5 to 6 days and then remains constant for a long time. This enables a prolonged use of the solution for obtaining films with the same properties, in contrast to alcoholic FFS.

An analysis of the absorption bands in IR spectra of Hacac kept at 333 K with a reflux condenser and of FFS prepared from Hacac–In(III)–Sn(IV) at 333 K in a thermostat and with a reflux (see figure) demonstrated that complexation of In(III) in a Hacac solution is only observed after heating the FFS with a reflux condenser to red-brown color. Presumably, the rate of complexation of In(III) with ketone and undissociated enol forms of Hacac increases because the FFS passes into the gas phase.

Films were prepared from these FFS and the properties of these films were studied (Table 4). As can be seen from Table 4, the surface resistance of In_2O_3–Sn(II, IV) films prepared from FFS kept at 333 K with a reflux condenser (complex ions exist in these FFS) is more uniform over the surface. The presence of the complex of indium(III) with Hacac in the FFS with Sn(IV) leads to formation of uniform films because of the better adhesion of the π-system on the surface of the cyclic enol form of the complex ion with the glass surface [10], compared with the solvated In^{3+} ion. As the number of layers deposited on the substrate grows, the surface resistance *R* of the films decreases. According to published data [11], the crystallites in a film grow in size, and, simultaneously, the charge carrier concentration increases as the films become thicker. The oxidation state of tin in an FFS affects the properties of the films, whereas the nature

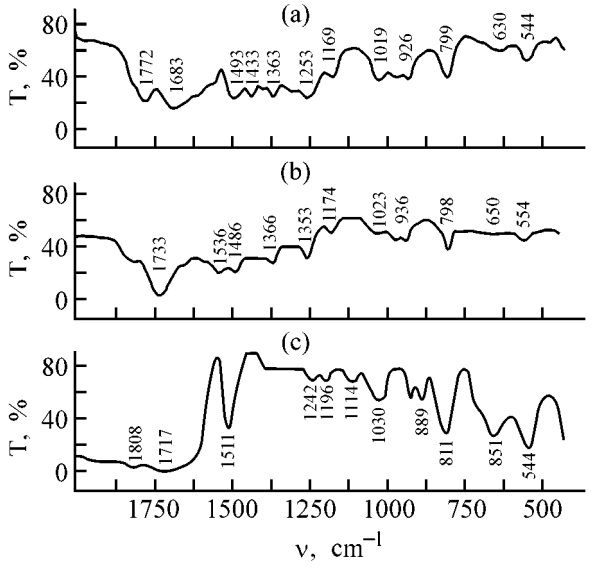

IR absorption spectra of (c) Hacac kept at 333 K with a reflux, (b) Hacac–In(III)–Sn(IV) kept at 333 K in a thermostat, and (a) Hacac–In(III)–Sn(IV) kept at 333 K with a reflux. (T) Transmission and (ν) wave number.

of the salt anion does not exert any significant influence. Films with a lower resistance are formed from Sn(II)-based FFS; however, the transparence of these films in the visible spectral range is lower than that of films obtained in FFS based on Sn(IV). A similar behavior was observed for films prepared from alcoholic solutions.

CONCLUSION

The influence exerted by the acidity, composition (concentration of acetylacetone and ethanol, oxidation state of tin), and thermal treatment of film-forming solutions on the electrical and optical properties of indium-tin oxide films was established. To obtain films with a relatively low resistance ($\leq$0.3 kΩ) and high transparence (up to 91%), it is necessary to use acetylacetone FFS prepared from Sn(IV), $In(NO_3)_3$, and $InCl_3$ and kept at 333 K with a reflux.

REFERENCES

1. Qiang Wei, Haixing Zheng, and Yjhing Hyang, *Solar Energy and Solar Cells*, 2001, vol. 68, pp. 383–390.
2. Nakamoto, K., *Infrared and Raman Spectra of Inorganic and coordination compounds*, New York: John Wiley & Sons, 1986. Translated under the title *IK spektry i spektry KR neorganicheskikh i koordinatsionnykh soedinenii*, Moscow: Mir, 1991, pp. 287–297.
3. Kostromina, N.A. and Salo, N.I., *Problemy khimii i primeneniya β-diketonatov metallov* (Problems of Chemistry and Use of β-Diketonatesof Metals), Moscow: Nauka, 1982, pp. 31–38.
4. Plotnikov, N.V., Kondratov, O.I., Petrov, K.I., and Olivkov, I.I., *Zh. Neorg. Khim.*, 1980, vol. 25, no. 7, pp. 1758–1764.
5. Kazitsina, L.A. and Kupletskaya, N.B., *Primenenie UF, IK i YaMR spektroskopii v organicheskoi khimii* (Use of UV, IR, and NMR Spectroscopies in Organic Chemistry), Moscow: Vysshaya Shkola, 1971.
6. Neiland, O.E. Stradyn', Ya.P., *et al.*, *Stroenie i tautomernye prevrashcheniya β-dikarbonil'nykh soedinenii* (Structure and Tautomeric Transformations of β-Dicarbonyl Compounds), Riga: Zinoine, 1991, pp. 171–174.
7. Kuznetsova, S.A., Skorik, N.A., and Kozik, V.V., *Zh. Prikl. Khim.*, 2000, vol. 73, no. 5, pp. 840–842.
8. Suikovskaya, N.V., *Khimicheskie metody polucheniya tonkikh prozrachnykh plenok* (Chemical Methods for Obtaining Thin Transparent Films), Leningrad: Khimiya, 1971.
9. Evstrop'ev, K.S., Kuznetsov, A.Ya., and Kruglova, A.V., *Opt.-Mekh. Prom–st.*, 1957, no. 2, p. 53.
10. Zandberg, E.Ya., Nezdyurov, A.L., Paleev, V.I., and Ponomarev, D.A., *Izv. Akad. Nauk, Ser. Fiz.*, 1994, vol. 58, no. 10, pp. 186–190.
11. Vaisfel'd, N.M., Sokolina, V.A., and Fialkovskaya, R.P., *Neorg. Mater.*, 1969, vol. 5, pp. 2095–2098.

Russian Journal of Applied Chemistry, Vol. 77, No. 10, 2004, pp. 1613–1617. Translated from Zhurnal Prikladnoi Khimii, Vol. 77, No. 10, 2004, pp. 1625–1629.

INORGANIC SYNTHESIS AND INDUSTRIAL INORGANIC CHEMISTRY

Extraction of Indium(III) from Sulfate Solutions with Organophosphorus Acids

V. F. Travkin, V. L. Kubasov, Yu. M. Glubokov, N. S. Busygina, L. A. Kazanbaev, and P. A. Kozlov

Lomonosov Institute of Fine Chemical Technology, Moscow, Russia
GINTsVETMET Institute, Federal State Unitary Enterprise, Moscow, Russia
Chelyabinsk Zinc Works, Open Joint-Stock Company, Chelyabinsk, Russia

Received February 9, 2004; in final form, July 29, 2004

Abstract—Extraction of indium(III) from sulfuric acid solutions with di-2-ethylhexyl hydrogen phosphate and isododecylphosphethanic and diisooctylphosphinic acids was studied. The effect of H_2SO_4 and In(III) concentrations in the aqueous phase, type and concentration of the extractant in the organic phase, temperature, and time of phase contact on the extraction of In(III) and impurity metal ions was considered. The In(III) extraction constants were estimated.

Extraction is widely used for recovering and concentrating In(III) from multicomponent process solutions [1–3]. Di-2-ethylhexyl hydrogen phosphate (HDEHP) is usually used as an extractant [2–6], although it exhibits poor selectivity. Along with In(III), HDEHP recovers Ga(III), Fe(III), Sb(III), and any other multicharged metal ions. In addition, the extraction with HDEHP has a slow kinetics and is often irreversible. Backwashing is performed with strong backwashing agents, such as HCl, H_2SO_4 + HCl, H_3PO_4, and $H_2C_2O_4$. Effective ways to eliminate the above disadvantages are sought for. Certain authors suggest to use, instead of pure HDEHP, its mixtures with monocarboxylic acids [7–10] or alkylamines [8]. In this case, a certain improvement of the backwashing conditions due to a decrease in the concentration of chloride ions in the backwashing solution is accompanied by a noticeable worsening of In(III) recovery and separation. Other researchers look for a better extractant than HDEHP [2, 11–13]. Such an extractant, while preserving HDEHP advantages, should ensure selective extraction of In(III) under milder conditions. Presumably, phosphinic acids, which are weaked than HDEHP, should meet the above requirements.

In this study, we examined the possibility of using isododecylphosphetanic (HIDDP) and diisooctylphosphinic (HDiOP) acids for In(III) extractive recovery from weakly acidic sulfate solutions.

EXPERIMENTAL

The In(III) sulfuric acid solutions were prepared by dissolution of metallic indium in aqueous H_2SO_4. They contained about 50 g l^{-1} In(III) and 290–320 g l^{-1} H_2SO_4. Less concentrated solutions were prepared by dilution of the initial solution with chemically pure sulfuric acid and distilled water. Such solutions contained 1–1.7 g l^{-1} In(III) and 9–14 g l^{-1} H_2SO_4, which corresponded to the composition of the process solutions of zinc production used for In(III) recovery.

Preliminarily purified HDEHP, HDiOP, and HIDDP (RH) were used as extractants. The content of the main substance in these acids was no less than 96 wt %. As a rule, 20 vol % solutions of these acids in kerosene were used. The dependence of the extraction on the extractant concentration was studied within the 5–30 vol % extractant content in kerosene. The above solutions were prepared by dilution of the extractants with dearomatizated kerosene. The main properties of the extractants are described in [14, 15].

The extraction and backwashing were performed in separating funnels. A mechanical shaker was used for phase mixing. For extraction, phases (unless otherwise indicated) were brought in contact once for 15 min at $20 \pm 1°C$ and 1 : 1 volume ratio of the aqueous to organic phase. After mixing, the phases were separated

1070-4272/04/7710-1613 © 2004 MAIK "Nauka/Interperiodica"

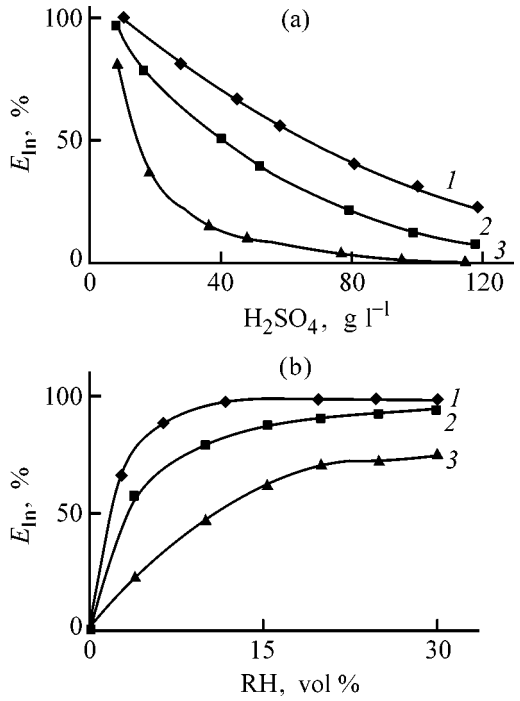

Fig. 1. Influence of the (a) H_2SO_4 concentration and (b) concentration of organophosphorus acids in kerosene on In(III) extraction E_{In}. Extractant: (*1*) HDEHP, (*2*) HIDDP, and (*3*) HDiOP; the same for Fig. 2.

by centrifuging. The initial and equilibrium aqueous phases were analyzed. The content of the metal ions and H_2SO_4 in the organic phase was found as the difference between their contents in the initial solutions and equilibrated aqueous phases, small changes in the phase volumes being neglected. A direct analysis of the backwashing solutions confirmed the validity of this procedure.

The effect of H_2SO_4 concentration in the aqueous phase, extractant concentration in the organic phase, time of phase contact, and temperature on In(III) extraction was studied. These parameters are the most important in evaluation of the process feasibility and in hardware design.

The In(III) extraction with phosphorus-containing acids proceeds by the cationexchange mechanism with the release of H_3O^+. Hence, the acidity of the aqueous phase should substantially affect the extraction.

It follows from the data obtained (Fig. 1a) that In(III) is well recovered from solutions containing approximately 10 g l^{-1} H_2SO_4: to 90–95% with HDEHP and HIDDP and to 70% with HDiOP. The recovery decreases as the acid concentration increases. The recovery of In(III) is virtually complete (>90%) with HDEHP and HIDDP at H_2SO_4 concentrations of up to 110 and 16 g l^{-1}, respectively.

As a rule, raising the extractant concentration leads to an increase in the metal ion recovery, but, at the same time, to a decrease in the rate of phase separation, which makes it necessary to use larger reactors, and, accordingly, a greater amount of the initially charged extractant.

The In(III) recovery is satisfactory with 20 vol % solutions of HDEHP and HIDDP and 30 vol % solution of HDiOP in kerosene (Fig. 1b). At extractant concentrations exceeding 30%, the phase separation substantially decelerates.

It is known that the extraction of M(III) ions, e.g., Fe(III), with HDEHP is slow [16]. Our data on In(III) extraction show that the equilibrium is virtually attained only after phase contact for >10 min (Table 1). The time in which the extraction equilibrium is estab-

Table 1. Effect of time of the phase contact, τ, on In(III) extraction

τ, min	In(III) concentration in equilibrium phases,* g l^{-1}		D**	E,** %	In(III) concentration in equilibrium phases,* g l^{-1}		D**	E,** %
	aqueous	organic			aqueous	organic		
	HDiOP				HIDDP			
1	0.58	0.45	7.8	43.7	0.460	0.70	22.8	50.3
3	0.25	0.78	31.0	76.7	0.038	1.12	40.0	90.7
5	0.22	0.81	37.0	78.6	0.011	1.15	92.7	98.4
10	0.19	0.84	44.0	81.6	0.009	1.15	119	99.2
20	0.15	0.88	59.0	85.4	0.010	1.15	122	99.1

* Initial aqueous phase: In(III) 1–1.2 g l^{-1}, H_2SO_4 11–12 g l^{-1}.

** (*D*) Distribution ratio and (*E*) degree of In(III) recovery.

Table 2. Influence of temperature on In(III) extraction

T, °C	In(III) concentration in equilibrium phases,* g l^{-1}		*D*	*E*, %	*T*, °C	In(III) concentration in equilibrium phases,* g l^{-1}		*D*	*E*, %	*T*, °C	In(III) concentration in equilibrium phases,* g l^{-1}		*D*	*E*, %
	aqueous	organic				aqueous	organic				aqueous	organic		
	HDiOP					HIDDP					HDEHP			
19	0.22	0.81	3.7	75.2	15	0.13	1.12	8.6	89.6	21	0.004	1.096	274	99.3
32	0.18	0.85	4.7	82.5	15	0.14	1.14	7.9	89.0	32	0.004	1.096	274	99.3
40	0.15	0.88	5.9	85.4	32	0.14	1.16	8.3	89.2	40	0.003	1.097	365	99.5
49	0.14	0.89	6.4	86.4	47	0.12	1.13	9.4	90.4	52	0.002	1.098	549	99.6

* Initial aqueous phase: In(III) 1–1.2 g l^{-1}, H_2SO_4 9–11 g l^{-1}.

Table 3. Distribution ratios of impurity metal ions

Extractant	Distribution ratio*							
	Fe(II)	Zn(II)	Cd(II)	Cu(II)	Ni(II)	Co(II)	As(III)	Sb(III)
HDEHP	0.01	0.01	0.02	0.01	0.01	0.01	<0.01	0.03
HIDDP	<0.01	<0.01	0.01	<0.01	<0.01	<0.01	<0.01	0.02
HDiOP	<0.01	<0.01	0.01	<0.01	<0.01	<0.01	<0.01	0.01

* Initial aqueous phase: M(II, III) 1 g l^{-1}, H_2SO_4 10 g l^{-1}.

lished depends on the type of the extractant and shortens as the organophosphorus acid strength increases, in the order HDiOP < HIDDP < HDEHP.

The temperature can strongly affect the extraction through the structure of the extractable complexes. For instance, heating improves the Co(II) recovery but does not affect the Ni(II) extraction with organophosphorus acids.

Varying of the temperature within the 20–40°C range does not noticeably affect the In(III) recovery. At higher temperatures, the extraction somewhat increases (Table 2).

The extraction isotherms obtained with feed solutions containing 1 to 15 g l^{-1} In(III) are shown in Fig. 2. As can be seen, the metal ion is recovered with HDEHP and HIDDP with a high distribution ratio providing a complete recovery up to a metal concentration in the aqueous phase of approximately 13 g l^{-1}. In the process, unsaturated extracts are formed. Thus, it is feasible to concentrate In(III) in the extraction step.

The process solutions contain, in addition to the target metal ion, In(III), such impurities as Fe(III), Fe(II), Zn(II), Cu(II), Ni(II), Cd(II), Co(II), Sb(III), etc. These ions mainly occur in the solution in the form of hydrated and partially hydrolyzed cations, and their extraction with acid organophosphorus extractants substantially depends on the acidity of the aqueous phase. Our study shows that the above ions are not noticeably recovered from weakly acidic sulfate solutions (Table 3).

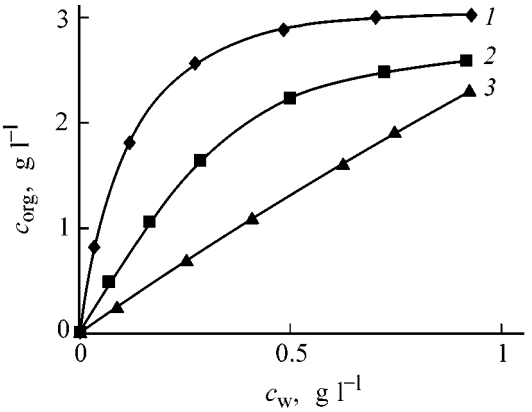

Fig. 2. Isotherms of In(III) extraction from 0.1 M H_2SO_4 with an extractant solution (20 vol %) in kerosene. (c_{org}, c_w) In(III) concentrations in the organic and aqueous phases.

Table 4. Extraction of Fe(III) with solutions of organophosphorus acids*

H_2SO_4, g l^{-1}	Fe(III) distribution ratio		
	HDEHP	HIDDP	HDiOP
5	170	21	17
10	100	9.0	7.2
15	38	5.1	4.0
50	1.0	0.3	0.2
100	0.2	0.1	0.15
150	0.1	0.05	0.03

* $c^0_{Fe(III)}$ = 2.06 g l^{-1}.

Table 5. In(III) backwashing with H_2SO_4 solutions

H_2SO_4 concentration in aqueous phase, g l^{-1}	In(III) concentration in equilibrium phases, g l^{-1}		D	E, %
	aqueous	organic		
HDiOP				
150	0.40	0.56	0.71	42
238	0.67	0.29	2.3	69
301	0.92	0.04	23.0	97
356	0.95	0.01	95.0	99
422	0.95	0.01	95.0	99
HIDDP				
165	0.79	0.32	2.5	72
204	0.91	0.19	4.8	83
252	0.99	0.11	9.0	90
301	1.02	0.08	12.7	93
348	1.04	0.06	17.3	95
HDEHP				
113	0.006	1.069	0.006	0.59
203	0.014	1.061	0.013	1.28
296	0.007	1.068	0.007	0.69
424	0.022	1.053	0.021	2.06

The most difficult-to-remove metal ion is Fe(III). Its distribution depends on the H_2SO_4 concentration (Table 4).

Thus, the recovery of admixtures, including Fe(III), increases in the order HDiOP < HIDDP < HDEHP.

The In(III) backwashing from the organic phase is an important factor in the assessment of the feasibility of using HDiOP and HIDDP as indium extractants. Table 5 shows that indium can be efficiently backwashed from an extract with 250–350 g l^{-1} H_2SO_4 solutions (without adding HCl), which is a substantial advantage over the system with HDEHP. This makes it possible to recommend HDiOP and HIDDP for extractive recovery and purification of In(III).

The mechanism of In(III) extraction from sulfuric acid solutions with HDEHP was considered in [13, 14]. With HDiOP and HIDDP, the mechanism is apparently similar:

$$In^{3+}_{(w)} + 3(RH)_{2(org)} \rightarrow InR_3 \cdot 3HR_{(org)} + 3H^+_{(w)},$$

where RH is HDEHP, HIDDP, and HDiOP.

Then, the extraction constant is given by

$$K = \frac{D_{In}[H^+]_{(w)} \cdot 2^3}{[(RH)_2]^3_{(org)}},$$

$$\log K = \log D_{In} + 3\log[H^+]_{(w)} + \log 8 - 3\log[(RH)_2]_{(org)}$$
$$= \log D_{In} + b,$$

where $b = 3\log[H^+]_{(w)} + \log 8 - 3\log[(RH)_2]_{(o)}$ is constant for all the extractants under the same conditions of the extraction.

This equation allows estimation of the extraction constants for different extractants at its known value for any one of these. From the data on the In(III) distribution between 0.1 M aqueous H_2SO_4 solution and 0.25 M RH solution in kerosene, we obtained the following extraction constants, K ($D_{In(III)}$): HDEHP 6.5×10^5 (99) [17], HIDDP 1.48×10^4 (2.45), and HDiOP 7.9×10^3 (1.31).

Taking into account the above results and the necessity for minimizing the alteration of the existing process scheme of In(III) recovery from sulfuric acid solution of zinc production, we can recommend the following basic operations:

(1) Fe(III) reduction to Fe(II);

(2) In(III) extraction with 20–30 vol % solutions of HIDDP or HDiOP in kerosene from sulfuric acid solutions containing Zn(II);

(3) Scrubbing of the organic phase with a 5–10 g l^{-1} aqueous solution of H_2SO_4;

(4) In(III) backwashing with H_2SO_4 (250–350 g l^{-1});

(5) In(III) recovery from backwashes by the existing process.

The basic process parameters of the process suggested for In(III) extractive recovery and concentration from sulfuric acid solutions are as follows:

Extraction

H_2SO_4 content in the aqueous phase	10–20 g l^{-1}
HIDDP or HDiOP concentration in kerosene	30 vol %
Organic-to-aqueous phase volume ratio (org : w)	1 : (1–2)
Time of phase contact	≥15 min
Temperature	20–40°C

Scrubbing of the organic phase

H_2SO_4 content in the scrubbing solution	5–10 g l^{-1}
org : w ratio	(10–15) : 1
Time of phase contact	10 min
Temperature	20–40°C

In(III) backwashing from the organic phase

H_2SO_4 content in the backwashing solution	350–400 g l^{-1}
org : w ratio	(10–15) : 1
Time of phase contact	≥10 min
Temperature	20–40°C

CONCLUSIONS

(1) A study of extraction of In(III) and concomitant metal ions with organophosphorus acids showed that HIDDP or HDiOP can be used instead of HDEHP as extractants for selective recovery and concentration of In(III), provided that Fe(III) is preliminarily reduced to Fe(II) and separated.

(2) The In(III) recovery increases in the order HDiOP < HIDDP < HDEHP. An increase in H_2SO_4 concentration in the aqueous phase leads to a decrease in the extraction of In(III).

(3) In(III) can be completely recovered from the resulting extracts by treatment with 2.5–3.5 M solutions of H_2SO_4.

REFERENCES

1. Fedorov, P.I. and Akchurin, R.Kh., *Indii* (Indium), Moscow: Nauka, 2000.
2. Paiva, A.P., *Sep. Sci. Technol.*, 2001, vol. 36, no. 7, pp. 1395–1419.
3. Sato, T. and Sato K., *Hydrometallurgy*, 1992, vol. 30, pp. 367–383.
4. Mihaelov, I. and Distin, P.A., *Hydrometallurgy: Overview*, 1992, vol. 28, pp. 13–27.
5. Lee, M.S., Ahn, J.G., and Lee, E.C.K., *Hydrometallurgy*, 2002, vol. 63, pp. 269–276.
6. Nishihana, S., Hino, F., and Hirai, N., *Ind. Eng. Chem. Res.*, 1999, vol. 38, pp. 1032–1039.
7. Judd, J.C.S. and Harbruck, D.D., *Sep. Sci. Technol.*, 1990, vol. 25, nos. 13–15, pp. 1641–1653.
8. Pashkov, G.L., Mikhnev, A.D., Kulmukhamedov, G.K., *et al., Tsvetn. Met.*, 1992, no. 2, pp. 44–45.
9. Kazanbaev, L.A., Pashkov, G.L., Kulmukhamedov, G.K., *et al., Izv. Vyssh. Uchebn. Zaved., Tsvetn. Met.*, 2002, no. 4, pp. 15–20.
10. Khol'kin, A.I., *Khim. Tekhnol.*, 2000, no. 9, pp. 41–47.
11. Inoe, R., Baba, Y., and Yoshizuka, K., *Hydrometallurgy*, 1992, vol. 29, pp. 393–399.
12. Sholi, K. and Saburo, K., *J. Min. Met. Inst. Jpn.*, 1998, no. 1207, pp. 601–605.
13. Rodriguez, M.A., Cote, G., and Bauer, D., *Solvent Extr. Ion Exch.*, 1992, vol. 10, no. 5, pp. 811–827.
14. Travkin, V.F., Kubasov, V.L., and Kotukhov, S.B., *Zh. Prikl. Khim.*, 1992, vol. 65, no. 7, pp. 1502–1509.
15. Devi, N.B., Nathsarma, K.C., and Chakravortty, V., *Hydrometallurgy*, 1998, vol. 48, no. 3, pp. 47–61.
16. Golinski, M., *Przem. Chem.*, 1973, vol. 52, no. 7, pp. 507–510.
17. Levin, I.S., Vorsina, I.A., and Azarenko, T.G., *Izv. Sib. Otd. Akad. Nauk SSSR*, 1967, vol. 12, no. 5, pp. 24–34.

Russian Journal of Applied Chemistry, Vol. 77, No. 10, 2004, pp. 1618–1622. Translated from Zhurnal Prikladnoi Khimii, Vol. 77, No. 10, 2004, pp. 1630–1633.

INORGANIC SYNTHESIS AND INDUSTRIAL INORGANIC CHEMISTRY

Thermodynamics of Cerium(III) Extraction with Naphthenic Acids

D. E. Chirkst, T. E. Litvinova, P. N. Devyatkin, and I. T. Zhadovskii

St. Petersburg State Mining Institute, St. Petersburg, Russia

Received February 25, 2004

Abstract—Cerium(III) extraction from dilute aqueous solutions with naphthenic acids in decane was studied. The dependence of the distribution ratio on the pH of the equilibrium aqueous phase was determined, and the extraction equilibrium constant and Gibbs energy were calculated.

The steady rise in the industrial demand for individual lanthanide and yttrium metals and for their pure compounds requires that lean raw materials [1], including eudialyte ore concentrate of the Kola peninsula, should be involved in the processing; however, the known procedures for recovery and separation of lanthanides by extraction with tributyl phosphate from nitrate solutions have low separation coefficients, 1.1–1.5 [2, 3]. Therefore, multiple repetitions of the extraction–backwashing cycles and too large expenditures for the equipment and chemicals are required. This stimulates a search for hydrometallurgical systems that would ensure higher distribution and separation coefficients of lanthanides. This search is based on a thermodynamic simulation and study of the extraction mechanisms. In this study, we examined the extraction of cerium(III) from dilute aqueous solutions simulating the composition of filtrates from acid leaching of eudialyte concentrates.

The initial aqueous solutions contained approximately 0.65 g l^{-1} Ce(III); the precise concentration was found photometrically. A 0.5 N naphthenic acid solution in decane was used as an extractant. The naphthenic acid was prepared by distillation of technical-grade Acidol-1 from Baku petroleum refinery at 165–190°C and a residual pressure of 5–7 mm Hg. The average molar weight of this fraction was 226 g mol^{-1} and the concentration, 4.4 M. In accordance with elemental analysis, the mean formula of the acid is $C_{13}H_{27}COOH$, and mean pK_a, 5.1 [4]. The pH of the aqueous phase was ajusted with NaOH and HCl solutions and monitored with a pH-150M pH-meter with a combined electrode. Chemically pure chemicals were used. The Ce(III) concentration was determined photometrically (λ 670 nm) on a KFK-3 photocolorimeter with Arsenazo III in an acetate buffer solution with pH 3 [5].

The cerium(III) content in the organic phase was determined as a difference between the Ce(III) concentrations in the initial and equilibrium aqueous phases with regard to the difference in the phase weights:

$$c_{org} = (c_0 - c_w)\frac{m_w}{m_{org}}, \quad (1)$$

where c_{org} is the equilibrium concentration of the metal in the organic phase (mol kg^{-1}); c_w, Ce(III) concentration in the equilibrium aqueous phase (mol kg^{-1}); c_0, initial content of cerium in the aqueous phase (mol kg^{-1}); and m_w/m_{org}, ratio of weights of the aqueous and organic phases (30 : 1 in our experiments).

The distribution ratio was calculated by the formula

$$D = c_{org}/c_w.$$

The liquid extraction of cerium(III) with the naphthenic acid solution in decane was studied within the pH 3–6.5 range (see scheme).

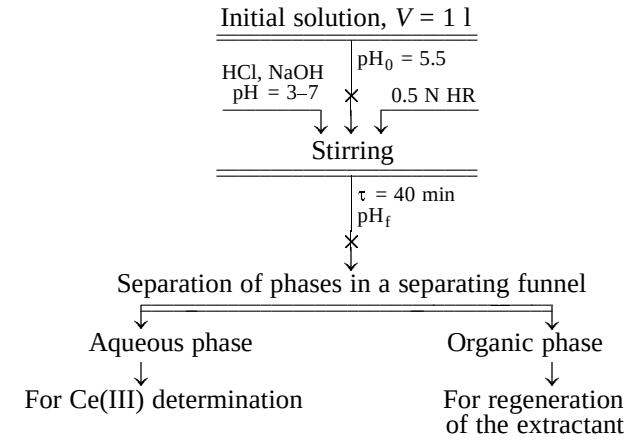

Scheme of the experiments on cerium(III) extraction.

1070-4272/04/7710-1618 © 2004 MAIK "Nauka/Interperiodica"

Table 1. Characteristics of cerium(III) extraction with a 0.5 M solution of naphthenic acid in decane at various equilibrium pH of the aqueous phase

Solution	pH	Ce(III) g l^{-1}	ε,* at indicated HR expenditure (with a 20% excess), mol mol^{-1} Ce(III)	
			2.4	3.6
Initial	3.0	0.652	–	–
Aqueous phase after phase separation		0.652** / 0.652	0	0
Initial	4.0	0.652	–	–
Aqueous phase after phase separation		0.652 / 0.652	0	0
Initial	5.0–5.1	0.648	–	–
Aqueous phase after phase separation		0.172 / 0.352	45.7	73.5
Initial	5.25	0.652	–	–
Aqueous phase after phase separation		0.212 / 0.378	42.0	67.5
Initial	6.0	0.648	–	–
Aqueous phase after phase separation		0.486 / 0.575	11.0	25.0
Initial	7.0	0.648	–	–
Aqueous phase after phase separation		0.648 / 0.648	0	0

* ε is the degree of Ce(III) recovery into the organic phase.

** Data for the HR expenditure of 3.6 and 2.4 mol mol^{-1} Ce(III) are given in the numerator and denominator, respectively.

The experiments were performed at various pH values and various expenditures of the naphthenic acid: at the expenditure equivalent to formation of neutral cerium(III) naphthenate in the extract, i.e., 3.6 mol of naphthenic acid per mole of cerium (20% excess), and at expenditure of 2.4 mol of naphthenic acid per mole of cerium, which corresponds to formation of basic cerium naphthenate. In the first case, an excess amount of free naphthenic acid was present, and in the second case, the acid was in deficiency and was fully bound into the solvate complex in the organic phase. Raisinh the pH to above 6.0 is not appropriate because of the precipitation of cerium(III) hydroxide, which begins at pH values close to 6 and is substantial at pH 6.5.

The experimental data are listed in Table 1. The dependence of the Ce(III) recovery into the organic phase on the pH of the equilibrium aqueous phase at various naphthenic acid expenditures is shown in Fig. 1. As can be seen, the maximum distribution ratio of cerium(III), 83.2 (degree of recovery 73.5%), is observed at pH equal to the pK_4 of naphthenic acid, 5.0–5.1. At the deficiency of the naphthenic acid with respect to the stoichiometry, the degree of Ce(III) recovery is lower by a factor of 1.5–2.

The dependences of the logarithm of the distribution ratio on the pH of the equilibrium aqueous phase

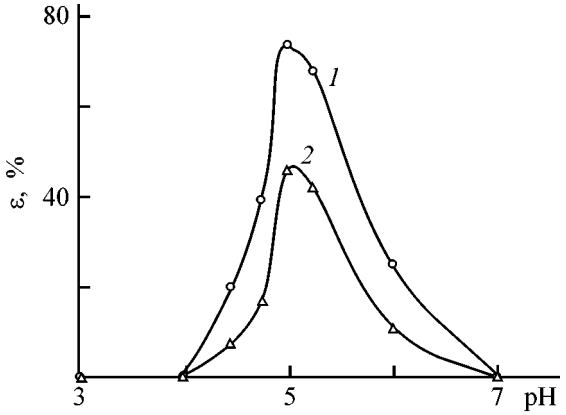

Fig. 1. Effect of pH on the degree of cerium(III) recovery ε. HR expenditure [mol mol^{-1} Ce(III)]: (*1*) 3.6 and (*2*) 2.4.

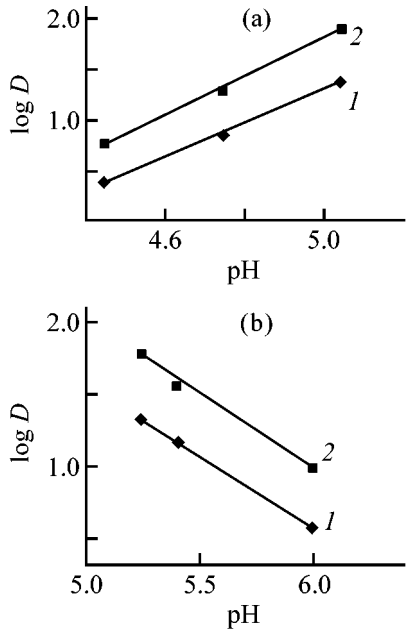

Fig. 2. Logarithm of the cerium(III) distribution ratio D vs. equilibrium pH of the aqueous phase at (a) pH < pK_a and (b) pH > pK_a.

were derived from the data of Table 1 (Figs. 2a, 2b). These dependences are described by the following linear equations with the confidence factors $R^2 > 0.99$:

$$\log D = 1.89\text{pH} - 7.654 \text{ (Fig. 2a, HR : Ce(III) = 3.6)}, \quad (2)$$

$$\log D = 1.67\text{pH} - 7.03 \text{ (Fig. 2a, HR : Ce(III) = 2.4)}, \quad (3)$$

$$\log D = -1.03\text{pH} + 7.16 \text{ (Fig. 2b, HR : Ce(III) = 3.6)}, \quad (4)$$

$$\log D = -1.00\text{pH} + 6.595 \text{ (Fig. 2b, HR : Ce(III) = 2.4)}, \quad (5)$$

It follows from the equation of formation of neutral cerium(III) naphthenate that the slope of these dependences should be 3. The experimental slopes [Eqs. (2)–(5)] are substantially lower, suggesting the extraction of cerium(III) hydroxo naphthenates. Hence, the following equations of extraction can be suggested:

$$\text{Ce(OH)}_{3-z}^{z+}\text{(w)} + z\,\text{HR(org)} \rightleftarrows \text{Ce(OH)}_{3-z}\text{R}_z\text{(org)} + z\,\text{H}^+\text{(w)}, \quad (6)$$

where z is the slope of straight lines described by Eqs. (2)–(5).

At pH < pK_a, this slope is positive, which means that, as the pH value increases, equilibrium (6) is shifted to the right, and at pH > pK_a, the slope is negative, and the equilibrium is shifted to the left. At pH = pK_a, the distribution ratio is at a maximum. The law of mass action for reaction (6) is

$$K = \frac{[\text{Ce(OH)}_{3-z}\text{R}_z\text{(org)}]a_{\text{H}^+}^z}{[\text{Ce(OH)}_{3-z}^{z+}\text{(w)}]\gamma_{z+}[\text{HR}]^z} = \frac{Da_{\text{H}^+}^z}{\gamma_{z+}[\text{HR}]^z}, \quad (7)$$

where the molal concentrations are denoted by brackets and γ_{z+} are the activity coefficients of cerium(III) hydroxo cations, calculated by the Davies equation [6]

$$\log \gamma_{z+} = -0.51z^2\left(\frac{\sqrt{I}}{1+\sqrt{I}} - 0.2I\right), \quad (8)$$

where I is the ionic strength of the solution.

The ionic strength of the aqueous phase was 0.018 ± 0.009 mol kg^{-1}. The calculated logarithms of the activity coefficients are -0.06 ± 0.01 and -0.24 ± 0.04 for $[\text{Ce(OH)}_2]^+$ and $[\text{Ce(OH)}]^{2+}$, respectively. Equations (4) and (5) describe the backwashing $[\text{Ce(OH)}_2]^+$ complexes, and Eqs. (2) and (3), extraction of a mixture of $[\text{Ce(OH)}_2]^+$ and $[\text{Ce(OH)}]^{2+}$ complexes in a 1 : 4 ratio, which is indicated by the slope of 1.8 ± 0.1. Therefore, we used $\log \gamma = -0.20$ in the calculations. For neutral molecules and solvates, the activity coefficients were taken be unity.

The concentration of naphthenic acid in the organic phase at the HR : Ce(III) molar ratio of 3.6 and 2.4 was 0.5 and 0.33 mol kg^{-1}, respectively.

The logarithmic form of Eq. (7) is

$$\log D = \log K + \log \gamma_{z+} + z\log[\text{HR}] + z\,\text{pH}. \quad (9)$$

It corresponds to empirical Eqs. (2) and (3).

The thermodynamic equilibrium constant was calculated from the absolute terms of Eqs. (2), (3) (they were denoted by a):

$$\log K = a - \log \gamma_{z+} - z\log[\text{HR}]. \quad (10)$$

Equations (4) and (5) correspond to the backwashing reaction, whose constant is equal to the reciprocal constant of the direct reaction. Then, we obtain from Eqs. (2) and (4), respectively:

$$\log K = -7.654 + 0.20 - 1.89\log 0.5 = -6.88,$$

$$\log K = -7.16 + 0.06 - \log 0.5 = -6.80.$$

The average value of the extraction constant from two independent empirical dependences is $(1.4 \pm 0.2) \times$

Table 2. Constants and Gibbs energies of cerium salt extraction

Extractant	pH	D	K	ΔG^0_{298}, kJ mol^{-1}
Naphthenic acid [Eq. (11)]	5.1	83.2	623 ± 60	-16.0 ± 0.2
TABAS [8], $c_{MgSO_4} = 2$ mol kg^{-1}	1.6–4	35 ± 4	35 ± 4	-8.9 ± 0.3
TBP [3], $c_{MgSO_4} = 2.5$–3 mol kg^{-1}	3	26.4 ± 0.4	10.9 ± 0.1	-5.92 ± 0.03

10^{-7}. The corresponding Gibbs energy is 39.04 ± 0.2 kJ mol^{-1}. We obtain from Eqs. (3) and (5), respectively:

$$\log K = -7.03 + 0.20 - 1.67 \log 0.33 = -6.03,$$

$$\log K = -6.595 + 0.06 - \log 0.33 = -6.05.$$

The average value of the equilibrium constant is $(9.1 \pm 0.2) \times 10^{-7}$. The corresponding Gibbs energy is 34.47 ± 0.2 kJ mol^{-1}. The difference in the constants and Gibbs energies at an excess and a deficiency of naphthenic acid can be accounted for by different mechanisms of the process. At the acid deficiency, anions of the cerium(III) salt can be incorporated into the solvate. Hereinafter we will use the thermodynamic characteristics obtained at the molar ratio of naphthenic acid to Ce(III) equal to 3.6, i.e., at a 20% excess of the extractant.

Taking into account the independence of the extraction constant and Gibbs energy on z within the range studied, $1 < z < 2$, we can calculate the Gibbs energy of formation of the solvate from simple ions by the reaction

$$Ce^{3+}(w) + (3 - z)OH^-(w) + zR^-(org) \rightleftarrows Ce(OH)_{3-z}R_z(org). \quad (11)$$

Calculations were performed for $z = 2$. The Gibbs energy of solvation is given by

$$\Delta_{solv} G^0_{298} = \Delta_{extr} G^0_{298} + \Delta_{compl} G^0_{298} - \Delta_{dis} G^0_{298}. \quad (12)$$

Formula (12) includes the Gibbs energies of solvation, extraction, formation of the hydroxo complex from Ce^{3+} ions, and dissociation of naphthenic acid, respectively. $\Delta_{compl} G^0_{298}$ was calculated from the reference data [7] to be –25.9 kJ mol^{-1}, and $\Delta_{dis} G^0_{298}$, from the dissociation constant, to be 29.1 kJ mol^{-1}. The Gibbs energy of solvation (from ions), was obtained equal to -16.0 ± 0.2 kJ mol^{-1}. It corresponds to the equilibrium constant of 623 ± 60. Since the maximum distribution coefficient of Ce(III) is 83.2 (this indicates the shift of the equilibrium toward extraction), it is reasonable to use the constant and Gibbs energy of formation of the solvate from simple ions, in accordance with Eq. (11), as the thermodynamic characteristics of the extraction.

The thermodynamic constants of cerium(III) nitrate extraction with neat tri-*n*-butyl phosphate (TBP) [3], 0.5 M solution of naphthenic acid in decane, and extraction of cerium(III) sulfate with a 0.5 M solution of trialkylbenzylammonium sulfate (TABAS) in *o*-xylene [8] are compared in Table 2.

As can be seen, the efficiency of extractants increases in the order TBP < TABAS ≪ naphthenic acid. The extraction with naphthenic acid proceeds without a salting-out agent. This gives an additional benefit and diminishes the pollution of the environment. In addition, TBP was used neat, and TABAS and naphthenic acid, as 0.5 M solutions in organic diluents; also the cost of naphthenic acid is hundreds of times lower than that of TBP and TABAS.

CONCLUSIONS

(1) The distribution ratio in extraction of cerium(III) with a 0.5 M solution of naphthenic acid in decane is at a maximum, 83.2, at pH = pK_a = 5.1 and the molar ratio of naphthenic acid to cerium(III) equal to 3.6. Under these conditions, a mixture of cerium(III) hydroxodinaphthenate and dihydroxonaphtenate at 4 : 1 molar ratio is extracted. The equilibrium constant and Gibbs energy of this process are 623 ± 60 and -16.0 ± 0.2 kJ mol^{-1}, respectively.

(2) The efficiency of extraction increases in the order tributyl phosphate (100%) < 0.5 M solutions of trialkylbenzylammonium salts in *o*-xylene ≪ 0.5 M solution of naphthenic acid in decane.

REFERENCES

1. Lebedev, V.N., Lokshin, E.P., Masloboev, V.A., *et al.*, *Tsvetn. Met.*, 1997, no. 8, pp. 46–51.

2. Masloboev, V.A. and Lebedev, V.N., *Redkozemel'noe syr'e Kol'skogo poluostrova i problemy ego kompleksnoi pererabotki* (Rare-Earth Raw Material of the Kola Peninsula and Problems of Its Integrated Processing), Apatity: Kol'sk. Nauchn. Tsentr Akad. Nauk SSSR, 1991.
3. Cirkst, D.E., Litvinova, T.E., Chistyakov, A.A., and Ionova, M.Yu., *Zh. Prikl. Khim.*, 2004, vol. 77, no. 8, pp. 1430–1434.
4. Devyatkin, P.N., Dibrov, I.A., and Voronin, N.N., *Tsvetn. Met.*, 2003, no. 7, pp. 52–57.
5. Savvin, S.B., *Arsenazo III*, Moscow: Atomizdat, 1966.
6. Vasil'ev, V.P., *Termodinamicheskie svoistva rastvorov electrolitov* (Thermodynamic Properties of Electrolyte Solutions), Moscow: Vysshaya Shkola, 1982.
7. *Termicheskie konstanty veshchestv: Spravochnik* (Thermal Constants of Substances: Reference Book), Glushko, V.P., Ed., Moscow: Akad. Nauk SSSR, 1978, vol. 8.
8. Dibrov, I.A., Chirkst, D.E., and Litvinova, T.E., *Zh. Prikl. Khim.*, 2002, vol. 75, no. 2, pp. 197–201.

Russian Journal of Applied Chemistry, Vol. 77, No. 10, 2004, pp. 1623–1626. Translated from Zhurnal Prikladnoi Khimii, Vol. 77, No. 10, 2004, pp. 1634–1637.

PHYSICOCHEMICAL STUDIES OF SYSTEMS AND PROCESSES

Complexation of Sterically Hindered Cobalt Porphyrin with 1-Methylimidazole along the Axial Coordinate and the Reaction of Reversible Binding of Oxygen

A. B. Valiotti and R. A. Abakumova

St. Petersburg State University, St. Petersburg, Russia

Received December 19, 2003; in final form, June 2004

Abstract—The complexation of a sterically hindered cobalt porphyrin with 1-methyl imidazole and its reaction of reversible binding of oxygen was studied. Spectrophotometry and potentiometry were used to determine the equilibrium constant of the oxygenation process.

In the last decade, methods for synthesis and study of properties of model compounds of natural porphyrins reversibly binding oxygen have been developed successfully. Synthetic oxygen transporting agents of this kind find use as blood substitutes, gas sorbents, and materials for recovery of oxygen from liquid media [1–4].

Monitoring the partial pressure of oxygen in gases, liquids, and semi-liquid media is an important task in most of biochemical investigations and technological processes. It is of indubitable interest, in this context, to develop a potentiometric sensor for measuring the partial pressure on the basis of a redox system that contains cobalt porphyrin and reversibly binds oxygen [5]. A necessary stage in this case is a study of the properties of the cobalt porphyrin.

The goal of this study was to examine the complexation of sterically hindered cobalt(II) meso-tetra(α,α,α,α-*ortho*-pivalamidophenyl)porphyrin [Co(II)TPivPP] with 1-methylimidazole along the axial coordinate and the reaction of reversible binding of oxygen.

EXPERIMENTAL

The meso-tetra(α,α,α,α-*ortho*-pivalamidophenyl)-porphyrin was synthesized by the procedure suggested by Collman [6]. The compound [Co(II)TPivPP] was obtained by heating free porphyrin with $CoCl_2$ in a flow of argon under constant stirring in a solution of tetrahydrofuran [7]. The purity of the products synthesized was verified chromatographically and using spectra. The complexation with 1-methylimidazole was studied spectrophotometrically. In the experiments, the dependence of the optical density of [Co(II)TPivPP] solutions in propyl cyanide on the concentration of 1-methylimidazole was determined at a fixed wavelength and analyzed. Propyl cyanide was chosen as the solvent because it has a sufficiently high dielectric constant (ε = 20.3) and does not react with metal porphyrins. As supporting electrolyte served tetrabutylammonium perchlorate (TBAP), c(TBAP) = 0.1 M. All the measurements were performed in quartz cuvettes of thickness 0.1 and 1.0 cm on an SF-18 spectrophotometer. The titration with a solution of 1-methylimidazole was performed directly in the cuvette. The titrant was added dropwise to a solution of [Co(II)TPivPP] in the atmosphere of argon and a spectrum of the solution was recorded upon each addition. All the measurements were carried out at a temperature of 20 ± 0.5°C. Figure 1 shows the experimental data in the form of a dependence of the optical density $A(\lambda_{532})$ of the [Co(II)TPivPP] solution on the concen-

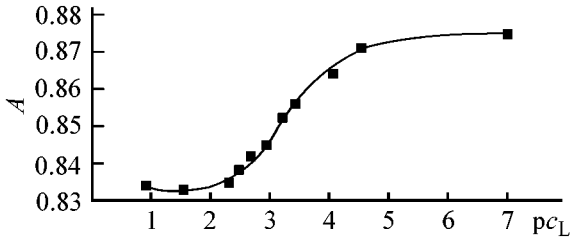

Fig. 1. Optical density A (λ = 532 nm) of the [Co(II)TPivPP] solution vs. the pc_L of 1-methylimidazole.

1070-4272/04/7710-1623 © 2004 MAIK "Nauka/Interperiodica"

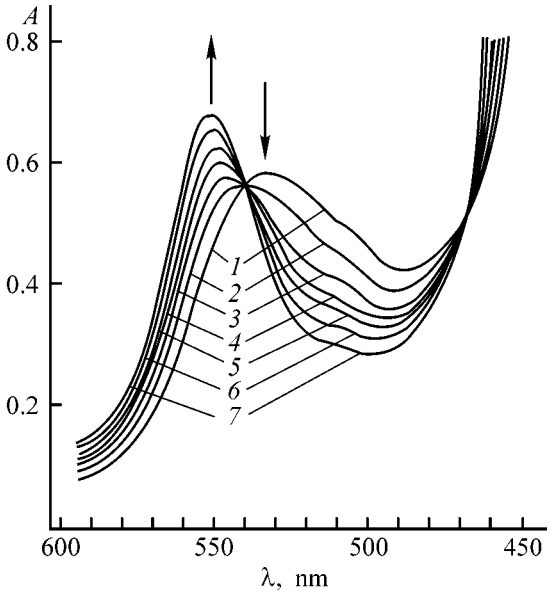

Fig. 2. Spectra of [Co(II)TPivPP] solutions in propyl cyanide in the presence of 1 M of 1-methylimidazole and 0.1 M of TBAP at different partial pressures of oxygen. (*A*) Optical density and (λ) wavelength. P_{O_2} (mm Hg): (*1*) 0, (*2*) 38, (*3*) 84, (*4*) 114, (*5*) 190, (*6*) 380, and (*7*) 760.

tration of 1-methylimidazole (pc_L). The first stage of the reaction of axial complexation of [Co(II)TPivPP] with 1-methylimidazole can be represented as

$$[\text{Co(II)TPivPP}] + \text{L} = [\text{Co(II)TPivPPL}], \quad (1)$$

where L is 1-methylimidazole.

Introduction of 1-methylimidazole into a porphyrin solution leads to a decrease in the optical density at λ = 532 nm. It can be shown, with account of this circumstance, that the dependence of the optical density of the solution on the ligand concentration c_L can be expressed as

$$A = \frac{A_0 + A_1 K_1 c_L}{1 + K_1 c_L}, \quad (2)$$

where A is the optical density measured in the experiment; A_0, optical density of a solution without ligand; A_1, optical density of a solution in which the complexation is complete; and K_1, complexation constant found from the equation

$$K_1 = \frac{[\text{Co(II)TPivPPL}]}{[\text{Co(II)TPivPP}][\text{L}]}.$$

The experimental dependence is described by a smooth single-step curve, which is due to the occurrence of the reaction of 1-methylimidazole addition by Eq. (1). The logarithm of the stability constant for [Co(II)TPivPP] with 1-methylimidazole, calculated by Eq. (2), is 3.3 ± 0.2. The data obtained suggest that, at a 1-methylimidazole concentration of 0.1 M, the complexation in the system constituted by porphyrin and 1-methylimidazole is complete. This result is of primary importance for a study of the reaction in which oxygen is reversibly bound in the presence of 1-methylimidazole.

The reversible binding of O_2 was studied by means of spectrophotometry in a hermetically sealed quartz cuvette. The partial pressure of O_2 was set by mixing argon and oxygen in various volume ratios at 1 atm in calibrated gas meters. Each mixture of gases, preliminarily dried over KOH, was bubbled through the cuvette for 20 min, and the spectrum of the solution was recorded after that. All the measurements were performed at a temperature of 20 ± 0.5°C.

It is known that, in the presence of an axial ligand, 1-methylimidazole, and O_2 in a [Co(II)TPivPP] solution, there exist the equilibrium

$$[\text{Co(II)TPivPPL}] + O_2 \rightleftarrows [\text{Co(II)TPivPPLO}_2], \left(K_{O_2}\right). \quad (3)$$

The fact that logarithm of the stability constant of [Co(II)TPivPP] with 1-methylimidazole has a value of 3.3 ± 0.2 shows that the complex [Co(II)TPivPPL] is formed to an extent exceeding 99% at a 1-methylimidazole concentration of 1 M. To determine K_{O_2}, spectra of a [Co(II)TPivPP] solution in propyl cyanide were recorded in the presence of 0.1 M of 1-methylimidazole and 0.1 M of TBAP at different partial pressures of O_2. Typical changes in the spectrum of a [Co(II)TPivPPL] solution in propyl cyanide in the presence of O_2 are shown in Fig. 2. It can be seen that, as the concentration of O_2 increases, the peak at 534 nm, associated with the deoxygenated form, is shifted to longer wavelengths, and a new peak associated with the oxygenated form appears at 552 nm.

Two clearly pronounced isobestic points are observed at 540 and 470 nm, which points to the presence of two interconvertible species in the solutions. In deoxygenation of the solution by bubbling of argon, the spectrum changes in the opposite direction and virtually coincides with the initial spectrum, i.e., the starting cobalt porphyrin is oxidized only slightly. It should be noted that the oxygenated form Co(II)TPivPPLO_2 and the oxidized species Co(II)TPivPPL^+ have the same spectrum. K_{O_2} was calculated using the Drago equation [6]

$$P_{1/2} = K_{O_2}^{-1} = P_{O_2}\left(\frac{[CoP]_{tot} l \Delta\varepsilon}{\Delta A} - 1\right), \quad (4)$$

where $[CoP]_{tot}$ is the total concentration [Co(II)TPivPP] in solution; l, cuvette thickness; $\Delta\varepsilon$, difference of the absorption coefficients of the oxygenated and deoxygenated species; and ΔA, difference of the optical densities at a certain P_{O_2} and in the absence of oxygen.

This equation is convenient in that it does not require any knowledge of the optical density of the oxygenated form, because the oxygenation is not complete even at P_{O_2} = 1 atm and 0°C. Transformation of Eq. (4) yields

$$P_{O_2} = [CoP]_{tot} l \Delta\varepsilon\left(P_{O_2}/\Delta A\right) - P_{1/2}. \quad (5)$$

The plot of P_{O_2} against $(P_{O_2}/\Delta A)$ is a straight line with a slope equal to $[CoP]_{tot} l \Delta\varepsilon$. This plot (Fig. 3) was used to determine K_{O_2}.

At a temperature of 20 ± 0.5°C in propyl cyanide in the presence of 0.1 M of TBAP, $P_{1.2}$ = 140 ± 7 mm Hg ($K_{O_2} = 7.2 \times 10^{-3}$).

The reversible binding of O_2 was also studied by means of potentiometry and, in particular, by the method of the oxidation potential [8]. The equation for the oxidation potential φ of the system Co(II)TPivPPL–Co(III)TPivPPL$^+$ can be written as

$$\varphi = \varphi^0 + \vartheta \log \frac{[Co(III)TPivPPL^+]}{[Co(II)TPivPPL]}, \quad (6)$$

where $\vartheta = 2.3RT/F$ and the concentrations of the oxidized and reduced forms of the redox system are given in the square brackets.

It was shown preliminarily that the oxidation potential of this system at a 1-methylimidazole concentration $c \geq 0.1$ M is independent of pc_L, which indicates the formation of complexes of the same composition for the oxidized and reduced forms. If reaction (1) is regarded as complexation of Co(II)TPivPPL with O_2, then the material balance equations can be written as

$$c^O = [Co(III)TPivPPL^+],$$

$$c^R = [Co(II)TPivPPL] + [Co(II)TPivPPLO_2]$$

$$= [Co(II)TPivPPL]\left(1 + K_{O_2}P_{O_2}\right), \quad (7)$$

where

$$K_{O_2} = \frac{[Co(II)TPivPPLO_2]}{[Co(II)TPivPPL]P_{O_2}},$$

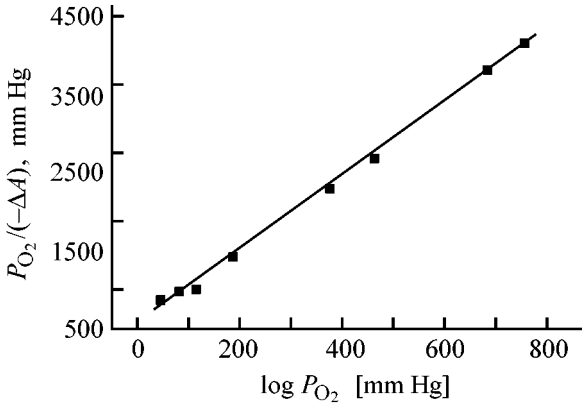

Fig. 3. $P_{O_2}/\Delta A$ vs. the partial pressure of oxygen, P_{O_2}. λ = 530 nm, c(TBAP) = 0.1 M, T = 25°C.

and c^O and c^R are the total concentrations of the oxidized and reduced forms of cobalt porphyrin.

With account of (7), the equation for the oxidation potential is transformed into

$$\varphi = \varphi^0 + \vartheta \log\left(c^O/c^R\right) + \vartheta \log\left(1 + K_{O_2}P_{O_2}\right),$$

and then, at constant concentrations c^O and c^R,

$$\varphi = \varphi_0 + \vartheta \log\left(1 + K_{O_2}P_{O_2}\right), \quad (8)$$

where $\varphi_0 = \varphi^0 + \log\left(c^O/c^R\right)$.

It follows from Eq. (8) that at high P_{O_2}, when $K_{O_2}P_{O_2} >> 1$, the dependence φ–log P_{O_2} must be linear with a slope equal to ϑ.

The experimental study consisted in finding the dependence φ–log P_{O_2}. The oxidation potential was determined by measuring the electromotive force of the galvanic cell Hg | Hg_2Cl_2, LiCl(sat.) || solution under study | Pt.

All the measurements were performed at 25°C. The concentration of 1-methylimidazole was 0.1 M. The ionic strength was maintained with 0.1 M of TBAP. The cobalt porphyrins Co(II)TpivPP and Co(III)TPivPP$^+$ were taken in a 1 : 1 molar ratio.

The experimental dependence E–log P_{O_2} is shown in Fig. 4. The oxidation potential φ is given relative to a saturated calomel electrode. It can be seen that this dependence is represented by a straight line at high P_{O_2}, in agreement with Eq. (8). At P_{O_2} = 0, φ = φ_0. The graphically found φ_0 made it possible to calculate, using Eq. (8), K_{O_2}($K_{O_2} = 1/P_{1/2}$) and, accordingly, $P_{1/2}$. The calculation was performed using the values of P_{O_2} falling within the range in which the dependence φ–log P_{O_2} is linear. The averaged value of

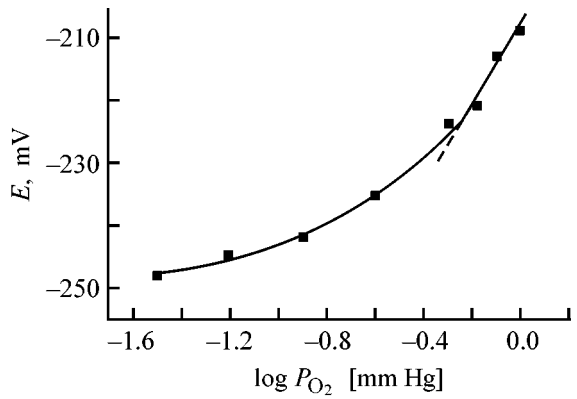

Fig. 4. Oxidation potential E of a solution of the redox system Co(II)TPivPPL–Co(III)TPivPPL$^+$ in propyl cyanide in the presence of 1-methylimidazole (1-MeIm) vs. log P_{O_2}. c(1-MeIm) = 0.1 M, c(TBAP) = 0.1 M, T = 25°C.

$P_{1/2}$ is 160 mm Hg, i.e., the results of spectrophotometric and potentiometric studies are in agreement within the experimental error.

CONCLUSION

The functional dependence of the oxidation potential of the redox system Co(II)TPivPPL–Co(III)TPivPPL$^+$ on the partial pressure of oxygen was determined on the basis of experimental data.

These results can be used to design a potentiometric sensor for molecular oxygen in aqueous solution and to assess the region and limits of its applicability.

REFERENCES

1. Bratushko, Yu.I., *Koordinatsionnye soedineniya 3d-perekhodnykh metallov s molekulyarnym kislorodom* (Coordination Compounds of 3*d*-Transition Metals with Molecular Oxygen), Kiev: Naukova Dumka, 1987.
2. Sokolova, T.A. and Rudkovskaya, G.D., *Zh. Vses. Khim. O–va*, 1976, vol. 21, no. 6, pp. 663–672.
3. Kurtikyan, T.S., Kazaryan, R.K., and Madakyan, V.N., *Izv. Ros. Akad. Nauk, Ser. Khim.*, 2003, no. 2, pp. 377–380.
4. Komatsu Teruyuki, Okado Tomoyuki, Moritake Miho, and Tsuchida Eishhun, *Bull. Chem. Soc. Jap.*, 2001, vol. 74, no. 9, pp. 1695–1702.
5. USSR Patent 1804622.
6. Collman, J.P., Gagne, R.R., Reed, C.A., *et al.*, *J. Am. Chem. Soc.*, 1975, vol. 97, no. 6, pp. 1427–1439.
7. Collman, J.P., Brauman, J.J., Doxsee, K.M., *et al.*, *J. Am. Chem. Soc.*, 1978, vol. 100, no. 9, pp. 2761–2766.
8. *Oksredmetriya* (Redoxmetry), Nikol'skii, B.P. and Pal'chevskii, V.V., Eds., Leningrad: Khimiya, 1975.

Russian Journal of Applied Chemistry, Vol. 77, No. 10, 2004, pp. 1627–1630. Translated from Zhurnal Prikladnoi Khimii, Vol. 77, No. 10, 2004, pp. 1638–1642.

SORPTION AND ION-EXCHANGE PROCESSES

Sorption of Light Fullerenes C_{60} and C_{70} on NORIT-AZO Carbon

K. N. Semenov, V. I. Seregin, O. V. Arapov, and N. A. Charykov

St. Petersburg State University, St. Petersburg, Russia

St. Petersburg State Technological Institute, St. Petersburg, Russia

Received April 29, 2004

Abstract—Sorption of fullerenes C_{60} and C_{70} from *o*-xylene, toluene, and dichlorobenzene solutions on NORIT-AZO carbons was studied.

Fullerenes can be regarded as a new form of hyperconcentrated carbon [1, 2]. Their molecules consist of five- and six-membered carbon rings forming balls. The ratio of hexagons and pentagons is determined by the isolated pentagon rule (IPR). Although the sp^2 orbitals are situated on a spherical surface, the fullerene molecules have a common π-electron system and are similar to aromatic compounds [3].

The fundamental parameters of fullerenes are the electron affinity *EA* and the ionization energy *IE*. For C_{60}, $EA = 2.667 \pm 0.001$ eV and $IE = 7.57 \pm 0.01$ eV [4]. It should be noted that the *EA* of fullerenes is higher than that of aromatic compounds, i.e., fullerenes are relatively strong electron acceptors. Since fullerenes have relatively high *EA* and low *IE*, they can be both donors and acceptors of electrons. In the solid state, C_{60} molecules are bound by van der Waals for us [5].

Isolation of pure fullerenes, i.e., by chromatographic separation of their mixtures is a problem of current interest [6]. The solution of this problem involves a study of fullerene sorption and development and synthesis of new sorbents. There are two types of sorption: physical sorption (van der Waals and electrostatic interactions between the adsorbate and adsorbent) and chemisorption (formation of chemical, usually covalent bonds between the adsorbent and adsorbate).

Apparently fullerenes C_{60} and C_{70} are physically sorbed from the solution on unmodified activated carbon. In this case, the adsorbent–adsorbate interaction is long-range and weak and the enthalpy of sorption is of the same order of magnitude as the enthalpy of condensation. The energy of separation can be transformed into vibrations of the sorbent lattice or released as a heat. Clearly, the first pathway prevails in our case.

The energy of intermolecular interaction consists of orientation, induction, and dispersion components

$$U(r) = U_{or} + U_{ind} + U_{disp}. \quad (1)$$

The dispersion forces are caused by fast fluctuations of the electron density in each atom which induce an electric moment in the nearest neighbor and thereby lead to interaction between atoms. The induction interaction is due to polarization of a molecule in the electrostatic field of another molecule. Since fullerene molecules (especially C_{60}) are relatively difficultly polarized, this interaction is weak. The orientation interactions are caused by permanent dipole moments of molecules. In our case, this interaction is absent, since all unsubstituted fullerene molecules are spheroids or quasiellipsoids of revolution and are nonpolar.

Sorption from solutions is a more complex process than sorption of gases. In this case, not only the force field of the solid phase but also intermolecular interactions in the liquid phase should be taken into account. In addition, sorption from the liquid phase is complicated by the competing sorption of the solvent [7, 8].

In this study, we examined the sorption of fullerenes C_{60} and C_{70} from oxylene, toluene, and dichlorobenzene solutions on NORIT-AZO carbon. This study was encouraged by the possibility of complete chromatographic separation of components of a fullerene mixture [9, 10].

EXPERIMENTAL

We used fullerene C_{60} containing 99.9 wt % main compound (0.1 wt % C_{70}) and C_{70} containing 99 wt %

1070-4272/04/7710-1627 © 2004 MAIK "Nauka/Interperiodica"

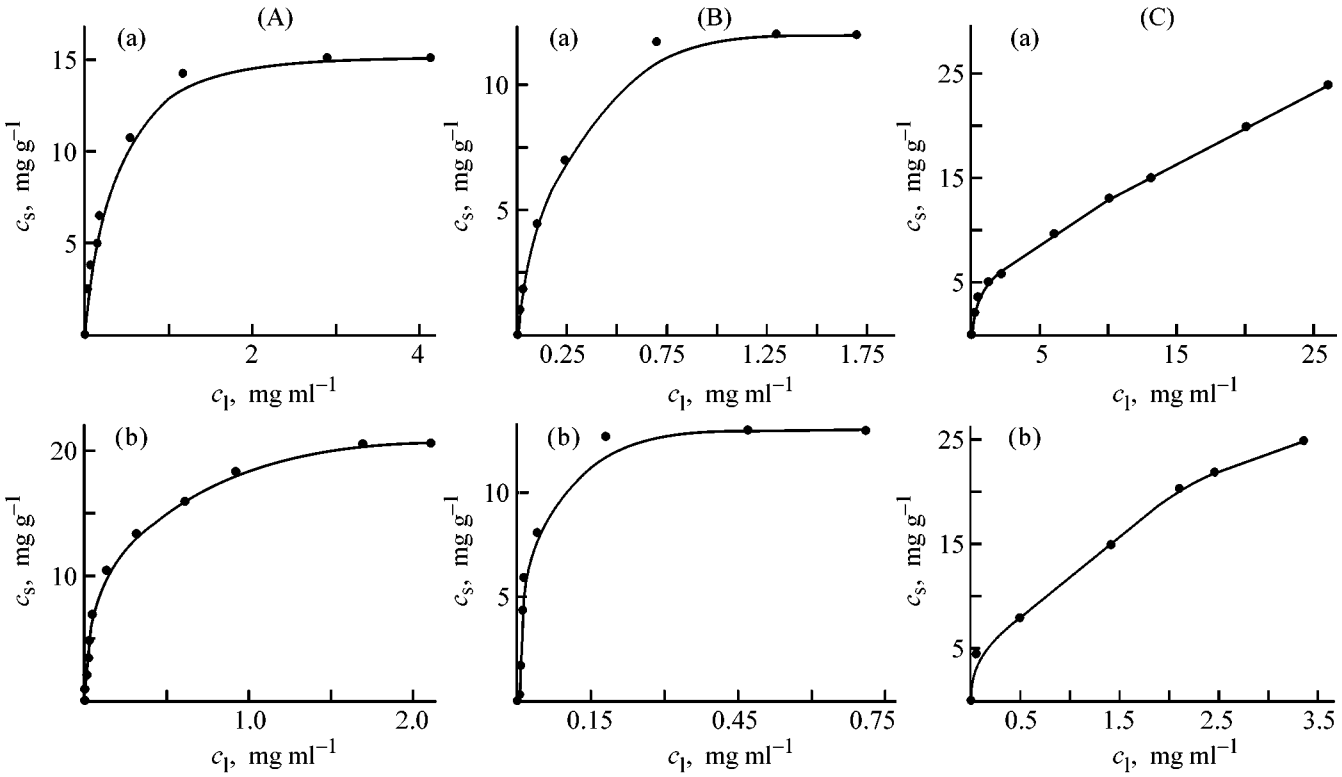

Fig. 1. Isotherms of adsorption of (a) C_{60} and (b) C_{70} from (A) *o*-xylene, (B) toluene, and (C) *o*-dichlorobenzene on NORIT-AZO carbon at 25°C. Sorbent weight $m \sim 1$ g, solution volume $V \sim 10$ ml. (c_s, c_l) Fullerene concentrations in the solid and liquid phases, respectively.

main compound (1 wt % C_{60}) (ILIP Joint-Stock Company). *o*-Xylene, *o*-dichlorobenzene, and toluene were of analytically pure grade. NORIT-AZO carbon (average grane size of the main fraction 75–90 μm, specific surface area ~250 m^2 g^{-1}).

To study the sorption properties of the carbon, concentrated stock solutions of the fullerenes in the above solvents were prepared by isothermal saturation at 25°C for 24 h. The concentration of C_{60} and C_{70} in *o*-xylene, toluene, and *o*-dichlorobenzene was 4.1 and 2.3, 1.3 and 0.46, and 26 and 3.3 g l^{-1}, respectively. Less concentrated solutions in all of these solvents were prepared by successive dilutions.

To weighed portions of the carbon (1 g) predried at 150°C for 3 h, 10 ml aliquots of the fullerene solutions of different concentrations were added. The mixture was magnetically stirred for 3 days at 25°C. This time is required for an equilibrium to be attained in the carbon–solution system. The mixture was filtered through a Schott filter (porosity 16) to remove the sorbent, and the fullerene content in the resulting solution was determined.

The content of C_{60} and C_{70} in the solutions before and after the sorption was determined spectrophotometrically on an SF-46 spectrophotometer operating at λ = 335.5 and 472.0 nm [11]. The concentrations were calculated by the following equations:

$$c(C_{60}) = 13.10(D_{335} - 1.808D_{472}), \quad (2)$$

$$c(C_{70}) = 42.51(D_{472} - 0.00810D_{335}), \quad (3)$$

where D_{335} and D_{472} are the optical densities of a 1-cm layer of the solution; $c(C_{60})$ and $c(C_{70})$ are the fullerene concentrations (g l^{-1}) [11].

The isotherms of fullerene sorption from *o*-xylene, toluene, and dichlorobenzene on ZORIT-AZO carbon are shown in Figs. 1A–1B.

In all the cases, except with *o*-dichlorobenzene solutions, the sorption isotherms exibit a sharp increase in sorption in the fist steps and smoother adsoption growth with further increase in the fullerene concentration in the solution. At fullerene concentrations $c < 0.1$ g l^{-1}, the slopes of the initial portions of the isotherms are approximately equal for both fullerenes, both in toluene and in *o*-xylene, and differences appear at higher concentrations.

It should be noted that the isotherms measured in toluene level of at lower fullerene concentration than the isotherms measured in *o*-xylene. The saturation of sorption isotherms in toluene is due to the physical sorption without specific adsorbate–adsorbent interactions. In *o*-dichlorobenzene, the sorbent is not saturated because of chemical interactions at high fullerene concentrations. In this case, fullerene association in the solution [19, 20] or layer-by-layer condensation of fullerenes on the sorbent surface is possible.

All sorption isotherms measured in toluene and *o*-xylene are of Langmuir type. This is not the case for *o*-dichlorobenzene solutions.

It should also be noted that adsorption of fullerenes depends on their solubility [12]. It is known [13, 14] that fullerenes dissolve by the cluster mechanism. Aggregation of fullerenes in a solution affects their thermodynamic parameters. As a result, the phase equilibrium is shifted and the fullerene solubility changes [15]. Fullerenes are almost insoluble in polar solvents [16]. The solubility of a fullerene is the highest if the ratio of the enthalpy of vaporization of the solvent to the volume of the solvent molecule is close to the similar ratio for the fullerene. The solubility of C_{60} and C_{70} in *o*-xylene, toluene, and *o*-dichlorobenzene at 25°C is 8.7 and 14.3, 2.8 and 1.4, and 27.0 and 36.2 g l^{-1}, respectively.

The effect of solubility on the sorption isotherms can be estimated by the height of the plateau (Figs. 1A–1C), which, in turn, characterizes the static sorption capacity of the carbon for the fullerenes. As can be seen from Figs. 1A–1C, the static sorption capacity for C_{60} and C_{70} in *o*-xylene, toluene, and *o*-dichlorobenzene (milligrams of fullerene per 1 g of the sorbent) is 15.5 and 21.3, 14.1 and 14.3, and >24 and >25, respectively. In *o*-xylene, the sorption capacity does not level off (Fig. 1C). These sorption capacities are appreciably higher than those of carbon sorbents studied previously [17–20].

The dependence of the distribution coefficients of C_{60} and C_{70} between NORIT-AZO carbon and *o*-xylene, toluene, and *o*-dichlorobenzene on the fullerene concentration in the liquid phase at 25°C is shown in Figs. 2a and 2b. The error of determination of the fullerene concentration in the solution and in the solid phase is 3 and 5 rel%, respectively. Hence, the determination error of the distribution coefficients is about 6 rel. %.

As can be seen from Figs. 2a and 2b, the distribution coefficients are only slightly dependent on the solvent (the curves almost coincide). The only difference is observed in dilute *o*-dichlorobenzene solution of C_{60}. In all cases, the distribution coefficients monotonically decreases with increasing fullerene concen-

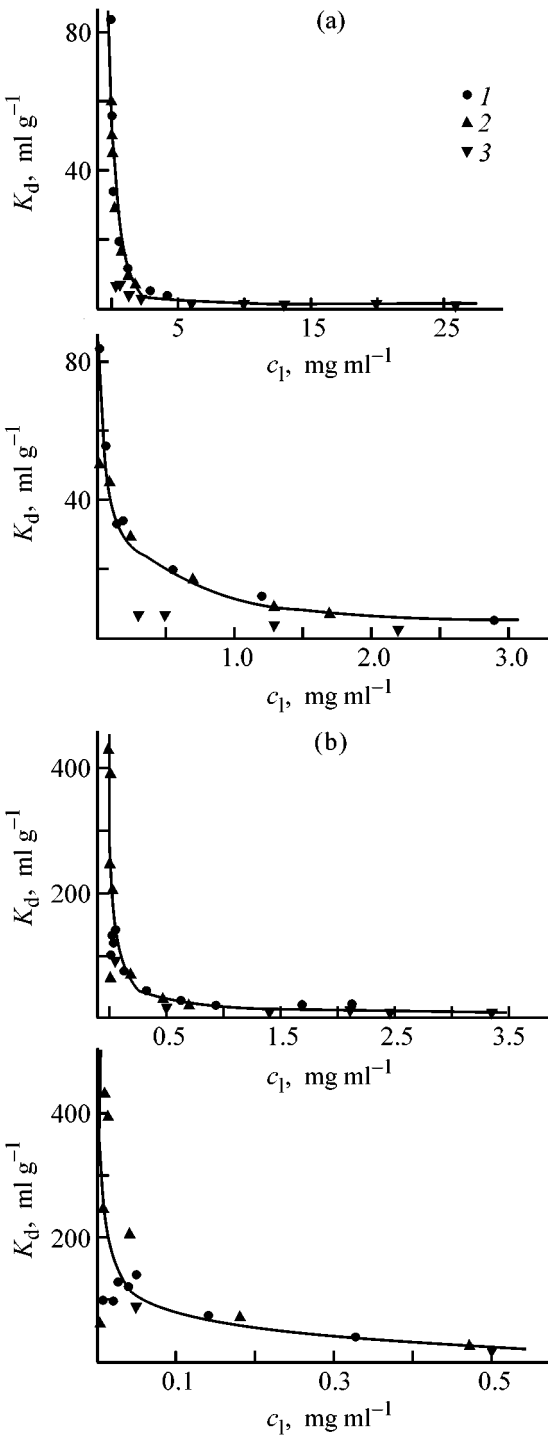

Fig. 2. Distribution coefficients $K_d = c_s/c_l$ of (a) C_{60} and (b) C_{70} fullerenes between NORIT-AZO carbon and (*1*) *o*-xylene, (*2*) toluene, and (*3*) *o*-dichlorobenzene vs. the fullerene concentration in the liquid phase c_l at 25°C.

tration in both phases. The distribution coefficients of C_{70} are almost always several times higher that those of C_{60}, which creates prerequisites for chromatographic separations of these fullerenes. The only exceptions are highly concentrated fullerene solutions (>5 g l^{-1}). In this case, the distribution coefficients of C_{60} and C_{70} become close, which makes chromatographic separation ineffective.

CONCLUSIONS

(1) Isotherms of fullerene adsorption from *o*-xylene, toluene, and dichlorobenzene solution at 25°C were measured and characterized.

(2) The sorption properties of NORIT-AZO carbons with respect to fullerenes are fairly good. The different sorption capacities of carbon for C_{60} and C_{70} fullerenes makes it promising for industrial separation of fullerenes.

ACKNOWLEDGMENTS

This study was financially supported by the Russian Ministry of Education, grant for Basic Research in the Field of Natural Philosophy and Exact Science (project E02-5.0-227) and by the Russian Foundation for Basic Research (project 03-05-65 164).

REFERENCES

1. Eletskii, A.V. and Smirnov, B.M., *Usp. Fiz. Nauk*, 1991, vol. 161, no. 7, pp. 1379–1391.
2. Bochvar, D.A. and Gal'perin, E.G., *Dokl. Akad. Nauk SSSR*, 1973, vol. 209, no. 3, pp. 610–612.
3. Hugh, Aldersey-Wiliams, *The Most Beautiful Molecules*, New York: Wiley, 1995.
4. Smit, W.A., Bochkov, A.F., Caple, R., *Organic Synthesis: The Science Behind the Art, The Royal Society of Chemistry*, Cambridge, 1998.
5. Kratschmer, W., Lamb, L.D., Fostiropolos, K., and Huffman, D.R., *Nature*, 1990, vol. 347, pp. 354–359.
6. Xu, Z.P., Chen, W.X., Wu, J., and Li, Y.B., *Chin. Sc. Bull*, 1994, vol. 99, no. 16, pp. 1347–1350.
7. Gregg, S.J. and Sing, K.S.W., *Adsorption, Surface Area and Porosity*, London: Academic, 1982.
8. Fridrikhsberg, D.A., *Kurs kolloidnoi khimii* (Course of Colloidal Chemistry), Leningrad: Khimiya, 1974.
9. Parker, D.H., Chatterjee, K., Wurz, P., *et al., Carbon*, 1992, vol. 30, no. 8, pp. 1167–1182.
10. Lazukhina, E.E. and Bubnov, V.P., *Izv. Ross. Akad. Nauk, Ser. Khim.*, 1995, no. 7, pp. 1223–1226.
11. Ponomarev, N., Yudovich, M.E., Charykov, N.A., *et al., Opt. Spectrosc.*, 2000, vol. 88, no. 2, pp. 195–197.
12. Ajie, H., Alvarez, M.M., Anzs, J., *et al., J. Phys. Chem.*, 1990, vol. 94, pp. 8630–8633.
13. Suvaramar, N., Dhamodaran, R., Kalippan, I., *et al., J. Org. Chem.*, 1992, vol. 57, pp. 6077–6079.
14. Bezmel'nitsyn, V.N., Eletskii, A.B., and Okun', M.V., *Usp. Fiz. Nauk*, 1998, vol. 168, no. 11, pp. 1195–2007.
15. Bezmel'nitsyn, V.N., Eletskii, A.B., and Stepanov, V., *Zh. Fiz. Khim.*, 1995, vol. 64, no. 4, pp. 735–741.
16. Konarev, D.V. and Lyubovskaya, R.N., *Usp. Khim.*, 1999, vol. 68, no. 4, pp. 569–573.
17. Samonin, V.V. and Slutsker, E.M., *Zh. Fiz. Khim.*, 2003, vol. 77, no. 7, pp. 1287–1293.
18. Samonin, V.V. and Marakulina, E.K., *Zh. Fiz. Khim.*, 2002, vol. 76, no. 5, pp. 888–893.
19. Golubkov, V.V., Shakhmatkin, B.A., Aksel'rod, B.M., and Charykov, N.A., *Zh. Fiz. Khim.*, 2001, vol. 75, no. 10, pp. 1819–1822.

Russian Journal of Applied Chemistry, Vol. 77, No. 10, 2004, pp. 1631–1634. Translated from Zhurnal Prikladnoi Khimii, Vol. 77, No. 10, 2004, pp. 1643–1646.

SORPTION AND ION-EXCHANGE PROCESSES

Thermodynamic Study of Adsorption of Nickel Complexes with Schiff Bases from Acetonitrile Solutions on Uncharged Graphite Surface

B. N. Afanas'ev, E. A. Aleksandrova, Yu. P. Akulova, and S. A. Logvinov

St. Petersburg State Technological Institute, St. Petersburg, Russia

Received December 17, 2003; in final form, April 2004

Abstract—Adsorption of nickel *N,N*-ethylenebis(salicylideneimine) complex from acetonitrile solution on expanded natural graphite powder at 273–313 K is studied.

The chemistry of conducting polymers and molecular modification of electrode surfaces are thriving branches of modern chemical science. In the last decade, a number of new complexes of transition metals with Schiff bases have been synthesized [1–4]. These polymeric compounds demonstrate high electron conduction, stability, and electrochromic and catalytic properties [3]. The polymerization is always accompanied by adsorption of monomers on the electrode surface. However, to our knowledge, there are no published data on the adsorption of the complexes indicated. Therefore, we examined in this study the adsorption of nickel *N,N*-ethylenebis(salicylideneimine) complex [Ni(SalEn)] on graphite.

Experimental data on adsorption of organic compounds on metal surfaces are often described by the Frumkin isotherm (1).

$$\frac{\Gamma}{\Gamma_{max}-\Gamma}\exp\left(-2a\frac{\Gamma}{\Gamma_{max}}\right) = Bc_{org} = BX_{org}\Sigma n, \quad (1)$$

where Γ and Γ_{max} are the current and limiting numbers of moles of a surfactant that can be adsorbed on unit surface area (mol); a and B, attraction and adsorption constants; c_{org} and X_{org}, concentration (M) and mole fraction of the surfactant; and Σn is the total number of moles contained in 1 l of the solution.

Since the common case is that $c_{org} \le 0.1$ M, it may be accepted that Σn is equal to the solvent concentration in the solution. It is known that

$$\ln(B\Sigma n) = -\Delta G_A^0/RT, \quad (2)$$

where ΔG_A^0 is the standard Gibbs energy of adsorption, corresponding to the asymmetric standard state in the bulk of solution [6]. At $a = 0$, the Frumkin isotherm transforms to the Langmuir isotherm [7]:

$$1/c_{org} = B\Gamma_{max}/\Gamma - B. \quad (3)$$

From experimental dependences of Γ on c_{org}, we can calculate the adsorption term B, and then, using Eq. (2), find the standard Gibbs energy of adsorption ΔG_A^0. In a previous communication [6], we suggested to calculate parameters Γ_{max}, a, and B of the Frumkin isotherm using the Origin software package.

If the symmetric standard state is chosen for the bulk of solution, the Frumkin isotherm should be represented as [6]:

$$\frac{\Gamma}{\Gamma_{max}-\Gamma}\exp\left(-2a\frac{\Gamma}{\Gamma_{max}}\right) = B'\gamma_{org}X_{org}. \quad (4)$$

Here $B' = \exp[-\Delta G_{ads}^0/RT]$ is the dimensionless parameter; ΔG_{ads}^0, standard Gibbs energy of adsorption, corresponding to the symmetric standard state; and γ_{org}, activity coefficient of the surfactant in the bulk of solution.

According to [6], if $c_{org} \le 0.1$ M, then

$$\Delta G_{ads}^0 \simeq \Delta G_A^0 + RT\ln\gamma_{org}^\infty, \quad (5)$$

where γ_{org}^∞ is the activity coefficient of the surfactant at infinite dilution.

The activity coefficient γ_{org}^∞ is the characteristic of the solution, which can range from unity to 10^3–10^5, depending on the nature of a surfactant and solvent [8]. The parameter ΔG_A^0 in Eq. (5) depends both on the properties of the surfactant solution and on the metal–surfactant binding energy, while the parameter

1070-4272/04/7710-1631 © 2004 MAIK "Nauka/Interperiodica"

$RT \ln \gamma_{org}^{\infty}$, only on the bulk properties of the solution. Therefore, the standard Gibbs energy of adsorption, ΔG_{ads}^0, characterizes the binding of the organic molecule to the metal.

If a surfactant is poorly soluble, the activity coefficient γ_{org}^{∞} can be approximately calculated by Eq. (6) [8].

$$RT \ln \gamma_{org}^{\infty} \approx -RT \ln X_{org}^{sat}, \quad (6)$$

where X_{org}^{sat} is the concentration of the saturated solution.

The standard enthalpy of adsorption can be calculated the using well-known equation [9]:

$$\Delta H_{ads}^0 = \Delta G_{ads}^0 + T\Delta S_{ads}^0, \quad (7)$$

where ΔS_{ads} is the standard entropy of adsorption.

Since the adsorption of a surfactant is always accompanied by displacement of ν solvent molecules from the metal or oxide surface to the bulk of the solution, we have

$$\Delta H_{ads}^0 = (\Delta H_{ads}^0)_{suf} - \nu(\Delta H_{ads}^0)_s. \quad (8)$$

where $(\Delta H_{ads}^0)_{sur}$ and $(\Delta H_{ads}^0)_s$ are the standard enthalpies of adsorption, related to adsorption of the surfactant and desorption of the solvent, respectively.

The goal of this study is to determine the parameters ΔG_{ads}^0 and ΔH_{ads}^0 characterizing the binding of Ni(SalEn) to the graphite surface. For this purpose it was needed to obtain the adsorption isotherms at various temperatures.

The numbers of moles of the adsorbed substance on the surface of the graphite powder was calculated by

$$\Delta n = (c_{org}^0 - c_{org})V, \quad (9)$$

where c_{org}^0 and c_{org} are the surfactant concentrations in the initial and equilibrium solutions, respectively; and V is the solution volume.

The Δn is accepted to be the surface concentration. Then we can write

$$\Gamma = \Delta n/A, \quad (10)$$

where A is the specific surface area of graphite.

The spectrum of monomeric Ni(SalEn) contains in its UV part three bands at 252, 325, and 420 nm. The optical density is a linear function of the monomer concentration, which allows determination of c_{org}^0 and c_{org} from Eq. (9). It was demonstrated in separate experiments that the band at 325 nm is best suitable for determining the monomer concentration in the solution bulk, and also that the time of contact of the solution with graphite can be reduced from 2 h to 10 min. The spectra were recorded on an SF-2000 spectrophotometer.

In the study, we used thermally expanded natural graphite of 99.9% purity.[1]

Above 150°C, the surface area of graphite increases dramatically. Incomplete removal of gases from the powder results in overestimation of the BET surface area of graphite. It is this circumstance that is responsible for such a low experimental value of A (0.4–1 $m^2 g^{-1}$; 0.7 ± 0.2 $m^2 g^{-1}$ on the average) determined by the BET method. For more exact determination of the specific surface area of the graphite powder, we studied the adsorption of β-naphthol from aqueous solutions at 19 ± 1°C. Then we calculated the parameters characterizing the adsorption of β-naphthol on graphite by Eqs. (1), (9), and (10) at $A_{ef} = 1$ $m^2 g^{-1}$ using the Origin software package. We obtained $\Gamma_{max}^{ef} = 2.65 \times 10^{-6}$ mol m^{-2}. The specific surface area of the graphite powder can be calculated by Eq. (11).

$$A = \frac{\Gamma_{max}^{ef}}{\Gamma_{max}} A_{ef}. \quad (11)$$

Our previous study of the adsorption of β-naphthol on the α-Fe_2O_3 surface [10] revealed that the surfactant molecules are oriented normally to the surface, since $\Gamma_{max} = 5.7 \times 10^{-6}$ mol m^{-2} and $\Delta G_A^0 = -24$ kJ mol^{-1} [Eq. (2)]. In studying the adsorption of β-naphthol on a smooth bismuth surface, Palm and Damaskin found [11] that $\Gamma_{max} = 3.1 \times 10^{-6}$ mol m^{-2} and $\Delta G_A^0 = -34$ kJ mol^{-1}. Changing the vertical orientation of the molecule for the horizontal orientation increases the absolute value of the Gibbs energy of adsorption. For the graphite powder, $\Delta G_A^0 = -28.8$ kJ mol^{-1}. Assuming the same type of orientation of β-naphthol as on bismuth and using Eq. (11), we obtain $A = 0.85$ $m^2 g^{-1}$. This value is somewhat overestimated, since $|\Delta G_A^0|_C < |\Delta G_A^0|_{Bi}$. Assuming the same type of orientation of β-naphthol as that on iron oxide, we obtain $A = 0.47$ $m^2 g^{-1}$. This value is underestimated, since $|\Delta G_A^0|_C > |\Delta G_A^0|_{\alpha\text{-}Fe_2O_3}$. The arithmetic mean $\bar{A} = 0.7 \pm 0.2$ $m^2 g^{-1}$. The results obtained suggest the following:

(1) The values of the true surface area of graphite $\bar{A}$, determined independently by two methods (BET and adsorption of β-naphthol) are well consistent. Therefore, we used in further study of Ni(SalEn) adsorption the value $\bar{A} = 0.7$ $m^2 g^{-1}$.

[1] Produced at the Unikhimtek.

Table 1. Parameters characterizing adsorption of Ni(SalEn) at different temperatures

T, K	Frumkin isotherm			Langmuir isotherm	
	B, M^{-1}	$2a$	$\Gamma_{max} \times 10^6$, mol m^{-2}	B, M^{-1}	$\Gamma_{max} \times 10^6$, mol m^{-2}
275	590 ± 220	~0	2.8 ± 0.6	540 ± 180	3.1 ± 0.5
283	890 ± 260	0.3	3.2 ± 0.3	690 ± 300	3.8 ± 1.0
293	250 ± 40	1.0	3.0 ± 0.4	240 ± 90	4.5 ± 0.5
304	220 ± 80	0.3	3.8 ± 0.8	350 ± 85	2.9 ± 0.3
313	150 ± 30	0.9	3.1 ± 0.3	200 ± 60	3.4 ± 0.4

(2) The porosity of graphite is small, since the specific surface area of the graphite powder is considerably lower than that of other materials. For comparison, A ($m^2\ g^{-1}$): α-Fe_2O_3 7–10, ZnO 6.8–9.4, W 2.7, graphitized carbon black (Vulkan 36-2700) 71.3 ± 2.7 [12], and activated carbon (Merck) 800–1000 [13].

To calculate the activity coefficients of Ni(SalEn) in acetonitrile by Eq. (6), it is necessary to have data on its solubility.[2] The solubility was measured over the temperature range 1–50°C. The saturated concentration of the monomer was determined using the optical density-vs.-concentration calibration curve. The dependence of the saturated concentration c^{sat} on t over the temperature range 0–50°C is described by Eq. (12).

$$c^{sat} \simeq 0.00624 - 0.000496t + 0.000049t^2 - 1.62 \times 10^{-6}t^3 + 2.33 \times 10^{-8}t^4 - 1.08 \times 10^{-10}t^5. \quad (12)$$

It follows from Eq. (12) that the solubility of Ni(SalEn) in acetonitrile is low. At 25°C, 1 l contains 19.024 moles of acetonitrile. Therefore, $\Sigma n \sim 19$ and $X_{org}^{sat} = c^{sat}/19$.

Acetonitrile (ultrapure grade) was used without further purification.

The adsorption parameters estimated by Eqs. (1) and (3) are listed in Table 1. As can be seen, the values of B and Γ_{max} are consistent within the errors indicated in the table, which is due to the fact that the attraction constant $a \leq 0.5$. Table 1 shows also that there is no clearly pronounced temperature dependence of Γ_{max}. Therefore, it may be accepted that Γ_{max} = constant over the temperature range 275–313 K. The arithmetic mean values of $\overline{\Gamma}_{max}$, corresponding to the Frumkin and Langmuir isotherms, are $(3.2 \pm 0.3) \times 10^{-6}$ and $(3.5 \pm 0.5) \times 10^{-6}$ mol m^{-2}, respectively. Then, the graphite surface area occupied by one Ni(SalEn) molecule is $(52 \pm 5) \times 10^{-20}$ m^2.

[2] Pure Ni(SalEn) was kindly provided by A.M. Timonov.

In the case of adsorption of the surfactant from the acetonitrile solution, Eq. (2) takes the form of Eq. (13).

$$\Delta G_A^0 = -RT \ln (19B). \quad (13)$$

The ΔG_A^0 values calculated this equation are listed in Table 2. The value of $RT \ln \gamma_{org}^{\infty}$ were calculated by Eqs. (6) and (12). The standard Gibbs energies of adsorption ΔG_{ads}^0 (symmetrical standard state) were found using Eq. (5). Table 2 shows that $|\Delta G_A^0| \gg |\Delta G_{ads}^0|$. Therefore, the coverage of the graphite surface with the Ni(SalEn) molecules is to a considerable extent determined by the effect of forcing-out of these molecules from the bulk of the solution to the interface. Since the parameter ΔG_{ads}^0 is small, the work expended for binding of monomer molecule to the graphite surface is close to that for breaking the bonds between ν acetonitrile molecules and the surface [ν is the number of acetonitrile molecules desorbed as a result of adsorption of one Ni(SalEn) molecule]. With decreasing temperature, the binding of Ni(SalEn) to the surface strengthens, since ΔG_{ads}^0 decreases.

It is commonly accepted [1–4, 14] that, in adsorption of Ni(SalEn), its molecule is horizontally oriented on the electrode surface. It can be found from

Table 2. Thermodynamic parameters of Ni(SalEn) adsorption

T, K	$-\Delta G_A^0$	$RT \ln \gamma_{org}^{\infty}$	ΔG_{ads}^0
	kJ mol^{-1}		
275	21.2 ± 0.4	18.4	2.8 ± 0.4
283	22.8 ± 0.7	19.9	2.9 ± 0.7
293	20.6 ± 0.4	19.6	1.0 ± 0.4
304	21.1 ± 0.7	19.1	2.0 ± 0.7
313	20.7 ± 0.4	19.7	1.0 ± 0.4

the structural formula of the monomer that, in the case of such an orientation, the Ni(SalEn) molecule covers about 70×10^{-20} m^2 of the surface, which noticeably exceeds the experimental value of $(52 \pm 5) \times 10^{-20}$ m^2 per molecule. Deviations from the horizontal arrangement of the adsorbed molecule may be due to the following factors.

(1) The larger the area occupied by a surfactant molecule on the surface, the greater the number of acetonitrile molecules to be transferred from the surface to the bulk of the solution, i.e., the higher the energy consumption.

(2) The experimental results obtained demonstrate that, in adsorption of Ni(SalEn), the prevailing effect is forcing-out of the molecules from the bulk to the surface, since $|\Delta G_A^0| >> |\Delta G_{ads}^0|$. The solvent tends to push out the maximum number of the molecules to the surface. This occurs at the vertical orientation of the molecule on the surface. In this case, the area occupied by the adsorbed molecule is the smallest. As a result of the simultaneous action of these two factors (interaction with the surface and forcing-out from the bulk of the solution), the adsorbed molecules can be differently oriented on the surface.

Finally, the thermal and vibrational-rotational motions of the adsorbed molecule can also alter its orientation.

Assuming that ΔS_{ads}^0 and ΔH_{ads}^0 are temperature-independent, we calculated these parameters by Eq. (7), using the experimental data for ΔG_{ads}^0 (Table 2). We obtain $\Delta S_{ads}^0 = -53 \pm 10$ J K^{-1} mol^{-1} and $\Delta H_{ads}^0 = -18 \pm 3$ kJ mol^{-1}.

Differentiation of Eq. (5) gives Eq. (14).

$$\Delta S_{ads}^0 = -\frac{d\Delta G_A^0}{dT} - R \ln \gamma_{org}^{\infty} - RT\frac{d\ln \gamma_{org}^{\infty}}{dT}. \quad (14)$$

Table 2 shows that, within the experimental error, $\Delta G_{ads}^0 \approx$ const, and, then, $\Delta S_A^0 = -d\Delta G_A^0/dT \approx 0$. Therefore, the change in ΔS_{ads}^0 is virtually totally accounted for by changes in the activity coefficients in the solution bulk. The high negative ΔS_{ads}^0 shows that the forcing-out of the Ni(SalEn) molecule from the bulk to the graphite surface results in ordering of the solution.

The observed negative ΔH_{ads}^0, corresponding to heat release in the course of adsorption, is virtually totally accounted for by the entropy factor.

CONCLUSION

The study of the adsorption of Ni(SalEn) on the graphite surface showed that the coverage of the surface with adsorbed monomeric molecules is controlled to a considerable extent by the effect of forcing-out of these molecules from the solution bulk to the interface. The observed high negative enthalpy of adsorption is accounted for by the entropy factor.

ACKNOWLEDGMENTS

The work was financially supported by the Basic Research Grant Program of the RF Ministry of Education (project E02-5.0-260).

REFERENCES

1. Popeko, I.E., Vasil'ev, V.V., Timonov, A.M., and Shagisultanova, G.A., *Zh. Neorg. Khim.*, 1990, vol. 35, no. 4, pp. 933–937.
2. Shagisultanova, G.A., Ivanova, M.E., Popeko, I.E., and Timonov, A.M., *Zh. Neorg. Khim.*, 1991, vol. 36, no. 12, pp. 3096–3101.
3. Popeko, I.E., Timonov, A.M., and Shagisultanova, G.A., *Zh. Prikl. Khim.*, 1990, vol. 63, no. 10, pp. 2207–2210.
4. Vasil'eva, S.V., Balashev, K.P., and Timonov, A.M., *Elektrokhimiya*, 2000, vol. 36, no. 1, pp. 85–91.
5. Damaskin, B.B., Nekrasov, L.N., Petrii, O.A., *et al.*, *Elektrodnye protsessy v rastvorakh organicheskikh soedinenii* (Electrode Processes in Solutions of Organic Compounds), Moscow: Mosk. Gos. Univ., 1985.
6. Afanas'ev, B.N., Akulova, Yu.P., and Yakovleva, O.R., *Zh. Fiz. Khim.*, 2003, vol. 77, no. 4, pp. 727–731.
7. Scchukin, E.D., Pertsov, A.V., and Amelina, E.A., *Kolloidnaya khimiya* (Colloid Chemistry), Moscow: Mosk. Gos. Univ., 1982.
8. Morachevskii, A.G., Smirnova, N.A., Balasheva, I.M., and Pukinskii, I.B., *Termodinamika razbavlennykh rastvorov neelektrolitov* (Thermodynamics of Dilute Nonelectrolyte Solutions), Leningrad: Khimiya, 1982.
9. *Fizicheskaya khimiya* (Physical Chemistry), Krasnov, K.S., Ed., Moscow: Vysshaya Shkola, 1982.
10. Afanas'ev, B.N., Akulova, Yu.P., Aleksandrova, E.A., and Yakovleva, O.R., *Proceedings, 4-ya Mezhdunarodnaya shkola-seminar "Sovremennye metody issledovaniya i preduprezhdeniya korrozionnykh razrushenii"* (4th Int. School "Modern Methods for Studying and Preventing Corrosion Damage"), Izhevsk: Udmurt. Univ., 2003, pp. 7–15.
11. Palm, U.V. and Damaskin, B.B., *Itogi Nauki Tekh.: Elektrokhimiya*, 1977, vol. 12, pp. 99–140.
12. Gregg, S.J. and Sing, K.S.W., *Adsorption, Surface Area and Porosity*, London: Academic, 1982.
13. Haghseresht, F., Nouri, S., Finnerty, J.J., and Lu, G.Q., *J. Phys. Chem.*, 2002, vol. 106, pp. 10 935–10 942.
14. Chepurnaya, I.A., Gaman'kov, P.V., Rodyagina, T.Yu., *et al.*, *Elektrokhimiya*, 2003, vol. 39, no. 3, pp. 348–353.

Russian Journal of Applied Chemistry, Vol. 77, No. 10, 2004, pp. 1635–1641. Translated from Zhurnal Prikladnoi Khimii, Vol. 77, No. 10, 2004, pp. 1647–1653.

SORPTION AND ION-EXCHANGE PROCESSES

Adsorption of Oligomeric Polyamineimide Binder and Its Monomers on the Surface of Nonstoichiometric Compounds of Titanium

A. V. Ishkov and A. M. Sagalakov

Altai State University, Barnaul, Altai krai, Russia

Received July 6, 2004

Abstract—Adsorption of an oligomeric polyaminoimide binder, PAIS-104, and its monomers, diaminodiphenylmethane and dimaleimidodiphenylmethane, on the surface of nonstoichiometric titanium carbides, nitrides, and carbonitrides was studied. The dependence of the oligomer adsorption parameters and strength properties of composites on the nature, composition, and specific surface area of the adsorbent and presence of various additives in the binder was examined.

The adsorption processes occurring on the surface of fillers in solutions and melts of oligomers and polymers predetermine numerous technological features of manufacture of composites and their properties [1, 2]. As is known, the properties of composites depend not only on the properties of the starting components, but also on surface phenomena at the phase boundary (wetting, adsorption, adhesion, etc.). The adsorption interaction of the components of a polymer solution with the filler surface is a first stage of formation of the phase boundary in composites, and, therefore, studying the adsorption of polymers on the filler surface is of high theoretical and practical importance.

Electrically conducting materials (ECM) occupy a particular place among composites with special properties. ECM are used to fabricate current-lead coatings, heat and radiation shields, film and bulk resistive heaters, and other articles of this kind [3]. However, a number of difficulties are encountered in manufacture and operation of articles fabricated from such composites. These difficulties are associated with the interactions at the interface between the polymer and the conducting filler, which lead to instability of the electrical properties of the material. For example, oxidation of filler grains is observed in ECM based on metal powders, which causes a decrease in the electrical conductivity of the material [4]. Therefore, obtaining new ECM with stable characteristics is, undoubtedly, a matter of current interest.

Previously, materials in which the part of the conducting filler is played by nonstoichiometric titanium compounds of the type of an interstitial phase have been suggested [5, 6]. Use of nonstoichiometric titanium carbides, nitrides, and carbonitrides exhibiting a metallic conductivity and high chemical and thermal resistance (up to 3500 K) in materials with a polymeric matrix based on a polyaminoimide binder makes it possible to obtain ECM with stable electrical properties in the whole temperature range of application of modern polymers. In addition, the ECM mentioned above have a new property of interest, self-adjustment, which makes them promising materials for fabrication of low-temperature heating devices [7]. Therefore, a study of adsorption properties in systems constituted by a nonstoichiometric compound of titanium and a polyaminoimide binder is of particular interest.

The aim of this study was to analyze the adsorption of an oligomeric polyaminoimide binder and its monomers on the surface of such fillers as high-melting nonstoichiometric compounds of titanium of the type of interstitial phases.

EXPERIMENTAL

As oligomeric polyaminoimide binder served a commercial specimen of PAIS-104 resin [TU (Technical Specification) 6-05-231-192–79], which is a powdered oligomer with an average molecular weight of 3.5×10^3. Content of free amino groups in the polymer ≤5%, drop temperature 103°C, gelatinization time 180 s.

1070-4272/04/7710-1635 © 2004 MAIK "Nauka/Interperiodica"

Table 1. Physicochemical properties of filler

Filler	Lattice constant, Å	Content, %			S_{sp}, $m^2 g^{-1}$
		Ti	C	N	
$TiC_{0.5}$	2.255	88.87	11.12	–	0.8
$TiC_{0.6}$	2.274	86.90	13.10	–	1.2
$TiC_{0.75}$	2.298	84.20	15.80	–	1.4
$TiC_{0.9}$	2.416	81.65	18.35	–	1.1
$TiN_{0.5}$	4.296	85.50	–	14.50	5.2
$TiN_{0.95}$	4.325	78.15	–	21.85	4.8
$TiC_{0.5}N_{0.4}$	2.795	80.56	10.09	9.35	2.5
$TiC_{0.4}N_{0.3}$	2.562	83.83	8.40	7.76	2.2

One of monomers of PAIS-104, diaminodiphenylmethane (DADPhM), was used after additional purification of the commercial chemically pure product by recrystallization from ethanol. Dimaleimidodiphenylmethane (DMIDPhM), the second monomer of PAIS-104, was obtained by reacting DADPhM with maleic anhydride in an ether solution in a 1 : 2 molar ratio, with the subsequent dehydration of the resulting diamide with a mixture Ac_2O : AcONa. The product thus obtained was purified by recrystallization from toluene to give a compound with a melting point of 155–156°C, which was identified by IR spectra [8, 9].

As nonstoichiometric compounds of titanium were used its carbides, nitrides, and carbonitrides obtained by means of a self-propagating high-temperature synthesis [10].

Titanium nitrides TiN_x ($0.5 \le x < 1$) were prepared by reacting powdered titanium of PTOM brand with nitrogen gas in a flow-through reactor under a nitrogen pressure of 0.2–0.5 atm at a controlled flow rate of the gas. Titanium carbides TiC_x ($0.5 \le x < 1$) were synthesized by burning mixtures of powdered titanium of PTK brand and carbon black of PM-50 brand, taken in 1 : 0.5, 1 : 0.6, 1 : 0.75, and 1 : 0.9 molar ratios, in argon. Titanium carbonitrides TiC_xN_y ($x + y < 1$) were obtained by reacting powdered titanium of PTK brand with technical-grade hexamethylenetetramine (urotropin) at 1 : 0.1 and 1 : 0.07 molar ratios of the reagents. The self-propagating high-temperature synthesis was initiated in all the systems with a thermit formulation.

The composition of the nonstoichiometric compounds was confirmed bu X-ray phase (DRON-2, Co_{K_α} radiation) and chemical analyses. Composites were prepared from titanium fractions with $d < 100$ μm. The specific surface area of the fillers was determined from the adsorption of surfactants.

The adsorption of PAIS and its monomers from solutions in DMF was performed in hermetically sealed volumetric flasks at a temperature of 20 ± 1°C and 10 : 1 mass ratio of the liquid and solid phases. Equilibrium solutions were separated from the adsorbent by centrifugation. The concentration of a polymer solution was determined by means of refractometry, using preliminarily obtained calibration plots. The concentration of DMIDDPhM solutions was determined using the procedure suggested in [11]. The content of DADPhM in solution upon adsorption was found photometrically, after combining the amine with β-naphthol [12].

Polymeric formulations for further studies were obtained by hot compaction of a mixture of powdered filler and binder at a pressure of 20–30 MPa and temperature of 200–220°C in the course of 1 h and at 240–250°C for additional 1 h.

The strength properties of the composites were determined on an R-0.5 tensile machine (rate of sample loading 10 mm min^{-1}, maximum load 500 kg) and a KM-0.5 pendulum impact testing machine by the standard procedures.

A specific feature of the compounds produced by self-propagating high-temperature synthesis is that their properties depend on various parameters of the technological process: powder dispersity, duration of agitation, and process temperature, and, therefore, any technological scheme of self-propagating high-temperature synthesis requires monitoring of the basic properties and the composition of the products obtained.

Table 1 lists the principal physicochemical parameters of the fillers synthesized. As can be seen from the data presented, the substances synthesized are nonstoichiometric and have a developed specific surface area, which predetermines their improved adsorption properties. With titanium nitrides and carbides, the prescribed compositions were well reproduced in synthesis. At the same time, the nonstoichiometric carbonitrides synthesized had a composition somewhat different from that expected. Presumably, this is due to sublimation and decomposition of a part of the organic substance at the temperature of synthesis and to different rates of assimilation of nitrogen and carbon by titanium in self-propagating high-temperature synthesis [10]. The nonstoichiometric titanium nitrides obtained have a 3.3–6.5 times greater specific surface area than the other compounds, which is accounted for by the higher dispersity of the starting titanium powder.

The attainment of the adsorption equilibrium in the systems under study was determined by measuring kinetic curves of adsorption. Figure 1 shows the kinetic curves of adsorption of the oligomeric polyaminoimide binder under study on the surface of some of the compounds in question. It was established that a constant value of the refractive index of the solution was observed during the first two to three days after solutions of PAIS-104 in DMF were brought in contact with the adsorbent, which indicates that the adsorption equilibrium was attained. Similar dependences were obtained for all the systems studied.

As is known, the rate at which the adsorption equilibrium is attained is determined by the nature of the adsorbent and by its dispersity and porosity. As the adsorbents studied have about the same dispersity and granulometric composition, the fact that the highest rate of adsorption is observed for the nonstoichiometric titanium nitrides $TiN_{0.5}$ and $TiN_{0.95}$ is accounted for by their larger specific surface area. The nature of adsorbent has a little effect on the kinetic parameters of adsorption of the polyaminoimide oligomer.

Similar studies were performed for systems constituted by a nonstoichiometric adsorbent and monomers of the polyaminoimide binder. It was established that the adsorption equilibrium is attained in this case during the first 1.5–2 h after DMIDPhM and DADPhM solutions are brought in contact with the surface of the adsorbent.

As the oligomer under study is a product obtained by reaction in a melt of DMIDPhM and DADPhM, it contains simultaneously amine and imide functional groups. In curing of PAIS-104, there simultaneously occur addition of amine groups to double bonds of imide rings and a competing reaction of autopolymerization of imide rings, which result in that structures of two types are formed in the polymer:

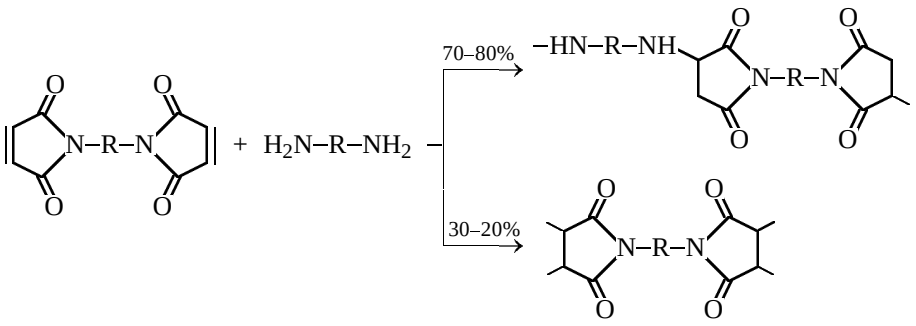

(I)

Therefore, a study of adsorption of the oligomeric polyaminoimide binder and its monomers could reveal the selective adsorption properties of the surface of the nonstoichiometric compounds with respect to amine and imide functional constituents of the oligomer.

As is known, adsorption by J. Gibbs is calculated as an excess amount of a solution component within the adsorption layer enveloping the surface of the adsorbent. However, the adsorption is calculated in actual practice as the amount of a substance adsorbed on a unit surface area of the adsorbent, using the formula

$$\Gamma_i = \frac{(c_0 - c_i)V}{mS_{sp}}, \quad (1)$$

where c_0 and c_i are the concentrations of the component in the initial solution and that in equilibrium with the adsorbent (mM); m, mass of the adsorbent (g); V, volume of the adsorption solution (l); and S_{sp}, specific surface area of the adsorbent ($m^2\ g^{-1}$).

Figure 2 shows adsorption isotherms of PAIS-104 and its monomers from diluted solutions in DMF on

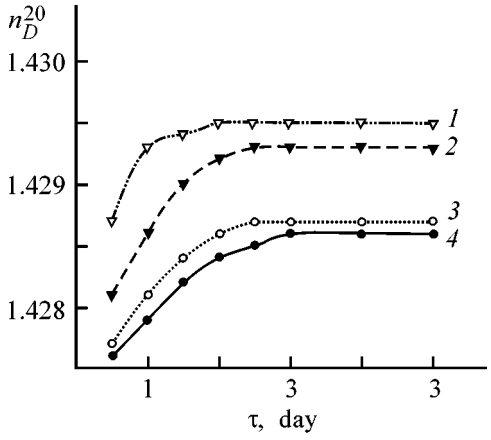

Fig. 1. Kinetic curves of PAIS-104 adsorption on the surface of fillers from solutions in DMF. (τ) Time. (*1*) $TiN_{0.5}$, (*2*) $TiN_{0.95}$, (*3*) $TiC_{0.5}N_{0.4}$, and (*4*) $TiC_{0.5}$.

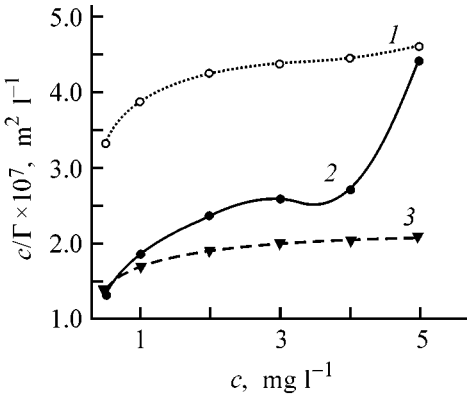

Fig. 2. Isotherms of adsorption Γ of PAIS-104 and its monomers on the surface of the carbide $TiC_{0.75}$. (*c*) Concentration of a component; the same for Fig. 3. (*1*) DADPhM, (*2*) PAIS-104, and (*3*) DMIDPhM; the same for Fig. 3.

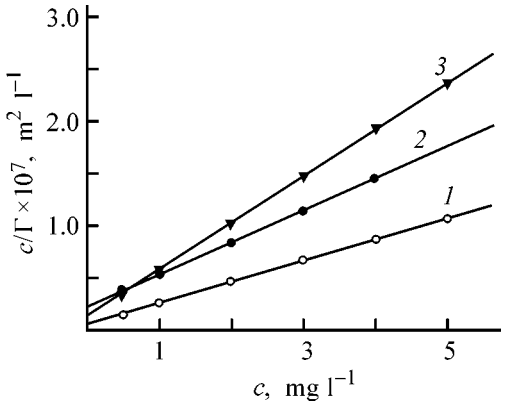

Fig. 3. Linear anamorphoses of the isotherms of adsorption Γ of PAIS-104 and its monomers on the surface of the carbide $TiC_{0.75}$.

the surface of a nonstoichiometric titanium carbide of composition $TiC_{0.75}$. Similar dependences were obtained for the other adsorbents.

As can be seen in Fig. 2, the adsorption isotherms of the monomers DMIDPhM and DADPhM have a typical shape with the adsorption approaching a limiting value. The adsorption isotherm of the polyaminoimide oligomer is S-shaped, which is typical of adsorption of sparingly soluble substances. Systems of this kind are commonly regarded as bulk-stratifying [13].

It is known [14] that all components of a mixture are sorbed simultaneously, but to varied extent, in adsorption of macromolecules from dilute solutions. Therefore, it is somewhat difficult to determine the limiting adsorption of the polymer. However, the adsorption isotherms of the polyaminoimide oligomer show a plateau with a nearly constant adsorption. If it is assumed that this part of the isotherm corresponds to dense filling of the surface of the adsorbents by macromolecules in a single layer, Langmuir's theory of monomolecular adsorption can be used to find the parameters of the adsorption equilibrium in systems of this kind. The equation describing the adsorption process is in this case as follows:

$$\Gamma = \Gamma_\infty[kc/(1 + kc)], \quad (2)$$

where Γ_∞ is the limiting surface concentration of the adsorbate (mmol m^{-2}); *k*, equilibrium constant equal to the ratio of the rate constants of desorption and adsorption; and *c*, volume concentration of the substance (mmol l^{-1}).

Equation (2) is linearized in the coordinates $c/\Gamma = f(c)$, which makes it possible to easily find values of its parameters.

Figure 3 shows linear anamorphoses of the adsorption isotherms of the polyaminoimide oligomer and its monomers on the surface of $TiC_{0.75}$. As can be seen from the plots shown in the figure, the experimental points fall with good precision on the theoretical straight line, which indicates that the model of monomolecular adsorption is adequate to the systems under study. Similar plots were constructed for the other adsorbents. The linear correlation factors found using the least-squares procedure were 0.985–0.998.

The linear form of Eq. (2) was used to find the limiting surface concentration of the components being sorbed and the adsorption equilibrium constants for all the nonstoichiometric compounds under study. The data on the limiting adsorption were used to calculate the thickness of the adsorption layer:

$$l = \Gamma_\infty M/d, \quad (3)$$

where Γ_∞ is the limiting adsorption (mg m^{-2}); *M*, molecular weight of the substance (g); and *d*, density of the substance (kg m^{-3}).

As can be seen from Table 2, the limiting adsorption depends not only on the specific surface area of the adsorbents, but also on the nature of a nonstoichiometric compound. Despite the large specific surface of nonstoichiometric titanium nitrides, the limiting adsorption of the polyaminoimide oligomer on their surface is lower than that on the surface of titanium carbonitrides and of the carbide of composition

Table 2. Parameters of adsorption of PAIS-104 and its monomers on the surface of fillers

Filler	PAIS-104			DADPhM		DMIDPhM	
	$\Gamma_\infty \times 10^7$, mg m^{-2}	k	l, Å	$\Gamma_\infty \times 10^7$, mg m^{-2}	k	$\Gamma_\infty \times 10^7$, mg m^{-2}	k
$TiC_{0.5}$	1.2	1.8	2.4	2.5	6.2	2.0	3.0
$TiC_{0.6}$	2.6	2.2	5.3	3.4	5.7	1.9	2.1
$TiC_{0.75}$	3.2	1.4	6.6	4.7	4.8	2.2	3.4
$TiC_{0.9}$	1.8	1.7	3.7	2.8	6.4	1.5	4.6
$TiN_{0.5}$	2.0	2.3	4.1	3.1	4.2	1.7	3.2
$TiN_{0.95}$	2.4	1.9	4.9	3.5	5.1	1.8	4.0
$TiC_{0.5}N_{0.4}$	2.5	1.2	5.1	4.2	3.8	2.0	3.7
$TiC_{0.4}N_{0.3}$	3.3	1.4	6.8	4.5	4.7	2.4	4.1

$TiC_{0.75}$. Another pattern is also observed: the farther the composition of a nonstoichiometric compound from the boundaries of the homogeneity region [15], the higher the limiting adsorption of the oligomer. The data of Table 2 also show that the adsorption of the amine functional constituents of the oligomer dominates over that of imide constituents. This is indicated by the values of the limiting adsorption of model compounds, monomers DMIDPhM and DADPhM. The low values of the equilibrium constants point to a comparatively weak interaction of binder molecules with the surface of the adsorbents, in agreement with published data [14]. The higher values of the constants for the model compounds indicate that desorption predominates over adsorption in the case of monomers. The thickness of the adsorption layer varies within the range 2–6 Å, which is due to orientation of oligomer molecules on the surface of the adsorbent in adsorption from dilute solutions and confirms once more the applicability of the monomolecular adsorption model to the systems studied.

As already noted, ECM based on a polyaminoimide binder and nonstoichiometric compounds are distinguished by stability of their electrical parameters, but also have some disadvantages: articles made of cured resins exhibit an increased brittleness, their processing by injection molding and extrusion is difficult [16]. These disadvantages can be obviated by modifying the polyaminoimide oligomer with various additives.

Oligooxypropylene glycol (OOPG), dioctyl phthalate (DOPh), and epoxydiane resin ED-20 were used as additives in this study. The adsorption equilibria in the systems constituted by a nonstoichiometric adsorbent, PAIS-104, and an additive were studied using the scheme described above. In this case, the adsorption isotherms were similar to those in Fig. 2. Their point-by-point linearization as far as the plateau region inclusive made it possible to determine the adsorption parameters for these systems.

Table 3 lists the parameters calculated similarly to those for the binary systems PAIS–filler: limiting adsorption, equilibrium constants, and thickness of the adsorption layer. As can be seen from the data presented, the adsorption of the polyaminoimide oligomer on the surface of the fillers studied is strongly affected by the composition of the binder. For example, introduction of a reactive additive OOPG and plasticizer additives DOPh and ED-20 raises the limiting adsorption by 40–60%, which is due to enhancement of the adsorption properties of the modified binder.

Noteworthy is the existence of a relationship between the limiting adsorption and the strength properties (adhesion strength and impact viscosity) of the

Table 3. Parameters of adsorption for systems with modifying additives

Filler	2.5% OOPG		1.5% DOPh		3% ED-20	
	$\Gamma_\infty \times 10^7$, mg m^{-2}	k	$\Gamma_\infty \times 10^7$, mg m^{-2}	k	$\Gamma_\infty \times 10^7$, mg m^{-2}	k
$TiC_{0.5}$	1.4	2.2	2.0	3.1	2.2	2.4
$TiC_{0.6}$	3.7	1.6	3.2	2.5	3.6	3.7
$TiC_{0.75}$	5.1	2.3	4.2	2.8	4.5	2.7
$TiC_{0.9}$	2.0	1.9	2.3	2.5	2.7	3.6
$TiN_{0.5}$	1.9	2.5	2.2	3.2	2.2	3.1
$TiN_{0.95}$	2.5	2.3	2.8	2.8	3.1	2.8
$TiC_{0.5}N_{0.4}$	3.0	1.8	3.0	2.7	3.2	2.9
$TiC_{0.4}N_{0.3}$	3.7	2.1	3.5	2.9	3.5	4.2

Table 4. Strength parameters of composites containing 50 wt % filler (n = 5)

Filler	Composite							
	no additive		2.5% OOPG		1.5% DOPh		3% ED-20	
	σ_{shear}, MPa	A, kJ m^{-2}	σ_{shear}, MPa	A, kJ m^{-2}	σ_{shear}, MPa	A, kJ m^{-2}	σ_{shear}, MPa	A, kJ m^{-2}
$TiC_{0.5}$	7	3.75	12	4.25	10	5.76	9	7.92
$TiC_{0.6}$	10	7.12	16	10.65	12	12.72	11	15.45
$TiC_{0.75}$	15	8.62	22	11.25	15	15.25	12	18.94
$TiC_{0.9}$	12	6.15	18	7.68	16	9.73	14	13.22
$TiN_{0.5}$	9	7.52	12	9.10	13	13.85	15	16.60
$TiN_{0.95}$	8	7.90	12	10.75	12	14.27	12	16.35
$TiC_{0.5}N_{0.4}$	10	7.24	12	12.15	18	13.88	20	16.30
$TiC_{0.4}N_{0.3}$	14	8.57	18	12.82	15	13.42	18	15.28

composite obtained. Table 4 lists the values of the adhesion strength in interlayer shear, σ_{shear}, and impact viscosity by Sharpy, A, for composites containing 50 wt % nonstoichiometric filler and similar composites with modifying additives. It can be seen that an increase in the limiting adsorption of PAIS-104 on a carbide of composition $TiC_{0.75}$ by a factor of 1.6 leads to an approximately 1.5 times higher strength in interlayer shear. A similar correlation is observed for other fillers and modifiers. The data in Table 4 can also be used to elucidate the relationship between the filler composition and the strength properties of the resulting composite. The increase in the strength of the composite can be attributed to a rise in the share of structures of the second type [Scheme (I)] in the cured polymer. These structures are formed upon blocking (as a consequence of specific adsorption) of radicals from the amine constituent of the oligomer on the surface of fillers, which enhances the process of autopolymerization of the imide.

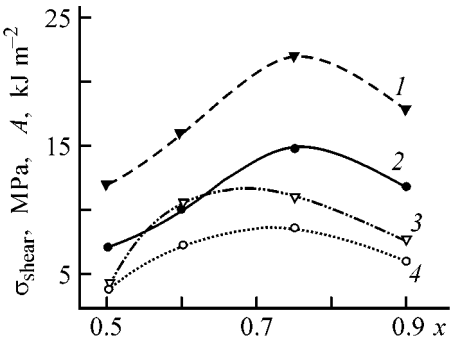

Fig. 4. Mechanical properties of composites vs. the composition of titanium carbide TiC_x: (*1*, *2*) adhesion strength σ_{shear} and (*3*, *4*) impact viscosity A. Material: (*1*, *2*) with 2.5% OOPG and (*3*, *4*) without additives.

Figure 4 shows how the strength properties of the composites obtained depend on the parameter x in the formula of nonstoichiometric titanium carbide. It can be seen that the maximum strength in interlayer shear and higher impact viscosity are observed for the material containing a carbide whose composition corresponds to the middle of the homogeneity region of the system Ti–C, i.e., $TiC_{0.75}$. This is in a good agreement with the previously established dependence of the adhesion strength of the material on the limiting adsorption of the polyaminoimide oligomer.

CONCLUSIONS

(1) Experimental data on adsorption of an oligomeric polyaminoimide binder PAIS-104 and its monomers on the surface of nonstoichiometric titanium carbides, nitrides, and carbonitrides were obtained for the first time.

(2) It was established that the adsorption of PAIS-104 on the surface of the fillers studied is adequately described by the monomolecular-layer model.

(3) It was found that the limiting adsorption of PAIS-104 is in the range $(1.2–5.1) \times 10^7$ mg m^{-2}, equilibrium constants are equal to 1.2–4.2, and the thickness of the adsorption layer is within 2.4–6.8 Å. The strength of the composites obtained, as well as the adsorption parameters of the binder, depend on the nature, composition, and specific surface area of the nonstoichiometric fillers and on the presence of modifying additives, oligooxypropylene glycol, dioctyl phthalate, and ED-20 resin.

REFERENCES

1. Lipatov, Yu.S., *Fizicheskaya khimiya napolnennykh polimerov* (Physical Chemistry of Filled Polymers), Moscow: Khimiya, 1977.
2. Lipatov, Yu.S., *Fiziko-khimicheskie osnovy napolnennykh polimerov* (Physicochemical Foundations of Filled Polymers), Moscow: Khimiya, 1991.
3. *Elektricheskie svoistva polimerov* (Electrical Properties of Polymers), Sazhin, B.I., Ed., Leningrad: Khimiya, 1970.
4. Gul', V.E. and Shenfil', L.V., *Elektroprovodyashchie polimernye kompozitsii* (Electrically Conducting Polymeric Formulations), Moscow: Khimiya, 1984.
5. RF Patent 2189998.
6. Ishkov, A.V., Perov, E.I., and Tuchkov, D.E., *Materialy VIII Mezhdunarodnoi nauchno-tekhnicheskoi konferentsii "Problemy mashinostroeniya i tekhnologii materialov na rubezhe vekov"* (Proc. VII Int. Sci.-Techn. Conf. "Problems of Machine Building and Materials Technology at the Turn of the Century"), Penza, 2003, pp. 85–87.
7. Kovalenko, N.A. and Syrovatskaya, I.K., *Trudy Vtoroi Mezhdunarodnoi nauchono-tekhnicheskoi konferentsii "Eksperimental'nye metody v fizike strukturno-neodnorodnykh kondensirovannykh sred, EMF 2001"* (Proc. II Int. Sci.-Techn. Conf. "Experimental Methods in Physics of Structurally Inhomogeneous Condensed Media, EMF 2001"), Barnaul: Alt. Univ., 2001, pp. 114–116.
8. Stenzenberger, H.D., Heinen, K.U., and Hummel, D.O., *J. Polym. Sci.*, Polym. Chem. Ed., 1976, vol. 14, pp. 2911–2925.
9. Kazitsina, A.A. and Kupletskaya, N.B., *Primenenie UF-, IK-, YaMR i mass-spektroskopii v organicheskoi khimii* (Application of UV, IR, NMR Spectroscopies and Mass Spectrometry in Organic Chemistry), Moscow: Mos. Gos. Univ., 1979.
10. *Khimiya sinteza szhiganiem* (Chemistry of Synthesis by Burning), Koidzumi, M., Ed., Translation from Japanese, Moscow: Mir, 1998.
11. RF Patent 2175124.
12. Korenman, I.M., *Fotometricheskii analiz: Metody opredeleniya organicheskikh soedinenii* (Photometric Analysis: Methods for Determining Organic Compounds), Moscow: Khimiya, 1975.
13. Fridrikhsberg, D.A., *Kurs kolloidnoi khimii* (A Course of Colloid Chemistry), Leningrad: Khimiya, 1974.
14. El'tekov, Yu.S., *Fizicheskaya adsorbtsiya mnogocomkomponentnykh faz* (Physical Adsorption of Multiponent Phases), Moscow: Nauka, 1972, pp. 214–221.
15. Gusev, A.I., *Fizicheskaya khimiya nestekhiometricheskikh tugoplavkikh soedinenii* (Physical Chemistry of Nonstoichiometric High-Melting Compounds), Moscow: Nauka, 1991.
16. *Tekhnologiya plasticheskikh mass* (Technology of Plastics), Korshak, V.V., Ed., Moscow: Khimiya, 1985.

Russian Journal of Applied Chemistry, Vol. 77, No. 10, 2004, pp. 1642–1645. Translated from Zhurnal Prikladnoi Khimii, Vol. 77, No. 10, 2004, pp. 1654–1658.

APPLIED ELECTROCHEMISTRY AND CORROSION PROTECTION OF METALS

A Study of the Kinetics of Electrochemical Dissolution of Aluminum Alloys in Alkaline Electrolytes

A. V. Krasnobryzhii, A. I. Rusin, V. N. Varypaev, V. V. Nikol'skii, and S. B. Alekseev

Akkumulyatornaya Kompaniya Rigel', Open Joint-Stock Company, St. Petersburg, Russia
St. Petersburg State Technological Institute, St. Petersburg, Russia

Received April 17, 2004

Abstract—Electrochemical dissolution of aluminum alloyed with tin, indium, and lead in a NaOH solution in the concentration range 4.4–12.0 M at 75°C was studied by the method of chronopotential and current–voltage curves. The influence exerted by alloying elements on the electrochemical parameters of the process was revealed.

The high electrochemical activity of aluminum, especially in alkaline solutions, makes it an attractive anodic material for standby chemical power cells [1, 2, 3]. Aluminum has a low electrochemical equivalent (0.336 g A^{-1} h^{-1}) and, consequently, a sufficiently high theoretical specific capacity (2.98 A h g^{-1}), and well surpasses zinc (0.83 A h g^{-1}), widely used as anode material, and the promising magnesium (2.20 A h g^{-1}). As regards its bulk characteristics, aluminum has a capacity of 8.00 A h cm^{-3}, compared with 5.88 A h cm^{-3} for zinc and 5.58 A h cm^{-3} for magnesium [1]. In addition, aluminum is a readily available and relatively inexpensive metal.

Until recently, the electrochemical dissolution of aluminum and its alloys has been mainly studied in a diluted NaCl solution modeling seawater [2–4]. In the last years, the interest of researchers in the behavior of aluminum in an alkaline medium has increased. This is due to the fact that the half-system Al/NaOH seems to be rather promising owing to its high electronegative standard potential, equal to –2.30 V [5]. However, the high energy capacity of aluminum cannot be used in full measure because of the pronounced difference effect, which markedly diminishes the utilization factor of the electrochemically active substance. Moreover, a shift of the anode potential toward the potential of the hydrogen electrode, which is –0.83 V at pH 14, is observed in this case.

To suppress the negative influence of the difference effect and the shift of the electrode potential in the negative direction, it is suggested to use alloying of aluminum with other elements in order to depassivate the surface and extend the range of anodic current densities, with the hydrogen evolution overvoltage simultaneously increasing. Of interest are studies by Klochkova's *et al.* [6, 7], who examined the anodic dissolution of aluminum and its alloys in alkaline solutions and pointed out, following Purenovich *et al.* [4], that use of indium as depassivator of the electrode surface in an anodic alloy and introduction of tin compounds as corrosion inhibitors into the electrolyte are promising methods.

This area of research is promising, which is confirmed by the patent literature. A number of patents are known, which suggest use of aluminum alloys containing gallium, thallium, tin, lead, and other alloying components for fabricating the active part of the anode in a chemical power cell [8, 9].

The present study is concerned with the electrochemical behavior of some aluminum alloys in a NaOH solution in a wide range of concentrations (4.4–12.0 M) and current densities (100–500 mA cm^{-2}).

EXPERIMENTAL

As objects of study were used aluminum–indium, aluminum–indium–tin, and aluminum–tin–lead alloys. The content of the alloying metals in some of the alloys studied is listed in Table 1. The aluminum–indi-

Table 1. Composition of the alloys studied (aluminum the rest)

Alloy	Content of alloying component, %		
	Sn	In	Pb
K16	0.20	0.25	–
K17	0.10	–	0.10
K18	0.20	0.06	–
K19	0.10	0.33	–
K20	–	0.60	–

1070-4272/04/7710-1642 © 2004 MAIK "Nauka/Interperiodica"

um alloy is a mixture of a solid solution and an indium–aluminum eutectic [6, 7]. At a mass fraction of indium of up to 0.2%, its solid solution with aluminum is a major component of the alloy. At higher indium concentrations, the fraction of the eutectic increases.

The electrode had the form of a $1.0 \times 4.0 \times 0.04$-cm plate with a working surface area of 2.0 cm^2 and the rest of the surface insulated with an alkali-resistant lacquer. Prior to each test the electrode surface was trimmed, degreased, and washed with distilled water. A NaOH solution of concentration 4.4, 8.0, and 12.0 M served as electrolyte. The working temperature of the electrolyte, equal to $75 \pm 1.0°C$, was maintained with a water thermostat. The polarization measurements were performed in a three-section electrochemical glass cell. A graphite rod was used as an auxiliary electrode, and a saturated silver chloride electrode, as reference. The anode under study was polarized with a B5-47 dc power supply. The voltage in the circuit constituted by the anode and the reference electrode was measured with a Shch-1413 high-input-resistance digital voltmeter. The loss of mass by the anode was determined gravimetrically by weighing the electrode on a VLR-200 balance before and after polarization.

Pure aluminum of A95 brand served for comparison of characteristics.

The chronopotential E–τ curves were obtained for the anodic dissolution of the aluminum alloys studied at current densities of 100–500 mA cm^{-2} and a polarization time of 600 s. The E–τ curves measured at a current density of 300 mA cm^{-2} in a 4.4 M NaOH solution are shown in Fig. 1a. All the potentials in the study are given relative to a standard hydrogen electrode.

It follows from Fig. 1a that the E–τ characteristics of alloys alloyed with indium and tin are stable (curves *1*, *3*–*5*). The chronopotentiograms lie at potentials in the range –1.54…–1.59 V, which indicates that there are no transient side processes, such as local semi-passivation by products of electrooxidation of the anode. It is important to note that the potential is stabilized during the first seconds of the electrode polarization. This means that the anodic activation of the electrode surface is not the rate-limiting process.

By contrast, the potential of the K17 alloy containing 0.1% tin and 0.1% lead (curve *2*) demonstrates a certain instability in the course of time, i.e., changes from –1.65 to –1.52 V in 600 s. However, even in this case, the electrochemical dissolution of the anode proceeds at potentials that are 0.15–0.20 V more negative than the potential of pure A95 aluminum (Fig. 1a, curve *6*).

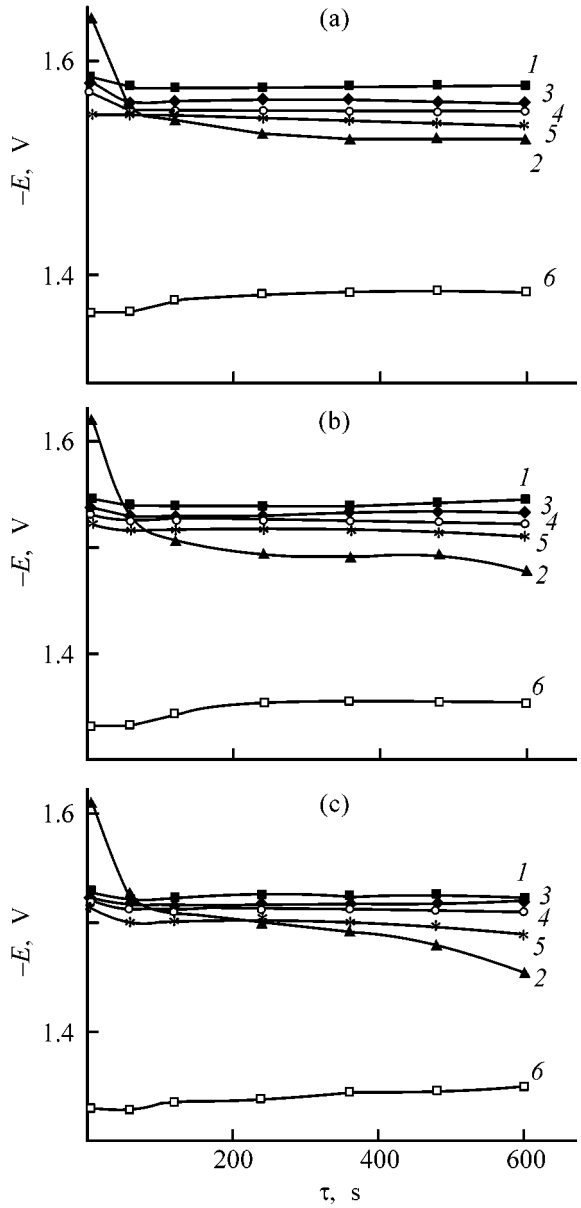

Fig. 1. Chronopotentiogram of anodic dissolution of aluminum alloys in a 4.4 M solution of NaOH. (*E*) anode potential and (τ) time. Current density (mA cm^{-2}): (a) 300, (b) 400, and (c) 500. Alloy: (*1*) K16, (*2*) K17, (*3*) K18, (*4*) K19, (*5*) K20, and (*6*) A95 aluminum.

The chronopotential curves obtained for the same alloys at current densities raised to 500 mA cm^{-2} (Fig. 1b, 1c) are not fundamentally different from the curves in Fig. 1a, except in the case of the lead-containing alloy K17 (curve *2*), which exhibits a stronger instability of the E–τ characteristics. For example,

Table 2. Potential of aluminum alloys at different concentrations of NaOH and current densities

c_{NaOH}, M	i, mA cm^{-2}	Potential $-E$, V, of indicated alloy			
		K16	K18	K19	K20
4.4	0	1.61	1.60	1.60	1.59
	100	1.60	1.59	1.59	1.56
	300	1.58	1.56	1.54	1.53
	400	1.57	1.55	1.54	1.52
	500	1.55	1.53	1.51	1.50
8.0	0	1.70	1.66	1.68	1.66
	100	1.65	1.63	1.64	1.62
	300	1.60	1.58	1.57	1.53
	400	1.56	1.54	1.53	1.50
	500	1.53	1.51	1.49	1.46
12.0	0	1.76	1.74	1.75	1.73
	100	1.70	1.67	1.69	1.63
	300	1.58	1.55	1.56	1.52
	400	1.55	1.52	1.53	1.48
	500	1.53	1.51	1.52	1.46

the change in the potential in 600 s at a current density of 500 mA cm^{-2} is as large as 0.17–0.20 V, whereas that for alloys with indium is 3–4 times smaller (curves *1*, *3–5*).

The chronopotential curves for the K16 and K18–K20 alloys are close, with the potential varying within the range ΔE not exceeding 0.05 V in each case. This confirms the decisive role of indium in the kinetics of electrochemical dissolution of the alloy, which has been noticed previously by Purenovich and coworkers [4]. The potential of each of the alloys in anodic polarization depends primarily on the relative rates of two processes, electrochemical dissolution of aluminum under the action of the external current by the reaction:

$$Al + 4OH^- \rightarrow AlO_2^- + 2H_2O + 3e \qquad (1)$$

and spontaneous dissolution of aluminum the electrochemical mechanism as a result of occurrence, on the anode surface, of two conjugate reactions

$$\left.\begin{aligned} Al + 4OH^- &\rightarrow AlO_2^- + 2H_2O + 3e, \\ 3H_2O + 3e &\rightarrow 3/2H_2 + 3OH^-, \end{aligned}\right\} \qquad (2)$$

which, combined, give the stoichiometric equation

$$Al + H_2O + NaOH \rightarrow NaAlO_2 + 3/2H_2. \qquad (3)$$

The anode potentials of the indium-alloyed aluminum (Fig. 1, curves *1*, *3–5*) are strongly shifted from the equilibrium potential of the hydrogen electrode in the negative direction with respect to the potential of pure aluminum. Therefore, the presence of indium as an alloying component makes lower the rate of spontaneous dissolution of aluminum by reactions (2). The mechanism of the influence exerted by indium is associated with the increase in the hydrogen evolution overvoltage on the surface of the indium-containing alloy. As regards pure aluminum (curve *6*), the side process (2) goes here at a noticeable rate, and, therefore, the E–τ curve is strongly shifted to less negative potentials.

Dependences similar to those plotted in Fig. 1 were obtained on raising the NaOH concentration to 12.0 M. The main results of these series of tests are listed in Table 2, which presents the average values of the potential in anodic polarization at a current density of 100 to 500 mA cm^{-2} for 600 s. The K17 alloy is omitted, as it has poorer characteristics than indium-containing alloys.

As the electrolyte concentration increases, the steady-state potential of the alloys shifts toward negative values and the variation of the potential with increasing current density becomes more pronounced. In a 4.4 M NaOH solution, the average potential at 100 mA cm^{-2} nearly coincides with the zero-current potential for all the alloys, whereas in a 12.0 M NaOH solution, E changes by 0.06–0.10 V, reaching a value of 0.23–0.27 V as the current density increases to 500 mA cm^{-2}. Most probably, the decrease in the anode potential is due to a rise in the concentration polarization as a result of an increase in the aluminum concentration in the near-anode layer, which is the more pronounced, the higher, the greater the current density. The increase in the electrolyte concentration is accompanied by a rise in the solution viscosity, which enhances the diffusion hindrance in the course of reaction (1). It should be noted, however, that the variation of the potential is, on the whole, quite acceptable. Also absent are any clearly pronounced indications of a partial passivation of the electrode surface, e.g., via formation of a sparingly soluble indium hydroxide.

The efficiency of the electrochemical dissolution of aluminum by reaction (1) can be conveniently evaluated by the utilization factor of the active substance, K_u, which is calculated by the formula

$$K_u = qi\tau S/\Delta m,$$

where q is the electrochemical equivalent of aluminum (g A^{-1} h^{-1}); i, current density (mA cm^{-2}); τ, duration of electrolysis (h); S, working surface area of the anode, (cm^2); and Δm, loss of mass by the anode through electrochemical and spontaneous dissolution (g).

The dependences of the utilization factor on current density in a 4.4 M NaOH solution are shown for the K16 and K18-K20 alloys and A95 aluminum in Fig. 2. When the current density increases from 100 to 500 mA cm^{-2}, the utilization factor clearly grows. The dependence is virtually linear within the range 200–500 mA cm^{-2}, which means that the rate of spontaneous dissolution of aluminum by reaction (3), accordingly, decreases. The deceleration of the spontaneous dissolution with growing current density in an alkaline electrolyte is typical of aluminum [10, 11].

As regards the data in Fig. 2, the K16, K18, and K19 alloys are indistinguishable (curves *1*–*3*) despite the different contents of indium (within the range from 0.06 to 0.33%). When the content of indium increases to 0.6% (K20 alloy, curve *4*), the utilization factor considerably grows (from 72 to 87% at a current density of 300 mA cm^{-2}). This is in agreement with the data obtained by Klochkova *et al.* [6, 7].

The utilization factor of A95 aluminum (curve *5*) exhibits a similar type of variation with increasing current density, but lies within 10–35%. This result agrees with the data in Fig. 1 (curve *6*).

At 8.0 M NaOH, the pattern of Fig. 2 is reproduced in every detail, and the utilization factors of all the four alloys change only slightly. A further increase in the electrolyte concentration to 12.0 M leads to a dramatic rise in the utilization factor of aluminum, K_u, in the alloys. At current densities of 300–500 mA cm^{-2}, the utilization factor is as high as 95–98%, with all the four alloys having closely similar characteristics. Thus, the rate of spontaneous dissolution of aluminum is at a minimum under these conditions.

CONCLUSION

A study of the electrochemical behavior of a number of the Al–Sn–In, Al–In, and Al–Sn–Pb alloys in a 4.4–12.0 M solutions of NaOH demonstrated that the efficiency of the anodic dissolution of aluminum largely depends on the nature and concentration of the alloying elements. The chronopotentiogram measured at current densities of 100–500 mA cm^{-2} is, as a rule, stable. The alloy containing 0.20% Sn and 0.25% In exhibits the most negative potentials of electrochemical dissolution, and that with 0.1% Sn and 0.1% Pb, the least negative anode potentials. The utilization factor of the active substance is the largest for the alloy with 0.60% In. As the electrolyte concentration increases, the efficiency of electrochemical dissolution of the alloys sharply grows.

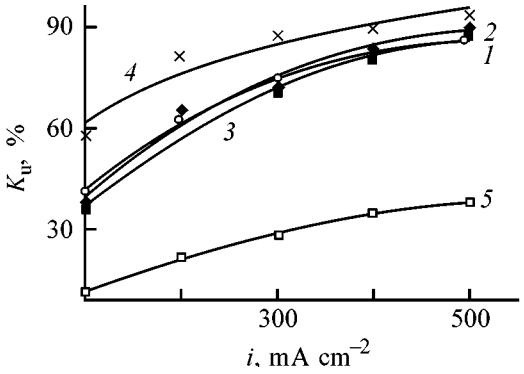

Fig. 2. Utilization factor K_u of the aluminum alloys vs. the current density i in a 4.4 M NaOH solution. Alloy: (*1*) K16, (*2*) K18, (*3*) K19, (*4*) K20, and (*5*) A95 aluminum.

REFERENCES

1. *Khimicheskie istochniki toka: Spravochnik* (Chemical Power Cells: Reference Book), Korovin, N.V., and Skundin, A.M., Eds., Moscow: Mos. Energ. Inst., 2003.
2. Ivanov, E.G., Berkman, E.A., and Petrova, G.M., *Sbornik rabot po khimicheskim istochnikam toka* (Coll. of Works on Chemical Power Cells), Leningrad: Energiya, 1974, issue 9, pp. 186–203.
3. Timonov, A.M., Cherepkova, I.A., Sysoeva, V.V., *et al., Sbornik rabot po khimicheskim istochnikam toka* (Coll. of Works on Chemical Power Cells), Leningrad: Energiya, 1981, pp. 53–56.
4. Purenovich, M.M., Despich, A.R., and Drazhich, D.M., *Elektrokhimiya*, 1976, vol. 12, no. 2, pp. 296–299.
5. *Spravochnik po elektrokhimii* (Handbook of Electrochemistry), Sukhotin, A.M., Ed., Leningrad: Khimiya, 1981.
6. Klochkova, L.L., Kulakov, E.B., Sevruk, S.D., *et al., Elektrokhimicheskie protsessy v khimicheskikh istochnikakh toka, elektrolizerakh i akkumulyatorakh: Sbornik nauchnykh trudov* (Electrochemical Processes in Chemical Power Cells, Electrolyzers, and Batteries: Coll. of Sci. Works), Moscow: Mosk. Ener. Inst., 1987, no. 135, pp. 72–82.
7. Klochkova, L.L., Koronik, V.V., Kulakov, E.B., *et al., Elektrodnye protsessy v novykh istochnikakh toka: Sbornik nauchnykh trudov* (Electrode Processes in New Power Cells: Coll. of Sci. Works), Moscow: Mosk. Energ. Inst., 1988, no. 169, pp. 28–33.
8. RF Patent 2035094.
9. RF Patent 2168811.
10. Kozlovskii, A.M., Kuritsyn, I.V, Terskii, V.M., *et al., Khimicheskie istochniki toka: Mezhvyzovskii sbornik* (Chemical Power Cells: Intercollegiate Coll.), Novocherkassk: Novocherk. Politekhn. Inst., 1981, pp. 46–49.
11. Gerasimov, V.V., *Korroziya alyuminiya i ego splavov* (Corrosion of Aluminum and Its Alloys) Moscow: Metallurgiya, 1967.

Russian Journal of Applied Chemistry, Vol. 77, No. 10, 2004, pp. 1646–1648. Translated from Zhurnal Prikladnoi Khimii, Vol. 77, No. 10, 2004, pp. 1659–1662.

APPLIED ELECTROCHEMISTRY AND CORROSION PROTECTION OF METALS

Choice of Electrolyte Composition for Liquid-Absorption Concentration of Mercury from Air for Subsequent Inversion-Voltammetric Determination

S. S. Ermakov, E. O. Averyaskina, and L. N. Moskvin

St. Petersburg State University, St. Petersburg, Russia

Received May 20, 2004

Abstract—An electrolyte composition is suggested for absorption recovery and concentration of mercury from air and its subsequent inversion-voltammetric determination on a gold electrode in a solution of the same composition.

In spite of the extremely high toxicity, mercury and its compounds find wide application in various fields of human activity: research, chemical industry, manufacture of chemical power cells, agriculture (treatment of seeds with mercury-containing fungicides), medicine, and cosmetics [1–3]. As a result, mercury comparatively frequently finds its way into the environment. Taking into account the volatility of elemental mercury, the problem of monitoring the content of mercury in the atmosphere arises most frequently. The maximum permissible concentration of mercury in the air of a working area is 10 $\mu g\ m^{-3}$ [4]. Combined with the wide demand for methods that can be used to monitor its contents in air, this circumstance imposes contradictory requirements to these techniques, namely, high sensitivity and simultaneous ready availability.

At present, the method of atomic-absorption spectroscopy in "cold" vapor has found the widest use for determination of mercury [5]. The main drawbacks of this method are the insufficiently high reproducibility of analytical data and the necessity for use of a comparatively expensive equipment [6, 7]. A new variety [8] of differential atomic-absorption spectroscopy opened up additional opportunities for making lower the detection limit in direct determination of traces of mercury in air. However, the cost of the analyzer increases in this case to an even greater extent, which makes this method inaccessible for most of laboratories engaged in ecological analysis. At the same time, inversion voltammetry with a gold electrode is known to be one of the most sensitive methods for determining mercury in aqueous media [9]. However, to apply this method for determining mercury in air, it is necessary to solve the problem of its liquid-absorption recovery from air. The composition of the absorbing solution should be as close as possible to the optimal composition of the background solution used in inversion-voltammetric determination of mercury.

The aim of this study was to choose a universal composition of the solution, which simultaneously enables absorption recovery of all possible chemical forms of mercury from air and its inversion-voltammetric determination on a gold electrode.

EXPERIMENTAL

To determine mercury(II) in solutions, we used an AKV-07 voltammetric analyzer (AKVILON NPKF, Moscow) with a three-electrode transducer: a rotating-disc working electrode in the form of a gold rod pressed in a fluoroplastic sheath, with a disc 1 mm in diameter as the working surface and a surface area of 0.8 mm^2; an auxiliary electrode in the form of a glassy carbon crucible serving simultaneously as a measuring cell; and an EVL-1M4 silver chloride electrode as reference. We prepared the surface of the indicator electrode as follows: after mechanical polishing of its surface with a fine emery paper, we polished the electrode electrochemically using the technique described in [10] and then additionally activated it directly in a mercury(II) solution to be analyzed, on the background of 1 M $HClO_4$ + 0.1 M HCl by electrode polarization at a potential of +1.3 V (1 min) in an agitated solution. The surface of the working electrode was cleaned between the measurements electrochemically in a solution of the same composition. We monitored the extent of cleaning by recording background voltammograms.

1070-4272/04/7710-1646 © 2004 MAIK "Nauka/Interperiodica"

A reference solution of mercury(II) with a concentration of 10^{-3} M was prepared from $Hg(NO_3)_2 \cdot H_2O$ and the concentration of the solution was determined by precipitation titration [11]. Chemically pure reagents were used, the solutions were prepared with twice-distilled water. A 10^{-3} M iodine solution was prepared by dissolving crystalline iodine in ethanol.

To choose conditions for absorption recovery of mercury with the aim of its subsequent inversion-voltammetric determination, we assembled a setup with in-series connected compressor, flask of mercury vapor generator, and two Tishchenko flasks. Flask no. 1 was used to absorb mercury, and flask no. 2, to test the completeness of absorption in the first flask. We used a flask blown through with air, with a drop of mercury on the bottom, as a generator of mercury vapor. To obtain reproducible results, air was blown above mercury into an exhaust hood for 1 min before each measurement and then the air flow with mercury vapor was directed into the absorbing Tishchenko flasks. The measurements were made and the flow rate of air was controlled with an RM-25GUZ-K rotameter. Compressors manufactured by AND and Barnant companies were used to inject air.

When choosing a universal composition of the solution, we used as the starting assumption that the inversion-voltammetric determination of mercury is usually carried out on the background of a mixture of perchloric and hydrochloric acids. The optimal composition of the background solution is 1 M $HClO_4$ + 0.1 M HCl [12]. However, all attempts to use a solution of such a composition as an absorbent even for recovery of mercury present in air in the elemental state appeared to be ineffective. This was indicated by the fact that, even after blowing air through the absorbing installation at a rate of 1 l min^{-1} for 10 min, the concentration of mercury in the background solution placed in Tishchenko flasks was about the same.

To make the catching of mercury more complete by converting atomic mercury into a nonvolatile ionic form, we tested as absorbent a solution into which nitric acid was introduced as an oxidizing agent. The background curves obtained in the solutions with HNO_3 introduced in concentrations higher than 1×10^{-4} M show (Fig. 1) an anodic peak dependent on the concentration of HNO_3 ($E_{peak} = 0.68 \pm 0.01$ V) is observed at potentials close to those of mercury ionization. This peak virtually disappears at HNO_3 concentrations $\leq 1 \times 10^{-4}$ M. The introduction of 1×10^{-4} M of HNO_3 into the absorbing solution was insufficient for complete absorption of atomic mercury from air. However, the ratio between the mercury concentrations in Tishchenko flask nos. 1 and 2 was improved (no. 1, ~80%; no. 2, ~20%).

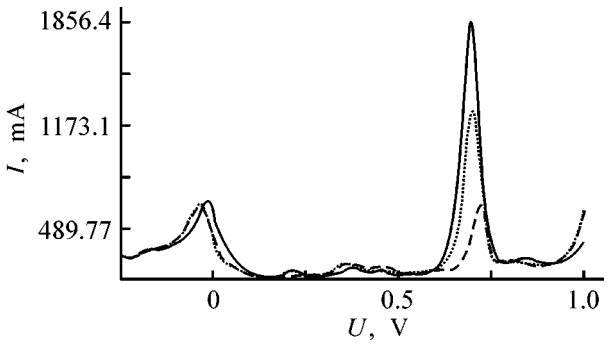

Fig. 1. Voltammogram obtained in a solution of composition 0.1 M HCl + 1 M $HClO_4$ + 1×10^{-3} M HNO_3 with addition of mercury. (I) Current and (U) voltage; the same for Fig. 2. Each curve corresponds to an increase in the concentration of nitric acid by an order of magnitude.

Therefore, we chose a solution of composition 0.1 M HCl + 1 M $HClO_4$ + 1×10^{-4} M HNO_3 for further experiments.

In our search for the conditions of absorption recovery of mercury, we took into account the known fact that virtually all forms of mercury are caught from air by activated carbon with elemental iodine absorbed on it [12]. By analogy, we studied the possibility of mercury absorption by a background electrolyte with addition of iodine. Molecular iodine was introduced into a solution of composition 0.1 M HCl + 1 M $HClO_4$ + 1×10^{-4} M HNO_3 by adding a solution of iodine in ethanol. The addition of iodine to the absorbing solution gave positive results. Mercury was found only in the solution contained in Tishchenko flask no. 1.

When choosing the optimal concentration of iodine, we started from the following. First, it was necessary to ensure a sufficient excess of iodine in the reaction mixture to effectively recover mercury from air and, second, the concentration of iodine should be not too high, because it is electrochemically active. In the presence of iodine, a peak is observed at +0.62 V in the voltammograms. Accordingly, at higher concentrations of mercury in air (>100 μg m^{-3}) and iodine in the absorbing solution (>10^{-5} M), an unresolved peak is observed in the voltammograms at 0.08–0.91 V (Fig. 2a). This peak corresponds to ionization of mercury with the formation of iodide complexes and to electrochemical conversion of iodine. In view of the fact that the mercury concentration range of practical interest for monitoring the content of mercury in air is in the range from several micrograms per cubic meter to tens of μg m^{-3}, we changed the conditions under which mercury vapor was generated. The area of the mercury mirror, over which the air was blown, was decreased from 400 to 16 mm^2. It was

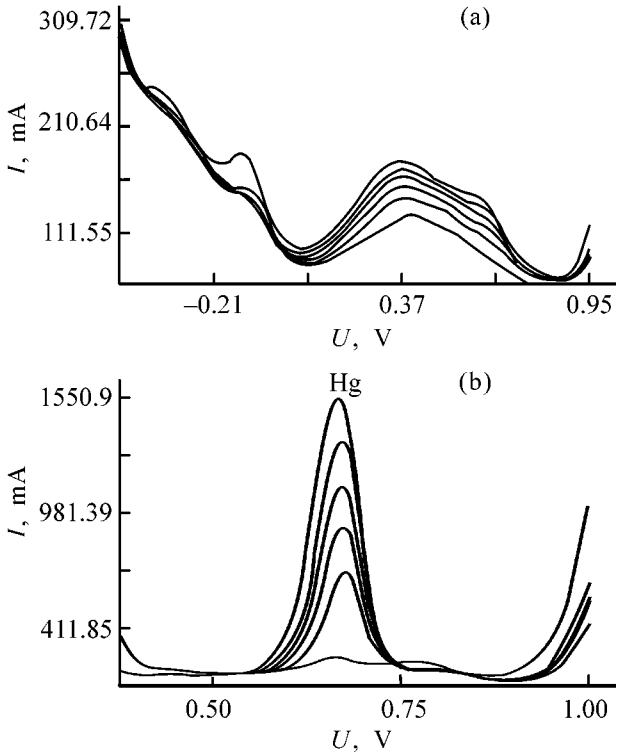

Fig. 2. Peak area in the voltammogram in bubbling air with a mercury vapor through a solution with a known concentration of Hg^{2+} ions. t_{acc} = 1 min. C_{I_2} (M): (a) 1×10^{-4} and (b) 1×10^{-6}.

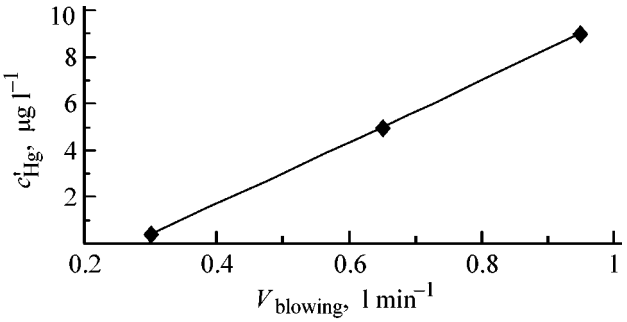

Fig. 3. Mercury concentration c'_{Hg} in a solution of composition 1 M $HClO_4$ + 0.1 M HCl + 2×10^{-4} M I_2 + 1×10^{-4} M HNO_3 vs. the rate of air blowing-through, $V_{blowing}$. t_{acc} = 60 s, flask no. 1.

found that the iodine concentration in solution, sufficient for complete recovery of mercury, is 1×10^{-6} M. No peak of iodine was observed in the voltammograms at this concentration (Fig. 2b).

A study of the concentration of mercury vapor in a solution at the outlet of the generator in relation to the blowing rate at a fixed volume of air (1 l) passed through the system gave the results presented in Fig. 3. It follows from the data obtained that the content of mercury at a blowing rate of 0.3–1 l min^{-1} varies in direct proportion to the blowing rate. Taking into account the experimentally confirmed completeness of mercury recovery with the solution of the chosen composition, we used a calibration plot constructed using data for reference solutions to determine the mercury concentration in air. This concentration, c'_{Hg}, was calculated by the equation

$$c'_{Hg} = c''_{Hg} \frac{V''}{V'},$$

where c''_{Hg} is the mercury concentration in the absorbate, found from the calibration plot; V'', volume of the absorbate; and V', volume of air blown through the system constituted by the generator and the absorbing vessel.

All the experimental data presented above suggest that the chosen solution composition provides for 100% mercury vapor catching in a wide range of mercury concentrations in air and allows inversion-voltammetric determination of mercury in a solution of the same composition.

REFERENCES

1. *Rtutnaya opasnost' – problema XX veka: Sbornik materialov* (Mercury Hazard, a Problem of the XX Century: Coll. of Materials), St. Petersburg, 1994.
2. Trakhtenberg, I.M. and Korshun, M.N., *Rtut' i ee soedinenniya v okruzhayushchei srede (Gigienicheskii i ekologicheskii Aspekty)* [Mercury and Its Compounds in the Environment (Hygienic and Ecological Aspects), Kiev: Vyshcha Shkola, 1990.
3. Isidorov, V.A., *Vvedenie v kurs khimicheskoi ekotoksikologii* (Introduction to Chemical Ecotoxicology), St. Petersburg: SPb Gos. Univ., 1997.
4. Bespamyatnov, G.P. and Krotov, A., *Predel'no dopustimye kontsentratsii khimicheskikh veshchestv v okruzhayushchei srede* (Maximum Permissible Concentrations of Chemical Substances in the Environment), Leningrad: Krismas+, 1985.
5. Antonovich, V.P. and Bezlutskaya, I.V., *Zh. Anal. Khim.*, 1996, vol. 51, no. 1, pp. 116–123.
6. Tatsii, Yu.G., *Partn. Konkurenty*, 2001, no. 4, pp. 22–26.
7. Khomik, L.I., Koval'skii, Yu.G., and Talovskaya, V.S., *Lab. Novost. Dal'n. Vost.*, 1999, no. 2, pp. 17–21.
8. Sholupov, S.E., Ganeev, A.A., Vergizova, V.S., *et al.*, *Zh. Anal. Khim.*, 1999, vol. 54, no. 1, pp. 61–69.
9. Peregud, E.A., *Khimicheskii analiz vozdukha* (Chemical Analysis of Air), Leningrad: Khimiya, 1996.
10. Grilikhes, S.Ya., *Elektrokhimicheskoe i khimicheskoe polirovanie* (Electrochemical and Chemical Polishing), Leningrad: Mashinostroenie, 1987.
11. Nemodruk, A.A., *Analiticheskaya khimiya mysh'yaka* (Analytical Chemistry of Arsenic), Moscow: Nauka, 1976.
12. Gladyshev, V.P., *Analyticheskaya khimiya rtuti* (Analytical Chemistry of Mercury), Moscow: Nauka, 1974.

Russian Journal of Applied Chemistry, Vol. 77, No. 10, 2004, pp. 1649–1652. Translated from Zhurnal Prikladnoi Khimii, Vol. 77, No. 10, 2004, pp. 1663–1666.

APPLIED ELECTROCHEMISTRY AND CORROSION PROTECTION OF METALS

Air Electrode of Chemical Power Cell as Oxygen Sensor

M. O. Danilov, G. Ya. Kolbasov, and N. V. V'yunova

Institute of General and Inorganic Chemistry, Ukrainian National Academy of Sciences, Kiev, Ukraine

Received February 21, 2003; in final form, April 2004

Abstract—The possibility of using the air electrode of a chemical power cell as an electrochemical oxygen sensor was studied.

The industrial development and ecological problems put forward, into a number of problems of current interest, the development of selective gas sensors for oxygen, hydrogen, and other gases [1, 2]. There exist two types of sensors: semiconductor [1, 2] and electrochemical [3, 4]. Semiconductor sensors have a semiconducting indicator element whose properties are changed under the action of a reagent to be determined. Electrochemical sensors intended for analysis of the gas composition of the atmosphere have the indicator electrode in which the electrode potential or the flowing current changes under the action of the reagent to be determined.

There exist electrochemical sensors of two types: potentiometric and amperometric. Amperometric sensors, in which the component to be determined is involved in a current-forming reaction, have the highest sensitivity among electrochemical sensors. Owing to the appropriate choice of catalysts for specific electrochemical reactions, amperometric sensors may have high selectivity and sensitivity. Electrochemical sensors based on a gas-diffusion electrode are preferable for analysis of gaseous media [4].

The goal of this study was to examine the possibility of using a porous gas-diffusion electrode, which is commonly applied in metal–air power cells and fuel cells, for analysis of oxygen-containing gaseous media. The prototype of such sensor is the air (oxygen) electrode of a chemical power cell.

The porous gas-diffusion electrode is a three-phase system electrode–electrolyte–oxygen [5]. The gas to be determined diffuses through a hydrophobic layer and enters into the current-forming reaction at the interface between three phases, gas–electrode–electrolyte.

As sensor for determining oxygen in the gas phase can serve a zinc–air chemical power cell or the oxygen electrode of a fuel cell working in a salt or acid electrolyte. The limitations associated with the use of an inert electrolyte are imposed in order to improve the selectivity of the sensor. This is because alkaline solutions can be carbonized in pores of the electrode by CO_2 present in the gas phase.

Let us consider the current-forming reaction at the air (oxygen) electrode in a neutral salt electrolyte:

$$O_2 + 4H^+ + 4e \rightarrow 2H_2O.$$

According to the data of [6, 7], where the kinetics of gas-diffusion porous oxygen electrodes is described, the current generated by this reaction is affected by the following factors: amount of fluoroplastic; electrode porosity; particle size of the catalyst, fluoroplastic, and carbon support; electrical conductivity of the electrolyte; and temperature. The electrode thickness and the dimensions of the current generation zone will also affect the current being generated. The dependence of the current on the electrode potential is determined not only by the Tafel slope but also by the relative values of the kinetic and transport coefficients of oxygen and the electrolyte.

Therefore, the oxygen sensor should have an inactive electrolyte, which poorly dissolves oxygen and does not enter into chemical reactions with possible impurities present in a gaseous medium. The indicator electrode should be composed of stable materials that are inert toward the gaseous medium. It should not include any oxygen-containing complexes and materials that can be involved not only in oxygen reduction, but also in a current-forming reaction, e.g., MnO_2.

As indicator electrode was used a combined matrix of the air electrode based on BAU activated carbon and

1070-4272/04/7710-1649 © 2004 MAIK "Nauka/Interperiodica"

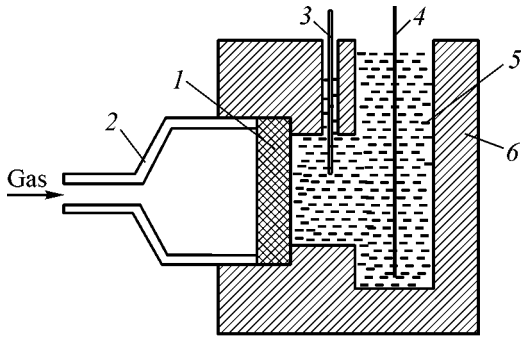

Fig. 1. Schematic of the electrochemical cell of the oxygen sensor: (*1*) indicator electrode, (*2*) gas-feeding chamber, (*3*) reference electrode, (*4*) auxiliary zinc electrode, (*5*) electrolyte, and (*6*) cell body.

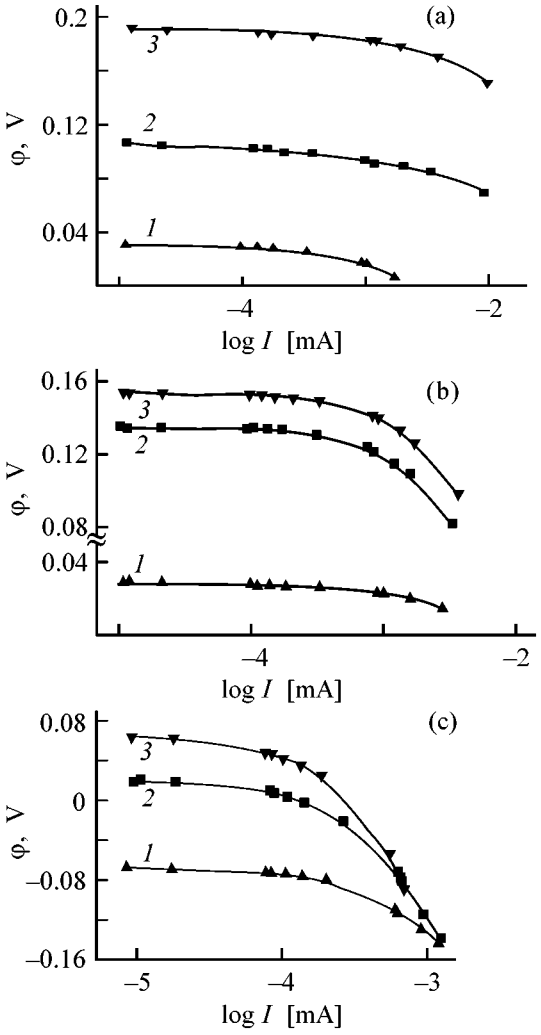

Fig. 2. Potential φ vs. current *I* for indicator electrode based on (a) BAU activated carbon, (b) polyaniline, and (c) combined matrix composed of polyaniline and BAU carbon in various gaseous media. (*1*) Argon, (*2*) air, and (*3*) oxygen.

electrochemically produced polyaniline. As shown previously [8], introduction of electrochemically produced polyaniline into the combined matrix gives a well-working air electrode. Therefore, a polyaniline matrix was used in the study. A salt electrolyte of composition 5 M NH_4Cl and 2 M $ZnCl_2$ was chosen. As auxiliary electrode served zinc, with the result that the sensor operated on the basis of an oxygen-zinc chemical power cell. The preparation of polyaniline and fabrication of the electrodes were described in [8]. All the potentials were measured relative to a silver chloride reference electrode. The indicator electrodes were fabricated from BAU activated carbon, pure polyaniline, and a combined matrix composed of polyaniline and BAU carbon.

The current–voltage characteristics of the oxygen sensor were measured in a three-electrode circuit in the current generation mode with a high-input-resistance voltmeter and microammeter.

The sensitivity of the air electrode based on the matrix was measured as follows. After the electrode was kept in argon, its potential (0.08 V relative to a silver chloride electrode) and the current at a load of 1×10^5 Ω were measured. Then, gaseous media were successively changed, the electrode was kept for 1 h, and the potential of the indicator electrode was adjusted to –0.08 V by making the load resistance lower. The current generated in the different media was recorded. The time of keeping in each medium was 1 h, although the potential varied noticeably only during the first 15 min.

The setup for testing the sensor is shown schematically in Fig. 1. The indicator electrode, composed of the matrix of the air electrode, was placed as a membrane between the gaseous medium and the electrolyte. The gas-feeding chamber, when tightened, firmly pressed the indicator electrode to the cell body. This chamber also served as a current lead.

The sensitivity of the oxygen sensor was tested in three gaseous media: oxygen-free atmosphere (argon), atmospheric air containing 21% oxygen, and a 100% oxygen atmosphere. The measurements were commenced in the oxygen-free atmosphere. Prior to a measurement, the electrode was kept for 2 h at a low pressure in the atmosphere to be analyzed. The excess pressure of the medium, created using an oxygen bag, was monitored with a gage.

The current–voltage characteristics of the indicator electrode in media with varied content of oxygen are shown in Figs. 2a–2c. Figure 2a demonstrates the cur-

rent–voltage dependence for the indicator electrode composed of activated carbon. As can be seen, at the minimum load of 300 Ω, on applying which the electrode is changed irreversibly, the potential corresponding to the argon atmosphere could not be reached in polarization with a flowing current in the atmosphere of air and oxygen. For the indicator electrode based on the electrochemically obtained polyaniline, it was possible to obtain rather close potentials at the minimum load (Fig. 2b, curves *2*, *3*) for air and oxygen, but it was impossible to reach the potentials corresponding to the atmosphere of argon (Fig. 2b, curve *1*).

The best coincidence of the potentials in argon, air, and oxygen (Fig. 2c, curves, *1*, *2*, and *3*, respectively) could only be achieved at the minimum possible load for the indicator electrode based on a combined matrix of activated carbon and polyaniline. As can be seen from Figs. 2a–2c, the current and potential of indicator electrodes respond to a certain extent to variation of the oxygen concentration in a gaseous medium. An analysis of Figs. 2a–2c demonstrated that the best suitable electrode for the oxygen sensor is a combined matrix composed of BAU activated carbon and polyaniline. With this electrode, a coincidence of the potentials in air and oxygen with the initial potentials in argon atmosphere was achieved at a load of 300 Ω and a polarization of 150 mV.

In this case, after switching off the polarization, the potentials of the matrix in different media returned to their initial values after a certain time at rest. This indicates that no irreversible changes occurred in the combined carbon-and-polyaniline matrix at a load of 300 Ω and a polarization of 150 mV.

The dependences of the potentials of the indicator electrodes composed of activated carbon, polyaniline, and a combined matrix on the oxygen concentration in the gaseous medium are shown in Fig. 3 (curves *1*, *2*, and *3*, respectively). As can be seen, the dependence is nonlinear for all the electrodes. This may be due to a change of the mechanism of oxygen diffusion in the hydrophobic layer toward the current generation zone on passing from a mixture of oxygen with the inert gas to pure oxygen.

The results obtained in measuring the sensitivity of the sensor with an indicator electrode based on a combined matrix composed of BAU activated carbon and electrochemically obtained polyaniline are presented in Fig. 4. An estimation of the sensitivity of this electrode from the dependence of the current on the oxygen concentration gives a rise in current by a factor of 180 on raising the oxygen concentration in air from 0 to 21%.

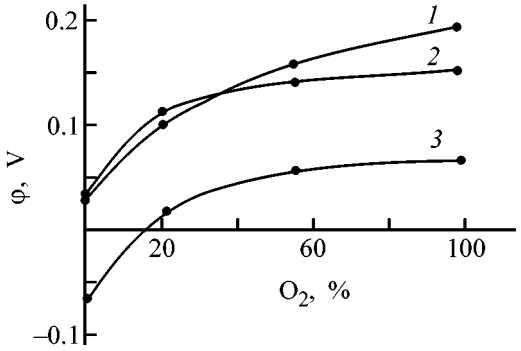

Fig. 3. Potential φ of the indicator electrode made of various materials vs. the oxygen concentration O_2 in a gaseous medium at a load of 10^5 Ω. Indicator electrode based on: (*1*) BAU activated carbon, (*2*) polyaniline, and (*3*) combined matrix composed of polyaniline and BAU carbon.

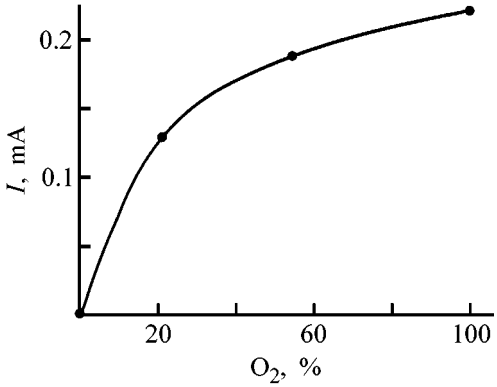

Fig. 4. Current *I* vs. oxygen concentration O_2 for the indicator electrode based on polyaniline and activated carbon.

CONCLUSIONS

(1) Electrochemical oxygen sensors can be created on the basis of the air electrode of a chemical power cell. For this purpose, it is necessary to use a neutral salt electrolyte or an acid electrolyte that does not react with the medium to be analyzed.

(2) Owing to the use of electrocatalysts for oxygen reduction, these sensors possess a high sensitivity for oxygen in the gaseous medium to be analyzed.

REFERENCES

1. Ermolaeva, T.N., Lavrent'eva, T.A., Seredkin, A.E., and Korenman, Ya.I., *Zh. Prikl. Khim.*, 2001, vol. 74, no. 2, pp. 197–202.

2. Rumyantseva, M.I., Bulova, M.N., Kuznetsova, T.A., *et al.*, *Zh. Prikl. Khim.*, 2001, vol. 74, no. 3, pp. 425–430.
3. Tailleferi, M., Luther, G.W., and Nuzzo, D.B., *Electroanalysis*, 2000, vol. 12, no. 6, pp. 401–412.
4. Chviruk, V.P., Zaverach, E.M., and Linyucheva, O.V., *Electrokhimiya*, 2001, vol. 37, no. 5, pp. 599–605.
5. Ksenzhek, O.S., Shembel', E.M., Kalinovskii, E.A., and Shustov, V.A., *Elektrokhimicheskie protsessy v sistemakh s poristymi matritsami* (Electrochemical Processes in Systems with Porous Matrices), Kiev: Vishcha Shkola, 1983.
6. Korovin, N.V., *Elektrokhim. Energet.*, 2001, vol. 1, nos. 1, 2, pp. 16–23.
7. Chizmadzhev, Yu.A., Markin, V.S., Tarasevich, M.P., and Chirkov, Yu.G., *Makrokinetika protsessov v poristykh sredakh* (Macrokinetics of Processes in Porous Media), Moscow: Nauka, 1971.
8. Danilov, M.O., and V'yunova, N.V., *Zh. Prikl. Khim.*, 2001, vol. 74, no. 2, pp. 335–337.

Russian Journal of Applied Chemistry, Vol. 77, No. 10, 2004, pp. 1653–1661. Translated from Zhurnal Prikladnoi Khimii, Vol. 77, No. 10, 2004, pp. 1667–1675.

APPLIED ELECTROCHEMISTRY AND CORROSION PROTECTION OF METALS

Characteristics of Surface Microprofile of Electrolytic Copper Foil with High Adherence to Insulator

L. A. Kuznetsova, I. V. Semiletova, and E. I. Makogina

Institute of Chemistry, Far Eastern Division, Russian Academy of Sciences, Vladivostok, Russia
Far Eastern State University, Vladivostok, Russia

Received August 12, 2004

Abstract—The topography of a copper electrolytic foil with varied adherence to an insulator was studied by the methods of statistical analysis of profilograms, by optical and scanning electron microscopies, and by coherent optics. The morphology of the deposit surface was revealed, and the microprofile constants responsible for the adhesion were determined. A method for obtaining a foil with high adhesion strength was suggested.

One of requirements imposed on the copper foil used in radio engineering and microelectronics for metallization of insulators is the high strength of copper adhesion to the substrate. The adhesion of dissimilar materials depends on the physicochemical affinity of substances brought in contact [1] and on their mechanical interaction associated with the structure and topography of the foil [2, 3]. The highest adhesion strength is observed for a foil with two- or three-layered structure [4]. It is obtained by depositing an "adhesion layer" of powdered copper on films of compact copper (so-called "raw" foil). Rather frequently, powder particles are passivated or coated with a thin "reinforcing" layer of various metals to prevent their fall-off [5, 6].

The aim of this study was to analyze the adhesion properties of various samples of a multilayer foil to reveal the microgeometric structure of the surface of its separate layers and to develop a morphological factor and a method for obtaining copper that would provide a high adherence of metal to a nonconducting support.

EXPERIMENTAL

The parameters of the foil samples studied are listed in the table. All the samples, except sample no. 1, were coated with copper powder, and sample nos. 3, 6, 7, with additional reinforcing copper (no. 3) and brass (nos. 6, 7) layers. Differences in sample preparation are unknown because of the foreign origin of sample nos. 4–7 (Germany, Luxembourg, and USA).

The foil was attached to the insulator and the adhesion strength was estimated according to GOST (State Standard) 10316–78 and 262460–89. On a foil-clad fiber-glass plastic produced by the method described in [7], a pattern was etched in the form of four copper strips 74 mm long and 3 mm wide, spaced by 10 mm. The etching was performed in a solution of ferric chloride (density 1.4 g cm^{-3}) at 50°C. After washing and drying, the steady load at which no less than 25–30 mm of the foil was detached was determined for each strip with a RMU-0.005 tensile machine at a motion velocity of the mobile clamp of 50 mm min^{-1}. The minimum load determined by measurements on four strips described above was taken as the adhesion strength. Three parallel measurements were made on each sample. The average values of the thus determined adhesion strength are listed in the table.

The structure of cross sections of the foil was studied on an MMP-4 metallographic microscope. The surface microgeometry was examined on an ISM-U3 scanning electron microscope (SEM) and a Kalibr-201 profilograph, and analyzed by means of coherent Fourier optics. The combination of these methods allowed monitoring of the wide variety of geometric irregularities on the surface, from elements of growth of crystal faces and single grains of the deposit to their conglomerates and microscopic waves caused by microscopic nonuniformities of the foil thickness.

An LA-70 analog-to-digital converter connected to a profilographic amplifier (±5 V) was used to obtain data arrays with a 1-μm step along a 1–1.5-mm trace

1070-4272/04/7710-1653 © 2004 MAIK "Nauka/Interperiodica"

Adhesion strength and parameters of the surface microprofile of foil samples, determined by profilometry* (Longitudinal tracing)

Sample no.	Adhesion strength, N m^{-1}	R_{am}	H_{rms}	R_z	H_{max}	L_{av}	S_{tr}/S_0	α, deg	N_0, mm^{-1}
		μm							
1	490 ± 30	0.881	1.042	3.946	4.304	23	1.069	7.448	43
1**		0.761	0.902	3.466	4.461	16		6.738	61
2	1140 ± 200	0.901	1.097	4.338	4.990	15	1.048	5.942	66
2**		0.763	0.944	3.780	4.340	18		6.389	56
3	1310 ± 100	–	–	–	–	–	–	–	–
3**		0.920	1.123	4.570	5.622	21		6.909	47
4	1640	0.748	0.939	4.064	4.999	19	1.069	7.933	51
4**		0.768	0.919	3.664	3.987	19		7.314	53
5	1830 ± 130	1.086	1.311	5.498	6.030	20	1.091	9.332	49
5**		1.043	1.319	5.416	7.170	23		8.663	43
6	2120 ± 150	1.018	1.256	5.292	6.780	16	1.095	9.757	60
6**		0.844	1.033	4.274	5.330	21		9.407	46
7	2190 ± 150	0.990	1.288	6.152	7.940	22	1.097	7.653	45
7**		1.108	1.355	5.582	6.970	19		9.192	51

* R_{am} and H_{rms}, the arithmetic mean and root-mean-square deviation of the profile, respectively; R_z and H_{max}, maximum height of irregularities; L_{av}, average width and α, average angle of inclination of the irregularities; l_{tr}, true length of the profile; S_{tr}, true surface area of the foil; and N_0, average number of iregularities per unit length of the trace.

** Transverse tracing.

of the microprofile in two mutually perpendicular directions, one of which coincided with the direction of motion of the foil in the electrolyte. The parameters characterizing the topography of the foil surface (see table) were determined by statistical processing of the data arrays, using a special software (based on formulas from [3, 8, 9]). The distribution of the metal along the height of the rough layer was characterized by plotting reference curves [8]. In addition, the distributions of the irregularities by height H, width L, and shape H/L were determined from the dependences of N/N_0 on H, L, and H/L, where N is the number of irregularities with the corresponding geometry.

A 35-μm-thick laboratory sample of foil was obtained by the method suggested previously [7] in pulsed electrolysis mode from an electrolyte of composition (M): $CuSO_4 \cdot 5H_2O$ 1 and H_2SO_4 0.5, on the polished steel cathode at 20°C. The current density was 6 A dm^{-2}, the pulse width, intervals between the pulses, and the total duration of electrolysis were 1 s, 5 s, and 2.7 h, respectively. To apply the adhesion layer, the electrode coated with raw copper was submerged in a 10^{-3} M solution of thiourea for 5 s. Then it was washed in distilled water and electrolysis was performed at 0.5 A dm^{-2} for 60 s at 18°C in an electrolyte containing (M): $CuSO_4 \cdot 5H_2O$ 0.02 and H_2SO_4 0.2.

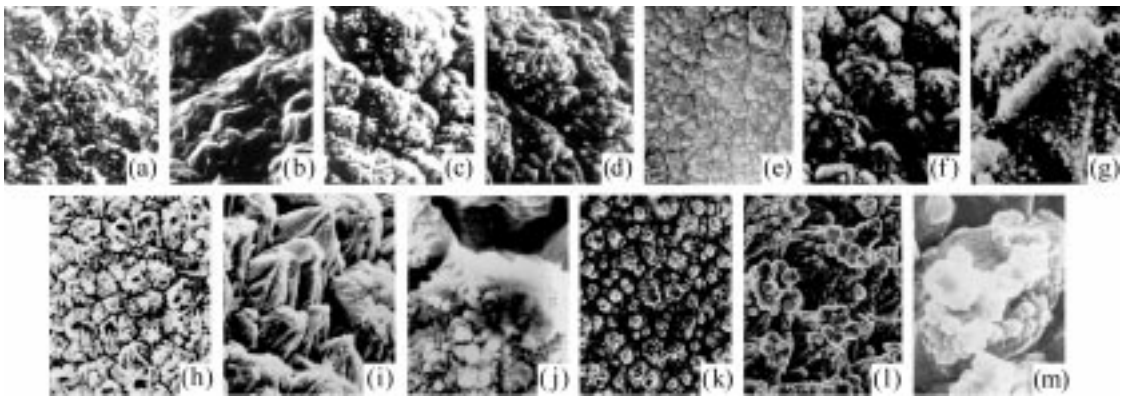

Fig. 1. Micrographs of the surface of the foil samples (a, b) no. 1, (c, d) no. 2, (e–g) no. 4, (h–j) no. 5, and (k–m) no. 6. Magnification: (k) 1500, (a, e, h) 2000, (c) 4000, (b) 4500, (f, i, l) 6000, (d, m) 12000, and (c, j) 20000. Measurement angle (deg): (a, e, h, j, k) 0 and (b–d, f, g, i, l, m) 45.

SEM micrographs of the foil surface are shown in Fig. 1. The surface of the raw foil with a low adhesion strength has loosely globular structure with a clearly pronounced nonuniformity of grains (grain size from 3 to 15 μm), which are speckled with Burgers dislocations and micropores (Figs. 1a, 1b). The layer of powdered copper, deposited on these structures, has the form of 0.3–0.4-μm grains of copper and copper oxide, which are uniformly distributed over the surface of flat crystals and somewhat decrease in size in going from projections to intergrain depressions (Figs. 1c, 1d). Deposition of a reinforcing layer of compact copper onto the powder has virtually no effect on structure of this foil.

Sample no. 4, like sample nos. 1–3, is not distinguished by high uniformity of the support grains (Figs. 1e–1g). At the same time, the scatter of their sizes, as also the size of the grains themselves (2.5–5 μm), considerably decreases. The powder layer has an extremely nonuniform distribution. The size of the powder particles is approximately 0.1–0.2 μm, i.e., a factor of 2–3 smaller than that of sample nos. 2, 3. At magnifications of about 20000, grains of raw copper in the form of faceted hexagonal pyramids with a conglomerate of powder particles at their vertices are clearly revealed (Fig. 1g). The insulator in which the foil is pressed may flow beneath such powder formations, with mechanical "locks" enhancing the adhesion produced as a result [3]. The adhesion strength is determined by the fraction of the surface, ν, occupied by the locks. This parameter can be evaluated by the ratio of the area under the lock to that occupied by a grain of the raw foil. Owing to the existence of a contact zone between the adhesion layer and the raw foil, the width of the lock is only a fraction of the width of a powder formation. This makes difficult finding the area under the lock, and, consequently, ν, too. We can roughly estimate ν by neglecting the above discrepancy and taking into account that the amount of the powder at the vertices and the zone of its contact with the grain grow simultaneously. In what follows, we name the powder formation the lock, thus emphasizing its function.

The minimum width of the lock for sample no. 4 is approximately 0.5–1 μm, i.e., 0.2 of the width of a raw foil grain, which corresponds to $\nu = 0.04$. As a base of the lock can serve any irregularity (projection or depression) making an acute angle with the visible surface of the foil [3]. In this case, even single particles of a uniformly distributed powder can act as locks if they are sufficiently large in size and have a granular structure similar to that in sample nos. 2, 3,. This seems to be a possible explanation of why the adhesion strength of the last two samples is better than that of sample no. 1.

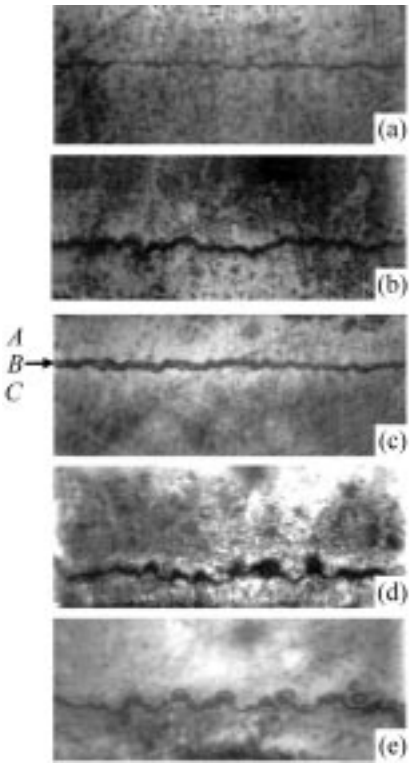

Fig. 2. Cross-sectional micrographs of the foil samples (a) no. 4, (b) no. 5, (c) no. 2, (d) no. 6, and (e) no. 7. Magnification: (a–c) 400 and (d, e) 600. (*A*) Raw foil, (*B*) powder, and (*C*) reinforcing copper sublayer.

A specific feature of sample nos. 5–7 (Figs. 1h–1m) is the pronounced uniformity of the substrate structure. The grains of the raw foil have a conical shape with the longitudinally folded facets. Their transverse dimensions are 4–6 μm (sample no. 5) or 5–7 μm (sample nos. 6–7). The copper powder is predominantly concentrated at projections of irregularities. The powder grain size of sample no. 5 is the same as that of sample no. 4 and five times less than that of sample nos. 6, 7. The micrographs of the foil clearly show the locks, each with small pits. The pits can enhance the adherence of the foil to the insulator, if their lateral faces make an acute angle with the bottom of a pit [3]. The minimum width of the lock is, similarly to sample no. 4, 0.2 of the grain width in the raw foil. The maximum width is markedly larger. It constitutes 0.3–0.5 of the width of the substrate grain.

Cross-sectional optical micrographs of foil samples (nos. 2, 4–7) are shown in Fig. 2. On sections prepared by the conventional procedure [10], two layers of compact copper with a dark layer of the powder in

between are clearly visible. One layer of compact copper is the raw foil, and the other, a the specially deposited reinforcing sublayer for preventing formation of roll-offs in polishing and finishing of the cross-sections of the samples to be studied. The surface of the raw foil is rough to a varied extent. The most pronounced roughness is observed for a foil with uniformly conical grains (sample nos. 6, 7), and the least rough surface, for a foil with extremely high size nonuniformity of grains of raw copper (sample no. 3). The adhesion layer reproduces the microprofile of the support, but its thickness and thickness uniformity vary between different samples. For example, a virtually uniform distribution of the powder over the irregularities of the raw foil is observed for sample nos. 2, 4, and 5, but the thicknesses of the powder layers are different. It is the same and equal to about 5 μm for sample nos. 2 and 5, and two times smaller for sample no. 4. A clearly pronounced nonuniformity in the distribution of the powder layer over microdefects of the substrate is observed for sample nos. 6, 7. In this case, globular formations of the powder with radius varying from 1 to 4 μm are present on microprojections of the raw foil. Apparently, they favor formation of locks. On the lateral edges and at microdepressions, the adhesion layer is, by contrast, virtually absent.

Thus, the results of our study of the surface morphology of a foil coated with a powder layer and of its cross-sections suggest that the adhesion strength is determined by the structure of the layers of both raw and powdered copper. The pointed crystals of the support ensure a reliable and deep penetration of the metal into the insulator. The nature of distribution of the powder particles over the grains of the raw foil provides formation of the mechanical locks of different shapes, from separate granular particles to conglomerates of various pointed irregularities. The highest adhesion is ensured by locks in the form of conical formations whose vertices are oriented toward vertices of raw copper grains and bases extend across voids of various sizes.

The microscopic study of the foil is mostly of descriptive nature. Obtaining the numerical parameters is limited to only the average size of structural elements. A more detailed quantitative description of the foil structure requires use of additional methods. In the study, the surface was examined by the method of contact profilography, with the subsequent statistical processing of the profilograms obtained.

The results of the statistical processing (see table) show that the parameters characterizing the height of the surface microprofile (R_{am}, H_{rms}, R_z, and H_{max}) are comparatively close for all the samples (R_{am} = 0.75–1, H_{rms} = 0.93–1.3, R_z = 3.5–6.1, and H_{max} = 3.9–7.9). Although no unambiguous correlation between the height of the microprofile and the adhesion strength can be revealed, a part of foil with an increased adhesion (sample nos. 5–7) has a somewhat more pronounced roughness (by 10–20%). No regular relationship is observed between the adhesion strength and the transverse dimensions of foil grains, which vary from 15 to 23 μm for different samples. For example, for foils with virtually the same average grain widths (sample nos. 1, 6) the strength of adherence to the insulator differs by more than a factor of 4. As indicated by the S_{tr}/S_0 ratio at S_0 = const, the true surface area of the foil coated with powder copper (sample nos. 2–7) steadily grows as their adherence capacity becomes higher. Only sample no. 1, which has no adhesion layer, falls out of the general trend. On the assumption that the irregularities have a triangular profile, it can be readily shown by a simple calculation that the ratio of S_{tr} to the apparent surface area S_0 is given by

$$S_{tr}/S_0 = (l_{tr}/l_0)^2 = (1/\cos\alpha)^2.$$

A similar result is obtained on the assumption of a spheroid shape of the irregularities.

$$S_{tr}/S_0 = (l_{tr}/l_0)^2 = [\alpha_1/2\sin(\alpha_1/2)]^2.$$

This means that the true surface area can be qualitatively characterized by the average angle of inclination of the irregularities, α, or by their curvature α_1. The greater α or α_1, the larger the true surface area, and statistical calculations do confirm this conclusion. As can be seen from the data in the table, the average angle of inclination of the irregularities varies similarly to S_{tr} as the adhesion increases. Another parameter indirectly characterizing the S_{tr} is the number of irregularities per unit length of the trace N_0 [3]. However, no correlation is observed between S_{tr} and N_0. This inconsistency may be due to the fact that profilography can give only a rough account of the true surface area of foil, which should be estimated [9] by considering simultaneously profilograhic data and those furnished by optical and scanning electron microscopies. Apparently, the method of contact profilography characterizes only that part of the surface which is formed by a conglomerate of grains. As to the true surface area of faces of grains themselves, coated with the powder, it can be qualitatively estimated from the secondary-electron emission spectra.

The secondary-electron emission spectra can be recorded simultaneously with sample surface imaging on a scanning electron microscope. These spectra are shown on the background of the surfaces studied in Figs. 3a, 3b. They look like profilographic traces on the surface of the samples at places indicated in the micrographs by solid lines. Special experiments on surfaces with undulate and steplike microprofiles showed that, unlike contact profilograms, the "optical profilograms" reflect neither areas with different heights, nor gently sloping waves. They are not affected by photographic magnification, either, and exhibit response solely to the angle of inclination of the irregularities and their curvature, i.e., to the true surface area of a foil. The stronger the average curvature of the irregularities, the larger S_{tr} and the higher the profile. This allows a qualitative estimate of the true surface area of crystals, which depends on the microgeometry and distribution of powder particles, by comparing the heights of optical profilograms.

The secondary-electron emission spectra, obtained from the surface of sample nos. 2–6 (Fig. 3), show that no unambiguous correlation exists between S_{tr} and the structure of the powder layer. Indeed, fine powder particles uniformly distributed over grains of raw copper (sample no. 3) exhibit a higher emission intensity than coarser particles irregularly covering the compact foil (sample no. 6). At the same time, sample nos. 2, 4, and 5 have, despite their different morphologies, spectra with virtually equal intensities, which is higher than those for sample nos. 3 and 6. Consequently, the true surface area associated with the powder structure and evaluated microscopically is not a factor determining the adherence of a foil to an insulator, unlike S_{tr}, which is found by profilography and takes into account profile elements with transverse dimensions of no less than 10 μm.

The results obtained in profilogram processing, which describe the distribution of the metal along the height of the rough layer and the distributions of the microprofile irregularities by size and shape are shown in Fig. 4.[1] The run of the reference curves (Fig. 4a) shows that the foil with higher adhesion strength (sample nos. 4–7) is distinguished by a steep drop of the deposit heights h at low and high fillings of the rough layer with the metal, l, at a length of the profile studied equal to l_0. This shows that high adhesion strength is typical of samples with roughness characterized by steeper projections and depressions. In this case, the size distribution of irregularities is uniform for all the foil samples, because the run of the reference curves is monotonic without sharp bends and inflections, which appear when microprofile elements of widely different sizes are present on the surface.

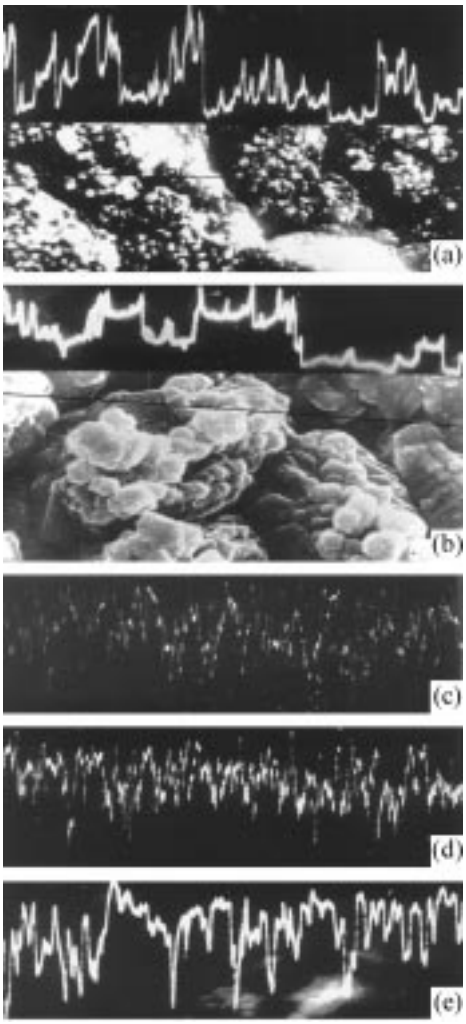

Fig. 3. Secondary-electron emission spectra of the foil samples (a) no. 3, (b) no. 6, (c) no. 4, (d) no. 5, and (e) no. 2 with (a, b) and without (c–e) the corresponding micrographs of the surface. Magnification: (c, d) 2000, (e) 10000, and (a, b) 12000.

The structural features of the foil roughness are the most clearly demonstrated by the curves of the height distribution of the irregularities (Fig. 4b). A foil with a high adhesion commonly has a larger fraction of higher irregularities (2.5–4 μm). Indeed, the foil with locks formed by copper powder (sample nos. 5, 7) has irregularities with a typical height of 2.5–3 μm, whereas on other samples (i.e., no. 2), the irregularities are lower.

[1] To make the perception of the statistical data in Fig. 4 easier, only selected curves clearly illustrating the conclusions based on the analysis of the whole body of the experimental data are presented of the whole variety of the dependences obtained.

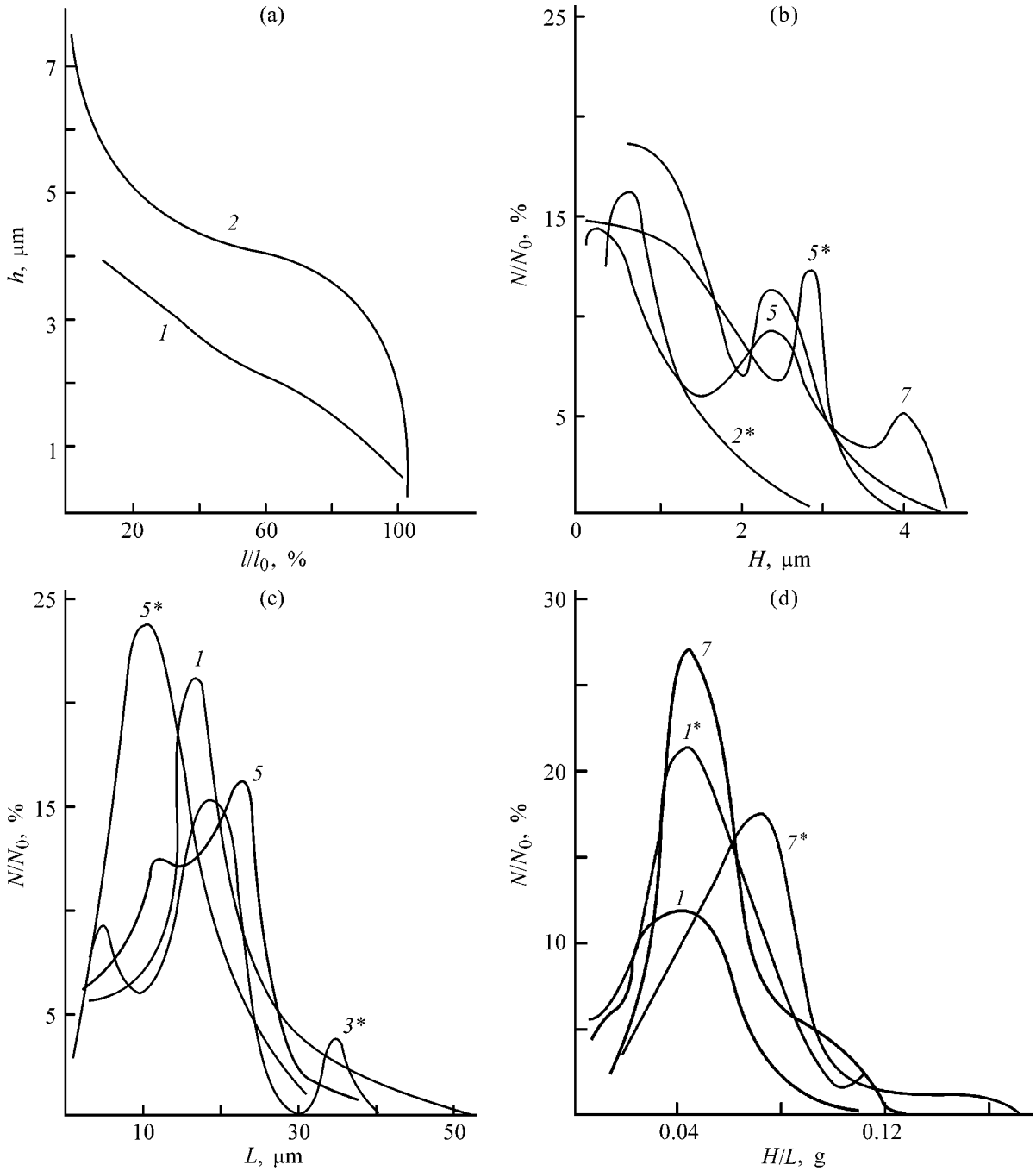

Fig. 4. (a) Reference curves h–l/l_0, the distributions of irregularities with respect to (b) height N/N_0–H, (c) width N/N_0–L, and (d) shape N/N_0–H/L. The *curve numbers* are the sample numbers [longitudinal and transverse (*) roughness].

The curves of the width distribution of the irregularities show a peak at around 10 μm for most of the foil samples (Fig. 4c). This indicates that, owing to the finite size of the probing tip of the profilograph, irregularities less than 10 μm in width are distorted or not recorded on the profilograms at all. This also confirms the predominance of small irregularities in the microprofile. Their dominating role in sample nos. 4–7 with a high adhesion strength is manifested as a clearly pronounced peak at L = 10 μm. This peak is always observed in transverse tracing of the foil surface with the profilograph tip. In longitudinal tracing, and also on foils with a lower adhesion strength, the peak is either broadened or shifted to larger L.

A study of the distribution of irregularities by sharpe (Fig. 4e) revealed a correlation between the adhesion strength and the profile structure. Indeed, the fraction of steep irregularities is commonly larger on the surface of foils with higher adhesion strength, compared with the other samples. For example, the number of irregularities with the ratio $H/L = 0.08$ is the following for sample nos. 4–7 (%): 27, 42; 24, 36; 9, 13; 7, 16, respectively; here the first and second figures in each pair corresponds to the longitudinal and transversal tracing of the foil surface, respectively. For the foil with an insufficiently high adhesion strength, the fraction of such irregularities constitutes only 2 and 9% for sample no. 1, 5 and 6% for sample no. 2, and 9% for sample no. 3 (transverse tracing). The percentage of even steeper irregularities with $H/L = 0.12$ varies from 2 to 22% on the surface of a foil with a high adhesion and does not exceed 1% of the total amount of defects in the profile for the foil with a low adhesion strength.

Notably, the surface of the foil studied is anisotropic. As can be seen from the data in the table, the anisotropy of the roughness parameters in the mutually perpendicular directions is small and does not commonly exceed 10–20%. This makes it possible to describe each parameter by only a single figure: the average of the values obtained in longitudinal and transverse tracings of the foil surface. The anisotropy also shows up in estimating the distributions of irregularities by height, width, and shape (Fig. 4). The anisotropy is an indication of the diffusion kinetics of formation of the majority of foils, which results in the appearance in their structure of heterogeneities caused by hydrodynamic flows in solution.

The profilographic method gives a notion of the anisotropy of the macroscopic elements of the microprofile. The method of coherent optics, which allows a study of the periodicities caused by growth of raw copper crystals and powder particles has great possibilities. An optical coherent spectral analyzer obtains information about the topography of a surface from its image on the photographic film in the form of a Fraunhofer diffraction pattern (FDP), which is a two-dimensional power spectrum of the frequencies present in the image [11]. The range of the periodicites recorded in FDP depends on the magnification of a photograph. With magnifications of 25 to 1500, the periodicites in the range from 40 to 0.1 μm can be studied.

The Fraunhofer diffraction pattern is a set of light spots of various shapes, whose brightness decreases from the center toward the periphery. Analysis of the shape of these spots reveals the anisotropy of the structure, its character, and orientation, indiscernible under visual inspection. It has been shown for electrolytic copper deposits that the spot is circular for an isotropic polycrystalline surface, [12]. Presence of clearly faceted crystals on the surface or similarly oriented profiles on the faces of these crystals (in the form of grooves or steps) leads to a redistribution of the light intensity in the directions that are normal to the structural elements and symmetric with respect to the FDP center. In the absence of a clearly pronounced faceting of the crystals, the surface anisotropy cannot be viewed visually, but is readily revealed by FDP, which acquires the shape of an ellipsoidal spot.

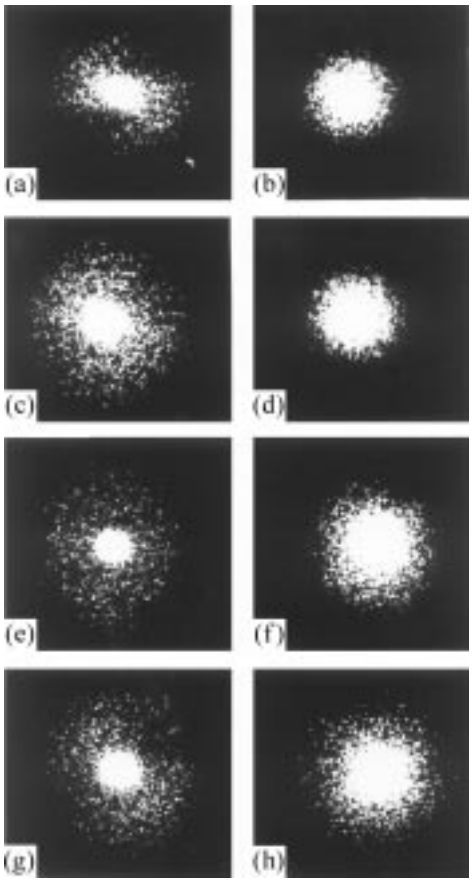

Fig. 5. Fraunhofer diffraction patterns and micrographs of the surface of the foil samples (a, b) no. 1, (c, d) no. 3, (e, f) no. 5, and (g, h) no. 6. Magnification: (e) 25, (g) 30, (a, c) 50, (b, d) 500, and (f, h) 1500.

The FDPs obtained in studying the surface of some foil samples are shown in Fig. 5. According to Fig. 5, the anisotropy is clearly manifested in all the samples at low magnifications. The anisotropy is the stron-

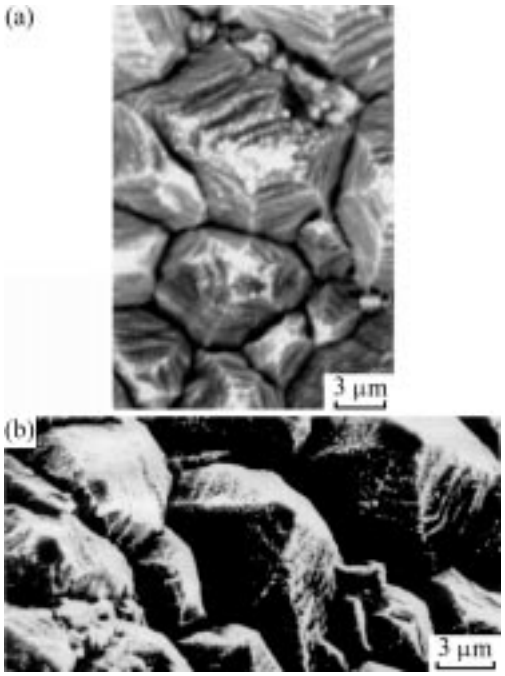

Fig. 6. SEM micrographs of the surface of a strongly adherent foil sample with a powder lock formed by preliminary modification of raw copper in an aqueous solution of thiourea. Measurement angle (deg): (a) 0 and (b) 5.

gest for the raw foil (sample no. 1), being less pronounced for sample nos. 3, 6 and, especially, sample no. 5. This indicates that the reason for the appearance of anisotropy is, for the most part, that coarse microstructural elements grow differently in the mutually perpendicular directions, in agreement with the profilographic data. Apparently, the anisotropy must impair the adhesion of the foil in certain directions. At the same time, it follows from the FDPs presented and from profilographic data that the anisotropy does not affect the adhesion by itself (within the limits recorded). Moreover, detailed analysis of the FDPs obtained from the photographs taken at large magnification shows that the ellipsoidal form is more clearly pronounced in samples with a high adhesion (Figs. 5f, 5h). This means that the ordered distribution of the powder particles over the coarse elements of the microprofile improves the adhesion strength of the foil.

Thus, to improve the adhesion strength of a foil, it is necessary, first of all, to ensure formation of conical or pyramidal grains of raw copper, which are uniform in size and have a width of 4–8 μm. In addition, a copper powder is to be deposited onto the foil to create mechanical locks that enhance the adhesion. The adhesion considerably increases in the case of a preferential deposition of the powder on tips of grains of the support. This occurs because the size of locks and the surface area occupied by them increase (ν changes from 0.04 to 0.15 in going from sample no. 4 to sample nos. 6, 7). The size of powder grains, which is not a crucial factor, varies within 0.1–1 μm. Spheroid granules are preferable. The reinforcing metallic layers must not make smoother the topography of the foil surface, formed upon powder deposition.

The pyramidal and conical structures of the raw foil can be easily formed if the sulfate copper plating electrolyte is purified to remove organic impurities and certain modes of pulsed electrolysis are used [13]. The copper powder is commonly obtained in the same electrolyte at the limiting current density, which is reached fast by making lower the concentration of Cu^{2+} ions, by intensifying the stirring of the solution, and by raising the concentration of sulfuric acid in the electrolyte [14]. The nonuniform distribution of the powder over the microirregularities of the cathode is favored by introduction of active depolarizing agents into the electrolyte [4, 6]. However, the incorporation of these additives into the deposit impairs its physicomechanical properties [8, 14], and their consumption in the course of electrolysis requires frequent corrections of the bath.

This stimulated a search for additional ways to control the distribution of powder copper over the electrode. The method suggested for production of foil is based on an unusual phenomenon in electrodeposition, which is associated with the ability of certain additives to rise to the surface of the deposit in the course of electrolysis, rather than being absorbed [15]. This ability is exhibited, in particular, by thiourea [16, 17]. This circumstance made it possible to separate the sorption and electrolysis processes and preliminarily modify raw copper having a pyramidal crystal structure in an aqueous solution of thiourea, with the subsequent deposition of the powder in a pure electrolyte, instead of introducing the additive into electrolyte [7]. In the course of sorption, thiourea decomposes to give Cu_2S [16]. Owing to the predominant diffusion of thiourea to the apices of microirregularities, copper(I) is preferentially formed there. When the amount of the sulfide present on the electrode surface constitutes a fraction of a monolayer, there occurs a prolonged (up to 10 min) depolarization of the subsequent electrodeposition of copper. As a result, the current density at apices of microirregularities is considerably higher during the above period, compared with that on the rest of the foil surface. Thereby, projections are formed at apices of the microirregularities to give locks in pressing of the foil in the insulator. When inspected under an electron microscope, these projections have the form of truncated pyramids (Fig. 6). The strength of adhesion

of such a foil to the insulator is 2160 N m^{-1}. Owing to the fact that additive is forced to the surface by the growing deposit [17], the concentration of sulfur incorporated in the deposit decreases [7], which makes lower the susceptibility of the foil to embrittlement and its possible corrosion activity.

CONCLUSIONS

(1) It was established that the highest adherence to the insulator is exhibited by a foil with uniform size and steep shape of conical or pyramidal grains of raw copper and extremely nonuniform distribution of copper powder particles over these grains. The powder, being concentrated at apices of microdefects, forms irregularities, and these irregularities give rise to mechanical locks in pressing of the foil in the insulator.

(2) A statistical study of the surface microprofile of the foil samples with a powder adhesion layer demonstrated that the strength of adhesion to the insulator increases when irregularities with an aspect ratio of 0.08–0.09 and an angle of inclination of no less than 7°–8° are present (in an amount of no less than 7%) in the microprofile and when the true surface area exceeds the apparent surface area by more than a factor of 1.048.

(3) An original method for obtaining copper foil with a high adhesion strength was suggested. This method is based on the prolonged influence exerted by thiourea preliminarily sorbed on the cathode on the copper electrodeposition from a sulfate solution. The forcing of the additive by the metal to the surface and its elimination from the electrolyte ensure that a lower amount of sulfur is incorporated in the deposit and improve the ecological conditions of the manufacture process.

ACKNOWLEDGMENTS

The authors thank A.V. Matokhin (Far Eastern State Technical University) for taking PDPs and N.Ya. Kovarskii (USA) for assistance and advice in discussing the results.

REFERENCES

1. Deryagin, D.V., Krotova, N.A., and Smilga, V.P., *Adgeziya tverdykh tel* (Adhesion of Solids), Moscow: Nauka, 1973.
2. Kragel'skii, I.V., *Trenie i iznos* (Friction and Wear) Moscow: Mashinostroenie, 1968.
3. Kovarskii, N.Ya, Kuznetsova, L.A., Sedova, S.S., *et al., Tsvet. Met.*, 1983, no. 6, pp. 34–36.
4. Golovin, I.N., Buzhinskaya, A.V., Mazurchuk, E.N., *et al., Tsvet. Met.*, 1980, no. 4, pp. 38–45.
5. USSR Inventor's Certificate, no. 338558.
6. UK Patent 1515361.
7. USSR Inventor's Certificate, no. 1387527.
8. Gnusin, N.P., and Kovarskii, N.Ya., *Sherokhovatost' elektroosazhdennykh poverkhnostei* (Roughness of Electrodeposited Surfaces), Novosibirsk: Nauka, 1970.
9. Kovarskii, N.Ya., Study of Microgeometric Defects of Electrodeposited Plolycrystalline Surfaces, *Doctoral Dissertation*, Moscow, 1975.
10. Popilov, L.Ya., and Zaitseva, L.P., *Elektropolirovanie i elektrotravlenie metallograficheskikh shlifov* (Electropolishing and Electroetching of Metallographic Sections), Moscow: Metallurgizdat, 1955.
11. Timakova, G.P., Yudina, L.A., Klenin, S.A., *et al., Fiz. Met. Metalloved.*, 1977, vol. 44, pp. 1198–1202.
12. Kovarskii, N.Ya., Yudina, L.A., Rudik, E.I., *et al., Elektrokhimiya*, 1981, vol. 17, no. 4, pp. 569–575.
13. Polukarov, Yu.M., Popkov, Yu.A., Grinina, V.V., and Sheshenina, Z.E., *Elektrokhimiya*, 1982, vol. 18, no. 9, pp. 1218–1223.
14. Kudryavtsev, N.T., *Elektrolitricheskie pokrytiya metallami* (Electroplating with Metals), Moscow: Khimiya, 1979.
15. Kuznetsova, L.A., and Semiletova, I.V., *Vestn. Dal'nevostoch. Otd., Ross. Akad. Nauk*, 2003, no. 1, pp. 41–49.
16. Kuznetsova, L.A., and Kovarskii, N.Ya., *Elektrokhimiya*, 1981, vol. 17, no. 11, pp. 1712–1716.
17. Kuznetsova, L.A., and Kovarskii, N.Ya., *Elektrokhimiya*, 1981, vol. 17, no. 11, pp. 1633–1637.

Russian Journal of Applied Chemistry, Vol. 77, No. 10, 2004, pp. 1662–1666. Translated from Zhurnal Prikladnoi Khimii, Vol. 77, No. 10, 2004, pp. 1676–1680.

PROCESSES AND EQUIPMENT OF CHEMICAL INDUSTRY

Filtration of the Extracting Agent in Porous Particles with Entrapped Gas at Low-Frequency Pressure Oscillations in the Extractor

E. V. Ivanov, M. V. Shvyrev, and M. A. Artemova

St. Petersburg State Chemical-Pharmaceutical Academy, St. Petersburg, Russia

Received April 18, 2003; in final form, September 2004

Abstract—A model of the process of filtration of the extracting agent in porous particles with entrapped gas was developed. This model takes into account pressure oscillations in the extractor.

The method of extraction with low-frequency pressure oscillations in the working volume of the apparatus finds increasing use for extracting target components from vegetable raw materials [1–6]. Compared with the conventional techniques, this method makes it possible to raise the mass-transfer rate, shorten the process duration, and diminish the energy expenditure. The available publications, as a rule, consider the hydrodynamics and mass exchange in separate capillaries [4–6]. The goal of the present study was to develop a model of filtration mass transfer in porous particles that would take into account pressure oscillations in the extractor.

Porous spherical particles, plates, and cylinders can serve as models of fruits and particles of a shredded raw material, leaves, and stalks, respectively. One or several zones of entrapped gas (as a rule, air), which are formed in impregnation of a vegetable raw material under the action of capillary forces, can be found within each particle in the initial stage of the process. Depending on how the pressure in the apparatus varies, the filtration of the extracting agent occurs in porous particles in different directions: from the periphery of a particle toward its center if the pressure in the apparatus increases, and vice versa. In the process, the gas in the entrapping zones is compressed or expands alternately. The difference between the maximum and minimum volumes of the zones with entrapped gas is equal (with account of the particle porosity) to the volume of the extracting agent entering a particle and exiting from it in a single cycle of variation of the external pressure.

Let us consider the filtration of the extracting agent in a spherical porous particle for the case when the zone of entrapped gas lies at its center. We assume that the particle and the extracting agent are incompressible, the structure of the particle is isotropic, and disregard the variation of the hydrostatic pressure along the particle height and the action of the gravity force on the filtration. The equations describing the filtration in a porous body in the spherical system of coordinates were presented in [7]. Taking into account the assumptions made and the symmetry of the spherical particles, we can transform these equations to obtain the following

$$\rho\varepsilon\left(\frac{\partial v_r}{\partial \tau} + v_r\frac{\partial v_r}{\partial r}\right) = -\varepsilon\frac{\partial p}{\partial r} - f_r s_V, \qquad (1)$$

$$\frac{\partial v_r}{\partial r} = -2\frac{v_r}{r}, \qquad (2)$$

where τ is time (s); r, running radius (m); v_r, velocity of filtration along the coordinate r (m s^{-1}); ρ, density of the liquid (kg m^{-3}); ε, volume fraction of pores; $\partial p/\partial r$, gradient of pressure along the coordinate r (Pa m^{-1}); f_r, specific force of interphase resistance, caused by friction of the liquid against the skeleton of a porous body (Pa); and s_V, specific internal volumetric surface area of the particle skeleton (m^2 m^{-3}).

In the laminar mode of motion of the extracting agent in a porous body, the specific resistance force is given by [7]

$$f_r = \frac{2\mu\xi^2 s_v}{\varepsilon} v_r, \qquad (3)$$

where μ is the dynamic viscosity coefficient (Pa s), and ξ is the tortuosity factor of the filtration path.

1070-4272/04/7710-1662 © 2004 MAIK "Nauka/Interperiodica"

On substituting Eqs. (2) and (3) into (1), we have

$$\frac{\partial v_r}{\partial r} - 2\frac{v_r^2}{r} + \frac{1}{\rho}\frac{\partial \rho}{\partial r} + Bv_r = 0, \quad (4)$$

where $B = 2\mu\xi^2 s_v^2/(\varepsilon^2\rho)$ is the coefficient characterizing the force of resistance to the motion of the liquid within a porous body (s^{-1}).

The filtration of a liquid within a porous particle is driven by the difference of pressures at the particle surface (external pressure P_{ext}) and inside a particle (in the zone of entrapped gas, P_{in}). Let us assume that the external pressure exerted by on the porous particle by the liquid varies by the law $P_{ext} = P_0 + \rho gh + \Delta P \sin\omega\tau$, where P_0 is the pressure at the initial instant of time or the average pressure in the extractor (depending on the principle of action of the extractor) (Pa); ρgh, hydrostatic pressure at a depth h at which a particle is situated (Pa); ΔP, amplitude of pressure oscillations around P_0 (Pa); and ω, angular frequency of pressure oscillations ($\omega = 2\pi f$) (rad s^{-1}).

The pressure within particles depends on the shape and diameter of pores, wettability of the particles with the solvent, and conditions of their impregnation. Let us designate the gas pressure within the porous particles at the initial instant of time (at the instant of impregnation with the extracting agent) as P_{in}.

In accordance with the Clapeyron equation, PV = const,

$$V_{pt}P_{in} = V_{tr}(P_{in} + P_c), \quad (5)$$

where V_{pt} and V_{tr} are the gas volumes in a dry porous particle in the entrapping zone of a wetted particle (m^3); $P_c = 4\sigma\cos\theta/\delta_c$, capillary pressure (Pa); σ, surface tension (N m^{-1}); θ, contact wetting angle (deg or rad); and δ_c, capillary diameter (m).

It follows from Eq. (5) that the volume fraction of entrapped gas at the instant of impregnation is given by

$$\alpha_0 = \frac{V_{tr}}{V_{pt}} = \frac{P_{in}}{P_{in} + P_c}. \quad (6)$$

If $P_{in} = P_0$, then

$$\alpha_0 = \frac{P_0 + \rho gh}{P_0 + \rho gh + P_c}. \quad (7)$$

If the particles are then placed in an apparatus with a pressure P_{ext}, the volume fraction of entrapped gas changes to

$$\alpha_{01} = \frac{P_{in}}{P_{ext} + P_c}. \quad (8)$$

If the shape of the gas entrapping zone gas is assumed to be the same as that of the particle itself, the radius of this zone can be found as

$$r_{01} = R\sqrt[3]{\alpha_{01}}, \quad (9)$$

where R and r_{01} are the radius of the particle and that of the gas entrapping zone at a pressure P_{ext} (m^3).

The gas pressure in the entrapping zone, P_{tr}, corresponds to the running radius r_0. By analogy with relation (5), $P_3 r_{01}^3 = (P_c + P_0 + \rho gh)r_0^3$, whence follows

$$P_{tr} = (P_c + P_0 + \rho gh)\left(\frac{r_0}{r_{01}}\right)^3, \quad (10)$$

where r_0 is the radius of the entrapping zone at the impregnation pressure (m).

The internal pressure exerted on the liquid in capillaries by the entrapped gas is lower than P_{tr} by the value of the capillary pressure P_c, which is oppositely directed:

$$P_{int} = (P_c + P_0 + \rho gh)\left(\frac{r_0}{r_{01}}\right)^3 - P_c. \quad (11)$$

Having integrated Eq. (2), we find how the velocity of the liquid being filtered varies along the particle radius:

$$\int_{v_R}^{v_r}\frac{\partial\omega_r}{\omega_r} = -2\int_R^r\frac{\partial\gamma}{\gamma}, \quad v_r = v_R\left(\frac{R}{r}\right)^2, \quad (12)$$

where ω_r and γ are auxiliary variables; v_r and v_R, velocities of filtration of the liquid across a spherical surface of radius r and on the particle surface (at $r = R$).

The velocities v_r and v_R are unknown functions; v_R is dependent only on time, and v_r, on time (via v_R) and radius [in accordance with formula (12)]. Substituting (12) into Eq. (4), we obtain

$$v_r'\left(\frac{R}{r}\right)^2 - 2v_R^2\frac{R^4}{r^5} + \frac{1}{\rho}\frac{\partial p}{\partial r} + Bv_R\left(\frac{R}{r}\right)^2 = 0. \quad (13)$$

Hence follows

$$\frac{1}{\rho}\frac{\partial p}{\partial r} = -\left[v_R'\left(\frac{R}{r}\right)^2 - 2v_R^2\frac{R^4}{r^5} + Bv_R\left(\frac{R}{r}\right)^2\right],$$

$$\frac{1}{\rho}\int_{P_{ext}}^{P_{int}}\partial p = -\int_R^{r_{01}}\left[v_R'\left(\frac{R}{r}\right)^2 - 2v_R^2\frac{R^4}{r^5} + Bv_R\left(\frac{R}{r}\right)^2\right]\partial r.$$

Upon integration and substitution of the values of P_{int} and P_{ext}, we obtain

$$v_R' R\left(\frac{R}{r_{01}} - 1\right) = (P_c + P_0 + \rho gh)\left[\left(\frac{r_0}{r_{01}}\right)^3 - 1\right]/\rho - \frac{\Delta P}{\rho}\sin\omega\tau + \frac{v_R^2}{2}\left[\left(\frac{R}{r_{01}}\right)^4 - 1\right] - Bv_R R\left[\left(\frac{R}{r_{01}}\right) - 1\right], \quad (14)$$

where $v_R' = \partial v_R/\partial\tau$.

Equation (14) involves an unknown quantity r_{01}, the running radius of the gas entrapping zone. As the velocity with which r_{01} changes coincides with the velocity of filtration at $r = r_{01}$, we obtain, taking into account formula (12) and introducing a dimensionless variable $z = R/r_{01}$, a system of two ordinary differential equations describing the process of filtration in a spherical porous particle with entrapped gas:

$$\begin{cases} \dfrac{\partial v_R}{\partial\tau} = \left[\Pi(Az^3 - 1) - \Delta\Pi\sin\omega\tau + \dfrac{v_R^2}{2}(z^4 - 1) - Bv_R R(z - 1)\right]/R(z - 1), \\ \dfrac{\partial z}{\partial\tau} = -\dfrac{v_R}{R}z^4. \end{cases} \quad (15)$$

The initial conditions are as follows: $\tau = 0$, $v_R = 0$, $z = R/r_0$.

The following designations are made in the system of equations (15): $\Pi = (P_c + P_0 + \rho gh)/\rho$, $\Delta\Pi = \Delta P/\rho$, $A = (r_0/R)^3$.

Equation (14) was numerically analyzed at different values of $\omega\tau$ and capillary diameters δ_c. The values of the physical variables appearing in Eq. (14) were taken to be as follows: $r_0 = 1 \times 10^{-3}$ m, $R = 4 \times 10^{-3}$ m, $\omega = 125.6$ rad s^{-1}, $\mu = 1 \times 10^{-3}$ Pa s, $\xi = 1.6$; $\varepsilon = 0.4$, $\theta = 0$; $\sigma = 73 \times 10^{-3}$ N m^{-1}, $\rho = 1000$ kg m^{-3}, $P_0 = 10^5$ Pa, $\Delta\rho = 0.25 \times 10^5$ Pa. s_v was calculated using the formula $s_v = 4\varepsilon/\delta_c$, which is valid for the case when the porous body is constituted by separate particles [8]. The hydrostatic pressure was neglected: $\rho gh = 0$; the capillary diameter was chosen in the range 10^{-3}–10^{-7} m. The contributions from the terms in Eq. (14) were evaluated with respect to that from the main terms $(P_c + P_0 + \rho gh)[(r_0/r_{01})^3 - 1]/\rho$ and $(\Delta P/P)\sin\omega\tau$.

It was established that, at different values of $\omega\tau$, the contributions of most of the terms are in the range 5×10^{-3}–5×10^{-7}% relative to the main terms and can be neglected. At capillary diameters $\delta_c \geq 1 \times 10^{-5}$ m, the term $Bv_R R[(R/r_{01}) - 1]$ can also be neglected. Then, formula (14) takes the form

$$(P_c + P_0 + \rho gh)\left(\frac{r_0}{r_{01}}\right)^3 = P_c + P_0 + \rho gh + \Delta P\sin\omega\tau, \quad (16)$$

whence follows, with account of (9),

$$r_{01} = R\left[\frac{(P_c + P_0 + \rho gh)\alpha}{P_c + P_0 + \rho gh + \Delta P\sin\omega\tau}\right]^{1/3}. \quad (17)$$

The relative (to the volume of liquid in the porous body at full impregnation) amount of the liquid drawn in and forced out of a porous particle in a cycle is given by

$$V_{rel} = \frac{\varepsilon V_{tr.max} - \varepsilon V_{tr.min}}{\varepsilon V_{pt}} = \frac{\alpha(P_c + P_0 + \rho gh)}{P_c + P_0 + \rho gh - \Delta P} - \frac{\alpha(P_c + P_0 + \rho gh)}{P_c + P_0 + \rho gh + \Delta P}, \quad (18)$$

where $V_{tr.max}$ and $V_{tr.min}$ are the maximum and minimum volumes of the gas entrapping zone, respectively; V_{pt}, volume of a porous particle; and ε, its porosity.

In a more compact form

$$V_{rel} = \frac{2\Delta P(P_c + P_0 + \rho gh)\alpha}{(P_c + P_0 + \rho gh)^2 - \Delta P^2}. \quad (19)$$

This relation can be used to calculate the maximum possible value of V_{rel}, which corresponds to a filtration mode without resistance to motion of the liquid in capillaries, i.e., is observed when equilibrium is attained at any instant of time between the gas pressures within the entrapping zone and in the bulk of the liquid. The same relations are obtained in solving the filtration equations for porous plates (model of leaves) and cylinders (model of stalks) at whose centers are situated gas entrapping zones.

The system of equations (15) was solved by the Runge–Kutta method. The values of the physical var-

iables corresponded to those presented above; the initial pressure in the apparatus was taken to be equal to the atmospheric pressure, P_0 = 0.1 MPa, and the magnitude of oscillations about this pressure, ΔP = 0.025 MPa. The actual relative amount of the liquid entering a porous particle and exiting from it in a cycle of pressure variation in the apparatus was found from the relation

$$V = \left(\frac{1}{z_{\min}^3} - \frac{1}{z_{\max}^3}\right), \qquad (20)$$

where $z_{\min}$ and $z_{\max}$ are the minimum and maximum values of z.

Figure 1 shows how the coefficient $K_v = V/V_{rel}$ depends on the diameters δ_c, angular frequency ω of pressure oscillations in the apparatus, and fraction α of entrapped gas. At low frequencies ω = 6.28 rad s^{-1} (f = 1 s^{-1}) and capillary diameters δ_c > 3 μm, V is comparable with V_{rel} and expression (19) can be used to calculate the relative amount of the liquid. ω = 251 rad s^{-1} (f = 40 s^{-1}), V is close to V_{rel} only for capillaries with a diameter δ_c > 50 μm. As δ_c decreases and ω increases, the coefficient K_v approaches zero. For example, this occurs at δ_c = 0.1 μm and ω = 6.28 rad s^{-1} or at δ_c = 1 μm and ω = 251 rad s^{-1}. The fraction of entrapped gas has only a little effect on the coefficient K_v, with V the closer to V_{rel}, the smaller α.

Data on the pore size distributions in particles of shredded vegetable raw materials of varied morphological structure were reported in [6, 8]. For saltwort, the fraction of pores of diameter exceeding 20 μm is 92%, and of those with diameters in the range from 100 to 600 μm, 63%. In the ginseng root, the fraction of >20 μm pores is 82.5%, and of those with diameters ranging from 100 to 2000 μm, 65%. Apparently, the loss of pressure is the same for motion of the extracting agent from the surface of a porous particle to the gas entrapping zone and in the opposite direction in capillaries of different diameters. Otherwise, the extracting agent would move along the path of least resistance and the flow rates through the capillaries would be redistributed until equalization of the pressure loss. In accordance with the Hagen–Poiseuille equation, the volumetric flow rates are proportional to capillary diameters raised to fourth power in a laminar motion of an incompressible liquid at equal resistances of the capillaries. Thus, the filtration of the extraction agent mainly occurs through coarse capillaries in extraction from vegetable raw materials under conditions of low-frequency pressure oscillations. These capillaries are formed in shredding of the raw material as a result of disintegration of its

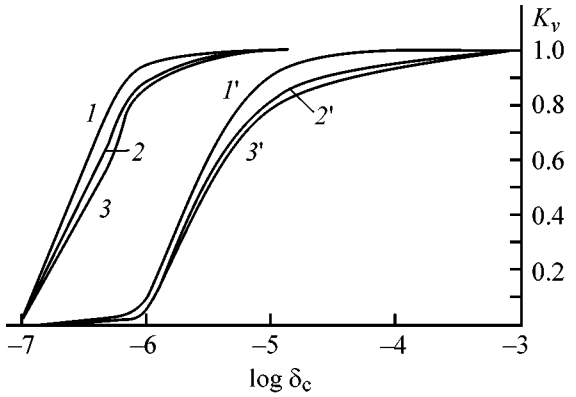

Fig. 1. Effect of the capillary diameter δ_c on the coefficient K_v. Curves *1*, *2*, and *3* are calculated for fractions of entrapped gas equal to 0.05, 0.15, and 0.25, respectively; unprimed for ω = 6.28 rad s^{-1} and primed for ω = 251 rad s^{-1}.

internal structure. In an unshredded vegetable raw material, coarse pores are virtually lacking, which is indicated by the closeness of the curves describing the kinetics of extraction of flavonoids from unshredded fruits of hawthorn, which contain entrapped air and are totally impregnated with the extracting agent (by their preliminary vacuum treatment and mixing with the solvent in a vacuum).

The experimentally found fractions of entrapped gas in capillary-porous bodies at the initial instant of time can be used to evaluate the capillary pressure P_c [formulas (6), (7)] in the gas entrapping zone (or zones) and the corresponding equivalent capillary diameter $\delta_{c.equiv} = P_c/4\sigma\cos\theta$. For various kinds of vegetable raw materials (unshredded fruits of hawthorn, leaves of birch, roots of licorice), $\delta_{c.equiv}$ = 0.8–1 μm, i.e., the capillary pressure in the gas entrapping zone is determined by the smallest diameters of pores in the raw material. This result is similar to the known results of experiments with impregnation from above of capillary-porous bodies with periodically narrowing and widening pores, in which the height of the capillary rise in the level of the liquid is determined by the diameters of the narrowest parts of the pores [9].

A solution of the system of equations (15) for filtration of an extracting agent in porous particles with capillary diameter exceeding 50 μm and gas pressure in the gas entrapping zone corresponding to P_c at $\delta_{c.equiv}$ = 1 μm demonstrated that formula (19) can be used to calculate V_{rel}. In the general case, when the magnitudes of drops ($\Delta P_{\min}$) and rises ($\Delta P_{\max}$) in the pressure in the apparatus relative to P_0 are not equal, formula (19) takes the form

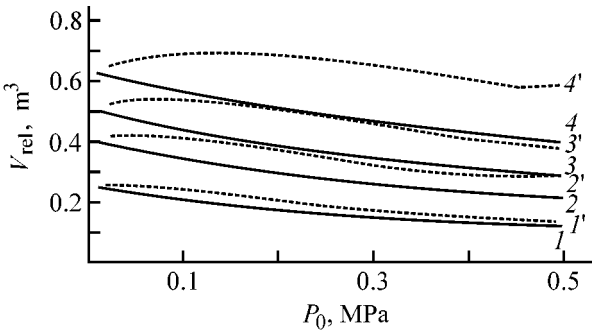

Fig. 2. V_{rel} in relation to the initial pressure P_0, total pressure difference, and way to produce pulsations. Curves *1*, *2*, *3*, and *4* correspond to pressure differences of 0.1, 0.2, 0.3, and 0.5 atm, respectively; unprimed, for apparatus with a pneumatic pulser, and primed, for those with piston pulser.

$$V_{rel} = \frac{(\Delta P_{max} + \Delta P_{min})(P_c + P_0 + \rho gh)\alpha}{(P_c + P_0 + \rho gh - \Delta P_{min})(P_c + P_0 + \rho gh + \Delta P_{max})}, \quad (21)$$

where P_c is the capillary pressure in the capillaries with the smallest diameter (MPa).

In accordance with Eq. (21), the volume of the extracting agent passing through porous particles is directly proportional to the fraction of entrapped gas, α, which steadily decreases in the course of time as a result of diffusion of the gas from a particle into the flow of the extracting agent. The magnitude ΔP_{min} may apparently fall within the range $0 \le \Delta P_{min} < P_0$. In apparatus with pneumatic pulsers, the minimum pressure is, as a rule, equal to the initial pressure P_0. When piston, plunger, bellows, or membrane pulsers are used, the pressure in the apparatus is related to the volume of the air cushion, following the law of adiabatic compression–expansion, by

$$(P_0 - \Delta P_{min})v_{max}^k = P_0 v_0^k = (P_0 + \Delta P_{max})v_{min}^k,$$

where v_{max}, v_0, v_{min} are the volumes of the air cushion in the apparatus at the minimum, initial, and maximum pressures, respectively (m^3); k is the adiabatic exponent.

Figure 2 compares the results of calculations of V_{rel} by formula (21) at $\alpha = 1$ for pneumatic and piston pulsers with equal values of $\Delta P_{min} + \Delta P_{max}$. The adiabatic exponent was taken to be $k = 1.4$, which is approximately equal to the adiabatic exponent of a vapor–air mixture over an aqueous solution (40%) of ethanol at 20°C. Depending on the initial pressure P_0 and the total pressure difference $\Delta P_{min} + \Delta P_{max}$, the values of V_{rel} for the piston pulser are 4–22% higher than the corresponding values for the pneumatic pulser. The volume of the extracting agent that has passed through porous particles grows as the initial pressure P_0 decreases and the total pressure difference increases. The highest values of V_{rel} can be obtained if the initial pressure in the apparatus is lower than the atmospheric pressure ($P_0 < 0.1$ MPa).

CONCLUSIONS

(1) The filtration of the extracting agent in porous particles, including those of vegetable raw materials, occurs only via coarse capillaries, which are for the most part formed as a result of shredding of the raw material.

(2) The volume of the extracting agent that passes through porous particles with entrapped gas in a single cycle of pressure variation in the apparatus is virtually independent of the frequency of pulsatory disturbances (at frequencies lower than 40 Hz), being determined by the volume of gas entrapped in particles, total pressure difference, initial pressure in the apparatus, and diameter of the narrowest pores in particles.

REFERENCES

1. Aksel'rud ,G.A. and Lysyanskii, V.M., *Ekstragirovanie (Sistema tverdoe telo–zhidkost')* [Extraction (Soid–Liquid System)], Leningrad: Khimiya, 1974.
2. Ostrovskii, G.M., Aksenova, E.G., and Abiev, R.Sh., *Mezhvuzovskii sbornik nauchnukh trudov "Protsessy, apparaty i oborudovanie pishchevoi promyshlennosti"* (Intercollegiate Coll. of Sci. Works "Processes, Apparatus, and Equipment of Food Industry"), SPbTiKhP, 1993, p. 20.
3. Ostrovskii, G.M. and Abiev, R.Sh., *Khim. Prom–st'.*, 1998, no. 8, pp. 468–478.
4. Abiev, R.Sh. and Ostrovskii, G.M., *Teor. Osn. Khim. Tekhnol.*, 2001, vol. 35, no. 3, pp. 270–275.
5. Abiev, R.Sh., *Zh. Prikl. Khim.*, 2001, vol. 74, no. 5, pp. 754–761.
6. Malyshev, R.M., Kutepov, A.M., Zolotnikov, A.N., *et al.*, *Dokl. Akad. Nauk*, 2001, vol. 381, no. 6, pp. 800–805.
7. Ostrovskii, G.M., *Prikladnaya mekhanika neodnorodnykh sred* (Applied Mechanics of Heterogeneous Media), St. Petersburg: Nauka, 2000.
8. Malyshev, R.M., Zolotnikov, A.N., Sedov, A.A., *et al.*, *Izv. Vyssh. Uchebn. Zaved., Khim. Khim. Tekhnol.*, 2001, vol. 44, no. 1, pp. 141–142.
9. Lykov, A.V., *Teplomassoobmen: Spravochnik* (Heat-and-Mass Exchange: Reference Book), Moscow: Energiya, 1971.

Russian Journal of Applied Chemistry, Vol. 77, No. 10, 2004, pp. 1667–1669. Translated from Zhurnal Prikladnoi Khimii, Vol. 77, No. 10, 2004, pp. 1681–1683.

ORGANIC SYNTHESIS AND INDUSTRIAL ORGANIC CHEMISTRY

Synthesis of Substituted Ureas from Urea and Halohydrins

A. M. Magerramov, R. T. Abdinbekova, M. M. Kurbanova, A. V. Zamanova, and M. A. Allakhverdiev

Baku State University, Baku, Azerbaijan

Received April 15, 2004; in final form, July 23, 2004

Abstract—Substituted ureas were prepared by reactions of 1,2-halohydrins with urea and were tested as antimicrobial additives to motor oils.

Substituted ureas attract researchers' attention thanks to a set of valuable properties allowing their use in industry, agriculture, and medicine. Substituted ureas are used as insecticides, as plant growth regulators, as effective additives of various purposes to hydrocarbon fuels, oils, and polymeric materials, as drugs, and as dyes [1].

Classical synthetic routes to substituted ureas are mostly based on reactions of amines with urea or with isocyanic acid derivatives, or on carbonylation of amino and nitro compounds [1]. These routes are diverse, but many procedures have certain drawbacks restricting their applicability. Development of new procedures is interesting from both scientific and practical viewpoints. In particular, synthesis of substituted ureas by direct reaction of aliphatic and aromatic alcohols with urea has been reported [2, 3]. However, there are no data on reactions of urea with alkoxy-substituted 1,2-halohydrins. These reactions are examined in our study.

Previously, we have studied the reactions of alkoxy- and alkylthio-substituted 1,2-chlorohydrins with thiourea in the presence of various acids [4–6]. Proceeding with analysis of the reactivity of ureas and thioureas [7], we prepared in this study *N*-substituted ureas by reactions of 1,2-halohydrins with urea in the presence of a mixture of H_2SO_4 and CH_3COOH.

The starting 1,2-halohydrins were prepared by reactions of appropriate alcohols with epichlorohydrin in the presence of $ZnCl_2$ at 65°C [8].

The yield of *N*-substituted ureas containing various functional groups (see table) can be optimized by varying the temperature (from 60 to 115°C), amount of H_2SO_4 (1–5 ml), and reaction time (4–8 h).

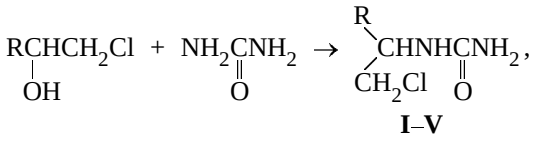

I–V

where R – H (**I**), CH_3OCH_2 (**II**), $C_2H_5OCH_2$ (**III**), $C_4H_9OCH_2$ (**IV**), $C_6H_5CH_2OCH_2$ (**V**).

By reactions of **I** with HCHO and $(C_2H_5)_3N$, we prepared *N*-hydroxymethyl-*N*'-chloroethylurea **VI** and cyclic urea **VII** (see table):

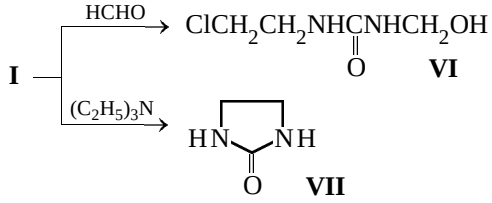

The compounds prepared were tested as antimicrobial additives to MS-11 lubricating oil [GOSTs (State Standards) 9.052–75 and 9.085–75]. The compounds showed a pronounced antimicrobial effect when present in low concentrations (0.5–1.0%); they are readily soluble in MS-11 oil and do not stimulate corrosion. Compounds **VI** and **VII** are more effective than the commercial antimicrobial additive, 8-quinolinol. With **VI**, the width of the suppression zone is 0.6–1.4 cm for bacteria and 1.0–1.9 cm for fungi. With 8-quinolinol, these parameters are 0.4–0.9 and 0.7–0.9 cm, respectively.

EXPERIMENTAL

The ^1H NMR spectra were recorded on a Bruker spectrometer (300 MHz, internal reference TMS). The

1070-4272/04/7710-1667 © 2004 MAIK "Nauka/Interperiodica"

Characteristics of **I**–**VII**

Compound no.	Yield, %	mp, °C	R_f	IR spectrum, cm^{-1}	^1H NMR spectrum, δ, ppm	Found, % / Calculated, %				Formula
						C	H	Cl	N	
I	65	200–207	0.54	3340 (NH) 3420 (NH_2) 1640 (C=O) 670 (C–Cl)	1.3–1.9 t (2H, CH_2Cl) 3.0–2.5 q (2H, CH_2) 6.5–7.5 c (3H,NH_2CONH)	29.12 29.38	5.93 5.71	29.17 28.97	22.59 22.85	$C_3H_7ClN_2O$
II	60	198–199	0.45	3325 (NH) 3490 (NH_2) 1650 (C=O) 700 (C–Cl)	1,7–1,8 c (3H, CH_3) 3.0–3.1 d (2H, CH_2O) 3.6–3.7 d (2H, CH_2Cl) 2.0–2.1 m (1H, CH) 6,5–7,5 s (3H, NH_2CONH)	36.26 36.03	6.42 6.60	21.46 21.32	16.61 16.81	$C_5H_{11}ClN_2O_2$
III	60	200–202	0.36	3330 (NH) 3460 (NH_2) 1600 (C=O) 650 (C–Cl)	1.0–1.3 t (3H, CH_3) 3.2–3.3 d (2H, CH_2Cl) 3.4–3.5 d (2H, CH_2O) 2.0–2.1 m (1H, CH) 6,0–8,0 s (3H, NH_2CONH–)	36.65 39.88	7.37 7.20	19.00 19.66	15.74 15.51	$C_6H_{13}ClN_2O_2$
IV	50	218–219	0.47	3320 (NH) 3480 (NH_2) 1640 (C=O) 600 (C–Cl)	1.0–1.2 t (3H, CH_3) 3.0–3.5 m (4H, $2CH_2$) 3.2–3.3 d (2H, CH_2Cl) 3.0–3.1 t (2H, CH_2O) 2.0–2.1 m (1H, CH) 6.5–7.7 s (3H, NH_2CONH)	46.17 46.04	8.27 8.15	17.23 17.02	13.66 13.42	$C_8H_{17}ClN_2O_2$
V	50	210–212	0.33	3340 (NH) 3500 (NH_2) 1600 (C=O) 600 (C–Cl)	7.2–7.4 d, 2t (5H, C_6H_5) 3.2–3.3 d (2H, CH_2Cl) 3.4–3.5 d (2H, CH_2O) 2.0–2.1 m (1H, CH) 5.5–7.5 s (3H, NH_2CONH)	54.28 54.43	6.31 6.18	14.44 14.63	11.72 11.54	$C_{11}H_{15}ClN_2O_2$
VI	80	240	0.52	3355(NH) 1600 (C=O) 700 (C–Cl) 3650 (OH)	1.3–1.9 t (2H, CH_2Cl) 2.5–3.0 q (2H, CH_2) 4.7–4.8 s (1H, OH) 3.5–4.0 t (2H, CH_2) 6.5–8.5 s (3H, NH_2CONH)	31.69 31.47	5.98 5.90	23.43 23.27	18.16 18.36	$C_4H_9ClN_2O_2$
VII	70	220–221	0.61	3350 (NH) 1655(C=O)	3,0–3,1 q (4H, $2CH_2$) 1.7–2.0 c (2H, 2NH)	41.99 41.86	7.17 6.97	– –	32.39 32.55	$C_3H_6N_2O$

IR spectra were measured on a Specord 75-IR spectrometer (mulls in mineral oil).

The compound purity and reaction progress were monitored by TLC (Silufol UV-254 plates, eluent isopropyl alcohol–hexane, 3 : 5).

Ureas I–III. A mixture of 0.04 mol of an appropriate halohydrin and 16.2 g of urea in 30 ml of AcOH was heated to 80°C, and 5 ml of H_2SO_4 (ρ = 1.84 g cm^{-3}) was added with vigorous stirring over a period of 10 min. Then the mixture was heated at 80°C for 4 h and cooled; the precipitate was filtered off and recrystallized from DMF or C_2H_5OH.

Ureas IV and V. A mixture of 0.01 mol of an appropriate halohydrin, 0.06 mol of urea, 15 ml of AcOH, and 1 ml of H_2SO_4 (ρ = 1.84 g cm^{-3}) was heated with stirring at 115°C for 8 h. The resulting mixture was worked up as described above.

Urea VI. A 30% aqueous solution of formaldehyde (1 ml) was added at 18–20°C with stirring to a suspension of 0.01 mol of **I** in 5 ml of water. The color-

less precipitate that formed in 1 h was filtered off, washed with water, and dried in air.

Urea VII. Triethylamine (10 mmol) was added to a suspension of 10 mmol of **I** in 25 ml of ether. The mixture was stirred at 18–20°C for 12 h, the precipitate of triethylammonium chloride was filtered off, the solvent was removed, and the product was filtered off and dried in air.

CONCLUSION

N-Substituted ureas improving the antimicrobial properties of MS-11 motor oil were prepared in good yields (50–80%) by reactions of 1,2-halohydrins with urea in the presence of a mixture of sulfuric and acetic acids.

REFERENCES

1. Vishnyakova, T.P., Golubeva, I.A., and Glebova, E.V., *Usp. Khim.*, 1985, vol. 54, no. 3, pp. 429–449.
2. US Patent 3673249, 1972, *Ref. Zh. Khim.*, 1973, 21N68P.
3. Bakibaev, A.A., *Zh. Obshch. Khim.*, 1996, vol. 32, no. 10, pp. 1486–1490.
4. Magerramov, A.M., Abdinbekova, R.T., Kurbanova, M.M., and Allakhverdiev, M.A., *J. Proc. Petrochem. Oil Refining*, 2003, vol. 3, no. 14, pp. 50–52.
5. Abdinbekova, R.T., Kurbanova, M.M., Magerramov, A.M., and Allakhverdiev, M.A., Abstracts of Papers, *XVII Mendeleevskii s"ezd po obshchei i prikladnoi khimii* (XVII Mendeleev Congr. on General and Applied Chemistry), Kazan, September 21–26, 2003, vol. 2, p. 75.
6. Magerramov, A.M., Abdinbekova, R.T., Kurbanova, M.M., and Allakhverdiev, M.A., Abstracts of Papers, *10 IUPAC Int. Symp. on Macromolecule–Metal Complexes (MMC-10)*, Moscow, May 18–23, 2003, P–25, p. 84.
7. Abdinbekova, R.T., Kurbanova, M.M., Magerramov, A.M., and Allakhverdiev, M.A., Abstracts of Papers, *Konferentsiya, posvyashchennaya 90-letiyu Z.G. Zul'fugarova* (Conf. Dedicated to Z.G. Zul'fugarov's 90th Anniversary), Baku, 2004, p. 203.
8. Farzaliev, V.M., Allakhverdiev, M.A., Khalilova, A.Z., and Guseinova, T.M., *Zh. Prikl. Khim.*, 1994, vol. 67, no. 6, p. 1049.

Russian Journal of Applied Chemistry, Vol. 77, No. 10, 2004, pp. 1670–1674. Translated from Zhurnal Prikladnoi Khimii, Vol. 77, No. 10, 2004, pp. 1684–1688.

MACROMOLECULAR CHEMISTRY AND POLYMERIC MATERIALS

Copolymerization of Sulfolane-containing Acrylamido Sulfonic Acid with Acrylamide and Acrylonitrile in Water

K. V. Shirshin, O. K. Kazantsev, A. V. Igolkin, V. L. Krasnov, and A. P. Sivokhin

Nizhni Novgorod State Technical University, Dzerzhinsk Branch, Dzershinsk, Nizhni Novgorod oblast, Russia

Received June 16, 2004

Abstract—Copolymerization of sodium 4-acrylamido-4-methyltetrahydro-1,1λ^6-dioxothiophene-3-sulfonate with acrylamide and acrylonitrile in water was studied. It was found the copolymer composition is mainly determined by association of the monomeric species.

Polymers derived from *N*-substituted acrylamides containing sulfo groups [primarily, copolymers of 2-acrylamido-2-methylpropanesulfonic acid (AMPSA)] are used in textile and paper industry, oil production, and wasterwater treatment [1]. A procedure for preparing a new monomer of this family, 4-acrylamido-4-methyltetrahydro-1,1λ^6-thiophene-3-sulfonic acid (ASA), has been developed recently [2].

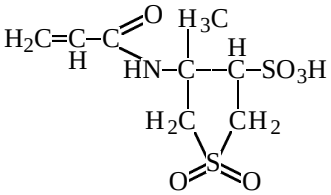

ASA

This compound contains not only sulfonic acid but also a sulfolane fragment, which imparts new valuable properties to the polymer.

Some features of copolymerization of the potassium salt of ASA with acrylamide (AA) were studied in [3]. It was suggested that copolymerization of these monomers in concentrated aqueous solutions can be affected by strong intermolecular interactions and, in particular, by formation of charge-transfer complexes of sulfonic anions with protonated monomers. It is of interest to study the influence exerted by the intermolecular interactions on the copolymerization of ASA with AA and AN in more detail. In this study we examined the monomer conversion and the copolymer composition as influenced by the ratio of the monomers in the initial reaction mixture.

EXPERIMENTAL

Na–ASA was prepared by the procedure described in [2]. AA was recrystallized from benzene prior to use. AN was purified by distillation. The physical constants of the purified monomers agree with published data. Copolymerization of NaASA with AA and AN was performed in glass ampules at 70°C. In all experiments, the total initial concentration of the monomers was 1 M. The initial AA–AN ratio ranged from 1 : 9 to 9 : 1. An ampule was purged with nitrogen and was charged with disodium salt of 4,4'-azobis-4-cyaopentanoic acid (0.5 mol % relative to the sum of the monomers). The concentrations of Na–ASA and AA in the reaction mixture were estimated by liquid chromatography, and the concentration of AN, by gas–liquid chromatography. The liquid chromatographic analysis was performed on a Praha chromatograph equipped with a UV detector (λ = 254 nm) and a 150 × 4.6-mm steel column packed with modified silica gel (Silasorb C_{18}, 10 μm fraction). Acetonitrile was used as the eluent. Gas–liquid chromatrograpic analysis was performed on a Tsvet-100 chromatograph with a flame-ionization detector and a 2-m steel column 3 mm in diameter, packed with 10% PEGA on Chromaton N–AW. The flow rate of the carrier gas (nitrogen) was 2×10^{-3} m^3 h^{-1}. The temperature of the vaporizer and columns was 70 and 40°C, respectively. The specific viscosity of monomer solutions was measured at 25°C on an Ubbelohde viscometer with a capillary 0.34 mm in diameter. The conductivity of the solutions was measured on a PRL T57-21

1070-4272/04/7710-1670 © 2004 MAIK "Nauka/Interperiodica"

conductometer with graphite electrodes, operating at 3500 Hz.

The dependence of the copolymer composition on the initial ratio of the monomers is shown in Fig. 1. At excess of AA, the copolymer composition differs from that of the initial mixture by no more than 2%. As the Na–ASA fraction in the initial mixture increases, the copolymer is slightly enriched with the nonionic units. However, the difference between the copolymer composition and that of the initial mixture of the monomers does not exceed 3–5 %.

Thus, the copolymerization of Na–ASA with AA occurs in a nearly azeotropic mode. In addition, the copolymer composition, does not change up to a 70% conversion, except in experiments with a large excess of AA (Fig. 2, curves *5*, *6*). It is known that the copolymer composition may be close to that of the initial mixture of the monomers. However, this is usually the case for vinyl monomers with about the same distribution of the electron density and sterically accessible C=C bonds [4]. In our system, the induction effect and steric accessibility of the amide groups in the acrylamide monomers substantially differ. The steric constant R_S of the $-NH_2$ group of AA and –NHR group of Na–ASA, determined by the procedure described in [5] are –0.98 and –2.93, respectively. The induction constants of these groups, σ^*, determined by the procedures described in [6] and [7], respectively, are 0.87 and 0.53. The bond distances were calculated by the MNDO procedure, using HyperChem software. Thus, we deal in the given case with "azeotropic" copolymerization of a nonionic monomer (AA), which has a small substituent at the C=C bond, with an ionic monomer (Na–ASA), which has at the C=C bond the much bulkier subsituent with substantially stronger electron-with-drawing properties.

We compared the results obtained with the data on copolymerization of AA with other vinyl monomers with sulfonic acid groups in aqueous solutions. The AA–(Na–AMPSA) copolymer is slightly enriched in the nonionic amide units. The composition of this copolymer remains virtually the same up to deep monomer conversions [8]. Kurenkov and Utikeeva [9] reported that AA–(Na–AMPSA) copolymers are enriched in the AA units. They also found that the copolymerization is accelerated as the AA fraction in the initial mixture grows, and the content of the nonionic units in the copolymer becomes higher with increasing total initial concentration of the monomers. This is due to a decrease in the fraction of free ions in the solution with increasing ionic strength. As a result,

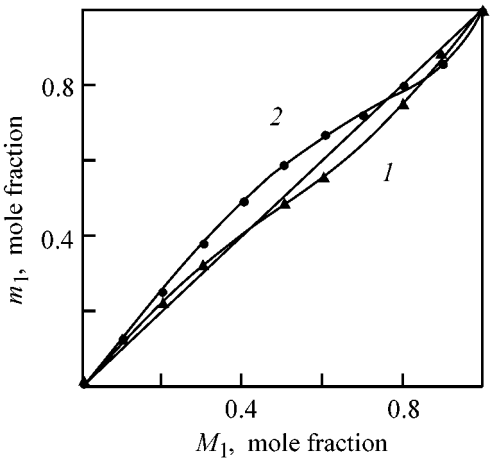

Fig. 1. Mole fraction of Na–ASA units m_1 in (*1*) Na–ASA–AA and (*2*) Na–ASA–AN copolymers prepared in water vs. the Na–ASA mole fraction M_1 in the initial reaction mixture.

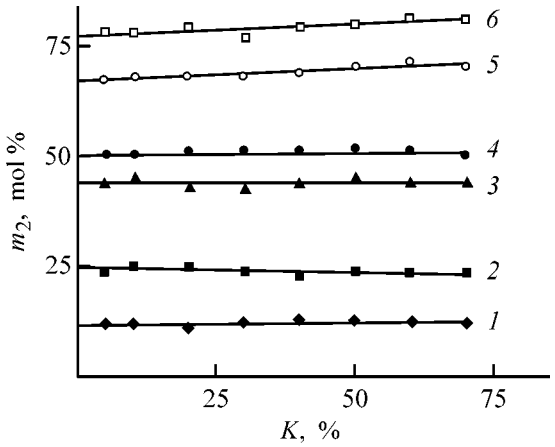

Fig. 2. Concentration of the AA units in Na–ASA–AA copolymer, m_2, vs. the monomer conversion K. Na–ASA : AA molar ratio in the initial mixture: (*1*) 90 : 10, (*2*) 80 : 20, (*3*) 60 : 40, (*4*) 50 : 50, (*5*) 30 : 70, and (*6*) 20 : 80.

the addition of the monomeric sulfonate to the macroradical with the terminal nonionic unit is accelerated. The composition of the AA–sodium vinylsulfonate copolymer remains constant up to approximately a 70% conversion [10]. In this case, the amide : sulfonate ratio in the copolymer exceeds by approximately a factor of 3 that in the initial mixture at all initial ratios of the monomers. Barabanova *et al*. [10] suggest that the copolymer composition of not only this copolymer but also all binary vinyl copolymers formed by homogeneous copolymerization in aqueous solutions should be almost independent of the monomer conversion and be determined by the ability of the monomers to penetrate into hydrophobic associates of the growing macroradicals. Since the penetration of charged sulfonate anions into these associates is dif-

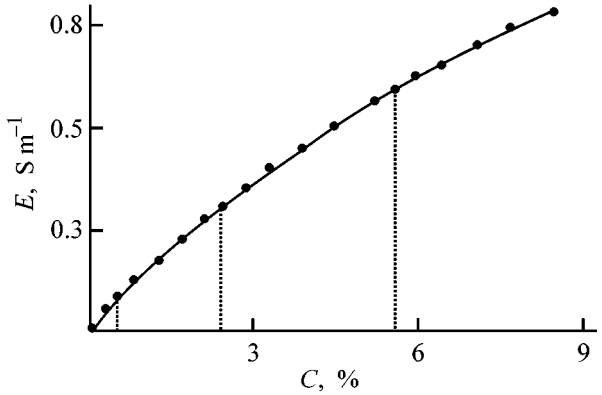

Fig. 3. Electrical conductivity E of aqueous Na–ASA solutions at 25°C vs. the Na–ASA concentration C.

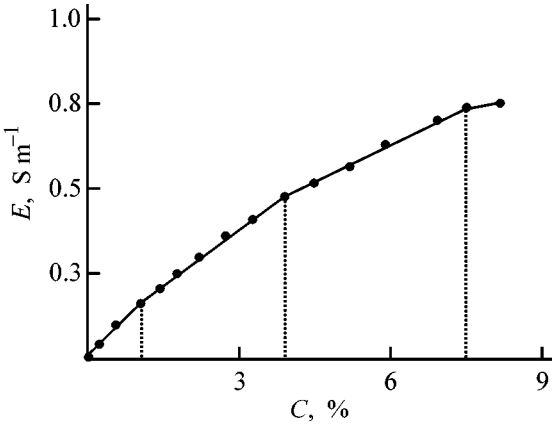

Fig. 4. Electrical conductivity E of aqueous solutions of Na–ASA and AA (Na–ASA : AA = 1 : 1) at 25°C vs. the Na–ASA concentration C.

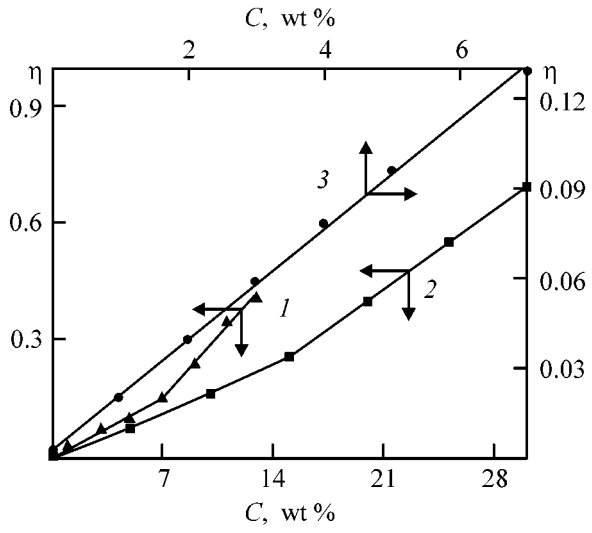

Fig. 5. Specific viscosity η of aqueous solutions of (*1*) Na–ASA, (*2*) AA, and (*3*) AN at 25°C vs. the monomer concentration C.

ficult, the reaction mixture in the vicinity of the reaction center is enriched with the nonionic amide.

It should be noted that these assumptions only partly account for the features of copolymerization of AA and vinyl sulfonic acid monomers. In particular, the copolymer composition markedly changes in some cases, e.g., in the AA–sodium sulfoethyl methacrylate system [8], in the course of copolymerization. Contrary to Kurenkov and Utikieva's hypothesis [9], the copolymer can be enriched in the nonionic units [see Fig. 1 or data on AA–(Na–AMPSA) copolymerization] or its composition may remain the same (AA–sodium vinylsulfonate system [10]) when the ionic strength of the solution becomes hidher, e.g., because of an increase in the fraction of the ionic monomer in the reaction mixture. In addition, the reaction orders with respect to the monomers in copolymerization of AA with potassium salts of ASA and AMPSA at the total monomer concentration of 20 wt % are abnormaly high (6.8 and 11.7, respectively) [3]. This fact cannot be understood in the framework of the above hypotheses.

The concentration effect and high reaction orders with respect to the monomers in copolymerization of Na–ASA with AA in water indicate that the monomer concentration is an important parameter of copolymerization. We suggest that the "prepolymerization" interaction of the monomers in aqueous solutions strongly affects the radical copolymerization. It is known [11] that vinyl monomers, which are not commonly classed with surfactants, i.e., contain no hydrophobic fragments with long hydrocarbon chain, along with polar hydrophilic groups, can be associated in aqueous solutions at the concentrations used in the copolymerization. In particular, association of acrylamide and some of its derivatives including AMPSA has been observed [12]. At the AA concentration in an aqueous solution exceeding 5.3 wt %, this monomer is associated to form mainly dimers [13]. Chapiro and Perec-Spritzer [14] suggest that AA forms dimers, trimers, and polymeric associates in aqueous solutions, with the polymer fraction increasing as the monomer concentration in the solution becomes higher.

Association of monomers can be judged from a nonlinearity of the concentration dependences of the viscosity, surface tension, electrical conductivity, and other physical properties of solutions. As can be seen in Figs. 3–5, Na–ASA and AA are associated in the solutions, with the structure of their associates changing with an increase in the concentration of these compounds. This is indicated by the "critical concentrations of association" (CCA), which are seen in the dependences of the electrical conductivity and vis-

cosity of solutions on the concentrations of Na–ASA and AA (Fig. 3, curve *5*). At these concentrations (about 1.0, 3.7, and 7.5 wt %), the dependence of the electrical conductivity on [Na–ASA] passes through inflection points (Fig. 3). At the concentration of 7.5 wt %, the concentration dependence of the viscosity (CDV) becomes nonlinear (Fig. 5, curve *1*).

The CDV of AA solutions (Fig. 5, curve *2*) has two inflection points at the monomer concentrations of 5% (in agreement with the data of [13]) and 15%. It should be noted that the concentration dependences of the physical properties of aqueous solutions of (meth)acrylate monomers that contain hydrophobic fragments (C_8 and longer) and, hence, exhibit surfactant properties also have several inflection points. These points are usually assigned to transformations of spherical micelles into anisotropic micelles and then into lamellas [15]. We suggest that the "critical concentrations" of AA solutions studied here are also due to transformation of AA associates with increasing monomer concentration.

Thus, copolymerization of ASA with AA should depend on the association of the monomers. It is known [11] that, in concentrated aqueous solutions of many monomers, their homopolymerization is sharply accelerated owing to close packing of molecules in the associates [11]. Probably, copolymerization in these associates is faster also. This mechanism accounts for the high total reaction order of copolymerization of K–ASA with AA [3]. The fact that the composition of Na–ASA–AA copolymer is close to that of the initial monomer mixture may be due to active formation of binary associates. As a result, although the individual capacities of pure monomers for association substantially differ, the composition of the binary associates is close to that of the initial monomer mixture. In such cases, the copolymer composition is similar to that of the coassociates. The constancy of the copolymer composition up to a high degree of monomer conversion can be explained as follows. Partial incorporation of monomers into hydrophobic polymeric chains stabilizes the monomer–polymeric associate. Hence, if the initial monomers readily associates, the process parameters will negligibly change with an increase in the conversion. Since AA monomers associate to a lesser extent than the sulfo monomer (Fig. 5), the total degree of the initial association at a low Na–ASA concentration (Fig. 2, curves *5* and *6*) starts to decrease and the copolymer composition slightly changes in the course of polymerization. This is due to a change in the composition of the monomer–polymer associates upon accumulation of the macromolecules (the total degree of association of the unchanged monomers gradually increases owing to hydrophobization).

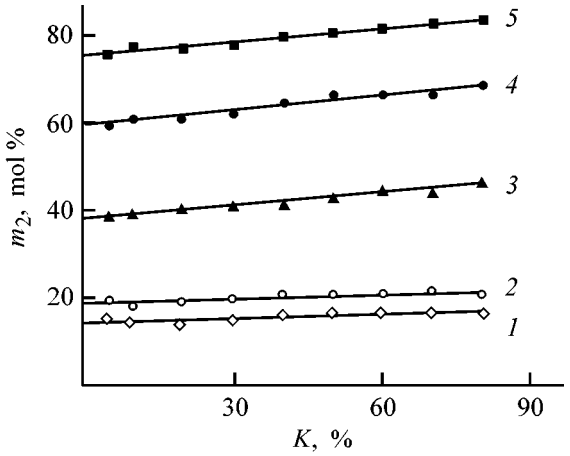

Fig. 6. Content m_2 of AN units in copolymers formed at the initial AN Na–ASA molar ratio of (*1*) 10 : 90, (*2*) 20 : 80, (*3*) 50 : 50, (*4*) 70 : 30, and (*5*) 80 : 20 vs. the monomer conversion K.

The formation of binary associates of the monomers is evident from the dependence of the electrical conductivity of the Na–ASA–AA–H_2O system on the monomer concentration. As in the case of a pure Na–ASA solution, three inflection points are observed (Fig. 4). However, the CCAs are shifted to lower concentrations, thus indicating the formation of Na–ASA–AA associates.

If Na–ASA copolymerizes with a monomer whose associating capacity is substantially lower than that of AA, the general aspects of the process will differ from those found for Na–ASA–AA system. We used AN as a such monomer. This compound does not associate in aqueous solutions (Fig. 5). The experimental data for the Na–ASA–AN system show that, unlike the first system, this system has a higher relative activity of Na–ASA. As can be seen from Fig. 1, the copolymer formed at the initial Na–ASA : AN ratios of 1 : 9 to 8 : 2 is enriched with the Na–ASA units. The copolymer composition changes in the course of copolymerization (Fig. 6).

Thus, copolymerization processes of Na–ASA–AA and Na–ASA–AN systems are strongly different. It is known that organic associates in aqueous solutions can both decompose and stabilize after introduction of substances of varied nature. We think that AN molecules, which do not form self-associates, are hydrophobic and can penetrate into Na–ASA associates. The stronger the hydrophobic properties of the associate, the higher the AN content in them. As the ini-

tial Na–ASA : AN ratio increases, the concentration of the readily associating Na–ASA monomer grows, and the molecules in the associates become more closely packed, which makes the aggregate more hydrophobic. As a result, a steadily increasing fraction of nitrile is incorporated into the associate (the degree of association increases), which leads to an increase in the content of the nitrile units in the polymer as compared to the systems with lower Na–ASA concentration in which the monomeric associates are "looser" and less hydrophobic.

CONCLUSIONS

(1) The composition of the Na–ASA–AA copolymer is close to that of the initial mixture of the monomers and remains the same up to high monomer conversions.

(2) The composition of the Na–ASA–AN copolymer changes in the course of the copolymerization. At the Na–ASA : AN ratio of 10 : 90 to 80 : 20 the copolymer is enriched with Na–ASA units, and at Na–ASA : AN = 90 : 10, with nitrile units.

(3) The capacity of Na–ASA, AA, and their mixtures for association revealed by analysis of the concentration dependences of the electrical conductivity and viscosity of their solutions.

REFERENCES

1. Lisovtsev, V.V., Rostokin, G.A., and Kulikova, A.E., *Khimicheskaya promyshlennost': Akrilaty i polivinilkhlorid* (Chemical Industry: Acrylates and Polyvinyl Chloride), Moscow: NIITEKhIM, 1984, pp. 1–22.
2. Kazakov, S.A., Kazantsev, O.A., Shirshin, K.V., *et al.*, *Zh. Prikl. Khim.*, 1999, vol. 72, no. 7, pp. 1168–1171.
3. Budanova, Yu.E., Shvetsov, O.K., and Maer, Zh.A., *Zh. Prikl. Khim.*, 2001, vol. 74, no. 7, pp. 1182–1185.
4. *Copolymerization*, Ham, G.E., Ed., New York: Interscience, 1964.
5. Galkin, V.A., Cherkasov, A.R., Sayakhov, R.D., *et al.*, *Zh. Obshch. Khim.*, 1995, vol. 65, no. 4, pp. 458–468.
6. Galkin, V.A., Cherkasov, A.R., Sayakhov, R.D., *et al.*, *Zh. Obshch. Khim.*, 1995, vol. 65, no. 4, pp. 477–479.
7. Galkin, V.A., Sayakhov, R.D., and Cherkasov, R.A., *Usp. Khim.*, 1991, vol. 60, no. 8, pp. 1617–1644.
8. McCormick, C.L. and Chen, G.S., *J. Polym. Sci. Polymer Chem. Ed.*, 1982, vol. 20, no. 3, pp. 817–838.
9. Kurenkov, V.F. and Utikeeva A.R., *Vysokomol. Soedin., Ser. A*, 2000, vol. 42, no. 4, pp. 587–593.
10. Barabanova, A.I., Gromov, V.F., Bune, E.V., *et al.*, *Vysokomol. Soedin., Ser. A*, 1994, vol. 36, no. 6, pp. 901–907.
11. Egorov, V.V., Zaitsev, S.Yu., and Zubov, V.P., *Vysokomol. Soedin., Ser. A*, 1991, vol. 33, no. 8, pp. 1587–1608.
12. Kazantsev, O.A., Igolkin, A.V., Shirshin, K.V., *et al.*, *Zh. Prikl. Khim.*, 2003, vol. 76, no. 7, pp. 1145–1149.
13. Arutyunyan, R.S., Grigoryan, Dzh.D., Simonyan, G.S., *et al.*, *Zh. Fiz. Khim.*, 2002, vol. 76, no. 5, pp. 846–849.
14. Chapiro, A. and Perec-Spritzer, L., *Eur. Polym. J.*, 1975, vol. 11, no. 1, pp. 59–69.
15. Batrakova, E.V., Orlov, Yu.N., Egorov, V.V., *et al.*, *Vysokomol. Soedin., Ser. B*, 1985, vol. 27, no. 2, pp. 87–93.

Russian Journal of Applied Chemistry, Vol. 77, No. 10, 2004, pp. 1675–1678. Translated from Zhurnal Prikladnoi Khimii, Vol. 77, No. 10, 2004, pp. 1689–1692.

MACROMOLECULAR CHEMISTRY AND POLYMERIC MATERIALS

Radical Copolymerization of Acrylic Acid with Derivatives of Monoethanolamine Vinyl Ether and *o*- and *p*-Chloranil

A. I. Nikitina, G. N. Zhunusova, S. A. Shoinbekova, B. A. Mukhitdinova, and E. E. Ergozhin

Bekturov Institute of Chemical Sciences, Ministry of Education and Science of the Republic of Kazakhstan, Almaty, Kazakhstan

Received July 20, 2004

Abstract—Radical copolymerization of derivatives of monoethanolamine vinyl ether and *o*- and *p*-chloranil with acrylic acid was studied. The parameter *p* for this system was determined by the Shtraikhman analytical graphic method; the copolymerization constants, Alfrey–Price specific activity and polarity parameters, probabilities of formation of various unit sequences in the macromolecular chain, lengths of sequences of similar monomeric units, and Harwood block structure parameters were calculated.

Although widely diverse synthetic ion exchangers are available today, improving their production processes and physicochemical characteristics and lovering of the production cost remain problems of current interest [1].

Previously, we have reported data on preparation of new quinoid derivatives of monoethanolamine vinyl ether (MEAVE) [2] and on their radical homopolymerization and copolymerization with available vinyl monomers [3–8]. In contrast to MEAVE, which shows virtually no tendency toward polymerization [9], and to quinones, which inhibit the polymerization, the redox monomers synthesized fairly readily enter radical homoand copolymerization. However, quinones differ in reactivity, depending on their structure.

The use of *o*- and *p*-chloranils for preparing redox ion exchangers is of large interest due to strong oxidative power of these compounds containing four chlorine atoms; the activity and redox potential of *o*-quinones are higher than those of their *p*-isomers [10].

In this study, we analyzed how the chemical structure (namely, position of carbonyl groups) affects the reactivity of redox monomers in copolymerization with acrylic acid (AA).

EXPERIMENTAL

3,4,5,6-Tetrachloro-1,2-benzoquinone (*o*-chloranil) (mp 125–130°C) was prepared as described in [11]. 2,3,5,6-Tetrachloro-1,4-benzoquinone (*p*-chloranil) (mp 289°C) was purchased from Aldrich and used without additional purification.

Redox monomers ($C_{10}H_8NCl_3O_3$) prepared according to [2] were cherry-lilac powders. The elemental composition and some physicochemical properties of derivatives of MEAVE and *o*- and *p*-chloranils (MEAVE–1,2-CA and MEAVE–1,4-CA), M 296.53, are listed in Table 1.

Azobis(isobutyronitrile) (AIBN) was recrystallized from absolute methanol, mp 102–103°C.

Table 1. Elemental composition and selected physicochemical properties of new redox monomers

Monomer	C	H	N	Cl	ρ, g cm^{-3}	mp, °C	Yield, %
	%						
MEAVE-1,2-CA	40.54*/40.38	2.70/2.85	4.73/4.68	35.90/35.15	–	138–140	43.60
MEAVE-1,4-CA	40.54/40.40	2.70/2.98	4.73/4.91	35.90/35.20	0.6111	168–170	67.10

* Numerator, calculated; denominator, found.

1070-4272/04/7710-1675 © 2004 MAIK "Nauka/Interperiodica"

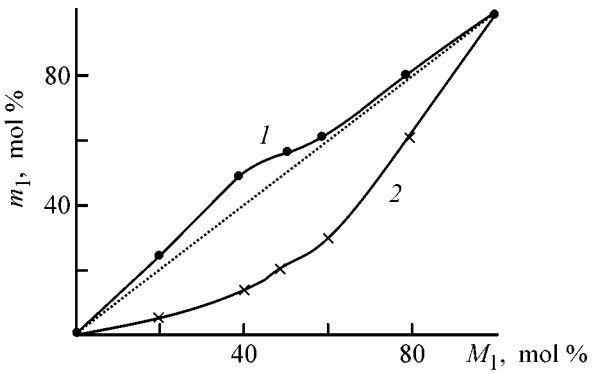

Monomer–copolymer composition diagrams. Content, mol %: (m_1) redox monomeric units in copolymers and (M_1) redox monomers in the monomer mixtures. (*1*) (MEAVE–1,2-CA)–AA and (*2*) (MEAVE–1,4-CA)–AA.

Acrylic acid had n_D^{20} = 1.421 after vacuum distillation.

The copolymerization of redox monomers (M_1) with AA (M_2) was performed in sealed ampules in DMF at 68°C in the presence of 6 wt % AIBN; the concentration of MEAVE–1,2-CA and MEAVE–1,4-CA was 20 g l^{-1}. The reaction was studied at the monomer ratio of 80 : 20 to 20 : 80. The conversion was evaluated by the concentration of the unchanged monomers, which was determined by polarography (redox monomers) and titration (AA).

Since it was difficult to record changes in the monomer concentrations in a short time, the first kinetic measurement was performed 30 min after the start of the reaction, and the experimental data were interpolated to 5 min from the start of the reaction.

The polarograms were measured in a temperature-controlled cell of a PU-1 polarograph at 25 ± 0.5°C using a mercury dropping electrode (capillary characteristic at open circuit $m^{2/3}t^{1/6}$ = 4.38 $mg^{2/3}$ $s^{1/2}$, with phosphate buffer solution (pH 7.4) in 25% DMF as supporting electrolyte. The reference electrode was a saturated calomel electrode. Prior to polarographic measurements, oxygen was removed from the solutions by bubbling of argon.

Viscometric studies were performed in Ubbelohde capillary viscometers in a temperature-controlled cell at 25°C in DMF.

The constants of relative activities of the monomers, which are important parameters of the copolymerization, characterize the relationship between the chemical structure of unsaturated compounds and their reactivity. The composition of the copolymers at various monomer ratios was determined by polarography and titration.

As seen from the figure, the systems do not form an azeotropic copolymer. In copolymerization of MEAVE–1,2-CA with AA, the composition curve lies above the azeotropic line, i.e., the copolymers are appreciably enriched in the units of the redox monomer ($r_1 > 1$, $r_2 < 1$) at any comonomer ratio. As the concentration of the redox monomer in the starting mixture is raised, the activities of both monomers become closer. In copolymerization of MEAVE–1,4-CA with AA, the composition curve lies below the azeotropic line, and the copolymer is enriched in the AA units ($r_1 < 1$, $r_2 > 1$).

Using the parameter p evaluated graphically by the Shtraikhman analytical method, we determined the copolymerization constants [12] and calculated from these data the Alfrey–Price specific activity and polarity parameters. For AA, we took Q_2 = 1.15 and e_2 = 0.77 [13]. The results are listed in Table 2.

As can be seen from Table 2, the *p*-chloranil-based copolymer shows a stronger tendency toward unit alternation, compared to the *o*-chloranil derivative, as indicated by the low product of the constants r_1r_2 and the large difference between the polarities of the two monomers, Δe (0.79).

For the monomeric system (MEAVE–1,2-CA)–AA, $r_1r_2 \approx 1$, i.e., "ideal" random copolymerization takes place, with low tendency toward alternation of the monomeric units. In such a copolymer, alternation of short blocks of the comonomers will be more typical. This system has a high specific activity Q_1; hence, MEAVE–1,2-CA is more reactive than MEAVE–1,4-CA.

The experimental data show that the reactivity of the redox monomers depends on the chemical structure of the quinones used for MEAVE modification. The mutual arrangement of carbonyl groups (*o*-, *p*-)

Table 2. Copolymerization constants and Q, e parameters for the systems constituted by redox monomer and AA (M_2)

Parameter	M_1 = MEAVE–1,2-CA	M_1 = MEAVE–1,4-CA
p	–1.81	–0.65
r_1	1.27	0.25
r_2	0.85	2.15
r_1r_2	1.080	0.538
$1/r_1$	0.79	4.00
$1/r_2$	1.18	0.46
Q_1	1.27	0.29
e_1	0.49	–0.02
Δe	0.28	0.79

Table 3. Probability of formation of various sequences in copolymers derived from redox monomers (M_1) and AA (M_2)

Starting mixture, mol %		Copolymer microstructure								
		$f_{M_1M_1}$		$f_{M_1M_2}$		$f_{M_2M_2}$		L_{M_1}	L_{M_2}	R
M_1	M_2	fraction	%	fraction	%	fraction	%			
(MEAVE–1,2-CA)–AA (r_1 = 1.27 and r_2 = 0.85)										
78	22	0.685	79.74	0.142	16.53	0.032	3.73	5.82	1.22	29.63
58	42	0.412	53.23	0.227	29.33	0.135	17.44	2.82	1.60	45.56
45	55	0.249	33.02	0.245	32.49	0.260	34.48	2.02	2.06	49.04
39	61	0.191	25.16	0.241	31.75	0.327	43.08	1.79	2.36	48.33
20	80	0.054	6.54	0.173	20.94	0.599	72.52	1.31	4.46	34.98
(MEAVE–1,4-CA)–AA (r_1 = 0.25 and r_2 = 2.15)										
80	20	0.289	40.20	0.282	39.22	0.148	20.58	2.02	1.52	56.64
60	40	0.109	14.89	0.268	36.61	0.355	48.50	1.41	2.32	52.45
49	51	0.061	7.93	0.232	30.17	0.476	61.90	1.26	3.05	45.18
40	60	0.035	4.34	0.194	24.07	0.577	71.59	1.18	3.97	36.38
20	80	0.006	0.66	0.097	10.74	0.800	88.60	1.06	9.25	18.40

and chlorine atoms in the quinone ring affects the donor–acceptor properties of the molecule; as a result, the electron density redistribution and the change in the polarization of the vinyl double bond in MEAVE–quinone derivatives are different.

Copolymerization yields different structural units, depending on the reaction conditions and monomer ratio: M_1M_1, M_1M_2, and M_2M_2. We calculated the microstructural characteristics of the copolymers: probability of formation of various diads f, mean lengths of blocks of similar units L_{M_1} and L_{M_2}, and Harwood parameters of block structure [14, 15]. The Harwood coefficient R is equal to the number of sequences of similar units per 100 units of the chain. The results are listed in Table 3.

At different monomer ratios, copolymers of different compositions are formed. Table 3 shows that, at an excess of redox monomers, MEAVE–1,2-CA and MEAVE–1,4-CA add to the "like" radicals more actively. The higher the content of redox monomers in the starting mixture, the larger L_{M_1}. The Harwood coefficients are the largest in compolymers with short lengths of units.

In the system (MEAVE–1,4-CA)–AA, in the range of the monomer ratios $M_1 : M_2$ from 80 : 20 to 60 : 40, copolymers of a more regular structure are formed. In the redox polymers containing 1,2-CA, the alternation of the monomers is regular at the monomer ratios $M_1 : M_2$ of 45 : 55 to 39 : 61. Table 3 shows that the microstructure of the copolymers can be controlled by choosing appropriate monomer ratios.

CONCLUSION

New unsaturated redox monomers, derivatives of monoethanolamine vinyl ether and *o*- and *p*-chloranil, differ in reactivity because of the different arrangements of the carbonyl groups in the quinoid rings; copolymerization of these monomers with acrylic acid proceeds differently.

REFERENCES

1. Kozhevnikov, A.V., *Elektronoionoobmenniki* (Electron and Ion Exchangers), Leningrad: Khimiya, 1972.
2. Kazakhstan Patent 8813.
3. Shoinbekova, S.A., Nikitina, A.I., Mukhitdinova, B.A., *et al., Zh. Prikl. Khim.*, 2001, vol. 74, no. 11, pp. 1847–1849.
4. Ergozhin, E.E., Mukhitdinova, B.A., Shoinbekova, S.A., *et al., Zh. Prikl. Khim.*, 2003, vol. 76, no. 3, pp. 475–478.
5. Nuranbaeva, B.M., Shoinbekova, S.A., Nikitina, A.I., *et al., Izv. Minist. Obraz. Nauki Resp. Kaz., Nats. Akad. Nauk Resp. Kaz., Ser. Khim.*, 2002, no. 3, pp. 111–115.
6. Nuranbaeva, B.M., Shoinbekova, S.A., Nikitina, A.I., *et al., Izv. Minist. Obraz. Nauki Resp. Kaz., Nats. Akad. Nauk Resp. Kaz., Ser. Khim.*, 2002, no. 4, pp. 91–99.
7. Ergozhin, E.E., Mukhitdinova, B.A., Shoinbekova, S.A., *et al., Izv. Minist. Obraz. Nauki Resp. Kaz.,*

Nats. Akad. Nauk Resp. Kaz., Ser. Khim., 2002, no. 2, pp. 108–114.

8. Shoinbekova, S.A., Nikitina, A.I., Nuranbaeva, B.M., *et al.*, *Izv. Minist. Obraz. Nauki Resp. Kaz., Nats. Akad. Nauk Resp. Kaz., Ser. Khim.*, 2002, no. 5, pp. 51–57.
9. Shostakovskii, M.F., *Prostye vinilovye efiry* (Vinyl Ethers), Moscow: Akad. Nauk SSSR, 1952.
10. Pullman, B. and Pullman, A., *Quantum Biochemistry*, New York: Interscience, 1963.
11. *Advances in Organic Chemistry. Methods and Results*, Raphael, R.A., Taylor, E.C., and Wynberg, H., Eds., New York: Interscience, 1961, vol. 2.
12. Shtraikhman, G.A., Vanshteidt, A.A., and Petrova, G.A., *Zh. Fiz. Khim.*, 1958, vol. 32, no. 3, pp. 512–519.
13. *Copolymerization*, Ham, G.E., Ed., New York: Interscience, 1964.
14. Gindin, L., Abkin, A., and Medvedev, S., *Zh. Fiz. Khim.*, 1947, vol. 21, no. 11, pp. 1269–1287.
15. Zil'berman, E.N., *Vysokomol. Soedin., Ser. B*, 1979, vol. 21, no. 1, pp. 33–36.

Russian Journal of Applied Chemistry, Vol. 77, No. 10, 2004, pp. 1679–1684. Translated from Zhurnal Prikladnoi Khimii, Vol. 77, No. 10, 2004, pp. 1693–1698.

MACROMOLECULAR CHEMISTRY AND POLYMERIC MATERIALS

Complexation of Anion Exchangers Based on Polyimines and Allyl and Epoxy Compounds with Transition Metal Cations

E. E. Ergozhin, T. K. Chalov, T. V. Kovrigina, R. A. Iskakova, and A. I. Nikitina

Bekturov Institute of Chemical Sciences, Education and Science Ministry of Kazakhstan Republic, Almaty, Kazakhstan

Received June 15, 2004

Abstract—Complexation of polymeric anion exchangers with transition metals was studied by polarographic and potentiometric titration techniques.

The wide use of ion-exchange sorption for recovering metals from process solutions and for solving various environmental problems stimulates studies of complexation of ion exchangers with metals. In choosing a sorbent suitable for efficient separation of metals with similar properties, data on the stability constants of sorbent–metal complexes, their composition, and factors influencing the complexation are required. These data are also taken into account in synthesis of sorbents selective for individual metal ions [1].

It is known that coordination compounds are mainly formed by transfer of an unshared electron pair from a ligand to a vacant orbital of a metal cation [2]. Sorbents containing amino groups (aliphatic or aromatic) are bound to metal ions via nitrogen atoms. Polymeric sorbents containing closely located amino groups can be coordinated to metals to give of strong five-membered chelate rings.

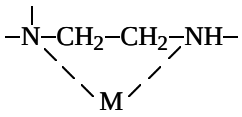

In this study, the complexation of polymeric polyfunctional anion exchangers with transition metal cations was examined by polarographic and potentiometric titration techniques. Anion exchangers were prepared by condensation of allyl glycidyl ether (AGE) with polyethylenimine (PEI) [AGE–PEI], AGE with poly(2-methyl-5-vinylpyridine) (PMVP) [AGE–PMVP], 4,4-isopropylidenediphenoldiglycidyl ether (ED-20) with PEI [ED-20–PEI], ED-20 with PVMP [ED-20–PVMP] and allyl haloides with PEI and PMVP.

EXPERIMENTAL

The polymeric anion exchangers used in this study were prepared by the methods reported in [3, 4]. A portion of the reaction mixture was taken in the precondensation stage and treated with diethyl ether to precipitate the polymeric sorbent. This sorbent was dried, and its solutions suitable for polarographic studies of its complexation with transition metals were prepared. The remaining reaction mixture was cured at 80°C to obtain an insoluble soild anion exchanger. The complexation of the cured sorbent with transition metals was studied by potentiometric titration.

The complexation of the anion exchangers obtained in the precondensation stage with transition metals was studied polarographically in 25% aqueous dimethylformamide (DMF) containing 0.01 N H_2SO_4. The anion exchanger concentration in these solutions was varied from 0.1 to 20 g l^{-1}. The concentration of transition metal salt ($CoSO_4$, $NiSO_4$, $CuSO_4$, and $ZnSO_4$) in these solutions was 2×10^{-3} M. A saturated calomel electrode was used as a reference electrode. The dropping mercury cathode had the following characteristic: $m^{2/3} t^{1/6} = 4.28$ mg$^{2/3}$ s$^{-1/2}$. The electrolytic cell was kept at 25 ± 0.1°C. The solutions used were deoxygenized by bubbling of argon for 10 min.

1070-4272/04/7710-1679 © 2004 MAIK "Nauka/Interperiodica"

Table 1. Effect of anion exchanger AGE–PEI on half-wave cathode potential of transition metal cations M^{2+} (M^{2+} concentration 2×10^{-3} M)

Cation	Anion exchanger content, g l^{-1}	$E_{1/2}$, V	Cation	Anion exchanger content, g l^{-1}	$E_{1/2}$, V
Cu^{2+}	0.00	–0.06	Co^{2+}	0.00	–1.31
	0.02	–0.10		0.02	–1.38
	0.04	–0.11		0.04	–1.39
	0.10	–0.12		0.10	–1.40
	0.40	–0.12		0.40	–1.41
	1.00	–0.15		1.00	–1.42
	4.00	–0.20		2.00	–1.43
	10.00	–0.23		4.00	–1.43
Ni^{2+}	0.00	–1.16		8.00	–1.44
	0.04	–1.18		10.00	–1.44
	0.10	–1.20	Zn^{2+}	0.00	–1.04
	0.40	–1.22		0.04	–1.13
	1.00	–1.24		0.10	–1.14
	4.00	–1.26		0.40	–1.16
	10.00	–1.28		1.00	–1.17
				4.00	1.19
				10.00	–1.21

Table 2. Shift of the half-wave cathode reduction potential of transition metal cations due to complexation with AGE–PEI anion exchanger (c_{resin} = 10 g l^{-1}, $c_{salt} = 2 \times 10^{-3}$ M)

Cation	$E_{1/2}$	$\Delta E_{1/2}$	pH
	V		
Cu^{2+}(I)*	–0.12	0.06	4.77
Cu^{2+}(II)	–0.23	0.17	7.12
Ni^{2+}	–1.28	0.12	6.90
Co^{2+}	–1.44	0.13	6.90
Zn^{2+}	–1.21	0.17	7.35

* c_{resin} = 0.10 g l^{-1}.

The apparent dissociation constant pK_a of the anion exchanger, the Bjerrum formation function *n*, and the stability constant *K* of the complex were calculated from potentiometric titration data by the technique reported in [5].

Table 1 shows how the half-wave cathode reduction potential of transition metal cations is influenced by addition of anion exchanger.

It has been shown [6] that the kind of transition metal cation significantly affects the half-wave cathode reduction potential of the forming transition metal complexes and its shift $\Delta E_{1/2}$ relative to the reduction potential of free metal ion $E_{1/2}$. As can be seen from Table 2, on adding AGE–PEI to solutions of transition metal salt, the largest $\Delta E_{1/2}$ is observed for Cu^{2+} and Zn^{2+}, i.e., these cations form the strongest complexes with the resin.

To elucidate the stability and composition of complexes formed by the AGE–PEI anion exchanger with transition metals, the $E_{1/2}$ of these metals was studied as a function of the resin concentration in the range 0.1–10 g l^{-1}. Figure 1 shows that, for Ni^{2+}, Cu^{2+} and Zn^{2+}, $E_{1/2}$ is a linear function of the logarithm of the resin concentration, i.e., only one strong complex of the anion exchanger with these metals is formed [7]. In the case of Cu^{2+}, the plot of $E_{1/2}$ against log *c* consists of three linear portions separated by two breaks. This plot shows that two complexes of the anion exchanger with copper are formed at pH 4.77 and 7.12, respectively.

The coordination number *p* of metal cations bound to the anion exchanger was determined from the slope of the plot of $E_{1/2}$ against log *c*, using the equation reported in [6, 7].

$$p = \frac{n}{0.059}\tan\alpha,$$

$$\tan\alpha = \frac{(E_{1/2})_2 - (E_{1/2})_1}{\log c_2 - \log c_1},$$

where *n* is the number of electrons transferred to the transition metal cation during cathodic reduction.

We found that, for Ni^{2+}, Co^{2+} and Zn^{2+}, only one amino group of the sorbent is coordinated with the metal. For Cu^{2+}, one or three amino groups can be coordinated with the metal depending on pH.

The stability constants of AGE–PEI complexes with metal cations, calculated by the equation reported in [8]

$$\log K = \frac{n\left(\Delta E_{1/2} + p\frac{0.059}{n}\log c\right)}{0.059},$$

are listed in Table 3.

Table 3. Coordination numbers p and stability constants ($\log K$) of AGE–PEI complexes with transition metals, determined by the polarographic technique (c_{resin} = 10 g l^{-1}, c_{metal} = 2×10^{-3} M)

Salt	p	$\log K$	pH	Salt	p	$\log K$	pH
$CuSO_4^*$	1	1.03	4.77	$CoSO_4$	1	5.58	6.90
$CuSO_4$	3	8.76	7.12	$ZnSO_4$	1	6.76	7.35
$NiSO_4$	1	5.07	6.90				

* c_{resin} = 0.10 g l^{-1}.

Table 4. Physicochemical characteristics of cured anion exchangers

Anion exchanger	SEC for 0.1 N HCl, mg-equiv g^{-1}		pK_a	m	SEC_M, mg-equiv g^{-1}			
	total	PT*			Cu^{2+}	Ni^{2+}	Co^{2+}	Zn^{2+}
AGE–PEI	7.5	7.3	5.3	1.9	6.1	4.8	4.3	1.7
AGE–PMVP	4.6	4.1	4.9	2.2	4.3	2.5	2.2	1.3
ED-20–AB–PEI	6.6	6.3	7.0	2.5	6.3	4.2	4.1	3.8
ED-20–AB–PMVP	3.2	3.0	3.6	2.3	2.8	2.0	1.8	1.3

* Determined from the potentiometric titration curve.

Figure 1 and Table 3 show the stepwise character of AGE–PEI complexation with Cu^{2+}. At the sorbent concentration below 0.1 g l^{-1}, one amino group is coordinated with the Cu^{2+} cation. At the sorbent concentration above 0.1 g l^{-1}, three amino groups of the anion exchanger are bound to one Cu^{2+} cation. Our polatrographic experiments showed also that, among transition metal cations, Cu^{2+} is the most strongly bound to the AGE–PEI sorbent. The stability of AGE–PEI-transition metal complexes decreases in the order $Cu^{2+} > Zn^{2+} > Co^{2+} > Ni^{2+}$. The ionic radii of these cations decrease in the same order: 0.96, 0.74, 0.72, 0.69 A [9]. This correlation shows that, as the ionic radius increases, the coordination power of the transition metal ion toward the AGE–PEI amino groups grows.

The characteristics of complexation of a cured (insoluble) AGE–PEI sorbent with transition metals (stability constant, composition of complexes) was studied by potentiometric titration of an aqueous suspension of this resin in the absence and in the presence of transition metals, with simultaneous monitoring of the content of free metal cations and pH.

The physicochemical characteristics of the cured anion exchangers are listed in Table 4.

It is known [10] that the shape of a potentiometric titration curve is sensitive not only to the concentration of titrable functional groups, but also to both the ionic strength of solution and the type of a supporting electrolyte. With the ionic strength increasing from 0.1 to 1.0 M, the electron-donor power of unprotonated amino groups increases, and their hydrate shells become looser. As a result, the complexation of the anion exchanger with transition metals is enhanced. Therefore, our sorption experiments were performed at the ionic strength of 1.0 M.

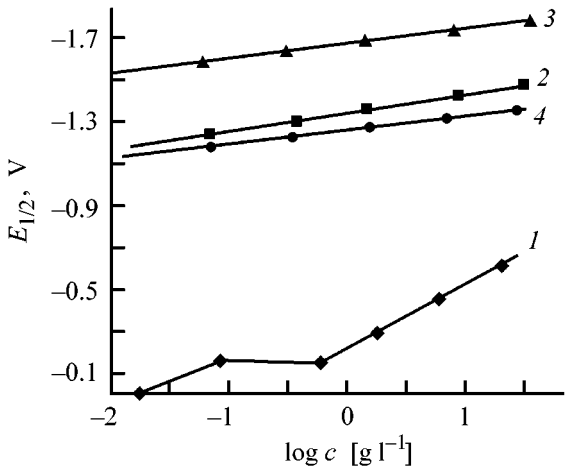

Fig. 1. $E_{1/2}$ of transition metal complexes vs. the anion exchanger concentration c: (*1*) Cu^+, (*2*) Ni^{2+}, (*3*) Co^{2+}, and (*4*) Zn^{2+}; the same for Fig. 4.

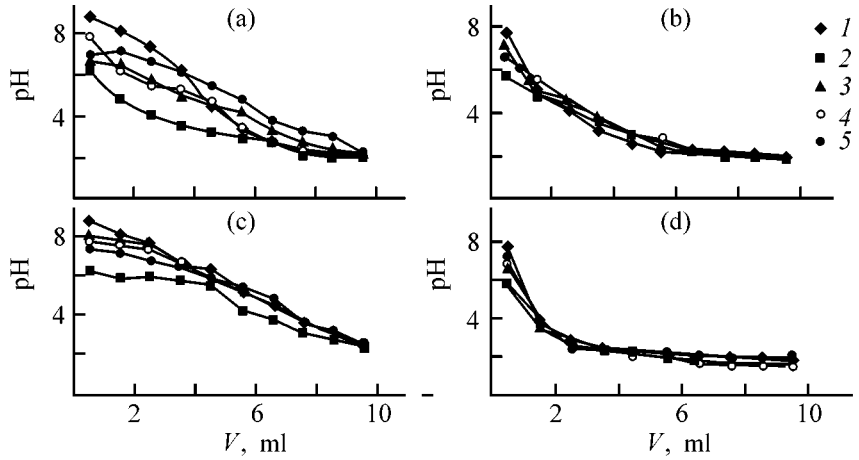

Fig. 2. Potentiometric titration curves of anion exchangers based on allyl and epoxy compounds in the absence and in the presence of transition metal cations. (*V*) aqueous acid volume. Anion exchanger: (a) AGE–PEI, (b) AGE–PMVP, (c) ED-20–AB–PEI, (d) ED-20–AB–PMVP. Metal: (*1*) none, (*2*) copper, (*3*) nickel, (*4*) cobalt, and (*5*) zinc.

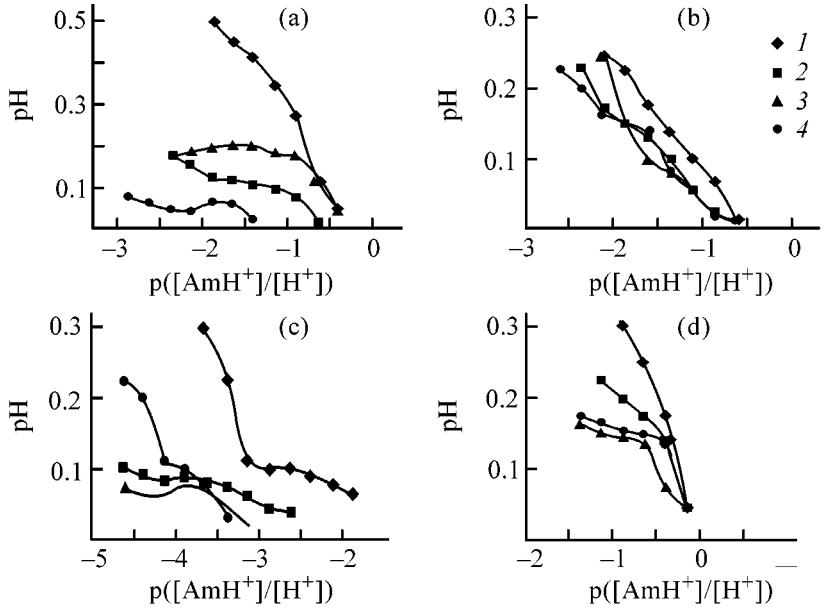

Fig. 3. Complexation functions. Metal cations: (*1*) copper, (*2*) nickel, (*3*) cobalt, and (*4*) zinc. Anion exchanger: (a) AGE–PEI, (b) AGE–PMVP, (c) ED-20–AB–PEI, and (d) ED-20-AB–PMVP.

Figure 2 shows the potentiometric titration curves of the cured anion exchanger based on AGE and ED-20 in an aqueous acid-containing suspension in the absence and in the presence of a transition metal. These curves show that both the complexation with metal and the protonation of the amino groups of the sorbent in the course of titration is accompanied by acidification of the liquid phase. The potentiometric titration curves obtained in the presence of metal are shifted to lower pH, compared to metal-free suspensions. This excess acidification becomes more pronounced with increasing metal concentration. The largest acidification in the presence of a metal is observed with AGE–PMVP and ED-20–PMVP anion exchangers. We believe that the excess acidification in the presence of metals is caused by a decrease in the sorbent basicity due to transfer of unshared electron pairs from the amino groups to metal cations. For all the sorbents under consideration, the sorption exchange capacity determined from the potentiometric titration curves at the equivalence point is less than the total exchange capacity. This difference can be caused by coordination of amino groups with metal cations and partial protonation of tertiary and secondary amino groups of the resin. The complexation curves of anion exchangers with copper, nickel, zinc and cobalt show (Fig. 3) that p tends to unity, i.e., the 1 : 1 complexes are predominantly formed. This means that one amino

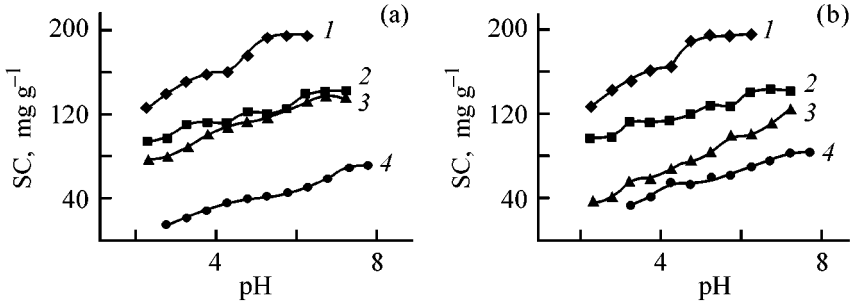

Fig. 4. Static exchange capacity SEC of anion exchangers as influenced by pH. Anion exchanger: (a) ED-20–AB–PEI and (b) AGE–PEI.

group, on the average, is coordinated with one metal cation. This stoichiometry is caused by the large excess of metal ions in the solution as compared with the content of sorbing sites in the sorbent. As the content of unprotonated amino groups in the sorbent becomes higher p increases to 1.5. This fact shows that the stoichiometry of complexation is sensitive to the content of sorbing sites in the resin. The chemical composition of sorbable metal complexes mainly depends on the ionic composition of the sorbing sites and on the metal cation speciation in the solutions. The higher the concentration of coordination-active ionic sites in the sorbent, the larger the amount of amino groups coordinated with metal cation.

Our calculations showed that the Bjerrum formation functions are too small for calculating the stability constants in our systems. In spite of this difficulty, we can suggest, based on published data [11], that in our systems the cross-linked anion exchanger complexation with transition metal decreases in the order: $Cu^{2+} > Zn^{2+} > Co^{2+} > Ni^{2+}$.

It is known [12] that sorption of cations on anion exchangers is dependent on the resin basicity. For example, zinc is sorbed on strongly basic anion exchangers only at the acidity exceeding 0.5 N, when anionic metal complexes are formed. By contrast, zinc is sorbed by weakly basic anion exchangers more strongly from weakly acidic aqueous solutions, and its sorption is enhanced when the acidity of the aqueous solution decreases. Therefore, to determine the pH ensuring the optimal metal sorption, we studied the transition metal sorption as influenced by pH. In these experiments, the distribution coefficients K_d and the degree of metal recovery, γ, were also determined (Table 5).

Table 5. Sorption of transition metal cations on AGE–PEI anion exchanger

Cation	Optimal pH	SEC_M, mg g^{-1}	K_d, ml g^{-1}	γ, %
Cu^{2+}	5–6	195	8203	94
Ni^{2+}	6–7	141	4976	91
Co^{2+}	7	126	3093	86
Zn^{2+}	7	72	2038	78

Figure 4 shows that, with increasing acidity of the aqueous phase, the sorption of metals decreases. This effect is caused by a decrease in the concentration of coordination-active (unprotonated) sorbing sites in the resin [13]. We found that the sorption of transition metals on the anion exchangers under consideration is the strongest at the following pH: Cu^{2+}, 5–6; Ni^{2+}, 6–7; and Zn^{2+}, 7.

CONCLUSIONS

(1) The complexation of polyfunctional anion exchangers based on polyimines and allyl and epoxy compounds with transition metals was studied by polarographic and potentiometric titration techniques. Copper was found to form the most stable sorption complexes.

(2) The distribution coefficients of transition metals between the aqueous phase and polymeric anion exchanger and the degrees of recovery of these metals were determined. The metal sorption was found to decrease with increasing acidity.

(3) Polyfunctional anion exchangers based on polyimine, allyl, and epoxy compounds can be recommended for industrial recovery of copper from aqueous solutions.

REFERENCES

1. Bjerrum, J., *Metal Ammine Formation in Aqueous Solution. Theory of Reversible Step Reactions*, Copenhagen: P. Haase, 1957.

2. Kukushkin, Yu.N., *Khimiya koordinatsionnykh soedinenii* (Coordination Chemistry), Moscow: Vysshaya Shkola, 1985.
3. Ergozhin, E.E., Chalov, A.K., Iskakova, R.A., and Kovrigina, T.V., *Zh. Prikl. Khim.*, 2004, vol. 77, no. 3, pp. 465–469.
4. Chalov, A.K., Ergozhin, E.E., Iskakova, R.A., and Kovrigina, T.V., *Izv. Minist. Obraz. Nauki Resp. Kaz., Nats. Akad. Nauk Resp. Kaz., Ser Khim.*, 2003, no. 3, pp. 78–84.
5. Ergozhin, E.E. and Menligaziev, E.Zh., *Polifunktsional'nye ionoobmenniki* (Polyfunctional Ion Exchangers), Alma-Ata, Nauka, 1986.
6. Shlefer, G.L., *Kompleksoobrazovanie v rastvorakh* (Complexation in Solutions), Moscow: Khimiya, 1964.
7. Heyrovsky, J. and Kuta, J., *Zaklady Polarografie*, Prague: Nakladatelstvi Ceskoslovenske Academie Ved., 1962.
8. Kovrigina, T.V., Iskakova, R.A., Sarsenov, S.K., and Chalov, A.K., *Vestn. Kaz. Gos. Nats. Univ., Ser. Khim.*, 2001, no. 2 (22), p. 341.
9. Goronovskii, I.T., Nazarenko, Yu.A., and Nekryach, E.F., *Kratkii spravochnik po khimii* (Concise Handbook on Chemistry), Kiev: Naukova Dumka, 1974.
10. Saldadze, K.M. and Kopylova-Valova, V.D., *Kompleksoobrazuyushchie ionity (kompleksity)* (Complexing Ion Exchangers (Complexites), Moscow: Khimiya, 1980.
11. Ergozhin, E.E., Chalov, A.K., Iskakova, R.A., and Nikitina, A.I., *Zh. Prikl. Khim.*, 2003, vol. 76, no. 2, pp. 216–219.
12. Saldadze, K.M., Pashkov, A.B., and Titov, V.S., *Ionoobmennye vysokomolekulyarnye soedineniya* (Ion Exchange Macromolecular Compounds), Moscow: Goskhimizdat, 1960.
13. Kopylova, V.D., Saldadze, K.M., and Asambadze, G.D., *Vysokomol. Soedin., Ser. A*, 1971, vol. 13, no. 7, pp. 1601–1611.

Russian Journal of Applied Chemistry, Vol. 77, No. 10, 2004, pp. 1685–1692. Translated from Zhurnal Prikladnoi Khimii, Vol. 77, No. 10, 2004, pp. 1699–1706.

MACROMOLECULAR CHEMISTRY AND POLYMERIC MATERIALS

Water-Soluble Polymer-Colloid Complexes of Aluminum Polyhydroxochloride and Polyacrylamide in Separation of Model and Real Dispersions

I. A. Novakov, S. S. Radchenko, and F. S. Radchenko

Volgograd State Technical University, Volgograd, Russia

Received March 1, 2004

Abstract—The activity of polymer-colloid complexes of aluminum polyhydroxochloride and polyacrylamide in separation of model kaolin dispersions and some real dispersions was studied under free and hindered particle sedimentation conditions.

The stability of dispersed systems is frequently controlled with flocculants, water-soluble macromolecular compounds, either natural or specially synthesized. Aluminum salts combined with certain polymers, above all polyacrylamide (PAA), have long been applied to water treatment [1, 2]. The main function of such components is to improve the flocculation in settlers and to reduce the water clarification time. However, the metal and the functional groups of the polymeric molecule of the flocculant can form ionic or coordination bonds. Schwartz and Francois [3] and Anufrieva *et al.* [4–6] studied reactions of a number of metals (Fe^{3+}, Ca^{2+}, Mg^{2+}, and rare-earth elements) with water-soluble polymers of various chemical structures and, in particular, with PAA. It was found that stable metal-containing polymeric complexes are formed in such systems via intramolecular complexation accompanied by a decrease in the conformational mobility of the macromolecules. Kudaibergenov *et al.* [7] studied the reaction between iron(IIII) chloride and nonionic and hydrolyzed PAA and showed that the coordination bond links the iron ions and the carbonyl groups of PAA. The resulting intramolecular ion-coordination cross-links are responsible for the compaction of the macromolecules: The hydrodynamic size of the particles of hydrolyzed PAA in water decreases from 2000 to 400 Å. At the same time, the conformation of the macromolecules and their hydrodynamic size in aqueous solutions are of primary importance in flocculation and sedimentation of dispersed particles. It has been shown [8–10] that the combined use of flocculants and inorganic coagulants in sedimentation of model kaolin and ocher dispersions can exert either synergistic or antagonistic effect, depending on the order in which the reagents are introduced.

More recent works [11–13] are concerned with formulations based on polyacrylamide and certain inorganic salts, whose high activity in flocculation and sedimentation of suspensions in potable water and wastewater treatment was noted by Gordeev-Gavrikov *et al.* [14]. Data on such formulations are scarce. These investigations are still in infancy, as suggested by the fact that the authors use terms like "alternative coagulants," "metal–polymer complexes," "composite organomineral coagulants," "inorganic polymeric flocculants," etc. [14, 15], which need to be defined more precisely.

We have shown previously [16] that mixing of aqueous solutions of PAA with aluminum polyhydroxochloride (APHC), as well as polymerization of acrylamide (AA) in an aqueous APHC solution, yields polymer-colloid complexes (PCCs) [16]. It was reasonable to test them both as flocculants for high-concentration dispersions and as coagulants for low-concentration aqueous dispersions (such as natural water).

EXPERIMENTAL

The poly complexes were prepared [16] by mixing aqueous solution of PAA (3 wt %) and APHC at room temperature or by polymerization of AA in an aqueous solution of APHC in the presence of an initiator, potassium persulfate. In both cases, the molar ratio of Al^{3+} to the PAA unit was varied from 0.25 to 10. The PCCs prepared were kept at room temperature for 2 days. The APBC obtained by the method described in [17] had the following characteristics: Al(III) content 12.8 wt %, Cl^{-1}/Al^{3+} atomic ratio 0.48, pH 4.5, ρ = 1330 kg m^{-3}, dry residue 46.5 wt %.

1070-4272/04/7710-1685 © 2004 MAIK "Nauka/Interperiodica"

Polyacrylamide was prepared by radical polymerization of AA (3% aqueous solution) in the presence of 0.1 wt % potassium persulfate at 45°C. The molecular weight of PAA was estimated viscometrically ($[\eta] = 6.8 \times 10^{-4} M^{0.66}$ [18]) at 520 000.

A kaolin dispersion (0.8 wt %) was prepared by swelling technical kaolin [GOST (State Standard) 19.608–84] in distilled water for 24 h. Before flocculation, we measured and, if necessary, adjusted pH to 7.4 by adding 5% $NaHCO_3$ or 0.1 N HCl solution. Before flocculation the dispersion was thoroughly mixed and poured into glass cylinders (V = 250 cm^3). A definite volume of a 0.1% solution of the flocculant was introduced into each cylinder, and the mixture was stirred for 1 min with a disk stirrer and allowed to stand for 20 min. The upper clarified layer was sampled with a pipet, and its optical density was measured on a Specol-10 spectrophotometer in a cell with a layer thickness of 1 to 5 cm at the wavelength of 460 nm. As flocculants served PCCs of various compositions, PAA and its copolymers (cation-active flocculants): Praestol-650, Zetag-92, and KF-99.

The flocculation of a concentrated kaolin suspension (5 wt %) was carried out in 100-cm^3 cylinders. A definite volume of the flocculant solution was introduced (0.1% solution) into each cylinder. After the cylinder was overturned 12 times, the time of migration of the interface between the clarified and thickened layers of the suspension was estimated using the graduation marks on the cylinders. Next, the kinetic plots were constructed in the distance (mm)–time (min) coordinates. The motion velocity of the interface was determined in the linear section of the curve at degrees of clarification within the range 20–60%.

To prepare a low-concentration kaolin dispersion, the previously prepared 0.8% kaolin dispersion was allowed to stand for 48 h. Then, the pH was measured and, if necessary, adjusted to 7.4. The upper clarified layer was decanted and filtered via a membrane filter to determine the content of the dispersed phase; it was estimated at 30–40 mg dm^{-3}. The coagulation was carried out by the same method as described above for a 0.8% dispersion. The settling time, after the reagent was added, was 40 min. Using the preliminarily constructed calibration plot [19], we recalculated the optical density into the turbidity (mg dm^{-3}). The flotation of the wastewater was carried out in a glass column (40 × 350 mm). The column bottom was a porous glass plate (Schott filter no. 4). Oil-containing wastewater (300 cm^3), preliminarily taken upstream of the process flotator, was poured into the column, whereupon a reagent dose was added; simultaneously, air was supplied via a porous plate. After a 20-min flotation, the sample was taken via the lower column cock, and the content of oil products in the sample was determined [20].

We studied poly complexes of PAA with APHC at various molar ratios of the reagents, prepared by mixing aqueous solutions of the reagents (PCMS) and by polymerization of AA in aqueous solutions of APHC (PCPs). Two particle sedimentation modes can be distinguished in flocculation, namely, free and hindered sedimentation at dispersed phase concentrations c_d under and over 1 wt %, respectively [21]. A number of parameters are used to quantitatively characterize the flocculation, among them the flocculation effect estimated from the rate of sedimentation of the particles and from accumulation of the precipitated mass on the pan of a torsion balance [9, 10]. However, the sedimentation rate was very high in the presence of PCCs and polycationic flocculants, which produced a strong scatter of the experimental data. Therefore, we studied the flocculation spectrophotometrically [22], by measuring the optical density of the supernatant liquid after the dispersion was allowed to stand a certain time with and without flocculant. Next, a dimensionless parameter, the clarification effect, was calculated:

$$E_{clar} = \tau_D^0/\tau_D - 1.$$

Here, τ_D^0 and τ_D are the optical turbidities of the supernatant liquid with and without the flocculant, respectively;

$$\tau_D = 2.3D/L,$$

where D is the optical density of the liquid; and L, length of the spectrophotometer cell.

The flocculation of the kaolin dispersion was carried out in the free sedimentation mode (dispersed phase concentration c_d = 0.8 wt %). Figure 1a presents the plots of the clarification effects for dilute kaolin dispersions as functions of the dose and composition of the poly complexes prepared by polymerization of AA in aqueous solutions of APHC. These dispersions are much more effective than PAA (Fig. 1a, curve *6*). The plots have peaks at the optimal content of the poly complex of 9–10 mg l^{-1}. At the poly complex concentrations above 10 mg l^{-1}, a secondary stabilization of the dispersion is observed, which is typical of all the flocculants. The poly complexes with the mole ratio of Al^{3+} to the PAA unit equal to 2 exhibit the maximum effect. Further increase in the content of aluminum in PCPs decreases the clarification effect (Fig. 1a, curve *5*). The poly complexes obtained by mixing

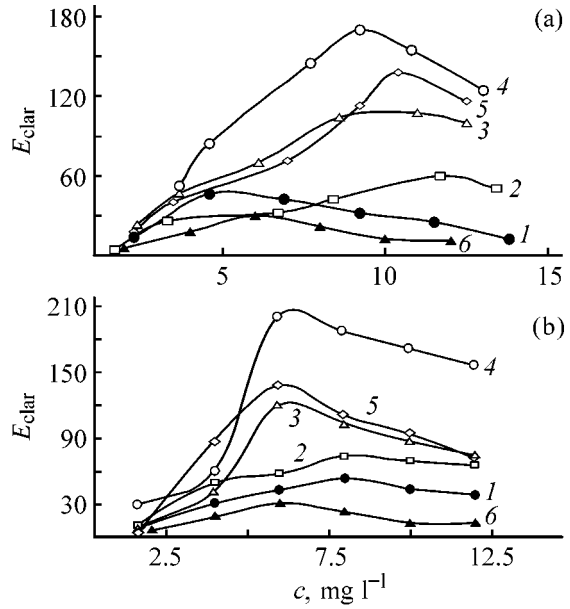

Fig. 1. Clarification effect E_{clar} for the kaolin dispersion (c_d = 0.8 wt %) vs. the concentration c and of the composition (Al^{3+} to PAA unit molar ratio, given below as hyphenated figures) of the poly complexes prepared by (a) polymerization of acrylamide (PCPs) and (b) mixing (PCMs). (*1*) PCP(PCM)-0.25, (*2*) PCP(PCM)-0.5, (*3*) PCP(PCM)-1, (*4*) PCP(PCM)-2, (*5*) PCP(PCM)-4, and (*6*) PAA.

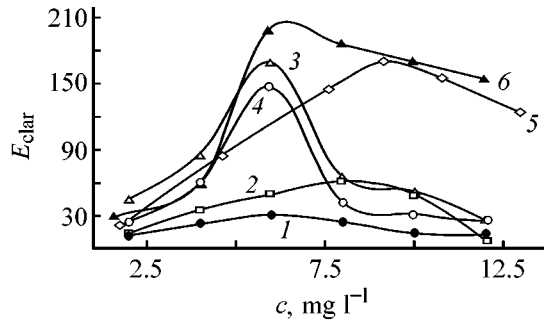

Fig. 2. Clarification effect E_{clar} for the kaolin dispersion (c_d = 0.8 wt %) vs. the concentration c and the type of flocculant. (*1*) PAA, (*2*) Praestol-650, (*3*) Zetag-92, (*4*) KF-91, (*5*) PCP-2, and (*6*) PCM-2.

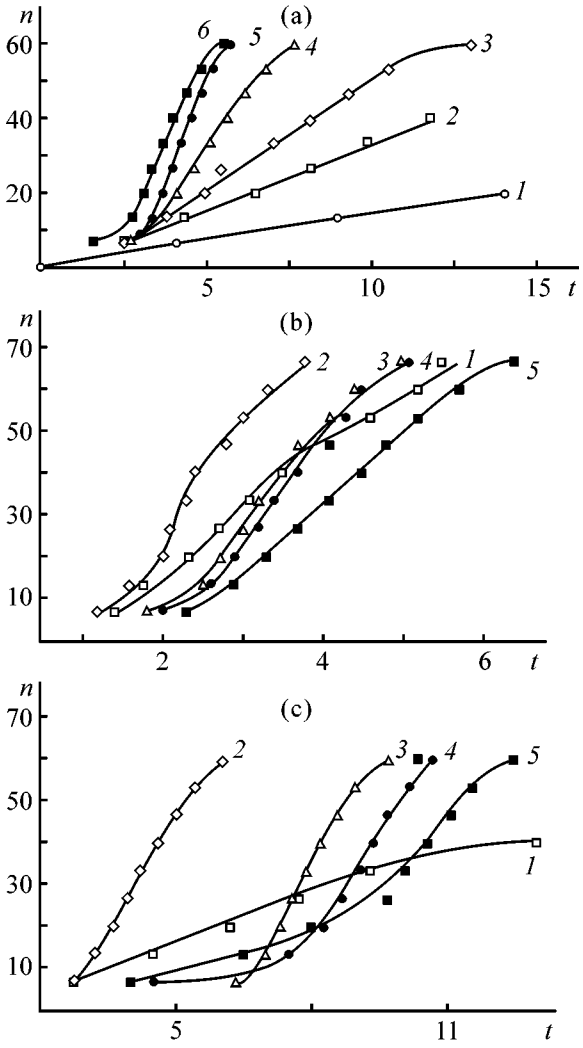

Fig. 3. Kinetic curve of sedimentation of a kaolin suspension (c_d = 5 wt %) in the presence of (a) PAA, (b) PCM-2, and (c) PCP-2. (*n*) Height of the clarified layer of the dispersion and (*t*) sedimentation time. Flocculant concentration, mg l^{-1}: (a) (*1*) 0, (*2*) 0.6, (*3*) 1.3, (*4*) 2.0, (*5*) 4.0, and (*6*) 6.5; (b) (*1*) 0.7, (*2*) 1.4, (*3*) 2.1, (*4*) 2.8, and (*5*) 3.5; and (c) (*1*) 1.0, (*2*) 2.0, (*3*) 3.0, (*4*) 4.5, and (*5*) 6.0.

aqueous solutions of PAA and APHC also exhibit high flocculation capacities. Figure 1b shows how the clarification effect for a dilute kaolin dispersion is influenced by the composition and dose of PCM. Similarly to PCPs, the clarification effect tends to grow with increasing APHC content in the poly complex and attains a maximum at the mole ratio of Al^{3+} to the PAA unit equal to 2. Further increase in the content of APHC in the PCs is accompanied by a decrease in the clarification effect. The optimal concentrations of the reagents in the case of PCMS are lower than for PCPs, namely, 6–8 mg l^{-1}.

It is known that the surface of the kaolin dispersion particles carries a negative charge [23], which makes cation-active flocculants the most effective reagents for their separation. Taking into account the nature of polymeric APHC particles, it can be assumed that the PCCs synthesized by us belong to cation-active reagents as well. In this context, we studied the flocculation capacity of PCP-2 and PCM-2 relative to the most widely used highly effective cationic flocculants Praestol-650, Zetag-92, and KF-91, as well as to nonhydrolyzed PAA (Fig. 2). We found that PCM-2 produces the strongest clarification effect,

Table 1. Clarification effects in sedimentation of the kaolin suspension with various flocculants

Flocculant	E_{clar} at indicated flocculant content, mg l^{-1}						
	0.5	1	1.5	2	3	4	5
PAA	1.6	3.0	4.5	8.5	13.5	14.7	14.2
Praestol-650	0.8	–	4.8	9.7	14.8	18.0	16.0
Zetag-92	–	6.1	10.8	12.8	14.5	32.5	28.7
KF-91	–	–	–	8.9	–	–	–
PCP-2	–	2.0	–	12.6	14.3	13.3	12.5
PCM-2	6.8	11.1	21.2	16.8	16.6	–	–

which significantly exceeds those of PAA and Praestol-650; it is no less effective than Zetag-92, even in a wider concentration range. Notably, PCM-2 was prepared from PAA of a relatively low molecular weight of 5.2×10^5 (according to viscometric data), against 20×10^6 for Zetag-92.

Of much importance for clarification of dispersions are kinetic parameters and, above all, the sedimentation rate of the dispersion particles in the presence of a flocculant. For concentrated dispersions (c_d = 5–8 wt %), this parameter is mostly estimated from the velocity of migration of the interface between the clarified and thickened layers of the suspension [24, 25]. We studied a kaolin dispersion prepared in distilled water with pH 7.35. In preliminary experiments, we determined the optimal flocculation conditions: kaolin concentration in water 5 wt %, and concentration of the flocculant solution to be introduced, 0.1 g l^{-1}. Figures 3a–3c show the kinetic curves for flocculation of a kaolin suspension in the presence of PAA, PCP-2, and PCM-2. Similar curves were obtained for Praestol-650, Zetag-92, and KF-91. Based on these data, we calculated the flocculation effects (see Table 1).

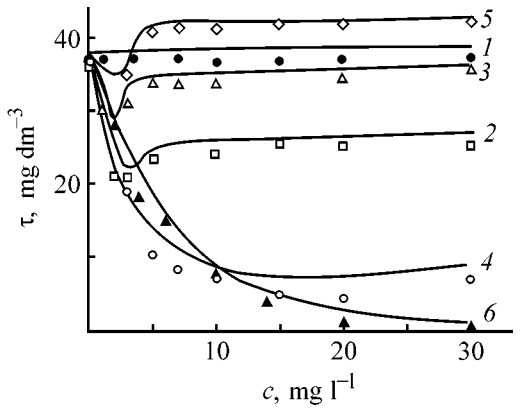

Fig. 4. Variation of the turbidity τ of the treated kaolin dispersion (c_d = 37 mg dm^{-3}) with the concentration c and type of the reagent. (*1*) PAA, (*2*) Praestol-650, (*3*) Zetag-92, (*4*) APHC, (*5*) PCP-0.5, and (*6*) PCP-2.

Table 1 suggests that the poly complexes exceed in the clarification effect PAA and some cationic flocculants and are equal in performance to Zetag-92. The flocculation capacity of the poly complex tends to grow with increasing molar ratio of Al^{3+} to the PAA unit and attains a maximum at the molar ratio of 2 (PCM-2, PCP-2).

The sedimentation of low-concentration dispersions (c_d < 1 wt %) predominantly occurs by the neutralization mechanism. The specific structure of the PCCs prepared (the relatively low molecular weight of PAA and charged particles arranged on the coil surface) can make them effective reagents in coagulation. In this context, we studied the performance of the PCCs in separation of a low-concentration kaolin dispersion prepared from a 0.8 wt % kaolin dispersion in distilled water. The content of the dispersed phase in the decanted liquid was 30–40 mg dm^3, and the particle size, 1.6–2.5 μm, according to the sedimentation analysis. On a certain assumption, such a system can be regarded as a model of natural water in terms of its dispersion composition [26]. The coagulation efficiency was estimated from the change in the water turbidity after treatment with the reagent. Figure 4 shows the plots of the turbidity of the water treated by various reagents at concentrations within 2–40 mg l^{-1}. It is seen that, under the actual conditions, PAA is inactive. Polycationic flocculants Praestol-650, Zetag-92, and PCP-0.5 cause coagulation when present in low concentrations, but the degree of purification is not high; an increase in the concentration results in stabilization of the system. As expected, APHC is an effective reagent under the actual conditions, but PCP-2 also exhibits a high coagulation activity: At concentrations above 12 mg l^{-1}, it exceeds APHC in the degree of purification, and at concentrations above 30 mg l^{-1}, all the reagents stabilize the system. Evidently, the ratio of the reagents (PAA and APHC) in the poly complex, required for attaining the maximum coagulation efficiency, can have an optimum, as in the case of flocculation. Therefore, we studied the coagulation activity of the PCCs (prepared by polymerization) at different molar ratios of the reagents (Al^{3+} to the PAA unit) (Table 2).

Table 2. Degree of purification in coagulation of a low-concentration kaolin dispersion with PCPs of various compositions

Reagent	Degree of purification, %, at indicated reagent content, mg l^{-1}									Reagent	Degree of purification, %, at indicated reagent content, mg l^{-1}								
	5	10	15	20	25	30	40	50	60		5	10	15	20	25	30	40	50	60
PCP-1	35	62	77	84	88	90	91	91	40	PCP-10	25	46	68	85	89	89	94	93	91
PCP-2	28	61	74	84	89	91	92	92	76	APHC	23	55	72	85	89	92	94	95	95
PCP-5	27	61	73	87	90	90	93	94	84										

Table 3. Degree of purification in coagulation of a low-concentration kaolin dispersion with PCMs of various compositions

Reagent	Degree of purification, %, at indicated reagent content, mg l^{-1}								
	2	3	4	6	8	10	16	20	30
PCM-1	8.1	16.2	20.5	30.4	38.5	46.0	65.0	70.2	73.0
PCM-2	16.2	–	43.2	54.0	–	70.2	83.8	89.2	96.0
PCM-3	29.6	–	57.3	69.0	76.7	–	90.5	92.0	96.0
PCM-10	40.5	73.0	82.4	–	89.2	90.5	–	98.6	99.0

Table 4. Degree of purification of a low-concentration kaolin dispersion as dependent on the type and concentration of the reagent

Reagent	Content, mg l^{-1}		Degree of purification, %	Reagent	Content, mg l^{-1}		Degree of purification, %
	Al^{3+}	PAA			Al^{3+}	PAA	
APHC	2.1	–	88.3	PCP-0.5	0.8	0.8	94.3
APHC + PAA*	0.8	1.6	90.0	PCP-2	0.8	0.4	96.7
				PCP-10	0.8	0.1	92.8

* Successive addition of the reagents.

Table 2 suggests that, at concentrations of 20 mg l^{-1} and over, virtually all the reagents are equally effective. The concentration of aluminum-containing coagulants of 20 mg l^{-1} is typical of breaking-down model kaolin dispersions [27]. The poly complexes prepared by mixing of the reagents also exhibit a high coagulation activity (Table 3).

Our experimental data suggest that the PCCs based on PAA and APHC, prepared both by mixing aqueous solutions of the reagents and by polymerization of AA in aqueous solutions of APHC, combine the properties of polymeric cationic flocculants and coagulants acting by the neutralization mechanism.

The known water treatment procedures involve a combined use of aluminum hydroxochloride and a flocculant, PAA [1]; it is recommended that the reagents should be introduced into the mixing chamber separately. Thus, a question arises as to whether such a treatment procedure will be similar to that in the case of PCCs. Table 4 compares the degrees of clarification, achieved with various reagents tested in coagulation of a low-concentration (30 mg dm^{-3}) kaolin dispersion. It is seen that introduction of PAA into the dispersion after its coagulation with APHC improves water purification, but the degree of purification in this case is lower, compared to PCCs. Notably, the concentrations of the reagents in the latter case are much lower.

Studies of model systems make it possible to tentatively by estimate the flocculation and coagulation capacities of a reagent or to compare these parameters

Table 5. Degree of purification of natural water as dependent on the composition and concentration of the reagents

Reagent	Content, mg l^{-1}		Turbidity* of treated water, mg dm^{-1}	Degree of purification, %
	Al^{3+}	PAA		
APHC + PAA**	2.0	0.58	1.32	93.8
PCP-0.5	0.5	2.35	1.50	94.0
	1.0	4.70	1.03	95.9
	2.0	9.40	1.44	94.2
	5.0	23.50	3.81	84.8
PCP-2	0.5	1.15	0.87	96.5
	1.0	2.30	0.56	97.8
	2.0	4.60	0.36	98.6
	5.0	11.50	1.25	95.0
PCP-10	0.5	0.14	19.10	92.4
	1.0	0.29	1.30	94.8
	2.0	0.58	0.82	96.7
	5.0	1.45	0.34	98.6

* GOST (State Standard) R 51232–98 prescribes potable water turbidities $\leq$ 1.5 mg l^{-1}.

** PAA according to TU (Technical Specifications) 76-01-1049.22.

Table 6. Sedimentation velocity and degree of purification of the wastewater from dielectric glove production as influenced by the composition and concentration of the reagents

Reagent	Content, mg l^{-1}		Sedimentation velocity, mm s^{-1}	Degree of purification, %
	Al^{3+}	PAA		
APHC + PAA*	50.0**	115.0	2.6	90.4
PCP-0.5	1.0	4.7	4.2	91.4
	50.0	253.0	8.0	97.4
PCP-2	1.0	2.3	5.5	97.6
	50.0	115.0	10.3	98.5
PCP-10	1.0	0.27	3.1	89.3
	50.0	13.5	5.9	96.6

* PAA according to TU (Technical Specifications) 76-01-1049.22.

** The concentration corresponding to the maximum degree of purification.

for a set of reagents under identical conditions. Under real conditions, the effect produced by a reagent is determined by the characteristics of the medium in which it is applied (pH, ionic strength, salt content, etc.). Natural water and wastewater are polycomponent systems, which prevents taking a uniform theoretical approach to selection of the concentrations and optimal conditions for their purification, despite the advancement of modern theories of coagulation and flocculation. In practice, empirical formulas are sometimes used for tentative estimation of the reagent concentration [28]. However, a commonly used method is test coagulation (flocculation) [29], whose modified version [30] is presently applied to real systems being treated.

In this study, we carried out an experiment in which we treated water with a turbidity of 25 mg dm^{-3} (taken from the Volga river in a flood period). The results (Table 5) suggest a better, compared to separate addition of the coagulant and the flocculant, performance of the PCCs in water treatment.

In this experiment, we also used two types of wastewater, namely, wastewater from production of dielectric gloves (prepared by depositing a latex composition onto molds covered with a fixative, containing up to 40% kaolin) and wastewater from an oil refinery.

The wastewater from glove production is distinguished by a high concentration of the dispersed phase and a complex composition, which is responsible for the high sedimentation stability of the dispersion. The treatment efficiency was judged from the motion velocity of the interface between the clarified and thickened layers of the suspension, as well as from the residual turbidity above the precipitate after the suspension was allowed to stand for 1.5 h. Table 6 shows that the PCCs afford a faster sedimentation and a higher degree of purification at much lower concentrations.

Wastewater containing emulsified oil products is frequently treated with aluminum sulfate or its mixture with cation-active macromolecular flocculants [31] and, in particular, a mixture of aluminum sulfate (AS) with VPK-402. Oil-containing wastewater is usually treated by pressure flotation [32]. In our experiment, we used wastewater samples taken in the wastewater treatment shop of an oil refinery. The treatment was carried out on a model installation simulating a pressure flotator [33]. Table 7 lists the experimental degrees of purification of the wastewater with various reagents at various concentrations of oil products at the flotator inlet. It is seen that the poly complexes are significantly more effective than other reagents tested in treatment of oil-containing water, and in much lower concentrations. In the PCC series, the efficiency tends to increase with increasing APHC content in the poly complex, from PCM-1 to PCM-6. The reason is that, in treatment of oil emulsions, the first stage of the process consists in breakdown of the

Table 7. Degree of purification of oil-containing wastewater in relation to the composition and concentration of the reagents

Reagent	c, mg l^{-1}	Content of oil products, mg l^{-1}		Degree of purification, %
		before treatment	after treatment	
AS + VPK-402	5.3 + 28	600	30.6	94.0
PCM-2	6.0	600	19.5	96.7
PCM-4	6.0	600	12.8	97.8
PAA	6.0	110	24.4	77.8
VPK-402	6.0	110	40.3	63.3
KF-99	6.0	110	12.7	88.4
PCM-4	6.0	110	7.1	93.5
PCM-6	6.0	110	2.6	97.6
AS + VPK-402	5.3 + 2.8	110	15.6	85.8
PCM-4	5.0	160	9.9	93.8
PCM-4	4.0	160	10.3	93.5
PCM-4	3.0	160	15.6	90.2

emulsion droplets and their coalescence [33]. Air bubbles are adsorbed on the surface of large oil droplets and float them as a foam. The role of demulsifiers is usually played in this case by ions of polyvalent metals (Al, Fe). When the molar ratio of Al^{3+} to the PAA unit in the PCCs is over 4, the solution contains particles of aquahydroxo complexes of aluminum, which are not bound to the PCCs. They act as demulsifiers and break down the oil emulsion, thereby enhancing the purification effect.

CONCLUSIONS

(1) The flocculation and coagulation activities of water-soluble polymer-colloid complexes of aluminum polyhydroxochloride and polyacrylamide were tested in separation of model dispersed systems and real media. These complexes effectively combine the properties of coagulants, destabilizing the colloid and emulsified systems, and of cation-active flocculants favoring faster and more exhaustive separation of dispersions and suspensions.

(2) The polymer colloid complexes synthesized from relatively inexpensive commercially produced reagents are suitable as highly effective reagents for water treatment and purification.

ACKNOWLEDGMENTS

This study was financially supported by the "Basic Research in Technical Sciences" Scientific and Technical Program (project no. T 02.-09.2-3731).

REFERENCES

1. Zapol'skii, A.K. and Baran, A.A., *Koagulyanty i flokulyanty v protsessakh ochistki vody* (Coagulants and Flocculants in Water Treatment), Leningrad: Khimiya, 1987.
2. Veitser, Yu.I. and Mints, D.M., *Vysokomolekulyarnye flokulyanty v protsessakh ochistki stochnykh vod* (Macromolecular Flocculants in Wastewater Treatment), Moscow: Stroiizdat, 1984.
3. Schwartz, T. and Francois, J., *Macromol. Chem.*, 1981, vol. 182, pp. 2775–2787.
4. Anufrieva, E.V., Gromova R.A., Kondrat'eva, E.V., *et al.*, *Vysokomol. Soedin., Ser. B*, 1976, no. 12, pp. 915–918.
5. Anufrieva, E.V., Gromova R.A., Nekrasova, T.N., *et al.*, *Zh. Prikl. Khim.*, 1996, vol. 69, no. 6, pp. 1014–1019.
6. Anufrieva, E.V., Nekrasova, T.N., Krakovyak, M.G., *et al.*, *Vysokomol. Soedin., Ser. A*, 2001, vol. 43, no. 5, pp. 875–882.
7. Kudaibergenov, S.E., Frolova, V.A., Kanan'yanova, G.Ya., *et al.*, *Izv. Akad. Nauk Kaz. SSR, Ser. Khim.*, 1987, no. 2, pp. 35–38.
8. Myagchenkov, V.A., and Bulidorova, G.V., *Khim. Tekhnol. Vody*, 1995, vol. 17, no. 5, pp. 583–587.
9. Kurenkov, V.F., Churikov, F.I., and Snigirev, S.V., *Zh. Prikl. Khim.*, 1999, vol. 72, no. 5, pp. 828–831.
10. Myagchenkov, V.A. and Proskurina, E.V., *Zh. Prikl. Khim.*, 2000, vol. 73, no. 12, pp. 2030–2035.
11. Fr Patent 2 788 779.
12. UK Patent 2 322 128.
13. Canadian Patent 1 331 124.

14. Gordeev-Gavrikov, V.K., Pedashchenko, D.D., and Bozhko, L.M., *Zhil. Kommun. Khoz.*, 2001, no. 2, pp. 34–38.
15. Young, S., Stanley, S., and Smith, D., *Voda Ekol.*, 2000, no. 4, pp. 2–12.
16. Novakov, I.A., Radchenko, F.S., and Papisov, I.M., *Vysokomol. Soedin., Ser. A*, 2003, vol. 45, no. 8, pp. 1340–1344.
17. RF Patent 2083495.
18. Minkova, O.B., Gromov, V.F., and Teleshov, E.N., *Plastmassy*, 1986, no. 8, pp. 10–12.
19. *GOST* (State Standard) *2874–82: Potable Water: Photometric Method of Determination of the Turbidity*, Moscow: Izd. Standartov, 1982.
20. *Kolichestvenniy khimicheskii analiz vod: Metodika vypolneniya izmerenii massovoi kontsentratsii nefteproduktov v probakh prirodnykh i ochishchennykh stochnykh vod* (Quantitative Chemical Analysis of Water: A Technique for Measuring the Weight Concentration of Oil Products in Samples of Natural and Treated Wastewater), PND F 14.1:2.116–97, Moscow: Gos. Kom. Ross. Feder. Okhr. Okruzh. Sredy, 1997.
21. Myagchenkov, V.A., Proskurina, V.E., and Bulidorova, F.V., *Uzv. Vyssh. Uchebn. Zaved., Khim. Khim. Tekhnol.*, 2001, vol. 44, no. 5, pp. 453–492.
22. Chernoberezhskii, Yu.M., Lorentsson, A.V., and Dyagileva, A.B., *Kolloidn. Zh.*, 2000, vol. 62, no. 5, pp. 707–710.
23. Nebera, V.P., *Flokulyatsiya mineral'nykh dispersii* (Flocculation of Mineral Dispersions), Moscow: Nedra, 1983.
24. Kurenkov, V.F. and Shipova, L.M., *Zh. Prikl. Khim.*, 1996, vol. 69, no. 6, pp. 1004–1007.
25. Myagchenkov, V.A. and Proskurina, V.E., *Kolloidn. Zh.*, 2000, vol. 62, no. 5, pp. 654–659.
26. Kul'skii, N.A., *Teoreticheskie osnovy i tekhnologiya konditsionirovaniya vody* (Theoretical Principles and Technology of Water Conditioning), Kiev: Naukova Dumka, 1980.
27. Khramenkov, S.V., Koverga, A.V., and Blagova, O.E., *Vodosnabzh. Sanit. Tekh.*, 2001, no. 3, pp. 5–7.
28. Maksimov, V.F., Vol'f, I.V., and Vinokurova, T.A., *Ochistka i rekuperatsiya promyshlennykh vybrosov* (Industrial Waste Treatment and Recovery), Moscow: Lesn. Prom–st., 1989.
29. *Rukovodstvo po khimicheskomu i tekhnologicheskomu analizu vody* (A Manual on Chemical and Technological Analysis of Water), Moscow: Stroiizdat, 1973.
30. Lorentsson, A.V., Chernoberezhskii, Yu.M., and Dyagileva, A.B., *Kolloidn. Zh.*, 2002, vol. 64, no. 1, pp. 94–96.
31. Abstracts of Papers, *Nauchno-prakticheskaya konferentsiya "Problemy nauchno-tekhnicheskogo obespecheniya neftepererabatyvayushchego i neftekhimicheskogo kompleksa* (Scientific and Practical Conf. "Problems of Scientific and Technical Provision for Oil-Refining and Petrochemical Complex"), Ufa, 1999, pp. 101–111.
32. Gandurina, L.V., Butseva, L.N., and Shtondina, V.S., *Neftepererab. Neftekhim.*, 1996, no. 2, pp. 27–31.
33. Skrylev, L.D., Skryleva, T.L., and Nebesnova, T.V., *Izv. Vyssh. Uchebn. Zaved., Khim. Khim. Tekhnol.*, 2001, vol. 44, no. 1, p. 143–146.

Russian Journal of Applied Chemistry, Vol. 77, No. 10, 2004, pp. 1693–1698. Translated from Zhurnal Prikladnoi Khimii, Vol. 77, No. 10, 2004, pp. 1707–1713.

MACROMOLECULAR CHEMISTRY AND POLYMERIC MATERIALS

Properties of a Film Material Based on Polyvinyl Chloride as Influenced by the Plasticizer

B. I. Lirova, E. A. Lyutikova, A. N. Degtyareva, V. A. Larionov, S. I. Degtyarev, and B. A. Berkuta

Gor'kii Ural State University, Yekaterinburg, Russia

Stroiplastpolimer Joint-Stock Company, Yekaterinburg, Russia

Received July 23, 2004

Abstract—The behavior of a film material based on polyvinyl chloride in air and aqueous media, as influenced by individual plasticizers and their binary mixtures, was studied by gravimetry, thermogravimetry, and IR spectroscopy. The effect of these factors on the frost resistance and other physicochemical properties of the films was studied.

Polymer films based on polyvinyl chloride (PVC) with a one-side adhesive layer are used for waterproofing and corrosion protection of oil, gas, and material pipelines [1, 2]. These films necessarily contain plasticizers and other low-molecular-weight additives, which can pass into air or wet soil during operation. The decrease in the plasticizer content can deteriorate the physicochemical properties and frost resistance of the polymer material [3, 4] and increase its cracking; as a result, the films can lose continuity and, hence, protecting properties. Water sorption is an important characteristic of a polymeric material operating in a moist environment. Small water sorption reduces the sensitivity of the polymer material to freezing-defrosting cycles typical of the Russian climate and favors preservation of its protecting properties.

One of procedures for preparing a polymeric material with required properties is its plasticization with a plasticizer mixture [3, 5]. The aim of this study was to improve the frost resistance of a PVC film for production of tapes with an adhesive layer by using mixtures of plasticizers of varied nature and to examine their behavior in air and aqueous media. We studied PVC films plasticized with individual plasticizers [di(2-ethylhexyl)-*o*-phthalate (DOP), dibutoxyethyl adipate (DBEA), dibutyl sebacate (DBS)] and their mixtures. Di(2-ethylhexyl)-*o*-phthalate is the common PVC plasticizer, whereas DBEA and DBS containing no aromatic groups, were used to improve the frost resistance of the films [3, 6].

EXPERIMENTAL

We studied plasticized PVC films with 100 : 45 PVC–plasticizer weight ratios, used in production of tapes with an adhesive layer. These formulations were prepared from industrial components: S-70 brand suspension PVC and DOP, DBEA, and DBS plasticizers. All the formulations contained talc as a filler and BAC-S-20 as a stabilizer.

The films were prepared by rolling on a laboratory masticating mill at 140°C for 10 min. The film thickness was about 0.3 mm. The samples were studied approximately three months after their preparation.

In this study, we determined the composition of compounds released from the film into air and aqueous media under various operation conditions.

The weight loss by the samples in air at normal atmospheric pressure was studied by gravimetry under the isothermal conditions at 90°C. The thermal analysis was performed in air on an MOM Q-1500 derivatograph (Hungary) in the 25–300°C temperature range at a heating rate of 10 deg min^{-1}, with Al_2O_3 as a reference.

The qualitative composition of the compounds released from the films into air and the kinetics of their liberation at 90°C under a dynamic vacuum (residual pressure ~30 Pa) were studied by IR spectroscopy in a heated vacuum cell [7]. In this procedure, a sample was placed on the bottom of the temperature-controlled

1070-4272/04/7710-1693 © 2004 MAIK "Nauka/Interperiodica"

Table 1. Brittle point T_{br} as influenced by the plasticizer composition

Plasticizer	Composition, %	T_{br}, °C
DOP	100	–40
DOP–DBEA	89 : 11	–40
	70 : 30	–50
	50 : 50	–50
DBEA	100	–50
DOP–DBS	89 : 11	–45
	70 : 30	–48
	50 : 50	–50
DBS	100	–50

cell and heated to a prescribed temperature. The volatile components of the sample condensed on the cooled KBr windows.

The spectrum of the condensate was recorded on a Specord 75-IR spectrophotometer. This procedure combines release of volatile compounds, their directed condensation, and recording of a spectrum without transfer of the condensate. The cell design allows operation at both atmospheric and reduced pressures.

To study the behavior of films in water, we recorded changes in the sample weight at room temperature and analyzed the composition of the liquid phase brought in contact with these samples. The weight changes Δm (%) of the samples in water were studied by gravimetry and calculated by the expression:

$$\Delta m = [(m - m_0)/m_0] \times 100,$$

where m_0 is the initial sample weight and m is the sample weight at a given time τ.

The relative weight Δm_r (%) of compounds liberated from the film in water during the experiment was calculated as follows:

$$\Delta m_r = [(m_0 - m_d)/m_0] \times 100,$$

where m_0 is the initial sample weight and m_d is the sample weight at the end of an experiment, after drying to constant weight at 50°C and atmospheric pressure.

Then, using Δm and Δm_r, we calculated the swelling index α (%) of the sample:

$$\alpha = \Delta m - \Delta m_r.$$

To determine the composition of compounds released from the film in water, the aqueous solution was evaporated at 50°C and atmospheric pressure to a solid residue. This residue was poured over with tetrahydrofuran (THF) and transferred onto a KBr window, after which THF was evaporated and the IR spectrum of the residue was recorded. The removal of THF was monitored spectrophotometrically.

The interaction of components in the films was judged from changes in the absorption bands of the functional groups in the IR spectra of model plasticizer-polymer systems. The model films were prepared by evaporation of 1% THF solutions on glass supports at room temperature. Then, the films were heated for 7 h at 70°C to remove the residual solvent; the THF content was monitored spectrophotometrically. The IR spectra were recorded on a UR-20 spectrometer.

The frost resistance was evaluated from the brittle point according to GOST (State Standard) [8].

The stress–strain curves were recorded at room temperature on an RT-250M-2 tensile-testing machine in the 0.0–0.5 kN load range. The extension rate was 25 mm min^{-1}. The samples were cut out as blades with 6.5-mm width of the working part. The stress in the samples was calculated as follows:

$$\sigma = P/S,$$

where σ is the stress (kPa), P is the load (kN), and S is the cross section of the working part of the sample at the beginning of an experiment (m^2).

The physicomechanical properties of the samples were characterized by the rupture stress σ_r and elastic modulus E characterizing the material rigidity and calculated from the following expression:

$$E = \sigma/\varepsilon,$$

where σ is the stress and ε is the strain in the initial section of the strain curve.

The data on the film frost resistance are listed in Table 1. As can be seen, the PVC films containing DBEA and DBS and their mixtures with DOP are more frost resistant then the films with DOP plasticizer.

Our further experiments were performed using the films containing individual plasticizers and their mixtures, with brittle point $T_{br} \approx 50$°C. We studied films with a smaller content of DBEA and DBS in the mixtures, because these plasticizers are more expensive than DOP.

Table 2. Deformation–strength properties of the films

Plasticizer	Composition, %	E, MPa	σ_t, MPa
DOP	100	63.6	18.2
DOP–DBEA	70 : 30	35.2	14.3
DBEA	100	18.0	12.1
DOP–DBS	70 : 30	28.8	13.2
	50 : 50	21.7	12.7
DBS	100	16.9	11.4

Table 3. Diffusion coefficients of plasticizers in PVC films and their volatility

Plasticizer	$D \times 10^{-15}$, $m^2\ s^{-1}$ (atmospheric pressure)	$D \times 10^{-12}$, $m^2\ s^{-1}$ (vacuum)	ν, $g\ cm^{-2}\ s^{-1}$ (atmospheric pressure)
DOP	0.3	0.3	0.2
DBEA	1.3	1.1	1.8
DBS	–	1.3	0.6

The stress–strain curves of the films are shown in Fig. 1, and their deformation–strength characteristics are listed in Table 2.

With addition of DBEA and DBS, the rigidity E of films decreases with a simultaneous decrease in their strength σ_s.

The kinetic dependences of the weight loss by the samples in air at atmospheric pressure and 90°C are shown in Fig. 2. In the samples plasticized with individual compounds, the weight loss changes in the following order DOP < DBEA << DBS. The samples containing mixtures of plasticizers occupy the intermediate positions. The IR spectra of the compounds released from the samples indicate that it is the plasticizers added to the polymer that pass into the atmosphere. Since the samples contain a stabilizer, we assumed that no HCl is liberated under the experimental conditions (90°C) due to PVC decomposition and the weight loss is related to migration of the plasticizers. This is also confirmed by the fact that the DTA curves of the films exhibit the endothermic peaks corresponding to the PVC degradation only at $T > 210$°C.

It is known that the plasticizer migration from the polymeric film involves diffusion of the compound from the film bulk to the surface and its removal from the surface. Under different conditions, the migration kinetics can be limited by the rate of one or another reaction [9, 10]. The weight loss by the films under the isothermal conditions (Fig. 1) was described by the following equation:

$$M_\tau/M_\infty = (4/\pi^{1/2})(D\tau/l^2)^{1/2}, \quad (1)$$

where M_τ is the amount of plasticizer released from the sample at moment τ, i.e., the weight loss by the sample; M_∞, initial plasticizer content in the sample; l, sample thickness; τ, experimental time; and D, diffusion coefficient of the plasticizer.

Equation (1) is a partial solution to the second Fick's law for diffusion in the initial stages of desorption ($M_\tau/M_\infty \le 0.6$) under certain initial and limiting conditions [11, 12]. The linear portions of the dependences $M_\tau/M_\infty = f(\tau^{1/2})$ for DOP and DBEA suggest that in these portions, the migration of plasticizers is controlled by their diffusion in the sample and allow calculation of the diffusion coefficients (Table 3),

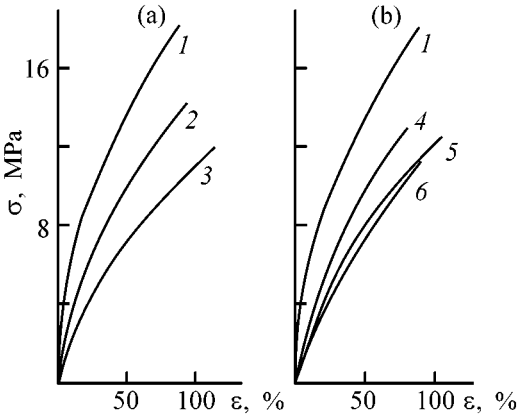

Fig. 1. Stress–strain curves for films containing (a) DOP–DBEA and (b) DOP–DBS. (σ) Stress and (ε) strain. (*1*) DOP, (*2*) DOP–DBEA, (*3*) DBEA, (*4*, *5*) DOP–DBS, and (*6*) DBS. Plasticizer ratio in the mixture, wt %: (*2*, *4*) 70 : 30, and (*5*) 50 : 50; the same for Fig. 2.

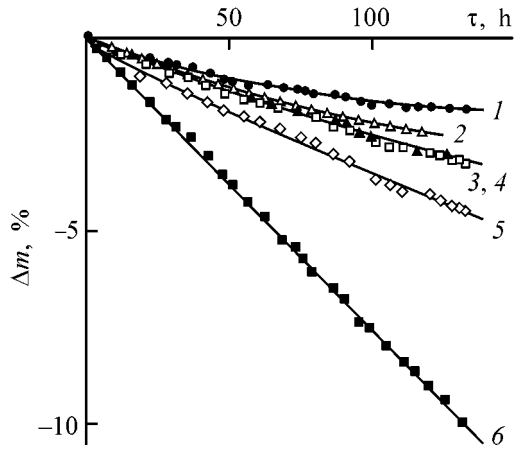

Fig. 2. Weight loss Δm in air at 90°C and atmospheric pressure vs. heating time τ of the samples containing (*1*) DOP, (*2*) DOP–DBEA, (*3*) DBEA, (*4*, *5*) DOP–DBS, and (*6*) DBS.

which can be used in this case as a criterion of migration rate [13, 14].

As can be seen, D_{DBEA} is greater than D_{DOP}. No linear portion was found for DBS plasticizer. This indicates that the migration of DBS in the film at 90°C and atmospheric pressure is limited not by diffusion in the sample, but by its removal from the surface, i.e., by its volatility.

We also studied the plasticizer recovery from the film under the conditions of its forced removal from the sample surface. For this purpose we performed experiments at 90°C under a dynamic vacuum, using a heated vacuum cell. The IR spectra of the volatile compounds released from the film containing DOP are shown in Fig. 3. As can be seen, the amount of DOP released from the sample grows with increasing time. Similar data were obtained with polymeric films containing DBEA and DBS. The spectroscopic results were presented as time dependences of the optical density of the absorption band of the plasticizer (~1720, ~1130, and ~1175 cm^{-1} for DOP, DBEA, and DBS, respectively) (Fig. 4a) and then in the coordinates of a modified Eq. (1):

$$A_\tau/A_\infty = (4/\tau^{1/2})(D\tau/l^2)^{1/2}, \quad (2)$$

where A_t is the optical density of the absorption band at instant of time τ and A_∞ is the initial optical density of the absorption band corresponding to the initial content of the plasticizer in the film (Fig. 4b).

The optical densities were determined taking into account the baseline of the corresponding absorption band [15], and A_∞ was calculated as follows:

$$A_\infty = A_e m_0/\Delta m_e,$$

where A_e is the optical density of the absorption band at the end of the experiment; m_0, initial plasticizer content in the sample; and m_e, weight loss by the sample at the end of the experiment, equal to the amount of the plasticizer released.

The initial nonlinear portion of the curve in Fig. 4b (~16 min) corresponds to the time in which the temperature in the heated vacuum cell increases from room temperature to 90°C. In contrast to the experiments at atmospheric pressure under the conditions of forced removal of plasticizer from the film surface, the linear portions [in the coordinates of Eq. (2)] are

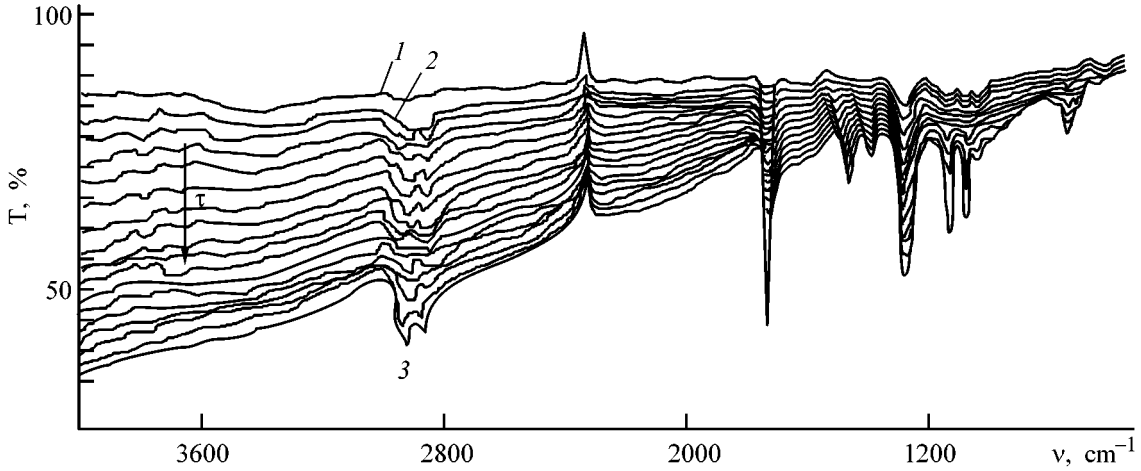

Fig. 3. IR spectra of the volatile compounds released from the film containing DOP. (T) Transmission and (ν) wavenumber. (*1*) Absorption of KBr windows, (*2*) spectrum recorded 7 min after the beginning of the experiment, and (*3*) spectrum recorded 245 min after the beginning of the experiment. The arrow indicates the order of recording of the spectra.

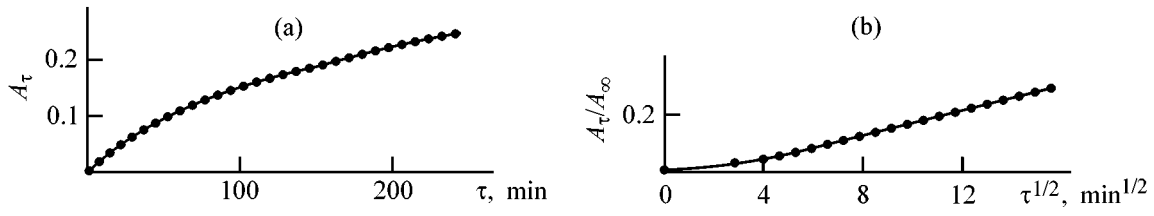

Fig. 4. Variation with time τ of the (a) optical density A_τ of the absorption band ν_{CO} (~1720 cm^{-1}) in the IR spectra of the plasticizer and (b) relative optical density in the coordinates of Eq. (2) for the film containing DOP.

observed with all the samples. This suggests that, under these conditions, migration of all the plasticizers, including DBS, is controlled by their diffusion in the sample. The diffusion coefficients D of the plasticizers, calculated from the linear portions of the curves, are listed in Table 3. An independent experiment showed that D values calculated using different absorption bands in the IR spectra of the recovered compound are similar. As can be seen from Table 3, D_{DBEA} and D_{DBS} are close and exceed D_{DOP}. Previously, we suggested that, the migration of DBS at atmospheric pressure, in contrast to that of DOP and DBEA, is controlled by its volatility. In this context, we studied the kinetics of the weight loss by individual plasticizers at 90°C and atmospheric pressure and calculated the plasticizer volatilities in 10 h (Table 3). The volatility of DBS appeared to be three times lower that that of DBEA. This confirms our assumption that the DBS volatility controls the plasticizer migration from the PVC film under the experimental conditions.

It is known [4, 13] that, the difference in the diffusion coefficients may be due not only to steric factors, but also to the chemical nature of the diffusion agent and, in particular, to the difference in interaction of its molecules with the polymer macromolecules. The IR spectra in the region of the stretching vibrations of the carbonyl group $\nu_{C=O}$ of individual plasticizers and of PVC-plasticizer mixtures are shown in Fig. 5 (curves *1* and *2*, respectively). The absorption bands of the plasticizers are complex because of the formation of molecular associates of various strengths [7, 16, 17]. In the presence of PVC, the absorption intensity is redistributed in all the systems toward the low-frequency component of the carbonyl band. The appearance of the low-frequency components of the $\nu_{C=O}$ bands is probably due to the formation of hydrogen bonds between the ester C=O groups of the plasticizer and CHCl groups of PVC [18]. However, we failed to evaluate unambiguously the contribution of this factor for all the plasticizers in question. Along with the formation of hydrogen bonds, an additional interaction is possible in the PVC–DOP system: formation of the donor–acceptor bonds between π electrons of the DOP benzene ring and free 3*d* orbitals of chlorine atoms in the PVC macromolecules [19]. Possibly, the stronger total interaction of PVC with DOP and the steric hindrance to diffusion of DOP in the film due to the presence of the benzene ring and branched hydrocarbon radicals lead to a decrease in the diffusion coefficient of DOP in comparison with DBEA and DBS.

The TG data for the films with individual plasticizers show that the weight loss by samples containing DBS begins at a lower temperature (~100°C), compared to DOP (~170°C) and DBEA (~160°C). However, the thermal stabilities of all the samples, defined as the temperature at which the sample loses 10% of its initial weight (TG data) differ only slightly.

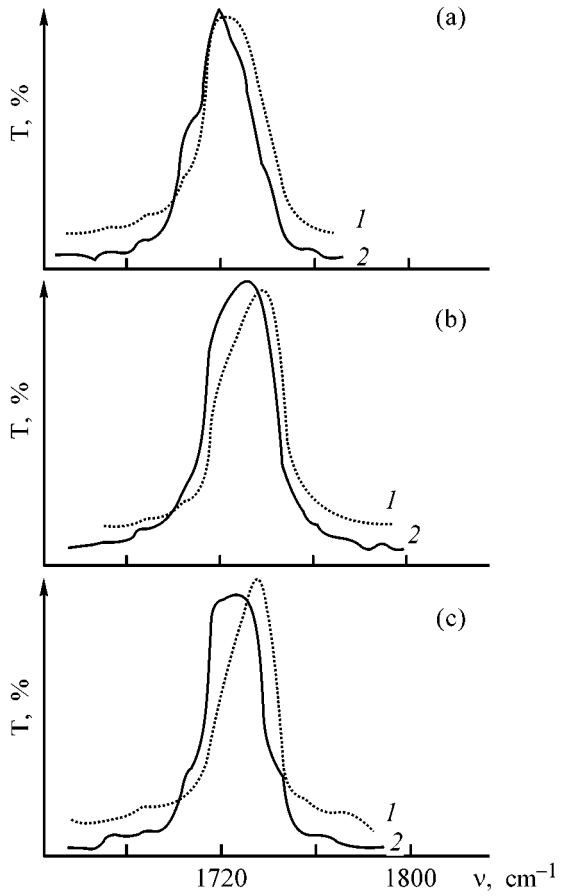

Fig. 5. IR spectra of (*1*) plasticizers and (*2*) PVC–plasticizer systems. (*T*) Transmission and (ν) wavenumber. Plasticizer: (a) DOP, (b) DBEA, and (c) DBS.

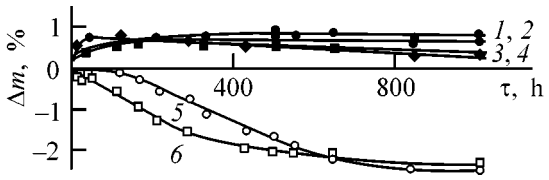

Fig. 6. Weight change Δm in water at room temperature vs. storage time τ of the samples containing (*1*) DOP, (*2*, *3*) DOP–DBS, (*4*) DBS, (*5*) DOP–DBEA, and (*6*) DBEA. Plasticizer ratio, wt %: (*2*, *5*) 70 : 30 and (*3*) 50 : 50.

These data suggest that the samples containing DBS are less stable in operation in air in comparison with the films containing DBEA and DOP plasticizers.

The changes in the film weight upon storage in water at room temperature are illustrated by Fig. 6. After storage, the weight of the films containing DOP and DBS increases by approximately 1%. With in-

Table 4. Weight changes of the films after storage in water at room temperature for 1000 h as influenced by the plasticizer

Plasticizer	Composition, %	Δm, %	Δm_w, %	α, %
DOP	100	0.9	0.8	1.7
DOP–DBEA	70 : 30	–2.4	4.0	1.6
DBEA	100	–2.4	4.1	1.7
DOP–DBS	70 : 30	0.8	1.1	1.9
	50 : 50	0.5	0.8	1.3
DBS	100	0.4	1.0	1.4

creasing DBS content in the film, the sample weight slightly decreases upon prolonged storage. After storage in water, the weight of the films containing DBEA and DOP–DBEA mixture decreases by ~2%. These changes in the sample weight are probably due to two opposite processes: swelling (α) increases the sample weight, whereas plasticizer washout (Δm_w) causes its decrease. The results of separation of the effects of these processes for the final point of the dependences (Fig. 6) are listed in Table 4.

As can be seen, the swellabilities of all the samples in water are similar, but the formulations containing DBEA exhibit a significant weight loss. The IR spectra of the dry residues show that the films release the plasticizer and a hydroxyl-containing compound, which is probably a component of the stabilizer. The stronger plasticizer washout from the films containing DBEA is due to the presence of the polar C–O–C groups accessible to interaction with water (in contrast to DOP) and smaller nonpolar fragments of the DBEA molecule [–$(CH_2)_4$–] as compared to DBS [–$(CH_2)_8$–].

CONCLUSIONS

(1) Properties of polyvinyl chloride films containing individual plasticizers and their mixtures and migration of plasticizers from the films into air and water strongly depend on the chemical structure of a plasticizer.

(2) Addition of dibutyl sebacate and dibutoxyethyl adipate to di(2-ethylhexyl)-*o*-phthalate increases frost resistance and decreases the strength of the films.

(3) Films containing mixtures of di(2-ethylhexyl)-*o*-phthalate with dibutoxyethyl adipate are more stable in air, whereas dibutyl sebacate enhances the stability of films in water.

ACKNOWLEDGMENTS

The study was financially supported by the US Civilian Research and Development Foundation (CRDF), grant no. EK-005-XI.

REFERENCES

1. *TU (Technical Specifications)* 952 322–92: *Polyvinyl Chloride Technical Tape with Adhesive Layer.*
2. *Spravochnik po plasticheskim massam* (Handbook on Plastics), Garbar, M.I., Akutin, M.S., and Egorov, N.M., Eds., Moscow: Khimiya, 1967.
3. Thinius, K., Chemie, *Physik und Technologie der Weichmacher*, Leipzig, Deutscher Verlag fur Grundstoffindustrie, 1963.
4. Starkman, B.P., *Plastifikatsiya polivinylkhlorida* (Plasticization of Polyvinyl Chloride), Moscow: Khimiya, 1975.
5. Egorov, A.N. and Khaliullin, A.K., *Plast. Massy*, 2002, no. 5, pp. 43–44.
6. Barshtein, R.S., Kirilovich, V.I., and Nosovskii, Yu.E., *Plastifikatory dlya polimerov* (Plasticizers for Polymers), Moscow: Khimiya, 1982.
7. Lirova, B.I., Lyutikova, E.A., Mel'nik, A.I., and Pyzh'yanova, L.G., *Vysokomol. Soedin., Ser. B*, 2002, vol. 44, no. 2, pp. 363–368.
8. *GOST (State Standard)* 16 214–86: *Polyvinyl Chloride Insulating Tape: Technical Specifications.*
9. Nazarov, V.G., Dedov, A.V., and Semenov, A.A., *Vysokomol. Soedin., Ser. B.*, 1991, vol. 33, no. 12, pp. 927–933.
10. Nazarov, V.G. and Dedov, A.V., *Vysokomol. Soedin., Ser. B.*, 2002, vol. 44, no. 4, pp. 729–732.
11. Malkin, A.Ya. and Chalykh, A.E., *Diffuziya i vyazkost' polimerov: Metody izmereniya* (Diffusion and Viscosity of Polymers: Measurement Procedures), Moscow: Khimiya, 1979.
12. *Physics and Chemistry of the Organic Solid State*, Fox, D., Labes, M., and Weissberger, A., Eds., New York: Interscience, 1965.
13. Chalykh, A.E., *Diffuziya v polimernykh sistemakh* (Diffusion in Polymeric Systems), Moscow: Khimiya, 1987.
14. Reitlinger, S.A., *Pronitsaemost' polimernykh materialov* (Permeability of Polymeric Materials), Moscow: Khimiya, 1974.
15. Smith, A.L., *Applied Infrared Spectroscopy: Fundamentals, Techniques, and Analytical Problem-Solving*, New York: John Wiley & Sons, 1979.
16. *Molecular Interactions*, vol. 2, Ratajczak, H. and Orville-Thomas, W.J., Eds., Chichester: John Wiley & Sons, 1981.
17. Lirova, B.I., Nokhrina, N.N., Lyutikova, E.A., *et al.*, *Zh. Prikl. Khim.*, 1996, vol. 69, no. 2, pp. 306–311.
18. Ganaik Baijayantimala and Sivaram Swaminathan, *Macromolecules*, 1996, vol. 29, no. 1, pp. 185–190.
19. Yushkova, S.M., Tager, A.A., Bessonov, Yu.S., *et al.*, *Vysokomol. Soedin., Ser. A*, 1982, vol. 24, no. 7, pp. 1373–1377.

Russian Journal of Applied Chemistry, Vol. 77, No. 10, 2004, pp. 1699–1703. Translated from Zhurnal Prikladnoi Khimii, Vol. 77, No. 10, 2004, pp. 1714–1718.

MACROMOLECULAR CHEMISTRY AND POLYMERIC MATERIALS

Correlation Analysis of Diffusion of Organic Solvents across Synthetic Low-Polar Polymeric Membranes

R. G. Makitra and R. E. Pristanskii

Pisarzhevskii Institute of Physical Chemistry, Ukrainian National Academy of Sciences, Lviv, Ukraine

Received April 6, 2004

Abstract—The influence exerted by physicochemical characteristics of organic solvents on their diffusion across polymeric membranes can be quantitatively using linear multiparametric equations.

There is a steadily growing interest in the problems of diffusion of liquids and gases in polymers, which is stimulated, in particular, both by the development of membrane technologies and by biochemical research concerning the penetration of ionic species, toxic substances, and drugs across cell membranes.

The diffusion of substances in a homogeneous medium has been thoroughly studied and can be described by well-known Fick's law, Einstein–Stokes equation, etc. However, the problem of quantitative evaluation of the effects of physicochemical characteristics of a penetrating liquid on its diffusion coefficient, even though being a subject of extensive studies, has not been satisfactorily solved as yet [1–3]. Khinnavar *et al.* [3] analyzed the transport of esters across ethylene–propylene membranes using the relationship

$$Q_t/Q_\infty = kt^n,$$

where Q_t and Q_∞ are the current and limiting solvent uptakes; and k and n, the constants.

It was found [3] that found $n = 0.5$, which suggests that this process obeys Fick's law. For films prepared from other materials (natural and synthetic rubber and polyurethane) $n \approx 0.6$, which points to partial transfer to so-called anomalous transport caused by different effects of particular units of the polymer chain on the sorption processes [3]. Even more pronounced deviations from Fick's law were observed in studying the diffusion of aromatic hydrocarbons and dimethylformamide across polyurethane membranes [1, 4].

Since the diffusion across a polymeric membrane follows the stage of sorption of a solvent, and these processes are interrelated, the diffusion parameters are commonly determined from the sorption kinetics, i.e., from the swelling data. Therefore, approaches to analysis of features of both processes are similar. Swelling of natural (rubber, coal) and synthetic polymers have been intensively studied in the last five decades, inparticular, in context of the problem of the stability of polymeric materials in various media. However, the traditional approaches based on the Flory–Huggins [5] and Hildebrand [6] theories allow only semiquantitative estimates, which is not surprising in view of the fact that these theories consider solely physical effects.

In fact, the solvation interactions occurring between a diffusing solvent and a polymeric material affect the energy-related parameters and the kinetics of diffusion. These interactions can be included in consideration semiempirically by using the principle of linear free energies (LFE). This approach is used, in particular, for generalization of data on the effect of solvents on rates of the chemical reactions, solubility of gases, distribution of substances between two phases, etc. Among such relationships, the Koppel–Palm equation is the most widely used. It includes the influence exerted by the polarity and polarizability of solvents and also by their capacity for acid–base interaction with a substrate. In studying the swelling of polymers and diffusion of solvents across polymeric membranes, it is necessary to take additionally into account the geometric factor (molecular size): the larger the size, the more difficult the penetration into the free volume of the polymer, whereas solvation of the polymer units will facilitate the diffusion. This suggestion logically follows from the Einstein–Stokes equation

$$D = kT/6\pi\eta r,$$

according to which the diffusion coefficient D in homogeneous media is inversely proportional to the

1070-4272/04/7710-1699 © 2004 MAIK "Nauka/Interperiodica"

Table 1. Experimental [9] and theoretical [calculated by Eq. (3)] coefficients of diffusion across ethylene–propylene–butadiene polymer

No.	Solvent	$-\log D^{exp}$	$-\log D^{calc}$	$\Delta\log D$
1	*n*-Hexane	5.977	6.047	0.071
2	*n*-Heptane	6.089	6.151	0.063
3	*n*-Octane	6.218	6.251	0.033
4	*n*-Nonane	6.406	6.356	–0.049
5	*n*-Decane	6.523	6.463	–0.060
6	*n*-Dodecane	6.708	6.673	–0.035
7	*n*-Tetradecane	6.845	6.887	0.042
8	*n*-Hexadecane	7.114	7.105	–0.008
9	Cyclohexanone	7.081	6.828	–0.253
10	Isooctane	6.465	6.267	–0.197
11	Cyclohexane*	6.322	–	–
12	Methyl acetate	6.695	6.387	–0.308
13	Ethyl acetate	6.467	6.479	0.012
14	Propyl acetate	6.635	6.677	0.043
15	Butyl acetate	6.666	6.678	0.012
16	Isoamyl acetate	6.857	6.937	0.081
17	Benzene	5.935	5.961	0.026
18	Toluene	5.982	6.116	0.134
19	*p*-Xylene	6.225	6.264	0.038
20	Mesitylene	6.342	6.404	0.062
21	Anisole	6.347	6.519	0.172
22	Fluorobenzene	5.960	5.951	–0.009
23	Chlorobenzene	5.922	6.003	0.081
24	Bromobenzene	6.107	6.032	–0.075
25	Tetralin*	6.606	–	–
26	Nitrobenzene*	6.947	–	–
27	Aniline	7.036	7.161	0.125

* Solvents excluded from calculation by Eq. (3).

radius *r* of a diffusing particle. Similar suggestions were also stated earlier [7, 8].

Aminabhavi *et al.* [9] studied the diffusion of various solvents in six different polymers. All these polymers, except polyurethane rubber, were vulcanized and contained (wt %) carbon black 50, zinc oxide 5, sulfur 2–2.5, and also some other additives. The diffusion coefficients in 0.1–0.15 thick membranes were determined at 25, 44, and 60°C.

log *D* values were calculated from the slopes of the linear portions of the sorption curves. They decrease in parallel with an increase in the molecular weight or molar volume V_M of the solvent. However, a satisfactory linear correlation between these parameters was observed only in the series of *n*-alkanes, and all efforts to extend this correlation to solvents belonging to other classes failed. Even data for isooctane and cyclohexane deviated from the linear correlation.

We attempted to generalize data on the diffusion coefficients of 27 solvents across a butadiene–styrene polymeric membrane [9], using the following six-parametric equation

$$\log D = a_0 + a_1\frac{n^2 - 1}{n^2 + 2} + a_2\frac{\varepsilon - 1}{2\varepsilon + 1} + a_3B + a_4E_T + a_5\delta^2 + a_6V_M. \quad (1)$$

Here $f(n)$ is the polarizability and $f(\varepsilon)$, polarity of the solvent, which are responsible for nonspecific solvation (*n* and ε are the refractive index and dielectric constant of the solvent); *B*, Palm's basicity [11], and E_T, Reichardt's electrophilicity index [12], which control the specific solvation; δ^2, squared Hildebrand's solubility parameter proportional to the cohesion energy density of the solvent; and a_1–a_6, regression coefficients.

Assuming that the penetrability of solvents decreases with increasing size of their molecules, we introduced the molar volume V_M as a parameter. This parameter appeared to be quite significant for generalization of data on swelling of polyethylene and butyl rubber in organic solvents [13]. Characteristics of the solvents were taken from the review [14]. Calculations were performed in accordance with the recommendations of the IUPAC Group on Correlation Analysis in Chemistry [15].

The use of Eq. (1) allowed a satisfactory generalization of data on the diffusion coefficients *D*,taken from [9] . Previously, we have shown [10] that, in accordance with the suggestion made by Aminabhavi *et al.* [9], the molar volume V_M has the most significant effect on log *D*. However, these are correlated, but not proportional parameters: for the entire set of 27 solvents, the pair correlation factor $r_6 = 0.708$, and for the set of 24 solvents, $r_6 = 0.858$. Therefore, to describe adequately the solvent effect, it is needed to take into account the factor of specific solvation. The sign "minus" at the corresponding terms of the correlation equation shows that an increase in the size of the organic molecules and also in their ability to nucleophilic solvation, i.e., in the basicity, results in decreasing log *D*. The term E_T, by contrast, stands with a sign "plus", which suggests that electrophilic solvation promotes the diffusion. This becomes clear in view of the presence of cyclic units with their π-electron systems in the structure of the butadiene–styrene rubber. However, further calculations showed that the capacity of solvents for nonspecific solvation has no significant effect on the diffusion.

To verify the applicability of this approach and also to study the possible interrelation between the structure of polymers and the significance of the factors included in Eq. (1), we generalized of the log *D* values for other hydrocarbon polymers studied in [9]. The results are summarized in Tables 1–3. In all

Table 2. Experimental [9] and theoretical [calculated by Eq. (5)] coefficients of diffusion across *cis*-isoprene polymer

No.	Solvent	$-\log D^{exp}$	$-\log D^{calc}$	$\Delta\log D$
1	*n*-Hexane	5.937	6.133	0.196
2	*n*-Heptane	6.072	6.209	0.137
3	*n*-Octane	6.166	6.285	0.119
4	*n*-Nonane	6.356	6.369	0.014
5	*n*-Decane	6.488	6.458	–0.030
6	*n*-Dodecane	6.686	6.637	–0.050
7	*n*-Tetradecane	6.836	6.823	–0.013
8	*n*-Hexadecane	7.076	7.016	–0.059
9	Cyclohexanone	6.672	6.687	0.016
10	Isooctane	6.387	6.310	–0.077
11	Cyclohexane	6.206	5.906	–0.300
12	Methyl acetate	6.695	6.442	–0.252
13	Ethyl acetate	6.467	6.507	0.039
14	Propyl acetate	6.635	6.666	0.032
15	Butyl acetate	6.666	6.656	–0.010
16	Isoamyl acetate	6.857	6.878	0.021
17	Benzene	5.864	5.848	–0.017
18	Toluene	5.864	5.990	0.127
19	*p*-Xylene	6.168	6.127	–0.041
20	Mesitylene	6.184	6.251	0.067
21	Anisole	6.153	6.314	0.161
22	Fluorobenzene	5.779	5.889	0.111
23	Chlorobenzene	5.813	5.847	0.034
24	Bromobenzene	6.025	5.822	–0.203
25	Tetralin*	6.424	–	–
26	Nitrobenzene*	6.674	–	–
27	Aniline	6.793	6.773	–0.020

* Solvents excluded from calculation by Eq. (5).

Table 3. Experimental [9] and theoretical [calculated by Eq. (7)] coefficients of diffusion across chloroprene polymer

No.	Solvent	$-\log D^{exp}$	$-\log D^{calc}$	$\Delta\log D$
1	*n*-Hexane	6.767	6.624	–0.143
2	*n*-Heptane	6.863	6.744	–0.119
3	*n*-Octane	7.009	6.864	–0.145
4	*n*-Nonane	7.187	6.993	–0.194
5	*n*-Decane	7.215	7.128	–0.087
6	*n*-Dodecane	7.620	7.400	–0.220
7	*n*-Tetradecane	7.721	7.680	–0.042
8	*n*-Hexadecane	7.721	7.970	0.248
9	Cyclohexanone	6.764	6.551	–0.214
10	Isooctane*	7.481	–	–
11	Cyclohexane*	6.883	–	–
12	Methyl acetate	6.385	6.328	–0.057
13	Ethyl acetate	6.378	6.475	0.097
14	Propyl acetate	6.533	6.700	0.167
15	Butyl acetate	6.623	6.776	0.153
16	Isoamyl acetate	6.896	7.056	0.160
17	Benzene	6.077	6.182	0.105
18	Toluene	6.086	6.354	0.269
19	*p*-Xylene	6.447	6.555	0.108
20	Mesitylene	6.535	6.722	0.187
21	Anisole	6.298	6.465	0.167
22	Fluorobenzene	5.959	5.958	–0.001
23	Chlorobenzene	5.953	5.959	0.006
24	Bromobenzene	6.119	5.971	–0.148
25	Tetralin*	6.770	–	–
26	Nitrobenzene*	6.660	–	–
27	Aniline	7.046	6.748	–0.298

* Solvents excluded from calculation by Eq. (7).

cases, the effect of solvent on the diffusion could be adequately by Eq. (1) after exclusion of the most deviating data for two or three solvents. In most cases, only two or three factors among the six were actually significant.

Table 1 lists the coefficients of diffusion of 27 solvents across the ethylene–propylene–butadiene copolymer (density 1.02 g cm^{-3}) at 25°C. For the entire set of the solvents studied, calculation by Eq. (1) gives a multiple correlation factor $R = 0.888$, which is unacceptably low. After excluding data for only three solvents (nitrobenzene, tetralin, and cyclohexane, as the most outlying), R increased to 0.972. In this case, we obtain Eq. (2) adequately describing the effect of solvents on the diffusion.

$$\log D = -6.01 + (3.77 \pm 1.45) f(n) + (0.01 \pm 0.92) f(\varepsilon) - (3.76 \pm 0.59) \times 10^{-3} B + (16.9 \pm 29.4) \times 10^{-3} E_T - (2.35 \pm 1.20) \times 10^{-3} \delta^2 - (6.90 \pm 0.57) \times 10^{-3} V_M, \quad (2)$$

$N = 24$, $R = 0.972$, standard deviation $S = 0.104$.

For comparison, the figure shows the experimental and theoretical [calculated by Eq. (2)] logarithms of the diffusion coefficients. The factors of polarity [$f(\varepsilon)$], cohesion energy density (δ^2), and capacity for electrophilic solvation (E_T) appeared to be insignificant, and

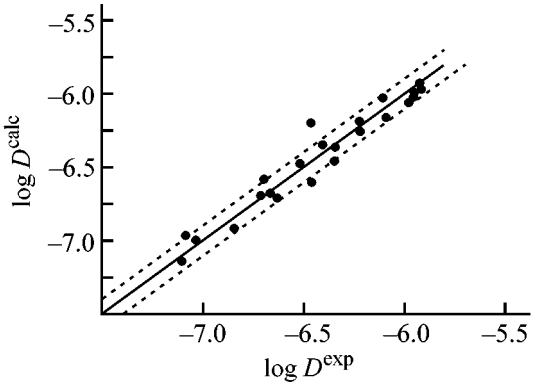

Comparison of theoretical [calculated by Eq. 2)] and experimental [9] diffusion coefficients D of various solvents across ethylene–propylene–butadiene polymer ($S = 0.104$).

their exclusion in accordance with the recommendations of IUPAC [15] only slightly decreased the multiple correlation factor. Therefore, we obtain a simplified three-parameter equation (3), which is also adequate.

$$\log D = -5.59 + (1.45 \pm 0.76) f(n) - (4.02 \pm 0.29) \times 10^{-3} B - (6.36 \pm 0.52) \times 10^{-3} V_M, \quad (3)$$

$R = 0.960$, $S = 0.114$.

The observed insignificant effect of E_T can be attributed to the fact that the ethylene–propylene copolymer contains no electron-donor structures capable of interacting with electrophilic solvents. Parameter $f(n)$ is relatively insignificant also. However, its exclusion decreases R more noticeably, to 0.953. It is seen that, as in the case of the butadiene–styrene copolymer, the most significant factors controlling (decreasing) the diffusion rate are the basicity and molar volume of the solvents. It should be pointed out that the polarizability factor has even less significant, but favorable effect on the diffusion.

Table 1 shows that the deviations of the diffusion coefficients calculated by Eq. (3) from the experimental data are mostly within $S = 0.114$. A more pronounced difference is observed only for three solvents, which were excluded from consideration.

The same approach appeared to be effective for generalization of data on the diffusion coefficients in membranes prepared from synthetic poly(*cis*-isoprene) (density 1.04 g cm^{-3}) (Table 2) and poly(chloroprene) (Neoprene) (density 1.42 g cm^{-3}) (Table 3).

In the former case, we obtain $R = 0.903$ for the entire set of 27 solvents. After exclusion of the most deviating data for nitrobenzene and tetralin we obtain a quite adequate equation.

$$\log D = -5.65 + (5.68 \pm 1.75) f(n) + (1.17 \pm 1.12) f(\varepsilon) - (2.91 \pm 0.71) \times 10^{-3} B - (19.9 \pm 34.8) \times 10^{-3} E_T - (2.19 \pm 1.43) \times 10^{-3} \delta^2 - (6.09 \pm 0.57) \times 10^{-3} V_M, \quad (4)$$

$N = 25$, $R = 0.956$, $S = 0.127$.

As in the case of the ethylene–propylene copolymer, the factors of polarity, cohesion energy density, and electrophilicity are insignificant, so that the effect of solvent on the diffusion can be adequately described by a three-parameter equation.

$$\log D = -6.03 + (3.07 \pm 0.85) f(n) - (3.51 \pm 0.32) \times 10^{-3} B - (6.69 \pm 0.57) \times 10^{-3} V_M, \quad (5)$$

$R = 0.947$, $S = 0.128$.

Table 2 shows the $\log D$ values calculated by Eq. (5) and their deviations from the experimental data.

In the case of chloroprene, the six-parameter equation for the entire set of solvents is characterized by lower R (0.875), so that exclusion of even four solvents (cyclohexane, isooctane, nitrobenzene, and tetralin) appears to be needed to obtain an adequate equation.

$$\log D = -5.12 + (3.91 \pm 2.81) f(n) + (3.53 \pm 1.75) f(\varepsilon) - (2.37 \pm 1.07) \times 10^{-3} b - (49.4 \pm 53.7) \times 10^{-3} E_T - (1.20 \pm 2.41) \times 10^{-3} \delta^2 - (9.52 \pm 1.06) \times 10^{-3} V_M, \quad (6)$$

$N = 23$, $R = 0.954$, $S = 0.189$.

In this equation, the δ^2 and E_T terms are insignificant, and, after their exclusion, we obtain an adequate four-parameter equation.

$$\log D = -6.26 + (2.06 \pm 1.25) f(n) + (1.85 \pm 0.76) f(\varepsilon) - (3.18 \pm 0.66) \times 10^{-3} B - (9.00 \pm 0.92) \times 10^{-3} V_M, \quad (7)$$

$R = 0.951$, $S = 0.185$.

Further exclusion of the parameter $f(n)$ decreases R to 0.943. Table 3 includes the $\log D$ values calculated by Eq. (7) and the corresponding $\Delta \log D$.

It is not improbable that, for the polymers studied, the components added in the course of vulcanization (carbon black, zinc oxide, etc.) can affect the diffusion parameters. However, their amounts are nearly the same in all the cases, and our thought is that the in the diffusion processes for separate polymers are apparently controlled just by their structure.

A similar generalization is possible for the diffusion coefficients determined in [9] at 44 and 60°C and also for the activation energies of diffusion, E_D, although in the latter case, the quality of the correlation appeared to be lower, evidently, as a result of insufficient accuracy of determination of the activation energies from $\log D$ values for only three temperatures.

The similarity of the diffusion mechanisms in the polymers studied is also supported by the fact that, in all the three cases, the most deviating data were obtained for the same solvents (nitrobenzene, tetralin, and cyclohexane), which were excluded to obtain a satisfactory quality of correlation. Most likely, this can be attributed to steric effects. For the solvents indicated, the theoretical values considerably exceed the experimental data. It is noteworthy that cyclohexanone also demonstrates a relatively large differ-

ence between the theoretical and experimental values. At the same time, the theoretical log D values for aromatic hydrocarbons with less bulky substituents (benzene, toluene, xylene, and even mesitylene) are in satisfactory agreement with the experimental data.

CONCLUSIONS

(1) The linear relationship between log D and the molar volume of solvents V_M, obtained by Aminabhavi *et al*. [9], is valid only for particular groups of solvents. At the same time, use of multiparametric equations taking into account various solvent effects allows generalization of the all available experimental data. Log D decreases in parallel with an increase in V_M. However, the process can be described adequately only if the effect of solvation of the polymer is taken into account.

(2) The correlation equations are similar for all the "hydrocarbon" polymers. The significant parameters are the basicity and molar volume of the solvents (their increase results in a decrease in log D); the coefficients at the corresponding terms of the simplified regression equations are close: $\sim 3.0 \times 10^{-3}$ at B and $\sim 6.0 \times 10^{-3}$ at V_M, which suggests a certain similarity of the diffusion mechanisms in these polymers.

(3) The approach suggested can be used for a rough estimation (on the basis of a limited body of experimental data) of the diffusion coefficients of organic solvents in various polymeric membranes.

REFERENCES

1. Aithal, U.S. and Aminabhavi, T.M., *Ind. J. Technol.*, 1990, vol. 28, no. 10, pp. 592–597.
2. Charlesworth, J.M., Riddel, S.Z., and Mathews, R.J., *J. Appl. Polym. Sci.*, 1993, vol. 47, pp. 653–665.
3. Khinnavar, R.C. and Aminabhavi, T.M., *J. Appl. Polym. Sci.*, 1992, vol. 46, pp. 909–920.
4. Aithal, U.S. and Aminabhavi, T.M., *Polymer*, 1990, vol. 31, no. 9, pp. 1757–1763.
5. Flory, P.J., *J. Chem. Phys.*, 1945, vol. 13, no. 6, pp. 453–465.
6. Hildebrand, J.K. and Scott, R.L., *Solubility of Nonelectrolytes*, New York: Reinhold, 1950.
7. Kotyukov, I.M., *Fizicheskaya khimiya* (Physical Chemistry), vol. 2, Tomsk: Sib. Nauchn. Mysl', 1933, pp. 713–725.
8. Gerasimov, Ya.I., Dreving, V.P., Eremin, E.I., *et al.*, *Kurs Fizicheskoi khimii* (Course of Physical Chemistry), vol. 1, Moscow: Khimiya, 1979, pp. 239–246.
9. Aminabhavi, R.H., Harogoppad, S.B., Khinnavar, R.C., and Balundgi, R.H., *JMS Rev. Macromol. Chem. Phys., Ser. C*, 1991, vol. 31, no. 4, pp. 433–498.
10. Makitra, R.G., Zaglad'ko, O.A., Midyana, G.A., and Protsailo, L.V., *Zh. Fiz. Khim.*, 2001, vol. 75, no. 12, pp. 2283–2287.
11. Koppel, L.A. and Palm, V.A., *Reakts. Sposobn. Org. Soedin.*, 1974, vol. 11, issue 1 (39), pp. 121–138.
12. Reichardt, Ch., *Solvents and Solvent Effects in Organic Chemistry*, Weinheim: VCH, 1988.
13. Makitra, R., Pyrih, Y., Zagladko, E., *et al.*, *J. Appl. Polym. Sci.*, 2001, vol. 81, no. 7, pp. 3133–3140.
14. Makitra, R.G., Pirih, Ya.N., and Kivelyuk, R.B., *Vazhneishie kharakteristiki rastvoritelei, primenyaemykh v uravneniyakh LSE* (Most Significant Characteristics Used in Linear Free Energies Relationships), Available from VINITI, December 29, 1985, Moscow, no. 628-V86; *Ref. Zh. Khim.*, 1986, 10B 3299.
15. Recommendations for Reporting the Results of Correlation Analysis in Chemistry Using Regression Analysis, *Quant. Struct. Act. Relat.*, 1985, vol. 4, p. 29.

Russian Journal of Applied Chemistry, Vol. 77, No. 10, 2004, pp. 1704–1707. Translated from Zhurnal Prikladnoi Khimii, Vol. 77, No. 10, 2004, pp. 1719–1721.

MACROMOLECULAR CHEMISTRY AND POLYMERIC MATERIALS

Composites Based on Vinyl Tetrazole–Acrylate Copolymers and Hollow Glass Spheres

M. V. Uspenskaya, N. V. Sirotinkin, and I. V. Masik

St. Petersburg State Technological Institute, St. Petersburg, Russia

St. Petersburg State Institute of Precision Mechanics and Optics, St. Petersburg, Russia

Received April 26, 2004

Abstract—Hydrogel composites based on sodium acrylate, 2-methyl-5-vinyltetrazole, and *N,N'*-methylenebisacrylamide, modified with hollow glass spheres during radical polymerization were prepared and studied. The influence of the modifying additives on the physicochemical properties of the composites was elucidated. A mechanism of modification of vinyl tetrazole–acrylate copolymers with hollow glass spheres was suggested. The materials synthesized are suitable for preparing articles with desired shape and good performance characteristics.

Tetrazole derivatives are promising heterocyclic modifiers of acrylic water superabsorbents, because, similarly to sulfo, phosphate, and other acidic groups, introduction of nitrogen-containing heterocyclic moieties into hydrogels increases the absorption power with respect to aqueous electrolyte solutions [1].

Modification of copolymers with various functional groups and other fragments by grafting or other procedures improves the physicochemical properties and thus extends the application field of these materials [2]. The modified materials are suitable as components of information-recording and environment-protection systems, as binders in high-energy-capacity formulaitions, and also as flocculants, ion-exchange resins, catalysts, and immobilizers of various media [3–5].

Among the most important characteristics of water superabsorbents are mechanical strength and water absorption rate. Gels can be strengthened by several procedures, e.g., by increasing the number of cross-links in the polymer or by introducing fillers into the copolymer. The former procedure can be performed by introducing a large amount of a cross-linking agent during polymerization or by additional cross-linking after the main polymerization to afford a denser cross-linking in the surface layer of the particles.

In the former case, gel strengthening is accompanied by a significant decrease in the absorption capacity, since the monomer mixture usually contains 0.2–1.0 mol % methylenebisacrylamide (MBAA) (in terms of the monomer). The tensile strength of the acrylonitrile–acrylamide copolymer is governed by the concentration of the cross-linked polymer in the gel, and, as the acrylonitrile content becomes higher, it increases to 500 kPa, which exceeds 4–5-fold the tensile strength of the polyacrylamide gel [6].

In the latter case, the gel can be strengthened via creation of additional cross-links after the main polymerization process.

A drawback of water superabsorbents based on acrylic acid is their low strength, which makes them unsuitable for production of articles with a desired shape: membranes, filters, sensor elements. In [7], it was shown that hydrogels based on alkaline metal acrylates have a surface strength of up to 800 Pa at water absorption of 650 g g^{-1}.

When active additives, such as chalk, are introduced during synthesis of water superabsorbents, a twofold effect is achieved, namely, the strength increases owing to additional cross-linking with the Ca^{2+} ion and the resulting copolymer is foamed by carbon dioxide released during neutralization of the acidic groups. The latter factor accelerates the absorption and reduces the time of drying of the water superabsorbent, but the mechanical strength increases insignificantly [8].

When an inert inorganic powder, such as silicon, titanium, or aluminum oxide, is introduced into

1070-4272/04/7710-1704 © 2004 MAIK "Nauka/Interperiodica"

Table 1. Deformation and strength characteristics of the acrylic hydrogel based films modified with glass spheres

Formulation			Tensile strength σ, MPa	Relative elongation ε, %
MBAA, wt % relative to [MVT + AA]	MVT, wt % relative to [MVT + AA]	glass spheres, wt % relative to AA		
0.2	0	80	5.5	750
0.2	0	0	5.0	1070
0.2	27	0	10.0	1175
0.2	27	80	18.5	360

the composition, the strength of the gel increases to 6 kPa, and the water absorption decreases to 350 g g^{-1} [9].

Glass fillers have a spherical shape (10–200 μm and more in diameter), low density, reasonable strength, and high adhesion to the majority of polymers, which make them widely applicable. Among the most important application fields for hollow glass spheres are preparation of polymer materials for various purpous, filling of varnishes and paints, and preparation of composite polymeric spackles, polymer compositions for electronics, and abrasives.

In this study, we prepared composites based on vinyl tetrazole–acrylate copolymers and hollow glass spheres and examined their physicochemical properties.

EXPERIMENTAL

Tetrazole-containing acrylic films filled with hollow glass spheres in the preparation stage were synthesized by copolymerization at 30°C. The glass spheres were introduced in an amount of 80 wt % with respect to acrylic acid (AA) into the prepared reaction mixture after adding the initiator, ammonium persulfate (APS).

Sodium acrylate and 2-methyl-5-vinyltetrazole (MVT) served as reagents, and *N*,*N*'-methylenebisacrylamide, as cross-linking agent. The degree of neutralization of acrylic acid with sodium hydroxide was 0.9. The fraction of monomers in the monomer mixture was 30 wt %; served as initiator the redox system constituted by ammonium persulfate and tetramethylethylenediamine. The MVT and APS concentrations were 10–50 and 0.8 wt %, respectively. Before polymerization, 2-methyl-5-vinyltetrazole was purified by recrystallization. The characteristics and methods of purification of other reagents, as well as the copolymerization procedure, were presented in [10].

The resulting films were dried at room temperature to constant weight. The moisture content of the films was 30%.

The degree of equilibrium swelling was measured by a standard gravimetric method and calculated by the formula

$$Q = \frac{m - m_0(1-\gamma)}{m_0(1-\gamma)}.$$

Here, Q is the degree of swelling of the hydrogel, g g^{-1}; m_0, initial mass of the gel sample, g; m, mass of the swollen sample, g; and γ, moisture content of the gel sample, weight fraction.

The degrees of swelling calculated for five analogous samples were averaged.

The rate and degree of swelling of hydrogels depend on the method and formulation of the reaction mixture of their synthesis, as well as on the medium in which the swelling occurs, and the swelling temperature and time. For the absorbents studied by us, the equilibrium swelling was reached within 6–13 h (for large pieces characterized similarly to films, within 24 h).

The tensile strength of the films was tested on an RMI-5 tensile machine. We prepared 1–1.5-mm-thick films, dried them at room temperature, cured, and cut into strips 6 cm long and 1 cm wide. The measurements followed GOST (State Standard) 270–75.

Table 1 lists the deformation and strength characteristics of the films based on vinyl tetrazole–acrylate gel and hollow glass spheres.

Table 1 shows that the acrylate films modified with glass spheres exhibit high deformation and strength characteristics. Upon introduction of glass spheres, the tensile strength of the film increases, but its relative elongation decreases twofold. The mutual influence of

Table 2. Characteristics of acrylic hydrogel-based films modified with glass spheres

Formulation			Equilibrium swelling degree Q, g g^{-1}, at 16°C		
MBAA, wt % relative to [MVT + AA]	MVT, wt % relative to [MVT + AA]	glass spheres, wt % relative to AA	in water		in 0.9% NaCl, rod
			film	rod	
0.2	0	80	240	270	50
0.2	0	0	300	600	65
0.2	27	0	320	640	85
0.2	27	80	285	480	80

the glass spheres, solvent, and cross-linked acrylate copolymer during synthesis of the composite is so specific that the results obtained can only be understood in terms of the polymer adsorption theory.

The low relative elongation of vinyl tetrazole–acrylate films is due to a strong intermolecular interaction of the carboxylate groups and tetrazole ring [11] with the hydrophilic groups of the glass spheres, as well as to dipole–dipole hydrophobic interaction between the glass sphere surface and the corresponding groups in the copolymer.

The improved strength characteristics may be due to the presence of additional "cross-links." Also, aggregation of the glass spheres in a strongly polar solvent (water in our case) cannot be ruled out, which additionally increases the strength.

The chemical properties of the composites are strongly dependent on the chemical composition of the surface of hollow glass spheres. The surface of hollow glass spheres has pH 8–9, and its alkalinity does not exceed 0.4–0.5 mg-equiv. g^{-1}. At a sufficiently high water concentration in the hydrogel, the surface can be neutralized by free carboxy groups, forming a strengthening adsorption-hydration layer, and the adjacent adsorption-hydration layers may overlap, which significantly strengthens new composites (see figure).

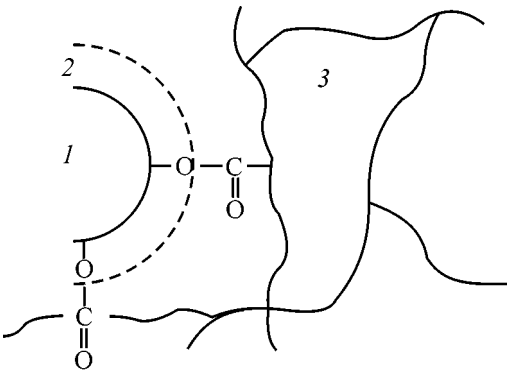

Formation of a strengthened structure of acrylic copolymers with hollow glass spheres: (*1*) a hollow glass sphere (*2*) adsorption-solvation layer (*3*) cross-linked acrylate copolymer.

The swelling rate of the films filled with hollow glass spheres exceeds by a factor of 1.5 that of the films without modifiers. Also, the film with glass spheres preserves its shape in the swollen state, which can be of great practical significance.

Table 2 presents the equilibrium degrees of swelling of the composites as dependent on their composition.

Table 2 suggests that the degree of equilibrium swelling of analogous cylindrically shaped hydrogel samples with a diameter of 2 mm, synthesized at 60°C, exceeds by a factor of 1.5–2 that of the film samples.

The degree of equilibrium swelling of the modified hydrogel samples is only slightly smaller than that of unfilled samples.

CONCLUSIONS

(1) Composites based on vinyl tetrazole–acrylate copolymers with hollow glass spheres were prepared for the first time.

(2) Introduction of glass spheres into tetrazole-containing acrylic hydrogels gives films with high deformation and strength characteristics, namely, tensile strength σ = 18.5 MPa and relative elongation ε = 350%.

REFERENCES

1. Kruglova, V.A., Annenkov, V.V., Saraev, V.V., *et al.*, *Vysokomol. Soedin., Ser. B*, 1997, vol. 39, no. 7, pp. 1257–1259.
2. Budtova, N.V., Suleimenov, I.E., and Frenkel, S.Ya., *Zh. Prikl. Khim.*, 1997, vol. 70, no. 4, pp. 529–539.
3. Annenkov, V.V., Kruglova, V.A., Kazimirovskaya, V.B., *et al.*, *Khim.-Farm. Zh.*, 1995, no. 1, pp. 38–40.
4. Kruglova, V.A., Annenkov, V.V., Vereshchagin, L.I., *et al.*, *Khim.-Farm. Zh.*, 1987, vol. 21, no. 2, pp. 159–163.
5. Kizhnyaev, V.N. and Kruglova, V.A., *Zh. Prikl. Khim.*, 1992, vol. 65, no. 8, pp. 1879–1884.
6. Samchenko, Yu.M., Baranova, A.I., and Ul'berg, Z.R., *Kolloidn. Zh.*, 1992, vol. 54, no. 1, pp. 134–138.
7. Jpn Patent 43606, *Chem. Abstr.*, 1986, vol. 105, no. 10, 79549.
8. Shvareva, G.N., Ryabova, E.N., and Shatskii, O.V., *Plast. Massy*, 1996, no. 3, pp. 32–35.
9. Jpn Patent 1103615, *Chem. Abstr.*, 1989, vol. 111, no. 24, 215103g.
10. Igrunova,, A.V., Sirotinkin, N.V., and Uspenskaya, M.V., *Zh. Prikl. Khim.*, 2001, vol. 74, no. 7, pp. 1170–1174.
11. Kurmaz, S.V. and Roshchupkin, V.P., Abstracts of Papers, *5-ya konferentsiya po khimii i fizikokhimii oligomerov* (5th Conf. on Chemistry and Physicochemistry of Oilgomers), Chernogolovka, October 4–6, 1994, p. 163.

Russian Journal of Applied Chemistry, Vol. 77, No. 10, 2004, pp. 1708–1710. Translated from Zhurnal Prikladnoi Khimii, Vol. 77, No. 10, 2004, pp. 1722–1724.

MACROMOLECULAR CHEMISTRY AND POLYMERIC MATERIALS

Specific Features of Vulcanization of Unsaturated Rubbers with Polymeric *p*-Dinitrosobenzene

G. E. Zaikov, O. R. Klyuchnikov, T. V. Makarov, and R. Ya. Deberdeev

Kazan State Technological University, Kazan, Tatarstan, Russia

Emanuel' Institute of Biochemical Physics, Russian Academy of Sciences, Moscow, Russia

Received June 1, 2004

Abstract—Conditions of vulcanization of unsaturated rubbers were studied.

p-Dinitrosobenzene (DNB), an agent for low-temperature vulcanization of rubbers and rubber–metal adhesives [1, 2], is produced in industry by oxidation of *p*-benzoquinone dioxime. *p*-Dinitrosobenzene is a straw-yellow finely dispersed polymeric substance [3] with the poly(*trans*-azo-*N*,*N*'-dioxy-1,4-phenylene) structure (poly-DNB) [4–7]:

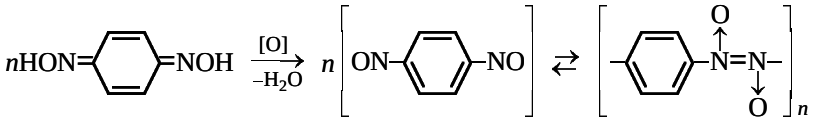

Poly-DNB is virtually insoluble in organic solvents under ordinary conditions [3–5], which complicates elucidation of its structure. Monomeric DNB is prepared by fast heating in xylene [3] or vacuum sublimation onto a surface cooled with liquid nitrogen; the resulting dark green monomeric DNB rapidly transforms at room temperature into straw-yellow poly-DNB [6].

Therefore, it was assumed that the molecular weight of poly-DNB should grow, and its vulcanizing activity change, in the course of storage. Indeed, we found that the vulcanizing activity of poly-DNB at low temperatures (20–60°C) is largely influenced by the time of its storage.

We compared the vulcanizing activity of poly-DNB produced in 1986 (Shostka Plant of Chemicals) and stored in dark glass bottles in a cold storehouse (DNB-sh) with that of freshly prepared DNB (DNB-fp) (for synthesis protocol, see [3]). The time elapsed from the synthesis of DNB-fp to its tests did not exceed 5 h. The analytical data for both samples were identical and consistent with the empirical formula $C_6H_4N_2O_2$. The IR spectra (Bruker Vector-22 IR Fourier spectrometer, KBr pellets) of both samples were, on the whole, similar; in particular, a characteristic strong band of *trans*-azo-*N*,*N*'-dioxy group was observed at about 1264 cm^{-1}. The difference was observed only in the region of 1533 cm^{-1} (stretching vibrations of monomeric nitroso groups [5]). In the spectrum of DNB-fp, the absorption in this region is approximately two times that in the spectrum of DNB-sh, which suggests for DNB-fp a higher concentration of monomeric nitroso groups, lower degree of polymerization,

Rate constants of vulcanization of NR solution

T, °C	*k*, s^{-1}	
	DNB-fp	DNB-sh
20	5.7×10^{-5}	–
30	1.3×10^{-4}	–
40	3.9×10^{-4}	1.4×10^{-5}
50	–	5.4×10^{-5}
60	–	2.1×10^{-4}

1070-4272/04/7710-1708 © 2004 MAIK "Nauka/Interperiodica"

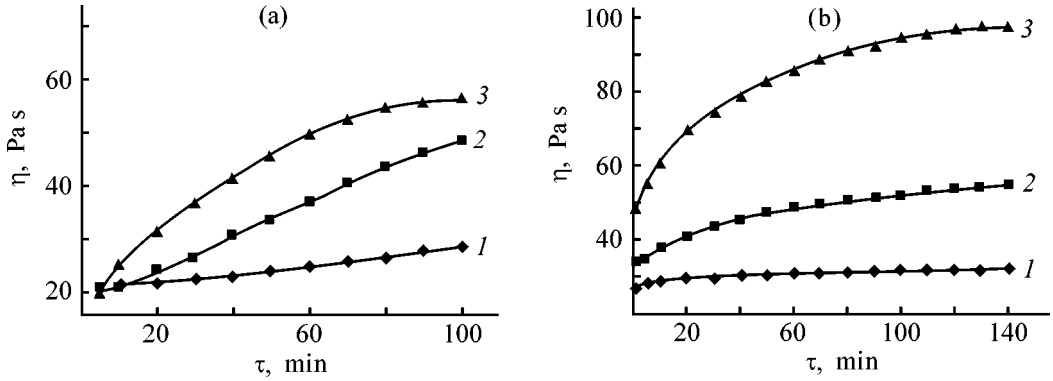

Fig. 1. Kinetic curves of NR vulcanization with (a) DNB-fp and (b) DNB-sh. (η) Viscosity and (τ) time. Temperature, °C: (a) (*1*) 20, (*2*) 30, and (*3*) 40; (b) (*1*) 40, (*2*) 50, and (*3*) 60.

and accordingly higher vulcanizing activity (or higher vulcanization rate constant).

The kinetic studies of vulcanization were performed with a 10% toluene solution of natural rubber (NR) preliminarily rolled out for 3–4 min. Poly-DNB was added to the solution in an amount of 1 wt % relative to the rubber. The growth of the solution viscosity with time was monitored on a Rheotron Brabender rotary viscometer at a cylinder rotation rate of 5 rpm. The kinetic curves were satisfactorily described by a first-order equation; the semilog plots were linear. The apparent rate constants of vulcanization k (s^{-1}) were calculated by the formula

$$k = \frac{1}{\tau} \ln \frac{\eta_{max} - \eta_0}{\eta_{max} - \eta_\tau}, \qquad (1)$$

where τ is time (s), and η_{max}, η_0, and η_τ are the maximum, initial, and running viscosities of the reaction mixture (Pa s).

The initial portions of the kinetic curves for vulcanization of NR with DNB-fp and DNB-sh are shown in Figs. 1a and 1b, and the rate constants of vulcanization are listed in the table.

The temperature dependences of the apparent rate constants of vulcanization are as follows:

$$k_{DNB\text{-}fp} = 10^{8.7} \exp(-72.8\ \text{kJ}/RT),$$

$$k_{DNB\text{-}sh} = 10^{14.3} \exp(-114.6\ \text{kJ}/RT).$$

As a quantity characterizing the reactivity of poly-DNB samples, we chose the temperature T_r (°C) at which the apparent rate constant $k = 1 \times 10^{-6}$ s^{-1}:

$$T_r = \frac{E}{19.142(6 + \log A)} - 273.15, \qquad (2)$$

where E is the activation energy, kJ. T_r is –15.1 and 22.6°C for DNB-fp and DNB-sh, respectively.

The quantity T_r also characterizes the thermal stability of the systems [8], in our case, the limiting temperature of storage of the system to be vulcanized, at which scorching leads to an approximately 2% rise in viscosity in 6 h.

DNB-fp appeared to be more active than DNB-sh also with respect to toluene solutions of other unsaturated rubbers: SKDK, SKN-3, and SKEPT-ENB.

The different T_r can be attributed to different degrees of polymerization of poly-DNB samples, which grow in storage, with the corresponding decrease in the relative concentration of monomeric terminal nitroso groups and in the apparent rate constant of vulcanization:

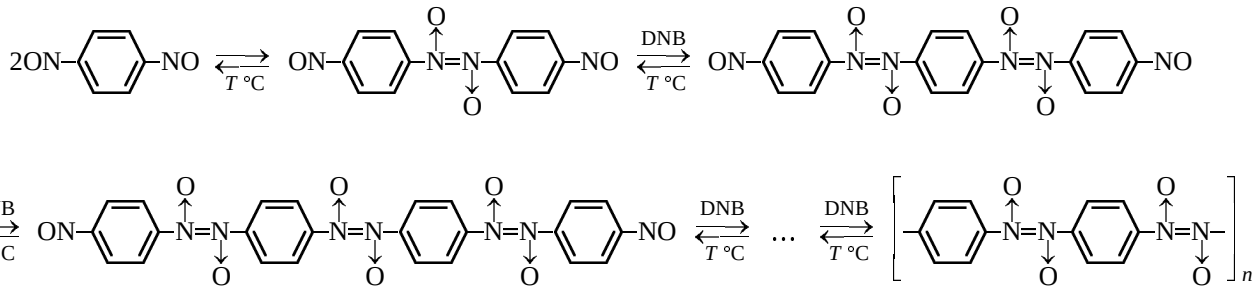

The vulcanizing activity of DNB-fp and DNB-sh at 100–130°C was studied with a Monsanto-100S rheometer. Samples were introduced into SKI-3 polyisoprene rubbers on cold rollers. The time of mixing on the rollers was 3–4 min.

In so doing, the major problem was to choose the optimal rolling time to ensure an effective mixing of the vulcanizing agent with the rubber and, at the same time, to avoid any appreciable scorching.

The kinetic curves were satisfactorily described by a first-order equation; the semilog plots were linear.

The apparent rate constants of vulcanization (s^{-1}) were calculated by the formula

$$k = \frac{1}{\tau_{90\%}} \ln \frac{M_{max} - M_{min}}{M_{max} - M_{90\%}}, \quad (3)$$

where $\tau_{90\%}$ is the time in which the vulcanization optimum (90%) is attained, s; M_{max}, M_{min}, and $M_{90\%}$ are the torque values: maximum, minimum, and that in vulcanization optimum (90% of the maximum), dN m.

Our study shows that, at relatively high temperatures (100–130°C), the apparent rate constants of vulcanization of SKI-3 with DNB-fp and DNB-sh do not differ appreciably: in both cases, $k_{130°C} = 6.4 \times 10^{-3}$ s^{-1}.

The temperature dependence of the vulcanization rate constant (s^{-1}) with DNB-fp and DNB-sh is

$$k = 10^{5.8 \pm 1} \exp(-6.2 \pm 8 \text{ kJ}/RT),$$

with $T_r = 0 \pm 10°C$.

According to previous data, DNB-fp, DNB-sh, and poly-DNB stored for 30 years show about the same activity in vulcanization of butyl rubber stocks in a mold at 100°C. The resulting vulcanizates had comparatively close values of the nominal tensile strength, $\sigma = 14 \pm 0.8$ MPa [9].

Apparently, under conditions of hot vulcanization, poly-DNB undergoes fast depolymerization, with the reaction of monomeric DNB with unsaturated rubber macromolecules being the limiting step.

REFERENCES

1. Gofman, V., *Vulkanizatsiya i vulkanizuyushchie agenty* (Vulcanization and Vulcanizing Agents) Moscow: Khimiya, 1968.
2. Tikhonova, N.P., Ginzburg, L.V., and Dontsov, A.A., *Kauchuk Rezina*, 1987, no. 3, p. 13.
3. Rugli, P. and Bartusch, G., *Helv. Chim. Acta*, 1944, vol. 26, no. 6, pp. 1375–1378.
4. Klyuchnikov, O.R., Thermolysis of *N*-Oxide Derivatives and Aromatic *C*-Nitroso Compounds, *Cand. Sci. Dissertation*, Kazan, 1990.
5. *The Chemistry of the Nitro and Nitroso Groups*, Feuer, H., Ed., New York: Interscience, 1969, part 1. Translated under the title *Khimiya nitro- i nitroozogrupp*, Moscow: Mir, 1972, pp. 103–104.
6. Hacker, N.P., *Macromolecules*, 1993, vol. 26, no. 22, pp. 5937–5942.
7. Klyuchnikov, O.R. and Deberdeev, R.Ya., Abstracts of Papers, *XVII Mendeleevskii s"ezd po obshchei i prikladnoi khimii* (XVII Mendeleev Congr. on General and Applied Chemistry), Kazan, 2003, vol. 1, p. 409.
8. Klyuchnikov, O.R. and Nikishev, Yu.Yu., *Khim. Geterotsikl. Soedin.*, 1995, no. 11, p. 1573.
9. Makarov, T.V., Klyuchnikov, O.R., Vol'fson, S.I., *et al.*, in *Materialy Yubileinoi nauchno-metodicheskoi konferentsii "III Kirpichnikovskie chteniya"* (Proc. Jubilee Scientific and Methodical Conf. "III Kirpichnikov Readings"), Kazan: Kazan. Gos. Tekhnol. Univ., 2003, pp. 390–392.

Russian Journal of Applied Chemistry, Vol. 77, No. 10, 2004, pp. 1711–1714. Translated from Zhurnal Prikladnoi Khimii, Vol. 77, No. 10, 2004, pp. 1725–1728.

MACROMOLECULAR CHEMISTRY AND POLYMERIC MATERIALS

Use of Latex Systems for Controlling the Properties of Urea–Formaldehyde Resins

S. S. Glazkov

Voronezh State Academy of Forestry Engineering, Voronezh, Russia

Received April 15, 2004

Abstract—The influence of latex formulations and a filler, Vulkasil, on the processing and physicochemical properties of urea–formaldehyde resins was studied.

Urea–formaldehyde resins (UFSs) are widely used for gluing of wood and wood materials in furniture and wood-working industry [1]. In world's production of chip boards and plywood, the consumption of these resins reaches 90% [2]. Despite the relatively high strength, UFRs have significant drawbacks: presence of cancerogenic free formaldehyde and low moisture and water resistance, especially under conditions of varying humidity and high temperatures. Numerous studies show that these drawbacks can be eliminated both in the synthesis stage [3] and by modification of the ready urea–formaldehyde oligomer [4]. The second alternative seems to be more promising, as it allows a comprehensive control over the properties of the resin and resin-containing wood materials depending on the conditions of service of ready items.

In this study we examined how a latex system based on butadiene–styrene copolymer affects the UFR properties.

EXPERIMENTAL

Latexes are colloidal systems [5]; the most readily available are butadiene–styrene latexes widely used in production of composite materials. However, in contrast to functional polymers, latexes require additional stabilization to enhance the stability of latex systems in contact with fillers and UFRs. The formula of an adhesive latex composition (ALC) based on a butadiene–styrene latex can include the following ingredients: thickener (protective colloid); agent that enhanced the adhesiveness; stabilizing emulsifier OP-10; trisodium phosphate (TSP, 20% solution); and active filler (Aerosil, Vulkasil). The stabilization of butadiene– styrene latexes is provided by introducing water-soluble polymers (polyvinyl alcohol; carboxymethyl cellulose, CMC; casein; etc.). In particular, it was shown for BS-65A latex (Fig. 1) that the stabilization of the colloidal system with 10% CMC solution is accompanied by changes in the surface tension σ and wetting angle θ. At CMC concentrations of 2 to 6%, these quantities pass through a maximum and a minimum, respectively. The thermodynamic work quantities pass in this range of CMC concentrations through maxima (Fig. 2), reaching the values that exceed those for the initial latex by a factor of 2–3. Acting as a protective colloid, CMC molecules link, via their polar (hydroxy) groups, the col-

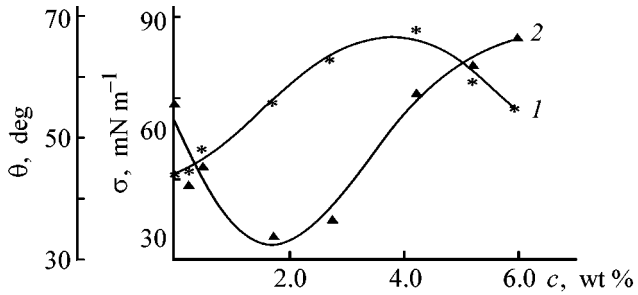

Fig. 1. Influence of CMC concentration *c* in the latex on (*1*) σ and (*2*) θ.

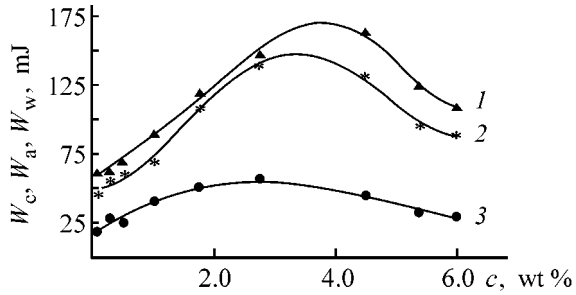

Fig. 2. Influence of CMC concentration c on the main kinds of thermodynamic works: (*1*) W_c, (*2*) W_a, and (*3*) W_w.

1070-4272/04/7710-1711 © 2004 MAIK "Nauka/Interperiodica"

Table 1. Physicochemical properties of UFRs

Parameter	ALC content, wt %									
	0	0.05	0.1	0.2	0.3	0.5	1.5	3.0	6.0	12.0
Time of outflow from VZ-4 viscometer, s	83	65	45	43	42	40	37	36	34	27
Content of free formaldehyde, %	1.10	0.75	0.60	0.55	0.85	0.85	0.90	0.95	1.00	1.05
Content of methylol groups, %	2.8	4.8	5.1	5.2	4.6	2.4	3.8	4.4	4.1	4.4
Gelation time at 100°C in the presence of 1.0 wt % NH_4Cl, s	78	76	69	58	62	65	66	68	70	82
Wetting angle, deg	76	72	67	65	70	69	68	65	62	60
Ultimate shear strength, MPa (after boiling in water for 2 h)	3.5	5.5	6.2	6.3	6.5	5.7	5.2	4.7	4.2	3.1

loidal particles of a latex into coarser agglomerates. The introduction of a polar compound and structural processes account for the shape of the curves for the works of cohesion W_c, adhesion W_a, and wetting W_w.

The sizes of wood capillaries (20–40 to 100–200 nm, depending on the kind of wood), interfibrillar pores (7–10 nm), and oligomer molecules (7–40 nm) are comparable [6]. Latex particles are coarser (100 to 1000 nm, depending on the kind of latex).

Thus, introduction of latexes into UFR-based binders will (1) of the the surface tension, wetting angle, and viscosity, which will favor better wetting and more uniform coverage of the external surface of the wood filler with the binder, and (2) retard penetration of the binder into the capillary-porous structure of wood particles, ensuring more uniform thickness of the adhesive layer.

According to the modern adsorption theory, the formation of a glue joint is a multistep process. Wetting of the substrate surface with the adhesive and the spill of the adhesive over the surface are accompanied by diffusion of polymer molecules and establishment of an adsorption equilibrium. Introduction of small amounts of latex compositions with the particle size reaching 300–400 nm (in synthetic latexes) should decrease the adsorption. Latex globules act as an active filler deposit on the substrate surface and plug the porous structure of the adsorbent, thus increasing the number of contact points. Acting as a peculiar "lock," latex particles favor an increase in the thickness of the adhesive layer and decrease the risk of formation of a discontinuous glue joint.

The specific adsorption (amount of the polymeric substance taken up by the wood filler) is at a maximum (0.17 g g^{-1}) for the straight resin. With the modified resin (KFZh brand), the specific adsorption steadily decreases as the latex content increases, amounting to 0.09, 0.058, and 0.042 g g^{-1} at a latex content of 0.05, 0.1, and 15.0 wt %, respectively. With straight latex, the specific adsorption is at a minimum: 1.5×10^{-2} g g^{-1}.

Latex formulations decrease the UFR viscosity (Table 1) and improve the wetting of the wood surface. The decrease in the wetting angle is apparently due to the effect of the emulsifier present in the latex.

Latex particles, being thermodynamically unstable, possibly initiate polycondensation processes. This is suggested by the shortening of the gelation time, i.e., by an increase in the UFR reactivity at low latex concentrations (Table 1). The modifying effect of the latex system is manifested in an enhanced strength of the glue joint (Table 1). The ultimate shear strength with the modified binder increases by 50–80% at the ALC content of up to 3–4%.

An examination of photomicrographs (Fig. 3) confirmed the assumed mechanism of the ALC effect on formation of a glue joint. In contrast to the initial UFR (Fig. 3a), which gives of discontinuous glue joint with large thickness and large penetration depth, the modified UFR (Fig. 3b) ensures a thinner and more uniform glue joint without apparent discontinuities.

The binder composition was optimized using the Statgraphics for Windows software.

As follows from Fig. 4, there exists an optimal latex content, determined primarily by the existence of extrema in the glue joint strength, free formaldehyde content, and gelation time. The influence of the filler (Vulkasil) content on the first two parameters is about the same but less pronounced, and the gelation time steadily increases with increasing filler content. Presumably, formaldehyde can by physically bound to

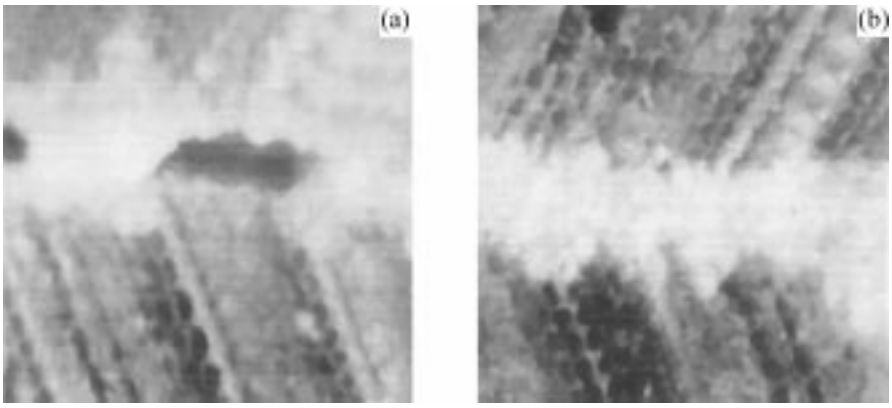

Fig. 3. Photomicrographs (×80) of glue joints obtained with (a) initial KFZh and (b) KFZh containing 4.0 wt % ALC.

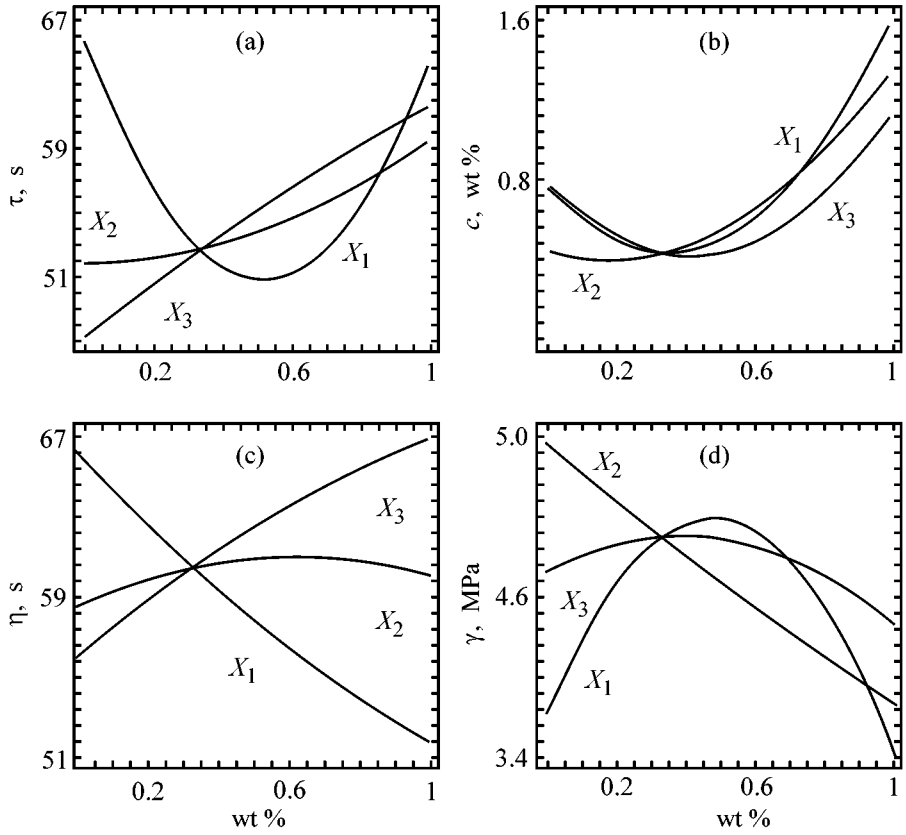

Fig. 4. Properties of the composite binder, plotted vs. the content of components in the pseudo-coordinates: (a) gelation time τ, (b) content of free formaldehyde *c*, (c) viscosity parameter η (time of outflow from VZ-4 viscometer), and (d) ultimate shear strength γ. (X_1, X_2, X_3) Contents of the latex composition, KFZh, and Vulkasil, respectively (wt %). Variation ranges: $0.5 \le X_1 \le 8.0$, $91.5 \le X_2 \le 99.0$, and $0.5 \le X_3 \le 0.8$.

with the surface of the latex particle. This is indirectly suggested by the fact that the content of the dispersed component (Fig. 4b, X_1) strongly affects that of free formaldehyde (decrease by almost a factor of 2, compared to the initial UFR). Figure 4b shows that this effect is similar in magnitude to that exerted by the filler, Vulkasil (X_3).

The optimal binder formulation was used in production of chip boards with various kinds of wood fillers (Table 2). At the optimal content of the latex system in the binder, the resulting boards based on secondary raw materials exhibit satisfactory chemical and physicomechanical characteristics and have decreased content of free formaldehyde.

Table 2. Physicomechanical and chemical properties of chip boards

Parameter	Filler								
	sawdust			buckwheat husk			sunflower-seed husk		
ALC content, wt %	0	2.5	5.0	0	2.5	5.0	0	2.5	5.0
Density of boards, kg m^{-3}	833	920	930	806	740	678	521	568	619
Water absorption, wt %, during a time, h:									
2	46.9	45.2	43.5	69.4	66.6	70.3	93.7	84.5	79.3
24	57.4	55.3	52.7	86.7	81.8	85.4	107.3	91.7	83.1
Swelling across the board, %, during a time, h:									
2	14.3	13.7	13.1	30.0	21.5	8.3	30.0	25.1	22.4
24	27.0	26.4	25.2	43.3	32.5	19.4	31.7	26.3	23.8
Ultimate bending strength, MPa	14.1	15.6	16.3	3.5	4.3	5.4	15.3	16.2	16.5
Ultimate tensile strength in the direction perpendicular to the surface, MPa	0.26	0.31	0.33	0.06	0.08	0.09	0.20	0.25	0.27
Formaldehyde emission, mg/100 g	40.1	9.8	8.7	63.4	13.2	10.7	38.7	15.6	12.1

CONCLUSIONS

(1) Introduction of the latex system based on BS-65A latex into urea–formaldehyde resin improves the processing and physicochemical parameters of the binder and of the composite as a whole.

(2) As the content of the adhesive latex composition in the urea–formaldehyde oligomer increases, the penetration of the oligomer into the wood substrate decreases, and thereby the distribution of the binder over the glue joint surface becomes more uniform.

(3) The vulkasil filler makes lower the residual formaldehyde content in the urea–formaldehyde oligomer and in finished chip boards.

REFERENCES

1. Temkina, R.Z., *Sinteticheskie klei v derevoobrabotke* (Synthetic Adhesives in Wood-Working), Moscow: Lesnaya Prom–st., 1971.
2. Beketov, V.D., *Tendentsii i prognozy razvitiya proizvodstva listovykh drevesnykh materialov: Obzornaya informatsiya. Plity i fanera* (Trends and Prognosis of Development of Production of Wood Sheet Materials: Review. Chip Boards and Plywood), Moscow: VNIPIEIlesprom, 1990, issue 7.
3. Glukhikh, V.V., Decreasing Toxicity of Wood Composites by Optimizing the Chemical Composition of Urea Binders, *Doctoral Dissertation*, Yekaterinburg, 1994.
4. Doronin, Yu.G., *Sovmeshchennye klei povyshennoi vodostoikosti dlya drevesnykh listovykh materialov: Obzornaya informatsiya. Plity i fanera* (Combined Adhesive of Enhanced Water Resistance for Wood Sheet Materials: Review. Chip Boards and Plywood), Moscow: VNIPIEIlesprom, 1987, issue 10.
5. Erkova, L.N., *Lateksy* (Latexes), Leningrad: Khimiya, 1983.
6. Ugolev, B.N., *Drevesinovedenie s osnovami lesnogo tovarovedeniya* (Wood Science with Fundamentals of Wood Merchandizing), Moscow: Lesnaya Prom–st., 1986.

Russian Journal of Applied Chemistry, Vol. 77, No. 10, 2004, pp. 1715–1720. Translated from Zhurnal Prikladnoi Khimii, Vol. 77, No. 10, 2004, pp. 1729–1734.

MACROMOLECULAR CHEMISTRY AND POLYMERIC MATERIALS

Synthesis of Polyurethanes with *B,P*-containing Polyols

S. N. Bondarenko, T. V. Khokhlova, S. A. Orlova, and O. I. Tuzhikov

Volgograd State Technical University, Volgograd, Russia
Volzhskii Polytechnic Institute, Volzhskii, Volgograd oblast, Russia

Received July 9, 2004

Abstract—Polyurethanes were prepared from diphenylmethane-4,4'-diisocyanate, poly(tetramethylene ether) glycol, and *B,P*-containing polyols. The structure and properties of these polyurethanes were studied in relation to the synthesis conditions, including the functional group ratio and temperature. The heat resistance of the polyurethanes was evaluated.

Preparation of polymers containing boron atoms in the macromolecule was discussed in an analytical review [1]; in particular, methods for preparing polyurethanes containing carborane and borinane structures were considered. Such polymers are synthesized from low-molecular-weight carborane-containing ethers and esters and aliphatic diisocyanates, or from carboranylene diisocyanates and various diols.

However, factors that control the lengthening of the polymeric chain and properties of the polymers prepared using oligomeric chain-lengthening organometallic agents were not analyzed comprehensively in [1].

Our goal was to reveal a relationship between the molecular parameters of the starting polyols containing borate and phosphonate groups, on the one hand, and the properties of polyurethanes prepared from these polyols, on the other.

EXPERIMENTAL

Polyurethanes were prepared by a two-step procedure. The reaction of a twofold excess of diphenylmethane-4,4'-diisocyanate (DMI) with poly(tetramethylene ether) glycol (PTMEG) yielded a macromolecular diisocyanate (MDC). The resulting MDC was brought into the reaction with a *B,P*-containing polyol (BPP) as a chain-lengthening agent.

Polyurethanes and MDC were prepared in a high-speed (1400 rpm) temperature-controlled mixer in an argon flow in dimethylformamide (DMF).

B,P-Containing polyols BPP-1, BPP-2, BPP-3, and BPP-4 were prepared according to [2] by reactions of glycols (ethylene glycol, diethylene glycol, glycerol, and 1,4-butanediol, respectively) with the phosphorus-containing oligomer [3]. The reaction occurs on heating of the equimolar amounts of the reactants under Ar at 453–463 K without a catalyst for 5 ± 1 h. The reaction products are viscous liquids with the color varying from light yellow to brown. The main physicochemical parameters of BPPs are listed in Table 1.

The structure of the BPPs obtained was confirmed by ^{1}H and ^{31}P NMR and by IR spectroscopy. The

Table 1. Physicochemical properties of *B,P*-containing polyols*

B,P-Containing polyol	n_D^{20}	ν, St	ρ_4^{20}, g cm^{-3}	MW	Content of OH groups, %	P content, %	
						found	calculated
BPP-1	1.4748	32.7	1.2573	820	6.6	29.4	28.9
BPP-2	1.4730	30.1	1.8839	910	6.2	26.8	26.2
BPP-3	1.4842	33.8	1.4486	890	8.2	27.8	27.3
BPP-4	1.4797	31.3	1.6243	880	6.6	28.1	28.7

* (ν) Viscosity.

1070-4272/04/7710-1715 © 2004 MAIK "Nauka/Interperiodica"

NMR spectra were recorded on a Bruker AC-200 spectrometer (working frequency for ^1H 200 MHz). The IR spectra of BPPs and polyurethanes were recorded on a Specord-M82 spectrometer.

Oligomer samples were dried at 353 K/0.66 kPa; the moisture content in BPPs did not exceed 0.02 wt%. Their molecular weight (MW) was determined cryoscopically in cyclohexanone. The molecular weight of polyurethanes was evaluated by the change in the viscosity of their solutions. The viscosity was measured with a Rheotest-2 cone–plate rheoviscometer in the shear rate range 5.6 – 4860 s^{-1}.

Diphenylmethane-4,4'-diisocyanate was distilled in a vacuum at 323–328 K/0.66 kPa and stored in sealed glass ampules. The urethane formation kinetics was monitored chemically (by consumption of isocyanate groups) and IR spectroscopically [by variation of the optical density at the wave numbers corresponding to the characteristic bands of the isocyanate (–N=C=O, 2275 cm^{-1}) and –NH (3400 cm^{-1}) groups]. The sol and gel fractions of the polyurethanes were separated in a Soxhlet apparatus.

Samples for tests were prepared as free films by casting from 65% DMF solutions according to GOST (State Standard) 14243–78. The mean film thickness was about 200 μm. Before tests, the films were heat-treated at 393 K for 6 h. The tensile characteristics of the materials were determined according to GOST 18299–72 at a loading rate of 20 mm min^{-1}. Each experimental point was obtained with no less than ten samples; the variance coefficients did not exceed 9% for the tensile strength σ and 15% for relative elongation at break, ε.

The heat resistance of polyurethane sample was evaluated under static (from the amount of oxygen taken up in 180 min at 453 K) and dynamic [by thermal gravimetric analysis in air, MOM derivatograph (Hungary), atmospheric pressure, 273–1273 K] conditions. The thermodynamic characteristics of the degradation processes were evaluated by the procedure described in [4].

B,P-Containing polyurethanes were prepared as follows.

First step:

$$2O{=}C{=}N{-}R{-}N{=}C{=}O + H{-}[{-}O({-}CH_2{-})_4]_n{-}OH \rightarrow O{=}C{=}N{-}R{-}NH{-}C(O){-}[O{-}(CH_2{-})_4]_n{-}O{-}C(O){-}NH{-}R{-}N{=}C{=}O,$$

Second step:

$$O{=}C{=}N{-}R{-}NH{-}C(O){-}[O{-}(CH_2{-})_4]_n{-}O{-}C(O){-}NH{-}R{-}N{=}C{=}O + HO{-}R_1\text{-}OH$$

$$\rightarrow O{=}C{=}N{-}[{-}R{-}NH{-}C(O){-}[O{-}(CH_2{-})_4]_n{-}O{-}C(O){-}NH{-}R{-}NH{-}C(O){-}O{-}R_1{-}O{-}]_m{-}H,$$

$$R = -\langle\bigcirc\rangle-CH_2-\langle\bigcirc\rangle;$$

$$R_1 = OH{-}[{-}R_2{-}O{-}P({=}O)({-}H){-}[{-}O{-}B({-}O{-}R_2{-}OH){-}O{-}P({=}O)({-}H){-}]_p[{-}O{-}B({-}OH){-}O{-}P({=}O)({-}H){-}]_q O{-}B({-}OH){-}O{-}P({=}O)({-}H){-}O{-}]_h R_2{-}OH;$$

$$R_2 = -CH_2{-}CH_2-,\ -CH_2{-}CH_2{-}O{-}CH_2{-}CH_2-,\ -CH_2{-}CH_2{-}CH_2{-}CH_2-,\ -CH_2{-}CH(OH){-}CH_2-;$$

where $n \approx 26$, $m \approx 10$, $p + q = 4–5$, $h = 1–2$.

The *B,P*-containing polyols used as chain-lengthening agents in the second step of polyurethane synthesis have close molecular weights and about the same content of terminal hydroxy groups. BPP-3 contains, along with primary hydroxy groups, also secondary groups; therefore, formation of a cross-linked polymer in the initial step of the synthesis can be expected, with a steeper rise in the viscosity of the reaction mixture. BPP-2 has a lower viscosity, which may be due to a higher mobility of oligomeric molecules containing ether fragments [5].

The reactions of MDC with BPPs were performed in DMF. The degree of conversion was evaluated from the consumption of NCO groups. With all the BPPs studied, the consumption of the isocyanate groups is determned by the amount of the BPP added and by the content of hydroxy groups in it (Figs. 1a, 1b). The higher rate of MDC consumption in the reaction with BPP-3 is apparently due to a higher content of hydroxy groups in this polyol.

The maximum molecular weight of polyurethanes prepared under conditions of migration polymerization is obtained at the [NCO]/[OH] molar ratio of 1 : 1. When the isocyanate groups are in deficiency, the MW of the polyurethanes is about 10^4 (left part of the curves, Fig. 2). Excess isocyanate groups, as shown in [6, 7], cause formation of allophanate fragments and give rise to branched structures.

The reaction temperature was varied within 333–363 K. The upper temperature limit was determined by the onset of side cross-linking reactions due to formation of allophanate branching sites, and also by the possibility of cyclization. The lower limit was determined by the polyaddition rate, which appreciably decreased below 333 K.

The variation of the concentration of NCO groups in the reaction mixture is shown in Fig. 3. Since the viscosity of the reaction mixture decreases with increasing temperature, the hydroxy groups are accessible in any position in the first step of the reaction. The gel fraction starts to be formed from the examined BPPs starts only after the residual content of NCO groups decreases to 0.6 wt % and less.

The intensity of consumption of NCO groups appreciably depends on the temperature and amount of BPP. Even at 363 K, the gel fraction content increases slowly, and the polyol preserves the weakly branched structure. Since the isocyanate groups cannot be determined by the chemical method in the final step of the polyaddition (residual content of NCO groups ≤0.6 wt %) because of the formation of a three-dimensional cross-linked structure, the completeness of consumption of the NCO groups was judged from the IR spectra of the polyurethanes.

The concentration of NCO groups was determined from the intensity of the absorption band at 2275 cm^{-1} [6, 8]. According to [9], the concentration of residual isocyanate groups in polyurethane does not exceed 0.1–0.12 wt %. The absorption bands at about 3400 and 3440 cm^{-1}, corresponding to the NH groups involved in hydrogen bonding and free NH groups, respectively, simultaneously grow in intensity. Accord-

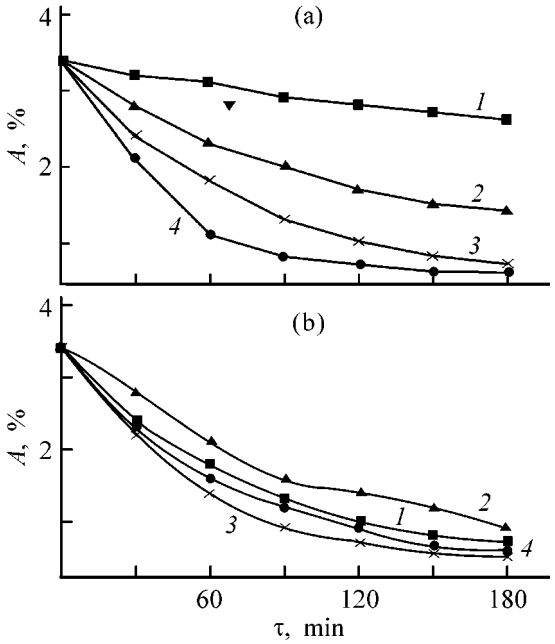

Fig. 1. Isocyanate number of the reaction mixture, *A*, vs. time τ of polyurethane synthesis. T = 343 K; c_{MDC} = 0.04 M. *B,P*-Containing polyol: (a) BPP-1, concentration, M: (*1*) 0.012, (*2*) 0.028, (*3*) 0.04, and (*4*) 0.08; (b) (*1*) BPP-1, (*2*) BPP-2, (*3*) BPP-3, and (*4*) BPP-4, all 0.04 M.

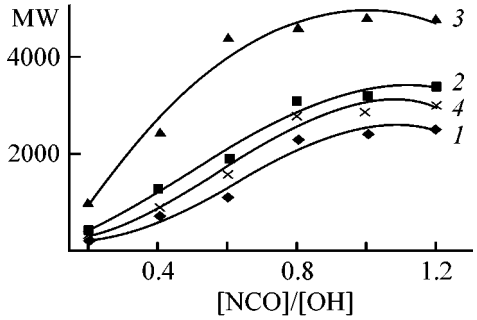

Fig. 2. MW of polyurethanes vs. the [NCO]/[OH] molar ratio. *B,P*-Containing polyol: (*1*) BPP-1, (*2*) BPP-2, (*3*) BPP-3, and (*4*) BPP-4; the same for Fig. 4.

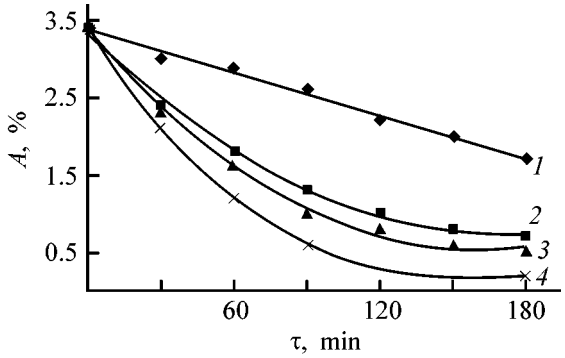

Fig. 3. Variation of the isocyanate number of the reaction mixture, *A*, with time τ. BPP-1 (0.04 M); c_{MDC} 0.04 M; temperature, K: (*1*) 333, (*2*) 343, (*3*) 353, and (*4*) 363.

Table 2. Thermodynamic parameters of polyaddition of the prepolymer to BPP

B,P-Containing polyol	E_a	$\Delta H^{\neq}$	$\Delta S^{\neq}$, J mol^{-1} K^{-1}	$\Delta G^{\neq}$, kJ mol^{-1}	*B,P*-Containing polyol	E_a	$\Delta H^{\neq}$	$\Delta S^{\neq}$, J mol^{-1} K^{-1}	$\Delta G^{\neq}$, kJ mol^{-1}
	kJ mol^{-1}					kJ mol^{-1}			
BPP-1	32.92	30.03	–152.4	109.58	BPP-3	28.61	25.71	–240.9	109.80
BPP-2	49.37	46.48	–124.5	94.90	BPP-4	30.82	27.93	–187.9	109.83

Table 3. Properties of polyurethanes based on BPPs

B,P-Containing polyol	[MDC]/[BPP] molar ratio	Gel fraction, %	σ_t, MPa	ε_{rel}	ε_{res}	σ_{tear}, MPa
				%		
BPP-1	1.4 : 1	77.4	55.2	582.1	10.8	–
	1.25 : 1	67.8	55.1	593.4	11.2	44.2
	1 : 1	57.7	50.2	610.1	13.1	–
BPP-2	1.4 : 1	78.5	50.4	527.2	15.2	–
	1.25 : 1	71.7	52.1	540.1	17.2	54.2
	1 : 1	63.5	47.3	590.2	21.4	–
BPP-3	1.4 : 1	88.4	61.7	536.4	9.2	–
	1.25 : 1	84.6	62.4	550.3	9.8	57.4
	1 : 1	72.4	57.3	600.1	10.3	–
BPP-4	1.4 : 1	78.1	52.8	495.5	8.2	–
	1.25 : 1	70.2	52.4	520.2	9.4	50.4
	1 : 1	66.4	50.3	580.4	10.2	–

ing to the IR data, the accumulation of NH groups corresponds to consumption of NCO groups, indicating that formation of allophanate and biuret structures is insignificant.

The temperature dependences of the reaction rate constants are linear in the Arrhenius coordinates (Fig. 4). From these data, we determined the thermodynamic parameters of the reaction (Table 2). The reaction rate constants were determined using a system of differential equations that describe the variation of the reactant concentrations in the initial period.

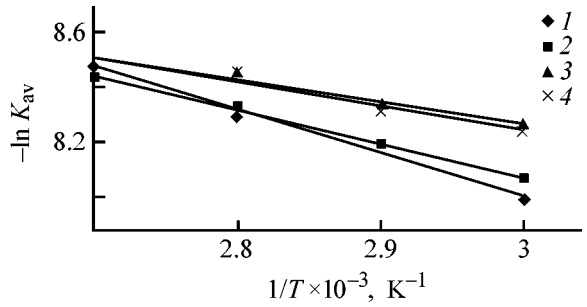

Fig. 4. Plot of $-\ln K_{av}$ vs. $1/T$ (c_{BPP} = 0.04 M).

The activation energies obtained show that the BPPs derived from 1,4-butanediol and ethylene glycol have close activities. The higher activity of the BPP derived from glycerol is apparently due to the higher content of hydroxy groups.

The IR spectra of polyurethanes derived from BPPs contain absorption bands at about 1730 (C=O), 1410–1480 (CH_2), and 3400–3500 cm^{-1} (–NH, both free and hydrogen-bonded with OH groups). Also present are the absorption bands belonging to the P=O (1230 cm^{-1}) and P–O–C (1008 cm^{-1}) groups; a medium-intensity band at about 2460 cm^{-1} is due to P–H stretching vibrations, and the band at 1456 cm^{-1} is assignable to B(III)–O stretching vibrations [10]. These bands somewhat differ in intensity and position, depending on the steric structure of BPP and the conformation of the chain fragments.

The differences in the properties of polyurethanes (Table 3) can be accounted for by structural features of the oligomers and polymers derived from them.

Table 3 shows that changing of the [MDC]/[BPP] molar ratio from 1 : 1 to 1.4 : 1 is accompanied by

Table 4. Parameters of thermal oxidative degradation of polyurethanes derived from BPPs and of a commercial polyurethane sample (PU)

Parameter	PU	BPP-1	BPP-2	BPP-3	BPP-4
Activation energy, kJ mol^{-1}	112.0	166.9	170.8	181.4	175.4
Temperature of decomposition onset, K	493	553	553	583	573
Temperature of weight loss, K:					
10%	513	583	573	593	583
20%	533	613	603	613	608
50%	558	653	643	663	663
Coke residue at 873 K, %	2	10	9	12	11

an increase in the gel fraction content; the tensile strength of the samples, σ_t, accordingly increases, and the relative elongation ε_{rel} decreases. Thus, at decreased content of BPP in the reaction mixture, MDC reacts with OH groups situated in different positions, which results in an increased cross-linking. At increased content of BPP, the gel fraction content decreases, which results in a decreased tensile strength and an increased relative elongation; consistent results were obtained in measuring the residual elongation ε_{res} (Table 3). The polyurethane derived from BPP-3 has a higher tensile and tearing strength, which is attributable to the more rigid three-dimensional structure of the polymer (maximum content of the gel fraction), due to the possibility of reaction of MDC with secondary OH groups of the glycerol moiety; this is also confirmed by the low residual elongation.

The resistance of the polymers to thermal oxidative degradation was studied under static and dynamic conditions. Figure 5 shows data on thermal oxidative degradation of BPP-based polyurethanes under static conditions; data for a commercial PU sample containing no BPP fragments are given for comparison. It is seen that the commercial sample (curve *5*) actively degrades after a short induction period. Thermal oxidative degradation of BPP-containing polyurethanes under these conditions is considerably slower (curves *1*–*4*).

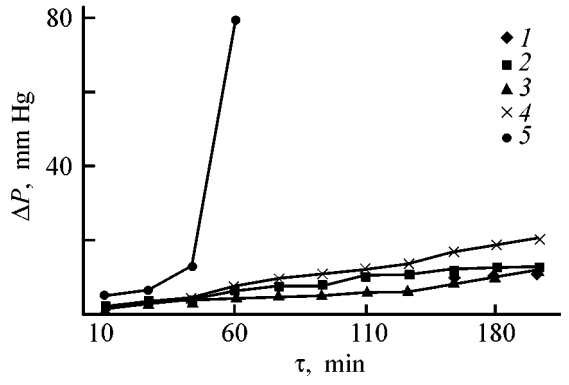

Fig. 5. Oxygen uptake ΔP vs. time τ at T = 453 K. Polyurethane derived from (*1*) BPP-1, (*2*) BPP-2, (*3*) BPP-3, and (*4*) BPP-4; (*5*) commercial PU.

The results of dynamic (TGA) experiments are given in Table 4. The BPP-based polyurethanes prepared at the [MDC] : [BPP] molar ratio of 1.2 : 1 have increased values of activation energy of thermal oxidative degradation, higher temperatures of decomposition onset and intense decomposition, and higher yield of the coke residue.

The oxygen index is 28.0–27.6% for polyurethane samples prepared at [MDC]/[BPP] ranging from 1 : 1 to 1 : 1.4 and 18% for the commercial PU sample.

CONCLUSIONS

(1) A macromolecular diisocyanate was prepared by the reaction of diphenylmethane-4,4'-diisocyanate with poly(tetramethylene ether) glycol and was then brought into reactions with *B,P*-containing polyols (chain-lengthening agents) to obtain elastic polyurethanes. The thermodynamic parameters of the polyaddition were determined.

(2) The polyurethanes synthesized exhibit improved physicomechanical properties and decreased combustibility.

REFERENCES

1. Korshak, V.V., Zamyatina, V.A., and Bekasova, N.I., *Boroorganicheskie polimery* (Organoboron Polymers), Moscow: Nauka, 1975.
2. Orlova, S.A., Bondarenko, S.N., Tuzhikov, O.I., *et al.*, Abstracts of Papers, *IV Mezhdunarodnaya konferentsiya "Polimernye materialy ponizhennoi goryuchesti"* (IV Int. Conf. "Polymeric Materials of Decreased

Combustibility"), Volgograd: Volgograd. Gos. Tekh. Univ., October 17–19, 2000, pp. 62–63.

3. Derbisher, V.E., Orlova, S.A., Bondarenko, S.N., *et al., Zh. Prikl. Khim.*, 1997, vol. 70, no. 10, pp. 1725–1728.
4. Kozlovtsev, V.A., Golovanchikov, A.B., and Bondarenko, S.N., *Ukazaniya po raschetu energii aktivatsii i poryadka reaktsii destruktsii polimerov* (Instructions on Calculation of Activation Energies and Orders of Polymer Degradation Reactions), Volgograd: Volgograd. Gos. Tekh. Univ., 1994.
5. Saunders, J.H. and Frish, K.C., *Polyurethanes. Chemistry and Technology, Part 1: Chemistry*, New York: Interscience, 1962.
6. Omel'chenko, S.I. and Kadurina, T.I., *Modifitsirovannye poliuretany* (Modified Polyurethanes), Kiev: Naukova Dumka, 1983.
7. Korshak, V.V. and Vinogradova, S.V., *Neravnovesnaya polikondensatsiya* (Nonequilibrium Polycondensation), Moscow: Nauka, 1972.
8. Badamshina, E.R., Stovbun, E.V., Lodygina, V.P., *et al., Vysokomol. Soedin., Ser. A*, 2000, vol. 42, no. 4, pp. 602–611.
9. Begishev, V.P., Ivanov, S.V., Romanova, V.A., and Karmanov, V.I., *Vysokomol. Soedin., Ser. B*, 1997, vol. 39, no. 6, pp. 1075–1077.
10. Musina, E.I., Litvinov, I.A., Balueva, A.S., and Nikonov, G.N., *Zh. Obshch. Khim.*, 1999, vol. 69, no. 3, pp. 429–436.

Russian Journal of Applied Chemistry, Vol. 77, No. 10, 2004, pp. 1721–1724. Translated from Zhurnal Prikladnoi Khimii, Vol. 77, No. 10, 2004, pp. 1735–1738.

MACROMOLECULAR CHEMISTRY AND POLYMERIC MATERIALS

Bleaching of Kraft Cellulose by the ClO_2–H_2O_2 Scheme

T. P. Shcherbakova and V. A. Demin

Institute of Chemistry, Komi Scientific Center, Ural Division, Russian Academy of Sciences, Syktyvkar, Komi Republic, Russia

Received April 22, 2004

Abstract—The influence of conditions of a two-stage treatment of deciduous and coniferous kraft cellulose (by the ClO_2–H_2O_2 scheme) on the degree of its delignification and bleaching was studied. The optimum ratio of reagents in each stage of the treatment was elucidated.

According to published data [1–3], the action of bleaching reagents on lignin involves parallel or successive attack of electrophilic and nucleophilic agents. It has been shown previously that the most efficient and selective processes of cellulose bleaching meet two conditions: first, alternation of the action of electrophilic and nucleophilic agents on the residual lignin in the successive stages of treatment; second, treatment with an electrophilic reagent in an acidic medium (acid catalysis), and with a nucleophilic reagent, in an alkaline medium (base catalysis) [4]. Along with alternation of the stages and catalysis conditions, the quantitative ratios of electrophic and nucleophilic agents in stages of treatment are very important for attaining the best whiteness and the highest degree of delignification with the minimum degradation of cellulose. In industry, the expenditure of reagents is commonly chosen empirically without considering their nature. Most of bleaching reagents-oxidants and, in particular, hydrogen peroxide in an alkaline medium, form numerous reactive species in oxidation of lignin. These include free radicals, singlet oxygen ($^{\cdot}OH$, $^{\cdot\cdot}OOH$, $^1O_2$), and hydroperoxide anion HOO^-. Free radicals induce cellulose degradation. To hamper the reactions of free radicals and to perform delignification of kraft cellulose in the stage of treatment with hydrogen peroxide by the ionic (nucleophilic) mechanism, H_2O_2 is stabilized with sodium silicate. The use of H_2O_2 for bleaching of kraft cellulose by this procedure offers some advantages over other industrially used procedures: it results in a 10–30% weaker degradation of cellulose and in a higher degree of delignification, allowing attainment of better whiteness [5, 6].

This study is aimed at examined the influence of the reagent ratio used in the successive stages of treatment (ClO_2 and H_2O_2) on the whiteness, degree of delignification, and selectivity of bleaching of coniferous and deciduous kraft cellulose.

EXPERIMENTAL

The conditions of the first stage were as follows: expenditure of chlorine dioxide 2% relative to the weight of absolutely dry cellulose, concentration of cellulose suspension 10 wt %, duration 120 min, and temperature 60°C.

The conditions of the second stage were as follows: expenditure of hydrogen peroxide 2.13, NaOH 1.3, and sodium silicate ($Na_2SiO_3 \cdot 9H_2O$) 5% relative to the weight of absolutely dry cellulose; concentration of a coniferous cellulose suspension 20 wt % (deciduous, 15 wt %); duration 120 min; and temperature 100°C. In the second mode of treatment, we used, along with H_2O_2, NaOH with the same expenditure (4% relative to the weight of absolutely dry cellulose); no sodium silicate was added.

The whiteness of the resulting samples was determined on an FKTsSh-M color comparator. In the standard methods, the reflectivity in blue light (457 nm) is taken as the degree of cellulose whiteness. A $MgSO_4$ plate whose whiteness was taken as 100% [GOST (State Standard) 30113–94] was used as a reference. The hardness of cellulose, which characterized the content of residual lignin in the sample, was determined by the method based on oxidation

Table 1. Quality characteristics of cellulose, in relation to depending on the conditions of bleaching with ClO_2–HO_2^- and ClO_2–($H_2O_2 \rightarrow O_2$)

Step I, ClO_2 expenditure, %	Step II, expenditure of reagents,* %			Cellulose			
	H_2O_2	NaOH	$Na_2SiO_3 \cdot 9H_2O$	whiteness	DP	hardness, p.u.	yield
Initial coniferous cellulose (121 p.u.)				28.0	1260	103	–
2.0	2.1	1.2	5.0	85.9	960	2.6	95.3
2.0	2.1	4.0	–	77.5	850	4.0	94.0
Initial deciduous cellulose (75 p.u.)				33.0	1170	75.0	–
1.6	2.0	1.2	5.0	85.0	950	2.2	98.1
1.6	2.0	4.0	–	78.1	870	2.4	96.5

* Expenditure of oxidants relative to the weight of absolutely dry cellulose.

Table 2. Influence of ClO_2 expenditure and treatment duration on the whiteness and hardness of coniferous cellulose*

ClO_2 expenditure, %	τ, min	Whiteness, %	Hardness, p.u.	ClO_2 expenditure, %	τ, min	Whiteness, %	Hardness, p.u.
0.00	0	28.0	103	2.00	60	47.0	24.0
1.00	60	–	38.1	2.50	80	50.1	16.3
1.54	60	–	28.4	2.75	90	53.2	12.5
1.75	60	42.9	26.2	3.12	120	57.8	9.8

* Temperature 60°C; treatment duration at high ClO_2 expenditure was increased to make complete the absorption of chlorine dioxide.

of the residual lignin in the cellulose material with $KMnO_4$ in an acidic medium, according to GOST 10070–74 (permanganate units, p.u.) [7]. The degree of polymerization of cellulose (DP) was evaluated from the viscosity of its solution in Cadoxene [8].

Here, we compare the results of treatment of non-whitened kraft cellulose with H_2O_2 by the ionic (pH ~10, in the presence of a stabilizing agent) and radical (pH ≥ 12) mechanisms in the two-stage scheme. The results are presented in Table 1.

As can be seen from Table 1, the maximum whiteness is reaches 85% for deciduous cellulose and almost 86% for coniferous cellulose (here, coniferous cellulose was treated at a higher concentration of pulp).

Then, we studied the characteristics of cellulose after the first step of treatment and the dependence of the whiteness on the ClO_2 expenditure in the range 1.0–3.1% ClO_2 relative to the weight of absolutely dry cellulose (Table 2, Fig. 1).

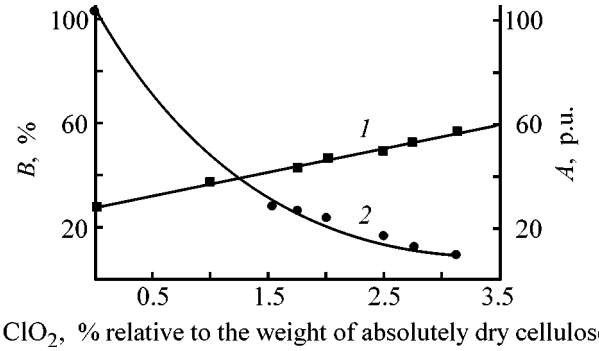

Fig. 1. Influence of ClO_2 expenditure on (*1*) whiteness *B* and (*2*) hardness *A*.

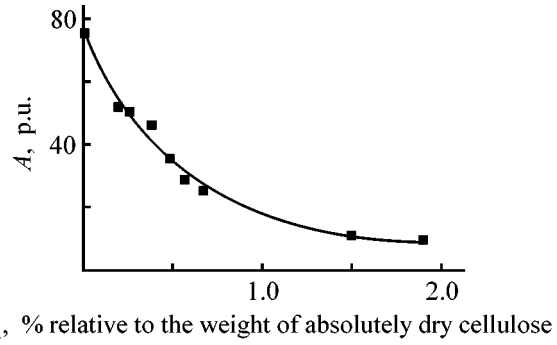

Fig. 2. Hardness of deciduous kraft cellulose *A* vs. ClO_2 expenditure for treatment (60°C, 1.5 h).

Table 3. Influence of ClO_2 expenditure on the whiteness and hardness of deciduous cellulose

ClO_2 expenditure, %	*T*, °C	τ, min	Whiteness, %	Hardness, p.u.	ClO_2 expenditure, %	*T*, °C	τ, min	Whiteness, %	Hardness, p.u.
1.00	60	60	55.5	28.0	1.50	80	120	61.7	18.0
1.50	60	120	57.2	21.5	2.00	80	120	65.9	14.7
1.75	60	120	59.8	19.0	2.50	80	120	69.1	10.1
2.00	60	120	61.3	16.8	3.12	80	120	72.0	7.7
2.50	60	120	67.9	13.4	1.50	80	120	52.3	22.0
3.12	60	120	71.6	9.8	2.00	80	120	58.0	17.9
1.50	70	120	65.5	19.3	2.50	80	120	66.4	12.3
2.00	70	120	67.8	12.5	3.12	80	120	68.7	9.2
2.50	70	120	69.6	10.7					
3.12	70	120	73.1	7.5					

Table 4. Conditions and quality characteristics of coniferous kraft cellulose whitened by the scheme ClO_2–HO_2^- *

Stage I			Stage II		Cellulose			
specific expenditure of ClO_2 ***	ClO_2 expenditure, %	ClO_2 ** expenditure	H_2O_2 expenditure, %	H_2O_2 ** expenditure	Whiteness, %	DP	Hardness, p.u.	Yield, %
0.067	1.75	4.60	2.44	5.09	83.2	890	4.3	95.0
0.077	2.00	5.26	2.13	4.45	85.9	960	2.6	95.3
0.096	2.50	6.58	1.50	3.13	84.0	1000	2.3	95.3
0.106	2.75	7.23	1.18	2.46	83.8	1040	2.3	95.3
0.120	3.12	8.21	0.72	1.50	81.4	1110	2.2	95.7

* Bleaching at a constant total expenditure of oxidants equivalent to 9.7% active chlorine relative to the weight of absolutely dry cellulose.

** Expressed in equivalent amounts of active chlorine.

*** Expressed in Kapp units.

Similar dependences were obtained for two samples of deciduous cellulose: at 60°C for the sample with a hardness of 75 p.u. (Fig. 2) and in the range 60–90°C for cellulose with a hardness of 84 p.u. (Table 3).

The results obtained suggest that there is no reason to raise the temperature of treatment with ClO_2 above 70°C. The minimum hardness of cellulose at this temperature is 7.5 p.u., and the maximum whiteness, 73.1%. In this case, the expenditure of ClO_2 is $3.12 \times 2.63 = 8.21\%$ active chlorine relative to the weight of absolutely dry cellulose.

It can be concluded from Fig. 2 that, in treatment of deciduous kraft cellulose with a hardness of approximately 75 p.u. with ClO_2, an increase in the ClO_2 expenditure above 1.5% does not result in any noticeable intensification of delignification.

The ClO_2 expenditure for the first delignification stage in treatment of kraft cellulose (both coniferous and deciduous) was estimated in the specific expenditures per unit degree of cooking by the Kapp method. The results of bleaching of kraft cellulose are presented in Table 4.

The index of cellulose whiteness has a maximum at the equivalent dose of ClO_2 equal to 55% of the total expenditure of oxidants. The maximum whiteness is 85.9%. An increase in the fraction of ClO_2 causes a noticeable increase in the degree of polymerization of cellulose (890–1110) and an insignificant increase in the yield of whitened cellulose, from 95.0 to 95.7%. Varying the fraction of ClO_2 in the total expenditure of oxidizing agents insignificantly affects the hardness of cellulose (4.3–2.2 p.u.), since virtually no lignin remains in cellulose.

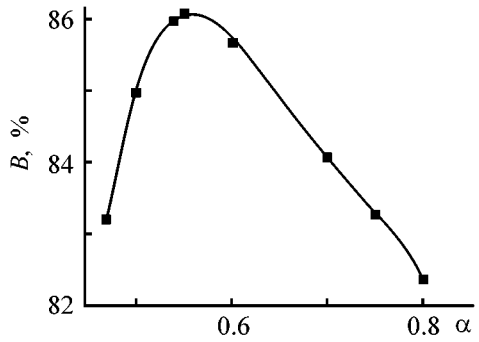

Fig. 3. Influence of the equivalent fraction of ClO_2, α, in the total expenditure of reagents on the whiteness of coniferous cellulose, *B*.

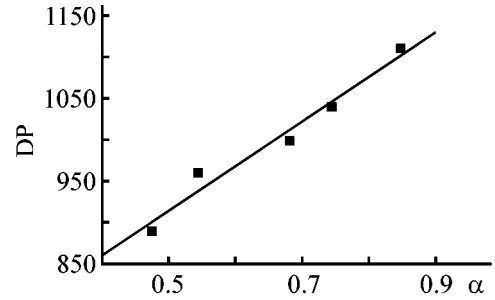

Fig. 4. DP of coniferous whitened cellulose vs. ClO_2 fraction α in the total expenditure of oxidizing agents.

The dependence of the whiteness of coniferous cellulose on the fraction of ClO_2 in the total expenditure of oxidants in two-stage bleaching is shown in Fig. 3.

The dependence of DP of the whitened coniferous kraft cellulose on the fraction of ClO_2 in the expenditure of oxidants is shown in Fig. 4. The degree of polymerization of cellulose increases in direct proportion to the fraction of ClO_2 in the total expenditure of reagents for bleaching. This confirms the well-known fact that, among bleaching reagents, ClO_2 is the most selective oxidant for lignin [9].

CONCLUSIONS

(1) Treatment of kraft cellulose with hydrogen peroxide in the presence of a stabilizing agent, sodium silicate, providing predominance of the ionic mechanism of delignification, results in a 7–8% higher whiteness of kraft cellulose, compared to that obtained under conditions favoring radical decomposition of hydrogen peroxide.

(2) The dependence of the whiteness of coniferous kraft cellulose on the fraction of chlorine dioxide in the total expenditure of reagents has a maximum. To reach the maximum whiteness, the fraction of ClO_2 should be approximately 0.5–0.6 (with respect to oxidation equivalents).

(3) The scheme of bleaching of kraft cellulose in two stages ClO_2–H_2O_2 (stabilizing agent), ensuring the whiteness index of 84% (deciduous cellulose) and 86% (coniferous cellulose), was developed.

REFERENCES

1. Gierer, J., *Holzforschung*, 1990, vol. 44, no. 5, pp. 387–394.
2. Gierer, J., *Holzforschung*, 1990, vol. 44, no. 6, pp. 395–400.
3. Gratzi, J.S., *Papier*, 1987, vol. 41, no. 3, pp. 120–130.
4. Demin, V.A., Shereshovets, V.V., and Monakov, Yu.B., *Usp. Khim.*, 1999, vol. 68, no. 11, pp. 1029–1050.
5. Demin, V.A. and German, E.V., *Khim. Drev.*, 1994, no. 3, pp. 38–45.
6. USSR Inventor's Certificate, no. 11 933 192.
7. Vlasova, T.E. and Nekhaichuk, A.D., *Tsellyuloza, Bumaga, Karton*, 1974, issue 9, p. 9.
8. Obolenskaya, A.V., Shchegolev, V.P., Akim, G.L., *et al., Prakticheskie raboty po khimii drevesiny i tsellyulozy* (Practicum of Chemistry of Wood and Cellulose), Moscow: Lesn. Prom–st., 1965.
9. Tumanova, T.A., *Fiziko-khimicheskie osnovy otbelki tsellyulozy* (Physicochemical Foundations of Cellulose Bleaching), Moscow: Lesn. Prom–st., 1984, p. 215.

Russian Journal of Applied Chemistry, Vol. 77, No. 10, 2004, pp. 1725–1728. Translated from Zhurnal Prikladnoi Khimii, Vol. 77, No. 10, 2004, pp. 1739–1742.

MACROMOLECULAR CHEMISTRY AND POLYMERIC MATERIALS

Polychronous Kinetics of Oxidative Delignification of Coniferous Kraft Cellulose with Hydrogen Peroxide

T. P. Shcherbakova, V. A. Demin, and A. I. Mikhailov

Institute of Chemistry, Komi Scientific Center, Ural Division, Russian Academy of Sciences, Syktyvkar, Komi Republic, Russia

Institute of Problems of Chemical Physics, Russian Academy of Sciences, Chernogolovka, Moscow oblast, Russia

Abstract—The kinetics of oxidative delignification of coniferous kraft cellulose with hydrogen peroxide in the temperature range 60–100°C was studied.

A study of kinetic features of oxidative delignification of kraft cellulose is of interest for improvement of the cellulose production process, in particular, cellulose bleaching, in which molecular chlorine, a source of dangerous pollution of the environment with toxic chlorophenols and polychlorodibenzodioxins, is still used in the Russian Federation.

New approaches based on the methods of polychromous kinetics, which take into account the dynamics of molecular motion and structural micro- and nanoheterogeneity of a matrix, have been developed recently [1–3] for kinetic studies of processes in solid and viscous media, among them polymeric materials. As applied to the kinetics of delignification of wood (cooking) and industrial cellulose (bleaching), the methods of polychromous kinetics have been developed for description of procedures of nitric acidic, soda, and kraft cooking and bleaching [4–7]. As chemical bonds and reaction centers in lignin (component of such a polymer composite as unbleached cellulose), are widely diverse, the formulation and correct solution of the direct kinetic problem for oxidative delignification is difficult. Therefore, it is appropriate to use in this stage of the study a phenomenological formalistic kinetic approach. The results obtained in studying the kinetics of oxidative delignification of deciduous kraft cellulose with hydroxoperoxide anions have been published previously [8]. Here, we studied the oxidative delignification of coniferous kraft cellulose produced by the Neusiedler Syktyvkar Joint-Stock Company.

Depending on the treatment conditions in alkaline medium, H_2O_2 reacts with the residual lignin localized in a cellulose fiber by two mechanisms: free-radical (in the absence of stabilizing agents) and ionic [9]:

$$H_2O_2 + OH^- \rightarrow HO_2^- + H_2O. \quad (1)$$

For lignin to be oxidized by the second mechanism, free-radical decomposition of H_2O_2 is suppressed by adding Na_2SiO_3. In this case, as shown previously [10], delignification of kraft cellulose under conditions of bleaching proceeds with a higher degree and selectivity and minimum degradation of cellulose.

Oxidative delignification of coniferous kraft cellulose with a hardness of 103 permanganate units (by Bjerkman) was carried out in an 88 mM H_2O_2 solution at pH 10.2 ± 2 in the presence of a stabilizing agent ($Na_2SiO_3 \cdot 9H_2O$ in the form of a solution with an expenditure of 5% relative to absolutely dry cellulose) with the liquor ratio of 200 : 1. We used a 20-fold excess of H_2O_2 with respect to lignin. Order of adding reagents: NaOH solutions (before thermostat), Na_2SiO_3, and H_2O_2. The temperature range was from 333 K to 373 K. A flask filled with cellulose and calculated amounts of water and alkali was placed in a temperature-controlled water bath. The bath was heated to the working temperature, Na_2SiO_3 and H_2O_2 were added and vigorously stirred to be mixed with the pulp; simultaneously with their addition, a stopwatch was switched on. The samples were with-drawn at certain intervals, rapidly washed on a porous glass filter, and dried. Then, the content of residual lignin in the resulting samples was determined on a KFK-3 photometer [11]. The experimental data were normalized to the initial content of lignin in kraft cellulose (Table 1).

The kinetic curves of delignification of kraft coniferous cellulose in bleaching with stabilized H_2O_2 are shown in Fig. 1.

1070-4272/04/7710-1725 © 2004 MAIK "Nauka/Interperiodica"

Table 1. Relative content of residual lignin in cellulose in relation to the treatment time and temperature

Time, s	Relative content of lignin in cellulose at indicated temperatures, °C (K)				
	60 (333)	70 (343)	80 (353)	90 (363)	100 (373)
0	1.00	1.00	1.00	1.00	1.00
60	0.95	0.89	0.89	0.86	0.80
300	0.90	0.88	0.86	0.80	0.80
900	0.84	0.78	0.79	0.75	0.68
1800	0.76	0.72	0.70	0.65	0.54
3600	0.69	0.64	0.60	0.52	0.36
7200	0.65	0.57	0.50	0.39	0.24
10 800	0.65	0.50	0.45	0.29	0.18
14 400	0.64	0.46	0.40	0.26	0.15
18 000	0.61	0.45	0.37	0.24	0.14

As can be seen from Fig. 1, in delignification of coniferous kraft cellulose, the reaction does not go to completion (kinetic termination).

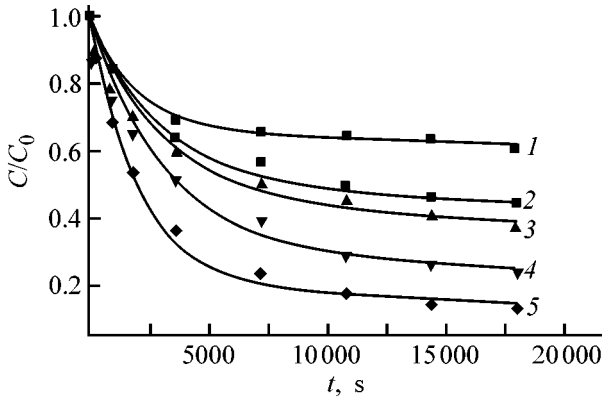

Fig. 1. Kinetic curves of delignification of kraft coniferous cellulose in bleaching with stabilized hydrogen peroxide. Temperature, K: (*1*) 333, (*2*) 343, (*3*) 353, (*4*) 363, and (*5*) 373; the same for Fig. 3. C_0 = 103 permanganate units; (*t*) time.

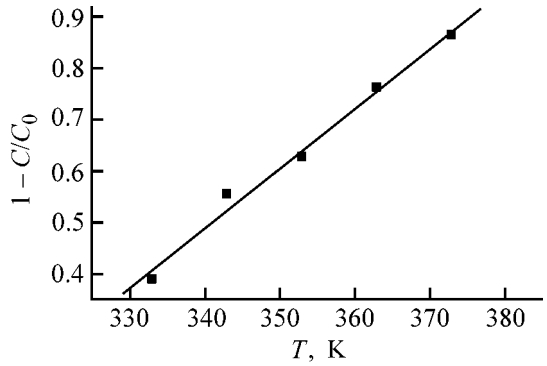

Fig. 2. Limiting degree of conversion $\theta_\infty = 1 - C/C_0$ vs. the process temperature *T*.

The reaction termination under isothermal conditions and the linear dependence of the limiting degree of conversion on temperature (defrosting curve, Fig. 2) allow a kinetic analysis of cellulose delignification by the polychronous kinetics method. The main concepts of the relevant theory, derivation of Eq. (2), and equations for calculations are given in [1–6].

$$n(t, T) = n_0 \int_{\ln K_{min}}^{\ln K_{max}} f(\ln K) G(K, t) d \ln K \approx n_0 \int_{\ln K_{min}}^{\ln K^*} f(\ln K) d \ln K, \quad (2)$$

where $n(t, T)$ is the amount of particles that mainly enter into the reaction within time *t* at a temperature *T*; $f(\ln K)$, the distribution function; $G(K, t)$, function describing the process kinetics in the isokinetic area, where $K \approx$ const; *E*, activation energy; K_0, preexponential factor; and $K(E) = K_0 \exp(-E/RT)$, rate constant. In the simplest case, *G* has the form $G_1 = \exp(-K_1 t)$ and $K^* = 1/t$.

The dependence $\theta = (1 - C/C_0)$–*T* is close to linear, which suggests a uniform (rectangular) distribution of ensembles of lignin macromolecules with respect to $\ln K$.

If the dependence $f(\ln K)$ has an almost rectangular shape in the range ($\ln K_{min}$, $\ln K_{max}$), then, under the condition of "strong polychronousness" (when $t \ll 1$, $tK_{max} \gg 1$, and the parameter of nonequivalence $S = \ln(K_{max}/K_{min}) > 1$ [2, 6]), we have

$$C(t, T)/C_0 = [\ln(K_{min}/K_{max})]^{-1} \ln K_{min} t. \quad (3)$$

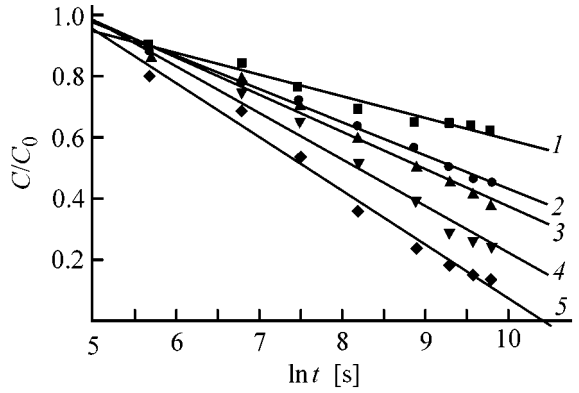

Fig. 3. Linearization of the kinetic curves of delignification of coniferous kraft cellulose in bleaching with hydrogen peroxide in the coordinates of the equation of polychromous kinetics.

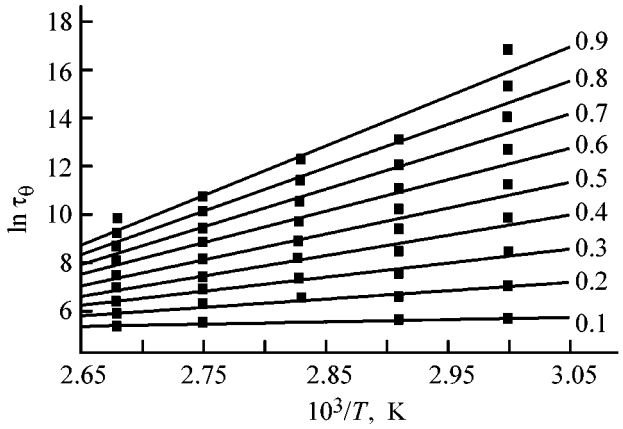

Fig. 4. Arrhenius plot of the characteristic time τ_θ for delignification of coniferous kraft cellulose with hydrogen peroxide at θ = 0.1–0.9.

The semilog plots of the delignification kinetics are shown in Fig. 3. It can be seen that most of experimental points are satisfactorily fitted by a straight line in the coordinates C/C_0–ln t.

With a horizontal section of the family of semilog plots in the coordinates C/C_0–ln t through the points corresponding to $C(t, T)/C_0 = \theta$, where θ is the lignin content corresponding to the considered portion of the kinetic curve, we obtain the temperature dependence ln τ_0–$1/T$ (Table 2).

Here, τ_0 is a characteristic time of the process in the given elementary group at a given degree of component removal θ; it is determined as an instant of time at which the kinetic curve for temperature T_i intercepts the axis $C/C_0 = \theta$.

A set of values of the characteristic time τ_θ, plotted in the Arrhenius coordinates ln τ_θ–$1/T$, allows us to obtain a set of activation energies $E(\theta)$ and preexponential factors $K_0(\theta)$ (Fig. 4, Table 2) for the spectrum of the rate constants of the process. From $E(\theta)$ and $K_0(\theta)$, we can obtain the inverse functions $\theta(E)$ and $\theta(\ln K)$, which are in fact joint integral distribution functions for the spectrum of kinetic constants of the process (Table 3).

The resulting spectra of effective activation energies E_{eff} and preexponential factors $\ln K^0_{\text{eff}}$ for delignification of coniferous kraft cellulose in bleaching with stabilized H_2O_2 are distributed in a wide range of values, which reflect a number of chemical and physical factors contributing to delignification and characterize the heterogeneity of properties of the lignocellulose matrix.

As shown previously [4–6], delignification is typically limited by the diffusion removal of the reaction products from the lignocellulose matrix. In this case, strongly overestimated values of E_{eff} and K^0_{eff} with the linear compensation dependence $\ln K^0_{\text{eff}}$–E_{eff}

Table 2. Values of characteristic time of conversion τ_θ

$10^3/T$, K^{-1}	ln τ_θ at θ				
	0.1	0.2	0.3	0.4	0.5
3.00	5.6	5.6	8.4	9.8	12.4
2.91	5.7	6.6	7.5	8.4	9.4
2.83	5.8	6.6	7.4	8.2	9.0
2.75	5.6	6.2	6.9	7.4	8.2
2.68	5.3	5.9	6.4	7.0	7.6

Table 3. Distribution of ensembles of residual lignin macromolecules with respect to activation energies and preexponential factors

θ	E_{eff}, kJ mol^{-1}	ln K^0_{eff}, s^{-1}
0.1	8.2 ± 5	–2.8 ± 2
0.2	28.7 ± 4	3.3 ± 1
0.3	48.9 ± 10	9.3 ± 2
0.4	70.3 ± 9	15.8 ± 3
0.5	89.8 ± 13	21.6 ± 4
0.6	110.1 ± 17	27.6 ± 6
0.7	130.6 ± 21	33.7 ± 7
0.8	154.6 ± 24	39.8 ± 8
0.9	171.2 ± 28	45.8 ± 10

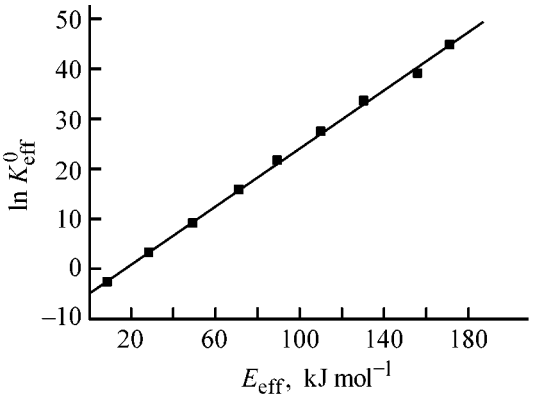

Fig. 5. Compensation dependence: (K^0_{eff}) preexponential factor and (E_{eff}) effective activation energy.

(Fig. 5) commonly originate from the so-called compensation effect in polymers at temperatures close to the softening point of the matrix [5], in particular, in transition of the lignocellulose matrix into the viscoelastic state, when the true values of activation energy E, governing the potential barriers for diffusion, begin to decrease with heating [$\partial E(T)/\partial T < 0$]. In this case, E and K_0 are determined according to the generalized Arrhenius–Voevodskii equation [12]:

$$E_{eff} = E - T(dE/dT),$$

$$\log K^0_{eff} = \log K_0 - (1/R)(dE/dT). \quad (4)$$

Thus, we made an adequate kinetic description of the process in wide time (60–18 000 s) and temperature (60–100°C) intervals in oxidative delignification of coniferous kraft cellulose with bleaching with stabilized H_2O_2 as bleaching agent. The experimental kinetic data and polychronous kinetic approaches allow a description and a forecast of delignification processes in microheterogeneous lignocellulose matrix. As can be seen from Fig. 1, the kinetic points evaluated from Eq. (3) are in good agreement with the experimental data.

CONCLUSIONS

(1) It was established in a study of oxidative delignification of kraft coniferous cellulose with hydrogen peroxide at 60–100°C that the process is polychronous and does not go to completion. Residual lignin macromolecules are kinetically nonuniform; they are characterized by a spectrum of activation energies and rate constants in the range from $\ln K_{min}$ (s^{-1}) equal to 48.3–171 to $\ln K_{max}$ (s^{-1}) equal to 4.6–8 (kJ mol)/RT. It was shown that $\ln K^0_{eff}$ and E_{eff} are related by a linear compensation dependence.

(2) It was foun that the kinetic nonequivalence of active centers, estimated from the parameter $S = \ln(K_{max}/K_{min})$ and E_{eff} value for all the ensembles of lignin macromolecules, decreases with increasing temperature. This suggests that there occurs a temperature rearrangement (defrosting) of the polymer lignocellulose matrix, accompanied by increase in the maximum degree of conversion, corresponding to kinetic termination of delignification of coniferous kraft cellulose in bleaching with hydrogen peroxide.

REFERENCES

1. Emanuel', N.M. and Buchachenko, A.L., *Khimicheskaya fizika molekulyarnogo razrusheniya i stabilizatsii polimerov* (Chemical Physics of Molecular Degradation and Stabilization of Polymers), Moscow: Nauka, 1988.
2. Mikhailov, A.I., Bol'shakov, A.I., Gol'danskii, V.I., and Lebedev, Ya.S., *Fiz. Tverd. Tela*, 1972, vol. 13, no. 4, pp. 1172–1179.
3. Kuzina, S.I. and Mikhailov, A.I., *Eur. Polym. J.*, 1990, vol. 26, no. 1, pp. 105–116.
4. Bel'kova, L.P., Gromov, V.S., and Mikhailov, A.I., *Khim. Drev.*, 1980, no. 6, pp. 50–58.
5. Bel'kova, L.P., Gromov, V.S., and Mikhailov, A.I., *Khim. Drev.*, 1980, no. 6, pp. 59–64.
6. Mikhailov, A.I., Kaplun, L.D., Kuzina, S.I., *et al.*, *Khim. Inter. Ustoich. Razv.*, 1993, no. 1, pp. 323–330.
7. Mikhailov, A.I., Demin, V.A., Kaplun, L.D., *et al.*, *Proc. Fifth Eur. Workshop on Lignocellulose and Pulp*, Aveiro (Portugal): Univ. Aveiro, 1998, pp. 79–82.
8. Karmanov, A.P. and Demin, V.A., *Khim. Inter. Ustoich. Razv.*, 1996, no. 4, p. 298.
9. Demin, V.A., Shershovets, V.V., and Monakov, Yu.B., *Usp. Khim.*, 1999, vol. 68, no. 11, pp. 1–22.
10. Demin, V.A., Ipatova, E.U., and Syutkin, V.N., USSR Inventors' Certificate, no. 1 193 192, *Bull. Izobret.*, 1985, no. 47.
11. Vlasova, T.E. and Nekhaichuk, A.D., *Tsellyulosa, Bumaga, Karton*, 1974, issue 9, p. 9.
12. Voevodskii, V.V., *Fizika i khimiya elementarnykh khimicheskikh protsessov* (Physics and Chemistry of Elementary Chemical Processes), Moscow: Nauka, 1969.

Russian Journal of Applied Chemistry, Vol. 77, No. 10, 2004, pp. 1729–1732. Translated from Zhurnal Prikladnoi Khimii, Vol. 77, No. 10, 2004, pp. 1743–1746.

MACROMOLECULAR CHEMISTRY AND POLYMERIC MATERIALS

Biochemical and Physicochemical Treatment of Flax Fibers

I. I. Shamolina, A. M. Bochek, N. M. Zabivalova, E. N. Vlasova, B. Z. Volchek, and A. P. Sinitsin

St. Petersburg State University of Technology and Design, St. Petersburg, Russia
Institute of Macromolecular Compounds, Russian Academy of Sciences, St. Petersburg, Russia
Moscow State University, Moscow, Russia

Received February 20, 2004

Abstract—Conditions were found for separating concomitant substances from cellulose in short flax fibers by treatment with surfactant and enzyme solutions. The chemical composition of the treated fibers was analyzed, and their structural organization was studied by IR Fourier spectroscopy.

The rise in production of linen textiles, observed in recent years, is accompanied by accumulation of wastes, such as short flax fibers and hardwood part of flax pedicels (boon). Short flax fibers can be used in textile industry instead of cotton fibers and in chemical industry as a raw material alternative to cotton linter.

There are two approaches to use of flax fibers in textile industry. The first approach is to develop appropriate equipment, which is very expensive. The second approach is to modify the properties of flax fibers (thickness, length, etc.) with the aim to process them on the existing equipment developed for cotton fibers.

One of the main problems that arises in utilization of flax fibers in chemical industry is their treatment to remove concomitant substances. Flax fibers differ from cotton fibers in the geometric parameters and chemical composition. Flax fibers, compared to cotton fibers, contain a considerably greater amount of fats, pectins, hemicelluloses, and lignin [1]. The concomitant substances can be removed by chemical, biochemical, and physicochemical methods.

Lignin can be removed from flax fibers by alkali treatment (by analogy with production of cellulose from wood). Pectin substances can be removed or recovered with aqueous solutions of mineral and organic acids, or of alkalis [2]. Fats and waxy substances are removed by treatment of fibers with organic solvents (ethanol, ethanol–benzene mixture) [3]. These compounds can also be removed by treatment of fibers with enzyme solutions. The latter procedure is preferable from the environmental viewpoint.

It is of scientific and practical interest to develop processes for treatment of bast fibers with the minimum use of organic solvents. In this study, we made a comparative analysis of biochemical and physicochemical procedures for removal of lignin, fats, and pectin substances from flax fibers with the aim to obtain purified fibers suitable for use in textile and chemical industries.

EXPERIMENTAL

As starting material we used short flax fibers with the degree of polymerization (DP) of cellulose equal to 1700, as determined viscometrically from the intrinsic viscosity [η] of cellulose in Cadoxen: $[\eta] = 7.0 \times 10^{-3}(DP)^{0.9}$ [4].

To separate concomitant substances from cellulose, we used Stearox nonionic surfactant and Celloviridin G2kh complex preparation (Promferment Ltd., preparation no. 1-67.2). Celloviridin is an ultraconcentrate of the culture medium of *Trichoderma reesei* fungus producing a complex of carbohydrases: cellullases, β-glucanases, xylanases, and pectinases. The CMCase (cellulase) activity of the preparation was 3000 units ml^{-1}; β-glucanase activity, 4100 units g^{-1}; xylanase activity, 2900 units g^{-1}; and polygalacturonase (pectinase) activity, 500 units g^{-1}. The activities were determined from the initial rate of hydrolysis of carboxymethyl cellulose (CMC), barley β-glucan,

1070-4272/04/7710-1729 © 2004 MAIK "Nauka/Interperiodica"

Composition of the initial flax fibers before and after treatment with surfactant and Celloviridin G2kh solutions

Treatment	Component composition of fiber, wt %				
	cellulose	pectins	fats, waxes	other hemicelluloses	lignin
No treatment	68.8	5.4	5.2	11.1	9.5
0.1 M acetate buffer, pH 5.0	68.2	4.9	4.9	12.7	9.3
Celloviridin G2kh (1 ml/100 ml buffer)	67.8	3.5	4.6	15.5	8.6
Celloviridin G2kh (2 ml/100 ml buffer)	67.7	3.4	4.1	16.2	8.5
Celloviridin G2kh (4 ml/100 ml buffer)	66.9	3.2	4.3	17.3	8.3
Stearox surfactant	70.4	4.3	3.7	12.8	8.8

birch xylan, and polygalacturonic acid, respectively (according to the procedures described in [5]). The fibers with Celloviridin G2kh were treated at 50°C and pH 5.0 (0.1 M acetate buffer) for 1 h. Celloviridin G2kh was used as 1, 2, or 4 vol % aqueous solutions. The fibers were treated with a surfactant solution at the boiling point for 1 h.

The short fibers were preliminarily analyzed to determine the component composition (see table). The cellulose content was determined by the Kürschner–Hoffer method; lignin content, by the Komarov method [3]; fat and moisture content, according to [2, 3]; and pectin content, by the calcium pectate method [2]. After treatment of the fibers with surfactant and Celloviridin solutions, the fibers were washed with distilled water and dried at 105°C, and then the content of cellulose and residual impurities (lignin, pectins, fats, hemicelluloses) was determined.

The structural changes occurring in flax fibers upon treatment with surfactant and enzyme solutions were monitored by IR Fourier spectroscopy. The spectra of cotton fibers pelletized with KBr were recorded on a Bruker FS-88 spectrometer.

The chemical compositions of fibers after various treatments are listed in the table. Since Celloviridin G2kh was taken in a buffer solution, we also checked in a blank experiment whether treatment with a straight buffer solution (0.1 M acetate buffer) affects the component composition of the fibers; no significant changes were revealed upon such a treatment.

Treatment of the flax substrate with Celloviridin G2kh solutions makes higher the content of hemicelluloses, which is due to the capability of enzymes to break down not only components characteristic of the given enzyme but also cellulose and concomitant compounds. Treatment with a surfactant solution involves a minimum degradation of cellulose. Treatment of flax fibers with enzyme solutions results in a partial removal of lignins, pectins, and waxes. With increasing concentration of Celloviridin G2kh working solutions, the lignin content decreases insignificantly, whereas the content of hemicelluloses grows from 11.1 to 17.3 wt %. After treatment of the fibers with the 4 vol % enzyme solution, the DP of cellulose decreased from 1700 to 1320. The Celloviridin G2kh solutions are more effective in removal of pectins.

Treatment with a surfactant solution results in the most complete removal of fats; lignin and pectins are removed partially. The content of hemicelluloses slightly increases. The results of chemical analysis, indicating that treatment with the enzyme and surfactant solutions results in a partial removal of fats and pectins, are confirmed by IR spectroscopy.

Figure 1a shows the IR Fourier spectra of the initial flax fibers and those treated with Celloviridin G2kh solutions. The IR spectrum of purified (whitened) cotton linter is shown for comparison.

Purified cotton cellulose exhibits a broad absorption band in the range 3000–3700 cm^{-1} (free OH groups of the polymer and those involved in intra- and intermolecular hydrogen bonds) and a band at 2900 cm^{-1}, which belongs to the CH_2 and CH groups of the oligomers; in the spectrum of pure cellulose, the latter band is symmetrical [6].

The IR spectra of crude wood cellulose and cellulose from flax pedicels contain characteristic lignin absorption bands at 1600, 1500, and 850 cm^{-1} [6]. In the samples of flax fibers, only the band at 820–830 cm^{-1} is well defined. The absence of bands at 1600 and 1500 cm^{-1} may be caused by considerably lower content of lignin in flax fibers, compared to the hardwood part (boon), and also by differences in the chemical composition of lignin in wood celluloses of different origins. The IR spectra allow qualitative detection of impurities in cellulose.

The characteristic bands of pectins are those at 1740 (free COOH groups of polygalacturonic acid),

1615, and 1410 cm^{-1} (symmetric and antisymmetric stretching vibrations of ionized COO^- groups). In the range 2850–2950 cm^{-1}, pectins exhibit one or two broad bands associated with CH_2 and CH groups [7]. Figure 1b shows on the enlarged scale the characteristic fragments of the IR spectra (1500–1800 and 2800–3000 cm^{-1}).

The IR spectrum of crude flax fibers contains an absorption band at 1740 cm^{-1}, which suggests the presence of pectins, and bands at 2920 and 2850 cm^{-1}, assignable to pectins and fatty acids. The presence of lignins may be judged by comparison of the IR spectra of crude flax fibers and whitened cotton cellulose. In contrast to cotton, all samples of flax fibers have IR spectra that contain a band at 820–850 cm^{-1}, which suggests the presence of lignin.

Treatment of fibers with a surfactant solution (Figs. 1a, 1b, spectrum *3*) affects the shape of the band at 2900 cm^{-1} (it becomes more symmetrical); the bands at 1740 and 820 cm^{-1} are preserved, which suggests that pectins and lignin are removed incompletely. Pectin substances are present not only in intercellular laminas but also in the primary wall of a single fiber. Therefore, more severe conditions are required to remove pectins binding single fibers of flax into bundles. Such a treatment, however, may cause appreciable degradation of cellulose.

The IR spectra of fibers treated with Celloviridin G2kh solutions of various concentrations only slightly differ from that of the initial flax fibers. The decreased intensity of bands characteristic of lignin, pectins, and fats is due to partial removal of these substances. The increased content of cellulose in the fibers is suggested by a more symmetrical shape of the band at 2900 cm^{-1} (for purified cellulose, this band is almost symmetrical [6]).

From the IR data, we can calculate the so-called crystallinity index of cellulose I_{cr} as the intensity ratio of the bands at 1372 and 2900 cm^{-1}, I_{1372}/I_{2900} [8]. This ratio correlates with the degree of ordering (or cristallinity) evaluated by X-ray diffraction. Since the cellulose samples were prepared for IR measurements under standard conditions (pelletization with KBr), this procedure can be used to reveal changes in the structural ordering of cellulose macromolecules after treatment of the fibers with various agents.

To evaluate the contribution of pectin substances to the absorption at 2900 cm^{-1}, used for calculating I_{cr}, we measured the IR spectra of milled purified cotton cellulose, pectin, and a model blend of cotton cellulose with 5 wt % pectin (Fig. 2). The bands at 2915

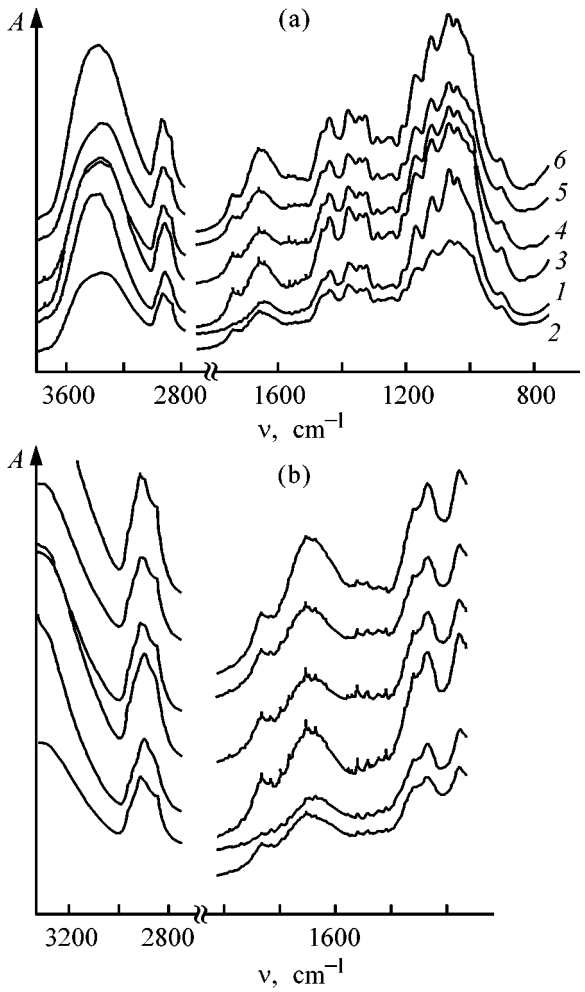

Fig. 1. IR Fourier spectra of (*1*) cotton linter fibers, (*2*) crude flax fibers, (*3*) flax fibers treated with Stearox surfactant, and (*4*–*6*) flax fibers treated with a solution of 1, 2, and 4 ml of Celloviridin G2kh, respectively, in 100 ml of 0.1 M acetate buffer (pH 5.0). (a) Total spectrum and (b) characteristic fragments (enlarged). (*A*) Absorption and (ν) wave number; the same for Fig. 2.

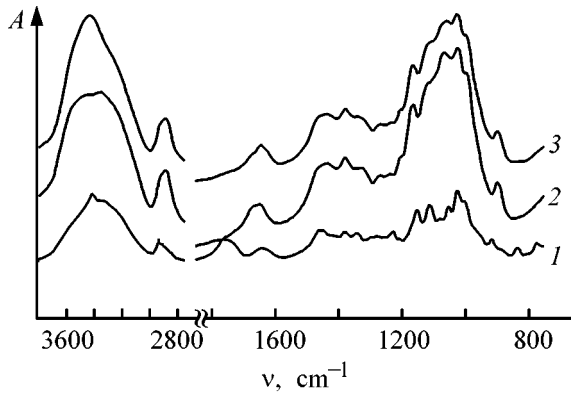

Fig. 2. IR Fourier spectra of (*1*) purified pectin, (*2*) cotton linter, and (*3*) a model blend of cotton linter with 5 wt % pectin.

and 2950 cm^{-1} observed in the IR spectrum of pectin do not make an appreciable contribution to the absorption at 2900 cm^{-1} in the spectrum of the blend. Indeed, the I_{cr} values calculated from the IR spectra of pure cellulose (0.44) and its blend with pectin (0.43) virtually coincide.

The crystallinity index of whitened cotton cellulose and crude flax fibers (Fig. 1a) is 0.64 and 0.54, respectively. After a treatment of the fibers with a surfactant solution, I_{cr} increased to 0.71. A treatment of the fibers with the enzyme solution (1 ml/100 ml buffer) increased I_{cr} to 0.83. However, as the enzyme concentration was raised further (2 and 4 ml/100 ml buffer), I_{cr} decreased to 0.64 and 0.60, respectively. The increase in I_{cr} upon treatment of flax fibers with surfactant and 1 vol % Celloviridin G2kh solutions and the decrease in I_{cr} upon treatment of the fibers with more concentrated enzyme solutions suggest that two processes occur. Partial removal of fats, pectins, and lignin results in that I_{cr} increases. However, further increase in the enzyme concentration accelerates the degradation of cellulose, which leads to disordering of the polymer macromolecules and formation of hemicelluloses having mainly amorphous structure. Thus, in treatment of flax fibers with surfactant and Celloviridin 2Kh solutions, it is necessary to find the optimal conditions under which the concomitant substances are partly removed from the fiber surface with minimum degradation and disordering of the cellulose macromolecules.

CONCLUSION

Treatment of short flax fibers with solutions of Stearox surfactant and Celloviridin G2kh complex enzyme preparation causes partial removal of concomitant substances (fats, pectins, lignin) from cellulose. However, treatment of fibers with Celloviridin G2kh solutions also causes an increase in the content of hemicelluloses and disordering of cellulose macromolecules.

REFERENCES

1. Bochek, A.M., Zabivalova, N.M., Shamolina, I.I., and Grishanov, S.A., *Zh. Prikl. Khim.*, 2002, vol. 75, no. 9, pp. 1549–1554.
2. *Spravochnik khimicheskoi tekhnologii obrabotki l'nyanykh tkanei* (Handbook of Chemical Technology of Treatment of Linen Fabrics), Fridlyand, G.I., Ed., Moscow: Legkaya Industriya, 1973.
3. *Prakticheskie raboty po khimii drevesiny* (Practical Works on Wood Chemistry), Nikitin, V.M., Ed., Moscow: Lesnaya Prom–st., 1965.
4. Bolotnikova, L.S., Danilov, S.N., and Samsonova, G.I., *Zh. Prikl. Khim.*, 1966, vol. 39, no. 1, pp. 176–180.
5. Sinitsyn, A.P., Gusakov, A.V., and Chernoglazov, V.M., *Biokonversiya lignotsellyuloznykh materialov* (Bioconversion of Lignocellulose Materials), Moscow: Mosk. Gos. Univ., 1995.
6. Zhbankov, R.G., *Infrakrasnye spektry tsellyulozy i ee proizvodnykh* (Infrafed Spectra of Cellulose and Its Derivatives), Minsk: Nauka i Tekhnika, 1964.
7. Aimukhammedova, G.B., Alieva, Dzh.E., and Shelukhina, N.P., *Svoistva i primenenie pektinovykh sorbentov* (Properties and Use of Pectin Sorbents), Frunze: Ilim, 1984.
8. *Cellulose and Cellulose Derivatives*, Bikales, N.M. and Segal, L., Eds., New York: Wiley–Interscience, 1971. Translated under the title *Tsellyuloza i ee proizvodnye*, Moscow: Mir, 1974, vol. 1, pp. 214–235.

Russian Journal of Applied Chemistry, Vol. 77, No. 10, 2004, pp. 1733–1735. Translated from Zhurnal Prikladnoi Khimii, Vol. 77, No. 10, 2004, pp. 1747–1749.

BRIEF COMMUNICATIONS

Thermodynamic Characteristics of the System $NaNO_2$–$NaNO_3$

V. I. Glazov, G. P. Dukhanin, M. Kh. Dkhaibe, and V. A. Losev

Volgograd State Technical University, Volgograd, Russia

Received May 11, 2004

Abstract—The activities and activity coefficients of the components of the system $NaNO_2$–$NaNO_3$, obtained from experimental saturated vapor pressures measured at 798, 823, and 848 K, were used to calculate the total and excess partial molar Gibbs energies $\Delta\overline{G}_i$, $\Delta\overline{G}_i^{ex}$, entropies $\Delta\overline{S}_i$, $\Delta\overline{S}_i^{ex}$, and total relative and excess thermodynamic properties ΔG, ΔG^{ex}, ΔS, ΔS^{ex} of the system.

Formation of a melt from pure components is accompanied by a change in the thermodynamic functions that characterize the given system. Of particular interest are changes in the Gibbs energy (ΔG), enthalpy (ΔH), and entropy of mixing (ΔS). If these quantities are known, the structure of the system and forces of ion–ion interaction between the components can be characterized.

The activities α_i and activity coefficients γ_i of the components of the system, determined by measuring the saturated vapor pressures [1–3], were used to calculate the total partial molar and excess partial molar Gibbs energies [4] for sodium nitrite and nitrate.

$$\Delta\overline{G}_i = 2.3RT \log \alpha_i,$$

$$\Delta\overline{G}_i^{ex} = 2.3RT \log \gamma_i.$$

The results of the calculation are listed in Table 1.

Table 1. Total and excess partial molar Gibbs energies and entropies of $NaNO_2$ and $NaNO_3$ in melts with$NaNO_3$ and $NaNO_2$, respectively

x, mol %	$\Delta\overline{G}_i$			$\Delta\overline{G}_i^{ex}$			$\Delta\overline{S}_i$			$\Delta\overline{S}_i^{ex}$		
	kJ mol^{-1}, at indicated temperature, K						J mol^{-1} K^{-1}, at indicated temperature, K					
	798	823	848	798	823	848	798	823	848	798	823	848
$NaNO_2$:												
10	20.55	19.58	19.46	5.30	3.84	3.26	25.75	23.79	22.95	6.64	4.67	3.84
20	14.63	14.49	14.37	4.09	3.38	2.93	18.33	17.61	16.95	5.13	4.11	3.46
40	9.19	8.70	8.48	3.07	2.53	2.03	11.52	10.57	10.00	3.85	3.07	2.39
50	7.14	6.80	6.63	2.55	2.16	1.75	8.95	8.26	7.82	3.20	2.62	2.06
60	5.43	5.16	5.03	2.09	1.70	1.49	6.80	6.27	5.93	2.62	2.06	1.75
80	2.66	2.44	2.41	1.16	0.96	0.83	3.33	2.96	2.84	1.45	1.17	0.98
90	1.16	1.12	1.05	0.49	0.43	0.29	1.45	1.36	1.24	0.61	0.52	0.34
$NaNO_3$:												
90	1.31	1.27	1.15	0.63	0.57	0.36	1.64	1.54	1.36	0.79	0.69	0.42
80	2.76	2.55	2.32	1.24	1.02	0.75	3.46	3.10	2.74	1.55	1.24	0.88
60	7.14	6.61	5.77	3.72	3.05	2.12	8.95	3.16	6.80	4.66	3.71	2.50
50	9.19	8.95	7.59	4.59	4.09	2.82	11.52	10.87	8.95	5.75	4.97	3.33
40	11.37	11.35	10.05	5.45	5.02	3.60	14.25	13.79	11.85	6.83	6.10	4.25
20	17.81	16.70	16.36	7.16	5.78	5.03	22.32	20.29	19.29	8.97	7.02	5.93
10	23.47	23.32	21.84	8.21	7.59	5.63	29.41	28.33	25.75	10.29	9.22	6.64

1070-4272/04/7710-1733 © 2004 MAIK "Nauka/Interperiodica"

Table 2. Total and excess integral molar Gibbs energies and entropies of the system $NaNO_2$–$NaNO_3$

x_{NaNO_2}, mol %	$-\Delta G$			$-\Delta G^{ex}$			ΔS			ΔS^{ex}		
	kJ mol^{-1}, at indicated temperature, K						J mol^{-1} K^{-1}, at indicated temperature, K					
	798	823	848	798	823	848	798	823	848	798	823	848
10	3.73	3.10	2.98	1.10	0.90	0.65	4.05	3.47	3.52	1.38	1.09	0.76
20	5.13	4.94	4.73	1.81	1.49	1.19	6.43	6.00	5.58	2.27	1.81	1.40
40	7.96	7.45	6.85	3.46	2.84	2.08	9.98	6.12	8.08	4.34	3.45	2.46
50	8.17	7.88	7.11	3.57	3.13	2.29	10.24	9.57	8.39	4.48	3.80	2.71
60	7.81	7.64	7.04	3.43	2.01	2.33	9.78	9.28	8.31	4.30	3.68	2.74
80	5.69	5.29	5.20	2.36	1.92	1.67	7.13	6.23	6.13	5.95	2.34	1.97
90	3.39	3.34	3.13	1.26	1.15	0.82	4.25	4.06	3.69	1.58	1.39	0.97

The resulting total and excess partial molar Gibbs energies were used to calculate the corresponding integral values

$$\Delta G = x_1\Delta\bar{G}_1 + x_2\Delta\bar{G}_2,$$

$$\Delta G^{ex} = x_1\Delta\overline{G_1^{ex}} + x_2\Delta\overline{G_2^{ex}},$$

where x_1 and x_2 are the mole fractions of $NaNO_2$ and $NaNO_3$ in the binary system.

The results of this calculation are listed in Table 2 and shown in Fig. 1a. The dashed line in Fig. 1a (curve *5*) represents the change in the integral molar Gibbs energy of the ideal system at a temperature of 798 K.

The partial molar total and excess entropies of mixing of $NaNO_2$ and $NaNO_3$ in their binary system were calculated [5]

$$\Delta\bar{S}_i = -2.3R\log\alpha_i,$$

$$\Delta\overline{S_i^{ex}} = -2.3R\log\gamma_i.$$

The results of this calculation are listed in Table 1.

These values of $\Delta\bar{S}_i$ and $\Delta\overline{S_i^{ex}}$ were used to calculate the integral molar total and excess entropies [5] for the system $NaNO_2$–$NaNO_3$

$$\Delta S = x_1\Delta\bar{S}_1 + x_2\Delta\bar{S}_2,$$

$$\Delta S^{ex} = x_1\Delta\overline{S_1^{ex}} + x_2\Delta\overline{S_2^{ex}}.$$

The results of this calculation are listed in Table 2.

Figure 1b shows the integral molar total and excess entropies for the system $NaNO_2$–$NaNO_3$. The dashed curve *5* shows how the integral entropy of mixing of the ideal system [5] varies at a temperature of 798 K.

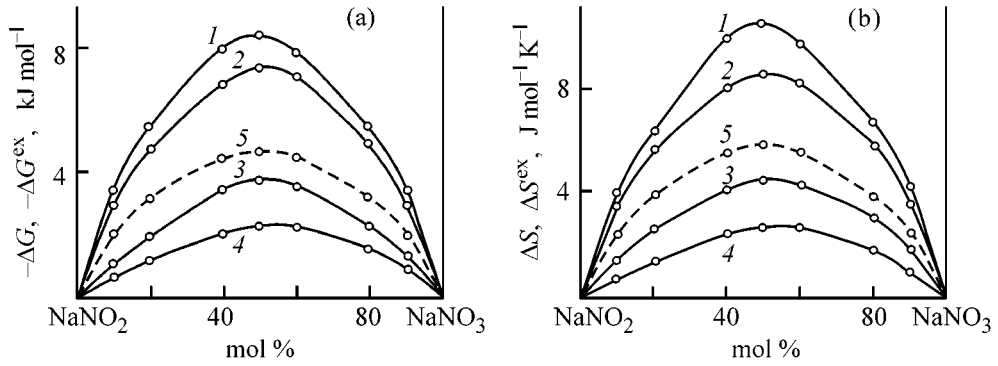

Fig. 1. (a) (*1*, *2*) Total and (*3*, *4*) excess integral molar Gibbs energies ΔG, ΔG^{ex} and (b) entropies of mixing ΔS, ΔS^{ex} for the system $NaNO_2$–$NaNO_3$. Curve *5*: (a) integral molar Gibbs energy and (b) entropy of mixing for the ideal system at 798 K. Temperature (K): (*1*, *3*) 798 and (*2*, *4*) 848.

As can be seen from Fig. 1a, the curves that represent the integral total and excess molar Gibbs energy exhibit negative deviations from the ideal behavior and a minimum at 50 mol %. The integral curves of the relative and excess molar entropies of mixing (Fig. 1b) exhibit positive deviations from the properties characteristic of the ideal system and a maximum at the same composition.

Such a behavior of the integral thermodynamic systems indicates that the arrangement of component species in the system under study is ordered to a certain extent.

The system $NaNO_2$–$NaNO_3$ shows larger negative deviations from ideality, compared with the previously studied system $NaNO_2$–KNO_3 [6]. Probably, this circumstance can be accounted for by the fact that the components $NaNO_2$ and $NaNO_3$ form a continuous series of solid solutions and a chemical compound, $2NaNO_2 \cdot 3NaNO_3$ [7], which does not decompose completely upon melting, but still exists in the form of complex ions [8].

REFERENCES

1. Glazov, V.I., Golod, V.F., and Golovanov, P.S., *Zh. Prikl. Khim.*, 1984, vol. 57, no. 6, pp. 2351–2352.
2. Glazov, V.I., Dukhanin, G.P., and Dkhaibe, M.Kh., *Zh. Prikl. Khim.*, 2003, vol. 76, no. 9, pp. 1445–1447.
3. Glazov, V.I., Dukhanin, G.P., Dkhaibe, M.Kh., and Losev, V.A., *Zh. Prikl. Khim.*, 2004, vol. 77, no. 2, pp. 335–337.
4. Morachevskii, A.G., *Termodinamika zhidkikh splavov* (Thermodynamics of Liquid Alloys), Leningrad: Len. Politekhn. Inst. im. M.I. Kalinina, 1981.
5. Morachevskii, A.G. and Sladkov, I.B., *Termodinamicheskie raschety v metallurgii* (Thermodynamic Calculations in Metallurgy), Moscow: Metallurgiya, 1993.
6. Glazov, V.I., Dukhanin, G.P., and Dkhaibe, M.Kh., *Zh. Prikl. Khim.*, 2003, vol. 76, no. 3, pp. 373–375.
7. Posypaiko, V.I., Alekseeva, E.A., and Vasina, N.A., *Diagrammy plavkosti solevykh sistem* (Fusibility Diagrams of Salt Systems), Moscow: Metallurgiya, 1979, part 3, p. 164.
8. Lantratov, M.F. and Alabyshev, A.F., *Zh. Prikl. Khim.*, 1953, vol. 26, no. 3, p. 263.

Russian Journal of Applied Chemistry, Vol. 77, No. 10, 2004, pp. 1736–1738. Translated from Zhurnal Prikladnoi Khimii, Vol. 77, No. 10, 2004, pp. 1750–1752.

BRIEF COMMUNICATIONS

Some Aspects of the Adhesion Compatibility of Hydrophobic and Hydrophilic Medicinal Materials

G. U. Ostrovidova, E. V. Zamyslov, and A. V. Makeev

St. Petersburg State Technological Institute, St. Petersburg, Russia

Received March 31, 2004

Abstract—The hydrophilicity and hydrophobicity of surfaces was studied after their treatment with solutions of NaOH and polyethylene.

The initial stage in design of medicinal composite materials consists in solving the problem associated with ensuring the adhesion compatibility of their constituent ingredients having different structures and surface properties, e.g., polymer–polymer, polymer–carbon, polymer–metal [1, 2].

The aim of this study was to solve the problem of adhesion compatibility between the hydrophobic surface of the composite based on polysiloxane of medical purity ($PDMS_{med}$) and bulk-modified with graphite of S-1 brand [3] and the hydrophilic polyvinyl alcohol (PVC) film coating deposited on the surface of the composite in an electric field [4].

EXPERIMENTAL

In order to enhance the biocompatibility of the composite [3], a hydrogel PVC coating was formed on its surface in an ac electric field with ultralow frequency (meander-type signal) [4, 5]. A polyvinyl alcohol of medical purity [TU (Technical Specification) 605-05-26–75) was used for this purpose. As cross-linking agent served glutaric aldehyde (GA) and boric acid. Glycerol was introduced to ensure plasticity.

The coating was formed in an electric field with the simultaneous immobilization of biologically active (trypsin, a proteolytic enzyme), medicinal (heparin, an anticoagulant; various antibiotics), and other substances, which made it possible to extend considerably the range of medical-biological properties of the starting material [4, 5].

To improve the adhesion of the hydrophilic polymer film coating to the hydrophobic surface of the composite, it was preliminarily treated with 5 and 10 M aqueous solutions of NaOH (special-purity grade) at 60–70°C for 2 h or with a 0.1–0.5% aqueous solution of polyethylene imine (PEI). Then the samples were washed with distilled water and dried at room temperature for 24 h.

X-ray photoelectric spectra (XPS) of the composite were measured on an ESCA LAB-5 spectrophotometer with excitation by Al_{K_α} radiation (Mekhanobr Research-and-Production Association). The accuracy with which the peak positions were determined was ± 0.1 eV. The accuracy of quantitative analysis was 10%.

The adhesion of the hydrogel polymeric film coating to the surface of the composite was evaluated by the method of lattice cuts [6] [GOST (State Standard) 15140–78].

As revealed in a study of the adhesion, raising the concentration of the NaOH solution used to treat the surface of the composite to more than 5 M has no essential effect on the adhesion compatibility of the materials in question, even though this leads to a considerable increase in the number of reactive hydroxy groups on the surface and in their penetration into the material. In addition, use of a 10 M NaOH solution causes changes in the microprofile of the surface of the composite, i.e., makes more pronounced its roughness, which adversely affects the hemocompatibility of the material.

1070-4272/04/7710-1736 © 2004 MAIK "Nauka/Interperiodica"

Table 1. Properties of the composite upon treatment of its surface with NaOH and PEI solutions (content of graphite 50 wt parts)

Material	Contact wetting, angle, deg	Electrical resistance, Ω m
Initial	72 ± 2	10^7
After treatment:		
with a 5 M NaOH solution	65 ± 2	10^6
with 0.5% PEI solution	70 ± 2	10^8

A preliminary treatment of the surface of the composite with PEI or NaOH solutions markedly raises the adhesion of the PVC film coating to the surface of the composite to 1 point.

The changes in some surface properties of the composite upon its treatment with NaOH or PEI solutions are illustrated by the data in Table 1. It can be seen that the electrical conductivity of the material increases by an order of magnitude upon its treatment with a 5 M NaOH solution, the wettability of the surface of the composite also grows. At the same time, treatment with a PEI solution makes higher its electrical resistance and changes its hydrophobicity only slightly. In this case, the adhesion of the hydrogel polymeric coating to the hydrophobic surface of the composite increases because of the hydrogen bonding and action of van der Waals forces [7, 8].

To reveal the reasons for the adhesion compatibility of the hydrophobic and hydrophilic surfaces, samples of the material were studied by XPS spectroscopy. XPS spectra of the surface of the composite, treated with a 5 M NaOH solution, are shown in the figure. For all of the samples, a peak at E = 532 eV is observed, which is related to the ≡Si–O–Si≡ bond (Figure, spectra *1–3*). Treatment with a NaOH solution gives rise to new peaks at E = 533 and 531 eV, which are associated with the ≡Si–OH and ≡Si–O–Na groups, respectively (see figure, spectrum *2*). In the course of a 2-h treatment of the composite, the following reactions occur on its surface [1]:

$$\equiv Si–O–Si\equiv + NaOH \rightarrow \equiv Si–OH + \equiv Si–O–Na, \quad (1)$$

$$\equiv Si–O–Na + H_2O \rightarrow \equiv Si–OH + NaOH. \quad (2)$$

The decrease in the intensity of the peak (E = 533 eV) associated with the ≡Si–OH group, observed upon deposition of a hydrogel layer on the surface of the composite (figure, spectrum *3*), suggests that polyvinyl alcohol chemically interacts, in the presence of glutaric anhydride, with hydroxy groups on the surface of the material, which appear upon treatment with a NaOH solution [9, 10].

The thus formed material was tested, as also were the starting components (composite and PVC film), for thromboresistance in *in vitro* experiments. The hemocompatibility of the surface of the materials obtained was evaluated by the method of activated partial thromboplastin time (APTT) [11]. A study of the thromboresistance of the resulting material by measuring the rate of coagulation of a plasma containing the basic coagulating proteins, brought in contact with various surfaces, demonstrated that materials with a hydrogel coating on a hydrophobic substrate do not activate thrombus formation (Table 2). The $PMDS_{med}$ shows an insignificant coagulation. The composite has better parameters, and the presence of a hydrophilic surface-type polymeric structure that is compatible with the hydrophobic surface of the composite makes this effect less pronounced, i.e., improves the hemocompatibility. This fact indicates that polymeric structures based on water-soluble polymers exert a positive influence on the interaction of blood with a foreign material. The hemocompatibility of the material can be considerably improved by introducing trypsin into

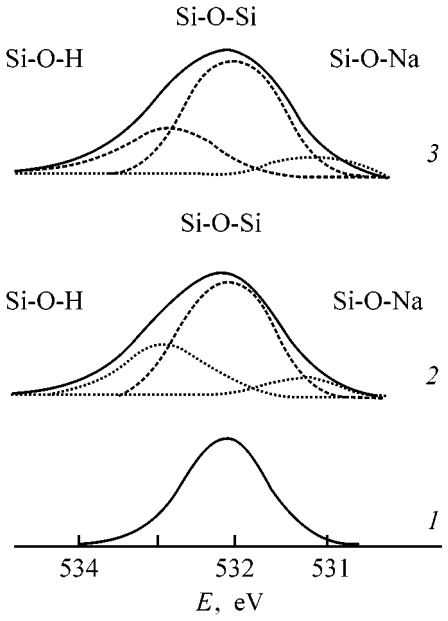

XPS spectra of composites. (*E*) Binding energy. (*1*) Before treatment, (*2*) after treatment with NaOH, and (*3*) with a PVC coating.

Table 2. Results of a study of a polysiloxane caoutchouc and the composite in combination with a hydrogel film coating (content of graphite 50 wt parts)

Material	APTT parameters, s	
	before incubation with the material	after incubation
$PDMS_{med}$, initial composite:	45	35
initial	45	44
treated with PEI, with a PVC+H_3BO_3 coating containing trypsin	45	55
treated with 5 M NaOH	45	>600
solution, with PVC coating containing heparin		
PVC film with heparin, formed in the electric field of a silicon wafer	45	>600

film coatings, and the effect exerted by the presence of heparin, an anticoagulanting agent, is apparent.

CONCLUSIONS

(1) It was established that the appearance of reactive hydroxy groups on the surface of the composite upon its preliminary treatment with a NaOH solution, and the resulting increase in hydrophilicity and electrical conductivity, make it possible to ensure the adhesion compatibility of the constituent ingredients of the composite obtained, which have different structural and surface properties, without changing the physicomechanical properties of the material.

(2) The compatibility of the hydrophilic and hydrophobic surfaces is provided by chemical bonding in the case of treatment of the latter with a NaOH solution in the presence of glutaric aldehyde in the polymeric coating and by van der Waals forces in treatment with a polyethylene imine solution.

(3) The materials obtained were tested in *in vitro* experiments and demonstrated a high level of thromboresistance.

ACKNOWLEDGMENTS

The authors thank A.V. Shchukarev and O.A. Bueva for assistance in certain experiments.

The study was supported by a Presidential Grant of the Russian Federation "Leading Scientific Schools of Russia," project NSh 2236.2003.3 "Chemistry of Highly Organized Substances."

REFERENCES

1. Miyaji, F., Iwai, M., and Kokubo, T., *J. Materials Sci., Materials in Medicine*, 1998, vol. 9, no. 2, pp. 61–65.
2. Ha, S.W., Eckert, K.Z., and Wintermantel, E., *J. Materials Sci., Materials in Medicine*, 1997, vol. 8, no. 12, pp. 891–896.
3. Zamyslov, E.V., Klochkov, V.I., and Ostrovidova, G.U., *Zh. Prikl. Khim.*, 1997, vol. 70, no. 7, pp. 1212–1214.
4. Ostrovidova, G.U., Makeev, A.V., and Shamtsian, M.M., *J. Materials Sci. Eng.*, 2003, pp. 23, pp. 545–550.
5. Ostrovidova, G.U., Makeev, A.V., Zamyslov, E.V., and Terukov, E.I., *J. Macromol. Symp.*, 1988, vol. 136, pp. 131–137.
6. Koryakina, M.I., *Laboratornyi praktikum dlya ispytaniya lakokrasochnykh materialov i pokrytii* (Laboratory Manual for Testing of Paint-and-Varnish Materials and Coatings),. Moscow: Khimiya, 1974.
7. Ostrovidova, G.U. and Kopylov, V.B., *Izv. Vyssh. Uchebn. Zaved., Khim. Khim. Tekhnol.*, 1986, vol. 29, no. 11, pp. 94–97.
8. Lopes Garcia, I., Batiston, M.J., and Mei, H.I., *Mat. 5th Eur. Polym. Federation Symp. on Polymeric Materials*, Basel, Switzerland, 1994, October 9–12, p. 234.
9. Ushakov, S.N., *Polivinilovyi spirt i ego proizvodnye* (Polyvinyl Alcohol and Its Derivatives), Moscow: Akad. Nauk SSSR, 1960, vols. 1, 2.
10. *Polimery meditsinskogo naznacheniya* (Medicinal Polymers), Manabu, S., Ed., Moscow: Meditsina, 1981.
11. Bueva, O.A., Zamyslov, E.V., and Ostrovidova, G.U., *Patofiziologiya mikrotsirkulyatsii i gemostaza* (Pathophysiology of Microcirculation and Hemostasis), Petrishchev, N.N., Ed., St. Petersburg: SPb. Gos. Med. Univ., 1998, pp. 447–453.

Russian Journal of Applied Chemistry, Vol. 77, No. 10, 2004, pp. 1739–1741. Translated from Zhurnal Prikladnoi Khimii, Vol. 77, No. 10, 2004, pp. 1753–1755.

BOOK REVIEWS

Kozin, L.F. and Volkov, S.V., *Khimiya i tekhnologiya vysokochistykh metallov i metalloidov* (Chemistry and Technology of High-Purity Metals and Metalloids), in 2 vols.: vol. 1, *Khimicheskie i elektrokhimicheskie metody glubokoi ochistki* (Chemical and Electrochemical Methods for Deep Purification, Kiev, Naukova dumka, 2002, 540 pp.; vol. 2, *Fiziko-khimicheskie i kristallizatsionnye metody glubokoi ochistki* (Physicochemical and Crystallization Methods for Deep Purification), Kiev: Naukova dumka, 2003, 350 pp.

The two-volume monograph devoted to methods for obtaining high-purity metals was written by professor L.F. Kozin and S.V. Volkov, an academician of the National Academy of Sciences of the Ukraine, who are well-known Ukrainia specialists in this field. High-purity metals and metalloids largely determine the development of quite a number of new fields of science and technology and branches of industry. The world's technological practice has produced a vast body of evidence concerning methods for obtaining high-purity metals and metalloids (with total impurity content of less than 1×10^{-5} wt %.

The first volume of the monograph comprises a foreword, introduction, three chapters, bibliographic list, and subject index. The foreword written by corresponding members of the National Academy of Sciences of the Ukraine, A.G. Belous and O.G. Zarubitskii, points to the importance of the problem under discussion. Rather stringent requirements to the purity of materials are imposed by nuclear and semiconductor industries: the total content of impurities should be on the order of 10^{-5}–10^{-6} and 10^{-7}–10^{-9} wt %, respectively. Of particular importance is the purity of metals for nanotechnologies, which are being developed all over the world. The brief introduction (pp. 5 and 6) outline the variety of elements whose deep purification is discussed in the first and second volumes of the monograph.

The first chapter of the first volume (pp. 7–33) presents a general information. It considers the main application fields of high-purity metals and metalloids, requirements imposed on their purity, accepted classifications of high-purity materials, and methods for analytical determination of their impurity content. Inversion voltammetry, whose theoretical foundations are being successfully developed in our country by A.G. Stromberg and his school, neutron-activation analysis, various spectral methods, and mass-spectrometry are discussed in the chapter. The second chapter (pp. 34–161) describes chemical methods for deep purification of metals and metalloids. These methods are based on chemical reactions in which substances are converted, with the accompanying impurities separated to give a high-purity main substance. A high separating capacity is characteristic of processes in which nonvolatile and volatile hydrides are formed, reactions of formation of organometallic compounds, and carbonyl processes. A considerable attention is given to halide processes; a hydrochemical technique for purification of simple and compound substances is considered. The theoretical foundations of all these methods are presented and particular examples are given.

The third chapter of the first volume (pp. 162–492) occupies in it the central position and contains evidence about the electrochemical methods for deep purification of metals and metalloids. The efficiency of deep purification by methods of this group primarily depends on the difference in the electrode potentials between the main component and the accompanying impurities. The same factor strongly affects the choice of an appropriate electrochemical refining technique. The authors analyze in detail the standard electrode potentials in aqueous solutions for a great number of electrochemical systems and discuss the influence exerted by various factors on the potentials. The kinetics of processes involving many-electron electrode reactions is described for specific examples. Anodic and cathodic processes involving bismuth, indium,

1070-4272/04/7710-1739 © 2004 MAIK "Nauka/Interperiodica"

gallium, tin, and iron and their ions in various states of oxidation are discussed in ample detail. The authors are mostly based on the results of their own studies. The fundamental aspects of electrodeposition and anodic dissolution of lead in various electrolytes and the electrochemical behavior of mercury have been described previously in special monographs [Kozin, L.F. and Morachevskii, A.G., *Fiziko-khimiya i metallurgiya vysokochistogo svintsa* (Physical Chemistry and Metallurgy of High-Purity Zinc), Moscow: Metallurgiya, 1991, 224 pp.; Kozin, L.F., *Fiziko-khimiya i metallurgiya vysokochistoi rtuti i ee splabvov* (Physical Chemistry and Metallurgy of High-Purity Mercury and Its Alloys), Kiev: Naukova dumka, 1992, 564 pp.] and are virtually not discussed in the book under consideration. The available published data on the kinetics and mechanism of discharge and ionization of zinc and on the electrochemical behavior of copper, silver, cadmium, palladium, rhodium, and gold are analyzed. It should be noted that the electrodeposition and dissolution of metals forming ions in various oxidation states have been the subject of a special monograph written by Kozin [Kozin, L.F., *Electroosazhdenie i rastvorenie mnogovalentnykh metallov* (Electrodeposition and dissolution of Polyvalent Metals), Kiev: Naukova dumka, 1989, 464 pp.]. The third chapter contains evidence about the kinetics and mechanism of the cathodic dissolution of metalloids: selenium, tellurium, arsenic, germanium, and antimony. In cathodic polarization of these elements in aqueous solutions, they are mostly reduced to hydrides. For example, selenium and its compounds can be reduced at the cathode in acid and alkaline media to give selenide ions Se^{2-}. The process of cathodic dissolution is strongly affected by the pH of the medium, material of the electrode, and potential of the cathode.

The same chapter (vol. 1, chapter 3) discusses the separation coefficients in purification of metals by electrochemical methods and, in particular, purification of metals by single-stage electrolysis with solid electrodes (zinc, cadmium, indium, thallium, silver, gold, palladium). To purify some metals, it is advisable to use singlestage electrolysis with liquid electrodes. Mercury is the most frequently used as a solvent for producing a liquid anode. This is a basis of the so-called "amalgam metallurgy." Also possible is use of gallium or low-melting formulations composed of a number of metals. Methods of the amalgam metallurgy can be used to purify zinc, cadmium, gallium, indium, and thallium to a rather high extent. In refining of tin, it is advisable to use the Wood alloy as a solvent for producing a liquid anode. The final part of the chapter is devoted to many-stage processes of deep purifica-tion of metals by electrolysis with liquid bipolar electrodes (zinc, cadmium, mercury, gallium, indium, thallium, tin, lead, bismuth). A special section of the chapter is concerned with deep purification of metals by reactive electrolysis. This technique is based on binding of impurities into electrochemically inactive compounds upon addition of some elements, as a rule, nonmetals. For example, introduction of sulfur, selenium, tellurium, or silicon into a metal being purified (lead, bismuth, cadmium, tin, indium, etc.) results in that the impurities contained in the metal form chalcogenides or silicides, being thus converted into an electrochemically inactive state. The impurities bound into chemical compounds are virtually not involved in the transfer of a metal being refined from the anode to the cathode.

Application of hydride electrochemical methods is discussed for the case of selenium, arsenic, and germanium.

The bibliographic lists (pp. 493–533) are composed separately for each of the three chapters. The total number of references in the first volume of the monograph is 1707. The volume ends with a subject index.

The second volume of the monograph has the same structure as the first volume: it comprises an introduction, two chapters, conclusion, bibliographic list, and subject index. The introduction (pp. 3 and 4) notes that the authors were the first to generalize and systematize the evidence concerning the theory and practice of deep refining of metals and metalloids by distillation, rectification, sublimation, and crystallization methods. In view of the involvement of metal systems in a liquid state in these processes, the authors found it appropriate to pay a considerable attention to a thermodynamic description of liquid alloys based on lead, cadmium, zinc, indium, tin, and antimony. The first chapter (pp. 5–210) is named "Physical methods for deep purification of metals and metalloids." Taking into account the existence of quite a number of monographs and spacious reviews devoted to the subject, Kozin and Volkov chose for consideration, among a great number of physicochemical methods, only techniques based on distillation, rectification, and sublimation. They described in detail the theory and technology of deep purification of zinc, cadmium, selenium, and tellurium by distillation and rectification; deep purification of arsenic by sublimation, distillation, and rectification; and purification of scandium, yttrium, and rare-earth metals by sublimation and distillation.

The second chapter of the second volume (pp. 211–320) is devoted to crystallization methods for separa-

tion and purification. These techniques are based on recrystallization of the starting component from melts (melt–solid) in a certain (optimal) temperature mode. The crystallization methods are mostly applied to metals and metalloids in the final stage of purification (finishing purification). The authors describe the theoretical and technological aspects of the crystallization purification; purification of lead, aluminum, gallium, indium, and noble metals; and crystallization purification of metalloids: sulfur, selenium, tellurium, arsenic, and antimony.

In the conclusion (pp. 321–323), the authors once again call attention to the complexity of processes used for obtaining high-purity metals and metalloids. It is commonly accepted that every subsequent decrease in the content of impurities in a high-purity material by an order of magnitude leads to an increase in its production cost by a factor of 2–5. The conclusion is also given in English (pp. 324–326). The bibliographic list for chapters of the second volume containes 808 references.

The monograph by Kozin and Volkov presents a detailed analysis of a wide variety of methods for obtaining high-purity metals and metalloids. In most detail are described the electrochemical behavior of metals in aqueous media and electrochemical refining techniques. At the same time, an impression is created, when reading the book, that part of the material presented could be excluded from the monograph without any noticeable sacrifice of understanding of the processes under consideration. Taking into account the earlier review and monographic publications of the authors, it would be appropriate to present in a considerably more concise form the section devoted to the kinetics and mechanism of electrode processes involving polyvalent metals (pp. 173–298) in the first volume. In the second volume, the thermodynamic evidence (pp. 7–93) given without any authors' concept are virtually unused in the subsequent presentation. These and some other curtailments would make the monograph more concise and closer to the technological practice.

After the year of 1991, the science experiences severe difficulties in all countries of the former Soviet Union, including the Ukraine. The major contribution by the authors in these not simple conditions deserves a deep appreciation. The book is of interest for a wide audience of specialists who deal with electrochemistry of aqueous solutions and production of high-purity metals and metalloids by various methods.

A. G. Morachevskii

Russian Journal of Applied Chemistry, Vol. 77, No. 11, 2004, pp. 1743–1745. Translated from Zhurnal Prikladnoi Khimii, Vol. 77, No. 11, 2004, pp. 1761–1763.

INORGANIC SYNTHESIS AND INDUSTRIAL INORGANIC CHEMISTRY

Pyrochemical Processing of Tungsten- and Cobalt-Containing Raw Materials

O. G. Zarubitskii, V. P. Orel, and B. F. Dmitruk

Vernadsky Institute of General and Inorganic Chemistry, National Academy of Sciences of Ukraine, Kiev, Ukraine

Received June 30, 2004

Abstract—A method for processing of secondary tungsten- and cobalt-containing materials is suggested. The optimal parameters of the processes involved and the consumption of chemicals are determined.

Processing of secondary tungsten-containing raw materials, and primarily the recovery of tungsten and cobalt from worn-out drilling and cutting tools, is an urgent problem.

Hydrometalurgical, pyrometallurgical, physical, and electrochemical methods for processing of tungsten–cobalt alloys of the VK type are known [1–5]. These processes are low-intensive, have low selectivity, and involve discharge of noxious substances (nitrogen oxides, hydrogen fluoride) into the atmosphere. The existing techniques are mainly applicable to processing of lump scrap of cutting tools, but show low efficiency in recovery of tungsten and cobalt from worn-out roller drill bits used in mining and geological prospecting. Chemical and electrochemical methods performed in melts based on alkali metal hydroxides show promise for processing of raw materials of this kind [6–12].

Of particular interest is recovery of tungsten from a tungsten-containing alloy by oxidative calcination. It has been suggested to perform this procedure at 780–820°C with subsequent leaching-out of tungsten compounds [13]. A technique for recovery of tungsten from lumps of high-alloy materials has been patented [14]. This technique consists in heating of the starting product in air at 800–900°C for 48 h followed by treatment of the oxidized products with a solution of an alkali metal hydroxide in an autoclave at 140–195°C for 6–10 h. The total duration of the process is 54–64 h.

EXPERIMENTAL

The method suggested for processing of worn-out roller drill bits (drilling tools) is based on oxidation of a hard composite alloy (tungsten carbide with a cobalt binder) in an air flow, mechanical disintegration of the brittle oxidized product, and removal of its residual amounts from sockets in an alkali melt.

Samples of the same type, 200–250-g fragments of roller drill bits, were used in the experiments. Each sample contained two picks made of a WC–Co hard-alloy formulation. Part of the samples contained picks 12 mm in diameter, embedded to a depth of 10 mm, and part, picks 8 mm in diameter, embedded to a depth of 5 mm. The roller drill bit from which the samples were cut was completely worn out: the picks were completely worn virtually to the level of the steel base. The samples were treated in a muffle furnace with apertures for in- and outflow of air. Air was pumped with a compressor through the aperture in the furnace at a flow rate of 10–30 l h^{-1}. The hydroxide melt was fused in a corundum crucible.

Worn-out roller drill bits were heated to 950–1050°C and kept in the furnace for a time sufficient for oxidation of the hard-alloy picks. The components of the hard alloy are oxidized by the reactions

$$WC + 2.5O_2 = WO_3 + CO_2, \quad (1)$$

$$CO_2 + Co = CoO + CO. \quad (2)$$

The oxidation product is formed as a kind of "columns" or "flowers" growing from the sockets and occupies a volume exceeding by a factor of 6 that of the initial hard alloy (Fig. 1). The above temperature interval is the optimal. At lower temperatures, the oxidation rate markedly decreases. The same occurs as the temperature is raised from 1050 to 1100°C, and upon further increase in temperature, the oxidation of

1070-4272/04/7711-1743 © 2004 MAIK "Nauka/Interperiodica"

(a)

(b)

Fig. 1. Roller drill bit (a) before and (b) after oxidative calcination at 1000°C.

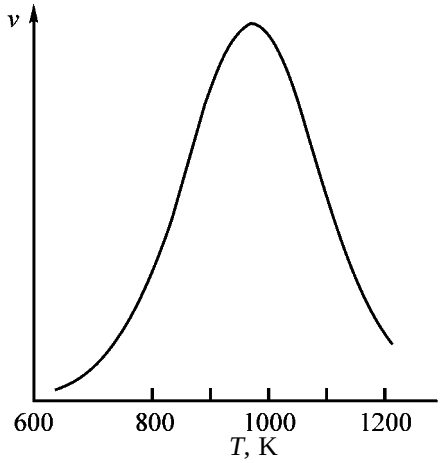

Fig. 2. Oxidation rate v of compact samples of the WC–Co alloy vs. temperature T.

the hard alloy is inhibited at all (Fig. 2). This is due to the formation on the pick surface of a thin dense layer of cobalt tungstate, preventing penetration of oxygen to the hard alloy. The tungstate is formed at approximately 1000°C by the reaction of tungsten(VI) and cobalt(II) oxides:

$$CoO + WO_3 \rightarrow CoWO_4$$

It was established experimentally that the rate of oxidation of VK alloys in air decreases at 1200°C by more than an order of magnitude, compared to 950–1050°C, with the reaction surface shielded by a layer of $CoWO_4$ (the salt was identified by X-ray phase analysis), in which the content of WO_3 is virtually zero.

The amount of oxygen theoretically necessary for oxidation of 1 kg of VK4, VK6, VK12, and VK15 alloys is 281, 279, 273, and 270 l, respectively. In terms of air, this amounts to 1.34–1.29 m^3. To ensure a high oxidation rate in practice, air is to be delivered at a 4–5-fold excess. For example, if oxygen is supplied at a fivefold excess, the volume V (m^3) of air, necessary for oxidation of hard-alloy picks in the roller drill bits, can be calculated by the formula

$$V = 66mc, \quad (4)$$

where m is the mass of roller drill bits (tons), and c is the average content of a hard alloy in the bits (%).

The rate of air delivery into the furnace, W ($m^3\ h^{-1}$), is given by

$$W = 66mc/\tau, \quad (5)$$

where τ is the duration of the stage of oxidation of hard-alloy picks (h).

The value of τ depends on the type of bits. In particular, picks inserted to a depth of 5 mm are completely oxidized in 4–5 h, and for those with insertion depth of 10 mm, the oxidation takes about 20 h.

Taking into account the consumption of atmospheric oxygen for oxidation of the hard alloy and, in part, for oxidation of the metal in the base of the roller drilling bits, it is desirable to maintain the content of O_2 in the outflowing air at about 12–16 vol %.

The mass of the oxidized product increases relative to that of the initial hard alloy by (%): 18.65 for VK4, 18.83 for VK6, 19.35 for VK12, and 19.63 for VK15. In calculating the heat balance of the furnace, it is necessary to take into account the fact that 5710–5950 kJ kg^{-1} is released as a result of chemical oxidation of the hard alloy alone.

After the oxidation of the hard-alloy picks is complete, the resulting oxidized product is disintegrated mechanically, for which purpose the roller drill bits

are subjected to one of the following types of treatment: barrel grinding, shot blasting, or water-jet treatment. The last two are preferable to barrel grinding. No less than 5/6 of the total mass of the oxidized product is disintegrated. The rest remains in the sockets.

The crushed mixture of tungsten and cobalt oxides with scale is subjected to magnetic separation. To diminish the capture of the oxides by the scale being separated, it is advisable to perform separation in an aqueous medium bubbled with air. This requires the subsequent settling, decanting, and drying of the finished product.

The oxidized product remaining in the sockets of roller drill bits is removed in a melt based on sodium hydroxide. To make lower the viscosity of the alkali melt, 4–8 wt % $NaNO_3$ and 1–3 wt % NaCl are introduced into the melt, so that it has the following composition (wt %): NaOH 89–95, $NaNO_3$ 4–8, and NaCl 1–3.

The drill bits are melt-treated at 450–550°C for 5–10 min. Tungsten(VI) vigorously reacts with the alkali by the reaction

$$WO_3 + 2NaOH = Na_2WO_4 + H_2O\uparrow. \quad (6)$$

The forming sodium tungstate has a high solubility in the melt. In processing of roller drill bits, the content of Na_2WO_4 is brought to 50–60 wt %, and after that the melt is discharged (cast into molds or iron drums). The solidified melt, which is an alkaline concentrate of sodium tungstate, is subjected to further processing [6]. In contrast to tungstic anhydride, cobalt oxide is only sparingly soluble in the alkali melt. Therefore, CoO precipitates in bath operation in the form of a slime, which is removed at regular interbals, together with the slime collector (pan), and directed to hydrometallurgical processing to give pure cobalt oxide [6].

CONCLUSIONS

(1) A method for processing of tungsten- and cobalt-containing secondary raw materials (roller drill bits) was suggested. This method includes the following main procedures: oxidative calcination at 950–1050°C and treatment in a NaOH–$NaNO_3$–NaCl melt at 450–550°C.

(2) An unusual effect of temperature on the oxidation rate of a hard-alloy formulation of the VK type (WC–Co) was observed. On heating the initial substance to 950–1050°C, the intensity of the process increases, but, on raising the temperature further, it falls dramatically because of formation on the sample surface of a dense layer of cobalt tungstate, which markedly hinders penetration of oxygen into the reaction zone.

REFERENCES

1. Shapiro, K.Ya., Kuz'micheva, K.I., and Evstigneeva, E.D., *Tsvetn. Met.*, 1970, no. 8, pp. 52–54.
2. Abrasheva, B., Chavdarov, G., Chavdarova, T., and Georgiev, G., *God. Inst. Tsvetn. Met.* (Plovdiv), 1984, vol. 22, pp. 92–104.
3. US Patent 4385972.
4. Satyvaldiev, A. and Asanov, U.A., *Zh. Prikl. Khim.*, 1995, vol. 68, no. 1, pp. 123–126.
5. Nikitina, L.S., *Tsvetn. Met.*, 1989, no. 9, pp. 84–89.
6. Orel, V.P., Dmitruk, B.F., Zarubitskii, O.G., and Kushkhov, Kh.B., *Ekotekhnol. Resursosberezh.*, 1994, no. 3, pp. 37–42.
7. Dmitruk, B.F., Zarubits'kii, O.G., and Dyachenko, N.M., *Vikorist. Vidkhod. Virobn.*, 1999, no. 4, pp. 98–101.
8. Ukrainian Patent 20016.
9. Ukrainian Patent 45189.
10. RF Patent 2102317.
11. Dyachenko, N.M., Zarubits'kii, O.G., and Dmitruk, B.F., *Viluchennya kol'orovikh, ridkisnikh ta dorogotsinnikh metaliv z vidkhodiv promislovikh ta yuvelirnikh virobnitstv Ukraini, Yalta, 25–27 veresnya 1988* (Recovery of Nonferrous, Rare, and Precious Metals from Wastes of Industrial and Jewelry Enterprises of Ukraine, Yalta, September 25–27, 1988), Kiev, 1988, pp. 10–12.
12. Zarubitskii, O.G., Dmitruk, B.F., Orel, V.P., and Dyachenko, N.M., *Joint Int. Meet. 192 ES USA and 48 ISE Paris*, Paris, September 5, 1997, vol. 97-2, p. 775.
13. USSR Inventor's Certificate no. 46045.
14. US Patent 3887680.

Russian Journal of Applied Chemistry, Vol. 77, No. 11, 2004, pp. 1746–1749. Translated from Zhurnal Prikladnoi Khimii, Vol. 77, No. 11, 2004, pp. 1764–1767.

INORGANIC SYNTHESIS AND INDUSTRIAL INORGANIC CHEMISTRY

Processing of Wastes from Manufacture of Cut Diamonds

O. G. Zarubitskii, B. F. Dmitruk, and N. M. Dyachenko

Vernadsky Institute of General and Inorganic Chemistry, National Academy of Sciences of Ukraine, Kiev, Ukraine

Received June 23, 2004

Abstract—Test experiments on recovery and purification of diamonds in melts based on alkali metal hydroxides and ammonium hydrofluoride were carried out. A method for processing of diamond-containing materials is suggested and apparatus for implementing this technology is described.

Manufacture of cut diamonds from natural diamonds mainly involves their physical and mechanical treatments: cutting, grinding, and faceting. In the process, a significant part of the starting material is transformed into a waste in the form of fragments, chips, and dust. The existing process for recovery of diamonds from industrial waste consists in the following. Wastes collected from working places together with contaminants are subjected to magnetic separation and manual sorting. After that, the waste is burnt in special furnaces. The heavy and light fractions of the resulting ash are separated in bromoform ($CHBr_3$). The heavy fraction is processed in boiling solutions of acids: hydrochloric (1 : 1), nitric (1 : 1), and concentrated sulfuric. The total duration of such a treatment is 5–7 h. A dried residue is leached by fusing it with sodium hydroxide at 600°C and dissolving the fusion cake in hot water. The solid residue is again treated with HCl, washed, and dried, with undissolved impurities removed and diamonds divided into fractions manually. Thus, the existing process is low-intense and multistage and involves the use of boiling concentrated solutions of strong acids; moreover, more than 10% of the diamond material is lost through etching.

In this context, it seems appropriate to develop effective chemical solvents that would ensure dissolution of all foreign substances in the diamond-containing waste without etching of the diamonds themselves. Solvents of this kind were sought-for taking into account the properties of diamonds and the composition of industrial wastes from manufacture of cut diamonds.

It should be noted that the most difficultly soluble substances among the foreign impurities contained in the waste in question are carbon (graphite), corundum, carbides (e.g., SiC), quartz sand, and minerals [1]. Removal of metallic and organic components presents no special problems. Of certain interest in this context are data on purification of synthetic diamonds. Commonly, an agglomerate containing firmly bound graphite, diamonds, catalyst, carbides, and the material of the high-pressure container (aragonite, silicon dioxide, silicates) is removed from the reaction mixture in synthesis of diamonds [2]. The first stage of purification consists in dissolution of the catalyst and the carbide phase with acids or mixtures of these. In the second stage, graphite is selectively oxidized with various reagents. In the third stage, compounds that are insoluble in water, solutions of acids (with the exception of hydrofluoric acid), and alkalis are removed, if the content of these compounds exceeds 1% of the total mass [3].

It is known that acid solutions, suspensions, and melts of alkali metal hydroxides, nitrates, and carbonates can be used to separate graphite from diamonds [3, 4]. According to the available data, etching of diamonds in alkaline solutions becomes noticeable at about 600°C, although in some papers lower temperatures are indicated [5, 6]. Of the other molten media used for purification of diamonds, mention should be made of molten mixtures based on sodium tetrafluoroborate, sodium peroxide, and halides of alkali and alkaline-earth metals. The first of these melts ensures removal of silicates and alumina-containing wastes at 700–1000°C. However, the strength of diamonds decreases and their cracking is observed because of the high working temperature in this case. The second of the above melts is used to recover diamonds from diamond-containing wastes at glass works. Unfortunately, the quality of diamonds is also impaired upon a purification of this kind [7].

1070-4272/04/7711-1746 © 2004 MAIK "Nauka/Interperiodica"

Table 1. Results obtained in purification of diamonds in alkali and alkali-salt melts

Run no.*	Melt composition, wt %				T, °C	τ, min	Sample mass, g		Weight loss, %
	NaOH	KCl	$NaNO_3$	$K_2S_2O_7$			before experiment	after experiment	
1	100				600	120	35.751	8.743	76.3
2	100				650	120	36.512	6.755	81.5
3	100				750	120	35.976	3.490	90.3
4	60		40		480	200	26.000	3.588	86.2
5	50	10	40		500	30	19.009	5.722	69.9
6	40		40	20	450	120	22.600	7.413	67.2
7	40		40	20	500	120	22.763	4.530	80.1
8	35		35	30	500	120	33.763	4.634	86.3
9	80			20	480	120	30.119	21.655	28.1

* In run nos. 1 and 2, the purification of diamonds is incomplete; in nos. 4–9, diamonds are etched; and in no. 3, diamonds are etched at incomplete purification.

EXPERIMENTAL

With account of the known data on the composition of solvents for processing of diamonds and diamond-containing mixtures, an attempt was made to use alkali and salt–alkali melts for recovery of diamonds from industrial wastes formed in manufacture of cut diamonds.

As additives to alkalis were used strong oxidizing agents: sodium and potassium nitrates, potassium persulfate and chromate, and sodium peroxide, as well as KCl and NaF. The range of working temperatures was 400–750°C. The results of selected experiments and conditions in which they were carried out are listed in Table 1. Similar results were obtained with molten potassium hydroxide and mixtures based on this compound. The treatment in melts was combined with that in an acid, hydrochloric or nitric. However, in no case could be simultaneously achieved the desired efficiency and quality of purification: at low temperatures, the process is insufficiently intensive, whereas at high temperatures and in the presence of an oxidizing agent, the quality of diamonds is impaired by their etching.

Having analyzed the possible solutions of the problem, we came to a conclusion that a low-temperature reaction medium is to be used in recovery of diamonds from wastes of jewel factories. As versatile solvent-reagent was taken ammonium hydrofluoride. The reactivities of aqueous solutions of NH_4HF_2 and of its melts were studied experimentally. It was established that ammonium hydrofluoride can vigorously react with metal oxides, including quartz, corundum, silicates, aluminosilicates, and, at elevated temperatures, even with carbon. The parameters of procedures used for treatment of diamond-containing wastes were chosen in solutions and melt of NH_4HF_2 at 100–200°C. Selected data are listed in Table 2. It can be seen that the intensity of impurity removal in a molten ammonium hydrofluoride grows as the temperature is raised. However, the volatility of the melt becomes noticeable at 175–180°C. Therefore, to preclude evaporation of NH_4HF_2, a new procedure was applied: its surface was covered with a layer of molten paraffin. It was established experimentally that effective purification of diamonds to remove foreign inclusions (impurities) should be performed at 140–200°C in the course of 1.5–3 h. No etching of the diamond surface occurs in this case.

Complete purification of diamonds also required an acid treatment in a boiling concentrated solution of HNO_3. The strongest effect was obtained upon direct dilution of the NH_4HF_2 melt (after the waste processing in this melt was complete) with hot (80–90°C) water taken in a 1 : 1 ratio. It was found that effective purification of diamonds is only achieved upon a combined treatment with the melt and the acid (Table 3). In this case, the duration of treatment in a solution of HNO_3 should be 1–1.5 h. The working capacity of the ammonium hydrofluoride melt was also determined experimentally. It was established that, for the process to be effective, the mass ratio of the melt and the raw material of process origin should be no less than 5 : 1.

The process developed in this study comprises the following steps: burning of the waste, separation of light fractions of the ash in bromobenzene, treatment of heavy fractions of the ash with molten ammonium hydrofluoride at 140–200°C for 1–3 h, dilution of the melt (fusion cake) with hot water taken in a 1 : 1 ratio, treatment of the dry residue with a boiling concen-

Table 2. Results obtained in purification of diamonds in ammonium hydrofluoride

Composition of reaction mixture, wt %		*T*, °C	τ, min	Sample mass, g		Weight loss, %
NH_4HF_2	H_2O			before experiment	after experiment	
50	50	100	60	25.150	17.555	30.2
50	50	100	180	17.553	8.497	51.6
50	50	115	60	25.009	12.705	49.2
50	50	115	120	12.705	5.298	58.3
87	13	130	120	5.003	3.060	61.2
87	13	150	120	31.939	8.686	72.8
87	13	150	120	8.686	2.962	65.9
100	–	130	60	25.021	15.413	38.4
100	–	130	60	25.000	14.702	41.2
100	–	150	60	25.000	13.906	44.4
100	–	150	60	25.105	12.452	50.4
100	–	150	60	12.452	5.915	52.5
100	–	150	60	5.915	3.117	47.3
100	–	150	60	3.115	1.786	42.7
100	–	175	120	25.363	2.688	89.4

Table 3. Results obtained in purification of diamonds by melt–acid treatment

Weighed portion of heavy fractions of the waste, g	Treatment in molten ammonium hydrofluoride		Duration of treatment with boiling HNO_3, h	Dry residue, g	Purification quality
	T, °C	τ, min			
25.02	125	4.0	1.5	4.12	Incomplete
25.30	140	2.0	1.5	3.57	″
25.05	140	3.0	1.5	2.60	Pure diamonds
25.16	140	4.0	1.5	2.64	″
25.08	140	3.0	1.0	3.18	Incomplete
25.10	140	3.0	2.0	2.62	Pure diamonds
25.00	175	2.0	1.25	2.58	″
25.12	200	1.0	1.0	3.39	Incomplete
24.97	200	1.5	1.0	2.43	Pure diamonds
25.05	200	1.5	0.5	3.25	Incomplete

trated solution of HNO_3 for 1–1.5 h, washing, drying, and separation of diamonds into fractions.

The apparatus for performing this process includes a purification bath (electric furnace with a container for the melt and a unit for monitoring and maintaining the prescribed temperature) and baths with an acid and warm flowing water. To improve the purification efficiency, the bath with the melt is equipped with a device for rocking the wire basket in which the raw material to be processed is placed. The rocking is carried out at a frequency of 20–40 min^{-1} in the vertical direction. To collect slime, a pan with perforated side walls covered on the inside with a fine nickel mesh is placed on the bath bottom.

The process developed for recovery of diamonds from the waste formed in manufacture of cut diamonds is efficient, with virtually zero loss of the diamond material. This technique can be used to recover, together with other diamond fractions, diamond dust. In addition, the full process cycle is shortened, compared to that presently used in the industry, by a factor of approximately 2.

CONCLUSIONS

(1) An effective low-temperature melt based on ammonium hydrofluoride is suggested. This melt ensures removal of the most part of foreign inclusions present in diamond-containing wastes from manufac-

ture of cut diamonds. A procedure precluding evaporation of NH_4HF_2 from the melt surface was developed.

(2) A technique for obtaining pure diamonds from secondary raw materials, waste from manufacture of cut diamonds, was developed. The method suggested rules out any loss of the valuable material being recovered, with the duration of the process decreasing by a factor of approximately 2, compared to the existing industrial technique. An apparatus for performing the procedure is suggested.

REFERENCES

1. Putyatin, A.A., Nikol'skaya, I.V., and Kalashnikov, Ya.A., *Sverkhtverd. Mater*., 1982, no. 2, pp. 20–28.
2. Novikov, N.V., Fedoseev, D.V., Shul'zhenko, A.A., and Bogatyreva, G.P., *Sintez almazov* (Synthesis of Diamonds), Kiev: Naukova Dumka, 1987.
3. Kruk, V.B., *Sint. Almazy*, 1975, no. 3, pp. 13–15.
4. Kruk, V.B., Lepikhova, T.G., and Vazhnev, V.P., *Sint. Almazy*, 1974, no. 2, pp. 11–13.
5. Karkina, M.I. and Maksakovets, Yu.P., *Dokl. Akad. Nauk SSSR*, 1983, vol. 183, no. 6, pp. 1311–1312.
6. Kukharenko, A.A. and Titova, V.M., *Uchen. Zap. Leningr. Univ., Ser. Geol. Nauk*, 1957, no. 215, issue 8, pp. 108–110.
7. Rudenko, A.P., Kulakova, I.I., and Balandin, A.A., *Dokl. Akad. Nauk SSSR*, 1965, vol. 163, no. 5, pp. 1169–1172.

Russian Journal of Applied Chemistry, Vol. 77, No. 11, 2004, pp. 1750–1753. Translated from Zhurnal Prikladnoi Khimii, Vol. 77, No. 11, 2004, pp. 1768–1771.

PHYSICOCHEMICAL STUDIES OF SYSTEMS AND PROCESSES

Distribution Coefficients of Phenol between Water and Hydrocarbons at 283–328 K

I. E. Dobryakova and Yu. G. Dobryakov

Research Institute of Chemistry, St. Petersburg State University, St. Petersburg, Russia

Received August 2, 2004

Abstract—Distribution of phenol between aqueous and organic phases at maximal dilution in the range 283–328 K was studied chromatographically. Ten systems containing saturated and aromatic hydrocarbons were examined.

The distribution coefficients of organic compounds in liquid–liquid systems are required for many purposes including development of extraction processes with organic solvents of various types and recovery, concentration, separation, and identification of substances. Distribution of a substance between immiscible solvents is determined by the difference in intermolecular interactions of this substance with the solvents. These interactions are studied by the solution theory. Ionization, hydration, and association constants [1–3] and activity coefficients [4] can be calculated form the distribution coefficients. Distribution coefficients in combination with gas chromatographic retention indices can be used to classify unknown organic compounds [5, 6]. Features of interphase distribution are extensively studied [7, 8]. The distribution coefficients are published in special handbooks [9, 10].

Phenol distribution in water–organic systems was extensively studied [11]. However, most of the distribution constants were measured at 20 ± 2°C. Data of different authors are sometimes inconsistent with each other. Many experiments were performed in acidified solutions and in solutions containing salt additives.

Improvement of procedures for determining distribution coefficients is also an urgent problem. Chromatographic analysis gives additional information on the presence of impurities, mutual solubility of the solvents, and occurrence of hydrolysis and other chemical reactions in the system [12].

The aim of this work was to develop a relatively simple and reliable chromatographic procedure for studying distribution of a low-volatile component between two phases and to determine the distribution coefficient of phenol between water and organic solvents at different temperatures. Saturated hydrocarbons (*n*-hexane, *n*-heptane, *n*-octane, and cyclohexane) and aromatic hydrocarbons (benzene, toluene, ethylbenzene, *o*-xylene, *p*-xylene, and *m*-xylene) were used as organic solvents. The distribution coefficients of phenol in 10 systems were measured at 10, 25, 40, and 55°C.

EXPERIMENTAL

The aqueous and organic phases were analyzed on a Multifract F-45 gas chromatograph (Perkin–Elmer, Germany) equipped with a flame ionization detector (FID). The samples were taken and injected in the chromatograph manually with the aid of a 10-μl Hamilton microsyringe. To keep the volume of injected liquid samples constant (2 μl), a special metal stop was fixed on the syringe rod.

The gas chromatographic analysis was performed under the following conditions: a 2-m metal column 3 mm in diameter was packed with Porapak P (50–80 mesh); flow rate of carrier gas (helium), hydrogen, and air was 25, 40, and 400 ml min^{-1}, respectively; the temperature of the column, detector, and injector was 200, 220, and 220°C, respectively; the detector sensitivity was 5×10^{-11} A; the analysis duration was 20 min. Under these conditions, the retention time of phenol is 13 min and its chromatographic peak is highly symmetrical. Each experiment was repeated at least four times. The electrical signal was treated with the aid of MultiChrom 1.5 for Windows software (Russia). The determination error of the peak area for the aqueous and organic samples was, on the average, 2 and 1.5%, respectively, and did not exceed 3%.

All organic solvents were distilled on a rotary distillation column with the 20 TP performance. The

1070-4272/04/7711-1750 © 2004 MAIK "Nauka/Interperiodica"

solvent purity was determined chromatographically. If the purity was insufficient, the solvent was distilled again. The main requirement to the solvent purity was low concentration of low-boiling impurities and the absence of compounds with the retention time close to that of phenol. Water was double-distilled from $KMnO_4$ on a 30-cm distillation column. Phenol was purchased from Merck (Germany) and used as received. The content of the main compound was 99.5%.

To determine the equilibrium distribution coefficients of phenol between the aqueous and organic phase at different temperatures, the phenol concentration in these phases was measured by gas chromatography [13]. The experiments were performed in a 100-ml glass cell (Fig. 1) whose temperature was controlled with a U-7c thermostat (Poland). The pipes were hermetically sealed with Teflon-coated silicon rubber seals and with screw stoppers. The cell had central and bottom lateral pipes to take upper (organic) and lower (aqueous) phases, respectively. The cell was equipped with a magnetic stirrer. To prevent emulsification, only the aqueous phase was vigorously stirred.

A stock 1% aqueous solution of phenol was prepared as follows. Solid phenol was melted (mp = 41°C). Liquid phenol (0.2 ml) was transferred with an automatic pipet into a 22.3-ml glass vessel and weighed. Double-distilled water (20 ml) was added, and the vessel was weighed again on an Ohaus Explorer electronic balance with an accuracy of 0.1 mg.

Double-distilled water (43 ml) was added into the cell with the aid of an automatic pipet. Then a 1% aqueous solution of phenol (2 ml) was added with a pipet, and the cell was loaded with organic solvent (45 ml). The resulting volume ratio of the phases was 1 : 1. The initial phenol concentration in the aqueous phase was about 5×10^{-3} M. At this concentration, phenol does not associate in the solution. The distribution coefficient of phenol between benzene and water at 25°C is almost independent of the phenol concentration up to 10^{-2} M [11]. In our experiments, the phenol concentration in the aqueous and organic phases was about 10^{-3} M. In this concentration range, the distribution coefficient is virtually constant and its determination error is lower than that in more dilute solutions.

The distribution coefficients were measured at 10, 25, 40, and 55°C. To attain the equilibrium, the system was kept for no less than 1 h. The cell was thermostatically controlled with an accuracy of ±0.05°C.

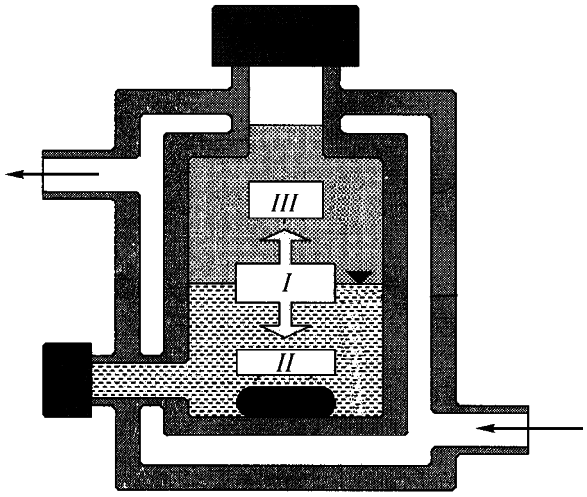

Fig. 1. Cell for study of (*I*) phenol distribution between (*II*) aqueous and (*III*) organic phases.

After the equilibrium was attained, the samples were taken with a microsyringe. Four to six samples of aqueous and then organic phases were analyzed chromatographically.

The phenol concentration in the aqueous and organic phases was determined from the peak area. Since the detector signal is proportional to the amount of the substance passed through the detector, the detector signal is proportional to the molar concentration of phenol in the sample. The ratio of the peak areas in the chromatograms of aqueous and organic phases will be equal to the distribution coefficient, if the detector works in the linear range and the sample volumes are the same:

$$S = kV_d c,$$

where S is the chromatographic peak area, V_d is the injected volume (ml), k is the coefficient, and c is the equilibrium concentration.

The molar distribution coefficient of phenol is calculated by the equation

$$K_d = \frac{c_{org}}{c_{aq}} \cong \frac{S_{org}}{S_{aq}}, \quad (1)$$

where c_{org} and c_{aq} are the equilibrium phenol concentrations in the organic and aqueous phases (M); S_{org} and S_{aq} are the peak areas of phenol in the chromatograms of the organic and aqueous phases.

The volume of injected samples was kept constant with the aid of a special metal stop fixed on the

Distribution coefficients of phenol between aqueous and organic phases

Solvent	$2K_d \pm \Delta K_d$ at indicated temperature, °C			
	10	25	40	55
n-Hexane	0.099 ± 0.004	0.148 ± 0.007	0.195 ± 0.006	0.244 ± 0.016
n-Heptane	0.098 ± 0.005	0.137 ± 0.005	0.186 ± 0.002	0.231 ± 0.007
n-Octane	0.091 ± 0.004	0.133 ± 0.006	0.169 ± 0.006	0.208 ± 0.010
Cyclohexane	0.119 ± 0.005	0.180 ± 0.007	0.241 ± 0.010	0.311 ± 0.008
Benzene	1.74 ± 0.07	2.06 ± 0.03	2.38 ± 0.09	2.64 ± 0.08
Toluene	1.10 ± 0.04	1.36 ± 0.02	1.63 ± 0.07	1.87 ± 0.06
o-Xylene	1.23 ± 0.02	1.47 ± 0.04	1.66 ± 0.03	1.85 ± 0.06
p-Xylene	1.11 ± 0.02	1.29 ± 0.03	1.46 ± 0.04	1.62 ± 0.05
m-Xylene	–	1.32 ± 0.02	1.47 ± 0.06	–
Ethylbenzene	0.89 ± 0.02	1.17 ± 0.02	1.34 ± 0.06	1.48 ± 0.02

syringe rod. The linearity of the concentration dependence of the detector signal in the range from 0.002 to 0.025 wt % was experimentally checked with five reference aqueous solutions of phenol.

It should be noted that, in this case, the distribution coefficient of phenol was determined without additional calibration of the chromatograph with external references and without taking the volume of the aqueous and organic phases into account, which made the determination more accurate [13].

The temperature dependence of the distribution coefficient of phenol in a water–benzene system is shown in Fig. 2 in comparison with the similar dependence determined in the aqueous HCl (pH 2)–benzene system by the photometric procedure. The phenol concentration ranged from 1×10^{-2} to 5×10^{-4} M. We used double-distilled water as the aqueous phase. The aqueous phenol solution was neutral. Since phenol is a weak acid ($K = 1.3 \times 10^{-3}$), its distribution coefficient should depend on the pH of the aqueous phase. However, calculations and the experimental data [11] show that only 0.1% of phenol molecules are dissociated at the phenol concentration of about

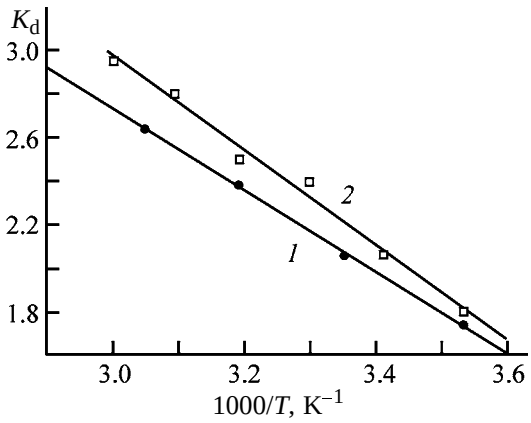

Fig. 2. Distribution coefficients of phenol in the benzene–water system, measured (*1*) in this work and (*2*) in [14]. (*T*) Temperature; the same for Fig. 3.

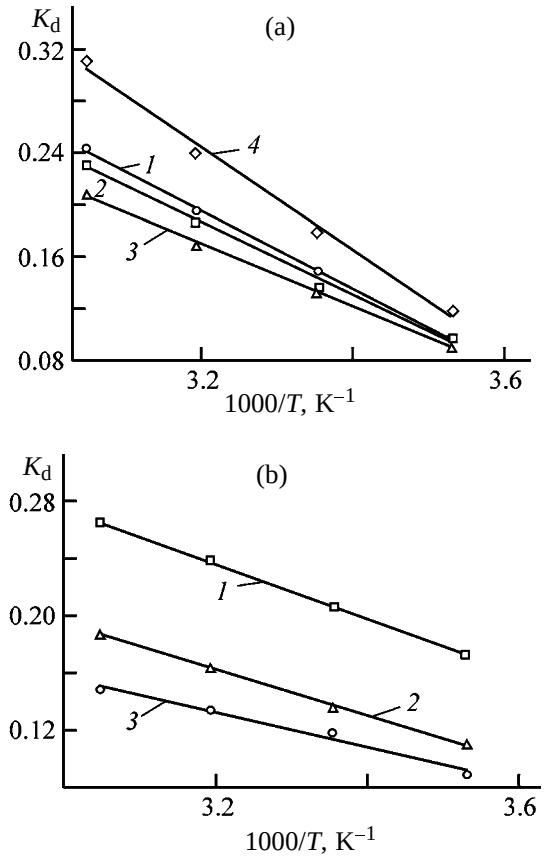

Fig. 3. Phenol distribution coefficient between aqueous phase and (a) alkanes [(*1*) hexane, (*2*) heptane, (*3*) octane, and (*4*) cyclohexane] and (b) aromatic hydrocarbons [(*1*) benzene, (*2*) toluene, and (*3*) ethylbenzene].

10^{-3} M and pH 7, which has virtually no effect on the distribution coefficient. Negligible discrepancy (7–8%) with the published data is likely due to the determination error and salting-out effect of hydrochloric acid.

The distribution coefficient of phenol in 10 systems at 10–55°C are summarized in the table.

The dependences of the distribution coefficient of phenol in water–alkane system and in water–aromatic hydrocarbon systems on the reciprocal temperature are shown in Fig. 3a and 3b, respectively. As seen from Fig. 3, the distribution coefficient decreases with an increase in the molecular weight or molar volume of the homologs.

It is known that the extracting power is determined by certain functional groups of the solvent. In the case of phenol extraction, this group is the aromatic ring. The distribution coefficients of phenol between saturated hydrocarbons and water are lower than 1 and decrease with an increase in the length of the hydrocarbon chain. In this case, the extraction depends on packing of phenol molecules in the solvent. The fact that the distribution coefficient of phenol in the cyclohexane-water system is higher than that in the *n*-hexane-water system is caused by this factor.

ACKNOWLEDGMENTS

We are grateful to N.A. Smirnova for discussion of the experimental results and useful comments.

This work was financially supported by the Federal Program "Leading Research Schools" (NSh-676. 2003.3) and Russian Foundation for Basic Research (project no. 02-03-32709).

REFERENCES

1. *Fizichsekaya khimiya* (Physical Chemistry), Nikol'skii, B.P., Ed., Leningrad: Khimiya, 1987.
2. Korenman, I.M., *Ekstraktsiya v analize organicheskikh veshchestv* (Extraction in Analysis of Organic Substances), Moscow: Khimiya, 1977.
3. Pimentel, G.C. and McClellan, A.L., *The Hydrogen Bond*, San Francisco: Freeman, 1960.
4. Aarna, A.Ya, Melder, L.I., and Ebber, A.B., *Zh. Prikl. Khim.*, 1979, vol. 52, no. 7, pp. 1640–1642.
5. Zenkevich, I.G. and Vasil'ev, A.V., *Zh. Anal. Khim.*, 1993, vol. 48, no. 3, pp. 473–486.
6. Zenkevich I.G. and Tsibul'skaya, I.A., *Zh. Fiz. Khim.*, 1997, vol. 71, no. 2, pp. 341–346.
7. Leo, A., Hansch, C., and Elkins, D., *Chem. Rev.*, 1971, vol. 71, no. 6, pp. 525–616.
8. Hansch, C. and Leo, A., *Substituent Constants for Correlation Analysis in Chemistry and Biology*, New York: Wiley, 1979.
9. Korenman, I.M., *Konstanty raspredeleniya organicheskikh veshchestv mezhdu dvumya zhidkimi fazami* (Distribution Constants of Organic Compounds between Two Liquid Phases) Gor'kii: Volro-Vyatskoe, 1979, issue 5.
10. Korenman, Ya.I., *Koeffitsienty raspredeleniya organicheskikh soedinenii: Spravochnik* (Distribution Coefficients of Organic Compounds: Handbook), Voronezh: Voronezh. Gos. Univ., 1992.
11. Korenman, Ya.I., *Ekstraktsiya fenolov* (Extraction of Phenols), Gor'kii: Volgo-Vyatskoe, 1973.
12. Ebber, A.V., *Tr. Tallin. In Politekh. Inst.*, 1976, no. 405, pp. 119–123.
13. Berezkin, V.G., Loshchilova, V.D., Pankov, A.G., and Yagodovskii, V.D., *Khromatoraspredelitel'nyi metod* (Chromatodistribution Method), Moscow: Nauka, 1976.
14. Korenman, Ya.I., *Zh. Prikl. Khim.*, 1970, vol. 43, no. 5, pp. 1100–1107.

Russian Journal of Applied Chemistry, Vol. 77, No. 11, 2004, pp. 1754–1756. Translated from Zhurnal Prikladnoi Khimii, Vol. 77, No. 11, 2004, pp. 1772–1774.

SORPTION AND ION-EXCHANGE PROCESSES

Sorption of Gold(III) Ions from Hydrochloric Acid Solutions by Aminated Shungite

A. M. Akimbaeva and E. E. Ergozhin

Bekturov Institute of Chemical Sciences, Ministry of Education and Science of Kazakhstan Republic, Almaty, Kazakhstan

Received August 4, 2004

Abstract—Sorption of gold ions by aminated shungite from chloride solutions was studied. The effects of the solution pH and process duration on the degree of recovery were considered.

Sorption methods of concentrating precious metals (PM) using various materials occupy a prominent place in their analytical chemistry [1–3]. The use of known organopolymer sorbents with good sorption characteristics for PM recovery involves certain problems associated with their swelling, low rate of the process, and insufficient desorption of metal ions [1]. Widely used activated carbons are able to sorb quantitatively microamounts of platinum metal and gold ions from solutions; however, the equilibrium is attained within a rather long time, and the carbon regeneration involves problems [4].

Recently we initiated studies of the sorption of PM ions by modified shungites, which appeared to be effective sorbents [4–6].

The sorption technology involving expensive AM-2B anion exchanger is in wide use at enterprises of gold mining industry of the Kazakhstan Republic and CIS countries. Therefore, along with the problem of increasing gold mining, the search for new available and cheap sorbents is necessary. We developed anion exchangers based on modified epoxy and amino derivatives of shungites abundant in our region [4–6]. The results of recovering silver and platinum ions by aminated natural sorbents showed that surface-modified shungite rocks quantitatively recover precious metal ions within a short time [5, 6].

The study of sorption parameters of the new sorbent based on aminated shungite containing polyvinylpyridine in granules showed that functional groups with nitrogen donor atoms determine its chemical and analytical properties and its ability to extract precious metal ions.

The aim of this work was a study of the properties of aminated shungite as a sorbent for gold(III) ions from standard solutions and the subsequent analytical determination of these ions.

A shungite concentrate containing 80% carbon was prepared by demineralizing natural shungite (20% carbon) with subsequent granulation [6]. Aminated shungite was obtained by the polymerization of 2-methyl-5-vinylpyridine in shungite granules. According to the elemental analysis, the content of nitrogen in the aminated product was 27.16%; the weight gain of the sorbent after polymerization was 2.51%.

We prepared the starting solution of gold(III) by dissolving gold metal in a mixture of hydrochloric and nitric acids (3 : 1) with subsequent boiling down with concentrated HCl. Working solutions of gold(III) were prepared by dilution of the starting $H[AuCl_4]$ solution. The required acidity was created by adding HCl and NaOH and was monitored by an EV-74 pH-meter with an ESL-43-07 glass electrode. The sorption of gold(III) ions was studied under static conditions. To study the process kinetics, we brought 0.5 g of the sorbent into contact with 50 ml of Au(III) solution (c_{Au} = 10 mg l^{-1}). The mixture was stirred with a magnetic stirrer at a rate of 400–500 min^{-1} at room temperature. At certain time intervals, we took samples and determined the metal ion concentration by the atomic adsorption method on an AAS-3 spectrometer in a propane–butane–air flame. The analytical signal of gold was measured by the resonance line at 242.8 nm at the spectral aperture width of 0.25 nm and the current of a lamp with a hollow cathode of 5 mA. The degree of gold(III) recovery was determined from the difference between the starting metal ion concentration and its residual concentration in the solution after sorption.

1070-4272/04/7711-1754 © 2004 MAIK "Nauka/Interperiodica"

We studied the process kinetics at room temperature with the aim to find the optimal conditions for the recovery of gold(III) ions with aminated shungite. The study of the dependence of the degree of gold(III) recovery on the process duration showed that the nature of the surface groups on the samples determines distinctions between the kinetic parameters of the process. An equilibrium in the distribution of Au(III) ions between the sorbent and the solution under the suggested conditions (c_{Au} = 10 mg l^{-1}, m_s = 0.5 g, V_l = 50 ml) is attained in 4 h with the starting nonmodified shungite, the recovery of gold(III) ions being 80%. At the same time, with the aminated sample Au(III) is recovered from the solution almost completely within 2 h (Fig. 1). Its high kinetic parameters are determined by the presence of chemically active groups and by the selectivity to precious metal ions. We emphasize that the time of half-saturation with the natural shungite is about 2 h, and with the modified sample it is 15 min. We have found that a high degree of recovery R (99%) of gold(III) ions from chloride solutions with the Au concentration of 10 mg l^{-1} is achieved on the aminated shungite. Therefore, this material shows promise for recovering traces of precious metal ions.

The proportion of various forms of gold(III) ions in the solution is predominantly affected by its acidity. In chloride media, gold(III) ions are known to exist as $[AuCl_4]^-$, $[AuCl_3OH]^-$, and $[AuCl_2(OH)_2]^-$ anions [7], which can react with functional groups of the sorbent. At pH > 3, Au(III) chloride complexes are hydrolyzed, the content of Au(III) hydroxochloride complexes increases, and the absorption of gold(III) ions decreases. Therefore, we studied their sorption behavior in the range of pH 1–3 (Fig. 2). We found that the optimal pH of the solution lies in the range 0.5–2.0. The examination of the dependence of the degree of gold(III) extraction by aminated shungite on the HCl concentration (0.5–4.0 M) confirms high efficiency and completeness of the extraction (99.8%).

The study of the sorption activity of gold(III) ions as a function of the solution acidity suggests that they pass into the solid phase owing to the complexation with functional groups (carbonyl and pyridine), and the acidity of the medium does not affect the process. This fact suggests that in this case the nitrogen atom of the heterocycle takes part in the sorption, which makes the ion-exchange mechanism of the process improbable. The Au(III) ions are recovered owing to complexation with the pyridine groups of the macromolecular ligand. Thus, gold(III) ions are recovered by the modified shungite predominantly owing to their coordination by the nitrogen atom of the pyridine ring and by the active surface centers of the natural sorbent.

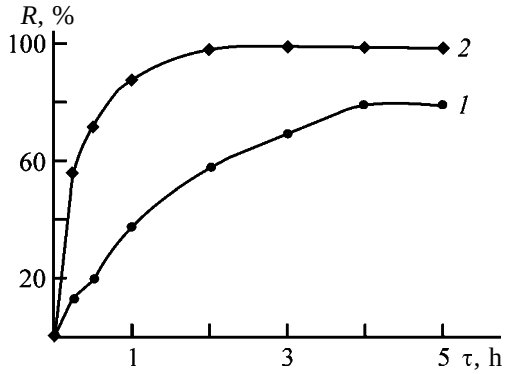

Fig. 1. Degree of Au(III) recovery R by shungites as a function of the process duration τ. c_{Au} = 10 mg l^{-1}, V_l = 50 ml, m_s = 0.5 g; the same for Fig. 4. Shungite: (*1*) natural and (*2*) modified.

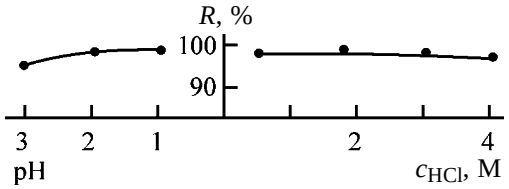

Fig. 2. Influence of the aqueous phase acidity on the degree of Au(III) extraction R by aminated shungite. c_{Au} = 10 mg l^{-1}, m_s = 0.5 g, τ = 24 h. c_{HCl} is the concentration of HCl solution (M).

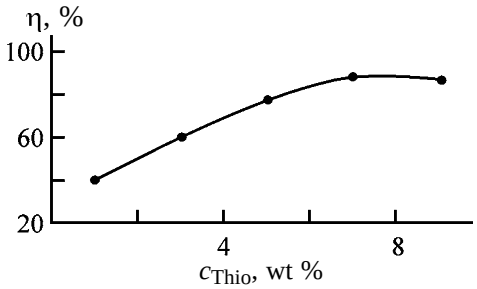

Fig. 3. Degree of Au(III) desorption η vs. thiourea concentration c_{Thio}. V_{el} = 50 ml, m_s = 0.5 g.

We examined the possibility of regeneration of aminated shungite for its multiple use and found that the sorbed gold(III) ions can be desorbed with a solution of thiourea in HCl. We have found that Au(III) is 90% desorbed with a thiourea solution (7 wt %) in 1 M HCl at room temperature (Fig. 3). An increase in the eluent volume by a factor of 2–3 results in complete desorption of gold ions (96–100%).

The pyridine group tends to form complex compounds via its nitrogen atom and shows a selectivity

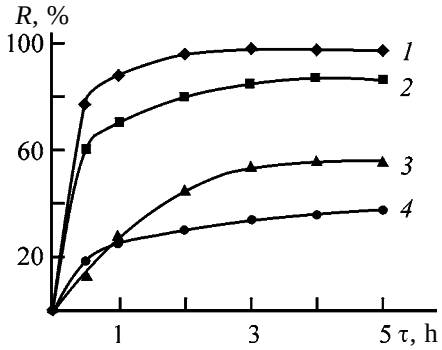

Fig. 4. Degree of Au(III) recovery R by aminated shungite vs. the process duration τ in the presence of concomitant metal ions: (*1*) Au(III), (*2*) Cu(II), (*3*) Co(II), and (*4*) Ni(II).

to transition metal ions. To determine the possibility of selectively recovering gold(III) ions on aminated shungite, we studied the kinetics of this process in the presence of copper(II), cobalt(II), and nickel(II) ions (the concentration of each metal ion was 10 mg l^{-1}) (Fig. 4). The comparison of the sorption curves shows that the selectivity of the sorbent under study varies in the order Au(III) > Cu(II) > Co(II) > Ni(II). Au(III) could be recovered completely, and the recovery of Cu(II), Co(II), and Ni(II) comprised 87, 56, and 38%, respectively. The sorbent is saturated with metal ions within 4–5 h.

It was shown in [3] that gold(III) ions can be quantitatively separated from transition metal ions [M(II)] in 0.5 M solution of HCl. Under the conditions of our experiments, the differences in the degree and rate of their sorption on the sorbent under study allow Au(III) to be determined in the presence of 10- and 50-fold amounts of M(II) (the table). The selectivity of the sorbent under study to the precious metal ions can be caused by the formation of an additional π-dative bond between Au(III) atoms and a π orbital of the pyridine ring. It has a positive effect on the recovery of Au(III) and allows us to separate the main body of the ions of concomitant elements.

Sorption of Au(III) on aminated shungite in the presence of concomitant metals. c_{Au} = 10 mg l^{-1}, m_s = 0.5 g, V_{el} = 50 ml, 0.5 M HCl

M(II)	M/Au	R(Au), %
Cu(II)	10	98.9 ± 1.1
	50	98.8 ± 1.2
Co(II)	10	98.9 ± 1.3
	50	98.9 ± 1.2
Ni(II)	10	98.9 ± 1.4
	50	98.9 ± 1.2

CONCLUSION

A shungite concentrate containing polyvinylpyridine in its granules efficiently sorbs gold(III) ions from chloride solutions. Its high selectivity makes it possible to concentrate gold(III) ions and to separate them from the concomitant elements Cu(II), Co(II), and Ni(II), even present in excess.

REFERENCES

1. Myasoedova, G.V. and Savvin, S.B., *Khelatoobrazuyushchie sorbenty* (Chelating Sorbents), Moscow: Nauka, 1984.
2. Pokonova, Yu.V. and Grabovskii, A.I., *Izv. Vyssh. Uchebn. Zaved., Tsvetn. Met.*, 2002, no. 7, pp. 38–40.
3. D'yachenko, N.A., Trofimchuk, A.K., and Sukhan, V.V., *Zh. Anal. Khim.*, 1995, vol. 50, no. 8, pp. 842–844.
4. Ergozhin, E.E., Akimbaeva, A.M., and Sadvokasova, A.B., *Izv. Vyssh. Uchebn. Zaved., Tsvetn. Met.*, 2003, no. 6, pp. 52–55.
5. Akimbaeva, A.M., Ergozhin, E.E., and Sadvokasova, A.B., *Izv. Vyssh. Uchebn. Zaved., Tsvetn. Met.*, 2004, no. 3, pp. 53–55.
6. Akimbaeva, A.M., Ergozhin, E.E., and Sadvokasova, A.B., *Izv. Vyssh. Uchebn. Zaved., Khim. Khim. Tekhnol.*, 2004, vol. 47, no. 1, pp. 110–112.
7. Efremov, S.A., Efremova, S.V., Kolesnikov, B.Ya., and Priz, E., Abstracts of Papers, *Mezhdunarodnaya konferentsiya po analiticheskoi khimii, posvyashchennaya 100-letiyu so dnya rozhdeniya O.A. Songinoi* (Int. Conf. on Analytical Chemistry Dedicated to the Centennial of O.A. Songina), Almaty, 2001, p. 52.

Russian Journal of Applied Chemistry, Vol. 77, No. 11, 2004, pp. 1757–1760. Translated from Zhurnal Prikladnoi Khimii, Vol. 77, No. 11, 2004, pp. 1775–1778.

SORPTION AND ION-EXCHANGE PROCESSES

Separation of Cerium-Group Rare-Earth Elements on PAN–FOSPAN Fibrous Sorbent

L. N. Skvortsova and E. V. Selivanova

Tomsk State University, Tomsk, Russia

Received April 2, 2004

Abstract—The selectivity of sorption of cerium-group rare-earth elements on acid- and base-treated fibrous complexing PAN–FOSPAN ampholyte from aqueous solutions containing acetate and butyrate anions was studied as influenced by pH. The possibility of separating Nd^{3+} from Eu^{3+} by eluent chromatography on PAN–FOSPAN was studied. The conditions for concentrating the sum of rare-earth elements on the resin were found.

The separation and preconcentration of rare-earth elements (REE) is an important analytical problem which, as a rule, is solved by chromatographic and extraction techniques. The growing interest in ion-exchange chromatography is stimulated both by the simplicity of regenerating the sorbents and possibility of performing sorption separation under dynamic conditions. The most efficient ion-exchange separation and preconcentration of lanthanides is reached using fibrous oxygen-containing complexing sorbents. These sorbents are characterized by high selectivity to REE and fast attainment of the sorption equilibrium.

The advantage of using the fibrous PAN–FOSPAN ampholyte for separation and preconcentration of Nd^{3+} and Yb^{3+} was shown in [1, 2]. We found that, on treatment of this sorbent with aqueous acid, its selectivity to REE ions at pH 3.5–4.5 strongly increases due to favorable modification of the sorbing sites (Table 1). It was found that, on treatment with acid, the amino groups in the resin remain unprotonated. The IR studies showed that sorption of REE on PAN–FOSPAN is caused by coordination of its functional groups with REE ions. In this work we continued our studies on sorption of REE on PAN–FOSPAN fibrous ampholyte. The aim of our experiments was to elucidate the possibility of separating cerium-group REEs.

The selectivity of ion-exchange separation of metal ions can be optimized by varying the chemical composition of the aqueous phase. This procedure allows variation of both the metal ion speciation in solution and composition and complexing power of the ionic sorbing sites in the sorbent. To improve the selectivity of sorption separation of metals, new approaches are being developed, based on competing complexing reactions in the sorption system [3]. It was found that the sorption selectivity of the resin is improved after adding appropriate complexing agents in the aqueous phase and varying pH. In this work, the selectivity of fibrous PAN–FOSPAN ampholyte to REE was studied as influenced by low-molecular-weight competing ligands (acetate and butyrate) added into solution, pretreatment of the initial sorbent with acid or alkali, and pH of solution [4]. The acetate and butyrate competing ligands were used as their buffer solutions. The physicochemical characteristics of PAN–FOSPAN fibrous ampholyte and chemical composition of its sorbing sites before and after treatment of the sorbent with acid and alkali are presented in Table 1.

EXPERIMENTAL

The initial fibrous sorbent PAN–FOSPAN was converted to the acid form by treatment with 0.1 M

Table 1. Physicochemical characteristics of PAN–FOSPAN* ampholyte

Functional groups		TEC, mmol g^{-1}	pK_a
acid form	base form		
–C(NH$_2$)=N–OH	–C(NH$_2$)=N–OH	3.50	4.8 ± 0.2
–CONHOH, –PO(OH)$_2$	–CONHOH, –PO(ONa)$_2$		8.4 ± 0.5

* PAN–FOSPAN was prepared at the St. Petersburg University of Technology and Design.

1070-4272/04/7711-1757 © 2004 MAIK "Nauka/Interperiodica"

Table 2. Influence of acetate anions on the selectivity of REE sorption on PAN–FOSPAN ampholyte in the acid and base forms

REE ion	Acid form		Base form	
	$D_M \times 10^{-3}$, ml g^{-1} (without adding acetate)	$D_M \times 10^{-4}$, ml g^{-1} (on adding acetate)	$D_M \times 10^{-4}$, ml g^{-1} (without adding acetate)	$D_M \times 10^{-3}$, ml g^{-1} (on adding acetate)
Pr^{3+}	9.2 ± 0.3	4.10 ± 0.10	3.85 ± 0.20	4.9 ± 0.3
Nd^{3+}	9.9 ± 0.5	4.30 ± 0.15	3.40 ± 0.20	4.6 ± 0.4
Sm^{3+}	9.4 ± 0.4	3.20 ± 0.20	2.30 ± 0.16	5.0 ± 0.2
Eu^{3+}	9.5 ± 0.3	2.15 ± 0.12	2.10 ± 0.15	4.7 ± 0.2

HCl and then washed with 10^{-3} M HCl to pH 3. To convert the sorbent to the base form, the initial PAN–FOSPAN was treated with 0.1 M NaOH and then washed with distilled water to decolorization of phenolphthalein.

To elucidate the separation power of the fibrous sorbent with respect to REEs, the distribution factor of these metals between the sorbent and aqueous phase was determined under static conditions. In these experiments, a weighed portion of PAN–FOSPAN (0.05 g) was equilibrated with a 5×10^{-4} M aqueous REE chloride (10 ml) at pH 4.5. In studies of the effect of acetate and butyrate anions on REE sorption separation, the REE chloride solutions in the acetate and butyrate buffers were used. The content of acetic and butyric acids and their salts in the buffer solutions was 0.1 and 0.25 M, respectively. The resin sample suspended in an REE-containing buffer solution was kept until the sorption equilibrium was attained. The REE content in the equilibrium liquid phase was determined spectrophotometrically with Arsenazo III. The REE amount sorbed on the fibrous sorbent was determined as the difference between the initial and equilibrium REE concentrations in the aqueous phase. The REE distribution factor was calculated by the equation $D_M = [\overline{M}]/[M]$, where $[\overline{M}]$ and [M] are the equilibrium REE contents in the sorbent (mmol g^{-1}) and aqueous phase (M), respectively. The REE separation factors K were calculated from the corresponding distribution coefficients.

In our sorption experiments, a weighed portion of the sorbent preliminarily saturated with REE under static conditions was packed in a temperature-controlled glass column (10 cm high and 0.8 cm in diameter) and washed with distilled water. The elution rate of 1.5 ml min^{-1} was maintained with a peristaltic pump. The REE content in the eluate was monitored spectrophotometrically. The elution curves were processed with the Statistica 5.0 computer program (Basic Statistics language), and the REE distribution factors were calculated. The sorption preconcentration of REEs was carried out on a microcolumn (15 mm high and 0.3–0.4 mm in diameter) packed with PAN–FOSPAN fibrous sorbent (50 mg). In these experiments, 10 ml of the initial aqueous REE solution (2×10^{-4} M) was pumped through the column at the required velocity. REEs were desorbed from the column with 0.1 M HCl.

The effect of acetate anions on the selectivity of sorption of cerium-group REEs on fibrous PAN–FOSPAN ampholyte in the acid and base forms is demonstrated in Table 2.

This table shows that, on adding acetate anions to the aqueous phase, the selectivity of fibrous resin in the acid form to REEs is improved. On the contrary, the selectivity of the resin in the base form is deteriorated under these conditions. The improvement of the selectivity of the resin in the acid form to REEs can be caused by the following competing reactions: (1) dissociation of the hydrogen phosphate functional groups of the sorbent, (2) protonation of acetate anions, and (3) coordination of acetate anions with REE^{3+}:

$$\overline{H}_2R \rightleftarrows \overline{H}^+ + \overline{H}R^-, \quad (1)$$

$$L^- + H^+ \rightleftarrows HL, \quad (2)$$

$$M^{3+} + 2L^- \rightleftarrows [ML_2]^+. \quad (3)$$

These reactions show that the protonation of acetate anions by equilibrium (2) shifts equilibrium (1) towards formation of deprotonated hydrohen phosphate groups in the ampholyte, and also destroys metal acetate complexes. As a result, the acetate anions favor the sorption of REE on the ampholyte. The selectivity of REE sorption on the resin was found to decrease in the order $Pr^{3+} = Nd^{3+} > Sm^{3+} > Eu^{3+}$. It should be noted that the stability of acetate complexes of these metals increases in the same sequence. The sorption power of the resin in the base form decreases in the presence of acetate anions. This effect can be caused by the shift of reaction (3)

toward formation of weakly sorbable bis(acetate) complexes. The maximal selectivity of the resin in the acid form to REEs in the presence of acetate anions was observed in separation of Nd^{3+} from Eu^{3+}.

Reactions (1)–(3) show that pH affects the ion-exchange sorption of REEs by affecting both the free ligand concentration in the solution and protonation of the sorbing sites. Figure 1 shows how pH of the acetate and butyrate buffer solutions influences the selectivity of PAN–FOSPAN in the acid form to Nd^{3+} and Eu^{3+}.

The low sensitivity of the distribution factor D_M to acidity of solutions in the pH range 3.0 – 4.0 is caused by protonation of both the weakly acidic functional groups of the sorbent and complexing anions in the buffer solution. The most efficient separation of neodymium from europium (separation factor 2.0) is reached in their sorption from acetate buffer solution with pH 4.5.

The comparison of the kinetic curves of Eu^{3+} sorption on PAN–FOSPAN ampholyte in the acid and base forms (Fig. 2) shows that the resin in the base form predominantly sorbs Eu^{3+} by the ion-exchange mechanism (sorption equilibrium is attained in 30 min), whereas sorption of europium on the resin in the acid form is complicated by complexation (sorption equilibrium is attained in 6 h).

The efficiency of separation of Nd^{3+} from Eu^{3+} by eluent chromatography on PAN–FOSPAN was estimated from the elution curves. In elution experiments, the acetate and butyrate buffer solutions (pH 4.5) and dilute aqueous HCl (0.01 – 0.1 M) were used as eluents. The elution of REE with buffer solutions was found to be inefficient due to high REE distribution factor between the sorbent and the buffer solutions ($D_M = n \times 10^4$). The resolution of the elution bands of Nd^{3+} and Eu^{3+} was reached in eluting REEs with aqueous HCl of various concentrations (Fig. 3). We found that, although the sorption selectivity slightly increases with decreasing HCl concentration, the column performance noticeably decreases. As seen from Fig. 3e, in flowing 0.01 M HCl through the column at 20°C, REEs are not eluted. Although the REE distribution factors calculated by us from the elution curves (6–20) are considerably lower than those determined from the static sorption experiments ($n \times 10^4$), their values remain too large to ensure the efficient elution of the metals. Upon heating the column to 80°C (Figs. 3b, 3d, 3f), the efficiency of eluting Eu and Nd noticeably increases, but the separation factor, as before, remains too low to reach the good resolution of the Eu and Nd elution bands.

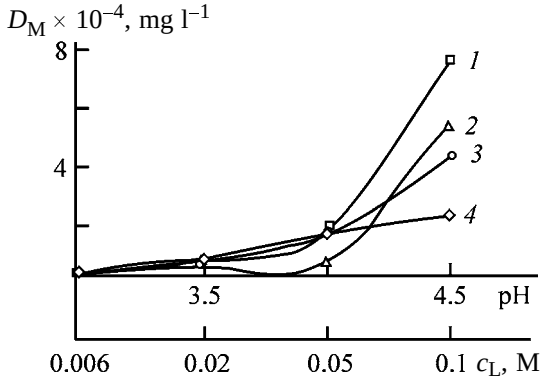

Fig. 1. Distribution factor D_M of (*1, 3*) neodymium and (*2, 4*) europium between PAN–FOSPAN in the acid form and buffer solution as functions of pH of (*1, 2*) butyrate and (*3, 4*) acetate buffer solutions and the butyrate and acetate concentration c_L.

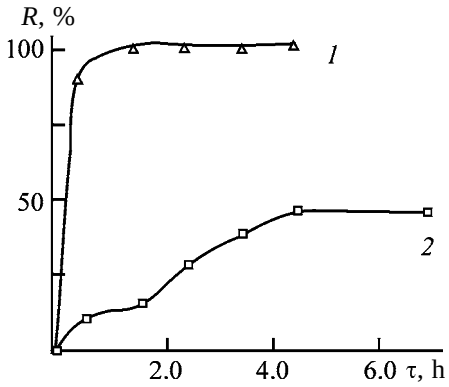

Fig. 2. Degree of europium sorption R on fibrous PAN–FOSPAN in the (*1*) base and (*2*) acid forms as a function of sorption time τ.

In order to improve resolution of chromatographic bands, we increased the sorbent bed height to 20 cm (Fig. 4). Under these conditions, the separation factor K increased to 2, which, however, was still insufficient for obtaining the resolution suitable for quantitative separation of Eu from Nd. From our experimental data, we calculated by the theory of the theoretical plates the resin bed height ensuring the acceptable degree of recovery of individual REE. For example, 99% of target REE can be recovered on a 60-cm column. To increase the degree of REE recovery to 99.95% , the resin bed height must be increased to 110 cm.

Table 2 shows that REEs can be concentrated by their sorption from acetate buffer solutions on PAN–FOSPAN ampholyte in both the base and acid forms. Figure 5 shows the degree of europium recovery vs. the filtration rate of europium-containing acetate buffer solution through the microcolumn packed with PAN–FOSPAN ampholyte. It is seen that the degree of europium recovery on the resin in the acid form is small even at very slow filtration. The inefficient

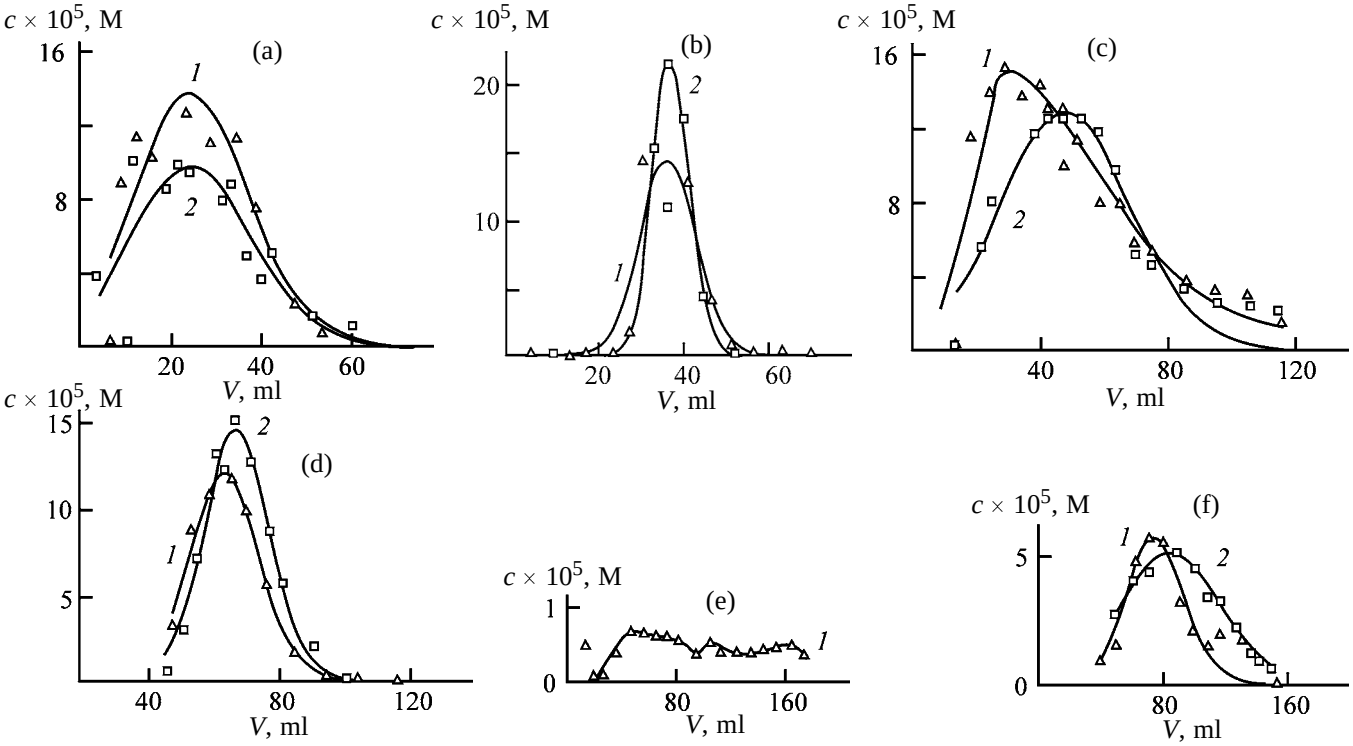

Fig. 3. Elution bands of (*1*) europium(III) and (*2*) neodymium(III) from PAN–FOSPAN ampholyte at (a, c, e) 20 and (b, d, f) 80°C with aqueous HCl. Column size 10 × 0.8 cm; the same for Fig. 4. (*c*) Metal ion concentration; (*V*) HCl volume; the same for Fig. 4. c_{HCl} (M): (a, b) 0.05; (c, d) 0.025, and (e, f) 0.01.

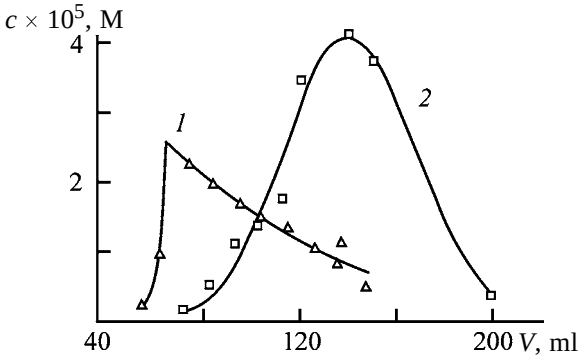

Fig. 4. Elution of Eu(III) and Nd(III) from PAN–FOSPAN ampholyte with 0.01 HCl at 80°C.

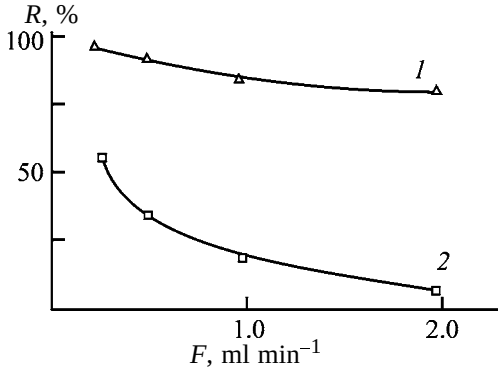

Fig. 5. Degree of europium(III) sorption recovery *R* vs. filtration rate of europium-containing solution *F* through PAN–FOSPAN in the (*1*) acid and (*2*) base forms.

recovery of europium can be caused by slow europium sorption due to its complexation with acetate anions. On the contrary, the efficient preconcentration of REEs on the resin in the base form can be reached at relatively slow filtration.

CONCLUSIONS

The fibrous PAN–FOSPAN ampholyte in the acid form is a promising sorbent for separating cerium-group REEs in acetate buffer.solution. Nd^{3+} can be separated from Eu^{3+} by eluting them from the resin with 0.01 M HCl at 80°C. The fibrous ampholyte in the base form can be used for efficient preconcentration of the sum of rare-earth elements.

REFERENCES

1. Chashchina, O.V., Bobkova, L.A., Skvortsova, L.N., *et al.*, *Zh. Anal. Khim.*, 1998, vol. 53, no. 3, pp. 278–280.
2. Skvortsova, L.N., Bobkova, L.A., Kiseleva, M.A., *et al.*, *Sorbts. Khromatogr. Prots.*, 2001, vol. 1, no. 1, pp. 35–45.
3. Janos, P., *J. Chromatogr. A.*, 1997, vol. 789, pp. 3–19.
4. Samuelson, O., *Ion Exchange Separation in Analytical Chemistry*, New York: Wiley, 1963.

Russian Journal of Applied Chemistry, Vol. 77, No. 11, 2004, pp. 1761–1764. Translated from Zhurnal Prikladnoi Khimii, Vol. 77, No. 11, 2004, pp. 1779–1782.

SORPTION AND ION-EXCHANGE PROCESSES

Sorption, Acid, and Catalytic Properties of a Sulfonic Cation Exchanger Supported on the Carbon Fiber

Yu. G. Egiazarov, L. N. Shachenkova, V. Z. Radkevich, B. Kh. Cherches, M. G. Gorbatsevich, and E. N. Ermolenko

Institute of Physical Organic Chemistry, Belarussian National Academy of Sciences, Minsk, Belarus

Received January 14, 2004; in final form, September 2004

Abstract—Distribution in strength of the acid centers in sulfonic cation in the form of exchanger granules and fibers was studied by the novel modification of the thermal desorption method.

Previously [1–3], we studied the activity of sulfonic cation exchanger granules and fibers in the synthesis of methyl *tert*-alkyl ethers and found that FIBAN K-1 surpasses in the activity KU2-8 (gel structure) in the synthesis of methyl *tert*-butyl ether (MTBE) and Dowex msm 31 (macroporous structure) in the synthesis of methyl *tert*-amyl ether (MTAE).

The main advantage of fibrous sulfonic cation exchanger FIBAN K-1 is that the fiber diameter is by approximately an order of magnitude smaller than the diameter of KU-2-8 and Dowex msm 31 granules. This decreases intradiffusion inhibition and intensifies mass exchange.

The diameter of the Carbopon fiber can be estimated as 5–10 μm, which is substantially smaller than FIBAN K-1 fiber diameter. Hence, sulfonic cation exchanger supported on Carbopon, when used as a catalyst of acid–base reactions, can provide more intense mass exchange than FIBAN K-1.

The performance of sulfonic cation exchanger substantially depends on its acidity, i.e., concentration and strength of acid centers. The literature survey [4–6] shows that the most adequate method of its determination is ammonia thermal desorption. However, for organic ion exchangers with a low thermal stability, ammonia is acceptable only for determination of weak acid centers. To determine strong acid centers, another thermal desorption method is required.

In this work, we studied sorption and acid properties and catalytic activity (by an example of MTAE synthesis) of two samples of sulfonic cation exchanger supported on Carbopon (sample I with gel structure and sample II with macroporous structure) in comparison with their structural analogs, fibrous (FIBAN K-1) and granular (Dowex msm 31) sulfonic cation exchangers.

EXPERIMENTAL

The sorption of various liquids with the initial Carbopon, synthesized samples of the supported sulfonic cation exchanger, FIBAN K-1 fibrous sulfonic cation exchanger with gel structure, and Dowex msm 31 granular sulfonic cation exchanger with macroporous structure was evaluated gravimetrically. A cation exchanger sample (~0.5 g) dried to the constant weight at 90°C was introduced into a test tube, 10 ml of a liquid was added, and the mixture was stored for 3 h. The sample was centrifuged (4000 rpm) for 15 min, weighed, and dried to the constant weight at 90°C. The sorption value, G_l ($g_l\ g^{-1}$), was calculated as the ratio of the liquid weight to the weight of dry sample:

$$G = \frac{m_1 - m_2}{m_2},$$

where m_1 is the sample weight after centrifuging and m_2, sample weight after drying at 90°C.

The average value of three parallel experiments was used in calculations. Along with G_l, the volume sorption V_l ($cm_l^3\ g^{-1}$) was also calculated.

As seen from Table 1, sorption of water with Carbopon is 0.64 $g_l\ g^{-1}$, which is substantially larger than sorption of methanol and the other components of the reaction mixture of the MTAE synthesis, and of *n*-octane taken as a nonpolar liquid. The V_l values show a clear correlation with the molecular size of liquids [i.e., molecular-sieve effect characteristic for

1070-4272/04/7711-1761 © 2004 MAIK "Nauka/Interperiodica"

Table 1. Sorption of liquids of various types with Carbopon and sulfonic cation exchangers

Liquid	Initial Carbopon	Sample I	Sample II	FIBAN K-1	Dowex msm 31
	G_l, $g_l\ g^{-1}/V_l$, $cm_l^3\ g^{-1}$				
Water	0.64/0.64	0.95/0.95	0.44/0.44	1.04/1.04	0.96/0.96
Methanol	0.34/0.44	0.47/0.60	0.20/0.25	0.67/0.85	0.59/0.75
Methylbutenes	0.19/0.29	0.22/0.34	0.14/0.21	0.26/0.40	0.23/0.35
Methanol : methylbutenes (1 : 1)	0.23/0.33	0.33/0.48	0.16/0.22	0.70/0.97	0.62/0.86
MTAE	0.19/0.24	0.27/0.34	0.14/0.18	0.42/0.53	0.41/0.52
n-Octane	0.19/0.27	0.16/0.23	0.15/0.21	0.14/0.20	0.08/0.11

finely porous sorbents (activated carbons, zeolites, silica gels) appears].

The effect of molecular size of liquid is preserved in samples of the sulfonic cation exchanger supported on Carbopon, and, in addition, the effect of the structure of the grafted copolymer can be observed.

Sample 1 (2% DVB, gel structure) sorbs more water (0.95 $g_l\ g^{-1}$) and the other polar components than does Carbopon. However, as expected, sample I sorbs nonpolar *n*-octane more weakly than does Carbopon. The fact that sample I is a weaker sorbent than its structural analog, fibrous FIBAN K-1, can be explained by lower exchange capacity (EC).

As compared to sample I and Carbopon, sample II (25% DVB, macroporous structure) sorbs water (0.44 $g_l\ g^{-1}$) and the other liquids substantially more weakly, probably due to a rigid cellular structure of the cation exchanger caused by the high degree of cross-linking of the polymer chains. The difference between the sorption properties of this sample and Dowex msm 31 can also be explained by differences in their EC (1.3 and 4.4 mg-equiv g^{-1}, respectively).

The novelty of the suggested method of the thermal desorption of bases consists in using a weak base, diethyl ether, as a desorbate to determine the concentration of strong acid centers. It is desorbed from the strongest acid centers of the dehydrated sulfonic cation exchangers at 120°C, i.e., under conditions of their thermal stability. In addition, diethyl ether is characterized by low adsorption power, due to small size of its molecule and low boiling point. Therefore, the sorbed ether is readily eliminated from the cation exchanger, which is important for obtaining correct results.

The concentration of weak acid centers is determined performed as follows. A cation exchanger (approximately 0.2 g) is charged into a glass reactor (70 mm long, 8 mm in diameter), and the reactor is attached to a carrier gas line in a chromatograph thermostat. Then the thermostat heating is switched on, and a sample is conditioned in a helium flow (30 ml min^{-1}) at 120°C for 2 h, cooled, and saturated with ammonia for 30 min at room temperature. Physically adsorbed ammonia is eliminated from the cation exchanger at room temperature in the helium flow. The course of desorption and its completion were monitored with a recorder. Then the stage of the thermal desorption of the chemisorbed ammonia begins. The temperature of the reactor is increased to 120°C, and the sample is kept for 1 h in a helium flow. The desorbed ammonia is trapped in a U-shaped glass condenser cooled with liquid nitrogen and, after heating at 90–95°C with hot water, is transported with helium flow to the katharometer, where it is monitored as a chromatographic peak. Using a calibration plot ammonia content–peak area, we determined the amount of ammonia desorbed and calculated from the weight of the ion exchanger sample and its EC the concentration (mmol g^{-1}) and percentage of weak acid centers in the sample.

To determine the concentration of strong acid centers, a cation exchanger sample is charged into a reactor arranged in the thermostat of a chromatograph, and the reactor is attached to an empty column functioning as a preheater of the carrier gas. After sample training in a dried helium flow (30 ml mim^{-1}) at 120°C for 2 h, the reactor is cooled to room temperature and detached from the column, and diethyl ether is added. After 1-h storage, excess ether is poured off, the reactor is attached to the column and flame-ionization detector, and the thermostat temperature is set at 75°C; the sample is kept in a helium flow until the recorder pen returns to the zero level, which indicates completion of ether desorption at this temperature. Then the temperature is sharply elevated to 100°C, and the peak of desorbed ether is recorded. After stabilization of the baseline, the temperature of the thermostat is elevated to 120°C, and the second desorption peak

Table 2. Acid properties of sulfonic cation exchangers

Sulfonic cation exchanger			Concentration and strength of acid centers							
sample	DVB, %	EC, mg-equiv g^{-1}	weak		medium		strong		very strong	
			mmol g^{-1}	%	mmol g^{-1}	%	mmol g^{-1}	%	mmol g^{-1}	%
I	2	1.7	0.27	16.3	1.16	69.2	0.16	9.4	0.09	5.1
II	25	1.3	0.17	13.3	0.97	74.8	0.10	7.9	0.05	4.0
FIBAN K-1	2	3.1	0.40	12.9	2.35	75.6	0.27	8.8	0.08	2.7
Dowex msm 31	25	4.4	0.86	19.5	3.32	75.4	0.18	4.1	0.04	1.0

is recorded. Then, using a calibration plot ether content–peak area, the amount of ether desorbed within the 75–100°C range is determined and the concentration and percentage of the strong acid centers in the sample are calculated from the sample weight and ion exchanger EC. Similarly, the amount of ether desorbed within the 100–120°C range is determined and the concentration of the very strong acid centers is calculated.

In accordance with the conventional classification, centers characterized by NH_3 desorption at temperatures of up to 120°C are weak acid centers, those characterized by diethyl ether desorption within the 75–100 and 100–120°C ranges are strong and very strong acid centers, respectively. The concentration of medium-strength acid centers was determined as the difference between the total amount the acid centers in the sulfonic cation exchanger (numerically equal to EC) and the sum of weak, strong, and very strong centers. It follows from Table 2 that the sum of the strong and very strong acid centers (strongly acidic centers) in sample I amounts to 0.25 and in sample II, to 0.15 mmol g^{-1}. In sulfonic cation exchangers FIBAN K-1 (gel structure) and Dowex msm 31 (macroporous structure), which are structural analogs of samples I and II, the concentration of strongly acidic centers responsible for the catalytic activity of the cation exchanger in the etherification reactions amounts to 0.35 and 0.22 mmol g^{-1}, respectively. Thus, the concentration of strong acid centers in samples with gel structure is higher than in macroporous samples. The content of strongly acidic centers in the cation exchangers considered decreases in the order FIBAN K-1 > sample I > Dowex msm 31 > sample II.

It is interesting to compare the acid characteristics of the sulfonic cation exchanger samples prepared with their catalytic activity. The experiments on MTAE synthesis were performed on a laboratory device of the flow type. The reaction unit of the device consisted of a catalytic reactor placed in a thermostat, a vessel for the starting compounds, a cooling system, and a product collector [2]. 1 g of fibrous sulfonic cation exchanger was loaded into the reactor, and the synthesis was performed under a pressure of 0.8 MPa to ensure the liquid state of the reaction system. In the case of granular sulfonic cation exchanger, the resin sample was mixed with ground glass of the same grain size to reach the volume of the compacted fibrous sample (1.4 ml). In the experiments, the process temperature was varied at a constant rate of raw material feeding, 4 g g_{ce}^{-1} h^{-1}, and CH_3OH : *i*-C_5H_{10} molar ratio of 1 : 1.

Methylbutenes were prepared by dehydration of isoamyl alcohol on γ-Al_2O_3 at 330°C. The mixture of isomers contained (%) 3-methyl-1-butene 45.8, 2-methyl-1-butene 19.4, and 2-methyl-2-butene 34.8.

The data on MTAE synthesis in the presence of sulfonic cation exchangers studied are listed in Table 3. The comparison of the sulfonic cation exchangers supported on Carbopon shows that sample I is more active: the maximal content of MTAE in the catalyzate reaches 42.4% at 80°C, while sample II gives 35.4% MTAE at 100°C. These results coincide with both the sorption properties of the samples and the concentration of strongly acidic centers. The decrease in the MTAE content as a result of the higher rate of the reverse reaction relative to the direct reaction rate on sample I is observed at 90°C. For FIBAN K-1 and Dowex msm 31, this decrease is observed at 100°C, and for sample II still higher temperature is required.

When the MTAE content in the catalyzate at 80°C is taken as a measure of the sulfonic cation exchanger activity, the following activity order is observed: sample I > FIBAN K-1 > Dowex msm 31 > sample II. As seen, the position of Dowex msm 31 and sample II in the catalytic activity series coincides with that in

Table 3. Synthesis of MTAE on sulfonic cation exchangers. Rate of raw material feeding 4 g g_{ce}^{-1} h^{-1}, molar ratio CH_3OH : *i*-C_5H_{10} = 1 : 1

Component	Content in catalyzate, wt %, at indicated *T*, °C			
	70	80	90	100
Sample I				
Methylbutenes	43.5	39.6	42.3	42.7
Methanol	19.9	18.0	19.3	19.6
MTAE	36.6	42.4	38.4	37.7
FIBAN K-1				
Methylbutenes	48.6	41.5	39.2	46.0
Methanol	22.2	19.0	17.9	21.0
MTAE	29.4	39.5	42.9	33.0
Sample II				
Methylbutenes	57.1	50.2	45.1	44.3
Methanol	26.0	22.9	20.7	20.3
MTAE	16.9	26.9	34.2	35.4
Dowex msm 31				
Methylbutenes	45.1	42.2	41.5	44.9
Methanol	20.0	18.8	18.7	19.9
MTAE	34.9	39.0	39.8	35.2

the series of acid properties. FIBAN K-1 suprasses all the other cation exchangers studied in the content of strongly acidic centers; however, it is inferior in the activity to sample I. Probably, in this case a size factor (the diameter of the Carbonpon fibers is by an order of magnitude smaller than that of FIBAN K-1 fibers), and the nature of sulfonic cation exchanger support (carbon or polypropylene fiber), which can affect the structure of the matrix formed, can contribute to the catalyst activity.

Thus, sulfonic cation exchangers supported on Carbopon show much promise, opening prospects for development of the theory and practice of the catalysis with cation exchangers.

CONCLUSIONS

(1) Sorption properties of sulfonic cation exchangers supported on carbon fiber depend on the degree of cross-linking of the styrene–divinylbenzene matrix: sample I (gel structure) substantially better sorbs polar liquids than does sample II (macroporous structure), whereas sorption of a nonpolar liquid (*n*-octane) with these sorbents is virtually the same.

(2) The study of the acid properties of samples I and II by the modified method of the thermal desorption of bases showed that the concentration of strongly acidic centers in sample I is substantially higher than in sample II.

(3) By an example of the synthesis of methyl *tert*-amyl ether, it was shown that the catalytic activity of sulfonic cation exchangers in acid–base reactions depends on both the resin acid properties and the diffusion factors affecting the intensity of the mass exchange.

REFERENCES

1. Cherches, B.Kh., Shunkevich, A.A., Belotserkovskaya, T.N., and Egiazarov, Yu.G., *Zh. Prikl. Khim.*, 1999, vol. 72, no. 4, pp. 623–627.
2. Cherches, B.Kh., Kovalenko, M.A., Shunkevich, A.A., *et al.*, *Neftekhimiya*, 2002, vol. 42, no. 1, pp. 28–31.
3. Egiazarov, Yu.G. and Soldatov, V.S., *Sorbts. Khromatogr. Prots.*, 2001, vol. 1, no. 4, pp. 591–599.
4. Tanabe, K., *Solid Acids and Bases. Their Catalytic Properties*, Tokyo: Kodansha, 1970.
5. Topchieva, K.V. and Thoang Kho Shi, *Aktivnost' i fiziko-khimicheskie svoistva vysokokremnistykh tseolitov* (Activity and Physicochemical Properties of High-Silica Zeolites), Moscow: Mosk. Gos. Univ., 1976.
6. Egiazarov, Yu.G., Savchits, M.F., and Ustilovskaya, E.Ya., *Geterogenno-kataliticheskaya izomerizatsiya uglevodorodov* (Heterogeneous Catalytic Isomerization of Hydrocarbons), Minsk: Nauka i Tekhnika, 1987.

Russian Journal of Applied Chemistry, Vol. 77, No. 11, 2004, pp. 1765–1768. Translated from Zhurnal Prikladnoi Khimii, Vol. 77, No. 11, 2004, pp. 1783–1786.

SORPTION AND ION-EXCHANGE PROCESSES

Choice of Optimal Conditions of Chromatomembrane Mass Exchange in the Liquid–Gas System for Saturation of Aqueous Solutions with Oxygen

L. N. Moskvin, G. L. Grigor'ev, O. V. Rodinkov, and K. Yu. Senchik

St. Petersburg State University, St. Petersburg, Russia
Pavlov State Medical University, St. Petersburg, Russia

Received July 23, 2004

Abstract—Fundamental aspects of the chromatomembrane mass exchange in the liquid–gas system are considered for the case of saturation with oxygen (oxygenation) of a physiological solution. The influence exerted by the geometrical dimensions and macroporous structure of a biporous matrix on the process efficiency is revealed.

At present, the membrane scheme of gas exchange is regarded as virtually the only possible way to remove gases from aqueous solutions and to saturate these solutions with gaseous components in flow-through analytical techniques [1] and as a unique principle of operation of blood oxygenators in medical practice [2–4]. However, this scheme has a common physicochemical disadvantage in all these cases, associated with the relatively low rate of molecular diffusion of oxygen across membranes. It is the limited rate of gas exchange across membranes that is responsible for the slow response of systems employed to monitor the composition of gases dissolved in water, for the need to use gas mixtures enriched in oxygen (compared with air) to saturate blood with oxygen, and for the insufficiently complete removal of carbon dioxide from blood in the course of oxygenation [4].

A scheme of mass-exchange processes in liquid–gas and liquid–liquid systems was suggested in the early 1990s as an alternative to diffusion membrane processes. This scheme was named the chromatomembrane mass-exchange (CMM) process [5]. It was demonstrated, already in the initial stage of investigations, that CMM can be, in principle, used for blood oxygenation [6, 7]. However, the problems associated with the efficiency of chromatomembrane oxygenation (CMO) and with the choice of optimal conditions of this process remained, on the whole, unsolved.

This study is concerned with fundamental aspects of the CMO process in model physiological solutions. Its goal is to determine the optimal porous structure of the mass-exchange bed and its geometrical dimensions and the best ratio of the flow rates of the liquid and gas phases.

EXPERIMENTAL

The scheme of the CMO process is shown in Fig. 1. The mass exchange between liquid and gas flows, which leads to saturation of the liquid with oxygen, occurs in a hydrophobic porous medium having the form of particles of porous polytetrafluoroethylene (PTFE), bound together in the course of repeated thermal annealing. Porous PTFE is formed in sintering of a PTFE powder formed in polymerization. Spaces between these particles constitute a system of open macropores along which moves an aqueous solution or, in the real oxygenation process, blood. The dimensions of these macropores can be arbitrarily varied by fractionation of particles of the porous PTFE obtained in the primary sintering. These particles contain open micro- and submicrometer pores comparable in size with particles of the polymerization powder. The micropores ensure the permeability of biporous matrices to air or gas mixtures. Biporous matrices are confined between the upper and lower microporous PTFE membranes impermeable to the liquid. The gas flow is fed into, and removed from, the microporous space of the matrices across these membranes.

The supply of the liquid into the micropores of the membranes and matrices is hindered by the capillary pressure arising because of the nonwettability of

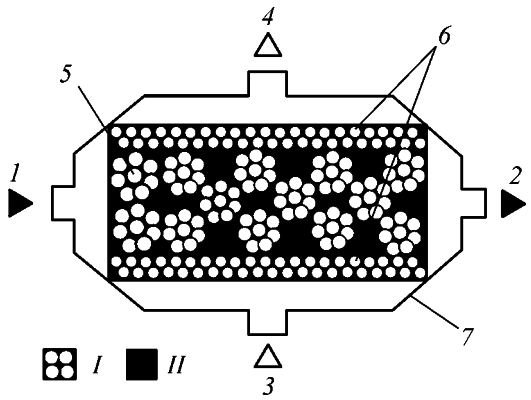

Fig. 1. Schematic of the chromatomembrane oxygenation process: (*1*, *2*) inlet and outlet of blood, (*3*, *4*) inlet and outlet of the air flow, (*5*) mass-exchange matrix, and (*6*) hydrophobic microporous membranes. (*I*) Microporous medium and (*II*) macropores.

PTFE with aqueous solutions and, in particular, with blood. In turn, the supply of the gas phase into macropores, in which the capillary pressure is negligible, is hindered by the pressure of the aqueous solution or blood filling the macropores. This pressure is maintained, according to the experimental conditions, at a higher level than the gas pressure. A more detailed information about the physicochemical principles and conditions under which chromatomembrane processes are performed can be found in [8].

The optimal conditions of the process, which would ensure the most effective saturation of the liquid phase with oxygen in CMM, were determined using the following physiological solution: 1 wt % NaCl + 4.5 wt % glucose. The physiological solution was passed through three in-series connected chromatomembrane cells (CMCs) with an independent feed of flows of the gas phase into each cell. The first CMC served for removing oxygen dissolved in the physiological solution with a flow of helium in order to determine the efficiency of the subsequent saturation of the solution with oxygen in the second CMC. It has been found previously that the CMO is more efficient than the conventional membrane scheme [6]. With account of these data, the physiological solution in the second cell was saturated with oxygen from the atmosphere, without its additional enrichment with oxygen. The third CMC was introduced into the hydraulic scheme to determine the degree of saturation of the physiological solution with oxygen in the second cell. For this purpose, a flow of helium was delivered into the third CMC through the line used to feed-in the gas phase. The flow of helium extracted dissolved oxygen from the physiological solution and then was directed into a gas chromatograph for analysis.

The results of a gas-chromatographic analysis were used to calculate, taking into account the fundamental aspects of CMM, the concentration c (mg l^{-1}) of oxygen dissolved in the physiological solution at the outlet of the CMC under study, using the formula

$$c = c_G W_L W_{G_0}, \quad (1)$$

where c_G is the concentration of oxygen in the flow of the extracting gas at the outlet of the third CMC according to gas-chromatographic data (mg l^{-1}); W_L, flow rate of the physiological solution through the chromatomembrane cells (ml min^{-1}); and W_{G_0}, flow rate of the extracting gas through the third CMC (ml min^{-1}).

The rates of gas flows through all the CMCs were varied with flow controllers and monitored using soap-film flow meters. The relative flow rate measurement error was ±1%. The flow rate of the physiological solution and blood through the CMC, W_L, was controlled with a peristaltic pump and measured with a measuring vessel and a stopwatch. The relative error in W_L measurements was ±1%.

The degree R of saturation of the liquid phase with atmospheric oxygen in the CMC under study was calculated by the formula

$$R = c/c_0, \quad (2)$$

where c_0 is the concentration of oxygen in water in equilibrium with air at a given temperature, known from reference data [9].

The biporous matrices of the CMC used in the study were in the form of parallelepipeds. The influence exerted on the efficiency of saturation with atmospheric oxygen by the ratio of the flow rates of the physiological solution and air through the CMC, by the dimensions of macropores in the biporous mass-exchange matrix, and by the length and height of this matrix was analyzed. The dimensions of the mass-exchange matrix in the directions of motion of the liquid phase and air and in that perpendicular to the first two were taken as length L, height H, and width, respectively.

The length and height of the matrices in the CMC under study, which are prototypes of chromatomembrane oxygenators, were varied from 20 to 100 mm and 10 to 30 mm, respectively, whereas the width remained constant (10 mm). The size of porous PTFE

particles constituting the matrix, which was taken as the macropore diameter, was varied in the range 0.25–1.5 mm.

The influence exerted by the ratio of the flow rates of air and physiological solution through the CMC on the degree of saturation of the latter with atmospheric oxygen is shown in Fig. 2. As expected, raising the flow rate of air through the CMC leads to an increase in the degree of saturation. In this case, the absolute values of the flow rates of air and the solution are unimportant and the degree of saturation depends only on their ratio. These data suggest that the maximum throughput of the CMC will be achieved at the maximum possible flow rates of the phases through the CMS, which are, in turn, determined by parameters of the porous structure of the biporous matrix. Degrees of saturation of the aqueous phase with atmospheric oxygen, equal to 95% and more, are easily obtained at a ratio of the flow rates of air and solution equal to 1 : 1 (and more).

The influence exerted by the length of the mass-exchange matrix on the efficiency of saturation of the aqueous solution with oxygen is illustrated by Fig. 3a. It can be seen that making the matrix and, accordingly, the CMC itself longer than 5 cm is virtually unfeasible because the degree of solution saturation changes in this case only slightly. The influence exerted by the height of the matrix is manifested in close association with that of its length. It was established that the height-to-length ratio of the mass-exchange bed, rather than the absolute value of the height, is of fundamental importance (Fig. 3b). It can be seen that the degree of saturation starts to decrease especially strongly when this ratio exceeds 0.5.

The size of macropores in the matrix affects the efficiency of saturation of the solution with oxygen only slightly (Fig. 4). By analogy with gas–liquid chromatography [10], this can be understood as follows: diffusion in the gas phase is the rate-determining stage of mass exchange. This circumstance makes reasonable use of CMC with coarse pores in chromatomembrane oxygenation to ensure high permeability of the mass-exchange bed to the liquid phase at minimum possible pressures, which rules out any damage to blood.

Thus, the optimal ratio of the flow rates of air and the liquid phase through the CMC is within the range 0.5–2. The height-to-length ratio of the matrix should not exceed 0.5; the sufficient length of the matrix is 50 mm; and, as shown previously [7], the width of the matrix affects the efficiency of mass exchange only slightly, and making it larger leads to a propor-

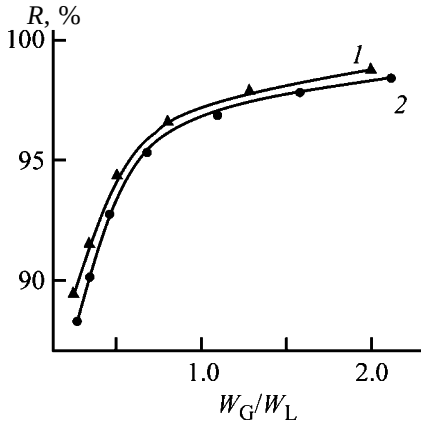

Fig. 2. Degree R of saturation of the physiological solution with atmospheric oxygen vs. the ratio of the flow rates of air and solution, W_G/W_L, through the CMC. Dimensions of the mass-exchange bed $30 \times 10 \times 10$ mm. Flow rate of the physiological solution (ml min^{-1}): (*1*) 5.0 and (*2*) 15.0.

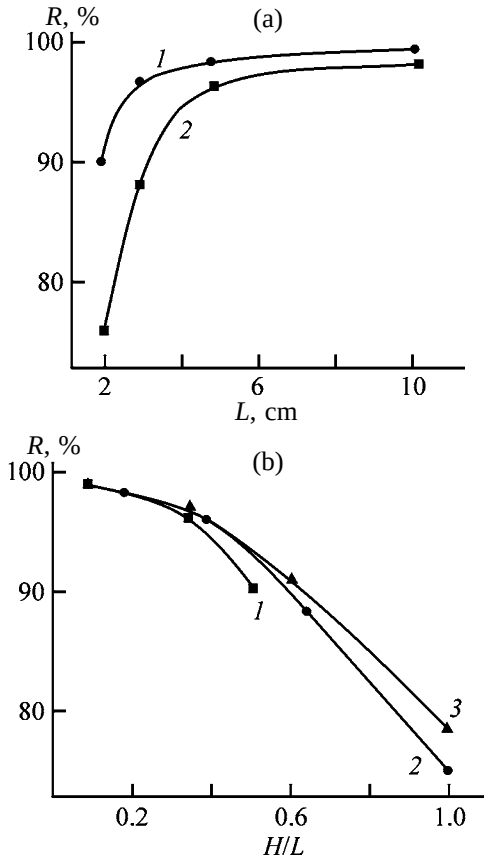

Fig. 3. Degree R of saturation of the physiological solution with atmospheric oxygen vs. (a) length L of the mass-exchange matrix of CMO and (b) matrix height to length ratio H/L. Height of the mass-exchange matrix (cm): (*1*) 1.0, (*2*) 2.0, and (*3*) 3.0.

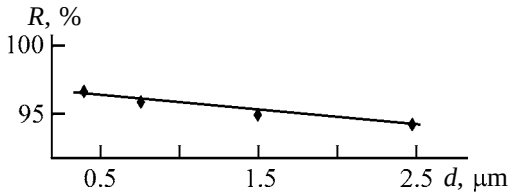

Fig. 4. Degree *R* of saturation of the physiological solution with atmospheric oxygen vs. size *d* of macropores in the matrix. Flow rate of air and solution 5 ml min^{-1}; length and height of the mass-exchange matrix 3.0 and 1.0 cm, respectively.

tional increase in the output capacity of the CMM process.

The results of experiments performed with donor blood on the same CMC and at the same flow rate ratios of blood and atmospheric air confirmed that, as in the case of physiological solutions, the prototype chromatomembrane oxygenators ensure higher efficiency of oxygenation than that obtained with their membrane analogues.

CONCLUSION

The size of macropores in the biporous mass-exchange matrix has virtually no effect on the efficiency of chromatomembrane oxygenation. The optimal ratio of the flow rates of air and the liquid phase being oxygenated across the mass-exchange bed is within the range 0.5–2. The aqueous phase is saturated with oxygen to virtually the equilibrium extent if the dimension of the mass-exchange bed in the direction of its flow exceeds by a factor of at least 2 that in the direction of flow of the gas phase.

ACKNOWLEDGMENTS

The authors thank the Russian Foundation for Basic Research (project no. 03-03-32 328) for support of this study.

REFERENCES

1. Moskvin, L.N. and Nikitina, T.G., *Zh. Anal. Khim.*, 2004, vol. 59, no. 1, p. 6322.
2. Kraewska, B., *Polim. Med.*, 1983, vol. 13, nos. 3–4, pp. 93–116.
3. Tanabe, T., *Nirpon Rinsho*, 1985, vol. 43, no. 1, pp. 213–226.
4. *Iskusstvennye organy* (Artificial Organs), Shumakov, V.I., Ed., Moscow: Meditsina, 1990.
5. Moskvin, L.N., *Dokl. Ross. Akad. Nauk*, 1994, vol. 334, no. 5, pp. 599–603.
6. RF Patent 2 023 488.
7. Bel'skikh, A.N., Moskvin, L.N., Katruzov, A.N., *et al.*, Abstracts of Papers, *Mezhdunarodnyi simpozium "Endogennye intoksikatsii"* (Int. Symp. "Endogenous Intoxications"), St. Petersburg, 1994.
8. Moskvin, L.N., *Ross. Khim. Zh.*, 1996, no. 1, pp. 67–76.
9. Lur'e, Yu.Yu., *Analiticheskaya khimiya stochnykh vod* (Analytical Chemistry of Wastewater), Moscow: Khimiya, 1984.
10. Giddings, J.C., *Dynamics of Chromatography*, part 1: *Principles and Theory*, New York: Marcel Dekker, 1965.

Russian Journal of Applied Chemistry, Vol. 77, No. 11, 2004, pp. 1769–1776. Translated from Zhurnal Prikladnoi Khimii, Vol. 77, No. 11, 2004, pp. 1787–1794.

SORPTION AND ION-EXCHANGE PROCESSES

Solubilization Compositions for Template Synthesis of Mesoporous Sorbents

N. A. Yaroshenko and V. G. Il'in

Institute of Sorption and Endoecology Problems, National Academy of Sciences of Ukraine, Kiev, Ukraine
Pisarzhevskii Institute of Physical Chemistry, National Academy of Sciences of Ukraine, Kiev, Ukraine

Received July 28, 2004

Abstract—The suitability of mixed solubilization compositions for template synthesis of mesoporous molecular sieves of various designations was demonstrated by analysis of published data and by the authors' experimental results.

Scientific approach and experimental methods in physical and colloid chemistry of surfactants are developed and improved mostly for individual substances, idealized models, and simple systems. In practice, it is more expedient, however, to use surfactant-based compositions, as, e.g., in production of detergents, flotation reagents, defoliants, emulsifiers, pharmaceuticals, and cosmetics [1–7].

The use of individual micelle-forming surfactants in template synthesis of mesoporous sorbents has been studied since 1992 [8, 9]. Beck *et al*. [8] and Huo *et al*. [9] suggested a number of basic schemes of interaction between a skeleton-forming inorganic reagent (I) and a micelle-forming surfactant (S), template. These authors assumed that the assembly (self-assembly) is controlled by electrostatic interaction of the ions in solution, namely, between charged polar groups of the surfactant and inorganic counterions. This interaction is the most efficient in the case of long-chain surfactants based on quaternary ammonium cations (S^+) and anionic silicate precursors (I^-), yielding hexagonal, cubic, of lamellar mesostructures. More recently, this concept was extended to include the views on the synthesis routes involving inversely charged reagents (S^-I^+), anionic surfactants such as sulfonates and phosphonates, as well as carboxylates and cations of inorganic precursors, buffer ions ($S^+X^-I^+$, $S^-M^+I^-$, where X is halogen, and M^+, alkali metal cation).

Irrespective of the scheme chosen, mesoporous sorbents are synthesized using insoluble/poorly soluble organic substances as auxiliary forming reagents. For example, Beck *et al*. [8] used trimethylbenzene (TMB) exerting a swelling (expanding) effect when added to a freshly synthesized template-containing mesophase: The diameter of the mesoporous molecular sieves (MMSs) increased from 4.0 to 6.5 nm. There is a good reason to assume that TMB is incorporated into the oil core of the micelle of the cationic surfactant.

Nonpolar aliphatic and aromatic hydrocarbons, for the most part, efficiently promote structure formation when introduced into freshly synthesized materials. Hydrocarbons with linear and branched radicals (C_5–C_{12}) yield an M41S phase mixture and/or cause the pore size to increase. At the same time, polar organic substances, in particular, alcohols, aldehydes, ketones, ethers, and esters, generally did not efficiently increase the pore size of the MCM-41 mesophase and, moreover, often yielded amorphous materials [10].

Kleitz *et al*. [11] prepared heat-resistant mesoporous oxides of transition metals (Ti and Zr) using binary organic additives, namely, 1-octanol as cosurfactant and toluene or TMB as swelling reagent. Both additives were introduced simultaneously with all the components (cetyltrimethylammonium bromide, CTMABr, acted as the basic template) into an acidic reaction mixture (RM). The ratio of the additives was varied and, since each additive was fixed at its specific place (cosurfactant was sorbed along the perimeter of the polar groups of the micelle, and TMB, codissolved in the CTMABr micelle core), these authors obtained composite mesostructures of Ti and Zr oxides with the pore diameter increased to 8.0 nm, while the degree of ordering of the hexagonal mesophase was not decreased. It was found that TMB increases the pore size more efficiently than toluene.

Kovalenko *et al*. [12] used organic hydrophobic cocondensing compounds in template synthesis for

1070-4272/04/7711-1769 © 2004 MAIK "Nauka/Interperiodica"

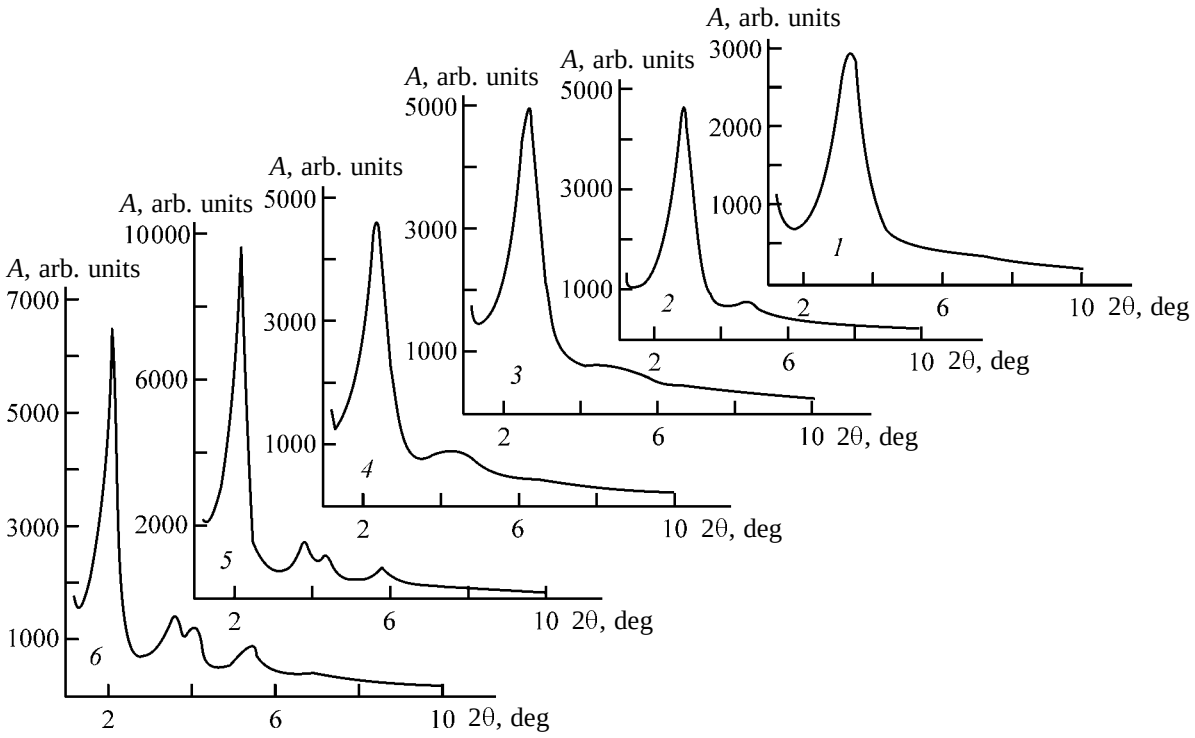

Fig. 1. X-ray diffraction pattern of the monotemplate mesophases prepared from (*1*) octyl-, (*2*) decyl-, (*3*) dodecyl-, (*4*) tetracyl-, (*5*) hexadecyl-, and (*6*) octadecylpyridinium halides. (*A*) Intensity and (2θ) Bragg angle; the same for Figs. 2 and 3. Diffraction pattern nos. correspond to those of the reaction compositions in Table 1 for even sample nos.

preparing a diversity of functionalized MCM-41 materials. In hydrolysis of the ether groups of vinyl- or allyltriethoxysilane, the radicals formed were localized for the most part in the surface layer of the CTMABr micellar structures. This allowed preparation of a material with enhanced catalytic activity by sulfonation of the vinyl (or allyl) groups.

Miyake *et al*. [13] solubilzied phenol and some other organic compounds in an aqueous CTMABr solution to synthesize spherical mesoporous silica with the external diameter of particles of ca. 500 μm. The maximal degree of solubilization of phenol corresponded to the maximal specific surface area (according to BET) of calcined spherical silica.

In our previous work [14] we used a micellar solubilization solution (solubilized were monoethanolamides of medium and higher *n*-aliphatic acids EAC_m with m = 10, 12, 14, 16) to increase the degree of ordering of the spatial organization of the substance rather that the mesopore diameter. This proved to be feasible under mixed solubilization conditions.

We analyzed published data and found that only a few authors used preliminarily prepared solubilization solution in template synthesis. By now, extensive information has been accumulated about template synthesis of MMSs, which allows changing to a meaningful search for and use of solubilization template compositions both for laboratory purposes and for development of an accessible method (technology) of commercial production of nanoporous sorbents. This constitutes the long-term goal of our work.

EXPERIMENTAL

The synthesis conditions and properties were studied most comprehensively for siliceous MMSs, primary mesophases (and further, mesoporous materials) formed by the S^+I^- mechanism, owing to efficient interaction between the cationic surfactants and anionic silicon-containing reagent. As surfactants served alkylpyridinium halide homologs (C_nPyHal) with an even number of carbon atoms in the hydrophobic radical (n = 8–18). In C_{18}PyHal, the counterion was bromide, and in all other homologs, chloride.

The critical micellization concentrations (CMC) of aqueous and aqueous-salt solutions of the surfactants were determined conductometrically.

The synthesis (to be regarded as bitemplate synthesis) differed from that known for the S^+I^- scheme [8, 9] in that a preliminarily prepared micellar solubiliza-

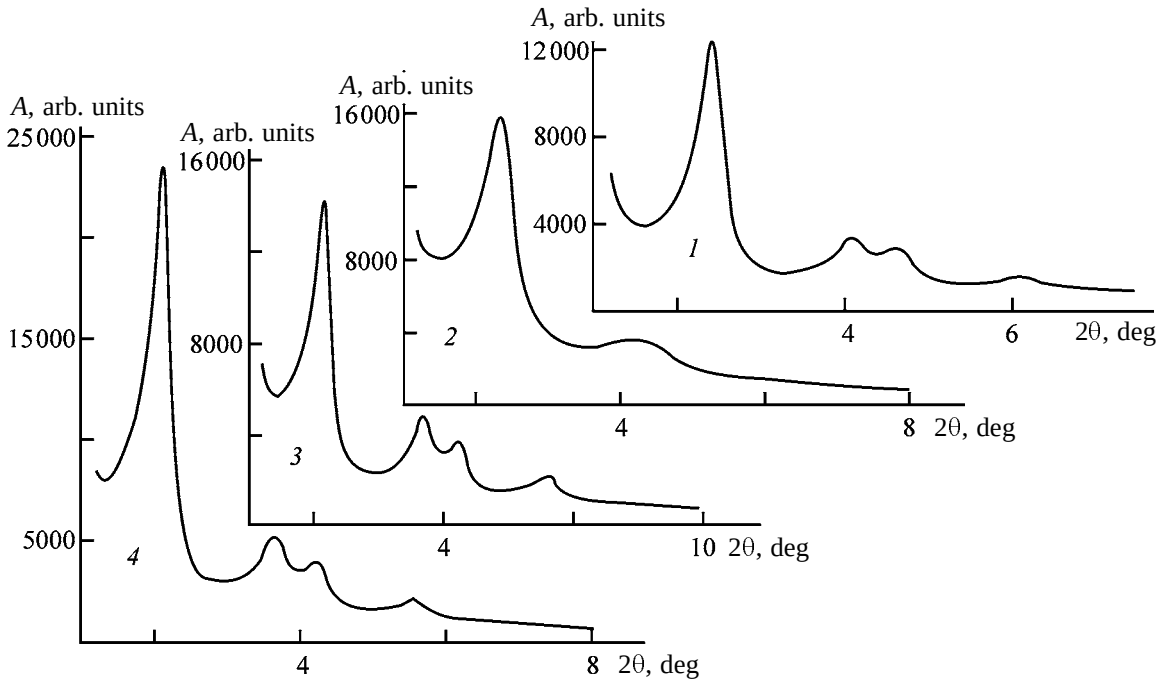

Fig. 2. X-ray diffraction patterns of the calcined samples synthesized from (*1, 2*) C_{16}PyCl and (*3, 4*) C_{18}PyBr monotemplates. HT treatment in (*1, 3*) water and (*2, 4*) mother liquor.

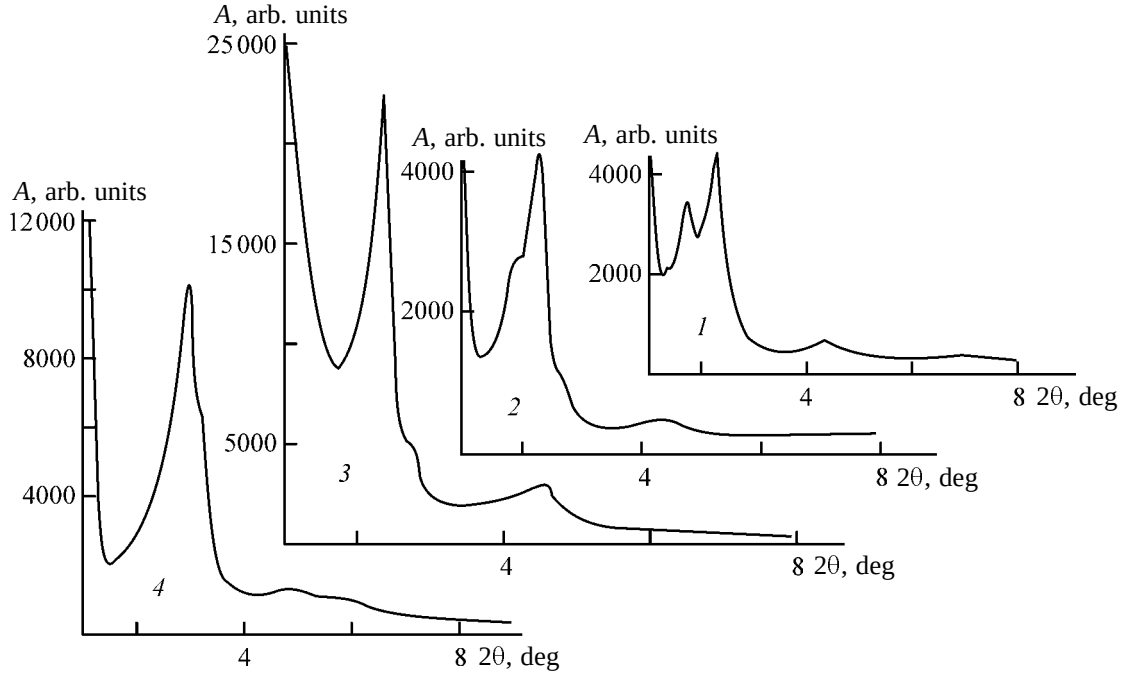

Fig. 3. X-ray diffraction patterns of the sample prepared from C_{10}PyCl solubilization composition and $EAC_{10–12}$ fraction. (*1*) Initial mesophase, (*2*) HT-treated sample, (*3*) HT-treated and calcined sample, and (*4*) sample prepared from a C_{10}PyCl monotemplate after similar HT and heat treatment runs.

tion solution was introduced into a dilute aqueous solution of sodium silicate. As solubilizate served monoethanolamides of saturated *n*-aliphatic acids (EAC_m) with the number of carbon atoms *m* within 10–16. We described the synthesis in detail in [14, 15].

The X-ray diffraction patterns of the freshly synthesized air-dry samples after hydrothermal (HT) and heat treatment were recorded on a DRON-3M diffractometer using monochromatized CuK_α radiation (Figs. 1–3). We assessed the perfection of the spatial

Table 1. Characterization of freshly synthesized alkylpyridinium-containing mesophases MCM-41*

Sample no.	Surfactant	Surfactant : silicate : water molar ratio	Initial solution concentration, mM		d_{100}, nm	a_0, nm	*A*/*W*
			surfactant	Na_2SiO_3			
1	C_8PyCl	1 : 1 : 1720	666	80	2.68	3.09	6
2		1.3 : 1 : 1720	3200	34	2.68	3.09	–
3	C_{10}PyCl	1 : 1 : 1720	333	80	3.15	3.64	29
4		1 : 1 : 1720	1800	34	3.05	3.52	–
5	C_{12}P-Cl	1 : 4 : 4000	14	1230	3.33	3.85	29
6		1 : 2 : 3000	1500	38	3.40	3.93	–
7	C_{14}PyCl	1 : 4 : 5000	12	432	3.68	4.25	32
8		1 : 4 : 5000	1000	44	3.68	4.25	–
9	C_{16}PyCl	1 : 4.3 : 3600	14	1230	3.84	4.44	160
10		1 : 4 : 8000	200	28	4.02	4.64	–
11	C_{18}PyBr	1 : 4 : 7430	7	120	4.21	4.86	31
12		1 : 6 : 8000	25	60	4.42	5.10	–

* a_0 is the hexagonal unit cell parameter of MCM-41.

organization of the initial mesophases and derivatives of MMSs from not only the number, intensity, and resolution of the main reflections, but also from the *A*/*W* parameter [16], i.e., the ratio of the intensity to full width at half maximum of the first diffraction line (corresponding to the interplanar spacing d_{000}) (Table 1). Notably, structure formation of the mesophases continues when the samples are being dried. Figure 1 and Table 1 (samples with even numbers) present the X-ray diffraction patterns and selected X-ray phase analysis (XPA) results for the monotemplate-containing materials after keeping (aging) air-dry for 2 months.

Naturally, it could be suggested that creative interaction is possible under specific (in the limit, optimal) ratio between the inorganic reagent, each subsequent surfactant homolog, and water, whose role in template synthesis is not restricted to that of a solvent. Though the overwhelming majority of the publications is concerned with synthesis of MMSs specifically by the S^+I^- scheme [8, 9, 17], there are no clear concept and methodology of synthesis of mesophases and, consequently, MMSs, to determine the nature of the corresponding changes in the RM composition on going from one surfactant (template) homolog to another, which afford the optimal structure and sorption and other characteristics of the intermediate and end materials.

One of the approaches, partially implemented in [18], consists in introduction (preferentially dropwise) with stirring of a concentrated [in the region of stable existence of platelike micelles (concentration $c > CMC_3$)], solution of the surfactant into a dilute aqueous solution of Na_2SiO_3 (density ~1.02–1.03 g cm^{-3}). This affords optimal charge localization and distribution and size and shape of the complex anionic moieties. In a dilute Na_2SiO_3 solution, the surfactant concentration decreases to that intermediate between CMC_2 and CMC_3 (CMC_2 refers to cylindrical micelles), which results in spontaneous formation and packing of the hexagonal micellar structure. Table 2 shows that CMC_3 of aqueous AlkPyHal solutions significantly (15–20-fold) exceeds CMC_1. Evidently, this can be helpful for extrapolation of the initial concentration of the surfactant solutions, if CMC_2 and CMC_3 data for the given ionic strength of solution are lacking. Beck *et al*. [8] and Romannikov [17] took alkyl(C_{12}–C_{18})trimethylammonium bromides at a fixed molar ratio of the components for preparing mesophase materials with a hexagonal unit cell parameter a_0 varying from 3.53 to 4.61 nm, and HT-treated materials with a_0 varying from 3.95 to 4.82 nm. These authors concluded that, under these specific conditions, the main stages and the entire mechanism of formation of silica-micellar mesophases are weakly dependent on the alkyl chain length and are governed by polycondensation during the HT and thermal treatments.

Successive lengthening of the linear alkyl radical by two methylene groups (2.6 Å) implies a certain interrelation between the d_{000} and a_0 parameters of the mesophase materials. For example, a proportional increase in these parameters is observed for the major axis of the spheroidal micelles of individual surfactants with lengthening hydrocarbon radical, as well as with changing other parameters.

Table 2. Critical micellization concentrations c^* of aqueous and aqueous-salt solutions of *N*-alkylpyridinium halides

System	c, mM			Ionic strength of solution at CMC_1
	CMC_1	CMC_2	CMC_3	
C_8PyCl–water	184.2	**		0.1842
C_8PyCl–0.2 M NaCl	184.2	**		0.3842
C_{10}PyCl–water	78.12	**		0.07812
C_{10}PyCl–0.2 M NaCl	23.44	**		0.22344
C_{12}PyCl–water	16.40	90.0	130.3	0.0164
C_{12}PyCl–0.2 M NaCl	4.93	14.1	61.6	0.20493
C_{14}PyCl–water	3.53	13.5	70.5	0.00353
C_{14}PyCl–0.2 M NaCl	0.96	8.0	48.1	0.20096
C_{16}PyCl–water	1.47	9.7	48.1	0.00147
C_{16}PyCl–0.2 M NaCl	0.21	**		0.20021
C_{18}PyBr–water	0.18	**		0.00018
C_{18}PyBr–0.2 M NaCl	0.03	**		0.20003

* At the actual ionic strength of solution.
** Micelles with more complex structure are not formed.

Table 1 summarizes the results of the syntheses of a number of mesophases with the hexagonal structure, attempted by us to further develop the synthesis concept suggested. Samples with odd numbers (1–11) are characterized by a maximum possible number of reflections for each homolog. Samples with even numbers (2–12) exhibit a proportionality between the first reflection intensity A, d_{000}, and a_0, but, unfortunately, they give a smaller number of reflections in the X-ray diffraction patterns. Notably, for both sample series the increment in d_{000} of the mesophases in going from the C_n to C_{n+2} template is much smaller than the length of two methylene groups of the two radicals whose ends meet at the center of the hydrophobic core ($0.26 \times 2 = 0.52$ nm). Probably, the hydrocarbon radicals get compressed in the oil core of the micelle and also undergo cross penetration and compaction.

Table 1 also shows that, upon lengthening of the template radical by two methylene groups, samples with odd numbers exhibit widely scattering differences between d_{000} (from 0.47 to 0.16 nm with an average of 0.30 nm) and, correspondingly, a_0 (from 0.55 to 0.19 nm, with an average of 0.36 nm). For the even sample series this scatter is much smaller, due, evidently, to a more perfect spatial organization of the substance (mesophase components).

We demonstrated earlier [14] that the perfection of alkylpyridinium-containing mesophases depends on the surfactant radical length. Materials with fairly perfect spatial organization can be prepared by templating $C_{16,18}$Py halides. After HT treatment for 72 h and calcination, the samples clearly exhibit four intense reflections in the X-day diffraction patterns (Fig. 2). Changes in the formation conditions, in particular, in the time of (co)mature, medium, and the HT and heat treatment temperature, markedly affect the perfection of the template-containing mesophases. We found that, for homologs with lower molecular weights, an efficient pathway lies in bitemplate synthesis based on mixed solubilization, when an insoluble/poorly soluble organic compound is solubilized in a solution of a typical micelle-forming surfactant. We listed the properties of the solubilizate and solubilizer, which afford mixed solubilization yielding mesophases with a fairly perfect three-dimensional structure.

To further develop this approach, we studied in more detail how the organoelemental solubilizate affects the perfection of the three-dimensional structure of the primary mesophases and MMSs thereof (Table 3). As organoelemental compounds served trialkylphosphine oxides $(H_{2n+1}C_n)PO$ with n = 8, 10, 12, 16. Their characteristic features affording mixed solubilization are as follows: a long linear radical; low water solubility (8–2 mg l^{-1} at 50°C for C_{10}–C_{16}); and a dipole moment of 2.66 D [19], which is responsible for dipole induction and formation of a stable polar shell of the micelle in interaction with the surfactant cation; the lack of substituents in the polar group and in hydrocarbon radicals, which could sterically hinder intermolecular interaction in the micelle; and the capability for hydrogen bonding with oxygen and hydroxy groups of the inorganic reagent. Trialkyl-

Table 3. Formulations of the bitemplate reaction mixtures and characterization of the structure of the nanoporous samples synthesized using insoluble/poorly soluble solubilizates. Calcination temperature 580°C

Sample no.	Reaction mixture formulation, AlkPyHal : $(C_m)_3P$: Na_2SiO_3 : H_2O, mol	HT treatment medium, 80°C	Structure characterization	
			d_{100}, Å	A/W
1	$C_{14}Py$, $(C_{10})_3P$; 1 : 0.05 : 5 : 3780	Mother liquor	38.81	43
2	$C_{12}Py$, $(C_8)_3P$; 1 : 0.09 : 2 : 1722	H_2O	35.40	48
3	$C_{16}Py$, $(C_{12})_3P$; 1 : 0.07 : 2 : 2556	Mother liquor	42.50	45
4	$C_{16}Py$, $(C_{10})_3P$; 1 : 0.09 : 4 : 5000	Mother liquor	44.35	40
5	$C_{14}P$-, EAC_{10}; 1 : 0.25 : 4 : 3333 [14]	H_2O	36.81	15

phosphine oxides also differ advantageously from aliphatic acid ethanolamides in enhanced thermal stability (because the C–P bond formed is stronger than C–C, and all the more than C–N) and in the specific stereochemical structure resembling a small shuttlecock, which favors expansion (increase in the volume) of the oil core of the micelle.

The organoelemental solubilizates with such properties, combined with a thermally stable surfactant (e.g., long-chain alkyltrimethylammonium bromide) as solubilizer, allow the temperature of HT treatment to be widely varied so as to reduce its time to 5–18 h. Table 3 shows that an organoelemental solubilizate with a relatively lower content in the micellar solubilization solution yields a mesoporous sorbent with improved structural characteristics.

The solubilization power and, thereby, the properties of the micellar structure, its interaction with inorganic reagents in the initial, ion-molecular stage of the mesophase formation can be controlled, in particular, by varying the composition of the medium and temperature. It is known that, with increasing solubilizate concentration in a solution of a neutral electrolyte, the specific solubilization S_{sp} of hydrocarbons and polar substances varies differently: With increasing concentration of a micellar surfactant S_{sp} tends to increase for hydrocarbons and decrease for polar solubilizates; with increasing amount of the neutral electrolyte S_{sp} also tends to decrease for polar solubilizates and increase for hydrocarbons [7]. In systems described by the relationships characteristic of mixed solubization, both trends in variation of the solubization power and several intermediate (transition) trends are observed, depending on the electrolyte and surfactant concentrations, the length of the hydrocarbon radical of the solubilizate and solubilizer, and some other factors [20].

Another approach to formulating solubilization compositions suitable for template synthesis of nanosorbents implies the use of close-cut surfactant fractions as both solubilizer and solubilizate. It should be noted that the use of wide fractions inevitably entails polytemplation and solubilization effect. Figure 3 illustrates how the solubilizate, with the example of monoethanolamide based on a low-molecular-weight fraction of C_{10}–C_{12} aliphatic acids, affects the structural characteristics of the end mesoporous sorbent, with decylpyridinium chloride serving as solubilizer. It is seen that, in the case of the solubilization bitemplate composition, the first reflection of the calcined sample grows in intensity manyfold compared to the freshly prepared sample. Compared to the calcined sample synthesized from the $C_{10}PyCl$ monotemplate, the reflection in the case of the solubilization bitemplate composition gets much more symmetrical and also grows in intensity (at the reagent molar ratio $C_{10}PyCl$: $EAC_{10–12}$: Na_2SiO_3 : H_2O = 1 : 0.5 : 1 : 1700; the mesophase was subjected to HT treatment in an aqueous medium at 80°C and calcined at 580°C).

The advantage of close-cut fractions of the solubilizate and solubilizer consists in that they form micelles with a more uniform surface (chemical nature, relief features, and curvature), characterized by a denser packing of the hydrocarbon radicals in the micelle core. Kryukova *et al*. [21] found that a significant portion of the radicals of an individual micelle-forming surfactant (40 – 60%, depending on its length) adjoins the polar group and contacts water. In the case of formation of a mixed two-component micelle ($C_{10}PyCl$ + $EAC_{10–12}$), the basic micelle-forming surfactant interacts with the surfactant fractions with shorter chains, i.e., water molecules are forced out of the hydrocarbon space. As a consequence, the micelle gets more "ideal." Once the optimal S_{sp} for several close-cut fractions of a specific solubilizate–solubilizer pair is determined, it is possible to formulate a series of solubilization composi-

tions for template synthesis of nanosorbents of various designations.

Thus, published data concerning the use of two- and multicomponent templates (mixtures of two micelle-forming surfactants and other versions) for synthesis of MMSs suggest the following. Cases of using preliminarily prepared and specially formulated solubilization solutions in the MMS synthesis were only few. The other researchers took advantage of one of the alternatives: codissolution of a hydrocarbon in the micellar core of the freshly formed mesophase [8, 10], introduction of a multicomponent template directly into the reaction [11], or utilization of cocondensing organic hydrophobic compounds in the synthesis [12]. In the latter case, localization of the hydrophobic–hydrophilic radicals in the surface layer of the micellar structures can be characterized as ad-solubilization. By this is meant, according to Esumi [22], formation of layers, adsorbed by surfactants, on hydrophobic particles, which favors incorporation of water-insoluble compounds into surfactant layers. The above-mentioned factors affecting the nature of ad-solubilization (surfactant structure, type of water-insoluble compounds, particle type) are generally close to those affording efficient solubilization, i.e., formation of a thermodynamically stable micellar solution of compounds insoluble in the given solvent. The suggested term "adsolubilization" implies cosorption of micelle-forming surfactants and water-insoluble compounds on the surface of hydrophobic particles.

On the whole, the use of solubilization compositions as templates seems to be an efficient and technologically sound method of preparation and, probably, production of a homologous series of organo–inorganic mesophases, micro- (template-containing) and mesoporous sorbents with regularly varying parameters of the spatial organization and pore structure, differing in the topography and nature of the sorption space surface, as well as of inclusion compounds and nanocomposites of various functional designations thereof.

CONCLUSIONS

(1) Solutions of micelle-forming surfactants in a specific for a certain homolog concentration range, corresponding to stable existence of plate-like micelles, are suitable for template synthesis of sorbents. The molar ratio of the reagents (surfactant : inorganic component) tends to increase on successively changing to a homolog with a higher molecular weight.

(2) The concept of bitemplate synthesis by mixed solubilization using solubilization solutions was further developed by studying how organoelemental solubilizate [trialkylphosphine oxide $(H_{2n+1}C_n)PO$ with n = 8, 10, 12, 16] affects the perfection of the structure of nanoporous silica sorbents.

(3) The close-cut fraction of carboxylic acid C_{10}–C_{12} monoethanolamides was tested as solubilizate for a bitemplate composition, and its influence on the structure formation of a low-molecular-weight (C_{10}PyCl) surfactant homolog and nanoporous materials thereof was elucidated.

(4) A technology of production of nanosorbents from bitemplate compositions comprised of a close-cut fraction of surfactants as solubilizer and a close-cut fraction of solubilizate was suggested and substantiated.

REFERENCES

1. *Emulsion Science*, Sherman, P., Ed., London: Academic, 1968.
2. Schwartz, A. M. and Perry, J. W., *Surface Active Agents. Their Chemistry and Technology*, New York: Interscience, 1949.
3. Schwartz, A.M., Perry, J.W., and Berch, J., *Surface Active Agents and Detergents*, New York: Interscience, 1958.
4. Stüpel, H., *Synthetische Wasch- und Reinigungsmittel. Chemie, Klassifikation, Technologie, Komposition, Anwendung, Untersuchungsmetoden und wirtschaftliche Bedeutung*, Stuttgart: Konradin, 1957.
5. Chwala, A., *Textilhilfsmittel; ihre Chemie, Kolloidchemie und Anwendung*, Wien: Springer, 1939.
6. Schönfeldt, N., *Oberflächenaktive Anlagerungsprodukte des Äthylenoxyds. Ihre Herstellung, Eigenschaften und Anwendung*, Stuttgart: Wissenschaftliche, 1959.
7. Rebinder, P.A., *Izbrannye trudy: Poverkhnostnye yavleniya v dispersnykh sistemakh: Kolloidnaya khimiya* (Selected Works: Surface Phenomena in Dispersed Systems: Colloid Chemistry), Moscow: Nauka, 1978.
8. Beck, J.C., Vartuli, W.J., Roth, M.E., *et al*., *J. Am. Chem. Soc*., 1992, vol. 114, pp. 10 834–10 843.
9. Huo, Q., Margolese, D.J., Ciesla, U. *et al*., *Nature*, 1994, no. 368, pp. 317–323.
10. Biz, S., and Occelli, M.L., *Catal. Rev.—Sci. Eng*., 1998, vol. 40, no. 3, pp. 329–407.
11. Kleitz, F., Czuryszkiewicz, T., Dufau, N., *et al*., *Deutsche Zeolith-Tägung*, 2002, March, pp. 6–8.

12. Kovalenko, A.S., Chernenko, Zh.V., Kochkin, Yu.N., *et al*., *Teor. Eksp. Khim*., 2002, vol. 38, no. 5, pp. 308–313.
13. Miyake, Y., Yumoto, T., Kitamura, H., and Sugimoto, T., *Phys. Chem. Chem. Phys*., 2002, vol. 4, no. 12, pp. 2680–2684.
14. Yaroshenko, N.A., Shvets, A.V., Solomakha, V.N., *et al*., *Kolloidn. Zh*., 2003, vol. 65, no. 4, pp. 563–568.
15. Bobonich, F.M., Yaroshenko, N.A., Solomakha, V.N., *et al*., *Kolloidn. Zh*., 2003, vol. 65, no. 4, pp. 448–453.
16. Cheng, C.F., He, H.Y., Zhou, W.Z., and Klinowski, J., *Chem. Phys. Lett*., 1995, vol. 244, pp. 117–120.
17. Romannikov, V.N., Fenelonov, V.B., and Derevyankin, A.Yu., *Izv. Akad. Nauk, Ser. Khim*., 1999, no. 10, pp. 1852–1856.
18. Ukrainian Patent 42372A.
19. Hudson, R.F., *Structure and Mechanism in Organophosphorus Chemistry*, London: Academic, 1965.
20. Demchenko, P.A. and Yaroshenko, N.A., *Kolloidn. Zh*., 1973, vol. 35, no. 4, pp. 751–753.
21. Kryukova, G.N., Kasaikin, V.A., Markina, Z.N., and Sineva, A.V., *Kolloidn. Zh*., 1981, vol. 43, no. 4, pp. 660–665.
22. Esumi, K., *J. Colloid Interface Sci*., 2001, no. 241, pp. 1–17.

Russian Journal of Applied Chemistry, Vol. 77, No. 11, 2004, pp. 1777–1780. Translated from Zhurnal Prikladnoi Khimii, Vol. 77, No. 11, 2004, pp. 1795–1798.

APPLIED ELECTROCHEMISTRY AND CORROSION PROTECTION OF METALS

Joint Electrolytic Deposition of Vanadium(V) and Chromium(III) Oxides from Aqueous Sulfate Solutions

V. M. Nagirnyi, R. D. Apostolova, A. S. Baskevich, and E. M. Shembel'

Ukrainian State University of Chemical Engineering, Dnepropetrovsk, Ukraine

Received June 4, 2004

Abstract—The conditions of the joint electrolytic deposition of vanadium(V) and chromium(III) oxides from mixed sulfate solutions at different concentration ratios of the main components were studied.

Vanadium(V) oxide deposited on the anode from oxovanadium(IV) sulfate solutions in the presence of Mn(II) and Ni(II) ions has the higher specific characteristics compared to the bulk oxide [1, 2]. This is due to the formation of complex nonstoichiometric oxide systems having high electrochemical activity. Therefore, the oxide system formed by the joint electrolytic deposition of V_2O_5 and chromium(III) oxide from mixed salt solutions is of interest. Cr_2O_3 has the positive effect on the specific discharge characteristics of the complex oxide systems based on manganese oxide and other systems [3, 4]. The oxide system under consideration is also of interest, since, as a rule, Cr_2O_3 is not spontaneously deposited in electrolysis of aqueous solution. Data concerning the given problem are lacking.

We studied two-component solutions of oxovanadium(IV) and chromium(III) sulfates with a total concentration of 0.20 – 0.25 M and the ratio of component concentrations (hereinafter, V : Cr) varied from 15 : 1 to 3 : 1. To prepare the solutions, we used pure grade and analytically pure grade chemicals and distilled water. The electrolysis was performed in a 200-ml temperature-controlled glass cell. The temperature was similar in all the experiments, $85 \pm 3°C$, and the pH was varied within 1.8–2.0. These conditions were chosen on the basis of the preliminary study [5]. Compact coatings were deposited onto both sides of smooth platelike anodes ($10 \times 10 \times 0.3$ mm). The cathodes were smooth plates of VT-1 technical-grade titanium with the ratio $S_a : S_c = 1 : 5$. The efficiency of the anodic process was estimated from the conventional current efficiency CE_{con} (wt %) assuming that in the total anodic process all the efficient current is spent for V_2O_5 formation. This assumption was made because determination of the electrochemical equivalent q [g (A h)$^{-1}$] of the anodic deposits studied was virtually impossible. The phase composition of the deposits was studied by X-ray diffraction (DRON-2 diffractometer, CoK_α radiation). These data were used to calculate CE_{con} by vanadium(V) oxide in the total anodic process at various ratios of the $VOSO_4$ and $Cr_2(SO_4)_3$ concentrations in the solution. The volt–ampere characteristics of the total anodic processes were taken with a 12Cr18Ni9Ti steel anode (S = 1 cm^2) finished to V 7–8 class and cathodes made of VT-1 titanium at the above parameters of the electrolysis within i_a = 0.5–50 mA cm^{-2}. The potentials were measured relative to a silver chloride reference electrode (E = +0.225 V) using a Shch-4315 digital device. The CE_{con} values were also used for constructing partial polarization curves.

The conventional current efficiencies CE_{con} by the double V–Cr oxide as functions of the current density i_a at various concentration ratios of oxovanadium(IV) to chromium(III) sulfates (under equal other conditions) are presented in Fig. 1. The dependences have a steep ascending branch and a nearly symmetric descending branch in the range i_a = 5–12.5 mA cm^{-2}. At higher current densities, the right branch shifts regularly to a certain minimum. At V : Cr from 1 : 0 to 4 : 1, the curves pass through a well-defined maximum at i_a = 7.5 mA cm^{-2} (curves *1*–*3*), and at V : Cr = 3 : 1, at i_a = 10 mA cm^{-2} (curve *4*). Comparison of the dependences (Fig. 1) shows that Cr(III) ions strongly affect the character of the anodic processes. This is revealed as change in the rate of formation of the anodic deposit in the solution on adding Cr(III) ions. At relatively low $Cr_2(SO_4)_3$ concentration in the solution (V : Cr = 8 : 1), CE_{con} by the anodic deposit (Fig. 1, curve *1*) is considerably higher than in the solution without Cr(III) ions (Fig. 1, curve *2*). However, as the Cr(III) concentration is in-

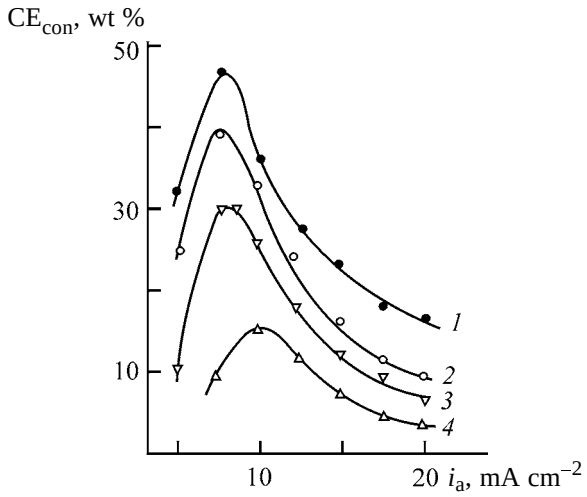

Fig. 1. Conventional current efficiency CE_{con} by the anodic deposit vs. the anodic current density i_a. Total concentration of the solutions 0.2–0.25 M, 85°C, pH 2.0; the same for Figs. 2–4. Concentration ratio of oxovanadium(IV) and chromium(III) sulfates (V : Cr): (*1*) 8 : 1, (*2*) 1 : 0, (*3*) 4 : 1, and (*4*) 3 : 1.

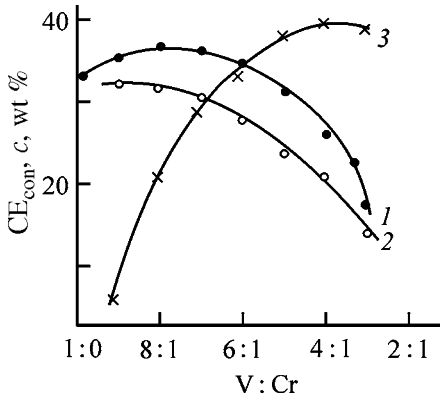

Fig. 2. Conventional current efficiency CE_{con} by (*1*) V–Cr double oxide and (*2*) vanadium(V) oxide, and (*3*) Cr_2O_3 content in the anodic deposit c vs. the V : Cr concentration ratio in the solution.

Conventional current efficiency by the anodic deposit V–Cr and relative and specific contents of Cr_2O_3 in the deposit at various V : Cr ratios in the solution and a prescribed conventional mass of the deposit*

V : Cr	CE_{con}, wt %	Conventional mass of deposit, mg	Amount of Cr_2O_3 in deposit	
			wt %	mg
1 : 0	35	3.5	–	–
8 : 1	37.5	3.75	20	0.75
6 : 1	35	3.5	33	1.15
4 : 1	32	3.2	37	1.18
3 : 1	28	2.8	40	1.13

* Data at i_a = 10 mA cm^{-2} and equal other electrolysis conditions.

creased further, CE_{con} considerably decreases and attains the critical value at V : Cr ≤ 3 : 1 (Fig. 1, curve *4*). This value agrees with the limiting content of Cr_2O_3 in the anodic deposit (Fig. 2, curve *3*). This trend is clearly seen when comparing CE_{con} by the anodic deposit and V_2O_5 as a function of the V : Cr ratio in the solution (Fig. 2, curves *1*, *2*). At V : Cr = 3 : 1, the corresponding values of CE_{con} are similar, which indicates that the total deposition rate and rate of V_2O_5 deposition become equal. Comparison of the CE_{con} values for various V : Cr ratios with the Cr_2O_3 content in the deposits (Fig. 2) shows that the specific mass of the doping component in the deposits remains virtually the same (see table).

The data presented (Fig. 1, 2) show that the V : Cr concentration ratio in the solution exerts a decisive effect on the kinetics of the anodic processes. This ratio determines the relative rate of the parallel reactions proceeding simultaneously at the anode: formation of the anodic deposit and O_2 evolution on the surface whose properties vary depending on the electrolysis conditions. The mutual influence of these reactions is complicated by redox processes of Cr(III) → Cr(VI) anodic oxidation and Cr(VI) → Cr(III) chemical reduction, which proceed simultaneously at the anode. The occurrence of these reactions is suggested, in particular, by the fact that the doping component in the anodic deposit is Cr_2O_3.

This conclusion is confirmed by the volt–ampere characteristics of the processes studied (Fig. 3). Their comparison shows that the curves of the total process and the partial curves of O_2 evolution are similar and have two ascending branches with a transition plateau between them (Fig. 3, curves *1*, *1*', and *4*, *4*'). Hence, it follows that the rate-determining reaction in the total process is O_2 evolution. The polarization is the lowest for the joint process of O_2 evolution and V_2O_5 deposition, and then it increases with decreasing Cr(III) content in a solution. For the curves of the total process and those of partial oxygen evolution, the current densities at the transition plateau decrease in the same order. On the surface with a preliminarily deposited layer, the polarization at the same V : Cr ratio in the solution is lower (Fig. 3, curve *4*''). In this case, clearly resolved inflections on the corresponding dependence are absent.

The partial curves of separation of the anodic deposit itself (Fig. 3, curves *1*'', *3*', *4*''') have sections which steeply ascend to certain limiting value and then pass a plateau. The limiting current densities decrease with increasing Cr(III) concentration in a solution. The exception is the partial curve of the V_2O_5

deposition with a steeper descending branch. The positions of extrema on the potential axis of the partial curves coincide with the analogous extrema in the total curves, which confirms similarity of the processes in each their section.

Analysis of the i_a–E_a curves presented here (Fig. 3) shows that their character is mainly determined by the relative rate of the joint anodic processes, which involves the formation of the anodic deposit, oxygen evolution, and probable redox reaction by the equations

$$2VO^{2+} + 3H_2O - 2e \rightarrow V_2O_5 + 6H^+, \quad E^0 = 1.1 \text{ V}; \quad (1)$$

$$2Cr^{3+} + 7H_2O - 6e \rightarrow Cr_2O_7^{2-} + 14H^+, \quad E^0 = 1.3 \text{ V}; \quad (2)$$

$$2H_2O + 2e \rightarrow O_2 + 4H^+, \quad E^0 = 1.23 \text{ V}; \quad (3)$$

$$18VO^{2+} + 2Cr_2O_7^{2-} + 19H_2O - 6e \rightarrow 9V_2O_5 + 2Cr_2O_3 + 38H^+. \quad (4)$$

The kinetic features of the anodic process consisting in that the anodic polarization in a solution containing small content of Cr(III) is lower than that in a pure oxovanadium(IV) solution are not fully understood. The same phenomenon was observed in anodic deposition of V_2O_5 from oxovanadium(IV) solution in the presence of Mn(II) ions [6]. This suggests that, at low concentration of Cr(III) ions (V : Cr = 8 : 1), the reaction (4) precedes reaction (2). Therefore, the forming Cr_2O_3 can block the anode surface and drastically decelerate the O_2 evolution; as a consequence, it can increase the anodic polarization. This corresponds to the extreme right position of the corresponding curves, i.e., total curve and partial curve of O_2 evolution (Fig. 3, curves *4*, *4*'). In the given case, the high O_2 overvoltage facilitates formation of the anodic deposit and exhaustion of the near-electrode space. For this reason, the limiting current density in the total curve is the lowest, and, on the contrary, that in the partial curve, the highest (Fig. 3, curves *4*, *4*'''). Apparently, this result is responsible for the fact that the limiting rate of formation of the anodic deposit is independent of E_a and that the relative rates of the anodic reactions, established correspondingly at each E_a value, are similar. Because the anode with a preliminarily deposited layer has the more developed surface, the blocking effect on it is lower and O_2 evolution occurs at lower polarization (Fig. 3, curve *4*'').

At higher concentrations of Cr(III) ions in a solution, consumption of dichromate ions by reaction (4) is delayed, and their excess amount appears in the near-surface layer of the anode. This may favor a decrease of the O_2 overvoltage by analogy with the effect observed in the course of the electrolysis of water [7]. Apparently, it can explain why with increasing Cr(III) concentration the limiting current densities increase and the total and partial curves shift to lower anode potentials (Fig. 3).

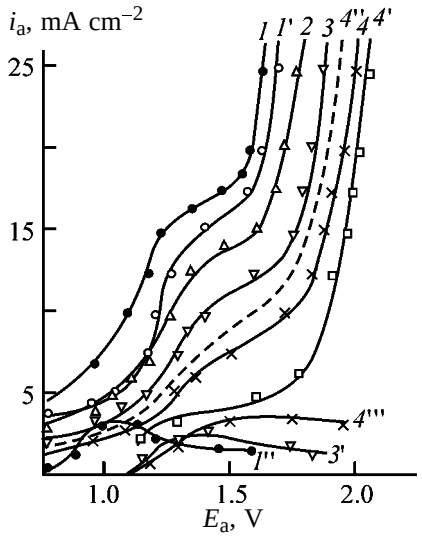

Fig. 3. i_a–E_a dependences taken in anodic deposition of (*1*) V_2O_5 and (*2*) V–Cr double oxide at different concentrations of the salts in a solution. V : Cr: (*2*) 3 : 1, (*3*) 4 : 1, (*4*) 8 : 1, and (*4*'') 8 : 1 (deposition onto the preliminarily formed film of the deposit). (*1*', *4*') Partial curves of the O_2 evolution with, respectively, vanadium(V) oxide and V–Cr double oxide (V : Cr = 8 : 1); (*1*'', *3*', *4*''') partial curves of the anodic deposit formation at V : Cr 1 : 0, 3 : 1, and 8 : 1, respectively.

The outward appearance and structure of the deposits studied directly depend on the electrolysis conditions. At the optimal values of the current densities (7.5–12.5 mA cm^{-2}) and V : Cr from 10 : 1 to 6 : 1, the deposits are characterized by the developed specific surface area having black color and amorphous structure typical of "pure" anodic deposits of V_2O_5.

At higher relative concentration of Cr(III) in the solution, the deposits become more compact and have clear crystalline structure. Increasing the current density above the limiting value makes the deposit surface nonuniform (i.e., results in appearance of regions of different color and roughness). This is manifested most clearly at V : Cr from 4 : 1 to 2 : 1 and is evidently associated with the increased concentration of Cr_2O_3 in the deposits. Also, this is manifested in the increased intensities of the reflections corresponding to the γ-Cr_2O_3 phase in the diffraction

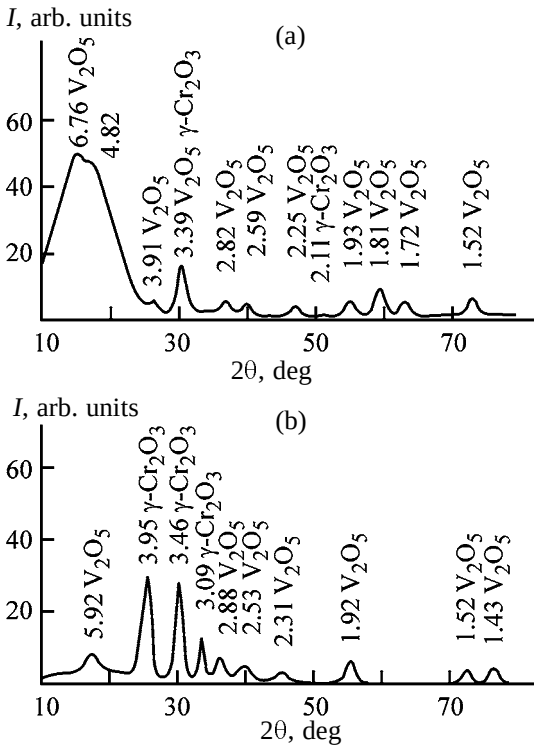

Fig. 4. Diffraction patterns of the V–Cr double deposits obtained at the V : Cr ratio in the solution of (a) 8 : 1 and (b) 4 : 1. (*I*) Relative intensity and (2θ) Bragg angle.

patterns of the precipitates obtained at higher concentration of Cr(III) ions in the solution (Fig. 4). According to the X-ray diffraction analysis, the deposits obtained under the conditions studied are two-phase systems V_2O_5–γ-Cr_2O_3, whose structure and phase composition are reasonably uniform for the given conditions of the electrolysis (Fig. 4). These data allow the materials studied to be classed with crystalline conglomerates whose constituting components enter into molecular interphase interaction.

CONCLUSIONS

The conditions for the formation of V–Cr double oxide materials from mixed sulfate solutions of the jointly deposited metals at the ratio of their concentrations V : Cr from 1 : 0 to 2 : 1 were studied. Reasonably compact coatings with the uniform structure can be deposited from the corresponding anode systems onto gauze and smooth platelike anodes made of 12Cr18Ni9Ti steel or aluminum with a current efficiency of 40–45 wt % in the course of the electrolysis from the above solutions at a total concentration of 0.2–0.25 M, concentration ratio V : Cr from 8 : 1 to 3 : 1, 80–85°C, pH 1.9–2.2, and the anodic current density of 7.5–12.5 mA cm^{-2}.

REFERENCES

1. Le Gal La Salle, A., Guyomard, D., Verbaere, A., and Piffard, Y., Abstracts of Papers, *9th Int. Meet. on Lithium Batteries*, Edinburg (Scotland), July 12–17, 1998, part II, Thursday, report no. 91.
2. Potiron, E., Le Gal La Salle, A., Piffard, Y., *et al*., Abstracts of Papers, *10th Int. Meet. on Lithium Batteries*, Como (Italy), May 28–June 2, 2000, p. 157.
3. Shembel, E., Nagirny, V., Apostolova, R., *et al*., Abstracts of Papers, *10th Int. Int. Meet. on Lithium Batteries*, Como (Italy), May 28–June 2, 2000, p. 105.
4. Shembel, E., Apostolova, R., Nagirny, V., *et al*., Abstracts of Papers, *10th Int. Int. Meet. on Lithium Batteries*, Como (Italy), May 28–June 2, 2000, p. 159.
5. Shembel', E.M., Nagirnyi, V.M., Apostolova, R.D., and Chaikovskaya, I.M., *Zh. Prikl. Khim*., 2000, vol. 73, no. 3, pp. 409–412.
6. Nagirnyi, V.M., Apostolova, R.D., Baskevich, A.S., *et al*., *Zh. Prikl. Khim*., 2002, vol. 75, no. 4, pp. 566–571.
7. Yakimenko, L.M., Modylevskaya, I.D., and Tkachek, Z.A., *Elektroliz vody* (Electrolysis of Water), Moscow: Khimiya, 1970.

Russian Journal of Applied Chemistry, Vol. 77, No. 11, 2004, pp. 1781–1785. Translated from Zhurnal Prikladnoi Khimii, Vol. 77, No. 11, 2004, pp. 1799–1803.

APPLIED ELECTROCHEMISTRY AND CORROSION PROTECTION OF METALS

Electrodeposition of Tin from Sulfate Electrolyte in the Presence of Syntanol, Formaldehyde, and Allyl Alcohol

G. I. Medvedev and N. A. Makrushin

Novomoskovsk Institute, Mendeleev Russian University of Chemical Engineering, Novomoskovsk, Tula oblast, Russia

Received April 23, 2004

Abstract—The elecrodeposition of tin from a sulfate solution containing $SnSO_4$, H_2SO_4, Syntanol, formaldehyde, and allyl alcohol was studied.

Organic substances ensuring formation of lustrous tin coatings can be chosen taking into account their first ionization potentials I [1]. It was established that obtaining lustrous tin coatings requires the presence of organic substances, luster-producing additives (LA), with I = 7.25 or 8.95–10.50 eV in an electrolyte containing Syntanol DS-10 and formaldehyde (37% solution).

We studied the influence exerted by allyl alcohol having I = 10.17 eV on the tin electrodeposition from a sulfate solution containing Syntanol and formaldehyde.

The study was performed in an electrolyte containing (g l^{-1}) $SnSO_4$ 10–50 and H_2SO_4 90–100. Organic substances were added into the electrolyte in the following amount: Syntanol DS-10 1–4 g l^{-1}, formaldehyde (37% solution) 1–10, and allyl alcohol 1–20 ml l^{-1}.

A 9–12-μm-thick tin layer was deposited onto copper samples. The polarization curves were taken with a P-5828 potentiostat. The degree of the coating luster was determined on an FB-2 photoelectric brightness-measuring device. The leveling power P of the electrolytes was determined by a direct method involving a profilographic measurement of the sample surface with a sine-shaped microprofile and calculation by the formula [2]

$$P = 2.3a/2\pi h_{av} \log (H_0/H_i),$$

where a is the amplitude of the wave of the sine-shaped microprofile; h_{av}, average thickness of the coatings (10 μm); H_0 and H_i, initial and final wave amplitudes of the sine-shaped profile, respectively.

The capacitance of an electrical double layer was measured in the course of electrolysis with a P-5021 ac bridge at a frequency of 30 kHz in a series equivalent chain.

The electrodeposition was performed at 18–25°C with and without agitation of electrolytes with a magnetic stirrer.

The influence exerted by organic additives on the outward appearance of the coatings was studied in an electrolyte containing (g l^{-1}) $SnSO_4$ 50 and H_2SO_4 100. It was found that the addition of Syntanol (1–4 g l^{-1}) to the electrolyte results in dull coatings. In the presence of formaldehyde (1–10 ml l^{-1}) or allyl alcohol (1–20 ml l^{-1}), or of both simultaneously, poor coatings are formed. The coatings with a considerably better outward appearance are formed in an electrolyte containing Syntanol (2–3 g l^{-1}), formaldehyde (6–8 ml l^{-1}), and allyl alcohol as additive. The influence of allyl alcohol is demonstrated in the table.

Influence of the allyl alcohol concentration c on the outward appearance of the tin coatings at various current densities. Electrolyte composition, g l^{-1}: $SnSO_4$ 30, H_2SO_4 100, Syntanol DS-10 2, formaldehyde (37% solution) 6 ml l^{-1}. Mechanical agitation

c, ml l^{-1}	j_c, A dm^{-2}	Outward appearance of coatings
1–5	1–2	Dull
	3–5	Semilustrous
	6–10	Dark gray
10–15	1–3	Dull
	4	Semilustrous
	5–10	Lustrous
	11–12	Lustrous with burn-on
20	1–4	Dull
	5–7	Lustrous
	8–10	Lustrous with burn-on

1070-4272/04/7711-1781 © 2004 MAIK "Nauka/Interperiodica"

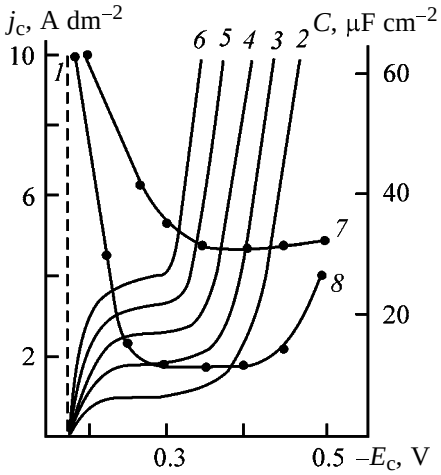

Fig. 1. (*1–6*) Cathodic polarization curves taken on a rotating Sn disk electrode and (*7, 8*) dependences of the electrical double layer capacitance C on the electrode potential relative to a standard hydrogen electrode E_c in the tin-plating electrolytes. (j_c) Current density. Electrolyte (g l^{-1}): $SnSO_4$ 30 and H_2SO_4 100. (*1, 7*) Electrolyte, (*2, 8*) *1* + 2 g l^{-1} Syntanol, 6 ml l^{-1} formaldehyde (37% solution), and 10 ml l^{-1} allyl alcohol; (*3, 4, 5, 6*) *2* at a rotation rate of the disk electrode (rpm) of 200, 500, 1000, and 2000, respectively.

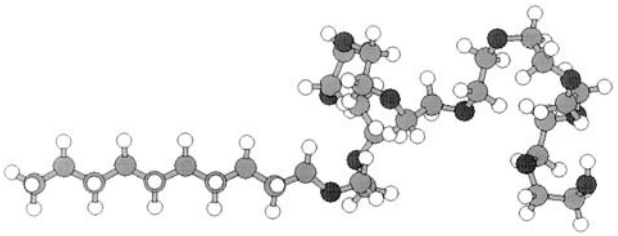

Fig. 2. Structure of Syntanol molecule according to quantum-chemical calculation. Hydrogen, carbon, and oxygen atoms are colored white, gray, and dark, respectively.

As seen, lustrous coatings can be obtained in the presence of allyl alcohol in certain modes of the electrolysis. The widest range (5–10 A dm^{-2}) of the current densities j_c ensuring formation of lustrous deposits is observed at an allyl alcohol concentration of 10–15 ml l^{-1}.

Deviations of the formaldehyde concentration from the above limit result in silvery coatings. At a Syntanol concentration below 1–2 g l^{-1}, the working interval ensuring formation of lustrous coatings is considerably narrower. At a Syntanol concentration above 3–4 g l^{-1}, the current density range in which lustrous coatings are obtained is the same, but foam formation in the electrolyte increases considerably, which complicates electrodeposition in the agitated electrolyte.

We studied the influence of the $SnSO_4$ concentration on the current density range ensuring formation of lustrous coatings. The study was performed in an electrolyte containing 2 g l^{-1} Syntanol, 6 ml l^{-1} formaldehyde, and 10 ml l^{-1} allyl alcohol. It was found that decreasing the $SnSO_4$ concentration makes j_c range ensuring formation of lustrous coatings narrower. For example, at a $SnSO_4$ concentration of 10–20 g l^{-1} lustrous coatings were formed in the current density range 2–4 A dm^{-2}, whereas at 30–60 g l^{-1}, they were formed in the 5–10 A dm^{-2} range. The H_2SO_4 concentration in the electrolyte must be within 90–100 g l^{-1}. Below 90 g l^{-1}, the electrolyte operation is instable, and the j_c range ensuring formation of lustrous coatings is narrower. At the H_2SO_4 concentration above 100 g l^{-1}, the range of the current densities ensuring formation of lustrous coatings does not vary.

It should be noted that high-quality lustrous coatings are obtained solely in an agitated electrolyte, and dull coatings are formed without agitation.

The current efficiency (CE) by tin in the electrolytes ensuring obtaining lustrous coatings decreases with increasing j_c and increases with increasing $SnSO_4$ concentration. At a $SnSO_4$ concentration varied within 10–20 g l^{-1} and at j_c = 2–4 A dm^{-2}, CE = 95–75%, and at the $SnSO_4$ concentration within 30–50 g l^{-1} and j_c = 5–10 A dm^{-2} CE = 95–90%.

The cathodic polarization curves on a rotating-disc electrode were obtained. As seen from Fig. 1, in the presence of organic substances, the cathodic polarization increases and the plateau of the limiting current appears on the cathodic polarization curve (curves *2, 3*). As the rate of rotation of the disc electrode increases, the limiting current density increases, whereas the cathodic polarization decreases (curves *2–6*). The limiting current in the polarization curves is due to adsorption of organic substances and formation of an adsorption layer on the cathode surface. This suggestion is confirmed by the results of measuring the capacitance of the electrical double layer. As seen from Fig. 1, curves *7* and *8*, the introduction of organic substances into the electrolyte results in the decrease of the double layer capacitance. In the potential range E from –0.3 to –0.4 V, the capacitance decreases from 32 to 11 μF cm^{-2}. At higher cathodic potentials, the organic substances desorb from the electrode surface, which makes the adsorption layer nonuniform and results in increased double layer capacitance.

To ascertain the nature of the adsorption layer formed on the cathode surface in electrochemical tin plating, we calculated the optimal structure of the

Syntanol molecule by the PM3 semiempirical quantum-chemical method [3, 4].

As seen from Fig. 2, the molecule consists of fibrillar hydrophobic nonpolar moiety (hydrocarbon radical $C_{10}H_{21}$) and hydrophilic moiety [globular oxyethylated fragment $(C_2H_4O)_{10}OH$]. The maximum size of the molecule lies within 2000 × 900 × 500 pm.

The surface of tin electrode was simulated by a rectangular cluster consisting of 48 tin atoms. The cluster was chosen as recommended in [5].

It was established that an adsorption layer on the tin surface is formed with planar orientation of the Syntanol molecule. In the process, formaldehyde, allyl alcohol, and Sn^{2+} ions are distributed in its globular moiety (Fig. 3). The calculation results show that, with the system Syntanol + allyl alcohol + Sn^{2+}, the interaction with the cluster surface is the strongest (E = 1009 kJ mol^{-1}). With formaldehyde introduced into this system, the interaction energy decreased by a factor of approximately 3 (E = 384 kJ mol^{-1}).

As known [6], formation of lustrous coatings is associated with the adsorption of organic substances on the electrode surface and with the complex physicochemical processes occurring in the near-cathode layer. The diffusion-hydrodynamic mode of delivery (removal) of ions changing the structure and properties of an adsorption layer on the cathode surface is also important [7]. The possibility of the electrochemical transformation of organic molecules must also be taken into account. In such a case, the products of transformation of the additive on the electrode, rather than the additive itself, can exert a luster-producing effect. Taking into account the experimental data obtained, the luster production in electrochemical tin plating can be explained by the adsorption–diffusion mechanism.

Unequal accessibility of different regions of the submicroprofile to LA is due to the adsorption film on the cathode [8]. The thickness of this film must be comparable with the size of ridges and pits, typical of lustrous surface.

As already noted, in a tin-plating electrolyte, the adsorption layer on the cathode is formed by Syntanol, formaldehyde, LA, and Sn^{2+}. Without agitation of the electrolyte, the thickness of the adsorption layer is large owing to polymolecular adsorption of organic substances (Fig. 4a). The layer formed in an agitated electrolyte has a smaller thickness, comparable with the size of ridges and pits (Fig. 4b). In this case, the adsorption layer plays the role of a diffusion layer in which a gradient of LA concentration is created. After

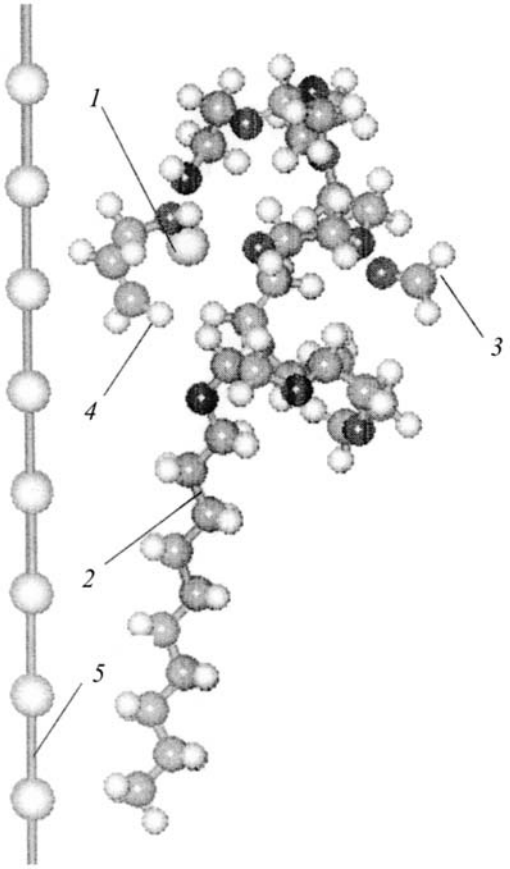

Fig. 3. System of (*1*) Sn^{2+}, (*2*) Syntanol, (*3*) formaldehyde, (*4*) allyl alcohol, and (*5*) Sn_{48} cluster. Planar orientation of the Syntanol molecule with respect to the cluster plane.

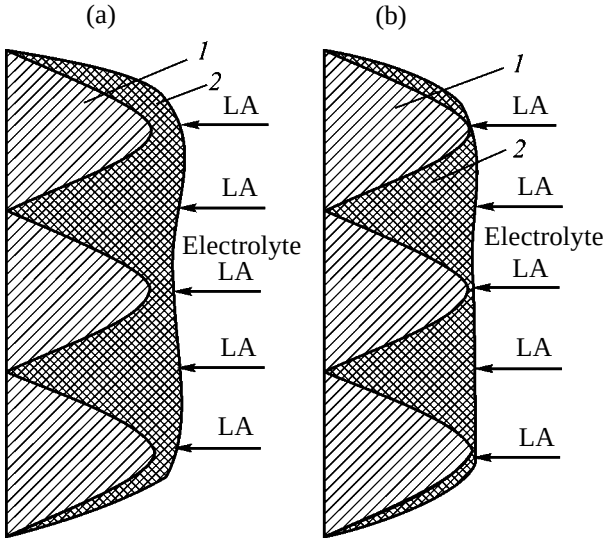

Fig. 4. Scheme of (*1*) ridges and pits of the submicroprofile in the presence of (*2*) adsorption layer (a) with and (b) without agitation of the electrolyte. Diffusion flow of LA is indicated by the arrows.

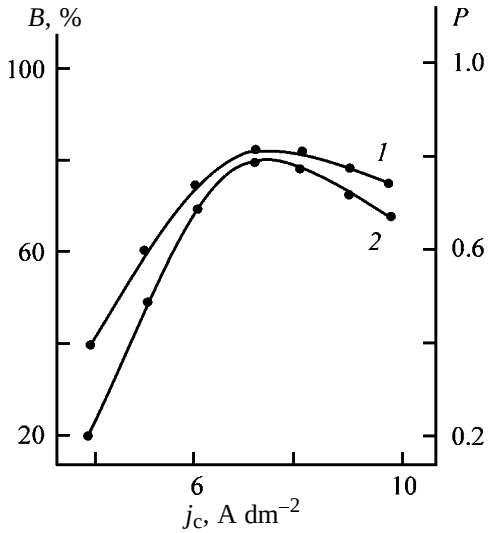

Fig. 5. (*1*) Degree of luster *B* and (*2*) leveling power *P* of the coatings vs. the cathodic current density j_c. Electrolyte: $SnSO_4$ 30 g l^{-1}, H_2SO_4 100 g l^{-1}, Syntanol 2 g l^{-1}, formaldehyde (37% solution) 6 ml l^{-1}, and allyl alcohol 7 ml l^{-1}; mechanical agitation.

the certain agitation rate is attained, the diffusion to the cathode will result in stronger adsorption of LA on ridges than in pits. As in adsorption–diffusion leveling theory [2], unequal accessibility of different regions of the microprofile is provided by consumption of LA in the diffusion-limited process, i.e., when the rate of LA consumption is equal to the limiting rate of its delivery to the cathode, with the consumption mechanism (incorporation of molecules into the deposit or their electrochemical reduction) insignificant. Since with increasing rotation rate of the disk electrode (and rate of the electrolyte agitation) the limiting current increases and the cathodic polarization decreases, it appears that inhibition on the ridges occurs to a lesser extent than in pits.

At the same time, despite the presence of the adsorption layer in them, a larger amount of tin will be deposited in pits than onto ridges (Fig. 4b). This is due to incorporation of tin ions Sn^{2+} into the adsorption film. Such redistribution of the metal makes the submicroprofile relief smoother and hence makes the surface lustrous.

We studied the leveling power of tin-plating electrolytes for obtaining lustrous coatings. It was found that they have the positive leveling power. The degree of luster and degree of leveling were studied in relation to the cathodic current density. Comparison of these parameters revealed their interrelation, i.e., the higher the degree of leveling, the higher the degree of luster (Fig. 5).

The phenomenon of leveling is associated with the luster of electrolytic coatings, since the luster production is also the process of the surface leveling. In the course of leveling, coarse microroughnesses, from 0.2 to 100 μm and larger, are removed. In the course of the formation of lustrous surface, very small submicroroughnesses, about 0.15 μm and smaller, are removed [9]. Thus, in a tin-plating electrolyte containing Syntanol, formaldehyde, and allyl alcohol, in the course of the tin electrodeposition the submicro- and microroughnesses of the cathode surface are smoothed.

Thus, we have developed a sulfuric acid tin-plating electrolyte of simple composition for obtaining lustrous coatings with a leveled surface. The electrolyte contains $SnSO_4$ 10–50 g l^{-1}, H_2SO_4 90–100 g l^{-1}, Syntanol (DS-10) 2–3 g l^{-1}, formaldehyde (37% solution) 6–8 ml l^{-1}, and allyl alcohol 10–15 ml l^{-1}. The process is performed with mechanic agitation of the electrolyte at the current density j_c = 2–10 A dm^{-2}. The current efficiency is 75–95% and the electrolyte temperature, 18–25°C. Above 25°C, the operation region of j_c in which lustrous coatings are obtained is narrower, the electrolyte becomes turbid wihtin a short time, and the deposit appears on the bath bottom. All the above impairs the quality of the coatings obtained. Anodes must be made of pure tin. To prevent the contamination of the electrolyte with sludge, it is necessary to place the anodes into jackets made of a polyvinyl chloride or polypropylene fabric.

The electrolyte should be adjusted with respect to $SnSO_4$, H_2SO_4, and formaldehyde on the basis of chemical analysis data [10]. The Syntanol amount in the electrolyte must be corrected after the amount of electricity of 100 A g^{-1} l^{-1} is passed; 1 g l^{-1} of Syntanol is added to the bath. The consumption of allyl alcohol is 0.02 ml A^{-1} h^{-1}.

CONCLUSIONS

(1) The study of the electrodeposition of tin from a sulfuric acid electrolyte containing organic additives showed that, when Syntanol, formaldehyde, and allyl alcohol are present simultaneously, the current densities at which lustrous coatings are formed vary within 2–10 A dm^{-2}, depending on the $SnSO_4$ concentration in the electrolyte.

(2) Lustrous coatings in tin electrodeposition are formed by the adsorption–diffusion mechanism.

(3) The leveling power of the sulfuric acid electrolyte containing organic additives was studied. It was

found that a tin-plating electrolyte containing Syntanol, formaldehyde, and allyl alcohol has the positive leveling power depending on j_c. It was shown that the degree of luster correlates with the leveling power: the higher the degree of luster, the higher the leveling power.

REFERENCES

1. Medvedev, G.I. and Makrushin, N.A., *Zh. Prikl. Khim.*, 2002, vol. 75, no. 11, pp. 1834–1838.
2. Kruglikov, S.S., *Itogi Nauki Tekh., Ser.: Khim., Elektrokhim.*, 1965, pp. 117–151.
3. Stewart, J.J.P., *J. Comput. Chem.*, 1989, vol. 10, no. 2, pp. 209–220.
4. Stewart, J.J.P., *J. Comput. Chem.*, 1991, vol. 12, no. 3, pp. 320–341.
5. Shapnik, M.S., *Elektrokhimiya*, 1994, vol. 30, no. 2, pp. 143–149.
6. *Blestyashchie elektroliticheskie pokrytiya* (Lustrous Electrolytic Coatings), Matulis, Yu.Yu., Ed., Vilnius: Mintis, 1969.
7. Gorbunova, K.M., Ivanovskaya, T.V., and Shishakov, M.A., *Zh. Fiz. Khim.*, 1951, vol. 25, no. 8, pp. 981–987.
8. Gerenrot, Yu.E., and Leichkis, D.P., *Elektrokhimiya*, 1977, vol. 13, no. 3, pp. 341–345.
9. Gnusin, N.P., and Kovarskii, N.Ya., *Sherokhovatost' elektroosazhdennykh poverkhnostei* (Roughness of Electrodeposited Surfaces), Novosibirsk: Nauka, 1970.
10. Vyacheslavov, P.M., and Shmeleva, N.M., *Kontrol' elektrolitov i pokrytii* (Control of Electrolytes and Coatings), Leningrad: Mashinostroenie, 1965.

Russian Journal of Applied Chemistry, Vol. 77, No. 11, 2004, pp. 1786–1789. Translated from Zhurnal Prikladnoi Khimii, Vol. 77, No. 11, 2004, pp. 1804–1807.

APPLIED ELECTROCHEMISTRY AND CORROSION PROTECTION OF METALS

Mechanism of Electrochemical Synthesis of Copper(II) β-Diketonates

N. N. Kostyuk

Sevchenko Institute of Applied Physical Problems, Belarussian State University, Minsk, Belarus

Received July 28, 2004

Abstract—Formation of copper β-diketonates in electrolysis of a solution of acetylacetone in acetonitrile in the presence of oxygen, with tetraethylammonium bromide as supporting electrolyte, was studied.

In [1–3], we reported on electrochemical synthesis of copper(II) β-diketonates in acetonitrile solutions of β-diketones. When the electrolysis was performed in an inert atmosphere (Ar, He), the copper anode dissolved but copper β-diketonates were not formed in noticeable amounts. The major process was copper transfer from the anode to the cathode. Since copper(I) β-diketonates are unstable, it was suggested that the transfer of Cu(I) ions to the cathode and their reduction to metal occur faster than their anodic oxidation to the double-charged state. Therefore, it seems necessary to use an oxidizing atmosphere. Passage of a moderate flow of dry air through the electrochemical cell in the course of electrolysis resulted in the successful synthesis. The yield of copper(II) β-diketonates as a function of current in most cases exceeded 100% [1–3], reaching in some cases 130%. This fact suggests [2] that a considerable amount of β-diketonates is formed not electrochemically but by the direct reaction of copper with the β-diketone under oxidative conditions. With low-active compact copper anode, the reaction is weak [2, 3], but formation of relatively active refined copper at the cathode and powdered copper in the near-anode space [due to disproportionation of Cu(I) ions] promotes the reaction [5]. This is indirectly confirmed by the fact that the excessive (over 100%) yield of copper chelates as a function of current increases in going to more acidic β-diketones [1] and by the possibility of electrochemical preparation of active Cu powders [6, 7].

The above data give certain insight into reactions involved in synthesis of copper(II) β-diketonates. It is unclear, however, how the oxidative atmosphere of air favors an increase in the yield of copper(II) chelates, can the mechanism of anodic oxidation of copper in aqueous solutions [5, 8, 1]] be applied to aprotic solvents [1–3] (taking into account the fact that an important role in electrochemical processes is played by intermediate metastable compounds, specific for aqueous and nonaqueous electrolytes [8, 9, 11]), and what chemical equations describe the processes occurring in the electrochemical cell.

EXPERIMENTAL

The electrolysis conditions, chemicals, and procedures for their preparation are described in [2]. The IR spectra of acetonitrile solutions of the electrolyte [1 M solution of acetylacetone (HAA) in acetonitrile, supporting electrolyte 0.1 M tetraethylammonium bromide], taken in various steps of the electrochemical synthesis, were recorded on a Specord IR-75 spectrophotometer using liquid cells with NaCl windows and 0.126 mm layer thickness. The X-ray phase analysis of powders was performed on a DRON-2 diffractometer (Mo radiation).

On applying the electric current, the steady state of the electrochemical system changes. New phases are formed on the electrode surface, and sometimes also in the bulk of solution [8]. In the case of electrolysis of aqueous solutions, a metastable compound containing hydroxide is formed at the anode [8]. The processes occurring with a copper anode are described in detail in [9]. The sequence of transformations can be schematically represented as follows:

$$\mathrm{Cu} \rightarrow (\mathrm{CuOH})_{ads} \rightarrow (\mathrm{CuOH^+})_{ads} \rightarrow (\mathrm{Cu^{2+}})_{ads} \rightarrow [(\mathrm{Cu^{2+}})_{aq}]_0 \rightarrow \mathrm{Cu^{2+}_{aq}}. \quad (\mathrm{I})$$

The first two transformations are electrode reactions, and their rates depend on the electrode potential. Scheme (1) involves oxidation of Cu to the Cu(II)

1070-4272/04/7711-1786 © 2004 MAIK "Nauka/Interperiodica"

state directly on the electrode surface, followed by migration of the Cu^{2+} ion into the solution. If copper is also oxidized by another pathway, along with scheme (1), the current density should increase with formation of a brown-red deposit on the anode surface [9], suggesting formation of various copper oxides:

$$Cu(CuOH)_{ads} \rightarrow (Cu_2O)_{ads} \rightarrow Cu(CuO)_{ads}$$

$$\text{and } (CuOH^+)_{ads} \rightarrow (CuO)_{ads}. \quad \text{(II)}$$

In earlier papers [5, 10], a somewhat different mechanism of anodic dissolution of copper was suggested:

$$Cu \rightarrow Cu^+ + e \text{ (fast) and } Cu^+ \rightarrow Cu^{2+} + e \text{ (slow). (III)}$$

In anodic polarization, the fast step of formation of Cu^+ is followed by the slow step of oxidation to Cu^{2+}. Stable Cu^+ ions can partially diffuse into the bulk of solution from the anode surface. Beyond the layer surface, their concentration increases, and the disproportionation $2Cu^+ \rightarrow Cu + Cu^{2+}$ starts near the anode, yielding a copper powder [5].

The electrolysis of an acetylacetone solution with a copper anode under oxidative conditions results in precipitation of $Cu(AA)_2$ as blue crystals. After the electrolysis completion, an equal volume of water was added to the electrolyte, and the blue precipitate was filtered off, dried in air, and recrystallized from chloroform [1, 2]. In recrystallization of large amounts of copper(II) acetylacetonate (products from several experiments were combined), formation of a black powder on the beaker bottom was observed; this precipitate was filtered off, washed successively with chloroform and acetonitrile, and dried in air at room temperature. According to X-ray phase analysis, the isolated black precipitate is CuO. No traces of Cu_2O were detected. The electrolysis in an inert atmosphere resulted in copper refining and formation of a small amount of a finely dispersed copper precipitate [1–3].

These facts are better consistent with mechanism (III) of anodic dissolution of copper. Apparently, bubbling of dry air results in copper oxidation:

$$2Cu + O_2 = 2CuO \text{ and } 4Cu^+ + O_2 = 2CuO + 2Cu^{2+}.$$

Simultaneously, a brownish red film formed on the anode surface, suggesting the occurrence of some reactions in accordance with mechanism (II), which is possible only in the presence of water. Since the starting chemicals were thoroughly dried and the cell was protected from atmospheric moisture, the only source of H_2O could be a chemical reaction in the course of electrolysis.

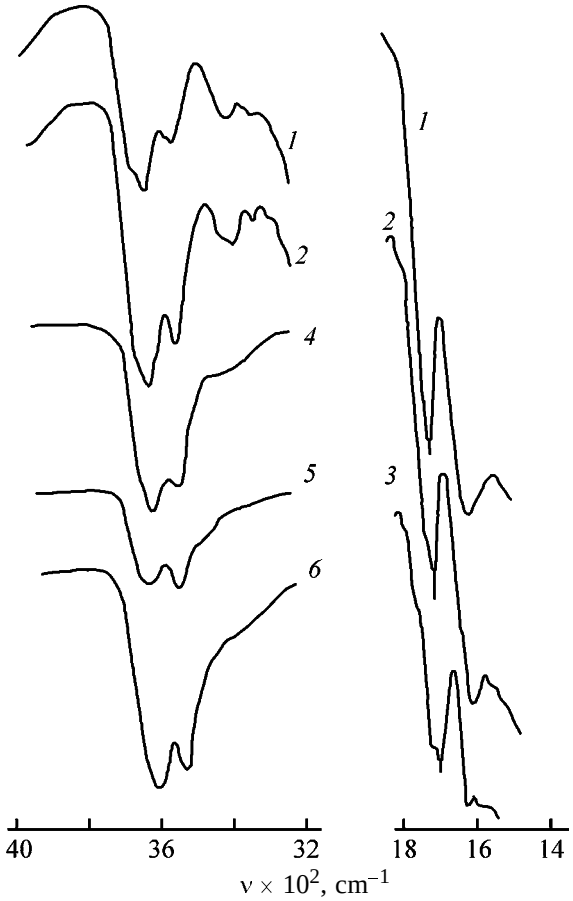

Fragments of the IR spectra of the acetonitrile electrolyte. (ν) Wave number. (*1*) Initial solution (sample 1), (*2*) after electrolysis for 15 min (sample 2), (*3*) after electrolysis for 30 min (sample 3), (*4*) subtraction of the spectrum of sample 1 (reference channel) from that of sample 2, (*5*) subtraction of the spectrum of sample 2 (reference channel) from that of sample 3, and (*6*) subtraction of the spectrum of sample 1 (reference channel) from that of sample 3.

The release of water during the electrolysis was confirmed by the IR spectra of the electrolyte. Samples were taken from the initial solution (sample 1) and in 15 (sample 2) and 30 min (sample 3) after the start of the electrolysis. The figure shows the fragments of the IR spectra of the samples in the ranges of stretching vibrations of hydroxy groups (3700–3300 cm^{-1}) and bending vibrations of water (1700–1500 cm^{-1}). In the IR spectrum of the initial electrolyte solution (sample 1), there is fairly strong absorption in the range of stretching vibrations of OH groups. Since the electrolyte solution was prepared with thorough protection from atmospheric moisture,

this absorption should be assigned to the enol form of acetylacetone [12–14].

The absorption in the range 3700–3000 cm^{-1} noticeably increases in going from sample 1 to sample 2, suggesting generation of OH groups. Simultaneously, a shoulder belonging to bending vibrations of water appears at 1700–1500 cm^{-1} [13–15]. The manifestation of the bending vibrations of water confirms its generation in the course of electrolysis and indicates that the increased absorption in the IR spectrum of sample 2 in the range 3700–3300 cm^{-1} is not due to keto–enol transformations of acetylacetone (the OH groups of the enol form do not absorb in this range) [12–15]. Longer electrolysis (30 min) results in a further increase in the absorption in the range of water stretching vibrations, though less pronounced than in the first 15 min. The generation of water in the course of electrolysis is demonstrated more clearly by subtraction of the spectrum of the initial electrolyte (sample 1) from the spectrum of the electrolyte subjected to 15-min electrolysis (sample 2). To obtain the differential spectrum, we recorded the spectrum of sample 2 with sample 1 placed in the reference channel. The resulting spectrum (curve *4*) is due to stretching vibrations of water generated in the first 15 min of the electrolysis. By recording the spectrum of sample 3 (solution after electrolysis for 30 min) with sample 2 placed in the reference channel, we obtained the spectrum of the stretching vibrations of water formed in the last 15 min of the electrolysis. The intensity of this spectrum is appreciably lower. This fact is consistent with a decrease in the current density in the potentiostatic mode of the electrolysis and the corresponding deceleration of the synthesis in the second 15 min [1]. The total amount of water generated in 30 min is reflected by fragment *6* (sample 1 in the reference channel, sample 3 in the sample channel). The IR spectra in the range 3700–3300 cm^{-1} well correlate with the spectra in the range of bending vibrations of water, 1700–1500 cm^{-1}. In going from the initial sample 1 to samples 2 and 3, first a shoulder (fragment *2*) and than a band at 1610 cm^{-1} (fragment *3*), belonging to $\delta(H_2O)$ [13–15], appear in the IR spectrum.

Since generation of water under conditions of dry air bubbling is possible only in the presence of hydrogen, it should be associated with the cathodic elimination of proton from the γ-position of acetylacetone. Actually, this reaction is reduction of dissolved oxygen [5].

Summing up, we can conclude that electrochemical preparation of copper(II) acetylacetonate in an acetonitrile solution is a complex process described by the following sum of electrochemical and chemical transformations:

Anode:

$$Cu = Cu^+ + e \text{ (fast)}, \quad (1)$$

$$Cu^+ = Cu^{2+} + e \text{ (slow)}, \quad (2)$$

$$Cu(CuOH)_{ads} \rightarrow (Cu_2O)_{ads} \rightarrow Cu(CuO)_{ads} \quad (3)$$

$$(CuOH^+)_{ads} \rightarrow (CuO)_{ads}. \quad (4)$$

Reaction (2) makes no appreciable contribution to the yield of the target product [1–3]. The direct reaction of the compact anode material with acetylacetone does not occur either, as follows from data of [2, 3] and from the thermodynamic data: In the electrochemical series of metals, copper stands to the right of hydrogen. Reactions (3) and (4) occur at the anode surface as water is accumulated [9] and are also weakly pronounced, although in some cases they can cause passivation of the anode.

Cathode:

$$O_2 + 4HAA + 4e = 4AA^- + 2H_2O. \quad (5)$$

This cathodic reaction corresponds to that suggested in [5].

Solution:

$$Cu^{2+} + 2AA^- = Cu(AA)_2, \quad (6)$$

$$Cu_{disp} + 2HAA = Cu(AA)_2 + H_2, \quad (7)$$

$$4H + O_2 = 2H_2O, \quad (8)$$

$$2Cu + O_2 = 2CuO, \quad (9)$$

$$4Cu^+ + O_2 = 2CuO + 2Cu^{2+}. \quad (10)$$

Reactions (6) and (10) are, apparently, the main final reactions yielding the target product. Reaction (7) of finely dispersed copper with acetylacetone may make approximately 30% contribution to formation of $Cu(AA)_2$, as judged from the current efficiency reaching 130%, and its contribution will significantly depend on the β-diketone acidity. With fine particles having a strong curvature, the direct reaction of Cu with an acid, thermodynamically forbidden with compact metal, may become allowed [16], as a new term related to the particle curvature radius appears in the expression for the Gibbs energy:

$$\Delta G(r) = \Delta G - \Delta g, \quad \Delta g = 2\sigma M/\rho r,$$

where σ is the surface energy; M, molecular weight; ρ, density; and r, curvature radius.

Thus, at low r, the Gibbs energy decreases. Reaction (2) will make a noticeable contribution to the generation of water, in addition to the cathodic reduction of oxygen. Reactions (9) and (10) occur in the near-anode space [5].

CONCLUSIONS

(1) A pattern of electrochemical and chemical reactions involved in electrochemical synthesis of copper(II) chelates was suggested on the basis of published data on anodic oxidation of copper, features of electrochemical synthesis of copper(II) β-diketonates, IR spectra of the acetonitrile electrolyte solutions taken in the course of electrolysis, and analysis of the by-products formed.

(2) The overall process can be described by ten reaction equations.

REFERENCES

1. Kostyuk, N.N., Electrochemical Synthesis and Physicochemical Properties of a Number of Transition Metal Chelates, *Cand. Sci. Dissertation*, Minsk, 1993.
2. Shirokii, V.L., Vinokurov, I.I., Kostyuk, N.N., *et al.*, *Zh. Obshch. Khim.*, 1996, vol. 66, no. 2, pp. 184–188.
3. Shirokii, V.L., Vinokurov, I.I., Kostyuk, N.N., *et al.*, in *Materialy mezhdunarodnoi nauchno-tekhnicheskoi konferentsii "Razrabotka importozameshchayushchikh tekhnologii i materialov v khimicheskoi promyshlennosti"* (Proc. Int. Scientific and Technical Conf. "Development of Import-Substituting Processes and Materials in Chemical Industry"), Minsk, October 20–22, 1999.
4. Peshkova, V.M. and Mel'chakova, N.V., *β-Diketony* (β-Diketones), Moscow: Nauka, 1986, p. 42.
5. *Prikladnaya elektrokhimiya* (Applied Electrochemistry), Rotinyan, A.L., Ed., Leningrad: Khimiya, 1974.
6. Fedushchak, T.A., Ermakov, A.E., Sedoi, V.S., *et al.*, Abstracts of Papers, *VII Mendeleevskii s"ezd po obshchei i prikladnoi khimii* (VII Mendeleev Congr. on General and Applied Chemistry), Kazan, September 21–26, 2003, vol. 2, p. 350.
7. Uglov, V.A., Specific Features of Electrolytic Preparation of Ultradispersed Copper Powders, *Cand. Sci. Dissertation*, Moscow, 1995.
8. Saadakov, G.A., *Teoriya metastabil'nogo sostoyaniya elektrokhimicheskikh protsessov v gal'vanotekhnike* (Theory of Metastable State of Electrochemical Processes in Electroplating), Moscow: Mashinostroenie, 1991.
9. Kiss, L., *Kinetics of Electrochemical Metal Dissolution*, Amsterdam: Elsevier, 1988.
10. Ershov, B.G., *Usp. Khim.*, 1981, vol. 50, no. 12, pp. 2137–2166.
11. *Elektrokhimiya metallov v nevodnykh rastvorakh* (Metal Electrochemistry in Nonaqueous Solutions), Kolotyrkin, Ya.M., Ed., Moscow: Mir, 1974.
12. Neiland, O.Ya., Stradyn', Ya.P., Silin'sh, E.A., *et al.*, *Stroenie i tautomernye prevrashcheniya β-dikarbonil'nykh soedinenii* (Structure and Tautomeric Transformations of β-Dicarbonyl Compounds), Riga: Zinatne, 1977.
13. Bellamy, L.J., *The Infra-Red Spectra of Complex Molecules*, New York: Wiley, 1957.
14. Bellamy, L.J., *Advances in Infrared Group Frequencies*, London: Methuen, 1968.
15. Nakamoto, K., *Infrared and Raman Spectra of Inorganic and Coordination Compounds*, New York: Wiley, 1978.
16. Lai, X. and Goodman, D.W., *J. Mol. Catal. A: Chem.*, 2000, vol. 162, p. 33.

Russian Journal of Applied Chemistry, Vol. 77, No. 11, 2004, pp. 1790–1792. Translated from Zhurnal Prikladnoi Khimii, Vol. 77, No. 11, 2004, pp. 1808–1810.

APPLIED ELECTROCHEMISTRY AND CORROSION PROTECTION OF METALS

Electrochemical Halogenation of 4-Hydroximino-2,2,6,6-tetramethylpiperidine

V. P. Kashparova, E. Sh. Kagan, and I. Yu. Zhukova

South-Russian State Technical University (former Novocherkassk Polytechnic Institute), Novocherkassk, Rostov oblast, Russia

Received November 19, 2003

Abstract—Electrochemical chlorination and bromination of 4-hydroximino-2,2,6,6-tetramethylpiperidine were studied.

Halogenation of amines attracts researchers' attention as a route to the corresponding halo derivatives and products of their further transformations. Numerous papers concern this reaction [1–3]. *N*-Halo derivatives of aliphatic amines are widely used in organic synthesis [2]; therefore, search for new halogenating agents is an important problem of applied organic chemistry. It was shown previously that electrochemical halogenation of 2,2,6,6-tetramethylpiperidine and its derivatives at pH 5–10 yields *N*-halo compounds of this series [4, 5], which are relatively stable and can be used as oxidants and halogenating agents [6, 7].

We studied electrochemical halogenation of 4-hydroximino-2,2,6,6-tetramethylpiperidine **I**. We found that electrochemical chlorination of **I** in acidic solution yields 4-nitroso-4-chloro-2,2,6,6-tetramethylpiperidine hydrochloride **II**, which is readily oxidized to 4-nitro-4-chloro-2,2,6,6-tetramethylpiperidine hydrochloride **III**. Compound **III** on treatment with a saturated sodium carbonate solution transforms into the corresponding amine **IV**:

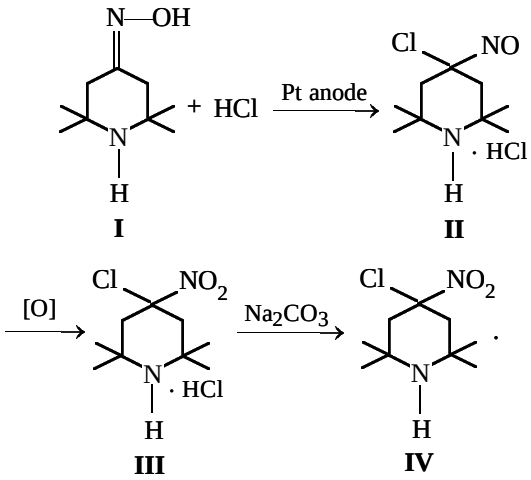

The electrolysis was performed at pH 4–5 at a platinum anode in a diaphragm electrolyzer in the presence of an organic solvent. After passing 2 F mol^{-1} of electricity, we isolated from the blue aqueous layer 4-nitroso-4-chloro-2,2,6,6-tetramethylpiperidine hydrochloride **II** in 70% yield based on **I**.

Apparently, the chlorinating agent in chlorination of **I** is 1-chloro-4-hydroximino-2,2,6,6-tetramethylpiperidine **V** formed by chlorination of **I** with molecular chlorine generated at the anode. Compound **V** is insoluble in water and passes into the organic phase. In the organic phase, apparently, compound **V** undergoes intramolecular chlorination or acts as a chlorinating agent with respect to substrate **I**. The resulting amine **II** passes into the aqueous phase from which it can be isolated as a salt. This reaction sequence is indirectly confirmed by cyclic voltammetry (CVA).

Chlorination of **I** in HCl solution could not be studied by CVA, because the process occurs in the potential range of discharge of the supporting electrolyte (1.0 V vs. silver chloride reference electrode). To study the process, we recorded the cyclic voltammograms of **I** in 1.5 M $HClO_4$. In this electrolyte, the oxidation wave of **I** was not observed (Fig. 1a). The background curve changed on adding a small amount of NaCl to the supporting electrolyte. In this case, the anodic current at 1.4 V increased, which is caused by the discharge of chloride ions (this peak grew with increasing concentration of Cl^- in the electrolyte), and a current wave appeared at 2 V. This wave is presumably related to oxidation of compound **V** formed by the reaction of chlorine with compound **I** added to the electrolyte earlier. Figure 1b shows the cyclic voltammograms of the solutions of **I** and 1-chloro-2,2,6,6-tetramethylpiperidine in the supporting electrolyte. Curve *2* in Fig. 1b, starting from 1.6 V, fully coin-

1070-4272/04/7711-1790 © 2004 MAIK "Nauka/Interperiodica"

cides with curve *2* in Fig. 1a, which counts in favor of formation of **V** as an intermediate.

To prepare compound **III**, the blue acidic aqueous solution of **II** was evaporated to dryness on a water bath. In the process, compound **II** was oxidized with atmospheric oxygen to **III**. On treatment of **II** with hydrogen peroxide in alkaline solution, 4-nitro-4-chloro-2,2,6,6-tetramethylpiperidine **IV** formed immediately. The structures of **II** and **III** were confirmed by elemental analysis and ^{1}H NMR spectroscopy.

The electrochemical chlorination of **I** in neutral and weakly alkaline solutions in the two-phase system probably occurs with the formation of 1,4-dichloro-4-nitroso-2,2,6,6-tetramethylpiperidine, which, being a practically neutral compound, passes to the organic phase. 1,4-Dichloro-4-nitroso-2,2,6,6-tetramethylpiperidine appeared to be unstable, and we failed to isolate it pure.

Attempted electrochemical bromination of **I**, similar to chlorination in acidic solution, failed. In alkaline solution, bromination did not occur either. In both cases, the hydrolysis of **I**, yielding 4-oxo-2,2,6,6-tetramethylpiperidine (triacetonamine), prevailed.

We were able to perform bromination of **I** in a neutral solution at a constant pH of the electrolyte in a diaphragmless electrolyzer. As electrolyte we used a two-phase system consisting of an aqueous solution of hydrobromide of **I**, potassium bromide, and methylene chloride.

Similarly to chlorination in a neutral solution, bromination of **I** involves intermediate formation of 1,4-dibromo-4-nitroso-2,2,6,6-tetramethylpiperidine **VI**. This compound dissolves in the organic layer of the electrolyte, imparting to it green color; then, according to TLC, compound **VI** transforms into 4-bromo-4-nitroso-2,2,6,6-tetramethylpiperidine **VII**. We failed to isolate **VII** because of its rapid oxidation to 4-bromo-4-nitro-2,2,6,6-tetramethylpiperidine **VIII** with atmospheric oxygen. The structure of **VIII** was confirmed by elemental analysis and ^{1}H NMR spectroscopy.

EXPERIMENTAL

4-Nitroso-4-chloro-2,2,6,6-tetramethylpiperidine hydrochloride II. The electrolysis was performed in a 150-ml diaphragm electrolyzer with platinum electrodes (anode and cathode, 10 and 6 cm^2 plates, respectively) and a power-driven stirrer.

The anode compartment was charged with 1.7 g (0.01 mol) of **I**, 0.5 ml of HCl (ρ = 1.19 g ml^{-1}), 70 ml of water, and 30 ml of methylene chloride. The cathode compartment was charged with 30 ml of 10% HCl. The electrolysis was performed with vigorous stirring at 20°C, current density 0.05 A cm^{-2} (current 0.5 A), and completed after passing 2 F mol^{-1} (0.52 A h) of electricity. After the electrolysis completion, the organic layer was separated, and the aqueous layer was evaporated in a vacuum to 1/3 of the initial volume, until blue crystals precipitated; the crystals were filtered off. Yield of hydrochloride **II** 1.68 g (70%), mp >250°C (dec.). The compound was identified by IR, UV, and ^{1}H NMR spectroscopy (comparison with an authentic sample [8]).

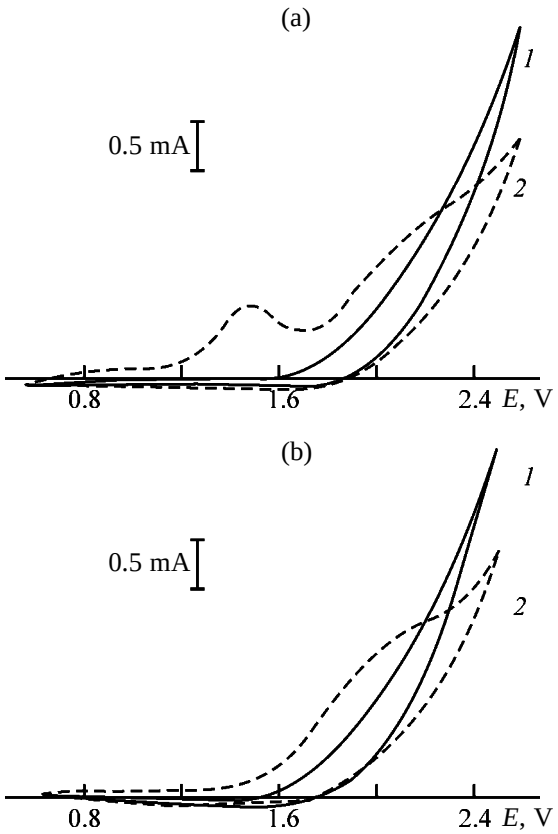

Fig. 1. Cyclic voltammograms of oxidation of **I**. (*E*) Potential. Pt anode; 20°C; potential sweep rate 0.2 V s^{-1}. (*1*) Supporting electrolyte (100 ml of 1.5 M $HClO_4$) + 2 × 10^{-4} M **I**; (*2*) the same + (a) 1 × 10^{-5} M NaCl and (b) 1 × 10^{-3} M 1-chloro-2,2,6,6-tetramethylpiperidine.

4-Nitro-4-chloro-2,2,6,6-tetramethylpiperidine hydrochloride III. An aqueous acidic solution (pH 4) of the electrolyte (70 ml), containing hydrochloride **II** (prepared as described above), was evaporated on a water bath to dryness; compound **III** was obtained as white crystals, yield 1.75 g (95%), mp 235°C (from ethanol). Mixing with an authentic sample gives no depression of the melting point [8].

4-Nitro-4-chloro-2,2,6,6-tetramethylpiperidine

IV. A suspension of 2.56 g (0.01 mol) of **III** in 30 ml of CH_2Cl_2 was treated with a concentrated Na_2CO_3 solution to pH 8–9. The organic layer was separated, and 40 ml of 30% H_2O_2 was added to it dropwise. After the blue color disappeared, the organic layer was separated, and the solvent was evaporated in a rotary evaporator; 2 g (94%) of **IV** was obtained, mp 45–46°C (from hexane). The ^{1}H NMR spectrum of the product coincides with that of an authentic sample [8].

4-Bromo-4-nitro-2,2,6,6-tetramethylpiperidine VIII. The electrolysis was performed in a 150-ml diaphragmless electrolyzer equipped with platinum electrodes (anode and cathode, 10 and 6 cm^2 plates, respectively) and a power-driven stirrer.

The electrolyzer was charged with 1.7 g (0.01 mol) of **I**, 1.5 ml of HBr (ρ = 1.39 g ml^{-1}), 2.4 g (0.02 mol) of KBr, 70 ml of water, and 30 ml of methylene chloride. The electrolysis was performed with vigorous stirring at 20°C, current density 0.05 A cm^{-2} (current 0.5 A), and completed after passing 2.5 F mol^{-1} (0.75 A h) of electricity. After the electrolysis completion, the organic layer was separated, washed with water (2 × 30 ml), and dried over sodium sulfate; the solvent was removed on a rotary evaporator. Compound **VIII** was obtained as white crystals; yield 1.35 g (60%), mp 106–108°C (from methanol).

Found, %: C 40.43; H 6.85; N 10.78.
$C_9H_{17}BrNO_2$. Calculated, %: C 40.8; H 6.45, N 10.55.

^{1}H NMR spectrum (CCl_4), δ, ppm: 1.09 s and 1.29 s (12H, MeC), 2.22 and 3.05 (4H, CH_2, *AB* pattern, J_{gem} 15 Hz, $\Delta\nu$ 63 Hz).

CONCLUSIONS

(1) Electrochemical chlorination of 4-hydroximino-2,2,6,6-tetramethylpiperidine in acidic solution (pH 4–5) yields 4-nitro-4-chloro-2,2,6,6-tetramethylpiperidine hydrochloride in 70% yield.

(2) 4-Nitroso-4-chloro-2,2,6,6-tetramethylpiperidine hydrochloride is oxidized with atmospheric oxygen to 4-nitro-4-chloro-2,2,6,6-tetramethylpiperidine hydrochloride; treatment of the latter with hydrogen peroxide in alkaline solution yields 4-nitro-4-chloro-2,2,6,6-tetramethylpiperidine.

(3) Electrochemical bromination of 4-hydroximino-2,2,6,6-tetramethylpiperidine in neutral solution yields 4-bromo-4-nitro-2,2,6,6-tetramethylpiperidine in 60% yield.

REFERENCES

1. Kovacic, P., Lovery, M.K., and Field, K.W., *Chem. Rev.*, 1970, vol. 70, no. 6, pp. 639–665.
2. Neale, R.S., *Synthesis*, 1971, no. 1, pp. 1–15.
3. Kagan, E.Sh. and Zhukova, I.Yu., *Elektrokhimiya*, 2000, vol. 36, no. 2, pp. 224–232.
4. Zhukova, I.Yu., Pozhidaeva, S.A., Kagan, E.Sh., and Smirnov. V.A., *Zh. Org. Khim.*, 1993, vol. 29, no. 4, pp. 751–757.
5. Zhukova, I.Yu., Kashparova, V.P., and Kagan, E.Sh., *Izv. Vyssh. Uchebn. Zaved., Sev.-Kavk. Region, Estestv. Nauki*, 2001, no. 2, pp. 44–45.
6. Minisci, F., *Synthesis*, 1973, no. 1, pp. 1–37.
7. Toda, T., Mori, E., Horiuchi, H., and Murayama, K., *Bull. Chem. Soc. Jpn.*, 1972, vol. 45, p. 1802.
8. Myshkina, L.A. and Rozantsev, E.G., *Izv. Akad. Nauk SSSR, Ser. Khim.*, 1980, no. 5, pp. 1175–1177.

Russian Journal of Applied Chemistry, Vol. 77, No. 11, 2004, pp. 1793–1796. Translated from Zhurnal Prikladnoi Khimii, Vol. 77, No. 11, 2004, pp. 1811–1814.

APPLIED ELECTROCHEMISTRY AND CORROSION PROTECTION OF METALS

Electrochemical Properties of Fibrous and Granulated Carbon Materials

A. P. Artem'yanov and I. V. Sheveleva

Far-Eastern State University, Vladivostok, Russia
Institute of Chemistry, Far-Eastern Division, Russian Academy of Sciences, Vladivostok, Russia

Received September 16, 2003; in final form, September 2004

Abstract—The influence exerted by the porous structure of fibrous and granulated carbon materials on the nature of the charging process and depth of penetration of the electrochemical process was studied.

Fibrous carbon materials have a unique porous structure and find wide application in widely diverse processes of chemical technology [1]. Use of carbon materials as sorbents makes it possible to intensify and improve the efficiency of the separation and concentration of mixtures by sorption and the recovery of impurities in utilization of industrial solutions. Rather promising is application of carbon fibers as electrodes in power cells and high-sensitivity electrochemical methods of analysis [2]. Use of carbon fibers as sorbents in the adsorption recovery of organic compounds, noble metals, and other inorganic compounds from aqueous solutions has been reported [3, 4]. In this case, the efficiency of fibrous carbon materials is due not only to their large surface area and high rate of adsorption, but also to the possibility of carrying out the process at a prescribed surface potential.

The possibility of implementation of the liquid-phase adsorption technology using carbon materials under conditions of electrochemical polarization largely depends on the efficiency of the process of charging of porous carbon electrodes. This study is devoted to comparative analysis of the electrochemical properties of granulated activated carbon (GAC) and activated carbon fibers (ACF).

EXPERIMENTAL

The electrochemical properties of carbon materials were studied by measuring charging curves and potentiodynamic curves in a standard three-electrode electrochemical cell. As electrolyte served a deaerated 0.1 N solution of potassium sulfate. The samples studied were placed on a gold grid serving as an inert current lead. A saturated silver chloride electrode was used as reference, and a porous carbon rod, as an auxiliary electrode. The compartments for the working and auxiliary electrodes were separated by an MB-2 biporous membrane. The electrochemical parameters were set and recorded with a PI-50 potentiostat.

As carbon materials to be studied served ACF of varied texture: bundle (Aktilen of brands A and B: AUV-A and AUV-B, respectively), felt (AUV-2), fabric (AUV-7), and GAC with a uniform porous structure.[1] The GAC samples were composed of uniformly porous carbon materials obtained by treatment of transition metal carbides with chlorine at elevated temperatures. Removal of volatile reaction products yields a carbon matrix whose uniform porous structure is determined by the crystal lattice of the starting carbide [5]. The uniformity of the porous structure makes it possible to interpret more unambiguously the effect of the porous structure on the electrochemical properties of carbon materials.

The structural parameters of the carbon materials under study are listed in the table. It can be seen that the porous structure of the samples changes from mostly mesoporous (granulated carbon GAU-2, GAU-3) to pronouncedly microporous (granulated carbon GAU-7 and GAU-6, carbon fibers).

The course of charging of the surface of GAC and ACF can be judged from galvanostatic charging curves $\Delta E = f(Q)$ obtained in the double-layer region,

[1] The GAC samples were fabricated at St. Petersburg Technological Institute. Carbon fibers AUV-A and AUV-B are semicommercial samples supplied by Khimvolokno Production Association (St. Petersburg); the carbon felt AUV-2 and fabric AUV-7 are fibrous materials manufactured at the Institute of General and Inorganic Chemistry (Minsk, Belarus).

1070-4272/04/7711-1793 © 2004 MAIK "Nauka/Interperiodica"

Parameters of the pore structure and electrochemical characteristics of carbon materials*

Material	r_{eff}, nm	Pore volume, $cm^3\ g^{-1}$		R, Ω	τ, s	$\tilde{\rho}$, Ω cm	λ, cm
		V_{micro}	V_{meso}				
GAU-7	1.10	0.19	0.01	960	2200	2100	0.04
GAU-6	1.30	0.44	0.06	760	1500	2000	0.04
GAU-2	3.00	0.02	1.08	245	320	640	0.20
GAU-3	5.00	0.09	0.51	80	45	210	0.41
AUV-2	0.57	0.36	0.05	990	1530	520	1.30
AUV-7	0.60	0.15	0.02	510	950	270	1.57
AUV-A	0.80	0.40	–	230	640	120	1.62
AUV-B	0.40	0.60	0.02	201	280	110	1.84

* V_{micro}, V_{meso} is the volume of micro- and mesopores, respectively; r_{eff}, effective pore radius; τ, characteristic charging time; and $\tilde{\rho}$, effective resistivity of the electrolyte in pores.

where Q is the quantity of electricity, and ΔE is the shift of the potential from the steady-state value (Fig. 1).

The nonlinear run of the dependence in the initial part of the curves corresponds to occurrence of transient processes and propagation of the "charging wave" across the thickness of the porous electrode [6]. The occurrence of pronounced transient processes in porous electrodes made of carbon sorbents results from nonuniform charging and is associated with the finite time of formation of an electrical double layer (EDL) in the pore space of the electrode. As a quantitative indication of the duration of these transient processes serves the characteristic charging time τ. The values of τ for the samples under study are listed in the table. At small radii of pores in the electrode, the hindrance to transport of ions in the interstitial space is significant, which makes the transient processes longer.

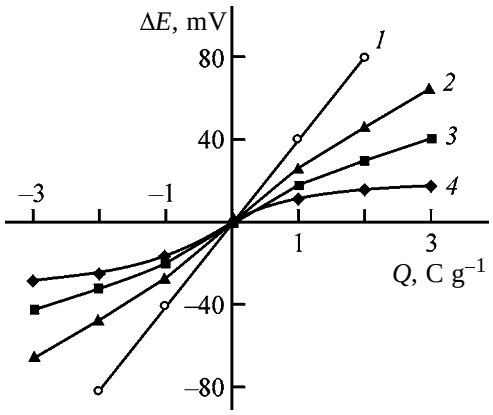

Fig. 1. Charging curves obtained on carbon fibers and activated carbon in 0.1 N K_2SO_4. (Q) Quantity of electricity and (ΔE) shift of the potential from the steady-state value. (*1*) GAU-3, (*2*) AUV-7, (*3*) AUV-2, and (*4*) GAU-7.

It can be seen from Fig. 1 that the dependence ΔE–Q is linear from virtually the very beginning for the mesoporous carbon GAU-3 (curve *1*) and carbon fiber AUV-3 (curve *2*). This indicates that the charging of the whole internal surface of the carbon samples is uniform, i.e., the rate at which the potential changes at any part of the internal surface of the porous electrode is comparable with the rate of EDL formation. The values of τ listed in the table for the given samples are comparatively short, as in the case of AUV-A and AUV-B fibers. Somewhat longer are transient processes on AUV-2 (Fig. 1, curve *3*). The nonlinear portion of the charging curve is very long for the microprous carbon GAU-7 (curve *4*), the small size of whose pores (r_{eff} = 1.1 nm) markedly limits the rate of transport of ions within the pore space and makes lower the rate at which the polarization is established across the thickness of the porous electrode.

The observed transient processes in charging of porous carbon materials are primarily due to the influence exerted by the porous structure on the rate and uniformity of the process of EDL charging and are independent of the degree of electrode impregnation with the electrolyte solution. The impregnation of the electrodes under study was complete because the electrodes were preliminarily kept in the electrolyte solution for a long time, and measurements were carried out 24 h after the electrodes were submerged in the electrolyte solution and a constant value of the stationary electrode potential was attained. After keeping the electrodes in the solution, the degree of impregnation reached a constant value and remained unchanged in the course of the experiment because the capacitance of EDL, determined for an electrode in different days, was the same.

All the carbon fibers under study have pores with small radii and would seemingly show a considerably longer duration of transient processes, comparable with that for a microporous sample GAU-7. However, this is not the case, which may be due to specific features of the pore structure of carbon fibers. Despite that the radius of micropores in carbon fibers is considerably smaller than that in activated carbon, the charging of fibers occurs more uniformly. This is favored by texture properties of ACF and, in particular, by the small thickness of threads and by the lability of the system of fibrils in the carbon fiber [6]. The effect of lability of the carbon fiber consists in that its porous structure changes in polarization because of the separation displacement of likely charged fibrils of the fiber and an increase in the dimensions of the transport pores. The manifestation of this effect favors a significant decrease in the hindering effect of the porous medium on the process of EDL formation and thereby leads to a faster establishment of a uniform polarization of the carbon fiber.

The relationship between the structure and nature of charging of ACF and GAC can be judged from the change in the capacitance of EDL in the electrode on raising the potential sweep rate. The capacitance of the EDL of the samples was determined by the method of potentiodynamic curves. Because of the increased ohmic resistance of the electrolyte in the pores, the rates of charging of the internal and external surfaces of the porous electrodes may differ. Beginning from certain small potential sweep rates, when the rate of EDL formation within the pore space starts to exceed the rate of polarization, the apparent capacitance of the carbon electrode corresponds to its whole internal surface area. As the polarization rate increases, the capacitance of the porous electrode decreases because the measured capacitance corresponds to only that part of the working surface which is involved in the electrochemical process and has enough time to be charged during the time of the potentiodynamic cycle.

Figure 2 shows that the capacitance of the EDL of the granulated carbon GAU-2 falls steeply and reaches rather small values as the polarization rate increases. This indicates that the charging process is displaced to the external surface. A considerably less pronounced decrease in the capacitance of the EDL is observed for AUV-7 and AUV-B, despite that the effective radius of pores in the fibers is severalfold smaller than that in carbon. The fact that high values of the capacitance of ACF are preserved in the whole range of potential sweep rates is a consequence of the lability of the

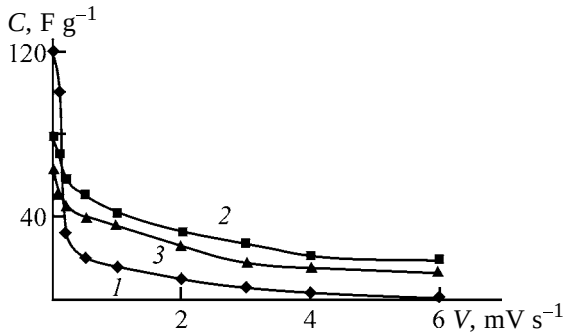

Fig. 2. Dependences of the capacitance C of the electrical double layer on the potential sweep rate V, obtained on carbon fibers (*1*) AUV-B and (*2*) AUV-A and (*3*) on activated carbon GAU-2.

structure of the fiber under polarization. The separation displacement of fibrils of a polarized carbon fiber and expansion of transport pores makes weaker the hindering influence of the porous medium and thus results in that rather high rates of current transport and mass exchange are preserved in polarized carbon fibers.

We calculated the parameters that make it possible to evaluate the efficiency of utilization of carbon materials under polarization. To these parameters belong the total resistance R and the effective resistivity $\tilde{\rho}$ of the electrolyte in the pores, the electrode capacitance C (F g^{-1}), and the characteristic time of charging ($\tau = RC$). The calculation was performed using a software that minimizes the deviation of experimental points from the theoretical curve describing the potentio-dynamic charging of a porous electrode in the double-layer range of potentials (range of ideal polarizability) [7]:

$$I = Cv\left\{1 - 2\pi^{-2}\sum_{k=1}(k + 0.5)^{-2}\exp\left[-\pi^2(k + 0.5)\frac{t}{RC}\right]\right\},$$

where I is the current (A g^{-1}); v, potential sweep rate (V s^{-1}); t, time; and k, summation index.

On calculating the values of C and R for each sample, $\tilde{\rho}$ was found by comparing the resistances R_i of the electrodes studied and that (R_0) of a model carbon adsorbent having sufficiently wide pores, which do not hinder the current transport and mass exchange. In this case, it can be assumed that $\tilde{\rho}$ of the model sample virtually coincides with the resistivity ρ_0 of the electrolyte in the solution bulk (found conductometrically). Then $\tilde{\rho}$ of the samples can be found using the relation

$$R_i/R_0 = \tilde{\rho} l_i S_0/(\rho_0 l_0 S_i),$$

where l and S are the thickness and cross-sectional area of the structural unit of the electrode (grains or fibers).

The calculated values of τ, R, and $\tilde{\rho}$ of the samples are listed in the table. It can be seen that the charging parameters found for the granulated carbons directly depend on the predominant pore radius. A decrease in the pore radius in carbons GAU-6, GAU-7, and GAU-1 leads to a steep increase in the effective resistivity $\tilde{\rho}$ of the solution in pores and in the characteristic time of EDL charging. At the same time, carbon fibers AUV-2, AUV-7, and AUV-B, which are sorbents with a clearly pronounced microporous structure in accordance with the values of the predominant pore radius, do not show so high values of $\tilde{\rho}$, which is presumably due to an increase in the size of transport pores in polarization of the fiber. Consequently, the structural lability of the fiber obviates ohmic limitations and allows a more uniform distribution of the polarization across the thickness of the porous electrode.

At strong polarizations (>0.1 V), at which Faraday processes occur in addition to the charging process, the effective depth λ of penetration of the electrochemical process was calculated for all the samples. This parameter characterizes the uniformity of distribution of the polarization across the thickness of the porous electrode [8]:

$$\lambda = (b/2\tilde{\rho} S i_0)^{1/2},$$

where b is the slope of the Tafel portion of the polarization curve (V); S, specific surface area of the electrode ($cm^2\ cm^{-3}$); and i_0, exchange current density ($A\ cm^{-2}$).

The value of λ and, consequently, the efficiency of polarization are determined by the size of structural units of the porous electrode and by the characteristics of the electrochemical process. The values of b and i_0 were found from cathodic polarization curves measured in a 0.1 N aqueous solution of K_2SO_4. Under the given conditions, the Faraday process is associated with discharge of water molecules. Comparison of the resulting values of λ (see table) shows that AFC are polarized considerably more efficiently than GAC. The better uniformity of AFC polarization in aqueous solutions, which is independent of the texture of fibers, is determined primarily by the very small thickness of carbon fibrils in the fibers, lability of their structure, and low exchange current densities, i.e., by the slow rate of water discharge on an energetically more uniform surface of carbon fibers.

Thus, fibrous carbon materials are rather promising for use as electrodes in various electrochemical processes, because they differ from granulated carbons in faster attainment of a prescribed polarization and in more uniform distribution of the polarization across the thickness of the carbon electrode.

CONCLUSIONS

(1) Comparison of the galvanostatic curves of charging of granulated carbons and carbon fibers shows that the time in which the equilibrium polarization is attained is shorter for carbon fibers.

(2) Analysis of the potentiodynamic curves reveals smaller hindrance to current transport and mass transfer in carbon fibers, compared to activated carbons.

(3) The calculated resistivity of the electrolyte in pores and the depth of penetration of the electrochemical process suggest that carbon fibers show more uniform distribution of the polarization across the thickness.

REFERENCES

1. Varentsov, V.K. and Varentsova, V.I., *Elektrokhimiya*, 2001, vol. 37, pp. 811–820.
2. Druzhinina, T.V., Tolkachev, A.V., Volodin, Yu.Yu., and Nazar'ina, L.A., *Zh. Prikl. Khim.*, 1999, vol. 72, no. 8, pp. 1303–1306.
3. Woodard, F., McMackins, D., and Jansson, R., *J. Electroanal. Chem.*, 1986, vol. 214, pp. 303–330.
4. Varentsov, V.K., *Intensifikatsiya elektrokhimicheskikh protsessov* (Intensification of Electrochemical Processes), Tomilov, A.P., Ed., Moscow: Nauka, 1988, p. 94.
5. Fedorov, N.F., Ivakhnyuk, G.K., and Gavrilov, D.N., *Zh. Prikl. Khim.*, 1982, vol. 55, no. 2, pp. 272–275.
6. Golub, D., Oren, Y., and Soffer, A., *Carbon*, 1987, vol. 25, pp. 109–117.
7. Posey, F.A. and Morozumi, T., *J. Electrochem. Soc.*, 1966, vol. 113, pp. 176–188.
8. Ksenzhek, O.S. and Stender, V.V., *Dokl. Akad. Nauk SSSR*, 1956, vol. 107, pp. 280–287.

Russian Journal of Applied Chemistry, Vol. 77, No. 11, 2004, pp. 1797–1800. Translated from Zhurnal Prikladnoi Khimii, Vol. 77, No. 11, 2004, pp. 1815–1818.

APPLIED ELECTROCHEMISTRY AND CORROSION PROTECTION OF METALS

Effect of Zirconium, Calcium, and Barium on Corrosion-Electrochemical Behavior of Aluminum

I. N. Ganiev, R. O. Barotov, and M. B. Inoyatov

Nikitin Institute of Chemistry, Academy of Sciences of Tajikistan Republic, Dushanbe, Tajikistan

Received March 16, 2004

Abstract—The effect of zirconium, calcium, and barium on corrosion-electrochemical properties of aluminum was studied. A positive effect of alloying aluminum by these metals was revealed.

The dissolution of aluminum in neutral media is described by the following equations [1, 2]:

$$Al + 3OH^- = Al(OH)_3 + 3e, \quad (1)$$

$$Al(OH)_3 + OH^- = Al(OH)_4^-. \quad (2)$$

The process is limited by the transport rate of OH^- ions to an electrode surface. Oxygen is a depolarizer in neutral aerated solutions. Its reduction at the metal|solution interface follows the equation

$$O_2 + 2H_2O + 4e = 4OH^-. \quad (3)$$

The process is limited by the diffusion of oxygen dissolved in an electrolyte, which finally determines the metal corrosion rate. The intermediate product of the reaction of aluminum with OH^- ions is hydrated oxide of the general formula $Al_2O_3 \cdot nH_2O$. Various modifications of aluminum oxides and hydroxides are readily soluble in alkaline and acid media, but they are practically insoluble in neutral solutions. Therefore, aluminum and its alloys can be used only in near-neutral media. In such solutions, oxide films on aluminum show high protective properties, and the corrosion of aluminum and its alloys, as a rule, is minor and occurs at separate defects of oxide films [1, 2]. The pitting corrosion is the most dangerous type of corrosion degradation of aluminum and its alloys.

According to [3, 4], a corrosion process proceeds on aluminum in alkaline media at rather negative potentials (–1.5 to –1.75 V), and the corrosion mechanism can be expressed as a system of two conjugated stages:

$$Al + 2OH^- \rightarrow Al(OH)^{2+} + 3e, \quad (4)$$

$$H_2O + e \rightarrow OH^- + 1/2H_2. \quad (5)$$

In alkaline solutions, corrosion occurs virtually fully under the conditions of hydrogen depolarization. The addition of the first electron to a water molecule is the slowest stage.

Thus, the corrosion of aluminum in various media has been extensively studied, but this is not true for its alloys, especially for low alloys. This makes difficult the choice of alloying components and alloy compositions.

This problem is complicated by the lack of the theory for basic principles of corrosion-proof doping of metals and alloys. The existing assumptions consist in an increase in the thermodynamic stability of the system and a decrease in cathode or anode areas on the alloy surface [5].

The most efficient way of increasing the corrosion resistance of aluminum alloys is the retardation of anode processes, i.e., the passivation. From the viewpoint of corrosion, it is preferable that the strengthening structural phase of alloys should be anodic with respect to the main (cathodic) bulk of the alloy. In such cases, the alloys must have the smallest possible relative surface area of the anodic component. The reduction of the surface area of anodes is attained by obtaining an alloy with narrower uniform grain boundaries, for example, by increase in the alloy purity or by an appropriate thermal treatment. Doping of a metal or an alloy with a stronger inhibiting alloying element also enhances the capability of the alloy for anodic passivation [5, 6]. For this purpose, anodic dopants are often used. In this work we chose calcium and barium, and also zirconium as anodic dopants because of their lower electronegativity [7] and high oxygen affinity [8] compared to aluminum. They were chosen owing to the fact that zirconium as a transition metal positively affects the strength, plasticity, and

1070-4272/04/7711-1797 © 2004 MAIK "Nauka/Interperiodica"

Table 1. Variation in time of the free corrosion potential of aluminum alloys with zirconium, calcium, and barium in 0.1 N NaOH

Content, wt %			E_{fc}, V, in indicated time, min					
Zr	Ca	Ba	0	5	30	60	120	steady-state value
0.01	0.03	–	1.510	1.380	1.352	1.342	1.320	1.312
0.01	0.05	–	1.510	1.385	1.356	1.346	1.323	1.318
0.01	0.02	–	1.480	1.345	1.225	1.183	1.160	1.145
0.01	–	0.04	1.515	1.485	1.465	1.455	1.453	1.453
0.01	–	0.04	1.500	1.428	1.388	1.383	1.383	1.383
0.01	–	0.04	1.510	1.442	1.405	1.394	1.386	1.383
0.01	–	0.06	1.500	1.420	1.400	1.397	1.395	1.395
Al (A5)	–	–	1.520	1.485	1.465	1.455	1.453	1.453

Table 2. Variation in time of the free corrosion potential of aluminum and its alloys in various media

Medium	Material	$-E_{fc}$, V, in indicated time, min					
		0	5	30	60	120	steady-state value
0.01 N NaOH	Al (A6)	1.450	1.375	1.342	1.358	1.335	1.335
0.01 N HCl	Al + dopant*	0.790	0.722	0.643	0.605	0.585	0.563
	Al (A6)	0.940	0.800	0.770	0.735	0.700	0.692
0.5 N NaCl	Al + dopant*	1.200	1.020	0.825	0.775	0.755	0.745
	Al (A6)	1.095	0.935	0.840	0.815	0.795	0.785

* Dopant content, wt %: Zr 0.05, Ba 0.03.

heat resistance of aluminum, whereas alkaline-earth metals act as refining and modifying agents and therefore positively affect physicomechanical properties and corrosion resistance of aluminum [9–12].

EXPERIMENTAL

The corrosion-electrochemical behavior of the synthesized aluminum alloys was studied according to [10, 11] in 0.01 and 0.1 N NaOH, 3% NaCl, and 0.01 N HCl using a PI-50–1 potentiostat operating at potential scan rates of 2 and 10 mV s^{-1}. A silver chloride electrode was used as a reference electrode, and all potential values were referenced to it. The corrosion rates of alloys were determined gravimetrically. The experimental data are shown in Tables 1 and 2.

It is known that the corrosion behavior of metals and alloys can be judged from various electrochemical parameters. The time dependence and steady-state value of the free corrosion potential can provide important data on the behavior of a metal in a corrosive medium. As a rule, a large shift of the corrosion potential to the positive region suggests that the anodic reaction rate can decrease owing to passivation. Such materials can be expected to be more corrosion-resistant under natural service conditions [13].

To select a corrosion medium, we first studied the behavior of Al in NaOH solutions of various concentrations.

Reduction of the NaOH concentration from 0.5 to 0.05 N results in decreasing corrosion current density, which suggests a decrease in the rate of aluminum corrosion. The sharpest decrease in the corrosion rate is observed in 0.05 N NaOH. If the sodium hydroxide concentration is less than 0.05 N, aluminum changes from an active state to a passive state owing to the accumulation of a film of aluminum hydroxide on the metal surface. These experimental data are in good agreement with the published data on aluminum behavior in KOH solutions [14, 15]. Taking these results into account, we carried out the further experiments in 0.1 N NaOH and in 3% NaCl.

The dynamics of free corrosion potential variation for low-alloyed aluminum alloys in 0.1 N NaOH solution (Table 1) indicates that a protective film on

Table 3. Electrochemical parameters of aluminum alloys with zirconium, calcium, and barium in 3% NaCl. Potential scan rate 10 mV s^{-1}

Content, wt %			$-E_{fc}$	$-E_{po}$	$-E_{cp}$	$-E_{pf}$	i_{po}	i_{cp}
Zr	Ca	Ba	V				mA cm^{-2}	
0.01	0.05	–	0.750	1.450	1.320	0.680	1.50	0.10
0.05	0.05	–	0.760	1.460	1.370	0.670	1.10	0.10
0.10	0.05	–	0.775	1.450	1.380	0.650	1.65	0.11
0.30	0.05	–	0.780	1.450	1.310	0.650	1.70	0.14
0.50	0.05	–	0.820	1.450	1.250	0.640	2.10	0.15
0.01	–	0.05	0.770	1.400	1.320	0.670	1.70	0.11
0.05	–	0.05	0.795	1.420	1.320	0.650	1.40	0.10
0.10	–	0.05	0.800	1.440	1.380	0.670	1.50	0.11
0.30	–	0.05	0.815	1.440	1.380	0.680	1.60	0.13
0.50	–	0.05	0.825	1.450	1.380	0.680	2.00	0.13
Al (A5)	–	–	0.760	1.420	1.320	0.680	2.10	0.15

their surface is formed slowly and the process is complete within 2–4 h and sometimes within a day. The alloys under study have a more positive free corrosion potential than the starting aluminum. The greatest positive shift of the potenial is observed within 5–30 min of the test in the corrosion medium.

Similar experiments were carried out in 0.01 N NaOH, 0.01 N HCl, and 0.5 N NaCl. In these media, free corrosion potentials of the alloys are also shifted to the positive region, the alloys showing more positive potential values than the pure metal (Table 2).

According to the experimental data, in particular, to the value of the steady-state free corrosion potential (Table 2), aluminum and its alloys have lower corrosion resistance in alkaline media than in acid media.

The results of the electrochemical study of aluminum alloys with various zirconium contents and constant barium and calcium contents in 3% NaCl are summarized in Table 3. The corrosion potentials of the alloys are shifted to the negative region as the zirconium content increases. Small amounts of zirconium scarcely affect the pitting formation potential E_{pf}, whereas the complete passivation potential E_{cp} somewhat decreases. With alloys, the passivation range is not reduced compared to aluminum. The alloys doped predominantly with 0.01–0.1% Zr have lower current densities of passivation onset i_{po} and of complete passivation i_{cp} than pure aluminum. Therefore, doping of aluminum with zirconium enhances the corrosion resistance of the alloys.

The modifying agents zirconium, calcium, and barium make alloy structures more finely dispersed and react with gases dissolved in aluminum. In the case of modified alloys, in contrast to nonmodified alloys, the intercrystallite corrosion is limited to the near-surface layer of the metal and is not developed significantly even after prolonged corrosion tests [16].

The role of zirconium as a dopant for aluminum alloys is not limited to its modifying action. It also sharply increases the recrystallization temperature of aluminum and its alloys after both hot and cold deformations, making it possible to obtain a non-recrystallized or partially non-recrystallized structure after thermal treatment and hence to enhance the corrosion resistance and mechanical properties. For example, the corrosion rate of the alloys of optimal composition under study after pressing (80% deformation) decreased from 0.0136 (initial state) to 0.0094 g m^{-2} h^{-1} after deformation.

REFERENCES

1. Käsche, H., *Die Korrosion der Metalle. Physikalisch-chemische Prinzipien und aktuelle Probleme*, Berlin: Springer, 1979.
2. Vyazovkina, N.V., *Zashch. Met.*, 1999, vol. 35, no. 5, pp. 493–499.
3. Izotova, S.T., Sysoeva, V.V., and Artyugina, E.D., *Zh. Prikl. Khim.*, 1985, vol. 58, no. 9, pp. 2115–2118.
4. Sysoeva, V.V., Artyugina, E.D., Gorodilova, V.G., and Berkman, E.A., *Zh. Prikl. Khim.*, 1985, vol. 58, no. 4, pp. 921–924.
5. Tomashov, N.D. and Chernova, G.P., *Teoriya korrozii i korrozionnostoikie konstruktsionnye splavy* (Corrosion Theory and Corrosion-Resistant Structural Alloys), Moscow: Metallurgiya, 1986.

6. Zhuk, N.P., *Kurs teorii korrozii i zashchity metallov* (Course of Corrosion Theory and Metal Protection), Moscow: Metallurgiya, 1976.
7. Pauling, L.C., *General Chemistry*, San Francisco: Freeman, 1970.
8. *Kratkii spravochnik fiziko-khimicheskikh velichin* (Concise Handbook of Physicochemical Quantities), Leningrad: Khimiya, 1983.
9. Ganiev, I.N. and Trubnyakova, E.D., *Zh. Prikl. Khim.*, 1986, vol. 59, no. 11, pp. 2545–2548.
10. Ganiev, I.N., Trubnyakova, E.D., and Karimova, T.M., *Zh. Prikl. Khim.*, 1987, vol. 60, no. 9, pp. 2114–2115.
11. Ganiev, I.N. and Shukroev, M.M., *Zh. Prikl. Khim.*, 1988, vol. 61, no 8, pp. 1916–1918.
12. Norova, M.T., Ganiev, I.N., and Nazarov, Kh.M., *Zh. Prikl. Khim.*, 2003, vol. 76, no. 4, pp. 567–569.
13. Sinyavskii, V.S., Val'kov, V.D., and Kalinin, V.D., *Korroziya i zashchita alyuminievykh splavov* (Corrosion and Protection of Aluminum Alloys), Moscow: Metallurgiya, 1986.
14. Rotinyan, A.L., Cherenkova, I.A., and Sysoeva, V.V., *Zh. Prikl. Khim.*, 1977, vol. 50, no. 11, pp. 2499–2501.
15. Fateev, Yu.F., Vrzhosek, G.G., and Antropov, L.I., in *Trudy 2 Ukrainskoi Respublikanskoi konferentsii po elektrokhimii* (Proc. 2nd Ukrainian Conf. on Electrochemistry), Novomoskovsk, 1978, p. 139.
16. Postnikov, N.S., *Korrozionnostoikie alyuminievye splavy* (Corrosion-Resistant Aluminum Alloys), Moscow: Metallurgiya, 1976.

Russian Journal of Applied Chemistry, Vol. 77, No. 11, 2004, pp. 1801–1807. Translated from Zhurnal Prikladnoi Khimii, Vol. 77, No. 11, 2004, pp. 1819–1825.

APPLIED ELECTROCHEMISTRY AND CORROSION PROTECTION OF METALS

Effect of Ozone on the Corrosion of Metals in an Acid Medium

G. O. Tatarchenko

Severodonetsk Technological Institute, Severodonetsk, Lugansk oblast, Ukraine

Received September 17, 2003; in final form, September 2004

Abstract—The corrosion-electrochemical behavior of steels and metals in sulfuric, hydrochloric, and acetic acids in the presence of ozone was studied.

In recent decades, one of directions of synthesis of oxygen-containing derivatives, oxidation of hydrocarbons and other organic compounds with ozone, which does not contaminate the products and the environment and makes it possible to improve the yield and quality of target products, has been developing successfully [1–3]. This poses an acute problem of the choice of structural materials and apparatus for organic synthesis in the presence of ozone. To fabricate the required equipment, it is necessary to use structural materials that would ensure prolonged and safe operation of the apparatus in chemical industries employing exceedingly corrosive media (sulfuric, hydrochloric, nitric, and acetic acids). Commonly, high-alloyed stainless steels (12Cr18Ni10Ti, 08Cr22Ni6Ti, and 06CrNi28MoCuTi), VT1-0 titanium and its alloys, and ADO aluminum and its alloys are used for this purpose. It is necessary to determine how such a strong oxidizing agent as ozone affects the corrosion resistance of these materials at different acid concentrations and temperatures and varied content of organic compounds, which may act both as corrosion inhibitors and as corrosion activators.

It should be noted that the materials mentioned above show different passivation mechanisms. The passivity of stainless steels is mostly due to chemisorption of the oxidizing agent on those parts of the surface which are enriched in chromium, whereas Ti and Al are passivated because of the formation of the oxides TiO_2 and Al_2O_3. The main factor that determines the rate of corrosion of the metals in nonoxidizing acids (H_2SO_4, HCl) is the hydrogen overvoltage on the cathodic areas of the metal. Ozone, which is an effective cathodic depolarizer, shifts the corrosion potential E_{cor} in the positive direction, with the result that the corrosion rate of a metal may increase if the metal remains in the region of active dissolution. At the same time, the facilitation of the cathodic process results in that the polarization of the anodic areas increases and may reach the critical current density and transfer the metal to the passive region.

The aim of this study was to determine how O_3, an exceedingly strong oxidizing agent, affects the corrosion-electrochemical behavior of steels, alloys, and metals in a corrosive acid medium.

EXPERIMENTAL

The following steels: 09Mn2Si, 08Cr17Ti, 12Cr·18Ni10Ti, 10Cr17Ni13Mo2Ti, and 06CrNi28MoCuTi, and metals: Ti, Ni, Cr, and Mo, were studied. As the acid media served hydrochloric, sulfuric, and acetic acids at 20–60°C. Polarization measurements were carried out in a three-electrode glass cell. The working electrodes were prepared using the standard procedure. The potential sweep rate was 1.44 V h^{-1}. Potentiometric and potentiodynamic curves were measured after the stationary corrosion potential E_{cor} was attained (10–15 min). The potentials are given relative to the standard hydrogen electrode. An ozone–air mixture was obtained in a laboratory glass ozonizer with a cooling water jacket from compressed cleaned and dried air. The concentration of O_3 in the mixture was varied by changing the feeding voltage with a laboratory one-coil transformer. The solutions were ozonized by bubbling with the ozone–air mixture at a rate of 0.07 m^3 h^{-1} during the entire time of experiment. The concentration of O_3 in the gas phase was 0.1 mol m^{-3}. The corrosion rate was found from the weight loss by samples kept in the solutions for 100 h.

The 06CrNi28MoCuTi alloy is corrosion-resistant in a 30% solution of H_2SO_4 at 80°C and an 80% solution of the same acid at 60°C. On the whole, introduction of O_3 into H_2SO_4 solutions improves the corrosion-electrochemical behavior of the alloy. However, the corrosion rate in a 70% solution of H_2SO_4 at 60°C

1070-4272/04/7711-1801 © 2004 MAIK "Nauka/Interperiodica"

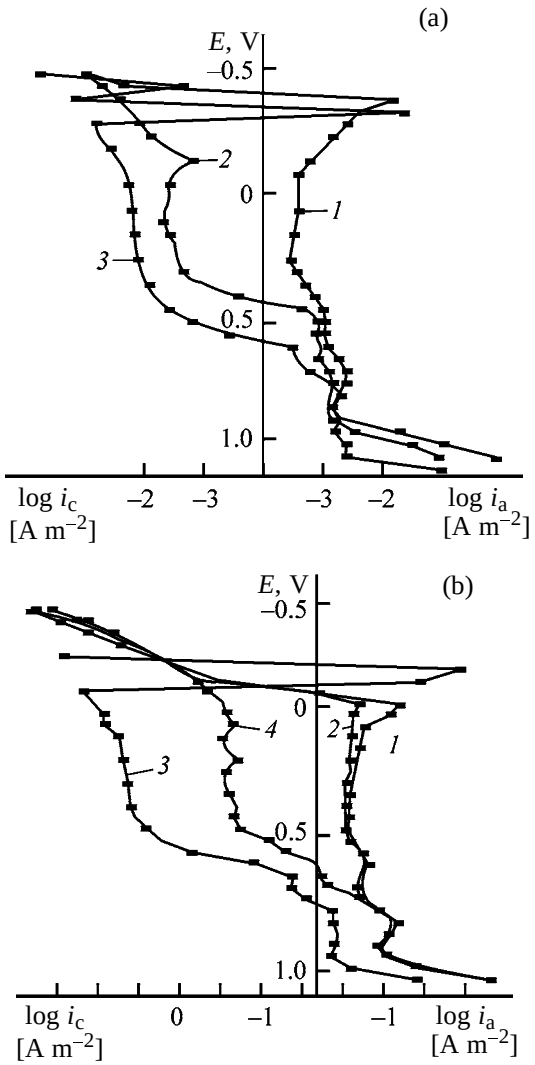

Fig. 1. Polarization curves for 12Cr18Ni10Ti steel in a 20% H_2SO_4 solution at 20°C. (i_c, i_a) Cathodic and anodic current densities and (E) potential; the same for Figs. 2–4. (a) H_2SO_4 solution: (*1*) subjected to aeration, (*2*) subjected to ozonation with agitation, and (*3*) subjected to ozonation. (b) Ozone concentration $c_0 \times 10^{-5}$ (M): (*1*) 1, (*2*) 4.8, (*3*) 25, and (*4*) 36.

increases from 0.07 to 0.49 g m^{-2} h^{-1} in the presence of O_3. The polarization curves show a noticeable increase in the width of the region of active dissolution, but the corrosion and repassivation potentials remain unchanged upon introduction of O_3 (E_{cor} = 0.4 V, E_p = 1.0 V) [4].

A study of the corrosion-electrochemical behavior of stainless steels in the medium subjected to ozonation revealed an ambiguous nature of the influence exerted by O_3. On the one hand, O_3, which is a strong depolarizer, transfers steels to the passive state; on the other hand, changes in the concentration of O_3, temperature, and pH of the medium can transfer the metal to the region of active dissolution, in which the rate of corrosion considerably exceeds that in an unozonized medium. For example, the 12Cr18Ni10Ti steel is in the region of active dissolution at 20°C in a 20% solution of H_2SO_4 and undergoes corrosion at a rate of 4.3 g m^{-2} h^{-1} (Fig. 1a, curve *1*). In a solution subjected to ozonation, the corrosion potential is shifted in the positive direction. However, a "cathodic loop" appears in the anodic curve, which is indicative of a state of unstable passivity (Fig. 1a, curve *3*). Agitation of a solution subjected to ozonation makes the cathodic reaction faster (the region of active dissolution disappears) and leads to a shift of E_{cor} into the passive region, but to a somewhat more negative value than that in an unagitated solution, with the rate of corrosion decreasing from 0.06 to 0.03 g m^{-2} h^{-1} (Fig. 1a, curve *2*). Agitation of solutions subjected to ozonation leads to an increase in the rate of cathodic processes; in the case of the 12Cr18Ni10Ti steel not only the cathodic, but also the anodic reactions become faster, with the rate of the anodic reaction increasing to a greater extent (Fig. 1a, curves *2*, *3*). However, as the current densities are low, the solution agitation affects the rate of corrosion significantly [5]. Raising the concentration of H_2SO_4 makes the influence exerted by O_3 weaker: the rate of corrosion in a 30% H_2SO_4 solution is half an order of magnitude lower than that in an unozonized solution, whereas in a 40% solution, the rates in ozonized and unozonized solutions are equal. Interestingly, the rate of corrosion of the 12Cr18Ni10Ti steel in a 70% H_2SO_4 solution is an order of magnitude lower than that in a 20% solution; however, the corrosion-electrochemical behavior in a medium subjected to ozonation is impaired.

Raising the concentration of O_3 from 10^{-5} to 3.6 × 10^{-4} M in a 20% H_2SO_4 solution leads to a gradual change of the anodic polarization curve (Fig. 1b). The range of concentrations at which the 12Cr18Ni10Ti steel is in the state of stable passivity is (0.10–3.6) × 10^{-4} M [5].

A study of the selectivity of dissolution of products formed in corrosion of the 12Cr18Ni10Ti steel demonstrated that the dissolution of Ni and Cr in ozonized solutions is lower in 30–40% H_2SO_4 solutions, compared to unozonized solutions, and that of Fe is lower in a 30% H_2SO_4 solution and higher in a 40% solution. However, the pattern changes in the 70% H_2SO_4 solution: with the total amount of dissolved products of corrosion of the 12Cr18Ni10Ti steel, the amount of Ni and Cr in ozonized media exceeds that in

unozonized solutions. In this case, the Fe : Cr : Ni ratio remains the same for virtually all the media, 1 : 0.08 : 0.02. Raising the temperature of the solutions makes the rate of steel corrosion considerably faster, the anodic polarization curves are shifted to higher currents.

The susceptibility of the stainless steels 12Cr18Ni·10Ti and 06CrNi28MoCuTi and their welded joints for intercrystallite corrosion (ICC) was studied in 20 and 40% H_2SO_4 solutions, respectively. Samples of the 12Cr18Ni10Ti steel were subjected to sensitization at 650°C for 6 h. The samples were tested for susceptibility to ICC in accordance with GOST (State Standard) 60-32.89. Sensitized samples exhibited no ICC after being kept in ozonized solutions for 100 h, but without O_3 ICC was observed [6]. Welded joints of steels did not undergo ICC in ozonized media, either.

The main alloying additives to stainless steels are Ni, Cr, and Mo; therefore, it was of interest to study the behavior of these metals in a medium subjected to ozonation.

Nickel is thermodynamically unstable in acid solutions; it may dissolve with formation of the Ni^{2+} ion and evolution of H_2. However, Ni is only slightly more electronegative in the electrochemical series with respect to the H^+/H_2 equilibrium. This means that the rate of dissolution of Ni in acid solutions will be low in the absence of oxidizing agents stronger than H^+. Indeed, the rate of Ni corrosion in 2–70% solutions of H_2SO_4 is low and virtually invariable, polarization potentiodynamic curves do not exhibit any significant differences either. As the concentration of H_2SO_4 increases, E_{cor} of Ni becomes more negative. The specific features of the electrochemical behavior of Ni are the dynamic instability, i.e., periodic oscillations of the current in a 2% solution of H_2SO_4 at potentials of 0.4–1.0 V, and anomalous phenomena in the dissolution of Ni, i.e., the absence of a Faraday correspondence between the quantity of electricity passed through Ni and the amount of dissolved metal. The corrosion rates calculated from the current differ by one or two orders of magnitude from those following from the weight loss, which can be attributed to the occurrence of an additional anodic process.

Introduction of O_3 shifts the corrosion potential in the positive direction by 0.1–0.15 V and leads to an increase in the density of the anodic dissolution current to 10 A m^{-2}. However, the rate of Ni dissolution cannot be determined from polarization curves, either. Comparison of polarization curves for Ni in a medium subjected to ozonation and that without O_3 does not show any significant difference in dissolution rates, whereas gravimetric analysis demonstrates that O_3 raises the corrosion rate by an order of magnitude and more.

The main reason for the decrease in the corrosion rate of Ni in an acid medium is adsorption of atomic hydrogen on atoms that occupy semicrystalline positions and block "active centers" on the surface [7]. At the same time, hydrogen dissolved in the metal partly dissociates into H^+ ions and electrons, and electrons can fill vacancies on the *d* level of Ni atoms. As a result, the metal loses its ability to chemisorb oxygen and hydrogenated Ni is activated in anodic polarization.

It was shown in [8] that, in corrosion of hydrogenated Ni with oxygen depolarization in the initial period of time, oxygen predominantly interacts with hydrogen that diffuses from the bulk of the electrode, and dissolution of Ni is hindered. Then binding of hydrogen and metal ions must occur at a higher rate in the presence of O_3, because atomic oxygen exists in the diffusion region in addition to molecular oxygen. The rate of variation of E_{cor} in solutions without O_3 in the first 10 min was 1 mV s^{-1} in the negative direction. In the presence of O_3, the rate of variation of E_{cor} was zero in a 2% solution of H_2SO_4, reached the highest value of 2 mV s^{-1} in the positive direction in a 20% solution, and again zero in a 70% H_2SO_4 solution [9]. In all probability, this is due to the following: In the 20% H_2SO_4 solution, the concentration of H^+ is sufficient for the reactions of O_3 reduction, with H^+ ions involved, and hydrogenation of the metal to occur simultaneously and for the rate of absorption of H^+ ions to be equal to the rate of diffusion supply of O_3 to the electrode surface. Ni samples preliminarily hydrogenated in a deaerated 5% H_2SO_4 solution were placed for 24 h in 5% H_2SO_4 solutions subjected to ozonation and aeration, and after that were analyzed by the vacuum method for the content of hydrogen. The volume of hydrogen in nickel was 20–30 cm^3 per kilogram of the metal in the presence of O_3, and 100 cm^3 without ozone, i.e., ozone diminishes the hydrogenation of Ni by a factor of 3–4, thereby making faster its dissolution [9].

Chromium belongs to metals that are easily passivated in an oxidizing medium, with the negative potential changing to positive relative to the standard hydrogen electrode; it has a higher electron deficiency of the *d* level (fraction of vacancies 0.8) than Ni (fraction of vacancies 0.6), and not only a chemisorbed layer, but also an oxide film can be formed on its sur-

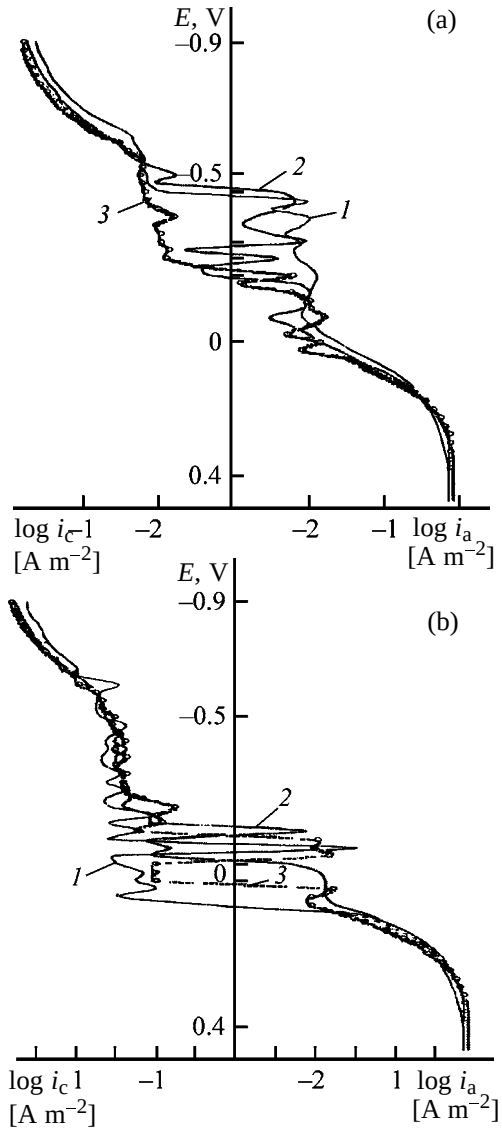

Fig. 2. Polarization curves for Mo in H_2SO_4 solutions subjected to (a) aeration and (b) ozonation at 20°C. Concentration of H_2SO_4 solutions (wt %): (*1*) 2, (*2*) 5, and (*3*) 10.

face. In the presence of oxygen-containing oxidizing agents (MnO_4^-, SeO_4^{2-}, H_2O_2) in a 0.05 M H_2SO_4 solution, the dissolution of Cr is accelerated because of the electroreduction of the oxidizing agent on the surface of chromium with formation of OH^- ions and discharge of H^+ ions [10, 11].

The polarization curves of Cr, obtained at different concentrations of H_2SO_4, exhibit a number of specific features. As the concentration of H_2SO_4 increases, the potentials of corrosion (E_{cor}) and repassivation (E_r) are shifted in the positive direction; the critical potential E_{cr} and the critical current density i_{cr} are virtually the same for all the concentrations (–0.5 V and 100 A m^{-2}), with the exception of the 70% H_2SO_4 solution: –0.35 V and i = 10 A m^{-2}. However, the region of active dissolution becomes in this case narrower and a cathodic loop appears in 5 and 10% solutions. The passive region lies within the range from –0.3 to 1.0 V. Introduction of O_3 into H_2SO_4 solutions does not change the E_{cor} of chromium, whereas i_{cr} decreases to 50 A m^{-2} for 2 and 5% H_2SO_4 solutions and remains unchanged for other concentrations. The cathodic loop becomes wider and the current densities in this region increase by an order of magnitude.

The best passivation characteristics are exhibited by Cr in a 20% H_2SO_4 solution subjected to ozonation. The corrosion rate of Cr in the presence of O_3 is lower than that in an unozonized medium, although Cr is stable in any of the solutions under study. The type of variation of E_{cor} with time demonstrated that the rate of electrochemical processes that occur on Cr is the highest during the first 10 min in a 70% H_2SO_4 solution and decreases as the acid concentration becomes lower. In the case of solutions subjected to ozonation, this dependence changes and the highest rate is observed in a 2% H_2SO_4 solution. The results obtained confirm the assumption that H^+ ions are actively involved in the cathodic reduction of O_3 [12].

In contrast to chromium, Mo has no region of active dissolution in the corresponding polarization curves. According to potentiodynamic data (Fig. 2), introduction of O_3 shifts the corrosion potential in the positive direction by 0.1–0.4 V. As the pH value is varied, E_{cor} remains virtually constant in the course of time for solutions subjected to ozonation (–0.2 V), being close to –0.5 V for solutions subjected to aeration. On introduction of O_3 into a solution (Fig. 2b), anomalous phenomena are manifested to a greater extent: the dissolution rate of the metal is independent of the potential in the region in which, obeying the laws of electrochemistry, the process would have been accelerated upon a shift of E in the positive direction (in accordance with the Tafel equation). For Mo in solutions subjected to ozonation, this region is observed at potentials from –0.6 to –0.3 V. It can be seen from Fig. 2 that, on the whole, the pH value of the solution exerts no influence on this effect. The corrosion potential of Mo in the presence of O_3 is more positive than that in solutions subjected to aeration, and the rate of the corrosion process in solutions subjected to ozonation exceeds by an order of magnitude that in solutions subjected to aeration. Ozone stimulates the corrosion process at the initial instant of time, with its subsequent deceleration, and then "shifts" Mo toward noble metals in the electrochemi-

cal series, acting as an agent passivating the corrosion process. In this case, the difference of the rates of variation of E_{cor} markedly decreases as the H_2SO_4 concentration increases, with the rates of variation of E_{cor} differing by a factor of only 2 in a 70% solution of the acid [13].

It would be appropriate to mention the effect of dynamic instability, observed at potentials in the range from –0.2 to 0.2 V. The frequency and amplitude of oscillations were different in different experiments, depending on their conditions (variation of the solution pH, presence or absence of O_3), but remained constant during each particular experiment. The data obtained suggest that, for solutions subjected to aeration, the amplitude of these oscillations increases with decreasing solution pH. The opposite tendency is observed for solutions subjected to ozonation, but ozonation makes wider the range of potentials at which the oscillations appear. Similar phenomena of dynamic instability, with oscillations of current or potential, have been described for iron [14]. However, no systematic experimental data on the conditions in which these oscillations appear are available at present, and no unambiguous explanation of this effect has been given, either.

According to reference data [15], Ti can be used as structural material in HCl solutions subjected to aeration at HCl concentrations of 10% at 35°C and up to 5% at 40°C. Analysis of the results obtained for stainless steels suggests that introduction of O_3 into HCl solutions will expand the region of the corrosion stability of Ti and its alloys. In the electromotive series, Ti is an active metal and is easily oxidized in the active state to pass into solution in the form of Ti^{3+} ions. The surface oxide film has properties of a semiconductor, which is mainly due to the presence of anionic oxygen vacancies and interstitial Ti^{3+} ions. They make the oxide an *n*-type semiconductor and, consequently, ensure its passive state. The disruption of the passivity of Ti is associated, on the one hand, with an increase in the activity of Cl^- ions, which penetrate into the chemisorbed layer through pores and defects more easily than O_2 or OH^- do and are adsorbed in competition with these ions. In this case, Cl^- ions, having reached the metal surface, favor hydration of metal ions and facilitate their transfer into solution, in contrast to the externally adsorbed oxygen. On the other hand, the solubilities of both O_2 and O_3, which provide the formation of the protective oxide film, decrease with increasing temperature. The decrease in the concentration of O_3 predetermines the diffusion control over electrochemical processes at potentials more positive than 0.1 V.

Bubbling of a 10% HCl solution with ozone at 20°C shifts the corrosion potential of VT1-0 titanium in the positive direction by 0.67 V, and that of the VT-5 and OT-4 alloys by 0.57 V, but all of them are passive at this temperature. However, the rate of corrosion in a 10% HCl solution at 40°C increases to 1.05 mm/year for VT1-0 and 1.85 mm/year for the alloys. The values of E_{cor} are –0.68 and –0.77 V, respectively, and the critical current densities i_{cr}, 0.76 and 2.10 A m^{-2}. On introduction of O_3 into the solution, the corrosion rate of Ti decreases to 0.06 mm/year (E_{cor} = 0.03 V), and the metal reaches the state of stable passivity. The electrochemical behavior of the alloys upon introduction of O_3 into solution exhibits a cathodic loop, which corresponds to the state of unstable passivity and to a lower rate of cathodic depolarization with ozone, compared to Ti [16]. The activity of Cl^- ions and the electrical conductivity of HCl reach the highest values at medium concentrations. Raising the concentration of HCl to 15–20% leads to a decrease in the corrosion resistance of Ti and its alloys, whereas in the presence of O_3 they remain in the passive state and can be used as structural materials. The presence of Al in Ti impairs its corrosion characteristics in solutions not subjected to ozonation, whereas in solutions subjected to ozonation at 20°C, there are no differences in the electrochemical behavior. At 40°C, the corrosion rate of VT1-0 is 2.56 mm/year, and that in the presence of O_3, 1.60 mm/year in a 15% HCl solution. A cathodic loop appears in the polarization curves, and the critical current densities of dissolution increase by an order of magnitude (Fig. 3).

Thus, presence of O_3 in HCl solutions favors passivation of Ti and its alloys and extends the limits of their applicability as structural materials.

It is known that steels of the 12Cr18Ni10Ti type are stable in acetic acid at any concentration up to 75°C; chromium stainless steels of the 08Cr17Ti type are stable only at low temperatures (30–40°C); St.3 and 09Mn2Si steels have low stability and are unstable in 5–10% solutions of acetic acid.

In a 5% CH_3COOH solution, the potentiodynamic polarization curve obtained for the 08Cr17Ti steel shows two peaks at E = –0.30 and 1.05 V at 20°C, i_{cr} = 1.22 A m^{-2}. Introduction of O_3 into the solution does not change the run of the polarization curve in the active dissolution region significantly. At more positive potentials, the anodic curve is abruptly shifted into the region of small current densities, with a cath-

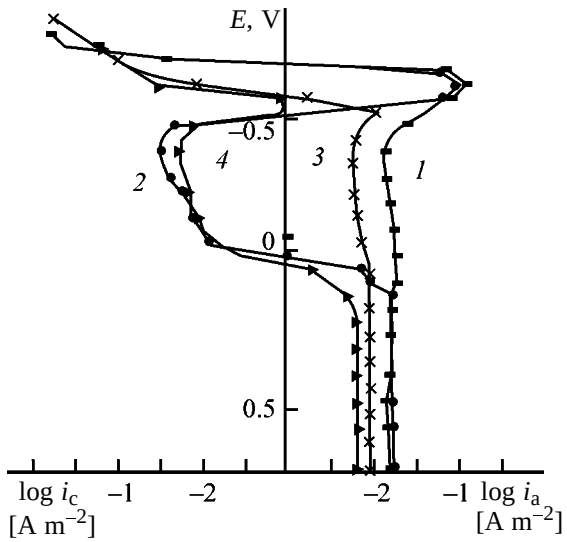

Fig. 3. Polarization curves for Ti in (*1, 2*) 15% HCl solution at 40°C and (*3, 4*) 20% HCl solution at 20°C. HCl solution: (*1, 3*) subjected to aeration and (*2, 4*) subjected to ozonation.

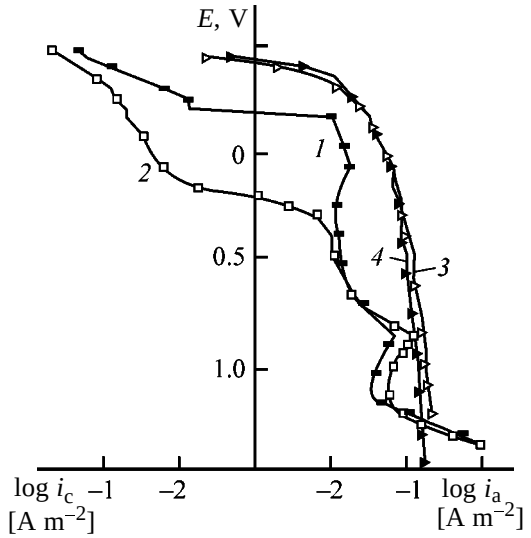

Fig. 4. Polarization curves of (*1, 2*) 08Cr17Ti and (*3, 4*) 09Mn2Si steels in an agitated 5% CH_3COOH solution at 25°C. CH_3COOH solution: (*1, 3*) aerated and (*2, 4*) ozonized.

odic loop formed both at 25°C and at 40°C. Vigorous agitation of a CH_3COOH solution subjected to ozonation makes it possible to eliminate the region of active dissolution because of the enhancement of the cathodic depolarization (Fig. 4). The corrosion rate of 08Cr17Ti steel in the presence of O_3 (0.009 g m^{-2} h^{-1}) somewhat exceeds that without O_3 at 25°C.

Low-carbon steels of the 09Mn2Si and St.3 types (Fig. 4) show a low stability in the presence of O_3, with their corrosion rate increasing by a factor of 2–3; consequently, they cannot be recommended for use in weakly acidic solutions subjected to ozonation. The differences in the corrosion rates of the 09Mn2Si and St.3 steels (100 h) and in the current densities in the polarization curves (1.5 h) are primarily determined by acceleration of the dissolution of the metals in the course of time because of the saturation of the near-electrode layer with ions of iron and manganese, which, being oxidized by ozone, are reduced on the metal and thereby enhance its corrosion.

Previously, a mechanism of reduction of O_3 in an acid medium to give H_2O_2 and OH^- ions in the near-electrode layer has been suggested [18]:

$$O_3 \longrightarrow O + O_2, \quad (1)$$

$$O + H^+ + 2e \longrightarrow OH^-, \quad (2)$$

$$OH^- + H^+ \longrightarrow H_2O, \quad (3)$$

$$O_2 + 2H^+ + 2e \longrightarrow H_2O_2, \quad (4)$$

$$H_2O_2 + 2e \longrightarrow 2OH^-. \quad (5)$$

The OH^- ions forming in the reaction zone favor transfer of the metal to the region of positive potentials, which leads to a decrease in the corrosion rate for metals that can be passivated, and to an increase in the corrosion rate for nonpassivated metals. In electroreduction of oxygen-containing oxidizing agents in acid solutions, the near-electrode concentration of H_3O^+ ions decreases, which leads to an increase in the pH value of the near-electrode layer.

CONCLUSIONS

(1) The action of ozone on metals and steels is determined by its high reactivity, as well as by the formation of not only molecular, but also atomic oxygen in the decomposition of O_3.

(2) The influence exerted by O_3 on the corrosion-electrochemical behavior of metals, steels, and alloys in an acid medium is determined by the concentration of O_3 in the medium, the pH value of the medium, the temperature of the medium, and diffusion into the double-layer region.

REFERENCES

1. Tyupalo, N., Yakobi, V., Bernashevskii, N., and Stepanyan, A., *Zh. Prikl. Khim.*, 1975, vol. 48, no. 5, pp. 1086–1090.
2. Tyupalo, N., *Dokl. Akad. Nauk Ukr. SSR, Ser. B*, 1980, no. 1, pp. 58–62.

3. Tyupalo, N., Yakobi, V., Bernashevskii, N., and Stepanyan, A., *Zh. Prikl. Khim.*, 1978, vol. 52, no. 3, pp. 700–702.
4. Shapovalova, I., Tyupalo, N., and Brodskii, A., *Fiz.-Khim. Mekh. Mater.*, Special Issue, 2001, no. 2, pp. 92–95.
5. Tyupalo, N., Tatarchenko, G., Gru, B., and Kuzub, V., *Zh. Prikl. Khim.*, 1991, vol. 64, no. 5, pp. 1085–1087.
6. Kuzyukov, A. and Tatarchenko, G., *Fiz.-Khim. Mekh. Mater.*, 1995, vol. 31, no. 3, pp. 114–117.
7. Kozachinskii, A., Pchel'nikov, A., Skuratkin, Ya., and Losev, V., *Zashch. Met.*, 1992, vol. 28, no. 2, pp. 191–194.
8. Markos'yan, G., Pchel'nikov, A., and Losev, V., *Zashch. Met.*, 1997, vol. 33, no. 5, pp. 503–505.
9. Tatarchenko, G., Cherkas, K., and Kuzyukov, A., *Fiz.-Khim. Mekh. Mater.*, 2002, no. 1, pp. 98–101.
10. Florianovich, G. and Kolotyrkin, Ya., *Dokl. Akad. Nauk SSSR*, 1964, vol. 157, no. 2, pp. 422–431.
11. Marshakov, A., Vysotskii, A., and Mikhailovskii, Yu., *Zashch. Met.*, 1988, vol. 24, no. 2, pp. 189–193.
12. Tatarchenko, G., Cherkas, K., and Pavlova, M., *Fiz.-Khim. Mekh. Mater.*, Special Issue, 2001, no. 2, pp. 97–101.
13. Tatarchenko, G. and Cherkas, K., *Fiz.-Khim. Mekh. Mater.*, Special Issue, 2002, no. 3, vol. 1, pp. 143–147.
14. Sazou, D., Diamantopulou, A., and Pagitsan, A., *Elektrokhimiya*, 2000, vol. 36, no. 10, pp. 1215–1228.
15. *Corrosion*, Shreir, L.L., Ed., London: Newnes–Butterworths, 1976, 2nd ed.
16. Tatarchenko, G., Makarova, Zh., and Kuzyukov, A., *Fiz.-Khim. Mekh. Mater.*, 2002, no. 3, pp. 97–101.
17. Tufanov, D., *Spravochnik* (Reference Book), Moscow: Metallurgiya, 1973.
18. Tatarchenko, G., *Fiz.-Khim. Mekh. Mater.*, Special Issue, 2000, no. 1, pp. 93–96.

Russian Journal of Applied Chemistry, Vol. 77, No. 11, 2004, pp. 1808–1814. Translated from Zhurnal Prikladnoi Khimii, Vol. 77, No. 11, 2004, pp. 1826–1832.

CATALYSIS

Hydride-Containing Silicas in Hydrosilylation of Olefin Monomers

Yu. N. Bol'bukh, V. V. Yanishpol'skii, and V. A. Tertykh

Institute of Surface Chemistry, National Academy of Sciences of Ukraine, Kiev, Ukraine

Received October 21, 2003; in final form, July 2004

Abstract—The kinetics of catalytic hydrosilylation of divinyltetramethyldisiloxane and 2-hydroxyethyl methacrylate with SiH groups fixed on the silica surface was studied. The influence exerted by the nature of the silica surface (initial and hydride-containing) on thermal and initiated [with a cobalt(II) acrylamide complex] polymerization of 2-hydroxyethyl methacrylate was examined.

Chemically modified finely dispersed oxides, in particular, those based on pyrogenic silicas containing active groups in the surface layer, are widely used for preparing filled polymer systems and nanocomposites with improved physicomechanical characteristics [1, 2]. Dispersed silicas with fixed ≡SiH groups (hydridosilicas) are studied in this respect insufficiently. At the same time, such modified silicas are of undoubted interest because of the possibility of hydrosilylation of various olefins with the surface ≡SiH groups under the action of catalysts, initiators, or temperature. Such an approach was used for immobilization on silicas of various functionalized olefins with the formation of hydrolytically stable surface compounds with a Si–C bond [3, 4]. The same type of the reactions can be used for formation of polymer–filler bonds (owing to direct reaction with the C=C bonds in polymeric macromolecules, or using appropriate bifunctional reagents for formation of cross-links). Participation of the ≡SiH groups fixed on the surface in chain termination and in polymerization of olefin monomers is also possible.

The behavior of silica fillers with the ≡SiH groups fixed on the surface in polymerization of olefin monomers is studied insufficiently. In particular, such examples of reaction systems hydridosilica–monomer were studied as catalytic hydrosilylation of styrene [5] and thermal addition of acrylic acid [6]. Previously we also initiated studies on reactions of hydridosilica with divinyltetramethyldisiloxane (DVTMDS) and 2-hydroxyethyl methacrylate (HEMA) in the presence of Speier catalyst [7, 8] and some reactive complexes of olefins with metal ions [9]. We used the cobalt(II) acrylamide complex, as it is catalytically active toward vinyl monomers in thermal polymerization [10] and tends to spontaneously polymerize by the radical mechanism with formation of highly rigid chains [11]. Recently the interest in silica–HEMA composites increased [12–14].

In this work we studied the kinetic features of solid-phase catalytic hydrosilylation of DVTMDS and HEMA. We also examined the effect exerted by silicon hydride groups present in the surface layer of silicas on thermal and initiated [with cobalt(II) acrylamide complex] polymerization of HEMA.

EXPERIMENTAL

The hydridosilica used in this study was prepared by chemical modification of nonporous finely dispersed silica (Aerosil, specific surface area 300 $m^2\ g^{-1}$, Oriana, Canada) with a solution of triethoxysilane (Kremniipolimer, Zaporozh'e) in ethanol at room temperature for 24 h, after which the solvent was removed by evaporation on a water bath. The content of silicon hydride groups grafted to the surface was controlled by the amount of the modifier added to the reaction medium. The concentration of the ≡SiH groups in the modified silicas was determined by titration. We prepared samples containing 0.25 and 0.64 $mmol\ g^{-1}$ silicon hydride groups. The degree of substitution of isolated silanol groups through which alkoxysilanes are mainly chemisorbed was about 30 and 80%, respectively. DVTMDS and HEMA (Fluka) were used without additional purification. DVTMDS can be considered as a model of bifunctional organisilicon compound with olefin groups. HEMA containing both hydrophilic and hydrophobic groups shows much promise in synthesis of nanocomposites with preset properties. The acrylamide (AAm) complex of cobalt(II) nitrate, $[Co(AAm)_4](NO_3)_2 \cdot 2H_2O$, was prepared in accordance with the recommendations of [11].

Catalytic hydrosilylation was performed in excess monomer (2–3 ml per 0.3–0.5 g of hydride-containing

1070-4272/04/7711-1808 © 2004 MAIK "Nauka/Interperiodica"

silica) in the presence of Speier catalyst (0.01 M $H_2PtCl_6 \cdot 6H_2O$ in isopropanol, 0.026 ml). The molar ratio of the catalyst to the amount of silicon hydride groups fixed on the Aerosil surface was 1 : 10000 [7]. The concentration of the ≡SiH groups fixed on the surface and the content of vinyl groups in the product were determined by bromide–bromate and iodometric titration [15]. Both methods are based on the reaction of an aqueous solution of a halogen with the surface functional groups, followed by titration of the unchanged reagent with $Na_2S_2O_3$ in the presence of starch. The choice of these methods was governed by their good reproducibility and sufficient sensitivity, especially in determination of low concentrations of fixed functional groups.

The volumetric method (treatment with alcoholic alkali and determination of the volume of the released H_2) gives less reproducible results and requires large amounts of the sample. It was shown [7] that the bromide–bromate method allows determination of the content of both vinyl and silicon hydride groups, and the iodometric method allows determination of the concentration of silicon hydride groups in the surface layer of modified silica at various reaction times after washing the product with ethanol and drying at 60°C. Since the monomer was taken in excess, the hydrosilylation can be considered as a pseudo-first-order reaction with respect to the concentration of the surface ≡SiH groups. The rate constants were calculated with the first-order equation by the least-squares method from the curves of the content of the surface silicon hydride groups vs. reaction time. The IR spectra of the starting compounds and modified silicas were recorded using KBr technique with a Nexus (Nicolet) IR Fourier spectrometer (diffuse reflection spectra) and a UR-20 spectrometer (absorption spectra, pellet weight 30 mg).

Taking into account the melting point and thermal stability limits of the cobalt(II) acrylamide complex [11], we performed the initiated polymerization of 2-hydroxyethyl methacrylate in air at 96–116°C and HEMA : $[Co(AAm)_4](NO_3)_2 \cdot 2H_2O$ weight ratio of 10 : 1. At certain intervals, we took 0.3-g samples, decanted the excess of the water-soluble monomer in the given volume of water, and determined the concentration of the C=C groups in solution by the bromide–bromate techniques [15]. The time of the sample setting (polymerization time) was extimated visually from the depth of indention of a glass rod into the final product.

Thermal and initiated [with cobalt(II) acrylamide complex] polymerization in the presence of the initial and SiH-modified Aerosil was performed at 106°C and 16 wt % filling. In initiated polymerization, the content of the cobalt(II) acrylamide complex was 10 wt % relative to the monomer. Prior to the reaction, the initiator and filler were thoroughly mixed in the required ratio and then added to the monomer. The reaction progress was monitored by determination of the content of the C=C bonds by the bromide–bromate method.

Catalytic hydrosilylation of olefins with the ≡SiH groups fixed on the silica surface follows the general scheme

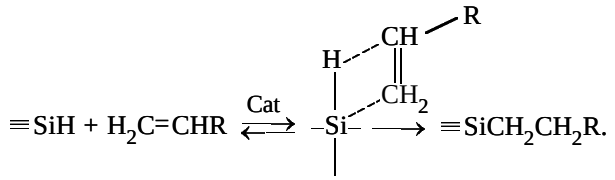

innvolving nucleophilic addition to the surface silicon atom.

The IR spectrum of $(H_2C=CH)(CH_3)_2SiOSi \cdot (CH_3)_2(HC=CH_2)$ contains characteristic absorption bands at 3060–2968 cm^{-1} corresponding to the stretching vibrations of the C–H bonds in methyl and methylene groups of the monomer. The bands above 3000 cm^{-1} belong to the vinyl C–H bonds. The spectrum of the starting hydridosilica contains a strong band with the absorption maximum at 2260 cm^{-1}, corresponding to the stretching vibrations of the surface Si–H groups. In the course of hydrosilylation, the band at 2260 cm^{-1} decreases in intensity, which corresponds to consumption of the surface SiH groups, and new bands corresponding to the grafted monomer molecules appear at 3060–2968 cm^{-1}. The spectrum of the final product after the 5-h reaction contains no Si–H band.

According to chemical analysis, the kinetics of variation of the concentration of the surface ≡SiH groups is satisfactorily fitted by a first-order equation. In Fig. 1, the calculated concentrations of the surface ≡SiH groups are shown by solid lines. Calculation by the empirical equation [16]

$$n = 1 - \frac{\log(\tau_2/\tau_1) - 1}{\log a_1}, \qquad (1)$$

($a_1 = c_1/c_0$, $a_2 = c_2/c_0$ are the fractions of the ≡SiH groups that remained unchanged by the time τ_1 and τ_2, respectively, with $a_2 = a_1^2$) also gives the first order of the reaction. The data characterizing the reaction kinetics are given in Table 1.

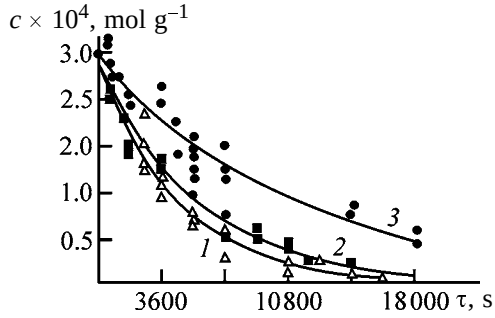

Fig. 1. Kinetic curves of hydrosilylation of DVTMDS with surface ≡SiH groups at (*1*) 80, (*2*) 60, and (*3*) 40°C. (*c*) Concentration of ≡SiH groups and (τ) time. Points are experimental concentrations of ≡SiH groups; solid lines are calculated by the equation $c = c_0 e^{-k\tau}$.

These data show that, as the reaction temperature is increased by 40°C, the rate of hydrosilylation of DVTMDS with the surface ≡SiH groups increases by a factor of slightly more than 2.

We found that, at a 0.25 mmol g^{-1} concentration of the surface ≡SiH groups in the initial hydridosilica, the content of grafter vinyl groups in the final product (the reaction for 5 h at 80°C) was also 0.25 mmol g^{-1}. These results, and also the IR data, indicate that all the surface ≡SiH groups were involved in the reaction. The surface immobilization of the vinyl groups in the amount equal to the content of the ≡SiH groups in the initial modified silica confirms that the hydrosilylation mainly follows the scheme

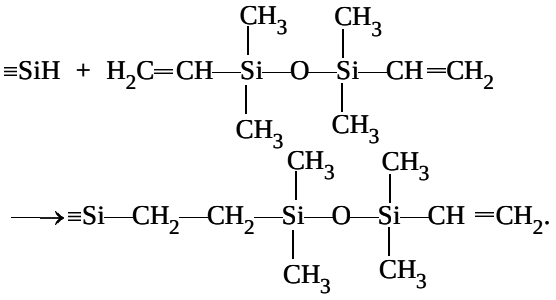

Table 1. Order *n*, rate constant *k*, and initial rate v_0 of hydrosilylation of DVTMDS with hydride-containing silica

T, °C	n_a^*	$k \times 10^4$, s^{-1}	$v_0 \times 10^8$, mol g^{-1} s^{-1}	
			$-\Delta c \Delta\tau^{-1}$, experiment	k/c_0, calculation
40	0.55–1	0.92 ± 0.076	3.33	2.30
60	1–0.83	1.77 ± 0.17	5.00	4.43
80	1.46–1	2.26 ± 0.24	7.50	5.65

* The reaction order was calculated by Eq. (1) at 36 and 60% conversion of the ≡SiH groups, respectively.

The activation energy of the hydrosilylation in the examined system, calculated from the temperature dependence (40–80°C) of the time corresponding to 20% conversion of the surface ≡SiH groups, is 72.2 ± 10.8 kJ mol^{-1}.

Catalytic hydrosilylation of HEMA with the ≡SiH groups fixed on silica is virtually complete in 0.5 h, and this time does not appreciably depend on the reaction temperature in the range 27–60°C [9]. The reaction rate measured at these temperatures 2–5 min after the start of the reaction is, on the average, (1.65 ± 0.18) × 10^{-7} mol l^{-1} s^{-1} (found from the equation $v = \Delta c \Delta\tau^{-1}$). At the same time, the maximal degree of conversion of the ≡SiH groups under these conditions does not exceed 90%. This is confirmed by the presence of a band at 2260 cm^{-1}, belonging to the residual ≡SiH groups, in the IR spectra of the final product. Also, the spectra contain bands at 1636 and 1717 cm^{-1} corresponding, respectively, to stretching vibrations of the C=C and C=O groups, which indirectly suggests the presence on the surface of both chemically fixed and physically adsorbed monomer molecules; the physical adsorption may involve hydrogen bonding with the residual silanol groups.

The chemical immobilization of the monomer molecules in the surface layer may also involve the reaction of the silanol groups with the hydroxy groups of HEMA. However, usually such reactions on the silica surface occur at higher temperatures or in the presence of bases [1]. In our case, because of mild hydrosilylation conditions, this reaction is improbable. Furthermore, the etherification will be hindered by relatively strong hydrogen bonds between the surface silanol groups and carbonyl groups of HEMA, formed in adsorption of HEMA on the silica surface. The complex mechanism of HEMA hydrosilylation is indicated by the reaction order calculated both in the $\log v = f(\log c)$ coordinates and with formula (1). Although the monomer, as in the previous case, was taken in excess, the reaction order *n* calculated by the two procedures was close to 2 (Table 2). The initial hydrosilylation rates given in Table 2 were determined from the *k* and *n* values found in the $\log v = f(\log c)$ coordinates. The high reaction rate in this system, compared to hydrosilylation of divinyltetramethyldisiloxane, may be due to the presence on the surface of a large amount of the adsorbed monomer and, correspondingly, to occurrence of the gel effect (increase in the reaction rate due to increase in the density of the medium [17]). Indeed, HEMA is adsorbed on the silica surface considerably more strongly than divinyl-

Table 2. Logarithm of the rate constant $\log k$, initial rate v_0, and order n of HEMA hydrosilylation

T, °C	n_a^*	n	$\log k$	v_0, mol g^{-1} s^{-1}	
				$-\Delta c/\Delta\tau^{-1}$, experiment	kc^n, calculation
20	1.88 ± 0.18	2.01 ± 0.10	0.81 ± 0.43	4.17×10^{-7}	4.52×10^{-7}
27	2.03 ± 0.13	2.06 ± 0.08	1.30 ± 0.31	7.50×10^{-7}	7.61×10^{-7}
40	1.82 ± 0.29	2.46 ± 0.33	2.96 ± 1.38	0.94×10^{-6}	1.49×10^{-6}
60	1.86 ± 0.04	2.37 ± 0.42	2.65 ± 1.69	1.04×10^{-6}	1.51×10^{-6}

* (n_a) Reaction order calculated by Eq. (1).

tetramethyldisiloxane, which may result in increased density of the medium in the surface layer. Furthermore, the possibility of densification of the adsorption layer due to partial polymerization of the monomer on the surface cannot be ruled out. With increasing temperature, the role of the gel effect weakens; as a result, the reaction rate measured 2–5 min after the start of the reaction remains virtually unchanged in the examined temperature range. The initial rate of this reaction, as that of hydrosilylation of DVTMDS, increases with temperature in the range from 20 to 40°C and remains virtually unchanged in the range 40–60°C. Hydrosilylation of HEMA can be represented by the general scheme

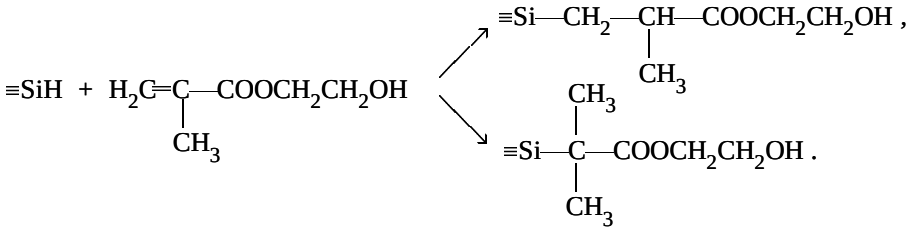

Applying our results to filled polymer systems, we can expect that, with disperse hydride-containing silicas as fillers of olefin polymers, it will be possible to provide additinal chemical cross-linking of the composites by formation of hydrolytically stable Si–C bonds between the filler surface and macromolecules.

When studying the kinetics of thermal (106°C, air) polymerization of 2-hydroxyethyl methacrylate, we observed a large scatter of the content of the C=C groups (Fig. 2). By analogy with thermal polymerization of methyl methacrylate [17], this may be due to condensation of the monomer molecules with formation of various intermediate states, affecting the polymerization rate. We can distinguish in the kinetic curve two portions characteristic of polymerization of vinyl monomers and corresponding, respectively, to the induction and acceleration (gel effect) periods.

Figure 3 shows the kinetic curves of HEMA polymerization initiated with the cobalt(II) acrylamide complex. The scatter of the experimental points is low, suggesting stable course of the process. On adding the initiator, the initial polymerization rate appreciably increases. However, as the temperature of initiated polymerization is increased, a short portion corresponding to the induction period appears in the time dependence of the concentration of vinyl groups (Table 3). It is believed [17] that deceleration of the initiated polymerization followed by an increase in the reaction rate may be due to the "cage effect" and considerable influence of the viscosity of the medium on the process.

The rate constant of radical polymerization (with

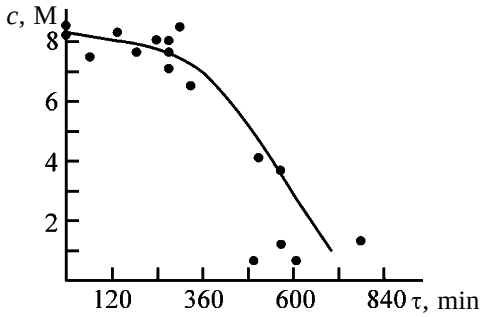

Fig. 2. Kinetic curves of thermal polymerization of HEMA at 96°C: (c) concentration of vinyl groups and (τ) time; the same for Figs. 3 and 4.

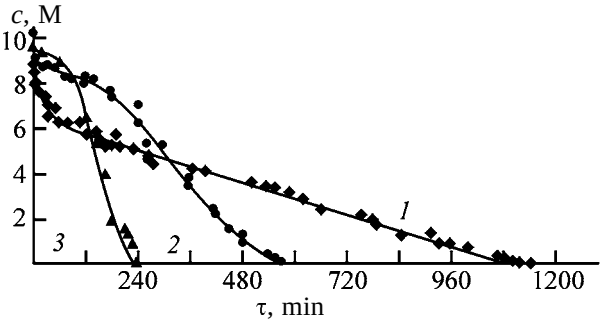

Fig. 3. Kinetic curves of initiated [with Co(II) acrylamide complex] polymerization of HEMA at (*1*) 96, (*2*) 106, and (*3*) 116°C.

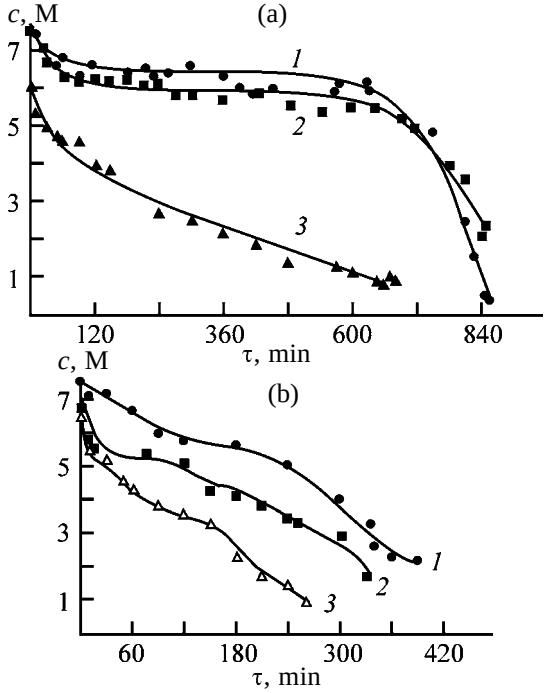

Fig. 4. Kinetic curves of thermal polymerization of HEMA at 106°C (a) in the presence of (*1*) Aerosil and (*2, 3*) hydridosilicas containing 0.25 and 0.64 mmol g^{-1} ≡SiH groups, respectively; (b) the same, with the cobalt(II) acrylamide complex as initiator. Composition (wt %) of the starting mixture: (a) monomer : filler = 6 : 1 and (b) monomer : filler : initiator = 1 : 0.16 : 0.1.

Table 3. Induction period τ_{ind}, monomer conversion half-time $\tau_{1/2}$, and time of complete curing τ in polymerization of HEMA initiated with the acrylamide complex of cobalt nitrate

T, °C	τ_{ind}	$\tau_{1/2}$	τ
	min		
96	–	270	1140
106	200	300	570
116	60	145	240

respect to the monomer) can be calculated using a first-order kinetic equation [18]

$$k = \frac{2.303}{\tau}\log(c_0/c),$$

where c and c_0 are the initial and final concentrations of vinyl groups (M); τ is the polymerization time (s).

The rate constant calculated by this equation is 5.55×10^{-5} s^{-1}. When calculating the overall rate constant of initiated polymerization without determining the rate constants of individual reactions, it is appropriate to use the general equation [16] based on variation of the monomer conversion (variation of the concentration of the vinyl groups). The rate constant of HEMA polymerization in the presence of 10 wt % initiator, calculated by the equation

$$\frac{1}{1-n}[(a^{n-1})^{-1} - 1] = k c_0^{n-1}\tau,$$

($a = c/c_0$ is the fraction of unchanged vinyl groups; $n = 1.5$ [17, 18]), was $(7.94 \pm 0.92) \times 10^{-5}$ s^{-1}.

In thermal polymerization of HEMA at 106°C in the presence of 16 wt % Aerosil, we observed a considerable weight loss (~60%), which prevented formation of a uniform material. According to [19], this effect may be caused by strong adsorption interaction of the polymer with the filler, decelerating curing near the surface and preventing formation of a three-dimensional network. Complete curing was attained in 14 h (Fig. 4, curve *1*). With addition of hydridosilica into the monomer (Fig. 4, curves *2*, *3*), the weight loss was insignificant. The curing time of the composite at a 0.25 mmol g^{-1} concentration of surface ≡SiH groups was 14 h, and at their concentration of 0.64 mmol g^{-1} it decreased to 11 h. Thus, the ≡SiH groups present on the surface of the modified silica favor thermal polymerization of HEMA.

Published data on the effect of a filler on initiated radical polymerization of vinyl monomers are contradictory. For example, according to [20], introduction of Aerosil does not affect the degree of radical polymerization of methyl methacrylate initiated with benzoyl peroxide, and the presence of functional groups (methacryloyloxypropyl, aminopropyl, mercaptopropyl) grafted to the filler surface decelerates the overall process, though increasing the percentage of the monomer molecules grafted to the silica surface. Different data on the effect of Aerosil on initiated polymerization of methacrylic monomers were reported by Almazova *et al.* [21]. It follows from their conclusions that finely dispersed silica is an active

Table 4. Times of attainment of 20% (τ_{20}), 50% (τ_{50}), and maximal (τ) conversion of the monomer and degrees α of thermal and initiated [with the cobalt(II) acrylamide complex] polymerization of HEMA in the presence of silica fillers

Filler	c_{SiH}, mmol g^{-1}	τ_{20}	τ_{50}	τ	α, %
		min			
Hydridosilica	0.24	250	750	840	68
	0.64	40	200	660	85
Aerosil + initiator	–	90	325	390	71
Hydridosilica + initiator	0.24	75	250	330	75
	0.64	10	150	270	86

filler accelerating structure formation and ensuring more stable properties of the composite. According to our results, in polymerization of HEMA initiated with the cobalt(II) acrylamide complex, addition of Aerosil decreases the time of complete curing of the samples from 9 to 6.5 h compared to the initiated polymerization without a filler; the monomer conversion in the presence of Aerosil increases (Fig. 4b). Addition of hydridosilica into the monomer, along with an increase in the monomer conversion, results in a considerable increase in the initial polymerization rate, i.e., it accelerates initiation, thus shortening the reaction time (Table 4). Acceleration of the process in the presence of hydride-containing silicas may be caused by formation of additional reaction centers at the surface ≡SiH groups of the modified silica.

It is not improbable that the ≡SiH groups fixed on the filler surface participate in formation of the Si–C bonds directly in the course of HEMA polymerization. However, whereas in thermal polymerization the ≡SiH and C=C groups can react similarly to catalytic hydrosilylation, in the graft polymerization initiated with the cobalt(II) acrylamide complex the pathways of reaction of the polymer with the filler can be different, since the C=C bonds are present not only in the monomer but also in the initiator. Both addition of the cobalt(II) acrylamide complex to the hydridosilica surface, followed by the reaction with HEMA, and the direct addition of the monomer molecules to the filler surface are possible.

CONCLUSIONS

(1) Catalytic hydrosilylation of divinyltetramethyldisiloxane is a pseudo-first-order reaction with respect to the concentration of the ≡SiH groups. These groups are fully involved in the reaction within 5 h at 80°C.

(2) Solid-phase hydrosilylation of 2-hydroxyethyl methacrylate is satisfactorily described by a second-order kinetic equation, suggesting a more complex mechanism of processes in the surface layer.

(3) As compared to the unfilled systems, addition of finely dispersed silica somewhat decelerates thermal polymerization of 2-hydroxyethyl methacrylate and, on the contrary, accelerates the process initiated with the cobalt(II) acrylamide complex.

(4) The silicon hydride groups present on the surface of the modified filler accelerate both thermal and initiated polymerization of 2-hydroxyethyl methacrylate.

REFERENCES

1. Tertykh, V.A. and Belyakova, L.A., *Khimicheskie reaktsii s uchastiem poverkhnosti kremnezema* (Chemical Reactions Involving the Silica Surface), Kiev: Naukova Dumka, 1991.
2. Vansant, E.F., Voort, P. van der, and Vrancken, K.C., *Characterization and Chemical Modification of the Silica Surface*, Amsterdam: Elsevier, 1995.
3. Tertykh, V.A. and Belyakova, L.A., *Adsorption on New and Modified Inorganic Sorbents*, Dabrowski, A. and Tertykh, V.A., Eds., Amsterdam: Elsevier, 1996, pp. 147–189.
4. Pesek, J.J., Matyska, M.T., and Takhar, S., *Chromatographia*, 1998, vol. 48, pp. 631–636.
5. Tertykh, V.A. and Tomachinsky, S.N., *Funct. Mater.*, 1995, vol. 2, no. 1, pp. 58–63.
6. Varvarin, A.M., Belyakova, L.A., Tertykh, V.A., *et al.*, *Colloids Surf.*, 1996, vol. 110, pp. 129–134.
7. Bol'bukh, Yu.N. and Tertykh, V.A., *Nauchn. Zap. NaUKMA*, 2002, vol. 20, pp. 29–33.
8. Tertykh, V.A., Yanishpolskii, V., and Bolbukh, Yu., *Macromol. Symp.*, 2003, vol. 194, pp. 141–146.
9. Bol'bukh, Yu.N. and Tertykh, V.A., *Khim., Fiz. Tekhnol. Poverkhn.*, 2003, no. 9, pp. 37–43.
10. Pomogailo, A.D., *Polimernye immobilizovannye me-*

tallokompleksnye katalizatory (Polymeric Immobilized Coordination Catalysts), Moscow: Nauka, 1988.

11. Savost'yanov, V.S., Ponomarev, V.I., Pomogailo, A.D., *et al.*, *Izv. Akad. Nauk SSSR, Ser. Khim.*, 1990, no. 4, pp. 762–768.
12. Saito, R., Kuwano, K., and Tode, T., *J. Macromol. Sci., Pure Appl. Chem.*, 2002, vol. 39A, no. 3, pp. 171–182.
13. Saito, R. and Mori, Y., *J. Macromol. Sci., Pure Appl. Chem.*, 2002, vol. 39A, no. 9, pp. 915–934.
14. Ji X.-L., Jiang S.-C., Qiu, X.-P., *et al.*, *J. Appl. Sci.*, 2003, vol. 88, no. 14, pp. 3168–3175.
15. Losev, I.P. and Fedotova, O.Ya., *Praktikum po khimii vysokomolekulyarnykh soedinenii* (Practical Course of Macromolecular Chemistry), Moscow: Gosizdat, 1962.
16. Berezin, I.V. and Klesov, A.A., *Prakticheskii kurs khimicheskoi i fermentativnoi kinetiki* (Practical Course of Chemical and Enzymatic Kinetics), Moscow: Mosk. Gos. Univ., 1976.
17. Bamford, C.H., Barb, W.G., Jenkins, A.D., and Onyon, P., *The Kinetics of Vinyl Polymerization by Radical Mechanisms*, London: Butterworth Scientific, 1958.
18. Odian, G., *Principles of Polymerization*, New York: Wiley, 1981.
19. Lipatov, Yu.S., *Fizicheskaya khimiya napolnennykh polimerov* (Physical Chemistry of Filled Polymers), Moscow: Khimiya, 1977, pp. 39–40.
20. Tsubokawa, N., Kimoto, T., and Koyama, K., *Colloid Polym. Sci.*, 1993, vol. 271, no. 10, pp. 940–946.
21. Almazova, T.P., Morozova, E.M., and Eliseeva, V.I., *Kompoz. Polim. Mater.*, 1985, no. 24, pp. 61–65.

Russian Journal of Applied Chemistry, Vol. 77, No. 11, 2004, pp. 1815–1817. Translated from Zhurnal Prikladnoi Khimii, Vol. 77, No. 11, 2004, pp. 1833–1835.

ENVIRONMENTAL PROBLEMS OF CHEMISTRY AND TECHNOLOGY

Use of Thermally Expanded Graphite in Water-Purification and Water-Treatment Systems

A. V. Yakovlev, A. I. Finaenov, E. V. Yakovleva, and E. V. Finaenova

Saratov State Technical University, Saratov, Russia
Technological Institute, Engels, Saratov oblast, Russia

Received April 7, 2004

Abstract—The adsorption and ion-exchange properties of thermally expanded graphite with respect to hardness cations and SO_4^{2-} and Cl^- anions were studied.

Thermally expanded graphite (TEG) is a product formed in thermolysis of graphite intercalation compounds (GICs). Modification of carbon to give GICs makes it possible to create new materials with unique combinations of physicochemical properties. One of the properties of this kind is the ability of GICs to form foamed structures having a developed surface, which creates prerequisites for their use as sorption materials. The bulk density d_{TEG} of the best samples of TEG is $(1–2) \times 10^{-3}$ g cm^{-3} [1]. This value largely depends on the preparation conditions and may widely vary, from 1×10^{-3}–5×10^{-3} to 2×10^{-2}–1×10^{-1} [2–5]. The degree of thermal expansion depends on synthesis conditions and composition of the GIC obtained, as well as on the structure and particle size of the carbon raw materials used [6]. The surface properties of the starting graphite are mainly determined by its purity and purification technique. According to the classical concepts [7], oxygen is chemisorbed on the surface of graphite, which ensures a positive potential when this graphite is subsequently submerged in aqueous solutions. In anodic oxidation of graphite, oxygen-containing surface functional groups (SFGs) are accumulated on its surface. The composition and concentration of these groups is determined by the mode in which the anodic treatment is carried out [8]. The subsequent washing of GIC leads to partial or total substitution of ions and molecules of an acid contained in the intercalate by hydroxide ions and water. Fast heating of GIC during thermal treatment must lead to virtually complete removal of SFGs and the intercalate. Thus, the surface properties of TEG again approach those of the starting graphite, being different only in a manyfold increase in the surface area [9].

As is known, virtually all carbon materials have a high adsorption capacity for numerous organic substances [10–13] and, at the same time, can retain metal cations by the ion-exchange mechanism [14, 15]. It is known that carbon materials can be not only adsorbents, but also anion and cation exchangers [15]:

$$\geqslant C–OH + Ca^{2+} + 2OH^- \rightarrow \geqslant C–O–Ca–O + H_2O, \quad (1)$$

$$–COOH + Ca^{2+} + 2OH^- \rightarrow COOCaOH + H_2O, \quad (2)$$

$$\geqslant C–OH + Cl^- \rightarrow \geqslant C–Cl + OH^-. \quad (3)$$

In this context, we studied the sorption and ion-exchange properties of TEG with respect to hardness ions and anions of mineral acids.

EXPERIMENTAL

GICs were obtained electrochemically in 13.5 M HNO_3 by anodic oxidation of a GSM-1 dispersed carbon material with particle size of up to 200 μm [GOST (State Standard) 1891–78; ash content $A \leq 0.1\%$, moisture content $W \leq 1$ wt %, yield of volatiles $X \leq 0.2\%$) in the potentiostatic mode at a potential of 2.1 V [16, 17]. A silver chloride electrode served as reference in electrochemical measurements.

GIC samples were washed with distilled water at 15–18°C and dried to constant weight at 60–70°C. Thermally expanded graphite was obtained by rapid heating of the samples to 900°C. The bulk density of TEG was determined by the standard procedure [OST (Branch Standard) 16–0689.031–74]. The specific surface area of the carbon materials was determined on a Tsvet-20 chromatograph from the adsorption of argon.

The initial composition and requirements to the water used in the study are listed in Table 1.

1070-4272/04/7711-1815 © 2004 MAIK "Nauka/Interperiodica"

Table 1. Parameters of untreated and purified water

Parameter	Water	
	untreated	purified
Chloride ion, mg l^{-1}	38	26–28
Sulfate ion, mg l^{-1}	115	45–50
Total hardness	22.5	32–48
pH	9.5–10.5	8.5–8.8

To purify water to remove hardness ions, a weighed portion of TEG (0.8 g) was placed in a funnel on a filter paper and 100 ml of water was passed. After that, samples were taken and the concentration of hardness ions was found complexometrically (GOSTs 4151–72 and 4389–72). The sorption capacity c was calculated by the equation [18]

$$c = (c_{in} - c_{fin})V/m,$$

where c_{in} and c_{fin} are the initial and final concentrations of a contaminant; V, volume of the solution passed; and m, mass of the sorbent.

The degree of recovery (%) was calculated by the formula [18]:

$$R = \frac{c_{in} - c_{fin}}{c_{in}} \times 100.$$

As follows from Table 2, passing water across a TEG bed ensures the water treatment to the required purity.

According to published data [14, 15], the removal of SO_4^{2-} and Cl^- ions with TEG proceeds via substitution of OH^- ions in the outer "plate" of the electrical double layer by contaminating anions. In this case, ion exchange undoubtedly plays an important role in overcoming the potential barrier in electrostatic approach of an anion to the positively charged surface of graphite. In [11], direct ion-exchange interaction of sulfate and chloride ions with the surface of graphite was reported.

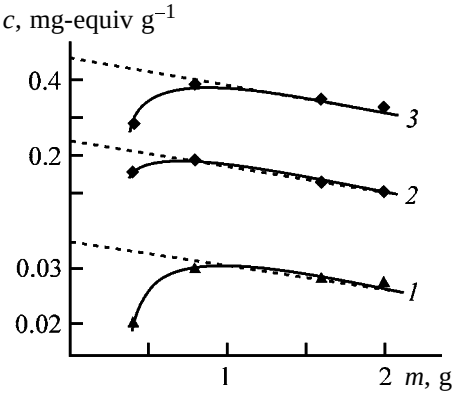

Sorption capacity c for different ions vs. mass m of TEG in the filter bed in passing 100 ml of water under study: (*1*) chloride ion, (*2*) sulfate ion, and (*3*) total hardness (Ca^{2+} + Mg^{2+}).

The dependences of the sorption capacity on the mass of TEG in the filter bed and on the filtration rate calculated in terms of the true surface area of the carbon material in passing a constant volume of water under study (100 ml) show that c first increases somewhat and then steadily decreases (see figure). Account should be taken of the fact that the filtration rate varies with the weight of TEG. Apparently, the recovery of contaminants and, accordingly, the value of c decrease because of the short time of contact between water and TEG at a small weighed portion of the carbon material (filtration rate is the highest). The further gradual decrease in the sorption capacity, observed for all the components (see figure), is due to an increase in the mass of TEG in the filter bed and to a decrease in the degree of saturation of the carbon surface with contaminants. Extrapolation of the linear portions of the curves in the figure to the ordinate axis makes it possible to approximately determine the limiting sorption capacity of TEG for SO_4^{2-} and Cl^- ions and hardness cations. The results of the graphical

Table 2. Change in the concentration of ions and pH upon filtration of water through TEG. d_{TEG} = 5 g dm^{-3}, S_{sp} = 43 m^2 g^{-1}

m_{TEG}, g l^{-1} of solution	Cl^- (c_{in} = 38 mg l^{-1})		SO_4^{2-} (c_{in} = 115 mg l^{-1})		Total hardness (c_{in} = 225 mg l^{-1})		pH
	c_{fin}, mg l^{-1}	R, %	c_{fin}, mg l^{-1}	R, %	c_{fin}, mg l^{-1}	R, %	
0.4	34.8	8.5	85.4	25.7	189	16.0	9.1
0.8	29.0	23.7	44.9	60.9	126	44.0	8.9
1.6	22.0	42.1	18.2	84.2	45.7	79.7	8.6
2.0	18.5	51.4	13.2	88.5	16.7	92.6	8.2

determination of the maximum sorption capacity for different ions in filtration of water across a TEG bed are presented below:

Ion	Chloride ion	Sulfate ion	Hardness cations
c_{max}, mg-equiv g^{-1}	0.033	0.23	0.42

According to the results obtained, the sorption capacity of TEG for hardness cations exceeds by a factor of more than 3 that of fibrous sorbents [19].

CONCLUSION

Thermally expanded graphite is an effective sorbent for removal of hardness cations. The sorption capacity for these cations is 0.42 mg-equiv g^{-1}, which allows use of thermally expanded graphite for practical purposes.

REFERENCES

1. Makhorin, K.E., Zayats, N.N., Donchak, S.S., *et al.*, *Khim. Tekhnol.*, 1990, no. 3, pp. 44–47.
2. Komarova, T.V., Puzyreva, E.V., and Puchkov, S.V., *Tr. Mosk. Khim.-Tekhnol. Inst. im. D.I. Mendeleeva*, 1986, vol. 141, pp. 75–83.
3. Makhorin, K.E., Kozhan, A.P., and Veselov, V.V., *Khim. Tekhnol.*, 1985, no. 2, pp. 3–6.
4. USSR Inventor's Certificate no. 767023.
5. Chernysh, I.G. and Buraya, I.D., *Khim. Tverd. Topl.*, 1990, no. 1, pp. 123–127.
6. Chung, D.D.L., *J. Mater. Sci.*, 1987, vol. 22, pp. 4190–4198.
7. Tarasevich, M.R., *Elektrokhimiya uglerodnykh materialov* (Electrochemistry of Carbon Materials), Moscow: Nauka, 1984.
8. Shapranov, V.V., Yaroshenko, A.P., and Kucherenko, V.A., *Elektrokhimiya*, 1990, vol. 26, no. 9, pp. 1130–1135.
9. Tarasevich, Yu.I., Bondarenko, S.V., Brutko, V.V., *et al.*, *Zh. Prikl. Khim.*, 2003, vol. 76, no. 10, pp. 1619–1624.
10. Makhorin, K.E. and Pishchai, I.Ya., *Khim. Tekhnol. Vody*, 1997, no. 2, pp. 188–195.
11. *Adsorbtsiya organicheskikh veshchestv iz vodnykh rastvorov* (Adsorption of Organic Substances from Aqueous Solutions), Koganovskii, A.M., Ed., Leningrad: Khimiya, 1990.
12. Savos'kin, M.V., Yaroshenko, A.P., Mochalin, V.N., and Panchenko, B.V., *Zh. Prikl. Khim.*, 2003, vol. 76, no. 6, pp. 939–938.
13. Savos'kin, M.V., Yaroshenko, A.P., Shologon, V.I., and Galushko, L.Ya., *Zh. Prikl. Khim.*, 2003, vol. 76, no. 7, pp. 1213–1215.
14. Tarkovskaya, I.A. and Stavitskaya, S.S., *Ross. Khim. Zh. im. D.I. Mendeleeva*, 1995, no. 6, pp. 44–51.
15. Tarkovskaya, I.A., *Okislennyi ugol'* (Oxidized Coal), Kiev: Naukova Dumka, 1981.
16. Yakovlev, A.I. and Finaenov, A.I., *Zh. Prikl. Khim.*, 1999, vol. 72, no. 1, pp. 88–91.
17. Yakovleva, E.V., Yakovlev, A.V., and Finaenov, A.I., *Zh. Prikl. Khim.*, 2002, vol. 75, no. 10, pp. 1632–1638.
18. Dubyaga, V.P., Perepechkin, L.P., and Katalevskii, E.E., *Polimernye membrany* (Polymeric Membranes), Moscow: Khimiya, 1981.
19. Skvortsov, N.G., Anan'eva, T.A., and Khabazova, T.A., *Zh. Prikl. Khim.*, 1989, vol. 62, no. 5, pp. 1161–1164.

Russian Journal of Applied Chemistry, Vol. 77, No. 11, 2004, pp. 1818–1821. Translated from Zhurnal Prikladnoi Khimii, Vol. 77, No. 11, 2004, pp. 1836–1839.

ENVIRONMENTAL PROBLEMS OF CHEMISTRY AND TECHNOLOGY

Radiolytic Gas Formation under γ-Irradiation of Oxalic Acid Solutions

N. N. Popova, Yu. V. Voronin, and I. I. Byvsheva

Vernadsky Institute of Geochemistry and Analytical Chemistry, Russian Academy of Sciences, Moscow, Russia

Institute of Physical Chemistry, Russian Academy of Sciences, Moscow, Russia

Received May 11, 2004

Abstract—Radiolytic gas formation under γ-irradiation (10^4–10^6 Gy) of 10^{-2}-10^{-4} M aqueous solutions of oxalic acid at 25–60°C was studied.

Substantial volumes of radioactive waste solutions containing oxalic acid are accumulated in the radiochemical industry, as oxalate precipitation is one of the final steps of spent nuclear material reprocessing [1]. In safe management of liquid radioactive wastes, liberation of explosive radiolytic gases should be taken into consideration. The features of radiolytic gas formation necessary in organization of safe transportation, storage, and reprocessing of radioactive solutions containing oxalic acid are poorly understood. In addition, a study of radiolysis of oxalic acid is of interest for its use as a dosimetric substance.

Previously [2–4], we studied the composition and yield of gases formed upon γ-irradiation of nitrate–acetate solutions simulating liquid radioactive wastes.

Irradiation of oxygen-free oxalic acid solutions at comparatively large doses gives the following products: CO_2, H_2, H_2O_2, formic, glyoxylic, and dihydroxymalonic acids, formaldehyde, and glyoxal. In the presence of oxygen and at lower doses, only CO_2, H_2, and H_2O_2 are formed [5, 6].

In this work, we studied features of radiation-chemical decomposition of oxalic acid in aqueous solutions at high doses, when the radiolysis products appear not only in the liquid, but also in gas phase, and examined the effect of temperature on the radiolytic gas formation.

EXPERIMENTAL

A GUG-120 γ-irradiation source with a dose rate of 9–12 kGy h^{-1} was used. The required doses were accumulated for several days (4–5 h per day). The dosimetry was performed with a bichromate dosimeter [7]. The error in the determination of the radiation-chemical yield did not exceed 20% at the confidence level of 0.95.

A glass reactor connected to a reference manometer for measuring the pressure rise due to liberated gas was charged with 400 ml of the solution. The mixture was purged with helium for 1 h and then irradiated in a thermostat at 15°C. The working solutions were prepared with chemically pure grade oxalic acid and double-distilled water.

After the irradiation, the composition of the gas phase was determined gas-chromatographically on an LKh-72 chromatograph (helium as a carrier gas, katharometer as a detector, columns with Porapak-Q and 5A molecular sieves) and IR spectroscopically with a Specord-80 spectrometer. The analysis sensitivity with respect to hydrogen was 10^{-3} vol % and relative error, ±10%. The processes in the liquid phase were simulated with an U-12F linear electron accelerator at the average dose rate of 12.5 Gy s^{-1}, which allowed substantial shortening of the irradiation time. The experimental method was described in detail in [8].

The concentration of oxalic acid in the solutions was determined by the reaction with copper benzidine complex [9]. The pH of solutions was measured with an EV-74 universal ion meter using standard buffer solutions.

Radiolytic gas formation at the γ-irradiation of oxalic acid solutions was studied within the ranges of the acid concentration 10^{-2}–10^{-4} M, absorbed dose 10^4–10^6 Gy, and temperature 25–60°C. The parallel experiments with the same solutions were performed

1070-4272/04/7711-1818 © 2004 MAIK "Nauka/Interperiodica"

Table 1. Yield and composition of radiolysis products at a total γ-irradiation dose of 120 kGy and 10°C depending on the concentration of the initial solution of oxalic acid

$[H_2C_2O_4]$, M	Total yield of products, %	Radiation yield G, molecules per 100 eV			Composition of reaction products	
		total	H_2	CO_2	H_2	CO_2
5.0×10^{-2}	94.7	0.76	0.17	0.59	21.9	78.1
5.0×10^{-3}	60.1	0.48	0.17	0.31	34.9	65.1
5.0×10^{-4}	12.0	0.048	0.02	0.028	42.5	57.5

at heating without irradiation to determine the contribution of thermal decomposition of oxalic acid.

Typical curves of radiolytic gas formation under γ-irradiation of oxalic acid solutions are shown in Fig. 1. As seen, oxalic acid decomposition increases with increasing total absorbed dose, gradually leveling out. CO_2 and H_2 are the main components of the gas mixture. The amount of the gas liberated increases with increasing oxalic acid concentration (Table 1). The yield and composition of radiolysis products at the total γ-irradiation dose of 120 kGy as functions of the concentration of the initial oxalic acid solution are shown in Table 1 and Fig. 2. The acid amount and absorbed dose affect the relative content of H_2 and CO_2 (Fig. 3). With increasing acid concentration, the hydrogen fraction decreases, whereas the fraction of CO_2 in the gas phase increases. The increase in the absorbed dose increases the CO_2 fraction and decreases the H_2 fraction.

At the total dose of γ-irradiation of 120 kGy, the total radiation-chemical yield of gases increases by a factor of almost 2 as the temperature is increased from 10 to 60°C (Table 2, Fig. 4). This trend is due to increase in the CO_2 yield, whereas the yield of H_2

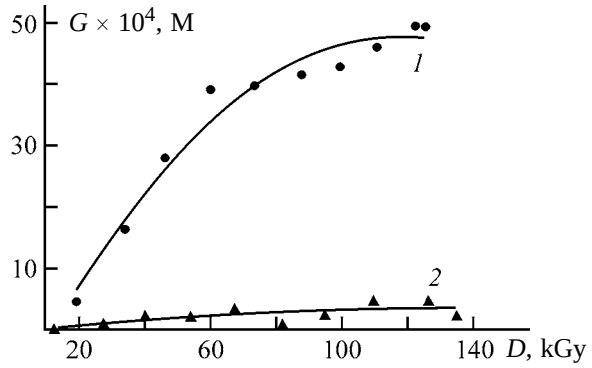

Fig. 1. Radiolytic gas formation under γ-irradiation of solutions of oxalic acid with various concentrations at 12°C as a function of the irradiation dose D. (G) Radiation-chemical yield. Oxalic acid concentration (M): (*1*) 5.0×10^{-3} and (*2*) 5.0×10^{-4}.

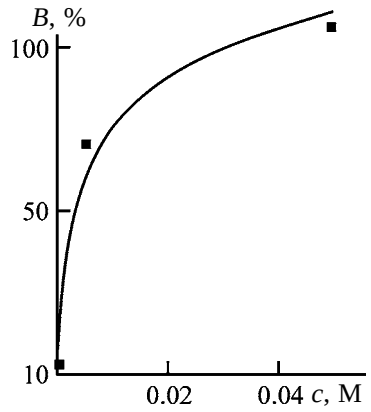

Fig. 2. Total yield of the oxalic acid radiolysis products B as a function of the initial acid concentration c in the solution at 10°C.

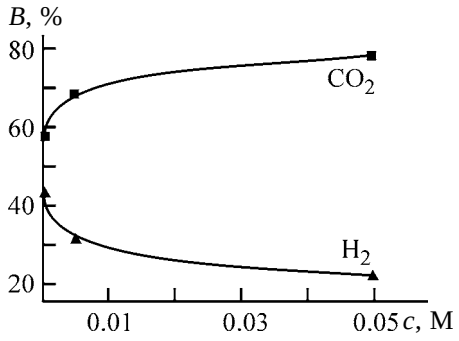

Fig. 3. Composition of oxalic acid radiolysis products as a function of the initial acid concentration c at 10°C. (B) Yield of products.

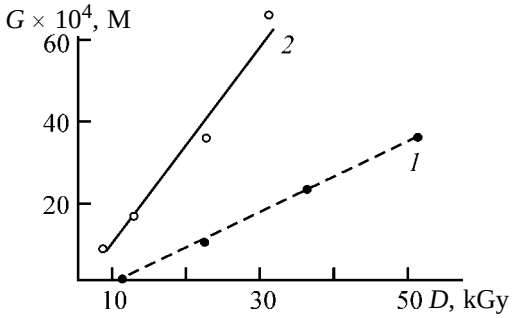

Fig. 4. Radiation-chemical yield G of decomposition of oxalic acid ($c = 5\times10^{-2}$ M) as a function of the irradiation dose D. Radiolysis temperature (°C): (*1*) 10 and (*2*) 60.

Table 2. Radiation-chemical yield of gases G in γ-radiolysis of oxalic acid solutions at 10, 12, and 60°C and dose of 0.06 MGy

Gas	5×10^{-3} M $H_2C_2O_4$			5×10^{-2} M $H_2C_2O_4$		
	$G_{12°}$	$G_{60°}$	$G_{60°}/G_{12°}$	$G_{10°}$	$G_{60°}$	$G_{60°}/G_{10°}$
	molecules per 100 eV			molecules per 100 eV		
H_2	0.27	0.203	0.75	0.17	0.157	0.03
CO_2	0.59	0.751	1.27	0.59	1.323	2.24
Sum of gases	0.86	0.954	1.11	0.76	1.480	1.95

decreases. Here, the change in the solubility of gases in water with temperature was not taken into account (the content of gases in the reactor free volume was determined).

It is known that the gas solubility decreases with increasing temperature; in going from room temperature to 60°C, the solubilities of hydrogen and CO_2 decrease by a factor 1.08 and 1.8, respectively [10]. As seen from Table 2, at the acid concentration of 5×10^{-2} M, the $G_{60°}/G_{10°}$ ratio for CO_2 is larger than 1.8, while the hydrogen yield in all the cases decreases with increasing temperature. In addition, the dose used is relatively high, and therefore the amount of gas in the solution is substantially lower than that in the free volume over the solution. It is known that an increase in the temperature from room temperature to 60°C and even higher only weakly affects the yield of the primary products of water radiolysis [11, 12], which allows a conclusion that the main cause of the observed change in the yield of the gaseous radiolysis products is the radiolytic transformation of the solutions studied, namely, the secondary radiolysis of oxalic acid.

The processes occurring in the system under irradiation can be represented by the set of the reactions written in [8, 11, 13]. In the deaerated solutions, the hydrated electrons depending on pH convert into H atoms or react with oxalic acid molecules. Under these conditions, hydrated electrons, OH radicals, and H atoms can participate in the oxalic acid decomposition. It was shown in [8] that hydroxy radicals are substantially more active in oxalic acid decomposition than hydrogen atoms. In addition, in some works [9, 13], the reactions with hydrogen peroxide to form CO_2 are assumed to occur during radiolysis.

Simultaneously, the thermal decomposition of oxalic acid under the same conditions without irradiation was considered. The most concentrated initial solution of the acid (5.0×10^{-2} M) was taken in order to observe the gas liberation (Table 3). The results obtained show that the gas liberation does not exceed 1% even at 60°C in 30 h. This amount cannot affect the radiolysis process under consideration.

Table 3. Yield of the products of the oxalic acid decomposition under γ-irradiation at a dose of 0.06 MGy and under heating without irradiation

T, °C	τ, h	Yield of products, %	
		γ-irradiation	without irradiation
10	30	94.7	–
40	12	–	0.19
	24	–	0.32
60	17	69.0	–
	30	–	0.72

CONCLUSION

Gas formation in irradiated aqueous solutions of oxalic acid starts at comparatively high doses, but gradually decelerates and the gas accumulation curve flattens out. Hydrogen formed exists as a mixture with CO_2. Therefore, hydrogen explosion in storage of dilute solutions of oxalic acid is unlikely. The results obtained should be taken into the consideration in storage and reprocessing of various systems containing oxalic acid.

REFERENCES

1. Zemlyanukhin, V.I., Il'enko, E.I., Kondrat'ev, A.P., *et al.*, *Radiokhimicheskaya pererabotka topliva AES* (Radiochemical Processing of Fuel from Atomic Power Plants), Shmidt, V.S., Ed., Moscow: Energoatomizdat, 1989.
2. Stel'makh, N.S., Kritskaya, V.E., Byvsheva, I.I., *et al.*, *Khim. Vys. Energ.*, 1997, vol. 31, no. 6, pp. 405–407.

3. Stel'makh, N.S., Kritskaya, V.E., Byvsheva, I.I., *et al*., *Khim. Vys. Energ*., 1998, vol. 32, no. 6, pp. 420–422.
4. Stel'makh, N.S., Byvsheva, I.I., Pirogova, G.N., *et al*., *Khim. Vys. Energ*., 1999, vol. 33, no. 4, pp. 312–314.
5. Pirogova, G.N., Zhestkova, T.P., Voronin, Yu.V., *et al*., *Khim. Vys. Energ*., 2002, vol. 36, no. 5, pp. 325–328.
6. Fricke, H., Hart, E.G., and Smith, H.P., *J. Chem. Phys*., 1938, vol. 6, pp. 229–232.
7. Pikaev, A.K., *Dozimetriya v radiatsionnoi khimii* (Dosimetry in Radiation Chemistry), Moscow: Nauka, 1975.
8. Zhestkova, T.P., Zhukova, T.N., Makarov, I.E., and Pikaev, A.K., *Dokl. Ross Akad. Nauk*, 2001, vol. 379, no. 5, pp. 635–638.
9. Holm, N.W., and Sehested, K., *Adv. Chem. Ser*., 1968, vol. 81, pp. 568–571.
10. *Spravochnik khimika* (Chemist's Handbook), Nikol'skii, B.P., Ed., Moscow: Goskhimizdat, 1952, vol. 3.
11. Pikaev, A.K., *Sovremennaya radiatsionnaya khimiya: Radioliz gazov i zhidkostei* (Modern Radiation Chemistry: Radiolysis of Gases and Liquids), Moscow: Nauka, 1986.
12. Pikaev, A.K., Kabakchi, S.A., and Makarov, I.E., *Vysokotemperaturnyi radioliz vody i vodnykh rastvorov* (High-Temperature Radiolysis of Water and Aqueous Solutions), Moscow: Energoatomizdat, 1988.
13. Draganic, I.G. and Gal, O., *Radiat. Res. Rev*., 1971, vol. 3, pp. 167–170.

Russian Journal of Applied Chemistry, Vol. 77, No. 11, 2004, pp. 1822–1825. Translated from Zhurnal Prikladnoi Khimii, Vol. 77, No. 11, 2004, pp. 1840–1843.

PROCESSES AND EQUIPMENT OF CHEMICAL INDUSTRY

Intensification of Gas–Liquid Processes in Tubular Turbulent Apparatus

V. P. Zakharov, K. S. Minsker, F. B. Shevlyakov, A. A. Berlin, G. G. Aleksanyan, B. L. Rytov, and A. A. Konoplev

Bashkir State University, Ufa, Bashkortostan, Russia
Semenov Institute of Chemical Physics, Russian Academy of Sciences, Moscow, Russia

Received July 1, 2004

Abstract—The fundamental aspects of intensification of the mass transfer in gas–liquid flows in tubular turbulent apparatus are revealed, and dependences of the gas absorption rate on the reactor geometry and method of reagent introduction are considered for the example of dissolution of atmospheric oxygen in water.

The chemical technology includes a large number of processes that occur in liquid–gas systems. To these, in particular, belong halogenation, hydrohalogenation, and oxidation, in which the main difficulty is encountered in creating a reaction mixture with a developed phase-contact surface. Taking into account the diffusion limitations in transport of reactants across the phase boundary is particularly important at high rates of the occurring chemical reaction. In this case, the apparatus dimensions are to be diminished to become comparable with those of the reaction zone (intensive dispersion zone) to eliminate dead zones. In addition, the process is to be carried out in the jet mode with an as short as possible time of residence of reactants in the apparatus in order to make lower the probability of occurrence of slower side reactions.

These requirements are satisfied in the optimal way by small-size tubular turbulent apparatus of diffuser–confuser design [1], which are highly efficient in fast chemical and mass-exchange physical processes in liquid–gas systems and, in particular, chlorination of butyl rubber with molecular chlorine, preparation of a homogeneous gas–liquid mixture for obtaining ethylene–propylene rubbers, chlorination and hydrochlorination of ethylene, production of nitrogen fertilizers, etc. [2, 3]. An analysis of experimental data and results of numerical calculations performed in [4] yielded an analytical expression for calculating the mass-transfer coefficient in the liquid phase, averaged over the volume of the diffuser–confuser channel. This coefficient exceeds by a factor of 1.5–2 the linear mass-transfer coefficients in volume mixing apparatus. At the same time, scientifically substantiated application of tubular turbulent apparatus in gas–liquid processes requires consideration of possible ways to control the efficiency of mass transfer in liquid–gas systems.

The aim of this study is to examine the fundamental aspects of intensification of the mass transfer in gas–liquid flows in tubular turbulent apparatus and analyze the dependence of the gas absorption rate on the reactor geometry and method of reagent introduction for the example of oxygen dissolution in water.

The efficiency of mass transfer in gas–liquid flows was evaluated using the sulfite technique [5] based on catalytic oxidation of sodium sulfite with atmospheric oxygen:

$$Na_2SO_3 + 1/2O_2 \xrightarrow{CuSO_4} Na_2SO_4.$$

Under the experimental conditions, sodium sulfite reacts with atmospheric oxygen under conditions of the diffusion control, i.e., the rate of the process is completely determined by the stage of oxygen transfer from the gas phase into the liquid. In view of the low solubility of oxygen in water, the mass-transfer coefficient is totally determined by the mass-transfer coefficient in the liquid phase (by the stage of oxygen diffusion from the phase boundary into the bulk of the liquid). As a consequence, changes in the oxidation rate of sodium sulfite are associated with the intensification of the mass transfer in the liquid phase.

The experimental setup was shown schematically in [6], but this was done for the case of recycling of the liquid phase, with the flow returned to the inlet of the apparatus in preliminary separation of the gas. The variation of the concentration of sodium sulfite in the

1070-4272/04/7711-1822 © 2004 MAIK "Nauka/Interperiodica"

reaction mixture was determined experimentally by iodometric titration during the operation of the setup till the instant of complete conversion of sodium sulfite into sulfate. As reactors were used tubular units of diffuser–confuser (length of diffuser–confuser section $L_s = 2d_d$, number of sections N) and cylindrical designs. As optimization parameters served the ratio of diameters of the wide (diffuser) and narrow (confuser) parts of the reactor, d_d/d_c (1–3 at d_d = 24 mm), and also the diameters of the radial tube, d_2 (0.8–7 mm), and of the coaxial tube, d_1 (5–10 mm), for supply of the liquid phase.

As a quantity characterizing the intensity of gas dissolution in a gas–liquid reaction mixture flowing in the apparatus, we chose the "sulfite number of the reactor," i.e., the amount of oxygen taken up by unit reaction volume in unit time [5]:

$$\mathrm{SuR} = 0.127\frac{\Delta c_{Na_2SO_3}}{\Delta\tau}\frac{v_\Sigma}{v_r},$$

where v_r and v_Σ are the volumes of the reactor and the reaction mixture, respectively; and $\Delta c_{Na_2SO_3}$ is the change in the concentration of sodium sulfite in a time $\Delta\tau$.

Simultaneously with evaluating SuR, the size of gas bubbles was determined photographically, with the images obtained subjected to digital processing and the volume–surface diameter of particles of the dispersed phase (d_{32}) found [6].

When the ratio of the flow rates at which the gas and liquid phases are introduced, w_g/w_l (gas-to-liquid ratio of the dispersed system), in a tubular turbulent apparatus of diffuser–confuser design is raised to about 0.1, the sulfite number SuR of the reactor increases, as also, consequently, does the efficiency of mass transfer of oxygen from the gas phase into the liquid (Fig. 1). This is apparently due to an increase in the rate of oxygen supply to the reactor and to the resulting rise in its amount in the reaction mixture, which accelerates the oxidation process. It should be noted that, as indicated by visual inspection, the process occurs in this case in the bubble mode, and the oxidation rate increases, despite that the average size of gas bubbles, d_{32}, grows to 1.4 mm as the w_g/w_l ratio becomes larger. Further increase in the content of gas in the reaction mixture (gas flow rate w_g) does not lead to any change in the sulfite number of the reactor, which is due to the following: the flow of the two-phase mixture passes into a densely packed bubble (foam) mode, whereas the volume–surface

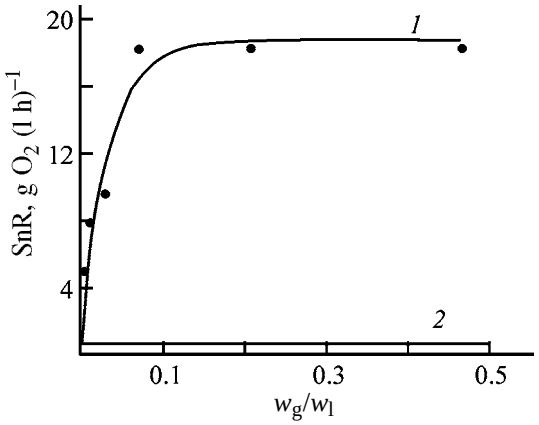

Fig. 1. Sulfite number of the reactor, SuR, vs. w_g/w_l in (*1*) tubular turbulent reactor ($w_l = 170 \pm 10$ cm^3 s^{-1}; N = 5; d_1 = 10, d_2 = 3, and d_c = 15 mm) and (*2*) volume mixing apparatus at a stirrer rotation rate of 1700 rpm (w_l/w_g = 3.3).

diameter of dispersed inclusions remains constant, $d_{32} \approx 1.4$ mm. It can be seen from the experimental data obtained that there exists the optimal ratio w_g/w_l, which apparently depends on the physical characteristics of the reacting components of the two-phase mixture, and there is no point in exceeding this value. This is especially important in working with aggressive gases, when the bypassing of the unreacted gas is impossible: in particular, in chlorination of butyl rubber with molecular chlorine in a hydrocarbon solvent [7].

The specific rate of uptake of atmospheric oxygen by water in a tubular turbulent reactor of the diffuser–confuser design (Fig. 1, curve *1*) exceeds by more than an order of magnitude that in a volume apparatus with a fast mechanical stirrer (~1700 rpm) (Fig. 1, curve 2). This is due to the following. In gas bubbling in a volume apparatus, including those with mechanical agitation, the zone of effective dispersion, which determines the rate of oxygen transfer, is considerably smaller than the reaction volume. In those parts of the apparatus which are remote from the zone of stirrer rotation in which effective dispersion occurs, gas bubbles coalesce and the area of the phase boundary decreases. In addition, zones of circulation of the two-phase mixture, which give rise to strong turbulent pulsations in the liquid phase, are absent in this case. As a consequence, tubular turbulent units of the diffuser–confuser design are distinguished by high values of the sulfite number of the reactor owing to the possibility of achieving a high-intensity dispersion throughout the reactor volume and to the presence of circulation zones in the diffuser–confuser sections.

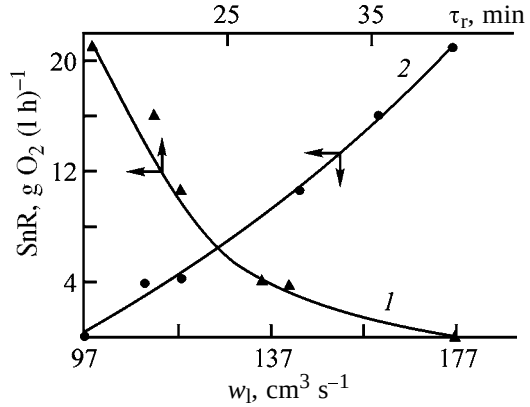

Fig. 2. Sulfite number SuR of the reactor vs. (*1*) residence time of the liquid in the reactor τ_r and (2) its flow rate w_l. w_l/w_g = 3.3; N = 5, d_1 = 10, d_2 = 3, and d_c = 15 mm.

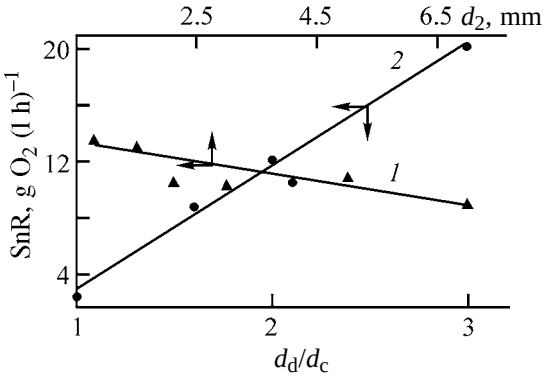

Fig. 3. Sulfite number SuR of the reactor vs. (*1*) diameter d_2 of the gas feed tube (d_d/d_c = 2) and (*2*) d_d/d_c (d_2 = 3 mm). w_l/w_g = 3.3, w_l = 140 cm^3 s^{-1}, N = 6, d_1 = 10 mm.

The small size of the tubular reactor ($v_r \approx 0.1$ l), compared to the volume mixing apparatus (v_r 4 l), allows metal saving and yields a higher (by a factor of more than 40) specific output capacity without a decrease in the time necessary for the oxidation to be complete.

The significant rise in SuR is observed when the flow rate of the reaction mixture increases at a constant content of gas in it (Fig. 2, curve *2*). In this case, the influence of shear deformation on gas bubbles is made stronger by the hydrodynamic energy of the flow, which leads to disintegration of particles of the dispersed phase in accordance with the exponential dependence and to an increase in the area of the phase-contact surface, as demonstrated for the example of emulsion formation [6]. In addition, gas uptake is virtually absent in the stratified mode of flow of the reaction mixture at low flow rates (<97 cm^3 s^{-1} in the given case), which is the lower limit to the output capacity of the reactor. At the same time, the maximum (plateau) in the SuR = $f(w_l)$ dependence is not reached at high w_l, i.e., there is no upper limit to the output capacity of the reactor. A characteristic feature of chemical and mass-exchange physical processes in tubular turbulent apparatus is that the rate of the process depends on the residence time of reactants in the reactor [2]. It can also be seen, for the example of dissolution of atmospheric oxygen in water, that SuR increases when the residence time of the reaction mixture in the reactor becomes shorter (Fig. 2, curve *1*). In this case, the reaction zone becomes "denser" as a result of diffusion control of the process.

As shown in [8], it is possible to effectively control the size of dispersion inclusions in liquid–liquid systems (specific area of the phase-contact surface) and, consequently, the efficiency of mass transfer by changing the method of reagent introduction. When gas–liquid flows move in tubular turbulent apparatus, raising the diameter of the gas feed tube results in that the sulfite number of the reactor diminishes only slightly (Fig. 3, curve *1*), which is determined by a decrease in the phase-contact area, because d_{32} increases by 15%. Similarly, when the diameter d_1 of the coaxial tube for supply of the liquid phase is reduced from 10 to 5 mm, SuR changes from 13.5 to 14 g O_2/(l h). Thus, the rate of oxidation of sodium sulfite by atmospheric oxygen in an aqueous solution is virtually independent of how the reagents are introduced. This is due to the fact that changing the method of introduction of the liquid and gas phases and, in particular, altering the diameters of feed tubes have no effect on the mass-transfer coefficient in the liquid phase.

In contrast to the method of reagent introduction, the geometry of the tubular turbulent apparatus and, in particular, the d_d/d_c ratio strongly affect the oxidation rate of sodium sulfite (Fig. 3, curve *2*). On passing from a cylindrical apparatus (d_d/d_c = 1) to that of a diffuser–confuser design with d_d/d_c = 3, the sulfite number of the reactor grows by nearly an order of magnitude. This is due to a rise in the mass-transfer coefficient in the liquid phase [4], which occurs because the coefficient of turbulent diffusion in the circulation zones of the diffuser–confuser sections grows as the depth of channel profile increases from d_d/d_c = 1 to d_d/d_c = 3 [3]. In addition, the size of dispersed inclusions decreases in this case by more than 70%. The rise in the efficiency of oxygen dissolution in water on passing from a cylindrical reactor to that of diffuser–confuser design is determined by the increase in the hydrodynamic energy of the flow. This is manifested in pronounced difference of the pressures at the apparatus ends (Fig. 4), which make higher the energy expenditure for a flow of the reaction mixture at the required linear velocity. However,

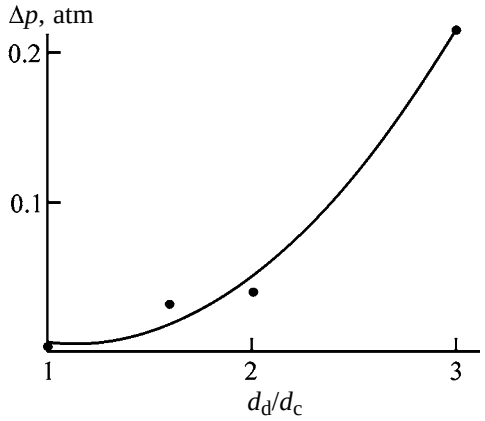

Fig. 4. Pressure difference across the ends of a tubular turbulent apparatus, Δp, vs. d_d/d_c (w_l = 140 $cm^3\ s^{-1}$).

the contribution of the expenditure for flow of the reaction mixture is insignificant owing to the small length of the tubular turbulent reactor, necessary for a fast chemical reaction to occur in high yield in the presence of a phase boundary, and to the high efficiency of mass transfer. Apparently, the best d_d/d_c ratio, from the standpoint of the efficiency of oxygen absorption in water (Fig. 3) and the optimal pressure difference across the ends of the apparatus (Fig. 4), is equal to 2.

Thus, tubular turbulent apparatus of diffuser–confuser design have a higher (by more than order of magnitude) specific rate of dissolution of atmospheric oxygen in water, compared to the volume mixing apparatus. An effective way to control the rate of oxygen absorption is to raise the flow rate of the two-phase reaction mixture (the output capacity of the reactor) and the depth of channel profile, expressed by the d_d/d_c ratio.

The results obtained in the study make it possible to recommend tubular turbulent apparatus for use in wastewater treatment by oxidation with atmospheric oxygen or ozone. In addition, the fundamental aspects of intensification of the mass exchange in liquid–gas systems, revealed in the study, enable effective use of tubular turbulent apparatus of diffuser–confuser design as reactors for fast chemical processes, as prereactors and external dispersion devices in order to make larger the area of the phase-contact surface in a two-phase reaction mixture, as internal circulation tubes in bubble-airlift (gas-lift) apparatus, as absorbers, etc.

CONCLUSIONS

(1) Tubular turbulent apparatus of diffuser–confuser design have a higher (by more than order of magnitude) specific rate of dissolution of atmospheric oxygen in water, compared to the volume mixing apparatus.

(2) Raising the flow rate of the reaction mixture leads to an increase in the sulfite number of the reactor, despite the decrease in the residence time of the reactants in the reaction zone, i.e., causes "densification" of the reaction zone.

(3) A decrease in the diameter of the radial tube for gas input by a factor of 9 and a threefold increase in the d_d/d_c ratio lead to a rise in the sulfite number of the reactor by factors of 1.5 and 9, respectively.

ACKNOWLEDGMENTS

The study was financially supported by the Russian Foundation for Basic Research (project no. 02-01-97913).

REFERENCES

1. Minsker, K.S., Zakharov, V.P., and Berlin, A.A., *Teor. Osn. Khim. Tekhnol*., 2001, vol. 35, no. 2, pp. 172–177.
2. Berlin, A.A., Minsker, K.S., and Dyumaev, K.M., *Novye unifitsirovannye energo- i resursosberegayushchie vysokoproizvoditel'nye tekhnologii povyshennoi ekologicheskoi chistoty na osnove trubchatykh turbulentnykh reaktorov* (New Unified Environmentally Clean Energy- and Resource-Saving Technologies Based on Tubular Turbulent Apparatus), Moscow: NIITEKhIM, 1996.
3. Minsker, K.S., Berlin, A.A., and Zakharov, V.P., *Vysokomol. Soedin.*, 2002, vol. 44, no. 9, pp. 1606–1627.
4. Berlin, A.A., Minsker, K.S., Mukhametzyanova, A.G., *et al*., in *Polimery-2003: Sbornik statei Inst. Khimicheskoi Fiziki Ross. Akad. Nauk* (Polymers-2003: Coll. of Works of the Inst. of Chemical Physics, Russian Acad. Sci.), Moscow, 2003, pp. 121–127.
5. Pavlushenko, I.S., Braginskii, L.N., and Brylov, V.N., *Zh. Prikl. Khim.*, 1961, vol. 34, no. 5, pp. 805–809.
6. Zakharov, V.P., Mukhametzyanova, A.G., Takhavutdinov, R.G., *et al*., *Zh. Prikl. Khim*., 2002, vol. 75, no. 9, pp. 1462–1465.
7. Berlin, A.A., Minsker, K.S., and Deberdeev, R.Ya., *Dokl. Ross. Akad. Nauk*, 2000, vol. 375, no. 2, pp. 218–221.
8. Zakharov, V.P. and Minsker, K.S., *Khim. Prom–st*., 2003, vol. 80, no. 6, pp. 38–42.

Russian Journal of Applied Chemistry, Vol. 77, No. 11, 2004, pp. 1826–1828. Translated from Zhurnal Prikladnoi Khimii, Vol. 77, No. 11, 2004, pp. 1844–1846.

PROCESSES AND EQUIPMENT OF CHEMICAL INDUSTRY

A Model for Calculation of Reverse Osmosis Apparatus of the Roll Type

O. A. Abonosimov, S. I. Lazarev, and A. S. Gorbachev

Tambov State Technical University, Tambov, Russia

Received January 26, 2004; in final form, May 2004

Abstract—A model of reverse osmosis apparatus of the roll type is suggested. The model makes it possible to calculate the working area of the membrane, perform sectioning of the apparatus, determine the working pressure in separating units, and find the energy expenditure for the separation process.

Together with the conventional methods for separation of liquid systems, such as distillation, extraction, and evaporation, membrane processes find increasing use [1]. This is due to a number of advantages of membrane separation processes over the conventional techniques. Membrane processes are less energy-intensive and have a good economic feasibility; membrane installations are simple, space-saving, reliable in operation, and can be readily automated. The most promising is the method of reverse osmosis with the use of separating units of the roll type.

However, wide industrial implementation of membrane separation methods is hindered by insufficient understanding of the mechanism of the process and by the lack of reliable engineering procedures for calculation of membrane separation apparatus. The existing methods for calculation of processes and apparatus for membrane separation were considered in sufficient detail in [2–5]. An analysis of these calculation methods demonstrated that all the existing models are mostly of strictly specialized nature. Therefore, the aim of this study was to develop a sufficiently simple and reliable model for calculation of reverse-osmosis apparatus of the roll type.

The primary problem in calculating reverse-osmosis installations of the roll type consists in determining the basic parameters of a reverse-osmosis apparatus. To these parameters belong the working area of the membrane, the working pressure in the separating unit, and energy expenditure for separation.

Roll apparatus in reverse-osmosis installations are equipped with separating units (Fig. 1). Separating units of the roll type comprise a permeate collector *1* (perforated solution-removing tube) with several multilayer sheets wrapped around. Each sheet comprises two layers of planar semipermeable membranes *2* of rectangular shape. The surface of a permeate collector *3*, made of a synthetic fabric, is placed between the membranes. A spacer *4* for the flow of the starting solution (promoter of turbulence in the starting solution) is placed on the face surface of the membrane. The permeate-collecting surface and the membranes are attached at one end to the permeate collector, with the edges of their three other sides glued together hermetically. Each multilayer sheet wrapped around the perforated solution-removing tube forms a spiral channel for the flow of the solution being separated.

The main parameter in calculation of a separating roll unit is the total working surface area of the semipermeable membrane. We determined the area using the basic mass-transfer equation [1, 6]

$$F_M = M/(\Delta PK), \quad (1)$$

where M is the mass of the substance; ΔP, driving force of the reverse osmosis; and K, mass-transfer coefficient.

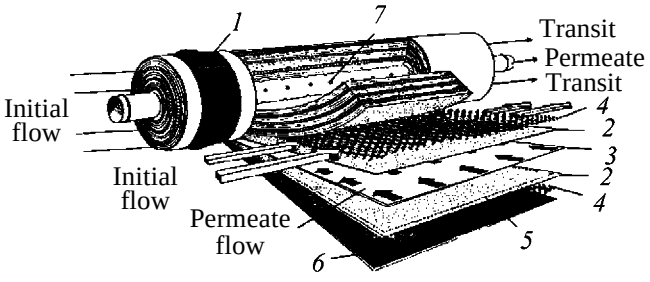

Fig. 1. Scheme of the roll-type separating unit: (*5*) adhesion line, (*6*) coating, and (*7*) seal; for the other designations, see text.

1070-4272/04/7711-1826 © 2004 MAIK "Nauka/Interperiodica"

We calculate the mass-transfer coefficient by the expression [6]:

$$K = \frac{1}{1/\beta + \delta/P_d}, \quad (2)$$

where β is the coefficient of mass transfer from the solution to the membrane surface; δ, membrane thickness; and P_d, the diffusion permeability coefficient of the membrane.

The diffusion permeability coefficients are calculated using approximating relations obtained in studies carried out on an industrial reverse-osmosis installation of the roll type [7, 8].

Experiments and calculations show that the kinetic characteristics of reverse osmosis depend on the longitudinal flow velocity in the intermembrane channel and on the pressure in the unit. The motion velocity and the flow mode of the solution in the intermembrane channel are taken into account in these calculations as usual, by means of the Reynolds number Re. The simplest way to take into account the pressure is to introduce the simplex

$$K_d = P_{work}/P_{st}, \quad (3)$$

where P_{st} is the standard pressure for which the rated throughput of the membranes is specified (P_{st} = 4 MPa).

More substantiated is use of the Euler number Eu

$$Eu = \Delta P/\rho w^2, \quad (4)$$

because Eu determines the forced transverse flow rate of the solvent and a number of other parameters.

However, simultaneous use of Re and Eu is inconvenient in processing of experimental data. Therefore, we used the following dimensionless combination instead of Eu:

$$K_{\Delta P} = Eu\,Re^2 = \Delta P \rho L^2/\mu^2. \quad (5)$$

Processing of calculated and analytical data on local mass-transfer coefficients made it possible to obtain rough approximating relations for the mass transfer coefficients averaged over the channel length. Having refined these relations on the basis of the experimental results, we obtained the calculation equation (error ±7%)

$$Nu = 1.84 \times 10^{-4} Re^{0.33} K_{\Delta P}^{0.18}. \quad (6)$$

Knowing the working area of a roll unit and taking into account the fact that the industrial reverse-osmosis apparatus consists of two units [9], we find the total number of apparatus in the membrane installation by the formula

$$n = F/2F_u, \quad (7)$$

where F_u is the working area of a single unit (m^2) (for the industrially used ERO-E-6.5/900A roll unit, this area is 6.5 m^2).

Further, we perform sectioning of the apparatus in the installation, based on the necessity for ensuring the same flow velocity of a solution being separated in each apparatus of each section and a constant decrease in the flow rate along the apparatus [6]:

$$L_i = (L_{in_i} + L_{fin_i})/2n_i = \text{const}, \quad (8)$$

$$q = L_{in_i}/L_{fin_i}, \quad (9)$$

where L_{in_i} and L_{fin_i} are the initial and final flow rates of the solution being separated in ith section; and n_i is the number of apparatus in ith section.

The value of q is chosen depending on the concentration coefficient k:

$$k = c_{fin}/c_{in}, \quad (10)$$

where c_{in} and c_{fin} are the initial and final concentrations of the solution being separated (the optimal value is q = 1.4).

The number of separation units in a section is calculated by the formula

$$n_i = \frac{L_{st}(1 - 1/q)}{q^{i-1}L_{per}}, \quad (11)$$

where L_{st} and L_{per} are the flow rates of the starting solution and the permeate in each apparatus.

To find the actual pressure in the reverse-osmosis apparatus, it is also necessary to calculate the loss of pressure for overcoming the hydraulic resistance constituted by the resistance of separating units, feed pipes, local resistances, etc. The major part of the pressure loss is accounted for by the hydraulic resistance of separating units, which can be calculated by the formula

$$\Delta P_\rho = \xi \rho w^2/2, \quad (12)$$

where ξ is a coefficient dependent on the design of a separating unit (type of the separating grid, drainage

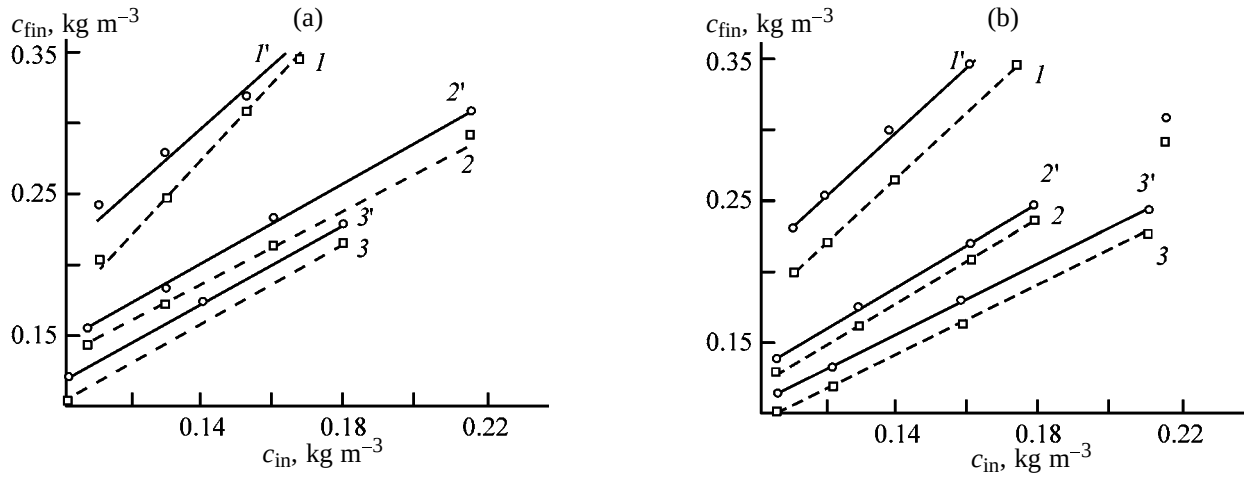

Fig. 2. Comparison of (*1*–*3*) calculated and (*1*'–*3*') experimental data for solutions of (a) $NiCl_2$ and (b) $NiCl_2$ + $K_2Cr_2O_7$. (c_{in}, c_{fin}) Initial and final concentrations of the solution being separated. Re: (*1*, *1*') 19, (*2*, *2*') 36, and (*3*, *3*') 55.

material, etc.); ρ, density of the solution being separated; and *w*, solution flow velocity in the intermembrane channel.

Knowing the actual pressure in the reverse-osmosis apparatus, we find the pump head:

$$H = \Delta P_{act}/\rho_{st} g, \quad (13)$$

were ρ_{st} the density of the initial solution.

The resulting data on the pressure and flow rate are used to select a pump for the reverse-osmosis installation.

The economical efficiency of the reverse-osmosis installation is evaluated by the total energy expenditure for separation, using the formula [10]

$$W_{eff} = VP/\varphi\eta, \quad (14)$$

where *V* is the volume of purified water; *P*, working pressure in a roll unit; φ, selectivity of retention; and η, efficiency of the pump unit.

The adequacy of the model for calculating reverse-osmosis apparatus of the roll type was assessed by comparing the experimental and calculated concentration dependences used in calculating the mass-transfer and diffusion permeability coefficients (Fig. 2). The calculated and experimental dependences for solutions of $NiCl_2$ and $NiCl_2$ + $K_2Cr_2O_7$ are shown in Fig. 2. It can be seen that the results are acceptable for engineering calculations.

REFERENCES

1. Dytnerskii, Yu.I., *Baromembrannye protsessy: Teoriya i raschet* (Baromembrane Processes: Theory and Calculation), Moscow: Khimiya, 1986.
2. Dukhin, S.S., Kocharov, R.G., and Gutierrez, L.E.R., *Khim. Tekhnol. Vody*, 1987, vol. 9, no. 2, pp. 99–103.
3. Volgin, V.D., Maksimov, E.D., and Novikov, V.I., *Khim. Tekhnol. Vody*, 1989, vol. 11, no. 3, pp. 222–225.
4. Murav'ev, L.L., *Khim. Tekhnol. Vody*, 1989, vol. 11, no. 2, pp. 107–109.
5. Lebrun, R.E., Bouchard, C.R., Rollin, A.L., *et al.*, *Chem. Eng. Sci.*, 1989, vol. 44, no. 2, pp. 313–320.
6. Baikov, V.I. and Znovets, P.K., *Inzh.-Fiz. Zh.*, 1994, vol. 72, no. 1, pp. 32–37.
7. Abonosimov, O.A., Korobov, V.B., and Konovalov, V.I., *Vestn. Tambov. Gos. Tekh. Univ.*, Tambov, 2000, no. 3, pp. 425–434.
8. Abonosimov, O.A., Lazarev, S.I., and Alekseev, A.A., in *Trudy Tambovskogo gos. tekhnicheskogo univ.: Sbornik nauchnykh statei molodykh uchenykh i studentov* (Coll. of Works of Tambov State Technical Univ.: Coll of Works of Young Scientists and Students), Tambov: Tambov. Gos. Tekh. Univ., issue 6, pp. 101–104.
9. Artemov, N.S., *Apparaty i ustanovki dlya membrannykh protsessov* (Apparatus and Installations for Membrane Processes), Moscow: Mashinostroenie, 1994.
10. Slesarenko, V.N., *Opresnenie morskoi vody* (Desalination of Seawater), Moscow: Energoatomizdat, 1991.

Russian Journal of Applied Chemistry, Vol. 77, No. 11, 2004, pp. 1829–1834. Translated from Zhurnal Prikladnoi Khimii, Vol. 77, No. 11, 2004, pp. 1847–1852.

PROCESSES AND EQUIPMENT OF CHEMICAL INDUSTRY

Effect of Change of Phase Resistances on the Kinetics of Mass Transfer with a Chemical Reaction across Spherical Phase Boundary in the Interphase Instability Mode

S. A. Ermakov, A. A. Ermakov, and V. A. Stepanov

Ural State Technical University, Yekaterinburg, Russia

Received June 28, 2004

Abstract—The influence exerted by the concentration of the binder reagent on the ratio of phase resistances in mass exchange across a spherical phase boundary in the liquid–liquid system was studied.

As is known, the reciprocal of the mass-transfer coefficient characterizes the resistance to mass transfer in the phase. Hence follows that the phase resistance is affected by such physicochemical parameters as viscosity of interacting phases, diffusion coefficient, hydrodynamic situation in the phases, and ratio of initial concentrations of the substance being transferred and the binder reagent. Studies of the mass transfer in the liquid–liquid system have shown [1] that introduction of a binder into the receiving phase leads to redistribution of the diffusion resistance to mass transfer among the phases. As the concentration of the binder reagent increases, the reaction front is shifted from the bulk to the phase boundary; as a result, the diffusion resistance of the receiving phase is eliminated and a change of phase resistances occurs.

Studies of the mass transfer with a chemical reaction at the planar phase boundary in the liquid–liquid system [2] have shown that the change of phase resistances leads to loss of the hydrodynamic stability of the phase boundary, and thereby conditions are created in the system that give rise to a spontaneous interphase convection (SIC) or intensify the already existing convection process.

The change of phase resistances was evaluated, as it was done before for the case of mass transfer across the planar phase boundary, by the parameter [3]

$$L = c_A/c_{Bp}, \quad (1)$$

where c_A is the initial concentration of the substance being transferred (kmol m^{-3}), and c_{Bp} is the critical concentration of the binder reagent (kmol m^{-3}).

This study is concerned with the influence exerted by the change of phase resistances on the conditions of appearance and intensity of SIC in mass transfer with a chemical reaction across a spherical phase boundary in the liquid–liquid system.

EXPERIMENTAL

The mass transfer across the spherical phase boundary on a single drop was studied in temperature-controlled glass columns of diameter d = 0.055 m and height p = 0.5 m at a temperature of 20 ± 0.1°C. The phase being dispersed was fed with a precision feeder of volume 8 cm^3, equipped, in order to eliminate pulsations, with two special bellows operating simultaneously, one in compression and the other in expansion. The height of drop fall was varied with a mobile capillary, which yielded experimental data for short times of phase contact. A column with a discharge pipe in its lower part (Fig. 1) was used in the experiment. The drop catchers in which the dispersed phase was collected had a diameter d_c = 0.007 m (in order to diminish the mass transfer across the planar phase boundary at place of drop coagulation). The volume of liquid in drop catchers was maintained constant (2–3 drops) by continuously removing the dispersed phase. The drop diameter was varied by selecting capillaries of different diameters (0.19×10^{-3}–0.32×10^{-3} m). The volume of the continuous phase was V_{cp} = 1100 ml; that of the phase being dispersed, V_{dp} = 50 ml; and that of a sample, W_s = 2 ml.

The experiments were performed with organic solvents and transferred substances of chemically pure and analytically pure grades, preliminarily purified by distillation. As binder reagent served chemically pure grade sodium hydroxide. The purity of all the chemicals was judged from their refractive indices and boiling points.

Prior to an experiment, the organic and aqueous

1070-4272/04/7711-1829 © 2004 MAIK "Nauka/Interperiodica"

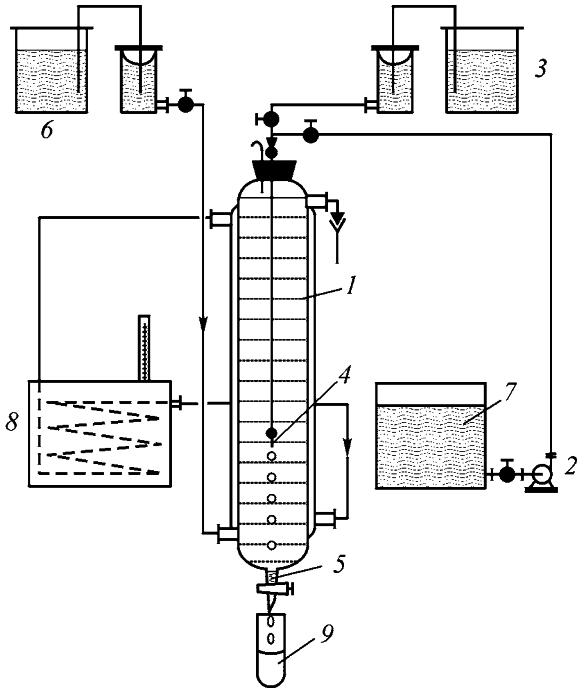

Fig. 1. Experimental setup for a study of the kinetics of mass transfer on a single falling drop. (*1*) Column, (*2*) precision feeder, (*3*) constant-level vessel for the dispersed phase, (*4*) capillary, (*5*) settler, (*6*) constant-level vessel for the continuous phase, (*7*) vessel for the starting solution of the dispersed phase, (*8*) thermostat, and (*9*) collector of the dispersed phase.

phases were mutually saturated (equal volumes of an organic solvent and distilled water were placed in a flask and kept there for 24 h) in order to eliminate the influence of mass exchange involving the solvents on the kinetic features of the mass exchange of the main substance being transferred. This substance was dissolved in the feeding (organic) phase, and the binder, in the aqueous phase. Before an experiment, the phases were thermostated for 30 min to eliminate the influence of the temperature factor.

The procedure used in the experiment on the laboratory setup consisted in the following: a certain height of ascent or fall of a drop (corresponding to a certain time of contact between the drop and the continuous medium) was set with a mobile capillary, and then the phase being dispersed was delivered into the capillary by a micropump, with separate drops formed in the continuous phase. After traveling a certain distance along the column height, the drop was caught with a drop catcher. The phase collected in the drop catcher was continuously discharged into the sampling device and analyzed. To determine the next point in the dependence of the concentration of the substance being transferred on the distance along the column height, the mobile capillary was moved into a new position and the procedure described above was repeated, with all the parameters (flow rate, time of drop formation, drop diameter, viscosity and density of phases) remaining unchanged. All the experiments were performed with the mass transfer directed from the drop into the continuous phase.

To determine the concentration of the substance being transferred, an aliquot (V_s = 1 ml) was taken from a weighing bottle with a pipet. The content of the substance in the aliquot was determined by potentiometric titration. The experimental error was found as root-mean-square error of the arithmetic mean to be $\leq$5%.

In a separate experiment, 100 to 200 drops were passed through the column, depending on the volume of the forming drops. The volume of a drop was 3–6 mm^3.

The time of drop formation, τ_{df}, was found as the total time in which the required number of drops was formed, divided by the number of drops formed.

The SIC was detected by three methods: visually, kinetically, and by the method of "strong surfactants."

As seen in Fig. 2a, the phase boundary is undisturbed in the case of mass transfer in the diffusion mode (diffusion-convective mechanism). In the case when the process occurs in the interphase-instability mode (Fig. 2b), waves are formed at the phase boundary, which is characteristic of SIC.

Figure 3 shows that interphase instability occurs in the presence of strong surfactants. It is known that some strong surfactants [polyvinyl alcohol (PVA) with 12.7% acetate groups, MW 47 800; Arkopol] can depress the interphase convection; however, mass exchange can proceed in this case in the diffusion mode [4]. As seen from Fig. 3, mass transfer occurs in the diffusion mode in the presence of polyvinyl alcohol (mass-transfer coefficient has a constant value); when mass transfer is performed in the same system without a surfactant, an increase in the mass-transfer coefficient is observed, which is characteristic of SIC.

In all the experiments, the kinetic method was used to detect the SIC [5]. This method consists in that the dependence $W = f(c)$ is plotted, where W is the rate of mass transfer and c is the driving force of mass transfer. A deviation from linear behavior points to occurrence of SIC (Fig. 4).

The experimental data obtained are presented in the form of kinetic dependences plotted in the c–h coordinates (c, concentration of the substance being transferred; h, distance along the height of column). With

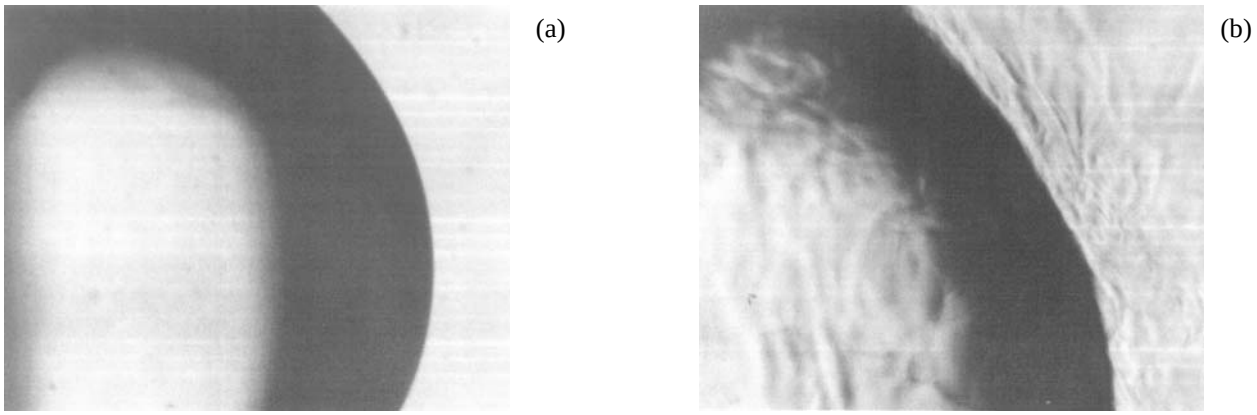

Fig. 2. Visual method for detecting SIC. Mass transfer of butyric acid (c_0 = 1 kmol m^{-3}) from CCl_4 to (a) water and (b) aqueous solution of NaOH (c_{NaOH} = 2 kmol m^{-3}).

the velocity of "free" motion of a single drop in the continuous phase and the distance traveled by the drop from the end of the capillary to the phase boundary known, the time of free motion of a single drop, τ_m, was calculated. The time of contact with the continuous medium was found by summing up the experimentally determined time of drop formation and the time of free motion of the drop:

$$\tau = \tau_f + \tau_m. \quad (2)$$

The experimental data were processed in the c–τ coordinates (c, as before; τ, process duration). The dependences obtained were approximated with a biexponential function by the least-squares method.

Further, using the resulting kinetic curve, we determined the averaged rates of the process and found the mass-transfer coefficients by the equation

$$-dc/d\tau = K_m S_{sp} c, \quad (3)$$

where K_m is the mass-transfer coefficient (m s^{-1}); S_{sp}, specific surface area of phase contact (m^2 m^{-3}); c, driving force of the mass-transfer process, equal to the concentration of the substance being transferred in the bulk of the feeding (limiting) phase [6] (kmol m^{-3}); and τ, process duration (s).

The specific surface area of phase contact was found as the ratio of the drop surface area to the drop volume by the formula

$$S_{sp} = 6/d_d, \quad (4)$$

where d_d is the average drop diameter.

The drop diameter was calculated on the following assumptions: the concentration of the substance in the continuous phase is constant during the experiment

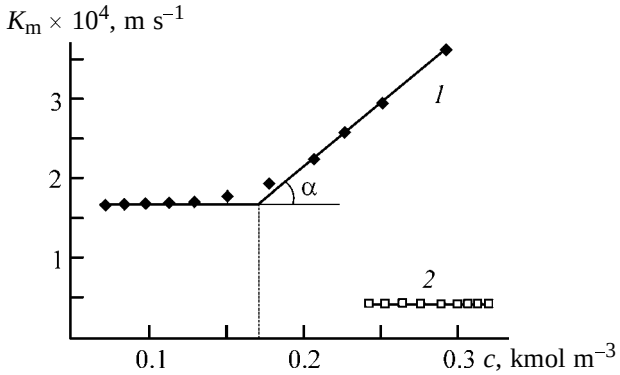

Fig. 3. Detection of SIC by the method of strong surfactants. (K_m) Mass-transfer coefficient and (c) concentration of the substance being transferred. Mass transfer of butyric acid (c_0 = 0.5 kmol m^{-3}) from CCl_4 into an aqueous solution of NaOH (c_{NaOH} = 2 kmol m^{-3}): (*1*) without surfactant and (*2*) in the presence of a surfactant (PVA, c_{surf} = 0.01 wt %).

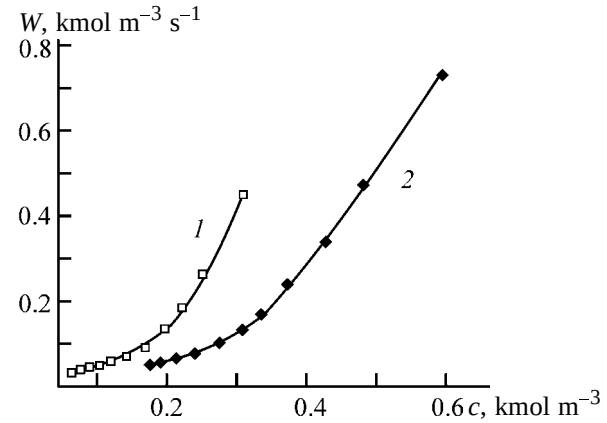

Fig. 4. Kinetic method for detection of SIC. (W) Rate of mass transfer and (c) driving force of mass transfer. Mass transfer from CCl_4 into an aqueous solution of NaOH. Substance being transferred: (*1*) acetic acid (c_0 = 0.7 kmol m^{-3}) and (*2*) butyric acid (c_0 = 1 kmol m^{-3}). c_{NaOH} (kmol m^{-3}): (*1*) 1 and (*2*) 2.

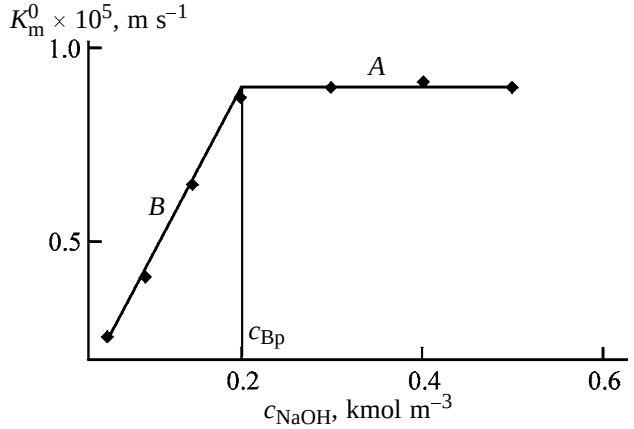

Fig. 5. Hatta curve: (K_m^0) initial mass-transfer coefficient and (c_{NaOH}) NaOH concentration; the same for Fig. 6. Mass transfer of benzoic acid (c_0 = 0.2 kmol m^{-3}) from toluene into aqueous NaOH (planar phase boundary): (*A*) diffusion region and (*B*) region of flows.

(the volume of the phase being dispersed was less than 4% of that of the continuous phase), the drop volume is constant during extraction (the drop density changed by less than 2%), and the phase boundary of the drop is spherical.

To determine the mass of drops dispersed in the column during an experiment, samples in weighing bottles were weighed on an analytical balance. The mass of the forming drop, m_d, was found by dividing the mass m_s of a sample taken by the number of drops that passed through the column during the time of drop formation. The mean arithmetic mass of a drop was found as the quotient of the total mass of drops in the experiments by the number of experiments. The error in determining the mean arithmetic mass of a drop was 2%.

With the average mass of a drop and its initial density known, the average drop diameter in an experiment was calculated by

$$d_d = (6m_d/\pi\rho_d)^{1/2}, \quad (5)$$

where ρ_d is the density of the drop (kg m^{-3}), and m_d, its mass.

The intensity of SIC and the conditions for appearance of an interphase instability were judged from the intensity coefficient ($K_{SIC} = \tan\alpha$, where α is the slope of the straight line plotted in the coordinates mass-transfer coefficient–driving force of the process) and the critical concentration c_{cr}, which are parameters of an empirical equation describing the process of mass transfer in the interphase-instability mode (Fig. 3) [7]:

$$J = \begin{cases} [K_D + K_{SIC}(c - c_{cr})] \text{ at } c > c_{cr}, \\ K_D c \text{ at } c \le c_{cr}, \end{cases} \quad (6)$$

where K_D is the coefficient of mass transfer in the diffusion mode (diffusion-convective mechanism) (m s^{-1}); K_{SIC}, coefficient taking into account the acceleration of the mass transfer in the interphase-instability mode (m^4 kmol^{-1} s^{-1}); c_{cr}, critical driving force (critical concentration) (kmol m^{-3}); c, driving force of the mass-transfer process (kmol m^{-3}); $K_D + K_{SIC}(c - c_{cr}) = K_m$, coefficient of mass transfer in the phase-instability mode (m s^{-1}).

In [8], it was suggested to evaluate the intensity of mass transfer in the phase-instability mode by the initial values of the mass-transfer coefficient, found graphically in the coordinates mass-transfer coefficient–driving force of the process at the point of intersection of the nonlinear portion of the curve for the mass-transfer coefficient with the driving force of the process at the initial instant of time.

In the present study, it is suggested to find the initial values of the mass-transfer coefficient, K_m^0 by extrapolating the function

$$K_m = -\frac{dc(\tau)}{d\tau}\frac{1}{S_{sp}c(\tau)}, \quad (7)$$

to the zero instant of time, which corresponds to the driving force of the process at the initial instant of time in the plot of the dependence of the mass-transfer coefficient on the driving force of the process.

The critical concentration of the binder component, c_{Bp}, was found from the plot of the dependence of the initial value of the mass-transfer coefficient on the initial concentration of the binder reagent, similar to the "Hatta curve" [1]. Two different portions can be seen in Fig. 5: portion *A*, parallel to the abscissa axis, corresponds to occurrence of a chemical interaction at the phase boundary, and sloping portion *B*, to the interaction of the reagent being transferred and the binder reagent in a certain volume of the extracting phase. The point of intersection of these portions corresponds to transition of the reaction front from some part of the volume of the receiving phase to the phase boundary. The critical concentration of the binder reagent, at which the change of phase resistances occurs, was found at the point of intersection of portions *A* and *B*.

Figure 6 shows a Hatta curve for mass transfer of carboxylic acids from a drop of carbon tetrachloride into an aqueous solution of NaOH. As seen from the

plot, raising the concentration of the binder reagent to the critical value for propionic and butyric acids leads to an increase in the initial values of the mass-transfer coefficient, which is accounted for by the appearance and development of SIC at approach of the front of the chemical reaction to the phase boundary. The decrease in the initial values of the mass-transfer coefficient under the conditions when the mass-transfer process is limited by the feeding phase (diffusion region) is due to hindrance to the turbulent motion of the liquid near the phase boundary. This hindrance is caused by the increase in the viscosity of the receiving phase. The quenching of the turbulization of the boundary layer diminishes the intensity of renewal of the contact surface by fresh portions of the binder reagent, which, in turn, makes less favorable the conditions of appearance and development of SIC. Accordingly, the intensities of interphase convection and mass transfer decrease.

The critical concentration of the binder reagent for the mass transfer of propionic acid (distribution coefficient $K_d = 4$) from CCl_4 into an aqueous solution of NaOH was $c_{Bp} = 0.7$ kmol m^{-3} (Fig. 6, curve *1*), i.e., the parameter L, which characterizes the change of phase resistances, is unity for propionic acid (initial concentration $c_0 = 0.7$ kmol m^{-3}). As seen in Fig. 6 (curve *2*), the change of phase resistances (transition of the limiting resistance from the receiving to feeding phase) for butyric acid (distribution coefficient $K_d = 1$) occurs at a critical concentration of the binder reagent, $c_{Bp} = 1.4$ kmol m^{-3}, i.e., at $L = 0.5$, as in the case of a planar phase boundary [2]. Comparison of the values of the parameter L for propionic and butyric acids shows that L decreases as the distribution coefficient of the substance being transferred becomes smaller, which coincides with the conclusions made in [3].

Now, the influence exerted by the change of phase resistances on the appearance conditions and intensity of SIC will be analyzed separately for substances being transferred, having different distribution coefficients.

As shown by the experiment (Fig. 7, curve *1*), the mass transfer of propionic acid in the absence of a binder reagent in the receiving phase or in its presence in low concentrations occurs under the SIC conditions, which is accounted for by the large distribution coefficient of the substance being transferred for the given system, i.e., the receiving phase does not hinder substantially the mass transfer of the main substance and thereby creates conditions under which SIC can appear and exist. At the critical concentration of the

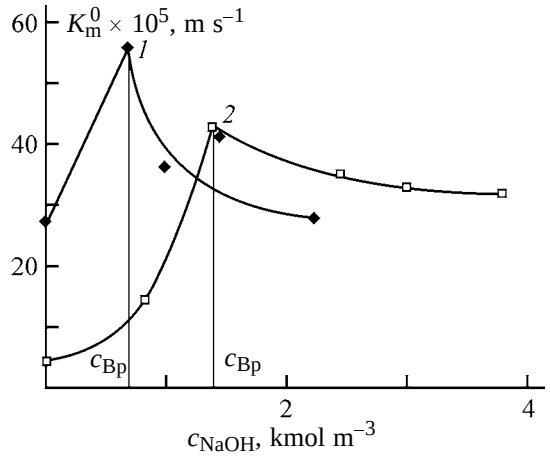

Fig. 6. Effect of the initial concentration of the binder reagent on the initial mass-transfer coefficient. Mass transfer from CCl_4 to aqueous NaOH: (*1*) propionic acid (c_0 = 0.7 kmol m^{-3}) and (*2*) butyric acid (c_0 = 0.7 kmol m^{-3}); the same for Fig. 7.

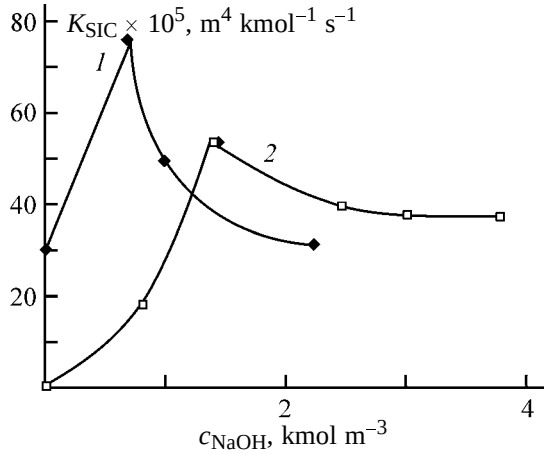

Fig. 7. Effect of the initial concentration of the binder reagent on the coefficient of SIC intensity, K_{SIC}. (c_{NaOH}) Concentration of NaOH.

binder reagent, $c_{Bp} = 0.7$ kmol m^{-3}, the maximum intensity of SIC is observed. As mentioned above, the decrease in the intensity of SIC is due to a rise in the viscosity of the receiving phase on raising the concentration of the binder reagent. The critical driving force, c_{cr}, i.e., the condition for appearance of SIC, is shifted to higher concentrations as the concentration of the binder reagent becomes higher (see table).

The mass transfer of butyric acid occurred in the absence of the binder reagent in the diffusion mode (diffusion-convective mechanism). Raising the concentration of the binder reagent from 0 to 3.8 kmol m^{-3} led to appearance of an interphase instability in the system and to intensification of mass transfer under the SIC conditions (Fig. 7, curve *2*). The absence of SIC in a system without a binder reagent is accounted

Effect of the concentration of the binder reagent on parameters of mass transfer with a chemical reaction under SIC conditions. Extracting system: CCl_4 + aqueous NaOH, c_0 = 0.7 kmol m^{-3}

Substance being transferred	c_{NaOH}, kmol m^{-3}	μ, mPa s	$K^0_m \times 10^5$, m s^{-1}	$K_{SIC} \times 10^5$, m^4 kmol^{-1} s^{-1}	c_{cr}, kmol m^{-3}	L
Propionic acid	0.0	1.00	27	30	0.01	1
	0.69	1.19	56	76	0.07	1
	1.0	1.26	36	49	0.14	1
	1.43	1.38	41	54	0.16	1
	2.25	1.67	28	31	0.18	1
Butyric acid	0.0	1.00	4.2	0	–	0.5
	0.81	1.21	14	18	0.05	0.5
	1.38	1.37	43	54	0.05	0.5
	2.45	1.74	35	40	0.02	0.5
	3.0	1.99	33	38	0.02	0.5
	3.79	2.45	32	37	0.02	0.5

for by the high diffusion resistance to mass transfer, exhibited by the receiving phase. Introduction of a binder reagent into the system results in that the process first occurs in the kinetic region. Then, at higher concentrations of the binder reagent, the reaction front is shifted to the phase boundary, and the process passes into the region of "flows" [3]. The occurrence of the mass-transfer process in this region creates conditions under which SIC can appear and develop. Raising the concentration of the binder reagent further leads to an increase in the coefficient of SIC intensity; at the critical concentration of the binder reagent, c_{Bp} = 1.4 kmol m^{-3}, there occurs a change of phase resistances (SIC has the maximum intensity) and the process passes into the diffusion region. As in the case of propionic acid, the decrease in the SIC intensity is due to an increase in the viscosity of the receiving phase on raising the concentration of the binder reagent. The critical driving force of the process decreases (see table).

CONCLUSIONS

(1) Raising the concentration of the binder reagent leads to transition of the limiting resistance from the receiving to feeding phase, i.e., to a change of phase resistances.

(2) The change of phase resistances in mass transfer of propionic acid leads to an increase in the intensity coefficient of spontaneous interphase convection. The conditions under which the spontaneous interphase convection can appear are shifted to higher concentrations.

(3) In mass transfer of butyric acid, the change of phase resistances creates conditions under which the spontaneous interphase convection can appear and the intensity of the already existing spontaneous interphase convection can considerably increase. The critical driving force of the process decreases.

(4) An increase in the initial concentration of the binder reagent in the diffusion region for propionic and butyric acids leads to a decrease in the intensity of spontaneous interphase convection, which is due to a rise in the viscosity of the receiving phase.

REFERENCES

1. Hatta, S., *Tech. Repts. Tohoku Imp. Univ.*, 1932, vol. 10, pp. 119–123.
2. Vaisov, D.V., Effect of Diffusion Resistances on Mass Transfer with a Fast Chemical Reaction under Conditions of Spontaneous Interphase Convection in Liquid Extraction, *Cand. Sci. Dissertation*, Yekaterinburg, 2002.
3. Skvirskii, L.Ya., Kremnev, L.Ya., and Abramzon, A.A., in *Protsessy khimicheskoi tekhnologii* (Processes of Chemical Technology), Moscow: Nauka, 1965, pp. 181–186.
4. Kremnev, L.Ya., Skvirskii, L.Ya., and Abramzon, A.A., in *Protsessy khimicheskoi tekhnologii* (Processes of Chemical Technology), Moscow: Nauka, 1965, pp. 186–191.
5. Ostrovskii, M.V., Abramzon, A.A., and Baradkov, I.I., *Izv. Vyssh. Uchebn. Zaved., Khim. Khim. Tekhnol.*, 1973, vol. 41, no. 6, pp. 955–960.
6. Astarita, G., *Mass Transfer with Chemical Reaction*, Amsterdam: Elsevier, 1967.
7. Ermakov, A.A., Kon'shin, Yu.A., and Nazarov, V.I., *Zh. Fiz. Khim.*, 1977, vol. 51, no. 8, pp. 2151.
8. Sherwood, T.K. and Wei, J.C., *Ind. Eng. Chem.*, 1957, vol. 49, pp. 1030–1034.

Russian Journal of Applied Chemistry, Vol. 77, No. 11, 2004, pp. 1835–1839. Translated from Zhurnal Prikladnoi Khimii, Vol. 77, No. 11, 2004, pp. 1853–1857.

ORGANIC SYNTHESIS AND INDUSTRIAL ORGANIC CHEMISTRY

Chlorinated Polyimides

B. A. Zhubanov, V. D. Kravtsova, and R. F. Mukhamedova

Bekturov Institute of Chemical Sciences, Ministry of Education and Science of the Kazakhstan Republic, Almaty, Kazakhstan

Received March 19, 2004

Abstract—Photoinitiated reaction of maleic anhydride with chlorobenzene and *o*-chlorotoluene in the presence of a sensitizer (benzophenone) was studied with the aim to prepare chlorinated tricyclodecenetetracarboxylic dianhydrides. New halogenated polyimides were prepared by the reactions of these products with various diamides in *N*-methyl-2-pyrrolidone in the presence of catalysts.

The chemistry of halogenated macromolecular compounds is a specific field of the polymer chemistry. It attracts researchers' attention because these compounds exhibit specific, often unique properties; this makes them indispensable in the modern engineering, medicine, and other fields. A particular place among such compounds is occupied by polyimides (PIs).

By now, the most studied are aromatic PIs. At the same time, certain studies show that alicyclic polyimides are also promising thanks to a favorable combination of chemical, physicomechanical, dielectric, and other properties [1, 2]. Some recent papers are devoted to fluorinated PIs; data on chlorinated PIs are virtually lacking.

The Diels–Alder reaction occurring upon sensitized UV irradiation of solutions of maleic anhydride (MA) in aromatic hydrocarbons yielded the corresponding chlorinated dianhydrides:

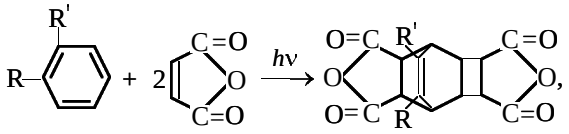

where R = H, Cl; R' = H, CH_3.

In this work we studied the specific features of preparation of chlorinated dianhydrides and PIs derived from them.

EXPERIMENTAL

The starting compounds and solvents were purified by standard procedures. The IR spectra were recorded on an IR-25 spectrometer; samples of the monomers were prepared as KBr pellets, and samples of the polymers, as 3–5-μm films. The ^{1}H NMR spectra were recorded on a Tesla BS-487B spectrometer in deuteroacetone (working frequency 80 MHz, internal reference hexamethyldisiloxane).

The reduced viscosities of 0.5% solutions of PI were measured in an Ubbelohde viscometer at 25°C in DMSO. Thermogravimetric analysis of the polymers was performed on a TGA SDTA Metler Toledo device at a heating rate of 8 deg min^{-1}. The temperatures of the onset of polymer degradation, $T_{o.d}$, were calculated from the TG curves.

The physicomechanical (tensile strength, relative elongation) and dielectric (dielectric loss tangent, dielectric permittivity) characteristics were studied under standard conditions [3, 4].

The dianhydrides were prepared by the Diels–Alder reaction upon irradiation of saturated solutions of MA in appropriate hydrocarbons in the presence of a sensitizer, benzophenone. 7-Chlorotricyclo[4.2.2.0^{2,5}]dec-7-ene-3,4,9,10-tetracarboxylic dianhydride [adduct of chlorobenzene (CB) and MA, ACB] was prepared in a temperature-controlled quartz glass reactor upon irradiation of a solution of MA (225.41 g, 2.30 mol) in 1000 ml of CB, containing 45.53 g (0.25 mol) of benzophenone, with a PRK-2M mercury quartz lamp (375 W) for 25 h. In the course of irradiation, a colorless crystalline precipitate formed, which was filtered off, recrystallized from acetic anhydride, washed with anhydrous diethyl ether, and dried in a vacuum at 80–90°C to constant weight; yield of ACB based on MA 74.2%.

7-Chloro-8-methyltricyclo[4.2.2.0$^{2.5}$]dec-7-ene-3,4,9,10-tetracarboxylic dianhydride [adduct of

o-chlorotoluene (CT) and MA, ACT] was prepared similarly, by irradiation of a solution of 186.01 g (2.00 mol) of MA in 1000 ml of CT, containing 36.42 g (0.20 mol) of benzophenone, for 30 h; yield of ACT based on MA 44.5%. Longer irradiation does not increase the yield of ACB and ACT.

Equivalent weight: ACB 154.43 (calculated 154.45), ACT 161.46 (calculated 161.47); mp: ACB 302–303, ACT 273–274°C.

Found, %: C 54.61; H 3.03; Cl 11.41.
$C_{14}H_9ClO_6$ (ACB).
Calculated, %: C 54.45; H 2.91; Cl 11.50.

Found, %: C 55.62, H 3.60, Cl 11.12.
$C_{15}H_{11}ClO_6$ (ACT).
Calculated, %: C 55.81; H 3.41; Cl 11.02.

IR spectra, ν, cm^{-1}: 1500 (benzene ring); 1775–1780, 1835–1840 (anhydride groups) [5]. ^1H NMR spectra, δ, ppm.: ACB 6.52 (1H), 2.82–3.61 (8H); ACT 1.97 (3H), 2.81–3.52 (8H).

The solvent, *N*-methyl-2-pyrrolidone (MP), was dried over 4 Å molecular sieves.

The polyimides were prepared in the presence of catalytic amounts of isonicotinic acid (INA) or triphenyl phosphate (TPP). Synthesis of PI derived from ACB and 4,4'-diaminodiphenyl ether (DADPE) was performed as follows. A three-necked flask equipped with a stirrer and a tube for feeding an inert gas was charged with 15.44 g (0.05 mol) of the dianhydride, 10.00 g (0.05 mol) of DADPE, and 1.52 g (5 wt % relative to the sum of the monomers) of INA, after which 76.3 ml of MP was added. The reaction flask was heated on an oil bath at 50°C for 15 min, after which the temperature was raised within 20 min to 160°C, and the mixture was heated at this temperature for 4.5 h. After cooling to room temperature, the PI was precipitated into acetone (chemically pure grade) and dried in a vacuum oven at 80–90°C to constant weight.

The elemental composition of the precipitated monomer corresponded to the theoretical calculation. The polyimide films were prepared by casting of solutions of the precipitated polyimides in MP (25 wt %) onto glass supports; to remove the solvent, the films were preliminarily dried in a vacuum oven at 80°C for 0.3 h and heated to constant weight at 150°C (1 h).

The polyimides derived from the other diamines in the presence of INA and TPP, and also the polyimides derived from ACT were prepared similarly; yield of the polymers 98.5–99.0%, degree of imidization about 100%.

Preparation of fluorinated alicyclic PIs from a an adduct formed by photochemical cycloaddition of MA to fluorobenzene was reported in [6]. Preparation of chlorinated dianhydrides of tricyclodecenetetracarboxylic acids has certain specific features. For example, synthesis of the photochemical adduct of CB and MA was attempted by other researchers [7], but they were not able to prepare ACB in a high yield; under the conditions used in [7], the yield of ACB did not exceed 5–7%, and the dianhydride derived from CT and MA was not obtained at all.

Photochemical synthesis of dianhydrides is two-step: First an unstable monoanhydride is formed (photochemical reaction), and then it is stabilized by addition of the second MA molecule (chemical step). In the initial period of the reaction (first 2.5–3 h), the rate constant in the temperature range 35–54°C is $(0.80–1.26) \times 10^{-5}$ s^{-1} for the CB + MA system and $(0.30–0.65) \times 10^{-5}$ s^{-1} for the CT + MA system. The activation energies are 53 and 79 kJ mol^{-1}, respectively. Such kinetic parameters are typical of reactions of MA with other aromatic hydrocarbons [2]. With CB, MA reacts at a higher rate; CT is less active, which may be due to the steric hindrance produced by the methyl group.

The conditions for preparing the adducts in the presence of two sensitizers, acetophenone and benzophenone, are listed in Table 1. As seen from Table 1, the yields of the process in the presence of benzophenone are 1.1–2.1 times higher, since the energy of the triplet state of this sensitizer (284 kJ mol^{-1}) is closer to the energy of the triplet level of the charge-transfer complex (CTC) between MA and aromatic hydrocarbons (280–284 kJ mol^{-1}). Furthermore, the spectrum of benzophenone covers the range of up to 420 nm, whereas acetophenone absorbs only up to 380 nm [8].

Examination of the influence of temperature on the reaction gave interesting results. As seen from Table 1, dianhydrides are formed virtually in the same, relatively narrow, temperature range. A decrease in the temperature to 30–35°C is accompanied by a decrease in the yield of the adducts; similar pattern is observed with increasing temperature to 60–65°C. A decreased yield of the dianhydrides at lower temperatures can be reasonably accounted for by the decreased solubility of the dienophile; in turn, too high temperatures may promote CTC decomposition, thus preventing the adduct formation. It should be noted

Table 1. Conditions for preparing chlorine-containing dianhydrides

Adduct	λ_{max}, nm	T, °C	c_{MA}, M	c_{sens}, M		Irradiation time, h	Adduct yield, %	
				acetophenone	benzophenone		acetophenone	benzophenone
ACB	280	45–50	2.30	0.30	0.25	25	64.2	74.2
ACT	284	50–55	2.00	0.30	0.20	30	20.6	44.5

that the CTC formed between the chosen addends is classed with so-called "contact" complexes, which are unstable and exist in solution virtually at the instant of contact of the donor and acceptor [9, 10]. If this time appears to be sufficient to receive the excitation energy from the sensitizer, formation of the monoadduct (and then bisadduct) becomes possible; if the CTC decomposes under the action of certain factors (increased temperature in our case), the yield of the final product decreases. We believe that these two factors are responsible for the narrow temperature range of the adduct formation.

Along with the direct influence on the CTC stability, the temperature exerts a still stronger influence on the second step of the process, stabilization of the monoadduct by addition of the second MA molecule. Heating causes the distances between the reacting species to increase, thus decreasing the probability and frequency of their contact. This fact is consistent with the previous data on the predominant influence of temperature on the second step of the process in photochemical synthesis of bisadducts of various structures [11].

A study of the reaction of MA with aromatic hydrocarbons showed that the MA conversion does not reach 100%. Along with the above factors, this is caused by side processes manifested in that the reaction mixtures turn yellow during prolonged irradiation (>35–40 h), and a tarry deposit (yellow to brown) is formed on the inner wall of the reactor. This product was identified as a low-molecular-weight product of photochemical polymerization of MA. Its yield is low (about 0.7–1 wt % relative to the final products), but it contaminates the dianhydrides, and their additional recrystallization from acetic anhydride becomes necessary.

Previously preparation of high-quality PIs from ACB and ACT was hampered by the lack of efficient synthesis procedures. However, in [6, 12] we showed that the polycondensation in polar aprotic amide solvents in the presence of catalytic amounts of INA allows preparation of PIs with high viscosity characteristics. In this paper, we consider the specific features of polymer preparation in the presence of INA and TPP. In the presence of TPP, acylation and cyclodehydration of the polyamido acids are accelerated, which may be due to the effect of the acidic ester formed by hydrolysis of the ester with water released in the cyclization [13]. The effect of the acidic ester is similar to that of the acid; the mechanism of polycondensation activation with carboxylic (in particular, pyridinecarboxylic) acids was discussed previously [13]. As solvent we chose MP in which PIs of the highest molecular weight are obtained (at 140–180°C) [12].

The optimal conditions of the synthesis of chlorinated PIs (CPIs) in the presence of INA and in the absence of a catalyst are listed in Table 2; the reduced viscosity of the PIs reaches 0.25–0.55 dl g^{-1}.

A study of the CPI formation showed that ACB is more active in polyacylation than ACT, due to higher electrophilicity of the anhydride groups. The CPIs prepared from ACB have higher viscosity characteristics. The reactivity of ACT decreases because of the presence of the alkyl group at the *endo*-ethylene bond.

In the presence of TPP, the polymers formed have a lower reduced viscosity (by 0.2–0.3 dl g^{-1}).

The compositions and structures of CPIs were proved by elemental analysis and IR spectroscopy. The IR spectra of CPIs contain absorption bands at about 1780 and 1720 (carbonyl groups of imide rings), 1360–1365 (–N<), 715–720 (imide ring), and 855 cm^{-1} (C–Cl). The absorption bands characteristic of the amido acid groups were lacking in the final polymers.

We have studied some properties of the new CPIs. We showed previously that the structural features of such halogenated PIs (presence of the fluorine atom) result in the lower glass transition point (T_g) compared to the nonfluorinated analog [6]. With the CPIs, the trend was similar (Table 3).

Relatively high reduced viscosities allowed us to cast films from the PI solutions and determine their main characteristics. The tensile strength of the CPI

Table 2. Optimal properties of CPI synthesis in the presence of INA*

Polymer no.	Dianhydride	Diamine	c_{mon}/c_{INA}, wt %/wt %	T, °C	τ, h	η_r, dl g^{-1}
1	ACB	DADPE	40/6.0	160	4.5	1.91
2	ACB	DADPM	40/6.0	160	4.5	1.78
3	ACB	*p*-PDA	40/5.0	155	4.5	1.61
4	ACB	*m*-PDA	40/5.0	145	4.0	1.45
5	ACB	*p*-XDA	35/3.0	120	2.5	1.11
6	ACB	HMDA	30/2.5	100	2.0	0.90
7	ACB	CDADPM	35/5.0	150	4.5	1.30
8	ACT	DADPE	40/6.0	150	5.0	1.25
9	ACT	DADPM	40/6.0	150	5.0	1.14
10	ACT	*p*-PDA	40/6.0	145	4.5	1.02
11	ACT	*m*-PDA	35/5.0	140	4.0	0.95
12	ACT	*p*-XDA	35/2.5	110	2.5	0.72
13	ACT	HMDA	30/2.0	90	2.0	0.68
14	ACT	CDADPM	40/5.0	140	5.0	1.01

* (DADPM) Diaminodiphenylmethane, (*p*-PDA) *p*-phenylenediamine, (*m*) *m*-phenylenediamine, (*p*-XDA) *p*-xylylenediamine, (HMDA) hexamethylenediamine, and (CDADPM) 3,3′-dichloro-4,4′-diaminodiphenylmethane.

films reaches 85–160 MPa depending on the diamine, and the relative elongation is 20–40%. The elastic modulus is within 2000–4100 MPa. We also determined some electrical characteristics: the dielectric loss tangent at 1 kHz and 25°C is 0.003–0.006, and the dielectric permittivity is 3.45–4.02.

It should also be noted that the samples prepared from the nonprecipitated polymers in the presence of TPP exhibit self-extinguishing properties. Furthermore, CPIs have lower oxygen index compared, e.g., to the fluorinated PI: The oxygen index of the PI derived from DADPE and the fluorinated dianhydride structurally related to ACB is 26; that of the PI derived from ACB, 0.30; and that of polymer no. 7, 0.40.

Table 3. Thermal characteristics of CPIs

Polymer no.	T_g, °C	$T_{o.d}$, °C	
		in air	under argon
1	310	375	420
2	307	370	410
3	318	370	405
4	325	365	400
5	285	330	375
6	265	311	340
7	320	360	390
8	305	365	395
9	300	360	390
10	311	365	395
11	320	350	390
12	276	317	345
13	255	290	323
14	312	355	380

CONCLUSIONS

(1) Chlorinated dianhydrides of tricyclodecenetetracarboxylic acids were prepared by UV irradiation of solutions of maleic anhydride in chlorobenzene and *o*-chlorotoluene in the presence of benzophenone as sensitizer.

(2) New chlorinated polyimides exhibiting fairly high viscosity, thermal, physicomechanical, and dielectric characteristics were prepared by single-step polycondensation of the chlorinated dianhydrides with various diamines in *N*-methyl-2-pyrrolidone in the presence of catalytic amounts of isonicotinic acid or triphenyl phosphate.

REFERENCES

1. Zhubanov, B.A., Arkhipova, I.A., and Almabekov, A.O., *Novye termostoikie geterotsiklicheskie polimery* (New Heat-Resistant Heterocyclic Polymers), Alma-Ata: Nauka, 1979.
2. Zhubanov, B.A., *Polym. Yearbook*, 1987, vol. 4, pp. 149–157.
3. Kalinina, L.S., Motorina, M.A., Nikitina, N.I., and Khachapuridze, N.A., *Analiz kondensatsionnykh polimerov* (Analysis of Condensation Polymers), Moscow: Khimiya, 1984.

4. Bradulina, L.G., Gavrilova, N.D., Vygodskii, Ya.S., and Matieva, A.M., *Vysokomol. Soedin., Ser. B*, 1999, vol. 41, no. 5, pp. 901–905.
5. Kazitsyna, L.A. and Kupletskaya, N.B., *Primenenie UF-, IK-, YaMR- i mass-spektroskopii v organicheskoi khimii* (Applications of UV, IR, NMR, and Mass Spectroscopy to Organic Chemistry), Moscow: Mosk. Gos. Univ., 1979.
6. Zhubanov, B.A., Kravtsova, V.D., and Bekmagambetova, K.H., *Polym. Sci.*, 2003, vol. 45/3-B, no. 4, pp. 75–81.
7. Shaikharzieva, V.Sh., Tal'vinskii, E.V., and Tolstikov, G.A., *Zh. Org. Khim.*, 1973, vol. 9, no. 7, pp. 1452–1458.
8. *Einführung in die Photochemie*, Berlin: Wissenschaften, 1976.
9. Eizenhal, K.B., *J. Chem. Phys.*, 1980, vol. 46, pp. 3268–3269.
10. Schmitz, L., Rehahn, M., and Bailaul, M., *Polymer*, 1993, vol. 34, pp. 646–649.
11. Logunova, V.I., Sokolov, L.B., and Savinov, V.M., *Vysokomol. Soedin., Ser. A*, 1976, vol. 18, no. 12, pp. 450–460.
12. Zhubanov, K.A., Abil'din, T.S., Bizhanova, N.B., *et al., Zh. Prikl. Khim.*, 2003, vol. 76, no. 8, pp. 1341–1345.
13. Zhubanov, B.A., Almabekov, O.A., Vorob'ev, V.D., *et al., Plast. Massy*, 1986, no. 3, pp. 40–42.

Russian Journal of Applied Chemistry, Vol. 77, No. 11, 2004, pp. 1840–1842. Translated from Zhurnal Prikladnoi Khimii, Vol. 77, No. 11, 2004, pp. 1858–1860.

ORGANIC SYNTHESIS AND INDUSTRIAL ORGANIC CHEMISTRY

Kinetics of Cleansing Action of Sodium Alkylbenzenesulfonate–Sodium Carbonate Binary Solutions

A. A. Kotomin, V. N. Naumov, and O. D. Yakimchuk

St. Petersburg State Technological Institute, St. Petersburg, Russia

Received May 24, 2004

Abstract—Kinetics of cleansing action of sodium alkylbenzenesulfonate–sodium carbonate binary solutions, as the most widely used components of synthetic detergents, is studied using the procedure based on direct determination of the weight fraction of pollutants removed from the fabric. The effective kinetic parameters of the cleansing process are determined.

Cleansing is one of the most important and complex colloidal chemical and physicochemical mechanical processes. It is of great scientific interest and practical significance [1–3].

Up-to-date synthetic detergents (SDs) represent complex multicomponent systems containing both surfactants with high detergent power and mineral and organic additives promoting cleansing action. Household detergents also contain additives imparting to them the desired consumer's performance characteristics such as solubility, friability, color, and odor [4–9].

Cleansing involves a series of successive stages providing removal of pollutants and their emulsification in the aqueous phase [3, 7–9]: (1) wetting of the surface and displacement of pollutants, (2) dispersion of pollutants, (3) stabilization of various pollutants in the aqueous phase, (4) protection of the solid surface, (5) solubilization, (6) chemical decomposition of pollutants, and (7) foaming.

Although the nature of these elementary events is clear at the qualitative level, there are no analytical relationships for their simulation. Presently, detergent compositions are mostly formulated empirically, which is due to the fact that the theory of cleansing is now developed only as a very general concept. Physicochemical mechanisms of each elementary stage of cleansing remain to be understood. All these do not permit prediction of properties of detergent compositions. Numerous attempts to develop a quantitative theory of cleansing action using the thermodynamic approach proclaiming, as a key point, energy gain on transferring pollutants from the surface to be cleaned to the cleansing solution, failed. Cleansing is a nonequilibrium process. Its activation energy can be determined from the temperature dependence of the rate constant. Despite the fact that kinetic study of cleansing action provides information only on the effective parameters of this complex process, such experimental data could fix the rate-determining stages.

Previously we demonstrated [10] that, similarly to other kinetically controlled processes, the temperature dependence of the cleansing effect is an exponential curve. This type of relationship is characteristic of temperature dependences of such parameters of various processes as the chemical potential, rate constant, solute concentration, viscosity, etc. The temperature dependence of the cleansing action can be written as

$$M = Ae^{-E_a/RT}. \quad (1)$$

where A is the preexponential factor, and E_a has a sense of the activation energy of cleansing action.

Therefore, the goal of this work is to determine the effective kinetic parameters of cleansing action: the activation energy and preexponential factor.

The cleansing effect is mostly determined by comparing the whiteness of the fabric samples before and after laundering. However, it is known that home pollutions can consist of both strongly and weakly tinted spots. In this case, it is difficult to unambiguously judge the degrees of pollution and cleansing only from the change in the whiteness. Therefore, in the kinetic study, it was necessary to employ a more objective method based on direct determination of the weight fraction of a pollutant washed away from the fabric surface. In this work, the cleansing effect was

1070-4272/04/7711-1840 © 2004 MAIK "Nauka/Interperiodica"

determined gravimetrically according to GOST (State Standard) 22 567.15–95, as applied to laboratory conditions. The quality of laundering was tested by comparison of the weight of the laundered cotton fabric sample (5×5 cm) with that of the initial and contaminated ones. The contaminant composition included highly dispersed lampblack, Syntanol DS-10, oleic acid, sunflower-seed oil, nujol, casein, and ammonia. Before laundering, the contaminated samples were matured at 110°C for 1 h.

A polluted sample was fixed on a gate agitator and laundered in a beaker in 500 ml of fresh cleansing solution at fixed temperature for 0.5–20 min. High rotation rate (200 rpm) provided uniform laundering of the entire sample surface. After completion of laundering, the sample was thoroughly rinsed and then dried and ironed. Three parallel experiments were performed with each fabric sample. Before the experiment, fresh fabric samples were pretreated by boiling in a chlorine-containing bleaching solution to remove the dressing coating.

The cleansing action was characterized by the relative weight of the pollutants removed from the fabric surface.

$$M = \Delta m / m_i, \quad (2)$$

where Δm and m_i are the weights of the removed and initial pollution, respectively.

In the kinetic experiments we used a binary solution containing 30 wt % sodium alkylbenzenesulfonate [$C_{10-14}(C_6H_4)SO_3Na$] and 70 wt % sodium carbonate (Na_2CO_3) as a rather simple model system. Now sodium alkylbenzenesulfonate is the surfactant most widely spread in detergent production. It is characterized by high cleansing power [11], good performance characteristics, and relatively low cost. Soda reduces the water hardness, preventing formation of water-insoluble complexes of sodium alkylbenzenesulfonate with alkaline-earth metals. It also establishes alkalinity of the cleansing solution and saponifies fatty pollutants, providing their solubilization. Furthermore, soda, being an electrolyte, promotes realization of the maximal surface activity of the surfactant, thus reducing its consumption.

Kinetic experiments were carried out at 25, 40, 60, and 85°C at a fixed concentration of 5 g l^{-1}. The experimental kinetic curves are given in Fig. 1.

From the experimental curves we estimated the effective kinetic parameters of cleansing: the activation energy E_a and preexponential factor A. The activation energy was determined by the standard procedure from the temperature dependence of the cleansing effect plotted in the coordinates $\ln M$–$1/T$ [12]. It follows from the table that the mean effective activation energy of cleansing is 5.2 ± 0.3 kJ mol^{-1}.

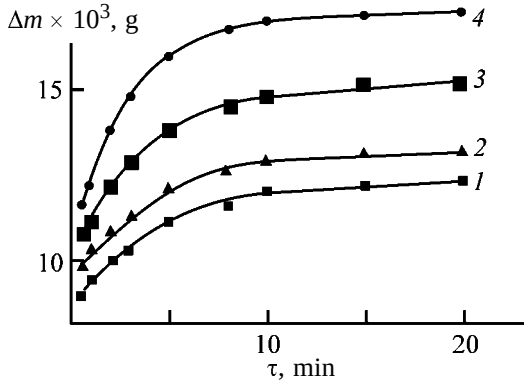

Fig. 1. Relative weight of pollutants removed Δm as a function of the time τ. Temperature (°C): (*1*) 25, (*2*) 40, (*3*) 60, and (*4*) 85.

As mentioned above, cleansing is a complex process involving a series of successive-parallel stages. Correspondingly, the activation energy is a function of all effective thermodynamic parameters controlling these stages. Determination of E_a allows fixation of the rate-determining stage of cleansing. We obtained E_a = 1–10 kJ mol^{-1}, which suggests that cleansing is a diffusion-controlled process. Previously [10], using the photometric method for determination of the whiteness of the fabric in the course of cleansing, we obtained the temperature dependence of the cleansing effect of sodium alkylbenzenesulfonate, its mixtures with sodium tripolyphosphate, and also of a complex composition based on sodium alkylbenzenesulfonate. This dependence is described by Eq. (3):

$$M^t_{max} = 8.65 M^{30}_{max} e^{-661.3/T}, \quad (3)$$

Estimated effective activation energy and preexponential factor at 298–358 K

τ, min	A	E_a, kJ mol^{-1}
0.5	2.35	4.87
1	2.75	5.15
2	2.82	5.03
3	3.03	5.37
5	3.36	5.21
8	3.49	5.14
10	3.65	5.15
15	3.71	5.20
20	3.68	5.19

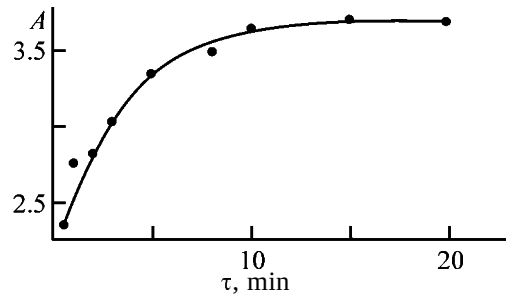

Fig. 2. Preexponential factor *A* as a function of the time of cleansing τ.

where M^{t}_{max} and M^{30}_{max} are the maximal cleansing effects of the substance at a fixed temperature and at 30°C, respectively, which practically correspond to its cleansing effect at a concentration above 50 g l^{-1}.

The activation energy of cleansing estimated by Eq. (3) for sodium alkylbenzenesulfonate and mixtures on its basis was found to be 5.8 kJ mol^{-1}. This value is consistent with that obtained in this work (5.2 ± 0.3 kJ mol^{-1}), also suggesting the significance of diffusion processes in cleansing.

Figure 2 shows the dependence of the preexponential factor *A* on the time of cleansing. As seen, *A* increases with time, but the growth decelerates starting from τ = 10 min, and the curve reaches saturation, suggesting that the process is unsteady in the initial stage (up to 10 min).

Nevolin [7] has demonstrated that, in all cases of laundering, mechanical activation is required to provide more uniform distribution of the cleansing solution and enhance wetting of the surface to be cleaned. The effect of agitation depends on the process time and natures of detergent and contaminated fabric. Generally, increasing agitation intensity accelerates removal of pollutants only in the first minutes of laundering, then having only slight effect. In parallel to desorption of pollutants, resorption occurs. Our results suggest that the preexponential factor *A* reflects the effect of mechanical activation. Furthermore, *A* can be affected by increasing viscosity of the cleansing solution as a result of formation of an emulsion and suspension of desorbed pollutants.

CONCLUSION

The estimated activation energy of cleansing (5.2 ± 0.3 kJ mol^{-1}) suggests that the process is diffusion-controlled. The value of the preexponential factor in Eq. (1) is a function of the intensity of mechanical activation and viscosity of the cleansing solution.

ACKNOWLEDGMENTS

The authors are grateful to N.P. Shirokova and M.B. Petel'skii for their help in the experimental work.

REFERENCES

1. Abramzon, A.A., *Zh. Prikl. Khim.*, 1993, vol. 66, no. 12, pp. 2794–2798.
2. Summ, B.D. and Goryunov, Yu.V., *Fiziko-khimicheskie osnovy smachivaniya i rastekaniya* (Physicochemical Principles of Wetting and Spread), Moscow: Khimiya, 1976.
3. Abramzon, A.A., *Chto nuzhno znat' o moyushchikh sredstvakh* (What One Should Know about Detergents), St. Petersburg: Khimiya, 1999.
4. *Poverkhnostno-aktivnye veshchestva i moyushchie sredstva: Spravochnik* (Surfactants and Detergents: A Handbook), Abramzon, A.A., Ed., Moscow: Giperoks, 1993.
5. Weuthen, M., *Parfum. Kosmet.*, 1990, vol. 71, no. 1, pp. 702–703.
6. Bulfori, M., *Riv. Ital. Sostanze Grasse*, 1995, vol. 72, no. 3, pp. 129–131.
7. Nevolin, F.V., *Khimiya i tekhnologiya sinteticheskikh moyshchikh sredstv* (Chemistry and Technology of Synthetic Detergents), Moscow: Pishch. Prom–st., 1971.
8. Bukhshtab, Z.I., Mel'nik, A.P., and Kovalev, V.M., *Tekhnologiya sinteticheskikh moyshchikh sredstv* (Technology of Synthetic Detergents), Moscow: Khimiya, 1988.
9. Kovalev, V.M. and Petrenko, D.S., *Tekhnologiya proizvodstva sinteticheskikh moyshchikh sredstv* (Processes for Production of Synthetic Detergents), Moscow: Khimiya, 1992.
10. Kotomin, A.A., Yakimchuk, O.D., Abramzon, A.A., *et al.*, *Zh. Prikl. Khim.*, 2002, vol. 75, no. 7, pp. 1151–1154.
11. Abramzon, A.A. and Kotomin, A.A., *Zh. Prikl. Khim.*, 2000, vol. 73, no. 11, pp. 1902–1904.
12. Krasnov, K.S., Vorob'ev, N.K., and Godnev, I.N., *Fizicheskaya khimiya* (Physical Chemistry), Moscow: Vysshaya Shkola, 2001, vol. 2.

Russian Journal of Applied Chemistry, Vol. 77, No. 11, 2004, pp. 1843–1846. Translated from Zhurnal Prikladnoi Khimii, Vol. 77, No. 11, 2004, pp. 1861–1864.

ORGANIC SYNTHESIS AND INDUSTRIAL ORGANIC CHEMISTRY

Colloid-Chemical Properties of 1,1-Dimethyl-1-Alkylhydrazinium Chlorides

M. G. Shcherban', A. V. Radushev, T. Yu. Nasretdinova, N. N. Teterina, and T. V. Bubyakina

Perm State University, Perm, Russia
Institute of Technical Chemistry, Ural Division, Russian Academy of Sciences, Perm, Russia
Galurgiya Joint-Stock Company, Perm, Russia

Received August 8, 2004; in the final form, March 2004

Abstract—The colloid-chemical properties [surface tension, surface activity, and critical micellization concentration (CMC)] of aqueous 1,1-dimethyl-1-alkyl(R)hydrazinium chlorides (R = $C_{10}H_{21}$–$C_{18}H_{37}$) were studied.

1,1-Dimethyl-1-alkylhydrazinium chlorides (DMAHCs) are quaternary hydrazinium salts. Owing to colloid-chemical features and low toxicity, these compounds are used in petroleum production [1] and also as flotation agents [2], detergents, antistatics, and biocides [3, 4]. 1,1-Dimethyl-1-alkylhydrazinium chlorides are efficient surfactants. In spite of wide practical application of DMAHC, published data on their colloid-chemical characteristics are scarce [1–3, 5]. In this work we attempted to obtain more complete set of colloid-chemical characteristics of DMAHCs belonging to a single homologous series.

EXPERIMENTAL

1,1-Dimethyl-1-alkylhydrazinium chlorides $[R(CH_3)_2NNH_2]Cl$, where R is C_nH_{2n+1}, n = 10, 12, 14, 16, 18, and mixture (12 + 14), were prepared by quaternization of 1,1-dimethylhydrazine with chloroalkanes [6]. The crude product was purified by 2–3-fold recrystallization from acetone. The content of the main substance in the final product determined by the technique reported in [7] was no less than 96%.

The surface tension at the aqueous dimethylalkylhydrazinium chloride–air interface was determined stalagmometrically [8]. The surface tension was calculated by the equation

$$\sigma = \sigma_0 \frac{m_x n_0}{m_0 n_x}, \qquad (1)$$

where σ_x and σ_0 are the surface tensions of aqueous DMAHC and water (mJ m^{-2}); m_x and m_0 are the weights (g) of aqueous DMAHC and water discharged from a certain volume of a stalagmometer; and n_x and n_0 are the numbers of drops of aqueous DMAHC and water discharged from the same stalagmometer volume.

In calculating the surface tension by Eq. (1), we used the reference value of the surface tension at the water–air interface [9]. The average values of aqueous DMAHC surface tension were calculated from the results of four replicate measurements; the relative determination error did not exceed 2%.

The critical micellization concentration (CMC) was determined by the point of rupture in the plot of the specific electrolytic conductivity of aqueous DMAHC vs. DMAHC concentration.

Figure 1 shows the surface tension isotherms of aqueous DMAHC (R = $C_{14}H_{29}$, curve *1*) and R = $C_{12}H_{25}$ + $C_{14}H_{29}$ (curve *2*). The surface tension isotherms of aqueous DMAHC with R = $C_{10}H_{21}$, $C_{12}H_{25}$, and $C_{16}H_{33}$ are similar to those presented in Fig. 1, except for the system with R = $C_{18}H_{37}$ (curve *2*).

As seen from Fig. 1, in the range of dilute DMAHC solutions, the surface tension sharply decreases with increasing surfactant concentration, and its further trend becomes relatively flat. The first portion of the isotherm reflects the saturation of the liquid–air interface with DMAHC molecules due to their sorption. Further addition of surfactant molecules is accompanied by their micellization in the bulk of the aqueous phase. This process is manifested as a flat

1070-4272/04/7711-1843 © 2004 MAIK "Nauka/Interperiodica"

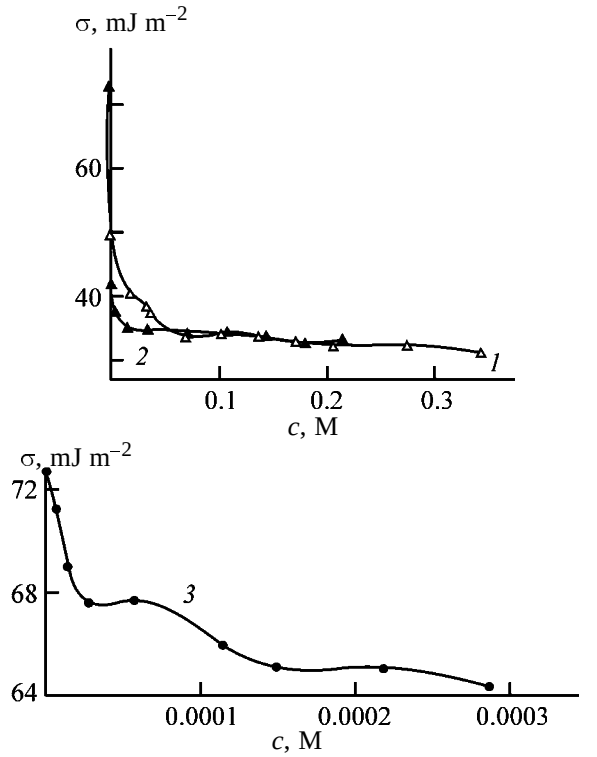

Fig. 1. Surface tension (σ) isotherms of aqueous DMAHC. (*c*) DMAHC concentration. Radical R: (*1*) $C_{14}H_{29}$, (*2*) $C_{12}H_{25}$ + $C_{14}H_{29}$ and (*3*) $C_{18}H_{37}$.

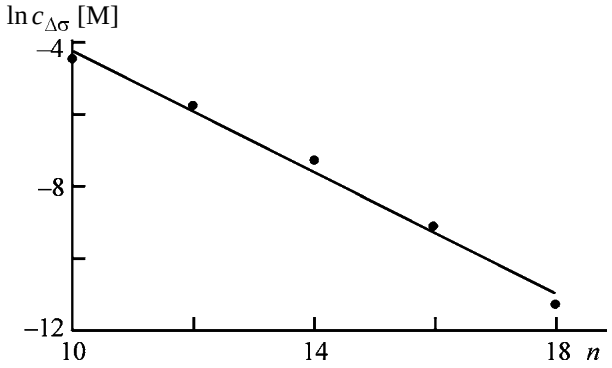

Fig. 2. DMAHC surface activity vs. the number of carbon atoms *n* in the radical R. (*c*) DMAHC concentration.

Table 1. Minimal surface tension of aqueous DMAHC at 20°C

Radical R	σ_{min}, mJ m^{-2}	c_{min} of DMAHC, M
$C_{10}H_{21}$	40	1×10^{-1}
$C_{12}H_{25}$	36	5×10^{-2}
$C_{14}H_{29}$	34	5×10^{-2}
C_{12}, C_{14}	34	2×10^{-2}
$C_{16}H_{33}$	34	2×10^{-3}
$C_{18}H_{37}$	66	1×10^{-4}

portion of the surface tension isotherm showing the insensitivity of the surface tension to micellization.

On further increasing the DMAHC concentration, the initial spherical micelles are apparently rearranged to nonspherical micelles influencing the state of the surface layer. This effect can be responsible for gradual decrease in the surface tension in the next portion of the isotherm.

Table 1 shows that, on adding DMAHC (R = $C_{10}H_{21}$, $C_{12}H_{25}$, $C_{14}H_{29}$, $C_{16}H_{33}$, and mixture R = $C_{12}H_{25}$ + $C_{14}H_{29}$] to water, the surface tension decreases to 35–40 mJ m^{-2}. This pronounced decrease in the surface tension shows that DMAHCs are active surfactants.

The surface tension isotherm of aqueous DMAHC (R = $C_{18}H_{37}$) (Fig. 1, curve *3*) has a small minimum at the surfactant concentration below CMC. We believe that this minimum is caused by the presence of impurity of a more active surfactant (presumably 1,1-dimethyl2-alkylhydrazine). It is known [8, 10] that the presence of even a trace of this foreign surfactant can significantly decrease the surface tension. After attainment of CMC, this impurity can be solubilized in the micelles. Therefore, σ slightly increases at DMAHC concentration exceeding CMC. Thus, the presence of a minimum in the surface tension isotherm of aqueous DMAHC suggests that the surfactant contains strongly surface-active impurities.

Each of the examined DMAHCs has two CMCs. The CMC_1 corresponds to formation of a monomolecular sorption layer filled with DMAHC molecules at the aqueous DMAHC–air interface. CMC_2 is manifested in the surface tension isotherms at DMAHC concentrations corresponding to formation of the nonspherical micelles. CMCs of aqueous DMAHC and the DMAHC concentrations corresponding to formation of the sorption layer at the aqueous DMAHC–air interface completely filled with DMAHC molecules are listed in Table 2. The published data show that the CMC values measured by various techniques differ [11]. For example, the CMC of aqueous DMAHC (R = $C_{12}H_{25}$ and $C_{16}H_{33}$) measured by the ring detachment technique is 9.4×10^{-3} M and 0.25×10^{-3} M, respectively. As seen from Table 2, these values considerably differ from the CMC values determined in this work stalagmometrically.

The surface activity of surfactants belonging to a single homologous series strongly increases with increasing number of carbon atoms in the hydrocarbon radical of the surfactant molecule [8]. Based on our

experimental data, we calculated the increment of the adsorption potential ΔW (contribution of the CH_2 group to the sorption work) for $\sigma_x = 68$ mJ m^{-2}. This value of the surface tension was chosen because it belongs to the linear portions of the surface tension isotherms of all the examined DMAHCs at $c_{DMAHC} \to 0$. The surface activity G can be calculated by the equation [8]

$$G = \lim_{c \to 0} (-d\sigma/dc) = RT\delta \exp[(W_0 + n\Delta W)/RT], \quad (2)$$

where δ is the adsorption layer thickness (m); W_0, work of adsorption of the polar groups of the surfactant molecule (J mol^{-1}); n, number of methylene groups; ΔW, contribution of one methylene group to the total work of sorption (J mol^{-1}); R, universal gas constant (J mol^{-1} K^{-1}); and T, temperature.

Equation (2) shows that, for the whole homologous series of surfactants, $\log c_{\Delta\sigma}$ is a linear function of n with the slope $\tan\alpha = \Delta W/RT$, where $c_{\Delta\sigma}$ is the surfactant concentration decreasing the surface tension by $\Delta\sigma$.

Figure 2 shows the plot of $\ln c_{\Delta\sigma}$ vs. n. The ΔW calculated from this plot is 2.1 kJ mol^{-1}, which is somewhat smaller than its theoretically calculated value (~2.7 kJ mol^{-1}) reported in [10]. We believe that this difference is caused by the fact that the surfactants used in our experiments (n = 10–18) have coarser molecules than the surfactant molecules used in the theoretical calculations (n = 3–6). The larger size of DMAHC molecules favors their sorption due to appearance of additional cohesion intermolecular interactions decreasing the sorption work.

In practice, surfactants are applied, as a rule, as their multicomponent mixtures. Owing to synergistic or antagonistic effects, the physicochemical characteristics of such mixtures can differ from the additive sum of characteristics of the individual surfactants. The multicomponent surfactants can exhibit higher micellization and solubilization power. Therefore, mixed surfactants often show enhanced performance. We studied as an example the surface tension of solution of commercial mixed DMAHC with $C_{12}H_{25}$ and $C_{14}H_{29}$ radicals. This multicomponent surfactant is used as flotation agent ChGS-1214 [2].

Figure 1 shows the surface tension isotherms of DMAHC (R = $C_{14}H_{29}$) and mixed commercial surfactant (R = $C_{12}H_{25}$ and $C_{14}H_{29}$). The comparison of these isotherms shows that the commercial surfactant has a high surface activity, which is governed by the contribution of the more active surfactant with R = $C_{14}H_{29}$. At a concentration of about 0.06 M, the surface tension isotherms of both the individual aqueous DMAHC and the commercial mixture become virtually indistinquishable. The commercial mixed surfactant decreases the water surface tension to 35 mJ m^{-2} at a concentration of 0.03 M, whereas with pure DMAHC (R = $C_{14}H_{29}$) this level of surface tension is reached at a concentration of about 0.06 M. The CMC of aqueous solution of mixed surfactant (R = $C_{12}H_{25}$ + $C_{14}H_{29}$) is lower than that of the individual DMAHCs, due to the higher micellization power of the mixed surfactant forming micelles of mixed kind.

Table 2. Critical micellization concentration of DMAHC and the aqueous DMAHC concentration corresponding to saturation of the sorption layer at the aqueous DMAHC–air interface with DMAHC molecules

Radical	CMC × 10^2, M		$c_1^{**} \times 10^2$, M
	CMC_1^*	CMC_2^*	
$C_{10}H_{21}$	7.0	27.0	9.0
$C_{12}H_{25}$	4.0	15.0	5.0
$C_{14}H_{29}$	4.5	14.0	5.0
C_{12}, C_{14}	2.7	6.1	3.0
$C_{16}H_{33}$	0.19	0.65	0.2
$C_{18}H_{37}$	4.2×10^{-3}	1.04×10^{-2}	3.5×10^{-3}

* Determined conductometrically.
** Determined from the surface tension isotherm.

CONCLUSIONS

(1) 1,1-Dimethyl-1-alkylhydrazinium chlorides are effective cationic surfactants. Their surface activity increases with increasing number of carbon atoms in the hydrocarbon radical. The increment of the adsorption potential is 2.1 kJ mol^{-1} per methylene group in the hydrocarbon radical.

(2) The critical micellization concentration of aqueous DMAHC corresponding to formation of the monomolecular adsorption layer at aqueous DMAHC–air interface was found. At DMAHC concentration exceeding CMC, the surface layer is rearranged due to formation of nonspherical micelles.

(3) With increasing number of carbon atoms in the DMAHC hydrocarbon radical, the micellization power of the surfactant increases.

(4) The surface activity of multicomponent commercial DMAHC (R = $C_{12}H_{25}$ + $C_{14}H_{29}$) exceeds that of the individual surfactants, which is mainly due

to the contribution of the more active surfactant, 1,1-dimethyl-1-tetradecylhydrazinium chloride.

REFERENCES

1. Tul'bovich, B.I., Kazakova, L.V., Radushev, A.V., *et al*., *Neft. Khoz*., 1995, no. 11, pp. 44–45.
2. RF Patent 2123893.
3. Lopyrev, V.A., Dolgushin, G.V., and Laskin, B.M., *Ross. Khim. Zh*., 2001, vol. 45, nos. 5–6, pp. 22–24.
4. Aleksandrova, G.A., Prokhorova, G.A., Lesnok, A.E., *et al*., *Khim.-Farm. Zh*., 1995, vol. 29, no. 11, pp. 22–24.
5. Kamayama, E. and Minegishi, Y., *J. Chem. Soc. Jpn., Ind. Chem. Soc*., 1968, vol. 71, no. 10, pp. 1671–1674.
6. RF Patent 2074174.
7. Siggia, S., and Hanna, J. G., *Quantitative Organic Analysis via Functional Groups*, New York: Wiley, 1979.
8. Shchukin, E.D., Amelina, E.A., and Pertsov, A.V., *Kolloidnaya khimiya* (Colloid Chemistry), Moscow: Mosk. Gos. Univ., 1982.
9. Ravdel', A.A. and Ponomareva, A.M., *Kratkii spravochnik fiziko-khimicheskikh velichin* (Concise Handbook of Physicochemical Quantities), Leningrad: Khimiya, 1983.
10. *Poverkhnostnye yavleniya i poverkhnostno-aktivnye veshchestva: Spravochnik* (Surface Phenomena and Surfactants: Handbook, Abramzon, A.A. and Shchukin, E.D., Eds., Leningrad: Khimiya, 1984, p. 7.
11. Aivazov, B.V., *Praktikum po khimii poverkhnostnykh yavlenii* (Laboratory Manual on Chemistry of Surface Phenomena), Moscow: Vysshaya Shkola, 1973.

Russian Journal of Applied Chemistry, Vol. 77, No. 11, 2004, pp. 1847–1853. Translated from Zhurnal Prikladnoi Khimii, Vol. 77, No. 11, 2004, pp. 1865–1871.

MACROMOLECULAR CHEMISTRY AND POLYMERIC MATERIALS

Synthesis of Perfluoroalkanes by High-Temperature Reaction of Graphite with Fluorine in a Fluidized Bed

D. S. Pashkevich, G. G. Shelopin, D. A. Mukhortov, V. B. Petrov, Yu. I. Alekseev, and V. S. Asovich

Prikladnaya Khimiya Russian Scientific Center, St. Petersburg, Russia

Received July 23, 2004

Abstract—Synthesis of lower perfluoroalkanes (tetrafluoromethane, hexafluoroethane, octafluoropropane, decafluorobutane) by high-temperature reaction of graphite with fluorine in a fluidized bed was studied.

Tetrafluoromethane, hexafluoroethane, octafluoropropane, and decafluorobutane are widely used in the modern industry as ozone-friendly refrigerants, propellants, dielectrics, and gas-phase fluorine carriers for semiconductor industry [1]. The annual world consumption of these substances reaches several thousand tons; therefore, development of efficient processes for their production is an urgent problem.

There exist several procedures for preparing these compounds. Tetrafluoromethane is prepared from the elements in the inverse wave of filtration combustion of graphite in fluorine, using a fixed graphite bed [2]. The feasibility parameters of this process are high.

Hexafluoroethane can be prepared by catalytic fluorination of fluorochloroethanes with HF [3]. The raw materials for these process destroy the ozone layer, and their production should be stopped. The process has also other drawbacks: large amount of hydrogen chloride waste and the necessity of regeneration and utilization of the environmentally hazardous chromium magnesium fluoride catalyst.

Octafluoropropane is produced by fluorination of hexafluoropropylene with cobalt trifluoride [4]. The production of hexafluoropropene also involves ozone-decomposing substances [1]. Furthermore, processes involving cobalt trifluoride as fluorinating agent have low productive capacity.

Decafluorobutane can be prepared by electrochemical fluorination of tributylamine in an HF solution [5]. However, the yield and productive capacity of the process are poor.

At the same time, it is known that all the above perfluorocarbons and solid carbon polyfluoride $(CF_x)_n$ are formed by high-temperature reaction of carbon with fluorine:

$$C(s) + F_2(g) \rightarrow (CF_x)_n(s) + CF_4(g) + C_2F_6(g) + C_3F_8(g) + C_4F_{10}(g) + ... \quad (1)$$

The boiling points of tetrafluoromethane, hexafluoroethane, octafluoropropane, and decafluorobutane are –128, –78, –37, and –2°C, respectively. In industrial implementation of reaction (1), separation of the products by distillation seems to involve no serious problems. Thus, commercial mastering of carbon fluorination will allow several different processes to be combined in a single process involving simple and cheap raw materials, with an efficient distillation system.

Published data on the composition of gaseous products of carbon fluorination are contradictory. However, most of the authors indicate that the major product is tetrafluoromethane. As an efficient process for tetrafluoromethane production has been commercially mastered [2], development of the process based on carbon fluorination is appropriate only if higher fluoroalkanes will be obtained in a yield comparable with that of CF_4.

Moissan was the first to perform the reaction of carbon with fluorine [6]; he found that amorphous carbon forms ignite in fluorine even at room temperature, whereas graphite and diamond are resistant to fluorine at normal temperature. Ruff reported in 1934 [7] that at 420°C graphite reacts with fluorine to form a solid compound, carbon polyfluoride $(C_xF_y)_n$. He also found that at 460–700°C the reaction occurs with explosion, and at temperatures above 700°C graphite burns in fluorine to form fluorocarbons, mainly tetra-

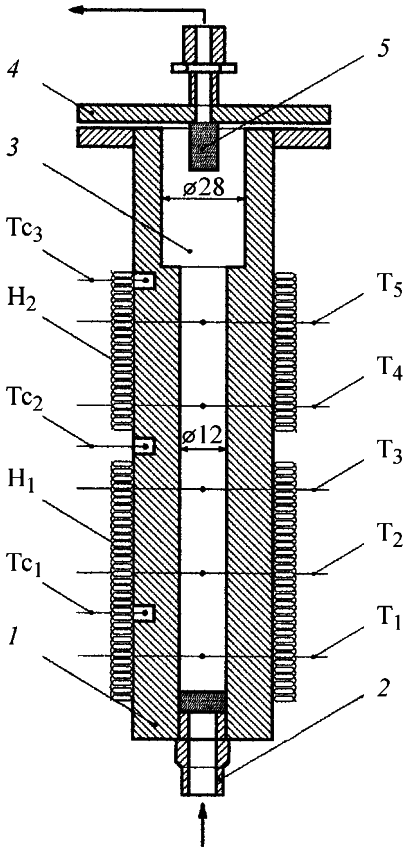

Fig. 1. Scheme of the reactor: (*1*) reactor body, (*2*) tube for feeding the fluorinating mixture, (*3*) chamber for separation of the gas and powder, (*4*) reactor lid, and (*5*) filter; (H_1, H_2) electric heaters, (T_1–T_5) thermocouples for the medium, and (Tc_1–Tc_2) thermocouples for the walls.

fluoromethane [8]. It was shown later [9] that the composition of carbon polyfluoride depends on the synthesis temperature and graphite particle size. Later, numerous papers concerning preparation of carbon polyfluoride were published; its composition, structure, properties, fluorination kinetics, and application fields were studied. Carbon polyfluoride found use as a solid lubricant and a cathodic material for lithium cells [10].

Thus, the majority of papers on fluorination of carbon were devoted to properties of carbon polyfluoride and procedures for its production; perfluoroalkanes were considered as by-products [11–13]. The available data are insufficient to determine the optimal conditions for preparing hexafluoroethane, octafluoropropane, and decafluorobutane from carbon and fluorine.

The goal of this study was to find conditions of carbon fluorination ensuring formation of a mixture of perfluoroalkanes containing tetrafluoromethane, hexafluoroethane, octafluoropropane, and decafluorobutane in commercially significant amounts.

The reaction of fluorine with carbon is strongly exothermic; in formation of CF_4, the thermal effect is 933 kJ mol^{-1}. The temperature of the reaction products in the adiabatic mode reaches several thousand degrees. Under these conditions, hexafluoroethane, octafluoropropane, and decafluoroethane decompose with the formation of other fluorocarbons, fluorine, and carbon.

To ensure the stability of the target products under the synthesis conditions, it is necessary to efficiently remove the released heat. This can be done by using dynamic (agitated) beds of powdered carbon.

Fluidization is one of the most advanced procedures for performing heterogeneous processes involving a solid phase. Systems fluidized with a gas flow are characterized by strong agitation inside the bed, provided by ascending gas "bubbles" [14]. Owing to the large surface area of solid particles, the heat exchange between them is very intense, and the difference between the temperatures of the fluidizing agent and solid particles is very small. To ensure stable fluidization, it is appropriate to use friable powders showing no tendency to sinter. Therefore, for laboratory tests we chose electrode graphite as a carbon material.

EXPERIMENTAL

For visual monitoring of the fluidization, experiments were performed in a model glass reactor. Stable fluidization without separation and removal of the particles is observed with the graphite fraction with the particle size less than 250 μm at a fluidizing gas velocity less than 15–20 cm s^{-1}. The contact time of the gas and powder varies from 0.5 to 3 s depending on the fixed bed height.

For fluorination experiments, we constructed a laboratory installation with a reactor containing a fluidized graphite bed. The reactor (Fig. 1) was a thick-walled pipe *1* from carbon steel of the following size: internal diameter 12 mm, external diameter 45 mm, and height 500 mm. The fluorinating mixture is fed through a porous insert *2* from pressed nickel powder, arranged in the bottom part of the pipe. In the top part, the pipe has an expansion *3* 28 mm in diameter for decreasing the gas velocity and separating the graphite particles. A filtering gauze is arranged at the reactor outlet.

To maintain the required temperature, two electric

Table 1. Composition of gaseous products of the reaction of fluorine with graphite in the steady-state isothermal mode as influenced by temperature. Contact time 3 s, fluorinating mixture 20% F_2 + 80% N_2

T, °C	CF_4	C_2F_6	C_2F_4	C_3F_8	C_3F_6	C_4F_{10}	$\Sigma S_{CF}/S_N$
	vol %						
410	49.9	16.8	–	18.2	–	15.1	0.018
425	50.8	18.1	–	18.8	–	12.3	0.019
450	44.7	20.2	–	20.4	–	14.7	0.024
460	53.8	15.9	–	15.9	–	14.4	0.019
465	57.7	15.5	–	16.4	–	10.4	0.026
490	62.4	17.1	–	15.1	–	5.4	0.017
495	63.8	17.1	0.2	13.0	–	6.0	0.074
520	64.0	17.3	0.1	13.8	–	4.8	0.075
540	64.1	17.7	–	14.7	0.5	3.0	0.080
560	63.6	15.2	–	13.6	1.5	6.2	0.084
585	58.2	21.2	–	13.6	1.2	5.8	0.081
590	59.1	19.2	–	13.5	1.5	6.7	0.084
610	62.9	20.8	–	11.2	1.5	3.6	0.088
635	66.2	22.0	–	8.3	1.5	2.0	0.084
670	70.2	19.8	–	7.0	1.6	1.4	0.090
720	75.9	14.2	–	7.3	1.1	1.5	0.092

heaters H_1 and H_2 are mounted on the reactor surface. The wall temperature is monitored with Chromel–Alumel thermocouples Tc_1 and Tc_2. The thermocouples in two-channel ceramic straws are arranged in wells 8 mm deep and 3 mm in diameter, so as to ensure reliable thermal contact between the thermocouple junction and well bottom.

The temperature of the reaction medium in the reactor volume is measured with Chromel–Alumel thermocouples T_1–T_5. The distance from the T_1 junction to the gas-feeding surface is 15 mm, and the distance between the junctions of the thermocouples, 115 mm.

As a fluidizing gas we used a mixture of fluorine and nitrogen, and as a carbon material, electrode graphite with the particle size less than 250 μm.

The expansion of the graphite powder bed was monitored with thermocouples T_1–T_5. If the bed expanded to occupy the whole channel height, the temperature became virtually equal throughout the reacting bed.

The experiment time was 25–30 min. In this time, the temperature of the reactor wall increased by no more than 15°C. Thus, fluorination of graphite was performed under approximately isothermal conditions.

Chromatographic analysis of the gaseous reaction products showed that the composition of the products changed during the first 5 min of the reaction. In the subsequent period, at constant feed rate and temperature, the composition of the gaseous products was stable and could be averaged.

The averaged (over the samples taken) composition of the gaseous products of the reaction of fluorine with graphite in the steady-state isothermal mode is given in Table 1 for various temperatures. At each temperature, we took three to five samples. When calculating the sample composition, we assumed the chromatographic correction coefficients to be unity for all the substances.

In Table 1 we also give the parameters $\Sigma S_{CF}/S_N$ characterizing the content of gaseous fluorocarbons in the gas flow. The parameter $\Sigma S_{CF}/S_N$ is the ratio of the total area of the fluorocarbon chromatographic peaks to the nitrogen peak area. The fluorine breakthrough was detected only at 410°C.

The dependence of the parameter $\Sigma S_{CF}/S_N$ on the fluorination temperature (contact time 3 s) is shown in Fig. 2.

Using the parameter $\Sigma S_{CF}/S_N$, we can qualitatively estimate the amount of fluorine consumed for formation of gaseous perfluorocarbons and solid carbon polyfluoride. This allows comparison of the rates of the synthesis and thermal decomposition of carbon polyfluoride and estimation of the accumulation of carbon polyfluoride in the reactor.

The molar ratio of fluorine and carbon in the gase-

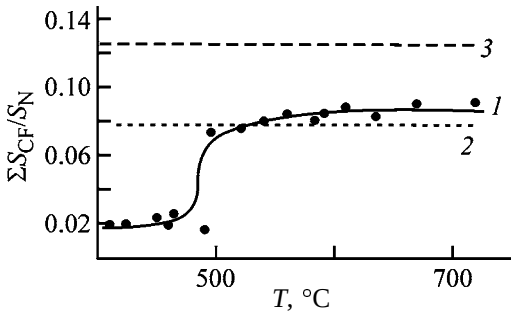

Fig. 2. Parameter $\Sigma S_{CF}/S_N$ as a function of temperature *T* at a gas–powder contact time of 3 s: (*1*) experimental dependence, (*2*) theoretical value corresponding to formation of $CF_{3.2}$ (which corresponds to the average composition of products obtained at 580–600°C), and (*3*) theoretical value corresponding to formation of CF_4.

ous reaction products at 550–600°C was 1 : 3.2 (Table 1).

Thus, the volume of gaseous fluorocarbons is by a factor of 3.2 smaller than the volume of fluorine consumed for their formation. The feed contained 20% fluorine, and the ratio of the volume of the gaseous reaction products to the volume of nitrogen, $\Sigma S_{CF}/S_N$, at a temperature close to 580°C should be

$$\frac{\Sigma S_{CF}}{S_N} = \frac{20/3.2}{80} = 0.078.$$

At 400–450°C, the theoretical value of $\Sigma S_{CF}/S_N$ is 0.083.

If the only fluorination product were tetrafluoromethane, the $\Sigma S_{CF}/S_N$ ratio would be the following:

$$\frac{\Sigma S_{CF}}{S_N} = \frac{20/2}{80} = 0.125.$$

At 400–450°C, the experimental value of $\Sigma S_{CF}/S_N$ is lower than the theoretical value by a factor of 4. This means that the fluorine fed into the reactor does not fully leave the reactor in the form of gaseous compounds. Hence, at this temperature the rate of formation of carbon polyfluoride is higher than the rate of its decomposition, and carbon polyfluoride accumulates in the reactor.

Table 2. Composition of gaseous products of the reaction of fluorine with graphite as influenced by temperature. Contact time 0.6 and 0.8 s

T, °C	CF_4	C_2F_6	C_2F_4	C_3F_8	C_3F_6	C_4F_{10}
	vol %					
565	59.2	20.9	1.6	11.8	1.3	5.2
590	62.3	17.9	–	13.3	1.0	5.4

At temperatures above 550°C, the experimental $\Sigma S_{CF}/S_N$ value agrees with the theoretical value; hence, the fluorine fed into the reactor fully leaves the reactor in the form of gaseous products. A slight increase in $\Sigma S_{CF}/S_N$ at temperatures exceeding 550°C is associated with an increase in the CF_4 content in the reaction products.

Thus, the gaseous products of graphite fluorination in a fluidized bed under the optimal conditions (550–600°C), when the CF_4 content is minimal and carbon polyfluoride does not accumulate, have the following composition (wt %): 40–45 CF_4, 20–25 C_2F_6, 20–25 C_3F_8, and 10–15 C_4F_{10}.

To estimate the minimal time of complete conversion of fluorine in a fluidized bed, we performed experiments with shorter contact times of the gas and powder: 0.6 and 0.8 s. The results are given in Table 2. No breakthrough of fluorine was observed. The composition of the gaseous products did not noticeably differ from that obtained at a contact time of 3 s.

Table 1 and Fig. 2 suggest that formation of gaseous perfluorocarbons involves intermediate formation of carbon polyfluoride, followed by its decomposition. To check this assumption, we performed experiments on synthesis and thermal decomposition of carbon polyfluoride. Carbon polyfluoride was prepared at 400–500°C in a fluidized bed for 35–40 min. The composition of carbon polyfluoride after the fluorination corresponded to the formula $(CF_{0.30–0.35})_n$.

Then we stopped the supply of gaseous fluorine and performed the decomposition at a higher temperature in a nitrogen flow ensuring fluidization and isothermal conditions. The decomposition of carbon polyfluoride was performed for approximately 10–100 min.

The composition of the gaseous products of thermal decomposition of carbon polyfluoride is given in Table 3.

These data confirm the assumption that perfluorocarbons containing more than one carbon atom are formed by synthesis and decomposition of carbon polyfluoride.

Tables 3 and 1 show that, as *x* in $(CF_x)_n$ decreases, the yield of tetrafluoromethane in decomposition of $(CF_x)_n$ increases. Also, the yield of tetrafluoromethane

Table 3. Composition of gaseous products of thermal decomposition of carbon polyfluoride in a fluidized bed as influenced by the reaction temperature and time. Nitrogen flow rate 6 $cm^3\ s^{-1}$

Run no.	τ, min	*T*, °C	CF_4	C_2F_6	C_3F_8	C_3F_6	C_4F_{10}	$\Sigma S_{CF}/S_N$
			vol %					
1	11	555	68.3	19.3	6.6	3.2	2.6	–
	19	590	70.2	20.8	5.6	2.0	1.4	–
	22	600	77.7	14.4	5.1	2.8	–	–
	25	620	81.6	14.9	3.5	–	–	–
	29	635	86.5	13.5	0.0	–	–	–
2	14	560	73.1	14.8	8.4	1.7	2.1	–
	19	600	74.0	17.2	5.5	2.2	1.1	–
	22	620	81.0	14.2	4.9	–	–	–
3	9	465	75.4	11.7	12.9	–	–	0.016
	23	465	77.8	11.7	10.5	–	–	0.016
	35	465	76.8	10.5	9.1	3.6	–	0.017
	51	465	75.9	10.6	6.9	4.4	2.2	0.015
	61	465	78.0	11.4	6.4	4.2	–	0.015
	80	530	74.0	15.0	7.1	2.3	1.6	0.205
	92	570	75.5	15.8	6.0	2.7	–	0.036
	102	580	86.7	7.9	3.7	1.7	–	0.013
4	13.5	478	62.7	16.9	14.4	–	6.0	0.016
	16.5	504	69.2	12.8	13.4	1.5	3.1	0.105
	23.5	540	73.1	15.3	7.1	2.3	2.1	0.133
	35.5	546	75.0	15.1	6.0	3.2	0.7	0.033
	54.5	562	82.1	9.9	2.7	2.5	2.8	0.010
	69.5	566	88.5	8.1	3.3	0.1	–	0.004
	77.5	568	82.0	12.3	3.9	1.5	0.3	0.004
5	12	530	73.5	13.4	8.8	2.0	2.3	0.051
	21	590	71.9	17.8	6.2	2.3	1.8	0.141
	27	620	82.9	10.8	2.7	3.6	–	0.018
	31	630	85.4	11.7	2.9	–	–	0.020

is higher in decomposition of $(CF_x)_n$ prepared in advance (Table 3) than in synthesis–decomposition of $(CF_x)_n$ at the same temperature (Table 1). These facts suggest the following.

When a graphite particle reacts with fluorine, a film of carbon polyfluoride with high x is formed on the particle surface, whereas the internal region of the particle remains unchanged. The lowest yield of tetrafluoromethane was observed in thermal decomposition of the film with a high x. If the film does not decompose rapidly and the particle occurs for a long time at approximately 500°C, the fluorine inside the particle is redistributed, i.e., the two-layer distribution pattern with $x \to 1$ at the surface and $x \to 0$ inside the particle changed for a uniform distribution of fluorine with a constant x throughout the particle volume. In thermal decomposition of such a sample of carbon polyfluoride ($x \ll 1$), the yield of CF_4 is high.

Thus, to decrease the yield of CF_4, it is appropriate to perform the thermal decomposition of the synthesized carbon polyfluoride as quickly as possible, so as to avoid equalization of x throughout the particle volume.

We performed experiments on fluorination of graphite in a fluidized bed using a fluorinating mixture with an increased fluorine concentration. The results are listed in Table 4. The temperature measurements showed that the fluorination occurred in the isothermal mode; no fluorine breakthrough occurred.

Comparison of Tables 1 and 4 shows that, as the fluorine concentration in the fluorinating mixture is

Table 4. Composition of gaseous products of reaction of fluorine with graphite in the steady-state mode as influenced by temperature. Contact time 3 s, fluorinating mixture composition 40% F_2 + 60% N_2

T, °C	CF_4	C_2F_6	C_2F_4	C_3F_8	C_3F_6	C_4F_{10}
	vol %					
580	75.43	13.9	0.02	7.37	0.57	2.49
590	75.65	14.18	0.06	6.72	0.4	2.99

increased, the product composition changes: the amount of CF_4 increases, and that of the other fluorocarbons decreases.

This experimental fact can be explained as follows. Two reaction zones can be distinguished in the reaction unit: the zone of the fluorine uptake in which solid carbon polyfluoride is formed and the zone of the carbon polyfluoride decomposition yielding gaseous perfluorocarbons. In a reactor with a circulating fluidized bed, the zone of decomposition of carbon polyfluoride occupies the whole reactor volume, whereas the zone of formation of carbon polyfluoride occupies only its part. These zones overlap (Fig. 3), and thermal decomposition of carbon polyfluoride occurs in a medium containing gaseous fluorine.

As the fluorine concentration in the fluorinating mixture is increased, the height of the zone of the fluorine uptake increases. Apparently, under the experimental conditions the gaseous fluorocarbons react with fluorine to give lower-molecular-weight perfluoro compounds. Therefore, at increased fluorine content in the fluorinating mixture, the yield of CF_4 is higher.

Thus, to increase the yield of perfluorocarbons containing more than one carbon atom, it is appropriate to perform the decomposition of the synthesized polyfluoride in the absence of fluorine in the decomposition zone.

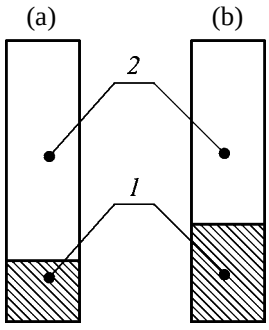

Fig. 3. Scheme of the distribution of the reaction zones in the reactor channel: (*1*) zone of fluorine uptake and (*2*) zone of decomposition of carbon polyfluoride. Fluorine concentration, %: (a) 20 and (b) 40.

CONCLUSIONS

(1) The major gaseous products of graphite fluorination are CF_4, C_2F_6, C_3F_8, and C_4F_{10}; the amounts of C_2F_4 and C_3F_6 do not exceed 2.0 wt %.

(2) At 550–600°C, the composition of the reaction products is as follows (wt %): 40–45 CF_4, 20–25 C_2F_6, 20–25 C_3F_8, and 10–15 C_4F_{10}.

(3) Synthesis of CF_4, C_2F_6, C_3F_8, and C_4F_{10} involves intermediate formation of $(CF_x)_n$ followed by its thermal decomposition.

(4) At temperatures above 550°C, solid carbon polyfluoride does not accumulate in the laboratory reactor.

(5) To increase the yield of perfluorocarbons containing more than one carbon atom, it is appropriate to perform the decomposition of $(CF_x)_n$ with $x \to 1$ under the isothermal conditions in the absence of fluorine.

REFERENCES

1. Maksimov, B.N., Barabanov, V.G., Serushkin, I.L., *et al., Promyshlennye ftororganicheskie produkty: Spravochnoe izdanie* (Commercial Organofluorine Products: Handbook), St. Petersburg: Khimiya, 1996.
2. RF Patent 2117652.
3. Trukshin, I.G., Vishnyakov, V.M., and Fedorova, S.G., *Abstracts of Papers, 2-ya Mezhdunarodnaya konferentsiya "Khimiya, tekhnologiya i primenenie ftorsoedinenii v promyshlennosti"* (2nd Int. Conf. "Chemistry, Technology, and Industrial Applications of Fluorine Compounds"), St. Petersburg (Russia), September 23–26, 1997, p. 35.
4. Asovich, V.S., Kornilov, V.V., Kostyaev, R.A., *et al.*, Abstracts of Papers, *1-ya Mezhdunarodnaya konferentsiya "Khimiya, tekhnologiya i primenenie ftorsoedinenii v promyshlennosti"* (1st Int. Conf. "Chemistry, Technology, and Industrial Applications of Fluorine Compounds"), St. Petersburg (Russia), May 30–June 3, 1994, p. 15.
5. Kaurova, G.I., Nikiforov, B.L., Nekrashevich, A.Yu., *et al.*, Abstracts of Papers, *3-ya Mezhdunarodnaya konferentsiya "Khimiya, tekhnologiya i primenenie ftorsoedinenii v promyshlennosti"* (3rd Int. Conf. "Chemistry, Technology, and Industrial Applications of Fluorine Compounds"), St. Petersburg (Russia), June 6–9, 2001, p. 155.

6. Moissan, H., *C. R. Acad. Sci. Paris*, 1890, vol. 110, p. 276.
7. Ruff, O. and Bretshneider, O., *Z. Anorg. Allg. Chem.*, 1934, vol. 217, pp. 1–18.
8. Ruff, O., *Trans. Faraday Soc.*, 1938, vol. 34, pp. 1022–1033.
9. Rudorff, O. and Rudorff, G., *Z. Anorg. Allg. Chem.*, 1947, vol. 253, p. 281.
10. Ishikawa, T. and Shimada, T., Abstracts of Papers, *5th Int. Symp. on Fluorine Chemistry*, Moscow, 1969, p. 68.
11. Kita, Y., Watanabe, N., and Fujii, Y., *J. Am. Chem. Soc.*, 1979, vol. 101, no. 14, pp. 3832–3841.
12. Simons, J.H. and Block, L.P., *J. Am. Chem. Soc.*, 1939, vol. 61, pp. 2962–2966.
13. Watanabe, N., Koyama, S., and Kawamura, T., *Bull. Chem. Soc. Jpn.*, 1980, vol. 53, pp. 3100–3103.
14. Gorbis, Z.R., *Teploobmen i gidromekhanika skvoznykh dispersnykh potokov* (Heat Exchange and Hydromechanics of Through Disperse Flows), Moscow: Energiya, 1970.

Russian Journal of Applied Chemistry, Vol. 77, No. 11, 2004, pp. 1854–1858. Translated from Zhurnal Prikladnoi Khimii, Vol. 77, No. 11, 2004, pp. 1872–1876.

MACROMOLECULAR CHEMISTRY AND POLYMERIC MATERIALS

Surface Structure and Thermal Oxidative Degradation of the Reaction Products of Polyethylene with PCl_3 and $VOCl_3$ Vapors

S. A. Trifonov, E. A. Sosnov, and A. A. Malygin

St. Petersburg State Technological Institute, St. Petersburg, Russia

Received September 24, 2004

Abstract—Reaction products of phosphorus(III) chloride and vanadium(V) oxychloride with low-density polyethylene were studied by chemical analysis and physicochemical (IR spectroscopy and atomic-force microscopy) methods. Thermaloxidative transformations of the initial and modified samples were studied by differential thermal analysis.

Modification of polymeric materials significantly expands their application field. The structure and properties of polymers can be modified in the desired direction either during synthesis or by introduction of fragments of different chemical nature into the macromolecules of final products. Since recently, special attention in development of polymeric materials with desired properties has been paid to modification of the polymer surface, because specifically the surface layer structure governs to a significant extent the behavior of polymers under exploitation [1]. Certain promise of enhancing the stability of polymers is offered by various methods of surface treatment, blocking the centers responsible for degradation of the material [2]. Among such methods is chemical gas-phase modification, in particular, molecular layer deposition (MLD) involving selective chemical reactions on the solid-phase matrix, which allow atom-by-atom assembly of fragments with the desired composition and structure [3].

Polyolefins, e.g., polyethylene, find wide commercial application due to their valuable properties such as good dielectric characteristics, chemical stability, frost resistance, strength, low specific weight, etc. The chemical activity of polyolefins is not very high. Among reactions by which various functional groups can be introduced into their macromolecules, halogenation, sulfochlorination, and phosphonation were studied in the most detail [4]. Modern physicochemical methods, e.g., atomic-force microscopy (AFM), allow not only examination of the surface layer structure [5] but also elucidation of the reactivity of the polymer with respect to low-molecular-weight compounds, as well as evaluation of the effect of modifying additives on the macroscopic, e.g., thermal oxidative, properties of the resulting products [6–8].

EXPERIMENTAL

In this work we studied chemical transformations of low-density polyethylene (LDPE) in reactions with phosphorus(III) chloride and vanadium(V) oxychloride vapors and elucidated how the thermal stability of the polymeric material is influenced by the inorganic structures synthesized. The choice of these specific modifiers was governed by the fact that phosphorus and vanadium compounds in various combinations are used for controlling the thermal oxidative properties of polymeric materials. Also, it was of interest to study the structure of the surface layer of polyethylene before and after its reactions with agents having different redox characteristics and to elucidate the interrelation between the chemical nature of the additives and the surface morphology, on the one hand, and the thermal oxidative characteristics of the products, on the other.

The element oxide groups were introduced in a flow-through reactor charged with the samples (40×20 mm films or specimens crushed to the particle size of ~4 mm). Gas-phase modification of the polymer was effected by phosphorus(III) chloride and vanadium(V) oxychloride vapors at 50°C in a stream of the carrier gas (air) dried to the dew point of –50 to –55°C. The degree of the chemical reaction between the low-molecular-weight modifiers and reactive groups of the polymeric material was estimated from

1070-4272/04/7711-1854 © 2004 MAIK "Nauka/Interperiodica"

the maximal concentration of the element in the modified samples. After modification, the polyethylene samples were treated with a stream of dried carrier gas until the initial chlorides and gaseous products formed were exhaustively removed from the reaction chamber. The chlorine-containing groups were replaced by hydroxyls via vapor-phase hydrolysis of the polymer matrix. The concentration of the nanoadditives in the material was determined on a PS-100 ICP spectrometer equipped with a computer accessory, upon preliminary degradation of the polymer in a solution of concentrated sulfuric and nitric acids in the microwave heating field (a Microdigest-301 instrument).

The IR spectra of the modified samples were recorded on an FSM-1201 Fourier IR spectrometer at 400–4000 cm^{-1}. The IR data and the results of chemical analysis furnished information about the composition and structure of grafted element-containing groups. The resistance of the initial and modified films to thermal oxidation was studied by differential thermal analysis (DTA) on an MOM (Hungary) instrument at 20–600°C at a heating rate of 5 deg min^{-1} in air. The AFM studies of the films were carried out on a Solver P47 Pro scanning probe microscope in the tapping mode, using a gold-plated silicon cantilever in two scanning modes: (1) topographic, to elucidate the surface morphology from the change in the frequency of the cantilever vibrations and (2) adhesive, to reveal the difference in the compositions of the sample surface segments from the changes in the slope of the cantilever to the surface under study, caused by adhesion interaction.

Chemical analysis[1] showed that, under the actual conditions, the total concentration of the elements in the samples attains a constant value within 15–20 min. The maximal content of phosphorus and vanadium in the polymer was estimated at 0.11 and 0.19 mmol g^{-1}, respectively.

Figure 1 shows the differential IR spectra of the films of the initial and modified polyethylene. The IR spectra of the polymer samples containing element oxide groups in the surface layer exhibit absorption bands near 1000 cm^{-1} due to stretching vibrations of the E–O bond in the E–O–Alk groups. Also, there are absorption bands with maxima at 1650 (stretching vibrations of the C=C bond upon introducing a new substituent) and 1455 cm^{-1} (bending vibrations of the C–H bond in substituted polyethylenes) [9], evidently,

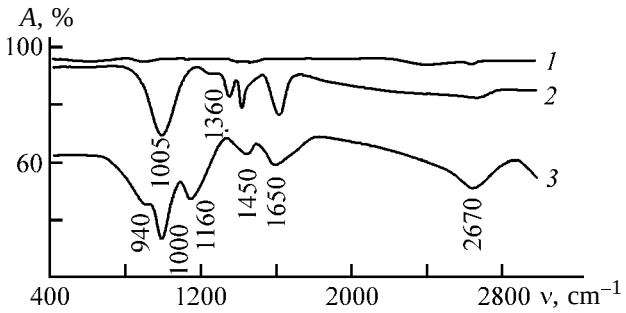

Fig. 1. Differential IR spectra of polyethylene. (*A*) Transmission and (*ν*) wave number. Sample: (*1*) initial, (*2*) vanadium-containing, and (*3*) phosphorus-containing; the same for Fig. 3.

due to the changes in the polymer matrix proper, caused by chemical modification (Fig, 1, curves *2*, *3*). Also, the spectra of phosphorus-containing polyethylene exhibit an absorption band near 1160 cm^{-1}, characteristic of phosphorus compounds (bending vibrations of the P=O bond). Vapor-phase hydrolysis of the modified films is responsible for appearance of the absorption bands due to vibrations of the OH groups at 2670 (stretching vibrations) and 940 cm^{-1} (out-of-plane bending vibrations) (Fig. 1, curve *3*).

The IR data evidence chemical grafting of the element oxide groups at the reactive centers of the polymer matrix. Our experimental results, together with published data, suggest that, for all the modified samples, element oxide groups are introduced via exchange reactions which can be represented as

$$[-CH_2-CH_2-CH_2-CH_2-]_n + ECl_m \longrightarrow [-CH_2-\underset{\displaystyle ECl_{n-m}}{\underset{|}{CH}}-CH_2-CH_2-]_n + (n-m)HCl, \quad (1)$$

$$[-\underset{|}{\overset{|}{C}}=\underset{|}{\overset{|}{C}}-]_n + ECl_m \longrightarrow [-\underset{\displaystyle Cl\ ECl_{m-1}}{\underset{|}{\overset{|}{C}}}-\underset{|}{\overset{|}{C}}-]_n. \quad (2)$$

Also, treatment of LDPE with a vapor of $VOCl_3$ (a modifier with a prominent oxidative power) causes partial oxidation of the reactive centers of the polymer, as evidenced by the presence in the IR spectra of an absorption band near 1360 cm^{-1} (symmetric stretching vibrations in the $CO-CH_3$ group) (Fig. 1, curve *2*).

When the modifying agents react with the polymer matrix by different mechanisms, they will, evidently, differently affect the structure of the surface layer of

[1] Chemical analysis was carried out at TsKP "Chemical Assembling of Nanomaterials", St. Petersburg State Technological Institute (TU).

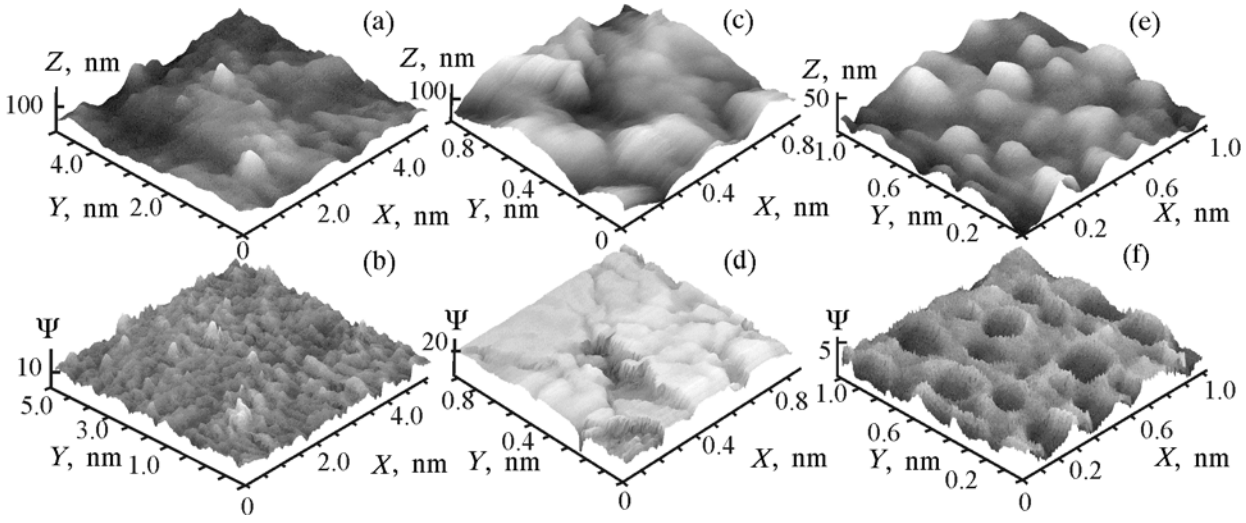

Fig. 2. AFM reconstruction of the surface of (a, b) initial and (c, d) vanadium- and (e, f) phosphorus-containing polyethylene. (a, c, e) Surface topography and (b, d, f) adhesion interaction pattern. (*X*, *Y*, *Z*) Axis coordinates and (Ψ) cantilever slope.

polyethylene as well. Redox reactions in synthesis of the vanadium oxide groups should, apparently, more profoundly transform the surface. Indeed, the AFM studies show that the initial film (Fig. 2a) is covered with projecting mutually fused crystallites; there are no profound relief defects and foreign inclusions affecting the adhesion interaction of polyethylene with the AFM probe (Fig. 2b). The surface roughness was estimated at 16–20 nm. Figure 2c suggests that, upon treatment with vanadium oxychloride, the surface exhibits clear intercrystallite boundaries; individual globules of modified polyethylene with a size of 200–250 nm are distinguishable. Also, up to 200 nm, deep caverns are observed, inside which the chemical composition sharply differs from that of the initial material, as suggested by a jumpwise variation of the slope of the cantilever to the surface at the cavern boundaries (Fig. 2d). These deep transformations of the structure of the surface layer are, evidently, due to the redox reactions with $VOCl_3$ vapor at the boundary separating the amorphous and crystalline areas in the initial matrix.

Chemical modification of the LDPE film with the PCl_3 vapor (Fig. 2e) yields on the surface spherically shaped islands 80–200 nm in diameter, in amount of 20–25 per quadratic micrometer. A sharp change in the slope of the cantilever when crossing the island boundary (Fig. 2f) also suggests the difference between the chemical compositions of the segments revealed and the surface of the initial polyethylene. Evidently, phosphorus-containing groups with a high hydrophilic power [10], when added to active centers of polyethylene, form a hydrate shell surrounding the grafted groups due to adsorption of water vapor from air. Since on the surface of the polymer matrix there are two fragments of different chemical compositions, which sharply differ in the strength and adhesion characteristics, it is fairly difficult to reveal the actual topography of the modified polyethylene surface from the AFM data. For example, the AFM reconstruction of the surface furnishes no information about the height of an individual phosphorus-containing island. However, it can be stated that, under the actual conditions, treatment of the material with the PCl_3 vapor does not cause degradation of the surface polymer layer, and phosphorus-containing groups add only to accessible active centers of the LDPE surface, which is in agreement with the results of chemical analysis.

The influence of the chemical modification on the heat resistance of the polymer was estimated both from the heat effects and from the change in the sample mass during thermal degradation. It should be noted that thermal oxidative degradation of polyethylene is a complex process due to the presence in its structure of amorphous and crystalline areas. It is known that first oxidized are amorphous areas of the material, which are more accessible for the oxygen molecule [11]. They act as a buffer protecting the crystalline areas from degradation.

The DTA curve for the initial polyethylene (Fig. 3, curve *1*) exhibits several segments corresponding to various degradation stages.

At 106°C, an endothermic melting peak is observed which is characteristic of LDPE [4]. The initial degradation stage due to low-temperature oxidation of

the material (exothermic effect with a maximum at 240°C) involves removal of the low-molecular-weight fraction contained in the polymer and degradation of weak bonds, which, in turn, initiates degradation of carbon–carbon fragments into free radicals. Upon further heating of the sample, the process acquires a more complicated multistage character, which is responsible for appearance in the DTA curve (Fig. 3, curve *1*) of a large number of exothermic (at 359, 392, 410, 435, and 452°C) and endothermic (at 425°C) peaks. These transformations are due to profound degradation of the skeleton and to removal of a wide spectrum of organic saturated and unsaturated volatile monomers. The third, final, stage involves complete (virtually 100%) degradation of polyethylene, and the corresponding exothermic peak is observed at 485°C.

Chemical modification of polyethylene with phosphorus(V) chloride causes virtually all the peaks due to thermal degradation of the polymer to shift by 20–90°C to higher temperatures (Fig. 3, curve *3*). The largest shift from 240 to 332°C, due, evidently, to decrease in the number of active centers of thermal oxidation [schemes (1) and (2)], is observed for the initial degradation stage. Upon further heating, the maxima of both exo- and endothermic effects in the DTA curve of the modified polymer (Fig. 3, curve *3*) shift by 20–40°C to higher temperatures. Also, exothermic peaks at 410 and 435°C disappear. These changes, together with the results of the previous studies, suggest active participation of phosphorus-containing additives in degradation processes both in the gas (deactivation of free radicals) and condensed (recombination of active centers at the gas–solid interface) phases [12].

The inhibiting action of the vanadium oxide fragments is manifested in the first and second stages of degradation of the polymeric material, as suggested by the following changes in the differential curve (Fig. 3, curve *2*). First, the exothermic peak shifts to higher temperatures from 240 (initial sample) to 280°C (vanadium-containing sample). This is evidently due to the preliminary partial oxidation of the polymer matrix and formation of more thermally stable fragments upon treatment of LDPE with $VOCl_3$ vapor. Second, the next degradation stage, similarly to the case of the phosphorus-containing sample, is characterized not only by shifts to higher temperatures of the exothermic (390, 430, 472°C) and endothermic (441°C) peaks but also by disappearance of the exothermic peaks with maxima at 392 and 435°C (Fig. 3, curve *2*). The influence of the modifying additive is, evidently, manifested in reactions with the oxidant

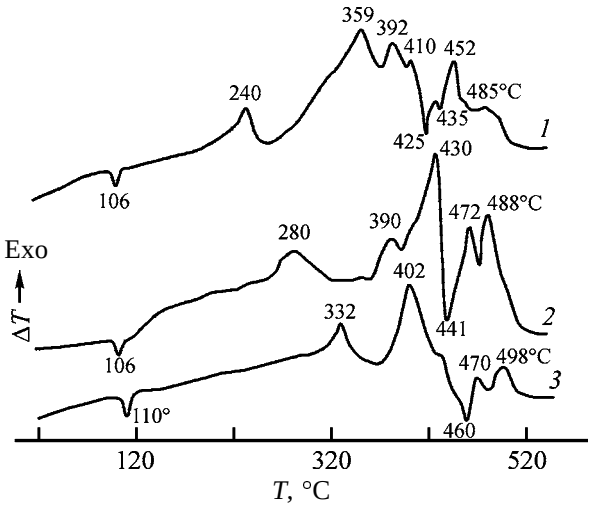

Fig. 3. DTA curves of polyethylene. (*T*) Temperature.

molecules, which, in turn, hinders formation of hydroperoxy radicals and degradation of the polymer chain.

Comparison of the derivatographic and AFM data for the modified polyethylene samples also revealed interrelation between their heat resistance and the surface layer structure, which is the most prominent in the initial degradation stage. For example, introduction of phosphorus-containing moieties is responsible for formation on the matrix surface of a uniform coating (Figs. 2e, 2f), which partially blocks the active centers of the degradation process. According to the DTA data, the temperature of the first exothermic effect significantly increases (by 92°C) relative to the initial polyethylene (Fig. 3, curve *3*). The AFM reconstruction for the vanadium-containing sample (Figs. 2c, 2d) clearly demonstrates etching of the polyethylene film surface, which can be responsible for the appearance of transport channels for atmospheric oxygen. This may be the reason for lowering of the temperature of the exothermic effect in the initial stage of degradation of this product relative to the phosphorus-containing sample (280 against 322°C) (Fig. 3, curves *2*, *3*). Partial degradation of the matrix surface on treatment with the $VOCl_3$ vapor, evidently, causes degradation of the internal layers of the polymeric material.

CONCLUSION

Chemical analysis and physicochemical studies of the reaction products of PCl_3 and $VOCl_3$ vapors with low-density polyethylene film samples suggest chemical grafting of the element oxide groups at the reactive centers of the polymer. Grafting proceeds both via

substitution reactions and, in the case of vanadium oxychloride, via redox transformations. Atomic-force microscopic studies reveal the difference in the morphologies of the initial and modified polymers and an interrelation between the chemical nature of the additive and the surface layer structure, on the one hand, and the thermal oxidative properties of polyethylene, on the other.

ACKNOWLEDGMENTS

This work was financially supported by the Russian Foundation for Basic Research (project no. 03-03-32 190).

REFERENCES

1. Povstugar, V.I., Kodolov, V.I., and Mikhailova, S.S., *Stroenie i svoistva poverkhnosti polimernykh materialov* (Structure and Properties of the Surface of Polymeric Materials), Moscow: Khimiya, 1988.
2. Grassie, N. and Scott, G., *Polymer Degradation and Stabilisation*, London: Cambridge Univ. Press, 1985.
3. Malygin, A.A., *Zh. Prikl. Khim.*, 1996, vol. 69, no. 10, pp. 1585–1593.
4. Sirota, A.G., *Modifikatsiya struktury i svoistv poliolefinov* (Modification of the Structure and Properties of Polyolefins), Leningrad: Khimiya, 1984.
5. Magonov, S.N., *Vysokomol. Soedin., Ser. B*, 1996, vol. 38, no. 1, pp. 143–182.
6. Trifonov, S.A. and Malygin, A.A., *Zh. Obshch. Khim.*, 1998, vol. 68, no. 12, pp. 1994–1998.
7. Trifonov, S.A., Lapikov, V.A., and Malygin, A.A., *Vliyanie khimicheskogo modifitsirovaniya khloridom fosfora(III) poverkhnosti polietilena na ego termookislitel'nuyu stoikost'* (Influence of Chemical Modification with Phopshorus(III) Chloride of the Polyethylene Surface on Its Resistance to Thermal Oxidation), Available from VINITI RAS, February 26, 2002, no. 374-V2 002.
8. Trifonov, S.A., Semenova, E.Yu., and Malygin, A.A., *Zh. Prikl. Khim.*, 1996, vol. 69, no. 11, pp. 1917–1920.
9. Kazitsyna, L.A. and Kupletskaya, N.V., *Primenenie UF-, IK-, YaMR i mass-spektroskopii v organicheskoi khimii* (Application of UV, IR, NMR, and Mass Spectroscopy to Organic Chemistry), Moscow: Mosk. Gos. Univ., 1979.
10. Van Wazer, I.R., *Phosphorus and Its Compounds*, New York: Wiley-Interscience, 1958, vol. 1.
11. Bryk, M.T., *Destruktisya napolnennykh polimerov* (Degradation of Filled Polymers), Moscow: Khimiya, 1989.
12. Trifonov, S.A., Malygin, A.A., and Gnatyuk, S.P., *Plast. Massy*, 1988, no. 7, pp. 35–36.

Russian Journal of Applied Chemistry, Vol. 77, No. 11, 2004, pp. 1859–1861. Translated from Zhurnal Prikladnoi Khimii, Vol. 77, No. 11, 2004, pp. 1877–1879.

MACROMOLECULAR CHEMISTRY AND POLYMERIC MATERIALS

Elemental Sulfur as a Stabilizing Agent for Vinyl Chloride Polymers

S. V. Kolesov, R. M. Akhmetkhanov, E. I. Nagumanova, N. N. Kabal'nova, R. R. Akhmetkhanov, and G. E. Zaikov

Bashkir State University, Ufa, Bashkortostan, Russia
Institute of Biochemical Physics, Russian Academy of Sciences, Moscow, Russia
Institute of Organic Chemistry, Ufa Scientific Center, Russian Academy of Sciences, Ufa, Bashkortostan, Russia

Received May 20, 2004

Abstract—The possibility of stabilization of some vinyl chloride polymers with elemental sulfur in their thermal and thermal oxidative degradation was studied.

Various sulfur compounds are widely used in chemical industry as initial components in synthesis of new products or as additives. In particular, to increase thermal and thermal oxidative stability of vinyl chloride (VC) polymers, some sulfur-containing compounds, dialkyl sulfides and sulfur-containing derivatives of dialkyltin [1, 2], are used as thermal stabilizing agents and antioxidants. Contrary to sulfur compounds, elemental sulfur is not used yet as an additive to polymers (only as vulcanizing agent for rubber [3]). There are published data on ability of sulfur to inhibit thermal oxidative degradation of polyethylene due to decomposition of hydroperoxides [4]. In this connection, it was appropriate to study the influence of elemental sulfur on thermal and thermal oxidative dehydrochlorination of hard and plasticized polyvinyl chloride (PVC) and some VC copolymers.

EXPERIMENTAL

Thermal and thermal oxidative dehydrochlorination of hard and plasticized PVCs were performed at 175°C in a bubbling-type reactor in nitrogen or air flow (3.3 $l\ h^{-1}$). The rate of dehydrochlorination and deacetylation was determined by the procedure described in [5]. Degradation of VC copolymer with 11.1 mol % vinyl acetate (VCVA-11.1) was estimated from the total rate of elimination of HCl and CH_3CO_2H. Titration of hydroperoxides was performed by the procedure described in [6]. Polymers of VC (PVC S-7059M, VCVA-11.1, and copolymer of VC with 28.8 mol % methyl acrylate VCMA-28.8) were washed with ethanol in a Soxhlet apparatus. Ester plasticizing agents, dioctyl phthalate (DOP) and dioctyl sebacate (DOC), were purified by filtration through a column packed with aluminum oxide. Elemental sulfur [GOST (State Standard) 127.1-93, content of main substance 99.98 wt %] and sulfur of ultrapure grade were not purified additionally.

Thermal oxidative degradation of PVC in the presence of sulfur may involve, along with dehydrochlorination and deacetylation, also formation of sulfur dioxide, which can affect the results of acid–base titration and thus can give overestimated rate of degradation of polymers. However, in a model experiment on oxidation of individual sulfur in air, the qualitative reaction on decolorization of $KMnO_4$ solution with products of sulfur oxidation at 175°C (at least in 80 min) gave negative result. The products of sulfur oxidation at 175°C, when bubbled through distilled water, did not change the color of the acid–base titration indicator (a mixture of Bromocresol Green and Methyl Red). The products of thermal oxidative decomposition of sulfur (175°C) did not also change the color of Congo Red indicator paper. Thus, we can conclude that, under the experimental conditions, sulfur dioxide is not formed and the resulting rates of PVC dehydrochlorination are correct.

Addition of sulfur to PVC results in an insignificant decrease in the rate of thermal dehydrochlorination of the polymer (Fig. 1); the kinetic curves for HCl elimination are linear. Using the indicator method with Congo Red, we showed that, under conditions of PVC degradation, sulfur has no accepting effect with respect to the released HCl.

1070-4272/04/7711-1859 © 2004 MAIK "Nauka/Interperiodica"

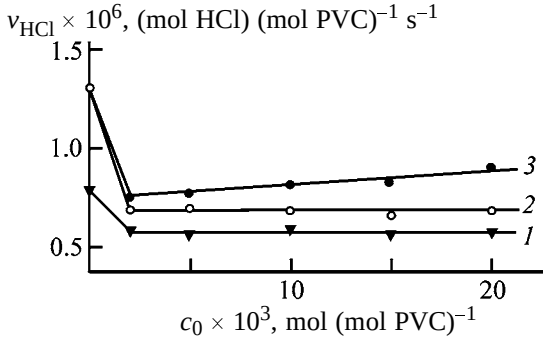

Fig. 1. Rate of (*1*) thermal and (*2, 3*) thermal oxidative dehydrochlorination of PVC v_{HCl} as a function of the content of (*1, 2*) elemental sulfur and (*3*) DPP c_0.

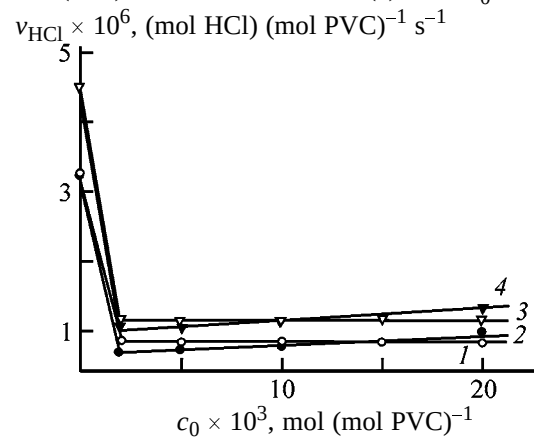

Fig. 2. Rate of thermal oxidative dehydrochlorination of PVC v_{HCl} plasticized (40 wt. parts per 100 wt. parts of PVC) with (*1, 2*) DOP and (*3, 4*) DOS as a function of the content of (*1, 3*) elemental sulfur and (*2, 4*) DPP c_0.

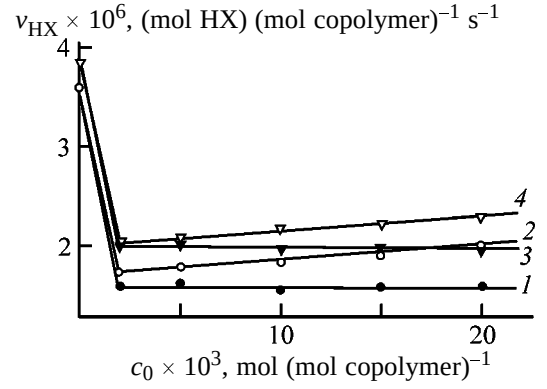

Fig. 3. Rate v_{HX} HX is HCl and CH_3COOH) of (*1, 2*) thermal oxidative dehydrochlorination of VCMA-28.8 and (*3, 4*) dehydrochlorination + deacethylation of VCVA-11.1 as a function of the content c_0 of (*1, 3*) elemental sulfur and (*2, 4*) DPP.

In thermal oxidative degradation of PVC, the stabilizing performance of sulfur noticeably increases and, in particular, exceeds the performance of a well-known antioxidant, diphenylolpropane (DPP) (Fig. 2). The kinetic dependences of thermal oxidative dehydrochlorination of PVC in the presence of sulfur remain linear.

The maximal decrease in the rate of PVC dehydrochlorination is observed at a sulfur content of 2 mmol per mole PVC and does not vary with a further increase in the sulfur content in the polymer. The dependence of the rate of thermal oxidative dehydrochlorination of PVC, v_{HCl}, on the sulfur content after reaching the minimum is linear, contrary to phenolic antioxidant DPP for which this dependence has an extremum. The rate of thermal oxidative dehydrochlorination of PVC decreases in the presence of sulfur practically to the values corresponding to the rate of thermal degradation of PVC, which is typical of antoxidants.

Stabilization of thermal oxidative degradation of VC copolymers with elemental sulfur is characterized by the same features as stabilization of PVC. However, the stabilizing performance of sulfur in VC copolymers is lower than that in PVC (Fig. 3). This is in agreement with the well-known fact that the inhibiting effect of stabilizers in VC copolymers is lower than that in PVC [7].

The problem of stabilization of plasticized PVCs in production of soft and semihard articles is mainly related to prevention of oxidative degradation of the plasticizer in polymer compounds by using antioxidants.

Introduction of elemental sulfur into PVC plasticized with ester plasticizers (DOP and DOS) results in an abrupt decrease in the rate of thermal oxidative dehydrochlorination of the polymer (Fig. 2). As in the case of degradation of nonplasticized PVC, the maximal decrease in the rate of dehydrochlorination of the plasticized polymer is observed at a sulfur content of 2 mmol per mole PVC. The stabilizing performance of sulfur in plasticized PVC materials is practically the same as the performance of DPP. It should be noted that the stabilizing effect is reached in introduction of sulfur into polymer composites in the range 0.02–0.05 wt % with respect to PVC, which is by an order of magnitude less than the weight concentration of the existing organic stabilizer-santioxidants for PVC. In this case, the stabilizing performance is independent of the sulfur origin (gas clumpy or natural clumpy).

The rate of thermal oxidative degradation of PVC decreases in the presence of elemental sulfur to substantially lower values corresponding to the rate of thermal oxidative degradation of nonplasticized PVC. It is evident that elemental sulfur efficiently prevents oxidation of the plasticizing agent (stabilizer-antioxi-

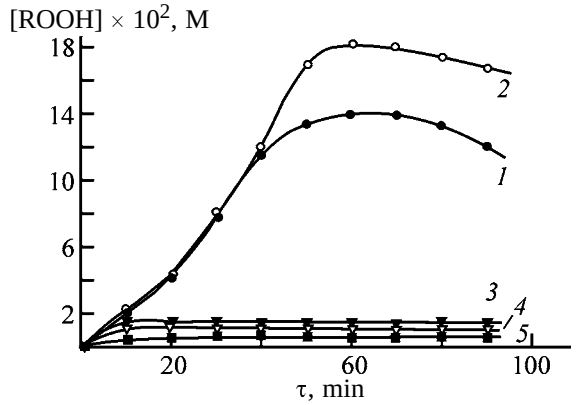

Fig. 4. Kinetic curves of accumulation of hydroperoxides (ROOH) in oxidation of plasticizing agents (*1*) DOP, (*2*) DOS, (*3*) DOP + 3.1 mM elemental sulfur, (*4*) DOS + 3.1 mM elemental sulfur, and (*5*) DOP + 1.4 mM 4-methyl-2,6-di-*tert*-butylphenol in DOP (oxygen feed rate 3.3 l h^{-1}, 165°C). ([ROOH]) concentration of hydroxoperoxides and (τ) process duration.

dant), which, in turn, enhances the thermal stability of PVC due to solvation stabilization (echo-stabilization of PVC [8]).

In stabilization of plasticized VC copolymers, the stabilization performance of elemental sulfur is also lower compared to plasticized PVC.

Iodometric titration of hydroperoxides formed in autooxidation of ester plasticizers, DOP and DOS, showed that introduction of sulfur into esters abruptly inhibits accumulation of hydroperoxides (Fig. 4). In the efficiency of inhibiting oxidation of ester plasticizers, elemental sulfur is comparable with the phenolic antioxidant 4-methyl-2,6-di-*tert*-butylphenol.

CONCLUSIONS

(1) Elemental sulfur has a high inhibiting effect in thermal oxidative degradation of hard and plasticized polyvinyl chloride, comparable with the inhibiting effect of phenolic antioxidants; it shows promise for practical use in production of polyvinyl chloride materials due to its availability and low coast.

(2) The stabilizing performance of elemental sulfur in polymer compounds based on copolymers of vinyl chloride is lower than that in stabilization of polyvinyl chloride.

REFERENCES

1. Minskler, K.S. and Fedoseeva, G.T., *Destruktsiya i stabilizatsiya polivinilkhlorida* (Degradation and Stabilization of Polyvinyl Chloride), Moscow: Khimiya, 1979.
2. Gorbunov, B.N., Gurvich, Ya.A., and Maslov, I.P., *Khimiya i tekhnologiya stabilizatorov polimernykh materialov* (Chemistry and Technology of Stabilizers of Polymer Materials), Moscow: Khimiya, 1981.
3. Blokh, G.A., *Organicheskie uskoriteli vulkanizatsii i vulkaniziruyushchie sistemy dlya elastomerov* (Organic Accelerators of Vulcanization and Vulcanizing Systems for Elastomers), Moscow: Khimiya, 1981.
4. Hawkins, W.L. and Sautter, H., *Chem. Ind.*, 1962, vol. 42, pp. 1825–1826.
5. Minsker, K.S., Abdullin, M.I., and Kraikin, V.A., *Plast. Massy*, 1980, no. 3, pp. 31–33.
6. Antonovskii, V.L. and Buzlanova, M.M., *Analiticheskaya khimiya organicheskikh peroksidnykh soedinenii* (Analytical Chemistry of Organic Peroxo Compounds), Moscow: Khimiya, 1978.
7. Minsker, K.S., Kolesov, S.V., Pancheshnikova, R.B., and Akhmetkhanov, R.M., *Dokl. Akad. Nauk SSSR*, 1982, vol. 266, no. 2, pp. 370–373.
8. Minsker, K.S. and Abdullin, M.I., *Dokl. Akad. Nauk SSSR*, 1982, vol. 263, no. 1, pp. 140–143.

Russian Journal of Applied Chemistry, Vol. 77, No. 11, 2004, pp. 1862–1868. Translated from Zhurnal Prikladnoi Khimii, Vol. 77, No. 11, 2004, pp. 1880–1886.

MACROMOLECULAR CHEMISTRY AND POLYMERIC MATERIALS

Composition and Properties of Water-Soluble Products Formed in the Reaction of Chitosan with Fe(III) in Aqueous $FeCl_3$ Solutions

G. R. Anpilogova and Yu. I. Murinov

Institute of Organic Chemistry, Ufa Scientific Center, Russian Academy of Sciences, Ufa, Bashkortostan, Russia

Received July 28, 2004

Abstract—The effect of preparation conditions on the composition and properties of products of Fe(III) reaction with chitosan was studied. The reaction was carried out by partial neutralization of moderately concentrated $FeCl_3$ solutions with chitosan followed by precipitation in an organic precipitant.

Some neutral and anionic polysaccharides form water-soluble compounds with Fe(III), thus preventing the precipitation of Fe(III) hydroxide and retaining considerable amounts of Fe(III) in aqueous solutions at physiological pH values of 1–8. This caused wide application of such compounds as medicines for treatment of iron-deficiency anemia: Imferon (iron–dextran) and Blutal (iron–chondroitin sulfate) [1]. The content of Fe(III) in dextran complexes reaches 12–31% [2, 3]. According to [4, 5], the polyaminosaccharide chitosan (CTS) at pH ≤ 7 is a stabilizer for colloidal FeOOH particles which are formed when 1–10 mmol l^{-1} $FeCl_3$ solutions containing chitosan hydrochloride in the molar ratio Fe : [CTS] ≤2 ([CTS] is chitosan monomeric unit) are neutralized with an alkali. Since the reaction of Fe(III) with CTS is a simple and economic method for obtaining nanosize (5–10 nm) spherical FeOOH particles [4], and since chitosan, being a polybase, can serve as a mild neutralizing agent for weakly acidic aqueous solutions of $FeCl_3$, it was of interest to prepare of water-soluble iron–chitosan compounds with a high Fe(III) content by partial neutralization of $FeCl_3$ solutions with chitosan.

In this work we studied how the preparation conditions affect the composition and properties of water-soluble products formed in the reaction of Fe(III) with chitosan as a result of a partial neutralization of moderately concentrated $FeCl_3$ solutions with chitosan followed by the precipitation in an organic precipitant.

EXPERIMENTAL

Chitosan was obtained from pure-grade chitin of Far East crabs (ash content 2.1 %) and conditioned by the procedure from [6]. According to the elemental analysis, air-dry conditioned CTS is characterized by the absence of ash and Cl and contains 37.4 and 6.4% C and N, respectively. The degree of CTS deacetylation, as determined by potentiometric titration, was 87 ± 3%; its viscosity-average molecular weight was 150 000. The CTS fraction with the particle size of $0.025 < d < 0.0315$ cm was used in the work.

Iron(III) solutions (0.050 and 0.10 M) were prepared by dissolution of the corresponding weighed portions of $FeCl_3 \cdot 6H_2O$ (pure grade) in water. The concentration of Fe(III) in aqueous solutions was determined by the EDTA titration with sulfosalicylic acid, and that in solid products of the Fe(III) reaction with CTS, also by EDTA titration after wet combustion of a weighed portion of the product [7]. The relative error of Fe(III) determination in solid products did not exceed 1.3%. Methanol purified by the procedure from [8], ethanol (rectificate), acetone, and isopropyl alcohol (chemically pure grade) were used as precipitating agents. Chitosan hydrochloride (CTS · HCl) was precipitated in acetone [9], washed with acetone in a vacuum, dried in air, and triturated. According to the elemental analysis, it contained 5.4% N and 12.3% Cl.

The pH values of solutions were determined on an OR-211/1 laboratory digital pH meter with an OR-0808R combined glass electrode. The electronic absorption spectra of aqueous solutions of $FeCl_3$, CTS · HCl, and products of the reaction between CTS and Fe(III) were recorded on a Specord M40 spectrophotometer against water in 0.2-cm-thick quartz cells. The IR spectra of chitosan-containing substances were

1070-4272/04/7711-1862 © 2004 MAIK "Nauka/Interperiodica"

taken in Nujol on a Specord M80 spectrophotometer in the range 4000–200 cm^{-1}. The X-ray phase analysis of iron–chitosan products and CTS·HCl was carried out on a DRON-3M diffractometer with a graphite monochromator; CuK_α radiation, angle range 2θ = 10°–80°, scanning step 0.1°, voltage 40 kV, current 20 mA. The thermogravimetric analysis of the substances and CTS was carried out on a Q-1500D derivatograph (MOM, Hungary) in air under with heating from 17 to 1000°C at a rate of 5 deg min^{-1} with an Al_2O_3 reference.

The products of the reaction of CTS with Fe(III) were obtained as follows. A weighed portion of CTS was introduced into a beaker with a $FeCl_3$ solution in the molar ratios Fe : [CTS] 1 : 3, 1 : 2, 1 : 1, and 2 : 1 at 16±1°C with vigorous stirring (an MM 2A magnetic stirrer). The chitosan completely dissolved wihtin 1 h. The dissolution was accompanied by an increase in viscosity and changes in pH (Fig. 1) and in the solution color from yellow to red-brown. The solution was stirred for the time τ_s, which usually corresponded to flattening out of the curve pH = $f(\tau)$ and was about 4–5 h (Fig. 1). Compounds of CTS with Fe(III) were isolated from aqueous solutions by precipitating in an organic precipitant. In this case, the volume of the precipitant was 2.5–4 times larger than the volume required for the beginning of the quantitative precipitation of the chitosan fractions $V_{0(min)}$ (Table 1). An aqueous solution was added dropwise to a precipitant with stirring; the mixture with the precipitate was stirred for 30 min and left for τ_{pr} = 20–24 h in a closed vessel for the precipitation. The voluminous orange-brown fibrous precipitate was filtered off and washed with the precipitant in a vacuum on a Büchner funnel to the negative reaction of the filtrate for the Cl^- ions with $AgNO_3$ and for Fe(III) with KCNS; then it was dried in a Petri dish to constant weight. Air-dry red-brown products were triturated and analyzed. The yield of the products based on CTS, as estimated from the content of nitrogen in the starting CTS and in the product, was no less than 96%. The elemental analysis data for the products obtained under various conditions are given in Table 2.

The dependence of the solution pH on the synthesis time for various molar ratios of chitosan amino groups and Fe(III) (Fig. 1) is typical for partially neutralized Fe(III) solutions at the corresponding molar ratios of an inorganic base to Fe(III) (OH : Fe) [10]. The increase in pH in the initial parts of curves *1–3* reflects the protonation of free CTS amino groups and simultaneous neutralization of solutions with the

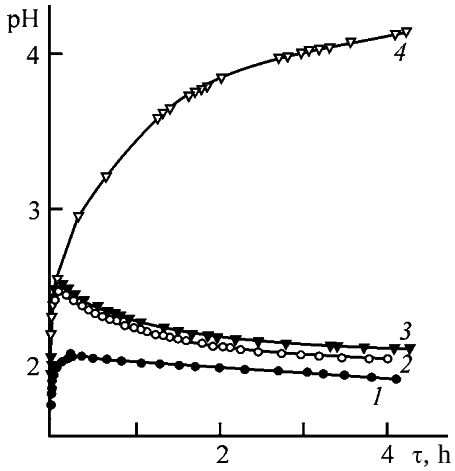

Fig. 1. Variation with time τ of pH of an $FeCl_3$ solution neutralized with chitosan. c_{Fe} (M): (*1*) 0.10 and (*2–4*) 0.05. Fe : [CTS]: (*1*) 2 : 1, (*2*) 1 : 1, (*3*) 1 : 2, and (*4*) 1 : 3. Mole ratio of chitosan amino groups to Fe(III): (*1*) 0.44, (*2*) 0.87, (*3*) 1.74, and (*4*) 2.61.

formation of nonequilibrium Fe(III) polynuclear hydrolysis products (PHP) imparting to the solution a red-brown color [10, 11]. The further pH decrease is caused by hydrolytic processes of aging of the partially neutralized $FeCl_3$ solutions. The maximal pH of solutions at Fe : [CTS] 2 : 1, 1 : 1, and 1 : 2 did not exceed 2.51 (Fig. 1), which corresponds to the degree of protonation of chitosan amino groups α = 1. The neutralization of the $FeCl_3$ solution by chitosan at the ratio Fe : [CTS] = 1 : 3 is accompanied by a monotonic increase in pH (curve *4*), as is the case with solutions neutralized with alkali at OH : Fe ≥ 2.5, and by the formation of a very viscous difficult-to-stir gelatinous solution. In this case, the pH of the solution obtained at τ_s ~4 days was 4.95, which corresponds to α ~0.96. Unlike solutions partially neutralized with alkali, the solutions partially neutralized with chitosan are stable against precipitation of Fe(III) hydroxide for a long time (no less than 3–6 months).

Table 1. Minimal volume of a precipitant $V_{0(min)}$ required for the beginning of quantitative precipitation of an iron–chitosan product from 0.10 M solution of $FeCl_3$ at Fe : [CTS] = 2 : 1; Fe(III) content in the product

Precipitant	ε(25°C) [9]	$V_{Fe} : V_{0(min)}$*	Fe(III) content, %
MeOH	32.6	1 : 4.0	7.1
EtOH	24.3	1 : (1.9–2.0)	8.1
Acetone	20.7	1 : (1.0–1.2)	7.3
i-PrOH	18.3	1 : (1.0–1.2)	11.5

* Volume ratio of an aqueous solution and a precipitant.

Table 2. Composition of iron–chitosan products

Product no.*	Preparation conditions						Fe	Cl	Fe : N : Cl
	c_{Fe}, M	pH_0	Fe : [CTS]	τ_s, h	precipitant, $V_{Fe} : V_{pr}$	τ_{pr}, h	%		
					Acetone:				
1	0.050	1.89	1 : 1	24	1 : 5	20	10.28	12.30	1 : 1.78 : 1.88
2	0.050	1.89	1 : 2	24	1 : 5	20	7.15	12.83	1 : 2.61 : 2.82
3	0.050	1.89	1 : 3	24	1 : 5	20	6.48	11.53	1 : 3.20 : 2.80
4	0.10	1.69	2 : 1	4.5	1 : 3.3	1	11.10	13.40	1 : 1.55 : 1.90
5	0.10	1.69	2 : 1	4.5	1 : 3.3	24	12.44	12.84	1 : 1.25 : 1.63
6	0.10	1.69	2 : 1	4.5	1 : 3.3	48	12.83	12.87	1 : 1.27 : 1.58
7	0.10	1.69	2 : 1	4.5	1 : 3.3	120	13.05	12.70	1 : 1.13 : 1.53
					Ethanol:				
8	0.10	1.69	2 : 1	5	1 : 5	21	9.36	12.30	1 : 2.02 : 2.07
9	0.10	1.69	2 : 1	4; 5 min at 90°C	1 : 5	21	19.18	11.58	1 : 0.87 : 0.95
10	0.050	1.92	1 : 1	4	1 : 5	21	6.94	13.29	1 : 2.65 : 3.02
11	0.050	1.92	1 : 2	4	1 : 5	21	6.06	13.26	1 : 3.20 : 3.45
12	0.050	1.92	1 : 3	93	1 : 5	21	7.10	12.13	1 : 3.11 : 2.69
13	0.10	1.47			Acetone, 1 : 8	24	43.84	10.64	1 : – : 0.38

* Product no. 9: after stirring for 4 h at 17°C, the solution was heated on a water bath at 90°C for 5 min and cooled to room temperature before precipitation; product no. 13: polynuclear hydrolysis products precipitated with acetone from a $FeCl_3$ solution aged in storage for 1 month.

In the IR spectra of the iron–chitosan products (Table 2), as well as in the spectrum of CTS · HCl, two absorption bands of medium intensity $\delta_{as}(NH_3^+)$ = 1624–1632 and $\delta_s(NH_3^+)$ = 1510–1522 cm^{-1} of protonated amino groups appear [4, 12, 13] instead of the absorption band $\delta_s(NH_2)$ = 1595 cm^{-1} of free amino groups, which is present in the CTS spectrum. This confirms complete or considerable protonation of CTS amino groups in the products and is consistent with the data [4] for iron–chitosan products isolated from solutions with pH 4.6 (α = 1).

As the degree of neutralization of $FeCl_3$ solutions increases, medium-intensity bands appear at 1618 and 1534–1540 cm^{-1} in the IR spectra of the isolated products (nos. 11 and 12) in the range of bending vibrations of the protonated amino groups. Piron and Domard [14] assigned these bands to the coordination of CTS free amino groups to the transition metal ions Ag(I), Cu(II), and Al(III). Therefore, we may assume that in these iron–chitosan products a small part of CTS amino groups are in the deprotonated form and are coordinated to Fe(III) ions.

The increase in the CTS concentration in the course of the synthesis (Fe : [CTS] = 1 : 3, product no. 12) is accompanied by an increase in the concentration of deprotonated amino groups and by an essential increase in the solution viscosity. The latter factor prevents the complete and uniform formation of the salt form CTS · HCl and the formation of a dense ionic atmosphere around the polyion [9], and also considerably retards the diffusion of mononuclear products of the $[Fe(H_2O)_5OH]^{2+}$ and $[Fe(H_2O)_4(OH)_2]^+$ hydrolysis and, hence, prevents the condensation and polymerization processes of the PHP formation [11, 15]. Such conditions seem to favor the formation of a certain amount of intraloop and interchain cross-links as a result of the formation of coordination bischelate complexes with mononuclear Fe(III) cations, in which Fe(III) ions are coordinated with two monomeric CTS units via the atoms of amine nitrogen and ring hydroxyl oxygen [16]. The formation of coordination cross-links is indirectly confirmed by a considerable decrease in the solubility of iron–chitosan products in water with increasing degree of neutralization of $FeCl_3$ solution with chitosan: for the products obtained at Fe : [CTS] 2 : 1, 1 : 2, and 1 : 3, the solubility at 20°C is 14.3–15.4, 11.0, and 2.7%, respectively.

The conclusion that Fe(III) in the iron–chitosan products is in the PHP form [4] is confirmed by the presence of the following bands in their IR spectra: weak absorption bands at 388–394 and 830–860 cm^{-1}, which can be assigned to ν_s and ν_{as} (Fe–O–Fe), respectively, in oxo-bridging PHP fragments [17], a broad complex band of medium intensity in the range

400–500 cm^{-1} (with maximuma at 416–418, 432–440, 455–460, and 480 and a shoulder at 495–505 cm^{-1}) corresponding to ν(Fe–O) in hydroxides and water-soluble PHPs [18, 19], and also a band of medium intensity in the range 650–680 cm^{-1}, which is observed in the spectrum of β-FeOOH [20]. The intensity of these bands increases with increasing Fe(III) content in the product, whereas the frequencies and the ratio of intensities correspond to those observed in the IR spectrum of Fe(III) hydroxo species precipitated with acetone from the aged solution (Table 2, compound no. 13) and also in the spectrum of β-FeOOH [20], cm^{-1}: 380–390 w, 488 m, 688 vs, and 864 m.

According to [4], water-soluble products forming upon partial neutralization of a solution containing $FeCl_3$ and CTS·HCl to pH 6.4 ($\alpha \approx 0.5$) can be considered as a sol of Fe(III) hydroxide protected by chitosan hydrochloride and possessing properties of a reversible colloid. Therefore, the solubility of iron–chitosan products in aqueous and aqueous-organic media should be defined by properties of a protective polymer [15, 21], in particular, by the degree of protonation of the amino groups and the degree of electrolytic dissociation of the polyelectrolyte CTS·HCl. For example, 1 g of the products dissolves (Tables 1 and 2) at 20°C in 100 ml of aqueous solutions of HCl and NaOH with pH 1–8 and of 0.85% NaCl. The products are insoluble in NaOH aqueous solutions with pH ≥ 10 because of complete deprotonation of chitosan amino groups and in 1 M NaCl because of suppression of CTS·HCl electrolytic dissociation by a high concentration of chloride ions. The degree of electrolytic dissociation of polyelectrolytes decreases as the permittivity of an aqueous-organic solvent decreases [15]. Therefore, a decrease in the relative permittivity ε of a precipitant makes it possible to reduce the precipitant consumption $V_{0(min)}$ in the series MeOH > EtOH > *i*-PrOH ≈ acetone (Table 1).

It is known that a decrease in ε of an aqueous-organic medium results in an increase in the formation constants of hydroxo complexes of transition metals [22]. This can be a reason for the fact that the increase in the Fe(III) content in isolated products observed in the series of alcohols under study (Table 1) and also when EtOH is replaced wiht acetone (Table 2, product nos. 8, 10, 11 and 5, 1, 2) correlates with a decrease in ε and in the hydrophilicity [8] of the precipitant. The study of how the time of precipitation in acetone affects the composition of products of the CTS reaction with Fe(III) (Table 2, products 4–7) has shown that an increase in τ_{pr} results in a parallel increase in the Fe(III) content and in a decrease in the Cl content

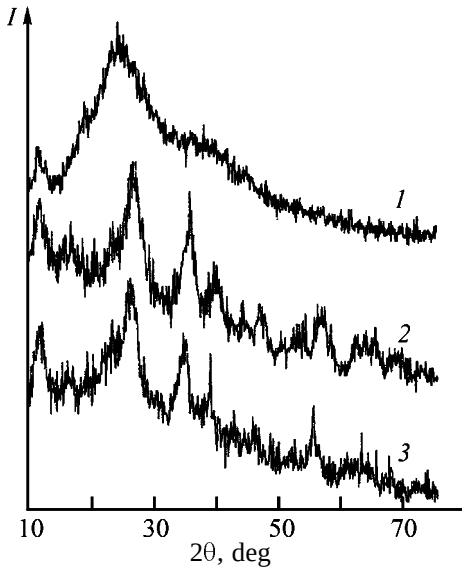

Fig. 2. X-ray patterns of (*1*) CTS·HCl powders and (*2, 3*) iron–chitosan product nos. 5 and 8, respectively. (*I*) Intensity and (2θ) Bragg angle.

at a constant molar ratio Fe : Cl_{exc} = 1 : (0.47–0.56) (Cl_{exc} is the superstoichiometric content of Cl relative to completely protonated amino groups).

According to [2], the presence of chlorine in the ratio Fe : Cl = 1 : (0.05–0.19) in water-soluble iron–dextran β-FeOOH-containing complexes obtained by the hydrolysis of $FeCl_3$ solutions is explained by a specific feature of the akaganeite structure. The increase in the content of Fe(III) in iron–chitosan products with increasing τ_{pr} seems to be caused by coprecipitation of hydrolyzed polymeric Fe(III) species forming in a aqueous acetone as a result of the decrease in ε of the solvent. Short heating of an iron–chitosan solution on a water bath at 90°C before precipitation increases the concentration and polynuclearity of PHP in aqueous solutions owing to acceleration of hydrolytic processes [10, 11] and makes it possible to precipitate water-soluble product no. 9 with a high Fe(III) content and a smaller Cl_{exc} content (Fe : Cl_{exc} = 1 : 0.20). The contents of Cl^- or NO_3^- anions, which are formed in partially neutralized Fe(III) solutions and compensate a high charge density in the nonequilibrium water-soluble PHPs of the composition $Fe_q(OH)_p^{(3p-q)+}$ ($p : q$ = 2.2–2.9), are known to decrease on aging of PHP solutions [10, 11].

According to the X-ray analysis (Fig. 2, Table 3), CTS·HCl is characterized by a noticeable crystallinity [23], and Fe(III) is present in the form of β-FeOOH in the products precipitated in acetone and ethanol. The higher relative intensity of β-FeOOH reflections at 2θ 12.0°–12.4° and 26.5°–26.7° for product

Table 3. X-ray phase analysis of CTS · HCl and iron–chitosan products precipitated in acetone (product no. 5) and ethanol (product no. 8)

CTS · HCl			Product no. 5			Product no. 8			β-FeOOH [20]		
2θ, deg	*I*	*d*, Å	2θ, deg	*I*	*d*, Å	2θ, deg	*I*	*d*, Å	*d*, Å	*I*	*hkl*
11.6	w	7.63	12.0	s	7.37	12.4	m	7.13	7.40	20	110
			16.8	m	5.28				5.26	20	200
24.7	s	3.61	26.5	vs	3.36	26.7	s	3.34	3.32	90	310
			35.2	s	2.55	35.4	m	2.54	2.54	100	211
			39.3	w	2.29	39.3	w	2.29	2.28	55	301
			45.5	w	2.08				2.07	10	321
			46.0	w	1.97				1.96	35	411
			55.9	w	1.65	55.9	w	1.64	1.64	45	521
			61.3	w	1.51				1.51	20	002
			62.5	w	1.49				1.48	w	112
											710
											550
			64.3	w	1.45				1.44	10	541

nos. 5 and 8, compared to the published data (Fig. 2, Table 3), is caused by overlapping with the reflections of CTS · HCl at 11.6° and 24.7°, respectively. The number of β-FeOOH reflections which are reliably identified in the X-ray pattern of product no. 8 is considerably less compared to product no. 5 (5 and 11 reflections, respectively), which is caused by a lower Fe(III) content and, probably, a smaller size of β-FeOOH crystallites in the product precipitated in ethanol, without significant coprecipitation of PHP from the aqueous-organic solution. The interplanar spacing corresponding to the first reflection for product no. 8 is less than that for β-FeOOH and CTS · HCl (Table 3), which seems to be due to a denser packing of CTS · HCl macromolecules [24] in iron–chitosan products as compared to CTS · HCl.

The TG and DTG curves of product nos. 5 and 8 are similar, which confirms the uniformity of their chemical and phase composition; at the same time, these curves essentially differ from the corresponding curves for CTS and CTS · HCl. The TG curves for CTS and CTS · HCl consist of three portions, and those for iron–chitosan products, of four portions, with different rates of weight loss. A broad endothermic effect in the DTA curves with a minimum at 83, 96 and 98–100°C corresponds, respectively, to the loss of physically bound water in the range 39–144°C for CTS (weight loss 11.2%), 30–156°C for CTS · HCl (17.5%), and (40–45)–188°C for product nos. 5 (16%) and 8 (11.3%). The increase in the weight loss with increasing Fe(III) content in product no. 5 (Table 2) suggests that in this temperature range, along with the physically bound water, the water forming by condensation of "ol" bridges in Fe(III) hydroxo species [25] is also removed. Intense decomposition of CTS and CTS · HCl starts at 200 and 170°C and comes to an end when they are completely burnt down at 530 and 541°C, respectively.

The features of the thermal oxidative degradation of CTS and CTS · HCl agree with the published data for CTS and its salt forms [26]. Intense exothermic degradation of product nos. 5 and 8 starts at 202–203 and comes to an end at 649 and 663°C, respectively. The weight of the residues is 21.7 and 14.2%, respectively, for product nos. 5 and 8. The content of Fe(III) in them is close to that in Fe_2O_3. Apparently, the residue of the decomposition products is hematite [20].

All the iron–chitosan products (Tables 1, 2) behave toward water as unrestrictedly swelling gels and form solutions stable against precipitation in storage for no less than 6 months. Saturated solutions of the products are very viscous and thick, they form films upon drying up. The viscosity of solutions considerably decreases on dilution by a factor of 2–3. Irrespective of the conditions of obtaining the products, their dilute aqueous solutions (0.5 g l^{-1}) have similar electronic absorption spectra and undergo equal changes with time and with changes in solvent pH in the range of physiological values.

Typical electronic absorption spectra of solutions of iron–chitosan products at various pH of a solvent (aqueous solutions of HCl, NaOH, and 0.1–0.15 M NaCl) are shown in Fig. 3. The spectra of solutions

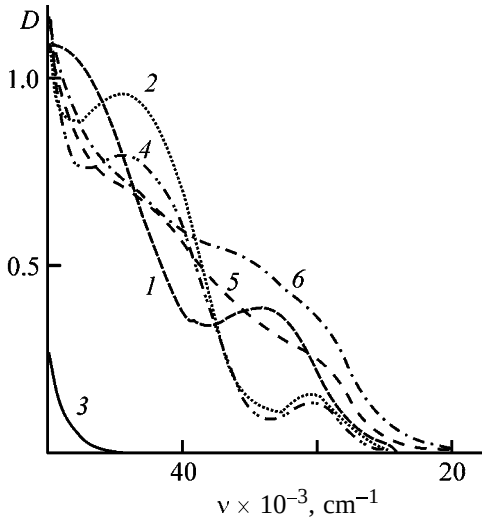

Fig. 3. Electron absorption spectra of solutions: (*1*, *2*) 1.04 M $FeCl_3$, (*3*) 0.5 g l^{-1} CTS·HCl, and (*4*–*6*) iron–chitosan product no. 8 in (*1*, *3*, *6*) water, (*2*, *4*) 0.1 M HCl, and (*5*) 0.01 M HCl. (*D*) Optical density and (ν) wave number. (*1*–*3*) Freshly prepared solutions and (*4*–*6*) 8 days after preparation (c_{Fe} = 8.4×10^{-4} M). pH: (*1*) 2.63, (*2*) 1.06, (*3*) 4.17, (*4*) 1.07, (*5*) 2.00, and (*6*) 3.87.

with the initial solvent pH of 4–7.7 resemble spectrum *6* and do not noticeably change with time (at least 20 days), which suggests that Fe(III) is present in the solutions in the PHP form [10, 27, 28]. The pH of these solutions decreases, compared to the pH of the solvents, to 3.8–4.1, which is caused by the hydrolysis of the CTS salt form (pH of the 0.5 g l^{-1} CTS·HCl aqueous solution is 4.17, which corresponds to the degree of salt hydrolysis about 4%), and also by the hydrolysis of Fe(III) PHPs isolated from acid solutions. These solutions do not show a qualitative reaction with KCNS for Fe^{3+} ions. The dialysis of the aqueous solution (initial pH of the solvent 6.1) of a product precipitated by acetone against water through a "100X" transparent cellophane film with the pore diameter of 2.0–3.5 nm has shown that chloride ions diffuse in water (test with $AgNO_3$) and low-molecular-weight Fe(III) species do not pass into water (test with KCNS in 0.1 M HCl). This confirms the hydrolysis of CTS·HCl and the absence of Fe(III) low-molecular-weight species in the solution of this product. At the initial solvent pH of 1–3, the pH values of solutions of iron–chitosan products correspond to those of the solvent and do not noticeably change with time. The electronic absorption spectra of such solutions suggest slow decomposition of PHPs as the solution acidity increases (Fig. 3, curves *4*, *5*). Within 3–4 h after preparation, the spectra of solutions of the products with pH 1 correspond to curve *5*, within 2 days they become more similar in shape of curve *4*, and within 8 days they become identical to curve *4* (molar extinction coefficients at ν 44400 and 30000 cm^{-1} are 4788 and 792, respectively) and to the spectrum of the $FeCl_3$ solution in 0.1 M HCl (curve *2*, molar extinction coefficients at ν 44480 and 29920 cm^{-1} are 4733 and 806, respectively), in which $FeCl_4^+$, $FeCl^{2+}$, and Fe^{3+} ions dominate [29]. Slow depolymerization of Fe(III) in the 0.1 M HCl solution indicates that PHPs in iron–chitosan products are considerably oxolated [11].

The high Fe(III) content in the iron–chitosan products studied, comparable to the content in commercial iron–dextran compounds (product no. 9), the solubility of products in aqueous solutions with physiological pH values, and the stability of their aqueous solutions on prolonged storage suggest that they are promising compounds for the use in medical and veterinary practice as drugs for treatment of iron deficiency anemia.

CONCLUSIONS

(1) Partial neutralization of moderately concentrated $FeCl_3$ solutions with chitosan results in formation of nonequilibrium polynuclear hydrolysis products stabilized in solutions by chitosan hydrochloride. Water-soluble iron–chitosan products with high Fe(III) content can be isolated by subsequent precipitation in an organic precipitant. The neutralization at the ratios Fe : [CTS] 2 : 1 and 1 : 1, a decrease in the precipitant permittivity, and short heating of the partially neutralized solutions before the precipitation result in a substantial increase in the Fe(III) content in the iron–chitosan products.

(2) The IR and X-ray phase analysis data show that a considerable part of chitosan amino groups in the isolated products is protonated, and Fe(III) is in the form of β-FeOOH.

(3) The dissolution of iron–chitosan products in aqueous solvents with physiological pH values is accompanied by slight aging of polynuclear hydrolysis products and by partial hydrolysis of the chitosan salt form in the range $4 \le pH \le 7.7$ and by slow depolymerization of polynuclear hydrolysis products in the range pH 1–3.

REFERENCES

1. Sipos, P., Pierre, T.G.S., Tombacz, E., and Webb, J., *J. Inorg. Biochem.*, 1995, vol. 58, no. 2, pp. 129–138.

2. Coe, E.M., Bowen, L.H., Bereman, R.D., *et al.*, *J. Inorg. Biochem.*, 1995, vol. 57, no. 1, pp. 63–71.
3. Knight, B., Bowen, L.H., Bereman, R.D., *et al.*, *J. Inorg. Biochem.*, 1999, vol. 73, no. 4, pp. 227–233.
4. Sipos, P., Berkesi, O., Tombacz, E., *et al.*, *J. Inorg. Biochem.*, 2003, vol. 95, no. 1, pp. 55–63.
5. Chan, P., Chua-anusorn, W., Nesterova, M., and Sipos, P., *Aust. J. Chem.*, 1995, vol. 48, no. 4, pp. 783–792.
6. Kolyadina, O.A., Murinov, K.Yu., and Murinov, Yu.I., *Zh. Fiz. Khim.*, 2002, vol. 76. no. 5, pp. 896–899.
7. Kalinina, L.S., Motorina, M.A., Nikitina, N.I., and Khachapuridze, N.A., *Analiz kondensatsionnykh polimerov* (Analysis of Condensation Polymers), Moscow: Khimiya, 1984.
8. Gordon, A.J. and Ford, R.A., *The Chemist's Companion. A Handbook of Practical Data, Techniques, and References*, New York: Wiley–Interscience, 1972.
9. Gamzazade, A.I., Sklyar, A.M., Rogozhin, S.V., and Pavlova, S.-S.A., *Vysokomol. Soedin., Ser. A*, 1985, vol. 27, no. 4, pp. 857–862.
10. Flynn, C.M., *Chem. Rev.*, 1984, vol. 84, no. 1, pp. 31–41.
11. Pykhteev, O.Yu., Efimov, A.A., and Moskvin, L.N., *Zh. Prikl. Khim.*, 1999, vol. 72. no. 1, pp. 11–21.
12. Guibal, E., Milot, C., Eterradossi, O., *et al.*, *Int. J. Biol. Macromol.*, 1999, vol. 24, no. 1, pp. 49–59.
13. Silverstein, R.M., Bassler, G.C., and Morrill, T.C., *Spectrometric Identification of Organic Compounds*, New York: Wiley, 1974.
14. Piron, E. and Domard, A., *Int. J. Biol. Macromol.*, 1998, vol. 22, no. 1, pp. 33–40.
15. Frolov, Yu.G., *Kurs kolloidnoi khimii: Poverkhnostnye yavleniya i dispersnye sistemy* (Course of Colloid Chemistry: Surface Phenomena and Disperse Systems), Moscow: Khimiya, 1989.
16. Bhatia, S.C. and Ravi, N., *Biomacromolecules*, 2000, vol. 1, no. 3, pp. 413–417.
17. Kurtz, D.M., *Chem. Rev.*, 1990, vol. 90, pp. 585–606.
18. Nesterova, M., Moreau, J., and Banfield, J.F., *Geochim. Cosmochim. Acta*, 2003, vol. 67, no. 6, pp. 1177–1187.
19. Brady, G.W., Kurkjian, C.R., Lyden, E.F.X., *et al.*, *Biochemistry*, 1968, vol. 7, no. 6, pp. 2185–2192.
20. *Gipergennye okisly zheleza v geologicheskikh protsessakh* (Hypergenic Iron Oxides in Geological Processes), Petrovskaya, N.V., Ed., Moscow: Nauka, 1975.
21. Pomogailo, A.D., *Usp. Khim.*, 1997, vol. 66. no. 8, pp. 750–791.
22. Peshchevitskii, B.I., Muzykantova, Z.A., and Nikolaeva, N.M., in *Termodinamika i struktura gidroksokompleksov v rastvorakh: Materialy III Vsesoyuznogo soveshchsniya* (Thermodynamics and Structure of Hydroxo Complexes in Solutions: Proc. III All-Union Meet.), Leningrad, 1983, pp. 138–144.
23. Piron, E., Accominotti, M., and Domard, A., *Langmuir*, 1997, vol. 13, no. 6, pp. 1653–1658.
24. Akopova, T.A., Rogovina, S.Z., Gorbacheva, I.N., *et al.*, *Vysokomol. Soedin., Ser. A*, 1996, vol. 38, no. 2, pp. 263–268.
25. Pechenyuk, S.I., *Sorbtsionnoe gidroliticheskoe osazhdenie platinovykh metallov na poverkhnosti neorganicheskikh sorbentov* (Sorption Hydrolytic Precipitation of Platinum Metals on the Surface of Inorganic Sorbents), Leningrad: Nauka, 1991.
26. Nikolaev, A.F., Prokopov, A.A., and Shul'gina, E.S., *Zh. Prikl. Khim.*, 1985, vol. 58. no. 8, pp. 1870–1874.
27. Mulay, L.N. and Selwood, P.W., *J. Am. Chem. Soc.*, 1955, vol. 77, no. 10, pp. 2693–2701.
28. Pykhteev, O.Yu., Efimov, A.A., and Sosnovskaya, E.V., *Zh. Prikl. Spektrosk.*, 1990, vol. 52, no. 4, pp. 581–586.
29. Gamlen, G.A. and Jordan, D.O., *J. Chem. Soc.*, 1953, no. 5, pp. 1435–1443.

Russian Journal of Applied Chemistry, Vol. 77, No. 11, 2004, pp. 1869–1872. Translated from Zhurnal Prikladnoi Khimii, Vol. 77, No. 11, 2004, pp. 1887–1890.

MACROMOLECULAR CHEMISTRY AND POLYMERIC MATERIALS

Initiation of Methyl Methacrylate Polymerization with the Systems Benzoyl Peroxide–Onium Salt and Benzoyl Peroxide–Aminostyrylpyridine

N. A. Turovskii, I. A. Opeida, O. V. Kushch, and E. L. Baranovskii

Litvinenko Institute of Physical Organic and Coal Chemistry, National Academy of Sciences of Ukraine, Donetsk, Ukraine

Received August 11, 2004

Abstract—Polymerization of methyl methacrylate in the presence of binary systems containing benzoyl peroxide and activators [4-(4-dimethylaminostyryl)pyridine, 4-(4-dimethylaminostyryl)pyridine *N*-oxide in chlorobenzene; triphenylbenzylphosphonium chloride, triphenylbenzylphosphonium bromide, tetraethylammonium chloride, tetraethylammonium bromide, tetraethylammonium benzoate in acetonitrile] at 303 K was studied. The rate constants of decomposition of benzoyl peroxide in the presence of activators, initial polymerization rates, initiation rates, and initiation efficiencies at 303 K were determined.

Binary systems consisting of peroxides and activators (amines, variable-valence metal compounds, phosphines, sulfides, onium salts) are widely used for initiation of radical-chain processes at temperatures close to room temperature.

Binary initiating systems containing peroxides are characterized by lower activation energies of radical generation (40–80 kJ mol^{-1}), compared to thermal decomposition of peroxides (120–170 kJ mol^{-1}), which allows fast polymerization at low temperatures. It was shown previously that quaternary ammonium salts and aminostyrylpyridines appreciably decrease the acrivation energy and temperature of decomposition of benzoyl peroxide (BP) and can be used as components of binary initiators [1–3].

In this work we studied polymerization of methyl methacrylate in the presence of binary systems containing BP and activators [4-(4-dimethylaminostyryl)-pyridine (DASP), 4-(4-dimethylaminostyryl)pyridine *N*-oxide (DASPO) in chlorobenzene; triphenylbenzylphosphonium chloride (TPBPC), triphenylbenzylphosphonium bromide (TPBPB), tetraethylammonium chloride (TEAC), tetraethylammonium bromide (TEAB), tetraethylammonium benzoate (TEABenz) in acetonitrile] at 303 K.

EXPERIMENTAL

Benzoyl peroxide was recrystallized two times from ethanol. 4-(4-Dimethylaminostyryl)pyridine and its *N*-oxide were prepared by the procedure suggested in [4] and recrystallized from dimethyl sulfoxide and benzyl alcohol. TEAC and TEAB were purified by reprecipitation. TPBPC and TPBPB were prepared from triphenylphosphine and the corresponding benzyl halide. The onium salts were dried over P_2O_5 under reduced pressure at 333 K and were stored in a glove box over P_2O_5. Technical-grade methyl methacrylate was washed 2–3 times with 10–15% aqueous alkali for complete removal of the inhibitor. Then it was washed 2–3 times with distilled water, dried over anhydrous calcium chloride, and distilled three times in a nitrogen flow under reduced pressure; the fraction boiling at 22 ± 0.2°C (25 mm Hg) was collected. Freshly distilled methyl methacrylate was used. The kinetics of methyl methacrylate polymerization was monitored dilatometrically to 3% conversion of the monomer (see figure). The monomer content in the reaction mixture was 25 vol %. Polymerization of methyl methacrylate in the presence of BP and salts was performed in acetonitrile, and that in the presence of BP and aminostyrylpyridines, in chlorobenzene. The concentrations of BP and salt in the salt-containing initiating systems were 2.5×10^{-2} and 5×10^{-3} M, and the concentrations of BP and DASP or DASPO in the systems with the pyridine derivatives, 7.5×10^{-3}, 2.5×10^{-4}, and 2.2×10^{-4} M, respectively.

The kinetic studies of decomposition of BP activated with quaternary ammonium and phosphonium salts were performed under the conditions of the

1070-4272/04/7711-1869 © 2004 MAIK "Nauka/Interperiodica"

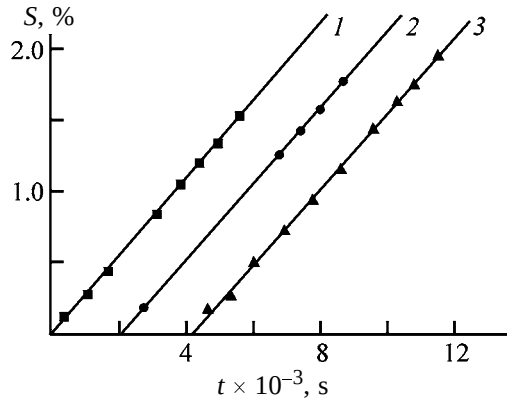

Inhibition of methyl methacrylate polymerization initiated with the system TEABenz–BP at 303 K. (*S*) Conversion and (*t*) time. [Inh], M: (*1*) 0, (*2*) 1×10^{-5}, and (*3*) 2×10^{-5}.

pseudo-first-order reaction with respect to the peroxide (291–313 K) at the initial BP concentration of 1.5×10^{-2} M. The initial concentrations of the salts were as follows (M): TEAC $(1.7–13) \times 10^{-2}$, TEAB $(2.6–10.34) \times 10^{-2}$, and TPBPC 9×10^{-3}. Triphenylbenzylphosphonium chloride is limitedly soluble in acetonitrile; therefore, the kinetic studies of BP decomposition in its presence were performed at a 1 : 1 concentration ratio of the peroxide and salt. The consumption of BP was monitored by a decrease in the intensity of the C=O absorption band (ν = 1764 cm^{-1}) in the IR spectrum (Specord 71-IR spectrophotometer, temperature-controlled 0.51-mm CaF_2 cells).

The kinetics of the reactions of BP with DASP and DASPO were monitored spectrophotometrically (Specord UV VIS) by consumption of DASP or DASPO (decrease in the absorption maximum: DASP, λ_{max} = 375 nm, $\varepsilon = 30\,000 \pm 600$ mol l^{-1} cm^{-1}; DASPO, λ_{max} = 395 nm, $\varepsilon = 32\,000 \pm 600$ mol l^{-1} cm^{-1}) in the presence of excess peroxide (0.01–0.4 M), at the initial amine concentration of 2.5×10^{-5} M.

The polymerization initiation rate W_{in} was determined by the method of inhibitors. As inhibitor we used 2,2,6,6-tetramethylpiperidyl-1-oxyl, a radical stable under the experimental conditions (303 K). The facts that the induction period is proportional to the initial inhibitor concentration, the inhibition period is not followed by deceleration in the examined concentration range (1×10^{-5}–1×10^{-3} M, see figure), and the transition from the induction period to the linear reaction course is fast allow the calculation of the initiation rates by the formulas valid for effective inhibitors:

$$W_{inh} = \mu[\text{Inh}]/\tau, \quad (1)$$

$$W_{inh} = nfW_d, \quad (2)$$

where τ is the induction period; W_d, initial rate of the initiatior decomposition; *f*, initiation efficiency; [Inh], inhibitor concentration; μ, stoichiometric coefficient equal to the number of chains terminated on one inhibitor molecule, μ = 1 in our case [5]; and *n*, number of radicals participating in the initiation.

The reaction of DASP and DASPO with BP yields two radicals capable to initiate polymerization of vinyl monomers. The amine radical cation generated in the process loses a proton, transforming into a radical which, along with the benzoyloxy radical, participates in the initiation [6]:

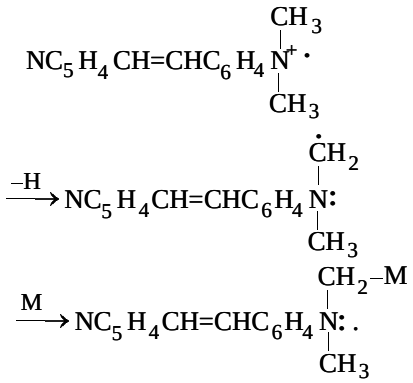

In decomposition of BP in the presence of quaternary salts, two pathways (catalytic and noncatalytic) are possible, both yielding two radicals:

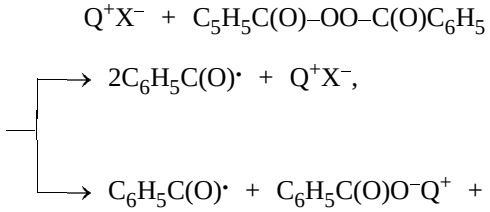

The initiation efficiency was determined by the equation

$$f = W_{in}/2W_d. \quad (3)$$

The rate of BP decomposition W_d was calculated by the equation

$$W_d = k_D[\text{BP}][\text{Act}].$$

The kinetic parameters of methyl methacrylate polymerization in the presence of BP–activator initiating systems and the initiation efficiencies are given in Table 1.

The initial concentrations of the peroxide and salt were the same in all the experiments (2.5×10^{-2} and

Table 1. Rates of benzoyl peroxide decomposition in the presence of activators W_d, initial polymerization rates W_{pol}, initiation rates W_{in}, and initiation efficiencies at 303 K

Activator	[Inh] × 10^5, M	τ × 10^{-2}, s	$W_{pol} \times 10^6$	$W_{in} \times 10^8$	$W_d \times 10^8$	*f*
			mol l^{-1} s^{-1}			
$(Me)_2PhCH{=}CHPy$	0	0	13.2 ± 0.01	–	0.9 ± 0.1	0.7 ± 0.2
	1	7.5	13.2 ± 0.04	1.3 ± 0.3		
	3	26	12.9 ± 0.03	1.16 ± 0.07		
$(Me)_2PhCH{=}CHPy{\rightarrow}O$	0	0	14.1 ± 0.01	–	1.0 ± 0.2	0.60 ± 0.04
	3	23	13.9 ± 0.01	1.29 ± 0.06		
	5	41	13.7 ± 0.01	1.22 ± 0.05		
$Ph_3(PhCH_2)P^+Cl^-$	0	0	8.2 ± 0.1	–	39 ± 2	0.02 ± 0.003
	1	6.2	7.41 ± 0.07	1.6 ± 0.1		
	2	12	7.11 ± 0.06	1.67 ± 0.05		
	3	18.3	5.81 ± 0.04	1.64 ± 0.03		
$Ph_3(PhCH_2)P^+Br^-$	0	0	6.39 ± 0.05	–	840 ± 16	0.003 ± 0.0005
	2	4	6.6 ± 0.1	5.1 ± 0.7		
	3	6	6.9 ± 0.1	4.9 ± 0.4		
	4	7.5	6.40 ± 0.33	5.3 ± 1.1		
$Et_4N^+Cl^-$	0	0	6.18 ± 0.03	–	38 ± 8	0.19 ± 0.05
	26	18	6.26 ± 0.07	14.5 ± 0.5		
	50	31	6.49 ± 0.06	16.2 ± 0.4		
	100	74	6.63 ± 0.01	13.50 ± 0.01		
$Et_4N^+Br^-$	0	0	9.11 ± 0.05	–	138 ± 4	0.05 ± 0.01
	26	18.7	8.79 ± 0.05	13.9 ± 0.2		
	50	37.8	8.81 ± 0.01	13.23 ± 0.01		
	740	55.5	8.96 ± 0.08	13.3 ± 0.2		
$Et_4N^+PhC(O)O^-$	0	0	6.30 ± 0.07	–	–	–
	1	20.5	6.52 ± 0.06	0.49 ± 0.02		
	2	41.3	6.26 ± 0.09	0.48 ± 0.01		

5×10^{-3} M, respectively), which allowed comparison of the initiation rates. Table 1 shows that the initiation rate is the highest in the presence of tetraethylammonium chloride, decreasing in the order $Et_4N^+Cl^- > Et_4N^+Br > Ph_3(PhCH_2)P^+Br^- > Ph_3(PhCH_2)P^+Cl^-$. At the same time, the initiation efficiency decreases in the order $Et_4N^+Cl > Et_4N^+Br^- > Ph_3(PhCH_2)P^+Cl > Ph_3(PhCH_2)P^+Br^-$.

The initiation rates with the systems BP + DASP and BP + DASPO are approximately equal and comparable with those observed with the systems containing onium salts, but the concentrations of BP and amines are lower: 7.5×10^{-3} and 2.5×10^{-4} M, respectively. It should be noted that the efficiency of initiation of methyl methacrylate polymerization in the presence of BP and aminostyrylpyridines is considerably higher than in the presence of the peroxide–salt systems.

Decomposition of organic peroxides under the action of activators is a complex process involving decomposition of the peroxide bond with the formation of free radicals, ions, and molecules; the ratio of the species formed depends on the kind of activator and properties of the reaction medium. In particular, recombination of the radicals in a solvent "cage" significantly decreases the fraction of active radicals diffusing into the bulk and thus decreases the initiation efficiency. For example, according to [7], the recombination rate in thermal decomposition of diacyl peroxides $[RC(O)O]_2$ sharply decreases in the series of peroxides with $R = CH_3 > C_6H_5 > n\text{-}C_4H_7$, and the results given in [8] reflect the trend that the efficiency of escape of radicals into the bulk increases in going from linear aliphatic radicals to branched radicals.

As seen from Table 1, in the systems DASP–BP and DASPO–BP the initiation efficiency is higher than in other related peroxide–activator systems [9–11], which may be due to hindered recombination of the generated radicals. Generation of bulky radicals from the initiator is preferable for polymerization initiation [8], because the recombination rate depends

Table 2. Content *c* of residual monomer in poly(methyl methacrylate) prepared in the presence of benzoyl peroxide–activator initiating systems

Activator	*c*, %
Thermal polymerization	0.94
$Et_4N^+Cl^-$	0.87
$Et_4N^+Br^-$	1.19
$Ph_3(PhCH_2)P^+Cl^-$	0.89

on the accessibility of the active centers of the radical and on the diffusion rate. For radicals of simple structure, generated in the systems BP–onium salt [$C_6H_5 \cdot C(O)O^\bullet$, $Br^\bullet$, $Cl^\bullet$], the accessibility factor prevails, and the initiation efficiency appreciably decreases.

The main application field of peroxide–amine binary initiators is curing and vulcanization, since the reaction products formed in the system are, as a rule, colored. Peroxide–onium salt systems can be used for preparing transparent high-purity poly(methyl methacrylate). The polymers prepared in the presence of peroxide–quaternary ammonium salt initiators were analyzed for the residual monomer content. Test poly(methyl methacrylate) samples were prepared by polymerization of methyl methacrylate in the bulk, initiated with systems containing BP and quaternary ammonium and phosphonium salts. The polymerization was performed at 303–318 K for 24–48 h. The monomer conversion under these conditions was 85–97% (GLC data). Under these conditions, no gel effect was observed. Afterpolymerization was performed at 393 K for 48–72 h. The BP–onium salt initiating systems ensure preparation of the transparent polymer at 303–313 K. The residual monomer in poly(methyl methacrylate) was determined by gas–liquid chromatography after dissolution of the polymer in chloroform. The results are listed in Table 2.

CONCLUSION

Data on the efficiency of initiation of methyl methacrylate polymerization with the binary systems benzoyl peroxide–onium salt and benzoyl peroxide–aminostyrylpyridine show that the rate of the peroxide decomposition and the yield of the radicals can be varied in a wide range by varying the structure of the catalyst.

REFERENCES

1. Leshin, V.V., Abramov, L.N., Kolegov, V.I., *et al.*, *Vysokomol. Soedin.*, 1985, vol. 27, no. 5, pp. 371–374.
2. Turovs'kii, M.A., Tselins'kii, S.Yu., Opeida, I.O, *et al.*, *Ukr. Khim. Zh.*, 1995, vol. 61, no. 5, pp. 67–71.
3. Turovskyj, M.A., Opeyda, I.O., and Kusch, O.V., in *New Developments in Chemistry and Biochemistry*, New York: Nova Sci., 2003, pp. 161–170.
4. Parker, E.D. and Furst, A., *J. Org. Chem.*, 1958, vol. 23, no. 2, pp. 201–203.
5. Plyusnin, A.N. and Chirkov, N.M., *Teor. Eksp. Khim.*, 1966, vol. 2, no. 6, pp. 777–782.
6. Sato, T. and Otsu, T., *Macromol. Chem.*, 1975, vol. 176, p. 561.
7. Oae, S. and Fujimori, K., *The Chemistry of Functional Groups: Peroxides*, New York: Wiley, 1983.
8. Kochkina, L.G., Loginova, N.N., Kulikova, N.M., *et al.*, *Zh. Prikl. Khim.*, 1983, vol. 56, no. 4, pp. 945–949.
9. Pryor, W.A. and Bickley, H.T., *J. Org. Chem.*, 1972, vol. 37, no. 18, pp. 2885–2893.
10. Pryor, W.A. and Hendricson, W.H., *J. Am. Chem. Soc.*, 1975, vol. 97, no. 6, pp. 1580–1582.
11. Pryor, W.A. and Hendricson, W.H., *J. Am. Chem. Soc.*, 1983, vol. 105, no. 24, pp. 7114–7122.

Russian Journal of Applied Chemistry, Vol. 77, No. 11, 2004, pp. 1873–1876. Translated from Zhurnal Prikladnoi Khimii, Vol. 77, No. 11, 2004, pp. 1891–1894.

MACROMOLECULAR CHEMISTRY AND POLYMERIC MATERIALS

Structure and Characteristics of Copolyamides Based on ε-Caprolactam and Diisocyanates

S. S. Galibeev, O. V. Barnyagina, A. M. Kochnev, V. P. Arkhireev, and L. R. Galimov

Kazan State Technological University, Kazan, Tatarstan, Russia

Received April 6, 2004

Abstract—The main supramolecular characteristics and the processing and service characteristics of copolyamides based on ε-caprolactam and hexamethylene diisocyanate were studied. The relation between the comonomer composition and supramolecular structure of copolymers was established.

Among numerous procedures of production of polyamides (PAs), one of the simplest is anionic polymerization of ε-caprolactam (ε-CL), which allows realization of practically 100% conversion and production of the polymer with high strength characteristics [1–5]. The resulting polycaproamide can be subjected to only mechanical treatment and cannot be molded to form items by standard procedures of processing of thermoplastics, which significantly narrows possible fields of its application. Therefore, so-called copolymers of ε-CL with other monomers, such as adipate, amimoenanthic acid, pyrrolidone, piperidine, etc., are of great practical significance. These copolyamides (CPAs) have lower melting points, which facilitates their processing and in some cases extends the fields of their application (films, fibers, etc.) [6, 7].

A procedure of production of CPAs based on ε-CL and a series of aliphatic and aromatic diisocyanates [hexamethylene diisocyanate (HMDI), 2,4-toluylene diisocyanate (TDI), and 4,4'-diphenylmethane diisocyanate (MDI)] in the presence of alkali metal (Na and Li) lactamates was developed previously [8, 9]. It was shown that, by varying the structure of PA macromolecule by introducing isocyanate component, its thermal characteristics, in particular, softening point, can be varied over a wide range.

In this work we examined the influence of the comonomer composition on the thermal, supramolecular, and mechanical characteristics of the resulting copolymers.

EXPERIMENTAL

The supramolecular structure of CPA was studied by differential scanning calorimetry (DSC; a DSK-D unit, heating rate 4 deg min^{-1}), differential thermal analysis (DTA), and X-ray analysis. The TG and DTG curves were obtained on an MOM derivatograph (Hungary) at a heating rate of 3 deg min^{-1}. The sample weight was 0.2 g. The X-ray analysis was carried out on a DRON-2 equipment (CoK_α radiation). The effective size of crystallites L, degree of crystallinity χ_c, and first-kind G_1 and second-kind G_2 defects were determined by the procedure described in [10]. The relaxation time was determined on a pulse NMR relaxometer operating at 20 MHz. The measurements were performed by the Carr–Purcell–Meiboom–Gill method and the running sequence method at 25°C [11].

The activation energy of failure U_0 was found using the Gul' equation [12]

$$\sigma_d = K_1 V_1^n e^{U_0/RT},$$

where V_1 is the extension rate, and K_1 and n are the parameters determined by the material nature and the sample size and shape.

Taking the logarithm of this equation, we obtain

$$\ln \sigma_d = \ln K_1 V_1^n + U_0/RT.$$

The slope of the straight line plotted in the coordinates $\ln\sigma_d$–$1/T$ is U_0/R. Hence, $U_0 = R\tan\alpha$.

The samples for determination of physicochemical characteristics were cut from plates produced by hot pressing. The samples were kept under a pressure for 5 min per 1 mm of the sample thickness. The physicomechanical characteristics were determined on an RM 500-T tensile-testing machine. The velocity of the tensile-testing machine clamps was 100 mm min^{-1}.

1070-4272/04/7711-1873 © 2004 MAIK "Nauka/Interperiodica"

Table 1. DTA data for CPA based on ε-CL and HMDI

HMDI content in initial monomer mixture, wt parts	$T_{o.m}$	T_m	ΔT_m	ΔH_m, kJ mol^{-1}
	°C			
–	200	243	43	77.9
5	190	237	47	59.9
10	143	193	50	17.2

Table 2. Diffuseness of melting of copolymers based on ε-CL and SKU (from the evidence of DSC)

SKU content in initial monomer mixture, wt.p.	ΔT_m, °C
–	14
10	20
15	39

The thermomechanical analysis was carried out with the samples 0.3 cm in diameter and 4 mm thick. The samples were cut from pressed plates and heated at a rate of 3 deg min^{-1}. The DTA and DTG curves were recorded at a periodical stress (period of stressing 0.25 min). The softening point was evaluated from the thermomechanical curves.

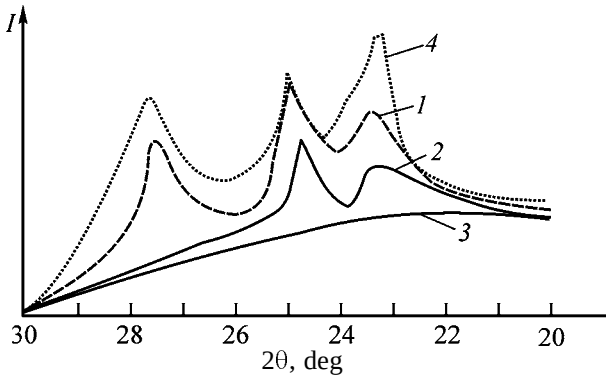

Fig. 1. Diffraction patterns (*1*–*3*) of copolymers based on ε-CL and HMDI at weight ratios of (*1*) 95 : 5, (*2*) 70 : 30, and (*3*) 50 : 50 and (*4*) of ε-CL homopolymer. (*I*) Intensity and (2θ) Bragg angle.

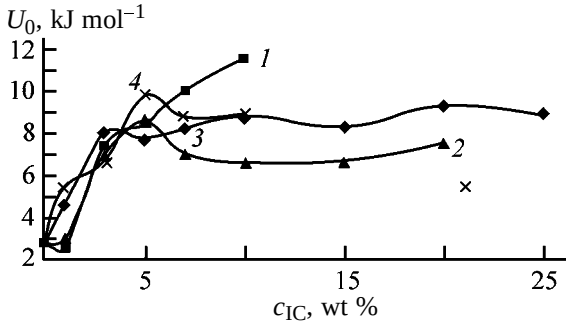

Fig. 2. Activation barrier of CPA failure as a function of content of ICs. (*1*) MDI, (*2*) SKU, (*3*) HMDI, and (*4*) TDI.

The synthesized CPAs are partially crystalline polymers. It was found that the degree of crystallinity of CPAs decreases with increasing content of isocyanates (ICs). This is apparently caused by growing steric hindrances appearing as a result of increasing branching of macromolecules, which is, in turn, determined by bifunctionality of the ICs used; this results in formation of polydisperse supramolecular structures. Thus, even at low content of HMDI in the initial monomer mixture, the heat of melting ΔH_m of the resulting CPAs significantly decreases; in this case, the temperature $T_{o.m}$ of the onset of melting and the equilibrium melting point T_m decrease and the melting diffuseness ΔT_m increases (Table 1). The similar variations are observed with an oligourethane SKU (the product of reaction of polyoxymethylene glycol and TDI) used as an isocyanate component (Table 2). The substantial changes in the supramolecular structure are evident from the diffraction patterns of the resulting polymers (Fig. 1). As seen, the copolymer of ε-CL with HMDI, similar to ε-CL hopolymer, has three reflections whose positions do not vary, only their intensities decrease.

With increasing fraction of ICs, χ_c of CPAs decreases, which, as mentioned above, can be caused by increase in branching of macromolecules. In parallel with decreasing fraction of crystallinity, the G_2 values caused by disordering in arrangement of the lattice points at long distances decrease and the G_1 values related, on the one hand, to displacement of the lattice points from the theoretical positions and, on the other hand, to nonuniformity in size remain practically the same (Table 3). The use of both sodium lactamate and lithium lactamate as a catalyst does not noticeably affect the trends in variation of the above characteristics.

An increase in the branching of macromolecules regularly hinders the conformation mobility. Thus, the spin–lattice relaxation time τ_1 of the synthesized CPAs in the temperature range in which they are in the hyperelastic state increases with increasing content of ICs in the initial monomer mixture (Table 4).

A decrease in the flexibility can be judged from a decrease in the activation barrier of CPA failure (Fig. 2). As seen, the copolymers prepared with all the ICs studied are characterized by increased U_0; in this case, the greatest increase occurs in the range of IC content in the initial monomer mixture from 1 to

Table 3. Data of X-ray analysis of CPA based on ε-CL and HMDI

HMDI content in initial monomer mixture, wt parts	G_1, %		G_2, %		χ_c, %	
	Na-CL	Li-CL	Na-CL	Li-CL	Na-CL	Li-CL
–	4.3	4.1	5.7	4.6	40	33
5	4.4	4.7	2.5	2.7	30	28
10	4.3	4.3	2.8	2.8	29	26
30	6.5	4.5	2.5	2.5	10	17

5 wt %. However, it is possible that the increase in U_0 is also caused by the increase in the cooperativity of deformation processes preceding the failure.

Changes occurring on the supramolecular level result in variation of the macroscopic characteristics. Thus, for CPAs with the HMDI content less than 20 wt parts, the shape of the stress–strain curves corresponds to crystalline polymers, while with increasing fraction of ICs it changes and becomes close to the shape typical of amorphous polymers (Fig. 3).

Table 4. Spin–spin relaxation time of CPA

HMDI content in initial monomer mixture, wt parts	τ_1, ms
–	130
1	142
3	145
5	147
7	160
10	152

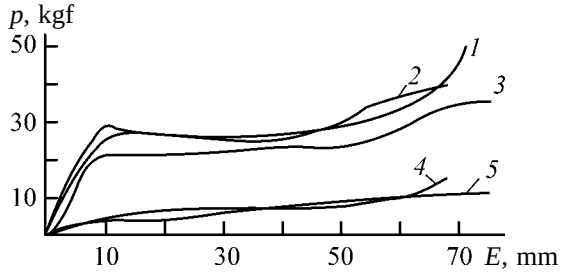

Fig. 3. Strain E–stress p curve of copolymers based on ε-CL and HMDI. HMDI content in the initial monomer mixture (wt parts): (*1*) 0, (*2*) 5, (*3*) 10, (*4*) 20, and (*5*) 30.

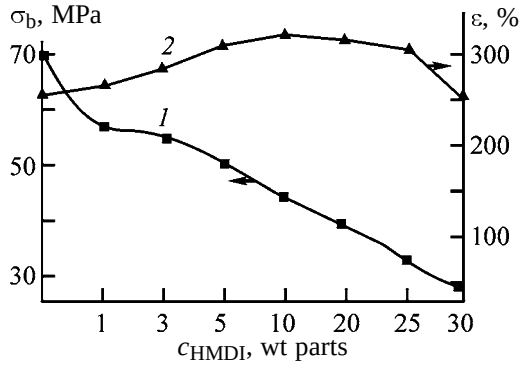

Fig. 4. (*1*) Breaking stress σ_b and (*2*) relative elongation ε of CPA as a function of HMDI content c_{HMDI} in the initial monomer mixture.

With increasing content of ICs, the softening point T_s determined from thermomechanical analysis monotonically decreases from 210°C for ε-CL homopolymer to 140°C on adding 20 wt parts HMDI. This decrease is apparently caused by variation in the structure of macromolecules. Introduction of IC into the polyamide chain results in appearance of bulky substituents with reactive NCO groups, which can cause branching of the macromolecule chain and, hence, decrease the intermolecular interaction in the resulting copolymer. This assumption is confirmed by the results of physicomechanical tests: the breaking stress σ_b decreases and the relative elongation ε slightly increases (Fig. 4).

CONCLUSIONS

(1) Copolymers with the supramolecular structure and characteristics varying in a wide range, depending on the ratio of the initial monomers, were prepared by anionic copolymerization of ε-caprolactam and diisocyanates.

(2) With increasing content of diisocyanates up to 30 wt parts, the crystalline polymers are formed. Further increase in the content of the isocyanate component results in complete disappearance of supramolecular formations.

REFERENECS

1. *Entsiklopediya polimerov* (Encyclopedia of Polymers), Moscow: Sov. Entsiklopedia, 1974, vol. 2.
2. Nikolaev, A.F., *Tekhnologiya plasticheskikh mass* (Technology of Plastics), Leningrad: Khimiya, 1977.

3. RF Patent 1 790 200, 1996.
4. Heda, K., Yamada, K., and Nahai, M., *Polym. J.*, 1996, vol. 28, no. 5, pp. 446 – 451.
5. Czechoslovak Patent 9424-87, 1991.
6. German Patent 624/89, 1993.
7. Czechoslovak Patent 228-89B, 1991.
8. Galibeev, S.S., Arkhireev, V.P., Barnyagina, O.V., *et al*., *Izv. Vyssh. Uchebn. Zaved., Khim. Khim. Tekhnol*., 2003, vol. 46, no. 4, pp. 88–90.
9. Arkhireev, V.P., Galibeev, S.S., and Barnyagina, O.V., Abstracts of Papers, *XVII Mendeleevskii s"ezd po obschei i prikladnoi khimii* (XVII Mendeleev Congr. on General and Applied Chemistry), Kazan, 2003, vol. 3, p. 44.
10. Martynov, M.A. and Vylegzhanina, K.A., *Rentgenografiya polimerov* (X-Ray Diffraction Analysis of Polymers), Leningrad: Khimiya, 1972.
11. *Issledovanie protsessov sinteza, struktury i svoistv VMS metodom YaMR: Metodicheskie ukazaniya* (NMR Study of Synthesis, Structure, and Characteristics of Macromolecular Compounds: Methodical Guideline), Kazan: Kazan. Khim.-Tekhnol. Inst., 1979.
12. Gul', V.E. and Kuleznev, V.N., *Struktura i mekhanicheskie svoistva polimerov* (Structure and Mechanical Characteristics of Polymers), Moscow: Labirint, 1994.

Russian Journal of Applied Chemistry, Vol. 77, No. 11, 2004, pp. 1877–1882. Translated from Zhurnal Prikladnoi Khimii, Vol. 77, No. 11, 2004, pp. 1895–1900.

MACROMOLECULAR CHEMISTRY AND POLYMERIC MATERIALS

Transport Properties of Cellulose Ester Membranes for Separating Gas and Liquid Mixtures

Yu. P. Kuznetsov, A. K. Khripunov, E. V. Kruchinina, V. M. Kuznetsov, L. D. Turkova, and A. V. Pen'kova

Institute of Macromolecular Compounds, Russian Academy of Sciences, St. Petersburg, Russia
St. Petersburg State University, St. Petersburg, Russia

Received April 29, 2004

Abstract—Mass-exchange characteristics of cellulose myristate or acetomyristate membranes in separating aqueous-organic, organic, or gas mixtures, particularly, in recovering aromatic hydrocarbons from binary mixtures with aliphatic alcohols, and also ethyl acetate from a mixture of esterification products, are studied.

There is a steady scientific and practical interest in cellulose-based membranes in recent six decades, which is caused by easy availability of cellulose raw material, and also by the possibility of directed synthesis of homologous series of various cellulose derivatives with desired physicochemical characteristics. Therefore, cellulose-based membranes with desired transport properties can be prepared as well. Microporous (diffusion) membranes are mostly formed on the basis of cellulose esters or mixed esters (diacetates, triacetates, acetobutyrates), regenerated cellulose, and chitosan [1–6]. Previously we demonstrated the possibility of using cellulose acetomyristate diffusion membranes for separating aromatic and aliphatic hydrocarbons using the pervaporation technique [7]. In this work we studied the transport properties of cellulose myristate (CM) and acetomyristate (CAM) membranes of different composition in separating gas, aqueous-organic, and organic mixtures.

EXPERIMENTAL

Cellulose myristate and acetomyristates were prepared according to the standard procedure [8]. Membranes as nonporous films of a fixed thickness were formed from chloroform solutions of the polymers on a cellophane support. The pervaporation experiments were carried out using a laboratory cell of the autonomous type (effective area of the membrane 12 cm^2) with stirring the mixtures over the membrane at a residual pressure under the membrane of 0.2 mbar. The permeate vapor (flow passed across the membrane) was condensed in a receiving vessel at the liquid nitrogen temperature and weighed, and the total flow $\prod$ ($kg\ m^{-2}\ h^{-1}$) was estimated. In the experiments we used binary mixtures ethanol–water, toluene–methanol, and benzene–ethanol of various compositions, and also a mixture of ethyl acetate, acetic acid, ethanol, and water. The compositions of permeates were analyzed on a refractometer or chromatographically using Porapak-Q or Reoplex columns. The partition factor α was estimated as

$$\alpha_{A/B} = (X_A/X_B)/(Y_A/Y_B),$$

where Y_A and Y_B are the concentrations of A and B in the initial binary mixture (wt %), and X_A and X_B, in the permeate (wt %).

The gas-permeability coefficient P and selectivity factor $\alpha_{A/B}$ of vapors were determined chromatographically using a column filled with 5A molecular sieve as a stationary phase at an excess pressure over the membrane of 10 mbar. The compositions of liquid permeates and gas-permeability coefficients were determined to within 5 and 10%, respectively.

To study the selectivity of CM membranes, we prepared a 1 m long chromatographic column with the CM stationary phase supported on Celite 22. The evolution of the chemical structure of cellulose esters on passing from cellulose diacetate to CM is accompanied by decreasing packing density of the polymer chains and increasing fraction of the free volume in the polymer matrix. This is caused by weakening of the network of the hydrogen bonds and disordering of the supramolecular structure, being reflected in a regular increase in the gas permeability with parallel decrease in the selectivity. These trends are illustrated

Table 1. Gas-selective characteristics of homogeneous cellulose acetomyristate membranes at 20°C

Parameter	CAM composition (acetate/myristate)		
	290/10	150/150	10/290
Permeability coefficient, barrer:*			
N_2	0.3	7.95	15.7
O_2	1.6	25.2	40.2
He	14.5	30.8	41.2
CO_2	17.5	139.3	193.5
Selectivity coefficient:			
O_2/N_2	5.3	3.2	2.55
He/N_2	42	3.9	2.6
CO_2/O_2	10.7	5.5	4.8

* 1 barrer = 1×10^{-10} cm^3 cm cm^{-2} s^{-1} cm^{-1} Hg.

Table 2. Separation of water–ethanol mixtures on cellulose acetomyristate membranes at 50°C

Parameter	CAM composition (acetate/myristate)		
	290/10	150/150	10/290
90 wt % EtOH			
Flow,* kg m^{-2} h^{-1}	5.6	1.4	1.1
H_2O in permeate, wt %	53	20	14
α_{H_2O}	10.2	2.3	1.5
50 wt % EtOH			
Flow,* kg m^{-2} h^{-1}	2.4	1.5	0.78
EtOH in permeate, wt %	20	80	85
α_{EtOH}	0.25	4.0	5.7
10 wt % EtOH			
Flow,* kg m^{-2} h^{-1}	2.8	0.48	0.36
EtOH in permeate, wt %	6	50	55
α_{EtOH}	0.6	9.1	11.1

* The flow is normalized to the membrane thickness of 10 μm.

in Table 1 with an example of CAM membranes of various compositions. The results demonstrate the opposite tendencies in the behavior of the gas-permeability coefficients *P* of the individual gases and of the selectivity factor α for various pairs of gases with increasing myristate content in the CAM membranes.

The maximal *P* values and the corresponding minimal α values were obtained for the 10/290 CAM membrane. In this case, the transport parameters approach those of the membranes based on polymers with low glass transition temperature, for example, polydimethylsiloxane [9] or cellulose diacetate plasticized with polyethylene glycol oligomers [6].

It is known that, in pervaporation separation of aqueous-organic mixtures, the direction of selective mass transfer is controlled not only by the kinetic diameter of molecules diffusing across the membrane, but also by the difference in the affinity of the components of the mixture with respect to the film-forming polymer. One of the parameters characterizing such an affinity can be the equilibrium swellability of the membrane in individual components of the mixture to be separated. This parameter with respect to water and ethanol is considerably different for cellulose diacetate and CM (6.5 and 0.3 wt %, and 10.7 and 3.7 wt %, respectively). Therefore, it was interesting to study the transport properties of CAM membranes with various acetate to myristate group ratios.

Table 2 shows the results of pervaporation separation of aqueous-ethanol solutions of various compositions. In separating the concentrated solution of ethanol, all the CAM membranes studied demonstrate dehydrating properties, even though the maximal α_{H_2O} = 10.2 is considerably lower than that of the known highly selective membranes used for dehydration [10, 11]. The tendency of α_{H_2O} to decrease in this series from 10.2 to 1.5 correlates with the increase in the hydrophobicity of the corresponding CAM membranes. At the same time, in separating more dilute solutions of ethanol with 150/150 and 10/290 CAM membranes, the direction of selective mass transfer changes for the opposite, demonstrating the tendency to increase in α_{EtOH} from 4.0 to 11.1, depending on the composition of the initial mixture and content of the myristate component in the membrane. The maximal α_{EtOH} = 11.1, obtained for 10/290 CAM membrane in separating 10 wt % EtOH–H_2O mixture, is well comparable with that of the membrane based on hydrophobic polymethylsiloxane [12]. Therefore, even higher selectivity could be expected for the CM membrane. However, its permeability with respect to both ethanol and water appeared to be very low, which is consistent with data on the equilibrium swellability of CM in these solvents, suggesting no practical interest.

The results obtained evidence the necessity in optimization of the hydrophilic–hydrophobic balance for membranes of this purpose, to attain a reasonable relation between their permeability and selectivity. Therefore, 150/150 and 10/290 CAM membranes are more suitable to concentrate ethanol from dilute aque-

ous solutions. It should be pointed out that, with an example of CAM membranes having a unitypical chemical structure regardless of the composition, we have demonstrated the possibility of changing the direction of selective mass transfer in separating water–ethanol mixtures.

Furthermore, it was interesting to compare the known methods for separating aqueous-organic and organic mixtures, such as rectification and distillation, with the pervaporation technique. Like distillation, in pervaporation the permeate is removed as a vapor, allowing comparative evaluation of the expediency of using this technique. In this case, we can compare the pervaporation diagrams characterizing the dependence of the permeate composition on the composition of the feed mixture with the liquid–vapor diagram of the same system.

Such a comparative analysis of the diagrams appeared to be most indicative for azeotropic systems. High efficiency of pervaporation separation in such systems was repeatedly indicated in the literature. Furthermore, there are numerous examples of industrial applications of membrane separation of azeotropic mixtures [13]. As an illustration, Fig. 1 gives the comparison of the liquid–vapor diagram [14] and the experimental data obtained for CAM membranes of various compositions in separating ethanol–water mixtures. For the CAM membranes demonstrating dehydrating and organophilic properties, the dependences of the permeate composition on the composition of the initial mixture are arranged below (Fig. 1, curve *2*) and above (curves *3* and *4*) the liquid–vapor equilibrium curve (curve *1*).

Comparative analysis of data presented in Fig. 1 shows some advantage of the 150/150 and 10/290 organophilic CAM membranes in the selectivity of separation of more dilute solutions of ethanol (Fig. 1, curves *3* and *4*) over equilibrium open evaporation. It is known from the literature [12, 15] that close arrangement of the pervaporation curves with respect to the liquid–vapor equilibrium curve is typical of a series of ethanol-selective membranes. In Fig. 1 (curve *5*) this is illustrated by an example of the membrane fabricated from Silar block copolymer, which was previously studied in separating ethanol–water mixtures over a wide composition range [16]. Our results (Fig. 1, curve *2*) also demonstrate relatively small advantage of the dehydrating 290/10 CAM membrane in the selectivity as compared to open evaporation.

At the same time, the advantage of pervaporation could be more pronounced just in dehydration of

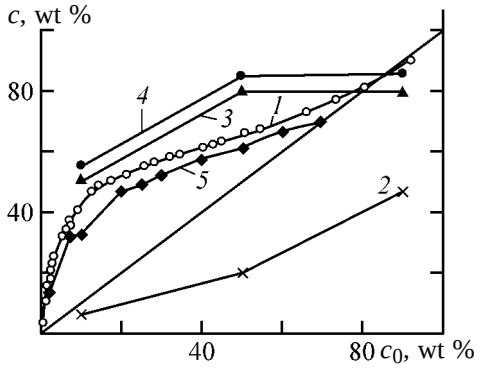

Fig. 1. Ethanol concentration c (*1*) in the vapor (liquid–vapor equilibrium in open evaporation) and in the permeate for membranes (*2*) 290/10 CAM, (*3*) 150/150 CAM, (*4*) 10/290 CAM, and (*5*) Silar as a function of the initial ethanol concentration c_0 in ethanol–water mixtures at 20°C.

water–ethanol mixtures. In this case, particularly in separating ethanol-rich mixtures close in their composition to the azeotropic mixture, the selectivity of membrane separation could be higher by 2–3 orders of magnitude than that in open evaporation. This is favored by the effect of diffusion mass transfer, i.e., by smaller kinetic diameter of the water molecules. From the practical standpoint, there is a wide spectrum of polymers and membranes on their basis [11, 17, 18] demonstrating strongly different affinity for water and ethanol, with the difference being considerably larger compared to dehydrating 290/10 CAM membrane (Table 2) and also to cellulose diacetate membrane [19].

Selection of binary systems showing more promise for pervaporation separation with the CM membrane was made using inverse gas chromatography (IGC). Roberts *et al.* [20] employed this technique using chromatographic columns with different polymeric stationary phases to predict the direction of selective mass transfer across the membranes fabricated from the same polymers in separating binary liquid mixtures. As a criterion they used the retention time (retention time of a component of the mixture on the column is in inverse proportion to its flow rate across the membrane). Therefore, we determined the retention times of a series of organic solvents on the CM column. The retention time increased in the order methanol < ethanol < benzene < toluene < ethyl acetate, being 105, 116, 126, 135, and 148 s, respectively. Knowing this parameter allowed prediction of the possibility of membrane separation of mixtures of toluene (or benzene) with methanol (or ethanol) with selective mass transfer directed in favor of the aromatic component, which was confirmed in the pervapora-

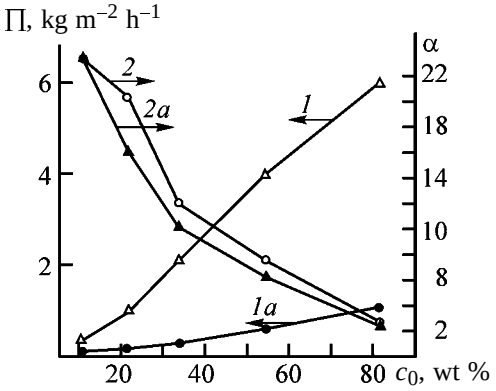

Fig. 2. (*1*, *1a*) Total flow ∏ and (*2*, *2a*) partition factor α in separating toluene–methanol mixture on the CM membrane as functions of the initial toluene concentration c_0 at 20°C. (*a*) For comments, see text.

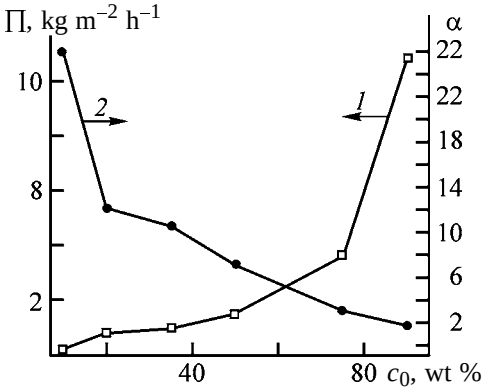

Fig. 3. (*1*) Total flow ∏ and (*2*) partition factor α in separating benzene–ethanol mixture on the CM membrane as functions of the initial benzene concentration c_0 at 20°C.

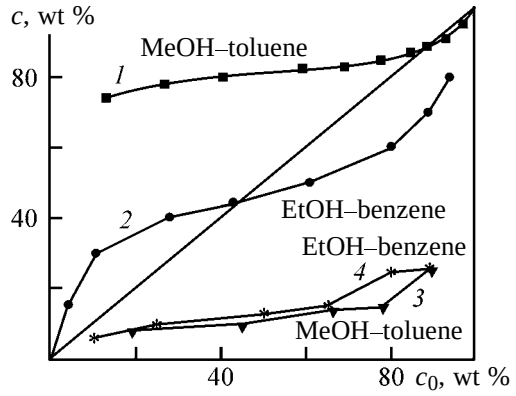

Fig. 4. (*1*, *3*) Methanol and (*2*, *4*) ethanol contents *c* in (*3*, *4*) permeate (CM membrane) and (*1*, *2*) vapor (liquid–vapor equilibrium in open evaporation) as functions of the initial methanol (or ethanol) concentration c_0 in mixtures with toluene and benzene, respectively, at 20°C.

tion experiments. Separation of such mixtures is of considerable scientific and practical interest, since these compounds form azeotropic systems and have similar boiling points (e.g., benzene and ethanol).

Figures 2 and 3 show the permselectivity α and total flow across the CM membrane ∏ as functions of the initial composition of the toluene–methanol and benzene–ethanol mixtures. As seen, over a wide concentration range, the CM membrane is selective with respect to the aromatic component of the mixture. Figure 2 demonstrates regular increase of the flow across the membrane (curve *1*) and parallel decrease in $\alpha_{toluene}$ (curve 2) with increasing toluene concentration in the initial mixture. Similar trend in the behavior of the transport parameters was observed also in separating the benzene–ethanol mixture (Fig. 3). It should be pointed out that, in separating the toluene–methanol mixture (Fig. 2), nearly the optimal relation between α and ∏ was obtained at the composition of the initial mixture close to the azeotropic composition (31 wt % toluene). For both systems, even at room temperature, 30–50 μm thick membranes allow sufficiently large flows in separating azeotropic mixtures, the attainable selectivity levels being well comparable with those of the membranes commonly used for this purpose [21].

Figure 2 (curves *1*, *2*) shows the dependences obtained in the pervaporation experiments on the same membrane with increasing toluene concentration in the initial mixture. Before passing to the next feed composition, the membrane cell was evacuated for a fixed time (10 min) to partially remove the solvents. Curves *1a* and *2a* were obtained at different evacuation time (1 h). As seen, longer drying of the membrane considerably affects the process characteristics, especially the flow ∏ (curve *1a*). The observed increase in the permeability at higher initial toluene concentration (Fig. 2, curve *1*) can be attributed to stepwise activation of the membrane structure at the supramolecular level with more penetrating component (toluene). Similar effect was observed previously [7] for CAM membranes in separating benzene–heptane mixtures.

In Fig. 4, the dependences of the permeate composition on the composition of the initial toluene–methanol (curve *3*) and benzene–ethanol (curve *4*) mixtures are presented along with the corresponding liquid–vapor diagrams obtained in the case of open equilibrium evaporation (curves *1*, *2*). A specific feature of pervaporation separation is that, over the entire feed composition range, the pervaporation curves are arranged considerably below the open evaporation curves, particularly, in separating the azeotropic mixtures. It should be pointed out that, in the frameworks of such comparative analysis, the pervaporation curves presented in Fig. 4 differ advantageously from those given in Fig. 2 for the system ethanol–water.

For the system toluene–methanol of the azeotropic compositions, we also studied the possibility of optimization of the transport properties with regard to the thickness of the CM membrane. The selectivity and flow across the membrane were determined at 20°C for 30-, 50-, and 690-μm thick membranes, and at 20 and 40°C for a 50-μm membrane. In each case, we determined the arbitrary production parameter as the product of ∏ and α. The maximal value of this parameter corresponds to the optimal relation between the flow across the membrane and the selectivity of separation. The production index appeared to be maximal for the 50-μm membrane (8.36 and 12.95 kg m^{-2} h^{-1} at 20 and 40°C, respectively).

In terms of the existing concept of the pervaporation mechanism, the immediate cause of the effect of the membrane thickness is associated with the penetrant concentration gradient across the membrane. In steady-state mass transfer, the penetrant concentration decreases in the direction to the permeate side of the membrane. Therefore, the surface of the membrane at the feed side occurs in the state maximally close to the condition of equilibrium swelling with regard to the components of the mixture. In this zone, the selectivity of separation is relatively low as a result of the plasticization of the surface layers of the membrane. In deeper layers, the degree of approaching the equilibrium swelling should decrease. As a result, "drier" layers at the permeate side are plasticized to a smaller extent, and the flexibility of the polymer chains or their segments in this zone is considerably lower, which should exert a positive effect on the separation selectivity. At the same time, with all other conditions being equal, with increasing concentration of more penetrable component in the mixture, the flow across the membrane increases. In this case, the concentration gradient and the thickness of the "dry" layer decrease, negatively affecting the selective properties.

This concept gives grounds to use the term "cross-membrane selectivity gradient." In each particular case of separation, the occurrence of such a gradient allows control of the transport characteristics of the membrane, including α. In this connection, it may be concluded that the use of the term "ideal partition factor" is incorrect with respect to pervaporation membranes as continuous nonporous films, since, with all other conditions being equal, α will increase with increasing thickness of the membrane.

To conclude, mixtures of aliphatic alcohols and aromatic hydrocarbons can be separated on pervaporation membranes in a single stage, to obtain the concentration of the aromatic component in permeate of up to 80–90 wt %. The resulting permeates can be then partitioned by, e.g., ordinary distillation. An alternative can be the use of methanol- or ethanol-selective pervaporation membranes in the second stage also. Furthermore, the IGC analysis revealed high affinity of CM for methyl acetate and ethyl acetate and low affinity for water and aliphatic alcohols. This difference could be of interest in view of the use of CM membranes in industrial processes in a series with a reactor, to shift the equilibrium of esterification and also to remove the target products from the reaction zone.

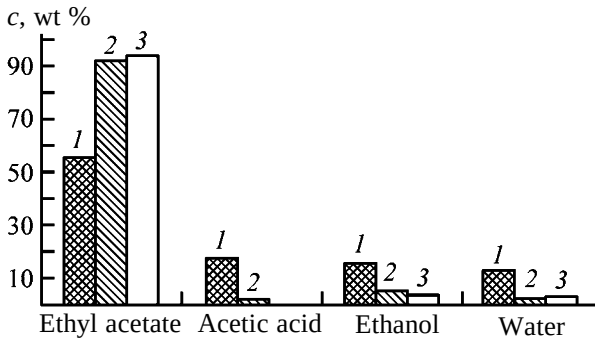

Fig. 5. Initial composition of the mixture ethyl acetate–acetic acid–ethanol–water compared to the compositions of permeates in separating the initial mixture in the pervaporation and evaporation modes with the CM membrane. (*c*) Component concentration. (*1*) Initial mixture; permeate composition: (*2*) pervaporation and (*3*) evaporation.

The histogram in Fig. 5 represents the results of separation of a four-component mixture whose composition models the esterification equilibrium realized in synthesis of ethyl acetate (55.0, 17.1, 15.4, and 12.5 wt % of ethyl acetate, acetic acid, ethanol, and water, respectively). The process was carried out at 20°C with direct contact of the simulated mixture with the surface of the CM membrane (pervaporation mode) or on a membrane in contact with vapor of this mixture (evaporation mode). In both cases, we observed considerable enrichment of permeate with ethyl acetate (from 55 to 91.6 and 93.8 wt %, respectively) with parallel significant decrease in the concentrations of acetic acid, ethanol, and water (1.5 and 0, 4.1 and 3.4, and 2.2 and 2.8 wt %, respectively). It is worth noting that the permeability of the membrane in the pervaporation and evaporation modes is considerably different (2 and 0.1 kg m^{-2} h^{-1}, respectively). Finally, our results are of interest in view of formation of composite CM membranes with higher permeability.

CONCLUSIONS

(1) The possibility of controlling the membrane permeability and selectivity with respect to some individual gases or their mixtures, as well as the direction of selective mass transfer in separating water–ethanol mixtures, was demonstrated with an example of cellulose acetomyristate membranes of various compositions.

(2) A comparative analysis is made of the selectivity of separation of binary organic and aqueous-alcoholic mixtures on cellulose myristate and acetomyristate membranes in the pervaporation and evaporation modes.

(3) The direction of selective mass transfer of components of organic mixtures across the cellulose myristate membrane can be predicted using the inverse gas chromatography.

(4) Cellulose myristate membranes are efficient for recovery of toluene and benzene from their mixtures with, respectively, methanol and ethanol, particularly from azeotropic mixtures.

(5) The separating properties of cellulose myristate membrane are studied with regard to a multicomponent mixture simulating the esterification equilibrium realized in synthesis of ethyl acetate. Ethyl acetate can be concentrated in permeate to 91.6–93.8 wt %.

ACKNOWLEDGMENTS

The authors are grateful to A.M. Toikka for valuable discussions. The work was financially supported by the Russian Foundation for Basic Research (project no. 03-03-32379) and the Federal Task Program "Integration" (project B0028/1365).

REFERENCES

1. Chaudry, M.A., *J. Membrane Sci.*, 2002, vol. 206, pp. 319–332.
2. Kim, S., Lim, G., Jegal, J., and Lee, K., *J. Membrane Sci.*, 2000, vol. 174, pp. 1–15.
3. Richau, K., Schwarz, H.-H., Aptel, R., and Paul, D., *J. Membrane Sci.*, 1996, vol. 113, pp. 31–41.
4. Mochizuki, A., Amia, S., Sato, Y., *et al.*, *J. Appl. Polym. Sci.*, 1990, vol. 40, pp. 633–643.
5. Kosutic, K. and Kunst, B., *J. Appl. Polym. Sci.*, 2001, vol. 81, no. 7, pp. 1768–1775.
6. Polotskaya, G.A., Turkova, L.D., Kuznetsov, Yu.P., and Nesterov, V.V., *Vysokomol. Soedin.*, 1990, vol. 32, no. 4, pp. 1733–1738.
7. Sidorovich, A.V., Baklagina, Yu.G., Khripunov, A.K., *et al.*, *Zh. Prikl. Khim.*, 2002, vol. 75, no. 12, pp. 1733–1738.
8. Khripunov, A.K., Koz'mina, O.P., Shtennikova, I.N., and Okhrimenko, G.I., *Zh. Prikl. Khim.*, 1970, vol. 43, no. 11, pp. 2581–2583.
9. Dytnerskii, Yu.I., Kagramanov, G.G., and Storozhuk, I.P., *Zh. Vses. Khim. O–va. im. D.I. Mendeleeva*, 1987, vol. 32, no. 6, pp. 684–692.
10. Karakane, H., Tsuyomoto, M., Maeda, Z., and Honda, Z., *J. Appl. Polym. Sci.*, 1991, vol. 42, pp. 3229–3239.
11. Kuznetsov, Yu.P., Kruchinina, E.V., Nud'ga, L.A., *et al.*, *Zh. Prikl. Khim.*, 2003, vol. 76, no. 11, pp. 1857–1862.
12. Uragami, T. and Moricava, T., *J. Appl. Polym. Sci.*, 1992, vol. 44, pp. 2009–2018.
13. Baker, R.W., *Membrane Technologies and Applications*, New York: McGraw-Hill, 2000.
14. Kogan, V.B., Fridman, V.M., and Kafarov, V.V., *Ravnovesie mezhdu zhidkost'yu i parom* (Liquid–Vapor Equilibria), Moscow: Nauka, 1966.
15. Yoshikawa, M., Wano, T., and Kitao, T.J., *Membrane Sci.*, 1994, vol. 89, pp. 23–36.
16. Aksenova, E.L., Kuznetsov, V.M., Kuznetsov, Yu.P., and Toikka, A.M., *Vestn. Sankt-Peterb. Gos. Univ.*, 2000, no. 4, pp. 87–92.
17. Ohya, H., Shibata, M., Negus, Hi Y., *et al.*, *J. Membrane Sci.*, 1994, vol. 90, pp. 91–100.
18. Lenk, W. and Meer-Haask, J., *Desalination*, 2002, vol. 148, pp. 11–16.
19. Masuda, T., Tang, B., and Higashimura, T., *Polym. J.*, 1986, vol. 18, no. 7, pp. 565–567.
20. Roberts, S.L., Koval, C.A., and Nobel, R.D., *Ind. Eng. Chem. Res.*, 2000, vol. 39, pp. 1673–1682.
21. Ruckenstein, E. and Sun, F., *J. Membrane Sci.*, 1995, vol. 103, pp. 271–283.

Russian Journal of Applied Chemistry, Vol. 77, No. 11, 2004, pp. 1883–1887. Translated from Zhurnal Prikladnoi Khimii, Vol. 77, No. 11, 2004, pp. 1901–1904.

MACROMOLECULAR CHEMISTRY AND POLYMERIC MATERIALS

Composition and Properties of Polysaccharides from Rice Husk

L. A. Zemnukhova, S. V. Tomshich, V. A. Mamontova, N. A. Komandrova, G. A. Fedorishcheva, and V. I. Sergienko

Institute of Chemistry, Far-Eastern Division, Russian Academy of Sciences, Vladivostok, Russia
Pacific Institute of Bioorganic Chemistry, Far-Eastern Division, Russian Academy of Sciences, Vladivostok, Russia

Received January 19, 2004; in final form, September 2004

Abstract—The composition and content of polysaccharides obtained from different samples of rice husk by successive treatment with water, ammonium oxalate (or oxalic acid), and alkali were studied. The chemical composition of the rice husk residues after the extraction was examined, and the possibility of their use for preparing amorphous silica or cellulose-containing products, depending on the hydrolysis conditions, was assessed.

Cleaning and polishing of rice grains involves formation of a large-tonnage waste, husk and dust, which is a valuable and renewable vegetable raw material for chemical industry [1–3]. It was shown previously that amorphous high-purity silica and xylitol can be prepared from rice husk [4], and phytin, from rice dust [5]. Rice husk and straw are also sources of polysaccharides [6]. Polysaccharides are widely used in various branches of industry, e.g., in production of fibers, films, adhesives, ethanol, and medicinals [6, 7]. Polysaccharides from higher herbs, including those from the Russian Far East, exhibit a broad spectrum of biological activity (immunomodulating, antiphlogistic, antiviral, antitumor, anticomplementary, wound-healing, etc.) [8, 9]. Data on the biological activity of polysaccharides recovered from vegetable waste, in particular, from rice husk, are virtually lacking.

This paper, continuing our studies on integrated processing of rice production wastes, concerns the chemical composition of rice husk polysaccharides recovered by various extraction proceduures and of the insoluble residues.

EXPERIMENTAL

We studied the composition and content of polysaccharides (PSs) in rice husk (RH-1, RH-2, RH-17) and dust (RD) samples taken in different years from the Primor'e and Krasnodar krais, and also of phytin recovered from rice dust without (phytin-1) and with (phytin-2) ultrafiltration by the method described in [5].

The RH samples usually contain an impurity of fine fractions of husk, grains, and dust (2–11 wt % depending on the equipment used). The husk particle size in our experiments was less than 2 mm. The RH samples were preliminarily washed with water and dried at 95°C in air to constant weight.

The RH and RD samples were treated successively with water, ammonium oxalate, an alkali. For this purpose, a sample was placed in water (weight ratio ~1 : 10) and heated on a water bath for 3 h. The solution was separated from the RH or RD residue by filtration and concentrated by evaporation on a rotary evaporator, after which the polysaccharides were precipitated with acetone (volume ratio of the solutions 1 : 4). The polysaccharide precipitate was separated by centrifugation, dissolved in water, and freeze-dried to obtain polysaccharides of aqueous extraction.

To the residue of RH and RD after treatment with water, we added a 0.5 N solution of ammonium oxalate (weight ratio ~1 : 10) and heated on a water bath for 3 h. The solution was separated from the undissolved residue by filtration and subjected to dialysis against running water (2–3 days) and then against distilled water (1 day). After that, the solution was concentrated, and a fourfold volume of acetone was added. The precipitate formed was separated by centrifugation, dissolved in water, and freeze-dried to obtain polysaccharides of oxalate extraction.

The solid residue of RH or RD after treatment with water and ammonium oxalate was suspended in 0.5 N NaOH and heated on a water bath for 2 h. The solution was separated by centrifugation (5000 rpm,

1070-4272/04/7711-1883 © 2004 MAIK "Nauka/Interperiodica"

Table 1. Monosaccharide composition and content of polysaccharides in extracts from RH and RD

Raw material	Treatment	PS yield based on raw material, wt %	Monosaccharide composition,* mol %					
			Rha	Ara	Xyl	Man	Glc	Gal
RH-1	H_2O	1.2	–	–	–	–	100	–
	$(NH_4)_2C_2O_4$	2.0	–	–	–	–	100	Traces
	NaOH	5.0	Traces	19	26	Traces	46	9
RH-2	H_2O	0.9	–	Traces	3	″	91	6
	$(NH_4)_2C_2O_4$	14.5	–	11	19	″	64	6
	NaOH	10.7	–	20	46	″	22	12
RD	H_2O	18.0	–	Traces	Traces	″	98	2
	$(NH_4)_2C_2O_4$	5.7	–	–	–	3	92	5
	NaOH	3.3	–	Traces	Traces	–	100	–

* Free polysaccharides: (Rha) rhamnose, (Ara) arabinose, (Xyl) xylose, (Man) mannose, (Glc) glucose, and (Gal) galactose; the same for Table 2.

20 min) and worked up as described above, to obtain polysaccharides of base extraction.

The isolated polysaccharides were subjected to acid hydrolysis, performed by treatment with 1 N trifluoroacetic acid (TFAA) at 100°C for 4–5 h. The qualitative and quantitative monosaccharide composition of the products was determined by paper chromatography (PC), gas–liquid chromatography (GLC), and gas chromatography–mass spectrometry (GC–MS) after conversion of the polyols to acetates. The descending PC was performed on Filtrak FN-12 paper in the system 1-butanol–pyridine–water (6 : 4 : 3 by volume). Monosaccharides were detected with an alkaline solution of silver nitrate. Gas–liquid chromatography was performed with an Agilent 6850 chromatograph (the United States) equipped with a flame ionization detector. An HP 5MS capillary column (30 m × 250 μm × 0.25 μm), was coated with 5% methylphenylsiloxane. The column temperature schedule was as follows: 150°C, 1 min; heating to 230°C, 3 deg min^{-1}; 230°C, 10 min. The GC–MS analysis was performed with a Hewlett–Packard 6890 chromatograph (the United States). The capillary column and temperature schedule were the same as in the GLC analysis. The chromatograph was interfaced with a Hewlett–Packard 5973 mass spectrometer (the United States).

Data on the polysaccharides obtained by aqueous, oxalate, and base extraction of RH and RD samples are given in Table 1. All the polysaccharides of aqueous extraction consist essentially of glucans. The polysaccharide of oxalate extraction from RH-1 is also glucan, and that recovered from RH-2 contains, along with glucose, also xylose, arabinose, and galactose. The polysaccharide recovered by oxalate extraction from RD consists of gluconate with a minor impurity of galactose and mannose. The polysaccharides recovered by base treatment of RH contain the residues of arabinose, xylose, glucose, and galactose; the monosaccharide ratio is different depending on the source of the raw material (RH-1, RH-2). The polysaccharides from RD are mainly glucans irrespective of the extraction procedure.

To develop an integrated scheme of utilization of rice production wastes, it is necessary to know the content in them of water-soluble low-molecular-weight carbohydrates (free monosaccharides, FMs). Below are data on the composition and content of FMs in RH depending on the treatment procedure. We studied the RH-17 specimen, which is of the same origin as RH-1, and a phytin specimen. We prepared and analyzed six samples of RH-17 treated as follows.

Sample no. 1 (RH-17, H_2O, 1 h, 60–90°C). A 5-ml aliquot of the solution was treated with KU-2(H^+) resin. A half of the aliquot was reduced with sodium borohydride, and the remaining part was hydrolyzed with a 1 N solution of TFAA (4 h, 100°C). In both cases, the polyols were converted to acetates, which were analyzed by GLC and GLC–MS.

Sample no. 2 (RH-17, 0.1 N NaOH, 1 h, 60°C). A 5-ml aliquot of the solution was neutralized with HCl, treated with KU-2(H^+) resin, and worked up as described above.

Sample no. 3 (RH-17, 0.1 N $H_2C_2O_4$, 1 h, 60°C). A 5-ml aliquot of the solution was neutralized with concentrated ammonia and treated with KU-2(H^+) resin. A half of the solution was analyzed without hydrolysis, and the other half, after acid hydrolysis, as described above.

Table 2. Composition and content of FMs recovered from RH-17, phytin-1, and phytin-2 as influenced by the treatment of the raw material

Sample	Treatment	FM + PS*	Content of monosaccharides, mol %						
			Rha	Ara	Xyl	Man	Glc	Gal	Int*
RH-17:									
no. 1	H_2O	FM	–	34	9	17	40	–	–
		FM + PS	–	33	20	15	22	10	–
no. 2	NaOH	FM	–	70	16	Traces	14	Traces	–
		FM + PS	5	23	31	4	24	13	–
no. 3	$H_2C_2O_4$	FM	–	72	10	4	11	3	–
		FM + PS	–	65	20	–	8	7	–
no. 4	H_2O, $H_2C_2O_4$	FM	–	95	5	–	Traces	Traces	–
no. 5	H_2O,	FM	–	Traces	–	–	″	–	–
	NaOH	FM + PS	8	30	45	Traces	9	8	–
no. 6	H_2O, $H_2C_2O_4$, NaOH	FM	–	–	–	–	–	–	–
Phytin-1	[5]	FM	–	Traces	–	–	Traces	–	Traces
			–	–	–	–	–	–	100
Phytin-2	[5]	FM	–	Traces	–	–	Traces	–	Traces
			–	″	–	38	18	–	45

* (FM) Without hydrolysis; (FM + PS) after hydrolysis.
** (Int) Inositol.

Sample no. 4 (RH-17, successive treatment with H_2O and 0.1 N $H_2C_2O_4$). The extract was treated similarly to sample no. 2; the aliquot was analyzed without hydrolysis by GLC and GC–MS.

Sample no. 5 (RH-17, successive treatment with H_2O and 0.1 N NaOH). The aliquot of the extract was treated similarly to sample no. 3. The monosaccharide analysis of the solution was performed both without hydrolysis and after acid hydrolysis.

Sample no. 6 (RH-17, successive treatment with H_2O, 0.1 N $H_2C_2O_4$, and 0.1 N NaOH). After neutralization of the solution and its treatment with KU-2 resin, the sample was analyzed without hydrolysis.

The results of analysis of the extracts for FMs are listed in Table 2. It is seen that low-molecular-weight carbohydrates are quantitatively recovered in the first extraction, irrespective of whether it was performed with water (sample no. 1), alkali solution (sample no. 2), or acid solution (sample no. 3). The monosaccharide composition only slightly depends on the RH-17 treatment procedure, but the quantitative ratios of the monosaccharides are different. In all the cases, polysaccharides are extracted together with FMs, as indicated by the difference in the quantitative ratio of FMs in the same RH-17 sample before and after hydrolysis.

In successive extraction of RH-17 with water and then with oxalic acid (sample no. 4), or alkali (sample no. 5), or with both acid and alkali (sample no. 6), FMs were detected only in extract no. 4. This can be accounted for by the fact that oxalic acid partially hydrolyzes polysaccharides present in the solution.

In the initial phytin samples (Table 2), inositol was detected by GLC in trace amounts, since it is present in the form of inositol phosphate. After acid hydrolysis, we identified in phytin-1 only inositol (100%), and in phytin-2, also mannose and glucose. Different composition of the phytin samples may be due to different procedures for their recovery from solution after acid hydrolysis of RD: phytin-1 was precipitated with ammonia from the crude hydrolyzate, and phytin-2, from the hydrolyzate purified by ultrafiltration. The hydrolyzate was purified by passing the solution, according to [5], through UAM-150 cellulose acetate membranes (pore diameter ~10–15 nm) permeable for molecules of a definite size. The molecular weights of inositol, mannose, and glucose detected in phytin-2 (Table 2) are equal (180). These data show that, to obtain a pure product from RD, ultrafiltration, giving a number of advantages in processing of the raw material [5], should be supplemented by washing of phytin to remove FMs.

Table 3. Yield of water-soluble substances from RH and content of inorganic elements in residues after different treatment procedures

Raw material	Treatment	Soluble substances	Residue	Ash residue from RH	SiO_2 content in ash	Content of elements in ash $c \times 10^3$, wt %						
		wt %				Fe	Al	Ca	Mg	Mn	Zn	Cu
RH-17	H_2O	12.5	87.5	14.0	96.7	51	46	620	85	26	25	0.1
	$H_2C_2O_4$	13.3	86.7	14.3	99.9	63	34	790	348	88	20	0.1
	NaOH	52.2	47.8	0.85	0.53	340	98	27 600	8220	2330	220	6.0
RH-1	H_2O, $(NH_4)_2C_2O_4$, NaOH	47.9	52.1	0.80	0.44	17	11	149	36	3	2	0.3
RH-2	H_2O, $(NH_4)_2C_2O_4$, NaOH	43.4	56.6	0.82	0.51	17	8	142	10	3	1	0.3

Comparison of our results with the data of [6, 10–12] shows that the chemical composition and content of water-soluble PSs and FMs in the rice production wastes depends on a number of factors: kind of the raw material (husk, straw, or dust), its origin (growth region; actually, apparently, the plant strain is concerned), and treatment procedure. In contrast to data from [6], uronic acids were detected only in trace amounts in some RH extracts.

The RH residues after extraction of water-soluble substances (cellolignin) are raw materials for production of amorphous silica [1–4] and, e.g., sorbents based on plant fibers [13–15]. Therefore, the RH residues after extractions were analyzed for the content of Si and metals by the procedures described previously [4] (Table 3).

The ash residue (oxidative calcination at 700–800°C [4]) from RH residue after aqueous or oxalate treatment is 10–12 wt % relative to the dry starting material. The content of amorphous silica in the ash is 96.7 wt % after aqueous extraction of RH and 98.3–99.9% after the oxalate treatment. The content of silica in ash of the RH residue after base hydrolysis does not exceed 0.6 wt %. The list of metals detected in the cellolignin ash and their contents are listed in Table 3.

CONCLUSIONS

(1) The chemical composition and content of water-soluble polysaccharides and low-molecular-weight carbohydrates in rice processing wastes depend on the kind of the raw material (husk, straw, dust), its origin (growth region, plant strain), and treatment conditions. Aqueous and oxalate polysaccharides mainly contain glucans.

(2) To obtain pure phytin from rice dust with ultrafiltration of the hydrolysis solution, it is necessary to include in the flowsheet the step of washing the product with water to remove free polysaccharides.

(3) High-purity amorphous silica can be prepared from rice husk after its pretreatment with water and acid. The content of the main substance, SiO_2, in the ash from the rice husk residue is 96.7–99.9 wt %, and the ash yield is 10–12 wt % relative to the dry starting material.

REFERENCES

1. Govindarao, V.M.H., *J. Sci. Ind. Res.*, 1980, vol. 39, no. 3, pp. 495–515.
2. Saprykin, L.V. and Kiseleva, N.V., *Khim. Drev.*, 1990, no. 6, pp. 3–7.
3. Okutani, T. and Nakata, Y., *Calorim. Therm. Anal.*, 1996, vol. 23, no. 3, pp. 117–127.
4. Zemnukhova, L.A., Sergienko, V.I., Davidovich, R.L., *et al.*, *Vestn. Dal'nevost. Otd. Ross. Akad. Nauk*, 1996, no. 3, pp. 82–85.
5. Kolzunova, L.G., Zemnukhova, L.A., Fedorishcheva, G.A., *et al.*, *Zh. Prikl. Khim.*, 2000, vol. 73, no. 10, pp. 1644–1651.
6. Sharkov, V.I. and Kuibina, N.I., *Khimiya gemitsellyuloz* (Chemistry of Hemicelluloses), Moscow: Lesnaya Prom–st., 1972.
7. Sharma, D.K., *Indian Cellul. Chem. Technol.*, 1989, vol. 21, no. 1, pp. 45–51.
8. Tomshich, S.V., Komandrova, N.A., Kalmykova, E.N.,

et al., *Khim. Prirodn. Soedin.*, 1997, no. 2, pp. 197–201.

9. Ovodov, Yu.S., *Bioorg. Khim.*, 1998, vol. 24, no. 7, pp. 483–501.
10. Juliano, B.O., Maningat, C.C., and Pascual, C.G., *Phytochemistry*, 1987, vol. 26, no. 12, pp. 3261–3263.
11. Haq, Q.N., Hannan, A., and Hoque, M.M., *Bangladesh J. Sci. Ind. Res.*, 1988, vol. 23, nos. 1–4, pp. 163–168.
12. Brylev, A.N., Adylov, D.K., Tukhtaeva, G.G., *et al.*, *Khim. Prirodn. Soedin.*, 2001, no. 6, pp. 488–489.
13. *TU* (Technical Specifications) *2164-003-02698192–69: RShMS Sorbents*, Moscow: Izd. Standartov, 1998, section L91, p. 193.
14. RF Patent 2117527.
15. Marshall, W.E., Champaque, E.T., and Evans, W.J., *J. Environ. Sci. Health*, 1993, vol. 28A, no. 9, pp. 1977–1992.

Russian Journal of Applied Chemistry, Vol. 77, No. 11, 2004, pp. 1888–1890. Translated from Zhurnal Prikladnoi Khimii, Vol. 77, No. 11, 2004, pp. 1905–1908.

MACROMOLECULAR CHEMISTRY AND POLYMERIC MATERIALS

Effect of Acidifying Agent on Autophoretic Application of Polymeric Composite Coatings

Zh. I. Bespalova, L. G. Miroshnichenko, Yu. A. Lovpache, and Yu. D. Kudryavtsev

South Russian State Technical University (former Novocherkassk Polytechnic Institute), Novocherkassk, Rostov oblast, Russia

Received August 4, 2004

Abstract—The effect of acidifying agent on autophoretic application of a polymeric composite material and protective properties of the resulting coatings is studied.

Studies concerning intensification of the existing processes for applying polymeric coatings to metallic surfaces and improvement of these processes with regard to environmental problems are directed primarily at searching for novel cost-efficient solutions. Among such new developments is the autophoretic method of applying polymeric protective coatings (PPCs) [1–3].

In this context, combining the unique properties of Teflon (corrosion resistant, antifriction, and antiadhesive) with the advantages of autophoretic deposition (no loss of the applied material, possibility of full automation, uniform thickness of PPC on articles of complicated geometry, reduced power consumption owing to utilization of the energy of the chemical reaction) is a topical scientific and applied problem.

The autophoretic process is realized by immersing metallic articles in an acidic aqueous composition containing an organic coating-forming material in the dispersed form, dispersing and acidifying agents, and an oxidant [4, 5].

Acidifying agents are introduced to form concentration and electric fields [6] that arise from a redox reaction occurring on the metallic surface and cause motion of the particles in autophoresis [7]. The autophoretic formation of a gel-like PPC is similar to electrochemical corrosion. In the presence of an acidifying agent, anodic dissolution of a metal ($M \rightarrow M^{z+} + ze$) and cathodic reduction of an oxidant or oxygen contained in the system proceed [8].

Therefore, ionization of a metal takes place only in the presence of an acidifying agent, being inseparably linked with autodeposition from acidic solutions. This process results in oxidation of a metallic support, which induces the charge and distorts the stability of the composition.

In this work we developed a composite Teflon-based material and studied its applicability to autophoretic deposition with regard to the nature of acidifying agent.

PPCs were applied to pretreated surfaces of 08KP steel.

The autophoretic bath was made from Plexiglas. The process was carried out at 18–25°C. A sample was fixed on a mechanical agitator using a specially designed holder and immersed in the polymeric coating-forming dispersion. The rotation rate was 60 rpm.

pH of the composition was measured with a pH-340 laboratory pH meter. The thickness of PPCs was determined by the magnetic method using an MT-2 instrument [9]; PPC yield, gravimetrically; and electrokinetic potential of dispersed particles, by the method of electrophoresis in a parallel-sided cell; and PPC adhesion to the metallic surface, by the shear stress according to GOST (State Standard) 14759–69. The tribotechnical characteristics were determined on an end friction-testing machine. The continuity of PPCs was measured using an LOK-1M electric-contact defectoscope; the viscosity, with an Ostwald capillary viscometer; and corrosion resistance, by the weight loss in corrosive media.

The composition used was found to be stable by the dry residue, viscosity, aggregation state, and kinetic parameters. Such a stable state was obtained after optimization of the composition.

As coating-forming agents we used aqueous suspensions of Teflon F-4D and Teflon F-4MD and a solution of polymethylphenylsiloxane in toluene; as mineral additives, carbon black, titanium dioxide, mica, and Aerosil; and as organic solvents, xylene, butyl Cellosolve, and furfuryl alcohol.

1070-4272/04/7711-1888 © 2004 MAIK "Nauka/Interperiodica"

To attain better compatibility and wetting of the polymer phase, the mineral additives were dressed with some modifiers, particularly, heterocyclic compounds of the vinylpyrrolidone series and oxyethylated alkylphenol. The dry residue of the initial composition was 55 wt %; viscosity, 16 s (VZ-246 viscometer); and pH, 6.5. The parameters of autophoretic deposition of PPC were optimized with the composition selected on the basis of preliminary experiments. The optimal pH of the composition was found to be 3 (Fig. 1).

The optimal temperature (380°C) and time (30–40 min) of heat treatment of PPC were established on the basis of experimental data on the swelling of PPC in acetone vapor and 10% nitric acid. All further experiments were carried out at these process parameters.

We studied the effect exerted on autophoretic deposition by such acidifying agents as phosphoric, tetrafluoroboric, hydrofluoric, and sulfuric acids, and a mixture of phosphoric and boric acids. The acids were added in amount sufficient to attain pH 3.

Our results showed that the nature of acidifying agent influences the ζ-potential of dispersed polymeric particles:

Acid	ζ-Potential, mV
H_2SO_4	–27.9
$H_3PO_4 + H_3BO_3$	–39.4
HF	–46.0
HBF_4	–54.0
H_3PO_4	–62.0

The observed increase in the absolute value of the ζ-potential on passing from sulfuric to phosphoric acid can be attributed to the anion effect on the adsorption of macromolecules of the coating-forming agents on the surface of mineral additives. Formation of the adsorption layer is controlled essentially by the ion-electrostatic factor. Evidently, the presence of phosphoric acid promotes adsorption to a larger extent as compared to other acids. This conclusion is supported by data on the effect of anion on the yield of PPC (Fig. 2).

As seen, the specific weight of PPC increases with increasing ζ-potential. The optimal deposition time was found to be 5–10 min regardless of the acid added. With further increase in the deposition time, the PPC weight reaches some critical value and then decreases, which can be attributed to the fact that, after reaching certain thickness, the polymeric coating no longer grows, since the concentration of Fe^{2+} and Fe^{3+} ions under the coating decreases below the coagulation threshold, and, despite the fact that autophoretic transport of particles goes on then, they do not precipitate [1]. Furthermore, in this case, some part of the particles leaves the surface as a result of weakening of the cohesion interaction of the components in the coating.

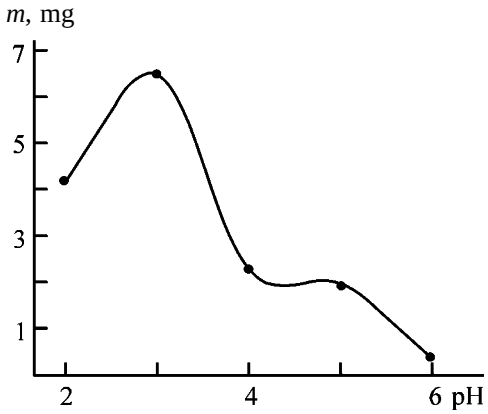

Fig. 1. Coating weight *m* as a function of pH of the composition at the optimal deposition time (5 min).

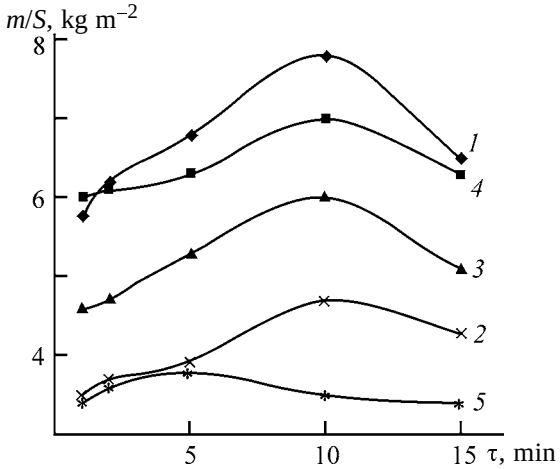

Fig. 2. Yield of the deposit *m*/*S* as a function of the time of deposition τ with various acidifying agents (acids): (*1*) H_3PO_4, (*2*) $H_3PO_4 + H_3BO_3$, (*3*) HF, (*4*) HBF_4, and (*5*) H_2SO_4; the same for Fig. 3.

The nature of the acidifying agent also affects the protective characteristics of PPC (Fig. 3). In the corrosion tests in 3 wt % HCl, the best protection characteristics were obtained for PPCs prepared with phosphoric acid. This is clear in view of the fact that phosphoric acid forms insoluble phosphates with metals, and phosphatization enhances the corrosion resistance and adhesion [10, 11]. Another reason is that, among the acids studied, phosphoric acid provides the highest yield of the deposit (Fig. 2).

The results of corrosion tests of the autophoretic coatings, prepared in the presence of phosphoric acid, in various corrosive media are given in Fig. 4.

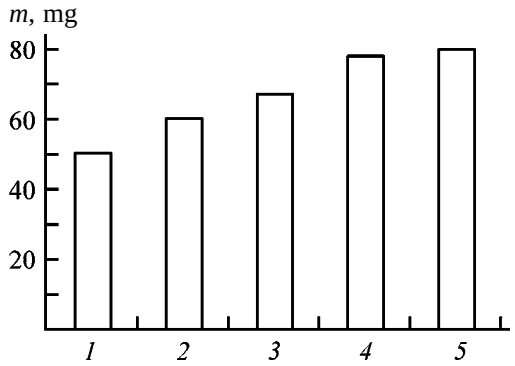

Fig. 3. Weight loss *m* in corrosion tests in 3 wt % HCl for coatings prepared in the presence of various acids.

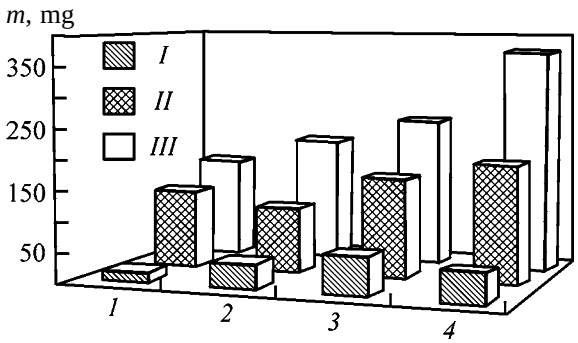

Fig. 4. Weight loss *m* in corrosion tests in (*1*) industrial atmosphere, (*2*) seawater, (*3*) 3 wt % NaCl, and (*4*) 3 wt % HCl. (*I*) PPC, (*II*) Teflon coating, and (*III*) uncoated steel.

As seen, the corrosion resistance of the polymeric composite coatings is higher by a factor of several tens as compared to uncoated steel, being several times higher than that of Teflon coatings prepared by immersing in aqueous suspensions of Teflon F-4D and F-4MD.

The adhesion tests of PPCs prepared with various acids also showed that phosphoric acid is the most effective acidifying agent. The adhesion of such coatings is rather high, ranging from 5.0 to 6.0 MPa:

Acid	Adhesion, MPa
H_3PO_4	5.9
H_3PO_4 + H_3BO_3	5.5
HF	5.0
HBF_4	4.9
H_2SO_4	4.5

CONCLUSIONS

(1) The nature of acidifying agent affects autophoretic deposition of polymeric composite coatings from compounded polymer dispersions, the effect being controlled by the adsorption characteristics of its anion.

(2) Among the acids studied, phosphoric acid is the most effective acidifying agent for applying coatings to 08KP steel, as providing the largest thickness of the coating and the highest adhesion and protective characteristics.

REFERENCES

1. Dvornichenko, G.L., Nizhnik, Yu.V., Slavikovskii, T.V., and Nikolaichuk, L.V., *Kolloidn. Zh.*, 1993, vol. 55, no. 1, pp. 45–48.
2. Verkholantsev, V.V. and Vedenov, S.S., *Lakokras. Mater. Ikh Primen.*, 1980, no. 3, pp. 29–32.
3. US Patent 3585084.
4. Ul'berg, Z.R., Dvornichenko, G.L., and Ivzhenko, I.I., *Lakokras. Mater. Ikh Primen.*, 1985, no. 3, pp. 29–31.
5. Liberman, A.I., Talanov, V.L., and Verkholantsev, V.V., *Lakokras. Mater. Ikh Primen.*, 1984, no. 1, pp. 35–38.
6. Kovalisko, Yu.M., Spryska, K.V., and Moravskaya, I.F., *Lakokras. Mater. Ikh Primen.*, 1978, no. 5, pp. 80–82.
7. Kozlov, V.A., Borisenko, S.I., and Panichev, E.P., *Lakokras. Mater. Ikh Primen.*, 1989, no. 1, pp. 82–84.
8. Rumyantseva, V.E., Study of the Effect of Acidifying Agent on Autophoretic Deposition of Polymeric Composite Coatings, *Cand. Sci. Dissertation*, Ivanovo, 1990.
9. Bagazhkov, S.G. and Sukhanova, N.A., *Praktikum po tekhnologii lakokrasochnykh pokrytii* (Practical Course on Technology of Paint Coatings), Moscow: Khimiya, 1982.
10. Panich, R.M. *et al.*, *Kolloidn. Zh.*, 1963, vol. 25, no. 4, pp. 76–81.
11. Dukhin, S.S. and Zueva, T.I., *Kolloidn. Zh.*, 1962, vol. 24, no. 4, pp. 443–445.

Russian Journal of Applied Chemistry, Vol. 77, No. 11, 2004, pp. 1891–1893. Translated from Zhurnal Prikladnoi Khimii, Vol. 77, No. 11, 2004, pp. 1909–1911.

MACROMOLECULAR CHEMISTRY AND POLYMERIC MATERIALS

Hydrolytic Copolycondensation of Ethyl Silicate with Copper Salts under Heterogeneous Conditions

V. A. Sviderskii, M. G. Voronkov, S. V. Klimenko, A. A. Khal'kova, and V. S. Klimenko

Kiev Polytechnic Institute, Ukrainan National Technical University, Kiev, Ukraine
Favorskii Institute of Chemistry, Siberian Division, Russian Academy of Sciences, Irkutsk, Russia

Received July 20, 2004

Abstract—Hydrolytic copolycondensation of ethyl silicate with copper salts in the presence of a base catalyst (NH_4OH) without organic solvent was studied.

Previously [1–3] we studied metal-containing (Cu, Co, Zn, Sn, Pb, etc.) siloxanes prepared by the sol–gel procedure involving homogeneous hydrolysis of ethyl silicate in 2-propanol in the presence of a base catalyst (NH_4OH) [1–3].

In practice, it is better to perform the sol–gel process without solvent. The advantage of the heterogeneous procedure is the absence of undesirable influence of the solvent impurities.

However, in the absence of solvent the reaction is substantially decelerated and the molecular uniformity of the products decreases. This is mainly due to phase segregation and emulsification.

Probably, a heterogeneous reaction can be promoted by choosing appropriate pH, temperature, and anion of the initial metal salt.

EXPERIMENTAL

The heterogeneous sol–gel process was simulated with commercial Etilsilikat-40 (partially hydrolyzed tetraethoxysilane) and copper salt crystal hydrates $CuSO_4 \cdot 5H_2O$, $CuCl_2 \cdot 2H_2O$, $Cu(NO_3)_2 \cdot 5H_2O$, and $Cu(OCOCH_3)_2 \cdot H_2O$.

As in our previous works, these salts were chosen because of formation of stable copper ammine complexes in a wide pH range. The preparation conditions were similar to those described in [3] except for the absence of the organic solvent. The products of hydrolytic copolycondenstaion were thoroughly washed by decanting and were dried at 120 ± 0.5°C to form xerogels. The xerogel was studied by thermal analysis in air (an MOM derivatograph, heating rate 10 deg min^{-1}) and by IR spectroscopy (a Specord IR-75 spectrophotometer, KBr pellets). To determine water absorption, the samples were kept at a 98% relative humidity for 72 h and then were weighed. The copper content in the xerogel was determined from that in the solution separated from the xerogel [4].

We found that the copper content in polycuprasiloxanes prepared by heterogeneous hydrolysis strongly depends on the anion of the initial salt, condensation temperature, and pH of the reaction mixture (Table 1). In the subsequent experiments we used polycupraethoxysiloxane prepared under the conditions (35°C, pH 12) that, on the average, proved to be the best.

Table 1. Degree of copper binding in polycupraethoxysiloxanes

Salt	pH of solution	γ, %, at indicated reaction temperature, °C			
		25	35	45	55
$CuCl_2$	11.5	67.6	69.8	66.2	56.1
	12.0	93.2	95.9	75.3	68.0
	12.25	69.8	73.5	65.3	49.7
$CuSO_4$	11.5	No cuprasiloxane formation			
	12.0	43.1	93.4	84.5	95.6
	12.25	68.5	90.4	86.7	91.0
$Cu(OCOCH_3)_2$	11.5	63.3	66.9	54.1	51.4
	12.0	61.0	81.6	77.1	68.8
	12.25	72.5	81.6	72.5	69.7
$Cu(NO_3)_2$	11.5	89.9	92.6	71.9	59.7
	12.0	89.5	90.0	77.2	76.2
	12.25	46.5	56.2	38.6	38.5

1070-4272/04/7711-1891 © 2004 MAIK "Nauka/Interperiodica"

Table 2. Shift $\Delta\nu$ of the ν_{as}(Si–O) band (1093 cm^{-1} in copper-free xerogels) in the IR spectra of polycupraethoxysiloxane xerogels

T, °C	$\Delta\nu$, cm^{-1}			
	$CuSO_4$	$CuCl_2$	$Cu(NO_3)_2$	$Cu(OCOCH_3)_2$
25	–7	–16	–29	–10
35	–13	–20	–27	–13
45	–13	–14	–13	–6
55	–13	–12	–13	–4

* Minus indicates the low-frequency shift

Table 3. Halfwidth $\Delta\nu_{1/2}$ and optical density *D* of the ν_{as}(Si–O) band (about 1093 cm^{-1}) in the IR spectra of polycupraethoxysiloxane xerogels

T, °C	$\Delta\nu_{1/2}$, cm^{-1}/D			
	$CuSO_4$	$CuCl_2$	$Cu(NO_3)_2$	$Cu(OCOCH_3)_2$
25	93/0.56	108/0.61	106/0.47	96/0.85
35	96/0.65	120/0.82	99/0.46	106/0.98
45	99/0.66	103/0.58	95/0.87	95/0.85
55	113/0.76	103/0.58	93/0.96	90/0.79

Table 4. Shift $\Delta\nu$ of the ν_s(Si–O) band (800 cm^{-1} in copper-free xerogels) in the IR spectra of polycupraethoxysiloxane xerogels

T, °C	$\Delta\nu$, cm^{-1}			
	$CuSO_4$	$CuCl_2$	$Cu(NO_3)_2$	$Cu(OCOCH_3)_2$
25	–14	–24	–35	–26
35	–20	–27	–27	–26
45	–27	–22	–24	–23
55	–27	–21	–20	–20

Table 5. Halfwidth $\Delta\nu_{1/2}$ and optical density *D* of the ν_s(Si–O) band (about 800 cm^{-1}) in the IR spectra of polycupraethoxysiloxane xerogels

T, °C	$\Delta\nu_{1/2}$, cm^{-1}/D			
	$CuSO_4$	$CuCl_2$	$Cu(NO_3)_2$	$Cu(OCOCH_3)_2$
25	23/0.04	26/0.04	26/0.02	26/0.05
35	25/0.04	30/0.06	26/0.04	26/0.05
45	26/0.04	23/0.07	25/0.06	25/0.06
55	26/0.05	23/0.08	25/0.11	23/0.07

The product of hydrolytic copolycondensation of ethyl silicate with copper salts in the presence of the base catalyst and in the absence of an organic solvent contains lattice and surface Si–O–Cu–O and Si–O–Si groups and minor amount of ethoxy groups. The presence of Si–O–Cu–O and Si–O–Si groups is indicated by the shift of the ν_{as}(Si–O) band (1093 cm^{-1}) with respect to this band in the spectra of silica xerogels free of copper. The shift depends on the anion of the initial copper salt (Table 2). The maximal shift of the ν_{as}(Si–O) band at 1093 cm^{-1} in the spectra of polycuprasiloxanes prepared from $CuSO_4$, $CuCl_2 \cdot 2H_2O$, $Cu(NO_3)_2$, and $Cu(OCOCH_3)_2$ is –13, –20, –29, and –13 cm^{-1}, respectively, and corresponds to the maximal copper content in the polycupraethoxysiloxanes (Tables 1, 2). The temperature dependence of the optical parameters of the ν_{as}(Si–O) band in the IR spectra of xerogels prepared at pH 12 correlates well with the copper content in these materials except for the xerogel prepared from $Cu(NO_3)_2$ (Tables 1, 2). In the latter case, the optical density of the ν_{as}(Si–O) band increases and its halfwidth $\Delta\nu_{1/2}$ decreases (Table 3). This is likely due to formation of cyclic fragments whose arrangement in the xerogel structure, unlike that of the other cross-linked structures, is three-dimensional or linear.

The structural transformations occurring mainly in the Si–O–Si groups are characterized by the optical parameters of the ν_s(Si–O) band at about 800 cm^{-1}. These data are consistent with the change in the optical parameters of the ν_{as}(Si–O) band (about 1093 cm^{-1}), i.e., the siloxane skeleton of the polymer changes simultaneously with the metallosiloxane structure and the changes depend on both the salt anion and the condensation conditions. The parameters of the ν_s(Si–O) band are presented in Tables 4 and 5.

Polycupraethoxysiloxane xerogels consists mainly of metal silicates. As determined by thermal analysis, the metal silicate content ranges from 80.7 to 92.1 wt %, depending on the anion of the initial copper salt. The weight loss at 200–450°C and the corresponding exoeffects in the DTA curves are due to the presence of residual ethoxy groups in the xerogels (Tables 6, 7).

The DTA curves of copper silicates prepared from copper nitrate and copper acetate contain a single exothermic peak at 300°C. Two exoeffcet in the range 290–320°C are observed in the DTA curves of xerogels prepared from copper chloride and copper sulfate. In all cases, these peaks are shifted to higher temperatures with increasing condensation temperature. The

Table 6. Weight loss Δm of polycupraethoxysiloxane xerogels at 200–450°C and the copper silicate content in the xerogels c

T, °C	Δm, wt %/c, wt %			
	$CuSO_4$	$CuCl_2$	$Cu(NO_3)_2$	$Cu(OCOCH_3)_2$
25	3.02/90.9	2.46/92.1	4.90/87.5	3.67/89.1
55	2.73/90.1	16.50/81.5	13.73/80.7	6.12/87.3

Table 7. Exothermic peak temperature T_{max} in the DTA curves of polycupraethoxysiloxane xerogels*

T, °C	T_{max}, °C			
	$CuSO_4$	$CuCl_2$	$Cu(NO_3)_2$	$Cu(OCOCH_3)_2$
25	290 s/330 s	300 s/320 m	300 s	300 s
55	300 s/340 s	360 s/550 w	320 s	335 s

* Intensity of the exothermic effect: s, strong; m, medium; w weak

xerogels, especially those prepared at 55°C, differ in the degree of condensation. The xerogels prepared at 55°C have a high degree of condensation and contain substantial amount of intraglobular alkoxy groups, which is indicated by the weight loss at 200–450°C (especially for copper silicates prepared from copper chloride and copper nitrate) and the shift of the exothermic peak to higher temperatures.

Thus, the structures of both siloxane skeleton and the Si–O–Cu–O–Si fragments of the polymers prepared at 25 and 55°C differ substantially. Either cross-linked or cyclolinear polymers are formed depending on the anion of the initial copper salt and the reaction conditions. The degree of copolycondensation (the copper content in the xerogel) depends on both the anion of the copper salt and the reaction conditions (temperature and pH of the reaction mixture).

Water sorption by the polycupraethoxysiloxanes depends on the anion of the copper salt. Xerogels prepared from $CuSO_4$, $CuCl_2$, $Cu(NO_3)_2$, and $Cu(OCOCH_3)_2$ adsorb 25.3, 21.7, 17.9, and 34.5 wt % water, respectively.

CONCLUSIONS

(1) The degree of hydrolytic copolycondensation of ethyl silicate with copper salts in the presence of a base catalyst (NH_4OH) without organic solvent and the composition and properties of the polycupraethoxysiloxanes are determined by the anion of the copper salt, temperature, and pH of the reaction mixture.

(2) Cuprasiloxanes prepared from $CuSO_4$, $CuCl_2$, and $Cu(OCOCH_3)_2$ have three-dimensional cross-linked structure. The structure of the polymers prepared from $Cu(NO_3)_2$ is cyclolinear.

REFERENCES

1. Sviderskii, V.A., Voronkov, M.G., Klimenko, V.S., and Klimenko, S.V., *Zh. Prikl. Khim.*, 1997, vol. 70, no. 10, pp. 1698–1703.
2. Sviderskii, V.A., Voronkov, M.G., Klimenko, S.V., and Klimenko, V.S., *Zh. Prikl. Khim.*, 2001, vol. 14, no. 7, pp. 1137–1141.
3. Sviderskii, V.A., Voronkov, M.G., Klimenko, V.S., and Bystrov, D.N., *Zh. Prikl. Khim.*, 2001, vol. 74, no. 12, pp. 2027–2030.
4. Marczenko, Z., *Kolorymetryczne oznaczanie pierwiastkow*, Warszawa: Naukowa-Techniczne, 1968.

Russian Journal of Applied Chemistry, Vol. 77, No. 11, 2004, pp. 1894–1895. Translated from Zhurnal Prikladnoi Khimii, Vol. 77, No. 11, 2004, pp. 1912–1913.

BRIEF COMMUNICATIONS

Solubility in the NaCl–$(C_2H_5)_2NH$–H_2O System at 50°C

V. A. Panasenko and S. A. Mazunin

State Research and Planning Institute of Basic Chemistry, Kharkov, Ukraine
Perm State University, Perm, Russia

Received February 21, 2003; in final form, June 2004

Abstract—The solubility in the system NaCl–$(C_2H_5)_2NH$–H_2O at 50°C was studied. The shape of the solubility isotherm was analyzed.

The NaCl–$(C_2H_5)_2NH$–H_2O system at 50°C, which determines the preparation conditions of a saturated solution of sodium chloride (mass fraction of NaCl is 26% [1–3]) and diethylamine, has not been described in the literature. The phase equilibria in the NaCl–$(C_2H_5)_2NH$–H_2O system are known only for 10, 20, and 30°C [1, 2].

The main method of studying solubility is the modified method of residue [3–5]. In the modified method, we used the compositions of the saturated solution and initial reaction mixture, instead of residue, to calculate the composition of the equilibrium solid phase. The mass ratio of the components in the initial mixture samples was chosen so that the compositions were heterogeneous and the mass ratios of the solid to liquid phase did not exceed 2 : 5. When studying the monotectic region, in which two liquid phases and NaCl crystals coexist, we used the half-sum of the contents of the system components in the upper and lower liquid phases. Equilibration was judged by constancy in three measurements of the refractive index of the liquid phase, which is a physical property of a medium that can be determined readily and accurately. The measurements were performed on an RL1 refractometer in 30-min intervals. The measurements started after thermostating for 3 h at 50 ± 0.1°C.

The Na^+ ions were determined by the flame photometry on a Zeiss photometer and an F-30 digital recorder. Practically, the determination was performed as follows: Three different weighed portions, sampled after the thermostating, were placed into 0.1 dm^3 volumetric flasks, and distilled water was added to the mark. Then the flame intensity was determined with samples from all the three flasks. After that, the intensity of 3–5 reference solutions was measured. We used reference NaCl solutions of the concentrations from 0.0001 to 0.1 mol dm^{-3}, prepared from reference samples.

The concentration of the Na^+ ions was determined from the linear dependence of the flame intensity on the logarithm of the concentration.

The molal concentrations of the sodium ions (mol kg^{-1}) in the weighed portions were calculated by the formula:

$$[Na^+] = \frac{c_{Na^+} VR}{m}, \quad (1)$$

where c_{Na^+} is the molar concentration of a sodium cation in the volumetric flask, as determined by the linear interpolation (mol dm^{-3}); V, flask volume (ml); R, dilution of the solution; and m, mass of the weighed portion m (g). The unknown quantity was determined as the mean of the three obtained values.

The content of the chloride ions was determined by argentometric titration [4, 5]. The equivalent point was determined from the functional dependence of the silver electrode potential on the amount of the $AgNO_3$ solution added. A glass electrode was the reference. The test solution was acidified with an 85% H_3PO_4 solution (1 ml). The potential of the silver electrode in the course of the titration was measured with an EV-74 pH meter.

The molal concentration (mol kg^{-1}) of the chloride ions was calculated by the formula

$$[Cl^-] = \frac{V_{AgNO_3} c_{AgNO_3} K_{AgNO_3} R}{m}, \quad (2)$$

where V_{AgNO_3} is the volume of $AgNO_3$ solution spent for titration (ml); c_{AgNO_3}, concentration of $AgNO_3$

1070-4272/04/7711-1894 © 2004 MAIK "Nauka/Interperiodica"

Solubility in the NaCl–$(C_2H_5)_2NH$–H_2O system at 50°C

Component content in liquid phases, wt %			Solid phase
NaCl	$(C_2H_5)_2NH$	H_2O	
8.7	22.7	68.6	–
6.0/13.9*	40.6/11.1	53.4/75.0	–
3.6/19.1	56.6/6.4	39.8/74.5	–
1.65/25.0	68.9/3.5	29.45/71.5	NaCl
1.3	73.9	24.8	NaCl
26.9	–	73.1	NaCl

* Numerator, component content in the upper liquid phase L_u; denominator, that in the lower liquid phase L_l.

solution (for titration we used a 0.05 M solution); K_{AgNO_3}, correction coefficient of $AgNO_3$ solution; *R*, dilution (part of the weighed portion taken for the titration); and *m*, mass of the weighed portion (g).

The diethylamine content was determined by direct potentiometric acidometric titration [5]. The functional dependence of the pH of the titrated solution on the amount of the acid solution added has a single pH jump. The titration was done on a T-108 automated titrator by determining the volume of a 0.1 M HCl solution spent for the titration to the equivalent point. The pH value was measured on a pH-121 device.

We used chemically pure grade NaCl and pure grade diethylamine distilled at the boiling point (55.6°C).

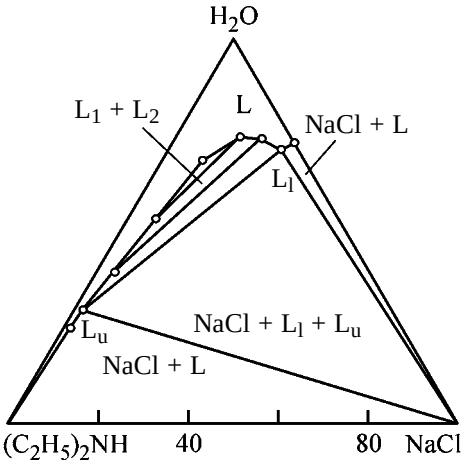

Solubility in the NaCl–$(C_2H_5)_2NH$–H_2O system at 50°C.

The experimental solubility data are presented in the table and in the figure.

The solubility isotherm of the system is monotectic. The following areas were revealed: the area of the unsaturated solutions L, the area of the two-phase liquid equilibrium $L_1 + L_2$, the three-phase area in which NaCl crystals and two liquid phases NaCl + L_l + L_u coexist, and the area of the NaCl (NaCl + L) crystallization, broken by the monotectic area into two parts.

The composition of the liquid phases in monotectic equilibrium with the NaCl crystals is as follows (wt %): NaCl 1.65, $(C_2H_5)_2NH$ 68.9, H_2O 29.45 (point L_u); NaCl 25.0, $(C_2H_5)_2NH$ 3.5, and H_2O 71.5 (point L_l).

As seen from the phase diagram, the largest area is occupied by the fields of the NaCl crystallization and by the monotectic field of the three-phase equilibrium; the field of coexistence of two liquid phases and the field of unsaturated solutions occupy a smaller area.

CONCLUSIONS

(1) The solubility in the NaCl–$(C_2H_5)_2NH$–H_2O system at 50°C was studied.

(2) The solubility isotherm is monotectic. Diethylamine exerts the salting-out effect on NaCl and forms a system of two liquid phases with NaCl solutions at 50°C.

REFERENCES

1. Vasong, T.M., and Shokin, I.N., *Izv. Vyssh. Uchebn. Zaved., Khim. Khim. Tekhnol*. 1970, vol. 13, no. 3, pp. 326–328.
2. Wasag, T., and Poleszczuk, G., *Chem. Stosowana*, 1974, vol. 18, no. 4, pp. 515–524.
3. Mazunin, S.A., Zubarev, M.P., and Panasenko, V.A., *Zh. Neorg. Khim*., 2000, vol. 45, no. 9, pp. 1576–1585.
4. Anosov, V.I., Ozerova, M.I., and Fialkov, Yu.Ya., *Osnovy fiziko-khimicheskogo analiza* (Basics of Physicochemical Analysis), Moscow: Nauka, 1976.
5. Charlot, G., *Les methods de la chimie analytique. Analyse quantitative minerale*, Paris: Masson, 1961, 4th ed.

Russian Journal of Applied Chemistry, Vol. 77, No. 11, 2004, pp. 1896–1898. Translated from Zhurnal Prikladnoi Khimii, Vol. 77, No. 11, 2004, pp. 1914–1916.

BRIEF COMMUNICATIONS

Preparation of Ultradispersed Transition Metals in Immobilized Microreactors

G. N. Al'tshuler and L. A. Sapozhnikova

Kemerovo Branch, Institute of Solid State Chemistry and Mechanochemistry, Siberian Division, Russian Academy of Sciences, Kemerovo, Russia

Received March 11, 2004

Abstract—Preparation of ultradispersed transition metals (20–100 nm) by reduction of metal complexes in molecular microreactors (cavities of immobilized calixarenes, polyelectrolytes) was studied.

Preparation and study of untradispersed metals and preparation of functional materials on their base are urgent problems of modern science [1]. It is known [2] that cross-linked polymers (polyelectrolytes) can be used as matrices for preparing ultradispersed metals. Cavities, complexes, and intercalated compounds contained in cross-linked polymers are immobilized microreactors providing certain spatial organization of molecules [3]. A study of processes occurring in immobilized microrecators gives insight into highly organized chemical transformations in supramolecular systems.

Previously [4] we prepared new cross-linked polymers with grafted *cis*-calix[4]resorcinolarene derivatives capable of forming intercalation compounds [5], i.e., having properties of a microreactor.

The aim of this work was to prepare ultradispersed transition metals in cross-linked polymers (polyelectrolytes), to study their catalytic activity in hydrogenation of organic nitro compounds, and to use *cis*-calix[4]resorcinolarenes immobilized in the polymeric matrix as microreactors for reduction and hydrogenation.

EXPERIMENTAL

Ultradispersed metals (Pd, Cu, and Ni) were prepared in pores of KU-2-12P and KU-23 sulfonic cation exchangers, AV-17 anion exchanger, and cross-linked polymer with immobilized *cis*-tetraphenylcalix[4]resorcinolarene groups. The Cu^{2+}, Ni^{2+}, and $[Pd(NH_3)_4]^{2+}$ cations were introduced in the sulfonic cation exchanger by the ion-exchange procedure. Reduction of palladium(II) tetraammine complex in the matrix yields 20–100-nm palladium particles. The X-ray pattern of KU-23 macroporous sulfonic cation exchanger containing palladium crystals is shown in Fig. 1.

The X-ray patterns were recorded on a DRON-2 diffractometer (copper radiation, voltage on the X-ray tube 30 kV, current 20 mA, scan rate 2 deg min^{-1}). The X-ray pattern contain reflections of crystalline palladium and a broad reflection of the amorphous polymer at 20°. The palladium content in the samples determined from the reflection intensity varies by an order of magnitude. The palladium dispersity calculated from the width of the reflection at 36° is 30–50 nm.

Pomogailo [2] showed that transition metal nanoparticles are formed by reduction of their cations in an ion-exchange matrix. When the dynamic ion-exchange capacity is completely saturated with transition metal amine complexes, the reduced metal particles form the metallic phase owing to short effective distance between the particles [2]. The catalytic activity of these materials is low. For the ultradisperse phase to be formed, palladium cations should occupy less than 0.2–0.3 of the total exchange capacity of KU-23 sulfonic resin. The catalytic activity at the palladium

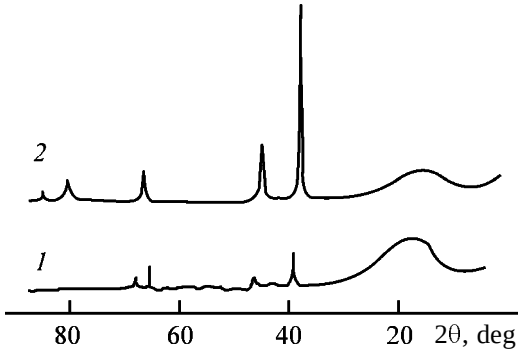

Fig. 1 .X-ray pattern of KU-23 30/100 macroporous sulfonic cation exchanger containing (*1*) 5.1 and (*2*) 34 g md^{-3} palladium(II). (2θ) Bragg angle.

1070-4272/04/7711-1896 © 2004 MAIK "Nauka/Interperiodica"

concentration corresponding to the total exchange capacity (65 g dm^{-3}) and at a low palladium concentration (<5 g dm^{-3}) is low.

We used KU-23 sulfonic cation exchanger containing Pd^0 as a heterogeneous catalyst for hydrogenation of nitro compounds that are intermediates in synthesis of dyes and pharmaceuticals (nitromethane, nitrobenzene, *p*-nitrobenzoic acid, and ethyl *p*-nitrobezoate). KU-23 30/100 sulfonic action exchanger containing 20–30 g dm^{-3} of 30–50-nm Pd^0 particles had the highest catalytic activity (2.6×10^{-3} mole H_2/min per gram of Pd^0).

The reactions occurring in a microreactor based on *cis*-calix[4]resorcinolarene can be described by the following scheme:

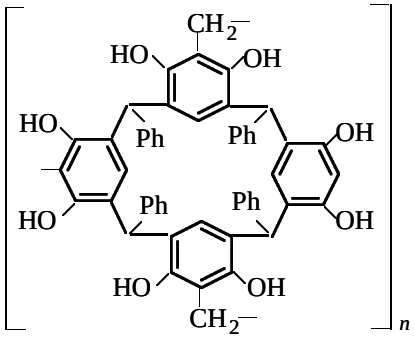

(1)

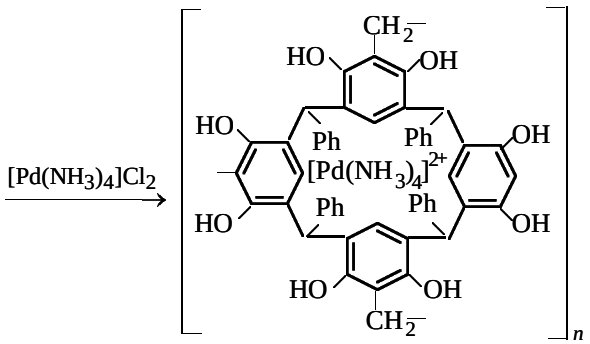

(2)

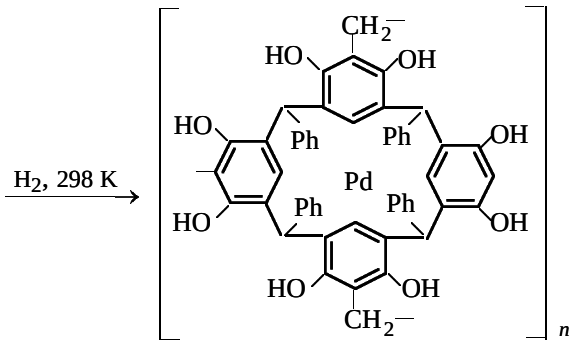

(3)

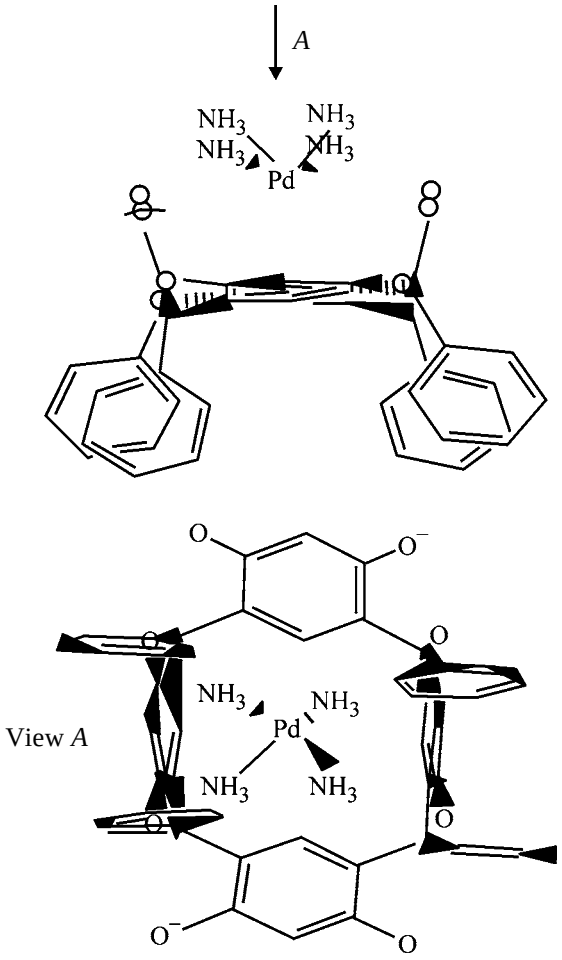

Fig. 2. Structure of the $[Pd(NH_3)_4]^{2+}$ complex with *cis*-tetraphenylcalix[4]resorcinolarene (MM2 calculation).

Three-dimensional cross-linked polymer (1) with grafted calixarene was prepared by polycondensation of *cis*-2,8,14,20-tetraphenyl-4,6,10,12,16,18,22,24-octahydroxycalix[4]arene with formaldehyde [4]. Metal ions were introduced in the polymer by sorption of Ni^{2+} and Pd^{2+} ammine complexes from aqueous solutions. The concentration of metal complexes in the solutions was chosen so as to provide the metal–polymer molar ratio of no more than 1. The structure of the $[Pd(NH_3)_4]^{2+}$ complex with *cis*-tetraphenylcalix[4]resorcinolarene, optimized by the MM2 method, is shown in Fig. 2.

Polymer (3) containing ultradispersed palladium is formed by hydrogenation of metal-containing polymer (2) at 298 K and 1 atm. Polymer (3) is hydrogenated at 600–650 K and 1 atm. The amount of consumed hydrogen, analysis of the thermolysis products, and the IR spectra of the polymers containing calix[4]resorcinolarene fragments [6] suggest formation of perhydroxanthene structures in the polymeric

matrix. These substances are new types of cavitands. Thus, palladium nanoparticles in polymer (3) catalyze hydrogenation of the surrounding benzene rings to form a new molecular reactor containing Pd^0 in the immobilized perhydroxanthene.

CONCLUSIONS

(1) Metal nanoparticles (20–100 nm) were prepared by reduction of transition metal (Pd^{2+}, Cu^{2+}, and Ni^{2+}) ammine complexes in the matrices of sulfonic cation exchnagers containing *cis*-calix[4]resorcinolarene fragments.

(2) KU-23 30/100 sulfonic cation exchanger containing 20–30 g dm^{-3} of 30–50-nm palladium(0) particles exhibits high catalytic activity in hydrogenation of nitro compounds.

REFERENCES

1. Sergeev, G.B., *Nanokhimiya* (Nanochemistry), Moscow: Mosk. Gos. Univ., 2003.
2. Pomogailo, A.F., *Ross. Khim. Zh.*, 2002, vol. 46, no. 5, pp. 64–73.
3. Buchachenko, A.L., *Usp. Khim.*, 1999, vol. 68, no. 2, pp. 99–118.
4. Altshuler, H., Ostapova, E., Sapozhnikova, L., *et al*., *Macromol. Symp.*, 2002, vol. 181, pp. 1–4.
5. MacGillivray, L.R. and Atwood, J.L., *J. Am. Chem. Soc*., 1997, vol. 119, no. 29, pp. 6931–6932.
6. Al'tshuler, G.N., Fedyaeva, O.N., Sapozhnikova, L.A., and Ostapova, E.V., *Vysokomol. Soedin., Ser. B*, 2001, vol. 43, no. 4, pp. 755–759.
7. Columbus, I. and Biali, S.E., *J. Am. Chem. Soc*., 1998, vol. 120, no. 13, pp. 3060–3067.

Russian Journal of Applied Chemistry, Vol. 77, No. 11, 2004, pp. 1899–1901. Translated from Zhurnal Prikladnoi Khimii, Vol. 77, No. 11, 2004, pp. 1917–1919.

BRIEF COMMUNICATIONS

Calorimetric Study of Polyvinyl Alcohols Used as Emulsifiers in Suspension Polymerization of Vinyl Chloride

K. V. Kir'yanov, Yu. D. Semchikov, A. G. Kronman, T. G. Ganyukhina, L. V. Leshina, and O. V. Orekhov

Lobachevsky Nizhni Novgorod State University, Nizhni Novgorod, Russia
Sibur-Neftekhim Joint-Stock Company, Nizhni Novgorod, Russia

Received July 20, 2004

Abstract—The heat effects of dissolution of two pairs of polyvinyl alcohols used as emulsifiers in suspension polymerization of vinyl chloride and the optical transmission of their stirred aqueous solutions as a function of time were determined.

One of the ways to improve the synthesis of suspension polyvinyl chloride (PVC) is the choice of emulsifying systems providing, in particular, production of a polymer with uniform grain size distribution with the minimal content or absence of so-called "fish eyes" having good ability to absorb the plasticizing agent. The following emulsifying systems are most frequently used: methyl cellulose derivatives [1], polyvinyl alcohols (PVAs) with various compositions and molecular weights [2–4], blends of PVAs with methyl cellulose derivatives [5–7], and blends of various PVAs [8].

In recent years, in synthesis of suspension PVC, preference is given to two-component emulsifying systems based on PVAs differing in the chemical structure and molecular weight. The component with a higher molecular weight, with the degree of hydrolysis of 70–80%, provides aggregative stability of the emulsion and polymer–monomer particles. The component with a lower molecular weight provides porosity of the polymer grain due to partial dissolution in drops of the polymerizing monomer. Here we attempted to find a criterion of choice of emulsifiers based on PVA by comparison of their characteristics with those of PVC to be synthesized. As the subjects of the study we used PVA of the Alcotex 72.5 and 552P brands (from here on, A-72.5 and A-552P) produced in the United Kingdom and of the L-9 and LM-20 brands produced in Japan. The first and the third are stabilizing agents for emulsion, and the second and the fourth are the modifying agents for morphology of the polymer grain. The characteristics of these products are given in the table.

EXPERIMENTAL

The enthalpy of solution was determined in a DAK-1A microcalorimeter of the Calvet type [9, 10]. The electric scheme of the measurement provides determination of heat release to no less than 98%. In each run, the calorimeter was calibrated by an electric current. The metrological characteristics were checked by measuring the standard enthalpy of solution of potassium chloride (chemically pure grade) in double-distilled water. The average determined from ten measurements was 17.7 ± 0.3 kJ mol^{-1} at 298.15 K. According to published data [11], this value is 17.58 ± 0.228 kJ mol^{-1}. The samples were prepared by grinding of PVA films prepared by casting. The films were dried in air to constant weight. The optical transmission of PVA solutions was determined on an FEK-3 photocolorimeter.

First and foremost, it was necessary to elucidate possible differences in the intensity of intermolecular

Characteristics of polyvinyl alcohols used in suspension polymerization of vinyl chloride

PVC	Color	Degree of hydrolysis, %	ΔH_{sol}, kJ g^{-1}
A-72.5	Lemon-yellow	72.4	31.6 ± 0.1
A-552P	Slightly colored solution	54.4	26.7 ± 0.1
Blend			28.4 ± 0.2
L-9	Brown	71.0	27.0 ± 0.5
LM-20	White	41.0	21.4 ± 0.1
Blend			23.3 ± 0.3

1070-4272/04/7711-1899 © 2004 MAIK "Nauka/Interperiodica"

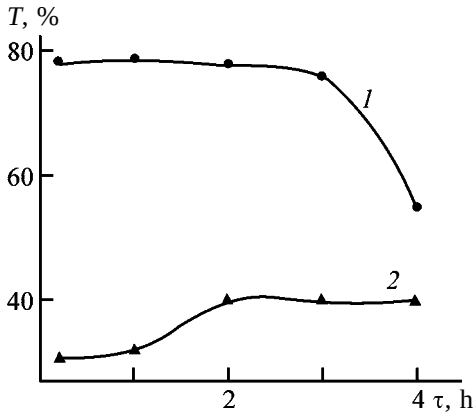

Optical transmission T as a function of time τ for aqueous solutions of PVC blends used as two-component emulsifying systems in suspension polymerization of vinyl chloride. (*1*) L-9 (0.18%)–LM-20 (0.06%) and (*2*) A-72.5 (0.15%)–A-552P (0.06%).

interaction between the components of two emulsifying systems and their solubility in the aqueous phase. It was assumed that both factors will affect the optical transmission of polymer solutions. The dependences of the optical transmission on time are shown in the figure. It is seen that the optical transmission of the solution of the blend of L-9 and LM-20 polymers abruptly decreases with time (with stirring of the solution), while for the blend of A-72.5 with A-552P the trend is inverse. These data suggest formation of associates of macromolecules in the first system and their degradation in the second system during stirring.

The enthalpies of solution of individual polymers and their blends are presented in the table. In their interpretation, account must be taken of the components of the total effect. According to published data [12], the energy of intermolecular interaction in PVA per hydroxy group is approximately 30 kJ mol^{-1}. The energy of hydrogen bonds of water molecules is 20–25 kJ mol^{-1}. Since dissolution of PVA is an exothermic process, it should be assumed that the strength of the hydrogen bonds formed by the hydroxy groups of this polymer with water is higher than the above values. Hence, we can conclude that, with increasing degree of hydrolysis of PVA, the exothermic effect of its dissolution in water increases. Indeed, PVAs of the L-9 and A-72.5 brands with a high degree of hydrolysis dissolve with a greater heat evolution as compared to PVAs of the LM-20 and A-552P types with an intermediate degree of hydrolysis.

The data listed in the table are in good agreement with this conclusion as applied to A-552P and LM-20. However, A-72.5 and L-9 have close degrees of hydrolysis and noticeably different enthalpies of solution. The deeper color of L-9 suggests higher degree of dehydration of this polymer compared to A-72.5. This change in color is equivalent to decreased degree of hydrolysis of PVA.

Thus, dissolution of PVA should be accompanied by energy evolution, which is the greater, the higher the degree of hydrolysis of PVA. These trends suggest an increase in the intensity of polymer–solvent interaction and a decrease in the polymer–polymer associative interactions (see figure). It is seen that the optical transmission of the stirred solution of the L-9 and L-20 blend decreases in time, while in the case of the polymer–polymer system the optical transmission increases. This suggests formation of aggregates of molecules in the first case and their degradation in the second case.

It was found that PVC prepared using a blend of L-9 with LM-20 does not meet the requirements of GOST (State Standard) imposed on granulometric composition, mainly due to the presence of a fraction of coarse particles, and also on the bulk density, which is equal to 0.39–0.45 g cm^{-1}, whereas the prescribed density is 0.45–0.55 g cm^{-1}. These deviations can be explained by a decrease in the relative amount of emulsifier macromolecules participating in stabilization of PVC drops, because of the tendency to polymer–polymer interaction caused by insufficient degree of hydrolysis. This follows from the calorimetric measurements and variation of the optical transmission of PVC solutions in stirring. The low degree of hydrolysis of the second component of this emulsifying mixture used as a modifying agent of PVC grain results in its increased affinity for the oil phase and, hence, in its increased content in PVC drops. As a result, the porosity of PVC particles increases.

Thus, we suggest a new approach to the choice of an optimal emulsifying system, based on determination of the enthalpy of solution and evaluation of polymer–polymer interactions of its components.

CONCLUSIONS

(1) A blend of polyvinyl alcohols of the A-72.5 and A-552 brands dissolves with a greater heat effect in comparison with a blend of L-9 and LM-20. For the first blend, the optical transmission of the stirred solutions increases with time, whereas for the second blend it decreases.

(2) Polyvinyl chloride prepared using the A-72.5 + A-552P blend meets all the requirements of GOST

(State Standard), while the polyvinyl chloride synthesized in the presence of a blend of L-9 and LM-20 does not meet the requirements imposed on the granulometric composition and bulk density, which is explained by the results of this work.

REFERENCES

1. Zil'berman, E.N., *Poluchenie i svoistva polivinilkhlorida* (Preparation and Characteristics of Polyvinyl Chloride), Moscow: Khimiya, 1968.
2. US Patent 4388442.
3. Dimitriu, I., Curcaneanus, S., Osanu, P., *et al*., *Mater. Plast*., 1983, vol. 20, no. 2, p. 100.
4. JPN Patent no. 23657.
5. JPN Patent Application no. 63156809.
6. US Patent 5100988.
7. US Patent 5096988.
8. US Patent 5087678.
9. Gal'perin, A.N., Kolesok, Yu.R., Shashkinov, L.B., and Germer, Yu.E., Abstracts of Papers, *IV Vsesoyuznaya konferentsiya po kalorimetrii* (IV All-Union Conf. on Calorimetry), Tbilisi, 1973, p. 533.
10. Calvet, E. and Prat, H., *Microcalorimetrie. Applications physico-chimiques et biologiques*, Paris: Masson, 1956.
11. Mishchenko, K.P. and Poltoratskii, G.M., *Termodinamika i stroenie vodnykh rastvorov elektrolitov* (Thermodynamics and Structure of Aqueous Solutions of Electrolytes), Leningrad: Khimiya, 1976.
12. Ushakov, S.N., *Polivinilovyi spirt i ego proizvodnye* (Polyvinyl Alcohol and Its Derivatives), Moscow: Akad. Nauk SSSR, 1960.

Russian Journal of Applied Chemistry, Vol. 77, No. 11, 2004, pp. 1902–1903. Translated from Zhurnal Prikladnoi Khimii, Vol. 77, No. 11, 2004, pp. 1920–1921.

BRIEF COMMUNICATIONS

Influence of Various Additives on Base Hydrolysis of Chlorine-Containing Organic Impurities in Naphtha Fractions

A. F. Gogotov, Ya. N. Silinskaya, V. Yu. Kolotov, and V. P. Tomin

Angarsk Petrochemical Company, Joint-Stock Company, Angarsk, Irkutsk oblast, Russia

Received June 30, 2004

Abstract—Degree of dechlorination of chlorine-containing naphtha fractions in the course of their base hydrolysis in the presence of phase-transfer catalyst and other compounds was studied. The optimal type of the phase-transfer catalyst was determined.

Recently, many oil refineries faced with a problem of refining of oil containing more than 20×10^{-4} wt % organochlorine compounds (OCCs) [1]. These compounds seriously disturbed operation of main oil-refining apparatus and made the facilities inoperative owing to strong corrosion. Procedures for removing organochlorine impurities from naphtha are intensively developed. One of these methods of dechlorination of straight-run naphtha fractions is base hydrolysis to form inorganic chlorides which can be extracted into an aqueous phase and then separated in reflux vessels by distillation of oil under atmospheric pressure.

The aim of this work was to increase the degree of hydrolytic removal of organochlorine compounds from naphtha fractions.

EXPERIMENTAL

In our experiments, we added di- and trichloropropanes to naphtha fractions. Naphtha fractions containing $(9.8–72.8) \times 10^{-4}$ wt % OCCs and boiling in the range 80–180°C were dechlorinated for 0.5–4 h in an autoclave under the static conditions in the temperature range 20–250°C. Alcohols, dimethyl sulfoxide (DMSO) of pure grade, and polyethylene glycol (PEG) and polypropylene glycol (PPG) with different molecular weights were studied as additives catalyzing the hydrolysis. The chlorine content in organic compounds was determined by the coulometric procedure [2].

The degree of hydrolysis of OCCs present in straight-run naphtha depends on their nature. Chlorinated paraffins are hydrolyzed at room temperature. The content of these compounds in naphtha decreases by ~17–18% after contact with 10% aqueous NaOH solution (Table 1, run no. 1). At 180°C, the degree of dechlorination γ increases to approximately 60% (Table 1, run no. 3).

It is known that PEGs of various molecular weights catalyze hydrolytic processes, e.g., hydrolysis of polychlorinated diphenyls [3]. Indeed, in the presence of PEG the content of organic chlorine in chlorine-containing naphthas can be decreased by ~60% at lower temperature (Table 1, run nos. 4 and 5). We studied hydrolysis of OCCs at various temperatures in the presence of a phase-transfer catalyst (PTC). The highest degree of dechlorination (85%) was observed at 210°C.

PEG was considered as both alcohol and alkylating agent [3]. At the same time, PEGs and PPGs of various molecular weights are PTCs along with tetraethylammonium salts, crown ethers, and other compounds [4]. To determine the function of PEGs in hydrolysis of OCCs (3 h, 180°C), we estimated the degree of hydrolysis in the presence of various alcohols and DMSO (Table 2).

The degree of OCC hydrolysis in the presence of

Table 1. Hydrolysis of OCCs in naphtha (50 ml) in the presence of 10% NaOH (0.5 ml). Hydrolysis time 2 h, [OCC] = 22×10^{-4} wt %

Run no.	T, °C	[OCC] $\times 10^4$, wt %	γ, %
1	20	18.1	17.7
2	130	11.4	48.2
3	180	8.6	61.0
4*	130	9.5	56.6
5*	150	8.8	59.9

* With PEG-600 additive (1 ml).

1070-4272/04/7711-1902 © 2004 MAIK "Nauka/Interperiodica"

Table 2. Hydrolysis of OCCs in naphtha (50 ml) at 180°C for 3 h in the presence of 10% NaOH (0.5 ml) and various additives

Run no.	$[OCC]_0 \times 10^4$, wt %	Additive	$[OCC] \times 10^4$, wt %	γ, %
6	10	Ethylene glycol	4.9	50.5
7	10	Diethylene glycol	4.7	53.4
8	10	Triethylene glycol	3.2	67.6
9	10	Butan-1-ol	7.2	27.6
10	10	Glycerol	–	–
11	10	Pentan-1-ol	10.9	–
12	10	Hexan-1-ol	–	–
13	10	Octan-1-ol	–	–
14	72.8	DMSO	13.8	81.0
15	72.8	Benzyl alcohol	48.7	33.1
16	72.8	Triethanolamine (TEA)	15.9	78.2
17	72.8	PEG-300	15.6	78.6
18	72.8	PEG-400	14.8	79.7
19	72.8	PEG-2025	49.5	32.0
20	72.8	PEG-1025	40.0	45.1
21	72.8	PEG-600	13.0	82.1
22	72.8	PEG-1500*	26.4	63.7
23	72.8	PEG-Polioks-100	18.3	74.9
24	72.8	PEG-1540	28.1	61.4
25	72.8	PEG-20 000	26.5	63.6
26	72.8	PEG-4000	26.4	63.7
27	72.8	PPG-4251	67.4	7.4
28	37.6	PEG-Keres 2000	13.6	63.8
29	37.6	PEG-Keres 3000	12.7	66.2

* Weight 1.4 g.

alcohols is substantially lower than that in the presence of PEG. Butan-1-ol, its higher homologs, and glycerol do not catalyze the hydrolysis. On the contrary, the catalytic effect of DMSO (run no. 14) and TEA (run no. 16) is similar to that of PEG. It is known that PEG, DMSO, and TEA create "superbasic" effect in alkaline solutions, i.e., provide the best conditions for a base-catalyzed chemical reaction. As seen from Table 2, the degree of OCC hydrolysis in the presence of PEG-600, PEG-400, and PEG-300 is maximal; its is slightly lower in the presence of PEG-Polioks, PEG-Keres 3000, PEG-Keres 2000, PEG-4000, PEG-1500, PEG-20 000, and PEG-1540. Polypropylene glycol PPG-4251 (run no. 27) cannot be used as PTC. In the subsequent experiments we used PEG-600, PEG-400, and PEG-300 as PTCs. In the presence of PEG-600, about 91% of OCCs is hydrolyzed at 210°C in 3 h.

CONCLUSIONS

(1) The degree of hydrolysis of organochlorine compounds in straight-run naphtha with sodium hydroxide solutions at room temperature is 17%. The degree of hydrolysis increases with temperature.

(2) The most promising additives catayzing the hydrolysis are polyethylene glycols with molecular weight from 300 to 600, dimethyl sulfoxide, and triethanolamine. In the presence of these compounds (2 wt %), about 80 and 90% of organochlorine compounds can be hydrolyzed in 3 h at 180 and 210°C, respectively.

REFERENCES

1. Kolotov, V.Yu., Tomin, V.P., Kolyvanova, E.M., and Krashchuk, S.G., *Nefterpererab. Neftekhim.*, 2003, issue 8, pp. 36–40.
2. Parashchenko, V.I. and Nemtsova, E.N., *Nefterpererab. Neftekhim.*, 2003, issue 11, pp. 24–26.
3. RF Patent 2 175 964.
4. Treger, Yu.A. and Sirovskii, F.S., *Zh. Vses. Khim. O–va. in. D.I. Mendeleeva*, 1986, vol. 31, no. 2, pp. 213–219.

Russian Journal of Applied Chemistry, Vol. 77, No. 11, 2004, pp. 1904–1906. Translated from Zhurnal Prikladnoi Khimii, Vol. 77, No. 11, 2004, pp. 1922–1924.

BRIEF COMMUNICATIONS

Oxidation of Propylene and Isobutylene in a Reactor with Barrier Discharge

S. V. Kudryashov, A. Yu. Ryabov, E. E. Sirotkina, and G. S. Shchegoleva

Institute of Petrochemistry, Siberian Division, Russian Academy of Sciences, Tomsk, Russia

Received April 20, 2004

Abstract—The oxidation of propylene and isobutylene in barrier-discharge plasma in the presence of octane was studied. The possible reaction mechanism was considered.

Recently, the interest in organic synthesis in electric discharges has been increasing. However, development of new technologies based on electric discharges is hindered by the lack of a sufficiently large body of data on the mechanisms and kinetics of conversion of organic compounds in plasma, which is, as a rule, caused by the low selectivity of the occurring reactions, tarring, and deep degradation of organic molecules.

We have shown previously that oxidation of hydrocarbons belonging to various classes without formation of tars and products of complete oxidation is possible in a barrier discharge [1]. This is achieved by effective removal of reaction products from the zone of the barrier discharge with a hydrocarbon film formed by condensation of supersaturated vapor of a hydrocarbon on the cooled reactor walls. For example, oxidation of hexane, cyclohexane, and cumene mainly yields hydroxy and carbonyl compounds: alcohols, aldehydes, and ketones with the same number of carbon atoms as that in the starting compound. The product formed in oxidation of cyclohexene is epoxycyclohexane (62 wt %).

It was shown in [2] that the selectivity of cyclohexene oxidation can be, in principle, controlled. The maximum yield of cyclohexene oxide was ~72%. However, products of oxidation of light olefins are of greater importance for petrochemical synthesis.

In this work we studied oxidation of propylene (PR) and isobutylene (IB) in a reactor with a barrier discharge.

EXPERIMENTAL

PR and IB were oxidized in the presence of octane to create a hydrocarbon film in which reaction products are dissolved and are thereby removed from the zone of the barrier discharge. A flow-through gas-discharge reactor of coaxial design was used. The experimental setup has been described in detail previously [1].

The starting parameters of the process were as follows: flow rate of oxygen, olefin, and octane through the reactor 3.0, 0.6, and 6×10^{-3} l h^{-1}, respectively; temperature of the reactor walls 10°C; atmospheric pressure; amplitude of voltage pulses 12 kV; pulse repetition frequency 500 Hz; specific energy of the discharge 1.3 Wh l^{-1}.

The liquid reaction products were analyzed by gas chromatography: heat-conductivity detector in the isothermal mode at 120°C; 1.2-m-long packed column with an inner diameter of 3 mm; sorbent Porapak-Q; carrier gas helium.

The conversions and the composition of products formed in oxidation of PR and IB are listed in the table. It can be seen that the main reaction products are the corresponding epoxides. In contrast to the oxidation of cyclohexene, the oxidation of PR and IB is accompanied by degradation of the olefin molecule to give methanol and formaldehyde. At the same time, no CO, CO_2, acids, or tarring products were found in the reaction products, which constitutes a fundamental difference between the results of this study and those of previous studies of oxidation of light olefins in electric discharges [3–5].

It should be noted that octane is oxidized simultaneously with the olefins. The conversion of octane is ~0.5 wt % in both cases. As a result, hydroxy and carbonyl compounds characteristic of octane oxidation products are formed [6].

A possible mechanism of cyclohexene oxidation

1070-4272/04/7711-1904 © 2004 MAIK "Nauka/Interperiodica"

was suggested in [2]. In this mechanism, the reaction products are formed by two pathways. The first of them yields cyclohexene oxide, cyclohexanone, and cyclopentylmethanal, and the second, cyclohexenone, cyclohexenol, and bicyclohexenyl.

No unsaturated oxygen-containing compounds were found in oxidation products of PR and IB, which suggests that the reaction predominantly goes by the first pathway involving activation of oxygen molecules by electron impact. This can be attributed to the higher dissociation energies of PR and IB molecules, compared with those of cyclohexene and oxygen molecules [7].

By analogy with the previously suggested mechanism of cyclohexene oxidation, the possible mechanism of PR oxidation can be represented as

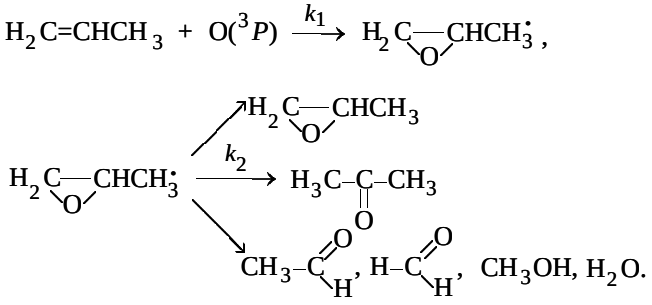

Acetaldehyde, formaldehyde, methanol, and water are formed by decomposition of a "hot" molecule of propylene oxide, with the resulting fragments subsequently involved in radical reactions. In the case of cyclohexene oxidation, the hot molecule of olefin oxide does not decompose [1, 2].

The validity of the suggested mechanism of PR and IB oxidation can be verified by simple calculations. For the oxidation of olefins, which occurs in a reactor with a steady flow mode, the following expression is valid:

$$w_1/w_2 = X_1/X_2, \quad (1)$$

where w_1, w_2, X_1, and X_2 are the oxidation rates and conversions of PR and IB, respectively.

In terms of the oxidation mechanism suggested, the following expression can be written for the oxidation rate of PR:

$$w_1 = \mathrm{d}[C_3H_5]/\mathrm{d}\tau = k_1[O(^3P)][C_3H_6]. \quad (2)$$

A similar expression can be written for w_2.

At a constant discharge power and all other experimental conditions being the same, the rates of generation of atomic oxygen in mixtures of oxygen with PR and IB will be the same, because their molecules have close cross sections of electron energy scattering. Therefore, the composition of the gas mixtures has no effect on the average electron energies. Hence, expression (1) can be written as

$$k_1'/k_1'' = X_1/X_2, \quad (3)$$

where k_1' and k_1'' are the rate constants of interaction of atomic oxygen with PR and IB, respectively. The results of calculation by expression (3) are given below:

$$\frac{k_1'}{k_1''} = \frac{2.2 \times 10^{12}\ \mathrm{cm^3\ mol^{-1}\ s^{-1}}}{2.2 \times 10^{13}\ \mathrm{cm^3\ mol^{-1}\ s^{-1}}} = 0.183\ [8],$$

$$X_1/X_2 = 1.56/6.74 = 0.231.$$

It can be seen that the calculation results reasonably agree with the experiment. The calculation error is 20.9%.

Conversions X and composition of products formed in oxidation of PR and IB*

Olefin	X, wt %	Oxidation products	Selectivity, wt %
Propylene	1.56	Propylene oxide	43.3
		Acetone	30.9
		Acetaldehyde	10.2
		Methanol	3.4
		Water + formaldehyde	12.2
Isobutylene	6.74	Isobutylene oxide	43.8
		2-Methylpropanal	23.9
		Acetone	19.2
		Methanol	4.6
		Water + formaldehyde	8.5

* Conversion obtained in a single pass of the starting mixture through the reactor at a time of contact with the discharge zone equal to ~10.5 s.

CONCLUSION

Oxidation of propylene and isobutylene by oxygen in the plasma of a barrier discharge allows synthesis of oxides of light olefins without formation of tars or complete oxidation.

REFERENCES

1. Kudryashov, S.V., Shchegoleva, G.S., Sirotkina, E.E., and Ryabov, A.Yu., *Khim. Vys. Energ.*, 2000, vol. 34, no. 2, pp. 145–148.

2. Kudryashov, S.V., Ryabov, A.Yu., Shchegoleva, G.S., and Sirotkina, E.E., in *Materialy V mezhdunarodnoi konferentsii "Khimiya nefti i gaza"* (Proc. V Int. Conf. "Chemistry of Oil and Natural Gas"), Tomsk, September 22–26, 2003, p. 485.
3. Weisbeck, V.R., *Chem. Ber.*, 1972, vol. 76, no. 11, pp. 1147–1155.
4. Junichi, I., Kazuto, T., and Satoru, T., *Bull. Chem. Soc. Jpn.*, 1977, vol. 50, no. 8, pp. 2183–2184.
5. Lyaskin, Yu.G., Mazanko, A.F., and Reznichenko, N.I., *Khim. Vys. Energ.*, 1983, vol. 17, no. 4, pp. 352–357.
6. Kudrjashov, S.V., Loos, D.A., and Sirotkina, E.E., *Contributed Papers, Int. Symp. on High Pressure Low Temperature Plasma Chemistry HAKONE VII*, Griefswald (Germany), September 10–13, 2000, vol. 2, p. 257.
7. *Khimiya plazmy* (Chemistry of Plasma), Smirnov, B.M., Ed., Moscow: Energoizdat, 1981, issue 8.
8. Herron, J.T. and Huie, R.E., *J. Phys. Chem. Ref. Data*, 1973, vol. 2, no. 3, pp. 465–514.

Russian Journal of Applied Chemistry, Vol. 77, No. 11, 2004, pp. 1907–1908. Translated from Zhurnal Prikladnoi Khimii, Vol. 77, No. 11, 2004, pp. 1925–1927.

INFORMATION

15th Annual BCC Conference on Flame Retardancy

The 15th Annual Conference on Flame Retardancy was held from June 6 to 9, 2004 in Stamford, Connecticut (the United States). The Conference was focused on recent advances in flame retardancy of polymeric materials (materials, applications, research and industrial developments, markets).

The conference started from performing the Intensive Short Course in Research, Production, and Marketing of Flame Retardancy of Polymeric Materials. The Course Director was Professor M. Lewin (the United States), and the Course Instructors were E.D. Weil, S. Levchik, and M.L. Janssens. The topics discussed in the Course were as follows:

(1) Principles of flammability and fire hazards: scheme of polymer combustion; energy balance; pyrolysis and structure of polymers; ignition and its sources; burn injury; spread of flame; smoke hazard.

(2) Flame retarding polymers: textile fabrics vs. plastics; processing systems; topical, reactive and nonreactive systems; flammability properties; other product properties.

(3) Review of flame-retardant chemicals based on: phosphorus, sulfur, halogens, antimony, nitrogen, boron, aluminum, magnesium, and others.

(4) Mechanisms of flame retardancy: gas-phase mechanism: radical scavenging in the flame; synergism in gas-phase systems: antimony trioxide, halogen blends; condensed-phase mechanism: reactions in the polymer phase, dehydration, char formation; intumescence and char properties, synergism in the condensed phase; mechanism based on physical effects in the gas phase; endothermic flame retardancy.

(5) Survey of flame retardancy of all significant plastics and textile fabrics: flame retardants in commercial use and some guidelines regarding their selection; problems of cost and effect on properties; unsolved or inadequately solved problems of interest for R&D.

(6) Discussion of material flammability, including effects of: heat and ignition sources; specimen size; shape and orientation.

(7) Standard-making and regulatory organizations: ASTM, ISO, ANSI, NFPA; Uniform building code; US Government, state regulatory; industry standards.

(8) Properties measured by fire tests: ignition; ease of extinction; flame spread; heat release rate; evolution of smoke and toxic or corrosive products.

(9) Fire test methods, grouped as: small scale, intermediate scale, full scale, and very large scale tests; research and development, regulatory, litigation.

The reports presented at the Conference were discussed in five sessions. Session I "General Mechanisms of Flame Retardancy" [chairmen: G.L. Nelson (the Unites States) and G. Camino (Italy)] included seven oral presentations. M. Nyden (the Unites States) in his lecture reported on the mechanism of the photolytic breakdown of decabromodiphenyl ether in plastics. Analysis of flammability of brominated epoxides was made in the lecture prepared by S. Stoliarov, R. Walters, S. Crowley, Q. Williams, and R. Lyon (the Unites States). The problems of charring and intumescence were discussed in the report of B. Schartel, M. Bartholmai, and U. Braun (Germany). The group of scientists (D. Price, T.R. Hull, G.J. Milnes, and L.K. Cunliffe) from the Center for Materials Research and Innovation (UK) reviewed current mechanistic and combustion product studies concerned with flame retardant systems. In his plenary lecture entitled Challenges in Flame Retardancy of Polymers, M. Lewin analyzed the future prospects in this field. Two last lectures of Section I were devoted to the problems of utilization of waste materials released in the course of intumescence [L.R.M. Estevro and R.S.V. Nascimento (Brazil); M. Le Bras, S. Bourbigot, and R. Delobel (France)] and of retardant release from materials [G.C. Stevens and J.L. Thomas (UK)].

Session II "Halogen- and Non-Halogen-Based FR Systems" [chairmen: G. Kirshenbaum and K. Shen (the Unites States) and T.R. Hull (UK)] included nine presentations. R.E. Lyon (the United States) reported on fire-smart chloral polymers, and the group of Hungarian researches (G. Marosi, A. Toldy, P. Anna, E. Zimonyi, S. Keszei, W. Krause, and S. Horold), on flame retardant mechanism and application of synergistic combinations of phosphinates. Flame retardant systems for textile back-coating applications were considered in the lecture prepared by R. Mazor, M. Peled, O. Ben-Vais, N. Zer-Zion, A. Shoshan, and I. Shalev (Israel). Yukihiro Kiuchi, Masatoshi Iji, and Makoto Soyama (Japan) reported on self-extinguishing

1070-4272/04/7711-1907 © 2004 MAIK "Nauka/Interperiodica"

epoxy resin compound and improvement of its flame resistance. The lecture prepared by the large German team (M. Doering, C. Kollann, M. Ahlmann, U. Dittrich, B.Just, H. Keller, V. Altstadt, H. Lengsfeld, R. Perez, D. Pospiech, and T. Hoffmann) was devoted to new phosphorous-containing flame retardants for epoxy resins. Reaction mechanisms of melamine-based flame retardants were discussed in the lecture prepared by N.J.J. Aelmans (Switzerland), N. Kaprinidis (the United States), and R. Kierkels and R. Steenbakkers (the Netherlands). R.L. Markezich (the United States) reported on low-smoke formulations for FR resins, and K.K. Shen and E. Olson (the United States), on the use of borates as fire retardants in halogen-free polymers. The last lecture of Session II [J. Kim (Korea)] was devoted to the effect of phenolic char former and oligomeric aryl phosphate mixtures on the flame retardance enhancement of ABS plastics.

Session III "Nano-Composites" [chairmen: D. Price (UK) and R. Kozlowski (Poland)] included six presentations. G. Camino (Italy) gave the lecture entitled Which Morphology for Nanocomposites FR C.A. Wilkie reported on advances in FR of polymer–clay nanocomposites. Researches from the United States (E.D. Weil, M. Lewin, K. Shen, and D. Rao) devoted their lecture to searching for interactive FR systems for EVA. The performance characteristics of PET/silica nanocomposites prepared via extrusion were considered in the lecture prepared by G.L. Nelson, Feng Yang, and C. Johnsrud (the United States).

The last two presentations of Session III were focused on the problems of evaluation of hydroxy double salts as fire retardant additives [J.M. Hossenlopp (the United States)] and flammability, degradation, and structural characterization of fiber-forming polypropylene nanocomposites [S. Zhang, A.R. Horrocks, T.R. Hull, B.K. Kandola, and D. Price (UK)].

Session IV "Consumer Focus/Industrial Products" [chairmen: C.A. Wilkie and S.V. Levchik (the United States)] included six presentations. Latest progress in rigid fire barriers was the subject of the lecture prepared by R. Kozlowski, B. Mieleniak, R. Gyrski, A. Przepiera, and K. Bujnowicz (Poland). T. Chen and T.J. Lynch (the United States) reported on the effect of surface treatment with magnesium hydroxide for flame-retardant wire and cable and TPO roofing compounds. C.Q. Yang, W. Wu, and H. Yang (the United States) considered applications of hydroxy-functional organophosphorus oligomers as a durable flame-retarding finishing agents for cotton and cotton/polyamide blends.

The next presentation was devoted to exploring issues surrounding flame retarded plastics used in electrical and electronic equipment [R.B. Dawson and S.D. Landry (the United States)]. S.V. Levchik reported on halogen-free printed wiring boards, O. Figovsky, V. Karchevsky, and D. Bellin (Israel) reviewed recent developments in waterborne compositions.

Finally, Section V "Testing/Standards/Methods" [chairmen J.S. Stimitz and M.M. Hirshler (the United States)] included eight presentation. R.H. White and M.A. Dietenberger (the United States) reported on cone calorimeter evaluation of wood products. G. Reznick, I. Finberg, A. Staimetz, Y. Bar Yaakov, and P. Georlette (Israel) discussed fire retardants for technopolymers of stricter fire safety and higher performance. Measurement of smoke production of low-smoke cables by means of present and future test methods was discussed in the lecture given by H. Breulet (Belgium). K. Battipaglia, J. Huczek, M. Janssens, and A. Sauceda (the United States) reported on using the cone calorimeter to predict FMVSS 302 performance of automotive materials. J.S. Stimitz and R.V. Wagner gave the lecture entitled Two New Test Methodologies To Evaluate Plastic Materials for Use in 42 Volt Auto Applications. The last two presentations of Session V were devoted to residential upholstered furniture hazards [M.M. Hirschler (the United States)] and to the regulatory status for flame retardants [R.B. Dawson, S.D. Landry, and V. Steukers (the United States)].

The poster presentations were made by researches from Germany, S. Korea, and the United States. Of particular interest was the presentation devoted to metal complexes of aromatic phosphinates as a newly developed class of fire retardants for engineering thermoplastics.

The Fifteenth Annual Conference on Recent Advances in Flame Retardancy of Polymeric Materials testifies to a continuous strong activity in various aspects of this field. It not only shows that the technical and commercial interest in flame retardancy is sustained but also indicates great vitality, as evidenced by the new and sometimes striking developments in the science and technology, and by the innovative applications, testing methods, and standards, presented and discussed at the conferences.

The next 16th Conference will be held in Stamford, Connecticut (the United States) early in June 2005.

G. E. Zaikov, L. L. Madyuskina, and M. I. Artsis

Russian Journal of Applied Chemistry, Vol. 77, No. 11, 2004, pp. 1909–1912. Translated from Zhurnal Prikladnoi Khimii, Vol. 77, No. 11, 2004, pp. 1928–1931.

HISTORY OF CHEMISTRY AND CHEMICAL TECHNOLOGY

Paul Sabatier (to 150th Anniversary of His Birthday)

A corecipient of the 1912 Nobel Prize in Chemistry, French scientist Paul Sabatier made an outstanding contribution to organic chemistry and heterogeneous catalysis, in particular, to studies of catalytic hydrogenation.

Sabatier was born in Carcassonne, in southern France, on November 5, 1854. His parents were farmers and, having lost their property, became merchants. He received his primary education at a lyceum in Carcassonne and went to a lyceum in Toulouse in 1868. He also attended there public lectures on physics and chemistry. Sabatier received higher education in Paris (Ecole Normale Supérieure, 1874–1877); he was the best student in his group and the first among the graduates in 1877. During the following year, Sabatier taught physics at a lyceum in Nice and then became an assistant of professor Marcellin Berthelot (1827–1907), an outstanding French chemist and statesman, at Collége de France. The first period of Sabatier's scientific activities (1879–1898) was associated with thermochemical and other studies of inorganic compounds. He earned his doctorate in 1880 for thermochemical studies of sulfur and metal sulfides. In 1881, Sabatier studied physics at the University of Bordeaux; he returned to Toulouse in 1882. In 1884, he became professor of chemistry at the University of Toulouse and occupied this position till his retirement in 1930. In 1905, he was appointed dean of a faculty.

In 1907, the French chemical sciences suffered a severe loss: H. Moissan (1852–1907, 1906 Nobel Prize in Chemistry) died on February 20, and M. Berthelot, on March 18. Both the scientists were members of the Paris Academy of Sciences and academies of many other countries and foreign corresponding members of the St. Petersburg Academy of Sciences; they were more than once elected Presidents of the French Chemical Society. Sabatier was invited to fill Moissan's position at Sorbonne or Berthelot's position at Collége de France. However, he preferred to remain in Toulouse. Sabatier's lectures enjoyed popularity. In 1901, he was elected a corresponding member, and in 1913, a full member of the Paris Academy of Sciences.

P. Sabatier

Sabatier's studies in the field of inorganic chemistry were widely diverse. He obtained pure hydrogen sulfide by vacuum distillation; studied sulfides, selenides, and nitrides of quite a number of metals, nitrogen oxides, and also nitrosodisulfonic acid and its salts. In 1895, Sabatier's attention was attracted by processes of recovery of metals by reduction of their oxides with hydrogen; he also obtained nickel carbonyl by direct action of carbon monoxide on finely dispersed nickel. However, Sabatier was made famous all over the world by his studies in the field of heterogeneous catalysis, which he and his co-worker J.B. Senderens (1856–1937) commenced in 1897 [1–3]. Initially, the studies involved only hydrogenation of unsaturated compounds, with various metals, and primarily nickel, used as catalysts. He obtained ethane from ethylene and the corresponding paraffins from a number of other olefins. He studied the condi-

1070-4272/04/7711-1909 © 2004 MAIK "Nauka/Interperiodica"

tions of catalytic hydrogenation of acetylene that ensured the maximum yield of ethylene. Of particular importance for organic synthesis were Sabatier's studies of hydrogenation of benzene and its homologs (1901); before that nobody could perform smooth hydrogenation. In 1902, the French scientist managed to reduce nitro compounds with the use of a nickel catalyst. In the same years, Sabatier and Senderens were the first to perform catalytic reduction of carbon monoxide to give methane. In 1902–1903, they found ways to reduce simplest aldehydes and ketones. Later, in 1907, Sabatier and co-workers studied in detail the ability of numerous oxides to catalyze dehydrogenation and dehydration processes.

Sabatier and his co-workers and disciples studied a large number of organic reactions and, as a rule, obtained target products in high yields. The experimental procedure they used was distinguished by its simplicity: It consisted in passing the vapor of a starting organic compound, mixed with hydrogen, through a tube containing a finely divided catalyst, mainly a metal, and heated to 100–190°C. For example, passing a mixture of benzene and hydrogen at 170–190°C over nickel ensured virtually 100% yield of cyclohexane.

In 1907–1911, Sabatier carried out a set of investigations in the field of catalytic conversion of alcohols. He established that magnesium, cadmium, manganese, and their oxides cause dehydrogenation of alcohols, whereas aluminum, tungsten, silicon, and their oxides lead to their dehydration. In 1909, Sabatier performed a vapor-phase catalytic hydrogenation of unsaturated organic acids.

Already by 1907, Sabatier's investigations in the field of catalytic hydrogenation were highly appreciated by the scientific community, and he was nominated for a Nobel Prize in 1907, 1909, and 1911. In 1909, Sabatier's closest associate, Senderens, also was among nominees. In 1912, Sabatier was awarded a Nobel Prize "for his method of hydrogenating organic compounds in the presence of finely disintegrated metals whereby the progress of organic chemistry has been greatly advanced in recent years." His corecipient was another French chemist, Victor Grignard (1871–1935). The statement of the Nobel Committee said that he was awarded "for the discovery of the so-called Grignard reagent, which in recent years has greatly advanced the progress of organic chemistry." This is related to wide use of organomagnesium compounds in preparative organic chemistry. Sabatier said in his Nobel lecture: "For the past fifteen years this idea of mine on the mechanism of catalysis has never left me, and it is to the inferences drawn from it that I owe all my useful results" [4–6].

A year after he was awarded a Nobel Prize, Sabatier summarized the results of his studies in the field of catalysis in the monograph *La catalyse en chimie organique* (Paris, 1913). The second, supplemented edition of Sabatier's monograph was published in France in 1920. The book was published in England and Germany. Later, in 1932, the monograph was translated into Russian [7]. The concept of heterogeneous catalysis, developed by Sabatier, contradicted the theory put forward earlier by W. Ostwald (1853–1932, 1909 Nobel Prize in Chemistry). According to Ostwald, adsorption of gaseous reagents in micropores of the catalyst plays an important role. In Sabatier's opinion, heterogeneous catalysis in hydrogenation is associated with formation of intermediate compounds on the external surface of catalysts. Unstable compounds then decompose to give the end product. The main results of Sabatier's investigations in the field of catalytic reactions are contained in compact form in [8].

In 1900, investigations in the field of heterogeneous catalysis, as applied to reactions involving organic substances, were commenced by one of the most prominent chemists of the first half of the XX century, V.N. Ipat'ev (1867–1952, academician since 1916). The commonness of interests and scientific purposes unites Sabatier's and Ipat'ev's investigations, which complement each other [1–3, 9]. However, the approaches of these scientists to solution of the problem of catalytic hydrogenation were fundamentally different. Sabatier and his co-workers mostly solved problems of preparative organic synthesis, with only the catalyst being the main factor affecting the course of the process and temperature being of secondary importance. At the same time, Ipat'ev and his disciples regarded the pressure and temperature as most important factors affecting the course of the catalytic reaction. In their first experiments, aluminum oxide was the most frequently used catalyst. Later, Ipat'ev used complex formulations as catalysts and studied the influence of various additives enhancing the activity of catalysts. The history of chemical science has shown that catalytic hydrogenation processes could not be used under industrial conditions without high temperatures and high pressures.

Sabatier demonstrated the applicability of heterogeneous catalysis in reactions performed under comparatively mild conditions, which are typical of the classical organic synthesis. To Ipat'ev belongs proof of the successful applicability of heterogeneous catal-

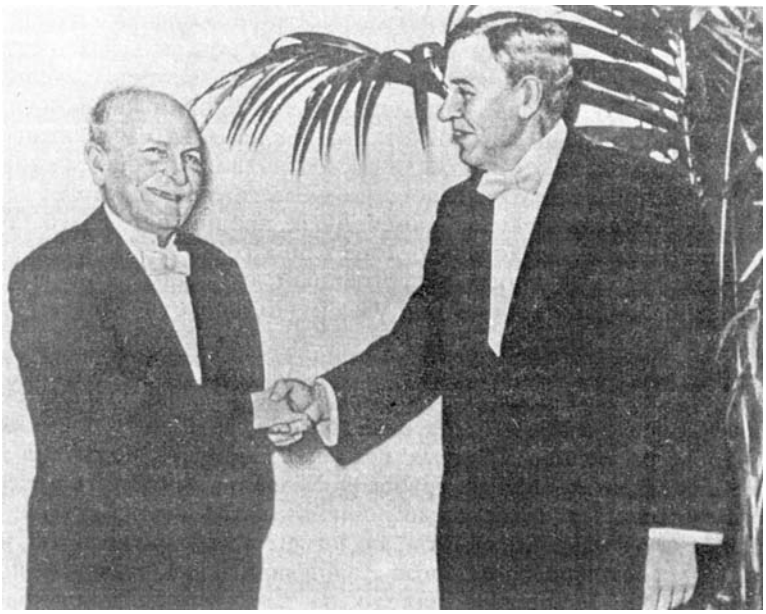

P. Sabatier (left) and V.N. Ipat'ev (right) (Paris, 1936).

ysis at high pressures and temperatures, i.e., under extreme conditions from the standpoint of an organic chemist of that time. Hydrogenation catalysis under atmospheric pressure, discovered and developed in detail by Sabatier in the very end of the XIX century, gave place, already in the 1920s–1930s, to catalytic hydrogenation by Ipat'ev's method [9]. The main results of investigations performed by the Russian scientist were summarized in the monograph [10]. Ipat'ev was nominated for a Nobel Prize in 1941, 1948, 1949, and 1950. However, he was not awarded the prize he undoubtedly deserved. The possible reasons were analyzed in [11]. According to recently published materials [12], the scientist himself, who was awarded a large number of scientific prizes and honorary titles of many countries, took this historical injustice rather calmly.

Having retired in 1930, Sabatier continued delivering lectures till the end of his life. Academies and scientific societies of many countries elected him their foreign honorary member (England, Spain, Italy, Romania, etc.), he had a degree of doctor of *honoris causa* from quite a number of universities [13]. In 1897 and 1905, Sabatier was awarded medals of the Paris Academy of Sciences; in 1915, the London Royal Society awarded him a Davy medal; in 1933, he received a Franklin medal (the United States). The scientist was honored with highest state awards of France.

Paul Sabatier died on August 14, 1941, in Toulouse at the age of 86. Unfortunately, biographic evidence concerning Sabatier in publications open to general use is very scarce [4, 13–15]. The reference literature contains repeated annoying inaccuracies [5, 6, 16].

REFERENCES

1. Kuznetsov, V.I., *Razvitie kataliticheskogo organicheskogo sinteza* (Development of Catalytic Organic Synthesis), Moscow: Nauka, 1964.
2. Bykov, G.V., *Istoriya organicheskoi khimii* (History of Organic Chemistry), Moscow: Nauka, 1978.
3. Levin, V.F., *Issledovaniya po istorii organicheskoi khimii* (Studies in the History of Organic Chemistry), Moscow: Nauka, 1980, pp. 68–85.
4. *Le Prix Nobel en 1912*, Stockholm, 1913.
5. *Laureaty Nobelevskoi premii: Entsiklopediya* (Nobel Prize Laureates: Encyclopedia), Moscow: Progress, 1992, vol. 2.
6. Zelenin, K.N., Nozdrachev, A.D., and Polyakov, E.L., *Nobelevskie premii po khimii za 100 let* (Nobel Prizes for Chemistry in 100 Years), St. Petersburg: Gumanistika, 2003.
7. Sabatier, P., *Kataliz v organicheskoi khimii* (Catalysis in Organic Chemistry), Orlov, N.A. and Petrov, A.D., Eds. and authors of supplements, Leningrad: Goskhimtekhizdat, 1932.
8. Sabatier, P., *Ind. Eng. Chem.*, 1926, vol. 18, no. 10, pp. 1005–1008.
9. Kuznetsov, V.I. and Maksimenko, A.M., *Vladimir*

Nikolaevich Ipat'ev: 1867–1952, Moscow: Nauka, 1992.

10. Ipat'ev, V.N., *Kataliticheskie reaktsii pri vysokikh temperaturakh i davleniyakh* (Catalytic Reactions at High Temperatures and Pressures), Moscow: Akad. Nauk SSSR, 1936.
11. Solov'ev, Yu.I., *Vestn. Ross. Akad. Nauk*, 1997, vol. 67, no. 7, pp. 627–642.
12. Kuksin, I., *Vestn. Ross. Akad. Nauk*, 1999, vol. 69, no. 2, pp. 175.
13. Taylor, H.S., *J. Am. Chem. Soc*., 1944, vol. 66, no. 10, pp. 1615–1617.
14. Le Necrologe, *C. R. Acad. Sci. Paris*, 1941, vol. 213, no. 8, pp. 282–284.
15. Partington, J.R., *Nature*, 1954, no. 4436, pp. 859–860.
16. *Dictionary of Scientific Biography*, Gillespie, C., Ed., New York: Charles Scribner's Sons, 1981, vol. 12, pp. 46–47.

A. G. Morachevskii

Russian Journal of Applied Chemistry, Vol. 77, No. 11, 2004, p. 1913–1914. Translated from Zhurnal Prikladnoi Khimii, Vol. 77, No. 11, 2004, p. 1932–1933.

OBITUARIES

Armin Genrikhovich Stromberg

On September 18, 2004, at the age of 94, passed away Armin Genrikhovich Stromberg, the oldest Russian electrochemist, founder of the world's most prominent scientific school in the field of stripping voltammetry, honorary professor of the Tomsk Polytechnic Institute, Honored Chemist of the Russian Federation, honorary Soros professor, and doctor of chemical sciences.

A.G. Stromberg was born on September 16, 1910, and spent his early childhood in St. Petersburg. After his father, an army doctor and privatdocent of the Military Medical Academy in St. Petersburg, died in action at the frontline in 1914, Stromberg's family moved to his mother's homeland, Yekaterinburg. In 1927, Stromberg entered the chemical department of the Ural Polytechnic Institute and graduated therefrom in 1930 as chemist-engineer. The first period of Stromberg's scientific activities (before 1941) was devoted to original investigations in the filed of high-temperature electrochemistry. He was the first to study electrocapillary phenomena for liquid metals in ionic melts and determined the zero-charge points. In 1939, Stromberg defended his candidate's (chem.) dissertation.

The postwar period of Stromberg's scientific activities is distinguished by wide use of polarographic techniques for studies of various objects. Particularly important was scientist's contribution to the theory and practice of amalgam polarography and to examination of the polarographic behavior of organic compounds. In 1951, Stromberg defended the dissertation "Theory and Practice of Polarography, and Amalgam Polarography in Particular," and the degree of a doctor of chemistry was conferred on him.

In the prewar years, and also in 1944–1949, Stromberg worked at the Institute of Chemistry and Metallurgy, Ural Division, Academy of Sciences of the USSR, and in 1950–1955, at the chair of physical and colloid chemistry of the Ural State University. In 1956, he was elected head of the chair of physical and colloid chemistry at Tomsk Polytechnic Institute. It is at this chair and at the Basic Research Laboratory for Physicochemical Determination of Microimpurities in Semiconductors and High-Purity Materials, created at the chair by Stromberg's initiative, that his talent as not only a theoretician, experimenter, and pedagogue, but also a head and organizer of a large team of researchers, capable of solving exceedingly complicated scientific and applied problems, displayed itself in full measure. Stromberg himself headed the laboratory for 24 years and then remained there as scientific consultant. The goal of all the staff members of the laboratory was the same, to improve thoroughly the method of stripping voltammetry: to elaborate upon the theory, and develop new apparatus and practical procedures for determining microimpurities. During the 40 years of existence of the basic-research laboratory, tremendous success was achieved, summarized in the collection of works *Tomskoi electrokhimicheskoi shkole i problemnoi laboratorii mikroprimesei sorok let (1962–2002)* (Tomsk Electrochemical School and Basic-Research Laboratory of Microimpurities Is Forty (1962–2002)) (Tomsk, 2004). The presentation of the book was made on the scientist's birthday, on September 16, 2004, two days before his death. In the last months of his life, Stromberg suffered from cardiac insufficiency, but did not terminate his scientific activities and continued to consult his co-workers.

Armin Genrikhovich Stromberg was a man of astonishing working capacity and devotion to science, his motto was "The life is short, so be in a hurry." Under scientist's supervision, near 100 candidate dissertations were prepared and defended, a number of

1070-4272/04/7711-1913 © 2004 MAIK "Nauka/Interperiodica"

his disciples became doctors of science and headed scientific teams in various cities and towns of Russia. Stromberg wrote more than 430 scientific articles and the textbook *Fizicheskaya khimiya* (Physical Chemistry), which has already run into five editions. The last three of these (in 1999, 2001, and 2003) were supplemented by the author with important sections: "Introduction to the Theory of Self-Organization of Matter. Elements of Synergetics" and "Introduction to the Theory of Fractals." In 1999 was published an original textbook *Sinergetika: Primenenie v khimii* (Synergetics: Application to Chemistry). These supplements manifested another important principle of the scientist: to learn incessantly, to be at the frontline of research. An exceedingly talented and well-organized person, Stromberg always took a rest in performing Chopin preludes in strictly fixed hours of every day, in supplementing his home library with books and journal articles devoted to an exceedingly wide variety of topics, and in reading of memoirs.

In the person of Armin Genrikhovich Stromberg, we lost a prominent scientist and a true representative of Russia's intelligentsia of the early XX century. His friends and colleagues will ever thankfully keep his memory.

A. G. Morachevskii, B. V. L'vov, and V. I. Kravtsov

Russian Journal of Applied Chemistry, Vol. 77, No. 12, 2004, pp. 1915–1919. Translated from Zhurnal Prikladnoi Khimii, Vol. 77, No. 12, 2004, pp. 1937–1941.

PHYSICOCHEMICAL STUDIES OF SYSTEMS AND PROCESSES

A Study of the Reactivity of Copper Nanopowders in Their Reaction with Glacial Acetic Acid

E. V. Mikubaeva, N. S. Kobotaeva, and E. E. Sirotkina

Institute of Petrochemistry, Siberian Division, Russian Academy of Sciences, Tomsk, Russia

Received August 11, 2004

Abstract—The reactivity of copper nanopowders obtained by mechanical treatment or electric explosion of a conductor was studied in their reaction with glacial acetic acid. Two parameters were used to evaluate the reactivity: heat effect of the reaction and the maximum rate of heat release.

Compared with compact substances, highly dispersed materials have an excess energy, and, therefore, they are frequently named energy-saturated systems or media [1, 2]. With the high energy content of dispersed particles, which is due, in particular, to the contribution of the surface energy, is associated a very important specific feature of ultradispersed media, i.e., their high reactivity.

Methods for preparing highly dispersed materials, including metal nanopowders, can be conventionally divided into physicochemical and mechanical techniques [3]. To the former belong processes in which powders are produced with a change in the chemical composition of the starting raw material or in its aggregative state, e.g., the method of electric explosion of a conductor (EEC). In mechanical techniques, the starting material is ground into a powder without any change in its chemical composition. The preparation technique used determines the size and morphology of particles, chemical composition, and physical and physicochemical properties of the powders obtained.

The electric explosion of a conductor consists in an abrupt change in the physical state of the metal because of the intensive release of energy in the conductor through which a pulsed current of high density is passed [4]. In the explosion stage, the metal is heated to above the melting point, with some part of the material of the wire evaporating and the rest flying apart in the form of liquid drops. The former phase yields, via condensation in a flow of a rapidly expanding gas, particles with exceedingly small size. Thus, the resulting particles are formed both via condensation (finer particles) and via dispersion (coarser particles). The relative amounts of these components depend on the type of disintegration of the conductor, which is determined by the process of energy introduction into the exploding conductor [5]. The energy introduced into the conductor is commonly characterized by the ratio of the density E of the energy introduced to the energy E_s of sublimation of the metal. This parameter, as well as the diameter of the wire being exploded, determines the specific surface area and size distribution of the resulting particles [5, 6]. The larger the ratio E/E_s, the greater the amount of finer particles (<30 nm) and the smaller that of coarse particles (≥100 nm). It should be noted that the particles formed in EEC have a regular spherical shape [5].

It is commonly believed that nanopowders produced by the EEC method have a very high excess energy [7], which exceeds severalfold the heat of melting of the same amount of substance in the bulk state. Such an excess of energy in nanopowders cannot be due to the contribution of only the surface energy. It is assumed, in particular, that the main component of the energy stored in electrically exploded powders is associated with charged structures [8], whose presence in the particles changes their electrochemical behavior.

Mechanical abrasion is the most productive method for obtaining powders of various materials in large amounts [4]. The grinding is commonly done with planetary, ball, and vibration mills. However, ordinary grinding is comparatively rarely used to obtain ultradispersed powders because of the existence of a certain limit of grindability [2, 9]. The grinding limit is an individual characteristic of a substance, which is commonly determined experimentally.

1070-4272/04/7712-1915 © 2004 MAIK "Nauka/Interperiodica"

Table 1. Preparation conditions of copper nanopowders

Nanopowder	Preparation technique	E/E_s, rel. units	Medium	Additive	MT duration, min
Cu-18	EEC	2.0	Nitrogen	–	–
Cu-19	EEC	1.0	″	–	–
Cu-8	EEC	1.0	″	–	–
Cu-13	EEC	0.8	Argon	–	–
Cu-11	EEC	1.2	Xenon	–	–
Cu-I	MT	–	Air	$H(CF_2CF_2)_2CONH_2$	10
Cu-II	MT	–	″	$H(CF_2CF_2)_2CONH_2$	20
Cu-III	MT	–	″	$H(CF_2CF_2)_2CONH_2$	30
Cu-1	MT	–	″	$CuCl_2$	10
Cu-2	MT	–	″	$CuCl_2$	20
Cu-3	MT	–	″	$CuCl_2$	30

Two opposite processes compete in grinding of a solid: (i) decrease in particle size in the disintegration of the material and (ii) aggregation of particles as a result of plastic flow. When the treatment duration increases, the specific surface area may behave differently, depending on the relative rates of these processes. For example, if the contribution from the second process starts to grow in the course of dispersion and becomes predominant at a certain level of dispersity, the time dependence of the specific surface area will pass through a maximum. In the case when the rates of disintegration and aggregation become equal and remain in this state during a certain period of time, the specific surface area reaches the largest possible, under the given conditions, value and further grinding does not reduce the particle size [10].

The relative contributions of these processes can be affected by varying such dispersion conditions as temperature (change in the flowability limit, transition from the plastic to the brittle state at low temperature), medium, and grinding in the presence of surfactants making lower the surface energy and mechanical strength of particles [2, 10]. As surfactants can act both inorganic and organic polar compounds: organic acids, alcohols, amines, and high-molecular-weight compounds containing acid, alcoholic, amine, and other fragments. For example, mechanical treatment of copper powders in the presence of fluorine-containing organic surfactants (in particular, amide of perfluorovaleric acid) leads to an increase in the specific surface area to 5.2 $m^2 g^{-1}$, which is comparable with that in EEC-produced powders [11]. Most of particles formed under high-energy impact (including mechanical treatment) have an irregular shape [9].

In this study, the reactivity of copper nanopowders obtained in various conditions of EEC and those produced by mechanical treatment (MT) toward glacial acetic acid was examined by means of microcalorimetry.

EXPERIMENTAL

As objects of study served copper nanopowders obtained using two methods: electric explosion of a conductor in an inert atmosphere (nitrogen, argon, or xenon) and mechanical treatment in an AGO-2 centrifugal-planetary mill at a power introduced by the balls equal to 55 $W g^{-1}$ (40 g) in the presence of amide of perfluorovaleric acid $H(CF_2CF_2)_2CONH_2$ (10 wt %) or $CuCl_2$ (15 wt %) ($CuCl_2$ was washed with ethanol after MT).[1] The preparation conditions of the nanopowders are listed in Table 1.

To evaluate the reactivity of copper nanopowders and examine its dependence on the conditions under which these nanopowders were obtained and on the methods used for this purpose, the reaction of copper with glacial acetic acid in the presence of atmospheric oxygen was chosen [12]. This reaction proceeds by the scheme

$$2Cu + 2CH_3COOH + O_2 \rightarrow Cu(CH_3COO)_2 \cdot Cu(OH)_2.$$

The reaction was performed in an MKDP-2 microcalorimeter in special cells [13]: 2 mg of copper powder were placed in 1.5 cm^3 of glacial acetic acid at 50°C. For each powder, measurements were carried out in five replications and the averaged values were

[1] Electrically exploded copper nanopowders were produced at the Institute of High-Current Electronics, Siberian Division, Russian Academy of Sciences (Tomsk), and those mechanically treated, at the Institute of Solid-State Chemistry and Mechanochemistry, Siberian Division, Russian Academy of Sciences (Novosibirsk).

Table 2. Results obtained in a study of the reactivity of copper nanopowders* in the reaction with glacial acetic acid at 50°C

Nanopowder	S_{sp}, $m^2\ g^{-1}$	d_s, nm	Completeness of the reaction, %	ΔH, kJ mol^{-1}	$W_{max} \cdot 10^4$, J s^{-1}
Cu-18	2.1	319	78	234.75	22.06
Cu-19	5.6	120	78	271.35	23.95
Cu-8	8.7	77	83	279.76	32.49
Cu-13	2.2	305	61	245.10	21.56
Cu-11	6.0	112	87	308.90	50.58
Cu-I	3.2	209	61	305.93	21.23
Cu-II	3.9	172	46	367.27	16.45
Cu-III	5.2	129	61	367.39	24.45
Cu-1	4.3	156	59	232.07	14.28
Cu-2	6.2	108	61	212.06	24.41
Cu-3	6.9	97	58	149.30	12.69

* S_{sp}, specific surface area found by BET; d_s, average particle diameter, $d_s = 6/\rho S_{sp}$, where ρ is the theoretical density, g cm^{-3}; ΔH, heat effect of the reaction; and W_{max}, maximum rate of heat release.

further analyzed. In all the experiments, the time of thermostating and that during which heat-release curves were recorded were the same: 80 min each. After the reaction was carried out in the microcalorimeter, an electronic absorption spectrum of the reaction mixture was recorded on a Specord M40 spectrophotometer and the absorption band of copper acetate (683 nm) was used to monitor the completeness of the reaction. The total heat of the reaction was found by integration of the heat-release curves, and the heat effect of the reaction was calculated with account of the completeness of the reaction. As a parameter for comparison of the reactivities of the copper powders served, in addition to the heat effect of the reaction, the maximum rate of heat release. It is known [14] that the heat flux is proportional to the reaction rate, and, therefore, the kinetics of the process can be judged from the experimental curve of the heat flux. The experimental curve obtained in studying a fast reaction, when the whole amount of heat is released during a time comparable with the time constant of the calorimeter, is to be corrected. In the case in question, with the reaction duration considerably longer than the time constant of the calorimeter (the time constant of the MKDP-2 microcalorimeter does not exceed 180 s), kinetic parameters can be calculated directly from the experimental curve. The maximum rates of heat release were calculated by integrating experimental curves in the vicinity of the peak heat release.

The results obtained in studying the reactivity of copper nanopowders by means of microcalorimetry are listed in Table 2. The experimental data obtained were used to plot the dependences of the heat effects of the reaction and the maximum rates of heat release on the specific surface area of the powders (Figs. 1, 2). One curve represents the results obtained for copper powders obtained by an electric explosion in the atmosphere of argon (curve *1*); the heat effects

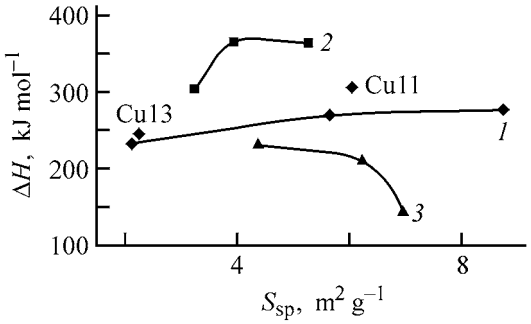

Fig. 1. Enthalpy of the reaction, ΔH, of copper nanopowders with glacial acetic acid at 50°C vs. specific surface area S_{sp}. Powder: (*1*) electrically exploded, (*2*) mechanically treated in the presence of amide of perfluorovaleric acid, and (*3*) mechanically treated in the presence of powdered $CuCl_2$; the same for Fig. 2.

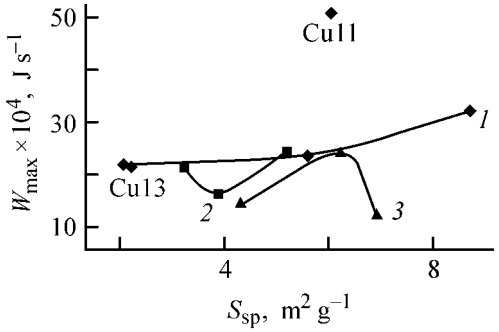

Fig. 2. Maximum rate of heat release, W_{max}, vs. the specific surface area S_{sp}.

of the reaction and the maximum rates of heat release for Cu-13 and Cu-11 powders prepared by an electric explosion in the atmospheres of argon and xenon, respectively, are plotted separately.

For the copper powders produced by electric explosion in the atmosphere of nitrogen, the heat effect of the reaction and the maximum rate of heat release grow as the specific surface area becomes larger (Figs. 1, 2; curves *1*). The values of the parameters ΔH and W_{max} for Cu-13 powder obtained in argon differ only slightly from the corresponding values for Cu-18 powder prepared by electric explosion in the atmosphere of nitrogen and having a specific surface area comparable with that of Cu-13. Thus, the reactivity of the copper powders produced by electric explosion in the atmosphere of nitrogen or argon grows with increasing specific surface area. An unexpectedly high reactivity is observed for Cu-11 powder obtained by electric explosion in the atmosphere of xenon. The highest heat effects of the reaction, fastest maximum rates of heat release, and highest yield of the product were obtained for this powder (Table 1).

It may be assumed that of decisive importance for the reactivity of electrically exploded powders with specific surface areas in the range studied and with the corresponding particle sizes (77 to 319 nm) is the medium in which the conductor is electrically exploded, rather than the specific surface area (or particle size), which is determined by the parameter E/E_s and by other conditions of the electric explosion [5, 6]. The highest reactivity is observed for Cu-11 copper powder produced by electric explosion in the atmosphere of xenon. Possibly, the electric explosion of a copper conductor in the atmosphere of xenon favors stabilization of metastable energy-saturated states to a greater extent than does the electric explosion in the atmosphere of other gases. It is also possible that presence of another type of impurities is important in this case. It was shown in [15], by means of radio-activation, chemical, and X-ray diffraction analyses and ESR and NMR spectroscopies that the particle of a powder produced by the EEC method is a metallic sphere of submicrometer size with a distorted crystal lattice, which also contains the amorphous phase of the metal and, in the bulk and on the surface, the gas in which the explosion was performed; air is adsorbed later, in storage. It is not improbable that powders produced by electric explosion in the atmosphere of xenon can be stored longer without loss of the initial properties.

Mechanically treated copper powders show a nonmonotonic variation of reactivity with increasing specific surface area of the powders (Figs. 1, 2; curves *2*, *3*). Among copper powders mechanically treated in the presence of amide of perfluorovaleric acid, the best combination of parameters is observed for Cu-III powder treated for 30 min and having the largest specific surface area. For copper powders produced by mechanical treatment in the presence of $CuCl_2$, the best results were obtained for Cu-2 powder treated for 20 min and not having the largest specific surface area among the three powders of this series.

Probably, the mechanical treatment of copper powders causes changes in their structure (e.g., accumulation of various kinds of defects and their subsequent relaxation [11, 16]), which lead, despite the continuing increase in the specific surface area, to a decrease in the reactivity of these copper powders. These changes are of cyclic nature, which is the reason for the nonmonotonic variation of the reactivity of the copper powders with increasing duration of mechanical treatment and, accordingly, with growing specific surface area of the powders. Although the highest reactivity is observed for Cu-III powder treated for 30 min in the presence of amide of perfluorovaleric acid, Cu-I powder treated for 10 min and having a considerably smaller specific surface area is inferior to Cu-III powder only in the heat effect of the reaction.

In addition, the mechanical treatment for 20 min in the presence of amide of perfluorovaleric acid leads to a decrease in the reactivity of Cu-II copper powder, as indicated by its maximum rate of heat release (the heat effect of the reaction is comparable with that obtained for Cu-III powder). At the same time, mechanical treatment for 20 min in the presence of $CuCl_2$, by contrast, causes an increase in the reactivity of the copper powder, because the resulting Cu-2 powder has the best reactivity as indicated by a combination of two parameters (ΔH and W_{max}). It may be assumed that the optimal duration of MT, yielding a copper powder with a high reactivity, depends on the type of additive in whose presence the copper powder is mechanically treated.

Comparison of the reactivities of copper powders obtained by different methods reveals the following specific features. As judged from the heat effects of the reaction of copper with glacial acetic acid, the reactivity is the highest for powders produced by mechanical treatment in the presence of amide of perfluorovaleric acid. However, as indicated by a combination of parameters chosen for evaluation of the reactivity, the most active are powders prepared by electric explosion: Cu-11 powder prepared by electric explosion in xenon and Cu-8 powder produced by

electric explosion in nitrogen and having the largest specific surface area.

CONCLUSIONS

(1) It is suggested to evaluate the reactivity of copper nanopowders toward glacial acetic acid by a combination of parameters determined by the microcalorimetric method: heat effect of the reaction and maximum rate of heat release.

(2) It is shown that the medium in which the electric explosion of a conductor occurs is of key importance for the reactivity of the resulting copper nanopowders. The highest reactivity is observed for a copper powder produced by electric explosion in the atmosphere of xenon. The reactivity of copper powders formed by electric explosion in the atmosphere of nitrogen or argon grows with increasing specific surface area of the powders.

(3) It is established that the reactivity of mechanically treated copper nanopowders varies nonmonotonically as the treatment duration becomes longer and, accordingly, the specific surface area of the powders grows. The optimal duration of mechanical treatment, necessary for obtaining the highest reactivity of a copper powder toward glacial acetic acid, depends on the type of additive in whose presence the copper powder is treated. As indicated by a combination of parameters, the reactivity is the highest for a copper powder produced by mechanical treatment for 30 min in the presence of amide of perfluorovaleric acid and that formed upon treatment for 20 min in the presence of $CuCl_2$.

REFERENCES

1. Pomogailo. A.D., *Usp. Khim.*, 1997, vol. 66, no. 8, pp. 750–791.
2. Tananaev, I.V., Fedorov, V.B., and Kalashnikov, E.G., *Usp. Khim.*, 1987, vol. 56, no. 2, pp. 193–215.
3. Andrievskii, R.A., *Poroshkovoe materialovedenie* (Powder Materials Science), Moscow: Metallurgiya, 1991.
4. Gusev, A.I, *Nanokristallicheskie materialy* (Nanocrystalline Materials), Yekaterinburg: Ural'sk. Otd. Ross. Akad. Nauk, 1998.
5. Kotov, Yu.A. and Yavorskii, N.A., *Fiz. Khim. Obrab. Mater.*, 1978, no. 4, pp. 24–29.
6. Valevich, V.V. and Sedoi, V.S., *Izv. Vyssh. Uchebn. Zaved., Fiz.*, 1998, no. 6, pp. 70–76.
7. Il'in, A.P., *Fiz. Khim. Obrab. Mater.*, 1994, no. 3, pp. 94–97.
8. Il'in, A.P., Trushina, L.F., and Rodkevich, N.G., *Fiz. Khim. Obrab. Mater.*, 1995, no. 3, pp. 122–125.
9. Andrievskii, R.A., *Usp. Khim.*, 1994, vol. 63, no. 5, pp. 431–448.
10. Pomogailo, A.D., Rozenberg, A.S., and Uflyand, I.E., *Nanochastitsy metallov v polimerakh* (Metal Nanoparticles in Polymers), Moscow: Khimiya, 2000.
11. Poluboyarov, V.A., Lapin, A.E., Korotaeva, Z.A., *et al.*, Abstracts of Papers, *VI Vserossiiskaya (mezhdunarodnaya) konferentsiya "Fizikokhimiya ul'tradispersnykh (nano-)sistem," Tomsk, 19–23 avgusta 2002 goda* [VI All-Russia (Int.) Conf. "Physical Chemistry of Ultradispersed (Nano)Systems," August 19–23, 2002], Moscow, 2002, pp. 77–78.
12. Ripan, R. and Chetyanu, I., *Neorganicheskaya khimiya* (Inorganic Chemistry), vol. 2, *Khimiya metallov* (Chemistry of Metals), Moscow: Mir, 1972.
13. Velikov, A.A. and Vavilkin, A.S., *Zh. Fiz. Khim.*, 1989, vol. 63, no. 1, pp. 282–284.
14. Khemminger, V. and Khene, G., *Kalorimetriya: Teoriya i praktika* (Calorimetry: Theory and Practice), Moscow: Khimiya, 1989.
15. Ivanov, G.V., Yavorskii, N.A., Kotov, Yu.A., *et al.*, *Dokl. Akad. Nauk SSSR*, 1984, vol. 275, no. 4, pp. 873–875.
16. Poluboyarov, V.A., Lapin, A.E., Korotaeva, Z.A., *et al., Khim. Interes. Ustoich. Razv.*, 2002, vol. 10, nos. 1–2, pp. 219–225.

Russian Journal of Applied Chemistry, Vol. 77, No. 12, 2004, pp. 1920–1923. Translated from Zhurnal Prikladnoi Khimii, Vol. 77, No. 12, 2004, pp. 1942–1944.

PHYSICOCHEMICAL STUDIES OF SYSTEMS AND PROCESSES

A Calorimetric Study of the Specific Heat of Cytisine and Enthalpies of Its Dissolution in Water and Ethanol

A. Zh. Abil'daeva, Sh. B. Kasenova, B. I. Tuleulov, S. M. Adekenov, and B. K. Kasenov

Institute of Phytochemistry, Ministry of Education and Science of the Republic of Kazakhstan, Karaganda, Kazakhstan

Received May 25, 2004

Abstract—The enthalpies of dissolution of an alkaloid cytisine at dilutions [mole of cytisine : moles of water; mole of cytisine : moles of 96% ethanol] equal to 1 : 9000, 1 : 18000, and 1 : 36000 were measured by means of calorimetry. The experimental data obtained were used to calculate the standard enthalpies of dissolution of cytisine in infinitely diluted (standard) aqueous and ethanolic solutions. The enthalpies of combustion, melting, and crystallization of cytisine were calculated. The method of dynamic calorimetry in the temperature range 198–298.15 K was applied to study the specific heat of the alkaloid, and an equation describing the dependence $C_p^\circ \sim f(T)$ was derived.

Quinolizidine alkaloids constitute a group of compounds with a broad spectrum of physiological proprties. The interest in this type of vegetable bases is due to the originality of their structure and existence of a large number of conformational and optical isoers [1]. A theoretically and practically important comound belonging to this class of substances is cytisine. Cytisine $C_{11}H_{14}N_2O$ is a secondary-tertiary acid base:

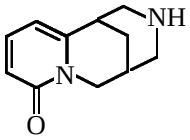

Numerous derivatives of cytisine have been studied in sufficient detail by PMR, IR, and UV spectroscopies [1]. However, no systematic thermochemical and thermodynamic studies of both cytisine itself and its derivatives have been reported in the literature.

In view of the aforesaid, the aim of this study was to make a calorimetric analysis of the specific heat and enthalpy of dissolution of cytisine in water and 96% ethanol and to evaluate its thermodynamic parameters.

The enthalpies of cytisine dissolution in water and 96% ethanol were studied on a DAK-I-IA calorimeter. The theory and practice of calorimetric investigations have been described in detail [2–5]. The main technical parameters of the calorimeter are as follows: range of working temperatures 25–200°C, ampule volume 8 cm^3, time of attainment of the steady state 5 h, sensitivity in the mode of direct measurement of the thermoelectric voltage no less than 0.12 $\mu V\,\mu W^{-1}$, sensitivity in the mode of automatic compensation of the thermoelectric voltage no less than 0.012 $\mu V\,\mu W^{-1}$, error in measurement of heat effects not exceeding 2%. The heat effects were recorded with a KSP-4 recorder and, in parallel, with an IP-4 precision integrator. The time of preliminary thermostating was 2 h.

The operation of the device was tested by measuring the ΔH of dissolution of thrice recrystallized KCl at dilutions of 1 : 1600, 1 : 2400, and 1 : 3200 (mole of salt : moles of water). The resulting ΔH of KCl dissolution (at 25°C), equal to 17860 ± 283 kJ mol^{-1}, is in a good agreement with the values obtained in [6, 7].

The experimental errors and the homogeneity of their variance were calculated using Student's and Barthlett's criteria [8].

The enthalpies of cytisine dissolution in water and 96% ethanol were determined experimentally at dilutions of 1 : 9000, 1 : 18000, and 1 : 36000 [mole of alkaloid : moles of water (ethanol)]. Table 1 lists the results of a calorimetric determination of

1070-4272/04/7712-1920 © 2004 MAIK "Nauka/Interperiodica"

Table 1. Enthalpies of cytisine dissolution in water and 96% ethanol at different dilutions [mole of alkaloid : moles of water (ethanol)]

Water			96% Ethanol		
mass of $C_{11}H_{14}N_2O$, g	ΔH_{dissol}, J	$-\Delta H^m_{dissol}$, kJ mol^{-1}	mass of $C_{11}H_{14}N_2O$, g	ΔH_{dissol}, J	$-\Delta H^m_{dissol}$, kJ mol^{-1}
Dilution 1 : 9000					
0.0059	0.264	8.37	0.0020	0.235	22.35
0.0057	0.248	8.28	0.0018	0.217	22.93
0.0057	0.245	8.18	0.0018	0.215	22.72
0.0061	0.268	8.36	0.0019	0.224	22.43
0.0060	0.258	8.18	0.0017	0.205	22.94
Average		–8.27 ± 0.11	Average		22.67 ± 0.34
Dilution 1 : 18 000					
0.0028	0.098	6.66	0.0010	0.141	26.82
0.0026	0.097	6.83	0.0011	0.153	26.46
0.0031	0.108	6.63	0.0009	0.126	26.63
0.0030	0.106	6.72	0.0010	0.142	27.01
0.0029	0.103	6.76	0.0009	0.127	26.84
Average		–6.72. ± 10	Average		26.75 ± 0.26
Dilution 1 : 36 000					
0.0015	0.034	4.31	0.0006	0.095	30.12
0.0013	0.029	4.24	0.0007	0.111	30.17
0.0014	0.031	4.21	0.0007	0.110	29.89
0.0012	0.027	4.28	0.0006	0.094	29.80
0.0016	0.036	4.28	0.0005	0.077	29.30
Average		–4.26 ± 0.05	Average		29.86 ± 0.43

the heat of cytisine dissolution at different dilutions.

The values of ΔH^m_{dissol} obtained for $C_{11}H_{14}N_2O$ at different dilutions (Table 1) were extrapolated to infinite dilution. Using the data reported in [9], the enthalpy of cytisine dissolution was calculated, using the equation $\Delta H^m_{dissol} = a + b\sqrt{m}$ (m is the molal concentration) in relation to the concentration of cytisine in water and ethanol (kJ mol^{-1}):

$$\Delta H^m_{dissol}(C_{11}H_{14}N_2O) = -(0.65 \pm 0.01) - (99.48 \pm 1.49)\sqrt{m}, \quad (1)$$

$$\Delta H^m_{dissol}(C_{11}H_{14}N_2O) = (36.13 \pm 0.47) - (311.83 \pm 4.05)\sqrt{m}. \quad (2)$$

Relations (1) and (2) were used to calculate the enthalpies of dissolution of cytisine in standard (infinitely diluted) solutions of water and 96% ethanol to be -0.65 ± 0.01 and 36.13 ± 0.47 kJ mol^{-1}, respectively.

The specific heat of cytisine was studied at 198–298.15 K on an IT-S-400 calorimeter. The duration of measurements in the whole temperature range, with processing of the experimental data, was about 2.5 h. The device was calibrated by determining the heat conductivity of the heat flow meter, K_{hfm} [10, 11]. For this purpose, several experiments were carried out with a copper sample and empty ampule. The heat conductivity was found using the formula

$$K_{hfm} = \frac{C_{Cu\ sample}}{\bar{\tau}_{hfm\ Cu} - \bar{\tau}^0_{hfm}}, \quad (3)$$

where $C_{Cu\ sample}$ is the total specific heat of the copper sample (J mol^{-1} K^{-1}); $\bar{\tau}_{hfm\ Cu}$, average time lag of the heat flow meter in experiments with the copper sample; and $\bar{\tau}^0_{hfm}$, the average time.

Table 2 lists the results obtained in determining the specific heat of cytisine. The rated error of the device in measuring the specific heat was ≤ to ±10% [11]. The device was tested by measuring $C^\circ_p(298.15)$

Table 2. Experimental values of the specific heat of $C_{11}H_{14}N_2O$

T, K	$C_p \pm \bar{\delta}$, J K^{-1} g^{-1}	$C_p^\circ \pm \Delta$, J mol^{-1} K^{-1}
198	0.7570 ± 0.0155	144 ± 8
223	0.9265 ± 0.0240	176 ± 13
248	1.0305 ± 0.0173	196 ± 9
273	1.1216 ± 0.0122	213 ± 6
298	1.1476 ± 0.0277	218 ± 15

of α-Al_2O_3. The experimental value of $C_p^\circ(298.15)$ of α-Al_2O_3, equal to 76.0 J mol^{-1} K^{-1}, is in a satisfactory agreement with the reference value of 79.0 J mol^{-1} K^{-1} [12].

The data in Table 2 were used to obtain the equation $C_p^\circ = f(T)$, which has the following form for cytisine at 198–298.15 K (J mol^{-1} K^{-1}):

$$C_p^\circ = (372.8 \pm 20.4) - (253.9 \pm 13.9) \times 10^{-3} T - (70.0 \pm 3.8) \times 10^5 T^{-2}. \quad (4)$$

To calculate $\Delta_f H^\circ$ (298.15) of $C_{11}H_{14}N_2O$, its standard heat of combustion was evaluated using the Karas and Frost methods [13], which are the most appropriate for taking into account the contributions of various groups to the heat of combustion. The results obtained were averaged to give a value of –6144 ± 232 kJ mol^{-1} for the heat of combustion of $C_{11}H_{14}N_2O$. Using the ΔH° of combustion by the Hess cycle for the reaction

$$C_{11}H_{14}N_2O_{(l)} + 14O_{2(g)} = 11CO_{2(g)} + 7H_2O_{(l)} + N_{2(g)}, \quad (5)$$

the standard enthalpy of formation of liquid $C_{11}H_{14}N_2O$ was calculated to be –189.7 kJ mol^{-1}. It is known that the Karas and Frost methods are applicable only to calculation of ΔH° of combustion of liquid hydrocarbons [13]. The data necessary for calculating $\Delta_f H^\circ(298.15)$ of $C_{11}H_{14}N_2O_{(l)}$ by Eq. (5), were taken, with the exception of ΔH° of combustion, from [14].

In view of the fact that cytisine is in the crystalline state at 298.15 K, $\Delta_f H^\circ(298.15)$ of solid cytisine was calculated. For this purpose ΔH°_{melt} of $C_{11}H_{14}N_2O$ was evaluated using the Gambill equation [15]:

$$\Delta H^\circ_{melt}/T_{melt} = 20.72 \times 10^{0.00324M}. \quad (6)$$

The value of ΔH°_{melt}, found for $C_{11}H_{14}N_2O$ by Eq. (6), is 36.6 kJ mol^{-1}. The equation

$$\Delta H^\circ(298.15)\, C_{11}H_{14}N_2O_{(s)} = \Delta_f H^\circ(298.15)\, C_{11}H_{14}N_2O_{(l)} - \Delta H^\circ_{melt} \quad (7)$$

was used to calculate the standard enthalpy of formation of crystalline cytisine, equal to –226.3 kJ mol^{-1}.

CONCLUSIONS

(1) The enthalpies of cytisine dissolution in water and ethanolic solution at different dilutions were determined experimentally and the corresponding values for the same solutions at an infinite dilution (standard solutions) were calculated. The standard enthalpies of formation of liquid and crystalline $C_{11}H_{14}N_2O$ and its heats of combustion and melting were also calculated.

(2) The method of dynamic calorimetry at 198–298.15 K was used to study the specific heat of cytisine, and an equation describing the dependence $C_p^\circ \sim f(T)$ was derived.

(3) The results obtained can be used in directed synthesis of biologically active compounds existing in the nature, for standardization and certification of preparations based on these compounds, and for loading of the data obtained into databases of fundamental constants and thermodynamic reference books.

REFERENCES

1. Sadykov, A.S., Aslanov, Kh.A., and Kushmuradov, Yu.K., *Alkaloidy khinolizidinovogo ryada* (Alkaloids of the Quinolizidine Series), Moscow: Nauka, 1975.
2. Skuratov, S.M., Kolesov, V.P., and Vorob'ev, A.F., *Termokhimiya* (Thermochemistry), Moscow: Mos. Gos. Univ., 1964, vol. 1.
3. Calvet, E. and Prat, H., *Mikrocalorimétric, Applications Physico-Chemiques et Bioloques*, Paris: Masson, 1956.
4. Topor, N.D. and Suponitskii, Yu.L., *Usp. Khim.*, 1984, no. 9, pp. 1425–1462.
5. *Zh. Fiz. Khim.*, 1959, no. 6, pp. 1161–1175.
6. Mishchenko, K.P. and Poltoratskii, G.M., *Termodinamika i stroenie vodnykh i nevodnykh rastvorov elektrolitov* (Thermodynamics and Structure of Aqueous and Nonaqueous Electrolyte Solutions), Leningrad: Khimiya, 1976.
7. *Termicheskie konstanty veshchestv: Spravochnik* (Thermal Constants of Substances: Reference Book), Glushko, V.P., Ed., Moscow: Nauka, 1987, issue 10, part 2.
8. Spiridonov, V.P. and Lopatkin, A.A., *Matematicheskaya obrabotka eksperimental'nykh dannykh* (Mathematical Processing of Experimental Data), Moscow: Mos. Gos. Univ., 1970.

9. Krestov, G.A., *Termodinamika ionnykh protsessov v rastvorakh* (Thermodynamics of Ionic Processes in Solutions), Leningrad: Khimiya, 1984.
10. Platunov, E.S., *Teplofizicheskie izmereniya v monotonnom rezhime* (Thermophysical Measurements in the Monotonic Mode), Moscow: Energiya, 1973.
11. *Tekhnicheskoe opisanie i instruktsii po ekspluatatsii IT-S-400* (Technical Description and Operation Manual of IT-S-400 Device).
12. Robie, R.A., Hewingway, B.S., and Fisher, J.K., *Termodynamic Properties of Minerals and Related Substances at 298.15 and 1 Bar (10^5 Pascals) Pressure and Higher Temperatures*, Washington, 1978.
13. Kazanskaya, A.S. and Skoblo, V.A., *Raschety khimicheskikh ravnovesii* (Calculation of Chemical Equilibria), Moscow: Vysshaya Shkola, 1974.
14. Ryabin, V.A., Ostroumov, M.A., and Svit, T.F., *Termodinamicheskie svoistva veshchestv* (Thermodynamic Properties of Substances), Leningrad: Khimiya, 1977.
15. Viktorov, V.V., *Metody vychisleniya fiziko-khimicheskikh velichin i prikladnye raschety* (Methods for Calculation of Physicochemical Constants and Applied Calculations), Moscow: Khimiya, 1977.

Russian Journal of Applied Chemistry, Vol. 77, No. 12, 2004, pp. 1924–1928. Translated from Zhurnal Prikladnoi Khimii, Vol. 77, No. 12, 2004, pp. 1945–1949.

PHYSICOCHEMICAL STUDIES OF SYSTEMS AND PROCESSES

Salting-out of Isopropyl Alcohol from Aqueous Solutions with Potassium Nitrate

S. I. Sinegubova, K. K. Il'in, D. G. Cherkasov, V. F. Kurskii, and N. V. Tkachenko

Chernyshevskii State University, Saratov, Russia

Received April 28, 2004

Abstract—The solubility of components and critical phenomena in a ternary system constituted by potassium nitrate, water, and isopropyl alcohol were studied by the visual-polythermic method in the temperature range 25–90°C. The formation temperature of the critical node of the monotectic equilibrium (critical solution–solid phase) and the solution compositions corresponding to the critical solubility points at different temperatures were determined. Isothermal solubility diagrams of the system were constructed, the previously suggested scheme of the topological transformation of the phase diagrams of ternary stratifying systems constituted by a salt and a binary solvent was confirmed, and the distribution coefficients of isopropyl alcohol at different temperatures were calculated.

Published evidence concerning the solubility of the components in the system KNO_3–H_2O–*i*-C_3H_7OH are scarce. A study has been reported [1] in which the solubility and density of mixtures of the components of this system were analyzed and it was suggested to use the system to obtain KNO_3. The onset temperature of the stratification of the system was determined. However, the pattern of the topological transformation of the solubility diagram of this system was not elucidated completely and no influence of temperature on the salting-out effect of KNO_3 was revealed.

EXPERIMENTAL

The polythermic study of phase equilibria in the ternary system constituted by potassium nitrate, water, and isopropyl alcohol was performed using the visual-polythermic method [2]. The experimental procedure consisted in the following. Mixtures of the three components were prepared by weighing on an analytical balance in 6-ml ampules made of a heat-resistant glass in such a way that the compositions of these mixtures varied along the chosen sections of the concentration triangle. The ampules with the mixtures were sealed and, by turns, placed in a 800-ml thermostated chemical vessel. Water was used as a heat-carrying agent. The temperatures of phase transitions were determined by successive heating and cooling of each mixture, with ampules shaken at regular intervals of time and the formation or disappearance of a liquid or solid phase fixed visually. Each value of the phase transition temperature, found with an accuracy of ±0.1°C, was an averaged result of several replicate measurements. The equilibrium in a heterogeneous mixture was considered to be attained when the results of measurements of the phase transition temperature became reproducible.

The results obtained in measurements for each section were used to plot the phase transition temperatures against the content of a component in mixtures of all the components of the system (polytherms). Using the resulting polytherms of phase states, the mixture compositions corresponding to phase transitions at chosen temperatures were found by graphical interpolation and isothermal phase diagrams of the ternary system were constructed. The relative error in determining these compositions was ±0.5–1.0%. The solution compositions corresponding to the critical solubility points were found by the method of phase volume ratios [3]. A mixture of the components, with a critical opalescence and equal volumes of the liquid phases in the vicinity (±0.1°C) of the phase transition temperature, was chosen. The solutions with a critical opalescence were studied in graduated ampules; the error in measuring the phase volumes was about 5%.

KNO_3 of analytically pure grade, additionally recrystallized, finely ground, and dried to constant weight in a vacuum over phosphorus(V) oxide at 100°C, was used in the study. The absence of moisture was

1070-4272/04/7712-1924 © 2004 MAIK "Nauka/Interperiodica"

verified by a thermogravimetric analysis. A salt sample prepared for study was stored over calcined $CaCl_2$ in a desiccator. A sample of chemically pure isopropyl alcohol (content of the main substance >99.8%) was dried over calcined K_2CO_3 for 24 h, separated from the precipitate by decantation, distilled on an installation with a rod-and-disk type fractionating column of height 0.3 m, and the fraction with a boiling point of 82.2–82.4°C was selected. The purified alcohol was stored over 4-Å molecular sieves. Water was obtained on a DEM-20 MERA-POLNA bidistiller. The solvents used were identified by their boiling points, refractive indices, and densities. The physical constants of isopropyl alcohol and water were in a good agreement with reference data [4].

The compositions of the component mixtures were varied along twelve sections of the concentration triangle of the system under study. The component mixtures belonging to sections *I–X* had a varying content of KNO_3 and constant mass ratios of isopropyl alcohol and water: 5 : 95 (*I*), 10 : 90 (*II*), 20 : 80 (*III*), 28 : 72 (*IV*), 36 : 64 (*V*), 50 : 50 (*VI*), 60 : 40 (*VII*), 70 : 30 (*VIII*), 80 : 20 (*IX*), and 90 : 10 (*X*). The component mixtures belonging to section *XI* had a varying content of the alcohol and a constant mass ratio of the salt and water (40 : 60), whereas the mixtures belonging to section *XII*, had a constant content of the salt (50.0 wt %) and a varying mass ratio of water to isopropyl alcohol.

For all the sections, polytherms of the phase states of the system were plotted. The polytherms of sections *XI* and *XII* made it possible to determine the temperature at which the critical node of the monotectic equilibrium (critical solution–solid phase) is formed, which corresponds to the onset of stratification in the system. The polytherms of the phase states of sections *I–IX* are similar.

Figure 1 shows as an example the polytherm of section *XII*. It comprises four curves that converge to a common point and delimit four fields of phase states, those of unsaturated solutions (*l*), saturated solutions ($l + S$), stratification ($l_1 + l_2$), and monotectic equilibrium ($l_1 + l_2 + S$). The solid phase has a composition KNO_3. In going from the saturated state ($l + S$) into the region of a monotectic equilibrium ($l_1 + l_2 + S$), critical phenomena in the system of two liquid phases were observed. The region of critical points corresponding to the compositions of the solutions with a critical opalescence is encircled with a dashed line, and the critical point corresponding to a mixture with equal volumes of liquid phases is denoted by a large circle and letter *K*. Apparently, point *K* corresponds to a mixture composition corresponding to

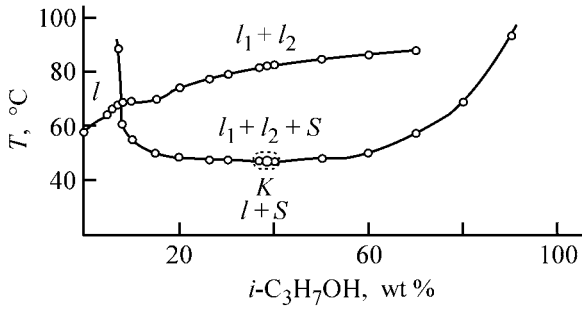

Fig. 1. Polytherm of the phase states of the system constituted by potassium nitrate, water, and isopropyl alcohol in mixtures of the components along section *XII* of the composition triangle. (*T*) Temperature and (i-C_3H_7OH) content.

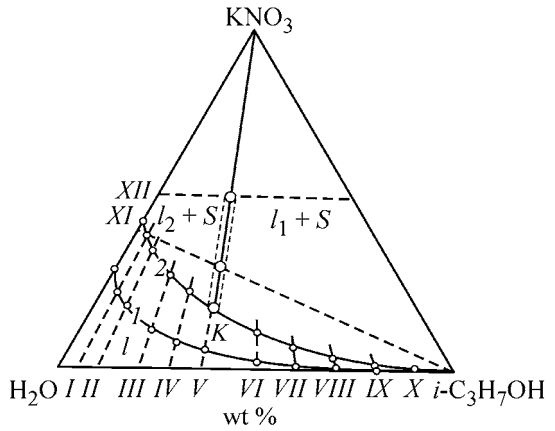

Fig. 2. Isotherms of phase states of the system constituted by potassium nitrate, water, and isopropyl alcohol at (*1*) 25.0 and (*2*) 47.2°C.

the critical node *KS* (critical solution–solid phase), which appears in the field of saturated solutions at 47.2°C.

The temperature dependence of the solution composition corresponding to the critical solubility point was found. For this purpose, component mixtures belonging to additional sections and having a varying content of the salt and a constant mass ratio of water to the alcohol were studied. It was established that the composition of the critical solution changes only slightly when the temperature is raised (see Table 1).

The polytherms and the temperature dependences of the composition of the critical solution were used to plot isothermal phase diagrams of the system at 25.0, 47.2, 50.0, 60.0, 70.0, 80.0, and 90.0°C. At temperatures in the range from 25.0 to 47.2°C, a simple solubility of potassium nitrate in mixtures of water and isopropyl alcohol is observed. For example, there is a field of homogeneous solutions (*l*), separated by a smooth curve *1* from the field of saturated solutions ($l + S$), in the isotherm at 25.0°C (Fig. 2).

Table 1. Solubility of the components of the ternary system constituted by potassium nitrate, water, and isopropyl alcohol*

T, °C	Composition of the saturated solution, wt %								
	KNO_3	H_2O	*i*-C_3H_7OH	KNO_3	H_2O	*i*-C_3H_7OH	KNO_3	H_2O	*i*-C_3H_7OH
25.0	27.2	72.8	0.0	7.5[a]	66.6[a]	25.9[a]	0.5[a]	29.8[a]	69.7[a]
	21.8[a]	74.3[a]	3.9[a]	5.5[a]	60.5[a]	34.0[a]	0.3[a]	19.9[a]	79.8[a]
	18.5[a]	73.3[a]	8.2[a]	4.7[a]	60.3[a]	35.0[a]	0.1[a]	10.0[a]	89.9[a]
	11.0[a]	71.2[a]	17.8[a]	2.6[a]	48.7[a]	48.7[a]	–	–	–
47.2	43.0	57.0	0.0	22.2[b]	56.0[b]	21.8[b]	5.8[d]	37.7[d]	56.5[d]
	38.7[b]	58.2[b]	3.1[b]	18.8[b]	51.4[b]	29.8[b]	3.3[d]	29.0[d]	67.7[d]
	34.0[b]	59.4[b]	6.6[b]	17.7**	51.8**	30.5**	0.9[d]	19.8[d]	79.3[d]
	26.6[b]	58.7[b]	14.7[b]	10.5[d]	44.8[d]	44.7[d]	0.3[d]	10.0[d]	89.7[d]
50.0	44.0	56.0	0.0	23.0[c]	55.4[c]	21.6[c]	7.0[d]	37.2[d]	55.8[d]
	40.7[b]	56.3[b]	3.0[b]	19.0[c]	51.8[c]	29.2[c]	4.0[d]	28.8[d]	67.2[d]
	38.0[b]	56.6[b]	5.4[b]	18.3**	51.5**	30.2**	1.5[d]	19.7[d]	78.8[d]
	36.7[b]	57.0[b]	6.3[b]	12.0[c]	44.0[c]	44.0[c]	0.5[d]	10.0[d]	89.5[d]
	28.3[c]	57.5[c]	14.2[c]	–	–	–	–	–	–
60.0	52.0	48.0	0.0	23.0[c]	55.4[c]	21.6[c]	7.5[c]	37.0[c]	55.5[c]
	47.5[b]	50.1[b]	2.4[b]	18.7[c]	52.0[c]	29.3[c]	3.8[c]	28.9[c]	67.3[c]
	41.7[c]	52.5[c]	5.8[c]	18.1**	51.5**	30.4**	1.3[d]	19.7[d]	79.0[d]
	37.0[c]	55.4[c]	7.6[c]	11.8[c]	44.1[c]	44.1[c]	0.5[d]	9.9[d]	89.6[d]
	27.2[c]	58.2[c]	14.6[c]	–	–	–	–	–	–
70.0	58.0	42.0	0.0	28.3[c]	57.4[c]	14.3[c]	7.3[c]	37.1[c]	55.6[c]
	55.0[b]	42.8[b]	2.2[b]	23.0[c]	55.4[c]	21.6[c]	3.7[c]	28.9[c]	67.4[c]
	50.0[c]	46.5[c]	3.5[c]	18.3[c]	52.3[c]	29.4[c]	2.0[d]	19.6[d]	78.4[d]
	42.0[c]	52.2[c]	5.8[c]	17.6**	51.8**	30.6**	0.6[d]	10.0[d]	89.4[d]
	36.7[c]	55.1[c]	8.2[c]	11.4[c]	44.3[c]	44.3[c]	–	–	–
80.0	62.8	37.2	0.0	28.8[c]	57.0[c]	14.2[c]	7.7[c]	36.9[c]	55.4[c]
	58.8[c]	39.1[c]	2.1[c]	23.0[c]	55.4[c]	21.6[c]	3.8[c]	28.9[c]	67.3[c]
	50.3[c]	46.4[c]	3.3[c]	18.7[c]	52.0[c]	29.3[c]	1.3[c]	19.6[c]	79.1[c]
	41.5[c]	52.7[c]	5.8[c]	17.8**	52.0**	30.2**	0.6[d]	9.8[d]	89.6[d]
	37.3[c]	54.8[c]	7.9[c]	11.2[c]	44.4[c]	44.4[c]	–	–	–
90.0	66.9	33.1	0.0	28.3[c]	57.4[c]	14.3[c]	7.3[c]	37.1[c]	55.6[c]
	58.5[c]	39.4[c]	2.1[c]	22.3[c]	55.9[c]	21.8[c]	4.0[c]	28.8[c]	67.2[c]
	50.0[c]	47.1[c]	2.9[c]	18.7[c]	52.0[c]	29.3[c]	2.0[c]	19.6[c]	78.4[c]
	41.7[c]	52.5[c]	5.8[c]	17.7**	52.1**	30.2**	0.7[d]	9.6[d]	89.7[d]
	36.8[c]	55.0[c]	8.2[c]	11.3[c]	44.4[c]	44.3[c]	–	–	–

* Phase transition: [a] $l \rightleftarrows l + S$, [b] $l \rightleftarrows l_2 + S$, [c] $l \rightleftarrows l_1 + l_2 + S$, and [d] $l_1 \rightleftarrows l_2 + S$.

** Critical solubility point.

Table 2. Compositions of the liquid phases of the monotectic equilibrium and distribution coefficients K_d for isopropyl alcohol in the ternary system constituted by potassium nitrate, water, and isopropyl alcohol

Composition of liquid phase in equilibrium with solid KNO_3, wt %						*T*, °C	K_d
aqueous phase			organic phase				
KNO_3	H_2O	*i*-C_3H_7OH	KNO_3	H_2O	*i*-C_3H_7OH		
17.7*	51.8*	30.5*	17.7*	51.8*	30.5*	47.2	1.0
32.0	58.0	10.0	7.7	37.3	55.0	50.0	5.5
45.3	50.9	3.8	5.0	25.7	69.3	60.0	18.2
53.0	43.8	3.2	1.3	20.0	78.7	70.0	24.6
59.7	37.8	2.5	0.3	15.7	84.0	80.0	33.6
63.8	34.9	1.3	0.1	10.7	89.2	90.0	68.6

* Composition of the liquid phase of the critical node of the monotectic equilibrium (critical solution–solid phase).

At 47.2°C, a critical point *K* appears on the solubility line *2* (Fig. 2). This point corresponds to a mixture in which two liquid phases, alcoholic (l_1) and aqueous (l_2), have identical compositions and properties. As the critical liquid phase *K* is in equilibrium with the solid phase *S* (KNO_3), there appears a critical node *KS* of the monotectic equilibrium. The composition of the critical phase *K* of node *KS* was determined graphically in the concentration triangle from the point of intersection of the critical node with the solubility line *2* for 47.2°C. This temperature is the onset temperature of stratification in the given system, and it coincides with that reported in [1].

As the temperature is raised, the critical node is transformed, as can be seen from the isotherm at 50.0°C (Fig. 3), into a monotectic triangle ($l_1 + l_2 + S$) with the adjacent fields of stratification ($l_1 + l_2$) and of saturated solutions ($l_2 + S$ and $l_1 + S$). As the temperature is raised further, the isotherms of phase states, measured at 60.0, 70.0, 80.0, and 90.0°C, do not change significantly, but the fields of the monotectic state and stratification increase in size, and those of saturated solutions become narrower (Fig. 4, isotherm at 90.0°C).

The results obtained in determining the solubility of the components of the system are listed in Table 1. Data on the solubility of KNO_3 were taken from a reference book [5]. The compositions of the liquid phases of the monotectic equilibrium (Table 2) were found graphically by plotting triangles of the monotectic equilibrium on the plane of the concentration triangle at different temperatures (Fig. 5). The dashed line *aKb* (Fig. 5), which reflects the variation of the compositions of the equilibrium liquid phases of the monotectic with temperature comprises two branches. The composition of the aqueous phase (l_2) varies along branch *Ka*, and that of the organic phase (l_1) along branch *Kb*. As the temperature increases, the aqueous phase is enriched with the salt and depleted of the alcohol, and the organic phase is enriched with the alcohol and depleted of water and the salt.

The distribution coefficient K_d of the alcohol was calculated as the ratio of the concentrations of the alcohol in the organic and aqueous phases of the monotectic equilibrium (Table 2). The fact that the distribution coefficient grows with increasing temperature indicates that the effect of salting-out of the alcohol with potassium nitrate from aqueous solutions is enhanced. Apparently, this is due to decomposition of alcohol hydrates [6, 7] and to a significant increase in the concentration of KNO_3 in the aqueous phase. A comparative analysis of the results of the poly-

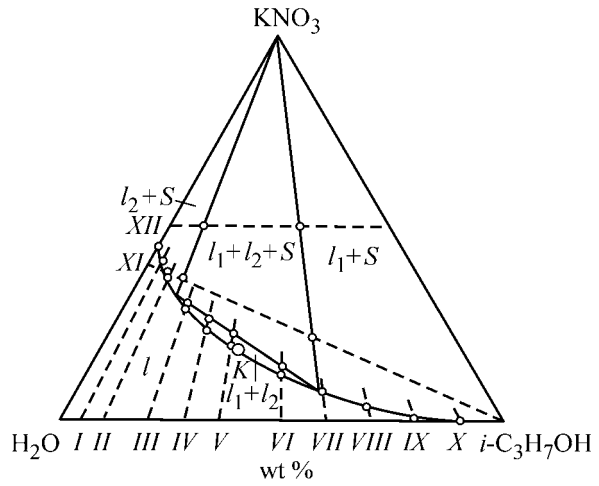

Fig. 3. Isotherm of phase states of the system constituted by potassium nitrate, water, and isopropyl alcohol at 50.0°C.

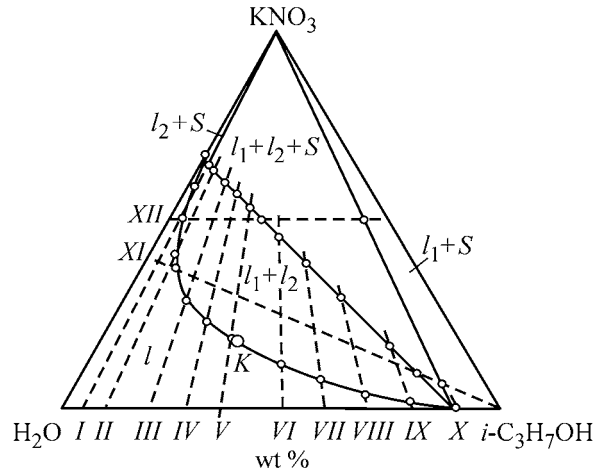

Fig. 4. Isotherm of phase states of the system constituted by potassium nitrate, water, and isopropyl alcohol at 90.0°C.

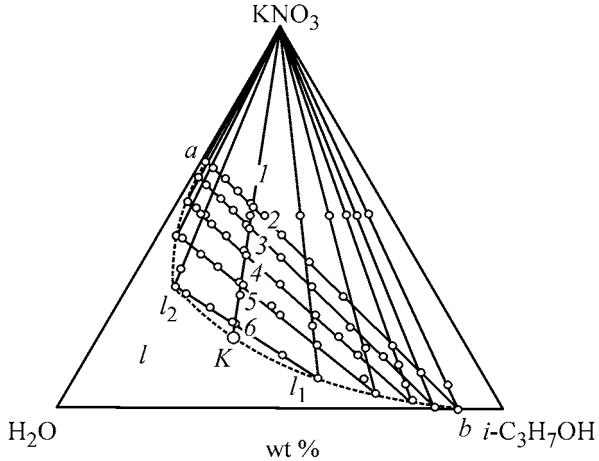

Fig. 5. Variation of the compositions of the liquid phases of the monotectic equilibrium and of the position of the monotectic triangle with temperature in the system constituted by potassium nitrate, water, and isopropyl alcohol. *T* (°C): (*1*) 47.2, (*2*) 50.0, (*3*) 60.0, (*4*) 70.0, (*5*) 80.0, and (*6*) 90.0.

Table 3. Distribution coefficients of isopropyl alcohol in ternary systems constituted by a salt (KCl, KBr, KNO_3), water, and isopropyl alcohol

T, °C	Distribution coefficient K_d		
	KCl	KBr	KNO_3
50.0	10.0	9.5	5.5
60.0	12.5	12.5	18.2
70.0	14.5	14.8	24.6
80.0	17.3	16.2	33.6

thermic study of phase equilibria in the system constituted by potassium nitrate, water, and isopropyl alcohol and in the previously studied ternary systems constituted by potassium chloride (bromide), water, and isopropyl alcohol [8] revealed an analogy between the topological transformations of their phase diagrams upon a change in temperature and confirmed the scheme suggested by Mertslin and Nikurashina [9] for ternary systems that are constituted by a salt and a binary solvent and exhibit salting-out. According to this scheme, the binary liquid system does not stratify in the entire temperature range of its liquid state. The difference is in the onset temperatures of stratification: 24.4°C in the system with KCl, 32.9°C in the system with KBr, and 47.2°C in that with KNO_3. Presumably, with the cation in the salts being the same, the energy of their hydration decreases in order of increasing radius of the anions, Cl–Br–NO_3^- [10], which leads to an increase in the onset temperature of stratification.

The values obtained for the distribution coefficients of isopropyl alcohol in the systems studied suggest that, at equal high temperatures (60–80°C), the salting-out of the alcohol with KNO_3 is stronger, and at equal low temperatures (50°C), weaker than that with KCl and KBr (Table 3). Apparently, this can be attributed to a higher temperature coefficient of the solubility of KNO_3 in aqueous-alcoholic mixtures, compared with that for KCl and KBr. Therefore, use of KNO_3 for salting-out of isopropyl alcohol from aqueous solutions is preferable at higher temperatures.

CONCLUSIONS

(1) The phase equilibria in mixtures of components along twelve sections in the composition triangle of the ternary system constituted by potassium nitrate, water, and isopropyl alcohol was studied in the temperature range 25–90°C by the visual-polythermic method and the temperature corresponding to the onset of stratification in the system was determined to be 47.2°C.

(2) The previously suggested scheme of the topological transformation of the phase diagrams of ternary systems that are constituted by a salt and a binary solvent and exhibit salting-out was confirmed. According to this scheme, the binary liquid system does not stratify in the entire temperature range of its liquid state.

(3) It was established that at 60–80°C the effect of salting-out of isopropyl alcohol from aqueous solutions with potassium nitrate is stronger than that with potassium chloride or bromide. Therefore, potassium nitrate can be effectively used to salt-out isopropyl alcohol from aqueous solutions only at high temperatures.

ACKNOWLEDGMENTS

The study was financially supported by the Russian Foundation for Basic Research (project no. 03-03-33128).

REFERENCES

1. Thompson, A.R. and Molstad, M.C., *Ind. Eng. Chem.*, 1945, vol. 37, no. 12, pp. 1244–1248.
2. Anosov, V.Ya., Ozerova, M.I., and Fialkov, Yu.Ya., *Osnovy fiziko-khimicheskogo analiza* (Fundamentals of Physicochemical Analysis), Moscow: Nauka, 1976.
3. Treybal, R.E., *Liquid Extraction*, New York: McGraw Hill, 1963.
4. *Khimicheskaya entsiklopediya* (Chemical Encyclopedia), Knunyants, I.L., Ed., Moscow: Sovetskaya Entsiklopediya, 1988–1998, vols. 1–5.
5. *Spravochnik po rastvorimosti: Binarnye sistemy* (Reference Book of Solubility: Binary Systems), Kafarov, V.V., Ed., Moscow: Akad. Nauk SSSR, 1961, vol. 1, book 1.
6. Krestov, G.A., *Termodinamika ionnykh protsessov v rastvorakh* (Thermodynamics of Ionic Processes in Solutions), Leningrad: Khimiya, 1984, p. 174.
7. Belgorodskaya, N.M., Shadskii, S.V., and Poltoratskii, G.M., Abstracts of Papers, *5-ya Respublikanskaya konferentsiya molodykh uchenykh-khimikov* (5th Republ. Conf. of Young Scientists-Chemists), Tallin, 1983, p. 205.
8. Il'in, K.K., Cherkasov, D.G., and Yakushev, S.A., *Zh. Obshch. Khim.*, 1998, vol. 68, no. 2, pp. 250–256.
9. Mertslin, R.V. and Nikurashina, N.I., *Fiziko-khimicheskie issledovaniya svoistv prostykh i kompleksnykh soedinenii RZE i troinykh sistem s razlichnym vzaimodeistviem komponentov* (Physicochemical Studies of Properties of Simple and Complex Compounds of Rare-Earth Elements and of Ternary Systems with Varied Interaction between the Constituent Components), Saratov: Sarat. Univ., 1968, p. 3.
10. Gordon, J.E., *The Organic Chemistry of Electrolyte Solutions*, New York: Wiley, 1975.

Russian Journal of Applied Chemistry, Vol. 77, No. 12, 2004, pp. 1929–1934. Translated from Zhurnal Prikladnoi Khimii, Vol. 77, No. 12, 2004, pp. 1950–1955.

PHYSICOCHEMICAL STUDIES OF SYSTEMS AND PROCESSES

Kinetics of Fluorination of Metallic Molybdenum with Elementary Fluorine

A. G. Rybakov, A. V. Seredenko, V. T. Orekhov, and B. S. Mironov

All-Union Research Institute of Chemical Technology, Federal State Unitary Enterprise, Moscow, Russia

Received March 10, 2004

Abstract—The kinetics of the heterogeneous reaction of metallic molybdenum with elementary fluorine under conditions close to those used in actual technological practice at a concentration of fluorine in the gas mixture equal to 20–50 vol % was studied. The kinetic parameters were evaluated using the Arrhenius equation. A regression equation was obtained using the statistical method of experimental design for practical calculations of the rate of fluorination of metallic molybdenum with elementary fluorine. This equation makes it possible to calculate the fluorination rate at any point of the factor space, at fluorine concentrations of 30–50 vol % and initial temperatures of 250–350°C.

A study of the kinetics of the heterogeneous reaction of metallic molybdenum with elementary fluorine to give gaseous molybdenum hexafluoride MoF_6 is of profound practical interest. Molybdenum hexafluoride is widely used in various fields of the national economy: for deposition of high-temperature- and corrosion-resistant Mo films of prescribed thickness on metallic articles, for obtaining ultrapure metallic powders, and as a fluorinating agent in synthesis of organofluorine substances.

In [1], the kinetics of fluorination of metallic Mo with elementary F_2 was studied at its concentration of 4 to 13 vol %. The kinetic parameters of the reaction (activation energy, reaction order) were determined. At a F_2 content in argon equal to 4–13 vol %, the concentration of MoF_6 in the gas flow is too low. This may present difficulties in the subsequent stages of isolation of molybdenum hexafluoride from the gas flow.

The goal of our study was to examine the kinetics of the heterogeneous reaction of powdered metallic Mo with elementary F_2 at real technological parameters of the fluorination process: concentration of fluorine in argon in the range 20–50 vol % and initial temperature of 250–350°C, by the classical and statistical methods.

EXPERIMENTAL

We performed the experiments aimed to study the kinetics of fluorination of metallic Mo with elementary F_2 on a "continuous weighing" setup shown schematically in Fig. 1.

The setup comprises a VLA-200M analytical balance *1*, induction transducer *2*, thermocouple *3*, reaction boat *4* with a sample *5*, furnace *6*, and table *7* for

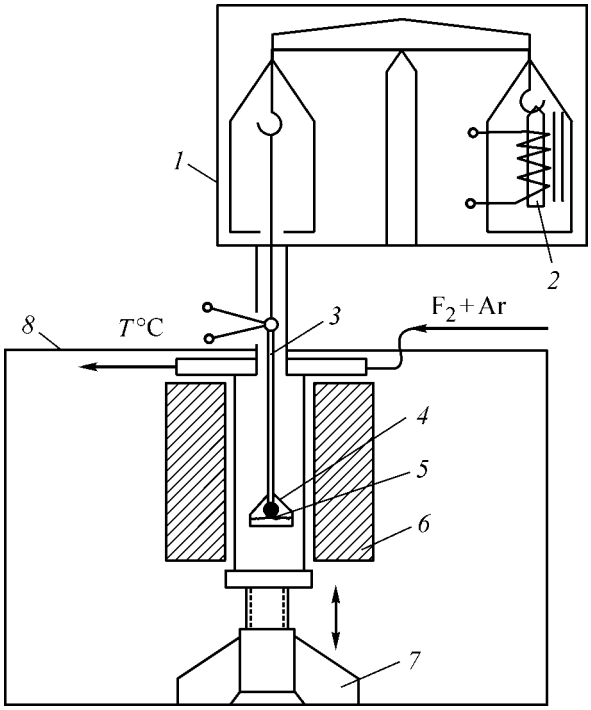

Fig. 1. Schematic of the continuous-weighing setup for studying the kinetics of the heterogeneous reaction of metallic molybdenum with elementary fluorine. (*8*) Exhaust hood; for other explanations, see text.

1070-4272/04/7712-1929 © 2004 MAIK "Nauka/Interperiodica"

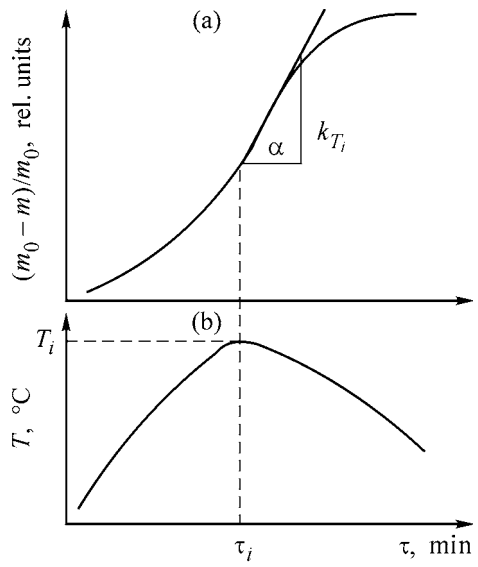

Fig. 2. Variation of the sample mass, $(m_0 - m)/m_0$, and of temperature T in the reaction between metallic molybdenum and elementary fluorine with time τ.

moving the reactor up and down in the furnace. The iron core of the induction transducer *2* is suspended on the right arm of the balance, and the thermocouple *3* and the reaction boat *4*, on the left arm.

The unbalance of the balance leads to motion of the iron core in the induction coil *2*, which gives rise to an induction voltage proportional to the change in the mass of the sample as a result of the reaction of metallic Mo with elementary F_2. The induction transducer *2* is connected into an arm of the differential-transformer circuit of a DSR-35 instrument. The linear portion of the plot of the change in mass against the induction voltage corresponded to variation of the sample mass in the range 0–500 mg. The conversion of the metallic Mo was determined from the loss of mass by the sample as a result of the formation of gaseous MoF_6. The variation of the mass of a sample of metallic Mo was continuously monitored with a secondary DSR-35 instrument. The completion of the reaction was judged from termination of variation of the sample mass.

A weighed portion (~400 mg) of powdered metallic molybdenum (particle size 20–50 μm) was charged into a cylindrical nickel boat 15 mm in diameter and 3 mm high. The boat with the sample was attached with a special clamp to the suspended Chromel–Alumel (ChA) thermocouple so that the thermojunction was close to the sample surface.

After that the fluorination reactor was hermetically sealed and heated to a required temperature in a flow of argon. The variation of temperature in the course of time was recorded with the ChA thermocouple and a secondary EPP-09 potentiometer. Then the zero level was set and the loss of mass by the sample in the course of fluorination was monitored. Fluorine with the content of the main component of 92–96 vol % was used in the study; argon of A brand served to dilute fluorine.

Before the experiments, we passivated the setup at a temperature of 300–400°C and F_2 concentration in argon of about 30 vol % until a stable fluoride film was formed on the surface. The ChA thermocouple was placed within a corundum "straw," with only its junction contacting with the fluorine–argon mixture. The error in weighing in the range 0–500 mg did not exceed 1–2%.

The heterogeneous reaction between metallic Mo and elementary F_2 occurs in accordance with the following overall equation

$$Mo + 3F_2 \rightarrow MoF_6.$$

At the technological parameters used in actual practice, the reaction of fluorination is strongly exothermic and, therefore, certain difficulties were encountered in experimental data processing. The results obtained using the procedure we suggested are shown in Fig. 2: after a stable temperature T_i was reached at an instant of time τ_i, the derivative of the curve describing the variation of the sample mass with time was found graphically at τ_i [2]. This derivative is numerically equal to the rate constant of fluorination, k_{T_i}, at a temperature T_i. The rate constants were determined at two temperatures and the apparent activation energy (kJ mol^{-1}) of the heterogeneous reaction between powdered Mo and elementary F_2 was calculated using the equation

$$E = \frac{19.1479 T_2 T_1}{T_2 - T_1} \log \frac{k_{T_2}}{k_{T_1}}. \quad (1)$$

We carried out more than 40 experiments, and typical S-shaped curves describing the variation of the mass of metallic Mo in the course of fluorination were obtained. During the first 2 min, there is no reaction, i.e., an induction period is observed. Further, the sample mass somewhat increases because of the formation of solid molybdenum fluorides MoF_5 and MoF_4. Then volatile MoF_6 starts to be formed, which leads to a decrease in the sample mass.

We processed the results of the experiments on the kinetics of fluorination of metallic Mo with

Table 1. Averaged calculated values of the kinetic parameters of fluorination of metallic molybdenum with elementary fluorine

Concentration of F_2 in argon, vol %	Apparent activation energy E, kJ mol^{-1}	Rate constant k, min^{-1}	Pre-exponential factor k_0, min^{-1}
20	55.447	6.7	2.237×10^4
30	76.221	9.7	1.392×10^5
40	84.108	12.9	4.196×10^6
50	95.497	14.1	1.651×10^7

Table 2. Matrix of the orthogonal CCD for two factors (c_{F_2}, T)

System	Run no.	c_{F_2}, vol %, X_1	T, °C, X_2	X_1^2	X_2^2	X_1X_2	$X_1^2 - \frac{\Sigma X_1^2}{N}$	$X_1^2 - \frac{\Sigma X_2^2}{N}$	Y, kg h^{-1} m^{-2}	Y_{calc}
	0	40	300							
	λ	10	50							
	+1	50	350							
	–1	30	250							
Complete factorial	1	–1	–1	1	1	+1	0.33	0.33	9.3373	9.4743
experiment	2	+1	–1	1	1	–1	0.33	0.33	15.6238	15.4383
	3	–1	+1	1	1	–1	0.33	0.33	9.0984	8.2243
	4	+1	+1	1	1	+1	0.33	0.33	13.7215	13.6483
Experiments at	5	–1	0	1	0	0	0.33	–0.67	8.6850	8.8493
star points	6	+1	0	1	0	0	0.33	–0.67	14.0453	14.2733
	7	0	–1	0	1	0	–0.67	0.33	13.1831	12.9838
	8	0	+1	0	1	0	–0.67	0.33	11.5654	11.7338
Experiment at the center of design	9	0	0	0	0	0	–0.67	–0.67	12.3486	12.3588

elementary F_2, using the Arrhenius equation [3–5]. The averaged values of the kinetic parameters are listed in Table 1.

The kinetic equation of the heterogeneous reaction of metallic Mo with elementary F_2 can be written in the general case as

$$k = k_0 e^{-E/RT}. \quad (2)$$

At technological parameters used in the actual practice, the reaction between metallic Mo and elementary fluorine proceeds with a considerable heat release, and reproducibility could not be achieved in parallel experiments. As a result, the error in determining the numerical values of the kinetic parameters was 35% at 20 vol % F_2 in the reaction mixture and about 60% at a concentration of 40–50 vol %.

In accordance with the values of the apparent activation energy (Table 1), the process is limited by diffusion of F_2 into a layer of metallic Mo. The reaction order with respect to F_2 is close to unity. Raising the concentration of F_2 in the gas mixture leads to a considerable exothermic effect.

Practical calculations of the rate of fluorination of metallic Mo with elementary F_2 require simpler and more precise relations. We solved this problem by using the experimental-statistical method of experiment design [6, 7], orthogonal central composite design (CCD). The necesary number of experiments can be calculated by the formula

$$N = 2^n + 2n + 1, \quad (3)$$

where n is the number of factors constituting a complete factorial experiment; $2n$, number of star points;

Table 3. Results of parallel experiments in studying the rate of fluorination of metallic molybdenum with elementary fluorine

Run no.	Parameter		Rate of fluorination kg h^{-1} m^{-2}				Y_{av}, kg h^{-1} m^{-2}	σ_j^2
	T, °C	c_{F_2}, vol %	Y_1	Y_2	Y_3	Y_4		
1	250	30	8.4389	8.3586	10.1925	10.3592	9.3373	1.1802
2	250	50	16.5513	15.9046	14.1456	–	15.6238	1.5621
3	250	40	13.1047	13.2017	13.2430	–	13.1831	0.0050
4	300	30	8.8785	8.8785	8.2912	–	8.6850	0.1123
5	300	40	12.8551	11.8449	12.3839	–	12.3613	0.2595
6	300	50	13.1047	14.2705	14.7608	–	14.0453	0.2813
7	350	30	9.6506	8.6229	9.0217	–	9.1029	0.1791
8	350	40	11.2030	12.4089	11.0840	–	11.5654	0.5372
9	350	50	14.5229	14.1304	12.5113	–	13.7215	1.1370
								Σ 5.2467

and 1 corresponds to an experiment at the center of design (at the point with zero level of the factors).

As independent parameters of the fluorination process were taken the concentration of F_2 in argon (c_{F_2}, vol %), X_1, and the initial temperature in the fluorination zone (°C), X_2. The rate of fluorination of metallic Mo, Y (kg h^{-1} m^{-2}), was chosen as the response function (output parameter).

It was established experimentally that the fluorination occurs on the outer surface of the sample, equal to the area of the reaction boat. This is also confirmed by the fact that, if the weighed portion (layer thickness) of metallic Mo is lowered by a factor of 2–4 (200, 100 mg) at initial temperatures of 250–350°C and F_2 concentration of 20–50 vol %, the fluorination rates remain virtually unchanged. The specific surface area of the metallic powder is apparently larger than the outer surface area of the sample, and, therefore, the calculated rates are underestimated. No quantitative estimates were performed.

The center of the design (zero level) corresponded to a F_2 concentration in argon of 40 vol % and the initial temperature in the reaction zone equal to 300°C; the range of variation of the independent parameters was taken to be 10 vol % for the concentration of F_2 and 50°C for temperature.

The regression equation obtained in this case with the use of an orthogonal CCD is as follows:

$$Y = b_0 + b_1X_1 + b_2X_2 + b_{12}X_1X_2 + b_{11}X_1^2 + b_{22}X_2^2. \quad (4)$$

The experimental conditions and the results obtained are listed in Table 2.

Each experiment in the design matrix was carried out no less than three times. The results of parallel experiments performed to study of the rate of fluorination of metallic Mo with elementary F_2 are listed in Table 3. Table 2 lists the averaged values of the rate Y [kg Mo/(h m^2)], calculated from the experimental data in Table 3. A statistical processing of the results obtained made it possible to calculate the rms deviation of the output response function to be σ_y^2 = 0.583, at a variance of the average, σ_y^2/n = 0.583/3 = 0.1943.

The reproducibility of the results of experiments is commonly verified by finding the ratio of the largest estimated variance to the sum of all estimates of variances (Cochrane criterion):

$$G_{calc} = \frac{\max \sigma_j^2}{\Sigma \sigma_j^2} = \frac{1.5621}{6.2467} = 0.29.$$

For the confidence probability P = 0.95, f = 3 – 1 = 2 and N = 9, G_{tab} = 0.478, and the experiments are considered to reproducible, and the estimates of the variance, to be uniform, because $G_{calc} \le G_{tab}$ (0.29 < 0.478).

The regression coefficients were calculated by the formulas

$$b_0 = 1/N \sum_{j=1}^{N} y_j, \quad (5)$$

$$b_0 = \frac{9.3373 + 15.6238 + 9.0984 + 13.7215 + 8.6850 + 14.0453 + 13.1831 + 11.5654 + 12.3613}{9} = 12.4386,$$

$$b_i = \sum_1^N x_{ij}y_j / \sum_1^N (x_{ij}), \quad (6)$$

$$b_1 = \frac{-9.3373 + 15.6239 - 0.0984 + 13.7215 - 8.685 + 14.0493}{6} = 2.7117,$$

$$b_2 = \frac{-9.3373 - 15.6238 + 9.0984 + 13.7215 - 13.1831 + 11.5654}{6} = -0.6265,$$

$$b_{ik} = \sum_1^N x_{ij}x_{ik}y_j / \sum_1^N x_{ij}x_{ik}, \quad (7)$$

$$b_{12} = \frac{9.3373 - 15.6238 - 9.0984 + 13.7215}{4} = 0.4159,$$

$$b_{ii} = \sum_1^N x_{ij}y_j / \sum_1^N (x_{ij})^2, \quad (8)$$

$$b_{11} = \frac{0.33(9.3373 + 15.6238 + 0.0984 + 13.7215 + 8.6850 + 14.0453) - 0.67(13.1831 + 11.5654 + 12.3613)}{0.33^2 \times 6 + (-0.67)^2 \times 3} = -0.7975,$$

$$b_{22} = \frac{0.33(0.3373 + 15.6238 + 0.0984 + 13.7215 + 13.1831 + 11.5654) - 0.67(8.685 + 14.0453 + 12.3613)}{0.33^2 \times 6 + 0.67^2 \times 3} = 0.2117.$$

To determine the significance of the coefficients obtained, we calculated their variances

$$\sigma_{bi}^2 = \sigma_{\text{av}}^2/N = 0.1943/6 = 0.0324,$$

$$\sigma_{bix}^2 = 0.1943/4 = 0.0483,$$

$$\sigma_{bii}^2 = 0.1943/[0.33 \times 6 + (-0.67)^2 \times 3] = 0.0971,$$

$$\sigma_{b0}^2 = 0.2549.$$

It is commonly believed that a regression coefficient is significant if the following condition is satisfied

$$|b| \geq \sigma_b t, \quad (9)$$

where t is the value of Student's criterion.

In the given case, for the confidence probability $P = 0.95$: $f = 9 - 1 = 8$, $t = 2.31$, $\sigma_{b0}t = 1.167$, $\sigma_{bi}t = 0.416$, $\sigma_{bik}t = 0.508$, $\sigma_{bij}t = 0.720$; $|b_0| = 12.3486 > 1.167$, $|b_1| = 2.7117 > 0.416$, $|b_2| = 0.6265 > 0.416$, $|b_{11}| = 0.7975 > 0.720$; $|b_{22}| = 0.2117 < 0.720$, $|b_{12}| = 0.4159 < 0.508$.

Thus, the regression coefficients b_{22} and b_{12} are nonsignificant and should be excluded from the regression equation.

The equation for the rate of fluorination of metallic Mo is written in the code variables as

$$Y = 12.3484 + 2.7117X_1 - 0.6265X_2 - 0.7975X_1^2. \quad (10)$$

Let us pass from the code variables to technological parameters:

$$X_1 = (c_{F_2} - 40)/10 = (0.1c_{F_2} - 4), \quad (11)$$

$$X_2 = (T - 300)/50 = (0.02T - 6). \quad (12)$$

Substituting the values of X_1 and X_2 in the code equation and simplifying it, we have

$$Y = 0.9092c_{F_2} - 0.0125T - 0.7975 \times 10^{-2}c_{F_2}^2 - 7.4992, \quad (13)$$

$$c_{F_2} = 30\text{–}50 \text{ vol \%}, \quad T = 250\text{–}350^\circ\text{C}.$$

Substituting the values of the independent parameters into this equation, we obtain the calculated fluorination rates (Table 4).

The adequacy of the equation was assessed by the Fisher criterion for a confidence probability of 0.95:

$$F_{\text{calc}} = 0.2549/0.1943 = 1.312.$$

Table 4. Calculated values of the fluorination rate

no.	$Y_{i\text{calc}}$	$Y_{i\text{exp}}$	$Y_{i\text{calc}} - Y_{i\text{exp}}$	$(Y_{\text{calc}} - Y_{\text{exp}})^2$
1	9.4743	9.3373	0.137	0.0188
2	15.4383	15.6238	–0.186	0.0344
3	8.2243	9.0984	–0.874	0.7640
4	13.6483	13.7215	–0.073	0.0054
5	8.8493	8.6850	0.164	0.0270
6	14.2733	14.0453	0.228	0.0520
7	12.9838	12.1831	0.801	0.6411
8	11.7338	11.5654	0.168	0.0284
9	12.3588	12.3613	–0.003	0.0001
				Σ 2.0392*

* $\sigma^2 = \sum_1^N 2.0392/(N-1) = 0.2549$.

At $f = 2$ and $N = 9$, the tabulated values of the Fisher criterion $F_{\text{tab}} = 4.26$ and, therefore, $F_{\text{calc}} \le F_{\text{tab}}$ ($1.312 \le 4.26$). Hence follows that the regression equation obtained is adequate to the experimental results. This equation can be used for calculating the numerical value of the rate of fluorination of metallic Mo ($\text{kg h}^{-1}\,\text{m}^{-2}$) at any point of the factor space: c_{F_2} = 30–50 vol % and T = 250–350°C.

CONCLUSIONS

(1) The kinetics of the heterogeneous reaction of metallic molybdenum with elementary fluorine was studied experimentally. The results obtained make it possible to calculate, using the Arrhenius equation, averaged values of the kinetic parameters (rate constant, apparent activation energy) for conditions close to those used in actual technological practice of fluorination. It was found that, as the concentration of F_2 in the gas mixture is raised from 20 to 50 vol %, the error in determining the kinetic parameters increases from 35 to 60%.

(2) A regression equation (13) for practical calculations was derived using the statistical method of experiment design. This equation relates the rate of fluorination of metallic Mo to temperature and concentration of fluorine. It can be used to calculate the rate of fluorination of metallic Mo at any point of the factor space at F_2 concentrations of 30–50 vol % and temperatures of 250–350°C.

REFERENCES

1. Andreev, G.G., Guzeeva, T.N., Krasil'nikov, V.A., and Makarov, F.V., *Sovremennye neorganicheskie ftoridy: Sbornik trudov, Sib. Otd. Ross. Akad. Nauk* (Modern Inorganic Fluorides: Coll. of Works, Sib. Div., Russian Acad. Sci.), Novosibirsk, 2003, pp. 26–29.
2. Batuner, L.M. and Pozin, M.E., *Matematicheskie metody v khimicheskoi tekhnike* (Mathematical Methods in Chemical Technology), Leningrad: Gostekhizdat, 1963.
3. Emanuel', N.M. and Knorre, D.G., *Kurs khimicheskoi kinetiki* (Course of Chemical Kinetics), Moscow: Vysshaya Shkola, 1962.
4. Panchenkov, G.M. and Lebedev, V.P., *Khimicheskaya kinetika i kataliz* (Chemical Kinetics and Catalysis), Moscow: Khimiya, 1985.
5. Shcherbakov, V.I., Zuev, V.A., and Parfenov, A.V., *Kinetika i mekhanizm ftorirovaniya soedinenii urana, plutoniya, neptuniya ftorom i galogenftoridami* (Kinetics and Mechanism of Fluorination of Uranium, Plutonium, and Neptunium Compounds with Fluorine and Halofluorides), Moscow: Energoatomizdat, 1985.
6. Nalimov, V.V. and Chernova, N.A., *Statisticheskie metody planirovaniya ekstremal'nykh eksperimentov* (Statistical Methods for Design of Extremal Experiments), Moscow: Nauka, 1965.
7. Sautin, S.N., *Planirovanie eksperimenta v khimii i khimicheskoi tekhnologii* (Experiment Design in Chemistry and Chemical Technology), Moscow: Khimiya, 1975.

Russian Journal of Applied Chemistry, Vol. 77, No. 12, 2004, pp. 1935–1938. Translated from Zhurnal Prikladnoi Khimii, Vol. 77, No. 12, 2004, pp. 1956–1959.

SORPTION AND ION-EXCHANGE PROCESSES

Surface Chemistry of Ultradispersed Diamonds

A. N. Eremenko, O. A. Besedina, and I. I. Obraztsova

Kemerovo Branch of the Institute of Solid-State Chemistry and Mechanochemistry, Siberian Division, Russian Academy of Sciences, Kemerovo, Russia

Received August 18, 2004

Abstract—The type and amount of functional groups on the surface of ultradispersed diamonds were determined. The adsorption of potential-determining ions was studied in relation to various factors, and the surface charge density was evaluated. The influence exerted by thermal treatment in argon and hydrogen on the functional composition of the surface was analyzed.

A new research area, "nano: -particles, -materials, and -technologies," has formed and has been generally accepted as a priority field of world's science.

By the term "nanotechnology" is understood creation and use of materials, devices, and systems whose structure is controlled on the nanometer scale. The primary goal is to reveal the principles governing the physicochemical properties of such materials and methods for their fabrication and to thereby master the prognostication of, and control over the properties of the objects obtained.

The specificity of the properties of the substances in question and the associated new physical phenomena are determined by the fact that the characteristic dimensions of the structural elements of nanoobjects are within the range 10^{-9}–10^{-7} m, which is comparable with the size of atoms and molecules in ordinary materials. Novel functional characteristics, markedly differing from those of ordinary materials, can be imparted to nanomaterials by controlling the dimensions and shape of nanostructures.

In the authors' opinion, ultradispersed diamonds (UDD) are the most interesting objects of study among all kinds of nanomaterials: they possess a unique combination of markedly anomalous chemical, physicochemical, and mechanical properties.

Ordinary (natural) diamonds are, as a rule, used only as abrasive and cutting materials or substrates in microelectronics. At the same time, the application field of UDD is rather wide. By chemical, barometric, or thermal treatment, various surface properties can be imparted to UDD. In this context, the attention of researchers is focused on a detailed study of parameters and properties of diamonds and on a search for new areas of their application. It is believed that the main application fields of UDD have not been found yet, and their wide use in future high-tech projects is expected [1].

Many physicochemical properties of diamonds strongly depend on the composition and properties of their surface, which is formed in synthesis and chemical treatment of the material. In a number of cases, this is the key issue in obtaining new diamond-containing composites with prescribed characteristics. The electrokinetic, ion-exchange, and sorption properties of diamonds are primarily determined by the nature and amount of surface functional groups. Despite the existence of numerous methods for studying the surface of detonation-produced diamonds (spectral, thermographic, potentiometric, polarographic), the available information about its chemical composition is of mostly qualitative nature [1].

In view of the importance of the surface chemistry of UDD for various applications, some quantitative characteristics of the chemical composition of the UDD surface were determined in the present study.

UDD with particle size of 3–5 nm were used; the method for their recovery from the detonation-produced diamond-carbon stock and subsequent purification has been developed previously [2, 3].

The type and amount of acid groups were found by reverse acid–base titration by selective neutralization with sodium hydroxide, hydrocarbonate, and carbonate by the Boem method [4] developed for carbon

1070-4272/04/7712-1935 © 2004 MAIK "Nauka/Interperiodica"

Table 1. Amount of protonogenic groups on the UDD surface, determined by the Boem method

Alkaline agent	NN, mg-equiv g^{-1}
KOH	0.55 ± 0.02
NaOH	0.67 ± 0.03
Na_2CO_3	0.34 ± 0.01
$NaHCO_3$	0.12 ± 0.01

Table 2. Effect of UDD treatment on the functional composition of the surface

Neutralizing agent	NN, mg-equiv g^{-1} at indicated *T*, °C			
	–	400	600	800
		Ar		
NaOH	0.67	0.28	0.04	0.04
$NaHCO_3$	0.18	0.05	0.03	0.00
NH_2OH	2.70	1.40	0.80	0.06
		H_2		
NaOH	0.67	0.25	0.07	0.06
$NaHCO_3$	0.18	0.05	0.03	0.00
NH_2OH	2.70	1.10	0.76	0.04

materials. It is assumed that sodium hydrocarbonate neutralizes stronger carboxy groups, and sodium carbonate, the same groups and weakly acidic carboxyls of lactone groups. Under the action of Na_2CO_3, the lactone ring is opened with a rearrangement and formation of an oxy and a carboxy groups. This accounts for the different acidities of surface carboxy groups. Sodium hydroxide neutralizes virtually all protonogenic groups. The difference of the neutralization numbers (NN) in neutralization with sodium hydroxide and carbonate, $NN_{NaOH} - NN_{Na_2CO_3}$, gives the amount of phenol groups.

It was revealed experimentally that 3 h is sufficient for equilibrium to be established after neutralization with sodium carbonate and hydrocarbonate, and 24 h, in the case of sodium hydroxide. The centrifuge effluent was titrated with a 0.1 N solution of HCl. The difference between the amounts of alkali in the starting solution and in the effluent was used to find the amount of neutralized surface groups, the neutralization number (mg-equiv g^{-1} UDD).

A comparison of the NN for surface groups in neutralization with the alkalis KOH and NaOH demonstrated that the neutralization with potassium hydroxide is weaker, in an agreement with the results [5] obtained for UDD purified to remove nondiamond carbon by liquid-phase oxidation with nitric acid and gas-phase oxidation. The results of experiments on reverse titration are listed in Table 1.

The data obtained were used to evaluate the amount of protonogenic groups (± 0.01 mg-equiv g^{-1}): carboxy 0.12, phenol 0.33, and lactone 0.22. The total neutralization number for NaOH is 0.67 mg-equiv g^{-1}.

The content of carbonyl groups was determined by the oximation method [6]. The analysis was based on the action of free hydroxylamine in an aqueous medium. Free hydroxylamine was obtained by neutralization of hydroxylamine hydrochloride with a strong base, NaOH. After the oximation was complete, the decrease in the alkalinity of the reaction medium was determined by titration with an acid, with Bromcresol Blue as indicator. The results of the analysis show that UDD has a considerable amount of surface carbonyl groups, 2.7 ± 0.02 mg-equiv g^{-1}, which is an order of magnitude higher that that of any of the previously determined groups.

The content of peroxy groups on the UDD surface (–O–O–) was determined by iodometric titration [7]. It was found that these groups are present on the surface of UDD in an insignificant amount, 0.034 ± 0.002 mg-equiv g^{-1}.

It is known that thermal treatment removes chemisorbed oxygen from the surface of UDD in the form of CO_2 (200–550°C) and CO (620–750°C). Carboxy groups, saturated with oxygen to the greatest extent are responsible for the evolution of CO_2 in thermal desorption, and carbonyl, hydroxy, and ester groups, for the evolution of CO [8].

A study of the influence exerted by thermal treatment of UDD in an atmosphere of oxygen, hydrogen, or argon on the amount of surface acid groups demonstrated that, in all cases, the total amount of protonogenic groups on the surface decreases. The NN in neutralization with sodium hydroxide at 400°C is as follows (mg-equiv g^{-1}): 0.28 in argon, 0.25 in hydrogen, and 0.30 in oxygen; strongly acidic carboxy groups (neutralization with sodium hydrocarbonate) are virtually absent.

For a more detailed study of the effect of thermal treatment on UDD, samples were calcined in a flow of argon or hydrogen at different temperatures. The results obtained are listed in Table 2.

It can be seen from Table 2 that thermal treatment in the atmosphere of argon or hydrogen at 800°C

leads to a virtually complete (>95%) removal of surface groups, which opens up a way to obtaining UDD with a monofunctional surface composition. This is very important for development of selective catalysts, sorbents, and composites on its base.

In addition to determining the types and amounts of functional groups on the UDD surface, some general characteristics used to assess the properties of carbon materials were studied.

In particular, potentiometric titration was used to study the adsorption of potential-determining ions $\Gamma_{OH^-H^+}$ (henceforth Γ) and evaluate the surface charge density on UDD [9], depending on the ionic strength of the electrolyte solution, pH value, and method used for pretreatment of UDD.

The specific adsorption of ions, Γ, was found using the formula

$$\Gamma = cV/m, \quad (1)$$

where c is the concentration of the alkali (KOH) solution; V, difference of volumes of KOH solutions added, in order to adjust pH to the prescribed value, to the dispersion and supporting electrolyte; and m, mass of a UDD portion.

The data obtained were used to evaluate the surface charge density σ_0:

$$\sigma_0 = \Gamma F/S, \quad (2)$$

where F is the Faraday number, and S, the specific surface area of the UDD powder (300 $m^2 g^{-1}$).

As shown above, thermal treatment of UDD leads to a significant change in the composition of surface groups, which is reflected on the specific adsorption and pH values of the suspensions studied (Table 3).

Table 3. Effect of thermal treatment on the specific adsorption Γ and pH of suspensions

Type of treatment	Γ (pH 8) mg-equiv g^{-1}	pH_{in}
No treatment	0.81	3.60
T = 400°C:		
Ar	0.20	7.18
H_2	0.10	7.32
T = 800°C:		
Ar	0.08	7.20
H_2	0.05	7.30

Table 4. Surface charge density on UDD, σ_0, in relation to the ionic strength of the solution, I_{KCl}, ultrasonic dispersion of the suspension, and temperature of the thermal treatment of UDD

UDD	I_{KCl}	σ_0, C m^{-2}	
		pH 7	pH 8
Suspension:			
after preparation	10^{-1}	0.24	0.34
24 h after preparation	10^{-1}	0.20	0.51
	10^{-2}	0.14	0.31
	10^{-3}	0.13	0.29
after ultrasonic dispersion	10^{-1}	0.27	0.56
	10^{-2}	0.19	0.34
	10^{-3}	0.12	0.25
Thermal treatment			
400°C, Ar	10^{-3}		0.064
400°C, H_2	10^{-3}		0.035
800°C, Ar	10^{-3}		0.026
800°C, H_2	10^{-3}		0.016

It can be seen from Table 3 that thermal treatment of UDD leads to a decrease in the adsorption capacity: the specific adsorption decreases by an order of magnitude, with a more complete reduction of active groups occurring in hydrogen.

It was found using potentiometric titration that, as the ionic strength of the electrolyte (KCl) or the solution pH increases, the specific adsorption becomes higher. In the first case, this is accounted for by an increase in the degree of exchange of hydrogen ions from the surface layer for K^+ ions with the concentration of the latter in solution, in an agreement with the results of similar experiments in which the adsorption capacity of natural diamond was studied [9]. In the second case, the dependence is accounted for by the increase in the degree of dissociation of surface groups having acid properties.

The data obtained were used to evaluate the surface charge density on UDD at pH 7 and 8. The results obtained are listed in Table 4.

Analysis of the results obtained shows that the surface of UDD in an aqueous suspension is strongly charged. The amount of charge is close to that for oxidized synthetic diamonds, 0.3 C m^{-2} at pH 8.6 [9]. The rise in the charge on a particle with increasing pH is apparently due to ionization of surface protonogenic groups.

With account of the fact that the 1% suspension of UDD has a pH 3.6, a calculation performed on the as-

sumption that the particle size is 2.5 nm and the density is equal to 3.5 g cm^{-3} indicated that there are 36 H^+ groups per a single UDD particle.

CONCLUSIONS

(1) The types and amount of functional groups on the surface of ultradispersed diamonds were determined.

(2) It was established that thermal treatment of ultradispersed diamonds in a flow of hydrogen or argon leads to significant changes in the composition and amount of surface groups, which is reflected on the specific adsorption and pH of the suspensions.

(3) It was shown that the surface of ultradispersed diamonds in an aqueous suspension is strongly charged, and the surface charge density depends on the ionic strength of the electrolyte, pH value, and method of preliminary treatment.

(4) It was found that thermal treatment of ultradispersed diamonds at 800°C leads to a virtually complete removal of surface groups, which opens up a way to obtaining ultradispersed diamonds with a monofunctional composition of the surface.

REFERENCES

1. Dolmatov, V.Yu., *Usp. Khim.*, 2001, vol. 70, no. 7, pp. 687–708.
2. RF Patent 2 081 821.
3. Obraztsova, I.I. and Eremenko, A.N., *Zh. Prikl. Khim.*, 2003, vol. 76, no. 3, pp. 443–445.
4. Boehm, H., *Advances in Catalysis and Related Subject*, Vol. 16, Eley, D.D., Pines, H., and Weisz, P.B., Eds., New York: Academic, 1966, pp. 179–274.
5. Chiganova, G.A., *Kolloid. Zh.*, 1994, vol. 56, no. 2, pp. 266–268.
6. Cheronis, N.D. and Ma, T.S., *Organic Functional Group Analysis by Micro and Semimicro Methods*, New York: Interscience, 1964.
7. Antonovskii, V.L., *Analiticheskaya khimiya organicheskikh peroksidnykh soedinenii* (Analytical Chemistry of Organic Peroxide Compounds), Moscow: Khimiya, 1978, p. 42.
8. Tarkovskaya, I.A., *Okislennyi ugol'* (Oxidized Coal). Kiev: Naukova Dumka, 1981.
9. Kuchuk, V.I., Golikova, E.V., and Chernoberezhskii, Yu.M., *Kolloid. Zh.*, 1984, vol. 46, no. 6, pp. 1129–1135.

Russian Journal of Applied Chemistry, Vol. 77, No. 12, 2004, pp. 1939–1944. Translated from Zhurnal Prikladnoi Khimii, Vol. 77, No. 12, 2004, pp. 1960–1967.

SORPTION AND ION-EXCHANGE PROCESSES

Natural Zeolites as Dehydrating Agents for Some Organic Solvents Used in Liquid Chromatography

T. G. Andronikashvili, L. G. Eprikashvili, and T. N. Kordzakhiya

Melikishvili Institute of Physical and Organic Chemistry, Georgian Academy of Sciences, Tbilisi, Georgia

Received July 15, 2004

Abstract—Possibility and conditions of dehydration of organic solvents [*N*,*N*'-dimethylformamide (DMF), tetrahydrofuran (THF), 1,4-dioxane, acetonitrile, ethyl acetate, and methyl ethyl ketone] with natural zeolites (analcite, laumontite, clinoptilolite, mordenite, and phillipsite) were studied.

The role of a mobile phase (solvent) in high-performance liquid chromatography, unlike gas chromatography, is multifunctional. The solvent not only transports substances, but also is actively involved in their separation [1]. Chromatographic separation is sometimes very sensitive to the composition of the mobile phase. Even insignificant variations in the water content of the solvent may noticeably change the capacity coefficient K^{I} and the degree of chromatographic separation [2]. Liquid, gaseous, and solid substances are exhaustively dried by different chemical and physical methods [3]. However, the most acceptable is the adsorption method which can be used for dehydration of solvents under both static and dynamic conditions [4]. The important advantage of this method is that the sorbents can be readily regenerated and repeatedly used as dehydrating agents.

Silica gels, zeolites, and, occasionally, alumina are currently used for drying [4]. Zeolites can sorb moisture at its low content in the sample, and their sorption capacity is substantially higher than that of other sorbents. Zeolites exhibit a molecular-sieve effect, i.e., they selectively sorb molecules whose diameter is smaller than their pore size [4–7]. Usually solvents used in liquid chromatography as the mobile phase are exhaustively dried. Synthetic zeolites, like NaA and especially KA [2, 6] activated by calcination at 420–450°C in a muffle furnace [2], are the best dehydrating agents for solvents. At the same time, natural zeolites of sediment origin also effectively dry various gaseous and liquid systems [8–10]. Sediment zeolites are naturally abundant and their industrial deposits are situated in Russia and countries of Former Soviet Union, including Georgia [8–12].

The aim of this study was to demonstrate the possibility and advisability of using natural zeolites of sediment origin from Georgian deposits to dehydrate some organic solvents used as the mobile phase in high performance liquid chromatography.

EXPERIMENTAL

We studied dehydration of the following solvents: dimethylformamide (bp 153°C, Snyder selectivity group III), tetrahydrofuran (bp 66°C, Snyder selectivity group III), 1,4-dioxane (bp 101°C, Snyder selectivity group VI), acetonitrile (bp 82°C, Snyder selectivity group VI), ethyl acetate (bp 77°C, Snyder selectivity group VI), and methyl ethyl ketone (bp 80°C, Snyder selectivity group VI). These solvents belong to different classes and have different molecular structures [2]. The water content in the initial solvents was 3.2–3.4%.

We studied the following zeolite-containing rocks abundant in Georgia [12]: (1) analcite containing rock of Kutaisi-Gelati region (western Georgia) with a 70–80% analcite content and prevalence of sodium in the cationic composition; (2) laumontite-containing rock from Tbilisi region (eastern Georgia) with a 60–70% laumontite content and prevalence of calcium in the cationic composition; (3) heulandite, clinoptilolite-containing rock from Tedzami deposit of Kaspi region (eastern Georgia) with a 70–90% clinoptilolite content and prevalence of calcium and sodium in the cationic composition; (4) mordenite-containing rock from Bolnisi-Ratevani region (easten Georgia) with a 60–80% mordenite content and prevalence of calcium and sodium in the cationic composition; and (5) phillipsite-containing rock from region of Shukhuti village

1070-4272/04/7712-1939 © 2004 MAIK "Nauka/Interperiodica"

Table 1. Physical properties of natural zeolites

Zeolite	Chemical composition	Channel size, nm	Free volume, %	Structure of channel system	Kinetic diameter, nm
Analcite	$Na_{16}(Al_{16}Si_{32}O_{96})\cdot 16H_2O$	0.26	18	Unidimensional	0.26
Laumontite	$Ca_4Al_8Si_{32}O_{48})\cdot 16H_2O$	0.46 × 0.63	0.35	″	0.23
Clinoptilolite	$(K_2Na_2Ca)_3Al_6Si_{30}O_{72}\cdot 22H_2O$	0.39 × 0.54	0.34	Two-dimensional	0.35
Mordenite	$Na_3KCa_2(Al_8Si_{40}O_{96})\cdot 28H_2O$	0.29 × 0.57	0.26	″	0.39
Phillipsite	$(K_2C`)_3(Al_6Si_{10}O_{32})\cdot 12H_2O$	0.28 × 0.49	0.30	Three-dimensional	0.26
NaA	$Na_{12}(Al_{12}Si_{12}O_{48})\cdot 27H_2O$	0.42	47	″	0.40

(westen Georgia) with a 60–90% phillipsite content and prevalence of calcium in the cationic composition.

The typical chemical composition of these zeolites and synthetic NaA zeolite and some physical parameters of these materials [5, 8, 10] are listed in Table 1.

We studied dehydration of model solvent–water (3.4%) systems in a special flow unit (see figure) [13] under dynamic conditions. The unit consists of three main parts: (*1*) dosing pump, (*2*) sorption column, and (*3*) sampler. The pump was made from 1-ml medical syringes *4*. Two plunger pumps were phase-shifted by half a period to smooth the pulsation. The pump was driven with an RD-09 electric motor via a system of pinions and a crank mechanism *5* built in a pinion. A solvent was fed by dosing pump from vessel *6* to adsorber *2* and passed from the bottom to the top of the sorbent bed. To determine the feed rate of the solvent, the dried solvent was fed into a graduated receiver *7*. To prevent penetration of atmospheric moisture into the system, it was equipped with drying tubes packed with $CaCl_2$.

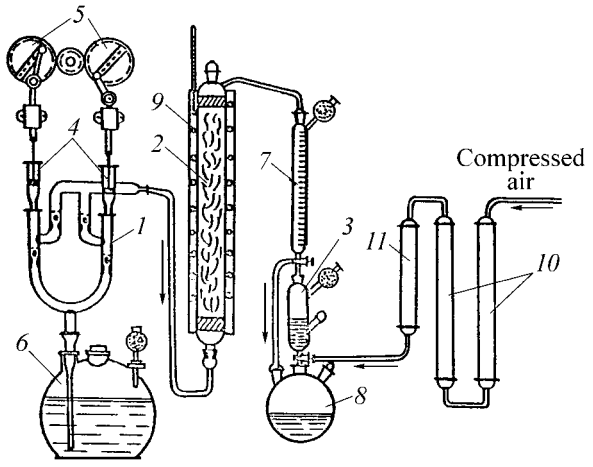

Scheme of the lab unit: (*1*) dosing pump, (*2*) sorption column, (*3*) sampler, (*4*) medical syringe, (*5*) crank mechanism, (*6*) vessel for solvent, (*7*) graduated receiver, (*8*) collector, (*9*) electrical furnace, (*10*) drying filters, and (*11*) color indicator.

The water content of the dried solvents was determined on an LKhM-8MD chromatograph [1.5-m column 3 mm in diameter, Porapak *Q* adsorbent (80–100 mesh), katharometer, carrier gas helium]. The column temperature and the flow rate of the carrier gas were set depending on the molecular weight and boiling point of the solvent. The water content in the dried solvents was 0.05%; 0.02% water passed through the sorbent.

The absorption column 1.0 cm in diameter was packed with a crushed zeolite (0.5–1.0-mm particles). The height of the sorbent bed was 24 cm. The zeolite was activated by heating at 300°C for 3 h in a flow of dry nitrogen. The solvent was passed through the sorbent bed at a rate of 1.3 ml min^{-1}. The column was isothermally heated in the range 25–100°C. Elution curves were plotted in the c/c_0–τ coordinates, where c is the concentration and τ is time. The experiment was continued to complete saturation of the sorbent, i.e., until the water concentration in the eluate became equal to that in the initial solvent c_0.

We determined the following interrelated parameters of adsorption dehydration of organic liquids: equilibrium (a_e, g/100 g) and dynamic (a_d, g/100 g) adsorption capacities of the column, height of the sorption layer H_s (cm), and degree of utilization of the active part of the sorbent bed η (%). The equilibrium adsorption capacity of the zeolite was calculated by the equation [14]

$$a_e = [w\tau_{bt}c_0 + w(\tau_s - \tau_{bt})c_0\varphi]v,$$

where w is the flow rate of the solvent (cm^3 min^{-1}); τ_{bt}, sorption time to breakthrough (min); τ_s, time to complete saturation of the sorbent (min); c_0, initial water concentration (wt %); v, sorbent weight (g); and φ, utilized fraction of the sorbent bed (symmetry coefficient) [4].

The dynamic sorption capacity of the sorbent bed is determined by the amount of substance absorbed

Table 2. Dynamic a_d and equilibrium a_e sorption capacity of zeolite bed for water in organic solvent–water systems at 25°C

Zeolite	Ethyl acetate	Butan-2-one	Acetonitrile	DMF	THF	1,4-Dioxane
Dynamic capacity, a_d, g/100 g						
NaA	13.32	14.61	13.00	18.56	21.75	20.05
Phillipsite	13.11	14.34	12.73	9.81	10.74	11.84
Mordenite	12.03	13.14	8.64	8.97	9.61	10.73
Clinoptilolite	8.51	9.21	9.70	6.82	7.28	7.16
Laumontite	2.34	2.42	1.98	2.04	2.31	2.09
Analcite	0.90	0.98	1.02	0.93	1.05	0.80
Equilibrium capacity, a_e, g/100 g						
NaA	14.20	15.55	14.82	20.05	23.10	21.05
Phillipsite	13.81	15.11	13.71	12.03	13.05	12.31
Mordenite	13.77	15.06	11.81	11.31	10.44	11.97
Clinoptilolite	11.20	12.00	12.10	9.94	8.19	10.38
Laumontite	4.20	4.31	3.17	4.01	3.40	3.74
Analcite	3.00	3.20	2.07	2.07	2.10	2.67

to breakthrough and is calculated using the equation [15].

$$a_d = a_e(1 - L_0/L),$$

where L is the height of the sorbent bed (cm), and L_0, height of the sorption zone (cm).

The height of the sorption zone, so-called height of the working bed, L_0, was calculated by the Michaels Treybal equation [4]

$$L_0 = L\frac{\Delta\tau}{\tau_s - (1-\varphi)\Delta\tau},$$

where $\Delta\tau$ is the time interval from the breakthrough (τ_{bt}) to saturation of the sorbent (τ_s).

The degree of utilization of the sorbent bed η (%) was calculated by the equation [4]

$$\eta = \frac{a_d}{a_e} \times 100.$$

To found the most effective desiccant for the organic solvents examined and to determine the best conditions of water adsorption, we considered the following parameters: type of a natural zeolite, type and molecular structure of a solvent, content of the main mineral in the rock, cationic composition of the zeolite, and column temperature. The dehydration efficiency of a zeolite depends on the spatial structure of the network of its channels and on the free volume and size of water-permeable pores of the sorbent.

Zeolites with a three-dimensional (3*D*) system of channels, large free pore volume, and, which is of particular importance, pore size allowing penetration of only water molecules (molecular-sieve effect) have the best dehydration properties.

However, the zeolites examined exhibit these properties incompletely. Zeolite A and phillipsite have a 3*D* system of channels. Zeolite A has relatively large free pore volume, and the size of its pores is larger than that in phillipsite (Table 1). Hence, zeolite NaA can adsorb not only water but also hydrocarbons with a linear chain structure. In this case, the competing sorption deteriorates the dehydration properties of the sorbent.

Phillipsite, unlike NaA zeolite, selectively sorbs water molecules (molecular-sieve effect). The dynamic and equilibrium sorption capacity of phillipsite for water in solvents with a linear molecular structure is similar to that of NaA (Table 2). However, the dynamic and equilibrium sorption capacities of NaA for water in the solvents with a cyclic or branched molecular structure (THF, 1,4-dioxane, DMF) are substantially higher than those of phillipsite. This is due to the fact that NaA zeolite selectively adsorbs water molecules (molecular-sieve effect) and its free pore volume is 50% larger than that of phillipsite.

Mordenite and clinoptilolite-containing rocks have a 2*D* system of channels. Unlike phillipsite, these zeolites have a more open pore structure (Table 1) and hence lower dynamic and equilibrium sorption capacity for water. This effect is more pronounced for clinoptilolite. In this case, both the competing sorption and the molecular-sieve effect are observed, depending on the molecular structure of the solvent.

Table 3. Equilibrium (a_e) and dynamic (a_d) sorption capacities of NaA zeolite and phillipsite for water

Zeolite	a_d	a_e	η	L_0	τ*
Ethyl acetate–water					
NaA	13.32	14.20	94	3.1	80
Phillipsite	13.11	13.81	95	3.2	75
THF–water					
NaA	21.15	22.10	95.7	2.8	122
Phillipsite	10.74	13.05	83.9	3.7	63

* τ is time to breakthrough.

Table 4. Dependence of the dynamic sorption capacity of the sorbent bed, a_d, for water in acetonitrile on the zeolite content in rock

Clinoptilolite		Phillipsite	
Content in rock, wt %	a_d	Content in rock, wt %	a_d
80–90	9.80	>85	12.85
70–80	9.70	70–80	12.73
60–70	9.12	60–70	12.10
50–60	7.20	50–60	11.21
40–50	3.12	40–50	5.20

Laumontite and analcite have a 1*D* system of channels, and their sorption capacity for water is low [16]. As can be seen from Table 2, these zeolites are unsuitable for dehydration of solvents. Although the size of their water-permeable pores is close to that of phillipsite, the free pore volume of the zeolites is very low (Table 1).

The parameters of water sorption on NaA zeolite and phillipsite from the ethyl acetate–water (competing sorption) and THF–water (molecular-sieve effect) systems are listed in Table 3. The parameters of dehydration by the competing sorption on NaA zeolite are close to those on phillipsite. Unlike synthetic zeolites in which the content of the crystalline phase is higher than 90%, the zeolite content of rocks varies widely, which undoubtedly affects the dehydration power. We determined to what extent the zeolite concentration in rocks can be decreased without affecting the performance in dehydration of organic solvents.

We determined the dynamic sorption capacity for water in acetonitrile of rocks with varied content of clinoptilolite and phillipsite.

As can be seen from Table 4, the dehydration efficiency of rocks with a 60–90% zeolite content is almost the same. However, in both cases, the dynamic sorption capacity sharply decreases at lower zeolite content. The sorption properties of a zeolite depend not only on its type but also on its cationic composition. Enrichment of clinoptilolite with various cations can increase its sorption capacity for water by 40–50% [17].

Since natural clinoptilolite contains potassium, sodium, calcium, and barium cations, we examined in this study clinoptilolites enriched with these cations.

To enrich clinoptilolite with the above-indicated cations, 0.5–1.0-mm zeolite granules were treated several times with a 0.1 N solution of appropriate metal chloride to maximum saturation with preservation of the zeolite lattice [18]. The composition of initial and modified zeolites based on 36 oxygen atoms, determined by chemical analysis [19, 20], is as follows: $Clin_{in}$ $C_{1.06}Mg_{0.36}Na_{1.10}K_{0.54}$, NaClin $Ca_{0.04}Mg_{0.05}Na_{1.52}K_{0.48}$, KClin $Ca_{0.04}Mg_{0.04}Na_{0.01}K_{3.58}$, CaClin $Ca_{4.93}Mg_{0.16}Na_{0.09}K_{0.05}$, and BaClin $Ca_{0.08}Mg_{0.07}Na_{0.1}K_{0.51}Ba_{1.31}$.

As can be seen from Table 5, the dynamic and equilibrium sorption capacity for water in organic solvents depends on the metal cation prevailing in the modified clinoptilolite. Based on these data, the zeolites can be ranked with respect to the selectivity of water sorption depending on the metal cation prevalent in their structure.

With the majority of the solvents examined (ethyl acetate, butan-2-one, 1,4-dioxane, THF, DMF), the selectivity of water sorption (dehydration efficiency) decreases in the following order: KClin > BaClin > CaClin > NaClin > $Clin_{in}$. With acetonitrile, this order in inverse: $Clin_{in}$ > NaClin > CaClin > BaClin > KClin.

In the first case, the enrichment of clinoptilolite with a specific metal cation improves the dehydration efficiency, with this effect being the strongest with potassium cations. The dynamic sorption capacity of the sorbent bed enriched with potassium increases, compared to the initial zeolite, by 39, 41, 22, 22, and 23% with ethyl acetate, butan-2-one, DMF, THF, and 1,4-dioxane, respectively. This positive effect is difficult to explain. We can only suggest the following. Only sodium and calcium (magnesium) cations can be exchanged with equimolar amounts of other cations [19, 20]. The position of a large portion of potassium atoms in the zeolite skeleton differs from those of Ca^{2+} and Na^{+}. In the course of ion exchange, potassium cations are localized deep in the channel *C* near the center of eight-membered rings, thus enlarging the free pore volume of the zeolite [21] and the kinetic diameter of zeolite pores.

Table 5. Dynamic (a_d) and equilibrium (a_e) sorption capacities of zeolite bed for cation-modified clinoptilolite in the system organic solvent–water

Zeolite	Ethyl acetate	Butan-2-one	Acetonitrile	DMF	THF	1,4-Dioxane
			Dynamic capacity, a_d, g/100 g			
Initial $Clin_{in}$	13.32	14.61	13.00	18.56	21.75	20.05
NaClin	9.60	10.50	8.90	7.32	7.88	7.77
KClin	11.80	12.94	7.32	8.33	8.91	8.77
CaClin	10.10	11.01	8.60	7.61	7.18	7.83
BaClin	0.63	10.74	8.42	7.80	8.50	8.25
			Equilibrium capacity, a_e, g/100 g			
Initial $Clin_{in}$	14.20	15.55	14.82	20.05	23.10	21.05
NaClin	10.90	11.90	11.90	10.31	10.45	11.89
KClin	14.31	15.61	9.00	11.31	10.92	12.54
CaClin	11.00	12.03	14.40	10.50	10.60	12.00
BaClin	11.70	12.2	10.20	11.0	10.80	12.64

Table 6. Increase (as compared to experiments at 25°C) in the dynamic sorption capacity of a bed of natural zeolites and synthetic NaA zeolite for water at the best column temperature T_{best}

Solvent	T_{best}, °C	Increase, a_d, %			
		NaA	clinoptilolite	mordenite	phillipsite
Butan-2-one	65	17.9	17.2	17.9	14.8
Ethyl acetate	65	15.6	15.2	14.7	13.9
Acetonitrile	65	13.1	12.6	12.2	14.1
1,4-Dioxane	70	11.4	10.9	11.0	11.7
DMF	90	8.6	14.3	10.0	10.2

It is also difficult to explain the fact that features of dehydration of acetonitrile with substituted clinoptilolites differ from those observed with the other solvents. Probably acetonitrile molecules specifically interact with cations present in clinoptilolite. As a result, water sorption on clinoptilolites enriched with potassium and barium cations is lower than that on the initial clinoptilolite.

In some cases, dehydration of solvents is accelerated with increasing temperature [22]. It is known that many organic compounds form associates with water. At elevated temperatures, water is redistributed between water–water and water–solvent associates; also, these associates partially decompose. Temperature affects the sorption rate in two ways. The limiting sorption of the absorbate decreases, and the sorption selectivity becomes worse with increasing temperature in the case of competing sorption. At the same time, the diffusion coefficient increases, the mass transfer is intensified, and the mass-transfer zone is shortened, and hence the dynamic sorption capacity of the sorbent increases. Hence, the temperature oppositely affects the equilibrium and dynamic sorption properties. The temperature effect is the most pronounced with high-boiling solvents. The viscosity of *N*,*N*'-dimethylformamide (bp 153°C) decreases by a factor of 3 upon heating to 90°C. As a result, the diffusion coefficient of water in this solvent increases and intramolecular and intermolecular hydrogen bonds are rearranged, thus improving the parameters of dynamic sorption dehydration.

To determine the maximum dynamic sorption capacity of a sorbent bed, the temperature dependence of its sorption properties should be studied. In the case of the solvents examined, the best sorption temperature is in the range 65–90°C (Table 6).

Since the boiling point of THF is low (66°C), we did not study the temperature dependences in this solvent.

As can be seen from Table 6, the increase in the dynamic sorption capacity for water of the examined zeolites at the best column temperature is almost the same.

The increase in the sorption capacity after modification of clinoptilolite tuffs with metal cations and the increase in the sorption capacity at the best column temperature are presented in Table 7. As can be seen from

Table 7. Change in the dynamic sorption capacity a_d in water–solvent systems of the initial and modified natural clinoptilolite at the best column temperature

Solvent	Increase in a_d as compared to the initial zeolite, %				T_{best}, °C	Increase in a_d at the best temperature, %				
	BaClin	KClin	CaClin	NaClin		$Clin_{in}$	KClin	CaClin	NaClin	BaClin
Ethyl acetate	25.06	38.70	17.50	12.80	65	13.9	18.38	15.60	14.40	12.61
Butan-2-one	19.54	40.20	16.61	14.00	65	14.77	17.43	14.80	15.24	12.61
1,4-Dioxane	15.21	22.5	9.40	8.50	70	10.30	10.26	10.34	9.65	13.3
DMF	13.8	21.6	11.1	6.90	90	9.6	18.0	21.0	20.6	21.9
Acetonitrile	–13.2	–7.2	–11.3	–8.2	65	14.1	23.3	10.3	14.7	13.3

Table 7, modification of the initial zeolite with sodium, calcium, barium, and especially potassium cations improves the efficiency of dehydration of all the solvents except acetonitrile. In acetonitrile, the sorption capacity of the modified zeolites is lower than that of the initial clinoptilolite. Thus, dehydration of solvents with natural clinoptilolite can be, in most cases, substantially improved by its modification with metal cations and by variation of the column temperature.

CONCLUSIONS

1. Dehydration properties of phillipsite are similar to those of synthetic NaA zeolite in the case of a competing sorption mechanism.

2. The efficiency of solvent dehydration with clinoptilolite can be substantially improved by modifying the zeolite with metal cations and performing sorption at the best temperature. The parameters of sorption performed under these conditions are similar to those obtained with synthetic zeolites.

REFERENCES

1. Sakodynskii, K.I., Brazhnikov, V.V., Volkov, S.A., *et al., Analiticheskaya kromatografiya* (Analytical Chromatrography), Moscow: Khimiya, 1993.
2. Styskin, E.L., Itsikson, L.B., and Braude, E.V., *Prakticheskaya vyisokoeffektivnaya khromatografiya* (Practical High-Performance Liquid Chromatography), Moscow: Khimiya, 1986.
3. Zhdanova, N.V. and Khalif, A.L., *Osushka uglevodorodnykh gazov* (Drying of Hydrocarbon Gases), Moscow, 1984.
4. Kel'tsev, N.V., *Osnovy adsorbtsionnoi tekhniki* (Foundations of Adsorption Methods), Moscow: Khimiya, 1984.
5. Breck, D.W., *Zeolite Molecular Sieves*, New York: John Wiley & Sons, 1974.
6. Dyer, A. *An Introduction to Zeolite Molecular Sieves*, New York: Wiley, 1988.
7. Andronikashvili, T.G., Skhirtladze, N.N., and Tabashidze, N.I., *Zavod. Lab.*, 1966, vol. 32, no. 10, p. 1211.
8. Tsitsishvili, G.V, Andronikashvili, T.G., Kirov, G.N., and Vilizova, L.D., *Prirodnye tseolity* (Natural Zeolites), Moscow: Khimiya, 1985.
9. Gottardi, G. and Galli, E., *Natural Zeolites*, Berlin: Springer, 1989.
10. Mumpton, F.A., *Proc. Nat. Acad. Sci. USA*, 1999, vol. 96, p. 369.
11. Kolodeznikov, K.E., *Tseolitnye provintsii Vostoka Sibirskoi Platformy* (Zeolite Provinces of Easten Siberian Platform) Yakutsk: Izd. Sib. Otdel. Ross. Akad. Nauk, 2003.
12. Skhirtladze, N.I., *Osadochnye zeolity Gruzii* (Sedimentary Zeolites of Georgia) Tbilisi: Izd. Tbilissk. Gos. Univ., 1991.
13. Tsitsishvili, G.V., Sabelashvili, Sh.D., Kordzakhiya, T.N., and Andronikashvili, T.G., *Soobshch. Akad. Nauk Gruz. SSR*, 1979, vol. 95, no. 2, pp. 349–352.
14. Stuchkov, G.S., Exhaustive Dehydration of Some Chlorine-Containing Substances with Synthetic Zeolites, *Cand. Sci. Dissertation*, Moscow, 1975.
15. Gel'ms, I.E., Krymov, P.V., Yudinson, R.N., *et al.*, *Khim. Tekhnol. Topliv Masel*, 1972, no. 6, pp. 16–19.
16. Galabova, I.M., Sheppard, R.A., and Haralampiev, G.A., *Poc. of the Sofia Zeolite Meeting 95*, Pensoft, Sofia-Moscow, 1997.
17. Tarasevich, Yu.I. and Rudenko, V.M., *Ukr. Khim. Zh.*, 1981, vol. 47, no. 6, pp. 603–609.
18. Tsitsishvili, G.V. and Andronikashvili, T.G., *Sinteticheskie tseolity* (Synthetic Zeolites), Moscow: Izd. Akad. Nauk SSSR, 1962.
19. Bish, D.L., *Clay Clay Minerals*, 1984, vol. 132, no. 6, p. 444.
20. Bish, D.L., *Occurrence, Properties and Utilization of Natural Zeolites*, Kallo, O. and Sherry, H.S., Eds., Budapest: Acad. Kiado, 1988.
21. Alberti, A. and Tschermark, K., *Min. Petr. Mitt.*, 1975, vol. 22, pp. 25–37.
22. Kordzakhiya, T.N., Gamkrelidze, L.A., Epikashvili, L.G., and Andronikashvili, T.G., *Zh. Fiz. Khim.*, 1996, vol. 70, no. 1, pp. 179–180.

Russian Journal of Applied Chemistry, Vol. 77, No. 12, 2004, pp. 1945–1950. Translated from Zhurnal Prikladnoi Khimii, Vol. 77, No. 12, 2004, pp. 1968–1973.

APPLIED ELECTROCHEMISTRY AND CORROSION PROTECTION OF METALS

Influence of Plasma-Electrolytic Treatment of Titanium on the Composition and Properties of Ruthenium-Titanium Oxide Anodes

M. S. Vasil'eva, V. S. Rudnev, L. M. Tyrina, N. B. Kondrikov, V. G. Kuryavyi, and E. V. Shchitovskaya

Far-Eastern State University, Vladivostok, Russia

Institute of Chemistry, Far-Eastern Division, Russian Academy of Sciences, Vladivostok, Russia

Received March 1, 2004

Abstract—Data on elemental and phase composition, morphology, and electrocatalytic behavior in dilute chloride solutions of ruthenium-titanium oxide anodes subjected to preliminary plasma-electrolytic treatment are presented.

The properties, including electrocatalytic ones, of ruthenium-titanium oxide anodes (RTOA), adhesion of an active layer, and oxidation of titanium at the interface between the active layer and titanium are determined by the ratio of titanium to ruthenium oxides [1–3], method of preliminary treatment of a titanium support [4], and conditions of electrolysis (concentrated or dilute sodium chloride solutions).

Corrosion-resistant oxide layers having different chemical compositions and good adherence to the substrate can be obtained on the surface of valve metals, including titanium, by means of the plasma-electrolytic deposition (PED) [5–7].

The first applications of PED showed that it can be used both to improve the adhesion of the active paste to the titanium support and decrease the oxidation of titanium [8] and to directly form electrodes with properties close to those of RTOA [9].

As shown previously [10], films formed by PED on titanium in a borate aqueous electrolyte contain only the rutile modification of TiO_2. Ruthenium oxides RuO_2 are isomorphic to the rutile modification of titanium oxide TiO_2, which is a prerequisite for further formation of coatings with electrocatalytic and catalytic properties.

In this study, we examined the composition, morphology, and electrocatalytic properties of electrodes obtained by depositing pure ruthenium hydroxo chloride or its mixture with titanium chloride onto oxide layers formed by PED on titanium in a tetraborate electrolyte.

EXPERIMENTAL

Samples of VT1-0 titanium ($2.5 \times 0.5 \times 1$ cm) were mechanically ground, chemically polished in a mixture of concentrated acids ($HF : HNO_3 = 3 : 1$) at 60–80°C for 2–3 s to remove the surface layer and standardize the surface, washed with distilled water, and dried in air.

Oxide films were formed on titanium by PED in a 0.1 M aqueous solution of sodium tetraborate in the galvanostatic mode at $i = 0.2$ A cm^{-2} and an oxidation time of 1–10 min. As current supply served a TEP4-100 : 46OH thyristor transducer with unipolar pulsed current. The process was performed in a 500-ml vessel made of a heat-resistant glass. As a cathode served a spiral tube made of Kr18Ni9Ti stainless steel and cooled with tap water. The temperature of the electrolyte was maintained within the range 10–50°C. The oxidized samples were washed with distilled water and dried in air.

An active layer was deposited onto oxidized titanium by means of thermal decomposition of ruthenium hydroxo chloride (RTOA1) or a mixture of ruthenium hydroxo chloride and titanium chloride taken in a molar ratio Ru : Ti = 30 : 70 (RTOA2) [4].

1070-4272/04/7712-1945 © 2004 MAIK "Nauka/Interperiodica"

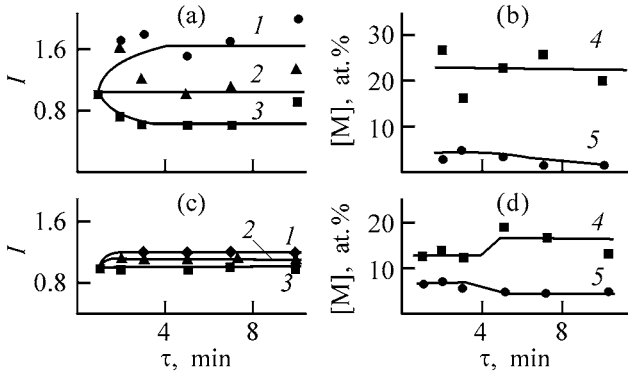

Fig. 1. Influence of the time of formation of the oxide sublayer, τ, on (*1–3*) phase and (*4, 5*) elemental composition of (a, b) RTOA1 and (c, d) RTOA2. (*I*) Relative content of a phase and [M] content of a component. (*1*) TiO_2 (rutile), (*2*) RuO_2, (*3*) TiO_2 (anataze), (*4*) Ti, and (*5*) Ru.

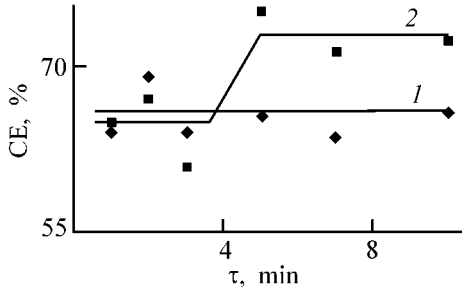

Fig. 2. Current efficiency CE vs. the time of formation of the oxide sublayer, τ, for (*1*) RTOA1 and (*2*) RTOA2.

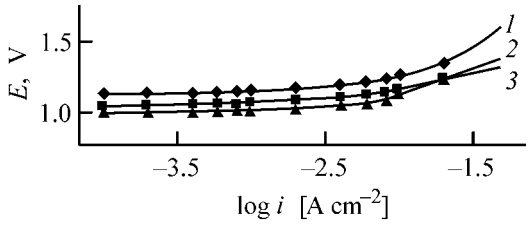

Fig. 3. Polarization curves measured on RTOA in a 3% solution of NaCl. Duration of PED 10 min. (*E*) Potential and (*i*) current density. (*1*) Standard RTOA, (*2*) RTOA1, and (*3*) RTOA2.

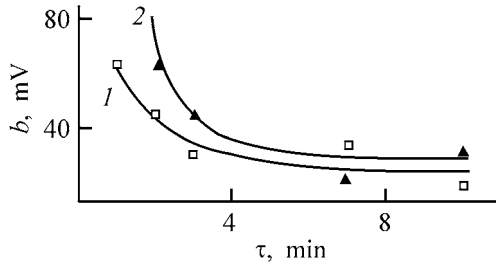

Fig. 4. Coefficient *b* vs. the time of formation of the oxide sublayer, τ, for (*1*) RTOA1 and (*2*) RTOA2.

The phase composition of the coatings was studied on a DRON-2.0 X-ray diffractometer (Cu_{K_α} radiation). The relative content of the crystalline phases was estimated from the ratio of the intensities of the strongest reflections present in the X-ray diffraction patterns of the samples being analyzed to the intensities of the same reflections in the X-ray diffraction patterns of the samples obtained on titanium oxidized for 1 min. The amount (wt %) of titanium and ruthenium in the surface layer was measured with a JXA-5A X-ray fluorescence microanalyzer. The atomic content of the elements was calculated on the assumption that the coatings contained oxygen, in addition to titanium and ruthenium.

An electron microscopic study was done on an LEO 430 scanning electron microscope.

Electrochemical measurements were performed in a 3% NaCl solution modeling sea water in a YaSE-1 standard electrochemical cell with a P-5827 potentiostat. An EVL-1M silver chloride electrode served as reference. The current efficiency (CE) by active chlorine was determined at a current density of 0.15 A cm^{-2} by iodometric titration.

The influence exerted by the time τ of PED pretreatment of a titanium support on the phase and elemental compositions of RTOA1 and RTOA2 is illustrated in Fig. 1.

In the case of RTOA1, an increase in τ, corresponding to a rise in the thickness of the original oxide layer, leads to a higher rutile content and lower anatase content, but does not affect the content of crystalline RuO_2 (Fig. 1a). In this case, the content of titanium, ruthenium, and oxygen (~76 at.%) in the analyzed layer remains virtually unchanged (Fig. 1b).

In the case of RTOA2, making longer the time of formation of an oxide sublayer has no effect on the phase composition (Fig 1c). At the same time, it should be noted that the elemental compositions of RTOA2 on the supports treated for less than 3 and more than 5 min are different (Fig. 1d). The content of titanium, ruthenium, and oxygen changes from 13 to 18, 7 to 5, and 80 to 77 at.%, respectively. At $\tau > 5$ min, the elemental composition of RTOA2 is close to that of RTOA1.

The current efficiency (CE) by active chlorine in electrolysis from a dilute chloride solution is independent of the time of oxidation of the titanium support for RTOA1, and markedly increases at $\tau > 5$ min for RTOA2 (Fig. 2). The current efficiency in deposition of a standard RTOA onto a titanium support

without a preliminarily formed oxide layer was 65–67% in the experiments described. Thus, pretreatment of the support by means of the PED method in a borate electrolyte at $\tau > 5$ min raises the selectivity of the chloride reaction by 6–8%.

The general run of the polarization curves obtained on the anodes under study (Fig. 3) corresponds to that the curves measured on standard RTOA under these conditions. As the time of formation of the oxide sublayer is made longer, i.e., the sublayer thickness increases, the coefficients b in the Tafel equation $E = a + b\log i$ decrease to become constant at $\tau > 5$ min (Fig. 4). In this case, they are equal to 0.03–0.04 V and correspond to the coefficients b for standard RTOA in dilute chloride solutions [10].

Figure 5 shows electron micrographs of PED coatings formed on titanium in a borate electrolyte at an oxidation time of 2 and 10 min, as well as those of samples with RTOA1 and RTOA2 deposited on the above sublayers. The surface of the oxide sublayer formed in 2 min is constituted by alternating projections and depressions (Fig. 5a). The difference of heights on the surface is as large as 0.5 μm. Pores, which are, in all probability, channels of electric breakdowns, open onto the surface. The distribution of pores over the surface is rather uniform, and their mouths are seen both on top of projections and on side slopes of depressions. The surface of the coatings formed in $\tau > 5$ min, which are thicker, has another profile (Fig. 5b). In this case, rather uniform areas of the surface, onto which pores open, also have microdepressions with pores seen on their bottom.

At a formation time of 2 and 10 min, the thickness of the coatings studied is 2–3 and 8–10 μm, respec-

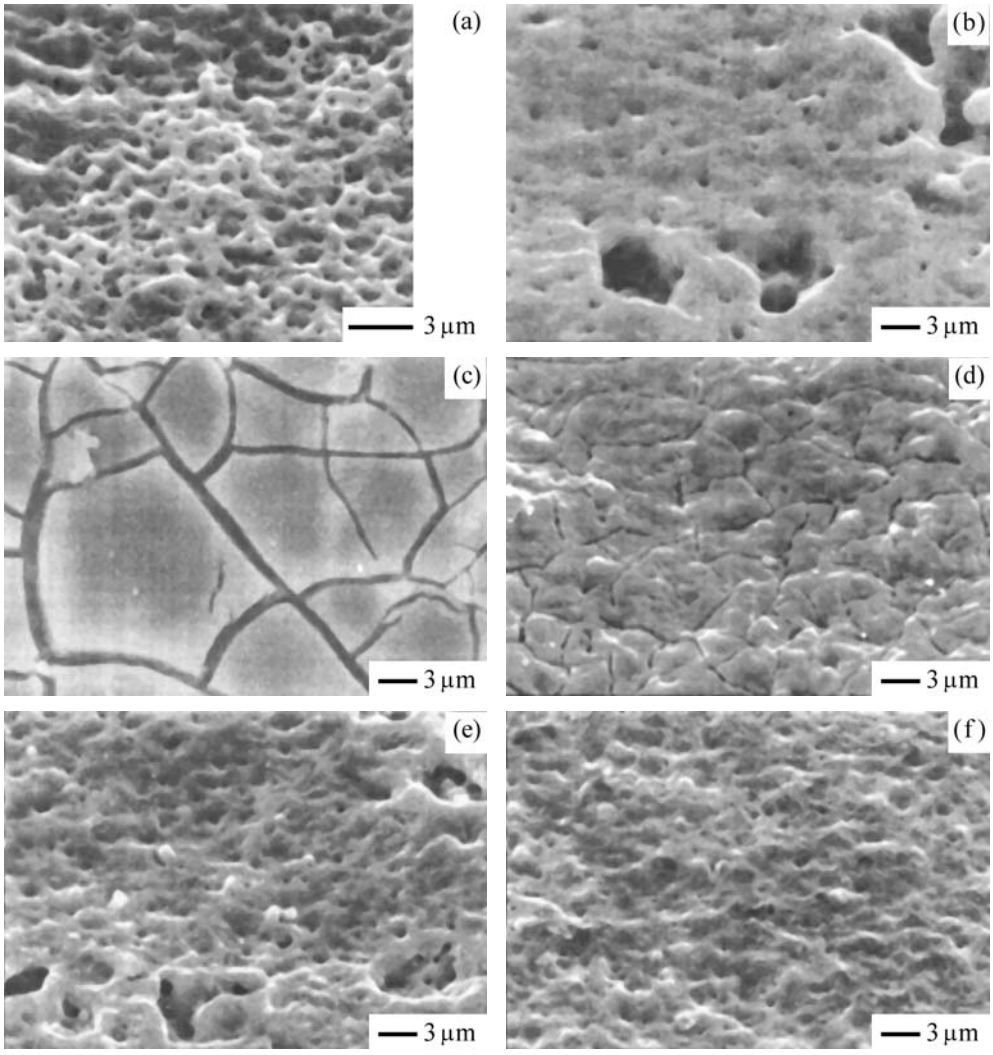

Fig. 5. SEM micrographs of the surface of (a, b) oxide sublayer, (c) standard RTOA, (e) RTOA1, and (d, f) RTOA2. Time of formation of the oxide sublayer (min): (a, d) 2 and (b, e, f) 10.

Results of an analysis of the SEM micrographs of the surface of titanium oxide and ruthenium-titanium oxide anodes subjected to PED

Parameter	Treatment time, min			
	TOA*		RTOA1, 10	RTOA2, 10
	2	10		
Most probable pores				
Diameter, μm	0.08	0.27	0.11	0.12
Number of pores, cm^{-2}	2.2×10^8	1.1×10^7	4×10^9	4×10^9
Surface porosity, %	2	0.6	0.4	0.5
Large pores (hollows)				
Average size, μm	–	3.8	2.9	–
Depth, μm	–	3.0	2.0	–
Number of pores, cm^{-2}	–	6×10^5	2×10^5	–

* TOA, titanium oxide anode.

tively. In both cases, the coating material resembles a partly molten glassy formation.

The results of an analysis of the electron micrographs are listed in the table. The calculated surface porosity of the oxide layers obtained is low, i.e., these layers should have satisfactory protective properties. If the formation time is made longer, not only the oxide layer thickness increases, but also the pore diameters grow, whereas the pore density (ratio of their total number to the micrograph area) and the surface porosity (ratio of the sum of the pore areas to the micrograph area) decrease. In this case, microdepressions ("hollows" or "large pores") are present on the surface of the anodic deposits formed at $\tau > 5$.

The deposition of the catalytically active material results in a change in the surface morphology of the oxide layers. As in the case of standard RTOA (Fig. 5c), isolated areas separated by cracks constitute the surface of both RTOA1 and RTOA2 at a time of formation of the oxide sublayer, $\tau < 5$ min (Fig. 5d). Under magnification, small pores can be seen on the bottom of cracks. On the surface of RTOA1 and RTOA2, the cracks are no more visible when the time of formation of the oxide layer exceeds 5 min (Fig. 5e, 5f). In these cases, the density of the most probable pores on the surface increases, whereas their diameter decreases, compared with the corresponding parameters of the oxide sublayer (see table), with the pore sizes and densities being the same for RTOA1 and RTOA2. When RTOA1 is deposited onto the oxide layers formed at $\tau > 5$ min, the depth and size of the hollows (large pores) decrease by about 1 μm. No hollows are observed on the surface of RTOA2 under these conditions.

In the general case, the oxide layer formed on titanium in an aqueous electrolyte under the action of electric breakdowns consists of a dense barrier layer with a thickness of no less than 1 μm, which is adjacent to the metal, and an outer layer transformed by breakdowns and pierced with pores, which contains titanium oxides with inclusions of compounds based on, or mainly composed of the solution components. The layers obtained on titanium by PED in the tetraborate electrolyte studied contain a rutile modification of TiO_2 [11]. As follows from the results obtained, pores open onto the surface of these layers. With increasing time of layer formation, the diameter of the most probable pores increases, whereas their number per unit surface decreases. Such oxide layers have a low electrical conductivity both in air and in a 3% NaCl solution, with the electrical resistance of the structures indicated not affected by annealing in air at 450°C for 1 h.

The deposition onto the given structures of both ruthenium hydroxo chloride and its mixture with titanium chloride (30 mol % RuO_2 and 70 mol % TiO_2), with the subsequent annealing for 1 h, results in a sharp decrease in the electrical resistance to values typical of the standard RTOA. The electrochemical parameters of the electrodes obtained are also close to those of the standard RTOA. This means that either the structures considered become electrically conduct-

ing throughout their bulk, or interconnected current-conducting regions or channels are formed in their structure. Apparently, these current-conducting regions are localized in pores (cracks) of the oxide sublayer and are associated with the presence of ruthenium oxide or with the formation of a TiO_2–RuO_2 solid solution both in voids and on the walls and bottom of pores (cracks). This assumption is confirmed by the observed correlation between the morphology of the oxide sublayer preliminarily formed in a tetraborate electrolyte and the properties of the anodes obtained. Probably, the conducting regions are formed in the barrier layer adjacent to titanium, owing to thermal diffusion of ruthenium ions into this layer in the course of the oxidative annealing at 400–450°C.

Both RTOA1 and RTOA2 compositions contain crystalline phases of TiO_2 in the rutile and anatase modifications and RuO_2 (Fig. 1). Presumably, the anatase modification is a product of oxidative annealing of the titanium support in air. In this case, the decrease in the amount of anatase, observed for RTOA1 when the formation time (thickness) of the oxide sublayer increases, indicates that its protective properties are improved. At the same time, the appearance of anatase may result from crystallization in the course of annealing of the amorphous phase in the oxide sublayer. It is noteworthy that the anatase phase is also recorded in the X-ray diffraction patterns of an annealed PED coating.

For RTOA1, the elemental composition (Fig. 1) and the current efficiency (Fig. 2) are virtually independent of the parameters and morphology of the oxide sublayer, despite the change in the phase composition. For RTOA2 at $\tau > 5$ min, the current efficiency increases from 65–67 to 72–75%. The change in the elemental composition, i.e., a decrease in the content of ruthenium in the surface layer and an increase in that of titanium (Fig. 1), and the morphological transformations, i.e., the appearance of large pores (hollows) on the surface of the oxide sublayer (Fig. 5b), correlate with these results. Presumably, the change in the macrostructure facilitates penetration of ruthenium into the oxide layer.

Calculations show that, in the RTOA1 surface layer analyzed, the Ru/Ti ratio (in at.%) is 0.23 on the average. For RTOA2, this ratio is 0.54 at $\tau < 5$ min and 0.28 at $\tau > 5$ min. When a mixture of ruthenium hydroxo chloride and titanium chloride is deposited to give a standard RTOA, this ratio is 0.43. The close electrocatalytic properties of the RTOA1 and RTOA2 electrodes, standard RTOA on titanium, and electrodes with a decreased content of Ru (e.g., at a Ru/Ti ratio of 0.23–0.28) possibly indicate that only certain parts of the electrode surface are active in the reaction of chlorine evolution.

An analysis of the SEM images shows that the morphologies of the RTOA1 and RTOA2 surfaces are, on the whole, similar (see table and Fig. 5). At $\tau < 5$ min, their surface, as also the surface of the standard RTOA, is covered with a network of cracks. At $\tau > 5$ min, the cracks are absent, but pore mouths emerge to the surface of RTOA1 and RTOA2.

The estimated pore sizes for the samples studied are listed in the table. Presumably, small pores on the oxide sublayer are craters of electric spark breakdowns, and larger pores, of micrometer size, are craters formed by arc discharges of higher power. As the number of pores per unit surface is two orders of magnitude larger on RTOA1 and RTOA2 and the sizes of these pores are smaller than those on the oxide sublayer, the pores on RTOA1 and RTOA2 are not associated with channels of electric breakdowns present on the oxide sublayer. In all probability, the pores on the surface of RTOA1 and RTOA2 result from evolution of gases (water vapor, chlorine, or HCl vapor) in the thermal treatment of the deposited aqueous solutions of ruthenium hydroxo chlorides or a mixture of ruthenium hydroxo chloride and titanium chloride. The change in the depth of large hollows upon deposition of the active paste was used to estimate the thickness of the deposited outer layer to be about 1 μm for RTOA1 and about 3 μm for RTOA2. These estimates agree with published data [12].

Cracking of RTOA (Fig. 5c), RTOA1, and RTOA2 on the thin, micrometer-thick oxide layers (Fig. 5d) is due to the drying of a wet layer, which tends to contract on a less contractible support. The absence of cracking in RTOA1 and RTOA2 deposited on relatively thick (8–10 μm) oxide sublayers means that the properties of these structures vary to a lesser extent. As a consequence, it would be expected that the adhesion of the active paste to the substrate should be higher in this case.

CONCLUSIONS

(1) Preliminary treatment of titanium in a tetraborate electrolyte by the method of plasma-electrolytic deposition does not deteriorate the electrochemical parameters of ruthenium-titanium oxide anodes in dilute chloride solutions.

(2) The surface structure of the oxide sublayer and the electrochemical characteristics of the ruthenium-titanium oxide anodes correlate.

(3) The results obtained suggest that an additional plasma-electrolytic treatment can be a promising method for improving the adhesion of the active paste and depressing the oxidation of a titanium support.

ACKNOWLEDGMENTS

The study was partly supported by the programs "New Materials" (project no. 02.02.032) and "Universities of Russia" (project no. UR-05.01.018), and by the Far-Eastern Division of the Russian Academy of Sciences (project no. 03-1-0-04-011).

REFERENCES

1. Yakimenko, L.M., *Elektrodnye materialy v prikladnoi khimii* (Electrode Materials in Applied Chemistry), Moscow: Khimiya, 1977.
2. Veselovskaya, I.E., Spasskaya, E.K., Sokolov, V.A., *et al.*, *Elektrokhimiya*, 1974, vol. 10, no. 1, pp. 70–73.
3. Razina, N.F., *Oksidnye elektrody v vodnykh rastvorakh* (Oxide Electrodes in Aqueous Solutions), Alma-Ata: Nauka, 1982.
4. Kondrikov, N.B., Shchitovskaya, E.V., Vasil'eva, M.S., *et al.*, *Elektron. Zh. "Issledovano v Rossii", 92*, 1005–1010, 2002, http://zhurnal.ape.relarn.ru/articles//2002/092.pdf.
5. Gordienko, P.S., and Gnedenkov, S.V., *Mikrodugovoe oksidirovanie titana i ego splavov* (Microarc Oxidation of Titanium and Its Alloys), Vladivostok: Dal'-nauka, 1997.
6. Gordienko, P.S., Bulanova, S.B., Khrisanfova, O.A., and Vostrikova, N.G., *Elektron. Obrab. Mater.*, 1991, no. 3, pp. 35–38.
7. Gordienko, P.S., Gnedenkov, S.V., Sinebryukhov, S.V., *et al.*, *Elektrokhimiya*, 1993, vol. 29, no. 8, pp. 1008–1012.
8. Tyrina, L.M., Tyrin, V.I., Gordienko, P.S., *et al.*, *Zh. Prikl. Khim.*, 1995, vol. 68, no. 6, pp. 949–952.
9. GDR Patent 273364.
10. Kalinovskii, E.A., Zhuk, A.P., and Bondar', R.U., *Zh. Prikl. Khim.*, 1980, vol. 53, no. 10, pp. 2233–2237.
11. Vasil'eva, M.S., Rudnev, V.S., and Tyrina, L.M., *Zh. Prikl. Khim.*, 2002, vol. 75, no. 4, pp. 583–586.
12. Busse-Machukas, V.B., Kubasov, V.L., L'vovich, F.I., and Mazanko, A.F., *Itogi nauki i tekhniki: Elektrokhimiya* (Advances in Science and Technology: Electrochemistry), Moscow, VINITI, 1982, vol. 20, pp. 84–111.

Russian Journal of Applied Chemistry, Vol. 77, No. 12, 2004, pp. 1951–1957. Translated from Zhurnal Prikladnoi Khimii, Vol. 77, No. 12, 2004, pp. 1974–1979.

APPLIED ELECTROCHEMISTRY AND CORROSION PROTECTION OF METALS

Electrocatalytic Oxidation and Amperometric Detection of Ethanol on Graphite Electrodes Modified with a Coating Composed of Hexacyanometallates

L. G. Shaidarova, A. V. Gedmina, I. A. Chelnokova, and G. K. Budnikov

Kazan State University, Kazan, Tatarstan, Russia

Received May 12, 2004

Abstract—The electrochemical behavior of methanol on graphite electrodes modified with a coating composed of (III) hexacyanoferrate and ruthenium(III) hexacyanoferrate(II) and hexacyanoruthenate(II) was studied. A method for electrochemical determination of ethanol on a carbon-paste electrode modified with a coating composed of ruthenium(III) hexacyanoruthenate(II) under stationary and flow-injection conditions was suggested.

Ethanol is commonly determined using a variety of techniques [1–3]: classical and modern physicochemical, including electrochemical methods. Direct voltammetry on metallic and graphite electrodes is not used to determine ethanol because of the oxidation overvoltage of this compound. Modifying the surface of solid electrodes with redox mediators markedly expands the analytical capacity of voltammetry. Various mediators are used for determining aliphatic alcohols: metals [3–6], metal complexes [7], or electron-conducting polymeric materials [8].

In the last years, a considerable attention has been given to electrodes modified with hexacyanometallates (HCM) [9–15]. Electrodes with a coating composed of ferric ferrocyanide [$KFe^{II}Fe^{III}(CN)_6$] are used as detectors or transducers in biosensors [9] The properties of these chemically modified electrodes (CME) are changed because of the alteration of the nature of metal ions in both the inner and outer coordination spheres. It has been established that the catalytic activity of HCM also changes because of the cross-linking of HCM species by ions of platinum-group metals [15, 16]. For example, introduction of ruthenium ions into the composition of a coating improves the catalytic activity of CME and makes their electrochemical response more stable [10–16].

The present study is concerned with the electrocatalytic properties of a carbon-paste (CPE) or a glassy carbon (GC) electrode with an electrodeposited coating composed of ruthenium(III) hexacyanoferrate(II) and hexacyanoruthenate(II) in oxidation of ethanol and with the possibility of using these electrodes to determine ethanol under stationary and flow-through conditions.

The electrochemical properties of hexacyanometallates deposited on the surface of GC, such as iron(III) hexacyanoferrate $KFe^{II}Fe^{III}(CN)_6$ (FeO–FeCN), ruthenium(III) hexacyanoferrate(II) $Ru_4[Fe(CN)_6]_3$ (RuO–FeCN), and ruthenium(III) hexacyanoruthenate(II) $Ru_4[Ru(CN)_6]_3$ (RuO–RuCN). A study of the electrochemical properties of ruthenium(III) hexacyanometallates established that ruthenium(III) oxidizes to oxidation states higher than 3+, with oxygen bridges formed between metal ions, such as Ru–O–Fe or Ru–O–Ru [15, 16]. Therefore, ruthenium ions in higher oxidation states are designated as oxo groups, e.g., –Ru(VI)O or –Ru(IV)O, and the designations RuO–FeCN or RuO–RuCN are commonly accepted for HCM coatings.

As can be seen in Fig. 1, the voltammetric curves obtained on HCM-modified electrodes are different. The voltammogram of an electrode with a FeO–Fe–CN coating contains two pairs of anodic and cathodic peaks (Fig. 1, curve *1*). The peak at E = 0.2 V is commonly attributed [17] to oxidation of a complex iron(II) ion, i.e., to the redox pair $Fe(CN)_6^{3-}/Fe(CN)_6^{4-}$ (E^0 = 0.36 V [18]), and the peak at E = 1.2 V is associated with oxidation of an outer-sphere ion of iron and is related to the redox pair Fe^{3+}/Fe^{2+} (E^0 = 0.77 V [18]).

1070-4272/04/7712-1951 © 2004 MAIK "Nauka/Interperiodica"

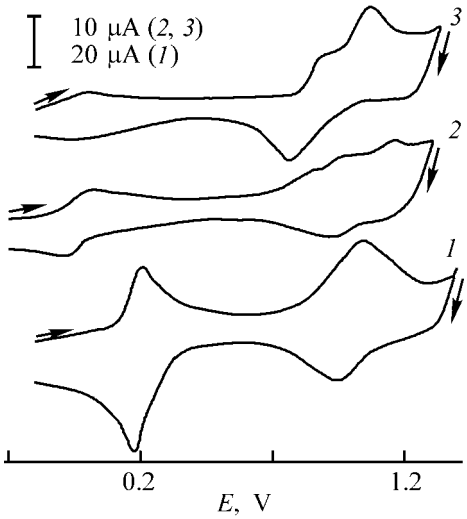

Fig. 1. Voltammograms obtained on GC with coatings composed of (*1*) $KFe^{II}Fe^{III}(CN)_6$, (*2*) RuO–FeCN, and (*3*) RuO–RuCN on the background of a 0.1 M solution of K_2SO_4 in the presence of 0.01 M H_2SO_4. (*E*) Potential; the same for Figs. 3, 4.

Introduction of ruthenium ions into the composition of an inorganic coating leads to an increase in the number of anodic and cathodic peaks in the cyclic voltammogram (Fig. 1; curves *2*, *3*). The voltammogram of an electrode with a RuO–RuCN coating contains three well pronounced anodic and reverse-cathodic peaks at potentials in the range from –0.2 to 1.5 V. Although data that could be used to assign each peak to a particular redox pair are still lacking, the electrochemical reactions occurring at a potential of 0.05 V are commonly attributed to the redox pair Ru(III/II), and peaks at 0.80 and 1.10 V, to oxidation of mixed-charge ruthenium ions bound to oxo and cyano groups to higher oxidation states. For example, it was assumed in [10, 13] that electron transfer occurs at E = 0.80 V, and Ru(IV) is oxidized to Ru(VI) at E = 1.05 V. An assumption was made in [11, 14] that the two current peaks observed at potentials of 0.6 to 1.2 V are associated with electrochemical transformations of the redox pairs Ru(III)/Ru(IV) and $Ru(II)(CN)_6/Ru(III)(CN)_6$. If account is taken of the similarity between the shapes of the voltammograms obtained on electrodes modified with Ru and RuO_2 species [19] and with a RuO–RuCN coating and published data obtained in studying these coatings by X-ray photoelectron spectroscopy [20] are analyzed, it may be concluded that the peaks observed in the curves are to be attributed to the following electrochemical reactions:

$$Ru(II) \rightleftarrows Ru(III) + e, \quad E = 0.05 \text{ V}; \qquad (1)$$

$$Ru(III) \rightleftarrows Ru(IV) + e, \quad E = 0.80 \text{ V}; \qquad (2)$$

$$Ru(IV) \rightleftarrows Ru(VI) + 2e, \quad E = 1.05 \text{ V}. \qquad (3)$$

The anodic and cathodic peaks recorded on GC modified with a RuO–FeCN coating (Fig. 1, curve *2*) are probably also associated with electrochemical reactions (1)–(3). The peak recorded at E = 0.2 V in the voltammogram of the electrode with a $KFe^{II}Fe^{III}(CN)_6$ coating (Fig. 1, curve *1*) and associated with oxidation of $Fe(CN)_6^{3-}$ ions is not observed in the voltammogram of the electrode with a RuO–FeCN coating. Possibly, the electrochemical reaction $Fe(CN)_6^{4-} \rightarrow Fe(CN)_6^{3-}$ occurs at potentials that are characteristic of the redox pair Ru(III)/Ru(II), which leads to a certain increase in the height and width of the peak at E = 0.05 V, compared with the peak observed on GC with a RuO–RuCN coating.

An HCM coating was deposited onto the surface of graphite electrodes electrochemically. The $KFe^{II}Fe^{III}(CN)_6$ coating was obtained using the procedure suggested in [17], and the RuO–FeCN coating, by the method described in [21].

The RuO–RuCN coating was deposited in two ways: potential sweeping in a fixed range or potentiostatic electrodeposition (Table 1). The voltammetric curves were compared by the peak observed at E = 1.05 V. When the first method was used, the potential was varied in a cyclic way in the range –0.2…+1.1 V. This is the optimal range of potentials. If the starting potential of sweeping was shifted into the anodic region, the current of the peak decreased at E = 1.05 V (Table 1). Using the potentiostatic electrodeposition instead of potential sweeping did not lead to any increase in the intensity of the peaks observed

Table 1. Conditions of electrodeposition of coatings composed of ruthenium(III) hexacyanoruthenate(II) on the surface of GC

Potential sweep		Potentiostatic electrodeposition	
potential, V	i_p, μA	potential, V	i_p, μA
+0.35…+1.1	7	+0.50	6
+0.20…+1.1	8	+0.70	9
+0.10…+1.1	10	+0.80	10
0.00…+1.1	13	+0.90	12
–0.20…+1.1	15	+1.05	16

Table 2. Characteristics* of electrooxidation of ethanol ($c = 1 \times 10^{-3}$ M) on GC modified with an HCM coating on the background of a 0.1 M H_2SO_4 solution

Coating	E_{mod}, V	i_{mod}, μA	E_{cat}, V	i_{cat}, μA	$(i_{cat} - i_{mod})/i_{mod}$
FeO–FeCN	0.25	38	0.25	38	0
	1.08	62	1.08	62	0
RuO–FeCN	0.9	1.4	0.9	1.4	0
	1.1	8.0	1.1	42	4.3
RuO–RuCN	0.8	15	0.8	15	0
	1.05	15	1.05	110	6.3

* E_{mod} and i_{mod}, potential and current of the oxidation peak of the modifier; E_{cat} and i_{cat}, potential and current of catalytic oxidation of ethanol on CME.

(Table 1). However, as can be seen in Fig. 2, this made it possible to shorten the time in which an inorganic coating was obtained by a factor of 2.

The coating is stable only in an acid medium. Figure 3 shows as an example voltammograms obtained on CME with a RuO–RuCN coating at different pH values. Making the pH higher impaired the shape of the peaks, with the anodic peaks becoming lower and the cathodic peaks even disappearing at all. In alkaline solutions, the coating disintegrates and repeated recording yields only the background curve characteristic of the unmodified GC.

A comparison of the properties of the coatings in question revealed that reproducible results are obtained on the electrode coated with FeO–FeCN when voltammograms are recorded in a narrow range of potentials: –0.5 to 0.5 V. In polarization of the electrode, the film disintegrates beginning at $E > 0.5$ V, which distorts the shape of the voltammogram and leads to a decrease in the intensity of the signal. Chemically modified electrodes with films containing oxo compounds of ruthenium can be used in a wider range of electrode polarizations, up to $E = 1.3$ V. The fabrication methods and the electrochemical and working properties of electrodes coated with RuO–FeCN and RuO–RuCN are similar in many respects. However, RuO–RuCN coatings are distinguished by a higher chemical and electrochemical stability. For example, the RuO–FeCN coating is stable during several days, and the RuO–RuCN coating, during several months, which is indicated by the good reproducibility of cyclic voltammograms obtained on the background of a 0.01 M H_2SO_4 solution. In addition, higher anodic and cathodic peaks are recorded on the electrode with this coating (Fig. 1).

Ethanol is not oxidized at potentials in the range from –0.2 to 1.4 V (Fig. 4, curve *1*) although the equilibrium potential of the redox system CH_3CHO/C_2H_5OH is 0.19 V [18]. A study of the electrooxidation of ethanol on electrodes coated with the HCM in question (Table 2) demonstrated that ethanol is not oxidized

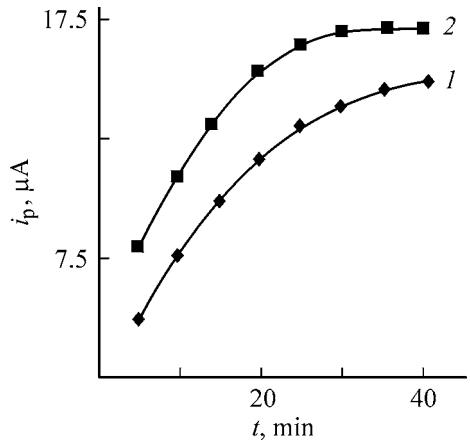

Fig. 2. Oxidation current i_p of the modifier at E_p = 1.05 V vs. the time t of electrodeposition (*1*) with potential sweeping in the interval –0.2…1.1 V and (*2*) in the potentiostatic mode at E_e = 1.05 V.

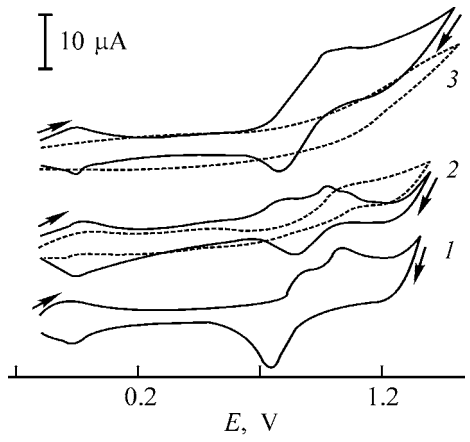

Fig. 3. Voltammograms obtained on GC with a RuO–RuCN coating on the background of (*1*) 0.1 M H_2SO_4 solution, (*2*) 0.1 M K_2SO_4 solution, and (*3*) borate buffer solution with pH 9.0. *Dashed line*: repeated sweep.

Table 3. Analytical parameters obtained in determining ethanol on GC modified with HCM coatings in stationary and FIA conditions [regression equation $i = a + bc$ (i, μA; c, M)]

Electrode	c, M	$a \pm \Delta a$	$(b \pm \Delta b) \times 10^4$	R
		Stationary conditions		
RuO–FeCN	1×10^{-3}–5×10^{-2}	4.03 ± 0.03	76 ± 0.2	0.997
RuO–RuCN	1×10^{-4}–5×10^{-2}	8.89 ± 0.02	19 ± 0.9	0.999
		FIA conditions		
RuO–RuCN	1×10^{-5}–5×10^{-2}	0.70 ± 0.06	2.1 ± 0.3	0.998

on CME coated with $KFe^{II}Fe^{III}(CN)_6$ and, therefore, the shape of the background voltammogram is not changed in the presence of the substrate. In oxidation of ethanol on CME with a RuO–FeCN or RuO–RuCN coating, a considerable increase in current is observed in the same range of potentials.

Figure 4 shows cyclic voltammograms obtained in the absence (curve *2*) and in the presence (curve *3*) of ethanol on an electrode modified with a RuO–RuCN coating. It can be clearly seen that electrocatalytic oxidation of ethanol occurs on CME. In this case, an increase in the peak current is observed at $E_p = 1.05$ V. At the same potential, the blank curve (Fig. 4, curve *2*) shows a current peak characteristic of the transition –Ru(IV)O → –Ru(VI)O, i.e., the substrate is oxidized in the oxidation region of this modifier. The peak

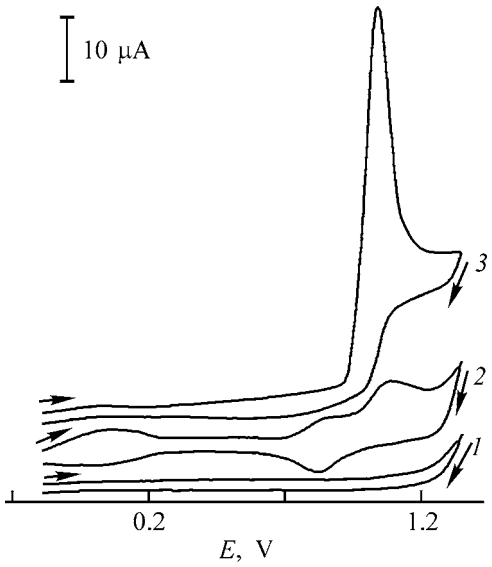

Fig. 4. Voltammograms of ethanol oxidation on (*1*) GC and (*3*) GC with a RuO–RuCN coating on the background of a 0.1 M H_2SO_4 solution. Ethanol concentration 5×10^{-2} M; the same for Fig. 5. (*2*) Blank curve obtained on GC with a RuO–RuCN coating.

current linearly depends on the ethanol concentration. The manyfold increase in the current, decrease in the overvoltage of substrate oxidation, and the value of the Semerano coefficient $\Delta\log i/\Delta\log v$ [22], equal to 0.3, suggest that the electrochemical process is of a catalytic nature.

The mechanism of ethanol electrooxidation is complicated and depends on the range of potentials in which the voltammograms are recorded [23]. In the first stage, ethanol oxidizes to an aldehyde, but deeper oxidation of the substrate to acetic acid is also possible. The scheme of the electrochemical reaction can be represented as

$$\text{–Ru(IV)O} \rightleftarrows \text{–Ru(VI)O} + 2e, \quad (4)$$

$$C_2H_5O + \text{–Ru(VI)O} \begin{cases} \rightarrow CH_3CHO + \text{–Ru(IV)O} + 2H^+, \\ \rightarrow CH_3COOH + \text{–Ru(IV)O} + 2H^+. \end{cases} \quad (5)$$

It should be noted that the catalytic effect, defined as the difference of the catalytic current i_{cat} and the peak current of modifier oxidation, i_{mod}, which is recorded in the background curve at $E = 1.05$ V, divided by i_{mod}, is observed on CME with RuO–FeCN and RuO–RuCN coatings (Table 2). However, the RuO–RuCN coating has a higher catalytic current, which makes the sensitivity of ethanol determination higher and the range of determinable ethanol concentrations wider.

A linear dependence of the catalytic current on the ethanol concentration is observed in the range 1×10^{-3}–5×10^{-2} M for RuO–FeCN and 1×10^{-4}–5×10^{-2} M for RuO–RuCN (Table 3). Moreover, the RuO–RuCN coating is more stable. Therefore, it is more appropriate to use CME with this type of coating for analytical purposes.

A chemically modified electrode based on ruthenium(III) hexacyanoruthenate(II) was used to determine

ethanol under conditions of a flow-injection analysis (FIA).

The FIA signal was recorded in the potentiostatic mode. Preliminarily, the influence exerted by hydrodynamic parameters on the magnitude of the FIA signal was studied. The maximum FIA signal is observed at a volume V of a sample injected equal to 0.6 ml (Fig. 5, curve *1*) and a flow rate u of 3.5 ml min^{-1} (Fig. 5, curve *2*).

The dependence of the current on the voltage applied to a CME with an electrodeposited RuO–RuCN coating was studied under these hydrodynamic conditions. The maximum current was observed at E = 1.05 V (Fig. 5, curve *3*). The data obtained were used to establish the working conditions of recording of a FIA signal on CME: u = 3.5 ml min^{-1}, V = 0.6 ml, E = 1.05 V.

The analytical parameters of the amperometric FIA determination of ethanol on a CPE modified with a RuO–RuCN coating are listed in Table 3. The magnitude of the FIA signal is a linear function of the substrate concentration in the range 5×10^{-2}–1×10^{-5} M, which is an order of magnitude wider than that under stationary conditions. The detection limit calculated using the 3s-criterion [24] is 8×10^{-6} M.

In assessing the metrological characteristics of different electrodes, the reproducibility of results of FIA determinations was analyzed. It was established that, in prolonged use (for 8 h) of a CME in a flow-through cell without renewal of the surface, the magnitude of the FIA signal remains virtually unchanged. The S_r calculated for the oxidation current in the case of ethanol (c = 0.05 M) does not exceed 3% (at n = 20).

Thus, graphite electrodes with a coating composed of ruthenium(III) hexacyanoruthenate(II) can be used for voltammetric determination and amperometric detection of ethanol under FIA conditions without preliminary sample preparation.

The method of voltammetric determination of ethanol on a graphite electrode coated with ruthenium(III) hexacyanoruthenate(II) was tested on ethanol-containing solutions. It was established that matrix components do not hinder the determination of ethanol. Most part of organic compounds present in solutions (carbohydrates, polyphenols, volatile organic acids, and mineral salts) exhibit no electrochemical activity and, therefore, have no effect on the results obtained when determining ethanol. Presence of alcohols (propanol, butanol, amyl alcohol), polyalcohols (sorbitol, mannitol, glycerol), aldehydes (e.g., acetaldehyde), oxy acids (tartaric, malic, and sorbic), and vitamins of groups B and C, which are all oxidized on the CME suggested does not affect the determination of ethanol without preliminary sample preparation, either, because the content of these components is considerably lower than that of ethanol.

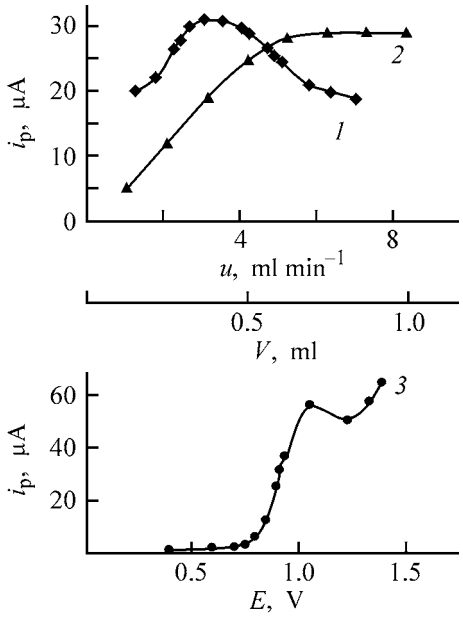

Fig. 5. FIA signal produced in ethanol oxidation on CPE modified with a RuO–RuCN coating vs. (*1*) flow rate u, (*2*) volume V of a sample injected, and (*3*) applied potential E on the background of a H_2SO_4 solution with pH 2.0. (i_p) Peak current.

The procedures developed for determining ethanol on CME with catalytic properties are distinguished by simplicity, high sensitivity, and short time of analysis (10 min); moreover, the necessary sample volume is small (V = 0.5 ml).

EXPERIMENTAL

A PU-1 polarograph and a PI-50-1.1 potentiostat were used to record dc voltammograms with linear and triangular potential sweep in a three-electrode cell. As indicator electrodes served GC and CPE with working surface areas of 0.1 and 0.09 cm^2, respectively, and CME. A silver chloride electrode served as reference, and a platinum wire, as an anode. The procedure used to fabricate the CPE was described in [19]. GC and CPE were used as supports in fabricating a film CME. By analogy with that described in [21], the method employed for this purpose consists in the following: first, the surface of a graphite electrode is polished on filter paper; then, the electrode is rinsed with distilled water and introduced into an el-

ectrochemical cell containing a freshly prepared solution: 1×10^{-3} M $RuCl_3$, 1×10^{-3} M $K_4[Ru(CN)_6]$ {or $K_4[Fe(CN)_6]$}, and 0.01 M H_2SO_4, and the potential is varied by means of sweeping in the range from –0.2 to 1.1 V at a rate of 100 mV s^{-1} for 40 min. Then the electrode is removed from the cell, rinsed with distilled water, and dried.

The FIA was performed on a setup comprising a peristaltic pump, injector, flow-through electrochemical cell, and recording unit [25]. The solutions used were delivered and discharged via flow-through lines made of silicone tubes with an inner diameter of 2.0 mm. The injection was performed with a microsyringe through a sealing membrane.

The standard ethanol solution (c = 1.0 M) was prepared from 96% ethanol. Solutions with lower concentrations were obtained by successive dilution of the standard solution.

To make the solutions electrically conducting, 0.1 M aqueous solutions of H_2SO_4, KOH, and K_2SO_4, and a borate buffer solution were used. The pH value was monitored with a pH-150 pH-meter.

CONCLUSIONS

(1) It was found that ruthenium(III) hexacyanoferrate(II) and hexacyanoruthenate(II) electrodeposited onto the surface of a graphite electrode exhibit a catalytic activity in oxidation of ethanol. A catalytic peak was observed at E = 1.0 V in the region of Ru(IV) oxidation. The conditions in which a chemically modified electrode with an inorganic coating composed of hexacyanometallates can be fabricated and the maximum catalytic current of ethanol oxidation on this electrode were determined.

(2) A method for voltammetric determination of ethanol on an electrode modified with a coating composed of ruthenium(III) hexacyanoruthenate(II) was developed. A procedure for amperometric detection of ethanol on this electrode under conditions of a flow-injection analysis was suggested. The electrochemical and hydrodynamic conditions for signal recording were established. A linear dependence of the catalytic current on the concentration of ethanol was observed in the range 1×10^{-4}–5×10^{-2} M under stationary conditions and 1×10^{-5}–5×10^{-2} M under conditions of a flow-injection analysis.

(3) It was established that the matrix components of ethanol-containing solutions do not hinder the determination of ethanol. The method suggested for determining ethanol is distinguished by simplicity, high sensitivity, good precision, short analysis duration, and use of samples with small volume.

ACKNOWLEDGMENTS

The study was supported by the Russian Foundation for Basic Research (grant no. 03-03-33116).

REFERENCES

1. Klimova, V.A., *Osnovnye makrometody analiza organicheskikh soedinenii* (Main Macromethods for Analysis of Organic Compounds), Moscow: Khimiya, 1975.
2. Siggia S., and Hanna, J. G., *Quantitative Organic Analysis via Functional Groups*, New York: Wiley Interscience, 1979.
3. Casella, I.G., Cataldi, T.R.I., Salvi, A.M., and Desimoni, E., *Anal. Chem.*, 1993, vol. 65, no. 21, pp. 3143–3150.
4. Avramov-Ivie, M., Jovanovie, V., Vlajnie, G., and Popie, J., *J. Electroanal. Chem.*, 1997, vol. 423, no. 1–2, pp. 119–124.
5. Jiang, J. and Kucernak, A., *J. Electroanal. Chem.*, 2003, vol. 543, no. 2, pp. 187–199.
6. Yanez, C., Gutierrez, C., and Urela-Zanartu, M.S., *J. Electroanal. Chem.*, 2003, vol. 541, nos. 1–2, pp. 39–49.
7. Ciszewski, A. and Milczarek, G., *J. Electroanal. Chem.*, 1997, vol. 426, nos. 1–2, pp. 125–130.
8. Beserlk, I., Suzer, S., and Kadirgan, F., *J. Electroanal. Chem.*, 2001, vol. 502, nos. 1–2, pp. 118–128.
9. Karyakin, A.A. and Karyakina, E.E., *Zh. Vses. Khim. O–va im. D.I. Mendeleeva*, 1998, vol. 42, nos. 1–2, pp. 86–94.
10. Cataldi, T.R.I., Centonze, D., Desimoni, E., and Forastiero, V., *Anal. Chim. Acta*, 1995, vol. 310, no. 2, pp. 257–262.
11. Cataldi, T.R.I., Campa, C., and Centonze, D., *Anal. Chem.*, 1995, vol. 67, no. 20, pp. 3740–3745.
12. Cox, J.A., Gray, T., and Kulkarni, K.R., *Anal. Chem.*, 1988, vol. 60, no. 17, pp. 1710–1713.
13. Cox, J.A., Alber, K.S., Brockway, C.A., *et al.*, *Anal. Chem.*, 1995, vol. 67, no. 5, pp. 993–998.
14. Kulesza, P.J., Grzybowska, B., Malic, M.A., *et al.*, *J. Electroanal. Chem.*, 2001, vol. 512, nos. 1–2, pp. 110–118.
15. Cataldi, T.R.I. and De Benedetto, G., *J. Electroanal. Chem.*, 1998, vol. 458, nos. 1–2, pp. 149–154.
16. Cataldi, T.R.I., De Benedetto, G., and Bianchini, A., *J. Electroanal. Chem.*, 1999, vol. 471, no. 1, pp. 42–47.
17. Kulesza, P.J., Zamponi, S., Malic, M.A., *et al.*, *J. Solid State Electrochem.*, 1997, vol. 1, no. 1, pp. 88–93.

18. Lur'e, Yu.Yu., *Spravochnik po analiticheskoi khimii* (Handbook of Analytical Chemistry), Moscow: Khimiya, 1971.
19. Shaidarova, L.G., Ziganshina, S.A., and Budnikov, G.K., *Zh. Anal. Khim.*, 2003, vol. 58, no. 6, pp. 640 – 645.
20. Abe, Toda, G., Tajiri, A., and Kaneko, M.T., *J. Electroanal. Chem.*, 2001, vol. 510, nos. 1–2, pp. 35– 42.
21. Shaidarova, L.G., Ziganshina, S.A., Tikhonova, L.N., and Budnikov, G.K., *Zh. Anal. Khim.*, 2003, vol. 58, no. 12, pp. 1277–1284.
22. Gorokhovskaya, V.I. and Gorokhovskii, V.M., *Praktikum po elektrokhimicheskim metodam analiza* (Manual of Electrochemical Methods of Analysis), Moscow: Vysshaya Shkola, 1983.
23. Lamy, C., Belgsir, E.M., and Leger, J.-M., *J. Appl. Electrochem.*, 2001, vol. 31, no. 4, pp. 799–809.
24. Charykov, A.K., *Matematicheskaya obrabotka rezul'tatov khimicheskogo analiza: Metody obnaruzheniya i otsenki oshibok* (Mathematical Processing of Results of Chemical Analysis: Methods for Detection and Evaluation of Errors), Leningrad: Khimiya, 1984.
25. Shaidarova, L.G., Zaripova, S.A., Tikhonova, L.N., *et al., Zh. Prikl. Khim.*, 2001, vol. 74, no. 5, pp. 728–732.

Russian Journal of Applied Chemistry, Vol. 77, No. 12, 2004, pp. 1958–1961. Translated from Zhurnal Prikladnoi Khimii, Vol. 77, No. 12, 2004, pp. 1980–1984.

APPLIED ELECTROCHEMISTRY AND CORROSION PROTECTION OF METALS

Carbon Nanostructures as Hydrogen Sorbent for Anode of a Chemical Power Cell

M. O. Danilov and A. V. Melezhik

Institute of General and Inorganic Chemistry, Ukrainian National Academy of Sciences, Kiev, Ukraine
TMspetsmash Ltd., Kiev, Ukraine

Received June 24, 2004

Abstract—Carbon nanofibers with a porous structure and a specific surface area of 300–475 $m^2 g^{-1}$ were synthesized by pyrolysis of acetylene on iron-containing catalysts. The possibility of using the carbon nanostructures synthesized as hydrogen sorbents to replace hydride-forming metal alloys in chemical power cells was analyzed.

Further development of electronics is impossible without use of power cells. Among them, alkaline batteries occupy an important place. In the European Community, the manufacture and use of nickel–cadmium and mercury-containing batteries has been prohibited since 1991. Therefore, rechargeable electrochemical systems with nontoxic electrodes and electrolytes are being intensively studied everywhere. The cells in which a cadmium electrode is replaced with a metal hydride electrode have a number of advantages over the conventional nickel–cadmium cells. These are, in addition to the similar technology of manufacture, the higher power and energy density and lower sensitivity to overcharging. Presently, metal hy- dride cells based on rare-earth metal alloys with AB_5 additives are produced with a capacity of 290–320 A h g^{-1}, and those based on Ti–Zr–Ni alloys with AB_2 additives, with a capacity of 385 to 450 A h g^{-1}. At the same time, all these alloys are complicated in preparation and have their own disadvantages.

Therefore, the search for the materials that can adsorb hydrogen electrochemically is being continued. The new structural modifications of carbon, developed in recent decades (Carbyne, fullerenes, nanotubes, and nanofibers), have received much attention of researchers as promising hydrogen accumulators in negatively polarized carbon electrodes in alkaline solutions [1–3]. It is known that, for activated carbon, the amount of adsorbed hydrogen grows with increasing specific surface area [2]. It has also been shown that carbon nanofibers (CNF) and nanotubes sorb a considerable amount of hydrogen at room temperature [3]. CNFs that can retain 10–13 wt % hydrogen at a pressure of 8–11 MPa [4] and 15 wt % [5] have been synthesized, which considerably exceeds the amount of hydrogen accumulated by such metallic alloys as $LaNi_5$.

Also, new carbon nanostructures, porous CNFs, have been described in the literature [6]. In principle, structures of this kind should be good hydrogen sorbents.

The type of a catalyst is known to determine the structure of carbon nanofibers formed by vapor pyrolysis of hydrocarbons. Classical carbon nanotubes, in which graphene layers are oriented along the axis, and CNFs with a crow-shaped and normal orientation of the carbon layers with respect to the fiber axis can be grown by choosing the composition and structure of a catalyst. According to the available data, it is the last two types of carbon nanostructures that are the most efficient hydrogen accumulators. It is assumed that hydrogen is incorporated into nanocavities between the graphene layers.

The aforesaid suggests that carbon nanostructures can be used as a hydrogen electrode in nickel–metal hydride power cells instead of metal alloys. The large specific surface area of nanoparticles and the high porosity and low apparent density of the electrode materials based on them suggest that carbon nanostructures are more efficient hydrogen accumulators than metal alloys.

The aim of this study was to develop methods for synthesis of carbon nanostructures promising as hy-

1070-4272/04/7712-1958 © 2004 MAIK "Nauka/Interperiodica"

drogen accumulators and to analyze the possibility of their use, instead of metal alloys, as electrode materials that can accumulate and store hydrogen in charging of a prototype chemical power cell.

EXPERIMENTAL

CNFs obtained by catalytic vapor deposition were chosen for study. Acetylene served as the source of carbon. It was found that pyrolysis of acetylene on catalysts with carbon and iron clusters on the surface of particles of finely dispersed pyrogenic silica yields porous CNFs. The catalysts were produced by pyrolysis of organometal compounds mechanochemically deposited on aerosil or aluminoaerosil. A thoroughly developed method for preparation of catalysts and the conditions of CNF deposition have been described previously [7]. The selectivity and output capacity of the process are reasonably high. For example, 75–100 g of CNFs at a virtually 100% conversion of acetylene into carbon were obtained in a lab reactor (2 l volume) at 620°C in 3–4 h. Admixtures of metals and silicon dioxide were removed from these materials by treatment in an alkali solution and then in hydrochloric acid. The resulting purified CNFs had a specific surface area of 300–475 $m^2 g^{-1}$ at a fiber diameter of 50–200 nm. The electrical resistivity of compacted powders was 0.08–0.4 Ω cm.

An electron micrograph of a typical nanostructure formed under the given conditions is shown in Fig. 1, and a thermogravimetric curve of a purified CNF sample with a specific surface area of 330 $m^2 g^{-1}$, obtained using a Fe/C/Al_2O_3–SiO_2 catalyst, in Fig. 2. It can be seen that the CNF sample heated in air starts to lose mass above 500°C. The inflections in the thermogravimetric curve are probably due to the presence of different nanostructural forms of carbon in the sample. However, no "amorphous" carbon, which is commonly rather rapidly oxidized by atmospheric oxygen beginning at 350–400°C, is present in the sample. The X-ray diffraction pattern of this sample is virtually identical to that of the CNF sample with a specific surface area of 460 $m^2 g^{-1}$ (Fig. 3, curve *1*) and contains a broadened band with the peak position corresponding to an interplanar spacing of 3.44 Å, which can be probably assigned to the 002 reflections of packages of turbostratified disordered graphene layers, and a wide halo peaked at around 5 Å. Possibly, these bands belong to different structural modifications of carbon, since nanofibers with X-ray diffraction patterns containing only the halo at around 5 Å were obtained on some catalysts (Fe–Sn/C/Al_2O_3–SiO_2).

The specific surface area of multilayer carbon nanotubes can be considerably increased, to 877–1184 $m^2 g^{-1}$, by activation with a KOH melt at 800°C and subsequent washing-out of potassium hydroxide [8]. It was assumed that activated nanotubes of this kind, with a well-developed surface, are promising

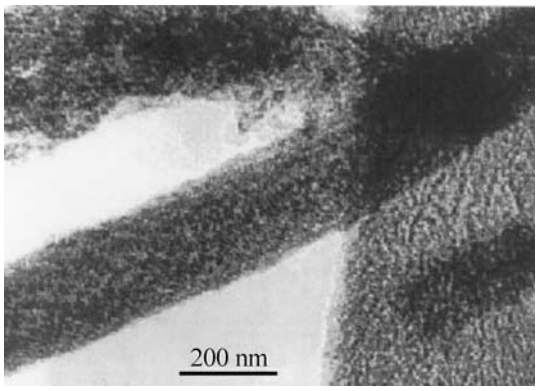

Fig. 1. Typical structure of carbon nanofibers obtained by pyrolysis of acetylene at 620°C on iron-containing catalysts.

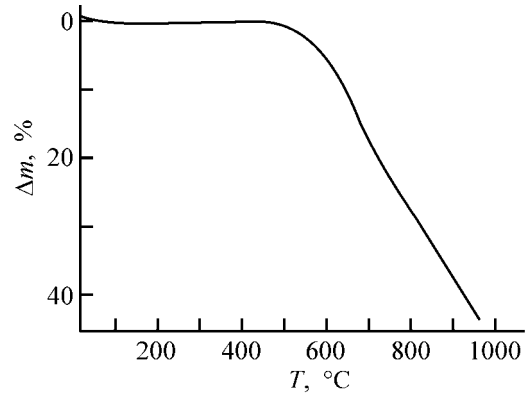

Fig. 2. Thermogravimetric curve of purified CNFs (specific surface area 330 $m^2 g^{-1}$). (Δ*m*) Loss of mass and (*T*) temperature.

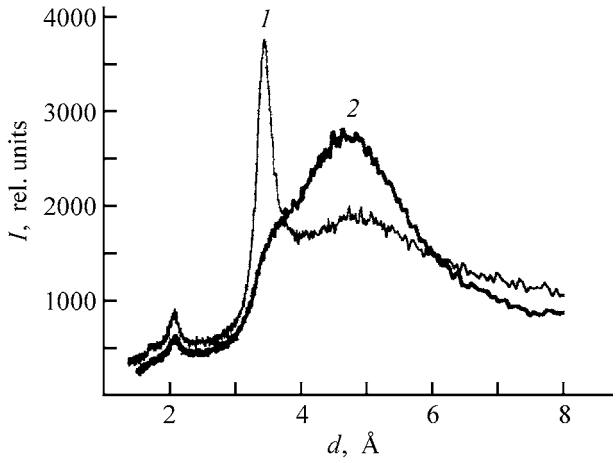

Fig. 3. X-ray diffraction patterns of a CNF sample (*1*) before and (*2*) after activation with a KOH melt. (*I*) Intensity and (*d*) interplanar spacing. Specific surface area ($m^2 g^{-1}$): (*1*) 460 and (*2*) 1700.

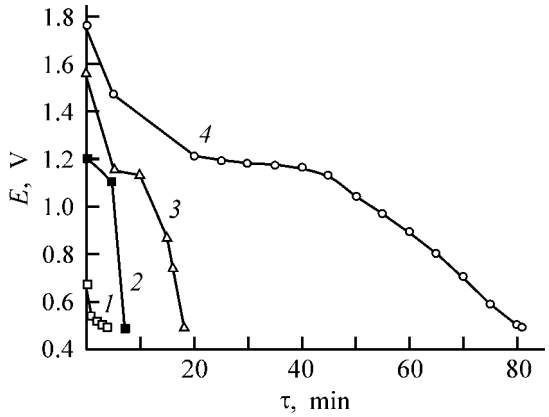

Fig. 4. Discharge curves measured on a prototype power cell with an anode made of carbon materials. (*E*) Potential and (τ) time; the same for Fig. 5. (*1*) Acetylene black, (*2*) activated carbon felt with a specific surface area of 1000 $m^2 g^{-1}$, (*3*) CNF with a specific surface area of 330 $m^2 g^{-1}$, and (*4*) activated CNFs with a specific surface area of 1700 $m^2 g^{-1}$.

electrode materials. The mechanism of activation remains unclear. Probably, carbon layers partly unfold to form nanocavities. We attempted to apply this method to obtain a more developed surface in CNF synthesized by the technique described above.

An X-ray diffraction pattern of CNF obtained by pyrolysis of acetylene on the $Fe/C/SiO_2$ catalyst (curve *1*) and that of the same carbon material activated with a KOH melt at 750°C in the atmosphere of argon (curve *2*) are shown in Fig. 3. It can be seen that the band at 3.44 Å virtually completely disappears upon activation, and the wide halo at around 5 Å becomes more pronounced. At the same time, the band at around 2.12 Å remains unchanged. Probably, the last band can be assigned to the 001 reflections from the graphene layers. Interestingly, the specific surface area of the material increases from 460 (starting CNFs) to 1700 $m^2 g^{-1}$, whereas the electrical resistivity of a compacted powder decreases from 0.4 to 0.05 Ω cm. These data indicate that activation with a KOH melt disrupts the parallel orientation of the graphene layers, which probably results in the formation of nanocavities between these layers. In the process, the layers themselves remain highly ordered, which is confirmed by the high electrical conductivity of the activated sample. The rise in the electrical conductivity of the sample upon activation is probably due to burning-out of a low-ordered carbon.

The nanocarbon electrodes were tested in a prototype Ni–MH battery in the galvanostatic mode. As a counter electrode served nickel oxide electrode with large area and capacity. As the electrolyte was used a 5 M potassium hydroxide solution containing 1 M lithium hydroxide. The test electrode was in the form of a tablet 30 mm in diameter, obtained by compaction at a pressure of 10 MPa on a nickel mesh. For this purpose, an emulsion of F-4D fluoroplastic was added as a binder to the CNF sample (5% fluoroplastic relative to the mass of CNF). All the potentials are given relative to a silver chloride reference electrode.

After fabrication, the electrode being tested was kept in the prototype battery for 1 h without loading. The cycle of study started from charging with a 50 mA g^{-1} current. All the charging cycles were 3 h long. After the charging was complete, the prototype remained unloaded for 5 min. Then, the discharge cycle was performed until the voltage on the prototype became 0.5 V, after which the charging was started. The discharge current (50 mA g^{-1}) was equal to the charging current.

The self-discharge of the hydrogen-sorbing electrode materials in the prototype battery was studied as follows. First, the prototype was charged with a current of 50 mA g^{-1} to a charging capacity of 450 A h g^{-1}. Then, the dc supply was switched off and the potential of the hydrogen electrode and the open-circuit voltage were measured. The prototype was stored for 24 h or a week, and after that the electrode potential and the open-circuit voltage were measured again. Then, the power supply was connected and the prototype was discharged with a current of 20 mA g^{-1}. After that, the discharge capacity of a prototype after storage was compared with that obtained directly after charging.

It is known from the literature that hydrogen is formed under these conditions of charging on the carbon electrode through reduction of water, and this hydrogen easily penetrates into nanopores present in the carbon material [1].

Hydrogen-sorbing electrodes made of acetylene black (AB), activated carbon felt (ACF, 1000 $m^2 g^{-1}$), CNF (330 $m^2 g^{-1}$), and activated CNFs (ACNF, 1700 $m^2 g^{-1}$) were fabricated and studied. Figure 4 shows the discharge curves measured on a prototype battery with electrodes made of AC (curve *1*), ACF (curve *2*), CNF (curve *3*), and ACNF (curve *4*). It can be seen that the hydrogen capacity of the traditional carbon materials (curves *1* and *2*) is very small, 3.2 and 9.2 mA h g^{-1} for carbon black and felt, respectively.

The electrical capacity was 16.7 for CNFs and 135 mA h g^{-1} for activated CNFs. The shape of the discharge and charging curves with a plateau and the potential in this region relative to that of the reference electrode show that there occurs an electrochemical reaction of oxidation–reduction of hydrogen.

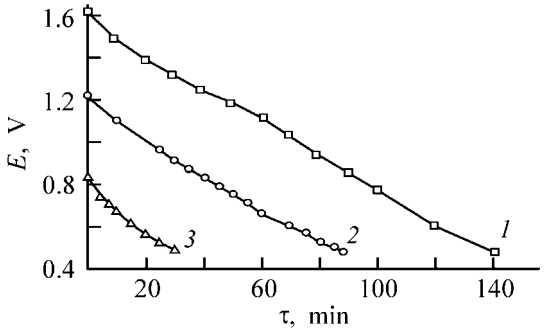

Fig. 5. Influence of the storage time on the self-discharge of the electrode made of activated CNFs with a specific surface area of 1700 $m^2 g^{-1}$ (discharge current 20 mA g^{-1}). Discharge curve: (*1*) measured immediately after discharge, (*2*) after 24 h of storage of a charged prototype, and (*3*) after 1 week of storage of a charged prototype.

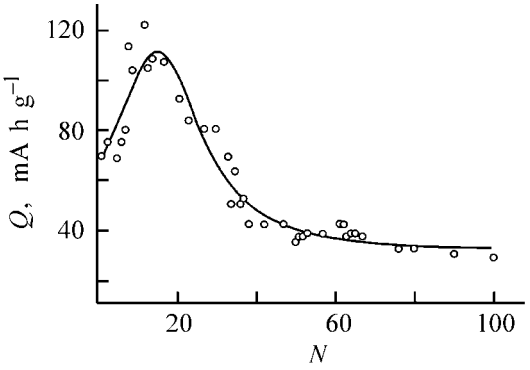

Fig. 6. Variation of the discharge capacity *Q* of a prototype power cell during cycling to complete discharge of the electrode made of activated CNFs with a specific surface area of 1700 $m^2 g^{-1}$ with the number of cycles, *N*.

As can be seen from Fig. 4, the CNFs have a considerably higher capacity, compared with carbon black and felt, despite that their specific surface area is smaller. The activation of CNF leads to a dramatic increase in the electrical capacity. For hydrogen electrodes based on carbon black and felt, the self-discharge was 100% in 24 h. For CNFs with a specific surface area of 330 $m^2 g^{-1}$, the residual capacity after 24 h was 3% of the initial value. It should be noted that the experiments were performed without hermetically sealing the prototype, so that the self-discharge is probably caused by diffusion of hydrogen from the electrode.

Figure 5 shows the results of a study of the self-discharge of a prototype power cell based on ACNF with a specific surface area of 1700 $m^2 g^{-1}$. As can be seen, the electrical capacity is 56% after 24 h of storage and 24% of the initial capacity after a week of storage.

The results obtained in a study of the self-discharge of the hydrogen electrodes made of CNFs show that, as the specific surface area of CNF increases (as a result of activation), the ability of the electrodes to store electrochemically accumulated hydrogen is improved.

Figure 6 shows how the electrical capacity of a prototype battery based on activated CNF with a specific surface area of 1700 $m^2 g^{-1}$ varies with the number of charging–discharge cycles. It can be seen that, after 100 cycles with a 100% discharge, the electrical capacity decreases by 25% of the initial value. In the process, the electrode crumbled, which is apparently due to the nonoptimal amount of binder in the hydride electrode.

It should be noted that the experiments described here were performed in an unsealed prototype power cell under atmospheric pressure. Probably, if charged under elevated pressure, the CNF electrodes could retain a considerably larger amount of electrochemically accumulated hydrogen.

CONCLUSIONS

(1) Pyrolysis of acetylene on catalysts containing carbon and iron compounds as clusters on supports made of finely dispersed pyrogenic silica yields carbon nanofibers with a porous structure.

(2) When the carbon nanofibers obtained are activated with a potassium hydroxide melt, the orientation of graphene layers changes, the specific surface area and electrical conductivity considerably increase, and the electrochemical parameters are improved.

(3) The resulting carbon nanofibers can be used as hydrogen sorbents in chemical power cells instead of a metal hydride anode.

REFERENCES

1. Frackowiak, E. and Beguin, F., *Carbon*, 2002, vol. 40, pp. 1775–1787.
2. Agarwal, R.K., Noh, J.S., Schwarz, J.A., and Davini, P., *Carbon*, 1987, vol. 25, pp. 219–245.
3. Dillon, A.C., Jones, K.M., Bekkedahl, T.A., *et al.*, *Nature*, 1997, vol. 386, pp. 377–386.
4. Fan, Y.-Y., Liao, B., Liu, M., *et al.*, *Carbon*, 1999, vol. 37, pp. 1649–1652.
5. Gupta, B.K. and Srivastava, O.N., *Hydrogen Materials Science and Chemistry of Carbon Nanomaterials: VIII Int. Conf., Sudak, Crimea, Ukraine, September 14–20*, 2003, pp. 794–795.
6. Yan, G., Li, H., Hao, Z., and Han, H., *Carbon*, 2002, vol. 40, pp. 787–803.
7. Ukrainian Patent Application 20031212313.
8. Raymundo-Pinero, E., Cazorla-Amoros, D., and Linares-Solano, A., *Carbon*, 2002, vol. 40, pp. 1597–1617.

Russian Journal of Applied Chemistry, Vol. 77, No. 12, 2004, pp. 1962–1966. Translated from Zhurnal Prikladnoi Khimii, Vol. 77, No. 12, 2004, pp. 1985–1989.

APPLIED ELECTROCHEMISTRY AND CORROSION PROTECTION OF METALS

Anodic Electrochemical Polymerization of Complexes [Ni(Salpn-1,3)] and [Cu(Salpn-1,3)]

L. P. Ardasheva, G. V. Vovk, L. G. Pchelova, and G. A. Shagisultanova

Hertzen Russian State Pedagogical University, St. Petersburg, Russia

Received July 9, 2004

Abstract—New experimental data characterizing the conditions of electrochemical synthesis of stable electrically conducting electrochromic polymeric film systems based on the complexes [Ni(Salpn-1,3)] and [Cu(Salpn-1,3)] [Salpn-1,3 is *N,N'*-propylenebis(salicylidenimine)] in a 0.1 M Bu_4NClO_4/CH_2Cl_2 solution are presented. The redox conductivity of the new polymers is characterized by the charge diffusion coefficient. The electrochemical stability of the polymeric films is analyzed in relation to the potential and time of accumulation, and also to the range of potential sweeping.

Studies of thin electrically conducting electrochromic metal-containing polymeric films on solid supports are of current interest because of the possibility of creating electro- and photocatalysts, sensors, and solid-phase galvanic cells for conversion of the energy of light on their basis [1, 2].

In the last fifteen years, polymeric film systems based on complex compounds of transition metals with macrocyclic ligands of varied composition and structure have been synthesized and rather extensively studied, including *N,N'*-ethylenebis(salicylidenes) [3–10], porphyrins [11], phthalocyanines [12], etc. Complexes with ligands of this kind are of the utmost interest to a researcher, because they are models and (or) analogues of most important natural organometallic compounds.

However, despite that a considerably body of experimental data has been obtained, the optimization of the synthesis conditions and analysis of the structure, stability, and functional features of organometallic polymers, including the best-studied compounds of copper(II) and nickel(II), remains a matter of current interest.

The present communication reports original results characterizing the synthesis conditions of polymeric systems based on the complexes [Cu(Salpn-1,3)] and [Ni(Salpn-1,3)], where Salpn-1,3 is *N,N'*-propylenebis(salicylidenimine)], in a solution of methylene chloride. It should be noted that the ability of the complex [Cu(Salpn-1,3)] to form, as a result of oxidation at the electrode, photosensitive electrically conducting polymers has been revealed previously [10], whereas the possibility, in principle, of polymerization of [Ni(Salpn-1,3)] is established for the first time.

The complexes [Ni(Salpn-1,3)] and [Cu(Salpn-1,3)]

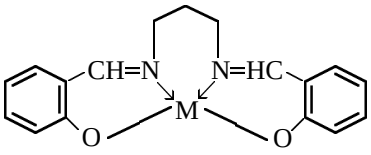

M = Ni(II), Cu(II)

were synthesized by the known methods [10]. The complexes were identified by electronic absorption spectroscopy in the visible and near-UV spectral ranges and by X-ray photoelectron spectroscopy (XPS). XPS spectra were obtained on an Axis Ultra electronic spectrometer (Kratos Analytical, UK) under excitation with monochromatic Al_{K_α} radiation (1486.6 eV).[1] During the experiments, the initial vacuum in the spectrometer was 5×10^{-7} Pa. The spectra obtained were processed with a Vision software package (Kratos Analytical). The scale of binding energies was calibrated against the C1s line of aliphatic carbon (E_b = 285.0 eV). The binding energies of photoelectrons and the atomic concentrations of selected components of the photoelectron spectra for the ligand H_2Salpn-1,3

[1] The XPS spectra were measured by A.V. Shchukarev (St. Petersburg State University)

1070-4272/04/7712-1962 © 2004 MAIK "Nauka/Interperiodica"

Table 1. Binding energies of photoelectrons and atomic concentrations of selected components of the XPS spectra of the starting compounds

Line	H_2Salpn-1,3		[Cu(Sapn-1,3)]		[Ni(Sapn-1,3)]	
	E_b, eV	atomic concentration, at.%	E_b, eV	atomic concentration, at.%	E_b, eV	atomic concentration, at.%
C1*s*	285.0	51.7	285.0	51.9	285.0	49.6
	286.4	28.5	286.4	28.6	286.5	22.4
					288.7	2.4
O11*s*			529.6	0.1		
	531.1	1.8	531.2	7.0	531.6	11.7
	533.0	7.9	532.1	0.5	533.0	1.5
N1*s*	399.1	7.1	399.5	7.2	399.5	6.0
	399.9	1.8				
	401.3	0.6	401.8	0.3	401.3	0.4
	402.9	0.6	403.5	0.6	403.5	0.6
Cu2*p*			934.7	3.7		
			936.7	0.1		
Ni2*p*					855.4	5.4

and the complexes [Cu(Salpn-1,3)] and [Ni(Salpn-1,3)] are listed in Table 1.

The presence of two components with binding energies of 531.1 and 533.3 eV in the spectra of O1*s* and two highest-intensity components with binding energies of 399.1 and 399.9 in the spectra of N1*s* for a free protonated ligand and H_2Salpn-1,3 can presumably be accounted for by the equilibrium transfer of a proton from an oxygen atom to a nitrogen, with the equilibrium shifted toward formation of hydroxy groups. The component with a binding energy of 402.9 eV in the spectra of N1*s* can be attributed to and electronically excited state of the π–π^* type, and the component with a binding energy of 401.3 eV is, in all probability, due to presence of trace amounts of the solvent used in synthesis.

The formation of the complexes [Cu(Salpn-1,3)] and [Ni(Salpn-1,3)] is accompanied by a change in the binding energies of the highest-intensity components in the spectra of O1*s* and N1*s*, compared with the case of a free ligand. For example, the binding energy of the N1*s* electron increases for both the complexes from 399.1 to 399.5 eV and that of the O1*s* electron decreases from 533.0 to 51.2 and 531.6 eV for [Cu(Salpn-1,3)] and [Ni(Salpn-1,3)], respectively.

Nickel has in the complex a binding energy of 2*p*-electrons equal to 855.4 eV, which corresponds to Ni(II) [11].

It follows from the spectrum of the [Cu(Salpn-1,3)] complex that copper is present in the starting compound in two different chemical states with binding energies of the Cu2*p* line equal to 934.7 and 936.7 eV. The main line with E_b = 934.7 eV can be attributed to the Cu(II) ion [11]. The line with a low intensity of the component with E_b = 936.7 eV is probably due to the presence of dimeric structures of the type Cu–O–Cu [12, 13].

The electrochemical measurements were performed with a PI-50-1 pulsed potentiostat with a PR-8 programming unit in the potentiostatic and potentiodynamic modes with a linear potential sweeping at sweep rate in the range 0.01–0.5 V s^{-1} in a three-electrode with separated spaces. A platinum wire (99.99% Pt) embedded in glass, with a surface area of 0.25 cm^2, was used as a working electrode, and a platinum wire, as an auxiliary electrode. All the potentials are given relative to a silver chloride glass electrode filled with a saturated solution of NaCl.

The concentration of the monomeric complex in the working solution was 1 mM. A 0.1 M solution of tetrabutylammonium perchlorate (Bu_4NClO_4) in methylene chloride (CH_2Cl_2), deaerated with high-purity argon, served as a supporting electrolyte.

Figures 1a and 1b show typical cyclic voltammograms reflecting the first 10 cycles of anodic polarization of the complexes [Cu(Salpn-1,3)] and [Ni(Salpn-1,3)], respectively, at potentials in the range 0.0 … +1.5 V. In the first cycle, two anodic processes with peaks at $E_{ap}(1) \approx +1.12$ V and $E_{ap}(2) \approx +1.25$ V and one cathodic process with a process at $E_{cp}(1) \approx$

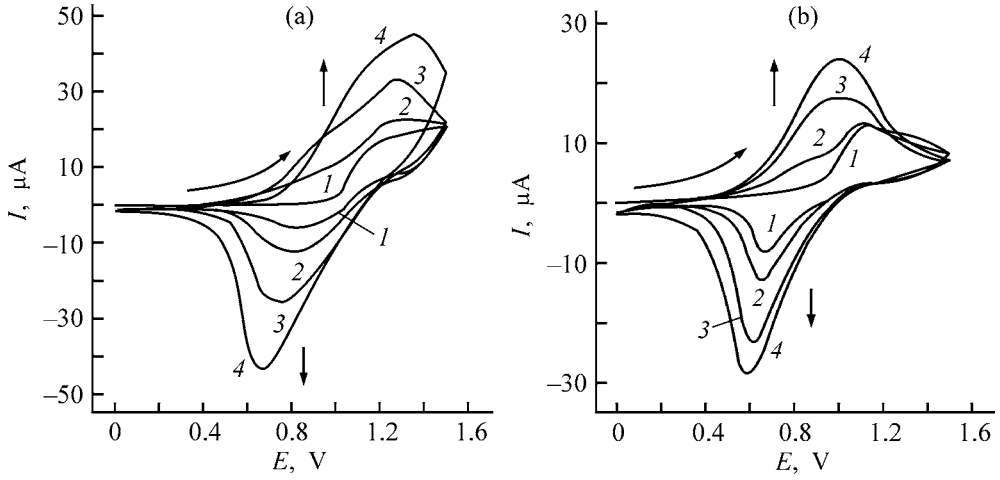

Fig. 1. Cyclic voltammograms reflecting the anodic polymerization of the complex (a) [Cu(Salpn-1,3)] and (b) [Ni(Salpn-1,3)] in potentiodynamic mode in a 0.1 M solution of Bu_4NClO_4 in CH_2Cl_2. $c_{complex} = 1 \times 10^{-3}$ M, $v_{sw} = 0.05$ V s^{-1}. (*I*) Current and (*E*) potential. Cycle of potential sweeping; (*1*) first, (*2*) second, (*3*) fifth, and (*4*) tenth.

+0.75 V are observed for [Cu(Salpn-1,3)] and one anodic and one cathodic peaks at $E_{ap} \approx +1.13$ V and $E_{cp} \approx +0.67$ V, respectively, for [Ni(Salpn-1,3)]. Further potential sweeping results in that a new broad wave at +0.6…+0.95 V without any clearly pronounced peaks appears in the anodic branch of the cyclic voltammogram and the intensities of all the current peaks observed in the first cycle increase. This effect indicates that a new solid substance is formed on the surface of an electrically conducting substrate. Visual inspection confirms the presence of a brightly colored film on the electrode surface. The color of the film is independent of the oxidation state of the substance on the electrode. For example, oxidized forms of poly[Cu(Salpn-1,3)] and poly[Ni(Salpn-1,3)] have a dark green and brown-yellow color, respectively, and the reduced forms are light green and pale yellow.

However, the rise in the peak currents virtually terminates for poly[Ni(Salpn-1,3)] by the tenth cycle, and the currents start to decrease. In the cyclic voltammograms reflecting the polymerization of [Cu(Salpn-1,3)], the anodic wave at $E = +0.7$ V is shifted, beginning with the fifth cycle of potential sweeping, to more positive potentials. Both the effects observed are probably due to a decrease in the redox activity of the polymeric film on the electrode surface, which is caused by an irreversible oxidation of the ligand or by passivation of the polymeric material. Nevertheless, films of poly[Ni(Salpn-1,3)] were found to be more stable than poly[Cu(Salpn-1,3)] at potentials in the range 0.0…+1.5 V. This is, in all probability, due to the role of the central metal atom. Comparison of the potentials at which the peaks of anodic currents of the first and subsequent cycles of polymerization are observed suggests that oxidation processes with the highest intensity (highest current strength) in poly[Cu(Salpn-1,3)] occur at more positive potentials than those in poly[Ni(Salpn-1,3)]. Apparently, the probability of overoxidation of the ligand environment decreases in the last case, and thereby the electrochemical stability of the polymer formed increases. Also to a decrease in the probability of overoxidation of the organic component of both the complexes can be attributed the fact that, as the range of potential sweeping is narrowed to 0.0…+1.3 V, electrochemically more stable films can be obtained in a larger (no less than 30) number of cycles than in the case of the 0.0…+1.5 V range.

The polymers were synthesized under potentiostatic conditions in a prescribed time at the experimentally established potentials with account of the potentials of the anodic peaks in the cyclic voltammograms of the first cycles. The presence of two peaks in the curve of a single cycling of [Cu(Salpn-1,3)] resulted in that two accumulation potentials, $E = +1.25$ and +1.1 V, were used in synthesis. As demonstrated by experiments, thick electrochemically active films cannot be obtained at $E = +1.25$ V. Already by the fifth minute of synthesis at this potential, the cyclic voltammogram of film-type poly[Cu(Salpn-1,3)] shows a significant decrease in the currents of the anodic and cathodic peaks and acquires a shape characteristic of a cyclic voltammogram recorded on a clean platinum electrode in a supporting electrolyte that does not contain the complex under study. At the same time, the accumulation potential of +1.1 V ensures accumulation of electrochemically stable polymeric systems based on both [Cu(Salpn-1,3)] and [Ni(Salpn-1,3)].

Table 2. Effect of the potential sweep rate on the potentials of the oxidation and reduction peaks of the solid phase of poly[Ni(Salpn-1,3)] and poly[Cu(Salpn-1,3)] on the electrode surface

Mode of the potentiometric synthesis of polymers, v_{sw} = 0.05 V s^{-1}		Mode of study of redox reactions in the solid phase* at indicated v_{sw}, V s^{-1}											
		poly[Ni(Salpn-1,3)]						poly[Cu(Salpn-1,3)]					
		0.01		0.05		0.20		0.01		0.05		0.20	
number of cycles	range of potential sweeping, V	E_{pa}	E_{pc}	E_{pa}	E_{pc}	E_{pa}	E_{pc}	E_{pa}	E_{pc}	E_{pa}	E_{pc}	E_{pa}	E_{pc}
		V											
10	0.0–1.5	0.93	0.70	1.02	0.55	1.22	0.35	1.10	0.90	1.28	0.73	1.45	0.60
1	0.0–1.3	0.85	0.75	0.88	0.70	0.93	0.62	1.05	0.90	1.12	0.85	1.25	0.70
10	0.0–1.3	0.93	0.70	1.05	0.55	1.25	0.35	1.10	0.90	1.25	0.75	–	0.55
30	0.0–1.3	0.94	0.65	1.12	0.48	–	0.25	1.15	0.85	–	0.60	–	0.45

* The range of potential sweeping corresponds to that in which the polymer was synthesized.

To determine the electrochemical parameters characterizing the individual substances poly[Cu(Salpn-1,3)] and poly[Ni(Salpn-1,3)], electrodes with the corresponding polymers synthesized were transferred into a solution of a pure supporting electrolyte and then cyclic voltammograms reflecting redox processes in the solid phase were recorded.

An analysis of the cyclic voltammograms obtained at different potential sweep rates on an electrode coated with poly[Ni(Salpn-1,3)] or poly[Cu(Salpn-1,3)] yielded the potentials of anodic and cathodic current peaks, which characterize the redox process in the polymers under study (Table 2). The data in Table 2 indicate that, as the potential sweep rate increases, the peaks of anodic currents are strongly shifted to more positive values, and the cathodic peaks, to negative values. This points to a considerable overvoltage of redox processes occurring in the solid phase of both polymers. This results from hindrance to motion in the polymer of ions of the supporting electrolyte, whose motion velocity is the rate-determining stage of charge transport in polymeric systems of this kind [14].

The thicknesses h of the polymers studied were calculated from the data obtained by integrating the areas of the anodic branch of the cyclic voltammograms by the known procedure [1] using the formula

$$h = NM/Sd = QM/FSd,$$

where Q is the amount of electricity consumed for the reduction, found by integrating the area under the anodic branch of the cyclic voltammogram; M, molecular weight of a fragment; F, Faraday number; S, surface area of the electrode; and d, density of the polymer (~1 g cm^{-3}).

For poly[Cu(Salpn-1,3)] and poly[Ni(Salpn-1,3)] with different thicknesses, the charge diffusion coefficient in the polymeric phase, D_{ct}, was calculated. This coefficient reflects the rate of charge transfer and is a characteristic of the redox conductivity of the polymers [1]. The value of D_{ct} depends on the polymer thickness, nature of the supporting electrolyte, and type of solvent [15].

The values of D_{ct} were calculated using data obtained in an analysis of cyclic voltammograms recorded at high potential sweep rates ($\geq$0.1 V s^{-1}), at which the film is not oxidized or reduced completely. In this case, the redox processes in the polymer occur in the semi-infinite-diffusion mode. In this mode, the peak currents in the voltammograms depend linearly on $v_p^{1/2}$, and it can be used to calculate D_{ct}. This calculation was done for both the anodic and the cathodic peaks by means of the Rendls–Shevchik equation [1]

$$I = 2.69 \times 10^{-5} n^{3/2} S D_{ct}^{1/2} v_{sw}^{1/2} c_0,$$

where I is the current of a cathodic (anodic) peak (A); n, number of electrons transferred in an elementary event; S, electrode surface area (cm^2); v_{sw}, potential sweep rate (V s^{-1}); and c_0, concentration of electrochemically active centers in the polymeric film (M).

The values calculated show that, for poly[Cu(Salpn-1,30] of thickness 0.05 and 0.12 μm, the values of

D_{ct} were 6.5×10^{-13} and 5.3×10^{-12} $cm^2\ s^{-1}$, respectively, for the anodic process, and 1.2×10^{-12} and 4.5×10^{-12} $cm^2\ s^{-1}$ for the cathodic process. Similarly, for [Ni(Salpn-1,3)] with h = 0.03 and 0.10 μm, the values of anodic D_{ct} were 3.3×1^{-13} and 3.5×10^{-12} $cm^2\ s^{-1}$, respectively, and those of the cathodic D_{ct}, 1.6×10^{-12} and 6.0×1^{-12} $cm^2\ s^{-1}$. Further increase in the polymer thickness leads to a decrease in the redox conductivity of the polymeric systems, because high potential sweep rates, at which D_{ct} is to be calculated, do not ensure oxidation of the polymeric phase. This is due to a pronounced hindrance to motion of ions of the supporting electrolyte in such a comparatively viscous solvent as methylene chloride.

CONCLUSIONS

(1) It was established that electrochemical synthesis of thin-film electrically conducting polymers based on the complex [Ni(Salpn-1,3)] is, in principle, possible.

(2) A study of the conditions of electrochemical synthesis of polymeric compounds based on the complexes [Ni(Salpn-1,3)] and [Cu(Salpn-1,3)] in the potentiostatic accumulation mode demonstrated that the optimal accumulation potential, at which polymeric films with the thickest electrically active layer are formed in unit time, is $+1.1 \pm 0.5$ V.

(3) It was established that the anodic and cathodic processes in poly[Cu(Salpn-1,3)] in a pure supporting electrolyte occur at more positive potentials than the processes in poly[Ni(Salpn-1,3)] synthesized in the same number of cycles.

(4) The rate of charge transport in poly[Cu(Salpn-1,3)] and poly[Ni(Salpn-1,3)] grows as the thickness of the polymeric phase increases.

(5) Poly[Cu(Salpn-1,3)] is electrochemically stable in a wider (up to +1.5 V) range of potentials than poly[Ni(Salpn-1,3)].

ACKNOWLEDGMENTS

The study was financially supported by the Ministry of Education of the Russian Federation (grant nos. E00.-5.0-210 and E03.-5.0-230).

REFERENCES

1. Abruna, H.D., *Coord. Chem. Rev.*, 1988, vol. 86, no. 1, pp. 135–189.
2 Shagisultanova, G.A., Taitz, A.M., and Timonov, A.M., *Coord. Chem. Rev.*, 1993, vol. 125, nos. 1–2, pp. 43–52.
3. Shagisultanova, G.A., *Teor. Prikl. Khim.*, 1991, vol. 27, pp. 330–338.
4. Shagisultanova, G.A., Orlova, I.A., and Borisov, A.N., *J. Photochem. Photobiol. A. Chem.*, 1997, vol. 103, no. 3, pp. 249–255.
5. Shagisultanova, G.A., Orlova, I.A., Ardasheva, L.P., and Popova, E.O., *J. Macromol. Phys. Macromol. Symp.*, 1998, vol. 136, pp. 91–97.
6. Shagisultanova, G.A. and Ardasheva, L.P., *Zh. Prikl. Khim.*, 2003, vol. 76, no. 10, pp. 1669–1674.
7. Shagisultanova, G.A., Ardasheva, L.P., and Orlova, I.A., *Zh. Prikl. Khim.*, 2003, vol. 76, no. 10, pp. 1675–1681.
8. Dahm, C.E. and Peters, D.G., *Anal. Chem.*, 1994, vol. 66, no. 19, pp. 3117–3123.
9. Vilas-Boas, M., Freire, C., de Castro, B., *et al.*, *Inorg. Chem.*, 1997, vol. 36, no. 22, pp. 4919–4929.
10. Popova, E.O., Orlova, I.A., and Shagisultanova, G.A., *Koord. Khim.*, 2000, vol. 26, no. 10, pp. 733–737.
11. *Handbook of X-ray Photoelectron Spectroscopy*, Chastein, J., Ed., USA: Perkin–Elmer Corp., 1992.
12. Shen, H.Y., Liao, D.Z., Jiang, Z.H., *et al.*, *Chem. J. Chinese Univ.*, 1999, no. 7, pp. 1017–1020.
13. Doca, R., Elias, H., Haase, W., *et al.*, *Inorg. Chim. Acta*, 1998, vol. 278, no. 2, pp. 127–135.
14. Shagisultanova, G.A. and Ardasheva, L.P., *Zh. Neorg. Khim.*, 2001, vol. 46, no. 3, pp. 411–419.
15. Ardasheva, L.P. and Shagisultanova, G.A., *Zh. Prikl. Khim.*, 2001, vol. 74, no. 2, pp. 311–319.

Russian Journal of Applied Chemistry, Vol. 77, No. 12, 2004, pp. 1967–1972. Translated from Zhurnal Prikladnoi Khimii, Vol. 77, No. 12, 2004, pp. 1990–1995.

APPLIED ELECTROCHEMISTRY AND CORROSION PROTECTION OF METALS

Sorption Purification of a Halide Cobalt Electrolyte with Organic Reagents Immobilized on Activated Carbon

F. D. Manilevich, L. F. Kozin, A. K. Bogdanova, V. Ya. Demchenko, and A. L. Makovetskii

Vernadskii Institute of General and Inorganic Chemistry, National Academy of Sciences of the Ukraine, Kiev, Ukraine

Dumanskii Institute of Colloid Chemistry and Water Chemistry, National Academy of Sciences of the Ukraine, Kiev, Ukraine

Received May 22, 2003; in final form, June 2004

Abstract—Purification of ammonium-chloride-bromide cobalt-containing electrolyte to remove ions of impurity metals with an adsorbent containing complexing organic reagents immobilized on the surface of synthetic activated carbon was studied.

Purification of solutions of cobalt(II) salts to remove impurities is an important technological process in manufacture of metallic cobalt and its compounds. The value of both metallic cobalt and its compounds is the better, the higher their purity. Therefore, methods for purification of cobalt-containing solutions, from which the target products are obtained, are being continuously improved [1]. Impurities are removed from electrolytes used in electrochemical production of cobalt by various methods based on the difference between the physicochemical properties of cobalt(II) ions or their compounds and those of ions of accompanying impurities or their compounds (recrystallization and precipitation, hydrolytic and sulfide purification, cementation and preliminary electrolysis, extraction and ion exchange). These methods have a limited capacity as regards both the amount of impurities extracted and the possible degree of extraction. As a rule, deep purification to remove all impurities from the electrolyte requires a combination of several complementary techniques.

In electrochemical recovery of cobalt from solutions of its salts, presence of impurity metal ions discharging at cathodes simultaneously with cobalt ions [Cu(II), Fe(II), Ni(II), Cd(II), Zn(II), etc.] in the electrolyte is undesirable for the electrolysis process and purity of cobalt obtained. A promising method for purification of cobalt electrolytes to remove impurities of this kind is their extraction from solution by selective sorbents. This study is concerned with purification of a cobalt-containing chloride-bromide-ammonium electrolyte (0.5 M $CoCl_2 \cdot 6H_2O$ + 2.0 M NH_4Br, pH 4.8 ± 0.1) to remove ions of some impurity metals with the help of organic reagents immobilized on the surface of synthetic activated carbon. As reagents of this kind served sodium dithiocarbamate, 8-oxiquinoline, 1,10-phenanthroline, and Xylene Orange. As a support for these reagents was used SKNP-2 synthetic activated carbon.

The organic reagents used form with metal ions stable (as a rule) chelate complex compounds, which is indicated by their high stability constants [2, 3]. According to published data on the stability constants of chelate complexes and to the stability series of complex compounds formed by doubly charged cations of transition metals with chelate-forming organic reagents (Irving–Williams series), the most stable complexes are formed by copper(II) ions: Mn(II) < Fe(II) < Co(II) < Ni(II) < Cu(II) > Zn(II) [4]. Consequently, it would be expected that a cobalt-containing electrolyte can be selectively and deeply purified with these reagents to remove Cu(II) even at a high background concentration of Co(II) cations.

However, the complexation involving chelate-forming organic reagents strongly depends on the solution pH, because reagents of this kind are weak acids or weak bases. Cu(II) ions form intracomplex compounds with sodium diethyldithiocarbamate at pH 4–11 [5, 6], 8-oxiquinoline at pH 5.33–14.55, and Xylene Orange

1070-4272/04/7712-1967 © 2004 MAIK "Nauka/Interperiodica"

at pH 5.4–5.8 [7]. Consequently, a weakly acidic cobalt-containing electrolyte can, indeed, be thoroughly purified to remove C(II) ions with the help of the organic reagents mentioned above. It is important that complexes of Co(II) cations with, e.g., sodium diethyldithiocarbamate and 8-oxiquinoline are formed at pH > 7 [8], and, therefore, Co(II) cations must not hinder the complexation of impurity metal cations with these reagents. As a result, it becomes possible to recover from a cobalt-containing electrolyte not only Cu(II) ions, but also ions of other impurity metals. For example, Zn(II) ions form a chelate complex with 8-oxiquinoline even at pH > 4 [4, 8, 9], and, for precipitation of Cd(II) ions with 8-oxiquinoline, it is recommended to acidify the solution with acetic acid (0.5% CH_3COOH) [10]. The complexation of 1,10-phenanthroline and Xylene Orange with cations of many impurity metals also occurs in the weakly acidic medium [4, 6, 9, 10].

The simultaneous use of several reagents makes it possible to recover a wider variety of impurity metals from electrolytes and creates prerequisites for occurrence of a synergetic effect in the process because of the mutual influence of the reagents. Apparently, organic reagents of this kind, immobilized on activated carbon, can be used to recover metal ions forming with the reagents both sparingly soluble and soluble, but little-dissociating compounds from solutions.

EXPERIMENTAL

SKN activated carbons [TU VV (Technical Specification) of the Ukrainian Soviet Socialist Republic 211.003.009–85] are spherical carbonates produced by carbonization of nitrogen-containing polymeric resins with the subsequent activation in a water vapor or in CO_2. These carbons have a high chemical resistance, mechanical strength, and adsorption capacity for a number of organic molecules of various sizes [11]. The immobilization of organic reagents on the surface of the SKNP-2 activated carbon consisted in adsorption of the reagents by the carbon from their saturated solutions. For this purpose, saturated solutions of the reagents in the following solvents were preliminarily prepared: water for sodium diethyldithiocarbamate; ethanol for 8-oxiquinoline; a 2 : 1.5 : 1 (by volume) mixture of $CHCl_3$, C_2H_5OH, and H_2O for 1,10-phenanthroline; and a 4 : 1 (by volume) mixture of H_2O and C_2H_5OH for Xylene Orange. The procedure used to prepare the carbon and to immobilize organic reagents on its surface has been described in detail previously [12]. Prior to sorption purification of a cobalt-containing electrolyte to remove impurities, modified activated carbons were mixed in such a way that the content of each organic reagent in the mixture was 2 wt %. The resulting mixture of carbons can be regarded as a modified carbon adsorbent with a variety adsorption centers.

The electrolyte was prepared using analytically pure $CoCl_2 \cdot 6H_2O$, chemically pure NH_4Br, and water twice distilled in a quartz apparatus. Solutions with a single impurity contained a $CuCl_2$ additive in amounts ranging from 1 to 55 mM. In multiple-impurity solutions, the following concentration of impurity cations were created (mM): Mn(II) 0.29, Cu(II) 0.3, Zn(II), 0.48, and Cd(II) 0.33. A weighed portion of a mixture of carbons and a certain volume of a solution to be purified were placed in a thermostated cell with a stirrer (180 rpm) and the purification was performed under static conditions. When studying the sorption kinetics, identical fresh portions of the solution being purified and the sorbent were used in each run. The content of impurities in untreated solutions and those after sorption purification was determined by means of atomic-adsorption analysis. The solution pH was measured with an EV-74 pH-meter.

The analytical data obtained were used to calculate the following sorption parameters: coefficient of sorption purification, η_{sr} (%); distribution coefficient of impurities, K_d; and adsorption by Gibbs, Γ:

$$\eta_{sr} = \frac{c_{in} - c_{eq}}{c_{in}} \times 100, \quad (1)$$

$$K_d = \frac{(c_{in} - c_\tau)V}{c_\tau m}, \quad (2)$$

$$\Gamma = \frac{(c_{in} - c_{eq})V}{m}, \quad (3)$$

where c_{in} and c_{eq} are the initial and equilibrium concentrations of impurity metal ions in solution (mM); c_τ, concentration of an impurity metal ion in solution at an instant of time τ (mM); V, solution volume (ml or l); and m, weighed portion of the adsorbent (g).

The adsorption by Gibbs [13] is equal to the excess of a component being sorbed (mol) in a certain solution volume near the adsorbent surface over that in the equal solution volume at a sufficient distance from the adsorbent surface.

To determine the optimal ratio between the weighed portion of the adsorbent and the volume of the solution to be purified, the dependence of the coefficient of sorption purification of a cobalt-containing electrolyte in the presence of 10 mM of Cu(II) on the V/m ratio was analyzed. The duration of purification under

static conditions at 298 K was 30 min. Figure 1 shows the η_{sr}–V/m dependence obtained in purification of the electrolyte to remove Cu(II) ions. It can be seen that the coefficient of sorption purification exceeds 95% at V/m less than 12.5 ml g^{-1}. Further experiments were performed at $V/m \leq 10$ ml g^{-1}.

To study the kinetic features of adsorption of impurity metals from a cobalt-containing electrolyte on the sorbent prepared, the dependences of the impurity concentrations in solution on the adsorption time τ were determined. This made it possible to calculate the impurity distribution coefficients at different instants of time. Figure 2 shows how the distribution coefficients of the ions Cu(II), Zn(II), Cd(II), and Mn(II) depend on the time of adsorption.

The initial concentrations of the four controlled impurities in the electrolyte solution are given above. The solution temperature was 298 K. The ratio between the volume of the electrolyte and the amount of the adsorbent was 3 ml g^{-1}. It can be seen from Fig. 2 that the distribution coefficients of Cu(II), Zn(II), and Cd(II) ions rapidly increase during the first 10–20 min of purification and then become constant (292, 129, and 50 ml g^{-1}, respectively). The content of Mn(II) in the electrolyte does not change significantly during 100 min of purification. This is, apparently, due to the fact that chelate complexes with Mn(II) are commonly formed at pH values exceeding that of the electrolyte being purified. For example, Mn(II) ions form complexes with sodium diethyldithiocarbamate at pH 6–8 [4–6] and with 8-oxiquinoline at pH 7.2–12.5 [14]. Making the pH values of the electrolyte higher will lead to hydrolysis of Co(II) ions and precipitation of basic salts of cobalt and Co(II) hydroxide [3]. Therefore, extraction of Mn(II) ions from a cobalt-containing electrolyte requires that other reagents, selective toward MN(II) ions in this electrolyte, should be used. These results indicate that the modified carbon adsorbent developed can be successfully used to purify solutions of Mn(II) salts to remove impurity metals. In the electrolyte under study, Mn(II) is not an interfering impurity because the standard electrode potential of manganese ($E^0_{Mn^{2+}/Mn^0} = -1.18$ V) is considerably more negative than the standard electrode potential of cobalt ($E^0_{Co^{2+}/Co^0} = -0.277$ V) [15].

The limiting values of the impurity distribution coefficients, which are reached upon a prolonged sorption purification of a cobalt-containing electrolyte and are equilibrium values, are in an agreement with the Irving–Williams series and with published data on the stability constants of chelate complexes with metal ions. The largest distribution coefficients were ob-

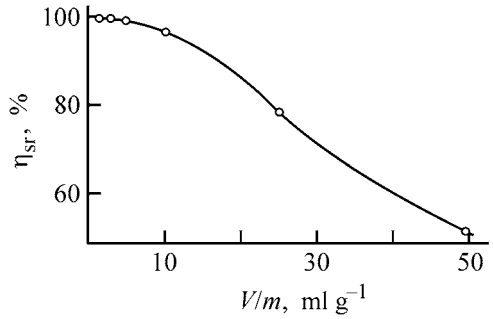

Fig. 1. Coefficient of sorption purification of a cobalt-containing electrolyte with a single impurity to remove Cu(II) ions, η_{sr}, vs. the ratio of the volume of the solution being purified to the sorbent mass, V/m. c_{in} = 10 mM, T = 298 K, τ = 30 min.

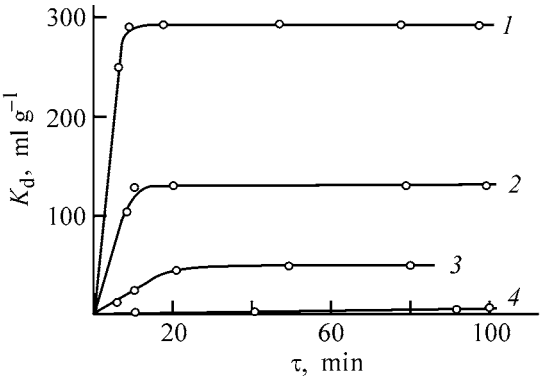

Fig. 2. Distribution coefficients K_d of (*1*) Cu(II), (*2*) Zn(II), (*3*) Cd(II), and (*4*) Mn(II) ions vs. the adsorption time τ in purification of a cobalt-containing electrolyte. T = 298 K, V/m = 3 ml g^{-1}.

tained in extraction of Cu(II) ions. These results can be regarded as a confirmation that it is chemical reactions of complexation of metal ions with organic reagents immobilized on the surface of activated carbon that are responsible for the binding of impurity metal ions with the sorbent developed.

A dependence similar to that in Fig. 2 was also obtained in purification of a cobalt-containing electrolyte solution with an initial concentration of Cu(II) ions equal to 10.3 mM. The equilibrium distribution coefficient for Cu(II) in purification of such a solution was 2027 ml g^{-1}, and 20 min were required to reach this value.

Figure 3 shows the experimental dependence of the concentration of Cu(II) ions in an electrolyte solution on the adsorption time, and also the dependence of $\ln c_\tau$ on τ. It can be seen that, in the initial stage of sorption purification of the solution to remove Cu(II) ions, their concentration in solution rapidly decreases; however, at an adsorption time exceeding 4 min, this

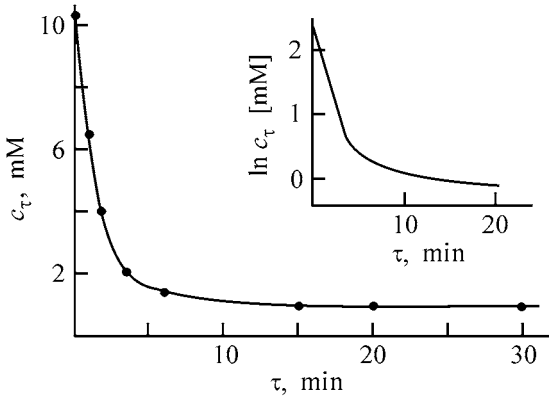

Fig. 3. Concentration c_τ of Cu(II) ions in a cobalt-containing electrolyte with a single impurity vs. the adsorption time τ. c_{in} = 10.3 mM, T = 298 K, V/m = 10 ml g^{-1}.

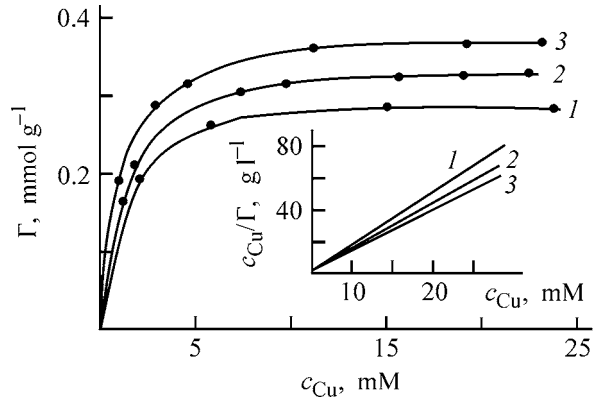

Fig. 4. Isotherms of Cu(II) adsorption Γ from a cobalt-containing electrolyte with a single impurity and the dependence of c_{Cu}/Γ on c_{Cu}. c_{in} = 1–55 mM, V/m = 10 ml g^{-1}. Adsorption temperature (K): (*1*) 283, (*2*) 298, and (*3*) 313.

decrease slows down and a constant value of c_τ is reached at τ > 20 min. As noted above, the adsorption of impurity metals on the adsorbent developed is based on reactions of their complexation. It is reasonable to conclude that it is these reactions that determine the rate of the purification process. At τ ≥ 4 min, the solution is depleted of Cu(II) ions, on the one hand, and the surface concentration of organic reagents on activated carbon decreases, on the other. As a result, there appears a transport hindrance associated with the deceleration of the delivery of Cu(II) ions to free active centers of the adsorbent. At τ > 20 min, the adsorbent is saturated with Cu(II) ions.

The initial portion (τ < 4 min) of the kinetic curve plotted in the ln c_τ–τ coordinates is linear (Fig. 3), and, consequently, this portion of the curve is described by a kinetic equation of a first-order chemical reaction [16]

$$\ln c_\tau = \ln c_{in} - k\tau, \quad (4)$$

where k is the rate constant.

The rate constant was found graphically as the slope ratio of the initial linear part of the dependence of lnc_τ on τ, and also was calculated using the equation

$$k = \frac{2.303}{\tau} \log \frac{c_{in}}{c_\tau}. \quad (5)$$

The calculation was done using the concentrations of Cu(II) ions in solution 1, 2, and 3.5 min after the beginning of adsorption. The resulting average calculated rate constant coincided with its graphically found value (0.46 min^{-1}), which points to a high rate of adsorption of Cu(II) ions in the initial stage of purification of a halide cobalt-containing electrolyte to remove these ions.

To obtain thermodynamic data on adsorption of Cu(II) ions from a cobalt-containing electrolyte on the adsorbent developed, the Gibbs adsorption of Cu(II) from the electrolyte under equilibrium conditions at 283, 298, and 313 K was determined. The initial concentrations of Cu(II) ions were in the range 1–55 mM, the V/m ratio was equal to 10 ml g^{-1}. The resulting values of adsorption were plotted against the equilibrium concentrations of Cu(II) ions in the electrolyte to give adsorption isotherms at the above temperatures (Fig. 4). These isotherms have a shape of type-I isotherms according to the classification of adsorption isotherms by Brunauer [17]. Isotherms of this kind can be described using the Langmuir equation. To make certain that this is the case, the isotherms were linearized in accordance with the Langmuir equation transformed to

$$\frac{c_{Cu}}{\Gamma} = \frac{1}{b\Gamma_m} + \frac{1}{\Gamma_m} c_{Cu},$$

where c_{Cu} is the equilibrium concentration of Cu(II) ions in solution; Γ_m, limiting adsorption; and b, adsorption coefficient.

The resulting plots of c_{Cu}/Γ against c_{Cu} are shown in the inset in Fig. 4. It can be seen that these dependences are linear and, consequently, the isotherms of Cu(II) adsorption can be described using the Langmuir equation. Below are given values of Γ_m, calculated from the slope ratios of the dependences of c_{Cu}/Γ on c_{Cu}, and values of the coefficient b, calculated from the intercept on the ordinate axis at a known Γ_m:

T, K	Γ_m, mM	b, mM^{-1}
283	0.300	0.667
298	0.325	1.538
313	0.387	1.290

As can be seen from Fig. 4 and from the data presented above, the adsorption of Cu(II) ions grows as temperature increases, which indicates that the adsorption process has a chemical nature. The adsorption isotherms obtained at several temperatures of the electrolyte make it possible to determine the isosteric heat of adsorption [13, 18] of Cu(II) ions, q_{st}:

$$q_{st} = RT^2(\partial \ln c_{Cu}/\partial T)_\Gamma, \quad (7)$$

where R is the universal gas constant, and T is the absolute temperature.

Because the temperature dependence of q_{st} can be disregarded in the case of a narrow temperature interval, the result of integration of Eq. (7) can be represented as

$$\ln c_{Cu} = \frac{q_{st}}{TR} + B, \quad (8)$$

where B is a constant.

It can be seen from Eq. (8) that the slope ratio $\tan\alpha$ of the dependence of $\ln c_{Cu}$ on $1/T$ is $-q_{st}/R$. Therefore, with $\tan\alpha$ determined, the isosteric heat of adsorption can be calculated by the equation

$$q_{st} = -R\tan\alpha. \quad (9)$$

Using the adsorption isotherms shown in Fig. 4, isosters of Cu(II) adsorption on the adsorbent developed were plotted for several values of adsorption (Fig. 5). These isosters are linear and their slope grows from 2100 to 3600 as the adsorption increases from 0.1 to 0.275 mmol g^{-1}. On substituting the values of $\tan\alpha$ in Eq. (8), the isosteric heats of adsorption of Cu(II) ions were calculated at the chosen amounts of adsorption. Figure 6 shows the resulting dependence of q_{st} on Γ. It can be seen that q_{st} varies from –17.459 kJ mol^{-1} at Γ = 0.1 mmol g^{-1} to –29.93 kJ mol^{-1} at Γ = 0.275 mmol g^{-1}, which indicates that the adsorption of Cu(II) ions occurs with an exothermic effect, which is the larger, the higher the amount of adsorption.

Thus, use of a carbon adsorbent modified with the organic reagents studied makes it possible to purify a cobalt-containing electrolyte to remove Cu(II), Zn(II), and Cd(II) ions. This adsorbent can also be successfully used to purify manganese-containing

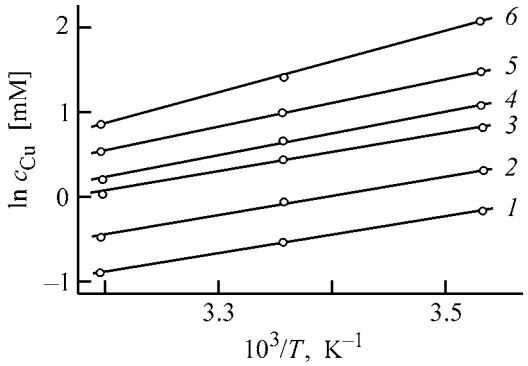

Fig. 5. Isosters of Cu(II) adsorption at different values of their adsorption by Gibbs. (c_{Cu}) Concentration of Cu(II) and (T) temperature. Amount of adsorption (mmol g^{-1}): (*1*) 0.100, (*2*) 0.150, (*3*) 0.200, (*4*) 0.225, (*5*) 0.250, and (*6*) 0.275.

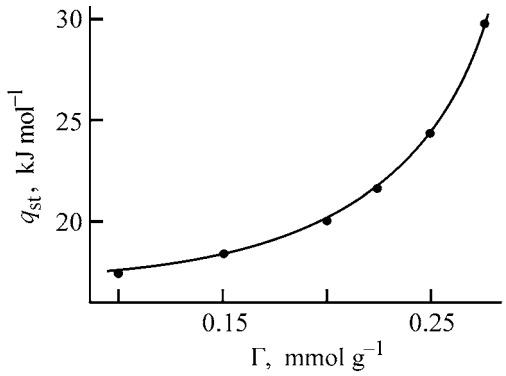

Fig. 6. Isosteric heat q_{st} of adsorption of Cu(II) ions vs. amount of adsorption by Gibbs, Γ.

solutions to remove impurity metal ions. The results obtained indicate that an adequate choice of reagents can yield selective sorbents for extraction of interfering impurities from electrolyte solutions used to obtain high-purity metals or their compounds.

CONCLUSIONS

(1) Extraction of impurity metals from a cobalt-containing electrolyte with complex-forming organic reagents immobilized on the surface of a synthetic activated carbon is a promising method for purification of electrolytes to remove ions of this kind.

(2) Adsorption of Cu(II) ions on a carbon sorbent modified with sodium diethyldithiocarbamate, 8-oxiquinoline, 1,10-phenanthroline, and Xylene Orange is a chemisorption process whose initial rate is described by the kinetic equation of a chemical reaction of first order with respect to these ions.

(3) The isosteric heat of Cu(II) adsorption is negative, and its magnitude is the higher, the larger the amount of adsorption, which indicates that the adsorption process is exothermic.

REFERENCES

1. Borbat, V.F., Volkov, V.I., and Kazanskii, L.A., *Proizvodstvo kobal'ta iz sul'fidnykh rud* (Manufacture of Cobalt from Sulfide Ores), Moscow: Metallurgiya, 1983.
2. Inczedi, J., *Analytical Application of Complex Equilibria*, Tyson, J., Transl. Ed., Budapest: Academia Kiado, Coll House: Ellis Horwood, 1976.
3. Lur'e, Yu.Yu., *Spravochnik po analiticheskoi khimii* (Handbook of Analytical Chemistry), Moscow: Khimiya, 1979.
4. Umland, F., Janssen, A., Thierig, D., und Wunsch, G., *Theorie und praktische Anwendung von Komplexbildnern*, Frankfurt am Main: Akademische Verlagsgesellschaft, 1971.
5. Byrko, V.M., *Ditiokarbamaty* (Dithiocarbamates), Moscow: Nauka, 1984.
6. Lazarev, A.I., *Organicheskie reagenty v analize metallov* (Organic Reagents in Analyses for Metals), Moscow: Metallurgiya, 1980.
7. Podchainova, V.N. and Simonova, L.N., *Med'* (Copper), Moscow: Nauka, 1990.
8. Holzbecher, Z., Divis, L., Kral, M., Sucha, L., and Vlacil, F., *Organicka cinidla v anorganicke analyze*, Praha: SNTL-Nakladatelstvi Technicke Literatury, 1975.
9. Zhivopistsev, V.P. and Selezneva, E.A., *Analiticheskaya khimiya tsinka* (Analytical Chemistry of Zinc), Moscow: Nauka, 1975.
10. Shcherbov, D.P. and Matveets, M.A., *Analiticheskaya khimiya kadmiya* (Analytical Chemistry of Cadmium), Moscow: Nauka, 1973.
11. Nikolaev, V.G. and Strelko, V.V., *Gemosorbtsiya na aktivirovannykh uglyakh* (Chemisorption on Activated Carbons), Kiev: Naukova Dumka, 1979.
12. Kozin, L.F., Mashkova, N.V., and Manilevich, F.D., *Zh. Prikl. Khim.*, 2000, vol. 73, no. 7, pp. 1098–1102.
13. *Eksperimental'nye metody v adsorbtsii i molekulyarnoi khromatografii* (Experimental Methods in Adsorption and Molecular Chromatography), Nikitin, Yu.S. and Petrova, R.S., Eds., Moscow: Mos. Gos. Univ., 1990.
14. Lavrukhina, A.K. and Yukina, L.V., *Analiticheskaya khimiya margantsa* (Analytical Chemistry of Manganese), Moscow: Nauka, 1974.
15. *Spravochnik po elektrokhimii* (Handbook of Electrochemistry), Sukhotin, A.M., Ed., Leningrad: Khimiya, 1981.
16. Perez-Bendito, D. and Silva, M., *Kinetic Methods in Analytical Chemistry*, Chichester: Ellis Horwood, 1988.
17. Von Kinle, H. und Bader, E., *Aktivkohle und ihre industrielle Anwendung*, Stutgart: Enke 1980.
18. Poltorak, O.M., *Termodinamika v fizicheskoi khimii* (Thermodynamics in Physical Chemistry), Moscow: Vysshaya Shkola, 1991.

Russian Journal of Applied Chemistry, Vol. 77, No. 12, 2004, pp. 1973–1978. Translated from Zhurnal Prikladnoi Khimii, Vol. 77, No. 12, 2004, pp. 1996–2002.

CATALYSIS

Influence of Silicate Ratio and High-Temperature Steam Treatment of Pentasil on Its Acid and Catalytic Properties in Conjugate Conversion of Lower Alkanes and Methanol

V. I. Erofeev, L. B. Shabalina, L. M. Koval', and T. S. Minakova

Department of Scientific and Technical Development, Tomskneftekhim Ltd., Tomsk, Russia
Tomsk State University, Tomsk, Russia

Received February 9, 2004

Abstract—The influence of aluminum content in the zeolite matrix of Pentasil on its acid and catalytic properties in conjugate conversion of lower alkanes and methanol was studied.

Studies of the conversion of lower alkanes and methanol on Pentasils into olefins and aromatic hydrocarbons have shown that their activity and selectivity are primarily determined by the structure of zeolite skeletons and the reaction conditions [1, 2]. The conjugate conversion of lower alkanes and methanol on Pentasil-containing catalysts allows the reaction to be performed under conditions of thermal neutrality and at lower temperatures owing to the formation of highly reactive intermediates from methanol, which initiate conversion of lower C_2–C_4 alkanes into C_2–C_4 alkenes, isoalkenes, and aromatic hydrocarbons [3–5]. The content of aluminum in the zeolite skeleton can be changed in the stage of the zeolite synthesis [6] or by thermal modification (high-temperature treatment of zeolite with air or steam) [7]. However, as applied to the above process, this possibility has virtually not been examined at all.

In this study, we examined the influence of the aluminum content in the matrix of the zeolite on its acid and catalytic properties in conjugate conversion of lower alkanes and methanol into hydrocarbons.

EXPERIMENTAL

High-silica zeolites (HSZ) with silica ratios (SiO_2/Al_2O_3) of 30, 50, 70, and 90 (HSZ-30, -50, -70, -90) were synthesized from alkaline aluminosilica gels, using an organic template by the method described in [6]. The Na-form of HSZ was transformed into the H-HSZ form by decationization with a 25% solution of ammonium chloride at 90°C for 2 h. Then the zeolite in the NH_4^+ form was dried at 110°C and calcined for 6 h at 600°C. The residual content of Na_2O in all the samples did not exceed 0.05 wt %, and that in the zeolite subjected to high-temperature steam treatment, 0.18 wt %. In accordance with data of X-ray diffraction analysis (Mo anode, Ni filter) and IR spectroscopy, the HSZs obtained were zeolites of the ZSM-5 type [8]. The degree of crystallinity of HSZ, found from the ratio of intensities of the absorption bands at 550 to 460 cm^{-1}, assigned to bending vibrations of SiO_4 and AlO_4 tetrahedrons, was no less than 90%.

The high-temperature steam treatment (HTST) of an HHSZ-30 sample was performed in a quartz reactor at 600°C in a flow of 100 wt % steam (space velocity of water supply 2 h^{-1}) for 4, 8, and 12 h (HHSZ-30-4, HHSZ-30-8, HHSZ-30-12). The Al fraction eliminated from the zeolite with steam into the steam condensate during HTST was determined colorimetrically on a KFK type photoelectrical colorimeter by the standard procedure. The acid properties of HSZ were studied by the thermal desorption of ammonia. HSZ samples (0.7 g) were charged into a quartz reactor and heated in a He flow (130 $cm^3\ min^{-1}$) at 600°C to eliminate volatile impurities from the sample surface. Then the reactor was cooled to 100°C, and NH_3 was sorbed to saturation of HSZ, with the subsequent removal of free ammonia. The thermal desorption of ammonia from HSZ was performed in a helium flow (130 $cm^3\ min^{-1}$) at a linear heating rate of 10 deg min^{-1}.

The conjugate conversion of lower alkanes and methanol in a flow unit consisting of a quartz reactor with a fixed catalyst bed (3 cm^3) was studied under the atmospheric pressure within the 500–650°C range.

1070-4272/04/7712-1973 © 2004 MAIK "Nauka/Interperiodica"

Table 1. Acid characteristics of HSZ with various silicate ratios

Catalyst	T_{max}, °C		Amount of acid centers, mmol g^{-1}			Fraction of strongly acidic centers, %
	form (I)	form (II)	form (I)	form (II)	sum	
HHSZ-30	208	411	0.683	0.532	1.215	44
HHSZ-50	208	420	0.585	0.529	1.114	47
HHSZ-70	206	415	0.439	0.445	0.885	50
HHSZ-90	203	391	0.353	0.363	0.716	51

The space velocity of methanol supply was 2 h^{-1}, and that of propane–butane fraction (PBF) with the composition (wt %): ethane 0.9, propane 58.3, isobutene 5.5, and *n*-butane 35.3, 200 h^{-1}. Under these temperature conditions, methanol is completely converted on HSZ into hydrocarbons, water, CO, and H_2. The PBF and reaction products were analyzed gas-chromatographically. Before studying the acid and catalytic properties, all the HSZ samples were activated in an air flow at 560°C for 2 h. The error of gas-chromatographic determination of the composition of PBF, products of PBF and methanol conversion, and the concentration of acid centers in the catalysts was 2.5%.

The TG and TGA curves of coked HSZ samples were recorded on an MOM-1500 (Hungary) derivatograph in a porcelain crucible in air within the 25–750°C range at a heating rate of 10 deg min^{-1}.

Influence of silicate module. A study of acid properties of HSZ with various silicate modules by the method of thermal desorption (TD) of ammonia showed that the TD spectra of all the samples contain mainly two peaks of NH_3 desorption. The low-temperature peak at 300°C is caused by ammonia desorption from weakly acidic centers (form I), which are mainly triple-coordinated aluminum atoms and residual sodium cations. The high-temperature NH_3 peak at temperatures above 300°C is caused by ammonia desorption from strongly acidic HSZ centers, including strong Broensted (B) and Lewis (L)-centers (form II) [9].

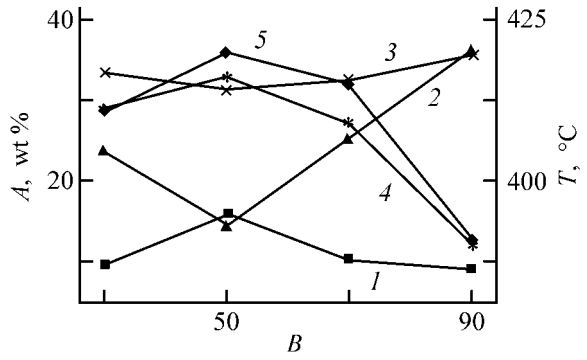

Fig. 1. Yield of products *A* of PBF and methanol conjugate conversion vs. silicate ratio *B*. (*T*) Temperature. (*1*) Methane, (*2*) Propane and butanes, (*3*) C_2–C_4 alkenes; and (*4*) arenes; (*5*) T_{max} of peaks of form II in the TD spectra.

Analysis of the concentration distribution of acid centers (Table 1) shows that, as the SiO_2/Al_2O_3 ratio in the zeolite is increased from 30 to 90, both the total acidity of the zeolites and the concentration of the acid centers corresponding to forms I and II of adsorbed ammonia decrease. This trend in the variation of the concentrations of the acid centers is caused by an increase in the content of the skeleton Al responsible for the formation of zeolite acid centers [8, 9]. All the zeolites synthesized, irrespective of the silicate ratio, are strongly acidic, because they contain a high fraction of strongly acidic centers; with increasing silicate ratio, this fraction also grows (Table 1).

The strength of the acid centers can also be estimated from the T_{max} values in the TD spectrum. T_{max} of the low-temperature peak of form I of NH_3 desorption shifts to lower temperatures with increasing HSZ silicate ratio, which indicates a decrease in the strength of the weakly acidic centers. HSZ with a silicate ratio of 50 has the highest strength of strongly acidic centers corresponding to form II of ammonia desorption (T_{max} = 420°C).

The results of the study of the HSZ activity in the conjugate conversion of PBF and methanol (600°C, space velocity of methanol supply 2 h^{-1}, and that of PBF supply, 200 h^{-1}) are shown in Fig. 1. It can be seen that the residual content of propane and butane in the reaction mixture passes through a minimum as the silicate ratio increases, i.e., changes in the opposite direction with respect to the strength of the acid centers of form II. A sample with SiO_2/Al_2O_3 = 50, which has strongest acid centers, is the most active among the zeolites studied in the propane and butane conversion. As the silicate ratio increase from 30 to 50, the yield of C_2–C_4 alkenes decreases from 33.4 to 31.3,

Table 2. Influence of high-temperature steam treatment on HSZ acid characteristics

Catalyst	T_{max}, °C		Content of acid centers, mmol g^{-1}			Fraction of strongly acidic centers, %
	form (I)	form (II)	form (I)	form (II)	sum	
HHSZ-30	194	367	0.841	0.325	1.166	28
HHSZ-30-4	174	338	0.369	0.128	0.496	26
HHSZ-30-8	174	333	0.364	0.136	0.499	27
HHSZ-30-12	169	300	0.236	0.109	0.345	32

and then increases from 31.3 to 35.7% at the silicate ratio increases from 50 to 90. The highest yield of lower alkenes is observed on a zeolite with SiO_2/Al_2O_3 = 90. The yield of arenes and methane varies in parallel with the strength of the strongly acidic centers (form II of ammonia desorption) and passes through a maximum for the sample a with silicate ratio of 50.

It should be noted that the influence of the silicate ratio on the yield of reaction products increases with temperature. The dependences of the yield of the main products of the conjugate process on the silicate ratio at the lowest and highest temperatures in the range examined are shown in Fig. 2. The yield of C_2–C_4 alkenes, C_3–C_4 alkanes, and arenes at 500°C on HSZs with a silicate ratio of 30, 50, and 70 changes insignificantly with increasing SiO_2/Al_2O_3. Raising the reaction temperature to 650°C favors activation of cracking reaction and hydrogen redistribution first of all for the HSZ sample with a silicate ratio of 50 containing the strongest acid centers, i.e., the rise in temperature activates just these centers.

A comparison of the acid characteristics of zeolites with their catalytic properties showed that the HSZ activity and selectivity (especially with respect to formation of aromatic hydrocarbons) in the conjugate process are largely governed by the strength of the acid centers, rather than by their concentration. On the whole, we can conclude that a decrease in the Al concentration in the zeolite skeleton in the stage of HSZ synthesis decreases the activity of the zeolite catalysts in the cracking and hydrogen redistribution reactions.

Influence of HSZ thermal-vapor treatment. The effect of thermal-vapor treatment (TVT) of HSZ is of interest as regards the possibility of controlling the Al content in the zeolite matrix (and thereby varying the zeolite acidity) and the change in the catalyst selectivity in conversion of hydrocarbon and methanol under the action of water formed in the reaction [10]. Determination of the content of aluminum transferred into the condensate during HTST under the above conditions showed that virtually the whole amount of Al remains in the zeolite. Only an insignificant, virtually the same for all the samples, part of Al (amounting to no more than 0.03 wt % Al in the HSZ sample studied) is carried away by steam.

Data on the acid properties of steam-treated HHSZ-30 zeolite are shown in Table 2 and Fig. 3. The TD spectra of ammonia (Fig. 3) for all HSZ samples con-

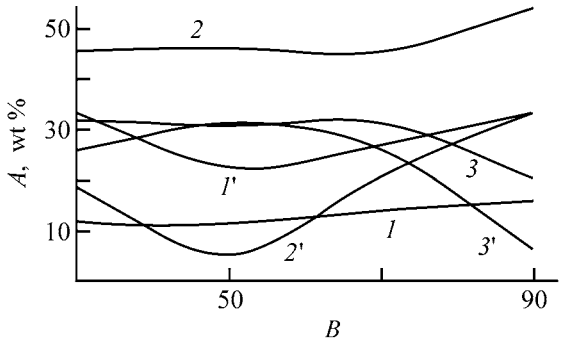

Fig. 2. Yield *A* of products of conjugate conversion vs. silicate ratio *B* at various temperatures: (*1*, *1*') C_2–C_4 alkenes, (*2*, *2*') propane and butanes, and (*3*, *3*') arenes. Temperature (°C): (*1*–*3*) 500 and (*1*'–*3*') 650.

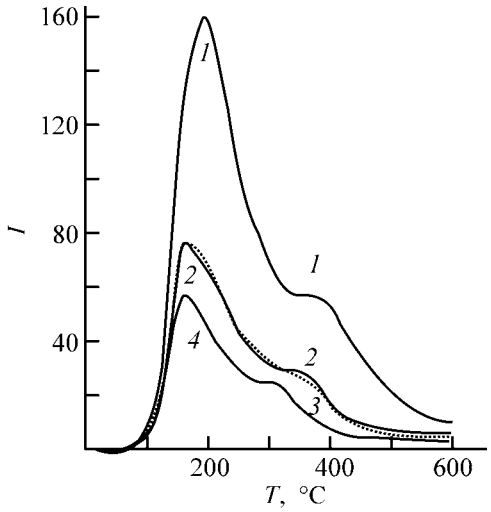

Fig. 3. TD spectra of ammonia from HSZ samples subjected to HTST. (*I*) Intensity and (*T*) temperature. (*1*) HHSZ-30, (*2*) HHSZ-30-4, (*3*) HHSZ-30-8, and (*4*) HHSZ-30-12.

Table 3. Effect of temperature and HTST on the yield of hydrocarbons in the conjugate conversion of methanol and PBF

Reaction product	HHSZ-30				HHSZ-30-4				HHSZ-30-8				HHSZ-30-12			
	temperature, °C															
	500	550	600	650	500	550	600	650	500	550	600	650	500	550	600	650
Gases:																
ΣH_2, CO	0.6	1.2	2.5	4.0	0.3	0.4	1.3	5.7	0.2	0.4	1.0	4.6	0.2	0.3	0.7	3.9
methane	5.0	7.6	11.6	15.8	1.9	3.4	7.6	14.9	1.9	3.2	6.0	13.5	1.2	2.2	4.8	12.1
ethane	1.7	1.4	1.3	1.0	0.6	0.6	0.9	0.9	0.6	0.7	0.8	0.9	0.4	0.6	0.8	1.0
propane	27.8	20.5	19.0	17.3	22.1	19.3	18.7	17.2	24.2	22.4	21.2	18.9	20.4	20.8	19.6	17.0
butanes	15.3	10.0	8.3	7.4	14.5	15.2	9.1	6.8	16.2	12.6	10.3	8.3	14.4	11.6	10.0	7.3
ethylene	4.9	13.9	13.1	11.4	8.4	11.1	14.5	11.6	8.3	11.4	13.2	10.9	8.8	12.8	15.3	13.7
propylene	6.1	9.7	12.3	11.2	11.1	13.6	17.2	13.8	11.7	15.6	17.8	14.3	13.3	18.9	22.2	17.3
butenes	4.8	5.0	4.2	3.0	8.5	7.5	6.5	3.7	8.8	9.1	7.1	4.2	9.5	9.9	8.5	4.9
Liquid products:																
alkanes C_{5+}	1.4	0.8	0.5	0.8	4.1	2.2	0.8	0.3	4.1	2.8	1.2	0.5	5.4	2.7	1.2	0.4
alkenes C_{5+}	0.9	1.1	0.8	0.7	3.0	2.5	1.4	0.5	2.9	2.9	1.8	0.8	3.6	2.8	1.9	0.6
cyclic C_{5+}	0.1	0.1	Traces		0.5	0.2	0.1	Traces	0.5	0.3	0.1	Traces	0.7	0.3	0.1	0.1
benzene	2.3	2.0	2.0	2.1	1.4	1.9	2.1	2.8	1.0	1.5	1.7	2.2	1.2	1.5	1.7	3.1
toluene	9.0	8.8	9.2	10.9	6.9	7.5	9.1	12.2	6.2	6.5	7.7	10.2	5.2	5.4	6.2	9.9
xylenes	14.6	13.5	12.1	12.7	12.3	11.7	8.9	8.5	8.9	7.8	8.3	9.6	11.1	7.9	6.0	7.3
arenes C_{9+}	5.2	4.2	2.9	1.6	4.4	2.8	1.5	1.0	4.4	2.7	1.7	1.0	4.5	2.3	1.0	1.4
naphthalenes	0.3	0.2	0.2	0.1	0.1	0.1	0.1	0.1	0.1	0.1	0.1	0.1	0.1	Traces		

tain two poorly resoved peaks because of the rather high residual content of sodium in the initial zeolite (0.18 wt %). The shape of the spectrum remains unchanged on going to more severe conditions of HSZ steam treatment. Hence, HTST does not affect the exchanging sodium cations in HSZ [11].

The temperatures T_{max} of ammonia desorption peaks and calculated amounts of acid centers of both forms are listed in Table 2. Their strength, qualitatively characterized by T_{max}, decreases during HTST. The longer the HTST time, the stronger the shift of T_{max} to lower temperatures and hence the higher the strength of acid centers. Our results also show that HTST of HSZ for 4 h sharply decreases the total amount of acid centers and the concentration of acid centers of both types. An increase in the time of HTST of HSZ gradually decreases the concentration of weakly acidic centers. However, after a 8-h steam treatment of HSZ, the concentration of strongly acid centers and the total acidity slightly increase as compared to the concentration of strongly acidic centers after a 4-h HTST. It is known [8] that HTST of HSZ first of all eliminates nonskeleton Al from the cationic sites and transfers it into the Al_2O_3 phase. Under definite conditions, HTST of HSZ can form centers with enhanced activity (EAC), including bridging OH groups and Al atoms whose bonds with the crystal lattice of the zeolite are partially (or completely) decomposed under HTST [11]. Probably, in our case, treatment of HSZ (HHSZ-30-8 sample) with steam for 8 h, similar strong centers leads to additional formation of and, as a result, their concentration somewhat increases.

The steam treatment at a higher temperature and for a longer time results in a further decrease in the zeolite acidity due to dealumination of the zeolite skeleton [13]. Indeed, an increase in the HTST duration to 12 h decreases the amount of strongly and weakly acidic centers and weakens their strength. The change in HSZ acid properties under HTST at a high temperature should change the zeolite activity and selectivity in the process studied. Data on the catalytic properties of the initial HHSZ-30 zeolite and its steam-treated samples are listed in Table 3.

As seen, the yield of products of the conjugate PBF conversion on HHSZ-30 and on HHSZ-30 after HTST correlates with the acid properties of the catalyst. Already with an HHSZ-30-4 sample, the yield of olefins sharply increases, and the yield of arenes and naphthalenes decreases within the entire temperature interval. The content of propane and butane (initial

Table 4. Derivatographic analysis of coked HSZ samples

Parameter	HHSZ-30	HHSZ-30-4	HHSZ-30-8	HHSZ-30-12
T_{min} (endotherms) in DTA curve, °C	100	80	80	–
T_{max} (exotherms) in DTA curve, °C	630	630	650	620
T_{max} in DTG curve, °C	170, 660–670	100–180, 620–660	100–200, 650	90–200, 630
Weight loss in stages, %, within the temperature range, °C:				
I stage	1.5/20–300	2.0/30–310	3.0/60–320	2.5/50–260
II stage	0.5/300–490	0.5/310–480	0.5/330–470	0.5/260–470
III stage	14.5/490–750	9.0/480–700	8.5/470–700	6.5/470–700
Total weight loss	16.5	11.5	12.0	9.5

components of the reaction mixture) changes insignificantly and fluctuates. Such a variation of the composition of the reaction products is probably caused by an increase in the concentration of B centers (due to dealumination of the zeolite skeleton) and strong L centers (aluminum at the cationic sites) responsible for olefin aromatization. However, in spite of a decrease in the total concentration of the acid centers in the zeolite, the fraction of strongly acidic centers increases (Table 2), and the residual amount of strongly acidic centers is sufficient for cracking of C_3–C_4 alkanes. Therefore, their yield remains virtually unchanged at varied HTST duration. The yield of methane and ethane on steam-treated HSZ samples substantially decreases as compared to the initial HHSZ-30, especially at $T \leq 600$°C.

Such a change in the product composition shows that HTST of the zeolite catalyst suppresses reactions of redistribution to lower alkanes and arenes on the strongly acidic centers [14]. It is interesting that, after a high-temperature steam treatment of a zeolite and with an increase in its duration, the fraction of heavy hydrocarbons increases in both liquid and gas phases of the catalyzate. For instance, on the background of general decrease in the content of C_{4+} alkanes among the reaction products, the amount of methane and ethane falls especially sharply. At the same time, on the background of general increase in the amount of C_2–C_4 alkenes, the amounts of propylene and butenes increase faster. A similar trend is observed for the liquid products. Among the aromatic hydrocarbons, the benzene content decreases faster. The contents of C_{5+} alkanes and C_{5+} alkenes increase with time of treatment within the entire temperature interval. Preliminary HTST of a zeolite catalyst changes not only its activity and selectivity but also stability, which is manifested in the character and degree of catalyst coking. The data obtained in DTA analysis of coked zeolite samples are listed in Table 4.

The pronounced exothermic effect at $T > 600$°C, corresponding to coke burning, is observed in the DTA curves of all the HSZ samples. Zeolite samples (excluding HHSZ-30-12) contain adsorbed water, and their DTA curves show an endothermic effect at 80–100°C. The decrease in the T_{min} of this effect for samples subjected to HTST, compared to the initial HHSZ-30, and the absence of such an effect for HHSZ-30-12 suggest an increase in the sample hydrophobicity because of dealumination of the zeolite skeleton.

The stages of the weight loss during calcination within the 25–750°C range were recorded for each HSZ sample. Stage I corresponds to loss of water and weakly sorbed reaction products. Features of the reaction course and the presence of methanol in the reaction mixture cause irregular deactivation of the catalyst along the bed. Three zones of methanol conversion on the zeolite catalysts can be distinguished: (A) zone of a spent catalyst, (B) zone of predominant conversion of methanol and dimethyl ether, and (C) zone of reactions of hydrogen redistribution [15]. Hence, the weight loss in stage II can be assigned to burning of the nonaromatic coke formed as a product of olefin oligomerization in zone C. With regard to high T_{max} of the exothermic effect, the weight loss in stage III corresponds to burning of the condensed aromatic coke formed in the zone of a spent catalyst (A).

The temperature of the completion of nonaromatic coke burning gradually decreases with increasing time of HTST. This can be connected with a decrease in the amount of B centers responsible for olefin oligomerization [12] because of a decrease in the aluminum amount in the zeolite skeleton. Although the amount of nonaromatic coke on all the zeolite samples remains constant, its condensation decreases with increasing time of HTST. The maximum amount of high-condensed coke was observed on HHSZ-30; it

decreases with increasing time of HTST. The total weight loss in calcination changes in parallel with the concentration of the strongly acidic centers (Tables 2, 4). Along with a decrease in the amount of B centers under HTST, their strength should increase in accordance with quantummechanical calculations [16]. Then, as noted above, formation of EAC is possible. In this case, the T_{max} of coke burning does not decrease smoothly with increasing time of HTST, but passes through a maximum (for HHSZ-30-8 sample). The subsequent decrease in the T_{max} of coke burning for HHSZ-30-12 confirms the suggestion [10] that these centers are unstable and decompose under the more severe conditions of TVT.

Thus, rather clear correlations between their acid and catalytic properties are observed for steam-treated HSZ samples. The selected catalytic properties of zeolites as functions of their acid characteristics change in the following order:

HHSZ-30-12 > HHSZ-30-4 > HHSZ-30-8 > HHSZ-30 →

Increase in total acidity of zeolites

In this series, the yield of C_2–C_4 alkenes at T = 500°C decreases, the yield of arenes at T = 500°C increases, and the total loss in calcination of the coked samples increases;

HHSZ-30-12 > HHSZ-30-8 > HHSZ-30-4 > HHSZ-30 →

Increase in the strength of acid centers of form II

In this series, the yield of C_2–C_4 alkenes at T > 500°C decreases, and the yields of arenes at T > 500°C and the yield of aromatic coke increase.

CONCLUSION

The activity of zeolites at low temperatures is controlled by the total concentration of the acid centers. With an increase in temperature (>500°C), the yield of the main products is controlled by the strength of acid centers. Similar trends are observed for samples with different silicate ratios, i.e., different contents of aluminum set in the stage of the zeolite synthesis.

REFERENCES

1. Minachev, Kh.M. and Dergachev, A.A., *Itogi Nauki Tekh. Ser.: Kinet. Katal.*, 1990, vol. 23, pp. 3–90.
2. King, D.L., Cusumano, J.A., and Garten, R.L., *Catal. Rev. Sci. Eng.*, 1981, vol 23, pp. 233–237.
3. Erofeev, V.I., Shabalina, L.B., Koval', L.M., and Minakova, T.S., *Zh. Prikl. Khim.*, 2002, vol. 75, no. 5, pp. 770–772.
4. Erofeev, V.I., Shabalina, L.B., Koval', L.M., and Minakova, T.S., *Zh. Prikl. Khim.*, 2002, vol. 75, no. 10, pp. 1680–1683.
5. Nowak, S., Gunschel, H., Lantzsch, J., and Anders, K., *Neftekhimiya*, 1987, vol. 27, no. 6, pp. 736–749.
6. Lomako, V.I. and Erofeev, V.I., Synthesis and Structure of High-Silica Zeolites, *Preprint of the Tomsk Division, Siberion Branch, Acad. Sci USSR*, 1985, no. 9.
7. Vos'merikov, A.V. and Erofeev, *Zh. Prikl. Khim.*, 1993, vol. 66, no. 10, pp. 2277–2281.
8. Breck, D.W., *Zeolite Molecular Sieves*, New York: John Wiley & Sons, 1974. Translated under the title *Tseolitovye molekulyarnye sita*, Moscow: Mir, 1976.
9. Topsoe, N.-Y., Pedersen, K., and Derouance, E.G., *J. Catal.*, 1981, vol. 70, no. 1, pp. 41–52.
10. Shabalina, L.B., Erofeev, V.I., Minakova, T.S., and Koval', L.M., *Zh. Prikl. Khim.*, 2002, vol. 75, no. 12, pp. 770–772.
11. Spiridonov, S.E., Khadzhiev, S.N., Yaralov, N.G., and Limova, T.V., *Kinet. Katal.*, 1986, vol. 27, no. 1, pp. 201–204.
12. Bragin, O.V., Kustov, L.M., Borovkov, V.Yu., *et al.*, *Kinet. Katal.*, 1988, vol. 29, no. 2, pp. 391–396.
13. Luk'yanov, D.B., Popkov, Yu.M., Rostanin, N.N., *et al.*, Abstracts of Papers, *IV Vsesoyuznaya Konferentsiya "Primenenie tseolitov v katalize"* (IV All-Union Conf. "Application of Zeolites in Catalysis"), Moscow: Nauka, 1989, pp. 65–67.
14. Ryabov, Yu.V., Korobitsyna, L.L., and Erofeev, V.I., *Zh. Fiz. Khim.*, 1987, vol. 61, no. 7, pp. 1817–1820.
15. Erofeev, V.I., Ryabov, Yu.V., Korobitsyna, L.L., and Bol'shakov, G.F., *Dokl. Akad. Nauk SSSR*, 1985, vol. 283, no. 1, pp. 148–151.
16. Kazanskii, V.B., *Kinet. Katal.*, 1982, vol. 23, no. 6, pp. 1334–1338.

Russian Journal of Applied Chemistry, Vol. 77, No. 12, 2004, pp. 1979–1986. Translated from Zhurnal Prikladnoi Khimii, Vol. 77, No. 12, 2004, pp. 2003–2010.

CATALYSIS

Thermocatalytic Decomposition of 1-Methylcyclohexyl Hydroperoxide

A. M. Syroezhko and O. Yu. Begak

St. Petersburg State Technological Institute, St. Petersburg, Russia

Mendeleev Russian Research Institute of Metrology, Federal State Unitary Enterprise, St. Petersburg, Russia

Received March 2, 2004

Abstract—A mathematical model of a multistage process of thermocatalytic decomposition of 1-methylcyclohexyl hydroperoxide in the presence of sodium stearate is developed. A procedure for calculating the unknown rate and equilibrium constants of the elementary and overall reaction stages is described. It is based on an analysis of the kinetic relationships in consumption of the initial products and accumulation of the intermediate and final products of thermocatalytic decomposition, with account of the known constants for individual stages.

Simulation in studies of the kinetics of chemical transformations involves solution of the forward and reverse problems of chemical kinetics. The forward problem consists in calculating the current concentrations of the components from their known initial concentrations and the known rate constants of the chemical reactions for all the elementary stages. The reverse problem consists in determining the unknown constants for selected stages from the known constants for the remaining stages and the experimentally estimated compositions of the multicomponent mixture at selected moments.

Let us formulate and analyze the forward problem. Let the dynamics of the component concentrations be described by the equations

$$db_1/d\tau = f_1(b_1, \ldots, b_n, k_1, \ldots, k_s),\ b_1\big|_{\tau = 0} = b_1^{in},$$

$$db_n/d\tau = f_n(b_1, \ldots, b_n, k_1, \ldots, k_s),\ b_n\big|_{\tau = 0} = b_n^{in}, \quad \text{(I)}$$

where $b_1, \ldots, b_n$ are unknown current concentrations; $b_1^{in}, \ldots, b_n^{in}$, known initial concentrations; $k_1, \ldots, k_s$, known constants; τ, time; and $f_1, \ldots, f_n$, preset kinetic functions.

A theoretical calculation of the current concentrations is confined to numerical integration of a system of ordinary equations (I), e.g., by the Euler method:

$$b_1/\tau = j\Delta\tau \equiv b_1^{(j)}, \ldots, b_n\big|_{\tau = j\Delta\tau} \equiv b_n^{(j)},$$

$$b_1^{(0)} = b_1^{in}, \ldots, b_n^{(0)} = b_n^{in};\ j = 1, 2, \ldots,$$

$$b_1^{(j)} = b_1^{(j-1)} + \Delta\tau f_1(b_1^{(j-1)}, \ldots, b_n^{(j-1)}, k_1, \ldots, k_s),$$

$$\ldots\ldots\ldots\ldots\ldots\ldots\ldots\ldots\ldots\ldots$$

$$b_n^{(j)} = b_n^{(j-1)} + \Delta\tau f_n(b_1^{(j-1)}, \ldots, b_n^{(j-1)}, k_1, \ldots, k_s), \quad \text{(II)}$$

where $\Delta\tau$ is the integration step.

However, this approach is practically unacceptable, since system (I) is typically a "rigid" system: It is characterized by a wide scatter of the matrix eigenvalues df_1/db_j. Thus, to obtain a stable numerical solution for (II), we have to use an extremely small step, namely, the time range of interest reduced by 6–10 orders of magnitude. Physically, this is due to the simultaneous occurrence of "slow" and "very fast" reactions with incomparable durations of 10^3 against 10^{-7} s, as well as to the need to coordinate the integration step with the smallest of these time periods.

One way to overcome these difficulties lies in the use of the method of steady-state concentrations, which consists in a physically valid simplification of the system (I) with the aim to eliminate the singularity. The method implies classifying all the components into unstable (free radicals, etc.) and stable. Next, it is assumed that, after a small induction period (10^{-2}–10^{-6} s), the system is characterized by the dy-

1070-4272/04/7712-1979 © 2004 MAIK "Nauka/Interperiodica"

namic equilibrium of the concentrations of the unstable components, when the rates of formation and consumption of these components are equal. The corresponding equilibrium concentrations depend on the current concentrations of the stable components and slowly vary in time with them.

Under the assumptions made, system (I) is transformed into

$$dc_1/d\tau = \varphi_1(c_1, \ldots, c_m, x_1, \ldots, x_k, k_1, \ldots, k_s),\ c_1\big|_{\tau=0} = c_1^{in},$$
$$\ldots\ldots\ldots\ldots\ldots\ldots\ldots\ldots\ldots\ldots$$
$$dc_m/d\tau = \varphi_m(c_1, \ldots, c_m, x_1, \ldots, x_k, k_1, \ldots, k_s),\ c_m\big|_{\tau=0} = c_m^{in},$$
$$dx_1/d\tau = 0 = \Psi_1(c_1, \ldots, c_m, x_1, \ldots, x_k, k_1, \ldots, k_s),$$
$$\ldots\ldots\ldots\ldots\ldots\ldots\ldots\ldots\ldots\ldots$$
$$dx_k/d\tau = 0 = \Psi_k(c_1, \ldots, c_m, x_1, \ldots, x_k, k_1, \ldots, k_s), \quad \text{(III)}$$

where $c_1, \ldots, c_m$, and $x_1, \ldots, x_k$ are the current concentrations of the stable and unstable components, respectively.

We will express the concentrations $x_1, \ldots, x_k$ from the second group of equations in system (III) as

$$x_1 = x_1(c_1, \ldots, c_m, k_1, \ldots, k_s),$$
$$x_k = x_k(c_1, \ldots, c_m, k_1, \ldots, k_s) \quad \text{(IV)}$$

and substitute them into the first groups of equations in system (III), which will yield eventually

$$dc_1/d\tau = \alpha_1(c_1, \ldots, c_m, k_1, \ldots, k_s),\ c_1\big|_{\tau=0} = c_1^{in},$$
$$dc_m/d\tau = \alpha_m(c_1, \ldots, c_m, k_1, \ldots, k_s),\ c_m\big|_{\tau=0} = c_m^{in}, \quad \text{(V)}$$

where $\alpha_1, \ldots, \alpha_m$ are the resultant kinetic functions.

System (V) is not rigid any more and can be integrated without difficulties by the Euler method with a fairly large step of 1–100 s. Physically, this transformation consists in changing from very fast to "infinitely fast" reactions, which allows us, via the limiting transition, to exclude from consideration small time scales and to remove the corresponding restrictions imposed on the integration step.

For the overwhelming majority of real problems of chemical kinetics, the dependences (IV) of the quasi-equilibrium concentrations on the currents concentrations of the stable components can be obtained analytically. Specifically this method should be preferred, since it not only significantly reduces the time required to solve the problem, but also makes it possible to reveal certain relationships.

By way of example, let us consider the mechanism of thermocatalytic decomposition of tertiary 1-methyl-1-cyclohexyl hydroperoxide (MCHP). The figure presents the kinetic curves of decomposition of MCHP and accumulation of the products formed. Based on the kinetic data, the composition of the MCHP decomposition products, and isotope analysis results, the MCHP decomposition mechanism can be represented by a set of 47 reactions [1–6] (Table 1).

Along with monomolecular thermal decomposition, MCHP undergoes bimolecular decomposition with a solvent involved, as well as catalytic decomposition in the ROOH · NaSt and 2ROOH · NaSt complexes [1–4]. Also, the MCHP dimers, $(ROOH)_2$, are involved in the decomposition. Oxygen-containing products (alcohols, acids) form inactive dimers $(ROH)_2$ and $(RCOOH)_2$ and complexes with MCHP (ROOH · RCOOH or ROOH · ROH). Alcohols and acids are incorporated into the coordination spheres of the initially formed complexes ROOH · NaSt to form ternary complexes ROOH · NaSt · RCOOH or ROOH · NaSt · ROH [2–6].

To simplify further calculations, we introduce the designations for stable and short-lived species (Table 2).

The rate constants of mono- and bimolecular decomposition of MCHP have been determined earlier [4, 5].

The rate constants $k_{17} = 10^6$ and $k_{20} = 1.6 \times 10^6$ l mol^{-1} s^{-1} of recombination of the secondary and tertiary peroxy radicals were calculated using the known partial oxidizabilities of methylcyclohexane $k_2/\sqrt{k_6}$ and independently determined chain propagation constants k_2 [1].

The estimated constants $k_{16} = 10^9$, $k_{19} = 2.5 \times 10^7$, and $k_{29} = 3 \times 10^2$, l mol^{-1} s^{-1}, were taken from [7]. We determined more precisely the constants k_{13}, k_{14}, k_{17}, k_{19}, k_{21}, and k_{24} later, when comparing the calculated and experimental rates of accumulation of the corresponding products of MCHP decomposition during the process.

The calculated kinetic curves of accumulation of the MCHP decomposition products at low conversions (up to 10–15%) coincide with the experimental data [the MCHP decomposition mechanism is described by reactions (1)–(29)].

Further calculations should take into account the influence of the reaction products [the MCHP decomposition mechanism in the developed process is supplemented by reactions (30)–(47)]. This affords an adequate description of the thermocatalytic decompo-

Table 1. Mechanism of thermocatalytic decomposition of MCHP (T = 130°C, $[NaSt]_0 = 4.7 \times 10^{-3}$ M, $[ROOH]_0$ = 0.3 M)

Reaction	Reaction*	Constant
(1)	ROOH → RO• + •OH	$k_1 = 9.5 \times 10^{-7}$ s^{-1}
(2)	ROOH + RH → RO• + H_2O + R•	$k_2 = 4 \times 10^{-7}$ l mol^{-1} s^{-1}
(3)	ROOH + RH → 2*t*-ROH	$k_3 = 1.5 \times 10^{-6}$ l mol^{-1} s^{-1}
(4)	2ROOH ⇄ $(ROOH)_2$	$K_4 = 8.1 \times 10^{-2}$ l mol^{-1}
(5)	$ROOH)_2$ → RO• + *t*-ROO + H_2O	$k_5 = 1.75 \times 10^{-6}$ s^{-1}
(6)	$(ROOH)_2$ → OH + *t*-ROO + *t*-ROH	$k_6 = 1.75 \times 10^{-6}$ s^{-1}
(7)	ROOH + NaSt ⇄ ROOH·NaSt	$K_7 = 1.57 \times 10^{1}$ l mol^{-1}
(8)	ROOH·NaSt → RO• + •OH + NaSt	$k_8 = 4.2 \times 10^{-4}$ s^{-1}
(9)	ROOH + NaSt → 1/2O_2 + *t*-ROH + NaSt	$k_9 = 1 \times 10^{-3}$ s^{-1}
(10)	ROOH·NaSt + ROOH ⇄ 2ROOH·NaSt	$K_{10} = 5.1 \times 10^{1}$ l mol^{-1}
(11)	2ROOH·NaSt → *t*-ROO• + RO• + NaSt + H_2O	$k_{11} = 2 \times 10^{-4}$ s^{-1}
(12)	2ROOH·NaSt → 2ROH + O_2 + NaSt	$k_{12} = 3.3 \times 10^{-4}$ s^{-1}
(13)	2ROOH·NaSt + RH → H_2O + Ac-$(CH_2)_4$Me + *t*ROO• + R•	$k_{13} = 7 \times 10^{-5}$ l mol^{-1} s^{-1}
(14)	RO• → Ac-$(CH_2)_4CH_2^•$	$k_{14} = 2 \times 10^{5}$ s^{-1}
(15)	Ac-$(CH_2)_4CH_2^•$ + RH → R• + Ac-$(CH_2)_4$Me	
(16)	R• + •OH → 1/4*s*-ROH + 3/4*t*-ROH	$k_{16} = 1 \times 10^{9}$ l mol^{-1} s^{-1}
(17)	2*t*-ROO• → 2RO• + O_2	$k_{17} = 1 \times 10^{5}$ l mol^{-1} s^{-1}
(18)	RO• + RH → *t*-ROH + R•	$k_{18} = 5 \times 10^{-4}$ l mol^{-1} s^{-1}
(19)	R•+O_2 → *s*-ROO• + 3/4*t*-ROO•	$k_{19} = 2 \times 10^{7}$ l mol^{-1} s^{-1}
(20)	2*s*-ROO• → *s*-ROH + Me-cycloC_6H_9=O	$k_{20} = 1.6 \times 10^{6}$ l mol^{-1} s^{-1}
(21)	ROOH + Ac–$(CH_2)_4$Me → RO• + Ac-$(CH_2)_4$Me	$k_{21} = 1 \times 10^{-3}$ l mol^{-1}s^{-1}
(22)	Me-C(O•)–$(CH_2)_4$Me → AcOH + $Me(CH_2)_3CH_2^•$ (OH)	
(23)	$Me(CH_2)_3CH_2^•$ + RH → $Me(CH_2)_3$Me + R•	
(24)	Ac-$(CH_2)_4$Me + R• → Ac-CH$(CH_2)_3$Me +RH	$k_{24} = 3 \times 10^{3}$ l mol^{-1} s^{-1}
(25)	Ac-CH$(CH_2)_3$Me + O_2 → Ac-CH(OO•)–$(CH_2)_3$Me	
(26)	Me-C(OO•)–$(CH_2)_3$Me → BuCHO + AcO•	
(27)	BuCHO + 1/2O_2 → $Me(CH_2)_3$COOH	
(28)	AcO• + RH → CH_4 + CO_2 + R•	
(29)	R• + ROOH → 1/4*s*-ROH + 3/4*t*-ROH + RO•	$k_{29} = 3 \times 10^{2}$ l mol^{-1} s^{-1}
(30)	ROOH + RCOOH ⇄ ROOH·RCOOH	$K_{30} = 2.1 \times 10^{1}$ l mol^{-1}
(31)	ROOH·RCOOH → RO• + •OH + RCOOH	$k_{31} = 3.0 \times 10^{-5}$ s^{-1}
(32)	ROOH·RCOOH → 1/2O_2 + *t*-ROH + RCOOH	$k_{32} = 2.7 \times 10^{-4}$ s^{-1}
(33)	ROOH + *t*-ROH ⇄ ROOH·*t*-ROH	$K_{33} = 2.1 \times 10^{1}$ l mol^{-1}
(34)	ROOH·*t*-ROH → RO• + •OH + *t*-ROH	$k_{34} = 1.16 \times 10^{-4}$ s^{-1}
(35)	ROOH·*t*-ROH → 1/2O_2 + 2*t*-ROH	$k_{35} = 2.09 \times 10^{-4}$ s^{-1}
(36)	ROOH + NaSt + RCOOH ⇄ ROOH·NaSt·RCOOH	$K_{36} = 8.8$ l^2 mol^{-2}
(37)	ROOH·NaSt·RCOOH → RO• + •H + NaSt + RCOOH	$k_{37} = 9.6 \times 10^{-5}$ s^{-1}
(38)	ROOH·NaSt·RCOOH → 1/2O_2 + *t*-ROH + NaSt + RCOOH	$k_{38} = 8.64 \times 10^{-4}$ s^{-1}
(39)	ROOH + NaSt + *t*-ROH ⇄ ROOH·NaSt·*t*-ROH	$K_{39} = 5.1$ l^2 mol^{-2}
(40)	ROOH·NaSt·*t*-ROH → RO• + •OH + NaSt + *t*-ROH	$k_{40} = 7.45 \times 10^{-4}$ s^{-1}
(41)	ROOH·NaSt·*t*-ROH → 1/2O_2 + 2*t*-ROH + NaSt	$k_{41} = 1.455 \times 10^{-3}$ s^{-1}
(42)	RCOOH + NaSt ⇄ RCOOH·NaSt	$K_{42} = 28$ l mol^{-1}
(43)	*t*-ROH + NaSt ⇄ *t*-ROH·NaSt	$K_{43} = 21.4$ l mol^{-1}
(44)	2RCOOH ⇄ $(RCOOH)_2$	$K_{44} = 8.18$ l mol^{-1}
(45)	2*t*-ROH ⇄ $(t\text{-ROH})_2$	$K_{45} = 1.15$ l mol^{-1}
(46)	*t*-ROH → H_2O + Me-cycloC_6H_9	$k_{46} = 1.5 \times 10^{-5}$ s^{-1}
(47)	*t*-ROH + CH_3COOH → H_2O + 1-Me-1-AcA-cycloC_6H_{10}	$k_{47} = 8 \times 10^{-4}$ l mol^{-1} s^{-1}

* RH and ROOH are methylcyclohexane and MCHP, respectively; R•, isomeric methylcyclohexyl radicals 1-Me-cyclo$C_6H_{10}^•$; RO•, alkoxy radicals 1-Me-1O•-cycloC_6H_{10}; *s*-ROO•-Me-cycloC_6H_{10}OO•; *s*-ROH, Me-cycloC_6H_{10}OH; *t*-ROO•, 1-Me-1-OO•-cycloC_6H_{10}; and *t*-ROH, 1-Me-1-HO-cycloC_6H_{10}.

Table 2. Designations for reagent concentrations

Reagent	Designation	Reagent	Designation	Reagent	Designation
ROOH	c_1	NaSt	c_{16}	$(RCOOH)_2$	c_{25}
RH	c_2	R$^\bullet$	x_1	Methylcyclohexene	c_{27}
$(ROOH)_2$	c_3	RO$^\bullet$	x_2	$(t\text{-ROH})_2$	c_{26}
ROOH · NaSt	c_4	t-ROO$^\bullet$	x_3	t–R–O–C–CH_3	c_{28}
2ROOH · NaSt	c_5	OH	x_4	ROOH	c_{1s}^{**}
t-ROH	c_6	s-ROO$^\bullet$	x_5	t-ROH	c_{6s}^{**}
$Ac(CH_2)_4Me$	c_7	$Ac(CH_2)_4CH_2^\bullet$	x_6	AcOH	c_{10s}^{**}
O_2	c_8	$Me(CH_2)_3Me$	c_{17}	RCOOH	c_{18s}
H_2O	c_9	RCOOH*	c_{18}	NaSt	c_{16s}^{**}
MeCOOH(AcOH)	c_{10}	ROOH · RCOOH	c_{19}	Me–C(OH)–$(CH_2)_4$CH	x_7
BuCOOH	c_{11}	ROOH · t-ROH	c_{20}	Bu$^\bullet$	x_8
CH_4	c_{12}	ROOH · NaSt · RCOOH	c_{21}	Ac$^\bullet$CHPr	x_9
CO_2	c_{13}	ROOH · NaSt · t-ROH	c_{22}	AcCH(OO$^\bullet$)Pr	x_{10}
s-ROH	c_{14}	RCOOH · NaSt	c_{23}	PrCHO	x_{11}
Isomeric methylcyclohexanones	c_{15}	t-ROH · NaSt	c_{24}	AcO$^\bullet$	c_{12}

* Sum of acetic and valeric acids.

** Monomeric form of the reagent not involved in intermolecular interactions.

sition of tertiary hydroperoxide until exhaustive conversion (see figure).

With increasing content of MCHP (0.1–0.35 M), when the NaSt content is varied within (4.72–236) × 10^{-4} M, the yields of alcohols grow relative to the uncatalyzed reaction (Table 3).

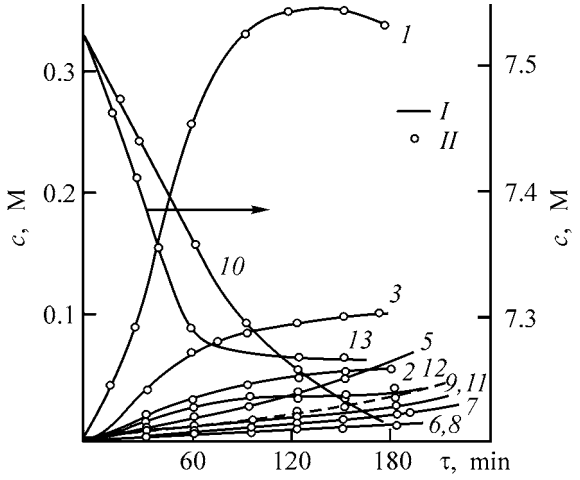

Kinetic curves of accumulation of the MCHP decomposition products. T = 130°C, [NaSt] = 4.7×10^{-3} M. (c) Concentration, and (τ) time. (*1*) Methylcyclohexanol, (*2*) secondary isomeric methylcyclohexanols, (*3*) 2-heptanone, (*4*) isomeric methylcyclohexanones, (*5*) water, (*6*) acetic acid, (*7*) valeric acid, (*8*) methane, (*9*) carbon dioxide, (*10*) MCHP, (*11*) 1-methylcyclohexyl acetate, (*12*) 1-methylcyclohexene, and (*13*) consumption of methylcyclohexane. (*I*) Experiment and (*II*) calculation.

An increase in the effective rate constant of MCHP decomposition in the presence of sodium stearate at 55–60% conversions is certainly due to formation and transformations of MCHP · ROH and MCHP · RCOOH associates and ROOH · NaSt · ROH and ROOH · NaSt · RCOOH complexes. The ratio of the radical and molecular routes in MCHP decomposition (and, consequently, the ratio of the main reaction products, 1-methylcyclohexanol : 2-heptanone) for these associates and complexes may differ from those for thermal and thermocatalytic process occurring at the initial moments of the reaction, when the influence of oxygen-containing reaction products can be neglected. Therefore, we carried out a series of experiments on catalytic decomposition of MCHP in the presence of 1-methylcyclohexanol and valeric acid. We estimated the limiting constants of the molecular and radical decomposition of 1-MCHP in the presence of these compounds: $k_{31} = 3 \times 10^{-5}$, $k_{32} = 2.7 \times 10^{-4}$, $k_{34} = 1.16 \times 10^{-4}$, and $k_{35} = 2.09 \times 10^{-4}$ s^{-1}.

Using the portions of the plot of W_Σ vs. the concentration of the monomeric form of acetic acid $[RCOOH]_m$, in which W_Σ grows with increasing concentration of the free (monomeric) acid, we estimated K_{30} at 21.0 ± 1.1 l mol^{-1}.

The rates of the radical and overall decomposition of MCHP without NaSt proved to be lower than those with NaSt. For example, at 130°C, [ROOH] = [RCOOH] = 6.5×10^{-2} M, and [NaSt] = 4.7×10^{-3} M, the limiting rate constants of the radical and overall decomposition of MCHP exceed by a factor of 3.2 those for decomposition of ROOH under identical conditions without NaSt. To understand why the rate of radical (overall) decomposition of MCHP in the presence of NaSt and RCOOH is independent of the hydroperoxide concentrations at high $[ROOH]_0$, we have to assume formation of mixed complexes NaSt · ROOH · RCOOH. In this case, the catalytic decomposition of MCHP in the presence of NaSt and ROOH is described by the scheme

$$ROOH_{free} + NaSt \overset{K_7}{\rightleftarrows} [NaSt \cdot ROOH]$$
$$\xrightarrow{k_8 + k_9} \text{free radicals and molecular products,} \quad (48)$$

$$[NaSt \cdot ROOH] + ROOH_{free} \overset{K_{10}}{\rightleftarrows} [NaSt \cdot 2ROOH]$$
$$\xrightarrow{k_{11} + k_{12}} \text{free radicals and molecular products,} \quad (49)$$

$$ROOH_{free} + RCOOH_{products} \overset{K_{30}}{\rightleftarrows} [ROOH \cdot RCOOH]$$
$$\xrightarrow{k_{31} + k_{33}} \text{free radicals and molecular products,} \quad (50)$$

$$ROOH_{free} + NaSt_{free} + RCOOH_{products}$$
$$\overset{K_{36}}{\rightleftarrows} [ROOH \cdot NaSt \cdot RCOOH] \xrightarrow{k_{37} + k_{38}} \text{products,} \quad (51)$$

$$RCOOH_{products} + NaSt_{free} \overset{K_{42}}{\rightleftarrows} NaSt \cdot RCOOH. \quad (52)$$

The constants K_7, K_{10}, k_8, k_9, k_{11}, and k_{12} were determined earlier.

The rate of the overall decomposition of MCHP is equal to

$$W_\Sigma = \frac{[NaSt]_0 [ROOH]_0 K_7(k_8 + k_9) + K_7K_{10}(k_{11} + k_{12})[ROOH]_0 + K_{36}[RCOOH]_{free}(k_{37} + k_{38})}{1 + K_7[ROOH]_0 + K_7K_{10}[ROOH]_0^2 + K_{36}[ROOH]_0[RCOOH]_{products} + K_{42}[RCOOH]_{free}}$$
$$+ K_{30}[ROOH]_0[RCOOH]_{free}(k_{31} + k_{32}). \quad (VI)$$

Using the plot of (VII) describing the catalytic decomposition of hydroperoxide, at known K_7, K_{10}, k_8, k_9, k_{11}, and k_{12}, under conditions (VIII), we obtained $K_{36} = 8.8 \pm 0.8$ l^2 mol^{-2}, and then, using the dependence of W_Σ on $[ROOH]_0$ in the presence of acids, all other constants being known ([NaSt] = 4.7×10^{-3} M), we obtained $K_{42} = 28 \pm 1.5$ l mol^{-1}:

$$W_\Sigma - K_{30}[ROOH]_0[RCOOH]_{products}(k_{31} + k_{32}) = f[RCOOH]_{free}, \quad (VII)$$

$$1 + K_7[ROOH]_0 + K_7K_{10}[ROOH]_0^2$$
$$+ K_{36}[ROOH]_0[RCOOH]_{products} \gg K_{42}[RCOOH]_{free}. \quad (VIII)$$

Likewise, we obtained $K_{33} = 21 \pm 1.1$ and $K_{43} = 21.4 \pm 1.2$ l mol^{-1} and $K_{39} = 5.1 \pm 0.3$ l^2 mol^{-2}.

The dimerization constants for acetic acid and 1-methylcyclohexanol were reported in [7]. The constants for the radical and molecular routes of decomposition of ternary complexes k_{37}, k_{38}, k_{40}, and k_{41} were determined experimentally.

We write the expression for the elementary rates of irreversible reactions in the mathematical model (the rates R_i and the rate constants k_i of the reaction are numbered in accordance with the numbers of the reaction equations in the model).

Rates of the elementary reactions of MCHP decomposition (IX)

$R_1 = k_1 c_{1s}$	$R_9 = k_9 c_4$	$R_{17} = k_{17} x_3^2$	$R_{29} = k_{29} c_{1s} x_1$	$R_{38} = k_{38} c_{21}$
$R_2 = k_2 c_{1s} c_2$	$R_{11} = k_{11} c_5$	$R_{18} = k_{18} c_2 x_2$	$R_{31} = k_{31} c_{19}$	$R_{40} = k_{40} c_{22}$
$R_3 = k_3 c_{1s} c_2$	$R_{12} = k_{12} c_5$	$R_{19} = k_{19} c_8 x_1$	$R_{32} = k_{32} c_{19}$	$R_{41} = k_{41} c_{22}$
$R_5 = k_5 c_3$	$R_{13} = k_{13} c_2 c_5$	$R_{20} = k_{20} x_5^2$	$R_{34} = k_{34} c_{20}$	$R_{46} = k_{46} c_{6s}$
$R_6 = k_6 c_3$	$R_{14} = k_{14} x_2$	$R_{21} = k_{21} c_{1s} c_7$	$R_{35} = k_{35} c_{20}$	$R_{47} = k_{47} c_{6s} c_{10s}$
$R_8 = k_8 c_4$	$R_{16} = k_{16} x_1$	$R_{24} = k_{24} c_7 x_1$	$R_{37} = k_{37} c_{21}$	

Note. k_{47} is the rate constant of accumulation of *tert*-methylcyclohexyl acetate.

It is seen that the expressions for R_{15}, R_{22}, R_{23}, and R_{25}–R_{28} are lacking; the rate constants of the corresponding reactions are unknown. We show below that, when the current concentrations of the radicals involved in the process are steady-state, there is no need to precisely know the absolute values of the rates of these reactions. They can be derived from the other, known rates of reactions describing the MCHP decomposition mechanism.

The initial concentrations are known: $[ROOH]_0$ = 0.3, $[RH]_0$ = 7.5, and $[NaSt]_0 = 4.72 \times 10^{-3}$ M. The concentration of the dissolved oxygen in solution was estimated experimentally at $(1 \pm 0.1) \times 10^{-4}$ M. The oxygen evolving during the process leaves the reaction zone.

We have to establish the dependences to be used for calculating for any moment the concentrations c_3–c_5, c_{19}–c_{26} for the complexes formed by equilibrium reactions. Also, we have to calculate the concentrations of free reactants (c_{1s}, c_{6s}, c_{10s}, c_{16s}, c_{18s}) at any moment.

We assume that the concentrations of the above-listed complexes are steady-state, and the reactions in which the complexes are consumed do not affect the equilibrium reaction of their accumulation. Then, the concentrations of the complexes can be expressed as

$$c_3 = K_4 c_{1s2},\ c_4 = K_7 c_{1s} c_{16s},$$
$$c_5 = K_{10} c_{1s} c_4,\ c_{19} = K_{30} c_{1s} c_{18s},$$
$$c_{20} = K_{33} c_{1s} c_{6s},\ c_{21} = K_{36} c_{1s} c_{16s} c_{18s},$$
$$c_{22} = K_{39} c_{1s} c_{16s} c_{6s},\ c_{23} = K_{42} c_{18s} c_{16s},$$
$$c_{24} = K_{43} c_{6s} c_{16s},\ c_{25} = K_{44} c_{218s},$$
$$c_{26} = K_{45} c_{26s}. \quad \text{(X)}$$

Next we determine the concentrations of free hydroperoxide, *tert*-methylcyclohexanol, acetic acid, and catalyst and also the sum of the concentrations of acetic and valeric acids (RCOOH) by the balance equations

$$c_1 = c_{1s} + c_3 + c_4 + c_5 + c_{19} + c_{20} + c_{21} + c_{22},$$
$$c_6 = c_{6s} + c_{20} + c_{22} + c_{24} + c_{26},$$
$$c_{10} = c_{10s} + c_{19} + c_{21} + c_{23} + c_{25},$$
$$c_{16} = c_{16s} + c_4 + c_5 + c_{21} + c_{22} + c_{23} + c_{24},$$
$$c_{18} = c_{18s} + c_{19} + c_{21} + c_{23} + c_{25}. \quad \text{(XI)}$$

We introduce a number of simplifications, namely, $c_4 + c_5 + c_{21} + c_{22} < c_{16} = 4.72 \times 10^{-3}$ M ($\tau = 0$), and the dimer concentration c_3 does not exceed 7.2×10^{-3} M, since it is equal to $K_4[ROOH]_2$, where $K_4 = 0.081$ l mol^{-1}. Then $c_{1s} \approx c_1 - c_{19} - c_{20}$ holds.

Analysis of K_{44} and K_{45} shows that the concentrations of the dimers c_{25} and c_{26} are low, and, hence, $c_{21} + c_{22} + c_{23} + c_{24} = 4.72 \times 10^{-3}$ M. This gives

$$c_{6s} \approx c_6 - c_{20},\ c_{10s} \approx c_{10} - c_{19},\ c_{18s} \approx c_{18} - c_{19}. \quad \text{(XII)}$$

Since $K_{30} = K_{33}$, we obtain

$$c_1 = c_{1s}(1 + K_{30} c_{18s} + K_{33} c_{6s}),\ c_6 = c_{6s} + K_{33} c_{6s} c_{1s},$$
$$c_{10} = c_{10s} + K_{30} c_{10s} c_{1s},\ c_{18} = c_{18s} + K_{30} c_{18s} c_{1s}, \quad \text{(XIII)}$$

or

$$c_{6s} = c_6/(1 + K_{33} c_{1s}),\ c_{10s} = c_{10}/(1 + K_{30} c_{1s}),$$
$$c_{18s} = c_{18}/(1 + K_{30} c_{1s}),$$
$$c_1 = c_{1s}[1 + K_{30} c_{18}/(1 + K_{30} c_{1s}) + K_{33} c_6/(1 + K_{33} c_{1s})]. \quad \text{(XIV)}$$

Hence,

$$c_1 = c_{1s}[1 + 21(c_{1s} + c_6 + c_{18})]/(1 + 21 c_{1s}). \quad \text{(XV)}$$

We obtain, eventually

$$c_{1s} = \sqrt{(D^2 + 84 c_1 - D)/42}, \quad \text{(XVI)}$$

where $D = 1 - 21(c_1 - c_6 - c_{18})$.

From the balance in the catalyst we obtain

$$c_{16s} = 4.72 \times 10^{-3}/(1 + K_7 c_{1s} + K_7 K_{10} c_{21s}$$
$$+ K_{36} c_{1s} c_{18s} + K_{39} c_{1s} c_{6s} + K_{42} c_{18s} + K_{43} c_{6s}). \quad \text{(XVII)}$$

All the assumptions suggest that, at the moment $\tau = 0$, when $c_6 = c_{6s} = c_{10} = c_{10s} = c_{1s} = c_{18s} = 0$ M, $c_{1s} = c_1 = 0.3$ M, which is not a very rigorous value.

We obtain a more rigorous value of c_1 by solving a transcendent equation ($\tau = 0$).

$$c_{1s} = c_1 - c_3 - c_4 - c_5,\ c_{16s} = c_{16} - c_4 - c_5,$$
$$c_3 = K_4 c_{1s2},\ c_4 = K_7 c_{1s} c_{16s},$$
$$c_1 = 0.3 \text{ mol dm}^{-3},\ c_{16} = 4.72 \times 10^{-3} \text{ M}. \quad \text{(XVIII)}$$

With $K_4 = 0.081$, $K_7 = 15.7$, and $K_{10} = 51$ l mol^{-1}, simple transformations give

$$c_{1s} + 0.081 c_{1s}^2 - 4.72 \times 10^{-3}/(1 + 15.7 c_{1s} + 791.28 c_{1s}^2)$$
$$- 0.29528 = 0. \quad \text{(IXX)}$$

We solve this equation and find $c_{1s} = 0.2887$ M $\approx c_1$, $\tau = 0$. Thus, the inaccuracy due to the assumptions made is very small and decreases with increasing reaction time τ.

The condition of steady state for the concentrations of the radicals x_i (i = 1, …, 12) gives

$$\left.\begin{aligned}
dx_1/d\tau &= R_2 + R_{13} + R_{14} + R_{18} + R_{21} - R_{16} - R_{19} - R_{29} = 0,\\
dx_2/d\tau &= R_1 + R_2 + R_5 + R_8 + R_{11} + 2R_{17} + R_{21} + R_{29} + R_{31} + R_{40} + R_{34} + R_{37} - R_{14} - R_{18} = 0,\\
dx_3/d\tau &= R_5 + R_6 + R_{11} + R_{13} - 2R_{17} + 0.75R_{19} = 0,\\
dx_4/d\tau &= R_1 + R_5 + R_8 + R_{31} + R_{34} + R_{37} + R_{40} - R_{16} = 0,\\
dx_5/d\tau &= 0.25R_{19} - 2R_{20} = 0,\\
dx_6/d\tau &= R_{14} - R_{15} = 0,\\
dx_7/d\tau &= R_{21} - R_{22} = 0,\\
dx_8/d\tau &= R_{22} - R_{23} = 0,\\
dx_9/d\tau &= R_{24} - R_{25} = 0,\\
dx_{10}/d\tau &= R_{25} - R_{26} = 0,\\
dx_{11}/d\tau &= R_{26} - R_{27} = 0,\\
dx_{12}/d\tau &= R_{26} - R_{28} = 0.
\end{aligned}\right\} \quad \text{(XX)}$$

Simple transformations yield

$$\left.\begin{aligned}
x_1 &= 8(R_2 + 0.5R_6 + R_{11} + R_{13} + R_{21})/K_{19}c_8,\\
x_2 &= (R_1 + R_2 + 2R_5 + R_8 + 2R_{11} + R_6 + R_{13} + 0.75K_{19}c_8x_1 + R_{21} + K_{29}c_1x_1 + R_{31} + R_{34} + R_{37} + R_{40})/(K_{14} + K_{18}c_2),\\
x_3 &= \sqrt{(R_5 + R_6 + R_{11} + R_{13} + 0.75K_{19}c_8x_1)/2k_{17}},\\
x_4 &= (R_1 + R_5 + R_8 + R_{31} + R_{34} + R_{37} + R_{40})/k_{16}x_1,\\
x_5 &= \sqrt{k_{19}x_1c_8/8k_{20}}.
\end{aligned}\right\} \quad \text{(XXI)}$$

Thus, knowing the concentrations of the molecular products and radicals x_i (i = 1, …, 5), we can obtain the desired R_i values.

We now write a system of differential equations describing the thermocatalytic decomposition of MCHP in the presence of sodium stearate in a methylcyclohexane solution under the starting conditions $c_{i(0)}$ at $\tau = 0$ $dc_n/d\tau$ (c_n is the current concentration of ith product, mM):

$$\left.\begin{aligned}
dc_1/d\tau &= -R_1 - R_2 - R_3 - R_5 - R_6 - R_8 - R_9 - R_{11} - R_{12} - R_{13} - R_{21} - R_{29} - R_{31} - R_{32} - R_{34} - R_{35} - R_{37} - R_{38} - R_{40} - R_{41},\\
&c_{1(0)} = 0.3 \text{ M};\\
dc_2/d\tau &= -R_2 - R_3 - R_{13} - R_{15} - R_{18} - R_{23} + R_{24} - R_{28};\\
&c_{2(0)} = 7.5 \text{ M};\\
dc_6/d\tau &= 2R_3 + R_6 + R_9 + 2R_{12} + 0.75R_{16} + R_{18} + 0.75R_{29} + R_{32} + R_{35} + R_{38} + R_{41} - R_{46} - R_{47},\\
&c_{6(0)} = 0,\\
dc_7/d\tau &= R_{13} + R_{15} - R_{21};\\
&c_{7(0)} = 0;\\
dc_8/d\tau &= 0;\\
&c_{8(0)} = 1 \times 10^{-4} \text{ M};\\
dc_9/d\tau &= R_2 + R_5 + R_{11} + R_{13} + R_{46} + R_{47};\\
&c_{9(0)} = 0;\\
dc_{10}/d\tau &= R_{22} - R_{47},\\
&c_{10(0)} = 0;\\
dc_{11}/d\tau &= R_{27},\\
&c_{11(0)} = 0;\\
dc_{12}/d\tau &= R_{28},\\
&c_{12(0)} = 0;\\
dc_{13}/d\tau &= R_{28},\\
&c_{13(0)} = 0;\\
dc_{14}/d\tau &= 0.25R_{16} + R_{20} + 0.25R_{29},\\
&c_{14(0)} = 0;\\
&c_{15(0)} = 0;\\
dc_{16}/d\tau &= 0,\\
&c_{16(0)} = 4.72 \times 10^{-3} \text{ M};\\
dc_{17}/d\tau &= R_{23},\\
&c_{17(0)} = 0;\\
dc_{27}/d\tau &= R_{46},\\
&c_{27(0)} = 0;\\
dc_{28}/d\tau &= R_{47},\\
&c_{28(0)} = 0;\\
c_{18(0)} &= c_{10} + c_{11} \text{ (at any moment).}
\end{aligned}\right\} \quad \text{(XXII)}$$

Thus, the set of equations (XXII) constitutes the mathematical model of MCHP decomposition in the presence of sodium stearate. Table 1 lists the reaction rate constants (determined experimentally and partially found in the literature).

To verify the adequacy of the mathematic model with a real process, it is necessary to solve the system of differential and nonlinear equations (XIV), (XVIII), (XX), (XXII) and compare the calculated concentrations of the reagents with the experimental data (see figure and Table 3). We solved the system on a PC. The solution was optimized in accordance with the criterion of the best agreement of the experimental and calculated data by more precisely determining the constants whose precise numerical values were unknown. The system of differential equations was solved by the Euler method:

$$c_i^{j+1} = c_i^j + (\mathrm{d}c_i/\mathrm{d}\tau)^j h \qquad \text{(XXIII)}$$

with a constant step h of 25 s for the time range 0–3 h.

For all the products yielded by MCHP decomposition, the calculated and experimental kinetic curve agree within 5% (see figure). Using the data obtained, we calculated the contributions from the radical F_R and chain F_C routes in the MCHP decomposition over the time range of interest:

$$F_R = -(R_1 + R_2 + R_5 + R_6 + R_8 + R_{11} + R_{13} + R_{29} + R_{31} + R_{34} + R_{37} + R_{40})/(\mathrm{d}c_1/\mathrm{d}\tau), \qquad \text{(XXIV)}$$

$$F_C = -R_{29}/(\mathrm{d}c_1/\mathrm{d}\tau). \qquad \text{(XXV)}$$

Our calculation showed that F_C asymptotically approaches zero, and F_R tends to 0.368 in the course of time, which is close to the experimental data.

CONCLUSION

A mathematical model of a multistage thermocatalytic process of decomposition of 1-methylcyclohexyl hydroperoxide in the presence of sodium stearate was developed, which adequately describes the experimentally observed relationships. A procedure for searching for the unknown rate and equilibrium constants of the elementary and overall reaction stages was also developed. The procedure utilizes the steady-state concentrations of the unstable components and kinetic relationships for analytical determination of the stable components (initial, intermediate, and final reaction products), using the known constants for selected elementary stages of the process of interest.

REFERENCES

1. Syroezhko, A.M., Liquid-Phase Oxidation of Alkanes, Cycloalkanes, and their Oxygen-Containing Compounds with Oxygen and Ozone in the Presence of Compounds of *s* and *3d* Elements, *Doctoral Dissertation*, Leningrad, 1985.
2. Syroezhko, A.M., *Zh. Prilk. Khim.*, 1977, vol. 50, no. 2, pp. 388–391.
3. Syroezhko, A.M., Proskuryakov, V.A., and Vakulova, O.M., *Zh. Prikl. Khim.*, 1977, vol. 50, no. 5, pp. 1115–1119.
4. Smirnov, P.A., Syroezhko, A.M., Potekhin, V.M., and Proskuryakov, V.A., *Izv. Vyssh. Uchebn. Zaved., Khim. Khim. Tekhnol.*, 1976, vol. 19, no. 9, pp. 1337–1339.
5. Smirnov, P.A., Syroezhko, A.M., Potekhin, V.M., *et al.*, *Zh. Prikl. Khim.*, 1976, vol. 49, no. 1, pp. 163–165.
6. Syroezhko, A.M., Proskuryakov, V.A., and Vakulova, O.M., *Zh. Prikl. Khim.*, 1977, vol. 50, no. 2, pp. 399–402.
7. Denisov, E.T., *Konstanty skorosti gomoliticheskikh zhidkofaznykh reaktsii* (Rate Constants of Homolytic Liquid-Phase Reactions), Moscow: Nauka, 1971.

Russian Journal of Applied Chemistry, Vol. 77, No. 12, 2004, pp. 1987–1993. Translated from Zhurnal Prikladnoi Khimii, Vol. 77, No. 12, 2004, pp. 2011–2017.

CATALYSIS

Complex Formation of Carbonyls, Carboxylates, and Acetylacetonates of Main-Group and Transition Metals with Hydroperoxides and Alcohols

A. M. Syroezhko and V. A. Proskuryakov

St. Petersburg State Technological Institute, St. Petersburg, Russia

Received February 2, 2004

Abstract—The thermodynamic and structural parameters of complexes formed by secondary and tertiary alcohols and hydroperoxides with carbonyls, carboxylates, and acetylacetonates of variable-valence metals were determined. The complexes of *s* and 3*d* elements with hydroperoxides have different structures.

The controlling role of 3*d*-element carboxylates and acetylacetonates in oxidation of *n*-alkanes and cycloalkanes is manifested in the stage of catalytic decomposition of hydroperoxides and in competitive reactions of $RO_2^{\cdot}$ radicals with the catalyst, initial substrate, and intermediates formed in oxidation [1]. The difference in the stability and lability of the resulting complexes is the key factor responsible for the specific controlling effect of these catalysts.

The aim of this study was to examine the reaction of transition metal carbonyls, carboxylates, and acetylacetonates with secondary and tertiary alcohols and hydroperoxides and to compare the catalytic activities of *s* and 3*d* elements in decomposition of tertiary hydroperoxides.

EXPERIMENTAL

The objects of study (ligands) were 1-methylcyclohexyl hydroperoxide (1-MCHP), cyclohexyl hydroperoxide (CHP), cyclohexanol (CH), and 1-methyl- and 4-methylcyclohexanol (1- and 4-MCH). Main-group and transition metal [Li(I), Co(II), Cr(III), Ni(II), Cu(II)] stearates and acetylacetonates, and also metal carbonyls $Cr(CO)_6$ and $Mo(CO)_6$ were used as complexing agents.

The ^{1}H NMR spectra of hydroperoxides in CCl_4 and *n*-heptane (0.625–2.0 M) were recorded on RYa-2310 and Tesla BS-497 spectrometers operating at 100 MHz in the temperature range from –50°C to 22°C; the ^{1}H NMR spectra of alcohols were taken at 15–50°C.

The broadening and shifts of signals in the ^{1}H NMR spectra of HO and HOO groups of alcohols and hydroperoxides dissolving the catalyst suggest the presence of labile paramagnetic complexes (Figs. 1–3). The position and linewidth of the NMR signals of hydroperoxide and alcohol molecules in complexes

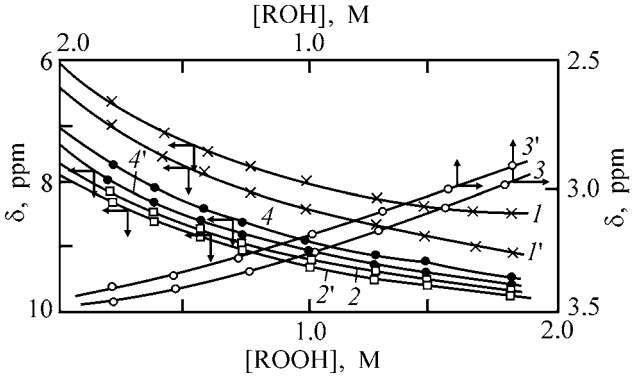

Fig. 1. Chemical shift δ of HO and HOO groups in the ^{1}H NMR spectra of alcohols and hydroperoxides vs. their concentrations [ROH] and [ROOH] in heptane at (*1*, *1*') –20, (*2*, *2*', *4*, *4*') –10, and (*3*, *3*') 23°C. Group: (*1*, *1*', *2*, *2*') OOH in 1-MCHP, (*3*, *3*') OH in 1-MCH, and (*4*, *4*') OOH in CHP; (*1*'–*4*') in the presence of 2×10^{-3} M $Mo(CO)_6$.

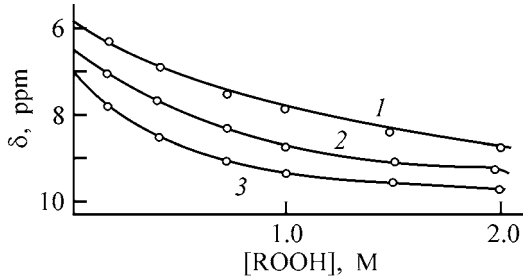

Fig. 2. Chemical shift δ of the HOO group in the ^{1}H NMR spectra of CHP vs. its concentration [ROOH] in heptane at -20°C (*1*) in the absence of a catalyst and in the presence of 2×10^{-2} M (*2*) $Mo(CO)_6$ and (*3*) $Co(acac)_2$.

1070-4272/04/7712-1987 © 2004 MAIK "Nauka/Interperiodica"

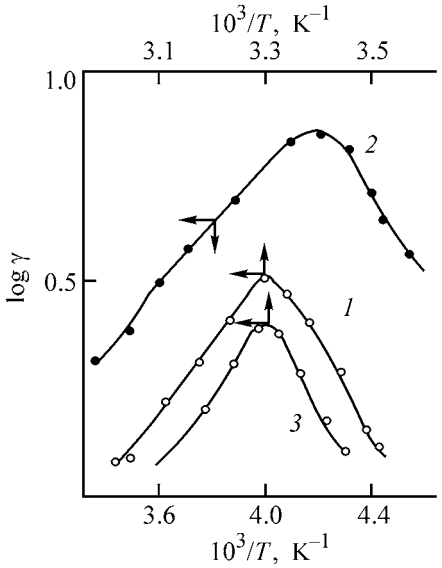

Fig. 3. Temperature dependence of signal broadening $\log\gamma$ in the ^{1}H NMR spectra of 1-MCHP and 1-MCH ([ROOH] = [ROH] = 0.25 M) in heptane in the presence of 2×10^{-2} M (*1*, *3*) $Mo(CO)_6$ and (*2*) $Co(acac)_2$.

are governed by the temperature and concentrations of the initial substrates.

The linewidths and shifts of signals in the ^{1}H NMR spectra are described by the Swift–Connick equations [2]. Consideration of special cases [3] under conditions of slow and fast exchange of ligands allows determination of the thermodynamic and structural parameters of complex formation in the systems: equilibrium constants K; enthalpy of complex formation, ΔH; lifetime of ligands in the coordination sphere of the metal, τ_1; activation energy of ligand elimination from the coordination sphere, E_a; and distances between the electron donor and acceptor in the complex, l.

The slow and fast ligand exchange can be distinguished by the temperature dependence of the linewidths of the ^{1}H NMR signals analyzed. In the first case, the linewidth increases with temperature, and in the second, it decreases. From the equation describing the complex formation

$$ML_n + XOH = ML_n \cdot XOH \quad (1)$$

[ML_n is a compound of a variable-valence metal, XOH is free hydroperoxide (ROOH) or alcohol (ROH), $ML_n \cdot XOH$ is paramagnetic labile complex], we can obtains provided that ML_n << [XOH], the complex concentration:

$$[ML_n \cdot XOH] = [ML_n]_0[XOH]_0/(1 + K[XOH]_0), \quad (2)$$

where $[XOH]_0$ and $[ML_n]_0$ are the initial concentrations of the ligand (hydroperoxide or alcohol, respectively) and variable-valence metal.

At a long lifetime of the ligand in the coordination sphere formed by the central atom ($\tau_1 >> \tau_{21}$, where τ_1 is the lifetime of ligand in the coordination sphere of the metal and τ_{21} is the transverse relaxation time of the ligand in the coordination sphere), the Swift-Connick equation for broadening τ_1/T_{2p} has a simple form

$$\tau_1/T_{2p} = P_1\tau_1^{-1}, \quad (3)$$

where P_1 is the mole fraction of ligands and τ_1/T_{2p} is paramagnetic broadening.

At a short lifetime of ligand in the coordination sphere of an ion ($\delta_{21} >> \tau_1$), the paramagnetic broadening and paramagnetic shifts (ppm) are given by expressions (4) and (5), respectively:

$$\tau_1/T_{2p} = P_1 2\pi(D + C), \quad (4)$$

$$\delta = -P_1\alpha a, \quad (5)$$

$$T_{2p} = 0.5(2\pi\Delta\gamma) = \pi\Delta\gamma, \quad (6)$$

where D is the contribution of the dipole-dipole electron-nuclear interaction in the complex of a transition metal with the ligand; C, the contribution of contact (isotropic) hyperfine interaction caused by delocalization of the unpaired electron of metal to the ligand; α, a coefficient; and $\Delta\gamma$, the line broadening measured at half-maximum (Hz).

From expressions (4) and (5) we obtain expressions (7) and (8) [4] allowing determination of the required thermodynamic and structural parameters of the complexes:

$$\delta^{-1}[ML_n]_0 = [-1/(\alpha a)](1/K + [ROOH]_0), \quad (7)$$

$$[ML_n]_0/\Delta\gamma = 1/2(D + C)(1/K + [ROOH]_0). \quad (8)$$

The dependences of the shifts $\Delta\delta$ and broadenings $\Delta\gamma$ on the concentration of alcohol or hydroperoxide, typical of the complexes studied, are shown in Figs. 1–4. The different directions of paramagnetic shifts of the ^{1}H NMR signals in complex formation with $Mo(CO)_6$ (downfield shift for ROOH and upfield shift for ROH) and the opposite signs of the signal shifts in complex formation of ROOH and ROH with $Co(acac)_2$ suggest different mechanisms of delocalization of the spin density from the metal to the ligand.

The distance between the oxygen atoms in ROOH is 0.1475 nm, and the O–H bond length is 0.095 nm. The quantum-chemical calculations by the extended Hückel method give the electronic structure of the ROOH molecule: the charge on the oxygen atoms is –0.59 (C–O) and –0.67 (O–H), and the charge on the hydrogen atom, +0.64.

The charge on atoms, the bond orders, and population of the –O–O bond vary only slightly with the structure of radical R•; however, introduction of polar substituents into radical R• has a noticeable effect. The electronic structure of ROOH is mainly characterized by two unshared pairs localized on the $2p_yO_\alpha$ and $2p_zO_\beta$ orbitals of oxygen atoms, which play an important part in the formation of the H–X bonds and in the weakening of the O–O bond in complexation with electron donors and acceptors. The lowest unoccupied molecular orbital is antibonding with respect to the O–O bond (it has a node located between the oxygen atoms), while the highest occupied molecular orbital is nonbonding and is close to the oxygen atomic orbital occupied by the unshared electron pair. The lower the energy level of the lowest unoccupied molecular orbital, the easier the reaction of the O–O group in ROOH with nucleophilic reagents. It would be expected that the associates of ROOH formed by H-bonds with bases should be preferentially formed along the 1*s* atomic orbital of hydroperoxide hydrogen and the $2p_z$ orbitals of the base heteroatom, and those with acids, along the $2p_yO_\alpha$ orbital of ROOH.

Applying Eqs. (7) and (8) to analysis of the ranges of fast exchange, we obtain the enthalpies of complex formation $H + E$ (E is the activation energy of electronic relaxation, equal to 4.2 kJ mol^{-1}). The hyperfine coupling constant a was determined from the dependence $[ML_n]/\delta = f[ROOH]$ (Fig. 4). From the concentration dependence of broadening under conditions of fast exchange (Fig. 5), we determine by Eq. (8) the sum (D + C), i.e., the dipolar and scalar contributions. In complexes with alcohols [5] under conditions of fast exchange, the scalar contribution ($S = 0.25a^2\tau$) can be neglected, and for complexes with ROOH (larger broadening in comparison with the shifts), all the observed broadenings in the ^{1}H NMR spectrum can be accounted for by the dipolar contribution D. Applying Eq. (3) to analysis of the ranges of slow exchange, we calculate the lifetime of ligands in the coordination sphere and the activation energy of ligand elimination from the coordination sphere.

In the complexes $Mo(CO)_6$–ROOH (CHP and 1-MCHP), $Co(acac)_3$–1-MCH, $Co(acac)_3$–4-MCH,

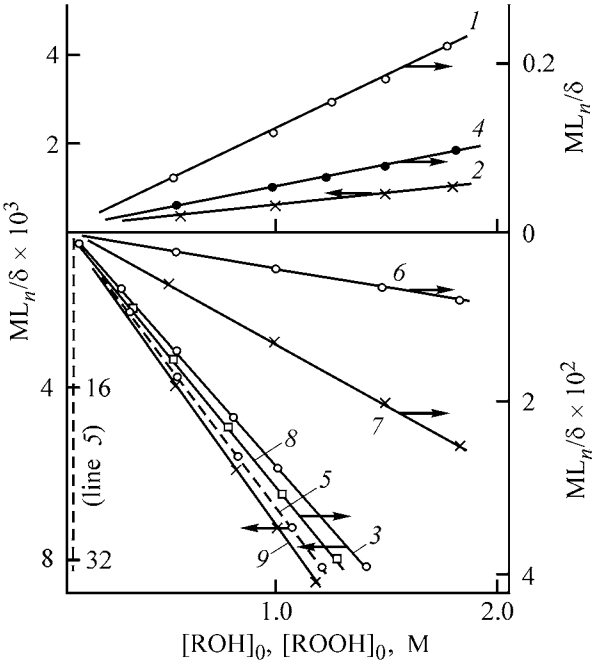

Fig. 4. Relative chemical shifts ML_n/δ of the signals in the ^{1}H NMR spectra of hyroperoxides and alcohols vs. the initial concentrations $[ROH]_0$ and $[ROOH]_0$ in the presence of complexing agents at various temperatures: (*1*) 1-MCH, (*2*, *3*, *6*) 1-MHCP, (*4*) CH, (*5*, *8*) CHP, (*7*) 4-MCH (*cis*), and (*9*) 4-MCH (*trans*). (*1*) $[Mo(CO)_6] = 1 \times 10^{-2}$ (23°C), (*2*) $[CoSt_2] = 7 \times 10^{-3}$ (26°C), (*3*) $[Co(acac)_2] = 1 \times 10^{-2}$ (–10°C), (*4*) $[CrSt_3] = 7 \times 10^{-2}$ (23°C), (*5*) $[Co(acac)_2] = 1 \times 10^{-2}$ (0°C), (*6*) $[Mo(CO)_6] = 2 \times 10^{-2}$ (–20°C), (*7*, *9*) $[Co(acac)_2] = 3.25 \times 10^{-2}$ (50°C), and (*8*) $[Mo(CO)_6] = 2 \times 10^{-2}$ M (–10°C).

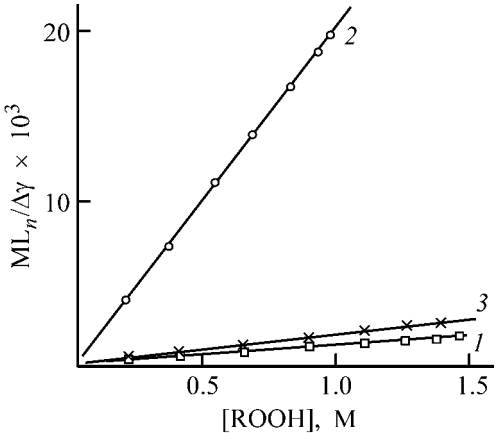

Fig. 5. Relative broadening $ML_n/\Delta\gamma$ in the ^{1}H NMR spectra of hydroperoxides and alcohols vs. their concentrations [ROOH] and [ROH] in the presence of complexing agents at various temperatures. (*1*) $[Co(acac)_2] = 1 \times 10^{-2}$ (–10°C), (*2*) $[Mo(CO)_6] = 2 \times 10^{-2}$ (–20°C), and (*3*) $[Cr(acac)_3] = 7 \times 10^{-2}$ M (23°C). (*1*) 1-MHCP, (*2*) CHP, and (*3*) 1-MCH.

Table 1. Structural parameters of complexes of ROOH and ROH with the compounds of variable-valence metals ([ROOH] = 0.05–2 M)

Complex	D + C, Hz	*l*, nm	*a*, Oe	*T*, °C	[Cat.] × 10^3, M
$Co(acac)_2$–1-MCHP in heptane	401	0.29	+2.7	–10	10
$Co(acac)_2$–CHP in heptane	503	0.28	+0.5	0	10
$CoSt_2$–1-MCHP in CCl_4*	796	0.26	–7.6	22	7
$CrSt_3$–CH in CCl_4		0.28	–0.34	22	70
$Mo(CO)_6$–1-MCHP	49	0.41	0.28	–20	20
$Mo(CO)_6$–1-CHP	59	0.40	0.375	–10	20
$Mo(CO)_6$–1-MCH	95	0.38	–0.16	23	20
$Cr(CO)_6$–CH	93	0.38	–	23	20
$Cr(acac)_3$–1-MCH	310	0.30	–0.25	23	70
$Cu(acac)_2$–1-MCH		0.24	–1.4	20	7
$Co(acac)_3$–4-MCH	672(*e*, *cis*)	0.265	1.18	50	32.5
	550(*a*, *trans*)		0.495	50	32
$Co(acac)_2$–1-MCH in *n*-heptane	400	0.29	1.92	23	20

* Evaluation by Eq. (7) is correct for complexes with an equimolar stoichiometric ratio.

and $Co(acac)_2$–1-MCH (downfield shift), the hyperfine coupling constant is positive. In complex formation of ROH and ROOH with acetylacetonates, the most probable is delocalization of the spin density along the conjugation system [4, 5]. In complexes of Co and Cu carboxylates with ROOH (Table 1), the spin density is delocalized by the polarization mechanism (parameter *a* is negative). The hyperfine coupling constant is affected by the steric hindrance in complex formation and also by the electron-donor power of the initial ligands. Of no small importance is the shielding of the coordinated 3d transition metal, which is evident from a comparison of the parameter *a* for metal carboxylates and acetylacetonates with the same ligands (Table 1).

Table 2. Thermodynamic parameters of complex formation of ROOH and ROH with carbonyls, carboxylates, and acetylacetonates of variable-valence metals

Complex	E_a, kJ × mol^{-1}	ΔH, kJ × mol^{-1}	$\tau_1 \times 10^4$, s (*T*, °C)
$Co(acac)_2$–1-MCHP	31.6	24.4	4.8 (–40)
$Co(acac)_2$–CHP	32.2	26.5	5.1 (–40)
$Co(acac)_2$-CH	38.7	34.5	
$Co(acac)_3$–4-MCH	18.5	14.3	2.35 (50)
$CrSt_3$–1-MCHP	28.2	24	3.1 (–23)
$Cr(acac)_3$–1-MCH	22.8	18.6	1.8 (23)
$Cr(CO)_6$–CH	21	16.9	–
$Mo(CO)_6$–1-MCHP	19.6	15.3	5.2 (–40)
$Mo(CO)_6$–CHP	20.6	16.4	–
$Mo(CO)_6$–1-MCH	21	16.8	6.5 (–40)
$Mo(CO)_6$–cyclohexene–1-MCHP	12.1	8.0	3.5 (–40)
$Cu(acac)_2$–1-MCHP	33.5	29.2	–
$Ni(acac)_2$–1-MCH	34.5	30.3	–

With account of the fact that, for the complexes studied, the dipolar interaction makes the main contribution to the linewidth of the ^1H NMR signal (D >> C) [5], the distance between the metal and the ligand nucleus in the complex (*l*) can be determined with a sufficient accuracy:

$$D = 4/3S(S + 1)(\gamma_e^2\gamma_n^2h^2/l^6)\tau_c, \quad (9)$$

where γ_e and γ_n are gyromagnetic ratios of electron and the nucleus, respectively; *h* is the Planck constant; τ is the correlation time of dipolar interaction varied in the range 10^{-11}–10^{-12} s [in calculations, τ_c and *S* (spin quantum number) are taken to be 10^{-12} s and 0.5, respectively].

From these data we calculated the structural parameters of the complexes studied (Table 1). From the temperature dependences of broadening of the ^1H NMR signals for HO and HOO groups of alcohols and hydroperoxides (Fig. 3), we evaluated the thermodynamic and kinetic parameters of the complexes (Table 2).

In the temperature range studied the hydroperoxides enter into a slow ligand exchange at low temperatures and into fast exchange at a higher temperature. The sum of dipolar and scalar contributions to the

signal broadening is greater for ROOH than that for structurally related ROH. The equatorial and axial stereoisomers of secondary alcohol (4-MCH) form with $Co(acac)_3$ complexes of varied stability. Complex formation with the sterically nonhindered equatorial *cis* isomer proceeds more easily (Table 1).

The activation energy of ROOH and ROH elimination from the coordination sphere of $Cr(CO)_6$ and $Mo(CO)_6$ is 19.6–21.0 kJ mol^{-1}. These values are typical of the energy of hydrogen bonds of metal cabonyls with hydroperoxides.

The lifetime of ROOH or ROH molecules in the solvation shell of $Mo(CO)_6$ is significantly longer than that of diffusion pairs in liquids. Since the lifetime of ligand in the coordination sphere of metal is nine orders of magnitude longer than the characteristic time of elemental events in chemical processes, it would be expected that the orientation of molecules due to outer-sphere complex formation should promote the catalysis.

The enthalpy of complex formation of ROOH and ROH with Co(II), Cr(III), Cu(II), and Ni(II) stearates and acetylacetonates is higher than that for similar complexes of $Mo(CO)_6$, and the distance between the donor and acceptor is shorter. All these characteristics are typical of "anisotropic" complexes intermediate between inner-sphere and outer-sphere complexes. The activation energy of ligand elimination from the coordination sphere of Co(II), Cr(III), Cu(II), and Ni(II) exceeds the energy of H-bond; however, this does not allow an unambiguous conclusion that of only a coordination bond exists. The thermodynamic parameters of complexes of 1-MCHP and CHP with the same catalyst are virtually the same. The data obtained (Table 2) show that there is a clear correspondence between the capability of a transition metal ion for complex formation and its catalytic activity in oxidation of alkanes and cycloalkanes and also decomposition of ROOH [1]. The activation energy of ROOH elimination from the coordination sphere of Cr(III) is lower, compared to the Co(II), Cu(II), and Ni(II) complexes. This can account for the enhanced activity of Cr(III) in catalytic decomposition of ROOH.

The presence of vacant *d*-electron levels in variable-valence metals determines their capability for complex formation with oxidation products of various hydrocarbons (saturated, olefin, and aromatic). With increasing electronegativity of 3*d* transition metals, the stability of complexes of their acetylacetonates with ROOH and ROH grows, compared to acetylacetonates of 3*d* transition metals with a small number of *d* electrons. The presence of various oxidation states (from 2 to 6) is typical of metals with a small number of *d* electrons (V and Cr). Delocalization of π electrons of the enol form of acetylacetonate and *d* electrons of the metal over the chelate ring is typical of inner-sphere coordination compounds [Mn(III), Fe(III), Co(III), and Cu(II) acetylacetonates], and delocalization of only π electrons over the chelate ring is more probable for Ni(II), Co(II), and Zn(II) acetylacetonates. Data on the mechanism of delocalization of the spin density in complexes of alcohols and hydroperoxides with compounds of 3*d* transition metals are contradictory [4–7].

The chemical shift is only a qualitative indication of changes in the electron density in formation of chemical bonds, since the local paramagnetic contribution arises from the anisotropy of electron density distribution at the atom for which the chemical shift is measured. The contact shift in octahedral complexes of 3*d* transition metal acetylacetonates is caused by delocalization of the electron density from the metal to ligand or from the ligand to metal. The charge transfer from the metal to ligand should give rise to delocalization of the positive spin. The charge transfer from the ligand to metal should give rise to delocalization of the positive spin for the d^5–d^9 configuration and delocalization of the negative spin for the d^1–d^4 configuration [7]. The more probable is the delocalization of the electron from the metal to ligand, involving π orbitals of the ligand, which only slightly differ in the energy from the nonbonding *d* orbitals of the metal, rather than σ orbitals.

The acetylacetonate anion and carbon monoxide are ligands in which the donor atom contains a pair of electrons capable of formation of σ bond and low-energy vacant π antibonding orbital which can accept an electron pair from a metal atom to form a dative bond. The acetylacetonate anion is a "hard" base, which is caused by the planar structure of the ring and conjugation due to strong π electron interaction along the ring. In the complex ROOH–catalyst, the ROOH anion is activated and decomposes homolytically, and the oxidation state of the transition metal ion changes by the mechanism of single-electron transfer.

In this reaction, *s* and 3*d* transition metal carboxylates are more active than the corresponding chelates, which is caused by the difference in the electron density at the central coordinating atom of the catalyst in these compounds and at the oxygen atom of the ROOH group (Table 1). The IR spectra of 1-MHCP [1], measured in the presence of Li(I), Co(II), and

Cu(II) carboxylates, show, in combination with the ^{1}H NMR data, that, in the presence of the above catalysts, the hydrogen bond in ROOH self-associates is replaced by hydrogen bonds of ROOH with oxygen atoms of the carboxylate. At the same time, the observed chemical shift of the OH group (upfield shift) suggests formation of a coordination bond between the metal ion (*s* and 3*d*) and the oxygen atom of the OOH group in ROOH. In complexes of *s* and 3*d* transition metal carboxylates with ROOH, the electron density on the oxygen atom of the OOH group of 1-MCHP increases.

In complex formation of lithium stearate with 1-MCHP, the shift of the electron density to the oxygen atom of the OOH group in ROOH [8] can be understood with account of the electrostatic effect of Li^+ ion, local polarity of the carboxylate anion, and polarizability of 1-MHCP as a result of formation of H-bond. In complexation of 3*d* transition metal stearates, this explanation is probably incorrect since the shifts of the ^{1}H NMR signals of OOH are significant. It is most likely that both donor and the acceptor properties of ROOH are manifested in complex formation.

The acceptor properties of hydroperoxides are manifested as a result of transfer of the electron density from the metal ion to the free antibonding orbital (nonbonding valence orbital) of the peroxide bond. In ROOH, this orbital has predominantly the $2p^*$ character. In this interaction, the occupied orbital of the donor overlaps with the vacant orbital of the acceptor. The efficiency of interaction is governed by the overlap integral. The overlapping orbitals should correspond to each other in symmetry. For ions of metals in the lower oxidation states [Cr(II), Fe(II), Cu(I), Co(II), and oxovanadium VO(IV)] in the reaction with H_2O_2, the overlap of the orbitals in the transition state ($d \rightarrow p^*_\sigma$) results in the formation of a π complex [9]. The probability of formation of this bond grows with increasing number of *d* electrons of the metal. Formation of π^* bonds with organic reagents is typical of Cu(I), Cr(II), Fe(II), and Co(II) ions [10]. It should be noted that we used the concept of σ and π bond by convention with account of the local symmetry of the O–O bond. "Hard" Lewis acids [Li^+, Na^+, K^+, Mg^{2+}, Ca^{2+}, Sr^{2+}, Ti(IV), etc] form no π bonds.

The appearance of electrons on the antibonding orbital of ROOH results in weakening of the O–O bond. As a result of its decomposition, a radical or a radical ion of the peroxy compound and an oxidized metal ion (M^{n+1}) are formed.

The donor properties of ROOH are related to the possibility of electron density transfer by the acceptor from the 2*p* nonbonding orbitals of the hydroperoxides. The population of oxygen *p* orbitals in ROOH, on which the unshared pair is localized [9], is close to that of pure atomic orbitals. In this case, the orbitals overlap at the electron transfer $p \rightarrow d$ from the nonbonding *p* orbital of ROOH to the vacant orbital of the 3*d* transition metal ion. This type of bonding is typical of 3*d* transition metals Cu(II), Mn(III), Fe(III), and Co(III). In these reactions, a one-electron reduction of metal is very probable. The data obtained show that the mechanism of donor–acceptor interaction is influenced by the geometry of 3*d* transition metal compound (acetylacetonate or carboxylate) and by the splitting of the central atom levels and the number of electrons on the valence orbitals. When σ bonds between ROOH and metal ion Co(II), Cu(II), Ni(II), or Mn(III) in high-spin octahedral complexes are formed, only decomposition of ROOH is observed. The π-bonding between the central atom of the catalyst and ROOH molecule in the case of Mo, W, V, and Cr compounds activates the ROOH molecule for its reaction with an olefin to form the epoxide. The ROOH molecule is activated by interaction of its π^* orbital with the t_{2g} orbital of the metal ion.

In complexation of Mo and Cr carbonyls, only the outer-sphere coordination of ROOH is possible. For example, in $Cr(CO)_6$ chromium atom uses six d^2sp^3 hybrid orbitals and forms a σ bond with six carbon atoms of CO groups octahedrally arranged around this atom. The filled *d* orbitals of chromium d_{xy}, d_{xz}, and d_{yz} have the same arrangement (symmetry) as the antibonding π^*_x and π^*_y orbitals of CO. The back donation of *d* electrons from the metal to the antibonding orbitals of CO ligands decreases the π bonding between the C and O atoms, so that the carbon-oxygen bond in the carbonyl is not triple. The ligands are strongly bound to the metal [11]. The M–C and C–O bond lengths in $Cr(CO)_6$ are 0.19 and 0.11 nm, and in $Mo(CO)_6$, 0.2 and 0.11 nm, respectively.

In the complexes studied, the distance between the central atom and ligand (ROOH and ROH) is 0.38–0.40 nm (Table 1). The structural parameters and energy characteristics obtained correspond to outer-sphere coordination, probably caused by H bonding. The structural parameters of the other complexes correspond to an intermediate state between inner- and outer-sphere complexes (Table 1). For example, the Co–O bond length in $Co(acac)_2$ is 0.205 nm, and that in $Co(acac)_2$–1-MCHP and $Co(acac)_2$–CHP, 0.29–0.28 nm, respectively. Cobalt(II) stearate coordinates 1-MCHP more strongly (l = 0.26 nm) than $Co(acac)_2$, which decreases the energy barrier of the reaction.

These results are in a good agreement with published data [7, 8, 12–14]. The products formed in decomposition of ROOH (alcohol and water) will competitively coordinate to the catalyst, which inhibits the reaction.

The shift of the electron density from the oxygen atom of ROOH to the metal in complex formation with $Co(acac)_2$ cannot be explained, since the charge on the α-atom of the OOH group should increase in this case [4]. In the complexes of $Co(acac)_2$ with ROOH, the pseudocontact interaction resulting in significant shift of the signal in the ^1H NMR spectrum plays an important role. In complexes of acetylacetonates with ROH, formation of an H bond is not ruled out [7].

The abnormal catalytic activity of chromium compounds [$Cr(ac)_3$, $CrSt_3$ (where ac is acetate and St is stearate anion), $Cr(acac)_3$, and $Cr(CO)_6$] can also be caused by the possible competitive formation of ROOH complexes with coordination through α- or β-oxygen atom [5]. It seems likely that, in the systems ROOH–catalyst, complexes of both types are formed and their ratio depends on the nature of metal and ROOH. The mobility of unshared electron pairs, i.e., the electron-donor power of both oxygen atoms in the hydroperoxide molecule, is virtually the same. The acceptor power of oxygen atoms of hydroperoxides varies: the energy level of the O_α atom is higher than that of the O_β atom. To compounds of metals with larger atomic numbers (Fe, Co, and Cu), ROOH should predominantly coordinate through the O_α atom, while with Mo(0), VO^{2+}, Cr(VI), and in part Cr(III) the coordination through the O_β atom is possible.

It is likely that the differences in the structure of the complexes studied and complexes of 3*d* transition metal acetylacetonates with methanol [4] are caused by the geometric structure and spatial arrangement of bulky compared to methanol, molecules of cyclic alcohols and hydroperoxides. A small molecule of coordinated methanol can approach the metal ion by 0.13–0.18 nm and enter into the inner coordination sphere. Bulky molecules of cyclic alcohol or hydroperoxide are situated at a significantly longer distance (0.24–0.30 nm). Contrary to published data [4] concerning the existence of two coordination spheres in the complexes $Co(acac)_2$–*tert*-butyl hydroperoxide and $Co(acac)_2$–*tert*-amyl hydroperoxide, for the cyclic alcohols and hydroperoxides studied here in the temperature interval examined we did not observed complete exchange of ligands between the inner and outer spheres.

CONCLUSIONS

(1) Acetylacetonates and stearates of 3*d* transition metals form anisotropic complexes with cyclohexanol and cyclohexyl hydroperoxide and their methyl-substituted derivatives, intermediate between inner- and outer-sphere complexes; molybdenum and chromium hexacarbonyls form labile outer-sphere complexes.

(2) In complex formation of hydroperoxides with carboxylates or acetylacetonates of 3*d* transition metals, both donor and acceptor properties of hydroperoxides are manifested, depending on the number of electrons on the *d* level of metal and its oxidation state. This results in different mechanisms of delocalization of the electron density.

REFERENCES

1. Syroezhko, A.M., Liquid-Phase Oxidation of Alkanes, Cycloalkanes, and Their Oxygen-Containing Derivatives with Oxygen and Ozone in the Presence of Compounds of *s* and 3*d* Elements, *Doctoral Dissertation*, Leningrad, 1985.
2. Swift, T.J. and Connick, R.B., *J. Chem. Phys.*, 1962, vol. 37, pp. 307–320.
3. Svitych, R.B., NMR Study of Paramagnetic Complexes in Solutions, *Cand. Sci. Dissertation*, Donetsk, 1978.
4. Yablonskii, O.P., Complex Formation and Its Role in Oxidation and Separation of Hydrocarbons, *Doctoral Dissertation*, Ivanovo, 1979.
5. Svitych, R.B., Buchachenko, A.L., Yablonskii, O.P., *et al.*, *Kinet. Katal.*, 1974, vol. 15, no. 5, pp. 1300–1306.
6. Gribov, A.A., Zolotov, Yu.A., and Noskova, MN., *Zh. Strukt. Khim.*, 1968, vol. 9, no. 3, pp. 448–457.
7. Bulgakova, G.M., Shchupik, A.N., Zamaraev, K.I., and Skibida, I.P., *Dokl. Akad. Nauk SSSR*, 1972, vol. 203, no. 4, pp. 363–367.
8. Smirnov, P.A., Timofeeva, T.N., Syroezhko, A.M., *et al.*, *Zh. Org. Khim.*, 1974, vol. 10, no. 9, pp. 1892–1896.
9. Lunenok-Burmakina, V.A., in *Neorganicheskie perekisnye soedineniya* (Inorganic Peroxy Compounds), Moscow: Nauka, 1975, pp. 27–38.
10. Sapunov, V.N., A Study of Hydroperoxide Epoxidation of Olefins, *Doctoral Dissertation*, Moscow, 1980.
11. Syrkin, V.G., *Karbonily metallov* (Metal Carbonyls), Moscow: Khimiya, 1983.
12. Mel'nichenko, N.A., Bazhanov, A.V., and Kupriyanov, A.S., *Zh. Strukt. Khim.*, 2003, vol. 44, no. 3, pp. 446–454.
13. Allakhverdov, G.R., *Zh. Fiz. Khim.*, 1996, vol. 70, no. 10, pp. 1828–1833.
14. Cao, Y., Gankin, M., and Betterton, E., *Health Perspect.*, 1995, vol. 103, no. 1, pp. 29–32.

Russian Journal of Applied Chemistry, Vol. 77, No. 12, 2004, pp. 1994–1996. Translated from Zhurnal Prikladnoi Khimii, Vol. 77, No. 12, 2004, pp. 2018–2020.

ORGANIC SYNTHESIS AND INDUSTRIAL ORGANIC CHEMISTRY

Kinetic Relationships in Synthesis of Dimethoxymethane

S. M. Danov, V. A. Kolesnikov, and I. V. Logutov

Dzerzhinsk Branch, Nizhni Novgorod State Technical University, Dzerzhinsk, Nizhni Novgorod oblast, Russia

Received July 15, 2004

Abstract—The kinetics of formation of dimethoxymethane by acetalization of formaldehyde with methanol, catalyzed by silicotungstic heteropoly acid, were studied.

Dimethoxymethane (DMM) is a colorless solvent with a low boiling point, low viscosity, and an excellent dissolving power. It finds application in organic and pharmaceutical syntheses, paint and varnish industry, as a washing solvent, as component of cleaning and degreasing solvents, in production of adhesives and plastics, as a fuel additive, and as a component of in technical aerosols and in household chemistry articles.

The starting reagents for preparation of DMM are formaldehyde (FA) and methanol (M). These are readily accessible and cheap chemicals, which, combined with their acceptable production costs, affords a cheap commercial DMM. The overall reaction of DMM formation can be represented schematically as

$$2CH_3OH + HCHO \overset{Cat.}{\rightleftarrows} CH_2(OCH_3)_2 + H_2O.$$

Since recently, commercial plants have been using as catalysts ion-exchange resins, which afford DMM in high yields but degrade during the reaction into small particles clogging the column, lose their activity under exploitation, and need either regeneration or replacement [1]. Also, inorganic acids such as sulfuric acid have been tested as catalysts, but they cause many nuisances like corrosion activity, environmental pollution, the need for neutralization of wastewater, and irreversible loss of the acid [2].

We believe that tungstic heteropoly acids and, in particular, silicotungstic heteropoly acid $H_4SiW_{12}O_{40}$ (STA), are suitable as catalysts. The trials on laboratory batch and continuous-operation units showed that tungstic heteropoly acids can be successfully applied as catalysts in synthesis of DMM.

In the context of development of the optimal procedure for isolation and purification of DMM, it is necessary to analyze the kinetic aspects of its synthesis, which constituted the aim of this study.

EXPERIMENTAL

In experiments, we used a water-methanol solution of formalin containing 37 wt % FA; the amount of FA was determined by the sodium sulfate technique, and that of M, by gas chromatography. We used M purified by distillation; gas chromatographic analysis showed that it contained residual water only. Analytically pure silicotungstic heteroply acid was dried by calcination at 250°C for 3 h.

The kinetic relationships were experimentally studied in a glass reactor (V = 100 ml) equipped with a water jacket, two ground-glass joints connecting the reactor with a reflux condenser and a thermometer, and a sampler. To exclude hot spots, the reaction mixture was stirred with a magnetic stirrer. A constant temperature in the reactor was maintained by water circulating between the thermostat and the reactor jacket, with the temperature monitored within the latter. A water thermostat connected to the reactor case was operated in the forced-circulation mode.

The reaction mixture was prepared by mixing M, FA, and water to achieve the desired ratio of the reactants, whereupon the required amount of the resulting mixture was sampled, weighed on an analytical balance, and placed in the reactor. When the desired temperature was established in the reactor, the required amount of STA was added, from which moment the time of the process was measured. Samples (0.2 ml) were taken at regular intervals; a sample was added to 5 ml of aqueous NaOH of the concentration required for neutralizing the acid contained in the taken volume of the reaction mixture, and the mixture contained in the test tube was thoroughly stirred.

All the samples were analyzed chromatographically on a Tsvet 500 gas chromatograph with a flame-

1070-4272/04/7712-1994 © 2004 MAIK "Nauka/Interperiodica"

ionization detector and a 2000 × 3 mm steel column packed with Polysorb (0.16–0.2 mm grains). The carrier gas was nitrogen; the flow rate of nitrogen and hydrogen was 30, and that of air, 300 $cm^3\ min^{-1}$. The temperatures of the column, detector, and vaporizer were 150°C. The relative error of analysis was 3%.

As mentioned above, DMM is formed by a two-stage reaction between M and FA:

$$HCHO + CH_3OH \underset{k_{-1}}{\overset{k_1}{\rightleftarrows}} HOCH_2OCH_3, \quad (1)$$

$$HOCH_2OCH_3 + CH_3OH \underset{k_{-2}}{\overset{k_1}{\rightleftarrows}} CH_2(OCH_3)_2 + H_2O. \quad (2)$$

The rate of formation of hemiacetal (HA) is very high [3], with the equilibrium strongly shifted toward its formation [4]. Since M was taken in excess in all the experiments, we assumed that the whole amount of FA was in the form of HA. Thus, we developed a kinetic model taking into account reaction (2) only. We described the DMM formation rate of by the differential equation

$$dc_{DMM}/d\tau = k_2' c_{PA} c_M - k_{-2}' c_{DMM} c_{H_2O},$$

where k_2' and k_{-2}' are the effective rate constants, $l\ min^{-1}\ mol^{-1}$; c_{PA}, c_M, c_{DMM}, and c_{H_2O}, concentrations (M) of PA, M, DMM, and water, respectively.

This equation was solved by the Runge-Kutta method. The rate constants were calculated by the least-squares method. Figure 1 shows the typical kinetic curves of DMM formation.

The dependence of the effective rate constants k_2' and k_{-2}' on the catalyst concentration was described by the equation

$$k_2' = k_2 c_{cat}^n, \quad k_{-2}' = k_{-2} c_{cat}^m,$$

where k_2 and k_{-2} are true rate constants, $l^2\ min^{-1}\ mol^{-2}$; c_{cat}, catalyst concentration, M; and n and m, reaction orders with respect to the catalyst.

Figure 2 shows that the logarithm of the effective rate constants linearly varies with the logarithm of the catalyst concentration. The orders with respect to the catalyst are identical for the constants k_2' and k_{-2}', namely, 1.43.

The constants k_2 and k_{-2} were calculated by the equations

$$k_2 = k_2'/c_{cat}^{1.43}, \quad k_{-2} = k_{-2}'/c_{cat}^{1.43}.$$

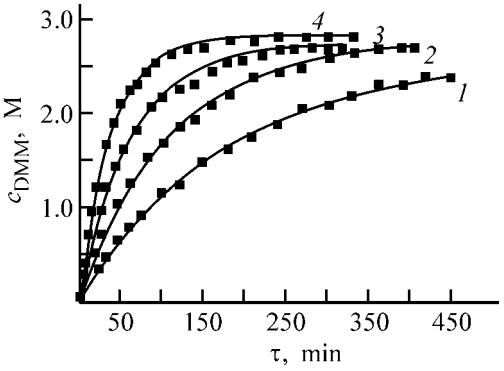

Fig. 1. Kinetic curves of DMM formation at (*1*) 303, (*2*) 308.3, (*3*) 313.3, and (*4*) 318.3 K. M : FA molar ratio 2 : 1. (c_{DMM}) DMM concentration, and (τ) time. (*Solid line*) Calculated values and (*black squares*) experimental values at c_{cat} = 0.1298 M.

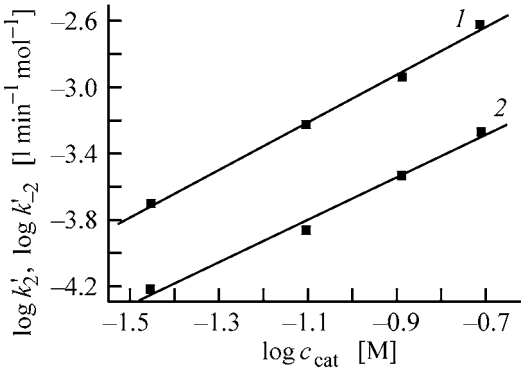

Fig. 2. Variation of the effective rate constants (*1*) k_2' and (*2*) k_{-2}', of DMM formation with the catalyst concentration c_{cat} at 313.3 K.

The temperature dependence of the rate constant is described by the Arrhenius equation (see table), and it was used for determining the expressions for $k_2 = f(T)$ and $k_{-2} = f(T)$ (activation energy, J mol^{-1}; temperature, K):

$$k_2 = 1.478 \times 10^{13} e^{-88\,800/RT},$$

$$k_{-2} = 6.798 \times 10^{11} e^{-84\,690/RT}.$$

Rate constants k_2 and k_{-2} at different temperatures

T, K	k_2	k_{-2}
	$l^2\ min^{-1}\ mol^{-2}$	
303	0.007421	0.001855
308.3	0.01318	0.002784
313.3	0.02226	0.005566
318.3	0.03897	0.008165
323.1	0.06679	0.01484

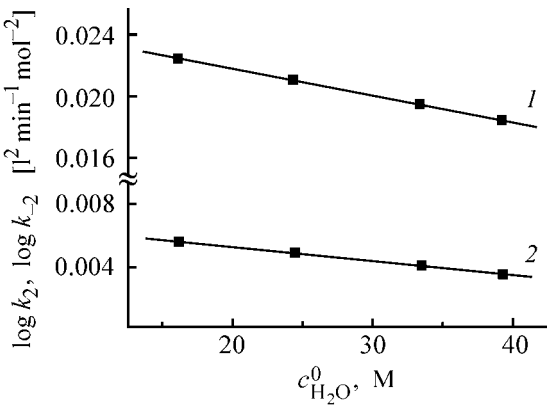

Fig. 3. Variation of the rate constants (*1*) k_2' and (*2*) k_{-2}', of DMM formation with the initial water concentration c^0_{H2O} at 313.3 K.

Using the dependences of k_2 and k_{-2} (T = 313.3 K) on the initial concentration of water in the system (Fig. 3), we derived the expressions

$$k_2 = 0.02493 - 0.000161c^0_{H_2O},$$
$$k_{-2} = 0.0069 - 0.00008454c^0_{H_2O}.$$

These dependences suggest that the rate constants k_2 and k_{-2} are weakly dependent both on the initial water concentration in the system and, evidently, on the composition of the reaction mixture as a whole.

CONCLUSION

A kinetic model was developed for synthesis of dimethoxymethane from methanol and formaldehyde, catalyzed by silicotungstic heteropoly acid $H_4SiW_{12}O_{40}$. The dependences of the rate constants of the process on the temperature and composition of the medium were obtained.

REFERENCES

1. Chinese Patent 688 041.
2. UK Patent 1 379 444.
3. Walker, J.F., *Formaldehyde*, 2-nd ed., New York: American Chem. Soc., 1953. Translated under the title *Formal'degid*, Moscow: Goskhimizdat, 1957.
4. Zhenghun Shan, Yanru Wang, Shouchang Qiu, *et al.*, *Fluid Phase Equil.*, 1995, vol. 111, no. 1, pp. 113–126.

Russian Journal of Applied Chemistry, Vol. 77, No. 12, 2004, pp. 1997–2000. Translated from Zhurnal Prikladnoi Khimii, Vol. 77, No. 12, 2004, pp. 2021–2024.

ORGANIC SYNTHESIS AND INDUSTRIAL ORGANIC CHEMISTRY

Nucleophilic Substitution of Chlorine with Hydrazine and Methylhydrazine in Chlorinated Pyridazines and Pyridazones

A. B. Baranov, V. G. Tsypin, A. S. Malin, and B. M. Laskin

Prikladnaya Khimiya Russian Scientific Center, St. Petersburg, Russia

Received August 18, 2004

Abstract—The reactions of methylhydrazine and hydrazine hydrate with chlorinated pyridazines and pyridazones were studied.

The reactivity of hydrazine and methylhydrazine toward aliphatic and aromatic compounds has been well studied [1, 2]. However, data on reactions of hydrazine and methylhydrazine with heterocycles and, in particular, with pyridazines are scarce. The interest in the chemistry of hydrazine is determined by its diverse applications in science and technology. In particular, hydrazine derivatives are widely used in medicine as physiologically active compounds exhibiting antitubercular, anticancer, radiation-protective, and other effects; in agriculture, as plant growth regulators and stimulants, as insecticides, fungicides, and hebricides; and in industry, for preparing synthetic fibers, films, and coatings [3, 4].

In this study we examined the reactions of hydrazine hydrate and methylhydrazine with some chlorinated pyridazines and pyridazones.

In the pyridazine series, available substrates for nucleophilic substitution are 4,5-dichloro-6-pyridazone **I**, 1-methyl-4,5-dichloro-6-pyridazone **II**, 3,4,5-trichloropyridazine **III**, 3,6-dichloropyridazine **IV**, and 3-methyl-6-chloropyridazine **V** [5–8]:

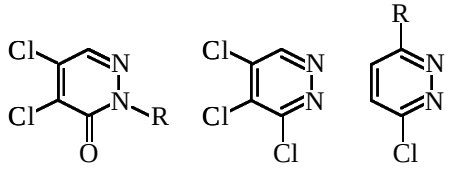

I, **II** **III** **IV**, **V**

where R = H (**I**), Me (**II**, **V**), Cl (**IV**).

It is known that pyridazone **I** reacts with ammonia [9], alkylamines [10], and hydrazine [11] selectively with chlorine substitution at the 4-position of the pyridazine ring. This is due to the activating effect of the keto group on the 4-position in **I** [10, 12]. However, it has been reported [13, 14] that the reaction of **I** with ammonia yields a mixture of 4-amino-5-chloro-6-pyridazone **VI** and 5-amino-4-chloro-6-pyridazone **VII**.

Our experiments showed that pyridazone **I** reacts with methylhydrazine in 2-propanol strictly specifically to give 4-(1-methylhydrazino)-5-chloro-6-pyridazone **VIII** in 95% yield. In methylation of **VIII** with dimethyl sulfate in methanol in the presence of sodium, the reaction occurs selectively at the 1-position of the pyridazine ring, giving 1-methyl-4-(1-methylhydrazino)-5-chloro-6-pyridazone **IX** in 37% yield.

It is known [11] that the reaction of **I** with 95% hydrazine in methanol yields exclusively 4-hydrazino-5-chloro-6-pyridazone **X**. Its structure was determined by hydrogenation (Pd/C) and independent synthesis of the dechlorination products. However, under the experimental conditions, the reaction of **I** with 100% hydrazine hydrate in ethanol yields a mixture of pyridazone **X** and 5-hydrazino-4-chloro-6-pyridazone **XI** in 29 and 48% yields, respectively, which is confirmed by the ^{1}H NMR and TLC data, and also by depression of the melting point, observed on mixing **X** and **XI**.

Then we performed methylation of **X** with dimethyl sulfate. The reaction was performed in the system 10% aqueous NaOH solution–$CHCl_3$ in the presence of Et_4NI. The reaction occurs selectively at the N^1 atom of the hydrazine moiety, yielding pyridazone **VIII**:

1070-4272/04/7712-1997 © 2004 MAIK "Nauka/Interperiodica"

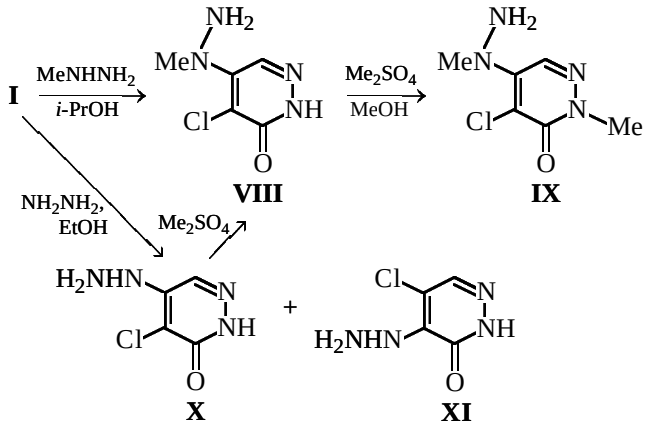

It is known that the reaction of pyridazone **II** with various amines occurs selectively with the substitution of chlorine at the 4-position of the pyridazine ring [10]. We also studied the reactions of pyridazone **II** with methylhydrazine and hydrazine hydrate. Pyridazone **II** does not react with methylhydrazine in refluxing alcohols (methanol, 56°C, 30 h; ethanol, 78°C, 30 h; 2-propanol, 86°C, 30°C; 1-butanol, 110°C, 30 h) and is recovered unchanged from the reaction mixture. The attempted reaction of **II** with 100% hydrazine hydrate in ethanol and 2-propanol results in tarring.

It is known that pyridazine **III** is synthesized by the reaction of **I** with $POCl_3$ [6]; acidolysis of **III** in glacial acetic acid eliminates chlorine from the 3-position of the pyridazine ring to give tion of **I**.

Our experiments showed that pyridazine **III** reacts with methylhydrazine in 2-propanol at 45°C selectively with substitution of the 5-Cl atom to give 5-(1-methylhydrazino)-3,4-dichloropyridazine **XII** in 40% yield. Acidolysis of **XII** in glacial acetic acid at 60°C gives pyridazone **VIII** in 10% yield:

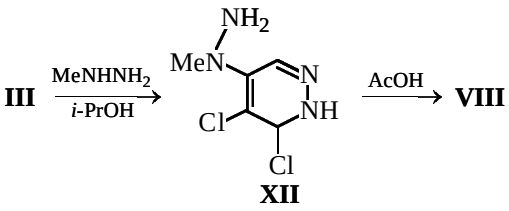

The starting substrates **IV** and **V** were prepared by the procedures described in [7, 8, 15]. We found that pyridazine **IV** in ethanol at 78°C reacts with methylhydrazine selectively with substitution of one chlorine atom to give 3-(1-methylhydrazino)-6-chloropyridazine **XIII** in 55% yield. The reaction of **V** with methylhydrazine in 1-butanol at 110°C gives 3-methyl-6-(1-methylhydrazino)pyridazine **XIV** in 32% yield:

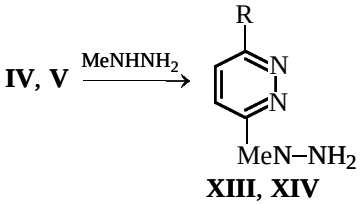

where R = Cl (**XIII**), Me (**XIV**).

EXPERIMENTAL

The ^1H NMR spectra were measured on a DPX-300 spectrometer (300 MHz), solvent DMSO-d_6, internal reference TMS. The elemental analysis was performed on a Hewlett–Packard automatic C, H, N analyzer. The melting points were determined on a PTP device. The TLC analysis was performed on Silufol UV-254 plates (eluent 90 vol % $CHCl_3$–10 vol % MeOH), development with UV light and iodine vapor.

4,5-Dichloro-6-pyridazone **I** and 1-methyl-4,5-dichloro-6-pyridazone **II** were prepared by the procedure described in [5].

3,4,5-Trichloropyridazine III. To 10 ml of $POCl_3$ we added with stirring 3 g of **I**. The mixture was stirred at 70°C for 6 h, after which excess $POCl_3$ was distilled off. The residue was cooled to 0–2°C and carefully neutralized with 5% aqueous NaOH. The precipitate of **III** was filtered off and dried in air; yield 1.45 g (43%), mp 56–58°C.

Found, %: C 26.10, H 0.01, N 15.20.
$C_4HCl_3N_2$.
Calculated, %: C 26.16, H 0.01, N 15.26.

4-(1-Methylhydrazino)-5-chloro-6-pyridazone VIII. (a) A 5-g portion of **I** was dissolved in 85 ml of 2-propanol, and a solution of 2.9 g of methylhydrazine in 15 ml of 2-propanol was added. The mixture was refluxed with stirring for 2 h, after which it was cooled and kept for 12 h at 0°C. The precipitate of **VIII** was filtered off and dried in air; yield 5.04 g (95%), mp 144–146°C (dec.). ^1H NMR spectrum, δ, ppm: 12.40 s (1H, NH in heterocycle), 8.19 d (1H, CH), 4.77 s (2H, NH_2), 3.40 s (3H, Me).

Found, %: C 34.31, H 0.04, N 32.05.
$C_5H_7ClN_4O$.
Calculated, %: C 34.38, H 0.04, N 32.09.

(b) A 2-g portion of **X** was dissolved in 20 ml of 10% aqueous NaOH, and 3.25 g of Et_4NI was added.

The mixture was heated with stirring to 30°C, and 2.1 ml of dimethyl sulfate in 20 ml of chloroform was added. The resulting mixture was stirred at 40°C for 10 h, cooled, and settled. The aqueous layer was treated with a 20-ml portion of chloroform. The extract was combined with the organic phase, the solvent was distilled off, and the precipitate of **VIII** was dried in air and recrystallized from ethanol; yield 0.21 g (10%).

(c) A 2-g portion of **XII** was dissolved in 50 ml of glacial acetic acid. The mixture was stirred at 60°C for 12 h, cooled, and kept at 0–5°C for 12 h. The precipitate of **VIII** was filtered off, dried in air, and recrystallized from ethanol; yield 0.19 g (10%).

1-Methyl-4-(1-methylhydrazino)-5-chloro-6-pyridazone IX. A 2-g portion of Na was dissolved in 30 ml of methanol, 3 g of **VIII** was added, the mixture was heated to 35–40°C, and a solution of 3 ml of dimethyl sulfate in 5 ml of methanol was slowly added with stirring. The mixture was stirred at 35–40°C for an additional 14 h and cooled; excess methanol was distilled off. The residue was mixed with 20 ml of 10% aqueous NaOH and treated with 50 ml of chloroform. Excess chloroform was distilled off, and the precipitate of **IX** was filtered off and dried in air; yield 1.22 g (38%), mp 136–137°C. ^{1}H NMR spectrum, δ, ppm: 8.19 s (1H, CH), 4.82 s (2H, NH_2), 3.57 s (3H, CH_3 in heterocycle), 3.38 s (3H, Me).

Found, %: C 38.15, H 4.72, N 29.68.
$C_6H_9ClN_4O$.
Calculated, %: C 38.19, H 4.77, N 29.71.

4-Hydrazino-5-chloro-6-pyridazone X and 5-hydrazino-4-chloro-6-pyridazone XI. A 3.3-g portion of **I** was dissolved in 60 ml of ethanol. This solution was heated to 70–75°C, and 3 g of 100% hydrazine hydrate in 10 ml of ethanol was added. The mixture was stirred at 70–75°C for 4 h and cooled; the precipitate containing a mixture of **X** and **XI** was filtered off and dried in air. To separate **X** and **XI**, the mixture was boiled in 50 ml of water and filtered while hot to separate difficultly soluble pyridazone **XI**. The mother liquor was cooled, and the precipitate of **X** was filtered off and dried; yield 0.95 g (30%), mp 195°C. ^{1}H NMR spectrum, δ, ppm: 12.30 s (1H, CH), 8.07 s (1H, NH in heterocycle), 7.63 s (1H, NH), 4.62 s (2H, NH_2).

Found, %: C 29.83, H 3.09, N 34.80.
$C_4H_5ClN_4O$.
Calculated, %: C 29.91, H 3.11, N 34.89.

For 5-hydrazino-4-chloro-6-pyridazone **XI**: yield 1.55 g (48%), mp 189°C. ^{1}H NMR spectrum, δ, ppm: 12.29 s (1H, CH), 8.07 s (1H, NH in heterocycle), 7.60 s (1H, NH), 4.50 s (2H, NH_2).

Found, %: C 29.90, H 3.10, N 34.85.
$C_4H_5ClN_4O$.
Calculated, %: C 29.91, H 3.11, N 34.89.

Mixing of **X** (R_f 0.11) and **XI** (R_f 0.35) showed 20°C depression of the melting point.

5-(1-Methylhydrazino)-3,4-dichloropyridazine XII. A 3-g portion of **III** was dissolved in 30 ml of 2-propanol. The solution was heated with stirring to 40°C, a solution of 1.87 g of methylhydrazine in 5 ml of 2-propanol was added, and the mixture was stirred at 45°C for 10 h, cooled, and kept at 0–2°C for 12 h. The precipitate of **XII** was filtered off and dried in air; yield 1.27 g (40%), mp 116–117°C. ^{1}H NMR spectrum, δ, ppm: 9.11 s (1H, CH), 4.99 s (2H, NH_2), 3.40 s (3H, Me).

Found, %: C 30.98, H 3.10, N 28.95.
$C_5H_6Cl_2N_4$.
Calculated, %: C 31.09, H 3.11, N 29.01.

3-(1-Methylhydrazino)-6-chloropyridazine XIII. A 30-g portion of **IV** was dissolved with stirring in 200 ml of ethanol, a solution of 19.4 g of methylhydrazine in 40 ml of ethanol was added, the mixture was stirred at 70–80°C for 1 h, and the solvent was distilled off. The residue was stirred with 200 ml of water at 50–60°C until it completely dissolved. The resulting mixture was cooled, and the precipitate of **XIII** was filtered off, dried in air, and crystallized from water or benzene; yield 17.5 g (55%), mp 110–111°C. ^{1}H NMR spectrum, δ, ppm: 3.33 s (3H, Me), 4.61 s (2H, NH_2), 7.23 d (1H, CH in heterocycle), 7.53 d (1H, CH in heterocycle).

Found, %: C 37.3, H 4.3, N 34.9.
$C_5H_7ClN_4$.
Calculated, %: C 37.9, H 4.4, N 35.1.

3-Methyl-6-(1-methylhydrazino)pyridazine XIV. A solution of 2.24 g of methylhydrazine in 10 ml of 1-butanol was added with stirring to a solution of 2.5 g of **V** in 25 ml of 1-butanol. The mixture was stirred at 108–111°C for 1 h, and excess solvent was distilled off. The residue was dissolved in 25 ml of water and treated with 50 ml of chloroform. Excess chloroform was distilled off, and the precipitate of

XIV was filtered off, dried in air, and recrystallized from CCl_4; yield 0.91 g (32%), mp 73–75°C. ^1H NMR spectrum, δ, ppm: 3.30 s (3H, Me), 4.38 s (2H, NH_2), 7.06 d (1H, CH in heterocycle), 7.39 d (1H, CH in heterocycle).

Found, %: C 52.3, H 7.1, N 40.4.
$C_6H_{10}N_4$.
Calculated, %: C 52.2, H 7.2, N 40.6.

CONCLUSIONS

(1) In the reaction of 4,5-dichloro-6-pyridazone with methylhydrazine, the nucleophilic substitution of chlorine occurs selectively at the 4-position of the ring to give 4-(1-methylhydrazino)-5-chloro-6-pyridazone (yield 95%), whereas the reaction of 4,5-dichloro-6-pyridazone with hydrazine hydrate gives a mixture of products of chlorine substitution at the 4-and 5-positions (yield 30 and 48%, respectively).

(2) 3,4,5-Trichloropyridazine reacts with methylhydrazine in 2-propanol selectively with substitution of the 5-Cl atom to give 5-(1-methylhydrazino)-3,4-dichloropyridazine in 40% yield. Acidolysis of 5-(1-methylhydrazino)-3,4-dichloropyridazione in glacial acetic acid gives 4-(1-methylhydrazino)-5-chloro-6-pyridazone (yield 10%).

REFERENCES

1. Ioffe, B.V., Kuznetsov, M.A., and Potekhin, A.A., *Khimiya organicheskikh proizvodnykh gidrazina* (Chemistry of Organic Hydrazine Derivatives), Leningrad: Khimiya, 1979.
2. Audrieth, L.F. and Ogg, B.A., *The Chemistry of Hydrazine*, New York: Wiley, 1951.
3. Soldatenkov, A.T., Kolyadina, N.M., and Shendrik, I.V., *Osnovy organicheskoi khimii lekarstvennykh veshchestv* (Fundamentals of the Organic Chemistry of Drugs), Moscow: Khimiya, 2001.
4. Mel'nikov, N.N., *Khimiya i tekhnologiya pestitsidov* (Chemistry and Technology of Pesticides), Moscow: Khimiya, 1974.
5. Mowry, D.T., *J. Am. Chem. Soc.*, 1953, vol. 75, no. 8, pp. 1909–1910.
6. Kuraishi, T., *Chem. Pharm. Bull.*, 1957, vol. 5, no. 4, pp. 376–378.
7. Mizzoni, R.H. and Spoerri, P.E., *J. Am. Chem. Soc.*, 1951, vol. 73, no. 4, pp. 1873–1874.
8. Overend, W.G. and Wiggins, L.F., *J. Chem. Soc.*, 1947, no. 2, pp. 239–244.
9. Kuraishi, T., *Chem. Pharm. Bull.*, 1958, vol. 6, no. 4, pp. 331–333.
10. Bourdais, J., *Bull. Soc. Chim. Fr.*, 1964, no. 9, pp. 2124–2132.
11. Osner, W.M., Castle, R.N., and Alduns, D.L., *J. Pharm. Sci.*, 1963, vol. 52, no. 6, pp. 539–540.
12. Shepherd, R.G. and Fedrick, J.L., *Adv. Heterocyclic Chem.*, 1965, vol. 4, pp. 145–423.
13. Castle, R.N. and Seese, W.S., *J. Org. Chem.*, 1958, vol. 23, no. 10, pp. 1534–1538.
14. Landguist, J.K. and Thornber, C.W., *J. Chem. Soc., Perkin Trans. 1*, 1973, no. 10, pp. 1114–1117.
15. Coad, P., Coad, R.A., Clough, S., *et al., J. Org. Chem.*, 1963, vol. 28, no. 1, pp. 218–221.

Russian Journal of Applied Chemistry, Vol. 77, No. 12, 2004, pp. 2001–2005. Translated from Zhurnal Prikladnoi Khimii, Vol. 77, No. 12, 2004, pp. 2025–2030.

ORGANIC SYNTHESIS AND INDUSTRIAL ORGANIC CHEMISTRY

Cleaning Action and Surfactant Properties of Alkyl Glucosides

O. D. Yakimchuk, A. A. Kotomin, M. B. Petel'skii, and V. N. Naumov

St. Petersburg State Technological Institute, St. Petersburg, Russia

Received September 24, 2004

Abstract—Cleaning action and surfactant properties of a series of alkyl glucosides, having high detergent power, emulsifying capacity, and biodegradability and low foaming capacity, were studied. The effects of various factors on the cleaning action of the surfactants and compositions on them were investigated, allowing prediction of the cleaning effect on the basis of data on physicochemical characteristics of the solutions and process parameters.

Today there is a tendency to reduce the use of certain classes of surfactants polluting the environment and to change them for new ones [1–3]. Accordingly, efforts are being made to develop new classes of surfactants with reduced foaming capacity and mild action, which operate at a lower temperature, with synergistic action of their components [3–6]. Such new surfactants should be environmental friendly and cost efficient.

Alkyl glucosides only recently started to be used in production of detergents, and, therefore, their properties are little studied. Some of them demonstrate very good surfactant properties [7–9]. These surfactants are stable in alkaline and acidic solutions and show careful action with respect to color retention. The use of this class of surfactants for production of detergents shows promise not only from the efficiency standpoint, but also in view of the environmental protection. Alkyl glucosides are characterized by high biodegradability, as being manufactured from natural raw materials. At the same time, these are mild, low-toxic surfactants providing no skin irritation. Large-scale application of alkyl glucosides was previously limited by their high cost. However, in recent years, the cost demonstrates a steady tendency to decrease.

Till now researchers mostly focused on long-chain alkyl glucosides with a broad distribution of the number of carbon atoms in the chain (C_{10}–C_{18}) [8, 9]. Short-chain compounds virtually have not been studied. However, such alkyl glucosides are of interest in view of the fact that they may have low foaming and good emulsifying properties.

In this study, we examined the relationships between the physicochemical characteristics of alkyl glucosides $C_6H_{11}O_5$–O–C_nH_{2n+1} and their cleaning properties. The results were then compared with those obtained for the known anionic and nonionic surfactants: linear sodium alkylbenzenesulfonate [SABS, C_{10-14}–(C_6H_4)–SO_3Na], sodium alkylsulfonate (C_{12-18}–SO_3Na), Syntanol DS-10 [C_{10-18}–$O(C_2H_4O)_{10}H$], Syntanol ALM-10 [C_{12-14}– $O(C_2H_4O)_{10}H$], and Neonol AF_9-12 [C_9H_{12}–C_6H_4–$O(C_2H_4O)_{12}H$]. We also studied the effect of the length of the hydrocarbon chain on the cleaning action and surfactant properties in the homologous series of alkyl glucosides with short (C_6, C_8, and C_{8-10}) and long (C_{8-16} and C_{12-14}) chains. It should be pointed out that the short-chain alkyl glucosides studied are new compounds, and their cleaning action and surfactant properties have not been investigated yet.

The cleaning action was determined from the whiteness of laundered cotton fabric samples [10]. Then the cleaning action in the test solutions was compared with that obtained in a reference solution, M_{ref}, under similar conditions. The reference solutions contained linear sodium alkylbenzenesulfonate (1 g l^{-1}) and sodium tripolyphosphate (2 g l^{-1}) in accordance with GOST (State Standard) 22 567.15–95. To eliminate some side effects, we used the relative cleaning action of a compound $M_{rel} = M/M_{ref}$ as a basic parameter in analysis of the results.

It follows from the concentration dependences of the relative cleaning action of alkyl glucosides (Table 1) that the cleaning effect increases as the hydrocarbon chain becomes longer. Short-chain alkyl glucosides (C_6 and C_8) demonstrate low cleaning action, while that of alkyl glucoside C_{8-10} is higher as compared to SABS and sodium alkylsulfonate

1070-4272/04/7712-2001 © 2004 MAIK "Nauka/Interperiodica"

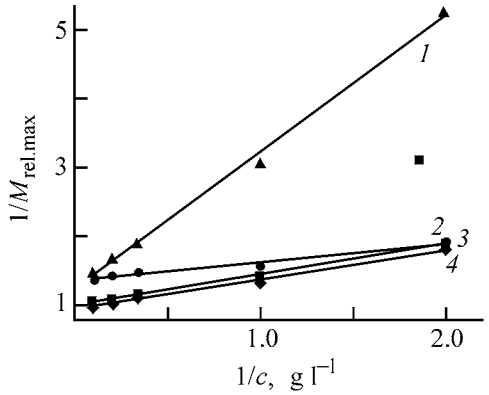

Cleaning effect of surfactants, $M_{rel.max}$, vs. their concentration c: (*1*) SABS, (*2*) Neonol AF_9-12, (*3*) alkyl glucoside $C_{8–16}$, and (*4*) alkyl glucoside $C_{12–14}$.

(Volgonate). Alkyl glucosides $C_{8–16}$ and $C_{12–14}$ demonstrated very high cleaning effect, which exceeded that of all the previously studied surfactants. The cleaning effect of alkyl glucoside $C_{12–14}$ was found to be slightly higher then that of $C_{8–16}$.

Previously, we have shown [10, 11] that, for surfactants and detergents, the dependence of the relative cleaning action M_{rel} on their concentration c in aqueous solutions, being plotted in the reciprocal coordinates, is a linear function expressed by Eq. (1).

$$M_{rel} = \frac{M_{rel.max}}{\alpha + c}, \quad (1)$$

where $M_{rel.max}$ and α are the parameters suggested as quantitative characteristics of the cleaning power of detergents.

Data on the cleaning effect of alkyl glucosides show that Eq. (1) is valid for this class of surfactants. The figure demonstrates the dependence of the reciprocal of $M_{rel.max}$ on the reciprocal of c for alkyl glucosides SABS and Neonol AF_9-12. As seen, the cleaning effect of alkyl glucosides $C_{12–14}$ and $C_{8–16}$ is higher.

The cleaning effect of the conventional anionic and nonionic surfactants (Table 1) depends on their structure and physicochemical characteristics, such as the work of adsorption W_a, limiting adsorption Γ_m, critical micelle concentration CMC, and work of micelle formation W_m. In this study, we examined whether the general structure-property relationships are valid for alkyl glucosides.

Table 1 summarizes the physicochemical characteristics of alkyl glucosides, determined from the experimental surface tension isotherms. The results reveal that the work of adsorption increases with increasing length of the alkyl chain of surfactants. Since the work of adsorption is a measure of the surface activity, which, in turn, controls the cleaning effect, it may be suggested that an increase in the work of adsorption causes to a significant extent an increase in the cleaning effect in the series of alkyl glucosides and formulations based on them.

The cleaning action is also associated with the critical micelle concentration. Cleaning requires a certain amount of a surfactant for wetting of the surface to be cleaned, emulsification of liquid pollutants and suspension of solid pollutants, foaming, and protection

Table 1. Relative cleaning effect M_{rel} and surfactant properties of alkyl glucosides and several anionic and nonionic surfactants*

Surfactant	M_{rel} at indicated c, g l^{-1}					$\Gamma_m \times 10^6$, mol m^{-2}	W_a, kJ mol^{-1}	c_{CMC}, g l^{-1}	W_m, kJ mol^{-1}
	0.5	1.0	3.0	5.0	10.0				
Alkyl glucoside:									
C_6	0.06	0.10	0.17	0.20	0.23	3.0	23.4	5.86	18.9
C_8	0.10	0.16	0.27	0.31	0.37	3.0	25.6	3.56	20.4
$C_{8–10}$	0.23	0.36	0.58	0.65	0.71	2.9	31.1	0.92	23.8
$C_{12–14}$	0.56	0.75	0.90	0.98	1.02	2.8	41.0	0.01	35.1
$C_{8–16}$	0.53	0.71	0.85	0.92	0.97	2.9	39.2	0.02	33.3
SABS	0.19	0.33	0.53	0.59	0.69	3.4	26.3	1.420	23.7
Volgonate	0.18	0.29	0.54	0.61	0.70	3.5	26.1	1.170	23.8
Syntanol DS-10	0.52	0.61	0.65	0.69	0.72	2.9	36.7	0.046	34.0
Neonol AF_9-12	0.53	0.65	0.68	0.70	0.74	2.6	38.5	0.061	33.0
Syntanol ALM-10	0.47	0.57	0.63	0.66	0.70	2.9	33.8	0.086	31.3

* (Γ_m) Limiting adsorption, (W_a) work of adsorption, (CMC) critical micelle concentration, and (W_m) work of micelle formation.

from resorption. After establishment of the critical micelle concentration, the fatty and solid pollutants are additionally stabilized in the surfactant micelles. With increasing surfactant concentration in the solution, the solubilization increases, as new coarser micellar structures are formed, providing an additional potential for retention of pollutants. Table 1 shows that, with increasing length of the hydrocarbon chain in the alkyl glucoside molecules, their CMC decreases and work of adsorption increases. Therefore, these factors can also enhance the cleaning effect with increasing length of the chain.

The limiting adsorption is controlled in our case by the chemical nature of the polar fragment of a surfactant, which is the same in all the alkyl glucosides studied. Therefore, the limiting adsorption should be constant throughout the homologous series (Table 1), being about 2.9 mol m^{-2}.

The hydrophilic–lipophilic balance (HLB) for the alkyl glucosides is as follows: C_6 17, C_8 16, C_{8-10} 14–12, C_{12-14} 14–12, and C_{8-16} 16–14, suggesting that these surfactants are direct-emulsion emulsifiers.

Alkyl glucosides C_{8-16} and C_{12-14} demonstrate a higher cleaning effect as compared to nonionic surfactants examined in this study (Table 1). Accordingly, they have a higher work of adsorption and lower CMC.

The cleaning effect of alkyl glucoside C_{8-10} is slightly higher than that of SABS. Correspondingly, this glucoside has a higher work of adsorption and lower limiting adsorption and CMC (Table 1).

Thus, the general structure–property relationships typical of the conventional nonionic and anionic surfactants are valid for alkyl glucosides too.

We also studied the cleaning effect of 1 : 1 (by weight) surfactant–soda binary mixtures. Table 2 shows that, for alkyl glucosides C_{8-10} and C_{12-14}, the cleaning effect of such mixtures is considerably higher over the entire experimental concentration range as compared to SABS–soda mixtures.

The foaming capacity of the alkyl glucosides was determined by the Ross–Miles method, which is accepted as a standard procedure in many countries. The measurements were carried out at a constant concentration (0.5 g l^{-1}) and temperature (20°C) (Table 3). As seen, short-chain glucosides demonstrate very low foaming capacity, allowing their use in those cases when foaming is undesirable. The foaming capacity of alkyl glucosides C_{8-10}, C_{12-14}, and C_{8-16} is lower than that of SABS, making it possible to use them instead of SABS in low-foam detergents. Alkyl glucoside C_{12-14} has a higher cleaning effect and lower foaming capacity as compared to C_{8-16}, which makes it preferable to use the former surfactant in production of detergents.

Table 2. Relative cleaning effect M_{rel} of 1 : 1 surfactant–soda binary mixtures

Surfactant	M_{rel} at indicated c, g l^{-1}				
	0.5	1.0	3.0	5.0	10.0
Alkyl glucoside:					
C_6	0.41	0.59	0.68	0.72	0.80
C_8	0.46	0.62	0.73	0.81	0.87
C_{8-10}	0.70	0.93	1.17	1.27	1.32
C_{12-14}	0.82	1.10	1.48	1.58	1.65
SABS	0.67	0.86	0.99	1.02	1.05

Table 3. Foaming capacity of alkyl glucosides and sodium alkylbenzenesulfonate

Surfactant	Foam height, mm, at indicated τ, min		
	0	3	5
Alkyl glucoside:			
C_6	2	0	0
C_8	4	0	0
C_{8-10}	90	79	78
C_{12-14}	98	86	83
C_{8-16}	109	96	94
SABS	118	105	100

We studied the cleaning effect of alkyl glucosides C_{8-10}, C_{12-14}, and C_{8-16} at 30°C (Table 4). The results show that the difference in the cleaning effect of the alkyl glucosides and SABS at lower temperature (30°C) becomes even stronger than that at 80°C. Therefore, these surfactants are preferable in production of low-temperature detergents.

Alkyl glucosides C_{8-10}, C_{12-14}, and C_{8-16} and mixtures based on them can be used as components of detergent formulations intended for strongly polluted surfaces, i.e., in those cases when highly concentrated detergents are needed. The high cleaning power of the alkyl glucosides and mixtures on their basis allows considerable improvement of the quality of formulations with the total amount of an active compound remaining unchanged. Furthermore, the use of alkyl glucosides allows reduction in the total surfactant

Table 4. Relative cleaning effect M_{rel} of surfactants at 30 and 80°C

Surfactant	M_{rel} at indicated c, g l^{-1}									
	0.5	1.0	3.0	5.0	10.0	0.5	1.0	3.0	5.0	10.0
	30°C					80°C				
Alkyl glucoside:										
$C_{8–10}$	0.20	0.29	0.46	0.51	0.57	0.23	0.36	0.58	0.65	0.71
$C_{12–14}$	0.45	0.59	0.70	0.77	0.81	0.56	0.75	0.90	0.98	1.02
$C_{8–16}$	0.43	0.57	0.68	0.72	0.77	0.53	0.71	0.85	0.92	0.97
SABS	0.13	0.21	0.37	0.41	0.48	0.19	0.32	0.53	0.59	0.69

Table 5. Basic factors controlling the cleaning capacity of surfactants and formulations and conditions necessary to enhance their cleaning effect

Stage of cleaning	Physicochemical characteristics and factors of influence	Investigated range	Conditions necessary to increase the effect*
Adsorption	Work of adsorption	26 – 41 kJ mol^{-1}	↑
	Limiting adsorption	$(2.6–3.5) \times 10^{-6}$ mol m^{-2}	↓
Wetting and replacement of pollutants	Surface tension at the cleaning solution–air interface σ_w	40 –29 mJ m^{-2}	$\sigma_{os} \geq \sigma_{wo} + \sigma_{ws}$
Emulsifying	Hydrophilic–hydrophobic balance	5–17	8–14
Solubilization	CMC	0.01–1.40 g l^{-1}	↓
Process conditions	Addition of alkali salt (surfactant/salt weight ratio)	25/75–75/25	50/50
	Temperature	30–85°C	$M^t_{max} = 8.65 M^{30}_{max} e^{-661/T}$
	Concentration	0.5–50.0 g l^{-1}	$M_{rel} = M_{rel.max} c/(\alpha + c)$
	Mechanical activation (agitation rate)	50–200 rpm	↑

* Increase (↑) or decrease (↓) in the factor value results in increasing cleaning capacity; (σ_{wo}, σ_{ws}, σ_{os}) surface tension at the aqueous surfactant solution–nonpolar pollutant, surfactant solution–solid surface, and pollutant–solid surface interfaces, respectively.

content with the quality of the formulation remaining unchanged. This is important not only from the standpoint of economy, but also in view of the environmental protection demands (discharge of organics to the environment decreases).

Short-chain alkyl glucosides C_6 and C_8 can be used as components facilitating dissolution of surfactants and various additives in water, i.e., as hydrotropes. The estimated HLB values suggest that short-chain alkyl glucosides can be effective emulsifiers of the first kind. As known, recently a need arose in development of low-foam surfactants [2]. Since the cleaning effect of short-chain alkyl glucosides considerably increases in the presence of mineral salts, they can be used in emulsifying low-foam detergents.

Based on data on the cleaning effect and surfactant properties of various classes of surfactants and formulations, we obtained the dependences of the cleaning capacity on various factors. The basic physicochemical characteristics, factors of influence, and conditions necessary to enhance the cleaning effect are summarized in Table 5. These results allow prediction of the cleaning power of surfactants and formulations based on them.

It can be seen that in the concentration range practically significant for laundering of fabric (0.5–5.0 g l^{-1}), the maximum cleaning effect and, accordingly, high $M_{rel.max}$ and low α [Eq. (1)] are demonstrated by surfactants having the following physicochemical characteristics: W_a = 38–

41 kJ mol^{-1}, $\Gamma_m = (2.6–2.9) \times 10^{-6}$ mol m^{-2}, and CMC = 0.01–0.06 g l^{-1}.

Addition of alkali salts (soda, sodium metasilicate, and sodium tripolyphosphate) enhances the cleaning effect of the mixtures by 30–100% as compared to the individual surfactants.

CONCLUSIONS

(1) A study of the cleaning effect and surfactant properties of a series of alkyl glucosides, C_6, C_8, $C_{8–10}$, $C_{8–16}$, and $C_{12–14}$ revealed that, with increasing length of the hydrocarbon chain, the critical micelle concentration of the alkyl glucosides decreases, the work of adsorption increases, and the limiting adsorption remains approximately constant. Accordingly, the cleaning effect increases. The surfactants studied demonstrate good cleaning and emulsifying properties and low foam. Recommendations are made on practical use of the alkyl glucosides in detergent formulations.

(2) Systematization is made of the basic factors controlling the cleaning properties of surfactants and formulations and also of conditions necessary to enhance the cleaning effect.

ACKNOWLEDGMENTS

The authors are grateful to N.P. Shirokova for her help in experiments.

REFERENCES

1. Bulfori, M., *Riv. Ital. Sostanze Grasse*, 1995, vol. 72, no. 3, pp. 129–131.
2. Croy, C., *INFORM: Int. News Fats, Oils Relat. Mater.*, 1995, vol. 6, no. 1, pp. 6–7.
3. Richard, D., *Chim. Oggi.*, 1993, vol. 11, nos. 7–8, pp. 34–36.
4. Hreczuch, W., *Chimik*, 1997, vol. 50, no. 2, pp. 42–46.
5. King Hillary, S.B., *Soap Cosmet.*, 2001, vol. 77, no. 12, pp. 63–65.
6. Hairston, D., *Chem. Eng.*, 1994, no. 7, pp. 65–67.
7. *Poverkhnostno-aktivnye veshchestva: Spravochnik* (Surfactants: A Handbook), Pletnev, M.Yu., Ed., Moscow: Firma Klavel', 2002.
8. Valesyan, E., *Byt. Khim.*, 2003, no. 12, pp. 26–31.
9. El'sner, M., *Byt. Khim.*, 2003, no. 13, pp. 15–16.
10. Abramzon, A.A. and Kotomin, A.A., *Zh. Prikl. Khim.*, 2000, vol. 73, no. 11, pp. 1902–1904.
11. Kotomin, A.A., Abramzon, A.A., and Yakimchuk, O.D., *Zh. Prikl. Khim.*, 2001, vol. 74, no. 12, pp. 2038–2042.

Russian Journal of Applied Chemistry, Vol. 77, No. 12, 2004, pp. 2006–2010. Translated from Zhurnal Prikladnoi Khimii, Vol. 77, No. 12, 2004, pp. 2031–2035.

ORGANIC SYNTHESIS AND INDUSTRIAL ORGANIC CHEMISTRY

Variation of pH in Reaction of Sodium Sulfide with Carbonyl Compounds

A. M. Ivanov, O. S. Altukhova, and I. A. Ivanov

Kursk State Technical University, Kursk, Russia

Research Institute of Leather, Kursk, Russia

Received November 26, 2003; in final form, July 2004

Abstract—The results of an experimental study of how pH varies in the course of a reaction between sodium sulfite and carbonyl compounds are presented.

It is commonly believed that, of all carbonyl compounds, only formaldehyde can react with sodium sulfite with a nearly quantitative yield [1]. However, this is far from being the case. A similar reaction proceeds to a large extent with acetaldehyde, too [2], even though at lower rates and smaller maximum conversion. If the HA acid is introduced dropwise, following a certain program, the process occurs quantitatively with numerous carbonyl compounds. [2–4]. As this process is used industrially, in particular, in manufacture of greasing and emulsifying formulations for leather and fur [5–7], it was of interest to study it in more detail.

The experiment was carried out as follows. A reactor with a mechanical or magnetic stirrer and electrodes for pH measurements was charged with a certain amount of a preliminarily prepared solution of Na_2SO_3 (commonly 100 ml of a 0.5–1.3 M solution) and agitation was switched on. After that, a calculated amount of a carbonyl compound (most frequently, also in the form of a preliminarily prepared solution) was introduced and the variation of the pH values was monitored. Commonly, these values increased rather rapidly. At some instant of this rise, a 5–10 N solution of a mineral or carboxylic HA acid started to be introduced in an amount equivalent to the content of Na_2SO_3 in the starting reaction mixture. The acid was introduced for 10–150 min. High concentrations of the HA acid were chosen in order to avoid a strong dilution of the reaction mixture and the inevitably resulting distortion of the results obtained. After about 90% of the calculated amount of the acid was introduced, the rate of its introduction was considerably lowered or a more diluted acid was used. This was done in order not to pass through the point corresponding to the 100% conversion of the carbonyl compound (see table). Simultaneously, the reaction mixture was sampled to determine the content of the carbonyl compound and the sum of Na_2SO_3 and $NaHSO_3$.

In those cases when the solubility of a carbonyl compound in water was insufficient, attempts were

Effect of the nature of a carbonyl compound on the pH value reached by the end of the 2nd minute after the introduction of this compound into a Na_2SO_3 solution (pH_1) and by the time of its nearly complete consumption (pH_2) (equimolecular amounts of the reagents)

Carbonyl compound, mole	pH_0^*	pH_1	pH_2
Aldehyde:			
acetic, 0.10	10.05	12.82	6.25
propionic, 0.10	10.25	12.65	6.21
benzoic, 0.10	10.02	11.42	6.23
meta-nitrobenzoic, 0.05	9.40	11.36	6.43
para-chlorobenzoic, 0.05	9.82	11.15	6.32
ortho-nitrobenzoic, 0.05	9.45	10.95	6.70
para-nitrobenzoic, 0.05	9.45	10.65	6.25
meta-bromobenzoic, 0.05	9.85	10.38	6.65
Ketone:			
acetone, 0.10	9.75	11.50	6.25
cyclohexanone, 0.10	10.43	11.51	6.15
methyl butyl ketone, 0.10	9.94	10.45	6.22
acetophenone, 0.10	10.25	10.46	6.55

* Before introduction of a carbonyl compound.

1070-4272/04/7712-2006 © 2004 MAIK "Nauka/Interperiodica"

made to raise the solubility by introducing 5–30 vol % water-soluble alcohols into the reaction mixture. When these attempts failed, the carbonyl compound was preliminarily dissolved in an appropriate organic solvent and the resulting solution was introduced, together with a Na_2SO_3 solution in a 1 : (1–1.5) ratio by volume, into the reactor, with the emulsion maintained by means of agitation in a state uniform throughout the volume. In some cases, in particular, when the densities of the aqueous and organic phases differed by a factor of 1.5 and more, the process under consideration was performed in a bead mill with occasional monitoring of the pH value of the aqueous phase outside the working zone of the reactor.

Figure 1 shows how the pH values in the systems Na_2SO_3–acetaldehyde and Na_2SO_3–acetone vary with the amount of acid introduced and the corresponding variation of the concentrations of carbonyl compounds. A significant change in behavior on passing from an aldehyde to a ketone is well seen. In the case of the aldehyde, the initial pH value is considerably higher and falls as the amount of the acid introduced increases at a substantially slower rate, whereas the concentration of the carbonyl compound, contrariwise, decreases faster. This behavior is observed until the conversion of the carbonyl compound exceeds 80–85%, and after that the dependences for the aldehyde and ketone are described by virtually the same curve.

In an aqueous solution of Na_2SO_3, there exists the equilibrium

$$Na_2SO_3 + H_2O \rightleftarrows NaHSO_3 + NaOH. \quad (I)$$

If a carbonyl compound is introduced into such a solution, the following reaction occurs:

$$\rangle C{=}O + NaHSO_3 \xrightarrow{k_2} \rangle C(OH)SO_3Na. \quad (II)$$

This reaction results in that the equilibrium of reaction (I) is shifted to the right, and this predetermines a rise in the pH value of the reaction mixture. For aldehydes with high reactivity in reaction(II), the rise in the pH value is rather significant. In particular, at the initial concentrations of acetaldehyde and Na_2SO_3 equal to 1 M, the pH value changes from 9.4 at $\tau = 0$ to 13.5 during the first 37 min and, further, to 13.7 at $\tau = 1500$ min. Such a variation of the pH value with time [the function $pH = f(\tau)$ was recorded automatically] can be easily recalculated to a kinetic curve of NaOH accumulation (for the case in question, this is the range 3×10^{-5}–~0.5 M),

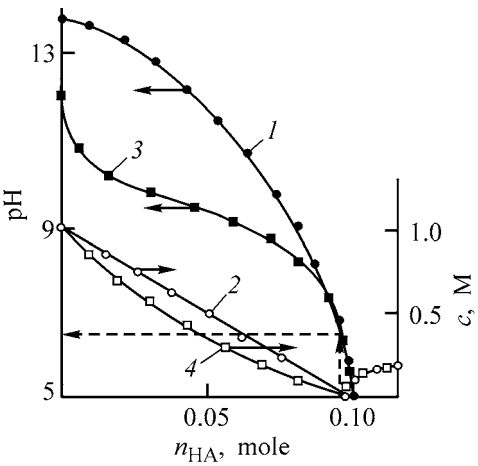

Fig. 1. (*1, 3*) pH value and (*2, 4*) the corresponding concentrations of carbonyl compounds vs. the amount n_{HA} of HCl introduced into the systems (*1, 2*) Na_2SO_3–acetaldehyde and (*3, 4*) Na_2SO_3–acetone. Dosage of each reagent 0.098 M; temperature 23°C, agitation with a magnetic stirrer.

which can be graphically differentiated to obtain values of $dc_{NaOH}/d\tau$.

Summation of the stoichiometric equations (I) and (II) yields the reaction equation

$$\rangle C{=}O + Na_2SO_3 + H_2O \rightarrow \rangle C(OH)SO_3Na + NaOH, \quad (III)$$

according to which the rate of NaOH accumulation must be equal to the consumption rates of both Na_2SO_3 and the carbonyl compound. This makes it possible to express the rate of reaction (II) in terms of the rate of NaOH accumulation:

$$\frac{dc_{NaOH}}{d\tau} = \frac{dc_{\rangle C=O}}{d\tau} = k_2 c_{NaHSO_3} c_{\rangle C=O}. \quad (1)$$

The concentrations of reagents in Eq. (1) are related to the concentration c_{NaOH} by the following expressions

$$c_{\rangle C=O} = c^0_{\rangle C=O} - c_{NaOH}, \quad (2)$$

$$c_{NaHSO_3} = \frac{6.3 \times 10^{-8}(c^0_{NaHSO_3} - c_{NaOH})}{c_{NaOH}}. \quad (3)$$

Substitution of Eqs. (2) and (3) into (1) gives the formula for evaluation of k_2. The value of k_2 for acetaldehyde was approximately 40 000 M^{-1}.

The value of k_2, estimated for acetone in a similar way, is approximately three orders of magnitude smaller. Therefore, the maximum conversion of a carbonyl compound by Eq. (III), α_{max}, is only several percent, against 40% and more for acetaldehyde. As $(0.7–0.8)\alpha_{max}$ is reached during the first several

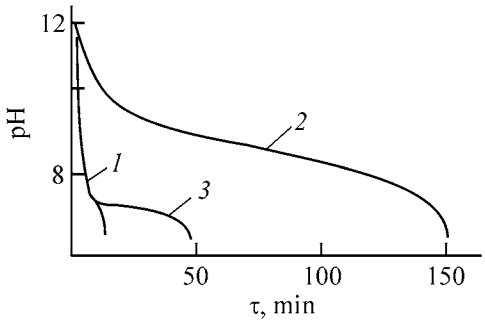

Fig. 2. Automatically recorded variation of the pH value with time τ at different concentrations of sulfuric acid introduced in the course of the reaction between acetone and Na_2SO_3 at 17°C. Dosage of each reagent 0.10 mole. H_2SO_4 concentration (equiv l^{-1}): (*1*) 8.6 and (*2, 3*) 1.05.

minutes, the corresponding rise in the pH value can be used for a rough estimate of the reactivity of a carbonyl compound under the chosen conditions (see table).

To raise the rate of the reaction between Na_2SO_3 and carbonyl compounds and make this reaction virtually quantitative, it is necessary to take the HA acid instead of water in the stoichiometric equation (III). This leads to the reliably practically substantiated stoichiometric equation

$$\rangle C{=}O + Na_2SO_3 + HA \rightarrow \rangle C(OH)SO_3Na + NaA. \quad (IV)$$

In accordance with this equation, for 1 mol of a carbonyl compound to be converted into a hydrosulfite derivative, it is necessary to introduce 1 mol of HA acid (1 mol-equiv for polybasic acids), in a good agreement with the data in Fig. 1.

Equation (IV) can be obtained by summing up the stoichiometric equations (I), (II), and (V):

$$NaOH + HA \rightarrow NaA + H_2O. \quad (V)$$

In this case, the role of the acid consists only in neutralization of the alkali accumulated in accordance with Eq. (III). However, such a function of the acid cannot be accepted as the only one, because it was established experimentally that reaction (IV) may occur quantitatively and at a comparable rate in a virtually anhydrous medium, i.e., between solutions of carbonyl compounds in organic solvents and solid Na_2SO_3 (with a bead mill as a reactor). As for the aqueous medium, reaction (V) accelerates reaction (II), and does so the more strongly, the larger the value of k_2. However, as shown by the experiment, the system of reactions (I) + (II) + (V) [or (III) + (V)] cannot ensure a quantitative extent of reaction (IV) by itself even at very large values of k_2. This occurs if the stoichiometric equation (IV) is represented as a sequence of reactions (II) and (VI):

$$Na_2SO_3 + HA \rightarrow NaHSO_3 + NaA. \quad (VI)$$

Most part of a carbonyl compound whose reactivity is comparable with, or is significantly lower than that of acetone is consumed in accordance with this scheme. Also by this scheme occur the final stages of reactions involving more reactive aldehydes (after curves *1* and *3* in Fig. 1 merge).

As mentioned in [8], more than 80–90% of the initial amount of Na_2SO_3 is selectively converted into $NaHSO_3$ under model conditions in the case of hydrochloric or nitric acids. The competitive capacity of reaction (VI) is high as compared with the reactions in which H_2SO_3 ($SO_{2(d)} + H_2O$ is formed from $NaHSO_3$ and spherical nickel hydroxide, or other mineral or carboxylic acids are used. This offers a clear view of why even high rates of introduction of the HA acid, $dn_{HA}/d\tau$, in systems with $c_{Na_2SO_3} > 0.2$ mol kg^{-1} do not lead to decomposition of the hydrosulfite derivative even in local zones formed immediately after the introduction of a drop of concentrated acid into the reaction mixture. And only at very low residual concentrations of Na_2SO_3 it is appropriate to make lower the rate of introduction of the HA acid, which can be most easily done by taking 0.5–1 N solutions instead of 5–10 N solutions and by maintaining a nearly constant rate of introduction of the solution itself. Naturally, the latter rate can be lowered too, which has no effect on the function $pH = \varphi(n_{HA})$, as demonstrated by a direct experiment.

The rate of introduction of the HA acid fully predetermines not only the process duration, but also the function $pH = f(\tau)$, as can be well seen in Fig. 2. One and the same process can be completed quantitatively in periods of time that differ by a factor of 10 and more. At a high rate $dn_{HA}/d\tau$, it is possible to pass, in the final stages, the point at which $c_{\rangle C=O} \approx 0$, with the concentration of the carbonyl compound increased because of the decomposition of the hydrosulfite derivative (Fig. 1). At low rate, the process duration may become too long. At the same time, it is possible to obtain a more acceptable (if not the optimal) variant by considerably lowering $dn_{HA}/d\tau$. Hence follows that process (IV) under consideration occurs in a clearly pronounced diffusion mode, with the mechanical introduction of the HA acid into the system being the rate-determining stage.

It was established that the quantitative characteristics of the function $pH = \varphi(n_{HA})$ are virtually in-

dependent of the nature of an HA acid (confirmed for hydrochloric, hydrobromic, formic, acetic, chloroacetic, trichloroacetic, sulfuric, oxalic, malonic, orthophosphoric, and citric acids; the differences in pK_a values between the first and subsequent stages of dissociation of polybasic acids are of no fundamental importance). Also unimportant is the presence in solution in amounts of up to 20 wt % of water-soluble organic substances (e.g., propanol-2, ethyl cellosolve). However, these characteristics strongly depend on the ratio of the initial concentrations of the carbonyl compound and Na_2SO_3. This is readily illustrated by the data in Fig. 3, in which the ratio between the number of mol-equiv of the acid introduced and the initial concentration of the reagent taken in deficiency is plotted along the abscissa axis. It was confirmed experimentally that, with the data presented in this form, it is the ratio of the initial concentrations of Na_2SO_3 and the carbonyl compound that is important. At different initial concentrations of these reagents, but equal ratios of these concentrations, the dependence in the coordinates of Fig. 3 will be represented by actually a single curve.

Curves describing how the pH value varies upon introduction of the acid in the case of reaction (VI) occurring under model conditions with the use of HCl and a number of other acids are plotted in Fig. 3 as auxiliary lines. For these curves, the quantity chosen to be plotted along the abscissa axis is also $n_{HA}/n^0_{Na_2SO_3}$. This is done to facilitate the interpretation of how the pH value varies in the case when the carbonyl compound and Na_2SO_3 are taken in excess in carrying out the main process.

As can be seen from a comparison of curves *1* and *2* in Fig. 3, the excess of acetone leads to higher pH values over virtually the entire range of variation of the molar ratio of the amounts of acid and a reagent taken in deficiency. The only exception are the values close or equal to unity, when the curves under consideration converge to a point. This circumstance is quite understandable, because such an excess will favor a decrease in the running concentrations of Na_2SO_3 and will shift the equilibrium of reaction (I) to the right; and the higher the reactivity of a carbonyl compound and its concentration, in the more alkaline medium will the process develop (Fig. 1).

In the case of an excess of Na_2SO_3, the amount of the acid introduced will be constituted by the amount consumed for a quantitative conversion of the carbonyl compound by reaction (IV) and for partial conversion of the excess amount of Na_2SO_3 into $NaHSO_3$ on reaching pH 6.3–6.5, which corresponds to the instant (denoted by the horizontal line) when the residual amount of the reacting carbonyl compound will approach to zero (see table).

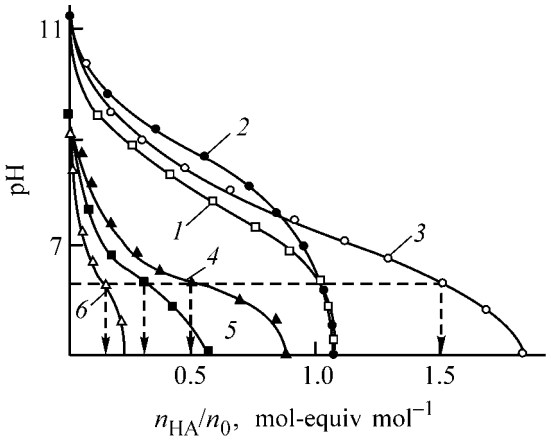

Fig. 3. Variation of the pH value in the course of (*1–3*) process (IV) and (*4–6*) its stage (VI) under model conditions with the relative amount of the acid introduced, n_{HA}/n_0 (n_0, amount of the reagent taken in deficiency). Temperature 23°C, agitation with a magnetic stirrer. Dosage (mole): Na_2SO_3: (*1, 2*) 0.05 and (*3, 6*) 0.10; acetone: (*1, 3*) 0.05 and (*2*) 0.10. Acid: (*1–4*) hydrochloric, (*5*) monochloroacetic, and (*6*) *para*-toluenesulfonic acid.

As can be seen in Fig. 3 (curves *4–6*), the fraction of Na_2SO_3 consumed in reaction (VI) by the instant of time when this pH value is reached depends on the nature of an HA acid used. It is about 50% for HCl, 40% for HNO_3, 33–35% for $NaHSO_4$ and $ClCH_2COOH$, 17% for *para*-$CH_3C_6H_4SO_3H$, etc. If the fractions corresponding to the above percentages are denoted by ε, the following formula can be suggested for calculating the number of moles (mol-equiv) of the acid to be introduced for reaching pH ~6.3–6.5 in the case of an excess amount of Na_2SO_3:

$$n_{HA} = n^0_{\rangle C=O} + \varepsilon(n^0_{Na_2SO_3} - n^0_{\rangle C=O}). \qquad (4)$$

Equation (4) is highly important for several reasons. First, the quantity n_{HA} is one of the most easily, rapidly, and accurately determinable in a kinetic experiment. At the same time, simultaneous monitoring of pH and n_{HA} can furnish a sufficient information about the course of the process in such an experiment. Second, the lower the reactivity of a carbonyl compound, the larger excess of Na_2SO_3 is necessary to faster obtaining a hydrosulfite derivative in a quantitative yield. In this case, not only the value of $n_{HA}/n^0_{Na_2SO_3}$ is important, but also that of ε. Naturally, the choice should ensure the highest value of ε. Third, Eq. (4) shows how the instant of completion of the target process can be determined if there are no other

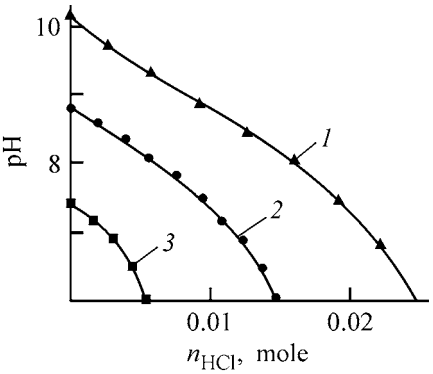

Fig. 4. pH value vs. the amount of hydrochloric acid, n_{HCl}, introduced in the course of reaction between *para*-oxybenzaldehyde with Na_2SO_3 at different amounts of *para*-oxybenzoic acid introduced with the aldehyde. *para*-Oxybenzoic acid impurity (mole): (*1*) virtually absent, (*2*) 0.010, and (*3*) 0.018.

reliable methods that can be used for this purpose: It is necessary to introduce a calculated amount of the acid in such a way that the intermediate pH value is not lower than 6.3–6.5.

A number of long-stored carbonyl compounds, especially aldehydes, contain as impurities products of their oxidation by atmospheric oxygen, which, in particular, include acids. As the strength of an acid in performing process (IV) is of no importance in a rather wide range of its values, acid impurities in aldehydes do not interfere with the process under consideration. The amount of a mineral or carboxylic acid to be introduced to ensure a quantitative conversion of a carbonyl compound into a hydrosulfite derivative is simply decreased by the number of mol-equiv of the acid coming as impurity with the aldehyde (Fig. 4).

CONCLUSIONS

(1) The variation of the pH value with time upon introduction of a water-soluble reactive aldehyde into a Na_2SO_3 solution makes it possible to estimate the rate constant of an exceedingly fast reaction of this aldehyde with $NaHSO_3$.

(2) In the case of a dropwise introduction of a mineral or carboxylic acid into the system constituted by sodium sulfite and a carbonyl compound, there exist two pathways of intermediate conversion of Na_2SO_3 into $NaHSO_3$. The competitive capacity of these pathways depends on the nature and reactivity of a carbonyl compound, Na_2SO_3 concentration (especially in the range ≤ 0.2 M), presence and amount of water in the system, but is virtually independent of the nature of an acid being added.

(3) Quantitative conversion of a carbonyl compound into a hydrosulfite derivative not only in a virtually anhydrous medium, but also in aqueous and aqueous-organic media, is provided by a fast reaction of Na_2SO_3 with an acid to give $NaHSO_3$ and a salt of the acid.

REFERENCES

1. Houben-Weyl, *Methoden der organischen Chemie*. Band 2: *Analytische Methoden*, Stuttgart: Georg Tieme, 1953.
2. Ivanov, I.A., Bobrineva, O.S., Zhmykhov, V.M., and Ivanov, A.M., *Izv. Kursk. Gos. Tekhn. Univ.*, Kursk: Kursk. Gos. Tekhn. Univ., 2003, no. 1(10), pp. 52–57.
3. USSR Inventor's Certificate, no. 541472.
4. USSR Inventor's Certificate, no. 1774616.
5. USSR Inventor's Certificate, no. 1759835.
6. RF Patent 2039087.
7. RF Patent 2099430.

Russian Journal of Applied Chemistry, Vol. 77, No. 12, 2004, pp. 2011–2016. Translated from Zhurnal Prikladnoi Khimii, Vol. 77, No. 12, 2004, pp. 2036–2041.

MACROMOLECULAR CHEMISTRY AND POLYMERIC MATERIALS

Binding of Protein to Polystyrene Particles in the Presence of Polyvinylpyrrolidone in the Surface Layer

A. Yu. Men'shikova, Yu. O. Skurkis, T. G. Evseeva, Z. P. Shkarubskaya, T. B. Tennikova, and S. S. Ivanchev

Institute of Macromolecular Compounds, Russian Academy of Sciences, St. Petersburg, Russia

Received May 11, 2004

Abstract—Adsorption and chemisorption of bovine serum albumin on polystyrene particles obtained by dispersion polymerization and containing graft polystyrene/polyvinylpyrrolidone copolymers and carboxy groups of the initiator in the surface layer were studied.

Binding of immunochemicals to the surface of micrometer polymer particles facilitates observation of immunochemical reactions, allows modeling of the behavior of biological objects and, in particular, bacteria or elements of blood, and improves the performance of diagnostic tests [1]. Such monodisperse polystyrene (PS)-based particles with a modified structure of the surface layer were obtained by dispersion polymerization of styrene in alcoholic solutions in the presence of polyvinylpyrrolidone (PVP) and 4,4'-azobis(4-cyanoisovaleric acid) (CVA) as an initiator [2]. The surface layer of these particles is composed by *in situ* formed graft PS/PVP copolymers, which, being diphilic, better stabilize the dispersion than the initial PVP. The carboxy groups of the initiator are localized at the ends of the side chains of PS, and, being ionized, impart a surface charge to the particles, thus providing their additional stabilization by virtue of the electrostatic factor. Hydrophilization of the particles through the effect of the PVP blocks of the graft copolymers can reduce the probability of nonspecific hydrophobic interactions in the surface layer in the course of immunochemical reactions.

Previously, we have shown [2] that the size of monodisperse PS particles, as well the concentration of the carboxy groups on their surface, can be controlled in the course of synthesis by varying the reagent concentrations, composition of the dispersion medium, and polymerization temperature. At the same time, it was found that these factors also influence the structure of the resulting graft copolymers. The structure of the surface of the resulting PS particles may determine their capacity for adsorption and covalent binding of proteins, and, therefore, their effectiveness as carriers for immunochemicals. Therefore, in order to obtain particles in which the structure of the surface layer would be optimal for binding of bioligands, we examined this study the effect of the graft copolymers on these characteristics.

EXPERIMENTAL

Polystyrene latexes were obtained by CVA-initiated dispersion polymerization of styrene at 351 ±1 K in ethanol containing 7 wt % double-distilled water. As an initial steric stabilizer we used medical grade PVP with MW 35 000 ± 5000 (Farmakon Joint-Stock Company, St. Petersburg, Russia). Synthesis, purification, and analysis of the resulting PS particles for their dispersity and surface functionality, and also the methods for partial extraction of the graft copolymers from the surface layer of the particles and of an IR spectroscopic and conductometric study of their structure and composition are described in detail in [2]. Table 1 listed the compositions of the reaction mixtures and characteristics of the resulting PS particles used to their capacity to bind protein.

As an adsorbate we employed bovine serum albumin (BSA), which is widely used in immunoassay as a carrier for small antigens and also as a blocking agent for protection of a hydrophobic surface from nonspecific interactions with proteins from the sample to be analyzed. Purification and analysis of BSA are described elsewhere [3]. Covalent binding of BSA to the surface of PS microspheres was carried out after preactivation of the surface carboxy groups with wa-

1070-4272/04/7712-2011 © 2004 MAIK "Nauka/Interperiodica"

Table 1. Conditions of synthesis and characteristics of PS particles*

Sample no.	[Styrene], M	[PVP], g l^{-1}	[CVA], wt % relative to [PVP]	Diameter, μm	Particle dispersivity		S_{sp}, m^2 g^{-1}	[COOH], mg-equiv m^{-2}	pH_{IEP}
					K	σ, %			
1	1.53	20	2.0	1.36	1.0011	3.4	4.20	1.7	2.0
2	1.72	20	2.0	1.46	1.0038	6.2	3.80	1.5	2.3
3	1.92	10	4.0	2.50	1.0013	3.6	2.28	2.8	2.2
4	1.92	15	2.7	1.90	1.0035	5.9	3.01	1.4	2.1

* (*K*) Polydispersity factor, $K = D_m/D_n$, where D_m and D_n are the weight-average and number-average diameters, respectively; (σ) room-mean-square variance; and (IEP) isoelectric point.

ter-soluble 1-[3-(dimethylamino)propyl]-3-ethylcarbodiimide hydrochloride (Sigma) in the presence of *N*-hydroxybenzotriazole (Sigma), which were taken in the equimolar proportion relative to the surface carboxy groups [4]. The process was carried out at 0°C in 10^{-2} M 2-(*N*-morpholino)ethanesulfonic acid (MESA, Reanal) (pH 5.5) for 15 min. Then these reagents were removed by centrifugation; the PS particles were redispersed in the MES solution; 0.05–1.50 mg ml^{-1} BSA solution in the same buffer was added; and the system was allowed to stand for 24 h at 20°C.

When the activation and covalent binding stages are performed separately, the carboxy groups of the protein are not activated and not involved in the chemical interaction leading to cross-linking of the protein globules and distortion of their native conformation. Adsorption was performed under the same conditions, but without preactivation of the carboxy groups. The protein concentration before and after the interaction with the particles was determined by high-performance monolithic chromatography (HPMC) on a CIMR DEAE anion-exchange membrane (BIA Separations, Ljubljana, Slovenia) [5, 6]. The BSA-modified particles were redispersed for storage in the phosphate buffer (pH 7.4) and then used for studying their surface electrical properties.

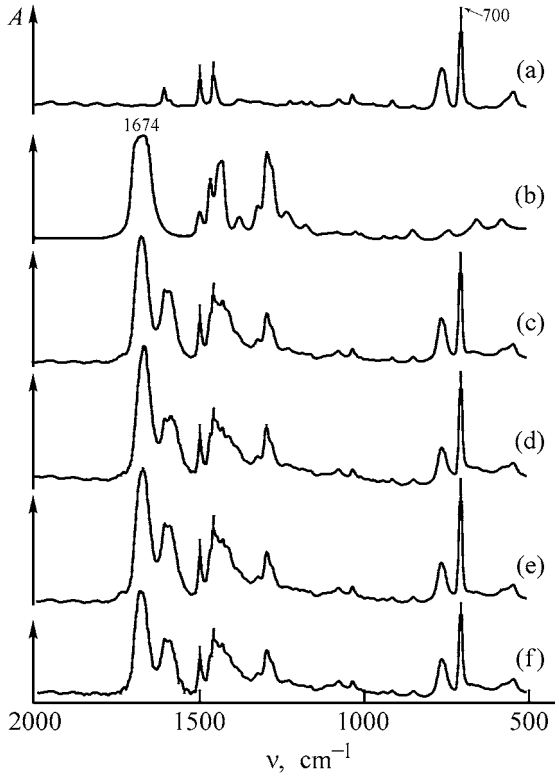

Fig. 1. IR spectra: (a) PS, (b) PVP, and alcoholic extracts from the surface of the latex sample nos. (c) 1, (d) 2, (e) 3, and (f) 4. (*A*) Absorbance and (ν) wave number.

The ζ potentials of the resulting particles before and after modification with BSA were determined by the standard microelectrophoresis method at a NaCl concentration of 10^{-3} and 10^{-2} M over the pH range 2.0–10.9. Calculation was performed by the Helmholtz–Smoluchowski equation [7]. In carrying out the microelectrophoresis, we used double distilled water with a conductivity of 1.2×10^{-4} Ω^{-1} m^{-1} and reference solutions of HCl, NaOH, and NaCl. Before the study, the latexes were equilibrated for 24 h with a NaCl solution of a given concentration and pH.

The interaction of the surface of the particles with the protein was studied with samples differing in the structure of PS/PVP graft copolymers in the surface layer (Table 1). Sample nos. 1 and 2 were prepared at a low styrene concentration and a sufficiently high PVP content in the reaction mixture, to obtain a structure with a large amount of grafted short PS chains [2, 8]. With increasing styrene concentration, the average length of the grafted PS chains grows (sample no. 2). With increasing PVP content in the reaction mixture (sample nos. 3 and 4), the grafting number decreases because of the decrease in the initiator/PVP ratio. Nevertheless, the weight percentage of the PVP and PS units in the graft copolymers extracted from the surface of the samples, determined from the IR

Table 2. Results of analysis of PS/PVP graft copolymers extracted from the surface of PS particles into alcoholic alkaline solutions

Sample no.	Content of PS/PVP copolymers in extract		I_{1674}/I^*_{700}	Content of PVP units, wt %	Sample no.	Content of PS/PVP copolymers in extract		I_{1674}/I^*_{700}	Content of PVP units, wt %
	% relative to the weight of PS particles	mg m^{-2}				% relative to the weight of PS particles	mg m^{-2}		
1	0.40	0.96	1.22	53	3	0.26	1.15	1.07	50
2	0.37	0.95	1.19	53	4	0.63	2.10	1.13	51

* Intensity ratio of the bands at 1674 (C=O of the lactam group in PVP) and 700 cm^{-1} (C–H bending vibrations of the aromatic rings in PS) [9].

spectra (Fig. 1), falls in a narrow range, only slightly deviating from the 1 : 1 ratio (Table 2).

Vigorous washing of the PS particles does not provide complete removal of the graft copolymers containing the PVP units from the surface layer, as demonstrated by the inversion of the sign of the ζ potential of the samples studied over the pH range 2.0–2.3 (Fig. 2, curves *1*, *2*). Note that such an inversion is not typical of the PS particles obtained by CVA-initiated polymerization, but in the absence of the steric stabilizer [10]. The lactam groups of PVP units on the surface are capable of protonation in strongly acidic solutions [11], which gives rise to a positive charge on the surface of the particles.

At the same time, preliminary washing of the particles before adsorption or chemisorption of the protein prevented washout of weakly bound copolymer chains from the surface and of their binding to BSA in solution, which was observed when the particles were washed only with water. This is supported by the lack in the HPMC chromatograms of the peaks of conjugates with a retention time longer than that of the initial BSA (Fig. 3).

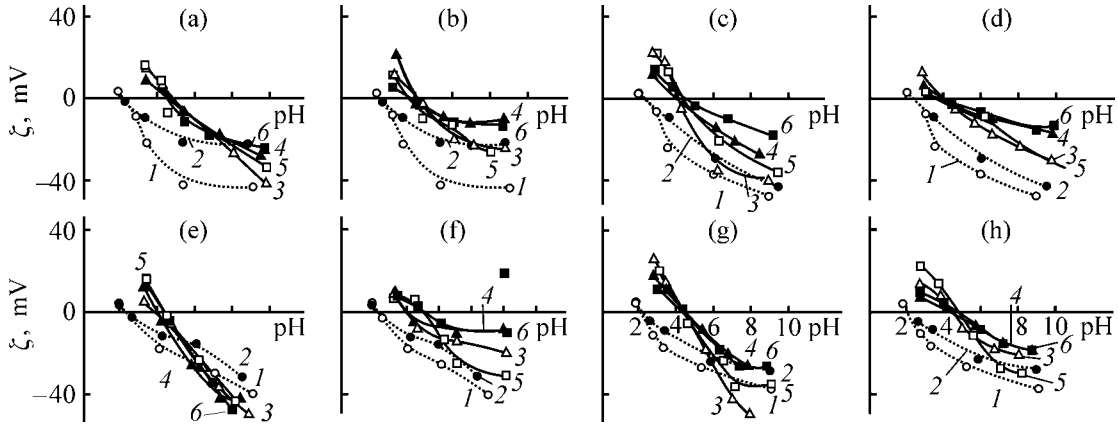

Fig. 2. Effect of pH on the ζ potential of the particles of latex sample nos. (a, b) 1, (c, d) 2, (e, f) 3, and (g, h) 4. NaCl concentration (M): (*1*, *3*, *5*) 10^{-3} and (*2*, *4*, *6*) 10^{-2}. Latexes: (*1*, *2*) initial, (*3*, *4*) modified by chemisorbed BSA, and (*5*, *6*) modified by physisorbed BSA under conditions of (a, c, e, g) minimal and (b, d, f, h) maximal sorption (Table 3).

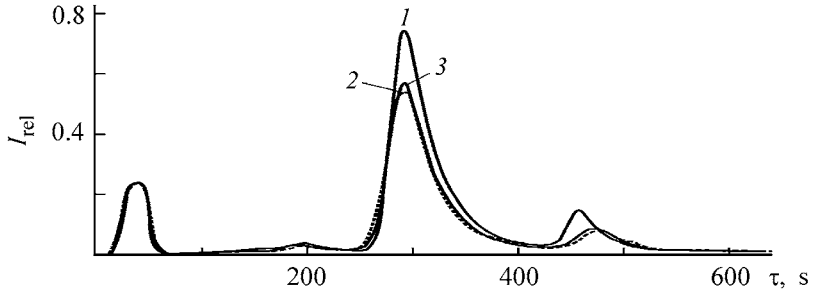

Fig. 3. Chromatograms of BSA solutions (*1*) before and (*2*) after interaction with latex sample no. 2, and (*3*) after chemisorption. (I_{rel}) Relative peak intensity and (τ) time.

Table 3. Adsorption and chemisorption of BSA on PS particles

Sample no.	BSA, c_0, g l^{-1}	BSA, c_{eq}, g l^{-1}		Γ_{BSA}, mg m^{-2}	
		adsorption	chemisorption	adsorption	chemisorption
1	0.30	0.18	0.17	0.57	0.60
	2.40	2.04	1.73	1.66	3.20
2	0.30	0.15	0.15	0.77	0.77
	2.40	2.05	1.84	1.79	2.86
3	0.15	0.10	0.12	0.28	0.17
	2.10	1.73	1.6	2.11	2.85
4	0.15	0.10	0.10	0.24	0.24
	2.10	1.54	1.60	2.66	2.37

Modification of the surface of the particles with the protein resulted in a drift of IEP of all the samples studied from pH 2.0–2.3 to 3.6–5.0. As the surface was covered with BSA, IEP changed, taking values mostly lower than IEP of the native protein (4.8–5.2) [12].

To elucidate the contribution of the graft copolymers of the surface layer to sorption, it was advisable to compare the chemisorption and adsorption isotherms of BSA (Fig. 4) and also the isoelectric points for various samples (Table 3).The limiting adsorption increases in the series of sample nos. 1–4 from 1.6 to 2.7 mg m^{-2}. For sample nos. 1 and 2, the chemisorption continues to increase over the entire experimental range of BSA concentration. The noticeable excess of the chemisorption over the adsorption at high BSA concentrations, observed for these samples (Figs. 4a and 4b, curves *1*, *2*), can be attributed to loosening of the surface of the particles in the course of activation of their carboxy groups and further interaction with BSA. Such a loosening is promoted by vigorous washing of the particles with hot alkaline alcohol, to extract graft copolymers weakly bound to the surface. In the case of sample no. 1, the extraction is facilitated by the presence of carboxylate anions at the ends of relatively short grafted PS chains (Table 2). The grafted chains of sample no. 2 are longer and are more tightly bound to the surface, and, therefore, the surface loosens to a lesser extent in this case. As a result, the difference between the chemisorption and adsorption decreases.

Sample nos. 3 and 4 show a knee in the initial section of the isotherm, suggesting hindered sorption at low protein concentration in solution (Figs. 4c and 4d, curves *1*, *2*). Insertion of small amounts of the protein into the surface layer may be unfavorable because

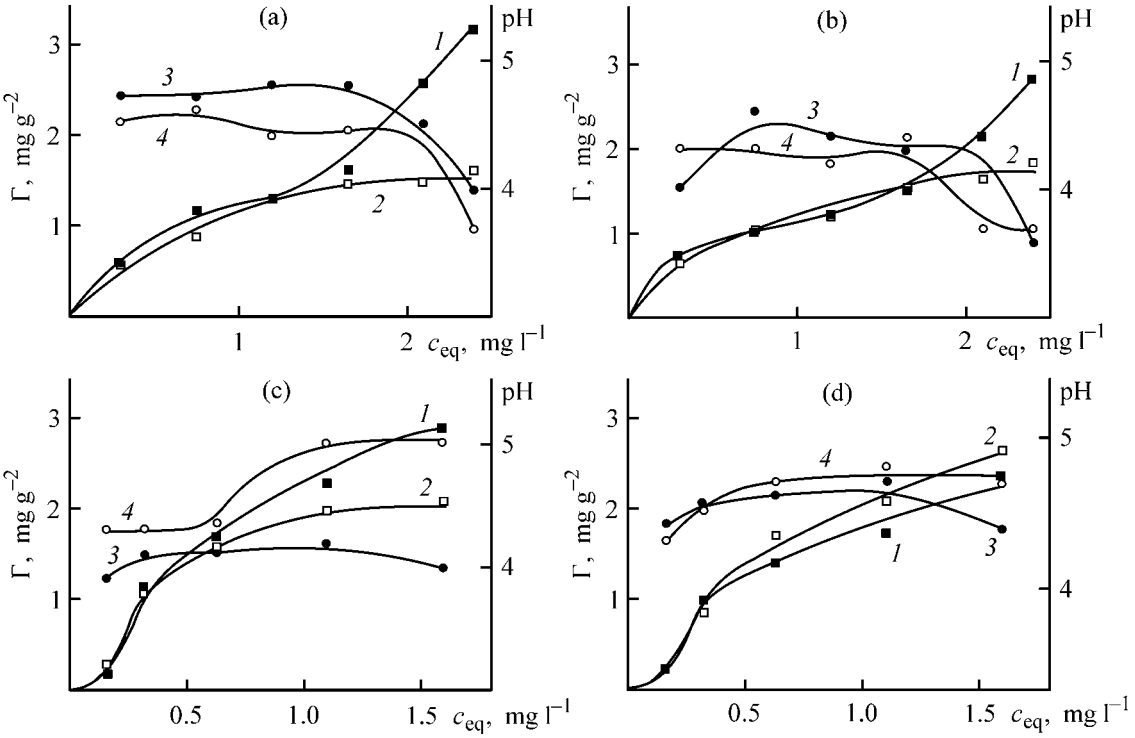

Fig. 4. Isotherms of (*1*) chemisorption and (*2*) physisorption Γ, and pH of isoelectric point of particles of latex sample nos. (a) 1, (b) 2, (c) 3, and (d) 4 after (*3*) chemisorption and (*4*) physical adsorption of BSA. (c_{eq}) Equilibrium concentration of BSA.

of the decreasing contribution of the entropy to the energy of the system as a result of a decrease in the flexibility of the hydrophilic segments of PVP graft copolymers. However, with increasing BSA concentration in solution, the amount of bound protein increases, and at the maximum chemisorption (2.9 mg m^{-2}, sample no. 3) and adsorption (2.7 mg m^{-2}, sample no. 4), 1 μm^2 of the surface contains as much as 2.3×10^4 and 2.5×10^4 BSA globules, respectively. These values reach the maximum amount of adsorption on the surface of the hydrophobic PS particles containing no graft copolymers in the surface layer (2.5×10^4 BSA globules per 1 μm^2 [12–14], suggesting a dense packing of the protein globules on the surface of the resulting particles. Thus, hydrophilization of the surface of the particles by virtue of PVP units of the graft copolymers does not hinder the effective binding of the protein. It should be pointed out that adsorption, i.e., concentration of the protein globules in the surface layer, is the first stage of interaction in covalent binding of the protein also. Therefore, the observed close values of the chemisorption and adsorption suggest that the conformation of BSA is preserved in the course of its binding by the standard carbodiimide method, since, in this case, the area occupied by one BSA globule in the surface layer remains unchanged and the size of the globule corresponds to the hydrodynamic radius of BSA (3.6 nm) [13].

The isoelectric point of sample no. 1, equal to 4.7–4.8 at the minimal chemisorption (Fig. 4a), falls in the IEP range characteristic of native BSA, suggesting that the surface is totally shielded by the protein. However, with the surface concentration of BSA increasing to 3.2 mg m^{-2}, 2.8×10^4 protein molecules per 1 μm^2 of the surface, IEP unexpectedly decreases to 4.0. This indicates that the effective specific surface area of sample no. 1 increases because of its loosening; the decrease in IEP suggests the formation of a loose mosaic structure, which permits both PS/PVP copolymers and BSA globules to move toward the slip boundary. For sample no. 2, the decrease in IEP with increasing chemisorption is slightly less pronounced (Fig. 4b), which is caused by the higher stability of the surface structure. The evolution of the IEP in sample nos. 1 and 2 with increasing adsorption of BSA is similar to that occurring in the case of chemisorption.

The isoelectric points of the samples modified by chemisorbed BSA may fall beyond the IEP range of native BSA for several reasons. Even in the case of full shielding of the substrate surface by the protein, this can be a result of chemical interaction of its amino groups with the carboxy groups of the surface. For example, in the case of sample no. 3, IEP is not higher than 4.1, being considerably lower than that of native BSA. At the same time, after the protein was adsorbed on this sample, IEP increased to 5.0 (Fig. 4c). However, for sample nos. 1 and 2, IEP decreased not only in the case of chemisorption, but also in adsorption, suggesting a noticeable effect on IEP of PS/PVP copolymers, which do not permit BSA to fully shield the surface of the particles. Only for sample no. 4, the constancy of high IEP values at any coverage of the surface with BSA and any type of binding suggests that BSA is well exposed at the slip boundary (Fig. 4d). It is obvious that the surface of the particles of this sample has the most stable structure, which was formed with participation of the grafted PS chains with the minimum amount of the longest grafted PS chains among all the samples studied (two chains 100 monomer units long, on the average [2]). The lack of surface loosening in the case of sample no 4 is also supported by the low difference between the adsorption and chemisorption throughout the isotherms. Since the graft copolymers have in this sample the minimum amount of grafted PS chains, free segments of the PVP backbone can interact additionally with the amino groups of BSA through coordination to the lactam groups. As a result, the adsorption of BSA is the highest for this sample.

The effects of the binding mode and BSA concentration in the surface layer of the particles (Table 3) on their ζ potential are shown in Fig. 2. As the sorption of BSA increases, the ζ potential of the particles decreases in absolute value for all the samples (Fig. 2, curves *3–6*), suggesting that the insertion of the protein globules into the surface layer of the particles causes a shift of the slip boundary toward the bulk of the solution. However, after chemisorption of a small amount of BSA, the negative ζ potential of the particles in the alkaline range appeared to be slightly higher in absolute value than after adsorption of the same amount of the protein (Figs. 2a, 2c, 2e, 2g). It may be suggested that, thanks to the spacer function of the PVP backbone, BSA globules chemically bound to the side PS chains of the graft copolymers via the terminal carboxy groups are more mobile. As pH increases, they can move toward the slip boundary with increasing negative charge of both the surface of the particle and the BSA globules. Quite the contrary, at high coverage of the surface of sample nos. 1 and 2 with BSA, the pH dependences of ζ potential, obtained for different binding modes, are virtually coincident (Figs. 2b, 2d), regardless of the large chemisorption. With the densest packing of BSA globules on the surface of sample nos. 3 and 4, the high neg-

ative ζ potentials are reached in the case of adsorption binding of the protein (Figs. 2f, 2h). These facts reveal the limited conformational flexibility in the surface layer, as it is saturated with the protein.

CONCLUSIONS

(1) Adsorption and chemisorption of bovine serum albumin on polystyrene particles allow reaching the adsorption capacity corresponding to the limiting adsorption. Therefore, hydrophilization of the surface through introduction of the steric stabilizer in the surface layer does not hinder the protein binding.

(2) The structure of the graft polystyrene/polyvinylpyrrolidone copolymer has a considerable effect on the stability of the surface structure of the particles and, accordingly, on the adsorption and chemisorption isotherms, and also on the surface electrical properties of the particles after the protein was bound.

(3) The most stable surface structure of the particles is formed when a small amount of long polystyrene chains is grafted to the polyvinylpyrrolidone chain. In this case, the resulting particles can effectively bind the protein through both chemical interaction of the amino groups of BSA with the surface carboxy groups and coordination interaction in physisorption. As a result, the adsorption and chemisorption isotherms are virtually coincident. The isoelectric points of the particles modified with BSA approach that of native BSA already at a low surface concentration of the protein and maintain their values until the complete coverage of the surface. This suggests that the protein globules are exposed at the slip boundary and, therefore, are accessible further immunochemical reactions.

ACKNOWLEDGMENTS

The study was financially supported by the Russian Foundation for Basic Research (project no. 04-03-33080) and Fundamental Research Program of the Chemistry and Materials Science Department of the Russian Academy of Sciences "Development and Research of Macromolecules and Macromolecular Structures of New Generation."

REFERENCES

1. Prokopov, N.I., Gritskova, I.A., Cherkasov, V.R., and Chalykh, A.E., *Usp. Khim.*, 1996, vol. 65, no. 2, pp. 178–192.
2. Men'shikova, A.Yu., Evseeva, T.G., Skurkis, Yu.O., *et al.*, *Vysokomol. Soedin., Ser. A*, 2004, vol. 46, no. 9, pp. 1479–1487.
3. Men'shikova, A.Yu., Dmitrieva, I.B., Kuchuk, V.I., *et al.*, *Kolloidn. Zh.*, 1999, vol. 61, no. 6, pp. 799–808.
4. Staros, J.V., Wright, R.W., and Swingle, D.M., *Anal. Biochem.*, 1986, vol. 156, no. 2, pp. 220–222.
5. Men'shikova, A.Yu., Evseeva, T.G., Ivanchev, S.S., *et al.*, *Zh. Prikl. Khim.*, 2001, vol. 74, no. 10, pp. 1677–1683.
6. Tennikova, T.B. and Freitag, R., *J. High Resol. Chromatogr.*, 2000, vol. 23, no. 1, pp. 27–38.
7. Grigorov, O.N., Karpova, I.F., Koz'mina, Z.P., *et al.*, *Pukovodstvo k prakticheskim rabotam po kolloidnoi khimii* (Practical Manual on Colloid Chemistry), Leningrad: Khimiya, 1964.
8. Jayachandran, K.N.N. and Chatterji, P.R., *J. Macromol. Sci., Polym. Rev.*, 2001, vol. 41, nos. 1–2, pp. 79–94.
9. Bellamy, L.J., *The Infrared Spectra of Complex Molecules*, New York: Wiley, 1957.
10. Shubin, V.E., Isakova, N.V., Sidorova, M.P., *et al.*, *Kolloidn. Zh.*, 1990, vol. 52, no. 5, pp. 535–541.
11. Kirsh, Yu.E., *Poli-N-vinilpirrolidon i drugie poli-N-vinilamidy* (Poly-*N*-Vinylpyrrolidone and Other Poly-*N*-vinylamides), Moscow: Nauka, 1998.
12. Suzawa, T. and Shirahama, H., *Adv. Colloid Interface Sci.*, 1991, vol. 35, no. 1, pp. 139–172.
13. Goode, N.P., Davison, A.M., Gowland, G., and Shires, M., *J. Immunol. Meth.*, 1986, vol. 92, no. 1, pp. 31–35.
14. Men'shikova, A.Yu., Skurkis, Yu.O., Kuchuk, V.I., *et al.*, *Kolloidn. Zh.*, 2001, vol. 63, no. 5, pp. 678–686.

Russian Journal of Applied Chemistry, Vol. 77, No. 12, 2004, pp. 2017–2021. Translated from Zhurnal Prikladnoi Khimii, Vol. 77, No. 12, 2004, pp. 2042–2046.

MACROMOLECULAR CHEMISTRY AND POLYMERIC MATERIALS

Treatment of Paper with Basic Agents in Alcohols and Supercritical Carbon Dioxide To Neutralize Acid and Prolong Storage Time

T. V. Dobrodskaya, P. A. Egoyants, V. K. Ikonnikov, N. D. Romashenkova, S. A. Sirotin, S. A. Dobrusina, and N. I. Podgornaya

Prikladnaya Khimiya Federal State Unitary Enterprise, State Scientific Center of the Russian Federation, St. Petersburg, Russia

Russian National Library, St. Petersburg, Russia

Received September 21, 2003; in final form, October 2004

Abstract—The efficiency of treatment of paper prepared from 100% sulfite cellulose with basic agents (solutions of magnesium alkoxides or methoxycarbonate in alcohols or in supercritical carbon dioxide) to neutralize acid was studied, as influenced by the following factors: concentration of a basic agent in the neutralizing solutions, repetition of impregnation of paper with a neutralizing solution and hydrolysis of the neutralizing agent after each impregnation cycle, temperature and pressure of supercritical carbon dioxide, mixing of a neutralizing agent with supercritical CO_2, and conditions (dynamic or static) the paper treatment with a neutralizing solution.

Numerous libraries all over the world, including Russia, have accumulated a great number of decrepit and damaged documents. It is known that paper is destroyed due to hydrolytic breakdown of cellulose catalyzed with acids. Acids of various origins are present in paper: auxiliary acid additives (bleaches, sizing compounds) used in paper making, acid inc, paints, and pigments. A paper can be acidified with atmospheric sulfur, carbon, and nitrogen oxides, its acidity can increase on heating, moistening, and illumination. In order to weaken the negative effect of acids accumulated in paper, we must not only increase its pH to 8, but also provide a sufficiently large excess bacisity (henceforth the base stock) (no less than 300 mg-equiv kg^{-1}) to decelerate paper aging and destruction in prolonged storage [1].

The modern high-performance technique must ensure large-scale treatment of stitched paper documents [2–5]. The simplest solution of this problem is to treat books and paper documents with a neutralizing agent in organic solvents. However, in large-scale treatment, this technique consumes a very large volume of an organic solvent. Furthermore, organic solvents destroy and deform covers, smear inc, and distort the color pattern.

Analysis of domestic and foreign data on large-scale conservation of paper documents by their treatment with various basic agents to neutralize acid [1, 2–11] shows that, in solution of this problem, the most promising neutralizing agents are alkaline-earth alkoxides and, in particular, magnesium alkoxides and their carbonate derivatives, in a supercritical carbon dioxide fluid. These compounds are the most effective and widely approved basic agents. In their use, the pH of the initial acid paper and the base stock can be raised to 8–10 and 200 mg-equiv kg^{-1}, respectively, depending on the kind and state of paper (age, pH), treatment procedures and also kind and concentration of alkaline-earth alkoxides [4–6, 8, 10].

The processing of paper with alkaline-earth alkoxides in supercritical carbon dioxide (SC CO_2) ensures its highly efficient, safe, and wasteless conservation. These advantages are governed by the specific properties of supercritical CO_2 as solvent [12]: (1) SC CO_2 dissolves the most effective basic agents suitable for neutralizing paper under controllable conditions; (2) the solubility of basic agent can be varied by varying the thermodynamic parameters (T, P) of supercritical CO_2 or introducing an additional organic solvent; (3) owing to low surface tension and high dif-

1070-4272/04/7712-2017 © 2004 MAIK "Nauka/Interperiodica"

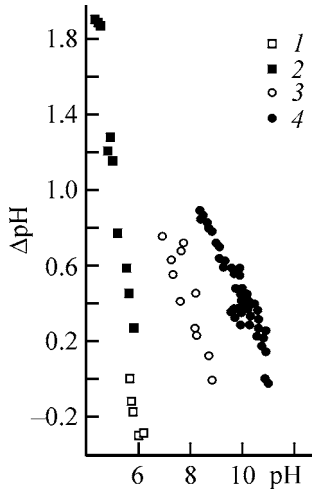

Fig. 1. Sign and value of the surface electrical charge of paper prepared from 100% sulfite cellulose (ΔpH) vs. pH of paper. (*1*) initial SFI paper, (*2*) treatment with water and alcohol, (*3*) treatment with NH_4COONH_2 in aqueous alcohol and (*4*) treatment with alcoholic solutions of $Mg(CH_3O)_2$ and $Mg(CH_3O)_2 \cdot nCO_2$ n = (0.6–1.0).

fusion coefficient of SC CO_2 molecules, the neutralizing agent in SC CO_2 quickly penetrates into pores and paper fibers and uniformly impregnates the paper; and (4) the basic agents in SC CO_2 can be easily regenerated and reused. Owing to these features of SC CO_2, the time-consumption of paper treatment considerably decreases and paper documents can be neutralized in the stitched state.

Carbon dioxide has low critical parameters (T = 31°C, P = 7.3 MPa) suitable for treatment of paper. The supercritical CO_2 fluid is chemically inert, nontoxic, odorless, fire and explosion safe, and commercially available.

The use of supercritical CO_2 in combination with other organic solvents instead of aqueous and organic solutions commonly used for neutralizing paper allows minimization of the negative effect of solvents on the color intensity and tint of inc, paints, and pigments and on the state of sizing compounds.

Although supercritical gases have come into use for treatment of paper documents in some countries; in Russia, supercritical gases are not applied in large-scale treatment of paper document in spite of a certain progress in this direction.

EXPERIMENTAL

In our experiments we used samples of paper prepared from 100% medium-porous sulfite cellulose (SFI) with pH 5.5–6.3.

Magnesium alkoxides (methoxide and ethoxide) and magnesium methoxycarbonate (MMC) were used as neutralizing basic agents.

The main characteristics of paper (pH, base stock, value and sign of the surface electric charge, physicomechanical parameters, reflection coefficient) were determined before and after processing the paper by standard techniques. It was reported in [1, 2, 11, 13] that there is a correlation between the pH of paper and its main characteristics (folding endurance, tensile strength, reflection coefficient). In our experiments, pH was determined in aqueous extracts from paper and directly on the surface of paper. The pH measured on the surface of paper characterizes the uniformity of impregnation of paper with the basic agent. The value and sign of the surface electric charge of paper were determined by the method of the suspension effect. The base stock in paper was determined either by titration with acid or by determination of magnesium content by atomic absorption spectroscopy. The same characteristics were also determined for paper samples subjected to artificial aging in a TABAI climatic chamber at 80°C and 65% relative humidity under conditions simulating a 75-year aging.

In separate experiments, we elucidated how basic agents are accumulated in paper and determined the amount of basic agent ensuring both the prescribed base stock and stability of paper in long-term storage. In the first experiments, paper samples were treated with methanolic and ethanolic solutions of magnesium alkoxides. For comparison, alcoholic solutions of ammonium carbamate were also tested. In these experiments, a standard sample of paper was immersed into a solution containing 0.1–5.0 wt % of basic agent and allowed to stand for 15–40 min. Our results are shown in Figs. 1 and 2.

Figure 1 shows that treatment of paper with basic agent changes the sign of the surface electric charge. Under these conditions, the zero-charge point shifts to the basic region. For both the initial paper and paper treated with water and alcohol the zero-charge point is observed at pH_{zcp} ~ 6. After processing of paper with alcoholic solutions of ammonium carbamate and magnesium alkoxide, the zero-charge point shifts to pH_{zcp} ~9 and ~11, respectively. Figure 1 shows a correlation between the surface electric charge of paper and its pH for different kinds of basic agents used for paper treatment. With the Mg^{2+} content in the paper increasing to 0.15–0.28 wt % , the pH of paper increases to 10–10.5, and the base stock, to 150–220 mg-equiv kg^{-1}. Further accumulation of

a basic agent in the paper does not affect the pH but leads to a steady increase in the base stock (Fig. 2).

The table shows how treatment of SFI paper (initial and artificially aged) with alcoholic solutions of magnesium methoxycarbonate (1.0, 2.5 and 5.5 wt %) affects its main characteristics. Similar effects were observed for paper treated with alcoholic solutions of magnesium methoxide and magnesium ethoxide of the same concentration.

We found that, after a single treatment of paper with alcoholic solutions of magnesium methoxycarbonate ($C \geq 2.5$ wt %), its pH exceeds 10 and the base stock becomes larger than 300 mg-equiv kg^{-1}. Testing of this paper sample showed that the single treatment of paper provides its stability during 75-year storage under common conditions.

In treatment of paper with dilute alcoholic solutions of magnesium methoxycarbonate (0.1–1.0 wt %), the base stock of ~300 mg-equiv kg^{-1} is reached only after repeated treatments with intermediate hydrolysis of the applied basic agent after each treatment cycle. Thus, the total base stock in paper is formed due to gradual accumulation of hydrolysis products of basic agent. We found that fivefold treatment of paper by the above-described procedures increases the base stock by an order of magnitude as compared to single treatment. These results were used in developing a technique for paper treatment with basic agent in supercritical carbon dioxide.

Figure 3 shows the scheme of our experimental device for paper treatment with a basic agent in supercritical carbon dioxide.

A supercritical carbon dioxide solution of a basic agent was prepared in a mixer *1* (350 cm^3) equipped with a magnetic stirrer. The treatment of paper with a basic agent in supercritical carbon dioxide was carried out in a reactor *2* (350 cm^3). The temperature was monitored with a TSP thermistor thermometer, and the pressure, with MTI-0.6 standard pressure gages and LKh-412 pressure sensors (grade of accuracy 0.6). All the parameters were recorded with a PC.

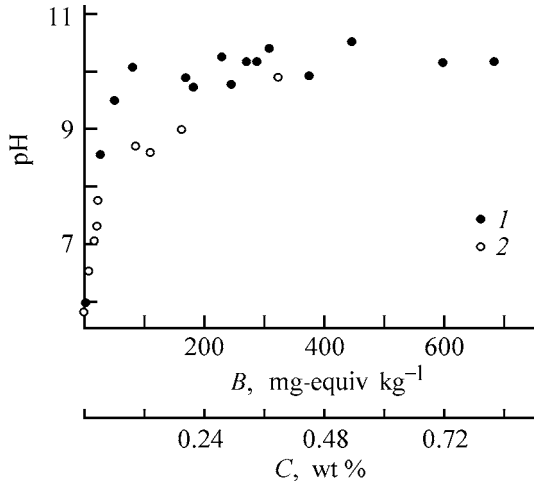

Fig. 2. pH of paper vs. base stock B and magnesium concentration C in paper. Basic agent: (*1*) alcoholic solutions of $Mg(CH_3O)_2$ and $Mg(CH_3O)_2 \cdot nCO_2$ (n = 0.6–1.0) and (*2*) $Mg(CH_3O)_2 \cdot nCO_2$ in super-critical CO_2 (n = 1.0–2.0).

In our experiments, the pressure was varied from 7 to 20 MPa; temperature, from 30 to 60°C; and the content of a basic agent in SC CO_2, from 8 to 30 wt %.

We tested various procedures for preparing supercritical carbon dioxide solutions of a basic agent: (1) a weighing bottle containing an alcoholic solution of the basic agent was placed in the mixing chamber; (2) an alcoholic solution of the basic agent applied to

Change in the characteristics of paper prepared from 100% sulfite cellulose (initial and artificially aged) after treatment with alcoholic solutions of magnesium methoxycarbonate

MMC, wt %	τ_{age}, days	Reflection coefficient R_{00}	Tensile strength, N	pH		Base stock, mg-equiv kg^{-1}
				contact method	extraction method	
Without treatment	0	0.725	77.2 ± 5.0	5.5	6.0	–
	9	0.606	65.0 ± 11.0	5.2	–	–
1.0	0	0.751	76.1 ± 5.2	10.1	10.0	115
	9	0.609	71.3 ± 10.3	8.5	–	Absent
2.5	0	0.739	79.6 ± 6.4	10.2	10.6	290
	9	0.568	76.6 ± 9.8	9.5	–	20
5.5	0	0.764	94.2 ± 6.5	10.2	10.2	610
	9	0.645	78.7 ± 9.4	10.3	–	70

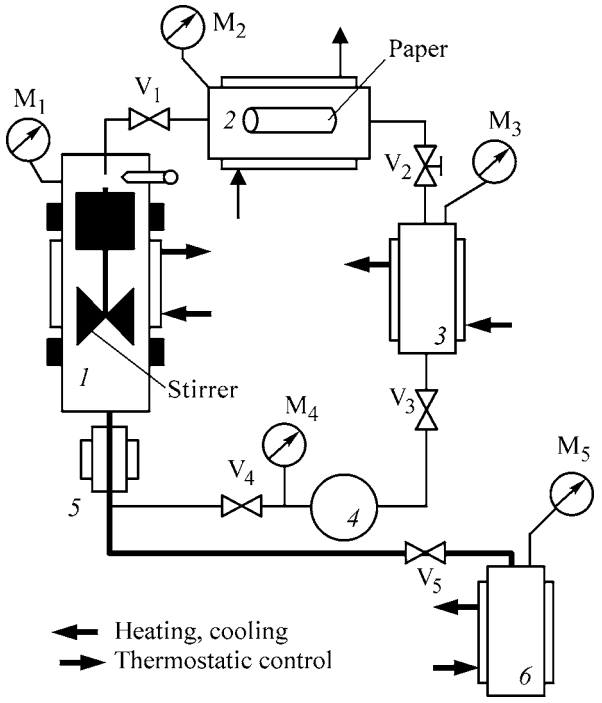

Fig. 3. Scheme of an experimental device for paper treatment with a basic agent in supercritical carbon dioxide to neutralize acid: (*1*) mixer, (*2*) reactor, (*3*) regenerator, (*4*) high-pressure pump, (*5*) heater, (*6*) thermocompressor, (V_1–V_5) shutoff valves, and (M_1–M_5) pressure gages.

a porous support was placed in a mixing chamber; and (3) an alcoholic solution of a basic agent was introduced in portions into the mixing chamber during pumping of CO_2. The introduced alcoholic solution of a basic agent was mixed with supercritical CO_2 fluid with a magnetic stirrer. Both static and dynamic procedures for application of alcoholic solution of a basic agent to paper were tested. The content of the basic agent in supercritical CO_2 was determined by gravimetric, atomic-absorption spectroscopic, chromatographic, and spectroscopic techniques.

We found that the maximum solubility of the basic agents under consideration in supercritical CO_2 containing 20% methanol or ethanol does not exceed 0.1 wt % even at the highest *T* and *P*. Therefore, after a single, even prolonged (8 h) processing of paper with the basic agent in SC CO_2, the base stock in the paper was relatively small (~100 mg-equiv kg^{-1}).

In order to increase the base stock, we used repeated impregnation of paper with a basic agent in SC CO_2, followed by hydrolysis of the basic agent after each impregnation stage. Such a procedure was preliminarily tested for treatment of paper with dilute alcoholic solutions of a basic agent. Under these conditions, the base stock increases to 300 mg-equiv kg^{-1} and more, depending on the treatment parameters.

In the course of our experiments, we optimized the separate process stages. We found that the largest base stock is reached in paper treatment under dynamic conditions, in pumping of CO_2 through a reactor at a rate of 300 $cm^3\ min^{-1}$ (temperature 38–40°C, pressure 11–13 MPa). To improve mixing of alcoholic solutions of a basic agent with SC CO_2, the mixing chamber was equipped with a magnetic stirrer.

The paper treatment with a basic agent in SC CO_2 was carried out in three stages: (1) treatment of paper with SC CO_2 containing approximately 1 wt % methanol to remove the soluble products of cellulose degradation; (2) treatment of the paper with a basic agent in SC CO_2, and (3) treatment of paper with pure SC CO_2. Each of these stages was carried out for no more than 0.5 h. The second and third stages were repeated 4–5 times, with intermediate pressure relief to atmospheric pressure and exposure of the paper to air for 1 h.

A methanolic solution of magnesium metoxycarbonate (up to 8 wt %) is recommended as the neutralizing agent solution. The tests of our technique for paper treatment showed its high efficiency: in a set of experiments, we obtained paper with pH 10.5 and the base stock of 300 mg-equiv kg^{-1}.

CONCLUSIONS

(1) The effective neutralization of paper (pH > 8, base stock 300 mg-equiv kg^{-1}) is reached by its repeated impregnation with dilute (<0.1 wt %) alcoholic or supercritical CO_2 solutions of a basic agent (magnesium methoxide or magnesium methoxycarbonate), with hydrolysis of the applied basic agent after each treatment stage.

(2) An experimental device for paper treatment with a basic agent in supercritical CO_2 to neutralize acid was constructed and the optimal conditions of neutralization of paper prepared from 100% sulfite cellulose were found: the use of magnesium methoxide or methoxycarbonate as basic agents, temperature 38–40°C, pressure 11–13 MPa, and CO_2 pumping rate 300 $cm^3\ min^{-1}$.

(3) The tretment of paper with a basic agent in supercritical CO_2 decreases the consumption of organic solutions of basic agents by almost two order of magnitudes; it decreases the detrimental environmental effect of the organic solvents and the cost of paper conservation. This technique shows much prom-

ise for developing a semicommercial installation for large-scale treatment of books and other paper documents.

REFERENCES

1. Kelly, G., *J. Am. Inst. Cons.*, 1972, vol. 13, pp. 16–28.
2. Dobrusina, S.A., in *Teoriya i praktika sokhraneniya knig v bibliotekakh: Sbormik nauchnikh trudov* (Theory and Practice of Preservation of Books in Libraries: Coll. Scientific Works), St. Petersburg: Ross. Nats. Biblioteka, 1992, pp. 67–77.
3. Bredereck, K., Haberditzi, A., and Bluher, A., *Restaurator*, 1990, vol. 11, no. 3, pp. 165–178.
4. US Patent 3676182.
5. Green, L.R. and Leese, M., *Restaurator*, 1991, vol. 12, no. 2, pp. 147–163.
6. US patent, no. 3939091.
7. US patent, no. 5137760.
8. EP patent, no. 0578736.
9. International Patent Application PCT WO 92-17640.
10. International Patent Application PCT WO 97-39190.
11. Bukovsky, V., *Restaurator*, 1997, vol. 18, no. 1, pp. 25–38.
12. Zhuze, T.P., *Szhatye gasy kak rastvoriteli* (Compressed Gases as Solvents), Moscow: Nauka, 1974.
13. Lienardy, A., *Restaurator*, 1990, vol. 11, no. 1, pp. 1–21.

Russian Journal of Applied Chemistry, Vol. 77, No. 12, 2004, pp. 2022–2024. Translated from Zhurnal Prikladnoi Khimii, Vol. 77, No. 12, 2004, pp. 2047–2049.

MACROMOLECULAR CHEMISTRY AND POLYMERIC MATERIALS

Inhibiting Effect of Fullerenes C_{60} and C_{70} on High-Temperature Oxidative Degradation of Copolymers of Methyl Methacrylate with Methacrylic Acid and Methacrylamide

B. B. Troitskii, L. V. Khokhlova, A. N. Konev, V. N. Denisova, and M. A. Novikova

Razuvaev Institute of Organometallic Chemistry, Russian Academy of Sciences, Nizhni Novgorod, Russia

Received June 24, 2004

Abstract—The inhibiting effect of fullerenes on thermal oxidative degradation of copolymers of methyl methacrylate with methacrylic acid and methacrylamide at 340°C was studied.

Fullerenes C_{60} and C_{70} are heat-resistant inorganic compounds consisting of 60 and 70 carbon atoms arranged on the surface of a sphere and an ellipsoid, respectively [1–9]. Both C_{60} and C_{70} inhibit radical chain reactions of anaerobic thermal decomposition of poly(methyl methacrylate) (PMMA) and polystyrene (PS), as well as branched chain reactions of thermal oxidative (in an oxygen atmosphere) degradation of PMMA, PS, and methyl methacrylate (MMA) copolymers.

The inhibiting effect of fullerenes on chain reactions of polymer degradation is due to reactions of C_{60} and C_{70} with macroradicals to form thermally stable diamagnetic compounds [7]. It has been shown that fullerenes C_{60} and C_{70} inhibit thermal oxidative degradation of PMMA only up to 320°C. This is the limit above which fullerenes are not effective as inhibitors of thermal oxidative degradation of PMMA [3, 4].

At high temperatures (290–320°C), C_{60} and C_{70} are more effective antioxidants in thermal oxidative degradation of PMMA than the known organic antioxidants: sterically hindered amines, phenols, and sulfur- and phosphorus-containing compounds [3–8]. Organic antioxidants inhibit the thermal oxidative degradation of polymers only up to 280–290°C [10, 11].

Experiments on thermal oxidative degradation of PMMA and of MMA copolymers with various comonomers at 304°C have shown [12, 13] that MMA copolymers with methacrylic acid (MAAc) and methacrylamide (MAAm) are more heat-resistant than PMMA.

Therefore, it seems appropriate to study the effect of C_{60} and C_{70} on thermal oxidative degradation of MMA–MAAc and MMA–MAAm copolymers at temperatures above 320°C.

EXPERIMENTAL

A procedure for preparing and purifying C_{60} and C_{70} has been described elsewhere [14, 15]. The purity of C_{60} was 99.9%, and that of C_{70}, 98%. The crude mixture contained about 80% C_{60} and 20% C_{70}.

Copolymers of MMA were prepared similarly to PMMA according to [1]. MMA and MAAc were separated from the inhibitors and distilled under reduced pressure; MAAm (commercial product) was used without additional purification.

Transparent films of polymers with and without C_{60} and C_{70} additives were prepared from polymer solutions by casting onto a glass surface, after which they were dried in a vacuum at 60–80°C; the film thickness was about 100 μm.

The oxidation of C_{60} and C_{70} was studied by differential scanning calorimetry (DSC) with a Perkin–Elmer DSK-7 device in the range 100–500°C at an oxygen flow rate of 40 ml min^{-1} and a heating rate of 5 deg min^{-1}. The thermal oxidative degradation of the copolymers was studied by thermal gravimetric analysis at 340°C and oxygen pressure of 200 mm Hg.

Figures 1a and 1b show the DSC curves characterizing the oxidation of C_{60} and C_{70}, respectively. It is seen that an appreciable oxidation of C_{70} starts

1070-4272/04/7712-2022 © 2004 MAIK "Nauka/Interperiodica"

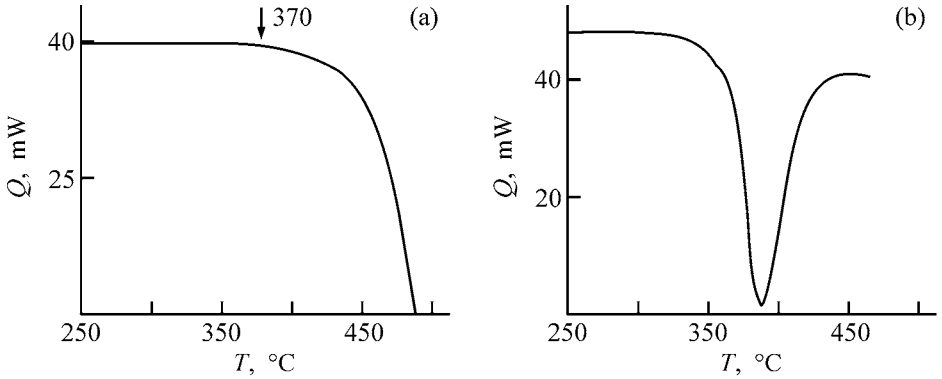

Fig. 1. DSC curves of (a) C_{60} and (b) C_{70} in oxygen: (Q) thermal flow and (T) temperature.

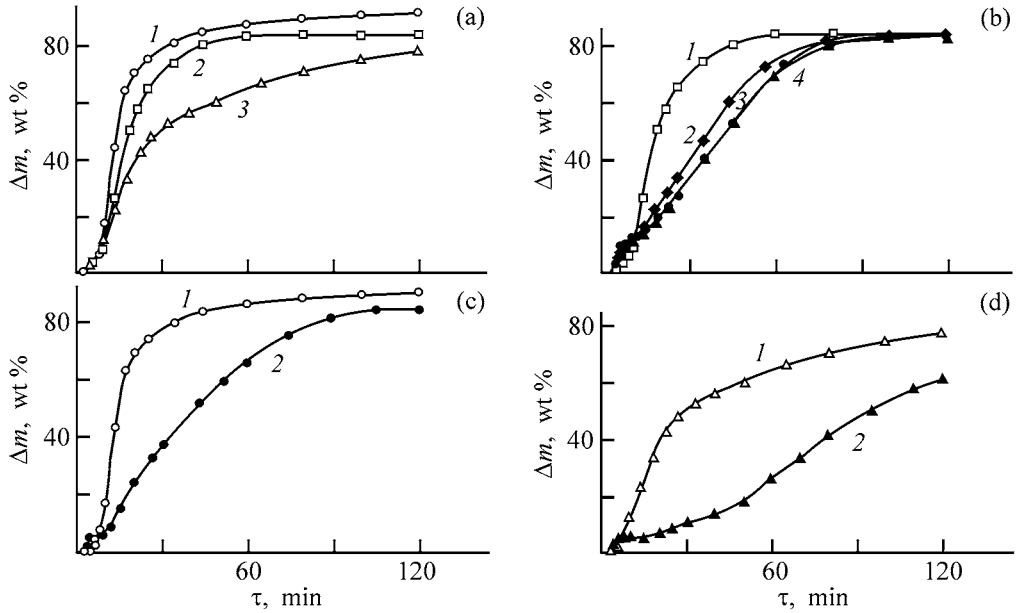

Fig. 2. Curves of the weight loss Δm in thermal oxidative degradation of copolymers. T = 340°C, p_{O_2} = 200 mm Hg. (τ) Time. (a) Copolymer of MMA with (*1*) 5 and (*3*) 10 mol % MAAm or (*2*) 15 mol % MAAc, no additives; (b) copolymer of MMA with 15 mol % MAAx (*1*) without additives and (*2–4*) with addition of fullerenes (mol kg^{-1}, $\times 10^3$): (*2*) C_{70} 8.3, (*3*) mixture of C_{60} with C_{70} 7.8, and (*4*) C_{60} 7.8; (c) copolymer of MMA with 5 mol % MAAm (*1*) without additives and (*2*) with addition of 11×10^{-3} mol kg^{-1} C_{60}; (d) copolymer of MMA with 10 mol % MAAm (*1*) without additives and (*2*) with addition of 9.5×10^{-3} mol kg^{-1} C_{60}.

at 340°C, with the maximum oxidation rate (dip in the DSC curve) observed at 388°C. Oxidation of C_{60} (Fig. 1a) starts at 370°C; the temperature of the maximum oxidation rate was not determined, because no dip was observed in the DSC curve, but it is apparently no less than 500°C. Our experimental data suggest that the theoretical temperature limits T_{lim} for C_{60} and C_{70} as high-temperature antioxidants will be in the range 340°C $\le T_{lim} \le$ 390°C for C_{70} and 370°C $\le T_{lim} \le$ 500°C for C_{60}.

Our experiments on thermal oxidative degradation of the copolymers were performed at 340°C, since the rate of oxidation of the more reactive fullerene C_{70} becomes appreciable at this temperature (Fig. 1b).

At 340°C and an oxygen pressure of 200 mm Hg, PMMA degrades completely in 10–15 min. Copolymers of MMA with 15 mol % MAAc and with 5 and 10 mol % MAAm are considerably more heat-resistant under these conditions (Fig. 2). It is interesting that the copolymer of MMA with 10 mol % MAAm, despite the lower content of the second comonomer, decomposes at a lower rate than the copolymer of MMA with 15 mol % MAAc (Fig. 2a, curves *2*, *3*). Deceleration of the degradation of the comonomers, compared to PMMA, is due to a reaction between the neighboring macromolecular units to give of six-membered rings containing anhydride (MMA–MAAc) and imide (MMA–MAAm) groups [12, 13].

The six-membered rings terminate the depolymerization process propagating along the macrochain. These rings inhibit, as shown in [7], the chain oxidation, catalyzing the molecular pathway of decomposition of hydroperoxides formed by oxidation of the polymer and thus decreasing the amount of free radicals in the reaction zone.

Fullerenes C_{60}, C_{70}, and $C_{60} + C_{70}$ (80 : 20) inhibit the thermal oxidative degradation of the MMA–15 mol % MAAc copolymer at 340°C; the inhibiting effect of the individual fullerenes and their mixture is the same (Fig. 2b). Fullerene C_{60} inhibits the thermal oxidative degradation of MMA–MAAm copolymers (Figs. 2c, 2d); in the case of the copolymer with a higher (10 mol %) MAAm content, there is a short induction period in the kinetic curve (Fig. 2d, curve *2*). The stronger stabilizing effect may be due to the formation of the six-membered imide ring, which probably decelerates the depolymerization more effectively than does the anhydride ring.

CONCLUSIONS

(1) In an oxygen atmosphere at 340°C, copolymers of methyl methacrylate with methacrylic acid and with methacrylamide degrade considerably more slowly than poly(methyl methacrylate).

(2) Fullerenes C_{60} and C_{70} and a crude mixture of these fullerenes decelerate the thermal oxidative degradation of the above copolymers.

REFERENCES

1. Troitskii, B.B., Troitskaya, L.S., Yakhnov, A.S., *et al., Eur. Polym. J.*, 1997, vol. 33, nos. 10–12, pp. 1587–1590.
2. Shibaev, L.A., Antonova, T.A., Vinogradova, L.V., *et al., Pis'ma Zh. Tekh. Fiz.*, 1997, vol. 23, no. 18, pp. 81–86.
3. Troitskii, B.B., Troitskaya, L.S., Yakhnov, A.S., *et al., Dokl. Ross. Akad. Nauk*, 1998, vol. 363, no. 1, pp. 79–81.
4. Troitskii, B.B., Troitskaya, L.S., Dmitriev, A.A., and Yakhnov, A.S., *Eur. Polym. J.*, 2000, vol. 36, no. 7, pp. 1073–1084.
5. Troitskii, B.B., Troitskaya, L.S., Yakhnov, A.S., *et al., Int. J. Polym. Mater.*, 2000, vol. 46, nos. 1–2, pp. 301–314.
6. Troitskii, B.B., Troitskaya, L.S., Anikina, L.I., *et al., Int. J. Polym. Mater.*, 2001, vol. 48, no. 3, pp. 251–265.
7. Troitskii, B.B., Domrachev, G.A., Khokhlova, L.V., and Anikina, L.I., *Vysokomol. Soedin., Ser. A*, 2001, vol. 43, no. 9, pp. 1540–1547.
8. Troitskii, B.B., Domrachev, G.A., Semchikov, Yu.D., *et al., Zh. Obshch. Khim.*, 2002, vol. 72, no. 8, pp. 1359–1364.
9. Ginzburg, B.M., Shibaev, L.A., and Ugolkov, V.L., *Zh. Prikl. Khim.*, 2001, vol. 74, no. 8, pp. 1293–1302.
10. Denisov, E.T., *Okislenie i destruktsiya karbotsepnykh polimerov* (Oxidation and Degradation of Carbon-Chain Polymers), Leningrad: Khimiya, 1990.
11. Shlyapnikov, Yu.A., Kiryushkin, S.G., and Mar'-in, A.P., *Antiokislitel'naya stabilizatsiya polimerov* (Antioxidative Stabilization of Polymers), Moscow: Khimiya, 1986.
12. Troitskii, B.B., Domrachev, G.A., Khokhlova, L.V., *et al., Zh. Obshch. Khim.*, 2003, vol. 73, no. 7, pp. 1154–1157.
13. Troitskii, B.B., Domrachev, G.A., Khokhlova, L.V., *et al., Zh. Obshch. Khim.*, 2003, vol. 73, no. 12, pp. 2013–2017.
14. Kaverin, B.S., Karnatsevich, V.L., and Kirillov, A.I., Abstracts of Papers, *Mezhdunarodnyi simpozium "Fullereny i atomnye klastery"* (Int. Symp. "Fullerenes and Atomic Clusters"), St. Petersburg, October 4–9, 1993, p. 78.
15. Lopatin, M.A., Karnatsevich, V.L., Davydov, V.Ya., and Filatova, G.N., Abstracts of Papers, *Mezhdunarodnyi simpozium "Fullereny i atomnye klastery"* (Int. Symp. "Fullerenes and Atomic Clusters"), St. Petersburg, June 19–24, 1995, p. 42.

Russian Journal of Applied Chemistry, Vol. 77, No. 12, 2004, pp. 2025–2028. Translated from Zhurnal Prikladnoi Khimii, Vol. 77, No. 12, 2004, pp. 2050–2053.

CHEMISTRY OF FOSSIL FUEL

Development of State Reference Samples of Mercaptan Sulfur Content in Petroleum Products

A. V. Bulatov, A. S. Rogotnev, V. A. Rogotnev, and A. G. Cherepova

Ekros Research and Production Association, Private Company, St. Petersburg, Russia
Ustinov Baltic State Technical University, St. Petersburg, Russia

Received June 16, 2004

Abstract—State reference samples were developed for determining the content of mercaptan sulfur in petroleum products, and a method for metrological certification of these samples by the certified measurement procedure was approbated.

One of the major tasks in assessment of the quality of petroleum products is to determine the content of the mercaptan sulfur (MS) because mercaptans cause corrosion and impair the strength of metals and other materials contacting them under conditions of production, application, and storage [1, 2].

The MS in petroleum products is mainly determined by potentiometric titration with an ammonia solution of silver nitrate, using a silver sulfide indicator electrode [3].

For metrological provision of procedures used to determine the MS content in petroleum products by analytical monitoring laboratories of petrochemical and oil-refining industry, state reference samples of MS content in petroleum products (MS SRSs) are required.

There are no samples of this kind in Russia today. Such samples, however, are demanded by fuel- and energy-producing enterprises for internal and external checkout in the assessment of the quality of petroleum products. This fact stimulated the development and production of MS SRS.

The goal of this study was to develop and metrologically certify the first batches of MS SRS.

EXPERIMENTAL

State reference samples SM-0.001-EK, SM-0.003-EK, SM-0.005-EK, SM-0.01-EK, and SM-0.03-EK with the rated MS content of 0.001, 0.003, 0.005, 0.010, and 0.030 wt %, respectively, were prepared by dissolution of an accurately weighed portion of phenylmethanethiol (Merck, Germany). As matrix material we used isooctane or decane (Merck, Germany).

An ammonia solution of copper(II) sulfate was prepared as described in [4]. A 3.9-g portion of copper(II) sulfate hydrate was dissolved in 700 ml of distilled water in a 1000-ml volumetric flask, a 25% ammonia solution was added until the precipitate of the basic copper(II) salt dissolved completely, after which an additional 50 ml of 25% ammonia was introduced, and the solution was brought to the mark with distilled water. The concentration of the ammonia solution of copper(II) sulfate was determined with a reference solution of sodium thiosulfate, which, in turn, was standardazied with a Grade 1 SRS of potassium bichromate (SRS 2215–81).

The certification of MS SRSs was performed by the measurement procedure[1] (MP) for determining MS in petroleum products [4]. According to this MP, a sample of MS SRS was weighed in a weighing bottle and quantitatively transferred into a 100-ml separatory funnel, for which purpose the weighing bottle was washed no less than three times with 2–3-ml portions of toluene. Then the titrant, ammonia solution of copper(II) sulfate, was added to the separatory funnel from a 2-ml Class 2 buret (scale division 0.01 ml) in the amount of 90% relative to the calculated amount required for the titration. The mixture was shaken

[1] Improved by the Ekros Research and Production Association; the procedure is hereinafter designated as EK 03-2003-NP; certified by the Ural Research Institute of Metrology, Federal State Unitary Enterprise (Certificate no. 253.12.02.129/2003).

Table 1. Metrological characteristics of MS SRSs

SRS	No. in State Register	MS,* %	Error,** rel. %
SM-0.001-EK	8415-2003	0.0009–0.0011	±10
SM-0.003-EK	8416-2003	0.0027–0.0033	±5
SM-0.005-EK	8417-2003	0.0045–0.0055	±5
SM-0.01-EK	8418-2003	0.0090–0.0110	±3
SM-0.03-EK	8419-2003	0.0270–0.0330	±3

* Certified range of weight percentage.

** Admissible error for a confidence level of 0.95.

with a PE-6410 agitation device (Ekros Research and Production Association) for 5 min. Then sodium chloride was added in portions in the amount required for complete phase separation in the separatory funnel, and titration was performed until the aqueous phase acquired a light blue tint not disappearing after vigorous shaking for 5 min.

MS in MS SRSs was determined by potentiometric titration [3] on an I-160M ion meter with a standard silver chloride (ESr-10 103) and the indicated silver sulfide (ESS-01) electrodes.

In the development of MS SRSs, we used a mixing procedure for their preparation. It involved preparation of the SRS material from the starting materials by their dissolution. First, we chose the matrix and substance materials ensuring the required MS content. Among the starting materials for preparing SRSs, we chose those with which the composition and structure of SRSs did not change after mixing [5].

Additional requirements to the matrix material were as follows: inertness to the material of vials (polyethylene terephthalate) used for MS SRS storage; availability and low cost of the chemicals. It is known that permanent components of light petroleum products are paraffin, naphthenic, and aromatic hydrocarbons [1]. From the viewpoint of these requirements, paraffin hydrocarbons seem to be the most suitable as the matrix material for MS SRSs.

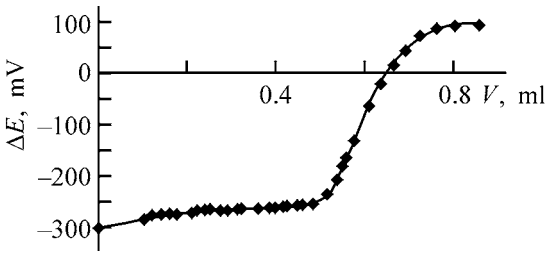

Potentiometric titration curve of an SM-0.001-EK SRS sample: (ΔE) Potential difference and (V) titrant (ammonia solution of silver nitrate) volume.

Among thiols, we chose phenylmethanethiol, as it has a relatively high boiling point (bp 194°C) and hence is relatively low-volatile; also, it meets the requirements formulated in [5]. Furthermore, the molecular weight of phenylmethanethiol is fairly high, which allows more accurate weighing in preparation of MS SRSs; it is also unlimitedly soluble in the available saturated hydrocarbons (e.g., isooctane, decane).

To prepare batches of reference samples, we developed a procedure ensuring preparation of SRSs with the metrological characteristics falling within the prescribed limits [6] (Table 1).

The first batches of MS SRSs were certified according to MP EK 03-2003-NP. Measurements were performed for all the rated values of the MS weight percentage. The experimental results obtained in certification of the MS SRSs are given in Table 2.

Taking into account the destination of the MS SRSs, we determined MS in these samples according to GOST (State Standard) R 52 030–2003 [3] by potentiometric titration with an ammonia solution of silver nitrate (see figure). Comparison of the results of MS determination in MS SRSs by the certified MP and by the procedure prescribed by GOST R 52 030–2003 (Table 2) shows that they are virtually identical.

Our next task was to assess the stability of MS SRSs. The stability of MS SRSs was determined according to the methodical instructions [7] by estimation of how the weight fraction of mercaptan sulfur in the samples $d_n = X_i - X_0$ and instability error $U_n = \alpha d_n + (1 - \alpha)U_{n-1}$ (where X_i is the current result of measuring the weight fraction of MS in MS SRS; X_0, control result; α, coefficient chosen in the range from 0.1 to 0.3 depending on the ratio $\sigma(\Delta)/\Delta X$ [7]) vary in storage. The weight fraction of MS in the samples was determined by the certified MP EK 03-2003-NP.

According to the methodological instructions [7], the number of measurements is chosen depending on the $\sigma(\Delta)/\Delta X$ ratio. Table 2 shows that this ratio is less than 0.5 for all the samples, i.e., the minimum number of measurements for estimating the instability error is four.

Taking into account this fact and expecting that the samples would be stable for no less than 2 years, we performed measurements at 6-month intervals. For the monitoring, we chose the samples with the lowest, highest, and medium rated weight percentage of MS: SM-0.001-EK, SM-0.005-EK, and SM-0.03-EK. The samples were stored under normal climatic conditions:

Table 2. Results of determining the weight fraction of MS in MS SRSs

SRS	MS content,* wt %				$\lvert(X_1 - X_2)/X_1\rvert$
	by MP EK 0.3-2003-NP		according to GOST R 52030–2003		
	X_1	S_r	X_2	S_r	
SM-0.001-EK	0.0101	0.025	0.00095	0.054	0.060
SM-0.003-EK	0.00302	0.012	0.00301	0.040	0.003
SM-0.005-EK	0.00499	0.004	0.00499	0.030	0
SM-0.01-EK	0.01001	0.003	0.00998	0.010	0.003
SM-0.03-EK	0.03005	0.002	0.02970	0.012	0.012

* Five replicate measurements, confidence level 0.95.

Table 3. Assessment of the stability of MS SRSs in storage

Storage time, months	X_i, %	$d_n = X_i - X_0$	αd_n	$(1 - \alpha)U_{n-1}$	U_n
		SM-0.001-EK			
0	0.00101	0	0	0	0
6	0.00100	10^{-5}	3×10^{-6}	0	3×10^{-6}
12	0.00101	0	0	2.1×10^{-6}	2.1×10^{-6}
18	0.00099	2×10^{-5}	6×10^{-6}	1.5×10^{-6}	7.5×10^{-6}
24	0.00101	0	0	5.3×10^{-6}	5.3×10^{-6}
		SM-0.005-EK			
0	0.00502	0	0	0	0
6	0.00502	0	0	0	0
12	0.00498	2×10^{-5}	6×10^{-6}	0	6×10^{-6}
18	0.00499	10^{-5}	3×10^{-6}	4.2×10^{-6}	7.2×10^{-6}
24	0.00498	2×10^{-5}	6×10^{-6}	5×10^{-6}	1.1×10^{-5}
		SM-0.03-EK			
0	0.03005	0	0	0	0
6	0.03002	3×10^{-5}	9×10^{-6}	0	9×10^{-6}
12	0.02997	8×10^{-5}	2.4×10^{-5}	6.3×10^{-6}	3×10^{-5}
18	0.02998	7×10^{-5}	2.1×10^{-6}	2.1×10^{-5}	2.3×10^{-5}
24	0.02997	8×10^{-5}	2.4×10^{-5}	1.6×10^{-5}	4×10^{-5}

temperature of 25 ± 10°C, relative humidity of ≤80% at 25°C, and atmospheric pressure of 100 ± 4 kPa.

The results obtained in assessing the stability of MS SRSs are listed in Table 3. These results show that the highest values of U_n for all the samples tested (7.5×10^{-6}, 1.1×10^{-5}, and 4×10^{-5}) do not exceed 2/3 of the certification errors (6.7×10^{-5}, 1.7×10^{-4}, and 6×10^{-4}, respectively), which, according to [7], indicates that the samples are stable for at least 24 months.

As noted above, the other MS SRSs developed are similar solutions of phenylmethanethiol in isooctane or decane with intermediate MS weight fractions. Therefore, there is good reason to believe that the SM-0.003-EK and SM-0.01-EK samples will also be stable for no less than 24 months. Thus, by now we can warrant that the shelf life of the MS SRSs developed is 2 years.

The SRSs developed successfully passed the metrological expertise at the Ural Research Institute of Metrology, were approved by the Scientific and Technical Committee of the RF Committee for Standards (Gosstandart), and were included in the State Register of approved reference samples (Table 1).

CONCLUSION

The procedures for preparation and certification of state reference samples with rated mercaptan sul-

fur content in petroleum products (SM-0.001-EK, SM-0.003-EK, SM-0.005-EK, SM-0.01-EK, and SM-0.03-EK; rated mercaptan sulfur content 0.001, 0.003, 0.005, 0.010, and 0.030 wt %, respectively) were developed. The first batches of separate types of the samples were obtained, and their metrological characteristics were determined. The admissible relative errors for these samples do not exceed ±10, ±5, ±5, ±3, and ±3%, respectively.

REFERENCES

1. Safonov, A.S., Ushakov, A.I., and Chechkenev, I.V., *Avtomobil'nye topliva* (Automobile Fuels), St. Petersburg: Nauchno-Proizv. Inform. Konsul't. Tsentr, 2002.
2. Chulkov, P.V. and Chulkov, I.P., *Kratkii slovar'-spravochnik po nefteproduktam* (Concise Dictionary and Handbook of Petroleum Products) Moscow: Politekhnika, 1997.
3. *GOST* (State Standard) *R 52 030–2003: Petroleum Products: Potentiometric Procedure for Determination of Mercaptan Sulfur*, Moscow: Izd. Standartov, 2003.
4. Rybak, B.M., *Analiz nefti i nefteproduktov* (Analysis of Crude Oil and Petroleum Products), Moscow: Gostoptekhizdat, 1962.
5. *MI* (Methodological Instructions) *1992–89: State System for Unification of Measurements: Reference Samples Prepared by Mixing: Certification by Preparation Procedure: Main Principles*, Sverdlovsk: Nauchno-Issled. Inst. Metrologii Standartnykh Obraztsov, 1989, p. 2.
6. *GOST* (State Standard) *8.207–76: Direct Measurements with Multiple Observations: Procedures for Processing of Observation Results*, Moscow: Izd. Standartov, 1981.
7. *MI* (Methodological Instructions) *1952–88: Methodical Instructions: Assessment of the Stability of Reference Samples of the Composition and Properties of Substances and Materials*, Yekaterinburg: Izd. Standartov, 1996.

Russian Journal of Applied Chemistry, Vol. 77, No. 12, 2004, pp. 2029–2030. Translated from Zhurnal Prikladnoi Khimii, Vol. 77, No. 12, 2004, pp. 2054–2055.

BRIEF COMMUNICATIONS

Surface Tension and Density of a Sodium Hydroxide Melt

B. V. Patrov and V. P. Yurkinskii

St. Petersburg State Polytechnic University, St. Petersburg, Russia

Received October 3, 2004

Abstract—The surface tension and density of a sodium hydroxide melt were determined experimentally in a wide temperature range.

A study of the surface tension of a sodium hydroxide melt is of theoretical and practical importance, because sodium hydroxide can be used as a component of a flux for brazing of zinc and zinc–aluminum alloys [1]. The surface tension to the adhesion ratio in Young's equation can be used to judge the wettability of the solid surface with a liquid. Data on the density of sodium hydroxide density in the temperature range from 620 to 730 K are available in the literature [2, 3].

The surface tension of a sodium hydroxide melt was measured by the method of the maximum pressure in a gas bubble [4], which is the most appropriate for corrosive media. The experiments were performed as follows. A corundum vessel sealed hermetically with a ceramic lid was placed in the furnace. A platinum–platinum-rhodium thermocouple for monitoring the temperature and a pipe for supply of argon to provide an inert atmosphere were introduced through the openings in the lid.

After the prescribed temperature was attained, a glassy-graphite crucible with sodium hydroxide (chemically pure grade) was lowered into the vessel. Prior to being used, it was vacuum-treated at 873–923 K for 4 h to remove water. After melting of sodium hydroxide, the melt was kept to equalize the temperature throughout the bulk of the melt. Then, a platinum capillary, through with argon passed, was moved down, until the lower end of the capillary touched the surface of the melt. This instant was indicated by a micromanometer as the rise in the level of the manometric liquid (ethanol). The formation of a gas bubble was accompanied by an increase in pressure. After the maximum pressure P_{max} was attained, the gas bubble detached from the capillary, and a pressure drop was indicated by the manometer.

The error in determining the surface tension was estimated to be ±2%.

The surface tension was calculated with account of the asphericity of the gas bubble by Cantor's formula:

$$\sigma = \frac{gP_{max}}{2}\left(1 - \frac{2}{3}\frac{\rho r}{P_{max}} - \frac{1}{3}\frac{\rho^2 r^2}{P_{max}^2}\right), \qquad (1)$$

where g is the gravity or the conversion coefficient from pressure (cm of water column) and radius (cm) to surface tension (mJ m^{-2}); r, radius of the capillary (0.1784 cm); and ρ, the density of the melt, determined experimentally by submerging the capillary in the melt.

The difference between the increased pressure P and P_{max} in contact with the surface of the liquid, $\Delta P = P - P_{max}$ (cm of water column) was determined by submerging the capillary to different depths Δh (cm): $\Delta P\rho_w = \Delta h\rho$. The density of the melt was calculated using the equation:

$$\rho = \frac{\Delta P}{\Delta h}\rho_w. \qquad (2)$$

The error in determining the density by this method was 2%.

Preliminary experiments yielded a satisfactory agreement between the experimental values of the surface tension and published values for chloride, carbonate, and nitrate melts [4], which confirms the reliability of the procedures used in measurements and salt preparation.

The experimental results averaged over two or three measurements at 673–1073 K are listed in the table. It can be seen that the surface tension and

1070-4272/04/7712-2029 © 2004 MAIK "Nauka/Interperiodica"

Surface tension and density of sodium hydroxide

T, K	σ, mJ m^{-2}	ρ, kg m^{-3}
673	150.2	1710
723	148.1	1684
773	145.8	1662
823	143.9	1633
873	142.0	1610
923	140.1	1591
973	138.0	1563
1023	136.2	1538
1073	133.8	1513

density decrease with increasing temperature. This decrease is linear and is described by the equations:

$$\sigma = A - BT, \quad (3)$$

$$\rho = A - BT. \quad (4)$$

The parameters A and B were determined by the least-squares method. In Eq. (3), they were found to be 1771.1 and 0.0402, respectively, at a confidence interval of 0.99963 and variance of 0.16068. Consequently, the temperature dependence of the surface tension (mJ m^{-2}) is described by the equation

$$\sigma = 177.1 - 0.0402T. \quad (5)$$

The parameters A and B in Eq. (4) are 2038.16 and 0.489, respectively, at a confidence interval of 0.99957 and variance of 2.10291, i.e., the temperature dependence of the density (kg m^{-3}) is described by the equation

$$\rho = 2038.16 - 0.489T. \quad (6)$$

A comparison of the densities of sodium hydroxide at 673 and 723 K with the published values [3] ρ_{673} = 1746 and ρ_{723} = 1723 kg m^{-3} demonstrated a disagreement of 2%, which does not exceed the error of density measurements. The agreement between the temperature coefficient of density, obtained in this study (0.489), and the value of 0.4784 from [3] can be considered satisfactory.

CONCLUSION

The temperature dependence of the surface tension and density of sodium hydroxide is linear and can be described by Eqs. (5) and (6).

REFERENCES

1. Lotsmanov, S.N., Petrunin, I.E., and Frolov, V.P., *Spravochnik po paike* (Handbook of Brazing), Moscow: Mashinostroenie, 1975.
2. Arndt, K., and Ploetz, G., *Z. Phys. Chem.*, 1926, vol. 121, nos. 1–2, pp. 439–455.
3. Morachevskii, A.G., *Spravochnik po rasplavlennym solyam* (Reference Book of Molten Salts), Leningrad: Khimiya, 1971, vol. 1.
4. Patrov, B.V., *Zh. Prikl. Khim.*, 1997, vol. 70, no. 11, pp. 1900–1902.

Russian Journal of Applied Chemistry, Vol. 77, No. 12, 2004, pp. 2031–2033. Translated from Zhurnal Prikladnoi Khimii, Vol. 77, No. 12, 2004, pp. 2056–2058.

BRIEF COMMUNICATIONS

Specific Features of Iodometric Methods for Determining the Content of Sodium Sulfite in Fixing–Bleaching Photographic Solutions

V. N. Kiryushov and L. I. Skvortsova

Institute of Solid Chemistry and Mechanochemistry, Siberian Division, Russian Academy of Sciences, Novosibirsk, Russia

Received July 9, 2004

Abstract—The conditions of oxidation of thiocyanate ions and thiocarbamide with iodine in aqueous solutions are discussed. The range of the pH values of the solutions, in which thiocyanate ions do not interfere with the iodometric determination of sodium sulfite in fixing–bleaching photographic solutions and the expenditure of iodine for oxidation of thiocarbamide can be taken into account correctly, is revealed.

Iodometric methods are widely used for determining the content of sodium sulfite in fixing solutions that contain, in addition to sodium sulfite, only a single component reacting with I_2, sodium or ammonium thiosulfate. The working principles of these methods were published in monographs [1, 2], manuals of the analytical chemistry of fixing solutions [3, 4], and a review [5].

Sulfite ions are commonly determined by the direct and back iodometry. In either method, two aliquots of a fixing solution being analyzed are titrated. In one of these, the total volume V of the standard I_2 solution spent for oxidation of sulfite and thiosulfate ions is determined, and in the other, V_1, the volume of the I_2 solution spent for oxidation of thiosulfate ions is found. In the second aliquot, sulfite ions are masked with formalin [1–5] or are precipitated in the form of a sparingly soluble salt $SrSO_3$ [5, 6]. The volume V_2 of the iodine solution spent for oxidation of sulfite ions is found from the difference $V_2 = V - V_1$.

Variants of iodometric procedures differ in the volumes of aliquots of a fixer and a masking formalin solution and in the acidity of the medium in titration of the sum of sulfite and thiosulfate ions. Being the most accurate, the back iodometry can be recommended for performing an arbitrary analysis. According to the current OST (All-Union Standard) 19-1–83, a direct volumetric method can be used to determine the content of Na_2SO_3 in fixing solutions.

In the last two decades, fixing–bleaching solutions have found wide use in color photography. Unlike other fixers, they contain, in addition to sodium sulfite and sodium thiosulfate, either of the two components that can be oxidized with I_2, potassium thiocyanate KSCN or thiocarbamide $(NH_2)_2CS$ (TC). The TC content in such a fixing solution can be varied within 2–6 g l^{-1}, and potassium thiocyanate is added in an amount of 10 g l^{-1}.

A method for determining Na_2SO_3 has been suggested for only a single composition of the fixing–bleaching solution, containing 6 g l^{-1} TC [6]. The general pattern of how the reaction of TC and thiocyanate ions with iodine affects the determination of the sulfite ion are not discussed here. Therefore, it is unclear whether or not this method can be used for determining Na_2SO_3 in other fixing–bleaching solutions.

The aim of this study was to discuss the mechanism of reactions of TC and thiocyanate ions with I_2 and to provide, on this basis, recommendations for determination of Na_2SO_3 in any type of fixing–bleaching solutions.

The mechanism of oxidation of thiocyanate ions by I_2 has been widely discussed [7, 8]. It was established that this mechanism depends on the pH value of the aqueous medium. In alkaline solutions with pH > 8, thiocyanate ions are oxidized in quantitative yield by the reaction [7, 8]:

$$KSCN + 4I_2 + 4H_2O \rightarrow H_2SO_4 + 6HI + KI + ICN. \quad (1)$$

Reaction (1) is the basis for quantitative iodometric analysis of thiocyanate-containing compounds.

1070-4272/04/7712-2031 © 2004 MAIK "Nauka/Interperiodica"

Results of determination of the known content of Na_2SO_3, c_0, in fixing–bleaching photographic solutions by direct titration in accordance with OST 19-1–83 (c_1) and by back titration with (c_2) and without (c_3) acidification of the aliquot of the fixing solution (n = 5, P = 0.95)

Interfering substance, g l^{-1}	c_0, g l^{-1}	$c_1 \pm \sigma$, g l^{-1}	S_r	$c_2 \pm \sigma$, g l^{-1}	S_r	$c_3 \pm \sigma$, g l^{-1}	S_r
KSCN, 10	2.16	2.3 ± 0.3	0.11	2.2 ± 0.1	0.04	3.3 ± 0.3	0.07
TC:							
2	2.08	1.9 ± 0.3	0.12	2.02 ± 0.12	0.05	4.2 ± 0.4	0.09
6	9.73	–	–	9.5 ± 0.3	0.02	16.4 ± 0.8	0.03

In weakly acidic solutions, at pH ≤ 5.0, thiocyanate ions do not react with I_2 [7], whereas at pH 5–8, the reaction product ICN partly reacts with I^- ions to give I_2:

$$ICN + HI \rightarrow I_2 + HCN. \quad (2)$$

The higher the solution acidity, the larger fraction of ICN is involved in the reaction to give I_2, which makes indeterminate the titrant volume spent for oxidation of sulfite ions. In [7], no products of oxidation of thiocyanate ions were found in a solution with pH < 5.0. Apparently, SCN ions will not interfere with iodometric determination of Na_2SO_3 in its titration in solutions with pH < 5. The fixing–bleaching solutions have pH 7–9 and their acidification with acetic acid to pH 3.5 is admissible. In more acidic solutions, thiosulfate ions react with H^+ ions to give S or SO_2, and, therefore, the results of analysis will be erroneous.

The mechanism of TC oxidation by iodine was discussed in [9, 10]. As in the case of thiocyanate ions, this mechanism is dependent on the solution pH. In an alkaline medium with pH > 8, TC is oxidized to carbamide by the reaction [9]:

$$(NH_2)_2CS + 4I_2 + 10NaOH \rightarrow (NH_2)_2CO + Na_2SO_4 + 8NaI + 5H_2O. \quad (3)$$

In weakly acidic and acid solutions, TC reacts with iodine in quantitative yield to form a salt of formamidine disulfide [10]:

$$2(NH_2)_2CS + I_2 + H_2SO_4 \rightarrow (NHNH_2)_2C_2S_2 \cdot H_2SO_4 + 2HI. \quad (4)$$

Thus, it is impossible to suppress the reaction of TC oxidation by varying the acidity of the medium in iodometric determination of Na_2SO_3 in the presence of TC. However, the volume of the iodine solution, V_3, spent for this process can be determined with a high accuracy. For example, if the same acidity of the medium (pH 3.5–5.0) is created in aliquots of a fixing–bleaching solution taken for determining either the total content of SO_3^{2-} and $S_2O_3^{2-}$ ions or that of only $S_2O_3^{2-}$ ions, then the volume of the I_2 solution spent for TC oxidation will be the same in both titrations. Therefore, the volume of the I_2 solution spent for oxidation of sulfite ions can be calculated from the difference of these titrations.

Indeed, the total volume of the I_2 solution spent for oxidation of the three components ($S_2O_3^{2-}$, SO_3^{2-}, and TC) can be written as $V_1 + V_2 + V_3$, and the volume spent for titration of an aliquot with masked sulfite ions, as the sum $V_1 + V_3$. Then the expenditure of I_2 for titration of Na_2SO_3 is the difference of volumes $V_1 + V_2 + V_3 - V_1 - V_3 = V_2$. Thus, the acidification of both the aliquots of a fixing solution to pH 3.5–5.0 in direct and back iodometry should eliminate the effect of thiocyanate ions and TC on the results obtained in determining of Na_2SO_3 in all types of fixing–bleaching solutions.

EXPERIMENTAL

To verify the correctness of this conclusion, different types of fixing–bleaching solutions containing 2 and 6 g l^{-1} TC or 10 g l^{-1} KSCN were analyzed by back iodometry. In one series of analyses, a 1-cm^3 aliquot of a fixing solution in which the sulfite ion was masked with formalin was acidified with 10% acetic acid (5 cm^3). In another series, an aliquot of a fixing solution, intended for determining the total volume of the standard iodine solution, was also acidified. The aliquots were treated with an excess amount (10–15 cm^3) of a 0.1 N iodine solution, which was then titrated with a 0.1 N solution of $Na_2S_2O_3$ in the presence of a starch solution as indicator. Simultaneously, some fixing solutions were analyzed for the content of Na_2SO_3 by direct iodometry in accordance with OST 19-1–83. In this method, the aliquots of a fixing solution were acidified with 10% acetic acid (10 cm^3). The compositions of the fixing solutions were reported in [6] and can be found in reference books on photography. The true content of Na_2SO_3 in a fixing solution prepared was calculated from the weight of the portion of this reagent, determined with high accuracy. The results of these determinations are listed in the table.

The data in the table show that use of the traditional back iodometry to find the total content of $S_2O_3^{2-}$ and SO_3^{2-} ions without preliminary acidification of the aliquot of a fixing solution yields erroneous results for the content of sodium sulfite (c_3) in all types of fixing–bleaching solutions containing thiocarbamide or potassium thiocyanate.

By contrast, the results obtained in determining the Na_2SO_3 content in accordance with OST 19-1–83 (c_1) and by back iodometry with acidification of all aliquots of fixing solutions (c_2) are well reproducible and correct, because the true value c_0 lies within the range of variation of the average values obtained by these methods.

CONCLUSIONS

(1) Thiocarbamide and salts containing thiocyanate ions interfere with iodometric determination of sodium sulfite in fixing–bleaching photographic solutions, because they are oxidized by iodine, together with the substance to be analyzed. The influence of thiocyanate ions can be eliminated by acidification of the solution being analyzed to pH 3.5–5.0. In such a medium, thiocyanate ions do not react with iodine.

(2) At pH 3.5–5.0, thiocarbamide is oxidized by iodine by the known reaction. The effect of this reaction can be taken into account when determining the total content of $S_2O_3^{2-}$ + SO_3^{2-} + $(NH_2)_2SC$ ions and that of only $S_2O_3^{2-}$ + $(NH_2)_2SC$ ions in the aliquots of fixing solutions acidified to these pH values.

(3) The determination in accordance with OST 19-1–83 meets these requirements, and, therefore, the content of sodium sulfite is correctly determined by this method.

(4) Back titration, in which the solution to be analyzed is acidified to pH 3.5–5.0 prior to the titration of the sum of $S_2O_3^{2-}$ + SO_3^{2-} ions, also yields correct results.

REFERENCES

1. Zolotnitskii, D.M., *Kontrol' protsessov obrabotki kinoplenki* (Monitoring of Film Development Processes), Moscow: Iskusstvo, 1986.
2. Russel, G., *Chemical Analysis in Photography*, London: The Focal, 1965.
3. Novatskaya, T.A., Filippova, N.I., and Shakhnazarova, A.S., *Metody kolichestvennogo analiza obrabatyvayushchikh rastvorov* (Quantitative Analysis of Developers), Leningrad: Len. Inst. Kinoinzhen., 1978.
4. Abramkina, I.V., Gas'kova, E.A., and Danilova, N.E., *Analiticheskaya khimiya veshchestv ispol'zuemykh v fotografii* (Analytical Chemistry of Substances Used in Photography), Leningrad: Len. Inst. Kinoinzhen., 1979.
5. Greyf, S., and Roosens, L., *Photo Korrespondenz.*, 1971, vol. 107, no. 1, pp. 5–10.
6. Grigor'eva, E.L., Oreshkina, G.N., and Strel'nikova, A.P., *Tekhn. Kino Televid.*, 1985, no. 10, pp. 10–13.
7. Tolstikov, V.P., and Epik, P.A., *Izv. Vyssh. Uchebn. Zaved., Khim. Khim. Tekhnol.*, 1962, vol. 5, no. 6, pp. 882–888.
8. Belcher, R., Liao, S-T., and Town Shend, A., *Talanta*, 1976, vol. 23, no. 7, pp. 541–543.
9. Joschi, M.K., *Anal. Chim. Acta*, 1956, vol. 14, no. 6, pp. 509–518.
10. Agorwa, R.R., and Gosh, S.K., *Chem. Anal.*, 1966, vol. 8, no. 3, pp. 141–142.

Russian Journal of Applied Chemistry, Vol. 77, No. 12, 2004, pp. 2034–2035. Translated from Zhurnal Prikladnoi Khimii, Vol. 77, No. 12, 2004, pp. 2059–2060.

BRIEF COMMUNICATIONS

A Procedure for Preparing *N*-Hydroxyethyl-Substituted Succinimide and Phthalimide

R. A. Gasanov and M. A. Allakhverdiev

Institute of Chemistry of Additives, National Academy of Sciences of Azerbaijan, Baku, Azerbaijan

Received May 13, 2004

Abstract—Conditions of synthesis of *N*-hydroxyethyl-substituted succinimide and phthalimide by reactions of dicarboxylic acid imides with aminoethanol were optimized.

Synthesis of *N*-hydroxyethyl-substituted succinimide and phthalimide has been the subject of numerous papers [1, 2]. *N*-(Alkoxyethyl)succinimides are used as SO_2 absorbents [3], and *N*-(2-hydroxyethyl)-phthalimide, as a synthetic precursor of *N*-vinylphthalimide, a monomer for preparing polymers with a high softening point (200°C) [4].

Condensation of 2-(diethylamino)ethanol with succinimide and phthalimide at 360°C yielded *N*-[2-(diethylamino)ethyl]succinimide **I** and *N*-[2-(diethylamino)ethyl]phthalimide **II** [1, 2]. The subsequent reactions of **I** and **II** with aminoethanol yielded *N*-hydroxyethyl-substituted succinimide **III** and phthalimide **IV**:

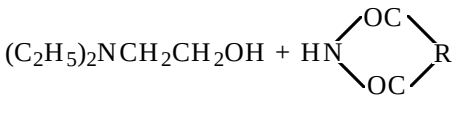

$\xrightarrow[-H_2O]{}$

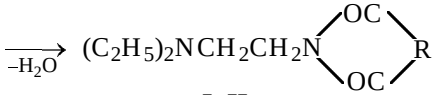

I, **II**

I, **II** + $H_2NCH_2CH_2OH$

$\xrightarrow[-H_2O]{}$ $(C_2H_5)_2NCH_2CH_2NH_2$

+ $HOCH_2CH_2N$

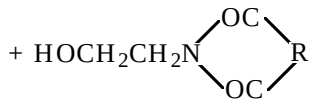

III, **IV**

where R = $(CH_2)_2$ (**I**, **III**), *o*-C_6H_4 (**II**, **IV**).

EXPERIMENTAL

We have developed a single-step procedure for preparing *N*-hydroxyethyl-substituted succinimide **III** and phthalimide **IV** by the reaction of aminoethanol with succinimide and phthalimide.

Freshly distilled aminoethanol (31 g) was added dropwise to an equimolar amount of phthalimide (73 g) or succinimide (49 g). The mixture warmed up and foamed owing to evolution of ammonia. Then the mixture was heated on a bath with Wood's alloy to 200–250°C. After the gas evolution ceased, the heating was stopped. In the case of **IV**, the mixture was poured into cold water. The crystalline precipitate was filtered off, dried, and twice recrystallized from benzene. Colorless crystals of **IV** were obtained in 87% yield (83 g); mp 127–128°C. In the case of **III**, the reaction mixture was cooled and vacuum-distilled; the fraction boiling at 178 (5 mm Hg) or 215°C (6 mm Hg) was crystallzed from hot benzene. The crystals of **III** were filtered off and dried; yield of colorless crystals of **III** 82% (58 g), mp 58°C:

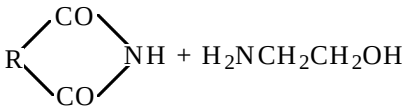

$\rightarrow$

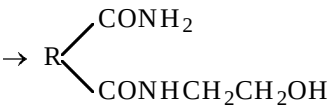

$\xrightarrow[-NH_3]{}$

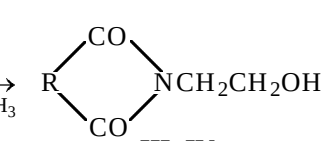

III, **IV**

The structures of **III** and **IV** were confirmed by IR and ^1H and ^{13}C NMR spectroscopy.

The IR spectra were recorded on a Specord M 80-IR spectrometer (liquid films and mulls in mineral

1070-4272/04/7712-2034 © 2004 MAIK "Nauka/Interperiodica"

oil) in the range 4000–600 cm^{-1}, using KBr and NaCl prisms. In the IR spectra of imides **III** and **IV**, we observed high-frequency absorption bands at 3600–3500 cm^{-1}, characterizing the free OH group. The bands at 1780–1710 cm^{-1} corresponded to the C=O stretching vibrations.

The ^{1}H NMR spectra were recorded on a Bruker spectrometer (300 MHz). The NMR spectra of **III** and **IV** contain, respectively, the signals of two methylene groups of the succinimide ring at 4.8–4.9 ppm and of the aromatic ring at 7.8–7.87 ppm. A broad singlet at 3.98–4.1 ppm is due to the hydroxy group. The methylene groups of the aminoethanol moiety give signals at 3.78–3.80 ppm. In the ^{13}C NMR spectra, the signals of the C=O groups are observed at 168–180 ppm.

CONCLUSION

A procedure was developed for preparing *N*-(2-hydroxyethyl)phthalimide and *N*-(2-hydroxyethyl)succinimide by the reaction of the corresponding imides with aminoethanol (yield 82–87%).

REFERENCES

1. Nakajima, K., *J. Chem. Soc. Jpn., Pure Chem. Sect.*, 1960, vol. 81, no. 2, pp. 323–327.
2. Nakajima, K., *J. Chem. Soc. Jpn., Pure Chem. Sect.*, 1960, vol. 81, no. 6, p. 962.
3. FRG Patent 1273501.
4. Nikolaev, A.F. and Ushakov, S.N., *Izv. Akad. Nauk SSSR*, 1957, vol. 10, pp. 1236–1239.

Russian Journal of Applied Chemistry, Vol. 77, No. 12, 2004, pp. 2036–2037. Translated from Zhurnal Prikladnoi Khimii, Vol. 77, No. 12, 2004, pp. 2061–2062.

BRIEF COMMUNICATIONS

Preparative Synthesis of (*Z*)-5-Decenyl Acetate

Zh. A. Chobanyan

Institute of Organic Chemistry, National Academy of Sciences of the Republic of Armenia, Yerevan, Armenia

Received July 14, 2004

Abstract—A procedure was developed for preparative synthesis of (*Z*)-5-decenyl acetate, the sex hormone of *Agrotis Segetum.*

The use of pheromones for plant protection from pests became possible after preparation of synthetic analogs of these natural compounds. Since that time, the chemistry of synthetic pheromones has been receiving a considerable attention [1].

Agrotis Segetum is a pest damaging various cereals under natural conditions and in storehouses. The principal component of its pheromone is (*Z*)-5-decenyl acetate **I**.

Procedures have been developed for preparing **I** using the Wittig reaction to obtain the (*Z*)-alkene moiety [2–4], by selective ozonolysis of (*Z,Z*)-1,6-cyclooctadiene [5], and by metal interchange with di(1-hexenyl)mercury [6]. Medarde *et al*. [7] reported a general procedure for preparing components of *Agrotis Segetum* pheromone from 1,4-butanediol [7]. The above procedures are multistep, difficult in implementation, and time-consuming; they involve formation of undesirable by-products, and the yield of the target products is low. We have developed a new procedure for preparing pheromones of this type, which is free of the above drawbacks.

The procedure suggested starts from butylacetylene **II** and follows the $C_6 + C_4$ scheme. In the first step, sodium butylacetylenide reacts with 1-iodo-4-chlorobutane in liquid ammonia at –50 to –60°C (under these conditions, iodochloroalkanes react selectively, with only the iodine atom substituted) to form 1-chloro-5-decyne **III**. This compound is treated with sodium acetate in refluxing dimethylformamide (DMF). The resulting 5-decynyl acetate **IV** is hydrogenated in a flow of hydrogen in the presence of nickel acetate treated with ethylenediamine and sodium borohydride; the reaction gives (*Z*)-5-decenyl acetate **I**, overall yield 44%.

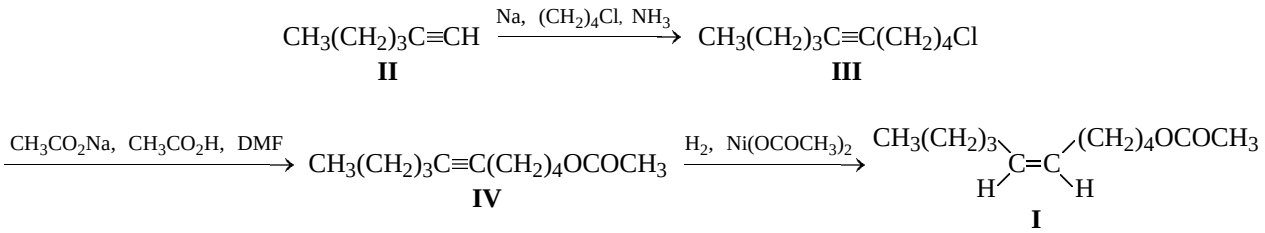

II **III** **IV** **I**

The process efficiency and yield of **I** essentially depend on the reaction temperature. At temperatures above –50°C, side reactions occur (dehydrochlorination, disubstitution), and below –60°C, the yield of **I** does not change further.

In the synthesis of 1-chloro-5-decyne **III** and 5-decynyl acetate **IV**, we took the reactants in an equimolar ratio, since an excess of any of the reactants had no appreciable effect on the product yield. The hydrogenation of 5-decynyl acetate **IV** to (*Z*)-5-decenyl acetate was performed according to [8].

According to GLC, the final product **I** contained the *Z* isomer only, which is confirmed by the IR data (presence of a medium-intensity band in the region of

1070-4272/04/7712-2036 © 2004 MAIK "Nauka/Interperiodica"

730 cm^{-1}; absence of a band at 980 cm^{-1}, characteristic of the *E* configuration) and by a characteristic multiplet of the (*Z*)-CH=CH protons in the ^1H NMR spectrum at 5.1–5.35 ppm (J = 11.5 Hz).

EXPERIMENTAL

The ^1H NMR spectra were recorded on a Varian Mercury-300 spectrometer (300 MHz) in $CDCl_3$, internal reference TMS, and the IR spectra, on a UR-20 spectrometer (thin films). The GLC analysis was performed on a Chrom-5 chromatograph equipped with a flame ionization detector and 25 000 × 0.2-mm glass capillary column coated with SE-30, carrier gas nitrogen, flow rate 30 ml min^{-1}.

1-Chloro-5-decyne III. Alkyne **II** (12.8 g) was added over a period of 15 min at –60°C to sodium amide prepared from 3.45 g of Na and 0.5 l of liquid ammonia; the mixture was stirred for 3 h. Then 32.8 g of 1-iodo-4-chlorobutane was added dropwise over a period of 2 h. The mixture was stirred for an additional 2 h and allowed to warm up. After evaporation of ammonia (15 h), 200 ml of anhydrous diethyl ether was added to the residue, and the mixture was refluxed with stirring for 3 h. After cooling, dilute HCl (pH 3) was added, and the mixture was extracted with diethyl ether (3 × 50 ml). The combined ether extracts were washed with a $Na_2S_2O_3$ solution and dried over magnesium sulfate. Distillation gave 18.1 g (70%) of **III** [9], bp 75–76°C (2 mm Hg), n_d^{20} = 1.4610.

5-Decynyl acetate IV. Chloroalkyne **III** (3.45 g) was added to a mixture of 1.64 g of sodium acetate and 10 ml of acetic acid in 50 ml of anhydrous DMF. The mixture was stirred at the boiling point for 10 h, the solvent was distilled off, 15 ml of water was added to the residue, and the mixture was extracted with diethyl ether (3 × 50 ml). The extract was washed with water to pH 7 and dried over magnesium sulfate. The solvent was removed. Vacuum distillation gave 3.2 g (82%) of **IV**, bp 92°C (2 mm Hg), n_d^{20} = 1.4460. IR spectrum, ν, cm^{-1}: 1745, 2250. ^1H NMR spectrum, δ, ppm: 0.9 t (3H, CH_3CH_2, J = 7 Hz), 1.4–1.7 m (8H, CH_2), 1.9–2.15 m (4H, $CH_2C{\equiv}CCH_2$), 1.85 s (3H, $COCH_3$), 4.1 t (2H, OCH_2, J = 6.8 Hz).

(*Z*)-5-Decenyl acetate I. A 0.32-g portion of $Ni(OAc)_2 \cdot 4H_2O$ in 10 ml of absolute ethanol was bubbled with hydrogen, after which 1.4 ml of a 1 M alcoholic solution of sodium borohydride was added in three portions. To the resulting black solution, we added 0.18 g of anhydrous ethylenediamine and 1.5 g of decynyl acetate **IV**; the mixture was stirred at 20°C in a flow of hydrogen. After the hydrogenation was complete, the catalyst was filtered off, the filtrate was evaporated, and the precipitate was diluted with 20 ml of water and extracted with diethyl ether (3 × 50 ml). The extract was washed with 10 ml of water and dried over magnesium sulfate; the solvent was distilled off. Yield of **I** 1.2 g (81%), bp 100–101°C (7 mm Hg), n_d^{20} = 1.4400. IR spectrum, ν, cm^{-1}: 730 m, 1150 s, 1245 s, 1370 m, 1390 m, 1465 m, 1658 w, 1745 vs, 3015 m. ^1H NMR spectrum, δ, ppm: 0.89 t (3H, CH_3CH_2, J = 7.1 Hz), 1.3–1.45 m (8H, CH_2), 1.95–2.25 m (4H, $CH_2CH{=}CHCH_2$), 1.96 s (3H, $COCH_3$), 4.01 t (2H, OCH_2, J = 6.8 Hz), 5.1–5.35 m (2H, CH=CH, J = 11.5 Hz).

REFERENCES

1. Franke, W. and Schulz, S., in *Comprehensive Natural Products Chemistry*, Amsterdam: Elsevier, 1999, vol. 8, pp. 197–261.
2. Bestman, H.J., Vostrowsky, K.H., Platz, H., *et al.*, *Angew. Chem.*, 1978, vol. 90, no. 10, pp. 815–816.
3. Ohloff, G., Vial, C., Naf, F., and Pawlak, M., *Helv. Chim. Acta*, 1977, vol. 60, no. 112, pp. 1161–1165.
4. Albores, M., Bestman, H.J., and Dohte, B., *Lieb. Ann.*, 1994, no. 3, pp. 231–235.
5. Odinokov, V.N., Galeeva, R.I., Sokol'skaya, O.V., *et al.*, *Dokl. Akad. Nauk SSSR*, 1985, vol. 280, no. 3, pp. 646–649.
6. Romanian Patent 78 763.
7. Medarde, M., Gordaliza, M., Castro, M.A., *et al.*, *Bol. San. Veg. Plagas*, 1988, vol. 14, no. 2, pp. 313–317.
8. Adams, J., Milette, S., Rokach, S., and Zamboni, R., *Tetrahedron Lett.*, 1984, vol. 25, pp. 2179–2182.
9. Taylor, W.R. and Strong, F.M., *J. Am. Chem. Soc.*, 1950, vol. 72, pp. 4263–4265.

Russian Journal of Applied Chemistry, Vol. 77, No. 12, 2004, pp. 2038–2040. Translated from Zhurnal Prikladnoi Khimii, Vol. 77, No. 12, 2004, pp. 2063–2065.

Professor Adam Vladislavovich Rakovskii (To 125th Anniversary of His Birthday)

A.V. Rakovskii, a corresponding member of the Academy of Sciences of the USSR and a professor of Moscow State University, performed a wide variety of experimental studies and made a major contribution to the formation of physical chemistry as an independent educational discipline and to the development of chemical education in Russia.

Adam Vladislavovich Rakovskii was born on December 23, 1879, at Mezhirech'e village of Sedletskaya Province (now in the Republic of Poland) into the family of a teacher. In 1896, he finished a classical gymnasium at the town of Bela in the same province and entered the natural department of the physicomathematical faculty at Moscow University. Rakovskii expressed the strongest interest in chemistry beginning from the first years of his education. At that time, chemical sciences were for the most part taught at the University by professor N.D. Zelinskii (1861–1952, academician of the Academy of Sciences of the USSR since 1929); V.F. Luginin (1834–1911), founder of a thermochemical laboratory at the University; and A.P. Sabaneev (1842–1923). I.A. Kablukov (1857–1942, honorary member of the Academy of Sciences of the USSR since 1932), a known physical chemist, was elected extraordinary professor of Moscow University only in May 1903.

In 1903, Rakovskii graduated from the University with a first-degree diploma and, on Zelinskii's recommendation, was taken on the staff of the Central chemical laboratory of the Ministry of Finance as a junior laboratory assistant. The main task of the laboratory was to monitor the quality of alcoholic drinks, in connection with the state monopoly on this kind of products, and also to control the work of provincial laboratories and to improve methods for rectification of ethanol. Most of the staff members of the laboratory were graduates from Moscow University, the operation of the laboratory was supervised by Zelinskii.

Already by the end of Rakovskii's education at the University his scientific interests were mainly focused on physical chemistry, even though no separate discipline of this kind existed at Moscow University in those years. When being an undergraduate, Rakovskii worked at the thermochemical laboratory;

he is the author of an unpublished manuscript "Heats of Combustion and Formation of Organic Substances in the Context of the Structural Theory" (Moscow, 1902) [1]. During his work at the laboratory of the Ministry of Finance, Rakovskii could, in addition to discharging his duties, prepare for publication his first study "Kinetics of Consecutive First-Order Reactions" (1907) [2]. In 1907–1910, the scientist published the results of seven more physicochemical studies. These included "Specific Heats of Solutions in Water and Ethanol" (1909) and "Purification and Rectification of Ethanol" (1909). In 1911–1914, a set of 11 publications concerned with the adsorption of water and aqueous solutions by starch appeared in *Zhurnal Russkogo Fiziko-khimicheskoro Obshchestva* (Journal of the Russian Physicochemical Society). The results of these studies were summarized in Rakovskii's master's dissertation "To the Theory of Adsorption" (1913), defended at Kiev University in 1914. Based on the results of his experiments, Rakovskii, in particular, concluded that the adsorption of water vapor by solid colloids occurs continuously and irreversibly. The irreversibility of the adsorption process is manifested in that there exists a hysteresis of the water content in the colloid. This set of publications devoted to adsorption was analyzed in detail by

1070-4272/04/7712-2038 © 2004 MAIK "Nauka/Interperiodica"

Ya.I. Gerasimov and A.V. Kiselev in the collection of works [2]. The authors highly appreciated Rakovskii's studies in the field of adsorption and thermodynamics of irreversible processes.

After the degree of master of science was conferred on Rakovskii, he became a privatdocent at the chair of chemistry of Moscow University and started to deliver lectures on chemical thermodynamics and application of mathematics to chemistry. Because of the beginning of World War I, Rakovskii took active part, as a staff member of the Ministry of Finance, in the equipment of plants for manufacture of the necessary medicines. In 1917, he was appointed head of the Central chemical laboratory of the Ministry of Finance and supervisor of chemical plants affiliated with this Ministry (beginning in 1918, People's Commissariat of Finance).

In 1919–1932, Rakovskii headed the laboratory of inorganic chemistry at the Institute of Pure Chemical Reagents, in whose organization he was directly involved. Beginning in 1920, the scientist started to pay increasing attention to Moscow University, without terminating his work at industrial research institutes. In 1920–1928, Rakovskii was a professor at the chair of inorganic chemistry of Moscow University; in 1928–1930, he headed this chair; and from 1930 till the end of his life, he headed the chair of physical chemistry of Moscow State University. From 1933 to 1937, he simultaneously occupied the positions of dean of the chemical faculty and director of the Institute of Chemistry at Moscow State University. Rakovskii was a talented and many-sided teacher.

During the period from 1919 to 1933, Rakovskii and co-workers carried out, mainly at the Institute of Pure Chemical Reagents, quite a number studies. He published in *Trudy Instituta* (Coll. of Works of the Institute), *Zhurnal Prikladnoi Khimii* (Journal of Applied Chemistry), *Zhurnal Obshchei Khimii* (Journal of General Chemistry), and other editions results of 33 studies. These include important investigations concerned with equilibria in water–salt systems, development of standards and standard procedures for testing of chemical reagents (including acids and alcohols), and a set of studies devoted to heteropolyacids and heteropolycompounds. All investigations performed by Rakovskii and his pupils are distinguished by extraordinary thoroughness in experimental work and assessment of the results obtained. Rakovskii made a major contribution to the organization of manufacture of various high-purity preparations. During several years, he was a consultant at Gintsvetmet and Giredment institutes. A collection of thermodynamic works carried out by staff members of the Gintsvetmet institute was published under Rakovskii's editorship (1935).

Rakovskii's services in organization of the higher chemical education in our country were great, he was actively involved in composition of curricula and programs of chemical higher-school institutions and paid primary attention to teaching of physics and mathematics to students of chemical specialities. Rakovskii was permanently concerned with problems of publication of educational literature in the field of inorganic and physical chemistry and chemical thermodynamics. Originally, his lectures from various courses were published as lithographic editions (1926–1935). In 1933, Rakovskii published (together with E.F. Krauze and A.V. Bogomolov) *Kurs obshchei i neorganicheskoi khimii* (Course of General and Inorganic Chemistry) (420 pp.). In 1938, he published a fundamental work *Vvedenie v fizicheskuyu khimiyu* (Introduction to Physical Chemistry) (679 pp.). The book comprised an extended and supplemented course of lectures delivered by the author at Moscow State University; it was widely used by postgraduate students and research workers. In 1939 was published a more concise *Kurs fizicheskoi khimii* (Course of Physical Chemistry) (544 pp.), recommended as a textbook for students of chemical specialities.

Rakovskii paid a considerable attention to translation of foreign publications into Russian; quite a number of textbooks and monographs were published under his editorship and with his supplements, which were rather significant in some cases. The book by A. Smith *Introduction to Inorganic Chemistry* was published in three editions in Russian translation under editorship and with supplements by Rakovskii (1928–1931). Rakovskii published a special supplement *Khimicheskaya kinetika i kataliz* (Chemical Kinetics and Catalysis) (1931, 84 pp.) to the Russian translation of A.P. van Eyken's *Foundations of Physical Chemistry* (*Osnovnye nachala fizicheskoi khimii*, 1929, 343 pp.). J.R. Partington's course of chemical thermodynamics was seriously reshaped [3]. This was the first experience of publication of a course of chemical thermodynamics in Russia; the translation was done by Rakovskii's closest associate Ya.I. Gerasimov (1903–1983, corresponding member of the Academy of Sciences of the USSR since 1953). The book simultaneously served as reference and strongly affected the development and level of the thermodynamic research in our country. Of considerable interest is Rakovskii's foreword to the Russian translation of the book by I.D. Van der Waals and F. Konstamm *Course of Thermostatics* (*Kurs termostatiki*;

1936, part I, 452 pp.; part II, 439 pp.) in which, in particular, editor's standpoint concerning important problems of the theory of solutions was presented.

Rakovskii's scientific activities were honored by his election a corresponding member of the Academy of Sciences of the USSR in 1933.

Adam Vlasdislavovich Rakovskii died of long and severe illness on June 7, 1941. He gave more than quarter of a century of his life to Moscow University, being one of the leading professors of the chemical faculty. Warmest recollections of Rakovskii, a brilliant pedagogue and talented scientist, were published by his closest pupils and co-workers Ya.I. Gerasimov, A.V. Kiselev, A.V. Frost, M.M. Popov, D.N. Tarasenkov, and others [2, 4, 5]. Rakovskii's accomplishments in organization of the chair of physical chemistry and, simultaneously, of the laboratory of chemical thermodynamics of Moscow State University (1930) are described in G.F. Voronin's essay devoted to the life and activities of Ya.I. Gerasimov who headed the laboratory of chemical thermodynamics for more than 35 years (since 1943) and the chair of physical chemistry of Moscow University for more than 30 years (since 1952) [6]. The collection of works [2] contains a full list of Rakovskii's scientific publications.

REFERENCES

1. Kipnis, A.Ya., *Razvitie khimicheskoi termodinamiki v Rossii* (Development of Chemical Thermodynamics in Russia), Moscow: Nauka, 1964.
2. *Adam Vladislavovich Rakovskii: Sbornik statei, posvyashchennykh zhizni i nauchnoi deyatel'nosti* (Adam Vladislavovich Rakovskii: Coll. of Articles Devoted to His Life and Scientific Activities), Gerasimov, Ya.I., Ed., Moscow: Mosk. Otd. Vses. Khim. O–va im. D.I. Mendeleeva, 1949.
3. Partington, J.R. and Rakovskii, A.V., *Kurs khimicheskoi termodinamiki* (Course of Chemical Thermodynamics), Moscow: Gos. Nauch.-Tekhn. Izd., 1932.
4. Frost, A.V., *Zh. Fiz. Khim.*, 1941, vol. 15, no. 9, pp. 981–982.
5. Gerasimov, Ya.I. and Tarasenkov, D.N., *Usp. Khim.*, 1942, vol. 11, no. 1, pp. 75–77.
6. Gerasimov, Ya.I., *Izbrannye trudy: Obshchie voprosy fizicheskoi khimii i termodinamiki: Termodinamicheskie osnovy materialovedeniya* (Selected Works: General Problems of Physical Chemistry and Thermodynamics: Thermodynamic Foundations of Materials Science), Voronin, G.F., Ed., Moscow: Nauka, 1988.

A. G. Morachevskii

Russian Journal of Applied Chemistry, Vol. 77, No. 12, 2004, pp. 2041–2042. Translated from Zhurnal Prikladnoi Khimii, Vol. 77, No. 12, 2004, pp. 2066–2067.

Zelenin, K.N., Nozdrachev, A.D., and Polyakov, E.L., *Nobelevskie premii po khimii za 100 let* (Nobel Prizes in Chemistry in 100 Years), St. Petersburg: Gumanistika, 2003, 873 pp.

In accordance with the will of Alfred Nobel (1833–1896), a Swedish engineer, chemist, and industrialist, international prizes have been annually awarded since 1901 for outstanding discoveries and achievements in physics, chemistry, physiology, or medicine; for creating the most important literary works, and for making a major contribution to friendship between peoples and consolidation of peace. Beginning in 1969, prizes in economic sciences in memory of Alfred Nobel are also awarded.

The changes in the political life of Russia in the last decade of the XX century affected the attitude of State structures toward the activities of the Nobel Committee and toward how these prestigious scientific prizes are awarded. In 1992, the encyclopedia *Nobel Prize Laureates*, published in the United States in 1987, was translated into Russian. The two volumes of this encyclopedia (vol. 1, 740 pp.; vol. 2, 854 pp.; Moscow: Progress) contain 564 articles with biographies of scientists, writers, and public and political figures, as well as information about institutions awarded Nobel Prizes in 1901–1986. This was the first fundamental publication in Russian about Nobel Laureates. It should be noted that the encyclopedia *Nobel Prize Laureates* is published abroad every five years. Following the encyclopedia, a number of publications devoted to A. Nobel's life and to the activities of the Nobel Prize Committee appeared in Russian. To these belong a Russian translation from English of R. Sulman's book *Alfred Nobel's Will. History of Nobel Prizes* (Moscow: Mir, 1993, 142 pp.) and translation from French of O. de Rudder's book *Alfred Nobel* (Rostov-on-Don: Feniks, 1997, 320 pp.). Of considerable interest is A.M. Blokh's monograph *Sovetskii Soyuz v inter'ere Nobelevskikh premii. Fakty. Dokumenty, Razmyshleniya, Kommentarii* (The Soviet Union in the Context of Nobel Prizes. Facts. Documents. Reflection, Comments), edited by A.I. Melua (St. Petersburg: Gumanistika, 2001, 608 pp.), which contains an exceedingly valuable documentary evidence. The author of the monograph, a known Russian Scientist, has been extensively and effectively working in the field of history of science. Among the books devoted to Nobel-related issues ("Nobelistics"), one more very well-compiled bibliographic publication: *Lektsii i rechi laureatov Nobelevskikh premii v russkikh perevodakh: 1901–2002. Bibliographicheskii ukazatel'* (Lectures and speeches by Nobel prize laureates in Russian translation: 1901–2002. Bibliographic Index), (St. Petersburg: Bibl. Akad. Nauk, 2003, 168 pp.) should be mentioned.

The book by Zelenin, Nozdrachev, and E.L. Polakov should be referred to reference books of mostly compiled nature. It contains evidence about laureates of 94 prizes in chemistry, awarded from 1901 till 2002. In the last century, Nobel prizes in chemistry were not awarded, for various reasons, only in 1916, 1917, 1919, 1924, 1933, 1940–1942. The book comprises an introduction, five chapters, and a supplement. The brief introduction (pp. 7–10) contains evidence about Alfred Nobel's family and possible reasons for the appearance of such a will. The first chapter (pp. 14–45) includes a rather detailed description of Alfred Nobel's life and activities. In the second chapter (pp. 46–61), the working mechanism of the Nobel Committee for Chemistry is described. The prerogative right to chose a laureate is vested in the Swedish Royal Academy of Sciences. Nominations can be made by Swedish and foreign members of the Swedish Royal Academy of Sciences, members of the Nobel Committee for Chemistry, professors of chemistry at universities and technological institutes of Sweden, Denmark, Finland, Island, and Norway, Nobel Laureates in Chemistry, professors of the Karolinska Institute in Stockholm, heads of chairs of a small number of other universities by choice of the Swedish Royal Academy of Sciences, and individual scientists by invitation of the Nobel Committee. Those invited personally as nominators should not discuss their decision with colleagues and nominees themselves. The information about the work of the Nobel Committee and about all the nominators and nominees becomes publicly accessible only in 50 years.

1070-4272/04/7712-2041 © 2004 MAIK "Nauka/Interperiodica"

The third chapter of the reference book by K.N. Zelenin and co-authors (pp. 62–100) considers the distribution of Nobel Prizes among the main fields of modern chemistry and different countries in 100 years. Particularly significant in the last 50 years is the share of works of chemical-biological nature, devoted to a study of the chemism of vital processes and of the functioning of living systems.

The first Nobel Prize in Chemistry was awarded in 1901 to one of the founders of modern physical chemistry, J.H. van't Hoff (1852–1911) (Netherlands), "in recognition of the extraordinary services he has rendered by the discovery of the laws of chemical dynamics and osmotic pressure in solutions." During the period from 1901 till 1950, the obviously leading position among the recipients of Nobel Prizes in Chemistry was occupied by German chemists (19 Nobel laureates). The Nobel Prize winners from Germany include such known chemists as A. von Baeyer (1835–1917), W. Ostwald (1853–1932), F. Haber (1868–1934), W. Nernst (1864–1941), and O. Hahn (1879–1968). Considerably smaller was the number of laureates from the United States (7), UK (7), and France (6). The situation changed fundamentally in the second half of the XX century. During the period from 1951 till 2000, Nobel Prizes in chemistry were awarded to 42 scientists from the United States, 16 scientists from the UK, and 8 from Germany. Among the American recipients of Nobel Prizes in chemistry were G.T. Seaborg (1912–1999) (together with E.M. McMillan) in 1951 "for their discoveries in the chemistry of the transuranium elements" and L. Pauling (1901–1994) in 1954 "for his research into the nature of the chemical bond and its application to the elucidation of the structure of complex substances." A recipient of a Nobel Prize in chemistry among Russian scientists was, in 1956, academician N. Semenov (1896–1986) [together with C.N. Hinshelwood (1887–1967)] "for their researches into the mechanism of chemical reactions." Here are primarily meant the works of these two scientists in the field of theory of chain reactions.

The fourth chapter (pp. 101–725) occupies the central position in the reference book under discussion. It contains scientific-biographical evidence about all the Nobel Prize laureates in chemistry. Each article of the chapter includes materials about a prize, the essence of the discovery, and the formulation of the Nobel Committee; discusses the importance of the discovery for the development of the related field of chemistry; and presents biographic evidence about the laureates. The volume and content of the biographical evidence are virtually the same as those in the two-volume encyclopedia mentioned above. The fifth chapter (pp. 726–738) describes the nationality, age, education, and working places of the Nobel Prize laureates in chemistry.

The supplement (pp. 739–865) contains, in particular, information about all scientists nominated for the Nobel Prize in chemistry in 1901–1950. Among the nominated Russian scientists were D.I. Mendeleev (in 1905, 1906, and 1907), P.I. Walden (1914), creator of the chromatographic method for separation and analysis of mixtures M.S. Tsvet (1918), outstanding microbiologist S.N. Vinogradskii (1921), and academician A.N. Frumkin (1946). One of the most outstanding chemists of the first half of the XX century, academician V.N. Ipat'ev, who was deprived of the Soviet citizenship in 1936 and worked in the United States, was nominated in 1938, 1941, 1948, 1949, and 1950. Unfortunately, he was not awarded the well-deserved Nobel prize. The possible reasons were analyzed by Yu.I. Solov'ev (*Vestnik Ross. Akad. Nauk*, 1997, vol. 67, no. 7, pp. 627–631).

The book by K.N. Zelenin, A.D. Nozdrachev, and E.L. Polyakov is of interest for a wide audience of readers; it is very well published and presents photographs of the laureates and other illustrative materials, but its edition of 500 copies is obviously insufficient for our country. Fundamental reference books of this kind are to be available at libraries of all higher- and secondary school institutions engaged in training of specialists in chemistry and chemical technology. Such books are to be accessible to teachers of chemistry and chemical disciplines of any level.

A. G. Morachevskii

Russian Journal of Applied Chemistry, Vol. 77, No. 12, 2004, p. 2043–2044. Translated from Zhurnal Prikladnoi Khimii, Vol. 77, No. 12, 2004, p. 2068.

BOOK REVIEWS

Naboichenko, S.S., Myamchenkov, S.V., and Karelov, S.V., *Mysh'yak v tsvetnoi metallurgii* (Arsenic in Nonferrous Metallurgy), Naboichenko, S.S., Ed., Yekaterinburg: Ural'sk. Otd. Ross. Akad. Nauk, 2004, 240 pp.

A certain amount of arsenic is contained in the form of various compounds in the majority of ores of heavy metals. As a rule, arsenic compounds are concentrated in the course of ore dressing or metallurgical processing of raw materials in various dumps, wastes, and wastewater. The existing methods for removal of arsenic from the production cycle are frequently far from satisfying the modern requirements to integrated use of raw materials and environment protection.

The book comprises an introduction, six chapters, and a bibliographic list. In the brief introduction (pp. 3 and 4), the authors emphasize that the integrated solution of the problem of utilization of arsenic in metallurgical processes includes a number of separate problems: expansion of its application fields, removal from technological processes, detoxication of arsenic-containing wastes, and purification of wastewater and technological gases to remove arsenic. The monograph being reviewed is devoted to finding ways to solve these problems.

The first chapter (pp. 5–53) contains general evidence concerning arsenic and its compounds and minerals. Also considered are the production and application fields of arsenic and its compounds, their hazard classes and toxicology.

The second chapter (pp. 54–111) summarizes technological evidence concerning the ways of removal of arsenic from the production cycle in processing of various ores and concentrates. In particular, the behavior of arsenic in manufacture of copper from oxidized and sulfide ores, in fire and electrolytic refining of copper, production of vitriol, manufacture of nickel and cobalt from various raw materials, processing of flotation zinc concentrates, and metallurgy of gold is considered.

The third chapter (pp. 112–118) very briefly discusses the published evidence concerning gas purification to remove arsenic. The fourth chapter (pp. 119–188) considers possible methods for purification of wastewater of varied nature to remove arsenic compounds. Quite a number of techniques are described: purification with manganese dioxide (pyrolusite), purification with compounds of calcium and iron(III), phosphate purification, precipitation of arsenic sulfides and sorption with sulfide minerals, use of inorganic and polymeric sorbents, extraction of arsenic compounds from acid solutions with tributyl phosphate, and electrolytic purification.

The fifth chapter (pp. 189–213) is devoted to processing of solid arsenic-containing wastes (dusts, sublimates formed in pyrometallurgy, products obtained in purification of gases to remove arsenic, precipitates formed in purification of wastewater, etc.). In view of the widely varying chemical composition of the solid products, their processing may present a highly complicated technological problem. The authors consider possible hydrometallurgical, pyrometalurgical, and combined methods. In the authors' opinion, the most promising, with account of the ecological requirements, are hydrometalurgical techniques. However, no versatile technology for processing of arsenic-containing metallurgical dusts has been developed yet.

The sixth chapter (pp. 214–24), which closes the monograph, discusses the important problem of burial of arsenic-containing wastes. According to the available published data, arsenic-containing substances constitute more than 97% of the whole amount of toxic wastes of nonferrous metallurgy. This means that transition to ecologically safer technologies for manufacture of nonferrous metals is impossible without finding a method for utilization of arsenic. At present, high-purity arsenic is manufactured in Russia in elimination of arsenic-containing chemical warfare, which will satisfy the demand for this element for many years to come. Recovery of arsenic from technological

1070-4272/04/7712-2043 © 2004 MAIK "Nauka/Interperiodica"

wastes of nonferrous metallurgy is economically unfeasible. The authors discuss possible variants of burial of arsenic compounds. The most appropriate way is to convert these compounds into a form that would rule out any possibility of contamination of the atmosphere and water reservoirs.

The bibliographic list (pp. 225–239) contains references to 309 studies of mostly domestic authors. The bibliographic descriptions of journal articles give their titles, which improves the information value of the bibliographic list. The monograph by S.S. Naboichenko and co-authors has a clearly pronounced technological orientation, its style of presentation makes it understandable for an exceedingly wide audience of engineers and technical workers at plants of nonferrous metallurgy. The book contains a vast body of reference data and a large number of examples of industrial nature; it is well published.

A. G. Morachevskii and I. N. Beloglazov

Russian Journal of Applied Chemistry, Vol. 77, No. 12, 2004, pp. 2045–2046. Translated from Zhurnal Prikladnoi Khimii, Vol. 77, No. 12, 2004, pp. 2069–2070.

INFORMATION

XIII Russian Conference on Physical Chemistry and Electrochemistry of Molten and Solid Solutions

On September 27 through October 1, 2004, in Yekaterinburg was held XIII Russian conference on physical chemistry and electrochemistry of molten and solid solutions. The organizers of the conference included: Scientific Council for electrochemistry, Russian Academy of Sciences; Institute of High-Temperature Electrochemistry, Ural Division, Russian Academy of Sciences; and Russian Foundation for Basic Research. Two hundred and seventy reports were submitted to the conference, extended abstracts of these reports are grouped in two volumes. The first of these (284 pp.) includes materials of 170 reports devoted to physical chemistry and electrochemistry of molten electrolytes, and the second volume (141 pp.), abstracts of reports concerned with solid electrolytes. In each volume, materials of plenary sessions and key reports delivered at sections are given separately.

More than 60% of all the reports were delivered by staff members of research institutes and higher-school institutions of Yekaterinburg. The leading position was occupied by the Institute of High-Temperature Electrochemistry (IVTE), Ural Division, Russian Academy of Sciences. Founded in 1958, the Institute of Electrochemistry (since 1992, Institute of High-Temperature Electrochemistry) has become a prominent reasearch center specialized in physical chemistry and electrochemistry of inorganic substances in the molten and solid state, molten and solid electrolytes. The investigations performed at IVTE are known worldwide. Large-scale investigations of high-temperature systems are also being conducted in Yekaterinburg at the Ural State Technical University and at the Institute of Metallurgy, Ural Division, Russian Academy of Sciences. A large number of reports were presented by staff members of Russia's research centers traditionally conducting investigations in the field of high-temperature electrochemistry. To these belong, in particular, the following: Institute of Chemistry and Technology of Rare Elements and Mineral Resources, Kola Scientific Center, Russian Academy of Sciences (Apatity); Kabardino-Balkar State University (Nalchik); Daghestan State University and Daghestan Scientific Center, Russian Academy of Sciences (Makhachkala); North-Caucasian State Technical University (Stavropol); Vyatka State University (Kirov). Among the authors or co-authors of quite a number of reports were scientists from Great Britain, Hungary, Italy, Netherlands, United States, France, Czech Republic, Japan, and also from Kazakhstan and Ukraine.

Opening the conference, the chairman of the Organizing Committee V.A. Khohlov (Yekaterinburg) emphasized that high-end technologies employing molten and solid electrolytes will play a steadily increasing role in solution and implementation of basic practical problems governing the technical progress in the XXI century: manufacture of new materials with prescribed properties; electrochemical power engineering ensuring direct and the most efficient interconversion of chemical and electrochemical kinds of energy; and deep processing of natural raw materials and those of technological origin, including regeneration of the nuclear fuel and processing of the radioactive waste.

Among the plenary and key sectional reports devoted to physical chemistry and electrochemistry of molten salts, the following can be mentioned. V.Ya. Kudyakov with a large group of co-authors (Yekaterinburg) analyzed the involvement of IVTE, in cooperation with other institutions, in the State program "The Strategy of development of nuclear power engineering in Russia till the middle of the XXI century." The report submitted by N.N. Batalov (Yekaterinburg) was devoted to achievements and difficulties in the development of chemical power cells with molten electrolytes. Kh.B. Kushkhov (Nalchik) considered the problem of manufacture of rare-earth metals, their alloys, and other formulations with the use of ionic melts. V.N. Prusakov discussed in his report the prospects for application of fluoride melts in regeneration of irradiated nuclear fuel. A.I. Afinogenov and co-authors (Yekaterinburg) demonstrated the possibility of using ionic-electronic melts as a medium for obtaining thermodiffusion coatings and powdered alloys. P.V. Polyakov discussed in detail in his report the tendencies in the development of the aluminum industry. Yu.P. Zaikov and co-authors (Yekaterinburg) considered the topical and rather promising problem of development of nonconsumable anodes for manu-

1070-4272/04/7712-2045 © 2004 MAIK "Nauka/Interperiodica"

facture of aluminum by electrolysis. In the authors' opinion, it is necessary to create new electrolytes with a melting point not higher than 800°C and solubility of alumina in the electrolyte not lower than 3–5 wt %.

O.I. Rebrin (Yekaterinburg) noted the broad informational opportunities furnished by the galvanostatic method of investigation of electrode processes with the use of modern equipment. A number of reports by O.M. Shabanov and co-authors were devoted to investigations of the influence exerted by strong electric fields on the physical properties of molten salts.

Sectional and poster reports devoted to investigations in the field of physical chemistry and electrochemistry of molten salts are grouped in the book of abstracts as follows: I. Theory and properties of molten electrolytes (43 reports); II. Phase equilibria (5); III. Interphase phenomena (6); IV. Electrochemical thermodynamics (6); V. Kinetics of electrode processes (42); VI. Reactions in melts (46); and VII. Processes and apparatus (12).

Quite a number of problems of current interest were analyzed in reports containing results of theoretical and experimental studies of thermodynamic, structural, and transport properties of solid electrolytes. A.B. Yaroslavtsev and co-authors (Moscow) reported new data on the ionic mobility and phase transitions in complex phosphates of polyvalent elements. A.K. Ivanov-Shits (Moscow) reviewed results of molecular-dynamic calculations of structural, thermodynamic, and kinetic characteristics of a number of ionic crystals and main classes of solid electrolytes with both cationic and anionic conduction. The report by S.I. Somov (Yekaterinburg) analyzed the practical application of solid electrolytes: in chemical power cells, in ionistors and capacitors, and in sensors for chemical analysis of gaseous and liquid media in the laboratory and technological practice. E.I. Burmakin (Yekaterinburg) reported results obtained in synthesis and studies of the crystal-chemical and transport properties of electrolytes with high conductivity by cations of alkali metals, which belong to the so-called skeleton structures. Complex oxygen-containing anions form a rigid three-dimensional skeleton whose voids accommodate highly mobile alkaline cations. The report by A.K. Demin (Yekaterinburg) was devoted to electrochemical power engineering based on solid oxide conductors. L.D. Yushina (Yekaterinburg) considered problems and promises of the solid-state chemotronics. A number of reports were devoted to solid electrolytes with protonic conduction.

The conference demonstrated that, despite all the difficulties encountered in the last 15 years by virtually all research groups in Russia, investigations in the field of physical chemistry and electrochemistry of molten salts and solid electrolytes are being performed at a sufficiently high level and cover quite a number of promising areas of research. Exchange of scientific information is performed on the regular basis. The coordination center of these investigations is the Institute of High-Temperature Electrochemistry, Ural Division, Russian Academy of Sciences.

A. G. Morachevskii